PTFE Nanocrystallines by Oriented Plasma Polymerization at Atmospheric Pressure

Ying Guo, Jingzhou Xu , Xinsheng Fang, Jing Zhang*

College of Sciences,Donghua University,Shanghai 20001, China

* Corresponding author: jingzh@dhu.edu.cn

Tel: 0086-21-62373947, Fax: 0086-21-62373623

Abstract

PTFE nanocrystallines with different morphology and crystal structures were rapidly formed by an Atmospheric Plasma Polymerization without any catalysts or templates. TEM and XRD results indicated single crystal phase of the nanocrystallines. FTIR and Polarization optical micrographs display their polymer properties. The atmospheric oriented plasma polymerization can serve as a common method for nanofabrication of many other single crystalline polymer systems.

Keywords: Atmospheric oriented plasma polymerization, PTFE, nanocrystallines, characterization

1. Introduction

1-D single crystalline nanostructure polymer could exhibit mechanical strength reaching its theoretical bonding strength [1]. Some novel optical and electronic properties could also be expected due to its high charge density, high carrier mobility, and unique quantum confinement effect [2-3]. The 1999 International Technology Roadmap for Semiconductors has set a goal to reach an effective dielectric constant of 1.6–2.2 for the 0.1 μm technology node by the year 2005, and fluoropolymers are a potential candidate [4]. PTFE has many desirable properties, including a low refractive index and dielectric constant, low coefficient of friction, excellent chemical resistance, and high thermal stability [5-7]. Thin films of PTFE offer advantages for applications as diverse as optical coatings [8], biopassivation coatings for implantable devices [9-10], and interlayer dielectrics in integrated circuits [11-12]. However, bulk PTFE's high melt viscosity and poor solubility make it difficult to process into thin, conformal, and uniform films[13]. Deposition of PTFE films has been explored in a number of other ways. Pulsed laser deposition from PTFE targets produced high quality films showing the structure and thermal stability characteristic of bulk PTFE [14-15]. Ionizationassisted evaporation of low molecular weight PTFE powders also yielded similar films [16].

Synchrotron radiation ablative photodecomposition of PTFE targets yielded films much like PTFE, although in that case CF3 chain ends were observed [17]. This is comparable to films produced by downstream plasma deposition using tetrafluoroethylene [18] and HFPO [19] as precursor gases. Thermolysis of bulk PTFE produced films consistent with the source material [20-21]. Films spin coated from aqueous nanoemulsion PTFE and commercialized by W. L. Gore as SPEEDFILMTM, have undergone several evaluation studies as a potential low dielectric constant material [22]. By contrast, OPP is capable of providing good control over film structure and morphology on a substrate. OPP provides yet another promising alternative. In this paper, rapid formation of single nanocrystallines of PTFE-Like polymer was achieved on a glass substrate by a novel synthesis, the so-called Oriented Plasma Polymerization (OPP) at atmospheric pressure. The entire process was completed within a short period of time ranging between a few seconds to several minutes. The surface morphology of the coated organic crystal film was controlled through the conditions such as discharge time, ratio of the monomer to carrier gas and power

2. Experimental

For the fluorocarbon films, a mixture of fluorocarbon (atom ratio of C: F is 1:1~1:4) and Argon were used as the precursor gases and fed into the reactor at a constant flow rate. The reactor used for the "oriented plasma polymerization" (OPP) was a home-made system. In this system, a gradient electric field with a high voltage of 10—50 KV and frequency of 10—100 KHz was applied to deposit the single nanocrystallines on the ordinary glass slides. Filament plasma streamers were generated between a high voltage strip electrode and a grounded plane electrode, both were covered with a dielectric barrier, the filament-to-substrate distance was maintained at 1.5 cm. After an initial period (a few seconds to several minutes), a uniform thin film was deposited onto the entire substrate.

3. Results and Discussion

Fig. 1 shows the TEM images of the nanocrystallines film on glass slide. As can be seen in Fig. 1a and Fig. 1b the ratio of the monomer to carrier gas is 3:100 and 7:100. The synthesis time needed for growing these nanocrystallines was only three minutes. The nanocrystallines on the substrate appear massive in quantity. Some of them tend to lie in parallel with the background particulate layer. Some of them grow vertically from the layer. There are a lot of uniformity of nanorods and nanotubes in Fig. 1a, c. These nanorods and nanotubes are about 10 m in length and 100 nm in diameter. In Fig. 1b, however, the nanorods are about

800nm in length and 250 nm in diameter. The morphology is dependent on the ratio of monomer to feed and reaction time. When the reaction time shortened from 3 minutes to 15s, the amount of the nanorods and nanotubes decreased obviously. The electronic energy inside the discharge core must be high enough to dissociate the monomers into active particles such as ions, radicals, metastable neutrals, and electrons. So the power of the discharge was very important to the form of the nanocrystallines. As can be seen in Fig. 1d, there were hardly any nanorods or nanotubes on the fluorocarbon polymer film. It was believed that the growth on the glass of fluorocarbon nanocrystallines effected by discharge conditions such as discharge power, time, ratio of the monomer to carrier gas on the nanocrystallines morphology.

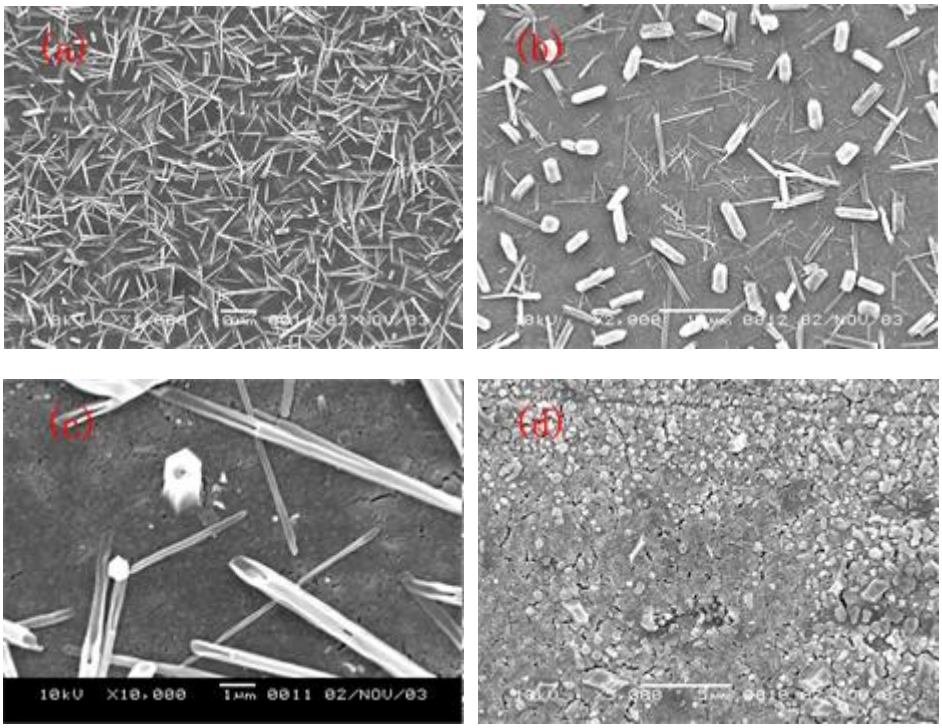

Fig 1 SEM images of fluorocarbon nanocrystallines

(a), (c) the ratio of the monomer to carrier gas is 3:100, for 3min at high power

(b) 7:100, for 3min at high power (d) for 3min at low power

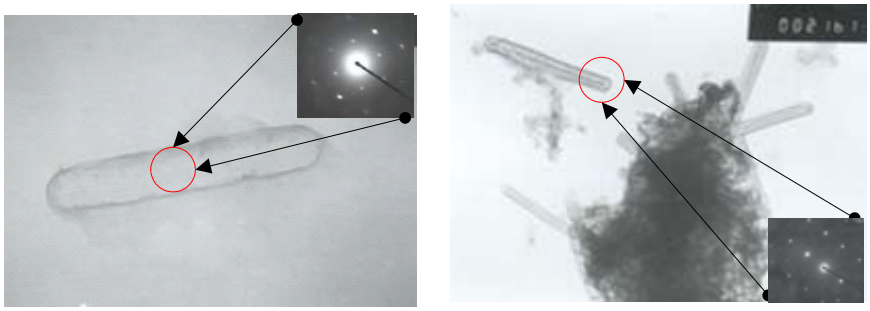

Fig 2 Transmission electron micrograph images and typical electron diffraction diagram

corresponding to single crystal (a) nanofibers, (b) nanotubes

Electron diffraction measurement in these nanotubes and nanofibers indicates that they are all single crystals. Fig 2a and Fig 2b shows diffraction pattern that the crystals growing on the substrate. Single crystals of fluorocarbon were prepared by a novel synthesis method--- Oriented Plasma Polymerization at Atmospheric Pressure. Each crystal yields a sharp electron diffraction pattern as shown in the images. Based on the d-spacing of the electron diffraction pattern, it was determined that the reflections corresponded to the hkl planes of a close-packed hexagonal (cph) structure.

The X-ray diffraction pattern of fluorocarbon films is presented in Fig. 3. The diffracted area also includes the background nanoparticulates on the substrate. Five main reflections sharp peaks can be found at 2θof about 18.620°, 15.520°, 21.099°, 20.100°and 31.3°. It can be index to a close-packed hexagonal (cph) structure.

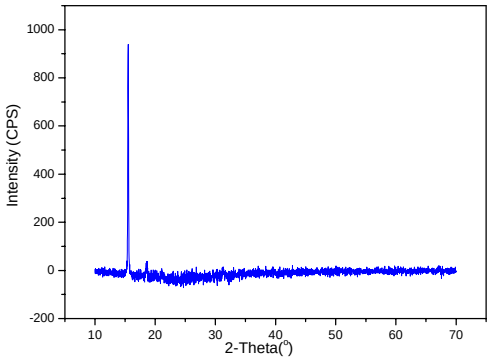

Fig.3 XRD diffraction pattern of nanocrystallines film

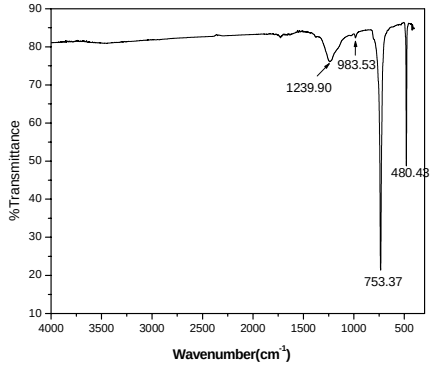

Fig.4 IR spectrum comparison of nanocrystallines film

The chemical composition of the coating is investigated through FTIR in Fig.4. The FTIR spectrum is shown in Figure 4. The feed gas is an unsaturated monomer. The peaks at 481 cm^{-1} and 735 cm^{-1} due to the CF deforming vibration are very strong. But the peak at 1368 cm^{-1} due to the CF stretching vibration in $-CF_2$ CF_3 group is only observed in the film deposited for 4 min., There is one new peak appearing at 983cm^{-1} attributed to –O-O- stretching vibration in aryl peroxide and another new peak at 1700cm-1 attributed to C=C stretching vibration in $–CF=CF_2$. These changes display that the C=C band is still remained in the deposited film. Besides, aryl peroxide group is combined into the film because of the strong oxidation during the deposition.

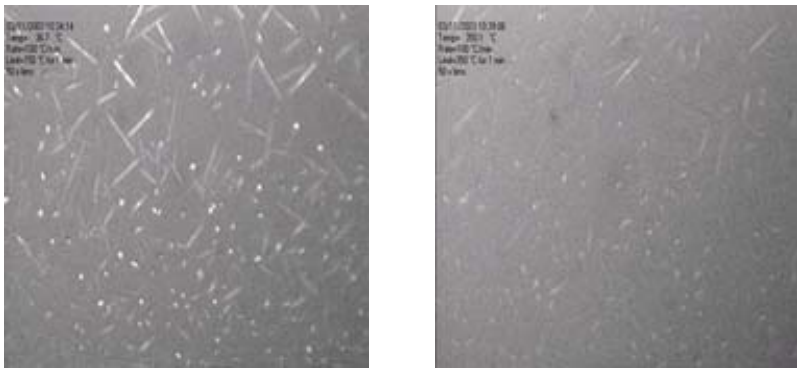

Fig.5 Comparison of thermal stability of observable nanotubes polymer slices through polarization micrographs at different testing temperatures (a) nanotubes at 36.7 °C; (b)nanotubes at 350.1 °C

The thermal stability of the as-obtained nanotubes was observed through the hot-stage polarized optical microscopy. As shown in Figure 5, the observable nanotubes with large size retain a needle-like morphology at 36.7°C (Fig. 5a) and exhibit high birefringence in the crystal edge region. Upon heating up to 350°C (Fig. 5b), the nanocrystallines layer appears melted and mobile in the vision field. But the nanocrystallines still display clear birefringence although not as strong as at 36.7°C.

4. Conclusion

The rapid formation of nanofibers or nanotubes is dependent on the monomer types and associated with plasma conditions. Discharge time, power and ratio of the monomer to carrier gas strongly influence the structure and morphology of fluorocarbon films. The “Oriented Plasma Polymerization” method opens a novel way of one-step fast formation of single crystal fluorocarbon nanotubes at Atmospheric Pressure. As a result, the physical morphology and structures of nanorods and nanotubes could be controlled through the conditions of the oriented plasma polymerization to some extent.

References

[1] F. C. Krebs and M. Jørgensen，Macromolecules 36, 4374(2003).

[2] H . Katagi et al, J. Macromol. Sci. Pure & Appl. Chem **34**, 2013(1997).

[3] C. J. Tonzola, M. M. Alam, B. A. Bean, and S. A. Jenekhe, Macromolecules 37, 3554(2004).

[4] International Technology Roadmap for Semiconductors ~International SEMATECH, 1999! can be obtained online at http://www.itrs.net/ 1999_SIA_Roadmap/Home.htm.

[5] Kerbow, D. L. In Polymeric Materials Encyclopedia; Salamone, J. C., Ed.; CRC Press: Boca Raton, FL,

1996; Vol. 9, p 6884

[6] Gangal, S. V. In Encyclopedia of Polymer Science and Engineering, 2nd ed.; Mark, H. F., Bikales, N. M., Overberger, C. G., Menges, G., Kroschwitz, J. A., Eds.; John Wiley and Sons: New York, 1989; Vol. 16, p 577.

[7] Scheirs, J. In Polymeric Materials Encyclopedia; Salamone, J. C., Ed.; CRC Press: Boca Raton, L, 1996; Vol. 4, p 2498.

[8] Martinu, L.; Poitras, D. J. Vac. Sci. Technol., *A* **2000**, *18*, 2619.

[9] Ocumpaugh, D. E.; Lee, H. L. In Biomedical Polymers; Marcel Dekker: New York, 1971; p 101.

[10] Gombotz, W. R.; Hoffman, A. S. Crit. Rev. Biocompat**. 1987**, 4, 1.

[11] Rosenmayer, T.; Huey, W. Mater. Res. Soc. Symp. Proc**. 1996**, 427, 463.

[12] Lau, K. K. S.; Gleason, K. K. Mater. Res. Soc. Symp. Proc**. 1999**, 544, 209.

[13] S.O. Kim et al, Nature **424**, 411 (2003)

[14] G. B. Blanchet, C. R. Fincher, Jr., C. L. Jackson, S. I. Shah, and K. H. Gardner, Science **262**, 719 ~1993.

[15] S. T. Li, E. Arenholz, J. Heitz, and D. Ba¨uerle, Appl. Surf. Sci. **125**, 17 ~1998.

[16] H. Usui, H. Koshikawa, and K. Tanaka, J. Vac. Sci. Technol. A **13**, 2318~1995

[17] T. Katoh and Y. Zhang, Appl. Phys. Lett. **68**, 865 ~1996.

[18] D. G. Castner, K. B. Lewis, Jr., D. A. Fischer, B. D. Ratner, and J. L.Gland, Langmuir **9**, 537 ~1993.

[19] C. I. Butoi, N. M. Mackie, J. L. Barnd, E. R. Fisher, L. J. Gamble, and D. G. Castner, Chem. Mater. **11**, 862 ~199

[20] W. de Wilde and G. de Mey, Vacuum **24**, 307 ~1973.

[21] T. C. Nason, J. A. Moore, and T.-M. Lu, Appl. Phys. Lett. **60**, 1866~1992.

[22] T. Rosenmayer and W. Huey, Mater. Res. Soc. Symp. Proc. **427**, 463 ~1996; W. L. Gore's website at http://www.gore.com/electronics/pages/techinfo/frameset_techarts.htm.

EFFICIENT PRODUCTION OF FULLERENES AND NANOTUBES BY MEANS OF THE *J*x*B* ARC DISCHARGE

T. Mieno[1], N. Matsumoto[1], M. K. H. Bhuiyan[1],T. Sakamoto[1], M. Takeguchi[2]

[1]Department of Physics, Shizuoka University, 836 Ooya, Shizuoka-shi 422-8529, Japan
[2]National Institute for Material Science, 3-13 Sakura, Tsukuba 305-0003, Japan

Abstract

Efficient production of fullerenes, endohedral metallo-fullerenes and single walled carbon nanotubes is realized by using the ***J***x***B*** arc-discharge method. By applying steady-state magnetic field perpendicular to the DC arc current, the ***J***x***B*** force jets out the sublimated carbon clusters and considerable increase of the production efficiencies is obtained, which would reduce the production cost of these new materials.

Keywords: production of fullerenes and carbon nanotubes, ***J***x***B*** arc discharge, efficient production, magnetic field, carbon clusters

1. Introduction

Recently, fullerenes and carbon nanotubes (CNTs) attract much interest in many branches of chemistry, physics and material science. [1] Applications of higher fullerenes and endohedral metallo-fullerenes are increasing, [2, 3] while production rates of these fullerenes are still very low with respect to that of C_{60}.

Therefore, high efficiency production of higher fullerenes and metallo-fullerenes should be developed. High quality single-walled carbon nanotubes (SWNTs) are also desired to supply good and cheap SWNT-materials for many kinds of applications. Here, in order to improve the normal arc-discharge method, the ***J***x***B*** arc discharge method has been developed to increase the production efficiencies of fullerenes [3, 4] and good-quality SWNTs. [5] Various production conditions are examined by this discharge method to obtain the high performance production.

2. Experimental setup and method

Fullerenes are produced by a revolver injector type fullerene producer (***RIT-FP machine***) [3] as shown in Fig. 1. It consists of three parts, (a) a cylinder-type arc-discharge chamber of 27 cm in diameter and 70 cm high made of stainless-steel, (b) a revolver-type carbon rod magazine of 35 cm in diameter and 45 cm long and (c) a control panel. A block type ferrite-magnet is set at outside of the middle chamber, which makes steady-state magnetic field of 10-50 Gauss perpendicular to the DC arc current and makes the ***J***x***B*** arc discharge. An anode carbon rod is 300 mm x 8 mmϕ and a carbon cathode is 30 mmϕ. For a standard arc condition, He pressure, $\boldsymbol{p}$(He)= 40 kPa, discharge current, $\boldsymbol{I}_d$= 120 A and gap distance $\boldsymbol{d}_G$ ~ 5 mm. In order to produce La metallo-fullerenes and Gd metallo-fullerenes, metal-oxide mixture carbon rods are used. [6] Carbon soot deposited on the chamber wall is collected and fullerenes in the carbon soot are extracted by the Soxhlet method with hot tri-chloro-benzene. A high pressure liquid chromatograph (HPLC) is used to measure fullerene contents in the extracted solution, and collection rates of fullerenes are obtained. A laser desorption TOF mass spectrometer is used to confirm separated

species. [7]

Carbon nanotubes are produced using a similar arc-discharge machine (RPX-machine), which consists of simpler configuration with a cylindrical arc chamber (18 cm in diameter and 20 cm high). [5] Metal-composite carbon rods (6x6x100 mm rectangular type, Ni/Y included carbon) are used to produce SWNTs.

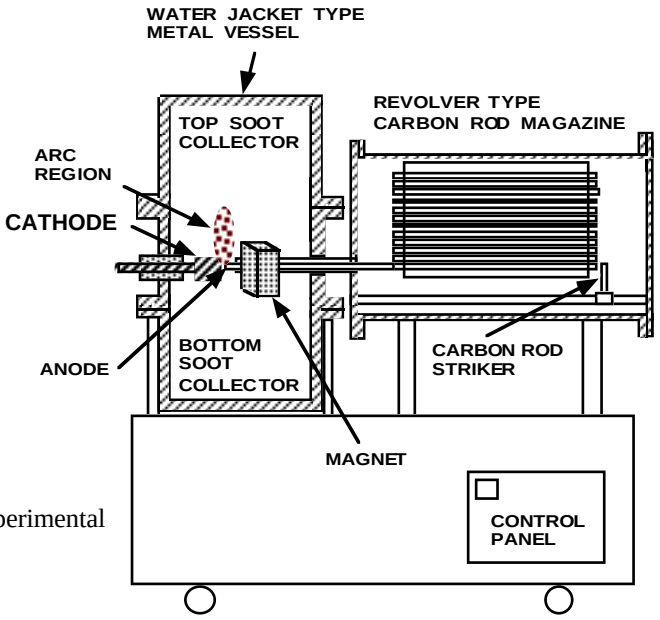

Fig. 1 Schematic of the experimental setup (***RIT-FP machine.)***

3. Experimental results and discussion

Collection rates of higher fullerenes (C_{60}, C_{70}, C_{76}, C_{78} and C_{84}) under the $\boldsymbol{J}$x$\boldsymbol{B}$ and $\boldsymbol{B}$= **0** conditions are measured and shown in Figs. 2 (a) and (b), where $\boldsymbol{I}_d$= 120 A, $\boldsymbol{p}$ (He)= 40 kPa and $\boldsymbol{d}_G$ ~ 5 mm. By applying the magnetic field, significant increase of the production rates is successfully obtained. [7] The effect of discharge current is examined. Collection rates of higher fullerenes as a function of discharge current ($\boldsymbol{I}_d$= 60-160A) are measured, where $\boldsymbol{p}$ (He)= 40 kPa, $\boldsymbol{d}_G$ ~ 5 mm with the $\boldsymbol{J}$x$\boldsymbol{B}$ arc. At $\boldsymbol{I}_d$= 120 A, optimum collection rates of higher fullerenes are obtained. Collection rates of higher fullerenes as a function of He pressure ($\boldsymbol{p}$ (He)= 5-95kPa) are measured where $\boldsymbol{I}_d$= 120 A, $\boldsymbol{d}_G$ ~ 5 mm with the $\boldsymbol{J}$x$\boldsymbol{B}$ arc. The collection rates become maximum at $\boldsymbol{p}$= 40kPa. In this experiment, collection rates of higher fullerenes to that of C_{60} are $\boldsymbol{C}(C_{70})$~ 0.3$\boldsymbol{C}(C_{60})$, $\boldsymbol{C}(C_{76})$~ $\boldsymbol{C}(C_{78})$~ 0.03$\boldsymbol{C}(C_{60})$ and $\boldsymbol{C}(C_{84})$~ 0.05$\boldsymbol{C}(C_{60})$. It can be confirmed that the production rates of these fullerenes increase about twice by the magnetic field. Pressure dependence and discharge current dependence of the production rates of C_{70} and C_{84} are shown in Fig. 3(a) and (b). It is confirmed that the relative collection rates of C_{70} and C_{84} have similar parameter dependence. They become maximum when the collection rate of C_{60} is maximum.

By using the La_2O_3 mixture carbon rod (15 mm in diameter), La metallo-fullerenes are produced by this method where $\boldsymbol{p}$ (He)= 40 kPa, $\boldsymbol{I}_d$= 300 A and $\boldsymbol{B}_0$= 12 Gauss. In this case, the collection rate of La@C_{82} is about 11 mg/h and the content is about 0.047w% (C_{60} content is 3.2 w%), where $\boldsymbol{p}$ (He)= 40 kPa and $\boldsymbol{I}_d$= 120 A. [6]

By using a catalyst-carbon mixture rod, SWNTs are produced [5] The discharge voltage gradually increases with increasing applied magnetic field. The discharge voltage also increases with increasing the gap distance as shown in Fig. 4. Production rate of soot including SWNTs versus applied magnetic field is shown in Fig. 5, where $\boldsymbol{p}$ (He)= 60 kPa and $\boldsymbol{I}_d$= 50 A. Clear monotonic increase of the production rate is obtained. Figure 6 shows a typical photo of SWNTs observed by a TEM, where $\boldsymbol{B}_0$= 0 Gauss. SWNTs, amorphous-like carbon and metal particles are observed. In order to make clear the quality of the samples, the Raman analysis is carried out and shown in Fig. 7. The radial breathing mode

(RB mode), G-band and D-band of the carbon soot are measured for the two magnetic-field conditions. From the RB mode, diameter distribution of the SWNTs can be confirmed. Form these figures, it is confirmed that SWNT of 1.40 nmϕ is predominantly produced by applying the magnetic field. From the ratio of the G-band intensity and the D-band intensity, content of disordered carbon in the soot is estimated, and it can be described that the disordered-carbon does not increase by applying the magnetic field.

4. Summary

It is shown that collection rates of higher fullerenes dramatically increase by means of the ***J***x***B*** discharge method. At the discharge current of 120 A, gap distance $\boldsymbol{d}_G$ ~ 5 mm and the He pressure of 40 kPa for 8 mmϕ rods, the production rate is optimum. SWNTs are also efficiently produced by this method and the SWNTs with 1.40 nmϕ are predominantly produced.

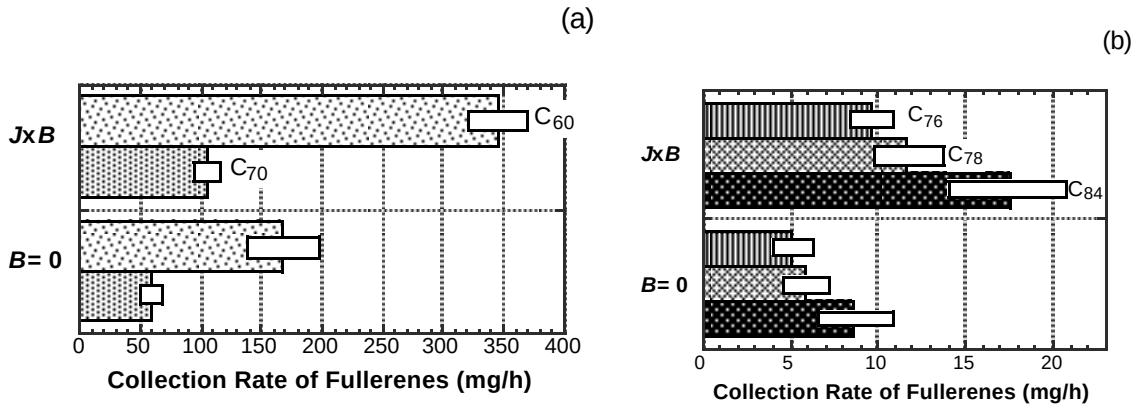

Fig. 2 Collection rates of (a) C_{60}, C_{70}, and (b) C_{76}, C_{78}, C_{84} for the two discharge methods from the produced soot. $\boldsymbol{I}_d$= 120A, ***p***(He)= 40 kPa, $\boldsymbol{d}_G$ ~ 5 mm.

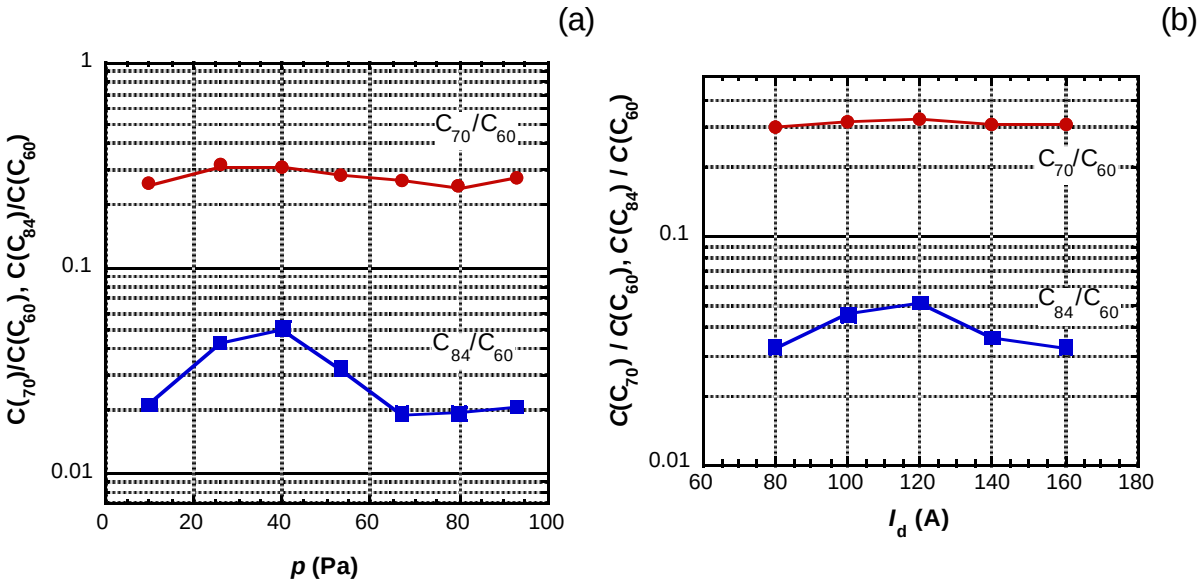

Fig. 3 Relative contents of C_{70}/C_{60} and C_{84}/C_{60} in the soot versus He pressure (a), where $\boldsymbol{I}_d$= 120 A. These contents versus discharge current (b), where ***p***(He)= 40 kPa.

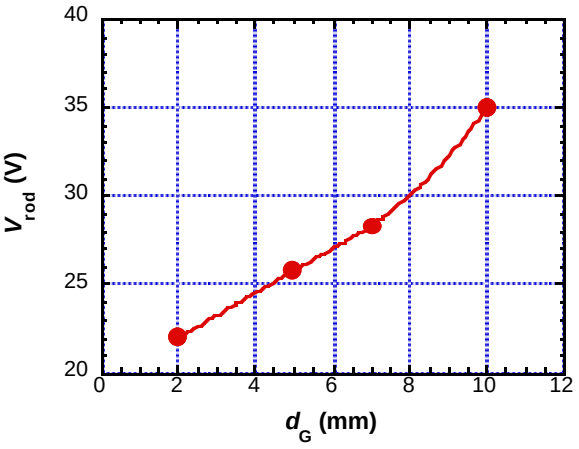

Fig. 4 Voltage betwene the two electrodes versus gap distance, where ***p***(He)= 60 kPa, I_d= 40 A, B_0= 22 Gauss.

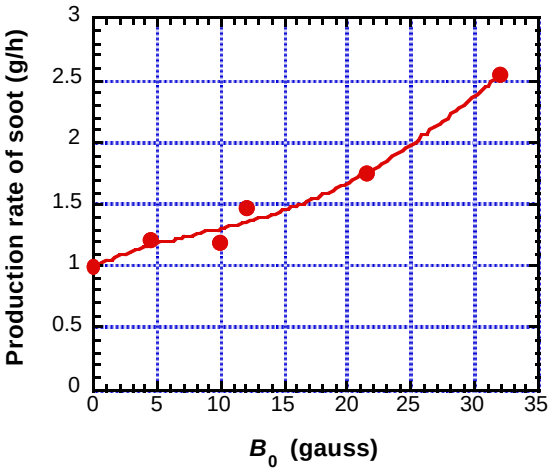

Fig. 5 Production rate of soot including SWNTs versus applied magnetic filed, where ***p***(He)= 60 kPa, I_d= 50 A.

Acknowledgments

We would like to thank Mr. H. Inoue of Dia-Vacuum Co. for his technical support. This study is partly supported by Grant-in-Aid for scientific research from MEXT, Japan and "Nanotechnology Support Project" of MEXT, Japan.

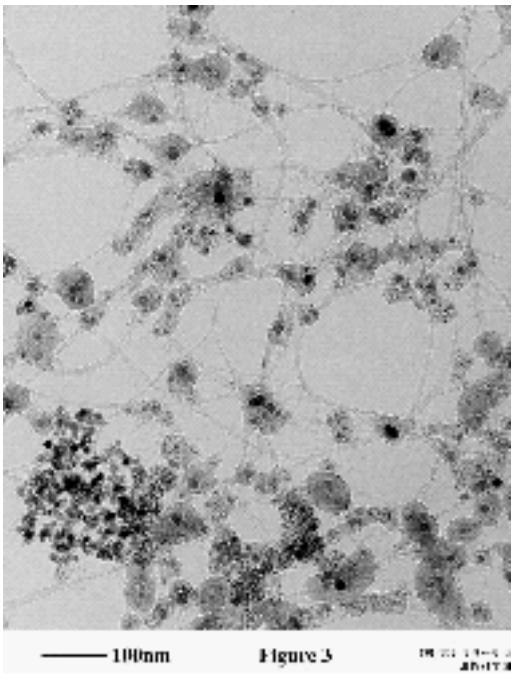

Fig. 6 Typical TEM photo of the produced soot with SWNTs. B_0= 0 Gauss.

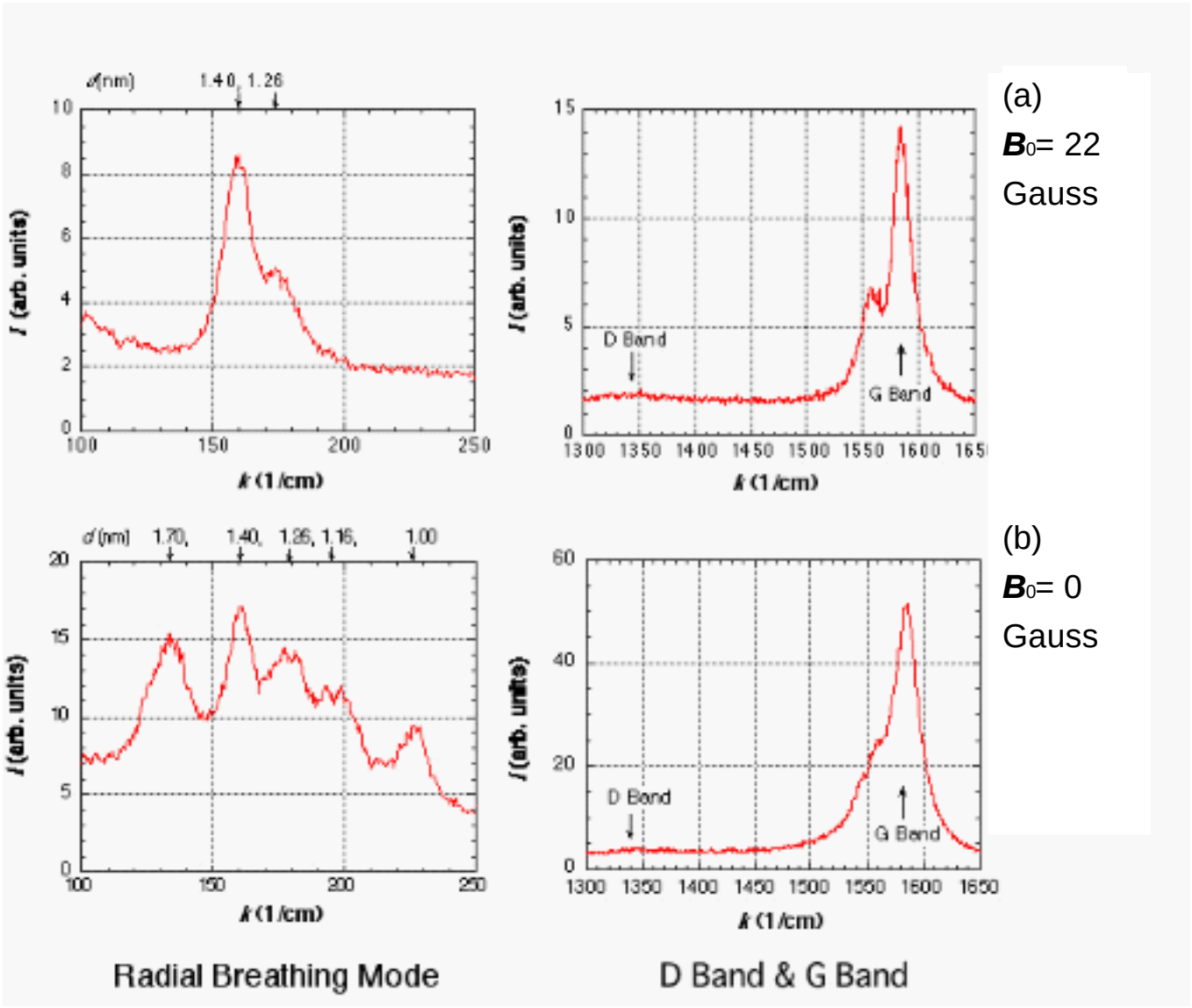

Fig. 7 Raman spectra of soot including SWNTs for the two magnetic fields (B_0= 0 and 22 Gauss). The radial breathing modes are shown in the left side of the figures, where the diameters of SWNTs are indicated on the top part. The G-band and D-band of the carbon are shown in the right-side. [5]

References

[1] R. E. Haufler ***et al.***, J. Phys. Chem. **94** (1990)8634.

[2] W. E. Billups ***et al***, ***Buckministerfullerenes*** (VCH Publishers, Inc., New York, 1993) p. 74.

[3] T. Mieno ***et al.***, Fullerene Sci. Technol., **4** (1996) 913.

[4] T. Mieno, Fullerene Sci. Technol., **3** (1995) 429.

[5] T. Mieno, N. Matsumoto & M. Takeguchi, Jpn. J. Appl. Phys. **43** (2004) L1527.

[6] T. Sakamoto, Master Thesis of Science & Technol Course, Shizuoka Univ. (2001) p.12.

[7] Md. K. Hassan Bhuiyan & T. Mieno, Jpn. J. Appl. Phys. **41** (2002)314.

Identification of vortex structures from plasma light emission

Vaclav Nenicka[1], Jiri Sonsky[1], David Kolman[2]
1 Institute of Electrical Engineering AS CR, Dolejskova 5, Prague, Czech Republic
2 Institute of Thermomechanics AS CR, Dolejskova 5, Prague, Czech Republic

Abstract

The key information about the mechanisms of the generation of structures of coherent character may be obtain from the time sequences of experimental data on the changing radiation intensity in the plasma. The variations of the radiation in time allow us to understand the dynamics of the structure movement in the plasma domain where the fluctuations of the radiation energy reach their maximum values.

Keywords Heat flow, vortex structure, radiation intensity, plasma jet

1. Introduction

The analysis of the vortex dynamics of the free stream is one of the exceptionally difficult problems of transition from laminar to turbulent flow. The transition between these two types of flow proceeds with a certain degree of organization (order) in the non-equilibrium working environment within the plasma generator. The degree of the organization of the movement in the free plasma stream depends on the gas throughput and on the energy supplied to the gas by the electric arc. The mathematical apparatus as well as the physical diagnostics tools must be designed in such a way as to respect the conditions under which the free plasma stream is generated. Therefore, it is desirable to select for the basic research such configurations of the plasma generating process that lead to the support of symmetric types of flow. The anisotropy of the processes is an inevitable complement of the interaction of the free plasma stream with the environment. The energy transport away from the central regions of the jet is influenced by the processes taking part in the outer regions of the free stream. These facts lead us to conclusions that the analysis of these processes must be performed by methods describing them in a certain spatial and temporal interval – i.e. not locally but globally.

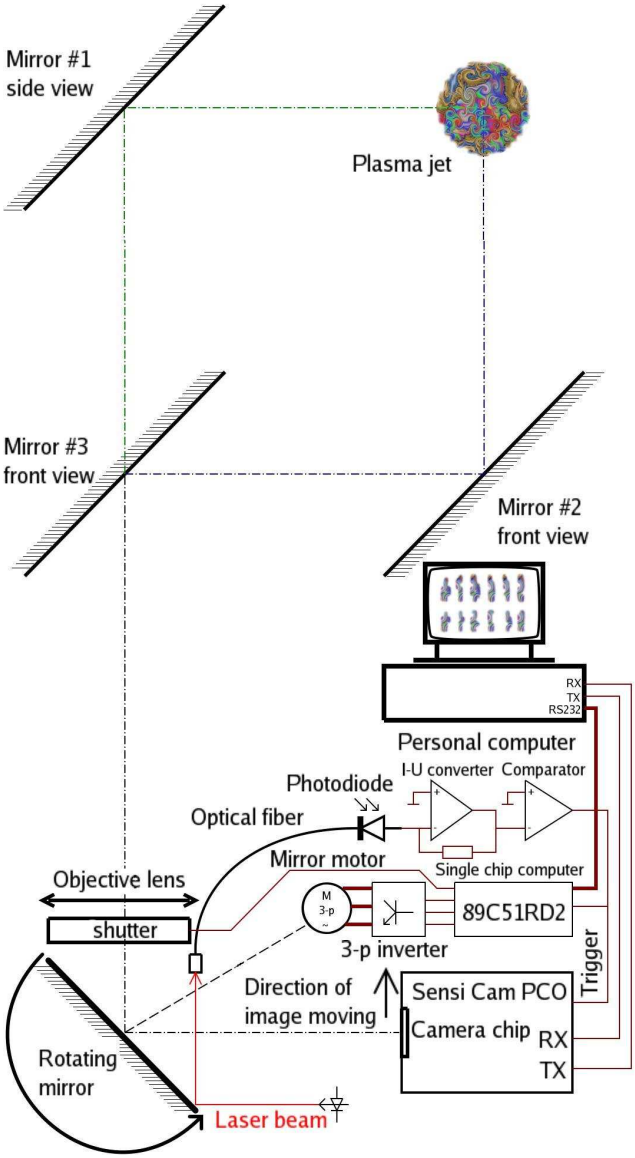

Fig. 1. Experimental setup.

Vortex motions make plasma flows fully three dimensional and complicated in general, and they play a dynamically important role in kinetic energy production and dissipation, mixing, diffusion and transport of mass, heat and momentum, plasma instabilities, and so on. Understanding of the dynamics of vortex structures in plasma, such as their generation, interaction and evolution mechanisms, is a prerequisite for flow prediction and control.

The basic components of the transport of the thermal energy in a flowing plasma are the heat flux and the tensor of the shear stresses of the velocity field. These two vector and tensor quantities, respectively, determine the dynamics of the development of the fluctuations of the velocity field and of the free energy in the plasma stream. The key information about the mechanisms of the generation of structures of coherent character may be obtain from the time sequences of experimental data on the changing radiation intensity in the plasma. The variations of the radiation in time allow us to understand the dynamics of the structure movement in the plasma domain where the fluctuations of the radiation energy reach their maximum values.

2. Experimental setup, imaging, and graphical representation methods of radiation structures in plasma

The heat flux in the free plasma jet depends on a number of thermodynamic and hydrodynamic quantities, first of all on the enthalpy and the vector of the macroscopic gas velocity. To determine it, we use the information about the radiation variation in the interval of 100 μs as captured on eight CCD snapshots. The image is swept through the CCD chip by a fast rotating mirror. An eightfold exposition produces a series of eight snapshots on a black background. The radiation intensity is used to identify the enthalpy values in the jet core where the jet possesses the highest internal energy and enthalpy. The shear layer region is characterized by fluctuations in the radiation intensity. These fluctuations result from macroscopic vortexes and, subsequently, from the fluctuation of the macroscopic velocity field. The instabilities of the velocity field thus become the source of the heat flux fluctuations.

In this situation, it is complicated to construct components of the three-dimensional heat flux vector from the CCD snapshots. The side view and the frontal view represent the image of the radiation dynamics in two directions. However, the determination of the radiation intensity in the horizontal projection is difficult and has not been performed by the CCD technique yet. Therefore, we have estimated the radiation values in the ground plane in the form of a square matrix from the values obtained in the vicinity of the nozzle orifice. The ground plane matrix is computed as a product of two vectors that are given by the radiation intensities in the side plane and the frontal plane in the nozzle vicinity. This method has several drawbacks that will be studied later.

The enthalpy of the gas mixture is strongly dependent on the mixture composition not only in the sense of chemical composition but, in the case under consideration, on the hydrodynamic processes that are related to macroscopic fluctuations resulting from the intense jet mixing. This means, in the same time, that the stress tensor also influences significantly the heat flux. The combination of these two factors focuses our attention to tomographic methods for the reconstruction of the radiation body of the free jet, ire. to the processing of the radiation signal based on Radon transformation. In this considerations, it is necessary to respect the differences between the vector and the scalar potentials.

We assume in the proposal for the phenomenological construction of the jet body that the changes in the radiation intensity are strongly influenced by the electric field in the chamber of the plasma generator, and, as far as the location of the vertical axis of the jet is concerned, also by the buoyancy forces. This leads to a break down of the isotropy of the heat transfer in the vertical direction as a consequence of the shear forces generated by the environment. Under these conditions, the location of the maximum radiation intensity in the side and frontal planes determines the coordinates of the maximum radiation intensity in the horizontal plane of the three-dimensional jet body. Via the determination of these couples of the locations of the maximum values we obtain the information about the location of the maximum radiation intensity along the axis of the jet. The three-dimensional matrix obtained from the multiplication of the side and frontal planes, resp., may be considered as a substitution of the spatial distribution of the radiation intensity in the vicinity of the maximum luminosity in the individual horizontal planes. Subsequent thoughts about the distribution of the heat flux vector are strongly determined by its dependence on the product of the velocity vector and the enthalpy of the working gas.

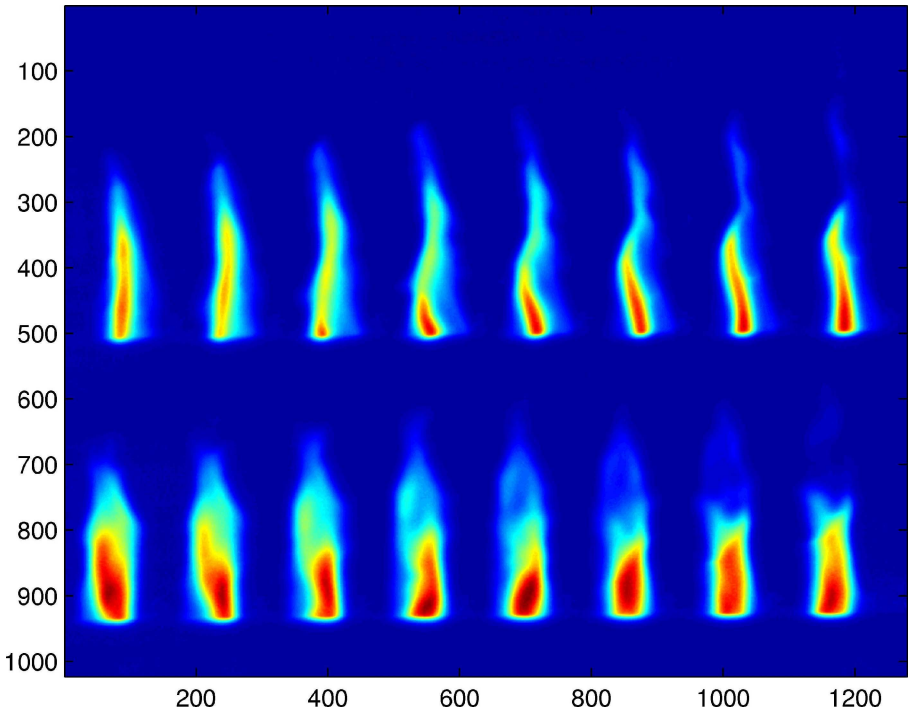

Fig. 2. Original image captured from CCD camera, 80 slm, 150A.

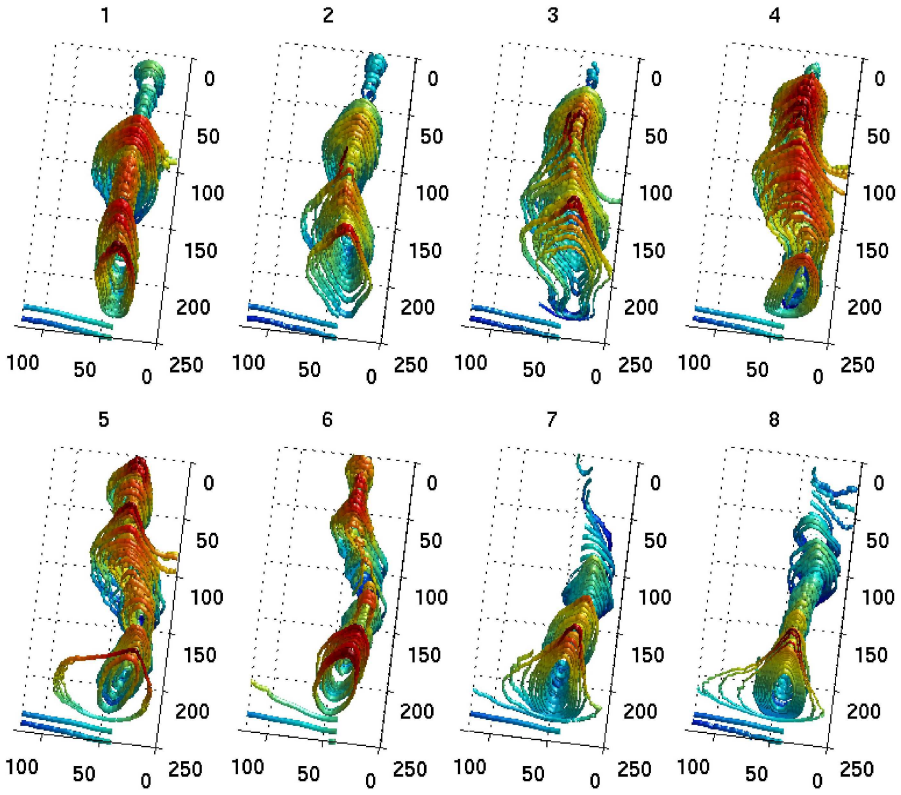

Fig. 3. Analysis of vortex structures, 80 slm, 150A.

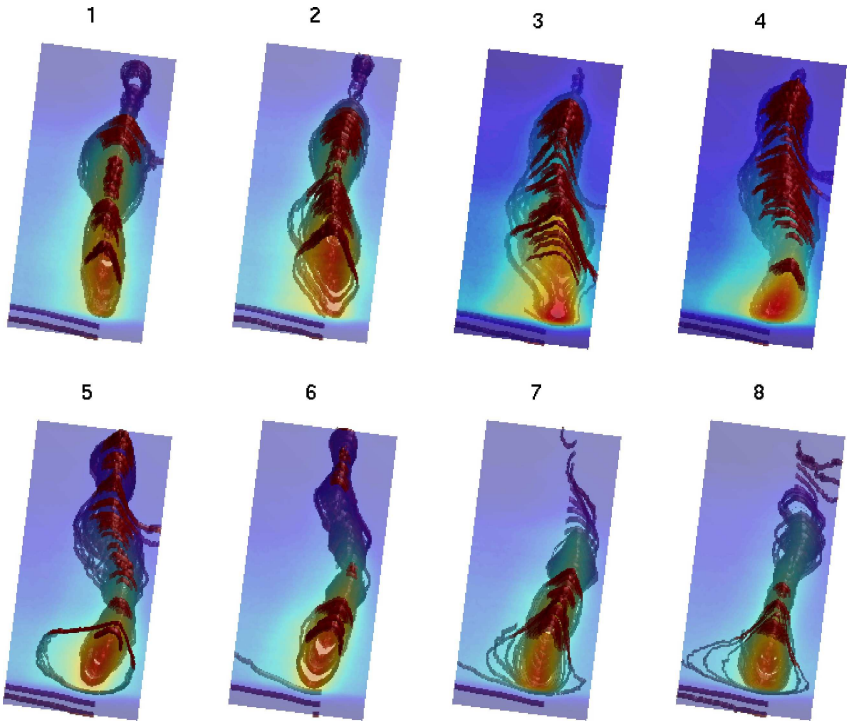

Fig. 4. Analysis of vortex structures together with a plane representating luminosity, 80 slm, 150A.

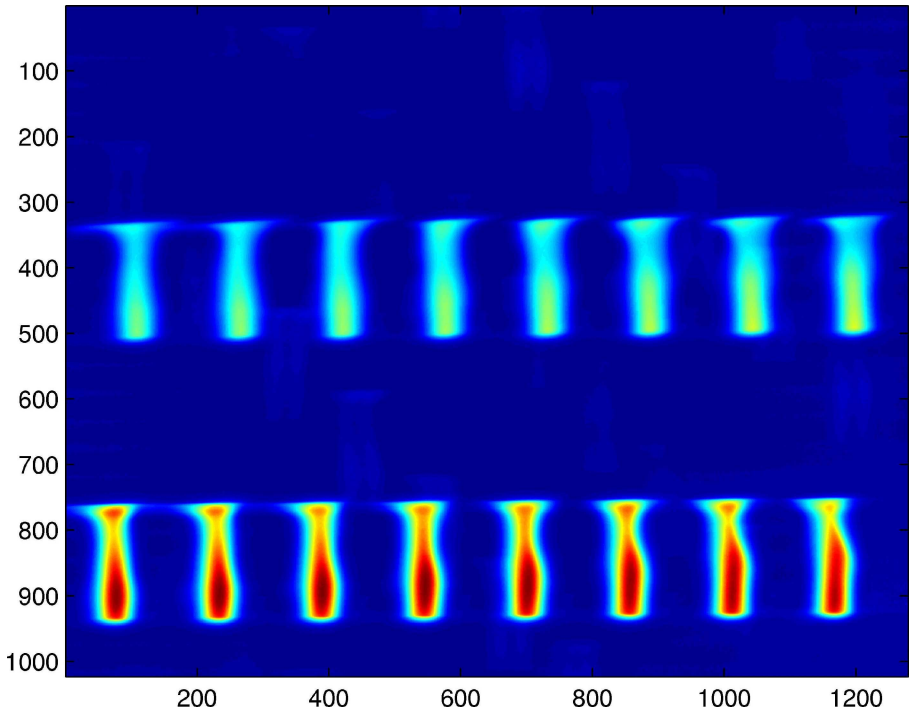

Fig. 5. Original image captured from CCD camera, 40 slm, 200A.

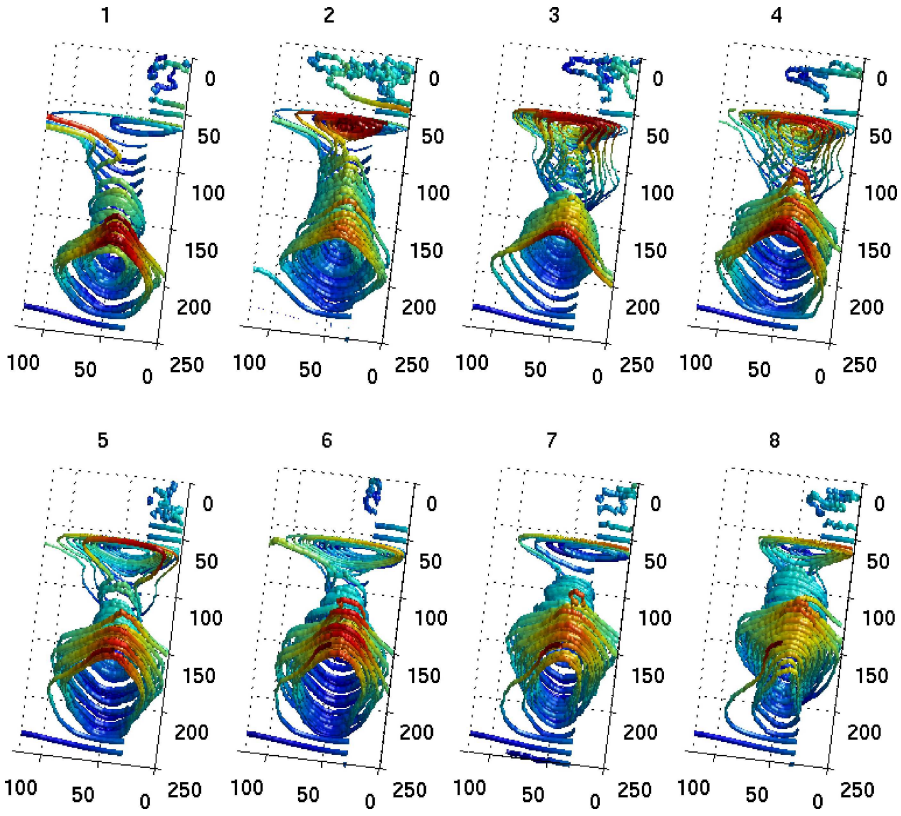

Fig. 6. Analysis of vortex structures, 40 slm, 200A.

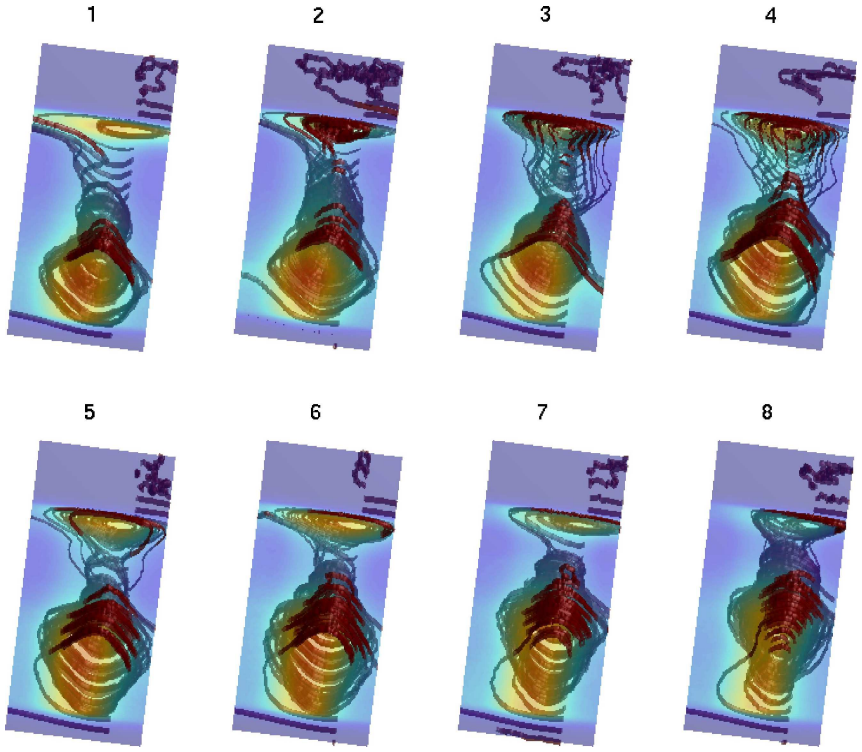

Fig. 7. Analysis of vortex structures together with a reconstructed plane, 40 slm, 200A.

Figures 5 - 7 show movement of heat flow vortex structures between the plasma jet and the barrier inserted into plasma flow. Snapshots 2, 3, and 4 in figures 5 - 7 illustrate the grow of vortex structures under the barrier, including the interaction of plasma jet with the vortex under the barrier. The barrier has a stabilising effect on the plasma jet, radial movements are minimized, in vertical direction we can see the movement of the vortex structure. Radial movements are influenced mainly by the presence of macroscopic scale vortexes in plasma jets outer shell, observed on figures 2 - 4 . The intensity of vortexes is increased if the mass flow rate of working gas goes up. For illustration we choose snapshot 5, figure 3 (mass flow rate 80 slm, current 150A). Radial transfers are dominant in structure dissipation, which is moving vertically (see snapshots 1 – 4). If we place a plane into plasma jet reconstruction in vertical direction, we obtain information about the stability changes in radial direction, and the velocity of movement of the structure in vertical direction.

The vector relations of the differential geometry for vorticity do not allow us, due to the properties of the scalar potentials, to perform such matrix transformations that rectify the measured values through scalar potentials as it holds that $rot(grad\phi)) = 0$ (ϕ is a scalar potential). Therefore, in the first phase of the application of the method based on the vorticity vector of the heat flux, we have retained only the components obtained as a product of the radiation body of the free jet – i.e. three-dimensional matrices – with two-dimensional matrices representing ground plane, frontal plane and side plane. Thereby we obtain a three-dimensional vector whose components contain the information about the enthalpy changes in the core and that modify the radial part of the free jet by the information about the stress tensor. The presence of the macroscopic vortexes in the vicinity of the jet body exercises the crucial influence on the stress tensor. This method as applicable namely to the identification of the different movement of the plasma features. We study structures of two types – emerging horizontal partitions, and structures of the free plasma jet whose dynamics is determined by the momentum in the closest vicinity of the nozzle exit. The discussion of the results is facilitated by drawing a plane through the jet body which allows to portray complex movements of the jet as opposed to the slower movement of the plasma features hold by the partitions. The selection of the planes intersecting the jet is done via a visual evaluation the graphical records shown in selected images. The selection is realized with Matlab.

3. Conclusion

The motion of heat flow vortex structures illustrated in Figs. 2 to 7 is influenced by forces of buoyancy, by shear forces due to macroscopic vortexes and by velocities corresponding to flow rates of gas. The value of the electric power input determines the stability of the system – with increasing the power input , the enthalpy of the system is on increase. The enthalpy is represented by the intensity of radiation in the central region of the jet , which allows for the reconstruction of the heat flow. A heat flow is considered as a vector whose anisotropy actuates towards establishing dynamic equilibrium. Experimental results need substantiating in terms of non-linear thermodynamics and kinetic theory [1] and are based on the changes of the radiation intensity of the jet. The geometrical correspondence between the volume features of the jet and the vorticity tubes of heat flow is from experimental results acceptable. Presented methods are very usefull for vorticity identification, and for velocity measurements. As non-contact method does not influence the plasma jet behavior, we are able to observe changes if a barrier is inserted into plasma flow.

Acknowledgement

This work has been suported by Grant Agency of the Academy of Sciences of the Czech Republic under Contract No. 202/04/1341.

References

[1] Byung Chan Eu, Nonequilibrium Statistical Mechanics – Ensemble Method, Kluwer Academic Publishers 1998

[2] Vaclav Nenicka, Jiri Sonsky: Correlation Analysis together with Vortex Geometry, Two Method for Tracing Structures in Plasma Heat Flows. Acta Technica, CSAV 49, 423-458 (2004).

Formation and reactions of radicals in the plasma treatment of polymers

A. Holländer and S. Kröpke

Fraunhofer-Institut für Angewandte Polymerforschung, Geiselbergstr. 68, 14476 Potsdam, Germany
email: andreas.hollaender@iap.fraunhofer.de

Abstract

The formation, the analysis, and reactions of radicals is reviewed briefly with respect to plasma processes. Polyethylene films were treated with an atmospheric pressure glow discharge. The formation of radicals and hydroperoxides was investigated by the derivatization with NO and SO_2, respectively, and XPS. It was found that the concentration of alkoxy radicals increases constantly with the treatment time to 4.2% of the C-atoms (5 min). A maximum of 0.7% C-atoms with a hydroperoxide group was measured.

1. Inroduction

Radicals play important roles in the plasma treatment of materials and in particular of organic materials. Some of the reactive particles in the plasma are radicals. They alter the surface chemistry of materials or form coatings. Oxygen atoms (biradicals) are crucial in cleaning and etching processes. On the other hand, most of the reactions that are initiated by a plasma in a solid are radical reactions. These radicals induce cross-linking or fragmentation and they readily react even with traces of oxygen in a chain reaction. But they also can be used to initiate graft polymerizations. In many plasma processes they are important intermediates.

In the present paper, we will briefly review the basics of radical chemistry before we will focus on reactions in solids. We will discuss methods for the analysis of radicals, which can be used for plasma-processed materials. Finally, we will show examples for the determination of radical concentrations and the radical structure in polyolefin surfaces after a plasma treatment.

1.1 Radical formation

Molecules or atoms are called radicals if they have one or more unpaired electrons. Usually they are formed by a homolytic scission [1] of a chemical bond. The energy necessary for the scission can be introduced thermally, by photons, or by a reactive chemical agent. This energy must be at least as high as the dissociation energy E_{dis} for the bond. The value of E_{dis} depends on the atoms that form the bond but also on the chemical environment of these atoms (see Table 1, [2]). If a molecule comprises different types of bonds, the ones with the smallest E_{dis} tend to be broken first. For example, the E_{dis} of a C-H bond of the methyl group at the end of a hydrocarbon polymer chain is higher by 27 % compared to the C-H bond at the tertiary carbon atom of a branch or linkage. Therefore, the hydrogen atom at the tertiary carbon atom is split off easier than others. Similarly, it

Table 1. Bond energies (E_{bond}) and dissociation energies (E_{dis}) of bonds in organic molecules [2]

Bond	E_{bond} kJ/mol	E_{dis} kJ/mol	eV
H–CH_3		436	4.52
H–CH_2CH_3		411	4.26
H–CH-$(CH_3)_2$		394	4.09
H–C-$(CH_3)_3$		381	3.95
H–CH_2-C_6H_5		322	3.34
C–C	348		3.61
C=C	594	246[a]	2.55
C≡C	778	184[b]	1.91
C–C–O		302	3.13
C–C=O – aldehyde		314	3.26
C–C=O – ketone		344	3.57
CH_3-OH		381	3.91
C–O–C		335	3.48
C=O – aldehyde	741	364[a]	3.77
C=O – ketone	749	372[a]	3.86
CH_3–NH_2		335	3.47
CH_3–F		453	4.70

[a] calculated as difference between the bond energy of the double bond and the single bond.
[b] calculated as difference between the bond energy of the triple bond and the double bond

takes less energy to produce radicals from multiple bonds than from single bonds because of the π-bond's smaller E_{dis}. C-O bonds and C-N bonds tend to break before C-C bonds and C-H bonds.

These purely energetic considerations are most important in the case of an excitation by photons. In the case of an attack by a reactive atom or molecule there are sterical influences, too.

In a plasma, there are particles and radiation which possess sufficient energy to break bonds and to form radicals. While the action of particles at polymer surfaces is mostly limited to a very shallow surface layer, photons can penetrate deeper. Vacuum ultraviolet radiation (wavelength between 100 nm and 200 nm) is usually absorbed in the outer 50 nm (90 % intensity loss [3]) of an organic material. It can produce radicals efficiently. Radiation with a longer wavelength can penetrate deeper into the material. However, the efficiency of initiating reactions in the solid is often small compared to the other plasma components and the contribution can be neglected. Many of the particle induced reactions and virtually all photon initiated reactions involve radicals.

1.2 Analysis of radicals

In general, the unpaired electrons are characterized by the spin. Electron spin resonance spectroscopy (ESR) is mostly used to analyze them. However, ESR analysis of real-world plasma treatments and plasma treated samples is difficult because the geometry of the spectrometer does not allow in-situ measurements. (There are reports in literature about experiments with plasma treatments in ESR cuvettes [4].) Experiments with quenching reactions which convert the radicals into stable structures are closer to real treatments. Diphenylpicrylhydrazyl (DPPH) was used for that purpose [5]. DPPH is an intensely colored and relatively stable radical which recombines with other radicals forming colorless products. The discoloration of a DPPH solution is used to quantify the amount of radicals in a sample. However, there are reports about DPPH not being useful for radical determination [6] because it reacts with other functional groups, too.

In previous papers we reported about the use of gaseous scavengers like iodine and nitric oxide (NO) for the analysis of radicals [7, 8]. These gaseous substances do not alter the surface in an unspecific way like a solvent does. Iodine can be determined very sensitively using XPS which provides the opportunity to identify small variations of the radical concentration. Unfortunately, the small iodine vapor pressure at room temperature limits the diffusion into the surface. If the radicals are not sufficiently stable and they diminish before there is iodine to react with, the absolute quantification is difficult. For example, the decay of radicals in the surface of polyethylene (PE) and polypropylene (PP) was investigated with iodine [8]. The radical decay rate was found to be in the same order of magnitude like the gross reaction rate with iodine. Consequently, the shape of the radical decay evolution was determined correctly while the absolute concentrations values were too small.

Nitric oxide is a gas under normal conditions and, therefore, it is easier to use. The reaction condition can be selected to meet the demands for the radical quenching at solid surfaces. These experiments provide absolute numbers for the radical concentration. Moreover, the reaction can be used to obtain information about the structure of the original radicals [7]. In the case of oxygen-free hydrocarbon polymers, the recombination of the carbon centered radical with NO is followed by rearrangement reactions. Depending on the structure, these reactions form different NO_x structures which can be distinguished by N1s-XPS.

1.3 Radical reactions

In general, we have to distinguish reactions which preserve the unpaired electron and such which result in the loss of the unpaired electron.

The addition of molecular oxygen starts a series of reactions that is called oxidation. From a practical viewpoint, it is the most important example for the first reaction type. For the understanding of the oxygen reactivity and the pathways of the reactions, it is important to note that molecular oxygen (O_2) is a biradical, i.e. the molecule has two unpaired electrons, one at each atom. The recombination rate of the carbon-centered radicals with O_2-radicals is several orders of magnitude higher than the value for the reaction with other molecules. Therefore, even traces of oxygen in a plasma chamber suffice to incorporate oxygen into the surface.

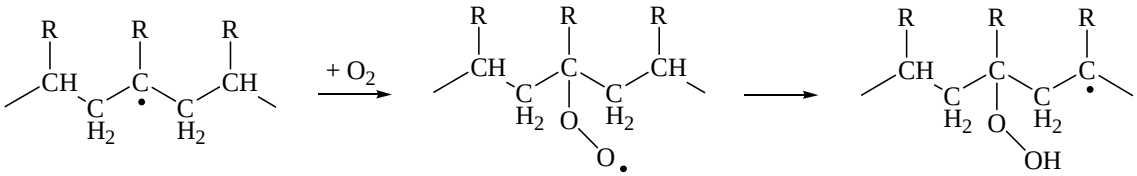

The reaction of a carbon radical with an oxygen molecule forms a peroxy radical. In the next step, the abstraction of a hydrogen atom preferably at the β-carbon atom results in a hydroperoxide and a new carbon radical, which again can react with O_2. This chain reaction continues until there are no more hydrogen atoms available. This means that several oxygen molecules are incorporated into the surface at the place of one single radical initiation site. For example, radicals which were produced by VUV photolysis in PE and PP result in the incorporation of about 20 and 10 oxygen atoms per radical, respectively [9].

Hydroperoxides degrade under the influence of heat or UV light. Depending on their structure, they can decay also at room temperature with a considerable rate. In the result, alkoxy radicals and hydroxyl radicals are formed. They react readily with neighboring molecules or parts of molecules in consecutive steps and form a variety of different functional groups. The type of these functional groups and their relative concentrations depend only partly on the structure of the first original radical, the initiation site.

There are two reaction types that result in the loss of the radical function: recombination and disproportionation. In recombination reactions the two unpaired electrons form a new bond. The disproportionation describes the transfer of a hydrogen atom from one radical to a second according to the following reaction scheme.

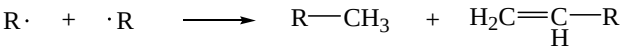

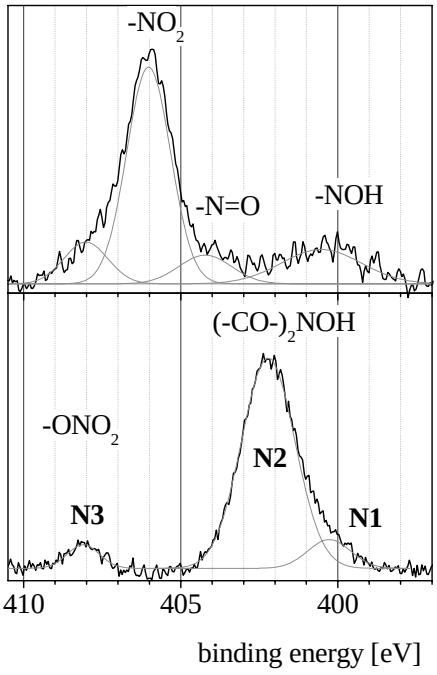

Figure 1. N1s-XPS of NO labeled PE which was treated with VUV (top, [8]) and with an atmospheric pressure glow discharge (bottom, 60 s).

While the recombination results in an increase of the molecular mass, the disproportionation tends to decrease it. In the case of a plasma treatment of polymers, the ratio between the two reactions decides whether the material gets cross-linked or etched. For example, a branched structure favors the disproportionation over the recombination. As a result of this tendency, in a plasma treatment polyethylene tends to be cross-linked while polypropylene forms low molecular weight volatile products. The etch rate is higher in the case of PP.

2. Radicals in the plasma treatment of polyolefins

In previous investigations [8] we studied the formation of radicals in VUV photolysis reactions of PE and PP and their decay in high vacuum (HV). With these experiments we were able to prevent oxygen from reacting with the radicals. This was a simulation of the subsurface conditions during a plasma treatment. With the NO reactions, it was found that at extended treatment times (60 min) the majority of radicals are located at tertiary carbon atoms (see upper part of Fig. 1), which is an indication for a substantial cross-linking. In the N1s X-ray photoelectron spectrum we observed highly oxidized nitrogen atoms, which are formed by multi-step reactions of the tertiary radicals with NO.

In the presence of oxygen, the reaction pathways during the treatment are much more complex. Considering what was discussed in the chapter above, the probability to find a carbon centered radical is rather low. We have to expect hydroperoxides and alkoxy radicals instead. In fact, we observe a completely different N1s-spectrum (Fig. 1, bottom) with samples, which were treated in an atmospheric pressure glow discharge (APGD) and then with NO. There is a

rather small fraction of oximes (400.4 eV) which are usually formed from radicals at secondary carbon atoms. The component at a binding energy of 402.2 eV suggests a nitrogen atom with one bond to an oxygen atom and two bonds to carbon atoms having one or two bonds to oxygen each [10]. Nitrogen in such a binding state has never been found in our experiments in HV. Therefore, we conclude that it is a result of the reaction of NO with an oxygen containing species. If we consider the evolution of this N1s component with the treatment time (see below), it seems reasonable to assume that alkoxy radicals are the origin of this feature.

Nitroso groups and nitro groups which are formed from tertiary radicals and which are prominent in the samples of HV experiments, were not found at all in the APGD experiments. This virtually complete absence of tertiary radicals suggests that there are no carbon based linkages at the polymer backbone within the analysis depth. If there is any cross-linking, it must be via oxygen bridges like ethers or esters.

The component at 408.1 eV must be attributed to nitrates [11]. In the HV experiments we observed nitrates, too. They were thought to be formed by the reaction of NO with nitroso groups. In the present samples, there were no tertiary radicals that could form nitroso groups and we did not find any nitroso groups. The source of the nitrates must be different. Comparing the two types of experiments, we see that the presence of O_2 gives rise to peroxy radicals and hydroperoxides which are both good candidates for the nitrate formation.

A typical evolution of the fractions of the 3 nitrogen components as a function of the duration of the APGD treatment is shown in Fig. 2. A short treatment time of some seconds gives rise to a relatively high concentration of the nitrate N3 component. Its concentration decreases at longer treatment times. The component N2 is formed more and more over all the treatment at least up to 300 s. N1 is small in all the samples but there might be a slight tendency to an increasing concentration value. These evolution characteristics fit reasonably well with the proposed structural features behind these components and their probable fate during an APGD treatment. In the very beginning of the treatment, the surface radicals react with O_2 and form peroxy radicals and hydroperoxides (N3). In the course of the treatment, the peroxy structures are destroyed and form alkoxy radicals (and other stable products). But the O_2 addition to carbon radicals continues although with a decreasing rate. The resulting peroxy structures decompose to alkoxy radicals which gives rise to a quasi-equilibrium concentration of the peroxy structures and to a steadily growing alkoxy radical concentration.

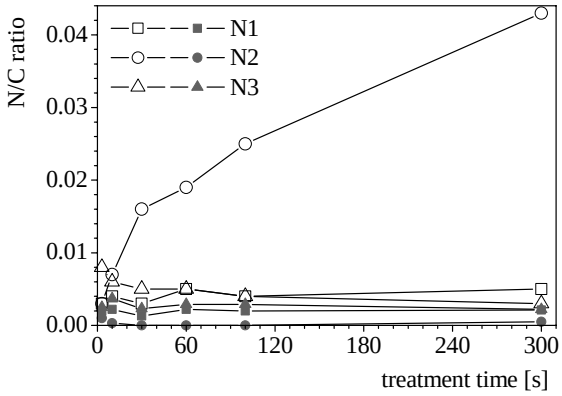

Figure 2. Evolution of the N1s component concentrations after the NO reaction as a function of the APGD treatment time of a PE film. open symbols: NO treated; filled symbols: NO treated and washed

A total of 2.3 at% of nitrogen from the NO reaction was found in the sample after the 300 s treatment. The oxygen concentration accounted for 20 at%. Washing the samples in ethanol reduced the oxygen concentration of all samples with treatment times > 10 s to about 8 at%. A maximum nitrogen concentration of 0.7 at% was found after washing the NO treated samples. It is worth noting that the component N2 is removed completely by the washing (filled symbols in Fig. 2).

In literature, there are reports about using sulfur dioxide for the investigation of hydroperoxides [12]. The sulfur inserts between the oxygen atoms and forms a hydrogen sulfate which can be determined by XPS. It was found that in a 30 s APGD treatment a hydroperoxide concentration of 0.7 % of the carbon atoms is present in the sample surface. This value is slightly higher than the one obtained from the NO reaction (N3: 0.5 %).

The hydroperoxides decompose during storage (Fig. 3). A 4 h heating to 89°C reduces the sulfur concentration to 0.29 % of the carbon atoms. At room temperature the decomposition is slower but still considerable. After a 24 h (1440 min) storage, we measured a value of 0.36%C.

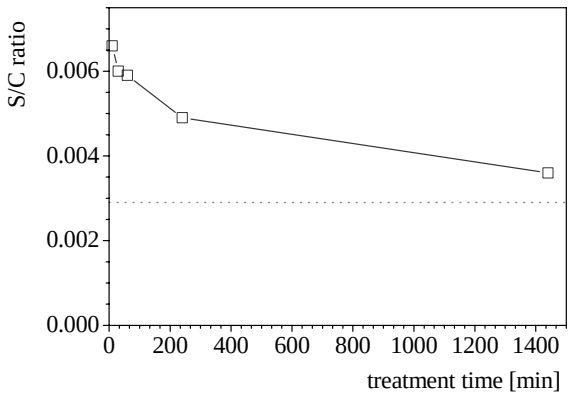

Figure 3. Sulfur concentration of SO_2 derivatized samples of PE films as a function storage time between APGD treatment and SiO_2 treatment. Dotted line: value for a 4 h storage at 89°C.

3. Conclusions

Gas phase derivatization reactions with nitric oxide NO and sulfur dioxide SO_2 can be used to obtain information about the concentration and the structure of radicals and the concentration of hydroperoxides at the surface of polymers.

Compared with previous studies in a strictly oxygen-free process, the reaction paths are more complex in the presence of oxygen. They are not completely understood yet and it requires further investigations on the reliability of the quantification data.

4. Experimental

The APGD equipment is described in detail elsewhere [13]. Briefly, a DC discharge (110 W) is generated between metal pin electrodes and a metal grid while blowing air through the discharge zone (250 m^3/h, 20 °C, 52 % rel. humidity). The sample film (polyethylene, 30 µm, Orbita-Film GmbH, Germany) located at a distance of 5 mm away from the discharge zone.

For the derivatization we used a 0.8 l stainless steel chamber which was pumped to < 1 mbar before filling with NO (99 % Linde AG, Germany) or SO_2 (99.98 %, Linde AG, Germany) to 200 mbar. After 15 min the chamber was pumped again to remove the gas. Then it was filled with argon and the samples were transferred to the XPS instrument.

Some samples were washed in ethanol in an ultrasound cleaner for 5 min.

The XPS spectra were recorded using an AXIS 165 instrument (Kratos Analytical, UK). A monochromatic Al Kα was used for excitation. The instrument was operated in hybrid mode (with magnetic and electrostatic lenses).

5. References

[1] The two electrons of the covalent bond remain one at each of the fragments. This contrasts the heterolytic scission in which one fragment takes both electrons. Then, the fragments carry opposite charges.

[2] A. Holländer, J. Thome in „Plasma Polymer Films“ Ed H. Biedermann, Imperial College Press, 2004, p. 248 and references there.

[3] R. Wilken, A. Holländer, J. Behnisch - Plasmas and Polymers, 7 2 (2002) 185.

[4] M. Kuzuya, J. Niwa, H. Ito - Macromolecules, 26 (1993) 1990.

[5] W. Lu, C. Huang, M. Roan - Surface and Coatings Technology, 172 2-3 (2003) 251.

[6] R. Teng, H. Yasuda - Plasmas and Polymers, 7 1 (2002) 57.

[7] R. Wilken; A. Holländer; J. Behnisch - Macromolecules. 31/ 22, 7613 (1998).

[8] R. Wilken; A. Holländer; J. Behnisch - Surface and Coatings Technology. 116-119, 991 (1999).

[9] R. Wilken, „Untersuchungen zur Oberflächenmodifizierung ausgewählter Modellpolymere durch VUV-Photolyse", („Investigation of the surface modification of some polymers by VUV photolysis“) PhD Thesis, Universität Potsdam, 1998.

[10] The precise structure is difficult to tell. We can exclude ammonium structures which hardly can be formed here. The nitrogen species must have a N1s electron density between the one of an oxime (>C=NOH) or hydroxylamine (R_2NOH) which have an binding energy of about 401 eV and nitrogen with 2 bonds to oxygen like a nitroso group (-N=O) with a BE of 403.7 eV.

[11] see NIST database http://srdata.nist.gov/xps.

[12] J. Mitchell, L.R. Perkins - Appl. Polym. Symp, 4 (1967) 167; L. J. Gerenser, J. F. Elman, M. G. Mason, J. Pochan. - Polymer, 26 (1985) 1162.

[13] S. Kröpke, Y. S. Akishev, A. Hollander - Surface and Coatings Technology, 142-144 (2001) 512.

Introduction of irregularities into plasma polymers by radiative and auto-oxidative processes

S. Krüger, R.-D. Schulze, K. Brademann-Jock, J. Friedrich
Bundesanstalt für Materialforschung und –prüfung (BAM), 12200 Berlin

Abstract
Thin plasma polymer films were deposited using the pulsed plasma (pp) mode. These plasma polymers should possess a more regular structure because of the lower monomer fragmentation during the plasma pulses and the chemical chain propagation during the plasma-less periods than those produced by the conventional continuous-wave (cw) mode. In addition to the use of the classic thin film characterization method XPS the new method of thermoluminescence was applied to characterize defects and structural specifics in the polymer films produced by pp or cw plasma mode. The thermoluminescence method was applied to functional groups-carrying plasma polymer layers, which are used in medical technology for forming biocompatible and bioactive coatings or in metal-polymer composites as adhesion-promoting interlayers.

1 Introduction

The process of plasmapolymerization was investigated in detail by Jesch, Yasuda, Westwood, Poll, Denaro, Shen, Bell, Tiller etc. [1-10]. It was recognized soon that plasmapolymers differ strongly in structure and composition from their classic reference polymers. Firstly, a complete fragmentation of monomers in the plasma phase was detected before the deposition occurs [10]. Secondly, it was observed that all fragments and atoms recombine randomly [8], so that the real structure of plasma polymers is far from that of classic analogues. Moreover, the deposited thin film is exposed to short-wavelength UV and to a bombardment of energetic plasma particles during the whole plasma process. These processes are responsible for the introduction of C-radical sites and irregular structures into the deposited polymer films. These trapped radical sites are points of initiation of auto-oxidation when the layers are exposed to the ambient air.

Using the pulsed plasma (pp) mode, the plasmapolymer deposition exhibits a new formation mechanism. Now, the plasma specific polymerization via fragmentation and polyrecombination is suppressed in favour of chemical chain propagation within the plasma-less periods of the pulsed mode. Here, short plasma pulses (100 µs-1000 µs) shall initiate the classic chain propagation of classic monomers as vinyl or acrylic monomers. By this way a more defined structure and composition were expected similar to those of classic polymers. This new quality could be confirmed using the above mentioned well-suited monomers, low power-input and short plasma pulses and long dark (plasma-less) periods (known as duty cycle $dc=t_{on}/t_{off}+t_{on}$) and analyzing these layers by surface-sensitive methods as XPS, NEXAFS, ATR etc. [11]. However, the use of integral (bulk) methods (UV, IR-transmission, FFF, TG or dielectric relaxation spectroscopy) had indicated stronger differences between pulsed plasma polymers and classic reference polymers. Thus, it was detected that more defined structures are formed at the surface whereas more irregular structures occur in the bulk, modified probably by the UV irradiation during each plasma pulse.

For the first time, pulsed plasma polymerized ethylene showed in its IR spectrum a weak doublet (721 and 738 cm^{-1}) characteristic for regularly structured sequences as occurring in classic polyethylene [11]. Using continuous-wave (cw) plasmas these bands could not observed anywhere [1]. The situation is improved when using allyl monomers as allylamine and allyl alcohol. It could be shown that the polymerization for these substances is more close to classic polymerization than that for ethylene [11].

Here, ethylene and allylamine plasmapolymers should be investigated for the retention of monomer structure or functional groups during the deposition process and vice versa for the formation of irregular structures in the layers. For this purpose, the thermoluminescence is well suited because of its sensitivity towards defects, irregularities and radical sites. Especially the comparison between continuous-wave and pulsed plasma polymerized layers and the influence of power-input were of interest.

Thermoluminescence from irradiated polymers is a powerful means widely used to investigate molecular motions with respect to the occurrence of phase transitions [12-14]. Recent reports have pointed out that the behaviour of light emission is related to and varies with the structure of materials [15]. Thus, thermoluminescence furnishes a new measure for the structural perfection of materials, i.e. in terms of the mode of releasing trapped electrons.

So far two references are found to deal with plasma, polymers and thermoluminescence [16,17]. However, structural changes of polymers caused by exposure to plasmas were investigated. Here, for the first time, thermoluminescence measurements of spectral distribution under isothermal conditions as well as measurements after exciting by irradiation in dependence on temperature were applied to pulsed plasma produced polymer layers.

2 Experimental

For measuring after the ITL-method (isothermal thermoluminescence, recording of decay-curves, spectral resolution in dependence on time) the samples are subjected to a vacuum chamber, which was pumped down to a pressure of 10^{-4} Pa and the polymer sample was cooled down to 30 K. For the irradiation of the polymer sample a low-pressure mercury-UV source (185, 248 nm; Hg-lamp HBO 200 W/4, Osram) equipped with a tunable shutter was used. After 3 min excitation the irradiation was stopped and the emitted radiation from the sample was collected and transmitted by flexible fibre optics to the monochromator connected with a cooled CCD cell. By this way the signal could be spectrally and temporally deconvoluted. Moreover, different temperature regimes could be adjusted (e.g. 30, 110, 150, 180 and 230 K).
Using the TL-Methode (thermally stimulated luminescence, glow curves, heating-up) a similar apparatus was used as described before. Only a new excitation source was introduced, an electron beam gun (7.5 keV; electron gun EGPS-14 B, Kimball Physics Inc.). In the same way as before, after 3 min electron-beam irradiation at 80 K, the decay curves were recorded. After slowing down of emission the heating-up process was started at 80 K up to room temperature and the glow curves were measured.
Plasma polymer layers were deposited in a cylindrical plasma reactor of 50 dm³ volume. The design of the plasma reactor has been described in detail in [11]. The reactor was equipped with a pulsed radio-frequency (r.f., 13.56 MHz) generator and an automatic matching unit as well as an r.f. bar antenna (length: 35 cm). The substrate foil was mounted on a continuously rotating, grounded steel cylinder (Ø= 10 cm, length= 35 cm, rotating frequency= 0.5– 1 s^{-1}) at 10 cm distance to the r.f. powered electrode. The duty cycle of pulsing was adjusted to 0.1 and the pulse frequency to 10^3 Hz. The power input was varied between P = 100 - 300 W. Mass flow controllers for gases and vapours, a heated gas/vapour distribution in the chamber, and control of pressure and monomer flow by varying the speed of the turbomolecular pump were used. The gas flow was adjusted to 75 - 125 sccm and the pressure was varied between 10 to 26 Pa depending on the respective polymerization or copolymerization process. The deposition rate and the film thickness were measured by a quartz microbalance.
These thin plasma polymer layers (thickness ≈ 125 nm) were deposited onto glass slides and analyzed by the thermoluminescence methods. Both continuous-wave and pulsed plasma mode were applied to produce the plasma polymers and deposit them onto glass slides. The plasmapolymer layers were produced from ethylene and allylamine to compare layers without functional groups and those with amino functionalities. The thickness of investigated layers ranged from 125 nm to 200 nm. TL investigations were performed immediately after finishing the plasma deposition, after 6 weeks and after 5-month exposure to the ambient laboratory air.

3 Results

3.1 Polyallyamine layers – isothermal TL, spectral resolution in dependence on time

At first the influence of the plasma polymerization mode, cw- or pp-plasma, on the spectral emission was investigated. The time-dependent ITL spectra of cw- and pp-plasma polymerized polyallylamine show significant differences, which are presented in Figs. 1 and 2.

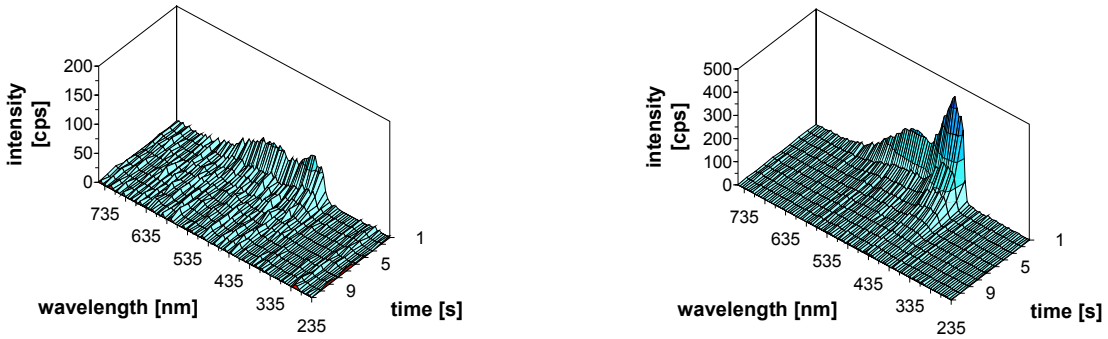

Figs. 1 and 2 Time-dependent ITL spectrum of polyallyamine that was deposited in the pulsed (left) and the cw-plasma mode (right)

The cw-plasma polymer shows a broad and continuous emission between 450-650 nm. Also in the range between 250 to 355 nm a very weak background emission is observed. Two broadened, not clearly resolved peaks at $\lambda \approx 435$ and 535 nm appear with moderate intensity (cf. Fig. 2). These two peaks are better resolved and much more intense if the polyallylamine was produced in the pulsed-plasma mode (Fig. 3). The intensity ratio of $peak_{435}$ and $peak_{535}$ is also changed if using the pulsed plasma. Applying the cw-mode the ratio 435/535 is roughly 1.2 : 1 and 2.1 : 1 for the pulsed mode.
In Fig. 3 the difference between the ITL-spectra of polyallylamine, produced in the cw-plasma mode or in the pulsed plasma mode, are obvious.

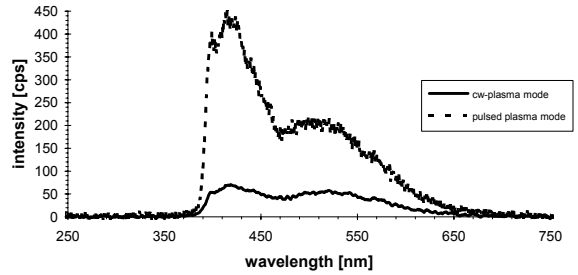

Fig. 3 ITL spectra of polyallylamine layers produced in the cw-plasma mode or in the pulsed plasma mode measured immediately after 3 min UV-irradiation at 30 K

The sharp peak at 435 nm and the broad peak at 535 nm are clearly pronounced. This behaviour is surprising because it means that using the pulsed plasma mode significantly higher concentrations of chromophores were formed. As described before the UV emission fraction is much higher than with the cw-plasma mode. Additionally, a shoulder at 375 nm becomes more intense whereas that at 445 nm shows slightly less intensity. The whole UV emission peak is slightly slimmer than that of the cw-plasma mode. Generally, the same emitting species are present in the two layers, which can be deduced from the shape and location of bands within the spectra.
The exponential decrease of light-emission in dependence on time ("fading") is presented in Fig. 4.

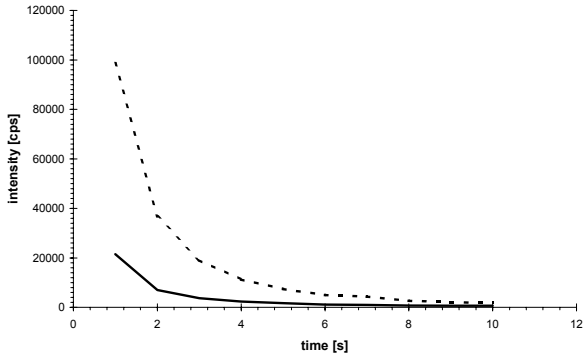

Fig. 4 Fading of total emission of polyamine layers produced in both the cw- and the pulsed plasma at 30 K and 3 min UV irradiation

Also in this case the two different produced polyallylamines show the same behaviour if the different start intensities are normalized. Therefore, it is to assume again that in both layers the same emitting species exist and the same decay rules are valid. Further work to this topic is in progress.

3.2 Storage of polyallylamine layers

The plasmapolymers were stored in a dark room with constant room temperature and humidity (20°C, 60%) and inspected by thermoluminescence in defined intervals. The ITL spectra of the cw-plasma mode produced polyallylamine exhibit a significant increase in intensity during the storage. The most important intensity increase is observed within the first 6 weeks of storing (Fig. 5).

Most likely this phenomenon is generated by the slow post-plasma auto-oxidation at exposure to the air. It should be remembered that there is a fast (primary) oxidation of trapped C radical sites at contact to oxygen [18]. This fast oxidation exceeds immediately during the transport of the samples from the reactor to the TL cell involving the contact to the air. At longer exposure of the plasmapolymer to air the slow auto-oxidation of the layer dominates [18]. After 5-month exposure to the air the intensity of emitted light only increases slightly in the UV range, however, the wavelengths of emitting species in the plasmapolymer do not change. The increase of the peak intensity at λ=398 nm to the dominant emission is obvious as presented in Fig. 5.

Figs. 5 and 6 ITL spectra of polyallylamine produced in the cw (left) and pulsed(right) plasma mode after 3 min UV irradiation in dependence on time of storage

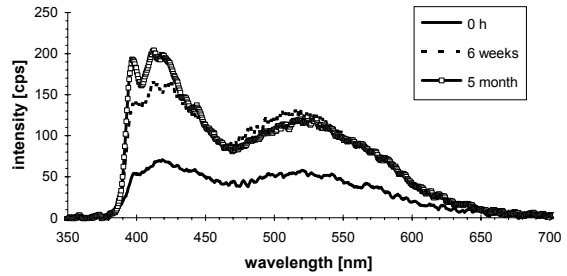

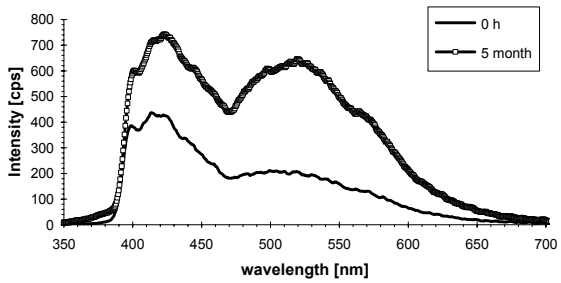

Investigating the pulsed plasma polymerized polyallyamine also the intensity of emitted light is increased, however, in this case in the visible range (λ>480 nm; $\lambda_{max}\approx$525 nm) more than in the UV region (Fig. 6). Moreover, the structure of the UV peak is different from that of the cw-plasma mode. The peak λ=398 nm does not increase so much as in the case of the cw-plasma mode produced sample. In contrast to it the emission at λ=420 nm increases super proportionally (cf. Fig. 6).

3.3 Time-dependence of ITL spectra

ITL spectra of cw-plasma mode produced polyallylamine are presented in dependence on the isothermal temperature used for measuring (Fig. 7). The temperature used varied between 30 and 230 K. The isothermal luminescence fading curves were recorded each after 3 min UV irradiation. With growing temperature the intensity increases in the first step (30→110 K) and then decreases dramatically (110→180→230 K) up to total quenching of emission (230 K). This behaviour is not surprising because the relaxation possibilities grow with temperature and, therefore, the radiation-less deactivation processes increase also. Moreover, the emission shifts to the visible (red-shifting) while the UV emission is completely quenched (cf. Fig. 7). This behaviour was prevailed for all investigated polymer layers. In the same manner the ITL spectra of cw-plasma mode produced polyallylamine are presented in dependence on the isothermal temperature using the UV activation but exposure the samples 6 weeks to the air. In contrast to unaged samples these layers show an unambiguous succession of decrease in intensity in dependence on increasing temperature (30→110→180→230 K). After 5-month exposure to the air the total emission in the ITL spectra of cw-plasma mode produced polyallylamine increases again for the measurements at 30 and 110 K, while the measurements at higher temperature lead to lower emission intensity.

Figs. 7 and 8 ITL spectra of polyallylamine produced in the cw (left) and pulsed (right) plasma mode and irradiated by UV for 3 min in dependence on isothermal temperature

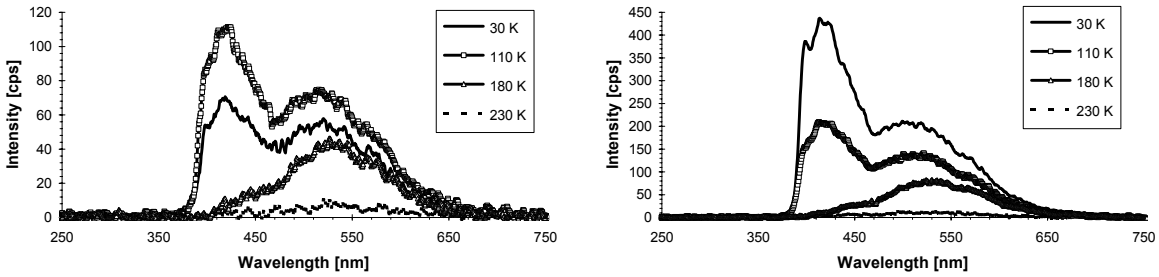

ITL spectra of pulsed plasma mode produced polyallylamine are also presented in dependence on the isothermal temperature (Fig. 8). A significant higher intensity was measured compared to the species those were produced in the cw-plasma mode and measured under the same conditions. These layers show a succession of decrease in intensity in dependence on increasing temperature (30→110→180→230 K). The peak at λ=398 nm decreases with growing temperature much more than that at λ=425 nm (30→110). At higher temperatures the two peaks disappear nearly completely and the broad visible peak λ=515 nm remains in lowered intensity. After 5 month exposure of the pulsed plasma produced polyallylamine layers to the air the global intensities become much more intense for each temperature. In general, the same situation exists as before without storage, the UV peak disappears with growing temperature and the broad peak in the visible range at λ=515 nm remains in lowered intensity

In the same manner the ITL spectra of cw- and pp-plasma mode produced polyallylamine are presented in dependence on the isothermal temperature using the electron beam activation before and after exposure the samples to the air. In Fig. 9, the decay curve is shown in dependence on the isothermal temperature at 80 K using the electron beam activation before and after exposure the samples to the air. As shown in Fig. 9 the exponential decrease in light emission of the cw-plasma mode produced polyallylamine is comparable for immediately measured and 6 weeks aged layers, however, starting with the twofold of emission in the case of the non-stored sample. The total intensity is low compared to that of Fig. 6.

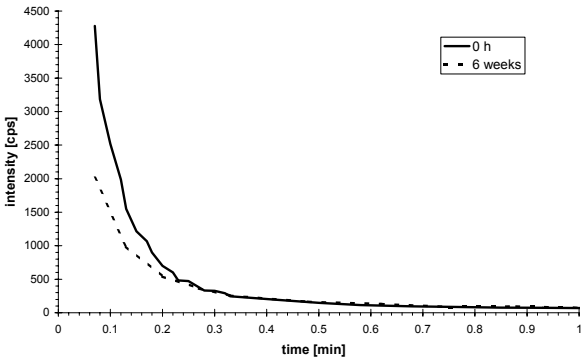

Fig. 9 Fading of the total emission of cw-polyallylamine before and after ageing

The glow curves of the two samples are also of low intensity. Both the non-aged as also the 5 weeks aged sample show a broad peak at about T≈130 K. The two curves differ insignificantly and do not change further at storage in air.

The type of traps (e.g. charge carrier traps) responsible for this luminescence emission is unknown. However, it is known from plasma chemistry that trapped radical sites play an important role. Obviously, considering Fig. 10, the types of traps and their "breaking" are identical for un-aged and aged. Thus, also the decaying of these traps is similarly, however, no concrete assignment to their nature is possible.

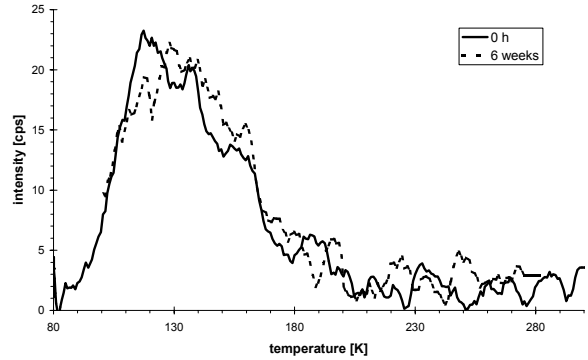

Fig. 10: Glow curve of emission from polyallylamine produced by the cw-plasma mode after 3 min electron beam irradiation (7.5 keV, 80 K)

In dependence on the mode of layer deposition different time-lag and intensities behaviours were found. The light emission obeyed kinetics of first order for the pulsed plasma mode produced species (lnI~t) and the cw-plasma mode produced layer was not unambiguously assignable to a defined kinetics.

The glow curves of the two species show also significant differences (Fig. 11). The cw-plasma produced species exhibit only a weak intensity and a broad diffuse peak at λ≈120 K.

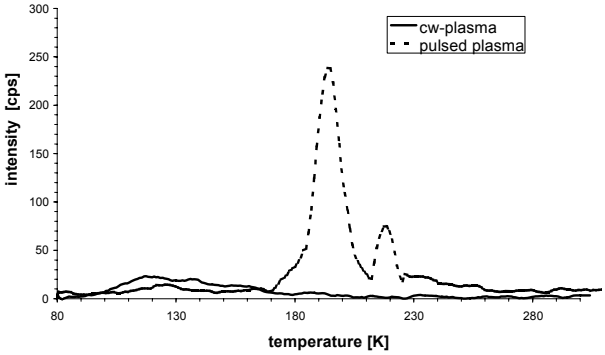

Fig. 11: Glow curves of polyallylamine produced by cw- or pulsed plasma mode after 3 min electron irradiation (7.5 keV) at 80 K

High intensities and characteristic peaks are manifested investigating the pulsed plasma polyallylamine (cf. Fig. 11). Obviously, complete different trap states were present, which are broken at higher temperatures (190 and 210 K). Together with the time dependence of total light emission and the glow curves the existence of significant different trap types can be derived and thus different chemical structures in the two layers can be concluded [19].

3.4 Polyethylene layers

Polyethylene sequences should be inserted as comonomer sequences in pulsed plasma polymerized allylamine-ethylene copolymers. By this way and varying the allylamine/ethylene proportion in the precursor mixture different concentrations of primary amino groups in the resulting polymer layers should be adjusted [20]. However, pulsed plasma polyethylene should be regularly structured and defect-free.

The intensity of light emission in dependence on time ("fading") showed a linear dependence when plotting it with 1/t. Thus, a tunnelling process was proposed as mechanism for the emission because of the 1/t dependence as described in [21-22]. The glow curves did not show significant emission before and after ageing. Around 130 K a broad maximum was visible.

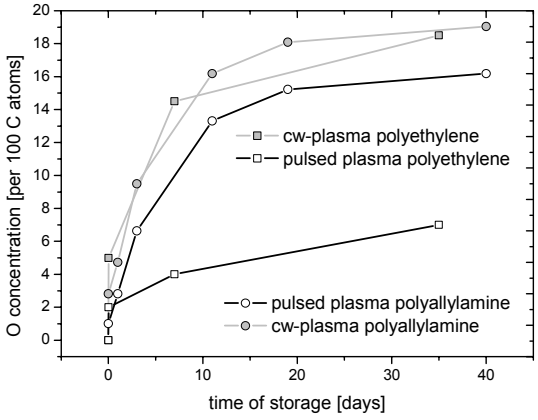

3.5. Results of XPS

It should be added that XPS measurements of these investigated polymer layers were performed to identify a correlation between ageing processes expressed in post-plasma attached oxygen and thermoluminescence features.

The two plasmapolymers, polyallylamine and polyethylene, are sensitive towards ageing. However, those one polymerized in the pulsed plasma mode pick up much lower amounts of oxygen as shown in Fig. 12.

Fig. 12 Introduction of oxygen into plasmapolymers during their exposure to the air measured by XPS

Primary amino groups containing polymers are generally sensitive towards oxygen. Thus, the broad shoulder at the high binding energy (BE) side of the C1s peak is attributed to the post-plasma formation of OH and ether groups (BE=286.3 eV), ketones and aldehydes (BE≈288 eV), esters and carboxylic acids (BE≈289 eV) as well as carbonates and peroxyacids (BE≈290 eV).

Now, it is assumed that the radiatively decaying centres in the plasmapolymers are connected with the post-plasma introduction of oxygen. Thus, the increasing emission after ageing of samples can be explained. Also the insignificant luminescence of pulsed plasma polyethylene is obviously resulted by the lower oxygen introduction if produced in the pulsed plasma mode.

4 Conclusions

The two investigated polymer layers, polyallyamine and polyethylene, show a noteworthy thermoluminescence. The original aim for production of such layers was to form structurally more perfect layers. However, the plasma process itself, known as "fragmentation-polyrecombination" polymerization, involves the co-formation of irregular structures and defects in the polymer layer. Using the pulsed plasma with short plasma pulses (a few hundred microseconds) and long plasma-off periods (a few milliseconds) these irregularities and defects should be minimized [20]. This was confirmed by XPS and NEXAFS measurements of the surface composition and structure of such layers [20]. On the other hand bulk-detecting analysis show more irregularities and defects. So, it is assumed that the deposited plasma polymers cover a number of analytically hidden defects, which are manifested at exposure to the air. These hidden defects may be C radical sites and other anomalities within the bulk of polymer layer. The other possibility of forming structural imperfections is the irradiation, which secondarily changes the structure of the growing plasma polymer by short-wavelength (λ<200 nm) UV from the plasma at each plasma pulse. Thus, C radical sites and cross linking were introduced into the deposited layer. In Toto the C radicals, wherever they come from, are source of post-plasma auto-oxidation. The results of thermoluminescence measurements confirm these earlier findings generally. Because of the high content of anomalous structures in plasma polymers an assignment of thermoluminescence (TL) features was not tried yet. The UV activated TL (ITL spectra) showed no principle differences in spectral intensity distribution. Generally, the pulsed plasma polymerized polyallylamine films emit with higher intensity compared to polyethylene. The ageing progression of both the pulsed and the cw-plasma species could be followed clearly when exposing the samples to the air. The longer aged the more intense are the ITL spectra in the case of polyallyamine. Here, a correlation of ITL spectra with the post-plasma XPS-measured introduction of oxygen is given when comparing Figs. 5 and 6 with Fig. 12. Therefore, the auto-oxidation of films during their storage seems to play an important role for the behaviour of ITL spectra. On the other hand, the concentration of implemented oxygen alone does not play the exclusive role because the intensity of ITL spectra of pulsed plasma produced polyallylamine is much stronger than that of the cw-plasma produced species and the XPS-measured O content is lower (cf. Fig. 12). Here, further investigations are in progress.

References

[1] K. Jesch, J. E. Bloor and P. L. Kronick, J. Polym. Sci., **A1**, 1487 (1966)
[2] A. R. Denaro, P. A. Owens and A. Crawshaw, Europ. Polym. J., **4**, 93 (1968); **5**, 471 (1969).
[3] D. D. Neiswender, Adv. Chem. Ser., **80**, 338 (1969)
[4] H.-U. Poll, Z. Angew. Physik, **4**, 260 (1970)
[5] A. R. Westwood, Europ. Polym. J., **7**, 363 (1971)
[6] H. K. Yasuda, C. E. Lamaze, J. Appl. Polym. Sci., **15**, 2277 (1971)
[7] L. F. Thompson and K. G. Mayhan, J. Appl. Polym. Sci., **16**, 2291 (1972)
[8] J. Friedrich, J. Gähde, H. Frommelt, H. Wittrich, Faserforsch. Textiltechn./Z. Polymerenforsch., **27**, 517 (1976)
[9] J. M. Tibbitt, M. Shen, A. T. Bell, J. Macromol. Sci., Chem. **A10**, 1623 (1976)
[10] H. K. Yasuda, J. Polym. Sci., Macromol. Rev., **16**, 199 (1981)
[11] J. Friedrich, G. Kühn, R. Mix, I. Retzko, V. Gerstung, St. Weidner, R.-D. Schulze, W. Unger, in: Polyimides and other High Temperature Polymers: Synthesis, Characterization and Applications, K. L. Mittal (Hrg.), VSP, Utrecht, 2003, S. 359-388
[12] R. H. Partridge, The Radiation Chemistry of Macromolecules, M. Dole (ed.), Vol. 1 (New York: Academic Press), 1973, p. 193
[13] A. Kadashchuk, Y. Skryshevskii, A. Vakhnin, N. Ostapenko, W. Arkhipov, E. V. Emelianova, H. Bassler, Physical Review, **63**, 11 (2001)
[14] A. Kadashchuk, D. S. Weiss, P. M. Borsenberger, N. Ostapenko, V. Zaika, Y. Skryshevski, Synthetic Metals, **109**, 177 (2000)
[15] E. Mandowska, A. Mandowski, J. Swiatek, Macromol. Symp., **212**, 251 (2004)
[16] A. A. Kalachev, S. Y. Lobanov, T. L. Lebedeva, N. A. PLATE, Appl. Surf. Sci., **70**, 295 (1993)
[17] I. V. Novoselov, V. N. Korobeinikova, Y. A. Sangalov, V. P. Kazakov, Doklady Akad. Nauk SSSR, Div. Chem. Sci., **39**, 1578 (1990)
[18] J. Friedrich, G. Kühn, J. Gähde, Acta Polymerica, **30**, 470 (1979)
[19] L. Zlatkevich: Luminescence Techniques in Solid State Polymer Research, Chapter 7, Marcel Dekker Inc., New York (1989)
[20] J. Friedrich, G. Kühn, R. Mix, W. Unger, Polymer Processing and Plasmas, **1**, 28 (2004)
[21] Y. Hama, Y. Kimura, M. Tsumura, N. Omi, Chem. Phys. **53**, 115 (1980)
[22] F. Kiefer, C. Lapersonne-Meyer, J. Rigant; Int. J. Radiat. Phys. Chem. **6**, 79 (1974)

Chemical synthesis at plasma modified polymer surfaces

Jörg Friedrich, Gerhard Kühn, Renate Mix
Bundesanstalt für Materialforschung und –prüfung, 12200 Berlin

Abstract
Polymer surfaces were modified in low-pressure glow discharge plasmas for introduction of monotype functional groups of different type and density. For this purpose three ways are selected, (**i**) oxygen plasma treatment followed by wet-chemical reduction of O functional groups to OH groups, (**ii**) plasma bromination for introducing C-Br groups and (**iii**) coating by deposition of thin plasma (co-) polymerized layers of functional groups-carrying monomers with OH, NH_2, COOH, epoxy etc. functionalities. Subsequently, these groups were used as anchoring points for chemical grafting of spacer molecules, oligomers, prepolymers, fluorescence labels, ionic and nucleic acid residues. This chemical grafting of organic molecules uses different simple chemical reactions. The yield in monosort functional groups at polymer surfaces ranged from 10-14 (process (**i**)), 20-45 (process (**ii**)) and 18-31 groups per 100 C atoms (process (**iii**)). The consumption of functional groups amounts 40-90% of all functional groups present at the surface and depending on the dimensions of grafted molecules. For infinitely variable tuning the number of functional groups process **iii** was executed as copolymerization of a functional group-carrying comonomer with a non-functionalized ("chain-extending") comonomer.

1 Introduction

Aim of this work was to introduce monotype functional groups at polymer surfaces and using them for subsequent chemical grafting of molecules, oligomers and polymers. The introduction of functional groups onto most often chemically inert polymer surfaces can be preferentially performed using plasmachemical processes. Such low-temperature glow discharge plasmas are well suited to attack the polymer surface, forming reactive sites, which are able to attach functional group-forming atoms or radical fragments from plasma. First attempts were made by Hollahan who used NH_3 plasma for introducing primary amino groups onto polypropylene surfaces and thus using these surfaces for interacting with heparin [1]. Later on it could be shown that the reaction of ammonia plasma with polymer surfaces always lead to the formation of co-existing N-functionalities of different types among them NH_2 groups not exceed a threshold concentration greater than 1-3 NH_2 groups per 100 C also for a total N-concentrations $\geq$ 20 N/100 C [2]. Attempts to unbalance this product distribution by feeding additional hydrogen to NH_3 yield without success [3]. The same is valid for introduction of O-functional groups onto polymer surfaces [4]. Also in this case a broad variety of O-functional groups is produced among them 2-4 OH groups/100 C are present. The formation of OH groups demands the preceding abstraction of H from the polymer thus the enormous rearrangements of the polymers well documenting. Also in this case an improvement in selectivity of the formation of only one type of O-functional groups is not realistic, otherwise the O-functionalization passes into polymer degradation and etching. Therefore, only a two-step process can be considered that repairs the unsatisfying result of the O_2 plasma modification by using a wet-chemical reduction process. This was firstly presented by Nuzzo and Smolinsky [5] and later perfected [6]. By this way 10-14 OH groups/100 C were synthesized (process **i**) with a maximum selectivity of about 60% within all O-functionalities [7].

An elegant one-step process was introduced by our group consisting of the polymer surface bromination by $HCBr_3$ (process **ii**) [8]. The tuning of the Br-concentration was reached by varying the treatment time. Thus, 20-45 covalently bonded Br-groups/100 C could be introduced onto the surface, with selectivities near 100%. Only traces of Br-anions were found as side-product.

A more complicated but very variable process (**iii**) was the pulsed plasma-initiated polymerization or copolymerization. Here, the wished monotype functional groups are provided by the monomer, which becomes polymerized in the pulsed plasma. The art of producing such 50 nm thick monotype functionalized polymer coatings consists in carrying out the plasma process so soft as possible to avoid fragmentations of monomers and to preserve and remain the functional groups of the respective monomer. This process uses short plasma pulses (0.1-1 ms), needed for monomer activation, and long plasma-off periods (1-100 ms), needed for a pure chemical chain propagation instead of the random recombination of fragments. Together with minimizing the plasma power-input the monomer fragmentation should be suppressed and the number of retained functional groups in the deposited plasma polymer layer should be maximum in comparison to the number of functional groups originally present in the monomer molecules. 60-95% of functional groups could be recovered at the polymer surface [9]. Now, the variety of

monomers suited for this "plasma-initiated" polymerization is similar to that of ordinary polymer chemistry. Thus, allyl alcohol, allylamine or acrylic acid produce OH, NH_2 or COOH groups, however, with the anomaly that under low pressure conditions the degradative chain transfer is absent, so that is possible to produce high-molecular weight allyl polymers. The same reaction principle is valid for copolymerization used to adjust the number of functional groups. Nevertheless, to a smaller content, the known disadvantages of all plasma techniques, as occurrence of trapped radical sites, auto-oxidation, crosslinking, irradiation defects etc. remain [10].

Now, the functional groups are open for derivatization and grafting for example using dioles and diamines (Br groups), silanes and isocyanates (OH groups), aldehydes (NH_2 groups) or alcohols (COOH groups).

2 Experimental

Plasma polymer layers were deposited in a cylindrical plasma reactor of 50 dm³ volume. The design of the plasma reactor has been described in detail in [11]. The reactor was equipped with a pulsed radio-frequency (r.f., 13.56 MHz) generator with an automatic matching unit and an r.f. bar antenna (length: 35 cm). The substrate foil was mounted on a continuously rotating, grounded steel cylinder (Ø= 10 cm, length= 35 cm, rotating frequency= 0.5– 1 s^{-1}) at 10 cm distance to the r.f. powered electrode. The duty cycle of pulsing was adjusted to 0.1 and the pulse frequency to 10^3 Hz. The power input was varied between P = 100 - 300 W. Mass flow controllers for gases and vapours, a heated gas/vapour distribution in the chamber, and control of pressure and monomer flow by varying the speed of the turbomolecular pump were used. The gas flow was adjusted to 75 - 125 sccm and the pressure was varied between 10 to 26 Pa depending on the respective polymerization or copolymerization process. The deposition rate was measured by a quartz microbalance.

Surface functionalization of PP foils in the O_2 plasma was performed in the continuous-wave (cw) mode. PP films, which were coated with plasma polymer layers of functional groups-carrying monomers, had been used without any additional plasma pretreatment. PTFE films were exposed first to H_2 r.f. plasma (continuous-wave mode) for 1 - 1800 s at a pressure of p = 6 Pa and a power of P = 300 W followed by deposition of adhesion-promoting plasma polymer layers.

The XPS and IR analyses have been described in detail elsewhere [12]. Here, only some important facts are summarized. The XPS data acquisition was performed with a SAGE 150 Spectrometer (Specs, Berlin, Germany) using a non-monochromatized MgK_α or AlK_α radiation with 12.5 kV and 250 W settings at a pressure $\approx 10^{-7}$ Pa in the analysis chamber. XPS spectra were acquired in the constant analyzer energy (CAE) mode at 90° take-off angle. Peak analysis was performed using the peak fit routine from Specs.

The FTIR spectra were recorded with a NEXUS instrument (Nicolet, USA) using the ATR (Attenuated Total Reflectance, 45° angle of incidence) technique with a diamond or a Ge cell ('Golden Gate', Specac, Kent, UK). The IR signal comes from a near-surface layer of the polymer film. The information depth depends on the material used as ATR crystal and amounts about <1.5 µm using Germanium and 2.5 µm applying diamond.

All solvents used were of analytical reagent grade. Toluene and THF were refluxed under N_2, and over sodium and benzophenone. Pyridine was distilled and stored over KOH pellets. Water was doubly distilled before use. All silanes were vacuum-distilled and all reactions were performed under N_2 atmosphere. Reactions on the polypropylene film were performed with pieces of 5 x 5 cm or for industrial applications with foils of 35 x 24 cm. Details of chemical synthesis are described in [6-10].

3 Results

3.1 Monotype functionalization

3.1.1 Reduction of oxygen plasma introduced O functional groups on PP and PE surfaces to OH groups by diborane

Using the oxygen r.f. pulsed-plasma modification the oxygen incorporation onto the surface of PP was identified by ATR-FTIR spectra. A strong carbonyl band (≈ 1700 cm^{-1}), alcoholic structures (≈ 1100-1200 cm^{-1}), a broad OH peak and adsorbed water related features (≈ 3100-3500 cm^{-1}) appear. Surfaces with an O/C ratio of about 0.2 were used for further chemical processing. The XP spectra of PP confirmed the plasma production of a strong O1s peak. After TFAA derivatization of plasma generated OH groups a small F1s peak at a binding energy of 689 eV is detected at the PP surface. The origin of this limited OH group formation in the oxygen plasma can be attributed to the largely absence of additional hydrogen sources, only abstracted hydrogen from the polymer backbone and hydrogen from dissociation of desorbed water are available. The diborane reduction strongly increases the yield of OH groups. Quan-

tification of this optimized process shows an improvement in OH yield from about 2-4 OH/100 C without further chemical post-plasma treatment to 13-14 OH/100 C maximum after chemical reduction with diborane under the best conditions. These conditions were the hydrolysis with NaOH and the oxidation of C=C in the presence of H_2O_2. $LiAlH_4$ increases slightly the yield in OH further.

3.1.2 Bromination

Polymer surface bromination using the bromoform plasma emphasized as a highly selective functionalization. Only negligible side-reactions were observed as the deposition of polymer layers, which was detected with a microbalance, as well as the formation of small quantities of bromide anions and traces of oxidized bromine as detected by means of XPS. The percentage of surface bromination could be varied between 0 and 45 Br per 100 C. Exposure to air causes a post-plasma addition of oxygen.

3.1.3 Williamson's ether synthesis to introduce spacers with OH end groups

Using the brominated PP surface, the C-Br groups reacted with sodium ethylene glycolates with n = 2,3,4,5 and 22 (PEG 1000) glycol units. Thus, this process forms spacer bonded OH groups. The concentration of these terminal OH groups can be compared to those, which are directly bonded to the surface (cf. with results presented in Sections 3.1-3.3) (Fig. 1). In the same way it is also possible using sodium hexamethylene diamine to produce a C_6 spacer with an amino end group (Fig. 1). Both end groups, OH and especially NH_2, are important for further biochemical synthesis. The synthesis was followed and controlled by XPS. In all these syntheses only 2 % Br was not consumed and remained at the PP surface. It was assumed that either steric problems played a role or these bromines were not situated directly at the surface. For all glycolate spacers a "functionalization density" of about 5 spacer bonded OH groups per 100 C was measured. Additionally, two directly at the surface bonded (without spacer) OH groups per 100 C atoms were also detected.

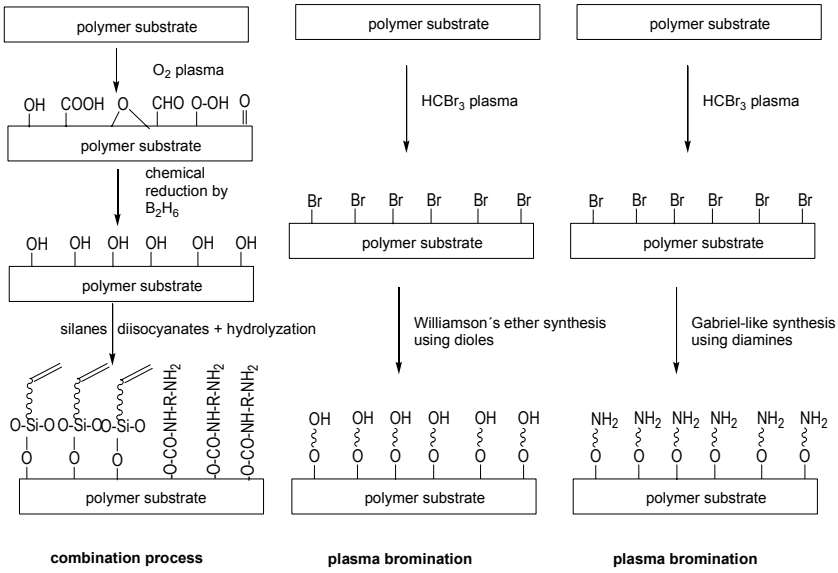

Fig. 1 Scheme of synthesis at brominated or hydroxylated polymer surfaces

3.1.4 Silane spacer

Undecenyltrichlorosilane was reacted with OH groups produced by oxygen plasma modification and hydroboration (B_2H_6/H_2O_2) (cf. Fig. 1). The yield of this reaction (attachment of C_{11} spacers) amounts to about 7. This means a selectivity of about 70% starting with 10 OH groups per 100 C. Additionally two OH groups directly bonded at the surface per 100 C atoms were also present. Subsequently, the undecenyl spacer was subsequently modified and now bearing bromo, cyano or amino groups in comparable yields and selectivities.

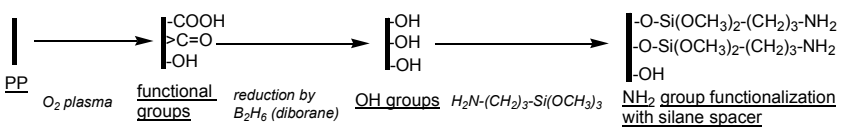

Fig. 2 Reaction scheme of covalent alanine grafting onto polypropylene surfaces

3.1.6 Azomethine group containing spacers and coupling of amino acids

Another synthesis, based on a hydroxylated polymer surface, consists in the attachment of γ-aminopropyltrimethoxysilane. This results in a polymer surface coated with primary amino

groups. These groups reacted with glutaraldehyde acting as a spacer. The spacer can facilitate the attachment of bioactive molecules such as phospholipids or amino acids and also can be used as a starting-point for biochemical synthesis. Therefore, simple amino acids, alanine and cysteine, were attached to the spacer (cf. Fig. 2). 4 to 6 carboxylic end groups were formed by this reaction pathway starting from 10 OH/100 C produced by oxygen plasma treatment and diborane reduction.

3.1.5 Isocyanate grafting

The consumption with diisocyanates (hexamethylene diisocyanate (HDI), methylene-di-*p*-phenylene isocyanate (MDI) and toluylene-2,4-diisocyanate (TDI)) is schematically shown in Fig. 3. Subsequently, different fluorescence labels (dansylchloride (DNS), dansylhydrazine (DNH) and dansylcadaverine (DNC)) were grafted. However, the reaction with HDI was too slow and the hydrolysis (Fig. 3a) not clearly reproducible. Using MDI and TDI the reactions 3b and 3c result in the attachment of ca. 1 fluorophore/100 C and in satisfying absorbance-fluorescence spectra.

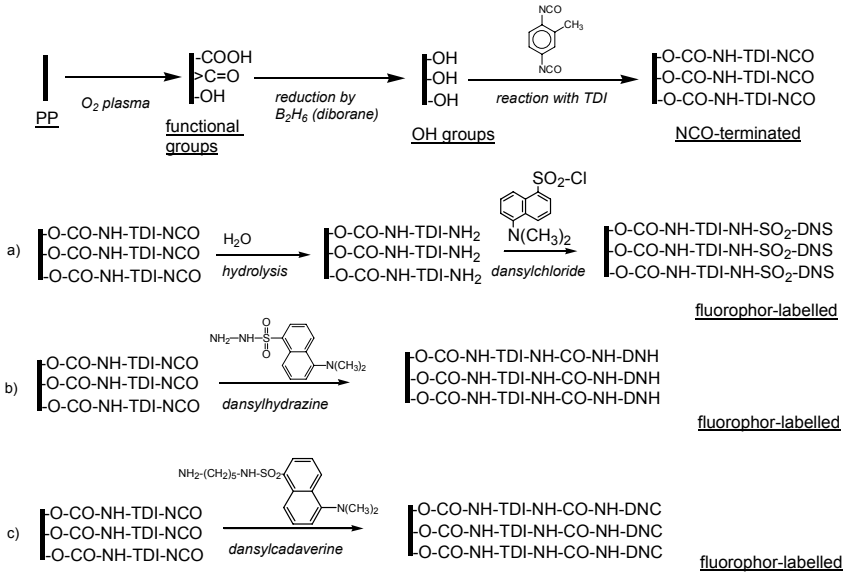

Fig. 3
Schematics of the reactions of hydroxylated PP surfaces with diisocyanates and fluorophores

3.2 Deposition of functional groups-carrying plasma polymers as anchoring points for grafting

3.2.1 Pulsed plasma polymerization

Allyl alcohol, allylamine and acrylic acid were pulsed plasma polymerised to retain a maximum in functionalities in the resulting plasma polymer. The respective pulsed plasma polymers were investigated for the retention or yield in functional groups. This retention was primarily measured by XPS including the chemical derivatization of these groups as described in Section 2. These layers were checked for side-products by respective IR spectra (Table 1).

Tab. 1 Absolute and relative yields in functional groups at the surface of deposited pulsed plasma polymer layers measured with XPS after derivatization (cf. Section 2, 100 W)

Group	Monomer	Theoretical stoichiometry	Measured stoichiometry	Yield in functional groups (per 100 C)	Characteristic side-products
OH	Allyl alcohol	100 C / 33 O	100 C / 3 O	31 (95%)	>C=O
NH_2	Allylamine	100 C / 33 N	100 C / 36 N / 4 O	21 (65%)	C-N-C, C≡N, C-O
COOH	Acrylic acid	100 C / 67 O	100 C / 60 O	26 (79%)	>C=O
-	Ethylene	100 C	100 C / 3 O	-	>C=O, C-O, C=C

3.2.2 Copolymerization

Exemplified with OH and COOH groups containing plasma polymer layers the qualification of these layers as models for monotype functionalized substrates with variable concentrations of functional groups should be proved. The plasma-initiated copolymerization of acrylic acid with ethylene or 1,3-butadiene is shown in terms of measured COOH- and OH-concentration as a function of the composition of the respective comonomer mixture (Fig. 4). Depending on the comonomer reactivity, a more linear correlation between precursor composition and produced COOH groups (butadiene) or a parabolic behaviour (ethylene) was observed. For each type and concentration of functional groups its concentration was determined by chemical derivatization followed by XPS analysis as described in Section 2. As shown in Fig. 4, similar tendencies were detected considering the allyl alcohol copolymerization with ethylene, butadiene or styrene. Here, different curve progressions are observed depending on the types of comonomers, their ratio in the precursor mixture and the plasma parameters. These deviations were attributed to the different copolymerization tendencies, for example expressed in copolymerisation parameters, which are also valid for the plasma-initiated gasphase copolymerization. Taking these curves as calibration it was possible to

adjust a defined concentration of functional groups in the deposited layer (Fig. 4). In the same way allylamine-copolymer and pure polyethylene-like layers were deposited. Also the nature and the quantity of side-products of these polymers were investigated. Generally, the number of side-products was minimum using low power values (cf. Tab. 2).

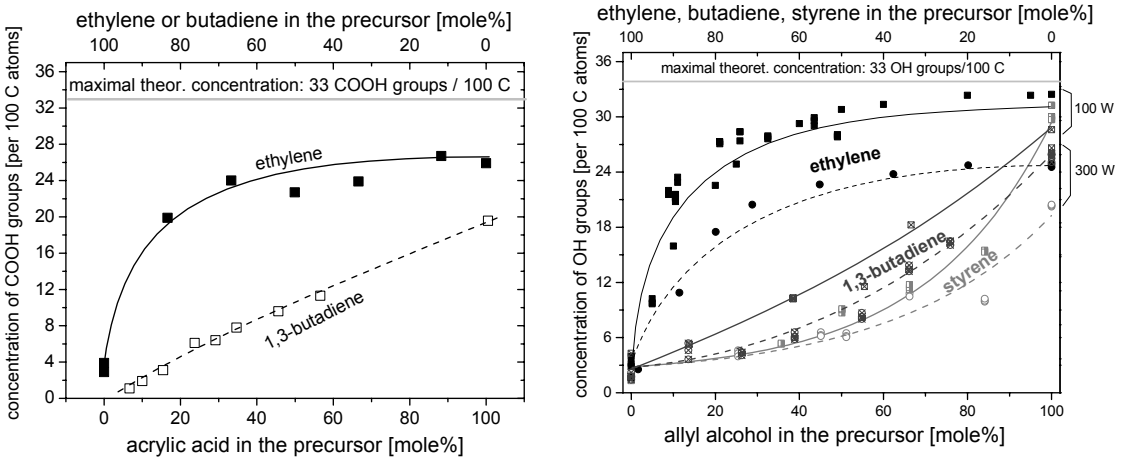

Fig. 4
Yield in COOH groups (a) and OH groups (b) in dependence on the composition of the precursor mixture and the types of comonomers (a – acrylic acid + ethylene or butadiene; b – allylalcohol + ethylene or butadiene or styrene)

Tab. 2 Comonomer pairs and yield in functional groups

Group	**Monomer**	**Maximum concentration (X per 100 C)**	**Suited comonomers**	**Range of concentration (X per 100 C)**
OH	Allyl alcohol	31	C_2H_4, C_4H_6, C_8H_8	0 - 31
NH_2	Allylamine	18	C_2H_4, C_4H_6, C_8H_8	0 - 18
	Diaminocyclohexane	12	C_2H_4	0 - 12
COOH	Acrylic acid	25	C_2H_4, C_4H_6, C_8H_8	0 - 25
Epoxy	Glycidylmethacrylat	10	-	-

The aim of this work was to produce defined layers with monosort functional groups, which can be used for grafting. Now, in contrast to the irregularly structured continuous-wave plasma polymers the structure of pulsed plasma polymers was so much improved that partial or complete solubility was observed. Therefore, the further chemical processing in solvents and water led to dissolving the layer. Here, also chemically crosslinking copolymers as butadiene, divinylbenzene and trivinylcyclohexane were necessary.

3.2.3 Introduction of fluorescence labels onto the surface of plasmapolymer layers

Fluoresceinisothiocyanate should be covalently bonded to polymer surface. For this purpose allylamine (and allylamine-butadiene copolymers – in process) polymer layers were deposited onto polypropylene foils (cf. Fig. 5). These layers were relatively stable at processing in aqueous solution or in THF. By means of derivatization of NH_2 groups with pentafluorobenzaldehyde or p-trifluoromethylbenzaldehyde their concentration was calculated to about 12 NH_2/100 C.

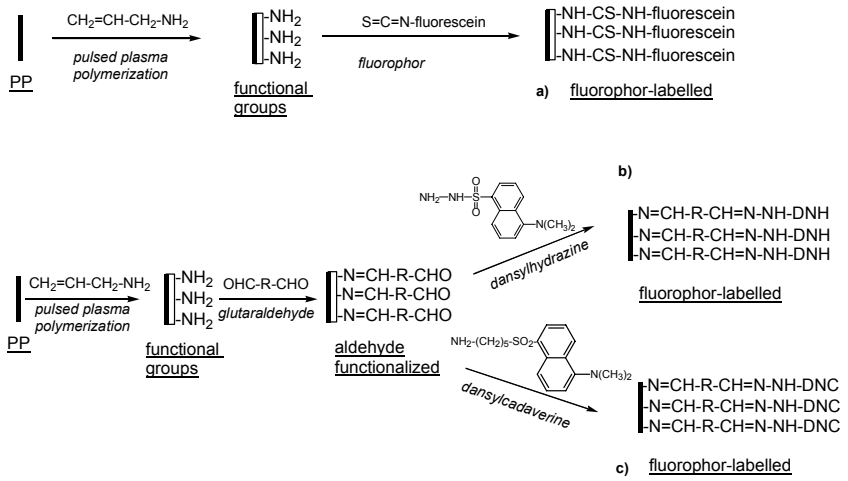

Fig. 5 Covalent bonding of fluorophores onto primary amino groups of allylamine pulsed plasma polymer layers (a-fluorescein bonding; b-dansylhydrazine bonding; c-dansylcadaverine bonding)

Two reaction pathways follow, the consumption with the thioisocyanate (a) and with glutaraldehyde and dansylhydrazine or dansylcadaverine (Fig. 5). Immediate transfer to wet-chemical processing avoided problems with the auto-oxidation of the amino group containing plasmapolymers, when exposed to air.

4. Conclusions

A few ways were presented for preparation of inert polymer surfaces with chemically reactive functional groups as Br, OH, COOH, NH_2 etc. It could be demonstrated that these functional groups are chemically available and, therefore, can easily react with organic molecules and prepolymers. The same is true for their reactivity towards metal atoms. First time, these functional groups are provided as more or less monotype functional groups. This monosort functionalization on polymer surfaces is a helpful pre-requisite for both to start graft reactions as well as to investigate metal-polymer interactions.

The functional groups could be formed by a combination process (plasma oxidation + chemical reduction, process **i**), by bromination (process **ii**) and by coating with monotype functional groups carrying polymer layers (process **iii**). The combination process leads to moderate yield in OH groups formation (10-14 OH/100 C) and shows moderate selectivity (60% of all O-functionalities appear as OH groups). On the other hand, this process allows it to covalently bond the OH groups directly onto the polymer molecules. The OH modification was stable if stored and exposed to air over longer periods (> 1 year). An adjusting of the OH group density at polymer surface was not reproducibly possible. The bromination was very selective and high concentrations could be introduced onto the polymer surface. The functional groups were also directly bonded to polymer backbones. Nearly all Br-sites were situated at the surface and, therefore, were open for chemical graft reactions. The concentration of C-Br groups was maximum compared with the other functionalization methods. Up to 40 C-Br/100 C could by produced with only negligible amounts of side-products. The concentration of C-Br groups could be slightly tuned by variation of the bromination time. Plasmapolymers from functional groups-carrying monomers allow a broad range of variation of both the type of monosort functional groups and the concentration. The concentration could be infinitely varied by copolymerization from 0 to 31 groups per 100 C atoms. In such a way OH and COOH groups carrying layers could be easily produced. They were resistant to long-time exposure to air. In contrast to that NH_2 groups containing layers show generally low yield in NH_2 formation, indications for reactions at the amino groups and a pronounced tendency of post-plasma oxidation. This oxidation during exposure to air may be ascribed to the auto-oxidation with oxygen from air initiated by trapped C radical sites in the layer.

Applications of these layers as targets for fluorescence sensor devices and biocompatible materials as well as for adhesion promotion have illustrated the ability of polymer surface chemistry.

References

[1] J. R. Hollahan B.B. Stafford, R. D. Falb, S. T. Payne, .J App.l Polym. Sci. 13, 807 (1969)
[2] J. F. Friedrich, J. Gähde, H. Frommelt, H. Wittrich, Faserforsch Textiltechn / Z Polymerenforsch 27, 604 (1969)
[3] A. Meyer-Plath, PhD-thesis, Ernst-Moritz-Arndt University Greifswald (2003)
[4] K. Rossmann, J. Polym. Sci., 19, 141 (1956)
[5] R. G. Nuzzo, G. Smolinsky, Macromolecules 17, 1013 (1984)
[6] G. Kühn, St. Weidner, R. Decker, A. Ghode, J. F. Friedrich, Surf. Coatings Technol., 116-119, 796 (1999)
[7] G. Kühn, I. Retzko, A. Lippitz, W. Unger, J. Friedrich, Surf. Coatings Technol., 142-144, 494 (2001)
[8] J. Friedrich, W. Unger, A. Lippitz, I. Koprinarov, A. Ghode, Sh. Geng, G. Kühn, Composite Interface, 10, 139 (2003)
[9] J. Friedrich, G. Kühn, R. Mix, W. Unger, Polymer Processing and Plasmas 1, 28 (2004)
[10] J. Friedrich, G. Kühn G, R. Mix, I. Retzko, V. Gerstung, S. Weidner, R.-D. Schulze, W. Unger, Plasma Polymer Adhesion Promoters to be used for Metal-Polymer Composites, in: Polyimides and other High Temperature Polymers: Synthesis, Characterization and Applications, K. L. Mittal (ed), VSP, Utrecht, pp 359-388 (2003)
[11] J. Friedrich, I. Retzko, G. Kühn, W. Unger, A. Lippitz, Metal doped plasma polymer films, in: Metallized Plastics, vol 7, K. L. Mittal (ed). VSP, Utrecht, pp 117-142 (2001)
[12] I. Retzko, J. Friedrich, A. Lippitz, W. Unger, J. Electr. Spectr. Rel. Phenom.,121, 111 (2001)

Control of the metal catalyst particles for CNT production in a supersonic DC thermal plasma torch

L. Guo, J-L. Meunier and D. Harbec

Department of Chemical Engineering, McGill University, Montreal (QC), Canada

Abstract

The existence of metal particles plays an important role in the carbon nanotube synthesis process. Not only the coexistence of the carbon and metal catalyst is a crucial requirement for the successful growth of CNT, but also the size of the metal catalyst has a very important impact on the morphology of the nanotubes. In order to have some insights of the production of CNT in a DC thermal plasma reactor, modeling work concerning the evolution of fine metal catalyst has been carried out. The results of an analysis on operating parameters are presented.

1. Introduction

It has now been over ten years since the first confirmation of the existence of single-walled carbon nanotube(SWNT) [1]. These SWNTs have many proposed applications in super-strong fibers, composites, catalysts, molecular wires, straws, gears, switches, nano-electronic and photonic materials [2]. However, success in most of these applications will be base on the ability to synthesize large-scale coherent, defect-free nanotubes or nanotube assembly. In recent years, many studies have been made to investigate methods of mass production of this fascinating novel material. From the published papers on the synthesis of CNT, we could tell that no matter how these are produced, the existence of metal particles plays an important role in the process. Zhang and Iijima [3] reported their results of using different components as target using a Nd:YAG laser. Their results indicated that when there was no metal catalyst used in the system, no CNT was produced. Metals used for the synthesis of CNT include for example transition metals Fe, Co, Ni and Cu and lanthanide metals Gd, Y, and La. Because the coexistence of carbon and a small percentage of metal is required in the CNT growth zone, catalytic growth is believed to be the mechanism of the CNT formation [4]. A widely accepted concept is that the metal particles satisfy the dangling bonds of carbon caps and stop the premature closure of the CNT. It is also highly believed that the size of the particles is one of the key parameters for determining the morphology of the CNT [5].

D. Harbec et al developed an approach of producing CNT based on the dissociation of carbon containing gas(carbon tetrachloroethylene, (TCE), C_2Cl_4 in this case) using a DC thermal plasma torch [6]. Experimental results showed that a large amount of CNT can grow inside the torch itself. In this system, though no external supply of metal species were added, CNT was produced. The erosion of the cathode and anode provided the source of metal catalyst. The metal vapor are transported by the main plasma flux to the torch exit nozzle. The geometry of the nozzle provides sudden expansion in its upstream section. This expansion produces a strong quench of the plasma gas and the metal vapor it contains, forming a zone of nucleation of metallic nanoparticles. These are rapidly brought in contact with carbon injected in a radial direction within the same nozzle. Due to the extremely high local temperature, the size and geometry of the nozzle, it is practically impossible to perform in situ diagnostics on the nucleation inside the nozzle. This paper presents modeling work on the evolution of the metal catalyst and the distribution of the carbon containing gas in the nozzle based on computational fluid modeling and fine particle nucleation modeling. The arc region is not investigated, we concentrate on the phenomena occurring within the nozzle only. The FLUENT and FPM codes were used as modeling platforms. In this report, we focus on finding appropriate operating conditions for attaining the desired size distribution of fine metal particles in this DC plasma torch system. The operating parameters include plasma gas flowrate, operating pressure and power level of the torch. These are connected with experimental results obtained on the plasma torch system [6,7,8].

2. Description of the Computational domain

The schematic of the computational domain is showed in Figure 1. The nozzle is water-cooled, cylindrical and shows a sudden expansion before the carbon-containing gas injection. The metal vapor, in the present case tungsten vapor, comes from the erosion process of the electrodes and enters the nozzle along with the plasma gases (argon or helium). The carbon containing gas comes into the system with the same carrier gas as the plasma gas. It will dissociate in the nozzle and provide C and Cl atoms and molecular species. In this paper we do not model the dissociation reaction of TCE, we consider instead the molecule as non-breakable and only consider its mass. The nozzle has a 100% change in diameter, changing from 0.5cm to 1cm upstream of the TCE injection. The high velocity of the plasma gas and the sub-atmospheric operating pressure in the reactor generates on the axis of the nozzle at node A a mach number as high as 5.37 (500 torr), and 1.52 (200 torr) in the case of helium plasma gas. We are in a supersonic region and the compressibility of the gas can not be neglected.

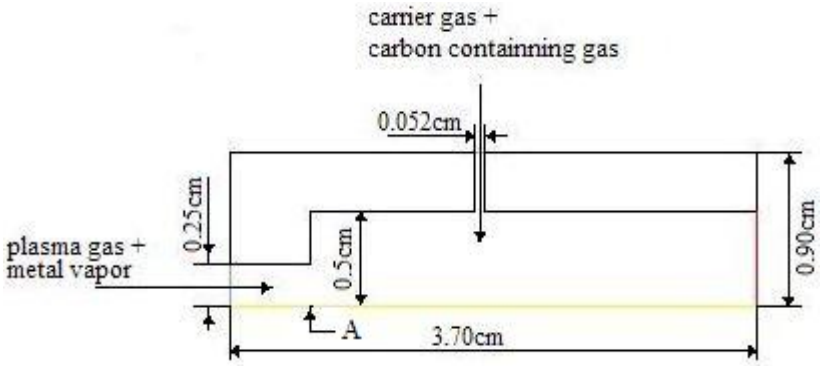

Figure 1. Computational domain.

3. Modeling work

3.1 Assumptions

In the modeling work, some major assumptions used are as follows:

(a) Plasma is at LTE, the process is operated under steady state, the nozzle is axisymmetric
(b) The radiative heat losses are negeleted
(c) The physical properties of the mixture follow the ideal gas mixing law, the fluid follows ideal gas law
(d) The particle size distribution is approximated by a lognormal distribution
(e) The particles are in thermal equilibrium with the plasma gas

3.2 Modeling approach

FLUENT(6.1.22) has been used to perform the modeling of the flow and temperature field, FPM is used to take care of the particle formation part. Classic K-ε model is chosen to calculate the effect of turbulence in sets of conservative equations. The conservative equations are solved with strong coupling to represent the effects of compressibility of the flow. Since the tungsten vapor comes from the erosion of the electrodes and has a very low concentration in the flow, the diffusivity of tungsten vapor in the gas phase is based on constant dilute approximation and is set as 2.88×10^{-5} (default value of FLUENT). In the case of TCE, the diffusivity is evaluated using [10]:

$$D_{AB} = \frac{2}{3}\left(\frac{k_B}{\pi}\right)^{3/2}\left(\frac{1}{2m_A}+\frac{1}{2m_B}\right)^{1/2}\frac{4T^{3/2}}{p(d_A+d_B)^2} \qquad (1)$$

In this equation k_B is Boltzmann's constant, p is the pressure in Pa, m_A and d_A are the mass and equivalent diameter of species A, respectively species B. In order to obtain a conservative estimate of the diffusion of the TCE, the molecular weight of TCE in non-dissociated form was applied in this equation. But since in this specific model the flow is turbulent, the laminar diffusivity should not influence the diffusion process very much.

In the modeling of particle formation, the carbon containing gas was not been taken into account, only the mass flowrate value of TCE was considered. Coagulation is calculated using Dahneke kernel function, Girshick model [11] has been chosen to deal with the particle nucleation, and particle condensation, thermophoresis and Brownian diffusion are all included in the calculation.

3.3 Calculation conditions

The chosen calculation conditions are as follows, based on experimental parameters:

The power added to the plasma gas is 45KW or 35KW, and the static pressure at the outlet of the nozzle is 200torr or 500torr. The mass flow inlet condition has been assigned to both plasma gas inlet (6.09×10^{-4} kg/s for helium plasma gas and 2.726×10^{-3} kg/s for argon plasma gas) and carbon containing gas with carrier gas. The torch efficiency is 75%, and the walls of the nozzle have a static temperature of 300K since they are all water-cooled. The mean mass ratio of tungsten vapor with respect to 225slpm helium plasma gas is 7.8095×10^{-5}, the molar flowrate of the carbon containing gas is 0.15 mol/min, while the flowrate of the carrier gas is 20slpm.

4. Calculation Results and discussion

Calculation results of static temperature fields are presented in Figure 2 for the case of helium plasma gas, plasma power level of 45KW, plasma gas flow rate of 225slpm, operating pressure 200torr and 500torr respectively. We can clearly see that there are shock waves inside of the nozzle. We see that under different operating pressures, the position of the first shock, the distance between each shock core and the number of shock waves in the nozzle is different. Since each expansion and compression of the gas correspond to regions of transfer between thermal energy and kinetic energy [3], the temperature and velocity fields vary enormously under different operating pressure and strongly influence the evolution of metal particles in the nozzle.

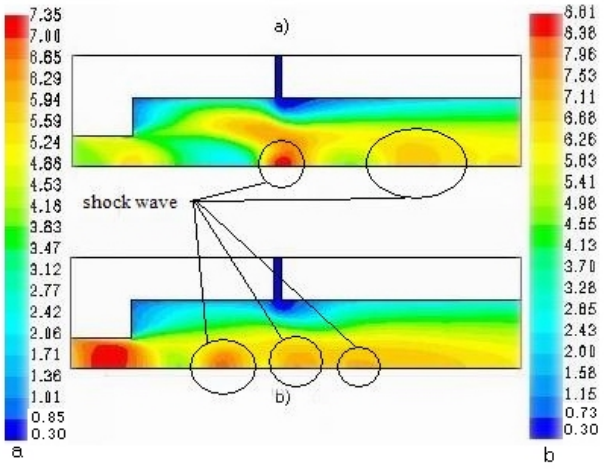

Figure 2. Static temperature contour for helium(10^3K)
(a. 200torr, b. 500torr)

The critical cluster size is defined as follows[12]

$$d_p^* = \frac{4\sigma_m v}{k_B T \ln S} \qquad (2)$$

where d_p^* the critical cluster size, σ_m the surface tension of the metal species, v the volume of a single metal atom, T is the local temperature. Parameter S is the saturation ratio of the metal vapor.

$$S = x_m * p / p_m \qquad (3)$$

where x_m is the molar ratio of metal vapor, p the local pressure, and p_m the saturated pressure of the metal.

In the model of the particle formation, we made the assumption that the particles which are smaller than the critical sized particles will not stay stable. From Equation 1 we can easily tell that the particle size and number distribution will change enormously in the supersonic area. This change could be favorable for maintaining the particle size to small values. Every compression area will have an extremely high temperature and particles coming into this area will re-vaporize to metal vapor or smaller particles and will re-grow in the following expansion zone. So the existence of the shock waves actually gives us opportunity to control the nucleation of the particles. As we can see in Figure 2, the position and number of the shock waves can be influenced by the operating pressure, which is a controllable parameter. And since the supersonic flow is also very closely related to the flowrate and energy of the flow, we will estimate the possibility of controlling the shock waves by adjusting these parameters so as to control the fine particle formation inside of the nozzle.

4.1 Changing operating pressure

As presented in Figure 2, the shock waves travel in the nozzle as the operating pressure changes. Figure 3. presents the contours of particle number density and particle size distribution in the nozzle under the same operating conditions as Figure 2. The expansion of the gas and the cold carrier gas generate a strong quenching for the plasma gas and create a strong temperature gradient inside of the small nozzle. The local partial pressure of the metal vapor also increases due to the decrease of the local pressure in the expansion area. These explain the reason why we obtained particle nucleation near the centre of the nozzle although the temperature is relatively high in this zone. However in the area of compression that follows, the formed particles vaporize because of the high local temperature and high local pressure in this zone. We can see from Figure 3 that there are "particle number shock waves", the density of the particles decreases and then increases again following the shock wave pattern. From Figure 2, we can see that strong temperature gradients exist near the water-cooled nozzle wall, this location providing favorable conditions for the nucleation of particles. From the calculation results of the tungsten particle number density and the mass distribution of carbon containing gas (as given in Figure 4), the area which is very close to the nozzle wall has a high tungsten particle concentration and a high ratio of carbon species. This correlates with experimental results showing a large quantity of carbon nanotube growing on the wall of the nozzle. Comparing the tungsten particle number density distribution under 200torr and 500torr, the formation of the particles is being pushed downstream with increasing pressure. This enables the possibility for producing the CNT inside the reactor instead of in the nozzle itself. This correlates with the results on the experimental reactor. One may note from Figure5 the relatively difficult penetration of the carbon precursor inside the main plasma flow. Under this configuration, 80% of TCE is mainly confined along the cold nozzle wall and induces and important carbon deposition in this zone, as observed experimentally [6]. Changing other parameters as mentioned can also change the size distribution of the particles inside the nozzle.

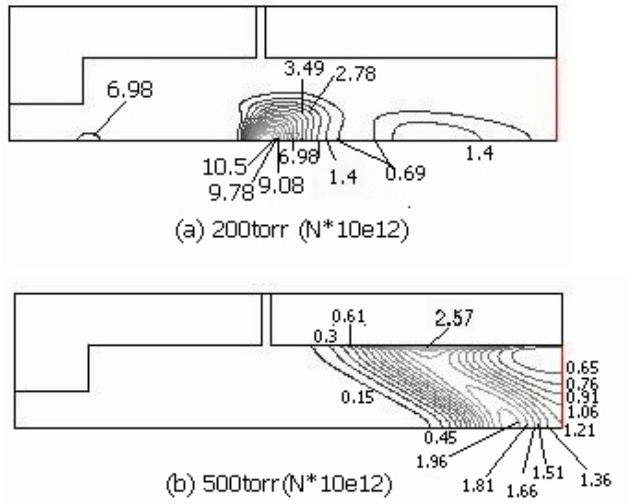

Figure 3: The number density distribution of particles in the nozzle(N/m^3).

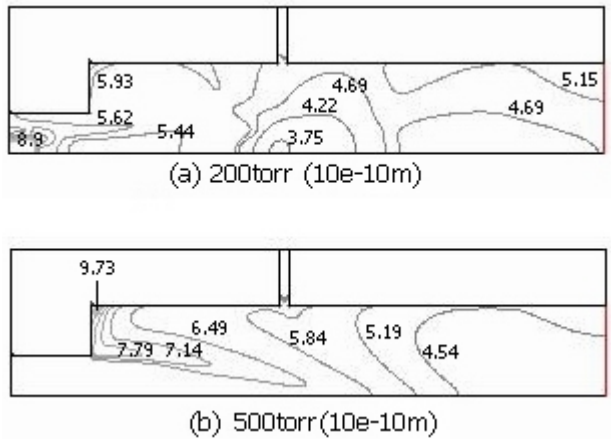

Figure 4: Size distribution of particles in the nozzle (m).

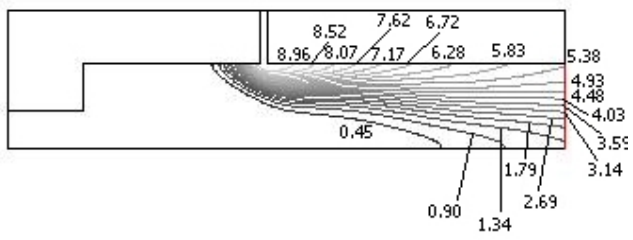

Figure 5: TCE mass ratio contour (45kW, 200torr)($x10^{-2}$).

4.2 Results with different plasma gas flowrates

Assuming all other conditions stay constant, we can study the effects of the plasma gas flowrates. Figure 6 shows the static temperature field, particle number density contour and particle size distribution field when the nozzle is operating under 200torr with a reduced helium plasma gas flowrate of 150slpm. Comparing with Figures 2(a), 3(a) and 4(a), we see first that the temperature is higher at this reduced flow rate since the power level is kept constant. As a

consequence, the particle number density is also lower, the high temperature is helping in this case to keep the metal species in the gas phase. There is not a strong difference between the two particle size distribution fields. Lowering the flow rate while keeping the power level constant can increase the energy of the plasma gas. It therefore helps to decrease the number of particles in the nozzle. More metal vapor would then be available to enter the reactor and grow catalyst particles outside of the nozzle.

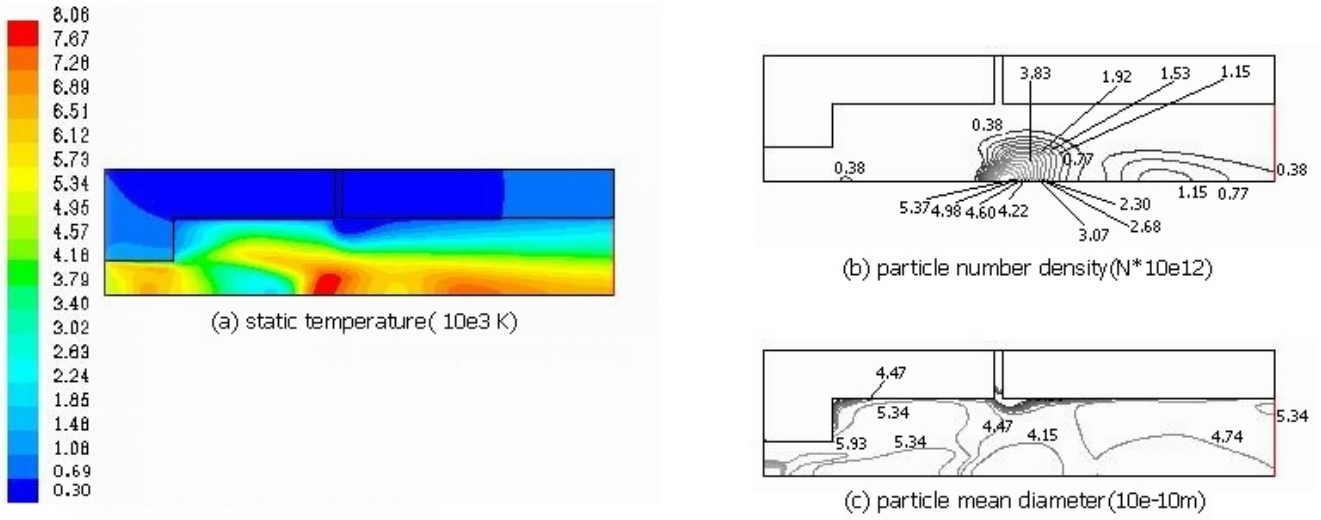

Figure 6. The temperature field (a), particle number density (b) and particle size distribution (c) under 200torr pressure, with a plasmas gas flow rate of 150slpm, and a power of 45kW.

4.3 The effect of change of the power level

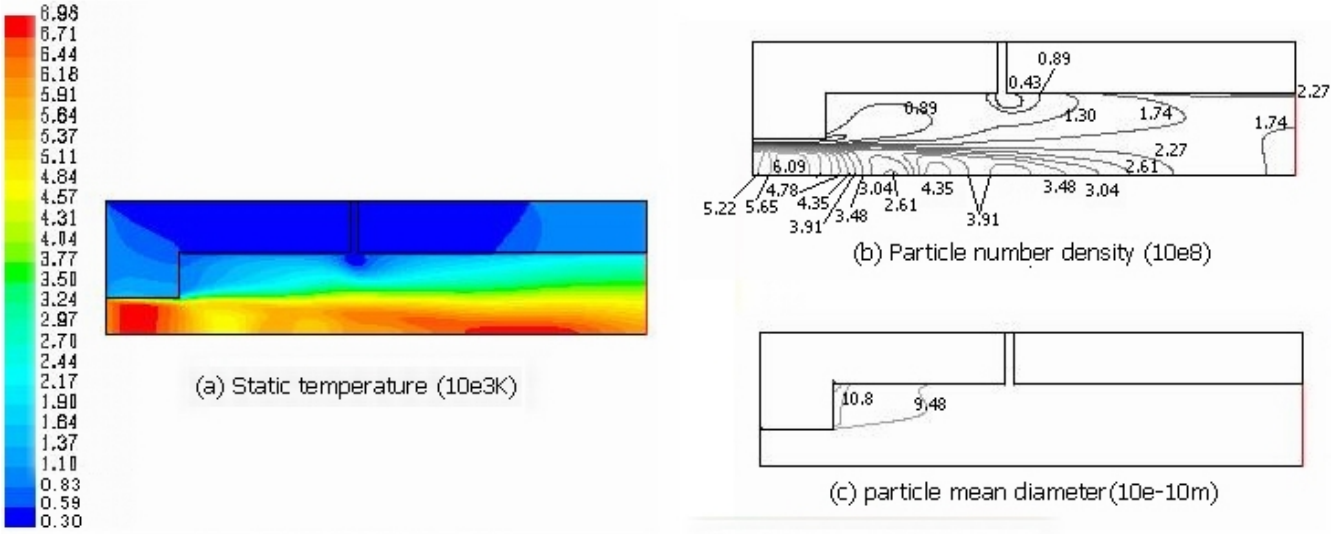

Figure 7. The temperature field(a),particle number density(b) and particle size distribution(c) under 500torr, with plasmas gas flowrate 225slpm, 35KW

Figure 7 shows the static temperature field, particle number density contour and particle size distribution field when the nozzle is operating under 500torr with a helium plasma gas flow rate of 225 slpm, a power level of 35KW. From the temperature field we can see that the shock waves are not as strong as what is observed at 45kW(Figure 2b). The position is pushed downstream, and both the temperature and temperature gradient are lower. When the power level is 35kW, the number density of the particles is quite low compare to the 45kW case. We can see from the temperature field that the high temperature area moves towards the outlet of the nozzle. As a consequence, the number density of the particle decreases along the main plasma gas flow. This is a favorable

condition for preserving the metal vapor into the reactor.

5. Conclusions:

The objective of this paper is to perform a parameter analysis with the aid of a CFD numerical model coupled to a particle nucleation model. Comparing the computational and the experimental results, one has a possibility to adjust operating parameters such as the pressure, power level and flow rate of the plasma gas, to modify the number and position of the shock waves inside the nozzle and the resulting evolution of the particles. Metal particles nucleate and grow in the expansion area but re-vaporize in the compression zone. From the calculation results, we come to a conclusion that higher operating pressures are favorable for pushing the formation of finer particles into the reactor along with the formation of CNT. This correlates well with experimental result [6]. From similar calculations, lower torch power is also favorable for preserving the metal vapor. The calculated particle sizes are smaller than the values obtained experimentally [6]. This could be attributed to the exclusion of the reaction energy term from the TCE dissociation. This contribution could also be an important factor behind the formation of nanometer-sized particles in the nozzle.

References:

1. Sumio Iijima, Nature, Vol.354(1991), P56-58
2. Pavel Nikolaev, Michael J. Bronikowski, R. Kelley Bradley, Frank Rohmund, Daniel T. Colbert, K. A. Smith and Richard E. Smalley, Chemical Physics Letters, 313(1999), P91-97
3. Y. Zhang, S. Iijima, Applied Physics Letters, Vol.75, No.20, P3087-3089
4. F. Kokai, K. Takahashi, M. Yudasaka, R. Yamada, T. Ichihashi, and S. Iijima, Journal of Physical Chemistry B, 103(1999), 4346-4851
5. Hongjie Dai, Andrew G. Rinzler, Pasba Nikolaev, Andress Thess, Daniel T. Colbert, Richard E. Smalley, Chemcial Physics Letters, 260(1996), P471-475
6. D. Harbec, J.-L. Meunier, L. Guo, R. Gauvin, N. El Mallah, J. Phys. D: Appl. Phys. 37, 15(2004), 2121-2126
7. D. Harbec, J.-L. Meunier, L. Guo, J. Jureidini, Proceeding of ISPC 17(2005)
8. D. Harbec, J.-L. Meunier, PCT Int. Appl., WO 2004046030. 32 pp (2004).
9. S. Selezneva, M. Rajabian, D.V. Gravelle, M. I. Boulos, J. Phys. D: Appl. Phys, 34, 2862-2874(2001)
10. R. B. Bird, W.E. Stewart, and E. N. Lightfoot, Transport Phenomena, Second Edition, 2002
11. S. L. Girshick, Journal of Chemical Physics, 94(1), P826-827(1991)
12. S. K. Friedlander, Smoke,dust and haze: fundamentals of aerosol dynamics, 2000

Application of laser Thomson scattering to thermal plasma studies

B.Pokrzywka[1], K.Dzierżęga[2], W.Zawadzki[2], K.Musioł[2] and S.Pellerin[3]

[1] Mt. Suhora Observatory, Cracow Pedagogical University, ul. Podchorazych 2, 30-083 Krakow, Poland
[2] M.Smoluchowski Institute of Physics, Jagellonian University, ul. Reymonta 4, 30-459 Krakow, Poland
[3] LASEP, Fac. des Sciences-Bourges, Université d'Orléans, BP 4043, 18028 Bourges Cedex France

Abstract

This work will present the experimental results of our investigations of the electron heating in Thomson scattering experiments obtained for atmospheric-pressure argon thermal plasma. The spatially and temporally (in time of the laser pulse duration) resolved LTS spectra enabled us to follow the evolution of T_e. These experimental results will be compared to the theoretical ones obtained with the model of Murphy.

1. Introduction

Thomson or incoherent scattering is the process of scattering of low energy photons ($\hbar\omega \ll m_e c^2$) on free electrons present in a plasma. These electrons, in a plasma, are not completely free but they are exposed to the electric microfields. This weak coupling causes coherent or collective scattering events. All electrons located in a sphere with the size of a Debye length λ_D oscillate in phase yielding a coherent scattered signal if, for the scattered wave $\lambda = \lambda_L/(2\sin(\theta/2))$ (see Fig. 1a), the condition $\lambda \gg \lambda_D$ is valid. In the opposite case, $\lambda \ll \lambda_D$, the scattering process is incoherent. The character (incoherent/coherent) of the scattering is measured by the so called scattering parameter $\alpha = \lambda/(2\pi\lambda_D)$ which determines the shape of the scattered spectrum (see Fig. 1). The theory of Thomson scattering has been presented in detail in many publications [1, 2, 3]. The interpretation of the experimental Thomson-scattered spectra is, in most cases, straightforward and gives direct access to the electron density n_e and the electron temperature T_e.

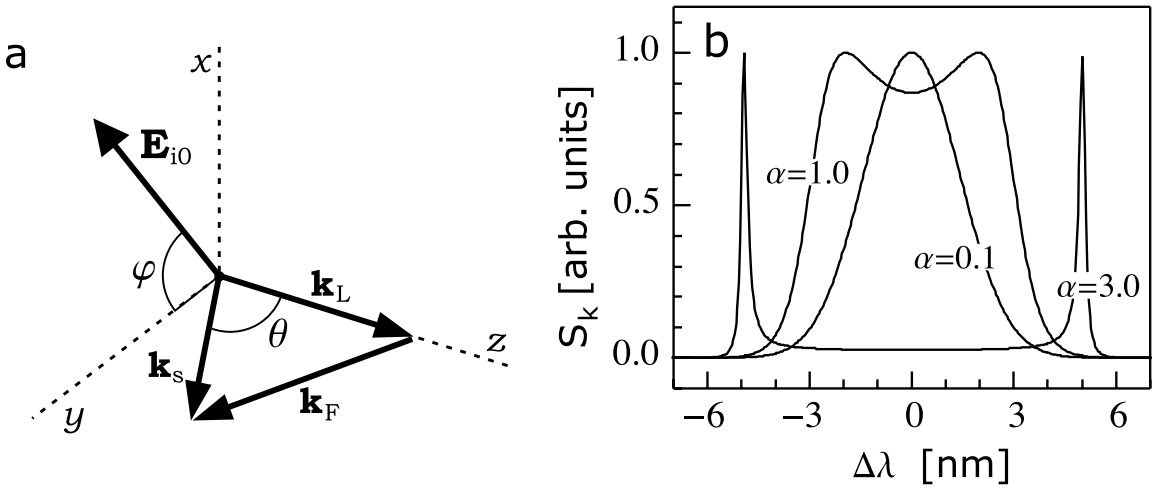

Figure 1: a). The Thomson scattering geometry and definition of the scattering angle θ and the angle φ between the plane of scattering and the polarisation vector $\mathbf{E}_{i0}$ of the incident laser beam. $\mathbf{k}_L$ and $\mathbf{k}_s$ are the wave vectors of the incident laser beam and the scattered light while $\mathbf{k}$ is the scattering vector ($\mathbf{k} = \mathbf{k}_s - \mathbf{k}_L$). b). The electronic part of the spectral density S_k calculated for $\theta = 90^o$, $\lambda_L = 532$nm and for different values of scattering parameter α.

The determination of n_e and T_e of thermal plasmas by spectrum analysis of the Thomson scattered light is attractive because it does not require any assumption about local thermodynamic equilibrium and, unlike optical emission spectroscopy, gives the spatially-resolved results. Moreover, since in thermal plasmas $k_B T_e > 1$ eV and $n_e > 10^{22}$ m^{-3} so $\alpha > 1$ and the electron temperature and density can be simultaneously determined based on the individual Thomson scattered spectrum. On the other hand, due to very low cross section for the Thomson scattering process ($\sigma_{Th} \equiv r_e^2 = 6.6 \times 10^{-25}$ cm^2), measurements require high power pulsed lasers in order to obtain a detectable signal level. However, it can result in significant disturbance of the plasma state predominantly due to electron heating by the laser pulse in the inverse bremsstrahlung process. The corrections of T_e for the laser power are commonly based on estimations made by Kunze [1]. According to these calculations the relative change in electron temperature is directly proportional to the laser power. Such dependence suggests measurements of Thomson-scattered spectra at different laser powers and then simple extrapolation of the determined electron temperature to the zero laser power. Such a linear extrapolation, in the case of thermal plasmas, yielded T_e well in excess of the expected values. These discrepancies were observed in many experiments with the laser Thomson scattering as a diagnostic tool [4, 5, 6].

The problem of the electron heating by the incident laser beam has been recently studied by Murphy [7]. He solved one-dimensional equation for the electron heating by absorption of laser radiation and cooling due to such processes as: electron thermal conduction, energy transfer to heavy particles by elastic and inelastic processes and by radiative emission. These calculations show highly nonlinear dependence of the derived electron temperature on the laser power and that the usual linear extrapolation leads to an overestimatation of T_e in thermal plasma.
The goal of our work was to give, at least qualitatively, some experimental evidence for plasma disturbance by the laser pulse. We also studied an evolution of the Thomson scattered spectra within the spatial and temporal profile of the laser beam which enabled to determine evolution of n_e and T_e.

2. Experimental setup

In our experiment we used a second harmonic of a Nd:YAG laser ($\lambda_L = 532$ nm) which delivered laser pulses of energy E_p up to 200 mJ and of about 6 ns duration time. The beam was passing through the beam attenuator and then it was focused to the spot of 150 μm on the plasma axis and a few millimeters z above the cathode tip. The scattered light was collected at a angle of 79.2^o with respect to the laser beam. The investigated plasma volume was imaged onto the entrance slit of a spectrograph (1.6 nm/mm reciprocal dispersion) with an enlargement factor equal 1. In order to improve S/N ratio the polarizer with the polarization axis parallel to the laser beam polarization vector was placed on the path of the scattered light beam. Finally, the scattered spectrum was registered using a gated two-dimensional intensified charged-coupled (ICCD) array with the gate width as short as 2 ns. The gate was delayed with respect to the triggering laser pulse.
In the experiment we can only measure the intensity of the scattered light integrated along a line of sight e.g. across the laser beam. In order to obtain some local values (spatially resolved Thomson spectra across the laser beam) we applied the Abel inversion transformation. The final spatial resolution across the laser pulse was limited by the pixel size of the ICCD camera which was $20\,\mu m \times 20\,\mu m$.
The details concerning plasma generator one can find in [8]. In the following presented results, the gate width of the ICCD camera was 2.5 ns and the arc was generally operated at I=100 A.

3. Results and Conclusion

Figure 2 shows the Thomson scattered spectra obtained from the plasma across the laser beam. The experiment was performed for the arc discharge current of 100 A and the axial region of plasma 4.0 mm above the cathode tip was studied. Energy of the laser pulse was set to 150 mJ while the gate width of the ICCD camera was 2.5 ns with 0 ns delay time with respect to the center of the laser pulse.
It is observed that both the distance between two peaks and their width increase while approaching the center of the laser beam. It follows that plasma parameters (n_e and T_e) vary with the laser beam which implies the disturbance of the plasma state by the laser pulse.

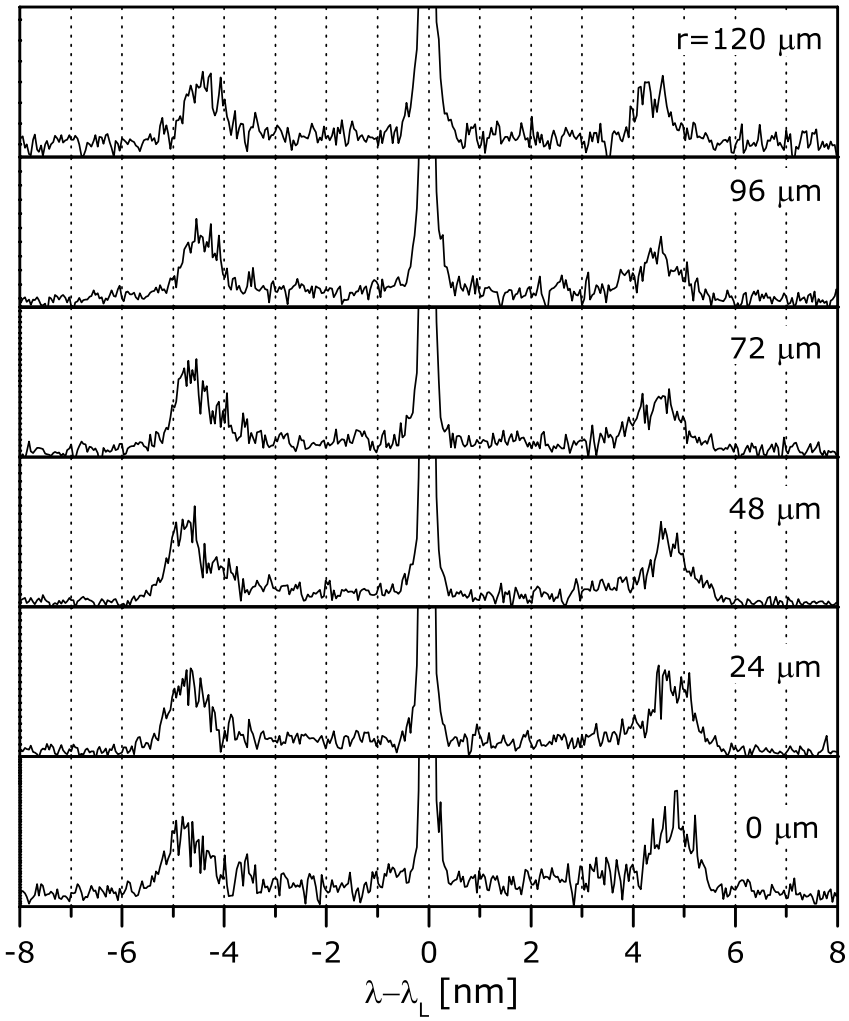

Figure 2: The Thomson scattered spectra determined for different positions across the spatial profile of the laser beam. Distances $r = 0\,\mu$m and $120\,\mu$m correspond to the center and the wing of the pulse, respectively [I=100 A; z=4.0 mm; E_p=150 mJ].

Under similar discharge conditions as in Fig.2 we investigated the temporal evolution of the Thomson scattered spectra setting the ICCD gate width to 2 ns and measuring the scattered light at different moments of the laser pulse. Figure 3 shows the Thomson scattered spectra determined for the central part (with the use of Abel transformation) of the laser beam. The delay of 0.0 ns corresponds to the maximum of the laser pulse while negative and positive delays correspond to its front and wing, respectively.
As one can observe the spectrum of the scattered light changes during the laser pulse. The spectral distance between two peaks and their width first increase with rising the pulse and then start to decrease at the delay time of +6.0 ns. This is the direct result of plasma temperature and electron density variations due to the interaction of plasma with the laser pulse.

The temporal evolution of plasma parameters (n_e and T_e) during the laser pulse was determined from the registered Thomson scattered spectra and is presented in Figures 5a-b. The gate width was set to 2.5 ns and the axial volume z=6.0 mm above the cathode tip was investigated at the discharge current of 100 A and at different energies of the laser pulse.

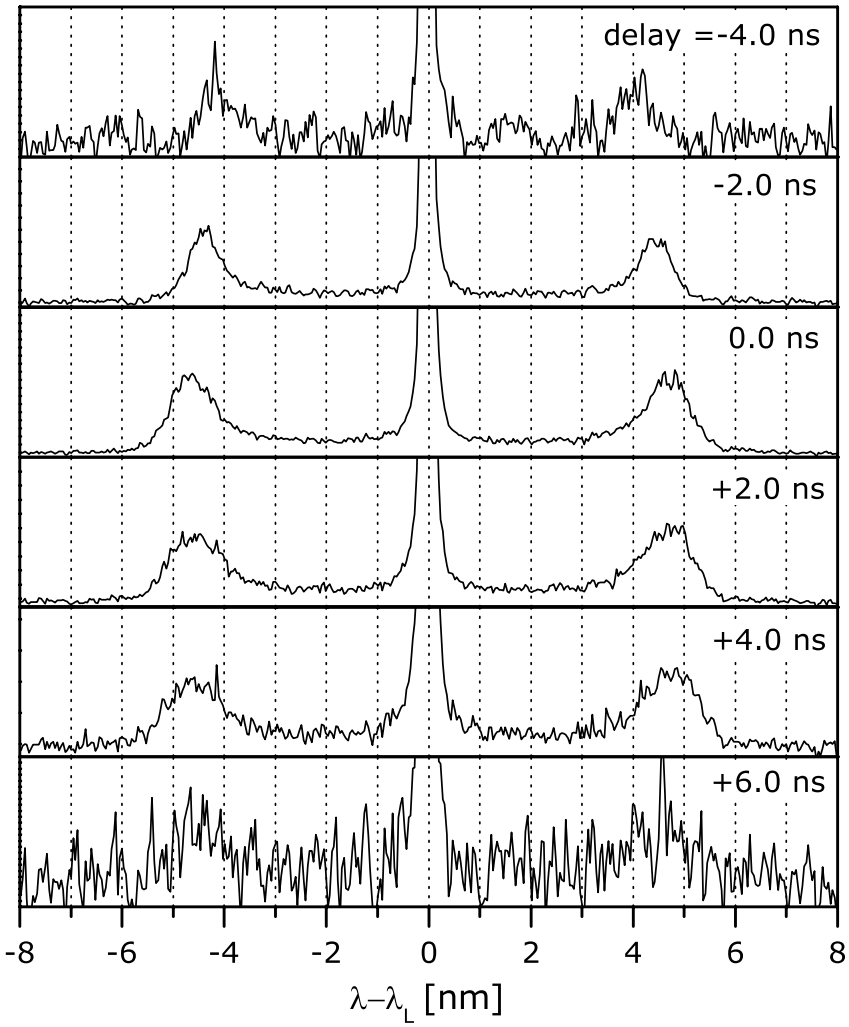

Figure 3: The Thomson scattered spectra determined at different moments of the laser pulse. Delay of 0.0 ns corresponds to the center of the laser pulse while negative and positive delays correspond to the front and the wing of the pulse, respectively [I=100 A; z=4.0 mm; E_p=150 mJ].

For the range of investigated energies of the laser pulse, T_e rapidly growths when the laser pulse is switched on. The higher laser energy the higher final temperature can be reached at given initial plasma parameters. Since the decay of T_e is slower than the decay of the laser pulse it follows that plasma processes are not fast enough to make it thermal at each moment of the laser pulse. At the same time the rapid increase of the electron density is observed only in the case of the highest laser energy ($E_L = 150\,\mathrm{mJ}$). No significant variation of n_e is observed during the laser pulse for the pulse energies E_p of 50 mJ and 20 mJ. It implies that for these lower energies photoionization processes are of minor importance unlike the electron heating by the laser pulse.

Acknowledgments
This work was supported in part by Polish Committee for Scientific Research (grant 1 P03B 090 26), Region Centre (France) and by project d'Action Intégreés-Polonium 01412ZH .

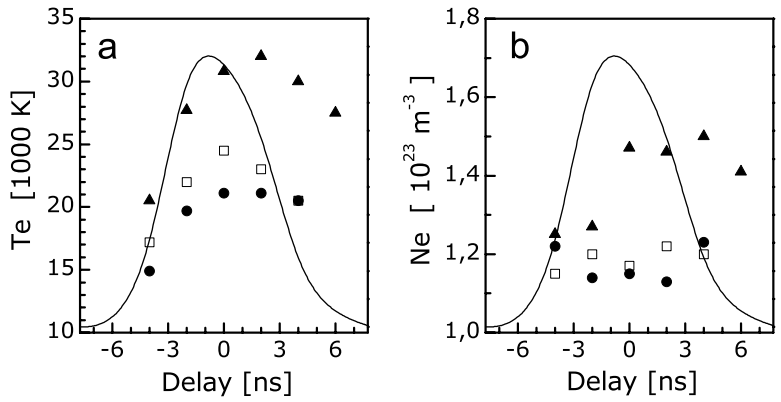

Figure 4: The electron temperature (a) and density (b) of plasma determined from the Thomson scattered spectra measured at different moments of the laser pulse.
E_p=150 mJ (▲), 50 mJ (□) and 20 mJ (•). The temporal evolution of the laser pulse is represented by the solid line [I=100 A; z=6.0 mm].

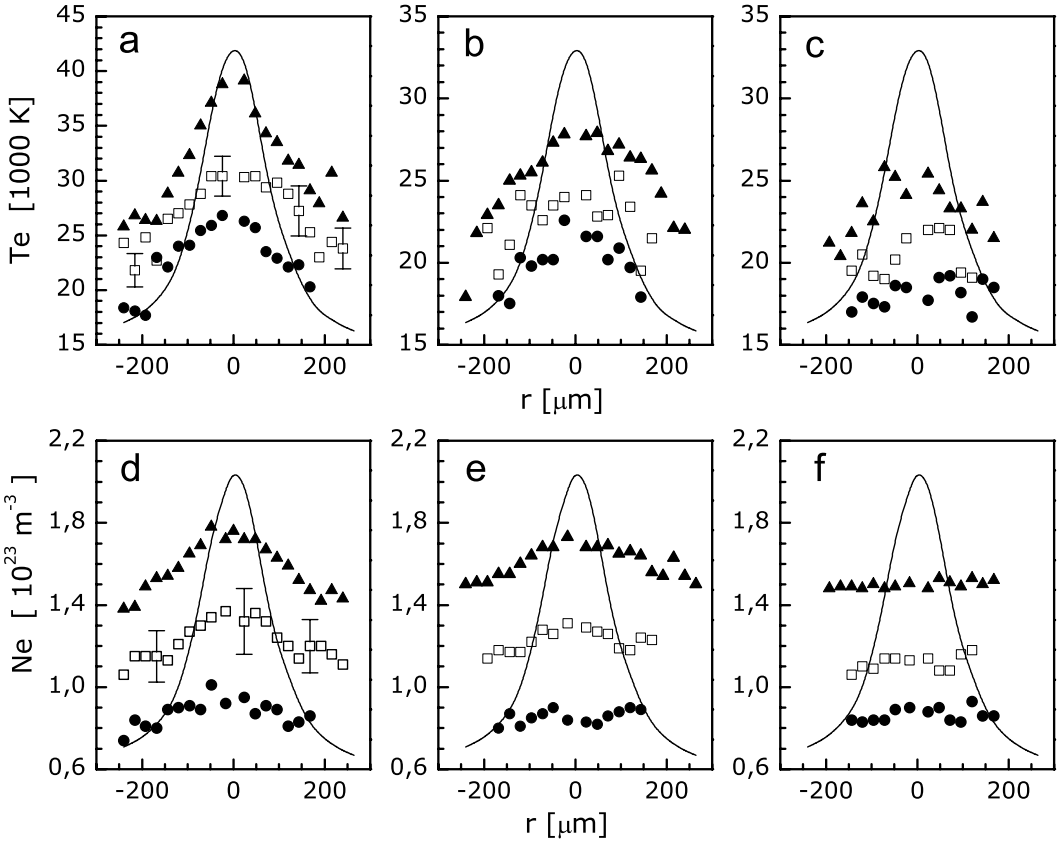

Figure 5: The distribution of the plasma parameters, T_e (a-c) and n_e (d-f), across the laser beam derived from the spatially resolved Thomson scattered spectra.
(▲) $I = 100$ A, $z = 4.0$ mm; (□) $I = 100$ A, $z = 6.0$ mm and (•) $I = 80$ A, $z = 6.5$ mm.
The measurements were performed for laser pulse energy E_p of 150 mJ (a,d), 50 mJ (b,e) and 20 mJ (c,f). The spatial profile of the laser beam is indicated by the solid line.

References

[1] H.J.Kunze, "The laser as a tool for plasma diagnostics," in *Plasma Diagnostics*, W. Lochte-Holtgreven, ed., pp.550–616, North-Holland Publishing Company, Amsterdam, 1968.

[2] D.E.Evans and J.Katzenstein, "Laser light scattering in laboratory plasmas," *Rep.Prog.Phys.* **32**, pp.207–271, 1969.

[3] J. Sheffield, *Plasma Scattering of Electromagnetic Radiation*, Acad.Press, New York, London, 1975.

[4] S.C.Snyder, G.D.Lassahn and L.D.Reynolds, "Direct evidence of departure from local thermodynamic equilibrium in a free-burning arc-discharge plasma," *Phys.Rev.E* **48**, pp.4124–4127, 1993.

[5] R.E.Bentley, "A departure from local thermodynamic equilibrium within a freely burning arc and assymetrical Thomson electron features," *J.Phys.D* **30**, pp.2880–2886, 1997.

[6] M.Tanaka and M.Ushio, "Plasma state in free-burning argon arc and its effect on anode heat transfer," *J.Phys.D* **32**, pp.1153–1162, 1999.

[7] A.B.Murphy, "Electron heating in the measurement of electron temperature by Thomson scattering: Are Thermal Plasmas Thermal ?," *Phys.Rev.Lett.* **89**, pp.025002, 2002.

[8] B.Pokrzywka, K.Musioł, S.Pellerin, E.Pawelec and J.Chapelle, *J.Phys.D* **29**, pp.2644-2652, 1996.

Quartz-like track deposition by micro-Jet Plasma CVD

Kamel Silmy, Andreas Holländer
Fraunhofer-Institut für Angewandte Polymerforschung, Geiselbergstr. 68, 14476 Potsdam, Germany
email: andreas.hollaender@iap.fraunhofer.de

Abstract
Quartz-like deposition tracks were produced from HMDSO/O_2 gas mixture (1:120) by means of micro-jet plasma chemical vapor deposition (MJPCVD) with a moving capillary. Virtually carbon-free quartz-like depositions were obtained at high power input. SEM analysis revealed a compact structure with some fine cracks. At a lower power input, uniform and densely packed nanospheres are produced and there are some traces of hydrocarbons in the deposition.

Keywords
Quartz-like deposition, micro-jet, plasma CVD, XPS

Introduction
The plasma deposition of SiO_2 using hexamethyldisiloxane (HMDSO) or tetraethoxysiloxane (TEOS) as precursor mixed with oxygen has been investigated extensively [1]. RF HMDSO/O_2 plasma deposition is widely used to produce a stable and long-life quartz-like deposition for gas barrier applications in packaging industries or for scratch resistance coatings of optical components. Such a SiO_2 deposition might possibly be used as an optical wave guide. However, a major source of attenuation of the wave propagation results from the morphology of the deposition. The chemical composition influences the optical quality, as well. Thus, a hazy layer will scatter the light [2, 3]. Plasma parameters as the oxygen flux or the power input influence the deposition of SiO_2 films, too.
Most of the plasma techniques target large area coatings. The preparation of a structured coating usually requires several steps such as the use of an appropriate mask followed by the dry-etching. A novel plasma technique for well-defined and localized deposition with extremely high deposition rate, called micro-jet plasma chemical vapor deposition (MJPCVD), was developed [4, 5, 6, 7]. This technique is based on the process gas injection through a capillary into a vacuum chamber and the RF plasma excitation of the jet. In this study, we report about our investigations of localized depositions of quartz-like coatings by means of MJPCVD as a function of the power input.

Experimental part
The MJPCVD experimental apparatus consists of a 4.63 dm³ stainless steel vacuum chamber with a home-made symmetric copper electrode configuration [7]. A shielded electrode which was powered by a 13.56 MHz RF generator and the grounded electrode were used to ignite the glow discharge. The chamber was pumped with a two stage rotary pump (Trivac DB16 from Leybold), and the pressure was measured with an absolute pressure transducer MKS Baratron (type 62A). A mass flow controller was used to control the gas mixture flow rate. The gas mixture comprises the organosilicone precursor hexamethyldisiloxane ($C_6H_{18}OSi_2$ 98.5% for gas chromatography from Fluka) and oxygen 3.5 (99.95 Vol. % pure). The oxygen was injected into a 0.785 dm³ stainless steel bubbler which contained the precursor liquid. The pressure in the bubbler was adjusted with the oxygen gas to p_1=5 bar. The resulting HMDSO concentration in the mixture was fixed at 120:1. The HMDSO, which has a vapor pressure of 4457 Pa at 20°C, was transported by the oxygen carrier gas.
The capillary position was accurately adjusted in front of the substrate and between the two electrodes, using an ultra-high vacuum motorized x-y-z manipulator (Huntington MPM-275). The 125 µm inner diameter and 5 cm length capillary, positioned normal to the substrate, was used to inject the reactive gas mixture into the vacuum deposition chamber and through the glow discharge. During the experiments, the capillary was maintained at 8.75 mm on the x-axis, corresponding to the injector-substrate distance. It was moved vertically along the substrate (y-axis) with a velocity of 175 µm/s to produce a one centimeter deposition track on the substrate.

The power input was varied up to 80 W, while the other parameters were maintained constant, namely the chamber pressure at 0.72 mbar and the flow rate at 50 sccm.
The deposition process was carried out onto substrates made of glass, aluminum or KBr. Except for the KBr, the substrates were cleaned in a solution of ethanol during 15 min in an ultra-sonic bath and then pre-treated with oxygen plasma for 1 min at 0.60 mbar with 60 W and 100 sccm O_2.
The Dektak³ST stylus surface profilometer was used to determine the surface topography of the deposition track. For the chemical characterization of the deposition we used Fourrier-transform infrared spectroscopy (FTIR) (in transmission mode with coated KBr), x-ray photoelectron spectroscopy (XPS), and scanning electron microscopy (SEM). FTIR spectra were obtained with a Perkin Elmer FTIR microscope system 2000 by means a 100 µm blind aperture. XPS spectra were obtained by using an Axis165 (Kratos Analytical, UK) with monochromatic Al Kα radiation (20 mA at 15 kV) in hybrid mode (with electrostatic and magnetic lenses). The spot size of approximately 0.3×0.7 mm^2 was applied to determine the relative concentration of elements from the integral intensities of photoelectrons. The sampling spot size was reduced to 120 µm in diameter for the laterally resoled measurements. The high resolution spectra were fitted with Gaussian curves after the subtraction of a linear background.

Results and Discussions

Profile

Figure 1 shows a profile of quartz-like deposition track. The width of the profile is approximately 2.6 times the inner diameter of the capillary. Less than 1 min is required to produce 1 cm long and 63 µm high quartz-like track with an extremely high deposition efficiency of 84 %. The average deposition efficiency reflects the conversion of the monomer to silicon oxide and can be expressed as follows:

$$Eff.(\%) = \frac{Quartz-like\ mass\ deposited}{SiO_2\ mass\ from\ the\ flow\ rate} \times 100$$

Eq. 1: Average deposition efficiency

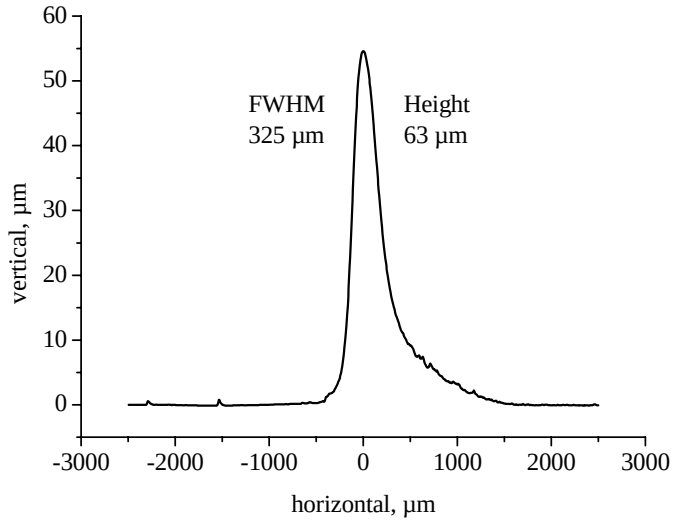

Fig. 1: Profile of a quartz-like deposition track (0.72 mbar, 50 sccm, 70 W)

Chemical composition

A XPS spectrum of quartz-like depositions from a O_2/HMDSO (120:1) mixture is shown in figure 2. Peaks of O1s, C1s, Si2s and Si2p core levels are distinguished. The high-resolution spectra of Si2p and C1s were fitted with Gaussian functions. Si2p peak was fitted only with the doublet $Si2p_{1/2}$ and $Si2p_{3/2}$ at 103.6 and 104.2 eV, respectively. There is no signal at 102.4 eV, which would be assigned to silicon atoms with bonds to carbon atoms like in methyl groups of the HDMSO molecule $(CH_3)_3$-Si-O-Si-$(CH_3)_3$. According to the peak fit, silicon atoms are surrounded by oxygen atoms only. The major component of the C1s spectrum was found at 284.91 eV (C-H/ C-C units). Minor quantities of C-O and O-C=O were detected, while there is no sign of carbon atoms with bonds to silicon C-Si (binding energy 284.5 eV). The carbon found in the spectrum (Fig. 1) is assumed to originate from surface contamination.

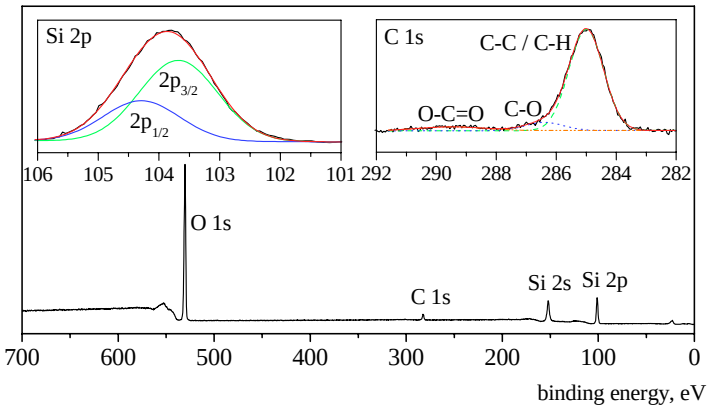

Fig. 2: Wide spectrum of a quartz-like deposition (capillary 125 µm × 5 cm, 0.72 mbar and 50 sccm O_2/HMDSO (120:1), 70 W and 7.95 mm injector distance)

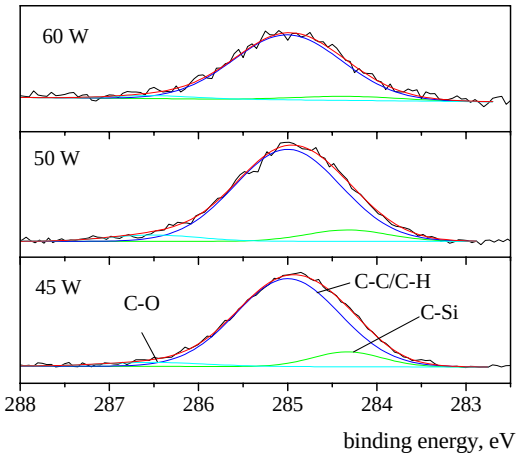

Fig. 3: C 1s spectra of quartz-like depositions prepared at varying power input.

The elemental surface compositions of the deposition track prepared at different power inputs reveal that the carbon content in the deposition decreases when the power input increases (Tab. 1). The ratio [C]/[Si] decreases from 0.29 to 0.06 for 45 and 70 W, respectively. The C 1s spectra show the various binding state components (Fig. 3). Most of the carbon atoms are bonded to carbon or hydrogen atoms and fewer to oxygen atoms. However, at low power input, the spectrum shows a small amount of C-Si bonds, which decreases when the power increases and it disappears completely at higher power (P>70 W). A low power input (P<70 W) results in the production of a more polymer-like deposition C-Si features in the C1s spectrum.

Table. 1: Element composition of the quartz-like deposition

	45 W		50 W	
	B.E. (eV)	%	B.E. (eV)	%
Si 2p	103.67	29.75 ± 0.1	103.67	30.19 ± 0.1
C 1s	285.01	8.82 ± 0.1	284.99	7.82 ± 0.1
O 1s	532.00	61.43 ± 0.1	532.00	61.99 ± 0.1
	60 W		70 W	
Si 2p	103.67	30.61 ± 0.1	103.67	33.01 ± 0.1
C 1s	284.96	6.81 ± 0.1	284.96	2.06 ± 0.1
O 1s	532.00	62.58 ± 0.1	532.00	64.93 ± 0.1

The FTIR spectra (Fig. 4) show the typical features of a quartz-like deposition. There are the major Si-O-Si stretching and bending absorption bands at 1090 and 1020 cm^{-1}, respectively (Tab. 2, V2). The silanol Si-OH stretching and bending bands at 3450 and 930 cm^{-1}, respectively, are present, too.
While the XPS spectra did not indicate the presence of Si-C bonds in the deposition track for a power input above 70 W, the V8 band at 804 cm^{-1} in the FTIR spectra clearly show a non-negligible amount of Si-C bonds from $Si(CH_3)_3$. The presence of $Si(CH_3)_3$ is supported by the wagging vibrations of methyl groups in $Si(CH_3)_3$ which cause the shoulder V5 on the absorption band V6 and by the CH stretching (V2). It is difficult to appraise the different results from the two techniques. The IR data represent all of the many microns thick deposition while with XPS we see the top-most layer only. But under the high vacuum conditions of a XPS measurement we remove a part of the adsorbed contaminants while they can remain on the high energy quartz surface during the recording of the FTIR spectra. It is quite possible that a material with a cauliflower surface morphology can adsorb substantial amounts of hydrocarbon contaminants from the ambient atmosphere.

Table. 2: List of bands observed in the quartz-like deposition

Notation	Wavenumber, cm^{-1}	Function
V8	804	Si-C from $Si(CH_3)_3$
V7	930	Si-OH bend
V6	1090 + 1020	ν_{as}(Si-O-Si)
V5	1277	Si-CH_3 wagging
V4	1633	
V3	2358	H_2O from air
V2	2981	$\nu_{as}(CH_3)$ stretching
V1	3450	OH stretch

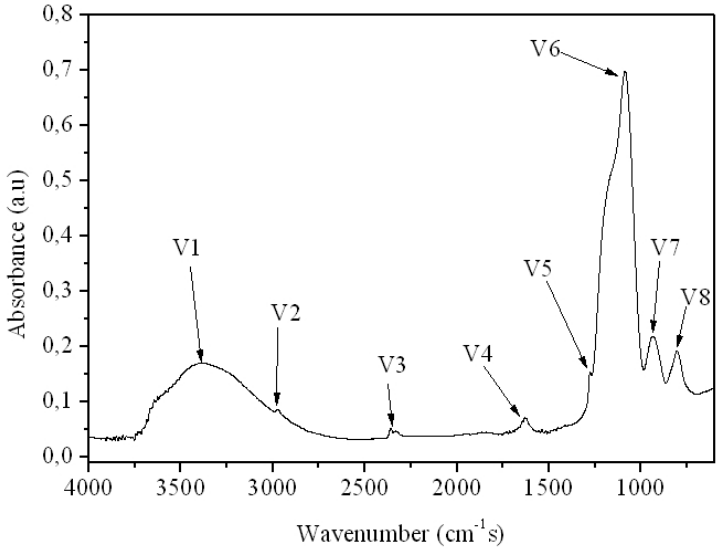

Fig. 4: FTIR spectrum of a quartz-like deposition (125 µm × 5 cm capillary, 0.72 mbar, 50 sccm O_2/HMDSO, 70 W)

Morphology
SEM images of the quartz-like depositions prepared at 60, 70 and 80 W show remarkable differences (Fig. 5). The 60 W sample is composed of mostly uniform and densely packed nanospheres. The average diameter of the nanoparticles measured on the SEM image accounts for about 30 nm. At 70 W, a cauliflower-like structure is obtained. However, the cauliflower-head is composed of nanoparticles, which have a about the same size as the nanospheres obtained at 60 W. At 80 W, a particle-free, compact structure with some fine cracks was produced.

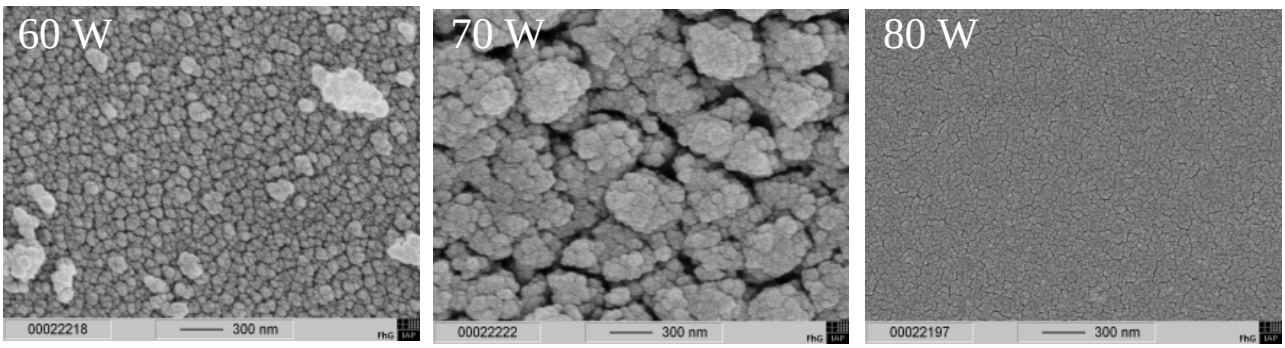

Fig. 5: SEM picture of quartz-like depositions at various input powers (0.74 mbar, 50 sccm O_2/HMDSO (120:1) employing the 125 µm × 5 cm capillary positioned 8.75 mm away from the substrate.

Conclusion

A localized quartz-like track deposition was produced by a micro-jet plasma CVD with a moving capillary. A parameter study has shown that the film quality is improved with increasing the applied energy. A transparent track which is either compact or it consists of nanoparticles, can be produced with a high efficiency.

Aknowledgements

We wish to thank Dr. Pinnow for the SEM images and Dr. Regenstein for microscopy FTIR spectra.

References

[1] A. M. Wróbel, M. R. Wertheimer, J.Dib, and H. P. Schreiber, J. Macromol. Sci.-Chem. A 14 (1980)
[2] L. F. Thompson and G. Smolinsky, J. of Appl. Phys., 16 (1972)
[3] A. M. Mearns, Thin Solid Films, 3 (1969)
[4] L. Bardos and V. Dusek, Thin Solid Films, 158 (1988) 265
[5] A. Holländer, L. Abhinandan, Surf. Coat. Technol. 174-175 (2003) 1175-1177
[6] L. Abhinandan, A. Holländer, Thin Solid Films 457 (2004) 241-245
[7] K. Silmy, A. Holländer, A. Dillmann and J. Thömel, Surface & Coatings Technology, 194 (2005)

Spectroscopic measurement of plasmas generated in supercritical carbon dioxide environments

T. Tomai, M. Sawada and K. Terashima

Department of Advanced Materials Science, Graduate School of Frontier Sciences,

The University of Tokyo, Chiba, Japan

Abstract

We applied optical emission spectroscopy (OES) to plasmas generated in high-pressure CO_2 environments up to supercritical condition. Two types of plasmas, namely, dielectric barrier discharge (DBD) and DC discharge were employed. Up to supercritical conditions, the spectra of C_2 molecule and atomic O were remarkable in intensity by optical emission spectroscopy of both types of discharge. Rotational temperature of C_2 was estimated as approximately 4000 K in DBD at 2.0 MPa.

Keywords: supercritical fluid (SCF), dielectric barrier discharge (DBD), optical emission spectroscopy (OES) and rotational temperature.

1. Introduction

Supercritical fluid (SCF) has attracted much interest in scientific and engineering fields due to its unique characteristics such as its transport properties intermediate between gas and liquid [1] and its high solubility. From the microscopic viewpoint, SCF consists of clusters of various sizes [2]. It results in the above-mentioned characteristics.

Up to present, we have succeeded in generating DC discharge [3] and dielectric barrier discharge (DBD) [4] in supercritical carbon dioxide ($scCO_2$, the critical point: 7.38 MPa, 304.2 K, the critical density: 0.46 g/cm^3) environments and observed unique phenomena such as a drastic decrease in breakdown voltage near the critical point [3]. Additionally, we have applied discharge in $scCO_2$ to fabricate nanostructured materials at temperatures lower than those in conventional $scCO_2$ processings [4, 5]. These interesting phenomena and chemical reactions are supposed to be caused by radical and ion clusters in SCF plasmas. Understanding its microscopic feature might bring an important indication for controlling its unique chemical reactions. However, there have been few reports on the microscopic features of this novel plasma.

In this study, we diagnose SCF plasmas by optical emission spectroscopy (OES). OES provides microscopic feature of plasmas, such as existence of species excited by plasmas and temperature of such species. In our previous work, we had measured emission spectra of DBD at high-pressure CO_2 environment up to the supercritical condition [4]. In present work, to investigate dependence of microscopic features of high-pressure CO_2 plasmas on pressure and type of discharge, we compared DC discharge, which might raise gas temperature, and DBD, which might maintain low temperature. In addition, to diagnose temperature of excited species in high-pressure CO_2 plasma, we attempted to estimate rotational temperature of C_2 from the emission spectrum of C_2 (0,0) Swan band taken from DBD.

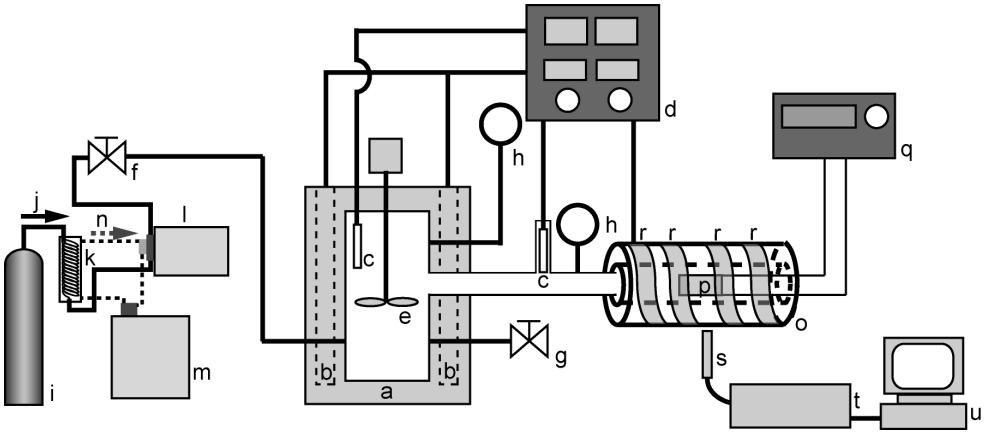

Figure 1. An apparatus for discharge generation in a high-pressure environment, (a) SCF cell, (b) cartridge heaters, (c) thermocouples, (d) temperature controller, (e) stirrer, (f) valve, (g) back pressure regulator, (h) pressure gauges, (i) CO_2 cylinder, (j) CO_2 flow, (k) condenser, (l) pump, (m) cooling unit, (n) cooling water flow, (o) sapphire tube, (p) electrodes, (q) power source, (r) band heater, (s) optical probe, (t) spectrometer, (u) PC.

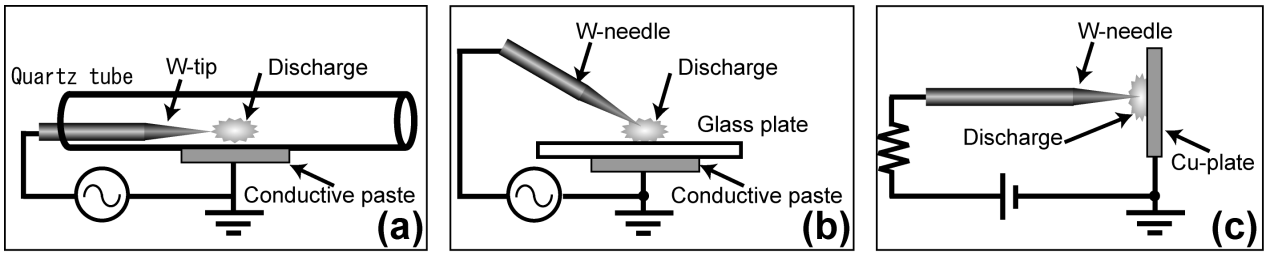

Figure 2. A schematic diagram of electrodes for (a), (b) dielectric barrier discharge and (c) DC discharge.

2. Experimental

Figure 1 shows a schematic diagram of the apparatus for generating discharge in a high-pressure environment. A stainless-steel cell, which has an internal volume of approximately 100 ml and can withstand conditions up to 10 MPa and 373 K, is employed as a reservoir. Electrodes are fixed in a sapphire tube connected with the reservoir. Liquefied CO_2 condensed in a condenser is pumped up to the reservoir and the sapphire tube. The reservoir and the sapphire tube are heated by cartridge heaters and band heater coiled around sapphire tube, respectively, to generate a high-pressure environment including supercritical conditions. Pressure and temperature in the reservoir and in the vicinity of sapphire tube are monitored using sensors and thermocouples, respectively, and controlled. The emission spectra of plasmas can be measured through the sapphire tube and optical fiber with a charged-coupled device (CCD) camera (Spec-10: 2KB/LN, Princeton Instruments Inc., NJ, USA) and a 500 mm spectrometer (SpectraPro-500i SP-556, Acton Research Corp., MA, USA). The spectra were recorded with a computer (PC).

A schematic diagram of the electrodes for identification of excited species in DBD is shown in Figure 2(a). The electrodes consist of a thin (outer diameter: 1 mm, and inner diameter: 700 μm) quartz tube as a dielectric barrier, conductive paste on the outside of the tube as the first electrode and a W-needle inserted into quartz tube as the second electrode. To generate DBD easier, the discharge gap, which is equal to the distance between the top of the W-needle and the tube, is reduced to approximately 100 μm. The details of

the electrodes are mentioned in Reference 4. The discharge is generated at the tip of the W-needle. In this study, applied ac voltage for generation of DBD was 0-15 kVp-p (frequency: 3 kHz, offset voltage: 0 V).

On the other hand, for measurement of rotational temperature of C_2, more accurate measurement is needed. Therefore, another type of electrodes for DBD is employed to remove optical obstruction such as quartz tube covering plasma. A schematic diagram of the electrodes is shown in Figure 2(b). The electrodes consist of a thin glass plate (thickness: approximately 150 μm) as dielectric barrier, conductive paste on one side of the glass plate as the first electrode and a W-needle, the tip of which is fixed ~100 μm away from the another side of the glass plate, as the second electrode.

A schematic diagram of the electrodes for DC discharge is shown in Figure 2(c). The electrodes consist of a W-needle and a Cu-plate. The distance between the W-needle and the Cu-plate is approximately 100 μm. Applied dc voltage for generation of discharge was 0-10 kV through a resistor (15 MΩ). The register is used to generate stable discharge.

3. Results and discussion

3.1 Identification of excited species in high-pressure CO_2 plasma

Before OES for CO_2 plasmas, we attempted to generate DBD and DC discharge in a high-pressure N_2 environment and measured the emission spectra of nitrogen to estimate the rotational temperature of N_2. The rotational temperature of N_2 can be measured from the intensity distributions in the rotational structure of the second positive system of nitrogen N_2 ($C^3\Pi_u$ (v' = 0) → $B^3\Pi_g$ (v'' = 2) transition) [6].

The rotational temperature of N_2 (nearly equal to gas temperature) in DBD is estimated as approximately 400 K under a various pressure (1-4 MPa) [4]. For example, in the case of our DC micro-discharge, in high-pressure N_2 environment (4.0 MPa), the rotational temperature of N_2 is estimated as approximately 800 K. Figure 3 is a schematic representation of gas temperature in various types of plasmas and environmental pressure. From Figure 3, it is found that our DBD, the distance of which is reduced to approximately 100 μm, can realize generation of low-temperature plasma in higher-pressure environment, compared to usual methods.

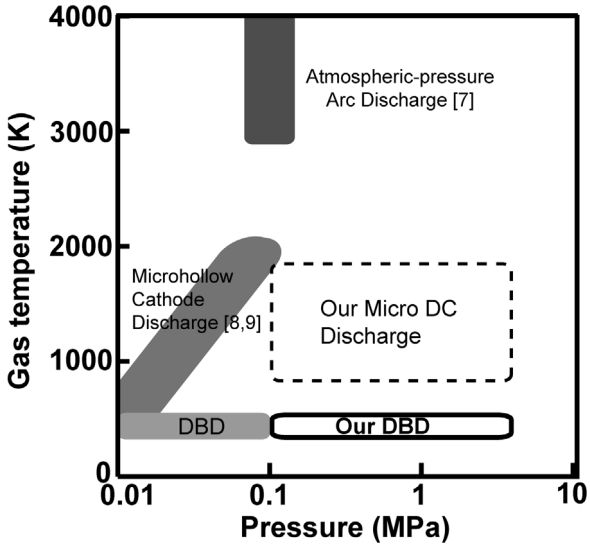

Figure 3. A schematic representation of gas temperature in plasmas and environmental pressure.

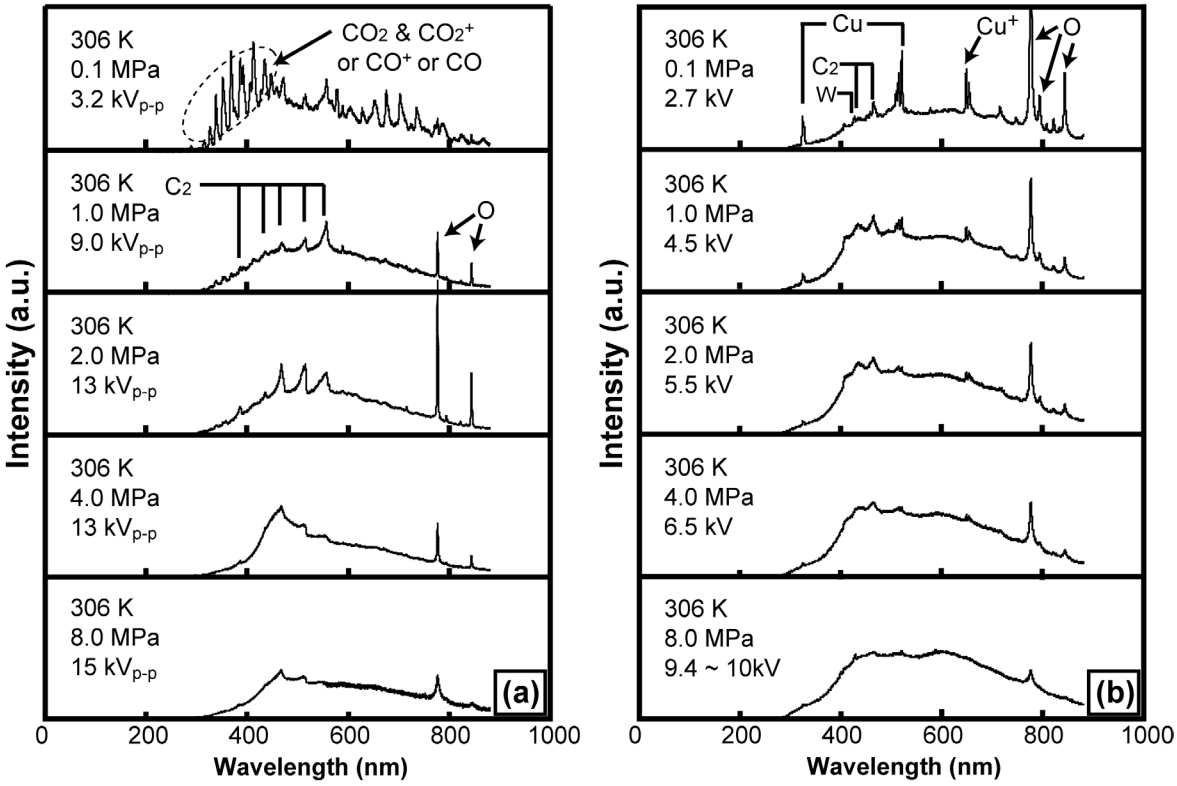

Figure 4. The emission spectra taken from (a) dielectric barrier discharge [4] and (b) DC discharge in high-pressure CO_2 environment up to the supercritical condition.

Figure 4 (a) and (b) show the typical emission spectra taken from DBD of previous work [4] and DC discharge in present work in high-pressure CO_2 environment up to supercritical condition, respectively.

At atmospheric pressure (0.1 MPa), the spectra taken from DBD and DC discharge are different obviously. In the case of DBD, the spectra of CO, CO^+, CO_2 and CO_2^+ are remarkable in intensity, in addition to the spectra of C_2 and O. On the other hand, as DC discharge, the spectra of C_2 and O are remarkable in intensity, in addition to the spectra of electrode materials, Cu and W. At higher than 1 MPa up to the supercritical condition, the spectra of C_2 molecule and atomic O become remarkable in intensity by OES of both types of discharge. In the case of DBD, the transition pressure from CO, CO+, CO_2 and CO_2+ to C_2 and O emissions probably exists in the range from 0.1 to 1 MPa. Generally, it shifts to a lower-pressure region with increasing gas temperatures. For example, it is approximately 500 Pa in the case of microwave induced plasma (MIP), whose gas temperature (600-1400 K) is higher than that of our DBD [10]. This transition pressure confirms that the gas temperature of our DBD is kept lower than 600 K in this DBD under a high-pressure CO_2 environment at least 1 MPa.

On the other hand, between the upper and lower sides of the critical point, any remarkable changes, which may result from the appearance of clusters in SCF, have hardly been observed. One of the conceivable reasons is as follows; With increasing pressure, collisional broadening of emission spectral lines becomes remarkable and the emission line tends to overlap neighbor lines. Therefore, the emission lines are difficult to identify, except for the emission line whose intensity is very strong, such as C_2 and O. Even if a tiny change between the upper and lower sides of the critical point exists, it may be hard to capture it.

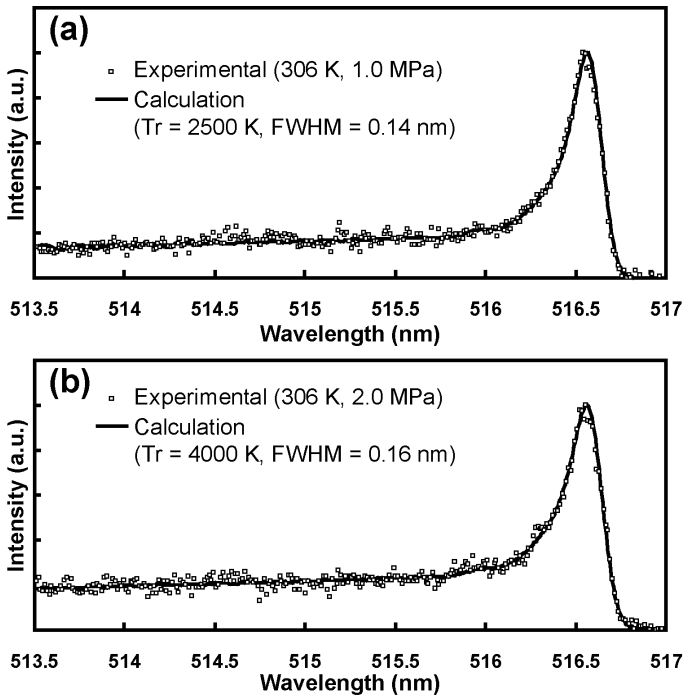

Figure 5. Observed and calculated spectra of C_2 (0,0) Swan band taken from dielectric barrier discharge in high-pressure CO_2 environments ((a) 1 MPa, (b) 2 MPa, environmental temperature: 306 K).

3.2 Measurement of rotational temperature of C_2

The determination of the temperature of excited species by OES gives valuable information on plasma processings. In this study, we attempted to estimate the rotational temperature of C_2 from the intensity distributions in the rotational structure of C_2 (0,0) Swan band, which was remarkable in intensity under the higher-pressure CO_2 environment than atmospheric pressure.

The C_2 (0,0) Swan band consists of P-, Q- and R-branches, and these bands belong to triplet transition. However, because the emission spectra taken by DBD under the higher-pressure CO_2 environment were noisy and broadened by collision with other particles, it was difficult to resolve these triplets sufficiently. Hence, to estimate the rotational temperature of C_2, we simulated these spectra with broadening by apparatus function and collisional broadening, and compared the calculated spectra with experimental spectra [11].

An observed spectra and calculated spectra of C_2 (0,0) Swan band taken from DBD at 1 and 2 MPa are shown in Figure 5. We revised FWHM (full width of half maximum) with increasing pressure, considering collisional broadening. In the case of DBD (applied voltage: 8 kVp-p) at 1 MPa, the rotational temperature of C_2 is estimated as 2500 ± 500 K (FWHM = 0.14 nm). In the case of DBD (applied voltage: 10 kVp-p) at 2 MPa, the rotational temperature of C_2 is estimated as 4000 ± 500 K (FWHM = 0.16 nm). At higher-pressure environment (more than 4MPa), the emission spectra of C_2 taken by DBD were noisier and spectra became broader, and it was hard to estimate the rotational temperature of C_2.

In general, DBD generates non-equilibrium plasma streamer: during the discharge hot electrons are created, while most of the gas stays at a temperature close to the environmental temperature. For example, Pellerin et al. reported that, in atmospheric pressure CH_4/CO_2-DBD plasma, the rotational temperature of C_2 was around 3000 K, which gave the temperature of the plasma streamer, while wall temperature was close to

the environmental temperature (≤ 350 K). In the case of our DBD, whereas the rotational temperature of C_2 was estimated as several thousands K under a high-pressure CO_2 environment (1, 2 MPa), melting of the electrodes employed for generation of DBD under a high-pressure CO_2 environment up to the supercritical condition, was not observed and the rotational temperature of N_2 was estimated as 400 K under high-pressure N_2 (1-4 MPa, 313K) environment up to supercritical condition (the critical point of N_2: 3.39 MPa, 126 K). Therefore, it is speculated that, in the case of our DBD, the temperature of plasma streamer is several thousands K, while most of the gas stays at several hundreds K under a high-pressure CO_2 environment up to the supercritical condition.

4. Conclusion

We applied optical emission spectroscopy to DBD and DC discharge generated in high-pressure CO_2 environment up to the supercritical condition. Under supercritical conditions, the spectra of C_2 molecule and atomic O are remarkable in intensity by optical emission spectroscopy of both types of discharge. We attempted to estimate the rotational temperature of C_2 from the emission spectra of C_2 (0,0) Swan band taken from DBD to diagnose temperature of excited species in high-pressure CO_2 plasma. The rotational temperature of C_2 was estimated as approximately 4000 K for DBD at 2.0 MPa. It is expected that the temperature of plasma streamer is several thousands K in the case of our DBD under a high-pressure CO_2 environment.

Acknowledgement

This work was supported financially in part by Specific Research of Priority Areas (Microplasma) (Grant No. 15075202) from The Ministry of Education, Culture, Sports, Science and Technology.

References

[1] C. A. Eckert, B. L. Knutson, and P. G. Debenedetti, Nature (London), **383**, 313 (1996).
[2] K. Nishikawa, I. Tanaka, and Y. Amemiya, J. Phys. Chem., **100**, 418 (1996).
[3] T. Ito and K. Terashima, Appl. Phys. Lett., **80**, 2854 (2002).
[4] T. Tomai, T. Ito and K. Terashima, Thin Solid Films, to be published.
[5] T. Ito, K. Katahira, Y. Shimizu, T. Sasaki, N. Koshizaki and K. Terashima, J. Mater. Chem., **14**, 1513 (2004).
[6] D. M. Phillips, J. Phys. D: Appl. Phys., **8**, 507 (1975).
[7] A. Schütze, J. Y. Jeong, S. E. Babayan, J. Park, G. S. Selwyn, R. F. Hicks, IEEE Trans. Plasma Sci., **26**, 1685 (1998).
[8] F. Leipold, R. H. Stark, A. El-Habachi and K. H. Schoenbach, J. Phys. D: Appl. Phys., **33**, 2268 (2000).
[9] C. Penache, M. Miclea, A. Braüning-Demian, O. Hohn, S. Schössler, T. Jahnke, K. Niemax and H. Schmidt-Böcking, Plasma Sources Sci. Technol., **11**, 476 (2002).
[10] E. A. H. Timmermans, J. Jonkers, A. Rodero, M. C. Quintero, A. Sola, A. Gamero, D.C. Schram and J. A. M. van der Mullen, Spectrochim. Acta Part B, 54, 1085 (1999).
[11] S. Pellerin, K. Musiol, O. Motret, B. Pokrzywka and J. Chapelle, J. Phys. D: Appl. Phys., **29**, 2850 (1996).
[12] O. Motret, S. Pellerin, M.Nikravech, V. Massereau and J. M. Pouvesle, Plasma Chem. Plasma Process., **17**, 393 (1997).

Topic 11：Plasma Chemical synthesis

Abstract ID: 380

The Conversion of Natural Gas to C_2 Hydrocarbons via Cold Plasma Technology*

Genhui Xu, Baowei Wang, Zhenhua Li , Yang Li, Changjun Liu

School of Chemical Engineering , Tianjin University,
Tianjin, 300072, P. R. China

Abstract

The focus of this research is to develop a process to convert methane to C_2 hydrocarbons (ethane、ethylene & acetylene) via cold (non-equilibrium)plasma technology at the room temperature and atmospheric。The experiments were carried out in the plug flow DBD reactor equipped the high voltage plasma generator, the feeding gas and reaction products were analyzed by GC on –line.

The experiment was found the power was enhanced the methane conversion was increased and the selectivity of C_2 hydrocarbons was decreasing. The experimental results show that the methane conversion was 47% and the selectivity of C_2 hydrocarbon was 40% under the proper condition using an atmospheric cold plasma technology for the natural gas convert to C_2 Hydrocarbons, it is possible.

Keywords: Natural gas, C_2 hydrocarbon, cold plasma

1. introduction

Natural gas reserves are found in abundant quantities in the world, natural gas is not only an increasing important role in energy and chemicals supplies but also the second major greenhouse gases. Natural gas, with methane as the primary constituent, has been paid more attention as a main source in chemical industry and energetic industry for several decades, with the lack of crude oil and the influence of greenhouse global warming effect . It is a deep significance of strategy that the development of natural gas utilization as the feedstock instead of crude oil for the production of chemical engineering. Industrial usage of natural gas is still limited to primarily a combustion fuel in China, the present industrial processes for the production of methanol and other hydrocarbons from methane are economically feasible in areas where large reserves of natural gas are available. The commonly considered and extensively researched direct conversion methods are:

Catalytic oxidative coupling	$2\ CH_4 + O_2 \rightarrow C_2H_4 + 2\ H_2O$
Partial catalytic oxidation	$CH_4 + 1/2\ O_2 \rightarrow CH_3OH$

The reactions above require the high temperatures with catalyst, because of the C-H bond in molecule of methane is very stable, however the high temperature required for methane activation drive the reaction to unavailing complete oxidation reaction at high methane conversion.

Selective activation from methane to C_2 hydrocarbons is very difficult due to the high dissociation energy of methane C-H bond, the reaction is an unfavorable reaction at the thermodynamics. The plasma

- **This work was supported by the Research Foundation of SINOPEC and**
- **The Research Foundation of Tianjin Science & Technology Committee support**

technology served as an unconventional catalysis has been used in natural gas conversion, because of the traditional catalytic research h of methane (the main component of natural gas) oxidative coupling must be required the high temperature, this stability of methane molecule causes difficulty in activating methane, so the high temperature with catalyst for methane activation drives the unavailing reaction to complete oxidation. The focus of this research is to develop a process to convert methane to C_2 hydrocarbons (ethylene and acetylene) with cold (non-equilibrium) plasma technology at the room temperature and atmospheric。

The preliminary studies have great contributions: Steven L.S. et al. studied the methane conversion to higher hydrocarbon using microwave plasma under the low pressure. [1] Oumghar A. et al. studied methane conversion by air microwave plasma. [2] Zhu A.M. et al. and Marafee A.,et al. studied with pulse corona plasma and DC corona discharge respectively for methane conversion. [3、4] Kozlov K.V. et al. and Yao S. L. et al. investigated the methane conversion using dielectric-barrier discharges (DBD) and high-frequency pulsed plasma respectively. [5、6] . In the present study is to develop a process of methane conversion to C_2 hydrocarbons (ethane、ethylene and acetylene.) via non-equilibrium plasma technology with DBD reactor under the without oxygen condition at room temperature and atmospheric, the reaction of methane coupling dehydrogenation as follows:

$$2CH_4 \rightarrow C_2H_6 + H_2$$

$$2CH_4 \rightarrow C_2H_4 + 2H_2$$

$$2CH_4 \rightarrow C_2H_2 + 3H_2$$

Above reactions are an electron & radical chain – reaction in the electric field enhanced plasma catalysis condition. This route of natural gas conversion to C_2 hydrocarbons via cold plasma technology could be offer an effective、simple and clean green chemical technology.

The experimental results show that the methane conversion was 47% and the selectivity of C_2 hydrocarbon was 40% under the proper condition using an atmospheric cold plasma technology for the Natural Gas convert to C_2 Hydrocarbons. This process is possible.

2. Experiment

The experiments were carried out in the dielectric-barrier discharges （DBD） plug flow reactor equipped the high voltage alternating current (AC) electric discharge plasma generator, the reactants were subjected to varying conditions of voltage (input power) and flow rates (reaction times), the range for the voltage under which the experiments were carried out was 20 – 200V. (power source), the voltage was controlled by a voltage regulator, the range of feed methane flow rate was 10 – 200 ml/min., the flow rate was controlled by an electronic mass flow controller. The gaseous product stream was analyzed using the HP 5890 GC, the GC was programmed to

take the gas samples automatically in-situ.

The experimental apparatus used for the steady state runs is shown in Figure 1.

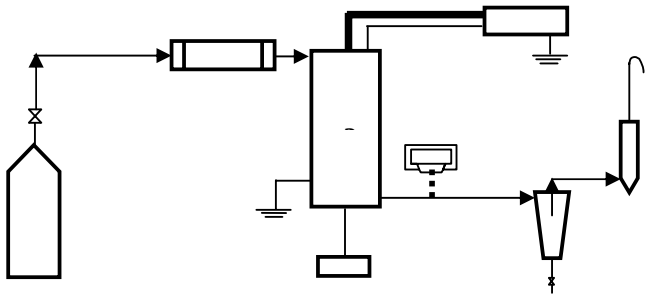

Fig. 1 Experimental Schematic Diagram

1.CH_4 Tank ; 2. Mass flow controller (MFC); 3. DBD Plasma Reactor ; 4. HV Plasma Generator ; 5. GC Analyzer 6. Thermocouple meter ; 7. Condenser ; 8. Flow meter;

The raw material methane from CH_4 tank 1. via MSC 2. was flowed to plasma reactor 3. which is consisted of a 10 mm ID quartz tube of 250 mm length, the gas methane molecule was excited to conversion C_2 hydrocarbon in the zone of plasma reaction, the outlet from the reactor through the condenser 7.

3. Results and Discussions

The experimental results were found that the parameters of electric field and the reaction conditions were effect on the conversion of methane and selectivity of C_2 hydrocarbons under the DBD plasma condition.

3.1 Effect of input power on the reaction results

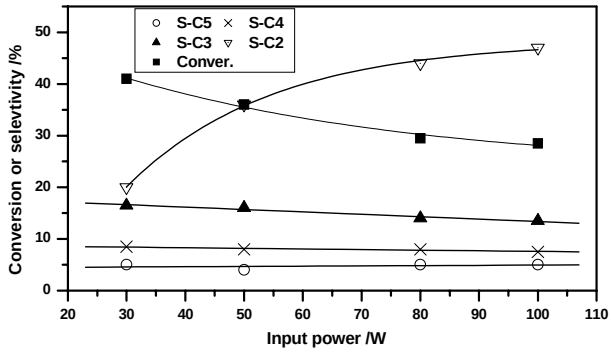

Figure 2. Effect of input power on the conversion of methane & Selectivity of Light hydrocarbons

Reaction temperature of 323K; Flow rate of 20ml/min

The experiment was found the characteristic of micro-discharge in DBD plasma condition for methane conversion, according to the Lissajous Voltage – Charge figure recorded by experimental data was obtained: the micro-discharge life of 20ns, current-diameter of 0.03mm, peak current of 0.4A., current density of 40000 A/cm^2, charge amount of 0.6 nC. , therefore the studies on above plasma parameters were helpful to understand the process of DBD plasma for methane conversion. The effect of input power on the conversion of methane and the selectivity of reaction were shown in Fig.2 and Fig.3.

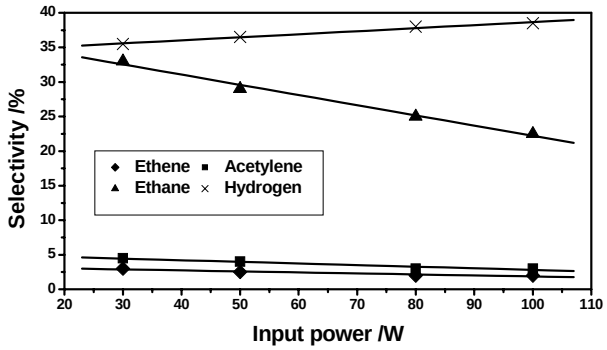

Figure 3. Effect of input power on the selectivity of C_2 hydrocarbons & H_2

Reaction temperature of 323K; Flow rate of 20ml/min

When the voltage was enhanced the methane conversion was increased and the selectivity of C_2 hydrocarbons was decreasing. The suitable voltage was provided 40-80 V. (input AC power 50W – 100W),. The experimental results show that the methane conversion was most to 47% and the selectivity of C_2 hydrocarbon was most to 40%

3.2 Effect of residence time on the reaction results

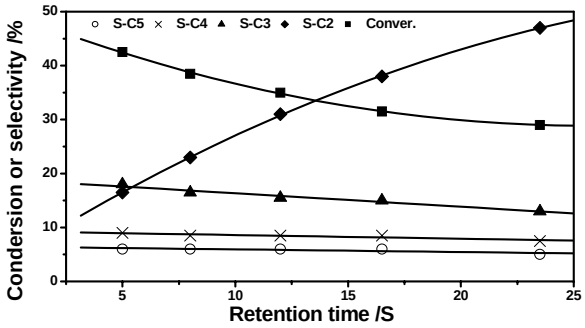

Figure 4 Effect of residence time on the conversion of methane & Selectivity of Light hydrocarbon

Reaction temperature of 323K; Input power of 100W

The experiment was varied in feed flow rate of methane, the methane conversion was decreased and the selectivity of C_2 hydrocarbons was increased with increasing of the inlet flow rate of methane in the above power condition. The proper extent of flow rate was 20-40 ml /min (corresponding residence time was 10 – 20 s) ,the experimental results were shown in Fig. 4 and Fig. 5.

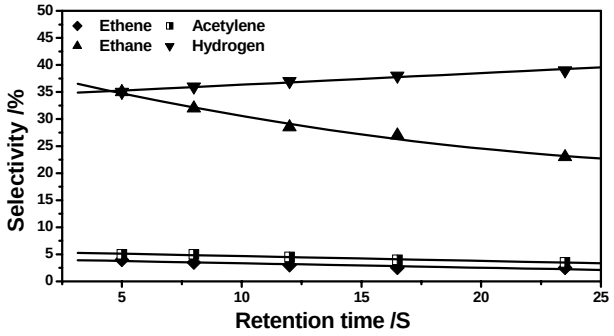

Figure 5. Effect of residence time on the selectivity of C_2 hydrocarbon & H_2

Reaction temperature of 323K; Input power of 100W

3.3 Effect of reaction temperature on the reaction results

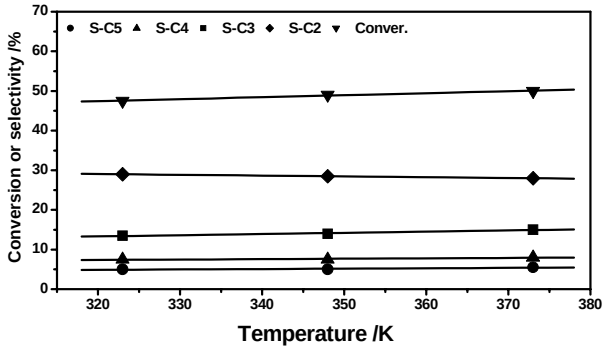

Figure 6 Effect of reaction temperature on the conversion of methane & Selectivity of Light hydrocarbon

The reaction temperature from the room temperature to 373K, but the experimental results were found the Effect of reaction temperature on the reaction results was not obviously at the condition of experimental range, in other words, the influence of temperature can be neglected for DBD plasma reaction. the experimental data were drawn in Fig. 6 and Fig. 7

Flow rate of 20 ml/min; Input power of 100W

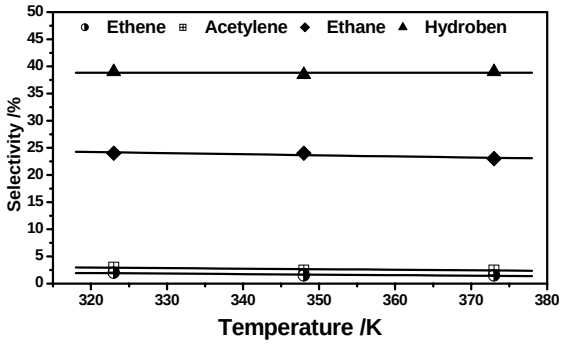

Figure 7. Effect of reaction temperature on the selectivity of C_2 hydrocarbon & H_2

Flow rate of 20 ml/min; Input power of 100W

The temperature action of DBD plasma reaction differs greatly from the traditional catalytic reaction, the

latter, on the contrary, the influence of temperature was very important.

3.4 Discussion

3.4.1．The breakdown voltage of methane under the AC cold plasma condition

As is known to all, the gas breakdown voltage $V_{B,min}$ is the minimal required voltage when the gas is beginning discharge, under the atmospheric and AC cold plasma condition the experiment was found that the breakdown voltage of methane $V_{B,min}$ was decided by the type of electrode and the discharge gap width, obviiiously, it can be used the Paschen law equation from the DC gas discharge deduced, the CH_4 breakdown voltage $V_{B,min}$ was alike at DC and AC plasma discharge condition.

Where: $V_{B,min} = BPd/\ lnAPd/\ ln[1+1/\gamma]$

P is the pressure of gas discharge

d is the distance between electrodes (the discharge gap width)

γ is Townsend's second ionization coefficient

A、B are the constants depending on the type of gas

Therefore, the breakdown voltage of methane under the experimental AC cold plasma condition, the $V_{B,min}$ equation was established:

$$V_{B,\min} = 26.186 \ln\left[1+\frac{1}{\gamma}\right]$$

γ is Townsend's second ionization coefficient, which is experimental volume also concerned with the type of gas. The $V_{B,min}$ volume is very important parameter in the conversion of natural gas to C_2 hydrocarbons with cold plasma reaction.

3 .4.2. The reaction route

The reaction of methane conversion to C_2 hydrocarbons (ethane、ethylene and acetylene.)

is very difficult at the normal condition due to the high dissociation energy of methane C-H bond, the reaction is an unfavorable reaction at the thermodynamics. Using non-equilibrium plasma technology under the without oxygen condition, the reaction route is the dehydrogenation & coupling reaction of methane, first the electron is accelerated by an electric field enhanced to turn into then high-energy electron e^*. The high-energy electron e^* with gaseous methane molecules react by means of the inelastic collisions and they are excited (or dissociation) to activity methyl、methylene、methine (CH_3^*、CH_2^*、CH^*)etc. radicals in silent discharge reaction area

$$CH_4 + e^* \rightarrow CH_3^* + H^* + e$$

$$CH_3^* + e^* \rightarrow CH_2^* + H^* + e$$

$$CH_2^* + e^* \rightarrow CH^* + H^* + e$$

The several activity radicals are associated each other to attract coupling to C_2 hydrocarbon as follow :

$$2\ CH_3^* \rightarrow C_2H_6$$

$$2\ CH_2^* \rightarrow C_2H_4$$

$$2\ CH^* \rightarrow C_2H_2$$

$$2\ H^* \rightarrow H_2$$

Above reactions are an electron & radical chain – reaction in the electric field enhanced plasma catalysis condition. This route of natural gas conversion to C_2 hydrocarbons was supposed

4. Conclusion

1. The experiment of the DBD plasma reaction for methane conversion was found that the input power and the residence time of reaction were key factor of influence reaction result, the suitable AC input power was 50 -80 W and the proper residence time of reaction was 10 -20 sec.

2. The experiment was considered the Effect of reaction temperature on the reaction results was not obviously under the DBD plasma reaction condition.

3. The experimental results show that the methane conversion was 47% and the selectivity of C_2 hydrocarbon was 40.0% under the proper condition using an atmospheric DBD cold plasma technology, this process of the natural gas convert to C_2 hydrocarbons was possible.

References

[1]. Steven L.S., Zerger R. P. "A direct, Continuous, Low-power catalytic conversion of methane to higher hydrocarbons *via* microwave plasma", J. Catal., 139(2), 383 – 391 (1993).

[2].Oumghar A., Legrand J.C., Diamy A.M.,Turillon N., "Methane conversion by an air microwave plasma", Plasma Chem. Plasma Process., 15(1), 87 – 91 (1995).

[3]. Zhu A. M., Gong W. M., Zhang X. L., Zhang B. A., "Coupling of methane under pulse corona plasma I: No oxygen", Science in China (B), 30(2), 169 - 173 (2000).

[4] Marafee A. , Changjun Liu, Genhui XU, Mallinson R., and Lobban L., "An experimental study on oxidative coupling of methane in a direct current corona discharge reactor over Sr/ La_2O_3 catalyst", Ind. Eng. Chem. Res., 36(3), 632 – 637 (1997).

[5]. Kozlov K.V., Michel P., Wagner H. E., "Synthesis of organic compounds from mixtures of ethane with carbon dioxide in dielectric – barrier discharges at atmospheric pressure", Plasmas and polymers, 5(3/4), 129 -150 (2000).

[6] Yao S.L., Nakayama A., Suzuki E., "Methane conversion using a high –frequency pulsed plasma: important factors", AIChE J., 47(2), 413 – 418 (2001).

Numerical Simulation of Radiation Power Density with Temperature Distribution emitted from Plasma Arc

S. Tashiro[1], T. Iwao[2], M. Yumoto[2], T. Inaba[1]

[1]*Department of Electrical, Electronic and Communication Engineering, Chuo University, Tokyo, Japan*
[2]*Department of Electrical and Electronic Engineering, Musashi Institute of Technology, Tokyo, Japan*

Abstract
The enormous radiation energy emitted from plasma arc is utilized as a heating device without combustion for the treatment of waste. In order to realize high radiation efficiency, precise controls of the radiation power and the spectrum of the radiation are required. In this paper, the MHD simulation of the dependence of plasma arc temperature and it's radiation power density on input current to the device is carried out in order to know the basic relationship of plasma torch between temperature distribution and radiation power. As a result, the temperature and the radiation power of plasma arc become higher near the cathode. The radiation power of this calculation agrees with it of experiment at the arc column.

Keyword : Numerical simulation, Radiation power, Plasma arc, Temperature

1. Introduction

The enormous radiation energy emitted from plasma arc is utilized as heating device without combustion for the treatment of waste. In order to realize high radiation efficiency, precise controls of the power and the spectrum of the radiation are required. In this paper, the MHD simulation of the dependence of plasma arc temperature and it's radiation power density on input current to the device are carried out in order to know the basic relationship of plasma torch between temperature distribution and radiation power.

2. Simulation model

In this simulation, 2-dimensional calculation domain in cylindrical co-ordinates is defined as shown in Fig. 1. The temperature of plasma arc and it's radiation power are evaluated using MHD equations and radiation equations. The flow is assumed to be laminar, steady and incompressible.

(a) mass continuity

$$\nabla \cdot (\rho \vec{u}) = 0$$

(b) momentum equation

$$\nabla \cdot (\rho \vec{u}\vec{u}) = -\nabla p + \vec{j} \times \vec{B} + \nabla \cdot \tau, \quad \tau_{\alpha\beta} = \eta \left(\frac{\partial u_\alpha}{\partial x_\phi} + \frac{\partial u_\beta}{\partial x_\alpha} \right)$$

(c) electron energy equation

$$\vec{u} \cdot \nabla \left\{ n_e \left(\frac{5}{2} k T_e + \varepsilon_i \right) \right\} = \nabla \cdot \left(k_e \nabla T_e \right) - \left\{ \varepsilon_i + \left(\frac{5}{2} + \frac{e}{k} \frac{\phi}{\sigma} \right) k T_e \right\} \dot{n}_e + \left(\frac{5}{2} + \frac{e}{k} \frac{\phi}{\sigma} \right) \frac{k}{e} \vec{j} \cdot \nabla T_e + \vec{j}\vec{E} - \frac{3 m_e}{m_i} n_e (\overline{\upsilon}_{ei} + \overline{\upsilon}_{en}) k (T_e - T) - \dot{R}$$

(d) heavy-species equation

$$\vec{u} \cdot \nabla \{ (n_e + n) k T \} = \nabla \cdot \left(k_a \nabla T \right) + \frac{3 m_e}{m_i} n_e (\overline{\upsilon}_{ei} + \overline{\upsilon}_{en}) k (T_e - T)$$

(e) diffusion equation

$$\vec{u} \cdot \nabla n_e + \nabla \cdot \left\{ \frac{e n_e D_{in}}{k T} \left(\vec{E} - \frac{1}{e n_e} \nabla p_i \right) \right\} = \dot{n}_e$$

(f) charge continuity

$$\nabla \cdot j = 0$$

(g) generalized ohm's law

$$\vec{j} = \sigma\left(\vec{E} - \frac{1}{en_e}\nabla p_e \right) + \phi \nabla T_e$$

(h) electric field strength

$$\vec{E} = -\nabla \phi$$

(i Maxwell equation

$$\nabla \times \vec{B} = \mu_0 \vec{j}$$

(j) Dalton's law

$$p = (n_e + n_i + n_n)kT$$

(k) quasi-neutrality condition

$$n_e = n_i$$

In addition, the anode sheath property is calculated using the method adopted in Ref[1]. The maximum temperature of the plasma arc is approximately 15000K. Therefore the plasma is assumed to be optically thin [2]. The simulation region is the plasma torch which has the cathode diameter 6.4mm, the inner diameter of nozzle 8.6mm and the electrode gap 20mm as shown in Fig. 1. The region is filled with 0.1MPa Ar gas. Input mass flow of 12NL/min. is introduced through a cylindrical area of radius 3.2-4.3mm in the face B-C. The gas flows out through the face D-F. Input current density distribution is defined on the boundary E-H. The current and potential distributions are calculated only in the region E-F-G-H. The temperatures of the anode and the cathode are set to be 1000K and 3000K, respectively. The boundary conditions of tye whole region are listed in Table 1.

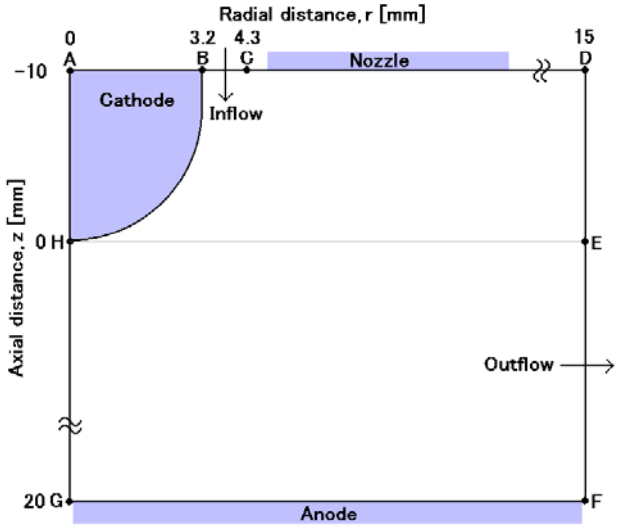

Fig. 1. Simulation region.

Table 1. Boundary conditions.

	T	φ	flow
A-B (Cathode)	3000K	-	u=v=0
B-C (Inflow)	1000K	-	v=0
C-D (Nozzle)	1000K	-	u=v=0
D-F (Outflow)	dT/dr=0	φ=0	u=0
F-G (Anode)	1000K	φ=0	u=v=0
G-A (Axis)	dT/dr=0	dφ/dr=0	v=0

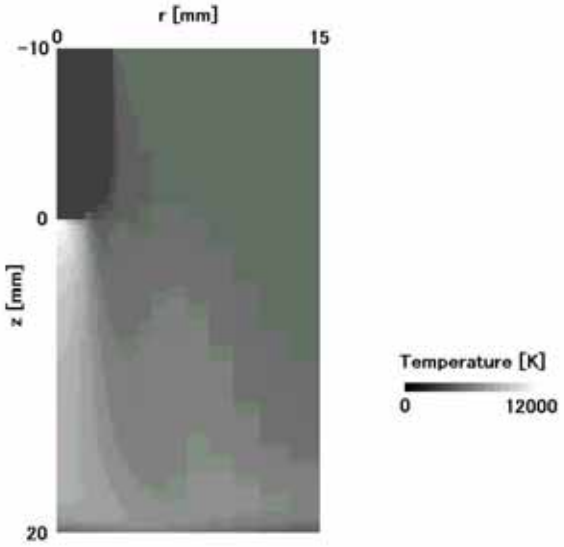

Fig. 2. 2-dimensional temperature distribution (I=100A).

3. Simulation results and discussion

The plasma arc temperature and radiation power density distributions of plasma arc are calculated in the case of 80, 100, 120A. Figure 2 shows 2-dimensional temperature distribution in the case of 100A. It is found that high temperature and small arc radius near the cathode are produced as a result of the arc column squeezed due to the inflow. Figure 3 shows temperature and radiation power density distributions along the axis(A-G). The experimental values by about 1,000 - 2,000K are cited from Ref. [4]. It is clear that calculated temperatures between z = 3mm - 20mm nearly agree with the experimental values. On the other hand, the experimental values near the cathode (z = 0 - 3mm) become higher than calculated values. One of the reasons for the difference is the strong dependence of the temperature near the cathode on the input current density distribution defined as the boundary condition. For more accurate calculation, it is necessary to define this boundary condition inside the cathode (A-B) to calculate current density distribution near the cathode. The temperature decreases gradually from the cathode to the anode. On the contrary, the radiation power density near the cathode decreases steeply apart from the cathode, because the radiation power density is reduced steeply when the temperature is lower than 10,000K [5] as seen near z=3 - 5mm. The radiation power of this calculation agrees with it of experiment at the arc column.

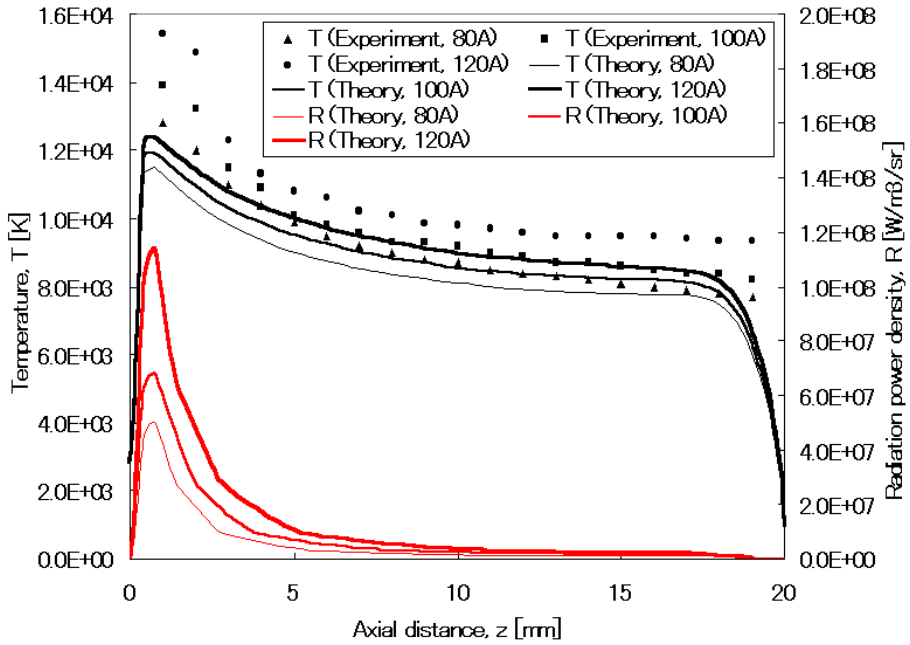

Fig. 3. Temperature and radiation power density distribution along the axis.

4. Summary

(1) The temperature and the radiation power of plasma arc become higher near the cathode.

(2) The radiation power density of this calculation agrees with it of experiment at the arc column.

(3) The axis temperature in calculation agrees with the experiments.

Acknowledgement

The authors wish to thank Prof. J. Heberlein of University of Minnesota and IEEJ International Conference Travel Grant.

References

[1] J. Jenista, J. V. R. Heberlein, E. Pfender: IEEE Trans. Plasma Sci. PS-25 (1997) 883.

[2] K. Ikeda, T. Amakawa, M. Shibuya: T. IEE Japan 120 (2000) 414 [in Japanese]..

[3] K. Konishi, T. Iwao, M. Yumoto, T. Inaba: The papers of Technical Meeting on Electrical Discharge, IEE Japan. ED-04-169 (2004)

[4] S. Honda, Y. Inoue, T. Iwao, M. Yumoto, T. Inaba: Proceedings of 2004 Annual Conference of Fundamentals and Materials Society, IEE Japan. VIII-3 (2004) pp.297-298 [in Japanese]

Radiation Component in Wavelength emitted from High Temperature Argon

S. Honda[1], T. Iwao[2], M. Yumoto[2], T. Inaba[1]

[1]*Department of Electrical, Electronic and Communication Engineering, Chuo University, Tokyo, Japan*
[2]*Department of Electrical and Electronic Engineering, Musashi Institute of Technology, Tokyo, Japan*

Abstract

When a reduction of the waste and dissolution of the iron are carried out by using a high temperature medium, the radiant power emitted from the medium should be suppressed. On the contrary, it is useful for lighting and treatment of hazardous wastes because it has a highly intense radiant energy. In this paper, we tried to calculate the radiant power density under consideration of atmospheric high temperature pure argon(Ar) which is frequently used for a plasma arc to know the basic theory of radiant power density for the development of the plasma treatment by using radiant power. The radiant power density of Ar I - Ar III is calculated with each rays and wavelength at 1,000 - 30,000 K and 200 nm - 1,000 nm in wavelength. The total radiation power density increases with increasing the temperature up to 15,000K and almost levels off over 15,000K. The continuum spectrum of Ar I increase up to 14,000 K with increasing the temperature. However, it decreases after 14,000K. The continuum spectrum of Ar II is ten times as high as the line spectrum of Ar I. The line and continuum spectrum of Ar III increases with increasing the temperature, and the latter levels off at 26,000K. The recombination radiation of Ar II-u_{fb} and Ar III-u_{fb} is higher than the bremsstrahlung Ar II-u_{ff} and Ar III-u_{ff}, respectively. The bremsstrahlung emitted from Ar I-u_{ff} is dominant in the continuum spectrum of Ar I. The u-Ar II is higher than u-Ar I and u-Ar III in UV rays. However, the u-Ar I reverses u-Ar II in IR rays. The Ar II-u_{fb} is higher than other continuum spectrum under 25,000K. Therefore, the recombination radiation is dominant with wavelength. The UV rays is to be 50% and the UV and VR:visible rays are dominant at 15,000K. Most UV and VR rays are emitted from Ar II-u_{fb}. Therefore, the radiation emitted from the UV rays of argon is dominant due to recombination radiation. The radiation emitted from argon could apply to waste treatment because of highly intense UV rays.

Keyword : Plasma Arc, Radiation Power, Radiation component, UV rays

1. Introduction

The plasma arc has a lot of excellent characteristics such as the high temperature, highly intense radiation[1-3] and high energy. When a reduction of the waste and dissolution of the iron are carried out by using a high temperature medium, the radiant power emitted from the medium should be suppressed. On the contrary, it is useful for lighting and treatment of hazardous wastes because it has a highly intense radiant energy. In this paper, we tried to calculate the number density and then the radiant power density under consideration of atmospheric high temperature pure argon(Ar) which is frequently used for a plasma arc to know the basic theory of radiant power density for the development of the plasma treatment by using radiant power.

2. Number Density and Radiation Power Density

Figure 1 shows the radiation power density with the temperature. The total radiation power density increases with increasing the temperature up to 15,000K and almost levels off over 15,000K. The continuum spectrum of Ar I increases up to 14,000 K with increasing the temperature. However, it decreases over 14,000K. The line one of Ar II does do. The continuum spectrum of Ar II is ten times as high as the line spectrum of Ar I over 12,000K. The line spectrum of Ar II goes to its maximum at 26,000K. The line and continuum spectrum of Ar III increases with increasing the temperature, and the value of the latter levels off at 26,000K. Figure 2 shows the component of continuum radiation power density. The recombination radiation of Ar II-u_{fb} and Ar III-u_{fb} is higher than the bremsstrahlung Ar II-u_{ff} and Ar III-u_{ff}, respectively. The bremsstrahlung emitted from Ar I-u_{ff} is dominant in the continuum spectrum of Ar I.

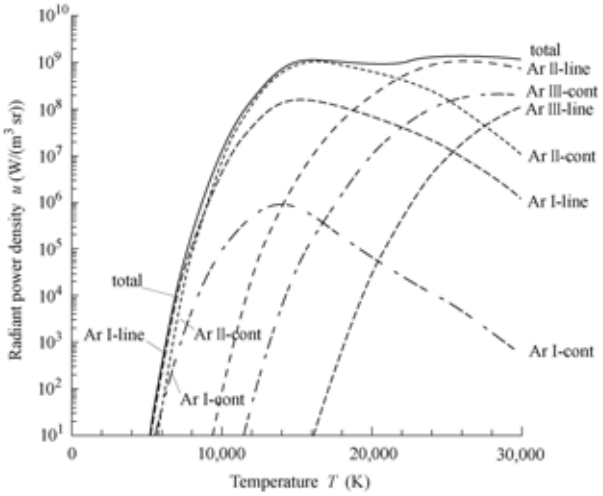

Fig. 1 Radiation power density with the temperature.

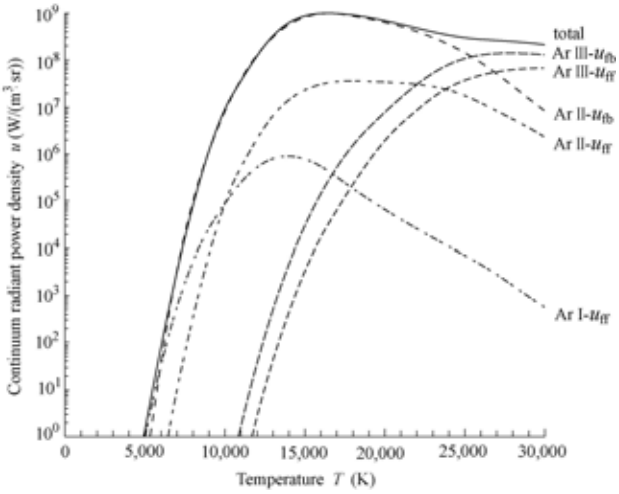

Fig. 2 Component of continuum radiation power density

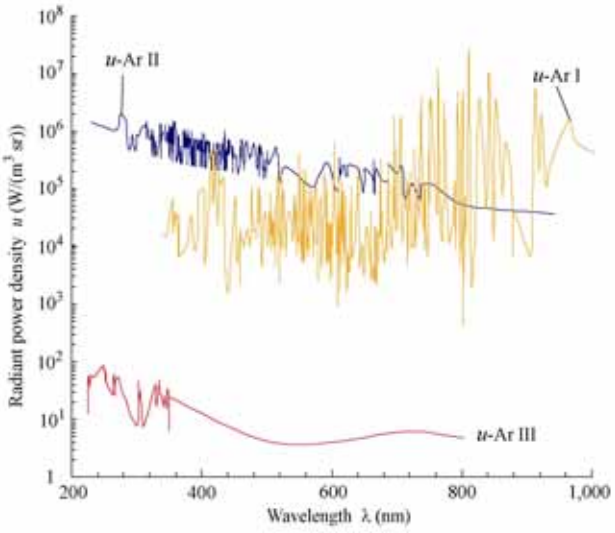

Fig. 3 Radiation power density emitted from Ar at each state as function of wavelength. (15,000K)

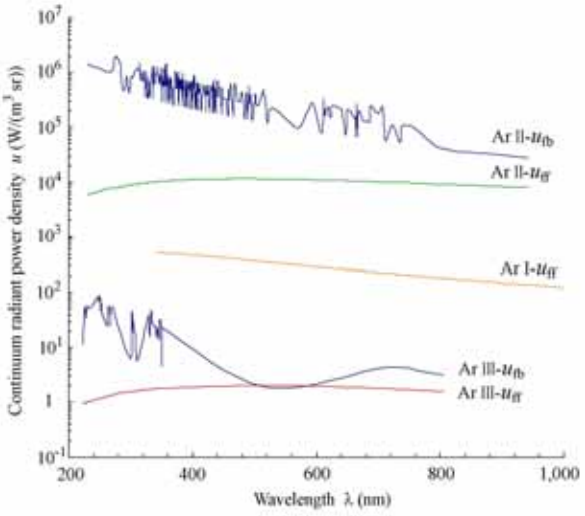

Fig. 4 Component of continuum radiation power density with wavelength. (15,000K)

3. Total Radiation Power in Wavelength

Figure 3 shows the radiation power density emitted from Ar at each state as a function of wavelength at 15,000K and 0.1MPa. The radiation power has a peak value at 15,000K. The UV rays under 380nm emitted from *u*-Ar II is about 10^6 W/(m^{3}sr) and higher than *u*-Ar I and *u*-Ar III. The VR rays between 380-780nm emitted from *u*-Ar I and *u*-Ar II is almost same value. The IR rays between over 780nm emitted from *u*-Ar III is almost constant to be 10 W/(m^{3}sr) and lower than it from *u*-Ar I and *u*-Ar II by 10^4 times. The UV rays emitted from *u*-Ar II is higher than *u*-Ar I and *u*-Ar III. However, the *u*-Ar I reverses *u*-Ar II in IR rays. Figure 4 shows the component of continuum radiation power density with wavelength at 15,000K. The Ar II-u_{fb} is higher than other continuum spectrum. Especially there are few Ar III-u_{fb} and Ar III-u_{ff}. Therefore, the recombination radiation is dominant with wavelength.

4. Component ratio of Radiant Power in Wavelength Region

Figure 5 shows the ratio of ultraviolet, visible and infrared rays emitted from Ar at 15,000K in order to know the component ratio of radiation power density in wavelength region. The UV rays is to be 50% and the UV and VR:visible rays are dominant. Most UV and VR rays are due to recombination radiation emitted

from Ar II-u_{fb}. The ratio of radiation power density becomes 48.6 % in UV(200-380nm), 38.6% in VR(380-780nm) and 12.8% in IR(780-1,000nm). The radiation power density emitted from u_{line}-*Ar I* is dominant in the IR region as shown in Fig.3, while the ratio of radiation power emitted from u_{fb} is dominant as shown in Fig.5.

Figure 6 shows the spectrum component of radiation power density from Ar at 15,000K. The UV component emitted from Ar II-u_{line} , Ar I-u_{ff}, Ar II-u_{ff} is dominant such as more than 60%.

Figure 7 shows the ratio of line and continuum to the total radiation power density about Ar I, Ar II, and Ar III. The IR rays are dominant due to the line radiation from Ar I. Although there is a little Ar II-u_{ff}, it is not effective and the ratio of other radiation component is to be less than 1%.

The UV radiation emitted from argon is dominant due to recombination radiation. The radiation emitted from argon could apply to waste treatment because of highly intense UV rays.

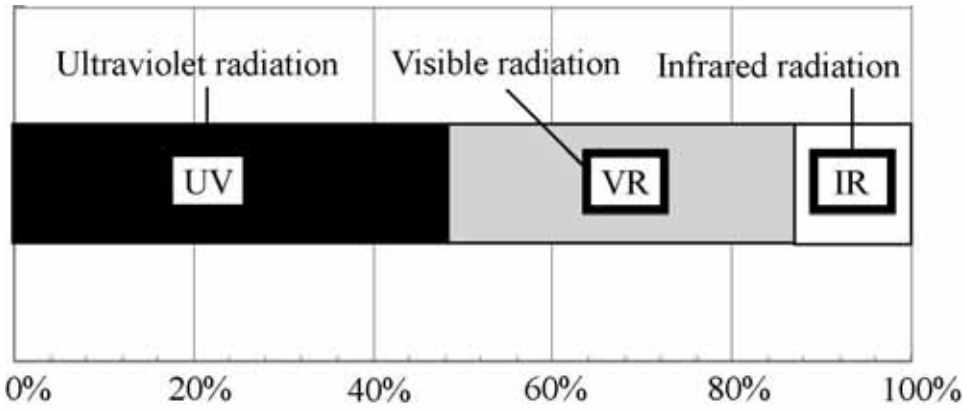

Fig. 5 Ratio of ultraviolet, visible and infrared rays emitted from Ar. (15,000K)

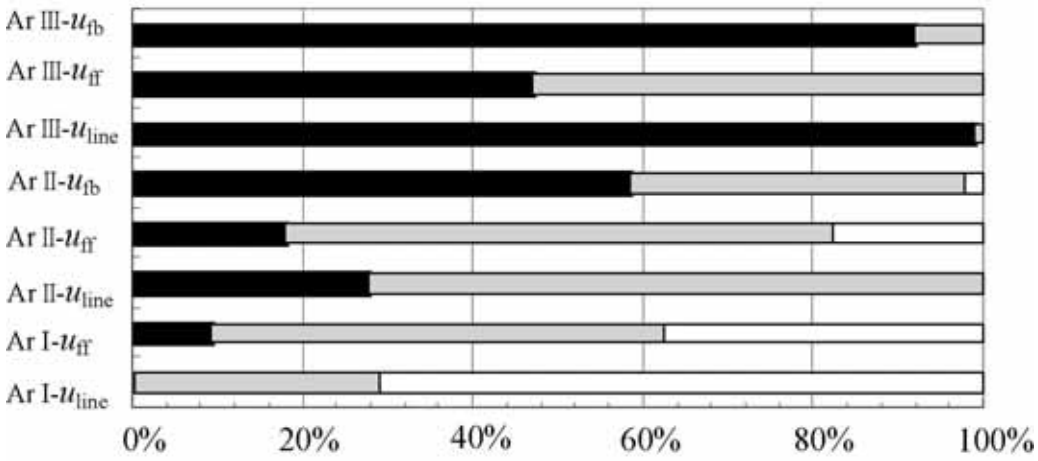

Fig. 6 Spectrum component of radiation power density emitted from Ar. (15,000K.)

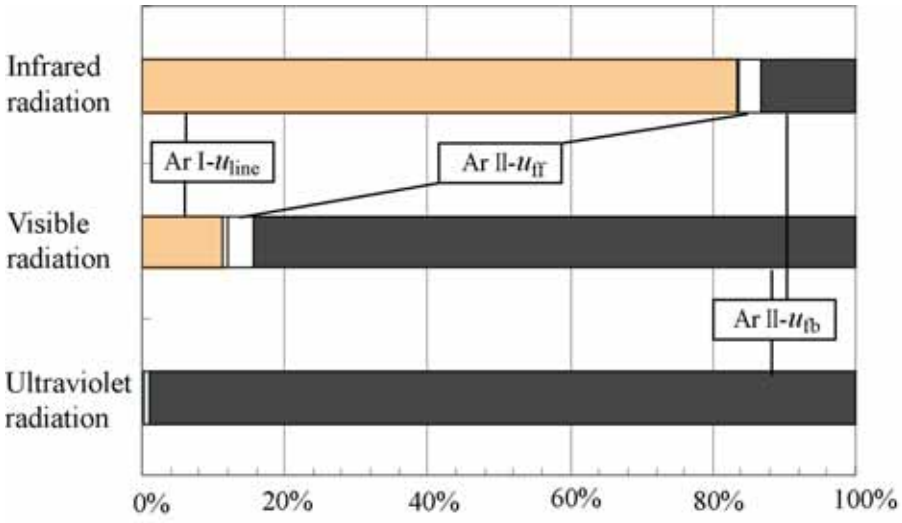

Fig. 7 Ratio of line and continuum to total radiant power density about Ar I, II and III.

5. Summary

The number density and radiant power density under consideration of atmospheric high temperature pure Ar which is frequently used was calculated for a plasma arc to know the basic theory of radiant power density for the development of the plasma treatment by using radiant power. The main results are shown below.

(1) The total radiation power density increases with increasing the temperature up to 15,000K and almost levels off. The continuum spectrum of Ar I increases up to 14,000 K with increasing the temperature. However, it decreases over 14,000K.
(2) The continuum spectrum of Ar II is ten times as high as the line spectrum of Ar I. The line and continuum spectrum of Ar III increases with increasing the temperature, and the latter value levels off at 26,000K.
(3) The recombination radiation of Ar II-u_{fb} and Ar III-u_{fb} is higher than the bremsstrahlung Ar II-u_{ff} and Ar III-u_{ff}, respectively. The bremsstrahlung emitted from Ar I-u_{ff} is dominant in the continuum spectrum of Ar I. The *u*-Ar II is higher than *u*-Ar I and *u*-Ar III in UV rays. However, the *u*-Ar I reverses *u*-Ar II in IR rays.
(4) The Ar II-u_{fb} is higher than other continuum spectrum under 25,000K. Therefore, the recombination radiation is dominant with wavelength. The UV rays is to be 50% and the UV and VR:visible rays are dominant. Most UV and VR rays are emitted from Ar II-u_{fb}.
(5) The UV radiation emitted from argon is dominant due to recombination radiation. The radiation emitted from argon could apply to waste treatment because of highly intense UV rays.

Acknowledgement

This research was supported by the High-Tec Project on High Temperature Plasma by The Institute of Science & Engineering of Chuo University, the Japanese Ministry of Education, the Japan Society for Promotion of Science and IEEJ International Conference travel grant.

References

[1] H.P. Schmidt, G. Speckhofer, IEEE Transactions on plasma science, Vol.24, No.4, pp.1239-1248(1996)
[2] E.J.Robinson and S.Geltman, Phys. Rev. ,153, pp.4-8(1967)
[3] G.J.Bastiaans, R.A.Mangold, Spectrochim Acta Vol.40B, No.7, pp.885-892 (1985)

Temperature Distribution of Twin Torch Plasma Arc near 100A

T. Iwao[1], M. Kikuchi[2], T. Inaba[2], M. Yumoto[1]

[1]*Department of Electrical and Electronic Engineering, Musashi Institute of Technology, Tokyo, Japan*
[2]*Department of Electrical, Electronic and Communication Engineering, Chuo University, Tokyo, Japan*

Abstract

The twin torch plasma arc can generate the high temperature and also treat non-conducting material, because it has a higher temperature arc column, even if it is a non-transfer type. Therefore, the twin torch plasma arc has been a more effective device for the treatment of hazardous waste. However, in the twin torch plasma arc, the arc mode is not easy to control. In this paper, the temperature distribution of twin torch plasma arc near 100A was measured. The high temperature region of the twin torch plasma arc is larger than that of a conventional single plasma torch. The plasma arc length can be changed as a function of plasma gas flow rate. The arc voltage is also changeable as function of current and plasma gas flow rate. The temperature of twin torch plasma was measured to be about 14,000K near the cathode, and 13,000K at the center point between the electrodes and near anode at 100A. The neutral bar under the arc column received the heat power of the amount of 280-500W, and the fraction of the total power transferred to the neutral bar of the total dissipated power is 12-18%.

Keyword : Twin Torch, Plasma Arc, Temperature Distribution

1. Introduction

The plasma arc has a lot of excellent characteristics such as the high temperature[1-5], highly intense radiation[6][7] and high energy. The conventional plasma torches have been developed, previously. However, they have some problems of ignition and generation of high temperature and highly intense arc for hazardous waste treatment[8-12]. Although the plasma jet in a non-transfer type can treat non-conducting material, it is difficult to generate the high temperature arc. In the case of the plasma torch in a transfer type[5], although it can generate the high temperature arc, it is difficult to treat the non-conducting material. Therefore, it is important to solve this problem immediately. Especially, the medical waste has complex such as knives, injectors, injector needles, diaper, blood etc.. Normally, the plastic is non-conducting material. Therefore, they should be treated and the off-gas should be clean. The twin torch plasma arc can generate the high temperature and also it can treat the non-conducting material, because it has a higher temperature arc column, even if it is a kind of non-transfer type. Therefore, the twin torch plasma arc is a more effective device for the treatment of hazardous waste. In this paper, the temperature of twin torch plasma arc near 100A is measured for the treatment of hazardous waste[1][2]. Metals such as knives and injection needles are electrically conducting materials. Therefore, they are treated easily by the electrical arc. However, the twin torch plasma arc is one of the non-transfer type arcs, i.e. it is not producing Joule heating of materials themselves. Therefore, the temperature of arc column must be high enough to treat the metals. Because the injector needle is very sharp, it is dangerous for workers and citizens. It is not enough to treat the injector needle by the normal incinerator, because the temperature is too low to treat the injector needle made of stainless steel.

2. Experimental arrangement

Figure 1 shows the experimental arrangement of twin torch plasma arc. And figure 2 shows an arrangement of nozzle electrodes. The angle between cathode and anode is 98 degrees. The argon is filled in the chamber at 0.1MPa. The twin torch plasma arc is generated between the cathode and anode. The conventional twin torch plasma arc has only two gas flow from the nozzle, and the twin torch plasma arc has more than three gas flow from the nozzle. The plasma gas is also argon and its flow rate of cathode, F_c, is 15slpm and 20slpm from nozzle electrode of cahode, and gas flow rate of anode, F_a, is constant to be 15slpm. The DC arc current of the twin torch plasma arc is varied from 30 to 100A. The neutral bar arranged at the middle point between the cathode and anode is used to measure the received power and derive the gas heating efficiency. The left electrode is anode and the right one is cathode. The neutral bar for a tentative treatment plate consists of a Th-W tip and a copper stem which is cooled by forced water.

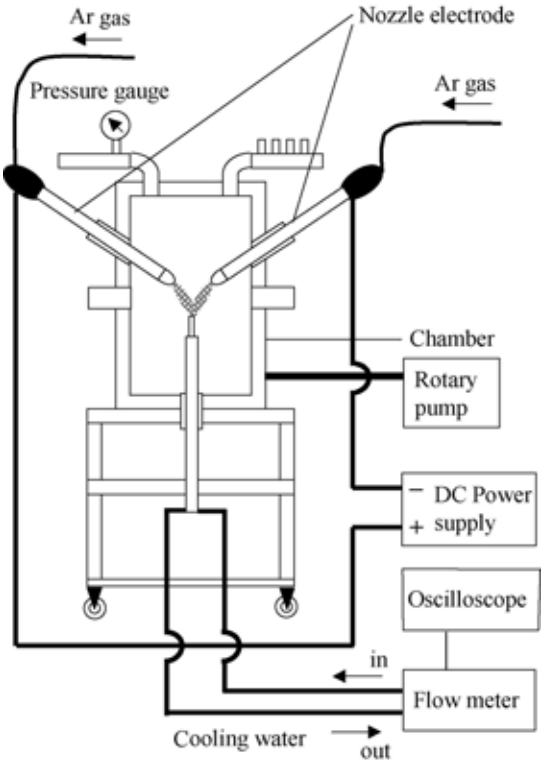

Fig. 1 Experimental Arrangement.

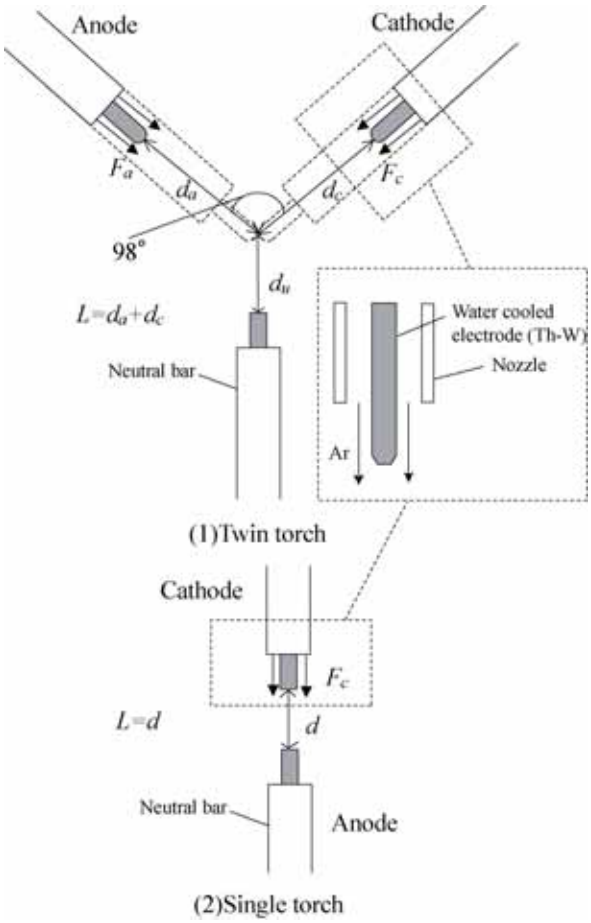

Fig. 2 Arrangement of nozzle.

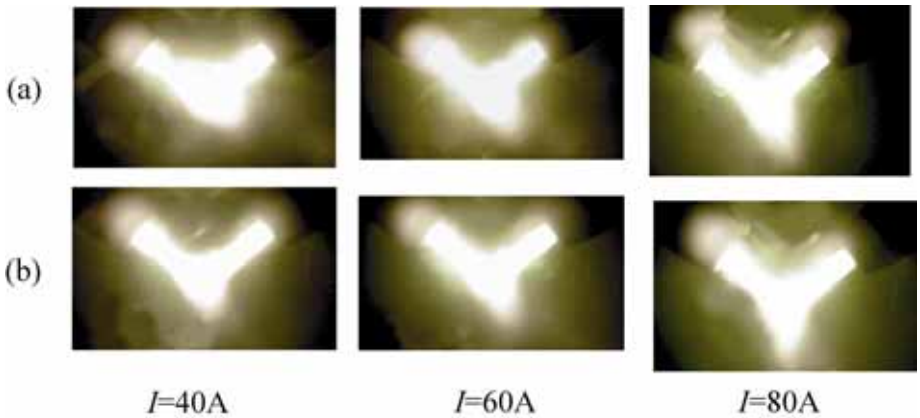

Left : Anode Right : Cathode

L=4cm, F_a=15slpm, (a) F_c=15slpm, (b) F_c=20slpm

Fig. 3 Conventional twin torch plasma arc mode.

3. Arc mode

The arc mode is changed by the gas flow surrounding the arc[13]. Figure 3 shows the conventional twin torch plasma arc modes. When the current increases, the arc appearance changes from a V to a Y mode. This means the high temperature region increases. When the gas flow rates of cathode and anode are the same, the arc modes don't become V and Y mode completely. However, when the gas flow rate from the cathode is 20slpm and it from the anode is 15slpm, the arc appears a V mode. This indicates that the electrode jet from the anode is bigger than that from the cathode.

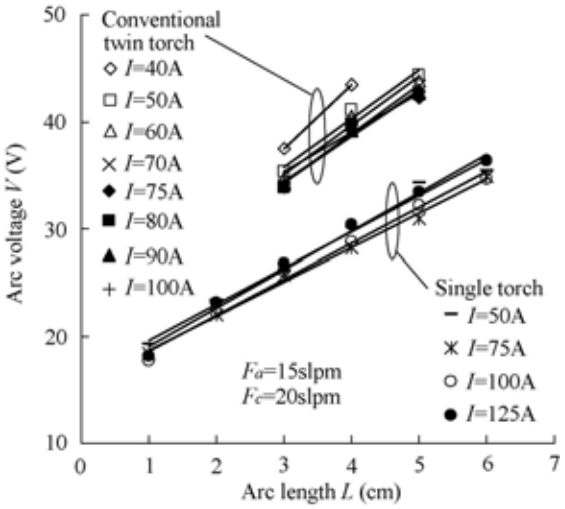

Fig. 4 Arc voltage as function of arc length.

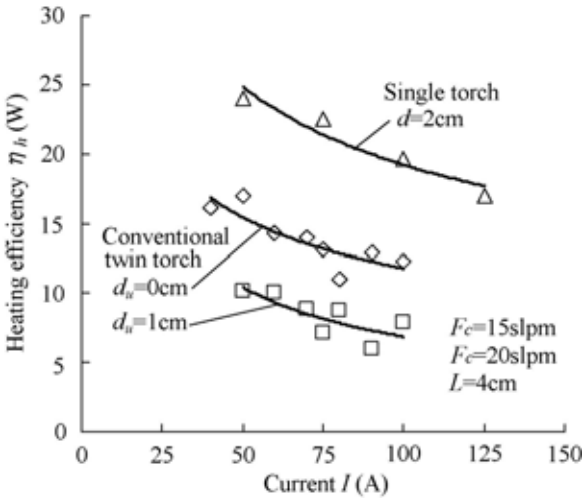

Fig. 5 Heating efficiency.

Therefore, the arc mode from anode is always strong. When the current increases from 40 to 80A, the high temperature region of arc expands. The anode spot was observed to be bigger than the cathode spot.

4. Arc Voltage

The arc voltage as a function of arc length as shown in Fig.4. The arc voltage of single torch plasma arc is almost constant around 30V. However, that of the twin torch plasma arc decreases with a current. These characteristics are similar to a wall-stabilized arc. Because the anode electrode has a nozzle, the radius of plasma arc is constricted due to the pipe type gas flow. Therefore, the voltage of twin torch plasma arc is larger than that of single torch plasma arc. However, the twin torch plasma arc can obtain more voltage and input power. The voltage and input power of twin torch plasma arc is 1.1, 1.4 times that of the conventional twin torch plasma arc and the single torch plasma arc, respectively, in the case of L=3cm and 100A. Figure 6 shows the arc voltage as a function of arc length. The arc voltages of single and twin torch plasma arc increase almost linearly with the arc length and the voltage gradients are almost constant at 4.5V/cm in the twin torch plasma arc and 3.4V/cm in single torch plasma arc in a range of 50-125A. They are almost the same when the current changes.

5. Heating efficiency

The flow rate of cooling water in the neutral bar, A, equals 233.3 g/s. Together with the temperature difference between input and output cooling water, $T_{\text{out}} - T_{\text{in}}$ (K), they indicate the quantity of heat power to the neutral bar, Q_{water} (W), as follows[14]:

$$Q_{water} = 4.185A(T_{out} - T_{in}) \qquad (1)$$

The received heat increases with the current. The received heat in the case of the twin torch is a little bit bigger than that of the single torch plasma arc. However, that of the twin torch plasma arc sharply decreases when the downward distance is bigger as d_{u}=1cm. The received heat is measured to be 280-500W at d_{u}=0cm. Figure 5 shows the heating efficiency, which is defined as the ratio of the received heat Q_{water} to the input power of the arc. The heating efficiency of the twin torch decreases with current and 18-12% at 40-100A, d_u=0cm. It is smaller in the case of the twin torch plasma arc than in the case of the single torch, because the Joule heating of materials exists in the case of single torch. When the heating efficiency is large enough, the twin torch plasma arc can treat the waste easily. If the neutral bar is changed into actual materials or a melting pot, the heating efficiency is expected to become double or more.

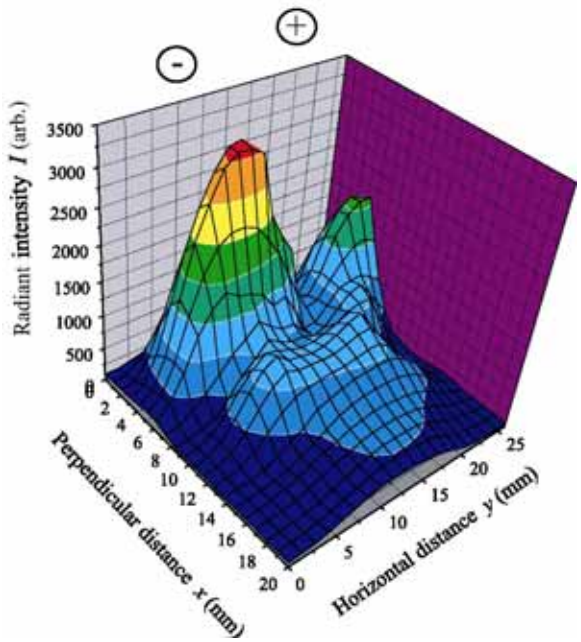

Fig. 6 Intensity distribution of spectrum (Ar I 706.7nm)

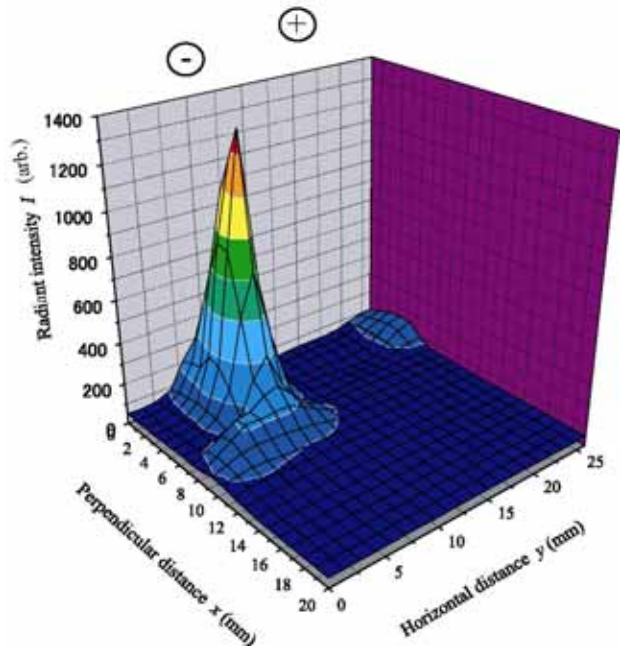

Fig. 7 Intensity distribution of spectrum (Ar II 434.8nm)

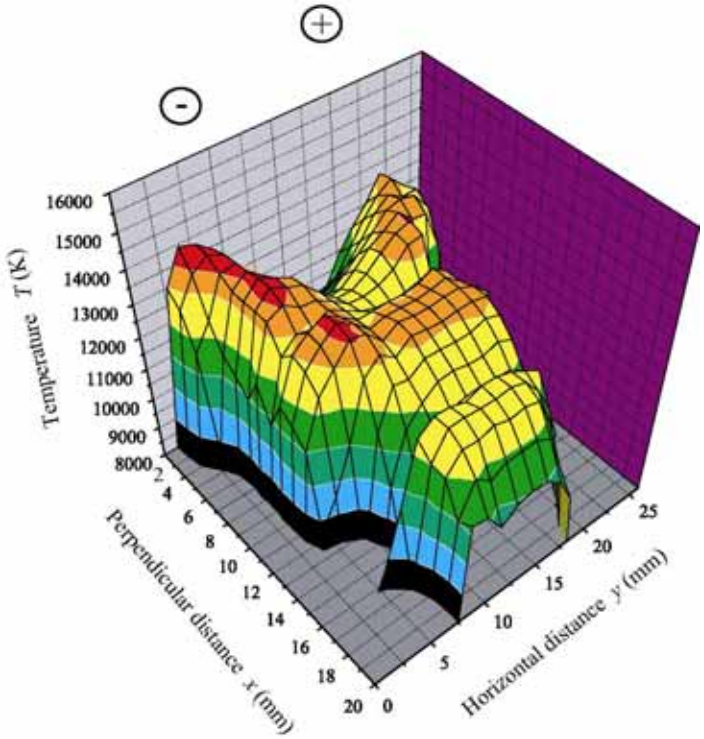

Fig. 8 Temperature distribution of twin torch plasma arc.

6. Temperature of Plasma arc

The temperature of twin torch plasma arc at 100A was measured by using spectroscope and line pair method. The intensity of spectrum Ar I(706.7nm) and Ar II (434.8nm) are shown in Figs. 7 and 8, respectively. The intensity of Ar I is higher than it of Ar II, and the intensity near cathode is higher than it near anode because the ionization and electron are dominated from 13,000K. The temperature becomes 14,000K near cathode. The center point of plasma arc, which is attachment point between the plasma arc from cathode and anode, and near anode is 13,000K.

7. Summary

The temperature distribution of twin torch plasma arc near 100A was measured for the treatment of hazardous waste. The main results are shown below.

(1) The high temperature region of the twin torch plasma arc is larger than that of a conventional single plasma torch and twin torch plasma arc.
(2) The plasma arc downward length can be changed by changing the plasma gas flow rate. The voltage is also changeable as function of current, plasma gas flow rate and arc length. The voltage gradient of twin torch plasma arc is about 4.5V/cm compared to 3.4V/cm in the case of the single torch.
(3) The temperature of the twin torch plasma was measured to be 14,000K near the cathode, and 13,000K at the center point between the electrodes and near anode at 100A.
(4) The heat power transferred to a neutral bar is 280-500W and its heating efficiency or the fraction of the total input power is 12-18% at d_u=0cm, 40-100A.

Acknowledgement

The authors wish to thank Prof. J. Heberlein of University of Minnesota and Prof. I. Miyachi of the Aichi Institute of Technology for their fruitful suggestions. This research was supported by the High-Tec Project on High Temperature Plasma by The Institute of Science & Engineering of Chuo University, the Japanese Ministry of Education, and the Japan Society for Promotion of Science, and IEEJ International Conference Travel Grant.

Reference

[1] H. Takizawa, S. Ando, Y. Yuza, T. Iwao, T. Inaba, “Voltage-Current Curve of Twin Torch Plasma Arc”, IEEJ National Convention, 1-096, p.103, 2004.
[2] H. Takizawa, T. Iwao, T. Inaba, “Received Heat Efficiency of Twin Torch Plasma Arc”, Plasma Application and Hybrid Functionally Materials, 13, pp.17-20, 2004.
[3] T. Iwao, T. Inaba, “Plasma length on characteristics of DC argon plasma torch arc”, Vacuum, 65, pp.299-304, 2002.
[4] T. Iwao, H. Miyazaki, T. Inaba, “Tungsten electrode erosion on DC horizontal short free arc in air”, Vacuum, 73, pp. 359-364, 2004
[5] T. Iwao, T. Ishida, T. Hayashi, T. Hirano, M. Endo, T. Inaba, “Examination for Radiation Power Emitted from Ar Torch Plasma as a Function of Length”, Trans. JIM, 63, pp.15-20, 1999.
[6] T. Iwao, H. Miyazaki, T. Inaba, “Radiation Characteristics as a Function of the Gas Flow Rate Emitted from Argon Torch Plasma Arc Discharge”, Electrical Engineering in Japan, 139, pp.1-8, 2002.
[7] T. Iwao, H. Miyazaki, T. Hayashi, T. Hirano, T. Inaba, “Radiation Power emitted from Ar Torch Short Plasma as a Function of In-put Power in Several kW”, Vacuum, 59, pp.88-97, 2000.
[8] Y. Liu, H. Qi, T. Iwao, H. Shindo, T. Inaba, “Sublimating Time for Decomposing Biphenyl Particles by a Hollow Cathode Argon Plasma”, Vacuum, 65, pp.463-468, 2002.
[9] T. Inaba, M. Nagano, M. Endo, “Investigation of Plasma Treatment for Hazardous Wastes such as Fly Ash and Asbestos”, Electrical Engineering in Japan, 126, pp.73-82, 1999.
[10] T. Inaba, T. Iwao, “Treatment of Waste by dc Arc Discharge Plasmas”, IEEE Trans. DEI, 7, pp.687-695, 2000.
[11] T. Iwao, H. Miyazaki, T. Ishida, Y. Liu, T. Inaba: “Proposal of Treatment for Hazardous Wastes Using the Highly Concentrated Radiation from Torch Plasma, Trans. ISIJ International”, 40, pp.275-279, 2000.
[12] T. Iwao, Y. Inoue, H. Kanda and T. Inaba, Development of highly intense radiant power equipment with a semi-oval reflector, Vacuum, 73, pp.347-351, 2004
[13] T. Iwao, P. Cronin, D. Bendix, J. Heberlein: Anode Attachment Stability and Anode Heat Fluxes for High Intensity Arcs with Helium, Nitrogen and Argon Gas Flow Parallel to the Anode, Proc. ISPC 16, Po12.52, 2003.
[14] T. Iwao, T. Beppu, S. Ishikawa, T. Inaba, Anode attachment of torch plasma arc with high-speed lateral gas air and axial plasma gas argon, J. Phys. D: Appl. Phys. 3, pp. 1158-1162, 2004

Gas influence on the behaviour of a MIG-MAG welding arc

S.Zielińska[1,3], N.Pellerin[2], S.Pellerin[3], K.Musioł[1], Ch. de Izarra[3]
F.Briand[4], F.Richard[4] and T.Opderbecke[4]

[1] Institut of Physics, Jagellonian Univ., ul. Reymonta 4, 30-459 Krakow - Poland
[2] CRMHT - 1D avenue de la Recherche Scientifique, 45071 Orléans cedex 2 - France
[3] LASEP - Centre Universitaire de Bourges, BP 4043, 18028 Bourges cedex 2 - France
[4] CTAS - Air Liquide Welding, Saint Ouen l'Aumone, 95315 Cergy-Pontoise cedex - France

Abstract

The type of the applied shielding gas has a strong influence on quality of the welding process. In particular, increase of the percentage of carbon dioxide in argon, involves increase of the transition current value from the globular to spray mode of metal transfer. These results show that the observed effects could be linked to the microstructural modifications of the anode tip during the MIG-MAG welding process as a function of the gas composition, and especially to the existence and disappearance of an insulating oxide "gangue" at the wire extremity.

The spectroscopic diagnostic of the welding arc is also necessary to understand the observed changes in the mode of droplet transfer. The use of an original diagnostic method allows to estimate the temperature and the electronic density distributions in the plasma without hypothesis on its equilibrium state.

1. Introduction

In the MIG-MAG ("Metal Inert Gas"-"Metal Active Gas") welding process, the plasma arc burns between the extremity of a fusible electrode (usually anode) and metal plate (usually cathode). The transfer mode of the metal melted in the arc depends mainly on nature of the used gas, electrode dimensions and composition, and the density of the welding current. Following the arc current and gas mixtures, the metal transfer can be made of three manners: the regime of transfer by short-circuits ("short-arc"), the "globular transfer" and the "spray-arc".

Composition of the applied shielding gas has a strong influence on physical properties of the plasma and parameters of the welding process. In particular, increase of the percentage of carbon dioxide in argon, results in increase of the transition current value while changing from the globular to spray mode of metal transfer during the welding process. In order to explain this phenomenon, the MIG/MAG welding arc plasma was investigated at different mixtures of argon and carbon dioxide in the shielding gas. Applying a fast camera, recording distribution of spectral lines of the plasma components, we have noticed some phenomena not described yet in the literature [1]. Particulary, results show in a very clear way that there is a limit of the percentage of relative concentration CO_2/Ar beyond which the shape of the arc is significantly modified.

Furthermore, the metal transfer mode can be characterized qualitatively by the shape of the plasma column and its attachement on the wire tip [1]: indeed, pictures show clearly in spray-arc a conical arc shape with a narrow attach zone on the anode, while the arc shape in globular transfer is rather like a bell with an attach zone largely increased on anodic wire, including the drop in the process of formation.

The current distribution inside the pendant attached droplet plays a decisive part on the drop behaviour due to the magnitude and sign of the induced electromagnetic force. The Lorentz force can act, either as a force of detachment (if current lines diverge), or on the other hand, as a force attaching the droplet to the wire electrode (if current lines converge) [*2*, *3*]. In this second case, the repelled metal transfer was observed during welding process using CO_2 shielding gas [4]. Detailed calculations made by Haidar [*5*] indicate that in dependence on welding conditions, the axial component of the electromagnetic force can perform this double function and its radial component is the dominant detaching force and directly determines the transition from globular transfer mode to the spray transfer mode. These results seem to show that the observed effects could be linked to the microstructural modifications of the anode tip during the MIG-MAG welding process as a function of the gas composition.

Also study of the anode erosion (detaching of electrodes pieces), formation of metallic droplets, their shape and their distribution in the discharge volume, are very valuable from the point of view of welding. One of the objectives of the present research was to identify microstructural characteristics for each transfer mode.

But a good knowledge of the welding arc plasma is also necessary to understand the observed changes in the mode of droplet transfer. The use of an original spectroscopic diagnostic method allows to estimate the temperature and the electronic density distributions in the plasma without hypothesis on its equilibrium state.

2. Experimental setup

The scheme of the experimental system is presented on Figure 1, and has been partially described in [1]. It is organized around a welding set SAFMIG 480 TRS PLUS [6, 7]. The welding was performed under reverse-polarity (wire-anode, workpiece-cathode) direct current in the constant current mode. The wire-anode was a mild steel consumable electrode (AWS A5.17) with 1.2 mm diameter. The distance between the contact-tube and the metal plate amounted 20 mm. The thickness of the workpiece was 8 mm for all measurements. The gas mixture based on the argon and the carbon dioxide, was provided by two bottles of industrial gas. Two mass flow meters allow measurement and control gas output. The measurements of voltage between the electrodes and arc current were carried out by a differential voltage and current probes, respectively.

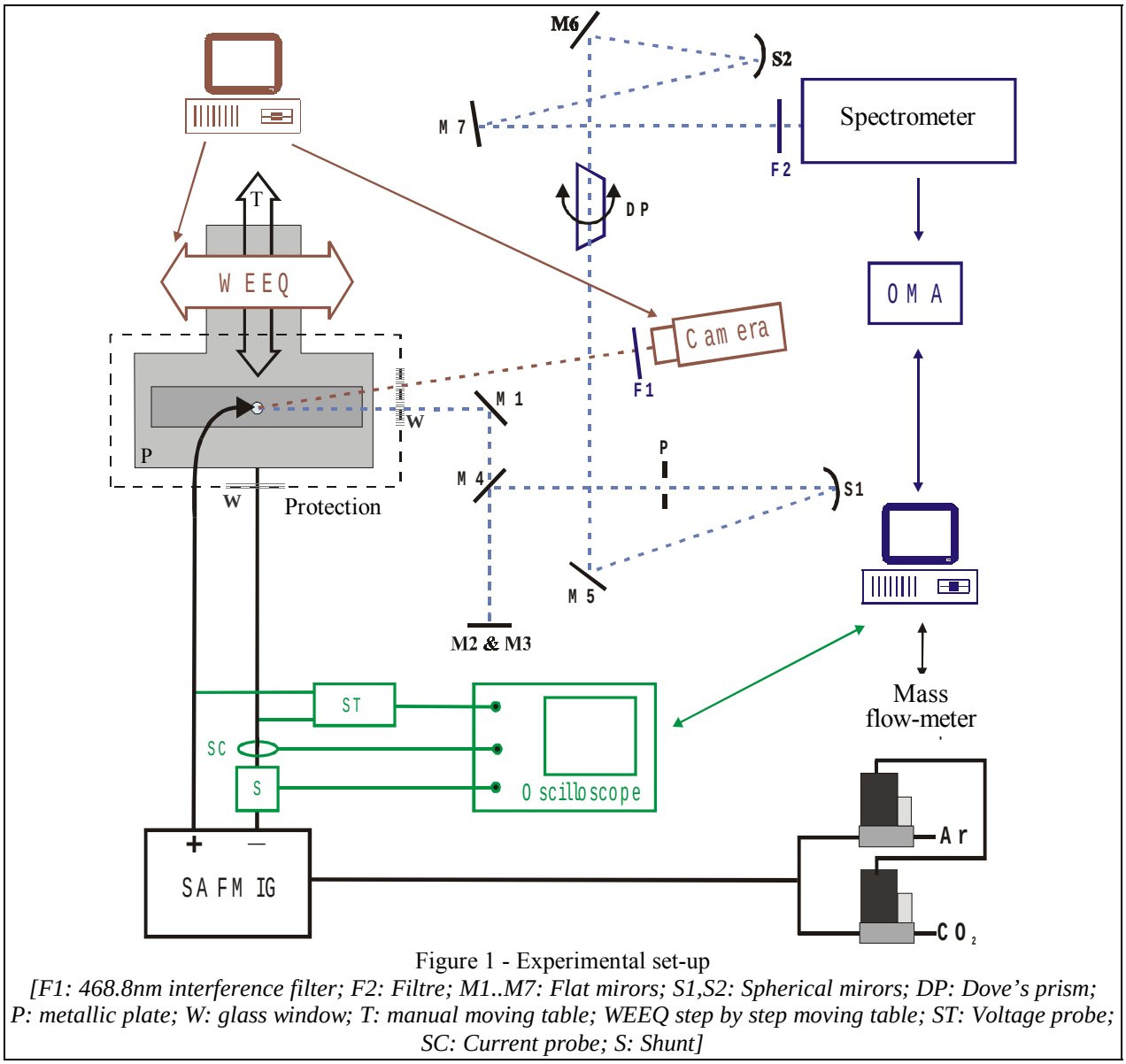

Figure 1 - Experimental set-up

[F1: 468.8nm interference filter; F2: Filtre; M1..M7: Flat mirors; S1,S2: Spherical mirors; DP: Dove's prism; P: metallic plate; W: glass window; T: manual moving table; WEEQ step by step moving table; ST: Voltage probe; SC: Current probe; S: Shunt]

3. Microstructural analysis

Working conditions of the process, such as the nature of the protective gas, the current, the wire moving speed, have direct consequences on the plasma, what induces an evolution of its shape and composition. So, they will give rise to some physicochemical transformations of the anode wire. We have studied in particular the microstructure and the elementary chemical composition of the drop derived from the steel quench into the working gas.

Microstructures have been examined by scanning electron microscope SEM (PHILIPS XL 40) coupled with an EDS (Energy Dispersive X-ray Spectroscopy) analysis. Observations are made on polished cross-sections according to wire axis. Chemical composition measurements are qualitative, with an incertitude in the order of 1% for metals and 5% on oxygen. Carbon detection is rather indicative. These measurements have been completed by quantitative analysis with an electron microprobe (CAMECA SX 50 microbeam).

Experiments in argon atmosphere allow to attain a spray-arc above 240 A in the case of steel anode wire 70S (cf composition in table). Decreasing the current, the arc behavior corresponds first to globular transfer mode then to short-arc for lowest currents (for 146 A for example). In spray-arc, the drops formed in quenching are very small and then can be supported at the tip of the wire on a section inferior to the normal wire section [Cf. Figure 2a]. Indeed, on the images of working arc, we can observe the tapering of the wire tip which discharges the drops. At the time of the quench, the liquid wire tip takes an equilibrium shape corresponding to a pendant drop which minimizes its surface energy, considering surface tension of the liquid. Reducing the current, more and more voluminous drops are obtained, and supported by the total wire section [Cf. Figure 2b and Figure 2c]. The largest are associated with the short-arc. However, remark that drop volume can be more or less important for same experimental conditions, in agreement with the kinetics of the drop formation and the time of the quench.

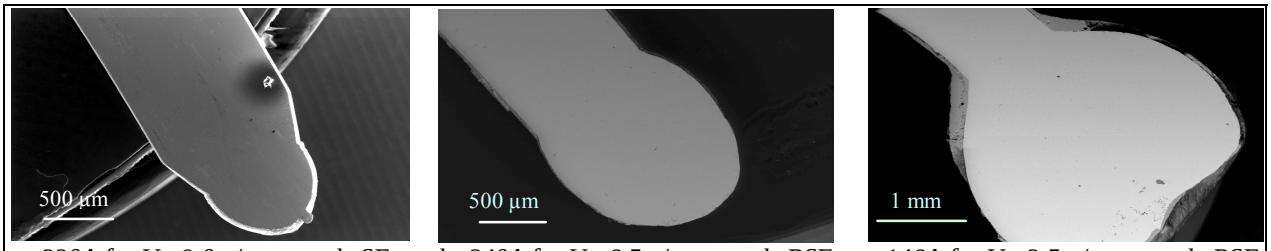

a: 330A for V_f=9.0m/mn - mode SE (Spray-arc) — *b: 240A for V_f=6.5m/mn - mode BSE (Globular transfer)* — *c: 146A for V_f=3.5m/mn – mode BSE (Short-arc)*

Figure 2 - Drop size comparison at different currents for MIG experiments in pure argon – SEM micrographs

When CO_2 is present in the protective gas, it is difficult to maintain the spray-arc. For low CO_2 contents (< 10 %vol) the current increase still allows to recover the spray transfer mode, but for higher CO_2 contents, we are limited by the available currents on the experimental device. At 330 A for example, spray-arc is maintained for 5 %vol CO_2, while the transfer mode is globular at 15.4 %vol. The microstructural analysis of drops formed in protective gas mixture Ar+CO_2 at different current values show that they have overall the same characteristics than in MIG experiments : precipitates, porosities and cracks, oxide gangue [Cf. Figure 3]. But in this case, the gangue presence is more systematic. It is constituted of oxides and its thickness increases when CO_2 content is higher at fixed current, or when the current decreases at constant CO_2 content in the protective gas. The trend is then the gangue disappearance towards the spray-arc.

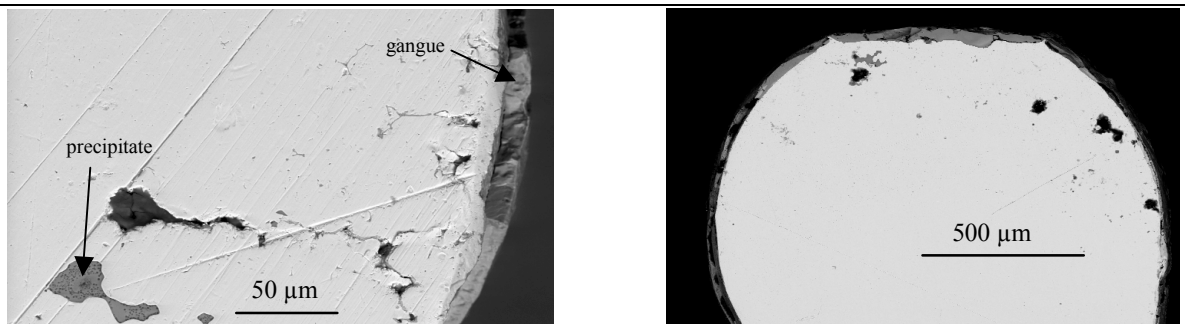

a: at 20% CO_2 vol. — *b: at 40% CO_2 vol. [V_f=9m/mn]*

Figure 3 - Drop microstructure for MAG experiment at 330A in gas mixture – SEM micrograph in BSE mode

In presence of oxide gangue, which is bad conductor, arc will need an attach zone larger to transfer the same current value. In globular transfer mode, we have effectively observed that arc attach zone includes largely the drop in the process of formation. This can explain the bell shape observed in globular transfer or short-arc, compared to conical shape characterizing the spray-arc.

To confirm these hypothesis, new recent experiments with another wire composition have been made. Very promising results have been obtained, and in few cases the transfer mode is observed close to spray at 330 A with 15 %vol CO_2.

4. Optical emission spectroscopic of the welding arc

The experimental diagnostic of the welding arc is necessary to understand the observed changes in the mode of droplet transfer. But the temperature measurements available in the literature, are dispersed, and do not seem to validate proposed models, for example by Haidar [8, 9]: from metallic lines emitted in the central region of the plasma, Lancaster [10] obtains temperatures in the order of 7000 K reaching 11000 K on the column axis with a mild steel consumable wire-anode, and closed to 17000 K on axis with an aluminium electrode. Haidar [8] puts these differences, that are not anticipated by the theoretical models, on the account of experimental uncertainties. It is therefore necessary to obtain precise informations on the plasma column behavior, and the not-intrusiv diagnosis methods of optical emission spectroscopy seem to be the alone methods adapted to the problem.

Spectral distribution of emitted light was measured in spectral range [260nm-760nm] using an Ebert type grating spectrometer equipped with a intensified two-dimensional CCD array of 512×512 contiguous photodiodes (19×19µm – effectiv size: 24×24 µm) designed by ROPPER SCIENTIFIC. The used CCD array recorded a spectral range of about 4 nm of the spectrum; therefore, the line profiles were measured up to their far wings.

The side-on measured intensity was converted into a radial emission distribution, pixel by pixel, using the numerical Abel inversion procedure with a cubic Spline data smoothing [11]. Then, the Voigt function on a linear continuous background was fitted to each inverted line profile, and allowed to determine automatically the total emission line profile (including line wings) and to obtain the Stark contribution to the effective line broadening, if the Doppler and instrumental broadening are known. Other broadening mechanisms, such as Van der Waals and resonant broadening, appeared to be negligible in the pressure and temperature range ($P \approx 1$atm, $T \leq 15000$K) of our experiments.

The use of an original method based on comparison of stark broadenings of the 696.543nm ArI line and 538.337nm FeI line spectral lines [12, 13], has allowed to estimate the temperature and the electronic density distributions in the plasma without hypothesis on its equilibrium state [14, 15]. So, the plasma diagnostic has been done on differents distances h from the cathodic plate for pure argon and for two Ar-CO_2 gas mixtures (Ar + 5.4% vol CO_2 and Ar + 20.2% vol CO_2), with a total gas flow rate D_g=20 l/min, and identical parameters of the process: wire speed V_f=9 m/min, $I_{ArcOrigine}$=330 A and average current I_{Mean}=326 A. An exemple of obtained results is given in Figure 4.

The temperature lowering in the center of the arc column, observed in the MIG-MAG arc under pure argon and with poor mixture in carbon dioxide, is well explained by the metallic vapours in the plasma that increase its electrical conductivity, but also of its emissivity [16, 17] and induces an increase of energy losses by radiation. Indeed, measurements realized in an TIG type's arc prove that the addition of less than 0.07% iron vapours to an argon plasma, lows its temperature approximately of 1500K [18].

Then, the temperature in the central part of the arc never seems to exceed the value of 15000 K, contrary to the values given in literature (T>20000 K on the axis). On the basis of these results, it is clear that the modelisations available in the literature [8, 9] do not represent the real situation: they are generally established in the local thermodynamical equilibrium (LTE) hypothesis in the case of the pure argon, and they do not take into account the metallic vapours influence and the induced temperature lowering.

Actually, to estimate the distribution of relative concentrations in argon and iron in the arc column, we try to verify the equilibrium state of the plasma using differents crossed diagnostic methods (Boltzmann plot, atomic to ionic lines ratio…). But the zone of most intense iron line emission is limited to the center of the arc column, and possibilities of MIG-MAG plasma diagnostic based on the emission spectrum of other metallic elements are limited.

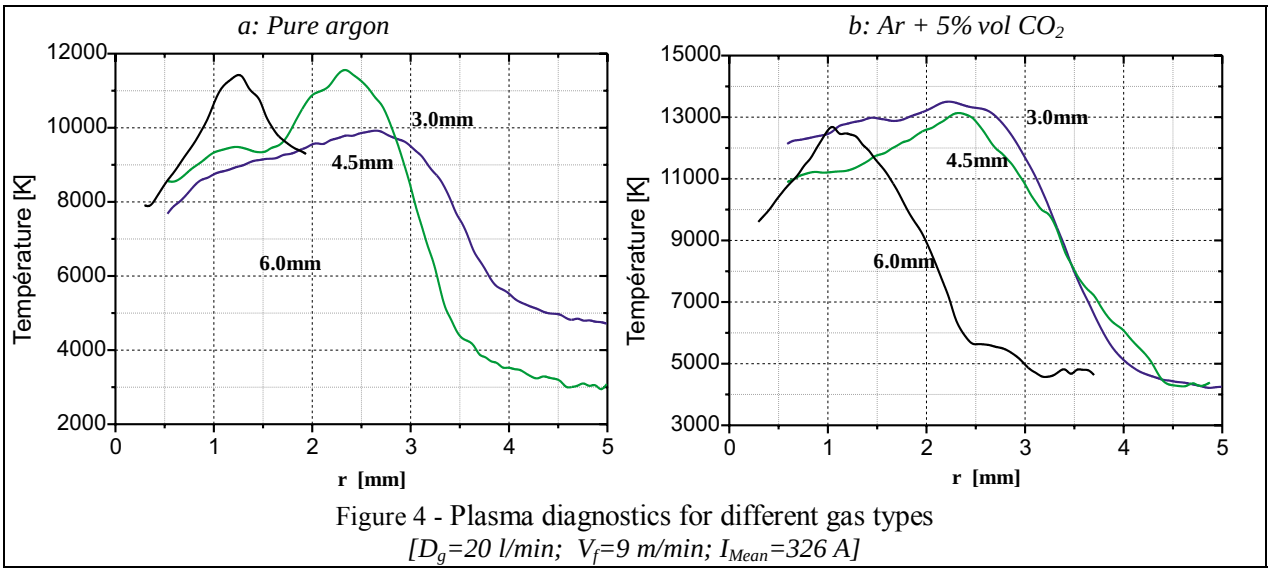

Figure 4 - Plasma diagnostics for different gas types
[D_g=20 l/min; V_f=9 m/min; I_{Mean}=326 A]

5. Conclusion

The comparison of metal transfer modes for experiments MIG in argon and MAG in argon+CO_2 shielding gas mixture shows an evolution from the short-arc to the globular transfer and then to the spray-arc when current values are increased. The transition between globular and spray transfer modes is observed towards 240 A in pure argon, and towards 410 A in gas mixture with 15%vol. CO_2.

SEM microstructural observations and EDX analysis, on quench drops for MIG-MAG experiments have allowed to characterize the physicochemical transformations of the anode wire, according to working conditions of the process, such as the nature of shielding gas and the arc current. The presence of oxide gangue, comparable to slag in iron metallothermy is typical of globular transfer and short-arc. CO_2 in protective gas favors its formation by chemical oxidation-reduction reactions. This bad conductor gangue hinders the current transfer and the arc needs a larger attach zone. That explains the bell arc shape associated to globular transfer or short-arc. The thickness of this gangue is decreasing when current value increases or CO_2 content decreases. So, it has not been observed in spray transfer mode for pure argon shielding gas. In this conditions, the plasma column has a well defined conical shape and the curvature on the current lines is clearly modified.

The plasma column diagnostic done by optical emission spectroscopy without hypothesis on the LTE state, show that, in the central part of the arc, the temperature never seems to exceed the value 15000 K, contrary to the values given in literature (T>20000 K on the axis). Among other results, we can note especially the deficit in excited argon close to the axis of arc when the amount of CO_2 in the shielding gas is less than 5%, the relative weakness of iron lines on the edge of the column, but also the increase of the FeII spectral lines in periphery of the arc. This work must be continued to study the LTE state in the plasma, and try to estimate the distribution of relative concentrations in argon and iron, and then the principal transport and thermodynamic characteristics (thermal and electrical conductivity, viscosity…) in the arc column.

Acknowledgment

This work was supported in part by CTAS-Air Liquide, Saint-Ouen l'Aumone (France), and by Integrated Action Project Polonium 958055E.

References

[1] S.Zielinska, S.Pellerin, K.Musiol, Ch. de Izarra & F.Briand, "Influence of the applied gas on the arc shape in MIG-MAG welding", 16th International Symposium on Plasma Chemistry, Taormina (Italie) – June 22/27, 2003 [Poster]

[2] V. A.Nemchinsky, "The effect of the type of plasma gas on current constriction at the molten tip of an arc electrode", *J.Phys.D* **29** (1996) 1202-1208

[3] J.H.Waszink & L.H.J.Graat, "Experimental Investigation of the Forces Acting on a Drop of Weld Metal", *Welding Journal* **62** (1983) 108s-116s

[4] Kim Y-S., Eagar T. W., "Analysis of Metal Transfer in Gas Metal Arc Welding", *Welding Journal* **72** (1993) 269s-278s

[5] J.Haidar, "An analysis of the formation of metal droplets in arc welding", *J.Phys.D* **31** (1998) 1233-1244

[6] Safmig 330TRS Plus / Safmig 480TRS Plus - Instruction de sécurité d'emploi et d'entretien , documentation technique SAF/Air Liquide Welding, Réf. 8695-0273, 1999.

[7] Kit Safmig 480TR 16 - Instruction de sécurité d'emploi et d'entretien , documentation technique Air Liquide, Réf. 8695-044, 1999.

[8] J.Haidar, *J.Appl.Phys*. **84** (1998) 3530

[9] J.Haidar, *J.Appl.Phys*. **84** (1998) 3518

[10] J.F.Lancaster, "The physics of welding", Pergamon Press, 1984

[11] J.Glasser, J.Chapelle & J.C.Boetner, *Appl.Opt.* **17**-23 (1978) 3750-3754

[12] S.Pellerin, K.Musiol, B.Pokrzywka & J.Chapelle, *J.Phys.B* **29** (1996) 3911-3924

[13] A.Lesage, J.L.Lebrun, J.Richou, *Astrophys.J.* **360** (1990) 737-740

[14] A.Sola, A.Gamero, J.Cortino, M.Sáez, C.Lao, M.D.Calzada, M.C.Quintero & J.Ballesteros, ICPIG XX Barga (Italy, 5-12 July 1991) Book of Contributed Papers p. 1147

[15] J.Torres, J.Jonkers, M.J.van de Sande, J.J.A.M.van der Mullen, A.Gamero and A.Sola, *J.Phys.D* **36** (2003) L55-L59

[16] A.Gleizes, J.J.Gonzalez, B.Liani, G.Raynal, *J.Phys.D* **26** (1993) 1921

[17] J.Menart & S.Malik, *J.Phys.D* **35** (2002) 867

[18] J.J.Gonzalez, M.Bouaziz, M.Razafinimanana & A.Gleizes, *Plasma Sources Sci.Technol.* **6** (1997) 20

Plasma etching of diamond-like carbon films on polyethylene terephthalate bottles and its plasma diagnostic

Kenji K. HIRAKURI, Kazuya TATSUTA, and Keisuke SATO

Department of Electronic and Computer Engineering, Faculty of Science & Engineering,
Tokyo Denki University
Ishizaka, Hatoyama, Saitama 350-0394, Japan
e-mail: hirakuri@f.dendai.ac.jp

Abstract

The etching of the DLC films deposited on the PET has been investigated by Atomic force microscopy (AFM), Raman spectroscopy, and infrared spectroscopy (IR). The DLC films were effectively etched by the reactive radicals in the glow discharge plasma of oxygen gas. The etching of the DLC films was easily carried out by the treatment of the plasma. The end point of the DLC etching was estimated by the plasma diagnostics because the damage of PET was given by the overexposure. The intensity of the optical emission was rapidly changed at the end of the etching treatment and it was able to monitor the etching process.

1. Introduction

The diamond-like carbon (DLC) films are coated at inner wall of the polyethylene terephthalete (PET) bottles because the DLC films protect degradation of inner soft drink against irradiation of ultra violet light and penetration of carbon dioxide gas through the PET[1]. By these advantages, the number of PET bottles with the DLC films is significantly increased for carriers of beverages with carbon dioxide gas such as soda, cola, and beer. These PET bottles become resource materials as synthetic fiber and resins. However, the DLC films act as contamination during recycling process of PET materials. Therefore the quality of regenerated PET is extremely deteriorated by the inclusion of the DLC residue. The removal of the DLC films is essentially required for recycling industry because it is big environmental problem against civil life. In order to recycle the PET bottles with DLC films, it is quite necessary to eliminate the DLC films before the treatment of recycling process. Furthermore, the base PET has to be analyzed after the removal of the DLC films from the PET substrates.

2. Experimental

Since the DLC films are easily deposited on the PET by using capacitive coupled radio frequency (r.f.) plasma discharge, the same r.f. plasma system is utilized for etching of the DLC films[2]. In this work, the oxygen gas was utilized for etching because radicals of oxygen plasma are very reactive with the carbon films. The power of the r.f. generator was kept constant at 100 W during etching. Optical emission

spectroscopy (OES) was used to obtain the end of the plasma etching treatment, and the results were applied to discuss the relationship between the etching treatment and the plasma diagnostic.

The etching of the DLC films on the PET has been investigated by atomic force microscopy (AFM), and Raman spectroscopy. The etching rate was calculated by the film thickness and plasma treatment time. It needs that the optimized time should be investigated for the etching because the PET is received the some damages by corrosion of ionic species for extra etching treatment. Therefore the end point of the etching treatment was estimated by the plasma optical diagnostic.

3. Results and discussion

The thickness of the DLC films was monotonously reduced with increase of the etching time as shown in Fig. 1. At the etching pressure of 10 Pa, the DLC films with thickness of 300 nm were completely removed by oxygen plasma for the treatment time of 6 minutes. The complete etching of the DLC films was also confirmed by Raman analysis. The etching of the DLC films in PET bottles is quit easy by using this technique. The etching time is estimated about 1 minute because the thickness of the DLC films in PET bottles is about several nanometers. The etching rate is approximately 50 nm/min by the etching time and thickness of the DLC film. The etching rate was dramatically decreased at 1 Pa because of the decrease of plasma density. The surface topography of the samples before and after the etching treatment was observed by AFM.

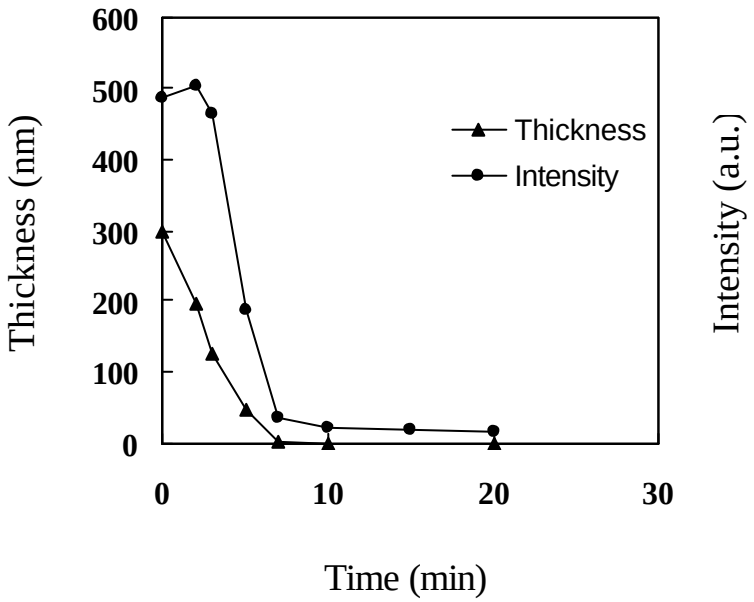

Fig. 1 The thickness of the DLC films and the intensity of CH optical emission at 430 nm as a function of the etching time. Both results of the thickness and the emission intensity obtained at pressure condition of 10 Pa.

In order to obtain the relationship between the etching result and plasma condition, the spectra of the OES measurements were recorded during etching. The emission intensity of CH at 430 nm as a function of the etching time is shown in Fig. 1. The optical emission peaks of the plasma were rapidly changed at the

end of the etching treatment. The intensity is dramatically decreased with the increase of the etching time and then it approaches to the saturation point. In particular, the intensity of the peak is the saturation value around the goal of the etching. The intensity of CH peak may be able to monitor the end point of the DLC etching by oxygen plasma.

Table I Etching rate and peak intensity ratio of optical emissions at each condition

Condition (Pa)	Intensity ratio CH/Hα (a.u.)	Etching rate (nm/min)
10	8.61	50.8
100	2.48	14.7

The etching rate is reduced at the higher pressure condition. At the etching pressure of 100 Pa, it needed for 20 minutes for etching of the DLC films with thickness of 300 nm. The etching rate in case of higher pressure condition (100 Pa) was a factor of one fourth lower than that of a low pressure condition (10 Pa). The etching rate at the pressure condition of 100 Pa is 15 nm/min. This decreasing effect can be explained by sputter removal through ions accelerated towards in the electrical field of bias voltage. Etching and deposition products are extremely influenced by the negative dc self-bias voltage which occurs on the powered electrode. The dc self-bias voltage is generally increased with decrease of the pressure in case of r.f .plasma. The relationship between the negative bias potential and the etching and deposition of some films is reported in detail[3,4].

The many peaks were observed from the OES of the oxygen plasma. The OES has intensive three peaks at 431.4, 486.1, and 656.3 nm. The peaks at 486.1 and 656.3 nm correspond to Hα and Hβ in hydrogen plasma, respectively. The peak at 431.4 nm is originated from CH radicals in the plasma. In order to monitor the etching process, the emission intensity ratio CH/Hα was measured at different pressure condition of 10 and 100 Pa. Table I shows the etching rate and peak intensity ratio of the optical emissions at different pressure condition. The intensity ratio CH/Hα of low pressure condition was higher than that of high pressure condition because the strong emission of CH peak was observed in case of 10 Pa. At lower pressure condition, the DLC films are exposed by the ionic species in the plasma that are accelerated to the film surfaces. The etching is enhanced by both ionic species and neutral radicals in the plasma.

On the other hand, the electrical neutral radicals are dominant at high pressure condition of 100 Pa. Since the etching of chemical reaction is mainly forwarded by the dominant radicals, the etching rate is decreased in comparison with lower pressure condition. The emission intensity ratio CH/Hα in case of high pressure is also greater than that of lower pressure condition. There is good agreement between both results of the etching rate and plasma optical diagnostic.

The root-mean-square (rms) roughness values used throughout the paper have been determined on areas of 1 μm x 1 μm. Figure 2 shows AFM images of the DLC film topographies obtained at different etching pressure. In the lower pressure region (10 Pa), pronounced protrusions were observed on the film surface. The estimated thickness is about 150 nm because of half time (3 min) of total etching time. The rms roughness was about 3.7 nm. In case of the high pressure condition (100 Pa), such pronounced features can not be observed at the surface. At this condition, the estimated thickness is about 150 nm from the etching rate of 15 nm/min because the etching

treatment is 10 min. The fine pronounced features can not be observed on the sample surface as shown in Fig. 2 (b). The decrease of the roughness with increase of pressure is obtained. The roughness at high pressure is approximately half than that of sample at low pressure. The decrease of the rms roughness from 10 Pa to 100 Pa is originated by the difference of the dc self-bias voltage and the energy of the ionic species. At low pressure condition, both weak and strong bonds of the films are sputtered and milled by the ionic species with high acceleration energy, and most of the ionic species attack to the surface without collision to any other molecules in the chamber. High etching rate was obtained at low pressure condition whereas the surface roughness was increased after the etching treatment.

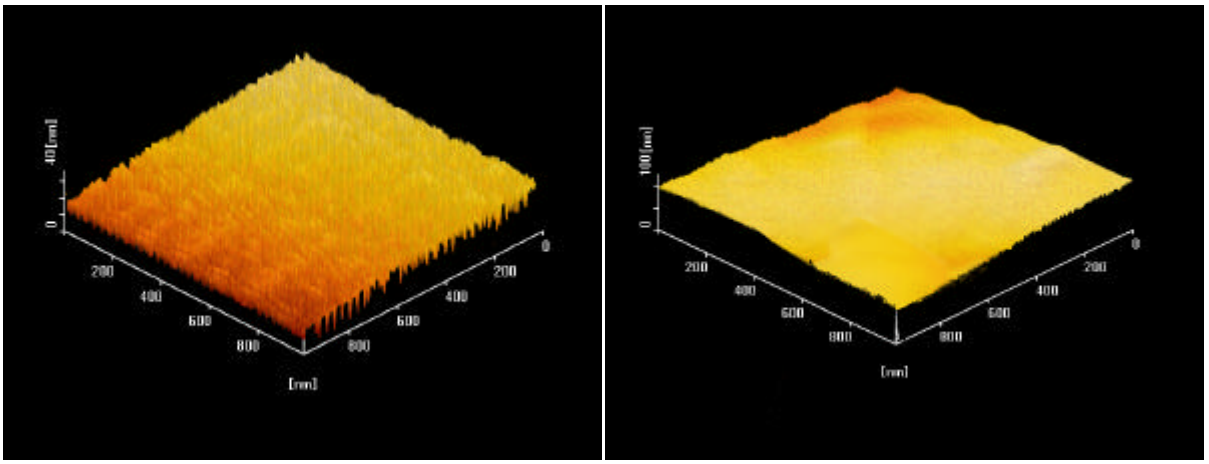

(a) etching time: 3 [min], pressure: 10 [Pa] Roughness: 3.7 [nm]

(b) etching time: 10 [min], pressure: 100 [Pa] Roughness: 1.9 [nm]

Fig. 2 AFM images showing the morphology of the sample surfaces.

4. Conclusion

The etching of the DLC films deposited in PET bottles has been investigated by using plasma process and optical emission spectroscopy. The etching thickness was increased with etching time of oxygen plasma and the etching rate at optimum condition is about 50 nm/min. The emission intensity of the plasma was proposed for monitoring the etching of the DLC films. The end of the etching is confirmed by the intensity ratio CH/Hα during etching. At high pressure condition, the etched surface of the substrate PET is smooth than that at low pressure condition with dependence on the dc self-bias voltage.

References

1. K. Tanaka, SEN'I GAKKAISHI 59 (2003) p-202.
2. Y. Ohgoe, and K. K. Hirakuri, J. Vac. Sci. Technol., A22 (2004) 2195-2200.
3. K. K. Hirakuri, T. Minorikawa, G. Friedbacher, and M. Grasserbauer, Thin Solid Films, 302 (1997) 5-11.
4. S. Yamanaka, S. Yoshida, M. Konagai, and K. Takahashi, Jpn. J. Appl. Phys., 158 (1987) 1107.

Microwave discharge in the co-axial wave-guide

S.I. Gritsinin[1], I.A. Kossyi[1], E.B. Kulumbaev[2], V.M. Lelevkin[2]

[1] *Institute of General Physics of the Russian Academy of Sciences, Moscow, Russia*
[2] *Kyrgyz-Russian Slavic University, Bishkek, Kyrgyz Republic*

Abstract
A two-dimensional magnet-gas-dynamic model for numerical calculation of the microwave discharge in argon at atmospheric pressure of co-axial waveguide with a short-cut internal electrode is offered. The output qualitatively agrees with experimental data.

Introduction

The microwave discharges with a co-axial electromagnetic power supply find a wide application in different scientific, technical and technological tasks [1-3]. The practice of different schemes of microwave discharges realization has shown that that plasma generation strives to "elongate" a short-cut electrode. For example, in a standard scheme of the co-axial microwave plasmatron the discharge is excited on the end of a short-cut internal water-cooling electrode. The stability of the plasma torch spatial localization is reached by a straight-jet or vortex work of gas flow supplied between the internal and external electrodes of co-axial line [2].

In Institute of General Physics RASc a new variant of the plasma torch generation is offered, where a short-cut internal electrode represents a tube, ensuring a plasma-generating gas flow (fig.1). The length of the internal electrode from entry in the co-axial part is taken so that the tube end was in maximum electric field of a standing wave, which arises without any discharge at reflection of a running wave from a zone of round below-cutoff waveguide. At relatively low microwave power (~ 1 kWt) the disruption is possible, that ensures generation of torch in different gases at different pressures, including the atmospheric. New modifications in the construction allowed an essential prolongation of generated microwave torch to 10-20 cm and perfection of the torch gas-dynamic stability. Experimental study of the discharge has shown that in every new power supply pulse (magnetron of 2.45 HHz) the torch passes stages of initialization, flaming, and propagation along the waveguide axis up to a certain end size. Visually, in atomic gas near a nozzle of the internal electrode a bright luminescence in a shape of a rod ("core") with a diameter of 1-2 mm and length 1-2 cm is realized; an expanded area of less luminescence follows it. In molecular gases the core as a sharply outlined area of bright luminescence is absent. The concentration of electrons in the core is 10^{16} cm^{-3}, and in the torch body outgoing from the core – 10^{14} cm^{-3}. Main part of the torch, elongated along axis of the waveguide system, is formed by the internal surface wave, which necessary condition for existence and propagation is increased critical concentration of plasma electrons.

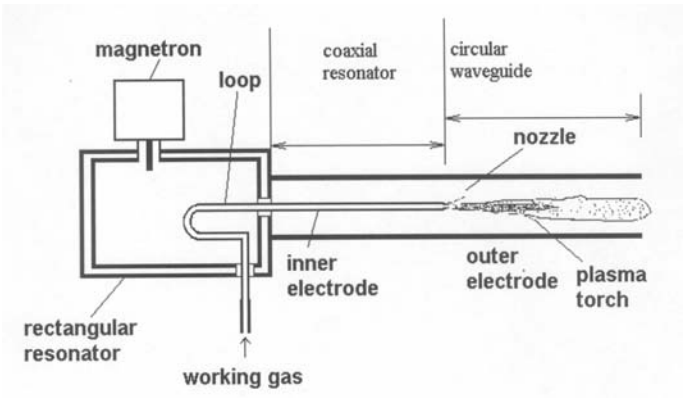

Figure 1. Microwave plasma torch launcher.

This model offers two-dimensional magnet-gas-dynamic (MGD) model of equilibrium microwave discharge in the co-axial wave-guide with a short-cut internal electrode. The discharge characteristics are calculated in argon at atmospheric pressure. The assessment of the numerical model adequacy to experimental properties of the discharge is carried out.

Model

Burning of the microwave discharge is considered in a driven by TEM-wave co-axial waveguide with a short-cut internal electrode made in a shape of tube for transporting plasma-generated gas with the discharge G_0 (fig.2). It is guessed that the electrodes material is ideally conductive, and a cylindrical wall of

the external electrode with the radius R_e is "transparent" for gas inflow and outflow. The axis-symmetrical equilibrium plasma jet, generated in a zone of a round below-cutoff waveguide, is guessed ensuring conditions for existence of electromagnetic field with components $\vec{E}(E_r; 0; E_z)\exp(i\omega t)$, $\vec{B}(0; B_\varphi = B; 0)\exp(i\omega t)$. A period of electromagnetic field change is much less than the time for establishing thermal gas-dynamic characteristics of the discharge.

Equations. The gas-dynamic, thermal and electromagnetic characteristics of the microwave discharge in axis-symmetrical MGD approximation are described on the basis of a set of stationary equations continuity, motion (Navies-Stokes), energy balance and wave equation:

$$\frac{1}{r}\frac{\partial}{\partial r}(r\rho v)+\frac{\partial}{\partial z}(\rho u)=0,$$

$$\rho\left(v\frac{\partial v}{\partial r}+u\frac{\partial v}{\partial z}\right)=-\frac{\partial p}{\partial r}-\frac{1}{4}\sigma\left(E_z B_\varphi^*+E_z^* B_\varphi\right)+\frac{2}{r}\frac{\partial}{\partial r}\left(r\eta\frac{\partial v}{\partial r}\right)-\frac{2\eta v}{r^2}+$$

$$\frac{\partial}{\partial z}\left[\eta\left(\frac{\partial u}{\partial r}+\frac{\partial v}{\partial z}\right)\right]-\frac{\partial}{\partial r}\left[\frac{2}{3}\eta\left(\frac{1}{r}\frac{\partial rv}{\partial r}+\frac{\partial u}{\partial z}\right)\right],$$

$$\rho\left(v\frac{\partial u}{\partial r}+u\frac{\partial u}{\partial z}\right)=-\frac{\partial p}{\partial z}+\frac{1}{4}\sigma\left(E_r B_\varphi^*+E_r^* B_\varphi\right)+2\frac{\partial}{\partial z}\left(\eta\frac{\partial u}{\partial z}\right)+\frac{1}{r}\frac{\partial}{\partial r}\left[r\eta\left(\frac{\partial u}{\partial r}+\frac{\partial v}{\partial z}\right)\right]-$$

$$\frac{\partial}{\partial z}\left[\frac{2}{3}\eta\left(\frac{1}{r}\frac{\partial rv}{\partial r}+\frac{\partial u}{\partial z}\right)\right],$$

$$\rho C_p\left(v\frac{\partial T}{\partial r}+u\frac{\partial T}{\partial z}\right)=\frac{1}{2}\sigma\left(E_r E_r^*+E_z E_z^*\right)-\varphi_e+\frac{1}{r}\frac{\partial}{\partial r}\left(r\lambda\frac{\partial T}{\partial r}\right)+\frac{\partial}{\partial z}\left(\lambda\frac{\partial T}{\partial z}\right),$$

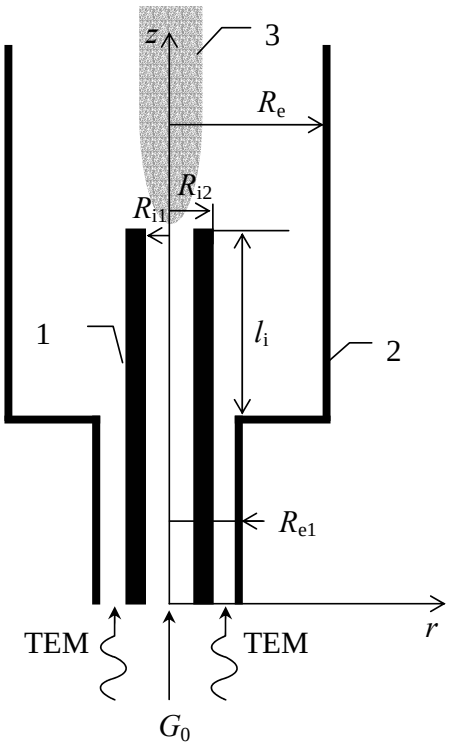

Figure 2. Schemes of accounted area of co-axial wave-guide with a short-cut internal electrode and electromagnetic power supply by TEM-wave: 1 – internal el.; 2 – external el-de; 3 – plasma; R_e, R_{e1}, R_{i1}, R_{i2}- radiuses of exterior and interior electrodes; l_i- length of the internal electrode emerging part; G_0- gas flow.

$$\frac{\partial}{\partial r}\left(\frac{1}{r\varepsilon_k}\frac{\partial rB}{\partial r}\right)+\frac{\partial}{\partial z}\left(\frac{1}{\varepsilon_k}\frac{\partial B}{\partial z}\right)+\frac{\omega^2}{c^2}B=0.$$

Components of the electric field intensity are found from the Maxwell equations:

$$E_r=\frac{i}{\omega\mu_0\varepsilon_0\varepsilon_k}\frac{\partial B}{\partial z},\qquad E_z=-\frac{i}{\omega\mu_0\varepsilon_0\varepsilon_k}\frac{1}{r}\frac{\partial rB}{\partial r}.$$

Notations: $\vec{V}(V_r=v,\ V_\varphi=0,\ V_z=u)$- velocity; T - temperature; p - pressure; $\omega=2\pi f$-frequency; ρ, λ, C_p, η, φ_e- density, thermal conductivity, thermal capacity, viscosity, emittance; $\varepsilon_k=\varepsilon-i\sigma/\omega\varepsilon_0$; $\varepsilon=1-\sigma/\varepsilon_0\nu_e$- dielectric permeability; $\sigma=K_\sigma e^2 n_e\nu_e/m_e(\omega^2+\nu_e^2)$- electro-conductivity; K_σ- kinetic correction; ν_e, n_e, e, m_e – effective collision rate, electrons concentration and mass; c – velocity of light; ε_0- electric constant; μ_0- magnetic constant; i – imaginary unit; upper index * means complex conjugate value.

Boundary conditions are given on all the contour of the accounted area (fig.2): for velocity – an adhesion on solid surfaces, radial gas inflow-outflow through the surface of the exterior electrode with radius R_e, poise flow in entry profile of the internal electrode tube; pressure in outflow profile is atmospheric; for temperature – conditions of coupling

with given temperature of exterior contour, excluding outflow boundary, where thermal equilibrium condition is given; for magnetic field induction – conditions of ideally conducting electrodes (tangential to the wall component of the electric field intensity is equal to zero), radiative conditions in ring profile of TEM-wave supply and in outflow profile. Boundary conditions are as follows:

$z = z_{\min}$, $R_{i2} < r < R_{e1}$: $\dfrac{\partial B}{\partial z} - ikB = -2ikB_I \dfrac{R_{i2}}{r}\exp(-ikz)$;

$z = z_{\max}$, $0 < r < R_e$: $\dfrac{\partial B}{\partial z} + ikB = 0$.

We guess that sizes of the co-axial R_{i2}, R_{e1} "ensure" for given field frequency the propagation only of the TEM-wave $B = B_I \dfrac{R_{i2}}{r}\exp(-ikz) + B_R \dfrac{R_{i2}}{r}\exp(+ikz)$: falling with amplitude $B_I = \sqrt{\dfrac{\mu_0 \omega P_I}{\pi k c^2 R_{i2}^2 \ln R_{e1}/R_{i2}}}$ and power P_I and reflected with amplitude $B_R = -\left.\dfrac{\partial B/\partial z + ikB}{\partial B/\partial z - ikB}\right|_{R_{i2}<r<R_{e1}}$ and power $P_R = \dfrac{B_R B_R^*}{B_I B_I^*} P_I$; $k = \omega/c$. On the outflow boundary a condition corresponds to the passed wave propagating along the plasma torch in positive direction of axis z with a number of longitudinal propagation k.

The integral balance of electromagnetic power was checked in accounts by the condition:

$P_I = P_R + P_T + P_d$,

where power of the "passed " wave and dissipated power are determined by the equations:

$$P_T = \frac{\pi}{\mu_0}\int_0^{R_e} E_r B^* r dr; \qquad P_d = 2\pi \int_0^{R_e}\int_0^{z_{\max}} \frac{1}{2}\sigma(E_r E_r^* + E_z E_z^*) r dr dz .$$

For *numerical solution a set of equations* is sampled by control volume method on a rectangular nonuniform grid. For velocity components the offset grids are used, and the pressure field is determined by the method SIMPLER [4]. On every pitch of the iteration procedure the discrete analogs of amendments for dependant variables are solved by the exclusion method of Gauss. Restriction conditions (less than 0.01%) for Euclidean norms of discrete analogs residual vectors made up on all control volumes for desired dependent variables are used for end criterion.

Results

The Characteristics of the microwave discharge in argon at atmospheric pressure are calculated as follows: f = 2.45 HHZ, R_{i1} = 1 mm; R_{i2} = 2 mm; R_e = 10 mm. Coefficients of the argon equilibrium plasma at atmospheric pressure are used from [5]. Particles concentrations are taken from calculation of equilibrium composition; electrons impingements frequency are calculated by the formula $\nu_e = \sqrt{\dfrac{8k_B T}{\pi m_e}}\left(n_a Q_{ea} + n_i Q_{ei}\right)$, where the impingements profile as in [5] are given by functions of temperature and concentrations. The output at $l_i = 3\lambda/4$ ($\lambda = 2\pi/k$); P_I = 800 Wt; G_0 = 10 l/min are shown in fig.3-4.

Following the accounts, the discharge is excited near the internal electrode profile (fig.3-4) because of high electric field concentration. The outflowing from the internal electrode plasma-generating gas results in formation of plasma torch front separated from the nozzle cut by "cold" space, which thermo-isolates the internal electrode. The isotherms field expands down the flow and then narrows with heat generation reduction (reduction of electromagnetic field intensity dissipation) and heating of surrounding gas at the expense of thermal conductivity and convective heat exchange. The electromagnetic field spreads up to area of plasma conductivity, which ensures conditions for further propagation and consequent dissipation of electromagnetic field energy in the thermal along the torch. In fig.3-4 is viewed that behind the internal electrode cut a complex electromagnetic field structure is formed. A zone of electromagnetic field energy dissipation: area with significant axial component of electromagnetic field intensity and radial vector

component of Umov-Pointing as well as area with prevailing radial electric field and axial electromagnetic energy flow, are distinguished. The periodicity of electromagnetic field structure along the discharge axis is considered. The isolines of the module of the electric field intensity

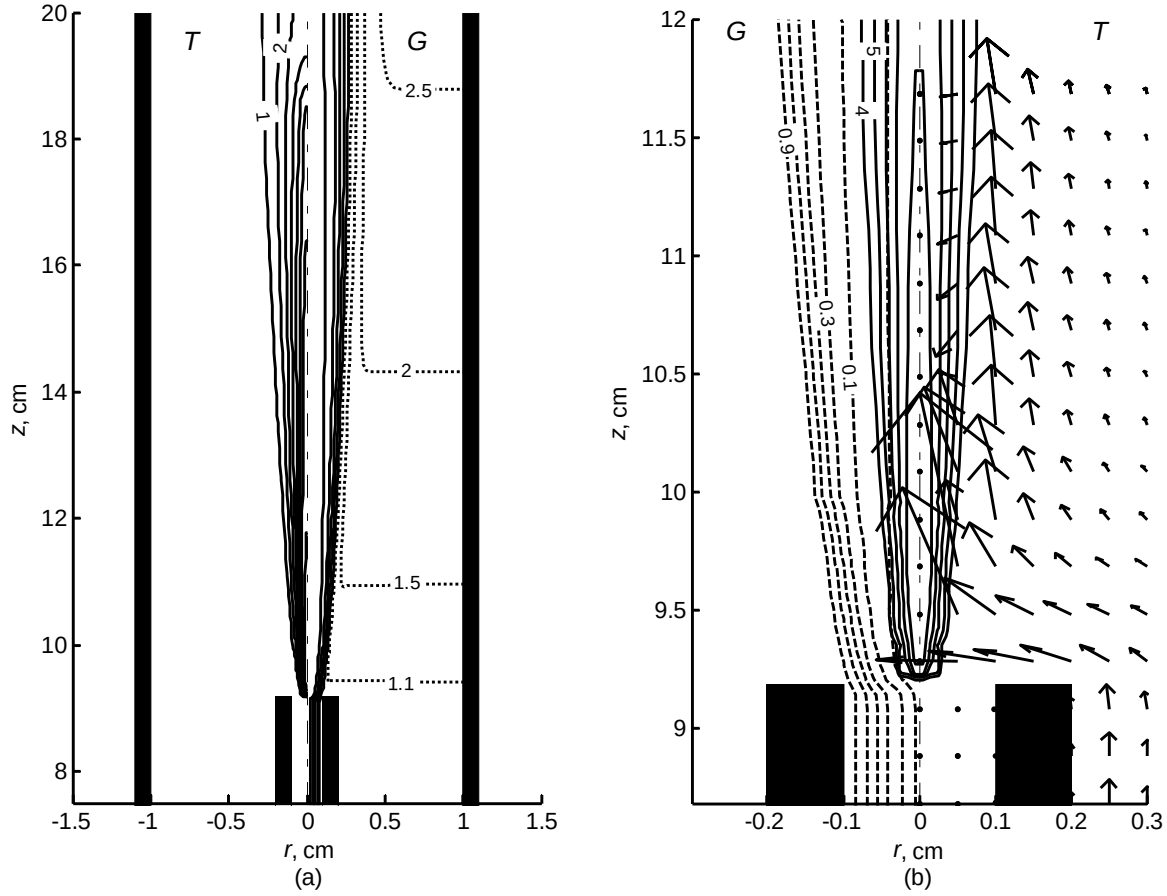

Figure 3. (a) Isotherms T/T_0 (pitch 1 kK) and gas flow lines G/G_0 (from 0.1, pitch 0.2); (b) field fragments of gas flow lines, isotherms and vector of Umov-Pointing (T_0 = 1kK, G_0 = 0.27g/s, S_m = 9.9 kW/cm^2, P_I = 800W, P_R = 493 W, P_d = 307 W, P_T = 0).

along the torch point to available concentration of the field near boundary of a zone of dissipation.

The picture corresponds to the mode of prevailing gas flow around discharge region: main amount of the transported on the internal electrode cold gas (more than 90%) flows around a high-temperature region (the isotherm 4 kK). The pressure increases sharply and goes down near the internal electrode cut on axis. On end surface of the electrode cut the pressure decreases and a surrounding air inflows (fig.3). The flow gasdynamic structure promotes spatial stabilization of the discharge (localization of main part and cross-section sizes fixation along the torch axis).

At power input increase or gas flow decrease, one consider a tendency to growth of radius of energy dissipation area along the torch axis.

When length of the internal electrode is $l_i = \lambda/2$ (fig.2) the numerical solution corresponds to a cold gas outflow from the internal electrode in free space at electromagnetic field energy dissipation absence and at full wave reflection from a zone of round below-cutoff waveguide ($z > l_i$). At $l_i = \lambda/4$ the account gives a solution, which is qualitatively similar to case $l_i = 3\lambda/4$. According to the scheme (fig.1, 2) a critical condition for the discharge existence is a choice of the internal electrode length that agrees with the experiment data. If the internal electrode length is equal to uneven number of quarters of wavelength, the electrode's end is in standing wave's electric field maximum, generated at reflection of TEM wave running from a zone of round below-cutoff waveguide. This choice of the internal electrode length can be considered as a necessary condition of the discharge burning.

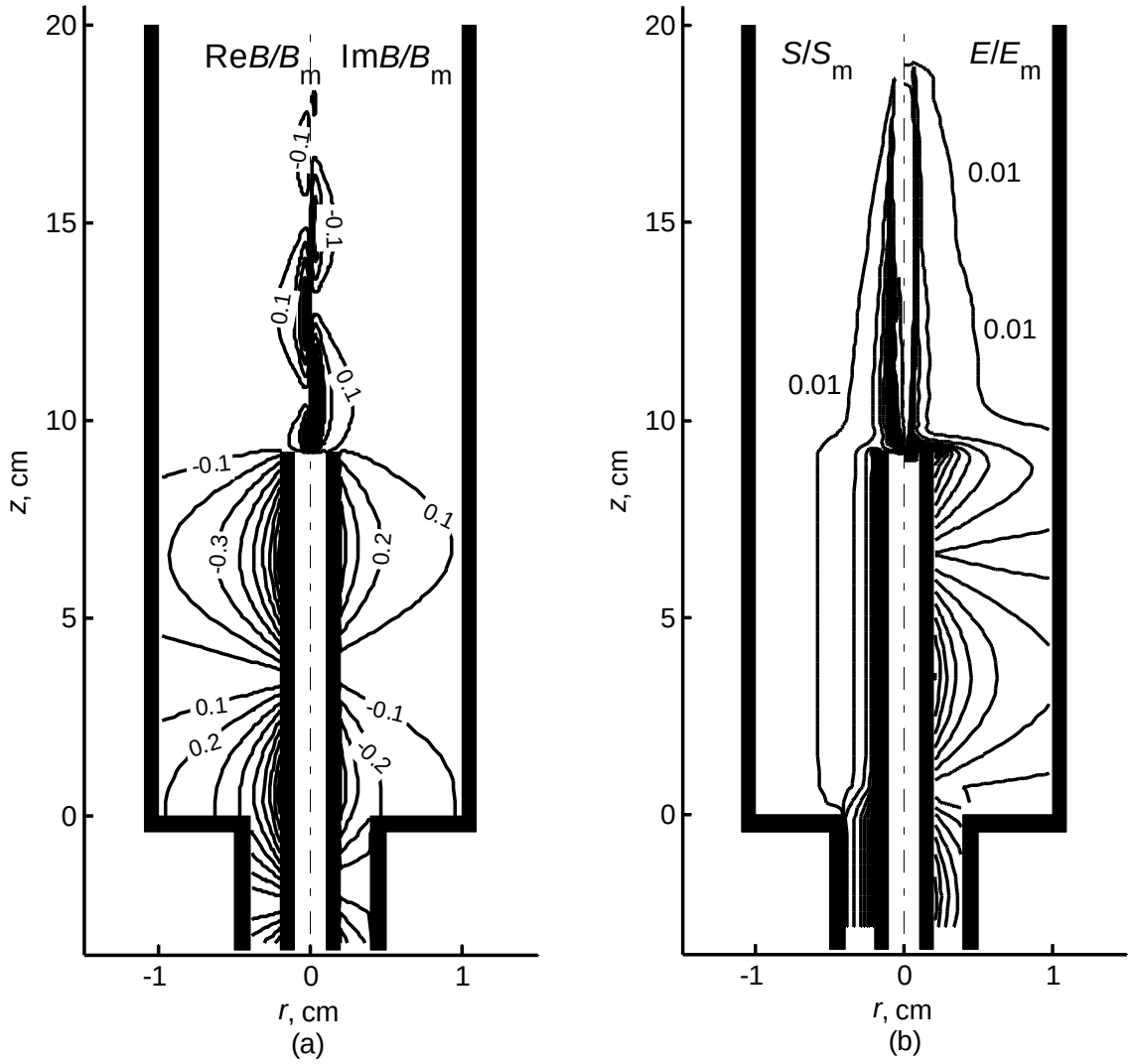

Figure 4. Given isolines of (a) magnetic field induction B/B_m (pitch 0.1); (b) vector of Umov-Pointing S/S_m (pitch 0.02) and electric field intensity E/E_m (pitch 0.02) (B_m = 1.09 mT; S_m = 9.9 kW/cm^2; E_m = 21.66 kV/cm).

Literature

1. V.M. Batenin, I.I. KlimovskiÏ, G.V. Lysov, and V.N. TroitskiÏ, *Microwave Plasma Generators: Physics, Technique, and Applications* (Énergoatomizdat, Moscow, 1988).
2. *RF and Microwave Plasmatrons*, Ed. by S.V. Dresvin, A.A. Bobrov, V.M. Lelevkin, *et al.* (Nauka, Novosibirsk, 1992), Vol. 6.
3. V.M. Lelevkin, D.K. Otorbaev, *Physics of Non-Equilibrium Plasmas* (North-Holland, 1992).
4. S. Patankar, *Numerical Heat Transfer and Fluid Flow* (McGraw-Hill, New York, 1980).
5. V.S. Éngel'sht, V.Ts. Gurovich, G.A. Desyatkov, *et al.*, *The Theory of Electric Arc Column* (Nauka, Novosibirsk, 1990), Vol. 1.

High-rate reactive magnetron sputtering of Al_2O_3 films

J. Musil[1,2], D. Heřman[1*], J. Šícha[1], P. Baroch[1]
[1]*Department of Physics, University of West Bohemia Univerzitni 22, 30614 Plzen, Czech Republic*
[2]*Institute of Physics, Academy of Sciences of the Czech Republic, Na Slovance 2, 18221 Praha 8, Czech Republic*
[*]*Corresponding author: Fax +420 37763-2202, e-mail: herman@kfy.zcu.cz*

Abstract
Aluminium oxide films were deposited by a dc pulsed reactive sputtering using a dual magnetron. High deposition rates (~100 nm/min) of Al_2O_3 films at the substrate-to-target distance $d_{s-t} = 100$ mm were achieved when the film deposition was carried out in a transition mode of sputtering. To avoid the hysteresis effect and to maintain the film deposition in the transition mode the process was controlled by the discharge voltage U_d. Transparent Al_2O_3 films with amorphous structure and smooth surface were successfully deposited. Optical and mechanical properties of Al_2O_3 films were determined.

Keywords: Al_2O_3 films, High deposition rate, Sputtering, Dual magnetron, Optical and mechanical properties

1. Introduction

At present, similarly as nitride films, the oxide films are a subject of great interest not only for their excellent properties such as a high chemical inertness, high thermal stability and corrosion resistance but also for their functional properties and particularly due to their enhanced mechanical, optical, electronic and catalytic properties. To understand fully the enhanced properties of oxide films, these films are intensively investigated in many world leading laboratories [1–7]. Simultaneously, a great attention is devoted also to the increase of a deposition rate a_D to ensure their low-cost industrial production. This concerns mainly the transparent oxide films which are usually produced in the oxide mode of sputtering with very low a_D.

The industry requires the transparent oxide films to be deposited with a_D of films at least 50 nm/min. However, this requirement is very hard to meet because (1) there is a jump transition from the metallic mode of sputtering (opaque films) to the oxide mode of sputtering (transparent films) and (2) the deposition rate of transparent oxide films in the oxide mode is very low $a_{D\,oxide} \leq (1/10)\, a_{D\,Me}$, where $a_{D\,Me}$ is the deposition rate of metallic films produced in the metallic mode of sputtering [8]. The transparent oxide films can be produced also in the transition mode of sputtering. However, due to the jump transition from the metallic to the oxide mode a special control system, which stabilizes the sputtering process, e.g. the system based on a plasma emission monitoring [6, 7], is needed. In addition, in the reactive magnetron sputtering of Al_2O_3 films, which are electrically insulating, a very serious problem is the charging of insulating islands and/or layers forming on uneroded areas of a sputtered target. The charging results in arcing on sputtered target that needs to be eliminated. A pulsed dual magnetron is an efficient tool which eliminates the arcing. It enables to produce insulating transparent oxides in the transition mode of sputtering without the arcing on sputtered target. This article reports on a high-rate deposition of the transparent Al_2O_3 films in the transition mode of sputtering using the magnetron discharge voltage U_d.

2. Experimental

The experiments were carried out in a deposition device schematically shown in Fig. 1. The dual magnetron, equipped with Al (99.99) targets of 50 mm in diameter, consists of two single unbalanced magnetrons tilted at 20° to the axis of substrate holder. In this system, both magnetrons were electrically insulated from the deposition chamber. The dual magnetron was supplied by a dc pulsed Advanced Energy 5 kW power supply and operated in a symmetrical bipolar mode at the pulse repetition frequency $f_r = 100$ kHz and pulse off time $t_2 = 5$ μs, i.e. the duty cycle $t_1 / T = 0.5$; here $T = 1 / f_r$ and t_1 is the pulse length. This means that each magnetron target acted alternatively as an anode and a cathode during the pulse cycle. Other deposition parameters were the

following: substrate-to-target distance $d_{s-t} = 100$ mm, substrate bias $U_s = U_{fl}$, substrate temperature $T_s = RT$ (unheated substrate), total gas pressure $p_T = p_{Ar} + p_{O2} = 0.5$ Pa and partial pressure of oxygen $p_{O2} = 0.06$ Pa; here U_{fl} is the floating potential. Ar and O_2 were introduced into the chamber at constant flow rates controlled by mass flow controllers MKS (type 1179 A). No automatic adjusting of the flow of O_2 was used when a film deposition was carried out. The microscopic glass slides (26x12x1 mm^3) and Si (100) (12x4x0.5 mm^2) plates were used as substrates. The thickness of films varied between 1000 and 5000 nm.

The film thickness and surface roughness were measured by a profiler Dektak 8 of the Veeco Instruments Inc. The structure of films was characterized by X-ray diffraction (XRD) in the Bragg-Brentano configuration with CoKα (λ=0.179021 nm) and the mechanical properties (hardness and Young´s modulus) were measured by computer controlled microhardness tester Fischerscope H 100. The optical properties (refractive index and optical transmittance) were measured by UV-vis spectrometer Specord M400.

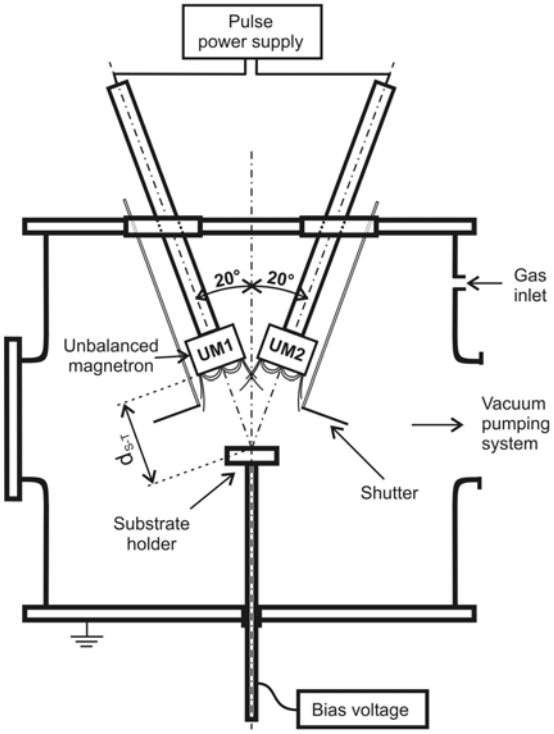

Fig.1. Schematic diagram of the experimental device.

3. Results and discussion

3.1. High-rate sputtering in transition mode

The dependence of p_{O2} on ϕ_{O2} measured prior to the film deposition at constant average discharge current I_{da} (average current over the pulse) and automatic regulation of the reactive gas (oxygen) flow rate ϕ_{O2}, which maintains the total gas pressure constant ($p_T = p_{Ar} + p_{O2} = const$), is displayed in Fig. 2. In this control of reactive sputtering, there is a jump transition from point A to point B when ϕ_{O2} increases, i.e. no stable operation in the transition mode is possible. This jump occurs due to an avalanche target poisoning, i.e. a conversion of the surface of Al target to Al_2O_3; for more details see, for instance, the reference [8]. From Fig. 2 it is clearly seen that this change in the chemical composition of sputtered targets is accompanied also by a jump change of the average discharge voltage U_{da} from 500 V (metallic mode) to approximately 300 V (oxide mode).

The difference in U_{da} occurring when films are sputtered in the metallic and oxide mode offers a possibility to ensure a stable sputtering in the transition mode. To achieve it, the magnetron must be supplied with the power supply with controlled output voltage, i.e. in the case when U_{da} is kept constant. This control makes it possible to adjust every value of p_{O2} from the interval between 0.025 Pa and 0.085 Pa, corresponding to the interval between points A and B (Fig. 2). The stable sputtering of Al_2O_3 films in this interval of p_{O2} is illustrated in Fig. 3. All film depositions in the transition mode of sputtering were carried out at a constant value of p_{O2} = 0.06 Pa. No change in p_{O2} with increasing ϕ_{O2} is due to a sorption of oxygen by sputtered Al atoms and formation of Al_2O_3 films.

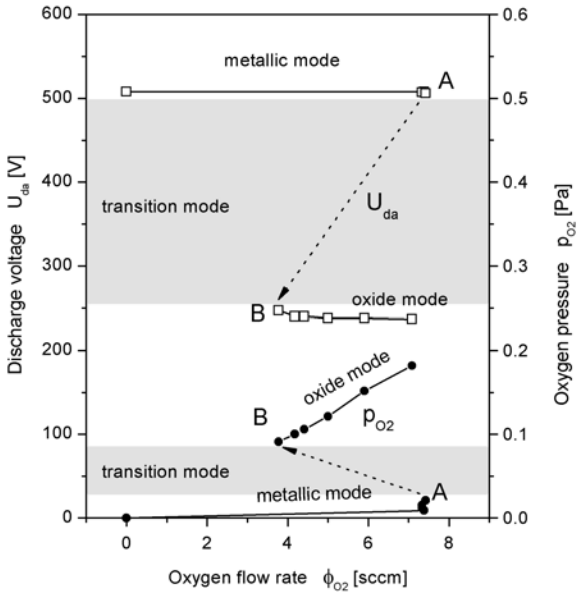

Fig. 2. Jump transition from the metallic to the oxide mode of sputtering due to p_{O2} control by ϕ_{O2} at I_{da} = 1.5 A and $p_T = p_{Ar} + p_{O2}$ = 0.5 Pa

Fig. 3 shows stabilized working points in the transition region with corresponding values of (i) the discharge voltage U_{da} and (ii) deposition rates of transparent Al_2O_3 films on substrates located at $d_{s\text{-}t}$ = 100 mm. As it is expected, U_{da} decreases and a_D increases with decreasing p_{O2}. The sputtering process controlled by U_{da} is more stable than that controlled by the discharge current I_{da}. Besides, it is worthwhile to note that the deposition rate of transparent Al_2O_3 oxide films produced in the transition mode is more than ten times higher than a_D of those produced in the oxide mode of sputtering, see Figs. 3 and 4. The increase of a_D of transparent Al_2O_3 films with increasing ϕ_{O2} up to a very high value $a_D \approx$ 100 nm/min at ϕ_{O2} = 7.8 sccm and p_{O2} = 0.6 Pa is clearly seen in Fig. 4. To increase a_D it is necessary to increase the magnetron target power loading to prevent full oxidation of its surface. To sputter transparent Al_2O_3 films with the high deposition rate $a_D \approx$100 nm/min, the magnetron must be operated at high target power loadings achieving up to 30 W/cm^2 (the average over the whole surface of a sputtered target during the sputtering pulse).

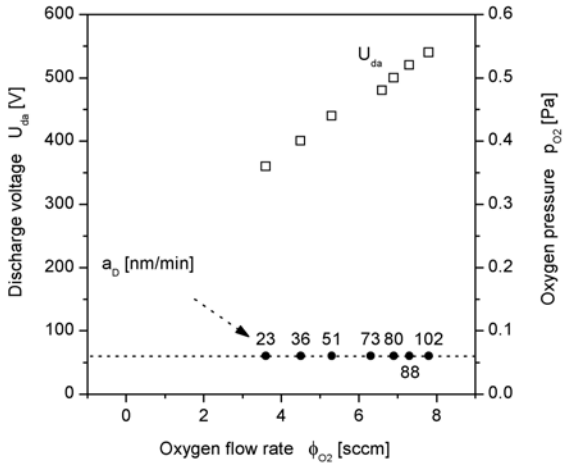

Fig. 3. Stable operation points in the transition mode of sputtering when p_{O2} is controlled by discharge voltage U_{da} at p_T = 0.5 Pa.

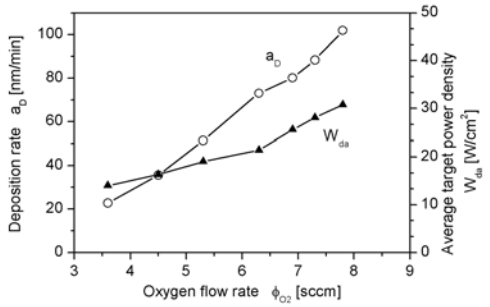

Fig. 4. The deposition rate of transparent Al_2O_3 films and the average target power density ($W=I_dU_d/S$) on oxygen flow rate at p_T = 0.5 Pa; S is the total area of target surface.

3.2. Mechanical and optical properties of transparent Al_2O_3 films

The Al_2O_3 films were deposited on unheated substrate. This is a reason why sputtered films exhibited an amorphous structure and relatively low hardness H of about 11 GPa. These results are in a good agreement with literature data which show that (1) amorphous Al_2O_3 films exhibit low (11 GPa) hardness and (2) $T_s \geq 500$ °C is necessary to produce crystalline alumina films [3]. All measured properties of sputtered Al_2O_3 films are summarized in Table 1.

Our measurements show that the hardness H and effective Young´s modulus E^* do not depend on the deposition rate a_D of their production, see Table 1. This fact indicates that mechanical properties of the films are determined by its structure which is amorphous in the whole range of a_D used in our experiment. The increase in a_D cannot stimulate the film crystallization because the energy of ions bombarding the growing film is inversely proportional to a_D and so decreases with increasing a_D [10].

Transparent Al_2O_3 films with amorphous structure have very smooth surface and excellent transmittance in visible spectrum, see Table 1. We report the index of refraction n at 550 nm for comparison with other author's studies. If we consider n = 1.70 at 550 nm of polycrystalline Al_2O_3 [11] as the bulk refractive index, we find that our sputtered amorphous Al_2O_3 films exhibit almost the bulk density. Also, the transmittance of sputtered Al_2O_3

films is very high and, in the system Al_2O_3 film/glass substrate (1 mm thick microscope glass plate), achieves approximately the same value of 87.5% for two (1140 and 5080 nm) very different thicknesses of Al_2O_3 films, see Fig. 5. This indicates that losses of light intensity inside the Al_2O_3 films are very low.

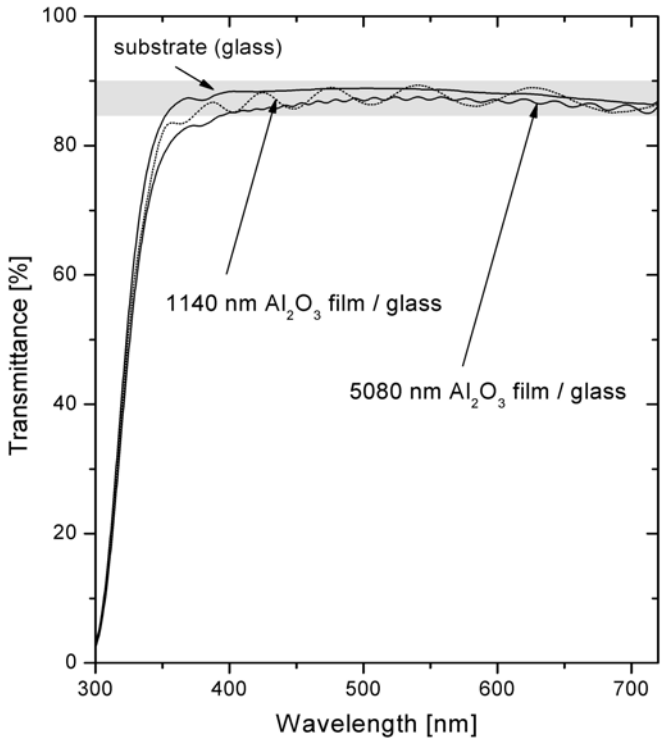

Fig. 5. Transmittance of the Al_2O_3 film/glass system with differnt film thickness h and sputtered with different a_D. a) h = 1140 nm, a_D = 22.8 nm/min and b) h = 102 nm/min.

4. Conclusions

Main conclusions of our study can be summarized in two points.

1. The operation of dual magnetron with discharge voltage control makes it possible the stable reactive sputtering of transparent Al_2O_3 oxide films in the transition mode of sputtering with a high deposition rate $a_D \approx 100$ nm/min. This deposition rate is more than ten times higher than that of transparent oxide films produced in the oxide mode of sputtering.
2. Transparent Al_2O_3 oxide films sputtered on unheated substrates are X-ray amorphous and their mechanical and optical properties do not depend on the deposition rate a_D of their production.

Table 1. Mechanical and optical properties of transparent Al_2O_3 films with amorphous structure sputtered in the transition mode.

p_{O2} [Pa]	$U_{da1,2}$ [V]	$I_{da1,2}$ [A]	a_D [nm/min]	h [nm]	R_a [nm]	T_{vis} [%]	n λ=550nm	H [GPa]	E* [GPa]
0.06	360	1.53	23	1140	1.0	87.8	1.66	11.8	155
0.06	480	1.75	73	3650	1.1	87.7	1.66	11.0	152
0.06	540	2.24	**102**	5080	0.8	87.3	1.65	11.2	154

Acknowledgement
This work was supported in part by the Ministry of Education of the Czech Republic under Project MSM# 4977751302.

References

[1] M.Scherer, P.Wirtz: Reactive high rate dc sputtering of oxides, Thin Solid Films 119 (1984), 203
[2] J.P.Lehan, R.S.Sargent, R.E.Klinger: High-rate aluminum oxide deposition by MetaMode™ reactive sputtering, J.Vac.Sci.Technol. A10(6)(1992), 3401
[3] J.M.Schneider, W.D.Sproul, R.W.J.Chia, M.S.Wong, A.Matthews: Very-high rate reactive sputtering of alumina hard coatings, Surf.Coat.Technol. 96 (1997), 262
[4] O.Zywitzki, G.Hoetzsch: Correlation between structure and properties of reactively deposited Al_2O_3 coatings by pulsed magnetron sputtering, Surf.Coat.Technol. 94-95 (1997), 303
[5] M.K.Olsson, K.Macak: Mechanisms for reactive dc magnetron sputtering of elements with different atomic mases: large area coatings of Al oxide and W oxide, Thin Solid Films 371 (2000), 86
[6] I.Safi: Recent aspects concerning dc reactive magnetron sputtering of thin films: a review, Surf.Coat.Technol. 127 (2000), 203
[7] J.Musil, P.Baroch, J.Vlcek, K.H.Nam, J.G.Han: Reactive magnetron sputtering of thin films: present status and trends, Thin Solid Films 475 (2005), 208
[8] P.Baroch, J.Musil, J.Vlcek, K.H.Nam, J.G.Han: Reactive magnetron sputtering of TiO_x films, Surf.Coat.Technol. 193 (2005), 107
[9] F.Fietzke, K.Goedicke, W.Hempel: Surf.Coat.Technol.: The deposition of hard crystalline Al_2O_3 layers by means of bipolar pulsed magnetron sputtering 86-87 (1996), 657
[10] J.Musil, H.Polakova, J.Suna, J.Vlcek: Effect of ion bombardment on properties of hard reactively sputtered Ti(Fe)N_x films, Surf.Coat.Technol. 177-178 (2004), 289
[11] CRC Handbook of Chemistry and Physics, 58th edition, Chemical Rubber, Cleveland, OH, 1978

Wear and tribological properties of air plasma sprayed nano and conventional zirconia coatings

M. A. Golozar[1,2], J. Mostaghimi[1], T.W. Coyle[1], and R. Soltani[1]

[1] *Center for Advanced Coating Technologies, University of Toronto, Toronto, ON, Canada*
[2] *Department of Materials Engineering, Isfahan University of Technology, Isfahan, Iran*
E-mail: golozar@mie.utoronto.ca , golozar@cc.iut.ac.irT

Abstract
Using pin-on-disc wear testing machine, wear and tribological characteristics of nano and conventional zirconia coatings were studied. Friction coefficient and weight loss were determined. Coatings were characterized before and after wear tests. Effects of wear distance, applied load, and pin materials were investigated. Results obtained revealed a pronounced effect of test variables and coating characteristics on the wear behavior of these coatings.
Keywords: Zirconia, Nanostructured, Air plasma spray, Wear, Tribology

1. Introduction

During the last decades, ceramic materials have been widely studied, developed, and applied as effective Thermal Barrier Coatings (TBC). The main application of thermal barrier coatings such as Plasma Sprayed Zirconia-base coatings (PSZ) are combustion system components such as: pistons, valves, piston fire decks in diesel engines, and piston rings, as well as cylinder liners [1-3]. These applications could extend durability of engine, increase engine efficiency, and reduce fuel consumption. The main advantage of plasma-spayed zirconia-base materials as TBC, stems from their unique properties such as: high hardness and wear resistance, high strength, excellent resistance to erosion, hot corrosion, and oxidation, as well as high thermal insulating characteristics and a thermal expansion coefficient close to that of the most metallic materials.
Regarding the development of TBCs for the above-mentioned applications, one of the main problems involved is the wear behavior. In this respect, the combined effects of intrinsic properties such as chemical composition, microstructure, and grain size, as well as the environmental parameters such as wear testing variables would be important [4-9]. Comparing the nanostructured and conventional 8wt.%yttria-partially stabilized zirconia coatings, it has been reported that at long wear distances such as 10km the former one showed better wear resistance and lower friction coefficient than the latter one [5]. Yang et al have shown that the wear resistance of tetragonal zirconia polycrystalline coating decreases with increasing grain size. They showed that the weight loss can be expressed in form of $R=nG^{-n}$, where G is the average grain size. The value of n is equal to 0.5 and 1.0 for fine and large grain size samples respectively [6]. Chen and his coworkers have reported a wear rate for nanostructured zirconia coating equal to two-fifths and half of traditional zirconia under applied load of 20-80N, dry and distilled water lubrication condition respectively. They have attributed the improved wear resistance of plasma-sprayed nanostructured zirconia coating to the optimization of microstructure and enhancement of mechanical properties [7-8]. Furthermore, Li et al have reported that the friction coefficient of the coatings spayed using the nanostructured powder were almost the same as those of the coatings spayed using the conventional powder. However, the former coatings were more wear resistant than the latter one [9].
The aim of this paper is to investigate and compare the wear and tribological behavior of Air Plasma Sprayed (APS) nanostructured and conventional 8wt% Yttria-Partially Stabilized Zirconia (Y-PSZ) coatings on stainless steel substrate.

2. Material and experimental techniques

Using Air Plasma Spraying (APS), and processing parameters shown in table 1, conventional and nanostructured 8wt.%Yttria Partially Stabilized Zirconia (Y-PSZ) coatings were deposited on pre-bond coated austenitic stainless steel (AISI 304) disc shape (75x4mm) substrates**.** Thickness of bond coat and topcoat were around 150µm and 250µm respectively**.** Conventional zirconia powder with particle size of 45-75 µm, and Ni-based bond coat powder with the particle size of 56-106 µm (purchased from Sulzer Metco Company) and

nanostructured powder consisted of agglomerated particles of 15-150μm in diameter (purchased from Inframeat Corporation) were used.
Using an X-ray diffractometer (Philips model PW2273) with Cu-k_α tube, phase analysis of powders and coatings produced were determined. Employing a computer controlled machine the coated substrates were subjected to pin-on-disc wear tests using silicon nitride (Si_3N_4) and zirconia balls (10mm in diameter) as the pin (Fig. 1). The coefficient of friction was recorded in real time. The weight loss of coated substrates was measured using initial and the final weight of coated substrates just before and after the wear tests, respectively. Coatings were characterized before and after subject to wear tests by various techniques including optical microscopy, scanning electron microscopy (SEM), energy dispersive X-ray spectrometry (EDX), and X-ray diffraction (XRD). Effects of experimental parameters such as wear distance, and applied normal load, were investigated.

3. Results and discussion

The XRD patterns obtained from coatings produced showed clearly the presence of tetragonal phase in the both coatings (Fig. 2). This phase is the most suitable phase for these types of ceramic coatings. Optical and scanning electron microscopy observations revealed an almost uniformly deposited bond and top coatings on the stainless steel substrates (Fig. 3)
Effect of wear distance on the weight loss for both coatings against silicon nitride and zirconia balls is shown in figures 4A and 4B respectively. As is observed, increasing the wear distance would increase the weight loss of both coatings. However, the wear rate of conventional coating against wear distance is higher than that of the nanostructured coating. This is more pronounced for coatings tested against silicon nitride ball. The lower weight loss (wear rate) obtained for nanostructured coating could be due to the finer microstructure as well as superior physical and mechanical properties of nanostructured zirconia compared with the conventional one. All worn tracks of coatings tested against silicon nitride and zirconia balls were examined using scanning electron microscopy. In the case of coatings tested against silicon nitride ball, a silicon containing film was observed on the worn surfaces (Figs. 5A and 5B). This film is less pronounced for short wear distances such as $\leq$ 5km. Conversely, for long wear distances such as 10km, a thick but very brittle silicon containing film is formed. Particles and wear debris produced due to cracking, fracturing and delaminating of this film at long wear distances could act as abrasive wear agents. The higher weight loss obtained for coatings tested for long wear distances against silicon nitride ball is believed to be due to presence of these wear debris.
Effect of applied normal load on the weight loss of nanostructured and conventional zirconia coatings against silicon nitride and zirconia ball is shown in figures 6A and 6B. As is observed, the effect of applied normal load on weight loss of coatings against silicon nitride and zirconia balls is quite different. In the case of silicon nitride ball (Fig. 6A), the rate of increasing the weight loss for applied normal loads greater than 40N is more than that of applied normal loads less than 40N. This is believed to be due to fracture and delaminating of silicon oxide containing film on the worn track surface at high-applied normal load. AS previously mentioned, these particles in the worn debris could act as abrasive wear agents, and therefore increase the wear rate of coatings. In the case of zirconia ball the weight loss of nanostructured and conventional coatings against applied load, for applied normal loads less than 40N increased. The rate of increase was more than that of coatings against silicon nitride ball. Conversely, for applied normal loads greater than 40N, the weight loss of nanostructured coating decreased while that of conventional coating remained almost constant. It is believed that at applied normal loads less than 40N, the wear debris act as abrasive wear agents. However, at applied normal loads greater than 40N, wear debris trap between the contact surfaces of ball and coating and redeposit on the worn track surface. This would reduce the weight loss measured.
In all cases, friction coefficients recorded for both coatings under various conditions tested in this paper represented a lower friction coefficient for nanostructured coating than that of conventional coating. However, the differences observed for various experiments were different from each other and were depended on the wear test conditions applied (wear distance, applied load, and ball material). Examples of friction coefficients recorded for nanostructured and conventional coatings are shown in figures 7A and 7B. As it is observed, under the conditions applied in figures 7A and 7B, the initial friction coefficient for both coatings is almost the same. However, in the case of nanostructured coating the friction coefficient against wear distance decreased more rapidly.

4. Conclusion

Under the wear conditions tested in this paper, the weight loss of nanostructured zirconia coating was observed to be lower than that of conventional zirconia coating. However, the difference obtained was observed to be a function of wears conditions applied, such as wear distance, applied normal load, and counterface material. Although the friction coefficients recorded for nanostructured coatings were observed to be lower than those of conventional coatings, the difference in some cases was negligible.

References

[1] A. Levy and S. Macadam, The Behavior of Ceramic Thermal Barrier Coatings on Diesel Engine Combustion Zone Components, Surface Coatings Technologies, 30, 51-61 (1987)

[2] F. Rasteger and A. E. Craft, Piston Ring Coatings for High Horse Power Diesel Engines, Surface Coatings Technologies, 61, 36-42 (1993)

[3] H. S. Ann, J. Y. Kim, D. S. Lim, Tribology Behavior of Plasma-Sprayed Zirconia Coatings, Wear 203-204, 77-87 (1997).

[4] J. F. Bisson, C. Moreau, M. Dorfina, C. Dambra, and J. Mallon, Behavior and Characterization of Two 7-8wt% yttria-Stabilized Zirconia Powders and Coatings Produced Using Plasma Spray Deposition, Thermal Spray, Ed. C. Moreau and B. Marple, ASM International (2003).

[5] M. A. Golozar, J. Mostaghimi, T. W. Coyle and R. Soltani, Wear Behavior of Nanostructured and Conventional Y-PSZ Coatings" Accepted for Presentation at "Materials Degradation: Innovation, Inspection, Control and Rehabilitation Symposium" in the COM 2005, 44th Conference of Metallurgists, August 21 to 24, 2005, Calgary, Alberta Canada.

[6] C. T. Yang, W. J. Wai, Effects of Material Properties and Testing Parameters on Wear Properties of Fine-Grain Zirconia, Wear 242, 97-104, (2000)

[7] H. Chen, Y. Ahang, C. Ding, Tribological Properties of Nanostructured Zirconia Coatings Deposited by Plasma Spraying, Wear, 253, 885-893, (2002).

[8] C. Ding, H. Chen, X. Liu, Y. Zeng, Plasma Sprayed Nanostructured Zirconia Coatings for Wear Resistance, Thermal Spay, Ed. C. Moreau and B. Marple, ASM International 455-458, (2003).

[9] J. F. Li, H. Liao, X. Y. Wang, B. Normand, V. Ji, C. X. Ding, C. Coddet, Improvement in Wear Resistance of Plasma Sprayed Yttria Stabilized Zirconia Coating Using Nanostructured Powder, Tribology International, 37, 77-87 (2004)

Table1- Wear processing parameters used to produce zirconia coatings.

Parameter	Conv. Coating	Nano Coating
Current (A)	740	740
Ar gas flow rate (slmp)	40	40
H_2 gas flow rate (slmp)	2.0	2.0
Ar carrier gas (slmp)	8	8
Distance (cm)	2.5	2.5
Mean velocity (cm/sec)	144.19	148.53
Mean temperature (ºC)	2809	2958

Figure1- The pin-on-disc wear testing machine used.

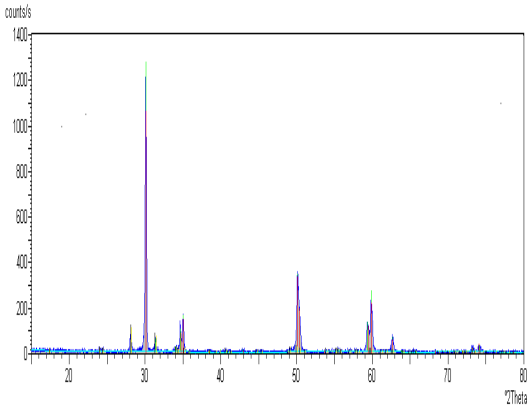

Figure 2 - An example of the XRD pattern obtained from coatings produced.

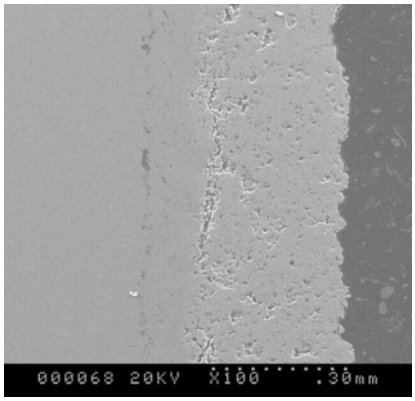

Figure3 - An example of the SEM micrograph showing the nature of bond coat and topcoat.

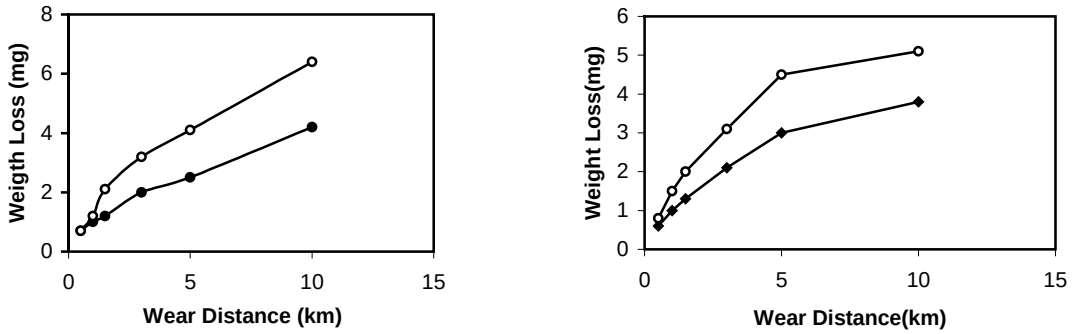

(A) (B)

Figure 4 - The weight losses against wear distance, 23 N applied load, 25ºC, 60 rpm, Silicon nitride ball (A), Zirconia ball (B), (○ Conv. Coating, ● Nano. Coating)

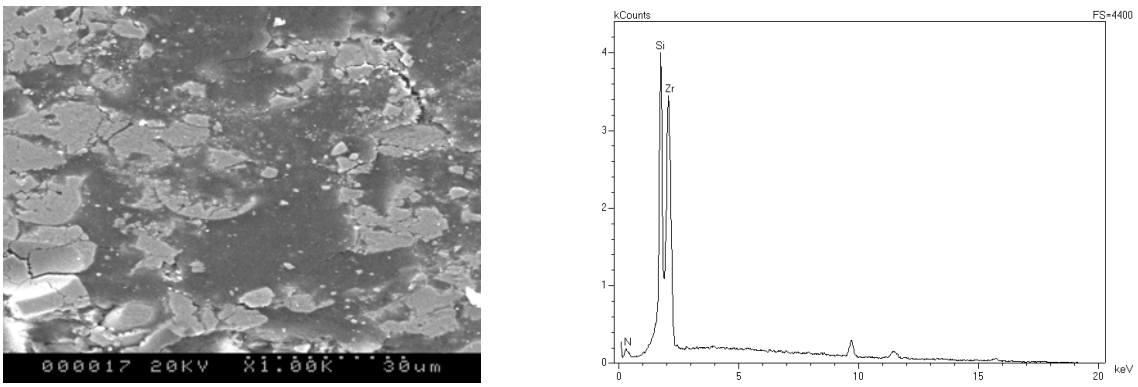

(A) (B)

Figure 5 - An SEM micrograph of the silicon oxide containing film on the worn track surface (A), and EDX analyzes of the film (B).

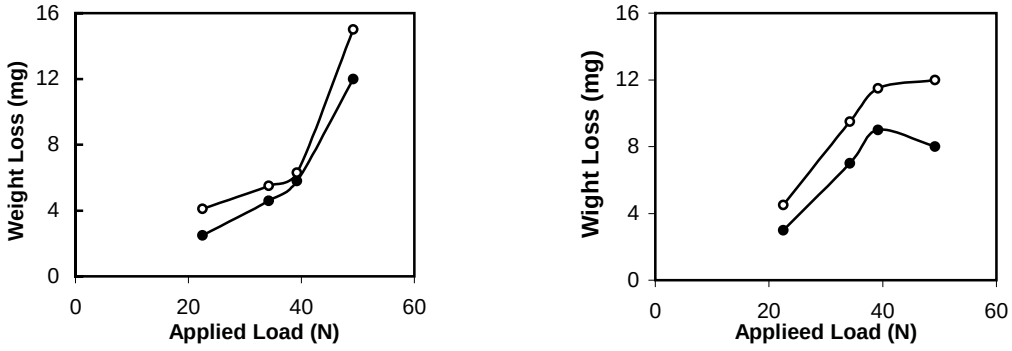

(A) (B)

Figure 6 - The weight loss against applied load, 5 km wear distance, 25ºC, 60rpm, silicon nitride ball (A), Zirconia ball (B), (○ Conv. Coating, ● Nano. Coating)

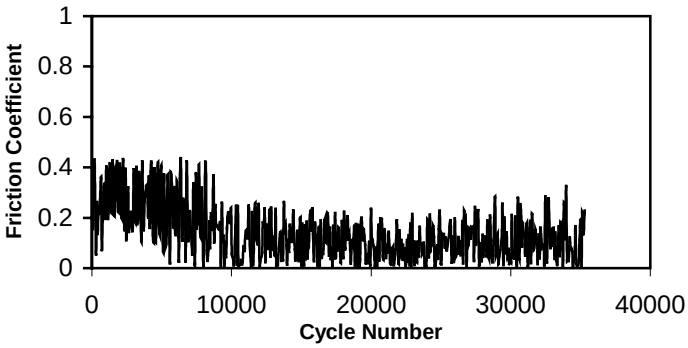

(A)

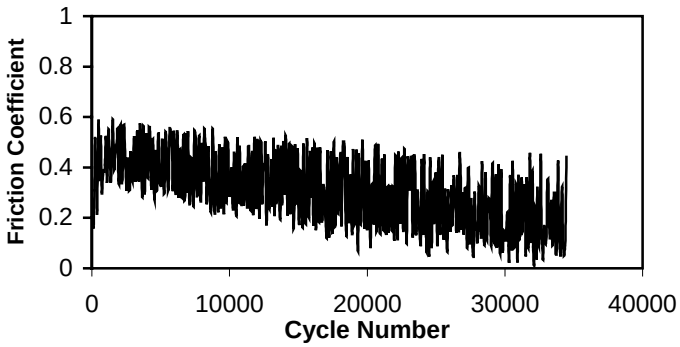

(B)

Figure 7 - An example of the friction coefficient against wear distance for nanostructured coating (A) and conventional coating (B), zirconia ball, 25ºC, 60rpm.

UV absorbance of titanium oxide-like films by plasma assisted deposition from mixtures of oxygen and titanium-tetrakis-isopropoxide

A. Sonnenfeld[1], R. Hauert[2], Ph. Rudolf von Rohr[1]

[1]*Swiss Federal Institute of Technology Zurich, Institute of Process Engineering, CH-8092 Zurich, Switzerland*
[2]*Empa, Materials Science and Technology, Überlandstrasse 129, CH-8600 Dübendorf, Switzerland*

Abstract
A radio frequency (RF) low pressure non-thermal plasma was used to deposit films by mixtures of oxygen and titanium(IV)isopropoxide (TTIP) at powers of 0.2 kW on polyethylene-terephthalat (PET). As to XPS, films deposited consist of TiO_x ($x \approx 2$). Spectral absorptance (309 to 500 nm) of films was studied. At 310 nm, the absorption coefficient obtained was 0.3% nm^{-1}. While keeping other parameters constant, the coefficient decreased by 0.05% nm^{-1} with an increase of the concentration of TTIP from 2% to 8%.

Keywords Titanium oxide, Plasma assisted chemical vapour deposition (PACVD), UV absorption, XPS

1. Introduction

Thin films of titanium oxide have many potential applications due to high dielectric constant, high refractive index and good chemical as well as thermal resistance of the material [1, 2]. Good quality films of titanium oxide are obtained in high temperature processes. However, as plastics are the material of choice in many domains of industrial production, this work addresses the deposition of titanium oxide-like films obtained by means of plasma assisted chemical vapour deposition (PACVD) in a low temperature environment.
Several polymers provide also excellent optical transmission in the visible range, and thus are convenient materials for substituting glass. However, polymers absorb very effectively ultraviolet (UV) light causing chain degradation and crystallization, accompanied by loss of flexibility and translucence.
In this regard, the absorption properties of films deposited by means of TTIP in mixtures with oxygen in an RF discharge are studied in the present work. Films were deposited in varying the concentration (the molar fraction) of TTIP in the discharge gas. In addition, chemical composition of films deposited was investigated by X-ray photoelectron spectroscopy.

2. Experimental

Experimental set-up for PACVD
Films were deposited in the set-up schematically shown in figure 1. Unless described differently, all parts of the set-up were made of stainless steel. The heart of the set-up is a double-walled chamber built on the basis of a T-piece pipe fitting for clamping flange (DN 250 ISO-K). Its side-flange is shut by a blanking flange acting as porthole. It is double-walled as well and gives access to the deposition chamber for maintenance and substrate exchange. The bottom flange of the chamber is sealed by a special flange which supports the feedthroughs of the annular gas shower and of the powered electrode. Inside the chamber, at 13 cm height from the chambers bottom, the cylindrical electric feedthrough meets the electrode, a circular plate of a diameter of 14 cm. Fitted into the dark space shield, gaskets of polytetrafluorethylen (PTFE) with fluorelastomer o-rings seal and centre the electric feedthrough as well as the electrode. The dark space gap obtained is 0.3 mm. The shield is fixed and grounded by thread-connection at the inner side of the blanking flange. Outside the vacuum chamber, the electric feedthrough of the powered electrode forms the pin of a plug shaped coaxial connector integrated in the blanking flange.This plug connects to the output socket of a LC-matching network (DRESSLER, VM 1500) right beneath the vacuum chamber. The matching is used to adapt the load impedance of the discharge configuration to the out-put impedance of the electric generator (DRESSLER, Cesar 1312). The generator supplies sinusoidal voltages of a frequency of f = 13.56 MHz and is connected to the matching unit by a coaxial cable. The gas throughfeeds support the annular gas shower which has a diameter of 23 cm. Since they are sealed by tube fittings with PTFE gaskets at the bottom of the vacuum chamber, the vertical position of the gas shower is variable. Gas throughfeeds and shower are made of ∅ 6 x 4 mm tube. By means of 24 holes (∅ 0.6 mm) in the shower, the gas is dispersed toward the center of the reactor and the substrate holder. The substrate holder is electrically

grounded and of the same diameter as the powered electrode. It is supported by a rod with rocket tail-shaped plates, which are fixed to the top flange of the vacuum chamber. By this means, the substrate holder is centre-positioned right beneath the exhaust gas exit of the chamber.

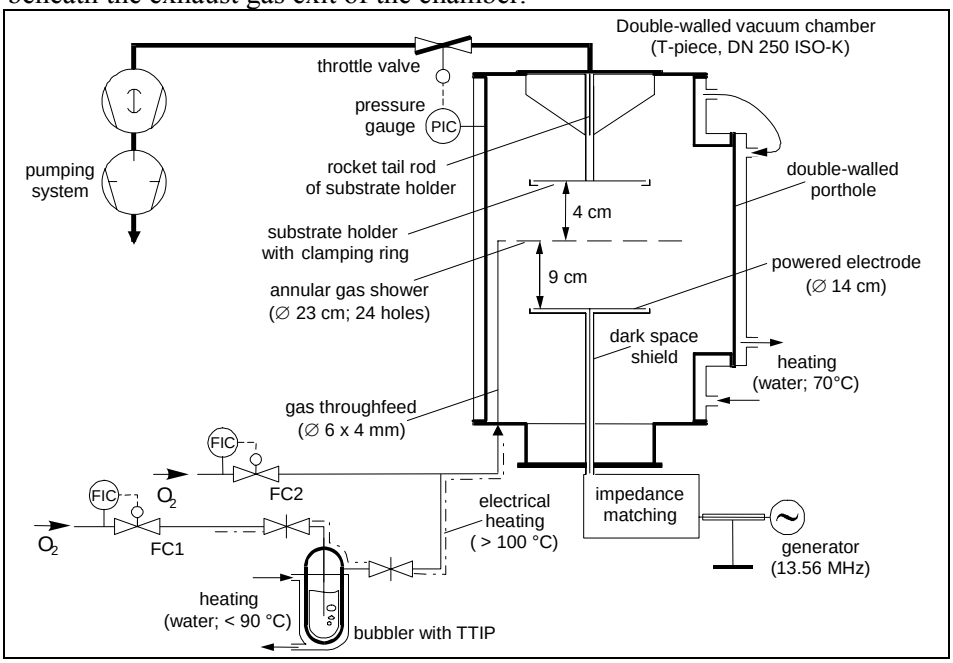

Figure 1 Scheme of the experimental set-up.

A triple stage pump system with a double stage pre-vacuum rotary pump (LEYBOLD, Trivac D 65 B) and a roots pump (LEYBOLD, RUVAC WS 1001) generates and maintains low-pressure environment. The base pressure of the chamber obtained is less than 10^{-3} mbar. The chamber pressure is measured by a capacitance diaphragm gauge (MKS, Baratron 626A, 10^{-3} – 10 mbar). It is connected to a pressure controller (MKS, 651C), and by means of a butterfly exhaust throttle valve (MKS, 653B, DN 100 ISO-F), the pumping speed is regulated. Therefore, the chamber pressure could be adjusted independently form gas flux.

The two mass flow meters (MKS, 1179B), in fig. 1, designated as FC1 ($Q_{FC1,max}$ = 10 sccm (N_2)) and FC2 ($Q_{FC2,max}$ = 100 sccm (N_2)) are controlled by a PR4000 (MKS). The gas flux delivered by FC1 is admixed to the gas flux of FC2 after passing through the bubbler containing the deposition precursor TTIP (purchased from SIGMA-ALDRICH with a purity of 97%). According to the dependence of its vapour pressure on temperature, a partition of TTIP is diluted in the through-streaming gas. Therefore, the precursor temperature T_{TTIP} has been controlled by means of a thermostat which pumps constantly water through the double-mantle of the bubbler. Since reference specifications concerning the vapour pressure are fragmentary and sometimes contradictory [3, 4, 5], we estimated the precursor concentration c_{TTIP} (molar fraction) in measuring the diminution of its volume ΔV_{TTIP} over time Δt at fixed values of T_{TTIP}:

$$c_{TTIP} = \frac{[TTIP]}{[TTIP] + Q_{tot}} \text{ with } [TTIP] = \frac{\sigma_{TTIP}}{M_{TTIP}} \frac{\Delta V_{TTIP}}{\Delta t} \qquad (1)$$

Here, Q_{tot} is the total flux of the diluting gas, i.e. oxygen, M_{TTIP} = 284.25 g/mol is the molar mass of TTIP, and σ_{TTIP} = 0.96 g/cm^3 its mass density. Hence, the resulting calibration function depending on Q_{tot} and T_{TTIP} is the basis for the values of the precursor concentration of TTIP given later on. All experiments described were conducted with an initial gas mixture of oxygen with TTIP admixed. Variation of c_{TTIP} = 0.4 to 8% was obtained by varying T_{TTIP} = 60 to 85°C at constant flux Q_{tot} = 50 sccm, and at constant value of T_{TTIP} = 80°C by varying Q_{tot} = 10 to 50 sccm. In order to prevent condensation of TTIP, the inner surface of the vacuum chamber was heated to 70°C by pumping water of a thermostat through the double-walled mantle of the chamber. The gas supply, however, was heated electrically to a temperature of more than 100°C.

During experiments the working pressure has been kept constant at $p = 4\times10^{-2}$ mbar. Comparing it to the base pressure of less than 10^{-3} mbar it would contribute to approximately 3% of residual gas in the initial gas

mixtures. But, purging with the process gas at the nominal pumping speed of several hundred cubic metres per hour reduces the residual gas to negligible amounts within seconds. Preliminary, pure streaming tests with different O_2/TTIP mixtures did not result in any detectable deposition although the sticking coefficient of TTIP below 300 K is nearly equal to unity [6]. This could only be achieved by operating the plasma. Experiments were conducted at a constant forwarded power of $P_f = 200$ W. The reflected power was adjusted to $P_r = 25$ W ± 3 W. By this means, an asymmetric RF discharge was operated between powered electrode and substrate holder (see fig. 1). The self bias voltage varied from experiment to experiment between 300 and 600 V. During a single experiment, however, it slightly increased by approximately 50 V. Films were deposited on PET films with a thickness of 12 µm. The PET films were attached to the substrate holder by a special clamping ring put to the edge of the substrate holder. Since in this orientation, substrates have been coated up side down, powder agglomeration on the substrate surfaces could be reduced. PET films were used as substrate for investigations of the light absorptance of films deposited. For XPS and ellipsometric analyses small pieces of Si(100) wafers have been fixed onto the surfaces of the PET films.

X-ray Photoelectron Spectroscopy

In order to determine the concentration and the chemical status of titanium, oxygen and carbon in the films deposited on pieces of Si(100) wafers, spectra were acquired on a Physical Electronics (PHI) Quantum 2000 photoelectron spectrometer. The samples were exposed to a monochromatized X-ray beam (Al-Kα: hν = 1486.6 eV). Low-energy electrons and argon ions were used simultaneously to compensate for electrical charging of insulating surface areas during analysis. Emitted photoelectrons were analyzed with a hemispherical electron energy analyzer equipped with a channel plate and a position sensitive detector. The electron take-off angle was 45°. The analyzer was operated in the constant pass energy mode at 58.7 eV giving a total energy resolution of 1.05 eV. The binding energy scale of the analyzer was calibrated for the Au 4f electrons to be at 84.0 eV ± 0.1 eV. The base pressure of the spectrometer was less than 5×10^{-9} mbar. Elemental concentrations are given in atomic percent (normalized to a total of 100%) using the photoelectron peak areas after Shirley background subtraction (Multi-Pack, Version 6.1, Physical Electronics Inc., Eden Prairie, MN, USA) and the built-in PHI sensitivity factors for the calculation. To remove adventitious carbon as well as surface oxide layer, prior to analysis the sample surfaces have been cleaned by 4 kV argon ion bombardment for 30 s. Due to residual charging of the samples during analysis, the actual peak positions had to be referenced to the Ar 2p peak at 241.9 eV.

Ellipsometry and Profilometry

A variable angle spectroscopic ellipsometer (J.A. WOOLLAM INC., M-2000F) was used to measure the film thickness. Measurements were performed at three different incident angles (65°, 70°, 75°) in the range of 245 nm to 995 nm. Best fit of the measured spectral dependencies of Δ and ψ have been found by adapting the spectral dependencies of the refractive index n and the extinction coefficient k of the deposited films.Film thicknesses obtained by ellipsometry could be validated by masking a portion of Si substrates during deposition and then measuring the resulting steps by profilometry (TENCOR P10).

UV-Vis spectroscopy

Spectral absorption of the films deposited on PET was determined by a double-beam spectrometer (PERKIN-ELMER, Lambda 35) operative in the ultraviolet and visible spectral range. The spectrometer is equipped with a deuterium (D_2) lamp for the UV range and a tungsten lamp for the visible spectrum. Spectral dispersions is obtained by a grating of 1053 lines/mm. Deposited films were investigated at a beam cross-section of 2 mm × 7.5 mm in the focal length of the sample compartment. Therefore, samples of 1.5 cm × 3.5 cm were cut out of the PET films coated. At these samples, spectra from 500 nm to 200 nm have been acquired and compared to the spectral absorption of the uncoated substrate material, namely PET film of 12 µm thickness.

3. Results

Chemical composition of the films

While keeping the temperature of TTIP constant at 80°C ± 1°C, the oxygen flow rate Q_{tot} was varied such as to vary the oxygen-to-TTIP ratio *q* in the range from 58 to 12. With regard to the chemical composition of the films deposited on PET, Si-wafer sample coated under these same conditions have been examined by XPS.

The obtained spectra reveal that oxygen, titanium and carbon are the major constituents in the films deposited. Apart from these elements, traces of nitrogen, chromium and silicon were observed at some coated samples. On the basis of the O1s, Ti2p and the C1s photo-electron peaks, their atomic concentrations were determined. In table 1, these values are listed in dependence on the concentration of TTIP during the plasma deposition process.

Table 1 Elemental composition (atomic-%) of films deposited at different precursor concentrations

c_{TTIP} [%]	1.7	1.9	2.6	3.8	7.4
O_2/TTIP ratio q [-]	57.8	51.6	37.5	25.3	12.5
C(1s) [%]	6.7	7.0	6.7	7.9	8
O(1s) [%]	58.8	58.5	59.7	58.5	57.9
Ti(2p) [%]	34.5	34.5	33.6	33.7	34.1
[O]/[Ti]	1.70	1.70	1.78	1.74	1.70

Despite a quadruplicating concentration of TTIP from approximately 2% to 7%, the resulting elemental composition of deposited films remains virtually unchanged. In comparison to the stoichiometry of TTIP, the carbon content is drastically reduced from nearly 74% to 8%. Consequently, the concentrations of oxygen and titanium have increased. However, the ratio [O]/[Ti] = 1.7 (tab. 1) is too low for being TiO_2.

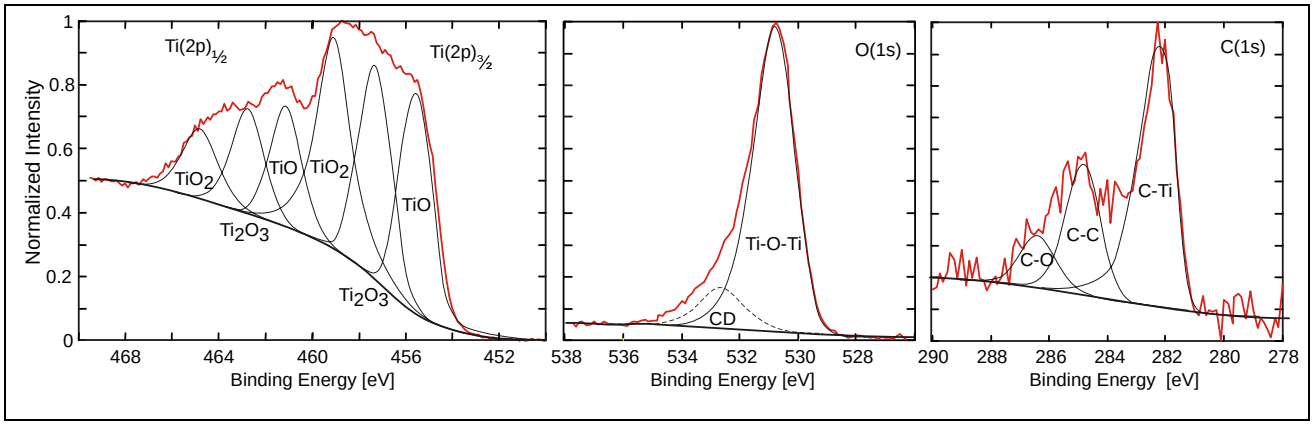

Figure 2 Spectra of the $Ti(2p)_{1/2}$ and $Ti(2p)_{3/2}$, O(1s) and C(1s) core level peaks. Peaks attribution to chemical structures has been done after [7, 8, 9].

Since peaks of the $Ti(2p)_{1/2}$ and $Ti(2p)_{3/2}$ core level are broad and overlapping each other (see fig. 2), the films seem to consist of a mixture of the oxides of titanium: Ti_2O_3, TiO_2 and TiO [7]. Further, the C(1s) spectrum features the chemical formations Ti-C, C-C, respectively C-H and C-O at binding energies of 282.2 eV [8], 285.0 eV and 286.2 [9].

The O(1s) spectrum, however, accounts for the presence of Ti-O-Ti structures typically observed of pure TiO_2. Indeed, the feature forming the shoulder of the O(1s) peak (at 535.3 eV) could represent Ti-O-C. However, considering the C(1s) spectrum, the occurrence of Ti-O-C seems to be rather improbable. Since the entire amount of carbon is always lower than 8%, the portion of C-O bonds attributable to the presence of Ti-O-C is too small to account for the shoulder in the O(1s) spectrum. In fact, it must be taken into account the effect of the argon ion bombardment which was applied to clean the film surfaces before spectrum acquisition.

Its influence has already been addressed in an earlier study [7]. It showed that (initially existing) TiO_2 becomes reduced due to preferential sputtering of oxygen at even lower ions energy of 2 kV. The by such means modified material showed the same characteristic XPS spectra as described above.Furthermore, it should be noted, that the effect of sputtering is not as noticeable in the O(1s) spectrum. In this case, the small peak shoulder accounts for charge transfer in TiO_x [7]. Consequently, it is likely that under the deposition conditions investigated all films obtained consist of TiO_2. Under this premise, the detected carbon is likely to descend from surface contaminations which become re-deposited and recombined under the influence of the argon sputtering.

Film thickness and growth rate

Apart from the chemical composition of the films deposited at different values of c_{TTIP}, the film thickness has

been derived by ellipsometry. In general, film thickness and growth rate were found to increase with precursor concentration. In figure 3, two deposition series at t_P = 5 and 10 min of deposition are compared. For the shorter deposition time, the growth rate increases linearly from 32 nm/min at c_{TTIP} = 2% to 48nm/min for c_{TTIP} = 8%.
In the sample series for 10 min deposition time, the deposition rate follows the characteristics for 5 min up to 4% of TTIP. However, at doubled concentration, the rate is by 8 nm/min smaller. This finding can be explained by the increase of powder formation with increasing precursor concentration, virtually observed in the gas phase. Gas phase nucleation reduces the flux of species contributing to deposition on the substrate.

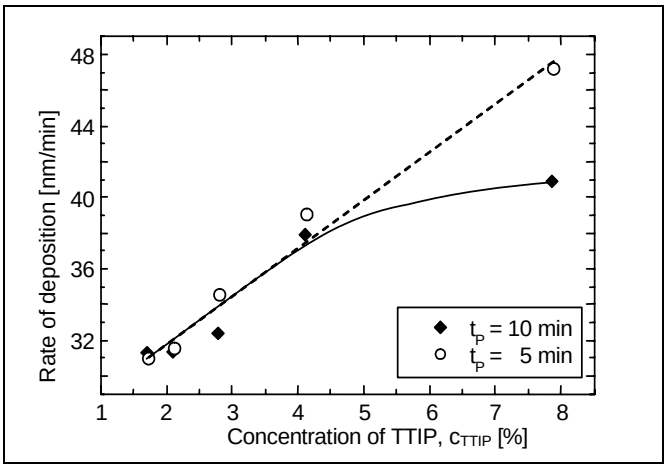

Figure 3 Dependence of the film growth rate on precursor concentration at different deposition times (t_P = 5 and 10 min) in O_2/TTIP gas mixture.

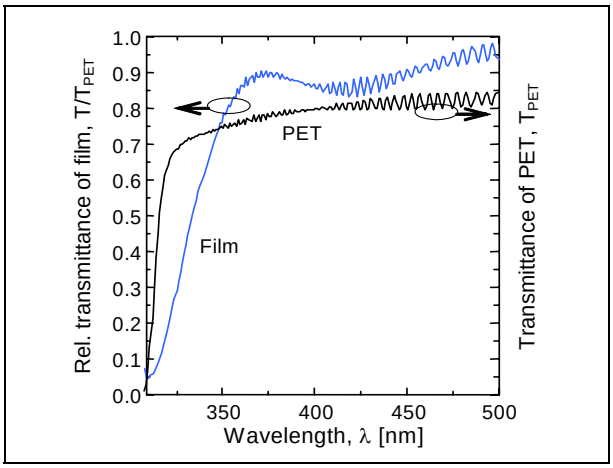

Figure 4 Relative transmittance of a film deposited at c_{TTIP} = 1.9% (t_P = 10 min in O_2/TTIP) compared to the transmittance of PET substrate.

Since number and size of particles will increase with progressing deposition time, the reduction of the film growth rate is inevitable. Surface profiling conducted to validate ellipsometric measurements, in addition, indicate the increasing role of gas phase nucleation with precursor concentration since a qualitative increase of surface roughness was observed.

UV and visible light absorption by deposited films

A typical transmittance spectrum of a film relative to the PET substrate is shown in figure 4. Due to the strong absorption of PET below 310 nm only the upper part of the spectral range acquired is presented here.

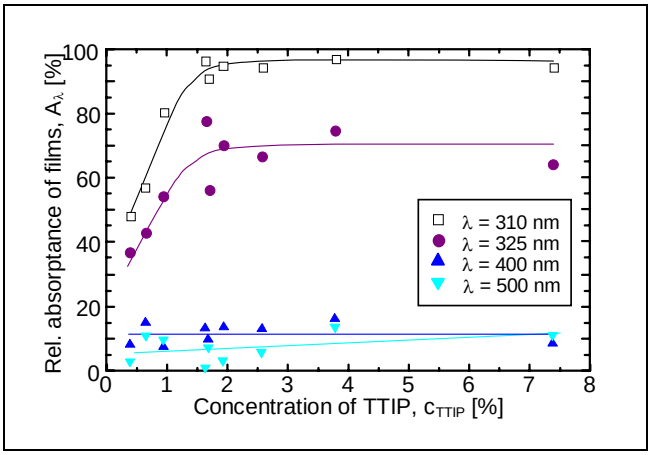

Figure 5 Dependence of the spectral absorptance on precursor concentration at different wavelengths.

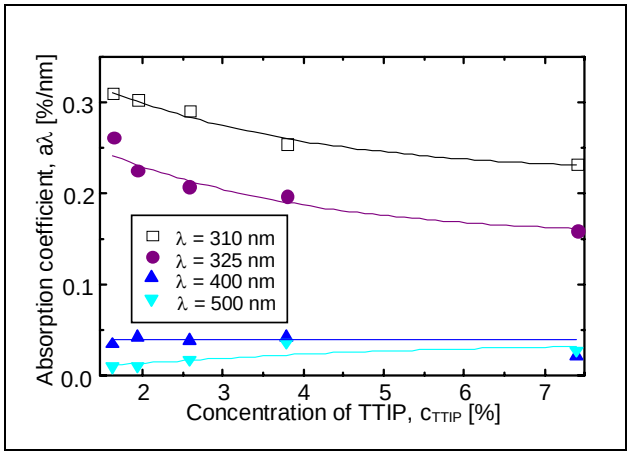

Figure 6 Absorption coefficient of films versus precursor concentration at different wavelengths.

Compared to PET, the relative transmittance of films deposited at c_{TTIP} > 0.6% is generally lower in the spectral range from 325 nm down to lower wavelengths. Therefore, cut-off (transmission reduced to the level of -3dB) occurs at higher wavelengths than 313 nm in the case of PET. The exact cut-off wavelength, however, has been found to alter in the range from 320 nm to 325 nm. Moreover, no cut-off was obtained for films deposited at

c_{TTIP} < 0.6%, although a reduction of transmission could be observed. In the spectral range from 350 to 500 nm, the relative transmittance of films is generally higher than that of PET, although it is not 100%. In this range the transmittance characteristics is strongly affected by interference effects as it can be seen in figure 4.
In order to study the influence of c_{TTIP}, spectral absorptance A_λ and absorption coefficient a_λ have been determined for λ = 310, 325, 400 and 500 nm. As shown in figure 5, absorptance at 310 nm and 325 nm rise with increasing value of c_{TTIP} up to an approximate concentration of 1.8%. Whereas the relative absorptance at 325 nm attains approximately 70% (cut-off value), the absorptance at 400 and 500 nm remains nearly constant at a level of 10%. Above c_{TTIP} = 1.8%, spectral absorptance remains nearly constant at all wavelengths. However, since the film thickness has been found to increase with precursor concentration, the efficiency of UV absorption of films deposited decreases with increasing precursor concentration above c_{TTIP} = 1.8%. This can be seen in figure 6, where the absorption coefficient is depicted. At λ = 310 nm, the absorption coefficient drops from 0.3% nm^{-1} (virtually 30% for a 100 nm thick film) to 0.25% nm^{-1} by an increase of the concentration of TTIP from 2% to 8% when keeping other parameters constant. In the same time, $a_{400\ nm}$ and $a_{500\ nm}$ appear to increase slightly.

4. Conclusions

As derived from XPS analyses, films deposited from oxygen-TTIP mixtures on PET films resemble the chemical structure of TiO_2 with small quantities of carbon containing inclusions. The origin of such contaminants could not be fully enlightened, and remains to further investigations. However, with respect to chemical properties of films, it was shown that good quality titanium oxide is also obtainable in a low-temperature process environment being preferable for coating of polymeric materials.
Since TTIP provides titanium already in chemical liaison to oxygen (at a ratio of 1:4), chemical composition of oxide films was found to be chemically invariant against the variation of precursor concentration (2% to 8%), and the variation of the mixing ratio of oxygen to TTIP (58 to 12), respectively.
Consequently, the cut-off wavelength of films analysed by UV-visible absorption spectroscopy showed little variation around 325 nm. However, detailed study of spectral absorptance and absorption coefficient of films shows an influence of the precursor concentration on optical properties. Accordingly, best UV absorptance the films deposited (at 310 nm more than 95%) was obtained above 2% of TTIP. Evaluation of the absorption coefficient revealed that the absorption effect of thicker films deposited at higher precursor concentrations is decreasing. Since chemical composition of films did not change significantly (see above), and profilometry showed increasing surface roughness with increasing precursor concentration, a decrease of the film density causing diminution of the absorption coefficient ($a_{310\ nm}$ from 0.3% nm^{-1} to 0.25 % nm^{-1}) is likely.

Acknowledgement

The authors wish to thank L. Feuz and Prof. M. Textor (ETH Zurich) for providing opportunity of and their support in ellipsometric measurements. Furthermore, access to the surface profiler used has been offered by U. Lang (ETH Zurich), whose helpfulness is gratefully acknowledged.

References

[1] Handbook of thin film process technology, Vol. 2, Ed.: D. E. Glocker, IOP Publishing (1995), X1.3.5:1
[2] Introduction to ceramics, Ed. H.K. Bowen, 2nd ed., Wiley, New York (1976)
[3] J. Lahouidak, Etude de couches minces de TiO_2 déposées par CVD et CVD assistée plasma, Thesis at University of Montpellier, Ecole nationale supérieure de chemie de Montpellier (1991), 51 – 54
[4] R.C. Smith, Tiezhong Ma, N. Hoilien, L.Y. Tsung, M.J. Bevan, L. Colombo, J. Roberts, S.A. Campbell, W.L. Gladfelter, Advances materials for optics and electronics 10 (2000), 105 – 114
[5] A. Goossens, E.-L. Maloney, J. Schoonman, Chem. Vap. Deposition **4(3)** (1998), 109 – 114
[6] Yuhan-Min Wu, D.C. Bradley, R. M. Nix, Applied Surface Science 64 (1993), 21 – 28
[7] P.R. McCurdy, L. J. Sturgess, S. Kohli, E. R. Fisher, Applied surface science 233 (2004), 69 – 79
[8] T. Zehnder, J. Patscheider, Surface and Coatings Technology 133-134 (2000), 138 – 144
[9] A. Sonnenfeld, T.M. Tun, L. Zajicková, K.V. Kozlov, H.-E. Wagner, J.F. Behnke, R. Hippler, Plasmas & Polymers **6(4)**, (2001). 237 – 266

UPDATING OF SURFACES OF ITEMS FROM STEEL BY PLASMA METHOD

V. Maslov, A. Lykov

«MATTEX», Kantemirovskaya st., 22, 1, 310, Moscow, 115522, Russia.

Abstract.

In the present work the results of an experimental research of the measurement of heat flows from the plasma generator with the external electrical arc which are controlled by magnetic fields are represented. Because of these data hardening the surfaces, subject to wear, of railway wheels and rails is conducted. The practical application of the given technology has shown it high efficiency.

1. Introduction.

The theoretical analysis of process of distribution of heat in a material [1] has shown, that for hardening of the surface it is necessary to create heat flows $(2\text{-}3)\cdot10^7$ W m^{-2}. And for want of heat flows more then $2\cdot10^7$ W m^{-2} the phase structure should consist in main of martensite. Using more "soft" conditions of heat treatment by the plasma generator it is possible to receive structures of metal practically without martensite, namely with troosomartensite, troostite, sorbite. This circumstance is extremely important for creation of a hardening stratum on details, which are subject to significant mechanical loads. For example, strengthening of crests of railway wheels or working surface of rails take place the formation of martensite. There are additional residual voltages [2], which can result in formation of cracks. The hardening of a surface of details without getting martensite creates conditions of their safe operation.

2. Experimental researches.

For deriving required structures in a hardened stratum of metal details it is necessary to select an appropriate source of plasma heat – plasma generator. After a selection of a construction plasma generator it is necessary to determine it of a regime parameter, which ensure required heat flows on a surface of an item for creation of required structures in a hardened stratum.

There are methods of determination of high intense heat flows, namely stationary and non-stationary. The non-stationary methods are based on a measurement of temperatures in the copper cylindrical gauge (or on an end face, or on a distance of several mm from it). After that the method of a solution of a return problem of a thermal conduction determines magnitude of a heat flow. In gauges of a stationary type by a way of calorimetric of water which is flowing past through the gauge determine magnitude of a heat flow. Restriction for gauges of such type are the heat flows 10^8 W m^{-2} and more, since melting a surface of the gauge.

In our researches the plasma generator with the born electrical arc was applied. The electrical arc in this construction "burns" between the tungsten cathode and rotated copper water-cooled anode. A breadth of processing, and intensity of heat of a surface are ensured with a system of constants and variable magnetic fields, which influence an electrical arc.

As the thermal effect on a surface is cyclical with magnitude of thermal impulse 10^8 W m^{-2} that application of non-stationary gauges of heat flows not probably because of reaching temperature of melting it by a surface for want of operation already of several thermal impulses (approximately 0,4 c)

The gauge of a stationary type was applied to definition of fields of heat flows in our experiments which found room (are located) in various points for want of working plasma generator.

The anode spot of an electrical arc of this construction of the plasma generator makes reciprocating movements on a surface of the electrode. Accordingly gauge of a stationary type measures the average integral for period magnitude of a heat flow.

The high-speed filming of movement of an electrical arc was made for determination of magnitude of a heat flow at the moment of passing an electrical arc (impulse heat flow).

The magnitude q_0 settled up under the formula

$$q_0 = QTV/2d, \quad (1)$$

where Q – an average integral heat flow, T - period of effect, d - it is the diameter. The magnitudes V and d were determined by a method of high-speed filming.

The field of heat flows Q represented in a fig. 1.

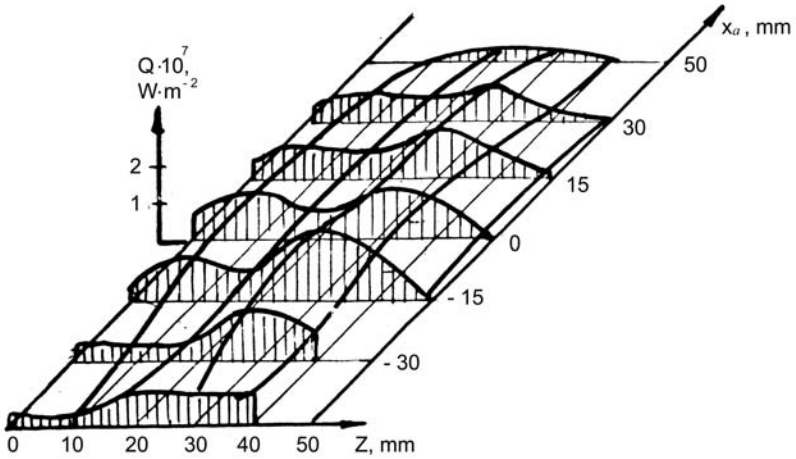

Fig.1. The field of heat flows

This field is uniform enough on a breadth of processing (x_a). The magnitude Q achieves $2 \cdot 10^7$ W m^{-2} for want of current of an electrical arc 400 A.

Influence of frequency of a variable magnetic field to heat flows Q and q_0 are indicated in a fig. 2.

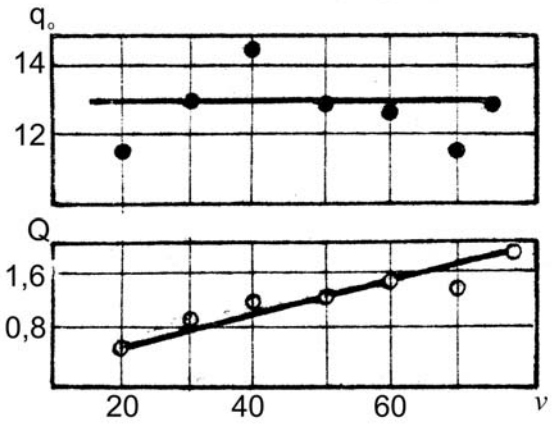

Fig.2. Influence of current frequency of magnetic field to the heat flows
in the point Z=0; Xa=0; I=400A;
q_0, $Q \cdot 10^7$, $W \cdot m^{-2}$; ν, Hz.

From Figures it is visible, that Q is increased approximately in 5 times for want of magnification of frequency n with 20 up to 100 Hz. On the other hand magnitude impulse of the heat stream remains practically constant $1{,}3 \cdot 10^8$ W m^{-2}. In the given construction of the plasma generator by a variation by a velocity of movement of an electrical arc, magnitude it of a current and degree of it approaching to a surface

of processing details is possible for changing magnitude of a heat flow in some times, that ensures technological flexibility of the given construction.

Leaning on data of a measurement of heat flows given to a construction of the plasma generator was applied to hardening crests of sprockets of locomotives with the purpose of magnification of term of their service.

The purpose was the hardening of a surface without formation of martensite .
The outcomes of such hardening are indicated in a fig. 3.

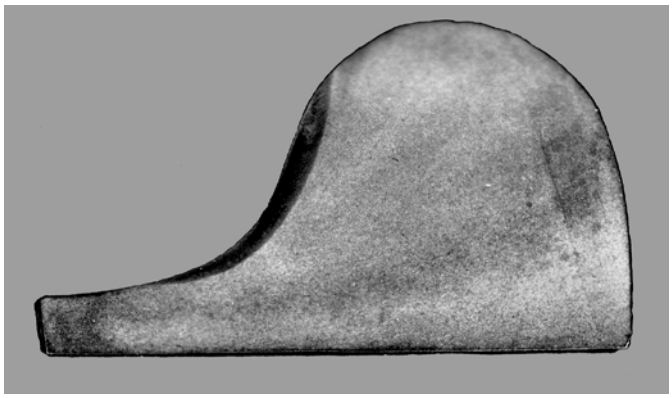

Fig.3 The structure of crest of the railway wheel.

Distributions of hardness on depth are given in a fig. 4.

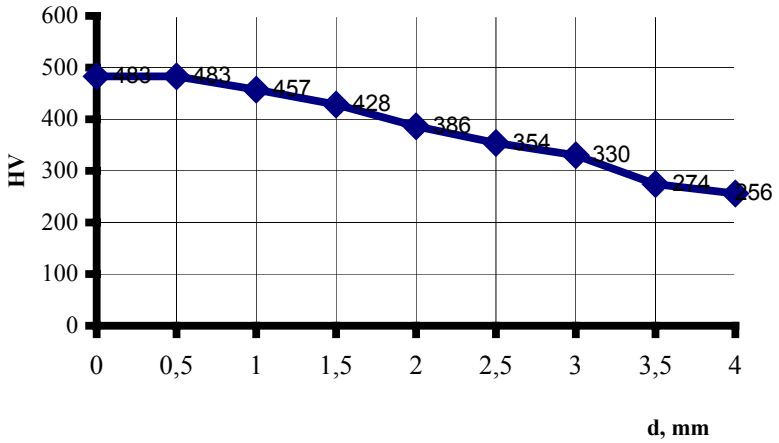

Fig.4 The dependence of hardness of treatment lays from depth of lays.

The data outcomes are obtained for want of optimum heat flows.
The current of an electrical arc made 270 A.

From Figures it is visible, that the obtained stratum has a thickness of 3 mm.
For want of it was hardened all surface of a crest, which is subject to wear. The phase structure of this stratum represented by: troosomartensite , troostite, sorbite .

For a diminution of defects on a surface of a rolling of carload sprockets it was hardened on a breadth up to 45 mm (fig. 4)

For want of magnification of a breadth of processing up to 45 mm the current of an electrical arc in this process was accordingly increased up to 400 A, and the frequency of a variable magnetic field made 50 Hz. Accordingly middle of the integrated heat flow in a material remained practically at the same level. The maximum hardness for want of hardening of a surface of a rolling made 520 HV. The depth of a hardened stratum made 3 mm.

With the purpose of a diminution of wear of a working surface of rails the processing by the plasma generator of the given construction was made it.

The outcomes of such hardening are indicated in a fig. 5.

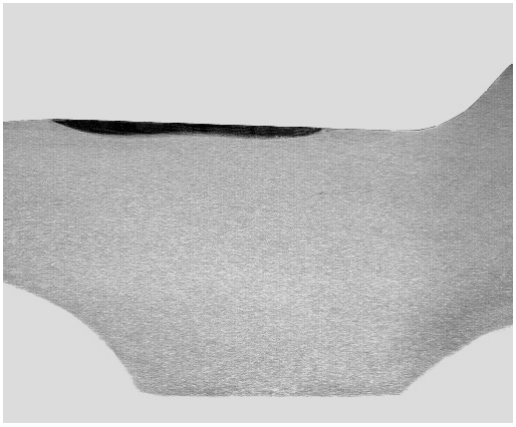

Fig.5. The structure of the running surface of the railway wheel.

The depth of a stratum makes 4 mm. The structure of metal in for heat treatment to a zone represented:
released martensite with hardness 670-592 HV (at a surface),
troosomartensite and troostosorbite with hardness 554-464 HV (in an average zone),
sorbite (at the basis of metal) with hardness 429-339 HV.

For the heat treatment of a horizontal and vertical surface of rails (fig.6)

Fig.6. The structures of the surface of the rail.

movement to an anode spot of an electrical arc added a Γ-figurative trajectory at the expense of an additional system of magnetic fields.

3. Practical application

The outcomes of researches were used for want of hardening of crests of sprockets of locomotives by the Far East railway. The wear of crests with plasma hardening has decreased in 1.5-3.0 times.

References.

1 A.M. Lykov, V.E. Maslov, O.I. Lobov. Plasma treatment of metalium materials. 15th International symposium on plasma chemistry. Gremy, CHRS/University of Orleans. 2001. Vol. 5. P 1941-1946.
2 S.N. Kiselev, A.V. Savruchin, G.D. Kuzmina., A.S. Kiselev. Influence of plasma processing on is intense deformed and structural condition of crests of bandages of sprockets of locomotives. Welding production. Moscow. 2001. №6. p. 9-17.

Wave-plasma power coupling in a low-pressure surface wave co-axial discharge.

S. Letout[1,2], C. Boisse-Laporte[1], A. Yanguas-Gil[3], G.Gousset[1] and L.L. Alves[2]

[1] *Laboratoire de Physique des Gaz et Plasmas, Université Paris-Sud, 91405 Orsay Cedex, France*
[2] *Centro de Física dos Plasmas, Instituto Superior Técnico, 1049-001 Lisboa, Portugal*
[3] *Inst. de Ciencia de Materiales de Sevilla, Consejo Superior de Inv. Científicas - Univ. Sevilla, Sevilla, Spain*

Abstract
The paper introduces an experimental work on surface-wave discharges, produced and sustained in a coaxial structure. Planar probes are used to investigate the existence and the directionality of a high-energy electron flux, which is expected to be generated within electron-plasma resonances. Emission spectroscopy measurements of argon line intensities are compared to the populations of different excited argon states, calculated using a Collisional-Radiative Model coupled to a 1D-moment method radial code.

Keywords Surface-wave, Electron-plasma resonance, Directional Langmuir probe, Emission spectroscopy, Collisional-Radiative Model.

1. Introduction

This paper analyses a microwave discharge sustained in a coaxial structure, which was initially developed as an additional ionization device for an Ionized Physical Vapor Deposition (IPVD) system [1]. We have decided to carry out a fundamental study on the electron population of low-pressure argon discharges produced in this device, as results may be extrapolated to similar high-density microwave discharges produced in large-scale planar reactors [2]. Such devices are interesting for material processing [3] specially because they may produce hot-electron fluxes, as reported in [4,5,6,7].
A definite advantage of this azimuthally symmetric structure was evidenced by the self-consistent description obtained in [8,9], which reported the development of an electron-plasma resonance in the vicinity of sheath regions. These resonances occur wherever $\omega_p \sim \omega$ (ω is the microwave excitation frequency; $\omega_p = \sqrt{n_e e^2/\varepsilon_0 m_e}$ is the electron-plasma frequency; e and m_e are the electron charge and mass, respectively; n_e is the electron density; and ε_0 is the vacuum permittivity), as a result of the strong radial gradient of n_e in sheath regions. The main interest with the coaxial configuration is that it leads to a resonance located near the centre of the discharge, where the local field is higher, thus enhancing its effect upon the local electron energy.
A preliminary experimental characterization of this discharge was previously reported in [10]. Cylindrical probe measurements yielded typical electron densities of 10^{11} to 10^{12} cm^{-3} and temperatures around 2 eV, for argon gas pressures ranging from 10 to 100 mTorr. Further probe measurements are presented in [11], where a planar probe configuration was used to investigate the anisotropy of the electron fluxes generated within field resonant regions. The projet also includes a numerical simulation analysis that uses a self-consistent 1D-moment method model to describe the radial deposition of energy in the plasma. Here, this model is coupled to a Collisional-Radiative Model (CRM), to compare calculated excited state populations with measured line intensities of argon gas.

2. Presentation

The coaxial structure presented in *Figre 1* is given by the superposition of 3 cylindrical layers - a 5 mm radius copper tube, a flowing air layer of 13 mm radius at atmospheric pressure and a 2 mm thick quartz tube - which act as propagation media for the surface-wave. A low-pressure chamber, delimited

by the quartz tube and an outer metalic shield, hosts a plasma with more than 60 mm radius. It is assumed that only the fundamental plasma mode TM_{00} propagates to sustain the discharge. The reactor is approximatively 70 cm long and operates for injected powers up to 1 kW.

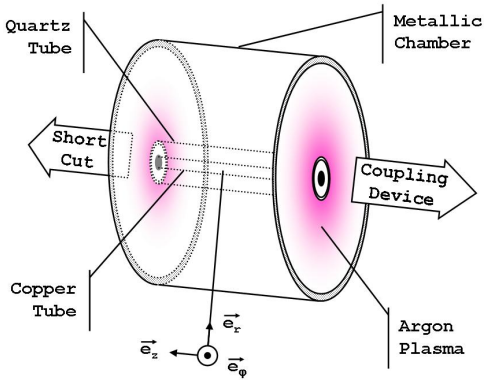

Figure 1. Longitudinal cut of the experimental setup.

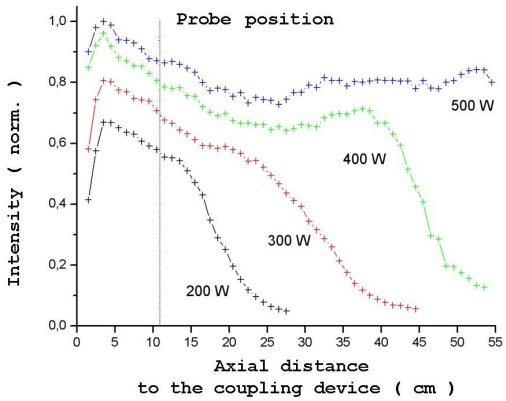

Figure 2. Experimental axial variations of the 3948.9 $\AA$ argon line at 30 mTorr pressure, and for different injected microwave powers (200, 300, 400, 500 W).

The experimental setup was designed as to allow Langmuir probe measurements across the discharge radius $\vec{e_r}$, for different positions along the axis $\vec{e_z}$, and emission spectroscopy measurements through a quartz window, set along the discharge axis on the outer metallic chamber. The probe measurements presented here were performed 11 cm away from the coupling device. As shown on *Figure 2*, emission spectroscopy measurements at 30 mTorr pressure reveal that, for low injected powers, the wave power is completely transferred to the plasma before reaching the ending shortcut, as the radiation intensity presents a rapid decrease with the axial distance.

The discharge radial description is given by a 1D - moment method code [8,9], which couples charged particle and energy transport equations to Maxwell's equations for the TM_{00} mode (taking into account the electron-plasma resonance) and to Poisson's equation for the electrostatic space-charge field. The local mean energy approximation [9] is adopted to introduce a radial dependence for the electron transport parameters and rate coefficients. The latter are calculated from the electron energy distribution function (EEDF), assumed Maxwellian, and are tabulated as a function of the electron mean energy ε. The radial map of the electron parameters is obtained by resorting to the profile $\varepsilon(r)$, as obtained from the charged particle transport model.

The calculated radial distribution of the electromagnetic field components is shown in *Figure 3*, where one can observe the resonance peaks of the radial electric field, located within the space-charge sheaths (near the quartz tube and near the outer metallic cylinder).

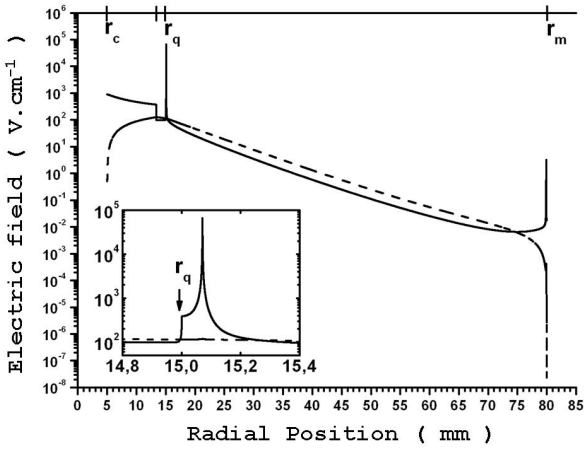

Figure 3. Calculated radial distribution of the wave electric field components, at 30 mTorr pressure and 5.7×10^{11} cm^{-3} radially averaged electron density. E_r : solid line, E_z : dashed line. The lower left graph is a blow-up of the inner resonance region

3. Planar probe directional measurements

Assuming as valid that the electric field in the plasma has no azimuthal component, presenting high intensity ratios of its radial to axial components in the resonance region near the quartz tube, we decided to check the possible anisotropy of the electron fluxes generated within this region. The study involved probe measurements that used Tungsten planar probes with 1 mm radius, as detailed in [11].

Two different planar probes were inserted at different axial positions, where they could move in the radial direction. The normal vector to the collection surface of the first probe (see *Figure 1* for axis references) was radially oriented (rad) $+\overrightarrow{e_r}$. The tip of the second probe was bent, so that the normal to its collection surface could point at different directions, by rotation around $+\overrightarrow{e_r}$: axially towards the coupling device (ax-cd) $-\overrightarrow{e_z}$; axially towards the short-cut (ax-sc) $+\overrightarrow{e_z}$; azimuthaly (azim) $\pm\overrightarrow{e_\varphi}$.

Figure 4 shows typical deformations of the probe characteristics, obtained at a fixed radial position of 2 mm away from the quartz tube, and for different probe orientations. The (azim) characteristic clearly corresponds to the case where only cold electrons are collected, with typical maxwellian temperatures that range between 1.5 and 2 eV, depending on the gas pressure. The different curves in this figure show very close plasma potentials V_{plasma} (see the inflexion points on the right), and a similar behaviour for the region of cold electron collection (at $V_{probe} \lesssim V_{plasma}$). At more negative probe potentials, we observe a strong increase in the characteristics obtained at both axial and radial directions (when compared to the corresponding azimuthal measurement), that can indicate an increase in the *number* of high-energy electrons overcoming the repulsive potential barrier of the probe sheath. Note that although such deformations may be associated to the existence of high-energy electrons, generated within the electric field resonance near the quartz tube, it is also possible to have the intense electric field in this region affecting current collection, or the probe itself modifying the local field.

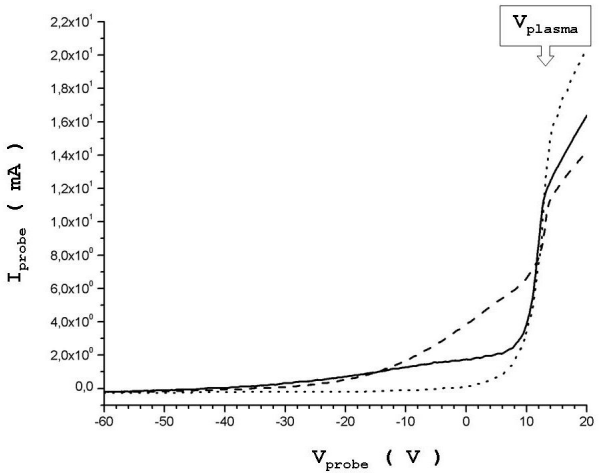

Figure 4. Planar probe characteristics at a constant radial position of 2 mm, for 30 mTorr gas pressure and 200 W injected power, and for different probe orientations: solid line (rad), dashed line (ax-sc) and dotted line (azim).

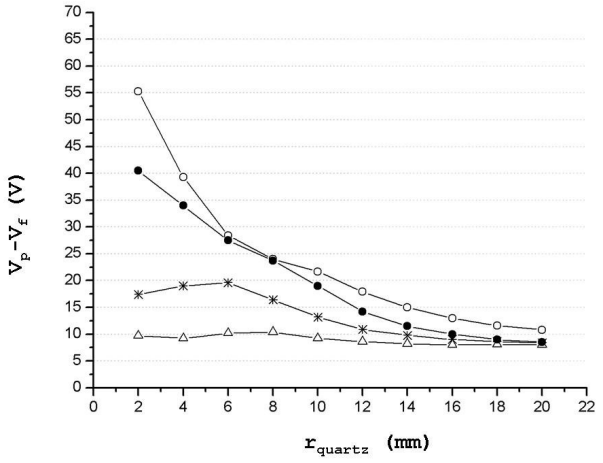

Figure 5. Deviation of the floating potential V_{float} with respect to the plasma potential V_{plasma}, as a function of the radial position, at 30 mTorr pressure and 200 W injected power, and for different orientations of the probe collection surface: empty circle (rad), star (ax-cd), triangle (azim) and full circle (ax-sc). Note that r_{quartz} is defined with respect to the outer radius of the quartz tube.

Further confirmation about the existence of high-energy electrons in the discharge is given by the radial evolution of V_{float} with respect to V_{plasma}. The floating potential V_{float} is defined as the potential at which the electron current exactly compensates the corresponding ion current. Considering that no external perturbation is affecting current probe collection, the quantity $\Delta V \equiv V_{float} - V_{plasma}$ is a simple parameter that relates to the *energy distribution* of electrons. *Figure 5* plots ΔV as a function of radial position, for different orientations of the probe collection surface. Far away from the quartz tube, the values of ΔV are independent of the probe orientation, which is consistent with the existence of a cold electron population, assuming that the plasma potential is constant across the radius. Near the quartz tube, however, one observes a strong increase in ΔV, for measurements carried out in all directions except the azimuthal one. In fact, the values of ΔV obtained in the azimuthal direction remain constant for all radial positions, thus indicating that probe measurements are not perturbed. Note that although the values of ΔV are comparable for measurements obtained at both axial (ax-sc) and radial (rad) directions (hence, suggesting similar electron energies), the number of cold electrons is higher is the latter case (see *Figures 4* and *5*).

4. Simulation results. Inclusion of the CRM

Preliminary comparisons have been carried out between simulation results and experimental measurements, obtained with both Langmuir probe and (radially averaged) emission spectroscopy diagnostics. It was shown [10,12] that the model predicts the correct trends of plasma density and electron mean energy profiles - see *Figure 6*, at various gas pressures and averaged electron densities. However, model predictions for the values of the electron mean energy were found to be systematically overestimated with respect to measurements, which was mainly attributed to the fact that stepwise electron-neutral (e-N) ionisation collisions were not taken into account.

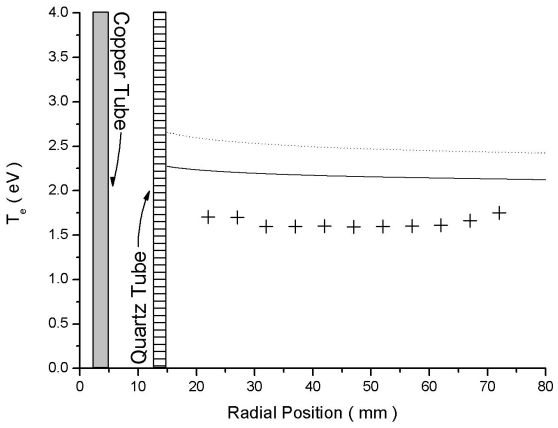

Figure 6. Radial mean electron energy profile (experimental - *cross*, calculated without CRM - *dotted line* and calculated with CRM - *full line*) for a gas pressure of 30 mTorr and injected power 700 W. Averaged electron density $< n_e > = 5.14 \times 10^{+}11\ cm^{-3}$.

In fact, the first excited levels of argon are expected to play a significant role in the electron energy balance, as they participate in stepwise e-N ionisation collisions that can contribute to lower the values of the electron mean energy required to sustain the discharge. In order to clarify the influence of these species, we have self-consistently coupled a CRM for argon gas to the 1D-moment method radial code, describing charged particle and energy transport. The CRM uses an updated set of cross-sections [13], taking into account 31 real and effective argon atomic levels - see *Fig.8*. The balance equation for each species includes electron impact inelastic processes (excitation and ionization, both direct and stepwise), radiative processes (taking into account resonant imprisonment effects) and diffusion of the two 3p5-4s metastable states toward the discharge walls. The flux boundary conditions assume total absorbing walls.

Level	Configuration	Energy (eV)
0	$3s^2p^6$	0
1	$4s[3/2]_2$	11.548
2	$4s[3/2]_1$	11.623
3	$4s'[1/2]_1$	11.723
4	$4s'[1/2]_0$	11.828
5	$4p[1/2]_1$	12.907
6	$4p[5/2]_3$	13.076
7	$4p[5/2]_2$	13.095
8	$4p[3/2]_1$	13.153
9	$4p[3/2]_2$	13.172
10	$4p[1/2]_0$	13.273
11	$4p'[2/2]_1$	13.283
12	$4p'[3/2]_2$	13.302
13	$4p'[1/2]_1$	13.328
14	$4p'[1/2]_0$	13.480
15	3d5s	14.019
16	3d'5s'	14.246
17	$5p[1/2]_0$	14.464
18	$5p[5/2]_3$	14.499
19	$5p[5/2]_2$	14.506
20	$5p[3/2]_1$	14.525
21	$5p[3/2]_2$	14.529
22	$5p[1/2]_0$	14.564
23	$5p'[3/2]_1$	14.681
24	$5p'[1/2]_1$	14.687
25	$5p'[3/2]_2$	14.688
26	$5p'[1/2]_0$	14.738
27	4d	14.780
28	6s	14.842
29	4f	14.906
30	4d'	14.967
31	$3s^2p^5$	15.76

Figure 7. Atomic levels of argon considered in the Collisional-Radiative Model.

Emission spectroscopy measurements were used for comparisons with the calculated populations from the CRM. Measurements were performed at an axial position of a 3 cm away from the coupling device. This corresponds to the position of the maximum of intensity of the plasma column, which does not change with pressure nor injected power, to ensure a similar spatial electromagnetic field configuration for comparisons. Injected power was set to 400 Watts.
Measurements are integrated over the discharge radius. Excited states populations are obtained from experimental line intensities using

$$n_p = \frac{4\pi}{V_p - V_q} \frac{I_{p \to q}}{A_p^q}$$

, where $I_{p\rightarrow q}$ is the experimental emission line corresponding to the transition from a level p to a level q, n_p is the excited state density, $V_{p,q}$ the respectively upper and lower state energy and A_p^q the corresponding radiative constant. Without the information of the spectral response of the acquisition system (optic fiber + CCD camera), only relative comparisons using the ratios of n_p excited states populations obtained from emitted lines which wavelengths are close to each other, are to be considered.

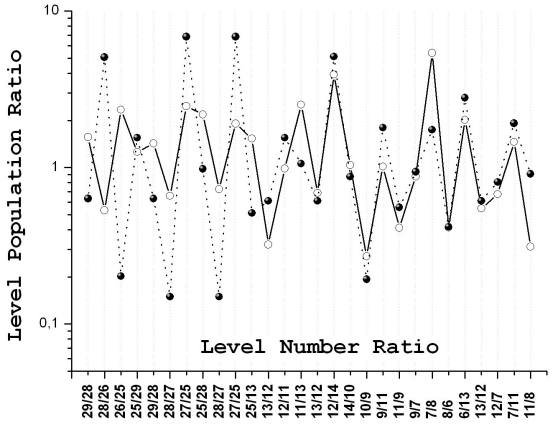

Figure 8. Ratio of excited states populations obtained from emitted radially averaged lines close to each other - *full line* - and from calculated radially averaged profiles using the CRM - *dotted line*. Gas pressure of 60 mTorr, injected power of 400 W. Corresponding averaged electron density $n_e = 7.0 \times 10^{+11}\ cm^{-3}$.

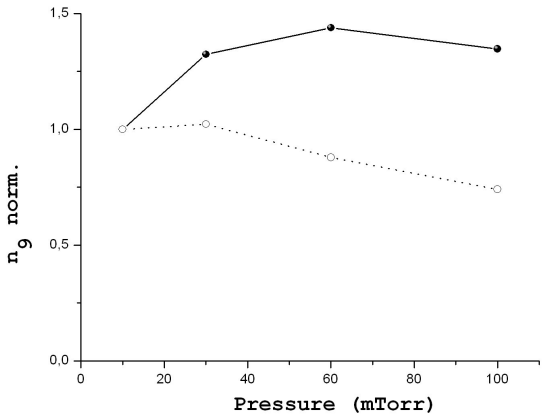

Figure 9. Normalized population of the level n° 9 as a function of gas pressure obtained from emitted radially averaged lines - *full line* - and from calculated radially averaged profiles using the CRM - *dotted line*. Averaged electron density $n_e = 7.0 \times 10^{+11}\ cm^{-3}$.

As one can notice on *Figure 8*, a good comparison between numerical and experimental results is achieved for the lower levels (ranging from number 6 to 14). This shows that the $4p$ levels are correctly described by the CRM. For levels ranging from number 25 to 29, a fair comparison is obtained as higher levels are not included in the model. The trend is similar for the different investigated pressures.
A typical evolution of both normalized calculated and measured populations as a function of gas pressure is shown on *Figure 9*. One can observe a similar qualitative trend for both cases where a maximum is reached around 30 mTorr for calculated populations and around 60 mTorr for measured populations.

5. Conclusion

Corroborating results obtained from a comparative study of planar probe characteristics show the existence of high energy electron fluxes [11] near the quartz tube of the coaxial structure of a low pressure microwave discharge. Still the global behavior of their generation process within the resonance regions is not clearly understood. The work indicates that an axial energetic electron flux is possibly generated along the discharge axis, which could induce changes in the radial energetic balance.
Despite a good qualitative agreement of both measured and calculated electron mean energy and low argon excited states description, one can notice a quantitative difference. Such discrepancy has been in part reduced by using a CRM, taking into account electron impact inelastic processes (excitation and ionization, both direct and stepwise). Further comparison work with experiment, including a precise spectral response of the acquisition system, is needed to evaluate the used cross sections relevancy.

As a first approximation, higher order terms have been neglected in the writing of the electrons and electron mean energy transport equations considered in the moment method model. A more complete description could result to an intensity increase in the regions of space charge separation and thus lead to a global diminution of the electronic temperature. It could also provide some usefull informations on the generation of more energetic electron fluxes in the resonance regions.

Aknowledgment The authors would like to express their most profound sadness as a result of the death

of G. Gousset. He was at the head of the *Laboratoire de Physique des Gaz et Plasmas*. This work is a consequence of the many projects he initiated. His enthusiasm, his rigorous analysis and his scientific vision will stay in our memories.

References

[1] C. Boisse-Laporte, O. Leroy, L. de Poucques, B. Agius, J. Bretagne, M. C. Hugon, L. Teulé-Gay, M. Touzeau, Surface and Coatings Technology 179, 176 (2004)
[2] M. Nagatsu, G. Xu, M. Yamage, M. Kanoh, H. Sugai, Jpn. J. Appl. Phys. 35, L341 (1996)
[3] I. P. Ganachev, H. Sugai, Plasma Sources Sci. Technol. 11, A178 (2002)
[4] J. Kudela, T. Terebessy, M. Kando, Appl. Phys. Lett. 76, 1249 (2000)
[5] T. Terebessy, M. Kando, J. Kudela, Appl. Phys. Lett. 77, 2825 (2000)
[6] T. J. Wu, W. J. Guan, C. M. Tsai, W. Y. Yeh, C. S. Kou, Phys. Plasmas 8, 3195 (2001)
[7] T. Terebessy, M. Sirý, M. Kando, J. Kudela, D. Korzec, Appl. Phys. Lett. 82, 694 (2002)
[8] L. L. Alves, G. Gousset, Proceed. MD5 (A.Ohl ed.), INP Greifswald, Germany, 2003, p.90
[9] L. L. Alves, G. Gousset, S. Vallée, IEEE Trans. on Plasma Sci. 31, 572 (2003)
[10] S. Letout, L.L. Alves, C. Boisse-Laporte, P. Leprince, ESCAMPIG 17th (2004), to be published
[11] S. Letout, L.L. Alves, C. Boisse-Laporte and P. Leprince, XXVIIth ICPIG 2005, The Netherlands
[12] S.Letout, L.L. Alves, C. Boisse-Laporte and P. Leprince, Bull. Am. Phys. Soc. (2004), Vol. 49, no. 5, p. 23
[13] A. Yanguas-Gil, J. Cotrino and L:L: Alves, J. Phys. D: Appl. Phys., in press (2005)

Crystallization of Organic Nanostructures by Atmospheric Orientation Plasma Polymerization

Jing Zhang*, Ying Guo, Xinsheng Fang, Jinzhou Xu

College of Sciences, Donghua University, 1882 West Yan-an Road, Shanghai 200051, China

*Corresponding author: jingzh@dhu.edu.cn

Abstract: In this paper atmospheric orientation plasma polymerization (APOP) has been selectively demonstrated, focusing on the controlling of crystalline phase structure and morphology of organic nanocrystals. We will concentrate on nanofabrication and crystallization of PTFE and pyrrole-like polymers through AOPP. Organic nanocrystallines with various shapes and crystal phase have been fast formed by AOPP. Special thermal or optical-active properties of the nanocrystallines were also found. This "oriented plasma polymerization" method opened another way for nanofabrication of crystalline polymers.

1. Introduction

Polymer nanostructures are mostly investigated for two purposes. One is to nanofabricate conjugated polymer structures with higher crystallinity for semiconductor or conductor applications such as FET's, LED's, molecular wires, molecular devices etc.. Another is to get nanostructures for insulating interconnections between other conducting or semiconduting nanostructures such as BCP's, nanocable shells, AFM tip coating, insulation coatings for biological implants such as integrated circuits, bond pads, wires, and neural probes etc.. PTFE-like polymers have many remarkable properties, including low dielectric constant, low friction coefficient, high thermal stability, good solvent or chemical resistance, low permeability constant, low surface tension and good biocompatibility etc..

Although there have been extensive efforts on the formation of polymer nanostructures with well controlled and specified nano dimensions, it is a great challenge to synthesize them with high crystallinity and purification. In most of the previous synthesis to get polymer nanostructures [1-6], it often requires confined templates, oriented polymerization catalysts, long and tedious post removing of the templates and catalysts after polymerization, and special requirement for monomers[7-11]. These post treatment process is usually not benefit to the purity and crystallinity of the nanostructures. It is therefore desirable to seek novel synthesis routes by which polymer single crystals with high purity can be formed reproducibly and efficiently.

Plasma method has been widely applied for etching or deposition in the microelectronics industry since 1960's. It has also played an important role in the fabrication of nanomaterials from the emerging of nanotechnology. Based on the strategy to assemble or etch small particles in the state of electrons, atoms, ions and excited molecules etc., it provides a convenient, effective, and low-cost vapor-solid or vapor-liquid-solid method for fabrication of nanomaterials. But most of the research concentrated on inorganic and metal nanostructures , especially on the fabrication of nanostructure arrays with the assistance of catalysts and templates. Only a few studies were related to its applications in the fabrication of organic or polymeric nanocrystalline structures. And it is normally considered that organic products by PECVD are pinhole-free and highly cross-linked amorphous structures[12].

Recently we have found that plasma discharge at atmospheric pressure with an inhomogeneous electric field and linear CxFy monomers could produce single crystalline PTFE-like polymer nanotubes. So in this paper, PECVD at atmospheric pressure (here it is called atmospheric orientation plasma polymerization (APOP)) has been selectively demonstrated, focusing on the controlling of the nanofabrication and crystallization of PTFE and pyrrole-like polymers through AOPP. Organic nanocrystallines with various

shapes and crystal phase have been fast formed by AOPP. Special thermal or optical-active properties of the nanocrystallines are also found. This “oriented plasma polymerization” method opened another way for nanofabrication of crystalline polymers.

2. Experimental

The apparatus used for the formation of single crystalline polymer nanoparticles was a home-made atmospheric plasma discharge reactor. In this reactor, a gradient electric field with a high voltage of 10—50 kV and a frequency of 10—100 kHz was applied to deposit the nanoparticles on ordinary glass slides or into water directly. Filament plasma was generated between a high voltage strip electrode and a grounded plane electrode, one of which was covered with a dielectric barrier at least. Perfluorocarbon compounds or pyrrole were used as the precursors and fed into the reactor through an argon carrier gas at a flow rate of 1:10. The flow rate of the mixture gas was controlled at 5 SLM through a mass flow controller. No vacuum was needed for the reactor system. After only a few seconds to several minutes, a thin film was deposited on the entire substrate, onto which a large quantity of nanoparticles were identified.

The morphology of as-grown nanoparticles was investigated by scanning electron microscopy (SEM) using a JSM-5600LV. Transmission electron microscopy (TEM) images were acquired at an accelerating voltage of 120 kV using a JEOL JEM-200CX. TEM samples of nanoparticles were prepared by dispersing them directly on a carbon film supported with Ni grids. The scattering selected area diffraction (SAD) pattern pictures were taken as soon as possible after focusing, otherwise the polymer nanoparticles experienced melting by the electron beam radiation. A Rigaku D/Max 2550V X-ray diffractometer (XRD) with Cu K radiation was used to characterize the synthesized film. The x-ray wavelength was 1.54 Å with a beam size of 3 mm. X-ray photoelectron spectroscope (American Physical Electronics, PHI 550) was used to characterize the chemical composition of the film containing nanoparticulates. FTIR measurement was carried out on a Nicolet NEXUS-670. Polarized optical micrographs were continuously taken by an Olympus B×51 with a hot stage at a constant heating rate. For comparing the thermal stability of the nanotubes with PTFE, small pieces of PTFE were cut off from PTFE polymer from 3F Company (melting point 310 °C) and also observed with polarized optical microscope. The heating rate was the same as in observing the deposition films. The UV-visible absorbency spectrum of the nanoparticle-water suspension solution was measured after 15 minutes ultrasonic treatment through a UV-3000 ultraviolet spectrophotometer (Shimadzu Corporation, Japan).

3. Results and discussions

3.1 Crystallization of PTFE-like Nanotubes by AOPP

Figure 1 shows the SEM images of the as-grown single crystalline nanotubes on a glass substrate. The synthesis time needed for growing these nanotubes was only three minutes. As can be seen in Fig. 1A and Fig. 1B, the nanotubes exhibit a hexagonal outer geometry with an open end. The outer diameter of these tubes is between 60-700 nm with a wall thickness of 50-120 nm. The maximum aspect ratio observed is on the order of 100:1. The nanotubes on the substrate also appear massive in quantity. Some of the nanotubes tend to lie in parallel to the background particulate layer. Portions of the nanotubes grow vertically from the layer. As can also be seen in Fig. 1C, these nanotubes protrude directly upward from the background film, indicating their close structural and compositional relationship with the background. Also observed in Fig. 1A and Fig. 1B is that the background film is composed of loosely-packed nanoparticles on the glass substrate. The loosely-packed nanoparticulates in the background have a mean particle size of about 50 nanometers.

Figure 2 shows the TEM image of the nanotubes (Fig. 2A) and the selected area diffraction pattern (SAD) within the nanotube (inset of Fig. 2A). Based on the sharp electron diffraction spots in SAD, it is clear that they

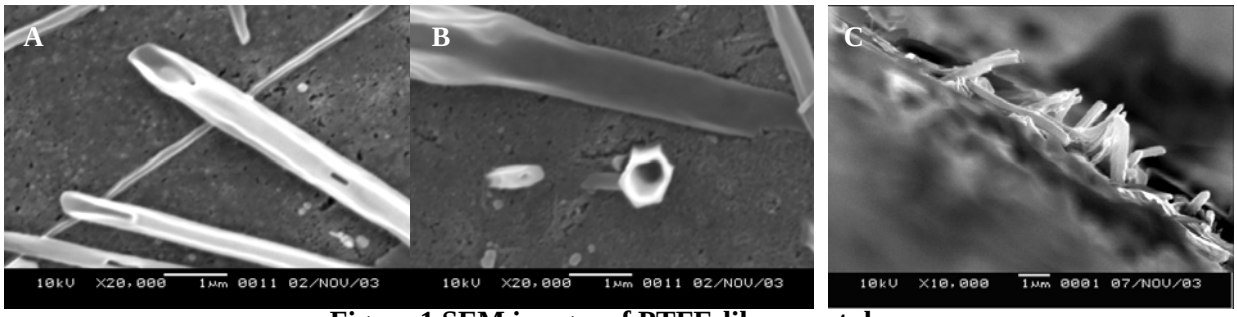

Figure 1 SEM images of PTFE-like nanotubes

A. PTFE-like nanotubes lying on the surface of a loosely-packed nanoparticulate layer
B. Cross-section of the broken PTFE-like Nonotubes, clearly showing hexagonal shape
C. Nanotube arrays grown from the nanoparticulate layer

have a single crystal phase, which is indexed to a hexagonal close-packed (HCP) structure with lattice constant of a=6.384 Å, c=10.231 Å and its axis direction of [011]. In sharp contrast, however, the diffraction pattern on the background nanoparticulates exhibits entirely different behavior. As shown in Fig. 2B, the ring patterns from these nanoparticulates on the substrate suggest a polycrystalline structure of a cubic structure with a unit cell parameter of 5.786 Å. Therefore there are two types of structures among the sample materials studied, namely, the HCP structure for the nanotubes and the cubic for the nanoparticulates, respectively. It should also be noted that both phases are well crystallized on the substrate.

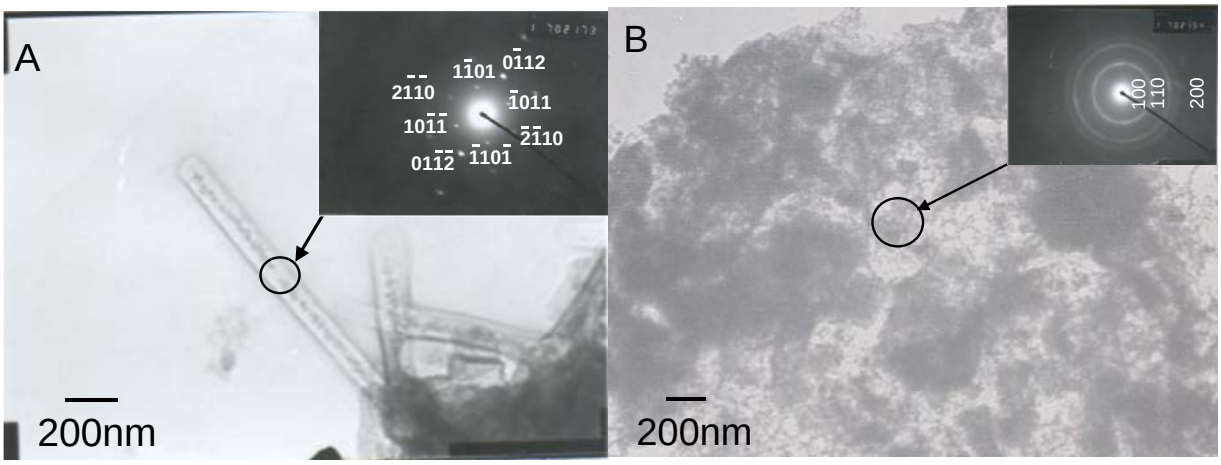

Figure 2 Crystal structure characterization of PTFE-like nanotubes through TEM

A. TEM image of PTFE-like single crystalline nanotubes and the SAD pattern (inset)
B. TEM image of PTFE-like polycrystalline nanoparticulates and the SAD pattern (inset)

The chemical structure of the film was characterized by Fourier infrared spectroscopy (FTIR). The FTIR spectrum is shown in Figure 3. As can be seen in this figure, the spectrum displays absorptions at 480.43 cm^{-1}, 753.37 cm^{-1}, 983.53 cm^{-1} and 1239.90 cm^{-1}, which can be assigned to CF_2 rock deformation, wag deformation, asymmetric stretch and symmetric stretch vibrations, respectively. Although the peak at 1750 cm^{-1} has considerably weak intensity, it is likely that it is associated with the oxygen-containing group. From the EDS experiment, the relative ratio of the C, O, F atom is about 51: 36: 13. Based on the FTIR and EDS results, the as-deposited film is identified to be a Teflon-like polymer structure .

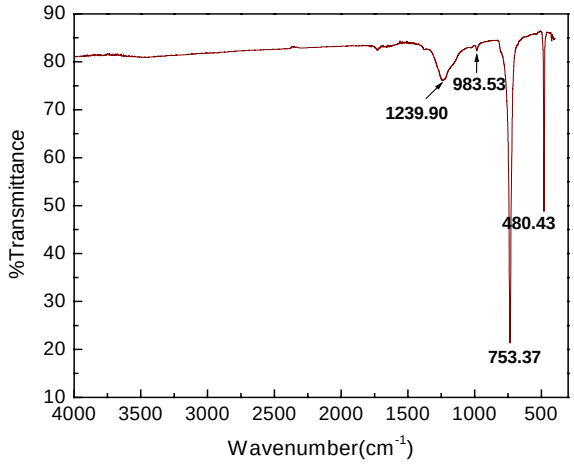

Figure 3FTIR spectrum taken from the as-deposited sample containing nanotubes and nanoparticulates on the glass substrate.

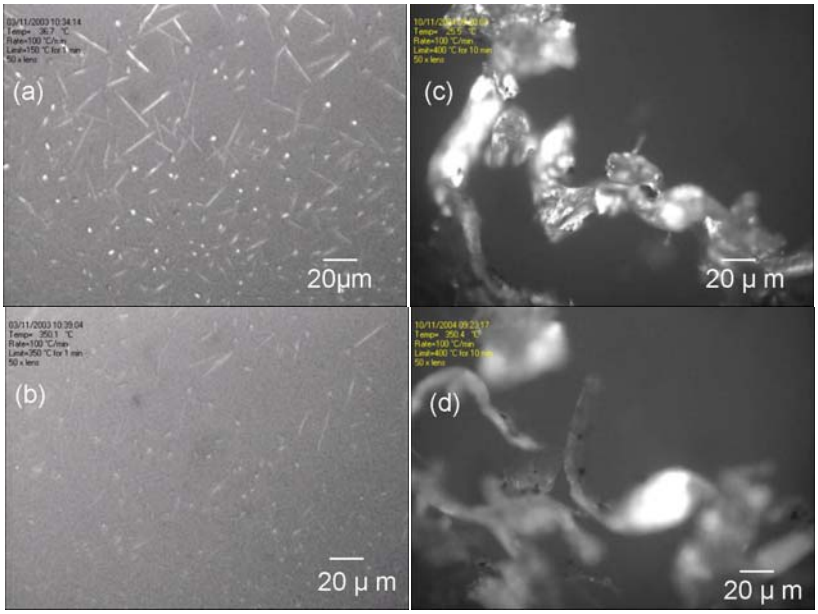

Figure 4 Comparison of thermal stability of observable nanotubes and PTFE polymer slices through polarization micrographs at different testing temperatures

A), Nanotubes at 36.7°C , B), Nanotubes at 350.1°C,

C) PTFE polymer slices at 25.5°C, D) PTFE polymer slices at 350.4°C

The thermal stability of the as-obtained nanotubes was observed through the hot-stage polarized optical microscopy. As shown in Fig. 4, the observable nanotubes with large size retain a needle-like morphology at 36.7 °C (Fig. 4a) and exhibit high birefringence in the crystal edge region. Upon heating up to 350 °C (Fig. 4b), the nanoparticulate layer appears melted and mobile in the vision field but the nanotubes still display clear birefringence although not as strong as at 36.7 °C. Small slices of PTFE exhibit high birefringence of polycrystalline at room temperature (Fig. 4c). Upon heating up to 350 °C, they also melt as the film(Fig. 4d). They completely melt when heating up to 370 °C. This implies significant thermal stability of the single crystal polymer nanotubes comparable to PTFE bulk polymer. The FTIR spectrum and XPS experiment data also display a PTFE-like polymer structure of the film (data not shown here).

3. 2Crystallization of Pyrrole-like Nanorods by AOPP

Figure 5 shows the SEM images of the as-grown single crystalline nanorods on glass substrates. The synthesis time needed for growing these nanotubes was only 2 minutes. As shown in Fig.5 A and Fig.5 B, the nanorods have a spindly shape. The diameter of the nanorods is between 300-400 nm and the maximum aspect ratio observed is about on the order of 8:1-2:1. The nanorods on the substrate also appear massive in quantity. As the same as observed in Fig. 1A and Fig. 1B there is also a background film which is composed of smaller nanoparticles on the glass substrate. The TEM of these nanorods displays that

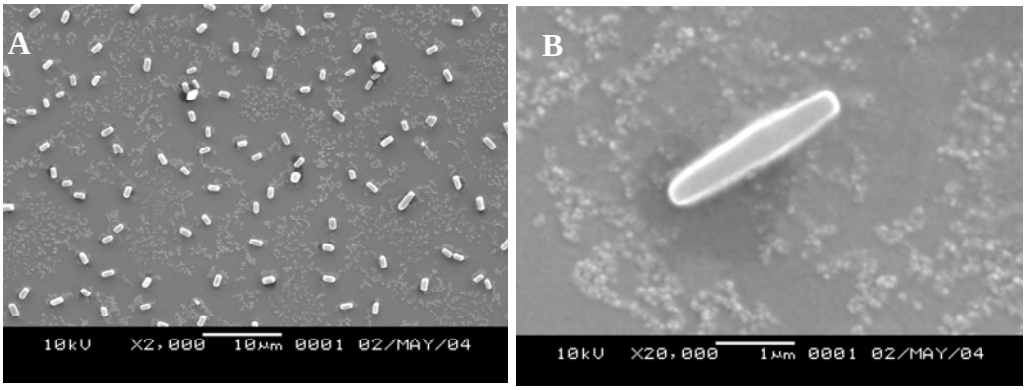

Figure 6 SEM images of pyrrole-like nanorods

When the product is led to water directly, the similar spindly shape nanorods are found in the suspension solution. Besides, the color of the nanorod-water suspension changes with time. As shown in figure 7, the color of

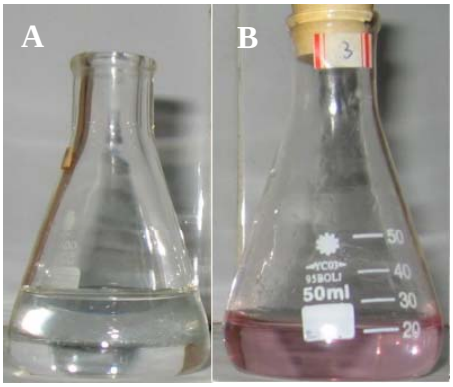

Figure 7 Color changes of pyrrole-like nanorod-water suspension after stored for 2 days

A) after reaction, B) after reaction for 2 days

the suspension changes to pink after stored for 2 days. No such phenomena is observed for pyrrole-water solution. The fluorescence intensity of the suspension increases with time, as shown in Figure 8. This demonstrates that these nanorods are optical-active.

3.3 Discussions

The atmospheric plasma discharge method has many unique advantages in nanofabrication of single crystalline polymer structures in comparison with other processes. It can be carried out at room temperature under atmospheric pressure on many kinds of substrates without any templates or catalysts at an exceptionally fast rate (within several minuets). The synthesized nanostructures by this method possess a high degree of crystallinity. It is suggested that the discharge streamers along the direction of the electric field act as temporary confined templates in the formation of the nanostructures and disappear after the discharge. The electron energy inside the discharge core is 2-5 eV and high enough to dissociate the monomers into active particles such as ions, radicals,

metastable neutrals, and electrons within the discharge channels. But compared with the plasma discharge in

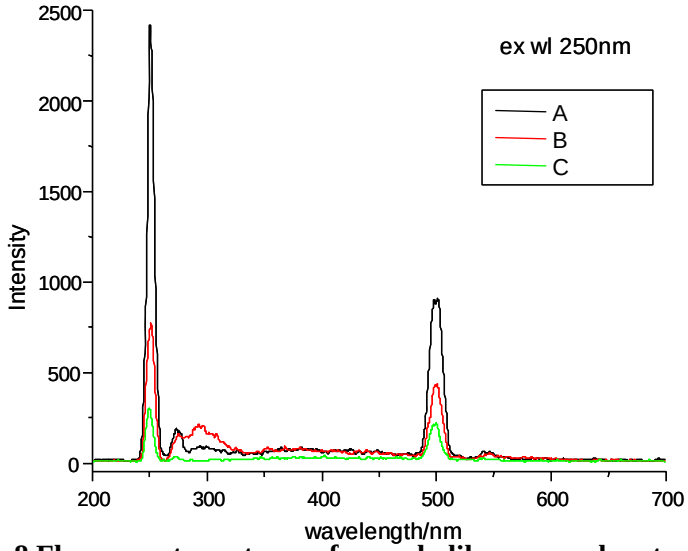

Figure 8 Fluorescent spectrum of pyrrole-like nanorod-water suspension

A) after reaction, B) after reaction for 1 day, C) after reaction for 2 days

vacuum, the mean free path of the electrons is only several micrometers. Therefore the dissociation of the monomers is not as severe as in vacuum plasma discharge. More organic functional groups containing oxygen, nitrogen, hydrogen or fluorine could be retained in the product. The density of the active species is also higher than that in vacuum plasma, leading to a high deposition rate. The initially formed active particles such as ions or radicals are polarized inside the numerous filament channels in the inhomogeneous electric field. Then they are oriented along the direction of the gradually-decreased electric field “head to tail”, react with each other and form the crystalline structures. So it looks like an “atmospheric oriented plasma polymerization”.

This AOPP method opens another approach in the one-step fast formation of single- or polycrystallines The rapid process is independent of monomer types and only associated with plasma conditions and the electric field gradient. Therefore, the novel plasma polymerization process can also be applied to the nanofabrication of other single crystalline polymers with potentially excellent properties and wide range of applications.

Acknowledgements

We are grateful to Wenqiang Wang, Prof Xiaojing Wu and Qiang Wu for their efforts in the SEM and TEM experiment. Jianzhong Lu for assistance in taking the polarized optical microscopic pictures. We are also grateful to Natural Science Foundation Of China (50473003) and Shanghai Nano Science and Technology Promotion Center for the financial support (0352nm035).

References

1. Okawa Y., Aono M., J. of Chem. Phys. 115, 2317 (2001).
2. Krebs F. C. and Jørgensen M., Macromolecules 36, 4374 (2003).
3. Kasaya M. A., Shimizu K., Watanabe Y., Saito A., Aono M., and Kuwahara1Y., Physical Review Letters 91, 255501 (2003).
4. Tonzola C. J., Alam M. M., Bean B. A., and Jenekhe S. A., Macromolecules 37, 3554 (2004).
5. Lee J., Liu Q.D., Motala M., Dane J., Gao J., Kang Y.J., and Wang S., Chem. Mater. 16, 1869 (2004).
6. Bradley K., Gabriel J. C. P., and Gru1ner G., Nano Letters 3, 1353 (2003).
7. Tessler N., Medvedev V., Kazes M., Kan S. H., Banin U., Science 295, 1506 (2002).
8. Kim S. O., Solak H. H., Stoykovich M. P., Ferrier N. J., de Pablo J. J. & Nealey P. F., Nature 424, 411

(2003).
9. Vito S. D. and Martin C. R., Chem. Mater. 10, 1738 (1998).
10. Steinhart M., Wendorff J. H., Greiner A., Wehrspohn R. B., Nielsch K., Schilling J., Choi J., Go¨sele U., Science 296, 1997 (2002).
11. Fu M. X., Zhu Y. F., Tan R. Q., Shi G. Q., Adv. Mater. 13, 1874 (2001)
12. H, Yasuda, Plasma Polymerization, American Academics, Orlando, 1985

The treatment of Li-ion battery waste in a transferred arc plasma reactor

Vittorio Silla and Richard J. Munz[1]

[1]*CREPE Department of Chemical Engineering, McGill University, Montreal, Quebec, Canada*

Abstract
A transferred arc process for the treatment of lithium-ion battery waste to recover cobalt was examined in a laboratory scale transferred arc plasma reactor. Batch operation under oxidizing conditions gave a recovery of 38% of the cobalt in a consolidated metal phase composed of 50 % Fe, 28 % Co, 12 % C and 7 % Cu and 3 % Ni. Operation simulating a semi-continuous process resulted in a Co recovery of 60% and a Co concentration of 57% in the metal phase.

Keywords – Li-Ion battery waste, transferred arc, cobalt, recycling, treatment

1. Introduction

In the new millennium, over 500 million rechargeable battery-operated and miniaturized pieces of electronic equipment will be in circulation. A battery market survey showed that the average annual growth rate of Li-ion batteries will increase by 118%. The millions of spent Li-ion batteries will cause an environmental waste management problem. The cathode metals, which have a high market value (41 US$ / kg cobalt) will leach into the earth when land filled. There is thus a great need to develop processes to recycle these batteries or at least render them harmless. This paper reports on a preliminary study of a transferred arc process to accomplish this. In this process the Li-ion battery waste would be separated into volatile, slag and metal phases using argon and/or oxygen as the plasma gas. The cobalt would be recovered in a metal phase while other elements would be either concentrated into an inert slag or volatilized and recondensed. Thermodynamic simulations and experimental test were carried out in both inert and oxidizing atmospheres.

2. Thermodynamic Simulations

Thermodynamic simulation of the process was performed using the FACT-Sage software [1] with free energy minimization calculations. The process was simulated at 1 atm and between 1000 and 2000ºC in both inert and oxidizing atmospheres using spent Sony Enertec lithium ion batteries. These batteries are commonly used in portable instruments such as laptop computers, camcorders, and digital cameras. The molar composition of the battery was : C 1.047, H 0.756, O 0.205, Fe 0.149, Co 0.126, Li 0.114, Al 0.057, Cu 0.021, Ni 0.003 and to this was added 5 moles of argon for inert operation and various amounts of oxygen for oxidizing conditions. Lithium was always volatilized at temperatures above 1600^{o}C. Inert conditions were unsuitable since although the valuable cobalt reported to the metal phase, it could not be separated from the other metals in the presence of carbon. Figure 1 below shows the predicted behavior of the most important metals at a temperature of 1800^{o}C as the oxygen added is varied from 0 to 2 moles. With the addition of oxygen, cobalt remains in the metal phase while iron is oxidized and copper is vaporized. Nickel reports primarily to the metal phase. With the addition of 1.1 moles of oxygen per standard battery at 1800^{o}C, the simulation showed that 98% for the Co could be recovered in the metal

phase but with contamination by 10 % Cu, 4 % Fe and 2 % Ni. At a temperature of 1600^{o} C the concentration of Co in the metal phase is reduced form 84% to 81% while at 2000^{o} C Co starts to be lost to the vapor phase.

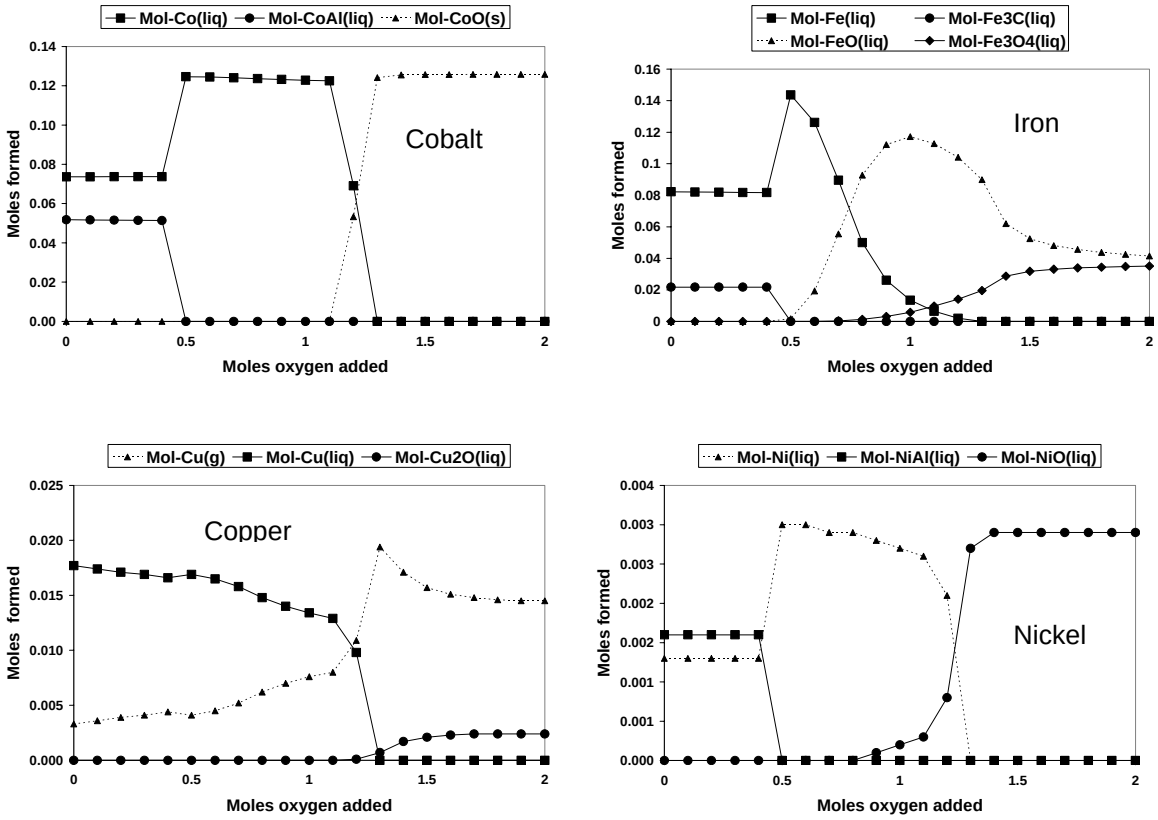

Figure 1: Predicted behavior of metals in system of ideal solutions at 1800^{o}C

3. Experimental Equipment

The experiments were conducted within a water-cooled stainless steel reactor vessel 30 cm in diameter and 38 cm long as shown in Figure 2. Further details are available elsewhere [2]. The vessel contained an inlet for oxygen at its midpoint and a gas exhaust as shown in the drawing. Two purged windows on the reactor lid were used for observations and pyrometric measurements. The arc was struck between a thoriated tungsten tip surrounded by an auxiliary anode and the crucible which contained the battery waste. The purpose of the auxiliary anode was to produce a non-transferred arc until the arc could be transferred to the waste. A data acquisition system monitored and logged the initial arc length, current, voltage, and bath temperature. A two wavelength pyrometer was used to obtain the reaction temperature after the arc was extinguished. The power was supplied by a DC power supply with an open circuit voltage of 600 V and a maximum power rating of 300 kW. The current supplied to the reactor was regulated using a remote control console. The arc was ignited with a high frequency generator in series with the dc power supply.

Two types of crucibles with identical interior dimensions were used. The cavity to receive the waste was in the shape of a truncated cone with a height of 2.54 cm, a bottom inner diameter of 2.54 cm and walls sloped at 21^{o} from the vertical. Graphite was used for inert gas operation while cast zirconia ceramic was used for oxidizing conditions. The graphite crucibles were placed in zirconia ceramic heat shield with an exterior diameter of 7.31 cm. The ceramic crucible bottoms contained a graphite rod with a diameter of 6.4 mm to provide conductivity to the charge.

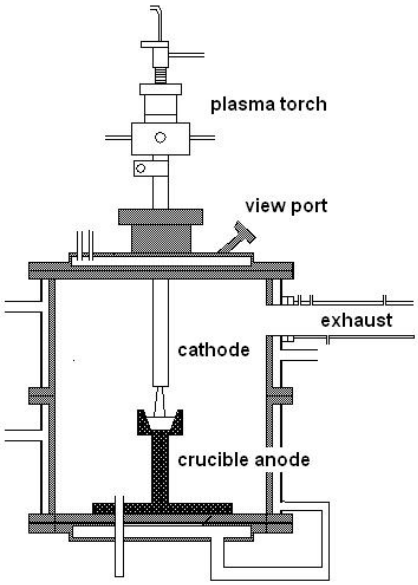

Figure 2: Transferred arc plasma reactor

4. Experimental Procedures

The batteries were first removed from their battery packs, and stripped of their plastic covering. They were then cut in two and dried in a vacuum oven for 24 hours at 80 ºC to eliminate the volatiles. After cooling, they were pressed in a stainless steel mould into 2.54 cm diameter by 2.54 cm high cylindrical pellets with a hydraulic press supplying 93 kN of force.

Before each experimental run the reactor was cleaned. The pellet was weighed and mounted in a weighed crucible. The reactor was then sealed and the torch adjusted to a position just above the pellet. The reactor was purged for 5 minutes at an argon flow of 9.3 slpm. For oxidizing runs, oxygen at a rate of 15.8 slpm was injected before igniting the arc. After arc ignition, the arc length and current were adjusted to the desired values to the appropriate run time. At the end of this time the arc current and gas were simultaneously stopped and an auxiliary stream of argon was injected into the reactor exhaust to avoid the inlet of air. This purging argon flow was continued for about 10 minutes during the cooling of the pellet and crucible to avoid any oxidation. The pellet temperature at shutdown was obtained by back-extrapolating the pyrometer readings after arc extinction to the time of extinction; pyrometer readings during arc operation were too biased by radiation from the arc to be reliable.

The treated samples were separated into their respective phases, weighed and analyzed by ICP emission spectroscopy, TOC, SEM-EDAX, and X-ray diffraction as was appropriate [2].

5. Experimental Results Inert Operating Conditions

The optimum operating conditions for inert conditions were treatment with 9.3 slpm of argon at 200 A for 20 minutes. The initial arc length was 3.0 cm and the voltage was 32.2±1.1V. The average temperature at the end of treatment was 1420^{o}C. Less current and time resulted in a less complete treatment while higher currents and time resulted in excessive vaporization. The combined results of four experiments are presented in Table 1 which gives the percentage of the initial elements reporting to each of the phases identified. These phases include a consolidated metallic phase, an essentially untreated hulk, a friable powder and the vaporized material. Only the first three phases were analyzed while the vaporized material behavior was obtained by difference. Overall 44±4% of the charge was vaporized and of the remaining material, 66±27% was consolidated, 23±26% was untreated while 11±1% remained as powder. The all important metallic phase contained 63% Fe, 16% C, 12% Co, 3% Ni, 4% Al and 0.68% Cu. The recovery of

the cobalt in this phase was only 19% and it was heavily contaminated. A comparison of the experimental results with the thermodynamic predictions suggested that the crucible contents were highly non-isothermal. It must be concluded that treatment under inert operating conditions is not successful.

Table 1: Inert operation - Elemental distribution among phases

Element	Consolidated (%)	Untreated (%)	Powder (%)	Vaporized (%)
Fe	87.89±5.91	10.82±1.89	0.97±0.07	0.33±7.98
Co	19.06±0.85	23.21±3.48	3.08±0.25	54.65±4.57
Cu	6.00±0.08	26.50±1.67	25.37±0.95	42.132.70
Al	26.79±0.12	19.85±0.57	6.74±0.14	46.62±0.83
Ni	93.02±2.06	5.81±0.22	2.22±0.01	0.00±2.29
Li	0.00±0	0.00±0	4.10±0.06	95.90±0.06
C	14.79±0.15	6.78±0.50	7.54±1.09	70.89±1.74

6. Experimental Results Oxidizing Operating Conditions

It was determined from exploratory experiments under oxidizing conditions that the optimum operating conditions were a current of 100 A, and initial arc length of 3.0 cm, an argon flow rate of 9.3 slpm, and a run time of 7 minutes. An oxygen flow rate of 15.8 slpm was used to reflect the thermodynamic simulations. The average arc voltage was 39.8±0.9 V and the average temperature at the end of treatment was 1510±210^{o}C. Lower arc currents were needed because of the insulating properties of the ceramic crucible and the heat of oxidation. The results presented below are based on three runs. Consolidated metal represented 31±11 % of the initial mass while 61±8 % was vaporized and 8±6 % formed oxides. The elemental distribution due to the oxidizing treatment is given below in Table 2. Because the amount of the oxidized phase was so small, it has been included with the vaporized material. The last column of Table 2 gives the composition of the product metal phase. The content of cobalt was much higher for oxidizing conditions but the product was still heavily contaminated with iron and copper. This is because the carbon was not sufficiently removed by oxygen. This was attributed to the poor mixing within the crucible and the nonisothermal conditions. Also, because the oxygen was not injected via the plasma gas, mass transfer resistances limited its contact with the product.

Table 2: Oxidizing operation – Elemental distribution among phases and composition of metal phase

Element	Consolidated Metal (%)	Vaporized and Oxidized (%)	Composition of Metal Phase (%)
Fe	62.0±6.2	38.0±6.2	49.63±4.93
Co	38.5±3.9	61.5±3.9	27.54±2.80
Cu	55.5±12.2	44.5±12.2	7.01±1.55
Al	2.2±1.3	97.8±1.3	0.32±0.20
Ni	100.0±37.6	0.0±0	2.77±0.31
Li	0.1±0	99.9±0	0.00±0
C	9.5±7.3	90.5±7.3	12.72±9.81

7. Experimental Results Oxidizing Operating Conditions with a Metal Heel to Simulate the Industrial Process

The experiments described above were necessarily batch while on an industrial scale the treatment was envisioned to be a semi-continuous process. Lithium ion battery waste would be continuously added to the system creating a large pool of liquid metal primarily composed of Co and an overlying slag layer. The metal and slag layers would be periodically tapped.

To better simulate the industrial scale process, a 10 g Co heel was added to the 40 g battery waste. During the treatment the Co heel would melt and act as a solvent, absorbing the liquid Co diffusing from the battery. It was found that because of the presence of the heel of Co, higher currents and oxygen injection rates could be used without damage to the crucible. Experiments were conducted at 100 A, 10 minutes of reaction, and oxygen flow rates of 15.8 as well as 23.3 slpm. This gave voltages of 42.3±2.5 V and 41.8 V respectively. As the flow rate of oxygen increased from 15.8 to 23.3 slpm, the percentages of consolidated metal, oxide and vaporized material changed from 41:8:51 to 25:11:64. Essentially the metal phase was reduced and the amount of material which was volatilized increased as more oxygen was added. The distribution of elements into the different phases and the compositions of the metal phases for the two operating conditions is given in Table 3 below.

It may be seen from the first set of conditions that the use of a heel improved the recovery of Co in the metal phase; it was increased from 39 to 59%. In addition, the contamination of the cobalt in the metal phase by other metals was less and the Co concentration increased to 57%. It is clear that there is still too much carbon in the product indicating poor mixing of the oxygen with the material in the crucible and within the crucible. Very little of the cobalt was lost to the oxide layer but a great deal, 40% was volatilized.

As the oxygen flow rate was increased to 23.3 slpm in the presence of a heel of cobalt, the overall recovery of cobalt decreased greatly from 59 to 35%; most of this was volatilized. The concentration of cobalt in the metal product increased marginally to 58% but the change was not statistically significant.

Table 3: Oxidizing operation with metal heel – Elemental distribution among phases and composition of metal phase at oxygen flows of 15.8 and 23.3 slpm

Element	Metal (%)		Oxide (%)		Vapourized (%)		Composition of Metal Phase (%)	
	15.8 slpm	22.3 slpm	15.8 slpm	22.3 slpm	15.8 slpm	22.3 slpm	15.8 slpm	22.3 slpm
Fe	64.9	15.1	0.6	1.0	34.5	83.9	30.87	32.43
Co	59.4	34.6	0.3	1.4	40.3	64.1	57.08	58.48
Cu	82.4	32.9	1.3	5.7	16.3	61.4	6.19	4.42
Al	1.1	0.1	8.0	10.9	90.8	89.0	0.10	0.03
Ni	98.8	100.0	0.0	0.0	1.2	0.0	1.82	1.96
Li	0.0	0.2	2.3	25.7	97.7	74.2	0.00	0.00
C	4.9	1.9	0.0	0.0	95.1	98.1	3.93	2.69

8. Conclusions and Recommendations

A transferred arc plasma process for the treatment of lithium-ion battery waste was examined using a thermodynamic simulation and a laboratory scale transferred arc reactor in the batch mode at power levels between 4.0 and 6.4 kW. Because of the small scale of the operation, a major challenge was to obtain a clean separation of the phases produced in the crucible. The system was nonisothermal in both time and space and this resulted in excessive vaporization in the vicinity of the arc and incomplete melting and consolidation at the edges. In experiments under oxidizing conditions, the flow of argon, which protected the tungsten cathode tip also partially, shielded the crucible contents from the oxygen injected into the reaction chamber.

The optimum operating conditions for oxidizing experiments gave a recovery of 38% of the cobalt in a consolidated metal phase composed of 50 % Fe, 28 % Co, 12 % C and 7 % Cu and 3 % Ni. The remaining Co was primarily volatilized.

To better approximate the proposed semi-continuous industrial process, experiments were also conducted with the addition of a 10 g Co heel. Operation the same conditions as above but for a run time of 10 minutes resulted in a consolidated metal phase of 41% of the original mass and a cobalt recovery of 60% and a Co concentration of 57% in the metal phase.

Future work should investigate possibility of moving the arc to improve treatment homogeneity and the use of an air or oxygen plasma to avoid the shielding effect of the argon plasma gas.

9. References

[1] C.W. Bale, P. Chartrand, S.A. Degterov, G. Eriksson, K. Hack, R. Ben Mahfoud, J. Melançon, A.D. Pelton and S. Petersen **"**FactSage Thermochemical Software and Databases", Calphad, Vol. 26, No. 2, pp. 189-228, 2002.
[2] V. Silla, 'The treatment of Li-Ion battery waste in a transferred arc plasma reactor' M.Eng. Thesis McGill University, Montreal, August 2004.

7. Acknowledgements

The financial assistance of the Natural Sciences and Engineering Council of Canada is gratefully acknowledged.

Amorphous Carbon Layer Embedded with Nano-Diamond Particles

N. Sakudo[1], N. Ikenaga[1], H. Yasui[2], K. Awazu[2], T. Kawabata[3], H. Hasegawa[3]

[1]Kanazawa Institute of Technology, AMS R&D Center, 3-1 Yatsukaho, Hakusan, Ishikawa 924-0838 Japan
[2]Industrial Research Institute of Ishikawa, Ro-1, Tomizumachi, Kanazawa,Ishikawa 920-0223 Japan
[3]Onward Ceramic Coating Co. Ltd., Wa-13, Yoshiharamachi, Neagari, Nomigun, Ishikawa 929-0111 Japan

Abstract
A new apparatus that has two types of plasma generators (RF and microwave) is developed for depositing on a silicon substrate a DLC (diamond like carbon) layer embedded with tiny diamond particles. The substrate temperature during deposition can be kept at around 200 degC [473 K]. According to the evaluation with Raman spectrometry both spectra of DLC and diamond are identified in the layer.
Key words: plasma, nano diamond, diamond like carbon, ion implantation

1. Introduction

Some machine tools and dies are coated with DLC or poly-crystalline diamond layer to improve their mechanical properties like hardness, friction and wear resistance. DLC coating lowers the coefficient of friction to make it possible to machine even soft and cohesive materials like aluminum. But it also lowers the surface hardness of the coated tools and dies, resulting in making it hard to machine usual hard materials. On the other hand the diamond coating that is usually made by thermal- or plasma-CVD (chemical vapor deposition) enhances hardness, but it also enhances friction. We develop a new coating method that takes in both advantages of the two coatings, i.e., very low friction and very high hardness.

2. Experimental setups

Usually DLC coating is carried out by PVD (physical vapor deposition) using hydrocarbon gases like ethylene, ethane, acetylene and so on. We constructed a new apparatus that has two kinds of plasma generators. One is an inductively coupled-plasma source with one-turn loop antenna driven by 13.56 MHz RF power, and the other is a 2.45 GHz microwave-plasma source with slotted rectangular waveguide surrounding the plasma chamber made of quartz cylinder. Fig.1 shows the photograph of the apparatus. The RF loop antenna is inside the plasma chamber. The sample holder that is placed at the center of chamber is supplied with negative high voltage pulses for performing PBII (plasma-based ion implantation). Thus, this apparatus can control the energies of charged-particles in plasma for a wide range. Whether the deposited carbon layer becomes DLC or diamond

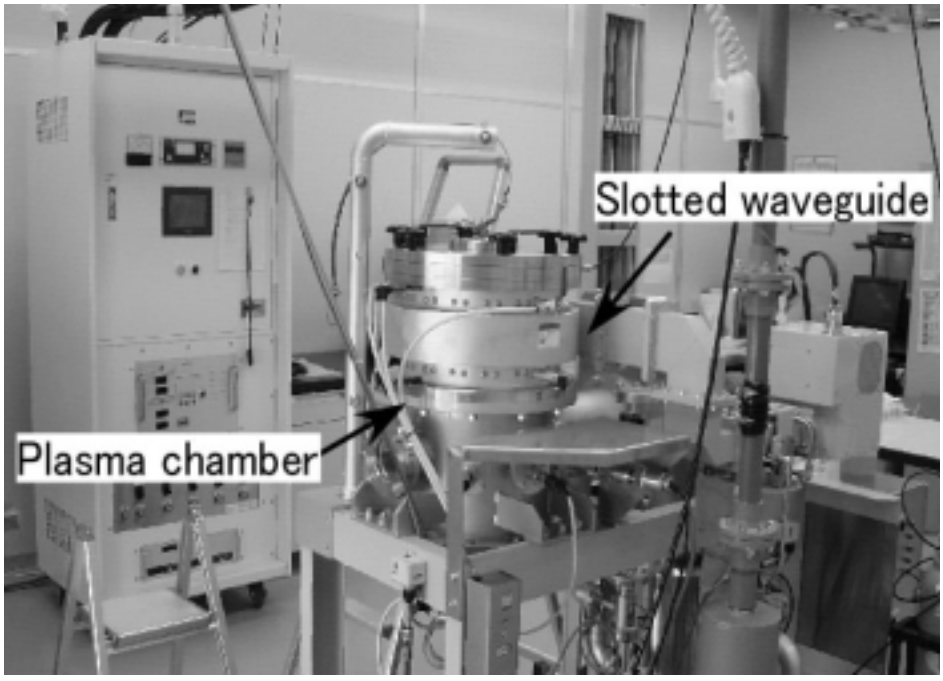

Fig.1 Experimetal apparatus

is considered affected by many factors such as gas pressure, energy distributions of particles, hydrogen-radical proportion in plasma and so on. High-density and high-electron temperature plasma is needed especially for depositing diamond films. Therefore, how efficiently microwaves are fed into vacuum is important. In order to find an appropriate microwave-feeding structure we made and compared two kinds of slotted waveguides as shown in Fig.2. Waveguide (a) in the figure has short slots on the H plane of rectangular waveguide. Since the waveguide end is short-circuited, standing waves exist in the waveguide. The slot positions coincide with where standing wave peaks of wall current are. On the other hand, waveguide (b) has a long slot on the E plane of rectangular waveguide. Since the waveguide end is not short-circuited, there are no standing waves. Microwaves that are progressing in the waveguide are emitted through any part of long slot on E plane into the plasma chamber. Plasma densities with waveguide (b) are more than 10^{11} cm^{-3} that are several times higher than those with waveguide (a). Thus, we adopt the waveguide (b) as the microwave plasma generator for this experiment.

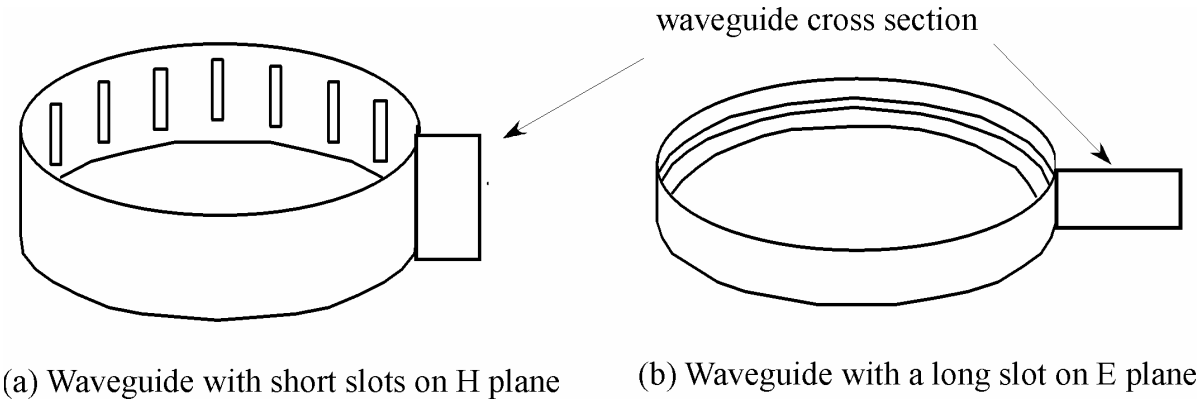

Fig.2 Selection of appropriate slotted waveguide

Another plasma generator, the RF plasma generator that is composed of 1 turn loop antenna, is placed under the microwave plasma generator around the sample holder.

3. Formation of DLC and diamond

3.1 DLC

DLC layer is easily deposited by either RF (13.56 MHz) or microwave (2.45 GHz) plasma with hydrocarbon gases like C_2H_2, C_4H_4 or C_6H_6 fed into the chamber [1]. In this case the gas pressure is around 1 Pa that is 1/100 the pressure for diamond deposition. Since ion bombardment at enegies of several tens to several thousands in eV is necessary in order to form DLC, negative-high voltage pulses of 1 to 2 kV are applied to the sample holder. Fig.3 shows comparison of Raman spectra from DLCs that are made with acetylene gas by both plasmas of RF and microwave (MW). The spectra are typical of DLC but have some differences each other. According

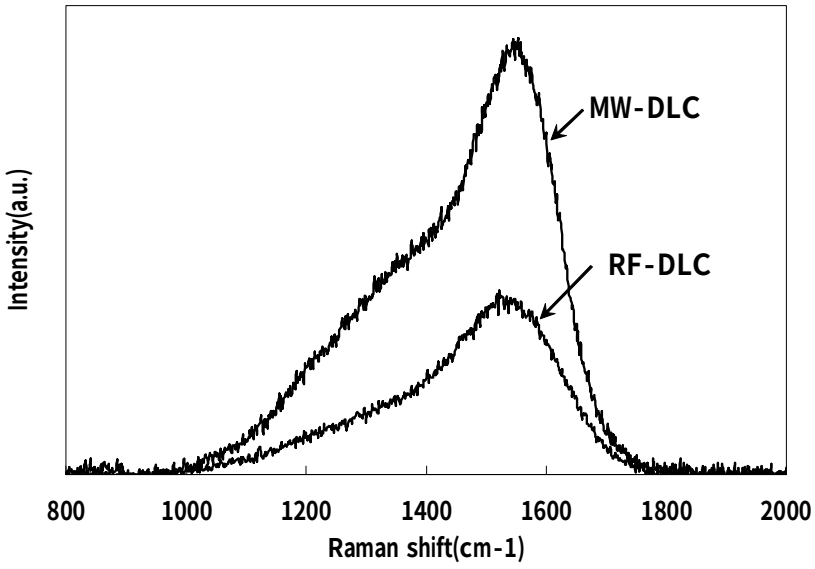

Fig.3 Raman spectra of DLCs made by different plasmas

to the component separation of the spectra by computer, microwave-plasma DLC contains larger percentages of small Raman shifts including disordered graphite component than RF-plasma DLC. Thus, the former has higher hardness as well as lower friction coefficient than the latter [2]. The typical hardness of DLC measured with super-micro hardness meter, Shimazu Co. DUH-W201, is about 25 GPa, and friction coefficient measured with CSEM Co. Tribometer is 1.0 to1.5.

3.2 Nano diamond

Diamond film has been usually formed on a substrate of higher temperature than 800 K by plasma process with methane and hydrogen mixture gas. In this case, the gas pressure is about 100 Pa. But since the percentage of methane is one to several %, the partial pressure of hydrocarbon (methane) is almost same as the presuure of acetylene for the above-mentioned DLC formation. For generating diamond, amount of CH_3 radicals or ions that have sp^3 mixed orbit for diamond combination must exist in the plasma [3]. Another difference of the diamond process from DLC is that the process needs low energies of plasma particles. Therefore, microwave plasma is advantageous over RF plasma. Because, microwave power of 2.45 GHz does not accelerate ions in plasma, but RF power of 13.56MHz does. For diamond formation high-voltage pulse bias is not applied to the sample holder from the same reason.

Using the new apparatus we deposited diamond layer that is composed of tiny particles of several to a thousand nm in grain size. Fig.4 shows the SEM image. We found out a new depositing condition where diamond particles are formed at a very low-substrate temperature of around 473 K (around 200 degC).

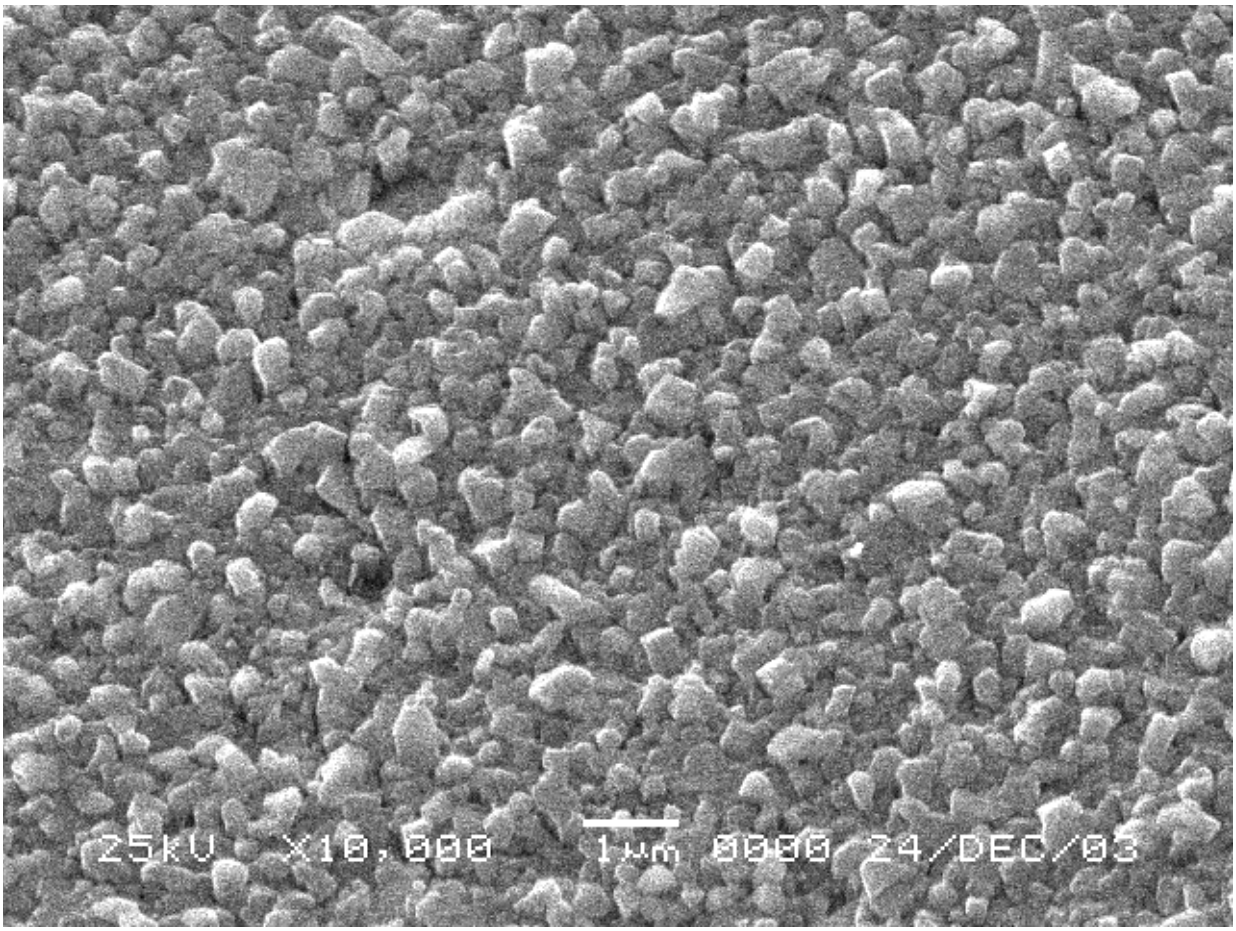

Fig.4 SEM image of nano-diamond deposit

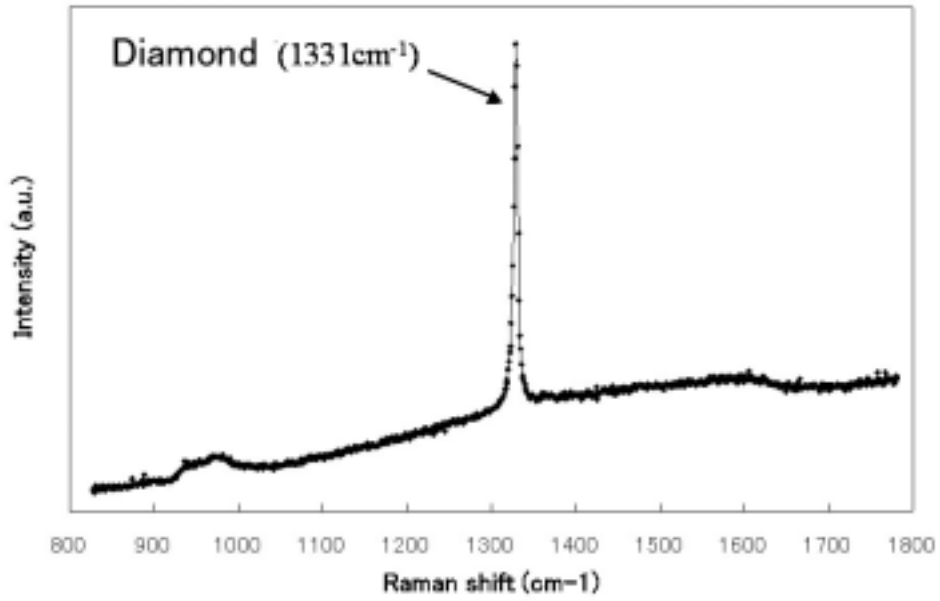

Fig.5 Raman spectrum of nano diamond deposition

The deposited material was measured with Laser-Raman spectrometer. Fig.5. shows a line peak at 1331 cm^{-1} that corresponds to diamond Raman shift. The slight inclination of base line implies that the deposition contains some amount of amorphous components of carbon. A lot of depositions are carried out by changing substrate temperature. It is found out that the grain sizes of nano diamond particles increase with substrate temperature as shown in Fig.6. Each black dot in the figure correponds to one sample datum. Even at a low temperature below 473 K [200 degC] nano deamonds of several tens of nm in grain size are deposited by this new plasma process, although diamond deposition has been until now carried out at a very high substrate temperature of over 1000 K.

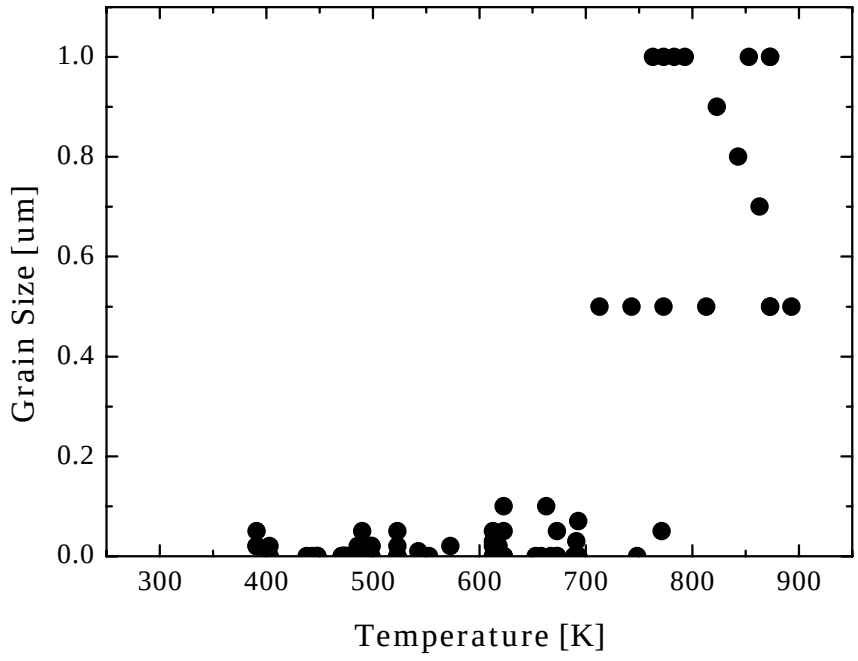

Fig.6 Dependence of nano-diamond grain size on substrate temperature.

Tribometric properties of nano diamond deposition are measured. The hardness is about 40 GPa, which is higher than that f DLC. But friction coefficient is about 4.0, which is 2 to 3 times higher.

4. Depositing DLC layer embedded with nano diamonds

In order to take advantages of both DLC and nano diamond we tried to combine both depositions. Two different plasmas are alternately generated; microwave plasma with methane-hydrogen mixture gas for nano diamond and RF plasma with acetylene gas for DLC. Resultantly, DLC layer that contains nano-diamond particles is deposited on a silicon substrate. Fig.7 shows the TEM (Transmission Electron Microscope) image of sliced sample of the deposited layer. The sample is sliced with a focused ion beam apparatus. The dark part on the left side of this figure is intermediate layer that is placed between Si substrate (not shown in this image) and the DLC layer embedded with nano diamonds. We can see a diamond particle of about 50 μm in grain size in the center. The part on the right side of this image is DLC deposition. The tribometric properties of this deposition are also measured. The hardness is almost same as that of the nano diamond deposition, and the friction coefficient is almost same as that of DLC.

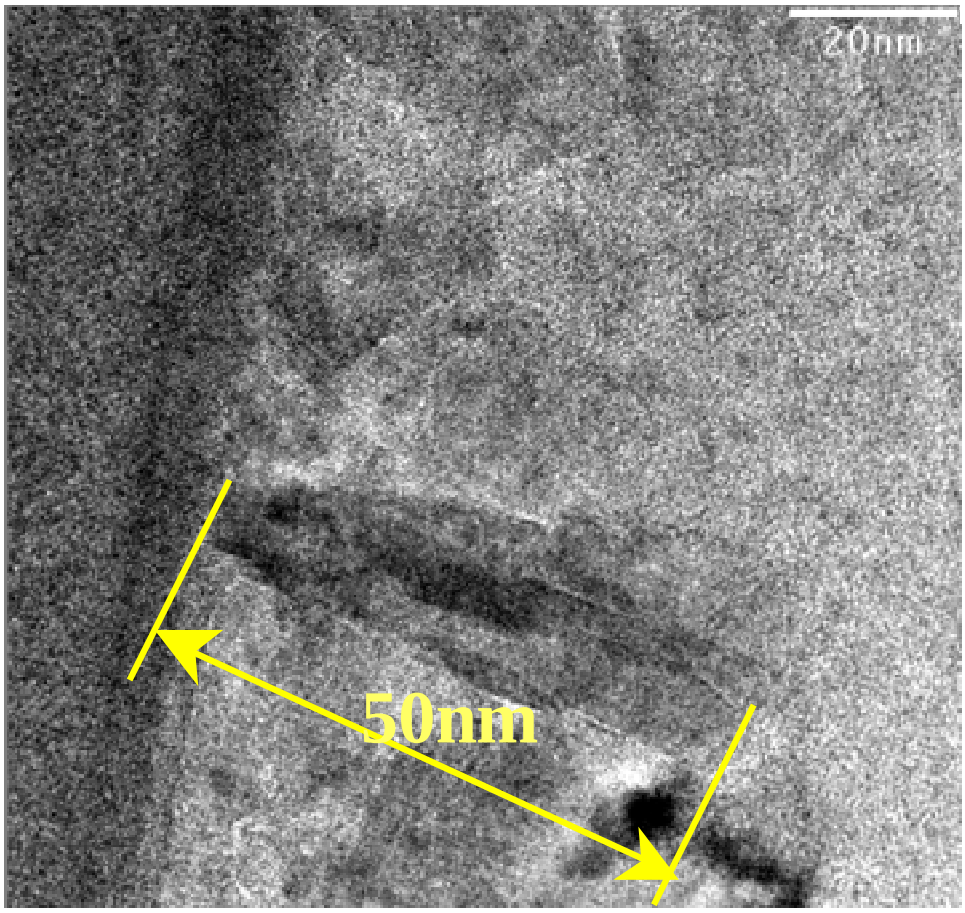

Fig.7 TEM image of sliced sample of habrid nano diamond layer

5. Conclusion

A new method to deposit a DLC layer embedded with nano-diamond particles is developed. The deposition is carried out at very low substrate temperature. The layer is expected to improve performances of machine tools and dies. It has low friction due to DLC as well as high local hardness due to diamond particle. Furthermore, the low temperature of substrate may enable the application of this new deposition to polymers that needs to be processed at a substrate temperature lower than 400 K.

Acknowledgement

This research was finantially supported by Japan Science & Technology Development Organization.

References

[1] N. Sakudo, D. Mizutani, Y. Yoshida, M. Yutani, K. Awazu and H. Yasui, Transactions of IEE Japan, Plasma Science and Technology, vol. 02-24 (2002) 49

[2] N. Ikenaga, K. Awazu, N. Sakudo, H. Yasui and T. Tabata, “Effect of electron temperature on the DLC film formation” to be published in Surface and Science Technology (2005)

[3] R. Mania, L. Stoibeiski and P. Panpuchi, J. Cryst. Growth, vol.62, (1981) 785

Partial oxidation of fossil and renewable fuels into the Synthesis Gas

A. Czernichowski, M. Czernichowski, P. Czernichowski[1]
ECP – GlidArc Technologies, La Ferté St Aubin, France

Abstract
The mixture of CO and H_2 is produced in our GlidArc (a High-Voltage discharge) assisted reformers *via* partial oxidation of various fuels with atmospheric air. Such process accepts almost any feed at up to 4% of Sulphur content. The feed conversion is total. No soot, coke or tars are produced. The assisting electric power presents less than 1% with respect to the power of the processed fuel.
Keywords: Synthesis Gas, Syngas, GlidArc, Reforming, Partial Oxidation

1. Introduction

The Synthesis Gas (SynGas, a mixture of mostly CO and H_2) is widely used as source of Hydrogen (*via* a simple extraction or when CO is water-shifted to CO_2 and H_2), as feedstock for chemical syntheses or as gaseous fuel for power generation. The last application can be performed, for example, in the Solid Oxide Fuel Cells (SOFC) that are capable of operating directly with the SynGas containing light Hydrocarbons and even some H_2S. The SOFC operating at high temperatures allow also a heat recycling for the primary fuel processing or other uses.

Conversion of liquid fuels into gaseous reformate for SOFC feeding is however difficult. High Sulphur and aromatic content of certain fuels deactivates classical catalytic processors and/or creates a significant soot appearance. Instead of removing thousands of Sulphur-organic molecules from fuels we propose a very simple plasma-assisted conversion of almost any fuels into the SynGas containing all initial Sulphur converted into the Hydrogen Sulphide. Such SynGas can be then very easily cleaned from H_2S, if necessary. Our High-Voltage discharge called GlidArc [1] assists first the cold-start of such processors when the full combustion of fuel is performed at high turbulence conditions. Once the reformer is sufficiently hot the discharge starts to assist only partial oxidation of the fuels with a reduced amount of oxidant. Such assistance allows the feed pre-reforming in the plasma zone so that the process achievement in the post-plasma zone containing an activated solid material may occur. Our electrically assisted process of partial oxidation accepts almost any feed at up to 4% of Sulphur content. The feed conversion is total. No water (or steam) needs to be added so that the process is simple.

Our tests with natural gas, cyclohexane, heptane, toluene, gasoline and Diesel oil (DO) were first published in [2]. Then we have presented a study on propane (LPG) [3] and natural gas [4]. The Rapeseed oil (Canola) conversion into SynGas was then tested [5] as example of various renewable fuels processing.

2. GlidArc-assisted reformers

Some experiments are now presented with a military aviation fuel and Rapeseed oil. We return also to our previous studies on the Diesel oil reforming and show our recent results. Here-presented tests are performed in small or medium-size reactors. A 0.6-L (internal volume) reformer is shown on the Fig. 1.

The plasma zone contains two flat electrodes that delimit a space filled with the gliding discharges. A feed + preheated air are mixed, blown into that space and flows along the diverging electrodes. The discharges ionize the air + partially vaporised fuel. Given the moderate temperature of the electrodes (not cooled) and a very short contact time of the discharge roots with the electrodes, we do not observe any deterioration (even at a high Sulphur presence) that may prevent the gliding of these current-limited discharges.

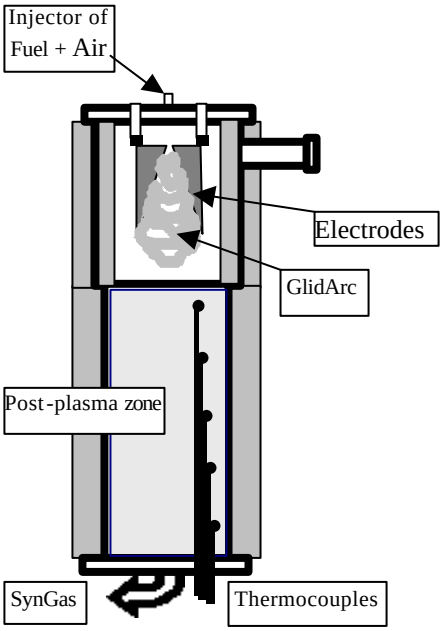

Fig. 1. Schematic of a 0.6-L GlidArc-assisted reformer.

[1] presently with Ceramatec Inc.

The plasma zone communicates with a post-plasma zone filled with activated packing (noble, rare or exotic elements are not used for activation). The flow of partially converted reactants containing long-living active radicals enters the zone where the conversion is completed by deactivation of all excited species. A 5 to 10kV power supply provides both ionisation of the air/fuel mix and then a transfer of the electric energy into the plasma. The time-averaged electric power is measured at the mains; it is less than 0.1kW for small reformers or up to 0.4kW for large ones.

The reformer is thermally insulated to keep it as hot as possible. Its total inside volume is 0.6L (1.8 to 6.6L for 20 or 80kW processor, the output power being accounted as the Lower Heating Value LHV of exiting reformate gas). No part of reactors is cooled in a forced manner. Some thermocouples measure the post-plasma zone temperatures. The output gas sample crosses white wool for soot presence checking. Other sample is analysed using a two-channel μ-GC dedicated to H_2, N_2, O_2, CH_4, and CO for one channel, and CO_2, C_2H_4, C_2H_6, C_2H_2, C_3H_8+C_3H_6, and residual moisture for the second one.

Figure 2 presents a picture of 6.6-L reformer that we are currently testing for up-to 1kg/h Hydrogen (+ roughly 14kg CO) production from the Soybean biodiesel or fossil Diesel oil. Such SynGas ($25m^3$(n) per hour equivalent to 80kW LHV) is devoted to clean up a NO_x-polluted exhaust from a 2MW Diesel engine. The GlidArc-assistance power is only 0.4kW.

Fig. 2. 6-L GlidArc-assisted reformer of various fuels.

3. Reforming

3.1.Aviation fuel

The JP-8 military aviation fuel can be considered as a logistic support for SOFC-based auxiliary power supply. The fuel has the following characteristics: relative density 0.800, average formula $CH_{1.94}$, aromatics 15.3 vol.%, total Sulphur 433ppm wt., initial BP 150°C, final BP 252°C, net heat of combustion (LHV) 43.2MJ/kg.

The explored ranges of inputs were: JP-8 @ 4.4–8.3g/min and air @ 23–41L(n)/min. The post-plasma zone of the processor contained 0.34L of activated refractory granules. The temperature of exiting SynGas (Reformate) reaches 725°C. As the result of various runs we have always observed the absence of soot, tar or non-reacted feed in the Reformate gas. The dry gaseous output (in vol.%) was:

H_2	10–16
CO	15–20
H_2+CO	6–35
N_2+Ar	5–68
CO_2	2.2–4.8
CH_4	0.7–2.8
C_2H_4	0.01–2.8
C_2H_6	0.00–0.19
C_2H_2, O_2, C_{3+}, others	absent

From the mass and enthalpy balances we deduce the output Reformate gas power (based on the LHV of all combustible components acceptable for SOFC): it can reach 4.4kW. Knowing the net heat of combustion (LHV) of the JP-8 we calculate the thermal efficiency of the JP-8 conversion into Reformate gas in our processor. This efficiency (defined as the ratio of the LHV of H_2+CO+light hydrocarbons at 25°C to the

LHV of the entering JP-8 fuel) is up to 78% for explored range of input parameters. Remaining energy content (chemical enthalpy) of the initial fuel is converted into the heat – but it is a compromise that we propose to accept for such a simple GlidArc-assisted soot-free and Sulphur-resistant technology.
The total GlidArc assistance power varied from 0.13kW at the cold-start of the process to some 0.05kW at the stabilized reforming conditions. The process power consumption related to the output Reformate gas power presents therefore only 1%. Figs. 3 and 4 show a typical composition of the Reformate gas (dry) and give an idea on the reformer output dynamics and its thermal efficiency.

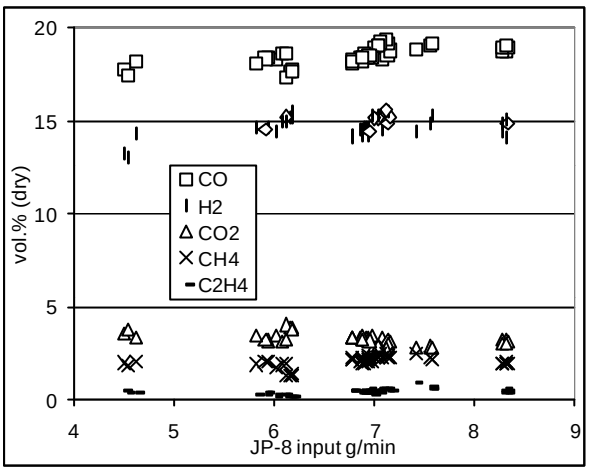

Fig. 3. Composition of the Reformate gas as a function of JP-8 fuel input rate.

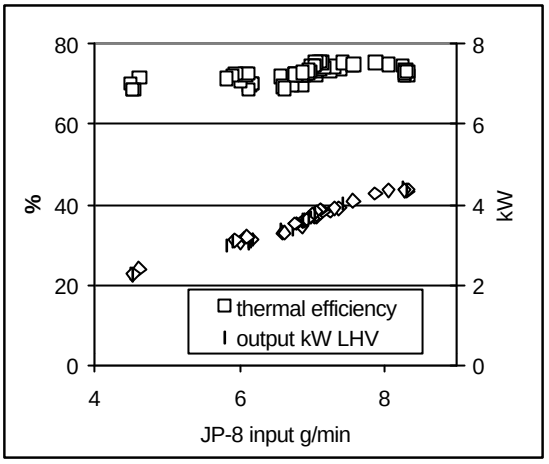

Fig. 4. Reformate output power and the thermal efficiency of the reforming as a function of JP-8 fuel input rate.

A 12-hours run at the constant air flow rate of 29L(n)/min and the constant fuel flow rate of 6g/min of JP-8 in 0.6-L processor at 3kW (LHV) output Reformate gas power and 60W GlidArc assistance was successfully preformed. No structural changes of the processor and its post-plasma zone after the run were found. Neither soot nor tars were produced.
We installed therefore this reformer for online feeding of a SOFC stack in a laboratory. Four series of tests were performed. No problems appeared after long runs during which several litres of this high Sulphur fuel crossed the reformer. Our 79 gas analyses showed a stable Reformate gas composition and the mass balance closure was typically 1%.The SOFC stacks were composed of a single 10-cell and then a dual 11-cell system. The stacks worked perfectly. Their performance were comparable to the Hydrogen baseline and the electric power output difference correlated well with higher steam content in our reformate gas. No soot was found in manifolds or electrodes after the stacks dismantling.

3.2. Diesel oil

Already in 2001-2 our feasibility tests with various road Diesel oils were successful [2] and further tests with a highly Sulphur-polluted heavy oil showed us that practically no harm is observed up to 4% Sulphur content. We performed then more detailed studies and long tests expanding the output Reformate gas power to >20-kW scale.
Our 1.8-L reformer is very similar to the previously described one. The plasma compartment (0.6L) contains two electrodes powered through one 10-kV power supply. The same activated material is used in the post-plasma zone of 1.2L volume. French road DO (from Total) is processed. Its average Carbon number is 15.6 (ranging from C_8 to C_{29}); an averaged formula can be written as $CH_{1.83}$, and the molecular mass is in the range of 210–220. This fuel has a quite high relative density of 0.826 and a high Sulphur content of 310ppm by weight. The DO (dosed by a metering pump) and compressed air (controlled by a mass flow meter) are simply mixed in a "T" connector and preheated up to 140-200°C before their injection to the GlidArc zone by an 8-mm (inner diameter) tube centred on the electrode axis. Through a porthole one can see the plasma discharge in the stream of the air + DO droplets. The droplets do not however affect our electric discharge. Explored inputs are:

Compressed air	48–146L(n)/min	Preheat	140–200°C
Diesel Oil	11–30g/min	GlidArc power	0.3–0.4 kW

As result we observe the following outputs at no sooting conditions and at total fuel conversion:

Bottom reformer temperature: ≤870°C

Reformate gas content (dry basis, vol.%):

H_2	16–20
CO	19–22
H_2+CO	38–41
CO_2	2.4–4.8
CH_4	0.8–3.3
C_2H_4	0.0–2.1
N_2+Ar	52–58
C_2H_2, O_2	absent

Reformate gas LHV power: 7-22kW.

Fig. 5 and 6 show the LHV power output of all combustibles (H_2, CO, CH_4, and C_2H_4) as a function of the DO input flow rate. They also illustrate the specific LHV energy output (in kWh per kg of DO) and the dry Reformate gas composition as a function of O_2/C molar ratio at the input (reflecting the air/fuel ratio).

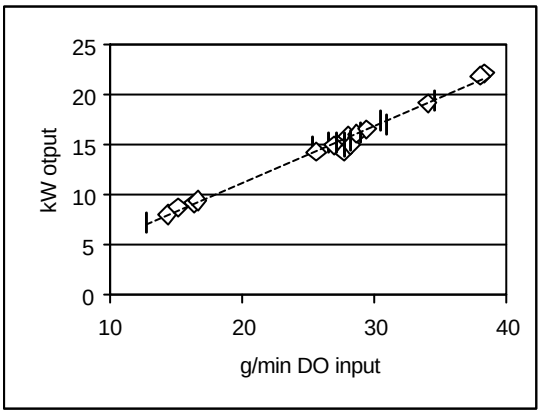

Fig. 5. LHV power output of 1.8-L processor as a function of the input flow rate of Diesel oil.

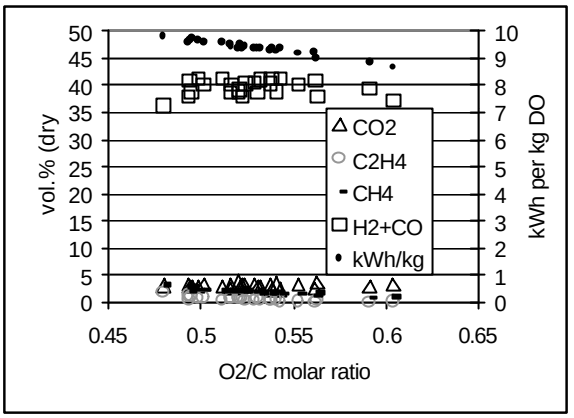

Fig. 6. Specific energy (LHV) output and the Reformate gas composition as a function of O_2/C at the input (right).

Our tests are successful: such quite highly Sulphur polluted Diesel oil is totally reformed at no water or steam added and at no soot or tars production (when checking the gas output with a white wool). To confirm that absence we dismantled several times our processor after its cooling and did not find any soot deposits inside. Our uninterrupted 24-hours test showed a good stability of the system. Other long-term tests are under way…

3.3. Rapeseed oil (Canola)

We use other 1-L reactor, similar to that shown on the Fig. 1. This processor contains three electrodes connected to 3-phase power supply 100 mA current to each electrode. No preheat is applied to any stream.

Several runs were preformed using an edible oil having the density of 913kg/m^3. At the accumulated runtime of 6 hours we never changed any part of the reformer. The process was always very stable. When soot was starting to appear at an insufficient air/oil ratio we just added more air (or reduced the oil flow) to establish the non-sooting reforming conditions. During these runs the air flow rate was comprised between 35 and 102 L(n)/min for the oil input flow rate between 11 and 30mL/min.

Fig. 7 shows temperatures T_1 (upstream) and T_2 (downstream, equal to exiting gas product temperature) such as observed when the thermal equilibrium of the reactor is achieved. Various tests are put together on the same graph showing therefore the explored range of the parameters. Fig. 8 presents the composition of the output gas (all successful tests are put into the same graph). In fact, the SynGas is always diluted by Nitrogen as we use air for reforming. The N_2 concentration at the output is typically in the 55–60 vol.% range (dry basis) depending on the air/oil ratio applied for the given test.

As results of the mass balances we calculate the output flow rate of 100% SynGas (H_2+CO only) for all runs as shown on the Fig. 9. The H_2+CO flow rate in the output can also be presented as the potential thermal output power. Such a power is therefore assimilated to the LHV. Our runs and reactor are not yet optimized but they indicate that we already obtain (at atmospheric pressure) as much as 11kW or 3.5m^3(n)/h of pure SynGas output. Higher outputs are expected for elevated pressures and/or preheat of the air and oil streams.

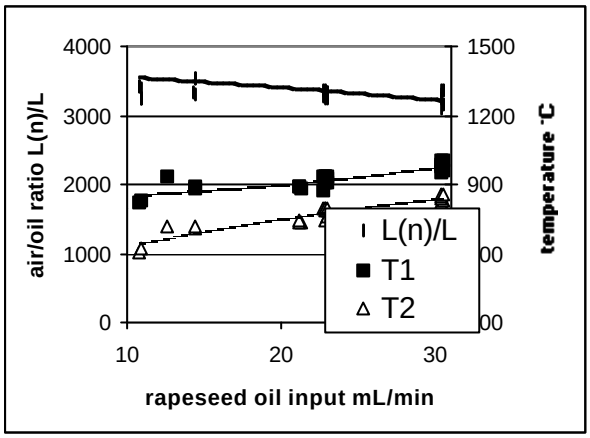

Fig. 7. Temperatures T_1 (upstream) and T_2 (downstream) inside the post-plasma zone as a function of the input flow rate of rapeseed oil. The left axis presents the air/oil ratio required for completely non-sooting reforming of the oil.

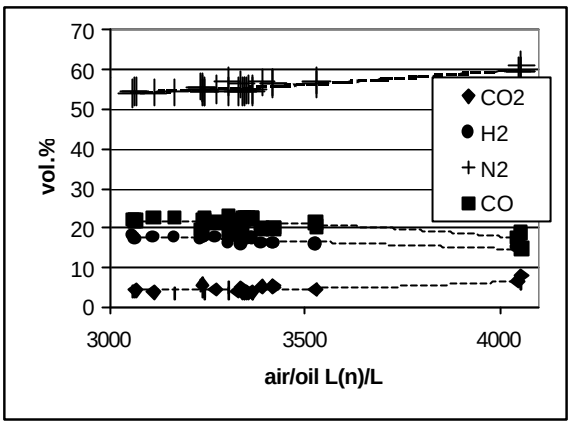

Fig. 8. Concentration of the main components (dry basis) in the output gas as a function of the air/oil ratio for all successful runs. Other gases are at minor concentrations: CH_4 0.5–1.0, C_2H_4 0.1–0.5, C_2H_6 0.01–0.03, and C_2H_2 0.001–0.005 vol.%.

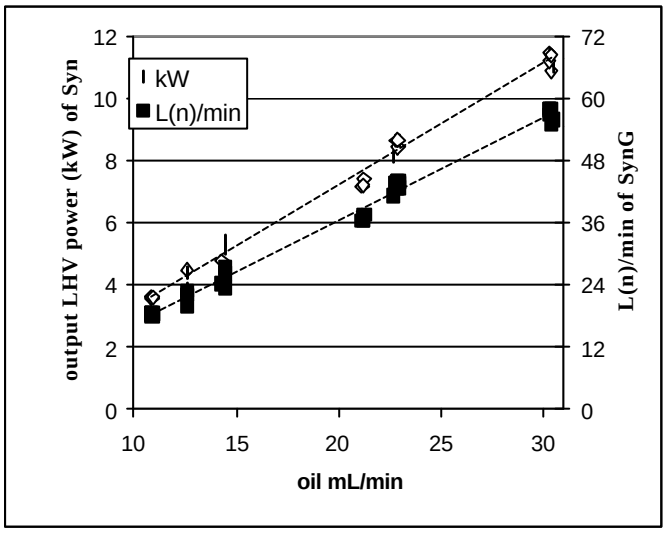

Fig. 9. Output flow rate of 100% SynGas (H_2+CO only) in L(n)/min and in kW for all runs at close-to the thermal conditions of the reformer.

The thermal efficiency of the reforming process can be estimated from these results. If one takes the LHV of the feed as 35MJ per kg then for our run at 30.4mL/min = 0.507mL/s = 0.463g/s the thermal input power corresponds to 16kW. For 11.4kW thermal power (LHV) output that we obtain as SynGas one finds therefore the thermal efficiency of the process at no sooting conditions equal to 70%. This quite high efficiency is based on only standard enthalpy heats (at 25°C) of the output H_2+CO combustion to CO_2 and steam (LHV) with respect to the standard heat of combustion (LHV) of entering oil. Such efficiency does not take into account any residual light hydrocarbon gas useful for SOFC or the sensitive heat content in the gas leaving the reformer. A part of that heat can certainly be reused to preheat entering feed and air so the thermal efficiency could be increased. No such heat exchange was used in this study.

3.4. Other feeds

We have already performed positive tests of reforming using 90% Ethanol, Glycerol, saturated Sugar/water solution, Soybean oil, Soybean diesel, and heavy bio-oil from the flash pyrolysis of wood. All that opens opportunities to upgrade some farm-issued products or waste biooils from various activities. ECP is presently fabricating a 30-L processor of about 0.5 MW output LHV power. Some last-minute results will be presented during the Symposium.

4. Conclusions

- Working hours or days we never changed any part of the reformer and/or its post-plasma zone loading. The technology is robust.

- Reformate gas appears after ~15min from a cold start or after ~2min when the reformer is kept hot. At such quick starts we do not obtain yet optimal performances – but the Reformate gas flow may be sufficient to start operate a SOFC (that also asks for a quite long heating and equilibration period).
- Thermal efficiency of the process is around 75%. An overall efficiency of our fuel processor + SOFC system can be increased thanks to some synergetic effects.
- Some methane and ethylene are present in the Reformate gas. They can be kept at quite low concentration, if necessary, by applying a higher O_2/C ratio at the input - but it would slightly lower the thermal efficiency of the reforming. These gases are however considered as good fuel for SOFC.
- Reformer works also when Sulphur is present in the feed. We proved it when reforming the JP-8 and Diesel oil at respectively 433ppm and 310ppm (weight) content. Our previous experiments show that even 4% of Sulphur in a heavy liquid carbonaceous feed (end distillation point of 600°C) is not harmful. In fact, even 100% H_2S can be processed using our GlidArc reactors for Hydrogen recovery from such waste gas [6].
- Conversion of the fuels is total, as we do not find any residual fuel or Oxygen at the exit. We do not produce soot, coke or tar and that is at no water or steam addition.
- Noble, rare or exotic elements are not used for activation of the solid mater present in the post-plasma zone of the reformer.
- Process is stable. The Reformate gas output flow and composition can be kept constant or match a required level by regulating the fuel and air flow rates. Drastic changes of the Reformate gas output flow and/or composition can be done in a fraction of minute.
- Electric assistance is low, around or less than 1% relative to the LHV of produced Reformate gas flow.
- According to our tests we can produce a flow of Reformate gas that is equivalent to 12kW LHV power per one Litre of inside reformer volume.

Here presented results show a simple way for a Reformate gas production from fossil or renewable matter. Our past tests show that pure Oxygen or O_2-enriched air can be used instead of atmospheric air. It opens some opportunities for more efficient GlidArc-assisted reformers and processes if such extra Oxygen is applied to reduce the Nitrogen content in the Reformate gas… One can also reduce the reformer volume or increase its output when working at higher pressures; we have some results at up to 6 bars.

References

[1] A. Czernichowski, M. Czernichowski, Further development of plasma sources: The GlidArc-III, this Symposium.

[2] A. Czernichowski, M. Czernichowski, P. Czernichowski, Non-catalytical reforming of various fuels into syngas, *France-Deutschland Fuel Cell Conf. on "Materials, Engineering, Systems, Applications"*, Forbach, France, 2002, p. 322-8.

[3] A. Czernichowski, M. Czernichowski, P. Czernichowski, GlidArc-assisted reforming of various carbonaceous feedstocks into synthesis gas. Detailed study of propane reforming, *14-th Annual U.S. Hydrogen Meeting*, 2003, Washington, DC, CD-proceeding, 8 pp.

[4] A. Czernichowski, K. Wesolowska, GlidArc-assisted production of synthesis gas through partial oxidation of natural gas, *First International Conference on Fuel Cell Science, Engineering and Technology*, Rochester, NY, April 21-23, 2003, p. 181-5.

[5] A. Czernichowski, M. Czernichowski, K. Wesolowska, GlidArc-assisted production of synthesis gas from Rapeseed oil, *Hydrogen and Fuel Cells Conf. and Trade Show*, Vancouver, Canada, 2003, post-conference proceedings (CD), 6 pp.

[6] A. Czernichowski, P. Czernichowski, M. Czernichowski, GlidArc-assisted removal and/or upgrading of Hydrogen Sulfide or Methyl-Mercaptan, 16th Int. Symp. on Plasma Chemistry, Taormina, Italy, June 22-27, 2003, poster, CD proceedings, 7 pp.

Further development of plasma sources: the GlidArc-III

A. Czernichowski, M. Czernichowski
ECP – GlidArc Technologies, La Ferté St Aubin, France

Abstract
A 45 years story of construction and development of various plasma sources for various applications is presented. It starts with a stabilized low-voltage but high-current intensity DC free-burning arc, a typical example of so-called "thermal plasma". Nowadays, we rather prefer our completely unstable AC high-voltage and very low-current plasma sources called "GlidArc". Third generation of this low-cost (and low-tech) devices is under development.
Keywords: GlidArc, plasma sources

1. Introduction

Since 46 years the first author has been involved in construction and/or development of various plasma sources for chemistry, metallurgy, atomic and molecular spectroscopy, deposition, assisted partial- or full-oxidation, and other. Under direction of Professor Wlodzimierz Trzebiatowski he started in 1959 with a DC free-burning low-voltage arc (up to 1500A in Argon) as a high-temperature source for some refractory minerals decomposition in Wroclaw's Technical University, Poland. Then he has successively built the first Polish DC plasma torch (1960) and started a study of the Argon plasma spectral emission. In 1962 he switched to an 800A DC arc in water- or Nitrogen-swirl; these plasma reactors were used for the Iron Titanate and Zirconium Silicate processing (Ph.D. thesis in 1966). Successively came a new DC torch having a Tungsten cathode and a segmented Copper anode (each segment actively power supplied at various electric potentials) for SiO_2, TiO_2 and ZrO_2 reduction in Hydrogen (1970). In turn a microwave torch for NO_x synthesis (3kW, 1973), an arc striking to the molten LiCl (1974), an induction-coupled torch (atmospheric pressure, 25kW, 1975), a metal-wall-stabilized arc for plasma spectroscopy (150A, 1975), a multiple-electrode and high intensity rotating/pulsating arc (1980), an unstable and very active transferred DC arc for Hydrocarbon or H_2S processing (1983), a high current circuit breaker (1983), an electro-burner for Methane flame over-heating (1985), and a semi-industrial 250kW DC transferred arc furnace (1987) took his attention…

In early 1980's the plasma-chemical community started to abandon the so-called "thermal plasma" devices for chemical applications, as it appeared that their high electric energy consumption cannot be accepted for most of industrial processes. Also the microwave and induction-coupled sources did not get a large approval because of their complex electric supplying, especially for higher power units. Other non-thermal ("cold" or "out-of-equilibrium") plasmas were demanded… Accordingly, the gliding arc device was proposed in 1988 [1]; it is now known under its short name "GlidArc".

2. Gliding Discharges

2.1. GlidArc-I

The GlidArc generates non-thermal plasma that enhances various processes through active catalytic species: electrons, ions, and excited atoms. This source has at least two diverging electrodes immersed in a fast gas or vapour flow. A high voltage and relatively low current discharge (up to 30kV, 0.05-5A, 0-20kHz) is generated across the flow between the electrodes as it is shown on the Fig. 1. The discharge forms at the closest point between the electrodes, glides along the electrode's edges, and disappears. Another discharge immediately reforms close to the initial spot. The discharge performs its own maintenance on the electrodes, preventing chemical corrosion and/or thermal erosion. The electrodes are not water-cooled so the electric power is directly and totally transferred to the processed feed. Any gas or vapour can be directly processed at 0.05-12bar range. Droplets, mists, and powders can be present. Feeds of any initial temperature are accepted.

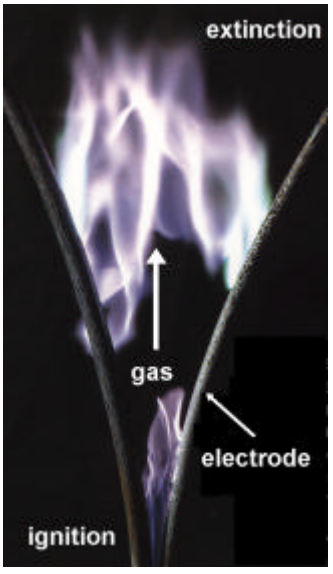

Fig. 1. The GlidArc-I

Gliding discharges of GlidArc-I type can be also installed between metallic electrodes and a conducting liquid [2]. Multiple electrode systems can be installed for large gas steams processing. Their electric powering is described in [3]. Structures of several dozens of electrodes can be organized as "clusters" forming some plasma heads for powerful AC plasma reactors supplied from unique 3-phase transformer [4].

2.2. GlidArc-II

In 1996 we started to develop an alternative way of gliding discharges generation using a rotating central electrode and "connecting" it, *via* high-voltage AC discharges, to several stationary electrodes located around the central electrode [5]. As result we have obtained a new GlidArc-II device. Figure 2 presents the principle of such cold-plasma source while the Fig. 3 shows a principle of multiple-stage reactor in which the processed fluid can cross several electric discharges to reach a suitable rate of conversion.

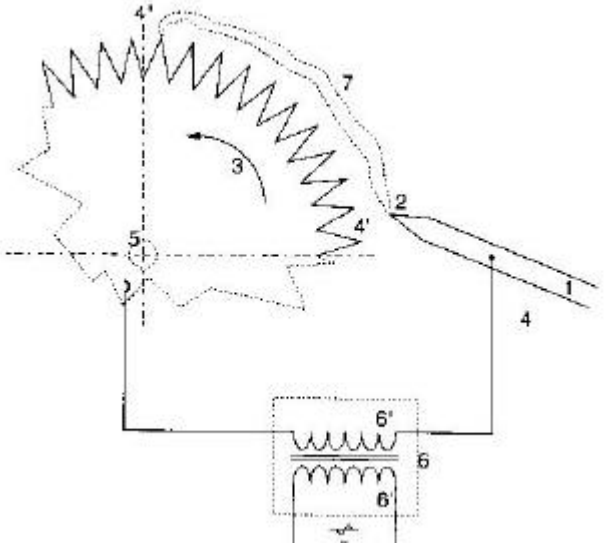

Fig. 2. Principle of the GlidArc-II device: 1 – stationary electrode, 3 – rotating electrode, 6 – power supply, 7 – high-voltage discharge filaments.

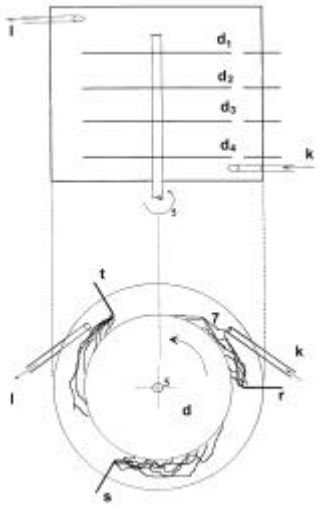

Fig. 3. Multiple-stages and multiple-electrodes GlidArc-II reactor: r, s, and t – three-phase-supplied stationary electrodes, k and l – input and output of the processed gas, d – rotating electrodes.

There are multiple advantages of the new structure. The high voltage discharges generation and the processed gas flow rates are no more self-dependent so that even a very low gas flow can now be accepted at any power as there is no more need to accelerate the gas at the proximity of electrodes. The mobile electrodes rotate in the range of 50–1000rad/s, which are acceptable speeds. The discharges can "touch" several times the same gas flux without any obligation to push the gas between the stages. The reactor is quite compact for even large gas flows. For example one can realize three 5A and 2kV discharges for one stage. When adding 4stages it makes us a 120kW reactor realized in a 0.3m diameter cylinder of 0.5m length (30L of volume). Such reactor can process roughly up to 2400 m^3/h of gas.

A 60-L stainless steel reactor was built by ECP for H_2S-related streams processing. This reactor presented on the Fig. 4 contains 9stages, each of them being powered by 3 stationary electrodes so that 36 active electrodes are present (including central electrodes).

First successive tests of this reactor were performed with an active participation of Piotr Czernichowski. We have obtained better than 50% conversion of an H_2S-rich acid gas into the SynGas.

Fig. 4. 60-L, 36-electrodes GlidArc-II pilot plant for Hydrogen Sulphide processing (SulfArc).

Several application tests and studies were performed in laboratory or pilot scale GlidArc-I and-II reactors for gases, vapours, liquids, and solids processing (decomposition, conversion, upgrading, activation) as well as for flames overheating or stabilization (flaring for example). More than twenty French and foreign patents protect some of GlidArc-I and -II principles, powering, and applications.

2.3. GlidArc-III

Since long time we have been also working on plasma assisted partial oxidation of various fuels into the synthesis gas [6]. During this process it appeared that soot or other solid particles could deposit on high-voltage insulators of the GlidArc-I electrodes. Generally, only two electrodes are needed for such application to ignite and then to support such partial oxidation at less than 1% dissipated electric energy with respect to the enthalpy of the SynGas. New GlidArc-III plasma source [7] solves this problem.

As shown on Fig. 5 we direct 5-20% of the air *(1)* to a vortex-like zone *(2)* that protects one central GlidArc-III electrode *(3)* while the remaining part of the oxidant is sent through *(4)*, together with the processed fuel, to the plasma zone *(5)* where the gliding and rotating high-voltage AC discharge strikes between the central electrode *(3)* and the surrounding metallic nozzle *(6)* being at the ground potential The fuel and its pyrolysis products cannot now harm the dielectric support *(7)* of the central electrode. A Diesel fuel conversion into Synthesis Gas was successfully performed this year.
Figures 5 and 6 present our GlidArc-III reformer for various fuels processing.

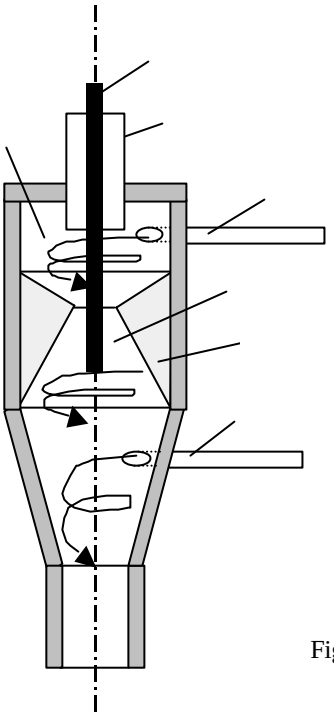

Fig. 4. Principle of the GlidArc-III.

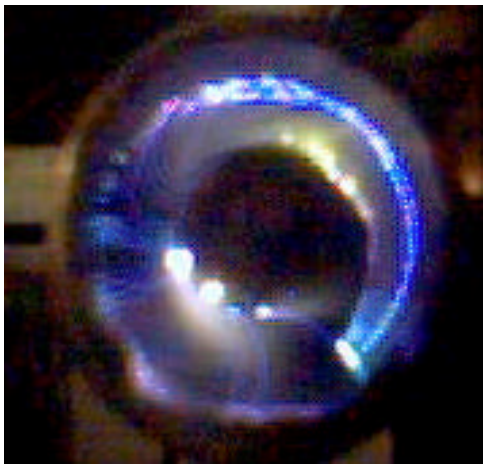

Fig. 5. GlidArc-III discharge.

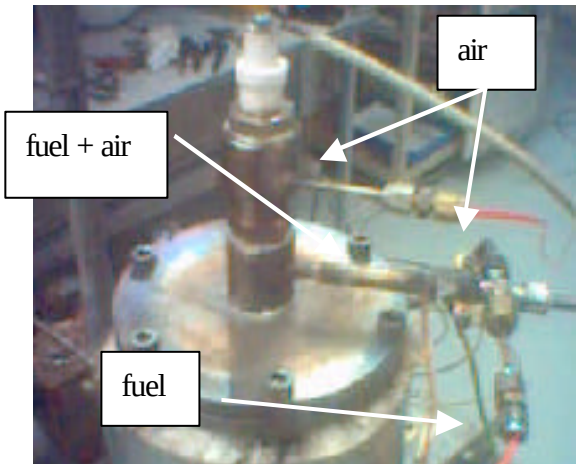

Fig. 6. GlidArc-III at the top of the Fuel Reformer body

3. Conclusion

A 45 years in-house story of construction and development of various plasma sources for various applications indicates that GlidArc-type generators are the best solution for plasma-chemical applications.

They can be as powerful as classical plasma torches while avoiding specific power supplying, water-cooling, electrode erosion, and quite complicated manufacturing. GlidArc instabilities rather help progressing the chemical processes by creating strong fluid turbulences (mixing) and generating very active catalytic species at quite low processed fluid temperature. We are proud to submit already three generations of these low-cost and low-tech devices to the Plasma Chemistry Community.

References

[1] H. Lesueur, A. Czernichowski, J. Chapelle, Dispositif de Génération de Plasmas Basse Température par Formation de Décharges Electriques Glissantes, French Patent No.2 639 172 (1988).
[2] A. Czernichowski, B. Hnatiuc, P. Pastva, A. Ranaivosoloarimanana, Générateurs et circuits électriques pour alimenter des décharges instables de haute tension, French Patent No. 2 817 444 (2000).
[3] A. Czernichowski, M. Czernichowski, Dispositif modulaire pour générer de multiples décharges électriques glissantes de haute tension, French Patent No. 2 842 389 (2002).
[4] J. Janca, S. Kuzmin, A. Maximov, J. Titova, A. Czernichowski, Investigation of the Chemical Action of the Gliding and "Point" Arcs Between the Metallic Electrode and Aqueous Solution, Plasma Chemistry and Plasma Processing, vol. 19(1) 53-67 (1999).
[5] A. Czernichowski, J. Sünnen, Procédé et dispositif de production d'un plasma hors d'équilibre, French Patent No. 2 763 778 (1997)
[6] A. Czernichowski, P. Czernichowski, Partial Oxidation of fossil and renewable fuels into the synthesis gas, this Symposium.
[7] A. Czernichowski, M. Czernichowski, K. Wesolowska, French application (2004).

Development of New Green Process for Methane Reforming Using Microwave Plasma / Solid Catalyst Combined Reactions

H.Nagazoe, M.Konuma, M.Kobayashi, T.Yamaguchi, K.Onoe

Department of Life and Environmental Sciences, Faculty of Engineering, Chiba Institute of Technology

Methane is irradiated with microwaves by using a microwave plasma reactor, and the selective synthesis of ethylene under the oxygen free condition is developed by the contact of active species with a Pt/Al_2O_3 catalyst, assuming that the concentration of the active species is sufficiently high. Furthermore, H-ZSM-5 is used as a zeolite catalyst, and oily matter can be produced with high yield.

1. Introduction

"Green Chemistry", namely the new chemical technology which does not give the load to the environments, has been promoted by many researchers. According to the suggestion of Anastas, the concept of reaction design with the aim of not only the consideration to the health but the lowering of environmental risk is summarized at twelve items [1]. From the viewpoint of the chemical reaction engineering, it seems to be necessary to carry out the development of the catalytic reaction process based on the new reaction mechanism. In a normal solid catalytic reaction, the material reaches the surface of the catalyst. However, the material is irradiated with microwaves, it will be converted to an active species before it reaches the surface of the catalyst. This suggests the possibility to develop a new reaction process by extracting higher performance from the catalytic activity.

Here, methane is attracting a great deal of attention as a next-generation carbon and hydrogen resources, and many researches have been investigated on the synthesis of C_2 hydrocarbon through oxidative coupling of methane (OCM) using solid catalysts since the early 1980's [2-5]. But the methane reforming to low-grade or long-chain hydrocarbons under the oxygen free condition is very important for an achievement of the clean process of non-discharging the unnecessary carbon oxides. If the advantage that "a raw material for a catalytic reaction is converted to appropriate active species before reaching the conventional catalysis field" outweighs the disadvantage that "external energy needs to be added", it leads to possibility of creating a new process.

In this study, a new oxygen-free green process combining the methane plasma decomposition with the solid catalytic reactions was developed. Features of this process reveal that three reaction zones exist. In the primary reaction zone, which is located in microwave-irradiated field, the supplied methane is decomposed into the hydrocarbon and hydrogen active species in the plasma state. In the secondary reaction zone, which is located between microwave irradiation field and packed bed zone of catalyst, the generated active species (mainly methine and hydrogen radicals) gradually convert to acetylene and hydrogen with an increase in residence time due to the individual progress of homogeneous couplings [6-10]. In the last reaction zone, the specified reactions among active species or between active specie and molecule are progressed on the surface of catalyst. In this paper, Pt/Al_2O_3 and H-ZSM-5 were chosen as catalysts. The concentrations of remaining hydrocarbon and hydrogen active species during the individual progress of homogeneous couplings are measured by the selective oxidation method using oxygen molecule, and the effects of the concentration of active species for the molecule on the catalytic activity are examined.

2. Experiment

2.1 Catalyst

0.5 wt% of Pt/Al_2O_3 pellet (2 mm in diameter with 3 mm in height, N. E. Chemcat. Co., Ltd. Japan) and a granular Al_2O_3 (Shinwa Kako Co., Ltd. Japan) were separately pulverized to 60-80 mesh and mixed together to produce a mixture with a Pt content of 0.05 wt%.

H-ZSM-5 (80 mesh under) was prepared by oxidation of NH_4-ZSM-5（Zeolyst Inter. Co., Ltd. US）under the air supplying. The ratio of Si/Al was 164.

2.2 Experimental apparatus

Figure 1 shows the experimental setup for the reduced-pressure continuous flow reactor, which consists of a gas supply system, a microwave-generator, a reaction tube and an analysis facility. Plasma was generated by irradiating a quartz reactor (an inside diameter of 25 mm, a thickness of 1.5 mm and a length of 500 mm) with microwave with a frequency of 2.45 GHz through a wave guide (a length of 54.6 mm and a width of 109.2 mm) installed horizontally. Non-irradiated gas was supplied from an alumina tube (an inside diameter of 4 mm) attached at the bottom of the quartz reactor. The catalyst was retained in silica wool and filled into the reaction tube (**Figure 2**).

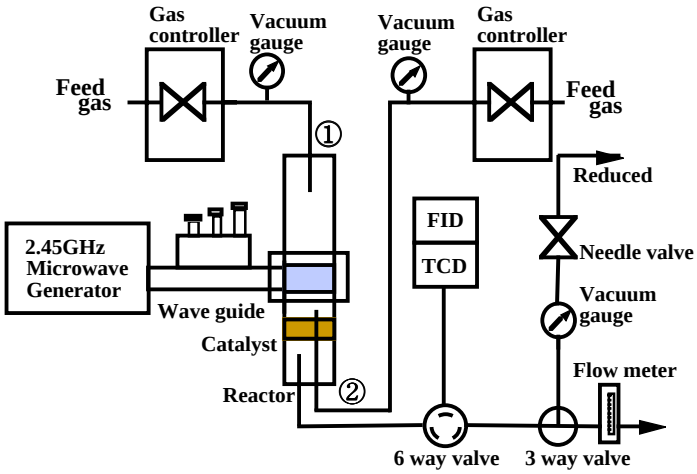

Figure 1. Experimental apparatus for combined reactions

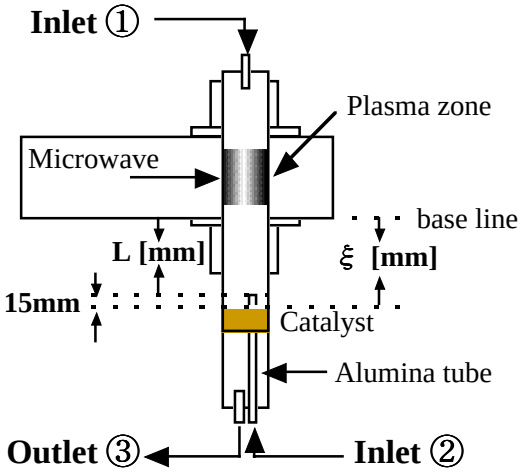

Figure 2. Detail of plasma reactor

2.3 Experimental procedures

2.3.1 Measurement of the concentration change of active species in the secondary reaction zone

The decreases in the concentrations of hydrocarbon species (HCS) and hydrogen species (HS) occurring

in the secondary reaction zone were estimated as follows: (a) The concentration decrease of hydrocarbon species was estimated on the produced amount of COx (CO and CO_2) using a set-up in which methane plasmas were contacted with the oxygen supplied from inlet ②, and the distance *L* from the lower-level of the waveguide to the inlet ② was changed. (b) Similarly, the concentration decrease of hydrogen species was estimated on the produced amount of water vapor when hydrogen and oxygen were supplied from ① and ②, respectively.

2.3.2 Combined reactions in the last reaction zone

Both the remaining active species and the generated molecules (acetylene and hydrogen) during the reactions in the secondary reaction zone were brought into contact with the surface of solid catalyst. Experiment was performed with varying the distance ξ between the lower-level of the waveguide and the upper-level of the catalyst bed.

When 5 g of Pt/Al_2O_3 catalyst was packed, the feed rate of methane was adjusted to 34.7 μmol/s and initial reaction pressure was set at 6.5 kPa. Microwave irradiation power was adjusted at 300 W. In the case of H-ZSM-5 (1 g) catalytic reactions, the methane feed rate was 4.95 μmol/s and initial reaction pressure was 4.0 kPa performed with keeping microwave irradiation at 150 W. The temperature of the catalyst layer was measured using a K-type sheathed thermocouple with its tip placed at 6 mm from the upper-level of the catalyst layer. The products were taken with an online sampler and analyzed by gas chromatography.

3. Results and discussions

3.1 Homogeneous reaction progress of active species into acetylene and hydrogen

When methane was supplied from inlet ① and the position of oxygen inlet ② was changed, the concentration of COx (mainly carbon oxide) formed by the selective oxidation of the carbon included in the hydrocarbon species was changed. **Figure 3a)** shows the concentration change of active hydrocarbon species (HCS) estimated from the yield of COx, where *L* means the distance between the lower-level of the waveguide and the upper of inlet ②. **Figure 3b)** shows the concentration of active hydrogen species (HS) estimated from the yield of water vapor measured when hydrogen was supplied from inlet ①. In both figures, "*" indicates that the supplied gas from inlet ① was converted to active species through the reaction induced by the microwaves. It was obtained that the concentration of hydrocarbon active species was decreased to 30 % at $L = 90$ mm, while that of acetylene increased with increasing *L*. The slight amounts of carbon dioxide and water vapor were detected. Assuming that the generation rate of carbon monoxide through a gas-phase reaction between the active hydrocarbon species and oxygen molecule is comparatively fast, which indicates that the molar fraction of carbon monoxide is positively correlated to the concentration of the reacted active hydrocarbon species. Similarly, the concentration of active hydrogen species was decreased to 35% at $L = 90$ mm, and it is assumed that the active hydrogen species turns into stable hydrogen molecules as it moves away from the microwave irradiation zone. These results in the secondary reaction zone are summarized that the concentrations of molecules (acetylene and hydrogen) which reaches the catalyst surface increases, while the concentration of the radical species decreases.

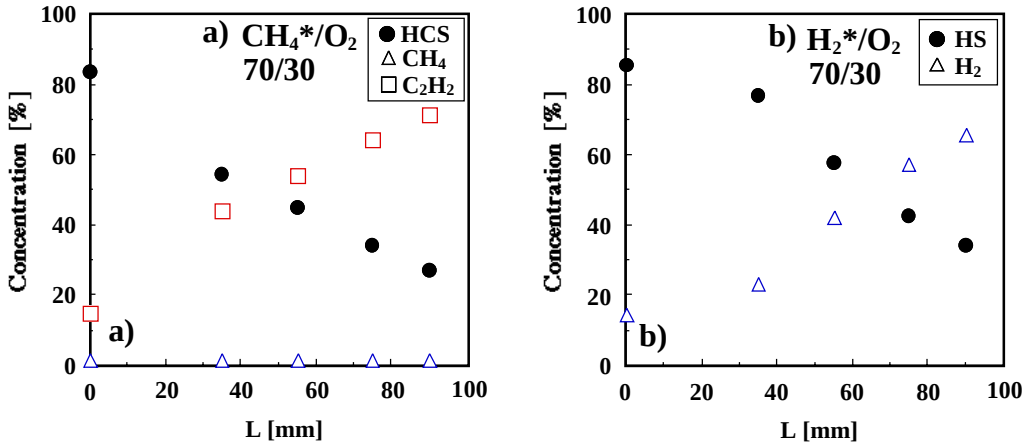

Figure 3. Concentration changes of a) hydrocarbon active species, and b) hydrogen active species

3.2 Comparison of products from the variation of solid catalyst

In the last reaction zone, microwave irradiated methane was introduced into the empty reaction tube [system I)] and the various packed bed zones [system II) Al_2O_3, III) Pt/Al_2O_3, and IV) H-ZSM-5], where the distance from the lower-level of the waveguide to the upper-level of packed bed (ξ) was set at -10 mm. **Figure 4** shows the comparison of the distribution of products in terms of the number of carbons. The trace amount of carbon deposition was observed in all experimental systems. In comparison with the experimental results in systems I) and II), the carbon distribution of the acetylene is almost equal, which indicated that the hydrogenation activity of alumina on the hydrocarbon active species is very low.d Meanwhile the yield of ethylene obtained in the system III) was up to 74.1%. This result indicates that active hydrocarbon and hydrogen species in contact with the Pt/Al_2O_3 catalyst can facilitate hydrogenation on the surface of catalyst. When H-ZSM-5 catalyst was used, the carbon distribution of oily product was remarkably increased (25.9 %).

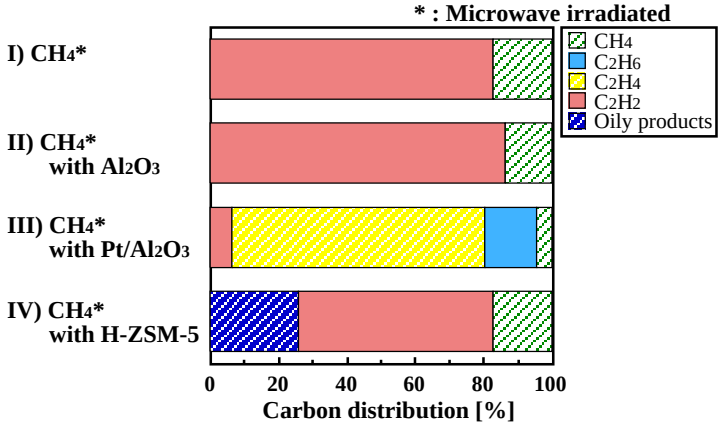

Figure 4. Comparison of carbon distribution in each system

3.3 Effect of the distance in the secondary reaction zone on catalytic activity of Pt/Al_2O_3

As described above, the concentrations of active species (active hydrocarbon and hydrogen species) produced in the primary reaction zone were decreased with increasing the distance in the secondary reaction zone. When Pt/Al_2O_3 catalyst was used, the effect of the distance ξ on the methane conversion (X_{CH_4}) and product yield are shown in **Figures 5a)** and **5b)**, respectively.

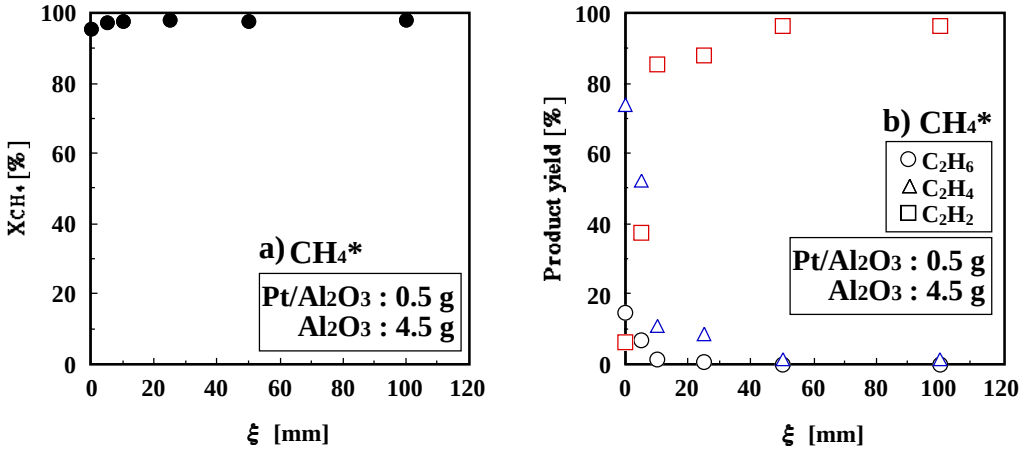

Figure 5. Effect of the packed position of catalyst on a)methane conversion and b)product yield

The methane conversion exceeded 90% in each experimental run. At ξ=0 mm, the yield of ethylene ($Y_{C_2H_4}$) was 78% and the temperature *T* of the catalyst layer was 785 K. These results are superior to the results obtained in the hydrogenation of acetylene using Pt/Al_2O_3 catalyst under microwave non-irradiated field (the maximum $Y_{C_2H_4}$ of 38.2% at *T* = 473K). At ξ= 100 mm, ethylene yield was 3% and *T* was 305 K. The decrease in ethylene yield with increasing ξ (*T* also decreases with increasing ξ) means that high yield of ethylene can be obtained by bringing into contact with the catalyst under high-density methane plasmas.

3.4 Effect of the distance in the secondary reaction zone on catalytic activity of H-ZSM-5

Figure 6 shows the effect of distance in the secondary reaction zone on product yield, where the methane conversion exceeded 80% in each experimental run. It was clear that the yield of the oily products exceeded 20% at ξ= -10 mm, which indicated that the catalytic activity of H-ZSM-5 for the production of oily compounds was increased with an increase in the concentration of active species. When the distance in the secondary reaction zone was set below –10 mm, the carbon deposition was remarkably observed on the surface of H-ZSM-5 catalyst.

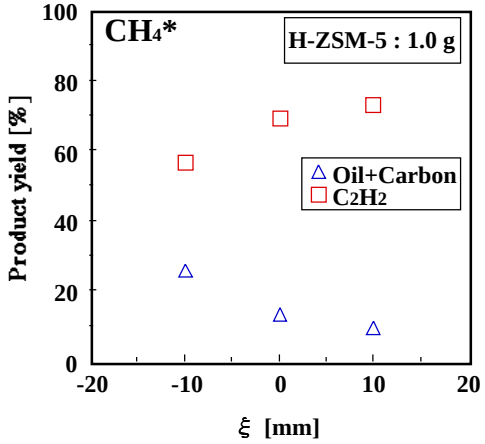

Figure 6 Effect of packed position of catalyst on product yield

Figure 7 shows the gas chromatogram of oily products (ξ=-10 mm). It was indicated by the measurement of the carbon number distribution of oily hydrocarbons that C_{14}-C_{45} of aliphatic hydrocarbons and C_{12}-C_{20} of aromatic hydrocarbons were obtained.

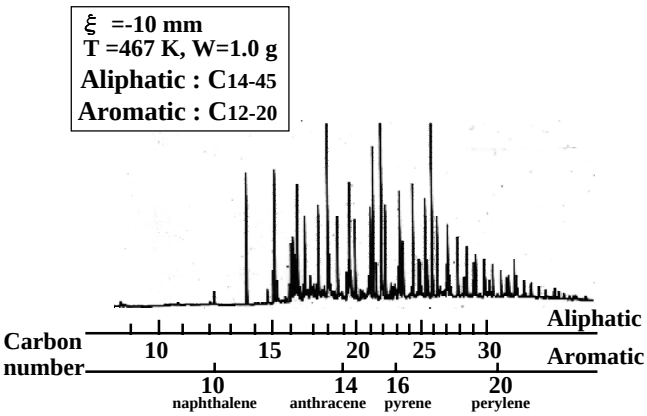

Figure 7 Gas chromatogram of oily product

4. Conclusions

Both active species of hydrocarbon and hydrogen produced by irradiating methane with microwaves were brought into contact with Pt/Al_2O_3 or H-ZSM-5 catalyst. From the results, the following findings were obtained.

a) In the primary reaction zone which is located in microwave-irradiated field,, the supplied methane is decomposed into the hydrocarbon and hydrogen active species (mainly methine and hydrogen radicals) in the plasma state.

b) In the secondary reaction zone which is located between microwave irradiation field and packed bed zone of catalyst, the generated active species gradually convert to acetylene and hydrogen with an increase in residence time due to the individual progress of homogeneous couplings.

c) When Pt/Al_2O_3 catalyst was packed in the last reaction zone, ethylene yield was increased with decreasing the distance in the secondary reaction zone. When H-ZSM-5 catalyst was used, the yield of oily product was increased compared with the Pt/Al_2O_3 catalytic reactions.

References

[1] Anastas P.T., J.C. Warner, Green Chemistry: Theory and Practice, Oxford University Press, New York, p. 30 (1998)

[2] Keller, G. E., M. M. Bhasin, J. Catal., **73**, 9 (1982)

[3] Guczi, L, R. A. van Senten, K. V. Sarma, Catal Rev-Sci Eng, **38**(2), 249 (1996)

[4] Krylov, O. V., Catal. Today, **18**, 209-302 (1993)

[5] Xu, L., S. Xie, S. Liu, L. Lin, Z. Tian, A. Zhu, Fuel, **81**, 1593 (2002)

[6] Larkin, D. W., T. A. Caldwell, L. L. Lobban, R. G. Makkinson, Energy & Fuels, **12**, 740 (1998)

[7] Fincke, J. R., R. P. Anderson, T. Hyde, B. A. Detering, R. L. Bewley, D.C. Haggard, W.D. Swank, Plasma Chemistry and Plasma Processing, **22**(1), 105 (2002)

[8] Kado, S., K. Urasaki, Y. Sekine, K. Fujimoto, T. Nozaki, K. Okazaki, Fuel, **82**, 2291 (2003)

[9] Onoe, K., A. Fujie, T. Yamaguchi, Y. Hatano, Fuel, **76**(3), 281 (1997)

[10] Nagazoe H., M. Kobayashi, T. Yamaguchi, H. Kimuro, K. Onoe, The Proceeding of International Symposium on Microwave Science and Its Application to Related Fields, No.O9-03 (2004)

Multi-electrode gliding arc plasma reactors powered from special transformers

Henryka Danuta Stryczewska, Grzegorz Komarzyniec, Jarosław Diatczyk
Institute of Electrical Engineering and Electrotechnologies, Lublin University of Technology,
20-618 Lublin, 38A Nadbystrzycka St., Poland, http:/volt.pol.lublin.pl

Abstract
Multielectrode reactor requires simultaneous ignition and sustaining the gliding arc discharge between many pairs of electrodes what is a difficult task for its electric power system and makes it complex and expensive. The proposed in the paper systems based on specially constructed transformer can fulfill requirements of industrial arc discharge reactors while representing simplicity of construction with high efficiency and reliability.
Keywords: non-thermal plasma reactor, gliding arc discharge, power supply systems, special transformers

1. Introduction

Industrial plasma-based technologies for pollution control require the non-equilibrium atmospheric pressure plasma to be produced directly in the big volume of polluted gases at conditions similar to whose the gases are emitted to the atmosphere during the industrial processes. Gliding arc discharges can be produced at DC and AC power supply conditions at commercial or increased frequency in the multi-electrode systems and can treat large volume of polluted gases, cold or hot, with moisture or dry without any previous gas preparation. Moreover, the possibility to treat very diluted substances, like VOC or CFCs components, simultaneous treatment of gas mixtures containing several pollutants, not very sophisticated requirements to power supply, all these make the gliding arc technology very promising tool in the environment pollution control [1].
The gliding arc discharges in the multielectrode and multistage configurations are especially suitable in the industrial pollution control applications. The technology is based on the arc discharge that is forced to glide by fast gas flow along electrodes of diverge form. The more electrodes are put into the discharge chamber the bigger volume of polluted gases can be effectively treated. Multi-electrode configuration allows gliding arc discharge to penetrate and to treat large volumes of polluted gases at atmospheric pressure and conditions typical for industrial processes.
It is a power supply system that determines the reliability and efficiency of the whole plasma generation installation and very often it just decides if the process has the prospects for common usage in industry. Reliability and low investment and exploitation costs are important factors, which shall be taken into consideration during design and construction process of the industrial plasma reactors' installations. Paper presents chosen solutions of arc discharge reactors' power systems. Their construction is based on single- and three-phase transformers, which magnetic cores' nonlinearity is the source of ignition voltage, so the additional arc ignition systems are not required and what makes the proposed systems very simple and reliable. The proposed systems are suitable to energize not only reactors with gliding arc discharge but also for plasmatrons with arc discharges of similar to gliding discharge current-voltage characteristic.

2. Gliding arc discharges in multielectrode and multistage configuration

Basic configuration of plasma reactor with gliding arc discharge, presented in Figure 1, comprises two knife-shaped working electrodes, **B,** connected to the power system, **Z,** and put in the discharge chamber, **A,** through which polluted gas, **D,** to be treated flows with velocity greater than 10 m/s. To assure required non-thermal plasma conditions, working electrodes should be energized with voltage of about 1-2 kV and current value lower than 10 A. Such values of voltage and current are not typical for arc discharge and the produced plasma is at non-equilibrium state similar to glow discharge rather than to arc discharge plasma. Moreover, the interelectrode voltage lower than 2 kV is not sufficient for discharge ignition and therefore it is necessary to introduce the additional ignition electrode, **C,** to the zone in which the discharge starts to move through electrodes. Presented in the Figure 2 typical voltage–current characteristic of the gliding arc discharge between two electrodes shows that voltage required for the discharge ignition (10,5 kV) is more than sixth times greater than for the discharge

sustaining (1,5 kV) at nominal current (2 A) and explains how the power supply system characteristics should be constructed to fulfill the plasma reactor requirements.

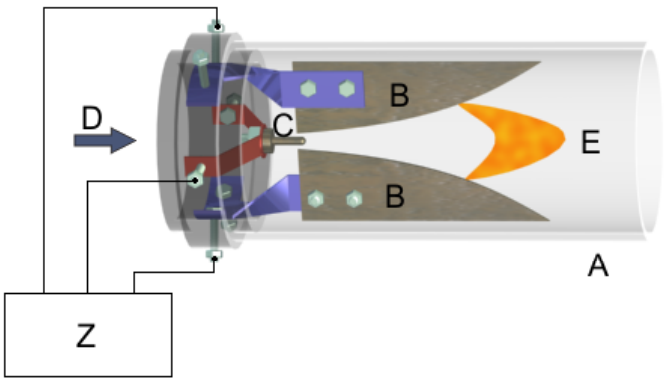

Fig. 1. Scheme of construction of the basic two–electrode gliding arc discharge reactor

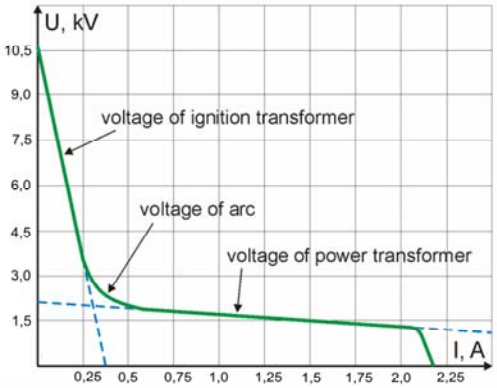

Fig. 2. Typical voltage–current characteristics of the gliding arc discharge

In industrial application, like for exhaust gas treatment, there is often the necessity to place more electrodes in the discharge chamber or more discharge chambers in parallel or in series to the flowing gas (e.g. inside the chimney). Multi-electrode and multi-stage configurations of the gliding arc reactors that could be applied in industrial practice are presented in Figure 3.

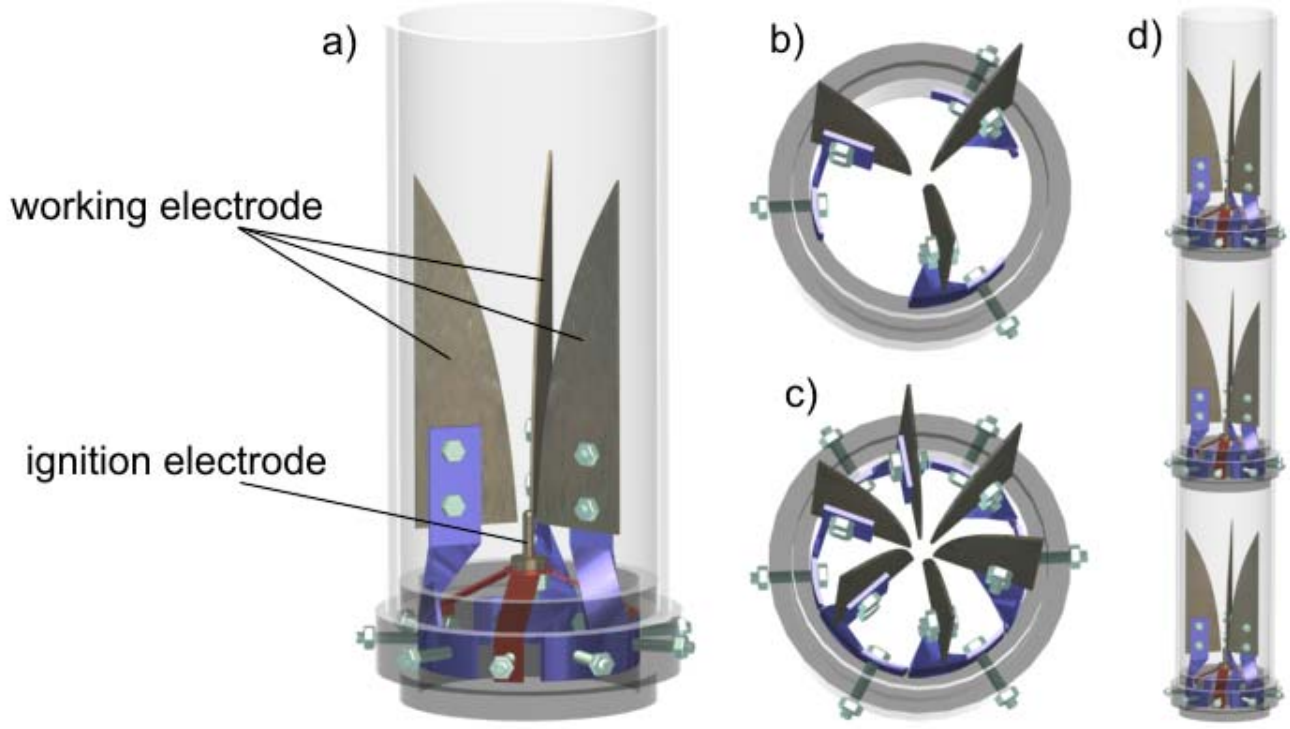

Fig. 3. Electrodes' configurations of gliding arc plasma reactor

Working plasma reactor with gliding arc discharge is strongly non-linear energy receiver of resistive nature. The multi-stage configuration loads power supply asymmetrically. Moreover, the interelectrode voltage is considerably distorted while current has close to sine form (Fig. 4a).

Voltage and current courses representative for two, (a), and three, (b), electrode configuration together with side view photo, (c), of the gliding arc discharge are presented in Figure 4.

a)

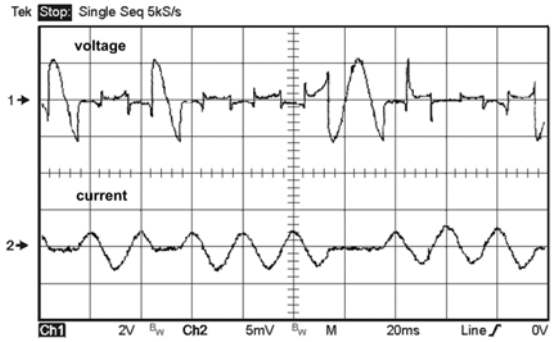

b)

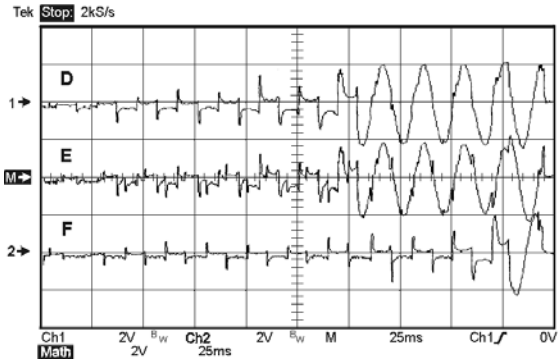

c)

Fig. 4. a), b) Courses of voltage and current of the gliding discharge in two and three electrode reactor, respectively, c) side view of the discharge

3. Power systems

Gliding arc discharge reactor as an electrical energy receiver differs considerably from the other plasma reactors and its cooperation with supplying system requires suitable analysis. The inter-electrode resistance depends on the gas ionization degree and during a single cycle of reactor operation its value changes significantly. It is the largest before discharge ignition when the gas is not ionized and after the ignition rapidly decreases. The increasing of the gap distance and the arc discharge resistance, when the discharge is displacing from the area of ignition to the area of extinction, are not sufficient for the extinction of the arc discharge. The decreasing of the supplying voltage is necessary, which means that the electrical supply of the plasma reactor should have very soft output characteristic, i.e. the voltage of which quickly decreases with the current increasing, like it is presented in Figure 2.

In spite of soft output characteristic, the power supply system should fulfill also the following requirements:

- to supply electrical energy at a high voltage of mains or increased frequency,
- to ensure the voltage varies in the wide range which enables the regulation of the plasma reactor productivity,
- to present high efficiency of energy transfer to the plasma
- to have low power consumption, capital and maintenance outlay
- to present simple servicing and safe operation,
- to cooperate properly with power grid
- to have possibility of controlling the operation of the whole system performance.

The basic unit of each power system of the discharge plasma reactor is a transformer. Its task is to supply energy to the discharge chamber at parameters required by an industrial process. Specially constructed transformer's based system of our invention, so called integrated system [6], can fulfill plasma reactor's requirements while representing high efficiency with simplicity of construction. In integrated power supply systems the functions of

preliminary ionization, ignition and discharge maintaining during operation cycle as well as a limiting the short-circuit current value are integrated in one device. The system employs the nonlinearity of the transformer cores to generate the tripled frequency preliminary ionization voltage, therefore, in one supplier the function of arc ignition and its maintenance are performed that makes them much more efficient in comparison to other power systems for industrial applications. Moreover, the system permits the arc suppression at the end of the electrodes at relatively low extinction current, limited by the transformer internal reactance, and prompt arc ignition at the least electrodes' distance [7].

a. Three-phase ninth-electrode system

The integrated power system of the triple-stage ninth- electrode reactor is presented in Fig. 5. The discharge chamber of the system comprises three triple-electrode segments. One out of three electrodes in each stage are for the arc discharge ignition and they are connected in parallel and energized from the ignition transformer, while two others are connected to line voltages of the three-phase power transformer. Thanks to this connection, the ninth electrode arc plasma reactor can be energized form the three-phase grid with single ignition transformer.

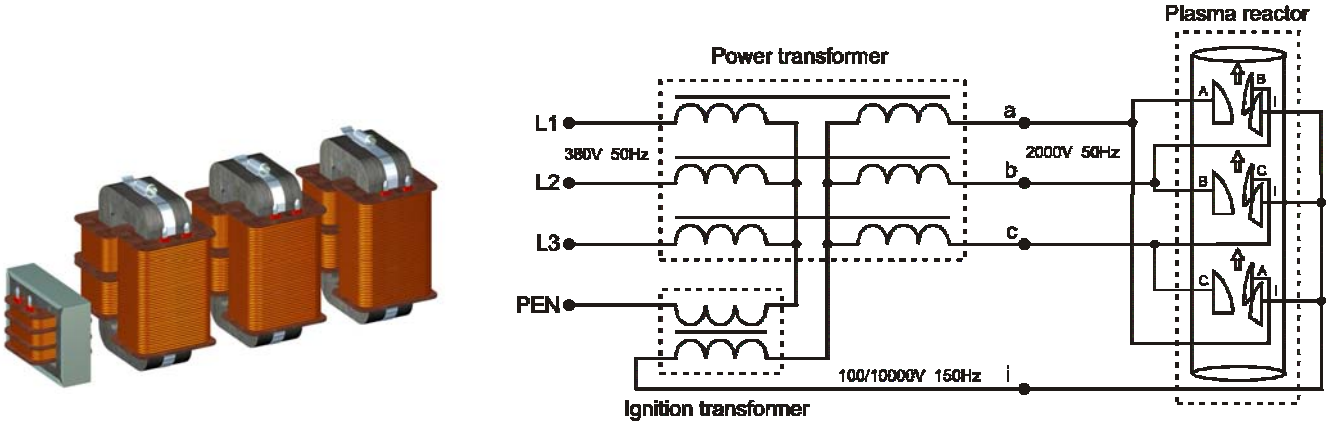

Fig. 5. The three-stage gliding arc reactor powered from integrated power supply system - one electrode in each stage operates as ignition electrode

b. Multi-stage system with individual ignition transformers

Sometimes, in the case of multi-stage systems, it would be better to detach the ignition system from the power supply and to equip each electrode system with separate ignition electrode, as it is presented in Fig. 6. In this solution, every ignition electrode of plasma reactor has its own power supply. The advantage of such solution is its high reliability, as when ignition power supply system breaks down only one segment of electrodes is out of operation.

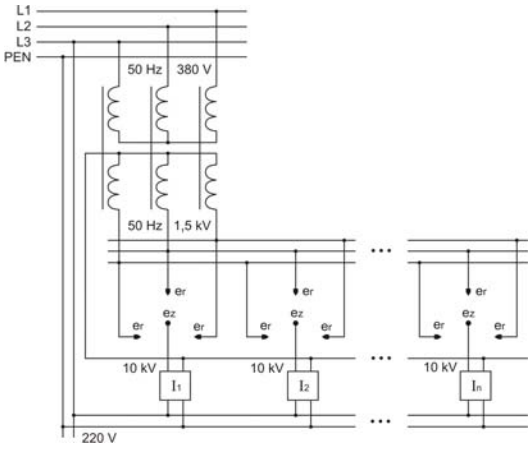

Fig. 6. Transformer–based power supply with separated ignition system, e_r-working electrode, e_z- ignition electrode, I_1, I_2, …I_n – discharge ignition systems

c. System based on five-limb transformer

Power systems, which have already been presented above, are based on the application of properly connected single-phase transformers. Solution presented in Figure 7 is taking advantage of the fifth-limb core of the three-phase transformer. The primary and secondary windings are put on three internal columns of transformer core and connected in star without neutral wire. The primary windings are energized from three-phase mains while the secondary supply the working electrodes of plasma reactor. In the connected in series windings, put on the core's external yokes, the ignition voltage is generated due to the magnetic flux distortion. The benefits of this solution are the tightness and simplicity of construction and the possibility to supply higher number of ignition electrodes compared to the other transformer-based systems.

a) b)

Fig. 7. Transformer with 5-limb core as a power system for triple-electrode gliding arc reactor

Experiments were carried out on the model of the power system from Figure 7a. Model consists of 4 rolled sheet metal cores with primary, secondary and ignition windings put on the core's columns as it is presented in Figure 7b. Magnetic flux and voltage induced in windings of the external columns' are distorted mainly by third harmonic (150 Hz) as it is shown in Figure 8.

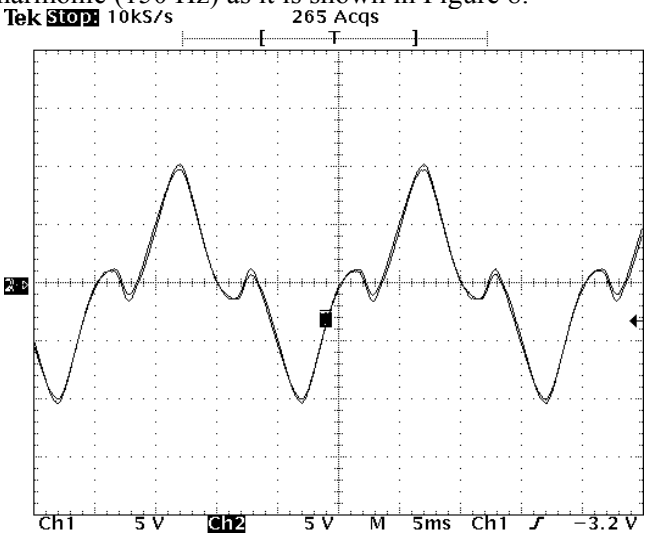

Fig. 8 Course of the voltage induce in the external columns of the 5-limb transformer under three-phase excitation

Voltage induced in the external columns' windings connected in series has enough value for pre-ionization of the interelectrode gap in the three-electrode reactor. It is possible to wind more ignition windings on the external columns which makes the system suitable also for multistage plasma reactors

5. Conclusion

Presented power supply systems for gliding arc plasma reactors are based on special construction single phase and three-phase transformers. The windings' connection and magnetic core construction assure proper operation of plasma reactor as well as expected plasma parameters. Proposed power systems take advantage of the three-phase power supply to energize multi-electrode and multi-stage gliding arc discharge reactors that are especially suitable treatment of large

volumes of polluted gases at atmospheric pressure, directly in the place of their emission. In the proposed power supply systems any auxiliary controls are not necessary which guarantees simplicity, reliability and low investment and exploitation costs of industrial plasma reactors with gliding arc discharge.

References

1. H. Lesueur, A. Czernichowski, J. Chapelle, French Patent 2639172
2. Stryczewska, H. D.: New Supply System of The Non-thermal Plasma Reactor with Gliding Arc", Archive of Electrical Engineering, No 4, pp. 384-399 (1997)
3. T. Janowski; H. D. Stryczewska; Ranaivosoloarimanana A.; Czernichowski A., Industrial Trials of the Glidarc Plasma Reactor, 12th International Symposium on Plasma Chemistry, University of Minnesota (USA), 1995, vol. 2, p. 825-830
4. Janowski, T., Stryczewska H. D: Plasma reactor supplier to carry out chemical processes, Polish Patent No 172152, 1997
5. T. Janowski, H.D. Stryczewska, A. Ranaivosoloarimanana and A. Czernichowski: Industrial Trials of the GlidArc Plasma Reactor, Proceedings of the 12th International Symposium on Plasma Chemistry, Minneapolis, vol. II, pp. 825-830 (1995).
6. Stryczewska H. D.: Układ zasilania reaktorów plazmy nietermicznej, Biuletyn Urzędu Patentowego, Patent Nr 317110, 2000
7. Stryczewska H. D. i inni, Multi-stage Gliding Arc Reactors for Environmental Applications, International COE Forum on Plasma Science and Technology, 5-7 April Nagoya 2004, Technical Session Proceedings, ed. by H. Sugai, P2-50, pp. 269-270

ATMOSPHERIC PRESSURE PLASMAS - ANALYSIS BY MODULATED MOLECULAR BEAM MASS SPECTROMETRY

Y. Aranda-Gonzalvo, M. E. Buckley, P. J. Hatton, J.A. Rees, D. L. Seymour, T.D. Whitmore

Hiden Analytical Ltd., 420 Europa Blvd., Warrington WA5 7UN, England
www.HidenAnalytical.com info@hiden.co.uk

1. Introduction

Atmospheric plasmas are increasingly used to process materials that are otherwise unsuitable for vacuum processing. Highly functional surfaces can be produced on a number of materials including textiles, plastics, polymers and nonwovens. Other applications include cleaning of polluted water, sterilisation of surgical instruments and localised treatment of biological tissues.

In all cases an understanding of the gas phase and surface chemistry involved is important in order to develop and refine a particular process. Compared with optical techniques, mass spectrometry has the distinct advantage of being able to provide simultaneous identification of the various plasma species that impinge on the substrate or workpiece. When coupled with energy analysis a detailed understanding of the process can be quickly achieved.

Molecular beam inlet systems consist of several differentially pumped stages coupled by sampling/collimating apertures and have been used previously to determine reaction kinetics of high pressure combustion and pyrolosis processes [1]. More recently they have been developed for accurate measurement of radical densities in low pressure plasmas [2,3]. In this work we describe a molecular beam mass spectrometer system for atmospheric plasma diagnostics. The instrument incorporates beam modulation in the form of a software controlled rotating disk chopper.

2. Diagnostic Apparatus

2.1. Molecular Beam Mass Spectrometer

The discharge was generated by a radio frequency driven atmospheric plasma source, based upon the design of Stoffels et al [4]. This original design was adapted to include a second, concentric gas inlet in order to study mixtures of gases. The low power discharge, around 7W, was produced between the plasma source and the entrance of the Molecular Beam Mass Spectrometer (MBMS) analyser.

Species created in the atmospheric discharge were sampled using a triple stage differentially pumped molecular beam inlet system and subsequently detected with the Hiden EQP mass/energy analyser. A schematic of the arrangement is shown in Figure 1. The chopper mechanism is omitted for clarity.

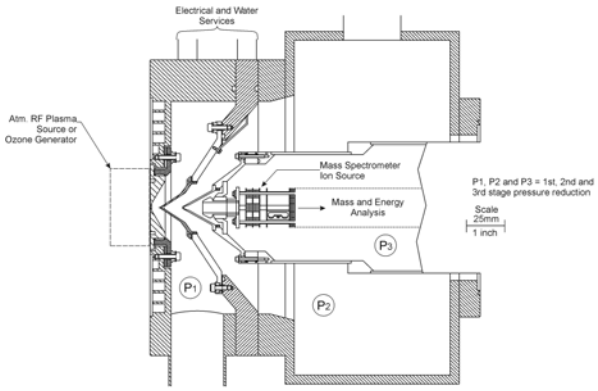

Fig. 1: Schematic of the MBMS Analyser.

2.2. Automated Beam Modulation Control

The beam chopper mechanism incorporates an opto-detector positioned on the opposite side of the rotating disk to the molecular beam aperture. This generates a synchronisation signal that is phase locked to the chopper movement and used by the mass spectrometer as two virtual detectors, *foreground* and *background*.

The mass spectrometer has one physical electron multiplier detector (SEM), which may be connected to either the foreground or background virtual detectors under the control of the gating system. The detectors are presented as separate inputs by the control software and related as follows;

$$\text{SEM} = \text{foreground} + \text{background} \quad (1)$$

$$\text{foreground} = \text{SEM} - \text{background} \quad (2)$$

$$\text{background} = \text{background} \quad (3)$$

The chopper synchronisation signal cannot be used to directly gate the mass spectrometer as its duty cycle does not exactly match the instrument's response to the beam chopper, and this would tend to reduce its differential sensitivity. To overcome this, two internal delayed pulse generators (100nsec resolution) are used to match the beam chopping cycle to the foreground and background gating, as shown in Figure 2.

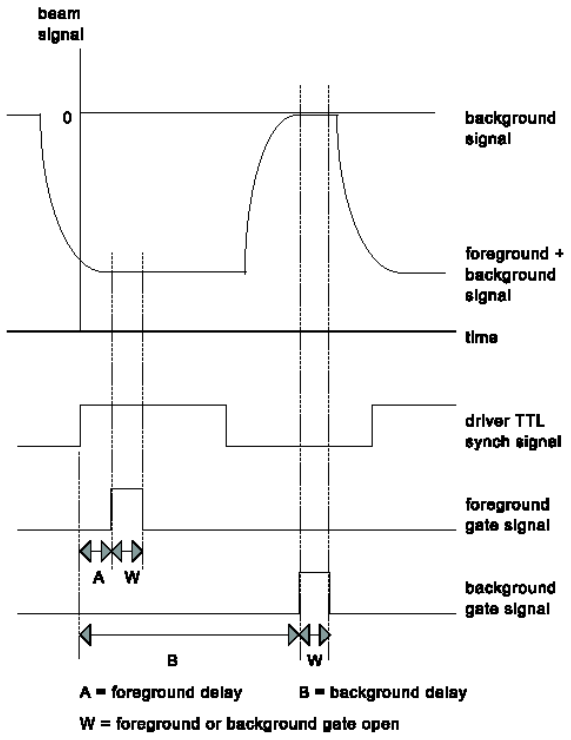

Fig. 2: Modulation timing diagram.

3. Results & Discussion

Figure 3 shows the measurement and display of SEM and background signals for N_2^+ for plasma on and off conditions. The foreground (beam) signal is derived in real time from (2).

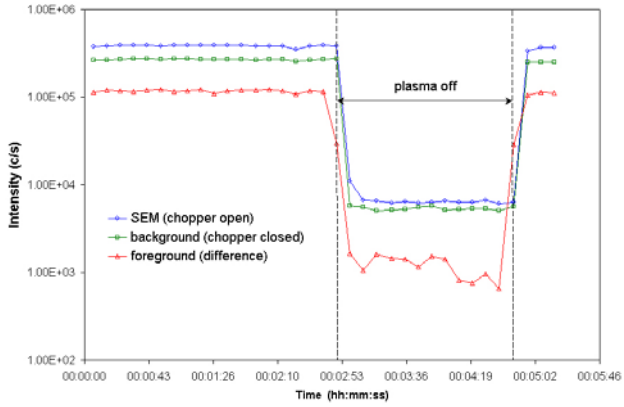

Fig. 3: Raw (SEM, background) and derived (foreground) signal intensities for N_2^+ for plasma on/off conditions.

Figure 4 shows the corresponding appearance potential scans for N^+ when the plasma is on. Again, the threshold ionisation foreground (beam) data is generated automatically. The two observed thresholds correspond to the direct and dissociative ionisation processes;

$N + e \rightarrow N^+ + 2e$ (Ei= 16.5 eV), and

$N_2 + e \rightarrow N^+ + N + 2e$ (Ei=25.2 eV)

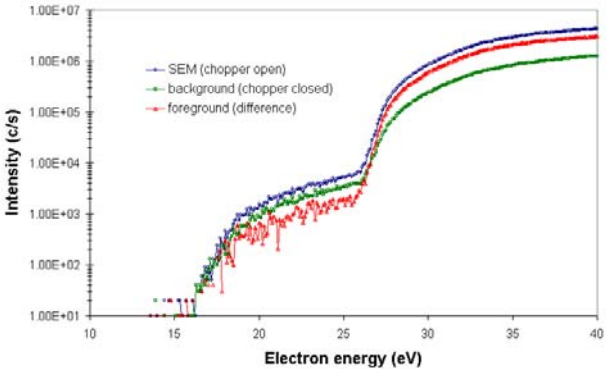

Fig. 4: Threshold ionisation curves for N^+ .

The beam-to-background ratio can be calculated from the slope of the linear fits between the above thresholds and gives a figure of merit for the sensitivity of the overall apparatus to the beam component [2]. This in turn determines the accuracy of absolute radical density calculations [3]. The value of 0.95 is obtained for the N^+ case above, clearly demonstrating the sensitivity of this apparatus for absolute radical density determination from atmospheric plasmas.

4. Conclusions

We have described a modulated molecular beam mass spectrometer that is suitable for diagnostics of atmospheric plasmas. Automatic control and processing of the modulated molecular beam signals allows rapid and accurate determination of beam/background components which are required to determine absolute radical densities.

5. References

[1] D. Dayton, W. Frederick, Energy & Fuels **10** (1996) 284.
[2] H. Singh et. al., JVST A **17**(5) (1999) 2447.
[3] S. Agarwal et. al., JVST A **22**(1) (2004) 71.
[4] E Stoffels et. al., Plasma Sources Sci. Technol, **11** (2002) 383.

Numerical Simulation of Low Pressure Inductively Coupled Plasma Sources for Nanocrystalline Diamond Deposition

Katsuyuki Okada, Shojiro Komatsu, and Takamasa Ishigaki

Advanced Materials Laboratory, National Institute of Materials Science, Tsukuba, Japan

Abstract
Numerical study on low pressure inductively coupled plasma (ICP) used for nanocrystalline diamond deposition has been performed with direct simulation Monte Carlo (DSMC) method and electron Monte Carlo simulation. Spatial distributions of electron density, electron temperature, and plasma potential are obtained. The electron energy distribution functions (EEDFs) are compared with the experimental results obtained with a Langmuir probe previously. The EEDFs of an Ar and a CH_4/H_2 plasma obtained from the simulation agree well with the measured data. The calculated EEDF of a CH_4/H_2 plasma at 50 mTorr exhibits a hump around 6 eV, which corresponds to a hump around 6 eV in the measured EEDF at the same pressure. It can be attributed to the resonant peak of the vibrational excitation cross section of CH_4 molecule.

Keywords
Low pressure inductively coupled plasma, Nanocrystalline diamond, Monte Carlo simulation

1. Introduction

We have applied a low pressure inductively coupled plasma (ICP) to deposit nanocrystalline diamond [1]. The sp^2/sp^3 bondings of the nannocrystalline diamond were evaluated with Raman spectroscopy [2] and electron energy loss spectroscopy [3]. Langmuir probe and mass spectrometric measurements were performed to characterize the ICP [4,5]. We obtained plasma parameters {electron density (N_e), electron temperature (T_e), and plasma potential (V_p)}, electron energy distribution functions (EEDFs), and ion energy distributions (IEDs). For better understanding of the ICP, we need a theoretical investigation such as modeling or numerical simulation. Economou et al. [6] used the direct simulation Monte Carlo (DSMC) method to demonstrate reactive neutral and ion flow in an ICP reactor. Nanbu et al. [7] also used the electron Monte Carlo method for obtaining the production rate of radicals. Takekida and Nanbu [8] reported the EEDFs of capacitively coupled Ar plasmas using particle-in-cell/Monte Carlo (PIC/MC) method.

In this study, we report on the numerical simulation of the ICP used for nanocrystalline diamond deposition using DSMC method and electron Monte Carlo simulation. Spatial distributions of N_e, T_e, and V_p are obtained. The calculated EEDFs are compared with the measured EEDFs.

2. Experiment and Simulation

Figure 1(a) illustrates the schematic diagram of the low pressure ICP-CVD system. The detailed description and the procedure of Langmuir probe measurement were reported previously [1,4]. To be brief, a low pressure ICP was generated in a growth chamber by applying 13.56 MHz rf powers of 1 kW to a three-turn helical antenna wound around a quartz tube. An Ar or a CH_4/H_2 (5:75 mixture) plasma was generated at pressures ranging from 10 to 50 mTorr. A Langmuir probe (Smart Probe; *Scientific Systems Inc.*) was utilized to measure plasma parameters and EEDFs.

The procedure of simulation is as follows. The flow, electromagnetic field, and plasma are assumed to be axisymmetric. The geometry of computational model is shown in Fig. 1(b). The height of the reactor is 110 mm. A three-turn helical coil wound around a quartz tube with 40 mm in diameter. The calculation was performed with DSMC method and electron Monte Carlo simulation. Collisions of e-Ar in an Ar plasma; e-H, e-H_2, e-CH_4, e-CH_3, e-CH_2, and e-CH are considered in a CH_4/H_2 plasma, respectively.

Surface reactions of radicals play a critical role in determining the concentrations and distributions of ions and radicals in a reactive plasma such as CH_4/H_2 plasma. The sticking of CH_3, CH_2, and CH radicals on the surface are taken into consideration in the calculation. The sticking coefficients of CH_4, CH_3, and CH_2 radicals are refereed to $1.0X10^{-4}$, $1.0X10^{-3}$, and $3.0X10^{-2}$ in the previous reports [9-11].

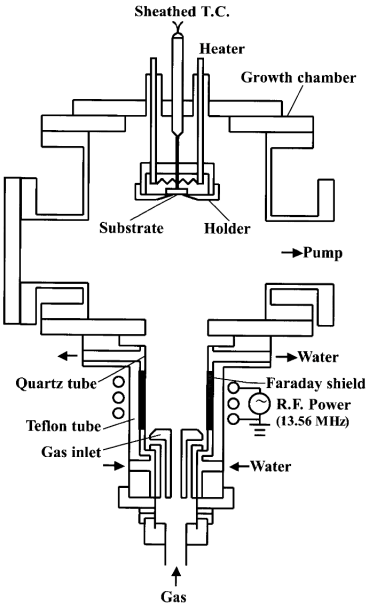

FIG. 1(a) Schematic diagram of low pressure ICP-CVD system.

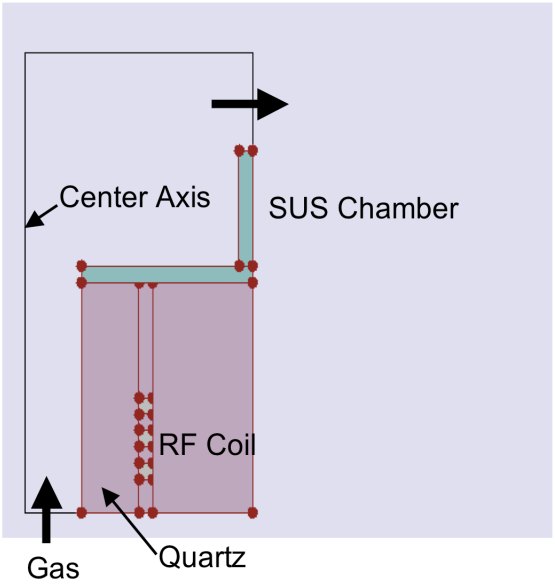

FIG. 1(b) Geometry of computational model.

3. Results and discussion

Figures 2(a) and 2(b) show the N_e and T_e of an Ar plasma at 50 mTorr, respectively. The N_e is concentrated near the rf antenna, and the T_e has a doughnut-shape distribution near the rf antenna. Figure 3(a) and 3(b) show the density of Ar^+ and Ar*, respectively. While the former has a similar distribution to the N_e, the latter spreads toward the growth chamber.

The N_e and T_e of a CH_4/H_2 plasma at 50 mTorr are shown in Fig. 4(a) and 4(b), respectively. The N_e is concentrated near the rf antenna similar to that of Ar plasma. The T_e is high along the quartz tube, which is different from that of Ar plasma. The density of H^+, CH_3^+, H*, and CH_3* are shown in Fig. 5(a), 5(b), 5(c), and 5(d), respectively. While the ion distributions are concentrated near the rf antenna, the radical distributions spread into the growth chamber. The distributions strongly depend on each radical.

Figure 6(a) shows the measured EEDF of an Ar plasma at 50 mTorr (closed circles) and the calculated one at the same pressure (open circles). The each EEDF is nearly a straight line, which means that the electron energy has a Maxwellian distribution. Although the calculated EEDF above 10 eV slightly deviates from a straight line, it is consistent with the measured EEDF.

Figure 6(b) shows the measured EEDF of a CH_4/H_2 plasma at 50 mTorr (closed circles) and the calculated one at the same pressure (open circles). They are different from the EEDF of an Ar plasma at the same pressure. There is a hump around 6 eV in both measured and calculated EEDF. Turner and Hopkins [12] reported the unusual structure of the EEDF. They found a dip around 4 eV in the EEDF of a N_2 plasma, which is interpreted as the electric absorption of N_2 molecule corresponding to the resonant peak of the vibrational excitation cross section. In the CH_4 vibrational excitation cross sections, $\sigma_v(1,3)$ and $\sigma_v(2,4)$ have a peak around 6 eV [13]. Therefore, the hump around 6 eV can be attributed to the electric absorption of CH_4 molecule analogous to the vibrational absorption of 4 eV electrons of the N_2 molecule.

The calculated EEDF of a CH_4/H_2 plasma agrees well with the measured one. Accordingly, the unusual structure around 6 eV in the calculated EEDF can also be attributed to the resonant peak of the vibrational excitation cross section of CH_4 molecule.

Acknowledgment

The authors would like to thank Mr. M. Tanaka and T. Takasaki of PEGASUS Software Inc. for their useful advice on the calculation.

References
[1] K. Okada, S. Komatsu, and S. Matsumoto, J. Mater. Res. **14,** 578 (1999).
[2] K. Okada, H. Kanda, S. Komatsu, and S. Matsumoto, J. Appl. Phys. **88,** 1674 (2000).
[3] K. Okada, K. Kimoto, S. Komatsu, and S. Matsumoto, J. Appl. Phys. **93,** 3120 (2003).
[4] K. Okada, S. Komatsu, and S. Matsumoto, J. Vac. Sci. Technol. **17,** 721 (1999).
[5] K. Okada, S. Komatsu, and S. Matsumoto, J. Vac. Sci. Technol. **21,** 1988 (2003).
[6] D. J. Economou, T. J. Bartel, R. S. Wise, and D. P. Lymberopoulos, IEEE Trans. Plasma Sci. **23,** 581 (1995).
[7] K. Nanbu, T. Morimoto, and M. Suetani, IEEE Trans. Plasma Sci. **27,** 1379 (1999).
[8] H. Takekida and K. Nanbu, Jpn. J. Appl. Phys. **43,** 3590 (2004).
[9] W. L. Hsu, J. Appl. Phys., **72,** 3102 (1992).
[10] H. Toyoda, H. Kojima, and H. Sugai, Appl. Phys. Lett., **54,** 1507 (1989).
[11] H. Kojima, H. Toyoda, and H. Sugai, Appl. Phys. Lett., **55,** 1292 (1989).
[12] M. M. Turner and M. B. Hopkins, Phys. Rev. Lett. **69,** 3511 (1992).
[13] W. L. Morgan, Plasma Chem. Plasma Process. **12,** 477 (1992).

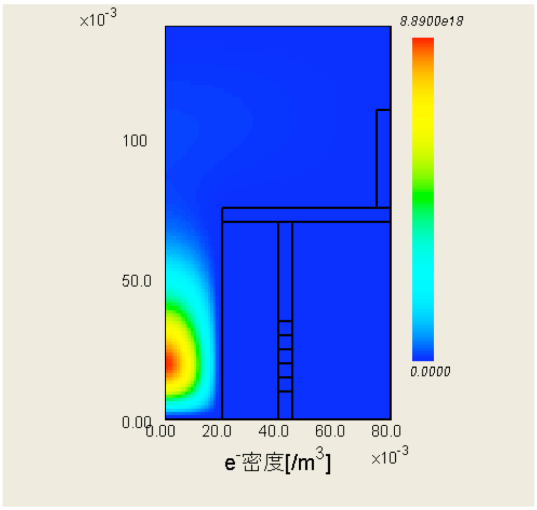

FIG. 2(a) Electron density of Ar plasma

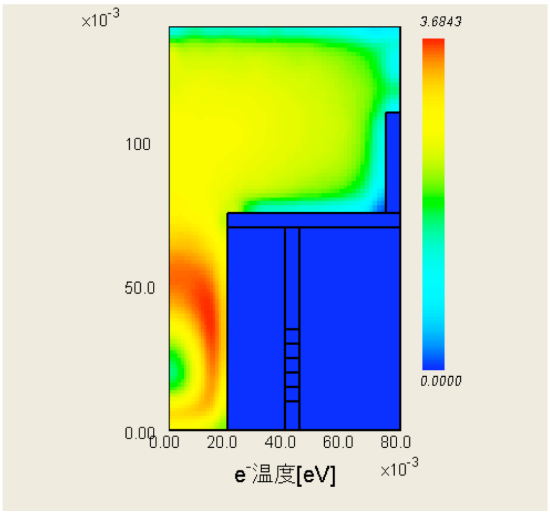

FIG. 2(b) Electron temperature of Ar plasma

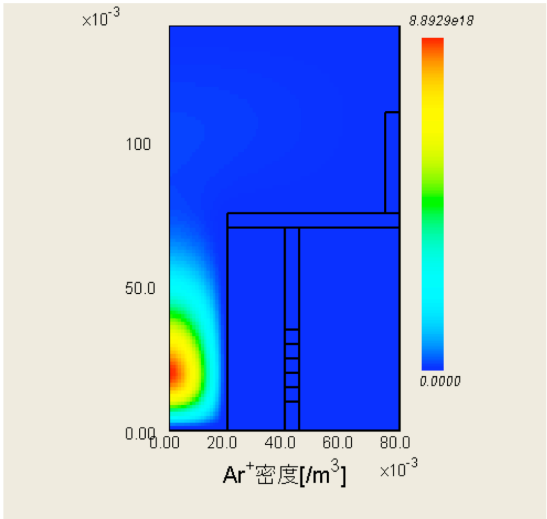

FIG. 3(a) Density of Ar^+

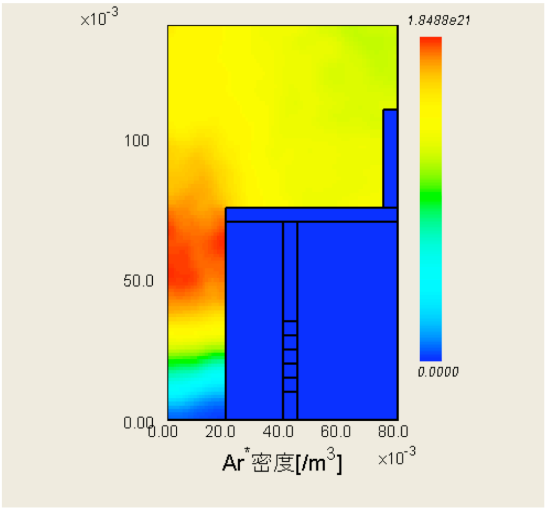

FIG. 3(b) Density of Ar*

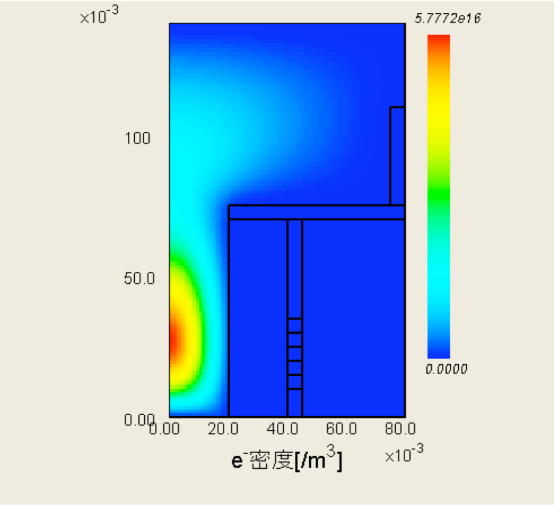

FIG. 4(a) Electron density of CH_4/H_2 plasma

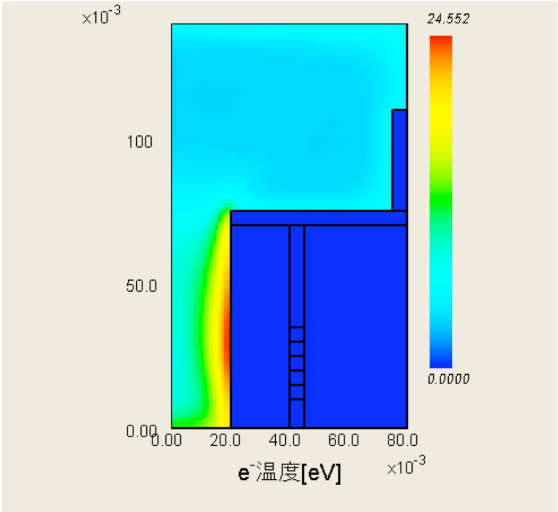

FIG. 4(b) Electron temperature of CH_4/H_2 plasma

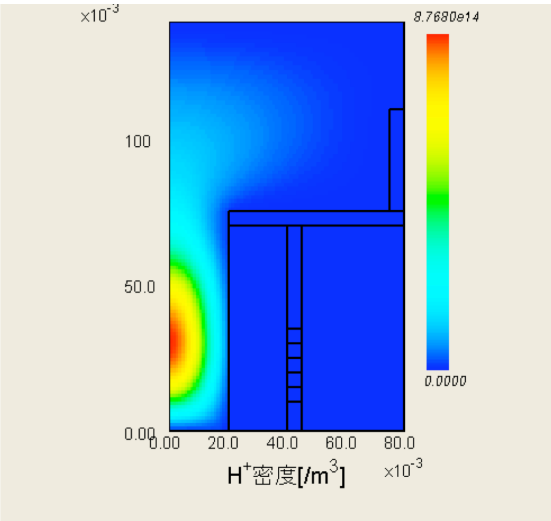

FIG. 5(a) Density of H^+

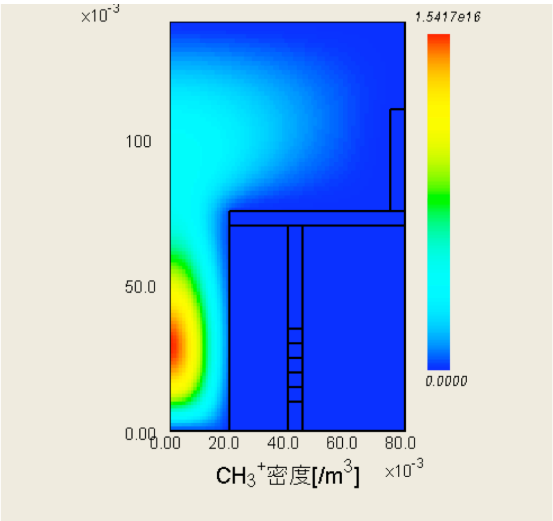

FIG. 5(b) Density of CH_3^+

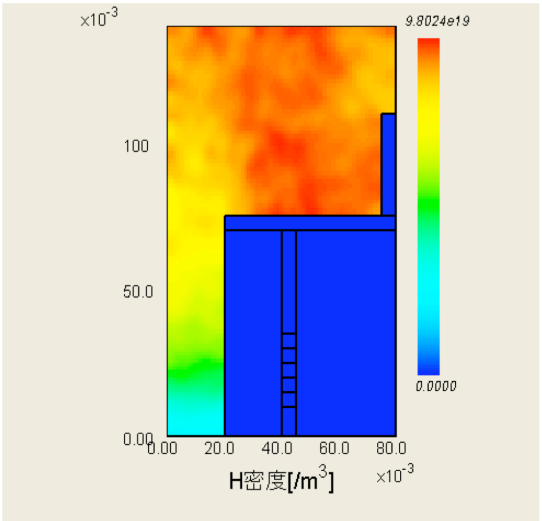

FIG. 5(c) Density of H*

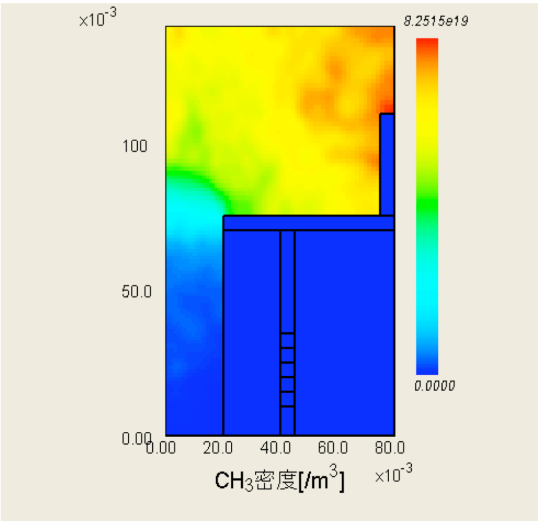

FIG. 5(d) Density of CH_3*

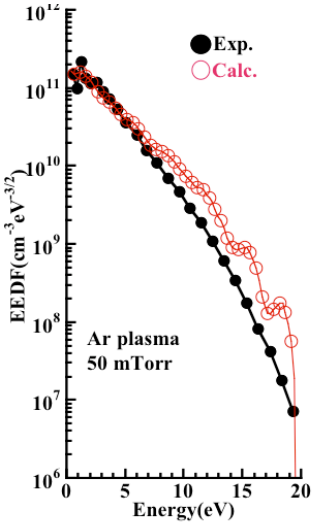

FIG. 6(a) The measured EEDF (closed circles) and the calculated EEDF (open circles) of an Ar plasma at 50 mTorr.

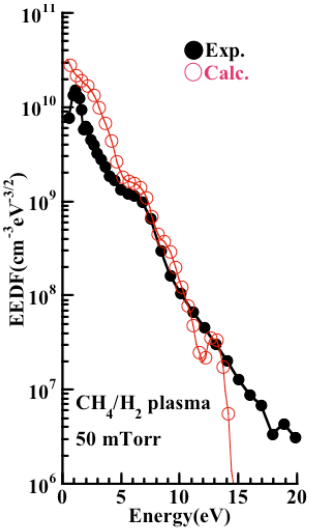

FIG. 6(b) The measured EEDF (closed circles) and the calculated EEDF (open circles) of a CH_4/H_2 plasma at 50 mTorr.

Characterization of a Plain-Jet Airblast Atomizer used in Hydrocarbons Pyrolysis by Induction Thermal Plasma

L. Merlo-Sosa[1,2], G. Cota-Sanchez [1,2], G. Soucy [1]

[1]*Department of Chemical Engineering, Université de Sherbrooke. 2500 Blvd. de l'Université, Sherbrooke, J1K 2R1, Canada. Tel. 819-821-8000, fax. 819-821-7955,*

[2]*Instituto Nacional de Investigaciones Nucleares. Carr. Mexico-Toluca km 36.5, Salazar, Edo. Mex., 52045 Mexico.*

Abstract

The characterization of a plain-jet air blast atomizer, as used for the pyrolysis of hydrocarbons in an induction thermal plasma reactor, has been performed. Experimental measurements of the mean droplet size, expressed as the Sauter Mean Diameter (*SMD*), were obtained using a light-scattering technique. A dimensionally consistent expression for the *SMD* estimation was determined as a function of the dimensionless numbers: *Re*, *We*, *ALR* and *X/do*. This empirical correlation permits the influence of the operating conditions of the liquids atomizer, on the quality of the atomization, to be described. Further, the final expression was subsequently and successfully used for the estimation of the size of droplets, produced during experimental tests of hydrocarbons pyrolysis by induction plasma.

Key words: liquid atomization, induction plasma, hydrocarbons pyrolysis.

Introduction

In an atomization process, a liquid is initially disintegrated by a gas stream into a multitude of small droplets, which are then dispersed into the gaseous medium, increasing the overall liquid phase surface area. As general rule, the performance of any given type of atomizer depends on its geometry and on the physical properties of the liquid and gas phases [1]. Various definitions of the mean droplet size are available [2], among them, the Sauter Mean Diameter (*SMD*) is one of those most widely used because it defines the volume/surface ratio of the spray and it has a special use in heat and mass transfer applications.

The majority of published investigations [3, 4, 5] into the droplet size distribution have been empirical in nature, and only a few of the more complex CFD models have been developed for large scale combustion processes. Very few reports have been published on the hydrodynamic performance of liquid atomizers when used under operating conditions typical of thermal plasma processes [6, 7]. Because the hydrodynamic performance of a liquid atomizer depends not only on the physical properties of the fluids employed, but also on the range of its operating conditions, a complete atomizer characterization becomes mandatory when it is desired to better understand the influence of vaporization on the physicochemical characteristics of the final products produced.

The primary purpose of this work is to evaluate the effect of the operating conditions, as well as the properties of the liquid phase, on the quality of atomization obtained for a new, plain-jet air blast atomizer. In addition, various experimental tests on the pyrolysis of hydrocarbons were performed in order to evaluate the influence of liquid droplet size on the type and quality of products, obtained in the plasma process.

Experimental

Experimental Set-Up

The experimental setup used in this study is shown in Figure 1. It consists of a liquid container, a liquids supply line, a pressurized air line, a specially designed air blast atomizer, a spray measurement system and a tunnel extraction system. The liquid flow rate was measured using precision flow meters, the air stream being separately introduced through a pressure regulator and a flow meter. The atomizer was horizontally oriented, thereby injecting the liquid into the collection system. It was designed to avoid undesirable droplet recirculation and to generate a quiescent environment.

The spray measurement system employed was a laser based, particle size analyzer (Malvern/Insitec Ensemble Particle Concentration and Sizes Instrument System) that measures suspended particles size distribution, via light scattering. The measurement error of this instrument is estimated to be ±2%, with an accuracy of 96% of the droplet size distribution. The experimental results were analyzed in terms of their *SMD* values, and the parameter known as Span (Δ), which is used as an indicator of the distribution width. The plain-jet air blast atomizer used in this study is an external-mixing-type nozzle. The liquid discharges

through a circular orifice of 6 x 10^{-4} m in diameter, while air is supplied through an annular slot of 1.2 X 10^{-4} m in diameter around the periphery, resulting in a conical discharge pattern.

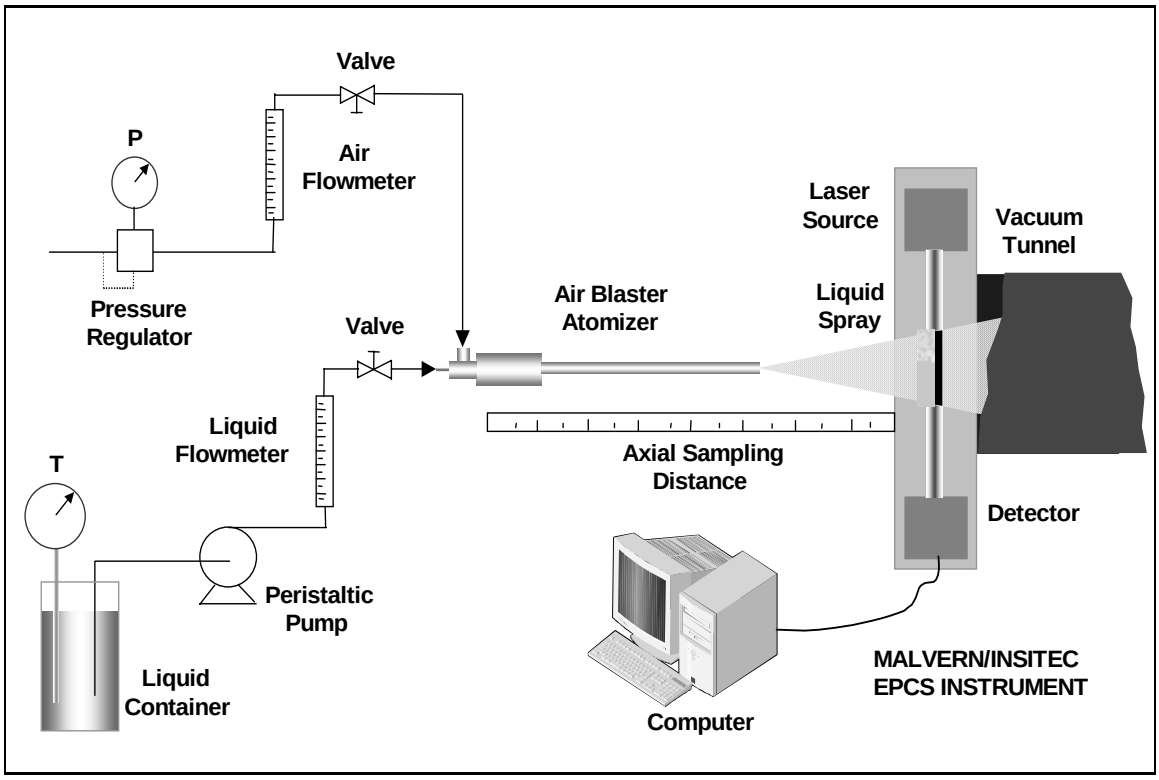

Figure 1. Experimental Setup for the Atomization Study

Continuing, the thermal plasma system used for the pyrolysis of hydrocarbons was composed of a Tekna PL-50 induction plasma torch, a water-cooled stainless steel reactor, and a filtration system. The complete experimental set up for the pyrolysis of hydrocarbons is described in more detail elsewhere [8, 9]. The final products, obtained after the plasma pyrolysis, were characterized by various techniques, including surface area, UV/Vis spectrometry and transmission electron microscopy.

Experimental Conditions

In the first series of experiments, an air-water system was used on which to conduct tests. The variable parameters were as follows: airflow rates (8.3, 12.5, 16.6, 20.8 slpm), liquid flow rates (*LFR*) (3.6, 9.0, 14.5, 20.5, 22.3 ml/min), and the axial distances from the nozzle exit (*X*) were (0.00, 0.04, 0.08, 0.12 m). In order to evaluate the influence of variations in the test liquid properties, a second set of experiments was performed, using dodecane ($C_{12}H_{26}$) and tetrachloroethylene (C_2Cl_4) as the test liquids. Due to safety considerations, a reduction in the overall number of tests performed with the two latter liquids was mandatory. Thus test conditions were; for the airflow rate, 8.3, 12.5 and 16 slpm, while for the liquid flow rate (*LFR*), values of 3.6, 9.0, 14.5 and 20.5 ml/min and 0,04 and 0.08 m for the axial distance (*X*) from the nozzle, were selected. All liquid flow rates were measured under ambient conditions (25°C and atmospheric pressure) and the delivered pressurized air was regulated at 412.7 kPa (60 psig).

On the other hand, the plasma operating conditions were maintained constant for all experimental tests conducted on hydrocarbons pyrolysis. Thus, flow rates of 8 and 25 slpm of argon, and 120 slpm of helium were used in the powder, central and sheath gas supplies, respectively. Plasma plate power was maintained at 40 kW, and the reactor pressure at 80 kPa. Various flow rates (5, 10 and 18 ml/min) of the liquids feeds were used to evaluate the effect of droplet size on the type and quality of the solid and gaseous products obtained in the plasma process.

Results and Discussion

Atomizer Characterization

The most important factor influencing the *SMD* is undoubtedly the air velocity. In general, *SMD* values decrease as the relative air velocity is increased. For instance, the influence of the relative air velocity on the *SMD*, for an axial distance of 0.04 m from the exit of the nozzle, is shown in Figure 2. It is clear that, for the three test liquids used, the *SMD* decreases when the air velocity is increased. Thus, for water, *SMD* values smaller than 25 μm are achieved at relative velocities greater than 220 m/s, while for $C_{12}H_{26}$ and C_2Cl_4, these values are already to be found at and above 160 m/s. This phenomenon can be explained by the differences in the physical properties of the various compounds examined.

It is generally accepted [3, 4, 5] that *SMD* be expressed in terms of dimensionless groups, such as the Reynolds (*Re*) and the Weber (*We*) numbers.

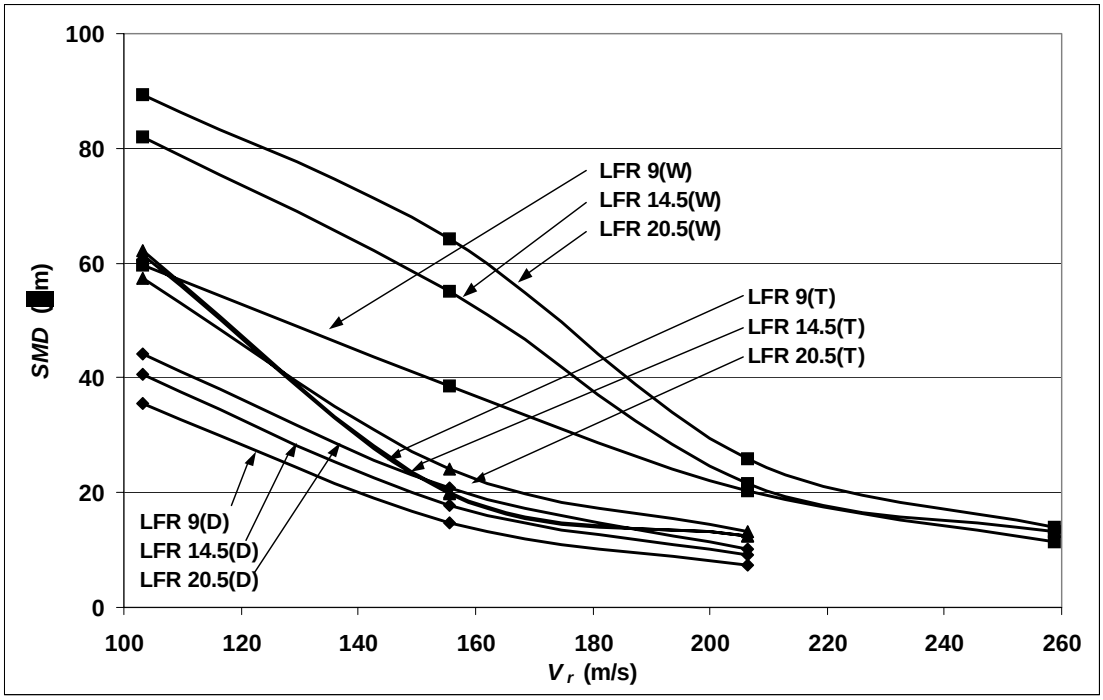

Figure 2. Variation in the Mean Droplet Size with the Relative Air Velocity (V_r)

In order to develop an empirical relationship, a dimensional analysis was performed by application of the Buckingham π-theorem method [10]. The variables used in this study are show in Table 1.

Table 1. Variables Used in the Dimensional Analysis

Variable	Symbol	Units	Dimensions
Air Mass Flow Rate	m_a	kg/s	m/t
Liquid Mass Flow Rate	m_l	kg/s	m/t
Liquid Density	ρ_l	kg/m^3	m/l^3
Gas Density	ρ_g	kg/m^3	m/l^3
Liquid Viscosity	μ	kg/ms	m/l t
Surface Tension	σ	kg/s^2	m/t^2
Discharge Orifice Diameter	d_0	m	l
Relative Velocity	V_r	m/s	l/t
Liquid Velocity	V_l	m/s	l/t
Axial Distance	X	m	l

There are ten variables and three reference magnitudes. Assuming that three dimensionless groups depend on one specific variable, the dimensional formula may then be expressed in terms of four dimensionless groups. The application of a multiple regression yields a regression coefficient of 96% and a standard error of 2.4 %.

$$SMD = 6.7 d_o \, Re^{-0.10} \, We^{-0.56} \, ALR^{-0.41} \left(\frac{X}{d_o} \right)^{0.003} \quad (1)$$

The range of the *Re* number for the operating conditions varies from 67 to 1376. It was observed that the effect of the *Re* number on the *SMD* strongly depends on the physical properties of the liquid. For instance, for liquids presenting smaller density/viscosity ratios, such as $C_{12}H_{26}$ (5.28 X 10^5 s/m^2), the *SMD* increases when the *Re* number values are increased. This means that, even when the liquid flow rate is increased, the inertial forces are not as strong as the viscous forces and the *SMD* values are thus increased. Here, the viscous forces control the disintegration process. In contrast, when a liquid, such as C_2Cl_4, with a higher density/viscosity ratio (1.9 X 10^6 s/m^2), is used, *SMD* values increase for small *Re* numbers.

The *We* number values varied from about 500 to 6500. In this case, surface tension of the liquid plays the most relevant role in determining the *SMD* value of the droplet. The surface tension force adversely affects the atomization process because it opposes the diffusion of air inside the liquid, preventing droplet disintegration. Additionally, *SMD* values decrease when the relative air velocities are increased. This result can be related to the high shear strengths produced at high values of relative air velocity.

In the case of the *ALR* effect, at a constant value of relative air velocity, the mean droplet size is inversely proportional to the *ALR* for values smaller than about 2, for any of the liquid compounds used. An increase in the *ALR*, and consequently in the *Vr* values, improves the atomization quality, due mainly to increases in the air mass, which favour the droplets' disintegration process.

According to equation 1, the modest value of the exponent (0.003) of the dimensionless number (X/d_o) indicates that *SMD* values are only slightly affected as the spray moves down wind. However, a narrowed droplet size distribution (decreasing Span (Δ) parameter), and hence a higher quality of atomization, is also achieved. Therefore, it is clear that atomizer position in the plasma torch plays a key role in the vaporization of further droplets and therefore, in determining the final energy consumption efficiency of the plasma process.

Hydrocarbons Pyrolysis Experiments

In order to evaluate the influence of droplet size on the synthesized product, four experimental tests of hydrocarbons pyrolysis were performed. Table 2 shows the liquid feed rates used in these experiments, along with the estimated *SMD* values and the most important experimental results for solid products.

Table 2. Experimental Tests for the Atomizer Performance Evaluation

Run	Compound	Feed Rate (ml/min)	Estimated *SMD* (μm)	Solid Product		
				Soot (wt%)	Surf. Area (m^2/g)	C_{60} (wt%)
1	$C_{12}H_{26}$	5.0	29	23	121	traces
2	$C_{12}H_{26}$	11.0	37	28	121	traces
3	C_2Cl_4	10.0	50	15	46	3.9
4	C_2Cl_4	18.0	60	21	58	2.1

Table 2 shows that higher liquid feed rates generate larger, average droplet sizes, which in turn, strongly affect the final composition of products. For example, results for $C_{12}H_{26}$ show that carbon soot yield increased when the $C_{12}H_{26}$ feed rate is greater, due in part to plasma cooling. The plasma temperature decreases because of the high-energy requirements required to vaporize the larger droplets and heat the gaseous species. According to thermodynamic and kinetic studies, found elsewhere [8, 9], lighter hydrocarbons, such as acetylene, are always favoured at higher temperatures.

Larger droplet sizes also generate products of incomplete $C_{12}H_{26}$ decomposition. In comparing Runs 1 and 2, it can be seen that both high $C_{12}H_{26}$ throughputs and large droplet sizes produced significant amounts of adsorbed polyaromatic compounds (PAHs), and some traces of C_{60} (MW = 720 uma) and C_{70} (MW = 840 uma) fullerene molecules. Richter et al. [11] suggested that acetylenic and olefinic compounds (C_2H_2 and C_2H_3) act as precursors in PAHs molecular growth.

In turn, the results of C_2Cl_4 pyrolysis tests also show that high liquid feed rates generate larger droplet sizes, which effectively quench the plasma tail, enhancing the formation of soot and favoring the synthesis of soot-adsorbed chloro-organic compounds. After toluene extraction, high concentrations of C_{60} and C_{70} fullerenes were observed. The formation of these higher molecular weight compounds may be similar to its non-chlorinated analogs, in which the small chlorinated species (C_2Cl_3 and C_2Cl_2) play key roles in the aromatic molecular growth.

Toluene extractions of soot samples were also analyzed by UV-spectrometry at 329 nm for the C_{60} determination. The results (Table 2) reveal that C_2Cl_4 enhances the formation of fullerenes, when compared with $C_{12}H_{26}$. This finding can be explained, taking into account the thermodynamic conditions at high temperatures. Equilibrium computations [8, 9] show that high concentrations of atomic hydrogen and small hydrocarbon radicals are found during the $C_{12}H_{26}$ pyrolysis. These radicals become competitive species for the C_2 and C_3 fullerene precursor molecules, inhibiting the fullerene growth-reactions.

The morphology and structure of the produced soot were evaluated by TEM. Figure 4 shows some of the typical synthesized carbon black aggregates. The shapes of these aggregates vary, from individual spheroidal particles to flat form particles, with some particles resembling crumpled paper. These forms are common in plasma-generated "blacks", reported earlier [12]. Figure 3(a), corresponding to $C_{12}H_{26}$ pyrolysis, shows the presence of "flat" forms of carbon particles. The high energy density of the induction plasma leads to the creation of growths of graphitized planar structure.

Interestingly, these flat particles were not observed (Figure 3(b)) in the soot collected when C_2Cl_4 was used as a raw material. Because of the higher flow rates and larger droplets generated in these tests, a greater plasma quenching effect was generated. Hence, the prevailing, lower plasma temperatures favored the formation of spherical amorphous carbon particles instead of the graphitized flat particles. The carbon black particle size also appears to depend on the particular feedstock used. The average spherical particle sizes are about 18 and 40 nm, for the $C_{12}H_{26}$ and C_2Cl_4 tests, respectively. Detailed inspection of the micrographs reveals the formation of hollow carbon shells, usually known as *giant fullerenes* [13], in $C_{12}H_{26}$ tests. While the pyrolysis of C_2Cl_4 mainly generated nanoparticles of amorphous carbon, the $C_{12}H_{26}$ tests produced a highly structured carbon black, which is usually characterized by its higher physicochemical properties [14].

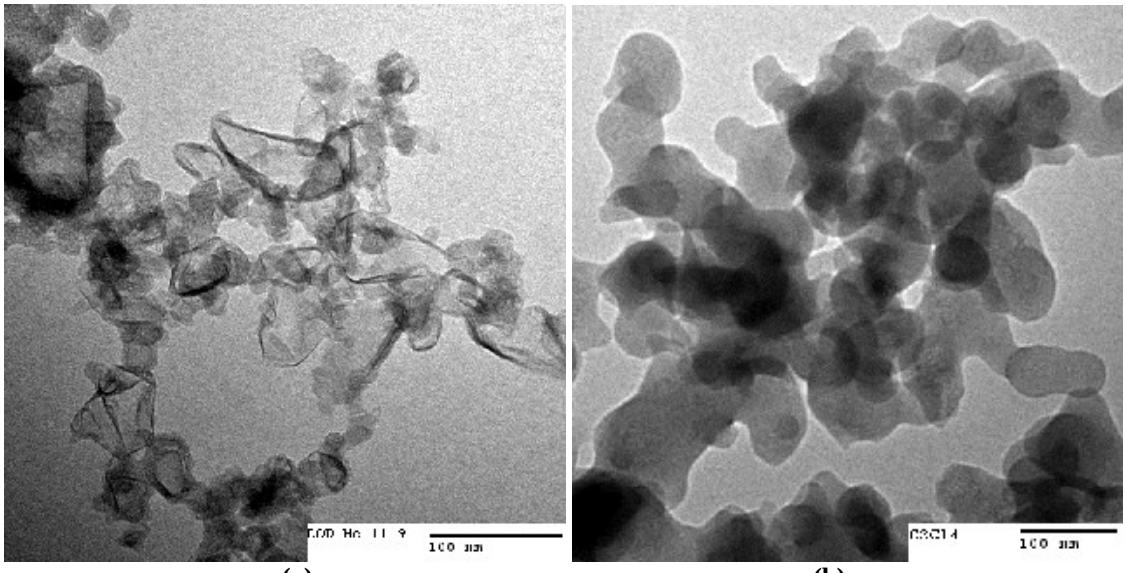

(a) **(b)**

Figure 3. TEM Images of Soot Samples Obtained in the Pyrolysis Processing of Liquid Hydrocarbons: a) Test 1 from Dodecane, b) Test 1 from Tetrachloroethylene.

Conclusions

The influence of the particular operating conditions of a liquid phase atomizer, on the quality of the achieved atomization, has been investigated. An empirical correlation, based on the relationship of *SMD* and dimensionless numbers, was also obtained, with a final correlation coefficient and standard error of about 96% and 2.4 %, respectively. While the *We* and *ALR* dimensionless numbers have the greatest influence on the final droplet product sizes, the dimensionless axial distance (X/d_o) has the smallest effect. However this term provides the opportunity for predicting the effect of the atomizer position on *SMD* values downstream

in the plasma reactor. The maximal *SMD* values were estimated for C_2Cl_4 atomization, while smaller values were estimated when $C_{12}H_{26}$ was used as the liquid feedstock, due to its particular physical properties. Experimental results also show that an increase in the liquid feed rate produces an increase in the *SMD* values. Both higher feed rates and larger droplet sizes strongly affect the composition and quality of the products finally obtained . When a higher *SMD* value of $C_{12}H_{26}$ was used, higher amounts of incomplete decomposition products were observed. Although the solid products obtained in all tests corresponded to the typical carbon black particles obtained at high temperatures, the morphology and particle size are strongly influenced by the *SMD* values of the liquid stream injected into the reactor. *SMD* values play a key role in both the hydrodynamics of the induction plasma torch reactor and in the thermochemistry of the system.

Acknowledgements

This work was supported by the NSERC of Canada and the CONACYT of Mexico.

References

[1] A. H. Lefebvre. “Atomization and Sprays”. Hemisphere Pub. Co., 238-244, (1989).
[2] A. H. Lefebvre. J. Eng. Gas Turbines and Power, **117**, 617-654, (1995).
[3] S. Nukiyama and Y. Tanasawa.. Trans. Soc. Mech. Eng., **5**, 68-74, (1939).
[4] G. E. Lorenzetto and A. H. Lefebvre. AIAA J., **15**, 7, 1006-1010, (1977).
[5] A. K. Jasuja. ASME Paper **78**-GT-83 (1982).
[6] V. Yargeau, G. Soucy and M. I. Boulos. Plasma Chem. Plasma Proc. **19**, 3, 327-340, (1999).
[7] E. Bouyer, G. Schiller, M. Müller and R. H. Henne. Plasma Chem. Plasma Proc. **21**, 4, 523-546, (2001).
[8] L. Merlo-Sosa and G. Soucy. (Accepted for publication in the Int. J. Chem. React. Eng.).
[9] G. Cota, G. Soucy, A. Huczko and H. Lange. Trans. Mat. Res. Soc. Jap. **29**, 2, 549-552, (2004).
[10] Buckingham. ASME Trans., **37**, 263-297, (1915).
[11] H. Richter, W. Grieco, and J. Howard. Combustion and Flame, **119**, 1-22, (1999).
[12] L. Fulcheri, Y. Schwob, and G. Flamant. J. Phys. III, **7**, 3, 491-503, (1997).
[13] L. Fulcheri, N. Probst, G. Flamant, F. Fabry, E. Grivei, X. Bourrat. Carbon, **40**, 2, 169-176, (2002).
[14] CABOT Co. North American Technical Report S-136, Special Blacks Division, (2001).

Mechanisms for the Surface Oxidation of Polypropylene

Mark Strobel[1] and Mary Jane Walzak[2]

[1] 3M Company, 3M Center, Building 208-1-01, St. Paul, MN 55144-1000, USA

[2] Surface Science Western, The University of Western Ontario, London, ON, Canada N6A 5B7

Abstract

We discuss five gas-phase surface treatment processes (flame, corona, plasma, UV/ozone and ozone) in terms of the speed of oxidation, the depth of treatment and the formation of low-molecular-weight-oxidized-material (LMWOM). These characteristics are then discussed in relation to the active species present in the initiation reaction, the gas-phase species available to react with the polymer radical and the ability of the treatment to generate alkoxy radicals. We derive a number of unifying concepts that assist in explaining the different effects on the surface of the polypropylene (PP) film**.**

Keywords: polypropylene, flame, corona, plasma, UV, ozone, surface oxidation, mechanism

Introduction

Oriented PP films ordinarily require some type of surface modification prior to commercial use. Surface oxidation is by far the most common type of modification imparted to PP. Oxidized PP surfaces have improved wetting and adhesion properties when compared with the unmodified polymer. There are five main gas-phase processes used commercially for the oxidation of PP: flame, corona discharge, air or oxygen plasma, ozone, and combined UV/ozone (UVO) treatments. Although all of these processes oxidize PP, there are significant differences between the surfaces formed by these techniques. Three major differences between the various surface-oxidation processes are the processing time required to generate a given amount of oxidation, the depth of that oxidation, and the extent of polymer chain scission that occurs during the oxidation process. Corona discharges, flames, and plasmas can rapidly oxidize PP surfaces, with characteristic processing times of < 1 s [1]. In contrast, the various UVO treatments appear to require exposure times that are orders of magnitude greater in order to achieve the same level of oxidation. Of the five techniques, flame treatment appears to incorporate the highest concentration of oxygen in the outermost surface of the polymer (~1-2 nm). Corona and plasma treatments appear to affect somewhat deeper areas of the PP(~3-10 nm). At the other extreme, the UVO treatments tend to modify considerably deeper into the bulk polymer (microns) [1].

Perhaps the most interesting difference between the five surface-oxidation processes is the propensity to form water-soluble low-molecular-weight oxidized material (LMWOM). LMWOM is the result of oxidation coupled with scission of the PP chains. The presence of LMWOM on PP can be detected by a number of analytical techniques performed in conjunction with washing of the treated surface. LMWOM is characteristically soluble in "polar" solvents such as water, alcohols, and ketones, but remains insoluble in non-polar solvents such as the alkanes and aromatics. More recently, we have demonstrated that LMWOM and other products of oxidative scission can be directly examined using atomic force microscopy (AFM). AFM images of unmodified biaxially oriented PP show a characteristic fine fibrillar network [2,3,4]. The presence of LMWOM on PP is characterized by a topography consisting of smooth, globular "mounds" that are completely removed by washing with water [2,3,4]. The size of these globular mounds often increases as the quantity of LMWOM increases, although this is not the only factor that influences the size of the mounds [2]. Of the surface-oxidation processes examined in this study, LMWOM is readily formed by corona discharge, air or O_2 plasma, and combined UVO treatment [2,3,5,6,].

In contrast, PP treated by flame or by ozone only has no detectable LMWOM within normal treatment-time regimes. Only after repeated treatments, in the case of flame treatment, or at abnormally long treatment times (1-2 hours), in the case of ozone-only treatment, can LMWOM formation be detected. Rather, a surface topography consisting of bead-like "nodules" is formed [2,7,8].

In this paper we will examine the similarities and differences between the PP surfaces treated using five gas-phase, oxidative processes and then attempt to rationalize these differences using our knowledge of the types of active species present in each of the gas-phase treatments and prior research into the mechanisms of oxidation. The comparison of the five surface-oxidation processes is facilitated by reference to two crucial portions of the overall oxidation mechanism, the initiation step and those reactions that lead to chain scission and the formation of LMWOM: the differences between the oxidation processes are most apparent when these two steps are examined.

The nomenclature of electrical discharges can be somewhat confusing. In this paper, we retain the historic "corona" terminology for atmospheric-pressure dielectric-barrier discharges that is overwhelmingly used in the polymer industry while we use the term "plasma" to denote high-frequency, alternating-current glow discharges sustained at reduced pressures.

Initiation Reactions

The initial step in the surface oxidation of PP is likely the formation of a polymer radical by hydrogen abstraction. Hydrogen can be abstracted from any of the primary, secondary, and tertiary sites on the PP chains to form an alkyl radical. The probability of abstraction scales as $H_{tert} > H_{sec} > H_{pri}$, with this ranking largely independent of the attacking radical [9,10,11]. As an example, H abstraction from atactic PP is approximately 20x faster at the tertiary site than at the secondary site [12].

We believe that all of the surface-oxidation processes are largely explained by free-radical chemistry. The rate-limiting step in surface-oxidation processes is probably the initial hydrogen-abstraction reactions. As implied by the data shown in Table 1, there are really only three effective gas-phase hydrogen-abstraction agents: OH, O, and H. Only these three species can account for the rapid reactions that occur in flames, coronas, and plasmas. UVO processes contain significant quantities of O but do not contain the OH or H reactive species. Ozone-only treatments do not contain significant quantities of any of the efficient hydrogen abstracting species. Much of the polymer-radical formation occurs through the reactions:

$$RH + OH \rightarrow R\bullet + H_2O \quad (1)$$

$$RH + O \rightarrow R\bullet + OH \quad (2)$$

$$RH + H \rightarrow R\bullet + H_2 \quad (3)$$

The excited state of atomic oxygen, $O(^1D)$, is extremely reactive and non-selective. Both OH and ground-state atomic oxygen, $O(^3P)$, are quite reactive but do tend to discriminate between the different types of C–H bonds[11]. PP is among the polymers most readily attacked by atomic O. Ozone and hydroperoxy radicals can also abstract hydrogen, but at rates that are orders of magnitude slower than H atoms. As shown in Table 2, given the relative concentrations of the hydrogen abstracting species in each of the gas-phase processes, one would expect treatment with UVO to be as effective as flame, corona and plasma in hydrogen abstraction.

Oxidation

Once a polymer alkyl radical ($R\bullet$) is formed, it will react with gas-phase species such as O_3, O_2, O, H, OH, $HO_2\bullet$, or H_2O_2. All of these reactions are likely to be fast, non-rate-determining reactions [10]. Therefore, the products formed by the reactions of surface alkyl radicals with these gas-phase species should be approximately proportional to the relative gas-phase concentrations of these various species. This is one of the key concepts that helps to explain the differing results obtained with each surface-oxidation method.

LMWOM

Each of the five gas-phase treatment processes produces an oxidized PP surface. LMWOM is not necessarily produced on the oxidized surface, indicating differing reaction mechanisms for each of the treatment processes.

For PP, it is widely accepted that chain scission and the lowering of the molecular weight of oxidized PP occurs primarily through the β-scission reaction [9,11]. The reaction rate constant for the β-scission of PP alkoxy radicals is ca. 10^3 L mol^{-1} s^{-1} [13]. Polymer alkoxy radicals should, therefore, be the main precursor to LMWOM. There are several routes to alkoxy-radical formation in PP oxidation mechanisms:

1. the direct formation of alkoxy radicals from the reaction of polymer alkyl radicals with atomicO:

$$R\bullet + O \rightarrow RO\bullet \quad (4)$$

2. the reaction of polymer peroxy groups with atomic O:

$$RO_2\bullet + O \rightarrow RO\bullet + O_2 \quad (5)$$

3. the reaction of peroxy groups to form hydroperoxy groups, which subsequently decompose to form alkoxy groups:

$$RO_2\bullet + R'H \rightarrow RO_2H + R'\bullet \quad (6)$$

$$RO_2H \rightarrow RO\bullet + OH \quad (7)$$

4. the reaction of ozone with alkyl radicals:

$$R\bullet + O_3 \rightarrow RO\bullet + O_2 \quad (8)$$

The reactions of either O or O_3 with polymer radicals are undoubtedly fast, with rate constants > 10^9 L mol^{-1} s^{-1} [14]. Gas-phase hydrocarbon alkyl radicals react with O_3 in the gas phase at rates of up to five times faster than the analogous reactions with O_2 [14]. When O_3 is present, route (4) to alkoxy formation is almost certainly important.

On the other hand, route (3) is quite slow. As shown by the kinetic data in Table 1, the formation and decomposition of hydroperoxides is considerably slower than the subsequent alkoxy β-scission reaction. The route to alkoxy formation from peroxy thus appears to be many orders of magnitude slower than the reactions involving atomic O or O_3. Therefore, extensive, rapid scission and the formation of detectable LMWOM may be strictly associated with reactions involving atomic O and O_3. If the scission process proceeds sufficiently, gaseous products such as H_2O, H_2, CO, and CO_2 will form, leading to the removal (ablation) of the polymer [15,16].

Process Comparisons

Based on this discussion of the routes and mechanisms available for the production of LMWOM, the five gas-phase modification processes were examined. Flame treatment does not result in the formation of LMWOM despite a high level of oxidation but the formation of nodules on the PP fibrils has been noted by AFM.

In a fuel-lean flame, hydrogen abstraction is primarily accomplished by OH radicals. Once the alkyl radical is formed, it reacts rapidly with O_2 and other gas-phase species in the flame. All of these reactions with the alkyl radical are fast, non-rate-determining reactions. Therefore, the mix of oxidized products that is formed on the PP surface should be in approximate proportion to the concentrations of the gas-phase species present at the PP surface. In a fuel-lean flame, O_2 is by far the most common oxidizing species and we will consider molecular oxygen as the species responsible for affixing most of the oxygen to the PP surface through the reaction:

$$R\bullet + O_2 \rightarrow RO_2\bullet \quad (9)$$

In earlier papers, we showed that, in flame treatment, the extent of surface oxidation best correlates with the gas-phase concentration of OH radicals near the PP surface [7,17]. Even though O_2 actually leads to most of the oxidation in flame treatments, the reaction of O_2 with alkyl radicals is not rate limiting. The rate-limiting step in the overall flame treatment process is hydrogen abstraction by OH radicals.

The reaction of PP in the ozone-only treatment process is a slow one, requiring many minutes of exposure to generate significant oxidation of the surface [18]. Even when the ESCA O/C atomic ratio of the ozone-treated PP becomes > 0.10 at long exposure times, no LMWOM is detected until the exposure times exceed 45-60 minutes [8]. Oxidation of PP by ozone is slow because there are no efficient hydrogen-abstraction agents present. The rate constant for the reaction of O_3 with PP is only 0.08 L mol^{-1} s^{-1}, which is many orders of magnitude slower than the reactions rates of O, OH, or H with PP (which are of the order of 10^8 – 10^9) [19]. The accepted reaction of O_3 with polyolefins is [18,19]:

$$RH + O_3 \rightarrow RO_2\bullet \quad (10)$$

The polymer peroxy radical ($RO_2\bullet$) subsequently reacts more slowly to form carbonyls, carboxylic acids, and hydroperoxides [18,19]. Only the formation of the carboxylic acid leads to chain scission:

$$ROO\bullet \rightarrow R{=}O,\ RCOOH,\ RO_2H \quad (11)$$

Flame treatment and ozone-only treatment do not show the formation of LMWOM within normal treatment regimes. The lack of LMWOM can be traced back to the fast formation of polymer peroxy radicals rather than alkoxy radicals at the surfaces of the PP in these two processes. Only one of the subsequent slow reactions of the polymer peroxy radical leads to chain scission. For the flame treatment, there is a fast hydrogen-abstraction reaction available which enables the reaction of the alkyl radical with O_2 to form the polymer peroxy radical. This set of reactions results in a high level of oxidation and no LMWOM formation. For the ozone-only treatment there is no fast route available for the formation of the alkyl radical: instead the oxidation of the surface proceeds slowly and directly from the reaction of the polymer with O_3 to form the polymer peroxy radical. This set of reactions leads to lower levels of oxidation and limited chain scission.

Study of the UVO treatment leads to some interesting observations. When PP is exposed to ozone in the presence of UV, LMWOM is formed readily and apparently to a great extent even though the O/C atomic ratio does not reach 0.12 quickly [18,20]. AFM images of PP treated with UVO show ample mounds of agglomerated LMWOM [3].

Léonard et al. suggest that an excess of oxygen atoms actually leads to limited stable functionalization (oxidation) of polyolefin surfaces because oxidative degradation and ablation of the polymer will predominate [21]. In other words, if scission initiated by O atoms is too vigorous, the polymer is etched away before a large number of oxygen-containing functional groups can be affixed to the surface. The UVO process is rich in O atoms, O_3 and O_2. The O atoms are available both for fast hydrogen abstraction and reaction to form polymer alkoxy radicals. Also freely available in the gas phase is O_3 at concentrations similar to the concentration of O atoms and O_2. The reaction mechanisms of all of these species have pathways that lead to the formation of polymer alkoxy radicals which are the precursors to the formation of LMWOM. The high concentrations of these reactive species, in conjunction with the observed formation of LMWOM before high levels of oxidation are reached, indicates that there may be an equilbrium process present that allows the formation of a large number of alkoxy radicals which in turn leads to massive amounts of LMWOM and ablation. This is consistent with the work of Holländer et al. in their study of the vacuum UV (VUV) induced oxidation of PP [10]. They suggest that the extent of surface oxidation can saturate at relatively low levels (as low as an ESCA O/C atomic ratio of 0.07) because of the continuous renewal of the PP surface by oxidative ablation. Low-molecular-weight products are continuously formed by the action of O atoms, then desorb from the surface, exposing new, less-oxidized PP molecules. A competition between oxidation, on one hand, and scission and desorption, on the other hand, leads to the behavior that we observe with UVO reactions.

The oxidation of PP by corona discharges is also primarily a free-radical process, with little contribution from ions or UV radiation. As shown by the modeling data in Table 2, a corona is characterized by high concentrations of O_3, O_2, O, HO_2, and H_2O_2, but a relatively low concentration of OH and virtually no H atoms. In a corona, as the RH increases, the concentrations of O_3 and O decrease while the concentrations of OH and H_2O_2 increase. In a corona, hydrogen abstraction is primarily accomplished by O with some contribution from OH, particularly at high RH:

$$RH + O \rightarrow R\bullet + OH \quad (12)$$

$$RH + OH \rightarrow R\bullet + H_2O \quad (13)$$

Once the polymer alkyl radical is formed, it will react with most gas-phase species in the corona at about the encounter frequency. Therefore, the oxidation of the PP occurs primarily by the reaction of R● with O_2 and O_3, which are present in large numbers relative to any of the other oxidizing species in the corona [22]:

$$R\bullet + O_2 \rightarrow RO_2\bullet \quad (14)$$

$$R\bullet + O_3 \rightarrow RO\bullet + O_2 \quad (15)$$

The reaction of O_3 with R● generates most of the RO● that then leads to scission and the formation of LMWOM. We now realize that there are simply not enough O atoms to accomplish all of the hydrogen abstraction and alkoxy formation that must occur in corona treatment, so that there must be another fast route to the formation of alkoxies. That route is through ozone reaction with alkyl radicals.

The smaller amount of LMWOM that is formed at higher RH is a result of lower [O_3], lower [O], more OH, and more H_2O_2. These trends in active species concentrations should reduce alkoxy formation and thereby reduce the amount of LMWOM formed. The concentration of O_2 should not be significantly affected by relative humidity, so O_2 must not have a major role in the formation of polymer alkoxy groups.

The reaction of PP in downstream air or oxygen plasmas has also been found to generate an oxidized surface similar to that of a corona. By locating the PP downstream of the plasma itself, the effect of the ions and electrons generated inside the plasma is negated. Downstream from the plasma, only the relatively long-lived electronically excited species exist long enough to react with the PP surface. Such species include atomic O which is efficient at hydrogen abstraction. Wertheimer and coworkers have shown that vacuum UV can cause hydrogen abstraction. They have also demonstrated that the action of UV and atomic O are synergistic [23]. Holländer et al. have observed that "the important step [in surface oxidation processes] is the formation of the alkyl radical in the presence of oxygen [24]. Whether this radical is formed by VUV photolysis, by hydrogen abstraction by any kind of radical including O atoms, or by an ion does not seem to be important for the following [oxidation] reactions."

Plasmas generate singlet O_2, O, various excited states of atomic O and vacuum UV, all of which can initiate the reaction sequence. Given the concentrations of the hydrogen abstracting species, it is likely that the O is the primary

abstraction species, possibly aided by VUV. A path to LMWOM formation involving primarily O seems easy to envision.

Summary

The rate-limiting step in all of the processes considered in this discussion is hydrogen abstraction. For a given process, the rate of overall oxidation is highly dependent upon which specific abstracting agent dominates the gas phase.

Once hydrogen is abstracted and a polymer alkyl radical is formed, the next gas-solid reaction step is fast, at about the encounter frequency. The specific reaction that occurs depends primarily upon the relative concentrations of all gas-phase species present near the PP surface.

Although reactions of alkyl radicals with O_2 may dominate the post-abstraction mechanism, the reactions of other species with lower gas-phase concentrations are also critically important. In fact, is it largely the reactions of these secondary gas-phase species that determine the differences between the various oxidation techniques. In particular, these secondary reactions determine whether or not LMWOM is formed during oxidation.

References

[1] M. Strobel, M. J. Walzak, J. M. Hill, A. Lin, E. Karbashewski and C. S. Lyons - J. Adhesion Sci. Technol. **9**, 365-383 (1995).

[2] M. Strobel, V. Jones, C. S. Lyons, M. Ulsh, M. J. Kushner, R. Dorai and M. C. Branch - Plasmas Polym. **8**, 61-95 (2003).

[3] H.-Y. Nie, M. J. Walzak, B. Berno, N. S. McIntyre - Applied Surface Science **144–145**, 627–632 (1999).

[4] R. M. Overney, R. Lüthi, H. Haefke, J. Frommer, E. Meyer, H.-J. Güntherodt, S. Hild, and J. Fuhrmann - Applied Surf. Sci. **64**, 197 (1993).

[5] M. Strobel, C. Dunatov, J. M. Strobel, C. S. Lyons, S. J. Perron and M. C. Morgen - J. Adhesion Sci. Technol. **3**, 321-335 (1989).

[6] R. Mahlberg, H. E.-M. Niemi, F. S. Denes, and R, M. Rowell - Langmuir, **15**, 2985-2992 (1999).

[7] M. Strobel, N. Sullivan, M. C. Branch, V. Jones, J. Park, M. Ulsh, J. M. Strobel and C. S. Lyons - J. Adhesion Sci. Technol. **15**, 1-21 (2001).

[8] H.-Y.Nie, M.J. Walzak, N.S. McIntyre - Journal of Materials Engineering and Performance, **13**, 451-460 (2004).

[9] J. F. Rabek, Polymer Photodegradation Mechanisms and Experimental Methods, Chs 2, 3, 6, and 7. Chapman & Hall, London (1995).

[10] A. Holländer, J. E. Klemberg-Sapieha and M. R. Wertheimer - J. Polym. Sci. A: Polym. Chem. **33**, 2013-2025 (1995).

[11] S. J. Moss, A. M. Jolly and B. J. Tighe - Plasma Chem. Plasma Process. **6**, 401-416 (1986).

[12] E. Nicki, C. Decker and F. R. Mayo - J. Polym. Sci.: Polym. Chem. **11**, 2813-2828 (1973).

[13] D. J. Carlsson and D. M. Wiles - J. Macromol. Sci. – Rev. Macromol. Chem. **C14**, 65-106 (1976).

[14] R. Paltenghi, E. A. Ogryzlo and K. D. Bayes - J. Phys. Chem. **88**, 2595-2599 (1984).

[15] F. Clouet and M. K. Shi, J. - Appl. Polym. Sci. **46**, 1955-1966 (1992).

[16] V. A. Titov, T. G. Shikova, E. V. Kuvaldina and V. V. Pybkin - High Energy Chemistry **36**, 354-357 (2002).

[17] M. Strobel, M. C. Branch, M. Ulsh, R. S. Kapaun, S. Kirk and C. S. Lyons - J. Adhesion Sci. Technol. **10**, 515-539 (1996).

[18] M. J. Walzak, S. Flynn, R. Foerch, J. M. Hill, E. Karbashewski, A. Lin and M. Strobel - J. Adhesion Sci. Technol. **9**, 1229-1248 (1995).

[19] S. D. Razumovskii, A. A. Kefeli and G. E. Zaikov - European Polym. J. **7**, 275-285 (1971).

[20] J. H. Hill, E. Kabashewski, A. Lin, M. Strobel and M. J. Walzak - J. Adhesion Sci. Technol. **9**, 1575-1591 (1995).

[21] D. Léonard, P. Bertrand, A. Scheuer, R. Prat, J. Hommet, J. Le Moigne and J. P. Deville - J. Adhesion Sci. Technol. **10**, 1165-1197 (1996).

[22] R. Dorai and M. J. Kushner - J. Phys. D: Appl. Phys. **36**, 666-685 (2003).

[23] Hollander, A., Klemberg-Sapieha, J. E., Wertheimer, M. R. - Macromolecules **27**(10), 2893-5 (1994).

[24] A. Holländer, H. Behnisch and M. R. Wertheimer, in: Plasma Processing of Polymers (NATO ASI series), R. d'Agostino, P. Favia and F. Fracassi (Eds), pp. 411-421. Kluwer Academic, Dordrecht, The Netherlands (1997).

Table 1. Reaction rate constants (in L mol $^{-1}$ sec^{-1}) for reactions pertinent to the surface oxidation of polypropylene.

For the gas-phase hydrogen abstraction from *n*-butane:	
by OH	1.6×10^9
by O (^{1}D)	$\sim 10^9$
by O (^{3} P)	1.3×10^7
by H	1.5×10^5
by HO_2●	1.0×10^1
by O_3	$\sim 10^{-2}$
by O_2	Negligible
For the reaction of liquid-phase macroalkyl radicals (R●):	
with O_2	10^7 - 10^8
For the solid-state polymer reactions:	
RO_2● + R'H → RO_2H + R'●	10^{-2}
RO_2H →RO● + OH or RO_2● + R'●	Slow
RO● → R=O + R●	10^3
RO● + R'H → ROH + R'●	10^2
RO● + RO_2H → ROH + RO_2●	10^2

Table 2:Comparison of the concentrations (in 10^{14} cm^{-3}) of gas-phase species in various surface-treatment processes

	Ozone Only	UVO	Corona (RH=1%)	Corona (RH=100%)	Flame (φ=0.94)	O_2 or Air Plasma
Exposure time (in s) needed to generate an ESCA O/C ratio of 0.12	1400	500	0.5	0.5	0.1	0.1
Presence of LMWOM	No	Yes	Yes	Yes	No	Yes
[O_3]	1400	1000	4700	1800	~0	
[O_2]	high	high	high	high	high	100
[O]	~0	1000	7.6	4.9	0.06	~0.5
[H]			0.002	0.2	3	
[OH]		v small	0.2	1.3	10	
[HO_2●]		v small	1.5	5	5.5	
[H_2O_2]		v small	5	16	3.5	

Nitrogen-doped zinc oxide deposition using an expanding thermal plasma: correlation between plasma chemistry and film properties

I.Volintiru[1], W.H. van Helvoort[1], M.Creatore[1], J.L. Linden[2], M.C.M. van de Sanden[1]

[1]Eindhoven University of Technology, Department of Applied Physics, Eindhoven, The Netherlands
[2]TNO TPD, Division Models and Processes, Eindhoven, The Netherlands

Abstract
Nitrogen-doped zinc oxide films were deposited in an $Ar/N_2/O_2$/DEZ expanding thermal plasma at different N_2/O_2 ratios. All films exhibit n-type conductivity, a high transmission in the visible and preferential *c*-axis orientation. For the ZnO films deposited at low O_2 flows the ERD/RBS measurements indicate a factor of 10 increase in the incorporated N and C levels, as compared to the undoped samples (from below 0.1% to about 1%). An explanation is given by the mass spectrometry results, which show high HCN concentrations in these working conditions. For high O_2 flows on the contrary, HCN is hardly present, while NO is predominantly formed. In contradiction with earlier predictions, the presence of NO in the deposition region leads to almost no N incorporation in the ZnO film.
Keywords nitrogen-doped ZnO, expanding thermal plasma, mass spectrometry

1. Introduction

Zinc oxide (ZnO) is a wide bandgap (3.2 eV) II-VI compound semiconductor, which gained a lot of interest in the last decades due to major advantages such as the low fabrication costs, the possibility of wet chemical etching, and stability during radiation exposure. Besides this, the large exciton binding energy (60 meV) makes ZnO a good alternative in terms of efficiency and stability to the widely used GaN (26 meV) for blue and UV solid-state emitters and in detector applications. For these applications, both high quality n- and p-type ZnO need to be fabricated.

Reproducible n-type ZnO material with high transmittance in the visible (>80%) and low resistivity (10^{-2}-10^{-4} Ωcm) has already been obtained using various deposition techniques, e.g. magnetron sputtering, atomic layer deposition, molecular beam epitaxy, and also expanding thermal plasma CVD [1-4]. This makes n-type ZnO a good alternative to the already commercially produced, but more expensive, indium tin oxide (ITO). Intrinsically, ZnO is n-type conductive, due to native donor defects, i.e. interstitial Zn/O vacancies and unintentional H incorporation [5]. The conductivity can be further increased by doping with Al, Ga, F. On the other hand, obtaining p-type ZnO is more complicated, because of the presence of native defects and a low dopant solubility [6]. Theoretical calculations have shown that nitrogen is the most suitable p-type dopant for zinc oxide [7]. Also other II-VI semiconductors, such as ZnTe and ZnSe, have been efficiently p-doped with nitrogen [8,9].

In this work the ZnO films are deposited using an argon-fed expanding thermal plasma, in which diethylzinc ($Zn(C_2H_5)_2$, DEZ) and oxygen gas are admixed downstream. This technique has the advantage of high deposition rates and has shown good reproducibility. Also, by adding nitrogen gas in the cascaded arc plasma source, the nitrogen molecules are dissociated to a high degree [10], leading to a high N radical density in the deposition chamber. For the p-type doping of ZnO the incorporation of nitrogen via N-radicals is desirable as N acts as an acceptor, while N_2 acts as a double donor [11].

Here we discuss the effect of nitrogen addition on the plasma chemistry and on the electrical and optical properties of the ZnO films deposited on glass substrates by expanding thermal plasma CVD, with the final aim of obtaining N-doped p-type ZnO.

2. Experimental

The ZnO films were deposited using an expanding thermal plasma, generated in an argon/nitrogen-fed high pressure (300-600 mbar) cascaded arc. The plasma expands supersonically in the low pressure (0.2-2 mbar) deposition chamber, where diethylzinc and O_2 are injected, via two separate injection rings, situated at 30 cm and 6.5 cm from the plasma source (figure 1). The diethylzinc is evaporated at constant rate by a control evaporating and mixing unit (CEM).

The substrate used for all films was 0.7 mm thick Corning 7059 glass. The deposition rate varied between 0.2 and 0.6 nm/s and the deposited films were between 400 and 600 nm thick. The substrate temperature was kept at 200^{o}C in all experiments. The experimental conditions are summarized in table I.

The film thickness was measured using a step profiler. The electrical properties, i.e. sheath resistance, carrier density and mobility, were measured at room temperature, using the van der Pauw method. The film crystallinity was studied by X-ray diffraction (XRD), while the film composition was determined by Elastic Recoil Detection (ERD) and Rutherford BackScattering (RBS) measurements. A double-beam spectrophotometer was used to acquire the transmission spectra in the 200-1100 nm range. The deposition process was monitored using a Balzers Prisma Quadrupole Mass Spectrometer (MS). The pressure in the MS measuring chamber was between $1.4 \cdot 10^{-5}$ and $2.2 \cdot 10^{-5}$ mbar. All the signals were normalised to the signal of He (4 amu) to account for variations in e.g. pressure or temperature. Before performing the measurements, the linear mass response with pressure in the chamber was checked.

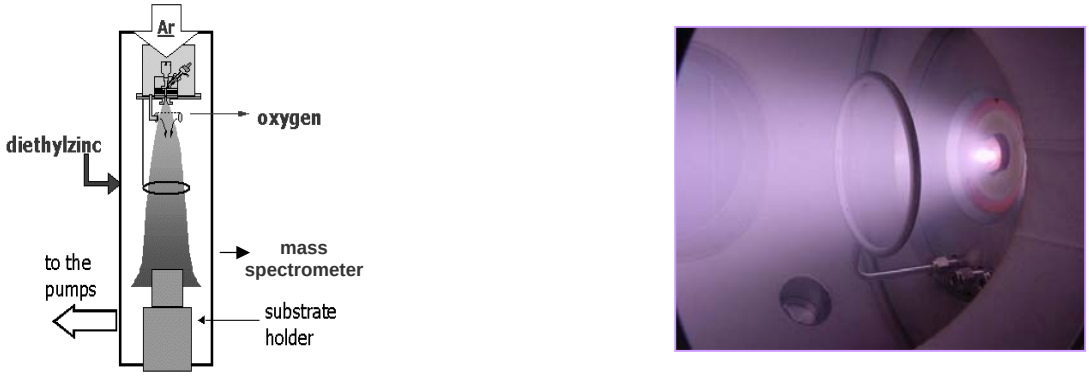

Figure 1. a) Schematic of the deposition reactor; b) Argon expanding thermal plasma (Φ_{Ar} = 1000 sccm, $p_{chamber}$ = 0.3 mbar); the O_2 ring and the arc nozzle are visible.

Table I. Overview of the experimental conditions

Plasma generation	
Argon gas flow (Φ_{Ar})	840-2000 sccm
Nitrogen gas flow (Φ_{N_2})	0-100 sccm
Arc current (I_{arc})	50 A
Plasma expansion & precursor injection	
Oxygen gas flow (Φ_{O_2})	20-150 sccm
DEZ flow (Φ_{DEZ})	2.5 g/h
Pressure in expansion chamber ($p_{chamber}$)	0.2-2 mbar

3. Results and Discussion

Hereby, we present our first attempts to incorporate molecular nitrogen in the expanding thermal plasma deposition process of ZnO. In order to understand how the interaction between species in the reactor takes place and how this influences the properties of the deposited films, preliminary studies of the stable species present in the reactor using mass spectrometry were performed. Their outcome is further correlated with the structural and electro-optical properties of the ZnO films.

3.1. Mass spectrometry

Mass spectrometry is used for monitoring the stable species present in the reactor. While the presence of atomic nitrogen in an Ar/N_2 expanding thermal plasma has already been demonstrated [10], it is not known what occurs in a more complex plasma chemistry, such as the $Ar/N_2/O_2/DEZ$ deposition plasma case. The aim of these measurements is therefore to investigate the presence of N-containing species when O_2 and DEZ decomposition products are present in the reactor.

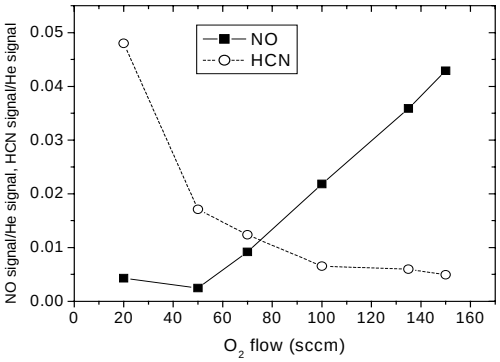

Figure 2. The NO and HCN relative intensities as a function of O_2 flow. The other conditions are Φ_{Ar} = 1000 sccm Ar, I_{arc} = 50 A, Φ_{N_2} = 50 sccm, Φ_{DEZ} = 2.5 g/h, $p_{chamber}$ = 0.6 mbar.

The only N-containing species which can be univocally identified in the mass spectra taken for an $Ar/N_2/O_2/DEZ$ plasma are hydrogen cyanide (HCN) and nitric oxide (NO). Their behavior with the O_2 flow shows two distinct regions (figure 2): for O_2 flow values lower than 60 sccm HCN is dominant, while for flow rates higher than 100 sccm, NO becomes dominant.

3.2. Film properties

The films are highly transparent (>80%) in the visible part of the spectrum for both undoped and nitrogen-mixed ZnO films, at all nitrogen mixing ratios (figure 3). The bandgap does not change significantly, the impurity concentration being probably too low for this effect to be detectable in a normal transmission measurement. Other more sensitive measurements, such as cathodoluminescence or photoluminescence at low temperature are necessary for the detection of the levels introduced by impurities inside the bandgap.

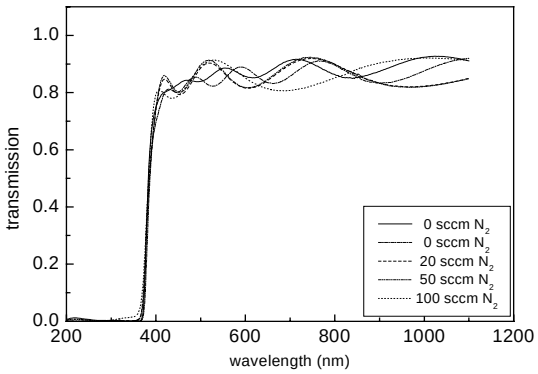

Figure 3. Transmission spectra for ZnO films deposited at different N_2 mixing ratios. The other conditions are Φ_{Ar} = 840 sccm, I_{arc} = 50 A, Φ_{O_2} = 50 sccm, Φ_{DEZ} = 2.5 g/h, $p_{chamber}$ = 0.6 mbar.

The XRD measurements (figure 4) show that all films are crystalline, with strong preferential orientation along the *c*-axis. The average crystallite size for all films was calculated from the (002) peak width using the Sherrer formula and is between 32 and 48 nm. This agrees with the values determined by other groups for polycrystalline ZnO [12].

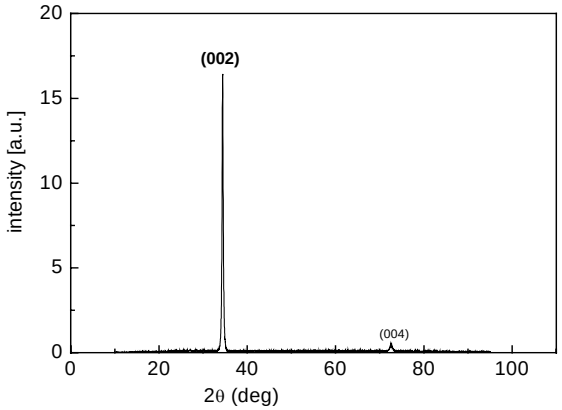

Figure 4. Typical XRD spectrum for an expanding thermal plasma-deposited ZnO film (for deposition conditions see table I).

The film resistivity gradually increases with higher nitrogen flow rates (figure 5a), while the carrier density is independent of the N_2 mixing ratio (figure 5b). The increase in resistivity can be attributed to a drastic decrease in mobility (figure 5c). This can be due to two effects: either a decrease in the grain size, the carrier scattering at grain boundaries being enhanced, or, very probable in our case, to an increased carrier scattering at impurities. These findings are in accordance with those of Sato *et al* [13]. For the sample deposited at 100 sccm N_2 flow and 50 sccm O_2 a Hall measurement could not be made with our system, probably due to a very low carrier mobility leading to a very low Hall potential. Also all samples deposited at high O_2 flow had resistivities outside the Hall measurement range.

The ERD/RBS measurements showed an N and C impurity level in the undoped ZnO films lower than 0.1%. For the films deposited at 50 sccm O_2 flow we observed an increase in the incorporated N and C to about 1%. On the contrary, for the films deposited at an O_2 flow of 150 sccm, no significant N and C incorporation is noticed.
Several articles already showed that NO potentially contributes to the growth of N-doped/p-type ZnO [14,15], while, to our knowledge, the influence of HCN on the ZnO film properties has not been reported yet.
After correlating the ERD results with the mass spectrometry measurements we can conclude that, for the films deposited at low O_2 flow, where the HCN concentration in the deposition region seems to be higher than the NO concentration, C and N incorporate easily, probably due to a high CN radical concentration. However, it is not clear what effect the additional carbon has on the N-doped ZnO films and what kind of bonds it forms in the material. Recent reports [16] give proves for CN incorporation in the ZnO film when similar mixtures are used. On the other hand, when NO is the dominant N-containing species in the plasma, almost no N or C are detected in our ZnO films. This seems to point out that, even when present in considerable amounts in the reactor, NO leads to almost no N incorporation in the ZnO film in these conditions.

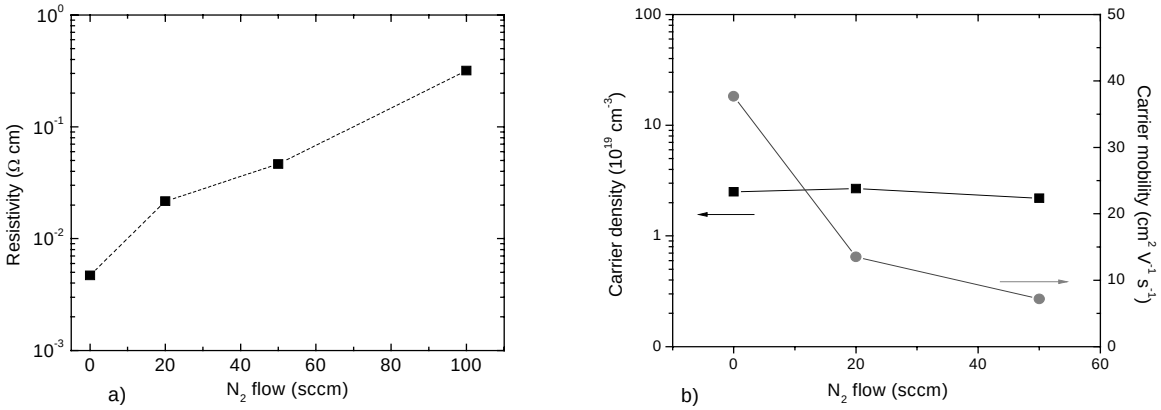

Figure 5. a) Resistivity of ZnO films as a function of the N_2 mixing ratio; b) The electron density and Hall mobility as a function of the N_2 mixing ratio; The other conditions are Φ_{Ar} = 840 sccm, I_{arc} = 50 A, Φ_{O_2} = 50 sccm, Φ_{DEZ} = 2.5 g/h, $p_{chamber}$ = 0.6 mbar.

4.Conclusions

We studied the N doped ZnO film deposition process in an $Ar/N_2/O_2$/DEZ expanding thermal plasma at different nitrogen mixing ratios. All films exhibited n-type conductivity, a high transmission in the visible and a preferential *c*-axis orientation. An increase of resistivity was also observed, probably caused by an increased carrier scattering at impurities. For the ZnO films deposited at low O_2 flows the ERD/RBS measurements indicated a factor of 10 increase in the incorporated C and N levels, as compared to the undoped samples (from below 0.1% to about 1%). This is in accordance with the mass spectrometry results, which showed considerable HCN concentrations in these working conditions. For O_2 flows higher than 100 sccm on the contrary, HCN is hardly present, while NO is predominantly formed. Working in these high oxygen flow-conditions, however, leads to almost no C and N incorporated, showing that, even when present in considerable amounts in the reactor, NO leads to almost no N incorporation in the ZnO film in these conditions.

Acknowledgements

The authors wish to thank W.M.Arnold Bik for the ERD/RBS measurements, as well as M.J.F. van de Sande, J.F.C.Jansen, and G.Kirchner for their technical assistance. This work was supported by the Netherlands Organisation for Applied Scientific Research (TNO) and the Eindhoven University of Technology (TU/e) through the the program for Sustainable Energy Technology (SET).

References

[1] K.Iwata, P.Fons, S.Niki, A.Yamada, K.Matsubara, K.Nakahara, T.Tanabe, and H.Takasu, J. Cryst. Growth. **214-215** (2000), 50

[2] S.Takeda and M.Fukawa, Thin Solid Films **468** (2004), 234

[3] B.Sang, A.Yamada, and M.Konagai, Jpn. J. Appl. Phys. **37** (1998), L206

[4] R.Groenen, J.L.Linden, H.R.M. van Lierop, D.C.Schram, A.D.Kuypers, and M.C.M. van de Sanden, Appl. Surf. Sc. **173** (2001), 40

[5] C.Van de Walle, Phys Rev. Lett. **5** (2000), 1012

[6] D.Laks, C. van de Walle, G.F.Neumark, and S.T.Pantelides, Appl. Phys. Lett. **63** (1993), 1375

[7] C.H.Park, S.B.Zhang, and S.Wei, Phys. Rev. B **66** (2002), 073202

[8] E.Tournie, P.Brunet, and J.P.Faurie, J. Cryst. Growth. **201-202** (1999), 938

[9] C.M.Rouleau and D.H.Lowndes, Appl. Surf. Science **127-129** (1998), 418

[10] G.J.H.Brussaard, M.C.M. van de Sanden, and D.C.Schram, Phys. Plasmas **4** (1997), 3077

[11] Y.Yan and S.B.Zhang, Phys. Rev. Lett. **86** (2001), 5723

[12] Z.Li and W.Gao, Mat.Lett. **58** (2004), 1363
[13] Y.Sato and S.Sato, Thin Solid Films **281-282** (1996), 445
[14] W.Xu, Z.Ye, T.Zhou, B.Zhao, and L.Zhu, J. Cryst. Growth **265** (2004), 133
[15] Y.G.Wang, S.P.Lau, X.H.Zhang, H.W.Lee, H.H.Hng, and B.K.Tay, J. Cryst. Growth **252** (2003), 265
[16] T.M.Barnes, J.Leaf, S.Hand, C.Fry, and C.A.Wolden, J.Appl.Phys. **96** (2004), 7036

OPTIMIZATION AND UP-SCALING OF PLASMA POLYMERIZATION PROCESSES

D. Hegemann, D.J. Balazs, M. Amberg, A. Fischer

EMPA Materials Science and Technology, Lerchenfeldstrasse 5, 9014 St.Gallen, Switzerland

Abstract
Progress in plasma polymerization processes can be made considering the reaction parameter power input per gas flow. This specific energy determines the plasma-chemical processes within the active plasma zone, known as concept of macroscopic kinetics. Regarding the geometry of plasma reactors and using well-defined, symmetric set-ups, a generalized activation energy is derived by evaluating the deposition rates of radical-dominated plasma polymerization processes. Thus, the presented concept enables the comparison of different processes such as HMDSO, methane, and acrylic acid discharges as well as their up-scaling.

Keywords: RF plasma, specific energy, activation energy, reactor geometry, pulsed plasma

Introduction

Plasma chemistry enables the deposition of thin films showing characteristics beyond wet chemical coatings. Using hexamethyldisiloxane (HMDSO), for example, chemical composition, cross-linking, and film thickness of SiOC:H films can be adjusted over a wide range [1,2]. Films with desired properties like wettability, elasticity, hardness, internal stresses, abrasion resistance, biocompatibility, and permeability can thus be designed. Different substrate materials and geometries like e.g. textiles, fibers, and membranes can be treated with high penetration [3]. However, the broad parameter range available as well as the distinct influence of reactor geometry complicates the process optimization and up-scaling. Therefore, a deeper understanding of process relevant correlations also on a macroscopic level is desirable.

As it is well-known, plasma polymerization – that means radical-promoted – processes are governed by the composite parameter power input per gas flow W/F, which relies on the concept of macroscopic kinetics [4]. This statistical approach considers the energy invested per particle within the active plasma zone yielding an excited state such as a radical and subsequent recombination in a passive zone yielding a stable product such as a deposition. A monomer depending activation energy E_a can be derived by evaluating the mass deposition rates R_m [1,2,5] considering that

$$\frac{R_m}{F} = G \exp\left(-\frac{E_a}{W/F}\right) \tag{1}$$

with a reactor depending geometrical factor G. An Arrhenius-type plot of Eq. (1) by variation of W/F parameters gives a straight line, where its slope corresponds to E_a (Fig. 1).

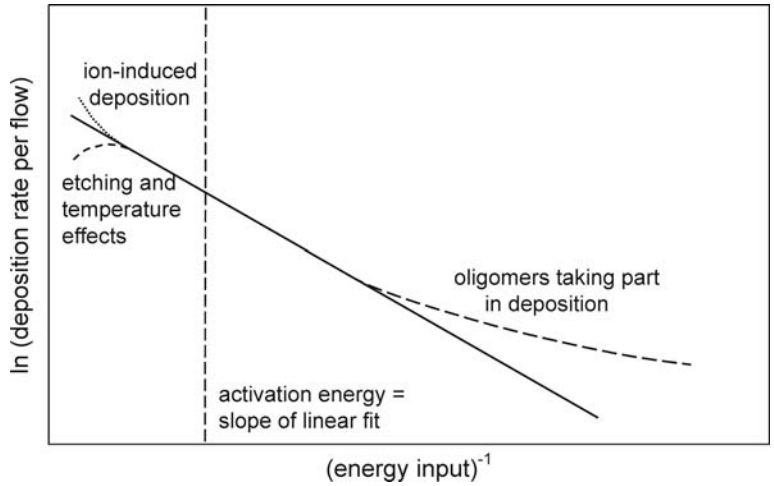

Fig. 1: Dependence of deposition rate (per gas flow) on (inverse) energy input. The straight line is given by Eq. (1) describing the deposition rates around the activation energy. Deviations might be found at low and high energy inputs.

While Eq. (1) agrees very well with experimentally found deposition rates at energy inputs around E_a, some deviations might be obtained at low power inputs due to different precursors or oligomers taking part in film growth and at high power inputs indicating ion-assisted or temperature effects. Hence, different effects can be observed using the evaluation of deposition rates.
At an energy input below the activation energy, for example, swellable hydrogel films can be deposited such as PEO-like coatings (Fig. 2). Increasing the energy input into the active plasma zone the degree of retention of functional groups can be controlled due to enhanced fragmentation at higher energies. While the hydrophobic properties of pp-HMDSO coatings slightly decrease at increasing energy input, the cross-linking and thus the mechanical properties can be enhanced. Further energy input leads to the formation of dense barrier coatings, when e.g. hydrocarbons are used as precursors.

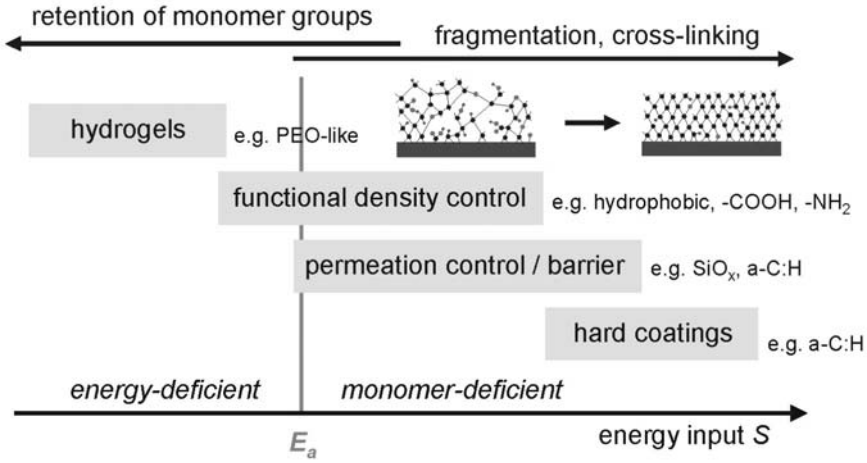

Fig. 2: Different regimes of functionality that can be covered by plasma polymerization.

Hence, the evaluation of the deposition rates to obtain the monomer-specific activation energy gives hints to find the optimum process parameters.
However, to obtain the generalized activation energy for a certain plasma polymerization process the real energy input within the active plasma zone that contributes to film deposition $S = W/F\,\big|_{dep}$ has to be known. Common plasma reactors often show power losses, e.g. due to the power coupling or secondary plasmas, and parts of the incoming particles might be pumped away without being activated, which might strongly affect the value of W/F. Therefore, geometrical considerations should be taken into account. Assuming a vertical flow of the gas particles towards the deposition area the real power delivered to the active plasma zone should be scaled by the expansion of the active plasma zone d_{act} above the electrode area A_{dep} to the total discharge volume V_{dis}, whereby the residence time of the monomer in the active plasma zone is regarded by

$$W\big|_{dep} = W\,\frac{A_{dep}\,d_{act}}{V_{dis}}\,. \tag{2a}$$

The real flow that contributes to film deposition should be scaled by the volume between gas inlet and electrode area $A_{dep}\,d_{gas}$ per total volume V_{gas} where the gas is flowing, using

$$F\big|_{dep} = F\,\frac{A_{dep}\,d_{gas}}{V_{gas}}\,, \tag{2b}$$

which finally leads to the similarity parameter [6]

$$S = \frac{W}{F}\,\frac{d_{act}\,V_{gas}}{d_{gas}\,V_{dis}}\,. \tag{3}$$

The derived geometrical correction is important e.g. for unconfined plasmas, corner-dominated discharges, where V_{gas} is larger than V_{dis}, and samples placed directly in the discharge (like in tubular reactors), where V_{gas} is smaller than V_{dis}. For volume-dominated discharges and small sheath length compared to the plasma expansion, on the other hand, the correction is close to one. In symmetric reactors, where the plasma fills the whole space between plane parallel electrodes, V_{gas} also equals V_{dis} and well-defined conditions are present. This work thus focuses on the evaluation of the deposition rates within different symmetric reactors using HMDSO, methane, and acrylic acid as monomers aimed for the optimization and up-scaling of plasma conditions.

Experimental

To obtain well defined plasma conditions capacitively coupled RF discharges (13.56 MHz) within symmetric reactor set-ups were considered. Three reactors with plane parallel electrodes which differ in size were compared. The two smaller reactors are cylindrical reactors, whereas the larger apparatus has rectangular electrodes. One electrode contains a gas shower yielding a vertical flow towards the counter electrode, where the substrates were placed at the distance d_{gas} from the gas inlet (Fig. 3a). Since the electrodes confine the vacuum chamber, the RF is directly coupled to the electrode without an electrical feed-through needed. V/I probe measurements thus reveal a 95% power conversion into the plasma. A small bias potential V_{bias} lower than 10% of the excitation voltage V_0 ($V_{RF} = V_0 \sin \omega t + V_{bias}$) was measured proving the symmetry of the set-ups. Moreover, homogeneous deposition rates over the entire deposition area A_{dep} were obtained. Due to the construction of the reactors, the whole vacuum chamber is filled by the discharge, and the gas volume V_{gas} equals the discharge volume V_{dis}. To obtain the length of the active plasma zone d_{act} the sheath widths can be observed, e.g. from the luminosity distribution (Fig. 3b). Some characteristics of the reactors are given in table 1.

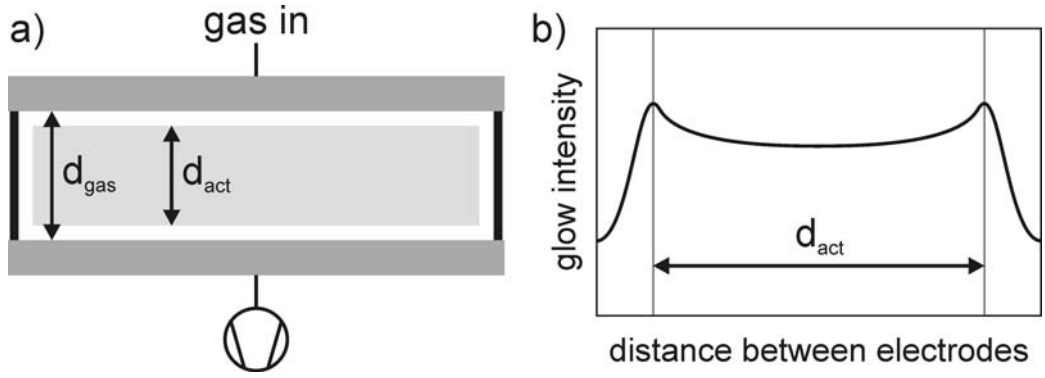

Fig. 3: (a) Schematic drawing of the reactor set-ups used. (b) The glow intensity indicates the plasma boundaries between sheath and bulk plasma and gives the length of the active plasma zone.

As monomers hexamethyldisiloxane (HMDSO), methane (CH_4), and acrylic acid (Aac) were used. Pure HMDSO and CH_4 discharges were run at a pressure of 10 Pa, while 30 Pa was used for the pure Aac discharge. The mass deposition rate was obtained by weighing the deposition on glass slides before and after plasma treatment.

Table 1: Characteristics of the used symmetric plasma reactors.

reactor	A_{dep} [cm^2]	$-V_{bias}/V_0$	d_{gas} [cm]	d_{act} [cm]		
				HMDSO	CH_4	acrylic acid
small	310	0.08	5.3	4.3		3.9
medium	700	0.05	5.0	4.0	3.2	
large	1150	0.05	8.5	7.5	6.7	

Results and discussion

At first HMDSO discharges were considered using all three symmetric reactors. Regarding the introduced similarity parameter $S = W\, d_{act} / F\, d_{gas}$ for $V_{gas} = V_{dis}$ it can be seen in Fig. 4 that the same slope of the mass deposition rates per monomer flow R_m/F in the Arrhenius-type plot was obtained for the different reactors. Thus, a generalized activation energy E_a can be derived which was found to be 55 J/cm^3 for HMDSO corresponding to 1230 kJ/mol (12.8 eV per molecule). This energy is exactly required to initiate HMDSO polymerization by breaking one Si-C (360 kJ/mol) and one Si-O bond (452 kJ/mol) and cross-linking by cleavage of a C-H group (435 kJ/mol). E_a is thus identified to be the minimum activation energy to start the polymerization process, i.e. to activate each monomer molecule and to avoid oligomerization [7].

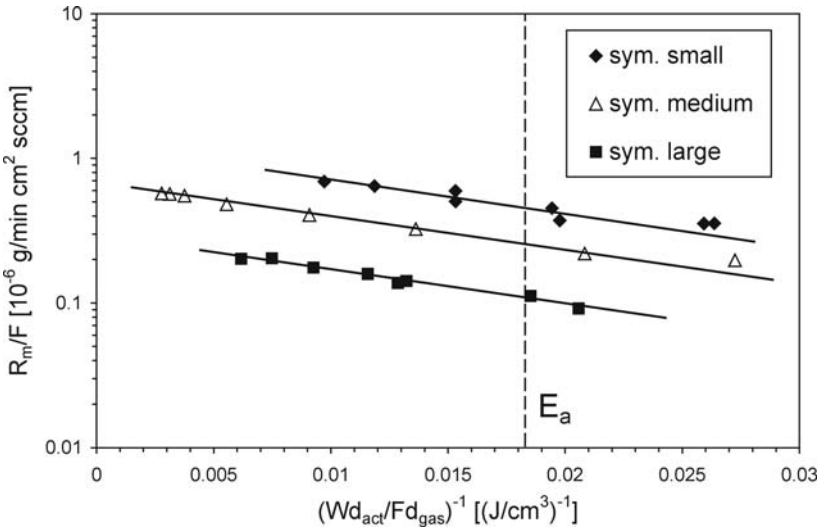

Fig. 4: Mass deposition rates per monomer flow depending on the similarity parameter (energy input) for pure HMDSO discharges within three different symmetric reactors.

Moreover, all three reactors were proven to show well defined deposition conditions. Note, that the proposed concept relates to the plasma chemistry taking place within the plasma zone determined by the activation energy. It is not related to the absolute deposition rate, which is further influenced by the interaction of energetic particles during film growth, by electric fields, conversion of monomer flow into film growth (by nucleation sites), and also by geometrical factors [2,3].

As a second monomer methane was used with two reactor set-ups (medium and large). Comparing both reactors, it can be shown that a generalized activation energy can be derived from the evaluation of the deposition rates (Fig. 5). E_a was found to be 23 J/cm^3 corresponding to 535 kJ/mol (5.3 eV per molecule).

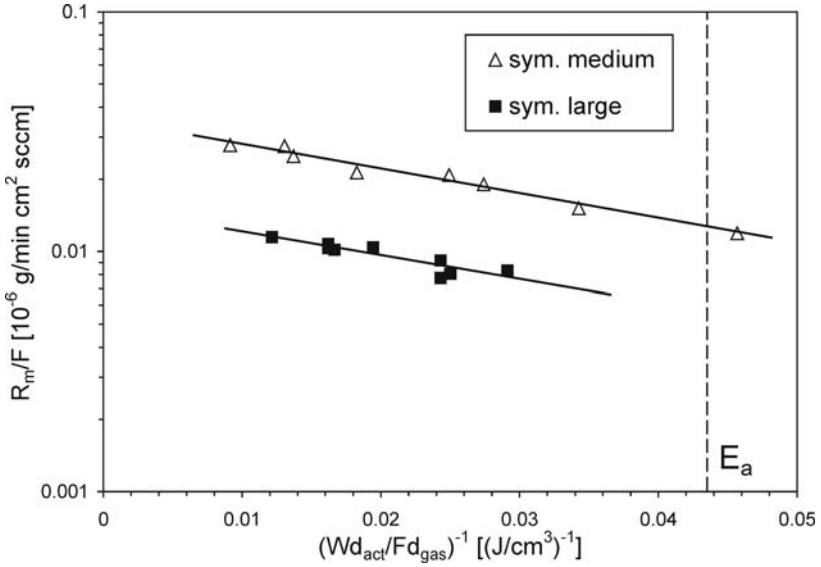

Fig. 5: Mass deposition rates per monomer flow for pure methane discharges within two different symmetric reactors.

To obtain CH_3 radicals in CH_4 discharges an energy of 435 kJ/mol is required. The additional energy might be used to break hydrogen molecules, since atomic hydrogen is considered to determine the hydrocarbon layer growth by transformation of higher hydrides into mono-hydrides yielding H/C ~1 for polymer-like films [8]. However, different precursors and growth zones (at different energies) are discussed for methane discharges [9]. As for the HMDSO discharges, higher absolute deposition rates were obtained for smaller reactors indicating a higher conversion of monomer flow into film growth.
The small reactor was also used to perform discharges with acrylic acid with the aim to retain carboxylic functional groups within the plasma. Therefore, not only continuous wave, but also pulsed plasma conditions were applied. While the on time was kept at 1 ms, the off time was varied between 1 and 40 ms to enable very low energy inputs into the plasma. At moderate energy inputs CW and pulsed plasmas can be compared. Regarding the deposition rate per flow a linear regime was obtained at energy inputs around the activation energy (Fig. 6). Here, Eq. (1) is applicable and E_a was found to be 33 J/cm^3 which corresponds to 740 kJ/mol (7.7 eV per molecule).

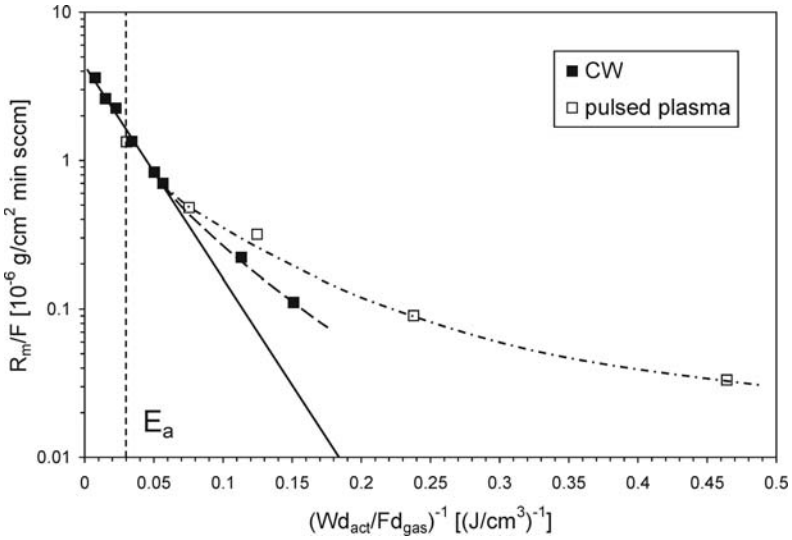

Fig. 6: Mass deposition rates per monomer flow for pure acrylic acid discharges for CW and pulsed plasma conditions. For pulsing the effective power input was used.

This energy is enough to open the double bond C=C in the acrylic acid molecule and to break one C-H bond for cross-linking reactions, while maintaining the carboxylic group in many molecules intact. For chemical and statistical reasons, however, the carboxylic group might also be dissociated. Therefore, many plasma groups investigate lower energy inputs by using power modulation. The usefulness of pulsed plasmas other than for reducing the average power input is controversially discussed within the literature. It is reported that deposition rates can be increased due to film growth during the off period [10,11], while others claim that no increase in the density of carboxylic groups can be obtained at comparable CW and pulsed plasma conditions [12]. As can be seen from Fig. 6, an increase in deposition rate can merely be observed at very low energy inputs for power modulated acrylic acid discharges. It can be assumed that oligomers strongly contribute to film growth (chain growth polymerization mainly during the off period). At moderate energies (around E_a), on the other hand, no difference in deposition rate is obtained and both CW and pulsed plasma conditions are comparable explaining the finding of similar functional densities [12]. While the highest retention of carboxylic groups can be obtained at energies around E_a [13], the stability of the films can be strongly enhanced using elevated energy inputs. More cross-linked films with a lower density of functional groups are able to withstand washing tests which is important for the use in bio applications [12,14].

Conclusions

In this work the introduced concept of a similarity parameter by considering the geometry of the discharge was proven for polymerizable gases such as a siloxane, hydrocarbon, and a vinyl-type monomer. Recently, we were able to show that the concept also works by addition of non-polymerizable gases such as O_2, N_2, Ar, NH_3, etc. by considering the modified flow $F = F_m + a\ F_c$ (F_m: monomer gas, F_c: non-polymerizable or

carrier gas), where the factor a (< 1) is experimentally determined [15]. A generalized activation energy for these different monomers can be derived by the evaluation of the mass deposition rates supported by the use of well-defined plasma conditions within symmetric reactors. For the use of asymmetric reactors it has to be regarded that the active plasma zone might expand into the plasma chamber at increasing energy inputs depending on gas flow and pressure [6,7]. Moreover, gas volume and discharge volume might differ and the true power absorption might not be known very accurately due to power losses within the reactor. Nevertheless, the evaluation of the deposition rates enables the identification of a process-specific activation energy that strongly facilitates up-scaling. Furthermore, the comparison of an asymmetric reactor with the well-defined symmetric set-ups increases the knowledge on the considered reactor with respect to power conversion and gas flow conditions using the introduced similarity parameter. For example, we demonstrated that the deposition of stable, hydrophobic pp-HMDSO coatings can be optimized using small, well-defined batch reactors, which was then scaled up to a large web coater to treat textile fabrics in a semi-continuous process [6].

We were able to demonstrate that the concept of macroscopic kinetics by evaluating the deposition rates depending on the specific energy shows many benefits:

- comparison and up-scaling of plasma polymerization processes [7,12]
- insight into plasma-chemical processes regarding the generalized activation energy [7,16]
- optimization of plasma polymerization processes with respect to the activation energy [1,6,7,16,17]
- detection of the influence of non-polymerizable gases on deposition or etching [15,17]
- detection of the influence of additional, e.g. ion-induced, effects [15]
- evaluation of pulsing conditions [12]
- design of functional gradient layers [2,18]
- optimization of power coupling and gas flow conditions (by comparison of activation energies) [7]
- conversion of monomer flow into film growth [2]
- advanced plasma reactor set-up [7]
- re-engineering (insights into old data sets or performed by different groups) [2]
- standard plasma process [7]

Acknowledgment

The authors gratefully acknowledge C. Oehr, Fraunhofer IGB, Stuttgart/Germany, where the experiments within the small and large reactor were performed (by the author).

References

[1] D. Hegemann, H. Brunner, C. Oehr, Plasma Polym. 6, 221 (2001).
[2] D. Hegemann, C. Oehr, A. Fischer, J. Vac. Sci. Technol. A23, 5 (2005).
[3] C. Oehr, D. Hegemann, M. Müller, U. Vohrer, M. Storr, in: Plasma Processes and Polymers, eds. R. d'Agostino, P. Favia, C. Oehr, M.R. Wertheimer, Wiley-VCH, Weinheim, 2005, p. 309.
[4] A. Rutscher, H.-E. Wagner, Plasma Sources Sci. Technol. 2, 279 (1993).
[5] Y.S. Yeh, I.N. Shyy, H. Yasuda, J. Appl. Polym. Sci.: Appl. Polym. Symp. 42, 1 (1988).
[6] D. Hegemann, in: Plasma Polymers & Related Materials, ed. M. Mutlu, Univ. Ankara, 2005.
[7] D. Hegemann, U. Schütz, A. Fischer, Surf. Coat. Technol. (2005).
[8] A. von Keudell, Thin Solid Films 402, 1 (2002).
[9] A. von Keudell, W. Jacob, Prog. Surf. Sci. 76, 21 (2004).
[10] H. Yasuda, Plasma Polymerization, Academic Press, Orlando, 1985.
[11] A.E. Lefohn, N.M. Mackie, E.R. Fisher, Plasma Polym. 3, 197 (1998).
[12] V. Sciarratta, D. Hegemann, M. Müller, U. Vohrer, C. Oehr, in: Plasma Processes and Polymers, eds. R. d'Agostino, P. Favia, C. Oehr, M.R. Wertheimer, Wiley-VCH, Weinheim, 2005, p. 39.
[13] C. Oehr, M. Müller, B. Elkin, D. Hegemann, U. Vohrer, Surf. Coat. Technol. 116-119, 25 (1999).
[14] L. Detomaso, R. Gristina, G.S. Senesi, R. d'Agostino, P. Favia, Biomater. 26, 3831 (2005).
[15] D. Hegemann, Plasma Proc. Polym., to be published.
[16] D. Hegemann, U. Schütz, C. Oehr, in: Plasma Processes and Polymers, eds. R. d'Agostino, P. Favia, C. Oehr, M.R. Wertheimer, Wiley-VCH, Weinheim, 2005, p. 23.
[17] D. Hegemann, H. Brunner, C. Oehr, Surf. Coat. Technol. 174-175, 253 (2003).
[18] D. Hegemann, H. Brunner, C. Oehr, Proc. 45th SVC Ann. Tech. Conf., 174 (2002).

70 μm Thick PZT Electron Emitter with 1 nm C-Au-S by Plasma Processes

S. Tsukahara, T. Suzuki, S. Kato, M. Suzuki, and S. Morita

Department of Electronic Information System, School of engineering Nagoya University, Nagoya 464-8603, Japan

e-mail: s_tukaha@echo.nuee.nagoya-u.ac.jp

Abstract

We succeeded in electron emission from PVDF with C-Au-S ultra thin film by a polarization inversion method, where the C-Au-S film was deposited by co-operation process of plasma CVD and sputtering. With using the electron, it is expected to excite luminescence substance as light emitting element. To realize the light emission, 70 μm thick and 5×5 mm^2 area PZT plate is used in this experiment, where the electron emission window is composed with a tooth type electrode and 1 nm thick C-Au-S semi-conductive layer.

Keywords: PZT, Ferroelectric Substance, Polarization Inversion, Electron Emission, Electro Luminescence

1. Introduction

Electron emission from ferroelectric materials is interested as a new electron source since the emission current of 7A and emitted electron energy of 3KeV were measured at CREN in 1988 [1]. Recently the emitted current was increased up to 200 A [2]. All report were concerned on in-organic substances like as $LiNbO_3$, PZT and others. It is known that PVDF (polyvinylidene fluoride) with ß-type crystal structure shows ferroelectric nature. However there is no report on electron emission from the organic ferroelectric substance like as PVDF.

Electron emission from PVDF was not easy to realize, even if same manner device system was constructed because there is large difference on the physical properties between in-organic and organic ferroelectric substances. Generally in-organic ferroelectric substance has large dielectric constant and small coercive field, but organic ferroelectric substance has small dielectric constant and large coercive field. In order to realize electron emission for organic ferroelectric substance, several problems must be solved.

In this paper, succeeded methods for electron emission from the PVDF will be reviewed. Then our efforts to realize a new light-emitting device will be introduced.

2. Experiment

2.1 Electron emission from PVDF through C-Au-S film [3~5]

PVDF with ß-type crystal structure shows ferroelectric nature, which have a small dielectric constant, large coercive field, and an insulating property. PVDF used in this experiment is flexible sheet with thickness of 40 μm. Sample was cut into size of 30×30 mm^2 from the sheet. PVDF sample was sandwiched by vacuum-evaporated Al film, but one side of electrodes was processed to a tooth-type electrode (10×10 mm^2 window area) using a photo-lithography process. The space between the teeth electrodes of the

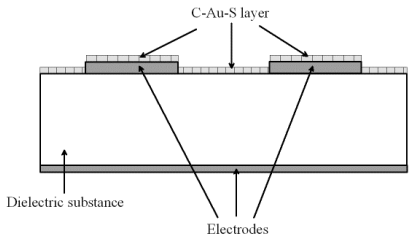

Fig.1. Cross section of sample with the C-Au-S layer.

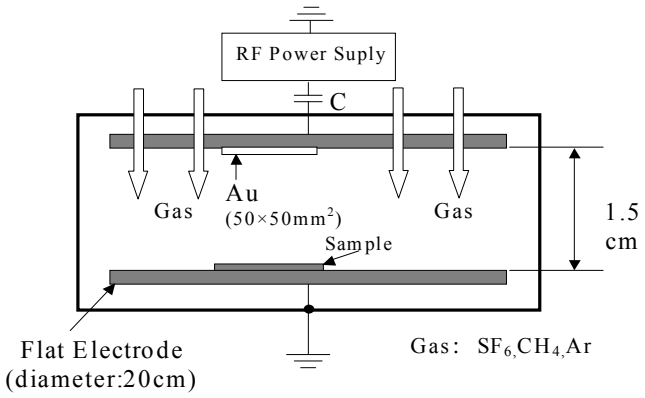

Fig.2 Cross section of sample holder in a vacuum

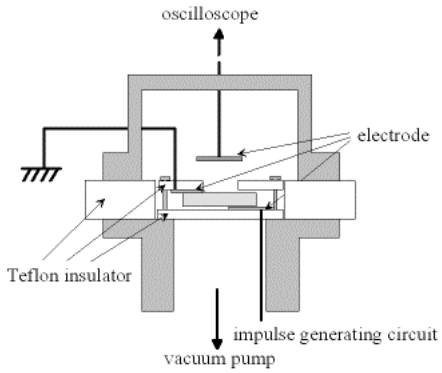

Fig.3 Cross section of sample holder in a vacuum chamber.

tooth-type electrode was set to 50 μm, similar to the PVDF film thickness. To prevent electrical contact between the electrodes on both sides, the rim of the Al film was etched off to maintain 15×15 mm^2 active area. When PVDF sample was polarized as flat-type electrode was negative and tooth-type electrode was positive, electric field induced along the surface of PVDF between teeth electrodes. However evidence of electron flow on the surface was not observed, the reason will be referred to high resistance of the PVDF surface.

To realize the current flow on PVDF surface, the surface with the tooth-type electrode was coated by semi-conducting film. From several candidates [3], the C-Au-S film was selected as a profitable semi-conducting film. As shown in Fig.1, the C-Au-S film, which is composed of C, Au and S atom at 63.7 10.5 and 25.8 atomic%, respectively, was coated on the PVDF surface by cooperation process of plasma CVD and sputtering at a pressure of 0.07 Torr for 3 sec. (Fig. 2) The film thickness was expected to be about 1 nm. Au atom disperses unanimously without forming a cluster in the film coated by this method. The semi-conductive C-Au-S film is adjustable by changing the content of Au in the film.

In the vacuum at 10^{-4} Torr or less, the sample was polarized at a voltage of 450 V. Thereafter, an opposite polarity impulse voltage of about –2400 V was added on the flat-type electrode to reverse the polarity, where the peak voltage was set higher than the voltage calculated by multiplying the coercive field of 50MV/m and

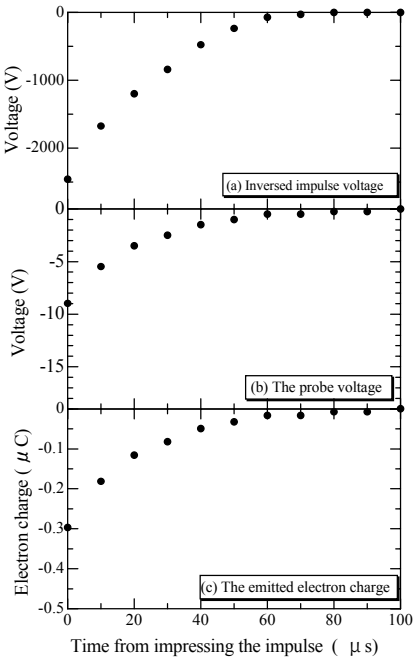

Fig.4 Time-dependence of applied impulse voltage, probe voltage and emitted electron charge for PVDF with the C-Au-S film

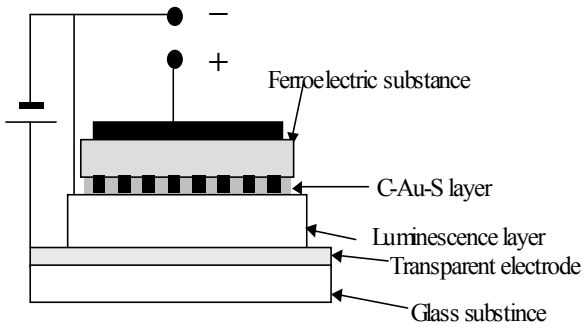

Fig.5 New light emitting device

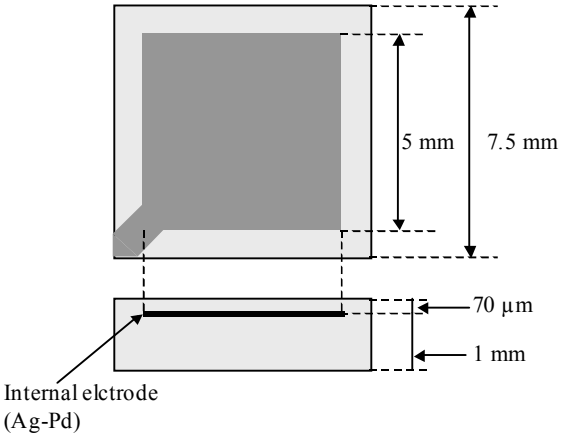

Fig.6 PZT Sample

a thickness of 40 μm. The prepared impulse voltage had a shape of 1-10 ns of wave front and 10-100 ms of wave tail. The electron emission was measured for the sample equipped in the vacuum chamber as shown in Fig. 3. The sample was placed on the Teflon holder while maintaining the tooth-type electrode side upward, where the probe electrode of copper plate (area 30×30 mm^2) was placed at 5 mm from the tooth-type electrode surface. The electron charges on the probe electrode were collected by a capacitor of 0.033 μF and the induced voltage on the capacitor was measured using a storage oscilloscope (Tektronix, 7834) with a memory system at response of sub-nanosecond. The applied voltage for reversing the polarization was used as shown in Fig. 4(a), which showed the peak value of 2400 V. The probe potential measured is shown in Fig.4(b), where the peak value is –9 V. By multiplying the capacitance of 0.033 μF, the emitted charge is shown in Fig.4(c). The total emitted electron charge was calculated to be 6.1×10^{-12} C, which is 5.2 % of the compensated charge on the PVDF surface.

2.2 Electron emission from PVDF through C-Au-S film

We propose a new light-emitting device, which has a new structure using ferroelectric electron emitter with C-Au-S layer. The device structure is shown in Fig.5. The electron will emit from a ferroelectric substance surface through C-Au-S 1nm thick film by a polarization inversion method and it is injected into the luminescence layer. If the electron energy is high enough to excite the luminescence substance, light will be emitted.

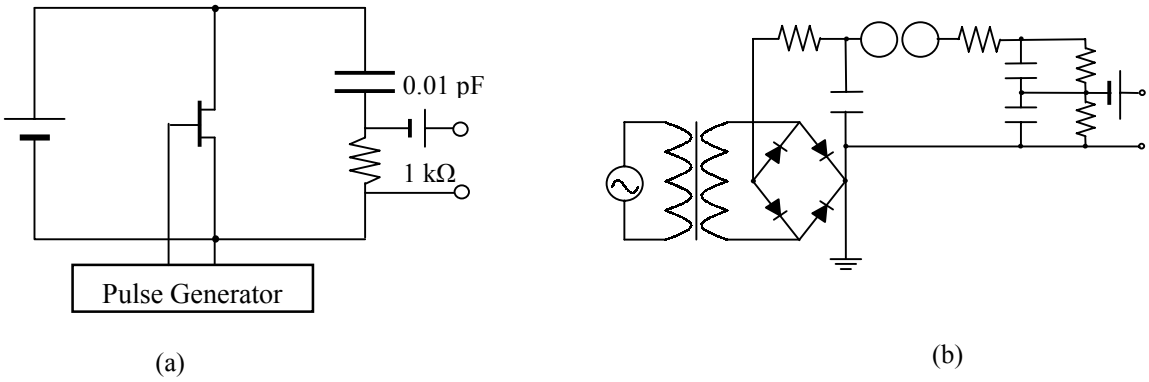

Fig.8 Impulse generation circuit

In this experiment, PZT was used as ferroelectric substance because of large dielectric constant. The PZT sample used for this experiment is shown in Fig.6. PZT has a dielectric constant of 1700 and small coercive field of 0.7 MV/m. Therefore, larger emitted electron charge and lower driving voltage are expected compared to the PVDF case. Ag-Pd flat-type electrode is sandwiched by PZT. The active PZT layer has 70μm thick in the are of 50×50 mm^2. Therefore, the coercive voltage is calculated to be 49 V. The tooth-type electrode was formed with evaporated Al film by photo-lithography processes. The line and space width of tooth type electrode was 50 μm. The C-Au-S film was coated on PZT surface with a tooth type electrode same as the PVDF at pressure of 0.08 Torr for 3 sec. The film thickness was 1 nm. ZnS and antracen were used as luminescence substances. These materials were coated on the C-Au-S film by a vacuum-evaporation method.

It needs to control emitted electron energy to excite luminescence layer, and two types impulse generator were prepared as shown in Fig. 8. The rise time of impulse voltage is estimated to be about 100 nsec for Fig.8 (a) and a few ns for Fig.8 (b), respectively. The poling voltage was 10-100 V, and the reversed polarization impulse voltage was 80-250 V.

The light emission has not been observed yet. The emission system and dimension must be optimized to realize the emission

3 Conclusion

Electron emission from PVDF could be observed by forming C-Au-S semi-conductive layer between the teeth electrode on the PVDF surface. With using same device system, a new electro luminescence device was proposed.

Acknowledgement

A part of experiments are carried out at the Center for Co-operation Research in Advanced Science and Technology, Nagoya University. Samples of PVDF and PZT were obtained from Kureha Chemical Industry Co. and NGK Spark Plug Co., respectively. We express our gratitude to all who contributed to this study.

Reference

[1] H. Gundel, H. Riege, E. J .N. Wilson, J. Handerek and K. Zioutas: Ferroelectrics **100**, 100(1989).

[2] Yasushi Hayashi, Donald Flechtner and Eiki Hotta :J.Phys.D: Appl.Phys.**35**, 281-286(2002)

[3] Kazuaki Omura, Md. Abul Kashem and Shinzo Morita:J. Photopolymer Sci. and Tech., **16**, 1, 55-60(2003).

[4] Kazuaki Omura and Shinzo Morita:Jpn. J. Appl. Phys., **43**, 5B, L689-L690 (2004).

[5] Shinzo Morita and Kazuaki Omura; IEICE Trans. on Electronics, **E87-C**, 12, 2103-2107 (2004).

Glow-Discharge Treated Polyethersulphone, Polycarbonate and Cellulose Acetate Ultrafiltration Membranes for Sugar Separation, Part I: Effect of Ethylenediamine and 2-Hydroxyethyl methacrylate as Precursors

Akdogan Ebru[1], Cokeliler Dilek[1], Aydın Emine[2], Tan Erdal[2], Mutlu Mehmet[1]

[1]*Hacettepe University, Engineering Faculty, Plasma Aided Bioengineering and Biotechnology Research Group, 06532 Ankara, Turkiye.*

[2]*Turkish Atomic Energy Agency, Ankara Nuclear Energy Research and Education Centre, Turkiye,*

Abstract

Polyethersulphone, polycarbonate and cellulose acetate membrane surfaces were modified in a glow-discharge plasma polymerisation system with a 13.6 MHz radio frequency using ethylenediamine and 2-hydroxyethyl methacrylate as monomers at a 20 W power and 10 min of exposure time. Surface properties were determined by AFM and contact angle measurements. Changes on permselective behaviours of the membranes were determined using a filtration system.

Keywords: Plasma polymerisation, sugar separation, glucose permeability.

1. Introduction

Sugar separation is a difficult and costly task in food industry. Among different separation methods, chromatography is the most used one for commercial sugar separation. Such methods are batch processes and imply expensive installations, low productivity and low yields of the desired products [1]. Alternative processes for sugar separation, such as zeolite adsorption [2], reverse osmosis [3], electro dialysis using borates to complex sugars[4], ion exchange membranes[5], plasticized cellulose triacetate membranes[6], liquid membranes[7], and supported liquid membranes [8-11] have been reported. Compared with the mentioned methods, the membrane processing has the advantages such as low energy demand, low capital and operating costs, easy scale up and continuous operation. Among membrane processes, supported liquid membranes are the most promising one but it is not commonly used in industrial applications because of the membrane instability due to the partition of the organic solvent/carrier to the aqueous phase [1].

The advantages of plasma processing of materials have been reported; it changes only the surface properties of the introduced material without affecting its bulk properties, it is a very efficient method and considered as environment friendly. When plasma is applied to a polymeric membrane, several kinds of reaction can take place on the polymer surface; breakage of covalent bonds along the chain, crosslinking, grafting, interaction of surface free radicals, alteration of existing functional groups and/or incorporation of chemical groups originated in plasma [12]. With the plasma polymerisation system, it is possible to prepare new membrane species, affinity membranes [13], reactive membranes [14], or membranes with brush-like surfaces [15].

Although plasma polymerisation technique is commonly used in the preparation and modification of different types of membranes for different purposes, to the best of our knowledge, no previous research studied on the effect of plasma polymerisation, so called glow discharge technique, modification of membranes for sugar separation. By plasma polymerisation technique we aimed to carry the separation technique of sugar beyond the state-of-the-art. In this paper, the effect of plasma polymerisation technique on the permselective behaviour of polyethersulphone, polycarbonate and cellulose acetate membranes to glucose by using ethylenediamine and 2-hydroxyethylmethacrylate as monomers was reported.

2. Materials and Methods

Cellulose acetate (CA) membranes were prepared by solvent casting method [12]. The composition of the casting solution was, 2% of cellulose acetate w/v (Acros organics, USA) in acetone (J.T Baker, Holland). Film formation was achieved by evaporation of acetone at room temperature (20ºC) and 80% relative humidity environment. Polyethersulphone (PES) membranes with a MWCO 100,000kDa and a diameter of 25 mm (Millipore Co., UK), Polycarbonate (PC) membranes, 0,03 µ pore size and 47 mm diameter (Poretics, USA) along with CA membranes were modified in a glass tubular reactor with the external plate electrodes and standard excitation frequency of 13.56 MHz (Fig.1). The reactor base pressure was 7x 10-2 mbar. The discharge power of the monomer gas (20 W), exposure time (10 min) and the flow rate were maintained constant for all of the modifications. Ethylenediamine (EDA) and 2-hydroxyethyl methacrylate (HEMA) (Sigma, Germany) were used as monomers.

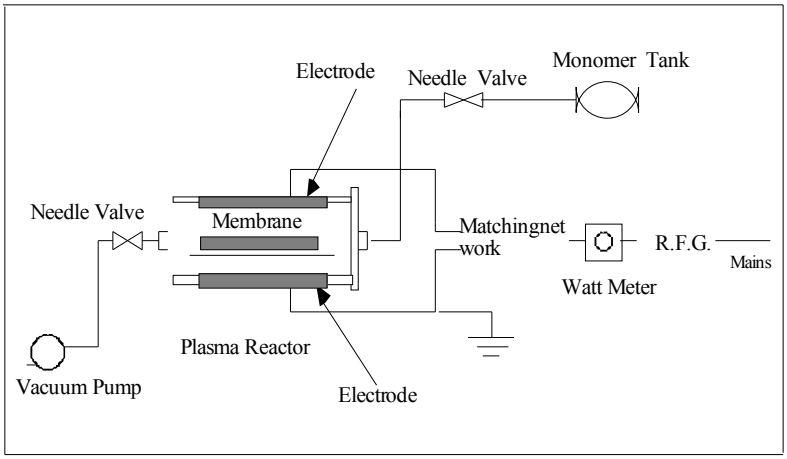

Fig. 1 Plasma Polymerisation System

Membranes, after storing in distilled water for 24 hr, were placed in filters (25 and 47 mm), filtration solution was fed to the system using an HPLC pump (Oriental Motor, Japan). A 0,1 M glucose (Acros organics, USA) solution in phosphate buffer (Sodium hydrogen phosphate, potassium dihydrogen phosphate, J.T Baker, Holland) at pH 7.5 and 50 ºC was used as the filtration solution. Glucose content of the permeates were determined using a sandwich type glucose electrode made in our laboratory. The preparation of the amperometric enzyme electrode is described elsewhere [12].

Contact angle measurements of the wetted membrane surfaces were performed by sessile bubble technique using an Intel®Play Q*3 Computer Microscope with distilled water and formamide (Sigma, Germany). Surface energies of the membrane surfaces were calculated using Young's and geometric mean equations [13].Atomic Force Microscopy (AFM) imaging was performed with using Topometrix TMX 200.

3. Results and Discussion

3.1 AFM

AFM images of PES membranes are given in Figure 2. Virgin PES membrane surface (Fig.2a) is rather smooth. After plasma treatment of membrane with both EDA (Fig. 2b) and HEMA (Fig 2c) at 20 W, 10 min some pores or pore like structures were appeared on the PES membrane surfaces. On the other hand no change on the porosity of the plasma modified PC membranes, when compared with virgin membrane (Fig 3a), occurred. AFM images of CA membranes showed a dense layer of deposition on the surfaces of both EDA and HEMA treated membranes (Fig4) making the surface smoother.

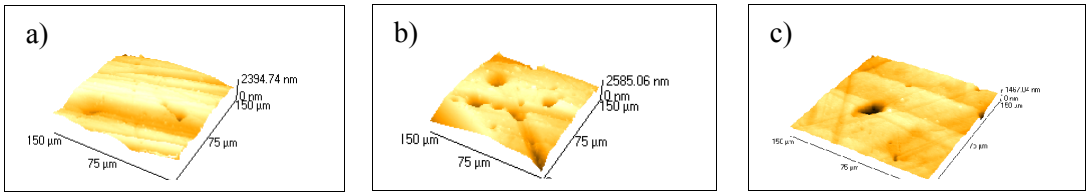

Fig.2. AFM images of PES membranes, a) virgin membrane, b)after modification with EDA 20 W 10 min, c) after modification with HEMA 20 W 10 min

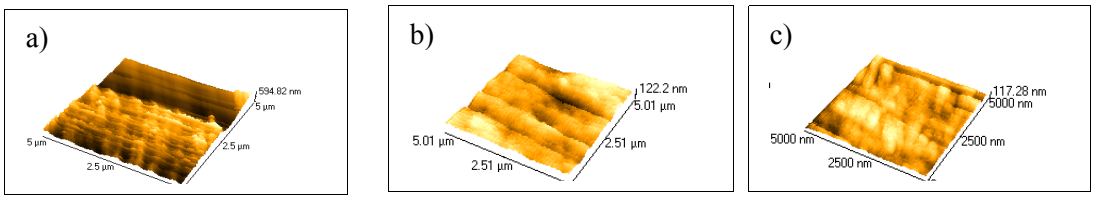

Fig.3 AFM images of PC membranes, a) virgin membrane, b)after modification with EDA 20 W 10 min, c) after modification with HEMA 20 W 10 min

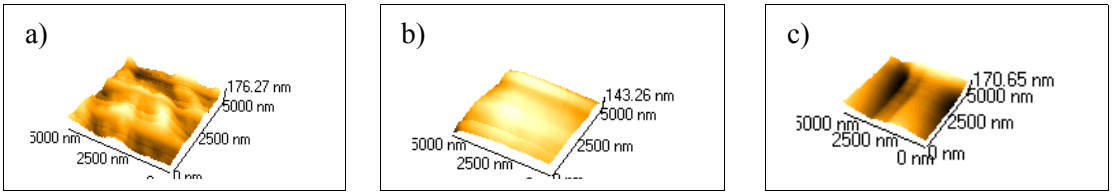

Fig.4 AFM images of CA membranes, a) virgin membrane, b)after modification with EDA 20 W 10 min, c) after modification with HEMA 20 W 10 min

3.2. Surface energies

Surface energy values of the virgin and modified membranes are given in table 1. After plasma treatment of PES membranes an increase in the surface energies is observed. The polarity of the EDA and HEMA treated PES membranes increased.

After plasma treatment, there was a little change in the SFE' s of the modified PC membranes, while their polarity decreased. The final SFE and polarity values of the EDA and HEMA modified membranes were close to each other.

Plasma treatment increased the SFE's and polarity of CA membranes. After treatment with EDA, the increase in the polarity was higher than the polarity of HEMA treated membrane while the SFE of EDA treated CA membrane was higher.

Membrane	γ^p_{pv}	γ^d_{pv}	γ_{pv}	**Polarity (%)** ($\gamma^p_{pv} / \gamma_{pv}$)
PES plain	15,6	28,2	43,8	35,62
PES EDA 20W 10'	37,7	5,24	42,94	87,8
PES HEMA 20W 10'	23,72	23,33	47,05	50,4
PC plain	26,73	9,55	36,28	73,7
PC EDA	16,32	18,23	34,55	47,24
PC HEMA	17,56	21,63	39,19	44,8
CA plain	28,73	39,19	67,92	42
CA EDA 20W 10'	42,51	3,92	46,43	91,6
CA HEMA 20W 10'	46,38	7,56	53,94	86

Table 1. SFE's and polarities of virgin and modified membranes

3.3. Glucose permeabilities

Changes in the glucose permeabilities of the membranes are given in Fig.5. There were no significant changes on the glucose permeabilities of the PC and PES membranes (Fig.5.b). Since PC membranes have a porous structure and the density of the pores on the surfaces is high, plasma may not have caused a deposition around those pores so the plasma treatment was not efficient on the surface for the applied plasma parameters.

AFM images of the CA membranes showed that a dense coating layer was formed after plasma treatment with both EDA and HEMA. A dramatic decrease was observed on the glucose permeabilities of the treated membranes probably due to this layer (Fig.5.c). When the permeability values of EDA and HEMA treated membranes were compared, it was seen that the glucose permeability values of HEMA modified membranes were higher than the glucose permeability values of EDA treated membranes (Fig.5.d.).

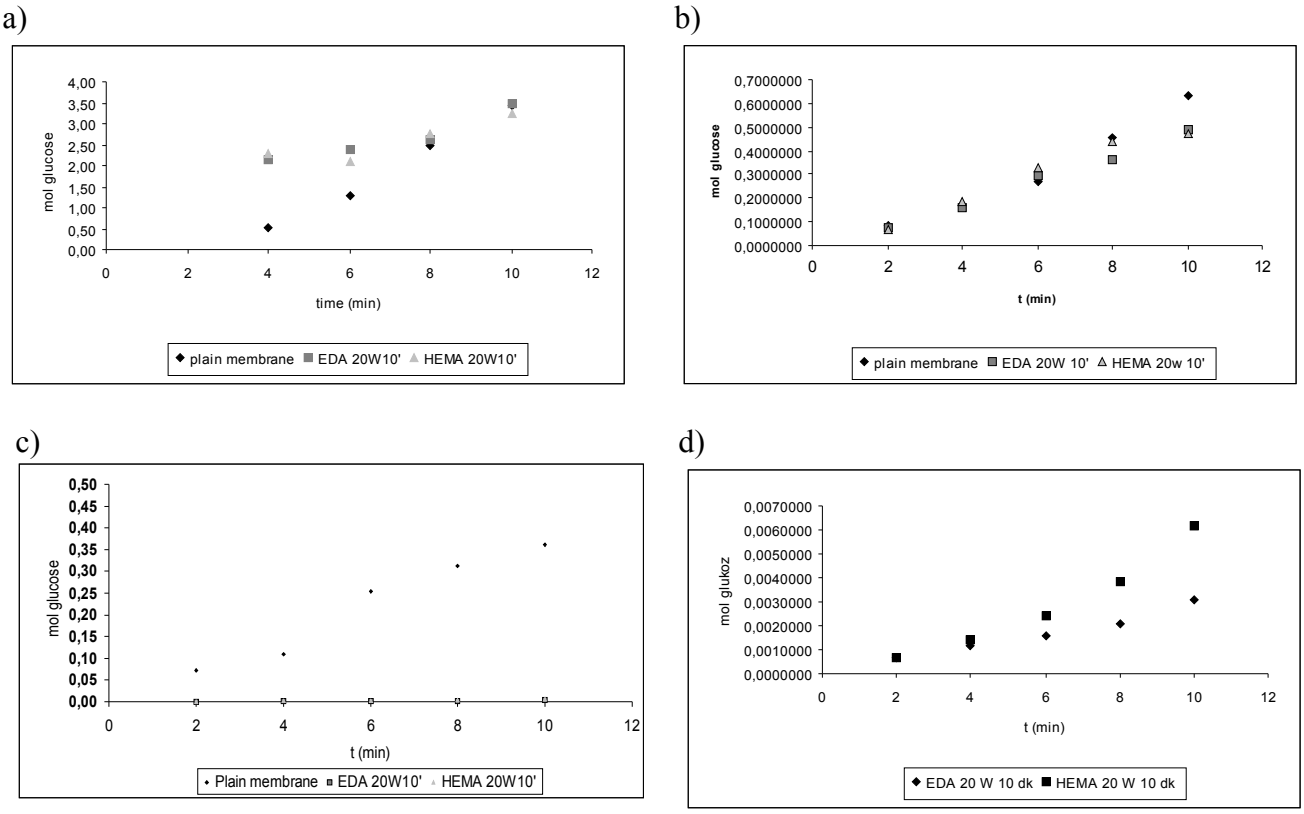

Fig.5. Changes on the glucose permeabilities of the membranes a)PES membranes, b)PC membranes c)CA membranes d)EDA and HEMA modified CA membranes.

4. Conclusions

The effect of glow discharge treatment on PES, PC and CA membranes at 20 W discharge power and 10 min exposure time was reported. Plasma treatment caused pore formation on the surface of PES membranes and making the surface more hydrophilic. The surface modification of PC and PES membranes was not efficient due to the membrane structures for the applied plasma parameters. Thus no significant change on the glucose permeabilities of the modified PC and PES membranes was observed. Glucose permeabilities of the EDA and HEMA modified CA membranes decreased compared to the virgin CA membrane, due to the coating layer formed after plasma modification. The hydrophilicity of EDA modified membrane was higher than the HEMA modified membrane but the permeability of HEMA modified membrane was higher. Monosaccharides are known to form complexes with OH groups. The reason of the glucose permeability value of the HEMA treated membrane was higher than EDA modified membrane may be the facilitated transport of glucose on the membrane surface due to the glucose-OH complex formation. For a better understanding of the transport mechanism on the membrane surface, XPS results are needed. Further studies will be performed using CA membranes as model membrane and with different monomers which are known to be carriers on sugar transport.

Acknowledgements

This project is funded by Hacettepe University Research Foundation, HUAF, (Project No: HUAFP 01 01 602 025).

AFM imagings were performed in Ankara Nuclear Research and Training Centre, TAEA.

References

1. M.Di Luccio, B.D. Smith, T.Kida, C.P.Borges, T.L.M.Alves, Separation of fructose from a mixture of sugars using supported liquid membranes. Journal of Membrane Science, 174 (2000), 217-224.
2. H.Odawara, Y.S.Noguchi, M.Ohno, Separation of fructose from a mixture of sugars. US Patent 4,014,711 (1997).

3. S.S.Kim, H.N.Chang, Y.S.Ghim, Separation of fructose and glucose by reverse osmosis. Ind.Eng.Chem.Fundamen., 24 (1985) 409-412.
4. D.Langev, M.Metayer, M.Labbe, C.Chappey, Electromembrane process for sugar separation: A preliminary study. Russian Journal of Electrochemistry. 32(2) 1996, 241-247.
5. Y.Shigemasa, S.Okamoto, H.Sashiwa, H.Saimoto, Uphill transport of carbohydrates across ion-exchange membranes. Chemical Letters. 3(1990), 433-436.
6. J.A.Riggs, B.D.Smith. Journal of American Chemical Society. 119 (1997), 2765-2766.
7. T.Shinbo, K.Nishimura, T.Yamaguchi, M.Sugiura, Uphill transport of carbohydrates across an organic liquid membrane. Journal of Chemical Society, Chemical Communications. 4 (1986), 349-351.
8. M.Di Luccio, B.D. Smith, T.Kida, T.L.M.Alves, C.P.Borges, Evaluation of flat sheet and hollow fiber supported liquid membranes for fructose pertraction from a mixture of sugars. Desalination, 148 (2002), 213-220.
9. S.J.Gardiner, B.D.Smith, P.J.Duggan, M.J.Karpa, G.J.Griffin, Selective fructose trasport trough supported liquid membranes containing diboronic acid or conjugated monoboronic acid-quaternary ammonium carriers. Tetrahdron. 55 (1999), 2857-2684.
10. T.Rhlalou, M.Ferhat, M.A.Frouji, D.Langevin, M.Metayer, J-F Verchere, Facilitated transport of sugars by a resorcinarene through a solid liquid membrane. Journal of Membrane Science. 168 (2000), 63-73.
11. M.Bryjak, G.Pozniak, I.Gancarz, W.Tylus, Microwave plasma in preparation of new membranes. Desalination 163 (2004), 231-238.
12. S.Mutlu, M.Mutlu, P.Vadgama, E.Piskin, Sandwich-type amperometric enzyme electrodes for determination of glucose, Diagnostic Biosensor Polymers, (1994), 71-83
13. H.A.Gulec, Wettability and surface energy measurements of plasma polymerisation modified surfaces. M.Sc. Thesis, Hacettepe University, Ankara, Turkiye, 2004.

Modeling of Chemical Vapor Deposition System Cleaning by Remote Plasma Source and/or In-Situ Plasmas

A. Chirokov, K. Iskenderova, A. Gutsol, A. Fridman
Department of Mechanical Engineering, Drexel University, Philadelphia, USA

Abstract:
The numerical study intended to assess the effectiveness of CVD chamber cleaning technology is presented here. The chamber cleaning process is of great importance since it can affect the quality of deposited film. To study the main aspects of the clean process, CFD plasma chemical model of High Density Plasma Chemical Vapor Deposition (HPD-CVD) chamber was developed. It was found that the clean time could be dramatically reduced by controlling on /off cycles of plasma discharges in the chamber.

Introduction
In recent years, semiconductor manufacturers have put in a great effort to improve the production worthiness and the effectiveness of the equipments. Equipment qualification procedures are quite expensive and lengthy. For Chemical Vapor Deposition (CVD) systems, the chamber cleaning process is very important not only because it affects the quality of the final product but also because it time consuming and technically costly.

In a typical cleaning procedure an inefficiently high flow rates of expensive gas are supplied into the chamber. Excess, unreacted cleaning gas is wasted, resulting in unnecessary operational costs. Also, inadequate usage of plasma sources leads to low etching rates and poor gas utilization. All these issues demand a detailed optimization of cleaning conditions to achieve maximum utilization for cleaning gas, high cleaning rates (i.e. low cleaning times) and maximum hardware lifetime. The objective of this work is to concern the main aspects of the problems involved in remote clean process achieving both superior chamber cleaning performance and improved environmental friendliness.

Up-to-date HDP-CVD chambers have a capability to ignite several plasma discharges in a turned on / turned off regime during the cleaning process. In order to minimize the damage to the chamber components caused by plasma, the use of remote plasma source was proposed. The method has clear benefits compared to in situ cleaning: due to the high efficiency of the microwave/RF excitation, the NF_3 gas utilization efficiency can be as high as 99% in standard operating conditions [1]. This ensures an extremely efficient source of fluorine, while virtually eliminating global warming emissions. With this “remote” technique, no plasma is sustained in the main deposition chamber and the clean of the chamber components is much “softer”, compared to an in situ plasma cleaning technology. The disadvantage of the remote cleaning technology is that atomic fluorine after being generated in remote plasma source has to be delivered to the main chamber trough a transport tube. The recombination of the F atoms in the transport tube decreases the effectiveness of these applications [2-4]. The recombination is affected by various factors such as wall material, pressure, flow rate, residence time, etc. In order to overcome this problem, in situ plasma is used to recover F-atoms that recombine in transport tube. While the usage of in-situ plasma allow to recover F-atoms lost in the transport tube and thus increase efficiency of the remote plasma clean technology it also leads to damage of chamber components. Thus cleaning process should be optimized to reduce cleaning time, increase F-atoms utilization and reduce damage to the chamber. In this article the possibilities of optimization of in situ cleaning process was studied using Fluent CFD commercial software.

Description of HDP-CVD Chamber:
The entire model of HDP-CVD was build using Fluent CFD commercial software with additional compiled user-defined functions for plasma chemistry modeling.
The CVD chamber considered in this study (Figure 1) is roughly cylindrical with diameter of 50 cm and the height of 20 cm. The diameter of the substrate is 35 cm while the diameter of the wafer is 30 cm. The gas enters the chamber with the temperature of 300 K through 72 nozzles (ID = 0.057 cm) and has the following

proportion: NF_3/Ar = 1/2, where NF_3 flow rate can vary from 0.7 slm (standard liter per minute) to 1.5 slm and Ar flow rate can vary from 0.35 slm to 0.7 slm. The system operating pressure is constant and equals to 2 Torr. The walls of the reactor, wafer region and the substrate are covered with the silicon (Si) deposits with the film thickness of up to 0.6 mkm (highest thickness of the deposits is on top of the chamber). There are two types of radio frequency (RF) discharges that could be ignited inside of the system: inductively coupled plasma (ICP) and capacitively coupled plasma (CCP). The first ICP discharge can be ignited at the top of the reactor from the flat antenna located on top of the chamber. The flat antenna generates a plasma power up to 5 kW with the frequency 2 MHz. The second ICP is toroidal-like discharge generated by the RF coils surrounding the chamber wall. The second ICP can also generate a plasma power up to 5 kW and frequency 2 MHz. The CCP discharge could be ignited at the region close to the substrate and the outlet zone of the chamber. This discharge operates at the frequency of 13.65 MHz and can generate a power up to 10 kW. For more details see [5].

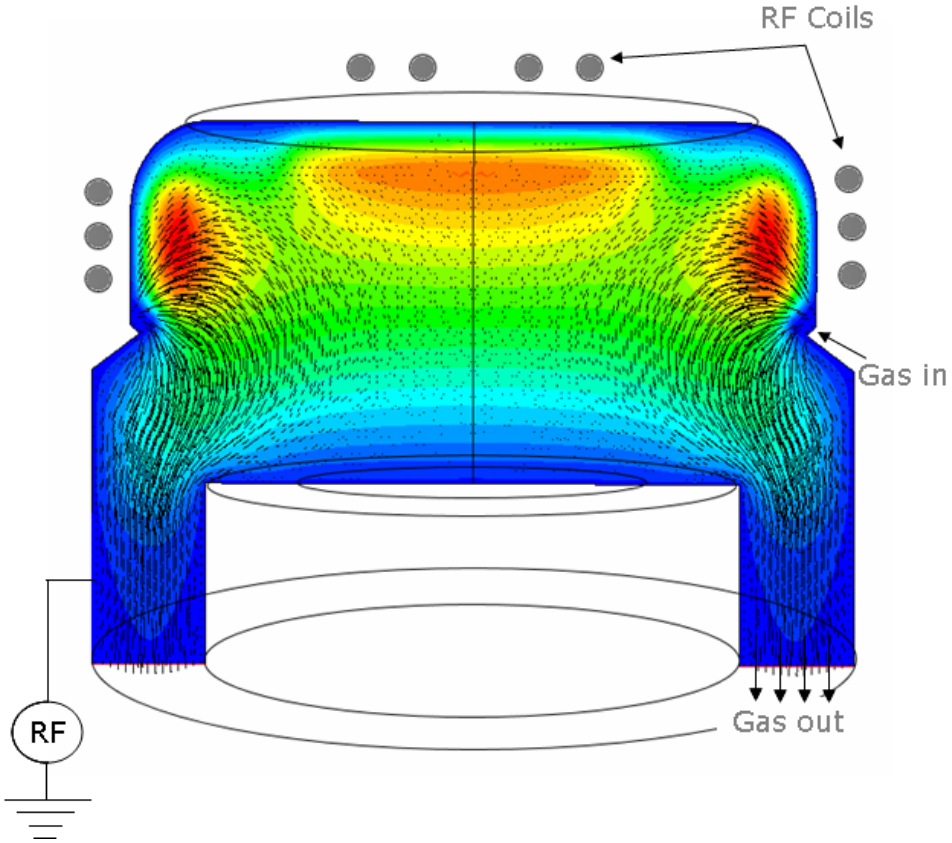

Figure 1: HDP-CVD chamber, with two ICP and one CCP discharge. Velocity vectors and temperature distribution are shown in case when all discharges are operational.

In Fluent CFD program, 2D steady-state laminar flow model was built and compiled together with the plasma-chemistry model. The analytically estimated energies and plasma volumes were implemented into CFD model as the source terms. ICP and CCP plasmas were represented in terms of heat sources and corresponding plasma-chemical reactions. Four global reactions describing overall plasma-chemical and etching process were selected and used in this model:

Reaction of electron-impact dissociation [6]:

$$e + F_2 \rightarrow F + F + e\,, \quad k_d = 1.18 \cdot 10^{-14} \exp\left(-\frac{6.88}{T_e} + \frac{1.11}{T_e^{\,2}} \right), \quad m^3/\sec \tag{1}$$

Reaction of thermal dissociation: [7]

$$F_2 \rightarrow F + F \quad (T > 1000K), \quad k = 7.52 \cdot 10^{-12} (cm^3/s) \cdot e^{-\frac{28.42(kcal/mole)}{RT}} \tag{2}$$

Reaction of volume recombination: [7].

$$F + F + M \rightarrow F_2 + M\ ,\ k = 2.76\times10^{-34}\ \mathrm{cm^6/s} \tag{3}$$

Surface etching reaction [8]:

$$Si + 4F \rightarrow SiF_4\ ,\ R = 2.91\cdot10^{-12}\cdot n_F\cdot T^{\frac{1}{2}}\exp\left(-\frac{0.108}{kT}\right),\quad \text{Å}/\min \tag{4}$$

Side Inductively Coupled Plasma: The Figure 2 (left) shows the contours of etch rates (4) in the side ICP discharge (main ICP discharge). In this regime the maximum etch rates are at the top of the chamber. The etch rates at the outlet walls are almost zero because of the shortage of reactive gas. Because of the high temperature in ICP discharge zone the volume recombination reaction rate of fluorine is very low having no effect on plasma volume kinetics and etching. The intermediate species formed with nitrogen atoms such as NF, NF_2 are very unstable and quickly decompose in a high temperature environment. The atomic fluorine mainly participates in the formation of SiF_4 molecules but still some amount of it recombines in the gas phase producing F_2 molecules. The main cleaning products outgoing from the system are F_2, N_2, Ar and SiF_4. The dilution gas such as argon (Ar) or helium (He) is always added to the plasma systems. The simulation results show that the highest etch rates comes with the minimum of dilution gas (Ar). On the other hand, the power consumption will increase dramatically without the presence of Ar. It was shown in [5] that for the reasonable result the ratio of etching gas (NF_3) and dilutant (Ar) should be 1/2.

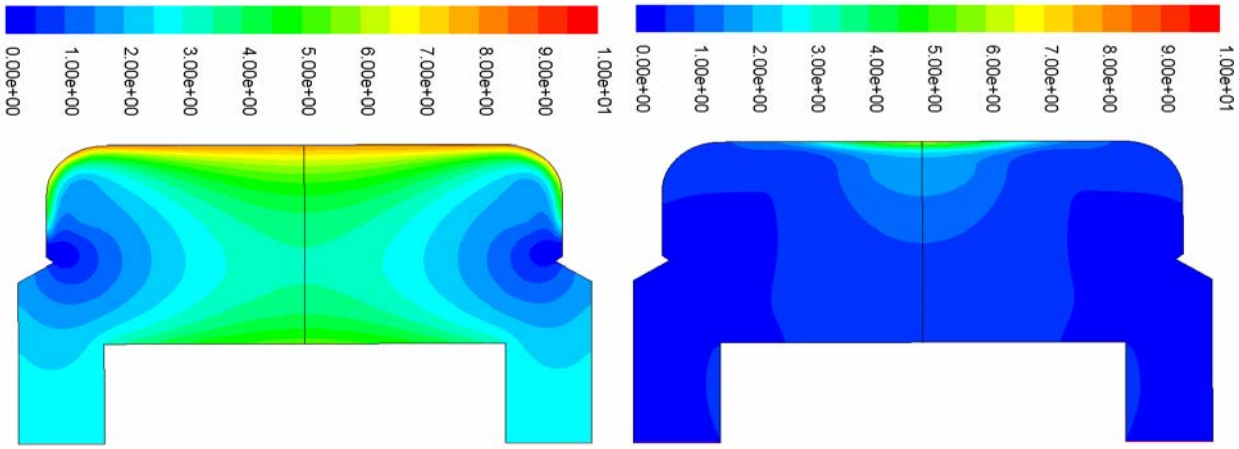

Figure 2: Contours of etch rates, kA/min. Only the side ICP is on (left). Only the upper ICP is on (right)

Upper Inductively Coupled Plasma. The abilities of secondary (upper) inductively coupled plasma are also explored in this study. The flow rates for the inlet gases are the same as is used for side ICP discharge. The corresponding contours of etch rates are shown in Figure 2 (right). As seen from the figure the upper ICP discharge is very local. The fluorine atoms produced in discharge do not propagate further through the system resulting in extremely low etching rates and overall cleaning efficiency. The low values of the flow velocity in the middle of the chamber result in discharge localization and low etch rates.

Side & Upper Inductively Coupled Plasmas. The results obtained from single side and upper ICP discharges show that the upper ICP can be used to increase the etch rates in the upper zones only (Figure 4). For this reason the simulation with both side and upper ICPs was performed. With both operational ICPs the etch time of upper chamber region could be essentially decreased. Although the upper ICP helps to decrease the etch time in upper region it has no effect on etch rates of lower zones.

Capacitively Coupled Plasma. The capacitively coupled plasma discharge is considered as low density (n_e = 10^8-10^9 $\mathrm{cm^{-3}}$) and high frequency (f = 13.56 MHz) discharge, used as a secondary discharge to increase etch rates in the lower zones of the chamber. The discharge is strongly non-equilibrium. The temperature of the gas in the discharge reaches only 600 K which means that thermal dissociation reaction of molecular fluorine will not

occur in this type of plasma. However, the fluorine recombination reaction is important here and affects the etching process. Due to strong influence of volume recombination reaction the optimal value for the flow rate should be investigated. For example, if we try to decrease the flow rate, the gas flows through the discharge slowly giving the time for proper dissociation, but once it passed the discharge zone it is also given a time for a proper volume recombination. If we try to increase the flow rate, the gas flows through the discharge quickly not having a time for proper dissociation, but once it passed the discharge zone it is also not given a time for proper volume recombination. In this situation there is an optimal solution for the gas flow rate and this solution is the maximum of some function depending on the flow rate or residence time. This function we are looking for is representation of the etch rates along the flow path. The highest value of the etch rate would give the most optimal value for the gas flow rate. The CFD modeling provides us with F-atoms concentration along the path line. The integral of F-atoms concentration basically represents the average value of the etch rate. The Figure 3 shows the integral of F-atoms over the flow path (etch rates) as a function of residence time (flow rates). The wide spectrum of flow rates was considered. The highest value of the residence time represents the lowest value of the flow rate and vise versa. The obtained function has the maximum value of the etch rate at the residence time of 5 sec. For the residence time of 5 sec the estimated total flow rate is 0.7 slm.

Figure **5** shows the contours of etch rates for capacitively coupled plasma discharge. Because CCP discharge is located near the outlet it affects only the lower zones of the chamber. Accordingly, the etch rates at the upper zones are very low while the etch rates at the lower zones have relatively high values.

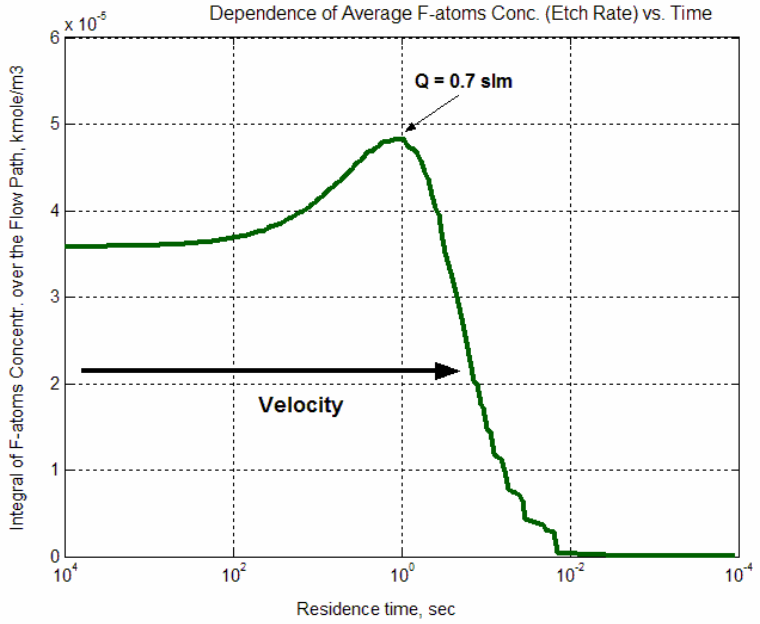

Figure 3: The dependence of average F-atoms concentration vs. residence time.

The Optimal Cleaning Regime: The control and manipulation of all considered discharges will give a reasonably optimal solution in overall cleaning time. It was found that for the system described above two stage cleaning procedure is the optimal solution. In a first time step which lasts 7 sec both side and upper inductively coupled discharges are operational. After that both inductive coupled discharges are turned off and the capacitively coupled discharge is turned on for additional 30 sec. Thus, the overall cleaning time of this process is about 40 sec. In the scope of the proposed method this can be the minimum time which could be achieved in remote cleaning technology with supported by *in situ* plasma.

Nowadays using NF_3-based remote cleaning technology without supported by *in situ* plasma the duration of cleaning time of HDP-CVD reactor reaches 2 min [9]. The multi-step plasma cleaning technology could save as much as 80 sec for each cleaning cycle. The cleaning time can be reduced further by igniting all three discharges

simultaneously, however, in this case due to the high etch rates in the upper reactor zones they will be cleaned off faster than the lower zones. Once the upper zones are cleaned the ICP discharges will continue to produce an excessive amount of F-atoms causing an overetching of upper zones resulting in equipment corrosion. Also igniting all three discharges simultaneously will significantly lower fluorine density in CCP discharge, since most of the fluorine will be dissociated in ICP discharges and F-atoms will be spent in upper zones [5].

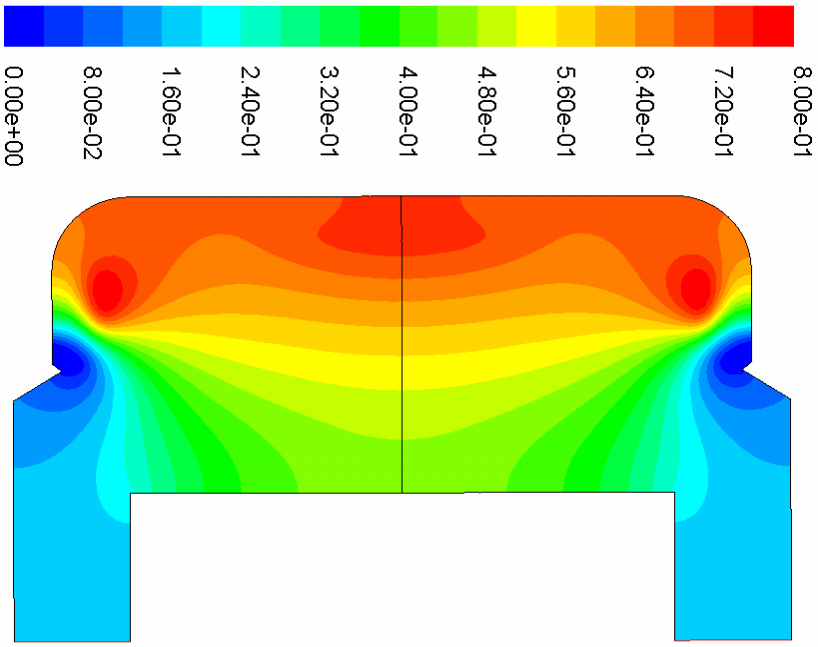

Figure 4: Contours of mole fraction of F atoms. Side and Upper ICPs.

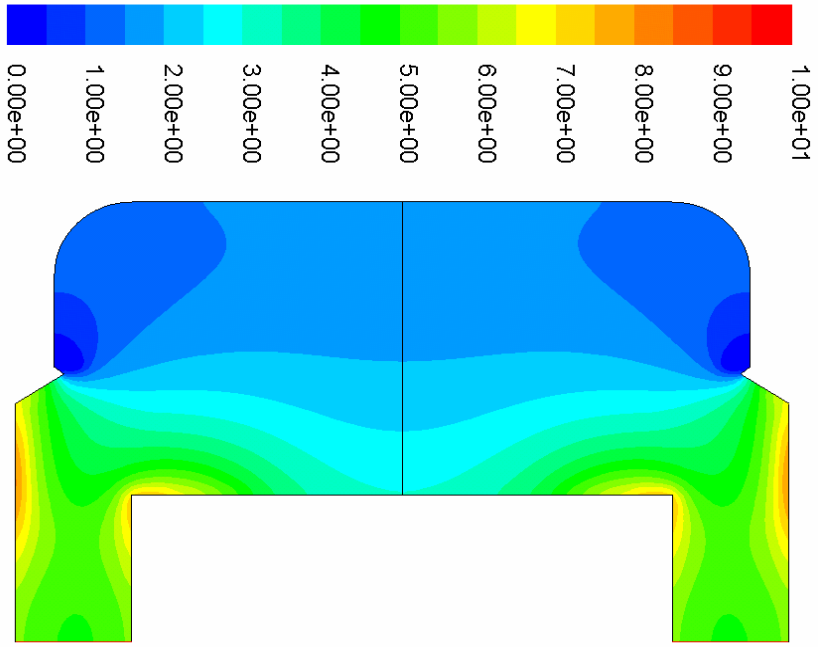

Figure 5: Contours of etch rate, kA/min. CCP discharge only.

In different HDP-CVD the optimal cleaning procedure can be different from the one proposed here, but it is clear that using multi-stage cleaning procedures instead of single strep procedures can dramatically lower cleaning time, reduce power consumption and significantly improve fluorine utilization.

References:

1. S. Raoux, T. Tanaka, M. Bhan, H. Ponnekanti, M. Seamons, T. Deacon, L-.Q. Xia, F. Pham, D. Silvetti, D. Cheung, K. Fairbairn, A. Jonhson, R. Pierce, J. Langan, "Remote microwave plasma source for cleaning CVD chambers: Technology to reduce global warming gas emissions". J. Vac. Sci. Technol. B 17, 477 (1999)
2. Gelb, A.; Kim, Shoon K. "Theory of atomic recombination on surfaces". Journal of Chemical Physics (1971), 55(10), 4935-9
3. Stueber, G. J.; Clarke, S. A.; Bernstein, E. R.; Raoux, S.; Porshnev, P.; Tanaka, T. "Production of Fluorine-Containing Molecular Species in Plasma-Generated Atomic F Flows". Journal of Physical Chemistry A (2003), 107(39), 7775-7782
4. Kastenmeier, B. E. E.; Matsuo, P. J.; Oehrlein, G. S.; Langan, J. G. "Remote plasma etching of silicon nitride and silicon dioxide using NF3/O2 gas mixtures". Journal of Vacuum Science & Technology, A: Vacuum, Surfaces, and Films (1998), 16(4), 2047-2056
5. K. Iskenderova, "Cleaning Process in High Density Plasma Chemical Vapor Deposition Reactor", Ph.D. Thesis, Drexel University (2003).
6. Ultee, C. J.. "The homogeneous recombination rate constant of fluorine atoms at room temperature". Chemical Physics Letters (1977), 46(2), 366-7
7. NIST chemical kinetic database, available online at: http://kinetics.nist.gov/
8. Donnelly, Vincent M.; Flamm, Daniel L.. "Studies of chemiluminescence accompanying fluorine atom etching of silicon". Journal of Applied Physics (1980), 51(10), 5273-6
9. Maria A Lester, Semiconductor International, Newton, Vol. 24, 44, Oct 2001b

Stability of the Atmospheric Pressure Dielectric Barrier Glow Discharges

A. Chirokov[1], A. Gutsol[1], A. Fridman[1], K. Sieber[2], J. Grace[2], K. S. Robinson[2]

[1]Department of Mechanical Engineering, Drexel University, Philadelphia, USA
[2]Eastman Kodak Company, Rochester, USA

Abstract:
Dielectric barrier discharges can exhibit two major discharge modes: filamentary mode and homogeneous or glow mode. Since stability of glow mode is very sensitive to gas composition, geometry, etc., most industrial DBD applications utilize filamentary mode despite the fast that glow discharge mode has obvious advantages over the filamentary one. Previously reported explanations of stability of glow DBD mode were inconsistent with experimental evidence. This article is an attempt to provide consistent explanation of glow mode stability.

Introduction
The dielectric barrier discharges (DBDs) are usually non-uniform and consist of many local microdischarges. Physics of these discharges is very sophisticated and is based on the initial avalanche-to-streamer transition that is followed by the formation of microdischarges and their arrangement in the specific pattern [1].
It was shown recently that dielectric barrier discharges can exhibit two major discharge modes: filamentary mode and homogeneous or glow mode [2]. The filamentary mode was a topic for active investigations in the past several years. A lot of experimental and theoretical work has been done in this area. Most industrial DBD applications utilize filamentary mode. However, for a homogeneous treatment of surfaces, or for the deposition of thin films, the glow discharge mode has obvious advantages over the filamentary one [3]. Unfortunately the glow mode is very unstable and prone to spontaneous transition to more stable filamentary mode.
Dielectric barrier discharges glow mode or atmospheric pressure glow discharges (APG) [4-6] with the average power densities comparable to those of filamentary discharges will be of enormous interest for applications if a reliable control over it could be achieved. Several approaches to generating stable APG were developed using helium as dilution gas and using special electrode structures [7]. Since usually use of helium is not practical due to its cost, alternative techniques of stabilizing APG are being actively researched. It is especially challenging to stabilize APG in electronegative gasses such as air. It was found in [8] that if concentration of oxygen in nitrogen discharge exceeds 0.1% the discharge can only operate in filamentary mode. Many APG stabilization criterion such as required preionization [9] and ion-trapping mechanism [10] were proposed but were inconsistent with experiment results [11, 12]. In this article we propose new explanation of the glow mode stability limitations based on the fluctuations of the local current densities.

Townsend Nature of APG:
Since streamer strike is immediately followed by formation of microdischarge, APG discharge operates when applied electric field exceeds Townsend criterion but is lower than Meek criterion [13] for the formation of streamers. The fact that in APG electric field must be below Meek and above Townsend criterion is consistent with experimental results [12]. Townsend breakdown criterion for the case of non-electronegative gas is well known and given by equation $(\exp(\int_0^d \alpha \cdot dx) - 1) \cdot \gamma > 1$, where γ is the coefficient of secondary electron emission (also known as the third Townsend coefficient) and α is ionization coefficient (also known as the first Townsend coefficient). In an electronegative gas the Townsend breakdown criterion becomes

$$\frac{\alpha}{(\alpha - \beta)} (e^{(\alpha-\beta)\cdot d} - 1) \cdot \gamma > 1 \qquad (1)$$

where β is an attachment coefficient (also known as the second Townsend coefficient). Most of APGs operate in the range of current densities of dark Townsend discharge (on the level of ~1 mA/cm^2), so electric field is not significantly disturbed by the space charge and is mostly affected by the charges deposited on the dielectric

surfaces. Deposited surface charge produces electric field which is opposite to the applied electric field. When voltage is higher then necessary for Townsend breakdown, electric current due to electron avalanches will grow exponentially until accumulation of charges on the dielectric surfaces collapses local electric field to the value below breakdown. So, there are similarities between DC and APG discharges and the major difference of APG from classical dark Townsend discharge [14] is that surface charges provide quenching mechanism for the discharge current.

Since positive ions are much slower than electrons, in addition to surface charge there is a positive space charge that form weak cathode layer and slightly increases electric field near the cathode. We do not consider space charge due to electrons since at typical APG operating frequencies 1-20 kHz electrons have enough time to leave the gap. Space charge due to electrons is important in discharge such as Atmospheric Pressure Plasma Jet (APPJ) since they operate at much higher frequencies [15]. Cathode layer formation leads to redistribution of the electric field and thus Townsend criterion can be satisfied for lower average electric field [14]. For more details about cathode layer formation in APG see [8].

The stability of APG can be considered as a balance between two effects: surface charges provide stabilization mechanism for the current density by collapsing local electric field while space charge provides destabilization by supporting discharge at lower average electric field. In order to simulate these effects detailed models based on drift-diffusion equations were developed [4]. Although these models can predict basic properties of APG discharge they fail to predict transition to filamentary mode. In these models discharge always appears to be stable, contradictory to experimental evidence. Thus there are physical effects that are not included in the model. We believe that this missing effect that influences the stability of glow mode is fluctuations of local current density. These fluctuations are the primary focus of this study. Also using a simple model the effect of these fluctuations on cathode layer formation and stability of APG was evaluated.

Effect of Electronegativity on Current Density:

Average number of electrons in an avalanche (avalanche "size") is $N = \exp((\alpha - \beta)d)$, and current density in given discharge location is proportional to the avalanche size. Multiplication of electrons in an avalanche and secondary electron emission from dielectric surface are statistical processes. Thus number of electrons in avalanche deviates from the average, causing fluctuation of the discharge current density (Figure 1). In order to estimate the standard deviation of the avalanche size from the average values we developed Monte-Carlo model similar to one described in [16]. In this model the electric field was assumed to be constant because the distortion of the electric field by the avalanche space charge becomes important at $(\alpha - \beta)d \approx 20$, and in the simulation $(\alpha - \beta)d = 5$. We choose to specify the value of $(\alpha - \beta)d$ instead of electric field in order not to be restricted by the particular gas mixture composition. The average size of avalanche in simulation is $\exp((\alpha - \beta)d) = \exp(5) \approx 148$ and Townsend criterion becomes $\gamma > 6.8 \cdot 10^{-3}$. Simulation results presented in Figure 1 and 2 clearly show the effect of attachment on the avalanche size distribution. An average size of avalanche is the same in both cases (with and without attachment) but standard deviation is much higher in the case with attachment, though it is very high (96%) even in the case without attachment. Also significant fraction ($\beta / \alpha = 3/8$) of the initial electrons in electronegative gas don't produce avalanches (Figure 1), because these electrons were attached on early stages of avalanche development.

Since current density at given discharge position is proportional to the total number of electrons in all avalanches at that position, fluctuations of current will be reversely proportional to the square root of number of avalanches and directly proportional to the standard deviation of the avalanche size:

$$\delta j \sim \frac{\sigma_{av}}{\sqrt{N_{av}}} \qquad (2)$$

where σ_{av} standard deviation of the avalanche size distribution and N_{av} is the total number of avalanches at given position.

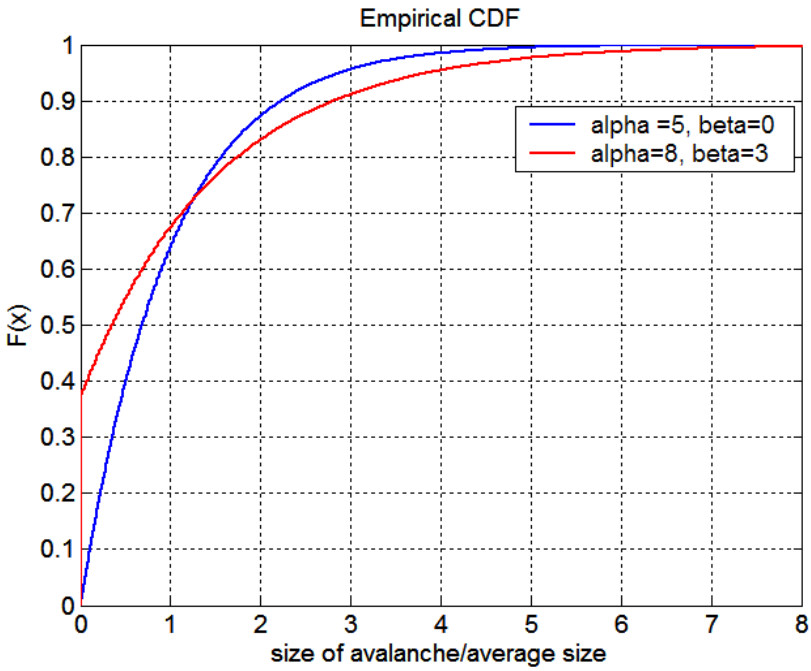

Figure 1: Empirical cumulative distribution function (CDF) of the avalanche size computed using Monte-Carlo simulation. Blue curve represent case without attachment, average avalanche size is $\bar{N} = 0.97 \cdot N_t$ while standard deviation is $s = 0.96 \cdot N_t$ where $N_t = \exp(5)$. Red curve represent the case with non dimensional attachment coefficient $\beta \cdot d = 3$, average size of the avalanche is the $\bar{N} = 0.96 \cdot N_t$ while standard deviation is $s = 1.41 \cdot N_t$.

Thus, for high current density these fluctuations become unimportant and this explains why these fluctuations are not usually considered for high current discharges. The stability limitations of high current discharges are usually related to thermal instability rather than to fluctuations of local current density and this is beyond the score of this study. In glow mode of dielectric barrier discharge typical peak current density is on the level of ~1 mA/cm^2 and can be as low as ~0.01 mA/cm^2 [4, 12].

Simple estimation shows that in case when $(\alpha - \beta)d = 5$, avalanche radius is about 0.1 mm in gap distance of 1 mm and electron drift velocity is 10^7 cm/sec, about 130 avalanches at a time needed to give electric current density of 1 mA/cm^2 and just one (1.3 on average) to give ~0.01 mA/cm^2. If there is only one avalanche on average at the same time at given location then fluctuations of current density will be proportional to fluctuations of the avalanche size at this location. Thus in this case standard deviation of local current density fluctuations will be equal to the average current density. In case when there are 100 avalanches at the same time standard deviation of the current density fluctuations will be according to (2) 10 times less than average current density. Accordingly local fluctuations of current density will be about 88% percent for current the density 0.01 mA/cm^2 in the conditions described above.

In non-electronegative gasses standard deviation of avalanche size is equal to the average avalanche size while in electronegative gasses standard deviation can be much higher (Figure 2). For example, if standard deviation is twice the average (Figure 2), number of avalanches in the same location has to be four time higher to have the same level of local current density fluctuations. Thus even small addition of electronegative gas to the APG can destabilize the discharge, by increasing local current density fluctuations and thus decreasing uniformity of discharge. It is clear that fluctuations of local current density in typical APG conditions can be very large and can not be neglected. Critical value of local current density fluctuations that causes filamentation of APG can not be specified based on this analysis alone because it obviously depends on the particular configuration of the discharge as well as parameters of external circuit.

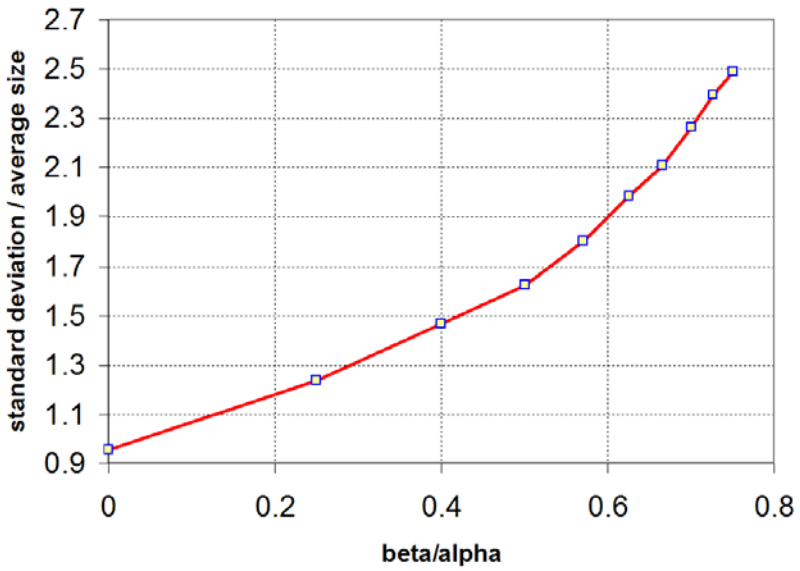

Figure 2: Standard deviation of the avalanche size distribution as a function of β/α parameter. Simulation was performed for $(\alpha-\beta)\cdot d=5$, parameter $\beta\cdot d$ was varied from 0 to 9 while parameter $\alpha\cdot d$ was varied accordingly. We found that variation of $(\alpha-\beta)\cdot d$ do not introduce any visible changes to this curve in the range from 3 to 5.

Effect of Current Density Fluctuation on Cathode Layer:

Although fluctuations of local current density disturb uniformity of the discharge they do not necessarily lead to the filamentation of the discharge, because current in the discharge gap can be stabilized by surface charges. The mechanism is the following: If current density at given location rises above the average, the amount of deposited surface charge increases. Since the surface charge decreases local electric field, thus it also decreases the non-dimensional parameter $(\alpha-\beta)d$. This lead to the decrease of the average size of electron avalanches and as a result to decrease of local current density, since average avalanche size exponentially depends on $(\alpha-\beta)d$. Stabilizing effect of surface charge can be canceled out by the formation of the cathode layer.

To illustrate the effect of current density fluctuations on the cathode layer, 1D steady–state model was developed. Space charge behavior can be understood with relatively simple model that consists of continuity equations for electrons, negative and positive ions (3) coupled with Poisson equation. Model does not take into account accumulation of surface charges. Flux of positive ions at the anode as well as flux of negative ions at the cathode was set to zero. Flux of the electrons from the cathode was equal to flux of positive ions to the cathode multiplied by the secondary emission coefficient. Simulation performed using MatLab boundary value ODE solver.

$$\begin{aligned}\frac{dj_e}{dx}&=(\alpha-\beta)\cdot j_e\\ \frac{dj_p}{dx}&=-\alpha\cdot j_e\\ \frac{dj_n}{dx}&=\beta\cdot j_e\end{aligned}\qquad(3)$$

Expression of ionization coefficient for helium as a function of electric field was taken from [12]; attachment coefficient was assumed to be independent on electric field and was specified as input parameter. Pressure in simulation was set to 1 atm, discharge gap was 1 cm and secondary emission coefficient was set to 0.01. Current density was specified as an input parameter while voltage drop in the gap was calculated during simulation for each value of current density.

Fluctuations of local current density were modeled by slightly changing input current density, and effect of fluctuation on voltage drop in the gap was recorded. Figure 3 shows how derivative of voltage with respect to current changes with different values of the attachment coefficient and different current densities. Expected voltage derivative is always negative, which means that lower voltage is needed to support discharge at higher current (falling voltage-current characteristic is typical for transition from dark to subnormal discharge). At low current densities, voltage derivative is much higher for electronegative gasses. This means that the same fluctuations of current density in case of electronegative gas produce higher 'overvoltage'. Term 'overvoltage' used here to describe the voltage that is higher than needed to satisfy Townsend criterion. Higher overvoltage in electronegative gas can be attributed to the much higher ionic space charge than in the case of electropositive gases. Comparing the effect of current density fluctuations on the cathode layer and the effect of surface charge accumulation the following relation can be obtained:

$$\Psi = j\frac{L_d}{\varepsilon\cdot\varepsilon_0} + U'\cdot\frac{\delta j}{dt} \qquad (4)$$

Here δj is current density fluctuation, U' is the derivative of voltage-current characteristics, L_d - total dielectric thickness, and value of Ψ described the balance between two effects mentioned above. For APG stability Ψ value should be higher than a certain "critical value" which depends on particular discharge configuration. It is clear from (4) that the higher value of current fluctuations and the slope of voltage current characteristics the harder it is to stabilize the discharge.

Concluding Remarks:

It was shown that fluctuations of local current density are important for understanding of APG discharge stability limitations especially in electronegative gasses and can not be neglected. These fluctuations strongly depend on the value of non-dimensional ratio of attachment over ionization coefficient. Combination of small average size and high density of avalanches results in less fluctuating current density and thus a favorable condition for obtaining APG. High density of avalanches means high number of initial electrons, so this condition is more general version of the "required preionization" condition [9, 16]. On the other hand, large size and low density of avalanches produces significant current density fluctuations and therefore such conditions should be avoided in order to obtain stable APG. Also it was found that in electronegative gases voltage-current characteristics is much more sensitive to current fluctuations than in non-electronegative gases. Our consideration shows that current fluctuations can be also a primary reason of instability of low current DC discharges.

It is important to emphasize that fluctuations are local with characteristic length scale equal to diameter of avalanche. So, fluctuations of total current in APG depend on the electrode area and can be negligibly small since usually this area is much larger than typical avalanche crossection (10^{-4} cm^2).

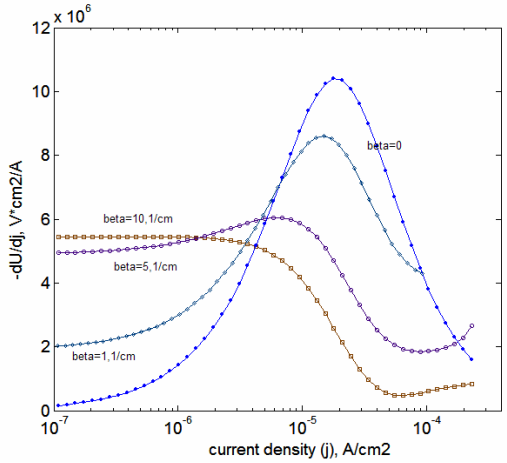

Figure 3: The plot of voltage derivative with respect to the current density as the function of current density, at different values of attachment coefficient.

References:

1. Chirokov, A.; Gutsol, A.; Fridman, A.; Sieber, K. D.; Grace, J. M.; Robinson, K. S. "Analysis of two-dimensional microdischarge distribution in dielectric-barrier discharges". Plasma Sources Science & Technology (2004), 13(4), 623-635
2. Kanazawa, S.; Kogoma, M.; Moriwaki, T.; Okazaki, S. "Stable glow plasma at atmospheric pressure". Journal of Physics D: Applied Physics (1988), 21(5), 838-40..
3. Martin, S.; Massines, F.; Gherardi, N.; Jimenez, C. "Atmospheric pressure PECVD of silicon based coatings using a glow dielectric barrier discharge". Surface and Coatings Technology (2004), 177-178 693-698.
4. Massines, F.; Segur, P.; Gherardi, N.; Khamphan, C.; Ricard, A. "Physics and chemistry in a glow dielectric barrier discharge at atmospheric pressure: diagnostics and modeling". Surface and Coatings Technology (2003), 174-175 8-14.
5. Massines, F.; Gouda, G. "A comparison of polypropylene-surface treatment by filamentary, homogeneous and glow discharges in helium at atmospheric pressure". Journal of Physics D: Applied Physics (1998), 31(24), 3411-3420.
6. T. Montie, K. Kelly-Wintenberg, and J. Roth, "An overview of research using the one atmosphere uniform glow discharge plasma (OAUGDP) for sterilization of surfaces and materials", IEEE TRANSACTIONS ON PLASMA SCIENCE 28, 41-50 (2000).
7. S. Okazaki, M. Kogoma, M. Uehara, And Y. Kimura, Journal Of Physics D-Applied Physics 26, 889-892 (1993).
8. K V Kozlov, R Brandenburg, H-EWagner, A M Morozov and P Michel, "Investigation of the filamentary and diffuse mode of barrier discharges in N2/O2 mixtures at atmospheric pressure by cross-correlation spectroscopy" J. Phys. D: Appl. Phys. 38 (2005) 518–529.
9. Levatter, Jeffrey I.; Lin, Shao-Chi. "Necessary conditions for the homogeneous formation of pulsed avalanche discharges at high gas pressures". Journal of Applied Physics (1980), 51(1), 210-22
10. Roth J R 2001 Industrial Plasma Engineering vol 2 (Bristol:Institute of Physics Publishing)
11. Wang, X., C. Li, et al.. "Study on an atmospheric pressure glow discharge." PLASMA SOURCES SCIENCE & TECHNOLOGY 12(3): 358-361(2003).
12. J. Shin and L. Raja, "Dynamics of pulse phenomena in helium dielectric-barrier atmospheric-pressure glow discharges," JOURNAL OF APPLIED PHYSICS, vol. 94, pp. 7408-7415, 2003.
13. J. M. Meek, "A theory of Spark Discharge," PHYSICAL REVIEW, vol. 57, pp. 722-728, 1940.
14. Y. P. Razer, "Gas Discharge Physics" (1987).
15. S. Babayan, J. Jeong, V. Tu, J. Park, G. Selwyn, and R. Hicks, "Characterization of the active species in the afterglow of a nitrogen and helium atmospheric-pressure plasma", PLASMA SOURCES SCIENCE & TECHNOLOGY 7, 286-288 (1998).
16. Brenning, Nils; Axnaes, Ingvar; Nilsson, J. Olof; Eninger, Jan E. "High-pressure pulsed avalanche discharges: formulas for required pre-ionization density and rate for homogeneity". IEEE Transactions on Plasma Science (1997), 25(1), 83-88

NO_x Oxidation/Reduction from Simulated Natural Gas Combustion Exhaust Gases by Trench Type Dielectric Barrier Discharge Plasma-Catalyst System

S. Ambridge[1], N. Debacher[1,2], K. Urashima[1], J. Hoard[3] and J.S. Chang[1]
[1] *Department of Engineering Physics, McMaster University, Hamilton, Canada*
[2] *Department of Chemistry, Universidade de Química, Florianópolis, Brazil*
[3] *Ford Motor Company Research Laboratory, Dearborn, USA*

Abstract:
Although natural gas is considered a cleaner source of energy than some solid and liquid fuels, there is still significant emissions emitted as a result of combustion that must be characterized and controlled. This research focuses on the treatment of simulated natural gas (NG) combustion exhaust gas by plasma-catalytic oxidation and reduction reactions produced by a trench type non-thermal plasma (NTP) reactor followed by a catalyst. The plasma-catalyst has been observed to be effective in the removal of NO_x using simulated NG exhaust gases.

1.0 Introduction

The development of an after-treatment technology for gas turbines (GTs) is critical since the large number of GTs being used today for commercial and industrial applications is only likely to increase over the next decade. The three pollutants of greatest concern for GTs are: nitrogen oxides (NO_x), carbon monoxide (CO) and volatile organic compounds (VOCs) including unburnt hydrocarbons. Although methods for controlling NO_x are available, none work efficiently in the oxygen rich, low temperature environment created by GTs. After treatment technologies for VOCs created by GTs are also limited, given the complexity of VOCs emitted by GTs and the overall cost of many of these technologies is too high to be cost effective. One of the technologies at the forefront of research for this application in non-thermal plasma in combination with a catalyst called a plasma-catalyst system.

It has been well established that non-thermal plasma reactors can efficiently reduce the NO concentration and convert NO to NO_2 by many researchers [1,2]. In order to convert the NO and NO_2 to elemental nitrogen and thus a harmless gas, research has focused on combining non-thermal plasmas with reduction or oxidation agents such as hydrocarbon additives [1, 2], ammonia [3, 4], hydrogen peroxide [9] and/or catalysts [1, 2, 10, 12].

The specific objectives of the present non-thermal plasma-catalyst experiments are to convert NO_x to less harmful substances such as N_2, O_2 and H_2O. The system also aims to convert CO to CO_2 and convert hydrocarbons and VOCs to aldehydes in order to activate the catalyst.

2.0 Experimental Facilities

Figure 1 shows the experimental set-up for the simulated gas test, where the test set-up capable of conducting real natural gas combustion with dust removal by the dust flow separated type electrostatic precipitator [13]. However, in the present work, a simulated combustion gas was used to investigate the potential to work at low gas temperature without soot generated from combustions. In this experiment N_2-NO 1.38% was introduced into the natural gas combustion test loop, with the combustor off, through an Edwards Datametrics 6100 flow controller. The air flow rate was controlled by a rotameter and introduced to the natural gas test loop. The air flow rate was set between 0-9.5 Nm^3/hr. The flow rate of the NO was accordingly adjusted to dilute the NO in the loop to approximately 20ppm. The non-thermal plasma reactor was then set to applied voltages between 10kV and 20kV, at a frequency of 60Hz. A Greenline combustion analyzer was used for exhaust gas analysis.

The sodium zeolite-Y catalyst coated on 400 cpsi cordierite monolith reactor was placed 30cm downstream of the trench type barrier discharge reactor [1] as shown in Figure 2. The sodium zeolite-Y reactor was then heated for a period of 2 hours by wrapping the catalyst chamber (steel) in standard electrical heating tape with an output of 300°C.

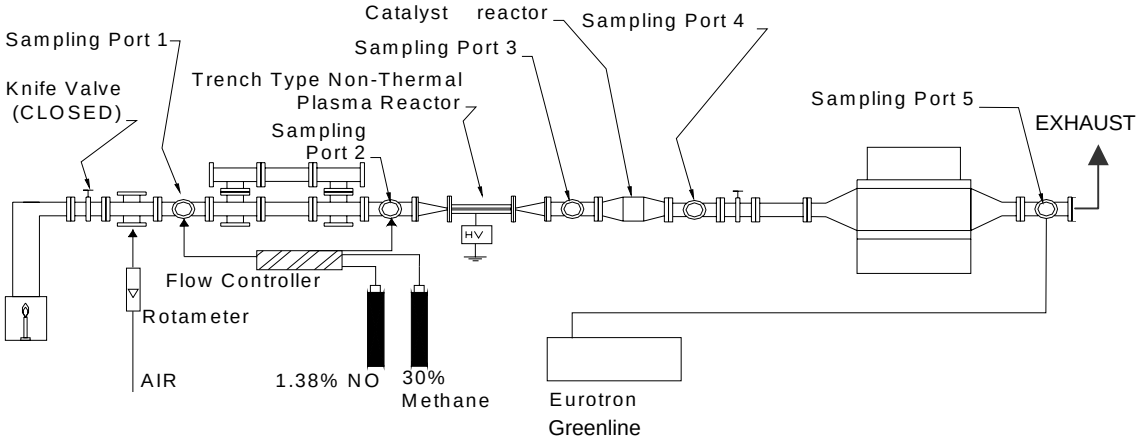

Figure 1: Schematics of Experimental Loop.

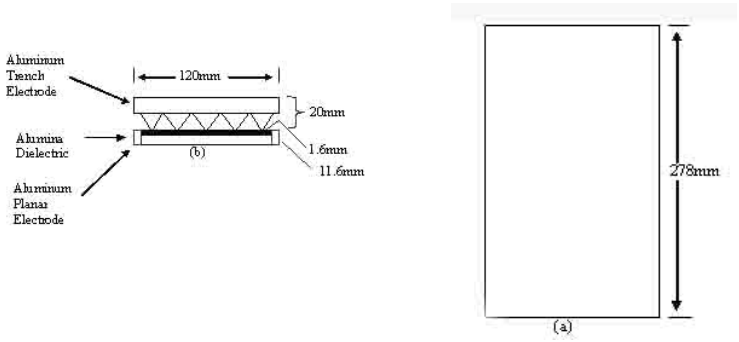

Figure 2: Trench type barrier discharge reactor (a) top view and (b) side view.

3.0 Experimental Results

3.1 NO_x removal in a N_2-O_2-NO System by Non-Thermal Plasma-Catalyst System

The NO_x removal efficiency of the trench type dielectric discharge non-thermal reactor followed by the sodium zeolite-Y catalyst is shown in Figure 3; where NO_x reduction versus the specific energy density (SED) for gas flow rates between 3.4-9.5Nm^3/hr at 23°C and 65°C, respectively is shown. Figure 3(a) shows that the NO_x removal efficiency increases with increasing SED and decreasing gas flow rates. The removal efficiency of NO_x increases with decreasing flow rates because the residence time is longer at lower flow rates. This increase in removal efficiency of NO_x occurs since there is a greater probability that the NO_x will interact with electrochemically excited nitrogen by reduction reactions, as well as further oxidation of NO_2 to N_2O, NO_3 and HNO_3 (with trace water content absorbed in the catalyst) by free radicals, [3,4] in the NTP reactor. Furthermore, the increase in residence time also increases the probability that the NO_2 formed by the NTP reactor will be absorbed in the catalyst surface and thus be removed by free radical reactions.

Figure 3(a) shows that the maximum removal efficiency of NO_x at flow rates 3.4 Nm^3/hr and 5.1 Nm^3/hr were the same at 65%, however the removal efficiency at 5.1 Nm^3/hr was achieved at a lower SED. This means that more gas was treated with the same electrical power injected into the plasma reactor, therefore the process was more effective at 5.1 Nm^3/hr than at 3.4 Nm^3/hr. By comparing Figure 3(a) to Figure 3(b) it can be observed that the NO_x conversion was greater at 23°C then at 65°C. The maximum NO_x removal at 23°C was 65%, whereas it was only 50% at 65°C. This is the opposite trend that was expected, as catalysts generally require elevated temperatures to operate effectively, however 65°C is still below minimum values for catalyst operation reported in literature. The test at 23°C may have been more effective for NO_x removal for two reasons. The cordierite monolith would have had a greater capacity to absorb at lower temperatures, thus resulting in more NO_x being absorbed at 23°C then at 65°C.

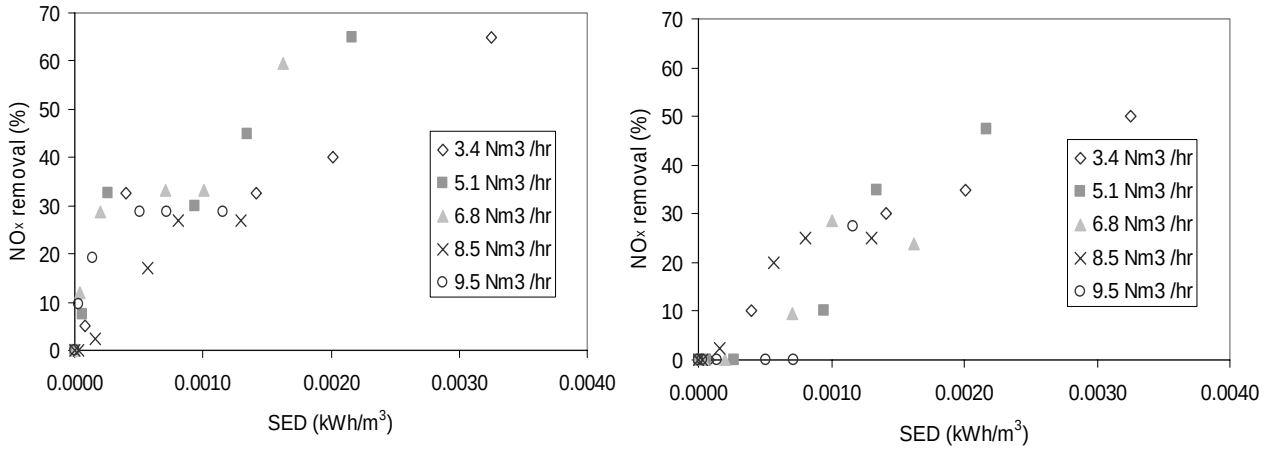

Figure 3: NO_x removal efficiency versus SED for trench-type non-thermal plasma-catalyst for gas flow rates between 3.4-9.5Nm^3/hr at (a) 23°C (left) and at (b) 65°C (right)

Figure 4 shows the energy efficiency of NO_x removal as a function of SED for various gas flow rates for gas temperatures of 23°C and 65°C, respectively. As can be observed from comparing Figures 4(a) and 4(b) the NO_x removed is greater for the test at 23°C than for 65°C at low SEDs. The maximum mass of NO_x removed at 23°C was 81g/kWh, whereas at 65°C the maximum NO_x removed was 8.5g/kWh. Again this large difference could be due to the effective mass of NO_2 and the other gas by-products absorbed on the surface of the catalyst, since absorption of gas decreases with increasing gas temperature. It can also be observed that at higher SEDs of about 0.001kWh/m^3 that the mass of NO_x removed is similar for both experiments. This trend can also be seen in Figures 3(a) and 3(b). This suggests that at higher SEDs there is not a significant difference between the NO_x removal efficiencies of the plasma-catalyst system.

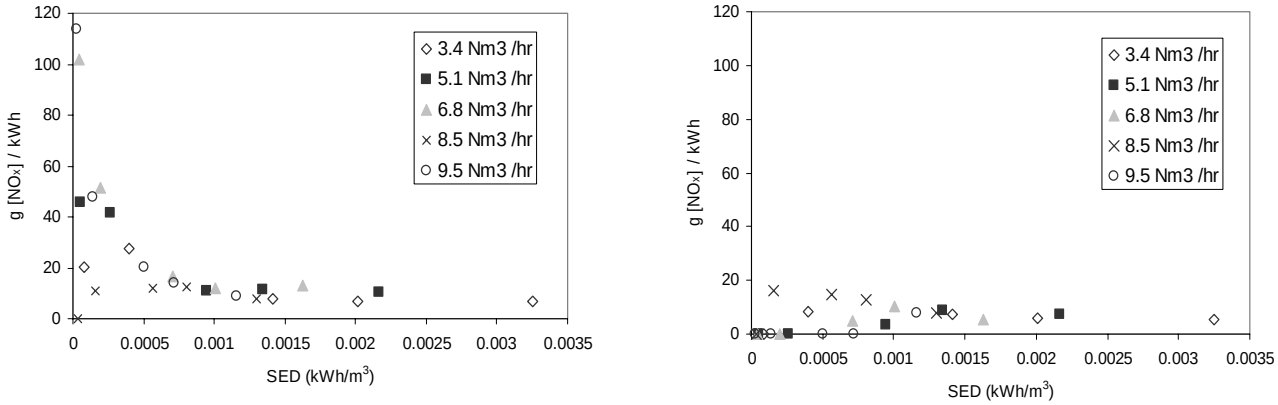

Figure 4: Energy efficiency of NO_x removal by mass versus SED for trench-type non-thermal plasma-catalyst for gas flow rates between 3.4-9.5Nm^3/hr at (a) 23°C (left) and at (b) 65°C (right)

3.2 NO_x removal in a N_2-O_2-NO-CH_4 system by Non-Thermal Plasma-Catalyst System

The NO_x removal efficiency of the plasma-catalyst system was examined during this test for various NO to CH_4 ratios at 23°C. Methane was injected into the system in order to create aldehydes to activate the catalyst [2]. The first large difference that was observed when compared to the previous test without CH_4, was the power injected into the NTP reactor. The power injected into the NTP reactor was approximately four times higher than the previous test. This was confirmed during the test and after with only air present in the NTP reactor. This change in the injected power may be due to the additional energy consumed by the CH_4 decomposition.

Figures 5(a) and 5(b) show the NO_x removal efficiency of the plasma-catalyst system for the addition of CH_4 for flow rates of 3.4 Nm^3/hr and 8.5Nm^3/hr, respectively. As can be observed from Figures 5(a) and 5(b), the NO_x removal efficiency increases with increases SED, as expected. As previously mentioned this

trend occurs both due to an increase in residence time in the plasma-catalyst system and because more power is being injected into the NTP reactor compared to the flow rate

The NO_x removal efficiencies are also lower than the previous test at 23°C without the addition of CH_4, as shown in Figure 5 ($[CH_4]/[NO]$ ratio = 0 for previous test). This result was expected as the addition of CH_4 should have allowed for the formation of aldehydes in the NTP reactor but could not activate the sodium zeolite-Y catalyst at low gas temperatures. As well, the plasma energy may be more effectively used to dissociate CH_4 then generating N* and N_2* radicals, hence NO_x removal may not be enhanced as has been observed by Ambridge et al [12].

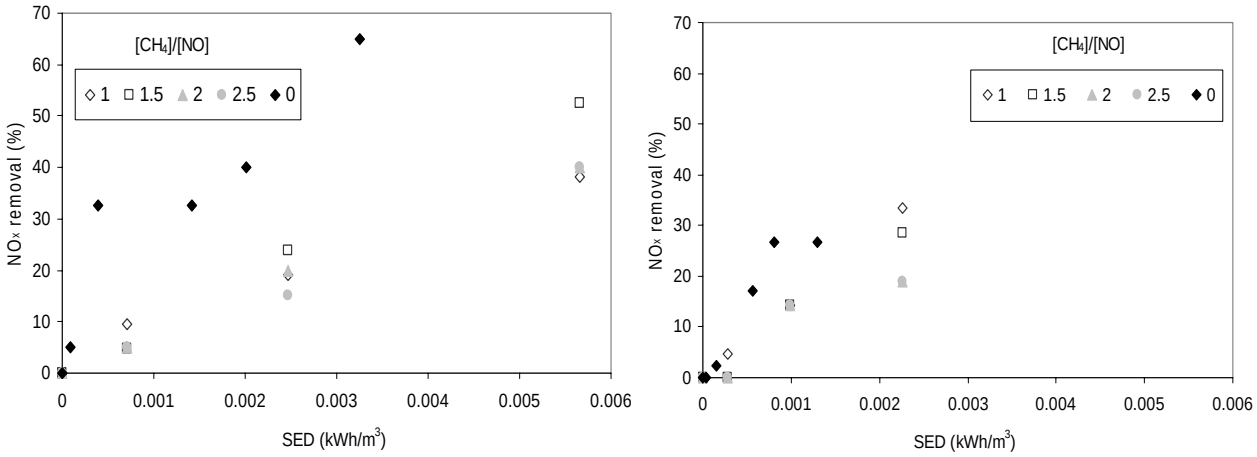

Figure 5: NO_x removal versus SED for non-thermal plasma-catalyst for gas a flow rate of (a) 3.4Nm^3/hr (left) and (b) 8.5Nm^3/hr (right) for various CH_4 to NO ratios

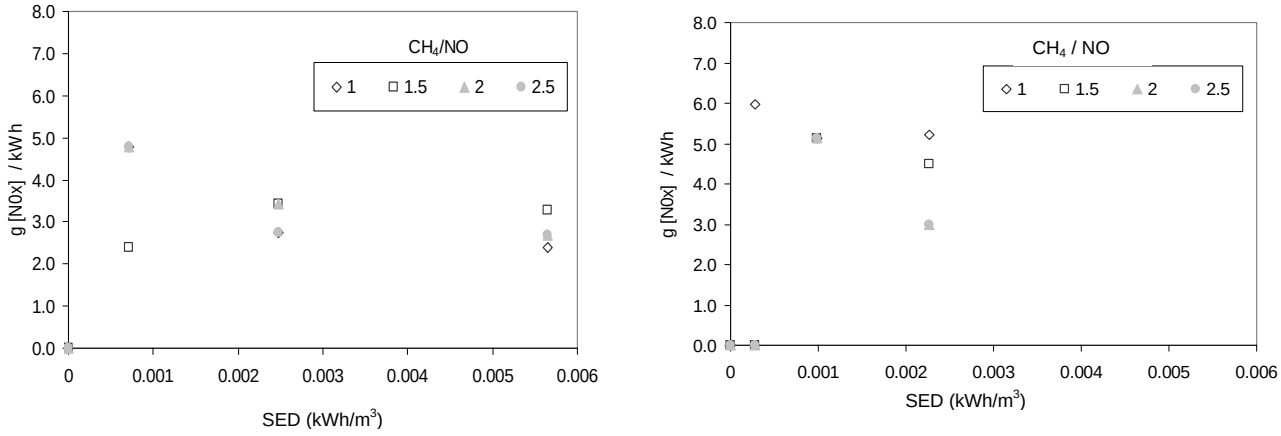

Figure 6: Energy efficiency of NO_x removal versus SED for non-thermal plasma-catalyst for gas a flow rate of 3.4Nm^3/hr (left) and 8.5Nm^3/hr (right) for various CH_4 to NO ratios

Figure 6 shows the energy efficiency of NO_x removed ($g[NO_x]/kWh$) versus the SED. The energy efficiency of NO_x removal decreases with an increasing CH_4 to NO ratio.

4.0 Conclusions

The plasma-catalyst system was observed to have a maximum NO_x removal energy efficiency of all experiments conducted was 120g/kwh at 23°C for the simulated exhaust gas without methane. The maximum NO_x removal energy efficiency observed at a gas temperature of 65°C was approximately 18 g/kwk. In the simulated exhaust gas treatment with methane, the maximum NO_x removal efficiency was observed to be 52% at 23°C with 30ppm of injected CH_4. It was observed during the test with NO and CH_4 that the removal of NO_x increased with increasing SED. It was also seen the concentration of CH_4 did not have a large impact on the NO_x removal efficiency in most cases at 23°C. At all flow rates, expect 8.5Nm^3/hr, the maximum

NOx removal occurred with a CH_4 concentration of 30ppm. The energy efficiency of NO_x removal decreases with increasing CH_4 to NO_x ratio.

Acknowledgment
Authors thank K. Yamada, M. Ara, S. Iwasaki, L. Guan, G. Ksiazek for technical assistant and D. Brocilo, D. Ewing, C.Y. Ching for valuable discussions and comments. Work supported by NSERC strategic Grant.

5.0 References

[1] K. Shimizu, T. Harano, and T. Oda, "Effect of Water Vapor and Hydrocarbons in Removing NO_x by Using Plasma and Catalyst," *IEEE Transactions on Industry Applications*, vol. **37**, no.2, pp. 464-471 (2001).

[2] J. Hoard and R. Tonkyn, "Two-Stage Plasma Catalysis for Diesel NO_x Emission Control," *Journal of Advanced Oxidation Technology*, vol. **6**, no.2, pp. 158-165 (2003).

[3] J. Y. Park, I. Tomicic, G. F. Round, and J.-S. Chang, "Simultaneous removal of NO_x and SO_2 from NO-SO_2-CO_2-N_2-O_2 gas mixtures by corona radical shower systems," *Journal of Applied Physics D: Applied Physics*, vol. **32**, pp. 1006-1011 (1999).

[4] Urashima, J.-S. Chang, and T. Ito, "Reduction of NO_x from Combustion Flue Gases by Superimposed Barrier Discharge Plasma Reactor," *IEEE Transactions on Industry Applications*, vol. **33**, no.4, pp. 897-886 (1997).

[5] M. B. Chang and S. C. Yang, "NO/NO_x Removal with C_2H_2 as Additive via Dielectric Barrier Discharges," *AIChE Journal*, vol. **47**, no.5, pp. 1126-1233 (2001).

[6] K. Takaki and T. Fujiwara, "Multipoint Barrier Discharge Process for Removal of NO_x from Diesel Engine Exhaust," *IEEE Transactions on Plasma Science*, vol. **29**, no.3, pp. 518-523 (2001).

[7] A. Mizuno, K. Shimizu, A. Chakrabarti, L. Dascalescu, and S. Furuto, "NO_x Removal Process Using Pulsed Discharge Plasma," *IEEE Transactions on Industry Applications*, vol. **31**, no.5, pp. 957-963 (1995).

[8] R. Dorai, K. Hassouni, and M. Kushner, "Interaction between soot particles and NO_x during dielectric barrier discharge plasma remediation of simulated diesel exhaust," *Journal of Applied Physics D: Applied Physics*, vol. **88**, no.10, pp. 6060-6071 (2000).

[9] H. H. Kim, K. Tsunoda, S. Katsura, and A. Mizuno, "A Novel Plasma Reactor for NO_x Control Using Photocatalyst and Hydrogen Peroxide Injection," *IEEE Transactions on Industry Applications*, vol. **35**, no.6, pp. 1306-1310 (1999).

[10] J. H. Kwak, J. Szanyi, and C. Peden, "Nonthermal plasma-assisted catalytic NO_x reduction over Ba-Y, FAU: the effect of catalyst preparation," *Journal of Catalysis*, vol. **220**, pp. 291-298 (2003).

[11] J.-S. Chang, P. Looy, M. Arquilla, I. Kamiya, and R. Sinko, "Ozone and the Other Gaseous By-products Generated from Dry Air by Trench Type Barrier Discharge Plasma Reactor," *Journal of Advanced Oxidation Technology*, vol. **2**, no.2, pp. 274-277 (1997).

[12] S. Ambridge, Y. Uchida, K. Urashima, D. Ewing, and J.-S. Chang, "Oxidation of NO_x and Hydrocarbon Emissions from Diesel Engines," Abstract Book of 53rd Canadaian Chemical Engineering Conference, Hamilton, Canada (2003).

[13] G.D. Harvel, J.S. Chang, L. Guan, M. Nock, and D. Brocilo", Dust Flow Separator Type Electrostatic Precipitator", Proc. 4th French Electrostatic Soc. Meeting, pp. 148-154 (2004).

Slow Oxidation of Alkanes in Stoichiometric and Lean Mixtures with Oxygen and Air under Nanosecond Discharge Action

N.B.Anikin[1] , S.M. Starikovskaia[1] , A.Yu. Starikovskii[1]

[1] *Physics of Nonequilibrium Systems Laboratory, Moscow Institute of Physics and Technology, Institutskii lane,9, Dolgoprudny 141700 Russia*

Abstract

The comprehensive experimental investigation of processes of alkanes slow oxidation in mixtures with oxygen and air under nanosecond uniform discharge has been performed. We have investigated kinetics of alkanes oxidation from methane to decane in stoichiometric and some lean mixtures with oxygen and air at room temperature. The discharge current, electric field and input energy have been measured with nanosecond time resolution. Time of full oxidation of alkanes was determined.

1 Experiment

The scheme of experimental setup is represented in the figure 1. The electric pulses yielded to the discharge cell through 50-Ohm RF cable with 20 m length. The discharge cell consisted of thin-wall quartz discharge tube with 5 cm inner and 4.7 cm outer diameters, metallic screen, high and low-voltage electrodes. The screen was made of eight brass rods with 12 mm diameters uniformly installed on the 7 cm distance from the cell axis. The high voltage electrode had conical form with 60^{O} opening angle. The low voltage one was a ring connected to the screen directly. The distance between the edges of the electrodes was 20 cm.

Electrical characteristics of the discharge were measured by capacitive gauge movable along discharge cell axis and back current shunt mounted into the break of the supplying cable screen. The back current shunt was installed on the distance from the discharge cell at which incident to the cell and reflected from it current pulses are separated in time.

In all mixtures the emission intensity of the discharge was measured both in time resolved (band pass of signal route was 150 MHz) and in integral regimes. Emission intensities were measured through the optical CaF_2 window mounted in the low-voltage ring electrode with using monochromator MDR-23 and photomultiplier FEU-100 (rise-time of signal was not longer than 3 ns, spectral sensitivity bandwidth was 200-800 nm).

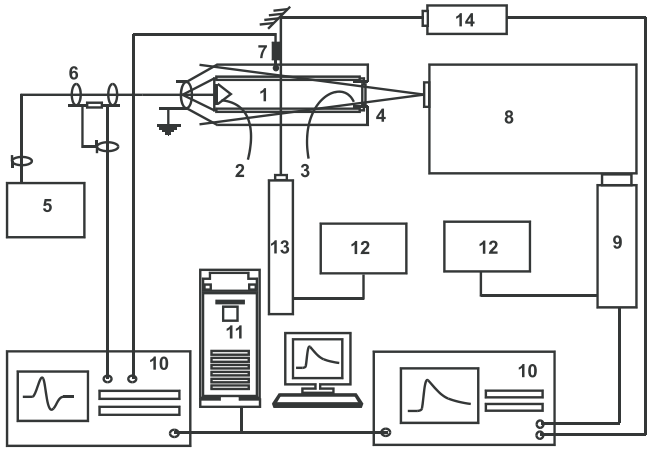

Figure 1: Experimental setup: 1 - discharge cell, 2,3 - electrodes, 4 - optical window (CaF_2), 5 - high-voltage generator, 6 - back current shunt, 7 - capacitive gauge, 8 - monochromator, 9 - photomultiplier FEU-100, 10 - oscilloscopes S9-8 and TDS-380, 11 - computer, 12 - power supplies, 13 - He-Ne laser ($\lambda = 3.3922\mu$m), 14 – photodetector Pb-Se.

In mixtures with methane absorption of He-Ne laser emission on 3.33922 μm was measured in addition to general set of parameters.

Time resolved signals were registered by oscilloscope Tektronix TDS 380 (band pass was 400 MHz). The integral measurements was fulfilled by oscilloscope S9-8 with 100, 200 and 400 s per scale.

Mixtures of heavy hydrocarbons were prepared under condition when partial pressure of an alkane lower than saturated vapor pressure at room temperature. A portion of an alkane was injected into the 10-liter vacuum-processed. The mass of the portion was smaller on 20% than mass of saturated vapor pressure of this alkane in this volume at room temperature. The control of pressure of gas in the volume allowed to measure the alkane concentration in the volume. Later we filled the volume by the oxygen up to the required pressure. The list of percentage of alkanes in all investigated mixtures is represented in the table 1.

2 Experimental methods

2.1 Finding of electric current, electric field and energy input

Typical oscillogram of the signal from the shunt is showed in the figure 2a. The first pulse of the current ("incident") is a pulse which moves from the high-voltage generator to the discharge cell. This pulse reflects from the discharge cell and returns to the shunt installation section in 100 ns. This is second pulse ("reflected") showed in the figure 2a. Further the pulse returns to the generator and reflecting from it returns to the shunt and later to the discharge cell. That is the process of pulse propagation repeats. Thus, the current shunt registers pair of pulses ("incident" and "reflected"), which come through it with period of 200 ns. The energy, which contributes in the gas in the first pulse, is equal to the difference of energies of "incident" and "reflected" pulses. The current, which passes through the discharge cell was obtained from the continuity equation of charge at the section of the high voltage electrode (figure 2). Taking into account directions of pulses propagation, which determine polarities of signals on the back current shunt:

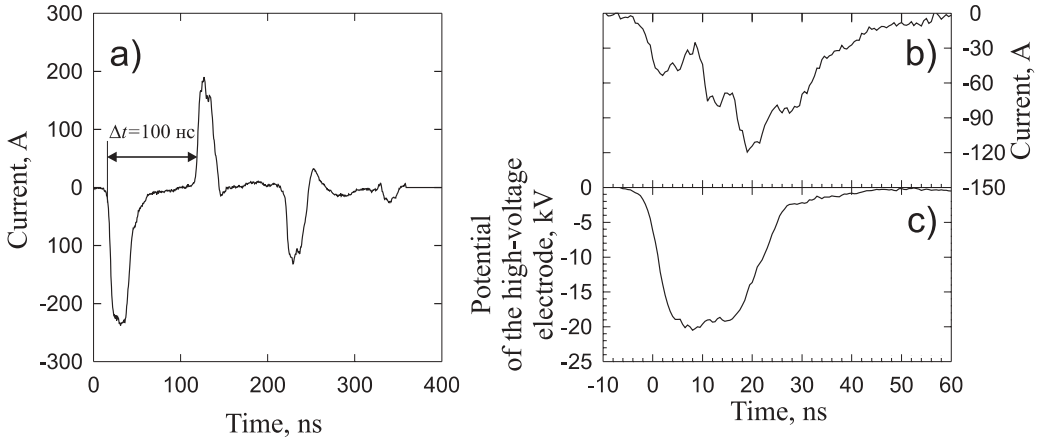

Figure 2: Characteristics measured by the current shunt: a) - the oscillogram of current in a cable, b) - the current through the high voltage electrode, c) - the high-voltage electrode potential. Initial pressure of the mixture CH_4+air is 1.51 torr.

$$J_0(t) = J_{\rm sh}(t) + J_{\rm sh}(t + 2\Delta t) \tag{1}$$

where $J_{\rm inc} = J_{\rm sh}(t)$ was the current in the incident pulse, $J_{\rm ref} = J_{\rm sh}(t+2\Delta t)$ is the current in the reflected pulse (figure 2), Δt is the time of the pulse propagation from the current shunt to the high-voltage electrode. Besides, the current shunt measurements allow to obtain as the current through the high electrode so the potential on the electrode U_0 (figure 2b), so electric field $E(t) = U_0(t)$ at the stage of short circuit.

Fulfilled analysis allowed to predicate that the main part of energy in the pressure range (0.76–10.6 torr), in which investigations were fulfilled, contributes in gas on the stage of short circuit in the first or the second pulse. At the same time nonuniformity of the discharge caused by cathode layer can be neglected. The noted feature allows measuring local electric field and current during the time of maximal energy contribution using only a back current shunt, that is especially important for investigation of chemical reactive mixtures, in which changes of a composition lead to the changes of electrodynamic characteristics. The electrical measurements,

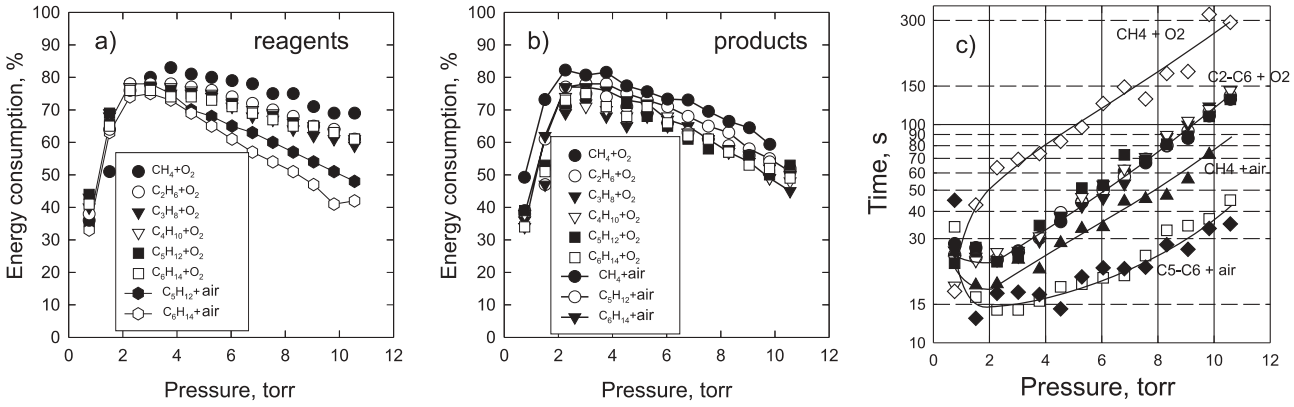

Figure 3: The sum of the energy input in the first and the second high-voltage pulses: a) in the initial mixture, b) in the mixture transformed by the discharge. Dependencies of alkanes full oxidation times on initial pressures of stoichiometric mixtures, obtained from $CO(B^1\Sigma \rightarrow A^1\Pi)$ band emission – c). The data for the stoichiometric mixtures of oxygen with alkanes from ethane to hexane are denoted as "C2–C6+O2", and data for the stoichiometric mixtures of oxygen with alkanes from ethane to hexane are denoted as "C5–C6+air" (see table 1)

which were fulfilled in the processed stoichiometric mixtures (from ethane to hexane) with oxygen or air, gave results, which are the same as the above-mentioned.

In the figure 3 the energy contribution is represented for all investigated mixture in the beginning of the discharge and after oxidation process. The total energy of the pulse reaches to 60 mJ. It is seen from the figure that in the beginning of the process of oxidation the energy contribution in any mixture with oxygen for pressures higher than 3 torr is systematically higher than for a mixture with air. With the growth of the pressure the difference increases and reaches 12% for the $p = 10.6$ torr. In processed mixtures variations of the energy contribution from a mixture to a mixture are negligible and even presence of nitrogen does not effect essentially. The energy contribution in the methane–oxygen processed mixture only is rather higher than one in other mixtures.

2.2 Experimental investigation of optical characteristics of the discharge

Full oxidation of alkanes in our conditions takes place under the action of a few thousands pulses (for tens and hundreds second), therefore integral over the time signal from the photomultiplier tube contains information about the hydrocarbons oxidation process. The control of emission intensity has been carried out for set of spectral transitions, at that some bands have been overlapped.

In addition in air-contained mixtures emission of $NO(A^2\Sigma \rightarrow X^2\Pi, \delta v = 3)$, $N_2(C^3\Pi, v' = 1 \rightarrow B^3\Pi, v'' = 7)$, $N_2(B^3\Pi, v' = 6 \rightarrow A^3\Sigma, v'' = 3)$ and $N_2^+(B^2\Sigma, v' = 0 \rightarrow X^2\Sigma, v'' = 2)$ have been controlled. It is necessary to note that intensities of the transitions of these molecules were so large that the emission of the overlapped bands was negligible.

In the case of essential overlap of the emitted bands to identify the band the emission intensities were measured in time-resolved regime for instants at the time when discharge switched on and when oxidation process was finished (when signal from the photomultiplier reached steady-state value). Also, measurements of emission intensities in time resolved regime were used for obtaining quenching constant rates in initial and final mixtures. Taking into account the constant rates of the quenching the excitation rates of higher states have been obtained.

Table 1: Investigated mixture.

Alkane	CH_4	C_2H_6	C_3H_8	C_4H_{10}	C_5H_{12}	C_6H_{14}
in mixture with O_2	33.3%	22.2%	16.6%	13.3%	11.1%	9.5%
n mixture with air	11.11%	–	–	–	3.03%	2.56%

2.3 Kinetics of alkanes oxidation in the discharge.

2.3.1 Stoichiometric mixtures

Time of full oxidation is defined as time at which the signal from photomultiplier reaches level of $0.95I_\infty$ for wavelengths (290 and 307,8 nm) corresponded to $OH(A^2\Sigma \rightarrow X^2\Pi)$ and $CO(B^1\Sigma \rightarrow A^1\Pi)$ transition and level $1.05I_\infty$ for wavelengths (430 and 518.6 nm) corresponded to $CO_2^+(B^2\Sigma \rightarrow X^2\Pi)$ and $CH(A^2\Delta \rightarrow X^2\Pi)$ transitions.

It is important to note that times of oxidation obtained from emission of different bands in the same experimental condition are rather different, owing to different influence of processes of excitation and quenching on different states during the mixture transformation, but times obtained from emission of the same band in different mixtures are practically the same within the experimental accuracy. Because of the fact that the experimental dispersion is minimal for the time obtained from $CO(B^1\Sigma \rightarrow A^1\Pi)$band emission, we designate time obtained from the emission of this band as the time of alkane full oxidation.

In the figure **??** times of full oxidation for different alkanes are represented. It is clearly seen, that time of methane full oxidation is nearly twice as large as times of full oxidation for other alkanes as in mixtures with oxygen so in mixtures with air. For other alkanes times of full oxidation are not differ with the experimental dispersion. In mixture with air times of full oxidation are twice or more as small as times in the same mixtures with oxygen. Taking into account that total quantity of alkanes smaller in stoichiometric mixtures with air than one in mixtures with oxygen, rates of allkanes in mixtures with oxygen oxidation are twice as small as one in mixtures with oxygen.

Thus, stoichiometric mixtures of alkanes with air and oxygen under nanosecond uniform discharge action at ambient temperature have been oxidized entirely. Oxidation of all alkanes beginning with ethane takes place for the same time in stoichiometric mixtures. The methane oxidizes in two times more slowly than other investigated alkanes.

2.3.2 C_4H_{10} oxidation in lean mixtures with oxygen under nanosecond discharge

As indicated above, oxidation of alkanes beginning with ethane under nanosecond discharge action proceeds for the same time under the same experimental conditions (initial pressure, energy input). One can explain this fact most logically in approximation of weak influence of excited and charged particles producing by electron impact to molecules of fuel in compare with influence of the impact to molecules of oxygen, intermediates and products, at first time water. It is known that electron impact thresholds of alkanes (in set methane–propane) dissociation reduce on 1 eV approximately with a increasing on a carbon's atom. Steric factor increases proportionally to a quantity of C atom in molecules of alkanes, at the same time a concentration of an alkane in stoichiometric mixture decreases inversely proportional to the quantity of C atom. Thus, it should be expected, that with change of stoichiometric mixtures from light to heavy alkanes the variation of an alkane concentration be compensated by variation of steric factor. However, with a quantity of carbon's atom in an alkane molecule increasing a dissociation threshold by electron impact is decreased. It should be expected, of course, faster oxidation of more heavy alkanes in compare with more lightly, which did not obtain in experiments. Let us consider possible explanation of this fact.

Excitation of molecular oxygen, its dissociation and ionization and so may be excitation and dissociation of products (at first time water) and intermediates entirely govern the alkanes oxidation. It is need to note, that in stoichiometric mixtures the quantity of oxygen is weakly varied from an alkane to another alkane and after processing in all mixtures the same quantity of water is produced. Difference in quantity of the carbon dioxide produced in oxidation process in all mixtures is negligible. So, the quantity of oxygen in stoichiometric mixture with ethane is 20% lower than it in mixture with hexane, on the same percents quantity of carbon dioxide produced in oxidation process is lower. It is necessary to note that water dissociates by electron impact more easily in comparison with carbon dioxide — water has lager absolute values of cross-sections of electron impact processes and essentially lowers thresholds; radicals generated from water are more active.

Thus, produced active particles of oxidant react with non-excited hydrocarbon's molecules, at that excitation, dissociation and ionization of hydrocarbons itself do not influence on oxidation rate. Using the methods described above, we have investigated oxidation of lean mixture of butane with oxygen. It has been shown that changes of energy input with equivalence ratio are not higher than 13% of pulse energy and specifically small for the range of maximum energy input in the initial mixture. And so we can assume that the discharge condition, which control excitation processes are not differ essentially for mixtures with different equivalence ratio from 0 to 1. In the figure 4 dynamics of the $CO(B^1\Sigma \rightarrow A^1\Pi)$ integral emission in the investigated mixtures is represented. It has clearly seen that with decreasing of the equivalence ratio the time of full oxidation decreases.

Time of full oxidation obtained from $CO(B^1\Sigma \rightarrow A^1\Pi)$ integral emission and time of of maximum of $CO(B^1\Sigma \rightarrow A^1\Pi)$ emission are represented in the figure 5. It is clearly seen that the time decreases linearly with

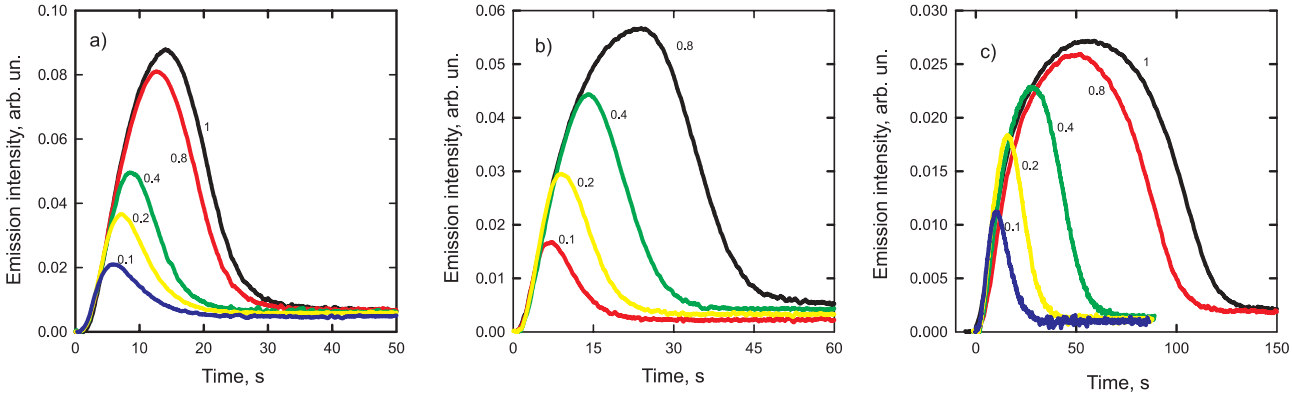

Figure 4: Integral over time emission intensities of transition $CO(B^1\Sigma \rightarrow A^1\Pi)$ in the discharge. The initial pressures of the mixtures are 1.51 torr for a), 5.29 torr for b) and 9.83 tor for c)

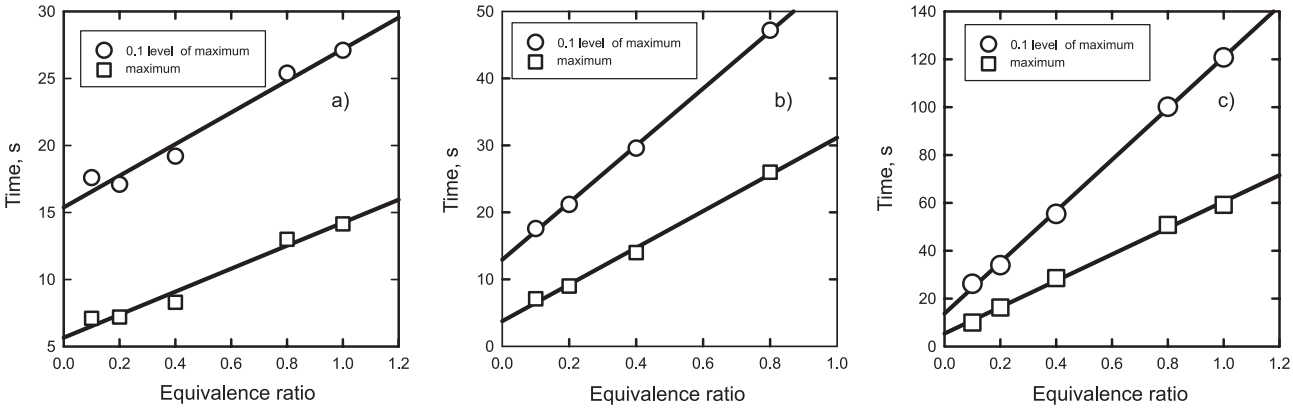

Figure 5: Time of full oxidation obtained from $CO(B^1\Sigma \rightarrow A^1\Pi)$ band emission - a) and time of $CO(B^1\Sigma \rightarrow A^1\Pi)$ band emission maximum versus initial pressure of butane with oxygen lean mixtures

decreasing the equivalence ratio that should be expected in the case of weak influence of excitation, dissociation and ionization of alkanes by the discharge. Really, the quantity of oxygen in stoichiometric mixture differs from it in mixture with equivalence ratio 0.1 on 11%, hence variations of concentrations of excited molecules, ions and atoms of oxygen no more than 11%. At the same time the concentration of butane changes in one order of magnitude, therefore dependence of time of full oxidation on equivalence ratio have to be linear with the good accuracy.

Thus, under our experimental condition, excitation, ionization and dissociation of an alkane by electron impact did not influence on the rate of the alkane oxidation.

2.3.3 $C_{10}H_{22}$ oxidation in lean mixture with oxygen under nanosecond discharge action

Real fuels used in internal-combustion engines consist of hydrocarbons C8-C16, therefore it should be examinate universality of above drawn conclusions on the example of alkane higher than C6. For this work we chouse n-decane $C_{10}H_{22}$. At 25^oC saturated vapor pressure of n-decane is equal 0.9 torr, and so the maximal pressure of stoichiometric mixture with oxygen is equal 18 torr. The preparation of the mixture was analogous as for hexane and pentane mixtures. A portion of decane was injected into the 10-liter vacuum-processed volume. The portion of decane was smaller than value of saturated vapor pressure of n-decane at 25^oC in 10-liter volume. Later we added oxygen into the volume. The mixture was mixed by ventilator. In spite of the forced mixing, concentration of decane increases very slowly, that we explained by very slow evaporation of decane under ambient temperature condition.

We controlled the concentration of decane by following method. The current mixture was oxidized in nanosecond discharge. The spectrum of emission of the mixture compared with spectra obtained in processed mixtures of butane and oxygen with different equivalence ratios. Emission intensities of OH and CO_2^+ bands in processed butane-oxygen mixtures upon equivalence ratio, which are used to obtain decane concentration depend on equivalence ratio essentially non-linearly. We explained this fact by the influence of concentration of

water on electron energy distribution function that is by changes of constants of excitation of these states by electron impact with water concentration changes. In this figure also emission intensities of processed decane oxygen mixture on the same wavelengths are represented. The emission intensities of different bands were interpolated between measured points and extrapolated to the zero point linearly. These dependencies allowed to obtain the equivalence ratio of the decane mixture. The concentration of n-decane obtained by this method amounted to 0.12 during 3 days of mixing. That is necessary 30 days to obtain the stoichiometric mixture of n-decane with oxygen.

Thus, there is no sense to prepare stoichiometric mixture of n-decan with oxygen in room temperature owing to very long preparation time, and so we investigated oxidation process in the mixture with 0.12±0.01 stoichiometric ratio. In the mixture was registered energy contribution and $CO(B^1\Sigma \rightarrow A^1\Pi)$ emission intensity. It is necessary to note that difference between energy inputs in initial and in processed mixtures is negligibly small owing to the oxygen is the main constituent of these mixtures.

The energy contribution in different mixture does not differ within the range of experimental data scattering. Thus, excitation of a gas occurred with the same intensity for all mixtures.

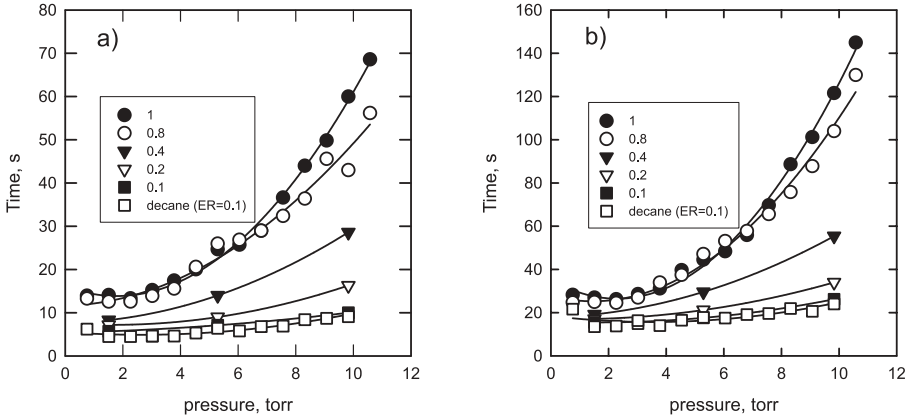

Figure 6: Time intervals between discharge beginning and $CO(B^1\Sigma \rightarrow A^1\Pi)$ emission maximum — a) and instants of full oxidation — b)

In the figure 6 times of full oxidation obtained by emission intensities of $CO(B^1\Sigma \rightarrow A^1\Pi)$ bands for butane-oxygen mixtures and for the decane-oxygen mixture are represented. It is clearly seen that time of full oxidation of n-decane is approximately equal to the time of full oxidation of butane in mixture with 0.1 equivalence ratio. Thus, the conclusions, which we have made for mixtures of alkanes C2-C6 early, can be extended on alkanes that are more heavy.

3 Conclusions

The kinetics of slow oxidation of alkanes under the action of the nanosecond pulsed-periodic discharge in stoichiometric and lean mixtures with oxygen and air at room temperature has been investigated experimentally.

It has been shown, that the alkanes under the nanosecond discharge action at ambient temperature are oxidized entirely. The times of the full oxidation with the same values of the energy contribution, mixture initial pressure and equivalence ratio were not differ for all alkanes large then methane. Methane was oxidized in two times more slowly than other alkanes. Alkanes oxidation in mixtures with oxygen passes approximately in two times more effectively than in corresponded mixtures with air. Times of full oxidation of alkanes are proportional to equivalence ratio under our conditions.

Acknowledgments

This work was partially supported Grants by PR0-1349-MO-02 EOARD/CRDF; Grant 02-3.2-97 by Ministry for Higher Education of Russian Federation; grant 02-03-33376 of Russian Foundation for Basic Research; Project 1440 by ISTC; Award MO-011-0 of the CRDF. Work of N.B.Anikin was partially supported in accordance with his grant Y1-C-11-09; work of S.M.Starikovskaia was partially supported by grant of President RF for young DrSc.

The Use of Nitrogen/Hydrogen Corona Treatment for the Surface Modification of Poly(tetrafluoroethylene)

Seth M. Kirk[1], Mark Strobel[1], Hyacinth Cabibil[1]

[1]*3M Corporate Research Laboratory, 3M Company, St. Paul, MN 55144*

1. Introduction

Fluoropolymer materials have many desirable properties such as low reactivity with chemical and biological compounds. However, these same non-reactive qualities also make it difficult to form an adhesive bond with a fluoropolymer surface to create a functional multi-layer construction. To successfully incorporate a fluoropolymer material into a multi-layer construction, a surface modification must be applied to the fluoropolymer.

Various processes are used for the surface modification of polymers, including solution-coating techniques, chemical etching, and the exposure of polymer surfaces to reactive gas atmospheres. The use of reactive gas atmospheres, such as plasmas and flames, is of significant interest for the high-speed industrial-scale surface modification of polymer films. Perhaps the most robust process for such surface modification is dielectric-barrier discharge treatment, commonly referred to as atmospheric-pressure plasma or corona treatment.

However, corona treatment technology has not been well developed for treating fluoropolymer films. Surface modification of fluoropolymer films has more typically been done with slow and costly wet-chemical etching or reduced-pressure plasma treatments. The use of commercial corona treatment technology for the surface modification of fluoropolymers is a lower-cost and higher-throughput process than other technologies. It is the aim of this paper is to demonstrate that by using a low-cost reactive atmosphere with commercial corona equipment, a robust and industrially viable polymer surface modification can be delivered to poly(tetrafluoroethylene) (PTFE) film.

2. Background

Although corona treating is a mature technology with multiple suppliers of commercial equipment, there has been limited work reported on the use of corona processing with controlled atmospheres. In particular, we are aware of no reported work on the use of corona treatment with hydrogen-containing atmospheres. Accordingly, the use of corona treatments in nitrogen/hydrogen atmospheres has been developed in 3M as a proprietary process [1].

There is a body of work that has examined reduced-pressure plasma treatment of fluoropolymers. Although the reactive environment of a reduced-pressure glow discharge is distinct from that of atmospheric-pressure corona, comparisons with the reduced-pressure work can be instructive. In particular, a comparison made by Inagaki [2] between “direct” plasma exposure and “remote” plasma exposure, shows that the remote plasma treatment, with diminished roles of ions and UV energy, produces a modified PTFE surface without a soluble surface component. Atmospheric-pressure corona discharges are understood to have minimal amounts of ions and reactive UV energy [3], and analysis of the samples reported here parallels the reported Inagaki results.

In work that directly compares hydrogen plasma to other reduced-pressure plasma chemistry, the use of hydrogen is noted to produce a uniquely high level of surface defluorination [4, 5]. However, defluorination of a PTFE surface followed exclusively by surface reaction with hydrogen does not result in the most reactive surface. Several researchers have demonstrated that a hydrogen plasma with other gaseous additives [6], including nitrogen [4], will produce a more functionalized surface than a pure hydrogen discharge.

2. Experimental

For the work reported here, we used a modified commercial corona treater. In this treater, PTFE film was transported on a grounded ceramic-covered water-cooled ground roll. The ground roll and two stainless steel shoe electrodes were enclosed in a housing that was purged with nitrogen and the optional addition of hydrogen. A sealing system on the treater enclosure enabled the polymer film to be transported into and out of the discharge while minimizing the amount of gaseous contaminants in the discharge atmosphere.

The most significant variables in corona processing are the composition of the atmosphere where the discharge occurs and the normalized energy. Normalized energy has units of Joules per square centimeter (J/cm^2) and is calculated from the net power P (in watts), the electrode width w (in cm) and the film velocity s (in cm/s):

$$\text{Normalized energy, } E = P/ws$$

All corona treatments reported here were done at 25 ºC, with a film velocity of 3.3 cm/s and a net power of 1870 watts delivered to 33-cm-wide electrodes, which corresponds to a normalized energy of 17 J/cm^2.

The surface composition of the films was analyzed by X-ray photoelectron spectroscopy (XPS), also known as Electron Spectroscopy for Chemical Analysis (ESCA). The ESCA spectra were obtained from a Kratos Axis Ultra system equipped with a monochromatic Al Ka X-ray source. The photoemitted electrons were detected at 90^o with respect to the sample surface. ESCA detected the presence of fluorine, carbon, oxygen, and nitrogen on the treated samples and only fluorine and carbon on the untreated sample.

Contact-angle measurements were made on the treated surfaces of the films using the Wilhelmy plate method on a ThermoCahn Radian DCA322 dynamic contact-angle instrument. Advancing and receding contact angles in air were made using deionized filtered water and high-purity hexadecane. A three-layer laminate was prepared using 3M Scotch Brand #666 double-coated tape to mount the treated sides of the film outward. The laminate was cut into a 2.5 x 2.5-cm square for analysis. The stage speed was 50 µm/sec with a travel distance of about 1 cm. At the position of the maximum travel, the motion of the stage was halted for 2 minutes prior to starting the retraction phase of the Wilhelmy cycle, thereby soaking the sample for a period of time. The contact angles were calculated using a software routine supplied with the ThermoCahn instrument that uses linear regression for the buoyancy correction. Typical standard deviations for the contact angles measurements were 2º.

3. Results

ESCA analyses show that corona treatments using nitrogen and nitrogen/hydrogen atmospheres result in the surface modification of the PTFE surface. The loss of fluorine is evident in Figure 1, which shows the changes in F/C atomic ratios as a function of the percent hydrogen in a nitrogen atmosphere. The use of a nitrogen discharge atmosphere with no hydrogen addition results in a surface with a F/C ratio just slightly lower that of the untreated PTFE surface, indicating a minor surface modification. The addition of increasing amounts of hydrogen results in a progressive loss of fluorine as shown by a substantial decrease in F/C ratios.

The defluorination is accompanied by the incorporation of nitrogen and oxygen to the polymer surface as shown in Figure 2, which plots the N/C and O/C ratios as a function of percent hydrogen in the nitrogen atmosphere. The incorporation of these atoms on the modified surface likely results from surface radicals (created by the removal of fluorine atoms) reacting with nitrogen and oxygen atoms formed in the discharge. Figure 2 also suggests that the maximum level of nitrogen and oxygen incorporation has been achieved at a hydrogen additive level of less than 1%.

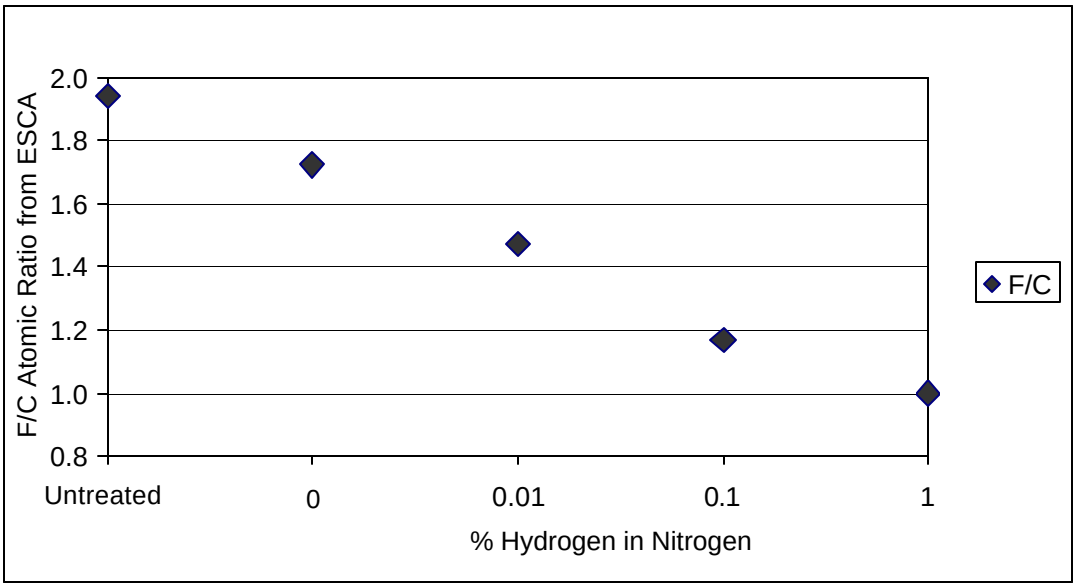

Figure 1. ESCA F/C atomic ratios of corona-treated PTFE

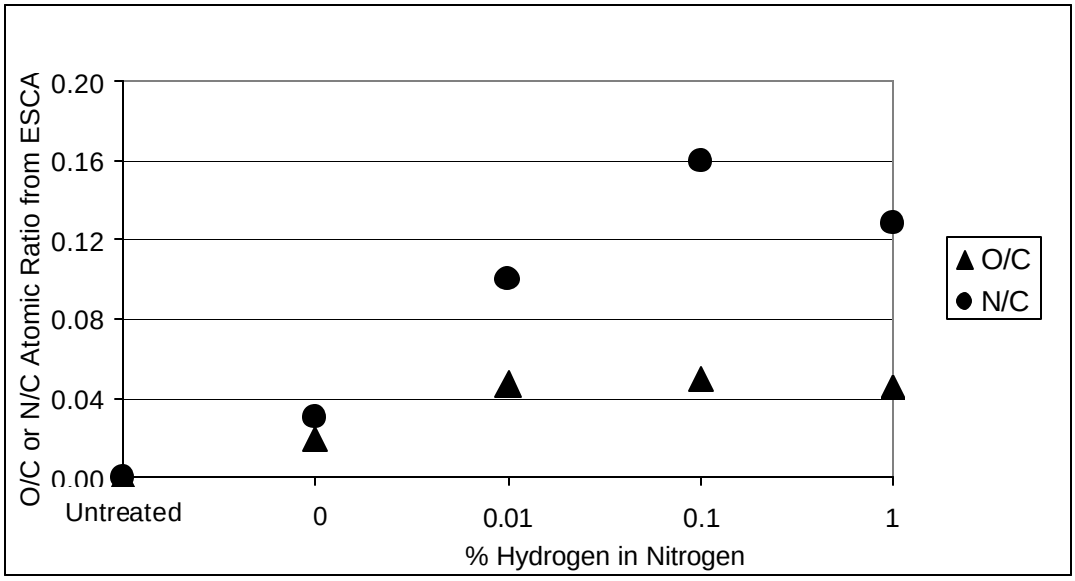

Figure 2. ESCA O/C and N/C atomic ratios of corona-treated PTFE

The loss of fluorine is also reflected in the ESCA carbon 1s spectra displayed in Figure 3, which shows the gradual decrease of the CF_2 peak from the untreated PTFE and the evolution of a broad peak on the lower-binding-energy side. The C 1s spectrum of the nitrogen corona treatment (no hydrogen added) is very similar to that of the untreated PTFE. A broad peak develops on the lower binding energy side of the C 1s spectra with the increasing addition of hydrogen to the nitrogen atmosphere. This broad peak includes contributions from carbon atoms in many different chemical environments. For example, –CF and C-CF_x bonding configurations may be present in addition to C-O, C-N, and C-C. The peak attributable to the C-C is most pronounced on the sample treated with the highest amount of hydrogen added to the corona atmosphere.

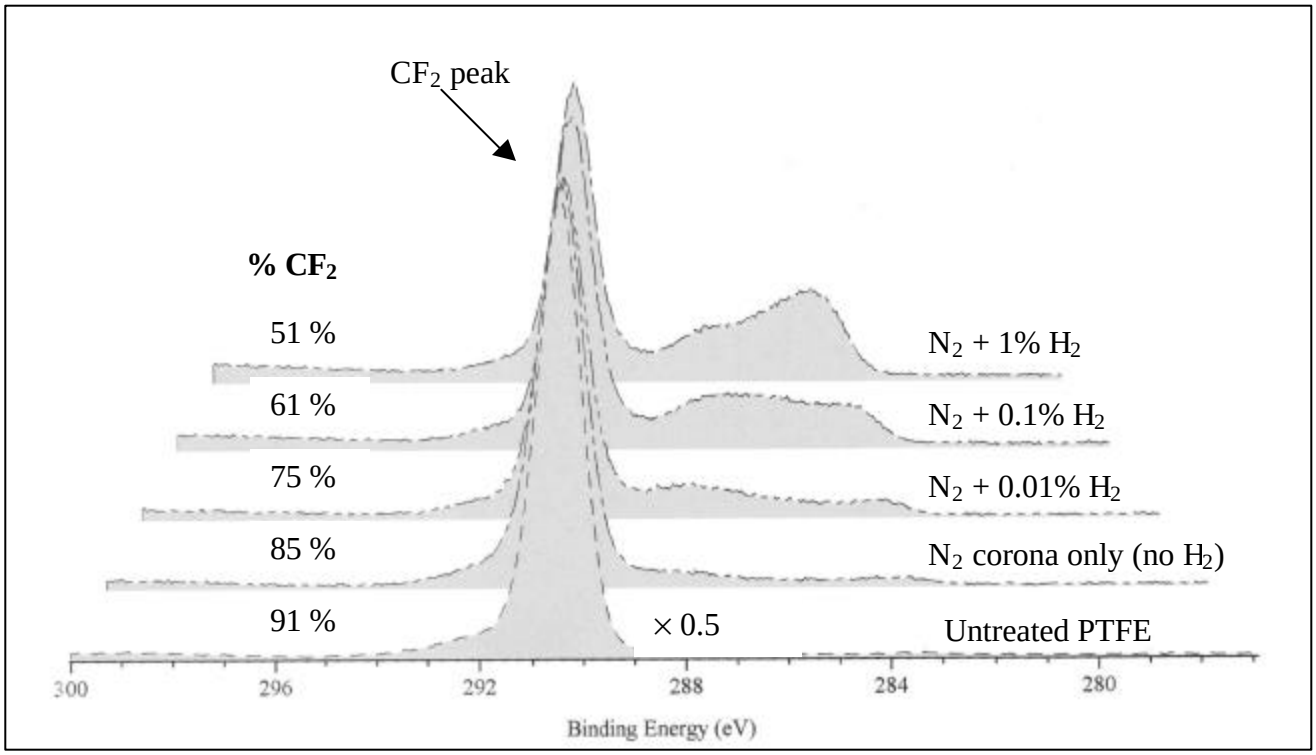

Figure 3. ESCA C1s spectra of PTFE treated with hydrogen/nitrogen coronas. Spectra not corrected for sample charging.

Corona-modified PTFE samples were further evaluated by measuring the advancing and receding contact angles of water in air, as shown in Figure 4. This analysis shows a decrease in the contact angles from treatment in the pure-nitrogen atmosphere and a continuing decrease in the contact angles with the addition of hydrogen to the discharge atmosphere. A more wettable, higher-energy surface develops with increasing additions of hydrogen to the nitrogen discharge.

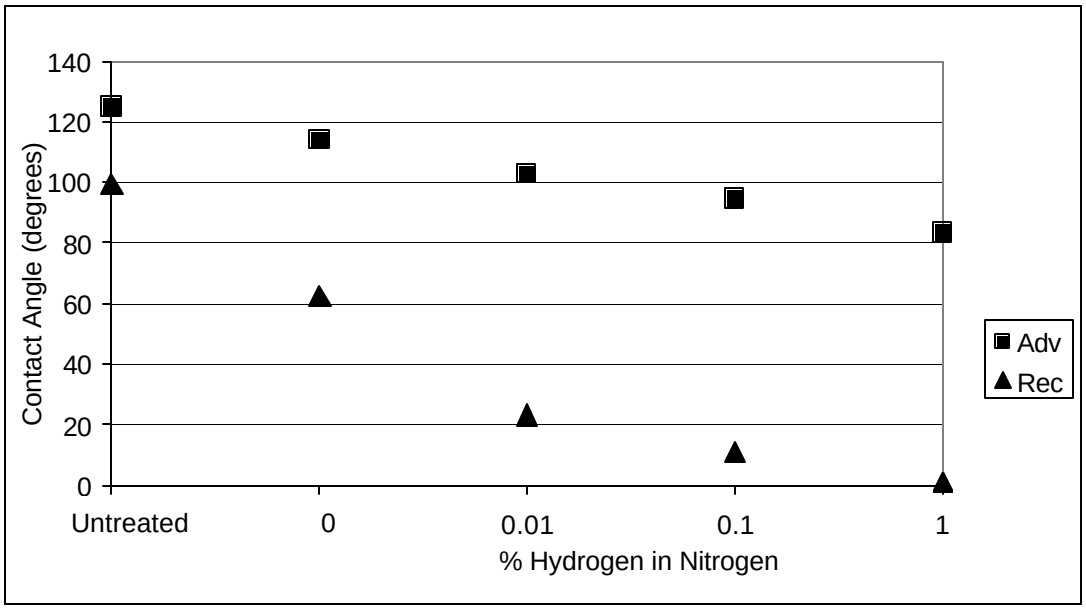

Figure 4. Advancing and receding water contact-angles in air of corona-treated PTFE

The same corona-modified PTFE samples were also evaluated by measuring the advancing and receding contact angles of hexadecane in air, as shown in Figure 5. This analysis also shows a decrease in contact angles from treatment in the pure-nitrogen atmosphere and a continuing decrease in contact angles with the

addition of hydrogen to the discharge atmosphere. The hexadecane contact angles respond strongly to the hydrocarbon functionalities on the modified PTFE surface and the 0º receding contact angles indicate the formation of hydrocarbon functionalities with hydrogen additions as low as 0.01%.

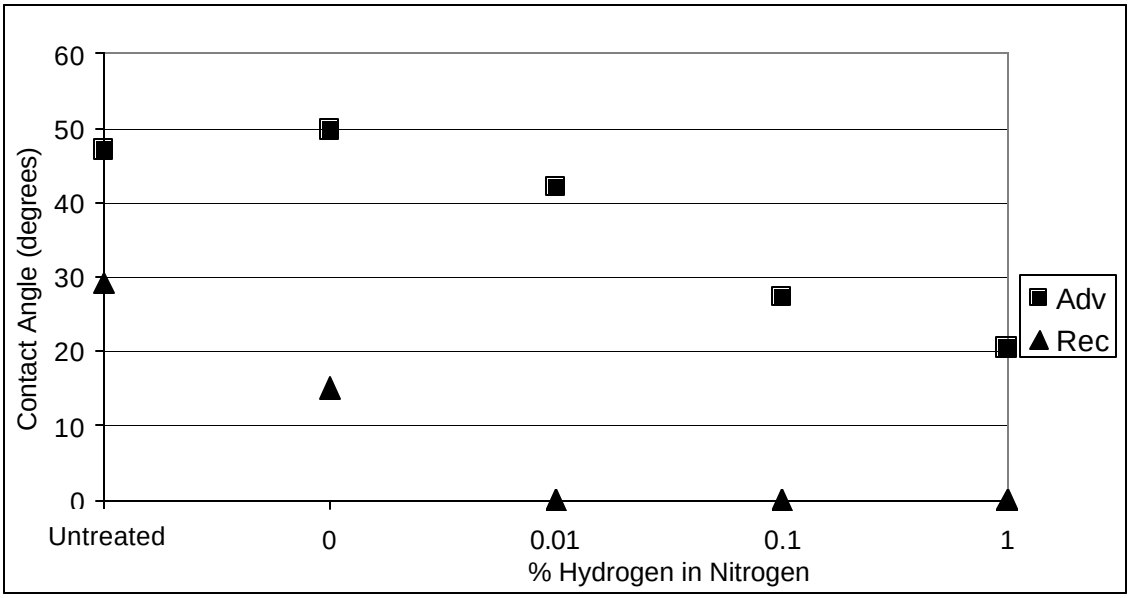

Figure 5. Advancing and receding hexadecane contact-angles in air of corona-treated PTFE

4. Discussion

The results presented here show that low concentrations of hydrogen in corona discharges can effectively defluorinate PTFE surfaces. Pure-nitrogen corona discharges have a minor effect on PTFE, indicating that the reactive species in these discharges cannot break significant numbers of C-F bonds. The addition of hydrogen to a nitrogen discharge allows the formation of hydrogen atoms that can break the C-F bonds on the surface of the PTFE. The decrease in surface fluorine resulting from increased hydrogen addition, combined with the limited role of ions and UV energy in the corona discharge, suggest that hydrogen atoms are primarily responsible for the removal of fluorine atoms from the surface of the treated polymer. The strongly bonded product species of this reaction, HF, removes surface fluorine and allows the other species in the discharge to react with the surface radicals formed by the abstraction of fluorine.

At low concentrations of hydrogen, the degree of surface modification is limited by the concentration of hydrogen introduced to the discharge atmosphere. As hydrogen is first introduced and increased, the increasing number of surface radicals formed from fluorine abstraction react with nitrogen and oxygen species in the discharge. As the hydrogen concentration continues to rise in the discharge atmosphere, surface defluorination increases, but the more abundant hydrogen atoms also compete with nitrogen and oxygen atoms for reaction with the surface radicals created by the fluorine abstraction. The result of this competition is seen in the ESCA results presented above, which show a point of maximum nitrogen and oxygen incorporation.

[1] S. M. Kirk, C. S. Lyons, R. L. Walter – U. S. Patent 5,972,176 (1999).
[2] N. Inagaki, S. Tasaka, T. Umehara – J. Appl. Polym. Sci. **71**, 2191-2200 (1999).
[3] M. Strobel, V. Jones, C. S. Lyons, M. Ulsh, M. J. Kushner, R. Dorai, M. C. Branch – Plasmas and Polymers **8**, 61-95 (2003).
[4] M.K. Shi, A. Selmani, L. Martinu, E. Sacher, M. R. Wertheimer, A. Yelon – J. Adhesion Sci. Technol. **8**, 1129-1141 (1994).
[5] M. E. Ryan, J. P. S. Badyal – Macromolecules **28**, 1377-1382 (1995).

[6] T. G. Vargo, J. A. Gardella, A. E. Meyer, R. E. Baier - J. Polym. Sci. A: Polym. Chem. **29**, 555-570 (1991).

Selective Removal of Acetylene from Ethylene via RF Plasma Derived Pd Catalysts

Ai-Min Zhu, Kliff Pittman, Monyka Macias and Ben W.-L. Jang*
Chemistry Department, Texas A&M University-Commerce, Commerce, TX 75429-3011, USA

Abstract

Plasma treatment for supported Pd/SiO_2 catalysts has been studied using a custom-designed 360° rotating RF plasma system. The treatments using O_2 plasma, Ar plasma and H_2 plasma can enhance the selectivity to C_2H_4 of acetylene hydrogenation. The catalyst treated with H_2 plasma without thermal reduction exhibits higher C_2H_4 selectivity and C_2H_4 concentration than those with thermal reduction. H_2 plasma treatment is promising for reduction of metal catalysts at low temperatures to fine tune catalytic activity and selectivity.

Keywords: plasma, Pd catalyst, selective hydrogenation, acetylene, ethylene

1. Introduction

Selective hydrogenation has been widely used for chemical processing and environmental applications. For examples, the removal of highly unsaturated hydrocarbons from the C_2-C_4 alkene feeds is highly desirable for petrochemical industry and the selective reductions of halogen containing compounds, NO_x and SO_x are required to meet stringent environmental regulations [1]. This study focuses on the development of Pd catalyst via the radio frequency (RF) non-thermal plasma technology for selective hydrogenation of acetylene in the presence of ethylene because plasma based techniques for catalyst preparation have recently been reported to develop catalytic materials with unusual catalytic properties including high metal dispersion and better stability [2,3]. The selectivity and stability of catalysts for acetylene removal from ethylene has been an important research subject due to its slight improvement representing a large revenue for the industry.

2. Experimental

20-40 mesh silica particles with 144 m^2/g surface area are impregnated with a calculated palladium nitrate solution using the incipient wetness technique. The resulted material followed by drying at 120 °C for 12 hours in static air is designated as untreated $0.05\%Pd/SiO_2$ catalyst. The obtained materials are treated with O_2, Ar and H_2 plasmas are designated as $0.05\%Pd/SiO_2(O_2)$, $0.05\%Pd/SiO_2(Ar)$, $0.05\%Pd/SiO_2(H_2)$, respectively. Some portion of un-calcined $0.05\%Pd/SiO_2$ is further calcined at 300 °C in air for half an hour and is designated as calcined $0.05\%Pd/SiO_2$.

Plasma treatments for catalytic materials were carried out in the custom-designed 360° rotating RF plasma system. The detail of the system is described in the previous publication [4]. The schematic of the system is shown in Figure 1. System pressure of 400 mTorr was used for plasma treatments in this study. Typically, one gram of catalysts is loaded in the plasma chamber for plasma treatments. The time for plasma treatment is set at 30 minutes with a continuous or pulsed (10 ms on duty and 50 ms off duty) waveform.

All catalysts are tested for the selective hydrogenation of acetylene. If not otherwise specified, the Pd/SiO_2 catalysts were reduced in situ in hydrogen from 25 °C to 300 °C or 400 °C with a ramp rate of 5 °C/min and held at 300 °C or 400 °C for half an hour before cooling to desired temperatures for testing of activity and selectivity. Reaction study was carried out with a space velocity of 84,000 sccm/h-g catalyst over 30 mg of catalyst. 40 sccm of the premixed gas consisting of 98.8% C_2H_4 and 1.2% C_2H_2 was mixed with 2 sccm of UHP H_2 to introduce

*Corresponding author: *Email*: Ben_Jang@TAMU-Commerce.edu (Ben W.-L. Jang)

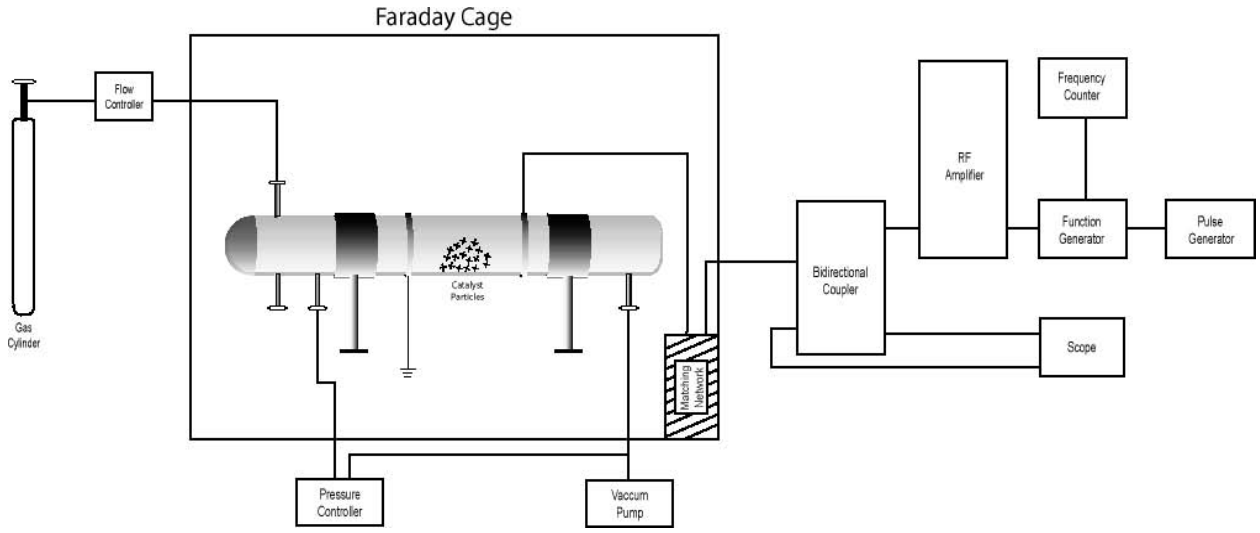

Fig.1 The schematic of the rotating RF plasma system for catalyst treatments

into the microreactor. All flows are delivered by mass flow controllers. The analysis of the gas components from the microreactor was performed by an on-line Shimadzu GC 17A equipped with a 30 m × 0.32mm (ID) ×1.50 μm GS-CARBONPLOT capillary column operating at 80 °C and a FID detector.

Possible products for acetylene hydrogenation are ethylene and ethane. The conversion of acetylene to ethylene is desirable. But, the conversion of acetylene to ethane or ethylene to ethane is not economical since they both reduce the net ethylene content, especially the hydrogenation of ethylene to ethane. The selectivity of acetylene hydrogenation to ethylene is defined as follows:

$$\%\ C_2H_4 \text{ selectivity} = (1 - \text{produced } C_2H_6 / \text{converted } C_2H_2) \times 100$$

Positive % C_2H_4 selectivity refers to a net gain of ethylene during the hydrogenation process and negative selectivity results in ethylene loss.

3 Results and Discussion

3.1 Effect of the Plasma Gas on Pd /SiO_2 Catalysts

Fig. 2a shows the activities of C_2H_2 conversion vs temperature on Pd /SiO_2 catalysts, including untreated and treated by O_2 plasma, Ar plasma, H_2 plasma and calcination. Compared to the untreated Pd /SiO_2 catalyst, the activity of Pd /SiO_2 treated with calcination is slightly improved. Yet, whether the plasma gas is O_2, Ar or H_2, plasma treated Pd /SiO_2 catalysts are less active than the untreated one. The activity order for the catalysts treated with plasma is O_2 plasma ~Ar plasma > H_2 plasma. As shown in Fig.2b, for any treated or untreated catalysts, the selectivity to C_2H_4 decreases with increasing temperature, which is in agreement with the literature [5]. The data also suggest that plasma treatment towards Pd/SiO_2 catalyst can lead to an improvement in C_2H_4 selectivity. However, the difference of C_2H_4 selectivity shown in Fig. 2b is affected by C_2H_2 conversion, which is also changing with different treatments on catalyst. To make this comparison meaningful, the selectivities of different catalysts should be compared at the same C_2H_2 conversion. As shown in Fig. 3, plotted as C_2H_4 selectivity vs C_2H_2 conversion, C_2H_4 selectivities of catalysts treated with O_2 plasma, Ar plasma, H_2 plasma and calcination appear to fall on one curve and are obviously higher than that of untreated catalyst. Results suggest that the plasma treatments towards Pd/SiO_2 catalyst using O_2 plasma, Ar plasma, H_2 plasma can enhance the selectivity to C_2H_4 of acetylene hydrogenation.

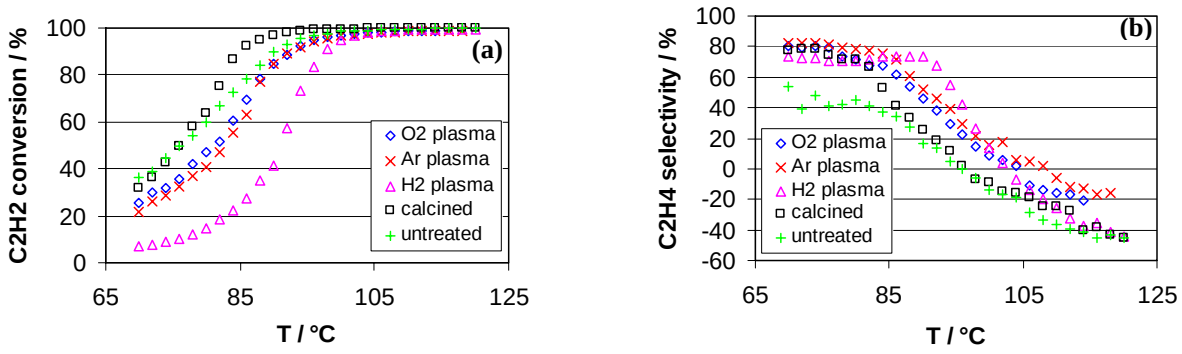

Fig.2 Curves of C_2H_2 conversion (a) and C_2H_4 selectivity (b) versus reaction temperature over untreated catalyst and catalysts treated by plasma or calcination. Plasma treatment conditions: pulsed waveform with 10 ms on duty and 50 ms off duty, 0.23 MHz of repetition frequency, 120 W, 400 mTorr, 0.5h. Calcination conditions: 300 °C, 0.5h

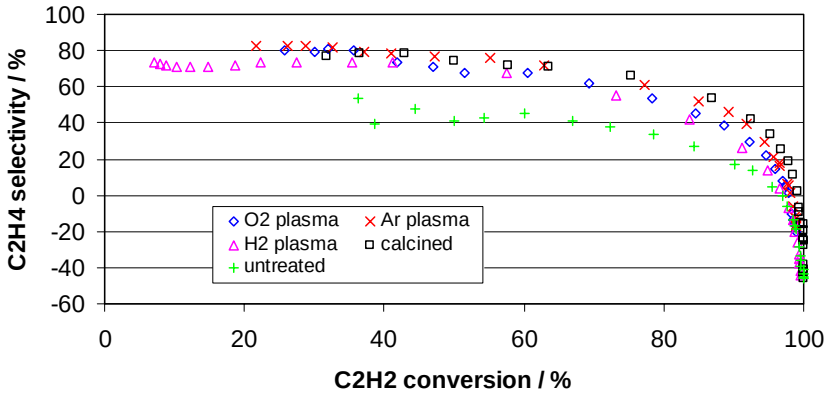

Fig. 3 C_2H_4 selectivity versus C_2H_2 conversion over plasma treated, calcined and untreated catalysts. The conditions are same as those in Fig. 2.

3.2 Effect of Reduction Temperature

The plasma employed to treat catalysts in this study belongs to a non-thermal equilibrium plasma (NTP) with much high electron temperature (>10^4 K) but rather low bulk gas temperature (R. T. ~ 400 K). Therefore, it is worthwhile to clarify whether high reduction temperature affects the catalytic performance of catalysts derived from plasma treatments or not. From this idea, untreated Pd/SiO_2 catalyst, calcined Pd/SiO_2 catalyst and $0.05\%Pd/SiO_2$ (O_2) catalyst were compared with 300 °C and 400 °C reduction temperatures. From Fig. 4a their activities with different reduction temperatures are comparable at same reaction temperatures. However, it can be seen from Fig 4b that the untreated Pd/SiO_2 catalyst reduced in H_2 at 400 °C shows higher C_2H_4 selectivity than that reduced at 300 °C at C_2H_2 conversion less than 80%. Reduction temperature, on the other hand, does not affect the C_2H_4 selectivity at C_2H_2 conversion higher than 80%.

For the calcined Pd/SiO_2 catalyst, it's found that the curves of C_2H_4 selectivity versus C_2H_2 conversion at 300 °C and 400 °C of reduction temperature appear to be similar as shown in Fig 5b, though the activity of catalyst reduced at 400°C is slightly lower (Fig 5a). In the case of the $0.05\%Pd/SiO_2(O_2)$ catalyst, activity and selectivity pattern is completely different from the calcined and untreated catalysts. As shown in Figure 6a, the selectivity of the catalyst reduced at 400°C decreases linearly with the increase in C_2H_2 conversion. These results in lower C_2H_4 selectivity of the catalyst reduced at 400°C at C_2H_2 conversion higher than 60% compared to the catalyst reduced at 300 °C. It indicates that catalysts derived from plasma treatments are quite different from those

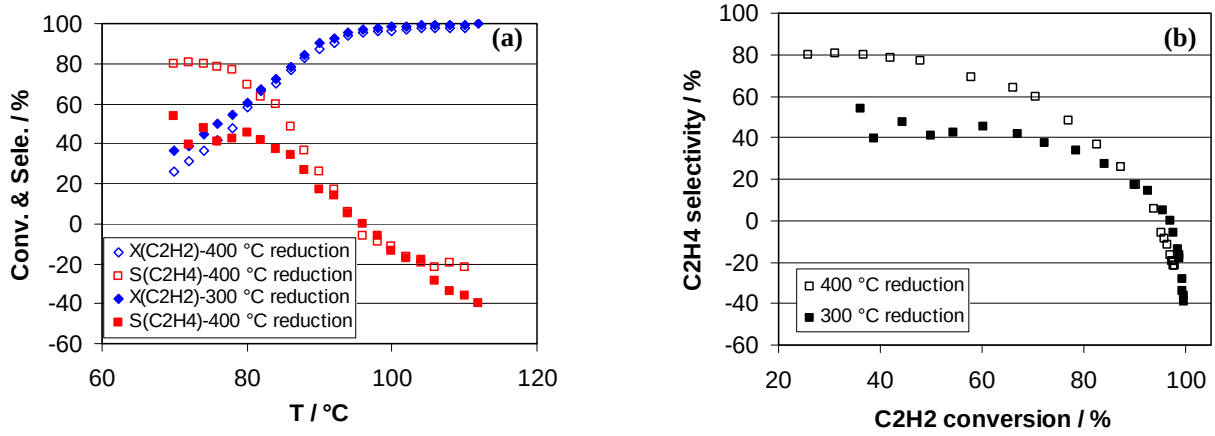

Fig. 4 Effect of reduction temperature over untreated Pd/SiO_2 catalyst. (a) conversion & selectivity vs temperature (b) C_2H_4 selectivity vs C_2H_2 conversion.

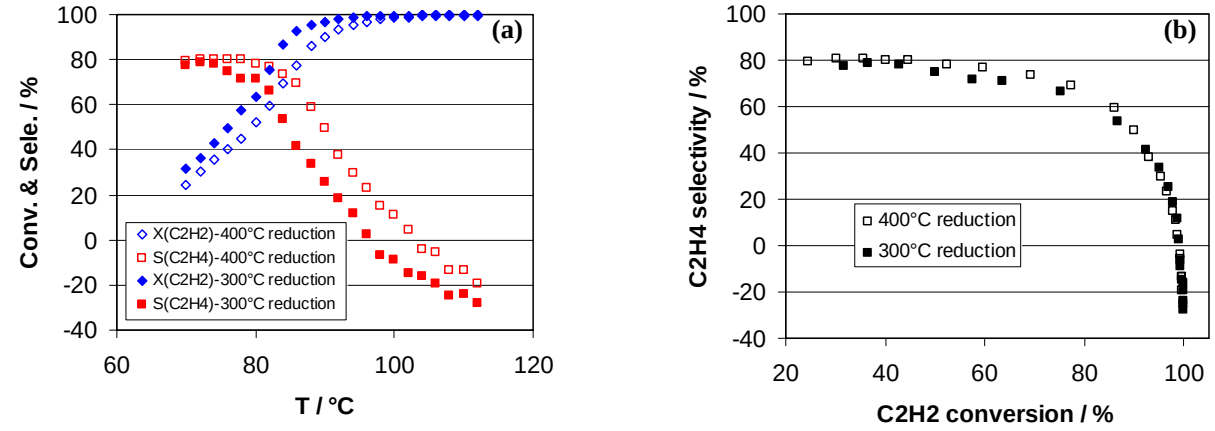

Fig. 5 Effect of reduction temperature over calcined Pd/SiO_2 catalyst (a) conversion & selectivity vs temperature (b) C_2H_4 selectivity vs C_2H_2 conversion.

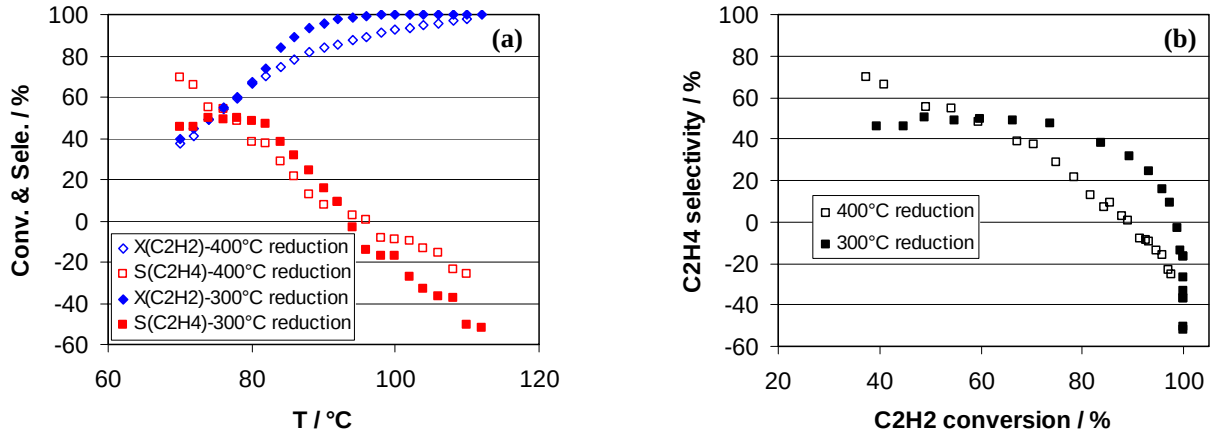

Fig. 6 Effect of reduction temperature over $0.05\%Pd/SiO_2(O_2)$ catalyst. (a) conversion & selectivity vs temperature (b) C_2H_4 selectivity vs C_2H_2 conversion. O_2 plasma treatment conditions: continuous waveform, 13.56 MHz, 160 W, 400 mTorr, 0.5h.

derived from conventional treatments and are more sensitive to reduction temperature than the latter. Catalysts treated by NTP may not be as stable as conventional catalysts in high temperature processes.

3.3 H_2 plasma reduction towards Pd/SiO_2 catalyst

As mentioned above, thermal reduction process may result in a decrease of catalytic selectivity and stability of catalysts treated with O_2 plasma. If H_2 is used as the plasma gas for plasma treatment of catalyst, can the thermal reduction process of Pd/SiO_2 catalyst be avoided? To answer this question, the catalytic materials treated by H_2 plasma with and without thermal reduction were compared. As shown in Fig.7a & b, the catalyst treated with H_2 plasma without thermal reduction exhibits higher C_2H_4 selectivity and C_2H_4 concentration (percentage of C_2H_4 in carbon-containing gaseous components) than those with thermal reduction either at 100°C or 300°C, though its activity is lower. It is suggested that the Pd precursor can be reduced by H_2 plasma to optimize the ethylene yield of acetylene hydrogenation. It is believed that H_2 plasma can likely reduce other metal catalysts at low temperatures and can be used to fine tune catalytic activity and selectivity.

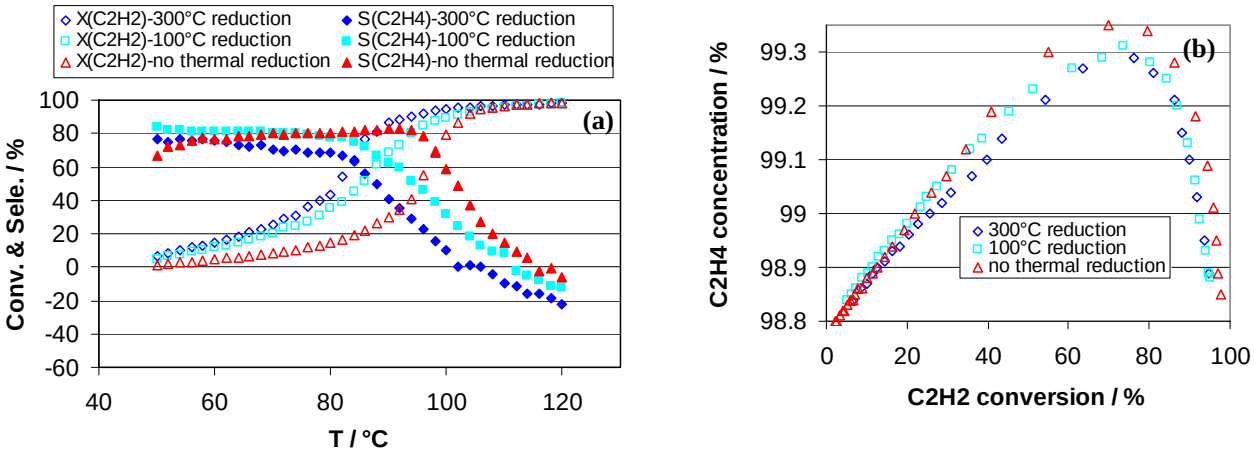

Fig.7 Effect of thermal reduction on (a) C_2H_2 conversion and C_2H_4 selectivity, (b) C_2H_4 concentration over catalysts treated by H_2 plasma. H_2 plasma treatment conditions: continuous waveform, 13.56 MHz, 160 W, 400 mTorr, 0.5h.

4. Conclusion

As compared to the untreated catalyst, the treatments towards $0.05\%Pd/SiO_2$ catalyst using O_2 plasma, Ar plasma, H_2 plasma can enhance the selectivity to C_2H_4 of acetylene hydrogenation and decrease their activity as the following order: O_2 plasma ~Ar plasma > H_2 plasma. The catalytic performance of catalysts derived from plasma treatments can be quite different from those derived from conventional treatments and is more sensitive to reduction temperature than the latter. Catalysts treated with plasma may not be as stable as catalysts obtained from conventional procedures for high temperature processes. The catalyst treated with H_2 plasma without thermal reduction exhibits higher C_2H_4 selectivity and C_2H_4 concentration than those with thermal reduction. It is suggested that the Pd precursor can be reduced by H_2 plasma to optimize the ethylene yield of acetylene hydrogenation. H_2 plasma treatment is promising for reduction of metal catalysts at low temperatures to fine tune catalytic activities and selectivities.

Acknowledgement The authors wish to acknowledge the financial support partly by the Welch Foundation and the Organized Research Grant of Texas A&M University-Commerce.

References

[1] M. L. Derrien, Stud. Surf. Sci. Catal. **27**, 313 (1986).

[2] C.-J. Liu, G. P. Vissokov, B. W.-L. Jang, Catal. Today **72**, 173 (2002).
[3] “Plasma Technology and Catalysis” edited by Jang et al., Catal. Today **89**(1-2), 1(2004).
[4] J. Zhan, P. Boopalachandran, B. W.-L. Jang, J. Cho, and R. B. Timmons, Am. Chem. Soc., Div. Of Fuel Chem. PREPRINTS, **49**(1),176 (2004).
[5] Y.-M. Jin, A. K. Datye, E. Rightor, R. Gulotty, W. Waterman, M. Smith, M. Holbrook, J. Maj and J. Blackson, J. Catal. **203**, 292 (2001).

Structure and energetics of the ingredients of the low-temperature plasma.

J. Jaroszyńska-Wolińska[1] and P. Borowski[2]
[1]*Department of Chemical Technology, Lublin University of Technology, Lublin, Poland*
[2]*Department of Chemistry, Maria Curie-Skłodowska University, Lublin, Poland*

Abstract
The DFT/B3LYP and *ab initio* CASSCF methods were applied in order to calculate the relative energies for a few reactions of ozone with nitrogen oxide (NO) and nitrogen dioxide (NO_2). The electronic energies of substrates and products were corrected for the zero point energy (ZPE) vibrations. The energy ΔE released during the reaction, calculated as $\Delta E=E_{\text{products}}-E_{\text{substrates}}$, was then obtained. All reactions considered in this work turned out to be exothermic.

Keywords: oxygen, ozone, nitrogen oxides (NO_x), energetics, DFT, CASSCF

1. Introduction

Within the problem of limiting of nitrogen oxides pollutants (NO_x) even the widest applied methods of catalytic reduction cannot be considered to be universal. Methods based on the destruction of nitrogen monoxide (or its higher oxides) are usually quite efficient but very expensive because of the need to break the N–O bond. Although nitrogen monoxide is an endothermic compound its decomposition to nitrogen and oxygen in a molecular forms runs through the stage of dissociation into atoms which is a strongly endoenergetic process. For economical reasons substances of high oxidizing potential were not used to oxidize tail nitrogen oxides in the nitric acid production process. Recent years of intensive investigations of ozone synthesis process have resulted in significant reduction of ozone generation costs at simultaneous widening of the production scale [1,2]. First attempts of ozone application appeared to be quite efficient but the subsequent experiments on semi-technological scale revealed some disadvantages such as a tendency to produce hardly removable aerosols. Another disadvantage is that ozone is an expensive oxidizer and needs to be used in excess in order to obtain the nitrogen pentoxide.

The utilization of NO_x from the gas-phase based on the oxidation using ozone nowadays seems to be a very promising method for both economical and technological reasons [3]. The determination of the main factors affecting its efficiency requires the detailed knowledge of the mechanisms of individual reactions. In principle the method can be modeled by a couple of reactions involving different nitrogen oxides and ozone (O_3), which lead to the formation of the nitrous acid (HNO_3). We consider the following reactions:

$$NO + O_3 \rightarrow NO_2 + O_2 , \quad (1)$$
$$NO_2 + O_3 \rightarrow NO_3 + O_2 , \quad (2)$$
$$NO_2 + NO_3 \rightarrow N_2O_5 , \quad (3)$$
$$2NO_2 + O_3 \rightarrow N_2O_5 + O_2 , \quad (4)$$
$$N_2O_5 + H_2O \rightarrow 2HNO_3 . \quad (5)$$

However, their mechanisms are complicated and yet not well known. In addition obtaining such information only from experimental data seems to be very complicated, time-consuming and expensive. On the other hand the theoretical investigations of these reactions, as well as proposing the relevant model for the method may to be more economical. The theoretical (quantum chemical) methods may turn out to be very useful with that respect. The calculation of the energetics of each of these processes is of particular significance. The modern theoretical techniques, involving the density functional theory (DFT) and *ab initio* multiconfigurational approach (MCSCF), are well suited for this kind of calculations. In the following we present our theoretical investigations of structures of the oxygen molecule, the ozone molecule and a few nitrogen oxide molecules, as well as the energetics of the reactions (1) – (4).

2. Computational details

The primary goal of our theoretical investigations was the determination of the relative energies, defined as $\Delta E=E_{\text{products}}-E_{\text{substrates}}$, for the reactions (1) – (4). This can be accomplished by calculating the equilibrium geometries and electronic energies of substrates and products: the oxygen molecule, the ozone molecule and a few nitrogen oxide molecules NO_x, as well as their zero-point vibration energy (ZPE).

First the optimal structures of oxygen and ozone molecules and all nitrogen oxide molecules involved in the reactions (1) – (4) were calculated at DFT [4] level of theory. In particular the so-called B3LYP exchange-correlation potential [5,6] was used. This method, called DFT/B3LYP, is known to give accurate molecular geometries and (relative) electronic energies. Note, that in the case of the open-shell molecules (O_2, NO, NO_2, NO_3) the unrestricted DFT procedure has to be adopted. The DFT calculations were carried out using 6-311G(d,p) basis set [7].

Next the correlated *ab initio* calculations of the optimal structures were carried out. We have chosen the CASSCF [8–10] method, a special case of the more general MCSCF [11] approach. This method is known to account for the major part of the so-called static (or non-dynamic) correlation effects, the effects of particular importance in the description of systems containing the lone-pair electrons. However, it does not incorporate the very important dynamic correlation effects and therefore the final results may suffer from this deficiency. It should be emphasized that for the CASSCF calculations to be of reasonable quality the adequate choice of the so-called active space (the CAS space) is of particular importance. This is especially true with regard to the description of the phenomena involving a few different potential energy surfaces. The balanced and consistent (in a well defined way) inclusion of the configurations into the wave functions of all species of interest is essential in obtaining reasonable values of the relative energies. For example the active space adequate in the treatment of the static correlation in the case of ozone molecule should consist of at least all *p*-derived orbitals, i.e. 6 orbitals from the σ space and 3 orbitals from the π space [12]. This active space may be referred to as the (6/3) active space. The distribution of 12 electrons among 9 orbitals leads to the CI expansion of the CASSCF wave function into approximately 670 configuration state functions (CSF's). Note that the size of the CI expansion has been reduced not only by the spatial symmetry but also by the spin symmetry of the configurations. However, the choice of the active space on the same grounds for the biggest molecule considered in this paper, i.e. the N_2O_5 molecule, becomes impractical. We managed to carry out this kind of calculations, called CASSCF(σ- and π-derived), only for O_2, NO, O_3 and NO_3 molecules. This means, that the CASSCF(σ- and π-derived) relative energies only for the reactions (1) and (2) were computed. Thus we decided to reduce the CI expansion of the MCSCF wave functions by including the excitations only within the π space for all systems. However, it is known [12,13] that, at least for the ozone molecule, any restriction of the active space below that of the (6/3) quality leads to substantial worsening of some of the calculated properties. Indeed, the π-derived active space turned out to be too small (*vide infra*). The CASSCF calculations were carried out using smaller, 6-31G(d,p) basis set [14].

In both DFT and CASSCF calculations the type of the stationary point was determined by frequency calculations. All calculated frequencies turned out to be real indicating that structures corresponding to local minima were found. It is also important to realize that dissociation/association processes may lead to the change of the number of the vibrational degrees of freedom when going from substrates to products. Thus the harmonic frequencies were also used in the calculation of the zero-point energy (ZPE) correction for substrates and products.

All DFT calculations were carried out using the parallel version of the PQS [15] quantum chemistry software. All CASSCF calculations were carried out using the DALTON [16] quantum chemistry software.

3. Results and discussion

3.1. Equilibrium geometries and vibrational frequencies

The equilibrium geometries of the molecules considered in this work are presented in figure 1. Note that only a few selected parameters of the N_2O_5 molecule are reported. The total electronic energies as well as the harmonic frequencies are reported in table 1. These values were used in the subsequent determination of the relative energies for the reactions (1) – (4).

The equilibrium bond length of the ground state ($^3\Sigma_u^-$) oxygen molecule is in good agreement (within 1%) with the experimental value. Apparently the DFT method seems to slightly overestimate, and the CASSCF method – slightly underestimate the attractive forces between atoms, causing the bond length to be shorter/longer, respectively than that found experimentally. As a consequence the harmonic frequency (cf. table 1) of the stretching mode is higher (1640 cm^{-1}, DFT) and lower (1545 cm^{-1}, CASSCF) than the corresponding experimental value of 1580 cm^{-1} [17]. The same trends regarding the bond length are observed in the case of the NO molecule in its (open-shell, $^2\Pi$) ground state. However, the comparison of the theoretical frequency with experimental value cannot be done – only the fundamental experimental frequency was available [18].

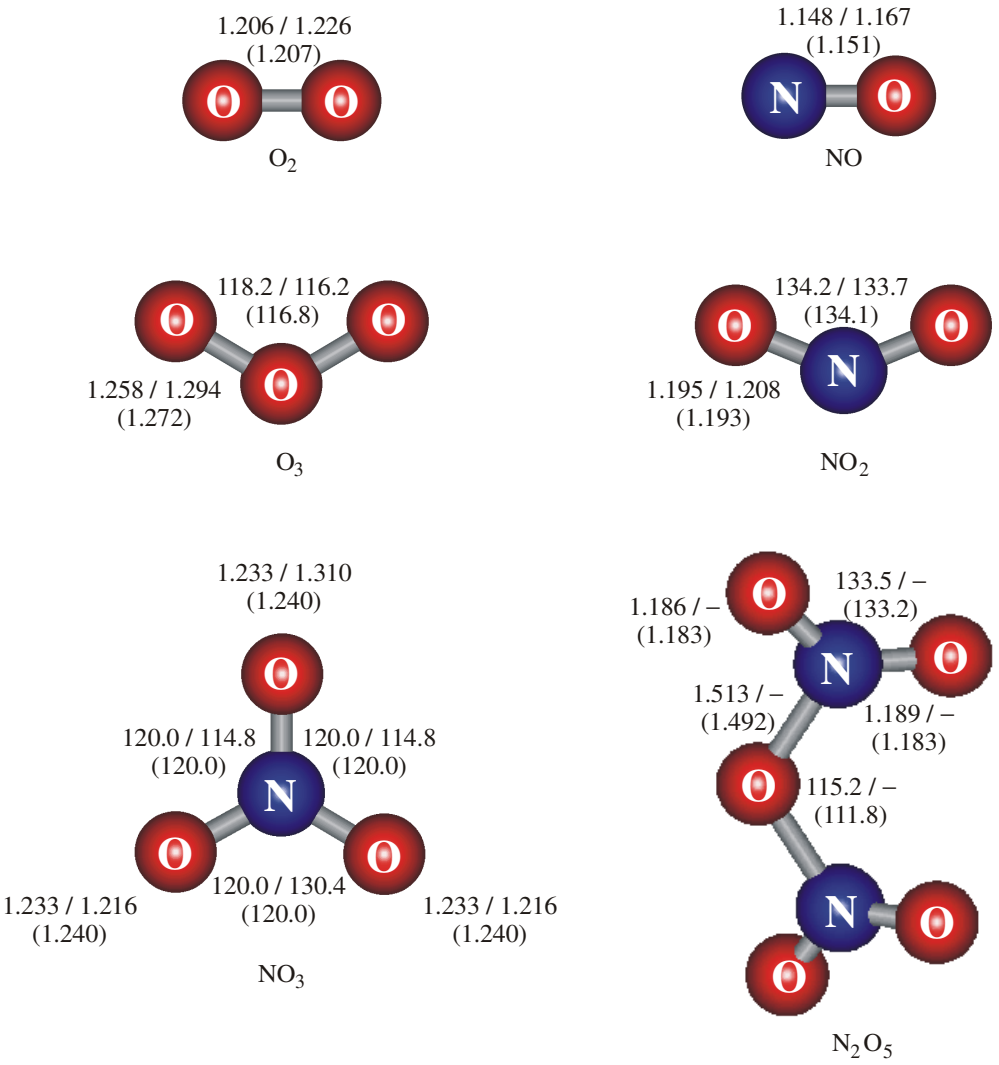

Figure 1. The geometrical parameters of the molecules considered in this work. The upper (separated by "/") are the theoretical values reported in the following order: DFT/B3LYP/6-311G(d,p) / CASSCF(σ- and π-derived)/6-31G(d,p). The experimental values (O_2: ref. [17], NO: ref. [18], O_3: [19], NO_2: [20], NO_3: [21], N_2O_5: [22]) are given in parentheses (bond lengths in Å, valence angles in deg).

In the case of the ozone molecule (in the $^1A_1$ ground state) the theoretically predicted bond lengths behave similarly – they are too short at the DFT level and too long at the CASSCF level. However, it should be noted, that much better agreement of the CASSCF results with experiment for both oxygen [23] and ozone [12] molecules was achieved using ANO-type basis set [24]. Consequently, the harmonic frequencies of two stretching modes (symmetric and antisymmetric) are higher at the DFT level of theory. They are 1249 cm^{-1} and 1191 cm^{-1} at the DFT level and 1078 cm^{-1} and 1015 cm^{-1} at the CASSCF level, respectively. These values are to be compared with experimental harmonic frequencies of 1135 cm^{-1} and 1089 cm^{-1} [25]. The theoretical (DFT and CASSCF) valence angle reproduces well the experimental value and the frequency of the symmetric bending mode is well accounted for. The theoretical geometry of the ground state ($^2A_1$) nitrogen dioxide molecule is also in good agreement with experiment, although the DFT method seems to perform slightly better than the CASSCF method. Somewhat worse performance of the CASSCF method may be due to the quality of the basis set – as was already pointed out the CASSCF calculations should be preferably carried out with a basis set of higher than 6-31G(d,p) quality. Again the comparison of the theoretical frequencies with experimental values cannot be done – only the fundamental experimental frequencies were available [20].

Table 1. The calculated at the DFT/B3LYP/6-311G(d,p) and the CASSCF(σ- and π-derived)/6-31G(d,p) levels of theory electronic energies and harmonic frequencies of oxygen, ozone and selected nitrogen oxide molecules used in the evaluation of the energy released during the reactions (1) – (4).

Molecule	Method	Energy [a.u.]	Harmonic frequencies [cm^{-1}]		
O_2	DFT/B3LYP	–150.364789	1640		
	CASSCF	–149.692351	1545		
	Exp. [17]	–	1580		
NO	DFT/B3LYP	–129.926701	1988		
	CASSCF	–129.351396	1919		
	Exp. [18][a]	–	1876		
O_3	DFT/B3LYP	–225.470791	748	1191	1249
	CASSCF	–224.475823	690	1015	1078
	Exp. [25]	–	716	1089	1135
NO_2	DFT/B3LYP	–205.132719	766	1398	1706
	CASSCF	–204.184820	746	1321	1663
	Exp. [20][a]	–	750	1318	1618
NO_3	DFT/B3LYP	–280.298553	258	258	802
			1121	1121	1135
	CASSCF	–278.993184	440	565	683
			946	1291	1695
N_2O_5	DFT/B3LYP	–485.465713	52	62	220
			344	384	570
			683	683	766
			812	894	1305
			1403	1797	1843
	CASSCF	–	–	–	–

[a]Fundamental frequencies

The NO_3 molecule in its ground electronic state ($^2A_2$') is planar. The experimental investigations [21] clearly demonstrate that the molecule belongs to the D_{3v} symmetry point group. Thus all N–O bond lengths should be the same and the O–N–O valence angles should be equal to 120°. Apparently the DFT/B3LYP approach is capable of predicting the proper structure of the molecule, both with regard to the symmetry of the ground state and the lengths of the N–O bonds. Oddly enough CASSCF is not! The structure predicted by the CASSCF method has C_{2v} symmetry (cf. figure 1). In addition the N–O bonds are substantially shorter than these predicted experimentally. Although all the frequencies turned out to be real, indicating that the local minimum was found, the final result seems to be an artifact of the CASSCF approach.

As can be seen (cf. figure 1) only the DFT/B3LYP geometrical parameters for the N_2O_5 molecule are available. Actually the DFT is a very efficient correlated method, which is used nowadays to carry out the calculations on molecules containing hundreds of atoms. Molecules as small as these considered in the present work should not bring any kind of problem. Indeed, the DFT molecular geometry (note that only a few selected geometrical parameters for N_2O_5 are reported on figure 1) is in good agreement with experimental one. It should be noted that the N_2O_5 molecule is not planar – the torsion O–N–O–N angle predicted by the DFT/B3LYP approach is equal to (approximately) 30° (or 150°). Next the CASSCF calculations were carried out. However, the CASSCF calculations are more complicated than the DFT calculations on account of the rapid growth of the CI expansion of the MCSCF wave function with the increasing size of the active space. As was already pointed out the choice of the σ- and π-derived active space turned out to be impractical for this molecule. Thus we decided to reduce the size of the active space. The choice of π-derived (only) active space for all the molecules led, however, to (*i*) substantial worsening of the results for other molecules and (*ii*) arriving at the saddle point (one complex frequency) rather than at the

local minimum on the N_2O_5 potential energy surface. Many attempts to extend slightly the active space beyond that of the π-derived quality were made. A physically justifiable choice of the active space can be made on the basis of the MP2 natural orbital occupation numbers: (*i*) orbitals with occupation numbers above certain threshold remain inactive, (*ii*) orbitals with occupation numbers below certain threshold remain virtual and (*iii*) the remaining orbitals constitute the active space. However, we failed to find the local minimum of the CASSCF potential energy surface of N_2O_5 for all (chosen in this way) active spaces that could be handled in our laboratory.

3.2. Relative energies

The DFT/B3LYP/6-311G(d,p) and the CASSCF(σ- and π-derived)/6-31G(d,p) relative energies and the relative energies corrected for the zero point vibrational energy for the reactions (1) – (4) are presented in table 2. The data necessary to calculate these energies can be found in table 1.

Table 2. Calculated at the DFT/B3LYP/6-311G(d,p) and the CASSCF(σ- and π-derived)/6-31G(d,p) levels of theory relative energies ($\Delta E=E_{products}-E_{substrates}$) and relative energies corrected for the zero point vibrational energy for the reactions (1) – (4).

Reaction	Method	ΔE [kcal/mol]	$\Delta E^{(ZPE)}$ [kcal/mol]
$NO + O_3 \rightarrow NO_2 + O_2$	DFT/B3LYP	−62.78	−62.31
	CASSCF	−31.36	−30.54
$NO_2 + O_3 \rightarrow NO_3 + O_2$	DFT/B3LYP	−37.56	−38.59
	CASSCF	−15.63	−14.69
$NO_2 + NO_3 \rightarrow N_2O_5$	DFT/B3LYP	−21.62	−16.90
	CASSCF	–	–
$2NO_2 + O_3 \rightarrow N_2O_5 + O_2$	DFT/B3LYP	−59.18	−55.49
	CASSCF	–	–

For all reactions considered in the present work the DFT/B3LYP energy of products is lower than that of substrates. Apparently all reactions are exothermic. The relative energies are ΔE=−61.83 kcal/mol for reaction No (1), ΔE=−39.62 kcal/mol for reaction No (2), ΔE=−12.18 kcal/mol for reaction No (3) and ΔE=−51.80 kcal/mol for reaction No (4). Apparently the most exothermic is the reaction of nitrogen oxide with ozone (reaction 1), the least – the reaction of nitrogen dioxide with nitrogen trioxide (reaction 3). It should be noted that during the reaction (1) the number of vibrational degrees of freedom is the same for substrates and products. Obviously the ΔE and $\Delta E^{(ZPE)}$ are close (cf. table 2). Somewhat bigger difference between these quantities is observed in the case of the reaction 2, in which an extra vibrational degree of freedom appears for products. However, the two low-energy (degenerate, on account of symmetry) vibrational modes cause that the ZPE correction for products is smaller than for substrates and consequently $\Delta E^{(ZPE)} > \Delta E$. 6 and 7 additional vibrational degrees of freedom are gained in the course of the reactions (3) and (4), respectively. Thus the ΔE and $\Delta E^{(ZPE)}$ values for these reactions differ by as much as 4.5 – 5 kcal/mol.

Although all reactions considered in the present work turned out to be exothermic (the total energy of products is lower than the total energy of substrates) they may not be spontaneous. In order to calculate the activation energy of the reactions (1) – (4) the search for the transition states was also carried out. No transition state was found for any of these processes even though numerous initial geometries were used and a few low-energy modes were followed in the iterative procedure. This is a strong indication of the spontaneous character of each of these reactions.

The relative CASSCF energies of only the first two reactions (due to the lack of the reliable data for the N_2O_5 molecule, *vide supra*) were calculated. They are much (more than twice as much) lower than the corresponding DFT/B3LYP energies. However, we are inclined to trust more the DFT/B3LYP energies due to the lack of the dynamic correlation in the CASSCF wave function.

4. Conclusions

In this work the relative energies, defined as $\Delta E = E_{\text{products}} - E_{\text{substrates}}$, for a few reactions involving nitrogen oxides and ozone were calculated at DFT/B3LYP/6-311G(d,p) and CASSCF(σ- and π-derived)/6-31G(d,p) levels of theory. It was demonstrated that the DFT/B3LYP is superior to the *ab initio* CASSCF approach. The DFT method provides an efficient way of estimating the (static and dynamic) correlation energy for the (strongly multiconfigurational) species, like these considered in the present work. Good agreement between the DFT/B3LYP and the experimental geometries as well as harmonic frequencies (if available experimentally) was achieved. On the other hand in some cases the CASSCF approach either (*i*) gives the wrong structure of the molecule (like NO_3 molecule) or (*ii*) cannot be applied due to the computational problems (like in the case of N_2O_5 molecule). The (ZPE corrected) relative energies for *all* reactions, i.e. reactions (1) – (4), were computed at the DFT level only. The negative values of the $\Delta E^{(\text{ZPE})}$ (exothermicity) along with the lack of the transition states provides a strong indication that the spontaneous character of all reactions considered in the present work.

Acknowledgements

The research has been supported by *The Ministry of Scientific Research and Information Technology* within the frame of the research project 4T 09B03425 in the years 2003-2006.

References

[1] J. Jaroszyńska-Wolińska, M. Wroński, *Pol. J. Chem. Tech.*, **4**, 8 (2002).
[2] J. Jaroszyńska-Wolińska, M. Wroński, J. Ozonek, I. Pollo, *Proc. Int. Symp. on High Pressure Low Temperature Plasma Chemistry, Hakone VIII*, Estonia, **2**, 210 (2002).
[3] J. Jaroszyńska-Wolińska, *Proc. Int. Symp. on High Pressure Low Temperature Plasma Chemistry, Hakone IX*, Padowa, 7P-02 (published as CD, 2004).
[4] See e.g. R.G. Parr, W. Yang, *Density-Functional Theory of Atoms and Molecules*, and Oxford University Press: New York (1989).
[5] A.D. Becke, *J. Chem. Phys.*, **98**, 5648 (1993).
[6] C. Lee, W. Yang, R.G. Paar, *Phys. Rev.* B, **37**, 785 (1993).
[7] R. Krishnan, J.S. Binkley, R. Seeger, J.A. Pople, *J. Chem. Phys.*, **72**, 650 (1980).
[8] B.O. Roos, P.R. Taylor, P.E.M. Siegbahn, *Chem. Phys.*, **48**, 157 (1980).
[9] B.O. Roos, *Int. J. Quantum Chem.*, **S14**, 175 (1980).
[10] P.E.M. Siegbahn, J.A. Almlöf, A. Heiberg, B.O. Roos, *J. Chem. Phys.*, **74**, 2384 (1981).
[11] A.C. Wahl, G. Das, *Adv. Quantum Chem.*, **261**, 5 (1970).
[12] P. Borowski, K. Andersson, P.-Å. Malmqvist, B.O. Roos, *J. Chem. Phys.*, **97**, 5568 (1992).
[13] K. Andersson, P. Borowski, P.W. Fowler, P.-Å. Malmqvist, B.O. Roos, A.J. Sadlej, *Chem. Phys. Lett.*, **190**, 367 (1992).
[14] P.C. Hariharan, J.A. Pople, *Theor. Chim. Acta*, **28**, 213 (1973).
[15] *PQS version 3.1, Parallel Quantum Solutions*, 2013 Green Acres Road, Fayetteville, Arkansas 72703.
[16] *Dalton, a molecular electronic structure program, Release 1.2*, (2001), written by T. Helgaker, H.J.Aa. Jensen, P. Joergensen, J. Olsen, K. Ruud, H. Aagren, A.A. Auer, K.L. Bak, V. Bakken, O. Christiansen, S. Coriani, P. Dahle, E.K. Dalskov, T. Enevoldsen, B. Fernandez, C. Haettig, K. Hald, A. Halkier, H. Heiberg, H. Hettema, D. Jonsson, S. Kirpekar, R. Kobayashi, H. Koch, K.V. Mikkelsen, P. Norman, M.J. Packer, T.B. Pedersen, T.A. Ruden, A. Sanchez, T. Saue, S.P.A. Sauer, B. Schimmelpfennig, K.O. Sylvester-Hvid, P.R. Taylor, and O. Vahtras.
[17] T.G. Slanger, P.C. Cosby, *J. Phys. Chem.*, **92**, 267 (1988).
[18] H.P. Huber, G. Herzberg, *Molecular Structure and Molecular Spectra. IV. Constants of Diatomic Molecules*, Van Nostrand Reinhold: Toronto (1979).
[19] T. Tanaka, Y. Morino, *J. Mol. Spectr.*, **33**, 538 (1970).
[20] D.R. Lide, ed. *CRC Handbook of Chemistry and Physics*, CRC Press, Inc., Boca Raton (1995)
[21] A. Stirling, I. Pápai, J. Mink, D.R. Salahub, *J. Chem. Phys.*, **100**, 2910 (1994).
[22] B.W. McClelland, L. Hedberg, K. Hedberg, K. Hagen, *J. Am. Chem. Soc.*, **105**, 3789 (1983).
[23] P. Borowski, M. Füscher, P.-Å. Malmqvist, B.O. Roos, *Chem. Phys. Lett.*, **237**, 195 (1995).
[24] J.A. Almlöf, P.R. Taylor, *J. Chem. Phys.*, **86**, 4070 (1987).
[25] A. Barbe, C. Secroun, P. Jouve, *J. Mol. Spectr.*, **49**, 171 (1974).

Dynamic Interaction Between Plasma and RF Source in Radio Frequency Inductively Coupled Thermal Plasma Generation at Atmospheric Pressure

M. Abdur Razzak[1], Shuichi Takamura[1] and Yoshihiko Uesugi[2]

[1]*Department of Engineering and Science, Graduate School of Engineering, Nagoya University, Furo-cho, Chikusa-ku, Nagoya 464-8603, Japan*
[2]*Department of Electrical and Electronic Engineering, Faculty of Engineering, Kanazawa University, 2-40-20 Kodatsuno, Kanazawa 920-8667, Japan*

Abstract

The dynamic interaction between plasma and a semiconductor-based radio frequency (rf) power source at the initial start-up phase of induction plasma at atmospheric pressure is investigated experimentally. A strong deterioration of power efficiency of the rf source is observed during the dynamic *E-H* mode transition, thereby decreasing the effective plasma production efficiency. Having employ a constant current immittance conversion circuit shows successful improvement of the power efficiency in induction plasma generation.

Keywords

dynamic interaction, inductively coupled plasma, thermal plasma, static induction transistor, radio frequency, atmospheric pressure, and *E-H* mode transition.

1. Introduction

A radio frequency (rf) inductive discharge operated at atmospheric pressure range requires high voltage in the initial start-up phase and high power during the steady state sustainment phase. It is thus necessary to ensure that the maximum possible rf power is injected to the high-pressure plasma from the power source, especially where the rf power is limited to few kilowatts. To understand the insight of this feature, it is necessary to investigate the dynamic interaction between plasma and rf power source at the initial start-up phase of induction plasma especially during the *E-H* mode transition period. With those in mind, we have studied the dynamic behaviors of atmospheric pressure (101 kPa) argon inductive discharges at the ignition stage experimentally, at a radio frequency of 1.2 MHz and a moderate rf power of about 3.5 kW.

High-power semiconductor-based radio frequency inverter power source [1] has become popular in the last decade with their application to various kinds of induction heating and plasma generation [2, 3] due to their high-efficiency and high-power operation. Inherent problems [4-6] are faced during high-pressure induction plasma generation using a in a static induction transistor (SIT) inverter-based rf power source. Because, at high operating frequencies in the MHz range, rf system behaves transient and strongly non-linear due to the presence of switching devices and reactive components in the power source, and non-linear interaction between plasma and rf source [7, 8]. With those in mind, in this article we investigate the transient behaviors of radio frequency (rf) inductive discharges generated by inductively coupled plasma (ICP) technique at the initial startup phase at atmospheric pressure. These analyses enable us finding a way to generate high-pressure (near one atmosphere) induction thermal plasmas with moderate rf power of few kilowatts. In this article, we discuss a simple and robust method by having employ a constant-current high-power immittance circuit [9] to enhance the power efficiency of the rf source as well as the power coupling efficiency between plasma and rf source, thereby generating the efficient rf induction thermal plasmas at atmospheric pressure in argon.

2. Experiment

In the present experiment, plasmas are sustained in a cylindrical Pyrex glass chamber with an inner diameter of 7 cm and length of 20 cm by applying a static induction transistor (SIT) inverter power source [1]. The rating of frequency range and maximum output power of the SIT inverter is 0.5–1.5 MHz and 20 kW (pulse operation), respectively. An induction coil consisting of 7 turns of a copper tube of ¼ inch outer diameter is used as the loop antenna. Argon gas is injected both axially and spirally into the discharge tube with a total flow rate of 20 lpm.

The neutral gas pressure is measured with a total pressure gauge by using a mechanical rotary pump. The rf power level is modulated with a 100 ms square wave pulse without applying any cooling system. Repetitive spark discharge, using the spark discharge technique [3], with a repetition frequency of 500 Hz and duration of 20 ms (total 10-pulse), is applied simultaneously with the rf modulating pulse to initiate the discharge. This task is performed by using a typical automobile spark plug, placed at the center of the top flange of the discharge chamber with a high-voltage transformer circuit. An *LC* matching network is employed to optimize the power coupling efficiency. For details experimental set up with block diagram, the readers are referred to Ref.5.

3. Dynamic Behaviors

At the initial phase of rf breakdown, a streamerlike electrostatic discharge (*E* discharge) develops by the strong axial electrostatic field (100-200 kV/m) due to the high rf voltage on the induction coil for several hundred microseconds, and then a rapid transition from electrostatic to electromagnetic mode occurs developing the ring-shaped electromagnetic discharge (*H* discharge) to form the volumetric induction plasmas [4-6].

The temporal plasma loading resistance and reactance indicating a dynamic transition from one mode to another is shown in Fig. 1(a). A rapid increase of the temporal coil loading resistance and decrease of the effective coil inductance, obtained by the rf input voltage to current ratio, are observed during the dynamic change from *E* to *H* mode. The resistance in the *E* mode is very small due to a weak coupling of electrostatic discharge and becomes high in the *H* mode due to the growth of the inductive plasma. The reactance, on the other hand, is slightly positive in the *E* mode, and decreases and becomes negative with the development of the *H* mode as shown in Fig. 1(a) due to plasma reaction by the induction current flowing in the azimuthal direction but opposite to that of the rf coil current, which decreases the original axial magnetic flux thereby decreasing the effective coil loading reactance and thus the inductance. The rf coil current, therefore, drops abruptly, as shown in Fig. 1(b), when the load changes from the capacitive to inductive mode due to the impedance rise thereby decreasing the rf power absorbed by the plasma and thus the power coupling efficiency.

The temporal change of coil loading inductance is shown in Fig. 2(a). Due to decrease of effective coil inductance, the driving frequency and thus the phase between inverter output voltage and current are shifted from their resonance value as shown in Fig. 2(b). The temporal change of driving frequency and phase difference during the *H* mode deviate from the resonance value about 15 kHz and $+\pi/4$ radian, respectively with a resonance frequency of 1.09 MHz at atmospheric pressure as shown in Fig. 2(b). From Fig. 2(b) it is seen that the phase of inverter output current (with respect to inverter output voltage), which is zero before plasma ignition due to resonance tuning, becomes slightly negative during *E* mode due to electrostatic coupling and becomes positive during the *H* mode due to electromagnetic coupling. The total load, therefore, becomes slightly capacitive during the *H* mode thereby increasing the switching losses of the SIT inverter elements present in the rf system. As a result, the inverter output as well as the dc-rf power conversion efficiency (P_{dc}/P_{rf}) strongly deteriorates as shown in Fig. 2(c).

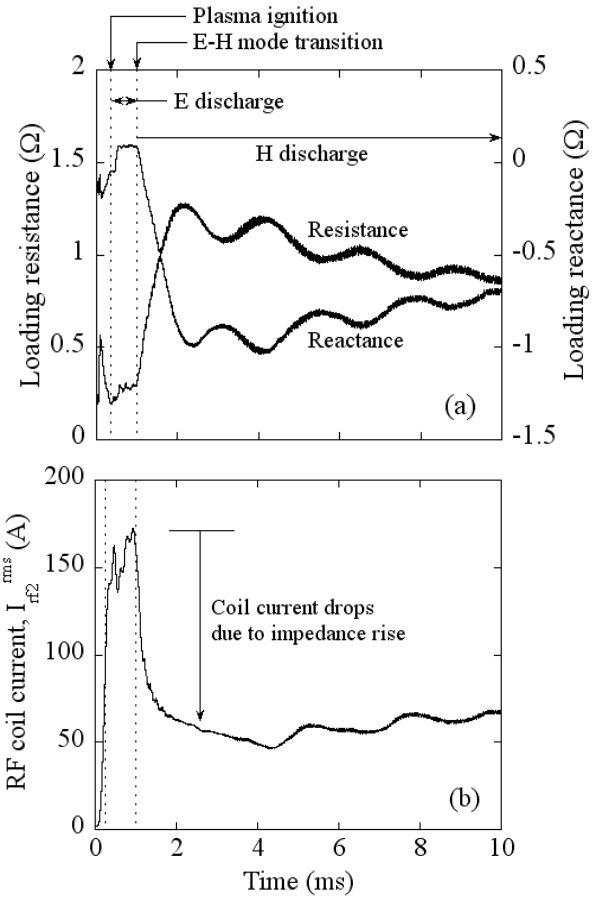

Fig. 1: (a) Temporal plasma loading impedance showing the different modes of operation; and (b) rf coil current waveform at the time of plasma ignition.

The dc-rf power conversion efficiency of the rf power source decreases from about 90% to a value of about 60% as shown in Fig. 2(c). This power conversion efficiency completely depends on the frequency and phase shift from their resonance value. Therefore, in some cases, the dc-rf conversion efficient drops to about 30% depending on the phase and frequency shift [7].

4. Enhancing the Power Efficiency

Having control gate driving frequency of SIT, the power efficiency of the rf source can be enhanced [4]. In this experiment, we use another simple and robust method by employing a high-power constant-current immittance circuit, which is shown in Fig.3, having other experimental conditions remain unchanged. Applying the resonance condition and assuming that the internal resistances of the inductors are negligible (r_{L1} = r_{L2} = 0), the voltage current relations can be obtained from Fig. 3 as

$$I_1 = V_1 Z_L / Z_0^2, \quad (1)$$

$$I_2 = V_1 / jZ_0, \quad (2)$$

where Z_L is the plasma loading impedance and $Z_0 = \sqrt{L_1/C_1}$ is the characteristic impedance determined by the primary inductance and capacitance.

From Eq.(2) it is seen that immittance circuit provides constant output current with a fixed voltage source since the characteristic impedance Z_0 is a constant. This confirms high output rf power thereby increasing the dc-rf power conversion efficiency of the rf source in induction plasma generation over the conventional series resonance circuit as shown in Fig.4. The time evolution of effective rf power using the immittance circuit with that of the series resonance circuit is compared in Fig. 4(a), from where the value of effective rf power, calculated from the rf power supply side, is found to be about 3 kW with immittance circuit, while about 1.2 kW with series resonance circuit after the plasma ignition under the same operating condition. Therefore, the effective rf power injected into the plasma is about three times larger in the case of immittance circuit than that of the series resonance circuit after the plasma ignition. Fig. 4 (b) shows the comparison of dc-rf power conversion efficiency (ratio of rf output power and dc input power) using immittance circuit with that of the conventional series resonance circuit, from where it is seen that the power conversion efficiency is about 90-92% using the immittance circuit, which is as much as three times than that of the conventional series resonance circuit (which is about 30%). Because, using the series resonance circuit, the total load behaves slightly capacitive due to the

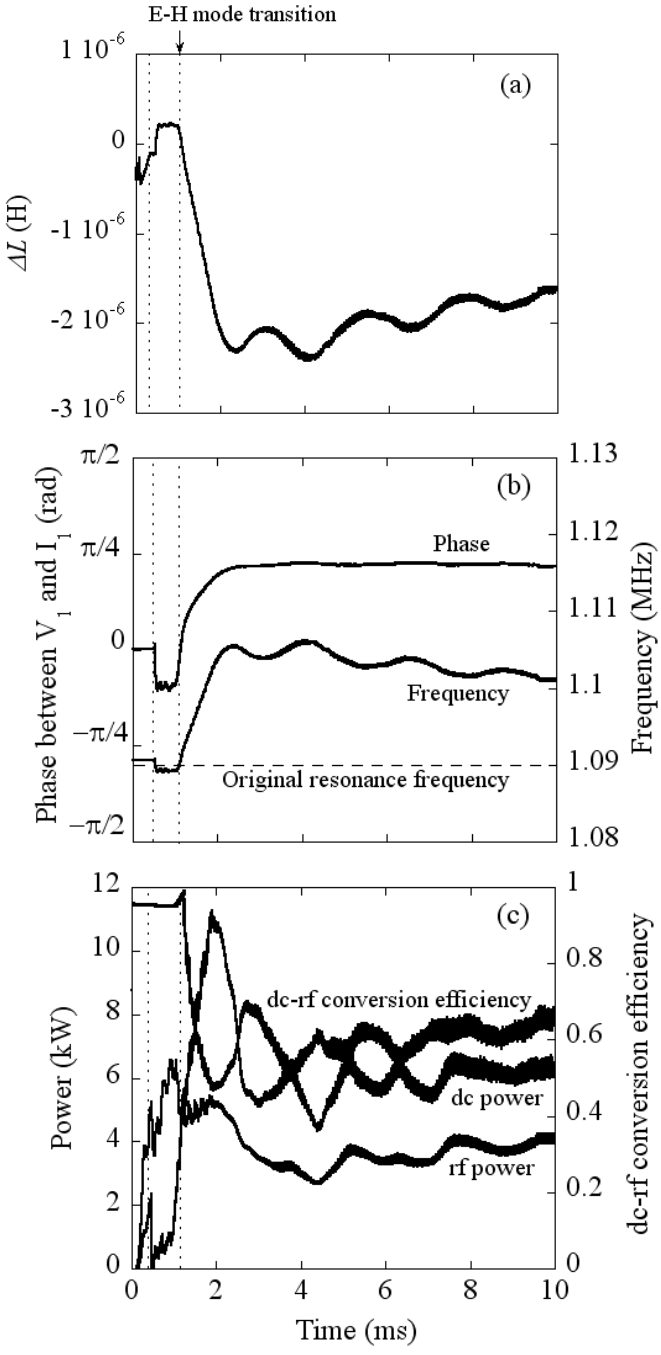

Fig. 2: (a) Temporal change of effective coil inductance; (b) Time evolution of frequency and phase; and (c) temporal rf output power and dc-rf conversion efficiency during *E-H* mode transition.

positive phase shift (about $+\pi/4$ radian) after the plasma generation, which increases the switching losses of the SIT inverter elements, thereby decreasing the rf output power and thus the dc-rf conversion efficiency. On the other hand, having the constant coil current properties as shown in Eq. (2), the immittance circuit helps to inject high rf power into the plasma thereby increasing the plasma heating efficiency as well as the plasma production efficiency.

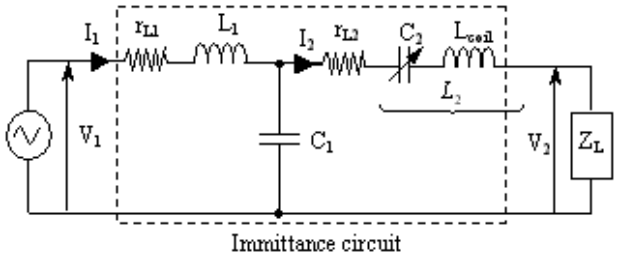

Fig. 3: Typical T-LCL immittance conversion circuit for constant current operation.

5. Conclusion

The dynamic interaction between plasma and a semiconductor-based radio frequency (rf) power source at the initial start-up phase of induction plasma at atmospheric pressure is investigated experimentally. A rapid increase of the plasma loading resistance and decrease of the effective loading inductance are observed during the dynamic change of plasma from electrostatic (*E*) to electromagnetic (*H*) mode, thereby deviating the output *RLC* circuit (including rf induction coil) from its ideal resonance condition. As a result, the power efficiency of the rf source strongly deteriorates from about 90% to 40%, thereby decreasing the effective plasma production efficiency. These analyses are very much helpful finding a way to generate of high-pressure (one atm or more) induction thermal plasmas especially where the rf power is limited to few kilowatts. In the present experiment, employing a constant-current high-power immittance conversion circuit shows successful improvement of the power efficiency in induction plasma generation (see Fig. 4).

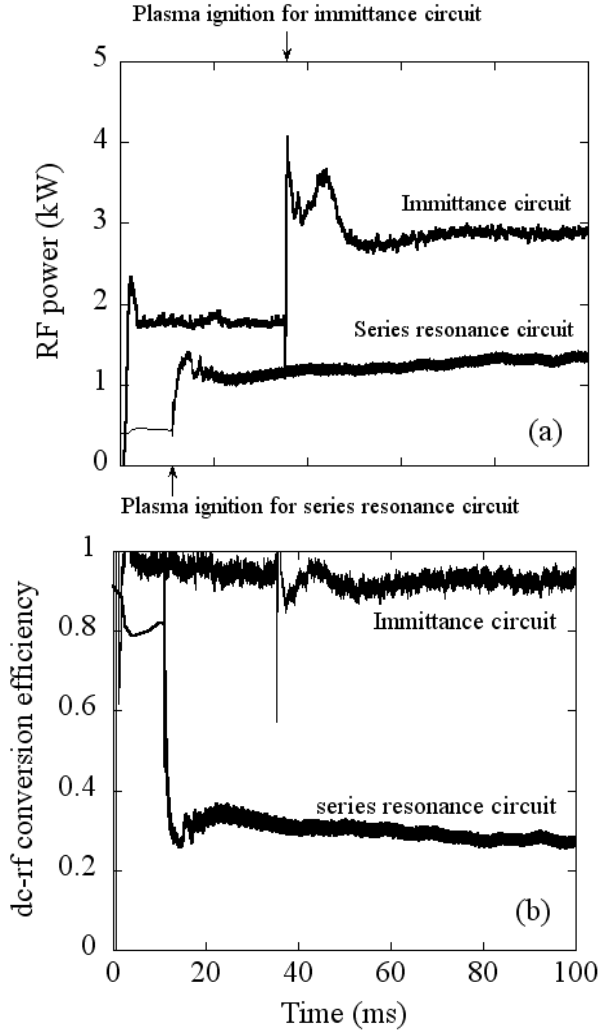

Fig. 4: Comparison of (a) rf output power; and (b) dc-rf power conversion efficiency using immittance circuit with that of the conventional series resonance circuit in high-pressure induction plasma generation.

References

[1] S. Watanabe, Y. Uesugi, S. Ohsawa and S. Takamura: Rev. Sci. Inst. **69**, 3555 (1998).

[2] Y. Uesugi, T. Imai, H. Sawada, N. Hattori, S. Takamura: *VACUUM*, **59**, 24 (2000).

[3] Y. Uesugi, T. Adachi, K. Kondo and S. Takamura: Trans. IEE Japan **122A**, 461 (2002) (in Japanese).

[4] M. A. Razzak, S. Takamura, and Yoshihiko Uesugi: *IEEE Tans. Plasma Sci.*, **33**, (2005).

[5] M. A. Razzak, K. Kondo, Y. Uesugi, N. Ohno and S. Takamura: J. Appl. Phys. **95**, 427 (2004).

[6] M. A. Razzak, S. Takamura, and Y. Uesugi: *J. Appl. Phys.*, **96**, 4771 (2004).

[7] M. A. Razzak, H. Ukai, Y. Uesugi, and S. Takamura: *Porc. Intl COE Forum Plasma Science Technology* (Nagoya, 2004) p. 83.

[8] M. A. Razzak, Y. Suzuki, S. Takamura, and Y. Uesugi: *Proc. XV Intl. Conf. Gas Discharge Their Appl.*, (Toulouse, 2004) p.505.

[9] H. Oguchi, R. Shimotaya, T. Shimizu, H. Takagi and M. Ito: *Trans. IEE Japan*, **121D**, 805 (2001)

Investigation of reactive hydrocarbon plasmas using THz-spectroscopy

J.-C. Schauer[1], M. Böke[1], S. Ebbinghaus[2], K. Schröck[2], E. Bründermann[2], M. Havenith[2] and J. Winter[1]

[1]*Lehrstuhl für Experimentalphysik II, Ruhr-Universität Bochum, Germany, email: js@ep2.rub.de*

[2]*Lehrstuhl für Physikalische Chemie II, Ruhr-Universität Bochum, Germany*

Abstract

For the first time we applied THz-spectroscopy as diagnostics in reactive plasmas. A 20 fs TiSa laser was used to produce short, broadband THz pulses via a GaAs emitter. The measurements were performed in a dust particle forming Ar-C_2H_2 plasma. We observed rotational lines of different hydrocarbons including ions and radicals.

1. Introduction

The formation of dust particles is of great interest in the field of thin film deposition or dry etching. But still the growth process is not completely understood. Today there is the following scenario for the growth of dust particles in the case of hydrocarbon plasmas: starting with negative ions (C_2H^-) big negative charged molecules are built through reactions with the neutral gas. Those molecules collapse and grow further through accretion. Especially for the first phase of dust formation sophisticated diagnostics are required to understand the nucleation process and to identify experimentally the nature of growth precursors of the particles. As a new diagnostic tool we used THz time-domain spectroscopy in reactive plasmas.

2. Experiment

Figure 1 shows the experimental set up. The dust particles were grown in a capacitively-coupled GEC-cell, powered by 20 Watt at 13.56 MHz. C_2H_2 diluted with Ar was used as precursor gas. The gases were introduced through the showerhead-like upper electrode, controlled by mass-flow controllers. The chamber was placed directly into the beam path of the laser. The laser pulses were transmitted through the plasma via methylpentene copolymer (TPX) windows installed at two opposite flanges. TPX was used because of its high transparency in the far IR and in the visible region. A femtosecond TiSa-laser (2) (KMLabs Inc. [1]) was used as the pulse source, pumped by a 532 nm Verdi laser (1). The mode locked laser emits a 80 MHz pulse train of 20 fs pulse width and 500 mW overall optical output power. The infrared laser beam is split into two parts of similar intensity by a beam splitter (3), one part for the emission of THz-radiation, the other part for coherent detection of the THz-pulse. The two beams are focussed on emitter (7) and detector (12), respectively. Emitter and detector are made of low-temperature grown Gallium Arsenide doped with CrO as the photoconductive substrate. An Au:Ge:Ni alloy is used for ohmic contact. A detailed description of the photoconductive antenna substrate and geometry and its correlation to the emitted THz-field is given in [2,3]. The size of the used photoconductive gap is 5x5 μm^2 and the length between the transmission lines is 20 μm. For the emission process the

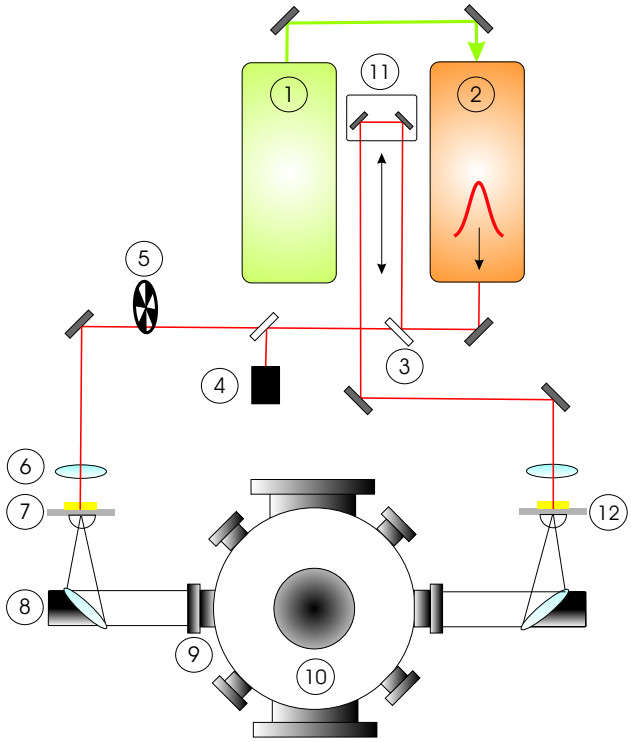

Figure 1: Experimental set up of the laser and the plasma chamber: (1) pump laser, (2) Ti:Sa femtosecond laser, (3) beam splitter, (4) Vis-IR spectrometer, (5) optical chopper, (6) microscope objective, (7) THz emitter (LTG-GaAs), (8) parabolic mirror, (9) methylpentene copolymer (TPX) window, (10) plasma chamber (GEC-cell), (11) delay line, (12) THz detector (LTG-GaAs).

photoconductive antenna of the emitter is contacted with 40 V DC bias. For coherent detection the induced photocurrent in the photoconductive antenna gap of the detector is measured using a lock-in amplifier. The emitted THz-pulse is collected and focussed using hemispherical high resistivity silicon lenses directly on the emitter. An off-axis parabolic mirror (8) focuses the beam through the TPX-windows and the plasma chamber. A second parabolic mirror and a silicon lens again focuses the THz-pulse on the detector, which is identical to the emitter. The transmitted THz-field is recorded by a variable delay between the first and second femtosecond pulse. The recorded electric field is transformed into the frequency domain using fast fourier transformation (FFT). For the measurements a pure argon plasma was ignited in the chamber as a reference (8 sccm Ar, 20 W rf power). The main measurements were performed in dusty plasmas, using 8 sccm Ar and 2 sccm C_2H_2 (20 W rf power, 10 Pa). After the ignition of the plasma the formation of dust particles starts immediately. After a while dust particles in the chamber between the electrodes could be detected by diffraction of HeNe laser light. Figure 2 shows dust particles collected in the chamber after the measurements. They consist mainly of carbon, are spherical and have a cauliflower-like

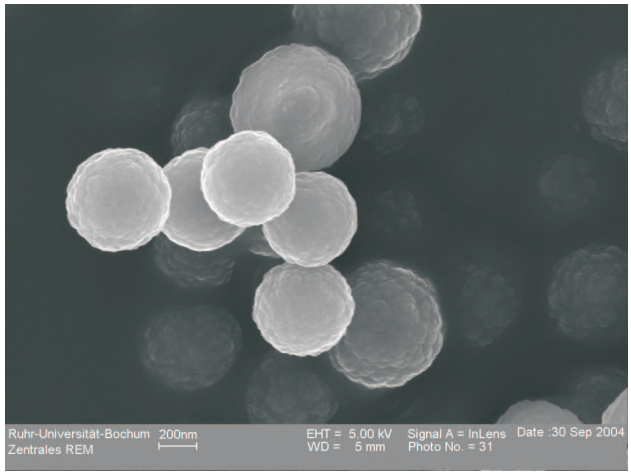

Figure 2: Dust particles collected from the chamber after the experiment

shape. Figure 3 shows a mass spectrum measured with a residual gas analyzer in the same set up. Besides C_2H_2 and its dissociation products also higher hydrocarbon molecules like C_4H_2 and C_6H_4 are observed. This gives evidence for the fact that dust particles are formed from chains of hydrocarbon molecules. C_2H^- ions are supposed to be a precursor for the dust formation [4]. They are built through dissociative electron attachment of C_2H_2. The C_2H^- molecules react with other gas molecules building larger molecules which collapse and grow further through accretion until macroscopic dust particles are generated [5]. Negative ions like C_2H^- are confined in the plasma and are therefore expected to have a long lifetime in the chamber.

The aim of the experiments is to monitor particles and molecules in the dusty plasma. The absorption and emission spectrum of the plasma was recorded and Fourier-transformed to obtain the THz spectrum between 3 and 35 cm^{-1}. The spectral resolution of the measurement was 0.05 cm^{-1}, scanning time was one hour. In order to eliminate background signals measurements with and without C_2H_2 were performed. The transmission function of the dusty plasma with respect to the pure argon discharge can be evaluated by comparing the squares of the electric fields or simply by dividing the two measured currents:

$$T(\nu) = \frac{I_{sample}}{I_{reference}}. \tag{1}$$

3. Results and Discussion

Figure 4 shows a measured spectrum in an Ar-C_2H_2 plasma. In this measurement we could assign several lines to the C_2H molecule, one to the CH^+ ion and one to the CH_2 molecule. In measurements with a different detector which could measure in a lower frequency region and with

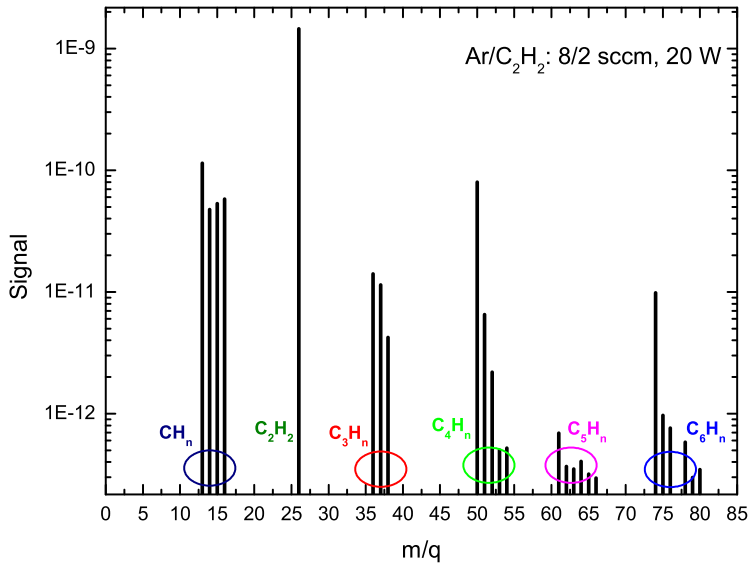

Figure 3: Mass spectrum of a discharge in an Ar-C_2H_2 discharge at 20 W rf power.

a higher resolution we were able to observe more lines of the above mentioned molecules and also lines of ArH^+ (41.3 cm−1) and of CH (18.3 cm^{-1} and 49.3 cm^{-1}). The origin of the observed lines are rotational transitions of molecules in the gas of the dusty plasma. Both emission and absorption are expected to be in the THz region. In the region from 3 to 35 cm^{-1} we observed emission, at higher wave numbers we saw absorption. Since only few data for rotational lines of hydrocarbon molecules in this frequency region are available, we were not able to assign the remaining lines. We assume the other lines also to be rotational lines of hydrocarbon molecules, including their ions.

4. Summary and Outlook

For the first time we performed THz spectroscopy in reactive plasmas. We observed several rotational lines of different hydrocarbons including positive ions and radicals. A whole set of lines in the region from 10 to 35 cm^{-1} could be attributed to C_2H (Fig. 4). Also other ions and radicals could be identified. We showed that THz spectroscopy is a powerful tool for the diagnostics of reactive plasmas. It is even possible to detect species like C_2H which are not easily detectable by mass spectrometry. With a higher resolution it is also possible to calculate the concentration and the temperature of the molecules and ions in the plasma.

In future we intend to detect possible eigenmodes of the nanoparticles which are assumed to lie in

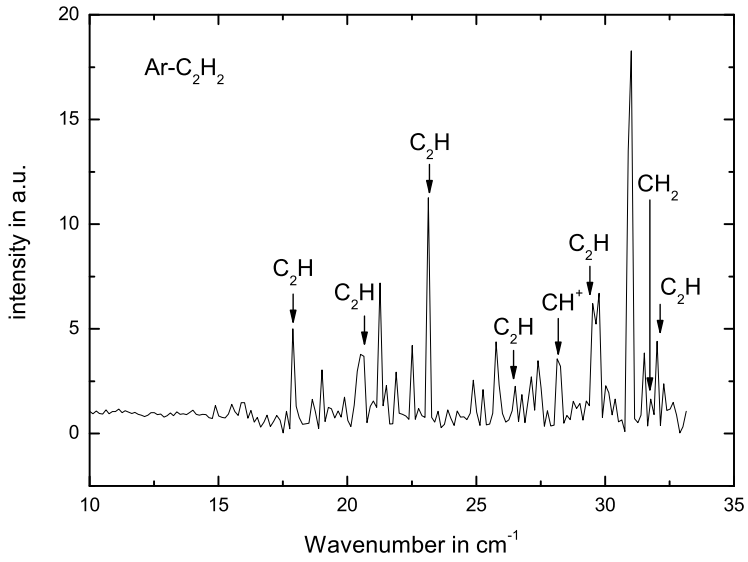

Figure 4: Measured spectrum in an Ar-C_2H_2 plasma. Several C_2H lines, one CH^+ line and one CH_2 line can be observed.

the THz frequency range in order to develop a diagnostic for very small dielectric particles which are not accessible by other optical methods (Mie-ellipsometry, laser light scattering). We think that THz spectroscopy offers a wide range of applications in the field of plasma diagnostics. It can close the gap between plasma ion mass spectrometry (up to 2000 amu) and Mie-ellipsometry (particles with diameter of 50 nm or bigger).

References

[1] M. T. Asaki, C. P. Huang, D. Garvey, J. Zhou, H. C. Kapteyn, M. M. Murnane: Generation of 11-fs pulses from a mode locked Ti:Sa laser, Optics Letters **18** (1993) 977

[2] M. Tani, M. Herrmann, K. Sakai: Generation and detection of terahertz pulsed radiation with photoconductive antennas and its application to imaging, Meas. Sci. Technol. **13** (2002) 1739

[3] P. U. Jepsen, R. H. Jacobsen, S. R. Keiding: Generation and detection of terahertz pulses from biased semiconductor antennas, J. Opt. Soc. Am. **13** (1996) 2424

[4] S. Hong, J. Berndt, J. Winter: Growth precursors and Dynamics of Dust Particle Formation in the Ar/CH_4 and Ar/C_2H_2 Plasmas, Plasma Sources Sci. Technol. **12** (2003) 46

[5] A. Bouchoule: Dusty Plasmas, Wiley, p. 78

Cold Atmospheric Pressure Plasma Nanoparticle Production

V. Vons[1,2], M. Barankin[1],Y. Creyghton[2], A. Schmidt-Ott[1]

[1] *Particle Technology, DelftChemTech, Delft University of Technology, Julianalaan 136, NL-2628 BL Delft, The Netherlands*
[2] *TNO Defence, Security and Safety, Lange Kleiweg 137, 2288 GJ, Rijswijk, The Netherlands*

Abstract
Two different cold plasma sources capable of operation at atmospheric pressure were tested for continuous production of both carbon and iron nanoparticles. These experiments were successful with both sources.

Keywords: Cold plasma, atmospheric pressure, nanoparticles

Introduction

In cold or non-equilibrium plasma, free electrons gain sufficient energy from the applied electric field for ionisation and molecular dissociation, while ions and molecules remain at almost the initial gas temperature. When applied to nanoparticle production, these free electrons dissociate a volatile precursor, for instance a metal organic complex or a hydrocarbon. Thus a supersaturated metal or carbon vapour is formed in the cold plasma, which, due to the low overall gas temperature, condenses to form nanoparticles. Subsequently, the particles can be coated with a different compound in the same plasma system [1].

So far, cold plasmas used for nanoparticle production have been low-pressure (usually <40 mbar [1]) microwave and radio frequency plasmas. This requires complicated vacuum systems, severely limits particle production rates and makes analysis of the particles rather difficult. Cold plasma at atmospheric pressure would allow continuous operation and simplification of the process. Generating stable, cold atmospheric plasmas is not an easy task, however, because the plasma has the tendency to tranfer to a (hot) arc discharge.

In the research presented in this report, two different cold atmospheric pressure plasma sources were used to produce nanoparticles. We tested these sources by the production of carbon nanoparticles from acetylene (C_2H_2), and iron particles from ferrocene ($Fe(C_5H_5)_2$). Carbon nanoparticles of various forms have a myriad of industrial applications. Carbon black, indispensable to the rubber, paint, and chemical industries, is also commonly used in inks [2]. Iron nanoparticles have many uses, from enhancing catalysis with their increased relative surface area, to special magnetic applications in micro- and nano-electronics [3, 4]. In this size range, particles of all materials have unique and valuable properties, which make them particularly well suited for special technological applications.

Experimental

Helium and argon were used as carrier gasses. The precursors were introduced into the plasma by mass controlled flow (acetylene), or by passing the carrier gas over the sublimating solid (ferrocene). Hydrogen could also be added to the plasma.

Behind the plasma, a differential mobility analyser (DMA) [5] and an aerosol electrometer (AEM) [5] or a condensation particle counter (CPC) [5] were used to determine particle size distributions. The DMA size selects charged particles by deflecting them in an electric field, the AEM or CPC then counts the particles in a certain size range. In this way a size distribution is obtained. By reversing the direction of the electric field inside the DMA, both positively and negatively charged particles can be analysed. Particles can be charged either by the plasma or using a Kr-85 radioactive neutralizer. A typical setup for particle size distribution measurements is

shown in figure 1. Particles were also collected on grids placed in the effluent of the plasma for transmission or scanning electron microscopy (TEM or SEM) analysis. TEM analysis is combined with energy dispersive X-ray spectroscopy (EDX or EDS), which gives an idea of the elemental composition of a sample.

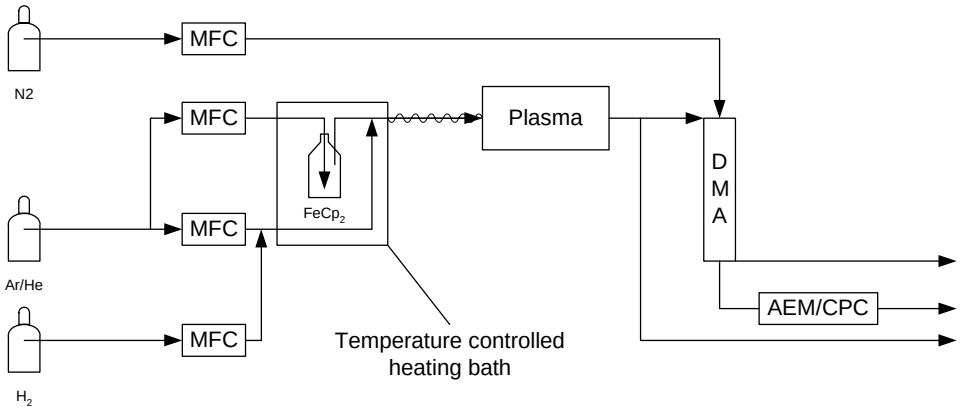

Figure 1: set-up for particle size distribution measurements for iron particles made from ferrocene

The two plasma sources that were used differ in the way the occurrence of unwanted arc discharges is prevented. The first source (for more details see [8]), in which the plasma is generated with a 13.56 MHz RF source [6], uses a high flow (> 20 L/min) to literally blow out the charged species before arcing can occur. This is a commercially available source and known as the Atmospheric Pressure Plasma Jet (APPJ). The RF power ranges up to 100 W at 13.56 MHz, and reflected power can be controlled on the source by a manually tuned matching network (set to minimal reflected power for each experiment). The plasma applicator has a diameter of 40 mm, and its exterior is electrically connected to the grounded electrode, as depicted in Figure 2 [7].

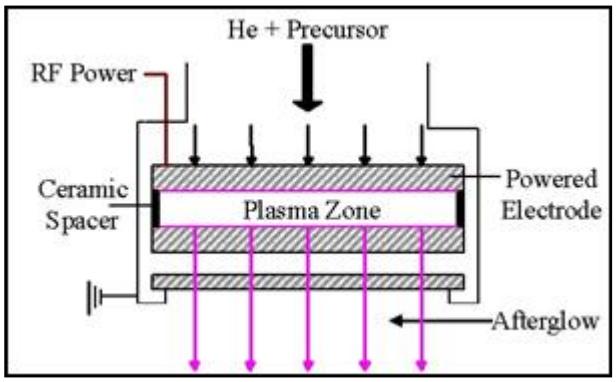

Figure 2: Electrode setup diagram of the APPJ.

In the second source, streamer-to-arc transition is prevented by dielectric barriers (DB) placed between the electrodes. The source used for iron particle generation consists of two concentric glass tubes (the dielectric barriers), between which there is a one-millimetre gap; through this gap the gas flows along the length of the tubes. The high voltage electrode is placed inside the inner tube, while the ground electrode is placed around the outer glass tube. Functionality for two plasma zones with intermediate coating precursor introduction was provided for. A 75 kHz high voltage AC power source is used to generate plasma. The source can be used with helium, argon and nitrogen as carrier gases, generally at a flow rate of 5 L/min. The discharge structure (homogeneous glow or filamentary streamer) depends strongly on gas composition. The structure of the plasma generated by this source was determined by analyzing the discharge current characteristics. A schematic of this plasma source is depicted in figure 3.

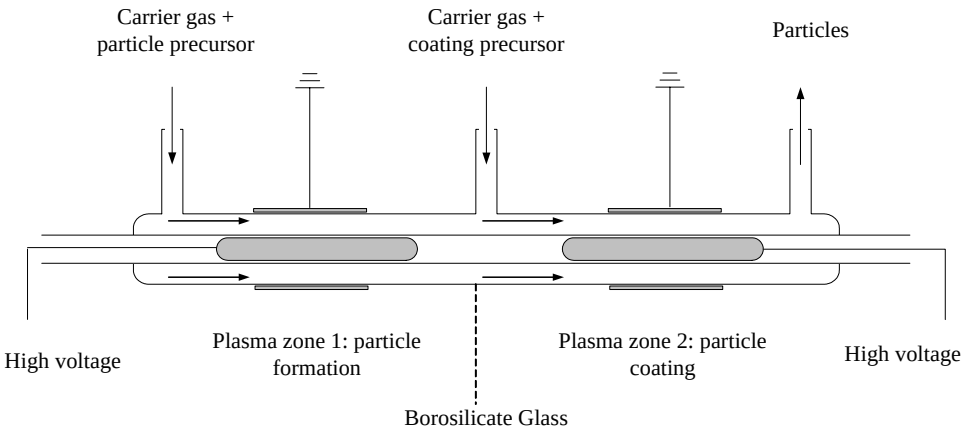

Figure 3: dielectric barrier plasma source used for iron particle production and coating

Results

Atmospheric Pressure Plasma Jet

Carbon nanoparticles sampled by plasma-enhanced deposition are depicted in Figure 4. The seven-minute deposition was made with 150 sscpm of Acetylene at 55 W applied power. The particles are highly agglomerated on deposition, and have primary diameters of ~15 – 30 nm. Closer imaging reveals no decipherable crystal structure, so it is presumed that the particles are amorphous in nature.

The effect of increasing Acetylene concentration has little effect on particle production. The mode of the distribution is decreased by only 1.5 nm, and total particle production is virtually unchanged. Nevertheless, a much finer distribution (smaller Full-Width Half-Maximum) is evidenced at the lower Acetylene flow. The effect of increased applied power is far more pronounced than that of precursor concentration. Overall nanoparticle production is drastically increased, with a slight decrease in average particle diameter. Finally, positively charged particle concentrations exceed those of negative ones in nearly every size range selected by the DMA. This is consistent with the excess of positive charge measured in the gas leaving a pure Helium plasma.

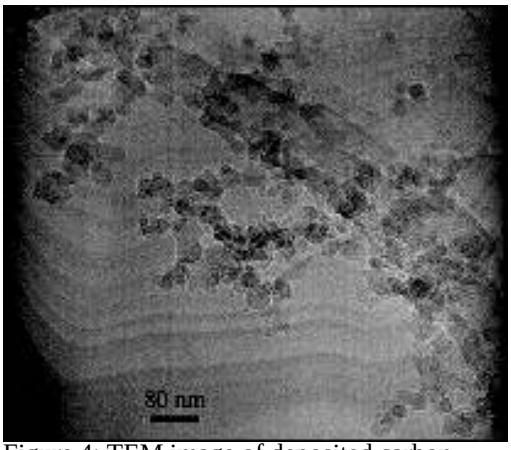

Figure 4: TEM image of deposited carbon nanoparticles made by APPJ

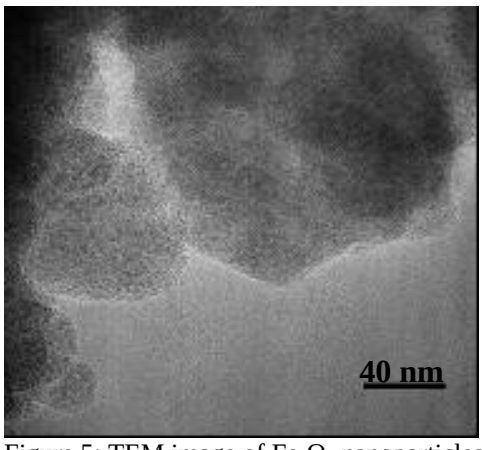

Figure 5: TEM image of Fe_2O_3 nanoparticles made by APPJ

Iron particles of approximately 20 nm were created from ferrocene. When the TEM grids on which the particles are collected are removed from the inert environment of the set-up, these iron nanoparticles are exposed to air and oxidize very rapidly. A pure amorphous iron particle converted fully to Fe_2O_3 will show a 29% increase in

diameter and a corresponding 115% growth in volume. This results in significant grain growth. Figure 5 depicts the resulting iron oxide nanoparticles; carrier gas flow rate through the ferrocene was set at 1.0 slpm He, and H_2 was fed at 400 sccpm for a 10 minute deposition. EDX analysis on samples not exposed to air indicates an extremely low presence of oxygen.

For iron, the generated particle size distribution (PSD) was observed as a function of ferrocene carrier gas flow, and H_2:He ratio. The experimental field is summarized in Table 1. Figure 6 indicates the resulting particle size distributions of produced iron nanoparticles. It is clear that an increasing relative hydrogen concentration causes a slight drop in average particle size and a drastic increase in the width of the distribution. The significant increase in overall charged particle production for increasing ferrocene concentrations is obvious. It is accompanied by an increase in particle diameter and a rise in the Full-Width at Half-Maximum (FWHM).

Table 1: Experimental field for Ferrocene.

Set	Settings		Results	
	Q_{Ferr} [slm]	H_2:He ratio [-]	d_p, at PSD maximum [nm]	FWHM [nm]
1	1.0	2:10	23.1	6.2
2	0.5	4:10	23.0	4.2
3	0.5	1:10	21.8	10.1

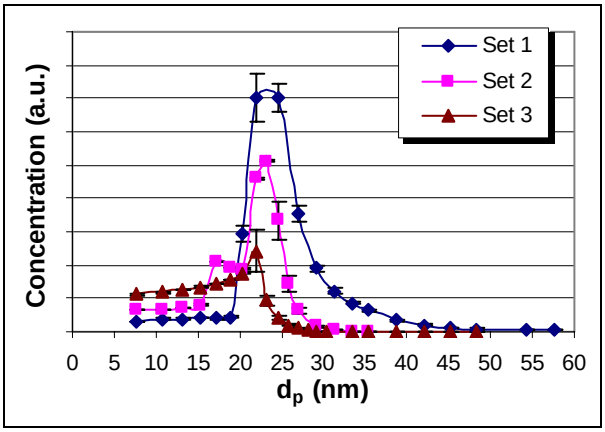

Figure 6: Iron distributions measured by AEM.

The particle charging properties of the ferrocene dosed plasma are similar to that of acetylene in so far as an excess of positively charged particles are produced. While the entire size range was not investigated, the concentration of the observed positively charged particles exceeds that of negatively charged particles at a nearly constant ratio of 2:1.

Dielectric Barrier Discharge

When helium is used as a carrier gas in conjunction with acetylene, the DMA/ CPC combination showed a large amount of particles, while none were seen with the scanning electron microscope. We speculate that the reaction only produces heavier hydrocarbons by acetylene oligomerization. These droplets are detected by the DMA/CPC but are invisible on SEM. When argon is used as a carrier gas, large amounts of amorphous carbon particles and agglomerates, with a primary particle size of 20-30 nm, were seen (Figure 7).

Nanoparticles were also produced successfully from ferrocene. TEM and EDX analysis proved these were iron-oxide particles. As for the APPJ, the original particles are assumed to be pure iron particles, the iron–oxide forming when the samples are removed from the set-up and exposed to air. Primary particle size of the iron oxide on TEM is generally between 6-11 nm, the original iron particles are therefore thought to be 5-9 nm in

size. On the TEM grid the particles form strange wire-like structures (figure 8). The reason for this kind of self-organization is not yet understood, but we believe that they originate from magnetic interaction between the superparamagnetic particles induced by an external magnetic field due to the Ni TEM grid applied.

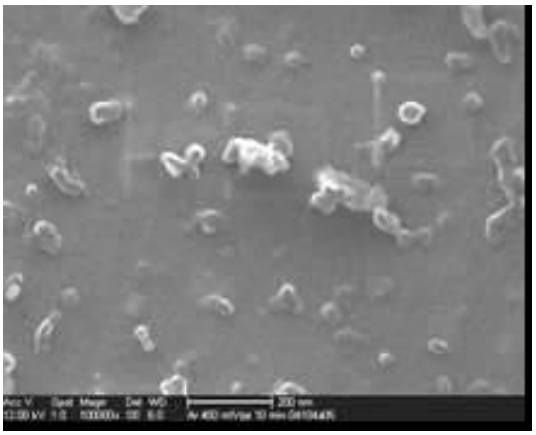

Figure 7: SEM image of carbon nanoparticles made with DBD

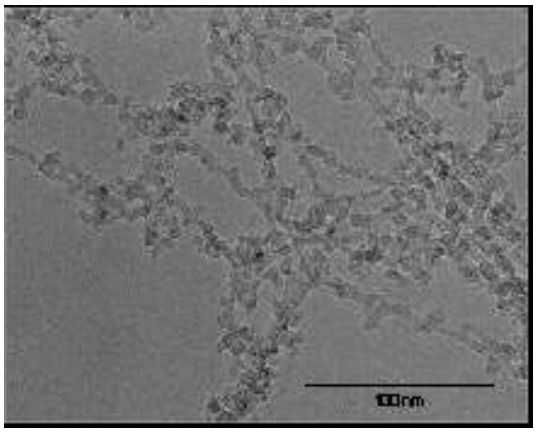

Figure 8: TEM image of iron (darker) and iron oxide (gray) particles

Although ferrocene is liable to form some carbon along with the iron, no carbon incorporation into the particles is detectable by EDX, and thus hydrogen is not needed to prevent this. Hydrogen does change the nature of the plasma and consequently the production rates, most noticeably for helium.

For a large number of different process adjustments, particle size distributions were recorded. Figure 9 gives representative PSDs for both argon and helium, both for positive and negative particles. Clearly, particle charge in an argon discharge is predominantly positive, while in helium the amounts of positive and negative particles are nearly equal. The larger positive space charge in the argon plasma is most likely the cause of this, although the exact mechanism of particle charging is not yet fully understood. Mean particle size for argon is generally lower than that for helium, even though the number concentration is much higher in the former case. We assume that the charge distribution in the plasma, which involves particles, ions and electrons, has a decisive influence on particle growth, but more experiments have to be carried out to to obtain results that are conclusive with respect to charge controlled growth mechanisms.

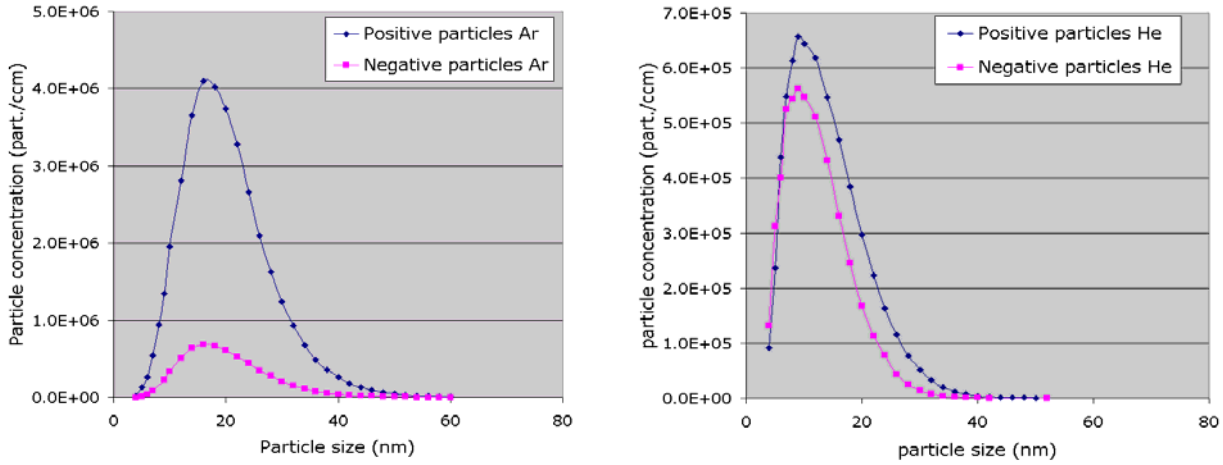

Figure 9: PSDs for both positive and negative particles in both argon (left) and helium (right). 4 ppm $FeCp_2$, no hydrogen, 4.8 kV applied voltage.

Mass production calculations were performed on the basis of the recorded size distributions; these seem to agree reasonably well with the amount of ferrocene that is introduced. The particle production rate is in the order of 10-100 μg/min. When argon is used as a carrier gas, the particle production rate is significantly higher than that for helium.

For both acetylene and ferrocene, a homogenous (glow) discharge was observed in helium. In argon, the plasma was an intermediate between glow and filamentary. In a filamentary plasma the actual plasma is localised in a large number of small micro-discharges about 100 μm in radius and a few nanoseconds in duration. A homogenous plasma, on the other hand, fills the entire volume between the electrodes. Given the fact that particle production was always higher for argon, even though the total power input into the helium plasma is higher, we believe that a filamentary discharge is more efficient in fully decomposing the precursor. This could have to do with the higher electron density and energy inside the filaments.

Conclusion

Cold atmospheric nanoparticle production is an interesting alternative for the production of nanoparticles. The possibility of carbon and iron nanoparticle production using cold atmospheric pressure plasma has been proven, and we expect that by choosing the right volatile precursors a large variety of nanoparticulate materials can be produced this way. Produced quantities are relatively high, and scale-up of the technology can be achieved by placing multiple plasma sources in parallel. Both the Atmospheric Pressure Plasma Jet as well as the Dielectric Barrier Discharge are relatively simple in design, construction and operation.

The higher flow of the APPJ leads to a higher particle production rate per unit plasma volume, but the high helium consumption would require recycling of the helium for the process to be economically feasible and sustainable. The dielectric barrier discharge can also operate with argon. In fact, the DBD operates even better using this more readily available and cheaper gas.

In the introduction of this article the possibility of directly coating produced nanoparticles was mentioned. In our experiments, particles were coated, first with polymethyl-methacrylate in the APPJ. This coating did not protect the particles from oxidation, as oxygen can diffuse through the small layer of polymer and oxidize the iron particles. This causes the iron particle to expand, breaking the polymer layer surrounding it. Therefore silicon/silicondioxide (from hexamethyldisiloxane, HMDSO) was tried as a coating. Although TEM indicated that some iron particles were covered, most of the silicon nucleated homogeneously. In future studies we will focus on a better mixing of iron particles and HMDSO vapour, which is expected to reduce homogeneous nucleation and moreuniform coating of nanoparticles.

Literature

[1] D. Vollath, D. Vinga Szabó. - in Innovative Processing of Films and Nanocrystalline Powders, ed. K.-L. Choy, p. 219, Imperial College Press, London, (2002).
[2] I. Pocsik, M. Veres, M. Fule, M. Koos, J. Kokavecz, Z. Toth, G. Radnoczi - Vacuum Surface Engineering, Surface Instrumentation & Vacuum Technology. **71,** 171-6. (2002)
[3] B. Schrick, B.W. Hydutsky, J.L. Blough, T.E. Mallouk - Chem. Mater. **16,** 2187-93 (2004)
[4] F.E. Kruis, H. Fissan, and A. Peled - Journal of Aerosol Science. **29**, 511-35 (1998)
[5] K. Willeke, P. A. Baron - Aerosol Measurement, Van Nostrand Reinhold, New York, 1993.
[6] A. Schütze, J.Y. Jeong, S.E. Babayan, J. Park, G.S. Selwyn, and R.F. Hicks - IEEE Transactions on Plasma Science. **26**, 6 (1998)
[7] G.R. Nowling, S.E. Babayan, V. Jankovic, R.F. Hicks, - Plasma Sources Science and Technology. 11, 97-103 (2002)
[8] M. D. Barankin, Y Creyghton, A Schmidt-Ott, Synthesis of Nanoparticles in an Atmospheric Pressure Glow Discharge, to be publ. In J. Nanoparticle Research, 2005

REACTION OF COPPER PRODUCED BY THERMAL EVAPORATION AND PLASMA SPUTTER DEPOSITION WITH TEFLON® PTFE, FEP AND PFA

D. G. Abreu[1], A. Entenberg[2], T. Debies[3] and G. A. Takacs[1*]

[1]Department of Chemistry, Center for Materials Science and Engineering, Rochester Institute of Technology, Rochester, NY, 14623
[2]Department of Physics, RIT, Rochester, NY, 14623
[3]Xerox Corporation, Webster, NY 14580

Abstract

Thin films of Cu were thermal evaporated and sputter deposited on Teflon® PTFE, FEP and PFA surfaces and analyzed with XPS. In contrast to thermal evaporation, the high energy Cu atoms from sputter deposition produced substantial yields of copper fluorides which were studied as a function of sputter parameters. The formation of copper fluoride bonds correlated with good practical adhesion of sputtered Cu with FEP and PFA compared to PTFE which was the most resistant to the production of fluoride ions.
Keywords: copper; Teflon® PTFE, FEP and PFA; fluoropolymers; copper fluoride; adhesion

1. Introduction

Fluoropolymers, like Teflon® PTFE (polytetrafluoroethylene), FEP (fluorinated ethylene-propylene co-polymer) and PFA (polytetrafluoroethylene-co-perfluoropropyl vinyl ether), have been extensively used in space applications, protective coatings, biotechnology, and microelectronic packaging [1]. In the latter application, the low dielectric constant properties of fluoropolymers have the advantage of producing faster package transmission speeds and less electrical interference from neighboring circuit lines [2, 3]. However, their low surface energy properties present considerable challenges for adhesion and wettability when bonding to other materials, such as, the conductor copper.

During recent investigations to control Cu adhesion using surface modification of PTFE [4, 5], FEP [6, 7] and PFA [8] with vacuum UV radiation from plasma systems, untreated FEP and PFA were found to show good practical adhesion, using Scotch tape peel tests, compared to PTFE with sputter-deposited copper. Therefore, this study was conducted to investigate the reaction of copper, using the different energies of metallization from thermal evaporation and plasma sputter deposition, with the untreated fluoropolymer surfaces.

2. Experimental

Commercially available films, 50.8 μm thick, of Teflon® PTFE [–(CF_2-CF_2)$_n$–], and the random co-polymers FEP, [–(CF_2-CF_2)$_x$-CF_2-$CF(CF_3)$-]$_n$ where x≅7, and PFA, [–(CF_2-CF_2)$_n$-(CF_2-$CFOC_3F_7$)$_m$–] (n/m= 39), were obtained from Saint-Gobain Performance Plastics and American Durafilm, respectively. Before attempting deposition of Cu, the samples were treated in ultrasonic baths of first methanol and then acetone at room temperature for 5 min each followed with over-night drying in air at room temperature to help remove potential contamination from lubricants employed in the processes to form the polymer mass into commercial film [8, 9].

Vacuum deposited copper films were either evaporated or sputtered. Deposition rates and film thicknesses were measured with Inficon (Syracuse, NY) quartz crystal monitors that were calibrated with a Sloan Dektak (Santa Barbara, CA) surface profilometer. Residual gas pressures were less than ca. 3.0×10^{-3} Pa.

Evaporated films were deposited with deposition rates (0.05 – 0.2) nm/s in a thermal evaporator manufactured by CVC Corporation, Rochester, NY. The substrates were mounted on a glass slide (for mechanical stability) and then placed in a substrate holder at a distance of 40 cm above a tungsten boat used to melt the copper. The boat and substrate holder were enclosed in a 50 l. glass bell-jar.

Sputtered films were vacuum deposited using deposition rates (0.01 – 0.5) nm/s with a MAK 3" DC planar magnetron manufactured by US Inc, Campbell, CA. The samples were placed on a grounded substrate holder which was 20 cm in front of a 99.99% pure, 7.5 cm diameter copper target. The magnetron and substrate holder were enclosed in a vacuum chamber. Research grade argon (99.997% pure) was introduced through a mass flow controller. After the sputtering plasma was ignited, the target was pre-sputtered, while a shutter covered the substrate, for ca. 2 min to allow the plasma to reach steady state during the establishment of the pressure and deposition rate. To change the energy of the sputtered Cu interacting with the substrate, the following parameters were varied: discharge voltage (273 – 377 V), current (0.1 – 0.95 A), power (40 – 365 W) and pressure (0.27 – 2.1 Pa).

The samples were analyzed *ex-situ* after Cu deposition with X-ray photoelectron spectroscopy (XPS), a surface analysis technique that provides elemental, chemical state and quantitative analyses for the top 2 – 5 nm of a sample's surface. A Physical Electronics Model 5800 XPS system was employed for the characterization. A region about 800 μm in diameter was analyzed. The films were prepared by cutting sections from the sample and mounting them beneath a molybdenum sample mask for exposing to the x-ray beam. The atomic percentages reported for carbon are precise to within 5% for major constituents and 10% for minor components. The samples were irradiated with monochromatized Al Kα radiation (1486 eV), treated with minimum XPS scan times and charge neutralized with a flood of low energy electrons from a BaO field emission charge neutralizer. These methods were employed so as to not over expose the post-metallization samples since such exposures have been reported to produce copper fluorides for evaporated copper on PTFE [10] but not for FEP or PFA [11]. High-resolution XPS spectra in the C 1s, O 1s, F 1s and Cu 2p regions were used to determine the chemical environment changes. The analysis was performed at an angle of 45° between the sample and analyzer. The spectra were curve fitted using the software package provided by the instrument's supplier. The software utilizes commercial Matlab© routines for data processing.

3. Results

The XPS analysis for the thin films of copper produced by thermal evaporation (1.5 – 4.5 nm) and plasma sputter deposition (0.5 – 2 nm) on the fluoropolymers revealed the presence of carbon, fluorine, oxygen and copper with a trace amount of tungsten for the evaporation experiments. The chemical state determination showed evidence for fluoropolymer, some hydrocarbon contamination, oxidized hydrocarbon containing the O-C=O moiety and copper oxides.

For the evaporation experiments, the F 1s spectra were nearly identical to the cleaned fluoropolymer samples. Single strong peaks due to the CF_2 moiety are observed as shown in Fig. 1. The F 1s peak due to FEP showed some broadening at low binding energy that could indicate a very low concentration of copper fluoride, but, in general, none of the fluoropolymers produced significant yields of fluoride ion at about 684 eV. The quantitative XPS analyses for these samples are given in Table 1.

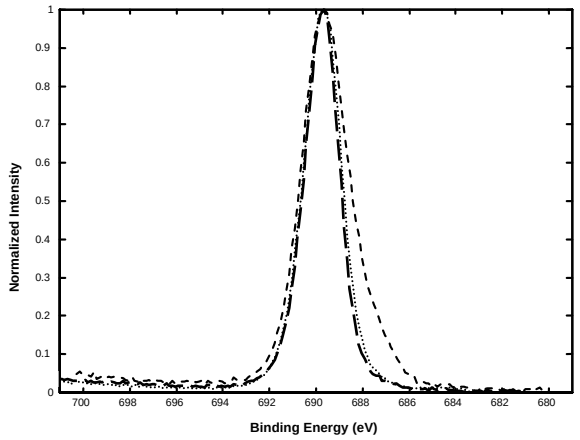

Figure 1. Overlapped F 1s Spectra for PTFE (_ _ _), FEP (- - -) and PFA (…) Post-Deposition by Evaporation of Copper

Table 1. Results of Quantitative XPS Analyses for Evaporated Copper on PTFE, FEP and PFA[1]

Sample	C (at%)	F (at%)	O (at%)	Cu (at%)	W (at%)
PTFE	30.2	29.2	24.5	14.8	1.3
FEP	29.0	24.2	30.3	14.6	1.8
PFA	30.9	36.4	20.7	10.6	1.5

[1]Evaporation Conditions: Pressure: 2.7 x 10^{-3} Pa.

In contrast to Cu deposited by thermal evaporation, sputter deposition, using the conditions reported in Table 2, formed substantial fluoride ions as shown in Fig. 2 which clearly demonstrates that PTFE does not react as readily with energetic Cu atoms as PFA and FEP.

Table 2. Results of Quantitative XPS Analyses for Sputtered Copper on PTFE, FEP and PFA[1]

Sample	C (at%)	F (at%)	O (at%)	Cu (at%)
PTFE	29.2	17.5	32.6	20.8
FEP	26.9	10.6	37.3	25.3
PFA	26.8	9.3	38.1	25.9

[1]Sputtering Conditions: Discharge Voltage: 381 V, Current: 0.24 A,
Pressure: 0.27 Pa.

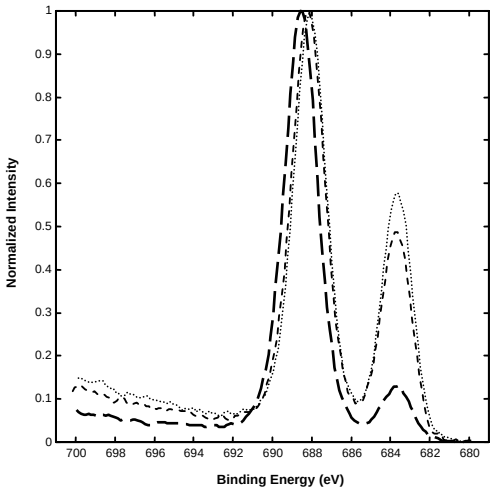

Figure 2. Overlapped F 1s Spectra for PTFE (_ _ _), FEP (- - -) and

PFA (…) Post-Plasma Sputter Deposition of Copper

Some experiments were conducted to investigate the effect of sputtering parameters on the production of fluoride ions. As an example, Table 3 and Figure 3 reports results for an experiment where the Ar pressure was mainly increased by a factor of about eight fold compared to the experimental conditions described in Table 2.

Table 3. Results of Quantitative XPS Analyses for "High Pressure" Sputtered Copper[1]

Sample	C (at%)	F (at%)	O (at%)	Cu (at%)
PTFE	29.1	28.4	23.7	18.9
FEP	28.1	25.2	25.8	20.9
PFA	28.0	23.4	27.0	21.7

[1]Sputtering Conditions: Discharge Voltage: 273 V, Current: 0.73 A,

Pressure: 2.1 Pa.

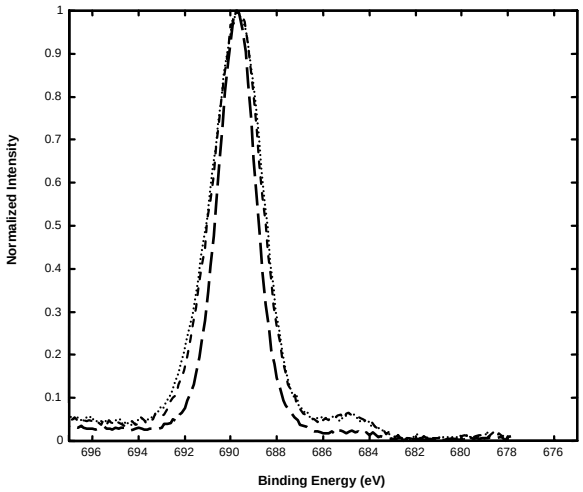

Figure 3. Overlapped F 1s Spectra for PTFE (_ _ _), FEP (- - -) and PFA (…)

Post-Plasma Sputter Deposition of Copper Using "High Pressure" Conditions.

4. Discussion and Conclusions

The lack of significant fluoride formation, when evaporated Cu is deposited on the fluoropolymers, correlates well with the observed poor practical adhesion of Cu to PTFE [4, 10, 12], FEP [11, 12] and PFA [11-13]. Quantitative measurements of the adhesion strengths have shown stronger adhesion of evaporated copper to FEP and PFA than PTFE which was attributed to the larger group electronegativities of CF_3 in FEP, C_3F_7O in PFA compared to F in PTFE [12]. The low chemical reactivity of vapor deposited copper to PTFE has been explained on the basis of the strength of the C-F bond compared to the heat of condensation [10]. No reaction of Cu with PTFE has been observed with temperatures up to 703ºK [14] while Cr-coated Cu foil reacts with glass-fiber-filled Teflon PFA laminates at 653ºK to produce metal fluoride formation [15].

In the sputter deposition experiments, the energy of the copper atoms is substantially greater than the C-F bond dissociation energy (ca. 5 eV [16, 17]) and the F 1s XPS analysis detected the formation of fluoride ions either as CuF and/or CuF_2 moieties. Because of the presence of copper oxides during the sputtering of Cu, there was too much interference to adequately detect CuF_2 by the Cu 2p XPS spectrum at 935 eV [18, 19]. Within the range of parameters studied, the presence of copper fluorides decreased with a decrease in discharge voltage, which would decrease the energy of the Cu atoms, and an increase in pressure, that due to collisions would also shift the energy distribution of Cu atoms to lower energies. Polycrystalline PTFE was found to be the most resistant to the formation of fluoride ions, again, consistent with the findings that poorer practical adhesion of sputtered Cu was observed with PTFE [4, 5] compared to the more amorphous FEP [6] and PFA [8]. Previously, copper fluorides were detected for sputter-deposited Cu on fluoropolymer Teflon®AF1600 [20] but not FLARE™1.0 where the breakage of the C-F bond resulted in the loss of fluorine at the interface instead of the formation of copper fluoride [21].

* To whom correspondence should be addressed. Phone: 585-475-2047, Fax: 585-475-7800.
E-mail address: gatsch@rit.edu.

References

[1] E. T. Kang and Y. Zhang, *Adv. Mater.*, **12**, 1481 (2000).
[2] C. R. Davis and F. D. Egitto, *Chemtech*, **44** (March) (1995).
[3] F. D. Egitto and L. J. Matienzo, *IBM J. Res. Develop.*, **38**, 423 (1994).
[4] S. Zheng, A. Entenberg, G. A. Takacs, F. D. Egitto and L. J. Matienzo, *J. Adhesion Sci. Technol.*, **17**, 1801 (2003).
[5] H. Desai, L. Xiaolu, A. Entenberg, B. Kahn, F. D. Egitto, L. J. Matienzo, T. Debies and G. A. Takacs, in: *Polymer Surface Modification: Relevance to Adhesion*, K. L. Mittal (Ed.), Vol. **3**, 139-157, VSP, Utrecht (2004).
[6] W. Dasilva, A. Entenberg, B. Kahn, T. Debies and G. A. Takacs, *Polymer Materials Science and Engineering*, **90**, 833 (2004); *J. Adhesion Sci. Technol.*, **18**, 1465 (2004).
[7] J. X. Chen, D. Tracy, S. Zheng, L. Xiaolu, S. Brown, W. VanDerveer, A. Entenberg, V. Vukanovic, G. A. Takacs, F. D. Egitto, L. J. Matienzo and F. Emmi, *Polym. Degrad. Stabil.*, **79**, 399 (2003).
[8] W. Dasilva, A. Entenberg, B. Kahn, T. Debies and G. A. Takacs, presented at 2004 Materials Research Society Fall Meeting, Boston, MA, Nov. 29 - Dec. 3 (2004).
[9] F. D. Egitto and L. J. Matienzo, *Polym. Degrad. Stabil.*, **30**, 293 (1990).
[10] C. C. Perry, J. Torres, S. R. Carlo and D. H. Fairbrother, *J. Vac. Sci. Technol.*, **A20**, 1690 (2002).
[11] M-K. Shi, B. Lamontagne, A. Selmani and L. Martinu, *J. Vac. Sci. Technol.*, **A12**, 44 (1994).
[12] C-A. Chang, Y-K. Kim and A. Schrott, *J. Vac. Sci. Technol.*, **A8**, 3304 (1990); C-A. Chang, Y-K. Kim and S. S. Lee, in: *Metallized Plastics: Fundamentals and Applications*, K. L. Mittal (Ed.), p. 345-354, Marcel Dekker, New York, NY (1998).
[13] M. K. Shi, A. Selmani, L. Martinu, E. Sacher, M. R. Wertheimer and A. Yelon, in: *Polymer Surface Modification: Relevance to Adhesion*, K. L. Mittal (Ed.), p. 73, VSP, Utrecht (1995).
[14] P. Cadman and G. M. Gossedge, *J. Materials Sci.*, **14**, 2672 (1979).
[15] J. M. Park, L. J. Matienzo and D. F. Spencer, *J. Adhesion Sci. Technol.*, **5**, 153 (1991).
[16] T. L. Cottrell, *The Strength of Chemical Bonds*, 2nd ed., Butterworths, Washington, D.C. (1958).
[17] W. A. Sheppard and C. M. Sharts, *Organic Fluorine Chemistry*, W. A. Benjamin, New York, N.Y. (1969).
[18] M. S. Silverstein, L. Sandrin and E. Sacher, *Polymer*, **42**, 4299 (2001).
[19] D. C. Frost, A. Ishitani and C. A. McDowell, *Mol. Phys.*, **24**, 861 (1972).
[20] D. Popovici, J. E. Klemberg-Sapieha, G. Czeremuszkin, E. Sacher, M. Meunier and L. Martinu, *Microelectronic Engineering*, **33**, 217 (1997); D. Popovici, J. E. Klemberg-Sapieha, G. Czeremuszkin, A. Alptekin, L. Martinu, M. Meunier and E. Sacher, in: *Metallized Plastics 5 & 6: Fundamental and Applied Aspects*, K. L. Mittal (Ed.), p. 237, VSP, Utrecht (1998).
[21] M. Du, R. L. Opila and C. Case, *J. Vac. Sci. Technol.*, **A16**, 155 (1998).

Atmospheric Pressure DBD gun and Its Application in the ink Printability

Qiang Chen, Erli Han, Yuefei Zhang, Yuanjing Ge
Laboratory of Plasma Physics and Materials, Beijing Institute of Graphic Communication, Beijing 102600

Abstract: In this paper, a plasma source discharging at atmospheric pressure and its characterization diagnosed by a Langmuir probe, a digital camera and a computer processing are presented. As an application the dielectric barrier discharge (DBD) gun modifying an ultraviolet (UV) cured resin surface for ink printability is reported.

Keywords: plasma source, application, ink printability

Introduction

Modifying polymer surfaces using plasma techniques is of great and increasing industrial relevance [1]. Appropriate plasma treatments are widely employed to modify polymer surface properties such as adhesion, friction, penetrability, wettability, dyeability, printability and biocompatibility, so as to adapt them to specific applications [2, 3]. Depending on the treatment parameters, rapid, clean, environmentally friendly plasma-based processes are able to induce physical and chemical surface changes in polymers through several concurrent actions (etching, grafting, polymerization, cross-linking, etc.), usually without modifying their original bulk qualities [4,5].

Among these various plasma applications, dielectric barrier discharges (DBDs) in air (or in other gases or vapors) that run at or near atmospheric pressure are demonstrably convenient for the activation or modification of polymer surfaces. Such discharges provide chemically mild and mechanically nondestructive means of altering surface properties targeting improved and desirable surface characteristics. Moreover, they are obviously attractive to the industry in that they avoid the high engineering costs usually associated with vacuum-based plasmas [6, 7].

Even through DBD techniques are used widely for surface modification/polymerization: for the treatment of polymers, for plasma coating, for thin-film deposition, for the cleaning and activation of substrates, for the sterilization of surfaces and materials [8-13], however, the shape of the electrodes, especially the small gap between the electrodes, is a demonstrable limitation of the DBD technique

application.

Thus the plasma torches/jets were appeared and generated deep inside discharging between the column electrodes for other unique applications. The working gas flow from the nozzle stabilizes the plasma jet, and a well-defined plasma channel is created downstream from the gas flow and therefore plasma interacts with the substrate for modification/deposition. Thermal torches and arcs, for example, which are high-temperature sources ($>10000^0$C) that are used for a variety of applications of coatings, welding and cuttings is well known [14]. Recently for practical requirements a capacitively coupled rf plasma jet, a kind of low temperature one, was studied in relation to bio-compatible plasma source at 13.56MHz [15]. Beside that a dc micro-hollow cathode discharge gun served as an efficient source of vacuum UV radiation was explored [16], and an rf discharge needle developed and performed in a small area treatment was also emphasized [17].

Taking into account the above discussion, we here present a plasma source dependent on the use of DBD gun, which is quite different from the ones described above. Unlike an RF atmospheric pressure glow discharge [18], or a plasma jet/needle [17, 19, 20], the DBD gun including a dielectric material between the electrodes can generate a stable glow plasma. With a digital camera and computer processing the uniformity of the plasma out of the nozzle is diagnosed. The electron temperature near the nozzle is detected by Langmuir probe. Then the plasma generating from DBD discharge in 26kHz without any vacuum demands at atmospheric pressure, for instance, has been used for a number of plasma chemical technologies, in particular modifying the UV cured resin for ink printability, with surprisingly good results.

Experimental

Experiments to study the optical and uniform properties of the DBD gun were done in Ar flowing into ambient air at atmospheric pressure. The setup is schematically depicted in Fig. 1 (a), where the gun consists of an inner electrode, a quartz glass tube (0.1cm wall thickness), and a foil metal cylindrical tube around the glass as outer electrode. Normally the gap was 0.5 cm between the inner electrode and the quartz glass. And the discharges were operated in a high-frequency power supply (0-5 kV, 26kHz) with Ar fed into the annular space between the two electrodes as working gas. The gas stream was directed onto silicon wafers located at the downstream from the nozzle and the flow rate was adjusted using mass flow controllers.

The optical of discharging gun was characterized by digital camera. Light was collected from the side of the plasma gun as showed in Fig. 1(a) thereby sampling the radiation from the outflow region. And then spectra were acquired by a computer processing.

The plasma treatment of UV cured resin was performed at atmospheric pressure with DBD gun. The samples were prepared by curing the resin in UV light at power of 150W for 15s on Si substrate prior to placement blow the plasma gun. Discharges were struck and maintained a constant current and voltage during the modification. After processing the substrates were characterized by Fourier transform infrared (FTIR), contact angle measurement and ink printability. An illustration of the discharging gun is shown in Fig. 1(b).

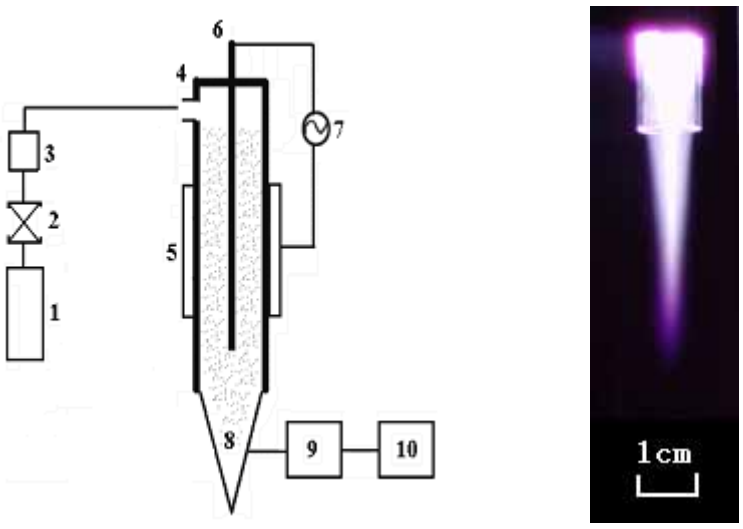

a **b**

Fig. 1 a-Schematic diagram of DBD plasma gun. a: 1-gas source; 2-valve;3-flow controller; 4-glass tube; 5-outer electrode; 6-inner electrode;7-high frequent power;8-plasma torch; 9-digital camera; 10- computer; b-the illustration of discharging torch

Results

The effect of discharge voltage and diameter of inner electrode on the torch length is shown in Fig. 2. It obtains that the variation of torch lengths with the discharging voltages exhibits clearly the distinctions as Fig. 2(a) shows: below 70V discharging voltage the torch length at the exit of the nozzle is relatively short and dependent on the gas effluent. But in higher voltage the change of length is relatively small and trend to the similarity for the three kinds of flow rates. In contrast, the variation of torch lengths influenced from diameters of the inner electrode is in a reverse way: the larger diameter of the inner electrode, the shorter length of the plasma torch. It can be explained by the resistance causing from decreased gap between the inner electrode and dielectric glass due to the increase of inner electrode diameter, and the less Ar effluent from the nozzle.

Fig. 2 (b) also demonstrates the plasma power obviously determined the torch length. For instance as Fig. 2(b) shows in 3mm diameter of inner electrode the torch length was 4.3cm

corresponding to 3.5kV discharging voltage but the length was only ca. 2.2cm in 2.6kV discharging voltage.

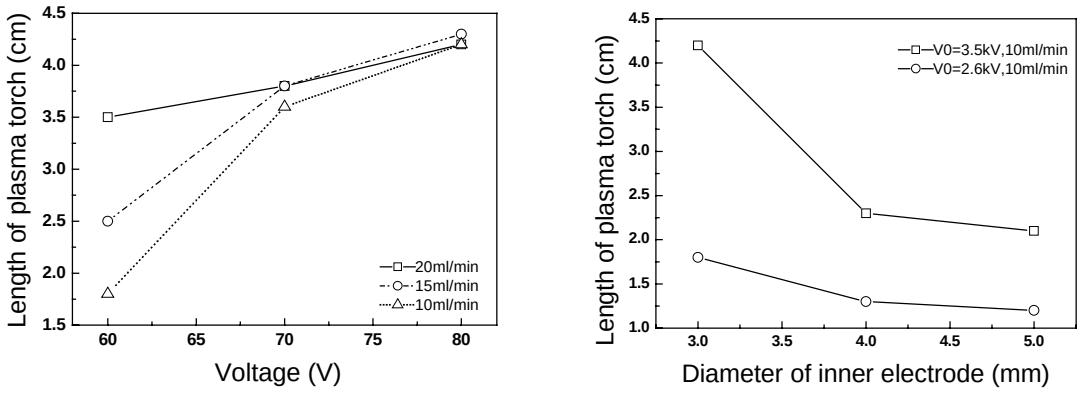

a **b**

Fig. 2 Relationship of plasma torch length with (a) applied voltages and (b) diameters of the inner electrode

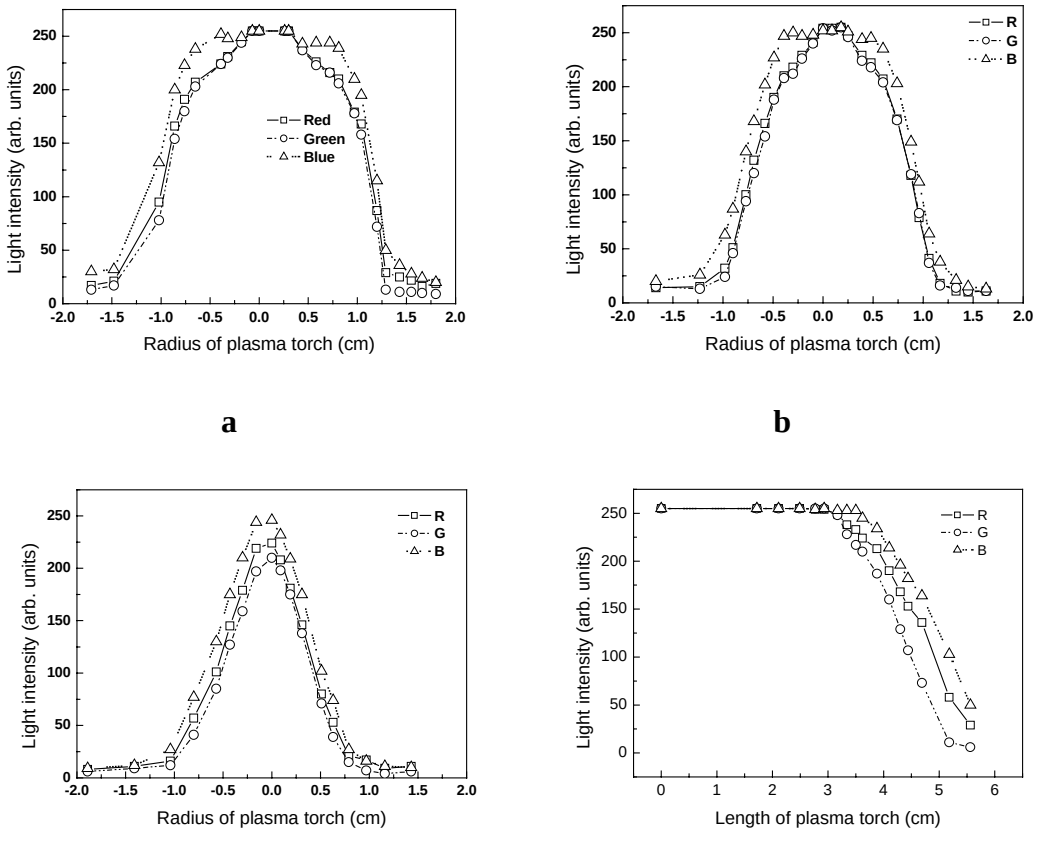

a **b**

c **d**

Fig. 3 Distributions of the three-light intensities versus the radius of torch at (a) 0.5cm; (b) 1.4cm and (c) 2.5cm from the gun mouth, and (d) the axial position from gun mouth (red light 600-700nm, green light 500-600nm, and B-blue light 400-500nm)

It is known that the light intensity is relevant to the electron density and the electron temperature in plasma. By a digital camera and processing in a computer the characteristics of the plasma in DBD gun is revealed quantitatively. Figure 3 shows the relationship of the three-light intensities (red light 600-700nm, green light 500-600nm and blue light 400-500 nm) with the distances from the nozzle to the detected site, and the distributions of light intensities in the radial and axial directions. It indicates from Fig. 3(a, b, c) that in a large region of plasma zone the light peaks are relatively flat and homogenous, and the intensities are demonstrably strong and uniform in the central areas of torches. In the axial direction, furthermore, Fig. 3(d) shows that the light intensity decreases also slowly along the flow direction outside the nozzle. It results that the DBD gun can generate a torch with relatively homogenous and uniform distributions of electron, ion and radicals in radial and axial directions.

Langmuir probe measurement reveals that the electron temperatures at 0.5cm site downstream from the nozzle were 0.3eV to 1.4eV depending on the probe position in the radus. It is simalar to the electron temperature measured in the rf capillary discharge of 0.2-1.2eV [20].

As an application, the DBD gun is used to treat VU cured resin for ink printability. Normally the UV cured resin has a surface energy blow $28\times10^{-3}N/m^2$ where the ink on the surface even cured by UV light is still easily being erased from the surface because of the poor adhesion causing by the low surface energy. Increasing the surface energy is an efficient and conventional method to improve the printability.

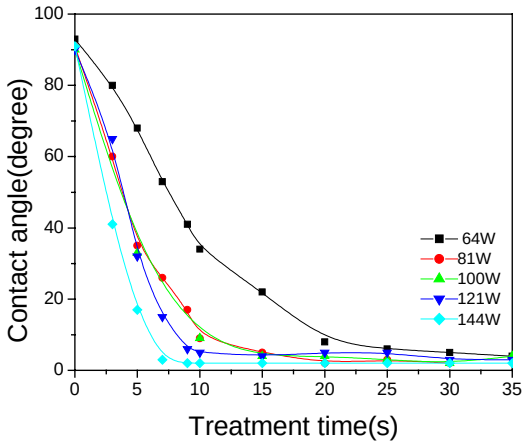

Fig. 4 Contact angles of the UV cured resin versus plasma powers (Ar flow rate 22.5L/min, 10mm between the substrates and the nozzle)

Fig.4 shows that the contact angles after Ar plasma treatment drastically decreased whereas the periods of plasma interaction were less than 5s for all incident powers. But after 20s exposure time, the contact angles

seem to be constant and negligible variation with the extension times.

The influence of Ar flow rates on contact angles in Fig.5 indicates that before ca. 5s exposure period the contact angle decreased greatly with the increase of flow rate. But after 5s the contact angle decreased relatively slow, similarity to the influence from plasma power. It derives that the surface modification of UV cured resin can be achieved in a short period, and means the DBD gun seems to be an effective tool to improve the surface energy. Moreover in this figure it notices that at flow rate 22.5 L/min a super hydrophilic surface can be obtain with the contact angle of 4^0.

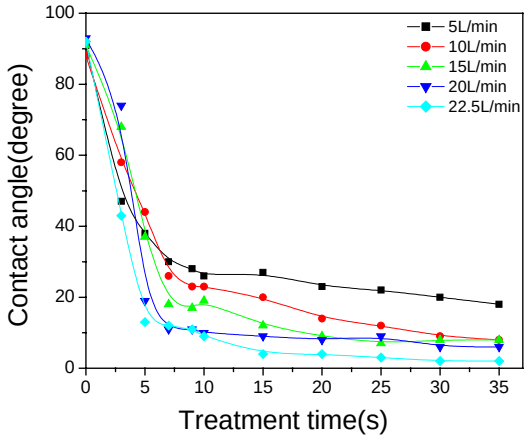

Fig. 5 Relationship of contact angles with Ar flow rates in DBD gun (conditions: 144W plasma power, 10mm between the substrate to the nozzle)

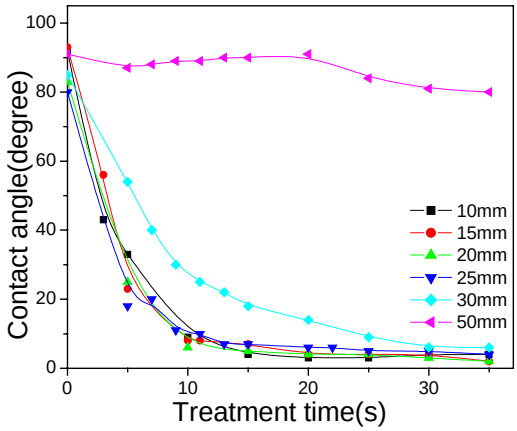

Fig. 6 Influence of the distance from substrates to the gun nozzle on the contact angles (plasma power 100W, flow rate 22.5L/min)

Due to the dependent of plasma densities on the distances from gun nozzle to substrate the

effect of distances on the contact angles is reasonable as Fig. 6 shows. When the substrates were placed less than 25mm form the nozzle in axis the efficiency of plasma modification were significantly strong by exponentially decreasing of the contact angles with the exposure times. But when the gap was beyond 30mm, the plasma interaction was relatively weak. Especially when the substrate was put 50mm under the nozzle, the contact angle shows a negligible variation after plasma treatment in Fig. 6.

The aging properties of UV cured resin after DBD plasma gun treatment are shown in Fig. 7. The recoveries of the contact angles were significant after DBD gun treatment. In particular at beginning when stored the sample the contact angles increased remarkably. After one day later the contact angles trended to stable and the recovery of contact angle was relatively slow. It can be explained by the polar groups in the surface turning into the body and stabilizing the surface [21], and the plasma generated from the gun occur the resin covalently grafted the polar groups on the surface and the dangling bonds remained on surfaces were much activity binding the species from the air to neutralize the polarity in the surface. Fig.7 also notes that the different exposure periods did not lead to any variable behaviors on the recovery of contact angles. The 15s period plasma treatment shows the same behavior as done in that 10s exposure period sample.

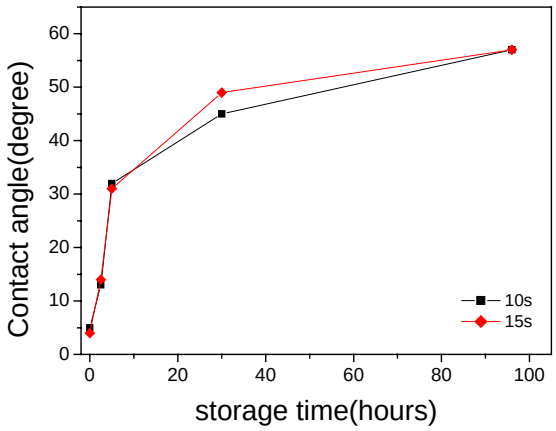

Fig. 7 Delay of contact angles after plasma treatment with the aging times (plasma power 144W, flow rate 22.5L/min, and distance was10mm between the substrate and the nozzle)

In Fig.8, Fourier transform infrared (FTIR) spectrum presents the comparison the structure change of UV cured resin before and after DBD gun treatment. The spectra exhibit a series of infrared

bands at 1060-1260 cm^{-1} which are due to O-H and C-H stretching, bending modes and hydrogen bond interaction [22]. That is indicative of the polar groups on the surface. In addition, infrared band seen at 3400cm^{-1} is assigned to the bending and stretching vibrations of hydroxyl groups. At peak 1450cm^{-1} C-O stretching, 1740cm^{-1} O=C rocking deformation clearly show the polar groups were grafted and significantly improved due to plasma interaction [23]. The very strong latter band can be attributed to polarized carboxyl and hydrogen bonding between neighboring hydroxyl and oxide groups.

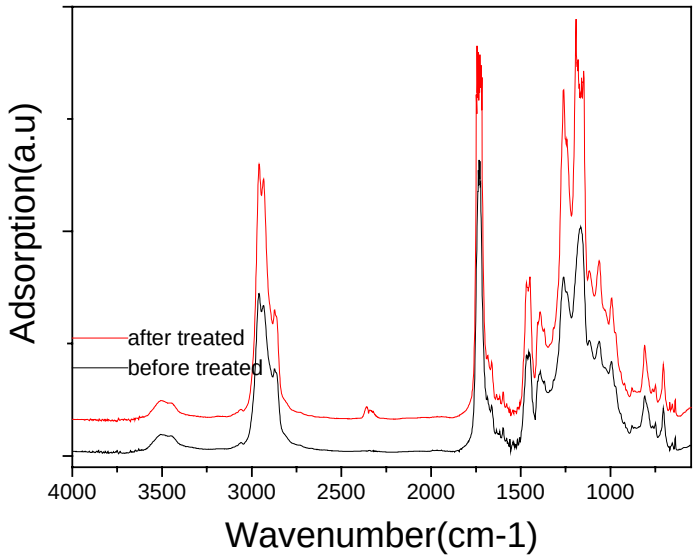

Fig. 8 FTIR spectra of UV cured resin before and after DBD gnu treatment

The surface energy measurement is established in Tensiometer K100, Germany. Table 1 shows the results in which testifying the features of FTIR spectrum. The grafted polar groups especially the carboxyl, hydroxyl and oxide groups increase the polar energy of UV cured resin and improve the ink printability.

Table 1 the surface energy of UV cured resin before and after DBD gun treatment

UV cured ink	surface tension（mN/m）	disperse part（mN/m）	polar part（mN/m）
untreated	27.2	24.3	2.9
treated	34.0	16.9	17.0

The ink printability was evaluated by printing the ink on surfaces and then measuring the ink

density. Fig. 9 shows that untreated substrate after ink printed visually appeared lots of blank sites on surface rather than the whole surface covered by ink in treated samples. The data in Table 2 indicates quantitatively the ink density on the treated surface increased ca. 27.3% after DBD gun treatment.

a **b**

Fig.9 Ink printability on UV cured resin a-before and b-after DBD gun treatment

Table 2 the density of ink on UV cured resin before and after DBD gun treatment

sample	1	2	3	4	5	average
before	1.945	1.823	2.035	1.953	1.951	1. 941
after	2.541	2.378	2.511	2.430	2.497	2.471
increased rate(%)	30.6	30.4	23.4	24.4	28.0	27.3

Discussion

After characteristic of the plasma generated by DBD gun with a Langmuir probe, the digital camera and computer processing, and then the application of the DBD gun to treat UV cured resins for ink printability, it obtains that the DBD gun is a very convenient tool for the controlled surface activation and modification of various categories of surfaces, where remarkably uniform treatment and relatively stable modified surface properties result over the entire treated area of the test surfaces.

Langmuire probe detected the electron temperatures in the gun were 0.3 to 1.3 eV near the mouth. It means the DBD gun is capable and suitable for polymer modification especially with its convenient and handable for a small zone. The measurements of light intensity along the axis of flow direction outside the nozzle reveal that concentrations of electron, ion and radicals in the downstream are quite homogenous and uniform when the substrates are near the nozzle. Increasing the distance, however, the concentration of species remarkably decreased. It is consistent with the contact angle measurement, where in long distances, for example 50mm between the substrate and nozzle, the contact angle showed a negligible variation after DBD gun treatment.

In the radial direction the species: electron, ion and radicals are concentrated in the core and

dispersed with the radii of nozzle and the distance from gun nozzle to detected site, which is intrinsic characteristic of torch plasma. Fig. 10 the droplets of distilled water visually demonstrate no dispersion around plasma interacted area and clearly indicates the plasma uniform under the nozzle. The circled area by droplets is consistent with the diameter of plasma torch.

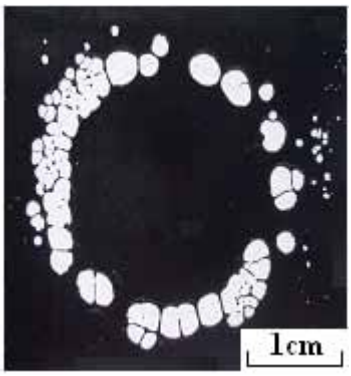

Fig. 10 Droplets of distilled water circling the plasma treatment zone

The FTIR spectrum reveal polar functional groups of carboxyl, hydroxyl and oxide grafted covalently on the surface contributed to resin printability and indicate even in a short exposure period and a relatively low power the DBD gun can achieve efficiently the surface modification in air at atmospheric pressure. The oxygen in the chemical structure of resin surface caused from the process carrying on the ambient environment whereas Ar as the working gas. The polar groups on the surface turning into body leaded to the modified resin aging, e.g. the contact angle increase very rapidly at beginning storage. Nevertheless, until now it is still to estimate of the species concentration in the atmospheric pressure DBD gun and cannot make any conclusions regarding the role of electrons, ions or radicals in the modification process.

Conclusion

The novel plasma source working at atmospheric pressure and its characteristic are presented. The high-frequency DBD gun and its applications as a unique instrument for interested works in printing are investigated. Langmuir probe detected the temperature of electrons near the nozzle is 0.3 to 1.3 eV. The digital camera and a computer processing reveals that the distribution of light intensity in the downstream of the nozzle is quite uniform and homogenous but depending on the distance from

the nozzle to detected site. The application of DBD gun treated UV cured resin for ink printability concludes that it can be utilized conveniently as a hand-operated tool to practically modify the micro-zone in printing industry such as a label on stamp surfaces.

References

[1] A. Fridman, A. Chirokov and A. Gutsol, J. Phys. D: Appl. Phys., 38 (2005) R1

[2] G. Greene, G. Yao, and R. Tannenbaum, Langmuir, 20(2004), 27395

[3] K.M. Baumgartner, J. Schneider, A. Schulz, J. Feichtinger, M. Walker, Surf. Coat. Technol., 142-144 (2001) 501

[4] A. J. H. Maas, M. M.Viitanen, H. H.Brongersma, Surf. Interface Anal., 30(2000)3

[5] M. L. Steen, A. C. Jordan, E. R. Fisher, J. Membr. Sci., 204(2002)341

[6] R. Foest, F. Adler, F. Sigeneger, M. Schmidt, Surface and Coatings Technology, 163 -164 (2003)323

[7] F. Massines, A. Rabehi, P. Decomps, R. Ben Gadri, P. Segur, Ch. Mayoux, J. Appl. Phys., 83 (1998)2950

[8] G. Borcia, C.A. Anderson, N.M.D. Brown, Applied Surface Science, 225 (2004)186

[9] E. Occhiello, M. Morra, G. Morini, F. Garbassi, P. Humphrey, J. Appl. Polym. Sci. 42(1991)551

[10] H. J. Griesser, R. C. Chatelier, T. R. Gengenbach, G. Johnson, J.G. Steele, J. Biomater. Sci. Polym., Ed., 5(1994)531

[11] H. Yasuda, Plasma Polymerization, New York: Academic Press, 1985

[12] B.D. Ratner, J. Biomater. Sci. Polym. Ed., 4(1) (1992)3

[13] C.-P.Klages, K.Hopfner, N. Klake, and R. Thyen, Plasmas Polym., 5(2000)79

[14] M. Boulos, IEEE Trans. Plasma Sci., 19(1991)1078

[15] E. Stoffels, A. J. Flikweert, W. W. Stoffels and G. M. W. Kroesen, Plasma Sources Sci. Technol., 11 (2002) 383

[16] M. Moselhy, W. Shi, R. H. Stark and K. H. Schoenbach, Appl. Phys. Lett., 79(2001) 1240

[17 E. Stoffels, I. E. Kieft and R. E .J. Sladek, J. Phys. D: Appl. Phys. 36 (2003) 2908

[18] J. Park, I. Henins, H. W. Herrmann, and G. S. Selwyn，Appl. Phys. Lett., 76(2000)288

[19] S. E. Babayan1, J. Y. Jeong, A Sch¨ utze, V J Tu, Maryam Moravej, G. S Selwyn and R. F. Hicks, Plasma Sources Sci. Technol. 10 (2001) 573

[20] J. Janča, M. Klima, P. Slaviček and L. Zajičková, Surf. Coat. Technol., 547-551(1999) 116

[21] N. Inagaki, Plasma Surface Modification and Plasma Polymerization, Pennsylvania: Technomic

Publishing Co, 1996

[22] M. Nitschke, A. Holländer, F. Mehdorn, J. Behnisch, and J. Meichsner, Journal of Applied Polymer Science, 59(1996)119

[23] C. Oehr, M. Mu¨ ller, B. Elkin, D. Hegemann, U. Vohrer, Surf. Coat. Technol., 116–119 (1999) 25

Non-Thermal Plasma Bio-Active Liquid Micro and Nano-Xerography

Gregory Fridman[1], Peter I. Lelkes[1], Gary Friedman[2], Alexander Fridman[3], Alexander Gutsol[3]

[1] *School of Biomedical Engineering, Science, and Health Systems*
[2] *Department of Electrical and Computer Engineering, College of Engineering*
[3] *Department of Mechanical Engineering and Mechanics, College of Engineering*

Drexel Plasma Institute, Drexel University, Philadelphia, Pennsylvania, USA

ABSTRACT

Method of biochemical patterning which allows for micro and nano-scale resolution on non-planar substrates is presented. Utilizing this method, bio molecules (including DNA, proteins, and enzymes) can be delivered to charged locations on surfaces by charged water buffer droplets. Charging of water droplets is accomplished using either Dielectric Barrier Discharge (DBD) plasma or Corona discharge. DBD and Corona were effectively stabilized in the presence of high concentration of micron-size water droplets. Discussed in this paper are the concepts of the proposed method as well as first experimental results supporting the idea.

Keywords: non-thermal plasma, biomedical applications, xerography

I. INTRODUCTION

Patterning of different biochemical molecules on surfaces has many applications ranging from biosensors, used in genetic discovery and monitoring of dangerous toxins, to tissue engineering constructs where surfaces control tissue assembly or adhesion of cells. Most existing methods of biochemical patterning are suitable only for planar surfaces. In addition, micro and nano-scale patterning often relies on complex sequences of lithography-based process steps.

Many methods are available for printing today. The most common ones, that led us to our idea, are Inkjet printing and its derivative – electro-spray technology, and Laser printing technologies. Disadvantages of Inkjet printing technology are splashing caused by droplets accelerated to high speeds hitting target surface, low precision caused by droplet diffusion, and, in many of the variations of the technology, like electro-spray – high dependence on chemical composition of the ink, i.e. printer has to be heavily modified to be able to print a slightly different substance. Laser printers address many of the issues brought up by Inkjets but raise many of their own – for example, toner particles undergo high mechanical strains that biochemical molecules and DNA are likely not to survive. There also is a multitude of issues associated with heating.

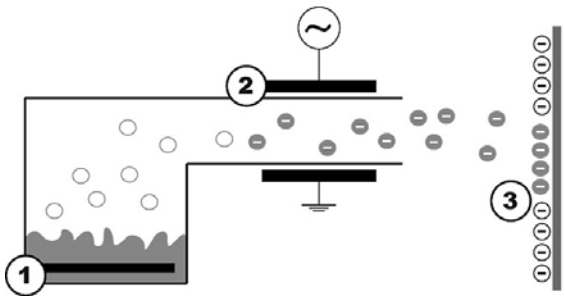

Fig. 1. Plasma "BioPrinter" prototype with
(1) droplet atomizer,
(2) DBD plasma reactor, and
(3) charged droplet deposition substrate.

We are developing a method of biochemical substance patterning, or printing, which allows for micro and nano-scale resolution on planar and non-planar substrates. Our goal is to print droplets of buffer containing bio-molecules (including DNA), peptides, and cells. We accomplish this by creating droplets with the molecules or cells in their respective buffer solution, then charging the droplets in cold atmospheric pressure discharges, like Dielectric Barrier Discharge (DBD) and Corona discharge plasma, and finally delivering them onto substrate with charge

pre-written onto the substrate via well-known xerography (micron-resolution) or charge stamping (nanometer-resolution) (Fig. 1).

DBD was selected as the plasma source because of its lower volumetric power – we are able to charge droplets in a more "gentle" way than competing technologies and more powerful plasma sources [1,5,7]. DBD is also a non-thermal discharge able to function under room temperature and pressure conditions which are required for survival of most bio-chemicals. In addition, DBD design allows us to charge large volumes and throughput more liquid than most available technologies resulting in faster printing. Finally, we have precise control of the droplet flow speed (carrier gas flow speed) and are able to virtually eliminate splashing problems that occur with other methods like electro-spray [2-5]. Slower droplet speeds also allow for better control over printing precision and rate. However, DBD plasma at atmospheric pressure is highly non-uniform, unlike a less powerful Corona discharge – we are currently investigating both discharges to determine optimal conditions for droplet deposition without biochemical damage.

II. EXPERIMENTAL SETUP

Experimental setup and schematic illustrations of the Plasma BioPrinter are presented in Fig. 2.1-2.3. In the experiments with Corona discharge, "grounded mesh" in Fig. 2.2, 2.3 is replaced with thin powered wire and "high voltage electrode" is disconnected.

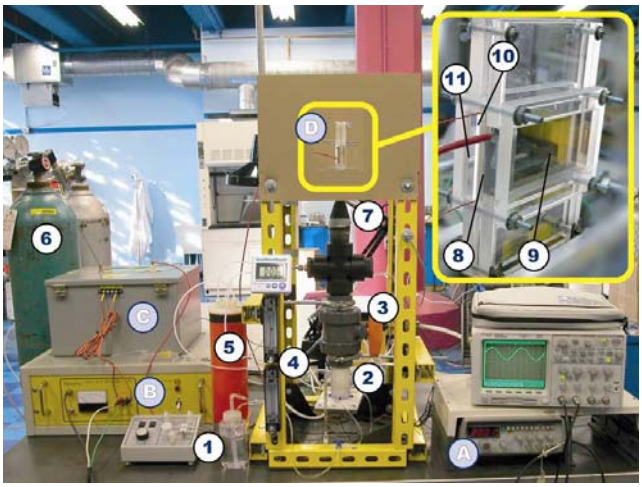

Fig. 2.1. Plasma BioPrinter Experimental Setup

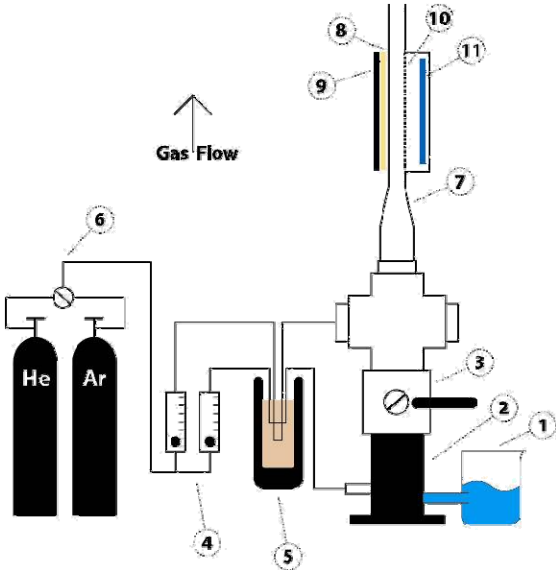

Fig. 2.2. Plasma BioPrinter Setup Schematic: (1) Liquid supply (bottle & variable flow pump); (2) Ultrasonic Nebulizer; (3) Droplet Flow control valve; (4) Gas Flow control; (5) Liquid Nitrogen cooler; (6) Carrier Gas Supply; (7) Flow conversion nozzle; (8) Quartz Dielectric Barrier; (9) High Voltage Electrode; (10) Grounded Mesh Electrode; (11) Target Substrate.

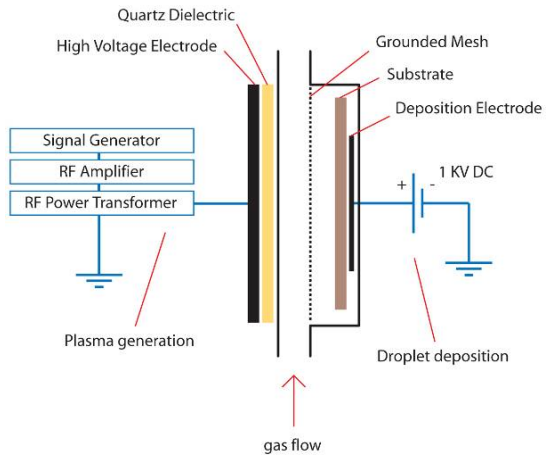

Fig. 2.3. Printer head setup schematic with DBD plasma.

Experimental process is as follows. Liquid is supplied by a variable flow mini-pump at 130 ml per hour (1). Piezoelectric Ultrasonic Nebulizer (atomizer) then produces 1-4 micrometer droplets (2). Aerosol flow into the system is controlled by the ball valve (3) and by supplying carrier gas into the Nebulizer (4). Carrier gas is supplied in two locations to allow control of the flow rate as well as droplet concentration via gas dilution (4). Air, Argon, or Helium can be used as carrier gases (6) which are cooled by liquid Nitrogen to ensure minimal water vaporization from droplets in the discharge (5). Our gas flow through plasma ranges from 1 to 2 liters per minute (4 to 8 cm per second flow speed through plasma gap), thus staying laminar with low Reynolds number; connection from Nebulizer to plasma is made in such a way as to ensure laminar flow (7). Plasma region consists of a 40x80 mm gap with 1 mm thick quartz dielectric (8). Gold was thermally evaporated onto quartz to act as one electrode (9). Second electrode is an open stainless steel mesh (10) which provides us with the ability to extract charged droplets from plasma onto target substrate (11) using an external electric field.

In plasma, droplets are charged to their "floating potential" – a potential at which flow of electrons onto a droplet is balanced by flow of positive ions. Bohm's sheath model [3,8] allows us to estimate floating potential as φ_{fl}:

$$\varphi_{fl} = -\frac{T_e}{2}\ln\left(\frac{M_i}{2\pi m_e}\right) = -4.7 \text{ V} \qquad \textbf{(1)}$$

where T_e – electron temperature, M_i – ion mass, m_e – electron mass. For droplet of radius r = 500nm we can estimate its charge to be:

$$q_{drop} = \varphi_{fl} c = \varphi_{fl} 4\pi\varepsilon_0 r \approx 1000 \text{ electrons} \qquad \textbf{(2)}$$

where c – droplet capacitance, ε_0 – permittivity of free space. In DBD discharge in Argon at room temperature and pressure, number of electrons $n_e \approx 10^{12}$ cm^{-3} and their velocity $v_e \approx 10^8$ cm/sec we can calculate electron flux [5,8]:

$$\Phi_e = 4\pi r^2 \frac{n_e v_e}{4} \approx 10^5 \ \frac{\text{electrons}}{\text{second}} \qquad \textbf{(3)}$$

Thus, a 500 nm radius droplet will gain 1000 electrons in $5\cdot10^{-3}$ seconds; and at the flow speed of 4 cm/sec through plasma we can estimate that the droplet will be charged after $2\cdot10^{-2}$ cm in plasma (more details on DBD plasma modeling and particle charging dynamics can be found in literature [4,5,8-12]). Even though plasma characteristics of a Corona discharge differ from DBD plasma, based on experimental evidence will assume that droplets gain similar charge [7].

Piezoelectric crystal in Ultrasonic Nebulizer vibrates at 2.4 MHz generating droplets of 1.7 micrometer diameter on average at room temperature and pressure [2]. Sonozap corp., makers of the crystal, measured droplet diameters to be in the 1 to 4 micrometer range (via light scattering). We plan to repeat those experiments at our lab in the near future. Nebulizer liquid throughput of 130 ml/hour and flow rate of 1 l/min yields droplet concentration of $7.8\cdot10^8$ droplets/cm^3 – droplet-carrier gas mixture is very dense and evaporates very slowly at the time scales relevant to our system [2,3,7].

Our droplets are too small to feel the effect of gravity during their residence in the system [3,7]. Neglecting the effect of gravity we notice that the only two forces are acting on the droplet: force exerted by the electric field pulling the droplet onto the substrate $F_{el} = Eq$ (E – applied electric field, q - charge) and drag force exerted by the gas on the droplet $F_{drag} = 6\pi\eta r v$ for low Reynolds number (η - dynamic viscosity, r – droplet radius, v – relative velocity) [2]. To find droplet's drift velocity let us equate the two forces:

$$Eq = 6\pi\eta rv \Rightarrow E\varphi_{fl} 4\pi\varepsilon_0 r = 6\pi\eta rv \Rightarrow$$

$$v = \frac{2}{3}\frac{\varphi_{fl}\varepsilon_0}{\eta} E \ \frac{\text{cm}}{\text{sec}} \qquad \textbf{(4)}$$

Thus we observe that charged droplet drift velocity under the influence of electric field will not depend on the size of the droplet. This allows us to control droplets motion more precisely as well as virtually eliminate splashing problems [2].

III. RESULTS

We have demonstrated our ability to ignite and sustain DBD discharge in Argon and Helium in the presence of water aerosol (Fig. 3.). The discharge operates at room temperature and pressure with power of 50-70 Watt in Argon and 15-25 Watt in Helium (Fig. 4.).

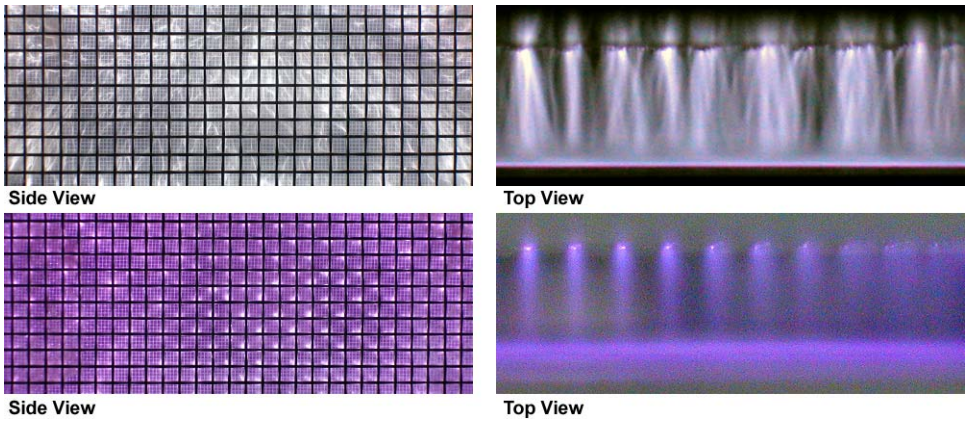

Fig. 3. DBD plasma with water aerosol at room conditions. Top: chilled Argon; bottom: chilled Helium.

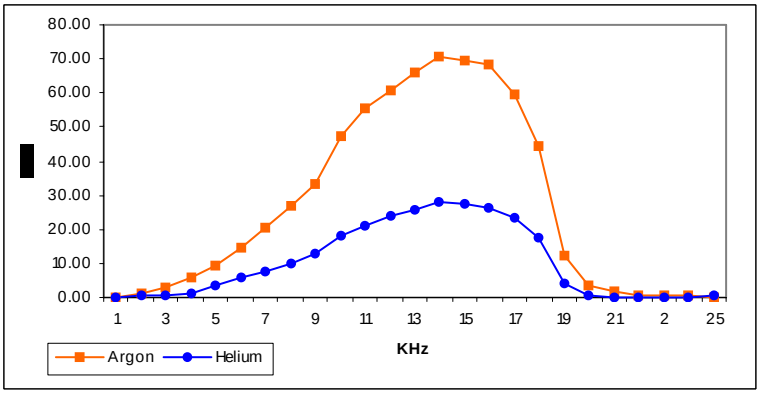

Fig. 4. Power of Argon and Helium discharges with water aerosol present.

We have demonstrated droplet deposition onto a 1 mm thick positively biased wire from DBD plasma and obtained similar results using a Corona discharge (Fig. 5.1, 5.2). This leads us to believe that our hypothesis of the droplets gaining a negative charge is, in fact, true; however, further testing is needed to ensure this fact. The obtained results did not differ between Argon to Helium.

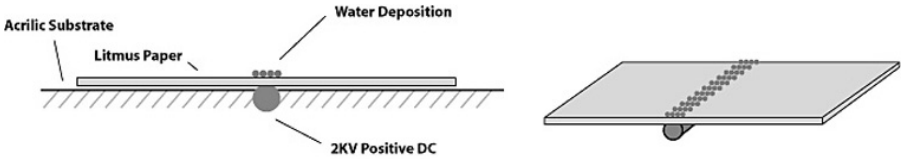

Fig. 5.1. Schematic of the substrate for deposition on positive electrode.

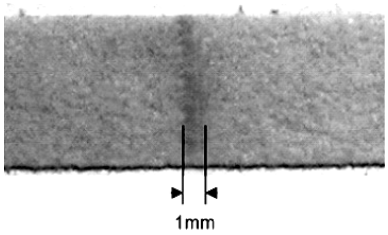

Fig. 5.2. Droplet deposition onto 1mm positively biased electrode.

Additionally we were able to demonstrate bio-active compound survival by printing Bovine serum albumin (BSA) onto a glass slide followed by fluorescein dye stain. BSA maintains its activity after passing through DBD plasma (Fig. 6.). However, more fragile molecules, like enzymes, rapidly loose their *activity* in DBD plasma (Fig. 7) – they still remain proteins but are no longer biologically active. This suggest that we need to keep residence time in plasma to a minimum to make sure bio-active molecules maintain their activity; however, this should not be a problem since our estimations show that droplet charging occurs in ~$5 \cdot 10^{-3}$ seconds which is significantly less time that required for Trypsin inactivation. Further testing of Enzyme inactivation rates in Corona discharge is pending.

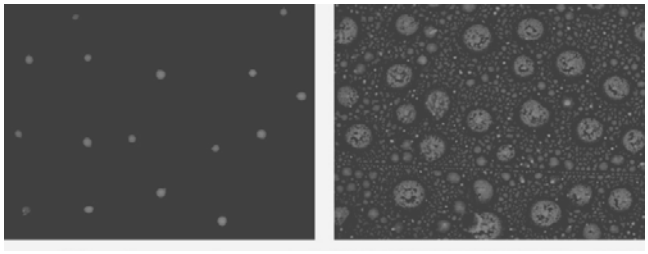

Fig. 6. Bovine Serum Albumin (BSA) fluorescein dye stain after deposition: (left) 15 second treatment; (right) 2 minute treatment.

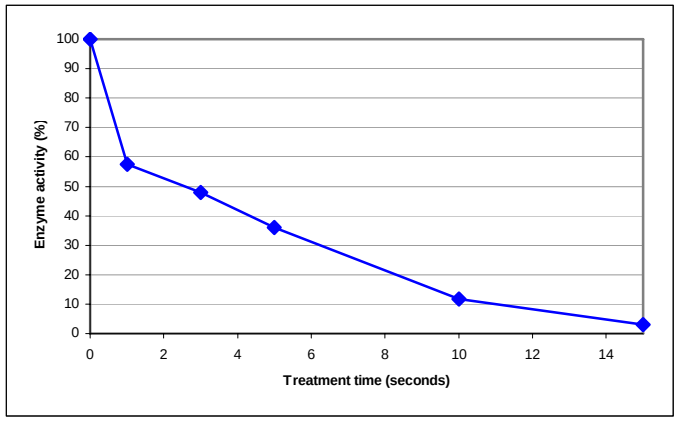

Fig. 7. Trypsin enzyme activity in plasma.

IV. CONCLUSION

Ignition of atmospheric pressure discharge in dense Argon and Helium atmospheres with dense liquid aerosol at atmospheric pressure and temperature was demonstrated. Droplet charging was demonstrated by droplet deposition controlled by electric field. Additionally it was demonstrated that DBD plasma in noble gases (under the discussed conditions) has little if any influence on bioactive compounds such as BSA (small protein). Detailed investigation of DBD plasma and Corona discharge inactivation of various protein and plasma influence on enzymatic activity of various bio-chemicals is being currently performed. Nano-precision is theoretically possible but was not yet demonstrated – our plans for near future include fabrication of charge-stamping setup – an existing and well-studied phenomenon that will provide us with nano-scale electrodes for charged droplet deposition.

ACKNOWLEDGMENTS

We would like to thank Ben Franklin Nanotechnology Institute for supporting this work, and Kurt Sieber of Eastman Kodak Company for his assistance with DBD plasma power supply construction.

REFERENCES

[1] A.Fridman, L.Kennedy, Fundamentals of Plasma Physics and Plasma Chemistry, Taylor & Francis, 2003.
[2] W.A.Sirignano, Fluid dynamics and transport of droplets and sprays, Cambridge University Press, 1999.
[3] A.V.Kozyrev, A.G.Sitnikov, Evaporation of a spherical droplet in a moderate pressure gas, Uspekhi Fizicheskikh Nauk, Russian Academy of Sciences, 2001.
[4] V.E.Fortov, Charge coupling and ordering in nonideal dusty plasmas, Institute for High Energy Densities, Russian Academy of Sciences, 2000.
[5] U.Kogelschatz, Dielectric-barrier discharges: their history, discharge physics, and industrial applications, Plasma Chemistry and Plasma Processing, Vol. 23, No. 1, Plenum Publishing, March 2003.
[6] M. Moravej, X. Yang, G. R. Nowling, J. P. Chang, R. F. Hicksa, S. E. Babayan, Physics of high-pressure helium and argon radio-frequency plasmas, J. Appl. Phys., vol 96.12, 2004.
[7] Kogelschatz U 1988 *Process Technologies for Water Treatment* ed S Stucki (New York: Plenum) pp 87–120
[8] Raizer Yu P 1991 *Gas Discharge Physics* (Berlin: Springer)
[9] Kunchardt E E and Tzeng Y 1988 *Phys. Rev.* A 38 1410
[10] Djermoune D, Samson S, Marode E and Segur P 1995 *11th Int. Conf. on Gas Discharges and their Applications (Tokyo)* vol 2, pp 484–7
[11] Kulikovsky A A 1994 *J. Phys. D: Appl. Phys.* 27 2556
[12] Babaeba N and Naidis G 1996 *J. Phys. D: Appl. Phys.* 29 2423

Use of Non-Thermal Atmospheric Pressure Plasma Discharge for Coagulation and Sterilization of Surface Wounds

Gregory Fridman[1], Marie Peddinghaus[3], Alexander Fridman[2], Manjula Balasubramanian[3], Alexander Gutsol[2], Gary Friedman[4]

[1] *School of Biomedical Engineering, Science, and Health Systems*
[2] *Department of Mechanical Engineering and Mechanics, College of Engineering*
[3] *Transfusion Services and Donor Center, College of Medicine*
[4] *Department of Electrical and Computer Engineering, College of Engineering*

Drexel Plasma Institute, Drexel University, Philadelphia, Pennsylvania, USA

Abstract

We demonstrate the ability of non-thermal plasma to promote blood coagulation and tissue sterilization in under 15 seconds of treatment. We demonstrate no gross (visible) or microscopic damage to tissue in as much as 5 minutes of plasma treatment. This procedure would be safe for patients since there are no exposed electrodes, discharge is cold, and current is low. Initial experimental results obtained using cadaver organs and donor blood support the fact that the DBD plasma can simultaneously sterilize skin and promote coagulation in bleeding tissue. This technique will decrease wound healing time and virtually eliminate wound infections with skin flora.

Keywords: non-thermal plasma, tissue sterilization, blood coagulation, wound healing

1. Introduction

In the last decade, advances in electrical discharge plasma systems allowed for many new applications. Such systems have been used for sterilization of surfaces, for biochemical surface functionalization, and for many other new applications [6-13]. Specifically, thermal plasma discharges are applied in the field of blood coagulation as a faster alternative to normal biochemical coagulation [7-9]. However, the use of thermal plasma is limited for two reasons: (a) the extremely high temperatures (2,000 K up to 10,000 K) cause severe tissue damage [7-9] (Fig. 1) and (b) the necessity of general anesthesia makes it inconvenient for wide-spread patient use, apart from the hospital setting [8,9].

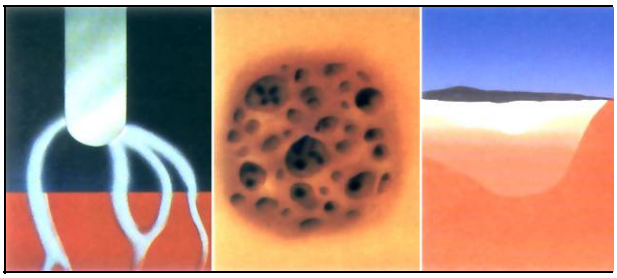

Fig. 1. Tissue damage by thermal plasma: tissue overheating, puncture and charring [7-9].

We have developed a Floating Electrode Dielectric Barrier Discharge (DBD) plasma (Fig. 2) system that promotes blood coagulation with simultaneous tissue sterilization for treatment of surface wounds. This treatment would be safe to patients because no exposed electrodes are involved and high frequency current is kept below a mili-ampere (see "Safety Considerations" below). Our initial experiments have shown that such plasma treatment hastens blood coagulation and causes simultaneous wound sterilization (probably via a large concentration of chemically active species in plasma [10-13] that are ions, radicals (O, OH, N) and electronically-excited atoms and molecules [1-6]). Fig. 3 and 6 display our prototype quartz-coated treatment electrodes for wound surface treatment by DBD plasma.

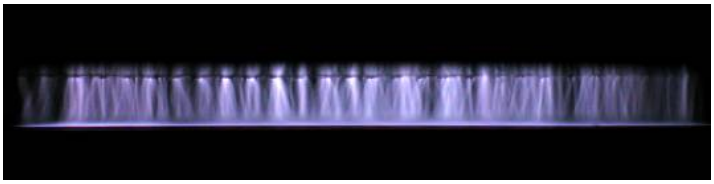

Fig. 2. Dielectric Barrier Discharge

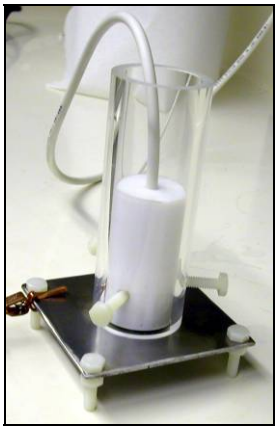

Fig. 3. Quartz-coated Treatment Electrode

This plasma technology can find many applications in the medical field. Within the hospital setting, this technology may prove useful in the operating room for patients suffering from bleeding not amenable to other methods of coagulation. Because of the potential for simultaneous sterilization, our device could also help prevent intra-operative infections. Sterilization effects of non-thermal plasma are well-known [10-13] and were confirmed, for example, in our research with NASA Jet Propulsion Lab [14]. In the future, we intend to develop a significantly smaller version of our power supply to create a portable, possibly battery-operated blood coagulator and wound sterilizer (Fig. 4). In addition, due to its ability to promote coagulation, the non-thermal plasma discharge device can be used for hemophiliac patients who have clotting difficulties or those who are on anti-coagulants.

2. Experimental Setup

Schematics of our experimental setup of the varying and fixed (Fig. 4) frequency, voltage, and power Floating Electrode DBD setups are presented. Power of both systems is approximately 1 W/cm^2 and the treatment surface varies from less than 1cm^2 to 10cm^2 depending on the attached electrode (Fig. 6). Utilizing the variable frequency, voltage, and power setup we are able to tune the setup for treatment dose appropriate for a specific application. I.e. for tissue sterilization we might want lower power with longer treatment time; while for blood coagulation we might want high power with low treatment time to stop "gushers" – large flow of blood; or lower power to coagulate blood in small cuts.

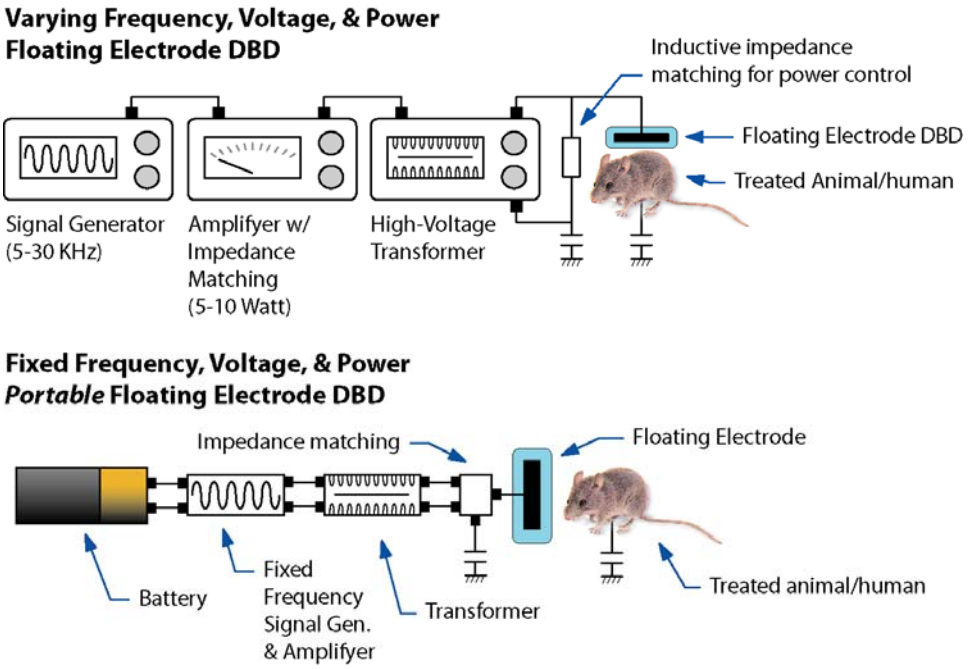

Fig. 4. Floating Electrode DBD schematic.

We started a fundamental study of mechanism of blood coagulation with the help of electrical discharge plasma. Fig. 5 presents our setup for treatment of small blood volumes – 500µl. While not wasting too much blood per test, this volume is a minimum required for standardized hematological tests we perform at the Drexel University Hahnemann Hospital hematology lab: PT (Prothrombin time), aPTT (activated partial thromboplastin time), and STA-Thrombin® (Diagnostica Stago proprietary Thrombin formation time test). In this setup we are able to precisely control the distance of Floating Electrode DBD to the treated blood sample for the purpose of

determining correct dose required for clot formation and to get reproducible results necessary for the fundamental study.

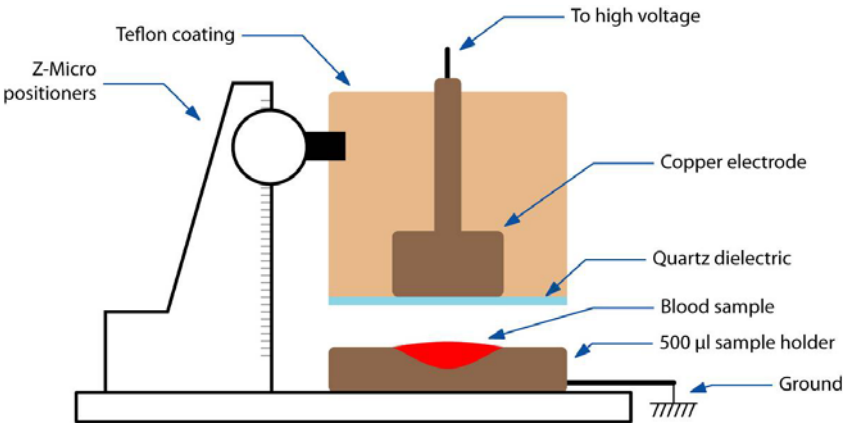

Fig. 5. Blood treatment experimental setup schematic.

Schematic representations of the three treatment electrode types used for this research are shown in Fig. 6. “Round” electrode is used for treatment of small areas and when distance between electrode and the treated surface is closely monitored (±0.1mm). “Wand” electrode is used in hand-held operation where distance and treated area are not precisely monitored. “Roller” is used for treatment of large flat areas.

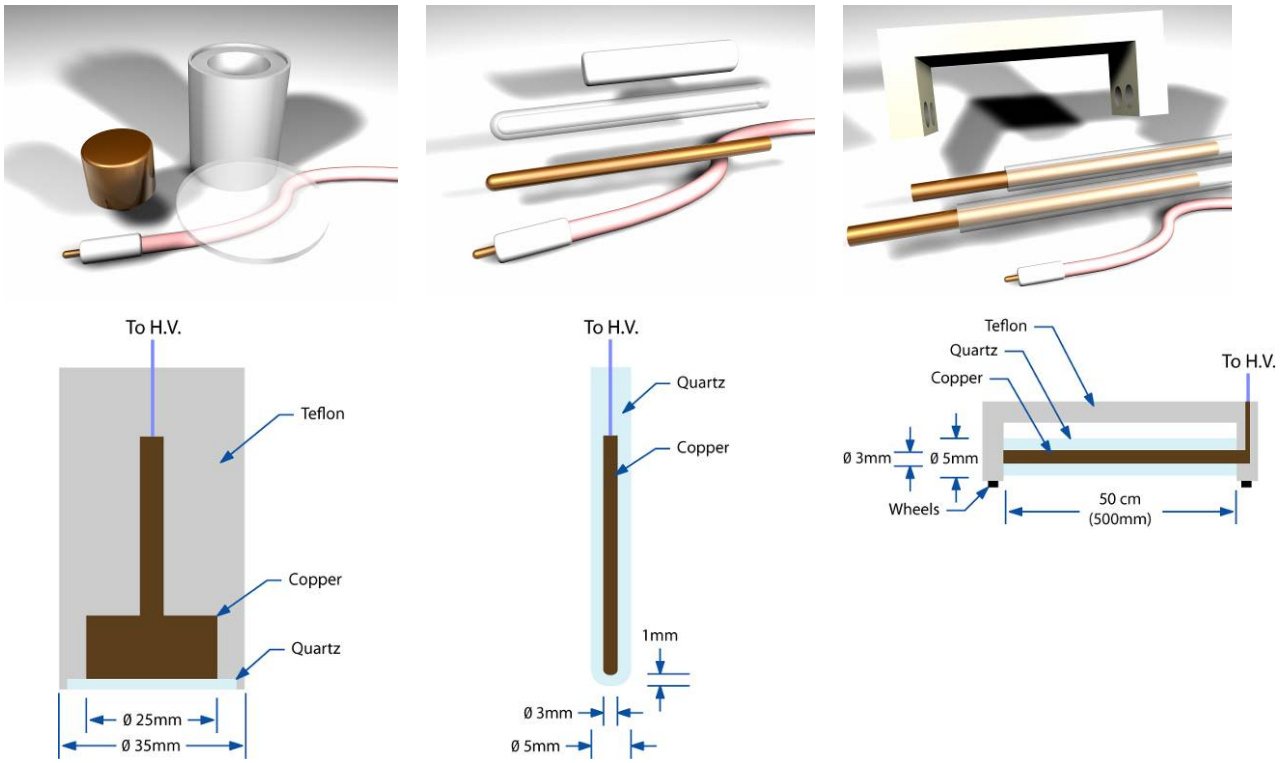

Fig. 6. Treatment electrodes. Top: 3D models; bottom: schematic representations;
left to right: “round”, “wand”, “roller”.

During treatment, tissue samples are placed directly on a grounded stainless steel plate. Blood samples are dispensed into 0.1 or 0.5 ml grounded stainless steel, aluminum, brass, or titanium containers (Fig. 5). For blood treatment we found titanium to be the best material where control blood sample coagulates the slowest.

3. Safety considerations

Safety of Floating Electrode DBD plasma electrode for humans needs to be considered for application in wound healing. Here we consider a simplified electric scheme to estimate conditions required for electrical safety. Once human approaches Floating Electrode, plasma ignites and at that point we can consider DBD plasma as capacitor and resistor in series and human as a resistor and capacitor in series (Fig. 7).

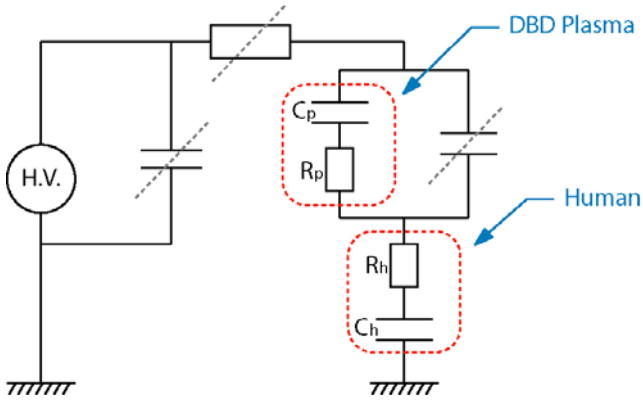

Fig. 7. Plasma/human interface principal schematic.

Total plasma resistance can then be estimated as a sum of capacitive and active resistances:

$$\overline{R}_p^{\Sigma} = \frac{i}{C_p\omega} + R_p$$

$$R_p^{\Sigma} = \sqrt{\left(\frac{1}{C_p\omega}\right)^2 + \left(R_p\right)^2}$$

Where R_p^{Σ} is total plasma resistance, C_p is plasma capacitance, R_p is plasma active resistance, and ω is the signal frequency. Similarly, total resistance of a human can be estimated as:

$$R_h^{\Sigma} = \sqrt{\left(\frac{1}{C_h\omega}\right)^2 + \left(R_h\right)^2}$$

Where R_h^{Σ} is total resistance of a human, C_h is human capacitance, and R_h is active resistance of a human. For the Floating Electrode DBD plasma device to be safe, total plasma resistance needs to be greater than total resistance of a human:

$$\sqrt{\left(\frac{1}{C_p\omega}\right)^2 + \left(R_p\right)^2} >> \sqrt{\left(\frac{1}{C_h\omega}\right)^2 + \left(R_h\right)^2}$$

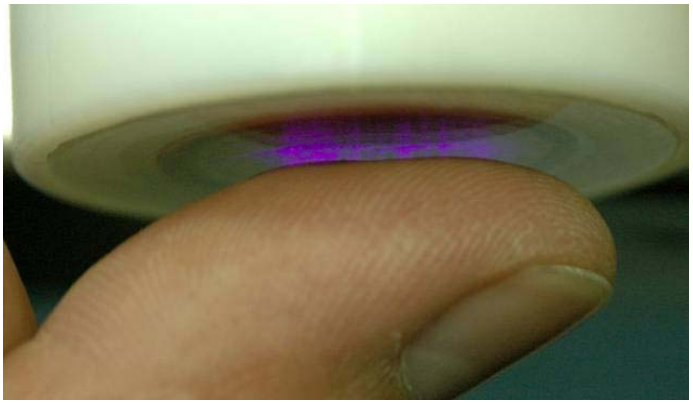
Fig. 8. Floating Electrode DBD: safe to touch.

Active resistance of a human is ~1 MOhm [15-17] and human capacitance is ~50 pF (though it ranges from 20 pF to 90 pF, depending on the surface human is standing on, thickness of his/her soles, and distance to nearest grounded object) [15,17]. For our frequency range, Floating Electrode DBD plasma active resistance can be estimated to 5 to 10 MOhm and its capacitance to ~50pF [18,19]. Thus at the operating frequency of 12 kHz we see that total resistance of a human (1.9 MOhm) is far smaller than total plasma resistance (5.3 MOhm), assuming C_h=50 pF, R_h=1 MOhm, C_p=50 pF, R_p=5 MOhm. Even in the case where human total resistance will increase for some reason, total current passing through the human will be very low because of a massive total resistance of the system. From this estimation we can conclude that even in the worst case where resistance of a human is approaching that of plasma, the overall system will still be completely safe from the electrical standpoint (Fig. 8).

4. Results

In our tests we have successfully accomplished the following:

- Designed and built a Dielectric Barrier Discharge (DBD) system capable of delivering 1 W/cm^2 of plasma power at operating frequencies of 10-30 KHz. While the system employs a power supply delivering voltage of up to 10 KV, it is perfectly safe as the high frequency plasma current is limited to below a milli-ampere.
- Developed treatment electrodes (Fig. 3-6) for treatment of blood and tissue samples.
- Performed blood coagulation tests on blood from cadaver organs (Fig. 9). The results consistently show faster coagulation when exposed to DBD plasma: for example, blood treated for 15 seconds completely coagulates in 2 minutes while untreated sample coagulates in 13 minutes.
- Performed blood coagulation tests on cadaver organs with subsequent gross and microscopic evaluation of tissue to test for damage. Our analysis demonstrates blood clotting within 15 seconds without gross or microscopic evidence of tissue damage (Fig. 10,11).
- Performed skin sterilization tests on cadaver skin with subsequent microbiologic culture. The results demonstrate complete sterilization of skin flora after 6 seconds of treatment by the plasma.
- Examined skin histology to find existence and/or extent of microscopic damage. No tissue damage was found after as much as 5 minutes of plasma treatment (Fig. 11).

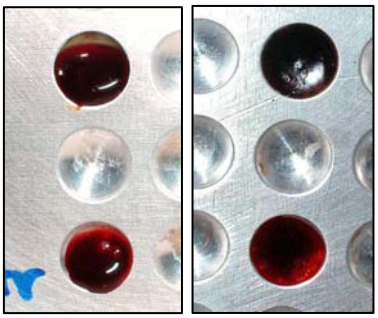

Fig. 9. Plasma-assisted blood coagulation with 15-second treatment (left) and 1-minute treatment (right); control drop on the bottom, treated drop on top.

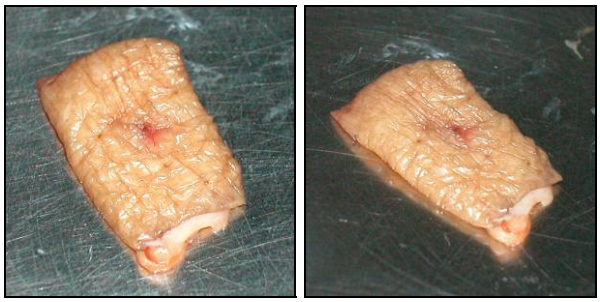

Fig. 10. 1-minute plasma treatment shows no visible tissue damage. Left: before treatment; right: after treatment.

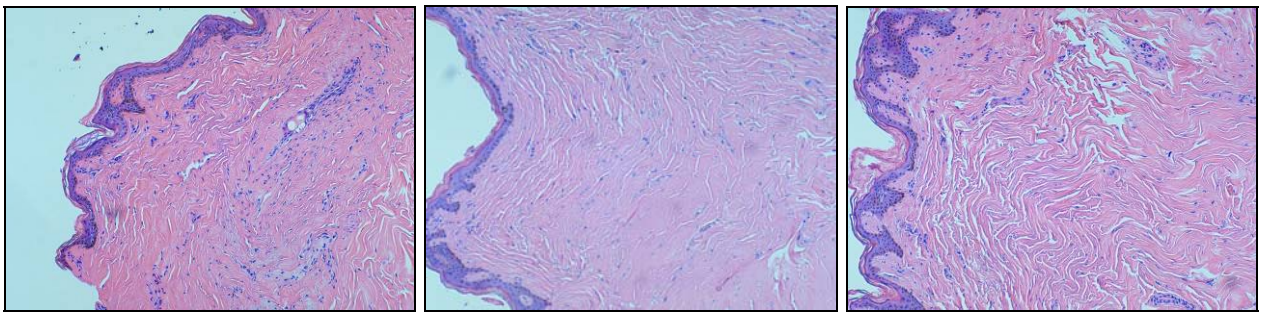

Fig. 11. Skin histology (left to right): control, 1 minute, and 5 minute treatment times show no detectable tissue damage.

5. Conclusion

This device can find many applications in the medical field, ranging from replacing high-power, high-temperature thermal plasma coagulators in the operating rooms to personal portable wound sterilizing and healing instruments. The scope of the presented research included only initial studies of plasma influence on blood coagulation and simultaneous tissue sterilization. However, these studies are essential in providing us with knowledge and expertise on the underlying processes.

At the present, we are actively working on developing a kinetic model of DBD plasma influence on Blood plasma coagulation cascade as well as DBD plasma role in the tissue sterilization process. We have interesting modeling results (that agree with experimental evidence) involving DBD plasma influence on Calcium ion

concentration and in turn on blood coagulation cascade. These results will be presented at the ISPC-17 conference.

Bibliography

[1] "Hydrogen peroxide as a topical hemostatic agent", Clin Ortop. 1984 Jun; (186):244-8. Hankin FM, Campbell SE, Goldstein SA, Matthews LS.

[2] "Clinical usefulness of 3% hydrogen peroxide in acute upper GI bleeding: a pilot study". Gastrointest Endos. 1999 Apr; 49(4 Pt l):518-21. Kalloo AN, Canto MI, Wadwa KS, Smith CL, Gislason GT, Okolo PI 3rd, Pasricha PJ.

[3] "Hydrogen peroxide is involved in collagen- induced platelet activation". Blood.I998 Jan 15;91(2):484-90. Pignatelli P, Pulcinelli FM, Lenti L, Gazzangia PP, Violi F.

[4] "Role of hydroxyl radicals in the activation of human platelets". Eur J Biochem. 1994 Apr l5; 221(2):695-704. Iuliano L, Pederson JZ, Pratico D, Rotilio G, Violi F.

[5] "H_2O_2 activity on platelet adhesion to fibrinogen and protein tyrosinephosphorylation". Biochim Biophys Acta. 2000 Feb 2; 1495(2): 1 83-93.

[6] "Free radicals contribute to platelet aggregation and cyclic flow variations in stenosed and endothelium-injured canine arteries". J Am Coil Cardiol. l994 Dec; 24(7):1749-56.

[7] "A plasma scalpel: comparison of tissue damage and wound healing with electrosurgical and steel scalpels". Archives of Surgery Vol 11 l No 4, Apr 1976. W.J. Link, F.P. Incropera, J.L. Glover.

[8] "The plasma scalpel: a new thermal knife". Lasers Surg Med. 1982; 2(1):I01-6. Glover JL, Bendick PJ, Link WJ, Plunkett RJ.

[9] "Evaluation of the plasma scalpel for intracranial surgery: a pilot study". Surg Neurol. I 979 Sep; 12(3):247-50. Payne NS, Tindall GT, Fleischer AS, Mirra SS.

[10] "Biological decontamination by non-thermal plasmas". IEEE Trans. Plasma. Sci., Vol. 28, No. 1, pp. 184-188, 2000. M. Laroussi, I. Alexeff, W. Kang.

[11] "A Remote Exposure Reactor (RER) for plasma processing and sterilization by plasma active species at one atmosphere". IEEE Trans. Plasma Sci., Vol. 28, No. 1, Feb 2000. J.R. Roth, D.M. Sherman, R.B. Gadri, F. Karakaya, Z. Chen, T.C. Montie, K. Kelly-Wintenberg, P.P.-Y. Tsai.

[12] "Use of one atmosphere uniform glow discharge plasma to kill a broad spectrum on microorganisms". J. Vac. Sci. Technol. A., Vol. 17, No. 4, Jul/Aug 1999. K. Kelly-Wintenberg, A. Hodge, T.C. Montie, L. Deleanu, D. Sherman, J.R. Roth.

[13] "Demonstration of a Hermetic Airborne Ozone Disinfection System: Studies on E. coli". AIHA J 64 no2 Mr/Ap 2003. W.J. Kowalski, W.P. Bahnfleth, B.A. Striebig, T.S. Whittam.

[14] Final Technical Report - NASA Contract NAS3-01068 – "Use of Non Thermal Plasma for Sterilization of Material Handling Devices"

[15] MARBLE, A. E., MACDONALD, A. C., MCVICAR, D., and ROBERTS, A., 1977, Phys. Med. Biol., 22, 365.

[16] "Bioelectrical impedance measurements in patients with gastrointestinal disease: validation of the spectrum approach and a comparison of different methods for screening for nutritional depletion", Petronella LM Cox-Reijven, Bernard van Kreel and Peter B Soeters, American Journal of Clinical Nutrition, Vol. 78, No. 6, 1111-1119, December 2003

[17] "Fusion Pore Conductance: Experimental Approaches and Theoretical Algorithms", Vladimir Ratinov, Ilya Plonsky, and Joshua Zimmerberg, Biophys J, May 1998, p. 2374-2387, Vol. 74, No. 5

[18] "Electrical Characterization of a Corona Discharge for Surface Treatment", LA Rosenthal, DA Davis, IEEE Trans. on Ind. Apps., Vol. IA-11, No. 3, May/June 1975.

[19] "Microdischarge behaviour in the silent discharge of nitrogen-oxygen and water-air mixtures", Z Falkenstein, JJ Coogan, J. Phys. D: Appl. Phys., 30 (1997) 817-825.

Generation of microwave excited atmospheric pressure air microplasmas with low microwave powers

Jaeho Kim[1] and Kazuo Terashima[2]

1 Department of Advanced Energy, Graduate School of Frontier Sciences, The University of Tokyo

2 Department of Advanced Materials Science, Graduate School of Frontier Sciences, The University of Tokyo

5-1-5 Kashiwanoha, Kashiwa-shi, Chiba 277-8561, Japan

Abstract

A 2.45GHz microwave excited microplasma at atmospheric air was produced using a SMMAP (stripline microwave micro atmospheric plasma) device based on microstrip technology. Plasmas were the self-ignition at a power of about 5W and were sustained at even under 1W. The rotational temperature of nitrogen molecules measured using optical emission spectroscopy (OES) was 480K with no flow of gas. A SMMAP device has been applied to polymer surface modification.

Keywords

microplasma, non-equilibrium plasma, atmospheric plasma, microwave excited plasma, wettability

1. Introduction

Atmospheric pressure microplasmas have offered many possibilities for the generation of new applications such as bio-MEM's sterilization, small-scale materials processing, propulsion of micro- and nanosatellites, and micro-chemical-analysis systems [1,2]. In addition, microplasmas can provide a large-scale non-equilibrium plasma the materials processing at atmospheric pressure using the array configuration. Recently, various microplasma sources have been developed including microwave excited microplasmas at atmospheric pressures based on microstrip technology [3-7]. Microwave excited microplasmas based on mictrostrip technology are with a long lifetime, stability, robustness, and simplicity, compared to other microplasma systems. Microstrip technology and a small semiconductor microwave source make it possible to achieve the low-power operation and the portability of the microplasma system. However, in these plasmas, He or Ar gases were used for the sustainment of stable plasmas at atmospheric pressure. Also, it is difficult to enlarge the plasma scale using the array configuration due to the configurations of their plasma systems used in these works.

While, in previous our work [8, 9], a SMMAP (stripline microwave micro atmospheric plasma) device was reported. Microplasmas at atmospheric air using the SMMAP device were ignited at over microwave power of 15W and were sustained at a microwave power of about 1W. The experimentally measured gas temperature using OES was about 800K. The SMMAP device permits the array configuration for enlarging of the plasma scale.

In this work, the SMMAP system has been improved to reduce the operation microwave power and to provide the plasmas with a lower gas temperature. The SMMAP has been applied to the modification of material surface such as a polymer for wettability, adhesion, bonding, and printability. In this paper, we report the results experimentally obtained recently.

2. Experimental setups

The SMMAP device consists of a dielectric plate, a stripline, a ground plane, and a discharge gap. The discharge gap is placed on a transverse cross-section of the dielectric plate between the stripline and the ground plane, which play the role of electrodes for generating plasmas. Figure 1 (a) shows the structure of the SMMAP device.

2.45GHz microwave power is introduced to the SMMAP device through a coaxial cable and a SMA connector and propagates along the inside of the dielectric plate between the stripline and the ground plane approximately in TEM mode. Electric fields are strongly concentrated at the discharge gap with smaller width than the thickness of dielectric plate. Electric fields are going from the stripline electrode to the ground electrode, resulting in the low radiation of electric fields to external space. Electric fields at the discharge gap become stronger by increasing the characteristic impedance of the transmission line. For the impedance matching, a three stub tuner, a stub matching, or a quarter-wavelength transformer have been used as shown in figure 1 (b), (c), and (d).

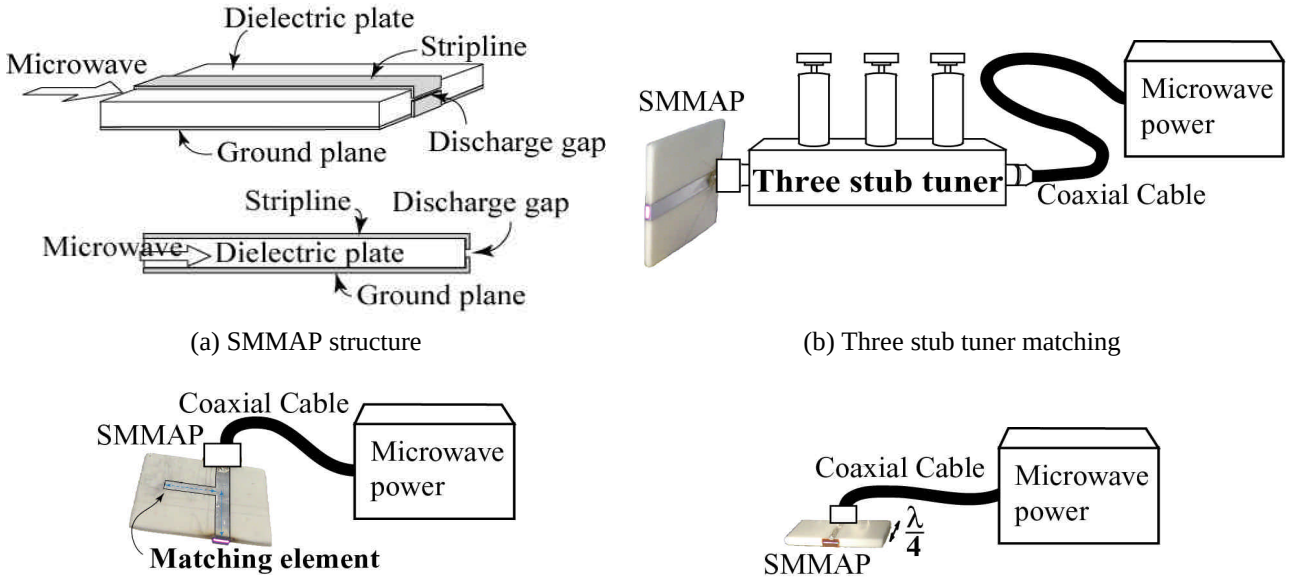

(a) SMMAP structure

(b) Three stub tuner matching

(c) Stub matching

(d) Quarter-wavelength transformer matching

Figure 1. SMMAP system.

Rotational temperatures of nitrogen molecules were measured to investigate gas temperatures in air plasmas by means of optical emission spectroscopy (OES). Rotational temperatures were obtained by fitting the experimentally observed spectrum of the second positive system with the numerically calculated one [10,11]. In this work, to obtain rotational temperatures in air plasmas, the second positive system of the nitrogen molecule was used. Rotational temperatures were investigated for the change in microwave powers at atmospheric pressure and the change in gas pressures at fixed microwave powers. Figure 2 (a) shows an experimentally observed spectrum. Figure 2 (b) shows a numerical fit and an experimentally observed spectrum.

A SMMAP device used in this work was modified from the previous structure [8,9]. The width of the stripline (1mm) was made smaller than that (5mm) in the previous structure, which provides stronger electric intensities at the discharge gap because a small width of a stripline increases the characteristic impedance.

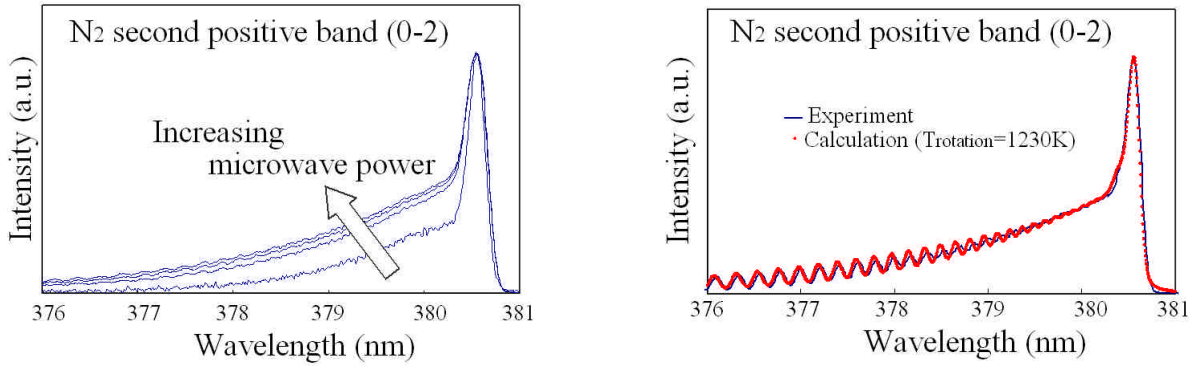

(a) (b)

Figure 2. (a) Experimentally observed spectrum and (b) a typical numerical fit and an experimentally observed spectrum.

3. Results

In this work, filamentary-like discharges were observed. Figure 3 shows the observed filamentary-like discharges. Filament-like discharges were observed with uniform plasmas simultaneous or were observed alone. The positions where the filament-like discharges happened were varied with times. These filamentary-like discharges cause some problems of the non-uniformity and the instability of plasmas. The sputtering of electrodes by the filament-like discharges was observed with naked eyes.

In order to avoid these problems, a dielectric plate was installed between two electrodes as shown in figure 4 (a). Uniform plasmas with no filamentary-like discharges were successfully produced at atmospheric pressure as shown in figure 4 (b). The plasmas was ignited at a microwave power of about 5W and was stably sustained under a microwave power of 1W.

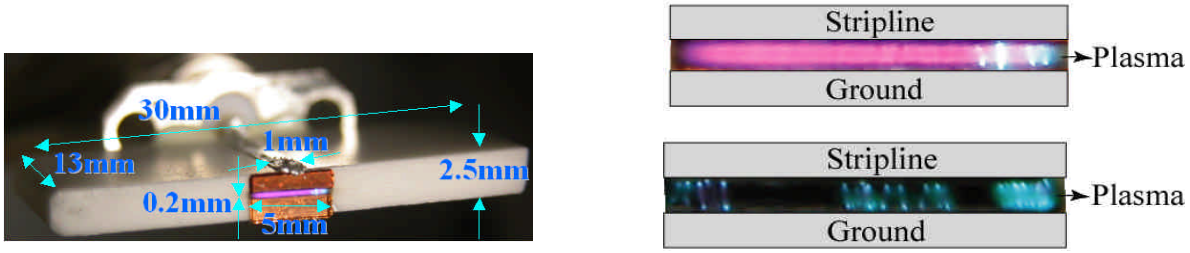

(a) (b)

Figure 3. Experimentally observed filament-like discharges: (a) a picture of a SMMAP and (b) magnified pictures of plasmas produced at a discharge gap.

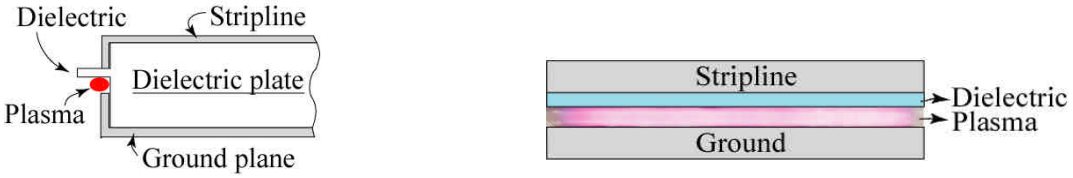

(a) (b)

Figure 4. (a) SMMAP device with the dielectric plate between two electrodes and (b) a picture of the uniform plasma.

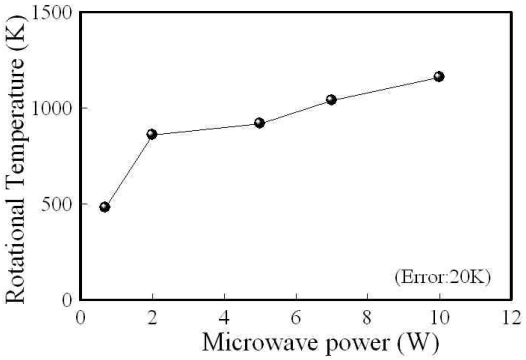

Figure 5. Rotational temperatures for the variation in microwave powers.

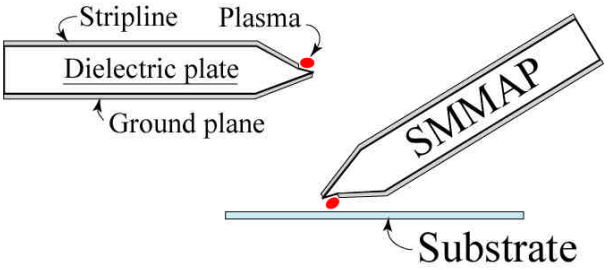

Figure 6. A modified SMMAP device by considering the processing of a substrate.

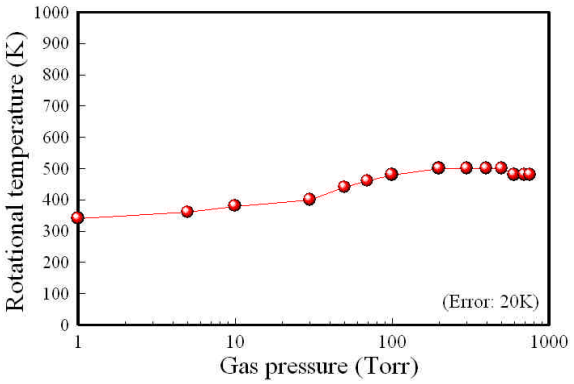

Figure 7. Rotational temperatures for the variation in gas pressure.

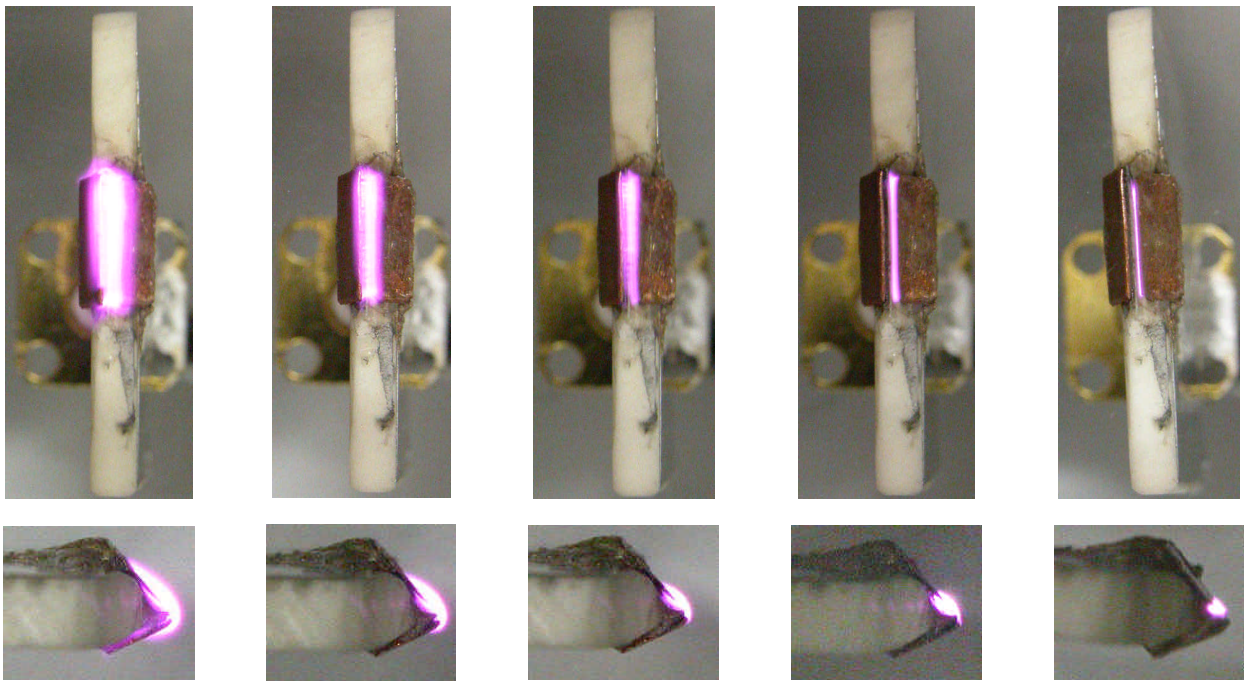

Figure 8. Pictures of plasma optical emission for the variation in gas pressure.

Figure 5 shows the changes in rotational temperatures of nitrogen molecules in air plasmas at atmospheric pressure as the changes in microwave powers. The rotational temperature of 1230K at microwave powers of 10W was reduced with the decrease of microwave powers. Under the microwave power of 1W, the temperature was 480K.

The SMMAP device shown in figure 4 was modified by considering the processing of a substrate as shown in figure 6. The modified SMMAP device was used to investigate the gas pressure dependence of plasma. Figure 7 shows the change of the rotational temperatures as the change of gas pressures from 760Torr to 1Torr. The microwave power was fixed at under 1W. As decreasing the gas pressure, the rotational temperature was decreased from 480K to 340K. Figure 8 shows the pictures of plasma optical emissions as changing gas pressures. The plasma region was diffused as the decrease in the gas pressure.

Moreover, a SMMAP device has been used for the of the polymer surface modification of wettability at the gas pressures of 10Torr to 760Torr. Figure 9 shows a typical photograph of water drops on a treated surface of a polymer film with air plasma treatment and on that without surface plasma treatment. It was found clearly that the surface wettability of a polymer film was improved by the treatment of air plasmas.

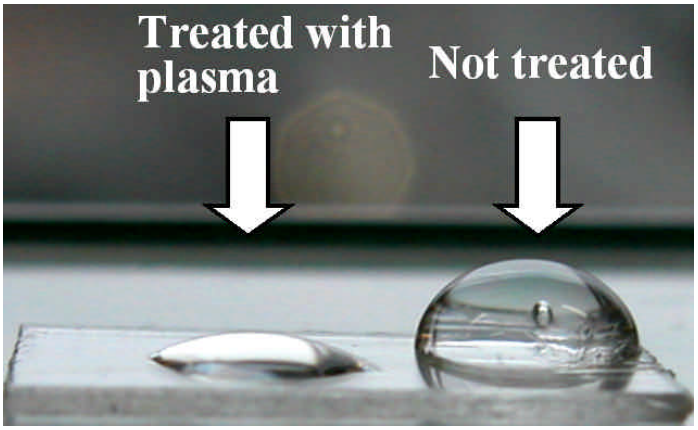

Figure 9. Water drops on a treated surface of a polymer film with plasmas and on a not treated surface.

4. Summary

A 2.45GHz microwave excited microplasma at atmospheric air was produced based on microstrip technology. Plasmas were the self-ignition at an input power of about 5W and were sustained at even under 1W. The rotational temperature of nitrogen molecules measured by using OES was 480K with no flow of gas. The wettability of a polymer film was improved by the treatment of air plasmas.

The optimization of the system is in progress for the ignition and the sustainment of plasmas with the lower microwave powers. The SMMAP device will provide a large-scale atmospheric non-equilibrium plasma using the array configuration and a potable plasma source.

References

[1] Proceedings of 2nd International Workshop on Microplasmas, NJ, USA, Oct. 2004 (Organizers: K.H.Becker, J.G.Eden, and K.H.Schoenbach).

[2] V.Karanassios, Spectrochimica Acta Part B, 59, 909-928 (2004).

[3] U.Engel, A.M.Bilgic, O.Haase, E.Voges, and J.A.C.Broekaert, Analytical Chemistry, 72, 193-197 (2000).

[4] A.M.Bilgic, E.Voges, U.Engel, and J.A.C.Broekaert, J. Anal. At. Spectrum, 15, 579-580 (2000).
[5] A.M.Bilgic, U.Engel, E.Voges, M.Kuckelheim, and J.A.C.Broekaert, Plasma Sources Sci. Technol., 9, 1-4 (2000).
[6] S.Schermer, N.H.Bings, A.M.Bilgic, R.Stonies, E.Voges, and J.A.C.Broekaert, Spectrochimica. Acta., Part.B, 58, 1585-1596 (2003).
[7] F.Iza and J.A.Hopwood, IEEE Transaction on Plasma Science, 31, 782-787 (2003).
[8] J.Kim and K.Terashima, Proceedings of 2nd International Workshop on Microplasmas, NJ, USA, p.62 (Oct. 2004).
[9] J.Kim and K.Terashima, Appl. Phys. Lett., to be published at May 2005.
[10] D.M.Phillips, J. Phys. D, Vol.9, pp.507-521 (1976).
[11] H.R.Griem, “Principle of Plasma Spectroscopy”, Cambridge, U.K.: Cambridge Univ. Press (1997).

Composite Pre-treatment on Metal Surface for Plasma Spray with Cathode Spots of Low Pressure Arc after grit Blasting

T. Inaba[1], M. Hara[1], Y. Kubo[1], K. Ogura[2], T. Iwao[3], S. Tobe[2]

[1]*Department of Electrical, Electronic and Communication Engineering, Chuo University, Tokyo, Japan*
[2]*Department of Mechanical Engineering, Ashikaga Institute of Technology, Tochigi, Japan*
[3]*Department of Electrical and Electronic Engineering, Musashi Institute of Technology, Tokyo, Japan*

Abstract

Cathode spots of a low-pressure arc can remove oxide layers and evaporate impurities on metal surfaces. Removal of the oxide layer using cathode spots is expected to solve recent obstacles to chemical and mechanical cleaning methods. Various phenomena of cathode spots have been investigated for pre-treatment of atmospheric pressure plasma spray (APPS). This study treated the surface shapes of oxide and non-oxide samples using a composite pre-treating method: cathode spots after grit blasting. In addition, the samples are compared with conventionally treated cathode spots and mechanical blasted surfaces. Results show that the roughness on the sample surfaces is higher concomitant with the initial oxide layer thickness. This fact reveals the factors that dominate bonding strength on the pre-treated surface using cathode spots of a low-pressure arc. Bonding strength is higher in relation to the arithmetical mean height of the surface roughness caused by the initial oxide layer thickness. Bonding strength is also higher when the mean spacing of profile irregularities is narrow. The bonding adhesive strength after treatment using cathode spots after the grit blasting is greater than 90 MPa, assuming over 100MPa.

Keywords : Low pressure arc, Plasma spray, Cathode spots, Oxide layer, Grit blasting, Pre-treatment

1. Introduction

Oxide layers accrete stably on steel material surfaces during manufacturing. Low-pressure arc cathode spots can remove oxide layers from metallic surfaces [1,2]. After removal of oxide layers, the surface is rough. For that reason, pre-treatment by thermal spray coating has been examined [3]. Grit blasting and chemical decontamination are widely used as pre-treatments, but these are environmentally unsound methods because they scatter sludge, create noise, and generate liquid waste. Application of a low-pressure arc creates neither noise nor sludge because pre-treatment is conducted in an enclosed space. Cathode spots are characterized [1,4] by: (1) numerous arc spots, (2) vapor emission of a cathode material because of the extremely intense arc power, (3) rapid movement of the spots on the cathode surface in a random manner [1,5], and (4) preferential formation on the oxides [1,6]. The oxides under the cathode spots are vaporized and removed instantaneously. Only a few reports have addressed the cleaning action of the cathode spots in the process of low-pressure plasma spray (LPPS)[3]. Removal characteristics of the oxide layer on stainless steel were reported recently [1]. In the present study, surface shapes of oxide and non-oxide samples of SS400 carbon steel were treated using cathode spots of a low-pressure arc with or without grit blasting. This study also compares the resultant surfaces with those of conventional and mechanically blasted surfaces [8].

2. EXPERIMENTAL ARRANGEMENT

2.1 Experimental set-up for removal of oxide layer by cathode spots

The experimental set-up comprises a vacuum chamber with electrodes inside, a water-cooled copper electrode as an anode, a DC power supply (open circuit voltage is 200 V) for the arc, and an evacuation system with a rotary pump, as shown in Fig. 1. The surface of the SS400 carbon steel sample has an oxide layer. It is connected with a negative pole of the power supply and serves as a cathode. The anode and cathode (steel) surfaces are maintained at 20 mm separation. The chamber with the specimen was evacuated to 30 Pa. Argon gas was introduced into the chamber to 0.1 MPa; it was evacuated again to 30 Pa. This operation was repeated. Adjusting the needle valve of the gas inlet controlled the chamber pressure. At this time, the pressure was adjusted to 100 Pa. A transferred-arc was ignited using an RF igniter. Then the arc-current was adjusted to 30 A in the constant current mode. Arc time was controlled by a timer at 0.1 s. For

measurement of the instantaneous removal rate, a sample was removed from and put back inside the chamber after each short arc duration. Areas of removed oxides are recognizable by their silver-metallic luster because the carbon steel oxide is black. The removal area was measured using a digital image scanner before, during, and after the removal process.

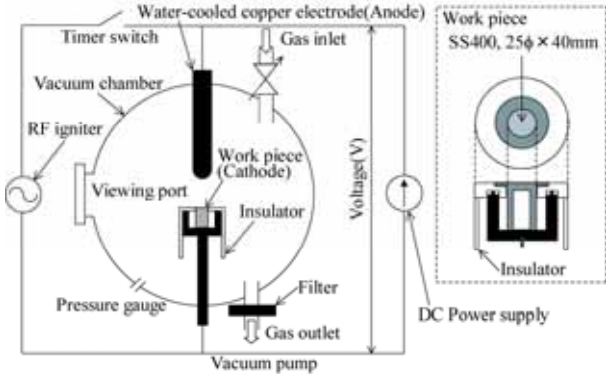

Fig. 1. Schematic illustration of experimental set-up

2.2 Oxide-layer covered samples

The chemical components of SS400 carbon steels were used as samples. Sample dimensions are 25 ϕ diameter and 40 mm height. The relationship of oxide thickness D_o with heating temperature T_h and component ratio of oxide layer on SS400 carbon steel are shown in below. First, the upper surface was polished using a buffing wheel; then ultrasonic cleaning with acetone was performed for several minutes. Finally, they were heated in an electrical furnace with heating temperatures T_h at 773, 873 and 973 K for 1 h. Thickness of oxides D_o was analyzed by glow discharge spectroscopy (GDS); its half value of the oxygen peak was adopted. The sample surfaces were covered uniformly with a black oxide. Oxide thickness was greater in geometric proportion to increased T_h. Furthermore the component ratio differed for each condition: main components were Fe_3O_4 or FeO for all temperatures.

The distribution of Fe and O elements in the depth direction along with a comparison of a sample and a real mill scale is measured by GDS. The oxide layer formed multi-layered iron oxides; it was Fe_2O_3, Fe_3O_4, FeO, in order from the surface on SS400 carbon steel. A real mill scale measurement of SS400 manufactured by hot rolling was carried out. Multi-layer components are similar.

3. ADHESIVE CHARACTERISTICS AND THE SURFACE FORM OF PLASMA SPRAY

3.1 Adhesive Strength for R_a Resulting From Surface Treatment

Figure 2 shows the adhesive strength for the average roughness, R_a, that is attributable to surface treatment using cathode spots and grit blasting. The current is 20 A, the distance between electrodes is 20 mm, and the oxide layer thickness is 6.7 μm. Arc times used here were 13–60 s. The R_a does not depend on the arc time. The surface temperature increases concomitant with the arc time. Consequently, the R_a changes only slightly. Furthermore, when the surface temperature becomes ca. 500 K [7], the cathode spot motion slows and the arc becomes constrictive. Adhesion between the sprayed film and the basic element increases with R_a for both treatments because of the anchor effect. Adhesion strength measurements have a margin of error for treatment with cathode spots from a low-pressure arc, but the values of R_a are almost equal. A margin of error also occurs in adhesive tests. The R_a that is obtained by treatment with grit blasting is sometimes greater than that by treatment with cathode spots. Therefore, the adhesive strength obtained through grit blasting is sometimes greater than that achieved using the low-pressure arc. Treatment of cathode spots after grit blasting is also shown in Fig. 2. The arc current is 20 A and arc times are 1–5 s. Adhesive strength is greater than 90 MPa because cement adhesion is dislodged by the combination of the cement and plasma spray. This is a limited combination. Therefore, this value should be greater than 90 MPa in most circumstances. The adhesive strength in the case of a composite of cathode spots after grit blasting is more than double that of conventional treatments by cathode spots or grit blasting.

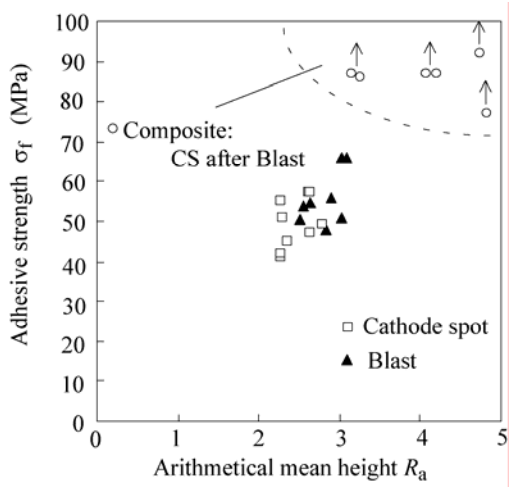

Fig. 2 Adhesion due to R_a attributing to surface treatment with cathode spots and grit blasting, and a composite.

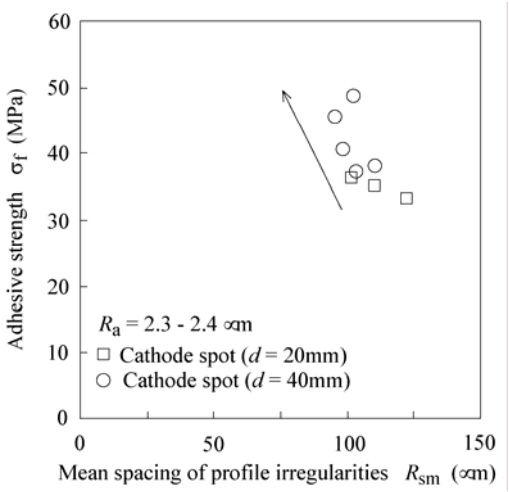

Fig. 3 Effect of R_{sm} on adhesive strength.

3.2 Effect of Adhesive Strength for R_{sm} in the case of equal R_a with Cathode Spots

Figure 2 shows that R_a has dispersion at 2.2–2.8 μm in the case of cathode spot treatment. Figure 3 shows the mean spacing of profile irregularities, R_{sm}, of the uneven surface. Figure 3 also shows effects of R_{sm} for adhesive strength σ for R_a of 2.3–2.4 μm. For equal R_a, the adhesive strength is greater when R_{sm} is smaller. In this example, when R_{sm} becomes less by 25 μm, increase of the adhesive strength is ca. 9.2 MPa. The adhesive strength is determined correctly here because of R_{sm} in the case of equal R_a. This relationship is influenced slightly by sample oxide thickness d. For lower d, σ_f is higher. Plasma spray particles are sprayed on the uneven areas, but also on the concave side. Thereby, a high adhesive strength is obtained for cases with large R_a and small R_{sm}. The maximum height of R_a and R_z changes greatly with R_{sm}, but the mean values of R_z are nearly equal: there is little dispersion of the mean R_z because of the constant standard deviation.

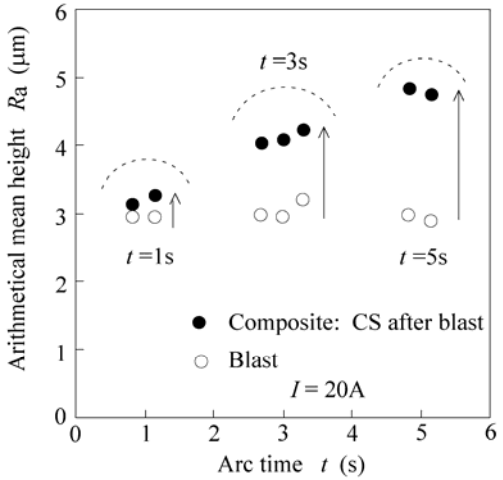

Fig. 4 R_a with composite treatment.

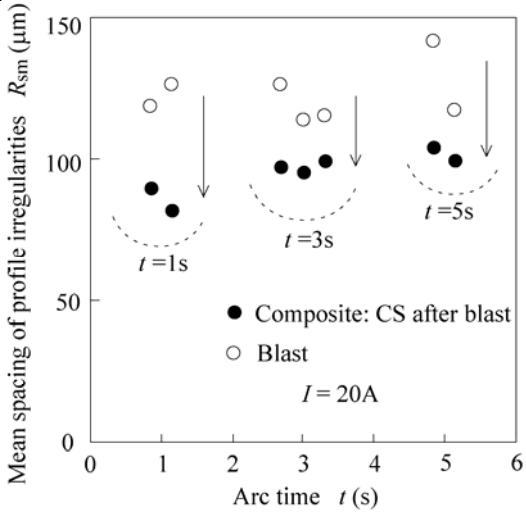

Fig. 5. R_{sm} with composite treatment.

Figure 4 and 5 shows the side and R_{sm} with cathode spots of low pressure arc after the grit blasting treatment. Although the mean R_a becomes around 3μm and the R_{sm} becomes around *120* μm with only the grit blasting treatment, the R_a increases with the arc time up to around 5 μm at 5s. The mean R_{sm} decreases to around 100 μm by 20% while the R_{sm} does not concern with arc time. Therefore the higher adhesive strength can be obtained with cathode spots of low pressure arc treatment after the blast to because the R_a increases and the R_{sm} decreases. The R_a and R_{sm} trend in change is the same in order to obtain the higher adhesive strength as shown in Fig.3.

4. SUMMARY

Surfaces samples with and without oxides were treated using cathode spots of a low-pressure arc after grit blasting. This study compared those surfaces with conventionally treated cathode spots and mechanical blasted surfaces. The main results are shown below.

(1) The roughness on the sample surfaces becomes greater for thicker oxide layers. The surface height has a maximum value at the final removal of the oxide layer. Bonding or adhesive strength of the sprayed surface is greatest in such a condition.

(2) Some factors dominate bonding strength on the surface pre-treated using the cathode spots of the low-pressure arc.

(3) Bonding strength increases with the mean value of surface roughness in a positive correlation to the initial oxide layer thickness.

(4) Bonding strength is greater when the mean spacing of profile irregularities becomes narrow when the arithmetical mean height of the surface pre-treated using the cathode spots is the same.

(5) The bonding adhesive strength of a sample treated by cathode spots after grit blasting is greater than 90 MPa, assuming over 100MPa, which is more than double that of previous treatments such as either cathode spot treatment or grit blasting.

Acknowledgement

The authors thank Prof. Takeda of Akita Prefectural University for his fruitful suggestions. This project is partly supported by Japanese Ministry of Education as High-tech project.

References

[1] I.I.Beilis: State of the Theory of Vacuum Arcs，IEEE Trans. on Plasma Sci., Vol.29, No.5, pp.657-670, 2001

[2] A.E.Guile，B.Juttner: Basic Erosion Processes of Oxidized and Clean Metal Cathodes by Electric Arcs，IEEE Trans. on Plasma Sci., Vol.PS-8, No.3, pp.259-269, 1980

[3] K.Takeda，S.Takeuchi: Removal of Oxide Layer on Metal Surface by Vacuum Arc，Mat. Trans., JIM, Vol.138, No.7, pp.636-642, 1997

[4] A.Itoh, K.Takeda, K.Itoh, M.Koga: Pretreatment of substrates using reversed transferred arc in low pressure plasma spray, Proc. of National Thermal Spray Conference (3rd), pp.245-251, 1991

[5] Y.Kubo, N.Kimitsuka, S.Furukawa, K.Adachi, M.Amakawa, T.Inaba: Cathode spot behavior of low pressure arc on carbon steels covered with oxide layer, Papers of Technical Meeting, IEE Japan, ED-03-258, 2003(in Japanese)

[6] Y.Kubo, T.Iwao, K.Takeda, T.Inaba: The removal characteristics of oxide layer on carbon steel by cathode spot in low vacuum, Proc. 16th Int. Symp. on Plas. Chem. (ISPC-16), Italy, No.Po1.12, (In CD-ROM), 2003

[7] K.Takeda: Effect of substrate temperature on the behavior of vacuum arc in surface cleaning, Proceedings of ISPC-15, pp.671-677, Orleans, France, 2001

[8] Y.Kubo, S.Maezono, K.Ogura, T.Iwao, S.Tobe, T.Inaba, Pre-treatment on metal surface for plasma spray with cathode spots of low pressure arc, Surface and coating Technology, Elsevier, 2005 (in printing)

Improvement of adhesive properties of HDPE samples by humid air plasma treatment

N. Benderdouche[1], B. Benstaali[2], B. Bestani[1], A. Addou,[1] J.L. Brisset[3], J.M. LeBreton[4]

[1]*Laboratoire des Sciences et Techniques de l'Environnement et de la Valorisation (STEVA), Faculté des Sciences de l'Ingénieur, Université de Mostaganem. 27000 Mostaganem, Algeria.*
[2] *Department of chemical engineering, College of engineering University of Bahrain, P.O. Box 32038 Kingdom of Bahrain.*
[3]*Laboratoire d'Electrochimie Interfaciale et de la Chimie Analytique, Faculté des Sciences, Université de Rouen 76821 Mont Saint-Aignan, France.*
[4]*CNRS UMR 6634, Technopole du Madrillet, BP 12, F-76801, St Etienne du Rouvray Cedex, France*

Abstract

In this investigation, carbon black filled high density polyethylene (HDPE) samples (2%) having a melt flow index of 0.77 g/10min used for the transportation of natural gas were exposed to plasma in humid air for different exposure times. Decohesion stress of the assembled samples as measured according to NFT 54-034 standard was shown to improve as a function of exposure time. Mechanically etched samples showed a higher decohesion stress for small exposure times to plasma. Epoxy assembled polyethylene pipes showed that the burst pressure increased from 14 bar for untreated assembled material to 33 bar for the 90 sec treated sample. Thermal stability study of plasma treated samples showed that oxidation induction time diminishes from 38 min for untreated samples to 17 min for 150 sec treated samples.

Keywords: Non thermal plasma, humid air, HDEP

I) Introduction

The application of non-thermal atmospheric plasma of glidarc type to polymeric surfaces modifies their physicochemical properties through cross-linking and formation of functional groups, which could have interesting adherence as well as selective permeability applications where a barrier effect to diffusion phenomena may take place. Reactive species mainly produced by electron-molecule collisions in such non-thermal equilibrium plasma were identified by emission spectroscopy technique, and predominantly correspond to OH° neutral radicals [1]. The presence of NO radicals is observed but in less quantity which confers to such humid air plasma interesting oxidising properties due to the overwhelming OH° highly reactive species created.
Several processes resort to plasma techniques that are now used for solutions processing in environmental applications and surface treatment for barrier diffusion creation and corrosion prevention. Previous investigation concerned humid air plasma-surface interaction where pure iron [2] and 304L and 316L stainless steel samples [3] were exposed at different treatment time and flow rate. Electrochemical and X-rays analysis reveal the presence of iron hydroxide $Fe(OH)_3$ at different proportions where it is more abundant on pure iron than on stainless steel surfaces. The presence of other chemical elements (Cr, Si, Mg, and others) seems to influence the interaction of the reactive species-iron atoms on the surface.
Polyethylene constitutes presently a large group of products exhibiting various characteristics. It has a very good chemical stability at a processing temperature lower than 60 °C and is not attacked by non-oxidant acids. The setting up of gas distribution networks requires the application of rigorous techniques, especially on pipe assembling such as electrofusion welding.

II) Materials and methods

II. a) Samples preparation and characteristics

In order to study the impact of plasma in humid air on the adhesive properties of carbon black filled high density polyethylene samples (2%) having a melt flow index of 0.77 g/10min used for the transportation of natural gas, samples from this plastic were cut out according to NFT 54-034 standard and exposed to plasma

in humid air for different exposure times. Figure 1 shows the samples used for plasma exposure. Some of the samples were pre-etched mechanically. The saturated humid air flow rate entering the high voltage set-up was 700 cm^3/min through two diverging aluminium electrodes 2 mm apart. The target samples were placed at a distance of 15 mm from the electrodes end.

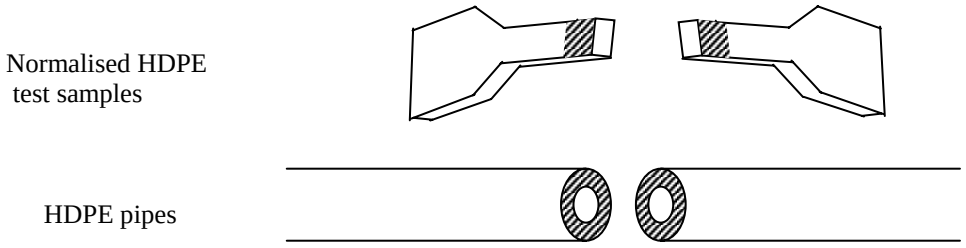

Fig. 1: HDPE samples exposed to plasma in humid air on the hatched area.

The commercial high density polyethylene was first characterised through the determination of carbon black content, melt flow index, tensile stress and Young's modulus (according to NFT 51-140, NFT 51-016, NFT 54-034 standards, respectively). Table 1 gives the experimental results obtained:

Table 1: Some HDPE characteristics.

Carbon black content (%)	Melt flow index (g/ 10 min)	Tensile stress (Mpa)	Young's modulus (Mpa)
2.05	0.77	18.46	125.20

According to these testing standard procedures, the values obtained for the HDPE samples are consistent with mean values.

II. b) Experimental methods

- **Decohesion tests:** The normalised samples were exposed to plasma in humid air as shown in Figure 2 for varying times ranging from zero to 100 seconds. They were subsequently assembled on the 15 mm^2 treated area with epoxy resin and let to settle down for 24 hours. Decohesion tests were performed using a Oroell Zwick machine according to NFT 54-034 standard.

- **Burst tests:**

Burst tests according to ISO 1167 standard were also performed at 20°C on plasma treated HDPE pipes (20 cm diameter) and assembled with the same epoxy resin.

- **Oxidation induction time**

Thermal stability tests were carried out on raw HDPE samples exposed to plasma, by differential scanning calorimetry according to NFT 58 – 003 standards.

III) Results and discussion

It can be noticed from Figure 2 that the decohesion stress improved as a function of exposure time passing from 3.02 MPa for untreated samples to 12.04 MPa for a plasma treatment time of 100 sec. In order to further assess the activating effect of such a plasma, similarly assembled samples were mechanically etched before plasma exposure and

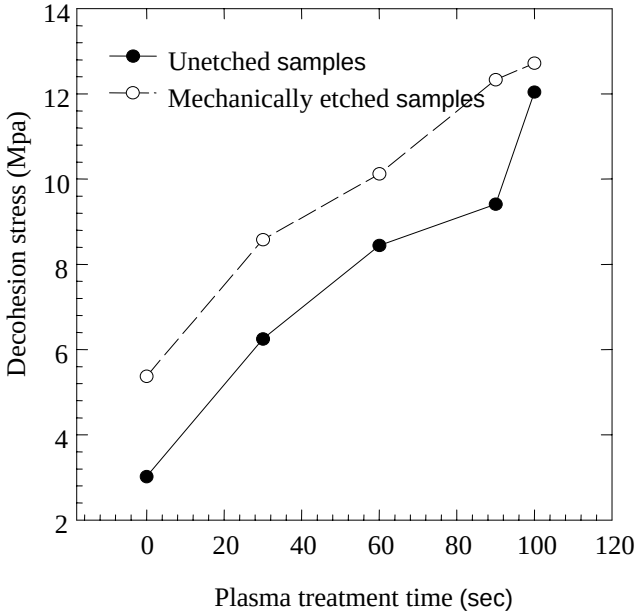

Fig. 2: Decohesion stress versus exposure time to plasma in humid air.

the results are also depicted in Figure 2. This mechanical treatment resulted in a higher decohesion stress for small plasma exposure times (5.01 MPa) but for 100 sec treatment time almost the same values were attained (12.4 MPa), highlighting the etching and activating effects of the plasma.

Burst tests (according to ISO 1167 standard) performed at 20°C on epoxy assembled polyethylene pipes 20 cm in diameter showed that the burst pressure increased from 14 bar for untreated assembled material to 33 bar for the 90 sec treated sample. For the pre-etched samples theses values varied from 15.33 to 37.50 bar as depicted in Figure 3. The burst pressure difference between unetched and pre-etched samples decreases versus plasma exposure times proving the activating efficiency of the plasma.

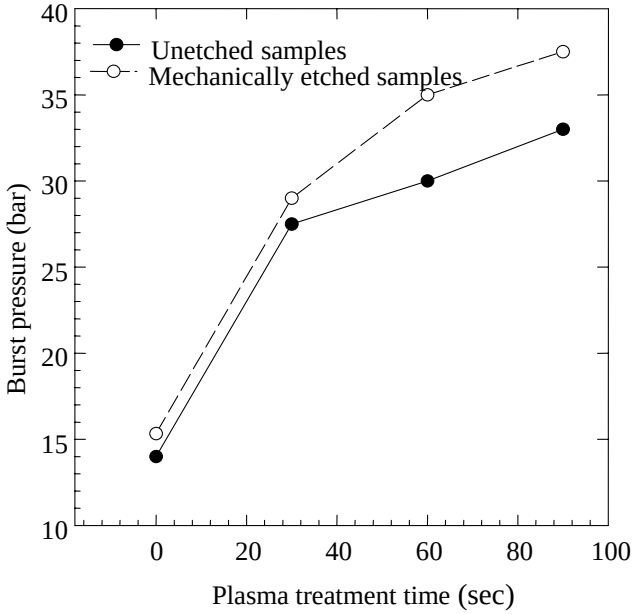

Fig. 3: Burst pressure versus exposure time to plasma in humid air.

On the other hand, thermal stability study (according to NFT 58-003 standard) using differential scanning calorimetry of plasma treated samples weighing 15 mg was performed under nitrogen flow rate of 50 cm^3/min at a heating rate of 20°C/min until a final temperature of 210°C was attained. After five minutes under nitrogen gas, thermograms were recorded under oxygen flowing at a rate of 60 cm^3/min until the exothermic peak attained its maximum. The results are presented in Table 2.

Table 2: Influence of plasma in humid air on the thermal stability of HDPE samples.

Plasma treatment time (sec)	0.00	90.00	120.00	150.00
Oxidation induction time (min)	38.00	24.00	19.00	17.00

It can be observed that oxidation induction time diminishes from 38 min for untreated samples to 17 min for 150 sec treated samples. The interaction of humid air plasma may create active radicals sites, chain scission resulting in new functional groups such as carbonyls and reaction of volatile products in the plasma. These results combined with earlier cited works confirm the interesting activating power of the plasma produced in these conditions, which can be profitably applied to activating polymers at an industrial scale. Their introduction to industrial scale is currently being developed as the production cost is constantly diminishing.

IV) Conclusion

The interaction of humid air plasma may create active radicals sites, chain scission resulting in new functional groups such as carbonyls and reaction of volatile products in the surface. In the case of polyethylene, the oxidised surface resulted in increased adhesive forces as shown through decohesion stress and burst pressure values. The oxidising power of such humid air plasma is also revealed through the oxidation induction time.

This work confirms the interesting activating power of the plasma produced in humid air and demonstrates the high oxidising ability of this kind of plasma, which can be profitably applied to activate polymers at an industrial scale.

Acknowledgements: The authors would like to thank the National Plastics Company for kindly providing the polyethylene samples and allowing laboratory tests.

References

[1] B. Benstaali, P. Boubert, B. G. Cheron, A. Addou, J.L. Brisset, "*Density and rotational temperature measurements of* $OH^{\bullet}$ *and* $NO^{\bullet}$ *radicals produced by a gliding arc in humid air*", Plasma Chem. Plasma Proc., 22, 4, (2002)

[2] Benstaali B., Benderdouche N., Breton, J.M., Chéron B., Addou A., Brisset J.L., "*Anti-corrosive properties of thin films produced on metal surfaces by cold atmospheric plasma of Glidarc type"*, 16th International Symposium on Plasma Chemistry, June 22-27 (2003) Taormina, Italy.

[3] B. Benstaali, A.Addou, J.L.Brisset, " *Electrochemical and X-rays investigation of austenitic 304L and 316L stainless steels treated by a gliding arc in humid air*", Materials Chemistry and Physics 78, 214 (2002).

Investigating the optical and electrical characteristics of plasma polymerised thin gradient films before/after thermal treatment

A. N. Chifen, W. Knoll and R. Förch
Max-Planck Institute for Polymer Research, Ackermannweg 10, Mainz 55128, Germany
chifen@mpip-mainz.mpg.de

Abstract
Deposition of gradient metal-oxide-like films with low carbon contents from HMDSO, TTIP and O_2 was carried out in a 13,56 MHz r.f. plasma. The aim was to structure the films to have specific chemical, optical and electrical properties. The chemistry and thermal stability of the films were investigated using FTIR and XPS. The surface roughness was examined using AFM. An interpretation of their electrical properties using EIS is presented.

Keywords: SiO_2, TiO_2, gradient metal-oxide films, electrical and optical properties

INTRODUCTION

Nano-structured gradient metal-oxide materials have new and often enhanced properties as compared to conventional TiO_2 and SiO_2. The properties of the tailored materials are related to their possible applications, e.g. leaf like structures in solar cell application [1], porous structures, consisting of nanoparticles used as gas sensors [2] and photocatalysts [3, 4].
Vacuum techniques such as co-sputtering, metalorganic chemical vapor deposition and plasma enhanced chemical vapor deposition (PECVD) have been used to fabricate gradient materials [5, 6, 7]. Titanium (IV) isopropoxide; $Ti(OC_3H_7)_4$, [TIPP] in combination with Ar, O_2 or N_2 as a carrier gas has previously been used as a precursor for the deposition of TiO_2 films in CVD processes and has high a refractive index *n* ($2 < n < 2.6$) [8].
Pure stoichiometric titanium dioxide (TiO_2) has numerous desirable properties e.g. low resistivity, high conductivity and refractive index, which can be correlated to the oxidation state of Ti and its crystal structure [9, 10]. SiO_2 films from HMDSO/O_2 have proven to be effective primer coatings for adhesion [11] and have a lower refractive index than TiO_2 ($1.4 < n < 1.6$).
Structuring the properties of thin gradient material would be of great importance in sectors such as adhesion, optical, microelectronic devices, biomaterials, protective coatings and thin film technology [12, 13].
In order to understand the interaction between the films, firstly, we study the depositions of each precursor, secondly the effect of the relative precursor ratio on the chemical composition, optical and electrical properties. Characterisation was done by Ellipsometry, Electrochemical Impedance Spectroscopy (EIS), X-ray Photoelectron Spectroscopy (XPS), Fourier transformed infrared (FT-IR) spectroscopy and Atomic Force Microscopy (AFM). The reasons for the thin gradient film structures are explained qualitatively.

EXPERIMENTAL

The precursors, TTIP and HMDSO were purchased from ACROS Organics (99,99 %). TTIP has been used for previous TiO_2 film deposition and it is less harmful in contrast to halides gases [4]. Simultaneous stirring and heating at 70 °C of TTIP outside the reactor assisted in the conveyance of the vapour into the reactor. The TTIP partial pressure was controlled by a needle valve (LV10K, EDWARDS) and a floating ball flow meter [Kobold Messring] was used to control the inlet concentration of HMDSO.
We therefore aimed at fabricating thin gradient films with definite refractive indices by varying the partial pressure of both monomers at constant input power (Ppeak). The reactor geometry is the same as earlier described [14], equipped with a temperature sensor [PT 100] built at the outlet. Depending on the characterisation technique, the films were deposited on evaporated gold

(BK7 glass) or Si-wafers. Figure 1 shows a schematic of the process step. The deposition of gradient films is divided into four steps; **1**) plasma pre-treatment process was used to clean and activate the substrate (30 sec. Ar:O_2 (10:1) and 40 W pPeak), **2**) TiO_2 like films were plasma polymerised (TTIP, 220 W, 300 sec, 0.07 mbar), **3)** SiO_2 like films were plasma polymerised (HMDSO:O_2 (1:10), 100 W, 10 sec, 0.02 mbar) to obtain an adherence layer for the gradient layers, **4**) co-deposition of HMDSO/O_2:TTIP: adding TTIP into the reactor, thus raising the total process pressure (0.07mbar, 220 W, ~ 260 °C). The partial pressure of the precursors in the reactor was varied between 0.025 and 0.07 mbar from step 3 to 4. Films between 25 and 70 nm thick, were deposited by varying the vapour flow of HMDSO and TTIP, while their total flow and other deposition parameters were kept constant.

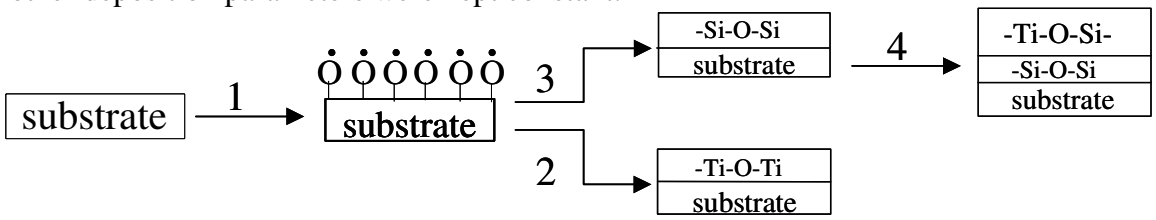

Figure 1: activation and deposition procedure of gradient films

Refractive index *n,* and thickness *d,* of the films were determined from the Ellipsometer ($\lambda = 450$, 630 nm) (Nanofilm Surface Analysis EP^3). The surface profiler (Tencor®) was used to approximate the thickness. To quantify our results, the thickness and refractive index determined were fitted using the surface analysis software based on the Cauchy model [15].

Chemical structure of the samples was analysed by X-ray photoelectron spectroscopy (XPS) using a ESCA 5600 (Physical Electronics GmbH) with a monochromated Mg Kα X radiation at 1253,6 eV beam operated at 300 W in a residual vacuum of $>5\times10^{-8}$ Pa with the analyzer in fixed transmission mode. Additional information was obtained by FTIR using a Nicolet Magna-IR spectrometer. The electrochemical impedance measurements were made in 0.1 M NaCl solution. The electrical properties of both the annealed and non-annealed deposited films were measured using Autolab PGSTAT 30 equipped with a Frequency Response Analyser (FRA) controlled by a PC with FRA software package (ecochemie). A Dimension 3100 Atomic Force Microscope was used to analyse the topology of the deposited annealed and non-annealed Ti-O-Si films. Contact angles for water (2µl/min) was measured using a Drop Shape Analyser (DSA 10-MK2, KRÜSS).

Results and Discussion

The results of refractive indices *n*, and thickness *d*, measured by ellipsometry are shown in Figure 2 and Figure 3 respectively. The film thickness was seen to increase with Ppeak (input power) for all pp films. The deposition rate of the Ti-O-Si (0.08nm/sec) film is lower than Si-O (0.5 nm/sec) film, which indicates that the mixture vapour requires longer interaction time (not shown here). The refractive indices of the Si-O and Ti-O film showed an increase with Ppeak in Figure 3. The isotropic arrangement of the molecules and structure is more decisive for the index of refraction rather than the thickness. This measurement was carried out at three different spots, which showed averaged error values less than 5% for both Si-O-Si and Si-O-Ti.

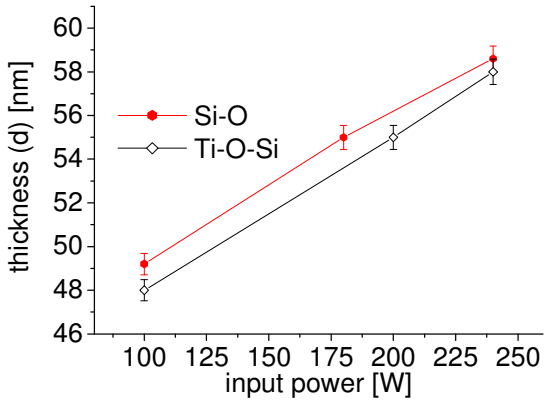

Figure 2: effect of power on the film thickness for Si-O-Si and Ti-O-Si thin films

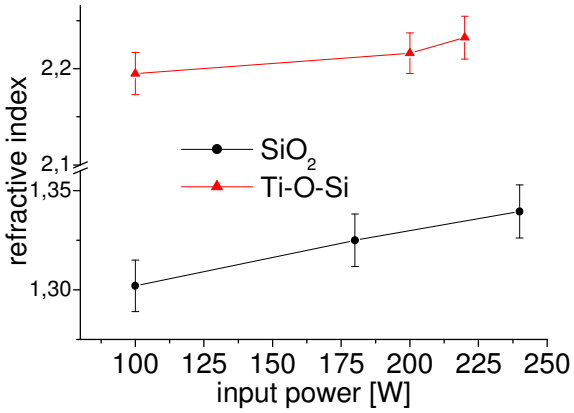

Figure 3: effect of refractive index of pp Si-O-Si and Si-O-Ti thin films

The chemical structures of the Si-O, Si-O-Ti films were analysed using detailed analysis of XPS and FTIR. Figures 4 and 5 show the data from XPS spectra of these films. Figure 4 shows that the concentration of Si atoms is increasing with plasma Ppeak. The oxygen atom ratio increases with Ppeak because the oxygen plasma promotes the loss of carbon, therefore creating more Si-O bonds. This increase in the oxygen ratio leads to the formation of cross-linked siloxane network. The ratios of Si:C and Si:O attained 6:1 and 1:2 respectively.

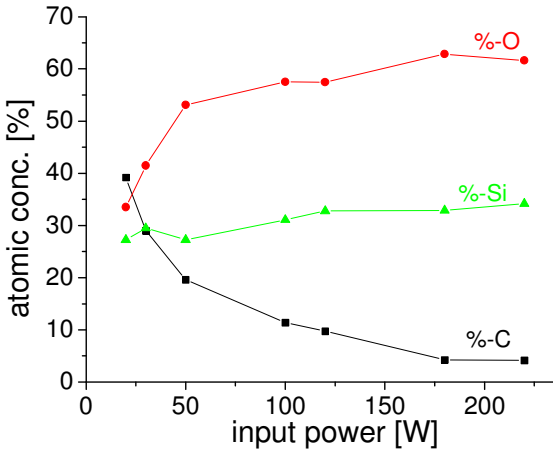

Figure 4: the effect of pPeak on atomic concentration for pp Si-O-Si film (50 nm)

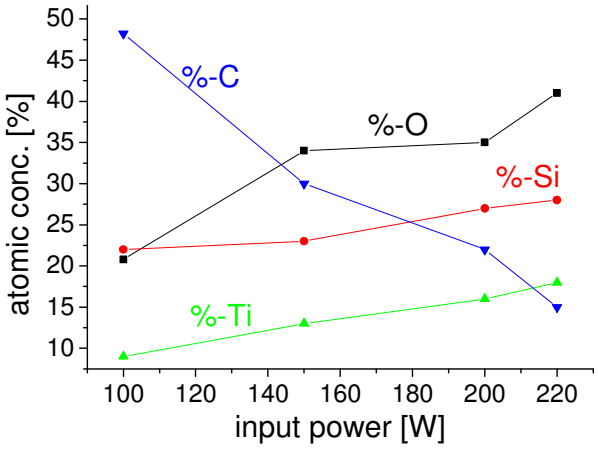

Figure 5: the effect of pPeak on atomic concentration for Ti-O-Si film (70 nm)

The data from XPS spectra of Ti-O-Si films in Figure 5 shows the relationship between Ppeak and atomic concentration. Increasing the pPeak was seen that the %-C decreases significantly but O, Si, and %-Ti increased because of the intensity of the oxygen plasma. The highest atomic concentration is oxygen, which suggest that a Ti-O-Si network is formed at the pp condition. The higher C-content in the Ti-O-Si film as compared to Si-O film may be related to the hydrocarbon components in the mixture and a higher temperature in the reactor, which is necessary for the fragmentation [9]. Furthermore, the elemental ratio for Ti-O-Si was $SiO_{1.4}C_{0.5}Ti_{0.6}$ compared to Si-O films with $SiO_{1.8}C_{0.12}$ showing lower %-C as a result of higher temperatures during the TTIP deposition. Figure 6 shows IR absorbance spectra of the pp SiO_2, TiO_2. The spectra interpretation of HMDSO film is based on well-known data [10]. The spectrum in Fig. 6(b) shows a shift of the Si-O peak to lower wavenumber and a new peak could be seen at 500 cm^{-1}.

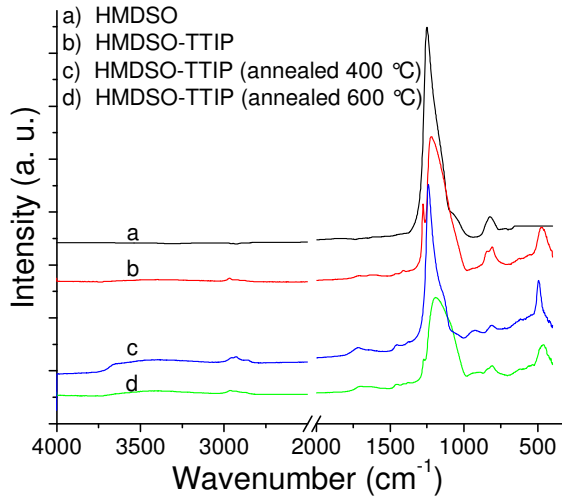

Figure 6: FT-IR spectra of pp-HMDSO+TTIP films

This shift and new peak can be attributed to Ti-O-Si bond formation, confirming a phase containing Ti, Si, and O [11]. Annealing at 400 and 600 °C, Fig. 6 (c & d) show that Ti-O-Si peak increased in intensity, indicating stability of Si and Ti network. This stability may be explained that Si and Ti atoms are randomly distributed in the network and bonded over an O-atom. Although the surface roughness (R_q) of Ti-O, Si-O and Ti-O-Si films analyzed were below 0.4 nm on polished silicon wafer, their surface morphology could not be distinguished using the AFM. The annealing effect showed relatively small changes with respect to surface analysis.

Electrical properties

Figure 7 shows the impedance spectra obtained for the deposited films as mentioned above having the same thickness. The ionic resistance of the Ti-O and Si-O is compared by the EIS. The spectra were numerically fitted using the equivalent circuit shown in Figure 7, with less than 5 % error for each component. The capacitance |Z| obtained from the fittings for a SiO_2 is lower than the TiO_2 film, which correlates the fact that TiO_2 has a higher dielectric constant than SiO_2. The fitted capacitance spectrum for the co-deposited film (Ti-O-Si) lies in between the Si-O and the Ti-O film spectra. The observed difference in the ionic resistance was related to the co-deposition of TTIP. A single RC time constant was observed for the Si-O-Ti film, suggested the ion penetration through the film consist of a single homogeneous material phase. The stability of the Si-O-Ti films was monitored over a period of time. For longer electrolyte (0.1M NaCl)-film (Ti-O-Si) exposure times, the film impedance measured was constant for over 25 hours, indicating that the Si-O film also served as an adhesion layer.

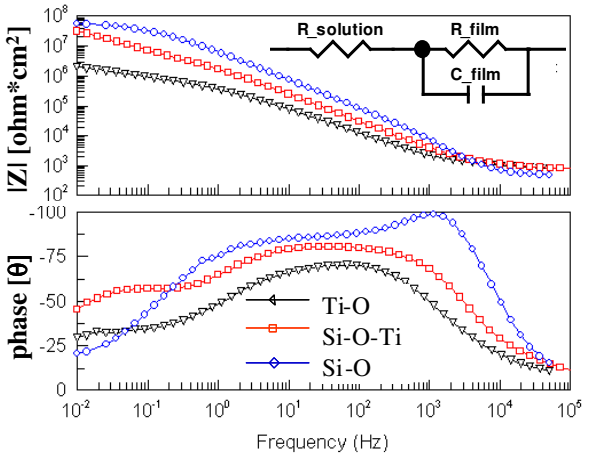

Figure 7: EIS spectra obtained from pp samples & equivalent circuit used for fitting

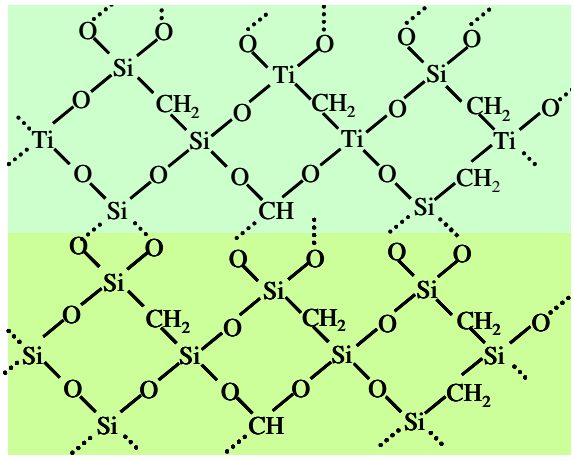

Figure 8: Theoretical model of Si-O-Si and Ti-O-Si films

CONCLUSIONS:

It should be therefore possible to polymerise films with desired index of refraction, if a relationship between the partial pressures of the precursors and the film composition and their effect on optical properties is well known. Valuable information regarding the surface morphology, chemical composition, optical and electrical properties, was achieved by the different method of analysis. Different refractive indices were attained due to input power increase or the monomer composition. From the electrical properties, the resistance of the co-deposited film (HMDSO/O_2 and TTIP) lies between the values of Ti-O and Si-O films. The phase angle spectra could be related to the homogeneity of the co-deposited films. A film network of Ti-O-Si could be concluded from the XPS and FT-IR analysis. No phase separation (stability) upon annealing from neither the FT-IR nor EIS spectra was noticed. The properties of Si-O-Ti films prepared by PECVD may be suitable for stable photo-optical and catalytic applications.

Acknowledgements

The authors wish to acknowledge the technical assistance of D. Moessner (IMTEK, Uni-Freiburg) for XPS measurement, Toda Masaya for fitting the ellipsometric data. We also thank Dr. J. Robertson for the helpful discussions about EIS.

References

1. T. E. Mallouk, Nature 353 (1991) 698
2. G. Vandrish, Key Eng. Mater. 122 (1996) 185
3. Y. Ohko, Fujishima, J. Phys. Chem. B. B 102 (1998) 1724
4. M. Nakamura, D. Korzec, T. Aoki, Appl. Surf. Sci. 175-176 (2001) 697
5. K.-H. Ahn, Y.-B. Park, D.-W. Park, Surf. & Coat. Technol. 171 (2003) 198
6. M. A. Rashti, D. E. Brodie, Thin Solid Films 240 (1994) 163
7. J. A. Ayllón, A. Figueras, S. Garelik, L. Spirkova, J. Mat. Sci. Letters 18 (1999) 1319
8. A. Sandell, M. P. Anderson, Y. Alfredson, M. K-J. Johansson, J. Appl. Phy (92) 6
9. U. Backman, A. Auvinen, J. T. Jokiniemi, Surf. & Coat. Technol. 192 (2005) 81
10. L. Zuri, M. Narkis, M. S. Silverstein, Polym. Eng. Sci. 1997, 37, 1188.
11. S. Larouche, H. Szymanowski, J. E. K-Sapieha, L. Martinu, S. Gujrathi, J. Vac. Sci. Technol. A 22(4) 1200W.
12. Gopel, Prog. Surf. Sci. 20 (1) 1985 9
13. J. Janca, L. Sodomka, Surf. & Coat. Technol. 98 (1998) 851
14. M.-I. Baraton, L. Merhari, J. European Ceramic Soc. 24 (2004) 1399
15. Z. Zhang, Q. Chen, W. Knoll, R. Foerch, R. Holcomb, D. Roitman, Macromol. 36 (2003)
16. J. Li, S-T. Wu, J. of Appl. Phy. 95 (2004) 3
17. S. Ichikawa, R. Doi, Catal. Today 27 (1996) 271
18. T. Oh, K. S. Oh, K-M. Lee, C. K. Choi, Thin Solid Films 468 (2004) 316
19.
20. Q. Fang, M. Meier, J. J. Yu et. al. Mat. Sci. & Eng. B105 (2003) 209
21. L. W, J. C. Yu, Journal of solid state chemistry 177 (2004) 2584
22. A. C. Bastos, C. Ostwald, L. Engl, Electrochimica Acta 49 (2004) 3947
23. C.-T. Lin, F. Li, T. D. Mantei, J. Vac. Sci. Technol. A 17(3) 735
24. J. C. S. Fernades, M. G. S. Ferreira, D. B. Haddow, Surf. & Coat. Technol. 154 (2002) 8
25. M. Gladys, P. Greig, P. Dastoor, J. Vac. Sci. Technol. A 18 (1) 257
26. R. Balkova, J. Zemek, V. Cech, Surf. & Coat. Technol. 174-175 (2003) 1159
27. S.-H. Cho, Z.-T. Park, J-H. Boo, Surface & Coat. Technol. 174-174 (2003) 1111
28. T. Fujii, M. Hiramatsu, M. Nawata, Thin Solid Films 343-344 (1999) 457
29. A. Takeda, T. Sato, S. Kaneko, Thin Solid Films 435 (2003) 211
30. M. F. A. M. van Hest, M. C. M van de Sanden, Thin Solid Films 449 (2004) 40

Investigating the properties of plasma polymerised films (e.g. Polystyrene, Allylamine) on organosiloxane polymer films

A. N. Chifen, W. Knoll and R. Förch
Max-Planck Institute for Polymer Research, Ackermannweg 10, Mainz 55128, Germany
chifen@mpip-mainz.mpg.de

Abstract

This report presents the deposition of plasma polymerised allylamine and polystyrene films on SiO_2-like films (patterned gradient films in a two step process) at 13,56 MHz r.f. plasma. The properties of both layer films are investigated, aiming to tailor stable films with specific combined properties, e.g. barrier, hardness, biocompatibility and insulating properties. The chemistry of the layer films was investigated using FTIR and XPS. The surface morphology was examined using AFM. An interpretation of their electrical and layer interface properties using EIS is presented.

Keywords: SiO_2, allylamine, polystyrene, thin layer films

INTRODUCTION

Plasma deposited organic films can be used to modify the surface of biomedical and synthetic polymers in order to attain specific properties in various sectors (e.g. biotechnology). Plasma-based coatings like SiO_2 have been applied to polymers as scratch and corrosion resistant, barrier or hydrophilic coatings [1, 2, 3, 4]. Investigating the properties of patterned allylamine or polystyrene films on plasma polymerised (pp) hexamethyldisiloxane (HMDSO) at different process parameters will clarify certain properties of tailoring patterned gradient films. The amine group in allylamine (AA) offer promising characteristics for a variety of biomedical applications [5] and Polystyrene (PS) is a disposable ware in medical diagnostic, primarily due to its optical transparency, durability, low cost, and good mouldability [6].
Using micro- and nano-patterning techniques to produce surfaces with pre-determined morphology and defined structured chemical functionalities, are increasingly demanded in these sectors, e.g. for specific bonding of bioactive molecules or protein or enzyme immobilization [1, 7, 8, 9, 10].

EXPERIMENTAL

The precursors, AA and styrene were purchased from ACROS Organics (99,99 %). The plasma source used was capacitively coupled plasma source. The vapour concentration delivered into the chamber was controlled using a floating ball flow meter [Kobold Messring]. A RF power supply operating at 13.56 MHz provided the power for the plasma generation. This reactor has been earlier described in literature [11, 12]. The films were deposited onto Si-wafer and Gold substrates. HMDSO was pp at 140W at 0,2 mBar for 30 sec, yielding 15nm (also serves as an adhesion layer). Previous results showed that SiO_2-like films were obtained at these conditions (see conference presentation No. 702).

AA was pp at constant monomer pressure (0.1mBar), different input power conditions, 5, 45 and 90W. Styrene was pp at 0,052mBar, (40, 80 180 W) and a film thickness of 50 nm was obtained depending upon deposition time (max. 600 and 60 sec for AA and styrene respectively). Approximately, 50 nm of AA and PS was deposited 20nm SiO_2-like films.

	Allylamine	Styrene	HMDSO/O_2
preesure/mBar	0.1	0.052	0.2
max. dep. time [sec]	600	60	25
Ppeak W	5	40	140
	50	80	
	90	180	
thickness/nm	50	50	15

Table 1: deposition parameter of pp films

The chemical characterization of the deposited film(s) was with conventional surface analytical tools such as contact angle goniometry, X-ray Photoemission Spectroscopy (XPS) and Fourier Transform Infrared Spectroscopy (FTIR). Surface morphology was studied using atomic force microscopy (AFM). Electrochemical Impedance Spectroscopy (EIS) was used to explain the interface and electrical properties of the multilayer structures.

Results and Discussion

The deposition of both thin films AA and styrene on SiO_2 film (pp) could be detected with FTIR spectroscopy. Figure 1 shows the spectrum of ppAA on SiO_2 (pp). Referring to Figure1, the broad absorption band between 1000–1200 cm^{-1} indicates the presence of Si-O-Si and also Si=O bonds. The multiple peaks with relatively low intensities around 830 cm^{-1} is due to the Si-C or Si-CH_3 strectching deformations. The peak around 2200 cm-1 indicates the presence of nitrile groups, while the bands at 1600 cm-1 are assigned to the bending modes of amines, the stretching of imine groups and the stretching of amide groups. The band intensities of the amine, imine and amide groups reduce with increase in input power. This indicates that the fragmentation of the amino functional group. The intensity of the Si-O band tends to be broader due to this conversion, formation of Si-H groups (at 1100 cm^{-1}). These band assignments are based on literature data [13, 14, 15].

The spectra in Figure 2 show the effect of increasing input power of ppPS on SiO_2 films. The peaks around 770 cm^{-1} indicate the presence of a benzene ring. This peak seems to disappear with increasing input power. The intensities of Si-C, Si-H, Si-O-Si bands seen around 1000–1200 cm^{-1} decreases with increasing power. The Si-C and Si-H bonds seem to be dissociating to form Si-O-Si bonds. The band at 1700 cm^{-1} may be attributed to aryl derivatives (R-CO) and stretching vibrations of C=C double bonds. The bands of the functional groups of the precursors (HMDSO and allylamine or HMDSO and styrene) could be seen in the spectra, indicating the presence of both films. Additionally, the film thickness was scanned using a surface profiler (figure 3 and 4).

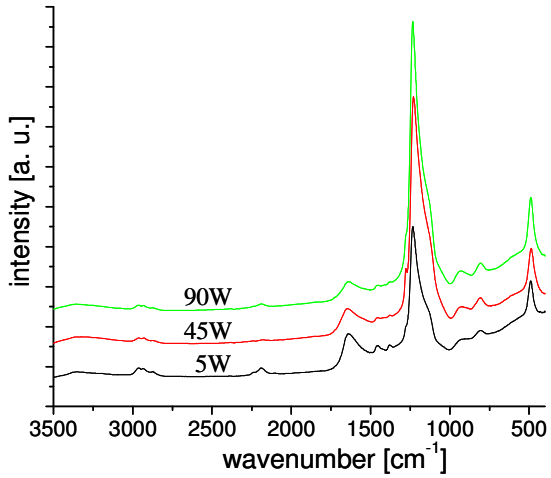

Figure 1: FTIR spectra of ppAA at different input power

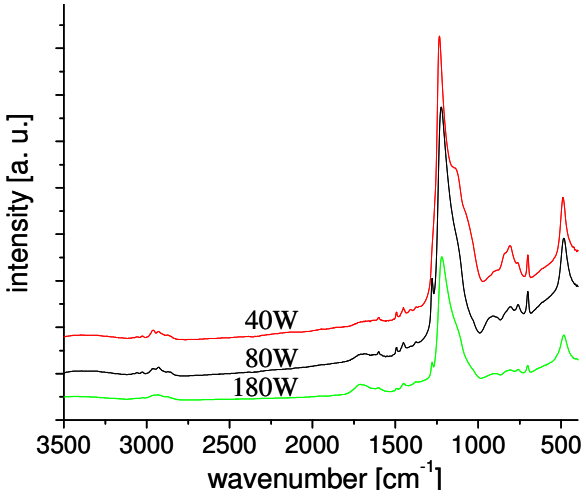

Figure 2: FTIR spectra of ppPS at different input power

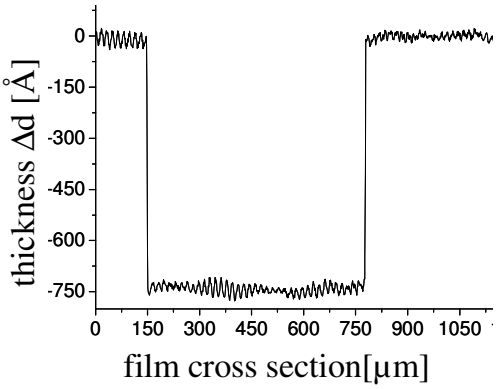

Figure 3: ppAA film thickness measured by the profiler

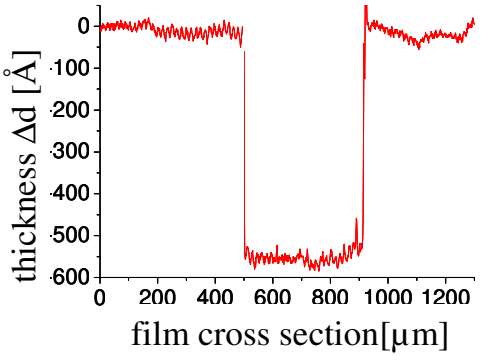

Figure 4: ppPS film thickness measured by the profiler

Figure 5 shows the impedance spectra obtained for the ppAA films on SiO_2. The impedance |Z| is relatively constant with increase in input power. A distinct trend of the ionic resistance plotted using the phase (θ) could not be distinguished with increasing power. A single RC time constant was observed for the films, the ion penetration through the film provides some information about the layer structure. Two "humps" could be distinguished on the phase spectra in Figure 5, indicating a heterogeneous material phase, low. The ppAA on SiO_2 films contact with the electrolyte (0.1M NaCl) seems to be considerably stable, because the impedance spectra are not distorted at low frequencies. This also indicates that the Si-O film also served as an adhesion layer.

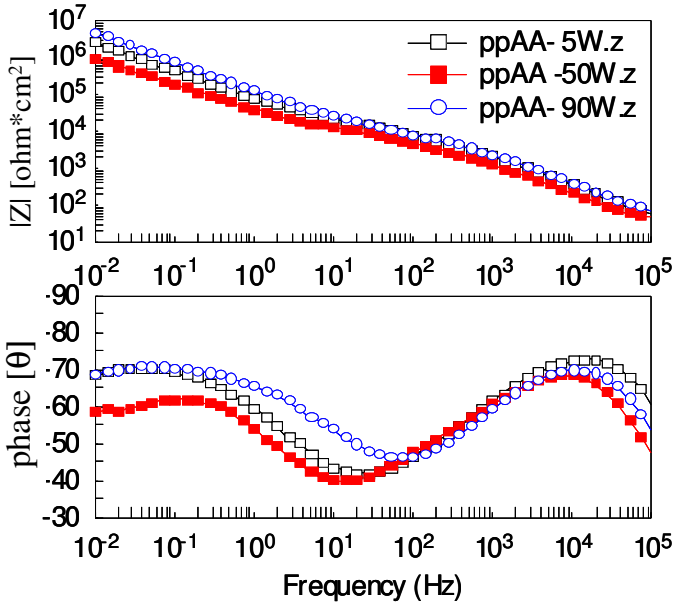

Figure 5: EIS spectra obtained from ppAA on SiO_2 film

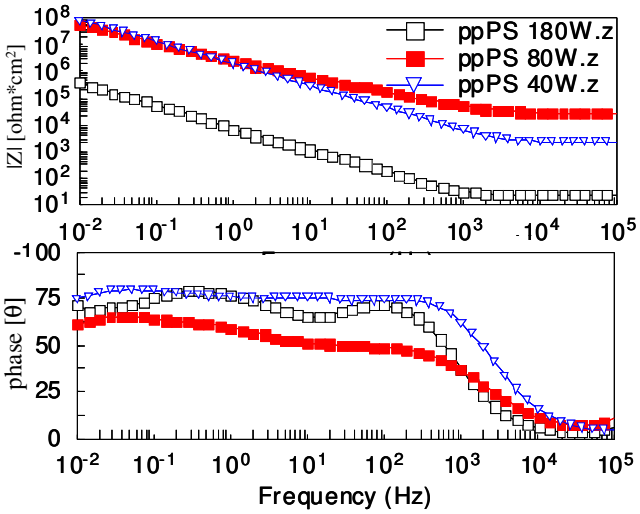

Figure 6: EIS spectra obtained from ppPS on SiO_2 film

Similar to Figure 5; Figure 6 illustrates the effect of input power on ppPS on SiO_2 films. At higher input power (180W), the impedance is lower than at 80 and 40W. This can be attributed to highly polymerised and closed network created during the plasma. Additionally, the scratch resistance of the films was measured using AFM cantilever tip (not shown here), showed that the films above 170W were harder to scratch than films below 100W. This maybe suggesting a higher degree of cross-linking causes lower impedance. The incorporation of the ppPS layer on the SiO_2 film was monitored with a single RC time constant, the ion penetration through the film provides some information about the layer structure. Two "humps" could be noticed for the films pp at 180W, whereas this cannot be seen at 40 and 80W. This cannot be explained here, but maybe films pp at lower input power is highly bonded to the SiO_2 films than the 180W pp film.

Figure 7 and 9 show images of the deposited ppAA and ppPS respectively at different input power. The results of AFM analysis show decreasing roughness with increasing input power (Table 2). This homogeneity may be due to plasma density because the more high plasma power can easily break monomer and cluster in the gas phase or on the surface. In summary, the contact angle of the thin films decreases with increasing input power, while the roughness decrease. This may be due to high cross-linking density with increasing input power.

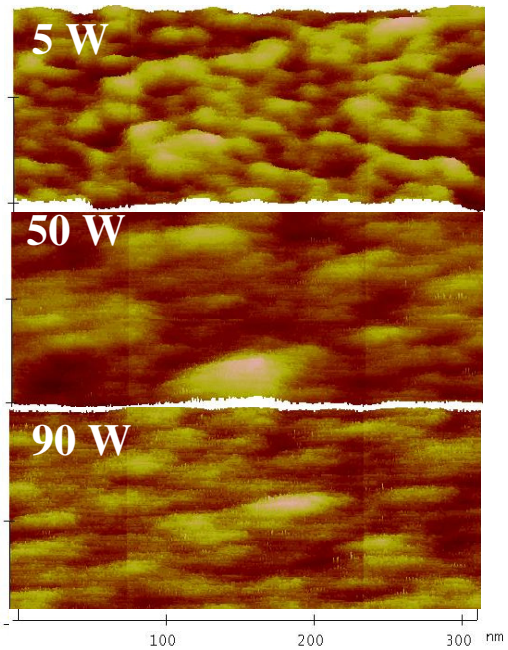

Figure 7: AFM images of ppAA on pp SiO2 deposited at different RF powers

ppAllylamine	
Power/W	Rz(500nm)
5	0.297
50	0.193
90	0.151

ppPolystyrene	
Power/W	Rz (500nm)
40	0.281
80	0.268
180	0.255

Table 2: surface roughness depicted from AFM images

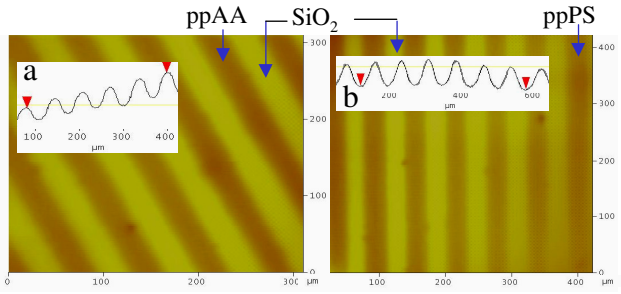

Figure 8: surface patterned with a grid a)ppAA, b)PS stripes

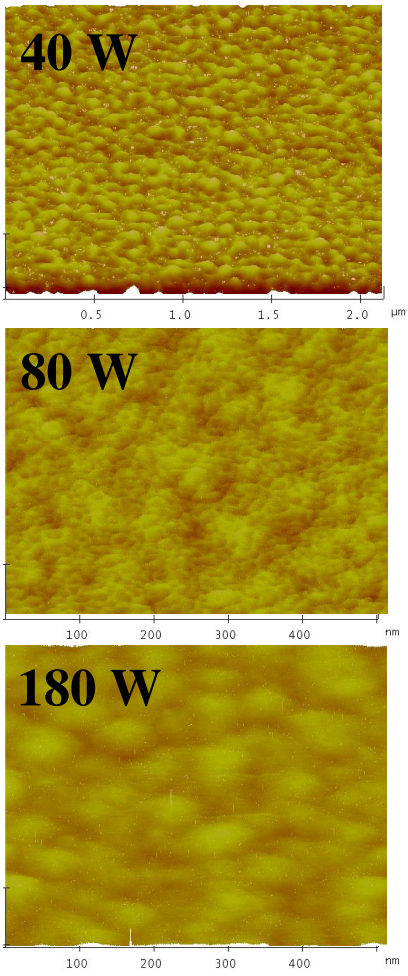

Figure 9: AFM images of ppPS on pp SiO2 deposited at different RF powers

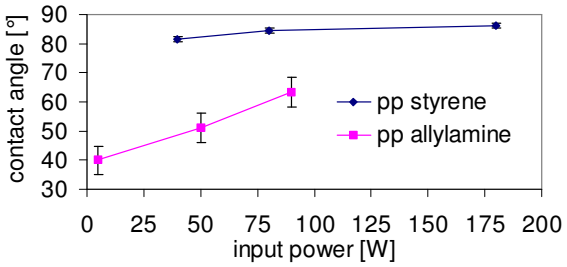

Figure 10: effect of input power on contact angle

Most notably in Figure 8 is the definite deposition of AA and styrene, which shows a constant profile obtained between the stripes. The contact angles between these stripes also showed that contact angle increases with decreasing surface roughness and oxygen content, existing C=O or C-O bond related species (see Figure 1 and 2).

Due the breakdown of the XPS equipment, the results will be belated. This will be presented on the poster.

CONCLUSIONS:

In this study, we especially compared two different films at various input power to determine their characteristics at different input power. This will deepen further studies to apply these films for adhesion or immobilization of protein. The FTIR spectra showed the plasma does not affect the SiO_2 film, but the spectra of the subsequent films (AA or styrene) were altered by the increasing input power, more evident were the amino and benzene bands. The EIS measurements showed that the impedance is relatively not affected by the input power, but analyzing the ion penetration depicted the interface layer information. The surface analysis (roughness and contact angle values) was correlated to the monomer fragmentation in the plasma and functional groups retention in the films. These surface characterisitics have a strong influence on the protein attachment. In the patterned surfaces, a definite deposition profile could was observed for both pp films, which also showed the properties determined for the non-patterned surface.

Reference

1. Y. Ikada (1984) Adv Polym Sci 57:104
2. R. D. Falb (1972) In: L. Wingard (ed), Enzyme engineering. Wiley, New York, p 177
3. D. Korzec, D. Theirich, F. Werner, K. Traub, J. Engemann (1995) Surf Coat Technol 74/75:67
4. E. P. Everaert, R. C. Chatelier, H. C. van der Mei, H. J. Buscher. (1997) Plasmas Polym 2:4117.C.
5. M.T. van Os, B. Menges, R. Foerch, R.B. Timmons, G.J. Vancso, W. Knoll, Mat. Res. Soc. Symp. Proc., 1999, 544, 45-50
6. S. B. Idage, S. Badrinarayanan. Langmuir 14 (1998) 2780-2785.
7. Oehr, B. Janocha, D. Hegemann, U. Vohrer, H. Brunner. (2000) Vakuum Forschung Praxis 5:313
8. Fischer J. P., Becker U.,Halasaz S. P.,Muck K. F., Puschner H. ,Rosinger S. , Smith A. , Suhr H. (1979) Polym Sci Polym Symp 66: 443
9. A. S. da Silva Sobrinho, M. Latrèche, G. Czeremuszkin, J. E. Klemberg-Sapieha, M. R. Wertheimer (1998) J Vac Sci Technol A 16:3190
10. Hegemann D., Vohrer U. , Oehr C. , Riedel R. (1999) Surf Coat Technol 116/119:1033
11. H. Schönherr, M. T. van Os, R. Förch, R. B. Timmons, W. Knoll, and G. J. Vansco, Chem. Mat. 12. 3689-3694 (2000) P-00-173
12. M.T. van Os, B. Menges, R. Förch, R.B. Timmons, G.J. Vancso, W. Knoll, Mat. Res. Soc. Symp. Proc., 1999, 544, 45-50
13. M. S. Silverstein, J. appl. Poly Sci. vol 62 2147- 2154
14. X. Yu, J. appl. Poly Sci vol 80 1434- 1438
15. Steffen T., Uni-Potsdam, IR Wizard, © 2000-2003, (chem.uni-potsdam.de/tools/index.html)
16. P. Hamerli, Th. Weigel, Th. Groth and D. Paul, Biomaterials 24 (2003) 3989- 3999
17. A. C. Bastos, C. Ostwald, L. Engl, Electrochimica Acta 49 (2004) 3947
18. J. C. S. Fernades, M. G. S. Ferreira, D. B. Haddow, Surf. & Coat. Technol. 154 (2002) 8

AN EXPERIMENTAL AND NUMERICAL STUDY OF SIO_2 NANOPARTICLES SYNTHESIS IN AN RF PLASMA REACTOR

B. M. Goortani[1], N. Mendoza[1], P. Proulx[1]

[1]*Department of Chemical Engineering, Université de Sherbrooke, Québec, Canada*

Abstract

Nanoparticles of SiO_2 were produced in an induction thermal plasma reactor. The resulting nanoparticles were characterized on the bases of their morphology and size distribution. Computational fluid dynamics (CFD) software Fluent™6.1 combined with a Fine Particle Model (FPM) developed by Chimera™, was used to simulate the whole synthesis process. The SiO_2 nanoparticles produced and collected at the exit lay in the size range of 20-150 nm, the predicted numerical results being in good agreement with the experimental revelations.

1. Introduction

Radio frequency (RF) thermal plasma processes may be used as a technique for the production of metallic and ceramic powder materials with particle sizes in the nanometric range [1]. To date, the control and understanding of such processes, which are of the vapor synthesis type, is still not well known and there is still a major challenge for achieving scale-up and subsequent industrial applications [2]. So far, a number of researchers in the field of nanoparticle production by aerosol methods have studied this kind of processes. Some examples are found in the literature [3,4], where the experimental work is combined with theoretical models. Such publications also present particle dynamics models implemented with Fluent™. Thus the synthesis of iron nanoparticles in a small scale RF reactor was studied by Girschick et. al. [1]. Ishigaki et al. [5] also experimentally studied the vaporization of Titanium Carbide in a much larger scale RF plasma reactor. In this present work, the study of SiO_2 nanoparticles synthesis in an RF induction plasma reactor is presented, followed by numerical simulation study of the process.

2. Experimental study

Figure 1 shows a schematic diagram of the complete experimental set up employed for the experiments. Micronised quartz particles (MIN-U-SIL 5™, US Silica Company) with an average diameter of 2 and maximum of 5 µm were used as the raw material in a methanol suspension of 50% solids.

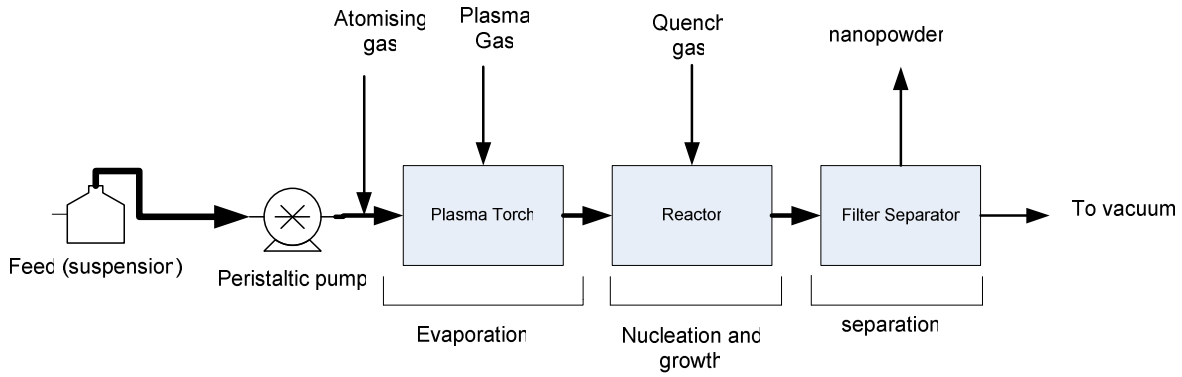

Figure 1. Schematic diagram of the experimental set-up for the production of SiO_2 nanoparticles.

The reactor set-up used here was a modification of that used by Jurewicz J. et al [6] (liquid circulation system were removed, demister was replaced by a Goretex^{TM} filter and the nozzle modified for quench gas injection). This was used with an induction plasma torch; model PL-50 (Tekna Plasma Systems, Sherbrooke, Qc, CA). The operating parameters of the reactor and the RF torch are summarized in table 1.

Table 1- Experimental conditions for the production of SiO_2 nanoparticles.

Process Parameter	*Value*
Plasma gas and Flow rate - Central Gas - Sheath gas	 Argon , 22.5 slpm Oxygen (75slpm), Ar (22.5 slpm)
Feeding rate and Mechanism	4.5 - 16 gpm SiO2 (a suspension of SiO2 in methanol)
Plasma Power Plate	40 kW
Reactor Pressure (absolute)	650 torr

Silica feed rates varied from 4.5 gpm (net SiO_2 injection) to about 16 gpm. Below 4.5 gpm it was difficult to achieve steady flow rates as a result of presence of higher pressures (related to atmospheric) in the induction zone of the torch. Oxygen, used as the "quench" gas, was injected counter-current into the reactor at its base. The nanoparticles produced were separated from gas suspension on the installed filter and the walls of the reactor.

- **Experimental Results**

Scanning electron Microscopy (SEM), Nitrogen adsorption (BET), X-ray diffraction and laser diffraction techniques were all used to characterize the resulting SiO_2 nanoparticles .

Figure 2 shows a typical product SiO_2 SEM image, for the case of 4.5 gpm quartz input feed rate. Product particles were sampled on the filter. In general, these particles are spherical and partially agglomerated (sintered). The average diameter of the primary particles lies in the range of 20-200 nanometers. By increasing the quartz feed rate, increased in sintering and agglomeration of product particles was observed.

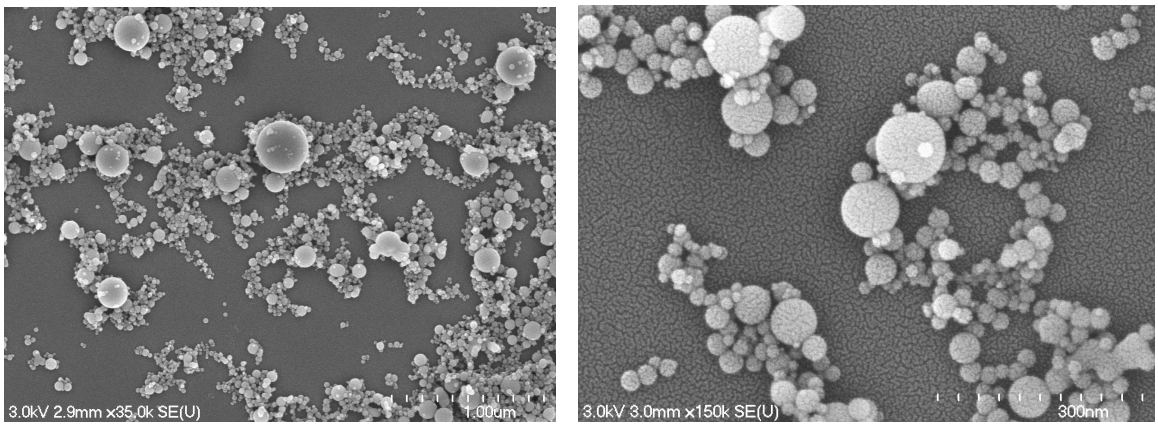

Figure 2. SEM image of the produced silica nanoparticles.

The results of X-ray diffraction studies show that the synthesized particles are completely amorphous in comparison the original input quartz particles that were fully crystalline. This

absence of original crystalline particles on the filter recovered product points to total process treatment of the input powder in the plasma zone. Nitrogen adsorption BET results later showed that, by increasing the quartz feed rate from 4.5 gpm to 16 gpm, the resulting specific surface area of the product powder decreases from 80 m^2/gr to 40 m^2/gr. Laser diffractometry also showed a similar behavior, i.e. by increasing the plasma process feed rate, the percentage of the produced nanoparticles (by volume) decreased.

3.Numerical study

The numerical model is applied to the torch and the reactor of the experimental set up, as described in figure 1. The synthesis process first initially consists of the evaporation of silica particles into the hot plasma formed from input oxygen and argon. In the following step, the mixture of plasma gas is transported to the second vessel (reactor in figure 1), in which condensation takes place and the product particles are produced.

The commercial CFD software Fluent™ 6.1, combined with a Fine Particle Model FPM developed by Chimera™, was used to simulate the overall synthesis process. The synthesis reactor is represented by a computational domain in figure 3, which is then split into discrete control volumes. The underlying computational grid consists of a total of 17598 cells, thereby assuring a high computational grid density. By integrating the governing equations on individual control volumes, algebraic finite difference equations result for the discrete unknown scalars. These discretized equations are solved with the Line Gauss-Seidel algorithm. Further details can be found in the software manuals (Fluent 6.1) or in the book by Bird et al. [7]. The whole model of SiO_2 nanoparticles synthesis involves the solution of fluid mechanics and particle dynamics equations.

The fluid mechanics part of the calculation concerns the solution of continuity, momentum, energy and species. In this approach, the model developed by S. Xue et al. [8] was used for the calculation of the electromagnetic fields, fluid mechanics, heat and mass transfer in the induction plasma generation zone. The evaporation of particles is considered with the model of discrete phase in a Lagrangian frame of reference, i.e. the Discrete Particle Model of Fluent™. The coupling between the phases and its impact on both the discrete phase trajectories and the continuous phase flow are included.

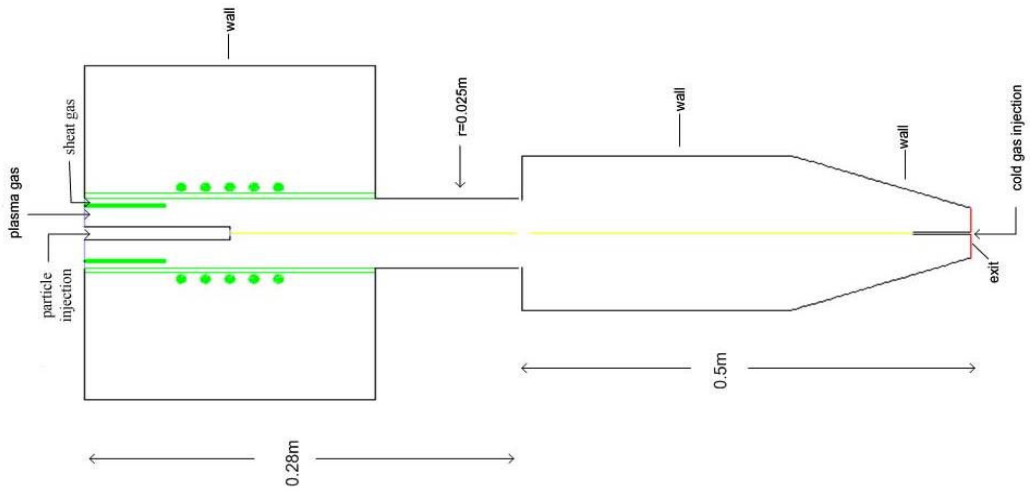

Figure 3. Calculation domain.

The particle dynamics part considers the effect of internal (nucleation, particle growth) and external (fluid convection particle diffusion and external forces) processes affecting particles within a homogeneous control volume. The FPM model for particles nucleation, growth and transport, based on the models of Whitby [9] and Wilck [10], is coupled also with the fluid mechanics.

The particles size distribution is represented using a modal approach. The evolution of particle distribution in space and time is governed by an equation known as the General Dynamics Equation for Aerosols (GDE) [11], which is transformed by applying the definitions for the integral moments of the modes into the Moment Dynamic Equation (MDE):

$$\frac{\partial \mathrm{M}_{j,k}}{\partial t} = conv_{j,k} + ext_{j,k} + diff_{j,k} + coag_{j,k} + cond_{j,k} + nuc_{j,k} + src_{j,k} \qquad (1)$$

This equation accounts for the changes of the size distribution moments $M_{j,k}$ due to external processes of convective transport (*conv*), transport by external forces (*ext*) and diffusion (*diff*), as well as the internal processes of coagulation (*coag*), condensation and evaporation (*cond*), homogeneous nucleation (*nuc*), and general source terms (*src*).

For the present simulation no source terms were involved. The coagulation coefficient is calculated with the transition regime provided by Dahneke [12]. The expression of Barret [13] is used to calculate the mass transfer rate for the condensation-evaporation mechanism. The expression of Girshick [14] for the homogenous nucleation rate is selected in this model. Finally, the equation provided by Talbot [15] is applied in this work for the thermophoresis velocity calculation.

- Assumptions

-Steady state.
-Axisymmetric flow.
-Laminar model for the induction zone and the k-ε turbulent model for the condensation zone.
-Particles are spherical.
-Particle temperature is uniform and equal to the fluid temperature.
-Particle velocity is the sum of convective and external-force velocities.
-Particle size distribution is represented using a lognormal distribution function.

- Boundary conditions

Pure argon is injected at the central entrance of the reactor with the solid particles. A mix of argon 25% and oxygen 75% is used for the sheath gas. Velocity profiles are given for each radial section at the entrance of the reactor: injection probe, plasma gas, sheath gas. The injected SiO_2 particles have a mean diameter of 2 μm. The induction zone is limited by water cooled walls (r=0.025 m). Gradients are assumed to be zero at the exit of the condensation tube. Radial gradients are assumed to be zero for all variables on the axis of symmetry. The condensation zone is limited by cooled walls (T=300K).

- Results of simulation

The results for a case with 4.5 gpm rate of SiO_2 particle injection without quench, are presented in this section. The temperature fields in the reactor are given in figure 4. The SiO_2 particles injected by the central probe are subjected to temperatures of more than 11000 K, which thereby assures complete melting and evaporation of the particles. The gas temperature decreases when the fluid reaches the condensation zone, thereby producing high temperature gradients. The mass

fraction of SiO_2 produced by evaporation of input raw material is decreased along the reactor length because of condensation, as shown in figure (5). Due to condensation, there is a "burst" of nucleation, thereby forming the new particles of SiO_2.

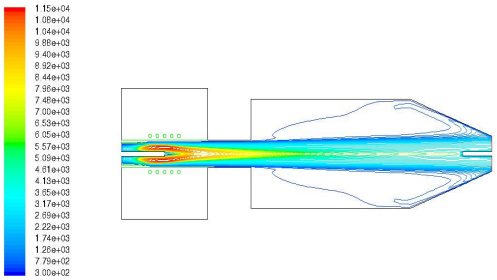

Figure 4. Contours of temperature (K)

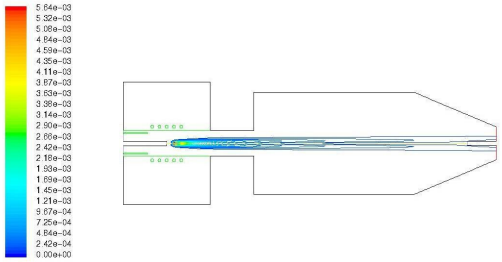

Figure 5. Contours of mass fraction of SiO_2

Particles start to grow and they attain sizes of up to 400 nm near to the reactor exit. This result is likely because the exit is the coolest zone of the reactor and the average residence time for particles is greatest here. Near the axis, slower cooling retards the onset of condensation. However the central cloud is gradually depleted by radial diffusion towards zones where the vapor is condensed. High particle concentrations are formed near the reactor walls. This is due to the presence of strong temperature gradients and thus the short time available to grow. Low temperature gradients at the axis lead to the formation of relatively large particles, even though the vapor concentration is reduced. In figure 6, the diameter isocontours of particles at any point of the reactor can be observed. An x-y plot for the final size of particles produced at the exit of the reactor is presented in figure 7, where the mean particle diameter is calculated as 160 nm. Further simulations, using higher particle feed rates shows similar tendencies, with larger SiO_2 particle sizes, but these results are not presented here.

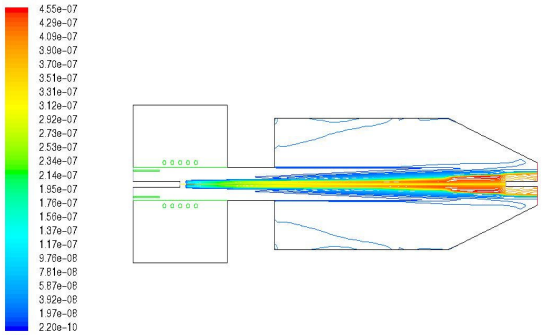

Figure 6. Contours of diameter (m)

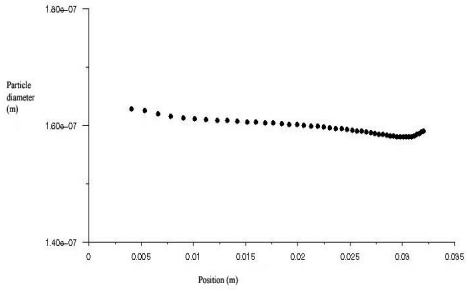

Figure 7. Particle size at the exit of the reactor

4. Conclusions

The overall process of nanoparticle synthesis has been studied both experimentally and numerically and the findings described. The experimental part accounted for the set up of the synthesis process reactor and several plasma conditions were examined. In respect of the numerical analysis part of the work, simulation was effected with low usage of computer time, easy access for parameters and geometry changes, and excellent visualization of the calculation results. This finding suggests that this model has distinct advantages in comparison with other classical models. Good agreement between the results of experimentation and simulation was observed. The final diameters of primary SiO_2 particles lie with the range of 20-200 nm for the cases studied. Finally, this work has helped to provide considerable insight into the phenomena occurring in the reactor and to point towards the appropriate direction for future work on this topic.

References

[1] Girshick S.L., Chiu C.P., Muno R., Wu C.Y., Yang L., Singh S.K., and Mcmurry P.H. "Thermal Plasma Synthesis of Ultrafine Iron Particles". J. Aerosol Sci., 24:367-382, (1993).

[2] Wendelin J.Stark, Sotiris E. Pratsinis "Aerosol flame reactors for manufacture of nanoparticles" Powder Technology, 126:103-108, (2002).

[3] Karsten Wenger, Bernhard Walker, Stavros Tsantilis, Sotiris E.Pratsinis "Design of Metal Naonoparticle Synthesis by Vapor Flow Condensation". Chemical Engineering Science, 57: 1753-1762, (2002).

[4] Tsantilis S., Pratsinis S.E. and Haas V, "Simulation of Synthesis of Palladium Nanoparticles in a Jet Aerosol Flow Condenser". J. Aerosol Sci, 30:785-803, (1999).

[5] Ya-Li Li, Ishigaki T., "Incongruent vaporization of titanium carbide in thermal plasma". Materials Science and Engineering, A305:301-308, (2003).

[6] Fortier A. and Jurewicz J. "Induction Plasma Synthesis of Nanosized Composite Oxides". 15th International Symposium on Plasma Chemistry (ISPC 15), Orléans (France), **VII:**2831-2836, (2001).

[7] Bird R.B., W.E. Stewart and E.N. Lightfoot. "Transport Phenomena". John Wiley & Sons, New York, (1960).

[8] Xue S., Proulx P., and Boulos M.I. "Extended-Field Electromagnetic Model For The Inductively Coupled Plasma". J. Phys. D: Appl. Physics. 34:1897-1906, (2001).

[9] Whitby W. "Modal Aerosol Dynamics Modeling". PhD thesis, University of Minnesota, Minneapolis (1990).

[10] Wilck M. "Modal Modeling Of Multicomponent Aerosols". Disertation, Univesitat Leipzig, VWF Verlag, Berlin (1999).

[11] Friedlander Sheldon K. "Smoke, Dust and Haze". John Wiley & Sons, New York, (1955).

[12] Dahneke B. "Simple kinetic theory of Brownian diffusion in vapors and aerosols2. Meyer, editor:97-133. Academic Press, New York, (1983).

[13] Barret J. C. and Clement C. F. "Growth rates for liquid drops". J. Aerosol Sci, 19(2):223-242, (1988).

[14] Girshick, S. L., Chiu, C. P., and McMurry, P. H. "Time-dependent aerosol models and homogeneous nucleation rates". Aerosol Science Technology, 13:465-477, (1990).

[15] Talbot, L., Cheng, R.K., Schefer R.W., and Willis D.R. "Thermophoresis in a heated boundary layer". J. Fluid Mechanics, 101(4):737-758, (1980).

Optical emission diagnostic of an impinging supersonic induction plasma jet

Y. Lakaf[1], S. Mhim[1], D.V. Gravelle[1] and M. I. Boulos[1]
[1]Energy, Plasma and Electrochemistry Research Centre (CREPE)
Université de Sherbrooke, Sherbrooke, Québec, Canada

Abstract:

The objective of the present study is to determine the temperature and plasma composition profile, using the emission spectroscopy method, across the thin boundary layer formed over the surface of a flat plate on which a supersonic plasma jet is impinging. The complex structure of the supersonic jet near the region of impact, such as the structure of the standing shock wave formed over the plate, motivates use of this non-intrusive diagnostic method. The radial profile of temperature obtained is very interesting comparing with those described in literature.

1. Introduction:

Supersonic plasma jets are characterized by very high temperature, velocity and pressure gradients which get them many advantages in industrial applications. They have been widely used for re-entry simulation studies and in the plasma spraying of high density nanostructured thin and thick coatings. In most of these applications, a fundamental understanding of the conditions in the boundary layer over the substrate is of critical importance for achieving the right conditions for the surface treatment and/or coating quality.

The supersonic plasma jets are produced by means of simple adjustment of the convergent-divergent nozzle and chamber pressure reduction. Optically the supersonic jet is narrow and fast. Downstream from the exhaust nozzle, it consists of an alternation of expansions and compressions zones, generated by the fact that the static pressure of the jet tends to balance with the medium of evolution. On the flat plate, the supersonic jet impingement includes very complicated phenomena, with the presence of multiple shock system that consists of the barrel shock, the plate shock, and the reflected shock, as well as the instability of a stagnation point. [1-2]

Previous studies [3-4] that have been conducted on the impinging flows have reported that the pressure and the local heat flux profiles along the plate both should have maxima at the center of the plate. However, it has also been reported in the literature [2] that the surface pressure distribution has the peripheral maximum due to the presence of bubble and it's also affected by the nozzle-to-plate distance. Indeed, if the plate is located in inside of some cycles of reflexion, the plate shock is formed. The flow downstream from this wave becomes subsonic and is allowed like the zone of stagnation of the flow. The fluid thereafter accelerates radially along the surface of the plate and possibly passes by again in supersonic mode. If it is the case, the radial expansion of the fluid makes so that the flow becomes again sonic at some distance. The bubble formation is the consequence of the very high gradient of velocity which surrounds it, dragged on its top by the high radial velocity.

Although it emerges from these studies a good comprehension of the impinging under-expanded gas jet dynamical properties onto the plate, it remains about it less concerning the heat transfer across the thin boundary layer formed over the surface of a flat plate on which an induction supersonic plasma jet is impinging.

The aim of this paper is to determine the temperature and plasma composition profile of supersonic plasma RF jet impinging on flat plate by the atomic emission spectroscopy nearest of the impact region and in the

stagnation bubble. The zone of interest is located at a few millimetres upstream from the plate where a very luminous structure is observed. Since we are interested essentially in the impact region where the plate shock wave appears, we have fixed the distance between the plate and the exit nozzle according to a relevant study reported in literature relatively to bubble appearance. [5]

Because of the plasma doesn't emit sufficiently, all of measurements were performed with no light in the diagnostic room, in order to be able to position our plasma on the slit entry of the spectrometer. So, the thinner boundary layer where the plasma doesn't emit, was estimated around 2 to 3 mm upstream the plate.

Spectroscopic measurement of inductively coupled plasma of pure Argon is carried out, and several plasma properties are determined from data. The radial excitation temperature (T_{LTE}) profile following Local Thermodynamic Equilibrium (LTE) assumption is determined along jet axis, and the electronic temperature T_e and density N_e are also estimated using the Boltzmann graph and the continuum emission, and confronted after with those giving by LTE assumption.

2. Experiment:

The experimental apparatus is shown in Fig1. The plasma is generated by RF plasma torch (PL-35 Tekna Plasma System) equipped with a convergent-divergent nozzle designed for Mach number of 4. The power is fixed at 16.65 kW and the pressure in the chamber was about 1.84kPa. The reactor supported the plasma torch is cylindrical and is fitted with the collecting pipe of exhausts gases connected in its turn with the system of vacuum. The reactor is provided with quartz port-holes laid out on the optical axis of spectroscopic measurements. The luminous rays coming from plasma are forwarded to a Jobin-Yvon monochromator of focal length of 1m via a system of lenses and mirrors disposed front of the plasma. The monochromator fitted with a grating having 1200groves/mm, makes it possible to break up the rebuilt image of plasma, with a factor of contracting of 1/8, in its emission spectrum. The resulting light intensities are read by a CCD detector with 1024x256 pixels, the rows and columns of this CCD correspond to the spectrum and radial emission profile of the plasma respectively. We were interested in the emission given by the spectrum of line of argon to a wavelength of 415.9 nm, 430.01 nm and 727.3 nm. Depending on the spectral wavelength, integration time of the CCD varied from 0.03 to 1s. The entrance slit width was kept at 8 μm.

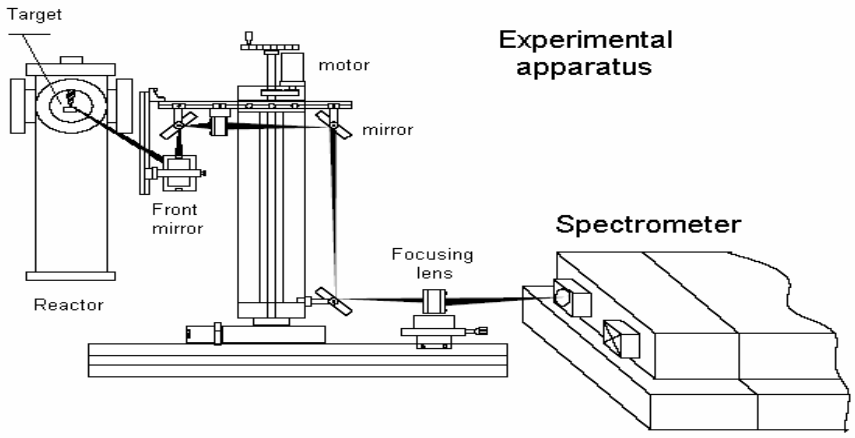

Figure 1: Schematic diagram of the reactor with the optical spectrometer instruments

In the vertical position, each diode recorded the signal corresponding to the light emitted by a cord of a slice of the plasma jet. The spectral width is equal to the product of the total height of the photodiodes

(0.027mm) and the linear dispersion of the monochromator (0.78 nm.mm^{-1}), i.e. 0.021mm. The absolute intensity of the line's radiation was obtained by calibration using a standard tungsten filament lamp.

3. Results and discussion:

Typical photographs of such chock waves formed for a Mach 4 supersonic plasma jet impinging on a flat plate located at a distances of 90 mm from the exit nozzle of the plasma jet are shown in Figure 2.

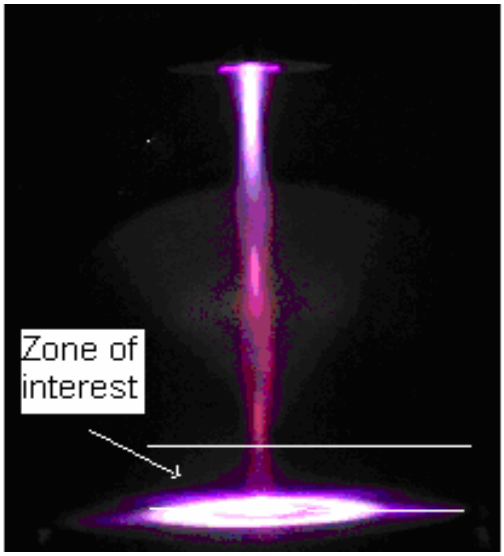

Figure 2: Mach 4 supersonic induction plasma jet impinging on flat plate placed at Z=90mm.

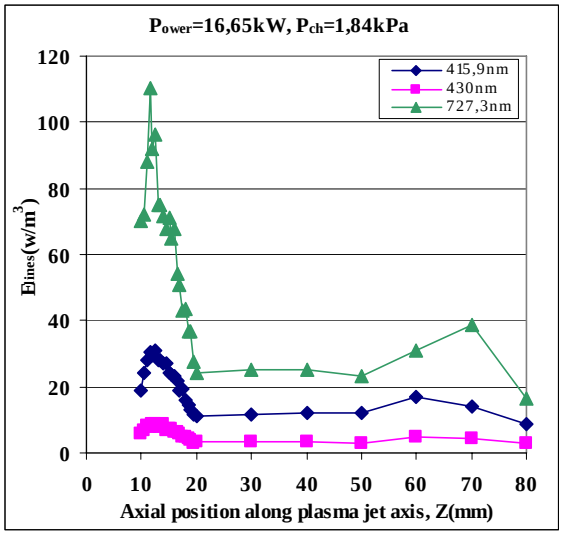

Figure 3: Emissivity lines of 415.9 nm, 430nm and 727.3nm vs. axial plasma jet position Z.

The figure 3 representing the emissivity lines of 415.9 nm, 430.nm and 727.3nm along the jet axis, shows the general structure of the impinging RF plasma jet, resulting in compression and expansion zones. The three profiles have shown the same phenomena. First plasma emission is observed at 10 mm away the from the plate, followed by a compression zone located at 12 mm , until a compression zone observed close to the nozzle exit at 70 mm from the plate. The emissivity increases to maximum, and then decreases till the 20 mm axial position, and then kept constant close to the first compression near the nozzle exit. The zone of interest is located within 20 mm from the plate surface where the measures were performed with axial displacement step of 0.5 mm, then the interval was increased to 10 mm between two measures, on the top region of interest.

The first attempt regarding the emissivity profile at 430.0nm line, after Abel inversion, as seen in Fig.4, shows interesting phenomenon occurring near the periphery of the plasma. The profile shows that the emissivity decreases with the radius, and then increases through the off axis maximum. This phenomenon has already been reported (Fig.5) through modeling and calorimetric measurements [6], showing an off axis maximum of heat exchange. This phenomenon results from lateral shock wave near the centre with peripheral off axis shocks, due to the radial plasma flow acceleration along the plate. [7]

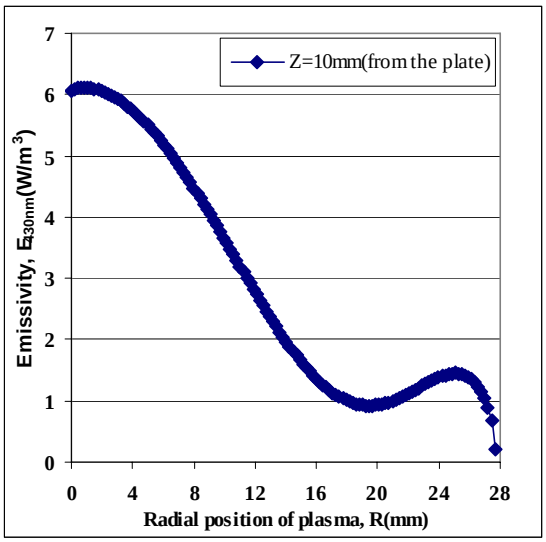

Figure 4: Emissivity of 430 nm lines from the centre of the impact zone. M=4.0, P_{ower} =16.65kW

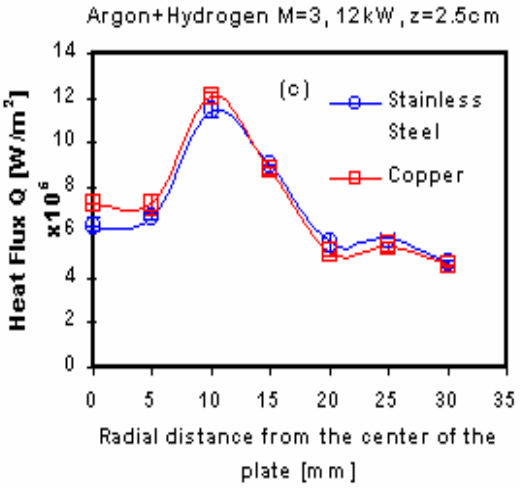

Figure 5: Heat flux calorimetric measurement along the radial distance from the centre of the plasma

The emissivity spectral lines of 415.9nm, 430nm and 727.3 nm are used to determine the temperature. Two methods were employed:

1- Atomic Boltzmann plot method
2- Absolute line intensity method, by solving a non linear system of equation given by Saha, Dalton and Boltzmann distribution, assuming LTE assumption.

For the first method, the plasma temperature can be obtained by plotting the equation:

$$y = \log \frac{N_m}{g_m} = \log\left(\frac{\varepsilon_{mi}\lambda_{mi}}{A_{mi}g_m}\right) = \ln A - \frac{E_m}{kT_e} \quad (1)$$

Where ε_{mi} are the absolute lines intensities (emissivity), and λ_{mi} are the wavelengths and E_m and g_m the excitation energy statistical weight of the upper atomic state respectively; K constant of Boltzmann.

The Boltzmann's diagram, while laborious, has the main advantage of not depending on the local pressure or composition in the measurement of plasma section. Then, the slope of the straight line obtained is inversely promotional to the temperature. We will call the temperature obtained, T_b, Boltzmann temperature. (See Figure5-6)

In the same time, are we getting the Boltzmann temperature, we can estimate the electronic density, by using the equation giving by the absolute continuum expressed as follow:

$$\varepsilon_{\lambda c} = C_1 \frac{N_e^2}{\lambda_u^2\sqrt{T}}\xi(\lambda_u, T_e) \quad (2)$$

Where $C_1 = 1.63.10^{-43}$ $Jm^4K^{1/2}s^{-1}st^{-1}$, and constant fro all Argon lines. λ_u is the continuum wavelength, and T_e the Boltzmann temperature.

These two properties (T and N_e) of plasma can be determined assuming LTE assumption near the central axis of plasma in the impact region. The plasma flow tends to stagnate in front of the plate, and the presence of the shock wave on the plate, resulting in the pressure increasing, allows to consider that the thermo dynamical non equilibrium plasma is approaching a temperature-equilibrium, one due to frequent energy transfer collisions among all particles species. The collision results by an increase from the temperature supporting by consequence of LTE assumption. [4]

The system of equation which allowed measuring excitation temperature, giving by the absolute line emission of 430nm, and the density of electron is given by equations (3, 4 and 5):

$$\varepsilon_{mn} = \frac{hc}{4\pi}\frac{N_0(T)}{Z(T)}\frac{A_{mn}\,g_m}{\lambda}\exp(-E_m/KT_{exc}) \quad (3)$$

$$\frac{N_e N_i}{N_0} = 2\frac{Z_i(T_{exc})}{Z_0(T_{exc})}\left(\frac{2\pi m_e K}{h^2}\right)^{3/2} T_{exc}^{3/2}\exp(-E_i/KT_{exc}) \quad (4)$$

$$\frac{P}{K} = N_e T_{exc}(N_i + N_0)T_{exc} \quad (5)$$

This system can be solved if the local pressure of the plasma is known. Because of the pressure in the stagnation pressure is unknown, and never reported in literature, we have used the pressure of the plasma environment which is the chamber pressure (1.84kPa), knowing well that is not represents the pressure of plasma.

The temperature of excitation and the density of electron are shown in the Figure (5-6)

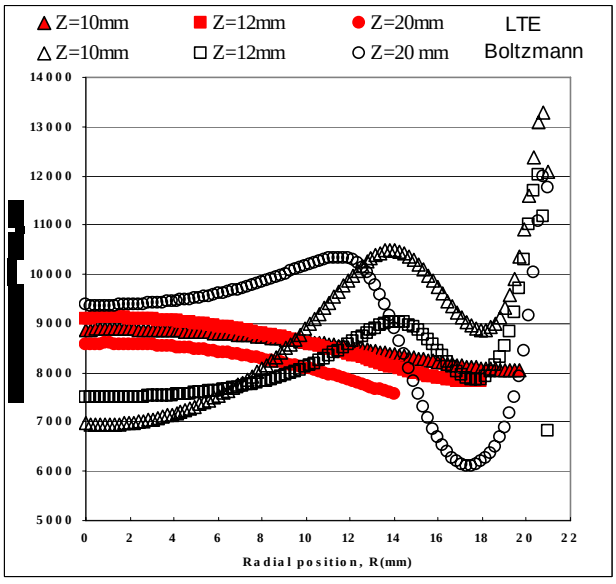

Figure5: Radial temperature profile at different axial position Z=2mm-4,5mm-12mm

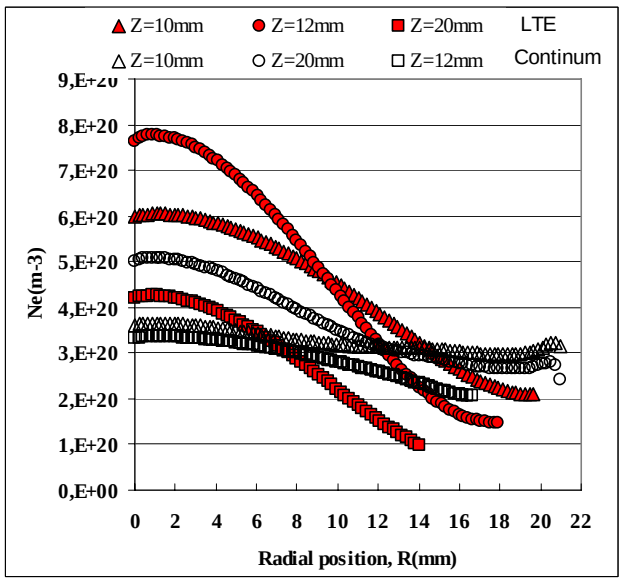

Figure6: Radial temperature profile at different axial position Z=2mm-4,5mm-12mm

In these graphics, three positions along plasma jet axis were chosen, relatively of expansion and compression zones apparition located at Z=10mm, 12mm and 20mm. The temperatures given by the two methods mentioned above were confronted. The Boltzmann temperature T_b (Fig.5), along the plasma jet centreline increases from 7000K to 9500K, due to shock plate formation, resulting by the formation of the stagnation bubble located upstream of the shock wave plate. Radially, the temperature profile also increases outward up to about 10500K at 12 mm in radius, for Z=10mm, over the plate. It is also valid for Z=10-12mm, where the same phenomena are observed, where the both temperature profiles passes from maxima to decrease then towards plasma periphery. This phenomenon has already been reported by the literature [2], due to the existence of cooled region near the jet periphery. Concerning the temperature given by solving the system of equation of Saha-Dalton-Emissivity distribution, following LTE assumption, this latter is shown in the Figure 5. Along the centreline plasma jet the T_{LTE} has a maxima at Z=12mm of about T=9100K before to decrease to T= 8600K at Z=20mm, according to the emissivity distribution along the centreline of plasma jet (Fig.4). Radially, the temperature profile T_{LTE} gradually decreases for all axial positions and have no great variation at these axial positions, compared with that given by T_b, until plasma periphery. However, towards the periphery of plasma profiles radial of temperature it's maximum in the direction of Z increasing.

The characteristics of the electron number densities shown in Fig.6, following LTE assumption, are almost similar to those of the temperatures. The electron densities distribution at the centreline of jet plasma for the three axial positions has peaks on the order of 4.10^{20} to 8.10^{20} m^3, and they gradually decrease radially outward to the order of 1.10^{20} to 2.10^{20} m^3. The profile at Z=20mm is greater that those at 10mm and 12 mm, because of the intensive collision transfer energy due to plasma jet compression.

Concerning the electron densities profile given by the Continuum equation, the same observation is observed, exception that the radial profile of the electron densities at Z=2mm almost equal to that at 12mm. radially all profiles decreases gradually and are much lower than those given by LTE.

4. Summary:

Optical emission spectroscopic measurements were performed to examine an impinging supersonic plasma induction jet over the flat plate. The complex phenomena characterising the impact region has motivated us to use this non-intrusive method of diagnostic. The spectral intensity response of the lines 415.9nm, 430nm and 727.3nm conducting throughout the thinner boundary layer at different axial position from the plate has permitted the temperature estimation at few millimetres upstream the plate. The radial profile of temperature has shown the existence of the shock wave at the periphery of the plasma nearest the plate due to radial acceleration of the plasma on the plate. The temperature pass from maxima at Z=12 mm due compression zone. Lastly, the electron number densities and temperature giving by the LTE do not give us entire satisfaction for their non conformity with those giving by the Bolztmann's temperature. This attempt to consider the LTE assumption is may be not applicable, and consist for further investigation.

References

[1] S.E.Selezneva, M.I.Boulos. M.I.J.Appl.Phys 91,5(2002).
[2] B.G.Kim. Journal of thermo physics and heat transfer, Vol.16, No.3, July-September 2002.
[3] B.Gon Kim. Trans.Japan Soc.Aero. Space.Sci. Vol. 38, No. 121, July 1994
[4] H.Tahara, Y.Ando, T.Yoshikawa. IEEE Transactions on plasma science, Vol. 31, No. 2, April 2003
[5] W.Masuda, E.Moriyama. JSME International Journal, Seies B, Vol. 37, No.4, 1994.
[6] S.E.Selezneva, J.Weber, M.I.Maher. IISPC 16, 22-27 June2003,Taormina, Toronto.
[7] Y.K.Chih. Journal of Fluids Mechanics, Vol.315,p.268.

Synthesis of Ferromagnetic Nanopowders from Iron Pentacarbonyl in Capacitively Coupled RF Plasma.

A.Kouprine, F.Gitzhofer, M.Boulos[a] and T.Veres[b].
[a]*Department of chemical engineering (CREPE), University of Sherbrooke, Québec, Canada*
[b]*Industrial Materials Institute, National Research Council, 75 boul. de Mortagne, Boucherville, Québec, Canada*

Abstract
Ferromagnetic nanopowders (NP), created with magnetically decoupled cores, are interesting for their further utilization in bulk nanostructured magnetic materials in low and high-frequency applications. Capacitively coupled RF discharges, at P=100-250 Pa, were used for the synthesis of binary iron/carbon NP from argon diluted vapors of iron pentacarbonyl ($Fe(CO)_5$). Obtained NP were investigated by TEM, XRD, TGA, FTIR and magnetization measurements. Diamagnetic NP, with ≈4% iron content, were obtained at lower pressures (100-130 Pa); increasing the pressure to 250 Pa resulted in the synthesis of ≈40% iron content NP with ferromagnetic properties (M_S ≈50 emu/gr). The first NP type is formed of particles some 10-50 nm long and several nm wide, being carbon/iron rods, covered by graphitic layers and integrated into an amorphous carbon matrix. The second ferromagnetic NP consist of isolated hexagonal shaped 20-60 nm crystals of the Fe_7C_3 or Fe_2C_3 carbides, embedded in an amorphous carbon. Factors, favoring the carbide NP formation are the temperature decrease, the shifting of the chemical equilibrium from non-bound *Fe* and its oxides towards the state of carburization, and the deceleration in the rate of removal of the *Fe* oxidation products towards the reactor walls.
Keywords: nanopowder, plasma, iron carbonyl, iron carbides, ferromagnetic.

1. Introduction
Binary or multi-component nanopowders (NP) attract interest as starting materials for the synthesis of composites with improved properties, e.g. advanced ceramics and ferromagnetics. Numerous methods for the composite NP fabrication, such as deposition from colloidal solutions [1], annealing [2], electric arc [3] and low power RF plasma treatment [4] and acoustic decomposition [5] have been developed. The plasma synthesis of binary NP can be processed with a variety of material couples and integrated into serial technological process. Such applications, for example in binary ceramics, are known since several years [6]. Encapsulation of the magnetic NP in carbon can protect them from oxidation and reduce the magnetic coupling between individual particles [2]. Bulk materials with new magnetic properties can be fabricated from such NP by densification. At [7] a capacitively coupled (CC) RF discharge in hydrocarbon gases was used for the in-flight coating of SiO_2 nanopowders with an *a-C:H* nanolayer. In the present work, a modified CC RF plasma system, operating under similar conditions, is applied for the synthesis of ferromagnetic NP, using iron pentacarbonyl as a gaseous precursor. $Fe(CO)_5$ is used for the fabrication of nanostructured materials by various methods, such as e^--beam assisted CVD [10] or ultrasound decomposition of the precursor [5]. The iron group metals are known as active catalysts for reactions involving graphitization and *CO* conversion [2, 9]. Hence, the application of $Fe(CO)_5$ combines the synthesis of ferromagnetic NP and the individual NP encapsulation in a carbon/graphite matrix. The NP cores may contain non-bound iron and a variety of iron carbides. The used plasma setup enables the control of the product composition, its magnetic properties and morphology.

2. Experimental setup
The capacitively coupled (CC) RF discharge facility used in this work can operate in various gases at pressures of 1000-10000 Pa, flow rates of 0.01-0.1 slpm and applied powers from 500 to 1800 W (5-20 W/cm^3). Detailed description of the facility is given at [7]. For the present work, iron pentacarbonyl was employed as the powder precursor for the synthesis of ferromagnetic powders. Saturated vapours of $Fe(CO)_5$, at corresponding partial pressure P_p ≈4000 Pa, were diluted with the argon, and the resulting mixture, of 5% vol. *iron* carbonyl and 95% vol. *Ar*, was supplied to the plasma reactor at 0.015-0.020 slpm. The plasma was operated under *P*=100-200 Pa and power density of 4-6 W/cm^3. Synthesized powder product was collected by a filter, located at the exit of the HF discharge quartz

tube. The iron carbonyl concentrations and exiting gases compositions were monitored by a *Baltzers* QMS 200 mass spectrograph. The *JEOL 100CX* 120 kV microscope, was used for the TEM, *Perkin-Elmer TGS-2* thermo-gravimetric analyzer for the TGA, *Philips* X'Pert MPD powder X-ray diffraction system for the XRD and *Nicolet 5DXB* FTIR spectrometer ofr the IR. A Quantum Design Physical Property Measurement System (PPMS) was used to measure the DC and AC magnetization for the T=2-300 K, for field strengths up to 9 Tesla. The resolutions are 2×10^{-5} emu in DC fields, and 1×10^{-8} emu for the value of AC magnetization. The DC magnetization was measured by utilizing the extraction method.

3.Results

The most abundant product of the $Fe(CO)_5$ processing is a tube walls deposit, observed mostly at the tube upper part in front of the high voltage electrode. Its elemental material was found to be Fe_2O_3; (XRD) capturing more than 90% of the initially introduced iron. The processing also results in the synthesis of smaller quantities of dispersed powders collected on the filter. This NP inception takes place in the reactor quenching zone, appearing as a disruption of the uniform plasma, creating instabilities in the form of swiftly moving and abruptly ceasing streamers. Typically, about 50 mg of black, ultra-dispersed powders were collected on the 2 cm^2 paper filter after the 1-hour experiments. This powder bound about 2-4% of the totally fed iron. TEM images of these powders, obtained in $Ar/Fe(CO)_5$ plasmas, are shown at Figs.1,2. Depending on the plasma conditions employed, the product represents two kinds of NP:

1. dense cores or rods ("nanocigars"), 10 to 50 nm long and several nm wide, encapsulated into layered cells and clustering into transparent flakes (Fig.1). For different conditions such clusters may represent 10 - 80 % of the observed NP. These NP were obtained under a lower plasma pressure, P=110 Pa, gas flow rate of 0.015 slpm and a power of 450-550 W for the total plasma volume of 60-70 cm^3.

2. dense, hexagonal shaped crystals, 20-60 nm in diameter, either individually covered by a transparent coating or integrated into transparent matrices. The conditions are: P=250 Pa, gas flow rate 0.020 slpm and applied power = 550-600 W of (Fig.2).

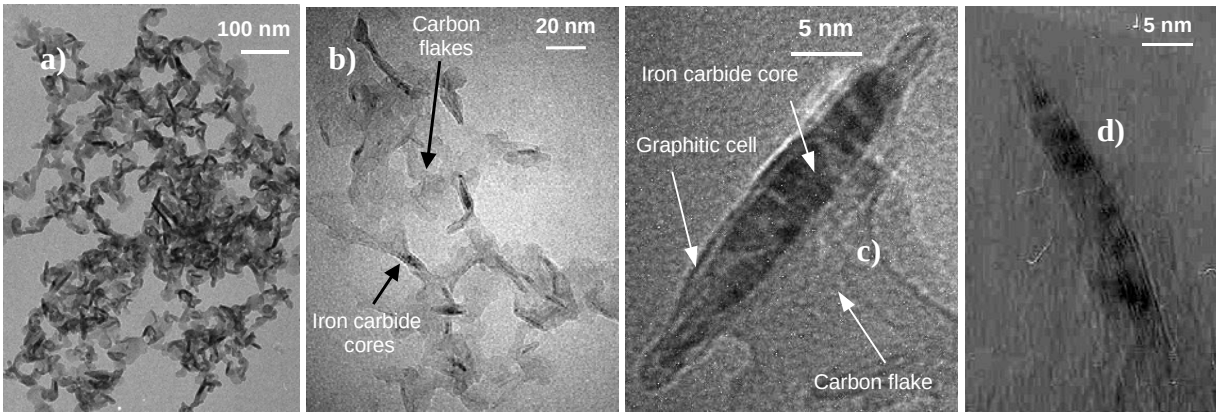

Fig 1. Powders synthesized at P = 110 Pa: iron containing "nanocigars" in graphitic cells integrated into the amorphous carbon matrix. a)-c) TEM; d) HRTEM .

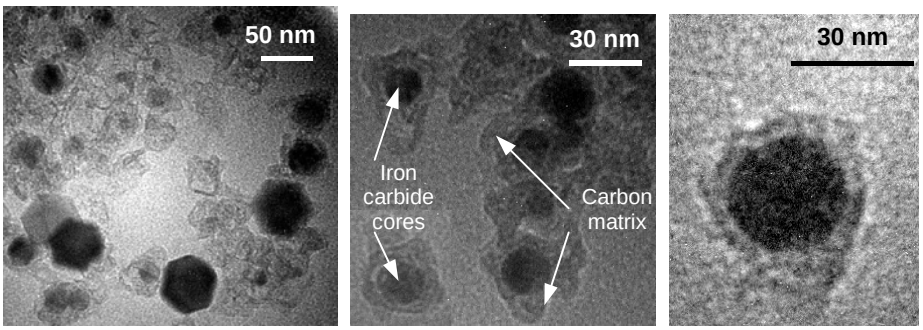

Fig. 2. Powders synthesized at P = 250 Pa; Fe_7C_3/Fe_2C crystals embedded in amorphous carbon.

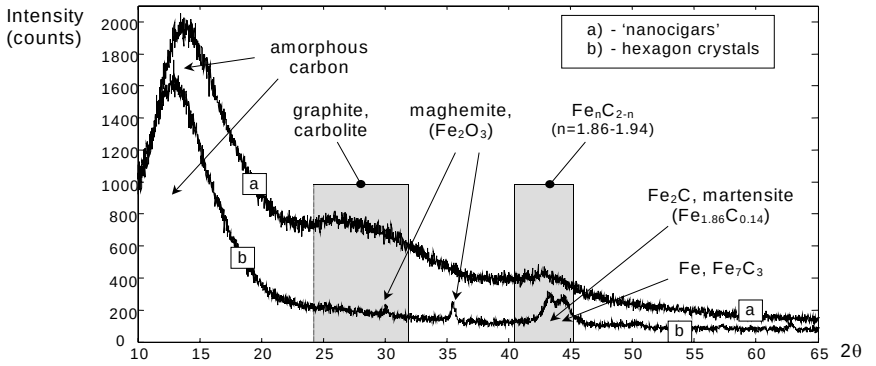

Fig. 3. XRD analysis. Typical NP synthesized at P=110 Pa (a-"nanocigars") and at P=250 Pa (b-hexagon crystals).

As detected by XRD (Fig.3b) and elementary analysis, for the first NP kind, the cores of "nanocigar" powder particles contain iron, either in the form of Fe_2C or as inter-phase surface *Fe* atoms, bound with carbon. The surrounding layered cells are graphite-like structures (detected by e^--diffraction), it correlates with the presence of graphitized carbon in NP (Fig. 3). Cell graphite planes have structural similarities with other metal carbide/graphite NP [13] or MWNT, with their graphite-like atomic bonding and hybridization. Core and cell layered structures are also observed by HRTEM (Fig. 1d). The surrounding flakes are amorphous, yielding to the intense diffuse XRD peak at 2θ =12-18° (Fig.3). Peaks at 22-28°, belong to graphitic structures. Both matrix carbon and iron carbides Fe_nC_{2-n} (n=1.86-1.94), contained in NP can contribute to the diffuse peak at 42-45°. The e^--diffraction pattern reveals as well the absence of structure, as is to be expected if the amorphous carbon forms the bulk of the matrix [14]. In the second kind of NP, the hexagonal shaped crystals consist of a mixture of iron carbides, the observed XRD peaks can be attributed: the 43.0-43.5° to Fe_2C or to martensite, $Fe_{1.86}C_{0.14}$; the 44.0-44.5° to iron, to Fe_7C_3 or to χ-Fe_5C_2 carbides [14]. Possible lattices for both Fe_2C and Fe_7C_3 (*bcc* pseudo-hexagonal) [15, 16] are consistent with the observed hexagons. The χ-Fe_5C_2 or Fe_7C_3 are the more stable phases among the mentioned carbides, they can also be final phases of Fe_2C transformation, presumably via $Fe_{2.2}C$ [8, 17]. Both ε-Fe_2C and ε'-$Fe_{2.2}C$ are thermally unstable hexagonal carbides [8]. Thus, the observed hexagon crystals are to be attributed to the Fe_7C_3, with a possible admixture of the Fe_2C phase. A similar composition of iron carbides' nanostructures has been obtained from $Fe(CO)_5$ by the e^--beam induced CVD [10]. The transparent matrices, embedding nanocrystals, should be associated with the amorphous carbon, yielding to the 2θ =12-17° peak (Fig.3). The traces of Fe_2O_3 /maghemite are also observed, with 30.2, 35.6, 63.0° peaks. This can result from the post-oxidation, suggesting that not all nanoparticles are completely coated by the carbon.

The Fig. 4 presents TGA of two kinds of synthesized NP. It is assumed that various carbon phases form volatile products of oxidation, while free and carbon bonded iron remain in the residuals. For the absolute mass loss data, in the case of hexagon crystals, the residual product constitutes ≈45% of the initial mass. Supposing this to be the Fe_7C_3 phase (XRD data), the iron mass fraction in the NP is ≈41%. In the case of "nanocigars", the residuals have only ≈4.1% (3.8% of iron mass fraction). A small 1% gain at T>700°C is related to the formation of non-volatile oxides and means that vulnerable to oxidation non-bonded iron is present in the "nanocigars". Differential gravimetry (Fig.4b) reveals at least one distinctive peak at 400-410°C common for both kinds of NP, and one extra peak at ≈500°C for "nanocigars". The 410°C peak should correspond to the combustion of amorphous carbon, the 500°C peak – to the combustion of graphite-like cells of "nanocigars" [12, 18]. This difference between the two kinds of NP is consistent with the TEM and XRD detection of a graphitic phase for the "nanocigars", and with the absence of this phase in the hexagonal crystal NP. Further separation of TGA peaks suggests that a third combustion peak exists at 280-320°C. This can be also attributed to the amorphous carbon phase [12,18].

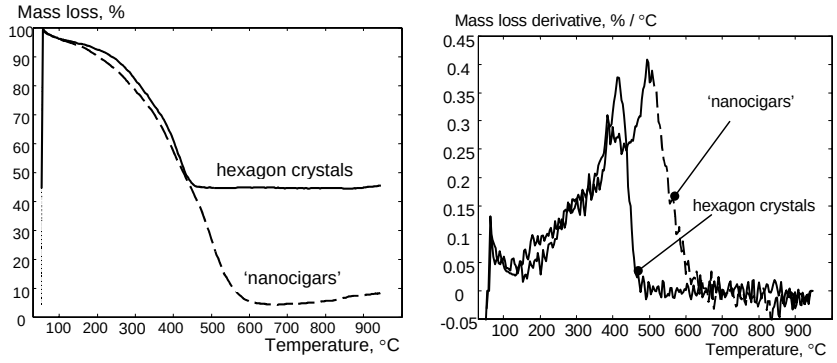

Fig. 4. TGA results for two kinds of powder a) mass loss b) differential mass loss. Two mass loss peaks at 410°C and 500°C correspond to the amorphous carbon matrix (both cases) and graphitic phase ("nanocigar" cells only).

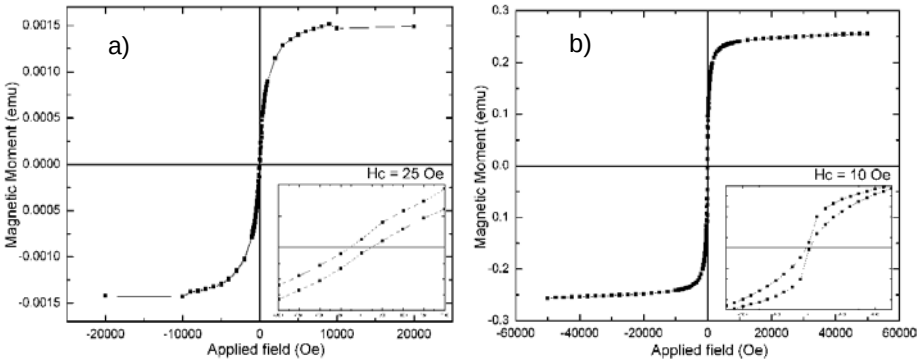

Fig. 9. Field dependence of the magnetization at 293 K for the two types of powder samples: a)"nanocigar" and b) hexagon. Mass of the sample m ≈ 6 mg.

The FTIR spectroscopy revealed two diffuse peaks of 1659 cm^{-1} and 1590 cm^{-1}, for all samples. They are associated with vibrational *C-O* bonds, arising from traces of oxygen. While the undisturbed CO_{vib} has apeak at 1659 cm^{-1}, the *Fe-CO* interaction results in its shift towards 1590 cm^{-1}, thus confirming the formation of carbon-iron chemical bonds [19]. The 1590 cm^{-1} peak relative intensity is higher than that of 1659 cm^{-1} for the hexagon crystals NP; therefore higher iron contents can be expected in this case, which corresponds to the higher iron content, as detected by TGA and XRD for this NP type.

Fig.9 presents results for induced magnetization of NPs as a function of the applied magnetic field. Powders synthesized at higher pressures have their magnetic moment saturation, M_S ≈50 emu/gr, typical for a variety of ferromagnetic NP [19, 20, 22]. The lower pressure synthesized "nanocigars" have a very low M_S value, ≈0.3 emu/gr and no ferromagnetic properties; the coercive forces H_C are 25 Oe and 10 Oe, respectively. The zero field cooling/field cooling (ZFC/FC) analysis of the hexagon crystal NP shows an intersection of the two curves, corresponding to a blocking temperature T_B, at ≈280 K. Thus the NP is ferromagnetic at $T<T_B$, and becomes superparamagnetic at $T>T_B$ when thermal fluctuations start to randomize the orientation of domains. The H_C is relatively high, meaning that each particle might contain several magnetic domains. The effective magnetic anisotropy constant (*K*) of the NPs can be estimated from T_B: $K=25kT_B/V$ (*V* is the particle volume). For the typical NP crystal sizes of 20-40nm a value for $K\approx 3000\text{-}5000\ erg/cm^3$ can be estimated, i.e. this powder has a relatively high magnetic anisotropy.

The mass-spectrography (MS) demonstrated complete $Fe(CO)_5$ decomposition; the iron supplied with the $Fe(CO)_5$ always remains bound within solid phases; the differences in the experimental conditions result in changes to the fractions of the exiting *CO* and CO_2 species. Increased pressure leads to the rise of the *CO* and CO_2 fractions, detected at the reactor exit, in comparison with that of *Ar*. Consequently, higher *Fe/C* ratios can be expected in those solid phases collected in the reactor under the higher pressure. It is consistent with the synthesis of ferromagnetic NP (hexagon crystals) exclusively from the higher pressure (250 Pa) plasma and is confirmed by the results of TGA and XRD measurements.

4. Discussion

The results obtained demonstrate that kinetics mechanisms for carbides and oxides formation in $Ar/Fe(CO)_5$ plasma may differ, and depend principally on the pressure conditions. Power input and gas flow rate in experiments are related with the pressure, to ensure the formation of the NP synthesis quenching zone. Experiments at the higher pressure (250 Pa) had, in comparison with these at 110 Pa, a 10% approximately higher power and a 30% higher gas flow rate and hence a 20% lower specific power value. Thus, higher pressure could result in lower gas temperatures. The gas temperatures for the present case are expected to be around 700-900 K (compare with the conditions of [7]), and electron temperatures $T_e \leq 1$ eV. For such a plasma, the part of the thermal conductivity λ, related to *CO* excitation and dissociation, can became pressure dependent [24], thus increasing the λ value for the higher pressure case. Hence, higher pressures can result in higher thermal losses and become a factor for the temperature decrease seen in the 250 Pa case. $Fe(CO)_5$ easily decomposes at temperatures >200°C, with *CO* decomposition following, via: 1) $CO^*+CO^* \rightarrow C+CO_2$; E_a=6eV, ΔH=5.5eV/mol and 2) $CO_2^* \rightarrow CO+1/2O_2$; E_{diss}=5.5 eV. Though the activation energies E_a of these reactions are quite high for the present non-thermal conditions (low T_{kin}), the reactions remain stimulated by the *Fe* nanoparticles, which are active graphitization catalysts, and through the vibrational excitation of the *CO* and CO_2. The latter factor is important because, from the results of [7], it can be presumed that for the plasma conditions of this present work: $T_e > 6000$ K >> $T_{gas} \approx$ 700-900 K.

Thus, the plasma chemistry considered represents competing processes for formation of iron carbides and oxides, in reactions involving *CO* and its reforming products. High rates of Fe_2O_3 deposition on the discharge tube walls mean an abundance of *Fe* oxidation products in the system. However, the formation of carbides (Fe_3C, Fe_2C, χ-Fe_5C_2 or Fe_7C_3), either directly from the gas phase or via transformation of iron particles, should remain a competing process at temperatures 700-1400 K [25]. For the range considered and up to 3000 K, the carbides' formation is endothermic, (e.g. for the Fe_3C $\Delta H^0_{solid} \approx$25 kJ/mol); while the formation of the presumed oxide species (FeO, Fe_2O_3, Fe_3O_4) is exothermic, with $\Delta H^0_{solid} \approx$-270, -820 and -1120 kJ/mol respectively [23, 26]. Hence, most of iron is bound within oxides, so forming the Fe_2O_3 wall deposit. Generally, temperature increase should decrease the carbides' fractions. Thus, the products of the reaction $3Fe + 2CO \rightarrow Fe_3C + CO_2$ are thermodynamically favored (ΔG<0) up to about T=1000K [27]; for higher T the equilibrium in the system is shifted towards free iron and its oxides. Formation of the higher carbides results, as a rule, in a greater decrease of entropy than formation of oxides, the latter process passes with lesser impact on the entropy [23, 27]. Reducing the entropy at higher T leads to greater impact on the rise of ΔG, therefore *Fe* carburization becomes less favored with rising temperature. The diffusive removal of the oxidation products, such as gaseous *FeO*, towards walls may also influence reactions chains. It is slowed by raising the pressure, thus shifting the equilibrium for oxidation reactions towards the initial species (free iron, *CO* and CO_2) [27, 28], thereby favouring the carbides formation. The estimation of mean free path χ for molecular *FeO* yields values of $\chi \approx 0.31$ and $\chi \approx 0.13$ mm for P=110 and P=250 Pa respectively. The turbulent mixing in the reactor tube (d=20 mm), can result in effective stirring. Then the mentioned change in the mean free path can drastically influence the removal of *Fe* oxides from the reaction zone, thus inhibiting further oxidation and favouring the carbide synthesis through the release of iron vapours.

We can conclude that the pressure rise changes the plasma kinetic processes in favor of volume formation of iron carbide solids. The NP properties change from the iron poor carbon clusters, with "nanocigars" (Fig.2), formed at 110 Pa pressure, to the synthesis of iron/iron carbide hexagon crystals (Fig.3) at 250 Pa. The appearance of less stable carbides instead of cementite (Fe_3C) in the ferromagnetic NP, can be favored by the carburizing environment containing up to 20 % vol of *CO*, shifting the phase balance of carbides from Fe_3C towards Fe_2C [25]. The presence of the less stable/intermediate carbides (Fe_7C_3, Fe_5C_2, Fe_2C) and the absence of cementite can also be related to the fast quenching of the plasma gas. For both kinds of NP, metal or carbide particles act as templates for the coating [25]. A possible formation mechanism for the graphitic cells of "nanocigars" is that of carbon dissolution in metal particles, followed by diffusion and precipitation of the graphitic phase on the surface. Oversaturation of the solution by carbon may also result in the formation of carbides, creating bulk particles or acting as a barrier against further penetration of carbon. The very low

saturation magnetization of "nanocigar" NP must be due to its very low *Fe* content and is probably due to the diamagnetic behaviour of the surrounding graphitic cells. A decrease in the M_S and a rise of the graphite fraction, for the temperatures over 1000°C, was observed for the CVD synthesis of nanostructures derived from $Fe(CO)_5$ [22].

5. Conclusions

A gas phase synthesis of nanosized powders, composed of iron/iron carbides embedded in carbon, was performed in RF CC plasma of $Ar/Fe(CO)_5$. Two kinds of nanopowders can be obtained: a) a high iron content NP (at over 40% mass of *Fe*), consisting of hexagonal carbide crystals (Fe_7C_3 or Fe_2C) embedded in amorphous carbon. This NP is produced under the P=250 Pa and demonstrates ferromagnetic properties; b) low iron content NP (less than 4% mass of *Fe*), formed from tiny nanorods of iron/iron carbides, surrounded by graphitic cells and integrated into the amorphous carbon matrix. This NP are produced under P ≈110 Pa and they are diamagnetic. The chemistry in the system is determined by the competing reactions of iron oxidation and carburization. Higher pressure conditions may: a) correspond to the lower gas temperatures, which favor the shift of the chemical equilibrium towards the formation of carbides; and b) slow the removal of *Fe* oxidation products to the reactor walls and thus shift the oxidation equilibrium towards non-bound iron and the formation of carbides. Adjusting the applied RF power, precursors' feed rates and the system pressure, provides control of the physical-chemical reaction kinetics and the powder product properties. The carbide particulates obtained at higher pressures are isolated and have no magnetic coupling. This NP can be applied as a precursor for the fabrication of bulk ferromagnetics with new magnetic permeability, hysteresis width or re-magnetization frequency. Using H_2 or CO admixtures in the plasma gas, and in scaling-up the processing facility, might reduce the co-fabrication of the amorphous carbon and increase the desirable NP output.

References

1. H. Fujii, K. Inata, M. Ohtaki, K. Eguchi, H. Arai. J. Mater. Science, v.36, p.527, 2001.
2. S, Tomita, M. Hikita, et al. Chem. Phys. Lett., v.316, p.361, 2000.
3. M. E. McHenry, S. A. Majetich, J. O. Artman, M. DeGraef. Phys. Rev. B 49, p. 11358, 1994.
4. D. Shi, S. X. Wang, W. J. van Ooij, Appl. Phys. Lett. 78, p. 1243, 2001.
5. A. Gedanken. Ultrasonics Sonochemistry, v. 11, n. 2, 2004, pp. 47-55.
6. D. Vollath, D. V. Szabó. Nanostructured Materials, v. 4, n. 8, pp. 927-938, 1994.
7. A. Kouprine *et al.* Plasma Chem. and Plasma Proc., v. 24, n. 2, pp. 189-215, 2004.
8. Sh. Jou, Chao Ken Hsu. Mater. Sci. and Engineering B, v. 106, n3, pp.275-281, 2004.
10. Z. Q. Li *et al.* Nanostructured Materials, v. 10, n. 2, 1998, pp. 179-184.
12. V. D. Blank *et al.*Diamond and Related Materials, v. 11, n. 3-6, 2002, pp. 931-934.
13. NRL Mater. science and technology division, 2004. http://cst-www.nrl.navy.mil/lattice/struk/Fe2C.html
14. E. Boellaard *et al.* Applied Catalysis A: General, v. 147, n. 1, 1996, pp. 229-245
15. H.J. Grabke. Mater. Corros. v. 49 , 1998, p. 303.
16. A.A. Zhukov *et al.* Acta Metallurgica, v. 21, n. 3, 1973, Pp. 195-197.
17. M. Takeguchi *et al.* Superlattices and Microstructures, Corrected Proof, available online 27.09.2004.
18. John D. Saxby *et al.* J. Phys. Chemistry. v.96, n.1, 1992, pp 17 – 18.
19. Yang-Long Hou and Song Gao. J. of Alloys and Compounds, v. 365, n. 1-2 2004, pp. 112-116,
20. Shaoyan Chu and Sara A. Majetich J. of Applied Physics, v. 93, n. 10, pp. 8146–8148, 2003.
22. Z. H. Wang *et al.* J. of Alloys and Compounds, v. 361, n. 1-2, 27 2003, pp. 289-293.
23. NIST Chemistry Web Book, 2004. http://webbook.nist.gov/chemistry
24. Raiser Y.P., Gas Discharge Physics. Berlin/New York. Springer-Verlag, 1991.
25. J. Zhang, A. Schneider and G. Inden. Corrosion Science, v. 45, n. 6, 2003, pp. 1329-1341.
26. FACTSAGE (2001), v. 5.0, CRCT, Montréal, Canada and GTT-Technologies, Aachen, Germany.
27. K. Mondal *et al.* Fuel Processing Technology, v. 86, n. 1, 2004, pp. 33-47.
28. NIST Kinetics Database, 2004. http://kinetics.nist.gov/index.php

Non-Equilibrium Model for Multi-Component Ar-H_2 Plasma under subsonic and supersonic flow conditions

Siwen Xue[1], Pierre Proulx[2], Anthony B. Murphy[3] and Maher I. Boulos[1,2]

[1] *Tekna plasma Systems Inc, Sherbrooke, Québec, Canada*
[2] *University of Sherbrooke, Department of Chemical Engineering, Québec, Canada*
[3] *CSIRO, Industrial Physics, Lindfield, NSW, Australia*

Abstract
A thermal and chemical non-equilibrium model, developed recently by the authors [1] of this paper, is applied to the modelling of multi-component supersonic induction Ar-H_2 plasma flows and to calculate the heat flux from the supersonic plasma flow to a copper substrate, which is put 45mm below the M4 supersonic nozzle exit. The model treats the subsonic discharge region above the supersonic nozzle and the supersonic region below the nozzle together. Three numerical schemes, provided by a commercial software, FLUENT, are used to the modelling of the supersonic plasma flow. It is found that FLUENT's coupled solver with second order upwind scheme, gives the best heat fluxes to the substrate, compared to the experimentally measured heat fluxes.

1. Introduction.

For the industrial and laboratory applications of induction plasma, such as, inductive plasma coatings, material processes, the formations of ultra-fine particles etc. a variety of mixtures of different gases are used as the working gas for the induction plasma torch and in some case the supersonic plasma flows, generated by the inductive plasma torch with a supersonic nozzle installed a few centimetre below the induction coil, are preferable for the applications [2]. The multi-component plasmas are normally neither in thermal equilibriums nor in chemical equilibrium, especially at low pressure. To predict the behaviours of these multi-component supersonic induction plasmas accurately a thermal and chemical non-equilibrium model is necessary.

In last a few decades, many publications [3-9] in the literature deals with the thermal no-equilibrium of the inductive plasma with pure argon as the working gas and some of the published papers in literature devoted to the modelling of supersonic plasma flow of pure argon under the thermal non-equilibrium without the treatment in the discharge region. A few publications reported the treatment of the multi-component Air[10-11]] and Ar-N_2[12] plasma under the thermal and chemical non-equilibrium state. In this paper, a thermal and chemical non-equilibrium model for multi-component argon-hydrogen[1] (Ar-H_2) plasma, developed recently, is applied to the modelling of argon-hydrogen supersonic plasma flow and to calculate the heat flux from the supersonic plasma flow to a copper substrate which is placed 45mm below the exit of M4 supersonic nozzle. The model for the inductive supersonic plasma flow modeling has been improved from the separate treatment[32] of discharge region and supersonic flow region to a united model, which treats the subsonic discharge region and the supersonic region below the nozzle together. The comparisons between the calculated heat fluxes from the model and the experimentally measured ones are made. Different numerical schemes are used to simulate the same supersonic flow and calculate the heat fluxes to the substrate it is found that FLUENT's coupled solver with second order upwind scheme, gives the best heat fluxes to the substrate, compared to the experimentally measured heat fluxes.

The thermal non-equilibrium model in the last half centuries remains almost the same, except for some improvements in transport properties used for non-LTE modelling. All the thermal non-equilibrium (two-temperature) models for pure argon plasma are similar to the first non-LTE model, proposed by M. Hoffert[13]. The only chemical reactions includes in the model for the pure argon plasma flow are the ionization of argon and the corresponding recombination. The rate coefficient of ionization is derived under the assumption that all bound electrons in the atom are thought to be ionized provided that they can reach the first excitation state and the recombination coefficient is derived through the condition that at Saha equilibrium electron density the net production rate of electrons equals to zero. The recombination coefficient thus derived become too big at low

temperature region near the quartz wall. At low temperature, Hoffert's recombination coefficients do not agree well with the experimental measurement[5]. For our present modelling, at high electron temperature region Hoffert's recombination coefficients are still used but in low temperature region the recombination coefficients from Biberman[14] for argon and from van de Sanden[15] for hydrogen, both are deduced from the experimental measurements and valid at low temperature, are used. In the modelling the smaller of the two recombination rate coefficients are used.

The accuracy of the model prediction depends on the accuracy of the transport properties. For thermal and chemical non-equilibrium multi-component plasma the transport properties are not only the function of electron and heavy species temperature but also the function of plasma compositions, electron density and pressure. Although the transport properties for many monatomic and diatomic gas plasmas, or their mixture, are available in the literature most of these data are obtained under that assumption of the plasmas being in LTE. Some authors calculated the transport properties by assuming two-temperature plasmas (non-LTE) but the Saha equilibrium electron density, calculated using the electron temperature, was still used. For induction plasma the electron density in discharge region is always different from the Saha equilibrium electron density at whatever pressure, otherwise there will be no electrons produced in the discharge region. And for supersonic plasma flow, the pressure change dramatically. Therefore, the available published transport properties data are not appropriate for non-equilibrium supersonic plasma modelling. That's a drawback in many of the published thermal non-equilibrium supersonic models. A proper way to get the transport properties for the supersonic plasma modelling is to calculate them directly from the collision cross-sections or the collision integrals between species in the mixture using the formulas, derived by Hirschfelder, Curtiss and Bird[16]. The transport properties thus obtained are used for our present thermal and chemical non-equilibrium model. The collision integral data are taken from publications[17-19] of Murphy, Devoto and Mason. The temperature in the data of collision integrals between two species is considered to be that of heavy species if no species in the two is electron, otherwise, the temperature is assumed to be the electron temperature because the collision integrals depends on the relative velocity between the two species. The binary mass diffusion coefficients between the species in the mixture are also calculated from these collision integral data. The effective mass diffusion coefficient of a species in the mixture is calculated using Stefan-Maxwell relations from the binary mass different coefficient and the Ambipolar electrical field is not included in the Stefan-Maxwell relations because it is difficult to get the effective mass diffusion coefficient from the full multi-component diffusion formulations[20] with the Ambipolar electrical field being included. Then the ambipolar effects of charged species are approximately taken into account by adding a factor of $(1+T_e/T_h)$ to their effective mass diffusion coefficient. Mass conservation equations are solved to obtain the mass fractions or mole fractions or the number densities of all the species except for electrons. The electron number density is determined by the condition of electrical neutrality, $N_e=N_{H+}+N_{Ar+}$. The electron electrical conductivity and thermal conductivity are calculated using Devoto's second order formulas [21]. The modelling of turbulence effect on the plasma flow is based on the Reynolds stress turbulence model[22-23] using standard wall function[24].

2. Description of the model

The multi-component plasmas includes six species: e, H, H+ H_2, Ar+ and Ar. It is assumed that all the species except for electron have the same temperature and all the species have the same convective velocity. The electron temperature is allowed to deviate from that of the heavy species. The plasma flow is assumed to be steady, axisymmetric and turbulent.

a. Model equations

Since the chemical reaction energies are treated as the source term, the energy conservation equations for electrons and heavy species take the following forms:

$$\nabla\cdot(\frac{5}{2}kn_e\vec{u}T_e)=\nabla\cdot((\lambda_e+\mu_t C_{pe}/\mathrm{Pr}_t)\nabla T_e)+P_{Ohmic}-P_{ir}-P_{eh}-P_{rad}+\vec{u}\cdot\nabla p_e \quad (1)$$

$$\nabla\cdot(\vec{u}\sum_j C_{pj}Y_jT_h)=\nabla\cdot\left\{(\lambda_h+\mu_t C_{ph}/\mathrm{Pr}_t)\nabla T_h-\sum_j C_{pj}Y_jT_h\vec{J}_j\right\}-P_{dr}+P_{eh}+\Phi_\mu+\vec{u}\cdot\nabla p_h \quad (2)$$

where the summation is over all the heavy species and n_e, T_h, p and λ are electron number density, heavy species temperatures, static pressure, and thermal conductivities, respectively. C_{pj} ,Y_j, J_j, μ_t and Pr_t are the specific heat, mass fraction and mass flux of species j, turbulent viscosity and Prandtl number, respectively. P_{eh} represents the energy exchange rate through elastic collision between electron and the heavy species, P_{ir}, the net ionization or three-body recombination energy exchange rate, P_{dr}, the energy exchange rate due to H_2 dissociation and the corresponding recombination, Φ_μ , the viscous dissipation, P_{rad}, the volumetric radiation losses and the last term in Eq.(1) and Eq.(2), the pressure work. The electron pressure work may be neglected because $\vec{u} \cdot \nabla p_e$ is related mainly to the energy transfer between the thermal energy and the mechanical energy of electrons. Even for supersonic flow, the mechanical energy of electrons is negligible due to their small mass.

The mass fraction Y_j of a species in the mixture are determined from the conservation equations of the species:

$$\nabla \cdot (\rho \vec{u} Y_j) = \nabla \cdot ((\rho D_{j,m} + \mu_t / Sc_t) \nabla Y_j) + R_j . \quad (3)$$

where $\rho = \sum_j \rho_j$ is the total mass density and $D_{j,m}$ is the effective mass diffusion coefficient of a species in the mixture. R_j is the net mass production rate of species j. Among the 6 species, only 4 mass fraction equations are solved. The principal species, argon, is determined by the condition that summation of mass fractions of all the species is unity and the electron number density is obtained by the condition of electrical neutrality. The mole fraction X_j of a species can be computed for the mass fractions:

$$X_j = (Y_j / M_j) \sum_j (Y_j / M_j)$$

And then the number density N_j of a species can be calculated by the following:

$$N_j = p \cdot X_j / (kT_h (1 - X_e) + kT_e X_e)$$

where $p=p_e + p_h$ is the total pressure and k is the Boltzmann constant.

$$p = kT_h \sum_{j \neq e} (N_j) + kN_e T_e$$

According to condition of electrical neutrality of charge:

$$N_e = N_{H+} + N_{Ar+}$$

The electromagnetic fields are obtained from solving the vector potential equation using the extended field model[25]. Momentum equations are same as these for pure argon plasma [26]. The Reynoids stress model equations used in the present modelling are described in Ref.[26].

b. Chemical reaction

Four chemical reactions are included in the modelling:

(1). The H_2 dissociation and the corresponding recombination induced by Ar:

$Ar+H_2 \leftrightarrow Ar+2H$

(2). The H_2 dissociation and the corresponding recombination induced by the H_2:

$H_2+H_2 \leftrightarrow H_2+2H$.

The forward and backward chemical reaction coefficients k_f and k_b for (1) and (2) can be found in Ref.[27].

(3) The argon ionization and the corresponding recombination

$Ar + e \leftrightarrow Ar^+ + 2e$

The forward reaction rate was given by Hoffert[13]. The backward reaction, the three-body recombination rate k_b coefficient is calculated based on the condition that at Saha equilibrium electron density, the net electron production rate is zero. In low temperature region, the backward coefficient thus obtained is too high and an experimentally deduced recombination coefficient[15], which is valid at T<5000K, is used

$k_b = 7*10^{-22} T^{-4.6}$ ($m^6 s^{-1}$)

In the modelling, the smaller of the two backward coefficients is used. The net electron production rate is:

(4) The hydrogen atom ionization and the corresponding recombination

$$H + e \leftrightarrow H^+ + 2e$$

For the ionization of hydrogen atom, the rate coefficient is calculated from the experimentally determined excitation cross-section of hydrogen atom[25]. It is assumed that the excitation rate coefficient from 1S to 2S and 2P equals to that of ionization. The way to calculate the backward coefficient is same as that to calculate backward coefficient of reaction (3). In the low temperature region [14]

$$k_b = 7*10^{-20}T^{-4.5}\ (m^6s^{-1})$$

In the same way, the smaller of the two backward coefficients is used in the modelling.

c. Transport properties

Since the published transport property data are obtained using either the condition of LTE or Saha equilibrium electron density or the both, the transport properties for our present modelling are computed directly from the collision integrals or the collision cross-section. The expressions, derived by Hirschfelder, Curtiss and Bird[16] and based on the first Chapman-Enskog approximation, are used to calculate the viscosity and translational thermal conductivity. The contributions of rotational and vibrational energies of hydrogen molecules to the thermal conductivity is calculated using Yos's mixing law[11,29]. The collision integral data are taken from publications[17-19] of Murphy, Devoto and Mason. The second approximation formulas [10, 21], given by Devoto in 1967 are used to calculate the electron thermal conductivities and electrical conductivity. The binary and effective mass diffusion coefficients (D_{ij} and D_j) are given by[20,30]

$$D_{ij} = \frac{3}{8}\left[\frac{(m_i + m_j)kT}{2\pi m_i m_j}\right]^{1/2} \frac{kT}{P\Omega_{ij}^{(1,1)}(T)} \qquad D_j = \frac{1 - X_j}{\sum_{i \neq j} X_i / D_{ij}})$$

If no species is electron, T is the heavy species temperature, otherwise T is the electron temperature. The effective mass diffusion coefficients D_j of a species in the mixture are computed from the binary mass diffusion coefficients using Stefan-Maxwell relation.

The ambipolar diffusion coefficient $\overline{D}_j$ of the charged heavy species may be written approximately as:

$$\overline{D}_j = D_j(1 + \frac{T_e}{T_h})$$

The boundary conditions are described on detail in Ref.[1, 22].

3. Computational results

The RF plasma torch, as used in this study, is the Tekna PL-35 with a M4 supersonic nozzle installed 25mm below the induction coil. The torch dimensions can be found in Ref.[31]. The working frequency of the power supply is 5.5MH_z. The gas flow rates used for the M4 supersonic plasma flow experiments (25.2kW plate power) are: the sheath gas flow rate, 50slpm Ar + 1slpm H_2. The swirling (75^0 relative to axis) central gas flow rate is 2.5slpm. The measured pressure from the working chamber is 13.5 torr (around 1800pascal).

The modelling results below are obtained from the FLUENT's coupled solver with second order upwind scheme. Under previously mentioned operation conditions the contours of stream function, pressure are shown in Fig.1. As can be seen from this figure, the pressure in the discharge region reaches 4.3 atmospheric pressures, while the minimum pressure (around 18mm above the substrate) in the working chamber is only 73 pascal. The pressure ratio reaches 5912. At such high pressure in discharge region, the electron and heavy species temperatures, shown in Fig.2 are almost the same. Fig.3 indicates the magnitude of velocity and Mach number. The maximum Mach number reaches 6.9. The mole fractions of H_2, H, H^+ and Ar^+ are shown in Fig.4 and Fig.5. As can be seen from Fig.4, almost all H_2 molecules are dissociated in discharged region. This is different from the case of low pressure[1], where only part of the H_2 molecules is dissociated even in high temperature region(T>6000K). The reason is simple, that is, at high pressure the H_2 molecules have enough time to dissociate before they are carried away to the downstream. Also in the case of high pressure (Fig.5), 28% charged particles are hydrogen ions. Fig. 6 shows the heat flux to the substrate from the supersonic plasma flow to the copper substrate. The heat fluxes

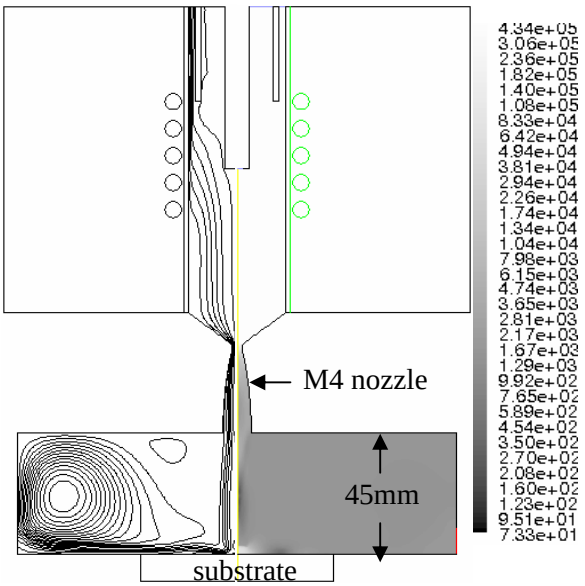

Fig.1 Left: stream function, Right: presure (pascal)

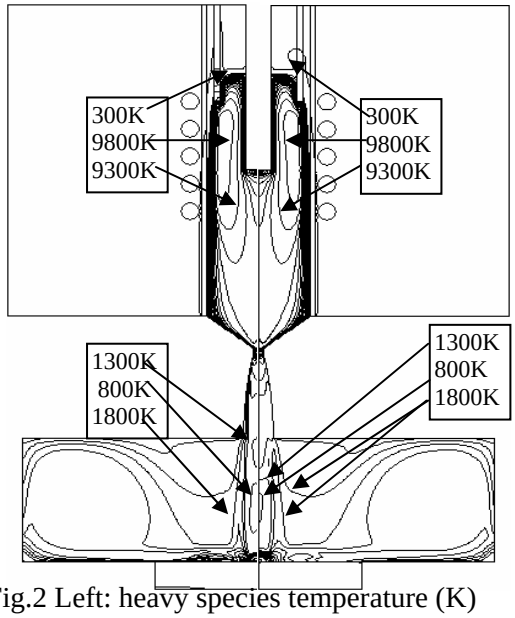

Fig.2 Left: heavy species temperature (K)
Right: Electron temperature (K)

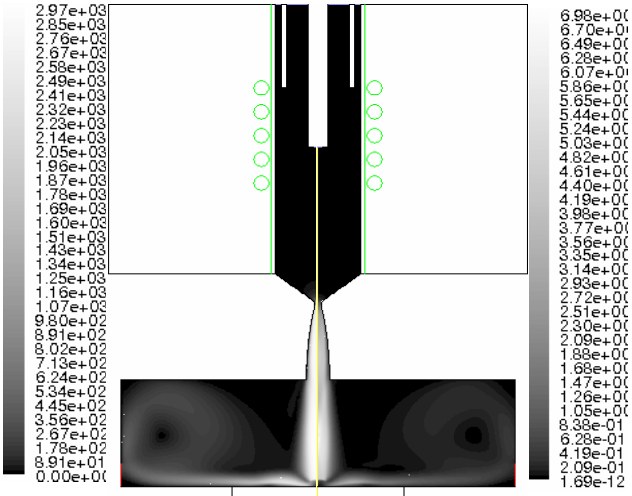

Fig.3 Left: Magnitude of velocity (m/s)
Right: Mach number

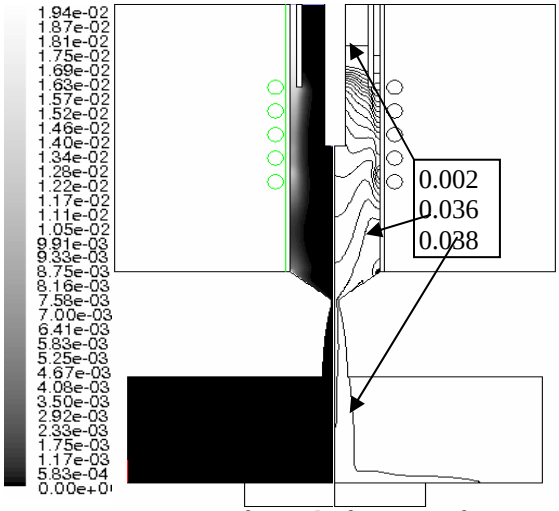

Fig.4 Left: Mole fraction of H_2
Right: Mole fraction of H

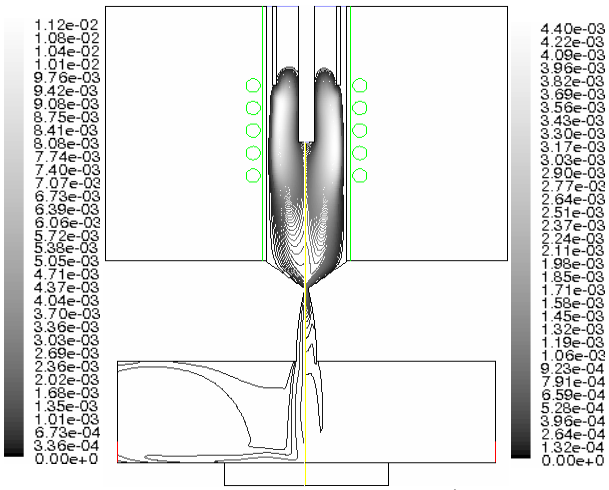

Fig.5 Left: Mole fraction of Ar^+
Right: Mole fraction of H^+

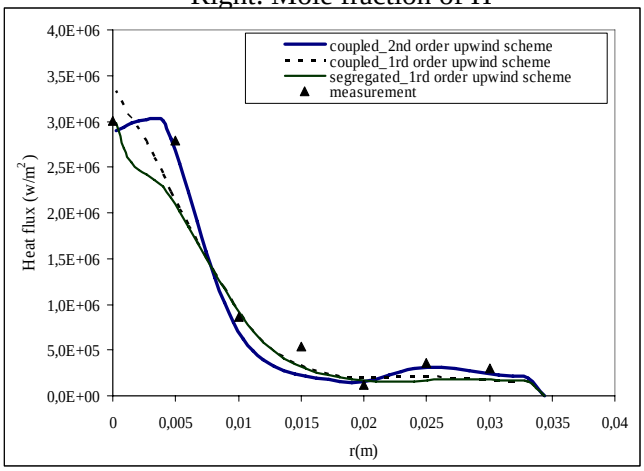

Fig.6 Radial profile of heat fluxes on the substrate

are obtained by using three different numerical schemes, the FLUENT's coupled solver with second order upwind scheme, the coupled solver with first order upwind scheme and the segregate solver with first order upwind scheme, for the modelling of the supersonic plasma flow. The measured heat fluxes are also shown in Fig.6. By the comparison with the measurement, FLUENT's coupled solver with second order upwind stream scheme gives the best heat fluxes.

References

[1] S. Xue, P. Proulx, A. B. Murphy and M. Boulos, International Thermal Spray Conference & Exposition, Basal, Switzerland, May 2, 2005.
[2]. M. I. Boulos, P. Fauchais and E. Pfender, Thermal plasmas, Fundamentals and Applications, Vol.1, (1994)
[3]. P. Hang and X. Chen,. Plasma Chem. and Plasma Processing, 21, 249(2001).
[4]. S.E. Selezneva et al. J. Phys D: Appl. Phys. 34, 2862(2001).
[5]. S.E. Selezneva et al. Plasma Source Sci. Technol. 12, 107(2003)
[6]. Y. Bartosiewicz, P. Proulx and Y. Mercadier, J. Phys D: Appl. Phys. 35, 2193(2002).
[7]. C. H. Chang and E Pfender, Plasma Chem. Plasma Processing. 10, 473(1990).
[8]. J. Mostaghimi and M. Boulos, J. Appl Phys, 68(6), 2643(1990).
[9]. J. Mostaghimi, et al., Appl Phys, 61(5), 1752(1987).
[10]. D. Vanden Abeele. Ph.D. thesis, University of Technology, Eindhoven, The Netherlands, 2000.
[11]. R. N. Gupta, J.M. Yos et al., Reference Publication 1232, NASA (Langley), Virginia, August 1990.
[12]. Y. Tanaka, J. Phys. D; appl. Phys. 37, 1190(2004).
[13]. M.I. Hoffert and M. Lien, Phys. Fluids. 10, 1769(1967).
[14]. L. M. Biberman, V. S. Vorob'evand I. T. Yakubov, 1987, Kinetic of non-equilibrium Plasmas (New York Plenum).
[15]. M. C. M. Van de Sanden, Ph.D. thesis, University of Technology, Eindhoven, The Netherlands, 1991
[16]. J. O. Hirschfelder, C. F. Curtiss and R. B. Bird, Molecular theory of gases and liquids, John Wiley, and Sons, New York, 1967
[17]. A. B. Murphy. Plasma Chemistry and Plasma Processing. 20, 279(2000)
[18]. R. S. Devoto, Physics of Fluids, 16(5), 616(1973).
[19]. E. A. Mason et al., Physics of Fluids, 10(8), 1827(1967).
[20]. J. D. Ramshaw and C. H. Chang, Plasma Chemistry and Plasma Processing. 13(3), 489(1993)
[21]. R. S. Devoto, Physics of Fluids, 10(10), 2105(1967).
[22]. M. M. Gibson and B. E. Launder, Ground effect on pressure fluctuation in the atmospheric boundary layer. J. Fluid Mech., 86, 491(1978).
[23]. B. E. Launder, Second-moment closure: Present and future? Inter. J. Heat Fluid Flow, 10, 282(1989).
[24]. B. E. Launder and D. B. Spalding. Lectures in Mathematical models of turbulence, Academic Press. London, England, (1972).
[25] Xue Siwen, Pierre Proulx and Maher I. Boulos,J. Phys. D: Applied Physics, **34**,1897 (2001).
[26] J. Mostaghimi and M. I. Boulos, Plasma Chemistry and Plasma Processing, **9**, 25(1989)
[27]. D. L. Baulch et al., J. Phys Chem. Ref. Data, Vol. 23, No. 6, 868(1994).
[28]. L. Vriens and A. H. M.Smeets, Phys. Rev. A, 22, 940(1980).
[29]. J.M. Yos, Contract Report AVSSD-0112-67-RM, Avoco Missiles, Space and electronics Corp. Wilmington, Massachusetts, April 1967.
[30]. J. Bzowski, et al., J. Phys. Chem. Ref. Data, 19(5), 179(1990)
[31]. R. Ye, Ph.D thesis, University of Sherbrooke, (2002).
[32] S. Xue, S. Mihm and M. Boulos, International Thermal Spray Conference & Exposition, May 10-12, 2004, Osaka, Japan

n-hexane soot oxidation reactivity in N_2/O_2 and $N_2/O_2/NO_2$ atmospheric pressure pulsed corona discharges

N. Aggadi, X. Duten, Ph. Marteau, M. Rédolfi, K. Hassouni
LIMHP, Université Paris Nord – CNRS UPR 1311 – 99 Avenue J.B. Clément – 93430 Villetaneuse (France)
E-mail:hassouni@limhp.univ-paris13.fr

Abstract
This paper discusses some aspects of n-hexane soot reactivity in a multi-pin to plate pulsed corona discharge working in the nanosecond regime. The soot-discharge interaction was quantified by measuring the densities of the resulting CO and CO_2. Results showed an enhancement of soot oxidation for $\%O_2$ greater than 10 and cathode temperatures above 150°C. A saturation effect in the treatment efficiency is observed at high power and $\%O_2$, which would indicate that the reactivity is kinetically limited by the de-sorption of CO and CO_2.

1. Introduction

The incomplete combustion of hydrocarbon fuels is known to produce carcinogenic compounds such as polycyclic aromatic hydrocarbons (PAH) and soot particles [1]. The emission regulation for these compounds are becoming more and more stringent, and new technological approaches for the removal of these pollutants from flue gas are needed to fulfil the emission limits expected in the near future.
Among these new technologies non-thermal plasmas techniques are certainly one of the most promising. Pulsed corona and dielectric barrier discharges have been indeed already used, sometimes as a part of a more complex process, to remove SO_x, NO_x and VOC compounds from flue gas [2-4]. Their use lies on their ability to produce a very active medium that contains highly reactive species, like O-atom and OH-radical, through electron-impact dissociation.
This work, is related to the investigation of n-hexane soot reactivity under atmospheric pressure pulsed corona discharges (APPCD). Its purpose is to assess the potentiality of APPCD process as a mean to remove soot particles from flue-gas.
The soot reactivity was investigated in term of the concentrations of CO and CO_2 that result from the interaction between the discharge streamers and the soot particles. The discharge parameters investigated was the oxygen percentages in the feed gas, the cathode plane temperature and the discharge frequency.
The paper is organized in 4 sections. In the next one the nanosecond pulsed corona discharge cell is described and its electrical characteristics are discussed. section 3 describes how n-hexane soot is synthesised and gives the main features of soot particles as derived from gas phase chromatography. section 4 reports a parametric study of soot gasification where the effect of oxygen in the feed gas, temperature and discharge frequency are investigated.
Results showed very weak soot reactivity for oxygen percentage below 10% in the feed gas. This reactivity becomes much more significant at higher O_2 percentage. Similarly, the soot reactivity strongly increases above 150 °C . The amount of CO_2 and CO produced from the interaction between the soot and the discharge increases linearly with the discharge frequency.

2. Main characteristics of the nanosecond pulsed corona discharge

The discharge investigated in this work is schematised in figure 1. It consists of a multi-pin anode, with up to 300 pins, and a plane electrode. The typical gap distance is around 0.7 cm and the plane-cathode on which soot particles are deposited may be heated up to 200 °C with the help of small cylindrical heating rod. The electrode system is placed in a 56 mm diameter cylindrical Pyrex cell. The feed gas enters the discharge cell from the bottom plane electrode and the flue gas resulting from the interaction between the discharge streamers and the soot exits from a second exit hole drilled in the cathode.
The pins are connected to a high voltage supply that may deliver up to 40 kV voltage steep front with a rise time of around 10 ns. To prevent transition to the arc regime a resistor is placed in parallel to the high voltage electrode, which enables to keep the discharge duration below 200 nsec. Figure 2 shows a typical voltage pulse used to produce the investigated discharge. The current corresponding to the voltage signal of figure 2 is shown in figure 3. The current pulse shows several oscillations with

maxima that reach 100 A. This value corresponds to an average current of 330 mA for each pin. The discharge current cancels after 200 ns duration. The energy absorbed by the discharge during a single pulse was evaluated by integrating the voltage-current product over the discharge duration. The values for the energy deposited in the discharge obtained for several oxygen percentages in the feed gas are shown in figure 4. They ranges between 45 and 60 mJ per pulse. For constant input voltage and electrode gap this energy decreases when increasing the oxygen percentage in the feed gas.

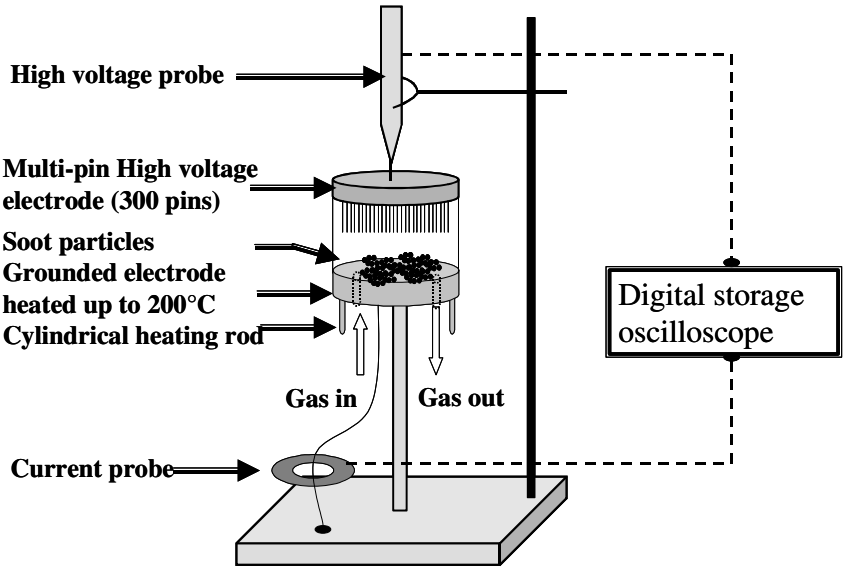

Figure 1. Schematic diagram of the experimental apparatus for the treatment of soot with a corona dicharge

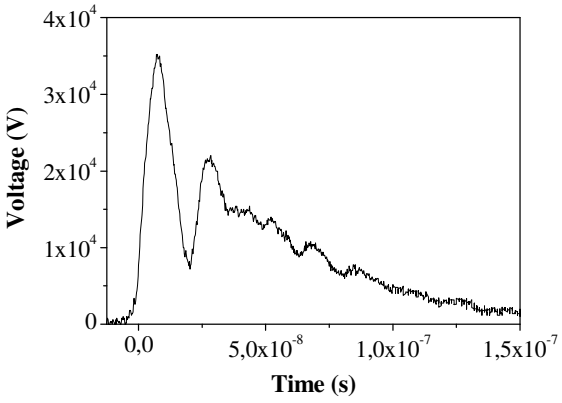

Figure 2. Voltage pulse as a function of time.

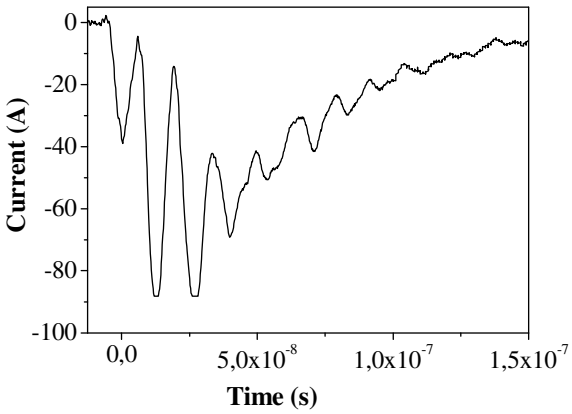

Figure 3. Current pulse as a function of time

3. n-hexane soot synthesis and characterization

Soot particles were synthesised from the combustion of liquid n-hexane. Figure 5 shows the FTIR spectrum of freshly produced soot. This spectrum exhibits several absorption bands associated to the aromatic C=C bonds (at 755 cm^{-1}, 840cm^{-1} et 880 cm^{-1}), the 1590 cm^{-1} which corresponds and the 3040 cm^{-1} and 1440 cm^{-1}bands that correspond to C-H bonds of aromatic compounds.

This first FTIR characterization would show that the soot is mainly composed of aromatic rings that may be substituted by radical groups and linked with anhydride bridges. This result is in quite good agreement with that of reference [4].

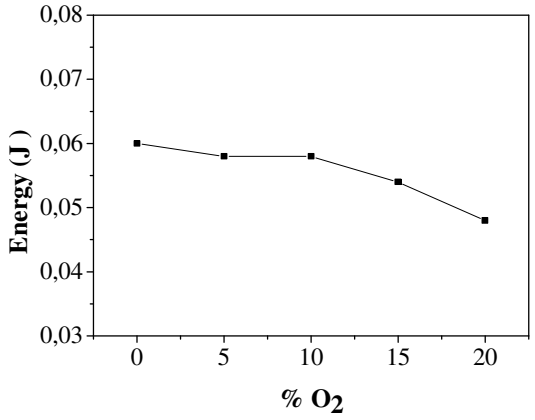

Figure 4: Energy deposited in the discharge as function of oxygen percentage

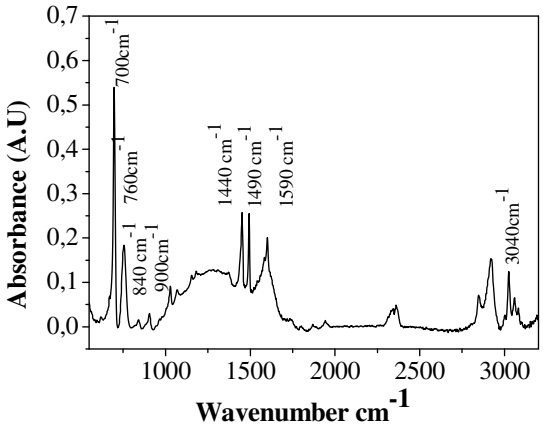

Figure 5 : FTIR spectrum of freshly produced n-hexane soot

4. A parametric study of soot particle reactivity in the pulsed corona discharge.

To investigate the reactivity of soot particles in the presence of the atmospheric pulsed corona, 40 mg of particles was introduced in the discharge vessel and placed on the cathode plane. They were subsequently treated by the discharge streamers produced in a N_2/O_2 mixture during several minutes. The total flow rate in the discharge vessel was set to 100 sccm and the cathode temperature was set at a constant value that was changed between 25°C and 200°C.

The soot reactivity was investigated in term of CO and CO_2 concentration in the flow exiting the discharge vessel. CO_2 concentration was measured by integrated infrared absorption spectroscopy while CO concentration was measured by a commercial electrochemical cell.

4. 1. Effect of oxygen amount in the feed gas

The variation of CO_2 concentration in the discharge cell outflow as a function of oxygen content in the feed gas for a plane cathode temperature of 200 °C and pulse frequency of 6 Hz is shown in figure 6. CO_2 concentration in the discharge cell outflow for pure N_2 discharge is around 30 ppm. This shows that there exists a small amount of CO_2 that desorbs from soot particles under interaction with streamer discharges. The increase of $\%O_2$ from 0 to 10 % leads to the increase of CO_2 concentration from 30 to 200 ppm. Further increase of $\%O_2$ between 10 and 20% leads to more than twofold variations of CO_2 concentration in the outflow.

The variation of CO concentration, x_{CO}, in in the discharge cell outflow is shown in figure 7. x_{CO} increases from 30 ppm to 140 ppm when $\%O_2$ varies between 0 and 20%. The soot oxidation leads therefore to much less CO than CO_2. It is also noteworthy to mention that the CO variation trends are somewhat different from CO_2 variation one. The variation of X_{CO} is indeed much smaller at high $\%O_2$, while CO_2 shows opposite behavior. This result could be expected since at high O_2 percentage the oxidation of soot is likely to result in a preferential formation of CO_2, which would consequently lead to the observed limited increase of CO concentration at high $O_2\%$.

4. 2. Effect of the discharge frequency

The discharge frequency ν_D was varied between 5 and 50 Hz. Figure 8 shows the variation of X_{CO} and X_{CO2} as function of ν_D at a cathode temperature of 140° C and 20% O_2 in the feed gas. Both CO and CO_2 concentrations increase quasi-linearly when ν_D is varied from 5 to 15 Hz and remain almost constant above this frequency. The maximum CO_2 and CO concentration achieved at this temperature of 140 °C are 250 and 400 ppm. This saturation effect would indicate that, for high oxygen content in the feed gas, the limiting step in the soot oxidation kinetics in pulsed corona discharge is not the production of oxidizing species which tends to keep increasing with power input in the discharge. This limitation may be well understood in the light of the surface chemistry model of reference [5]

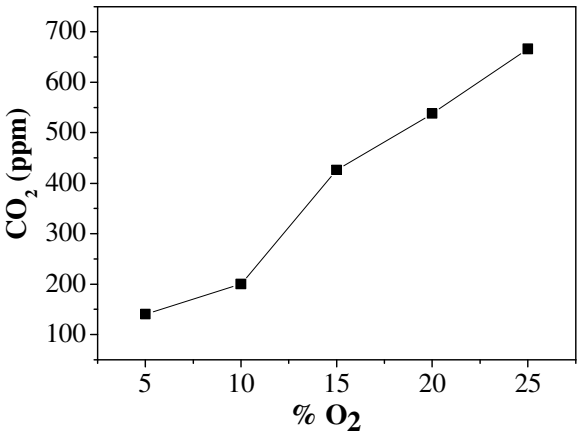

Figure 6: CO concentration in the discharge cell outflow as a function of oxygen at a cathode temperature of 200° C

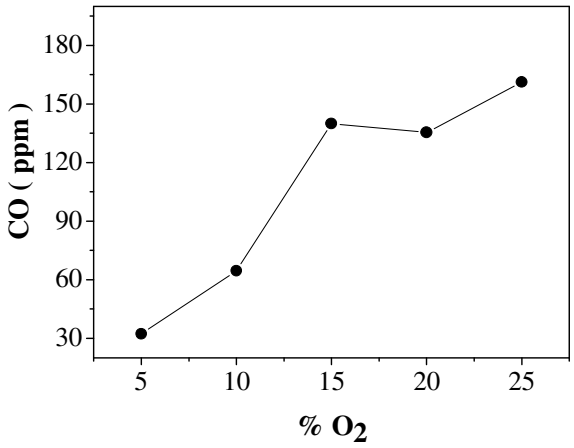

Figure 7: CO_2 concentration in the discharge cell outflow as a function of oxygen at a cathode temperature of 200° C

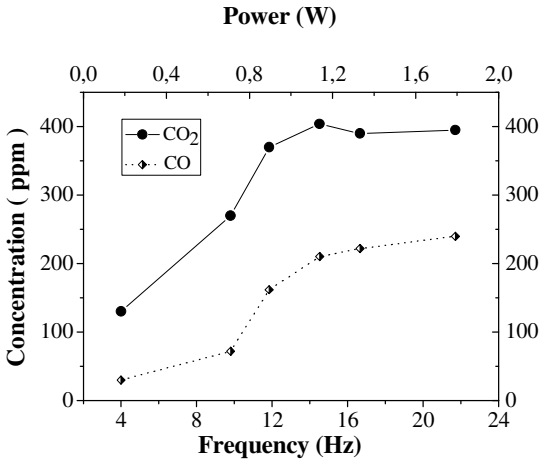

Figure 8: variation of X_{CO} and X_{CO2} as function of ν_D at a cathode temperature of 140°C and 20% O_2

5. Conclusion

The present study showed that soot particles may be oxidized at fairly low temperature by a pulsed corona discharge working in a nanosecond regime. The pulsed corona discharge used are characterized by a discharge pulse duration of 200 ns, a discharge frequency ranging between 4 and 60 Hz and a discharge current that may reach 100 A. The average current per streamer is around 300 mA. FTIR characterization showed that the n-hexane soot investigated in this wok was mainly composed of aromatic rings linked by anhydride functional groups. Results showed that the oxidation of soot mainly lead to the formation of CO_2. The amount of CO is also significant even though it remains below the obtained CO_2 concentration for all the investigated discharge conditions. This result is quite surprising since a preferential CO production was expected at low oxygen concentration in the feed gas. The increase of O_2 in the feed gas leads to a quasi-linear increase of CO and CO_2 in the flow exiting the discharge cell at low discharge frequency, i. e. average input energy. A saturation effect in the increase of CO and CO_2 is however observed in the high energy/high oxygen concentration regime. This would indicate that the soot oxidation kinetics is governed (or limited) by the de-sorption of the oxidation product and not by the production active species in the discharge. This means that further improvement of soot oxidation under discharge conditions would require to enhance the de-sorption kinetics. This may be obtained by increasing the temperature. This solution would however cancel the main benefit that motivates the use of APCCD : the low temperature discharge conditions.

Further effort is therefore needed to find the discharge conditions that would favour both the production of active species and the de-sorption of the products of the oxidation reactions at the soot surface.

Reference

[1] J. P. A. Neeft, M. Makke, J. A. Moulijn, 'Diesel particulate emission control', Fuel Processing Technology, **47**, 1 (1996).

[2] E. A. Filimonova, RH Amirov, HT Kim et IH Park, 'Comparative modeling of NO_x and SO_x removal from pollutant gases using pulsed corona and silent discharges', J. Phys. D: Appl. Phys. **33**, 1716 (2000).

[3]T. Hammer, *' Non-thermal plasma application to the abatement of noxious emissions in automotive exhaust gases", Plasma Sources Science and Technology,* **11**(3A): A196 (2002).

[4] M. G. Sobacchi, ,-A. V. Saveliev, A. A. Fridman, A. F. Gutsol, L. A. Kennedy, '*Experimental assessment of pulsed corona discharge for treatment of VOC emissions*', Plasma-Chemistry-and-Plasma-Processing. **23**(2), 347 (2003).

[5] D. M. Smith and A. R. Chughtai, 'The surface structure and reactivity of black carbon', Colloids and Surfaces A: Physicochemical and Engineering aspects, **105**, 47 (1995).

[6] R. Dorai, K. Hassouni, M. J; Kushner, 'Interaction between soot particulate and NO_x during dielectric barrier discharge processing of simulated diesel exhaust' J. Appl. Phys. **88**(10), 6060-6071 (2000).

New powder port holder geometry to avoid lump formation in APS.

I. Choquet[1], S. Björklund[1], J. Johansson[2], J. Wigren[2]

[1]*Department of Technology, Trollhättan/Uddevalla University, Trollhättan, Sweden*

[2]*Volvo Aerospace Corporation, Trollhättan, Sweden*

Abstract

A new geometry of the powder port ring holder used in atmospheric plasma spraying has recently been designed to avoid lump formation, and successfully tested for a set of process parameters associated with Ni-5Al powder used in production to form bond coat [1]. But with ZrO_2 powder used to made top coat, improvements were not enough satisfactory. Here, we investigate numerically the cause of the remaining defects, and further improve the ring geometry to prevent lump from forming in any part of the coating.

Keywords

1. Introduction

During atmospheric plasma spraying (APS), powder is injected into a plasma jet, melted and deposited onto a substrate. Under standard operation conditions, a back-stream of powder may return to the spray gun, leading to clogging of the nozzle wall. Under certain operation conditions a dramatic increase of clogging frequency can be observed [2]. Typically, this occurs when the carrier gas flow rate is increased above some limit to built-up coatings with enhanced tensile bond strength. When clogging occurs during operation (see figure 1a), the powder clogged on the nozzle or on the end piece of the spray gun aggregates in larger droplets, which are liquid due to the high wall temperature. The droplets are pulled by gravity, get loose and are ejected into the plasma jet. They cause disturbances in the spraying process, resulting in blisters and lumps being generated in the coating (see figure 1b). As these coating defaults are unacceptable, the damaged work-piece must be stripped and re-coated.

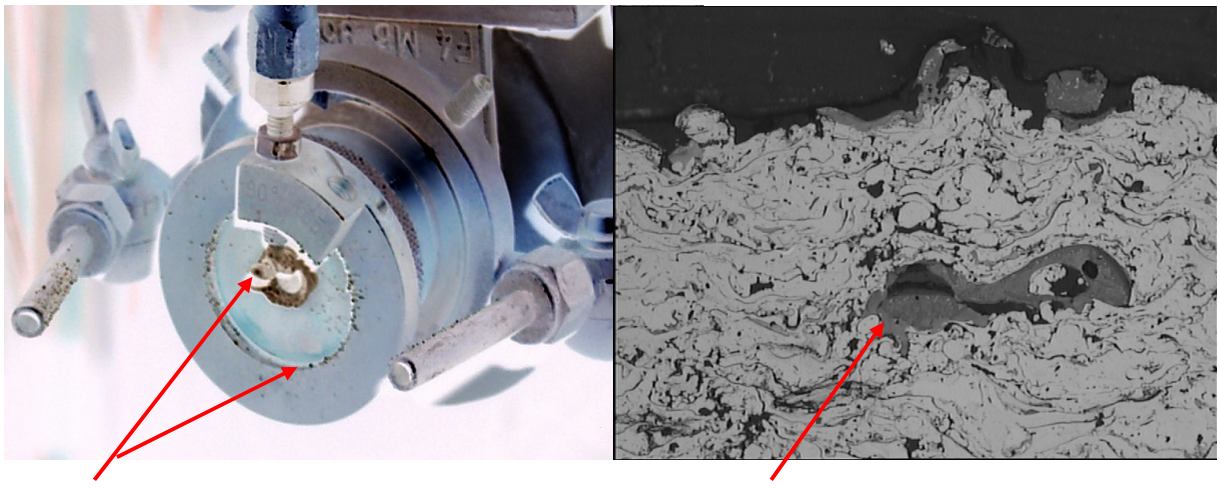

Fig. 1: a) Nozzle wall of a spray gun with traces of clogging that can be observed after operation. **b)** Optical microphotographs; 768x576 µm. Microstructure for a ZrO_2 top coat sprayed with 32 slpm of argon through the powder port ring holder.

A previous study was focused on the understanding of the cause of lump formation, and the development of a solution for avoiding it [1]. The coating baseline used in this investigation was a standard Ni-5Al one used in Volvo Aero production, operating with an F4 atmospheric plasma spray gun manufactured by Sulzer Metco Ag (Wholen Switzerland). This spray gun is equipped with a Sulzer Metco annular holder ring with

one or two threads for assembly of up to two powder injectors, figure 2a. The ring is fixed at the nozzle exit; the powder is thus injected downstream the nozzle.

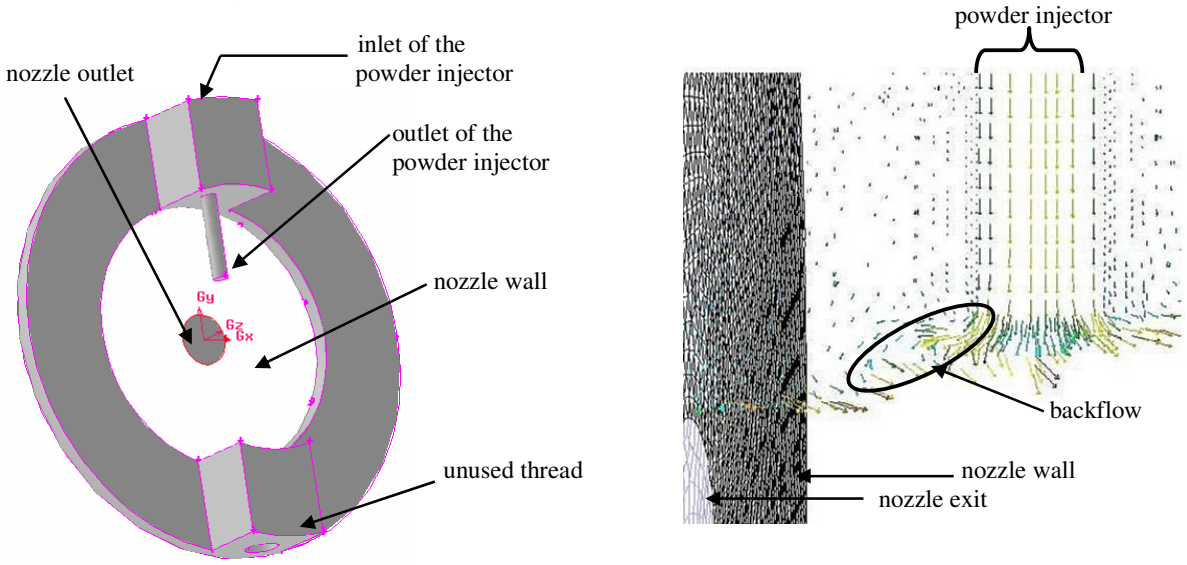

Fig. 2: **a)** CAD representation of a ring with two powder port holders, only one powder port injector, **b)** velocity vectors (calculated numerically with Fluent 6.1) showing the carrier gas backflow at the powder pipe outlet (the plasma flow is not plotted here).

Numerical simulations showed that beyond some critical value of the carrier gas rate, the carrier gas starts expanding towards the nozzle as it exits the injector, figure 2b, and entrains some powder particles. The solution proposed in [1] to prevent this backflow of powder from clogging the nozzle wall consisted in applying a screen between the nozzle wall and the powder pipe injector. The intention was to divert from their path the small fraction of powder flowing backwards, while keeping the coating quality. For this purpose, a new geometry of the powder port ring holder has been designed. It allows the injection of a gas through the ring to form a protective layer in the vicinity of the nozzle wall. When properly formed, this gas layer prevents the powder back-stream from reaching the nozzle wall and thus from initiating lump formation.

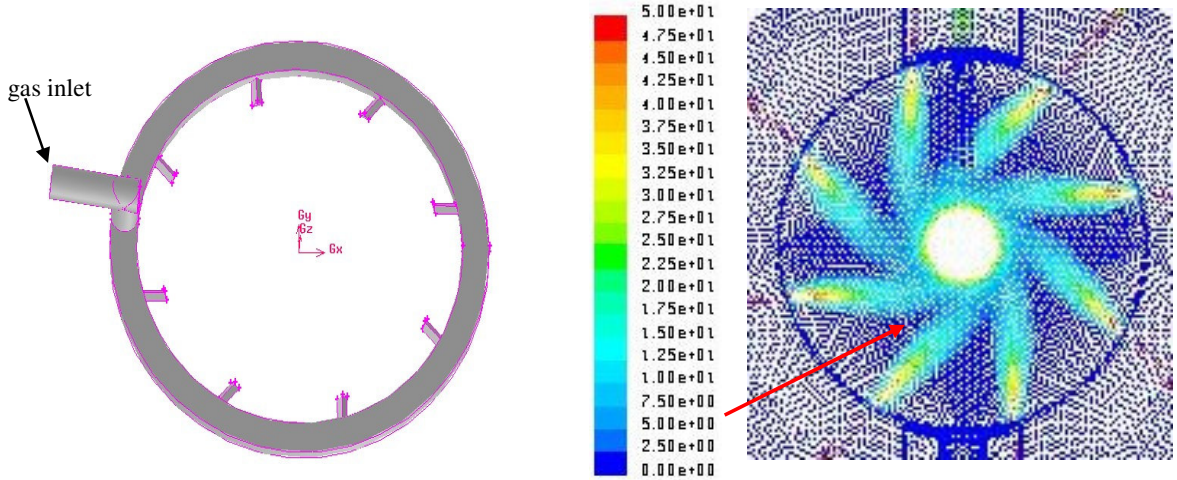

Fig. 3: **a)** CAD representation of the channels allowing to inject the protective gas layer through the powder port ring holder, **b)** velocity vectors of the protective gas layer formed at the nozzle wall (calculated numerically with Fluent 6.1) showing areas (red arrow) hat should be further protected (the plasma flow is not plotted here).

The new ring has been designed in [1] starting from a standard annular powder port ring holder. It has been made by milling grooves in a Sulzer Metco ring with two threads, figure 2a, to form a path for the gas layer

injection. When sealing the ring on the nozzle exit, the grooves result in channels, plotted figure 3a. They link the pressurized gas inlet, via a circular channel of rectangular section (1 mm x 3 mm), to eight gas channels of triangular section (right isosceles of base 1.8mm) opening on the inner radius of the ring. The eight inner gas injection channels are evenly angularly distributed along the circumference of the ring. They are oriented along a non-radial direction, such that the injected gas flows in the close vicinity of the outer periphery of the plasma jet, as illustrated by the velocity vectors of figure 3b. This orientation allows avoiding any direct interaction between the gas injected through the ring and the plasma jet. So the protective gas layer should: *i*) prevent from lump formation in the coating, *ii*) not modify the properties of the powder particles prior to impact on the substrate (velocity, temperature, oxidation, etc.) and thus *iii*) preserve the coating quality.

These properties have indeed been successfully verified experimentally when spraying a bond coat on Titanium coupons with the commercially available powder NiAl Amdry 956 from Sulzer Metco, [1]. No lump was observed when using the new ring with a gas rate of 32slpm to form the protective layer. No difference was noticed when using a protective gas layer of argon or air. The measured properties of the coating microstructure remained within the required quality range.

Other experimental tests have been carried out building the top coat with the commercially available powder ZrO_2 Amperit 827.873 from HC Starck. When sprayed with a standard ring, this powder leads to more severe clogging problems than NiAl Amdry 956. Using the new ring and the same gas flow rate as for the bond coat, a significant reduction of the number of lumps was reached. But this improvement was not sufficient since lumps could still be observed in some coupons, as illustrated figure 1b. ZrO_2 Amperit 827.873 is characterized by particles of smaller size than NiAl Amdry 956. Plotting the protective gas layer formed at the nozzle wall (such as the velocity vectors calculated numerically with Fluent 6.1, figure 3b) we can observe, in the vicinity of the plasma jet, areas of the nozzle wall that are poorly protected by the gas layer. So we assumed that the finest powder particles could still find a path through these weakly protected areas. The purpose of this study was thus to further optimize the geometry of the channels through the ring in order to prevent lump from forming in the coating when spraying powder lots containing very small particles. The two constraints we fixed are: to maintain the quality requirements for the coating and design a solution based on a standard annular powder port ring holder.

2. Simulation model

APS processes are composed of three separate sub-processes: the plasma generation by an arc discharge [3], the plasma/powder particle interaction, and the formation of the coating [4]. In this work the plasma generation was modeled by imposing profiles at the nozzle outlet, and the plasma/powder particle interaction was calculated up to the substrate location. The models used to simulate both the atmospheric plasma and the powder particles are summarized in [5]. They have been widely studied and validated by comparisons with experimental data; related references are also given in [5].

Three species were taken into account in the calculations: the plasma gas, the surrounding air and the carrier gas. The plasma gas was formed by the ionization of a mixture of argon and diatomic hydrogen (here 24.5% of H_2 in volume). The carrier gas was pure argon. The gas used to form the protective layer at the nozzle wall was either argon or air. Each of these gases was supposed to be in local thermal and chemical equilibrium.

The system of equations governing these fluids was the complete set of turbulent Navier-Stokes equations. The turbulence closure was a k-epsilon model in its RNG formulation, supplemented by a corrective term for the k-conservation equation [6]. Quantities such as the transport coefficients were derived from kinetic theory as in [7]. This system was solved using a finite volume method (Fluent 6.1, [8]) and numerical schemes of second order accuracy in space.

The computational domain was 3-dimensional and started from the wall at the exit of the plasma gun. It included the powder port ring holder fixed at the nozzle outlet. The geometrical dimensions were the same as in [1].

The boundary conditions at the nozzle exit were imposed profiles of temperature, velocity, turbulence kinetic energy and dissipation rate. Their expressions are detailed in [1]. The maximum temperature was $T_{max} = 12575$ K and the maximum velocity $U_{max} = 2167$ m/s. These quantities were derived from the

operating conditions of the arc generator, as explained by Nylén [5]. The boundary equations for the turbulent kinetic energy and the dissipation rate are also reported in [5].
Pure argon was injected through the inlet of the powder injector. This boundary condition was set assuming a constant temperature of 300 K and a parabolic velocity profile corresponding to an average velocity of 26.2 m/s for the figures presented here. Concerning the hole of the ring that was not occupied by a powder port, the boundary condition was, as for the surrounding, air at rest and 300 K. The wall of the nozzle was assumed to be at a constant temperature of 1000 K.
The powder feed rate was 54 g/min. The particles were modeled as described by Nylén [5]. However, the calculations did not account for all phenomena involved such as vaporization or oxidation of the particles. This powder feed rate is low enough to avoid any loading effect. A weak coupling between plasma and powder particles was thus retained: heat and momentum were transferred from the plasma to the particles, but the effect of the particles on the plasma was neglected.

5. Numerical results

The first change we did to obtain a more extended protective gas layer around the plasma jet at the nozzle wall was to increase the number of triangular channels (from 8 to 16), reduce their section area by two, and keep the same total inlet gas flow rate. As illustrated by the argon mass fraction, and the argon velocity vectors, figures 4a and b, the evenness of the protective gas layer gets worst than with only 8 triangular channels. Similar disappointing results are obtained with air rather than argon to make the gas layer.

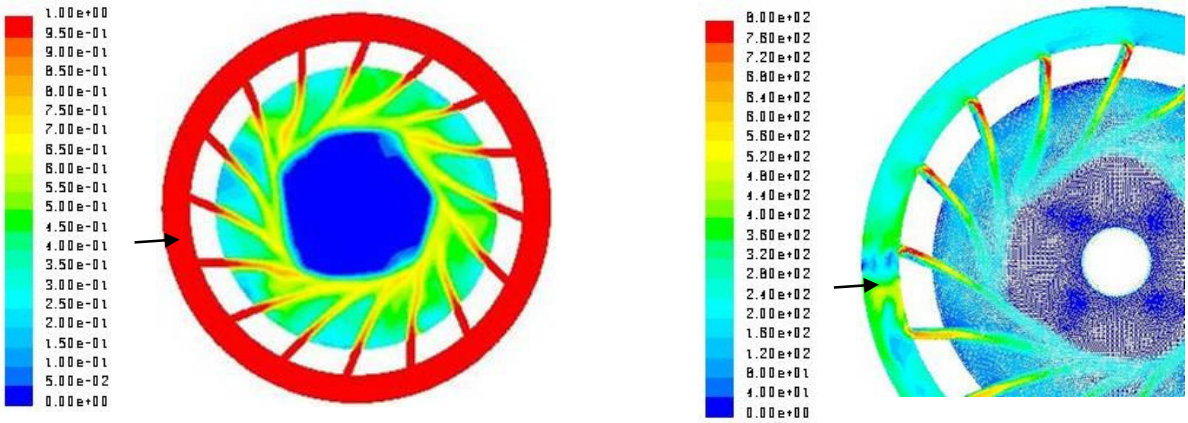

Fig. 4: Protective gas layer made of argon at the nozzle wall (calculated numerically with Fluent 6.1) with 16 triangular channels. The arrow indicates the location of the gas inlet. **a)** argon mass fraction, **b)** velocity vectors (zoom; the plasma flow is not plotted here).

We observe that the gas layer is far away from the plasma jet. The gas jets leaving the triangular channels vary significantly from one channel to the next. This non-uniformity is already important at the junction between the circular channel and the triangular ones.
So we did a second change: inject the gas through two inlets rather than only one. The gas inlets are located on the circular ring, symmetrically, each being equidistant from two neighboring triangular channels. This modification results in the gas flows at the exit of the triangular channels being more similar. Then, the central area (i.e. at the center of the nozzle wall) that is not covered by the protective gas layer becomes circular, as required. However its radius is twice larger than the nozzle exit, so the screen extension is not sufficient to prevent powder particles from reaching the nozzle wall.
A part of the kinetic energy given to the gas at the inlet is indeed lost on the way through the ring. This loss is here too large to form an efficient protective gas layer. The channels used here are short. Many changes occur along the gas path though the ring: in direction, in shape, and in size. The minor losses are thus more important than the major ones. But they can be reduced at various levels. For instance by changing the bending angle of the pipe for gas injection into the circular channel from 90 degrees to 45 degrees, and adjusting properly the distance from the bended edge to the circular channel, figures 5a and b. An additional way to reduce losses is to force the gas to flow mainly along the external radius of the circular channel (which is smooth), rather than the internal one (that contains all the triangular channels inlets). This can be achieved inserting a conical shape in the circular channel, on its internal side, and vertically aligned with the

injection pipe (see figure 6.a). In this way the turbulent flow is confined to the vicinity of the connection between the inlet channel and the circular channel, figure 6.b. Notice that the injection pipe bend angle, the distance from this bend to the circular channel, the size and location of the conical shape are dependent parameters.

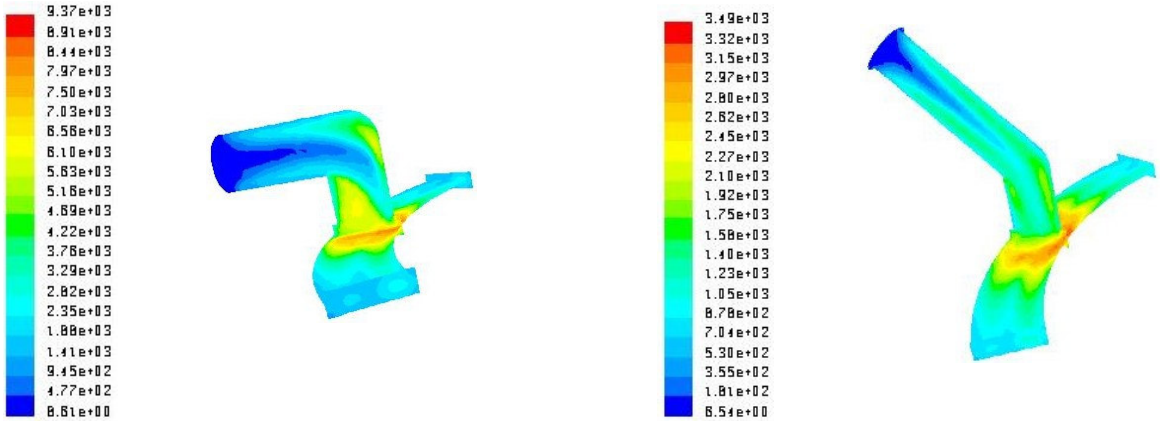

Fig. 5: Turbulence intensity in the pipe for gas injection and a section of the circular channel for a gas injection pipe bended at **a)** 90 degrees, **b)** 45 degrees.

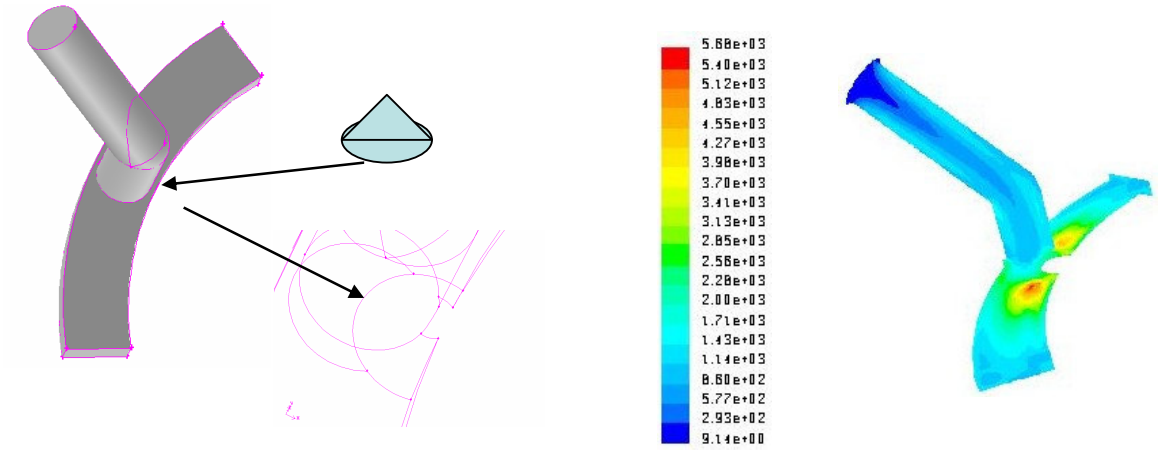

Fig. 6: **a)** Schematic representation of the conical shape inserted at the junction between injection channel and circular channel to redirect the flow, **b)** turbulence intensity in the pipe for gas injection and a section of the circular channel obtained with the channels geometry 6.a.

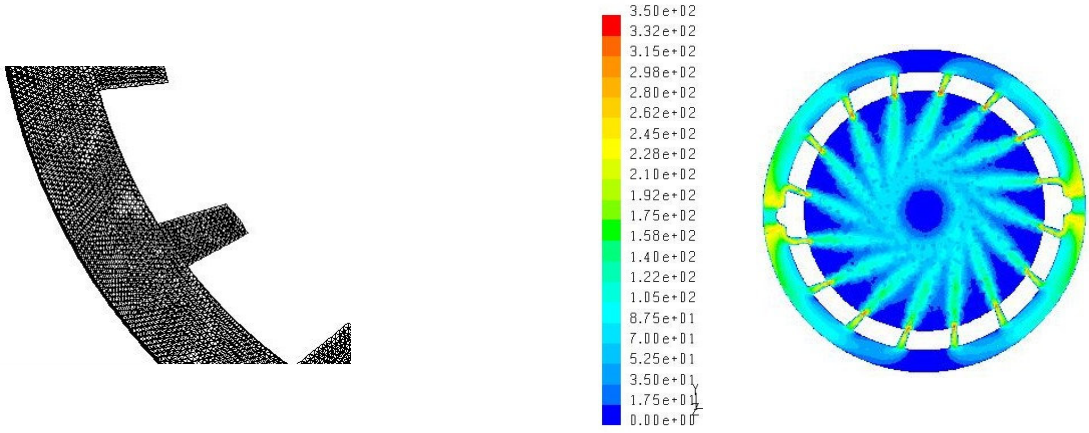

Fig. 7: **a)** A section of the circular channel and a triangular convergent channel, **b)** velocity vectors (zoom; the plasma flow is not plotted here) obtained with the modified geometry.

Unfortunately these changes are not enough to sufficiently reduce the losses. To go further we could also use more than two pipes for gas injection through the ring, but this does not seem to be very convenient. We could also change the section of the circular pipe, from a rectangle to a square, but this is not consistent with our whish to use a standard ring. A thicker ring would indeed be needed. Another source of loss is the large difference in sections between a triangular channel and the circular one. For this reason, the triangular channels are instead modified by increasing regularly their section in the direction of the circular ring. This last modification reduces losses, also accelerates the gas flow since the triangular channels now act as nozzles. As a result, the protective gas layer becomes sufficiently extended to cover the nozzle wall up to the vicinity of the plasma jet, figure 7.b.

These modifications result in a gas layer that better screens the nozzle wall between the powder injector outlet and the plasma jet. The non-radial orientation of the triangular channels is determined so that plasma jet and protective gas layer do not directly interact. The numerical results show that the properties of the powder particles (such as velocity, temperature) prior to impact with the substrate are kept unchanged (when using or not the protective gas layer). During preliminary experiments, no lump formation could be observed in top coats sprayed with the new system of 16 channels through the ring. Other experiments are in progress to further validate this numerical study.

6. Conclusion

The efficiency of the proposed solution to avoid lump formation in coatings built up using APS (with powder injection downstream the plasma nozzle) depends on the evenness of the protective gas layer. To completely eliminate lump formation, a minimum number of channels used to form the screen, and a minimum flow rate through these channels are needed. These minimum values depend on the distribution in size of the powder particles. The solution suited to Ni-5Al Amdry 956 powder from Sulzer Metco used to form bond coat [1] was not sufficient for the finer powder ZrO_2 Amperit 827.873 from HC Starck. The present numerical investigation indicates that a few modifications in the channels geometry designed in [1] are needed to sufficiently improve the screen quality to avoid lump formation with these finer powders. Preliminary experiments with ZrO_2 Amperit 827.873 support this numerical study.

A key issue is also to maintain the coating properties. It has been checked numerically that just prior to impact with the substrate, the average temperature and velocity of the powder particles are kept unchanged when using the new ring (with either argon or air) compared to a standard ring. So the coating quality should not be affected by the injection of gas through the ring. Experiments are in progress to confirm this last point.

References

[1] I. Choquet, S. Björklund, J, Johansson, J, Wigren: Nozzle exit geometry and lump formation in APS, International Thermal Spray Conference ITSC2005, to appear.

[2] Langhammer, C.: Optimisation of the deposition efficiency and deposition rate for PM 919-20 sprayed with the multi-local radial injection system. Volvo Aero Corporation (2002), Report TC-02-227.

[3] Choquet, I., Lucquin-Desreux, B.: Hydrodynamic limit for an arc discharge at atmospheric pressure, Journal of Statistical Physics, to appear.

[4] Mingheng, L., Panagiotis, D. C.: Multiscale modelling and analysis of an industrial HVOF thermal spray process, preprint.

[5] Nylén, P.: The prediction of Fluid flow, particle in-flight and coating characteristics in atmospheric plasma spraying, PhD thesis (1999), Chalmers University, Sweden.

[6] Bolot, R., Li., J., Coddet, C.: Modeling of thermal plasma jets: a comparison between PHEONICS and FLUENT, International Thermal Spray Conference (2004), Osaka, Japan.

[7] Boulos, M.I., Fauchais, P., Pfender, E.: Thermal plasmas. Fundamentals and applications (1994), Vol. 1, Plenum Press.

[8] Fluent users guide, Fluent Incorporated, Evanston, Ill., U.S.A.

Non-Thermal Plasma Applications in Air-Sterilization

Michael J. Gallagher[1], Alexander Gutsol[1], Gary Friedman[2], Alexander Fridman[1]
1 Department of Mechanical Engineering & Mechanics, Drexel University, Philadelphia, PA
2 Department of Electrical & Computer Engineering, Drexel University, Philadelphia, PA
Drexel Plasma Institute, Drexel University, Philadelphia, Pennsylvania, USA

Abstract

In our present study, two non-thermal plasma devices, dielectric barrier discharge and magnetically-rotated gliding arc, are being used to sterilize air containing high concentrations of viral and bacterial bioaerosols. A Pathogen Detection and Remediation Facility was designed for bioaerosol generation, containment, and sampling during plasma sterilization experiments.

Keywords: non-thermal plasma, sterilization; decontamination, airborne virus, bacteria, influenza

1. Introduction

The improvement of indoor air quality has been a challenge since the dawn of heating, ventilation, and air conditioning (HVAC) systems. Incidents like the infamous outbreak of Legionnaires disease in 1976 in Philadelphia and the recent increasing threat of bioterrorism have raised awareness of the dangers of airborne microorganisms in indoor environments. In recent years, non-thermal atmospheric pressure plasma has been the focus of research as an improved method for the sterilization of air from biological contaminates. Non-thermal plasma has been proven to inactivate many different types of microorganisms, such as viruses and bacteria, on surfaces of materials, but there have been few scientific studies of air sterilization using non-thermal plasma. Also, of the few researchers that have been able to use plasma to decontaminate a moving air stream, many rely on high efficiency particulate air (HEPA) filters to remove a large portion of microorganisms. HEPA filters are effective at trapping particles down to 0.5 microns in size; however, studies have shown that they are not as effective at capturing airborne viruses, which are among the smallest (20-300nm) known microorganisms [1]. HEPA filters also cause significant pressure losses in HVAC systems giving rise to higher energy and maintenance costs. There are several alternative methods for air cleaning, which include electrostatic precipitators, Ultraviolet Germicidal Irradiation (UVGI) devices, and some portable negative air ionizers, that are all capable of reducing particulates and even certain levels of microbial contamination in indoor environments. However, many of these methods are not proven as an efficient and cost effective means of eliminating airborne viruses. In this ongoing scientific study, we will examine the sterilization effect of two types of non-thermal plasma; dielectric barrier discharge (DBD) and magnetically-rotated gliding arc on air contaminated with high concentrations of aerosolized Influenza A virus. A non-pathogenic unicellular bacterium known as Synechococcus Elongatus, or Cyanobacteria, was also used in initial trials to demonstrate the decontamination ability of active chemical species generated from dielectric barrier discharge for bacteria in water and to provide benchmark data regarding bioaerosol sampling efficiency.

2. Non-thermal plasma for air sterilization

Although Dielectric Barrier Discharge (DBD) and magnetically-rotated Gliding Arc [2] are quite different in terms of current-voltage characteristics and operational power levels, both devices can provide a high concentration of active chemical species, which are a necessary component of the sterilization process. There are two main sterilization effects that bioaerosols are subjected to as they are passed through each plasma device: the direct interaction with the lethal environment of the discharge itself and the downstream interaction with active chemical species, such as ozone (O_3) and hydroxyl (OH), produced by the discharge. Figure 1 below shows a photo of the DBD device which consists of a thin plane of wires with equally spaced air gaps of 1.5 mm. The high voltage electrodes are coated with a quartz capillary dielectric that has an approximate wall

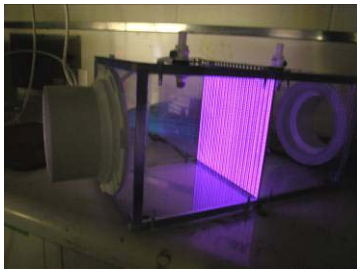

Figure 1. Dielectric Barrier Discharge for air sterilization

thickness of 0.5 mm and the device requires 14 kV for breakdown while consuming less than 200 watts of power. DBD is a low temperature discharge that is very efficient for the production of ozone, which is a strong oxidizer and proven microbial disinfectant [3-6]. The second discharge, magnetically-rotated Gliding Arc, generates a transitional non-thermal plasma and has a relatively low translational gas temperature with a high electron temperature. Gliding Arc uses a strong magnetic field to rotate and elongate an initial thermal arc resulting in rapid convective cooling, keeping the passing air flow near room temperature. This type of discharge has a large power density that can work at atmospheric pressure, but is still very efficient in providing active species. The Gliding Arc device is eight inches in diameter which keeps air velocity low allowing for greater uniformity of treatment. In figure 2, the arc is partially elongated at the center electrode. Additionally, both DBD and gliding arc devices have been designed to prevent an air pressure loss during operation and are capable of retrofit into existing HVAC systems.

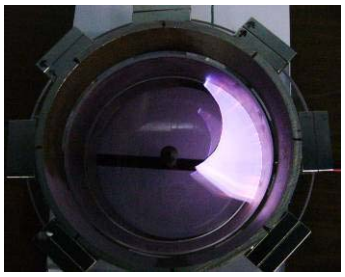

Figure 2. Magnetically Rotated Gliding Arc

3. Preliminary experiments with plasma-water decontamination

To understand the decontamination effectiveness of DBD, we designed a simple experiment to test the effect of active chemical species generated from this discharge on cyanobacteria suspended in liquid growth medium. Approximately 35 ml of liquid with cyanobacteria was placed in a Petri dish at a distance of 30 mm from the surface of the plasma discharge. A small fan forced air through the discharge at a direction normal to the surface of the liquid. Figure 3 shows a diagram of the experimental setup. The DBD discharge produces 0.11 mg of ozone per liter of air, most of which was directed toward the liquid-gas interface as the solution was stirred with a magnetic stir bar. After 3.9 minutes of treatment, we demonstrated more than a 2-log reduction (99.3%) of bacteria in the solution. We attribute ozone as the main active specie responsible for the inactivation of bacteria in this case because of its longer lifetime in comparison to hydroxyl. A similar experiment was performed by Moreau, et al. [7] to demonstrate the lethal effect of a gliding arc discharge on strain of a bacterial plant pathogen, Erwina, suspended in a liquid medium.

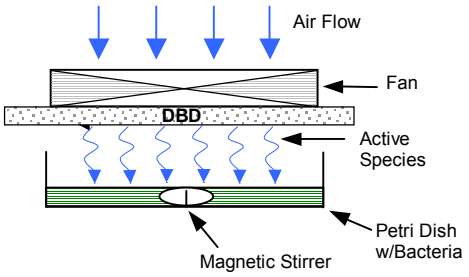

Figure 3. Water decontamination experiment using Dielectric Barrier Discharge (DBD).

4. Air Decontamination / Sterilization

In order to prove that non-thermal plasma is the main factor responsible for sterilization, one must first build a system that is capable of creating, handling, and analyzing dense concentrations of viable bioaerosols. Designing and building an air sterilization system is challenging because there are many factors that contribute to losses of aerosolized microorganisms in moving air streams. These factors include diffusion of aerosol to walls of the air flow system, desiccation stress on the microorganism due to evaporation of bioaerosol droplets in flight, and inertial and gravitational forces which can remove larger droplets from the air stream. The factors causing these losses must be carefully considered in order to avoid misinterpretation of sterilization data and may also be one reason why bioaerosol sterilization studies are limited in comparison to studies involving water or surface sterilization. Careful attention to these potential sources of error will yield greater accuracy and validity in distinguishing non-thermal plasma as the true sterilizing agent. Figure 4 below shows a scheme of the Pathogen Detection and Remediation Facility (PDRF) which is a plug flow reactor that was designed for

bioaerosol generation, containment, and sampling. It was designed to simulate conditions commonly found in an HVAC system: it has an overall volume of 250 liters, and can operate at flow rates up to 25 liters per second. The PDRF houses interchangeable non-thermal plasma devices, DBD and Magnetic Gliding Arc, which are connected to the system with four inch (10 cm) diameter flexible piping. At a flow rate of 25 L/s, the residence time, that is, the time for one droplet to make one revolution through the system, is approximately 10 seconds. An air sampling system is included in the PDRF and was designed to take as large volume air sample as possible (~ 1 liter) in a short period of time (~ 1 second) so that we do not disturb the flow inside the system and can evaluate the viability of the bioaerosol as a function of treatment time.

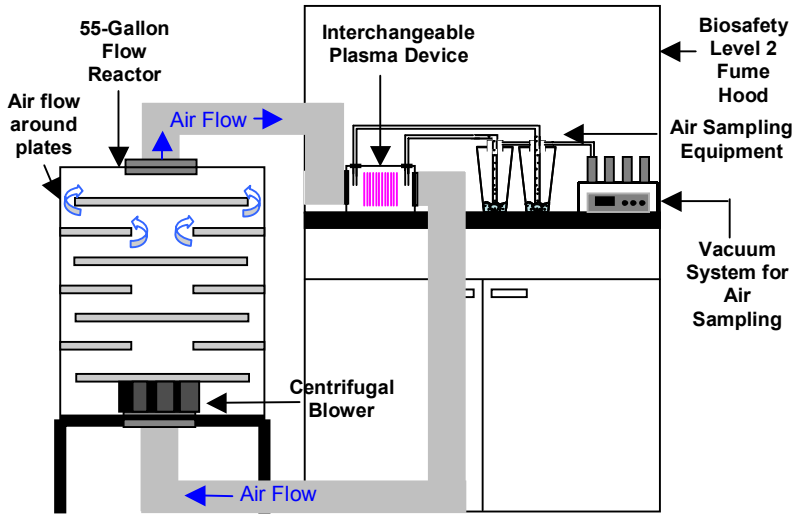

Figure 4. Pathogen Detection and Remediation Facility (PDRF)

Liquid impingement was chosen as the air sampling method for our system, as opposed to filtration or impaction, because it minimizes dessication stress and allows for the direct deposition of the microorganism into growth media. The AGI-30 liquid impinger is a commonly used bioaerosol sampler and it operates by drawing a sample of air through in inlet tube submerged in a solution, thereby causing the air stream to strike the liquid bed trapping aerosols in the solution through forces of inertia [8]. The AGI-30 impinger contains a critical orifice that contains one exit port and limits the maximum air sampling rate to 12.5 liters per minute [9]. To accommodate our desired sampling rate of 1 liter per second, we modified the AGI-30 by increasing its overall volume and replacing the standard critical orifice with a hollow spherical tip with several exit ports. Several calibration experiments performed with our modified AGI-30 impinger demonstrated reproducibility in terms of sampling efficiency. In these experiments, a Collison nebulizer was connected directly to the modified liquid impinger and after five minutes of continuous sampling in each trial, we obtained a stable sampling efficiency rating of 3.5%. Some may not consider this as an optimal efficiency rating, however, when sampling bioaerosols, reproducibility is often considered more important than the efficiency rating because the final conclusions are derived from internal comparisons between various data collected using the same samplers [9].

Several additional calibration experiments were performed in which cyanobacteria aerosol (droplet size: 1.5 micron) was injected into the Pathogen Detection and Remediation Facility (PDRF) not for the purpose of sterilization, but to identify all bioaerosol losses from diffusion, inertia, and evaporation, thereby establishing accurate controls before non-thermal plasma is introduced. In these experiments, a Collison nebulizer was used to generate the bioaerosol, the air flow rate was fixed at 25 liters per second, and the lifetime of droplets was measured by periodic air sampling with two modified liquid impingers. For all experiments described here, the system was prehumidified with sterile de-ionized water until the internal surface of the system walls were wet prior to input of the bioaerosol. Initial results showed a very poor recovery of cyanobacteria bioaerosol from the PDRF in comparison to air sampler calibration experiments. When examining the sources of loss: diffusion, inertia, and evaporation, we ruled out inertial forces because air velocity is relatively low and the aerosol droplets are small (1-2 microns). Also, our estimate of droplet diffusion time to the wall is approximately 40 minutes, well beyond the upper time limit of these trials. The effect of small droplet evaporation, however, can be prominent because the saturation pressure around a small droplet is high in comparison to the saturation pressure near the wet walls of the system. To test the effect of evaporation on the survivability of cyanobacteria, we performed two experiments: the first (Experiment A) in which additional humidity was applied continuously with the bioaerosol using an additional nebulizer with with sterile de-ionized water, and the

second (Experiment B) without additional humidification. Our results, which are described in figure 5 below, show that additional humidification reduces the rate of inactivation of aerosolized cyanobacteria, by dessication stress compared to the results of experiments without additional humidification.

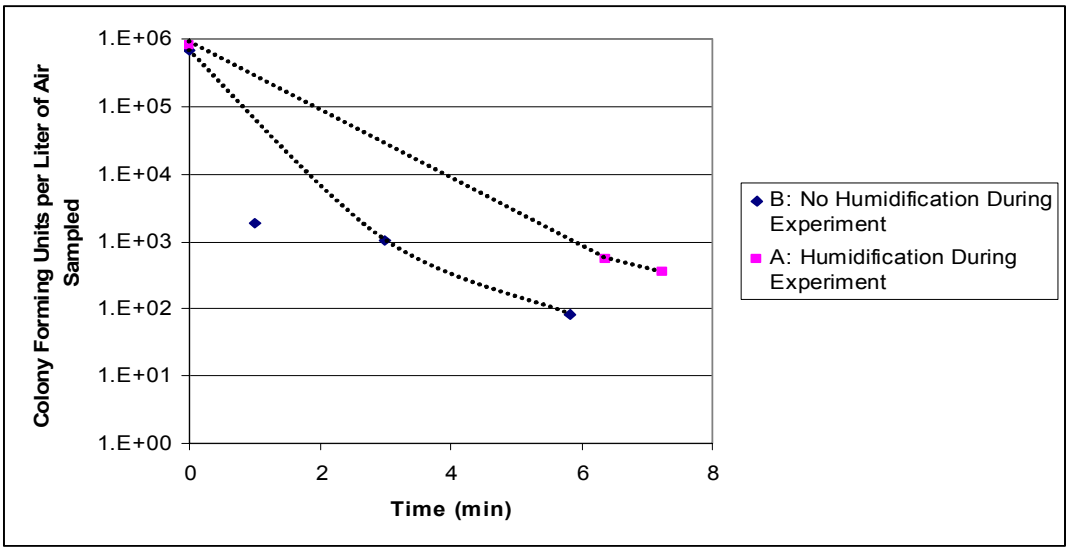

Figure 5. Evaluation of the effect of droplet evaporation on the survivability of aerosolized cyanobacteria. Experiment A minimizes evaporation by providing constant humidity.

The experimentally estimated maximum lifetime of aerosolized Cyanobacteria is 10 minutes, which is far below the estimated diffusion time of droplets to the walls of the system. We desire to have the ability to recover viable cyanobacteria over an extended period of time (tens of minutes) so that when we perform sterilization experiments with non-thermal plasma, we have enough time to take several air samples and thus acquire many data points to accurately describe the rate of inactivation. To determine if the droplets were indeed still present in the air flow after 10 minutes, we added a laser to the system to characterize the optical density of the bacterial aerosol over time. Figure 6 shows an image of the illuminated laser beam at the first minute of the experiment when the concentration of viable Cyanobacteria is high. Illumination from the laser beam slowly decayed over a period of nearly 2 hours indicating that aerosolized bacteria were still present in the flow, however, they were non-viable. Similar results were reported by Ehresmann & Hatch, who described the optical density of aerosolized unicellular bacteria lasting up to four hours at high humidity (92-94%) with viability lasting only minutes [10]. These calibration experiments with Cyanobacteria provided us with a basic understanding of the flow characteristics of the Pathogen Detection and Remediation Facility and efficiency of our air sampling system. This was a necessary step before working with viral bioaerosols because immunoassay detection methods used to quantify viruses are less accurate than the serial dilution methods used to quantify Cyanobacteria in these calibration experiments. Sterilization experiments with Cyanobacteria and Influenza A virus are in progress and we expect to have results in the summer of 2005.

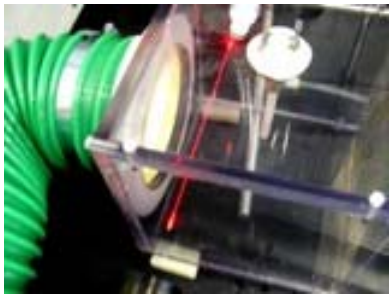

Figure 6. A laser beam illuminates the dense concentration of bioaerosol

5. Plasma chemistry sterilization modeling

The results from our experiments with the PDRF will be used to verify a model of plasma chemical sterilization [11]. We have composed a physiochemical model of the oxidizing effects of the active chemical species

generated by non-thermal plasma on many different types of microorganisms. We are investigating the individual sterilizing effects of hydroxyl radicals (OH), ozone (O_3), ultraviolet radiation (UV) as there is a large amount empirical data regarding the role of each of these components for the sterilization of various bacteria, viruses, and spores in various media. Our model combines this data with the chemical kinetics of non-thermal plasma to predict the rate of destruction of microorganisms under varying conditions.

This research is supported by Telemedicine and Advanced Technology Research Center of the US Department of Defense (TATRC of DoD) through Civilian Medical Response Center (CiMeRC).

References

[1] Harstad, J.B. Evaluation of air filters with submicron viral aerosols and bacterial aerosols. American Industrial Hygiene Association Journal. May-June (1969).

[2] Gangoli, S., Gutsol, A. and Fridman A. Rotating Non-Equilibrium Gliding Arc Plasma Disc for Enhancement in Ignition and Combustion of Hydrocarbon Fuels, ISPC-17, August 7-12, 2005, Toronto, Canada.

[3] Kowalski, W.J., Bahnfleth, W.P., and Whittam, T.S. Bactericidal effects of high airborne ozone concentrations on escherichia coli and staphylococcus aureus. Ozone Sci. Engin. 20 (1998).

[4] Kowalski, W.J., W.P. Bahnfleth, B.A. Striebig, and T.S. Whittam. Demonstration of a hermitic airborne ozone disinfection system: studies on E. coli. American Industrial Hygiene Association Journal. March-April (2003).

[5] Ishizaki, K., Shinriki N., and Matsuyama H. Inactivation of bacillus spores by gaseous ozone. Journal of Applied Bacteriology 60 (1986).

[6] Burleson G.R., Murray T.M., Pollard M. Inactivation of viruses and bacteria by ozone, with and without sonication. Applied Microbiology 29, 3 (1975).

[7] Moreau M., Feuilloley M.G.J., Orange N., and Brisset J.-L. Lethal effect of the gliding arc discharges on Erwinia spp. Journal of Applied Microbiology. 98 (2005).

[8] Perry, J.H. Chemical engineers' handbook, 2nd ed. McGraw-Hill, New York. (1941).

[9] Cown WB, Kethley TW, Fincher EL. The critical-orifice liquid impinger as a sampler for bacterial aerosols. Applied Microbiology 5 (1957).

[10] Ehresmann D.W., Hatch M.T. Effect of relative humidity on the survival of airborne unicellular algae. Applied Microbiology 29:3 (1975).

[11] Gangoli, S., Gallagher, M., Dolgopolsky, A., Gutsol, A. and Fridman A. Sterilization of Microorganisms using Non-Thermal Dielectric Barrier Discharge Plasma – Statistically based Chemical Kinetics Model, ISPC-17, August 7-12, 2005, Toronto, Canada.

Electrical and optical analysis of a double spark ignition system

B.Hnatiuc[(1)], S.Pellerin[(2)], E.Hnatiuc[(1)] and J.Chapelle[(2)]

[(1)] Univ.Techn. "Gh.Asachi", Catedra de Bazele Electrotehnici, Bd.D.Mangeron nr. 51 - 6600 Iasi, Roumanie
[(2)] LASEP - Centre Universitaire de Bourges, Rue G.Berger - BP 4043 -18028 Bourges cedex 2, France

Abstract

The spark that ignites the combustible mixtures is a glow discharge produced between the electrodes of a spark plug, connected to the secondary of a coil at the high voltage. A good combustion require a frank spark, in a volume as large is as possible and with a maximum of energy.

We propose a solution to increase the plasma volume and present electrical discharge parameters as function of inter-electrode distances, pressures in the test-reactor and the electrical pulses width of the power supply.

1. Introduction

To ignite an air-combustible mixture into the combustion room of an engine it is necessary to have an unshaken spark discharge between the electrodes of the spark plug that assure as higher energy as possible. This is a minimum condition to burn up and to increase the engine power.

The classic ignition uses a contact breaker and a coil boosting supplied at 12-13V that provide in secondary 15-20kV. This level of high voltage is required to breakdown the spark between electrodes. This could happen only if the high voltage exceeds a threshold value imposed by the dielectric constant of the mixture.

The ignition timing must be very precise. The optimum work could reduce the ignition consumption (power feed). Besides it is possible to replace the rich mixtures used so often with poor mixtures resulting an important diminution of the poluant emissions (HC, CO, NO_x) and a lower consumption [1]. However, for a good combustion is necessary to inject higher ignition energy that in the case of the classic spark plug [2].

The production of an economic and clean engine need a quick and efficient combustion of the poor mixtures at high pressure. The evolution of the combustion depends on the interactions between the flame and the plasma movement. However the used electric spark rest located ($\approx 1mm^3$) and could not assure the perfect (best) ignition for an air-hydrocarbure mixture to increase the engine performances.

Few solutions to improve these incovenients have already been proposed [3, 4, 5, 6, 7, 8, 9], but for many of them, it is difficult to believe that could become industrial applications. Nevertheless, the work of Nakamura [10] which analyze the influence of many ignition points with a device containing few classic spark plugs by cylinder has shown that the combustion cycle takes place more quickly, thereby is possible to increase the ratio. The use of poor mixtures reduces certain pollutants and the combustible efficiency was increased.

The purpose of this study concerns the conception and the realisation of a plasma ignition system for a combustion engine room, increasing the plasma volume and the electrical power injected into the discharge in order to have a quick and efficient combustion ignition. We have been interested to simultaneously produce two sparks at high pressure ($\leq$9atm), by a high voltage pulsed power supply. This power supply does not allow the transition of the spark to an electric arc. The preliminary experiments have been done in air.

2. Experimental arrangements

2.1. Schematic structure of the ignition spark plug with double spark

The experimental device [Cf. Figure 1] uses a third auxiliary electrode ③, not connected to the power supply, placed between the main electrodes ① - high voltage electrode and ② - ground electrode of a typical spark plug supplied by a pulsed high voltage power supply ⑨ through the medium of a coil ⑧. A such geometry assure the existence of two spark discharges ④ respectively between the electrodes ① and ③, called “first discharge” (referenced by *1*), and between the electrodes ③ and ②, called “second discharge” (referenced by *2*). The double spark is produced after an horizontally direction that could also help the combustion of air-combustible mixture [11].

The ceramics insulated passages ⑥ fixed by epoxy resin ⑤ assure the electric connections. The spark plug manufactured in this way is placed and fixed in a combustion room by a classic screwed ⑦.

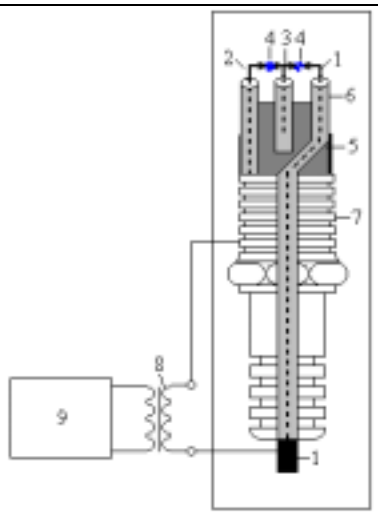

Figure 1 - New type of spark plug

① HV Electrode ; ② Ground Electrode ; ③ Auxiliary Electrode ; ④ Sparks ; ⑤ Epoxy Resin ; ⑥ Insulated passages ; ⑦ Fixative screwed ; ⑧ Coil ; ⑨ Pulsed high voltage power supply

The pulsed high voltage supply allow to provide in the secondary of the coil a high voltage up to U_d=50kV at the frequency of f_d=100Hz with an adjustable pulse width τ_d between 0.05 and 6 msec. Furthermore, to study the breakdown of each spark, the experimental device has used a time relay (opened t_{on}≈15ms and closed t_{off}≈10s). The measurements have been taken in this way in order to eliminate any luminescent post-discharge inffluence due to the metastable atoms persistance or any others species with important life time (typicaly few miliseconds [12]) into the milieu.

2.2. Experimental device for electric and optic measurements

The distance d_1 between the electrode at high voltage ① and the auxiliary one ③ is fixed by construction at 1.5 or 2mm and the distance d_2 between the auxiliary electrode ③ and the grounded one ② is adjustable between 0 and 4mm by a micrometric screw. The adjustment of the distance can modify the volume of one spark and it is possible to establish the best adapted distance under a given pressure corresponding to the necessary level of the high voltage delivered by the power supply.

The instantaneously values of spark voltage *u(t)* and discharge current *i(t)*, have been measured respectively using a differential high voltage probe [Max.: 100kV; Atenuation: 1/3300], and a shunt (RCH50 56Ω 5%MD). They were stored by a numerical oscilloscope TEKTRONIX TDS210 to get the evolution of the instantaneously power *P(t)* injected in the sparks, its average value and even the spark resistance *R(t)*.

The sparks have been studied optically using an adapted device and two fast photodiodes, whose signals were stored on a digital oscilloscope LECROY Waverunner-2 LT584L. Each of these optical signal records permit to determine simultaneously the total time T_1 of the first spark between the beginning of the positive front and the end of the negative one; the numbers N_1 and N_2 of breakdowns (discharges) corresponding to the first and second spark, resp.; the delay Δt between the first and the second discharge breakdown, but also their respective lifetimes, τ_1 and τ_2, measured between the end of the positive front and the beginning of the negative one; and eventually the lifetimes t_2', t_2'' of each discharge composing the second spark, and the past times Δt_1, Δt_2 between the negative front of one discharge and the positive front of the next discharge of each spark. Under certain conditions (only for pressures between 2 and 6atm) some anomalies of sparks behaviour have been observed.

The electrical and optical parameters have been simultaneously recorded on the computer, and the absolute pressure into the measurement chamber is controlled by a manometer sensitive from 1 to 10atm.

2.3. The structure of the power supply

The used pulsed power supply uses controller unit based on a special circuit (βAA145) or on AT89C2051 microcontroller. It allows modifying the number of pulses, the pulse width and the phase of the pulse by the microcontroller software. The last adjustment is very important for a good concordance between the pulses and the synchronization signal.

3. Experiment Results

3.1. Preliminary measurements and results

The records of electrical and optical parameters of the spark on computer allow observe the good time correlation between the electrical current and the optical spark signal.

The evolution of the all spark parameters depends on the total distance d between electrodes, and the air pressure p in the experimental device [CF. Figure 2]. The observed oscilations on the electrical parameters strongly depend on the using coil. Particularly, using a new one design by Volkswagen, they completely disapear.

The breakdown minimum voltage U_d for a normal electrical discharge between two electrodes spaced of d, is given by the Paschen law [13, 14]. It depends on the $p.d$ and has one breakdown voltage minimum. It was already proved that the maximum distance between electrodes could be increased using different geometries of the electrodes [15, 16] that allow the breakdowns of the electrical discharges. These previous results have lead to the geometry of the spark plug proposed in this paper.

During the breakdown of the first spark between the electrodes ① and ③ all demanded conditions are achieved for producing the second spark breakdown between the electrodes ③ and ②. The spark aspect strongly depends on the experiment pressure.

For the next experiments, the distances between electrodes have been fixed to d_1=d_2=1.5mm and then we have obtained the breakdown for absolute pressures up to 9atm.

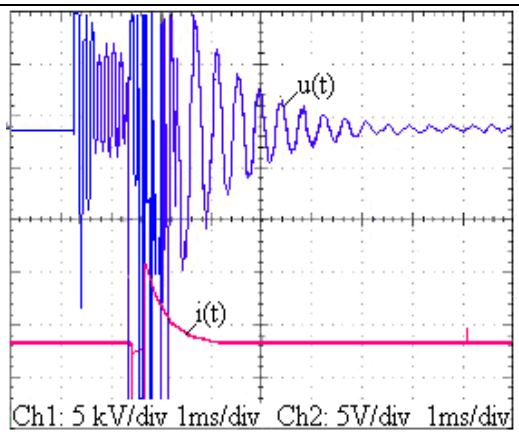

a/ d=3mm; p=3atm

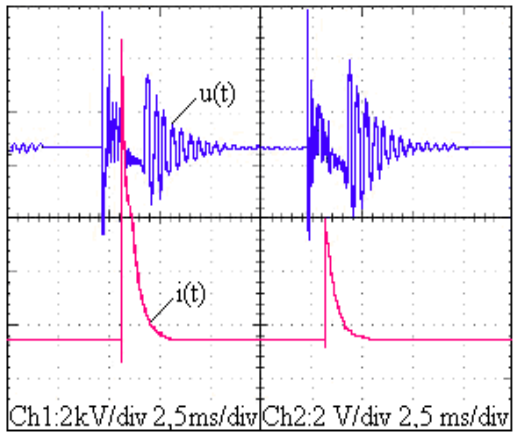

b/ d=3mm; p=1atm

Figure 2 – *u(t)* and *i(t)* for different air pressures

3.2. Breakdown delay between ①-③ and ③-② electrical discharges

For a good work of the experimental device, it is important to verify the breakdown delay between the two sparks: if the delay is too high the second spark could not influence the ignition, so the efficiency of the ignition system will not increase.

The measurements of the Δt breakdown delay between the sparks and their lifetime τ_1 and τ_2 have been done for a τ_d imposed and adjustable value of the pulse width given by the power supply.

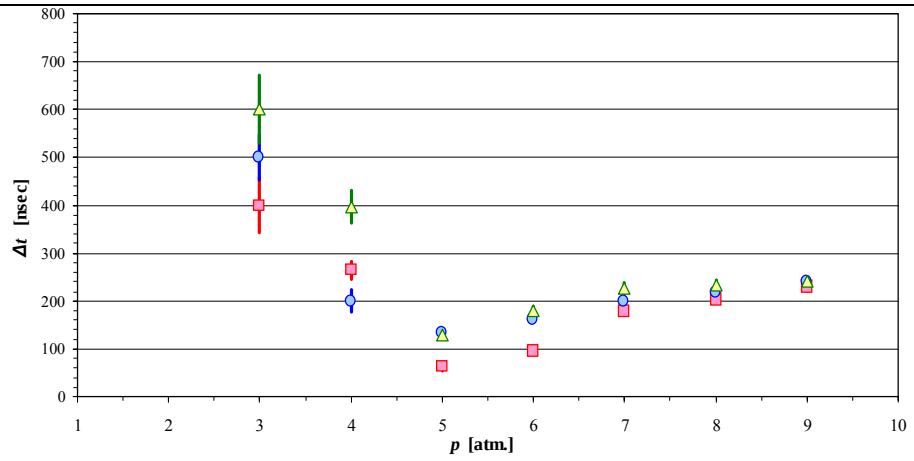

[□ τ_d=3.0ms ; ○ τ_d=4.5ms ; △ τ_d=6ms]

Figure 3 - Breakdown spark delay Δt as a function of pressure p *[d_1=d_2=1.5 mm]*

Usually the sparks breakdowns are simultaneously ($\Delta t \approx 0$). However, if there is a delay, it is always between the first and the second spark. For different pulse width we have obtained almost the same results, but the delay depends on the pressure variation [Cf. Figure 3, where data are averaged on important number of acquisitions, and incertitudes are due to measurements and process repetability].

The measurements done at pressures nearby 1atm are relative dispersed and it is very difficult to have the accurate values of Δt. However if the pressure increase the delay Δt reach a minimum near p=5atm and trends to $\Delta t \approx 240$ns at maximum high pressure.

These results are extremily hopefully for the future of our ignition device because the ignition into the engine chamber takes always place at high pressure (p>7atm). Besides for an air-methane mixture [17] the combustion needs few millisecondes so the both sparks will interfere to the mixture ignition. It is oviously that the results obtained using the air could be not exactly the same like for an air-combustible mixtures that have a bigger dielectric constant. But our last tests with a double spark ignition system applied to an monocylinder engine have shown very encouraging results.

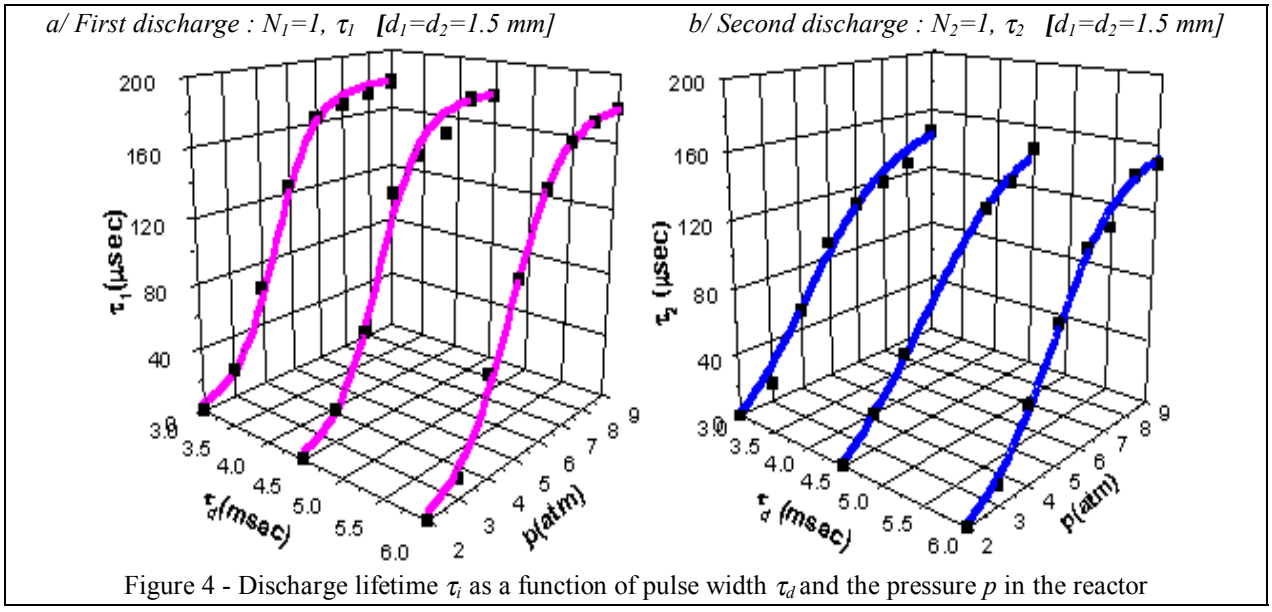

Figure 4 - Discharge lifetime τ_i as a function of pulse width τ_d and the pressure p in the reactor

3.3. Lifetime of ①-③ and ③-② sparks for one pulse

The evolutions of spark lifetimes $\tau_1(p, \tau_d)$ and $\tau_2(p, \tau_d)$ as a function of pressure p and pulse width τ_d, are given in Figure 4, where the experimental data have been fited with the same law of variation for all the family characteristics. One can observe the similar evolutions of each spark optic signal, with maximum spark lifetimes for the higher values of the air pressures.

It is obviously that the modification of pulse width τ_d does not strongly influence the work of the ignition system. The lifetime of the discharges varies from $\tau_1 \approx \tau_2 \approx 10$µs at normal pressure to $\tau_1 \approx 180$µs and $\tau_2 \approx 150$µs for 9 atm pressure. This evolution depends on the gaz type, the pressure, the distance between electrodes and the physical phenomenon inside the reactor. However, if the pulse width is too narrow, the breakdown of the sparks won't be produced. The time of the first spark breakdown, is linked to the negative front of the pulse width.

3.4. Average number and mean lifetimes of ①-③ and ③-② sparks for one electric pulse

For the most part of the experiments, we have obtained $N_1=N_2=1$. But it is possible to obtain multiple successiv sparks during the same electrical pulse (N_2, $N_1 > 1$), especially at intermediary pressure. Then, we have verified that the mean discharge time $<\tau_i>=\tau_i/N_i$ by spark is not significally modified; but on result, the total discharge time τ_i during one electrical pulse is increases compare to the case with only one spark.

The delays Δt_1 and Δt_2 between two consecutive breakdownss of each spark when $N_1,N_2>1$, have no clear dependance on the pressure: then, they seem quite independent on p, but increasing with the pulse width τ_d [Cf.Figure 5]. So, to profit of this situation, it could be necessary to adjust the τ_d value in order that the the second sparks (and the following ones) interfere with mixture ignition and not only with burned gases.

Nevertheless, we must noted that above p=6atm, it is to tell at necessary pressures for the ignition into an engine chamber, these multi-sparks effet doesn't take place.

τ_d [ms]	Δt_1 [µs]	Δt_2 [µs]
3.0	94 ± 34	70 ± 28
4.0	94 ± 41	89 ± 22
4.5	153 ± 32	157 ± 34
6.0	288 ± 34	263 ±50

[Mean values of Δt_1 and Δt_2 following pressure dependance, when N_1,N_2>1]

Figure 5 – Delay between consecutive breakdowns during one electric pulse

4. Discussion

Few conclusions of the first experiments realized at high pressure with dry air are the following:

- The order of the spark breakdowns is always the same: firstly it occurs the spark *1* and then the spark *2*.
- Once the sparks started the discharge voltage decreases and his tendency is to follow the minimum value to hold the discharges; it is possible to observe also that the discharge voltage oscillations increase with the value of the pressure into the experimental device so the instantaneous values of the electric field will increase with the pressure;
- At low pressures (p < 2atm) there are parasite discharges, D.B.D. type, produced around the ceramic insulation of the main high voltage electrode ①. These perturbations produce few difficulties for the electrical parameters measurements.
- For one pressure the sparks become instable and will stopped if the distance d_2 between the electrodes ② and ③ is constant increased.
- For one inter-electrodes distance, the sparks become instable to the variation of the pressure. The spark established between the electrodes ② and ③ is more sensitive to this variation than the other spark.
- The utilization of the auxiliary electrode ③ permits to increase the maximum breakdown distance between the electrodes, at atmospheric pressure from d_{max}=23 mm to $d_{max}=d_1+d_2$=28 mm. In this case the electrical power injected into the sparks is from (2÷10)W for energy up to 60mJ [18].
- The sparks breakdown has been done for a maximum absolute pressure of 9 atm at a maximum distance between electrodes $d_{max}\approx d_1+d_2$=2+2 mm=4 mm.
- The sparks have a red-violet color at atmospheric pressure, and becomes blue and more shining when the pressure increases.
- During the breakdown of the sparks all the energy accumulated in the magnetic field of the coil is consumed, after a transient process to the gas, the secondary coil resistance and the shunt.
- There are three successive frequencies on the records of discharge voltage [See Figure 2]: The first one at ≈8kHz is due to the breakdown and the power supply corresponding to an energy charge regime. The second corresponds to the physical behavior of the sparks. The third one, like a relaxation phenomenon at ≈2.5kHz is influenced by the coil and electrical circuit parameters. We have considered that the plasma is physically equivalent with a diode in series with a low (dissipation) resistance and the oscillations appear because of the energy transfer into the electromagnetic field [19] and the coil characteristics [20].

6. Conclusion

The presented double spark ignition system seems to be well adapted for the combustible mixtures ignition and it could assure a better combustion by its two simultaneously discharges, therefore a bigger plasma volume for ignition. We have observed that the first spark breakdowns always before the second and it is more stable and with a longer lifetime.

The total distance between the electrodes has been increased from 0.7 mm to about 2 mm. Furthermore, the duration of the two discharges is much lower than the electrical pulse widths τ_d: this phenomena allows to generate under intermediary pressures successiv ignitions in each electrodes gap.

Under certain conditions (intermediary pressures) it was observed more that one breakdown corresponding to the sparks for one pulse. All the observations have been found on both electrical and optical parameters

evolution. Then the maximum number of discharges N_{1max} and N_{2max} is limited to 1 for normal pressure and high pressure and could be 3-4 for pressures between 2 and 6 atm. The pulse width has no influence on this evolution (variation). The case with just one discharge for each spark was found much more often (90% of cases).

Our results were encouraging for the air pressure bigger than 7 atm. In this case, there is only one breakdown for each spark for one command pulse applied to the coil from the power supply. We intend to continue the study with the chemical results of the combustion and the sparks diagnostic obtained for modulated pulses train (2 or 3). The last experiments already done proved good results in real conditions with a BRIGGS & STRATON engine for upper breakdown pressure (breakdown at 7-8 atm pressure). Therefore, we have used a controller unit, based on AT89C2051 microcontroller, to ensure synchronisation of the ignition with the maximum pressure into the cylinder obtained during the compression time. In these conditions, we have verified that the purposed double sparks system provides bigger energy than with the classic system.

Acknowledgment

This research work has been developed in the frame of an Integrated Actions Programme (PAI Brancusi N°7/2003-2004) and has been supported by the 'Agence Universitaire de la Francophonie' (Post-Doctoral bourse accorded by A.U.F.).

References

[1] N.Docquier & S.Candel, *Progress in Energy and Combustion Science* **28** (2002) 107-150.
[2] A.Glassman, in "Combustion", Academic Press London (1996)
[3] http://www.lcd.ensma.fr/opmot2.html
[4] J.D.Dale, M.D.Checkel & P.R.Smy, *Progress in Energy and Combustion Science* **23** (1997) 379-398
[5] J.D.Dale, P.R.Smy & R.M.Clements, *Trans. SAE paper 780\329* **87**-2 (1978) 1539-1548
[6] J.R.Smith, *Sandia Laboratories Report SAND 79-8715* (1979) The Combustion Institute - Berkeley CA. 1-31
[7] E.Sher, J.Ben-Ya'Ish & A.Pokryvailo, *SAE paper 920\810*
[8] J.Ianca, C.Tesal, F.Hosek & B.Dolejsi, *Internal report - Department of Physical Electronics*, Faculty of Science, Masaryk University, Kotlarska 2, 61137 Brno, Czech Rep.
[9] bougie BOSCH Super 4**,** http://www.bosch.fr/ et http://www.bosch.com.br/br/autopecas/produtos/velas/popup_super4.htm
[10] N.Nakamura, T.Baika & Y.Shibata, "Multipoint spark ignition for lean combustion" *SAE paper 852\092*
[11] Activity report from the division of Combustion Physics 1999 – 2000, Department of Physics at Lund Institute of Technology, Lund, Sweden
[12] N.Gherardi, V.Puech, "DBD filamentaires et luminescentes", Atelier "Traitement de surface par plasma à pression atmosphérique", 1-2 decembre 2003, Aspen , France
[13] A.von Engel, "Ionised gases", Clarendon press, 1965
[14] J.D.Cobine, "Gaseous conductors", Dover publications, New York, 1958
[15] A.Czernikowski, B.Hnatiuc, P.Pastva & A.Ranaivosoloarimanana, "Générateurs et circuits électriques pour alimenter des décharges instables de haute tension", Brevet français N° 00 15537 et 2817444 en France, US2002093294 aux Etats-Unis
[16] E.Hnatiuc & B.Hnatiuc, "Sistem multielectrod pentru realizarea reactoarelor electrochimice cu plasma rece si circuit pentru comanda si reglarea functionarii acestuia", Brevet de Inventie OSIM nr. 112225B, Romania, 1996
[17] J.–B.Liu, P.–D.Ronney & M.–A.Gundersen, "Premixed flame ignition by transient plasma discharges", 29th International Symposium on Combustion, Sapporo, Japan, July 21 – 26, 2002
[18] B.Hnatiuc, S.Pellerin, M.Brassart, J.Chapelle, „Système d'allumage par plasma pour moteur d'automobile", FRAPOL'04, 16–19 juin 2003, Bourges, France
[19] B.Hnatiuc & S.Pellerin, «Electrical modelling and diagnostic of a luminescent discharge at high pressure», 9th IC Optimization of Electrical and Electronic , Brasov (Roumanie) - 20/22 mai 2004
[20] B.Hnatiuc, "Système d'allumage par plasma pour moteur d'automobile", Stage Postdoctotal (AUF) – 01/10/2003-31/07/2004, LASEP-Université d'Orléans, France

Suspension Plasma Spraying of finely structured coatings

C. Delbos, R. Etchar-Salas, V. Rat, J.F. Coudert, P. Fauchais
Laboratoire Sciences des Procédés Céramiques et de Traitements de Surface
(SPCTS) UMR-CNRS 6638, University of Limoges, France

Abstract
This paper reports the study of the influence of two particle size distributions of powders (submicron and micron, respectively) on the microstructure of coatings produced by Suspension Plasma Spraying. It is shown that finely structured coatings are reached by carefully adjusting plasma spraying parameters for both powders.

1. Introduction

Since the beginning of the eighties, the plasma spraying process has increasingly been used in many manufacturing industries such as aeronautics, nuclear, chemistry, oil, textile, automotive[1,2]. Despite this large field of applications, the plasma sprayed coatings always contain a network of connected porosities and reach thicknesses between 100 µm and 1 mm. This is due to the coating growing which consists in a layering of splats resulting from melted particles with diameters ranging between 5 and 50 µm impacting the substrate. That is why, for a few years, research efforts have been devoted to develop the Suspension Plasma Spraying (SPS) process which aims at reaching thin (e.g., one order of magnitude smaller in thickness than in conventional plasma spraying) and finely structured coatings. The flexibility of this process should offer the possibility to adjust the porosity rate in coatings [3,4] as well as its chemical composition provided that the suspension injection is controlled.
This paper is devoted to show that finely structured coatings can be built by carefully choosing the plasma spraying parameters as function of particles sizes contained within suspensions.

2. Experimental facilities

In this section, first, the powder characteristics and their preparations are described as well as that of the corresponding suspensions. Second, the experimental set-up and the operating conditions are given.

2.1 Powders

Two different powders are used in this study to obtain finely structured coatings. The first one consists of submicron particles and the second one of micron particles. The former results from a sedimentation technique of a commercial Yttria Stabilized Zirconia (YSZ with 13.5wt% Yttria) powder provided by Tosoh Corp. (Japan). Figure 1-a shows a picture obtained by Scanning Electron Microscopy (SEM) of the submicron particles after sedimentation. It highlights particles with a few hundreds of nanometer in diameter.

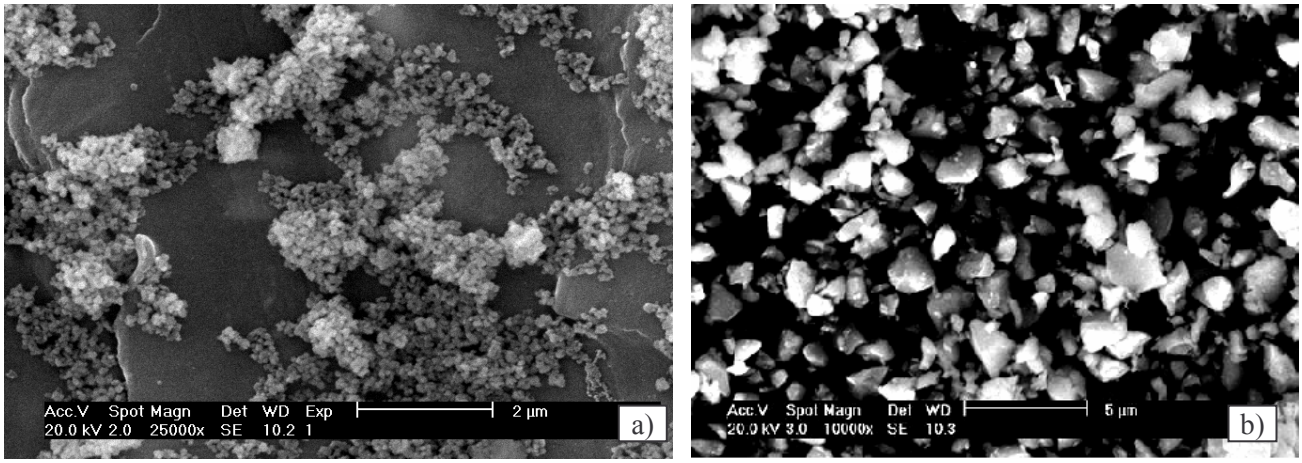

Figure 1: Pictures obtained by scanning electron microscopy of a) the submicron powder and b) the attrition milled powder

Figure 2 shows a volume particle size distribution of the submicron particles. This powder is mainly composed of particles with diameter smaller than 600 nm, with a large amount of particles with diameters ranging between 100 and 300 nm.
The second powder containing micron particles is obtained using an attrition milled technique. Fused and crushed particles are attrition milled to achieve a narrow particle size distribution centred on 3 µm. A -22+5µm YSZ powder was attrition milled during 13 hours (see the SEM picture in Figure 1-b). The Figure 2 shows that this powder is mainly composed of micron particles. Less than 10vol% particles have a diameter smaller than 1 µm, whereas the maximal diameter does not exceed 5 µm.

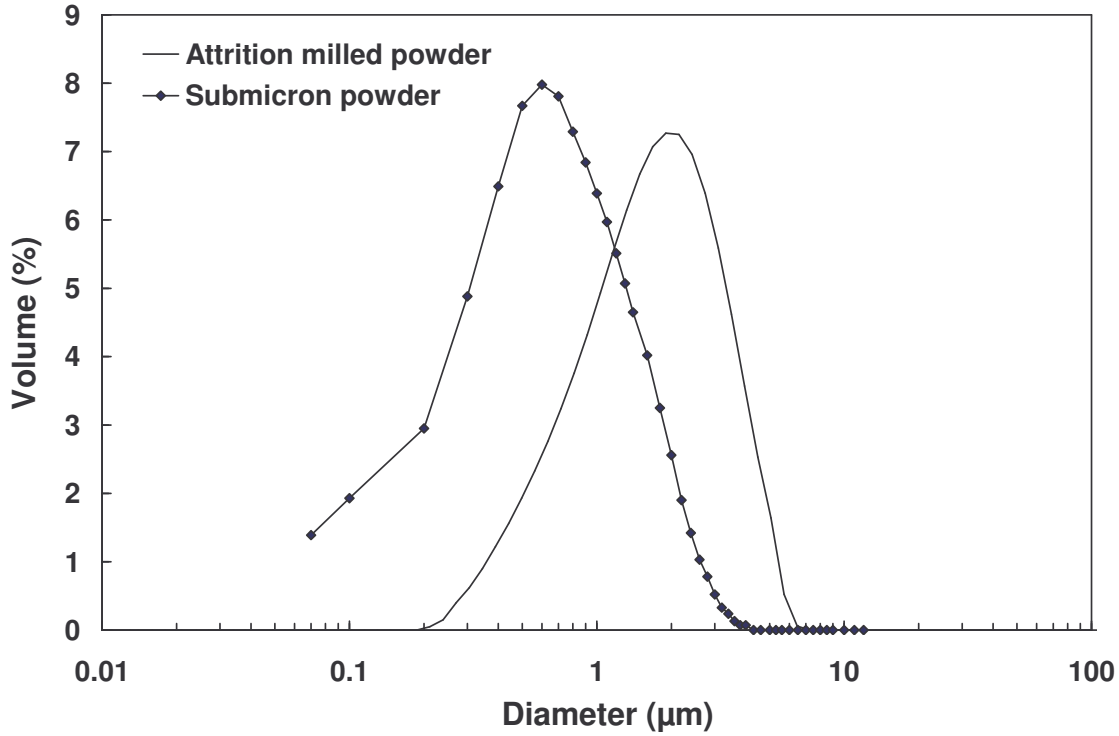

Figure 2 : Powder size volume distributions of the attrition milled powder and submicron powder.

The suspensions are produced according to the following criteria: they must be time-stable, maintaining good particle dispersion (without agglomeration), have the lowest viscosity, for a given particle loading, corresponding to an optimum dispersion and enabling an efficient injection, and, have a high particle loading to increase the deposition efficiency. Suspension of YSZ particles consist of a solvent, e.g. ethanol, in which solid particles are dispersed using a dispersant, e.g. an ester phosphate. The stabilization mechanism is based on an electrical charge balance produced at the surface of particles [5] and a stabilizing effect induced by the polymeric chains of the dispersant [6]. Chartier *et al.* [6] explains that the lowest viscosity of ceramic/dispersant/solvent systems corresponds to the best degree of deagglomeration and the highest stability. They show that the dispersant behaves as anionic dispersants by partially dissociating when immersing it within the solvent and liberating hydronium ions (H_3O^+). Ceramic particles initially presenting a negative charge on the surface, the hydronium ions adsorb to charge positively the surface of the particles. Then, ceramic particles attract the anionic dispersant molecules which present long polymeric chains. Consequently, the latters prevent the particles from falling into the van der Waals attraction potential at close distance of the particle surface (steric repulsion).
Suspensions of YSZ powders were prepared with a powder mass percentage of 7% of the ethanol and powder mass. The mass percentage of the phosphate ester selected for use is 2 % of the powder mass for both powders.

2.2 Experimental set-up

The plasma spraying set-up (Figure 3) consists of a PTF4 plasma torch, four suspension feeders and, either a splat collector or a deposition system. The internal diameter of the anode nozzle is 6 mm. The operating conditions are summarized in Table 1.

The pressure of the tank of the suspension feeders can be varied to modify the drop injection velocities. Three tanks are used to spray different suspension compositions only by switching tank valves. The fourth is filled only with solvent to clean the injection nozzle (150 µm in internal diameter) when the injection of a given suspension is finished.

The suspension is counter-flow injected, with a 15° angle with respect to a vertical axis. Moreover, in order to ensure the repeatability of experiments, the injector position is rigorously controlled by micro-positioning it with respect to the plasma torch.

In respect of the deposition system, a micro-controlled table carrying the substrate can be moved in the three space coordinates (x,y,z). Moreover, the plasma torch voltage V and current I as well as the thermal losses Q at the electrodes are controlled and measured on-line. The torch efficiency η can be deduced from the following equation: $\eta = 1 - Q/VI$, as well as the specific enthalpy $\bar{h}$ of the plasma jet from $\bar{h} = \eta VI/\dot{m}$ where $\dot{m}$ is the total plasma forming gas mass flow rate. The plasma voltage decreases with the deposition time due to the erosion of electrodes, resulting in a reduction of the available specific enthalpy inducing mainly a decrease of the plasma velocity and a lowering of the heat transfer to particles. This is compensated for by increasing the arc current to keep the specific enthalpy constant. For new electrodes without erosion, Table 1 gives the specific enthalpy of plasma jets used.

The local heat flux absorbed by the coating is measured. The measurement simply consists in measuring the total heat flux received from the plasma jet by a copper target rapidly crossing it. The temperature rise ΔT is measured by means of a thermocouple inserted within the copper target. It is assumed that the heat uptake is rapidly and homogeneously transferred within the target interior. Moreover, a pseudo-stationary temperature state is assumed to exist within the copper target after exposure to the plasma since its natural cooling period is much longer (3 to 4 orders of magnitude) than its heating one.

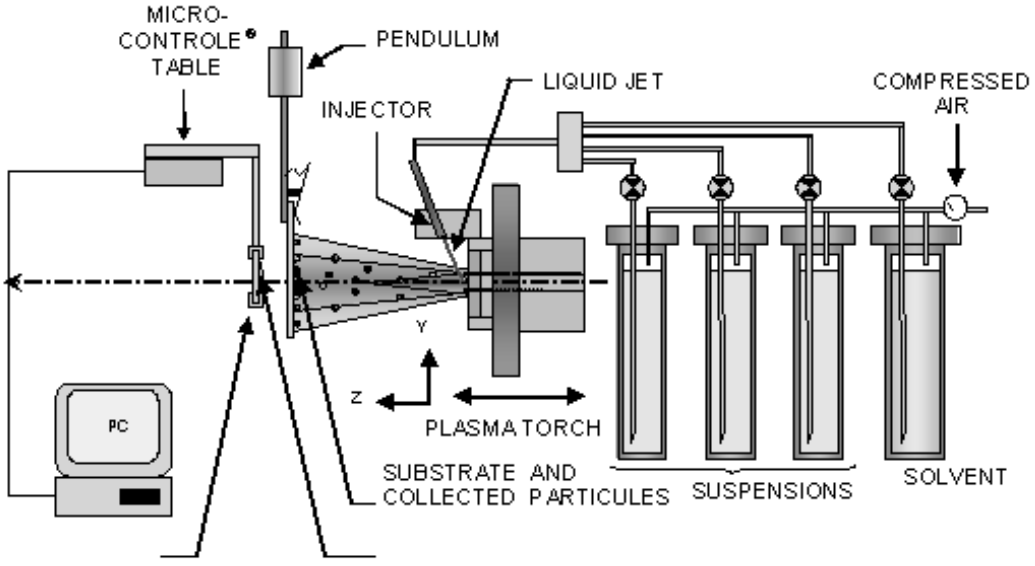

Figure 3: Experimental set-up

The copper target crosses the plasma jet without suspension injection at the same location as a normal coating. Crossing distances are respectively at 40, 50 and 60 mm from the nozzle exit. The heat, ΔQ, transferred to the copper target is calculated using the relation $\Delta Q = mc_p\Delta T$ where m (kg) and c_p ($J.kg^{-1}.K^{-1}$) are respectively the mass and the specific heat of the copper target. The exposure is time is 31.25 ms and the copper target exposed area is about 2.10^{-4} m^2. It has to be pointed out that this area is related to the plasma area intercepted by the target which is not precisely defined because it has been evaluated from the trace left by the plasma jet on the copper target.

Table 1: Spray parameters

Internal nozzle diameter (mm)	6	6
Stand-off distance (mm)	40	40
Plasma forming gas (slm)	Ar-He (40-80)	Ar-H_2-He (40-10-50)
Powders	Submicron	Attrition milled
I (A)	300	500
Power (kW)	18.6	37.5
Specific enthalpy (MJ/kg)	13	20.6

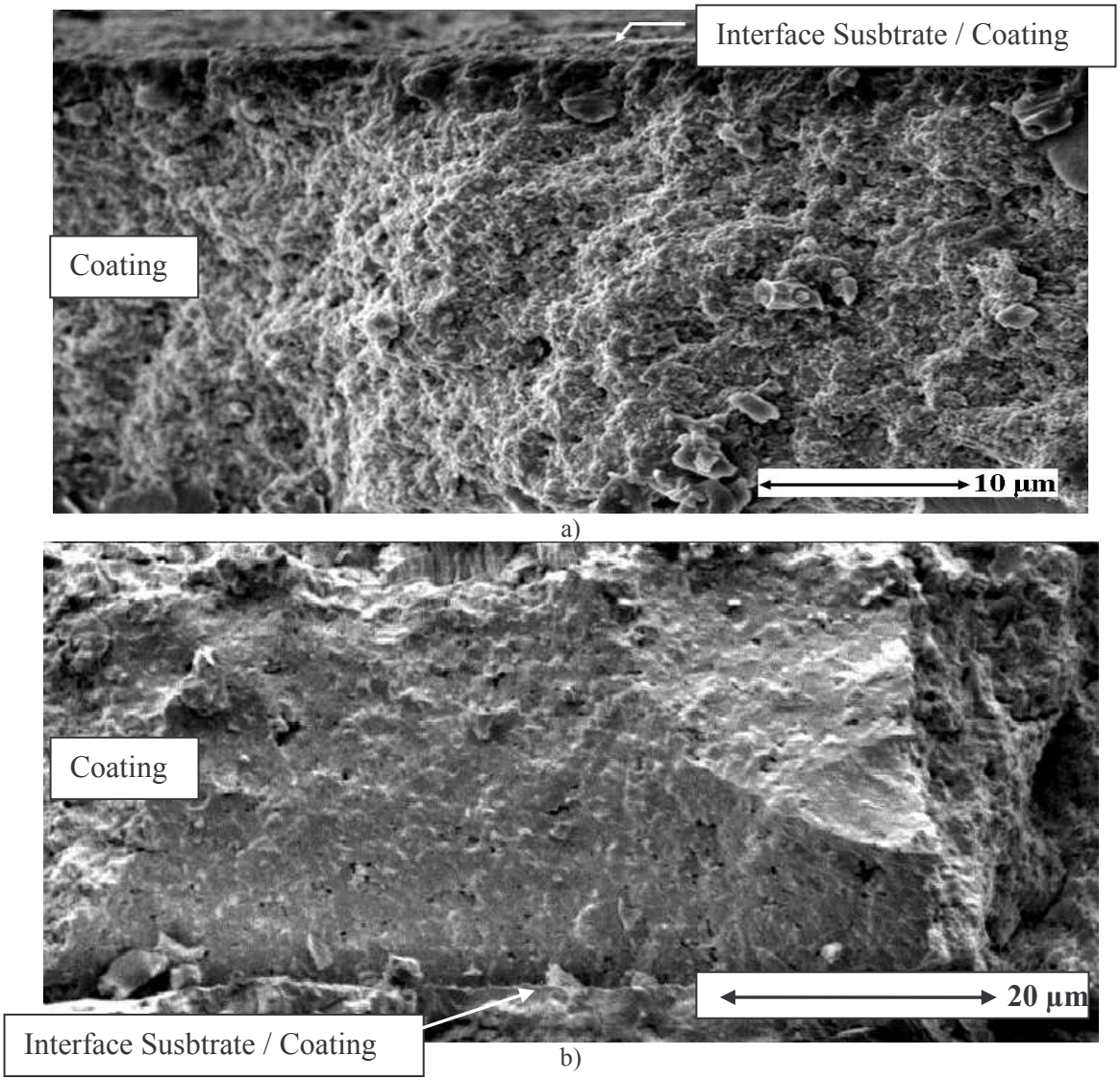

Figure 4: Fractured cross-section of coatings sprayed at 40 mm dowstream of the nozzle exit with a) the submicron powder and b) the attrition milled powder.

3. Results and discussion

3.1 Coatings

Coatings are produced following both operating conditions given in Table 1. The suspension containing submicron particles is sprayed onto a smooth (Ra=0.05 µm) and pre-heated (350 °C) stainless steel substrate. The suspension consisted of the attrition milled particles is sprayed onto a conventionally plasma sprayed YSZ substrate.

Figure 4 shows the fractured cross-section of coatings sprayed with the submicron powder and the attrition milled powder, respectively in Figure 4-a and 4-b. First, no layering of splats is observed in both coatings as obtained in conventional plasma spraying when using particles with a few tens of microns in diameter.

Both coatings exhibit a granular microstructure without interconnected porosities and micro-cracks. However, despite a different scale between both figures, Figure 4-a seems to highlight a more finely structured microstructure and less dense than in Figure 4-b

The choice of plasma parameters for the submicron powder is devoted to obtain a reduced available specific enthalpy within the plasma jet which allows treating submicron particles limiting their vaporization. That is why a higher specific enthalpy is used in the case of the attrition milled powder where particles are one order magnitude higher in diameter than within the submicron powder. Moreover, in order to homogeneously treat the particles, the helium plasma forming gas is used because it tends to limit the voltage fluctuations and to generate a more stable plasma jet as shown in Figure 5 [7]. It shows that the voltage amplitude relatively to the mean voltage is almost twice higher when using a plasma forming gas with hydrogen than when using helium alone. It has to be noted that the heat and momentum transfer characteristic times of particles is proportional the square of their diameter. Submicron and micron particles are therefore much more sensitive to changes in momentum and heat transfers than particles used in conventional plasma spraying.

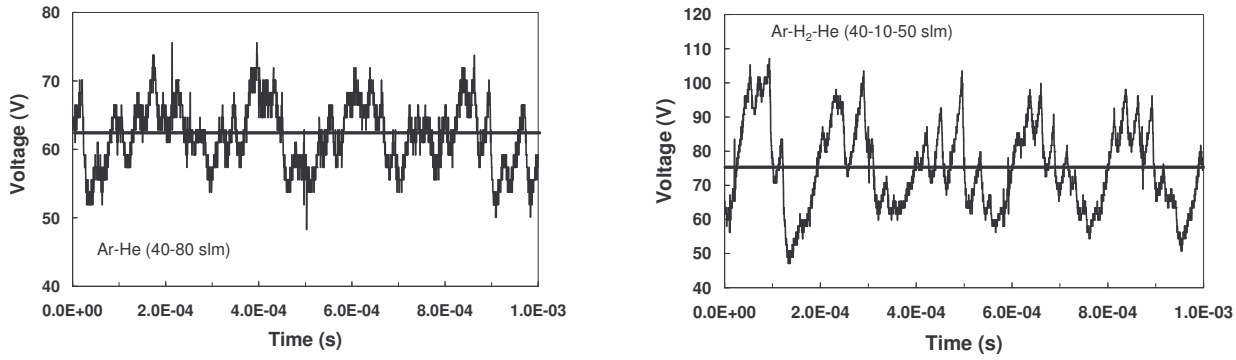

Figure 5: Torch voltage fluctuations as function of the plasma gas composition

3.2 Heat Fluxes

It is expected that the convective transfers between the plasma jet and the coating should be of great importance due to the short stand-off distance (40 mm downstream of the nozzle exit). That is why heat fluxes are measured as function of the stand-off distance for both plasma compositions, Ar-H_2-He (40/10/50 slm) and Ar-He (40/80 slm), as explained in section 2.2.

Figure 5 shows the heat flux transferred to growing coatings under the above mentioned experimental conditions. At 40 mm from the nozzle exit, for the Ar-H_2-He plasma, the heat flux to the copper target reaches 17 $MW.m^{-2}$, this flux level being some 10 times larger than that used in conventional plasma spraying where the coatings are generally deposited at a stand-off distance of 100-120 mm. These very strong heat fluxes probably involve drastic increases in the surface temperature of the deposited YSZ pass (of only about 0.8 µm thickness) which should either be higher than the sintering temperature of zirconia (about 1500 °C) or keep the sprayed pass melted resulting in a quite dense coating. The heat flux induced by the Ar-He plasma is less important than that of the ternary mixture permitting the conservation of the fine microstructure.

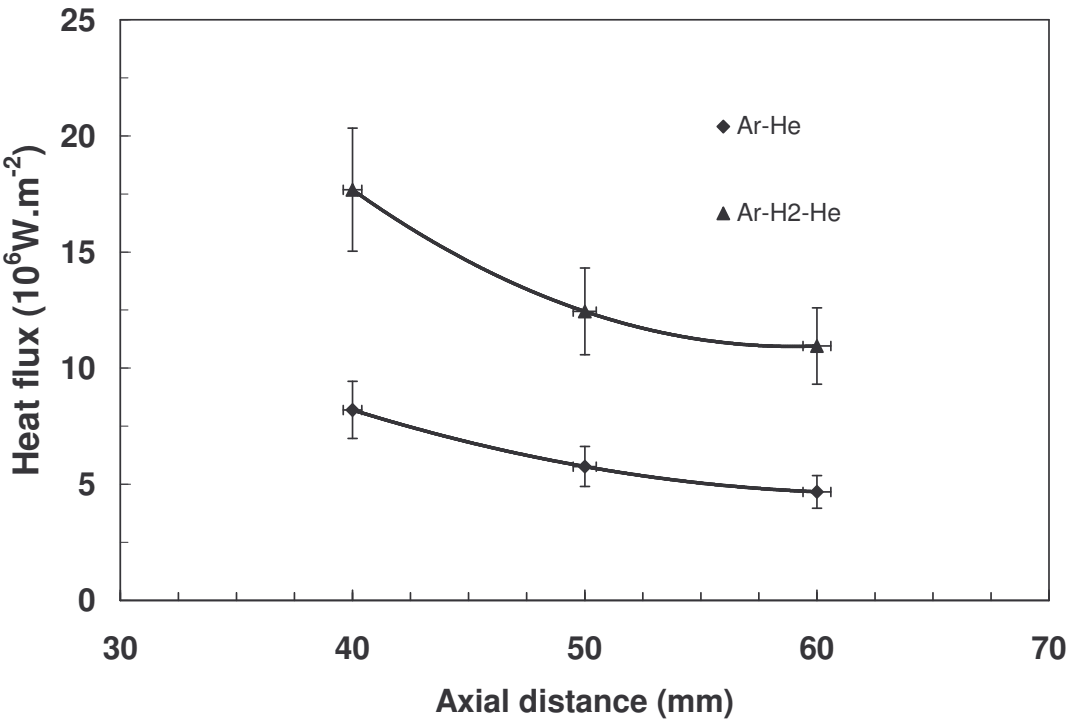

Figure 5: Evolution along the torch axis of the heat fluxes imposed to the substrate with three plasma forming gases: Ar-H_2, Ar-H_2-He and Ar-He.

4. Conclusion

Suspension Plasma Spraying (SPS) is a novel process which aims at producing coatings with intermediate thicknesses of a few micrometers up to a few tens of micrometers. Actually, it fills the gap between the Chemical/Physical Vapor Deposition processes and the thermal spraying processes. The main characteristic of SPS is the possibility to plasma treat submicron particles by a thermal plasma jet provided that the particles are injected within the core of the plasma. This paper shows that finely structured coatings are obtained using SPS by analyzing the microstructure of coatings. The latters are produced by injecting suspensions of powders with narrow micron and submicron particle size distributions. It is shown that finely structured coatings are obtained for both powders but, choosing a set of plasma spraying parameters adapted to the size of particles. For submicron particles, it has to be recommended a reduced specific enthalpy available within the plasma jet to limit particle vaporization as well as a more stable plasma source. However, for micron particles, even if the last condition should be maintained, an enhanced specific enthalpy must be used. Consequently, in this case, it is shown that the plasma jet should contribute to increase the density of coating during its growing due to the strong heat flux transferred from the plasma to the coating.

References

[1] P. Fauchais and A. Vardelle, IEEE Trans. Plasma Sci. **25**, 1258 (1997).
[2] E. Pfender, Plasma Chem. Plasma Process. **19**, 1 (1999).
[3] V. Rat, C. Delbos, C. Bonhomme, J. Fazilleau, J.F. Coudert, and P. Fauchais, J. High Temp. Mat. Process. **8**, 95 (2004).
[4] C. Delbos, V. Rat, C. Bonhomme, J. Fazilleau, J.F. Coudert, and P. Fauchais, J. High Temp. Mat. Process **8**, 397 (2004).
[5] A. Kitahara and A. Watanabe,"Electrical Phenomena at interfaces," Marcel Dekker, INC. New York and Basel (1984).
[6] T. Chartier, E. Streicher, and P. Boch, Am. Ceram. Soc. Bull. **66**, 1653 (1987).
[7] Z. Duan and J. Heberlein, J.Thermal Spray Technol. **11**, 44 (2002).

session # 13

Feasibility Study of Plasma Assisted Fuel Reforming Technique

Y-H. Song, M-S. Cha, K-T. Kim, D-H. Lee, and S-J. Kim

Emission Control Group, Korea Institute of Machinery & Materials
171, Jang-dong, Yusung-Gu, Daejeon, 305-343, Korea

Abstract; performance of CH_4 conversion with pulsed corona, dielectric barrier discharge, microwave torch plasma, gliding arc, and micro-hollow cathode plasma are compared. After the comparison tests, O_2 is added into the reactor, which leads to 1) elevated temperature conditions through exothermic partial oxidation reactions and 2) higher CH_4 conversion rate and H_2 yield.

Introduction

A small-scale plasma reformer has great potential to apply in advanced combustors. Fig. 1 shows the effect of syngas (hydrogen and carbon monoxide) on the unstable flame. Here, the syngas is produced from CH_4 using the small-scale plasma reformer. The emitted gas compositions from the reformer are 66.9 % N_2, 15.1 % CH_4, 8.1 % O_2, 3.4 % H_2, 3.0 % CO, and C2, C3 chemicals. As shown in fig.1, even the small amount of syngas is effective to stabilize the unstable flame. Flame stabilization has been one of the most critical issues in combustion study, since flame stability problems frequently occur in developing low NOx combustors, high throughput combustors, low emission engines and gas turbine combustors, etc. Fig. 1 clearly shows that flame stabilization technique with plasma reformer could be an alternative approach to conventional flame stabilization techniques.

(a) (b)

Fig. 1 modification of flame stability, (a) plasma reformer off, (b) plasma reformer on

Plasma reforming technique has inherent advantages in applications of syngas assisted

combustors for the capability of fast start-up and low cost of device. However, operating cost for producing syngas could be problems for practical applications. As reviewed by Cormier et al [1], operating cost of plasma reformer is higher than those of conventional catalytic steam reformer by several factors of magnitudes. The objective of the present study is to search for the approaches to reduce the operating cost, i.e. specific electrical power consumption for producing hydrogen. In the early stages of the study, numerous types of atmospheric pressure plasma have been tested and compared. The tested plasma generation techniques are pulsed corona, spark, DBD (Dielectric Barrier Discharge), microwave torch plasma, micro hollow cathode plasma, and gliding arc. In this comparison study, hydrogen is produced through methane direct decomposition, $CH_4 \rightarrow C + 2H_2$. Methane conversion rates, compositions of products, and specific power to produce hydrogen are varied depending on the types of plasma. After the comparison tests, syngas was obtained through partial oxidation process of methane, $CH_4 + 1/2\ O_2 \rightarrow 2H_2 + CO$. Here, modified gliding arc, i.e., rotating arc is adopted for generating plasma.

Comparison of plasma generation technique

Fig. 2 (a) shows typical shapes of plasma reactor for generating DBD and pulsed corona. The length of the electrode is 10 cm, and the dia. of the quartz tube is 30 mm. For CH_4 decomposition tests, up to several hundred kJ/L of specific input power are needed, which used to cause break down of the quartz tube. In order to protect the quartz tube and to run the test for the long periods, cooling water is supplied into the inner and outer electrodes. When generating DBD, medium frequency (10 kHz) and high voltage (up to 10 kV) AC power supply is used. When generating positive pulsed corona, pulsed power supply is used to produce 20 kV peak voltages with 100 nsec pulse width. Fig. 2 (b) shows typical images of positive pulsed corona taken by ICCD. The gate time of the ICCD is 100 msec, which is long enough to superpose multiple images of corona. So-called non-thermal plasma, shown in fig. 2, can produce relatively high electron energy and low gas temperature. Detailed numerical and optical analysis showed that the mean electron energy of the streamer head is about 10 eV and the electron number density of streamer head is about $10^{13} - 10^{14}$ cm^{-3} [2]. These conditions of electrons are good enough for decomposing CH_4 that is relatively inert compared to other hydrocarbons. The calculation also predicts that the life-time of the single pulsed corona is about several tenth nano seconds. This means that the plasma zone in a fixed time is quite small, considering the actual volume of the reactor shown in the figure.

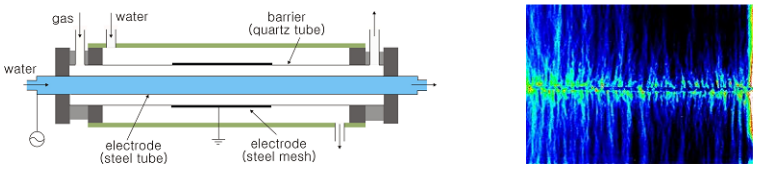

(a) (b)

Fig. 2 (a) Schematics of pulsed corona and DBD reactors, (b) images of positive pulsed corona taken by Intensified CCD (gate time: 100 msec)

Fig. 3 shows micro-hollow cathode plasma, microwave torch plasma, gliding arc and spark, respectively. These plasma reactors are fabricated in the lab for the present study. We expect that effective chemical reactions induced by plasma need 1) high electron energy, and 2) dense plasma zone in the reactors. Unfortunately, none of typical atmospheric pressure plasma produces such ideal conditions. Mean electron energy of non-thermal plasma is high, but the effective reaction volume occupied by such high electron energy inevitably small, as shown in fig. 2. On the other hand, even though the mean electron energy of the plasma shown in fig. 3 is relatively low, the pathways of the treated gas are filled with plasma. Since none of the previous studies compared the performance of the above types of plasma while producing syngas, we need a preliminary test for choosing an appropriate plasma sources for producing syngas.

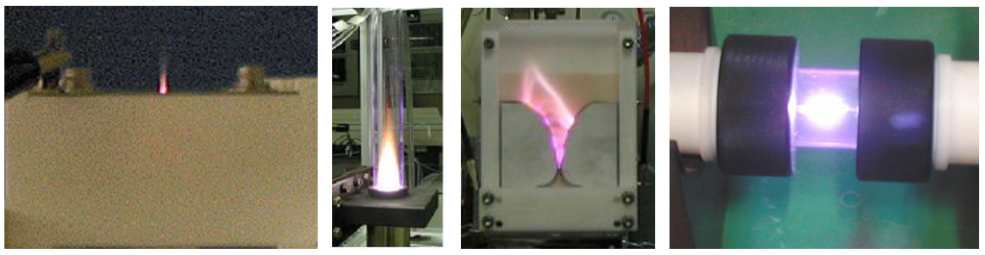

(a) (b) (c) (d)

Fig.3 (a) micro hollow-cathode plasma; hole dia. 1 mm, 22 kV, 60 Hz AC power supply is used, (b) microwave torch plasma, (c) gliding arc, 10 kV, 60 Hz AC power supply is used, and (d) spark generated by a pulsed power supply.

Hydrogen produced from CH_4 can be obtained through several different chemical reaction pathways; direct CH_4 decomposition ($CH_4 \rightarrow C + 2H_2$), partial oxidation ($CH_4 + 1/2\ O_2 \rightarrow CO + 2H_2$), steam reforming ($CH_4 + H_2O \rightarrow CO + 3H_2$), etc.. Among these pathways, we tested direct CH_4 decomposition to determine which types of plasma could be appropriate for hydrogen production. Fig. 4 showed the CH_4 conversion rate and the specific input power, kJ/L. In the cases of the microwave torch plasma, gliding arc, and micro-hollow cathode

plasma, the inlet gases are diluted by 93 - 95 % of nitrogen. We observed that ignition and continuous operation of the present microwave torch is difficult when CH_4 concentration is higher than 10 %. Without dilution, continuous operation of gliding arc and micro-hollow cathode plasma was also difficult due to carbon deposition on the reactor wall. Some modifications of reactor configurations might be helpful to solve these problems, but such efforts were not tried in the present comparison tests.

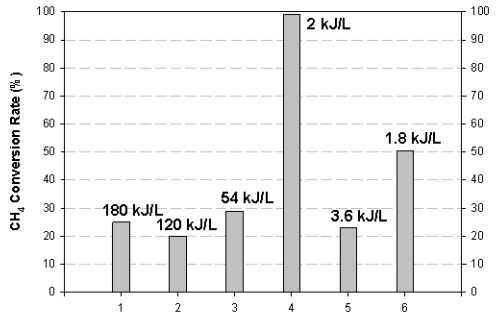

Fig. 4 CH_4 conversion rate and specific input power along with different types of plasma, (1): DBD, (2) Pulsed Corona, (3) Pulsed Spark, (4) microwave torch, (5) gliding arc, (6) micro-hollow cathode plasma

Several characteristics of direct CH_4 decomposition can be verified based on the fig. 4 result. Non-thermal plasma sources, which generate DBD and pulsed Corona, are not effective for producing H_2, since the input power of these plasma sources are higher than those of other types of plasma by orders of magnitudes. In addition, these plasma sources also produce unwanted by-products, i.e., C_2H_6, C_2H_4 and C_3H_8, which result in lower H_2 selectivity. On the other hands, plasma sources with relatively high gas temperatures, which are microwave torch, gliding arc, and micro-hollow cathode plasma, consume small electrical power. H_2 and C_2H_2 selectivity with these plasma sources is also high. In the case of the pulsed spark, the highest C_2H_2 selectivity is obtained among the tested plasma sources, and is about 50 %. An additional test shows that C_2H_2 selectivity tends to decrease and H_2 selectivity tends to increase when the gas residence time in the reactors increases. In conclusion, the plasma sources with relatively high gas temperature and longer gas residence time are desirable for hydrogen production process.

O2 addition test

Gas temperatures of the plasma sources can be significantly increased by addition of O_2, since partial and complete oxidation process of CH_4 with O_2 is exothermal reactions. A rotating arc

reactor shown in fig 5 was used in the present O_2 addition tests. The arc generated in the reactor is rotated by tangentially injected gas, as suggested by Hnatiuc et al [3]. The rotating arc can produce relatively high gas temperatures like gliding arc, and can be operated continuously without the problems of carbon deposition on the wall. Another advantage of the rotating arc is that the gas residence time can be longer than that of the two dimensional gliding arc reactor shown in fig. 3, since the area of the outlet section of the rotating arc reactor is larger than that of the two dimensional reactor. The power supply used in the present test operated with 10 kHz of high voltage (5 – 10 kV) AC power. Fig. 6 shows the schematics of the test apparatus. In order to measure the outlet gas compositions, quartz tube is located after the reactor. Gas sampling and temperature measurements are conducted through the quartz tube.

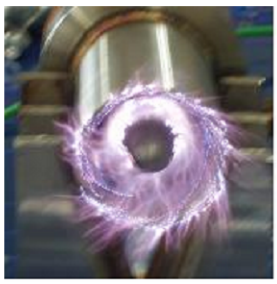

Fig. 5 rotating arc reactor (gas: Nitrogen)

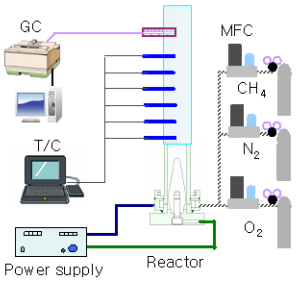

Fig. 6 Schematics of test apparatus

Temperatures measured at the outlet of the reactor are increased by the O_2 addition, as expected. The temperature measured at the closest port to the outlet of the reactor is 500 °C when O_2/C ratio is 0.5. The temperature increases up to 1,000 °C when O_2/C is 1.0. Here, O_2/C = 0.5 is the O_2/C ratio of the partial oxidation, $CH_4 + 1/2\ O_2 \rightarrow CO + 2H_2$, and O_2/C=2 is the O_2/C ratio of the complete combustion, $CH_4 + 2\ O_2 \rightarrow CO_2 + 2H_2O$. CH_4 conversion rate, H_2 yield, and CO yield also increase, as the O_2/C ratio increases, as shown in fig. 7. In the tests, total gas flow rates are 10 lpm. When O_2/C ratio is 0.5, the inlet gas consists of N_2: 70 %, CH_4: 20 %, O_2: 10 %. The input power is 200 W, which corresponds to 1.2 kJ/L of the specific input power. Considering CH_4 conversion rate, H_2 yield, and the specific input power, the performance of the O_2 addition test is much higher than the test results shown in fig. 4. Such enhanced performance could be attributed to the increased temperature caused by the heat released by the partial oxidation or combustion. A chemical equilibrium calculation also predicted that the CH_4 conversion rate and H_2 yield increase as the temperature increases. This simple explanation, however, might not be sufficient, since strong interactions between plasma and oxidation (combustion) are expected in the reactor. At present we do not have information of electron energy distributions and number densities at the elevated temperature conditions. In a further study, clarifying of such phenomena is expected.

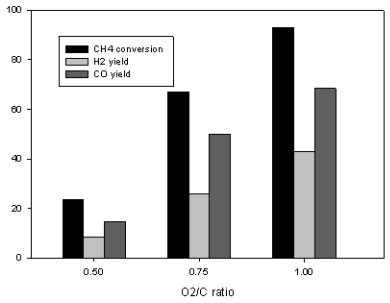

Fig. 7 CH_4 conversion, H_2 and CO yield at different O_2/C ratio

Conclusion

Numerous types of plasma generation techniques are investigated to search for appropriate plasma sources for hydrogen production. Comparison test results showed that so-called non-thermal plasma is not effective for CH_4 conversion and H_2 production. This could be attributed to the fact that 1) non-thermal plasma produces relatively low gas temperature and 2) effective reaction zone, e.g. streamer head, is small compared to the total reactor volume. Microwave torch plasma, gliding arc, and micro-hollow cathode plasma, which produce relatively high gas temperature, are effective for CH_4 conversion and higher H_2 yield, although these plasma sources generate relatively lower mean electron energy. After the comparison test, we performed O_2 addition tests that generated higher temperature conditions in the reactor. The increased temperature, which is caused by the heat released by partial oxidation and combustion, are effective to enhanced performance of CH_4 conversion and higher H_2 yield.

Acknowledgements: This study is supported by Korea Ministry of Commerce, Industry and Energy

References:

1. J. M. Cormier and I. Rusu, "Syngas production via methane steam reforming with oxygen: plasma reactors versus chemical reactors", J. Physics D: Appl. Phys. 34 (2001), 2798-2803

2. Y.H. Kim, W.S. Kang, J.M.. Kang, S.H. Hong, Y.H. Song, S.J. Kim, "Experimental and Numerical analysis of Streamers in Pulsed Corona and Dielectric Barrier Discharges", IEEE Trans. Plasma Sciences, Vol. 32, No. 1, 18-24, Feb. 2004

3. E. Hnatiuc, B. Cheron, B. Hnatiuc, R. Burlica, J.L. Brisset, "Cold Plasma Electrochemical Reactor with Rotary Discharge", Proceedings of HAKONE VIII

A Miniature RF Atmospheric Pressure Glow Discharge Torch (APGD-*t*)

S. Coulombe and V. Léveillé

Department of Chemical Engineering, McGill University, Montréal (QC), Canada

The interest in the development of atmospheric pressure glow discharge plasma sources has grown considerably over last few years [1,2]. Ideally, such sources would offer the principal benefits of the "classical" low-pressure glow discharges with additional advantages associated with the operation outside vacuum chambers (lower equipment and operation costs, compact size and portability, ease of sample handling). There is in fact an interest to develop such sources for the treatment of biological surfaces since those are particularly difficult to handle under low-pressure conditions, and/or require *in-situ* treatment. Some examples of actual (or potential) applications in this field are the sterilization of contaminated surfaces [3], the removal of cells and biofilms, the momentarily disruption of the cell adhesion properties [4], the surface functionalization of polymer surfaces for the microcontact printing of proteins, and the disruption/acceleration of biochemical processes. This paper reports recent research activities that led to the development of a miniature atmospheric pressure glow discharge torch (APGD-*t*) suitable for the precise treatment of biological surfaces.

Figure 1 shows a schematic of the atmospheric pressure glow discharge torch (APGD-*t*) and its electrical circuit. The torch consists of a quartz confinement tube which downstream end is shaped into a convergent nozzle (final I.D. = 500 μm). The central stainless steel tube serves two purposes: as powered electrode and for the injection of reactive gaseous species into the afterglow plasma jet. A silver epoxy painted on the external surface of the quartz tube serves as the ground electrode. Two zones with distinct functions are created with this geometry: a plasma-forming zone where electrons, excited neutral He and metastables are formed, and a recombination zone (the afterglow plasma jet) where the active species formed in the plasma-forming zone recombine and loose their energy to excite the reactive gaseous species injected through the capillary. From the electrical standpoint, the torch assembly forms a concentric electrodes capacitor having a theoretical capacitance value of ≈1.5 pF. A pulsed RF (13.56 MHz) excitation is used to sustain a stable glow discharge jet of various power levels in the flowing plasma-forming gas (He). A homemade series inductor is used in order to provide near-resonance circuit conditions. The power delivered to the torch is determined from the measurement of the torch voltage, circuit current and phase angle between both signals. Due to the extremely low electrical capacitance of the torch and the use of 13.56 MHz excitation, the voltage probe (Tektronix P3169A, 10X, 10 MΩ, 8 pF) has a drastic effect on the operating conditions and thus, has to be accounted for. Detailed circuit analyses and experimental investigations showed that an inductance value of 6.3 μH gives rise to reasonable operating conditions.

The measured breakdown voltage of the APGD-*t* operating with 1 SLM He fed in the quartz tube is ≈67 $V_{pk\text{-}to\text{-}0}$. This low value is attributed to the geometrical amplification of the electric field at the capillary electrode surface. In fact, the estimated value for the electric field at the breakdown voltage is ≈1.6×10^5 V/m thanks to a 4.4X geometrical amplification factor. This minimum electric field value compares well with the value of ≈2×10^5 V/m one obtains by extrapolation of the Paschen's curve data reported for the high-frequency breakdown of He [5]. At 10% pulse duty cycle, the measured RMS torch voltage, RMS circuit current (Tektronix CT-2 current transmitter, 1mV/1mA into 50Ω) and phase shift between both signals were 382 V_{rms}, 410 mA_{rms} ($|Z|$=910 Ω) and -86°, respectively ("ON" period only). The torch/voltage probe system thus represents a highly-capacitive complex impedance in the circuit. The torch's resistance (R_T) and capacitance (C_T), and resistive power dissipated in the torch (P_T) and voltage probe (P_P) were determined from the circuit analysis. Values of R_T ≈160 Ω, C_T ≈5.1 pF, P_T ≈ 450 mW and P_P ≈640 mW were obtained. The power density of the glow discharge is thus ≈6 W/cm^3.

Fig. 2 shows telemicroscopic images of the plasma jet for three sets of conditions: 1 SLPM He in the quartz tube (top); 1 SLPM He in the quartz tube with 1 SCCM O_2 injected through the capillary electrode (middle); and 1

SLPM He + 1 SCCM O_2 injected in the quartz tube (bottom). When no reactive gas is injected in the plasma-forming region, a bright plasma jet extending ≈2.5 mm downstream of the nozzle exit is observed. This jet appears symmetric and laminar. The presence of a structure similar to a bow shock requires further investigation since the flow is subsonic. Experiments carried out under similar conditions but using a metallic mesh as ground electrode instead of the silver epoxy paint showed that the glow discharge fills the entire inter-electrode volume (≈76 mm^3). The bluish appearance of the jet is attributed to the entrainment and excitation by He metastables of N_2 molecules from the ambient air. The injection of small quantities of O_2 through the capillary electrode does not lead to a significant alteration of the jet though atomic oxygen is detected further downstream (by OES). The injection of the same amount of O_2 to the plasma-forming gas causes a quench of the optical emission of the plasma jet. Thorough studies of the plasma jet characteristics by optical emission spectroscopy and laser-absorption spectroscopy and of the interaction of the jet with a biological surface are currently under progress.

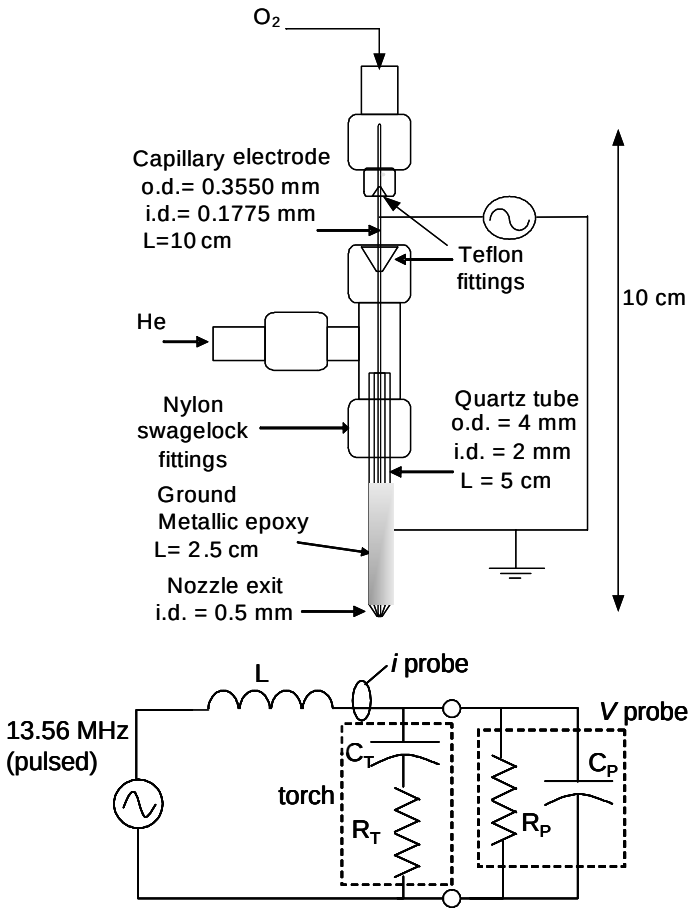

Fig. 1. Schematic view of the APGD-*t* and associated Electrical circuit.

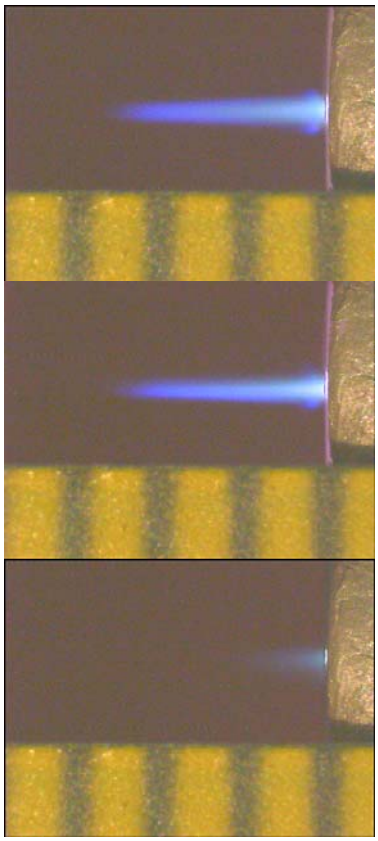

Fig. 2. Telemicroscopic images of the He plasma Plasma jet discharging into air.
Top: He, Middle: He + O_2 (Capillary),
Bottom: He + O_2 (Quartz)

References

[1] A. Fridman, A. Chirokov, A. Gustol – J. Phys. D: Appl. Phys. 38, R1 (2005).
[2] F. Massines – J. Phys. D : Appl. Phys. 38, E01 (2005).
[3] M. Laroussi, D.A. Mendis, M. Rosenberg - New J. Phys. 5**,** 41.1 (2003).
[4] E. Stoffels, I.E. Kieft, R.E. Sladek - J. Phys. D: Appl. Phys. 36, 2908 (2003).
[5] S.C. Brown - *Basic Data of Plasma Physics*, New York: AIP Press (1993).

Modeling zirconia melt droplet – substrate interaction

A.N. Cherepanov, V.N. Popov, O.P. Solonenko
Institute of Theoretical and Applied Mechanics, SB RAS, Novosibirsk, Russia

Abstract
Thermal and hydrodynamic processes that occur during impingement of the liquid metal and metal oxide droplets onto a multilayered substrate were numerically studied. The model developed is based on the Navier-Stokes equations for an incompressible liquid and on 'substrate–particle' heat transfer equations that take into account the surface tension forces and solidification of a melt. The simulation results are found to be in satisfactory agreement with experimental data.
Key words: micro-droplet, melt, substrate, collision, spreading, cooling, solidification, splat formation

1. Introduction

During the last one and half decades, increasingly growing interest was expressed to the problem of ultra-rapid quenching of melt micro-droplets of various materials upon their impingement on a surface [1-17]. This phenomenon is basic to many advanced technologies such as plasma, arc, detonation and flame spraying, powder micro-atomization, solder-drop-printing in microelectronics, production of microcrystalline and amorphous materials and high-temperature superconductors. Also, it is of great interest for heterogeneous plasma chemistry and materials science when it is necessary to study non-equilibrium state diagram of different alloys and composite materials under extreme exposures. It was recognized that further progress in improving both quality and structure of sprayed materials largely depends on our understanding of processes that occur during interaction of liquid particles, carried by a high – temperature jet, with substrates.

Characteristic features of this system are the fine particulates, the wide range of velocities and temperatures of droplets at their interaction with a surface and, as a consequence, the presence of many factors essentially complicating the analysis of the attendant phenomena. The interaction proceeds under extreme conditions like the high rate of droplet deformation, cooling, phase changes, and abnormal high local density of thermal fluxes and drastically variation of the physical properties of particle and substrate materials. Therefore, as the result of heating a particle in high-temperature jet and its subsequent quenching under impact with substrate, a spread out and solidified droplet, what is known as splat, can be in specific cases in metastable or amorphous state.

In this connection, it seems to be an urgent matter to further develop hydrodynamic and thermophysical concepts for the interaction between a liquid particle and a solid surface. Since a detailed experimental study of the majority of processes that occur in a melt particle and in the near – surface region of base (a substrate or already deposited layer) is extremely difficult, the only way to get a better insight into the phenomenon is to perform numerical experiments together with derivation of model analytical solutions [10,15,16].

The main goal of the paper presented is to develop and testing the physical and mathematical model and numerical method for unsteady conjugated conductive – convective heat transfer and phase transitions that occur during impingement of liquid micro-particles onto solid surfaces.

2. Physical and mathematical model

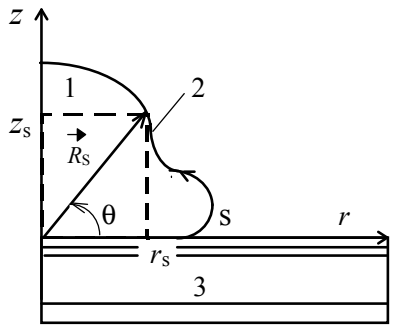

Fig. 1. Diagram of deforming droplet after collision with multi-layer substrate.

Let's assume that spherical droplet impinges onto a wet rigid substrate. The trajectory of the drop is normal to the substrate surface, and the initial substrate temperature is lower the melting point of the particles' material. After collision, a drop surface starts deforming, and an initial liquid flow develops in the drop (Fig. 1).

Viscous fluid dynamic equations. To numerical study the dynamic of a liquid drop after its impingement onto solid surface, we use the Navier-Stokes equations for a viscous incompressible fluid. We suppose the flow in the droplet to be laminar and the values of the thermophysical properties of the melt to be constant and equal to their mean values in the temperature range under consideration.

With allowance for the assumptions used, the equations of the fluid flow in the cylindrical coordinates shown in Fig. 1 have the following dimensionless form [18, 19]:

$$\frac{\partial U_z}{\partial \bar{z}}+\frac{1}{\bar{r}}\frac{\partial\left(\bar{r}U_r\right)}{\partial \bar{r}}=0,\quad \frac{1}{\bar{r}}\frac{\partial}{\partial \bar{r}}\left(\bar{r}\frac{\partial P}{\partial \bar{r}}\right)+\frac{\partial^2 P}{\partial \bar{z}^2}+\frac{1}{\bar{r}}\cdot\frac{\partial^2(\bar{r}U_r^2)}{\partial \bar{r}^2}+\frac{2}{\bar{r}}\frac{\partial^2(\bar{r}U_rU_z)}{\partial \bar{r}\partial \bar{z}}+\frac{\partial^2 U_z^2}{\partial \bar{z}^2}=0,$$

$$\frac{\partial U_z}{\partial \tau}+\frac{\partial U_z^2}{\partial \bar{z}}+\frac{1}{\bar{r}}\frac{\partial\left(\bar{r}U_rU_z\right)}{\partial \bar{r}}+\frac{\partial P}{\partial \bar{z}}-\frac{1}{\mathrm{Re}}\left[\frac{1}{\bar{r}}\frac{\partial}{\partial \bar{r}}\left(\bar{r}\frac{\partial U_z}{\partial \bar{r}}\right)+\frac{\partial^2 U_z}{\partial \bar{z}^2}\right]+\frac{1}{\mathrm{Fr}}=0, \tag{1}$$

$\tau=tu_{p0}/D_p, \bar{r}=r/D_p, \bar{z}=z/D_p, U_r=u_r/u_{p0}, U_z=u_z/u_{p0}, P=p/(\rho_{pm}^{(l)}u_{p0}^2)$. System (1) is solved with the dimensionless boundary conditions:

$$\begin{aligned}&U_r=0,\quad U_z=-1,\quad P=4/\mathrm{We}\ \text{ for }\tau=0,\\ &U_r=0,\quad \partial U_z/\partial \bar{r}=0,\quad \partial P/\partial \bar{r}=0\ \text{ for }\bar{r}=0,\\ &U_r=0,\quad U_z=0\ \text{ for }\ \bar{z}=\zeta(\bar{r},\tau),\quad \zeta(\bar{r},0)=0,\end{aligned} \tag{2}$$

$\bar{z}=\zeta(\bar{r},\tau)$ is the solidification front. The last relations are supplemented by the conditions at the free surface of liquid particle:

$$\left(P-\frac{2K}{\mathrm{We}}-\frac{2}{\mathrm{Re}}\frac{\partial U_r}{\partial \bar{r}}\right)n_r-\frac{1}{\mathrm{Re}}\left(\frac{\partial U_r}{\partial \bar{z}}+\frac{\partial U_z}{\partial \bar{r}}\right)n_z=0,\left(P-\frac{2K}{\mathrm{We}}-\frac{2}{\mathrm{Re}}\frac{\partial U_z}{\partial \bar{z}}\right)n_z-\frac{1}{\mathrm{Re}}\left(\frac{\partial U_r}{\partial \bar{z}}+\frac{\partial U_z}{\partial \bar{r}}\right)n_r=0. \tag{3}$$

Here n_r and n_z are the components of a unit vector normal to the free surface of the droplet, along the *r* and *z* axes, respectively, and the dimensionless curvature of drop surface is given by the relation [7]

$$K=\left\{x_s^2(x_s'y_s''-y_s'x_s'')+[(x_s')^2+(y_s')^2]x_sy_s'\right\}/\left(2x_s^2[(x_s')^2+(y_s')^2]^{3/2}\right),$$

where the prime denotes the derivative with respect to the dimensionless arc length $S=s/D_p$ and $x_s=r_s/D_p$, $y_s=z_s/D_p$ are dimensionless projections of the vector R_s/D_p onto the $\bar{r}$ and $\bar{z}$ axes, respectively (Fig.1).

Heat transfer equations. We determine the change in the temperature field in the droplet – substrate system from the solution of the conjugate heat transfer problem posed both in the liquid and solid phases of the particle, which undergoes solidification, and in the substrate. We take into account the liberation of the latent crystallization heat during the phase transition by introducing an effective heat capacity [20].

We write the heat transfer equations in the melt (*i*=1), in the layer that has already solidified (*i*=2), and in the substrate (*i*=3) in the following dimensionless form:

$$c_{eff}\left(\frac{\partial\vartheta_1}{\partial\tau}+U_r\frac{\partial\vartheta_1}{\partial \bar{r}}+U_z\frac{\partial\vartheta_1}{\partial \bar{z}}\right)=\frac{1}{\mathrm{Pe}_1}\left[\frac{1}{\bar{r}}\frac{\partial}{\partial \bar{r}}\left(\bar{r}\frac{\partial\vartheta_1}{\partial \bar{r}}\right)+\frac{\partial^2\vartheta_1}{\partial \bar{z}^2}\right],\ c_{eff}\frac{\partial\vartheta_i}{\partial\tau}=\frac{1}{\mathrm{Pe}_i}\left[\frac{1}{\bar{r}}\frac{\partial}{\partial \bar{r}}\left(\bar{r}\frac{\partial\vartheta_i}{\partial \bar{r}}\right)+\frac{\partial^2\vartheta_i}{\partial \bar{z}^2}\right], \tag{4}$$

where $\mathrm{Pe}_i=D_pu_{p0}/a_i$ is the Peclet number, $\vartheta_i=T_i/T_{pm}$ (*i*=2,3), and $\tau=u_{p0}t/D_p$ is the dimensionless time. The effective heat capacity c_{eff} is defined by the relations

$$c_{eff}=\begin{cases}1, & \vartheta>1+\Delta\vartheta/2,\\ 1+\mathrm{Ku}_p^{(l)}/\Delta\vartheta, & 1-\Delta\vartheta/2\le\vartheta\le1+\Delta\vartheta/2,\\ c_2/c_1, & \vartheta<1-\Delta\vartheta/2,\end{cases} \tag{5}$$

where $\Delta\vartheta=\Delta T/T_{pm}$ is dimensionless temperature interval over which the phase transition is "smeared" [20]. To describing crystallization of the droplet one may use the Stefan-problem approximation, assuming that the temperature at the solid-liquid interface coincides with the equilibrium solidification point, the crystallization front is macroscopically smooth, and the nucleation in the liquid metal may be ignored.

Equations (4) should be supplemented with the following boundary conditions.

1. Initial values of the droplet and substrate temperatures: $\vartheta_1|_{\tau=0}=\vartheta_{p0}$, $\vartheta_3|_{\tau=0}=\vartheta_{20}$. (6)

2. Adiabatic condition at the free surface of the drop: $\bar{\lambda}_i\left(\frac{\partial\vartheta_1}{\partial r}n_r+\frac{\partial\vartheta_1}{\partial z}n_z\right)=0.$ (7)

3. Condition of heat transfer between the drop and the substrate:

$$\bar{\lambda}_i \frac{\partial \vartheta_i}{\partial \bar{z}}\Big|_{\bar{z}=+0} = \lambda_3 \frac{\partial \vartheta_3}{\partial \bar{z}}\Big|_{\bar{z}=-0} = \mathrm{Bi}(\vartheta_i - \vartheta_3). \tag{8}$$

Hear $\bar{\lambda}_i = \lambda_i / \lambda_1$ (i=1 for $\vartheta \geq 1$, i=2 for $\vartheta < 1$), $\mathrm{Bi} = \alpha D_p / \lambda_1$ is the Biot number, $\alpha = 1/\sum_j \delta_{sj} / \lambda_{sj}$ is the coefficient substrate-to-particle heat transfer through the previously deposited layer(s), and δ_{sj}, λ_j are the thickness and thermal conductivity of the jth sub-layer, respectively.

4. Conditions of heat transfer at the lower, side and upper substrate surfaces, respectively:

$$\partial\vartheta / \partial\bar{z}|_{\bar{z}=-L} = \partial\vartheta / \partial r|_{\bar{r}=\bar{r}_3} = \partial\vartheta / \partial r|_{\bar{z}=0} = 0. \tag{9}$$

Here $\bar{L} = L / D_p$, $\bar{r}_3 = r_3 / D_p$ (L, r_3 are the thickness and radial dimension of the substrate; $r_3 >> D_p$).

5. Symmetry condition at the z axis in the droplet spreading and substrate:

$$\frac{\partial \vartheta_i}{\partial \bar{r}}\Big|_{\bar{r}=+0} = 0, \quad i = 1, 2, 3. \tag{10}$$

The heat-transfer equations (4) with boundary conditions (6)-(10), together with Navier-Stokes equations for the liquid part of the particle (1), govern the droplet cooling and solidification process.

3. Numerical method

The numerical algorithm for computing the problem formulated was describe in [18]. It is based on a finite-difference approximation of the Navier-Stockes and heat-transfer equations with an implicit scheme of order $O(\tau, h)$. The region occupied by the unsteady flow of melt is marked with successively enumerated particles-markers located along the droplet free surface and moving with the local fluid velocity. To satisfy the monotonicity conditions for the finite-difference scheme, the special derivatives in the inertial terms are approximated by using the "up-wind" scheme. The diffusion terms are approximated by their second-order difference analogs. In this approach, no limits are imposed by Reynolds numbers on the stability of the numerical calculations.

Having determined the velocity field, we calculate the temperature field in the drop and substrate in accordance with the Eqs. (4)–(10). The thermal problem is to be solved in two conjugated computational domains, in the drop and in the substrate. The match the temperature distributions in the two domains, no more than three iterations were sufficient. The new coordinated of the markers, $r_m^{(n+1)}$ and $z_m^{(n+1)}$, at the (n+1)-th time step are calculated by the relations

$$r_m^{(n+1)} = r_m^{(n)} + u_m^{(n)} \Delta\tau_{n+1}, \quad z_m^{(n+1)} = z_m^{(n)} + v_m^{(n)} \Delta\tau_{n+1}, \quad m=1,\ldots, M(t_n).$$

Here $u_m^{(n)}$ and $v_m^{(n)}$ are the particle velocities determined in accordance with the mean local velocities in a small vicinity of each of the markers and $M(t_n)$ is the number of markers at the time t_n. At each time step, we have to either remove or add some part of markers, in order to obtain their uniform distribution over the droplet contour, and re-enumerate them. Throughout the whole computational domain, a spatial grid h_z=h_r=0.01·D_p was used. At the time moment t_{n+1}, the time step $\Delta\tau_{n+1}$ was computed by the formula

$$\Delta\tau_{n+1} = \min\{h_z, h_r\} / K_0 \max\{|u_m^{(n)}|, |v_m^{(n)}|\}, \quad K_0=20.$$

Following [20], we chose the region over which the boundary between the phases was "smeared" so that the region included two or three nodes of the spatial grid. This could be achieved through preliminary estimation of typical temperature gradient. In the computer program, the temperature interval ΔT was chosen automatically. It should be noted that, in the calculations, the mean value of this parameter was around 5°C.

At each time step, the system of algebraic equations is solved using an iterative procedure. The computations were terminated on reaching the relative error of 0.002.

The simulation results are found to be in satisfactory agreement with different experimental data (low and high Reynolds and Weber number). In particular, it is possible to simulate the droplet's oscillation during splat formation. The results of computational experiment allow to analyze the influence of the key physical parameters (KPPs) - and thermophysical properties of particle and substrate materials on morphology of splat, the time of its formation, the size of contact spot splat-substrate, etc. A typical CPU time of one running using conventional PC computer (f ~ 1-2 GHz) is 2-3 hours.

4. Results and discussion

In accordance with [21], the following four basic scenarios of splats formation are possible, depending on the temperature $T_{c0} = (T_{p0} + K_{\varepsilon}^{(b,p)} T_{b0})/(1 + K_{\varepsilon}^{(b,p)})$ of the particle/substrate interface and melting points of particle (T_{pm}) and substrate (T_{bm}) materials (Fig. 1):

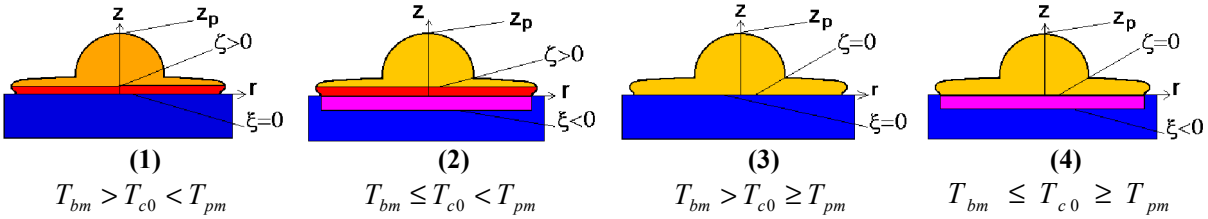

(1) $T_{bm} > T_{c0} < T_{pm}$ (2) $T_{bm} \le T_{c0} < T_{pm}$ (3) $T_{bm} > T_{c0} \ge T_{pm}$ (4) $T_{bm} \le T_{c0} \ge T_{pm}$

Fig. 2. Possible scenarios of splat formation.

(1) – spreading of the droplet over the solid surface of the base and its simultaneous solidification;
(2) – spreading of the droplet over the surface, its simultaneous solidification, and partial sub-melting of the base at the base/particle contact spot;
(3) – spreading of the liquid particle over the solid surface, followed by cooling and solidification of the flattened drop with simultaneous recoiling of its edges;
(4) – spreading of the liquid droplet over the surface with simultaneous sub-melting of the base, followed by their cooling and solidification.

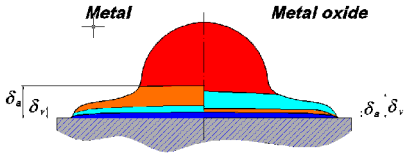

Fig. 3. Relative thickness of thermal (δ_a) and hydrodynamic (δ_v) boundary layers under metal (Pr<<1) and metal oxide (Pr>1) splats formation.

For each of the above-mentioned scenarios, two characteristic regimes of heat transfer between the melt and the solid wall (either the particle solidification front surface $\zeta(r,t)$ or the substrate z=0) are possible depending on the ratio between the thicknesses of the dynamic and thermal boundary layers in the melt flow (see Fig.3), whose value, in a first-order approximation, can be estimated as $\delta_v / \delta_a \approx \sqrt{\mathrm{Pr}}$.

4.1. Testing the model and numerical method

The proposed model was tested for adequacy by comparing the droplet shape computed for different times after its impingement onto copper substrate with the experimental data previously reported in [15].
It was carried out the additional model numerical experiments to study the deviation of experimentally measured and numerically predicted splats' diameter and morphology at reduced We and Pe numbers in order to study the influence the surface tension on splat formation on stainless steel substrate (see Figs. 4–7). It takes place a rather good agreement between experimental and numerical results. As evident from the results of comparison, the influence of a surface tension is negligible at We > 200 and Pe>250.

4.2. Modeling zirconia splats formation

The next series of computer simulation has been fulfilled regarding the zirconia splats' formation. The results of calculations presented in Figs. 8–10 establish a fact a rather satisfactory agreement between experimental and numerically predicted final diameter and morphology of splats.

(a)

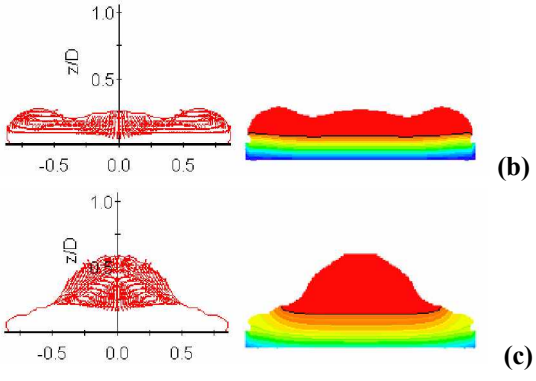

(b)

(c)

Fig. 4. The final experimental tin splat morphology - (a), at KPPs: D_p=1.55 mm, u_{p0}= 0.75 m/sec, T_{p0}=535 K, T_{b0}=290 K; the numerically predicted spreading and solidifying droplet at time moments 2 msec, - (b), and 9 msec - (c). We=11, Pe=67, Re=4381.

(a)

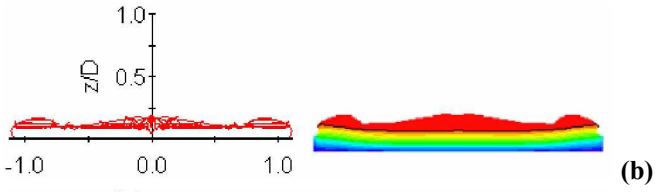

(b)

Fig. 5. The final experimental tin splat morphology - (a), at KPPs: D_p=1.55 mm, u_{p0}= 1.16 m/sec, T_{p0}=532 K, T_{b0}=290 K; the numerically predicted spreading and solidifying droplet at time moments 2 msec - (b), and 4 msec - (c). We=27, Pe=104, Re=6772.

(a)

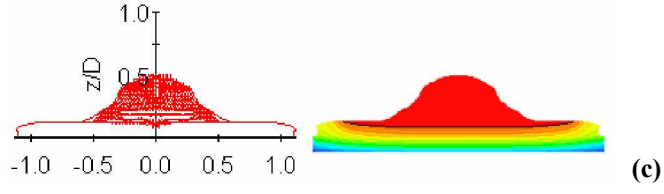

(c)

Fig. 6. The final experimental tin splat morphology - (a), at KPPs: D_p=1.55 mm, u_{p0}= 1.64 m/sec, T_{p0}=528 K, T_{b0}=290 K; the numerically predicted spreading and solidifying droplet at time moments 1 msec - (b), and 2 msec - (c). We=54, Pe=147, Re=9603.

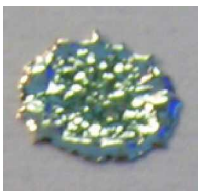

(a)

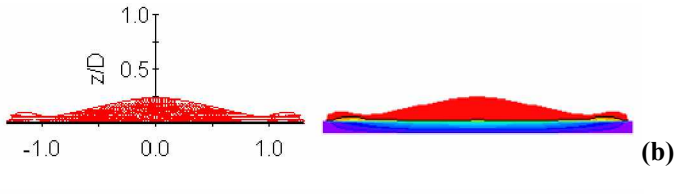

(b)

Fig. 7. The final experimental tin splat morphology - (a), at KPPs: D_p=1.55 mm, u_{p0}= 3.08 m/sec, T_{p0}=515 K, T_{b0}=290 K; the numerically predicted spreading and solidifying droplet at time moments 1 msec - (b), and 2 msec - (c). We=189, Pe=276, Re=18045.

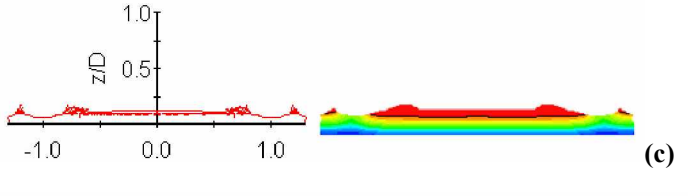

(c)

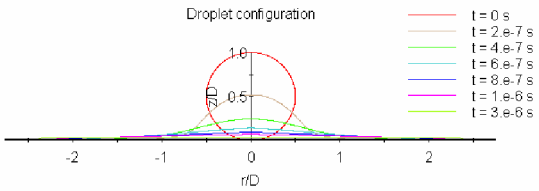

Fig. 8. Dynamics of ZrO_2 droplet spreading and solidification calculated at following value of the KPPs: D_p=54.3 μm, u_{p0}=146 m/sec, T_{p0}=3380 K, T_{b0}=624 K.

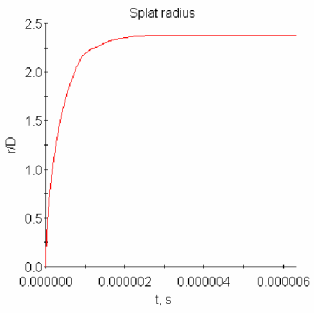

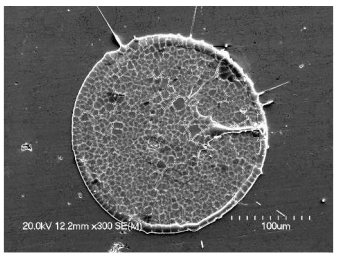

Final splat D_s/D_p=4.71

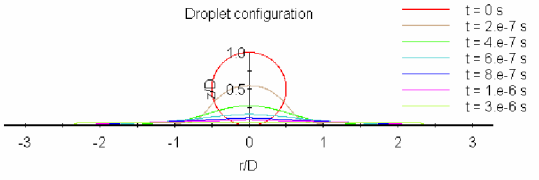

Fig. 9. Dynamics of ZrO_2 droplet spreading and solidification calculated at following value of the KPPs: D_p=45.6 μm, u_{p0}=114 m/sec, T_{p0}=3120 K, T_{b0}=586 K.

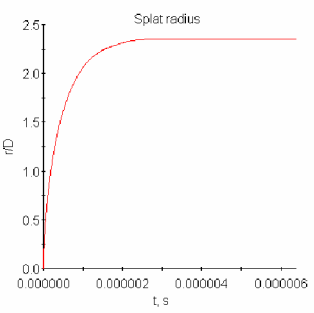

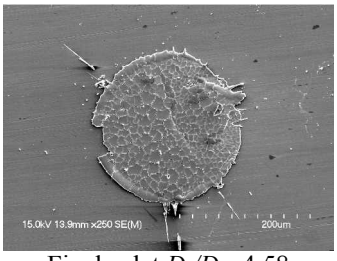

Final splat D_s/D_p=4.58

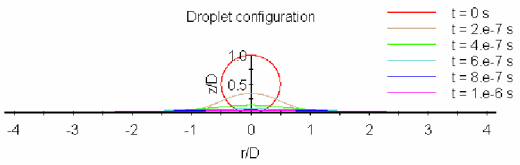

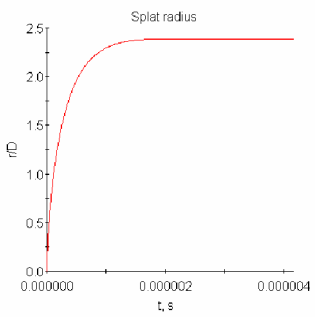

Fig. 10. Dynamics of ZrO_2 droplet spreading and solidification calculated at following value of the KPPs: D_p=36 μm, u_{p0}=130 m/sec, T_{p0}=3540 K, T_{b0}=612 K.

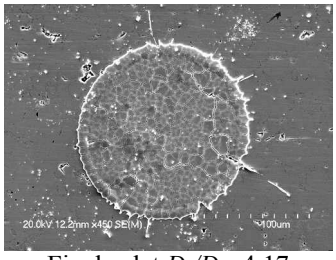

Final splat D_s/D_p=4.17

5. Conclusions

Thermal and hydrodynamic processes that occur during impingement of the liquid metal and metal oxide droplets onto a multilayered substrate were numerically studied; the model developed is based on the Navier-Stokes equations for an incompressible liquid and on 'substrate–particle' heat transfer equations that take into account the surface tension forces and solidification of a melt. The model and numerical method developed were tested on example of tin droplets impacting with stainless steel substrates.

The simulation of the ZrO_2 splats formation on a nickel substrates were carried out using the mathematical model and numerical method developed. The results obtained are in a reasonable good agreement with the experimental data [22].

Acknowledgement

The present study was supported by Siberian Branch of Russian Academy of Sciences (Integration Program No.93 on 2003-2005) and by Russian Academy of Sciences (Program of Prezidium of RAS No.8 on 2003-2005).

Referenecs

[1] G.Trapaga, J.Szekely – Metal. Trans. B22 (1991), p.901-914.
[2] M.Rein – Fluid Dynamics Research, 12 (1993), p.61-93.
[3] D.J.Hayes, D.B.Wallace, M.T.Boldman, R.M.Marusak – Int. J. Microcircuits and Electronic Packaging, 16 (1993), p.173-180.
[4] F.Gao, A.A.Sonin – Proc. of Royal Society, London, 444 A (1994), p.533-554.
[5] O.P.Solonenko – Thermal Plasma and New Materials Technology. Vol.2. Investigation and Design of Thermal Plasma Technologies, Ed. by O.P.Solonenko and M.F.Zhukov, Cambridge, England, Cambridge Interscience Publishing (1995), p.7-96.
[6] M.Pasandideh-Fard, Y.M.Qiao, S.Chandra, J.Mostaghimi – Physics of Fluids, 8 (1996), p.650-659.
[7] Z.Zhao, D.Poulikakos, J.Fukai – Int. J. of Heat and Mass Transfer, 239 (1996), p.2771-2789.
[8] J.M.Waldvogel, D.Poulikakos – Int. J. of Heat and Mass Transfer, 40 (1997), p.295-309.
[9] J.Mostaghimi – Pure and Applied Chemistry, 70, 6 (1998), p.1209-1215.
[10] O.P.Solonenko, A.V.Smirnov – Dokl. RAN, 63 (1998), p.46-49 (in Russian).
[11] D.J.Hayes, D.B.Wallace – Chip Scale Review, 2 (1998), p.75-80.
[12] V.V.Sobolev, J.M.Guilemany – J. of Thermal Spray Technology, 8, 1 (1999), p.87-101.
[13] V.V.Sobolev, J.M.Guilemany – J. of Thermal Spray Technology, 8, 2 (1999), p.301-314.
[14] S.D.Aziz, Chandra – Int. J. of Heat and Mass Transfer, 43 (2000), p.2841-2857.
[15] M.R.Predtechensky, Yu.D.Varlamov, S.N.Ul'yankin, A.N.Cherepanov, V.N.Popov – J. Eng. Thermophys., 11, 1 (2002), p.83-103.
[16] O.P.Solonenko – Int. J. of High Temp. Mat. Processes, 7, 2 (2003), p.187-194.
[17] P.Fauchais – J. Phys. D: Appl. Phys. 37 (2004), p.R86-R108.
[18] V.Popov – Matematicheskoye modelirovaniye, 13, 9 (2001) (in Russian).
[19] M.Predtechensky, A.Cherepanov, V.Popov, Yu.Varlamov – J. of Appl. Mechanics and Technical Physics, 43, 1 (2002).
[20] A.Samarsky, B.Moiseenko – Zh. Vychisl. Mat. Mat. Fiz., 5, 5 (1965) (in Russian).
[21] O.P.Solonenko, Thermal Spray: International Advances in Coating Technology, USA, ASM International (1992), p.787-792.
[22] O.Solonenko, A.Mikhalchenko, E.Kartaev, M.Bondar', K.Ogawa, T.Shoji, M.Tanno – Materials Transactions, 44, 11 (2003).

Analysis of Capability of the Polychromatic Pyrometry Method to Measure Temperature of Single Particle in High-Temperature Flow

E.V. Kartaev, A.A. Mikhalchenko, O.P. Solonenko
Institute of Theoretical and Applied Mechanics, SB RAS, Novosibirsk, RUSSIA

Abstract. The main goal of the paper presented is to model the procedure of measuring the temperature of alumina particles by implementing the 4-color pyrometry technique as well as to analyze the applicability of photo electronic multipliers (PEM-83) in comparison with that of Si-based avalanche photodiodes (APD S5344). The conducted numerical analysis regarded 4-color pyrometry technique as being promising for measuring the "non-gray" particle temperature, with APD S5344 being used as particle radiation detector.
Keywords: plasma, single particle, temperature, modeling, 4-color pyrometry, spectral emissivity.

1. Introduction

The reliable in-situ measurement of velocity, temperature and size of single in-flight particle in high-temperature flows, including plasma ones, is still of major interest since in a number of cases the information about an individual particle needed instead of statistical estimates of above parameters of the representative particle ensemble. In particular, this problem appears when the mechanisms of formation of splat as flattened and solidified melt droplet is studied as function of the key physical parameters (KPPs) of particle collision with a substrate [1].

Particle temperature in high-temperature dust-laden flows is measured by detecting the particle thermal radiation. Here, the radiation intensity is simultaneously recorded in two spectral bands and the ratio of spectral intensities is derived to determine particle color temperature. The latter is equal to a real particle temperature assuming the particle behaves as "gray" radiator. The error of the method is primarily affected by spectral dependence of particle emissivity, an essential temperature gradients within the particle (for instance, in semi-transparent particles of alumina or YSZ) and chosen band centers for two-color pyrometry as well. The mentioned spectral particle emissivity in measurement procedure is commonly considered to be indeterminate.

In order to reduce both an instrumental error and that of the method one should increase the number wavelength bands to detect. The recording of particle thermal radiation in three bands is regarded as giving the optional feature in particle temperature measurement. This is due to using of an expanded scope of operating spectral bands as well as implementing the two independent methods of signal processing [2]. Assuming particle as "gray" body these methods allow one to match three independent particle temperatures (two color temperatures and 3-color one) having differed instrumental errors and those of the methods.

In the present work by simulating the measurement procedure of particle temperature the analysis of the method of multicolor pyrometry taking into account the 4 wavelength bands is conducted, with spectral particle emissivity being as $\varepsilon(\lambda,T)=a_o+a_1\lambda$.

2. Modeling and comparative analysis

The comparative analysis of measuring the temperature and size of alumina particles (original powder being close to mono-disperse one) have revealed the three-color pyrometry as having the least instrumental error of particle temperature measurement. Here the alumina powder was chosen as its optical properties in wide spectral region for vast variety of temperatures are most accurate, for instance, the effective absorption cross-section [3]. Attempting to take into consideration a "non-gray" radiation of particle by applying the linear approximation of its emissivity ($\varepsilon(\lambda,T)=a_o+a_1\lambda$) have shown to be stipulated unsatisfactorily which is pronounced by several minima within noise "grass" [2]. It is dealt with the excess of number of unknown parameters (particle temperature and size, the coefficients of linear approximation of spectral emissivity) over the number spectral bands to detect the particle radiation (3 wavelengths).

Detecting the particle radiation in four spectral bands enables one to provide the comprehensive survey of particle thermal state owing to the both enhanced spectral scope and three independent methods of signal data processing. The total error in measuring the particle temperature is caused by following factors: addition of detector shot noise to the pyrometric signal, plasma background noise, the violation of "gray" behavior of the particle radiation.

In the present paper the 4-color pyrometry technique assuming a linear spectral dependence of particle emissivity $\varepsilon(\lambda,T)=a_o+a_1\lambda$ is used in order to test whether it is capable to estimate average temperature of

alumina particles' ensemble more precisely. The latter is urgent when detecting YSZ particle radiation for which corresponding optical properties in wide spectral region for vast variety of temperatures are rather scarce. Moreover, when traveling in plasma jet the temperature gradients inside the YSZ particles are likely valuable. This influences the YSZ particle emissivity [5].

To investigate a potential of diagnostic setup presented in [2] intended for detecting the particle parameters in plasma spraying, the photo electronic multiplier (PEM-83) used by this time and the avalanche photodiode (APD S5344 commercially available by Hamamatsu Inc.) were separately analyzed as detectors based on the multicolor pyrometry technique. The basic characteristics of both detectors are denoted in Table 1.

Table 1. The basic features of the detectors

Detector	Spectral response bandwidth, μm	Dark current, nA	Gain M	Cut-off frequency band Δf at 50 Ω load resistance, MHz	Photo sensitivity $S_{\lambda i}$, mA/Wt			
					λ_1= 0.5145 μm	λ_2= 0.6328 μm	λ_3= 0.7212 μm	λ_4= 0.8906 μm
PEM-83	0.4-1.2	500	$4 \cdot 10^5$	100	0.6	1.5	2.4	1.9
APD S5344	0.2-1.2	20-100	50	25	410	420	400	140

As the development of [2] the simulation of the measurement procedure of alumina particle temperature by detecting the signals with different noise levels for each of stated detectors has been executed. This was done to analyze an influence of noise level on the error of temperature estimate. The original particle parameters to be restored: size, velocity and temperature. Particle diameter and velocity, plasma background temperature were supposed to be constant (D_p= 50 μm, u_p= 100 and 200 mps, T_g= 2000 K), whereas particle temperature was varied within the range of T_p= 2400÷2800 K. The intensity P_{0i} of modeled signal per each spectral range was calculated in accordance with formula (1) below:

$$P_{0i} = f(D_p, u_p, t)\varepsilon(\lambda_i, T)\int_{\lambda_i-\Delta\lambda_i}^{\lambda_i+\Delta\lambda_i}\Phi_i(\lambda)\frac{C_1 d\lambda}{\lambda^5\left[\exp(C_2/\lambda T)-1\right]},\ i = 1 \div 4, \tag{1}$$

where $f(D_p,u_p,t)$ is the function that describes passing of the image of a spherical particle of diameter D_p in the plane of the intake diaphragm in time as a function of its velocity u_p, this function is proportional to the area of the particle image sequentially truncated by slits S_1 and S_2 (Fig.1) of the intake diaphragm; $\varepsilon(\lambda_i, T_p)$, ($i$=1÷4) – the emissivity of particle substance at the center of the spectral region of the i-th interference filter with measured transmission factor $\Phi_i(\lambda)$, $\lambda \in [\lambda_1 - \Delta\lambda_i/2;\ \lambda_i + \Delta\lambda_i/2]$.

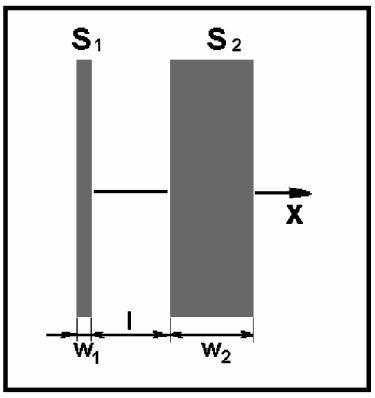

Fig.1. Geometry of the intake diaphragm. The S_1 slit width w_1= 100 μm, S_1 slit width w2= 800 μm, the inter-slit distance I= 800 μm, the diaphragm height – 3 mm.

The modeled signals are considered to be superimposed additively by a normally distributed noise with the relative mean-root-square error being expressed as following:

$$\sigma_{ni} / P_{0i} = P_{0i}^{-1} \sqrt{PkT_g \Delta f + 2e(P_{0i} + P)(1+B)\Delta f / S_{\lambda i}}\ , \qquad (2)$$

where P – average power irradiated by plasma background at i-th spectral region, i=1÷4; k = 1.38·10^{-23} J/K - Boltzmann constant; e = 1.6·10^{-19} A·sec - electron charge; (1+B)=2.5 - the coefficient including shot noise of PEM-83 dynodes; $S_{\lambda i}$, A/Wt - spectral sensitivity of PEM's photocathode; Δf = 20 MHz - the transmittance bandwidth of the electronic channel. In Fig.2(a) the typical profile of current signal of detected particle thermal radiation at λ_3= 0.7212 μm when using APD S5344 as the passive detector is drawn, in Fig.2(b) the corresponding current signal at PEM-83 photocathode is shown. In both cases the parameters of irradiating particle were following: D_p= 50 μm, u_p= 100 mps, T_p= 2400 K and ε(λ) =0.1.

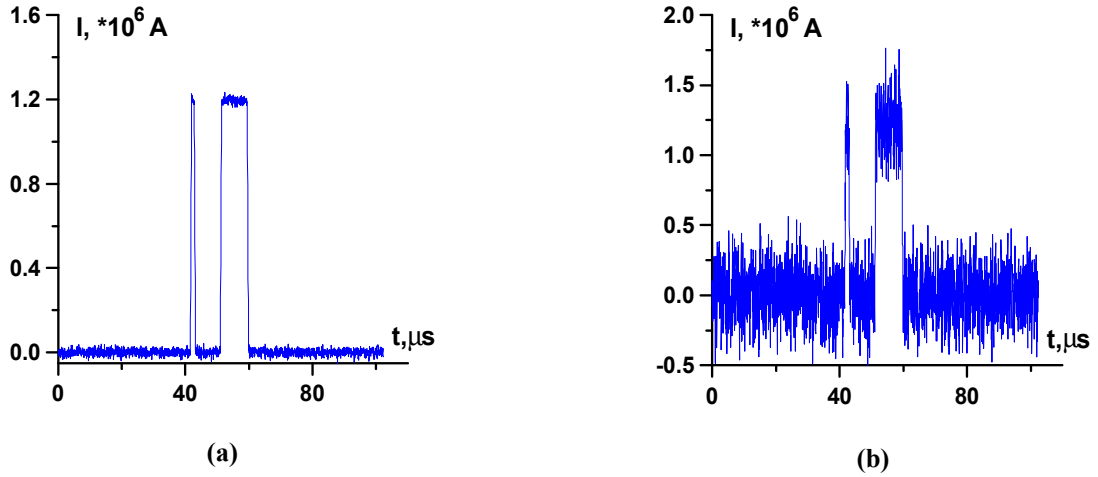

Fig.2. The typical signals of current for detecting the particle radiation at λ_3= 0.7212 μm when using APD S5344 as the passive detector – (a); the corresponding current signal at PEM-83 photocathode – (b). Parameters of irradiating particle: D_p= 50 μm, u_p= 100 mps, T_p= 2400 K and ε(λ) =0.1.

In the expression for relative noise mean-root-square error of APD S5344 the value allowing the APD magnification to be dependent on selected wavelength should replace (1+B) value in (2). It is physically caused by distinguished depth of penetration of light with different wavelengths in photosensitive area in silicon. In further modeling the particle thermal radiation this factor was neglected.

Within the restrictions of the model proposed by authors of [6,7] and described in detail in [8], the estimates of 3-color temperature T_{3c} using least square method for the same spectral regions λ_2=0.6328 μm, λ_3= 0.7212 μm, λ_4 = 0.8906 μm were obtained assuming particle as "gray" body. With the object of considering the real spectral dependence of emissivity of single Al_2O_3 particle, this model have been generalized for the case of $\varepsilon(\lambda)=a_0+a_1\lambda$ by means of complementary information on the base of the particle radiation intensity at λ_1=0.5145 μm. 4-color temperature T_{4c} is complied with minimum of the following discrepancy:

$$\Delta(r_p, \varepsilon, T) = \sum_{i=1}^{4} \left\{ \pi r_p^2 \varepsilon(\lambda_i, T) \int_{\lambda_i - \Delta\lambda_i/2}^{\lambda_i + \Delta\lambda_i/2} \Phi_i(\lambda) \frac{C_1 d\lambda}{\lambda^5 [\exp(C_2/\lambda T) - 1]} - \overline{P}_i \right\}^2 / \sum_{i=1}^{4} \overline{P}_i^2, \qquad (3)$$

where πr_p^2 - the area of irradiating particle, $\overline{P}_i$ - average power irradiated by the particle at i-th spectral region on the signal "plateau" corresponding to traveling the full particle image through wide slit S_2 (see Fig.1). Previously when calculating 3-color temperature the constancy of particle emissivity $\varepsilon(\lambda) = a_0 = const$ was postulated. The authors of [6] maintain yet the minimum of $\Delta(r_p,\varepsilon,T)$ to be determined in the best way when the linear approximation $\varepsilon(\lambda,T)=a_o+a_1\lambda$ is used.

Numerical algorithm of computing the minimum of (3) by analogy with that in [7] comprises the plotting 3D grid with nodes (q_i, p_j, T_k), i=1,…N_1, j=1,…N_2, k=1,…N_3 within the area of varying the quantities $q_i = a_{oi}\pi r_p^2$, $p_j = a_{1j}\lambda\pi r_p^2$ and T_k corresponding to some discrepancy Δ_{ijk}. The sought values of q^*, p^* $T_{4c} = T^*$ are supposed to be adequate the minimization of $\Delta^* = \min \Delta_{ijk}$ determining the instrumental error of the given model.

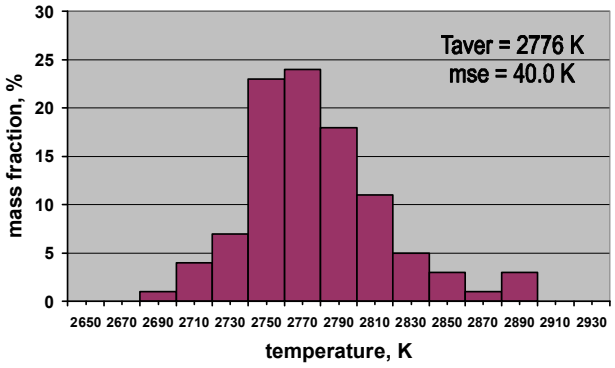

(a)

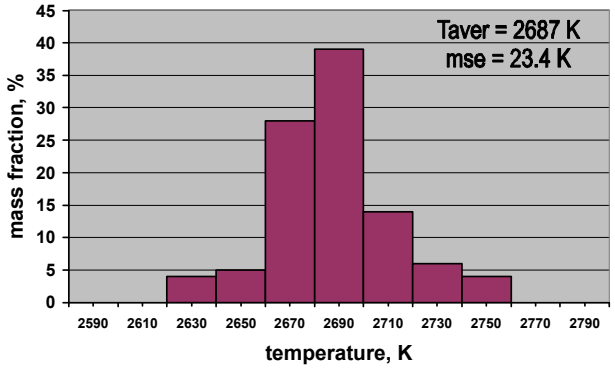

(b)

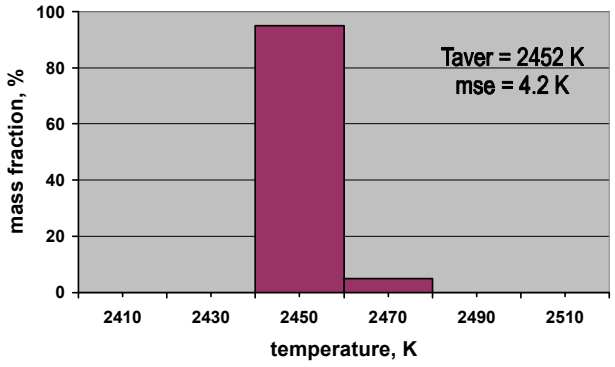

(c)

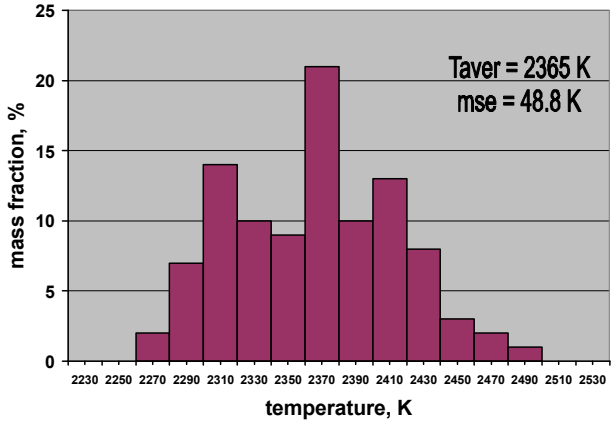

(d)

Fig. 3. Bar charts of particle temperature distributions of 10 μm alumina powder: *a*, *b* – color temperatures T_{c34} and T_{c24}; *c*, *d* – T_{3c} and T_{4c} calculated for 3 and 4 spectral regions respectively.

To estimate the potential limits of diagnostics of alumina particles using APD S5344 the modeling of 100 in-flight single particles with fixed parameters (D_p= 510 μm, u_p= 100 mps, T_p= 2350 K), with chosen spectral emissivity of alumina particle ε(λ) = 0.15-0.1λ (μm) being close to that in [3]. This has a descending slope of spectral emissivity for selected Al_2O_3 particle size and temperature. Here the modeled signals had following noise levels relative to useful ones in spectral regions of interest in the view of transmission bandwidths of filters: $\sigma_{n1} / \overline{P}_1 = 0.18$, $\sigma_{n2} / \overline{P}_2 = 0.11$, $\sigma_{n3} / \overline{P}_3 = 0.07$, $\sigma_{n4} / \overline{P}_4 = 0.08$.

The results of statistical data acquired for color temperatures T_{c34}, T_{c24}, 3-color temperature T_{3c} ("gray" body assumption) as well as 4-color temperature T_{4c} taking into consideration spectral dependence ε(λ) are depicted in Fig.3. The estimate of averaged velocity of particles' ensemble was 197 mps, with standard velocity deviation being about 6 mps.

As seen from the bar charts of the temperatures that averaged 4-color temperature T_{4c} is close to the real temperature of the particles modeled, nevertheless it has a relatively wide standard "3σ" data scattering of ±150 K. For given noise level the procedure permitted to restore certainly the negative slope of dependence $\varepsilon(\lambda)$. At the same time the absolute emissivities at each wavelength had been restored with averaged error of ~20-25%. The selected averages of as 3-color temperature as either color temperature are still biased from the real temperature. The error of estimation of T_{3c} is entirely specified by methodical error of the "gray" body approach. Though it had a very narrow data scattering (±15 K), conditioned by presence of shot noise of the detector. The errors of estimates of the color temperatures are much greater than that of T_{3c} in average and in data scattering too as already notified in [8].

The modeling for the same particle parameters assuming "gray" particle with emissivity of $\varepsilon(\lambda) = a_0 = 0.1$ demonstrated almost complete coincidence of all the temperatures. Here the sensibility of the 4-color technique seemed to be too weak on order to estimate accurately the quantity of particle emissivity. Data scattering for ε was about 20-30%. The corresponding modeling of particles' diagnostics with the help of PEM-83 shown clearly the diagnostic complex as being unable to detect these particles with given parameters.

The comparative modeling of the procedure of detecting 50 μm alumina particles at higher temperatures illustrated more evidently the preference of implementing the avalanche photodiodes in respect to the reduction of instrumental error for both 3- and 4-color pyrometry techniques. Further modeling investigation is required to analyze thoroughly 4-color technique sensibility to varying particle parameters. Although the above stated estimates are promising from the point of view of applying these techniques under real conditions of plasma spraying.

The small instrumental error and low threshold of determination of 3-color temperature T_{3c} when using APDs as detectors compared with those obtained for PEMs are primarily resulted from higher level of APD spectral sensitivity. For this reason APDs are preferable as detectors in diagnostics of particles to be sprayed. The basic APD shortcomings are an insufficient gain and some narrow cut-off frequency band Δf. These could be overcome by matching the conventional units of amplifying.

Acknowledgements

The present study was supported by Siberian Branch of Russian Academy of Sciences (Integration Program No.93 on 2003-2005) and by Russian Academy of Sciences (Program of Prezidium of RAS No.8 on 2003-2005).

References

[1] O.P. Solonenko – Thermal Plasma and New Materials Technology. Vol.2. Investigation and Design of Thermal Plasma Technologies, Ed. by O.P. Solonenko and M.F. Zhukov, Cambridge, England, Cambridge Interscience Publishing (1995), p.7-96.

[2] O.P. Solonenko, A.A. Mikhalchenko, E.V. Kartaev – Proc. of 16th Int. Symp. on Plasma Chemistry, June 22-27, 2003, Taormina, Italy.

[3] V.P. Pinchuk, N.P. Romanov – J. of Appl. Spectroscopy. 27,1 (1977) (in Russian).

[4] A.B. Shigapov – J. of Thermophysics of High Temperature. 36, 1 (1998) (in Russian).

[5] L.A. Dombrovsky, M.B. Ignatiev – TVT, 39, 1 (2001) (in Russian).

[6] D.Ya. Svet, Yu.N. Pyrkov, V.G. Plotnichenko – Reports of Rus. Ac. Sci. 361, 5 (1998) (in Russian).

[7] A.S. Leonov, S.P. Rusin - J. of Thermophysics and Aeromechanics. 8, 3 (2001) (in Russian).

[8] O.P. Solonenko, A.A. Mikhalchenko, E.V. Kartaev, K. Ogawa and T. Shoji - Proc. of the 5th JSME-KSME Fluids Engineering Conf., November 17-22, 2002, Nagoya, Japan.

Diamond like carbon films preparation by thermionic vacuum arc for MEMS applications

C. P. Lungu[1], I. Mustata[1], G. Musa[1, 3], C. Surdu Bob[1], A. M. Lungu[1], C. Moldovan[2], C. Rotaru[2], R. Vladoiu[3], V. Ciupina[3] and G. Prodan[3]

[1]*Low Temperature Plasma Physics Laboratory, National Institute for Lasers, Plasma and Radiation Physics, Bucharest, Romania*
[2]*National Institute for Micro and Nanotechnology, Bucharest, Romania*
[3]*Department of Physics, Ovidius University, Constanta, Romania*

Abstract
A novel method based on thermionic vacuum arc plasma was developed to grow carbon films for MEMS applications. Carbon films deposited on mirror-polished Si and glass substrates were identified as DLC phase with sp^3 bonds up to of 89% and diamond crystallites size of 3-11 nm. Atomic force and electron transmission microscopes, Raman and X-ray photoelectron spectroscopes, were used to characterize the morphology and the phase composition of the samples after the growth stages.

1. Introduction

Microsystems domain represents a growing interest due multiple applications in health care, environment, automotive and aero-spatial industries, etc. being developed in the frame of many European programs.

MEMS (Micro-Electro-Mechanical-Systems) technology is about 80% based on Si. Even Si can be used in many applications its usage is limited due to the low mechanical and high wear resistances and high coefficient of friction between Si and SiO_2. These problems can be solved by using new materials with enhanced tribological properties [1-2] ensuring lubrication and hydrofobicity to prevent adhesion. High value of hardness and low coefficients of friction determine a longer liftime. Materials with high tribological properties are: diamond like carbon (DLC), diamond, cubic boron nitride, silicon carbide, carbon nitride, aluminum nitride. DLC is an extremely interesting prospective material for MEMS due to its superior wear-resistant qualities, hydrophobicity, resistance to stiction (i.e. a combination of stickiness and friction) and potential as a biocompatible material that could be used inside the human body for medical purposes without generating an allergic reaction. Thermionic vacuum arc (TVA) method [3-5] was adopted to prepare DLC films on Si and glass substrates

2. Experimental set-up

One of the most important characteristics of TVA method is the presence of energetic ions in the pure carbon vapor plasma. Moreover, the energy of ions can be fully controlled from outside of the discharge vessel via the control of the arc voltage drop value. It results that during film preparation, just during deposition, the growing thin film is bombarded by energetic ions with an in advance established value of the energy of ions. The bombarding ions are just the ions of the depositing material (carbon). A Whenelt cylinder is used to focus the electrons on the anode surface. A bright discharge is established in high vacuum conditions in the cathode-anode space. Due to the high energy dissipated in the unit volume plasma, the material is strongly dispersed and completely droplets free. The obtained thin film is very smooth and in some experimental conditions has a nanoscale structure.

Coatings on mirror-polished Si (size of 20 mm x 20 mm x 0.5 mm) and glass substrates (size of 8 mm x 60 mm x 0.5 mm) were performed. The main working parameters are presented below: Anode material; graphite rod of 10 mm diameter and 200 mm in length; Cathode material: W + 0.2% Th, 1.5 mm in diameter; Distance between cathode and anode (2 -10 mm); Angle between the electron beam and the horizontal line (30 – 45^o); Intensity of the heating current of the cathode filament (100 – 120 A); TVA applied voltage (1-6kV); TVA

discharge voltage (1.5 – 2kV); Intensity of the TVA current (0.1 – 1 A); Distance between anode and substrate holder (100-300 mm); Deposition rate (0.2 – 3 nm/s).

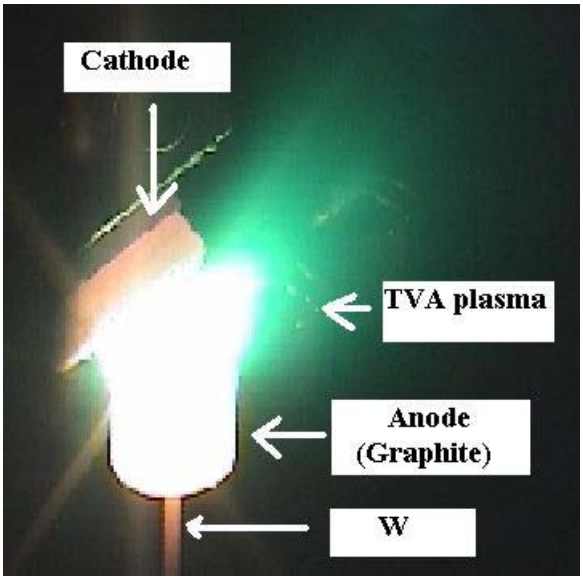

Fig.1 Photograph of TVA running in pure carbon atoms.

The obtained films were analyzed by Raman and X-ray photoelectron spectroscopy (XPS), transmission and atomic force microscopy (TEM and respectively AFM), microindentation and tribological tests.

3. Results and discussion

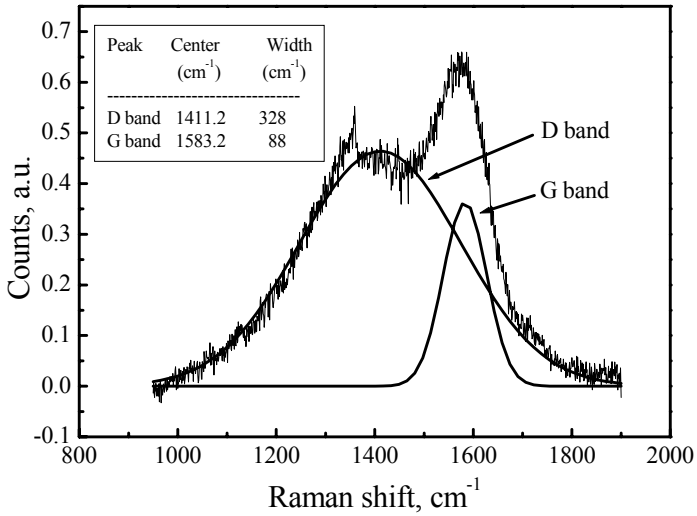

Fig. 2 Typical Raman spectrum of the DLC film

Raman spectroscopy was used to identify the C phase of the deposited films. Raman spectra were obtained in a back-scattering configuration using the 514.5 nm line of an Ar^+ laser with 5 mW power and 50 μm spot diameter. The signal was detected with a photomultiplier using a standard photon counting system with the acquisition time of 60 s. Carbon was identified as DLC phase, as defined recently by Ferrari and Robertson [6] with a large ratio of characteristic D-band/G-band intensities. Figure 2 shows a typical spectrum of the prepared

films and a Gaussian fit made in order to separate the D and G-bands. The D and G-bands are characteristic of the sp^2 sites of all disordered carbons at about 1411 and about 1583 cm^{-1}, respectively. Development of the D-band indicates disordering of graphite due to the formation of sp3 bonds between graphitic adjacent planes but ordering of an amorphous carbon structure; its intensity is proportional to the number and size of sp^2 clusters, while its width is more related to a narrower distribution of clusters with different order and dimensions. The G-band involves the in-plane bond-stretching motion of pairs of carbon sp^2 atom; this mode does not require the presence of sixfold rings and so it occurs at all sp^2 sites [6].

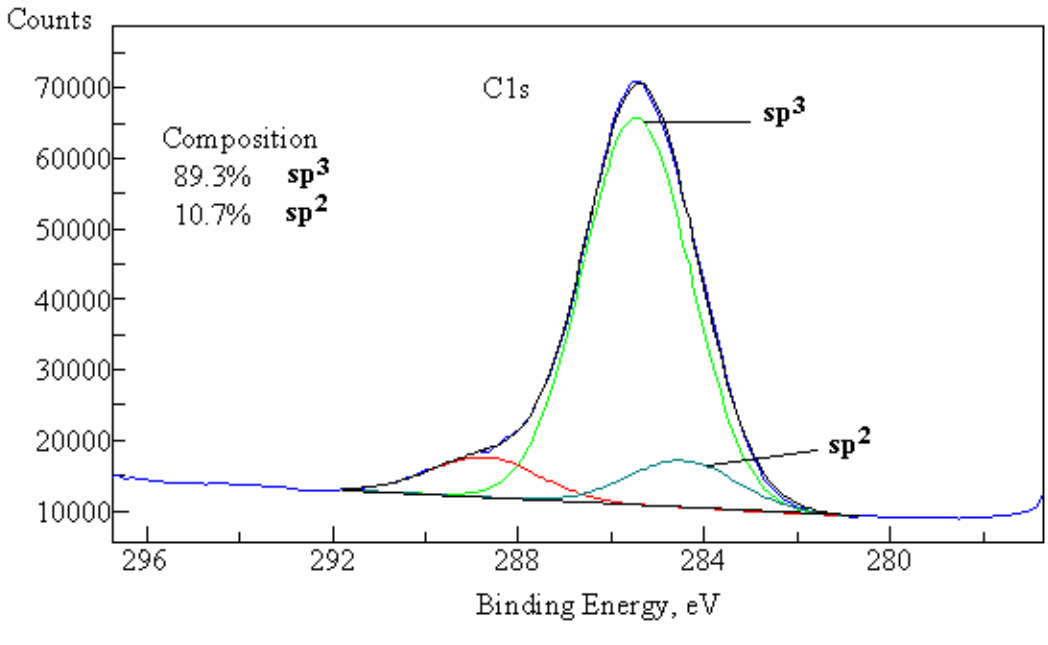

Fig.3 C1s peak deconvolution

The sp^3 bonds were found in the range of 89% compared with 11% of the sp^2 bonds after calibration and deconvolution of the C1s peak of the XPS spectrum of the prepared film as can be seen in Fig. 3.

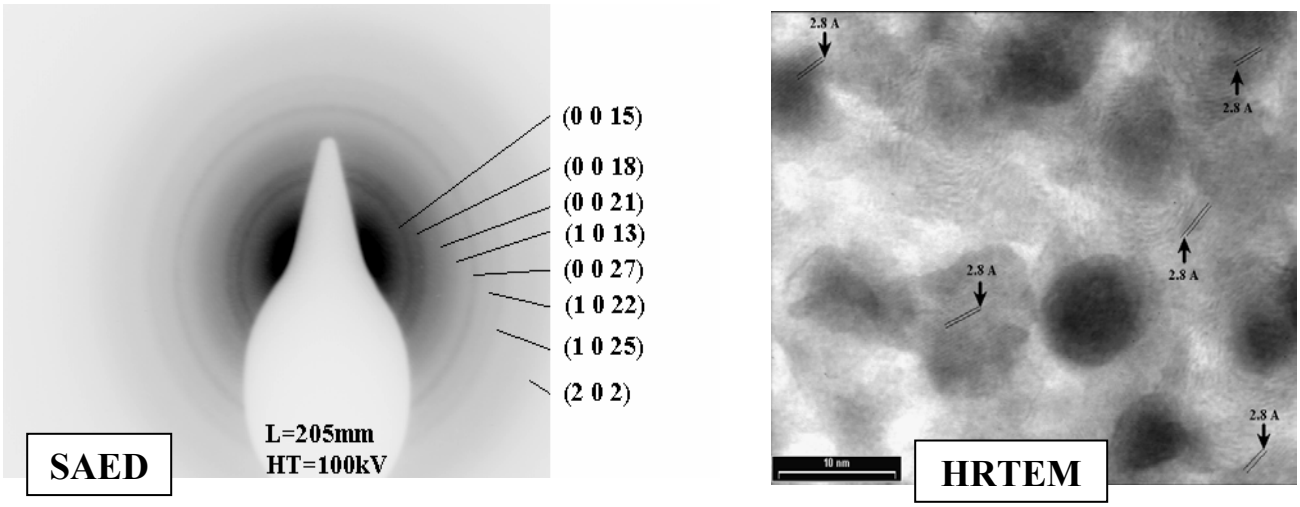

Fig. 4 Rhombohedra structures of the film with following parameters: a = 0.25221 nm, c = 4.3245nm (ASTM pattern: 79-1473) corresponding to diamond/carbon, determined by SAED (selected area electron diffraction) and HRTEM (high resolution transmission electron microscopy)

HRTEM images analysis shows the interference fringes given by the complex crystallites included into the amorphous carbon (Fig. 4). The arrows show the interplanar distances corresponding to the crystalline structure. The particles, 3-11 nm in diameter, were embedded into the film containing amorphous carbon. .

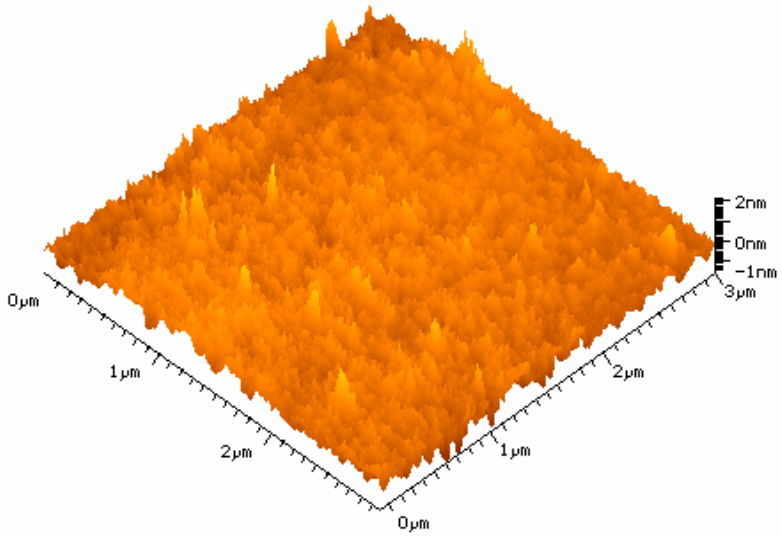

Fig. 5 AFM image of the analyzed film

The AFM image presented in Fig.5 shows the DLC film surface with a the peak-to-valley roughness in the 2-3 nm range.

The hardness of the deposited films was found in the range of 50-60 GPa, typically values for the DLC films.

The coefficient of friction of the deposited films tested by a flat to flat tribometer in dry conditions was in the range 0.05 -0.1. This suggests the predominant influence of the DLC acting as a solid lubricant in dry friction.

4. Conclusions

We can conclude that TVA method can be used successfully for preparation of DLC films for MEMS applications. High resolution TEM images of the deposited films using TVA reveals nanostructured particles with 3-11 nm diameter size, embedded in the amorphous carbon film. Super hard (50-60 GPa) nanostructured carbon films with low value of roughness and coefficient of friction can be obtained quite easily. Further developments will be related mainly to the improvement of the TVA stability at the transition from electron bombardment heating of carbon rod to the TVA arc plasma ignition and running.

Acknowlegements

The financial support under the MATNANTECH 4-249 national program for research and development is greatly acknowledged.

References

[1] C. P. Lungu, K. Iwasaki, K.Kishi, M. Yamamoto and R.Tanaka - Vacuum, **76**, Issues 2-3, 119-126 (2004).
[2] C. P. Lungu, I. Mustata, G. Musa, V. Zaroschi, Ana Mihaela Lungu and K. Iwasaki -Vacuum, **76**, Issues 2-3, 127-130, (2004).
[3] G. Musa, H. Ehrich, M. Mausbac, J Vac Sci and Techn., **A12**, 2887-2895 (1994).
[4] G.Musa, I. Mustata, A.Popescu, H.Ehrich, J.Schumann - Thin Solid Films, **333**, 95-102 (1998).
[5] H. Ehrich, G. Musa, A. Popescu, I. Mustata, A. Salabas, M. Cretu, G. F. Leu - Thin Solid films, **344**, 63-66 (1998).
[6] A. C. Ferrari, J. Robertson, Phys. Rev. B **61,** 14095 (2000).

MICROSTRUCTURAL STUDY OF SILICON NITRIDE WHISKERS PRODUCED BY NITRIDATION OF PLASMA-SPRAYED SILICON LAYERS

M.S.Alaee [1,2]
[1] *Department of Physics, Azad University, Karaj, Iran*
[2] *Department of Physics, University of Tehran, Tehran, Iran*

Abstract
plasma-sprayed silicon layers have been used to produce silicon nitride with fiberous microstructure which optimizes fracture toughness and strength. In order to study the oxygen contamination effect as well as other contaminants introduced during spraying and nitridation processes, surface sensitive analysis techniques like AES and XPS have been used to determine concentration of these contaminants. SEM examination of the specimens shows that the surface is covered by fine needles and whiskers of Si_3N_4.
Keywords: plasma spray, silicon nitride, whiskers, surface analysis, microstructure, contamination

1. Introduction

Silicon nitride whiskers offer the advantages of high melting point, low density and high moduli which makes it an important reinforcing material in composites [1]. Silicon nitride layers have been studied extensively in recent years on account of the potential uses as a material which has many desirable properties such as strength, light weight, low coefficient of friction and high wear resistance and fracture toughness, which make it one of the more promising candidates for high temperature structural materials. Silicon nitride is a hard material with low expansion coefficient and possesses high strength by comparison with other ceramic materials. The reaction-sintered form of silicon nitride which is known as the first engineering form of silicon nitride has some 15-30% porosity which limits the strength of the material. This problem may be overcome by taking advantage of the inherent capability of the plasma spraying technique to produce layers with low porosity. On the other hand, to some extent, low porosity hinders the nitridation. Plasma sprayed silicon subjected to nitridation has been shown to be promising technique for developing layers of silicon nitride of thickness in the micron to sub-micron range. Due to the low porosity of the plasma sprayed silicon layers, nitridation of the whole body seems impossible; however, this technique is suitable for applications where only a thin layer of silicon nitride is desired. Commercial production of silicon nitride by conventional methods takes place very slowly by the reaction of nitrogen gas and silicon in a nitridation furnace. The long time needed for this process to take place can provide a relatively impure product as well as an increase in the cost of silicon nitride. In this work we have shown that parameters effecting the development of silicon nitride are: temperature, positive pressure of nitrogen gas, particle size of the starting silicon powder and the firing time. The characterization of the layers has been carried out using: (I) X-ray diffraction (XRD) to determine the crystalline structure of the silicon nitride layers, (II) scanning electron microscope (SEM) to show the morphology and surface structure of the samples, (III) Auger electron spectroscopy (AES) to determine the elements in the ultra thin layers and (IV) electron spectroscopy for chemical analysis (ESCA) to determine the surface chemical composition of the specimens.

2. Experimental Procedure

Silicon powder was prepared from semiconductor grade billets with 99.9% purity .The billets are crushed into small ingots using a standard jaw crusher. To pulverize the smaller ingots a ceramic milling machine was used. The powder is then acid washed to remove the iron contamination introduced during pulverization process and then sieve separated into 75-105mm powder sizes.

The Metco type 3M plasma flame spray equipment is used in this work which is an integrated group of modular units consisting a type 3MB plasma gun, type 6MC plasma flame spray control unit and type MP powder feed unit. The plasma forming gases used are argon as the primary gas and the hydrogen as the secondary gas. The addition of about 10-20 % hydrogen gas has shown to act as a useful deoxidizing agent.

Layers of silicon, 0.5-2.0 mm thick are plasma sprayed onto an ultrasonically cleaned alumina substrates placed at some 10-15 cm away from the plasma gun. The alumina substrates are then heated in order to separate the silicon layer from the substrate.

The nitridation process is carried out in a gas tight Metal Research furnace type PC A10 with molybdenum heating element and inner alumina tube. The samples are placed in the alumina boat and are then introduced into the furnace. Before nitridation, the furnace is out-gassed in vacuum at 700^{o}C for five hours and then backfilled with nitrogen gas (99.999%) to a slightly positive pressure which continued all through the nitridation process. Nitridation was carried out for eight hours at 1150-1350°C. Too rapid an increase in temperature involves sample damaging, either from gross melting of silicon or torsion in the sample.
XPS (ESCA) & AES analysis of the samples which are well known methods of surface chemistry studies have been carried out using a VG ESCALAB 200 and MICROLAB 300. All measurements were performed at pressures lower than 10^{-8} Torr in the analysis chamber.

3. Results and discussion

AES microanalysis of the samples

Important chemical information can be obtained from Auger spectra. The chemical effect will appear either in the form of a simple peak shift or a change in peak shape and in many cases as both. Fig.1 shows the AES general spectra after the removal of about 50 nm of the surface layer, both KLL and LMM peaks show a shift in position between pure silicon and the silicon in the form of silicon nitride. For the LMM peak there is a shift of about 8 eV between pure silicon and silicon in the form of silicon nitride. There is also a change in the peak shape and width. In the case of silicon oxide, due to an electron beam induced effect, oxygen has been lost from the surface and Si LMM spectra from silicon oxide show distinct peaks in the elemental silicon position at 91 eV. In the case of silicon nitride it is somewhat different, because a distinct shift of about 4 eV in the Si LMM peak due to silicon and silicon nitride is clearly observed. The Si KLL data obtained is shown in fig.2. Careful curve fitting of the Si KLL line shows the silicon oxide peak at the kinetic energy of 1605.8 eV and silicon nitride at 1612.3 eV. The AES spectra clearly show that the nitrogen is depleted in the near-surface layer. This effect is more pronounced in the AES depth profile than in the ESCA due to a better depth resolution and signal to noise ratio in the AES spectra.

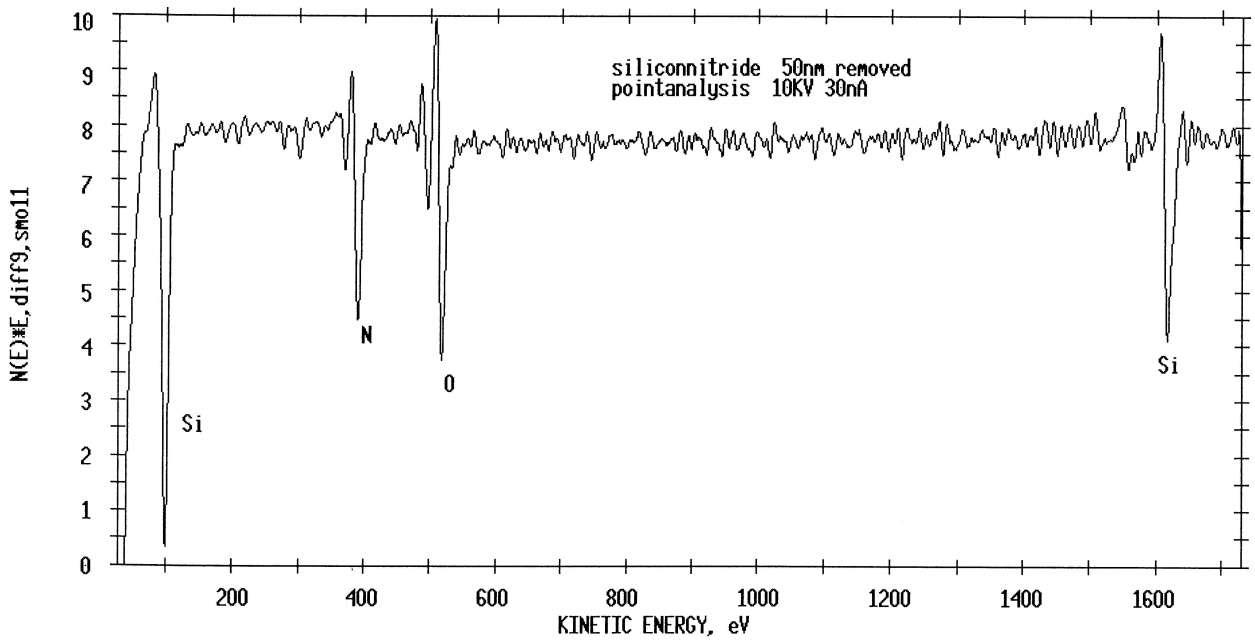

Figure 1. General AES spectra indicating the presence of Si KLL, N, O & Si LMM

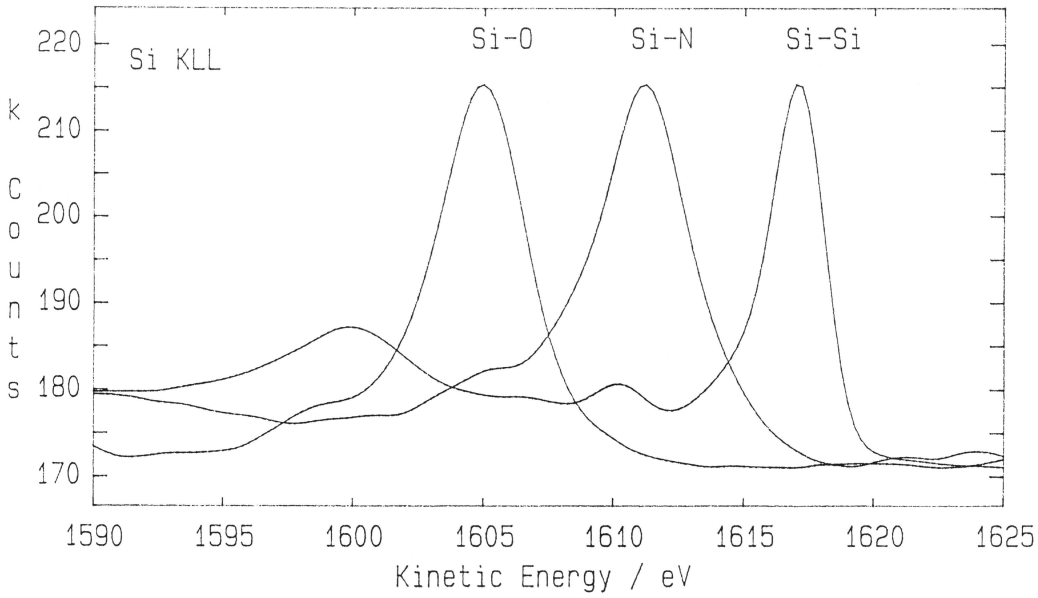

Figure 2. AES spectrum showing the chemical shift in the Si KLL peak for the nitride and oxide

ESCA analysis of the samples

The chemical state of Si in the nitrided sample was determined from the value of the Si binding energy after a 50 nm layer was removed from the surface. The formation of silicon nitride was explained by the binding energy of the Si $2p^{3/2}$ peak referred to ESCA handbooks and standard samples [2]. The binding energy of Si 2p was measured to be 104.5 eV compared with 99.3 eV for pure silicon. According to the binding energy of the Si 2p peak, the Si in the sample is thought to be silicon nitride with some mixed amount of silicon oxide and oxynitride. Due to the presence of Si, SiO_2 and Si_3N_4 the assignment of the peaks in the Si 2p spectrum cannot be easily accomplished. The difference in binding energy of the two peaks is only a few electron volts. The Si 2p peak shows the presence of silicon nitride at 105.6 eV. Computer curve fitting of the Si 2p spectra has been used to obtain the relative intensities of the Si 2p oxide and nitride components. Fig.3 is a XPS montage of sputtered depth profile analysis of the Si 2p peak which shows the shift in the binding energy from a higher value (106 eV) due to the Si-O bond, towards the lower binding energy (103 eV) being due to the Si-N bond.

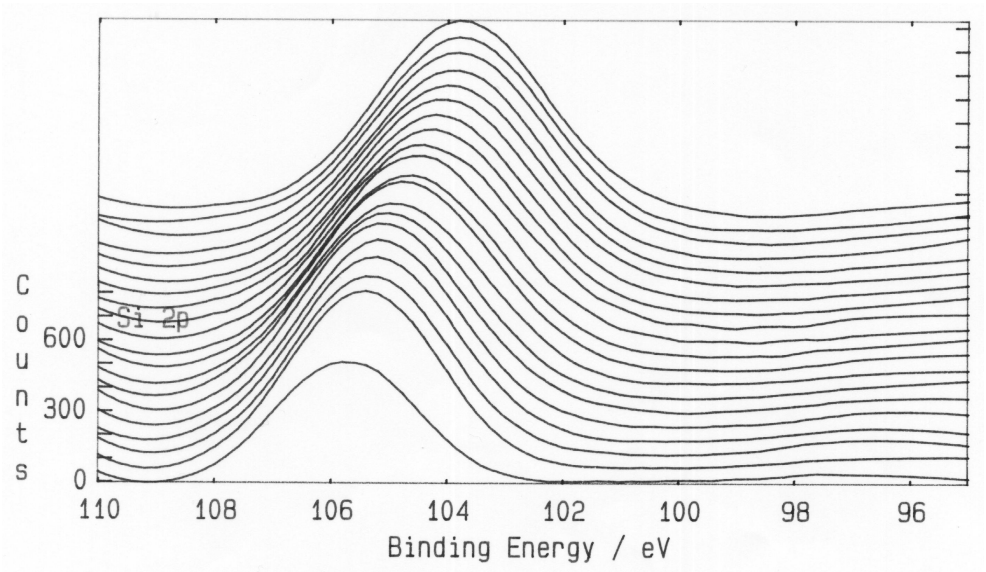

Figure 3. XPS montage of sputtered dept profile showing Si 2P peak shift

Surface structure of the samples

The surface morphology of the nitrided silicon has been investigated by SEM and shows that the orientation of the whiskers in the matrix is nearly three dimensionally random as shown in fig.4. The diameter of each whisker is about 300 nm having various lengths.

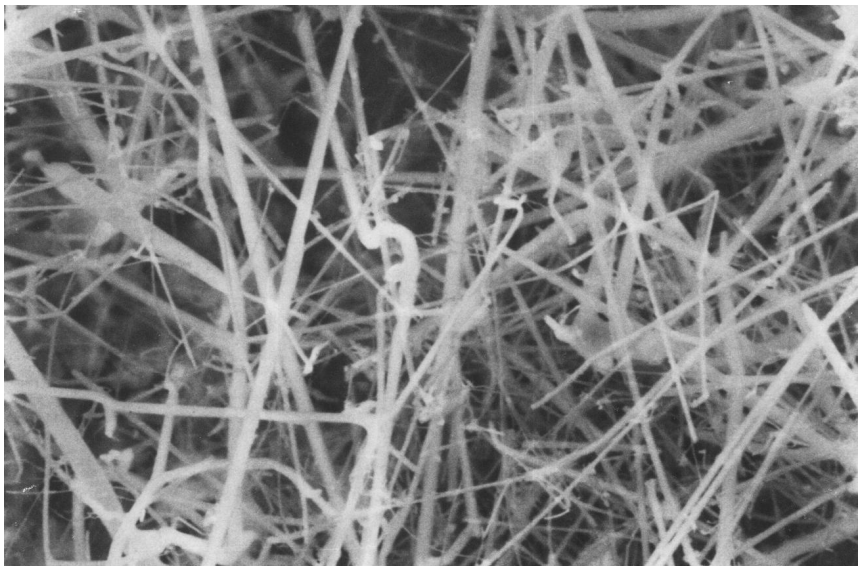

Figure 4. SEM micrograph of whiskers (Mag. 6 k)

It is well known that the reaction of SiO_x vapour with carbon and nitrogen always produces alpha and not beta silicon nitride [3]. In the absence of impurities in the reactants, formation of beta and oxynitride is completely suppressed. There are no liquid phases in the Si-O-N-C system in the temperature range used for the production of silicon-nitride layers, but small amounts of impurities have a pronounced effect on the melting temperature [4]. Iron is also known to influence both the phases formed as well as the rates of reaction. When the sample crucible is removed from the furnace after the reaction, the exposed inside surface of the graphite crucible as well as the top surface of the specimen pellet (containing excess carbon) are covered by fine white needles of alpha-silicon nitride.

This product provides clear evidence that the mechanism of formation of alpha Si_3N_4 is by a solid-gas mechanism. The crystal shapes produced within the sample pellet are twisted and faceted which is due to restricted growth within pores and cavities, but when grown on a free surface such as on the top of the pellet or on the crucible walls, perfect whiskers and needle growths are produced.

Silicon oxide film formed on the surface of the plasma sprayed silicon samples was analyzed prior to nitridation using AES and ESCA [5]. The results showed that silicon powder particles acquired oxygen in the plasma-spraying environment to form a thin layer of oxide on the periphery of each particle upon splat quenching on the substrate.

Beta-silicon nitride was the dominant phase [6]. The alpha silicon nitride whiskers are easily distinguished by the ribbon-like morphology with about one micron in width and less than 0.1 micron in thickness. The growth direction of the alpha silicon nitride whiskers is <211> as determined by XRD. Since single crystals usually include much less impurities than other forms; therefore, it can be concluded that the samples made contain whiskers of pure silicon nitride. The microstructure also contains many small globules, which appear to have been liquid during reaction and in some cases the globules are seen to be attached to the ends of needles. Scanning Auger Microanalysis (SAM) reveals that the globules are composed of Si, N, O and some iron (Fe) content [7]. Although the precise composition could not be obtained by microanalysis, it is suggested that the iron is present in the matrix in the form of a Fe-Si intermetallic phase. The iron-silicon phase diagram contains four eutectics at about 1250 degree centigrade and the formation of Fe-Si phases at the reaction temperature is therefore possible.

4. Conclusion

The main advantage of the present method is its potential to develop relatively thin layers of silicon nitride on complex shaped bodies which is otherwise impossible to form by other conventional methods i.e. powder compaction or hot pressing. Data obtained shows that this method is a promising one for producing submicron to a few micron thick fiberous films of silicon nitride.

The nitridation process should be carefully controlled, since it has been recognized for some time that the exothermic nature of the nitridation reaction plays a significant role in the process. This behavior may cause some spots to be melted once the temperature of the sample approaches the melting point of silicon. It is predicted that the critical defects in reaction-sintered silicon nitride were large pores that resulted from melting of particles of unreacted silicon when the temperature of the sample exceeded 1400 °C. It has been reported that a more complete nitridation and generally higher nitriding rate can be obtained by using the variable atmosphere in the nitrogen-demand nitriding runs by decreasing nitrogen partial pressure [8]. By using an isothermal nitriding run it was found that a more complete nitridation was obtained with reduced nitrogen partial pressure.

Plasma sprayed silicon for the purpose of producing layers of silicon nitride by nitridation has shown to be a promising technique for developing layers of silicon nitride from submicron to a few micron thick. Due to the low porosity of the plasma sprayed layers, nitridation of the whole body of the sample seems impossible. However, this technique is suitable for applications where only a thin layer of silicon nitride is desired.

The plasma spraying technique has enabled us to produce silicon nitride from plasma sprayed silicon bodies having various shapes and sizes. By analyzing various spots on the surface of the samples, it was found that the Si_3N_4 whiskers formed are relatively homogeneous in composition.

References :

[1] H.H.K. Xu, J.B. Quinn, D.T. Smith, et.al., Dental Materials. **19**,5 (2003)
[2] P.M. Williams, Handbook of X-ray and UV Photoelectron Spectroscopy(Ed. D. Briggs) (1977)
[3] G. Sucik, D. Hrsak, T. Kuffa, Metallurgija . **39**,1 (2000)
[4] T. Hashishin, H. Iwanaga, Y. Yamamoto, Journal of Material Research. **18**,12 (2003)
[5] M.S. Alaee, et.al., Journal of Material Science Letters. **2** (1983)
[6] J. Dusza, P. Sajgalik, Z. Bastl, et.al., Journal of Material Science Letters. **11**,4 (1992)
[7] S.A. Siddiqi, A. Hendry, Journal of Material Science. **20** (1985)
[8] J.A. Mangles, Am.Ceram.Soc.Bull. **60** (1981)

Modelling of Fracture in Plasma Spray Coating Systems Subjected to Thermal Loading: Use of Finite Element Technique

[1]A Mimaroglu, [2]H Unal, [3]O Iyibilgin and [4]K Yilmazcoban
*University of Sakarya, Faculty of Engineering, Esentepe Kampusu, Adapazari, Turkey
Tel: (90) 264-3460354, Fax: (90) 264- 3460351, e-mail: mimarog@sakarya.edu.tr

Abstract:

In this study, general-purpose finite element code ANSYS with coupled solution has been employed to analysis fracture in ceramic coating subjected to thermal loadings. Coatings with substrate material Tungsten, coating materials Diamond, Si_3N_4 and interlayer materials NiAl were modeled. The aim was to evaluate the stress intensity factors in different coating systems. The result showed that the shorter the crack length and the better material combinations the sounder is the coatings.
Keywords: Thermal loading, Fracture, finite element

Introduction

Plasma coating systems are used for many severe engineering applications. Most of these applications are in the form of thermal barrier coatings, which allow for higher engine temperatures and better efficiencies [1]. The strength of the bonded system is governed by a number of variables; the thermal and elastic mismatch, the plastic flow stress of the metal [2], the relative substrate/coating thickness[3], thickness of interlayers [4], elasticity of interlayers [5], the fracture resistance of the interface, and the flaw distributions in the ceramic and at the interface [6]. Most failures in the thermal barrier bond coatings system also depend on processing parameters, i.e. contact temperature, surface composition, solidification of sprayed particles [7]. A main problem of such coatings has been the failure in the form of debonding and spalling from the substrate [8-9]. In most cases the failure appears to be close to the interface between the ceramic and the metal. More recent experimental observations [5] suggest that the crack have strong tendency to extend into the substrate and propagate parallel to the interface. The fracture and crack propagation in homogenous elastic brittle materials is well understood , while that of bimaterials is still the subject of much debate. The general approach for the bimaterial fracture mechanics [10] is that increase the flow orientation in affects of crack propagation through the coating, interfaces and substrate. Evans [11] , investigated the fracture energy of bimaterial interfaces. They concluded that the fracture energy is influences on many problems of technological importance, particularly the mechanical properties of composites [2,11,12] and the decohesion of films and coating [10] as well as the strength of bonds [12]. In case of thermal stresses, it is well known that the thermal stresses are generated at the interfaces when dissimilar materials are bonded together. Most studies in this area have considered steady-state excursions. More recently, the thermal stresses in ceramic-metals bonds has been analysed by taking into account the transient nature of the heat transfer process [11,12]. Again the principlesof fracture mechanics is used to determine the effect of a transient thermal load on the interface [13].

Diamond and Si_3N_4 based ceramic coatings are most used as thermal barrier coatings because of their low thermal conductivity which reduces the detrimental interfacial stress [14]. In this investigation ANSYS finite element packet programme was employed to analyse the influence of interfacial crack length and material properties on fracture toughness of ceramic coatings. The results showed the significant influence of the thermal expansion coefficient, thermal conductivity and crack length on the stress intensity factors K_I and K_{II}.

Analysis

A general purpose finite element code ANSYS, is employed to obtain thermal/structure coupled solution. A half of a disc sample was modeled using 4-node, plane strain, quadratic elements see Figure 1a,b. The ends of the model were constrained and the loads were applied by cooling down the model from 600 °C to room temperature in very short time using an 30 W/m^2 °C heat transfer coefficient at the top end of the model. To avoid bending problems an coating to substrate materials thickness ration of geometries with 1/10 and three different crack lengths 1.2, 2.4 and 4.8 mm were modeled to evaluate the influence of the crack length. A transient coupled thermal/ structure finite element analysis was executed for the coating and for all different geometry models. The stress intensity factors K_I and K_{II} were obtained and compared. Table 1 present properties of the materials used in this investigation.

Results and Discussions

Figure 2 represents K_I and K_{II} stress intensity factor - time curves for reference coatings Diamond-W and Si_3N_4-W coating systems. This figure shows a 5% decrease in the K_I value for about a times 14 increase in thermal conductivity of the coating material. This effect is hardly noticeable in K_{II} value. This is explained as the thermal stresses are significantly effected by the thermal expansion at the end of homogeneous heating period.

Figure 3 shows the influence of coating thermal expansion coefficient value on the stress intensity factors K_I and K_{II} for models with 0.2 mm coating thickness, 1.2 mm crack length and α values of $3.5x10^{-6}$ and $1.75x10^{-6}$ /°C. It is clear from this figure that a times two decrease in thermal expansion coefficient value lead to 220% increase in K_I and K_{II} values. Because as mentioned before, thermal stress values are largely dependant on the thermal expansion mismatch in bimaterial systems.

Figure 4 represent the influence crack length on K_I and K_{II} stress intensity factor values for Si_3N_4 coating material of 0.2 mm coating thickness and 1.2, 2.4 and 4.8 mm crack length. This figure shows a 100% increase in K_I and a 75% increase in K_{II} values for a times 3 increase in crack length. It is clear that stress intensity factors are influenced by the crack length.

Conclusions:

1- Under thermal stress conditions, the stress intensity factors K_I and K_{II} decreases with the increase in thermal conductivity of the coating material.
2- The stress intensity factors K_I and K_{II} increases with the decrease in the thermal expansion coefficient of the coating material.
3- It is clear that stress intensity factors are influenced by the synergetic effect of crack length and material properties mismatch.

References

[1] T.M. Yonushonis, conference Proceedings, 1988.
[2] A. Bennett, Materials Science & Technology, 2 (1986) 257-261.
[3] E. Benger, N. Perrin, M. Boussuge, H. Burlet, Proc. of Third International Symp., Ceramic Material & Components for Engine, Las Vegas, 1987, pp.528-537.
[4] J.K. wright, R.L. Williamson, K.J. Maggs, Materials Science and Engineering, A187 (1994) 87-96.
[5] M. Meyer, S. Schmauder, Scripta Metallurgica, 28 (1993) 743-745.
[6] Y. Huang, H.W. Zhang, Acta Metallurgica, 43 (1995) 1523-1530.
[7] H.D. Steffens, B. Wielage, J. Drozak, Surface and Coatings Technology, 45 (1991) 291-308.
[8] G. McDonald, R.C. Hendricks, Thin Solid Films, 73 (1980) 491-496.
[9] R.A. Miller, C.R. Lowell, Thin Solid Films, 95 (1982) 265-273.
[10] K.L. Hoang, D.P. Roehling, T.M. Yonushonis, B.E. Dulin, ASME Paper No. 88-KE-20, 1988.
[11] A.G. Evans, M. Rühle, B.J. Dalgleish, P.G. Charalambides, Materials Science and

Engineering, A126 (1990) 53-64.
[12] K. Kokini, R.W. Perkins, J. of Computers and Structures, 19 (1984) 531-534.
[13] M.D. Thouless, A.G. Evans, M.F. Ashby, J.W. Hutchinson, Act Metallurgica, 35 (1987) 1333-1341.
[14] H. Herman, N.R. Shankar, Materials Science and Engineering 88 (1987) 69-74.
[15] J Chanderasekar, Ceramic for magnetic recording,386-389

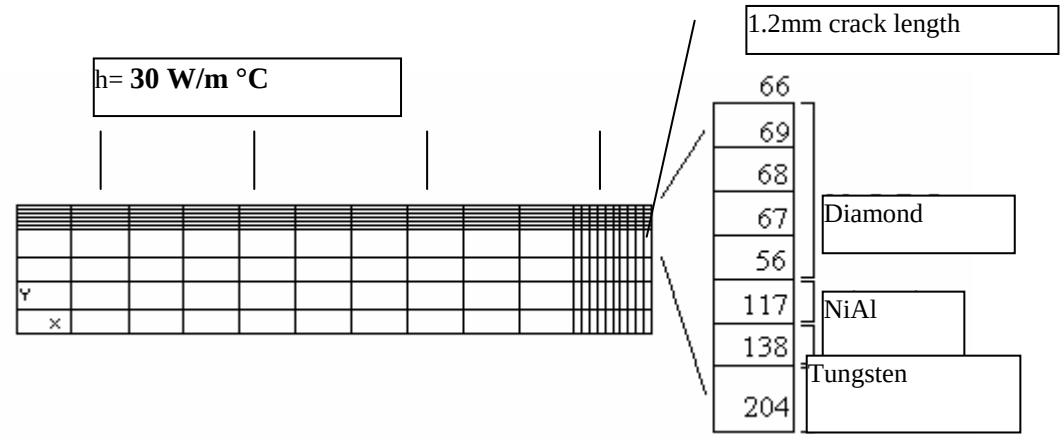

(a)

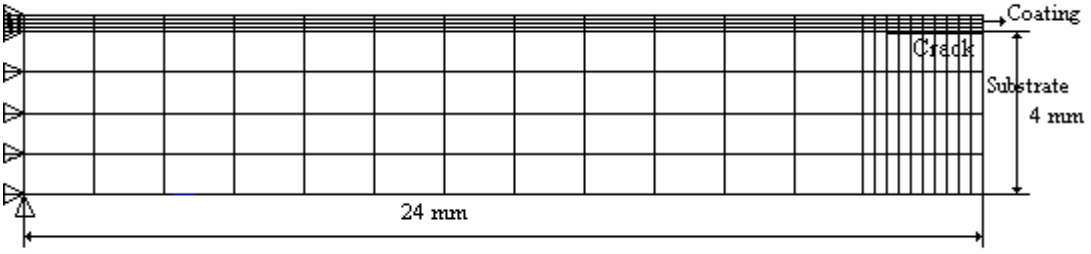

(b)

Figure 1a,b Finite element model.

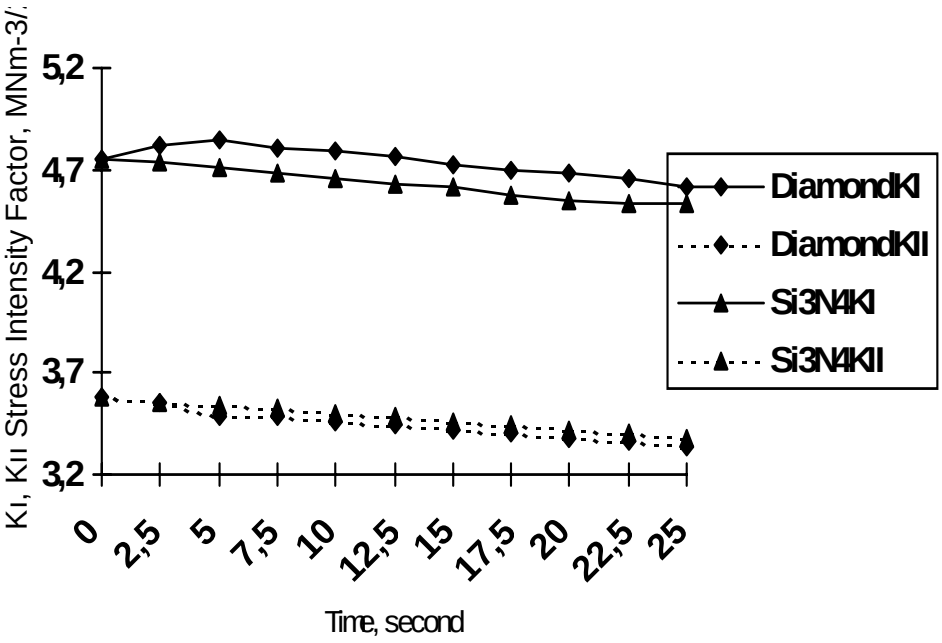

Figure 2 Influence of coating thermal conductivity value on the stress intensity factors K_I and K_{II}, for model with 0.2 mm coating thickness, 1.2 crack length and K value of 2 and 28 W/m°C

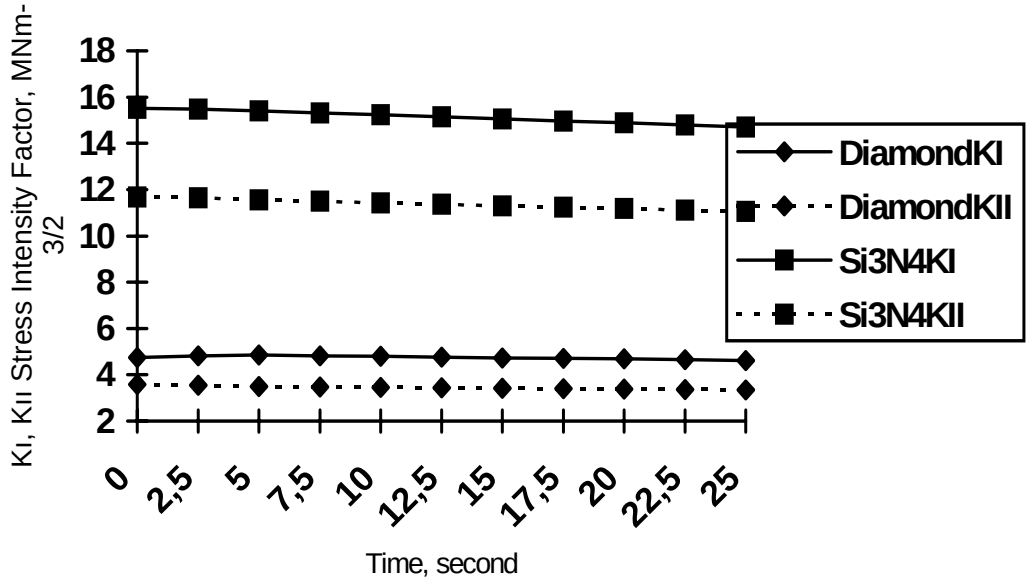

Figure 3 Influence of coating thermal expansion coefficient value on the stress intensity factors K_I and K_{II}, for models with 0.2 mm coating thickness, 1.2 crack length and coating α values of 3.5×10^{-6} and 1.75×10^{-6} /°C

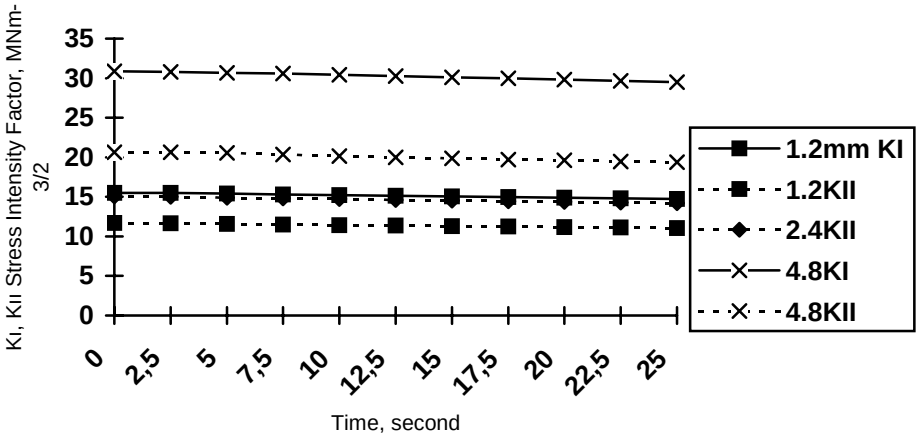

Figure 4 Combined influence of thermal expansion coefficient and crack length on the stress intensity factors K_I and K_{II}, for models with 0.2 mm coating thickness, 1.2 , 2.4 and 4.8 mm crack length and coating α value of 1.75×10^{-6} /°C

Table 1. Coatings system material properties used in FE analysis[4,15]

Material	Coating (Si_3N_4)	Substrate (Tungsten)(W)	Diamond	NiAl
Elasticity Modules, E, (GPa)	230	410	1050	103
Poisson Ratio, ν	0.26	0.28	0.20	0.17
Thermal Expansion Coefficient, α, (/ °C)	3.5×10^{-6}	4.5×10^{-6}	1.75×10^{-6}	14.6×10^{-6}
Density, ρ, (Kg/m^3)	2200	15800	3500	5800
Thermal Conductivity, K, (W/m°C)	28	29	2	5.3
Specific Heat, Cp (J/Kg°C)	720	200	525	593

2-D Photonic Crystal with using C-Au-S–PMMA Dielectrics

Takeshi Suzuki, Mikinori Suzuki, and Shinzo Morita

Department of Electronic Information System, School of engineering Nagoya University, Nagoya 464-8603, Japan

E-mail: kenji_s@echo.nuee.nagoya-u.ac.jp

Abstract

C-Au-S film formed by cooperation process of plasma CVD and sputtering showed a large refractive index like as 3.5, which can be used for a photonic crystal at a visible light range because of transparency and process compatibility. 2D photonic crystal with C-Au-S-PMMA dielectrics processed by plasma processes can be used as an optical wave-guide and other optical devises at a visible light wavelength range. 2D photonic crystal pattern with beehive type at around 500 nm was successfully fabricated.

Key Words: Photonic Crystal, C-Au-S Film, Cooperative Process of Plasma CVD and Sputtering, Refractive Index

1. Introduction

Optical computing integrated circuit or optical integrated circuit is named as OIC. The OIC device size is limited by the light wavelength. However the computing speed is very fast composed to a silicon-computing device. The OIC technology is used for an optical inter-connection circuit between the silicon integrated circuits, an optical sensing system and so on. Therefore the OIC minimizing technology is important to realize new devices.

Photonic crystal introduced by E. Yablonovitch [1], S. John [2] etc. in 1987 is expected to be a new and important element for optical device. The crystal has a periodic refractive index distribution in 1-D, 2-D, 3-D structure and shows photonic band gap (PBG) property. By using the 2-D or 3-D photonic crystal, curved optical waveguide is fabricated by introducing linear crystal defects array. Therefore the circuit become very small compared to a thin film wave- guide. Additionally, The photonic crystal acts as photon traps and emitters depending on the defect size at the wavelength level if point defect is introduced near the wave-guide in the 2-D photonic crystal [3]. These photonic crystals can be utilized to the OIC.

For the photonic crystal, high refractive index material must be used. In this work, C-Au-S (carbon-gold-sulfur) film [4] was used because it is optically transparent in the visible light range, high refractive index and process compatibility for oxygen plasma etching. The C-Au-S film was fabricated by co-operative process of plasma chemical vapor deposition (CVD) with using CH_4, SF_6 and Ar mixture gas and sputtering Au plate discharge electrode. The optimized optical properties of film were a refractive index of 3.5 and transmittance of 51 % at a wavelength of around 500 nm.

Using the C-S-Au film, 2-D beehive photonic crystal was designed and fabricated by an electron beam lithography with using two-layer resist system of negative resist and evaporated Al film, which works as an oxygen plasma etching stopper. The 2-D beehive photonic crystal pattern has hexagonal structure, which is effective for both of TM and TE mode light propagation [5]. These theoretical and experimental

investigations on the photonic crystal structure are reported variously [5-8]. The 2-D beehive (hexagonal) structure for 500 nm light is shown in Fig. 2.

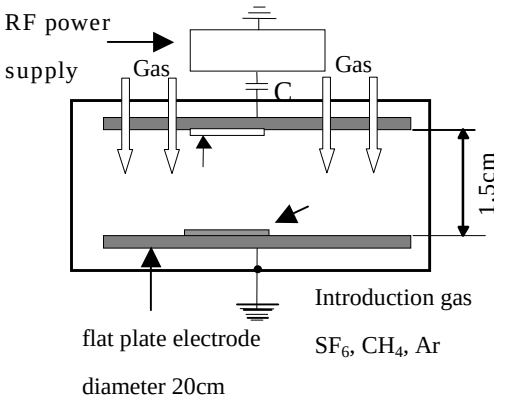

Fig. 1 Plasma CVD apparatus

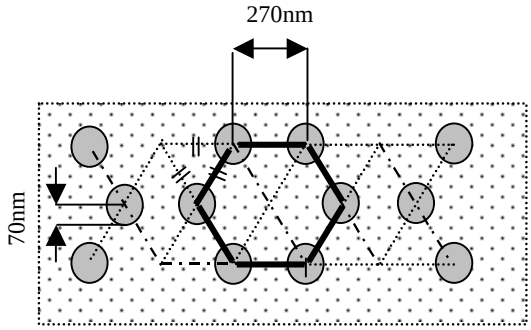

Fig. 2 The photonic crystal for 500 nm light

2. Structure and fabrication of beehive type photonic crystal

The C-Au-S film was formed by plasma CVD reactor (ULVAC CPD-1108). The plasma CVD reactor has a parallel plate electrode with 20 cm diameter and 1.5 cm gap distance between the two electrodes. A gold plate with area of 50×50 mm^2 was set on the upper electrode which was made of graphite and connected to the RF power source of 13.56 MHz. Substrates of Si wafer were located on the lower electrode grounded and electrically connected to the reactor vessel of stainless steel.

The C-Au-S film with a refractive index of 3.5 was fabricated as followings. The deposition condition was kept to be constant at a pressure of 0.1 Torr, a discharge power of 100 W, and a discharge duration of 30 min. The flow rate of CH_4 was 10 SCCM, the flow rate of Ar and SF_6 were 15 SCCM. The C-Au-S film was characterized by measuring the refractive index using an ellipsometer.

2-D photonic crystal was fabricated as followings. After Al film evaporated on the C-Au-S film, which works as etching stopper, negative resist (SHIPLEY SAL601) was spin coated on the Al film at 4000 rpm and pre-baked at 105°C for 60sec. Then electron beam patterning apparatus (JEOL JBX-6000SG) was used for patterning of 140 nmϕ poles at six apex of hexagonal with 270 nm sides as a single cell as shown in Fig. 3. The pattern delineation was performed at an acceleration voltage of 50 kV and a current of 100 pA. After the pattern delineation on the resist, it was post-baked at 115°C for 60sec. The pattern was developed by SHIPLEY MF CD-26 and rinsed by pure water to made the pattern clear. Al film was etched off through the resist pattern by etching liquid of HNO_3 5%, HF 3% and H_2O 92%. The C-S-Au film with around 500nm thickness was etched through the Al patterns by oxygen plasma with using RIE (SAMCO RIE-1C) at 13.56 MHz. The etching rate of this film was measured at oxygen flow rate of 10 SCCM and a pressure of 0.09 Torr as a function of discharge power.

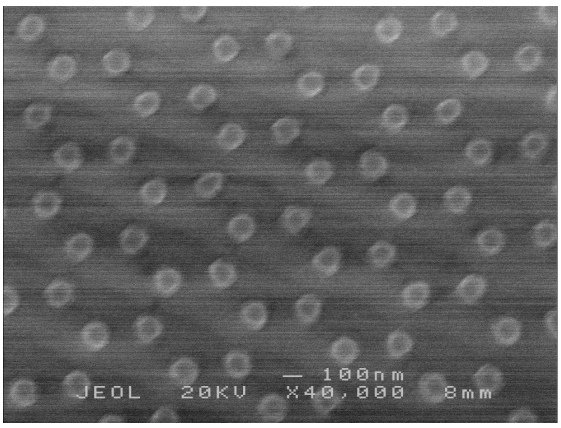

Fig. 3. The SEM photograph after negative resist etching

3. Integrated optical wave-guide with a light source

EL light source will be fabricated on the 2-D photonic crystal to fabricate the OIC. For the device, the beehive type C-Au-S structure surface must be flattened. For the filling substance, the refractive index must be lower then that of C-Au-S. Therefore, PMMA was selected as a low refractive index substance because the refractive index of PMMA is 1.5. Also, PMMA can be filled in the 2-D beehive C-Au-S photonic crystal structure by spin coating. EL element is formed on the flatted surface. Then a transparent wave-guide with a light source is formed on the crystal. The cross-section view of the device is expected as shown in Fig.4. Where the amorphous carbon layer was formed to separate the wave-guide from the substrate with large refractive index. The refractive index of amorphous carbon is about 1.5~1.6.

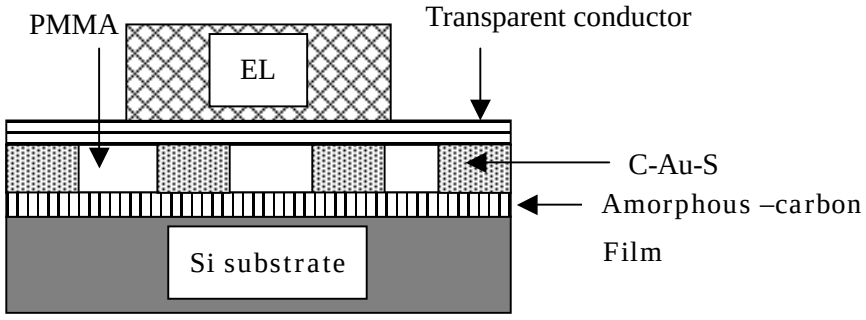

Fig.4 Basic structure of OIC with EL light source on the 2-D photonic crystal

4. Conclusion

The C-Au-S film was synthesized by co-operation process of plasma CVD and sputtering with using methane, SF_6 and Ar mixture gas and gold plate on the discharge electrode. We found that the C-Au-S film was etched by oxygen plasma RIE and has high refractive Index. The 2-D beehive type (hexagonal) photonic crystal was successfully fabricated for a visible light wavelength range at 500 nm. The photonic crystal of C-Au-S – PMMA with EL element will be proposed for the OIC element.

Acknoledgement

The lithography works were carried out at the center for Cooperation Research in Advanced Science and Technology, Nagoya University. We express our gratitude to all who contributed to this study.

References

[1] E. Yablonovitch, Phys. Rev. Lett. **58**, 2059 (1987).

[2] S. John, Phys. Rev. Lett. **58**, 2486 (1987).

[3] S. Noda, A.Chutinan, and M. Imada, Nature **407,** 608 (2000).

[4] M. Matsushita, Md. Abul Kashem and S. Morita, Thin Solid Films **407**, 50 (2002).

[5] D. Cassagne, C. Jouanin, and D. Bertho, Phys. Rev. B **52**, R2217 (1995).

[6] D. Cassagne, C. Jouanin, and D. Bertho, Phys. Rev. B **53,** 7134 (1996).

[7] D. Cassagne, C. Jouanin, and D. Bertho, Appl. Phys. Lett. **70**, 289 (1997).

[8] Jia-Yu Ye, Vygantas Mizeikis, Ying Xu, Shigeki Matsuo, Hiroaki Misawa, Opt. Commun. **211**, 205 (2002).

Oscillations in the low-frequency Townsend mode of DBD

D. Nikandrov, L. Tsendin
St.Petersburg State Polytechnical University, Polytechnicheskaya 29, 195251, St.Petersburg, Russia

Abstract
The physical mechanism and scaling laws for the non-linear relaxation oscillations in the Townsend mode of DBD are presented. The fact that the space charge can be neglected with respect to the surface charge on the dielectric, allows to derive analytic dependences and to perform the comparison with the numerous experiments. The analysis is valid for an arbitrary time dependence of the applied voltage *U(t)*.
Keywords: Dielectric-barrier discharges; silent discharges, non-linear oscillations.

1. Introduction

Dielectric Barrier Discharges (DBD) are characterized by the presence of dielectric layer(s) between the gas and metal electrode. These discharges are widely used in industrial applications [1].
The Townsend mode DBDs are usually oscillatory. The oscillatory mode of traditional DC Townsend discharges results from the falling static Volt-Ampere Characteristic (VAC) [2-5]. These oscillations can be considered as a result of development of instability of the homogeneous stationary discharge mode; so their evolution can be continuously traced, starting from the small-signal linear stage up to the amplitude saturation.
The oscillations physical mechanism in the DBDs, in which the static VAC is altogether absent, is quite different. These oscillations exist only in the strongly non-linear form, and no continuous transition from the linear to the non-linear mode can be traced.

2. Simple model

The frequency restriction:

$$\tau = \frac{L}{E_{br} b_i} << \frac{2\pi}{\omega}. \qquad (1)$$

is considered here. E_{br} – the breakdown field; b_i - the ion mobility; ω - the applied voltage frequency; τ - the ion transit time at $E = E_{br}$.
The born in the discharge gap ions are collected on the dielectric surfaces (Fig. 1), resulting in the surface charges with densities.

$$\sigma_1(t) \approx -\sigma_2(t). \qquad (2)$$

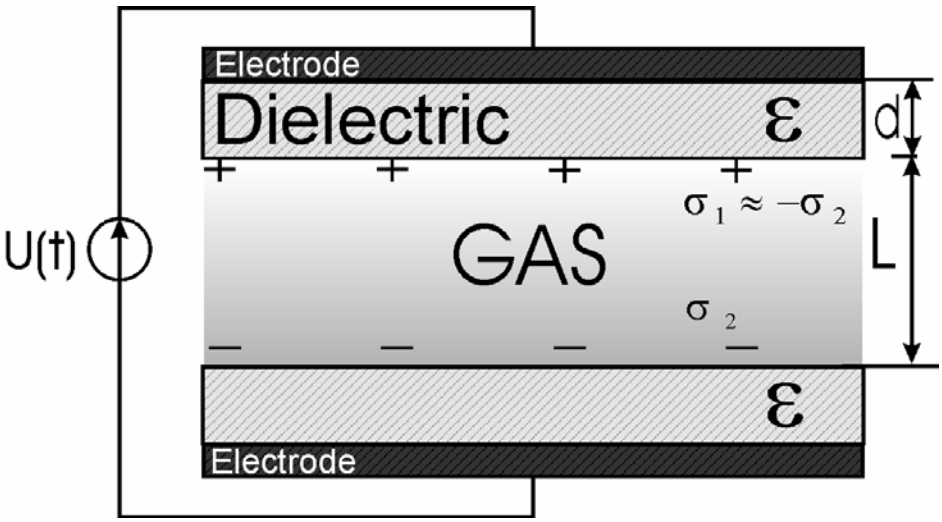

Fig. 1 Discharge cell

Due to (1), the electric field in the discharge gap is created mostly by the surface charges, and the space charge field can be neglected. So the field can be considered as spatially uniform: $E = E(t)$. From the Gauss' theorem the relation between the applied voltage $U(t)$, the electric field in the discharge gap E, and the surface charge follows:

$$E = U\frac{1}{L+\frac{2d}{\varepsilon}} + \sigma\frac{8\pi}{L+\frac{2d}{\varepsilon}}\frac{d}{\varepsilon}. \qquad (3)$$

At the time scale exceeding τ the conductivity current behaves as

$$j \propto \exp\left(\int^{t}\frac{M-1}{\tau}dt\right), \qquad (4)$$

where the multiplication factor M equals to the electrons number generated by one cathode-emitted electron during τ. If the standard local approximation for the ionization rate is valid,

$$M = \gamma\left(e^{\alpha(E)L}-1\right). \qquad (5)$$

As the Townsend's coefficient α itself depends exponentially on the field, the dependence (4), (5) is extremely steep, and the surface charges are piled up fast, which, according to the Le Chatelier principle, reduce the field back to the value E_{br}. So the crudest model corresponds to the assumption that

$$|E(t)| \le E_{br}. \qquad (6)$$

This crude discharge scenario for the sinusoidal $U(t)$ is sketched in Fig. 2, Fig. 3.

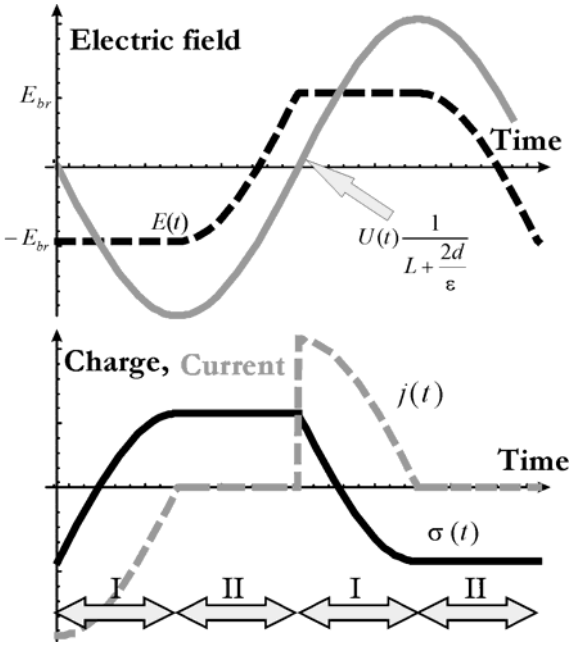

Fig. 2 Crude model of a discharge evolution

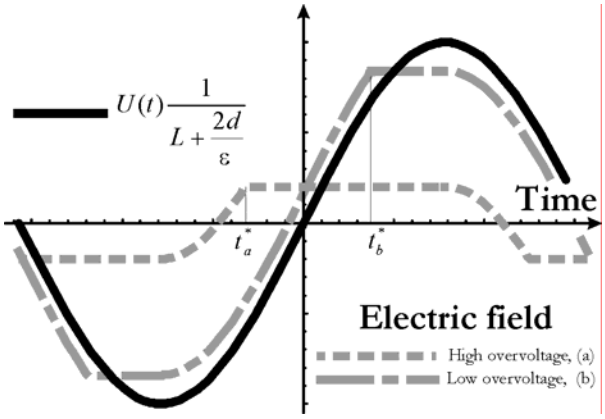

Fig. 3 Evolution dependence on overvoltage

The passive phase II corresponds to a low field; the ionization at this stage is absent, and the surface charge remains constant. During the active phase I the current which creates the surface charges and maintains $|E(t)| \approx E_{br}$, flows.

The moment t* (Fig. 3), when the breakdown starts, is defined by equation

$$U(t^*) = \left(2E_{br}\left(L+\frac{2d}{\varepsilon}\right) - U_{\max}\right). \qquad (7)$$

At low overvoltage, when

$$U_{\max} < 2L\left(1+\frac{2d}{L\varepsilon}\right)E_{br} \tag{8}$$

the moment t* is later, than the moment when $U(t)=0$; in the opposite case, the breakdown occurs when the gap field is opposite to the applied voltage.

For the description of the phase I this approach is oversimplified. Since the background electron density at t=t* is extremely low, it takes a rather long time, which considerably exceeds τ, for the current to rise enough to influence on the surface charge and to initiate the field reduction. According to (3), it means that during the time of the order of several τ after the exponential current rise starts, the surface charge remains practically unchanged, and the gap field $E(t)$ continues to rise. The storage of the surface charge starts to reduce the field, when $E(t) > E_{br}$. When the field reaches the value $E(t) = E_{br}$, a considerable current continues to flow; which is maximal at this moment. It takes some time (again of the order of several τ) for the current to fall off, and to start the following $E(t)$ rise process. As the current flow continuously reduces the field, this rise starts from the low value, $E(t) < E_{br}$. So during the active phase I the non-linear relaxation oscillations arise.

3. Oscillations characteristics

The conductivity current during the phase I, when the oscillations occur, is given by expression:

$$j(t) = \int_{-\infty}^{t} \frac{j_{ext}(t')}{\tau} \exp\left(\int_{t'}^{t} \frac{\ln M\left(E\left(t''\right)\right)}{\tau} dt''\right) dt' \tag{9}$$

where j_{ext} is the external (independent from the discharge) electron current from the cathode. Equation (9) is equivalent to

$$\tau \frac{dj}{dt} = -j \ln M(E) + j_{ext}. \tag{10}$$

By differentiating (3) we obtain

$$\frac{dE}{dt} = \frac{dU}{dt}\frac{1}{L+\frac{2d}{\varepsilon}} - j\frac{8\pi}{L+\frac{2d}{\varepsilon}}\frac{d}{\varepsilon}. \tag{11}$$

Introducing the dimensionless variables: time $\theta = \frac{t}{\tau}$, field $\mathrm{E} = \frac{E}{E_{br}}$, applied voltage $\Phi = \frac{U}{1+\frac{2d}{\varepsilon L}}\frac{1}{E_{br}L}$, external current $\imath = \frac{j_{ext}}{j\big|_{t=0}}$ and parameter:

$$\kappa = \frac{8\pi\, d}{\left(\varepsilon L + 2d\right)}\frac{j\big|_{t=0}}{E_{br}}\tau, \tag{12}$$

we obtain the equation for the oscillatory discharge phase I.

$$\begin{cases} \dfrac{d^2\mathrm{E}}{d\theta^2} - \dfrac{d^2\Phi}{d\theta^2} - \ln\left(M(\mathrm{E})\right)\left(\dfrac{d\mathrm{E}}{d\theta} - \dfrac{d\Phi}{d\theta}\right) = -\imath\,\kappa; \\ \mathrm{E}\big|_{\theta=0} = 1, \qquad \left.\dfrac{d\mathrm{E}}{d\theta}\right|_{\theta=0} = \left.\dfrac{d\Phi}{d\theta}\right|_{\theta=0} - \kappa \end{cases} \tag{13}$$

According to (1), the term $\frac{d^2\Phi}{d\theta^2}$ can be neglected, and the oscillations characteristics follow adiabatically value of $\frac{d\Phi}{d\theta}$. Since during the active phase I the external current is negligible, the right-hand side of (13) can be replaced by zero, and the undamping oscillations result. Their mechanical model corresponds to the particle motion with non-linear friction force, which changes its sign at $\mathrm{E}=1$. The expressions for the maximal and minimal electric field values, and the oscillations frequency can be derived.

In small oscillation case $M(\mathrm{E}) \approx 1 + M'(\mathrm{E}-1)$ simple expressions for the amplitude (in units E_{br}):

$$\mathrm{E}_{\max} = 1 + \sqrt{\frac{2\Phi'\left(\ln\frac{\Phi'}{\kappa} - 1\right)}{M'}}; \quad \mathrm{E}_{\min} = 1 - \sqrt{\frac{2\Phi'\left(\ln\frac{\Phi'}{\kappa} - 1\right)}{M'}} \tag{14}$$

and the oscillations period (in units τ):

$$\sqrt{\frac{8\ln\frac{\Phi'}{\kappa}}{\Phi' M'}} \tag{15}$$

follow.

On the other hand, if the dependence $U(t)$ is meander-like, the oscillations disappear.

4. Comparison with experiments

In experiments [6] with He at 730 Torr, frequency of the external voltage (for the triangular (a) and sinusoidal case (b)) was 1.5 kHz, L=0.2 cm, d=0.23 cm, ε=5. In Fig. 4 and Fig. 5 the experiment comparison with the calculations is presented.

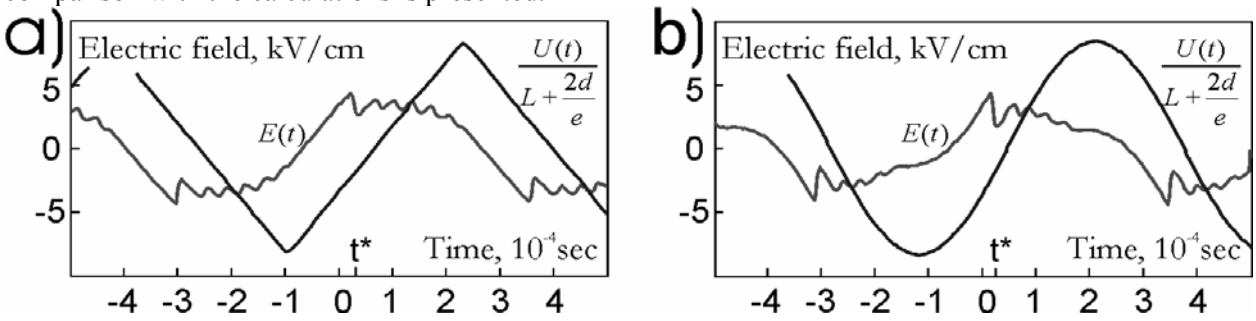

Fig. 4 The oscillations onset (7) is shown

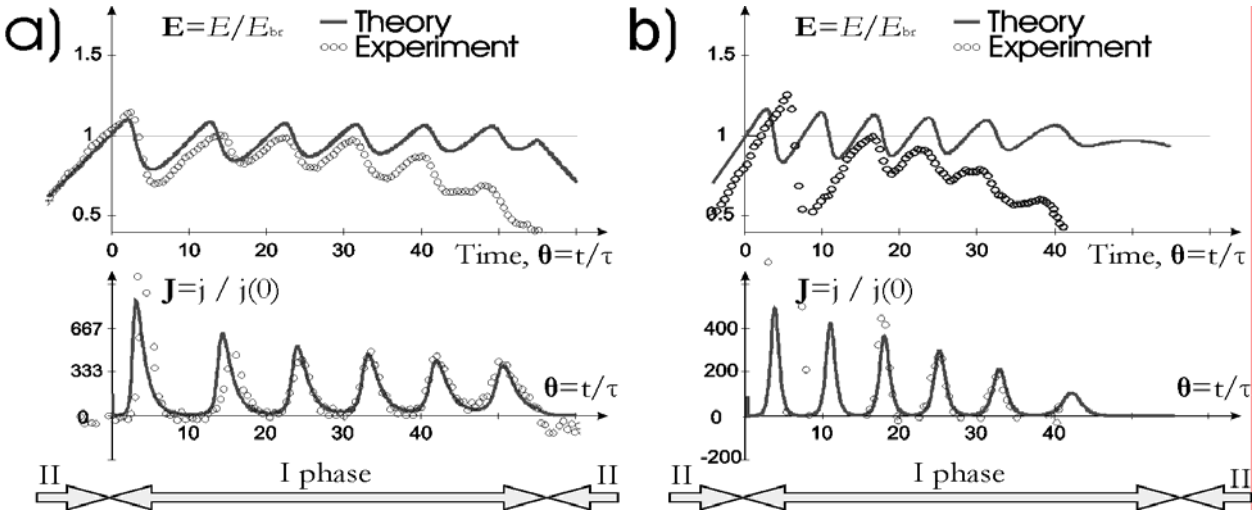

Fig. 5 Oscillations characteristics

In the experiments [7] DBD in methane at 0.75 Torr, L=0.5 cm, d=0.5 cm, f=1.4 kHz, was used. In Fig. 6, Fig. 7 the comparison of the experiment with the calculations is presented.

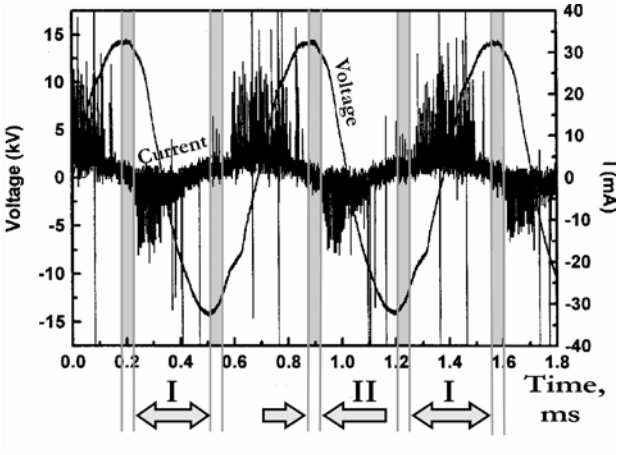

Fig. 6 Phase separation (on active I, and passive II)

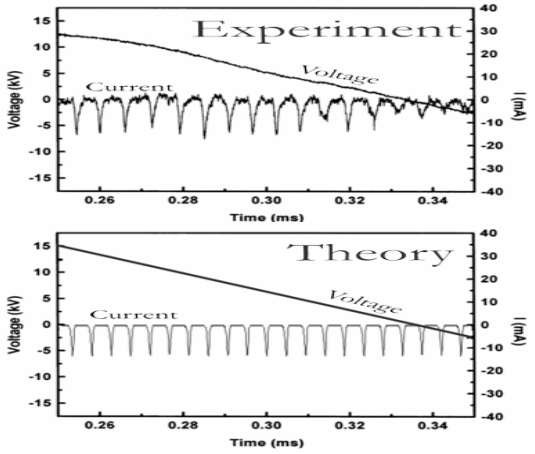

Fig. 7 Oscillation characteristics

In the experiments [8] the DBD in He at atmospheric pressure, L=0.3 cm, d=0.23 cm, ε=7.63, γ=0.01. For the voltage frequency of 100 Hz and 500 Hz in the Fig. 8 the comparison experiment and theory is presented. In the Fig. 9 the scaling for the pulses number during the phase I is shown for different discharge parameters. The agreement for the 3 mm gap looks reasonable, but for the 5 mm gap agreement is considerably worse. This fact can be attributed to the rise of the field distortion by the space charge with the gap length increase.

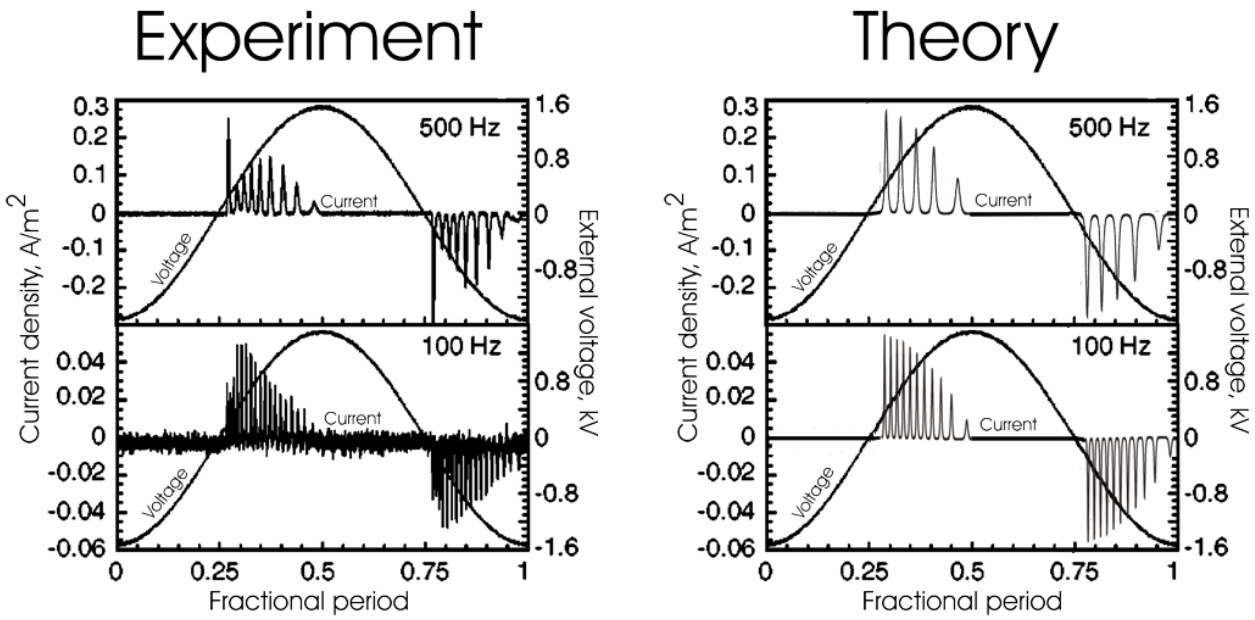

Fig. 8 Oscillation pattern

Since the calculation results depend on j_{ext} logarithmically, they are rather insensitive to its precise value. In all the calculations the values of j_{ext} in the range $10^{-4} \div 10^{-5} \frac{mA}{cm^2}$ was used.

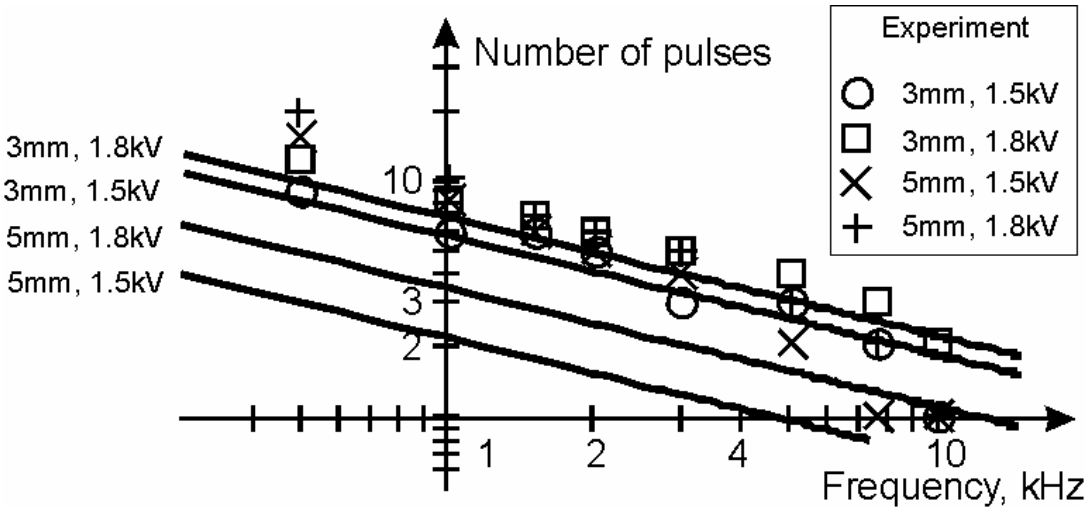

Fig. 9 Scaling for the pulses number

The paper was supported by RFBR, Project 04-02-16483-a; CRDF NS grant N RP1-567-ST-03 and ISTC grant 3098.

References

[1] U. Kogelschatz, Plasma Chemistry and Plasma Processing, Vol. **23**, No. 1, March 2003.
[2] V. Melekhin, N. Naumov, Sov. Phys. Tech. Phys., **29**, 888, (1984).
[3] Z. Petrovic and A. Phelps, Phys. Rev. E, **47**, 2806–2815 (1993).
[4] A. Phelps, Z. Petrovic, and B. Jelenkovic, Phys. Rev. E, **47**, 2825–2838 (1993).
[5] A. Kudryavtsev, L. Tsendin, Technical Physics Letters, **28**, 1036–1039 (2002).
[6] G.Visentin, L.Mangolini, K.Orlov, U.Kortshagen and J. Heberlein. Proc. of 15th Int. Symp. on Plasma Chemistry (Orleans, France, July 10-13 2001) V.**8** p.3251-3256.
[7] Dongping Liu, Tengcai Ma, Shiji Yu, Yong Xu and Xuefeng Yang, J. Phys. D: Appl. Phys. **34** 1651–1656, (2001).
[8] Jichul Shin and Laxminarayan L. Raja., J.Appl.Phys. **94**(12), 7408-7415 (2003).

Plasma arc beam characteristics in hybrid plasma and laser deposition

Ying-ping Qian, Hai-ou Zhang, Gui-lan Wang
State Key Lab. of Plastic Forming Simulation and Die & Mould Technology,
Huazhong University of Science and Technology, Wuhan 430074, China

Abstract
In order to research the characteristics of plasma arc in the hybrid plasma and laser deposition manufacturing (PLDM) process of high temperature alloy, the high speed CCD camera was used to obtain the picture around the plasma arc. And then the clear sketch of picture was obtained through dealing with the plasma arc picture. The effect of laser parameters, such as average power, pulse width and pulse repetition frequency on the plasma arc appearance was studied experimentally. The results show that the modality of plasma arc is influenced markedly by laser beam.
Key words: Hybrid plasma and laser deposition manufacturing (PLDM), Characteristic, Modality

1. Introduction

In the late 1980s, the emerging of RP (Rapid Prototyping) technology provided a new idea for the rapid development of high-temperature components. Now the RMP (Rapid Metal Prototyping) has become the advanced manufacture in RP technological research [1-5]. In terms of RMP, there are various kinds of RMP, in which we can mainly gain LENS (Laser Engineering Net-Shaping), electron beam deposition technology, PDM (Plasma Deposition Manufacturing) and the other technologies that can fabricate components with high density [6-8]. The LENS technology adopts the high-power laser to melt the powdered metal that is sent to a substrate and then solidifies quickly and finally forms a work-piece by depositing layer by layer. The density of the work-piece is far higher than that in the SLS (Selective Laser Sintering) method, and the mechanics performance reaches formal casting standards. But because of the overheating power, the shaped work-piece is easy to fracture. Besides, there exist several problems such as non-full densification, low surface quality and too much investment in equipment. The electron beam deposition method adopts the electron beam with 4KW power to melt metal powder materials. According to the computer model, the control system exerts the electromagnetic field, controls the movement of the electron beam to scan layer by layer until the end of the whole component shaping. The porosity is about 0.5%. However, the process condition is required strictly. It has to move in vacuum to limit the prototype length, and the expense of the equipment is very high. The PDM adopts highly compressed and centralized plasma beam, to heat metal powder and melt the metal in a molten pool on the substrate, then the metal-prototype or component is deposited and formed layer by layer, which has such features as materials to be more widely used, higher shaping efficiency, fuller density and lower cost of equipment than those of LENS and electron beam deposition methods [9-10]. But this technology has some problems such as lack of forming energy, arc stability and centralization of the beam when using the micro-plasma arc to shape precision and thin walled component. Therefore, the PLDM (Hybrid Plasma and Laser Deposition Manufacturing) as a new direct metal prototyping technology is proposed in this paper. The characteristics of the PDM technology are applied, and the better collective laser beam as a supplemental energy resource is adopted to make the high temperature material prototype with high quality. The effects of laser beam parameters, such as average power, pulse width and repetition frequency on the performance characteristics of plasma arc in the process of hybrid plasma and laser deposition manufacturing are studied

experimentally.

2. The principle of PLDM

The principle of PLDM technology is shown in Fig.1. The conception model is gained by means of concept design first, and then work out a CAD model. According to the requirement of the component's dimensional accuracy, the CAD model is dealt with slices and transferred into an STL document. In accordance with the shape of every layer, the control system draws up route, generates the CNC code to control the movement of the NC machine. On the one side of the plasma arc, the laser beam is focused on the plasma arc into the molten pool through adjusting the optical path for light transmitting and focusing. The deposition and shaping are then carried out under the controlling of the parameters such as movement of worktable, plasma arc-stream, shielding gas flow, carrying powder gas flow, electric current according to the design in advance. The high-temperature alloy powder is sent to the molten pool to melt and solidify into a compact metal layer rapidly, then continue repeating the lamination until all the three-dimensional component's layers are formed.

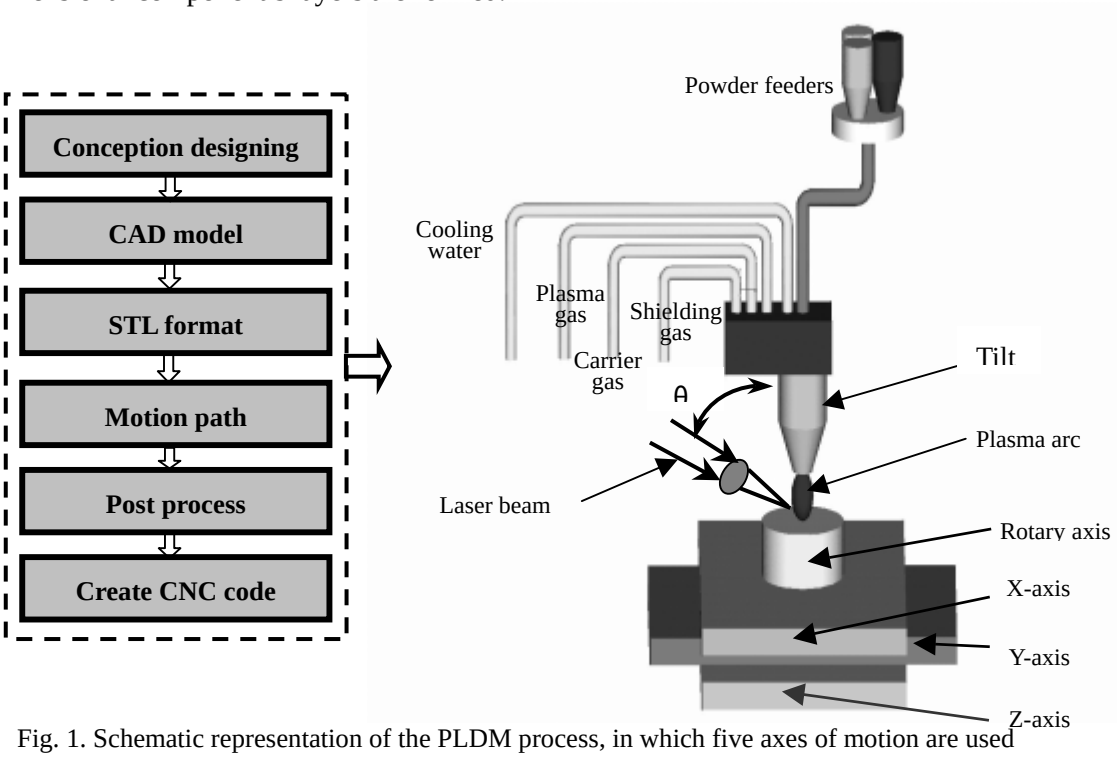

Fig. 1. Schematic representation of the PLDM process, in which five axes of motion are used

3. The condition and method of experiment

3.1. Experimental material

The experimental material was nickel-chromium-cobalt high-temperature alloy powder, with the characteristics of greatly high yield and creep strength under the lower 800℃, crack resistance while strain aging, satisfactory performance of fatigue when it was heated. And the main elements were shown in table 1.

Table 1.Chemical composition of nickel-chromium-cobalt alloy powder

Composition	Al	Co	Cr	Mo	Si	Mn	Mo
Wt (%)	0.59	20.56	19.79	5.88	<0.40	<0.60	5.88
Composition	W	Fe	Nb	Ti	Ti+Al	Ni	Ti
Wt (%)	<0.20	<0.7	<0.25	2.14	2.73	Bal.	2.14

3.2. Condition of experiment

The parameters of plasma arc deposition shaping process remained unchangeable during the experiment. The pressure ratio of ion air, protection air, argon as carrying-powder air was 1:1:1, electric current of transferred arc: 80-200A, moving speed of worktable: 200mm/min, feeding quantity of powder: 25g/min. A pulse YAG laser was adopted and the parameters values were shown in table 2.

Table 2. The laser parameters in the experiment

Average power (W)	4	39	91	160	254	-
Pulse width (ms)	0.3	2	4	6	8	-
Repetition frequency (Hz)	1	10	30	50	70	99

3.3. Method and device of experiment

The laser beam was focused on the molten pool, which remaining the parameters of the plasma; changing the laser average power, pulse width and repetition frequency. The high-speed CCD camera was used to obtain the picture around the plasma arc. And then the clear sketch of the picture was gotten after dealing with the plasma arc picture. By means of the obtained picture sketch, the diameter of plasma arc was measured and the influence of the laser parameters on the plasma arc shape was analyzed. The position using measure the diameter of the plasma arc was selected at the same distance below the nozzle of plasma gun.

The PLDM equipment with five-axis numerical controlling function as shown in the fig. 1 was used in the experiment. The range of the laser average power was from 4W to 280W, the transmission and focus of laser could be adjusted freely in the optical path system.

4. The result and discussion of experiment

4.1. The influence of the laser average power

Fig.2 (a) shows the relationship between plasma arc characteristics and laser average power. Fig.2 (b) is the plasma arc sketch dealt with by Gauss-Laplace method. The relationship between average power and plasma arc diameter is shown in fig.3. It is clear that the plasma arc is becoming small when the laser average power is increasing, which means that the laser has the compression effect on the plasma arc. The reason is that the increase of the laser average power makes the energy absorbed by the plasma arc increase, which improves ionization and magnetic effect compression, and then results in the reduction of the plasma arc diameter.

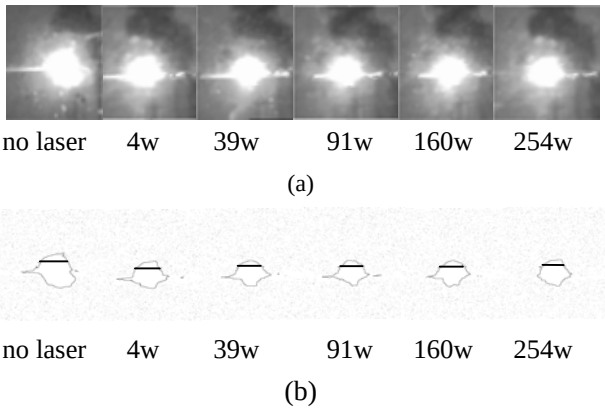

Fig. 2. The plasma arc pictures under the condition of different laser average power (a), and the plasma arc sketch dealt with by Gauss-Laplace (b).

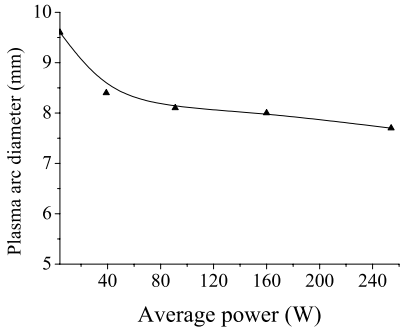

Fig. 3. The relationship between laser average power and plasma arc diameter

4. 2. The influence of the laser pulse width

Fig.4 (a) is the plasma arc under the different pulse width conditions and fig 4 (b) is plasma arc sketch dealt with by Gauss-Laplace method. The relationship between the different pulse width and plasma arc diameter is given in fig.5. As shown in the picture, the plasma arc diameter is reducing with the increasing of the laser pulse width, which means that the compression of plasma arc increases as the pulse width increases. The reason is that the increasing of the pulse width increases the energy of the single pulse, and the average power equals the single pulse energy multiplied by repetition frequency. Therefore when the pulse width increases, the energy absorbed by the plasma arc also increases. As a result, the plasma arc diameter reduces while the plasma arc has a further compression.

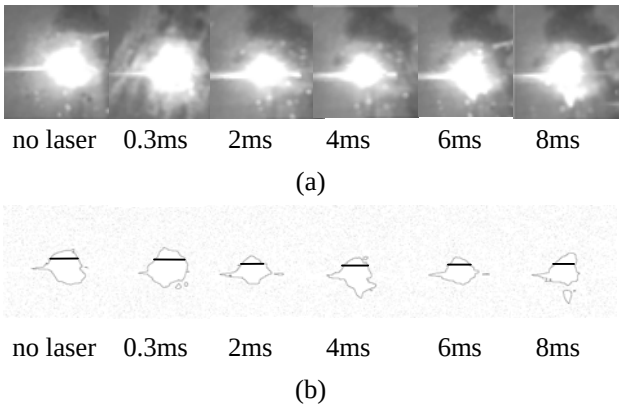

Fig. 4. The plasma arc picture under the condition of different laser pulse width (a), and the plasma arc sketch dealt with by Gauss-Laplace (b).

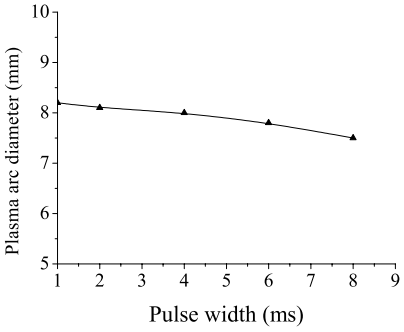

Fig. 5. The relationship between laser pulse width and plasma arc diameter

4. 3. The influence of the laser repetition frequency

Fig.6 (a) is the shape of plasma arc under the condition of the different laser repetition frequency and Fig.6 (b) is the plasma arc sketch dealt with by the Gauss-Laplace method. The relationship between the repetition frequency and the plasma arc diameter is shown in Fig.7. From the figure, the plasma arc diameter becomes reducing when

the laser repetition frequency increases. But with the increasing of the repetition frequency to a certain range (about 50Hz), the plasma arc diameter begins tending to increase. This means that the increasing of the laser repetition frequency makes the plasma arc compress at the beginning, but the compression effect gradually goes down. When it goes over a certain value, the plasma arc begins to extend reversal. The reason is that during the compounding of the laser and plasma, first the plasma arc absorbs laser energy through the inverse bremsstrahlung absorption mechanism, then the plasma arc ionization and magnetic compression effects increase, and the plasma arc compresses effect and arc diameter reduce. On the other hand, the plasma induced by the interaction of the laser and substance has a process of generating, extending and disappearing. Under the unchangeable condition of the electronic arc plasma, and under the condition of using low laser repetition frequency, the influence of laser repetition frequency on the plasma arc is not obvious. The magnet compression effect of electronic arc plasma plays an important role, thus the plasma arc diameter reduces. When the laser repetition frequency increases further to a valve value, the ionization of the electronic arc plasma will reach a maximum value, and the electron density and temperature will reach the valve value. The electron density and temperature no longer increase with the increasing of the repetition frequency. And then the magnetic compression effect no longer increase. However the interval between every laser pulse becomes smaller and the laser average power becomes greater with the repetition frequency increasing more, which makes the energy accumulated in the laser function area more and more and the temperature of the laser pulse function area higher and higher. At the same time, the plasma induced by laser extends towards outside at a rapidly increasing speed. So after counteracting the magnetic compression effect of the electronic arc plasma, the diameter of the plasma arc becomes greater.

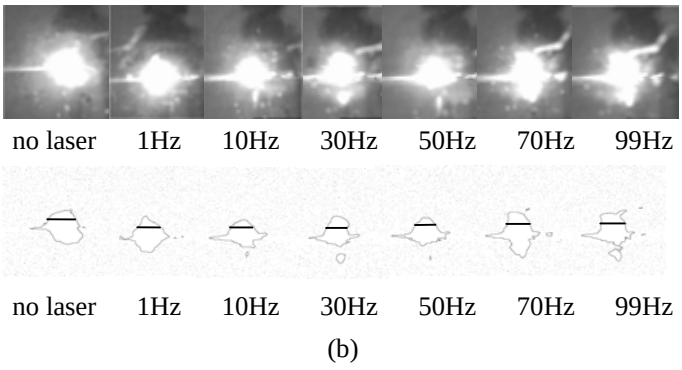

Fig. 6. The plasma arc picture under the condition of different laser repetition frequency (a), and the plasma arc sketch dealt with by Gauss-Laplace (b).

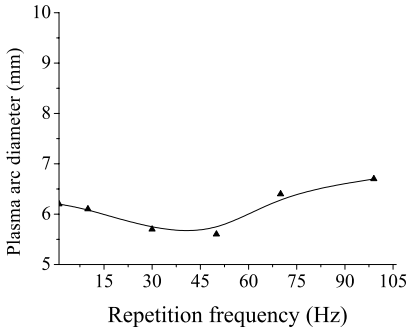

Fig. 7. The relationship between laser repetition frequency and plasma arc diameter

5. Conclusion

(1) Hybrid plasma and laser will bring about a plasma arc compression effect. This compression effect has related to the laser average power, pulse width and pulse frequency, and also has an important influence on the plasma arc beam shape.

(2) The compression of the plasma arc increases with the increasing of the laser average power, pulse width. The increasing of the laser repetition frequency causes the plasma arc compression effect to reduce. When the repetition frequency exceeds a certain value, the plasma arc will begin to extend contrarily. This effect and the inverse bremsstrahlung absorption effect of plasma has related to the ionization degree.

Acknowledgements

The authors would gratefully appreciate the contribution of the National Nature Science Foundation of China under project No.50474053 and the State High-Technology Development Program of China under project No. 2003AA421150.

References

[1] H.O. Zhang, G. L. Wang, Y.H. Luo - Thin Solid Films 390 7 (2001).
[2] H. Zhang - Surface and Coating Technology 171 112 (2003).
[3] M. Allahverdi, S.C. Danforth, M. Jafari - Journal of the European Ceramic Society 21 1485 (2001).
[4] M. Zhong - Journal of Materials Processing Technology 147 167 (2004).
[5] H. Muller, J. Sladojevic - Journal of Material Processing Technology115 97 (2001).
[6] S. Das - Rapid Prototyping Journal 4 112 (1999).
[7] A. Bernard, A. Fischer - Annals of the CIRP 51 635 (2002).
[8] D. I. Srivastava, T. H. Chang, M. H. Loretto - Material and Design 21 425 (2000).
[9] J. Schlosser - Fusion Engineering and Design 49 337 (2000).
[10] J. Hur, K. Lee, H. Zhu, - Computer-Aided Design 34 741 (2001).

Quenching the Inductively Coupled Thermal Plasma for Nanoparticle Synthesis

St. Siegmann, M. Leparoux, C. Schreuders, J.-W. Shin, L. Rohr

EMPA - Swiss Federal Institute for Materials Research and Technology,
Feuerwerkerstrasse 39, CH-3602 Thun, Switzerland

Abstract
Temperature evolution during nanoparticle synthesis by thermal plasma has an enormous influence on the final size, size distribution, and phases of the generated products. The influence of several quenching parameters, like two gas jets or eight nozzles quench ring, different gas flow rates and chemical composition, quench jet positions on the resulting temperature profiles has been investigated. The modelling has been supported and validated with experiments, in-situ diagnostics, and ex-situ measurements.

Keywords: quenching, inductively coupled plasma, nanoparticles

1. Introduction

The worldwide activities in nanoparticles research increased dramatically during the last 5 to 10 years. Among the different routes for nanoparticle production, the main directions envisaged are mechanical milling, wet chemical reactions or gas phase processes. Each of these processes has its specific advantages and limitations. Mechanical milling and wet chemical reactions are typically time intensive and batch processes, whereas gas phase processes by flames or plasma can be carried out continuously and fast.
Materials of interest are mainly oxides, carbides, nitrides, and pure metals or alloys. Nano-ceramics are attractive candidates for application in coating technologies due to the expected higher coating toughness, better thermal shock and wear resistance. Inductively coupled plasma (ICP) facility provides a versatile tool for nanoparticle formation by controlling the heating, evaporation, quenching, and chemical composition of the atmosphere.

2. Experimental

The thermal plasma techniques, especially the inductively coupled plasma (ICP) process, offer many advantages compared to other gas phase techniques [1]. A high temperature and energy density enable the processing by vaporisation/condensation of high refractory materials and the use of inexpensive commercial available solid precursors [2]. Furthermore, the electrodeless operation of the ICP torch generates high purity products. The processability even under reduced pressure or reactive atmosphere offers some distinct advantages compared to other processes.
The induction plasma equipment consists of a plasma torch (PL-35, TEKNA Plasma System Inc., Canada) operated at a frequency of 13.56 MHz with an electrical input power of up to 35 kW. This torch is mounted on a modular vacuum synthesis chamber equipped with numerous view ports for in-situ monitoring. Finally the off gases are passing an on-line sampling filter or alternatively a large mass filtration unit [3] to retain the produced nanopowders. The detailed description of the experimental set-up is published elsewhere [2, 3].
A photograph of the setup is shown in *Figure 1*.

Figure 1: Photograph of the inductively coupled plasma (ICP) equipment for nanoparticle synthesis.

One important factor influencing the chemical and physical properties of the generated nanoparticles is quenching. Quenching can be carried out using different approaches e.g. using a cold surface [4], an expansion nozzle [5], or cold gas quenching [6] for nanoparticle condensation. The quench gas jets have some advantages like for instance easy positioning, variable quench gas flow rates, use of a reactive quench gas, etc. Only few references are available on this topic among them e.g. Hansen et al. [6] reporting on modelling of quench ring designs for a flame reactor or Soucy et al. [7] investigating the axial and radial mixing of two gas streams.

In this work two different quench nozzle designs are compared, i.e. a two jet nozzle and a ring type nozzle with eight holes. The influence of the different conditions on the plasma temperature and velocity field was measured by enthalpy probe technique [8]. The modelling of the temperature and velocity of the plasma flow field and quenching designs was carried out using the commercial CFD software Fluent 6.1.18. As quench gas Ar and N_2 have been investigated for the simple two jet nozzles as well as for the eight nozzles quench ring.
Commercially available tungsten carbide (WC) powder (d_{50} = 1.1µm) was used as precursor. The powder was injected into the plasma at the height of the first induction coil with a feed rate of approximately 300-350 g/min. The plasma conditions where the following (*Table 1*):

Table 1: Plasma parameters used for the study:

Parameters	**Values**
Central gas: Ar	27 slpm
Sheath gas (Ar / H_2)	80 slpm / 6 slpm
Electrical net power	15 kW
Chamber pressure	40 kPa
Powder carrier gas: Ar	5 slpm

3. Results:

The symmetric two jet nozzles positioned in opposite directions have shown good agreement between experimental observations *(Figure 2a)* and the 3D model exhibiting the splitting of the plasma jet (*Figure 2b)* at an Ar quench gas flow rate of 56 slpm. The asymmetry in *Figure 2a* is caused by a small deviation from the symmetry axis.

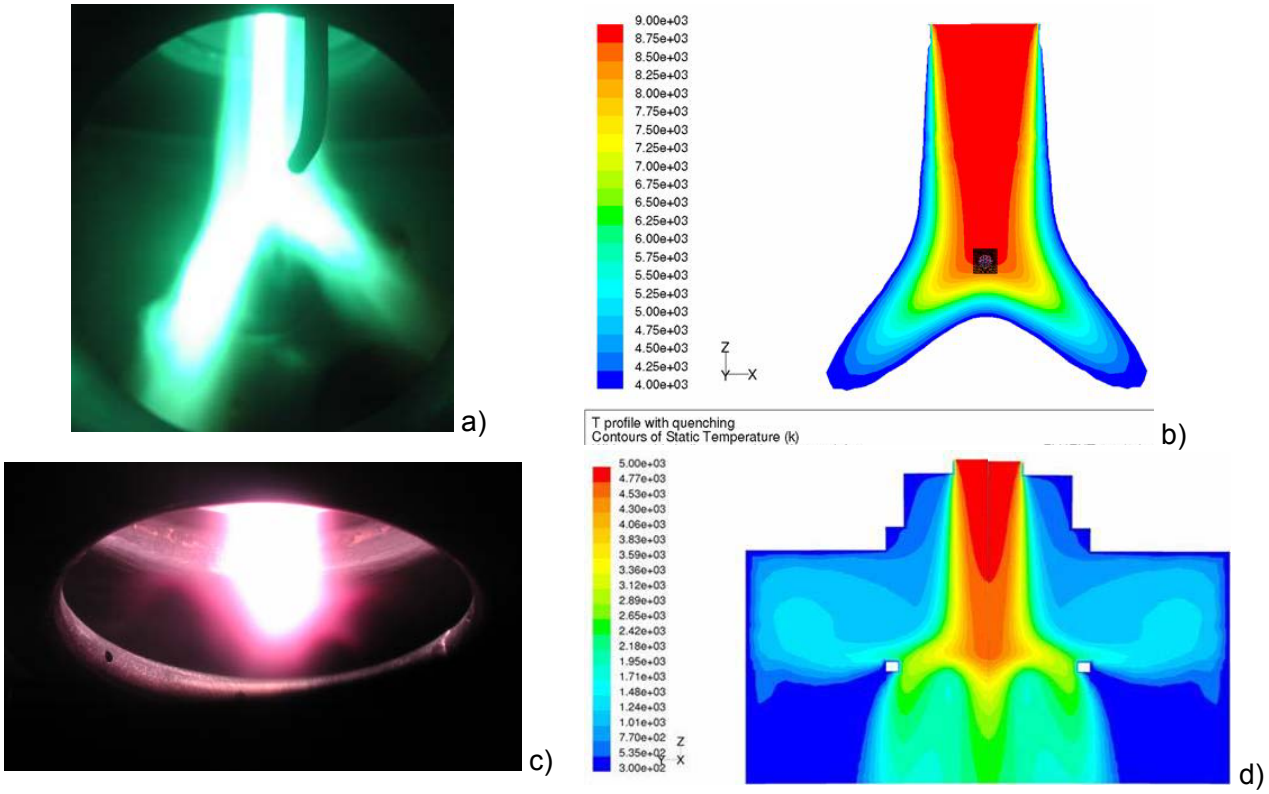

Figure 2: Comparison between a) photograph of two jet quenching and b) 3D temperature modelling and c) photograph of plasma jet quenched by an eight nozzles quench ring and its modelled trend in d).

The eight nozzles quench ring performed a more homogeneous and symmetrical quenching of the hot plasma. Figure 2c) shows a photograph of the plasma at the same quench gas flow rate level (56 slpm) like the two jets in Figure 2a). The two jets nozzle intersects the plasma in two parts giving rise to uncontrolled cooling and strongly variable and broad temperature and velocity profiles. In the case of the eight nozzles quench ring, the condensed particles are forced to flow through the ring. A better control of the nanoparticle size and size distribution is expected than for the 2 jets geometry.

The influence of quenching on the resulting size of the products is shown in *Figure 3*. Without quenching a particle growth is observed compared to the precursor. The non-quenched product also shows a smaller size distribution due to nucleation of the vapour on the non-vaporised, i.e. cold particles. A clear reduction of the particle size is visible when quenching has been used. The size distribution depends on the temperature and velocity profiles followed by the particles.

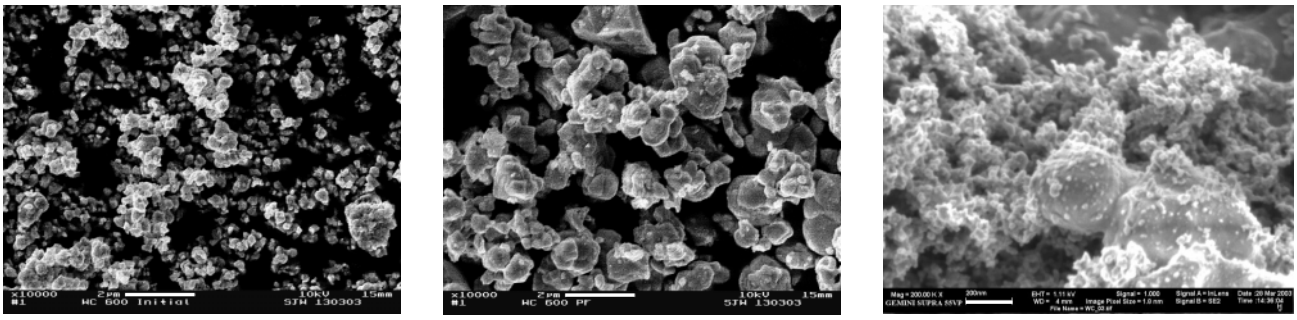

Figure 3: (left) SEM picture of WC precursor; (middle) plasma processed and grown WC without quench; (right) HR-SEM picture of plasma processed WC with 2 jets quench (white bars correspond to 2 μm in the SEM pictures and 200 nm in the HR-SEM picture).

As expected, quenching does not only influence the particle size and distribution, but also the chemistry. The XRD spectra in *Figure 4* show the phase composition of plasma processed WC as a function of the quenching gas flow rate and gas chemical composition.

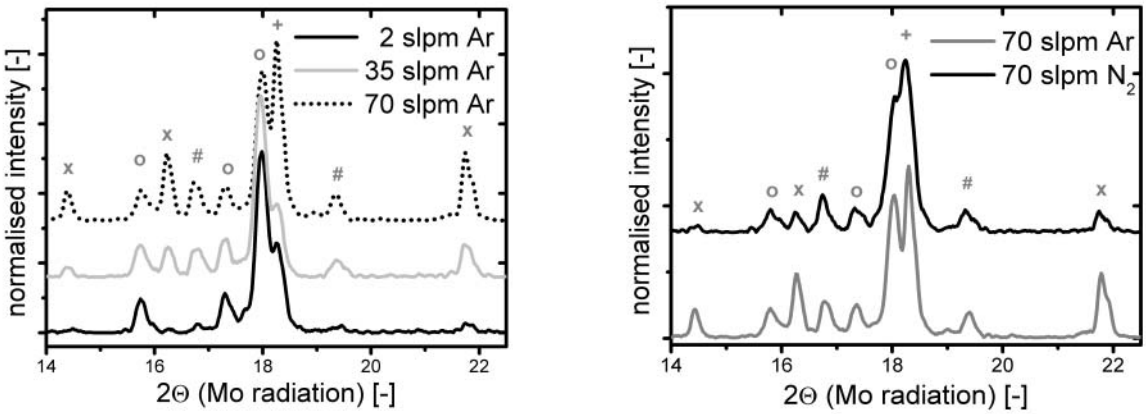

Figure 4: Phase composition determined by XRD of the synthesised WC powders for (left) different Ar quench gas flow rates and (right) comparison between 70 slpm of Ar and N_2 quench gas (X: WC, #: WC_{1-x}, O: W_2C, +: W).

4. Conclusions:

The optical observations, enthalpy probe measurements [9], and CFD modelling showed all good agreements between each other. The developed CFD model allows further optimizing the quenching of the plasma by adjusting the position, the geometry and the flow rates for controlled nanoparticle synthesis.

5. Acknowledgements:

The Commission for Technology and Innovation (CTI) of Switzerland is acknowledged for partial financial support of the projects “Top Nano 21: #5978.2 and #6740.1.
J.-L. Dorier and C. Hollenstein are gratefully recognized for lending of the enthalpy probe device and for helpful discussions.

References:

1. M. I. Boulos, *High Temperature Material Processes* **1**, 17-39 (1997).
2. C. Schreuders, M. Leparoux, J.-W. Shin, M. Dvorak, S. Siegmann, Partec 2004 - International Congress for Particle Technology, Nürnberg, GER (2004).
3. M. Leparoux, S. Siegmann, Filtech Europa 2003 - International Conference and Exhibition Filtration and Separation Technology, Düsseldorf, GER (2003).
4. A. Singhal, G. Skandan, N. Glumac, B. H. Kear, *Scripta Materialia* **44**, 2203-2207 (2001).
5. K. Wegner, S. E. Pratsinis, *AIChE Journal* **49**, 1667-1675 (2003).
6. J. P. Hansen, J. R. Jensen, H. Livbjerg, T. Johannessen, *AIChE Journal* **47**, 2413-2418 (2001).
7. G. Soucy, J. W. Jurewicz, M. I. Boulos, *Plasma Chemistry and Plasma Processing* **14**, 43-58; 59-71 (1994).
8. M. Rahmane, G. Soucy, M. I. Boulos, *Review of Scientific Instruments* **66**, 3424-3431 (1995).
9. C. Schreuders, M. Leparoux, J.-W. Shin, H. Miyazoe, St. Siegmann, 16th International Plansee Seminar 2005 - Powder Metallurgical High Performance Materials, Reutte, A, 45-58 (2005).

Preparation of supported $TiO_2/\gamma–Al_2O_3$ photocatalyst by plasma driven surface reaction using dielectric barrier discharge at atmospheric pressure

Long-Hui Nie [a], Xiu-LingZhang[a], Ai-Min Zhu[*ab], Chuan Shi[ab], Zhi-Min Song[a], Yong Xu[ab], Xue-Feng Yang[ab]

[a] *Laboratory of Plasma Physical Chemistry, Dalian University of Technology, Dalian 116024,China*

[b]*Center for Nano Materials and Science , Dalian University of Technology, Dalian 116024,China*

Abstract: At atmospheric pressure and room temperature, dielectric barrier discharge induced plasma driven surface reaction (PDSR) for the preparation of $TiO_2/\gamma–Al_2O_3$ photocatalyst has been investigated. $TiCl_4$ and O_2 were used as reagents in successive cycles. The adsorbed-state $TiCl_4$ may be oxidized by O_2 plasma to form Cl_2 and TiO_2, which exhibits high activity in the photocatalytic degradation reaction of formaldehyde. It has been found that there is an optimum cycle number to obtain the highest photocatalytic activity.

Keywords: dielectric barrier discharges, photocatalyst, TiO_2, plasma driven surface reaction

1. Introduction

Chemical vapor deposition (CVD) has been widely studied for depositing TiO_2 thin films on the supports with various geometric shapes[1-8]. In these studies, most TiO_2 films were prepared by thermally activated low-pressure (10^1-10^2 Pa) CVD at 573K followed by heat treatment or atmospheric pressure CVD (APCVD) at 773-923 K. Plasma enhanced CVD (PECVD) has been known to activate the deposition process more effectively than that of thermally driven CVD, because it makes use of low temperature, non-thermal equilibrium plasmas that provide energetic species to activate reactant molecules at temperature compatible with a wide range of substrate materials. However, PECVD have been studied in the preparation of TiO_2 films for photocatalyst mainly using radio frequency (RF) or microwave (MW) discharges at low pressure (10^2-10^3 Pa) [9,10]. Recently, a hybrid process of EFCM (electrostatic formation of ceramic membrane) and SPCP (surface corona discharge induced plasma chemical process) was proposed and successfully utilized to prepare TiO_2 photocatalytic membrane at atmospheric pressure[11]. In our previous paper, the supported $TiO_2/\gamma–Al_2O_3$ photocatalyst prepared by dielectric barrier discharges (DBD) induced PECVD at atmospheric pressure and room temperature has been explored, and exhibits high photocatalytic activity[12].

Generally, for the dominant TiO_2 deposition pathway in low-pressure CVD, it is believed that a Ti precursor molecule collides with another molecule in gas phase to form a more active intermediate species. They in turn react with the surface active site to produce deposited TiO_2 onto the surface of the support. But for atmospheric pressure CVD, in most case, another pathway is easy to take place that TiO_2 powders are generated in gas phase and settle down on the support surface. This pathway leads to very poor adhesion of TiO_2 to the support and should be avoided. For this purpose, in this work, DBD induced plasma driven surface reaction (PDSR) for the preparation of supported $TiO_2/\gamma–Al_2O_3$ photocatalyst at atmospheric pressure and room temperature has been investigated.

[*]Corresponding author. *E-mail*: amzhu@dlut.edu.cn

2. Experimental

The experimental setup designed for this work has been reported previously [12]. The discharge chamber consists of an outer quartz tube (*i*. *d*. 17 mm, *o*. *d*. 20 mm), a stainless steel tube (*i*. *d*. 4 mm, *o*. *d*. 6 mm) placed along the axis of the outer tube as the high-voltage electrode and 6 ml of γ–Al_2O_3 pellets (ϕ1 mm) filled between the two tubes. A copper wire mesh (height 30 mm) wound on the outside surface of the quartz tube was used as the ground electrode. The DBD power supply source is capable of supplying a bipolar sine wave output with 0–40 kV peak-to-peak voltage (U_p) at an a.c. frequency (f) of 5-20 kHz.

Titanium tetrachloride ($TiCl_4$) was chosen as the precursor. $TiCl_4$ was stored in a separate container and introduced into the PDSR reactor by bubbling 10ml/min of Ar carrier gas through. The temperature of $TiCl_4$ was kept at 340K using a water bath.

The preparation of TiO_2/γ–Al_2O_3 photocatalyst by DBD induced PDSR was performed at atmospheric pressure and room temperature. After the γ–Al_2O_3 pellets were loaded into the PDSR reactor, if not otherwise specified, $TiCl_4$ was first introduced and absorbed onto the supports for 30 min and then purged residual $TiCl_4$ vapor in the reactor by 18 ml/min of Ar for 15 min . Afterwards 20ml/min of O_2 together with 8ml/min of Ar was introduced into the PDSR reactor and the dischargestarted and lasted for 30 min (discharge conditions: f = 5 kHz, U_p=12kV).

This experiments for TiO_2/γ–Al_2O_3 preparation were carried out in a cyclic way. The above mentioned operation is just for1 cycle.

To determine the loading amount of titanium on the surface of γ –Al_2O_3, the coated γ –Al_2O_3 pellets were placed in warm $(NH_4)_2SO_4$-H_2SO_4 mixture solution, then the solution was heated up boiling for 2 h. The dissolved titanium was quantified by colorimetric method [13].

The photocatalytic activities of the TiO_2/γ–Al_2O_3 photocatalysts were evaluated by the photocatalytic degradation of formaldehyde solution. 10 ml of 3.0 mg/l formaldehyde solution, together with 1.3 g of TiO_2/γ–Al_2O_3 photocatalyst, were irradiated by a ultraviolet lamp (254 nm, 8 W) for 0.5 h. The concentrations of formaldehyde were determined by colorimetric method. It is worthwhile to point out that there is no need for heat treatment for the TiO_2/γ–Al_2O_3 photocatalyst prepared by the PDSR process at room temperature.

The optical emission spectrometer (Acton, SP-300i) was composed of an optical collection and a transmission system. The collection of the light was carried out with a lens (diameter ϕ 30 mm), by which the collected light was focused onto the input slit of the monochrometer through a group of supplement lens. After being amplified by a DC-amplifier, the out-put signal of the optoelectron multiplying tube (PMT) was sent to a computer. The wavelength scanning range of the monochrometer was 200-900 nm with highest resolution 0.1nm. The response scope of the PMT was 200-900 nm. The mass spectrometry (Balzers, Omistar^{TM} 422) was used to determine the products of PDSR.

3. Results and discussion

3.1 Comparison of two synthesis routes of PDSR process

Generally, in thermal CVD process[3], $TiCl_4$ was first introduced and absorbed onto the porous supports, then water vapor was brought through to start the hydrolysis of those absorbed $TiCl_4$ species. In the PDSR process, whether $TiCl_4$ is absorbed followed by discharge in O_2-containing gas (designated as Route A) or O_2 is absorbed

followed by discharge in $TiCl_4$-containing gas (designated as Route B), this should be first determined by a comparative experiment. As shown in Fig.1, formaldehyde conversions of $TiO_2/\gamma–Al_2O_3$ photocatalyst prepared by Route A and B are 83% and 4%, respectively. This result strongly supports that Route A is much more advantage than Route B for $TiO_2/\gamma–Al_2O_3$ photocatalyst preparation using PDSR process. Thereby, Route A was employed in all the following experiments.

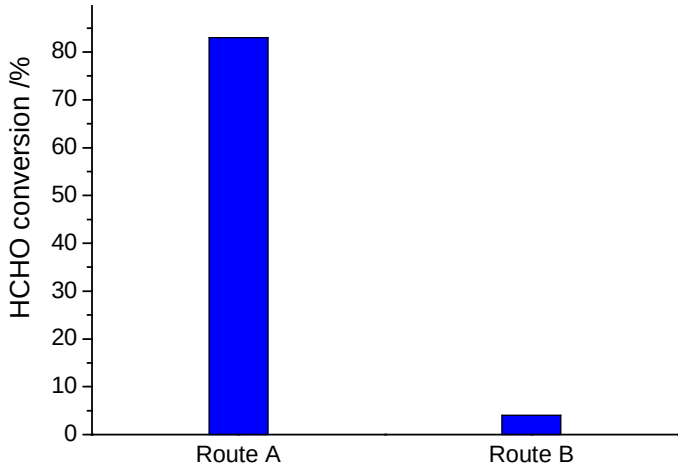

Fig. 1 Comparison on photocatalytic activity of $TiO_2/\gamma–Al_2O_3$ photocatalysts prepared by Route A and B (2 cycles of adsorption-PDSR)

3.2 Effect of the number of PDSR cycles

Fig.2 shows TiO_2 loading amount and formaldehyde conversion of $TiO_2/\gamma–Al_2O_3$ photocatalyst versus the number of adsorption-PDSR cycles. The TiO_2 loading amount increases with increasing the cycle number. This result differs from the work using the Chemical Surface Coating (CSC) method in literature [14], where it was reported that the uptake of Ti is linearly during the first 6 reaction cycles and afterwards no further uptake of Ti was found. In the CSC process, $TiCl_4$ and H_2O were used as reactants. But, $TiCl_4$ is too reactive with water to handle the reaction rate. In the PDSR process, O_2 was employed instead of H_2O and the reaction of adsorbed-state $TiCl_4$ and O_2 driven by plasma was easy to control.

It can be also seen that there is an optimum number of PDSR cycles to obtain the highest photocatalytic activity, which is around 6 cycles. When further increasing the cycle number, the TiO_2 loading layer becomes thicker and it is more difficult for UV light to penetrate and for formaldehyde molecules to diffuse through. Furthermore, with increasing the loading amount, the small TiO_2 crystals tend to agglomerate which also has an disadvantage effect on the performance of the catalyst.

3.3 Mechanisms of TiO_2 coating in the PDSR process

Generally, the overall oxidation reaction for $TiCl_4$ is

$$TiCl_4 + O_2 \rightarrow TiO_2 + 2Cl_2 \quad (1)$$

and can be carried out in the gas phase or on a solid surface. To shed light upon the reaction mechanism in the

PDSR process, the gas phase stable species were monitored in situ by mass spectrometry and optical emission from plasma of PDSR was measured.

In the process of PDSR, no peak related to $TiCl_4$ appears in the mass spectrum at *m*/*e* =190 ($TiCl_4^+$), *m*/*e* =153 ($TiCl_3^+$), *m*/*e* =118 ($TiCl_2^+$), *m*/*e* =83 ($TiCl^+$). Fig.3 shows the peaks of the gas effluent from PDSR reactor, these include: the peaks related to Ar appears at *m*/*e* =40 (Ar^+) and *m*/*e* =20 (Ar^{2+}); the peaks related to Cl_2 appears at *m*/*e* =70 (Cl_2^+), 72 (Cl_2^+), 35 (Cl^+); the peaks related to O_2 appears at *m*/*e* =32 (O_2^+) and *m*/*e* =16 (O^+).

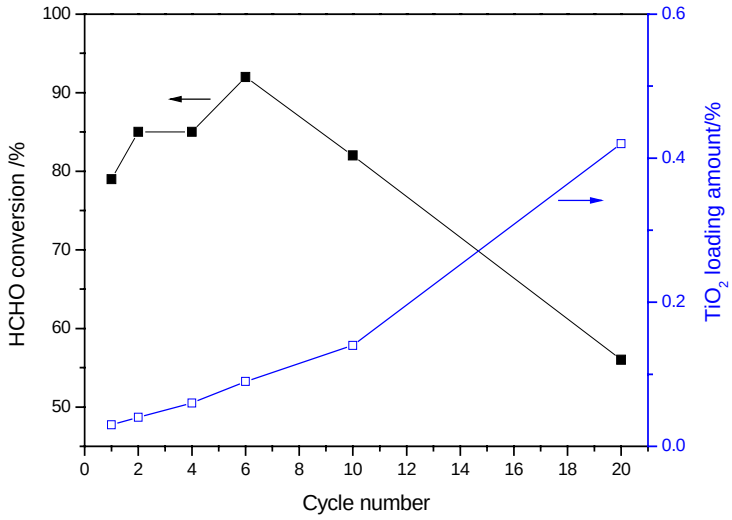

Fig.2 TiO_2 loading amount and formaldehyde conversion of $TiO_2/\gamma–Al_2O_3$ photocatalyst as functions of the number of adsorption-PDSR cycles.

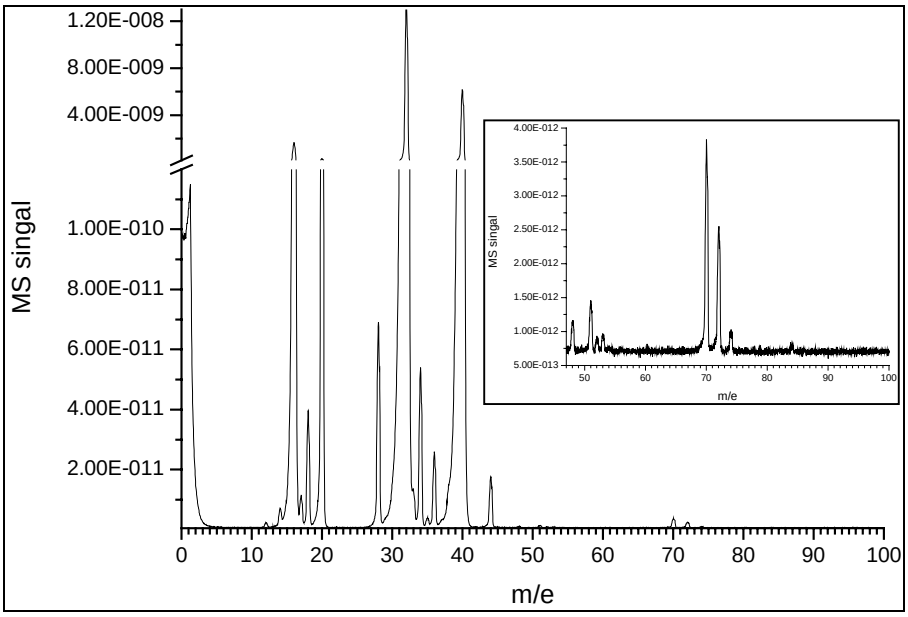

Fig.3 Typical mass spectrum of the gas effluent from PDSR reactor

Fig.4 exhibits peak intensity of Cl_2, the oxidation product of $TiCl_4$, changes with time. In a PDSR cycle, with the increase of discharge time, peak intensity of Cl_2 rises rapidly to the maximum and decreases slowly, which implies that $TiCl_4$ adsorbed onto the γ–Al_2O_3 surface was being consumed and getting less and less. As shown in Fig.5, the emission spectrum of O (778.0 nm) and Ar (772.8 nm, 795.4 nm) from the plasma of the PDSR process is observed.

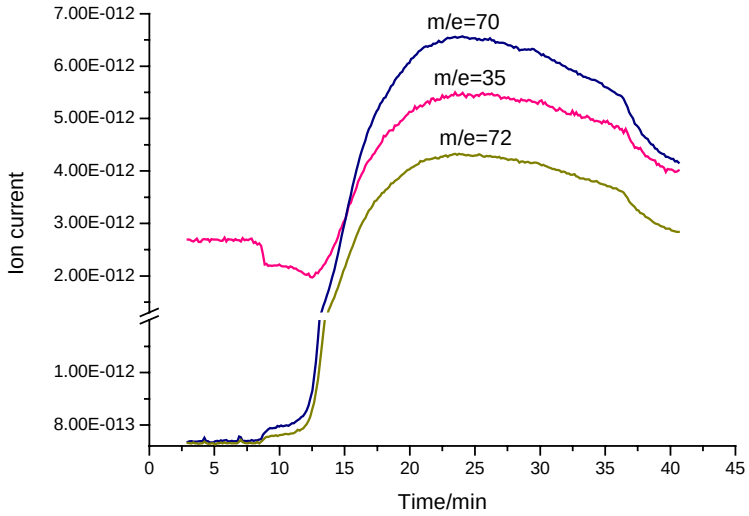

Fig.4 Intensity of peaks related to Cl_2 at *m*/*e* =70, 72 and 35 versus time

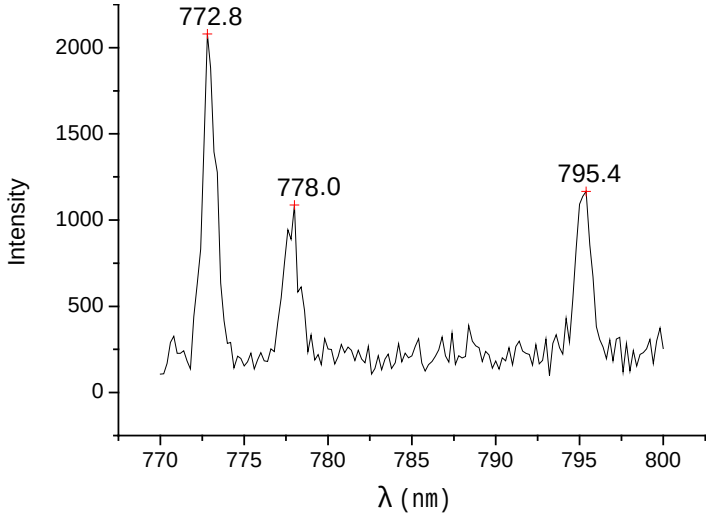

Fig.5 Optical emission spetra from the plasma of the PDSR process

Based upon the above experimental results, the mechanism for the adsorption and PDSR process can be explained as follows:

$TiCl_4$ first adsorbs on γ–Al_2O_3 surface

$$TiCl_4\ (g) \rightarrow TiCl_4\ (ad) \qquad (2)$$

Adsorbed-state $TiCl_4$ is oxidized by oxygen atom derived from the collision of O_2 molecule with energized

electron in the plasma

$$TiCl_4\ (ad) + O \rightarrow TiCl_2O\ (ad) + 2Cl \quad (3)$$

$$TiCl_2O\ (ad) + O \rightarrow TiO_2\ (s) + 2Cl \quad (4)$$

The recombination of Cl atom from reaction (3) and (4) forms Cl_2

$$2Cl \rightarrow Cl_2 \quad (5)$$

4. Conclusion

$TiO_2/\gamma-Al_2O_3$ photocatalyst was prepared by means of DBD induced plasma driven surface reaction at atmospheric pressure and room temperature. By plasma-driven reacting adsorbed-state $TiCl_4$ with O_2 in a cyclic way, a TiO_2 coating is formed which is chemically bound to the support and exhibits high activity in the photocatalytic degradation reaction of formaldehyde. It has been found that there is an optimum cycle number to obtain the highest photocatalytic activity. There is no need for heat treatment for the $TiO_2/\gamma-Al_2O_3$ photocatalyst prepared by the PDSR process at room temperature.

Acknowledgements The project supported by the National Natural Science Foundation of China (Grant No. 50177003).

References

[1] A. Mills, N. Elliott, I. P. Parkin, S. A. O'Neill and R. J. Clark, *Journal of Photochemistry and Photobiology A: Chemistry*, **151**, 171(2002).

[2] L. Lei, H. P. Chu, X. Hu and P.-L. Yue, *Ind. Eng. Chem. Res.*, **38**, 3381(1999).

[3] Z. Ding, X. Hu, G. Q. Lu, P.-L. Yue and P. F. Greenfield, *Langmuir*, **16**, 6216(2000).

[4] Z. Ding, X. Hu, P.-L. Yue, G. Q. Lu and P. F. Greenfield, *Catalysis Today*, **68**, 173(2001).

[5] V.G. Bessergeneva, I. V. Khmelinskiia, R. J. F. Pereiraa, V. V. Krisukb, A. E. Turgambaevab and I. K. Igumenov, *Vacuum*, **64**, 275(2002).

[6] D. Byun, Y. Jin, B. Kim, J. K. Lee and D. Park, *Journal of Hazardous Materials*, **B73**, 199(2000).

[7] B. Kim, D. Byun, J. K. Lee and D. Park, *Jan. J. Appl. Phys.*, 41, 222(2002).

[8] S. Motojima, T. Suzuki, Y. Noda, A. Hiraga, S. Yang, X. Chen, H. Iwanaga, T. Hashishin and Y. Hishikawa, *Journal of Materials Science*, **39**, 2663(2004).

[9] M. Morstein, M. Karches, C. Bayer, D. Casanova and P. R. von Rohr, *Chem. Vap. Deposition*, **6**, 16(2000).

[10] M. Karches, M. Morstein, P. R. von Rohr, R. L. Pozzo, J. L. Giombi, and M. A. Baltanás, *Catalysis Today*, **72**, 267(2002).

[11] T. Moriya, T. Matsuyama and H. Yamamoto, *Journal of Electrostatics*, **58**, 185(2003).

[12] A.-M. Zhu, L.-H. Nie, X.-L. Zhang et al., *Plasma Science & Technology*, **6**, 2546(2004).

[13] N. B. Jackson, C. M. Wang, *J. Electrochem. Soc.*, Vol. 138. No.12, 3660 (1991).

[14] K. Schrijnemakers, N. R. E. N. Impens and E. F. Vansant, *Langmuir*, **15**, 5807(1999).

THEORETICAL STUDY OF AR/O_2 MIXTURES IN ECR PLASMAS: IS IT POSSIBLE TO USE OPTICAL EMISSION SPECTROSCOPY AS A QUANTITATIVE DIAGNOSIS TOOL?

A. Yanguas-Gil[1], J. Cotrino[1,2] and A. R. González-Elipe[1]

[1)] *Instituto de Ciencia de Materiales de Sevilla (CSIC - Univ. Sevilla), Sevilla, Spain*
[2)] *Dep. Física Atómica, Molecular y Nuclear, Univ. Sevilla, Sevilla, Spain*

Abstract

In this work a collisional-radiative model of Ar and O_2 is used to model low pressure microwave ECR discharges for these gases and their mixtures. The model is formed by two parts which are self-consistently solved, one global model of the discharge zone and a 2D model of the downstream region. The model is able to reproduce the trends experimentally observed for the different parameters of the discharge, but further refinements are needed in order to find a quantitative agreement with the Optical Emission Spectrocopy measurements carried out in the same reactor.

1. Introduction

Low pressure Ar/O_2 discharges are frequently used for applications such as etching or thin film deposition of different oxides. In our laboratory, in the past five years an ECR reactor in an SLAN configuration has been successfully used for such purposes[1,2]. One of the advantages of these devices is that the discharge is generated inside a quartz chamber that is connected to the metallic reactor in which the reactive process takes place (Fig. 1), so that Optical Emission Spectroscopy (OES) measurements can be easily made in the discharge region. However, in PECVD and etching processes it is interesting to get further information not only about the species that are present in the plasma, but also of the active species that are reaching either the substrate or the etched material.

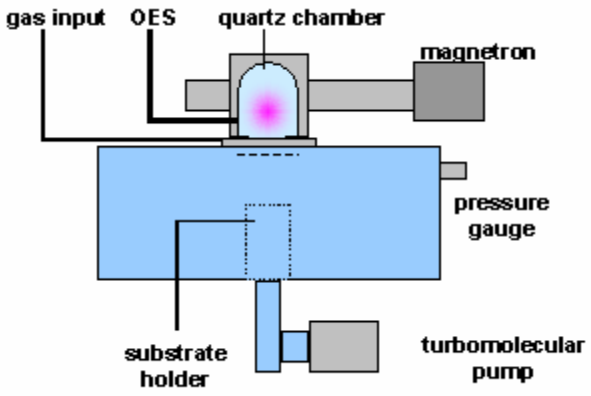

Figure 1: Scheme of the experimental set-up

Optical emission spectroscopy is a non-intrusive characterisation tool that has been used in many works to characterise the excited species that appear during the deposition process[2]. In oxygen discharges, quantitative information has been obtained from the optical emission spectroscopy by techniques such as actinometry. Other works have tried a different approach, using theoretical models of the main plasma kinetics in order to get information of some of the key parameters of the discharge (i. e., electron density or electron temperature) from experimentally measured emission intensities.

In this work we have followed this second approach, so that a collisional radiative model for Ar, O_2 and Ar/O_2 mixtures has been developed in order to get the populations of the different species as a function of the main experimental parameters, that is, microwave power, pressure and mixture composition. The model would serve as a starting point to identify Ar and O emission lines that could be used to check the theoretical results obtained with OES experimental measurements[3].

2. Theoretical model

The discharge zone is studied using a global model in which the electron energy distribution function and a collisional-radiative model taking into account the main species for discharges in Ar and O_2 are solved self-consistently. For the case of argon, the kinetic model includes 32 argon levels, so that the populations of the excited states responsible of the argon main emission lines are considered[4]. We have included a coherent cross-section set including the most recent experimental data available which has been previously tested and compared with other collisional-radiative models[5].

In the case of oxygen, seven species have been included in the model: O_2 (X), O_2 (a), O_2 (b), O_2^+, O, O^- and O_3. The oxygen kinetics has been modeled following the models presented by Capitelli et al[6] and the references cited therein. Ar and oxygen models have been linked through three main reactions[6,7]: charge transfer process between Ar^+ and O_2^+, metastable dissociation of O_2 molecule and O three-body recombination with Ar as the third body.

In order to study the evolution of the different species in the downstream region, the global model previously described is coupled to a 2D model of the deposition chamber. Populations of the different species are calculated in the difussion approximation with an effective diffusion coefficient D_e[8]. Milne boundary conditions have been used at the walls of the reation chamber. In the case of charged particles and metastable states of Ar and O_2, the wall recombination and de-excitation probability has been taken into account as in the work of Takechi and Lieberman[9].

The use of these two different approaches in the calculations is justified by the presence in the experimental reactor of a grounded grating between these two regions, so that the glow zone is confined in the quartz reactor. Both models are solved for the geometry and the conditions used in our laboratory as described in previous works. Averaged values of the electron density and temperatures as well as density profiles of some key species in the downstream are obtained using microwave power, pressure, gas temperature and Ar/O_2 ratio as input parameters.

3. Results

The model described above has been solved for different conditions. Pressure and power are the two parameters with greatest interest from the experimental point of view, along with the Ar/O_2 fraction when mixtures are studied. Gas temperature is also another parameter that may have an important influence on the discharge, especially due to the strong dependence of the wall recombination probability with the wall temperature. However, as can be seen in Fig. 2, measurements of the outer wall temperature of the quartz carried out in our reactor show that it is almost independent of the pressure and the electromagnetic power. Therefore, taking into account the high thermal conductivity of quartz, all results presented here correspond to a gas temperature of 300 K.

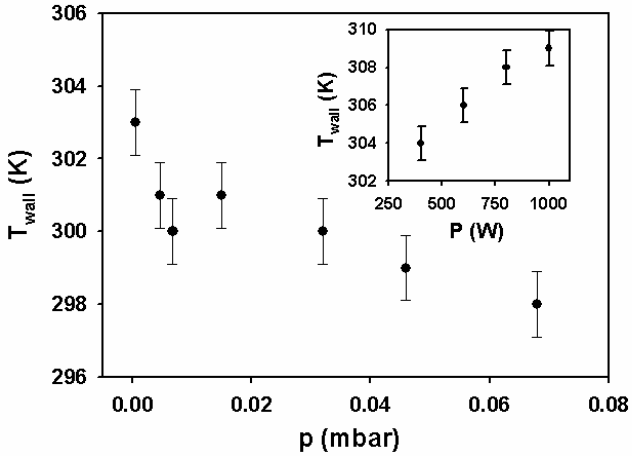

Figure 2: Wall temperature measurements

In Figure 3, the electron density ne and the population of atomic oxygen n_O are presented as a function of pressure and power for a pure oxygen discharge. Both depicts a characteristic behaviour reaching a maximum value for intermediate pressures, in contrast with the behaviour of the electron temperature, which decreases when increasing pressure.

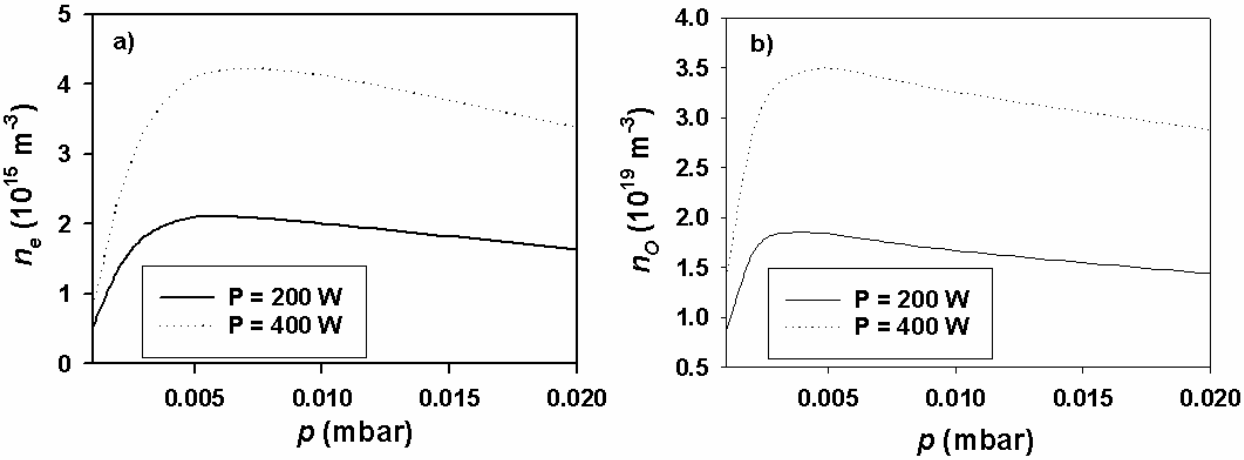

Figure 3: Electron density (a) and atomic oxygen population (b) as a function of pressure

The case for pure argon is presented in Figure 4. The electron density, in contrast with the behaviour of the oxygen discharge, increases with pressure and the values agree well in order of magnitude with the experimental measurements carried out by other autors for the SLAN plasma source. The electron temperatures presented follow the same trend as in the case of oxygen, but their values are lower than the obtained for O_2 discharges.

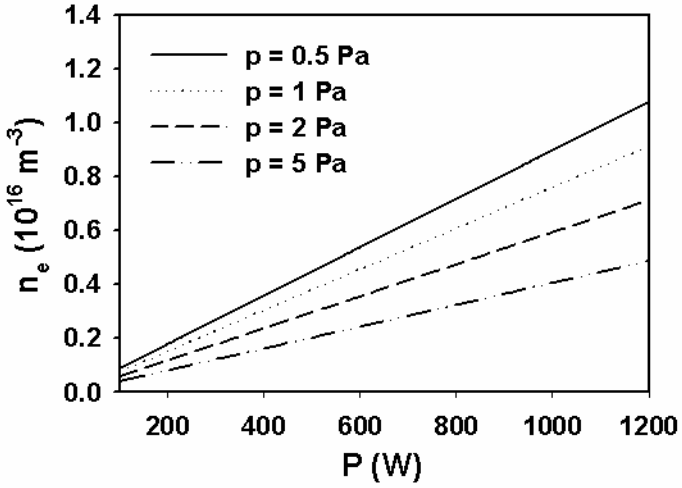

Figure 4: Electron density as a function of power for an Ar discharge

The presence of oxygen affects to both the electron temperature and the electron density of the discharge. In Ar/O_2 mixtures the charge transfer process between Ar^+ ions and O_2^+ is very effective, so that the population of O_2^+ ions in higher than that of Ar^+.

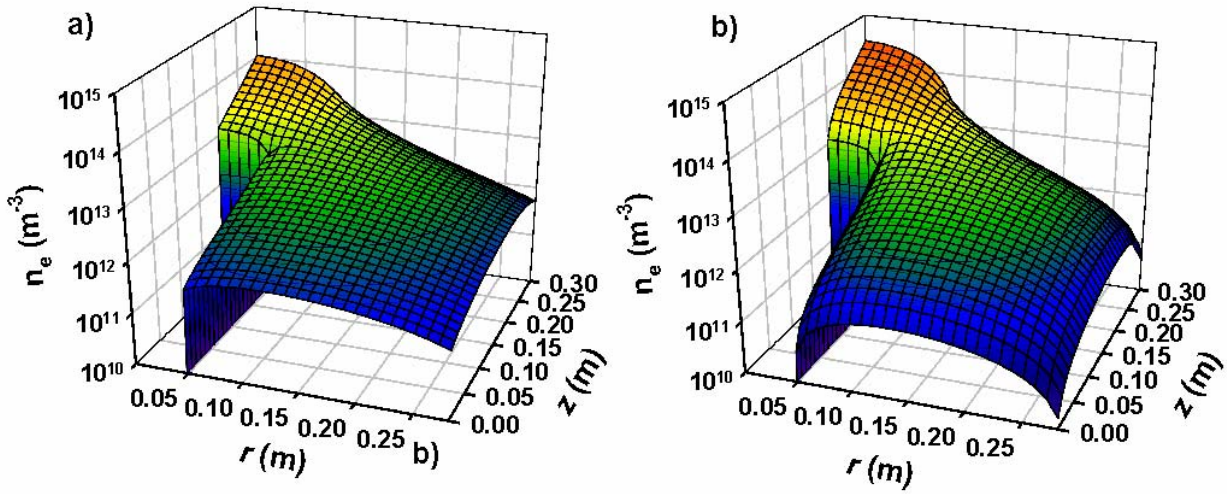

Figure 5: Downstream electron density profiles for two different pressures: (a) 10 mtorr; (b) 50 mtorr

Pressure is the main parameter affecting the evolution of the active species of the discharge in the downstream region. In Figure 5, the profiles for the electron density are presented for a pure argon discharge at two different pressures: tal and tal mbar. As a consequence of the increase on pressure the discharge is almost confined to the glow zone, and the flow of ionized particles onto the substrate-holder decreases significatively. Contrary to what happens with electron density, populations of metastable Ar are very important in the position of the substrate-holder. In this regard, in Figure 6 the joint flows of the Ar metastable levels of the 4s configuration, Ar 4s($^3P_0$) and Ar 4s($^3P_2$) is presented along the position of the substrate holder along with the flow of charged species for a pure argon discharge. The flow of Ar metastable states onto the substrate holder are almost an order of magnitude higher than the flow of charged

particles.

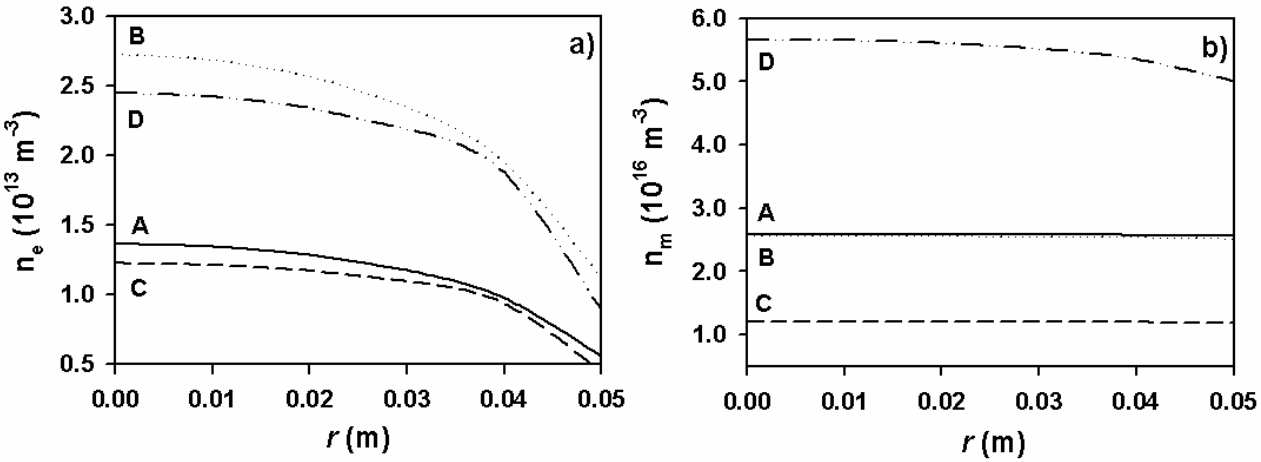

Figure 6: electron density and metastable population over the substrate holder: A 10 mTorr, 200 W; B 10 mTorr, 400 W; C 50 mTorr, 200 W; D 50 mTorr, 400 W

4. Discussion:

According to the model electron density behaves with pressure in a different way for argon or oxygen discharges. In this latter case, there are optimal conditions in which the electron density and the atomic oxygen reach their maximum value. In this regard, Optical Emission Spectroscopy measurements carried out in our SLAN reactor show that both the 777 nm and the 845 nm atomic lines of O present a similar behaviour with pressure, as well as the deposition rate in the case of SiO_2 thin films. In contrast, argon atomic lines do not exhibit such behaviour, in agreement with the monotonally increasing variation of the electron density with the pressure for argon plasmas.

Pressure is the main parameter that controls the evolution of the different species of the discharge in the afterglow. As the diffusion coefficients of Ar^+ and O_2^+ are similar, the variations in the populations of charged species in the afterglow are more influenced by total pressure than by the specific composition of the Ar/O_2 mixture. Due to their long mean lifes, these species are strongly affected by both the boundary conditions and the diffusion coefficients.

One of the limitations of the present model is that no detailed description of the kinetics of the excited states of the O_2 molecule has been included: in general, most of previous models found in literature either consider effective rate coefficient for the ionisation or neglect the contributions of the excited levels over the $O_2(b)$ excited state. In the case of argon, it has been found that the step-wise ionisation can be very effective, and when the full collisional-radiative model is considered, the electron temperatures theoretically calculated are lower and closer to the experimental data. Without having an accurate description for step-wise ionisation for the molecular oxygen the electron temperatures calculated are expected to be higher than the real ones. Although this is not very important when trying to reproduce the trends experimentally observed, this is an important issue if a quantitative agreement is desired.

References:

[1] A. Martín, J. P. Espinós, A. Justo, J. P. Holgado, F. Yubero and A. R. González-Elipe, Surf. Coatings Technol. 151-152, 289 (2002).
[2] A. Barranco, J. Cotrino, F. Yubero, J. P. Espinós, J. Benítez, C. Clerc and A. R. González-Elipe, Thin Solid Films 401, 150 (2001).
[3] K. Kano, M. Suzuki and A. Akatsuka, Plasma Sources Sci. Technol 9, 314 (2000).

[4] S. Letout, C. Boisse-Laporte, A. Yanguas and L.L. Alves, "*Characterization of Low-pressure Microwave Discharges in Argon*", 57th Gaseous Electronics Conference, September 26-29, Shannon, Ireland (2004).
[5] A. Yanguas-Gil, J. Cotrino and A. Yanguas-Gil, J. Phys. D: Appl. Phys, *In Press*.
[6] M. Capitelli, C. M. Ferreira, B. F. Gordiets and A. I. Osipov, Plasma kinetics in atmospheric gases (Springer, 2000).
[7] A. V. Vasenkov and M. J. Kushner, J. Appl. Phys 95, 834 (2004).
[8] C. H. Muller, III and A. V. Phelps, J. Appl. Phys. 51, 6141 (1980).
[9] K. Takeshi and M. A. Lieberman, J. Appl. Phys. 90, 3205 (2001).

A new Surface Tension Measurement Technique for High-Melting-Point Materials

A. Moradian[1], J. Mostaghimi[2]

[1] *Centre for Advanced Coating Technologies, University of Toronto, Toronto, Canada*
[2] *Centre for Advanced Coating Technologies, University of Toronto, Toronto, Canada*

Abstract
A new experimental/numerical method is proposed to measure the surface tension coefficient of high-melting-point materials. In the proposed method, radio-frequency-Inductively Coupled Plasma (rf-ICP) is employed to melt materials. Dynamics of melting is photographed. The surface tension dominant phenomenon of melting is then numerically modeled. Interfacial tension, as the major parameters governing the dynamics of melting, is estimated by comparison between the theory and observation. The results for copper generally agree with those obtained in previous studies. Preliminary findings suggest promising application of the method for ceramics.
Keywords: Surface tension measurement, radio-frequency plasma, dynamics of melting

1. Introduction

Because of the relatively high temperatures involved and the reactivity with any container, measurement of the surface tension of high-melting-point materials poses special challenges. Therefore, only a few of the common methods can be implemented at high temperatures [1,2]. Metal manufacturing and fabrication industries are increasingly using computational based mathematical models to obtain a better understanding or control of their processes, or to predict defects in their final products. These models are highly developed in terms of the mathematical equations used, but they rely on the accuracy of the physical and physico-chemical property data of materials they are modelling. In many cases these data are not available, and this is particularly true in the case of surface tension and viscosity of high-melting-point materials. These properties are the critical factors in the modelling of the processes of interest. According to the limitation imposed because of melting temperature of materials, methods for the measurements at high temperatures should be container-less. Using atmospheric rf-ICP samples can be heated to high temperatures. Figure 1 shows the heating of a ceramic sample by a rf-ICP torch.

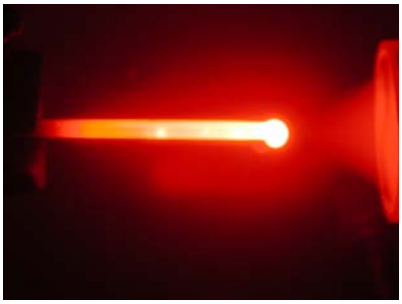

Fig. 1: Plasma heating of a ceramic sample

Details of the methods available for measuring surface tension of ordinary liquids have been reviewed [3,4] and will not be repeated here. Because of the relatively high temperatures involved and their reactivity with any container, surface tension of high-melting-point materials pose special challenges. Therefore, only a few of the common methods can be implemented at high temperatures. The maximum bubble pressure has frequently been employed in experimental determination of the surface tension of liquid metals and alloys. The maximum drop pressure method has been applied for determining the surface tension of highly reactive, low melting point metals, but it is limited to about 1000 K because of difficulties related to the design of equipment for high temperatures. The capillary rise method is not commonly used for metallic liquids; because the exact knowledge of contact angel is required. This angle is often more difficult to measure than surface tension [5]. The pendant drop method and the drop weight methods are applicable to most transition metals. The sessile drop method has

been extensively used for measuring surface tension of melts. In addition to the common methods many sophisticated techniques have been developed. For example, levitating drop method in which electro-magnetic levitators employ inhomogeneous radio frequency electro-magnetic field to heat and position samples. Such a field induces eddy currents within the material which due to Ohmic losses eventually heat up the samples (inductive heating). In addition, the field exerts a force on the sample and pushes it towards region of lower strength of the filed (Lorentz force). The latter effect produced by a strong magnetic field can be used to compensate for the 1 g gravitational force [6].

A brief review of the traditional methods manifests the drawbacks in using the methods for high temperature materials. Problems such as contamination, economic issues, equipment limitations and unexpected instabilities are the reasons that makes the levitation method deficient for high melting point materials.

Also, by using the theoretical relations for axisymmetric profile of pendant drops proposed by Young (1805) and Laplace (1805), surface tension of fluids can be measured. To this end, a comparison between the experimental drop profile and the theoretical profiles results in an appropriate capillary constant. Hence, having the density of the fluid interfacial tension will be calculated

The earliest efforts in the analysis of axisymmetric drops were those of Bashforth and Adams (1883) [7]. Hartland and Hartley (1976) [8] also investigated the interfacial tension measurement of axisymmetic fluid-fluid menisci. Based on their pioneering approach, Rotenberg et al. (1983) developed a technique called Axisymmetric Drop Shape Analysis-Profile (ADSA-P). The ADSA-P technique fits the measured profile of a drop to a Laplacian curve [9].

To quantify the equilibrium condition used in the drop weight method, Tate (1864) [10] proposed the following relationship.

$$m^* g = \pi d \sigma \qquad (1)$$

Where m^* is the mass of total pendant volume and d is the diameter of the wire at the melting point. However, this simple form does not allow for true determination of surface tension, which let Harkins (1919) to introduce a correction factor F, as “a fraction of the ideal drop separating from the rod” with using m (the mass of the collected drop) instead of m^*; therefore $F = \frac{m}{m^*}$ [11].

Harkins & Brown (1919) showed that the $f(R_0/a)$ is better correlated with a third-order polynomial. Their method led to the well-known “drop-weight” method to determine surface tension. Garandet et al. (1994) showed that the Harkins’ empirical correction factor F can be derived from a momentum balance written just before release [12].

Present study deals with the melting of copper samples by using the plasma torch, observation of the melting dynamics through high-speed imaging, extracting the profiles which are the result of full Navier-Stokes equations, and producing the analytical Young’s profiles. Figure 2 shows the digitally reproduced pendant drop based on image post processing and a numerically simulated pendant drop at the end of a horizontal rod.

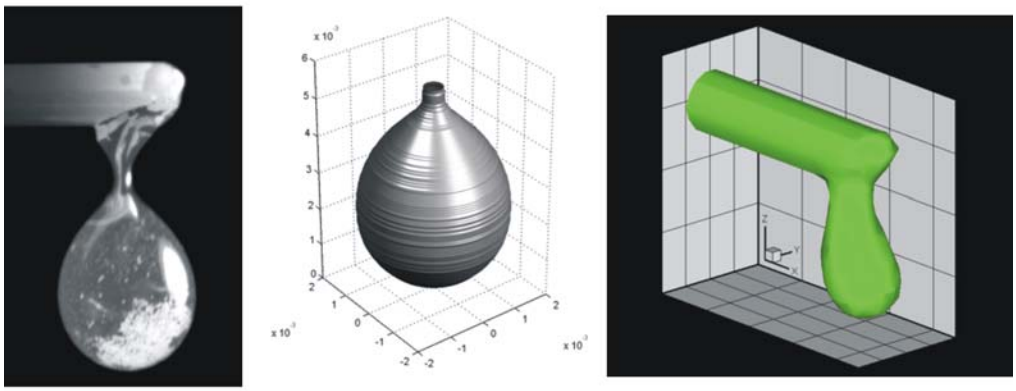

Fig.2: Schematic of the new container-less surface tension measurement method, left to right; copper drop, reproduced experimental profile in an image analysis process, and numerically simulated melting dynamics

2. Experimental setup

Atmospheric 40 MHz argon rf-ICP plasma with a maximum power of 1 kW is used to melt copper rods. Argon flows at 1.2 and 7.6 *slpm* as plasma and sheath gases, respectively. The rod is aligned with the axis of symmetry of the rf-ICP (see Figure 1). Initial studies were conducted on copper rods of 1.6 mm diameter with a melting point of 1370 K. The argon radio frequency plasma produces the required high temperatures for melting the rod. In addition, the flow of argon prevents the samples from oxidations. The rf quartz torch (Delta Scientific Laboratories, Mississauga) has a diameter of 18 mm. The rf power supply (Advanced Energy Industries, Inc., Co) generates up to 1 kW forward power at 40 MHz. A CCD video camera (Sensicam, Optikon Corporation Ltd., Kitchener, ON) equipped with a 90 mm macro lens with an intensified CCD chip capable of recording 30 frames per second and a resolution of 1280 by 1024 pixels is used to record the dynamics of the process. The camera was triggered by an external digital time delay generator (DG 535 Stanford Research Systems, Sunnyvale, CA) at 50 Hz frequency. Dynamics of melting phenomenon is also recorded by a high-speed camera (PHOTRON FASTCAM-ultima 1024, Corporation Ltd., Kitchener, ON) at rates of 500, 1000, and 2000 frames per second.

3. Governing Equations

3.1. Numerical simulation

An axisymmetric two fluid model based on finite volume method [13] is used to solve the full Navier stokes equations. The incompressible interfacial flows in such two immiscible fluids (melt and surrounding gas) are separated by an interface. The present numerical model uses a one-field volume of fluid tracking method based on the one fluid volume of fluid (VOF) method modified by Youngs. It is assumed that only one of the fluids governed the motion of the fluids which is a reasonable assumption in dealing with incompressible and immiscible fluids. The numerical code is based on RIPPLE with the modified volume tracking and surface tension implementing. Surface tension is applied by using the continuum surface force (CSF) method. This method applies the surface tension force as a body force on a limited region around the interfacial cells. In the one-field method, the concept of mixed properties is used to represent cells containing multiple fluids.

Process of melting is modeled by a continuous injection of liquid from a nozzle with a diameter equal to the diameter of the rod. The interface is continuously under oscillations during the growing period. The oscillations (capillary waves) are the result of interacting injected momentum and restoring surface tension force. Injecting flow rate is changed during the process to decrease the inertia forces acting on the motion of the pendant drop. In order to decrease the CPU time of the simulation and obtaining a quasi-equilibrium condition velocity is defined by a step function.

$$V_i = \begin{cases} V_{i1} & ;\ t < t_c \\ V_{i2} & ;\ t > t_c \end{cases} \qquad (2)$$

where; $V_{i2} < V_{i1}$.

Reducing the velocity after the time t_c improves the possibility of comparing the resulting profiles with the Young's profiles while the inertia forces became very small. This will also decrease the oscillations due to the momentum of the injected liquid and restoring force of interfacial tension. Therefore, the pendant drop will be closer to the equilibrium state presumed in the Young analytical profiles.

3.2. Theoretical pendant drop profile

Based on the Young-Laplace equation the profile of a pendant drop can be represented by a set of three simultaneous nonlinear, non-homogeneous, and first order ordinary equations [8] which can be solved simultaneously to calculate three unknowns, (φ, X, Z) while S is the independent variable measured from the apex (see figure 3); and B is the curvature at the apex.

$$\frac{d\varphi}{dS} = \frac{2}{B} - Z - \frac{\sin\varphi}{|X|} \tag{3}$$

$$\frac{dX}{dS} = \cos\varphi \tag{4}$$

$$\frac{dZ}{dS} = \sin\varphi \tag{5}$$

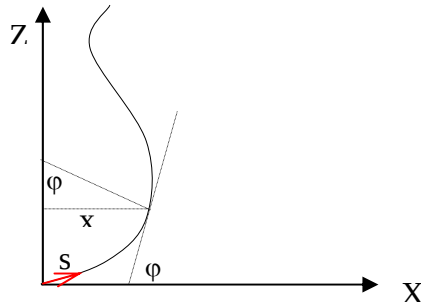

Fig. 3: Theoretical profile of a pendant drop

4. Results and discussions

An image analysis program is developed to obtain the evolving profile of the melting portion from the high-speed recorded movies [14]. Then the program fitted an optimized theoretical profile based on the Young-Laplace equation on each image. The curvature at the apex and an scaling factor are adjusted to improve the fitting process. Therefore, the scaling factor, $\sqrt{\frac{\Delta\rho g}{\sigma}}$, is used to measure the dynamic surface tension. Fitting the profiles is evaluated based on an error defined as:

$$e = \frac{1}{N}\sum_{i=1}^{N}\left|\frac{R_{\text{exp.}} - R_{young}}{R_{\text{exp.}}}\right| \times 100 \ \ \% \tag{6}$$

Figure 4 shows one images which is fitted by Young-Laplace profile. Accordingly, the surface tensions measured during the melting process is depicted in figure 5. Dots (red) in the figure are surface tension values based on the drop weight method using the detached drops which were quenched in water.

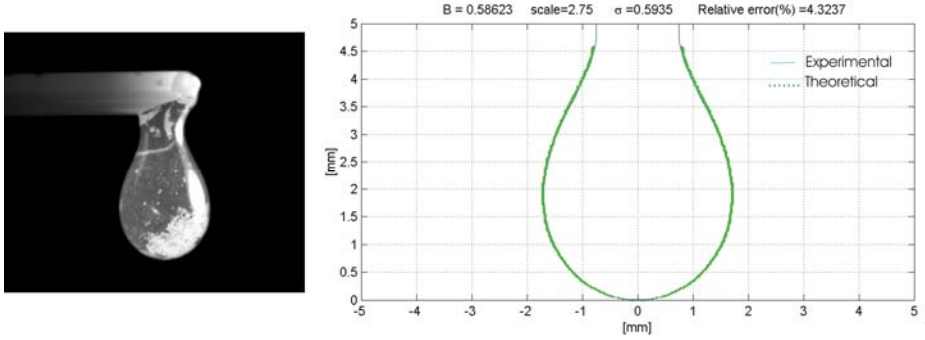

Fig. 4: Pendant drop of the copper sample (left), fitted analytical profile on the experimental profile (right)

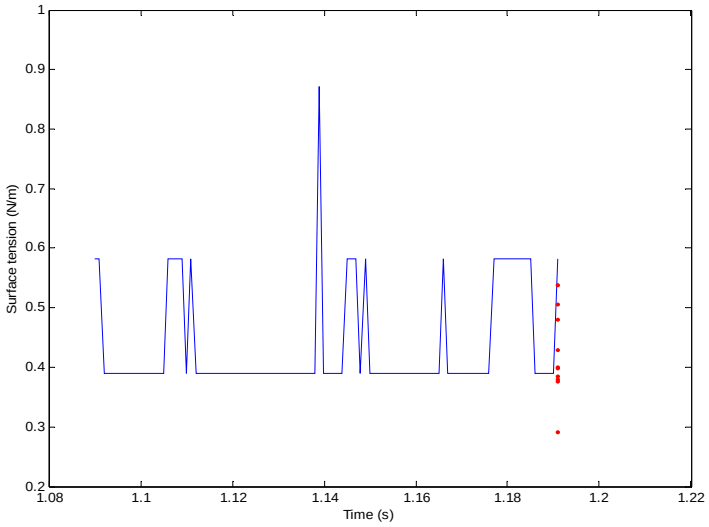

Fig. 5: Surface tension measured based on fitting theoretical profiles on the experimental profiles during the melting process (continues line), surface tension measured based on the weight of detached drops

The profiles are also produced by solving the flow field equations. Figure 6 shows a numerically generated profile at a specific time during the growth process by solving the axisymmetric Navier-Stokes equations. While the Young-Laplace equation ignores viscous and inertia effects it is expected that the numerical profiles do not match during the whole process of melting (injection).

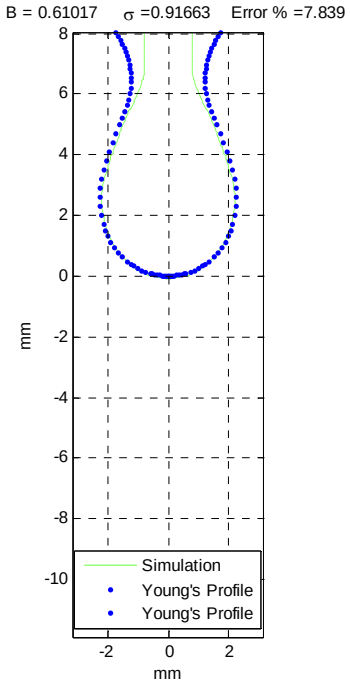

Fig. 6: Fitting the simulated and the theoretical profiles

5. Conclusion

The results show a good agreement in surface tension value measured for the sample by different methods. While the method is not influenced by the limitations imposed because of a container or lack of a high temperature source the method is applicable to very high melting point materials such as ceramics and alloys. However, more investigations are still needed to determine the effect of melting rate, surrounding gas, temperature, and effect of oxidation at the elevated temperature in both the experimental and numerical approaches.

References

[1] Allen B.C., "The surface tension of liquid metals" in: Liquid metals, chemistry and physics, Dekker, New York (1972).

[2] Passerone A. and Ricci E., "High temperature tensiometry" in: drops and bubbles in interfacial research, Elsevier Science (1998).

[3] A. I. Rosanov and A. Prokhorov, Interfacial Tensiometry, Elsevier, (1996).

[4] J. Drelich, Ch.Fang, C.L.White, "Measurement of interfacial tension in fluid-fluid systems, in Encyclopaedia of surface and colloid science, Marcel Dekker Inc. NY, pp. 3152-3166, (2003).

[5] T.Lida, R.I.Guthrie, "The physical properties of liquid metals", Oxford Univ. Press, pp. 1-13, (1998).

[6] I.Egry, G.Lohofer, I.Seyhan, S. Schneider, B.Feuerbacher, "Viscosity and surface tension measurements in microgravity, 20(4), pp. 1005-1015 (1999).

[7] F. Bashford and J. C. Adams, An attempt to test the theory of capillary action, Cambridge University Press and Deighton Bell & Co., Cambridge, (1883).

[8] S. Hartland and R. W. Hartley, Axisymmetric fluid-liquid interfaces, Elsevier, Amsterdam, (1976).

[9] A. Neumann and J. K. Spelt, Chap.10: Axisymmetric Drop Shape Analysis (ADSA), in Applied surface Thermodynamics, Vol. 63, Marcel Dekker Inc., 1996.

[10] T. Tate, On the magnitude of a drop of liquid formed under different circumstances, Phil. Mag. 27, 176-180, (1864).

[11] W.D.Herkins, F.E.Brown, "The determination of surface tension (free surface energy), and the weight of falling drop", J. Am. Chem. Soc., 41, pp. 499-524, (1919).

[12] J. P. Garandet, B. Vinet, and P. Gros, Corrections on the Pendant Drop Method: A New Look at Tate's Law, J. Colloid Interface sci., 165, 351-354, (1994).

[13] V. Mehdi-Nejad, Modeling flow and heat transfer in two-fluid interfacial flows, with applications to drops and jets, Ph.D. Thesis., (2003).

[14] A. Moradian, J. Mostaghimi, High-temperature Tensiometry by a coupled modeling and experimental approach, Proceeding of International Thermal Spray Conference, Basel, Switzerland, May 02-04, (2005).

Control of the stability of Plasma Polymerized Acrylic Acid coating deposited in a low frequency discharge on Polyethylene (PE) films

R. Jafari, M.Tatoulian, F. Arefi-Khonsari

Laboratoire de génie des procédés plasmas et traitement de surface, ENSCP, UPMC, 11 rue Pierre et Marie Curie, 75005 Paris, France

Abstract

Plasma polymerized acrylic acid (PPAA) coatings were deposited on PE films, in a 70 kHz low pressure plasma reactor with an asymmetrical configuration of electrodes, at various plasma powers. The COOH retention of PPAA coatings and its stability to washing in water were investigated by XPS, WCA (water contact angle), SEM analyses. The results have shown that the use of higher powers leads to an increase of the stability of the coating due to a high degree of cross-linking. Optical emission spectroscopy measurements (OES) have shown good correlation between the CO density in the gas phase and the carboxylic content of PPAA coating. Under optimized conditions, it is possible to obtain stable PPAA coatings which resist to washing with a COOH retention rate of 15 %, which is much higher than the coating deposited in a 13.56 MHz discharge.This high stability of the coatings is probably due to the ions which play an important role in such discharges.

Keywords: stability, selectivity, plasma polymerisation, acrylic acid, ions

Introduction

The plasma polymerization of acrylic acid to produce thin coating with carboxylic functions has been an active area of research for applications in biomedical and biosensors [1-5]. The objective of this work is therefore to produce a surface containing a high density of COOH functions on the polymer films (PE) for the covalent immobilisation of biomolecules. For such applications, there is a strong need to obtain stable plasma polymerised acrylic acid coating, resistant to washing with water. M.R. Alexander et al. have found stable crosslinked polymers formed by copolymerising a mixture of acrylic acid –and 1,7-octadiene under high plasma power [6]. They have obtained a percentage of COOH less than 6 % after rising in water. L. Detomaso at al. studied the increase of power and of duty cycle in a modulated plasma for the deposition of acrylic acid ; they obtained a surface containing 3-4 % of COOH groups after washing [7]. All the studies have been carried out at 13.56 MHz. At this high frequency, the ions cannot follow the fluctuation of the electrical field. In this work, we have used a low frequency discharge of 70 kHz with an asymmetrical configuration of electrodes in order to obtain coatings from acrylic acid precursor. Different physicochemical analyses have been used such as water contact angle measurements (WCA), XPS, OES and SEM analyses to characterize the PPAA coatings deposited under different experimental conditions. Special attention will be paid on the level of retention of the carboxylic acid functionality and on the stability of the coating upon washing.

Experimental

A bell-jar reactor with an asymmetric blade-type configuration of electrodes was used for the plasma polymerisation of acrylic acid. It has been described in details elsewhere [8]. The stainless steel blade is hollow and serves for the introduction of the gases. It faces a grounded stainless steel cylinder (length 22 cm and diameter 3.5 cm) onto which the polymer film to be covered is rolled on. The gaseous mixture was produced by bubbling Argon at a rate of 10 sccm in a 10 ml round bottom flask containing the acrylic acid monomer (Sigma Aldrich, 99% pure). The flow rate of the acrylic acid was around 0.06 sccm. The main chamber was evacuated by a TPH 170 (Balzers) turbo molecular pumping system and a base pressure of 10^{-3} Pa was obtained. The operating pressure was maintained at 0.1-0.2 mbar by a 2012 AC chemical pump.

Plasma emission was monitored through an optical fiber (diameter : 200 µm, Incident angle = 47°). The radiation transmitted was analysed by a spectrophotometer SpectraPro-500i (Acton Research

Corporation) equipped with a 3600 and 1200 grooves/mm holographic grating for the analysis of the 300-450 nm spectral domain.

Surface characterization

The XPS spectra were acquired on a Thermo VG ESCALAB 250 spectrometer. The XPS spectra were recorded with the monochromatized Al Ka X-ray source (1486.6 eV, size 650 µm) and a combination of electron and argon ion flood guns for charge compensation. Quantitative surface and interface analyses were performed using the peak areas of the high-resolution spectra and the Manufacturer's sensitivity factors. Sample charging was corrected by positioning the hydrocarbon peak component of the C_{1s} signal at 285.0 eV.

Contact angle measurements were performed with an image processing system using bi-distilled water liquid (liquid droplet: 2 µL). The reported values correspond to the average of four measurements of the static contact angle, on different parts of the samples rinsed in water and dried.

Results and Discussion

Plasma polymerised acrylic acid coating was produced on the PE films at different plasma powers and analysed by XPS. A peak-fitted spectrum for the C_{1s} core level is shown in Figure 1. The high-binding energy structure is indicative of the existence of carbon-oxygen bonds. The spectrum can be satisfactorily fitted by a combination of four distinct peaks: the peak at 285 eV (C_0) corresponds to C-C and C-H moieties, the peak at 286.5 eV (C_1) to C-OH and C-O-C functional groups, the peak at 287.8 eV (C_2) to C=O groups and the peak at 289.4 V (C_3) is due to COOH and/or COOR groups. Some authors have distinguished the contribution of the acid form from that of the ester by a derivatization experiments with trifluoro-ethanol [9,10]. Their investigations have shown that the contribution of the carboxylic acid form represented more than 90 % of the component at 289.4 eV. In our case, we have then assumed that the ester contribution in the C_3 component was absent or negligible.

The well resolved feature at 289.4 eV of an unwashed PPAA deposited at low power (13 W) (figure 1a) is indicative of a high carboxylic acid group retention : the COOH/C_{1s} ratio is around 28.0 % compared to a theoretical maximum of 33 % for a conventional poly acrylic acid. The latter corresponds to a COOH retention rate of around 80 %. Since the stability of the polymerized coating to solvents is essential for biotechnological applications, we have therefore investigated the resistance of the films to washing in water. Figure 1b showed a sharp decrease of the COOH content that passed from 28 % to 7-8% after washing.

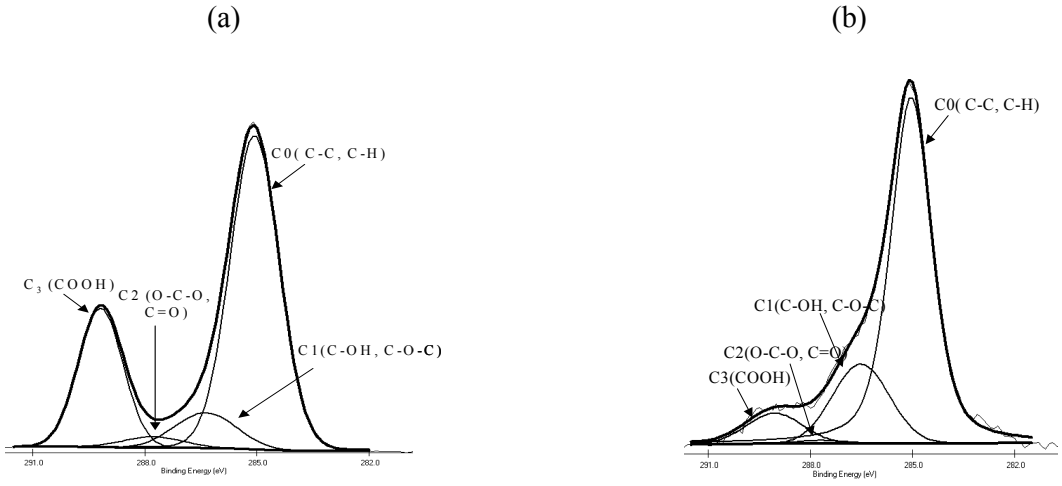

Figure 1: C1s spectra of PPAA deposited at 13 W before (**a**) and after (**b**) washing the samples with water (p = 0.4 mbar, t = 10 s, Q_{Ar} = 10 sccm, $Q_{\text{acrylic acid}}$ = 0.06 sccm)

The use of a plasma pretreatment of the PE films in Ar or N_2 before the plasma polymerization of acrylic acid has shown negligible effect on the COOH retention. This indicates that the instability of

the coating was not due to a weak adhesion between the PPAA coating and the PE film. At a low frequency of 70 kHz, the PE film at the first stage but also the growing polymer are constantly bombarded by energetic ions during the process. This first of all leads to an activation of the underlying PE film which favors the formation of covalent binding with the coating. Secondly the ion bombardment results in a more crosslinked and cohesive PPAA coating. In a previous study, we have clearly pointed out the role of the ions in the functionalization process of PP films in a NH_3 discharge by comparing the grafting process at two different frequencies [11]. This is why at 70kHz there is no need to have a pretreatment of the substrate in order to ensure a good stability of the PPAA coatings. On the contrary complementary results done in a 13.56 MHz reactor show the necessity of carrying out a pretreatment in order to have a good retention of carboxylic groups [12]. OES has been used to estimate the energetic character of our 70 kHz discharge as compared to a 13.56 MHz one, by calculating the ratio of the first negative system of N_2^+ (B) line at 391.4 nm and that of the second positive system of N_2 (C) at 394.3 nm. Figure 2 clearly shows that the N_2^+/N_2 ratio, which is an indicator of the mean electron temperature, is much higher in a low frequency system explaining the formation of a coating which is crosslinked and presents a good adhesion to the substrate as well.

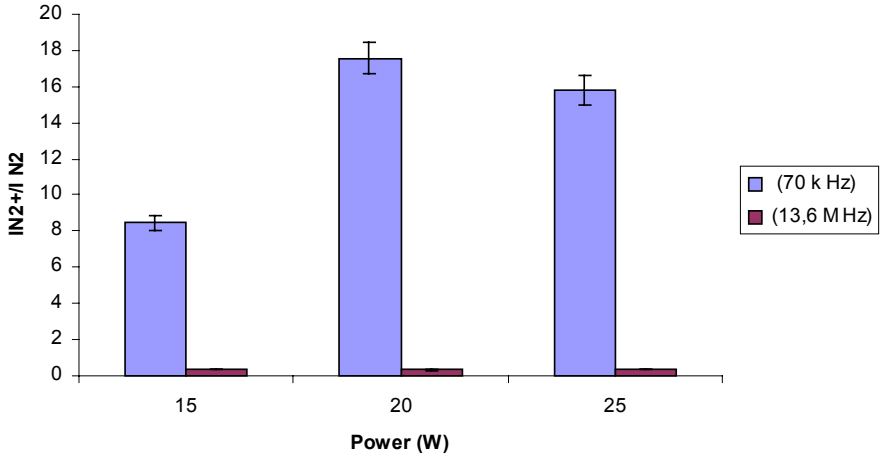

Figure 2 : N_2^+/N_2 ratio as a function of power at two frequency system

SEM analyses have been used in order to look at the change of morphology of the coatings upon washing due to a partial removal of the soluble deposits (figure 3). Figure 3b corresponds to an unwashed PPAA coating ; the film is thick, homogeneous and covers the porous zones of the untreated PE film (figure 3a). After rinsing the coating in water (figure 3c), porous zones of the underlying PE film appear, revealing a partial solubility of the coating in water ; this phenomenon may be due to the formation of low molecular oxidized fragments weakly bonded to the growing film.

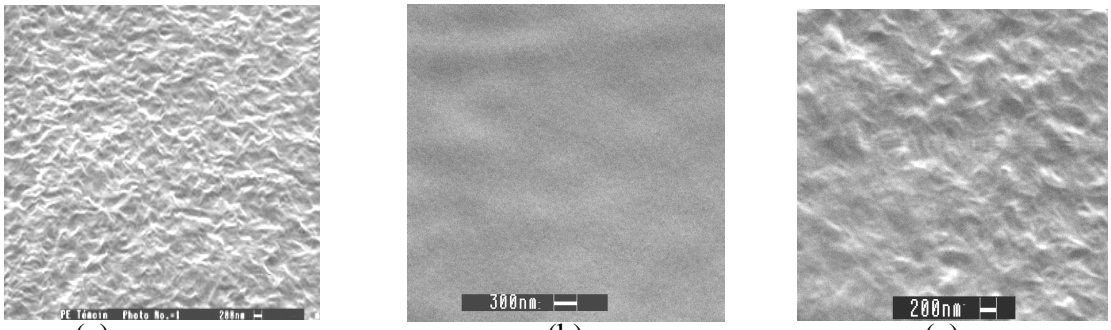

(a) (b) (c)

Figure 3 : SEM analysis of a non treated PE (a), and PPAA deposited on PE films before (b) and after washing in water (c). (P= 13 Watts, Q_{argon}=10sccm, $Q_{acrylic\ acid}$ = 0.06 sccm, treatment time = 10 s, p=0.4 mbar)

In order to increase the cohesive strength of the coating, we have increased the input power of the discharge during the plasma polymerization of acrylic acid. The XPS analyses of unwashed and rinsed deposits presented in figure 4, illustrates that the increase of the input power renders the deposit less soluble ; the COOH content deposited at a power of 25 Watts, is around 15 % for both deposits, which is in agreement with a high stability of the coating.

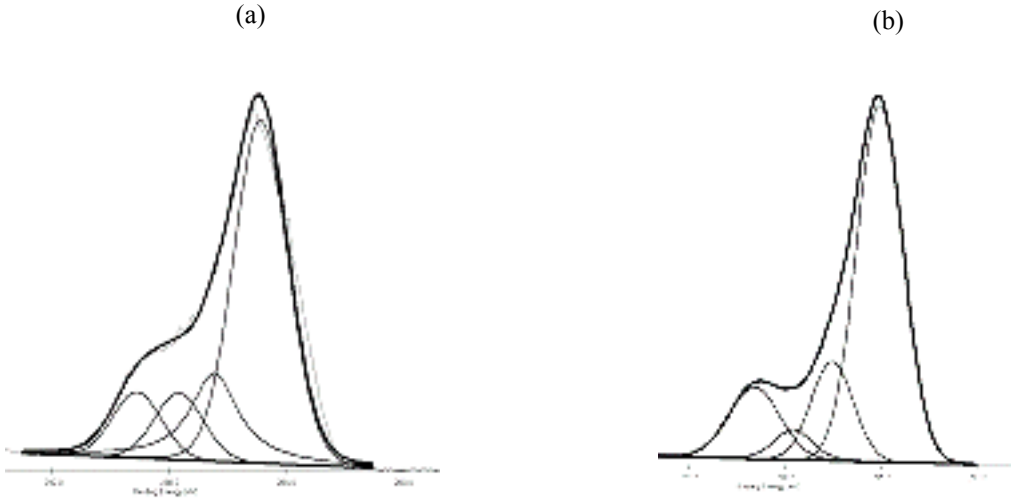

Figure 4 : C1s spectra of PPAA deposited at high power (25 W) before (**a**) and after (**b**) washing the samples with water (p = 0.4 mbar, t = 10 s, Q_{Ar} = 10 sccm, $Q_{\text{acrylic acid}}$ = 0.06 sccm)

Some authors [9,13] have explained that this phenomenon results from an increase of the degree of cross-linking in the film. SEM analysis of the rinsed deposit confirmed this hypothesis (figure 5) since the coating still remains on the substrate after rinsing. In our work, the increase of cross-links in the coating was confirmed by the formation of cracks in the PPAA film which is consistent with a more brittle coating.

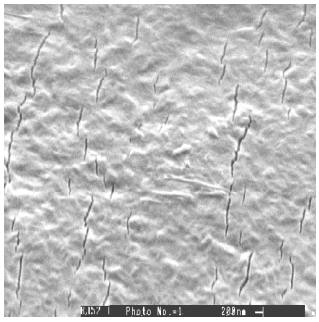

Figure 5 : SEM analysis of a washed PPAA deposited on PE at high power (P = 25 Watts, Q_{argon}= 10 sccm, $Q_{\text{acrylic acid}}$ = 0.06 sccm, t = 10 s, p = 0.4 mbar)

In order to have further information about the deposition process, Optical Emission Spectroscopy (OES) was used to study the fragmentation of acrylic acid in the plasma in function of the power. The OH ($A^2\Sigma^+$-$X^2\Pi$ at 306.6 nm), the CH ($A^2\Delta$-$X^2\Pi$ at 431.4 nm) and the CO ($B1\Sigma$-$A^1\ \Pi$ at 519.8 nm) lines were followed in order to link these results with the monomer functionality [9, 10]. Figure 6 shows that the acid fragmentation (CO and OH products) increases with the power injected in the plasma. The emission intensity of CO increases linearly with the applied power within the experimental range but the emission intensity of OH reaches a plateau at high power.

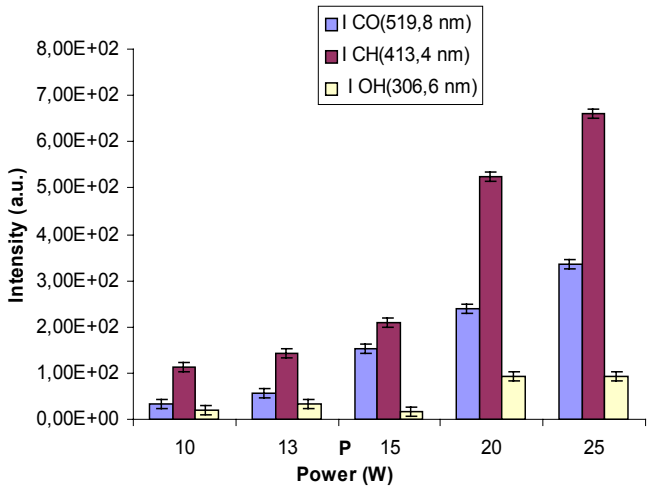

Figure 6 : Evolutions of CO, CH and OH emission intensities with plasma power (Q_{argon}=10sccm, $Q_{acrylic\ acid}$ = 0.06 sccm, p=0.4 mbar)

F. Palumbo et al [9] have shown that the I_{CO}/I_{Ar} ratio in a 13.56 MHz discharge could be advantageously used as a process control parameter to monitor the retention of the carboxylic groups in the film. We have also found that at 70kHz there exists a good correlation between this ratio which is proportional to the density of CO species in the fundamental state, and the carboxylic groups content in the PPAA coating (figure 7). An increase of the power leads to a decrease of the I_{CO}/I_{Ar} ratio (Fig.6), indicating a more fragmented AA monomer in the gas phase ; as a consequence, the carboxylic groups in the PPAA coating decreases since instead of being incorporated in the films, are fragmented in the discharge in the form of CO species which ate pumped out of the reactor.

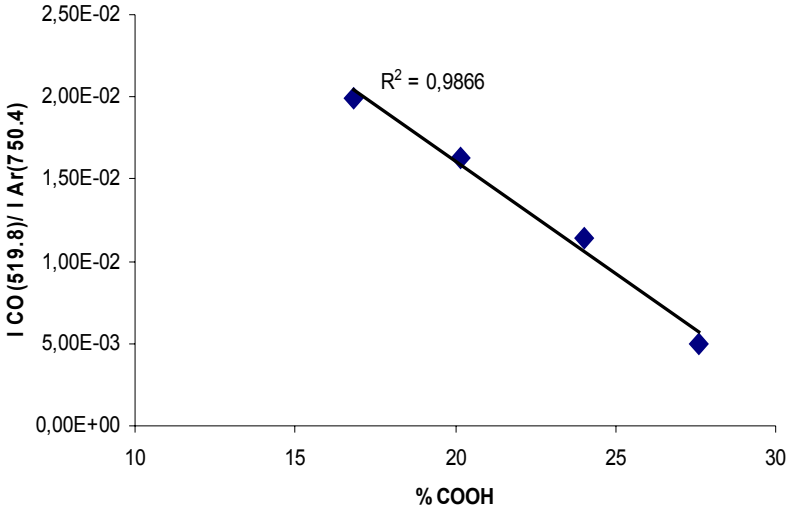

Figure 7: Correlation between the I_{CO}/I_{Ar} ratio and the carboxylic content in the PPAA coating, as measured by XPS. (Q_{argon}=10sccm, $Q_{acrylic\ acid}$ = 0.06 sccm, p=0.4 mbar)

Conclusion

Numerous studies on PPAA have been carried out for applications in the field of biotechnology and biomedical. However, the majority of the studies have been performed in 13.56 MHz pulsed or continuous discharges and which report on the fact show that their stability is highly affected by washing. In this work, the plasma polymerization of AA has

shown to be very efficient for the retention of carboxylic groups. Under optimized conditions, it is possible to obtain a stable PPAA coating upon washing with a COOH retention rate of 15 %. This high stability of the coatings is probably due to the ions which play an important role in such discharges.

Acknowledgement :

The authors would like to acknowledge the European commission for having financed this work in the framework of the IFCA project No. GRD1 2001-40680.

References:

[1] B. Gupta, C. Plummer, I. Bisson, P. Fery, J. Hilborn, *Biomaterials***, 2002,** 23, 863-871
[2] J. D.Whittle, N. A. Bullett, R. D. Short, C. W. Ian Douglas, A. P. Hollander, J. Davies, *Journal of Materials*, **2002**,12, 2726-2732
[3]L. De bartolo, S. Morelli, L. C-. Lopez, L. Giorno, C. Campana, S. Salerno, M. Rende, P. Favia, L. Detomaso, R. Gristina, R. d'Agostino, E. Drioli, *Biomaterials*, **2005**, 26, 4432-4441.
[4] R. Daw, S. Candan, A.J. Beck, A.J.Devlin, I.M.Brook, S. MacNeil, R.A. Dawson, R.D. Short, *Biomaterials*, **1998**, 19, 1717-1725.
[5] H. Muguruma, I. Karube, *Trends in analytical chemistry*, **1999**,18,1, 62-68.
[6]. M. R. Alexander, Tran M. Duc, *polymer*, **1999**,40, 5479-5488.
[7] L. Detomaso, R. Gristina, G.S. Sensi, L.C. Lopez. P. Favia, R. d'Agostino, *plasma process and polymers, Willy-VCH*, **2005**, 389-402.
[8] Arefi, F., Tatoulian, M., André, V., Amouroux, J. and Lorang, G., In Metallized Plastics 3: Fundamental and Applied Aspects*,* Mittal, K. L., Ed.; Plenum Press: New York, **1992**; 243-256.
[9] F. Palumbo, P. Favia, A. Rinaldi, M. Vulpoi, R. d'Agostino, *Plasmas and polymers*, **1999** , vol. 4, No.2/3, 133- 145
[10] M.R. Alexander and T.M. Duc, *J. Mater. Chem*., **1998**, 8,37
[11] M. Tatoulian, N. Shahidzadeh, F. Arefi-Khonsari and J. Amouroux, Intl. *J. Adhesion Adhesives*, **1995**, 15, p 177 – 184.
[12] R. Jafari, M. Tatoulian, F. Arefi-Khonsari, unpublished results
[13] S. Cansan, AJ. Beck, L. O'Toole, RD. Short, *J. Vac. Sci. Tech. A*., **1998**, 16,1702

Silicon nanocrystal formation on post-annealed substoichiometric SiO_x layers deposited in SiH_4-N_2O radiofrequency discharges

M. Bedjaoui, B. Despax

Laboratoire de Génie électrique (UMR 5003), Université Paul Sabatier, 118 Route de Narbonne, F-31062 Toulouse Cedex, France

Abstract
SiO_x films grown using Plasma Enhanced Chemical Vapor Deposition (PECVD) in SiH_4-N_2O-He discharges were thermally annealed at 1000°C for 1h. The chemical composition was dominated by silicon suboxide containing Si-N and Si-H bonds. Raman spectra and spectroscopy ellipsometry measurements showed that the SiO_x films exhibited the amorphous state in the as-deposited samples and a mixture of (i) amorphous materials (ii) silica (iii) silicon nanocrystals in the annealed samples.
Keywords
PECVD, SiO_x, Silicon nanocrystals, FTIR, Raman, Spectroscopic Ellipsometry.

1. Introduction

Recent developments of new forms of silicon have brought about renewed interest in the fabrication of integrated devices. The main goal of the new electronic technology is to integrate micro-structures showing appropriate electronic, chemical and structural properties and compatible with the well established silicon micro-electronics. Therefore, after the initial studies in porous silicon [1], growing attention has been paid to nano-structured silicon thin films with desired properties. This attention has been motivated mainly by their promising optical and electronic properties [2]. Indeed, these materials can be produced in a wide range of systems and involve various scientific communities. In the field of nanocrystalline materials, significant effort has been focused on the formation and characterization of silicon nanocrystals. Among the various Si nc fabrication techniques [3,4,5], a process that has been widely used for Si nanocrystal formation involves high temperature annealing of substoichiometric SiO_x thin films. Subsequently, an intensive research activity has been devoted to study the properties of silicon suboxide thin films, in particular the possibility of varying their composition with the operating process conditions which is of great interest for the control of Si nc formation. Recently, Iacona et al. [4] reported some detailed works on the structural and optical properties of silicon nanocrystals formed by high temperature annealing of substoichiometric silicon oxide produced by PECVD. In particular, they showed a good correlation between structural data, including crystal radius and width size distribution, and the optical properties of the films. In the same way, C. Bonafos et al. [5] using ion implantation of Si^+ in SiO_2 draw similar conclusions.
In this work, we report a detailed study of the physical, structural and optical properties of thin silicon rich SiO_x films within a large range composition. They were produced by PECVD using SiH_4 and N_2O as precursors. The formation of silicon clusters embedded in a dielectric silicon oxide matrix is investigated. The properties of as-deposited films and annealed films were studied by Fourier Transform Infrared (FTIR) spectroscopy, Raman spectroscopy, Transmission Electron Microscopy (TEM) and Spectroscopic Ellipsometry (SE). We have found that by varying the flow ratio of the gaseous precursors it is possible to change the properties of the film, therefore the size of the Si nc.

2. Experiments

Silicon-rich silicon oxide SiO_x thin films were prepared by PECVD at a low temperature in silane-N_2O-He discharges. The reactor shown in Fig. 1 [6] is a rectangular parallelepiped box placed under a vacuum bell jar ($1x10^{-7}$ Torr). An electrode driven by a 13.56 MHz signal splits the inside of the box into two symmetrical plasma zones since the rest of the box is grounded. In order to obtain homogenous gas flows on each side of the driven electrode, the gas first enters a buffer-zone, then flows through two small slits in the plasma zones and finally flows out through two other identical slits. The size of a single plasma zone is 25.6 cm x 25.6 cm with an electrode spacing of 3.9 cm. The silicon substrates were placed on the grounded walls. The electrode was capacitively coupled to a 13.56 MHz RF generator by means of a LC matching box. 200-350 nm thick SiO_x films were grown

on intrinsic silicon substrates and silica substrates. All deposition processes were performed at 380°C, under a pressure of 0.5 Torr and a RF power of 5 Watt. The source gases used were SiH_4, N_2O and He, the N_2O gas flow rate was kept constant at 40 sccm for all the samples. After deposition, the SiO_x films were annealed for 1 hour at 1000°C in nitrogen atmosphere.

The SiO_x film composition ($0<x<2$) was controlled by varying the SiH_4/N_2O flow rate ratio ($\gamma = Q_{SiH4}/[Q_{N2O}+ Q_{SiH4}]$). Physico-chemical, structural and optical absorption properties of SiO_x films, as-deposited and subjected to thermal annealing, were investigated by FTIR spectroscopy, Raman spectroscopy, TEM and SE. The infrared analyses were performed by means of a BIORAD QS 300 FTIR spectrometer. The IR absorbance spectra of the silicon oxide films were compared in the range of 400-4000 cm^{-1} (1.3-12.3μm) with a resolution of about 4 cm^{-1}. The Raman measurements were carried out with a Dilor UV spectrometer equipped with a charge-coupled device multichannel detection system and a microprobe focused on the sample with a spot surface of 1 μm^2. The incident beam at 363 nm line of argon laser was used for the excitation. Dark-field plan-view TEM analyses were carried out with a CM30 Philips microscope to determine the nanocrystals size distribution. The SE experiment is based on the measurement of the ratio "ρ" of the Fresnel reflection coefficients, $\rho=r_p/r_s=\tan(\Psi)\exp(i\Delta)$ where r_p and r_s are, respectively, the Fresnel reflection coefficients for a plane wave polarized parallel and perpendicular to the plane of incidence. The ellipsometric angles Δ and Ψ characterize the phase difference between the two polarizations and the amplitude ratio, respectively. Ellipsometric functions $\tan(\Psi)$ and $\cos(\Delta)$ were measured in the spectral range from 200 to 880 nm at 75° angle of incidence, using a rotating polarizer spectroscopic ellipsometer SOPRA GES-5 with tracking analyzer.

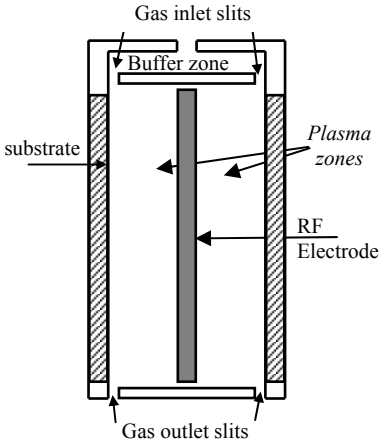

FIG.1. Schematic representation of the plasma reactor.

3. Results and discussion

3.1 Chemical and structural characterization

FTIR spectroscopy was used as a non destructive technique to obtain further information about the structural and compositional properties of films, and the types of chemical bond present. The spectral positions of the absorption bands correspond to the vibrational frequencies of the chemical groups present in the layer, their intensity to the concentration of such groups. As a matter of fact, a lot of works [7, 8] were carried out to ascribe the positions of the infrared bands present in amorphous SiO_x and SiO_xN_y. A particular attention was paid to the position of the stretching mode for the Si-O-Si, the SiH and SiN band which varies in relation to the O/Si ratio of SiO_x films. Figure 2 shows the IR spectrum of a $SiO_xN_yH_z$ film obtained under the same operating conditions but for different flow rate ratio, γ, as-deposited Fig. 2(a) and after annealing Fig. 2(b). The analysis of the spectrum of the as-deposited sample exhibits a dominant absorption band around 1020-1030 cm^{-1} which can be attributed to the Si-O-Si stretching mode [9]; a subsidiary band located between 810-820 cm^{-1} due to the Si-O-Si bending mode [9] and also the Si-O-Si rocking in the range 440-460 cm^{-1} [9]. Another band that should be mentioned is the Si-H bending in the range of 640-660 cm^{-1} correlated to the Si-H stretching between 2100-2260 cm^{-1} [10]. Besides, the IR spectrum shows the presence of nitrogen in the as-deposited films; indeed; the absorption region at about 860-880 cm^{-1} is due to the stretching vibration of the Si-N bonds [11], while a weak peak of the N-H stretching 3385 cm^{-1} [12] is observable only for the sample with $\gamma = 0.15$.

For the lowest values of γ ($\gamma = 0.15$), the Si-N band contribution (860-880 cm^{-1}) with respect to the Si-O stretching band in the spectra appears very low. Conversely as γ increases, the Si-N peak becomes significant and the IR spectrum of the as-deposited films also characterized by other relevant absorption bands at around 2100-2127 cm^{-1} and 640-660 cm^{-1} suggest the presence of H-Si≡Si3 groups

in the layers [7]. Hydrogen incorporation has been found to be more efficient in SiO_x films having the highest silicon content [4].

After annealing, the stretching absorption bands shift towards higher frequencies in the range of 1050–1075 cm^{-1}. This effect accounts for the evolution of the amorphous phase present in the as-deposited SiO_x films towards a Si/SiO_2 mixture. Another major effect is the disappearance of the Si-N bonds and the Si-H bonds. This behavior of the spectrum is due to the partial conversion of the Si-N and Si-O phases to a mixed Si-O-N phase and the effective elimination of hydrogen from the films after the annealing treatment. These last observations could explain the unusual broadening of the band at 1070 cm^{-1} after annealing due to a residual SiO_x network containing Si-O-N and Si-Si bonds.

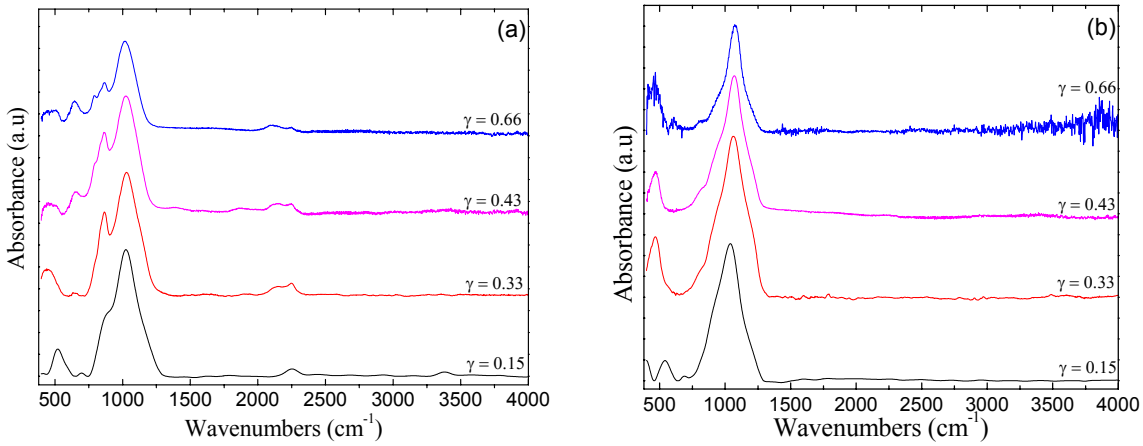

FIG.2. Transmission infrared spectra of SiO_x films obtained for different flow rate ratioγ, as-deposited (a) and annealed at 1000°C for 60 min in N_2 atmosphere (b).

Although Si-Si vibrations cannot be directly detected by IR spectroscopy, they can easily be detected by Raman spectroscopy. Raman scattering provides a fast and non destructive method for detecting the presence and studying the structure of silicon particles in the deposited layers [13]. Figure 3 shows typical Raman spectra of SiO_x films as-deposited and annealed at 1000°C during 60 min on silica substrate under a flow rate ratio, $\gamma = 0.43$. The Raman scattering shows essentially two components, a broad band at around 490 cm^{-1} for the as-deposited sample (Fig.3, dashed spectra), indicating that it is amorphous [13, 14], and a sharp peak at 513 cm^{-1} (Fig.3, solid spectra) after annealing, that we attributed to the incorporation of nanosilicon in the SiO_x films [13, 14]. The band shape modification of the Raman spectra has been used in the past for the evaluation of the average size of nc-Si. This can be achieved by using different theoretical models [15, 16]. Let us take the peak position in crystalline silicon at around 520 cm^{-1}. When the flow rate ratio decreased from $\gamma = 1$ (polysilicon) to $\gamma = 0.43$, the position of these nanocrystalline silicon peaks were shifted down by approximately 7 cm^{-1}. It suggested a decrease in the silicon nanocrystallite size by a few nanometers. According to the Zi's confinement model [15] and Viera's studies [16], the crystallite size is about 2 nm and about 3.6 nm, respectively. The Raman results indicate that the SiO_x films obtained by PECVD exhibit the amorphous state of the as-deposited samples and a mixture of two phases, an amorphous matrix and ordered silicon domains or nanocrystallites of the annealed samples.

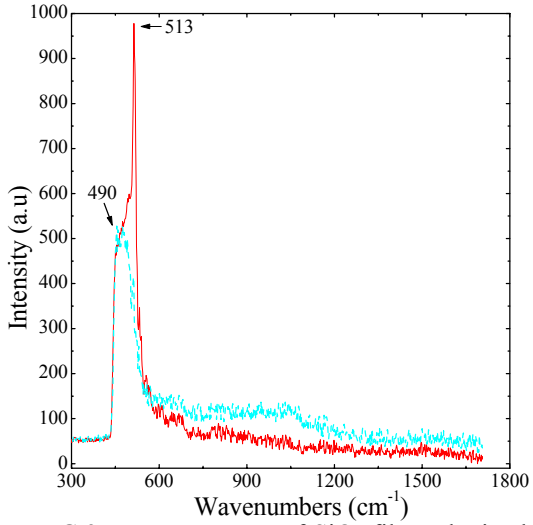

FIG.3. Raman spectra of SiO_x films obtained for a flow rate ratio $\gamma = 0.43$, as deposited (dashed spectra) and annealed at 1000°C for 60 min in N_2 atmosphere (solid spectra).

In order to map the presence of Si nanocrystals

embedded in the SiO_x layers after the annealing process and to exclude any crystallization induced by the laser in the Raman measurements, we used a High Resolution Transmission Electron Microscopy (HRTEM). Figure 4 reports the TEM image relative to SiO_x film obtained with a flow rate ratio, γ = 0.43, after annealing 1 hour at 1000°C. This sample was deposited under the same experimental conditions as the sample characterized by Raman spectroscopy (Fig. 3). The analysis of the TEM image showed clearly that the amorphous SiO_x contained a high density of small clusters which could be identified as Si nanocrystals. The statistical analysis of the crystal size distribution (histogram reported in Fig. 4) obtained from the TEM micrograph shows a distribution of crystal size that range from 3 to 6 nm, and a mean radius of 4 nm, in good agreement with the particle size calculated from the Raman measurements with the Viera's model [16]. The distribution had a standard deviation σ of 0.7 nm, accounting for all the different crystal sizes detected in the micrograph.

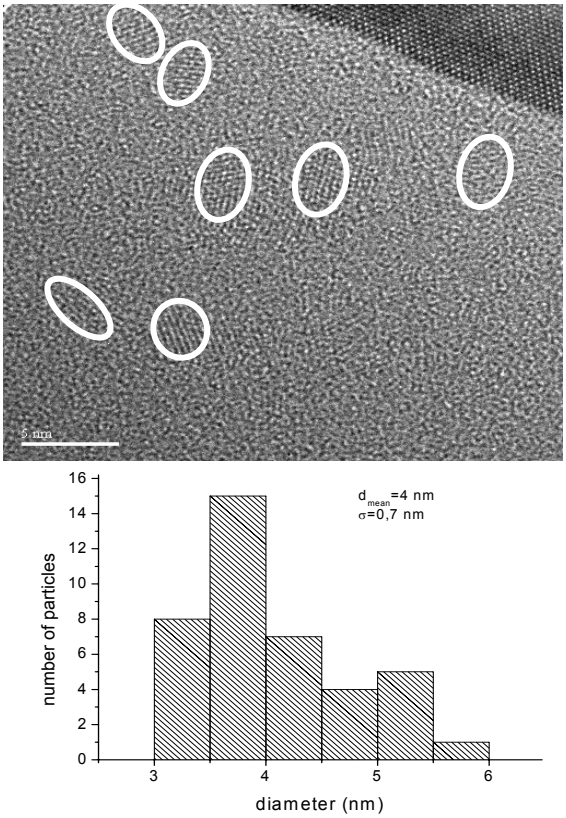

Fig. 4. HRTEM micrograph and relative Si-nc size distribution of a SiO_x film with a flow rate ratio γ=0.43 annealed at 1000°C for 1h in nitrogen atmosphere.

3.2 Optical analysis of thin films

The measurements of SiO_x optical properties allow an evaluation of the dielectric function in addition to the determination of the volume fraction of constituents, cristanallity of the layers and consequently, the effect of the incorporation of nc Si in an amorphous phase. Most of the studies aiming at determining the optical properties of nc-Si have been performed either by the use of a mixture of known materials [17] or by a direct inversion of the optical parameters of thin film [18], or else by a theoretical calculation [19]. Ellipsometry is a nondestructive, rapid and highly sensitive method often used for studying properties of silicon-based films. Therefore, it would be interesting to apply it to the analysis of nanocrystal silicon formation in thin SiO_xN_y films. Up to now, *Ex situ* spectroscopic ellipsometry measurements were performed in order to determine the thickness, composition and optical properties of the films. In this work, the complex optical index N is defined as $N = n - ik$ where n is the refractive index and k, the extinction coefficient. The optical constants of the as-deposited and post-annealed silicon compounds are obtained by fitting spectroscopic ellipsometry measurements with an appropriate model in the wavelength range from 200 to 880 nm. For the determination of N in $SiO_xN_yH_z$ films, the first step concerned the choice of a correct and suitable optical model for the dispersion law of layers. In agreement with our previous Raman spectra analysis, the as-deposited films consist of amorphous $SiO_xN_yH_z$ layers whereas the annealed films can be modeled as mixtures of poly-silicon crystals, amorphous silicon compounds, and SiO_2. In this part, two classes of models were selected and tested to describe the sample optical properties. One class uses the Forouhi dispersion model [20]. In this, we assumed that the films were homogenous and the as-deposited films can be based on this model. Another model uses Bruggeman Effective Medium Approximation (BEMA) [21] which can be utilized to describe the optical properties of the annealed films. In this case, the fit parameters are the layer thickness and the volume fraction of the different materials constituting the effective medium. Therefore, the complete physical model should take into account the surface roughness and possible surface oxidation. Thus, a two layer model plus a topmost layer with a void fraction are required to reproduce the optical data of the as-deposited and annealed films. The film thickness deduced from the fit compares very favorably with the value that we determined experimentally by measuring the height of the step by profilometry technique.

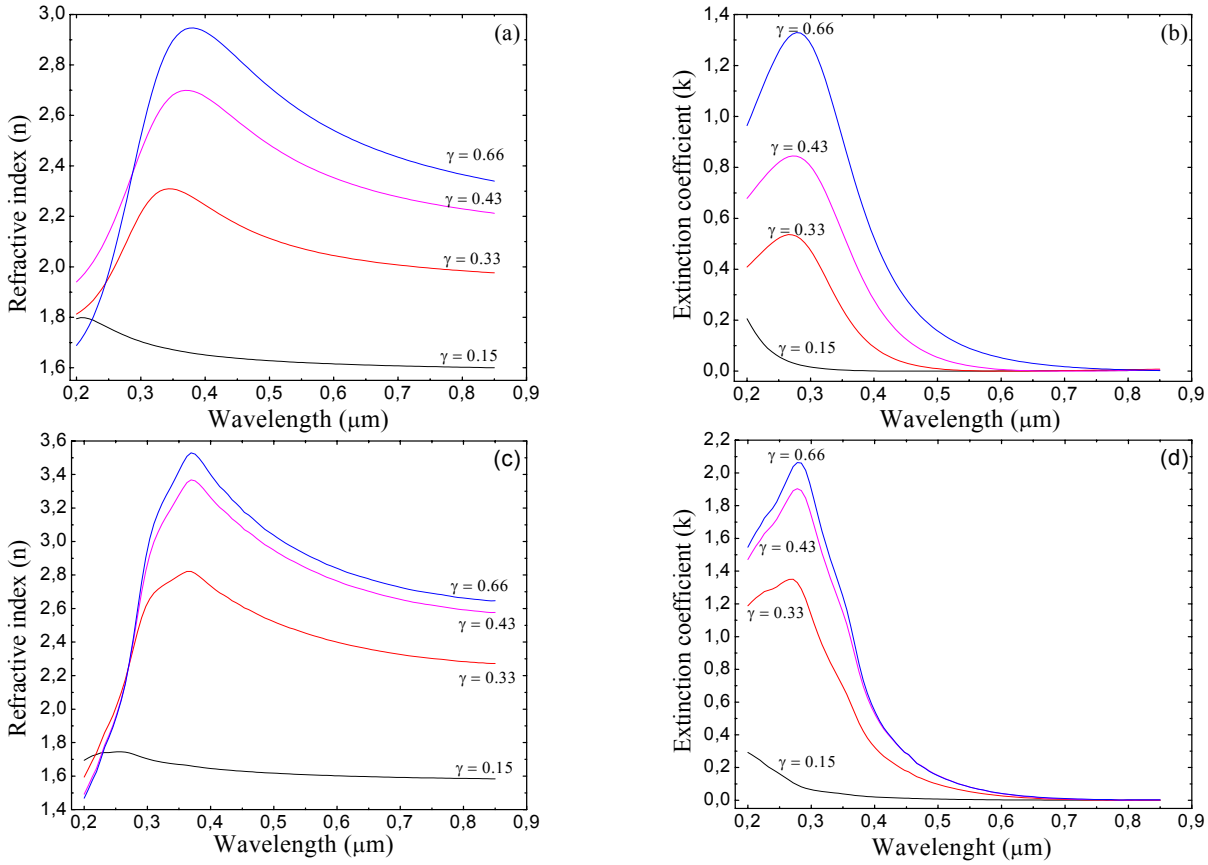

FIG.5. Refractive index (a, c) and extinction coefficient (b, d) as a function of wavelength for the SiO_x films obtained for different γ, flow rate ratio, as-deposited (top panel) and annealed at 1000°C for 60 min in N_2 atmosphere (bottom panel).

We present in Fig. 5 the optical constants n and k of samples obtained under the same operating conditions at different flow rate ratios, as-deposited (Fig. 5(a,b)) and annealed (Fig. 5(c,d)), derived from the BEMA and Fourouhi fits. At first above λ = 0.25 μm, a simple comparison of the spectra shows that the both n and k coefficients increase with increasing flow rate ratio. In fact, the increase of the n and k amplitudes is due to the layer compactness related to the silicon concentration increase (Fig. 5(a,b,c,d)). Besides, we also observe that the shapes of the optical spectra n and k of the annealed SiO_xN_y films are quite different from those of the as-deposited films. In agreement with our previous FTIR and Raman observations, this difference may be attributed to the phase separation between SiO_2 and silicon after thermal annealing process. On the other hand, we also observe that with increasing flow rate ratio the polycrystalline silicon volume fraction increases and the SiO_2 volume fraction decrease (see Table 1). However in each case, a small amount of residual amorphous phase (a-SiO_x) remains present.

Actually, in agreement with the very low standard deviation between Fourouhi modeling results and experimental results, the refractive index curves of as-deposited films are a smooth and structureless spectra bump [17], confirming an amorphous state. After the 1000°C annealing process of suboxide layers, we know that the silicon is crystallized [17, 22]. The n and k values of the annealed films with respect to the amorphous films are higher when the wavelength decreases from 0.7 μm to 0.3 μm [17]. The optical layer behavior is conveniently simulated by BEMA model involving appropriate mixtures of SiO_2, a-SiO_x and poly-Si. The BEMA modeling results shows an increasing contribution of poly-Si and a decreasing contribution of SiO_2 and a-SiO_x with increasing γ. These calculated optical constants from the annealed samples lead with respect to the amorphous optical constant to a shift of the spectral hump to low energies and, at the same time, to an increase in the absolute value of the refractive index and the extinction coefficient. According to the above observations, we can conclude that the annealed films converge from a structure dominated by the SiO_2 for the lowest γ, flow rate ratio, to a structure dominated by the polysilicon crystals for the highest γ.

TABLE.1. Fit values for the SiO_x films obtained for different flow rate ratios, γ, as-deposited and annealed at 1000°C for 60 min in N_2 atmosphere.

γ	sublayer thickness (nm)		layer thickness (nm)		optical gap E_g(ev)		Bruggeman mixture (%)		
	as-deposited	annealed	as-deposited	annealed	as-deposited	annealed	SiO_2	a-SiO_x	p-Si
0.15	2.3	4.3	265	249	2.58	1.67	91.3	2.6	6.1
0.33	2.4	7.1	331	282	2.02	1.56	57	17.2	25.8
0.43	4.6	15	280	226	1.84	1.5	44.1	17.6	38.3
0.66	3.6	11	247	217	1.78	1.48	29.1	17.4	52.5

It is known that the variations of the optical properties are due to the size reduction of nanocrystals [23]. In order to clarify this assumption, we have reported in Table 1 the optical band gap of several samples. The optical gap E_g is determined using the absorption coefficient α, and from an intercept on the energy axis of $\sqrt{\alpha \times E}$ versus E plot. Before annealing, the optical gap decreased as the γ, flow rate ratio, increased. This expected phenomenon could be explained by the change of size and distribution of the particles formed. Other studies [4, 19] attribute this behavior to the quantum confinement effect, e.g. the gap energy is conditioned on the size of the nanocrystals although, from the present result, it can be concluded that reducing the size of the silicon clusters induced a variation in the electronic band structure which is quite different from that of bulk silicon.

4. Conclusion

SiO_x layers were grown by PECVD technique by varying the flow rates of SiH_4 precursor gases and keeping N_2O constant at 40 sccm. Using Infrared and Raman spectroscopy, Transmission Electron Microscopy and Spectroscopic Ellipsometry the films were found to consist of an amorphous state in as-deposited and of very small crystals (3-6 nm) embedded in an amorphous SiO_2 matrix formed after a high-temperature annealing. In particular, it has been established that the value of γ, flow rate ratio, strongly affects both physico-chemical and optical properties of the SiO_x films. This effect is a serious drawback in determining the Si nc size.

References

[1] L.T. Canham, Appl. Phys. Lett. 57, 1046 (1990).
[2] P. Roca i Cabarrocas, Phys. stat. sol. 5, 1115 (2004).
[3] E. Edelberg, S. Bergh, R. Naone, M. Hall, and E. S. Aydil, J. Appl. Phys. 81, 2410 (1997).
[4] F. Iacona, G. Franzo, and C. Spinella, J. Appl. Phys. 87, 1295 (2000).
[5] C. Bonafos et al, J. Appl. Phys. 95, 5696 (2004).
[6] K. Radouane, L. Date, M. Yousfi, B. Despax, and H. Caquineau, J. Phys., D 33, 1332 (2000).
[7] D.V. Tsu, G. Lucovsky, and B.N. Davidson, Phys. Rev. B 40, 1795 (1989).
[8] M.I. Alayo, I. Pereyra, W.L. Scopel, and M.C.A. Fantini, Thin Solid Films 402, 154 (2002).
[9] G. Lucovsky, M.J. Mantini, J.K. Srivastava, and E.A. Irene, J. Vac. Sci. Technol. B5, 530 (1989).
[10] E. San Andréas et al, J. Appl. Phys. 94, 7462 (2003).
[11] M. Ribeiro, I. Pereyra and M. I. Alayo, Thin Solid Films 426, 200 (2003).
[12] F. Ay, A. Aydinli, Optical Materials. 26, 33 (2004).
[13] D. Nesheva et al, J. Appl. Phys. 92, 4678 (2002).
[14] N. Chaâbane, P. Roca i Cabarrocas and H. Vach, J. Non-Cryst. Solids 338, 51 (2004).
[15] J. Zi, H. Busscher, W. Ludwing, K. Zhang, and X. Xie, Appl. Phys. Lett. 69, 200 (1996).
[16] G. Viera, S. Huet, and L. Boufendi, J. Appl. Phys. 90, 4175 (2001).
[17] D. Amans et al, J. Appl. Phys. 81, 4173 (2003).
[18] U. Rossow et al, Appl. Surf. Sci 104-105, 552 (1996).
[19] C. Delerue, G. Allan, and M. Lannoo, Phys. Rev. B 48, 11024 (1993).
[20] A.R. Fourouhi, and I. Bloomer, Phys. Rev. B 34, 7018 (1986).
[21] A.G. Bruggeman, Ann. Phys. (Leipzig) 24, 636 (1935).
[22] B. Gallas et al, Thin Solid Films 455, 335 (2004).
[23] A. En Naciri, M. Mansour, L. Johann, J.J. Grob, C. Eckert, Thin Solid Films 455, 486 (2004).

Modeling of Chemical Reactions for Plasma Coating of Nanoparticles

B. Rovagnati[1], A. L. Yarin[2], and F. Mashayek[1]

[1]*Department of Mechanical and Industrial Engineering, University of Illinois at Chicago, Chicago, IL, USA*
[2]*Faculty of Mechanical Engineering, Technion-Israel Institute of Technology, Haifa, Israel*

Abstract
A hybrid model of kinetic theory and continuum theory for predicting coating of nanoparticles by plasma enhanced chemical vapor deposition in low-pressure conditions is presented. The model is used to investigate the important phenomena occurring during the surface deposition on a single submicron particle immersed in non-equilibrium CH_4/H_2 plasma. Self-consistent electric field, chemical composition of the gas, species fluxes towards the particle, rate of deposition, and particle charging are calculated.
Keywords: nanoparticle, film deposition, chemical vapor deposition, plasma reactor.

1. Introduction

Plasma processing is nowadays considered as a critical technology for a large number of industries, which are attracted by its remarkable capability to modify matter at submicron or nanometer scales. Nanoparticles are the important constituents of many chemicals, ceramics and metal composites, pharmaceutical and food products, energy related products, and electronics related products, to name a few. Particle's surface modification may improve properties such as corrosion/oxidation resistance, adhesion, electrical properties, hydrophobicity, printability, etc. In particular, surfaces of particles can be coated with other materials allowing for example removal of metal ions from water when ZnO particles are coated with acrylic film [1], reinforcing of materials using SiC particles coated with metallic nickel and copper for aluminum-based metal matrix composites [2, 3], controlling pharmaceutical dosage by using microcapsule coated with composite latex membrane [4], or improving energetic properties of solid fuels for combustors if aluminum nanoparticles coated with carbon are used [5].

Among various techniques, plasma enhanced chemical vapor deposition (PECVD) is an attractive route for substrate coating. In PECVD, low-pressure (order of 100 mtorr) and low-temperature (300-600 K) conditions allow the achievement of a wide range of highly reactive chemical species capable of sticking onto surfaces, producing surface features in the nanometer range and maintaining excellent purity control. In particular, a low-pressure plasma process was applied for depositing films with thicknesses of the order of few to several hundred nanometers on micron and sub-micron particles [6, 7]. However, the ever-growing interest in dust particle surface deposition during industrial processing calls for further investigation. In order to improve the deposition process, plasma modelling can be of great use by predicting the composition of the plasma and by optimizing the plasma parameters, i.e. pressure, temperature, gas mixture, etc.

The present work aims to model the time-dependent deposition of amorphous carbon layers onto a sub-micron particle in a CH_4/H_2 low-pressure plasma. A detailed chemical kinetics scheme of the reactions occurring in plasma is considered [8] along with a "sticking model" that accounts for surface reactions and coating.

2. Description of the Model

A hybrid model of kinetic theory and continuum theory is proposed to evaluate effective fluxes of species towards the particle, since only a fraction of the species molecules reaching the proximity of the particle collides with it (Fig. 1). To a distance longer than the mean free path, λ, from the surface of the particle, the diffusion approximation is used,

$$\frac{\partial C_j}{\partial t} = -\frac{1}{r^2}\frac{\partial}{\partial r}\left(r^2\Gamma_j\right) + \omega_j, \quad j = 1, 2, \cdots, 20, \;\; r \geq \lambda \tag{1}$$

where r and t are the radial coordinate and time, respectively. C_j is the concentration of species j in m^{-3}, [H, H_2, H_2^+, H_3^+, CH, CH_2, CH_3, CH_3^+, CH_4, CH_4^+, CH_5^+, C_2H_2, $C_2H_2^+$, C_2H_4, $C_2H_4^+$, C_2H_5, $C_2H_5^+$, C_2H_6, C_3H_8, e^-],

and the source terms ω_j correspond to the species reaction rates of reactions shown in Table 1. The fluxes Γ_j, in $\mathrm{m^{-2}s^{-1}}$, are defined as

$$\Gamma_j = -\mathcal{D}_j \frac{\partial C_j}{\partial r} \pm C_j \mu_j E_r, \quad j = 1, \cdots, 20, \tag{2}$$

where μ_j is the mobility coefficient, and E_r is the local radial electric field strength, plus is for ions and minus is for electrons. The electric field has no effect on neutral species for which μ_j=0. The diffusion coefficient, $\mathcal{D}_j$ in $\mathrm{m^2/s}$, is defined for species j in a mixture with all other species and is calculated by first determining the separate binary diffusion coefficient, as reported in [9],

$$D_{ij} = \frac{3k_B T_{gas}\sqrt{4\pi k_B T_{gas}/2\mu_{ij}}}{16 P_{tot}\pi\sigma_{ij}^2 \Omega_D(\Psi)}, \tag{3}$$

where k_B is the Boltzmann's constant, T_{gas} is the gas temperature in K, P_{tot} is the total pressure in Pa, $\mu_{ij} = \frac{m_i m_j}{m_i + m_j}$ is the reduced mass in amu, and $\sigma_{ij} = \frac{\sigma_i + \sigma_j}{2}$ are the reduced Lennard-Jones length scale parameters in Å. $\Psi = \frac{T_{gas}}{\epsilon_{ij}}$, with $\epsilon_{ij} = \sqrt{\epsilon_i \epsilon_j}$ and ϵ_i's denoting the Lennard-Jones energy parameter. The parameter Ω_D and various Lennard-Jones parameters are found and evaluated as described in [9]. The diffusion coefficient of a neutral species j in the whole mixture is given by

$$\frac{P_{tot}}{\mathcal{D}_j} = \sum_{i=\text{background}} \frac{P_i}{D_{ij}}, \tag{4}$$

where the summation is carried out over all the background gases i. The partial pressure P_i of species i is determined via concentrations C_i and the equation of state. The ion mobilities, μ_j in $\mathrm{m^2/V{\cdot}s}$, are calculated similarly to the diffusion coefficients of the neutrals,

$$\frac{P_{tot}}{\mu_j} = \sum_{i=\text{background}} \frac{P_i}{\mu_{i,j}}, \tag{5}$$

The binary mobility, $\mu_{i,j}$, of ion j in each of the background gases i is calculated as

$$\mu_{i,j} = 0.514 \frac{T_{gas}}{P_{tot}\sqrt{\mu_{ij}\alpha_i}}, \tag{6}$$

where α_i is the polarizability of neutral i in $\mathrm{Å}^3$. Diffusion coefficients of ions, $\mathcal{D}_j$, and of electrons, $\mathcal{D}_e$, are defined as

$$\mathcal{D}_j = \frac{k_B T_{ion}}{e}\mu_j, \quad \mathcal{D}_e = \frac{k_B T_e}{m_e \nu}, \tag{7}$$

where e is the electron charge, $T_{ion}(= T_{gas})$ and T_e are ion and electron temperatures, respectively, and m_e is the electron mass. The collision frequency, ν, is estimated as ([10], p. 352)

$$\nu = c_\nu 10^{-6} B T_e^{-3/2} \sum_{j=1}^{20} C_j, \tag{8}$$

where the dimensionless constant B is about 10 ([10], p. 181). In Eq. (8), T_e is in eV and C_j is in $\mathrm{cm^{-3}}$, while ν is obtained in $\mathrm{s^{-1}}$. The $\sum C_j$ term relates the dependence of electron collision frequency to the presence of various species. The dimensionless coefficient c_ν is introduced to obtain correct estimates of the electron diffusion coefficient as can be found in previous works [11]. Finally, integrating the Poisson equation, the total electric field strength E_r can be calculated as,

$$E_r = \frac{1}{4\pi\epsilon_0}\frac{Q_p}{r^2} - \frac{e}{\epsilon_0 r^2}\int_{r_p}^{r} \xi^2 \left[C_{elec} - \sum_{i=\text{ions}} C_i\right] d\xi, \tag{9}$$

where ξ is a dummy variable, r_p is the particle radius, and Q_p is the particle charge.

Inside the so-called vacuum sphere, $r_p < r < \lambda$, a molecular-kinetic approach is implemented. Accordingly, the species j at $r = \lambda$, moving towards the particle and absorbed at the particle surface, are characterized by the flux

$$\Gamma_{\lambda j} = -C_{\lambda j} \left(\frac{8 k_B T_j}{\pi m_j} \right)^{1/2} \left(\frac{r_p}{2\lambda} \right)^2 \gamma_j, \tag{10}$$

where m_j is the considered species, and it is assumed that $r_p/\lambda \ll 1$. The factor γ_j accounts for the possible interaction between charged species and charged particle, and is calculated following [12].

Inside the vacuum sphere it may be shown that charged species are represented by a spatially uniform effective concentration $C_{\lambda j}\gamma_j$. Thus, the modified electric field strength outside the vacuum sphere $r > \lambda$ can be calculated using Eq. (9) by replacing Q_p with the effective charge

$$Q_{\text{effective}} = Q_p - e\frac{4\pi\lambda^3}{3} \left[C_{\lambda \text{elec}} \gamma_{\text{elec}} - \sum_{j=\text{ions}} C_{\lambda j} \gamma_j \right]. \tag{11}$$

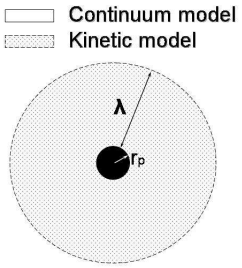

Figure 1: Kinetic and continuum models are implemented on the inside and outside of the vacuum sphere with radius λ, respectively.

Table 1: The reaction mechanism

Reaction	Rate constant (m^3/s)	Reaction	Rate constant (m^3/s)
electron-neutral:		$H_2 + H_2^+ \rightarrow H_3^+ + H$	2.5×10^{-15}
$e^- + CH_4 \rightarrow CH_4^+ + 2e^-$	$f(\epsilon)^*$	$H_3^+ + CH_4 \rightarrow CH_5^+ + H_2$	1.6×10^{-15}
$e^- + CH_4 \rightarrow CH_3^+ + H + 2e^-$	$f(\epsilon)^*$	$H_3^+ + C_2H_6 \rightarrow C_2H_5^+ + 2H_2$	2.0×10^{-15}
$e^- + CH_4 \rightarrow CH_3 + H + e^-$	$f(\epsilon)^*$	$H_3^+ + C_2H_4 \rightarrow C_2H_5^+ + H_2$	1.9×10^{-15}
$e^- + CH_4 \rightarrow CH_2 + 2H + e^-$	$f(\epsilon)^*$	*neutral-neutral:*	
$e^- + H_2 \rightarrow 2H + e^-$	$f(\epsilon)^*$	$CH_3 + CH_3 \rightarrow C_2H_6$	3.7×10^{-17}
$e^- + H_2 \rightarrow H_2^+ + 2e^-$	$f(\epsilon)^*$	$CH_3 + H \rightarrow CH_4$	7.0×10^{-18}
$e^- + C_2H_6 \rightarrow C_2H_4^+ + H_2 + 2e^-$	$f(\epsilon)^*$	$C_2H_5 + H \rightarrow CH_3 + CH_3$	6.0×10^{-17}
$e^- + C_2H_6 \rightarrow C_2H_5 + H + e^-$	$f(\epsilon)^*$	$C_2H_5 + CH_3 \rightarrow C_3H_8$	4.2×10^{-18}
$e^- + C_3H_8 \rightarrow C_2H_4 + H_2 + CH_4 + e^-$	$f(\epsilon)^*$	$CH_2 + H \rightarrow CH + H_2$	2.7×10^{-16}
$e^- + C_2H_4 \rightarrow C_2H_4^+ + 2e^-$	$f(\epsilon)^*$	$CH + CH_4 \rightarrow C_2H_5$	1.0×10^{-16}
$e^- + C_2H_4 \rightarrow C_2H_2 + 2H + e^-$	$f(\epsilon)^*$	$CH_2 + CH_4 \rightarrow CH_3 + CH_3$	1.7×10^{-17}
$e^- + C_2H_2 \rightarrow C_2H_2^+ + 2e^-$	$f(\epsilon)^*$	$CH_2 + CH_4 \rightarrow C_2H_4 + H_2$	1.7×10^{-17}
ion-neutral:		$CH_4 + CH \rightarrow C_2H_4 + H$	1.0×10^{-16}
$CH_4^+ + CH_4 \rightarrow CH_5^+ + CH_3$	1.5×10^{-15}	$CH_3 + CH_2 \rightarrow C_2H_4 + H$	3.3×10^{-17}
$CH_3^+ + CH_4 \rightarrow C_2H_5^+ + H_2$	1.2×10^{-15}	$C_2H_5 + H \rightarrow C_2H_4 + H_2$	3.0×10^{-18}
$CH_5^+ + C_2H_6 \rightarrow C_2H_5^+ + CH_4 + H_2$	5.0×10^{-16}	$CH_2 + CH_2 \rightarrow C_2H_2 + H_2$	1.1×10^{-16}

* $f(\epsilon)$ expressed as the first term of Taylor series approximation of the mean electron energy.

The boundary conditions for different species are defined as follows. At an infinite distance from the particle at which electroneutrality is restored, species of H_2 and CH_4 are continually supplied so that their concentrations are constant at $r = \infty$. Also, since the ionization process has not been modeled in the present work, an electron concentration is assumed so that C_{elec} balances $\sum_{ions} C_j$ at $r = \infty$. For all other species, $\partial C_j/\partial r = 0$, which guarantees that none of these species are supplied to or from infinity.

At $r = \lambda$, for those species which are absorbed at the particle surface, the concentration $C_{\lambda j}$ is found via matching the diffusion, Eq. (2), and molecular-kinetic, Eq. (10), fluxes. At the particle surface, the species' flux is given by

$$\Gamma_{pj} = \Gamma_{\lambda j} \left(\frac{\lambda}{r_p} \right)^2. \tag{12}$$

For all other species j not absorbed at r_p, it is imposed $\Gamma_{\lambda j} = 0$. To calculate the growth rate of the coating, we make use of a "sticking model" [13]. Following Herrebout *et al.* [9], for radicals R assumed to be responsible for

film growth, i.e., CH_3, CH_2, and C_2H_5, the sticking coefficient s is 0.01, 0.025, and 0.01, respectively. Thus, the layer thickness h in m/s is calculated from

$$\frac{dh}{dt} = -\sum_R s_R \Gamma_R v_R, \tag{13}$$

where v_R's are radicals volumes in m^3, taken all to be equal to 10^{-24} m^3.

3. Results and Discussion

The species transport equations, valid where plasma is considered as a continuum, are integrated in a radial symmetric geometry by means of a splitting algorithm, accounting separately for the diffusion term and for the reaction source term. The discrete region has been taken into consideration through the appropriate matching boundary conditions, as described in section 2. Both species transport and Poisson equations have been solved on a nonuniform grid. Typical results of the present model are the concentrations of various species, the electric field generated by charge distribution, and electron density as a function of space and time. Moreover, information is obtained about the fluxes of the different species towards the nanoparticle, and the growth rate of the amorphous carbon layer at the particle surface and its composition.

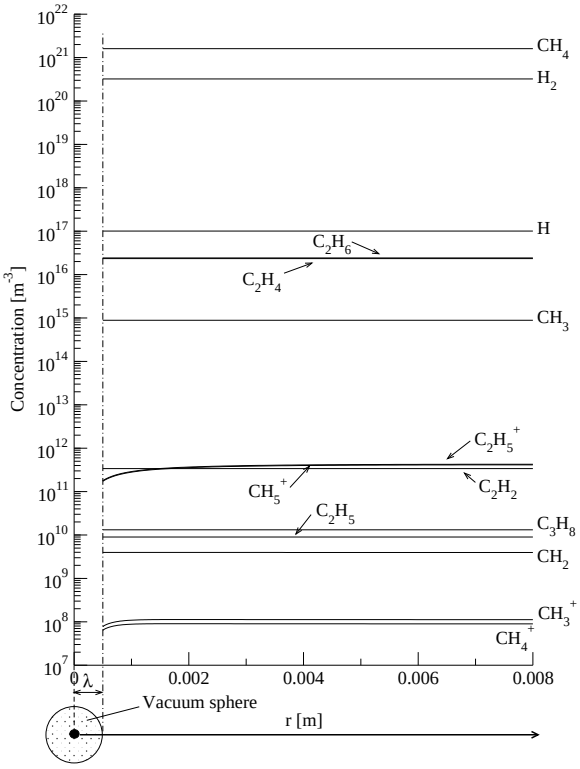

Figure 2: Concentrations of non-radical neutrals, radicals and ions as functions of distance from the dust particle.

Figure 2 illustrates the calculated concentration of the non-radical neutral molecules, the radicals and the ions for the particle radius r_p=100 nm, P_{tot}=100 mtorr, T_{gas}=T_{ion}=500 K, and the electron energy ϵ=1 eV (equivalent to the electron temperature T_e=11600 K). A constant ratio $[CH_4]/[H_2]|_\infty = 0.2$ was imposed so that together with equation of state, the concentration of CH_4 at infinity equal to 1.6×10^{21} m^{-3}. From Fig. 2, non-charged species are found to be almost homogeneously distributed within the domain. This is due to the low fluxes of such species from/towards the particle, which affects only their magnitudes. Similarly to Herrabout *et al.* [9], also for particle coating, the most important radical is found to be CH_3, with a concentration of 8.4×10^{14} m^{-3}. Smaller contributions to the film growth are given by CH_2 and C_2H_5, whose concentrations are 3.9×10^9 m^{-3} and 8.9×10^9 m^{-3}, respectively. Finally, in Fig. 2, only the most important ions are shown, for which $C_2H_5^+$ and CH_5^+ are the most dominant ones. In proximity of the particle, ions are characterized by a decreasing profile as they feel the effect of the generated electric field. In fact, due to the higher speed and mobility of electrons as compared to ions, the dust particle in a plasma acquires a negative charge and a negative potential with respect to the unperturbed plasma. However, the potential adjusts such that, by repelling the mobile electrons and attracting positive ions, the dust particle is being surrounded by an overall positive charge within the vacuum sphere. Outside this region, ion and electron concentrations are distributed as seen in Fig. 3a, and a positive electric field is generated in the continuum domain (Fig. 3b). In Fig. 3a, it is shown that as $r \to \infty$ ions and electrons balance each other, and electroneutrality is restored as expected. In the order of 6-8 mm the charged particle is completely screened by the ion-electron cloud, and no electric field is felt at these distances.

In this framework, the time-dependent charging of the particle can be calculated, as shown in Fig. 3c. After less than a second a steady-state value of -235.6e is reached. In a longer run, also growth-rate (dh/dt) approaches a value of approximately 0.49 nm/min (Fig. 3d). Thus, at long times the layer thickness vs. time (Fig. 3e) approaches a linear behavior, in accordance to [6], and after 200 sec, a layer of approximately 2.96 nm is deposited.

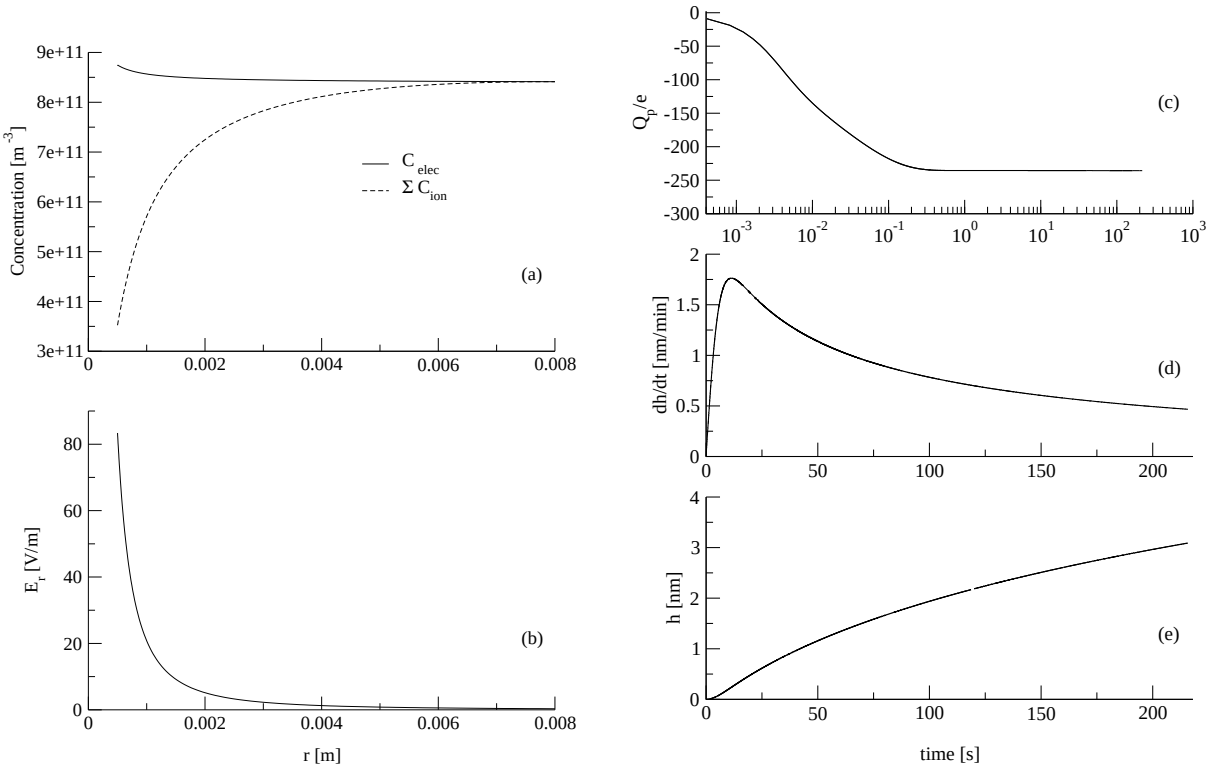

Figure 3: (a) Spatial variation of electron and total ion concentrations. (b) Spatial variation of electric field. (c) Temporal variation of particle charge. (d) Temporal variation of the coating growth rate. (e) Temporal variation of the coating thickness.

4. Conclusions

A kinetic/continuum theory model for predicting coating of nanoparticles by PECVD in low pressure conditions has been presented. Species transport phenomena were considered along with kinetics of chemical reactions consisting of 20 species. Electron-neutral, ion-neutral, and neutral-neutral reactions were counted in a total of 31 reactions, whereas vibration excitation electron-neutral reactions have been ignored to limit the number of species. Plasma-particle interaction of radicals was included by means of sticking coefficients and surface reactions. It was found that the thickness growth rate of the coating approaches a constant behavior as the system moves towards a constant at about 200 sec. For pressure P=100 mtorr, after 200 sec, a layer of approximately 2.96 nm was deposited, and a quasi constant growth rate deposition of $\simeq$0.49 nm/min was calculated.

Acknowledgments

This work was supported by grant CTS-0422900 from the U.S. National Science Foundation with Dr. T.J. Mountziaris as the program Director.

References

[1] D. Shi, P. He, J. Lian, L. Wang, and W. J. Van Ooij. Plasma Deposition and Characterization of Acrylic Acid Thin Film on ZnO Nanoparticles. *Journal of Materials Research*, 17:2555–2560, 2002.

[2] C. C. Chen and S. W. Chen. Nickel and Copper Deposition on Al_2O_3 and SiC Particulates by Using the Chemical Vapour Deposition-Fluidized Bed Reactor Technique. *Journal of Materials Science*, 32:4429–4435, 1997.

[3] Y. W. Yen and S. W. Chen. Nickel and Copper Deposition on Fine Alumina Particles by Using the Chemical Vapor Deposition-Circulation Fluidized Bed Reactor Technique. *Journal of Materials Science*, 35:1439–

1444, 2000.

[4] K. Jono, H. Ichikawa, M. Miyamoto, and Y. Fukumori. A Review of Particulate Design for Pharmaceutical Powders and Their Production by Spouted Bed Coating. *Powder Technology*, 113:269–277, 2000.

[5] A. Ermoline, M. Schoenitz, E. Dreizin, and N. Yao. Production of Carbon-Coated Aluminium Nanopowders in Pulsed Microarc Discharge. *Nanotechnology*, 13:638–643, 2002.

[6] J. Cao and T. Matsoukas. Deposition Kinetics on Particles in a Dusty Plasma Reactor. *J. Appl. Phys.*, 92(5):2916–2922, 2002.

[7] J. Cao and T. Matsoukas. Seeded Growth in Dusty Plasma with a Distribution of Surface-Deposition Rates. *J. Vac. Sci. Technol. B*, 2003. submitted.

[8] V. Ivanov, O. Proshina, T. Rakhimova, A. Rakhimov, D. Herrebout, and A. Bogaerts. Comparison of a One-Dimensional Particle-in-Cell–Monte Carlo Model and a One-Dimensional Fluid Model for a CH_4/H_2 Capacitively Coupled Radio Frequency Discharge. *J. Appl. Phys.*, 91(10):6296–6302, 2002.

[9] D. Herrebout, A. Bogaerts, M. Yan, R. Gijbels, W. Goedheer, and E. Dekempeneer. One-Dimensional Fluid Model for an RF Methane Plasma of Interest in Deposition of Diamond-like Carbon Layers. *J. Appl. Phys.*, 90(2):570–579, 2001.

[10] F. F. Chen. *Introduction to Plasma Physics and Controlled Fusion, Volume 1: Plasma Physics*. Plenum Press, New York, 2nd edition, 1984.

[11] J. D. P. Passchier and W. J. Goedheer. A Two-Dimensional Fluid Model for an Argon rf Discharge. *J. Appl Phys.*, 6:3744–3751, 1993.

[12] T. Matsoukas. The Coagulation Rate of Charged Aerosols in Ionized Gases. *J. Colloid Interface Sci.*, 187:474–483, 1997.

[13] G. J. Nienhuis, W. J. Goedheer, E. A. G. Hamers, W. G. J. H. M. van Sark, and J. Bezemer. A Self-Consistent Fluid Model for Radio-Frequency Discharges in SiH_4–H_2 Compared to Experiments. *J. Appl. Phys.*, 82(5):2060–2071, 1997.

Thickness dependence of optical properties of TiO_2 thin films prepared by PECVD and AFM analysis with scaling parameters

A. I. Borrás[1], A. Yanguas-Gil[1], J. Cotrino[1], T. Girardeau[2] and A.R. González-Elipe[1]

[1] *Instituto de Ciencia de Materiales de Sevilla (CSIC-USE), Sevilla (SPAIN).*
[2] *Université de Poitiers, UFR Molecular Sciences, SP2MI LMP UMR 6630, CNRS , Poitiers (France).*

Abstract

This paper describes the optical behaviour of TiO_2 thin films prepared by PECVD. The refraction indexes of these thin films generally decreases with thickness. Changes in microstructure and surface roughness are related with the scaling behaviour of these thin films. Differences are found depending on the plasma composition (O_2 or mixtures O_2/Ar) and interpreted within the concepts of the Dynamic Scaling Theory (DST).

1. Introduction

It is known that refraction index of oxide thin films may change with deposition time. Thus, thick films of a material may have distinct refraction index that another thin film made under identical conditions. Although there are some works in literature that have reported about the variations with thickness of the refraction index of evaporated films [1], the importance for practical purposes of this feature is not always recognised. Even less information is avalaible about the factors that influence such a behaviour. The present paper constitutes a first contribution trying to account for these observations and the causes that produce them in thin films prepared with Plasma Enhance Chemical Vapour Deposition.

Since roughness, along with porosity, is one of the factors that affects refraction index, in the present paper we have compared the evolution of this parameter for TiO_2 thin films grown by Plasma Enhanced Chemical Vapour Deposition (PECVD) for different periods of time with the evolution of the surface roughness. PECVD is a well established method for the preparation of TiO_2 thin films. With this technique different working parameters can be modified for an effective control of thin film compactness (and, therefore, refraction index). Here, besides deposition time, we have investigated the influence of using oxygen or argon/oxygen mixtures as plasma gas on the thin film properties. From Dynamic Scaling Theory (DST) [2] it is also known that the increase of the roughness with thickness until reaching a saturation value is a common behaviour in thin films growth.

The analysis of AFM images of the surface of samples grown for increasing periods of time under the concepts of DST has shown that no saturation of surface roughness is attained under our working conditions and that the surface morphology is mainly controlled by shadowing effects and not by surface diffusion. This agrees well with the SEM observation of the microstructure of the thin films.

2. Experimental

TiO_2 thin films were prepared by PECVD in a reactor with a downstream configuration. The plasma source is a SLAN type [3]. It was operated at a power of 400W with either pure O_2 or mixtures Ar/O_2 (90% Ar) as plasma gas. Titanium isopropoxide was used as titanium precursor [4]. Due to its low vapour pressure at room temperature, to dose this precursor into the chamber oxygen was bubbled though it while heated. Both the bubbling line and the shower-type dispenser used to dose the precursor were heated at 373K to avoid any condensation in the tube walls. Total pressure during deposition was $4x10^{-3}$Torr either with pure oxygen or Ar+O_2 mixtures as plasma gas. Films were deposited at room temperature simultaneously on quartz and silicon substrates.

The optical properties of the samples were determined by UV-Vis absorption spectroscopy (Perkin-Elmer Lambda 12 Spectrometer) and by spectroscopic ellipsometry (SOPRA). These two techniques yielded similar values of the refraction index except for differences of the order of 0.01 in some determinations. These differences will not be considered explicitely in the rest of this work. AFM images were collected in a Topometrix Explorer 3000 in non contact mode using high frequency levers. SEM cross section and normal images were measured for TiO_2 thin films grown on silicon.

3. Results

Fig. 1 shows the refraction index values measured for TiO_2 thin films prepared for increasing periods of time with different compositions of the plasma gas. It is apparent in this figure that the refraction index of the films decreases with deposition time and that this decrease is more pronounced for the samples prepared with mixtures $Ar+O_2$ as plasma gas. In relation with this behaviour it is interesting to note that the growing rates for the films grown in pure O_2 (5nm/min) were greater than in $Ar+O_2$ mixture (2.4 nm/min for 10% of O_2).

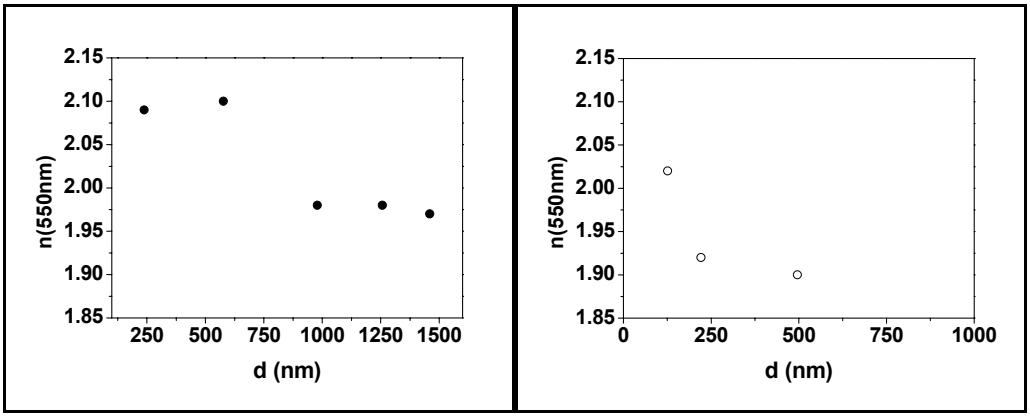

Figure 1: Variation of the refraction index with the film thickness for three experimental conditions: pure oxygen (left) and Ar/O_2 mixtures (right)

Another characteristic of the thin films that changed with deposition time was surface roughness. Fig. 2 shows a series of AFM images taken for TiO_2 thin films prepared with a Ar/O_2 mixture with 90% of Ar and for increasing periods of time. Meanwhile a comparison between the surface morphology of TiO_2 films grown with pure oxygen and Ar/O_2 mixtures is presented in Fig 3.

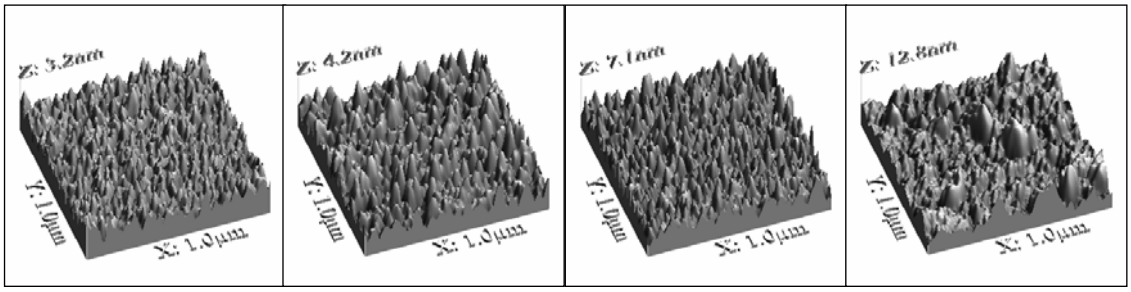

Figure 2: Increase of surface roughness with film thickness (Ar/O_2 mixture with 10% of oxygen): (a) 50 nm; (b) 126 nm; (c) 221 nm; (d) 496 nm

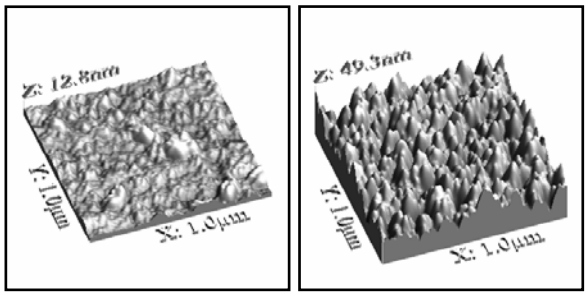

Figure 3: Comparison of the surface morphologies between TiO_2 films grown with Ar/O_2 mixtures (left, 10% O_2, 496 nm) and pure O_2 (right, 577 nm)

The average roughness was calculated from these images according to the expression:

$$w = \sqrt{\langle h_i^2 \rangle - \langle h_i \rangle^2}$$

where w is the roughness and h_i the height of each point of the surface [2]. The evolution of roughness with time is plotted in Fig. 4 in a logarithmic scale. The resulting plots define two straight lines whose maximum values do not saturate even after deposition for long periods of time.

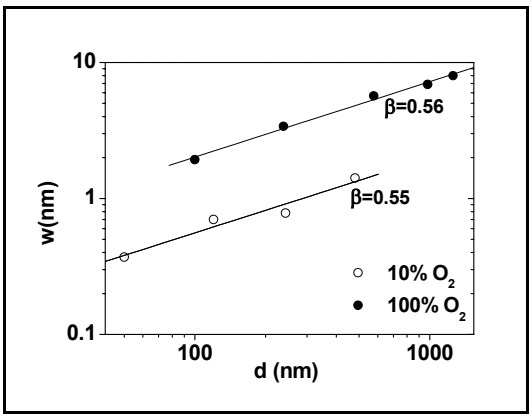

Figure 4: Roughness evolution with film thickness for 10% and 100% of oxygen

According to the DST, the slopes of this kind of plots define the value of the exponent β, the so called *growth exponent* [2], that serves to characterise the scaling behaviour of growing surfaces. In the present case, the values determined for the two series of samples were β =0.56± 0.03 for pure oxygen and β =0.55± 0.08 for the Ar/O_2 mixture.

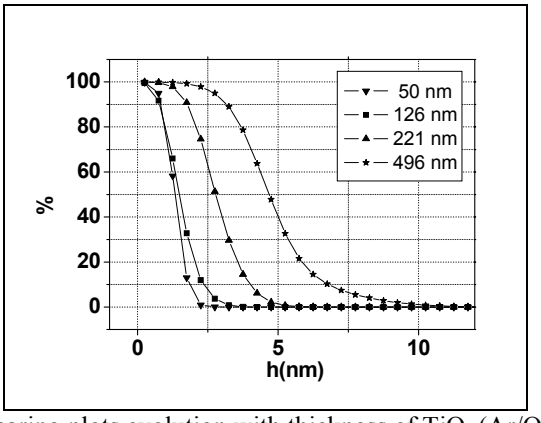

Figure 5: Bearing plots evolution with thickness of TiO_2 (Ar/O_2) samples.

Besides roughness, another interesting parameter that can be derived from AFM images is the particle size distribution. This is typically done by the so called Bearing plots as those represented in Fig. 5 for the series of samples prepared with this Ar/O_2 mixture. It is apparent from these series of diagrams that average particle size increases with the deposition time.

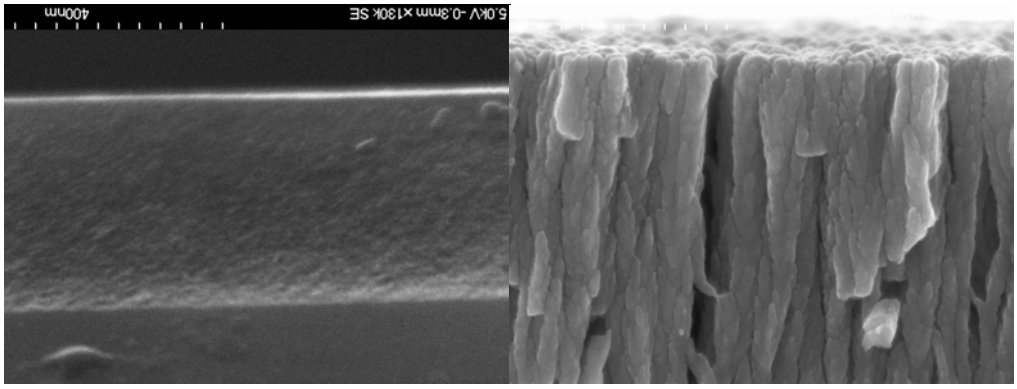

Figure 6: SEM cross sections of two TiO_2 films: 10% of O_2 (left) and 100% (right)

The behaviour depicted in Fig. 4 for the films grown with pure oxygen or with Ar/O_2 mixtures is congruent with the cross section SEM images presented in Fig. 6. This figure clearly shows that the TiO_2-O_2 films are characterised by a columnar microstructure with columns having a relatively big size. By contrast, TiO_2 - Ar/O_2 samples do not have a well defined columnar structure.

4. Discussion

The two sets of samples prepared in this work present different values of their refraction indexes and surface roughness, but also depict quite different microstructures. All these differences must be a consequences of the growth mechanism occuring in each case. However, a preliminary interpretation of the growth processes based on the application of the DST concepts does not reveal significant differences. The two sets of samples are characterised by a similar growth exponent $\beta \approx 0.55$ and a non-saturation behaviour of roughness. In previous reports in literature [5,6] these two features have been associated with growth processes characterised by very high sticking probabilities of the fragments/particles reaching the surface and the eventual development of a columnar microstructure. In this case, surface diffusion is restricted or supressed and the incoming particles remain in the same place where they have touched the surface. This is certainly the case for TiO_2-O_2 samples characterised by homogeneus columns that grow in height from practically the interface with the substrate up to the surface films. The slight decrease in n found in these samples when their thickness increase has probably to be associated with the continuous increase in surface roughness found for the samples. On the other hand, the high growing rate found in this case (i.e. 5 nm min^{-1}) points out to a high efficiency of the plasma to induce the fragmentation and oxidation of the titanium isopropoxide precursor in the gaseous phase.

Samples TiO_2-O_2/Ar show a globular microstucture and low values of n that sharply decrease with the thickness of samples. The presence of Ar in the plasma must be the reason for these differences as well as the most important factor for decreasing the growing rate of these samples (i.e. 2.4 nm min^{-1}). Characterization of the O_2 and O_2/Ar plasmas in our experimental set-up has shown that the electron density is greater in this latter case. It is therefore likely that the plasma particles arriving to the surface have a higher perpendicular component of velocity when the concentration of Ar in the plasma is important. Under these conditions the columnar growth is hindered even though the sticking coefficient of titanium fragments is high (columnar growth mechanisms are typically recognised as the result of a random distribution of the velocity direction of

the incoming particles). In addition, the high rate and momentum of the Argon particles may induce a certain sputtering of surface, a feature that is also reflected by the lower growing rate of these samples.

The considerable decrease in n found for the TiO_2-O_2/Ar films as they grow in thickness reveals an accumulation of voids and pores. Meanwhile, the much lower values of surface roughness found in these samples as compared with TiO_2-O_2 discard that roughness is a significant parameter for the control of n. We rather believe that the increase in the particle size that occurs as the thickness of samples increases (cf. Fig. 5) is the inmediate cause of this increase in porosity. The study of these and other sets of samples is still being carried out at present based on a more thorough characterisation of the scaling behaviour of the different families of thin films.

References

[1] A. Álvarez-Herrero, G. Ramos, F. del Monte, E. Bernabeu and D. Levy, Thin Solid Films 455-456, 356 (2004).
[2] A. L. Barabasi and H. E. Stanley, Fractal Concepts in Surface Growth (Cambridge University Press, 1995).
[3] A. Brockhaus, D. Korzec, F. Werner, Y. Yuan and J. Engemann, Surf. Coatings Technol. 74-75, 431 (1995).
[4] F. Gracia, J. P. Holgado and A. R. Gonzalez-Elipe, Langmuir 20, 1688 (2004).
[5] M. Kondo, T. Ohe, K Saito, T Nishimiya and A. Matsuda, J. Non-Cristalline Solids 227-230, 890 (1998).
[6] F. Ojeda, R. Cuerno, R. Salvarezza and L. Vázquez, Phys. Rev. Lett. 84-14, 3125 (2000).

Characteristics of an AC Three-Phase GlidArc Plasma Generator

L. Lin[1)*], B.Wu[1)], C. Yang [1)], C. K. Wu [1)], P. Zhang [2)], Y. Q. Wang[2)]

[1)]*Institute of Mechanics, Chinese Academy of Sciences, Beijing 100080*

[2)]*Shenyang Aircraft Research Institute, Shenyang 110035*

E-mail: LinLie@imech.ac.cn

Abstract

An AC three-phase GlidArc discharge plasma generator and its characteristics are described. Some experimental results about the GlidArc discharge of the plasma generator were obtained. This type of GlidArc plasma generator is potentially used in air pollution treatment processes and treatment of medical waster.

1. Introduction

GlidArc discharge plasma is a type of non-equilibrium plasma near atmospheric pressures, and has many applications in chemical industry and environment engineering [1-3]. The non-equilibrium plasma near atmospheric pressure is the so-called non-thermal plasma in between the thermal plasma and cold plasma. In general, the GlidArc discharge was powered by a DC power source supply[3-6]. In this paper, a novel AC three-phase GlidArc plasma generator is presented. The principle of the plasma generator is analyzed. The main advantages of AC GlidArc discharge plasma are simplicity of the power supply system and its low cost.

This AC three-phase GlidArc plasma is potentially used in air pollution treatment processes and treatment of medical waster.

2. Electrical device and GlidArc plasma generator

The experimental set-up of the GlidArc plasma generator is shown in Fig.1. It consists of a GlidArc discharge plasma generator, an AC three-phase main power supply, a high voltage ignition power supply and a gas supply. The AC three-phase main power supply included a variable transformer, three transductors and a main transformer. The GlidArc discharge plasma generator included a water-cooling center electrode, three water-cooling outside electrodes, a gas injection device and an electric discharge chamber. The shortest distance between the center electrode and outside electrodes is 2-3 mm. When a high voltage ignition power supply of 10000 volts is attached to the center electrode and the outside electrodes, the arc will be ignited at the shortest distance and then driven towards the exit of the setup by the gas flow and electromagnetic force created by own arc current. The force on the electric arc by gas flow per unit length is

$$F_g = \frac{1}{2} c_d \rho (v_g - v_a)^2 d \qquad (1)$$

where c_d is the resistance coefficient of gas flow on the electric arc, ρ is the density of gas, v_g is the velocity of gas flow , v_a is the velocity of electric arc, d is the diameter of the electric arc.

This work is supported by National Nature Science Foundation of China №.90205026，№.10375082.

The electromagnetic force by own arc current per unit length is

$$F_e = IB_i \qquad (2)$$

Where I is the arc current, B_i is the magnetic field strength created by own arc current. When the arc current is low, the electromagnetic force is much lower than the force of gas flow.

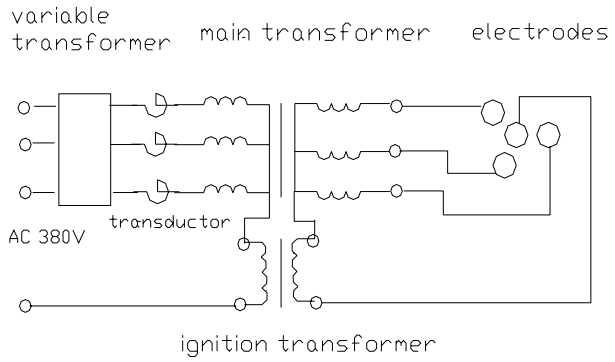

Fig.1 Experimental set-up of the AC three-phase GlidArc discharge plasma

Parameters of the AC three-phase power supply and the high voltage ignition power supply are given in Table 1. The gas flow-rate for the plasma generator is 8-10m^3/h, and the gas medium is air.

Table 1. Parameters of the AC three-phase power supply and the ignition power supply

	Voltage (V)	Current (A)
AC Three-phase power supply	1000	10
Ignition power supply	10000	0.1

The configuration of the AC three-phase GlidArc plasma generator is shown in Fig.2. The diameter of the plasma generator is 120mm, and length is 220mm. Six holes for gas injection with 2mm diameter are set on the top of the generator.

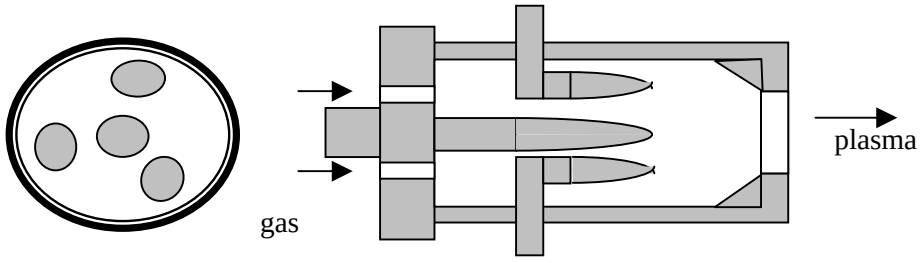

Fig.2 Schematic diagram of AC three-phase GlidArc discharge plasma generator

Fig.3 shows the photograph of the AC three-phase plasma generator. The average electric power of the plasma generator is 3-8kW.

Fig.3 Photograph of the AC three-phase GlidArc plasma generator in operation

3. Characteristics of discharge

Fig.4-5 show the current and voltage curve of the discharge recorded with a digital oscilloscope. Fig.4 shows that the discharge current has some oscillator when the instantaneous voltage is low. If the arc voltage is high enough, the oscillator of the arc current will decrease. Fig.5 shows that after arc current be ignited the voltage of the arc will be near a constant.

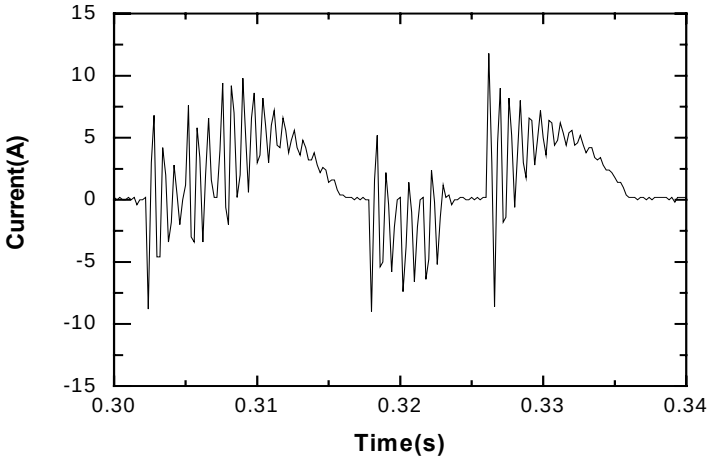

Fig.4 Current curve for the AC GlidArc discharge

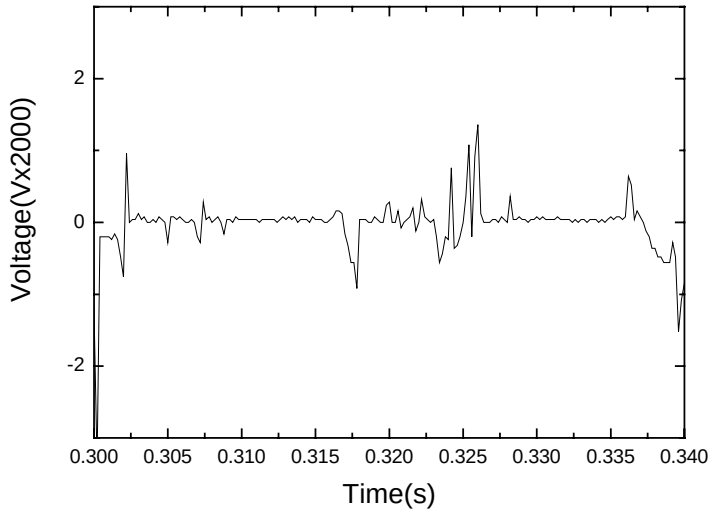

Fig.5 Voltage curve of the AC three-phase GlidArc plasma generator

4. Discussion

We report here an AC three-phase GlidArc plasma generator and some results of experiment for GlidArc discharge. This type of three-phase GlidArc discharge plasma generator has some advantages (for example, simplicity of the power supply system and its low cost, uniform temperature distribution of the plasma at the exit cross-section of the plasma generator.) and offer good application prospect in environment engineering.

References

[1] S Pellerin, et al., "Heat string model of bi-dimensional DC GlidArc", J. Phys. D: Appl. Phys. 33(2000) P.2407

[2] T.Janovski, et al., "Industrial trials of the GlidArc plasma reactor", ISPC-12 1995, P.825-830

[3] Ph. G. Rutberg, et al., "Construction of three-phase single –chamber plasma torch with tubular copper electrodes for work on air and oxidizing media", ISPC-16, 2003, CD-No.670

[4] Lin Lie，Wu Cheng-kang, " Study on Characteristics of Rotating GlidArc Discharge at Atmospheric Pressure", ISPC-13, Beijing , 1997, P.807-811

[5] Lin Lie, Wu Bin, Wu Chengkang, Pan Wenxia, "Experimental Study on Propagation Characteristics of Microwave in GlidArc Discharge Plasma", In the proceeding of 16th International Symposium on Plasma Chemistry, Italy, 2003

[6] L. Lin, B.Wu, C. Yang, C. K. Wu, P. Zhang, Y. Q. Wang, "Distribution of Temperature in Glidarc Discharge Plasma", 7th APCPST&17th SPSM, 2004 June, Japan

Plasma Surface Activation of Polymer Using Atmospheric Pressure Glow Discharge

M. Šíra, P. Sťahel, Z. Navrátil, F. Zlámal, D. Trunec
Department of Physical Electronics, Masaryk University, Kotlářská 2, 611 37 Brno, Czech Republic, e-mail pstahel@physics.muni.cz

Abstract
APGD was used for surface modification of polycarbonate (PC). The discharge was generated in pure nitrogen or in nitrogen–hydrogen mixture. The surface properties of treated and untreated samples were investigated by surface free energy measurements, X-ray photoelectron spectroscopy. The influence of the treatment time and the aging on the surface properties of PC was studied. The surface free energy of PC increased from 30 to 53 mJm^{-2}. The decrease in the surface free energy during the ageing was approximately 10%.

Introduction

Polycarbonate is widely used material in different branches of industry. This thermoplastics material is used everywhere high impact resistance and transparency is required. However, surface properties of polycarbonate (e.g. wettablity and adhesion with deposited metallic or dielectric films) are not suitable for every application. Plasma surface treatment is very promising technique for adhesion improvement. Most of reported works with plasma activation of different polymers [1] especially polycarbonates were made in different types of low-pressure plasma [2, 3]. The disadvantage of the low-pressure techniques is their demand of expensive vacuum pumping systems. Moreover, the difficulties in arranging the system for large area treatment have to be overcome. Recently, plasma activation of polymers at atmospheric pressure has become a promising technology due to its economical and ecological advantages.

Dielectric barrier discharges at atmospheric pressure are widely used in various applications such as depolution, ozone production, surface treatment and thin film deposition. Two modes of barrier discharge can occur: filamentary and glow. In the filamentary mode the treatment is not homogeneous so its application is limited for surface activation and plasma depositions. The atmospheric pressure glow discharge (APGD) allows homogenous treatment of the surface however this kind of discharge is possible to obtain only under certain specific conditions.

The main objective of this paper was to investigate the effect of the plasma surface treatment in APGD on the surface properties of polycarbonate. The influence of the treatment time and the aging on the surface properties of PC was studied. The surface free energy of PC increased from 30 to 53 mJm^{-2}. The decrease in the surface free energy during the ageing was approximately 10%.

Experimental

The atmospheric pressure glow discharge was generated in a reactor chamber between two brass electrodes. The upper electrode was covered by a dielectric (pyrex glass) 1 mm thick and the bottom one was covered with the polycarbonate sample. The discharge was generated in pure nitrogen or in pure nitrogen with small admixture of hydrogen (3%). The bottom electrode was periodically moving with sample during the treatment to achieve higher homogeneity and to increase the treated area. The distance between electrodes was 1 mm. The operating frequency was kept at 10 kHz and the input power density was kept at 0.8 $W.cm^{-2}$ in all cases. The treatment time varied from 4 to 100 s.

So called Acid Base Regression method [4] was used to calculate the total surface free energy γ and its components (Lifshitz-van der Walls γ^{LW}, acid-base γ^{AB}, acid part γ^{+} and base part γ^{-}) from contact angles measured by means of Surface Energy Evaluation System [5]. The topology of treated and untreated samples was studied by means of AFM and SEM and chemical changes were investigated by XPS.

The discharge properties were studied by means of the optical emission spectroscopy. The spectra emitted by the discharge were recorded with the Jobin-Yvon TRIAX 550 spectrometer with a CCD detector.

Results and discussion

Typical spectrum of the nitrogen discharge with 3 % hydrogen admixture is displayed in Fig. 1. The spectrum consists only of the molecular bands of the second positive system of nitrogen ($C\ ^3\Pi_u \rightarrow B\ ^3\Pi_g$). Neither hydrogen atomic lines nor hydrogen molecular lines were registered, although the integration time was exaggeratedly raised. This is probably due to the complex structure of nitrogen molecule excited states, which absorbs the most of the supplied energy.

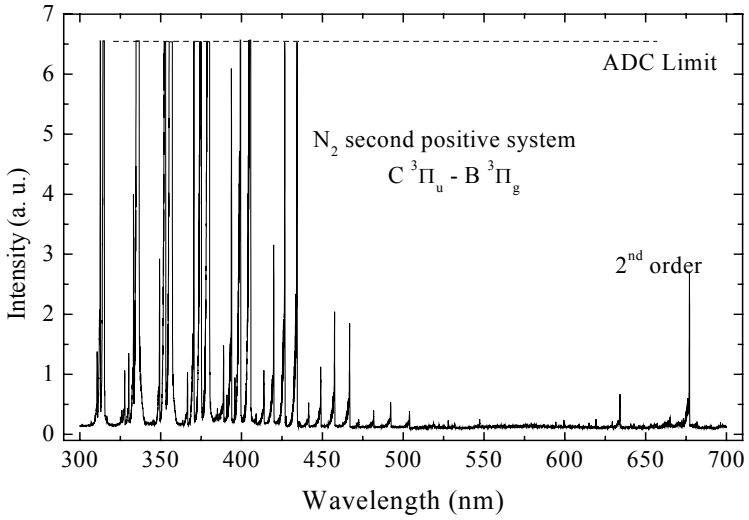

Figure 1. Overview spectrum of APG discharge in nitrogen with 3 % hydrogen admixture. Whatever the hydrogen admixture was, only nitrogen emission was observed.

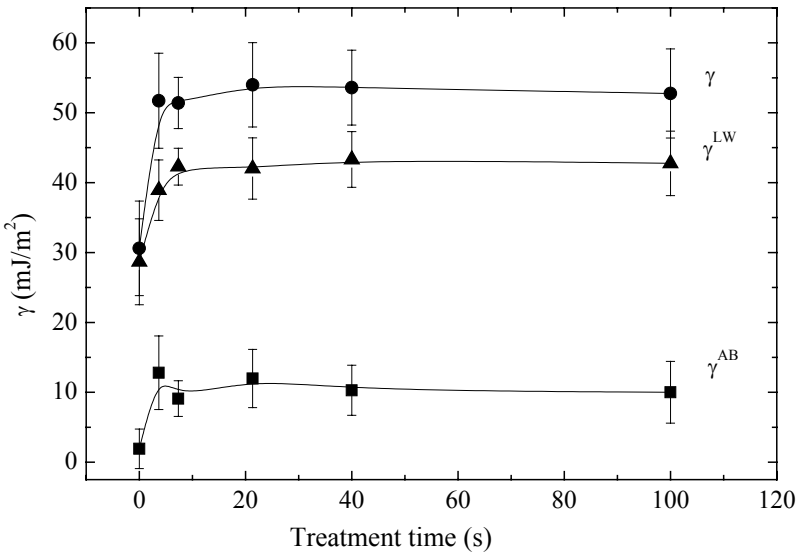

Figure 2. *SFE of sample versus treatment time. γ is total surface free energy, γ^{LW} is Lifshitz-van der Walls component and γ^{AB} is acid-base component.*

The surface free energy (SFE) of treated polycarbonate as a function of the plasma treatment time in nitrogen-hydrogen mixture is shown in Fig. 2. The total surface free energy γ and also its components (γ^{LW} Lifshitz-van der Walls and γ^{AB} acid-base component) rapidly increased during the first 7 s of treatment then reached saturation.

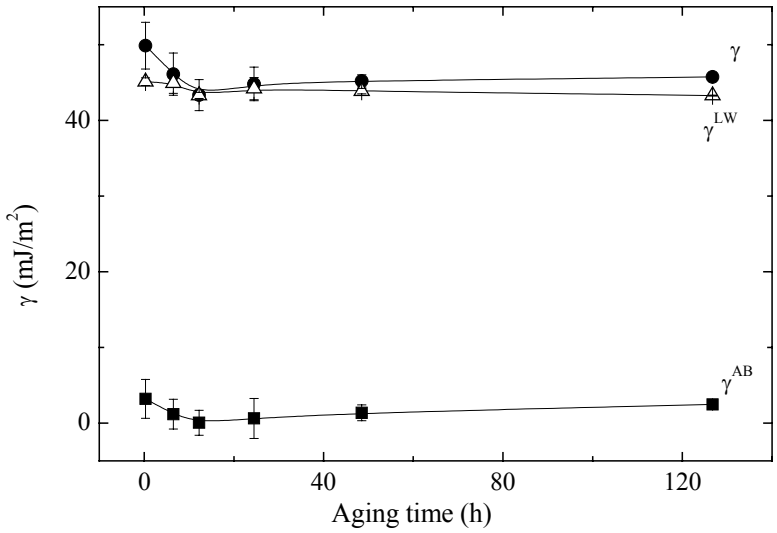

Figure 3. *SFE of sample versus aging time. γ is total surface free energy, γ^{LW} is Lifshitz-van der Walls component and γ^{AB} is acid-base component. Plasma treatment time of sample was 100 s.*

The time stability of treated samples was also investigated (see Fig. 3). The total surface free energy and its components slightly decreased during the first 12 hours of the aging and remained constant. The stable value of SFE of aged sample was considerably higher then the value of SFE of untreated sample. We suppose the good stability is caused due to croslinking effect.

The surface atomic concentration of samples was measured by X-ray Photoelectron Spectroscopy using Mg K_α photon beams. The results are in Tab.1.

Tab. 1: *Atomic concentration of virgin sample and treated samples. Plasma treatment time of samples was 100 s.*

Sample	**C**	**O**	**N**
	%	**%**	**%**
virgin PC	83.2	16.8	0.0
PC treated in N_2	72.1	17.9	10.0
PC treated in N_2+H_2	68.1	16.9	15.0

Conclusion

Polycarbonate samples were activated in the atmospheric pressure glow discharge. The surface free energy of treated samples increased from 30 to 53 $mJ.m^{-2}$. The treated samples showed out only low ageing effect. The saturated value of SFE of samples plasma treated in APGD was comparable with saturated value of

SFE of samples treated in low-pressure discharges. The benefit of the technique based on APGD is short-process time and low aging effect in contrast to low-pressure techniques.

Acknowledgment

This work was supported by Grant Agency of Czech Republic No. 202/05/0777 and 202/02/D097.

Reference

[1] Lehotský M. , Drnovská H. , Lapčíková B. , Barros-Timmons A. M. ,Trindade T. , Zembala M. , Lapčík Jr. L. : Colloids and Surfaces A: *222,*125 (2003)
[2] Zajíčková L. , Subedi D. P. , Buršíková V. , Veltruská K. : Acta Physica Slovaca *53, 6*, 489 (2003)
[3] Klemberg-Sapieha J. E. , Poitras D. , Martinu L. , Ymasaki N.L.S. , Lantman C.W. : J.Vac.Sci.Technol *A15,3*, 985(1997)
[4] Navrátil Z. , Buršíková V. , Sťahel P. , Šíra M. , Zvěřina P .: Czech. J. Phys. *54*, C877 (2004)
[5] http://www.seesystems.wz.cz

A parametric study of carbon nanotubes produced from the thermal plasma dissociation of tetrachloroethylene

D. Harbec, J.-L. Meunier, L. Guo, J. Jureidini
CRTP / Department of Chemical Engineering, McGill University, Montreal, Quebec, Canada

Abstract
We produce carbon nanotubes (CNT) using a nominal 100 kW dc non-transferred plasma torch and tetrachloroethylene as carbon raw material. The erosion of the torch electrodes emits tungsten vapours that nucleate *in situ* into catalytic nanoparticles within the plasma jet. CNT mass yield values are based on thermogravimetry analysis correlated using electron microscopy and Raman spectroscopy. This led us to conduct a parametric study and determine the influence of the different operating parameters on the yields of carbon nanotubes. Formation of a supersonic jet, high vapour pressures of carbon and a control of the temperature profile within the torch nozzle enable the rapid growth of CNT.

1. Introduction

Carbon nanotubes (CNT) are long hollow tubes that contain hundreds of carbon atoms. Their nanometric diameter and their micron-size length give them a one-dimensional structure. Single-Walled Nanotube (SWNT) consists of the roll-up of a graphene sheet and closed on itself, whereas a Multi-Walled Nanotube (MWNT) constitutes an arrangement of concentric SWNT. Due to their 1-d hollow structure, CNT possess interesting properties. They feature mainly high modulus of elasticity, high tensile strain, superconductor and semiconductor behaviours, high thermal conductivity and storage capabilities. Novel applications are being developed in advanced materials [1-3], electronic components [4-5], and storage applications [6-7]. The availability and the high cost of CNT however limit the development and the commercialization of most applications. Our objective is to contribute in solving this problem through the development of a manufacturing process that can produce CNT on an industrial level based on thermal plasma torch technology.

In this paper, we present CNT catalytically produced using tetrachloroethylene (TCE) as carbon raw material injected in the nozzle of a dc plasma torch. Researchers widely use metallic nanoparticles to catalyze the formation of CNT. These metallic nanoparticles enhance the yields of CNT by anchoring the tip of the CNT structure. These mainly inhibit the formation of pentagonal rings preventing a premature closure of the CNT structure into by-products and allowing an efficient elongation and CNT growth [8-10]. Here, the erosion of a thermal plasma torch electrode emits metallic vapours that nucleate *in situ* into catalytic nanoparticles within the plasma jet [11-12]. In this simple scheme, the tungsten particles act as the metal catalyst within the graphitic deposit formed on the internal wall of the torch nozzle, thereafter called the "nozzle deposit". Here, we present results regarding the mechanism of formation of CNT within the torch nozzle using the particular tungsten/TCE precursors, and implementation of a method to quantify and characterize yields of CNT. This makes possible to conduct a parametric study and investigate the effect of the various operating parameters on the yields of CNT.

2. Experimental

As outlined in the introduction, we produce CNT from the thermal plasma dissociation of TCE. We inject TCE vapours using 20 slpm of carrying argon gas in the water-cooled nozzle of a dc non-transferred thermal plasma torch (*Pyrogenesis Inc.*, model RPT-2) operating with 100 slpm of plasma-forming argon and a torch power of 30 kW. Upstream of the torch nozzle, the arc plasma erodes both the anode and the cathode made of tungsten and supplies tungsten vapour as a source for catalyst nanoparticles for the growth of CNT. The arc current controls the supply of tungsten in the process [11-12]. We characterize CNT and the catalyst nanoparticles using electron microscopy (EM): Transmission Electronic Microscopy (TEM) and Field-Emission Scanning Electronic Microscopy (FE-SEM).

We quantify yields of CNT using thermogravimetric analysis (TGA; *Perkin Elmer* TGA 7) and characterize the diameter distribution of CNT using Raman spectroscopy (*Renishaw inVia*). Raman spectra are recorded on raw soot using the 514 nm wavelength of an Ar-ion laser. The results are then confirmed using a 785 nm wavelength

laser, this yielding a higher signal-to-noise ratio compared to the 514 nm Ar-ion laser. For the mass evaluation of CNT, 15-18 mg of raw soot is placed in the TGA crucible. A temperature ramp rate of 5°C/min from 50°C to 1000°C and an air flow rate of 60 cc/min are used. Weight loss in wt.% is recorded as a function of furnace temperature, thereafter called the TG curve. The derivative of the TG curve with respect to temperature yields the DTG curve. The DTG curve shows peaks associated to the weight-losses of each carbonaceous species contained in the raw soot, the peak temperature representing the burning temperature of the related carbonaceous species. CNT are identified using EM techniques on samples taken before and after a given TGA peak, and using a TGA analysis on purified samples having similar morphology.

3. Formation of CNT

We previously reported that the flow and the temperature conditions within the torch nozzle enable a good dispersion of tungsten and the synthesis of large concentrations of long MWNT, carbon onions and carbon nanoparticles within the nozzle deposit [11]. Using TEM, these MWNT are typically 50μm long and their internal and external diameters are respectively 2-3 nm and 10-20 nm. TEM micrographs (Figure 1a) show nanoparticles of tungsten carbide (C_xW_y) encapsulated at the tip of CNT. These particles likely play a role of catalyst in the growth of CNT. The mechanism of formation of the CNT occurs most probably in a similar fashion as Kataura *et al.* [8], Gavillet *et al.* [9] and Larouche *et al.* [10]. Upon cooling, the carbide nanoparticles segregate their excess of carbon to their surface at their eutectic temperature. The segregated carbon graphitizes and forms CNT at the surface of the carbide nanoparticles. The growing CNT continuously uses the segregated carbon and carbon in the gas phase as building blocks to elongate their structure and CNT grows from the surface of the carbide particles until the temperature become too low. Below a certain temperature level, the nanoparticles solidify and stops further growth of the CNT. On Figure 1b, an electron diffraction pattern of the nozzle deposit using TEM shows good resonance of the diffracted light. This reveals a highly graphitic arrangement of the carbon atoms and a negligible content of amorphous carbon in the nozzle deposit.

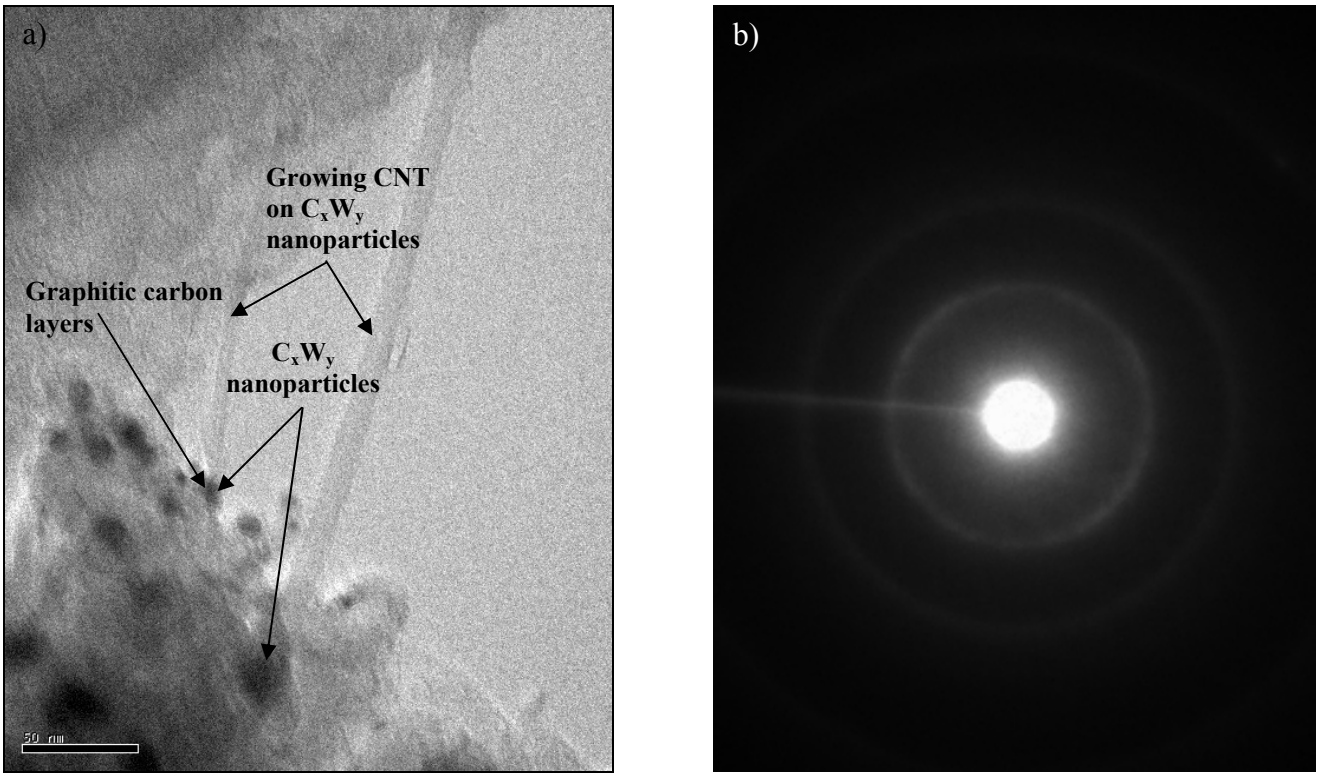

Figure 1 a: Nanoparticles of tungsten carbide at the tip of CNT promoting the growth and the elongation of CNT. **b:** Electron diffraction analysis demonstrates that the nozzle deposit contains carbon in graphitic and crystalline forms.

The Raman spectrum using the 514 nm and the 785 nm lasers of an as-produced nozzle deposit effectively confirms that this method of production promotes the growth of MWNT (Figure 2). The absence of peak in the RBM mode at both wavelengths indicates the absence of SWNT in the nozzle. The spectrum obtained with the 785 nm laser particularly consolidates this affirmation due to its higher signal-to-noise ratio. The G mode peaks (Raman shift @ 1582 cm^{-1}) inform about the relative content of graphitized carbon: MWNT, carbon nanoparticles and onions. Due to the small amount of amorphous carbon in the nozzle deposit, the D mode peak (Raman shift @ 1357 cm^{-1}) reflect most probably the relative content of the amount of pentagonal rings of carbon and defects in the sample. As indicated above, the as-produced MWNT show a defect-free morphology over lengths exceeding 50 µm [11], and are less likely the source material for the D peak intensity. The D mode rather indicates the relative amount of carbon nanoparticles and onions.

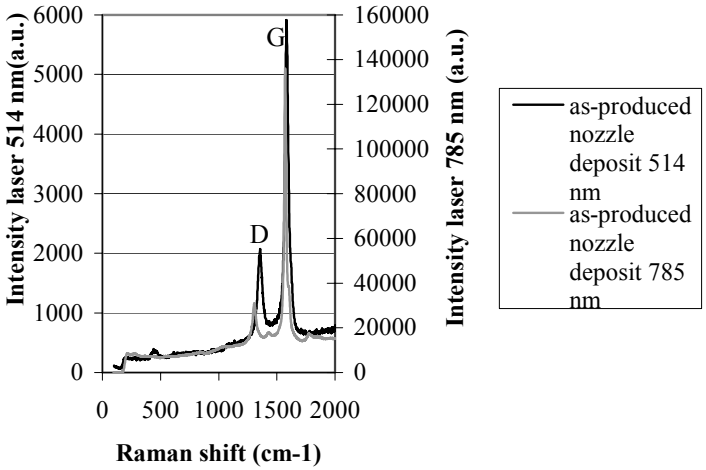

Figure 2: Raman spectra using the 514 nm laser and the 785 nm laser of an as-produced nozzle deposit.

On Figure 3, CFD modeling of the temperature profiles within the nozzle using *Fluent 6.1* demonstrates for two pressure conditions that a strong quench upstream of TCE injection ports is induced by a supersonic plasma jet expansion followed by two shock waves. According to the average velocity of the plasma jet, the upstream expansion cools the plasma at rate of ≈50x10^6 K/s, while rates of 2-4.5x10^6 K/s are calculated for the two subsequent shock waves (see related ISPC-17 paper [13]). Such quench rate values at or above 10^6 K/s were evaluated by Larouche *et al* [10] as a requirement for CNT synthesis. From these considerations, we stipulate the growth of MWNT in the nozzle occurs as the following. The plasma arc erodes the tungsten electrodes and generates tungsten vapours upstream of the nozzle within the plasma torch. Nanoparticles of tungsten nucleate in the quench zone generated by the supersonic expansion and in the cold areas along the nozzle walls. Most of the particles generated are transported to the nozzle walls by thermophoresis effect from the strong temperature gradients, and by the cold gas recirculation loops upstream in the nozzle. Meanwhile, the plasma jet atomizes the injected TCE and provides atomic carbon contamination to the tungsten particles. A fraction of the carbon vapours also nucleate in the cold wall areas into carbon nanoparticles and onions. The tungsten carbide (C_xW_y) particles having suitable temperature and size will be the site of CNT growth. These particles attached to the nozzle wall are characterized by very long residence times in a given high temperature window, together with a continuous supply of atomic carbon. This temperature window is presumably the eutectic temperature of C-W mixture being 2700K. Such a situation should lead to the observed CNT showing average lengths exceeding 50 µm and defect-free morphology because of the high temperature of this tungsten-based nucleation.

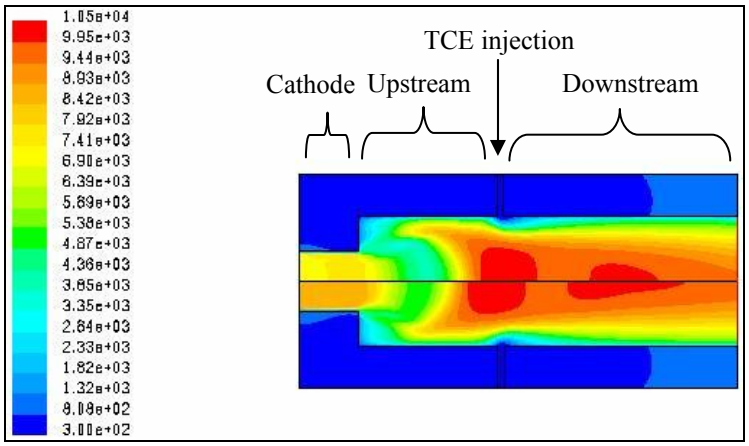

Figure 3: CFD modeling temperature profile inside the torch nozzle. Upper part: 200 torr, bottom part: 500 torr.

4. Quantification of CNT

Quantification of CNT still remains a challenge due to its insolubility in most solvent and difficulty to extract them. Here, we use a simple method to quantify these using TGA. TGA of the nozzle deposit as shown on

Figure 4 typically shows DTG curves with two steps weight loss between 50°C and 1000°C. The first one occurs at 575°C and the second, at 830°C. We are thus in presence of two specific types of carbonaceous species in the nozzle deposit. To identify the morphologies associated to these peaks, we performed TGA analysis of pure MWNT sample having similar size characteristics to those found in the nozzle deposit (*Nanostructured & Amorphous Materials Inc. #1228MNG*). The combustion of the pure MWNT sample occurs characteristically at 575°C. EM observations of the TGA samples taken above and below the peak temperature confirm the disappearance of MWNT at a temperatures of 690ºC (Figure 5). Only a few carbon fibers and particles remain in the sample. These evaluations allow associating the first weight-loss peak occurring at around 575°C to the combustion of the MWNT contained in the nozzle deposit, and the second to the combustion of the by-products such as the carbon nanoparticles and onions. We exploit in the following section the area under the weight-loss peak at 575ºC to quantify the concentration of MWNT in the nozzle deposit.

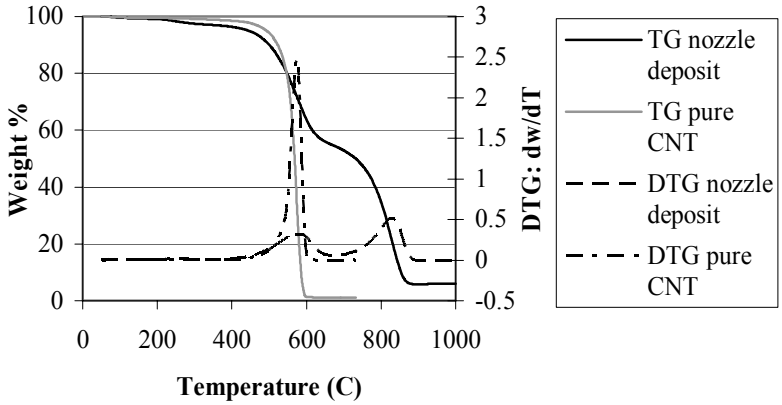

Figure 4: Typical TG and DTG curves of the nozzle deposit and the pure MWNT sample obtained after TGA.

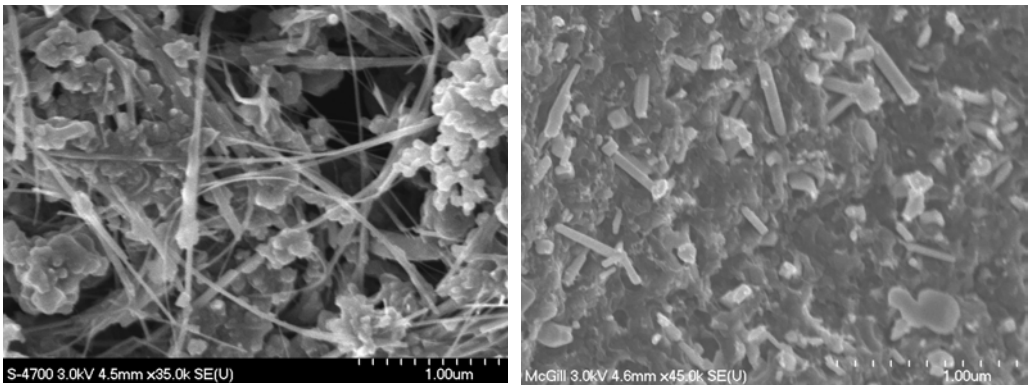

Figure 5 left: Fe-SEM micrograph of nozzle deposit prior TGA. **Right:** after TGA up to 690ºC

5. Parametric study

The influence of process parameters such as the reactor pressure, the TCE feed rate and time are evaluated using the MWNT yield from the TGA analysis. MWNT condense mainly on the internal wall of the torch nozzle. The mass of the soot collected following 5 minutes of TCE injection experiments remains relatively constant around 1 g. Table 1 summarizes the concentration of CNT obtained from TGA and the averaged I_D/I_G intensity ratio calculated from the Raman spectra for the different operating parameters investigated.

Table 1: Concentration of MWNT in the nozzle deposit and I_D/I_G as a function of the process parameters

Investigation	TCE feed rate (mol/min)	Pressure (Torr)	Time (min)	MWNT conc. from TGA (wt.%)	I_D/I_G from Raman spectra
Effect of pressure and TCE feed rate	0.15	200	5	49.8%	1.00
	0.15	500	5	43.9%	0.94
	0.05	200	5	38.6%	0.64
	0.29	200	5	51.3%	1.07
Effect of time of operation	0.15	200	1	1.9%	N/A
	0.15	200	2	0.1%	0.10
	0.15	200	3	0.1%	0.04
	0.15	200	4	8.16%	0.26

I_D/I_G rises as increasing the MWNT concentration. EM observations reveal that the concentration of carbon nanoparticles and onions increases with the MWNT concentration. These two by-products are synthesized in similar conditions as the CNT without the use of metal catalyst [14-15]. Their synthesis occurs due to the lack of metal catalyst in the plasma jet and the I_D/I_G becomes a tool for the appreciation of the experimental conditions for the growth of MWNT.

- *5.1 Effect of the reactor pressure*

We perform experiments using two different reactor pressures, 200 torr and 500 torr. We compare the yields of CNT in the nozzle deposit synthesized at these two pressure levels and at a constant TCE feed rate of 0.15 mol/min. Calculations of the area under the weight-loss peak at 575°C indicate that the reduction of the reactor pressure tends to increase the yield of MWNT. For the experiment performed at 500 torr, we evaluate the yield at 43.9% and for the experiment performed at 200 torr, 49.8%. The I_D/I_G for both experiments are respectively 0.94 and 1.00. From Figure 3, the quench produced by the supersonic expansion at the nozzle entrance cools the plasma jet to a lower temperature at 200 torr. This quench reduces the temperature of the plasma jet from ≈7000K to ≈3350K at 200 torr, respectively from ≈8000K to ≈4890K for 500 torr. The stronger quenching effect at 200 torr enables a more efficient nucleation of tungsten particles from the tungsten vapours provided by the arc erosion. A larger amount of metal catalyst nanoparticles is expected to be available at this pressure for the growth of CNT [13].

- *5.2 Effect of the TCE feed rate*

In order to investigate the TCE feed rate on the MWNT concentration in the nozzle deposit, we conducted three experiments at three different levels of TCE feed rate: 0.05, 0.15 and 0.29 mol/min. We performed these at constant pressure (200 torr), flow of plasma-forming argon (100 slpm) and torch power (30 kW). The concentration of MWNT in the nozzle deposit increases with the increase of the TCE feed rate. On table 1, the TGA of the nozzle deposits synthesized at TCE feed rate of 0.05, 0.15 and 0.29 mol/min respectively indicate a concentration of 38.6%, 49.5% and 51.3%. The Raman spectra respectively indicate an I_D/I_G of 0.64, 1.00 and 1.07. The increase of the yield of MWNT with the increase of the TCE feed rate means that the vapour pressure of carbon is a parameter to consider in the growth of MWNT here. At a high TCE feed rate, a high vapour pressure of carbon presumably favours higher carbon concentration in the tungsten nanoparticles for the initial nucleation stage, and a better supply of carbon to feed the growing tube. The present method of production of CNT uses a relatively small amount of metal catalyst compared to the carbon feed. According to the erosion rates outlined previously [11], the quantity of tungsten vapour in the system varies from 0.01% to 0.2% of the carbon fed. This is much smaller than the range suggested by Pacheco [16] for the graphite arc process giving percentages of metal catalyst over the carbon fed between 0.4% and 13% for an efficient CNT synthesis. The lack of available metal catalyst particles is most probably the reason behind what seems to be a levelling of the curve of CNT production when moving to the highest carbon feed at 0.29 mol TCE/min.

5.3 Effect of time of operation

We investigated the effect of time on the concentration of MWNT grown in the nozzle deposit in performing experiments at constant flow rate of plasma-forming argon (100 slpm), torch power (30 kW), TCE feed rate (0.15 mol/min) and pressure (200 Torr). We stopped the experiments at interval of 1 minute after TCE injection and perform these tests up to 5 minutes. Table 1 shows the evolution of the concentration of MWNT and of the I_D/I_G as a function of time of operation. Small concentrations of MWNT are observed during the first 3 minutes of TCE injection, and then an increase is observed during the 4^{th} minute of operation followed by a drastic increase in the 5^{th} minute of operation. The thickness of the nozzle deposit also gradually increases with the time of operation. We collected 0.02g of soot after the 1^{st} minute of operation and 1g after the 5^{th} minute. The small quantity of soot produced after only 1 minute of operation does not allow the measurement of a Raman spectrum. One may thus estimate that the quantity of CNT reported in Table 1 for experiments lasting 5 minutes are in fact produced over a 1-2 minutes timescale achieved after a temperature ramp up period. Although the present operating conditions and metal/carbon precursors are exploratory and not optimized particularly with

respect to the availability of metal catalyst, this corresponds roughly to a generation rate between 24-30 g/h of CNT in continuous operation.

CFD modeling as shown on Figure 3 indicates that the temperature of the plasma jet is in the order of 2400K near the internal wall of the torch nozzle. This temperature is actually colder than the eutectic temperature of the tungsten-carbon alloy (C-W) varying around 2700K. During the first minutes of operation, thin layers of graphitized carbon condense in the nozzle due to the relatively cold temperature near the internal wall of the nozzle. The nozzle deposit thickens during operation and accumulates condensed nanoparticles of tungsten carbide. This wall deposit acts as an additional thermal resistance between the water-cooled nozzle wall and the hot plasma, and will tend to increase in temperature as the layer grows in thickness. The temperature of the nozzle deposit eventually reaches the eutectic temperature of the C-W mixture and enables the growth of MWNT at the surface of the nanoparticles of tungsten carbide. According to the TGA, this moment occurs during the 4^{th} and the 5^{th} minute of operation due to the drastic increase of the MWNT concentration in the nozzle deposit. The long MWNT synthesized showing lengths in the 50μm scale [11] indicates that the catalyst nanoparticles of tungsten carbide are available for growth over a long period within their eutectic temperature window.

6. Conclusion

In summary, our process based on the thermal plasma torch technology uses the supersonic expansion of the plasma to generate *in situ* the metal catalyst particles and simultaneously treat large amounts of carbon containing gas for conversion into CNT. This process can operate under a continuous operation regime and has the potential for scale increase, thermal plasma torch technologies currently operating at the megawatt level. The supersonic expansion of the plasma realizes quenching rates up to $50x10^6$ K/s that lead to the nucleation of the metal catalyst nanoparticles. We implemented a quantification method for the CNT mass based on TGA calibration with purifies samples, electron microscopy and Raman spectroscopy. This method enabled a parametric study to determine the effect of some operating parameters on the yields of CNT. Optimal conditions in argon are achieved at 200 torr pressure and TCE feed rate of 0.29 mol/min. An important time evolution in the 5 minute experiments is observed on the yield of CNT. In the present conditions, we believe that this time evolution results from a temperature increase of the carbon deposit reaching the eutectic temperature of the tungsten catalyst.

References

1. N.-H. Tai, M.-K. Yeh, J.-H. Liu, Carbon, **42**, 2735 (2004).
2. X. Xu, M.M. Thwe, C. Shearwood, K. Liao, Appl. Phys. Lett., **81**, 2833 (2002).
3. M.J. Biercuk, M.C. Llaguno, M. Radosavljevic, J.K. Hyun, A.T. Johnson, Appl. Phys. Lett., **80**, 2767 (2002).
4. T. Matsumoto, T. Komatsu, K., Arai, T. Yamazaki, M. Kijima, H. Shimizu, Y. Takasawa, J. Nakamura, Chem. Commun., **840** (2004).
5. M. Freitag, Y. Martin, J.A. Misewich, R. Martel, Ph. Avouris, Nano lett., **3**, 1067 (2003).
6. H. Zhang, Y. Chen, S. Li, X. Fu, Y. Zhu, S. Yi, X. Xue, Y. He, Y. Chen, J. Appl. Phys, **94**, 10, 6417 (2003).
7. D. Pantarotto, C.D. Partidos, J. Hoebeke, F. Brown, E. Kramer, J.-P. Briand, S. Muller, M. Prato, A. Bianco, Chem. Biol., 10, **961** (2003).
8. H. Kataura, Y. Kumazawa, Y. Maniwa, Y. Ohtsuka, R. Sen, S. Suzuki, Y. Achiba, Carbon, **38**, 1691 (2000)
9. J. Gavillet, A. Loiseau, C. Journet, F. Willaime, F. Ducastelle, J.-C. Charlier, Phys. Rev. Lett., **87**, 275504-1 (2001).
10. F. Larouche, O. Smiljanic, X. Sun, B.L. Stansfield, Carbon, **43**, 986 (2005)
11. D. Harbec, J.-L. Meunier, L. Guo, R. Gauvin, N. El Mallah, J. Phys. D: Appl. Phys. **37**, 2121 (2004).
12. D. Harbec, J.-L. Meunier, PCT Int. Appl., WO 2004046030. 32 pp (2004).
13. L. Guo, D. Harbec, J.-L. Meunier, Proc. ISPC-17, Paper FileCode **155**, Toronto, 2005.
14. D. Ugarte, Carbon, **33**, 7, 989 (1995).
15. N. Hatta, K. Murata, Chem. Phys. Lett., **217**, 4, 398 (1994).
16. M. Pacheco, PhD Thesis, Université Paul-Sabatier, Toulouse, France (2003).

Improvement of Gas Barrier Properties of Polymers by Microwave Plasma CVD

A. Ogino, T. Tanaka, T. Matsuda, M. Nagatsu

Department of Electrical and Electronics Engineering, Shizuoka University, 3-5-1 Hamamatsu, 432-8561 Japan

Abstract

We have carried out the experiments of the gas barrier coating by hydrogenated amorphous carbon (a-C:H) thin films prepared with surface-wave plasma (SWP). The SWP allows to perform the large-area film deposition at low temperature. According to the gas permeation experiments, it was found that the gas barrier properties of polyethylene terephthalate (PET) sheets were improved by a-C:H thin film coating by a factor of 150~200 compared with one of uncoated PET sheets.

Keywords: Microwave plasma chemical vapor deposition; Amorphous carbon; Gas barrier film; Polymer

1. Introduction

Recently, the replacement of glass to transparent plastics, e.g. polymetylmethacrylate (PMMA), polycarbonate (PC) and polyethylene terephthalate (PET), are demanded due to their properties, such as low weight, good impact resistance and forming with ease in medical or industrial fields. However, these polymer materials have a weakness for the impermeability of oxygen or carbon dioxide gases. Polymers with high gas barrier properties are required for packaging of foods or drinks, protecting the environmental pollution of cars, organic light emitting display (OLED) and so on. For example, a water vapor transmission rate (WVRT) of 10-50 g/m^2·day is enough for the dampproof packaging sheet for the products to contain fats and oil [1], on the other hand, in order for the transparent panels of OLED to have reliable performance and practical lifetime, an oxygen transmission rate (OTR) of below 10^{-5} cm^3/m^2·day and WVTR of approximately 10^{-6} g/m^2·day at 39 ºC and 95% RH are required [2]. It is well known that organic light emitting device structures and other active display materials degrade in the presence of oxygen and moisture.

In order to improve the gas barrier properties, various coating techniques, such as plasma-enhanced chemical vapor deposition (PECVD) [3-6], ion implantation or ion-assisted deposition [7-9], DC or RF magnetron sputtering [10, 11], and so on, have been studied. And also, various type of thin films grown on polymer substrates, such as diamond like carbon (DLC) or tetrahedral amorphous carbon (ta-C) [12,13], hydrogenated amorphous carbon (a-C:H) [3-5,14,15], and aluminum or silicon oxide (AlO_x or SiO_x) films [16-19], and so on, have been investigated. Among these techniques, surface wave plasma chemical vapor deposition (SWP-CVD) is one of the most suitable techniques for low temperature not to deform polymer substrate with low heat resistance, and allows large area thin film deposition. Therefore, we have carried out making the gas barrier coating by a-C:H films which can be prepared by SWP-CVD of helium and methane mixture gas at low pressure. In this paper, we have reported on the deposition and the gas barrier properties of a-C:H film coated on high density polyethylene (HDPE) and PET sheets.

2. Experimental set up

In this study, we have employed the SWP-CVD system for the deposition of a-C:H films at low temperature. A schematic drawing of the experimental setup is shown in Fig. 1. The SWP was produced in a 400 mm diameter, cylindrical vacuum chamber by introducing a 2.45 GHz microwave through a quartz window via slot antennae [20]. A rectangular quartz window with inner dimension of 109 mm x 380 mm is used as vacuum sealing on the top metal plate. Five transverse slots are cut vertically to the waveguide axis with a spacing of one-half of the waveguide wavelength, and four pair of longitudinal slots are also cut

between the transverse slots. The length and width of each slot are 61 mm and 10 mm, respectively. The vacuum chamber was evacuated to ~10^{-6} Torr using a turbo molecular pump.

In the SWP, the microwave introduced through the slot antennae damps exponentially below the quartz window where the electron density exceeds the cutoff density [21]. The high density plasma with uniform electron density more than 10^{11} cm^{-3} was formed in the vacuum chamber and broadened in the downstream region due to the particle diffusion.

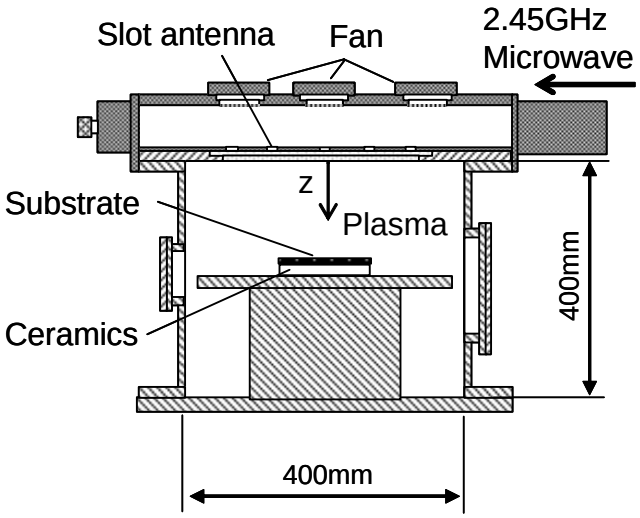

Fig.1. Schematic drawing of the experimental setup.

Film deposition was carried out on HDPE and PET substrates with a thickness of 1.0 mm placed on the substrate stage at 185 mm below the quartz window. The launched microwave power was typically 650 W and the total gas pressure was 2.0 Torr, where the gas flow rates were 280 sccm for helium and 6 sccm for methane.

To investigate the characteristics of the deposited films, we carried out the measurements of Fourier-transform infrared spectroscopy (FT-IR), the atomic force microscope (AFM) and gas permeation. FT-IR spectra of the deposited films were obtained with a JASCO FT/IR-550 spectrometer used in transmission mode in the spectral wave number form 1000 to 4000 cm^{-1}. In the FT-IR measurements, samples deposited on silicon substrate were used. The absorbency of the silicon substrate was subtracted from the measured spectral absorption curves. The morphologies of deposited films were characterized by AFM (SEIKO SPI3700). The gas transmission rate (GTR) was measured as an index of the gas barrier effectiveness of polymer sheet by manometer method. The measured polymer sheet was installed to vacuum chamber for the measurement of GTR and sealed using a vacuum rubber ring. The vacuum chamber sealed with the polymer sheet was pumped to 1×10^{-6} Torr, and it was closed by a valve. After then, the increase in pressure of the vacuum chamber was monitored with a pressure gauge. The measurements were curried out for polymer sheets and SUS plate without gas permeation. The increase in pressure in the case of SUS plate is considered that the effect of gas release from the plate surface and the inner wall surface of the chamber appeared significantly. The GTR of polymer sheets can be estimated by subtracting the outgas effect of chamber wall from the results of polymers.

3. Results and discussion

In the CVD experiments, a small amount of methane gas was added into helium gas at a pressure of approximately 2.0 Torr. Polymer sheets used in the coating were cut in a size of 70 mm x 70 mm. The special uniformity of amorphous carbon film thickness is less than ±5% over a diameter of 100 mm. The deposition rate is approximately 11~13 nm/min.

The polymer sheet is easily influence by heating, and the glass transition temperature and softening temperature of polymers are considerably lower than the melting of them. The glass transition temperature of PET and the softening temperature of PE are around 77 ºC and 130 ºC, respectively. Therefore, it is necessary to make a coating of polymer sheets at the low temperature of 75 ºC or less to avoid the change of physical properties and the transformation of shape by heat. Figure 2 shows the temperature measured by thermal labels attached to a glass plate on substrate stage. The temperature of substrate and the deposition rate depend on the position of substrate and the microwave power. In the condition of z=185 mm and the microwave of 650 W, the temperature changed from 20 ºC at room temperature to 75 ºC with the 15 minutes

of plasma irradiation as shown in Fig. 2. In addition, polymer sheet was warped at higher than 75 ºC, the height of swelled rule in PET sheet was from 2.0 mm to 2.7 mm after the deposition of 20 minutes. The measured maximum temperature in the deposition of 20 minutes was 80 ºC. On the other hand, the change of swelled rule in PE sheets was not so large after CVD, i.e. less than 0.1 mm.

In order to investigate the bonding structures of the carbon film, FT-IR measurement was carried out. Figure 3 shows the FT-IR transmittance spectrum of the deposited films. The prominent absorption bands are observed between 2800 and 3000 cm^{-1} corresponding to sp^3 C-H bond, which indicate a bond in diamond with tetrahedral geometry. The absorptions at 2870, 2930 and 2960 cm^{-1} are corresponding to sp^3-CH_3 symmetric, sp^3-CH_2 asymmetric and sp^3-CH_3 asymmetric C-H stretching [5,14], respectively. Also, the absorption band ranged from 3000 to 3100 cm^{-1} is typical for sp^2-bonded carbon [22]. A weak absorption corresponding to sp^2 C-H asymmetric C-H stretching appears in the 3050 cm^{-1} region [23]. In the region between 1000 and 1800 cm^{-1}, broad asymmetric peaks are observed, which are typical characteristics of amorphous carbon films [24]. The absorption at 1580 cm^{-1} is assigned to C=C double-bond stretching vibration [25], which indicates non-graphite bonding of carbon [26]. The distinct absorption bands ranged from 1640 to 1900 cm^{-1} are assigned to be due to C=O. [27] The absorption centered around 2357 and 2140 cm^{-1} can be ignored because they result from background noise, corresponding to the CO stretching vibration. The result of FT-IR spectrum shows that the film structure is composed of hydrogen linked to carbon mainly in sp^3-CH_x bonding, which is consistent with the polymer like amorphous carbon [25]. According to NMR analysis of a-C:H films under a gas flow rate of 280 sccm in helium and 6 sccm in methane, a fraction of sp^2-carbon bonding was approximately 25% and that of sp^3-carbon bonding was approximately 75%, respectively [28].

Figure 4 shows AFM image of the surface morphology of a-C:H film deposited on silicon substrate with film thickness of 0.43 μm when the

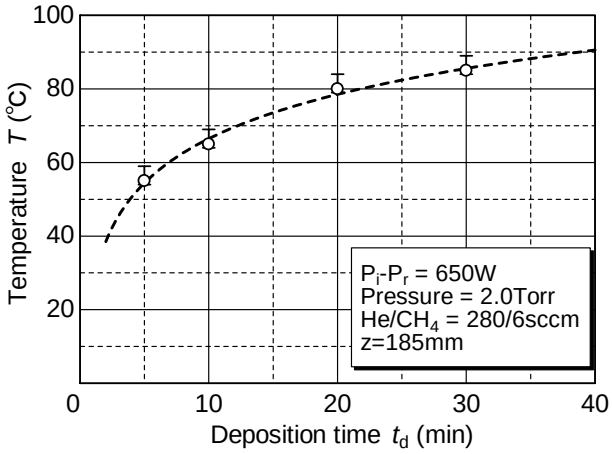

Fig.2. The relation between stage temperature and the deposition time.

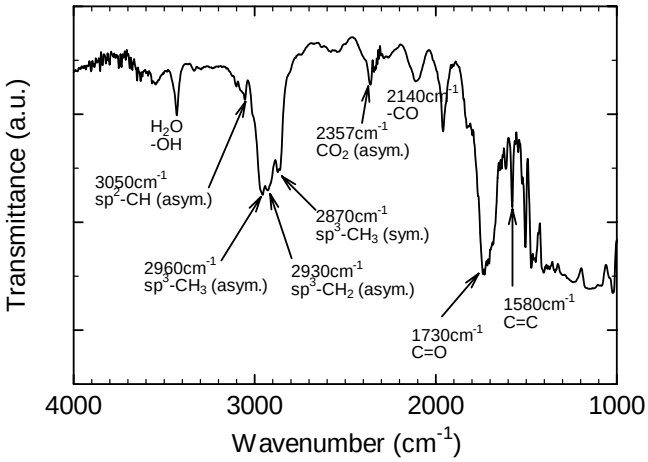

Fig.3. FT-IR transmittance spectrum of a-C:H film deposited at the microwave of 650 W, He/CH_4= 280/6 sccm, pressure of 2. 0 Torr, z=185 mm and film thickness of 620 nm.

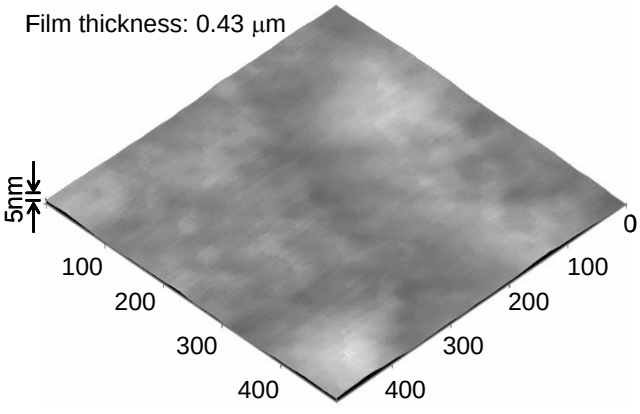

Fig.4. AFM image of a-C:H film deposited on silicon substrate with film thickness of 0.43 μm.

gas flow rates were He/CH_4 =280/6 sccm. The surface morphology of a-C film is considerably flat and smooth with the surface roughness of a few nm.

The downstream pressure p_g changes due to the permeation of air through (a) HDPE and (b) PET sheets covered with different thickness of a-C:H film are plotted as a function of time after closing the valve in Fig.5, where the increase in the extra pressure due to the outgas from chamber wall was subtracted. In the present experimental conditions, though air was used for the gas permeation measurement, the permeating gas particles could be considered to be mainly oxygen molecules considering the composition ratio of air and the gas species dependency of permeability, diffusivity and solubility [29]. The GTR is obtained from the gradient dp_g/dt of these curves which are proportional to it. In all cases the film deposition of a-C:H results in a reduction of gas permeation. It was found that the GTR had decreased from 135 to 5.8 $cm^3/m^2 \cdot day \cdot atm$ when HDPE sheet surface was covered with the a-C:H film thickness of 620 nm. From the results, it was found that the gas barrier properties of the HDPE sheet had been 2~23 times better than uncoated one depending on film thickness. Furthermore, the a-C:H coating on PET sheet shows better barrier property about 0.27 $cm^3/m^2 \cdot day \cdot atm$ at film thickness of 207 nm. The gas barrier performance of coated polymers depends on coating film thickness and substrate roughness. Rougher surfaces require thicker coating for maintained barrier properties. However, thicker coating tends to result in cracking. When the film thickness becomes 310nm and 620nm, it seems that the effect of cracking decreases in adhesion of a-C:H films or thermal stress during plasma irradiation appears sensitively.

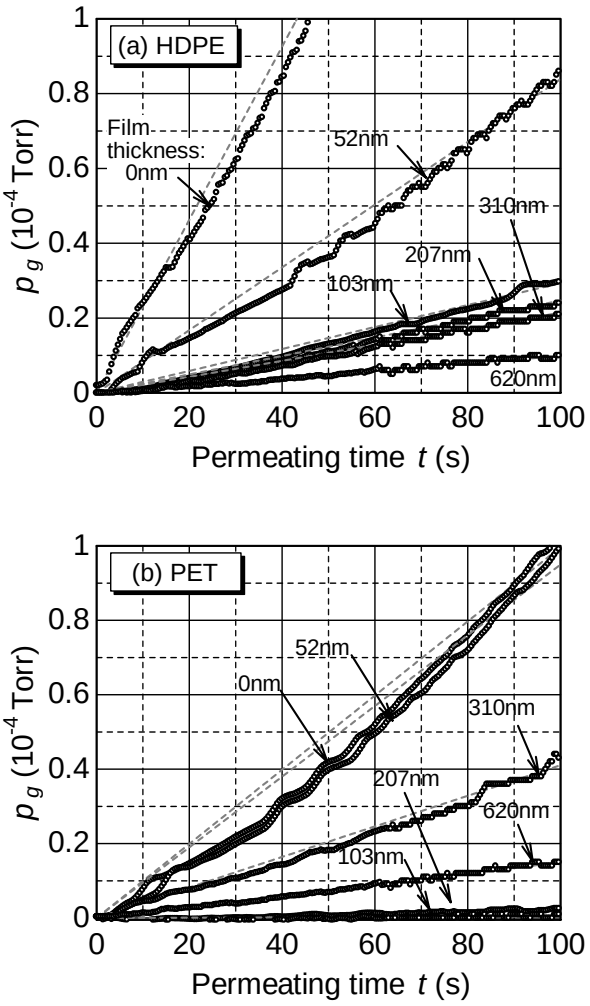

Fig.5. The downstream pressure p_g changes due to the permeation of air through (a) HDPE and (b) PET sheets covered with different thickness of a-C:H film under the conditions of 15~18 ºC and ~40%RH.

4. Conclusion

In this study, we carried out making the gas barrier coating by a-C:H thin films which can be prepared by SWP-CVD of helium and methane mixture at low temperature. The launched microwave power was typically 650 W and the total gas pressure was 2.0 Torr, where the gas flow rates were 280 sccm for helium and 6 sccm for methane. The temperature of substrate stage at 185 mm below the quartz window changed from 20 ºC at room temperature to 75 ºC with the 15 minutes of plasma irradiation. According to FT-IR measurements, the a-C:H film structure is composed of hydrogen linked to carbon mainly in sp^3-CH_x bonding. The a-C:H film possesses polymer-like structure. Gas permeation measurements show that the GTR of polymers covered with a-C:H film has been improved compared with uncoated one. It was found that the GTR of HDPE had decreased from 135 to 5.8 $cm^3/m^2 \cdot day \cdot atm$ with the a-C:H film thickness of 620 nm. The gas barrier properties of the HDPE sheet had been 23 times better than uncoated one. The GTR of PET

sheet with 207 nm a-C:H film was about 0.27 $cm^3/m^2 \cdot day \cdot atm$. However, the present GTR is far away from 10^{-5} $cm^3/m^2 \cdot day$ for the enough lifetimes of flexible and lightweight OLEDs.

Acknowledgments

The present work has been partly supported by Faculty of Engineering, Shizuoka University as one of advanced research projects. The authors would like to thank Mr. W. Tomoda of Shizuoka University for the FT-IR analysis.

References

[1] U. Moosheimer, Ch. Bichler, Surf. Coat. Technol. **116–119**, 812 (1999).
[2] R.S. Kumar, Mark Auch, Eric Ou, Guenther Ewald, Chua Soo Jin, Thin Solid Films **417,** 120 (2000).
[3] E. Tomaslla, C. Meunier, S. Mikhailov, Surf. Coat. Technol. **141**, 286 (2001).
[4] N.K. Cuong, M. Tahara, N. Yamauchi, T. Sone, Surf. Coat. Technol. **174-175**, 1024 (2003).
[5] E. Tomaslla, C. Meunier, S. Mikhailov, Surf. Coat. Technol. **141**, 286 (2001).
[6] M. Creatore, F. Palumbo, R. d'Agostino, P. Fayet, Surf. Coat. Technol. **142-144**, 168 (2001).
[7] M. Yoshida , T. Tanaka, S. Watanabe, M. Shinohara, J. W. Lee, T. Takagi, Surf. Coat. Technol. **174-175**, 1033 (2003).
[8] J.R. Conrad, J.L. Radtke, R.A. Dodd, F.J. Worzala, N.C. Tran, J. Appl. Phys. **62**, 4591 (1987).
[9] R. Hatada, K. Baba, Nucl. Instr. Methods Phys. Res. B **148**, 655 (1999).
[10] E.M. Moser, R. Urech, E. Hack, H. Kunzli, E. Mullerq, Thin Solid Films **317**, 388 (1998).
[11] E. Fortunato, A. Goncalves, A. Marques, A. Viana, H. Aguas, L. Pereira, I. Ferreira, P. Vilarinho, R. Martins, Surf. Coat. Technol. **180-181**, 20 (2004).
[12] A. Kimura, H. Kodama, T. Suzuki, J. Vac. Sci. Technol. A **21**, 515 (2003).
[13] G.A. Abbas, J.A. McLaughlin, E. Harkin-Jones, Diamond Relat. Mater. **13**, 1342 (2004).
[14] K. M. Krishna, H. Ebisu, K. Hagimoto, Y. Hayashi, T. Soga, T. Jimbo, M. Umeno, Appl. Phys. Lett. 78, 294 (2001).
[15] S.V. Borucki, W. Jacob, C. A. Achete, Diamond Relat. Mater. **9** 1971 (2000).
[16] A.G. Erlat, B.M. Henry, J.J. Ingram, D.B. Mountain, A. McGuigan, R.P. Howson, C.R.M. Grovenor, G.A.D. Briggs, Y. Tsukahara, Thin Solid Films **388**, 78 (2001).
[17] M. Benmalek, H.M. Dunlop, Surf. Coat. Technol. **76-77**, 821 (1995).
[18] P. Zhu, M. Teranishi, J. Xiang, Y. Masuda, W.S. Seo, K. Koumoto, Thin Solid Films **473**, 351 (2005).
[19] A.P. Roberts, B.M. Haenry, A.P. Sutton, C.R.M. Grovenor, G.A.D. Briggs, T. Miyamoto, M. Kano, Y. Tsukahara, M. Yanaka, J. Memb. Sci. **208**, 75 (2002).
[20] M. Nagatsu, T. Sano, N, Takada, W. X. Gunang, T. Hirao, H. Sugai, Jpn. J. Appl. Phys. **39** L929 (2000).
[21] M. Nagatsu, G. Xu, I. Ghanashev, M. Kanoh, H. Sugai, Plasma Source Sci. Technol. **6** 427 (1997).
[22] B. Dichler, E. Bayer, J. Appl. Phys. **68** (3), 1237 (1990).
[23] Y Hayashi, K. Hagimoto, H. Ebisu, M. K. Kalaga, T. Soga, M. Umeno, T. Jimbo, Jpn. J. Appl. Phys. **39**, 4088 (2000).
[24] W. J. Yang, Y. H. Choa, T. Sekino, K. B. Shim, K. Niihara, K. H. Auh, Material Letters **57**, 3305 (2003).
[25] Y. Bounouh, M.L. Theye, A. Dehbi-Alaoui, A. Matthews, J.P.Stoquert, Phys. Rev. B **51**, 9597 (1995).
[26] M. P. Nadler, T. M. Donovan, A. K. Green, Thin Solid Films **116**, 241 (1984).
[27] Y. Wu, Y. Inoue, H. Sugimura, O. Takai, H. Kato, S. Murai, H. Oda, Thin Solid Films **407**, 45 (2002).
[28] M. Nagatsu, T. Sano, N, Takada, Wang, N. Toyoda, M. Tanga, H. Sugai, Diamond Relat. Mater. **11**, 976 (2002).
[29] X.-G. Li, M.-R. Huang, I. Kresse, J. Springer, Polymer **42**, 8113 (2001).

Preparation of solution containing luminescent nanocrystalline silicon particles for medical application

K.Shinoda, S.Yanagisawa, K.Sato, and K.Hirakuri

Department of Electronic & Computer Engineering, Tokyo Denki University
Ishizaka, Hatoyama, Saitama 350-0394, Japan

Introduction

Semiconductor nanoparticles have attractive characteristics for a luminescent phenomenon, i.e., size-depended luminescence. Especially, nanocrystalline silicon (nc-Si) particles are useful candidate materials for medical applications such as cancer cells observation and drag delivery system because they have good biocompatibility. The nc-Si particles, however, are inexpedient for medical applications to exist in the thin film under the general synthesis methods. Therefore, the condition of nc-Si should be changed from thin film form to particle structure owing to supply in the medical fields.

In this study, we report a synthesis technique for the particle shape of nc-Si using plasma processing and wet process. Moreover, the shape and photoluminescence (PL) property of the nc-Si particles will be discussed.

Experiments

The solution containing the nc-Si particles was fabricated by manufacturing process as shown in Fig. 1. Samples were deposited on a p-type Si (100) substrate using a radio frequency (RF) sputtering method which is one of dry process [1]. A sputtering target used 36 pieces of p-type Si (100) chips with 5 mm × 5 mm placed on a SiO_2 with purity of 99.99 % and 100 mm diameter. The Si chips/SiO_2 target was sputtered in argon (Ar) atmosphere at a gas pressure of 1.33 Pa and a RF power of 200 W for 240 min. To form the nc-Si particles the sample, subsequently, was annealed at 970 ℃ in Ar atmosphere for 60 min. The nc-Si particles were prepared in a SiO_2 layer with thickness of 3 μm (Fig. 1(a)). The thick SiO_2 layer, then, was etched by hydrofluoric (HF) acid steam (wet process) for 5 min to uniformly extract the nc-Si particles on substrate surface (Fig. 1(b)) [2]. After the HF treatment, the nc-Si particles were shaken off from the substrate into the solution by supersonic wave treatment and thereby they were dispersed in the solution (Fig. 1 (c)).

The size and shape of nc-Si particles was confirmed by using high-resolution transmission electron microscopy (HRTEM). The PL spectra of nc-Si particles in the solution were detected by using a photonic multichannel analyzer. The light source was utilized a Xenon lamp with an optical band-pass filter of 313 nm.

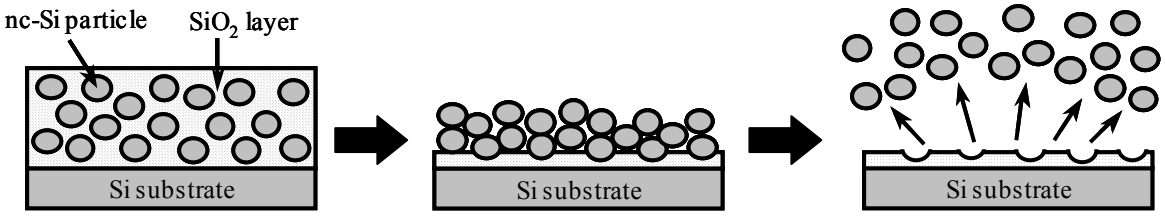

Fig. 1 Schematic illustrations of manufacturing process for the solution with nc-Si particles form: (a) annealing at 970 ℃ ; (b) HF treatment; (c) supersonic wave treatment.

Results and discussion

The existence of the nc-Si particles was confirmed by the presence of regular lattice fringes by the HRTEM observation. The lattice fringes were corresponded to (111) plane of cubic Si (diamond structure) with correct atomic spacing of 0.314 nm. The nc-Si was uniformly dispersed with a spherical form. Moreover, the average size of nc-Si particles was approximately 2.5 nm.

Figure 2 shows the PL spectra for the solution containing the nc-Si particles. The solution exhibited the strong and stable red PL with a peak of 670 nm. The PL peak wavelength of the solution was as same as that of the thin film form with the nc-Si. This result indicates that the PL spectra of both particle form and thin film form is originated from same radiative recombination process between electron and hole.

From the above results, the condition of nc-Si could freely change from the thin film form to the particle form by using the processes of dry and wet. And the nc-Si particle was stably existed without the transform of shape in the solution. This leads to stable and strong red luminescence. Consequently, the nc-Si particles fabricated in this study would be sufficiently adapted to apply for medical fields.

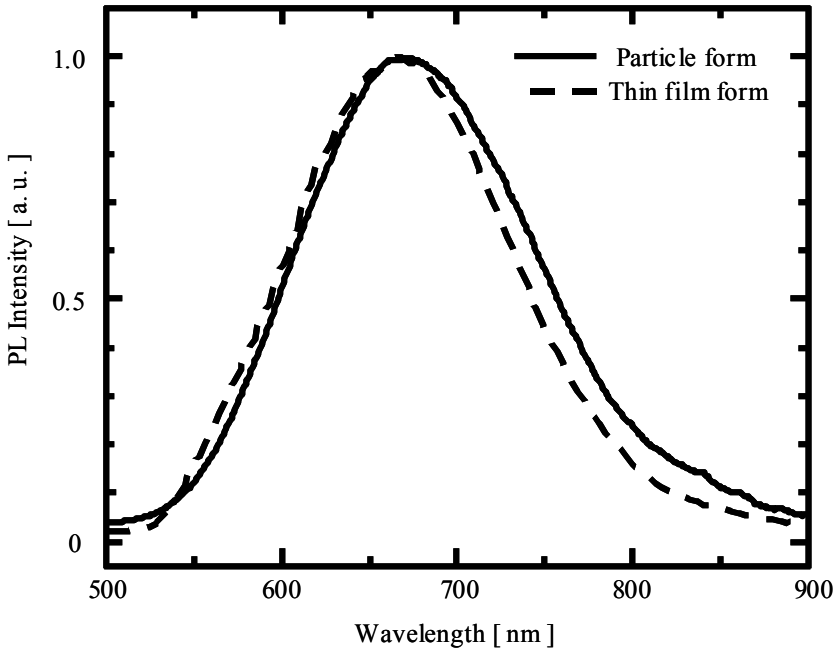

Fig. 2 PL spectra of the thin film form and the particle form.

Conclusions

We have investigated the formation condition and PL property of the solution containing the luminescent nc-Si. The nc-Si particles with size of 2.5 nm were uniformly formed with the spherical form. The solution with the nc-Si particles strongly and stably emitted the red light.

Acknowledgment

We would like to thank Mr. Tsuneo TOYA and Mr. Shinya KOBAYASHI of Tokyo Denki University for the technical assistance on the FT-IR measurement and cytotoxicity test, respectively. This work was partially supported by a grant from the Tokyo Denki University Frontier Research and Development Center.

Reference

1. K.Sato, Appl. Sur. Sci. 216, p376-381 (2003)
2. K.Sato, Mat. Res. Soc. Proc. Vol.789, p221-226 (2004)
3. W.Theiβ ,Surf.Sci.Rep. 29, 91 (1997)

Keywords: *nanocrystalline silicon particles, RF sputtering method, wet process, visible luminescence, medical application*

Identification number of the session topic: ***10 (Clusters, particles and powders)***

Investigations into the vibrational populations of the N_2 A-state ($^3\Sigma_u^+$) and the N_2^+ ground state ($^2\Sigma_g^+$)

L. Thornton[1], G. Hancock[1], R. Peverall[1] and G.A.D. Ritchie[1]

[1]*Physical and Theoretical Chemistry Laboratory, Oxford University, Oxford, United Kingdom*

Session Topic 2: Gas Phase Plasma Diagnostics

The populations of the $v = 0$, 1, 3 and 6 levels of the $^3\Sigma_u^+$ state (the A-state) of N_2 have been studied as a function of plasma power and pressure in an inductively coupled plasma (ICP) chamber. This was achieved using tunable diode lasers to probe the $^3\Pi_g \leftarrow {}^3\Sigma_u^+$ (B ← A) transition at the wavenumbers listed in table 1. The low concentrations of these species required the use of cavity enhanced absorption techniques to enhance the effective pathlength through the plasma chamber.

In Cavity Enhanced Absorption Spectroscopy (CEAS), laser radiation is injected into the back of one of a pair of AR-coated high reflectivity mirrors (typically R = 99.94) and the cavity is then intentionally mis-aligned to produce a highly congested mode structure. Leakage of the light out of the second mirror is incident upon a PMT. Rapid scanning of the laser radiation across the transition and subsequent averaging produces the absorption feature. The laser radiation background, I_0, and the optical emission from the plasma, γ, must both be removed from the raw data to enable analysis to be undertaken using equation 1.

Table 1: Transitions frequencies of the vibrational bands

Line	Band Centre (cm^{-1})
$v = 3 \leftarrow 0$	14580.7
$v = 3 \leftarrow 1$	13147.9
$v = 6 \leftarrow 3$	15133.0
$v = 7 \leftarrow 6$	12699.1

$$\text{CEAS Signal} = \frac{I_0 - I(v)}{I(v) - \gamma} = \frac{\alpha L}{1 - R} \qquad (1)$$

Conversion of the resultant signal into an absorption coefficient α is achieved with a knowledge of the physical length of the cavity (L) and the reflectivity of the mirrors (R). The latter is obtained using Cavity Ring-Down Spectroscopy (CRDS) where, upon mode excitation, an Acousto Optic Modulator (AOM) is used as a fast switch to cut-off the laser radiation being fed into the cavity. This allows the decay of the light intensity from the cavity to be recorded as a function of time using a PMT, an example trace of which is shown in figure 1. The spectra of the bands are assigned using a simulation program [1] and spectroscopic constants [2], [3] taken from the literature. Figure 2 shows a section of the (3, 1) band.

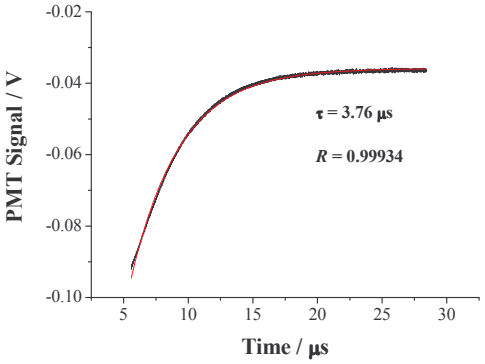

Figure 1: CRDS trace taken at 13149 cm^{-1} to obtain the mirror reflectivity (R).

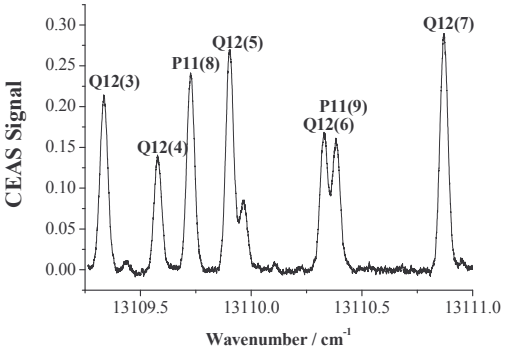

Figure 2: A section of the (3, 1) band taken at 300 W and 10 mTorr plasma power and pressure.

The absorption coefficients are converted into absolute concentrations of the ro-vibrational levels using cross-sections taken from the literature [4], [5], [6]. Conversion of these into the total concentrations of the various vibrational levels was achieved assuming a Boltmann distribution over rotational levels, weighting for the nuclear spin and inputing the rotational temperature which is obtained from comparing the intensities of two different rotational lines. This temperature was found to be independent of plasma pressure (~ 350 K for 100 W) but increased with plasma power (from ~300 K at 50 W to ~ 500 K at 500 W). The translational temperature is calculated from analysing the Doppler Widths of the absorption profiles and is found to be in agreement with the rotational temperature. Figures 3 and 4 show how the concentrations of these vibrational levels vary with plasma parameters.

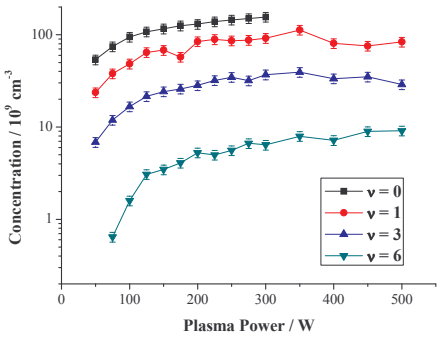

Figure 3: Vibrational populations measured at 25 mTorr plasma pressure.

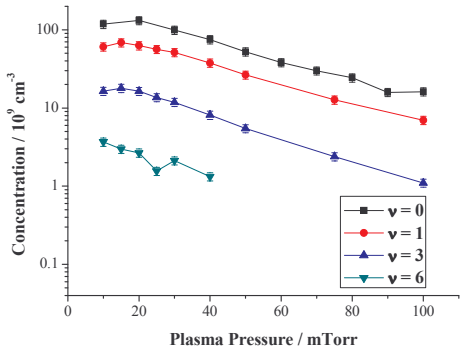

Figure 4: Vibrational populations measured at 100 W plasma power.

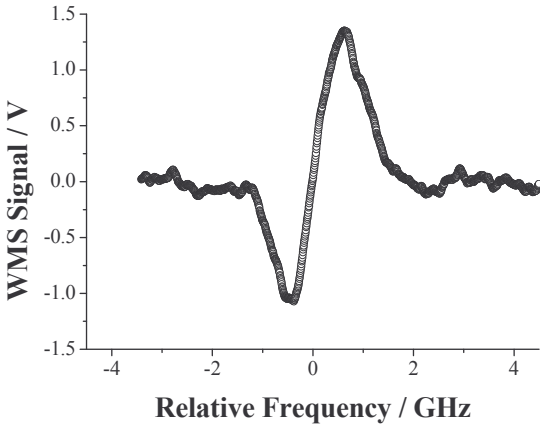

Figure 5: CEAS/WMS 1st harmonic trace taken at 10 mTorr and 400 W plasma pressure and power.

The technique of CEAS is combined with wavelength modulation spectroscopy (WMS) in an observation of the $v = 0$ level of the ground state ($^2\Sigma_g^+$) of N_2^+, utilising a diode laser at 12677 cm^{-1} corresponding to the (2, 0) band of the $^2\Pi_u \leftarrow {}^2\Sigma_g^+$ (A ← X) transition. The use of WMS is expected to improve the sensitivity as the noise in the system is dominated by plasma emission, and the detectivity increased from $\alpha_{min} = 3.49 \times 10^{-8}$ cm^{-1} $Hz^{-1/2}$ for homodyne CEAS to $\alpha_{min} = 3.91 \times 10^{-9}$ cm^{-1} $Hz^{-1/2}$ for CEAS combined with WMS. A typical trace is shown in figure 5. The spectra can be assigned to N_2^+ using [7] and a cross-section calculated using constants found in the literature [5], [6] to extract a total N_2^+ concentration of $(2.68 \pm 0.32) \times 10^9$, which shows a weak increase with plasma power and a weak decrease with plasma pressure. Electron density measurements taken previously with a Langmuir probe suggest a value for $[e^-]$ of $\sim 5 \times 10^9$ cm^{-3}, which may present evidence for the existence of other charged species inside the plasma.

References

[1] Roux et al, J. Mol. Spec., **97**, 253, (1983).
[2] http://spider.ipac.caltech.edu/staff/laher/fluordir/fluorindex.html
[3] Diatomic version 1.02, Xiaofeng Tan, (2001).
[4] Foissac et al, J. Phys. D: Appl. Phys., **33**, 2434 (2000).
[5] Laux et al, J. Quant. Spectrosc. Radiat. Transfer, **48** (1), 9, (1992).
[6] I Kovacs, Rotational Structure in the Spectra of Diatomic Molecules, Adam Hilger Ltd., (1969).
[7] Bachir et al, J. Mol. Spec., **166**, 88, (1994).

Microarc plasma treatment of magnesium and aluminum surfaces in electrolytes

V.Anita[1,2], N.Saito[3] and O.Takai[2]

1 - Department of Plasma Physics ,Optics and Material Science, "Al.I.Cuza"University, Iasi, 700 506, Romania
2 - EcoTopia Science Institute, Nagoya University, Furo-cho, Chikusa, Nagoya 464-8603, Japan
3 - Department of Molecular Design and Engineering, Graduate School of Engineering, Nagoya University, Furo-cho, Chikusa, Nagoya 464-8603, Japan

Abstract

Magnesium and aluminum are very important in technology but are characterized by very low hardness and wear resistance. By using microarc discharges in different ecologically safe electrolytes the properties of magnesium and aluminum surfaces were improved by growing thick oxides films. Results about the properties of microarc discharges and on the properties of treated surfaces obtained under different experimental conditions are reported.

Keywords: Magnesium; Aluminum; Microarc discharge; Electrolyte

1. Introduction

The micro arc discharge oxidation of materials is gaining increased attention as a new and innovative technique for depositing thick, dense and hard ceramics on metals from valve family (Al, Mg, Ti, V) and a wide range of their alloys. This process combines an electrochemical process (anodic oxidation) with a plasma process (micro arc discharge) and the resulted coating exhibit superior mechanical properties and superior adhesion on the substrate as compared with the classic anodic oxide coating. The ceramic coatings obtained by using the above technique are characterized by many useful properties as controllable thickness, high hardness and wear resistance, low friction coefficient, improved corrosion resistance and high resistivity at high temperature [1]. All these properties recommend this process as being of real interest to different industries and many applications can be developed for chemical, mechanical, thermal, electrical, food processing, aerospace, environment protection and electronics industries.

By applying a positive voltage to a sample made from metal of the valve family, immersed in a low concentration alkaline electrolyte, the oxidation of surface occurs and forms an oxide layer at the anode-electrolyte interface. When the applied voltage exceeds a threshold value and, on a local area of the anode, the electric field is greater than the dielectric breakdown field for the oxide, micro arcs develop as a result of dielectric breakdown of the growth oxide film. This process is accompanied by visible light emission and by a high frequency noise. The voltage threshold value is dependent on electrolyte concentration and on the nature of treated material. These micro arc discharges are short-lived, move randomly on the treated surface and promote plasma-chemical reactions on the surface of anode. The high locally electric field determines that OH^- anions to be drawn into discharge micro channel. Positive metal ions from the substrate and negative OH^- ions from the electrolyte react and form oxides in the places where micro arcs develop. The growth oxide film is formed mainly by conversion of the substrate material and by deposition of electrolyte components. The material in the channel is heated by locally high density plasma up to temperatures higher as 10^4 K [2]. Locally developed transient high temperatures melt the anode material, enter the micro channel and get oxidized, growing the oxide layer into the substrate and improving the adherence. The low temperature electrolyte in contact with the melted material determines a very high cooling rate and different nano crystalline phase are promoted in the growth film together with amorphous material. The reaction products are deposited onto the walls of micro channels. The location of the micro discharge moves randomly on the all anode surface and promotes the increase in the coating thickness. Oxygen and steam gases, anodically produced, determine the growth oxide layer to be porous with porosity dependent on the discharge parameters.

2. Experimental details

The treatments were performed by using an electrochemical cell (1) with treated surface as anode (3) and a stainless steel plate (4) with a much higher area as cathode (Fig.1). The temperature of electrochemical cell was kept at low temperature (approximately 10°C) by a stainless steel coil with circulating cooling fluid (6).

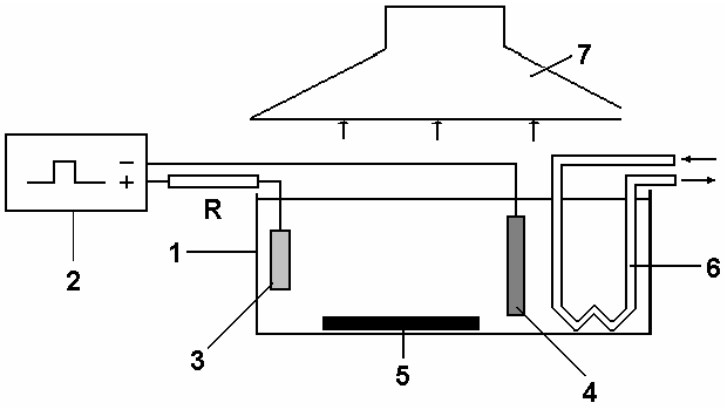

Fig.1. Experimental set-up for micro arc discharge treatment of aluminum and magnesium surfaces
1- electrolytic cell; 2 –pulsed power supply; 3 – Al or Mg treated substrate as anode; 4 - high area stainless steel cathode; 5 – magnetic stirrer, 6 – cooling coil; 7 – ventilation system

In order to homogenize the electrolyte composition and temperature, an external propelled magnetic stirrer was utilized (5). A variable frequency, pulsed power supply in constant current, voltage or constant power modes was utilized in the time of process (2). Low concentration of sodium hydroxide and tri-sodium phosphate in distilled water were utilized as electrolytes. The pH of solutions was controlled in the time of process and kept at high values between 8 and 12. The properties of microarc discharge were characterized by measuring current – voltage characteristics. A high speed digital camera was utilized to obtain information about the evolution of microarcs onto the surface of the anode. The properties of treated surfaces were analyzed by different techniques: Field Emission Scanning Electron Microscopy interfaced with Energy Dispersive X-ray analyzing system (FESEM - EDX, JEOL JSM- 6330F), X-ray difractometry (Rigaku X-ray Difractometer) and nanoindentation (TriboScope ^{TM} Nanomechanical Test Instrument).

3. Experimental results and discussion

Current-voltage characteristics revealed three regions in the operation of the treatment process (Fig.2). In the first region, for low input voltages, the current intensity was low and only oxygen evolution on the anode and hydrogen evolution on the cathode surfaces were observed. This first region is characterized by a low slope of current-voltage characteristic. In the second region, by increasing the applied voltage, the current intensity and the quantity of evolved gasses increases rapidly and also the slope of current voltage characteristic has a high value. When the applied voltage exceeds a threshold value, dependent on the anode material, electrolyte and electrolyte concentration, microarcs begin to develop on the surface of the anode. This process is accompanied by visible light emission and by a high frequency noise. At the end of second region all the surface of the anode was covered by micro arcs. By increasing the applied voltage the slope of current intensity variation changed to a lower value in the third region and the intensities of light and sound emitted by micro arcs developed on the treated surface increased. The behavior of current-voltage characteristics do not changes with the increase of electrolyte concentration, only the thresholds values of voltages between regions change to lower values, while the maximum current intensity increases. In the second and third regions the process is accompanied by intense heat generation, determined by the high temperature micro arcs developed on the anode, by ohmic lost in the electrolyte, from condensation of water steam generated in the vicinity of micro arcs and in the cooling time of melted oxide.

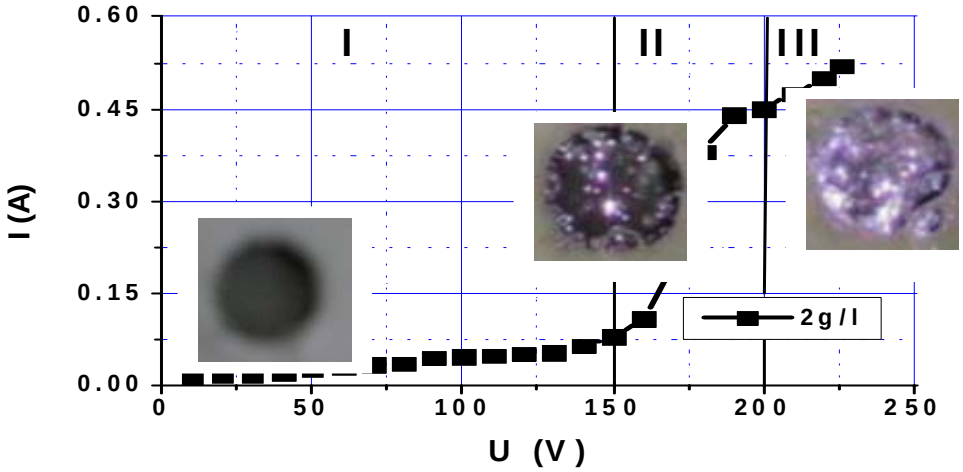

Fig.2. Current – voltage characteristic of microarc discharge (Al anode, NaOH electrolyte)

The amount of produced heat increased in the second region of current - voltage characteristics and attended maximum value in the third region. Electron microscopy images revealed that a porous oxide layer was formed onto the samples surface after the microarc plasma treatment of both materials (Fig.3 – FESEM images of surface and cross section of treated Mg substrate).

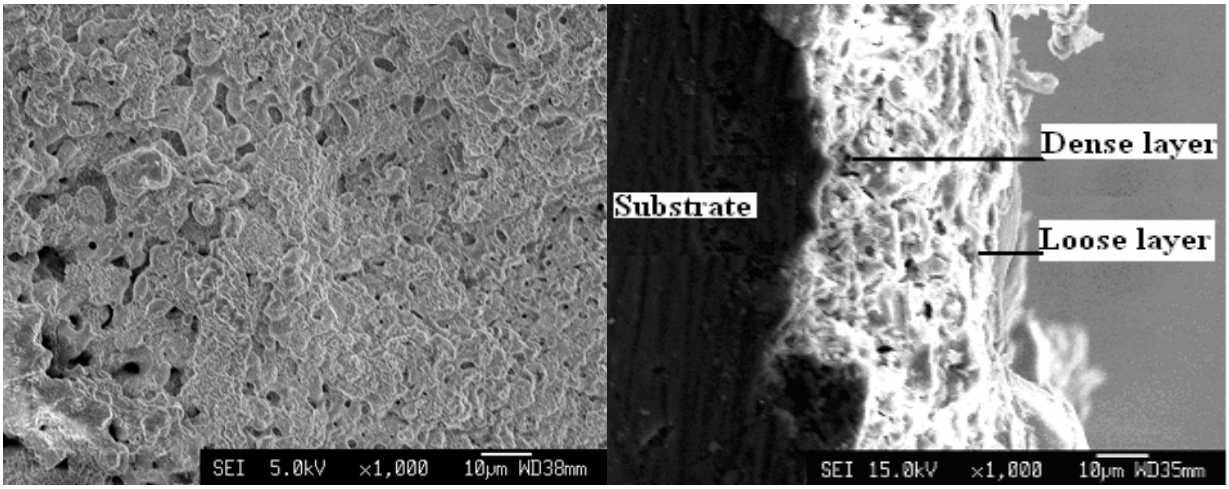

Fig.3. FESEM image of surface and cross section of treated magnesium sample

The morphology of surfaces was also dependent on the current density during the treatment (Fig.4, Al substrate). For low discharge current the porosity is high (Fig.4.a) and by increasing the discharge current the porosity decreases as a consequence of melting of produced oxide under the influence of high temperatures developed in the place of micro discharges (Fig.4.b). Two kinds of pores were observed: one in micrometer scale and

another one in nanometer scale. The pore diameter decreased with the increase of current intensity and, for a constant applied current, the thickness of the oxide film increased almost linearly with the time of treatment.

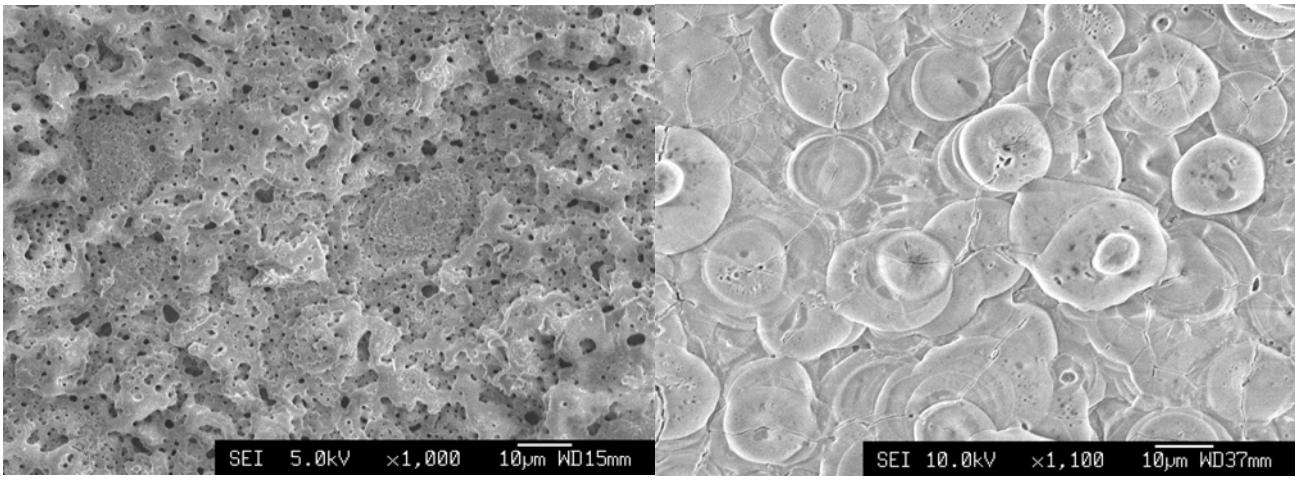

(a) (b)

Fig.4. FESEM images of treated aluminum sample

Higher growing rates as 1.5 μm/min was obtained for both substrates. XRD measurements of treated aluminum substrates indicated the presence of $\alpha - Al_2O_3$ and $\gamma - Al_2O_3$. The peak intensity of $\alpha - Al_2O_3$ was higher, indicating a high content of this phase and confirmed the high temperature developed in microarc discharge. This higher content of alpha phase in aluminum oxide film could explain the high value of hardness obtained from nanoindentation measurements (approximately 30 GPa) because alpha form of aluminum oxide is characterized by a high hardness. XRD measurements of treated magnesium substrates indicated the presence of MgO, the peak intensity increasing with the treatment time. EDX mapping indicated the presence of oxides on treated surfaces and a small amount of cations from utilized electrolytes.

Conclusion

The micro arc discharge in different electrolytes was utilized to treat the surfaces of aluminum and magnesium. The current – voltage characteristics indicated three region of the process. In the first region a normally anodization occurs. The micro arc discharge develops in the second and third regions of the process and is accompanied by intense heat generation. The growth rate of both aluminum and magnesium oxides was high and higher values as 1.5 μm/min were obtained. Deposited thin films presented a layered and porous structure. The external layer was with low strength and with high porosity. The internal layer was harder and well adherent to the substrate because the micro arc melts the growing film in the substrate. Different textured surfaces were obtained by controlling the growth condition of oxides. The measurements indicated that surface properties of light metals as magnesium and aluminum were improved by micro arc plasma treatment in different electrolytes, demonstrating a big potential for the treatment of complex configuration components as those utilized by aero spatial, ship and car industries.

References

1. A.L.Yerokhin, A.Shatrov, V.Samsonov, P.Shashkov, A.Leyland, A.Matthews, Surface and Coatings Technology, 182 (2004) 78-84

2. A.L.Yerokhin, L.O.Snizhko, N.L.Gurevina, A.Leyland, A.Pilkington and A.Maththews, J.Phys.D: Appl.Phys. 36 (2003) 2110 - 2120

Diamond like carbon thin films deposition by hollow cathode plasma enhanced CVD

V.Anita[1,2], Nina Andreeva[3], N.Saito[4], O.Takai[2]
1 - Department of Plasma Physics, "Al.I.Cuza" University, Iasi -700 506, Romania
2 - EcoTopia Science Institute, Nagoya University, Furo-cho, Chikusa, Nagoya 464-8603, Japan
3 – Chemnitz University of Technology, Nationen Str. 62, Chemnitz 09111, Germany
4 -Department of Molecular Design and Engineering, Graduate School of Engineering, Nagoya University, Japan

Abstract
The properties of diamond like carbon thin films obtained with a hybrid method by combining the hollow cathode discharge and plasma enhanced chemical vapor deposition are presented. Methane and pyrrole were utilized as precursors for DLC thin films synthesis. The conductivity of deposited films increases in the low impedance state of discharge as a consequence of higher nitrogen content in deposited films resulted from the decomposition of pyrrole precursor.

Keywords: Diamond like carbon; Hybrid process; Hollow cathode; Plasma enhanced chemical vapor deposition; Mechanical and electrical properties;

1. Introduction

One of the main problems in the case of deposition of diamond like carbon (DLC) thin films by the most utilized capacitively coupled plasma enhanced chemical vapor deposition methods is the low deposition rate. In this case DLC thin films are deposited on powered electrode and this geometry determines a big connection between deposition rate and the properties of deposited thin films. This connection is determined by the importance of ion energies on the content of sp^3 bonded carbon atoms in deposited films. To increase the deposition rate it is necessary to increase the input power and the self bias voltage, responsible for ion energies, increases also. Optimum carbon ion energies, approximately 100 eV, were suggested by much experimental work in order to obtain high sp^3 content in thin films [1]. In a capacitively coupled RF powered CVD the self generated bias voltage is a measure of ion energies and, as an example, - 150 V bias voltage is obtained for only 50 W input power. For this input power the deposition rate is very low (8 nm/min) [2]. A possibility to overcome this problem is to use a hollow cathode discharge, characterized by high decomposition and ionization rates of precursor gases. In this case the reactive gases enter in the reaction chamber passing through high density plasma established inside of the hollow cathode and radicals and ionized reactive species forms DLC thin films on a separate biased substrate. In this way the substrate bias can be independently controlled in the view to obtain DLC thin films with desired properties.

2. Experimental set-up

The utilized experimental set-up is presented in Fig.1. A graphite tube with 8 mm external diameter, 5.5 mm internal diameter and 35 mm in length was utilized as cathode. This hollow cathode was capacitive coupled to a 13.56 MHz frequency and a variable power supply (0 - 400 W) or to a DC power supply. Thin films were deposited at different distances in the front of the cathode on a water cooled substrate holder. Methane (CH_4) and pyrrole (C_4H_5N), one of the most known monomer for conductive polypyrrole polymer processing, were utilized as precursors. Nitrogen was utilized as supplementary doping element in order to influence the conductivity of deposited DLC films. The properties of obtained thin films were compared with those prepared only with capacitively coupled plasma chemical vapor deposition system without hollow plasma enhancement. The substrates holder was biased by the same RF power supply and the measured bias voltages were utilized as indicator of ions energies involved in the growth of thin films. Thin films were deposited onto silicon and Al_2O_3 substrates in different experimental conditions: maximum 100 sccm mass flow rate of reactive gases, 10 to 400

W variable applied RF power on hollow cathode and variable negative substrate bias voltage between - 10 and - 800 V.

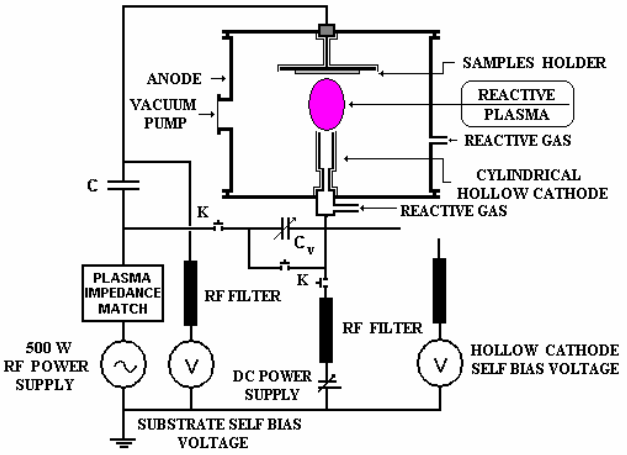

Fig.1. Experimental set-up

The surface morphology of DLC thin films was observed with an atomic force microscope (AFM; JSPM – 5200 T, JEOL). The deposition rate was estimated by measuring the thickness of deposited thin films using a surface profilometer (Surfatest SV-600, Mitutoyo). The infrared spectra of the films were analyzed in order to characterize carbon - hydrogen bonding in thin films (FTS 175 C, Bio- Rad). Raman spectra were recorded using a Jobin Yvon spectrometer with 514.5 nm laser excitation line and 10 mW output power. The spectra were fitted with curve fitting software, based on two Gaussian curve shapes, to identify the G and D peaks positions, to measure and compare the intensities (GRAMS/AI^{TM} from ThermoGalactic). The hardness and Young's modulus of the DLC films were determined from loading-unloading curves on a nanoindentation instrument (TriboScope, Hysitron). Ten indentations were made for each sample and the hardness and Young's modulus were calculated by averaging the measurements.

2. Experimental results and discussion

The hollow discharge presented two stable regimes: one with high impedance and another one with low impedance. The evolution of self bias voltage developed on the hollow cathode evidences very clearly this particularity: for a given pressure the self bias voltage increases with the increase of input power and then, at a specific power, suddenly decreases to a lower value. The bias voltage increases again with the increase of input power, as indicated in Fig.2.a. The reactive gas pressure influences the threshold values of input power for transition from normal plasma with high impedance (external to the cathode) to low impedance plasma (mainly inside of the cathode). This value increases with decreasing internal diameter of hollow cathode and by increasing the pressure of reactive gas. The low impedance state of discharge is explained by the increased plasma density induced by the multiple reflections of secondary electrons inside of hollow cathode. The transition in the low impedance state is accompanied by an increase of cathode temperature to very high values, as indicated in Fig.2.b, by the red color of graphite cathode. This behavior is determined by the increase of dissipated power inside the cathode. In the high impedance state the discharge is outside of the hollow cathode, as indicated in Fig.2.c (image obtained after the transition from low impedance state). As a characteristic of this geometry is the non uniformity of thin films. The highest thickness is obtained on the axis of hollow cathode with a radially decreasing tendency. Deposition rate increases after the transition in the low impedance state, being determined by the increased decomposition of precursors in high density plasma developed inside the hollow cathode. The nature of reactive gas precursor influences the deposition rate and the biggest value of 294 nm/min was obtained from pyrrole. This behavior can be explained by the content of five carbon atoms in

pyrrole molecule as compared with only one carbon atom in the methane molecule. Also the ionizing potential is different: 8.8 eV in the case of pyrrole and 12.2 eV in the case of methane. This difference influences the plasma density obtained for the same input power, the biggest value being obtained in the case of pyrrole precursor.

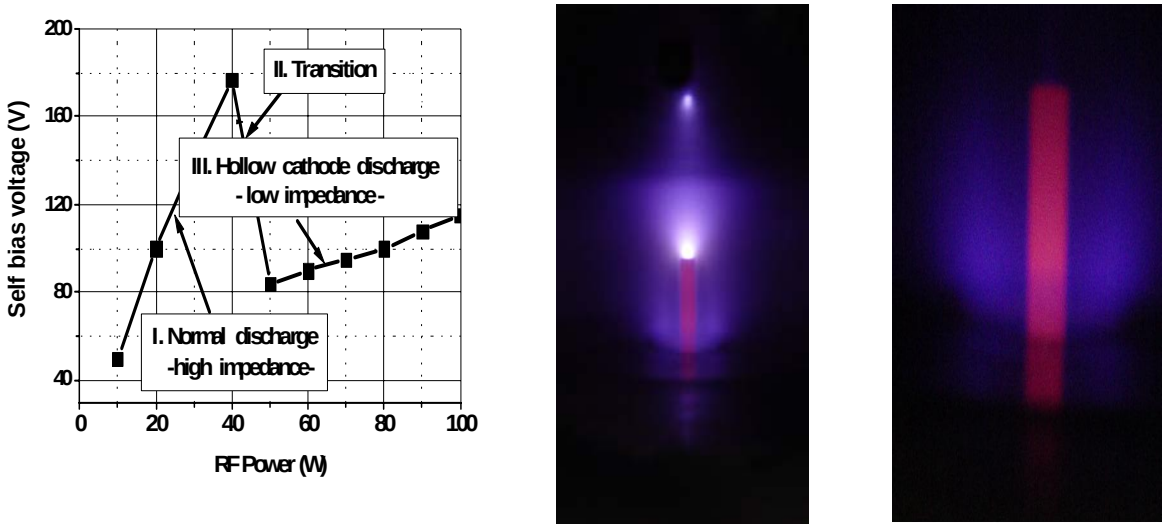

(a) (b) (c)

Fig.2. a - Transition modes of hollow cathode discharge;
b - Image of the discharge in low impedance state;
c – Image of the discharge after the transition from low to high impedance state

The deposition rate increases with the increase of input power on hollow cathode and the bias voltage applied on the substrate. The deconvolution of Raman spectra presented in Fig.3 reveals the presence of graphitic and disordered graphitic components in thin films (G band, I_G - 1580 cm^{-1} and D band, I_D - 1370 cm^{-1}). The integrated intensities ratio I_D/I_G increases with the increase in the input power suggesting a decrease in the sp^3 fraction and the increase of disordered sp^2 fraction in deposited DLC thin films.

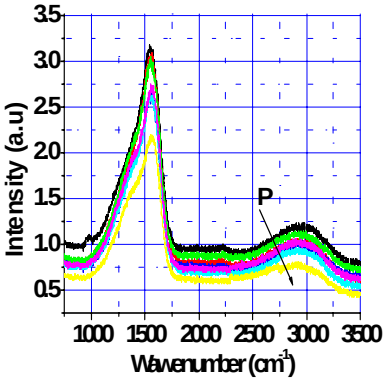

Fig.3. Raman spectra of DLC thin films obtained from pyrrole for increased input power

The infrared transmission spectra at wave numbers from 700 to 4000 cm^{-1} were analyzed in order to characterize the bonding of hydrogen and nitrogen with carbon in thin films. The deposited films were transparent in the infrared range. The spectra are characterized by absorption peaks centered at 1400 cm^{-1}, 2189 cm^{-1}, 2955 cm^{-1} and 3368 cm^{-1}. The high intensity and large absorption peak at 1400 cm^{-1} is a superposition of unsolved bands situated in this region, determined mainly by N-H bending and C=C stretching. The intensity of this peak increases with the increase of input power, suggesting the increase of nitrogen content in thin films. The peak registered at 2189 cm^{-1} was assigned to CN triple bonds stretching. The intensity of this peak increases with the increase of the input power or by adding nitrogen in the discharge, indicating the increase of nitrogen content in thin films. The peak at 2925 cm^{-1} was associated with the C-H stretching of sp^3 - CH_3 (2885 cm^{-1}), with sp^3 - CH_2 (2920 cm^{-1}) and sp^3 - CH_3 (2955 cm^{-1}) group. The peak at 3368 cm^{-1} was associated with the pyrrole monomer not decomposed in the plasma and included in thin films. The intensity of this peak decreases at higher input powers, indicating the decrease of residual pyrrole in thin film. Also, the adding of nitrogen in the discharge induces the decrease of the intensity of the peak situated at 3368 cm^{-1}, indicating a more efficient decomposition of pyrrole monomer. AFM measurements reveal a very smooth surface of thin films obtained from both precursors without important change with the increase of input power and bias voltage. RMS roughness of deposited thin films decreases with the increase of bias voltage (from 4.5 nm at - 50 V bias voltage to 0.8 nm at - 400 V bias voltage). From nanoindentation measurements resulted the increase of hardness with the increase of bias voltage with a maximum value of 16 GPa obtained at - 150 V bias voltage. The main advantage of hollow cathode plasma enhanced chemical vapor deposition geometry, high deposition rate, is diminished by the nonuniformity of thin films deposited in static mode, without the movement of substrate in the front of the cathode. To overcome this disadvantage, a twin hollow structure with parallel connected hollow cathodes was designed and tested. The influence of the distance between cathodes on the uniformity of deposited films was investigated. A distance of 10 mm between the axes of hollow cathodes was found as optimum for a nonuniformity less than 10% in the thickness of deposited thin films. To obtain larger uniform thin films by utilizing this geometry it is necessary to move the substrate in the front of a multi hollow structure, the number of parallel connected hollow cathodes being determined by the dimensions of substrates. Electric measurements of DLC films deposited onto aluminum oxide substrates showed that the resistivity was very high for low values of bias voltages ($\rho > 10^7$ k Ω·cm at -100 V) in the case of DLC films obtained from both precursors and decreased for higher values of input power, the bigger decrease being obtained in the case of pyrrole ($\rho \approx 55$ kΩ·cm at – 700 V). Nitrogen addition in the pyrrole discharge induces a further decrease of the resistivity, 3.5 kΩ·cm being obtained for 20 sccm mass flow, suggesting that nitrogen acts as a weak donor element.

3. Conclusion

By using a hollow cathode plasma enhanced chemical vapor system and a plane cathode plasma enhanced chemical vapor deposition system, DLC thin films were deposited from methane and pyrrole. DLC with similarly mechanical and electrical properties were obtained by using both geometries. DLC films were transparent in IR spectrum, with absorption peaks characteristic for carbon bonding with hydrogen and nitrogen. The deposited films were nonuniform as a consequence of axially symmetric geometry of generated plasma, with the maximum thickness on the axis of the hollow cathode. To obtain larger uniform thin films by utilizing this geometry it is necessary a multi hollow structure with the movement of the substrate, the number of parallel connected hollow cathodes being determined by the dimensions of the substrate. From the experiments made with a twin structure with parallel connected hollow cathodes, a distance of 10 mm between the axes of hollow cathodes was found as optimum for nonuniformity less than 10% in the thickness of deposited thin films.

References

[1] J.Robertson, Materials Science and Engineering, R37 (2002) 129-28

[2] V. Anita, T.Butuda, T. Maeda, K.Takizawa, N.Saito, O. Takai, Proceedings of the 9th International Conference on New Diamond Science and Technology (ICNDST-9), Diamond and Related Materials, 13 (11-12) (2004) 1993-1996

Electrochemical probe into DLC thin films

T. Butsuda[1], V. Anita[2,3], N.Saito[4] and O. Takai [3]

1 - Department of Materials, Physics and Energy Engineering, Graduate School of Engineering, Nagoya University, JAPAN
2 - Department of Plasma Physics, Optics and Material Science, "Al.I.Cuza"University, Iasi, 700 506, ROMANIA
3 - EcoTopia Science Institute, Nagoya University, JAPAN
4 -Department of Molecular Design and Engineering, Graduate School of Engineering, Nagoya University, JAPAN

Abstract

Results about mechanical, electrical and electrochemical properties of diamond – like carbon thin films obtained by plasma enhanced chemical vapor deposition (PE-CVD) method are presented. The overpotential for hydrogen and oxygen evolution is larger than that of graphite electrode. The electrochemical window of DLC (approximately -1.0 to + 2.5 V vs. Ag/AgCl electrode) is lower than that of diamond electrode (about -1.25 to + 2.30 V) and is higher as electrochemical window of graphite electrode (- 0.40 to + 1.60 V).

Keywords: Diamond like carbon; Plasma enhanced chemical vapor deposition; Mechanical, electrical and electrochemical properties;

1. Introduction

Diamond like carbon (DLC) is a promising material for application in different fields as mechanics, electronics, optics, tribology and chemistry. DLC thin films are characterized by many properties similarly with diamond: high hardness, high elastic modulus, transparency in infrared region of electromagnetic spectrum and chemically inertness [1, 2]. The deposition rate of diamond thin films is very low and the production cost is high and this particularity restricts the area of applications. On the contrary, DLC thin films are widely utilized in various fields since the deposition rate is much higher than that of diamond and the production cost is much lower. The high chemical stability of DLC recommends this material for electrochemical applications: DLC is not destroyed by acids (or mixed acids as acid etch), alkalis solutions at high temperature and also by organic solvents. As a result of their chemical resistance DLC thin films can be utilized as corrosion resistant coatings. Generally, DLC is characterized by high resistivity. The electrical property can be controlled by changing the ratio between sp^2 and sp^3 bonded carbons, by controlling the concentration of bonded hydrogen and by doping with nitrogen or different metallic elements. By using different doping elements as nitrogen, boron, transition metals and metals from platinum group, the resistivity can be decreased and DLC thin films can be successfully utilized for electrochemical applications in aqueous solutions.

2. Experimental details

The DLC thin films for this investigation were fabricated onto low resistivity Si (111) substrates through the radio frequency capacitively coupled plasma chemical vapor deposition method. A RF variable power generator (50 – 400 W) and fixed frequency (13.56 MHz) was utilized as power supply (Fig.1). The power supply was connected to the cathode of discharge by using a manually matching box in the view to adapt the variable plasma impedance to the fixed 50 Ohm output impedance of the generator. A fixed value capacitor was utilized between matching box and the cathode in the view to permit the measurement of self developed bias voltage. The measured bias voltage was utilized as indicator of ions energies involved in thin films growth. Methane, acetone and toluene were utilized as precursors and the pressure of reactive gases was kept at 25 Pa in the time of process. The pressure was monitored by using a capacitance manometer. Nitrogen was utilized supplementary as a doping element in the view to increase the conductivity of thin films. The film

thickness was adjusted to approximately 1μm by controlling the input power and the deposition time.

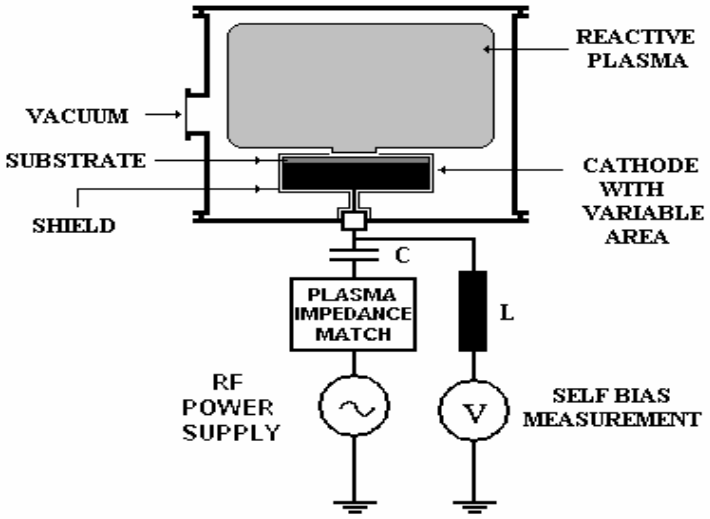

Fig.1. PE-CVD reactor for DLC thin films deposition

The electrical properties of deposited thin films onto high resistivity aluminum oxide substrates were evaluated by a two point method by applying a constant current between silver electrodes deposited by magnetron sputtering and by measuring the developed voltage. The surface morphology, structure and bonding states of DLC thin films deposited under various RF input power were analyzed using atomic force microscope (AFM; JSPM – 5200 T, JEOL), Field Emission Scanning Electron Microscopy (FESEM; JSM- 6330F; JEOL), Fourier Transform Infrared Spectroscopy (FTIR, FTS 175 C, Bio-Rad) and visible Raman spectroscopy (Nanofinder®,TOKYO INSTRUMENTS INC., with 488 nm argon ion laser line and 10 mW output power). The hardness and Young's modulus of the DLC films were determined from loading-unloading curves on a nanoindentation instrument (TriboScope, Hysitron) using a Berkovich diamond tip. The hardness and Young's modulus were calculated by averaging the measurements of ten indentations on different area for each sample. Electrochemical properties were investigated by cyclic voltammetry. The voltammograms were obtained with the electrodes immersed within a conventional electrochemical cell with three electrodes. Cyclic voltammetry were carried out in 0.1M H_2SO_4 solution by using a computer controlled potentiostat and function generator (Solartron 1280Z). In advance, the back sides of substrates were etched in HF solution and aluminum was deposited in the view to improve electric contact. DLC thin film was sealed with an open area surface of 5 mm in diameter. The potential of working electrode was varied over a certain range with respect to a reference Ag/AgCl electrode and a platinum mesh was utilized as counter electrode. I - V characteristics were obtained at a scan rate of 20 mV/sec.

3. Experimental results and discussion

The deposition rate increases with the increase of input power up to values as higher as 45 nm/min in the case of CH_4 precursor. The highest deposition rate was obtained in the case of toluene (350 nm/min) and acetone (70 nm/min) at 400 W input power. By adding nitrogen in the time of deposition the deposition rate increased (50 nm/min in the case of $CH_4 - N_2$ mixture) and this behavior was associated with an enhancement of the plasma density and in more active plasma.

The hardness of DLC thin films increases with the input power, attains maximum and then decreases. At about 150 W input power the hardness of DLC thin films deposited from methane reach maximum values (13 GPa). In the case of toluene the maximum hardness (17.5 GPa) was obtained at 400 W and in the case of acetone the maximum hardness (12.5 GPa) was obtained at 100 W input power. The nitrogen adding in the time of process decreases the values of hardness and elastic modulus.

The infrared transmission and absorbance of DLC thin films at wave numbers from 400 to 4000 cm^{-1} were analyzed in order to characterize the strength bonding of hydrogen with carbon. For DLC films obtained from all precursors the peak of absorption spectra are centered at approximately 2920 cm^{-1} which is associated with the majority presence of hydrogen in the form of $sp^3 - CH_3$ and $sp^3 - CH_2$ group. The peak intensity decreases with the increase of input power for films obtained from all precursors. For the same input power the peak intensity was different for films obtained from different precursors, decreasing from toluene to acetone and methane. By adding nitrogen in the time of process the intensities of this peak decreased, suggesting an induced dehydrogenation by the nitrogen included in thin films.

Raman measurements revealed a large luminescence background of thin films obtained at low input power and the high slope of this luminescence background suggests a high content of hydrogen. The ratio of disordered graphite component and graphite component intensities in thin films obtained from both precursors decreases with the input power suggesting the decrease in sp^3 and the increase in sp^2 components.

Electrical measurements of DLC thin films deposited on high resistivity aluminum oxide substrates showed that films obtained in methane, acetone and toluene plasma has very high resistivity ($\rho \approx 16x10^6\ \Omega.cm$). Addition of nitrogen decreases the resistivity of thin films to lower values ($12.5\ x10^3\ \Omega.cm$ for 10 sccm of nitrogen mixed in 100 sccm methane). In the case of acetone precursor the smallest value of resistivity was only $55\ x\ 10^3\ \Omega.cm$ at 40 sccm nitrogen added in methane precursor and no significant variation of resistivity was registered in the case of toluene plasma. These results suggest the necessity to increase the input power in order to increase the graphite component in thin films in order to obtain a lower resistivity. The decrease of thin film resistivity obtained from methane and acetone with the increase of nitrogen mass flow suggests that N acts as a weak donor and improve the conductivity.

No visible grain features could be observed under FE-SEM measurements. AFM measurements revealed a very smooth surface of DLC films, without big modification with increased input power. As generally characteristics, RMS roughness decreases with input power (Fig.2). In the case of methane plasma RMS decreased from 0.47 nm at 50 W to 0.30 nm at 400 W and in the case of toluene plasma RMS decreased from 1.23 nm at 50 W to 0.75 nm at 400 W input power.

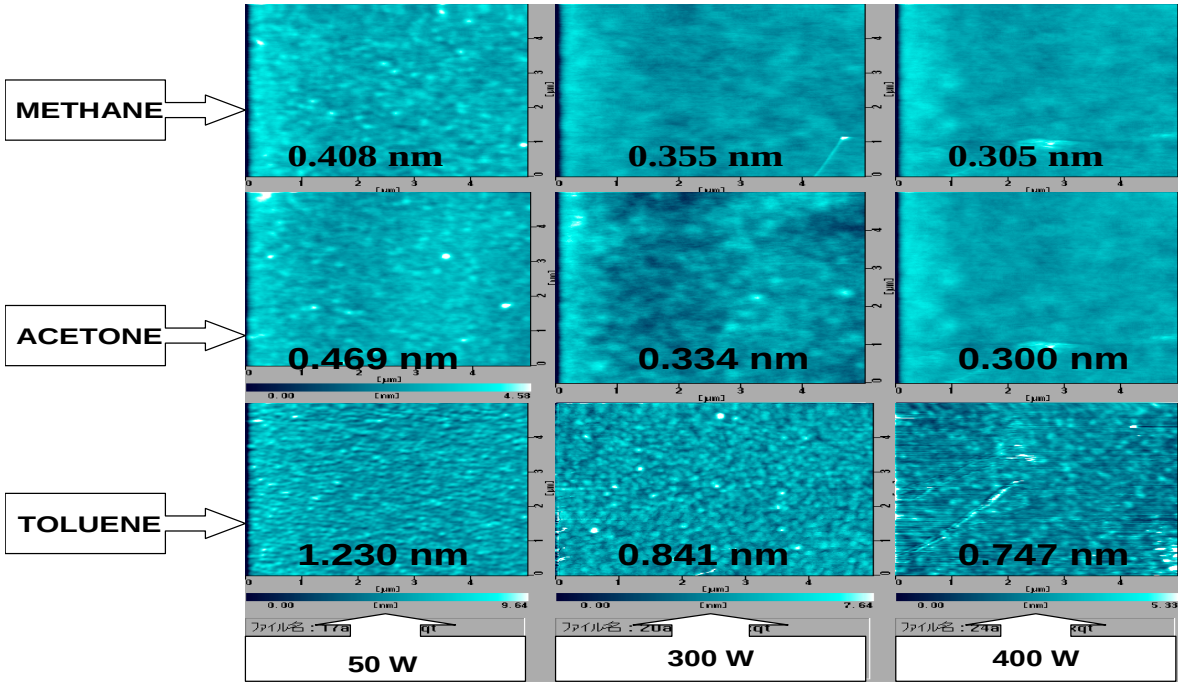

Fig.3. RMS roughness values for DLC thin films obtained from different precursors

A characteristic cyclic voltammogram of DLC film in 0.1M H_2SO_4 solution is presented in Fig.3.

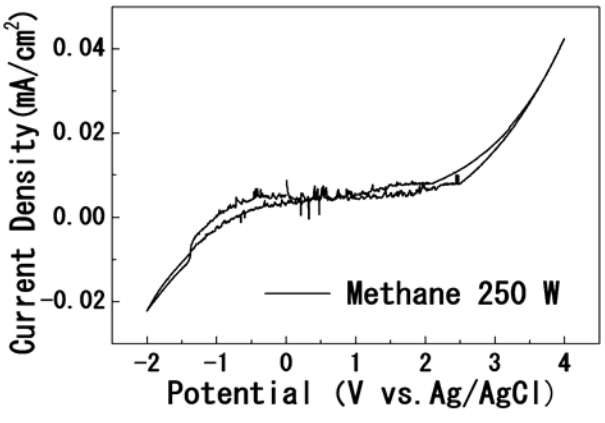

Fig.2. Cyclic voltammograms of DLC electrode

The overpotential for hydrogen and oxygen evolution on DLC thin films is larger than that of graphite electrode. The typical average potential limit corresponds to a current density of $20\mu A/cm^2$. For a DLC electrode, a broad potential range (approximately -1.0 to + 2.5 V vs. Ag/AgCl electrode) is observed over which no significant water decomposition occurs. The wide electrochemical window of DLC is lower than that of diamond electrode (about -1.25 to + 2.30 V) and is higher as electrochemical window of graphite electrode (- 0.40 to + 1.60 V). As evidenced by measurements, DLC electrodes present catalytic activity for Cl^2/Cl^- evolution and also high sensibility for Pb^{2+}/Pb^0 in the trace lead solutions. High hardness, good adherence on silicon substrates and large electrochemical window in aqueous solution recommends DLC thin films as environmental-friendly disposable electrochemical electrodes. Another important feature of DLC electrochemical electrode is the possibility to reuse the substrate or to repair the destroyed thin films by re - depositing the active film.

4. Conclusion

By using plasma enhanced chemical vapor deposition, hard and very smooth DLC thin films were deposited on different substrates. Mechanical, electrical and electrochemical properties were investigated and correlated with the plasma properties. Hardness and elastic modulus were dependent on the value of radio frequency input power. The maximum values were different for different precursor, the highest values of hardness being obtained in the case of toluene, H = 17.5 GPa. FTIR measurements indicated the decrease of hydrogen content in deposited films as a consequence of intense ion bombardment at high input power. Raman measurements indicated high hydrogen content in thin films obtained at low input power and an increase of disordered graphite component with the increase of input power. The adding of nitrogen in the time of process decreased the hardness and elastic modulus and increased the conductivity of thin films. Electrochemical measurements revealed that the overpotential for hydrogen and oxygen evolution on DLC electrode is larger than that of graphite electrode. The electrochemical window of DLC electrode is lower than that of diamond electrode and is higher as electrochemical window of graphite electrode.

References

1. A.Grill, Diamond and Related Materials, 8 (1999) 428-434
2. J.Robertson, Materials Science and Engineering, R37 (2002) 129-281

THERMAL BEHAVIOR AT IMPACT OF MICROMETRE AND MILLIMETRE SIZED PARTICLES, INFLUENCE OF SUBSTRATE ROUGHNESS AND SKEWNESS

J.Cedelle[1], M.Vardelle[1], P.Fauchais[1], M. Fukumoto[2]

[1]S.P.C.T.S Laboratory, University of Limoges, France
[2]Advanced Joining Process Laboratory, University ot Toyohashi, Japan

Abstract :

Two different techniques have been developed in order to study plasma sprayed particle behavior at impact. The first one (SPCTS lab.) allows direct studying under dc plasma spray conditions, while the latter one, based on the millimeter sized free falling drop, enables the visualization of flattening phenomena, but at larger scale (time and dimensions about 3 order of magnitude larger). These two techniques bring complementary approaches and results.

Introduction :

The increasing request for more and more plasma sprayed coatings with improved service properties, requires a better understanding of phenomena at impact [1]. Although the experimental data are difficult to obtain on micrometer sized droplets impacting at velocities in the hundreds of m/s range, they are absolutely necessary for a better understanding of impact phenomena. Leading in parallel a study on millimetre sized particle enables to observe phenomenon at a larger scale. That's why a collaboration between the SPCTS Laboratory in France and the Advanced Joining Process Laboratory in Japan was realized. SPCTS Laboratory developed a new experimental set-up for the investigation of the splashing processes under direct current (dc) plasma conditions using an imaging technique composed of two fast shutter cameras and two long distance microscopes. The study of millimetre sized drop at impact using a free falling drop experiment was realized in Advanced Joining Process Laboratory in Japan.
The impact splashing is exclusively observed with the first technique when the particle impacts with high velocities (>100 m/s) [1,2]. The second technique presents other advantages, like comparing nickel drop cooling rates for different substrate characteristics. Results show that the quenching rate seems to be equivalent on a hot (673 K) or on room temperature substrate once preheated to 673K and higher than that measured on a room temperature substrate. The formation of peaks of oxide (positive skewness) resulting from the preheating seems to improve the contact with the droplet resulting to a disk shaped splat. The recalescence phenomenon can also be observed in few cases.

Experimental procedure :

- **Description of the experimental set up developed at SPCTS Laboratory (Limoges, France):**

This study is focused on the impact of a single droplet in plasma spraying. The research is carried out using an imaging technique with fast CCD cameras (PCO Sensicam) aimed both parallel to the substrate or almost orthogonal to it, in order to visualize all phenomena generated at impact. The correlation of the images with the results of a set of measurements allowing determining in-flight a single particle parameters just prior to its impact allow a better understanding of the splashing and flattening processes. All the difficulties of such investigations are linked to the fact that the impact of a single droplet in plasma conditions is not a reproducible event (in conventional spray condition between 10^6 and 10^8 particle/s, depending on their positions within the sprayed spot). A change in the particle mass causes a variation in the temperature and velocity of the droplet and can modify the morphology of the resulting splat. That's why a significant number of experiments should be realized to draw general tendencies.
Plasma spraying is carried out using a direct current plasma torch (PTF4 type) with a 7 mm internal diameter nozzle. The plasma torch is operated between 300A and 600A, and the inlet plasma gas flow consists of a mixture of 45 L/min Ar and 10 L/min H_2. An yttria partially stabilized zirconia's powder (8 wt % Y_2O_3) with

fused and crushed particle sizes ranging between 22 µm and 45 µm is used in this study. These spray conditions result in fully melted particle with velocities at impact ranging between 100 and 300 m/s [2].
The powder is injected 2 mm upstream from the nozzle exit and the argon carrier gas flow rate is adjusted to the torch working parameters in order to achieve a mean trajectory making an angle of about 3,5° with the torch axis (optimum value). The internal diameter of the injector tube is 1.8 mm. Besides, to limit the number of impacting particles, the powder flow rate is only 10 g/h (instead of a few kg/h in spraying conditions !).

Splats are collected on a substrate at a distance of 85 mm. Only particles following the trajectory close to the plasma jet axis are selected thanks to a moving water cooled shield positioned at 70mm downstream the torch nozzle exit and a another one positioned 11 mm upstream of the substrate with a 1.5 mm hole.
The experimental set-up for a single particle is two fold : in flight characterization by an optical sensor head and a fast (50ns) two-color pyrometer and flattening characterization by a two color pyrometer and two imaging systems, i.e fast CCD cameras triggered by the velocity signal

Measurement techniques :
The parameters of a single molten droplet are measured prior to its impact, with the experimental set-up already described in previous paper [3].

Synchronisation – Triggering of cameras :
Camera triggerings are generated by external TTL signals (5 V) in order to catch images at the impact moment. The latter are produced by a LabVIEW® program which creates TTL pulses from the velocity signal described in figure 2b. This procedure allows being sure that images come from the same particle, which velocity has been calculated.
It is necessary that cameras are activated as the particle impacts on the substrate. Knowing the particle velocity and the position of the substrate, it would then be possible to calculate the delay to be allocated to one pulse TTL for the release of both movie cameras. All this work is made possible thanks to a LabVIEW® program which allows, after the acquisition of the velocity signal, calculating the speed of the particle and thanks to a simple calculation the delay necessary in the release of movie cameras. All this is performed takes about 20 µs with a precision of the order of 0,1 microseconds.

- **Description of the experimental set up developed at Advanced Joining Process Laboratory (Toyohashi, Japan):**

The experiment has been described in details in previous paper [4]. Commercially available pure Ni and Cu wires (diameter 2 mm, > 99,99% purity) are used in this study. These wires are heated and melted by a radio frequency heating equipment. The mirror polished substrate (using 0,3 µm Al_2O_3) AISI 304 stainless steel substrate can be heated and its temperature is measured by a K-type thermocouple. The experiment is performed in a nitrogen atmosphere to eliminate oxidation. The impact velocity is calculated from the falling distance. It can be varied between 2 and 5 m/s. In order to maintain fluid and thermal similarity with the thermal spray process, i.e. analogy of Reynolds and Peclet numbers, the droplet velocity and diameter are adjusted.
Temperature measurements are obtained using the same fast two color pyrometer technique as that used with the thermal spray process : the temperature of the droplet just prior to its impact and that of the resulting splat are calculated from the ratio of the two signals obtained thanks to the optical head focused on the substrate surface. The main cooling rate of the splat is estimated from the time-temperature evolution of the lamella. For the observation of the flattening process, a sequence of images is recorded with a high speed camera (4500 frame/s).

Results

- **Plasma-sprayed particles**

Spraying a single particle on a preheated smooth stainless steel substrate using the experimental conditions summarized in table 1 allows understanding impact phenomena thanks to events chronology :

Table 1: Experimental conditions

Plasma gas	Ar /H_2 36/12
Arc Current	500 A
Voltage	55 V
Substrate	Smooth stainless steel
Ceramic powder	Zirconia
Powder granulometry	50-63 µm

Lamella formation on a preheated substrate :
In this first case, lamella formation with a disk shape is expected by preheating the substrate to 673 K which is higher than the transition temperature T_t (550 K) [5] To determine exactly when the cameras are triggered ,only pyrometer signal (fig 1a) and the TTL pulse (fig 1b) need to be recorded. The intrinsic delay of cameras must be taken into account in order to determine precisely when the image acquisitions start. This delay is 4,98 µs for a fast shutter camera PCO Sensicam. Dotted line on the left side corresponds to cameras acquisition beginning. In this experimentation the time exposure of cameras was 2 µs, so the second dotted line corresponds to the end of exposure

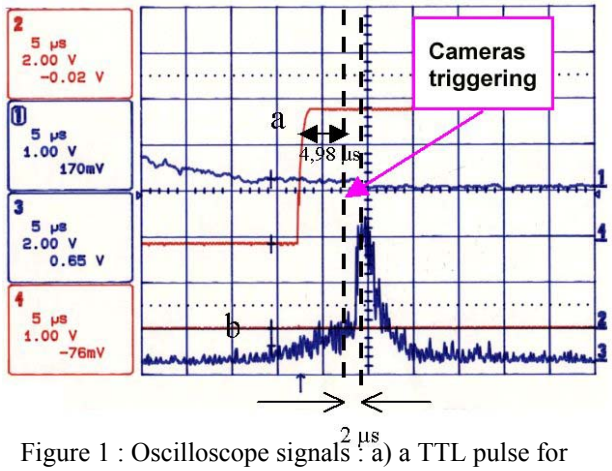

Figure 1 : Oscilloscope signals : a) a TTL pulse for cameras triggering, b) pyrometer signal

A correlation between the oscilloscope signals and the image makes it possible to see the very short period of the lamella formation. The disk shape of the flattening particle is already perfectly drawn (see figure 2a) and different as the acquisition of the photo ends, i.e., at the end of the flattening period (see figure 2b). The resulting splat of the selected droplet is immediately located on the substrate in order to be analysed. If this image is compared with that of the same lamella observed after impact with an exposure time of 1 ms, it can be noticed that the diameters are identical. It seems to mean that the complete spreading of the droplet is achieved in 2 µs and that the maximum diameter is 200 µm. During the spreading, the nuances of luminosity between the centre and the peripheral crown testify of a difference of temperature and allow saying that the cooling seems to begin during the phase of spreading. The resulting splat which is observed by optical microscopy presents microcraks in the central zone of about equal thickness and a rim in its periphery .This observation shows that a homogeneous and fast cooling took place in the central part while the warm and liquid material was still present (see fig 2a) at the outside crown 2 µs after impact (curling of the splat inducing a poor contact of its rim with the substrate).
Flattening velocity of the droplet after impact can be estimated thank to this imaging technique : within 2 µs after impact, droplet has spread on a distance of 100µm from the centre, which corresponds to a mean velocity of 50 m/s for the flattening stage.

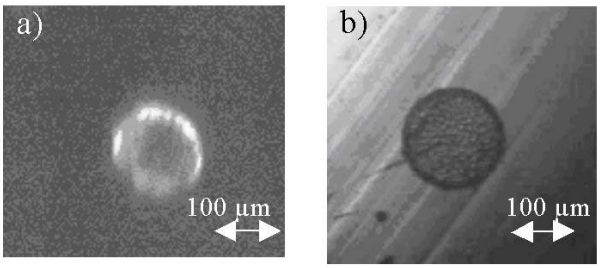

Figure 2: Disk shape obtained on a hot substrate. a/ Image of the spreading droplet (camera 1,time exposure 2 µs) velocity prior impact : 97 m/s, size range :50 – 60 µm. b/Resulting splat

Splashing on a room temperature substrate :
With the same experimental conditions, spraying a particle on a room temperature (300 K) substrate doesn't result in a regular disk shape splat but in impact and flattening splashing. The oscilloscope

signals presented in figure 3 show that cameras were triggered at the impact moment and that acquisition of each image had a 3 µs duration.
Both obtained images (fig 4, parallel and orthogonal to the substrate) show splashing phenomena. The resulting splat is extensively fingered and present a poor adhesion to the substrate. In order to have a better understanding of the splashing, a more precise study has been realized using longer time exposures for image acquisition.

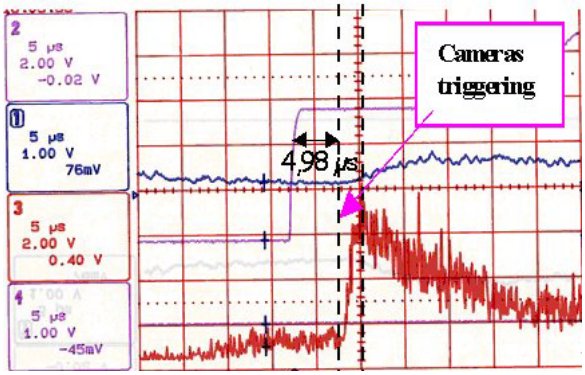

Figure 3 : Oscilloscope signals

Camera 2, parallel to y substrate axis makes it possible to visualize ejected matter generated just after collision. This kind of splashing called "impact splashing" [5] in the following, is associated with tiny droplets ejection (d~1µm). Results obtained with zirconia (22 – 45 µm) particles in conjunction with room temperature stainless steel substrate (flat surface Ra< 0,05 µm) confirms C. Escure ones with alumina particles [5]. These ejections seem not only to be in the impact direction (fig 4) but also in a direction with a 45 ° angle with substrate surface.

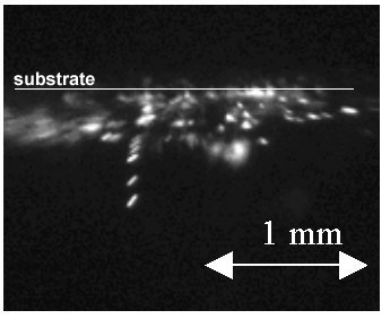

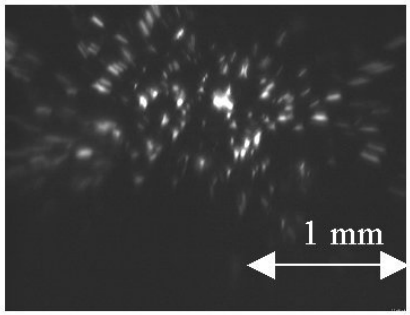

Figures 4a and 4b: Splashing observation : time exposure 3 µs, velocity prior impact : 102 m/s, size range : 50-60 µm

In order to materialize these matter emission, photographs were taken with a multiple exposure operation (10 shots exposure : 5 µs , delay 5 µs) (fig 5). The latter allows estimating the mean velocity of these ejections. It appears that they are a ten factor less than droplet impact velocity ($v_{ejection}$ = 15-20 m/s). These tiny droplets are ejected up to one millimetre over the substrate. The origin of this phenomenon is probably due to wave propagation at impact which velocity is estimated to be 3000 m/s for a liquid droplet. These observations confirm Armster et al. collision theory [6] which introduced expansion waves notion which can result in the formation of appreciable tensions within the liquid in the first phase of impact.

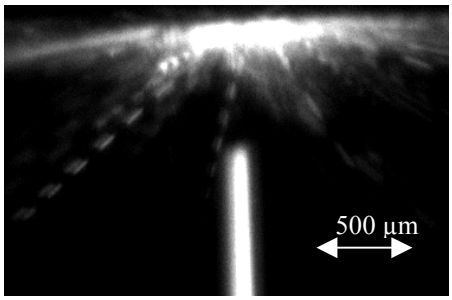

Figure 5 : Multiple exposure operation to materialize matter ejection

Substrate temperature seems to affect flattening splashing but not impact splashing. Wave regime is probably little or none dependent of substrate properties whereas the latter may govern flattening splashing [3].
To have a better understanding of the disk shape formation which presents a good contact with the preheated smooth stainless substrate, work with bigger drops was undertaken measuring in parallel their temperature and shape evolution.

- **Millimetre-sized drops**

The following results were obtained with the free-falling drop apparatus. The advantage of such an experimental study of flattening process is to work with millimetre sized droplets impacting with velocities about a few m/s. The time ranges are one thousand more important than in plasma spraying conditions, allowing following the flattening process with a camera speed of 4500 frame/s.
Using the high speed camera aimed parallel to the substrate surface makes it possible to realize a more precise study of directions of matter ejections in case of a splashing process.
Results obtained show that these ejections are mainly parallel to the substrate surface. Instabilities responsible of such ejections appear at the very early stage after impact (about 0,5 ms) but first secondary droplets are ejected only 2,2 ms after impact, i.e., more than 1 ms after the end of flattening stage. If these results are compared with those obtained under plasma conditions, it can be seen that using a falling-drop experiment does not allow the impact splashing visualisation, but only flattening splashing. These observations confirm the wave propagation theory for impact splashing in case of a particle impact with high velocities (150- 300 m/s).
The following results present pyrometric signals and temperature calculations, for millimetre sized nickel droplets impacting on a mirror polished substrate. Three different conditions were studied: impact of a 1,5 mm sized drop on a preheated substrate (673 K), on a room temperature substrate and a room temperature substrate once preheated at 673 K (fig 6).
Cooling rates can be calculated thanks to the temperature evolution of the resulting lamellae.(See table 2)
Results obtained thanks to the two colour pyrometer technique show that cooling rates measured for the resulting splats after flattening seem to be equivalent for a preheated substrate and for that once preheated at 673 K. The latters are more important than those obtained with a room temperature substrate. These results confirm Fukumoto et al [4] last ones concerning the link between splat morphologies and substrate surface roughness. They recently showed the effect of the physical change of the substrate surface due to its preheating (see fig 7).

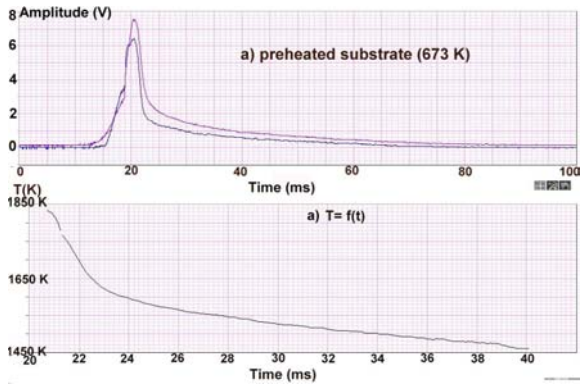

Figure 6: Pyrometric signals obtained with a millimetre-sized Nickel droplet impacting on a mirror-polished stainless steel substrate

Table 2 : Quenching rate calculation

Substrat Temperature	**R.T (room temperature)**	**Preheated at 673 K**	**R.T Once preheated at 673 K**
Lamella temperature after flattening stage	1770 K < T < 1880 K		
Quenching rate calculation	6-16.10^3 K/s	50-75.10^3 K/s	35-50.10^3 K/s
Resulting splat morphology	Fingered shape	Disk shape	Disk shape

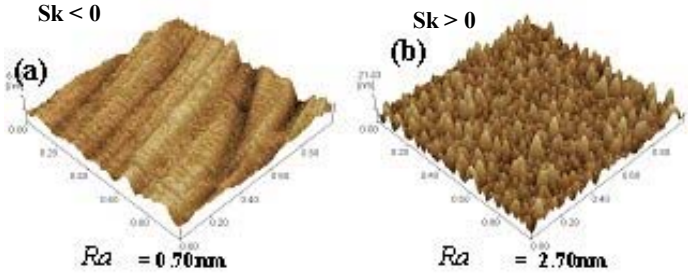

Figure 7 : Measurements of surface roughness on AISI 304 substrate by AFM. ***Fukumoto et al. [4]*** (a) as polished with 0.3µm Al2O3, (b) once heated to 673K after polishing with 0.3µm Al2O3

As it can be seen in figure 7, many oxide peaks were formed on once heated substrate. If the results for the corresponding splat cooling are compared, it can be imagined that these more numerous peaks with less undercuts induce more contact points between the splat and the substrate which enable a better quenching phenomenon. The transition temperature effect seems to improve the contact by surface modification in nm scale.

Fukumoto et al [4] showed that the skewness S_k value modification by preheating the substrate corresponds well to the splat shape for each substrate. Increasing the quantity of contact points between the substrate and the flattening droplet enables a rapid cooling and results in a columnar growth. As for the spraying case, in the free falling drop experiment, flattening splashing does not occur for a substrate temperature $T_s > T_t$.

Using the free falling drop experimental set up, recalescence phenomenon was also observed in some cases. For example, the results obtained with a millimetre-sized copper droplet exhibits a less conventional shape in case of impact on a room temperature substrate. Figure 8 presents the pyrometric signals and the calculated temperature evolution after the end of the flattening stage for a 2 mm diameter sized droplet impacting at 4m/s. Thanks to these time temperature evolution calculations, it can be seen that the second dump which appears after the droplet was in the supercooling stage (temperature reached 1280K) corresponds to a small increase of temperature which can be associated to the release of the latent heat of solidification of the material at the end of its undercooling. A dump is also observed in the case of a nickel droplet impacting on a glass substrate. This recalescence phenomenon seems to be linked to a bad wettability of the drop corresponding to a high thermal contact resistance between it and substrate.

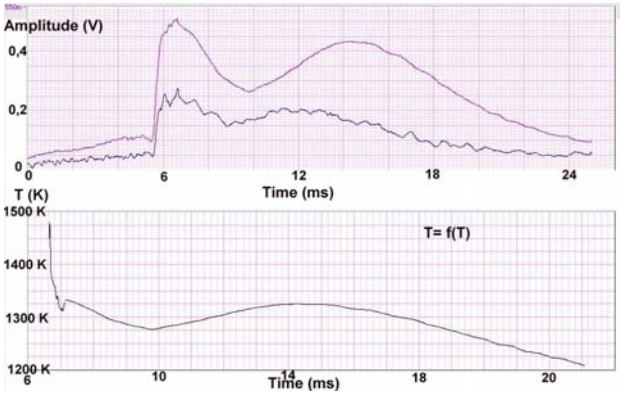

Figure 8 : Pyrometric signals obtained with a millimetre sized copper droplet and time-temperature evolution of the resulting splat.

Conclusion

The impact splashing is exclusively observed with the plasma spraying impact technique when the particle impact with high velocities (>100 m/s). The millimetre-sized drop impact technique presents other advantages, like comparing nickel drop cooling rates for different substrate characteristics. Results show that the quenching rate seems to be equivalent on a hot (673 K) or on room temperature substrate once preheated to 673K and higher than that measured on a room temperature substrate. The formation of peaks of oxide resulting from the preheating seems to improve the contact with the droplet resulting to a disk shaped splat. The recalescence phenomenon can also be observed in few cases. Future experiments will study the latter under d.c. plasma conditions with micrometer sized droplets. However, depending on the kinetic of these phenomena, it is not sure that they could be observed on the pyrometric signals.

Acknowledgement

A part of this work was supported by the Japan Society for Promotion of Science. SPCTS Laboratory would like to thanks the members of The Advanced Joining Process Laboratory (University of Toyohashi, Japan) for their collaboration.

References

[1]. Fauchais P., Fukumoto M., Vardelle A. and Vardelle M., Knowledge concerning splat formation, An invited review, J. Thermal Spray Technology, 2004,vol 13 (3),pp 337-360.
[2]. Fauchais P., Vardelle A. and Dussouds B., Quo Vadis Thermal Spray, J. Of Thermal Spray Technology, 2001,vol 10 (1), pp 44-66.
[3]. Cedelle J, Vardelle M, Pateyron B, Fauchais P., Study of droplet behaviour at impact in plasma spraying, J.of High Temperature Material Processes, 2004, vol 8 (3) pp 353-380.
[4]. Fukumoto M., Ohgitani I. and Yasui T., Effect of substrate surface change on flattening behaviour of thermal sprayed particles, Materials Transactions, 2004, vol 45 (6), pp 1869-1873.
[5]. Escure C., Vardelle M. and Fauchais P., Experimental and Theoretical study of the impact of alumina droplet on cold and hot substrates, Plasma Chem. Plasma Process., 2003, vol 23 (2), pp.185-221.
[6]. Armster S.Q, Delplanque J.P, Rein M., and Lavernia E.J, Thermo-fluid mechanisms controlling droplet based materials processes, International Materials Reviews, 2002, vol 47 (6) pp 265-304.

Micrometer-scale discharge plasma in high pressure H_2O and Xe up to a supercritical condition

M. Sawada, T. Tomai, T. Ito, H. Fujiwara, and K. Terashima

Department of Advanced Materials Science, Graduate School of Frontier Sciences,
The University of Tokyo, Chiba, Japan

Abstract

We performed the generation of micrometer-scale discharge plasma in high pressure H_2O and Xe up to a supercritical condition. Compared with conventional Paschen's curves, there exist two peculiar features in breakdown voltages. The first one is the shift from the right-hand branch of Paschen's curve and the second one is the drastic decrease near the critical point. We discussed these features by employing gaseous breakdown theory and the density fluctuations, which are caused by the clustering of the particles.
Keywords: micrometer-scale discharge, **s**upercritical fluid (SCF), H_2O, Xe, and density fluctuation

1. Introduction

Supercritical fluid (SCF), the intermediate state between gas and liquid, has received great attention because of its unique characteristics, such as a drastic change of thermal conductivity and high dissolving power near the critical point. From the microscopic viewpoint, SCF consists of the clusters of various-size particles and it produces large density fluctuations, which contribute the above-mentioned characteristics. Due to these characteristics, the applications of SCF have widely spread in many fields, especially in environmental science, nanotechnology, and chemical engineering. For instance, supercritical fluid extraction using supercritical carbon dioxide ($scCO_2$) as the solvent, substitutes for the conventional extraction process [1].

We have succeeded in generating discharge plasma in high-pressure CO_2 (critical point: 7.38 MPa and 304.2 K) up to a $scCO_2$ condition with a micrometer-scale gap electrode, and discovered that, near the critical point, its breakdown voltage was about 1/4 at the lowest of the value expected from conventional Paschen's curve [2, 3]. In addition, we have succeeded in fabricating carbon nanotubes and some other carbon nanostructured materials without any catalysts by discharge plasma in $scCO_2$ [4]. Although there had been few reports about discharge plasma in SCF yet, some groups have recently started reporting their interesting studies on this topic, which indicates that the unique features of SCF-plasma have recently been recognized in various fields [5, 6].

In this study, we performed the generation of micrometer-scale discharge plasma in high pressure H_2O (critical point: 22.12 MPa and 647.3 K) and Xe (critical point: 5.84 MPa and 289.8 K) up to supercritical conditions to compare the results with our previous work, which focused on CO_2 [2]. The main purpose of this study is to clarify that the unique phenomena of SCF-plasma, which were observed in the $scCO_2$ experiment, are general and analyze the differences among H_2O, Xe, and CO_2.

2. Experimental

Fig. 1 shows a schematic illustration of the apparatus for the discharge in high-pressure H_2O. The apparatus consists of a hastelloy cell with approximately 10 ml inner volume, heaters, thermocouples, pressure sensor, direct current (dc) generator and coplanar film electrodes (CFE), whose gap distance, thickness, and width are 1 μm, 1μm, and 50μm, respectively. CFE is produced with platinum on a sapphire substrate by lithography technique [7]. The procedure of the experiment is as follows. Ultra pure H_2O is injected into the cell and heated by four heaters. The pressure and temperature in the cell are controlled within the accuracy of ±0.07 MPa and ±2.5 K, respectively. The dc voltage applied to CFE generates the micrometer-scale discharge plasma. The radiation of the plasma is observed through a sapphire window, which is attached to the cell.

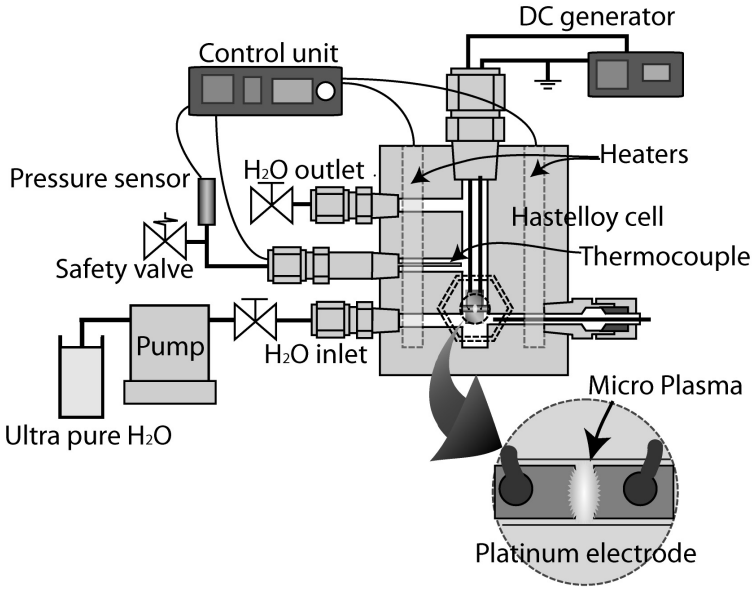

Fig. 1 A schematic illustration of the apparatus for the discharge in high pressure H_2O

Fig. 2 is a schematic illustration of the apparatus for the discharge in high-pressure Xe. The experimental setup is basically the same as that of H_2O except that we employ tungsten CFE on a quartz substrate for Xe experiment and Xe gas is once liquefied by liquid N_2 before injecting into the cell. The pressure and temperature of the environment are controlled within the accuracy of ± 0.07 MPa and ±1.0 K, by cooling the cell, which is surrounded by the ice and water. These parameters are also monitored all the time by using a pressure sensor and thermocouples.

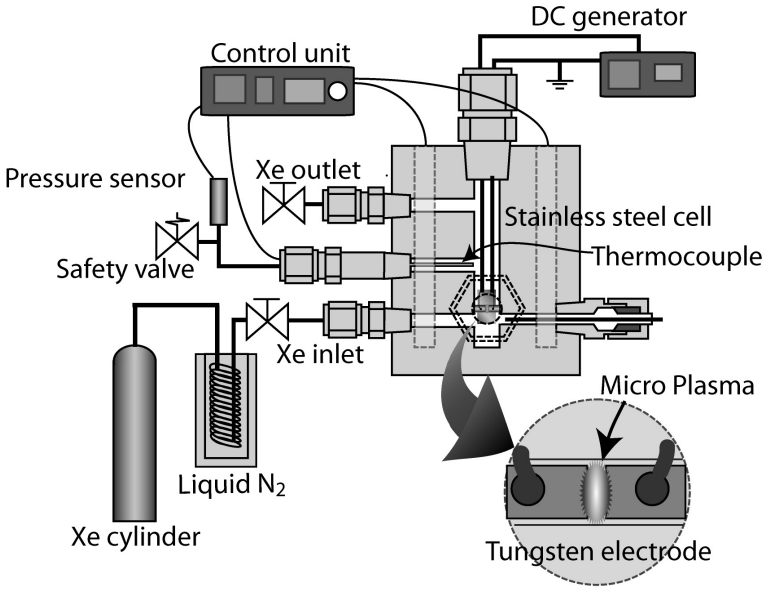

Fig. 2 A schematic illustration of the apparatus for the discharge in high pressure Xe

3. Results

Fig. 3 (a) and (b) show the breakdown voltages as the functions of environmental pressures for (a) H_2O, and (b) Xe, respectively. Fig. 3 (c) is from our previous report for CO_2 [3]. These three experiments were performed at 650.65 K ($T/T_c = 1.005$) for (a) H_2O, 292.15 K ($T/T_c = 1.008$) for (b) Xe, and 305.65 K ($T/T_c = 1.005$) for (c) CO_2, respectively, which were close to the critical temperature of each gas. The insets show the density fluctuations of each gas at the above-mentioned temperature. According to the results, there exist two peculiar features in not only CO_2 but also in H_2O and Xe. The first one is the shift from Paschen's curve above around 3MPa. The second one is the drastic decrease of the breakdown voltages in the vicinity of the critical pressure. Accordingly, these two unique features probably are general phenomena for the micrometer-scale discharge plasma under high-pressure gases up to supercritical conditions.

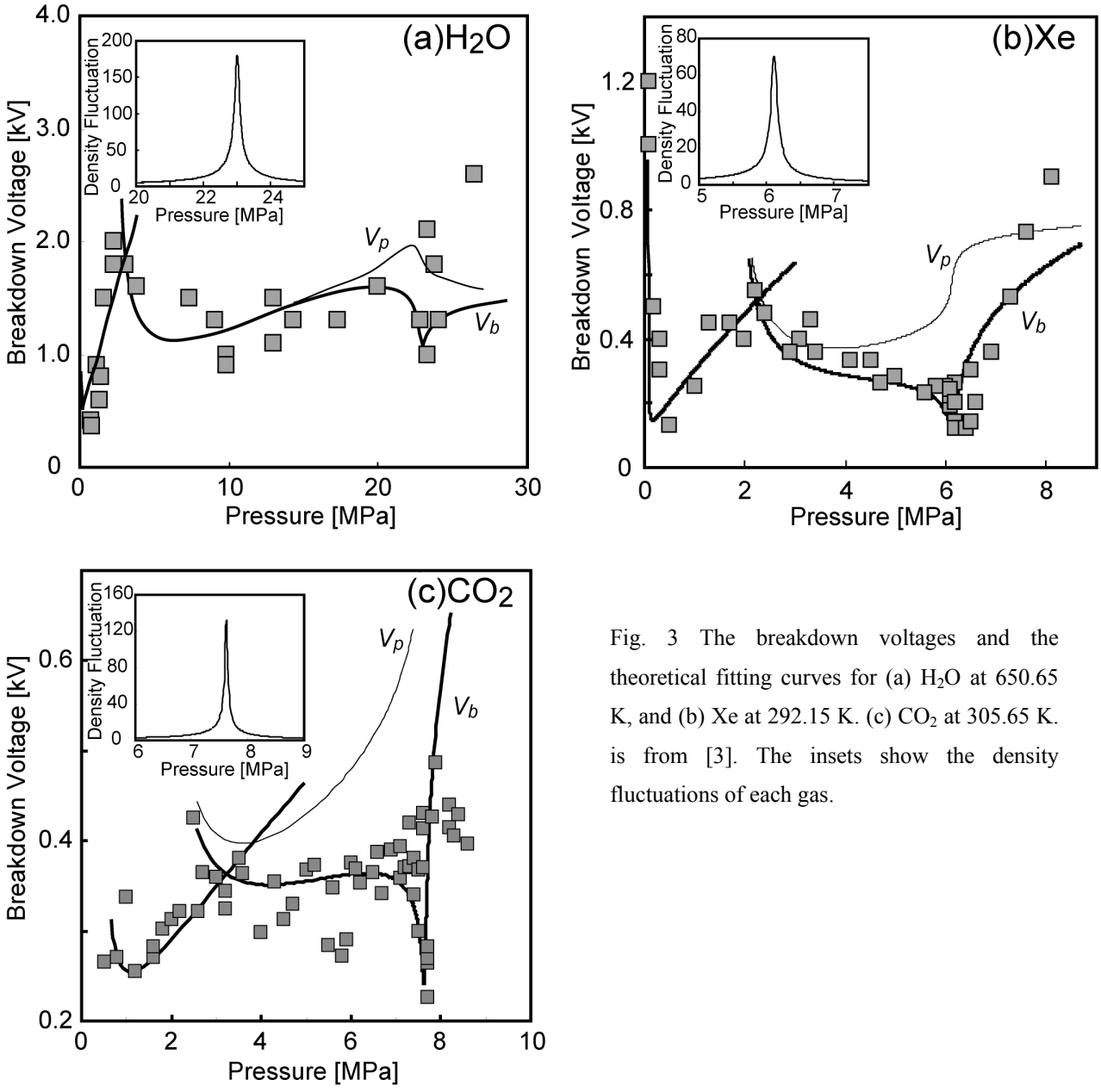

Fig. 3 The breakdown voltages and the theoretical fitting curves for (a) H_2O at 650.65 K, and (b) Xe at 292.15 K. (c) CO_2 at 305.65 K. is from [3]. The insets show the density fluctuations of each gas.

According to the gaseous breakdown theory (Townsend's theory), the breakdown voltage V_p is generally described as [8]

$$V_p = \frac{dn\sigma\psi_i}{AB}\left\{\frac{1}{\ln(dn\sigma) - \ln\left(\ln\left(1/\gamma' + 1\right)\right)}\right\}, \tag{1}$$

where d is the gap distance of the electrode, n is the number density, σ is the electron-to-particle cross section, φ_i is the ionization potential, γ' is the secondary Townsend coefficient, A is the effective coefficient related to the electrode sharpness, and B is the coefficient associated with the dielectric constant.

The trough locations of the breakdown voltages in Fig. 3 are fairly close to the pressures, at which the density fluctuations take the maximum. In our previous report, which was about CO_2, the drastic decrease of the breakdown voltages near the critical point was analyzed systematically by employing Townsend's theory and the density fluctuations due to the clustering of the molecules [3]. The density fluctuation F_D is calculated from the equation [9]

$$F_D = \left\langle (\Delta N)^2 \right\rangle \Big/ N = (N/V)\kappa_T k_B T = \kappa_T / \kappa_T^0, \tag{2}$$

and the isothermal compressibility κ_T is calculated from the equation [10]

$$\kappa_T = (-1/V)(\partial V/\partial P)_T, \tag{3}$$

where N is the number of molecules, V is the volume, k_B is Boltzmann's constant, T is the temperature, κ_T^0 is the compressibility of a ideal gas, and P is the pressure. To explain the drastic decrease near the critical point, we proposed the correlation between the conventional breakdown theory and the density fluctuations as

$$V_b = \alpha V_p F_D^{\beta}, \tag{4}$$

where α and β are individual coefficients [3]. Also in this study, we employ this equation (4) to analyze the unique phenomena of the breakdown voltages near the critical point.

The lines in Fig.3 (a) show the theoretical fitting curves for H_2O at 650.65 K. The fitting curves V_p and V_b are calculated from the equations above. In the region higher than around 3 MPa, σ of 1.5×10^{-20} m^2, and γ' of 1.0×10^{-18} are assumed for agreement with the experimental results, while σ of 1.9×10^{-19} m^2, and γ' of 8.0×10^{-8} are employed under the lower pressure. The dielectric constant is calculated from [11]. φ_i of 12.62 eV, A of 1.2, α of 1, and β of –0.15 are employed for all estimations. The location of the inflection in Fig.3 (a) agrees with the pressure, at which the electron mobility decreases because of the electron attachment to the clusters [12]. We discussed this inflection at 3 MPa, taking into consideration of the possibility of the electron attachment as were done in our previous report [3].

On the other hand, the lines in Fig.3 (b) show the theoretical fitting curves for Xe at 292.15 K. The fitting curves V_p and V_b are calculated from the equations above as H_2O. In the region higher than around 2 MPa, σ of 3.0×10^{-20} m^2, and γ' of 1.0×10^{-6} are employed for agreement with the results, while σ of 3.3×10^{-19} m^2, and γ' of 4.5×10^{-3} are employed in the region lower than around 2 MPa. The dielectric constant is calculated from the Clausius - Mossotti function [13]. φ_i of 12.1 eV, A of 1.2, α of 1, and β of –0.25 are employed for all estimations. We discussed the inflection of the breakdown voltages at 2 MPa,

taking into consideration of the possibility of the electron attachment to the clusters as we did for CO_2 and H_2O.

4. Discussion

We discussed two unique behaviors (the inflection at around 2~3 MPa and the drastic decrease near the critical point) of the micrometer-scale discharge with the electron attachment to the clusters and the change of the discharge space, respectively.

Firstly, as the shift from the conventional breakdown theory above 2~3MPa, according to the results, there must be some environmental changes at this pressure. V. Giraud, et al. reported that the density-normalized mobilities of these gases rapidly decrease at the pressure above 2~3 MPa [12, 14, 15]. This is believed to result from the electron attachment to the clusters. Therefore, at the pressure above 2~3MPa, some clusters in the discharge space have negative charges and it makes the electron to difficult to collide to the clusters. Consequently, the electron could acquire sufficient energy for ionization because the actual cross section becomes smaller and the mean free path extends enough. The attached electron might be emitted mainly from the cathode edge. Therefore, the emitted electrons may work more effectively as we employ the smaller electrode because the ratio of the number of the electron to the molecules in the discharge space becomes higher. In fact, the shift from the conventional Paschen's curve has not been observed when the gap distance was longer than several μm [3]. Therefore it indicates that our micrometer-scale discharge plasma may be the peculiar and different from the conventional one.

As the drastic decrease of the breakdown voltages near the critical point for these three gases, there is the possibility that the discharge space changes by the density fluctuations. In other words, the discharge space becomes sufficiently large for electrons to be accelerated in SCF, compared to the space estimated from the average density. Hamaguchi, et al. also reported, according to the simple calculations, that the discharge space might become sufficient and the discharge plasma could be generated with low voltages near the critical point [16]. Table 1 shows the individual coefficients α and β for H_2O, Xe, and CO_2, respectively. The values of β are different from one another. As shown in equation (4), $F_D{}^{\beta}$ expresses the ratio of V_b to V_p. In these three gases, Xe is the closest to the ideal gas, while H_2O and CO_2 have the polarities and the internal bonding angles. Therefore, Xe is reflected by the density fluctuations directly, compared to the other two gases. As the value –0.35 (~-1/3) of β for Xe, it might be explained by the dimension of the density fluctuation and the electric field. Though the density fluctuations express the deviation of the number of molecules per unit volume, it affects only to the direction of the electric field. Hence, the influence of the density fluctuations to the breakdown voltage might become approximately 1/3. As the differences in the value of β among these gases, there are two reasonable possibilities. The first one is that CO_2 and H_2O have the polarities and accordingly, the actual voltages, which accelerate the electrons, might become smaller than the displayed voltages applied to the electrode because the molecules or clusters which have polarities, changes the electric field slightly. Therefore, it prevents the electrons from being accelerated enough for ionization. The second one may be the differences in the packing structure due to the shapes of the molecules. Xe molecules, which have

Table 1 The individual coefficients for H_2O, Xe, and CO_2

	H_2O	Xe	CO_2
α	1	1	1
β	-0.15	-0.35	-0.25

spherical shapes, make a neat and tight structured cluster. On the other hand, CO_2 and H_2O molecules make less efficient clustering because these molecules have the limitations for gathering.

5. Summary

In this study, we succeeded in generating dc discharge plasma under H_2O and Xe environments from the atmospheric pressure up to supercritical pressure with a micrometer-scale gap electrode, and confirmed that there were the shifts from the conventional Paschen's curve at the pressure above 2~3 MPa, and near the critical point, the breakdown voltages were extraordinary low. We proposed the possibility of the electron attachment to the clusters and the changes of the discharge space for understanding of these unique features of micrometer-scale discharge plasma in a high-pressure environment up to a supercritical condition.

Acknowledgement

This work was supported financially in part by Specific Research of Priority Areas (Microplasma, Grant No. 15075202) from The Ministry of Education, Culture, Sports, Science and Technology.

References

[1] K. Zosel, Angew. Chem. Int. Ed. Engl. 17, 702 (1978)

[2] T. Ito, and K. Terashima, Appl. Phys. Lett., 80, 2854 (2002).

[3] T. Ito, H. Fujiwara, and K. Terashima, J. Appl. Phys., 94, 5411 (2003).

[4] T. Ito, K. Katahira, Y. Shimizu, T. Sasaki, N. Koshizaki, and K. Terashima, J. Mater. Chem., 14, 1513 (2004).

[5] E. Lock, A. Saveliev, and L. A. Kennedy, abstract of 2nd International Workshop on Microplasmas, in New Jersey 65 (6/Oct/2004) edited by K. H. Becker, J. G. Eden, and K. H. Schoenbach.

[6] H. Akiyama, M. Goto, T. Namihara, M. Sasaki, T. Heeren, B. C. Roy, T. Kyan, and K. Sunao, abstract of 2nd International Workshop on Microplasmas, in New Jersey 44 (6/Oct/2004) edited by K. H. Becker, J. G. Eden, and K. H. Schoenbach.

[7] T. Ito, T. Izaki, and K. Terashima, Thin Solid Films, 386, 300 (2001)

[8] Y. P. Raizer, *Gas Discharge Physics*. Springer-Verlag, Berlin, 1991

[9] H. E. Stanley, Introduction to Phase Transitioins and Critical Phenomena. Oxford University Press, 1971.

[10] F. Huang, M. Li, L. L. Lee, K. E. Starling, and F. T. H. Chung, J. Chem. Eng. Jpn. 18, 490 (1985)

[11] IAPWS Release on the Static Dielectric Constant of Ordinary Water Substance for Temperatures from 238K to 873K and Pressures up to 1000MPa (1997)

[12] V. Giraud, and P. Krebs, Chem. Phys. Lett., 86, 85 (1982).

[13] J. Hout, and T. K. Bose, J. Chem. Phys., 95, 2683 (1991)

[14] F. M. Jacobsen, G. R. Freeman, J. Chem. Phys., 84, 6, 3396 (1986).

[15] S. S. Huang, G. R. Freeman, J. Chem. Phys., 68, 1355 (1978).

[16] S. Hamaguchi, and S. C. Sharma, abstract of Symposium of Micro plasma in liquid, in Tokyo, 10 (22/Sep/2004) edited by K. Tachibana, (in Japanese)

Control of arc root attachment mode at the anode surface: application to the synthesis of ultra fine particles by plasma transferred arc technique

C. Chazelas, J. F. Coudert, J. Jarrige, P. Fauchais

Laboratoire Science des Procédés Céramiques et Traitement de Surface. UMR 6638
123 avenue Albert Thomas 87060 Limoges cedex
E mail : Christophe.chazelas@unilim.fr

ABSTRACT

Gas to particle conversion refers to production of particles from individual atoms or molecules in the gas phase. In the current work, a transferred arc is used to produce nanometric particles from the condensation of metallic vapours obtained by controlling the evaporation of the anode material of a d.c. transferred arc. The synthesis of desired particles requires both the control of the heat transfer and more precisely the heat flux to the anode and its stability, which depend on properties of the cold boundary layer close to the anode surface. That's why a new and original experimental set-up was built in order to control cold boundary layer properties close to the anode surface, and so the vapour production and its thermal history.

I-Introduction

Ultra fine powders are used in many fields. For example, catalysts, sensors, sintered parts and electric insulators under high temperature would perform better if ultra fine particles (UFP) were used as materials. Several processes can be used for producing ultra fine particle, such as sol-gel process [1], ball- milling [2], and gas phase synthesis [3-4]. Gas to particle conversion refers to production of condensed particles from individual atoms or molecules in the gas phase. Particle formation is driven by the cooling of a supersatured vapour or by the generation of atoms and molecules by chemical reaction of gaseous precursors. Once particles form in the gas phase, further growth depend of the properties of the flow into which they are imbedded. Thermal plasma based vapour condensation methods which utilize a transferred arc, have not been successful up to now to generate fine or ultra fine powder of materials such as metals, alloys, ceramics or composites on a commercial scale because of rudimentary control of powder properties such as particles size and distribution, shape and cristallinity [5-6]. As the synthesis of ultra fine particles with desired size and composition requires reactive species production control, a good understanding of the heat transfer mechanisms to the anode, which depends of properties of the cold boundary layer and arc roots dynamic is of prime importance. In plasma transferred arc devices, it is well known that there are two distinct types of anode attachment modes, namely the diffuse and the constricted mode. It appears that the cold boundary layer properties and particularly its thickness govern both the dynamic and geometry of the arc root attachment. In previous works [7-9], the cold boundary layer modifications were obtained by several ways such as the addition of diatomic gases, the variation of the electrode gap and the internal diameter of the exit nozzle, or the use of constrictor tube [8] or with a superimposed cross flow [9]. In this work, its modification is performed by the inclination of the torch assembly to the normal of the anode surface. By increasing the angle, for given arc working conditions, the normal velocity of the plasma flow close to the anode surface decreases as well as the fraction of the convective heat transfer, thus modifying the arc root attachment, from the diffuse one to the constricted one. Beyond the modification of the heat transfer mechanisms and so vapour production, this inclination allows controlling the jet orientation of the metallic vapours towards a pressure and temperature controlled zone. Hence, the synthesis of particles with controlled characteristics may become possible, by controlling their thermal history.

II-Experimental set-up

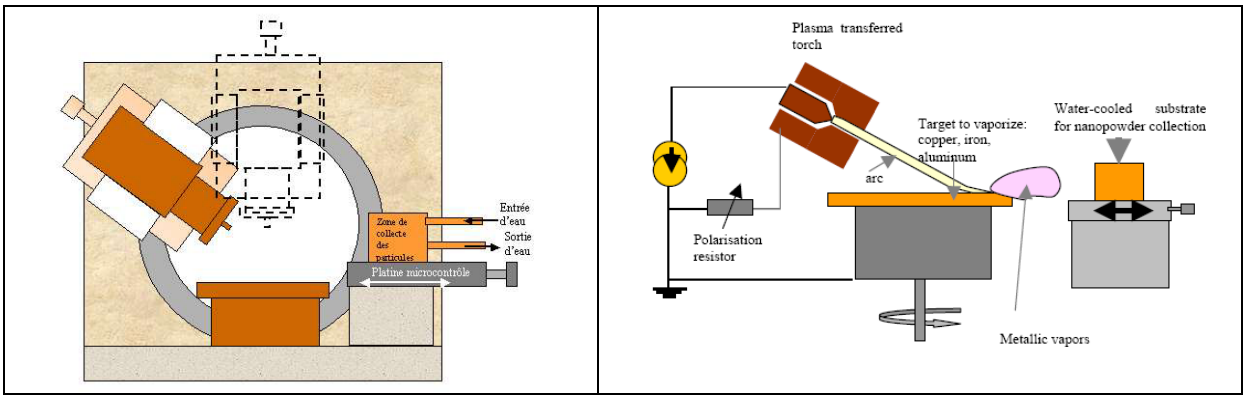

Figure 1: experimental set up developed

A transferred arc reactor (see fig 1) was designed to generate a stable arc jet, less than 3mm in diameter, using pure argon, argon-hydrogen mixture or nitrogen as plasma forming gases (4-10 slm) and power supplied by a current regulated source (I = 15-40A). The arc, stabilized by a superimposed plasma jet, is transferred between the cathode made of thoriated tungsten and the main anode precursor, made of the material to be eventually proceeded and situated perpendicular to its axis. According to the nozzle internal diameter (1.6mm or 2.5mm) used to constrict the arc, the jet velocity is over 1000 $m.s^{-1}$.The pilot arc offers several advantages, such as arc ignition and arc column stability. The pilot arc, first started, feeds the gap between the exit nozzle and the anode precursor with hot gases. Hence, it becomes easier to transfer low current intensity to the anode precursor. The heat flux density transferred to the anode can also be regulated by mean of the electrical resistor R, distributing the current between the stabilization anode-nozzle and the main anode. Furthermore, the arc pilot allows rising the plasma jet momentum, allowing its inclination. As the torch assembly is mounted on "ball bearings", the angle between the jet axis and the normal to the anode surface can be changed continuously from $\theta = 0°$ to 85°, whereas the electrode gap can vary from 1 mm to 25 mm. Thus, for given working conditions, the normal velocity varies between V_p and $V_p.\cos\theta$, where V_p corresponds to the plasma jet velocity. Beyond the orientation of the metallic vapors towards a pressure and temperature controlled zone, the inclination allows controlling cold boundary layer thickness and so the heat transfer at the anode. Hence, the control of vapours production and their thermal history becomes possible [10]. Besides the target is rotating, permitting the temperature control at the arc attachment, and thus, the vaporization flux. The particles are collected onto a water-cooled substrate, mounted on micrometric displacement in order to modify the residence time of particles imbedded in the flow. Ultra fine particles synthesized must be characterized. This requires control of size and size distribution, as well as composition. Micro structural features of the particles were studied using the scanning electron microscopy (Philips XL 30). If the particles synthesized were too small to be visualized on SEM microscopy, the collected powder was dispersed ultrasonically in alcohol and then allowed to settle on carbon coated copper grids for investigation by transmission electron microscopy (TEM JEOL 2010). The chemical composition of the particles was obtained by XRD diagrams. The diffraction pattern of the powder was recorded at a speed of $0.04°.s^{-1}$ using Cu Kα radiation.

III- Experimental results

Thermal vapour history could be achieved either by blowing the arc root by a superimposed cross flow or by tilting the angle between the jet issued from the cathode and the normal to the anode surface. As the plasma jet is stabilized by a superimposed plasma jet, it can be tilted. This inclination allows the orientation of the metallic vapours toward a pressure and temperature controlled zone. Hence, the control of vapours thermal history becomes possible.

.

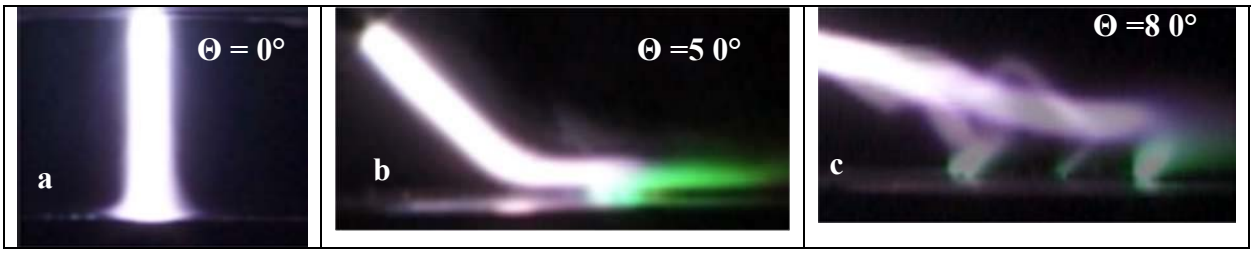

Figure2: different arc root attachment mode: (a) diffuse stable, (b) constricted stable, (c), constricted unstable, Ar plasma, I=20A, arc length L=15mm.

It is then suggested by pictures of figure 2 that it is possible to go continuously from a steady mode, for normal or low inclination, to a transient mode, where the arc root jumps from place to place, as soon as the arc length overcomes a critical value. As already discussed in former work [8-9], arc root dynamic and geometry are strongly dependent on the cold boundary layer properties (flow affected zone) close to the anode precursor. For angle $\theta < 30°$, the diffuse attachment is observed and no vapour production can be noticed in that case. The plasma forms symmetrically beneath the nozzle exit and a diffuse and stable arc root attachment is observed. For angle between 30° and 65°, the diffuse attachment changes to a constricted and stable one. The constriction, which appears as soon as the cold boundary layer becomes visible, leads to an enhanced heat flux and the anode material evaporates, as testified by green copper vapours It must be understood that the cold boundary layer disappears for normal incidence and increases in thickness as the normal component of the plasma jet velocity decreases. This clearly demonstrates that cold boundary layer thickness is governed by thermal effects for low values of θ.

Nevertheless, when the angle overcomes a critical value, appreciatively 65° for the actual plasma parameters, plasma flow acts tangentially onto arc root attachment and normal impact jet velocity tends to zero. Hence, cold boundary layer thickness is mainly governed by thermal effects and no more by mechanical effect. The arc root is still constricted but becomes unstable. In such configuration, the electrical connexion is submitted to the drag force induced by the plasma flow and also to the Laplace interaction of the magnetic field induced by the column and the current density at the wall, giving rise to a backward force. The cold flow pushes the arc root, and in the same time, the arc voltage increases together with the electric field in the cold boundary. When the field overcomes a given value, the breakdown in the sheath initiates a new path for the arc and the attachment jumps to another place. The arc root is still constricted but becomes unstable. It is then believed that the same phenomena occur inside the nozzle of a plasma torch, because the recorded time resolved voltage shows the same waveform. This unsteady mode, termed “restrike” mode, is accompanied by a saw tooth shaped voltage, showing linear increasing ramps followed by sudden negative jumps, this scheme being repeated in a few kilohertz range. It can be seen, following that example that phenomena inside the sheath participate to the arc column instability. Finally, three arc root attachment behaviours can be distinguished, as shown on figure 3, depending of the cold boundary layer thickness close to the anode: diffuse or constricted and stable ones, or stable or unstable constricted once.

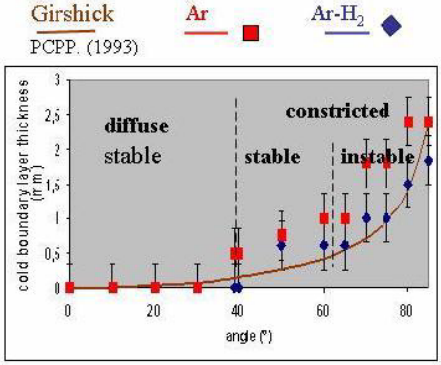

Figure 3: evolution of the “cold boundary layer thickness as a function of the inclination for Ar or Ar-H_2 plasma forming gas

Figure 3 shows the evolution of the arc root dynamic and geometry as a function of the cold boundary layer thickness, for argon and argon-hydrogen mixture as plasma forming gas. As the arc current intensity and plasma forming gas could be imposed by the nature of the particles to be produced, it could be interesting, for given working parameters, to visualise their effects on arc root attachment properties. The main result is that adding hydrogen delays the shifting from one mode to another. That must be explained by the fact that shifting from argon to argon-hydrogen as plasma forming gas result into a better heat transfer and a higher plasma jet velocity of the superimposed plasma jet. Hence, cold boundary layer is governed longer by mechanical effect and higher angles are needed for reducing the normal impact jet velocity at the anode and then shifting from one mode to another. Same results are obtained both by increasing arc current intensity or decreasing exit nozzle internal diameter. The role which is played by the sheath may be completely different following the kind of confinement of the arc column as it is the case either for a free burning arc or for a wall stabilized arc. In the last case, the electric field in the cold boundary layer may be high enough to give rise to the breakdown of the gas, which initiates another pass for the electric current.
As the key-point of this process consists in keeping the heat flux at a critical value for which anode erosion is only due to its vaporization, minimizing droplet ejection, the angle is set-up in order to obtain a constricted and stable arc root for powder synthesis. Stable arc root allows both the reproducibility and vapour phase production whereas constricted arc root enhances by one order of magnitude the heat flux transferred to the anode precursor.

III-2 Alumina particles synthesised

Synthesis of particles with controlled sizes and compositions requires the control of the vapour flux and its thermal history. Nevertheless, as experiments presented here were performed at atmospheric pressure, in air; control of chemical composition is not possible. The experimental parameters are summarized in table1.With such parameters, the arc root is constricted and stable. Due to the high power level transferred to the anode precursor, vaporisation of anode precursor occurs. The vapours are naturally canalised by the plasma flow towards the collecting substrate.

Plasma gas	Intensity transferred (A)	Total voltage (V)	Gas flow rate (L/min)
Ar	15 A	50V	4 L/min
Nozzle internal diameter (mm)	Collection distance	Rotating speed ($cm.s^{-1}$)	Angle
2.5 mm	20 mm	$0.5cm.s^{-1}$.	45

Table 1 : working parameters for alumina synthesis

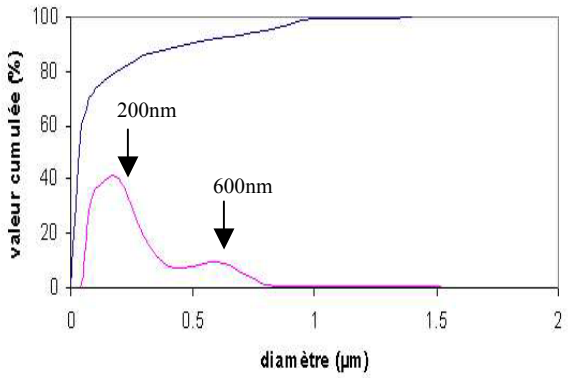

Figure 4 : Particles size distribution

Particle size distribution of the processed powder is shown in figure 4. It comes that vapour phase production and orientation allow decreasing the mean averaged size of the particles and their granulometric distribution. It is obvious from figure 4 that all the particles are in the submicrometer range. That must be explained by the very good control of the vaporization step, avoiding droplet ejection, and by the dissociation of the vaporization and nucleation/growth event. By the way, it must be said that the reproducibility of the experiments is achieved. Two main peaks can be distinguished, centred respectively at 200 nm and 600 nm.

Ultra fine particles have an inherent tendency to form agglomerates and aggregates, and very often, the results of particle size distribution studies by laser scattering mostly gives the size distribution of these agglomerates. The actual size of the individual particles in the clusters can be determined by electron microscopy (figure5).

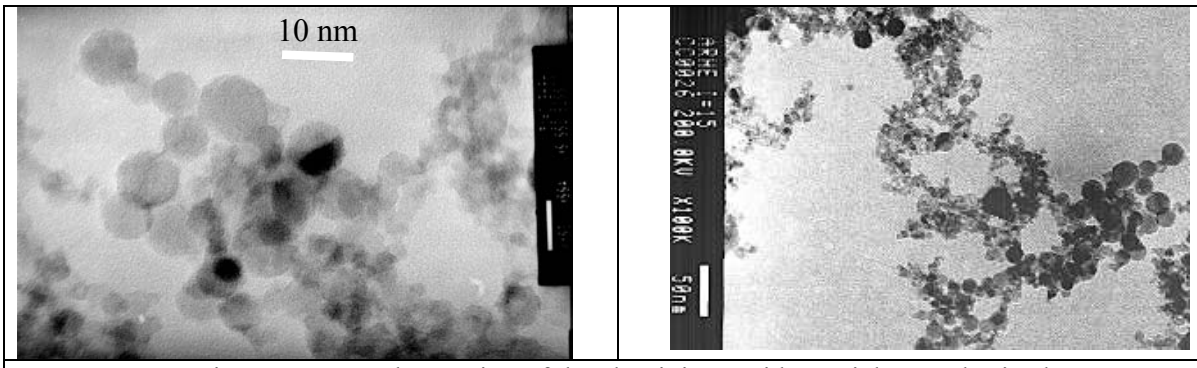

Figure 5: TEM observation of the aluminium oxide particles synthesized

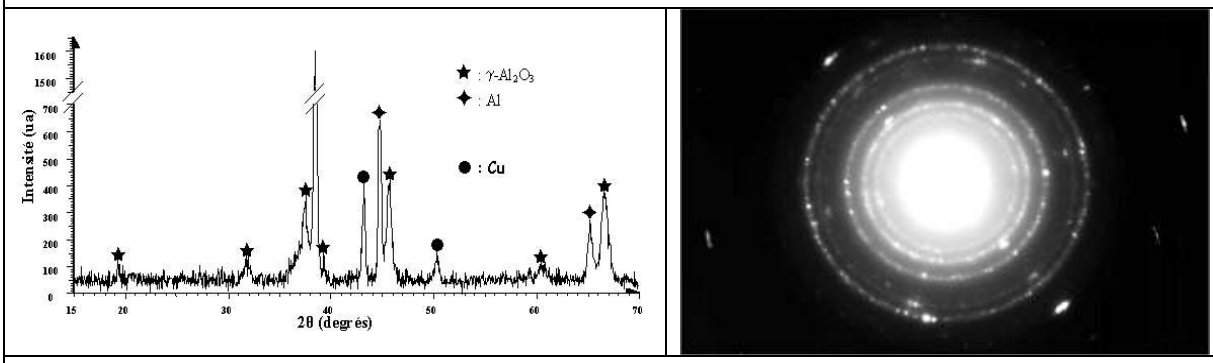

Figure 6 : XRD of powder synthesized

Particles synthesized are clearly nanoparticle chain aggregates, whose compactness depends on ramifications orientation, composed of primary particles that are approximately 10 nm, even if particles with diameters reaching 40 nm can be observed. The spherical or near spherical morphology of the powder is evident. X ray diagram (figure 6) proved that particles are well crystallized, even if some of them are not. The presence of discontinuous rings, as well as broadened peaks from normal X ray patterns, proves that the particles are crystallized and in nanometric range (below 40nm). X-rays diffraction results of the powder indicate that they are heterogeneous. The presence of copper can be explained by the fact that the aluminium precursor is an alloy with 4% of copper (AU 4G). The analysis of diagrams tends to prove the existence of the gamma alumina phase. As no oxygen has been introduced in the plasma plume during the experiments, formation of aluminium oxide can be explained as follow. For appropriate working parameters, vaporization of aluminium precursor occurs. These vapours are naturally orientated by the plasma flow towards the water cooled substrate for collection. Nevertheless, due to viscous strength, air penetrates in the fringes of the plasma and diffuses inside the core, where it is dissociated. Hence, atomic oxygen can react with atomic aluminium vapour to form aluminium oxide. The formation of gamma phase is consistent with the highly non equilibrium nature of the process. Vapours of aluminium react with oxygen to form aluminium oxide, which crystallizes in the metastable γ phase due to of the rapid quenching associated with the process. The formation of the metastable γ phase, in preference to the thermodynamically stable α phase has also been observed in fine alumina powder prepared by other high temperature techniques, such as plasma spraying, arc discharge and electrodynamic atomization.

IV- Conclusion

Ultra fine powder has been synthesized and the product has been characterized. As synthesis of powder with controlled size and composition requires the dissociation of the vaporization and

nucleation events, a new experimental set up has been developed. The process developed consists in keeping the local heat flux at a critical value for which anode erosion is only due to its vaporization. Orientation and so dissociation of nucleation event is achieved by tilting the angle between the jet issued from the cathode and the anode. Experiments showed that it was possible to control arc root attachment geometry and stability close to the anode surface by modifying cold boundary layer thickness at the anode. It becomes then possible to generate diffuse or constricted stable arc root attachment, and so vapour production. Nevertheless, when the angle overcomes a critical value, approximatively 65° for the actual plasma parameters, plasma flow acts tangentially onto arc root attachment and normal impact jet velocity tends to zero. Hence, cold boundary layer thickness is mainly governed by thermal effects and no more by mechanical effect.
The vapours produced are naturally canalised and orientated towards a temperature controlled zone, where they are collected onto water cooled substrate. The powder synthesized is heterogeneous, because oxygen is the limiting reactive specie. Results of X-ray powder diffraction studies show that the particles are nano-sized and are mainly crystallized under the gamma phase. Particles synthesized are clearly nano-particle chain aggregates initially about few hundred nm long, composed of primary particles that are approximately 10 nm, even if particles with diameter reaching 40 nm can be observed. In some applications, such as catalysis, agglomerates with an open structure like those are desired. However, in many potential applications non-agglomerated spherical nano-particles of uniform size are needed. More experimental studies are needed using a wider range of materials and operating conditions. Nevertheless the most important result may be the fact that reproducibility of the experiments is achieved.

References

[1] Zhai Yongqing, Yao Zihua, Ding Shiwen, Qiu Mande and Zhai Jian, « Synthesis and characterization of Y_2O_3 : Eu nanopowder via EDTA complexing sol–gel process », Materials Letters, 57, (19), (2003), 2901-290

[2] C. Lam et al., large scale synthesis of ultrafine Si nanoparticles by Ball-milling, Journal of cristal growth, (220), (4), (2000), 466-470

[3] Zachariah, M. R., Shull, R. D., McMillin, B. K. and Biswas, P. In situ characterization and modeling of the vapor-phase formation of a magnetic nanocomposite Nanotechnology :Molecularly Designed Materials (Edited by Chow, G. and Gonsalves, K.), ACS Series, 622, (3), (1996b), 42-64. American Chemical Society, Washington, DC

[4] S. Martelli, A. Mancini, R. Giorgi, R. Alexandrescu, S. Cojocaru, A. Crunteanu, I. Voicu, M. Balu and I. Mor, « Production of iron-oxide nanoparticles by laser-induced pyrolysis of gaseous precursors », Applied Surface Science, 154-155, (2000), 353-359

[5] Ageorges et al., Plasma Chemistry and Plasma Processing,. 13, (4), (1993), 613-632

[6] Francesco J. Moura and Richard J. Munz, Vapor phase synthesis of nanosize Alumunuim Nitride particles Using a Two-Stage Transferred Arc Reactor, J. Am. Soc., 80, (9), (1997), 2425-28

[7] Hartmann R. M and Heberlein J., quantitative investigations on arc-anode attachments in transferred arcs, 2001 J. Appl. Phys. **34** 2972-78.

[8] Heberlein J and Pfender E 1997 IEEE Trans. Plasma Sci. **5** 171-80

[9] Hartmann R. M and Heberlein J., Experimental Investigation of Anodic Arc Attachment Instabilities, 15th Int. Symp. Plasma. Chemistry, 2 (2001), p. 497-502. orleans.

[10] Da Cruz et al., IEEE Trans. On Plasma Sciences, 1997, 25, (5), 1008-1016.

THE MODIFICATION OF GLASS FIBRES BY PLASMA POLYMERISATION FOR COMPOSITE GLASS FIBRE/ACRYLIC RESIN

D. Çökeliler[1], S. Erkut[2], J. Zemek[3], A. Choukourov[4], D. Slavinska[4], H. Biederman[4] and M. Mutlu[1]

[1]*Plasma Aided Bioengineering and Biotechnology Research Laboratory, Engineering Faculty, Hacettepe University, Ankara, Türkiye*
[2]*Department of Prosthodontics, Baskent University, Ankara, Türkiye*
[3] *Academy of Sciences of the Czech Republic, Institute of Physics, Prague, Czech Republic*
[4] *Department of Macromolecular Physics, Charles University, Prague, Czech Republic*

Abstract

Plasma treated E-glass fibre to improve the mechanical properties of acrylic resin denture base material, polymethylmethacrlyate was studied. Three different types of monomers 2-hydroxyethyl methacrylate, triethyleneglycoldimethyl-ether, and ethylenediamine were used in the plasma polymerisation modification of glass fibres. Results revealed that treatments had significant effect ($p<0.001$) on the flexural strength. SEM was used to examine the microstructure and XPS was used for chemical analysis of surface.

Keywords: Plasma polymerisation; Glow discharge; E-glass fibres; Ethylendiamine, 2-hydroxyethyl methacrylate, triethyleneglycoldimethyl-ether

Introduction

The addition of glass fibre reinforcement is known to improve the stiffness, strength, and the high temperature performance of polymeric materials [1,2]. In general, the advantages of glass fibres compared with other competing fibres are high tensile and compressive strengths and, especially, low cost. Glass fibres are also effective in improving the mechanical properties of polymethylmethacrlyate (PMMA). PMMA is the most commonly used material in the construction of dentures. The reinforcement of PMMA through the addition of glass fibres has been shown to be effective in enhancing the mechanical properties of the assembly [3,4]. One of the drawbacks observed in the composites is poor compatibility between glass fiber and polymeric matrix, and difficulty to distribute glass fiber uniformly**.** The interfacial adhesion between the glass fiber and polymer is not strong enough, which affects the mechanical properties of the composites. A strong interface generally leads to the best composite properties, and many effective interfacial coupling agents that are capable of forming strong interface have been identified for single component polymer matrices. The need for techniques to bond glass fibers to polymer matrices is recognized since glass fibers were first used as reinforcement. Silane coupling agents are widely used for this purpose [5]. The enhancement of the adhesion between a polymer matrix and a plasma-treated fiber is caused by both physical and chemical modifications. The physical modification is the surface roughening of the fiber by the sputtering effect, producing an enlargement of contact area that increases the friction between fiber and the polymer matrix. The chemical modification is the implantation of active polar groups on the fiber surface, reducing the surface energy and promoting chemical bonding between the fiber and the polymer matrix. This difficulty can be avoided by emloying the plasma polymerization technique, which has advantages of being cost-effective and environmentally friendly. The main purpose of plasma surface treatment of fibres or whiskers used as reinforcements in composite materials is to modify the chemical and physical properties of their surface with tailoring fibre-matrix bonding strength, yet without affecting their bulk mechanical properties. Oxygen or argon plasma gas treatment has been most commonly used to introduce hydroxyl functional groups in the surface of materials. Wettability can also affect considerably the interfacial adhesion between the fiber and the matrix [6,7]. Radio frequency (RF) glow discharge plasma is one of the most widely used sources for surface modification. In our previous study, two different agents 2-hydroxyethyl methacrylate (HEMA) and air were used for the modification of glass fibres by RF glow discharge treatment [8]. The deposition of plasma polymers by hexamethyldisiloxane and vinyltriethoxysilane plasmas was also studied [9,10].

In this study, three different types of monomers, 2-hydroxyethyl methacrylate (HEMA), triethyleneglycoldimethylether (TEGDME) and ethylenediamine (EDA) were used for the plasma polymerisation modification of glass fibres. The plain and surface modified glass fibres were incorporated into the PMMA structure and the effect of modification was tested in terms of mechanical properties, surface chemical composition change and microstructure.

Material and Method

The Modification of glass fibers

In the study, glass fibers were treated in a glow discharge reactor by plasma polymerisation technique to change the surface properties. The reactor was a glass tube with two external cupper electrodes. A 13.6 MHz radio frequency generator was used to sustain plasma in the reactor. Power losses were minimized by means of a matching network. The reactor was evacuated to $2x10^{-3}$ mbar and monomer vapor allowed to fill the reactor until the pressure in the reactor to reach a level of $8x10^{-3}$ mbar. Then, RF power was adjusted to 25 W and the glass fibers were exposed to glow discharge for 30 min. The preliminary studies of our group to optimize the plasma polymerisation conditions for reinforcement of the PMMA based denture materials were reported elsewhere [4]. At the end of process the RF generator was turned off and the system was fed with Argon gas for 20 min. to deactivate free radicals. Monomers: HEMA, TEGDME and EDA were used for surface modification of reinforcement material glass fibers.

The testing of mechanical properties of plasma modified glass fibers

For testing mechanical properties, fibers were incorporated in the PMMA with %1 (w/w) loading. Specimens were prepared using standard gypsum moulds of 3x0.5x0.8 cm in dimension. Glass fibers were wetted with 1 ml of methyl methacrylate monomer and mixed with 2,4 g of polymer. The mixture was allowed to reach the dough stage and loaded in to the mould in a dental flask. The upper portion of the flask was placed over the lover and two portions were pressed in a hydraulic press. The flask was placed in a heated water bath during the polymerisation. The polymerized specimens were removed from the gypsum and their dimensions were checked. Each group consisted of 8 specimens. Control group contained no fibers. Specimens were stored dry at room temperature the mechanical testing. In order to test record the load of the fracture, each specimen subjected to three-point-bending test in an universal testing system Machine (AGS-J, Shimadzu Co., Kyoto, Japan) of 10 KN capacities with bending apparatus at a crosshead speed of 5mm/min. The ultimate flexural strength σ (MPA) of each specimen was determined with the formula (Philips Science of dental materials).The results were compared statistically by one way analysis of ANOVA (SPS Inc., Chicago, Illinois, USA). The Duncan post hoc test was used to analyze the statistically significant differences between the flexural strenght values (α=.05).

The Surface characterisation of plasma modified glass fibers

An X-ray photoelectron spectrometer ADES-400 ADES-400, by Mg Ka and Al Ka excitation sources and a hemispherical energy analyzer was used to obtain information about the composition and the chemical bonding of elements found in a surface region of unmodified and plasma treated samples. The thickness of a surface region from which information can be obtained depends on kinetic energy of photoelectrons in question and on the material analyzed. For carbon-based polymers the thickness can reach ~10 nm. Photoelectrons in the present work were excited by Mg Ka radiation (1253.6 eV, 200 W), the incidence and the emission angles were set at 70∞ and 0∞, respectively, both measured from the surface normal. Photoelectron spectra were recorded with the analyzer operated with constant pass energy of 100 eV or 20 eV. The atomic concentrations of unmodified and plasma treated glass fiber surfaces were determined from background-subtracted Si 2p, O 1s, C 1s and N 1s peak areas [11] corrected for the photoelectric cross-sections and the photo emission asymmetry [12]. The electron inelastic mean free paths [13] and for the measured transmission function of the spectrometer which comprises all instrumental factors influencing the measured quantity [14].

The surface morphology of modified glass fiber was investigated by using scanning electron microscope (SEM) (JSM-820, JEOL Ltd, Tokyo, Japan). Fibers were coated with a thin layer of gold by using sputter coater (VG Microtech Polaron SC500, USA) and photographed in the electron microscope with x4000 magnification. Beside this, the unmodified and modified with EDA glass fibers, which inserted in the PMMA was used for the imaging with SEM.

Results

The mechanical tests results given in Figure 1 show that the tensile strength of the denture texture reinforced with EDA plasma treated glass fibres was improved by 36%. Also, the surface treatment using TEGDME plasma improved the reinforcement properties of glass fibres by 15%.

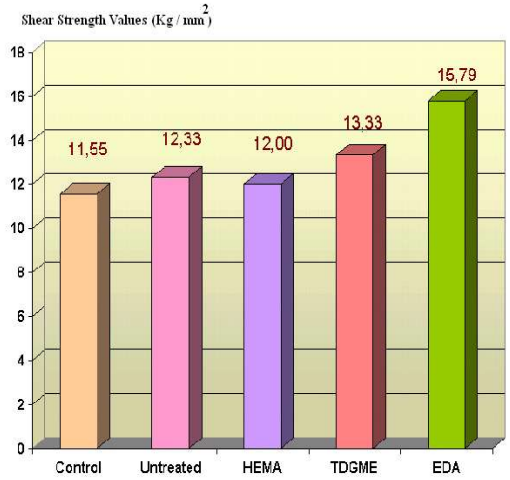

Group	Treatment	Shear strength values (kg/mm2)	% Change
1	Control	11.55±2.09	0.00 %
2	Untreated	12.33±1.87	6,75%
3	HEMA	12.00±2.14	3,89%
4	TGME	13.33±2.15	15,41%
5	EDA	15.79±2.63	36,71%

Fig1 Mechanical Test Results of Glass Fibres

The results of XPS quantitative analysis for untreated and plasma modified glass fibres are summarised in Table 1. The high resolution C 1s, O 1s and N 1s spectra are obtained. The C 1s spectra are asymmetric indicating carbon-oxygen (C-O, C=O) and carbon-nitrogen bonding environments. The O 1s lines are rather wide including different types of oxygen bonding, such as O-C, O=C, -OH. The N 1s peak position is corresponding to the N-C bonding [8]. A slight decrease of silicon and oxygen concentrations and a slight increase of carbon concentration indicate a development of thin plasma polymer film on the glass fibre surface. The most pronounced changes in composition were found for EDA plasma treated glass fibre. In this case, very weak Si 2p signal was recorded. In addition, nitrogen concentration was calculated as high as 15.5 at. %. Therefore, the EDA plasma treatment of the glass fibre surface appears to be more efficient, also in accordance with the improvement of mechanical properties already mentioned.

Table 1 Chemical Composition of Surface

Sample	%C	%O	%N	%Si
Untreated	44.1	39.9	0.0	16.0
EDA	63.7	16.1	15.5	4.7
TEGDME	47.8	37.4	0.0	14.7
HEMA	44.4	39.5	0.0	16.1

Besides the changes of the chemical structure of the surface, the physical changes have been visualized by using SEM analysis. Figure 2, 3, 4 and 5 showed the change in the surface characteristic of glass fibers by changing the monomer used in plasma polymerisation respectively. In the case of monomer EDA surface roughness of the glass fiber was increased much more than in the case of the other monomers.

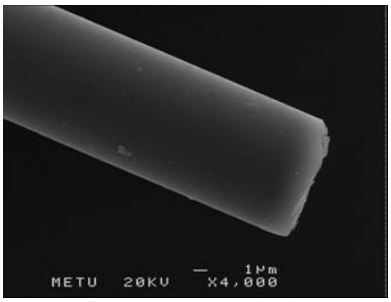

Fig2. Unmodified Glass Fibre

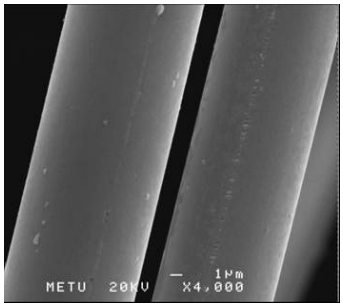

Fig3. Modified glass fiber with HEMA

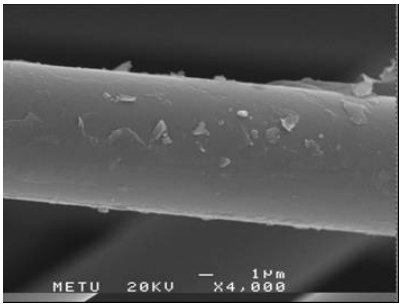

Fig4. Modified glass fiber with TEGDME

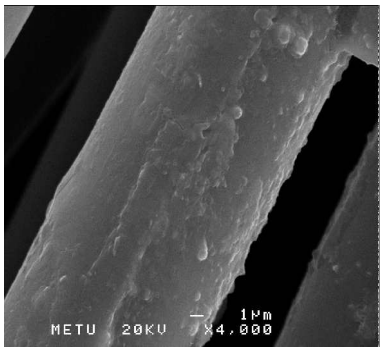

Fig5. Modified Glass Fibre with EDA

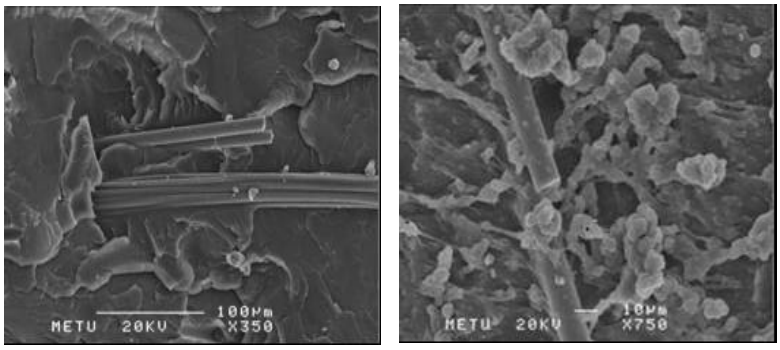

Fig6. Glass fibers in PMMA structure; i.)unmodified ii.)modified withEDA

Glass fibers that were modified with EDA showed uniform distribution in PMMA structure while not modified glass fibers suffered from aggregation in the PMMA matrix (Fig6).

Mechanical tests results showed that the tensile strength of the denture texture reinforced with monomer EDA treated glass fibers were improved by 36%. Also, the surface treatment using monomer TEGDME improved reinforcement properties of glass fibers by 15%. In XPS results the most significant change occurred by EDA treatment. The composition of untreated glass fiber surfaces corresponds to an air-exposed SiO_2, as expected. The glass fiber surfaces modified by HEMA showed no difference in the composition with respect to the reference sample. It indicates that the modified surface layer is very thin or that the surface modification process was, in this specific case, less efficient. The plasma surface treatment using TEGDME monomer resulted in slight changes in the surface composition with respect to the reference sample surface. A slight decrease of silicon and oxygen concentrations and a slight increase of carbon concentration indicate a thin modified film on the glass fiber surfaces. The most pronounced changes in composition were found for EDA plasma treated glass fiber surfaces. In this case, very weak Si 2p signal was recorded. In addition, nitrogen concentration was calculated as high as 15.5 %. Therefore, the EDA plasma treatment of the glass fiber surface appears to be more efficient, also in accordance with the mechanical properties already mentioned. Also the SEM results show that all plasma treatment cause the change of the physical topology on the surfaces. And also, most significant change occurs on EDA treated surfaces. EDA has been found to be the most effective monomer from those here investigated for the increase of mechanical properties of the PMMA based denture material. So, for the increasing bonding properties of the glass fibers to the PMMA denture materials, the physical changes could be effective factor. The researchers of this study are planning further studies focusing on EDA and EDA like amine group containing monomers with different plasma polymerisation parameters, such as discharge power, pressure and exposure time.

Conclusion

In this study, mechanical tests show that shear strength of PMMA can be improved by coating of glass fibers in a glow-discharge system. We also showed that, the treatment of glass fibers with an amino group containing monomer such as EDA is an alternative method to maintain a higher strength dental material. The chemical structure of the surface especially increasing the amount of -N could give an idea that for the amine film deposition which facilitates the improvement of mechanical properties.

References

[1] M.J. Folkes, In: Miles IS, Rostami S, editors. Multicomponent polymer systems. Essex: Longman Scientific and Technical, (1992).
[2] H. Krenchel, Copenhagen Akademisk Forlag, 86, (1964).
[3] P.K. Vallittu, Symposium book of the European Prosthodontic Association, 22nd Annual Conference. Biomaterials Project., (1998).
[4] G. Uzun, N. Hersek, T. Tinçer, J Prosthet Dentistry, 81, (1999).
[5] Plueddemann EP. Silane coupling agents, 2nd ed. New York: Plenum Press,(1991)
[6] Luner PE and Oh E. Characterization of the surface free energy of cellulose ether films. Colloid Surf., 181, (2001).
[7] Clint JH. Adhesion and components of solid surface energies. Current Opinion in Colloid Interface Science, 6, (2001).
[8] F. Keyf, G. Uzun, M. Mutlu, Journal of Oral Rehabilitations, 30, (2003).
[9] V. Cech, R. Prikryl, R. Balkova, A. Grycova, J. Vanek, Composites Part A: Applied Science and Manufacturing, 33, (2002).
[10] R. Prikryl, V. Cech, R. Balkova, J. Vanek, Surface and Coatings Technology, 173 –174, (2003).
[11] J. Zemek, M. Jelínek, V. Vorlíek, M. Trchová, Lanok, Diamond and Related Material, 9, (2000).
[12] Shirley DA. High-resolution X-ray photoemission spectrum of the valence bands of gold. Phys. Rev. B, 5, (1972).
[13] Band IM, Kharitonov YI and Trzhaskovskay MB. Photoemission cross sections and distributions. Atomic Data Nucl. Data Tables, 23, (1979).
[14] Tanuma S, Powell CJ and Penn DR. Surf. Calculations of electron inelastic mean free paths. 5. Data for 14 organic-compounds over the 50-2000 eV range. Interface Anal., 21 (1994).

Plasma Processing Prior To Wire Bonding and Underfill

A. Dr. Jack Zhao, B. Dr. James D. Getty
March Plasma Systems, 2470-A Bates Avenue, Concord, CA 94520 USA
www.marchplasma.com

Abstract
The market demand for smaller and faster IC devices drives the microelectronic packages smaller and more complicated, resulting in more substantial challenges in the advanced packaging process. To ensure high device reliability and minimize manufacturing costs, it is important to ensure a well prepared surface for increasing bond strengths in wire bonding or enhancing the underfill performance in flip chip package. In this paper, how plasma improved the wire bonding and underfill processes in advanced packaging has been demonstrated.

Key words: Plasma, wire bonding, underfill, and reliability

Introduction
Integrated circuits continue to shrink in size, and the associated decrease in size of the wire bond pad on both the die and substrate presents substantial challenges in the manufacturing process. To ensure high device reliability and minimize manufacturing costs, it is important to optimize the wire bonding process to ensure good bond strengths and yields. Poor bond strengths and low yields are often due to the selection of materials in advanced packaging or upstream contamination sources.

In the flip-chip packaging process, capillary underfill is traditionally used to ensure the highest reliability. However, the underfill dispensing process presents challenges, particularly with advanced chip designs including die size, gap, bump density, and differing die passivation materials. Specific challenges include wicking speed, fillet height and balance, and underfill adhesion to various materials. All of these challenges are related to the properties of the substrate, underfill fluid, and flip chip device [1].

Plasma is a partially ionized gas that has an electrically neutral mixture of physically and chemically active gas phase species. These reactive radical species are capable of chemical work, whereas the ionized atom and molecular species are capable of physical work through sputtering. As a result, plasma can perform numerous surface modification processes including surface activation; contamination removal; cross-linking; etch by chemical reaction; and physical bombardment [2].

Plasma is widely used for applications such as surface cleaning, activation and modification for enhancing surface adhesion, improving surface bondability, and tailoring surface energy. Plasma has proven to improve the pull strength and uniformity of wire bonds; increase fillet height and uniformity; increase underfill adhesion for flip chip devices; and alter surfaces for better adhesion in mold and encapsulation processes.

Two plasma modes, downstream and direct plasma, can be chosen in actual application. In direct plasma mode, the substrate is directly exposed in the glow discharge zone. Since both ions and free radicals are involved in the process, the direct plasma process is an aggressive, faster and effective plasma process. However, it may not be suitable for certain devices that are sensitive to ultraviolet (UV) light and ion bombardment.

In downstream plasma mode, including ion free plasma (IFP), the substrate is placed outside the plasma glow discharge zone, normally downstream of the gas flow. Downstream plasma is a mild plasma process since most ions and UV light are filtered before the activated species reach the substrate surface. This process is safe for some devices which are very sensitive to UV light and ion bombardment.

Plasma Prior To Wire Bonding

Generally, poor wire bond strength and bonding yield are attributed to surface contamination on the bond pad. Bond pad contamination is mainly from epoxy bleed-out from the die attach step. This organic resin bleed can be removed with oxygen-based plasma. The oxygen radicals generated in the plasma oxidize the organic resin, producing gas phase carbon dioxide and water. Typical results of pull strength improvement for a quad flat no-lead (QFN) package is displayed in Figure 1. The die was attached with conductive epoxy; oven cured; direct plasma treated; and wire bonded with 25-micron wire. A statistically valid set of samples yielded a mean pull strength of 10.00 grams with a CpK of 2.07 with plasma, compared to a mean pull strength of 3.89 and CpK of 0.03 without plasma.

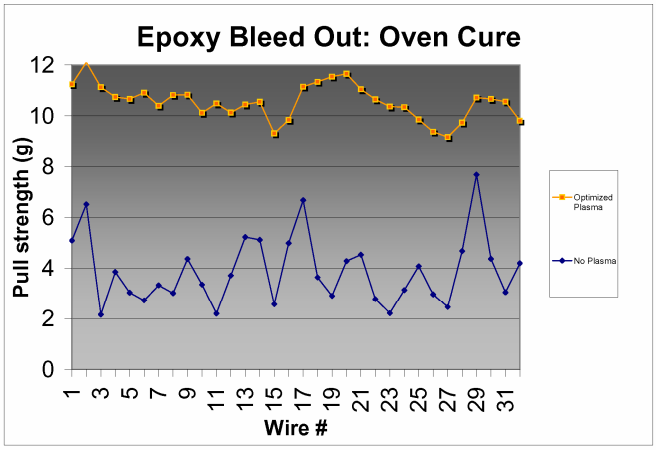

Figure 1

When an identical QFN package was attached with conductive adhesive, the package was snap-cured and wire bonded with 25-micron wire. The pull strengths for this package with and without plasma are displayed in Figure 2. Comparing Figures 1 and 2, both the oven-cured and snap-cured samples yield similar mean pull strengths and CpK after plasma treatment. However, the relative increases when compared to the no-plasma condition are dramatically different. The snap curing process has less epoxy bleed-out than the oven curing process, resulting in less surface contamination on the bond pad and higher mean pull strength in the wire bond process. These results highlight the importance of understanding the upstream processes and how significant the plasma treatment can be in overall wire bond yield improvement.

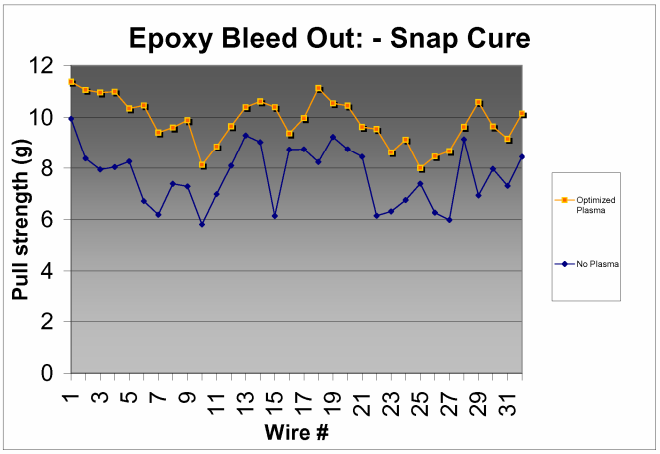

Figure 2

Wire bonding pull strength is sensitive to the substrate's bond pad metallization. Precise control of the plasma treatment process is necessary to achieve the best wire-bonding strength (see Table 1). The samples used for this evaluation were identical QFN packages with wire bond pads consisting of 25 nanometers of gold on palladium. The package was die attached with conductive adhesive; oven cured; treated or not treated with direct plasma; and wire bonded with 25 micron wire.

Table 1

Sample Conditions	Mean Pull Strength (grams)	CpK
No Plasma	3.72 g	0.07
Under Treated	4.67 g	0.35
Optimized	8.52 g	2.15
Over Treated	4.82 g	0.45

The pull strength data in Table 1 was collected with a constant plasma power, pressure and argon source gas while varying the plasma process time. The "Under Treated" sample showed some improvement over the "No Plasma" sample, but did not remove all of the epoxy bleed when compared to the "Optimized" conditions. The "Over Treated" sample yielded poor pull strengths due to the removal of the thin gold film on the palladium bond pad.

It is necessary to precisely control the direct plasma condition. If the sample is over-treated, the thin film gold on palladium will be removed, resulting in decreased wire bonding strength. In ion-free plasma, the QFN will only be exposed to the chemically active radicals, thus limiting the effect of sputtering the gold.

Figure 3 displays pull strengths for these QFN packages under the following conditions: no plasma; optimized direct oxygen plasma; and IFP oxygen plasma. In both plasma cases, the wire bond pull strength and CpK improve dramatically when compared to the no-plasma condition. However, the direct plasma condition is slightly better in this case, possibly because bond pull strength not only depends upon the removal of the organic resin bleed, but also relates to the other surface characteristics such as surface roughness.

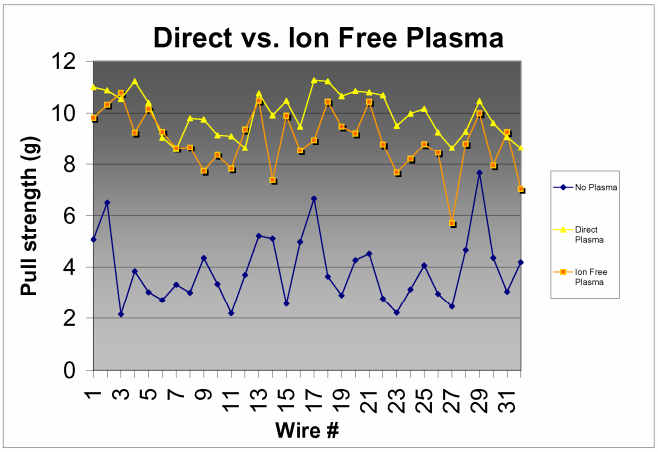

Figure 3

When applying plasma for pre-wire bonding applications, the sensitivity of the semiconductor device to all the active components contained in a direct plasma must be taken into consideration. In very specialized applications, the semiconductor device may be sensitive to either UV light exposure or ion exposure. In this case, IFP plasma technology can be employed to improve pull strengths for applications with epoxy bleed-out. Figure 4 compares the pull strength distribution of no plasma and IFP plasma-treated samples. In this study, a low temperature co-fired ceramic (LTCC) multi-chip module was populated with seven different active die; the

conductive epoxy was oven cured; no plasma or IFP plasma treated; and wire bonded with 25-micron wire. A sensitive pre-programmed EEPROM device was monitored for device erasure. In all IFP plasma processes, the EEPROM device was not erased, and with optimum plasma conditions an improvement of pull strengths was observed (Figure 4).

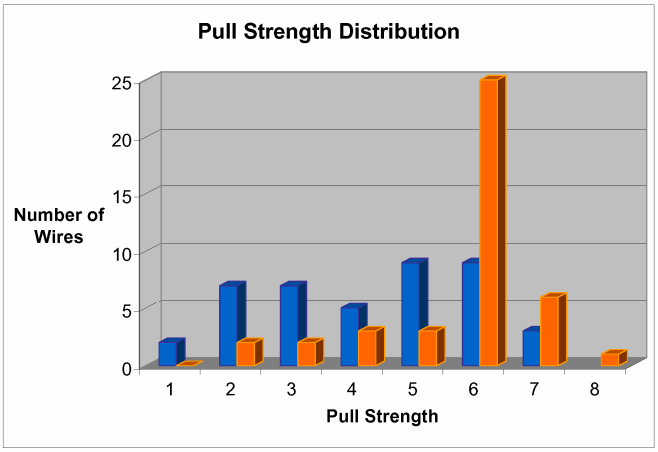

Figure 4

Plasma Prior to Underfill

The underfill process is very important for successful flip chip packaging since it can increase the mechanical and thermal reliability and improve the quality of the package itself. However, the flip chip process also meets challenges related to the surface properties of the die and substrate such as low wicking speed, lower and unbalanced fillet height, and possible delamination.

It has been proven that plasma can increase the surface energy, improve bondability, and enhance the interface adhesion. However, the gap between the die and substrate in the flip chip package is very small. Answers to the following questions are required: "Can plasma modify the surface properties beneath the die in the flip chip package?" and "Does a plasma-modified surface promote the underfill process?"

The surface wettability under the flip chip die depends on the geometry of the flip chip, materials, and plasma chemistry. Figure 5 displays contact angle data for plasma conditions of pure argon, pure oxygen, and pure nitrogen with two different die sizes. The die surface has a polyimide passivation layer with solder balls, and the substrate is FR-4 material. It is clear that chip size affects the surface cleaning effectiveness in flip chip packaging. With the increase of die size, the surface contact angle on the center of both the die and substrate increases, meaning that the plasma cleaning effectiveness decreases with increased die size. The activated species have more difficulty reaching the center of the flip chip due to the larger physical barrier of the large die.

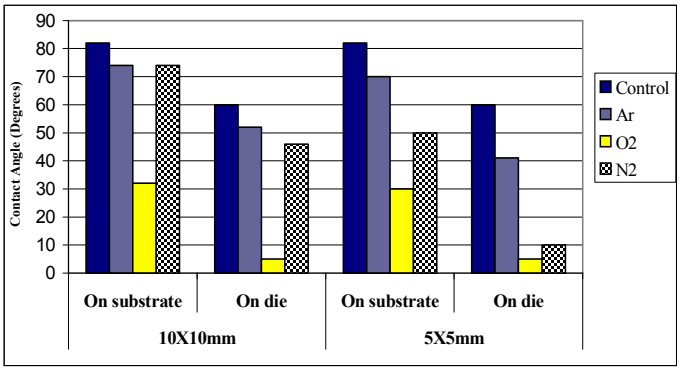

Figure 5

Contact angle vs. die size, substrate materials and plasma chemistry

The surface material also affects the surface contact angle after plasma treatment. Under the same plasma condition, the surface contact angle on the die is lower than that on the substrate surface. It is also clear that the surface contact angle at the center of the die and on the substrate beneath the flip chip is impacted by the plasma source gas. In general, the oxygen-based plasma has a greater impact on the contact angle than either nitrogen or argon. The contact angle trend is: O_2 plasma > N_2 plasma > Ar plasma.

The plasma processes can be characterized by two key surface mechanisms: physical bombardment and chemical reaction. An argon plasma process is a pure physical process where the argon ions generated in the plasma perform surface changes through ion bombardment. The Ar ions must penetrate beneath the die and still have sufficient energy to be effective. This process is inefficient as very few activated species penetrate into the gap between the die and substrate. As a result, the treatment performance of Ar plasma under the flip chip is not effective.

When oxygen is used for the process, both physical bombardment and chemical reaction work on the surface, but the chemical process plays a more important role. Oxygen-free radicals can diffuse and move in all directions since the free radicals are uncharged particles and not confined by an electric field. This random movement results in many activated species penetrating into the gap between the die and substrate, producing better surface contact angles than those achieved with argon plasma.

The treatment performance of nitrogen plasma is between the oxygen plasma and argon plasma. It is likely that the free radicals generated in the nitrogen plasma are less effective in chemically changing the surface. As a result, the surface contact angle beneath the die is different with differing gas chemistry. The cleaning performance trend is O_2 plasma > N_2 plasma > Ar plasma when considering treatment under a flip chip package.

The data shown in Figure 5 indicates that plasma can modify the surface beneath the die in flip chip packages. The specific challenges from the underfill process include wicking speed, fillet height, fillet uniformity and underfill adhesion between the underfill and die passivation.

Wicking speed is inversely proportional to the flow-out time, which is proportional to the contact angle. The relationship between the flow-out time and flip chip condition can be expressed by the following formula:

$$T = 3\mu L^2/h\gamma\cos\theta \quad (1)$$

T is flow-out time in seconds; μ is fluid viscosity; L is flow distance; h is gap or bump height; γ is surface tension of liquid vapor interface, and θ is the contact and wetting angle.

For certain flip chip packages, the lower the contact angle the faster the wicking speed, and therefore, the higher the production line throughput.

Plasma-induced surface energy changes are employed to increase wicking speed. In Case Study 1, 20x20-mm die with silicon nitride passivation were plasma treated with oxygen for both chemical cleaning and surface activation. The contact angle on the center of the die under the flip chip package was 40 degrees before plasma, and 20 degrees after plasma treatment. The reduction in contact angle translated into a reduction in flow-out time from 60 to 22 seconds, a 270-percent improvement (Table 2). This flow-out time enhancement will have a dramatic impact on the production line throughput.

Table 2

Case Study 1		
Experimental conditions		
Equipment	Batch plasma treatment system	
Plasma	Oxygen plasma (Chemical cleaning and surface activation)	
Conditions	AP-1000*, 500 Watts, 13.56 MHz, 50 CFM pump	
Loading	6 magazines of 10 Auer boats each (four flip chip per boat)	
Flip Chip Package	20 X 20 mm die	
	Silicon nitride die passivation	
	Bump height: 80 μm, Bump pitch: 200 μm, No. bumps: 2400	
Results		
Item	**No plasma**	**Plasma treated**
Contact angle on center of die surface	40°	20°
Flow out time	60 seconds	22 seconds
Voids?	Yes	No
Fillet height and uniformity	Poor	>40% fillet height with ± 4% uniformity

**The AP-1000 is a batch plasma system from March Plasma Systems.*

Although plasma treatment improves the flow-out time, the effect of other parameters, such as material types and bump density, can impact the magnitude of improvement as shown in Table 3. In Case Study 2, the substrate material and die passivation layer differed, as did the pitch pattern. There was a significant reduction in contact angle from 90 degrees on the untreated sample to 28 degrees on the plasma-treated flip chip. However, the improvement in flow-out time was only 14 percent, indicating that material sets are very important when considering flow-out time.

Typically, a more uniform fillet results in a more reliable packaged device. Non-uniform fillet heights often result in uneven stresses on the chip, which could cause fillet cracking and package failure. The low surface energy of both the substrate and die impacts both fillet height and uniformity. Table 3 shows both fillet height and uniformity with and without plasma treatment. The fillet height and imbalance were defined by the following equations:

$$\underline{\text{Fillet Height}}: \quad \text{Dispensing Side: } H_d = (H_{disp}/H_c) \times 100\% \qquad \text{Opposite Side: } H_o = (H_{opp}/H_c) \times 100\% \tag{2}$$

$$\underline{\text{Imbalance}}: \text{ Fillet height of dispensing side} - \text{Fillet height of opposite side} = H_d - H_o \tag{3}$$

where H_c is the thickness of the die, H_{disp} is the fillet height on the dispensing side and H_{opp} is the fillet height on the opposite side.

For these experiments, a single-line dispense was performed. With single-line dispense, the fillet on the opposite side of the die will often be lower than the dispensed side. The objective is to provide not only sufficient fillet height (> 20-percent of the height of the die) but also an imbalance lower than 30 percent.

As shown in Table 3 with plasma versus no plasma, there was a 220-percent improvement in fillet height on the opposite side and significant improvement in imbalance.

Table 3

Case Study 2						
Equipment	In-line plasma treatment system					
Plasma	Oxygen downstream plasma					
Conditions	XTRAK-IFP**, 45 sccm, 200 mTorr, 200 W, and 60 seconds					
Loading	Auer boat (Ten flip chips per boat)					
Flip Chip Package	Polyimide passivation layer on the Flip chip					
Result						
	Statistics	Contact angle	UF flow time	Fillet Height		Imbalance
				Dispensed side (%)	Opposite side (%)	(H_d-H_0)
		(degree)	(seconds)	H_d	H_0	(%)
Control	Avg.	**90**	**59**	**56.6**	**12.4**	**44.2**
	Stdev.	---	1.41	3.89	8.66	7.49
	Max.	---	60	64.8	26.1	58.4
	Min.	---	58	49.5	0.3	34.6
Plasma Treated	Avg.	**28**	**51**	**40.3**	**27.7**	**12.6**
	Stdev.	---	0.0	6.54	4.32	4.58
	Max.	---	51	60.6	35.9	22.1
	Min.	---	51	31.7	20.2	6.25

***The XTRAK-IFP is an in-line plasma system from March Plasma Systems.*

Adhesion and Voiding

Delamination of a flip chip package is often seen between the underfill and die passivation, typically around the edges of the die. There are numerous factors that impact underfill adhesion, including surface contamination and passivation layer material type. However, plasma can treat these surfaces to both remove contamination and chemically modify the surface to enhance adhesion. CSAM analysis indicated that the O_2 plasma-treated sample did not show any delamination after 3000 temperature cycling testing. The temperature cycling range is 0 to 100 °C.

Table 4 illustrates the difference between the control set and the oxygen plasma-treated polyimide passivation layer on the flip chip. Plasma treatment changes the surface composition through modification of the surface chemical functional groups. After oxygen treatment, the oxygen composition on the substrate surface increased approximately 36 percent. The surface functional group analysis indicates that the total oxy-functional group increased by 19 percent. The increase in these chemical functional groups is likely responsible for the improved adhesion of the underfill fluid to the polyimide passivation.

Table 4

	Surface composition			Surface functional group			
	C	N	O	OC=O	OCO, C=O	C-O-	C-C
Control	79.5 %	5.9 %	14.6 %	2.2 %	11.7 %	25.9 %	60.2 %
Treated*	74.8 %	5.4 %	19.9 %	0.9 %	17.4 %	29.1 %	52.6 %

*Sample treated in XTRAK-IFP system with oxygen plasma condition, 45 sccm, 200 W, 60 seconds.

Generally, oxy-functional groups on the surface interact and chemically bond the underfill materials during the underfill process. Therefore, the greater the concentration of oxy-functional groups, the less likely it is for delamination to occur. Removing contaminants on the interfaces and chemically activating the surface minimize delamination. Additionally, this process improves wettability under the die resulting in a reduction in the incidence of voiding as shown in Table 2.

Conclusion

Plasma treatment can be successfully applied to the wire bonding and capillary underfill processes. Plasma improves the bond strength and increases the CpK in wire bonding. It has also been demonstrated that various plasma chemistries improve the fillet height and uniformity, but oxygen chemistry is the most effective at lowering the contact angle under the die. The use of oxygen chemistry for improved wicking speed and enhanced adhesion performance has been demonstrated.

References

1. Jack Zhao, James Getty, and Daniel Chir, "Plasma Processing for Enhanced Underfill," Chip Scale Review, July 2004.
2. James Getty, "How Plasma-Enhanced Surface Modification Improves the Production of Microelectronics and Optoelectronics," Chip Scale Review Jan/Feb 2002.

Author Biographies

Dr. Jack Zhao

Dr. Zhao is an Applications Scientist for March Plasma Systems. He is responsible for process development, technical support and R&D. Dr. Zhao holds a doctorate in chemical engineering and has worked in the semiconductor industry for four years and plasma application field for ten years. Email: jzhao@marchplasma.com

Dr. James D. Getty

Dr. Getty is Director of Applications Engineering and Business Development for March Plasma Systems. He is responsible for cooperative development programs, business development, new process development and the applications laboratories worldwide. Dr. Getty holds a doctorate in physical chemistry and has worked in the semiconductor industry for over 15 years.

Chemical reactivity of atmospheric pressure water plasma as a function of temperature monitored by emission spectroscopy

I. G. Koo, M. S. Lee, J. M. Lee and W. M. Lee

Department of Molecular Science and Technology, Ajou University, Suwon, Korea,443-749

Abstract

Chemical reactivity of water in an electrical discharge was studied by allowing hot water vapor to pass through micro hollow cathode (MHC) array. Atmospheric pressure water vapor heated up to 700^{o}C, often mixed with sulfur dioxide SO_2, was introduced to the electrode assembly and the resulting plasma flame was studied using emission spectroscopy. The experimental results in this study include the current-voltage profile as a function of the medium temperature and emission spectra of the species such as OH, H, O and SO also as a function of the temperature.

Keywords: atmospheric pressure discharge, micro hollow cathode, emission spectra, water dissociation.

1. Introduction

Chemical reactivity of water vapor heated to high temperature, often near 800^{o}C, is an interesting subject particularly when the heating is coupled with electrical discharge from the standpoint of utilization of nuclear heat as a means of dissociating water [1]. The excitation of water molecules by thermal as well as electrical means could provide an alternate reaction path for their dissociation. Plasma-chemical reactions of water molecules in electrical discharge have been encountered in applications such as hydrogen isotope exchange reaction [2,3], non-thermal removal of NOx in presence of water [4] and water-stabilized plasma generators [5]. When thermal excitation of water molecules is coupled with electrical excitation it is not difficult to foresee that such combined effect can first result in improved sustainability of the MHC discharge and can also bring in enhanced reactivity of the molecules. First, the discharge can be sustained using less power as the medium temperature goes up due to an increase in the rate of thermal ionization and the ion flux. Second, the population distribution at vibrational energy levels of water molecules should shift somewhat to higher states with increase of temperature and particularly, the existence of non-thermal electrons in MHC discharge should help bring in further excitation of their quantum states of the involved molecules. Third, the net charge accumulated at the electrode surface for the MHC discharge helps a certain orientation of water molecules residing at the electrode surface. With such regularity in the alignment of water molecules adsorbed at the surface the added molecules to the system such as SO_2 would also orient themselves in a regular fashion configuration wise in reference to the water molecules. Consequently the whole reacting system consisting of metal-water-SO_2 would have drastically modified potential energy surface so that the temperature effect of the system on the reactivity would be more clearly manifested.

2. Experimental

The electrode design for generating large-area atmospheric pressure plasma was based on micro-hollow electrodes assembly[6]. The assembly consisted of two stainless steel disks, 100 μm thick and 1 cm^2 surface area, separated by a mica sheet of 200 μm thickness. Holes of 300 μm diameter, the spacing between them to be about 1 mm, were bored through the assembly for the gas passage. A DC power supply was connected to the electrodes and the voltage and current during the sustained discharge were measured at various temperature. The hot water vapor in temperature range of 100-700^oC was introduced into the electrode assembly, at the flow rate of 400 ml min^{-1}, after passing through ceramic tubing placed in a furnace. In some experiments the water vapor was mixed with SO_2. The resulting plasma flame generated out of the electrode assembly was guided into a chamber at which optical probe was attached. The emitted light from the reactor was collected and transmitted through an optical fiber to Monochromator with the resolution of 0.01-0.05 nm attached to CCD camera. The whole experimental design is schematically depicted in Fig. 1.

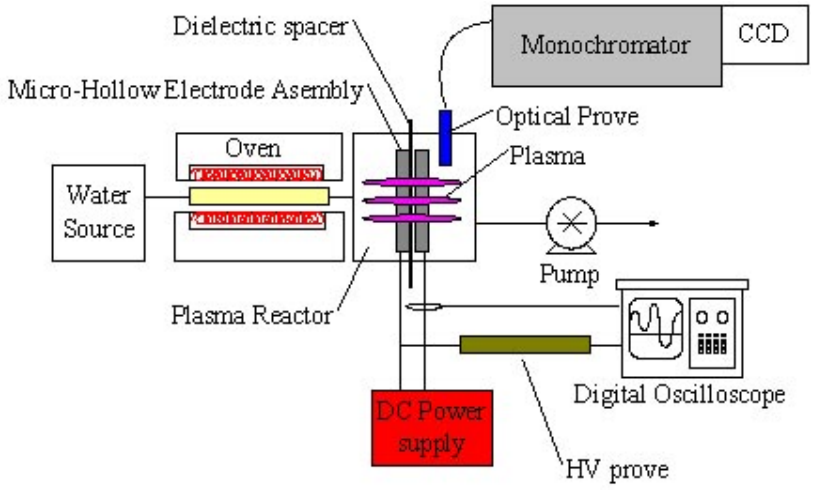

Fig.1 Schematic experimental setup

3. Results and discussion

The current and the voltage between the electrodes during the sustained discharge were measured as a function of the water vapor temperature as shown in Fig. 2. As the temperature went up from 200^oC to 530 ^oC, the power decreased from 4.5 to 2.5 W, accompanying more than 40% reduction. As explained before the discharge requires less power as the medium temperature goes up due to an increase in the rate of thermal ionization and the ion flux. The power of 2.5 W is equivalent to 9 kJ of the electrical energy if the discharge is continued for one hour, a time span during which about 0.3 moles of water, as the flow rate is fixed at 400 ml min^{-1}, is electrically excited. Since electrolyzing 0.3 mol of water requires about 80 kJ of electrical energy, the power consumption exhibited in MHC discharge is rather encouraging if most of the excited water molecules can undergo dissociation.

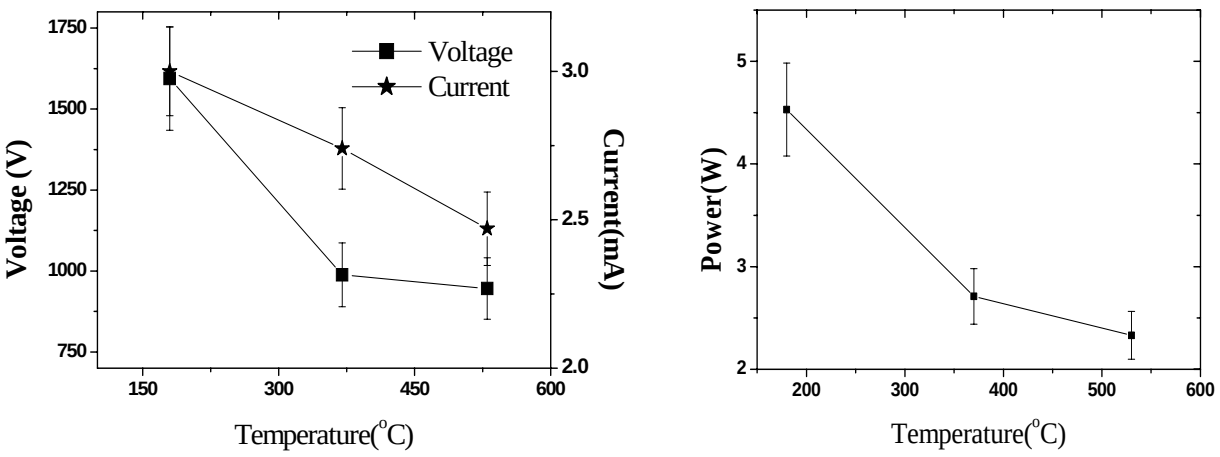

(a) (b)

Fig.2 Power consumption for MHC discharge as a function of the medium temperature: (a) I-V characteristics (b) Power.

In our experimental setup the vapor is introduced into the micro hole of the gas-in electrode, generating the glowing plasma microjet while it leaves the hole of the gas-out electrode. The emission measurement of this glowing region showed that the intensity of various peaks depends on the polarity of the gas-out electrode. For example, Fig. 3 shows that the intensity ratio of oxygen(777.1nm) to hydrogen(486nm) peak, I_o/I_H, varies from 2.4 to 1.0 as the polarity of the gas-out electrode switches from anode to cathode, respectively. With the reversal of the polarity no such change of the relative intensity was observed when He was used as the working gas. Thus, tentatively we came to a conclusion that the chemical reaction of the water plasma depends on the polarity of the gas outlet[7].

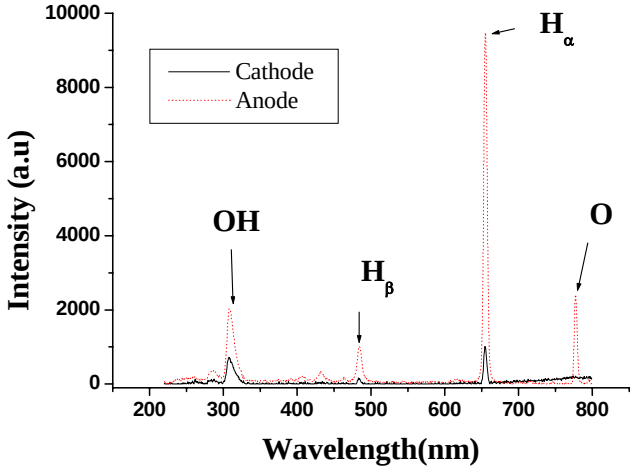

Fig.3 Dependency of the emission spectra intensity on the polarity of the gas-out electrode (T= 150°C).

With the polarity of the gas-out electrode set as the anode the electron density of the plasma microjet was determined by measuring "the half width half maximum (HWHM)" of the gauss-fitted H beta line(486.13nm). The electron density, 1.14×10^{14} cm^{-3}, was obtained from its relationship to the HWHM [8]. It turned out that the density changed very little as the medium temperature was raised from 300 to 700°C.

Fig. 4 shows the dependency of the relative intensity of different lines of the emission spectra on the medium temperature. With the polarity of the gas-out electrode set as anode the spectra shows that the intensity of OH lines at 306 and 600 nm and O line at 771 nm decreases with increase of the temperature whereas the intensity of H lines at 486 and 656 nm increases [9]. This trend is attributed to increase of the rate of the $OH + O \rightarrow O_2 + H$ reaction with the increase in temperature (the thermodynamic prediction does not support the shift of the reaction to the forward direction.) With the polarity reversed the spectra shows the appearance of O_2^+ band as the temperature is over 500 [10]. Formation of the O_2^+ band with polarity reversal clearly indicates that the chemical reactions in the plasma region is sensitive to the polarity of the nearby electrode, which in turns could dictate the electric field contour of the region, and possibly the electron density profile.

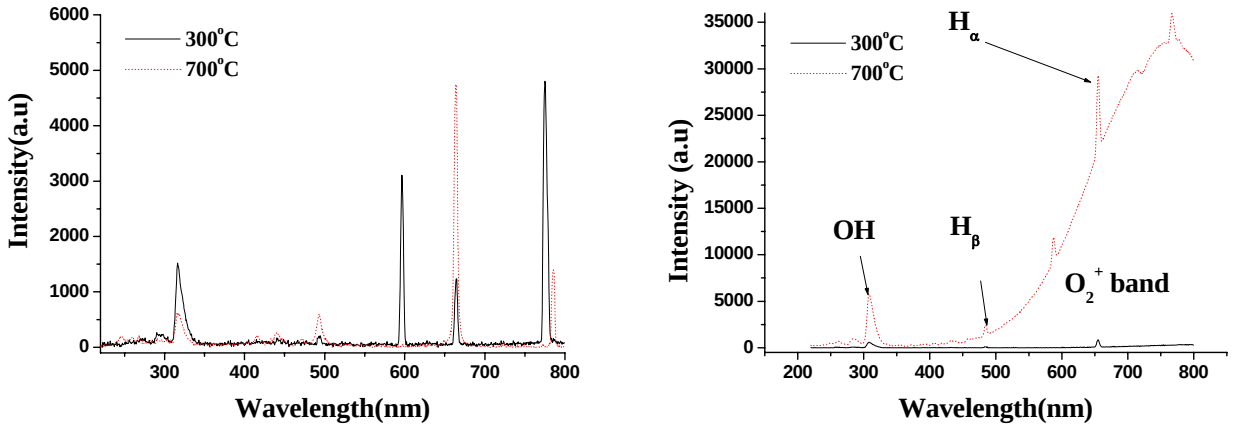

(a) (b)

Fig. 4 The emission spectra at different medium temperature with polarity of the gas-out electrode set as (a) anode or as (b) cathode.

When SO_2 was added to the water vapor some changes were observed in the emission spectra, as shown in Fig. 5. With the addition of SO_2 the OH lines almost completely disappeared, indicating that OH species could have reacted with the added species [7,9,10].

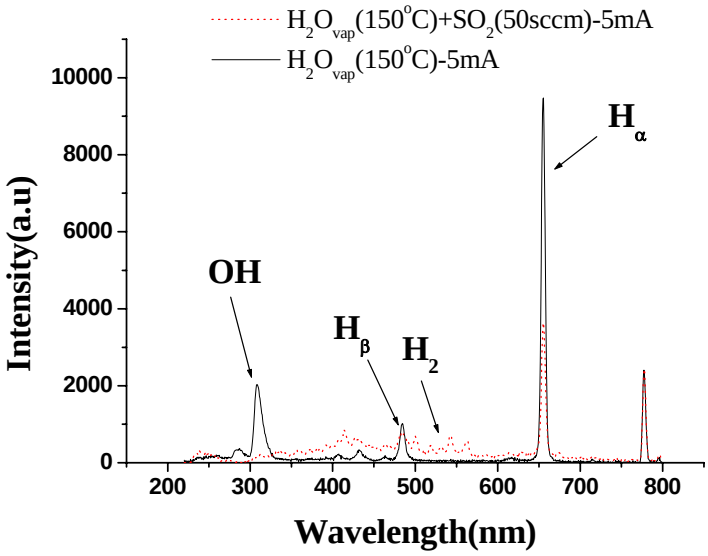

Fig. 5 Disappearance of OH line with SO_2 to the water vapor. The gas-out electrode is set as the anode.

Acknowledgments

This study was supported by Korea Institute of Science & Technology Evaluation and Planning (KISTEP) and Ministry of Science & Technology (MOST), Korean government, through its National Nuclear Technology Program.

References

[1] M. Roth and K.F. Knoche – Int.J. Hydrogen Energy **14**, 545 (1989)

[2] H.J. Kim, Y.D. Park and W.M. Lee - Plasma Chem. Plasma Process. **20**, 259 (2000)

[3] I.G. Koo and W.M. Lee - Plasma Chem. Plasma Process. **24**, 537 (2004)

[4] B.M. Penetrante and S.E. Schultheis - *Non-Thermal Plasma Techniques for Pollution Control*, Springer-Verlag, Berlin (1993).

[5] M. Hrabovsky – Pure & Appl. Chem. **70**, 1157 (1998).

[6] R. H. Stark and K. H. Schoenbach – J. Appl. Phys. **85**, 2075 (1999).

[7] K. Kobayashi, Y. Tomita and M. Sanmyo – J. Phys. Chem. B. **104**, 6318 (2000).

[8] H. R. Griem – Plasma Spectroscopy, McGraw-Hill Book Company, New York (1964).

[9] W. T. Shin, S. Yiacoumi, C. Tsouris and S. Dai – Ind. Eng. Chem. Res. **39**, 4408 (2000).

[10] R. W. Pearse and A. G. Gaydon – The Identification of Molecular Spectra, John Wiley & Son Inc, New York (1950).

Atmospheric pressure plasma-chemical preparation of Pt nanoparticles in liquid phase

I. G. Koo, J. H. Shim, M. S. Lee, K. W. Joung, Y. J. Kim and W. M. Lee

Department of Molecular Science and Technology, Ajou University, Suwon, Korea.443-749

Abstract

We have developed a novel method for preparing nano-sized Pt catalysts based on a plasma-chemical method. Pt nanoparticles were prepared in H_2PtCl_6 solution when electrical discharge powered by 60Hz AC was sustained between two electrodes, one outside the solution and the other placed in the solution, using atmospheric pressure H_2/He gas mixture as the working gas. The average particle size was in the range of 2.2 and 3.5 nm with the solution temperature maintained between 10^oC and 40^oC.

Keywords : platinum nanoparticles, atmospheric pressure plasma, plasma-chemical reduction, liquid phase discharge.

1. Introduction

Metal nanoparticles, particularly noble metals, have drawn increasing interest due to their potential use in preparation of high surface area electrodes and to some unique properties different from those of bulk materials [1]. The use of Pt as an electrocatalyst requires that the active area remains stable with time of operation and that the utilization of expensive Pt metal is most efficient. It is well-known that the catalytic activity of the metal is strongly dependent on the particle size, shape, and size distribution. Thus, numerous methods to produce and utilize Pt nanoparticles have been developed [2]. We are proposing a novel method for preparing nano-sized Pt catalysts based on a plasma-chemical method. Our work was motivated for a search of a method that warrants simple and fast preparation of Pt nanoparticles without using stabilizers and reducing agents, which could be toxic, so that the whole process would involve simplest possible chemical system. The critical step in preparation of its colloidal solution is the reduction of the metal by various reducing agents under the protection of stabilizers. Our group recently showed that $PdCl_2$ can be reduced to metallic Pd when the chloride reacts with hydrogen plasma. The plasma-chemical conversion of 3 μm thick $PdCl_2$ film coated on alumina substrate into Pd film took only 30 seconds without heating the reacting system; atmospheric pressure hydrogen plasma was generated by RF discharge through H_2/He working gas in contact with the film [3]. We extended this technique to plasma reactions at liquid-vapor interface so that hydrogen plasma in contact with aqueous Pt salt solution can possibly reduce the metal complex ions. We used the ionic compound, hexachloroplatinic acid (H_2PtCl_6), as the precursor. The novelty of the approach is manifested in fast kinetics, low temperature reaction, and no use of stabilizing agents. In this note we present the outline of the approach and some evidence of the nanoparticles produced under the circumstances described.

2. Experimental

Fig. 1 shows the experimental setup used in our work. A similar discharge system has been reported by other groups to generate non-thermal air plasma [4]. Pt nanoparticles were prepared in H_2PtCl_6 solution when electrical discharge powered by 60Hz AC was sustained between two electrodes, one outside the solution and the other placed in the solution, using atmospheric pressure H_2/He gas mixture as the working fluid. The total power consumption needed to sustain the discharge was less than 10 W. The gap between the upper electrode and the surface of the solution was maintained to be 5 mm. The inside of the tubular upper electrode (2mm OD, 1.5 mm ID) shielded by alumina provided the path through which the mixture of He and H_2 flew at the rate of 500 and 100 ml/min, respectively, with their total pressure approaching the atmospheric value. The surface of the metal salt solution acted as the water electrode while a stainless disk placed at the bottom of the solution completed the electrical connection to the power source. The temperature of the solution under constant stirring with a magnetic bar was set at 10 ± 0.1 ^oC or 40 ± 0.1 ^oC using a water bath (JEM-2010). The voltage and current were measured by a Tektronix 400Mhz digital oscilloscope with current prove.

The Pt colloidal formation in the solution and the plasma reaction were monitored using UV-Vis spectrometer (Scinco UV-2100). Pt colloids collected on carbon grids were examined using TEM (JEOL JEM-2010) and EDX.

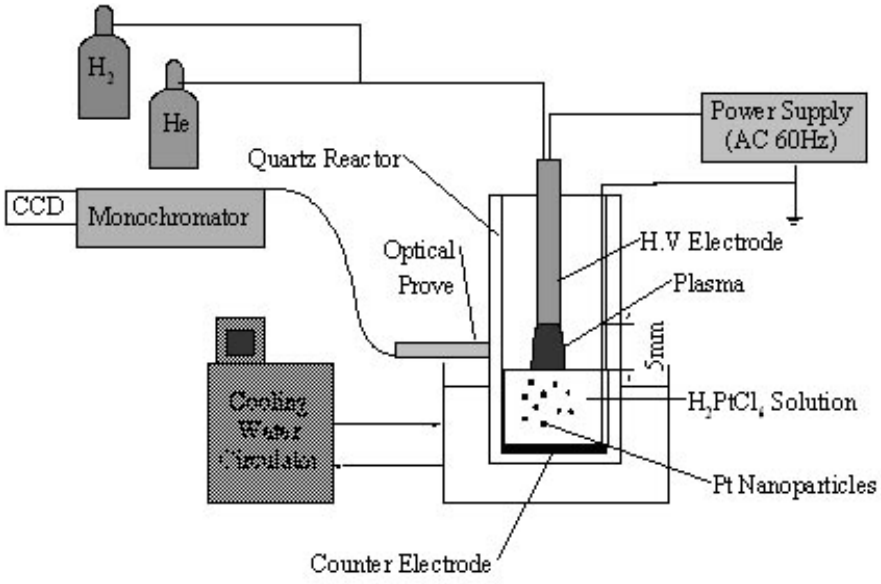

Fig.1 Schematic experimental setup

3. Results and discussion

The plasma-chemical generation of Pt nanoparticles, apparently at the interface region of the plasma and the solution as shown in Fig. 2, was achieved within 10 seconds during which most of the platinum chlorides in the solution was converted into Pt particles, evidenced by color change of the solution. The clear yellow aqueous H_2PtCl_6 solution changed to dark gray upon hydrogen plasma-chemical reaction. Fig. 3 shows that the

characteristic absorption peak of $PtCl_6^{2-}$ at around 260 nm disappeared 5 minutes after the onset of the discharge. The reduction rate of the metal salt was estimated to be about 1.2 x 10^{-5} mol/min from the change of UV/Vis absorbency. The black particle formation took place at the interface where the plasma touched the solution and the spread of the particles to other regions of the solution was clearly observable. The plasma formed with He gas alone without H_2 did not engage any reaction with the metal salt solution. As a plausible reaction mechanism it is proposed that the excited hydrogen species existing in the plasma helped, even at ambient temperature, fast dissociation of Pt-Cl bonds in $[PtCl_6]^{2-}$ ions producing Pt nanoclusters and HCl.

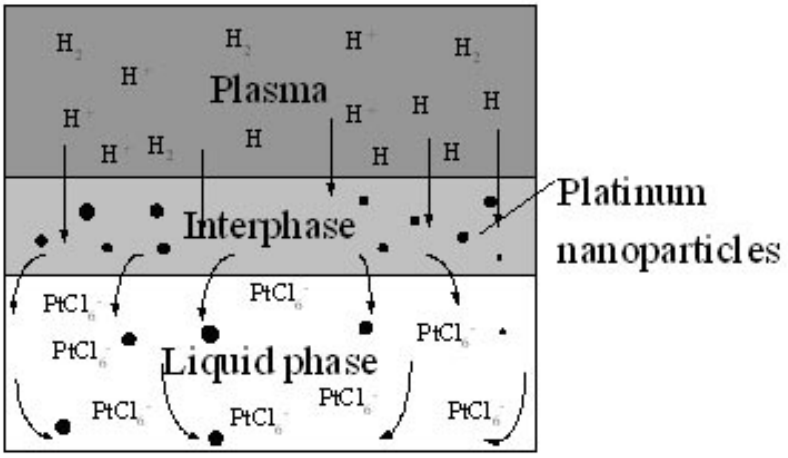

Fig.2 Plasma-chemical reaction

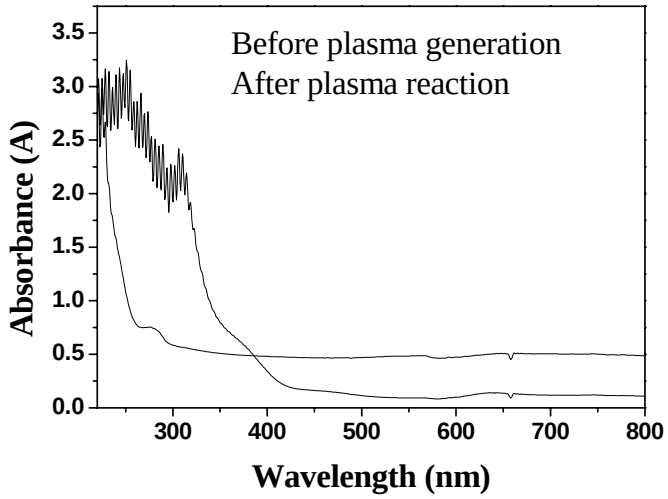

Fig. 3 UV-vis absorption spectra of solution containing H_2PtCl_6 before and after plasma-chemical reduction.

The formation of pure Pt particles was confirmed first by EDX profile taken on the Pt sample collected on

carbon conductive tab. The profile showed the peaks of only carbon and Pt, confirming that the chloride was completely converted to pure metallic phase as shown in Fig. 4. Fig. 5 shows the TEM images of the Pt particles. The TEM image discloses that the particles are not completely separated from one another since no stabilizer was used, but they are not coalesced into tight agglomerates, allowing size measurements of each particulate to be still possible. The particle size distribution determined from the image of Fig. 5 clearly indicates that it decreases as the solution temperature is lowered; the average size was around 2.2 and 3.5 nm at 10^{o} C and 40^{o} C, respectively.

.

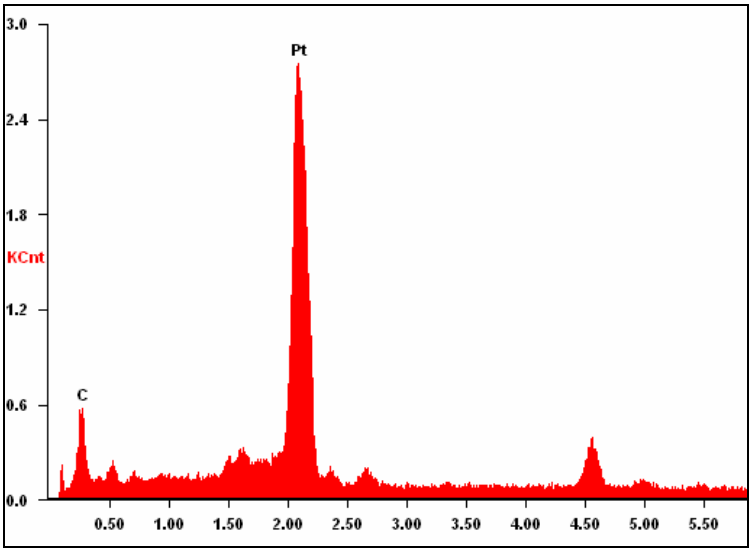

Fig. 4 EDX profiles of Pt nanoparticles.

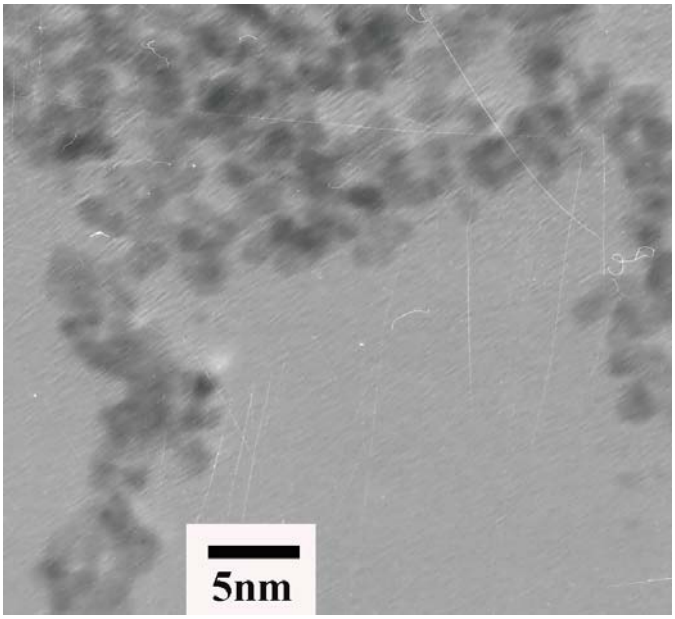

Fig. 5 TEM images of the Pt nanoparticles.

Acknowledgments

This study was supported by Korea Institute of Science & Technology Evaluation and Planning (KISTEP) and Ministry of Science & Technology (MOST), Korean government, through its National Nuclear Technology Program.

References

[1] Henglein - A. Chem. Rev. **89**, 1861 (1989).

[2] H. A. Andreas and V. I. Birss - J. Electrochem. Soc. **149**, A1481 (2002).

[3] I. G. Koo, M. S. Lee and W. M. Lee – Thin Solid Films. (2005) Inpress.

[4] M. Laroussi, X. Lu and C. M. Malott – Plasma Sources Sci. Technol. **12**, 53 (2003).

[5] Y. Sawada, H. Tamaru, M. Kogoma, M. Kawase and K. Hashimoto- J. Phys. D: Appl. Phys. **29**, 2539 (1996).

[6] T. Teranishi, M. hosoe, T. Tanaka and M. Miyake- J. Phys. Chem. B. **103**, 3818 (1999).

Spectroscopic Analysis of Capillary Underwater Discharges

F. De Baerdemaeker[1], C. Leys[1] and M. Šimek[2]

[1] *Department of Applied Physics, Ghent University, Rozier 44, B-9000 Ghent, Belgium, Christophe.Leys@UGent.Be*
[2] *Laboratory of Pulse Plasma Systems, Institute of Plasma Physics, Za Slovankou 3, 18221 Prague, Czech Republic simek@ipp.cas.cz*

Abstract
A capillary underwater discharge in solutions of distilled water and $NaH_2PO_4.2H_2O$ (conductivity: 50 ÷ 1000 $\mu S.cm^{-1}$), sustained with AC (50 Hz) voltages up to 15 kV, was investigated by time-resolved ICCD spectroscopy. Preliminary measurements indicate that this discharge concept might be an efficient source of OH, H^I and O^I radicals. For the negative pulsed microsecond discharge regime, most radicals are generated during the first few hundreds of nanoseconds after the breakdown event. The average plasma duration is of the order of a few microseconds. For the glow-like discharge regime the rotational distribution of $OH(A^2\Sigma^+, v=0)$ state deviates from a single Boltzmann distribution.
Keywords: water, capillary, AC discharge, OH emission

1. Introduction
The past few years witnessed an increasing interest in underwater plasmas, but compared to the broad knowledge on discharges in the gas phase, the physics of underwater discharges is still largely unknown. Electrical discharges above water surface or underwater can be generated in several ways [1-6], e.g. excited with either short or slow rising voltage pulses and by using various electrode geometries. Envisaged application areas include water purification and shock wave generation.
An approach that allows generating underwater plasmas with DC or low frequency AC voltages at atmospheric pressure is the 'diaphragm' discharge. The principle relies on forcing the electrical current to flow through a narrow bore in a dielectric material between two submerged electrodes. When the current density is sufficiently high, local boiling and subsequent vapour breakdown results in the formation of a plasma within this pin-hole. A variant is the 'capillary' discharge, generated in a bore with large length-to-diameter ratio.

2. Experimental set-up
In this study an AC capillary underwater discharge was investigated in solutions of distilled water and $NaH_2PO_4.2H_2O$. The applied high voltage (up to 15 kV rms) is obtained by stepping up the 220 V (50 Hz) mains, and is varied using an autotransformer. In series with the capillary a 50 Ω resistor is placed which allows measuring the electrical current flowing through the capillary. Dimensions of the Macor glass ceramic capillary are 0.5 mm inner diameter and 5 mm length. The electrodes are aluminium bars, and both water vessels are cooled to room temperature (see figure 1). Two different discharge regimes occur, depending on the conductivity and the excitation voltage, ranging from repetitive microsecond discharge pulses at a frequency of 100 Hz to a quasi-continuous discharge with a glow-like voltage-current characteristic [7]. Electrical conductivity was varied in the range 50 ÷ 1000 $\mu S.cm^{-1}$ and the excitation voltage was varied in the range 5 ÷ 15 kV.

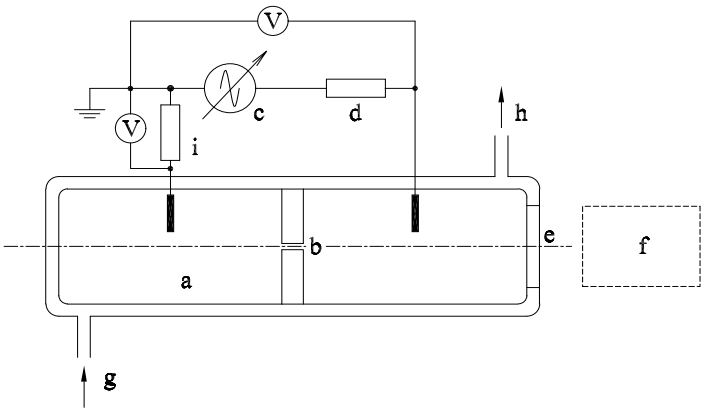

Fig. 1. Experimental set-up: (a) cooled water vessels, (b) dielectric capillary, (c) high voltage source (*U*: 0-15 kV rms, 50 Hz), (d) 100 kΩ resistor, (e) quartz window, (f) ICCD spectrometer, (g) cooling water inlet, (h) cooling water outlet, (i) 50 Ω resistor.

Optical characterization of plasma induced emission for the negative pulsed microsecond discharge regime was carried out for varying conductivity and excitation voltage by time-resolved ICCD spectroscopy. Furthermore, time-averaged measurements were performed to evaluate rotational temperature by analyzing emission of OH radical. The CHROMEX-500i imaging spectrometer equipped with an intensified TE/CCD-1024 TKB/UVAR/1 two-dimensional charge-coupled device detector (gated through a PI PG-200 gate pulse generator) monitored the emission coming out along the symmetry axis of the discharge through quartz optics and color-glass filters. Spectra acquisition was performed through a PI ST-138 controller and WinSpec software. Spectra were corrected for the detection sensitivity by means of a tungsten ribbon lamp (OSRAM Wi 17/G).

3. Results and discussion

3.1. Basic emission features

Spectroscopic measurements of the plasma induced emission performed without time-resolution indicate that this kind of 'underwater' plasma might be an efficient source of OH, H^I and O^I radicals (see figure 2). Clear evidence is given by observing radiation produced in 280-900 nm spectral range. The most intense emissions are produced by OH, H^I and O^I electronically excited species (see figure 2).

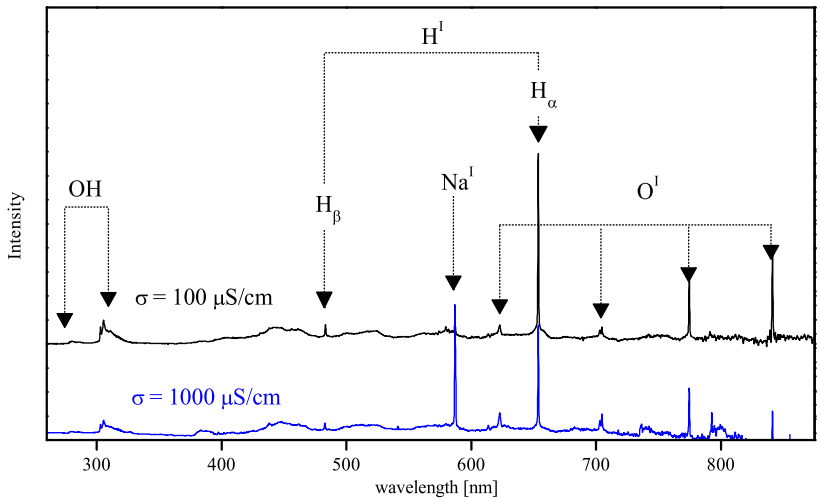

Fig. 2. Time-averaged ICCD spectrum of the glow-like capillary discharge regime;
a) σ =100 μS.cm^{-1} (upper trace; U = 8.5 kV (50 Hz)) and b) σ =1000 μS.cm^{-1} (lower trace; U = 5.5 kV (50 Hz)).

3.2. Time evolution of OH and H_α emission

Characterization of the evolution of the plasma induced emission intensity and the average plasma duration for the negative pulsed microsecond discharge regime was performed using time-resolution which was defined by the opening gate of an ICCD intensifier. A time-resolution was selected as a compromise between necessity to acquire spectra with both high time-resolution and sufficient S/N ratio during reasonably long accumulation period (typically 2-10 min/spectrum). Figure 3 shows typical evolutions of OH and H_α emissions for the negative pulsed microsecond discharge regime at two different conductivities (100 and 200 μS.cm^{-1}) and at an applied AC voltage of 8 kV rms. Time evolution of the applied AC voltage and current signal for this pulsed microsecond discharge regime is shown in figure 4. All time evolutions shown in figure 3 were normalized to 1 for the first point of each curve. The measurements indicate that radiative species are mostly generated during the first few hundreds of nanoseconds of plasma generation. All acquired emission intensities clearly show a two slope decay characteristic with characteristic time-constant of initial fast part τ = 0.2-0.4 μs. Due to internal delays and jitters of the used diagnostic instrumentation, the plasma induced emission could not be explored with sufficient time-resolution for discharge onset delays lower than ~200-400 ns, consequently we are missing the initial development of emission intensities. The average duration of plasma emission induced by the breakdown event for the negative pulsed microsecond discharge regime is however clearly of the order of a few microseconds.

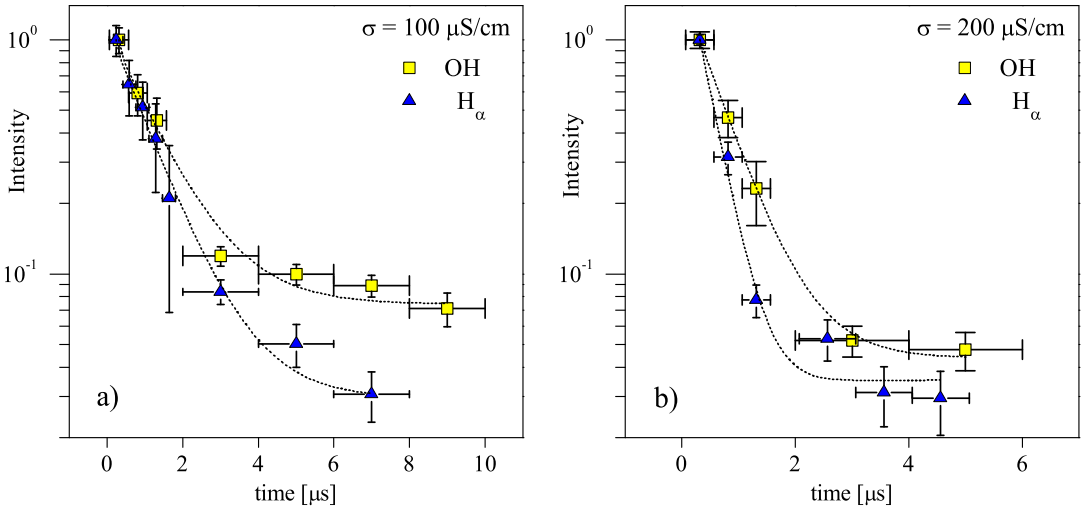

Fig. 3. Characteristic evolutions of OH and H_α emission intensities acquired for the negative pulsed microsecond discharge regime at an applied AC voltage of 8 kV for water solution conductivities of a) 100 and b) 200 µS.cm^{-1}.

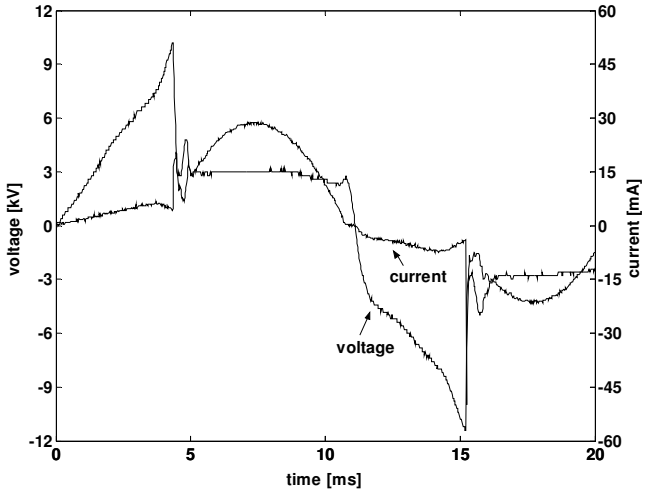

Fig. 4. Voltage and current signal for the pulsed microsecond discharge regime for water solution conductivity of 100 µS.cm^{-1} at an applied AC voltage of 8 kV rms.

3.3. Rotational distribution of OH($A^2\Sigma^+$, v=0) state

Partially resolved profile of OH($A^2\Sigma^+$,v=0 → $X^2\Pi$,v=0) band is often being used to evaluate rotational temperature T_{rot} in order to estimate, especially in high-pressure discharges, the gas temperature T_g. We attempted to evaluate T_{rot} by means of a synthetic model [8]. However, we found it impossible to reproduce well the overall (0,0) band-profile using a single Boltzmann rotational temperature T_{rot} as a fitting parameter. As the resolution of the 0.5 m spectrometer is not sufficient to resolve fully most intense rotational lines arranged in R_{11}, R_{22}, Q_{11} and Q_{22} branches, we had to resort to a set of very weak $^SR_{21}$ satellite lines occurring, quite well isolated, in 302-306 nm spectral region, just in front of the first band head at 306.26 nm (figure 5).

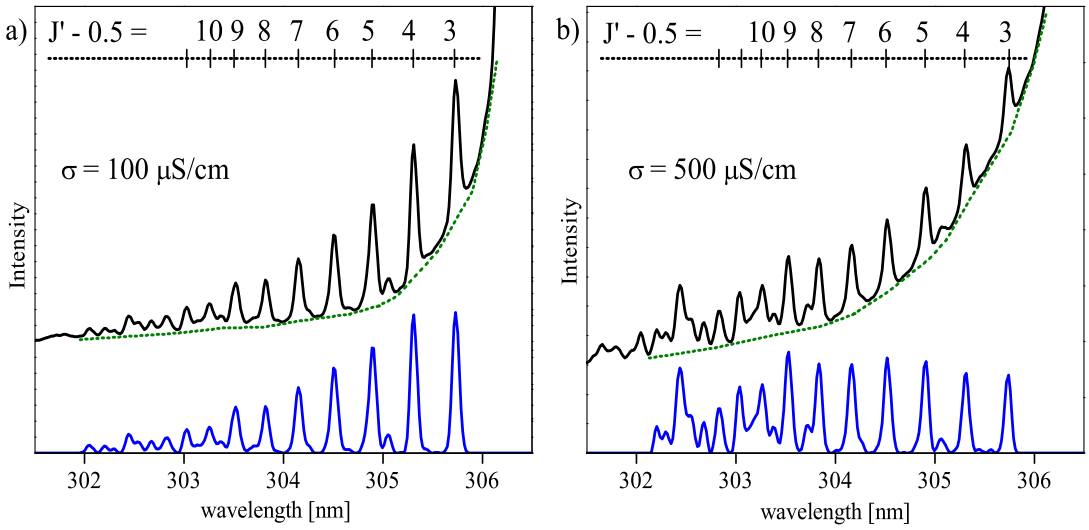

Fig. 5. Characteristic, partially-resolved OH emission through the $^{S}R_{21}$ branch of the OH($A^2\Sigma^+$,v=0 → $X^2\Pi$,v=0) band. Spectra acquired for the glow-like discharge regime for water solution conductivity of a) σ= 100 μS.cm^{-1} (U = 8.5 kV (50 Hz)) and b) = 500 μS.cm^{-1} (U = 8 kV (50 Hz)).

The rotational distributions plotted as a function of the roto-vibronic energy of $A^2\Sigma^+$ state levels are shown in figure 6. They were derived from spectra shown in figure 5. The distribution shown for water solution conductivity σ= 100 μS.cm^{-1} can be quite well fitted with a straight line (least-square fitting procedure applied to $^{S}R_{21}$(J'=3.5, 4.5, 5.5, 6.5, 7.5, 8.5) corresponding to a Boltzmann rotational temperature T_{rot} = 1530 K (figure 5a). Higher levels (J'= 9.5 - 12.5) show deviations from a single Boltzmann slope. A qualitatively very different distribution, obtained for water solution conductivity σ= 500 μS.cm^{-1}, is shown in figure 5b. It is apparently a highly non-Boltzmann distribution with the initial slope (evaluated from $^{S}R_{21}$(J'=3.5) and $^{S}R_{21}$(J'=4.5) line intensities) corresponding to T_{rot} = 2660 K. Here we have to note that the two distributions shown in figure 6 have been selected among many others as the two extreme cases (with all other distributions in between those two extremes). Furthermore, source spectra were acquired as time and space (along the capillary axis) averaged data; therefore they cannot be identified, at the moment, with any local discharge parameter.

4. Concluding remarks

Discharge generation in a thin dielectric capillary filled with liquid water solution driven by an AC high-voltage power supply presumably involves a breakdown of a water vapour bubble. The bubble is formed inside the capillary as a consequence of local heating of water solution due to increased current density. During the breakdown, various species may be formed through electron impact dissociation processes. Except of H_2O molecules, we have to consider other species as, e.g., NaH_2PO_4, N_2/O_2 (dissolved air molecules) and fragments of dielectric Macor glass ceramic (borosilicate glass + fluorophlogopite mica).
We investigated the discharge sustained with AC (50 Hz) voltages up to 15 kV rms by employing ICCD spectroscopy. Our measurements performed for water solution conductivity in the range 50-1000 μS.cm^{-1} indicate that this discharge concept might be an efficient source of OH, H^I and O^I radicals. The rotational distribution of OH($A^2\Sigma^+$, v=0) state for the glow-like discharge regime deviates from a single Boltzmann distribution. The rotational temperatures we have derived from the beginning of OH($A^2\Sigma^+$, v=0) rotational distribution indicate that quite high gas temperatures might be achieved during the breakdown event. This is consistent with observing a progressive erosion of Macor capillary profile after several hours of discharge operation. For the negative pulsed microsecond discharge regime, most emitting species are generated during the first few hundreds of nanoseconds after the breakdown event. The average plasma duration for the negative pulsed microsecond discharge regime is of the order of a few microseconds.

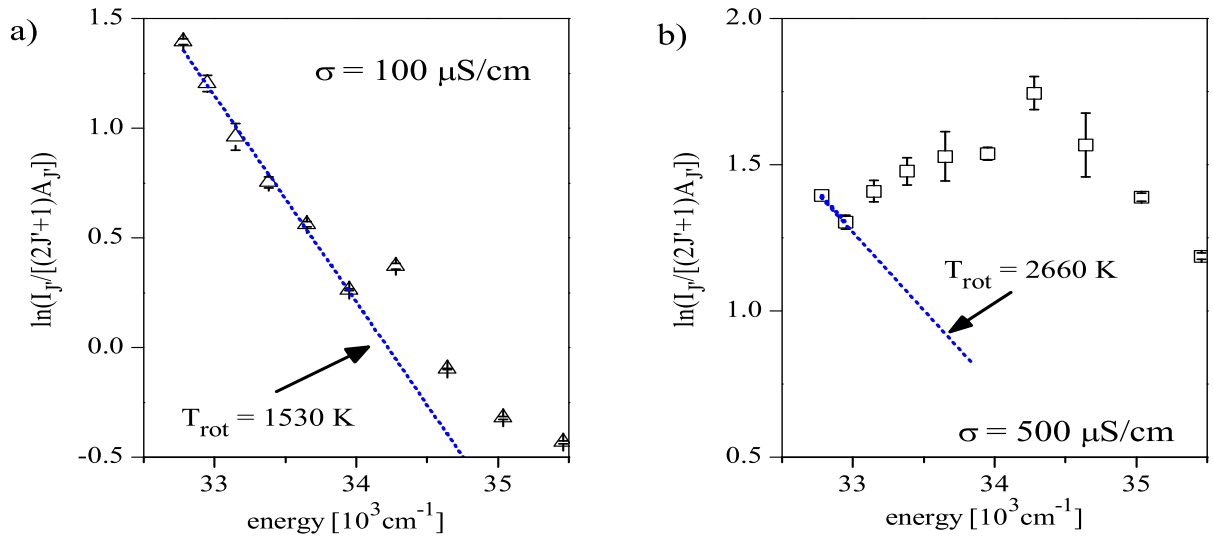

Fig. 6. Rotational distribution of OH($A^2\Sigma$,v=0) electronic state as derived from isolated lines belonging to $^{S}R_{21}$ branch of the OH($A^2\Sigma^+$,v=0 → $X^2\Pi$,v=0) band in the case of a) σ= 100 μS.cm^{-1} (U = 8.5 kV (50 Hz)) and b) σ= 500 μS.cm^{-1} (U = 8 kV (50 Hz)).

Acknowledgement

This work has been supported by the Bilateral Scientific and Technological Cooperation Programme between Flanders and the Czech Republic (contract no. 2004-2005-03).

References

[1] J.S. Clements, M. Sato and R.H. Davis: IEEE Trans. Ind. Appl., **IA-23**, 224 (1987).
[2] B. Sun, M. Sato and J.S. Clements: J. Electrost. **39**, 189 (1997).
[3] A.A. Joshi, B.R. Locke, P. Arce and W.C. Finney: Journal of Hazardous Materials **10**, 3 (1995).
[4] W.F.L.M. Hoeben et al.: J. Phys. D: Appl. Phys. **32**, 133 (1999).
[5] P. Šunka et al.: Plasma Sources Sci. Technol. **8**, 258 (1999).
[6] P. Šunka: Physics of Plasmas **8**, 2587 (2001).
[7] F. De Baerdemaeker et al.: Czech. J. Phys. **54**, C1062 (2004).
[8] M. Šimek: Proc. XVth Int. Conf. on gas discharges and their applications, Toulouse (France), Vol. 2, 853, (2004).

Modeling nanoparticle effects on a low-pressure plasma

S. J. Warthesen and S. L. Girshick

Department of Mechanical Engineering, University of Minnesota, Minneapolis, MN.

Abstract

The interactions between a plasma and nanoparticles are discussed here in the context of plasma-enhanced chemical vapor deposition. Results are obtained from a 1-D plasma model coupled to an aerosol transport model. The influence of nanoparticles on plasma properties is reviewed, and the charge distribution for 2-5 nm diameter particles is presented. A significant fraction of particles are found to be positively charged in a region of the sheath, close to the electrode.

1. Introduction

Nanoparticle-plasma systems are of interest for various processes, such as hypersonic plasma particle deposition, plasma etching, and plasma-enhanced chemical vapor deposition. Particles may be detrimental to plasma processes, causing contamination problems, or may be desired for the production of nanostructured materials and devices. In either case, the industrial goal is to control the nanoparticles in the plasma. Ultimately, this requires the study of formation, growth, and transport of nanoparticles, and their influence on the plasma parameters driving the process of interest. The focus of this research is to model the interactions between nanoparticles and plasma in the context of plasma-enhanced chemical vapor deposition (PECVD). During PECVD of silicon thin films using a silane or diluted silane plasma, nanoparticle formation can occur in the gas-phase. The mechanisms of nanoparticle nucleation, growth, and transport, as well as the interaction between nanoparticles and the plasma, form a complex system resulting in several interesting phenomena. These include the formation of trapped particle layers within the plasma and a drastic increase in electron temperature in the presence of particles (α-γ' transition) [1]. Several research groups have investigated the nanoparticle-silane plasma system, including many numerical studies. Akdim *et al.* developed a one-dimensional plasma model describing the influence of 2-μm-radius particles on the plasma characteristics [2]. De Bleecker *et al.* extended this model to include silane plasma chemistry predicting particle nucleation [3]. They equated nuclei formation with particles in the 10-100 nm size range and discussed the development of particle trapping layers for various particle sizes. Bhandarkar *et al.* predicted nucleation of particles using an extensive chemical clustering mechanism, and coupled this to an aerosol growth model in 0-D [4]. Both modules are solved consistently with bulk plasma parameters, predicting the temporal evolution of particle concentration and size and charge distributions. The focus of this research is the extension of this 0-D model to 1-D to describe spatial variations of the plasma and particle properties during particle nucleation, growth, transport, and charging. Preliminary results of this development are discussed here, focusing on the interaction between the plasma and nanoparticles in the 2-5-nm-diameter range in a parallel plate PECVD reactor.

2. Model Description, Plasma Module

Our model describes a radio frequency, capacitively-coupled plasma in a parallel plate reactor. The reactor is assumed to have large electrode diameters compared to the electrode separation distance. Thus, the analysis is reduced to solving the governing equations in the axial direction between electrodes, as the system varies in time. Time-varying profiles of electron and ion concentrations, electron energy, and electric field are computed in the plasma module by solving the continuity equation for each species at each location in the discretized computational domain (for example, refer to [2, 5, 9]). The species flux terms are estimated by the drift-diffusion approximation. Ions, large compared to electrons, cannot follow the instantaneous electric field due to inertial effects. Thus, an effective electric field, described by Richards *et al.* is used in the drift-diffusion approximation in place of the local instantaneous electric field [5]. The loss of ions and electrons to particles is accounted for as a sink in each continuity equation, and is calculated according to collision frequencies discussed below. The electron energy balance is solved to calculate the electron temperature, and includes the energy absorbed by

electrons when intercepted by particles (to overcome the particle potential). Poisson's equation is solved to determine the electric field from the space charge, and accounts for charges residing on particles as well as free electrons and ions.

3. Particle Module

The change in size distribution and concentration of aerosols in space and time is described by the aerosol general dynamic equation. Mechanisms accounted for in the transport of neutral particles include diffusion, convection, and thermophoresis. Additional transport mechanisms are incorporated in the model to account for particle interaction with the plasma, including ion drag and electrostatic effects. Coagulation and surface growth are not included in these preliminary results. For computational ease, the complex chemistry mechanism is not included here. Instead, nucleation occurs at a prescribed rate.

The charge distribution of particles at a given location in space is calculated by assuming spherical particles and applying orbital-motion-limited (OML) theory to calculate ion and electron interception rates by the nanoparticles [6]. The collision frequency of electrons with a nanoparticle of radius r_p and potential V_p depends on electron concentration N_e and electron temperature T_e.

$$\nu_e = \pi r_p^{\,2} N_e \left(\frac{8 k_B T_e}{\pi m_e} \right)^{1/2} \alpha \qquad (1)$$

$$\alpha = \exp\left(\frac{eV_p}{k_B T_e} \right) \text{ for } k < 0 \qquad \alpha = \left(1 + \frac{eV_p}{k_B T_e} \right) \text{ for } k > 0 \qquad (2)$$

In the above equations, ν_e is the electron-particle collision frequency, m_e is the electron mass, k_B is Boltzmann's constant, and α is an enhancement or retardation factor, depending on the sign of the particle charge, k. For ions, the collision frequency equation is similar. However, the energy acquired by positive ions in the plasma sheath is taken into account by calculating the ion energy, E_o, based on the ion drift velocity, v_D, and using it in the collision frequency calculation below, where ν_i is the ion-particle collision frequency, m_i is the ion mass, T_i is the ion temperature (assumed to be the same as the gas temperature), N_i is the ion concentration, and β is the charge dependent enhancement or retardation factor.

$$E_o = \left(\frac{8 k_B T_i}{\pi m_i} \right) + \frac{1}{2} m_i v_D^{\,2} \qquad (3)$$

$$\nu_i = \pi r_p^{\,2} N_i \left(\frac{2 E_o}{m_i} \right)^{1/2} \beta \qquad (4)$$

$$\beta = \left(1 + \frac{eV_p}{E_o} \right) \text{ for } k < 0 \qquad \beta = \exp\left(\frac{-eV_p}{E_o} \right) \text{ for } k > 0 \qquad (5)$$

By assuming that the particle charging process is in equilibrium with the local plasma properties, a recursive relationship is defined for the distribution of charges on particles of a given size, equation (6), where $\nu^k_{e\,(i)}$ is the collision frequency of electrons (ions) with a particle that has k unit charges. Subsequently normalized, F_k, represents the fraction of particles with k unit charges, providing a discrete charge distribution function [7]. The effect of secondary electron emission is not currently accounted for in this calculation, but may slightly shift the charge distribution toward positive charge values, depending on the reactor conditions [8].

$$F_{k+1} = \frac{\nu_i^k}{\nu_e^{k-1}} F_k \qquad (6)$$

The ion and electron continuity and electron energy equations are solved using the Scharfetter-Gummel scheme [9, 10]. These equations, as well as Poisson's equation for potential, are discretized and solved in a tridiagonal matrix solver. As suggested by Akdim and Goedheer, a time stepping procedure is implemented in two stages [2]. One time step is applied to the plasma balance equations, and a second, larger time step is applied to the nanoparticle module. Plasma parameters, such as the electric field, ion and electron concentrations, and electron temperature are time-averaged over the nanoparticle time step. The time-averaged profiles are applied to nanoparticle transport and charging calculations, since particles are too slow due to inertial effects to follow the high frequency oscillations of the plasma.

4. Results

Results presented here correspond to a typical PECVD reactor under conditions of particle formation. The electrode separation is 3 cm. The upper electrode (x = 3 cm) is the RF-powered electrode, while the lower, representing the film substrate, is grounded (x = 0). The RF voltage and frequency are 200 V and 13.56 MHz, respectively. The reactor pressure is ~13 Pa (100 mTorr), with a uniform gas temperature of 300 K. The plasma is modeled as an argon plasma in a static gas (excluding convection effects). The ion drag force has been shown to have a negligible influence on the transport of particles in this size range under these conditions [3], thus it is excluded from the present calculations for computational simplicity. Initially, the plasma is established by running the simulation without particles for several cycles. Once a periodic steady state for the non-contaminated plasma is obtained, particles are introduced at low concentrations (less than that of the electron concentration). An initial population of particles is placed in a region approximating the bulk plasma (indicated in Figure 1), and subsequent nucleation is assumed to occur only in this region. This assumption is consistent with the simulation results of De Bleecker *et al*, who showed that nucleation in a diluted silane plasma, for similar conditions, mainly occurs in the plasma bulk [11]. The nucleation rate applied to the system is estimated from results of quasi-1-D simulations coupling the chemical clustering mechanism to aerosol and plasma modules [4].

In Figure 1, the period-averaged ion and electron concentrations are compared to the particle concentration at 0, 10^{-3}, and 10^{-1} seconds after nucleation began. N_+ represents the ion concentration (Ar^+), N_e is the electron concentration, and N_p represents the concentration of particles within the reactor. Particles here are 2 nm in diameter, with a constant production rate (~ nucleation) of 10^{11} $cm^{-3}s^{-1}$. As time proceeds, an increase in particle

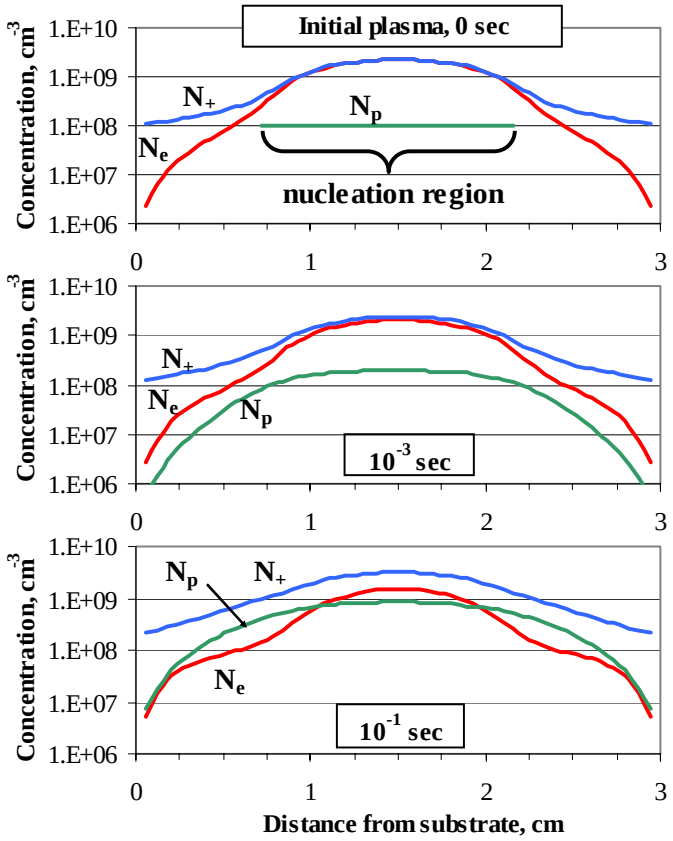

Figure 1. 2-nm-diameter particle concentration (N_p) in the reactor at various times. Initially $N_p = 10^8$ cm^{-3}, with a nucleation rate of 10^{11} $cm^{-3}s^{-1}$. Concentration is compared to ion and electron concentration (N_+, N_e) in the plasma. The electron concentration drops slowly in time, while the ion concentration increases.

concentration occurs throughout the reactor as particles nucleated in the center region are transported due to diffusion and electrostatic force. The period-averaged electron temperature, T_e, and ionization rate corresponding to profiles in Figure 1 are displayed in Figure 2. When particles are present, electrons are lost to particles and they become negatively charged. Ions are also lost to particles, but to a much lesser degree than electrons because of the electron:ion mobility ratio. In the center of the plasma, where the electron concentration is highest, electron loss results in a slight increase in T_e. In this region, T_e, increases slowly from 2.1 to 2.6 eV over 0.1 seconds, as seen in Figure 2a. Contrastingly, in the sheath region, T_e quickly increases from 2 to 4 eV. Since the electron concentration in the sheath is significantly lower than in the plasma center, the electron temperature is more sensitive to particle charging effects. The increase in T_e causes an increase in ionization rate, which is maximum in the plasma center where the electron concentration is highest (Figure 2b). The ion concentration increases with ionization rate (a factor of 1.5 – 2 over 0.1 seconds), as does the power absorption in the plasma (the RF voltage is maintained, allowing absorbed power to change).

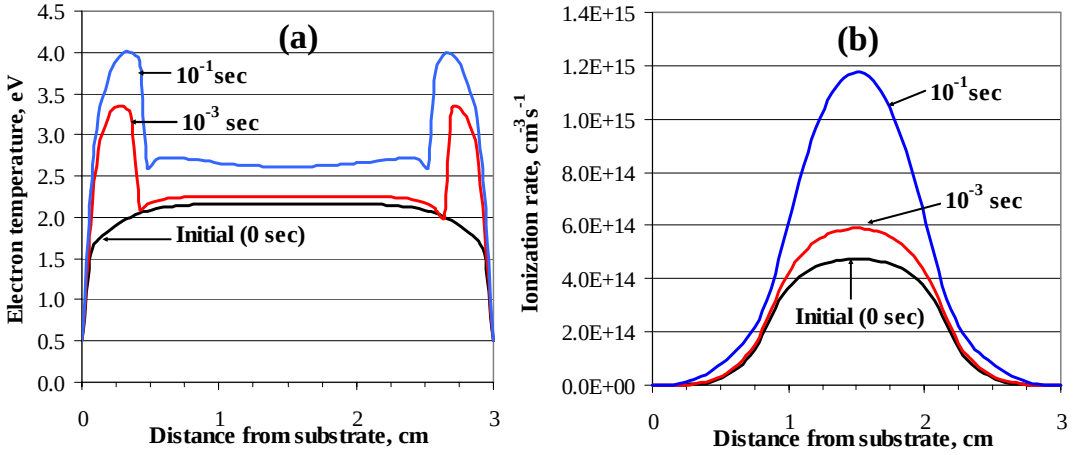

Figure 2. Variation of plasma properties as particle concentration increases. (a) Electron temperature increases quickly in sheath, and slowly in the plasma bulk. (b) Ionization rate increases in time.

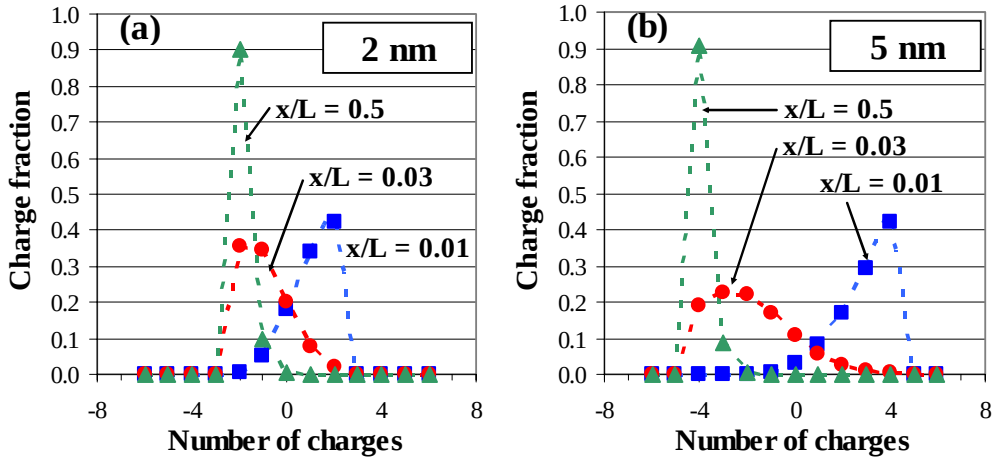

Figure 3. Charge distributions, at 0.1 s, for particles at three locations within the reactor (for position x relative to electrode separation L); near the electrode, within the sheath, and in the plasma center. Particles have a diameter of (a) 2 nm and (b) 5 nm. Near the electrode, particles may acquire a positive charge due to the increased energy of ions and small electron concentration in the sheath. Lines are added to the discrete charge distributions for visual clarity.

The charge distribution of 2-nm-diameter particles is shown for various locations (close to electrode, mid-sheath, and plasma center) in Figure 3a, where *x/L* indicates the position in the reactor *x* relative to the electrode separation *L*. The charge distribution is shown at 0.1 seconds, and changes little over the time simulated here. It is interesting to note that due to low electron concentrations and high ion velocity in the sheath, particles are likely to become positively charged. The contribution of ions to charging is mostly due to their energy acquired in the sheath (equation 3). If only the thermal energy of ions is considered, the calculated charge distribution remains almost completely negative. Figure 3b shows the charge distribution for nanoparticles with a diameter of 5 nm. The charge distribution was taken after 0.1 seconds under conditions similar to those described for the 2-nm simulation. The same three locations are shown in Figures 3a and 3b. It is assumed that 2-nm particles are limited to a maximum of 2 charges, while 5-nm particles are allowed to hold up to 4 charges [12]. Both sizes show similar charge distribution characteristics. In the plasma center, the electron supply is sufficient such that most particles are charged to their negative charge limit. As particles move into the sheath, however, the competition for electrons among particles shifts the distribution to a less negative charge. As particles continue to move toward the electrode, the contribution of ions becomes significant, and both negatively and positively charged particles are likely to exist (*x/L* = 0.03, Figure 3). Very close to the electrode, the particle charge distribution is almost completely positive. Particles are present in low concentrations here, thus there is little or no competition among particles for charges. In both the 2- and 5-nm case, most particles attain their maximum allowed charge, now positive as opposed to the negative charge in the center of the plasma. Thus, a region of one or two millimeters extends from both electrodes into the plasma where positive particles are likely. These positive particles will be quickly rejected from the plasma due to the electric field. This mechanism of particle loss will influence the growth of particles in the reactor as well; small particles are likely to diffuse to the sheath region and can be expelled before growing to larger sizes. For example, compare the *x/L* = 0.03 charge distribution for 2 and 5-nm diameter particles. If a 2-nm particle grows to 5 nm near this location, it is more likely to acquire a negative charge and be transported toward the center of the plasma for further growth. In addition to the effect on growth mechanisms, the existence of a positive charge region near the electrode has significant implications for plasma processing of materials. Even if the number concentration of particles is low in the sheath, a high percentage of them may have high velocities upon deposition or impaction on the substrate.

5. Summary

This research attempts to simulate nanoparticle behavior during PECVD of silicon films. In development of a more complete model, we have presented preliminary results using a one-dimensional plasma model coupled with an aerosol transport and charging model. Using this model, simulations have been presented and the interaction between nanoparticles and a plasma have been explored. It is found that ionization rate increases as particles become more populous, and the electron temperature increases drastically in the sheath. In the bulk plasma, the electron temperature is also increasing, but more slowly and to a lesser magnitude than the sheath electron temperature. Finally, charge distributions have been presented, discussing the existence of positively charged particles in the sheath. Positively charged particles are likely to escape and reduce the overall growth rate of particles in the reactor. Also, positive particles can significantly affect the quality of the film being deposited due to the high energy acquired by positively charged species over the large electric field of the sheath.

This research is supported by NSF under IGERT grant DGE-0114372 and MRSEC grant DMR-0212302, by DOE under grant DE-FG02-00ER54583, and by the Minnesota Supercomputing Institute.

References

[1] A. A. Fridman, L. Boufendi, T. Hbid, B.V. Potapkin, and A. Bouchoule, J. Appl. Phys. **79**, 1313 (1996).
[2] M. R. Akdim and W. J. Goedheer. J. Appl. Phys. **94**, 104 (2003).
[3] K. De Bleecker, A. Bogaerts, and W. Goedheer. Phys. Rev. E, **70**, 056407 (2004).
[4] U. Bhandarkar, U. Kortshagen, and S. L. Girshick. J. Phys. D: Appl. Phys. **36**, 1399 (2003).
[5] A. D. Richards, B. E. Thompson, and H. H, Sawin. Appl. Phys. Lett. **50**, 492 (1987).
[6] J. E. Allen. Phys. Scr. **45**, 497 (1992).

[7] T. Matsoukas, M. Russel, and M. Smith. J. Vac. Sci. Technol. A. **14**, 624 (1995).
[8] U. Kortshagen and U. Bhandarkar. Phys. Rev. E. **60**, 887 (1999).
[9] D.L. Scharfetter and H. K. Gummel. IEEE Trans. Electron. Devices, **ED-16,** 64 (1969).
[10] J. P. Boeuf. Phys. Rev. A, **36**, 2782 (1997).
[11] K. De Bleecker, A. Bogaerts, and R. Gijbels. Phys. Rev. E, **69**, 056409 (2004).
[12] *Aerosol Technology*. W. C. Hinds, (John Wiley and Sons Inc, New York, 1999).

Numerical Study of the Transition from Filamentary Dielectric Barrier Discharges to Uniform Glows in Helium at Atmospheric Pressure

Peng Zhang, Uwe Kortshagen

Department of Mechanical Engineering, University of Minnesota, Minneapolis, USA

Abstract

The transition from filamentary dielectric barrier discharges to uniform glow discharges in atmospheric helium has been studied by a two–dimensional fluid model. Influences of different operating parameters have been investigated. The results show that for a filamentary discharge the number of filaments increases with the frequency and the voltage. The overlap of the filaments favors the formation of a uniform glow. For dielectric barriers with lower permittivity, the number of filaments decreases, resulting in a uniform Townsend discharge.

Keywords

Dielectric barrier discharge, atmospheric pressure glow, two-dimensional fluid model

1. Introduction

The dielectric barrier discharge (DBD) is a non-equilibrium discharge in which one or both electrodes are covered with an insulating layer [1]. At atmospheric pressure, DBDs typically have a filamentary structure, characterized by a large number of short-lived microdischarges. This behavior is highly transient and non-uniform over the electrode surface; hence high-pressure DBDs are of limited use for applications that require high plasma uniformity [2, 3]. Operated in similar reactor set-ups as DBDs, atmospheric pressure glow (APG) discharges have attracted great attention [4-7]. Typical APGs have a structure similar to low-pressure glow discharges. Being transversely homogeneous, they have a unique advantage over the filamentary DBDs for applications that require uniform plasma treatment such as thin film deposition [8], VLSI processing [9, 10], biological sterilization or decontamination [11].

Dielectric barrier discharges have been studied for many years [3, 12-15]. Under certain conditions, self-organized filaments can be formed. Brauer *et al* simulated the formation of self-organized filaments and demonstrated that for large *pd* values the discharge had a natural tendency to become filamentary [14]. An increasing number of filaments were reported for increasing voltage by T. Shirafuji *et al* [15]. However, so far no comprehensive numerical study of transition from filamentary to glow discharge has been reported.

The two-dimensional modeling of APGs is still in an early stage. Highly disparate time-scales have to be satisfied for capturing both the instantaneous and long-term behaviors of the discharge. A first successful effort was made by Schweigert and Kortshagen [16]. In this work, the time-dependent two-dimensional distribution of electrons and ions was obtained for the first time. However, with only electrons and atomic helium ions considered, the kinetic model was too simple to represent the real experimental situation, where experimental results have revealed the existence of strong nitrogen emission in otherwise high purity helium atmospheres. More sophisticated kinetic models were developed in later works by other groups [17-19]. With those the breakdown process of the APG in helium [17] and in nitrogen [19] has been reproduced. However, limited information was given on the discharge evolution up to reaching a periodic steady state, which typically takes several ac cycles.

In the current paper, based on a two-dimensional fluid model, the transition between a filamentary DBD and a uniform APG is investigated. Influences of operating parameters such as the driving frequency, the amplitude of the applied voltage, and the dielectric constant of the dielectric barrier material are studied. The paper is organized as follows: Section 2 describes the model and elementary processes, section 3 presents the numerical results and their interpretations, and section 4 summarizes the main conclusions.

2. Model and Elementary Processes

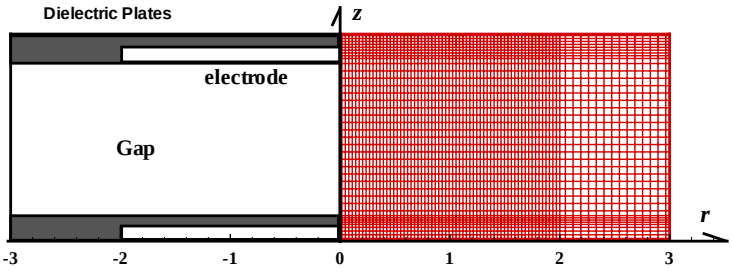

Fig. 1. Numerical simulation domain.

A two-dimensional fluid model has been developed for the simulation of APGs. Based on the experimental setup (see ref. [20] for details), the numerical simulation domain is selected, which includes two 1mm-thick dielectric barriers and a 5mm discharge gap as shown in Fig. 1. The electrodes are embedded in the dielectrics. The radius of the electrodes and the dielectrics are 2cm and 3cm, respectively. The gap is filled with atmospheric-pressure helium. Assuming azimuthal symmetry, cylindrical coordinates *(r-z)* are used. A non-uniform mesh of 81x121 nodes is used with the minimum node spacing being 62 μm.

For a pure helium discharge, due to the small leak rate of the experimental system, the known effects of nitrogen impurities must be considered in the simulation. The following species are used for the model: electrons (e^-), atomic and molecular helium ions (He^+, He_2^+), helium metastables (He^*), and molecular nitrogen ions (N_2^+). Here helium excited states of 2^3S and 2^1S are lumped into one single state for simplicity (denoted He^*). The model involves the self-consistent solution of the Poisson equation for the electric field and the continuity and momentum equation for all the species. The momentum equations are simplified by using the drift-diffusion flux approximation. The governing equations are:

$$\nabla^2\phi = -\frac{e(n_i - n_e)}{\varepsilon_0} \tag{1}$$

$$\frac{\partial n_e}{\partial t} = G_e - L_e + \nabla\cdot(-\mu_e n_e \nabla\phi - D_e \nabla n_e) \tag{2}$$

$$\frac{\partial n_i}{\partial t} = G_i - L_i + \nabla\cdot(\mu_i n_i \nabla\phi - D_i \nabla n_i) \tag{3}$$

$$\frac{\partial n_m}{\partial t} = G_m - L_m + \nabla\cdot(-D_m \nabla n_m) \tag{4}$$

Here ϕ is the electric potential, n is the number density, μ is the mobility, and D is the diffusion coefficient. The subscript *e*, *i*, and *m* represent the electrons, ions, and metastables in the discharge, respectively. The generation term $\boldsymbol{G}$ and loss term $\boldsymbol{L}$ are determined by the elementary processes inside the discharge. The reactions and the corresponding rate coefficients are the same as in ref. [20].

The secondary electron emission at the dielectric surface due to ion bombardment is regarded as a main source of electrons sustaining the glow discharge. The space charge deposited on the plates is obtained from the drift-diffusion flux to the dielectrics. The surface sticking coefficients of the electron and ions is set to 1 for simplicity.

The simulation was started with one electron avalanche located at cathode, with a maximum electron density equal to 10^6 cm^{-3}. For all the cases, a sinusoidal alternating current (ac) voltage was applied. The nitrogen concentration was assumed to be 20ppm. The simulations were stopped once a periodic solution was reached, usually occurring after 8-10 ac cycles.

The transport terms in the continuity equations are discretized using the Scharfetter-Gummel exponential scheme [21] on a non-uniform mesh. To increase the time-stepping efficiency, an adaptive time step and a semi-implicit

time integration scheme [22] are adopted. All the numerical simulations were implemented on an IBM Power4 supercomputer at the University of Minnesota Supercomputing Institute.

3. Results and discussion

In the following, we study the influence of frequency, voltage amplitude, and dielectric material, which are all important parameters that can affect the discharge behavior.

3.1 *Driving frequency*

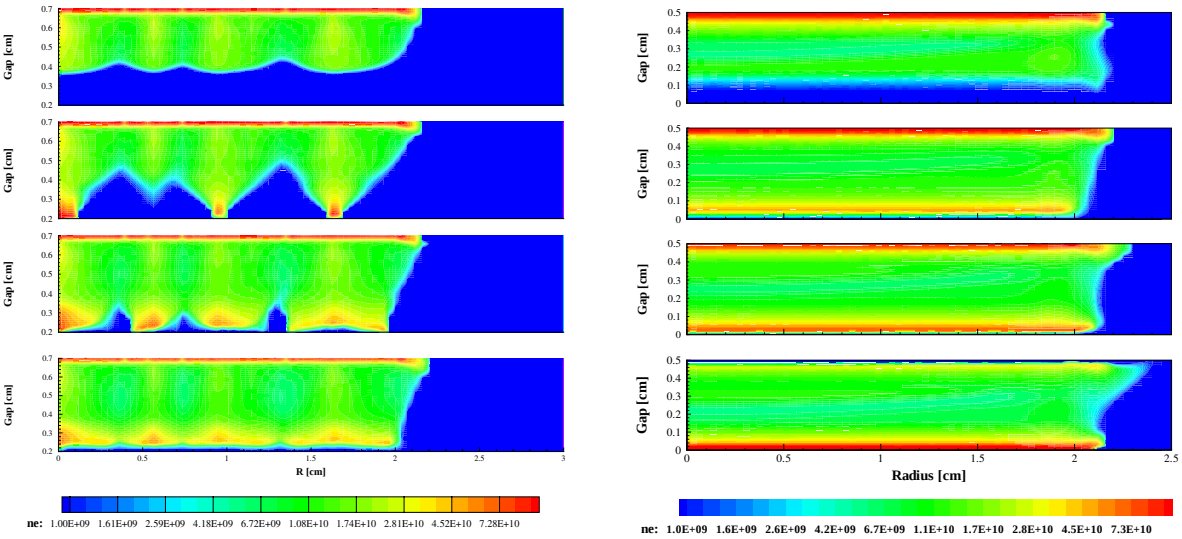

(a) (b)

Fig. 2 Electron density profiles at different times for f =15kHz (a) and f =30kHz (b).

To study the influence of the driving frequency, the applied voltage amplitude is fixed at 1.8kV. Alumina dielectrics are used with a relative permittivity equal to 9. Fig. 2(a) shows the electron density profile at different times for a 15kHz frequency. Four self-organized filaments are observed in the discharge gap. The location of the filaments is balanced by the repulsive force between the filaments and the confining potential as stated in [15]. The number of filaments increases as f increases to 18kHz, 20kHz, 23kHz (Fig. 3). Eventually, when the frequency reaches 30kHz, numerous filaments are formed. The coalescence of these filaments finally leads to the uniform appearance as shown in Fig.2 (b).

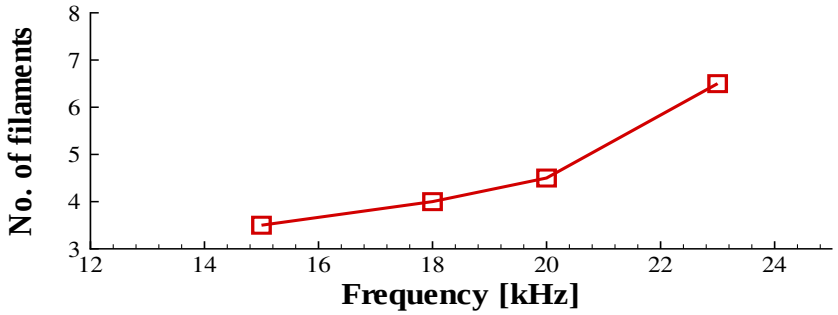

Fig. 3 Number of filaments as a function of frequency.

It should be pointed out that the trend we observe here, namely, the number of filaments increasing with driving frequency, is consistent with the results obtained by other researchers [14, 16]. The observed trend is based on two mechanisms: The first is the increasing pre-ionization with frequency since at higher frequency there is less time between discharge pulses for the density to decay through recombination. The second is related to the ion

transport and diffusion, which are limited at a higher frequency, resulting in a smaller separation between filaments and an increasing number of filaments.

3.2 Amplitude of the applied voltage

For the formation of a glow discharge at atmospheric pressure, a Townsend breakdown is required instead of a filamentary breakdown. For this purpose, the applied voltage has to be only slightly larger than the breakdown voltage. Too large an overvoltage will result in a filamentary breakdown and thus an inhomogeneous filamentary discharge.

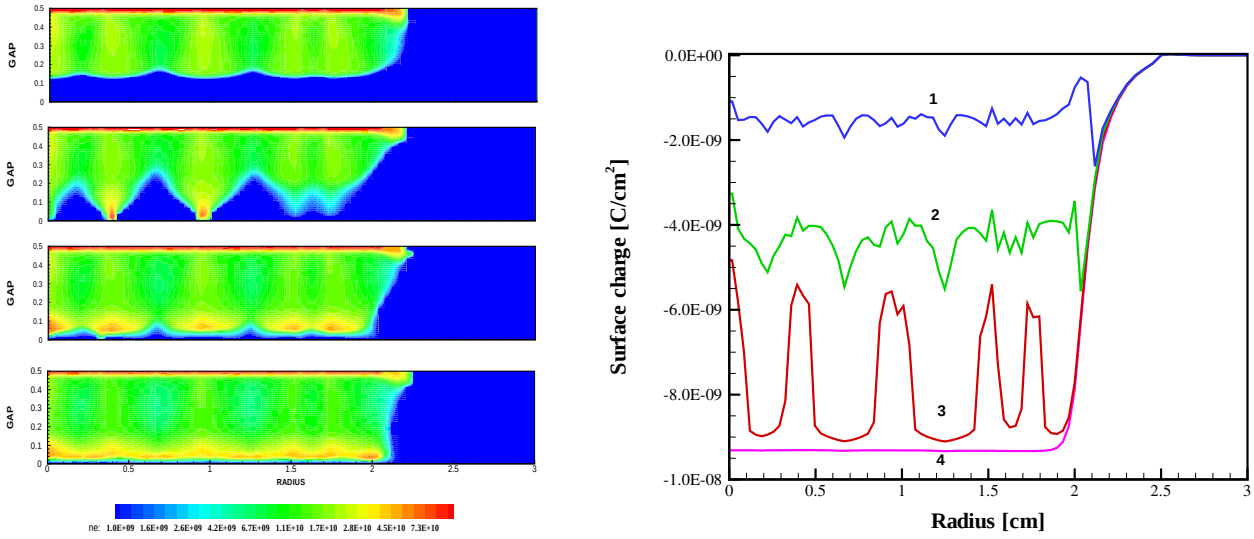

(a) (b)

Fig. 4. Electron density (a) and surface charge density on the powered dielectric (b) at different times for a 2.5kV voltage.

For a self-organized filamentary discharge, the discharge appearance also changes with the voltage amplitude. If the voltage for the case in Fig. 2 is elevated to 2.5 kV, the number of filaments increases from 4 to 5 along the electrode radius as shown in Fig. 4(a). This effect may be explained by the limited capacitance for a unit area of the dielectric. Because the gap breakdown voltage remains approximately constant, a higher voltage drop occurs across the dielectrics with increasing voltage amplitude leading to an increase in the total surface charge on the dielectrics. As a consequence, the number of surface charge spots increases. These results are consistent with [15, 23]. Fig.4 (b) shows the surface charge density on the powered dielectric. Five localized negative surface charge spots are observed. The non-uniformity of the surface charge is one important reason for the non-uniformity of the discharge, as it reinforces the inhomogeneity of the electric field in the discharge gap.

3.3 Relative permittivity of the dielectric

As discussed before, we expect the surface charge pattern on the dielectrics to affect the electric field distribution. If the non-uniformity of the surface charge is smoothed out the discharge is more likely to become uniform. Starting from the case in Fig. 2, fewer filaments are formed when the relative permittivity ε_r is decreased. A uniform glow appears when ε_r equals 2.0 (see Fig. 5(a)). Fig. 5(b) shows the current density–voltage waveform with one current pulse per half cycle, the typical V-I profile for an APG.

The reduced number of filaments with decreasing relative permittivity can be explained by the increased impedance of the dielectrics. This leads to an overall slower increase of the gap voltage and a slower evolution of the breakdown compared to a dielectric with larger ε_r. This slower evolution of the breakdown allows for more time for the inhomogeneity in the gap and on the surface to be smoothed out. The reduced inhomogeneity

is accompanied by weaker gradients in the plasma density which otherwise may give rise to strong space charge fields, which again non-linearly enhance the inhomogeneity through increased ionization.

Even when starting from a filamentary discharge (15kHz, 1mm thick alumina dielectrics), a uniform discharge can be obtained either by increasing the driving frequency or replacing the dielectrics with a material that has a lower permittivity. However, the mechanisms leading to this transition are different. In the former case the uniform discharge is related to the overlapping of the numerous filaments. In the latter case it is due to the reduction of the number of filaments. These two uniform discharges actually belong to different regimes. Fig. 6 shows the axial profile of the electric field and helium metastable production rate for these two uniform discharges. The 30 kHz case shows a typical dc glow discharge structure, with a high electric field in a narrow cathode layer and a relatively low electric field in the positive column. The helium metastable production rate has a similar structure (Fig. 6(a)) following the behavior of the electric field. However, for the case with ε_r equal to 2.0, a much broader cathode layer is formed and the positive column is missing as shown in Fig. 6(b). Correspondingly, the helium metastable production has only one peak, which is located inside the cathode layer. This structure is similar to a Townsend discharge, although it has the same V-I characteristic as an APG in the glow mode.

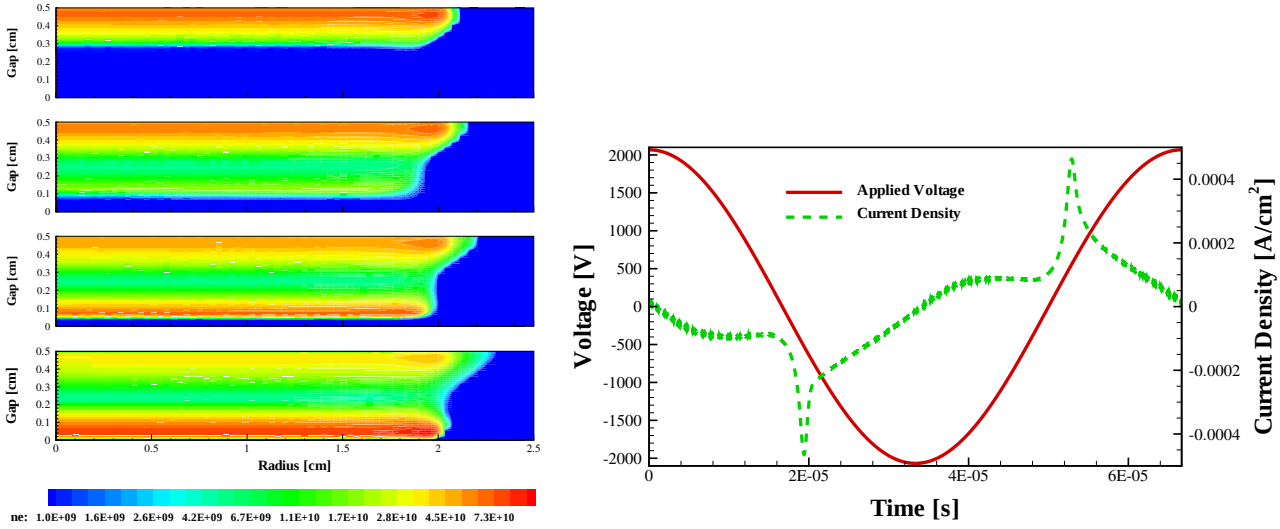

(a) (b)

Fig. 5 Electron density profile at different times (a) and voltage-current wave form (b) for the case with ε_r=2.0

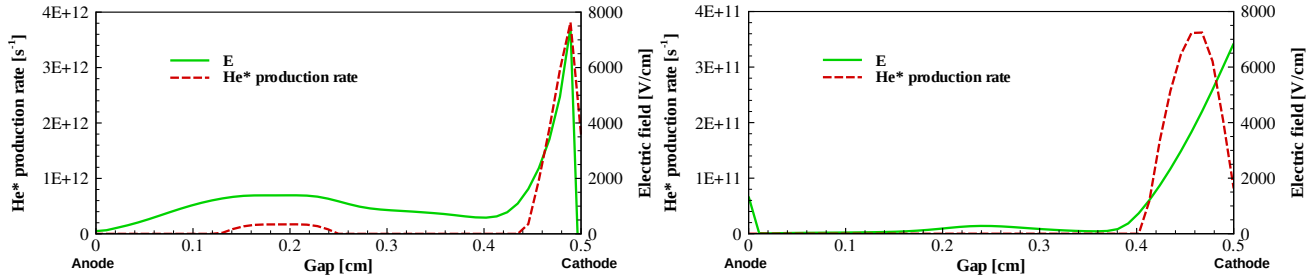

(a) (b)

Fig. 6 Electric field and helium metastable production rate at current maximum for glow discharge (a) and Townsend discharge (b). In (a), f=30kHz, ε_r=9.0; in (b), f =15kHz, ε_r=2.0.

4. Conclusion

A two-dimensional fluid model was used for the study of the transition between filamentary dielectric barrier discharges and uniform atmospheric pressure glows in a helium atmosphere. The influences of the driving frequency, voltage amplitude and the dielectric material were investigated. For self-organized filaments, the number of filaments was found to increase with increasing frequency. This is due to the less pronounced drop of the pre-ionization level and the limited ion diffusion and transport at higher frequency. Once a large enough number of filaments was formed, the overlapping of the filaments gave a uniform appearance of the discharge. The influence of the voltage amplitude manifests in a decreasing number of filaments at lower voltage amplitude. The dielectric material also influences the discharge appearance. Fewer filaments were formed for materials with lower permittivity, as the slower increase of the gap electric field tends to smooth out the non-uniformity of the surface charge and of the gap plasma density. The localized surface charge is believed to be one important reason for the formation of the non-uniform filamentary discharge.

Although increasing frequency and decreasing permittivity of the material both favor a uniform plasma, the resulting discharges fall into different regimes. A glow discharge was formed on increasing the driving frequency, while a Townsend-like discharge appeared for a lower permittivity material.

Other than the above operating parameters, intrinsic properties of the background gas also have a large influence on the discharge behavior. A study in this direction is now in progress.

5. Acknowledgement

This work is supported by the Department of Energy under grant DE-FG02-00ER54583 and by the University of Minnesota Supercomputing Institute.

References:

[1] B. Eliasson and U. Kogelschatz, IEEE Trans. Plasma Sci. **19**, 309 (1991).
[2] U. Kogelschatz, IEEE Trans. Plasma Sci. **30**, 1400 (2002).
[3] U. Kogelschatz, Plasma Chem. Plasma Process **23**, 1 (2003).
[4] F. Massines, A. Rabehi, P. Decomps, R.B. Gadri, P. Segur and C. Mayoux, J. Appl. Phys. **83**, 2950(1998).
[5] D. Trunec, Z. Navratil, L. Zajickova, V. Bursikova and J. Cech, J. Phys. D: Appl. Phys **37**, 2112 (2004).
[6] X.X. Wang, C.R. Li, M.Z. Lu and Y.K. Pu, Plasma Sources Science & Technology **12**, 358 (2003).
[7] N. Gherardi and F. Massines, IEEE Trans. Plasma Sci. **29**, 536 (2001).
[8] T. Yokoyama, M. Kogoma, S. Kanazawa, T. Moriwaki and S. Okazaki, J. Phys. D: Appl. Phys. **23**, 374 (1990).
[9] Y. Sawada, S. Ogawa and M. Kogoma, Journal of Physics D: Applied Physics, **28**, 1661 (1995).
[10] Y. Sawada, H. Tamaru, M. Kogoma, M. Kawase and K. Hashimoto, J. Phys. D: Appl. Phys. **29**, 2539 (1996).
[11] M. Laroussi, G.S. Sayler, B.B. Glascock, B. McCurdy, M.E. Pearce, N.G. Bright and C.M. Malott, IEEE Trans. Plasma Sci. **27**, 34 (1999).
[12] J. Li and S.K. Dhali, J. Appl. Phys. **82**, 4205 (1997).
[13] J. Li, W.M. Sun, B. Pashaie and S.K. Dhali, IEEE Trans.Plasma Sci. **23,**672 (1995).
[14] I. Brauer, C. Punset, H.-. Purwins and J.P. Boeuf, J. Appl. Phys. **85**, 7569 (1999).
[15] T. Shirafuji, T. Kitagawa, T. Wakai and K. Tachibana, Appl. Phys. Lett. **83**, 2309 (2003).
[16] V.A. Schweigert and U. Kortshagen, Proceedings Hakone VIII (International Symposium on High Pressure Low temperature Plasma), 154 (2000)
[17] Y. Honda, F. Tochikubo and S. Uchida, Jap. J. Appl. Phys. Part 2-Lett. **41**, L1256 (2002).
[18] Y.B. Golubovskii, V.A. Maiorov, J. Behnke and J.F. Behnke, J. Phys. D: Appl. Phys. **36**, 975 (2003).
[19] Y.B. Golubovskii, V.A. Maiorov, J.F. Behnke, J. Tepper and M. Lindmayer, J. Phys. D: Appl. Phys. **37**, 1346 (2004).
[20] L. Mangolini, C. Anderson, J. Heberlein and U. Kortshagen, J. Phys. D: Appl. Phys. **37,** 1021 (2004).
[21] D.L. Scharfetter and H.K. Gummel, IEEE Trans. Electron Dev. **16**, 64 (1969).
[22] M.S. Mock, Analysis of mathematical models of semiconductor devices, Dublin: Boole press, 1983.
[23] I. Muller, C. Punset, E. Ammelt, H.-. Purwins and J.P. Boeuf, IEEE Trans. Plasma Sci. **27**, 20 (1999).

High-Yield Synthesis of Luminescent Silicon Quantum Dots in a Continuous Flow Non-thermal Plasma Reactor

L. Mangolini, E. Thimsen and U. Kortshagen

Department of Mechanical Engineering, High Temperature and Plasma Laboratory
University of Minnesota, Minneapolis, MN 55455

Abstract

Light-emission from nanostructured silicon has sparked intense research ever since its discovery about 15 years ago. The lack of a simple high-yield synthesis approach for luminescent silicon nanocrystals has so far hampered their widespread application in such diverse areas as opto-electronics, solid-state lighting for general illumination, and fluorescent agents for biological applications. In this paper we discuss a non-thermal plasma process for the synthesis of luminescent silicon nanocrystals.

Introduction

Silicon is a material with rather poor optical emission and absorption properties due to its indirect band gap, which requires that photon emission and absorption involve a momentum balancing phonon. This fact has so far prevented the development of silicon-based opto-electronic devices, which would have the potential to enable a new level of integration of silicon electronics with optical devices on one chip. Hence first reports of room temperature light-emission from quantum confined silicon structures were met with great enthusiasm. Initial processes for the production of luminescent silicon nanostructures used magnetron sputtering of silicon in a hydrogen atmosphere [1] and the production of porous silicon [2, 3]. Other reports of luminescence from quantum confined silicon nanostructures such as surface oxidized nanocrystals [4, 5] and silicon/insulator superlattices [6] soon followed. Since then the proof of concept of the silicon based light emitting diode was given [7], and the observation of optical gain from silicon nanocrystals was reported [8]. While initially light emission from silicon was studied mostly with regards to the role of quantum confinement, more recently increased attention has been paid to the important influence of the surface conditions of silicon nanocrystals [9].
A wide range of synthesis approaches has been proposed for silicon nanocrystals both in the liquid and in the gas phase. Liquid phase approaches range from the synthesis in inverse micelles [10], to the synthesis in high temperature supercritical solutions [11], to the oxidation of metal silicide [12], to the reduction of silicon tetrahalides and other alkylsilicon halides [13]. However, liquid phase approaches are often time-consuming and sometimes have a low yield of crystalline material. Gas phase approaches range from the pyrolysis of silane in furnace flow reactors [4, 14], to the decomposition of silane or disilane through laser light irradiation (photolysis) [15], to the laser pyrolysis using high power infrared lasers [16, 17]. These approaches often have faster processing times, but particle agglomeration in the gas phase may annihilate the desired quantum confinement properties. A high rate laser pyrolysis process was proposed in ref. [17] with yields of up to 200 mg/h., however, particles required post-process etching to reduce the particle size. The resulting effective yield of luminescent material was significantly lower than the original synthesis yield.
Here we report an approach based on a non-thermal plasma. This approach benefits from the unipolar negative charge distribution acquired by the particles immersed in the plasma [18]. The negative charge is required to ensure a steady state balance between electron and ion fluxes to the particle surface, and the subsequent unipolar distribution significantly decreases the agglomeration rate and reduces particle growth through coalescence. Moreover, the recombination of electrons and ions at the particle surface and the weak convective cooling in the low pressure environment leads to a significant heating of the nanoparticles, whose temperatures can be several hundreds of Kelvin above the surrounding gas temperature [19]. The intense particle heating leads to the synthesis of nanometer-sized silicon crystals between 2-8 nm on timescales of a few milliseconds.

Experimental set-up

The schematic of the plasma reactor is shown in figure 1. An argon-silane gas mixture is passed through a reactor which consists of a 3/8" O.D. quartz tube with an inner diameter of 1/4". Two copper rings with an intermediate gap of 1/4" serve as electrodes. The plasma exhibits an intense emission between the electrodes and downstream of the electrode pair. Weaker emission is also observed upstream of the ring electrodes. The residence time of the gas is estimated based on the distance between the grounded ring electrode and the fitting of the quartz tube to the vacuum chamber. This distance is kept constant at 1". The plasma is typically generated at a pressure of 1.4 Torr. The total gas flow rate is adjusted between 12 and 60 sccm, changing the residence between ~7 and ~1.2 ms. The discharge is operated in a SiH_4-Ar mixture and the silane partial pressure is adjusted between 10 and 60 mTorr. The RF power is delivered to the discharge through a T-type matching network, and the discharge is excited at a frequency of 27.12 MHz. The power consumption, read from the power meter of the matching network, is 200 W, with <5 W of reflected power. However, this power reading does not correctly reflect the power absorbed by the discharge, since it does not account for the power reflected from the discharge back into the matching network, and for the power losses through heat dissipation and radiation. Measurements of the RF current and voltage indicate that the power consumption in the plasma is of the order of only a few W. Given the very small discharge volume (<1 cm^3), a considerable power density is achieved in the plasma region. The particles produced in the plasma are collected on a fine stainless steel mesh placed about 1" downstream of the discharge. After a few minutes of deposition, the mesh is completely coated with particles. After deposition, the mesh is extracted from the system and the particles are rinsed into vials with methanol or ethanol. For transmission electron microscopy (TEM) studies, TEM grids can be placed onto the filter. Grids are exposed to the aerosol flow typically for 2-6 seconds which results in a coverage sufficient to obtain a reasonable statistic for particle size distribution measurements using a TEM image analysis software.

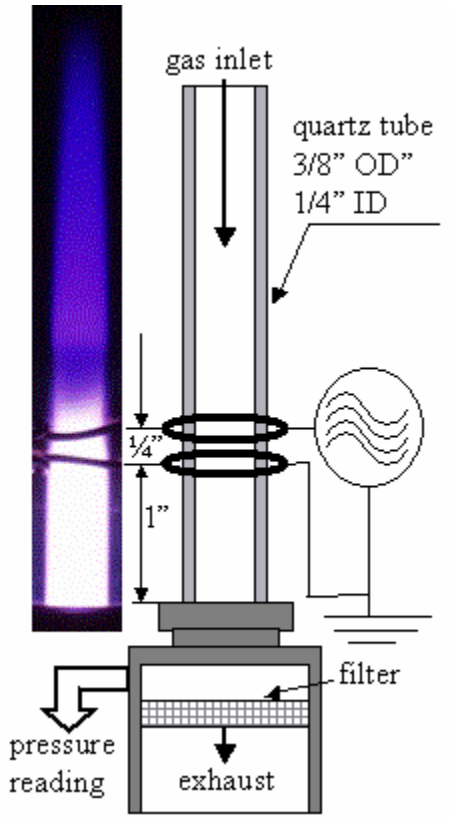

Figure 1: Schematic of experimental apparatus with digital picture of the argon-silane discharge during operation

Results and discussion

Particles produced in our system do not immediately show photoluminescence. When particles are collected on the filter or on a piece of glass and exposed to the air, luminescence sets in after a few minutes of exposure. When particles are collected on the filter and rinsed into vials with methanol, luminescence sets in later typically after several minutes to a few hours. We interpret this delay in the onset of luminescence as being caused by the formation of a native silicon oxide that passivates surface states that otherwise quench photoluminescence. The photoluminescence emission spectra for different experimental conditions are shown in figure 2.

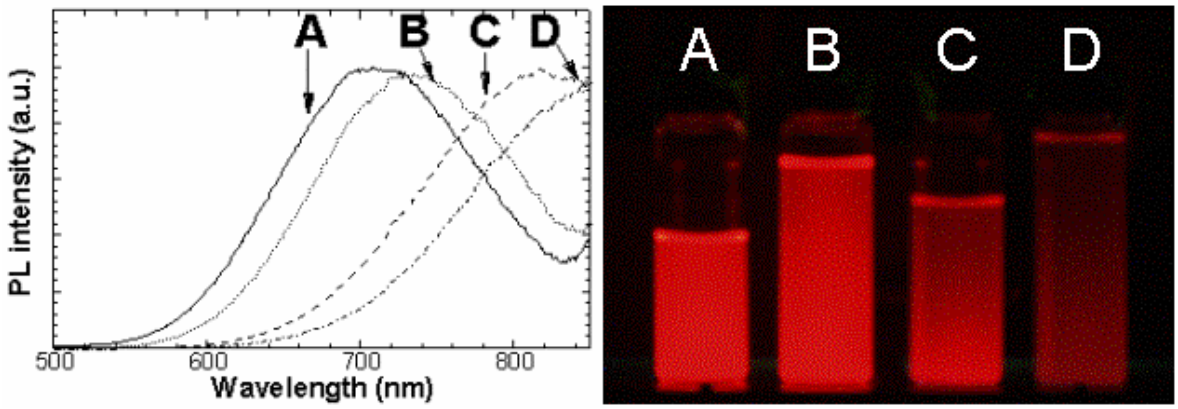

Figure 2: Photoluminescence of silicon particles produced for: (A) 50 sccm Ar, 10 sccm Ar-SiH4 (95:5); (B) 40 sccm Ar, 8 sccm Ar-SiH4 (95:5); (C) 30 sccm Ar, 30 sccm Ar-SiH4 (95:5); (D) 24 sccm Ar, 24 sccm Ar-SiH4 (95:5); pressure= 1.4 Torr, 200 W RF power.

The particles luminesce in the red-orange range, as it is expected for silicon particles with a native oxide layer on the surface [9]. The influence of oxygen on the quantum dot electronic structure has been extensively studied since the luminescence from porous silicon was first observed. Oxygen is known to introduce a large Stokes shift between the absorption band gap edge of the particles and the energy at which the particles emit. Oxygen terminated quantum dots are not expected to shown luminescence at wavelength shorter than that corresponding to orange emission [9]. The change in the peak emission wavelength with the experimental conditions is consistent with the change of the silicon nanoparticle size. Sample A and B were produced at the same SiH_4 partial pressure (11 mTorr), with a residence time of 1.48 ms for A and 1.85 ms for B. For C and D the partial pressure was increased to 35 mTorr which leads to larger particles, shifting the peak emission to longer wavelengths. Our result is consistent with the current understanding of the optical properties of silicon quantum dots.

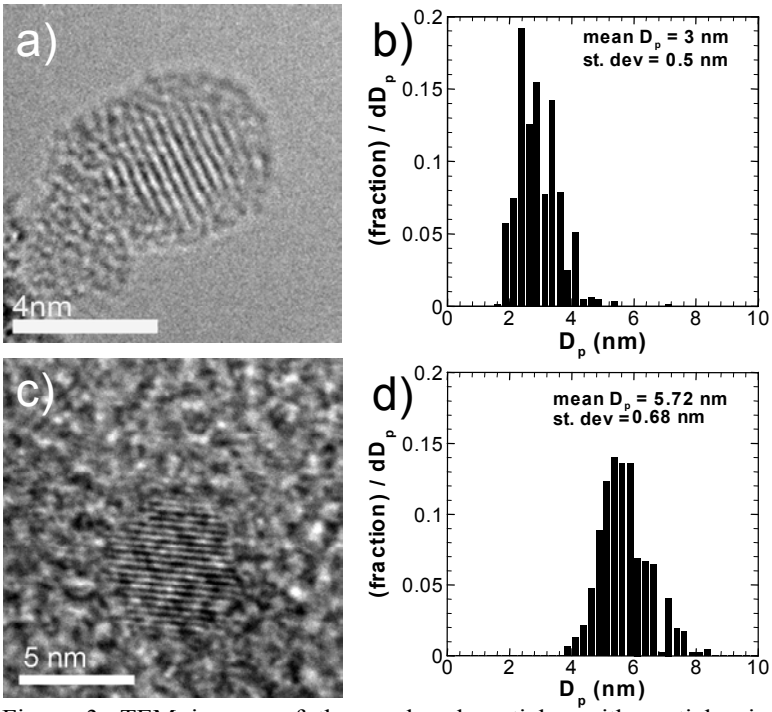

Figure 3. TEM images of the produced particles with particle size distribution as obtained from micrograph analysis. a) and b) were obtained for 40 sccm Ar, 8 sccm Ar:SiH4 (95:5); c) and d) for 10 sccm Ar, 2 sccm Ar:SiH4 (95:5). (Image b) courtesy of Dr. C. Perrey taken on a 300 kV Tecnai F30).

The particle size distribution and the particle crystallinity were studied by TEM analysis. Figure 3 shows high magnification micrographs as well as the particle size distributions for both a short and a long residence time case. For figure 3 a) and b) the Ar flow rate is 40 sccm and the Ar-SiH_4 (95:5) flow rate is 8 sccm. Under these conditions the residence time is 1.85 ms. For figure 3 c) and d) the Ar flow rate is 10 sccm and the Ar-SiH_4 (95:5) flow rate is 2 sccm, the residence time is 6.8 ms. The partial pressure of silane is the same for these two cases and equals 11 mTorr.

It can be seen that reducing the residence time leads to a decrease of the particle size from an average of 5.7 nm to 3 nm. The size distribution is relatively monodispersed, with a standard deviation of 0.5 nm for the short residence time case, and 0.68 nm for the long residence time case. Particles observed for these two

cases are almost exclusively crystalline. Figure 3 c) shows fringes from the (111) plane of a 5-nm silicon particle deposited on a regular carbon film grid. The particle in figure 3 a) has a crystalline core of around 2 nm in diameter and an amorphous layer of about 1 nm in thickness which is likely a native oxide. This result shows that the non-thermal plasma process can produce sub-5 nm silicon crystallites. A crystalline fraction of ~100% is observed for the long residence time case. At the shorter residence time less than 100% of the particles are crystalline. Decreasing the residence time of the particles in the plasma leads to the production of smaller particles, however, these particles are less likely to be crystalline.

Mass spectroscopy and direct mass measurements have been performed to determine the process yield. Measurements with a mass spectrometer show that the plasma dissociates virtually 100% of the fed silane precursor. A flow rate of 40 sccm of Argon and 8 sccm of Ar-SiH_4 (95:5) corresponds to a mass flow rate of silicon of 30 mg/hour. The deposition rate on the filter was measured to be 14.4 mg/h. At the same time, a silicon film was deposited in the reactor tube at a rate of 14.7 mg/h. This result indicates that slightly less than 50% of the silane is converted into silicon nanocrystals, while another 50% are deposited as a silicon film on the reactor walls. For slightly larger nanocrystals with emission wavelength peaking at 800 nm we achieve a net yield of ~40 mg/h.

While it is still not clear which processes lead to the formation of crystalline silicon particles at relatively low gas temperatures, we have recently pointed out that the heating of the particles by electron-ion recombination at the particle surface can be a significant heating process [19, 20]. The time dependent energy balance for a particle immersed in a plasma is given by:

$$\rho c V_p \frac{d(T_p - T_{gas})}{dt} = J_i A_p E_{ion} + G_m A_p E_{bind} - \frac{1}{4} n_g v_g A_p \frac{3}{2} k_B (T_p - T_{gas}) \qquad [1]$$

ρ and c are the material density and specific heat, V_p is the particle volume, T_p the particle temperature, T_{gas} the background gas temperature. The first term on the right hand side describes the particle heating due to electron-ion recombination at the particle surface, where J_i is the ion flux to the particle, A_p the particle surface area and E_{ion} the ionization potential (15.76 eV in the case of Argon). The second term on the right hand side describes the heat of condensation released during the particle growth. G_m is the flux of monomers to the particle surface, for the case of silicon each monomer releases an energy of 4.07 eV when it binds to the particle. The last term describes the gas cooling, n_g and v_g are respectively the background gas density and its thermal velocity.

In order to estimate the particle heating rate a good estimate of the plasma density is needed. The plasma density was measured with the help of a capacitive electrostatic probe. This technique is described in details in ref [21], and in contrast to other probe diagnostic methods is not perturbed by the silicon film which is inevitably deposited on the probe. A 5 mm long 0.4-mm diameter wire was placed in the plasma and connected to an external test capacitor. By coupling an RF signal to the probe, the probe is charged negatively with respect to the plasma in a process similar to that of RF biasing of silicon wafers in microelectronics processing. The negative potential on the probe also charges the test capacitor. After the turn-off of the RF signal, the free positive ions in the plasma discharge the capacitive probe and the test capacitor. From the rate of discharge of the capacitor, the plasma density can be determined. For typical conditions that yield luminescent nanocrystals a plasma density of $\sim 5 \cdot 10^{10}$ cm^{-3} was found.

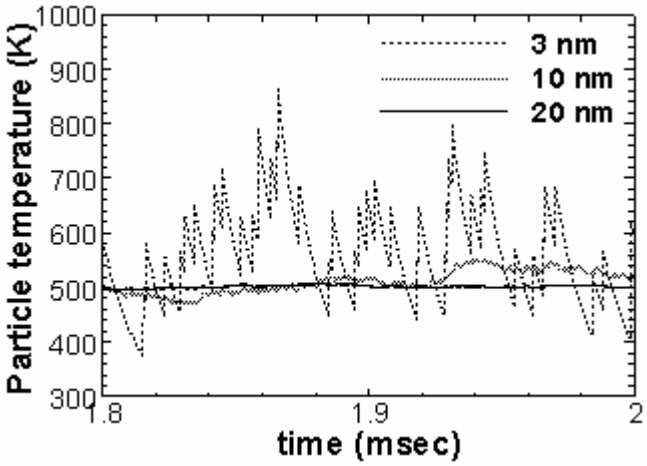

Figure 4: Simulation results of the temperature history of nanoparticles of different size in an argon-silane plasma. Gas pressure is 1.4 Torr, the gas temperature is assumed to be 300 K, the plasma density is $5 \cdot 10^{10}$ cm^{-3}.

Using this plasma density and assuming a gas temperature of 300 K and pressure of 1.4 Torr, the particle energy balance was solved. Results of this simulation are presented in Figure 4. The time-

dependent simulation was performed assuming that the ion flux to the particle is well described by the orbital motion limit (OML) theory, from which the average frequency of recombination events ν_+ is calculated. The electron-ion recombination occurs in stochastic time-intervals at the particle surface such that the average recombination frequency is equal to the calculated ν_+. The calculated temperature history shows that small particles of 3 nm diameter undergo significant temperature fluctuations while immersed in the plasma. Small particles never reach a steady temperature and their instantaneous temperature can be much larger than the gas temperature. This heating of the particles is likely responsible for the efficient synthesis of crystalline particles.

Conclusions

A continuous flow, non-thermal plasma reactor has been developed for the production of silicon nanocrystals. Nanoparticles are synthesized in a simple, single-step flow-through reactor on the time-scale of a few milliseconds. The low pressure plasma environment serves to prevent particle agglomeration and leads to an efficient heating of the particles through electron-ion recombination at the surface. Production yields on the order of several tens of milligrams per hour can be achieved.

Acknowledgements

This work was supported in part by the MRSEC Program of the National Science Foundation under award number DMR-0212302, by NSF under IGERT award number DGE-0114372, and by InnovaLight, Inc. We acknowledge Dr. Christopher R. Perrey and Professor C. Barry Carter for support with high-resolution TEM and Professor David Norris and Ms. Lijun Zu for support with photoluminescence measurements.

References

1. Furukawa, S. and T. Miyasato, *Three-dimensional Quantum Well Effects in Ultrafine Silicon Particles*, in *Jpn. J. Appl. Phys.* 1988. p. L2207.
2. Canham, L.T., *Silicon quantum wire array fabrication by electrochemical and chemical dissolution of wafers.* Appl. Phys. Lett., 1990. **57**(10): p. 1046-1048.
3. Cullis, A.G. and L.T. Canham, *Visible light emission due to quantum size effects in highly porous crystalline silicon.* Nature, 1991. **335**: p. 335-338.
4. Littau, K.A., P.J. Szajowski, A.J. Muller, A.R. Kortan, and L.E. Brus, *A Luminescent Silicon Nanocrystal Colloid via a High-Temperature Aerosol Reaction.* J. Phys. Chem., 1993. **97**: p. 1224-1230.
5. Wilson, W.L., P.F. Szajowski, and L.E. Brus, *Quantum Confinement in Size-Selected, Surface-Oxidized Silicon Nanocrystals.* Science, 1993. **262**(5137): p. 1242-1244.
6. Lu, Z.H., D.J. Lockwood, and J.-M. Baribeau, *Quantum confinement and light emission in SiO_2/Si superlattices.* Nature, 1995. **378**: p. 258-260.
7. Hirschman, K.D., L. Tsybeskov, S.P. Duttagupta, and P.M. Fauchet, *Silicon-based visible light-emitting devices integrated into microelectronic circuits.* Nature, 1996. **384**(6607): p. 338-341.
8. Pavesi, L., L. Dal Negro, C. Mazzoleni, G. Franzó, and F. Priolo, *Optical gain in silicon nanocrystals.* Nature, 2000. **408**: p. 440-444.
9. Puzder, A., A.J. Williamson, J.C. Grossman, and G. Galli, *Surface Chemistry of Silicon Nanoclusters.* Phys. Rev. Lett., 2002. **88**(9): p. 097401-4.
10. Wilcoxon, J.P. and G.A. Samara, *Tailorable, visible light emission from silicon nanocrystals.* Appl. Phys. Lett., 1999. **74**(21): p. 3164-3166.
11. Holmes, J.D., K.J. Ziegler, C. Doty, L.E. Pell, K.P. Johnston, and B.A. Korgel, *Highly luminescent silicon nanocrystals with discrete optical transitions.* J. Am. Chem. Soc., 2001. **123**: p. 3743-3748.

12. Pettigrew, K.A., Q. Liu, P.P. Power, and S.M. Kauzlarich, *Solution Synthesis of Alkyl- and Alkyl/Alkoxy-Capped Silicon Nanoparticles via Oxidation of Mg2Si.* Chemistry of Materials, 2003. **15**(21): p. 4005-4011.
13. Baldwin, R.K., K.A. Pettigrew, J.C. Garno, P.P. Power, G.-y. Liu, and S.M. Kauzlarich, *Room Temperature Solution Synthesis of Alkyl-Capped Tetrahedral Shaped Silicon Nanocrystals.* Journal of the American Chemical Society, 2002. **124**(7): p. 1150-1151.
14. Ostraat, M.L., J.W. De Blauwe, M.L. Green, L.D. Bell, M.L. Brongersma, J. Casperson, R.C. Flagan, and H.A. Atwater, *Synthesis and characterization of aerosol silicon nanocrystal nonvolatile floating-gate memory devices.* Applied Physics Letters, 2001. **79**(3): p. 433-435.
15. Batson, P.E. and J.R. Heath, *Electron energy loss spectroscopy of single silicon nanocrystals: the conduction band.* Physical Review Letters, 1993. **71**(6): p. 911-14.
16. Ehbrecht, M. and F. Huisken, *Gas-phase characterization of silicon nanoclusters produced by laser pyrolysis of silane.* Physical Review B: Condensed Matter and Materials Physics, 1999. **59**(4): p. 2975-2985.
17. Li, X., Y. He, S.S. Talukdar, and M.T. Swihart, *Process for Preparing Macroscopic Quantities of Brightly Photoluminescent Silicon Nanoparticles with Emission Spanning the Visible Spectrum.* Langmuir, 2003. **19**(20): p. 8490-8496.
18. Kortshagen, U. and U. Bhandarkar, *Modeling of particulate coagulation in low pressure plasmas.* Phys. Rev. E, 1999. **60**(1): p. 887-898.
19. Bapat, A., C. Anderson, C.R. Perrey, C.B. Carter, S.A. Campbell, and U. Kortshagen, *Plasma synthesis of single-crystal silicon nanoparticles for novel electronic device applications.* Plasma Phys. and Controlled Fusion, 2004. **46**(12): p. B97–B109.
20. Mangolini, L., E. Thimsen, and U. Kortshagen, *High-Yield Plasma Synthesis of Luminescent Silicon Nanocrystals.* Nano Letters, 2005.
21. Braithwaite, N., J.P. Booth, and C. Cunge, *A novel electrostatic probe method for ion flux measurements.* Plasma Sources Sci. Technol., 1996. **5**: p. 677-684.

Low-pressure plasma synthesis of silicon nanoparticles and fabrication of a field-effect transistor using a single silicon nanoparticle.

Ameya Bapat[1], Yongping Ding[2], Ying Dong[2], Chris Perrey[3], C.Barry Carter[3], Stephen Campbell[2], Uwe Kortshagen[1]

[1] *Department of Mechanical Engineering*
[2] *Department of Electrical and Computer Engineering*
[3] *Department of Chemical Engineering and Materials Science*
University of Minnesota, Minneapolis, MN 55455

Abstract

Semiconductor nanoparticles are candidates of interest in a range of applications in the fields of nano-electronics and nano-optoelectronics. This paper describes a constricted-mode capacitive plasma synthesis process for making single-crystal cubic silicon nanoparticles. Single-nanoparticle field-effect transistors are fabricated using these nanoparticles. Operation and electrical characterization of these devices are also described.

Keywords

Nanoelectronics, Nanoparticles, Plasma synthesis, Transistor.

Introduction

Semiconductor nanoparticles are attracting research interest due to a wide range of potential applications [1-3]. Silicon especially is important due to its low toxicity and maximum compatibility with current semiconductor manufacturing processes. A number of gas-phase methods such as laser ablation of a silicon target, thermal pyrolysis and laser pyrolysis of silane have been tried for the synthesis of silicon nanoparticles [3-7]. Formation of amorphous particles and particle agglomeration are reported to be the main problems.

Non-equilibrium silane plasmas have been widely used in the semiconductor industry. They were primarily studied to prevent gas phase particle nucleation [8-10]. Nanoparticle synthesis using such non-equilibrium plasma based methods, however, can overcome issues associated with other methods because plasmas tend to unipolarly charge suspended nanoparticles and prevent agglomeration. Plasmas can also heat the particles to high temperatures leading to particle crystallization. Plasmas processing is widely used in the semiconductor industry, making it easier to for it to adopt a plasma-based process.

We have developed a novel non-thermal plasma process for silicon nanocrystal synthesis that can produce freestanding, defect-free, cubic silicon nanoparticles in a size range from 20nm-80nm. Such freestanding, defect-free, silicon nanoparticles are good candidates for new methods for fabricating microelectronic devices, such as vertical transistors and LEDs. These particles are synthesized separately and could potentially be intermixed with other materials to form novel nanocomposite heterostructures and devices.

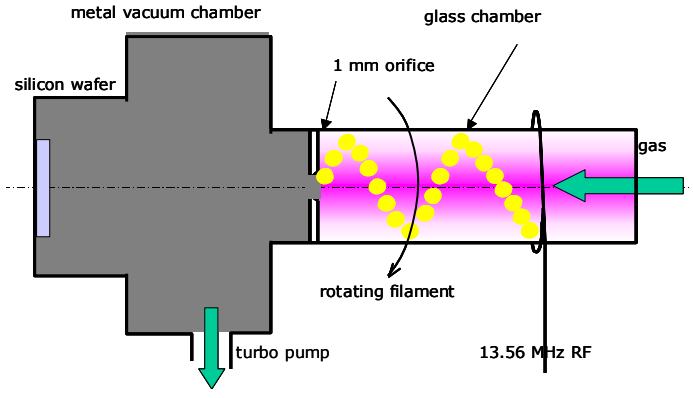

Fig.1 Sketch of constricted plasma setup used for nanoparticle deposition on silicon wafers

In this paper we describe the synthesis process for producing single crystal nanoparticles and the current understanding of the particle heating and crystallization mechanism. A prototype vertical Schottky-barrier field effect

transistor (FET) is fabricated using these nanoparticles. The paper describes the fabrication process and the electrical characteristics of the fabricated devices.

Particle Synthesis

The nanoparticle synthesis process employed here has been described in detail elsewhere [11]. To explain in brief, silicon nanoparticle synthesis is done using a 13.56 MHz constricted-mode RF capacitive discharge in 5% silane diluted in helium. Argon is used as a carrier gas. A 2 sccm flow of silane-helium and 3 sccm flow of argon are used to produce a pressure of 1.5 Torr in the discharge chamber. The substrate is kept in the downstream chamber that is evacuated to a much lower pressure of 10^{-3} torr. A 1mm diameter orifice separates these two chambers. The plasma is formed between a powered electrode shaped in form of a ring and a metal flange as ground as shown in Figure 1. The discharge runs at around 100-200W RF power to form a single luminous filament, which consists of ten to twenty individual plasma globules. The discharge may be a high-density plasma thermal instability as described by Raizer [12]. The filament is unsteady and oscillates at frequencies of up to 150 Hz.

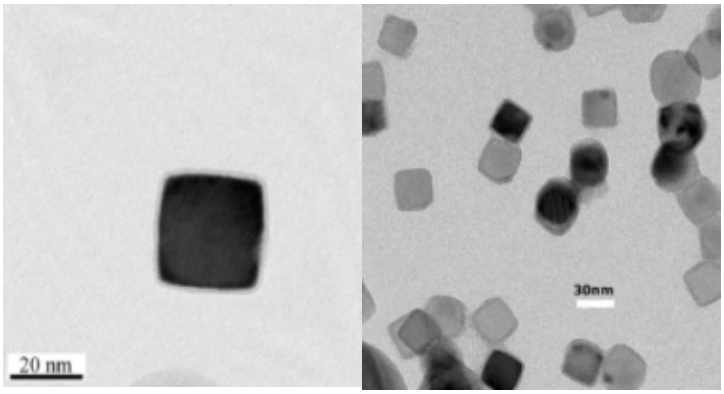

Fig.2 TEM images of cubic nanoparticles.

Silane undergoes dissociation and subsequent nucleation reactions in the plasma to form a nanoaerosol of silicon particles. This aerosol accelerates through the orifice to form a high-speed beam of particles in the substrate chamber. Particles are then collected by inertial impaction. For characterization, particles are collected on electron microscope grids, whereas for device fabrication particles are deposited on to patterned silicon substrates. The discharge is run for up to 2 minutes to achieve requisite particle density on the silicon substrate.

Varying process parameters such as residence time of particles in the discharge and the plasma chamber tube diameter can control the particle size and morphology to a certain extent.

Particle characterization and analysis

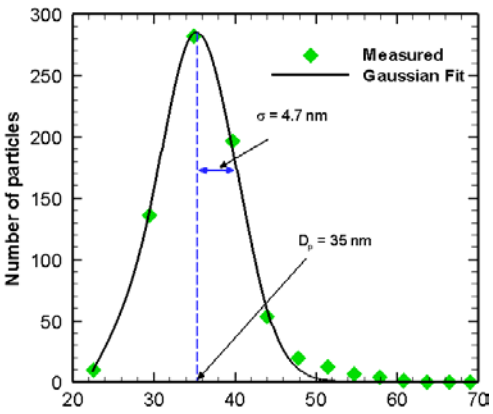

Fig.3 Particle size distribution centered at 35 nm with a standard deviation of 4.7 nm.

Nanoparticle characterization is primarily done using e*x-situ* transmission electron microscopy (TEM). Particles are deposited on TEM grids (01822-F ultra-thin carbon type–A from *Ted Pella Inc.*) TEM analysis is carried out using a JEOL 1210 (120kV accelerating voltage) and an FEI Tecnai T12 (LaB_6 filament, 120 kV)

Fig. 2 shows electron micrographs with cube shaped particles. It is seen that particles are monodisperse and single crystal. Fig.3 shows a plot of a typical size distribution obtained from a TEM image analysis using NIH ImageJ [13] The nanoparticles are diamond-cubic silicon with (100)-plane faces. Particles are highly oriented with no line or planar defects. Defect-free particles are necessary for electrical devices because the nanoparticle acts as the channel of the device, and any defects would create trap states, affecting device performance. Selected area electron diffraction and high resolution TEM are used to characterize the crystal structure and defects, if any.

The constricted-mode discharge is a non-equilibrium plasma where the electron temperature is greater than the gas temperature. Thermometrically measured gas temperature in the discharge is around 450K, which is substantially lower than the melting point of silicon of 1783K. This indicates that a unique heating mechanism is at play. Particle heating most probably occurs via argon ion-electron recombination on the particle surface. Each recombination event heats a particle with an energy equivalent to the ionization energy of argon (15.75eV). The primary cooling mechanisms on the other hand are conduction heat loss to the gas, and radiative heat transfer to the surroundings. A simple energy balance calculation using eqn.1 for a single particle yields particle temperatures that are 500-1000K higher than the gas temperatures. The left hand side term accounts for the heating of the particle due to the release of argon ionization energy E_{ion} during each recombination event. The first term on the right hand side is for conduction heat loss, whereas the second term is radiative heat loss. A detailed analysis of this process is described elsewhere [11].

$$n_i v_b A_p E_{ion} = \frac{1}{4} n_g v_g A_p \cdot \frac{3}{2} k_B (T_p - T_g) + \sigma (T_p^4 - T_g^4) \quad (1)$$

Transistor Fabrication

As shown in Fig.5, a vertical transistor using platinum silicide (PtSi) as a Schottky barrier for source and drain electrodes is fabricated using these nanoparticles. Freestanding, monodisperse, cubic particles are synthesized with the constricted mode plasma and deposited on to an oxide (SiO_2) patterned, Pt-coated silicon wafer. The pattern essentially is a window in the covering SiO_2 layer, where the bottom Pt layer is exposed. These windows serve as sites for fabricating clusters of silicon nanoparticle based transistors. The nanoparticles from the reactor get deposited either on the Pt or on the CVD oxide as shown in Figure 6(a). The substrate then is heat treated at 165ºC for 30 minutes during which the nanoparticles deposited on the Pt react with the metal to form a few nanometer thick layer of PtSi The particles deposited on the oxide are unchanged. The next step is removal of the unwanted particles deposited on the oxide. For that, the whole substrate is coated with SiO_2. (Figure 6(b)) The surface is then planarized using chemical mechanical polishing (CMP). CMP is carried out until the thickness of covering SiO_2 layer is equal to or less than the original thickness before nanoparticle deposition, as illustrated in Figure 6(c).

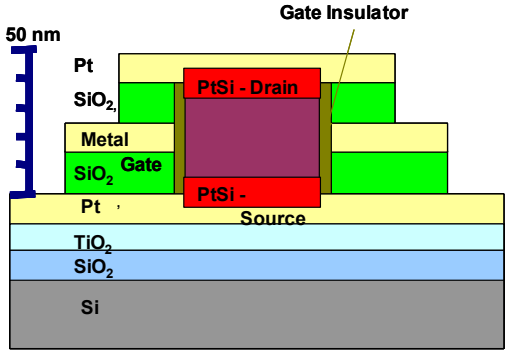

Fig.5 Cross-section schematic of the vertical PtSi Schottky source/drain SiNP-MOSFET

The number of nanoparticles in a window depends on its area and the time of particle deposition. The area of the windows is defined in a series from 5x5 μm^2 up to 20x20 μm^2. An average density of about 160 nanoparticles/100μm^2 is obtained after a one-minute deposition. That means, even for 5x5 μm^2 window, there are about 40 silicon nanoparticles. For ease of electrical contact and characterization of the nanoparticle device, all the nanoparticles in the same window are developed into nanoparticle transistors that are connected in parallel.

After the CMP planarizing, a dry etch process with high SiO_2/Si selectivity is performed to etch back the SiO_2 uniformly, and is stopped at point where the thickness of remaining thin SiO_2 layer is 10 to 15 nm, which is about a third the height of the 45 nm side cubic nanoparticles. Two-thirds of the

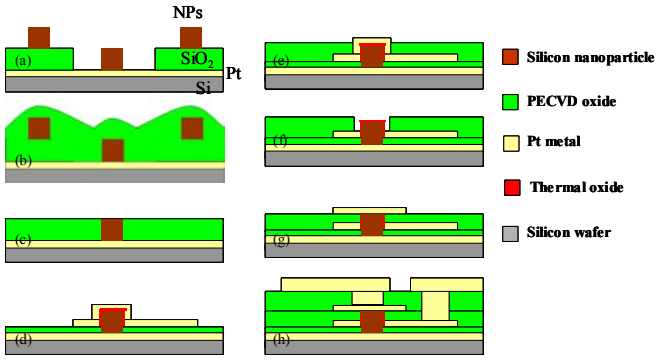

Fig. 6. Schematics of the process flow of the fabrication

height of the nanoparticle is now exposed. This SiO_2 serves as an insulating layer between the Pt layer *source* at the bottom and the metal *gate* electrode which is not yet deposited. The control of the thickness of the CVD oxide by dry etching is a challenging step, especially considering the additional requirement of a very small surface roughness. AFM characterization is employed to monitor this step. It is found that the height of exposed silicon nanoparticles is around 26 nm and the mean roughness (R_q) of the fresh SiO_2 surface after etching is ~1.5 nm or less. A higher R_q value might lead to short-circuiting of the source and gate.

The next step is to build the surround gate structure. But before that, a layer of gate insulator is necessary between the gate and the nanoparticle channel. The gate insulating layer is formed on the exposed nanoparticles by first immersing the substrate into boiling H_2O_2 for 30 minutes and then heat treating it at temperature of 500^0C under an oxygen atmosphere for another 30 minutes. The same oxidation process, done on a Si monitor wafer reveals nearly a 2 nm thick thermal silicon oxide on surface. This oxide has a leakage current of 1.8 x 10^{-5} A/cm^2 at a bias voltage of 0.5 V. This electrical performance satisfies the requirement of gate insulator of the proposed transistor. After that, surrounding the thermal oxide coated nanoparticles, a 15 nm thick metal layer is deposited to serve as the gate, as shown in Figure 6(d). Both Pt and Cr have been used as gate electrodes. The metal workfunction significantly affects the turn-on voltage of the device.

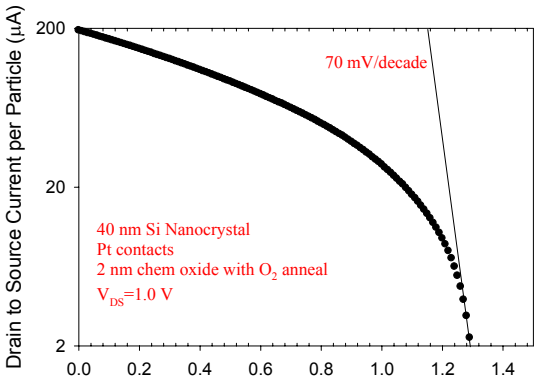

Fig.7 Single SiNP transistor's I-V characteristics showing turn off characteristic of p-channel device.

It is necessary to note that before this deposition, the substrate is patterned with photoresist. The pattern is nearly the same as the windows mentioned above, but with an extension for electrical contact pads. A lift-off process is employed at this step to remove the extra Pt. A second CVD oxide is then deposited to isolate the gate and drain electrodes. CMP is performed to planarize the oxide surface. A second etch back of the planarized surface is done to expose the top of the metal-coated nanoparticles. See Figure 6(e). Subsequently, wet etching in diluted aqua regia is done to remove the metal coating on the top of the nanoparticles first and later along the side of the nanoparticles. A result for this step is as shown in Figure 6(f) where the gate metal is in close contact with nanoparticles, but no longer covers the particles on the top and side. These steps are particularly important to avoid a short circuit between the gate and the drain electrodes.

Insufficient etching and over-etching of the metal gate will both result in a failure of the transistor either through short circuit or due to loss of field effect control by the gate.

During this wet etching a recess might be introduced in the gate insulator oxide, but a subsequent SiO_2 CVD is used to fill it up. CMP is used a third time over to expose the tip of nanoparticles prior to laying down the top Pt electrode. Finally, this top Pt layer slightly reacts with the tip of the silicon nanoparticle to form Schottky junction for the drain electrode, as shown in Figure 6(g).

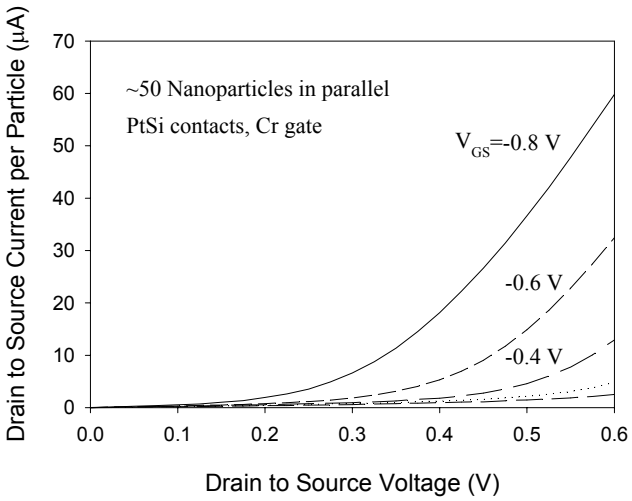

Fig.8 Family of curves for a single SiNP transistor using a Cr gate. The nonlinear behavior at low voltage is believed to be due to the Schottky contacts.

Transistor Characterization

Microprobes are used for electrical characterization of the nanoparticle devices. In order to get reliable test results under microprobes, a test structure is built for the devices, by which a direct

contact of the microprobes onto the drain or gate is avoided. A passive layer of 500 nm thick CVD SiO_2 is deposited, patterned and etched to realize the gate and drain contact via. Pt/Al bi-layers are deposited both as via and as test pads, as shown in Figure 6(h).

Typical transistor behavior of drain/source current I_d controlled by the gate-source voltage V_{gs} has been successfully demonstrated (Fig.7). The I_d-V_{gs} characteristic shown is for a single device, after accounting for the multiple devices fabricated in a single window. Electrical measurements show turn off characteristics of a p-channel device. Reasonable turn-off behavior is observed although leakage occurs, particularly through the chemical gate oxide. The device transconductance is roughly 80 μA/V per 40 nm particle or $5x10^6$ amp/V-cm^2. To the best of our knowledge, this is the first time that such a transistor has been reported that is built using a plasma synthesized single crystal Si nanoparticle.

Conclusion

In conclusion, a reliable plasma process has been established to synthesize high quality cube shaped, single crystal, nanoparticles. The particles have been used to successfully fabricate a prototype single particle vertical surround gate nanoelectronic FET. The p-channel device shows gate controlled drain-source current characteristics. This demonstrates the ability of non-equilibrium plasmas to synthesize high quality, high throughput nanomaterials, having a wide range of potential applications.

Acknowledgements:

This work is supported by NSF and NIRT grant DMI-0304211 and under grant CTS-9876224. Partial support of NSF-MRSEC program under Award Number DMR-0212302 is also acknowledged.

Reference:

1. A.P.Alivisatos, *Semiconductor Clusters,Nanocrystals and Quantum Dots.* Science, 1996. **271**: p. 933-936.
2. F.E.Kruis, H.Fissan, A.Peled, *Synthesis of nanoparticles in the gas phase for electronic, optical and magnetic applications - a review.* Journal of Aerosol Science, 1998. **29**: p. 511-535.
3. M.Swihart, *Vapor-phase synthesis of nanoparticles.* Current Opinion in Colloid and Interface Science, 2003. **8**: p. 127-133.
4. Y.Nakata, J.Muramoto, T.Okada, M.Maeda, *Particle dynamics during nanoparticle synthesis by laser ablation in a background gas.* Journal of Applied Physics, 2002. **91**(3): p. 1640-1643.
5. Takeuchi, D.; Mizuta, T.; Makimura, T.; Yoshida, S.; Fujita, M.; Hata, K.; Shigekawa, H.; Murakami, K., *Deposition dynamics of droplet-free Si nanoparticles in Ar gas using laser ablation.* Applied Surface Science, 2002. **197-198**: p. 674-678.
6. M.L.Ostraat, JW De Blauwe, M.L.Green, L.D.Bell, M.L.Brongersma, J.Casperson, R.C.Flagan, H.A.Atwater, *Synthesis and characterization of aerosol silicon nanocrystal nonvolatile floating-gate memory devices.* Applied Physics Letters, 2001. **79**(3): p. 433-435.
7. Ledoux G, Gong J, Huisken F, Guillous O, Reynaud C, *Photoluminescence of size-separated silicon nanocrystals: Confirmation of quantum confinement.* Applied Physics Letters, 2002. **80**(25): p. 4834-4836.
8. A.Bouchoule, L.Boufendi, *Particulate formation and dusty plasma behaviour in argon-silane RF discharge.* Plasma Sources Science and Technology, 1993. **2**: p. 204-213.
9. L.Boufendi, A.Bouchoule, *Particle Nucleation and growth in a low-pressure argon-silane discharge.* Plasma Sources Science and Technology, 1994. **3**: p. 262-267.
10. E.Stoeffels, W.Stoeffels, G.M.W.Kroesen and F.J.De Hoog, *Dust formation and charging in an Ar/SiH_4 radio-frequency discharge.* Journal of Vacuum Science and Technology - A, 1996. **14**(2): p. 556-561.
11. Ameya Bapat, Curtis Anderson, Christopher R Perrey, C Barry Carter, Stephen A Campbell and Uwe Kortshagen, *Plasma synthesis of single-crystal silicon nanoparticles for novel electronic device applications.* Plasma Physics and Controlled Fusion, 2004. **46**: p. B97-B109.
12. Y.P.Raizer, *Gas Discharge Physics*. 1st edition ed. 1997, Berlin: Springer-Verlag.
13. Rasband, Wayne, *NIH Image J*. 2003, National Institute of Mental Health.

Short-time plasma surface modified polymer powders – Improved bonding and wettability

C. Arpagaus, Ph. Rudolf von Rohr

ETH Swiss Federal Institute of Technology Zurich, Institute of Process Engineering, ETH Zentrum, Sonneggstrasse 3, CH-8092 Zürich, Switzerland

Abstract
Hot-melt adhesive HDPE and CoPA polymer powders were short-time plasma surface modified (0.1s) to improve wettability and adhesive bonding strength of polymer glued textile laminates and aluminum plates simultaneously. Peel strength of polymer glued textile laminates increased up to 25% for CoPA powder. Aluminum adhesive bonding strength increased up to 85% for HDPE after plasma exposure. Increased interfacial bonding is attributed to stronger chemical bonds of plasma formed polar groups on the powder and cross-linking.

Keywords: plasma surface modification, polymer powder, XPS, wettability, bonding, adhesion, viscosity

1. Introduction

Recently, a Plasma Downer Reactor (PDR) has been developed to allow the study of powder-plasma interaction in short-timescale (0.1sec) processing [1]. HDPE (high density polyethylene) and CoPA (co-polyamide) polymer powders were examined, which are used as thermoplastic hot-melt adhesives in paste dot coating applications in textile interlining industry. The feasibility to increase water wettability of the polymer powders was shown. XPS studies confirmed the formation of polar functional groups on the particle surface after O_2/Ar plasma exposure (Fig. 1). O/C-ratio on HDPE powder increased from 0.0 (no oxygen on untreated HDPE) up to 0.15 and from 0.1 up to 0.27 for Co-PA [2]. Ageing (hydrophobic recovery) occurred for treated HDPE powder mainly in the first 7days of storage due to a diffusion-like process of oxygen into the bulk of the polymer [3]. However, powder was still water wettable after 40days of storage.

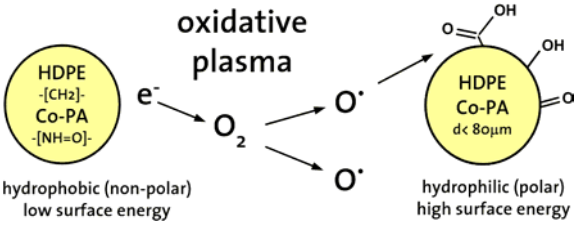

Figure 1: Incorporated hydrophilic groups on polymer particles (HDPE, CoPA) by plasma-assisted surface modification.

Besides conditioning of water-based pastes out of polymer powders, beneficial improvement of their adhesive strength is expected. Results of flat polymers showed that wettability has often been used as an estimate of bonding quality for adhesives. Lap-shear bonding strength of flat polymer-polymer bonds using epoxy adhesives improved significantly after various plasma treatments e.g. HDPE from 2.2 to 21.6N/mm^2, Nylon from 5.9 to 27.6N/mm^2 [4] or PP from 0.2 to 1.4N/mm^2 [5]. Moreover, plasma oxidation is known to enhance metal-polymer adhesion [4, 5, 6]. Reaction of adhesives with surface species during curing leads to covalent metal-oxygen-carbon (M-O-C) bonds. Fourfold improvement of epoxy bonding peel strength of PE or PP to aluminum was measured [4].
In this study, the objective was to treat hot-melt adhesive polymer powder by reactive plasma (mixtures of N_2, O_2 and Ar) in the PDR, thereby enhancing interfacial compatibility to materials like aluminum and textile fabrics (cotton). Wettability was quantified by water contact angle measurements. Lap-shear aluminum bonding tests and textile peel tests were used to study the adhesion strength of glued adhesive powder. Rheological tests of molten powder were performed to investigate possible changes in viscosity. XPS measurements were applied to determine the chemical elements of the modified surfaces.

2. Experimental

2.1 Materials and plasma treatment

HDPE (Schätti Fix 1820) and CoPA (Schätti Fix 5000) powder were used as model substances supplied by Schätti AG (Wallisellen, CH). Particle sizes were smaller than 80µm with a mean of 50µm. Manufacturers melt flow rates were 20g/10min (HDPE, 2.16kg, 190°C) and 15g/10min (CoPA, 2.16kg, 160°C) with a melting point between 120°C and 130°C. Plasma treatment of the powders was conducted in the PDR. Powder is fed into a vertical glass-tube reactor and simply moves downwards by gravity and gas acceleration forces through the plasma treatment zone. Efficient contact between reactive plasma species and particle surfaces is provided by nozzle-dispersion into the reactor. Plug-like flow regime ensures a narrow residence time distribution in the plasma zone. More details on the reactor setup can be found elsewhere [1]. Main operating parameters for this study were 100W RF power, 5kg/h powder throughput, 1.7mbar pressure, 500sccm gas flow rate and O_2, Ar, N_2, (technical purity) process gas.

2.2 Methods

Wettability was quantified by water contact angle measurements on a tensiometer (K100, Krüss GmbH, D) according to the liquid penetration method into a porous media [7]. Contact angles were measured at 25°C using hexane as perfect wetting liquid to determine the geometric constant. Reported water contact angles are average values of two measurements. The errors were calculated by proper error propagation of the modified Washburn equation [7]. The method procedure was described in detail previously [3].

Bonding strength of the adhesive powders was examined by **single overlap shear tests** on **aluminum plates** (Anticorodal 110, AlMgSi1, 1.5x25x100mm). Joint preparation, geometry and testing were in agreement with ISO 4587 [8]. Prior to bonding, aluminum plates were sandblasted (quartz sand 100µm) to provide better mechanical interlocking and washed with acetone. To ensure a constant bond thickness a 0.2mm thick wire was placed in the glued joint in direction of the load. A fixing device provided a parallel 12.5x25mm shear plane overlap of the samples. The joints were glued in a laboratory hot-press (THB400, Fontijne, NL) at 170°C under 5kg/cm^2 pressure for 20min. After cooling to room temperature, lap-shear strength of the joints was tested on a material-testing machine (Zwick 1474, Zwick GmbH, D) at constant test speed (2mm/min.) until sample failure. Maximum load was determined for each powder from an average of five specimens. Commercial epoxy adhesive (Araldite 2011, Ciba SC, Basel, CH) was used to compare the bonding strength of plasma treated adhesive powder. Araldite manufacturers lap shear strength on aluminum at 23°C was given to be 19N/mm^2 (at 1h cure cycle and 60°C).

Hot-melt adhesives strength on **textile bonding** was examined by **peel tests**. Cotton-cretonne fabric (black, 150g/m^2, 16x5cm) was used as textile model. In the case of CoPA, cotton tapes were equally sprinkled with powder dots out of a perforated sieve. HDPE powder was uniformly strewed in plane on the cotton tapes through a metal sieve. Total weight of the powder coating on the tapes was 15g/cm^2 for both powders. After sintering at 140°C two tapes were fixed one upon the other and were fused in a fusing press (PR1, Gygli AG, CH) for 15s at 150°C and 0.5bar overpressure. Reported textile peel test data are average values of 3 samples.

Rheological behavior was investigated using melt mass-flow rate (MFR) (Meltflixer LT, Haake, D) and shear-viscosity measurements (MCR300 rheometer, Anton Paar Physica, D). MFR is expressed in grams per 10min. at 190°C (HDPE) and 160°C (CoPA) with 2.16kg piston load according to ISO 1133 [9]. MFR data are means of two values. Cone-plate arrangement was adopted for shear-viscosity measurements with a cone angle of 4°. Testing specimens (pills) were prepared by melting cold pressed tablets in a hot press (THB400, Fontijne, NL) under vacuum conditions (<5x10^{-2}mbar) for 15min. at 150°C and 5MPa. The rheometer chamber was purged with dry nitrogen during measurement to avoid oxygen degradation. Strain controlled angular frequency sweep tests of 0.1 to 400rad/s at 10% strain amplitude were performed. The measuring temperature was 150°C and polymer densities were 0.78g/cm^3 (HDPE) and 1.05g/cm^3 (CoPA). Reported shear-viscosity data are average values of at least two measurements with the same powder.

XPS analysis was performed using a PHI Quantera SXM photoelectron spectrometer (Scanning X-ray Microprobe, ULVAC-PHI, Inc.). The residual pressure in the spectrometer during data acquisition was $<10^{-7}$ Pa. The X-ray source was monochromatic AlKα (1486.6eV), run at 25W and 15kV. The spectrometer was operated with 280eV pass energy for survey spectra. The electron take-off angle was 45°. For analysis, polymer powder was fixed on indium foil. X-ray spot size was 100µm in diameter. Charging of polymer surface during X-ray exposure was controlled using a flood gun and ions. Spectra were referenced to aliphatic carbon C1s signal at 285.0eV.

3. Results and Discussion

3.1 Wettability results

Figure 2 shows the effect of RF power on water contact angle after 1hour (fresh) and 45days of treatment. HDPE data show a decrease in contact angle from >90° (untreated powder was not-wettable) down to 70° indicating more hydrophilic surface. At higher power both mean electron energy and density increase in the plasma and more energetic chemically reactive species are formed through dissociation reactions of oxygen, suggesting higher incorporation of oxygen functionalities and better wettability [10, 11]. Increase of oxygen atom concentration is therefore a key factor to increase the modification rate. CoPA data show no significant dependency on power. Water contact angle remained stable between 77° and 80°. A low power is sufficient to activate the surface since CoPA possess inherently polar amide groups. After 45days of storage HDPE water contact angles reverse back to 80°. Hydrophobic-recovery (ageing) is attributed to mobility of plasma introduced polar species in the surface, which was confirmed by XPS in a previous work [3].

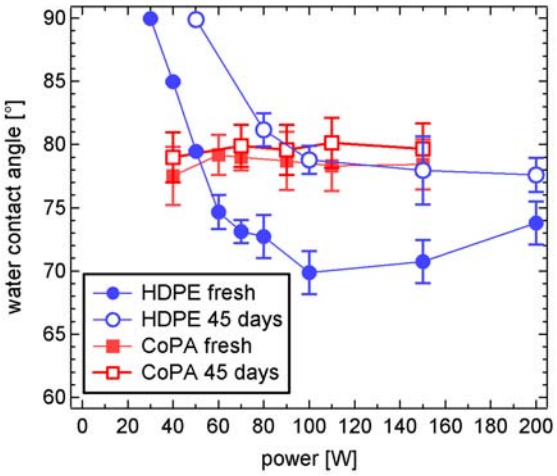

Figure 2: Water contact angles of HDPE and CoPA powder vs. RF power in the plasma after 1 hour (fresh) and 45 days of treatment (experimental conditions: 1.7mbar, 500sccm, HDPE 90%O_2/10%Ar, CoPA 30%O_2/70%Ar)

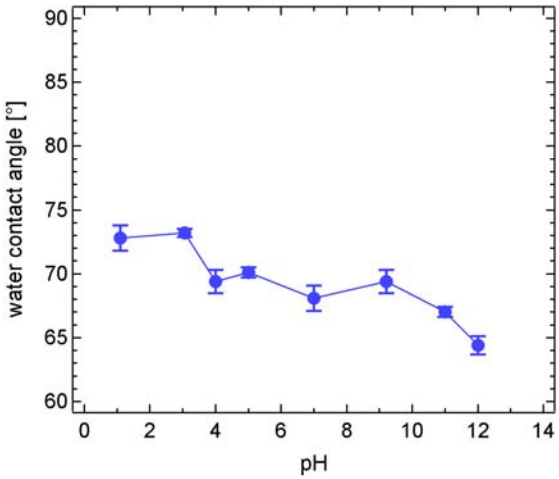

Figure 3: Water contact angles of fresh (within 1hour) O_2-plasma treated HDPE power vs. pH of buffer aqueous solutions (DURACAL buffers, Hamilton, CH).

In order to determine the existence of new functions on plasma modified HDPE powder a series of contact angles with buffered aqueous solution and different pH was measured (Figure 3). After O_2 plasma treatment a tendency of lower contact angle at higher pH was detected suggesting an acidic character to the surface. At higher pH functional groups (carboxylic acid) on the HDPE surface may dissociate and are capable of undergoing liquid solid acid-base interactions leading to a contact angle decrease. This information is at least qualitatively for HDPE powders in agreement with acid-base studies at interfaces between water and surface-functionalized PE-films as a function of pH of buffered water drops [12, 13].

Table 1 reports wettability results derived after O_2/Ar, N_2/O_2, N_2 and Ar plasma treatment of the powders. The best wettability conditions were found with O_2/Ar treatment for HDPE and N_2/O_2 for CoPA. Those powders were examined further for bonding and rheological tests.

Gas composition	HDPE	CoPA
untreated	>90° (no water penetration)	
O_2/Ar	90%/10%	30%/70%
	69.9° ± 2.0°	78.5° ± 1.4°
90%N_2/10%O_2	86.1° ± 1.1°	70.1° ± 0.8°
100%N_2	> 90°	84.6° ± 0.8°
100%Ar	> 90°	> 90°

Table 1: Water contact angle data of plasma treated HDPE and CoPA powder vs. different process gases.

3.2 Bonding results

Figure 4 shows the variation of mean lap shear bond strength of aluminum/powder/aluminum joints (12.5x25mm overlap) with different plasma gases (from Table 2) compared to untreated powder and araldite. After treatment mean shear strength increased for HDPE from 6.8 to 12.5MPa (+85%) and 12% improvement was observed for CoPA. However, strength was almost constant regardless of the treatment gas and lower than araldite joints. Improved adhesion is attributed to formation of hydrogen and chemical bonds between polar functional groups at the polymer surface and the aluminum oxide layer. Microscope analysis of failed bonds suggested the locus of failure for treated HDPE and CoPA within the polymer (cohesive failure) rather than in the bond line of the interface polymer/aluminum. Untreated HDPE did not adhere properly to sandblasted aluminum and failure was more like adhesive, due to its non-polar character. Untreated CoPA showed cohesive failure.

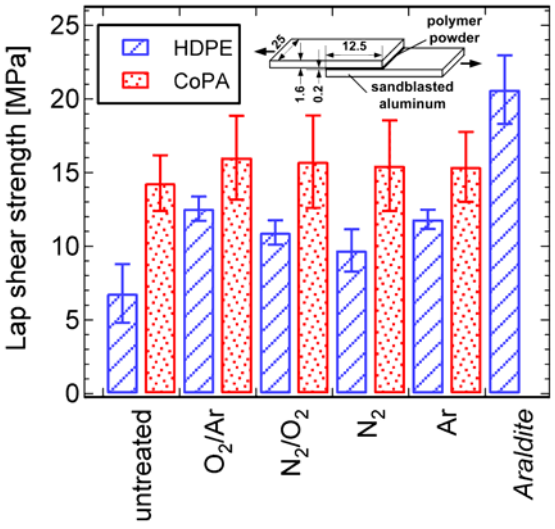

Figure 4: Influence of plasma gas composition on aluminum/adhesive powder/aluminum lap-shear force for HDPE and CoPA powder

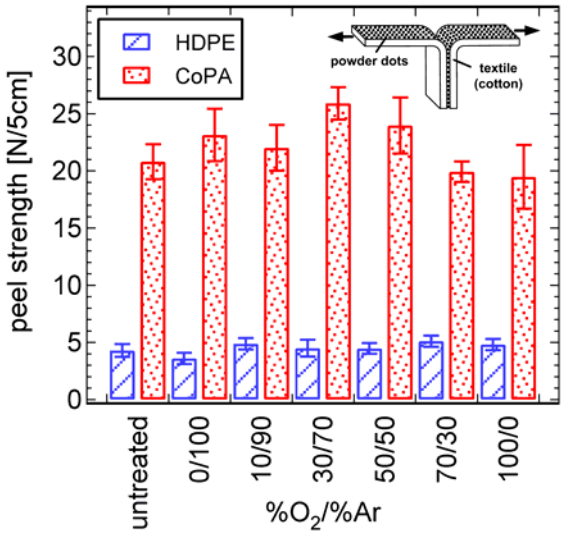

Figure 5: Peel strengths of bonded cotton tapes with HDPE and CoPA powder adhesive vs. O_2/Ar plasma gas composition. (15s fusing time, 0.5bar pressure, 150°C (HDPE), 140°C (CoPA))

Ar and N_2 plasma data revealed that good bonding was possible to obtain even with poor water wetting. A general correlation between improved wettability and bonding-strength could not be established.

Figure 5 shows the influence of O_2/Ar gas composition on the powders as a function of peel strength of powder glued cotton tapes compared to untreated powder. Data indicate a slight improvement of bonding strength after treatment (HDPE: from 4.3 to 5.1N/5cm, +19% and CoPA: from 20.8 to 25.9N/5cm, +25%). However, the improvement was not as high as for aluminum bonding. Failure locus was identified between powder dots and cotton fabric suggesting adhesive bond failure in the bond line. During short-time plasma treatment only a very thin particle surface layer is modified, the inner part remains untreated. A low volumetric ratio of surface modified shell to bulk (in the order of 1% for a spherical 50µm particle and a modification depth of 100nm) is a sign that a dilution effect of surface functional groups occurs in the molten state of the powder.

3.3 Viscosity results

Figure 6 and Figure 7 present typical shear-viscosity results $\eta^*(\omega)$ (with included MFR values) for a set of HDPE and CoPA powder as a function of different plasma gas treatment. HDPE viscosity did not appear to be significantly affected by the treatment. Except for pure Ar a slight increase (+8%) compared to the untreated was detected but the effect was barely above the limits of measurement accuracy. The change in MFR was in the same range. CoPA shear-viscosity raised significantly from 1279 to 1646Pas (+25%) due to plasma exposition. MFR decreased from 16.4 to 12.3g/10min. Since polymer zero shear viscosity η_0 depends on average molecular mass M_W according to $\eta_0 \sim M_W^{3.4}$ [14] (exponent 3.4 is an empirical factor), treated CoPA suggests a 7% increase in the average molecular weight caused by plasma treatment.

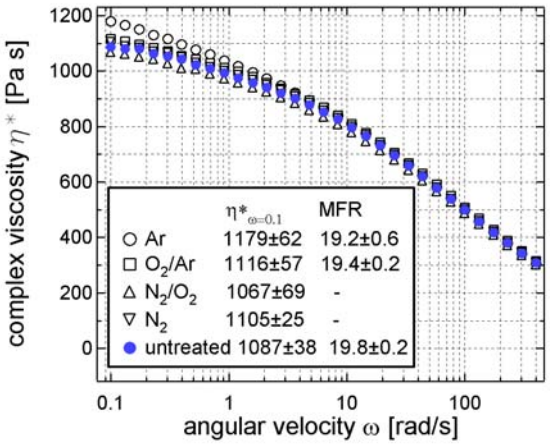

Figure 6: Influence of process gas composition on the viscosity function of HDPE powder (at 150°C)

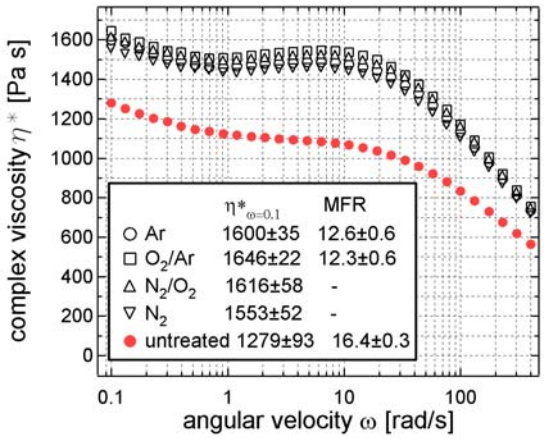

Figure 7: Influence of process gas composition on the viscosity function of CoPA powder (at 150°C)

There is evidence for vacuum-UV-radiation (VUV λ<200nm) in plasmas [15], whereby VUV emission spectra overlap with VUV absorption spectra of polymers [16]. VUV photons are responsible for change in the depth of a polymer. C-C or C-H bonds undergo scission reactions leading to free radical sites. These can in turn react with plasma gas species or crosslink, e.g. to form C=C bonds, which work as chromophores [17]. Powder exposed to reactive gas plasma (O_2, N_2/O_2, N_2) showed clear discolouration (dark-yellow colour) after melting. The yellowing effect is stronger at higher RF powder and is attributed to the presence of new chromophores, such as C=O and C=C, caused by photo degradation and ageing at elevated temperatures in the melted state.

3.4 XPS results

Figure 8 shows XPS survey spectra of HDPE powders plasma treated with 90%N_2/10%O_2 and 100%N_2 process gas composition. Untreated HDPE showed no oxygen or nitrogen indicating a pure polymer. After plasma treatment the properties of the powder surface changed with process gas composition. Oxygen and nitrogen were detected in the polymer surface.

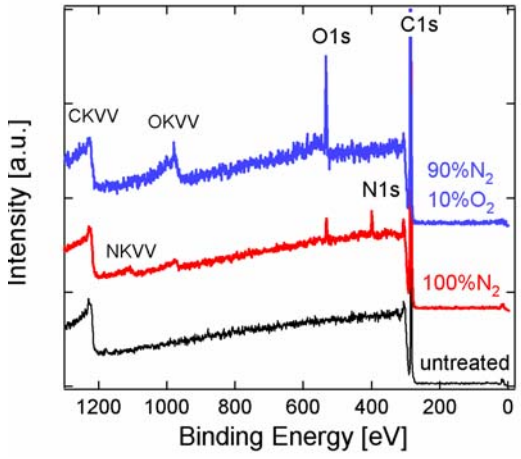

Figure 8: XPS survey spectrum of HDPE powder after different plasma gas treatments.

4. Conclusions

In a novel short-time plasma modification system for polymer powders (hot-melt adhesive HDPE and CoPA) it was shown that wettability and adhesive bonding strength could be improved simultaneously. Water contact angles reduced from >90° down to 70° (HDPE) and 78° (CoPA). Peel strength of polymer glued textile laminates (cotton tapes) increased slightly up to 25% for CoPA. Adhesive bonding strength increased up to 85% for HDPE based on aluminum lap shear tests. Failure mode analysis indicated changes from separation of polymer/aluminum interfacial bond (adhesive failure for untreated HDPE powder) to cohesive failure after plasma treatment. Increased shear-viscosity of melted CoPA (+25% compared to raw material), lower MFR (-25%) and yellowing effect provided evidence to plasma induced crosslinking reactions in the material due to plasma VUV radiation. Higher interfacial bonding is attributed to stronger chemical bonds based on incorporation of oxygen and nitrogen into the powder surface.

Aknowledgements

This work was supported by the Claude & Giuliana foundation. We would like to thank Prof. Antonella Rossi for the XPS measurements, Dr. Thomas Schweizer for the use of the rheometer, Dr. Gerhard Kuhn for lap-shear test analysis and our material supplier Schätti AG.

References

[1] C. Arpagaus, A. Sonnenfeld, Ph. Rudolf von Rohr: Chem. Eng. Technol. **28**, 1, 86-87 (2005).
[2] C. Arpagaus, Ph. Rudolf von Rohr, A. Rossi: Surface & Coatings Technology (2005) in press
[3] C. Arpagaus, A. Rossi, Ph. Rudolf von Rohr: Applied Surface Science (2005) in press
[4] E. M. Liston, L. Martinu, M.R. Wertheimer: J. Adhesion Sci. Technol. **7**, 10, 1091-1127 (1993).
[5] M. Morra, E. Occhiello, L. Gilla, F. Garbassi: J. Adhesion, **33**, 77-88 (1990).
[6] C.K. Cho, B.K. Kim, K. Cho, C.E. Park: J. Adhsion Sci. Technol. **14**, 8 (2000).
[7] E.W. Washburn: The Physical Review. **17**, 3, 273 (1921).
[8] ISO 4587: Determination of tensile lap-shear strength of rigid-to-rigid bonded assemblies (2003).
[9] ISO 1133: Determination of the melt mass-flow rate (MFR) of thermoplastics (1997).
[10] S.H. Park, S.D. Kim: Polym. Bull. **33**, 249-256 (1994).
[11] S. H. Jung, S.H. Park, D.H. Lee, S.D. Kim: Polym. Bull. **47**, 2, 199-205 (2001).
[12] G.M. Whitesides, H.A. Biebuyck, J.P. Folkers, K.L. Prime: J. Adhesion Sci. Technol. **5**, 1, 57-69 (1991).
[13] R. Prat, M.K. Shi, F. Clouet: J.M.S.- Pure Appl. Chem. **A34**, 3, 471-488 (1997).
[14] P.J. Carreau, D.C.R. De Klee, R.P. Chhabra: Rheology of Polymeric Systems. Carl Hanser (1997).
[15] M.R. Wertheimer, A.C. Fozza, A. Holländer: Nucl. Instr. and Meth. B. **151**, 65-75 (1999).
[16] S. Onari: J. Phys. Soc. Japan. **26**, 2 (1969).
[17] J.F. Rabek: Photodegradation of Polymers. Springer (1996).

Kinetic Study of the Flowing Afterglow of a N_2-CH_4 Microwave Discharge for Metal Nitrocarburizing

C.D. Pintassilgo[1, 2], C. Jaoul[3], T. Czerwiec[3], T. Belmonte[3] and J.Loureiro[2]

[1]*Dep. Física, Faculdade de Engenharia, Univ. Porto, 4200-465 Porto, Portugal*
[2]*Centro de Física dos Plasmas, Instituto Superior Técnico, 1049-001 Lisboa, Portugal*
[3]*Laboratoire de Science et Génie des Surfaces,CNRS UMR 7570, 54042 Nancy Cedex*

Abstract

This work presents experimental and calculated results of the concentrations of N and C atoms in a flowing N_2-CH_4 afterglow of a microwave discharge. Two situations are investigated: methane is added to N_2 in the downstream afterglow; methane is added to the discharge. There is a very good agreement with the predictions of our model for [N] in situation 1, as well as in situation 2 for very small values of CH_4. However, our model fails to predict the efficient production of carbon atoms in these two situations.

1.Introduction

The study of a N_2-CH_4 afterglow has an actual interest due to the large number of applications in different fields, such as in the study of the atmospheric chemistry of Titan [1], detoxification of gases [2], and metal surface nitrocarburizing [3]. The afterglow resulting from a methane-nitrogen flowing microwave discharge can be very efficient in metal nitrocarburizing, since this treatment can be improved with the presence of carbon and hydrogen atoms [3,4]. Recently, various papers have reported experimental values for these active species when small concentrations of CH_4 are added to N_2, either in the discharge or in the afterglow [4,6]. In this work, we present theoretical and experimental results for the concentrations of N and C atoms in a N_2-CH_4 flowing afterglow, due to the importance of these two species in the formation of carbonitrides ε-Fe_{2-3} (C,N) and γ′-Fe_4(C,N) in metal nitrocarburizing processes. We consider two different situations: methane is added to N_2 in the downstream afterglow (set-up I); methane is added to the discharge (set-up II).

2.Experiment

The experimental device is presented in Figure 1. The originality of this set-up is the possibility of heating the post-discharge in order to reach the temperatures of nitriding and nitrocarburizing treatment. The gas mixture is introduced into a 5 mm inner diameter quartz tube. The gases (N_2 and CH_4) are considered to be pure (99.995%) and the flow rates are controlled by mass flow meters. The discharge is produced using a surfatron device connected to a microwave generator (2.45 GHz). The post-discharge is analysed at about 200 mm downstream from the discharge in a quartz tube (26 mm internal diameter and 600 mm length). The methane can either be mixed with nitrogen before the discharge cavity or introduced in the post-discharge. The central part of the afterglow can be heated up to a temperature within the range 300 - 850 K using a cylindrical furnace. The gas temperature corresponding with the furnace temperature has been measured by means of a thermocouple with the discharge off. Several holes in the furnace allow the collection of the light emitted in the heated post-discharge. Optical Emission Spectroscopy (OES) is carried out in the post-discharge using a HR640 Jobin Yvon spectrometer with a CCD detector. Our observations take place mainly in the quartz tube of 26 mm diameter that constitutes the post-discharge reactor, at a distance of 540 mm from the discharge gap. The total pressure is 2670 Pa and the N_2 flow rate is 1000 sccm. The microwave power is kept constant equal to 150 W.

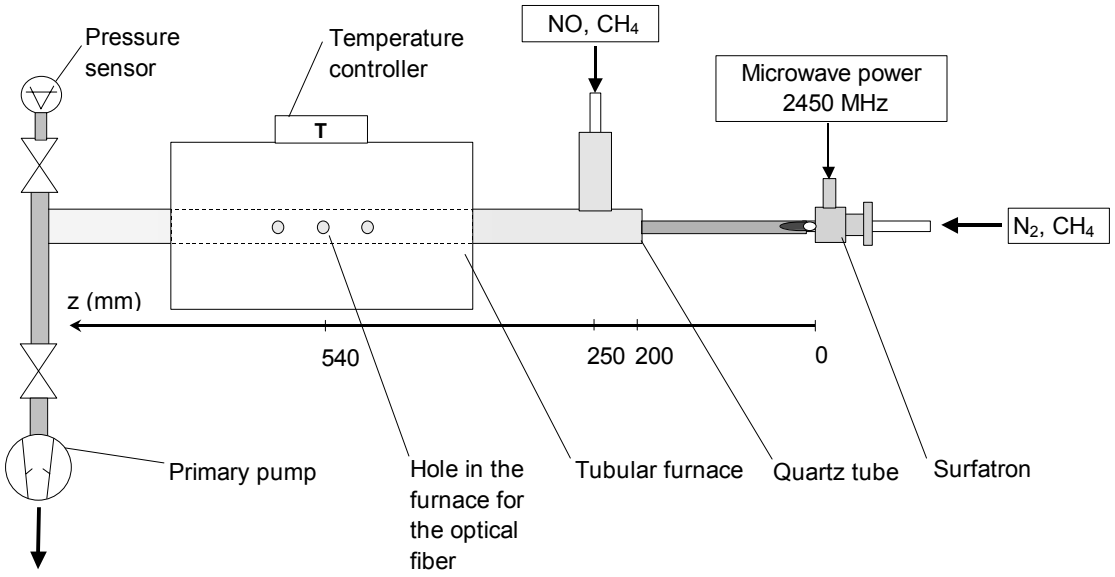

Figure 1: Experimental set-up.

The densities of carbon and nitrogen atoms in late post-discharge can be inferred from OES measurements of the first positive system of N_2 for different wall temperatures [4]. Briefly, the nitrogen atoms density is obtained from the emission of the $N_2(B^3\Pi_g,11) \rightarrow N_2(A^3\Sigma_u^+,7)$ transition at 580.4 nm, by assuming that $N_2(B^3\Pi_g,11)$ is exclusively populated by three-body re-association of N atoms. On the other hand, by means of a simple kinetic model, the carbon atoms density is deduced from the intensity of the CN violet band $CN(B^2\Sigma,7) \rightarrow CN(X^2\Sigma,7)$ at 384.7 nm, by assuming that the $CN(B^2\Sigma,7)$ state is populated via the three-body reaction $C+N+N_2 \rightarrow CN(B^2\Sigma,7)+N_2$ for low CH_4 content (< 5 vol.%). These relative measurements are then calibrated by an absolute measurement of N atoms density using NO titration. It is possible to obtain the evolution of the densities of nitrogen and carbon atoms under different reactive conditions. Uncertainties on the determination of the atomic densities by this method are approximately 20% for N atoms density and 40% for C atoms density.

3. Kinetic Model

Since we consider two different situations, in which the methane is introduced either in the afterglow or in the discharge (set-up I and II, respectively), we have developed two different models. In the first case, we considered the self-consistent determination of the active species concentrations in the discharge for pure N_2, by solving the Boltzmann's equation for the electrons coupled to a set of rate balance equations for the various molecular and atomic species produced in the discharge, including the different ions produced and the vibrational distribution of $N_2(X^1\Sigma_g^+,v)$ molecules. The sustaining electric field in the discharge is self-consistently determined as well. The electron density in the discharge is assumed to be equal to the critical value for surface wave mode propagation in a quartz tube, which is equal to 3.74×10^{11} cm^{-3} at $\omega/2\pi=2.45$ GHz. Once the concentrations of the various neutral and ionic species at the end of the discharge are obtained, the relaxation of the most populated heavy species is studied in the afterglow by considering a system of coupled time-varying kinetic master equations, in which the electron impact processes are neglected [7]. This has been done in two parts: first we determine the heavy species concentrations in the discharge and analyze their relaxation in the near afterglow in which only N_2 exists; then we consider the introduction of a small methane percentage into the post-discharge, at 250 mm downstream from the end

of the discharge (see figure 1). At this point we replace the former system of time-varying kinetic rate balance equations for pure N_2 with another for a N_2-CH_4 mixture, in which methane dissociation occurs in the presence of nitrogen together with several other reactions leading to formation of HCN, $CN(X^2\Sigma)$, $CN(B^2\Sigma)$, etc [8]. In order to describe the dissociation of CH_4 in the nitrogen afterglow and to interpret the measured values of carbon atoms, we need to consider among other reactions, the following processes:

$$N_2(A)+CH_4 \rightarrow N_2(X)+CH_3+H$$

$$N_2(A)+CH_4 \rightarrow N_2(X)+CH_2+H_2$$

$$N_2(a')+CH_4 \rightarrow N_2(X)+C+2H_2 \quad .$$

The first two processes are responsible for the production of the active species CH_3 and CH_2 in the afterglow [8], whereas the third process, as suggested in [5, 6], can be an important reaction leading to C atoms formation. In our calculations we assume that the introduction of methane occurs at $t=10^{-3}$ s downstream from the end of the discharge, which is a value obtained from the molecular flow rate used in the experiment. The gas temperature has been assumed equal to 620 K and 320 K in discharge and post-discharges zones, respectively.

In what concerns now the set-up II, in which a flowing microwave discharge is conducted in a N_2-CH_4 mixture, since we are dealing with very small relative concentrations of methane introduced in the discharge ($[CH_4]_0/N_g<0.5\%$, with $[CH_4]_0$ and N_g denoting the initial methane concentration and the gas number density), we assume that the electron energy distribution function (EEDF) in the mixture is the same as in pure N_2 for identical discharge parameters. Thus, once the EEDF is obtained in the discharge, we determine the electron impact rate coefficients for excitation of N_2 and CH_4 states, dissociation and ionization. These electron rate coefficients are then considered in a system of time-dependent rate balance equations used to describe the evolution of the most important heavy species produced in a nitrogen-methane discharge [8]. This is done by solving this time-dependent kinetic model between the times t=0 and t=0.1 s, with the initial conditions $[N_2(X,v=0)]=[N_2]$ and $[CH_4]=[CH_4]_0$. The correctness of the present approach has been confirmed by checking that steady-state solutions are obtained for $t<0.1$ s. Finally, the afterglow kinetics in N_2-CH_4 is described by considering the relaxation of the same time-varying system of rate balance equations used in the mixture, neglecting electron impact processes.

4. Results and Discussion

Figure 2 shows the concentrations of nitrogen and carbon atoms 540 mm away from the end of the discharge, as different values of methane concentration are introduced at 250 mm from the end of the discharge, which is in the near afterglow (see figure 1). The marked points correspond to experimental values, whereas the plotted curves are our calculated values obtained at the equivalent flowing time of $3x10^{-2}$ s with its origin taken at the end of the discharge. We note that this equivalence between post-discharge distances and afterglow times is an estimation since the flow velocity is not kept constant along the post-discharge. This figure shows a slightly decrease of the nitrogen atom concentration when small CH_4 concentrations are added to the afterglow. This effect mainly results from collisions between N atoms and active species resulting from methane dissociation.
With respect to carbon atoms, their observed concentration increases with added CH_4. Although our model shows a very good agreement between the experimental values for nitrogen, our calculations for carbon atoms concentration are several orders of magnitude lower than the respective measured values. We obtain typically $[C] \sim 10^8$-10^9 cm^{-3}, whereas the experimental values are $\sim 10^{12}$ cm^{-3}. Hence, we decided to represent in this figure only the measured values.

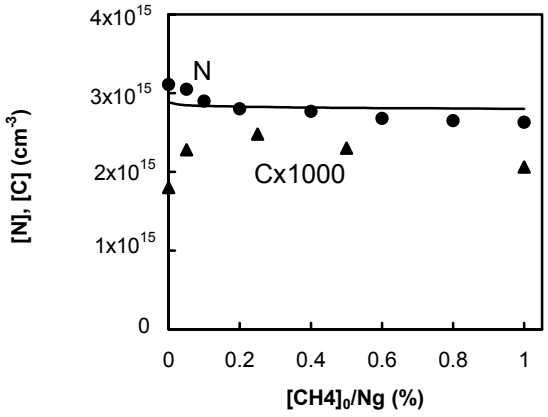

Figure 2: Concentration of nitrogen and carbon atoms 540 mm away from the end of the discharge as a function of the percentage of CH_4 introduced in the near afterglow of a pure N_2 discharge with p=2670 Pa and $\omega/2\pi$=2.45 GHz. The points represent experimental values, [N] (●) [C] (▲), and the curve is the calculated values for [N] .

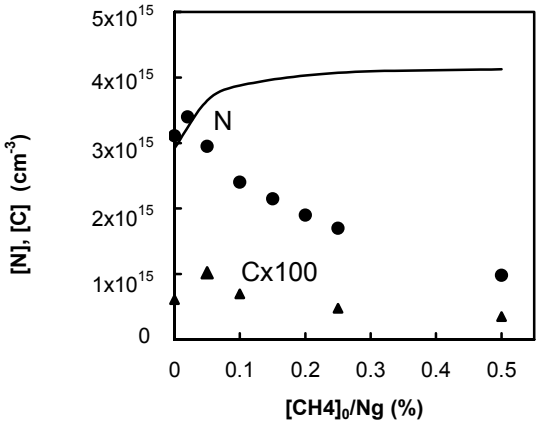

Figure 3: Concentration of N and C atoms 540 mm away from the end of a N_2-CH_4 microwave discharge, as a function of CH_4 concentration introduced in the discharge with p=2670 Pa and $\omega/2\pi$=2.45 GHz. The points represent experimental data, [N] (●), [C] (▲) , whereas the curve is the calculated value for [N].

Figure 3 shows the concentration of N and C atoms in the post-discharge 540 mm away from the end of a N_2-CH_4 discharge (set-up II), for different values of methane concentration added to the discharge. The points represent experimental values, while the curve corresponds to calculated values for [N]. The measurements show to exist a maximum in both the nitrogen and carbon atoms concentrations for added methane percentages equal to 0.02% and 0.05%, respectively. As the CH_4 percentage increases beyond these values, it is observed a smooth decrease in the concentrations of both these species. Our model predicts the magnitude of the measured N atoms concentration, but it fails to reproduce the maximum occurring at very small concentrations of CH_4, although the initial increase is also observed. As in figure 2 the calculated concentrations of C atoms are considerably smaller than those measured here.

The rapid increase of the measured N concentration for $[CH_4]_0/N_g \sim 0.02\%$, as observed in figure 3, is predicted by the model and it results from an increase of the dissociation rate by direct electron impact on $N_2(X)$ molecules, when CH_4 is added to the discharge. In fact, the methane addition leads to a reduction of the contribution from associative ionization, since the excited states $N_2(A)$ and $N_2(a')$ that are able to participate in such a process are strongly quenched by the species resulting from methane decomposition, in particular by collisions with H_2 molecules. Consequently, the electric field needs to increase in order to maintain the discharge, which leads to an increase of the electron impact dissociation rate. However, this effect cannot explain the measured decrease observed in figure 3 for the N-atoms concentration at $[CH_4]_0/N_g > 0.02\%$. This behaviour is probably a consequence of the increase of the probability for wall re-association of nitrogen atoms, γ_N, as small concentrations of CH_4 are added to the discharge. In our model, we do not take into account the complex surface kinetics and the probability γ_N is assumed to be constant.

The concentration of N and C atoms in the flowing afterglow of a N_2-0.05%CH_4 microwave discharge is presented in figure 4.

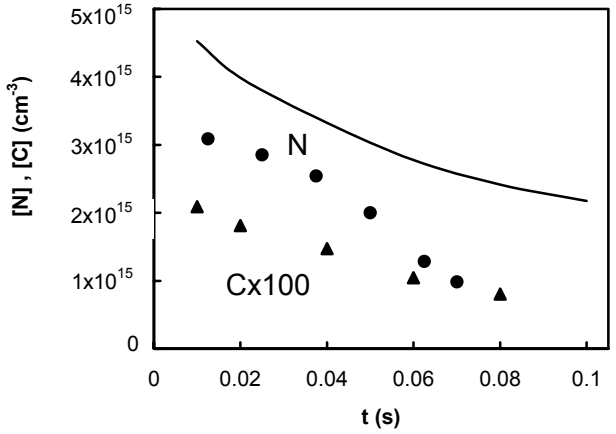

Figure 4: Concentration of N and C atoms in the flowing afterglow of a N_2-0.05%CH_4 microwave discharge, with p=2670 Pa and $\omega/2\pi$=2.45 GHz. The points and curves represent our experimental ([N] (●), [C] (▲)) and calculated data, respectively.

This figure shows a decrease in the measured concentrations of both species during the afterglow, which is in qualitative agreement with the predictions from the model for the N-atoms concentrations. However, the model predictions for the concentrations of C atoms are clearly underestimated by some orders of magnitude, so that they are not shown here. Although the production of C atoms through the reactions $CN(X)+N_2 \rightarrow C+N+N_2$ and $N_2(a')+CH_4 \rightarrow N_2(X)+C+2H_2$ have been both included in the model, we found a strong decomposition of CH4 in parallel with a depopulation of CN(X), which avoid that the C atoms may be produced. Hence, explanations are still lacking to explain the important creation of C atoms measured in both situations 1 and 2. This discrepancy can also result from a still little rigorous evaluation of the map of flow velocities in the reactor. The work is in progress to improve this point.

[1] W.R.Thompson, T.J.Henry, J.M.Schwartz, B.N.Khare and C.Sagan, ICARUS 90, 57 (1991)
[2] M.E. Fraser, D.A.Fee and R.S.Sheinson, Plasma Chem. Plasma Process. 5, 163 (1985)
[3] A.Ricard , J.E. Oseguera-Pena, L.Falk, H.Michel and M.Gantois, IEEE Trans.Plasma Sci 18, 940 (1990)
[4] C. Jaoul, T.Czerwiec, T. Belmonte, A.Ricard and H.Michel, Eur. Phys. J.Appl Phys. 26, 227 (2004)
[5] A.-M.Diamy, L.Hochard, J.-C. Legrand and A.Ricard, Surf. Coat. Technol. 98, 1377 (1998)
[6] A.-M.Diamy, R.Hrach, V.Hrachova and J.-C. Legrand, Vacuum 61, 403 (2001)
[7] V. Guerra, P.A.Sá and J.Loureiro, Phys. Rev. E (2001)
[8] C.D.Pintassilgo, G.Cernogora and J.Loureiro, Plasma Sources Sci.Technol. 10, 147 (2001)

Radial characterization of a magnetized chlorine high-density plasma sustained by electromagnetic surface-waves

A. Quintal-Léonard[1], L. Stafford[1], J. Margot[1], K. Giroux[1], J.-S. Poirier[1], F. Meunier[1], & M. Chaker[2].

[1]*Groupe de physique des plasmas, Université de Montréal, Québec, Canada.*
[2]*INRS-Énergie, Matériaux et Télécommunications, Varennes, Québec, Canada.*

Abstract

The radial structure of a chlorine high-density plasma sustained by electromagnetic surface waves was investigated using various plasma diagnostics. While the radial distribution of Cl^+ and Cl_2^+ are relatively similar in magnetized plasmas sustained at low pressure (~0.5 mTorr), the radial profile of Cl_2^+ significantly differs from that of Cl^+ at higher pressure (~5 mTorr). On the other hand, in the absence of magnetic field, the radial structure of Cl^+ and Cl_2^+ remains similar over the whole range of pressures investigated. This behavior is found to result from the changes in the driving kinetics of the positive ion species that depends on both pressure and magnetic field intensity.

Introduction

The last two decades have seen the development and characterization of high-density plasma sources aimed at improving the performance of etching in the high technology industry, particularly for the replication of deep sub-micron features in microelectronics. However, experimental plasma characterization and modeling remains quite limited even though they are crucial for the development and optimization of advanced plasma etching tools.

In this context, over the last few years, we have carried out exhaustive experimental investigations of the concentration of neutral and charged species in a magnetized high-density plasma sustained by electromagnetic surface waves. In this work, we specifically investigate the influence of the gas pressure and magnetic field intensity on the radial structure of the plasma, having in mind to provide a comprehensive picture of the kinetics driving the various charged species. This work is performed for pure chlorine plasmas that we have recently modeled.[1]

Experimental setup and diagnostics

The high-density plasma under investigation is produced at 190 MHz by an electromagnetic surface wave excited in a 15 cm diameter fused silica tube opening in a 28 cm stainless steel chamber (see Fig. 1). Both in the source region and the downstream chamber, the plasma can be confined by the action of an axial magnetic field, whose strength B_0 can be varied continuously from 0 to about 1 kG. In the present work, the absorbed RF power is kept constant at 250 Watts (yielding a power density of about 2.5 mW/cm^3). The gas pressure can be varied from 0.1 to about 10 mTorr by adjusting either the chlorine flow rate (between 5 and 10 sccm), or a throttle valve located at the entrance of the pumping system.

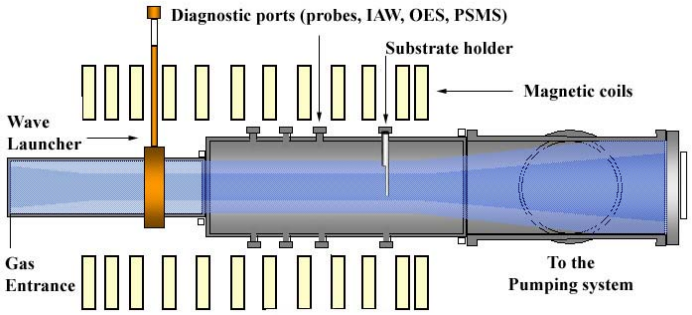

Fig 1 : Schematic drawing of the high-density plasma reactor.

The diagnostics used for plasma characterization are the following: *(i)* ion mass spectrometry using a plasma sampling mass spectrometer (PSMS) to obtain the relative density of Cl_2^+ and Cl^+ and *(ii)* electrostatic probe for the total positive ion density. More details on the use of such diagnostics in our experimental conditions can be found elsewhere.[1,2]

Results and discussion

Figure 2 shows the radial structure of the Cl^+ and Cl_2^+ density at two gas pressures: 0.5 mTorr (Fig. 2a) and 5.0 mTorr (Fig. 2b). These results have been obtained by using PSMS and Langmuir probes as in refs. [1,2]. At 0.5 mTorr (Fig. 2a), the density of both species slowly decreases between 0 and 6 cm, exhibits a peak at about 6-8 cm, and rapidly decreases beyond. The presence of the peaks in the density profiles of positive ion species was reported and modeled in ref. [3] for argon and SF_6 plasmas. It was attributed to a combination of two factors: (*i*) the fact that ionization is essentially peripheral (i.e., the ionization frequency is maximum at the edge of the fused silica tube in which the wave is launched, a common feature in surface-wave plasmas produced in large diameter tubes), and (*ii*) the anisotropy of the diffusion process in the presence of a magnetic field. This phenomenon can be either enhanced or smoothed out when further considering the volume losses for molecular gases. Finally, even though the radial distributions of Cl^+ and Cl_2^+ do not significantly differ from each other, Cl^+ remains however the main positive charge carrier between 0 and 8 cm while Cl_2^+ becomes slightly larger than Cl^+ from 8 cm.

In contrast, at 5 mTorr (Fig. 2b), the Cl^+ and Cl_2^+ density profiles are similar up to about 6 cm, while Cl^+ falls much more rapidly than Cl_2^+ beyond this position. In addition, Cl_2^+ dominates the positive ion composition for any radial position.

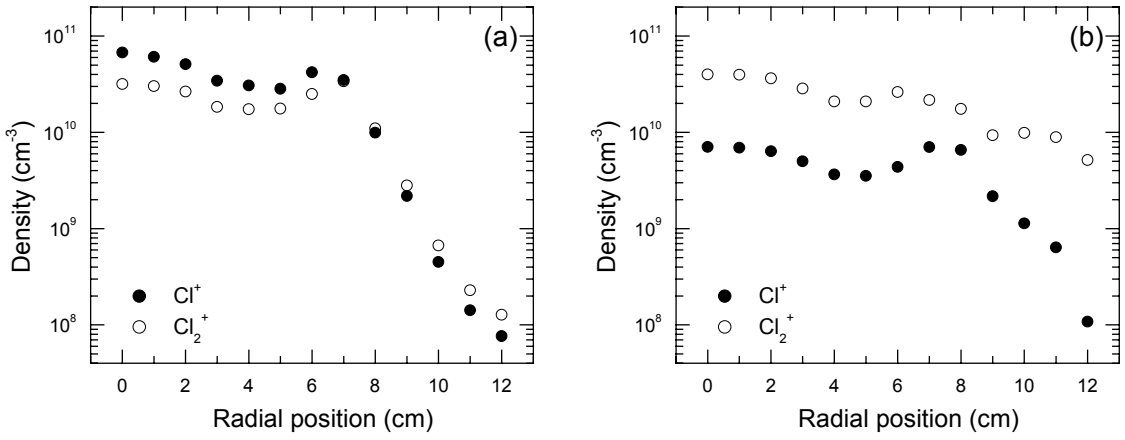

Fig. 2 : Radial distribution of the Cl^+ and Cl_2^+ density for B_0=600 G at two gas pressures: 0.5 mTorr (Fig. 2a) and 5 mTorr (Fig. 2b).

In order to more precisely examine how the gas pressure influences the radial profiles of the positive ions, we show in Fig. 3 the radial distribution of the ratio n_{Cl+}/n_{Cl2+} in the region 6-14 cm where the differences in the profiles are the most significant. Clearly, when moving to the wall, n_{Cl+}/n_{Cl2+} monotonously decreases by typically a factor of 5-7 for pressures up to about 1 mTorr. At 5 and 10 mTorr, the ratio is drastically different. Not only it shows a maximum (~ 8 cm), but it also decreases very rapidly when moving to the wall.

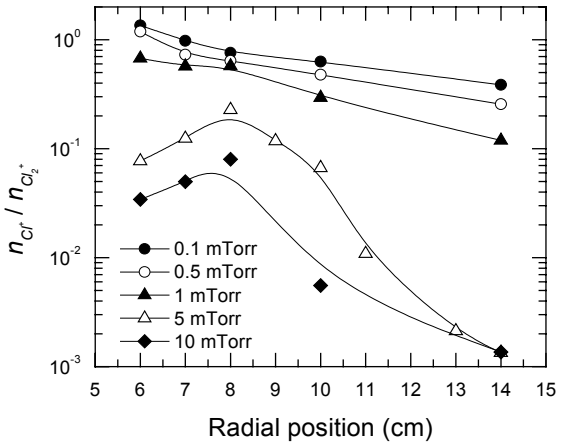

Fig. 3 : Radial distribution of n_{Cl+}/n_{Cl2+} at various gas pressures for B_0=600 G.

In order to gain insights into the meaning of the results presented in Figs. 2 and 3, we resume here the predictions of a simple fluid model recently developed for describing magnetized Cl_2 high-density plasmas. The reader is referred to previous works for details.[1] This model allows to determine the dependence of the density of electrons, Cl, Cl_2, Cl^+, Cl_2^+ and Cl^- on the experimental conditions (e.g. gas pressure, magnetic field intensity, and absorbed power). The reaction set used in the model is presented in Table 1 (from refs.1,2,4).

#	Mechanism	Reaction	Rate (cm^3/s)
1	Electron-impact ionization of Cl_2	$Cl_2 + e^- \rightarrow Cl_2^+ + 2e^-$	$\beta_1 = 9.214\times10^{-8}\exp(-12.9/T_e)$
2	Electron-impact ionization of Cl	$Cl + e^- \rightarrow Cl^+ + 2e^-$	$\beta_2 = \sqrt{T_e/12.96}\exp(-12.96/T_e)\sum_{i=0}^{5} a_i\left[\log\left(12.96/T_e\right)\right]^i$ $a_0 = 1.419\times10^{-7}$; $a_1 = -1.864\times10^{-8}$; $a_3 = 3.306\times10^{-8}$ $a_4 = -3.54\times10^{-9}$; $a_5 = -2.915\times10^{-8}$
3	Dissociative ionization of Cl_2	$Cl_2 + e^- \rightarrow Cl^+ + Cl + 2e^-$	$\beta_3 = 3.881\times10^{-8}\exp(-15.5/T_e)$
4	Electron-impact detachment	$Cl^- + e^- \rightarrow Cl + 2e^-$	$\beta_4 = 2.627\times10^{-8}\exp(-5.375/T_e)$
5	Dissociative recombination	$Cl_2^+ + e^- \rightarrow 2Cl$	$\beta_5 = 5.1\times10^{-7}(0.025/T_e)^{0.43}$
6	Dissociative attachment	$Cl_2 + e^- \rightarrow Cl^- + Cl$	$\beta_6 = 3.69\times10^{-10}\exp\left(\sum_{i=1}^{5} a_i/T_e^i\right)$ $a_1 = -1.68$; $a_2 = 1.457$; $a_3 = -0.44$; $a_4 = 0.0572$; $a_5 = -0.0026$
7	Ion-ion recombination	$Cl_2^+ + Cl^- \rightarrow Cl_2 + Cl$	$\beta_7 = 5\times10^{-8}$
8	Ion-ion recombination	$Cl^+ + Cl^- \rightarrow 2Cl$	$\beta_8 = 5\times10^{-8}$
9	Polar dissociation	$Cl_2 + e^- \rightarrow Cl^- + Cl^+ + e^-$	$\beta_9 = 8.549\times10^{-10}\exp(-12.65/T_e)$
10	Charge transfer	$Cl^+ + Cl_2 \rightarrow Cl_2^+ + Cl$	$\beta_{10} = 5.4\times10^{-10}$
11	Electron-impact dissociation	$Cl_2 + e^- \rightarrow 2Cl + e^-$	$\beta_{11} = 3.80\times10^{-8}\exp(-3.824/T_e)$
12	Surface recombination	$Cl + Wall \rightarrow 1/2\ Cl_2$	

Table 1 : Chlorine reaction set involved in the model presented in ref. [1].

In the magnetized plasma conditions examined in Figs. 2 and 3, the model predicts that the creation of Cl^+ is governed by electron-impact ionization. On the other hand, the creation of Cl_2^+ results only from electron-impact ionization of Cl_2 at very low pressure (~0.5 mTorr) and from both electron-impact ionization and charge transfer at higher pressure (~5 mTorr). In addition, even though diffusion dominates the losses for both Cl^+ and Cl_2^+ at low pressure, it can be ignored above about 1 mTorr. In these conditions, Cl^+ and Cl_2^+ are lost by charge transfer and recombination (ion-ion and dissociative), respectively.[1]

Based on the predictions of the model, the charged particle balance equation for Cl^+ and Cl_2^+ can be considerably simplified. At 0.5 mTorr (low-pressure regime), assuming that Cl^+ and Cl_2^+ diffuse at a similar rate, the Cl^+-to-Cl_2^+ density ratio can be approximated by

$$\frac{n_{Cl^+}}{n_{Cl_2^+}} = \frac{\beta_2 n_{Cl}}{\beta_1 n_{Cl_2}}. \qquad (1)$$

Since n_{Cl} and n_{Cl2} are independent of the radial position, the radial distribution of n_{Cl+}/n_{Cl2+} is uniquely determined by the radial variation of β_2/β_1.This ratio depends on the electron temperature distribution through the individual dependence of the rate coefficients on T_e (see Table 1).

We have calculated β_2/β_1 as a function of the electron temperature. The results of Fig. 4 show that β_2/β_1 increases with T_e. In our experiments, we found that T_e decreases with increasing radial position in the 6-12 cm region as shown in Fig. 5 for a gas pressure of 0.5 mTorr. Therefore, β_2/β_1 also decreases when moving from 6 to 14 cm. As a consequence, for low-pressure conditions, the ratio n_{Cl+}/n_{Cl2+} must correspondingly decrease, as observed experimentally in Fig. 3. Note that according to Eq. (1), the absolute value of n_{Cl+}/n_{Cl2+} also depends on n_{Cl}/n_{Cl2}, which is an increasing function of pressure.[1,2] Thus, at any radial position, n_{Cl+}/n_{Cl2+} must increase with pressure, in agreement with the experimental data presented in Fig. 3. These results are a clear indication that Eq. (1) adequately describes the plasma kinetics of positive ion species in the low-pressure regime.

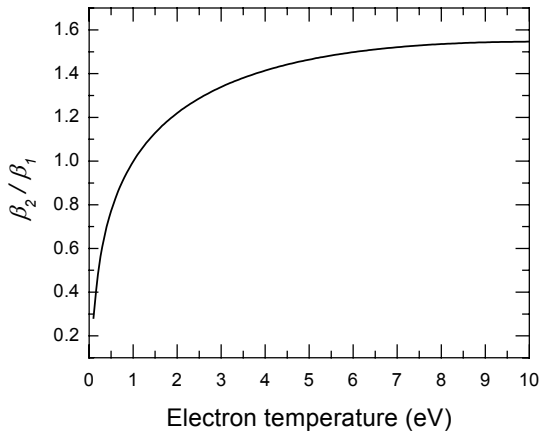

Fig. 4 : β_2/β_1 as a function of T_e

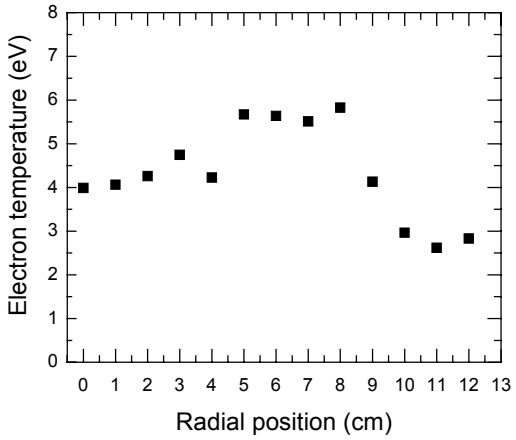

Fig. 5 : Radial distribution of T_e for B_0=600 G and a gas pressure of 0.5 mTorr.

On the other hand, at 5 mTorr, the Cl^+-to-Cl_2^+ density ratio is given by

$$\frac{n_{Cl^+}}{n_{Cl_2^+}} = \left(\frac{\beta_2 n_e n_{Cl}}{\beta_{10} n_{Cl_2}}\right)\left(\frac{\beta_5 n_e + \beta_7 n_{Cl^-}}{\beta_1 n_e n_{Cl_2} + \beta_{10} n_{Cl_2} n_{Cl^+}}\right). \qquad (2)$$

Clearly, Eq. (2) cannot be reduced to a simple form as Eq. (1). Therefore, it is not possible to identify the specific reactions responsible for the difference between the Cl^+ and Cl_2^+ profiles. However, the weakest dependence of the Cl_2^+ profile on the radial position as compared to that of Cl^+ underlines the importance of reactions independent of the electron temperature, i.e. charge transfer, ion-ion and dissociative recombination.

Finally, Fig. 6 shows the radial distribution of n_{Cl+}/n_{Cl2+} in unmagnetized plasma conditions. Clearly, n_{Cl+}/n_{Cl2+} monotonously decreases over the whole range of pressures investigated. This indicates that Eq. (1) correctly describes the positive ion kinetics even at pressures up to 10 mTorr. As shown in ref. [1], this is because for B_0=0 G, the creation of positive ion species remain governed by electron-impact ionization and the losses by diffusion up to about 10 mTorr in comparison to about 1 mTorr for B_0=600 G.

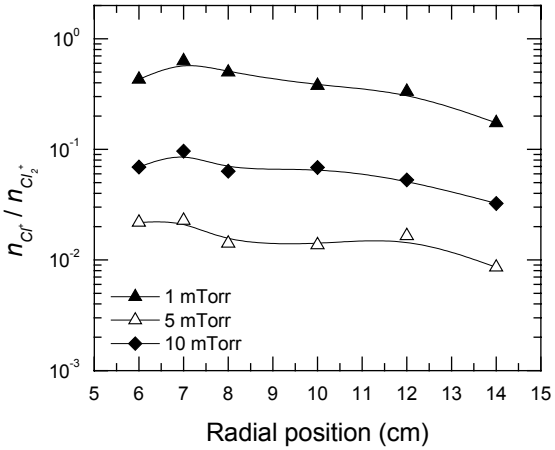

Fig. 6 : Radial distribution of n_{Cl+}/n_{Cl2+} at various gas pressures for B_0=0 G.

Conclusion

In summary, we have shown that in chlorine plasmas, the radial distribution of Cl^+ and Cl_2^+ strongly depends on the gas pressure and the magnetic field intensity due to changes in the driving kinetics of charged species with the experimental conditions. To further understand the radial structure of such plasmas, this work needs to be extended to the characterization of the negatively charged carriers. Preliminary results obtained from ion acoustic waves measurements [1,5] seem to indicate that at low pressure, the radial distribution of all positive and negative species are similar. At higher pressure, Cl^- and Cl_2^+ are closely correlated, whereas the electron and Cl^+ radial profiles are similar. This investigation is in progress.

References

[1] L. Stafford, J. Margot, F. Vidal, M. Chaker, K. Giroux, J.-S. Poirier, A. Quintal-Léonard, and J. Saussac, submitted to J. Appl. Phys. 17/03/2005 ; Preliminary results in L. Stafford, F. Vidal, J. Margot, & M. Chaker, CD-Proceeding of the 16th Int. Symp. on Plasma Chemistry (ISPC), 22-27 June 2003, Taormina (Italy).

[2] L. Stafford, J. Margot, M. Chaker, and O. Pauna, J. Appl. Phys. **93**, 1907 (2003).

[3] L. St-Onge, J. Margot, and M. Chaker, Plasma Sources Sci. Technol. **7**, 154 (1998).

[4] C. M. Lee and M. A. Lieberman, J. Vac. Sci. Technol. A **13**, 368 (1995).

[5] L. St-Onge, J. Margot, and M. Chaker, Appl. Phys. Lett. **72**, 290 (1998).

Influence of the hydrogenated plasma treatment conditions on chemical and electrical properties of multicrystalline photovoltaic silicon

S. Darwiche[1], M. Nikravech[1], D. Morvan[1], J. Amouroux[1], D. Ballutaud[2]
[1]*Laboratoire de Génie des Procédés Plasma et Traitement de Surface*
Université Pierre et Marie Curie. ENSCP 11 rue Pierre et Marie Curie 75005 Paris, FRANCE
[2] *Laboratoire de Physique des Solides et Cristallogenèse, 1 place Aristide Briand-92195 Meudon, FRANCE*

Abstract
Multicrystalline silicon (mc-Si) samples were submitted to hydrogen plasma under various conditions. The role of exposure time, and gas composition on photovoltaic properties were determined. Impedance spectroscopy, SIMS, hydrogen effusion and EBIC techniques showed the presence of optimal conditions to improve the quality of mc-Si by exposing to hydrogen. Soft hydrogenation improves the electrical conductivity and the diffusion length, while severe hydrogenation decreases the properties by creation of acceptors defects. Hydrogen effusion spectra showed the presence of 2 peaks confirming the formation of 2 kinds of Si-H bonds. Deuterium depth profile measured by SIMS SHOWED D concentration on the surface reaches 7×10^{19} atoms/cm^3 and 2×10^{17} atoms/cm^3 at 4000 nm depth.
Keywords
Silicon**,** hydrogen, plasma, impedance spectroscopy, SIMS, minority carrier diffusion length.

1. Introduction

It is well admitted that hydrogen plays an important role in improving the electrical properties of silicon for photovoltaic devices [1-4]. Incorporation of hydrogen into the silicon bulk can be achieved commonly by direct hydrogen plasma processes [5-8]. Atomic hydrogen diffuses from plasma into silicon and interacts with a variety of defects in the bulk, especially with grains boundaries. The exact mechanism of passivation is not well understood for many defects, but reaction of hydrogen with defects can be roughly classed as passivation of unsatisfied bonds (or dangling bonds). The passivation of these defects can reduce their recombination activity and increase the minority carrier diffusion lengths [9-11].
The objective of this work is to review, in relation to photovoltaic properties, the effects of the hydrogenated plasma treatment on mc-Si. The samples were treated by an inductive RF hydrogen plasma. The influence of exposure time and gas composition were studied.
In order to determine the electrical properties of the silicon's surface, we choose Electrochemical Impedance Spectroscopy technique that has widely been used for electrochemical measurements specially to determine the electrical characteristics of solid oxide fuel cells [12].
The hydrogen diffusion was studied by Secondary Ion Mass Spectrometry (SIMS). SIMS profiles show that the hydrogen concentration at the surface reach to 10^{20} atoms/cm^3 and diffuses in depth more than 4 µm. Hydrogen effusion permits to identify the silicon-hydrogen bonds. The combination of these two techniques gives information's about the hydrogen concentration into silicon samples.
The Electron Beam Induced Current (EBIC) is a powerful technique to extract the minority carrier diffusion length from the collection efficiency versus the applied voltage of electron beam.

2. Experiments

The investigations were carried out on multicrystalline silicon mc-silicon (so-called polix) made by Photowatt International S.A. that were p-type, boron doped to 3×10^{16} cm^{-3} and whose mean grain size was about 5 mm, and the thickness of the wafer was 300 µm.
The set-up consisted of an inductive radiofrequency (40MHz) plasma source with typical power between 100-500 Watts and a glass tube with 50 mm in diameter. A substrate-holder equipped with an electrical heater and a temperature sensor (type K) were placed in the center of reactor at 5 cm below the RF coils. The pressure was ranged between 0.7 and 1.3 mbar by the mean of a vacuum pump and a MKS pressure gauge (figure 1). Prior to measurements, the surface of a polycrystalline boron-doped silicon samples was cleaned during 6 min by a mixture of (HNO_3+2%HF) to eliminate the native oxide layer. The impedance spectroscopy was used as a new method to determine the electrical properties of mc-Si surface. The device consisted of a potentiostat Solartron SI 1287 coupled with a frequency analyzer Solartron 1250. An alternative voltage of 100 mV between 2 platinum electrodes applied on surface of the samples using silver

glue. In turn, the current is measured while the frequency swiped from 1 Hz to 65 kHz. Data are presented in the form of imaginary impedance, Z", versus real impedance, Z'. The electrical resistance values are given from the intercepts of the curves with the Z' axis at low frequency [13].
During the tests we observed that the measurements were very sensitive to light, temperature and atmosphere. So we carried out measurements in dark under nitrogen atmosphere at constant temperature.
The deuterium profiles were obtained by SIMS, using a CAMECA IFS4f apparatus, the primary ions was Cs^+. For this analysis, deuterium was used as a readily identifiable isotope which can duplicate the chemistry of hydrogen. Effusion spectra were obtained either through linear (13.5°C/min) or isothermal heating of the deuterated samples. EBIC was performed using JOEL JSM 840 scanning electron microscope. The collections junctions were obtained by vacuum evaporation of a 100 nm thick aluminium layer to perform the EBIC measurements. The excitation electron beam current was less than 10^{-10} A. The minority carrier diffusion lengths at the junction were deduced by fitting the variation of the collection efficiency as a function of beam voltage.

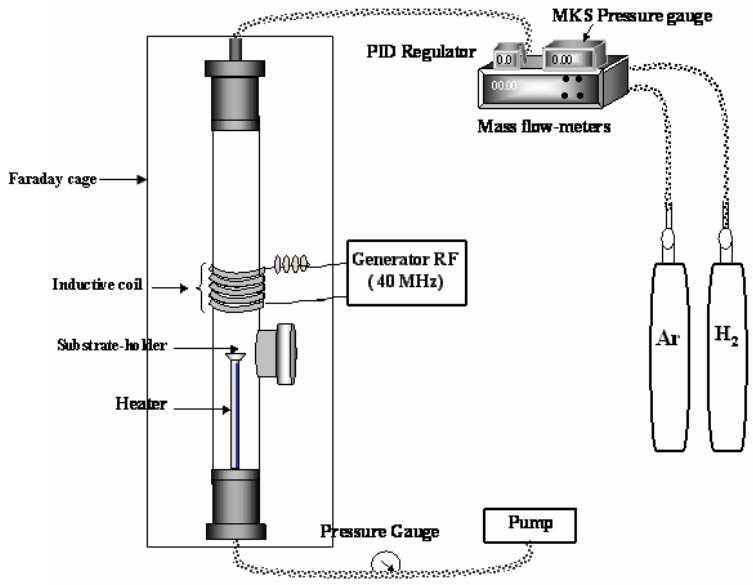

Figure 1 : Experimental set-up for treatment of silicon wafer by a low pressure plasma

3. Results and discussion

Figure 2 shows the impedance data for a silicon sample before and after exposure to pure hydrogen plasma. The electrical resistance is obtained by the intersection of the curve and Z' axis. Before hydrogenation, the electrical resistance of the silicon sample is 22000 ohm. After 1 minute exposure to hydrogen plasma at 85°C, the electrical resistance decrease to 9000 ohm.

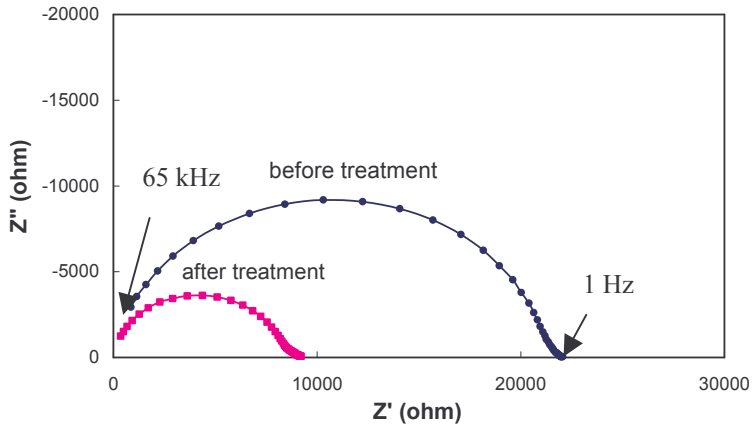

Figure 2 : Impedance data for a mc-Si sample treated 1 minute by hydrogen plasma (P=1.25 mbar, 120 W, 85°C).

In order to elucidate the role of the hydrogenation time, silicon samples were exposed to hydrogen plasma and the electrical resistance was measured as a function of exposure time. Typical reduced electrical conductivity (σ/σ_0) curve is shown in figure 3 at 180°C, σ_0 represents the conductivity of the untreated sample. We observed the same behavior at various temperatures from 150 to 400°C.

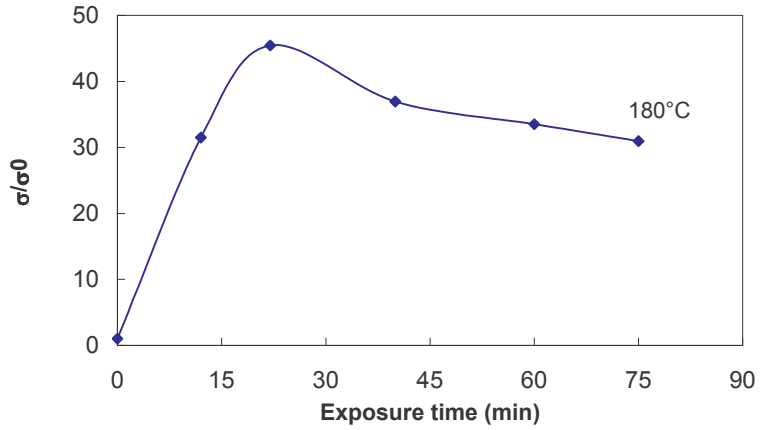

Figure 3 : The reduced electrical conductivity of poly-Si during various exposure times under pure hydrogen plasma at 180°C (1.25 mbar, 120W)

The reduced conductivity exhibits a steep increase after 12 minutes exposure to hydrogen plasma. With increasing hydrogenation time, σ/σ_0 reaches a maximum (about 22 minutes) and decays on a longer time. The observed conductivity enhancement is due to migration hydrogen atoms in the silicon host. Moreover, since the treated samples are boron-doped, hydrogen introduces from the plasma diffuses in the positive charge state, H^+, donating electrons according to the reaction $H \longrightarrow H^+ + e^-$, that indicates the passivation of grains boundaries causes an increase of the electrical conductivity [14,15].
Whereas, after a longer hydrogenation time, the reduced electrical conductivity decays exponentially. This effect, also observed by Nickel et al. [16], could be explained by a generation of new acceptors defects due to the excess of hydrogen concentration in the bulk.
In order to elucidate the effect of hydrogenation exposure time, we carried out SIMS measurements on silicon samples exposed to deuterium at 250°C. The data in figure 4 reveal that with increasing the exposure time from 15 min to 60 min, the deuterium concentration increases at the near-surface by an order of magnitude (from 2×10^{18} to 2×10^{19} atoms/cm^3). This effect is also visible until 4000 nm.

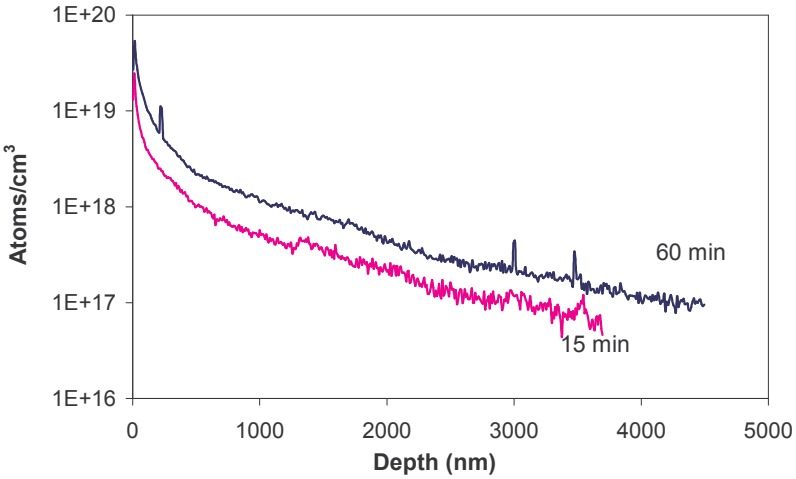

Figure 4 : Time dependence of deuterium depth profile. The samples were deuterated by plasma (50%Argon-50%Deuterium) : P = 120 W, P = 1.25 mbar, T = 250°C at indicated times.

Deuterium effusion spectra obtained for these samples were shown in figure 5. Two peaks were observed at 400°C and 550°C. In a quite similar case reported for p-type hydrogenated amorphous silicon by Stutzmann and Brandt [17]. These authors attribute the first peak (at 400°C) to clustered Si-H bonds, and the second peak to stable Si-H bonds. Accordingly, as a prelude to the desorption process, the formation of H_2 molecules from neighbouring Si-H bonds occurs at low temperature and is responsible for the 400°C peak. The hydrogen concentration in the sample calculated from Effusion spectra after 15 minutes is 1×6.10^{17} atoms/cm^3 while the sample treated 60 minutes contains 3×10^{17} atoms/cm^3.

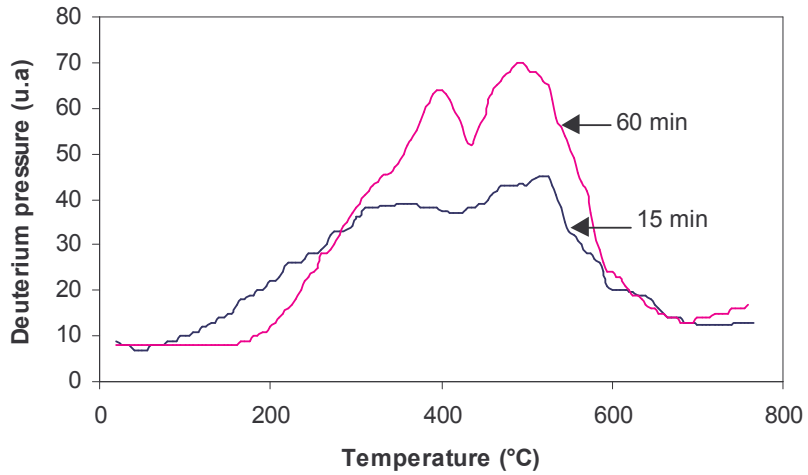

Figure 5: Deuterium effusion spectra.The samples was deuterated at 1.25 mbar, 120 Watts and 250°C at indicated times

Then, EBIC technique was used in order to control the photovoltaic properties of material. The diffusion length was measured before and after 15 and 30 minutes hydrogenation. The experimental curves of the EBIC collection efficiency as a function of accelerating voltage measured in the center of a grain are reported in figure 6. The strong increase of collection efficiency after hydrogenation treatment was characteristic of an improvement in the minority carrier diffusion length at the junction. The mean diffusion length was improved up from 72 µm (curve a) to 110 µm for 15 minutes hydrogenation time (curve b) and seems to decrease for longer times (curve c).

In order to explain this phenomena, we compared this results to those obtained by Impedance Spectroscopy in figure 3. We can conclude that, at 180°C, for a short hydrogenation time (15 minutes), the hydrogen leads to decrease the recombinant activity of grains boundaries which improve the mean diffusion length. However, for a longer time, the amount of hydrogen into silicon exceeds the density of defects and leads to a generation of new defects, that results in a decrease of mean diffusion length.

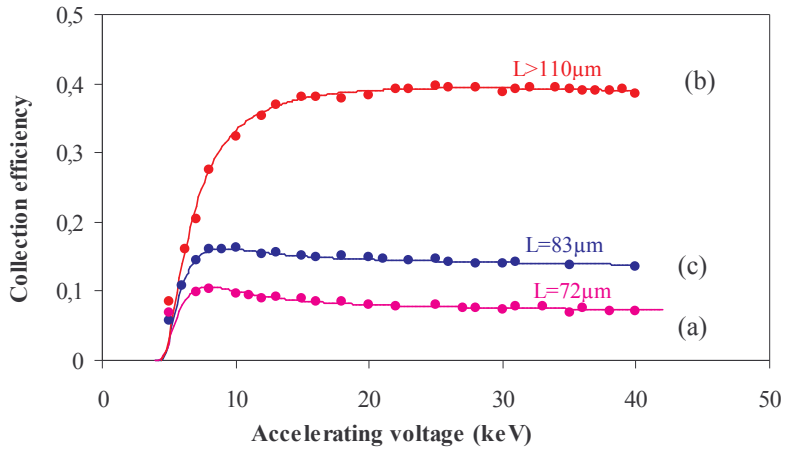

Figure 6 : Collection efficiency vs. accelerating voltage before and after treatment at different times. (a) untreated sample, (b) mc-silicon treated by pure hydrogen plasma (P = 1.25 mbar, P = 120 W, T = 200°C, t=15minutes), (c) mc-silicon treated by pure hydrogen plasma (P = 1,25 mbar, P = 120 W, T = 200°C, t=30minutes).

Experiments were carried out to study the influence of deuterium molar fraction in plasma gas on the profiles of D concentration in silicon samples. A comparison of depth profiles of deuterium is shown in figure 7. In this figure, we observed a higher concentration of deuterium on the surface of Si specimen after treatment by 100% D plasma, especially at depth below 3000 nm than that sample exposed to plasma containing 50%D. It decreases from 1.6×10^{21} to 1.1×10^{19} atoms/cm^3 with the reduction of D molar fraction in the plasma by factor 2.

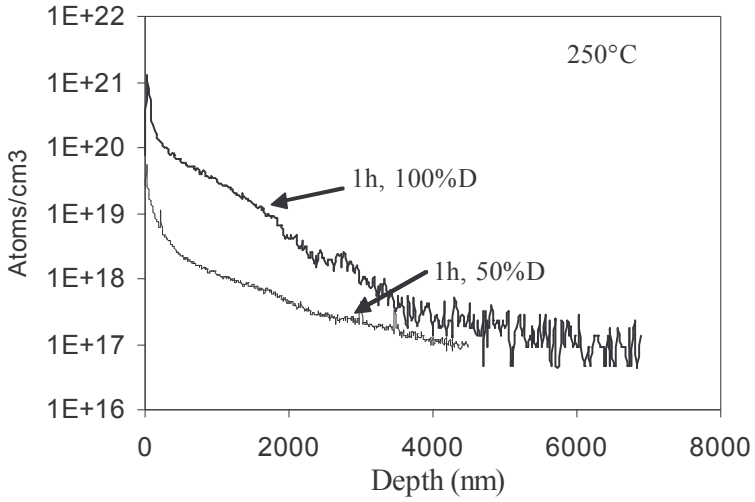

Figure 7 : Depth profiles of deuterium in mc-Silicon. The samples were exposed to deuterium non-equilibrium plasma (at various D rate), for 1hour at 250°C

EBIC measurements was used in order to elucidate the effect of plasma composition on the electronic properties of mc-silicon (figure 8). Results show that, after a treatment by pure hydrogen plasma, the mean diffusion length was smaller than this obtained after a treatment by a plasma (Ar-50%H_2). This effect is probably related to the hydrogen concentration in plasma. When the molar fraction of hydrogen in plasma is large, the hydrogen diffusion into silicon is more important, and its amount exceed that of the defects. In this case, the hydrogen can generate a new defects or reduce the diffusion length.

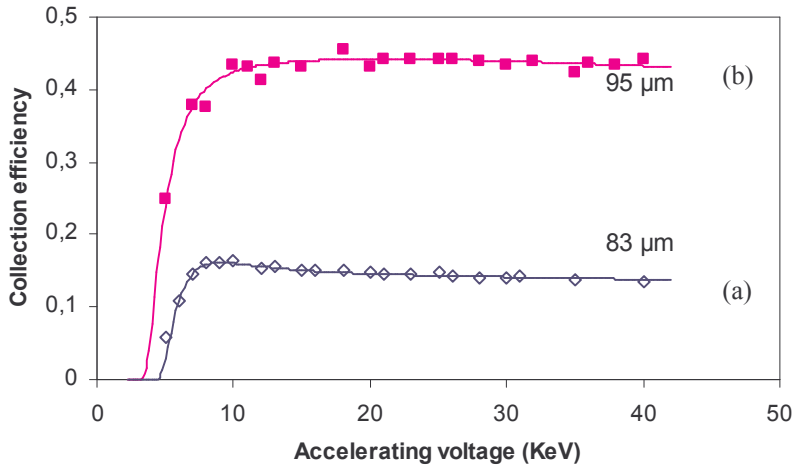

Figure 8 : Collection efficiency vs. accelerating voltage before and after treatment for different plasma composition (a) mc-silicon treated by pure hydrogen plasma (P = 1,25 mbar, P = 120 W, T = 200°C, t=30minutes), (b) mc-silicon treated by plasma (50%Ar+50%H_2) (P = 1,25 mbar, P = 120 W, T = 200°C, t=30 minutes)

4. Conclusion

In summary, we have presented an investigation of the effects of hydrogen plasma on the properties of silicon surface. Impedance spectroscopy was used as a new method to determine the electrical properties. The electrical conductivity of silicon surface depends strongly on the hydrogenation time. SIMS measurements were also carried out in order to confirm the impedance data. We observed a strong influence of the experimental parameters (exposure time, Deuterium rate) on deuterium concentration at the surface. Hydrogen effusion exhibit the presence of two kinds of silicon-hydrogen bonds. The electron beam induced current have been applied to control the electronic properties of our material. The collection efficiency as deduced from EBIC analysis allowed us to extract the minority carrier diffusion length. We have shown that the effective diffusion length can be strongly improved by plasma hydrogenation. Results obtained by these techniques show that there exists an optimum time for hydrogen incorporation and minimum defect generation.

5. References

[1] B. Pajot, B. Clerjaud, J. Chevallier, Bulletin de la S.F.P **131**, p.26-31, 2001
[2] R. Street, Hydrogenated amorphous silicon. Cambridge : Cambridge University press 1991
[3] A. Mimura, N. Konishi, K. Ono, J.-I. Ohwada, Y. Hosokawa, Y.A. Ono, T. Suzuki, K. Miyata, H. Kawakami, IEEE Trans. Electron Devices **36**, p. 351, 1989
[4] K. Pandya, B.A. Khan, J. Appl. Phys. **46**, p. 5247, 1987
[5] D. Kaplan, N. Sol, G. Velasco, R.A. Thomas, Appl. Phys. Lett. **39 (1)**, p. 73-75, 1981
[6] M. Benmansour, E. Francke, D. Morvan, J. Amouroux, D. Ballutaud, Thin Solid Films **403-404**, p. 112-115, 2001
[7] R. Pandya, B.A. Kahn, J.Appl.Phy. **62**, p. 3244, 1987
[8] J. W. Corbett, J. L. Lindström, S. J. Pearton, Solar Cells **24**, Issues 1-2, p. 127, 1988
[9] A. Coreirra, D. Ballutaud, A. Boutry-Forveille, Appl. Phys. Lett. **39 (1)**, p. 2394-2396, 1995
[10] J. Weber, Solid State Phenomena **37-38**, p. 13-24, 1994
[11] S. Martinuzzi, A. Räuber, 9th Photovoltaic Solar Energy Conference, Freiburg, p. 3, 1989
[12] M. Nikravech, F. Rousseau, D. Morvan, J. Amouroux, J. of Phys. and Chem. of Solids **64**, Issues 9-10, p 1771-1775, 2003
[13] J. R. Macdonald, Impedance Spectroscopy, Wiley – New York, 1987
[14] C. G. Van de Walle, P. J. H. Denteneer, Y. Bar-Yam, S. T. Pantelides, Physical review B **39**, n°15, p. 10791, 1989
[15] S. Martinuzzi, I. Périchaud, F. Warchol, Solar Energy Materials and Solar Cells **80**, p. 343, 2003
[16] N. H. Nickel, N. M. Johnson, J. Walker, Physical Rev. Lett. **75**, n° 20, p. 3720, 1995
[17] M. Stutzmann, M. S. Brandt, J. Appl. Phys. **68**, p. 1406, 1990

6. Acknowledgements

The authors would like to thank Dr D. Ballutaud for her contribution on analysis mentioned in this work (SIMS, hydrogen effusion, EBIC).
This work is financially supported by the French Agency for environment and energy development (ADEME).

Aligned CNT synthesis by Plasma Enhanced CVD

A.F. Pal[1], N.N. Dzbanovsky[2], V.V. Dvorkin[2], A.V. Filippov[1], N.V. Suetin[2], M.A. Timofeev[2]
[1]*Troitsk Institute for Innovation and Fusion Research, Troitsk, Moscow reg., Russia*
[2]*Nuclear Physics Institute of Moscow State University, Moscow, Russia*

Abstract
The paper is devoted to study of the growth of the aligned CNT in the anode sheath of the glow DC discharge on silicon substrate and in the MW discharge using porous Al_2O_3 template. Numerical simulation of transport processes in the anode sheath for conditions of CNT growth is carried out. It was found that the alignment of CNT was induced by the electric field in the near anode sheath region under plasma enhanced chemical vapor deposition (PA CVD) process.
Keywords
Carbon nanotube, DC glow discharge, anode sheath, chemical vapour deposition, microwave discharge

1. Introduction

Considerable interest to highly-aligned carbon nanotubes (CNT) is due to the possibility of using them in the field electron emission [1], micro- and nanoelectronics [2], filter mediums [3], electrical super-capacitors as well as for super-hydrophobic surfaces [4]. At present different synthesis methods are developed for production of CNT. These methods basically use different plasma sources (see review [5]), such as direct current (DC), radio-frequency (RF) and microwave (MW) discharges, inductively-coupled RF discharges. It is widely believed that electric field plays key role in aligning CNT by PA CVD. But possible mechanisms for the influence of the electric field upon aligned CNT growth do not understand yet. We have studied the properties of anode sheath region of DC discaharge and the possibility of aligned CNT growth in MW discharge.

2. Aligned CNT synthesis in the DC glow discharge

The scheme of the experimental setup is presented in fig.1. In the DC glow discharge the electrodes were made from molybdenum. The anode of 2.7 cm in diameter was grounded; the 2.4 cm diameter cathode cooled by water was fed with the negative voltage from the DC source. The deposition time was varied from 1 up to 15 minutes. The working pressure in the chamber was within 100-140 Torr and the substrate temperature was within 960-1080°C.

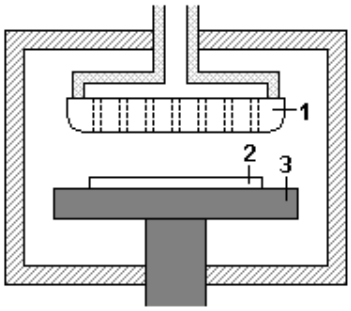

Figure 1. The scheme of the setup: 1 is the water-cooled cathode containing holes for loading the working gases; 2 is the substrate; 3 is the anode.

Before the deposition of CNT the Si substrates were successively coated by magnetron sputtering with layers of titanium (as a barrier layer and for a better adhesion) and nickel (the latter is one of the best catalysts for CNT growth). After that the substrate was placed into the chamber of a DC discharge, and the annealing process was performed in pure hydrogen for 10-15 minutes under the pressure of 120 Torr and the temperature of $T \sim 980$°C. This procedure resulted in the modification of solid nickel film to nanoparticles of 20-30 nm in size.

Then methane was added to the working gas and deposition of CNTs was performed. In Fig.2 there are SEM image of the chip of the film grown by this procedure and consisting of the oriented CNT. Deposition was performed for 15 minutes, the discharge current was 1.35 A, the discharge gap voltage was 720 V, flow rate of hydrogen was 30 l/hour, that of methane was 2.7 l/hour. The deposited nanocarbon films were also studied with the transmission electron microscopy (TEM) and Raman spectroscopy.

3. Numerical simulation of the DC discharge anode sheath

The gas density in our experiments under the conditions of growing nanotubes was about 10^{18} cm^{-3}, so in the $10\%CH_4+90\%H_2$ mixture the free path length of electrons was equal to $l_e \approx 8$ μm , and that of ions to

$l_i \approx 20$ μm. Therefore, the hydrodynamic approximation can be used to describe transport processes of charged particles in the anode sheath. To determine the distribution of the potential and the electrical field strength as well as of the density of electrons and ions in the anode sheath the following self-consistent system of equations was used:

$$\frac{\partial n_e}{\partial t} = \frac{\partial^2 \left(D_e n_e\right)}{\partial z^2} + \frac{\partial \left(k_e n_e E\right)}{\partial z} + \nu_{ion} n_e - \beta_{ei} n_e n_i \,, \tag{1}$$

$$\frac{\partial n_i}{\partial t} = -k_i \frac{\partial \left(n_i E\right)}{\partial z} + D_i \frac{\partial^2 n_i}{\partial z^2} + \nu_{ion} n_e - \beta_{ei} n_e n_i \,, \tag{2}$$

$$\frac{\partial \left(n_e \varepsilon_e\right)}{\partial t} = \frac{\partial^2 \left(G n_e\right)}{\partial z^2} + \frac{\partial \left(\beta n_e E\right)}{\partial z} - e j_e E - n_e W_S \,, \tag{3}$$

$$\frac{\partial E}{\partial z} = 4\pi e \left(n_i - n_e\right), \tag{4}$$

where n_e, n_i, k_e, k_i, D_e, D_i are the densities, the mobilities and the diffusion coefficients of electrons and ions respectively, ν_{ion} is the frequency of gas ionization, β_{ei} is the coefficient of electron-ion recombination, ε_e is the mean energy of electrons, β is the thermal electricity coefficient, W_S is the rate of energy loss in elastic and inelastic collisions, E is the electrical field strength, e is the absolute value of the electron charge.

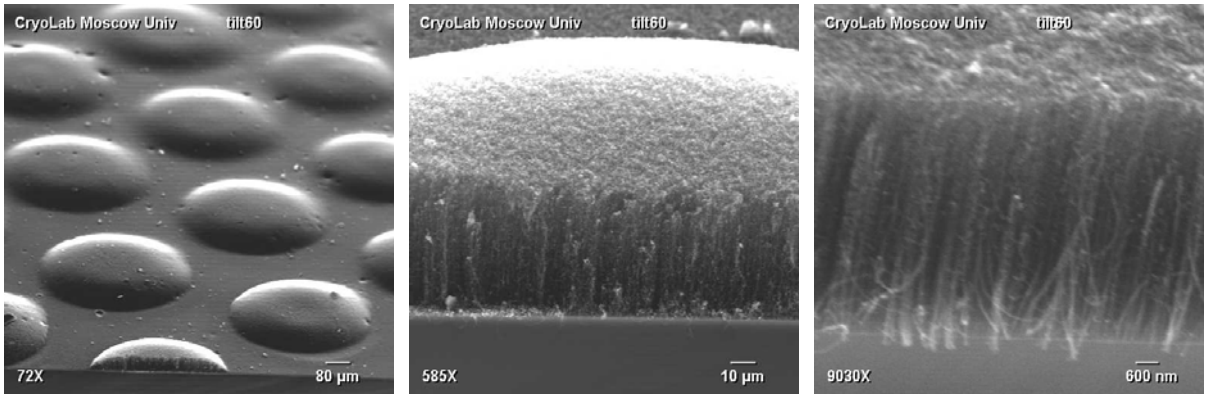

(a) *(b)* *(c)*

Fig.3. SEM images of grown nanotubes.

System of equations (1)-(4) was completed with the following boundary conditions:

$$\left[n_e - \gamma_e l_e \frac{\partial n_e}{\partial z}\right]_{|z=z_0} = 0 \,, \left[n_i - \gamma_i l_i \frac{\partial n_i}{\partial z}\right]_{z=z_0} = 0 \,, \left[p_e - \gamma_\varepsilon l_e \frac{\partial p_e}{\partial z}\right]_{|z=z_0} = 0 \,; \tag{5}$$

$$n_{e|z=z_\infty} = n_{e\infty}, \quad n_{i|z=z_\infty} = n_{i\infty}, \quad \varepsilon_{e\,|z=z_\infty} = \varepsilon_{e\infty}, \; E_{|z=z_\infty} = E_\infty \,; \tag{6}$$

where $p_e = n_e T_e$ is the pressure of the electron gas; T_e is the electron temperature defined by $T_e = 2\varepsilon_e/3$, γ_e, γ_i, γ_ε are the coefficients which, for the case of the plane geometry, are equal to the Hopf constant

$$\gamma_{e(i)} = \left(2D_{e(i)} / l_{e(i)} \upsilon_{T,e(i)}\right)\Big|_{z=z_0} \approx 0.7104 \,; \; \gamma_\varepsilon = \left(G_e / l_e \upsilon_{T,e} T_e\right)\Big|_{z=z_0} \,; \tag{7}$$

$\upsilon_{T,e(i)}$ is the thermal velocity of electrons (ions), z_0 is the anode coordinate, z_∞ is the coordinate of the point after which the influence of the electrode (anode) upon the positive arc column can be neglected. The values with the subscript "infinity" are the positive column values.

During this stage we do not consider negative ions, because it is conventional view at present that the methane-hydrogen mixture that is being studied is an electropositive gas [1,3-5]. In principle the system can be easily supplemented by the balance equation for negative ions. Usually the ion diffusion in transport processes in the DC glow discharge does not play any role; therefore, to increase the calculation rate and to avoid numerical instabilities (those of Gibbs type), for ions we solved the first-order balance

equation with the boundary condition in the anode. It is supposed that the basic positive ion is $C_2H_5^+$ with the dissociative recombination coefficient

$$\beta_{ei} = 7.4\times10^{-7}\left(T_e/300\right)^{-1/2}\ \text{cm}^3/\text{s}$$

(the temperature of electrons is in K). The mobility of ions was calculated from the equation:

$$k_i = \left(\chi_{\text{H}_2}/k_{i,\text{H}_2} + \chi_{\text{CH}_4}/k_{i,\text{CH}_4}\right)^{-1},$$

where the numerators contain the fractions of the corresponding molecules in the mixture, and the ion mobilities reduced to normal conditions for pure gases was derived from the Langevin relationship:

$$k_i = 36/\sqrt{\alpha\mu}\ \text{cm}^2/\text{V s},$$

where α is the polarizability of hydrogen (α_{H2}=0.819) or methane (α_{CH4}=2.6) molecules in atomic units, μ is the reduced mass of the ion and the selected molecule.

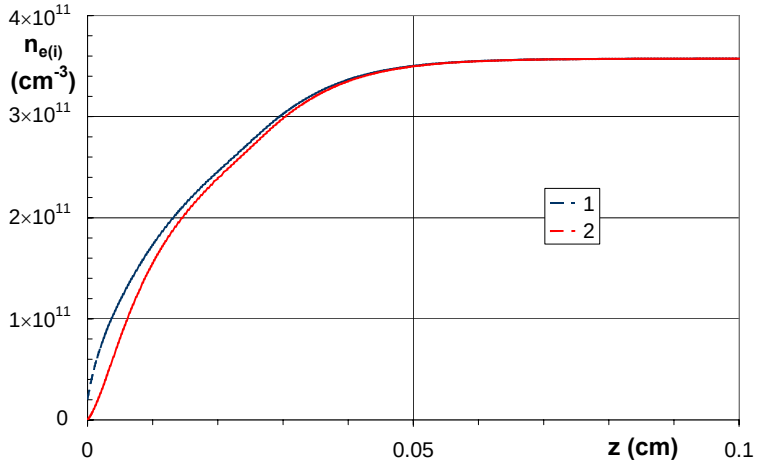

Fig.3. Distributions of electron (1) and ion (2) densities in the anode sheath of the glow discharge in the 10%CH_4+H_2 mixture.

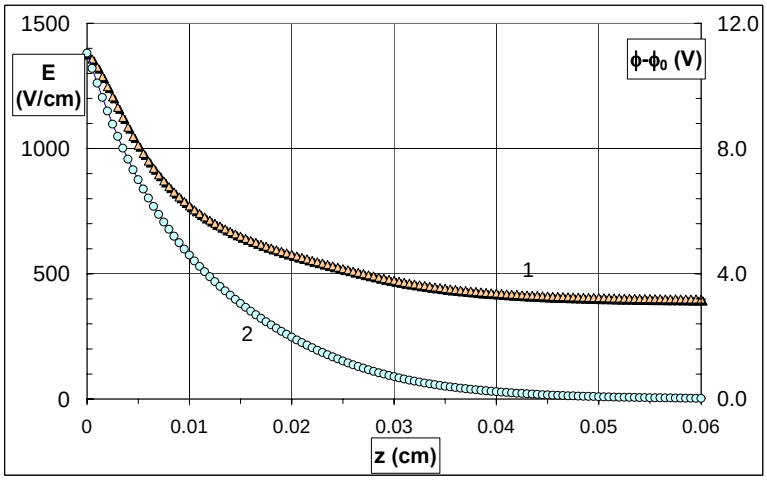

Fig.4. Distributions of electric field strength (1) and potential (2) in the anode sheath of the glow discharge in the 10%CH_4+H_2 mixture. The ϕ is the total potential, the ϕ_0 is the potential of the homogeneous external field without considering the net charges

In figures 3-5 there are results of numerical calculations in the H_2:CH_4=1:9 mixture under the following input parameters: the pressure was p = 120 Torr, the gas density $N = 9.474\times10^{17}$ cm^{-3}, the gas temperature T_{gas} = 1250 K, the discharge current density in the positive column j_d = 670 mA/cm^2. Such parameters were maintained in experiments in growing oriented nanotubes. Then these parameters were used in

numerical calculations to determine the reduced electrical field strength, the electron density and temperature in a positive column, which were equal to the following:

E_{pc} = 404.5 V/cm, $E_{pc}/N = 4.27\times10^{16}$ V cm^2, $T_{e,pc}$ = 1.444 eV, $n_{e,pc} = n_{i,pc} = 7.91\times10^{11}$ cm^{-3},.

It is clearly seen from the presented figures that the size of the anode sheath in the mixture is about several hundreds of microns, which is considerably larger than the height of highly oriented nanotubes.

According to the present literature data there is opinion (for example, [2]), that the electrical field considerably influences upon the growth of nanotubes, but there is no recognized mechanism for this influence. It was shown in [2] that the growth of the oriented nanotubes only occurred under the electrical field strength of 0.1-0.15 V/μm, and no nanotubes grew under the electrical field of 0.07 V/μm.

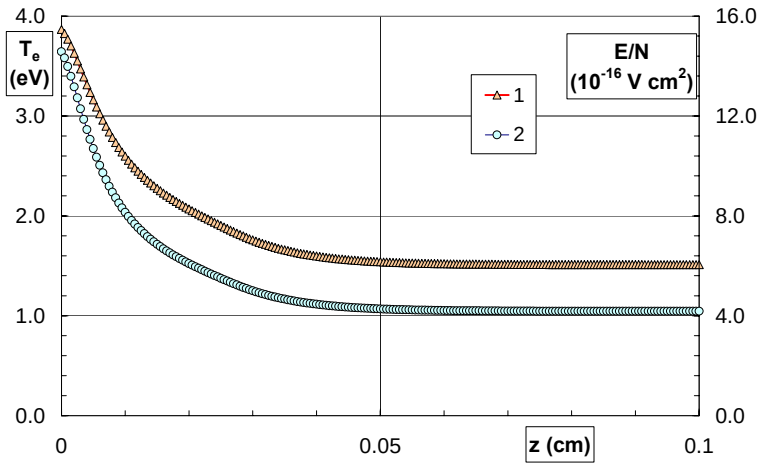

Fig.5. Distributions of electron temperatures (1) and reduced electric field strength (2) in the anode sheath of the glow discharge in the 10%CH_4+H_2 mixture.

According our simulations aligned CNTs in the anode sheath grow in the electric field with the strength of about 1.4 kV/cm (fig.4). The interaction energy of a nanotube with such a field is negligible, about 10^{-5} eV, therefore the ponderomotive force cannot be the reason for the aligned growth of nanotubes. Consideration of possible mechanisms of electric field effect on the oriented CNT growth showed that the ordered alignment of the nanotube array could result in our conditions from the collective Coulomb interaction of charges induced by the electric field on nanotube heads. It was found that aligned CNTs could only grow within the rather narrow temperature range of 960-1000^{o}C. Termination of the aligned CNT growth could be due to the fact that the increase of CNTs height is accompanied by enhanced heating of nanotubes by the electrons and the hot gas from plasma.

4. Aligned CNT synthesis in the MW discharge

The basic advantage of MW discharge is the plasma purity due to absence of electrodes, which is important in using deposited film in microelectronics. Among the basic features of the MW discharge the following ones stand out: high ionization and dissociation degree under relatively low gas temperature, which is caused by a considerable difference in gas and electron temperatures. For typical deposition processes under the gas pressure of 50 Torr those are 2000 K and 18,000 K respectively. In comparison with other types of discharges this results in great dissociation degree of hydrogen, which is a strong etching agent for sp^2 carbon phase. The influence of these conditions is particularly negative for CNT formation process. In the same way, relatively high energy acquired by electrons influences the composition of the gas phase, where low molecular compounds are dominating, owing to which the formation of complex structures such as, for example, fullerene complexes, is complicated.

As a result, the basic difficulty to grow CNT in the MW discharge is the necessity to decrease the rate of etching CNT by atomic hydrogen, which is formed in the dissociation process of both hydrogen molecules and carbon containing gas (for example, methane). The etching effect is increased with the rise in the working pressure, which results in the impossibility of producing CNT under high pressures (about

100 Torr) in the gas mixture of hydrogen-methane. It should be noted that the concentration of etching components in plasma should be sufficient to provide appropriate purification of the deposited film surface from growth sites of unsuitable phases, which decrease the quality of the CNT structure.
The following three methods can be used to decrease the concentration of atomic hydrogen near the substrate under high pressures: (a) growing CNT under the graphite grid, (b) adding the gas substituting hydrogen into the working mixture and (c) using the pulsed mode (PM) for gas excitation.
The first method consists in placing a graphite grid with holes of about 1 mm in diameter and a step of 2 mm within 1-2 mm above the substrate surface (see the fig.6). The grid supplies additional amount of carbon into the growth region and at the same time screens atomic hydrogen within the graphite surface. The mechanism of the grid action has not yet been studied completely.

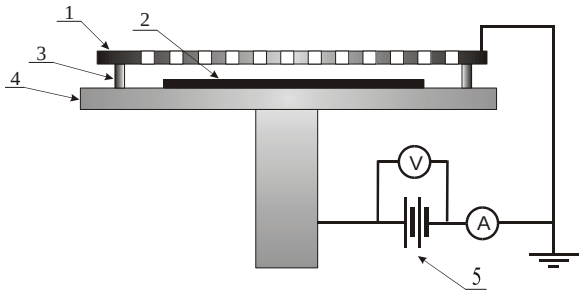

Fig.6. Arrangement of sample holder . 1 – graphite grid; 2 – Si sample; 3 – spacer; 4 – Mo plate; 5 – DC power supply.

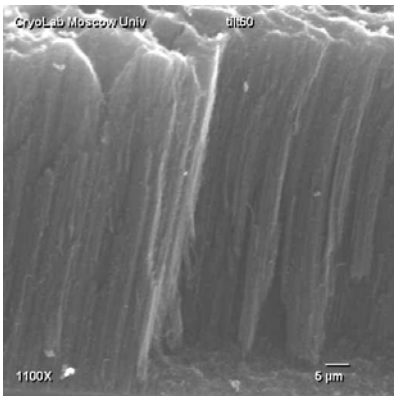

Fig.7. Aligned nanotubes produced with graphite grid.

The grid can also provide an electrical shift for the oriented growth of CNT. Fig.7 shows SEM image of produced CNT film. The Si substrates were the same as used in DC CVD. It was found that growth of aligned CNT are only possible when the Si resistivity is no more than 10 kΩ.
Lately the second method is rather widely used. The hydrogen in a standard methane-hydrogen mixture can be substituted partially or completely by nitrogen, oxygen containing gas or rare gases (usually Ar is used). The use of mixture of methane and carbon dioxide shows good results. Oxygen binds atomic hydrogen forming OH, and, in addition, results in enrichment of the mixture with carbon. In such a mixture growing CNT occurs within a wide range of deposition parameters, also under low temperatures of a substrate.
The third method is based on the difference in time dependence of formation and recombination rates for radicals and ions in plasma. By varying the duration of pulses and the interval between them it is possible to influence considerably the radical composition of discharge, and hence, the structure of the film formed. The pulse mode (PM) MW CVD provides also a possibility of low-temperature nanomaterials growth. This is especially urgent for the case of glass substrate, which could be easily built into present-day electronic technology. In continuous mode decrease in the substrate temperatures is connected with MW energy decrease, which leads to decreasing plasma volume and essential change in plasmochemistry. Using PM it is possible to eliminate both of these factors: increasing on-off ratio one can decrease average MW power and, hence, substrate temperature, keeping pulse power constant and, thus, preserving plasmochemistry and discharge volume. In such a way we successfully perform the CNT growth at a substrate temperature of 370-400^0 C.
When CNTs arrays are used as emitters of electrons, there occurs mutual electric shielding of separate nanotubes. Deposition of a solid layer of nanotubes leads to considerably weakening the effect of the electric field increase on nanotube tips and to the higher emission threshold for the specimen coated with such a film. Besides, there is the natural fluctuation in the length of grown CNTs, as a result the emission homogeneity also becomes worse. This problem can be solved by separating individual emitters. One of the effective approaches to solve this problem is growing nanotubes through the pores of the anodic Al_2O_3

(porous anodic alumina – PAA). In our experiments PAA substrate 30-40 μm thick was covered with Mo film 20 μm thick to form an electrode. The Co catalyst was cathodically deposited into the nanopores of PAA.

The growth of CNTs was performed by MW CVD in continuous mode with graphite grid or pulse mode. In the first method the deposition conditions were the following: CH_4:H_2 gas mixture with methane concentration of about 16%, total pressure of 80 Torr. Substrate temperature was equal to 780°C. The deposition time was about 10 min. The negative bias applied to the substrate holder relative to the grounded grid electrode was about 100 V. The bias current reached 5 mA.

The pulse mode of plasma excitation makes it possible to change the C_2/CH radicals concentration, that allows the optimization of the CNT deposition conditions. Using the optical emission spectroscopy we found out that changing of the modulation frequency made it possible to manipulate the [C_2]/[CH] ratio within 15% range (fig.8). The CNT were grown in CH_4:CO_2 gas mixture (1:1) under the following conditions: total gas pressure was 30-40 Torr, average MW power 100 W, modulation frequency 1.5 kHz, on-off ratio of 4, the substrate temperature was 500°C. Fig.9-11 show SEM images of the chips of the films grown and Raman spectrum of CNT.

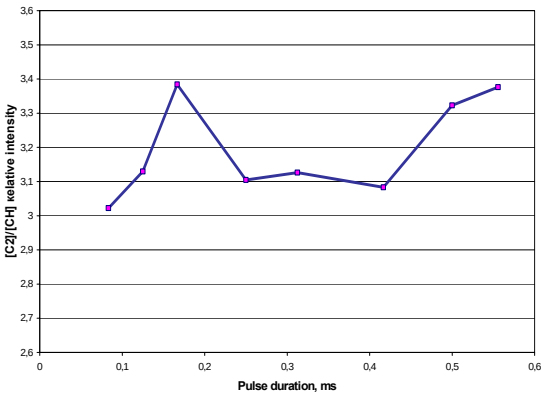

Fig.8. Dependence of [C_2]/[CH] from MW pulse duration in CH_4:H_2 plasma.

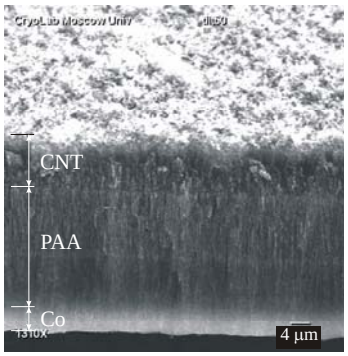

Fig.9. CNT grown in the continuous mode.

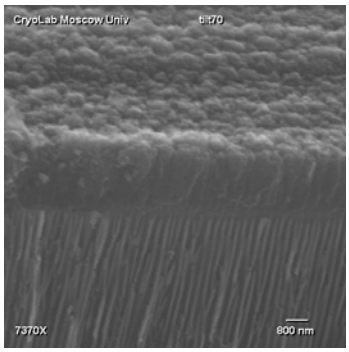

Fig.10. CNT grown in the pulse mode.

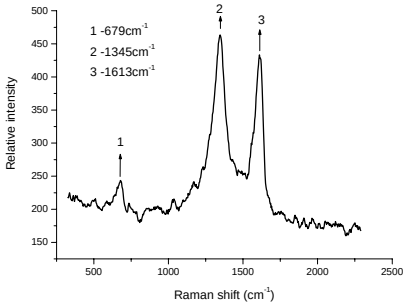

Fig.11. Raman spectrum of CNT film grown in the pulse mode.

Practically through each pore of the PAA an individual nanotube grows about 10 μm height over the template (fig.9).

Acknowledgements

This work was supported by International Science and Technology Center, project 2484.

References

[1] M.A. Guillorn, A.V. Melechko, V.I. Merkulov, at al. - Appl. Phys. Lett. 81, 3660 (2002).
[2] J. Koehne, H. Chen, J. Li, at al. - Nanotechnology 14, 1239 (2003).
[3] L. Zhang, A.V. Melechko, V.I. Merkulov, at al. - Appl. Phys. Lett 81, 135 (2002).
[4] K.K.S. Lau, J. Bico, K.B.K. Teo, at al. - Nano Lett. 3, 1701 (2003).
[5] M. Meyyappan, L. Delzeit, A. Cassel, D. Hash - Plasma Sources Sci. Technol.; 12, 205 (2003).

Water treatment by radical injection with atmospheric micro plasma generated in fast oxygen flow

Atsushi Yamatake, Jeremy Fletcher, Koichi Yasuoka and Shozo Ishii

Department of electric and electronic engineering, Tokyo Institute of Technology, Tokyo, Japan

Abstract

In this study, a new water treatment method by O radical injection with DC driven micro plasma was examined. This method can realize stronger oxidation than an ozone process because of O and OH radicals. The effect of radical injection was measured by using a water solution of acetic acid (CH_3COOH). This was examined with various parameters (discharge current, gas flow rate, hole diameter), and the results indicated that high gas flow velocity was important to inject short-lived radicals into water effectively.

1. Introduction

Atmospheric plasma is used for various fields such as decomposition of toxic substances. In the plasma, molecules are dissociated by high energy electrons and radicals. One of the methods for decomposition of toxic substances is using ozone which is produced by oxygen discharge. Oxygen atoms (O radicals) and ozone molecules are generated by following equations.

$$e + O_2 \rightarrow O + O + e \quad (1)$$

$$O + O_2 + M \rightarrow O_3 + M \quad (2)$$

Ozone is useful for oxidation processes such as water purification because it is stronger than chlorine and harmless to the environment. However, ozone cannot perfectly decompose organic substances, so it is impossible to decompose persistent substances such as dioxin. Therefore stronger oxidants than ozone are needed for advanced oxidation process, such as O and OH radicals.

We have studied radical sources with atmospheric micro plasma such as micro hollow cathode discharge [1]. Oxygen molecules are decomposed in the plasma and ozone molecules are generated at the downstream of the plasma when feeding oxygen into the plasma at high speeds [2][3]. In this case, O radicals, whose life is very short, can be directly used within several millimeters from the electrode. In this study, direct water treatment with O radical was achieved. It is considered that OH radicals are also generated in water by Eq. (3).

$$O + H_2O \rightarrow OH + OH \quad (3)$$

2. Experimental setup

Fig. 1 shows the structure of the discharge electrode. The upper electrode (cathode) is molybdenum with a thickness of 200 μm, and there is a small hole at the center. The lower electrode (anode) is separated from the upper electrode with alumina of 500 μm thickness. Plasma is generated in the hole when DC high voltage is applied. Oxygen gas is injected into the discharge and radicals are emitted from the hole.

The experimental setup is shown in Fig. 2. DC high voltage was applied to the electrode with a DC high voltage source through a ballast resistor. Oxygen was supplied with a mass flow controller. Water was on the electrode and treated directly by radical injection.

The treated water was a solution of acetic acid (CH_3COOH) as a persistent substance. To detect the decomposition of the acetic acid, TOC (Total Organic Carbon) concentration in the water was measured by a TOC analyzer (Sievers 810) because a decrease of TOC means decomposition of acetic acid.

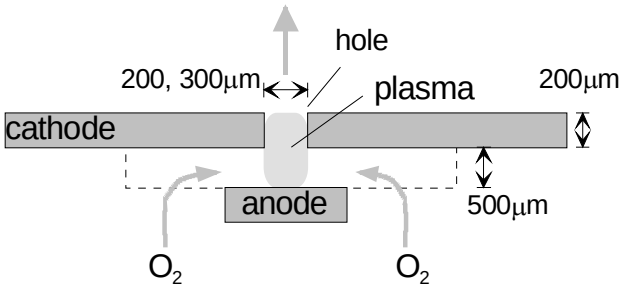

Fig. 1 Schematic of electrode

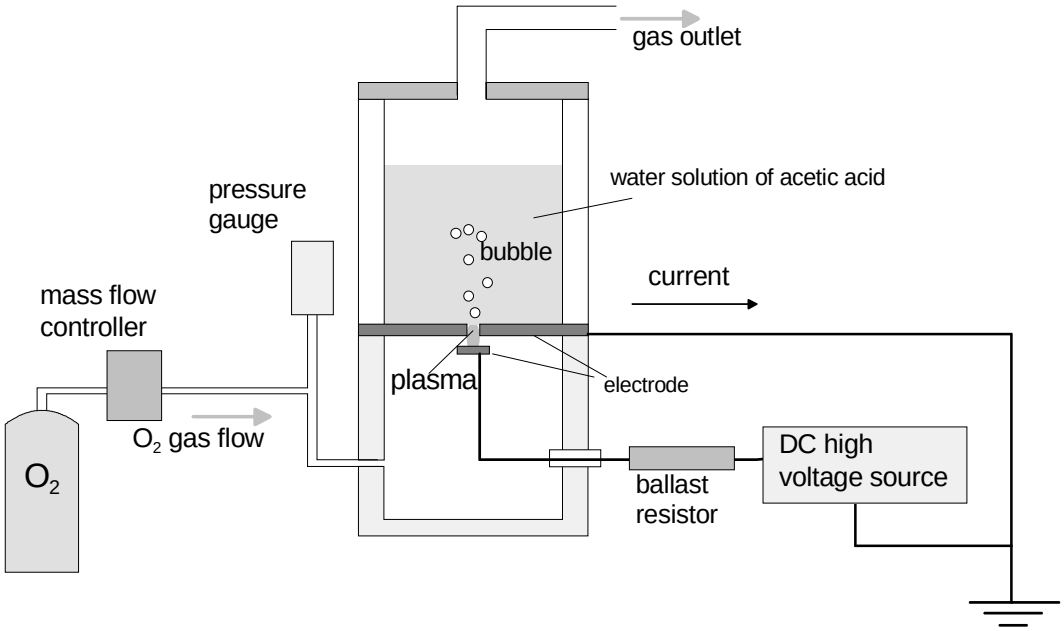

Fig. 2 Experimental setup

3. Results and discussion

First, sustaining voltage was measured by oscilloscope at various currents with water and oxygen gas flowing through the hole. The results are shown in Fig. 3. A stable plasma was generated even when the electrode was in contact with water. The plasma was not in direct contact with the water because of the high gas flow rate and surface tension of the small hole. But the stability was less than that of plasma generated in the atmosphere.

Fig. 4 shows the result of decomposition of TOC. Initial TOC concentration was 10 ppm, and the water volume was 10 mL. In this case, oxygen gas flow rate was 500 sccm. When gas flowed without discharge, TOC didn't decrease because acetic acid isn't decomposed by only bubbling. The symbol of "O_2 + O_3" means injecting ozone which was generated in another place, and TOC didn't decrease because ozone can't decompose acetic acid. When plasma was made at the electrode and oxygen was fed through, the effect of decomposition was measured. It was found that this system has the ability to inject radicals into water. The decomposition rate became higher after increasing the discharge current. That can be explained that the amount of O radicals generated at the plasma being larger because the electron density was higher.

In order to compare various results, the energy efficiency of decomposition was calculated by the results and below equation [4]:

$$\eta = \frac{w\Delta C / m}{IV\Delta t} \tag{4}$$

where η[mol/J] is energy efficiency for decomposing acetic acid, w[g] is the weight of sample water, ΔC is the variation of TOC concentration, m[g/mol] is the weight of carbon in 1 mol (m=24 in case of CH_3COOH), I[A] is discharge current, V[V] is sustaining voltage and Δt[s] is processing time.

Fig. 5 shows the energy efficiency calculated by the results of Fig. 4. The efficiencies were not largely changed with various discharge currents.

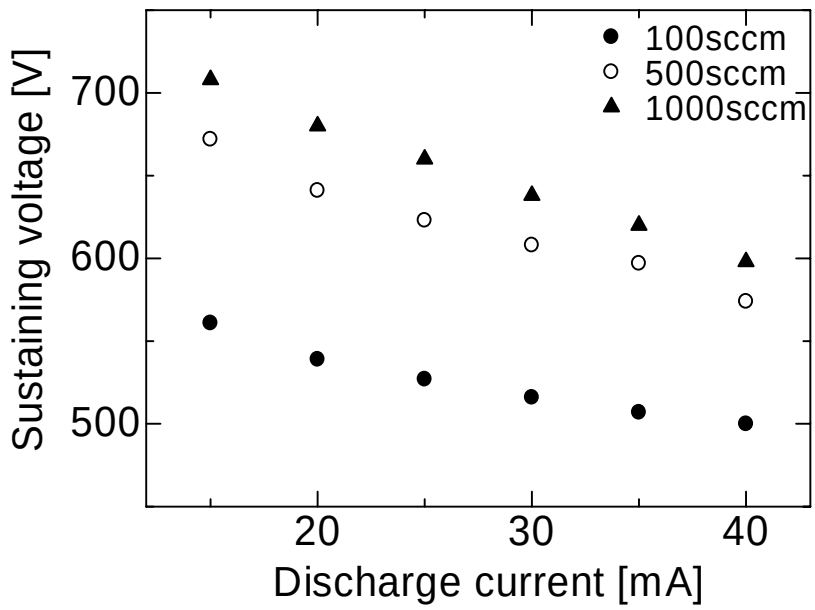

Fig. 3 *V-I* characteristics

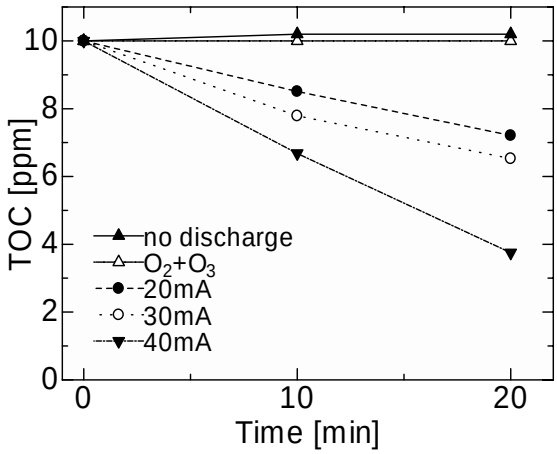

Fig. 4 Time dependences of changing of TOC (hole diameter is 200 μm, gas flow rate is 500 sccm)

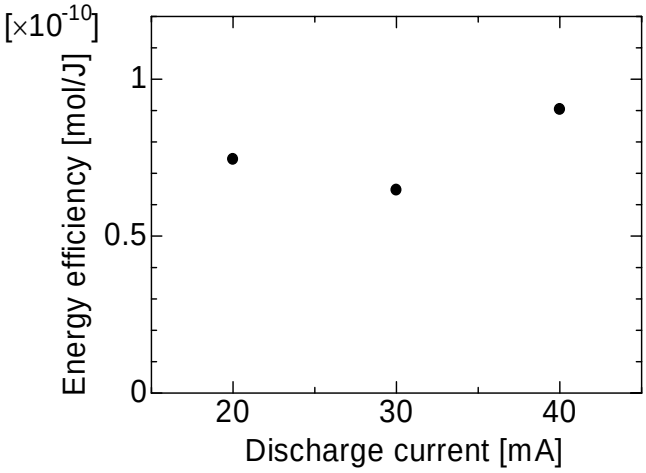

Fig. 5 Energy efficiency of decomposition with various currents

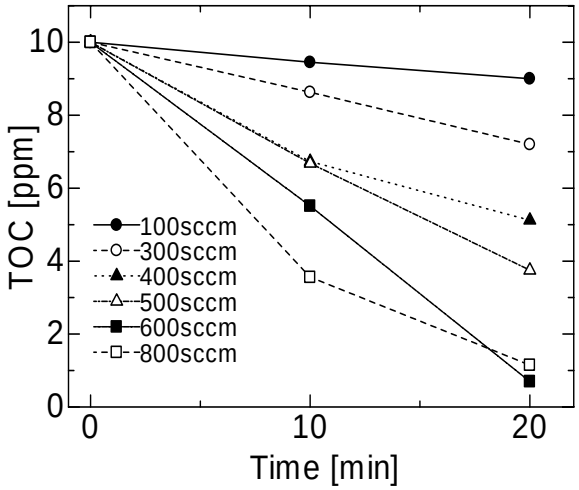

(a)ϕ200 μm

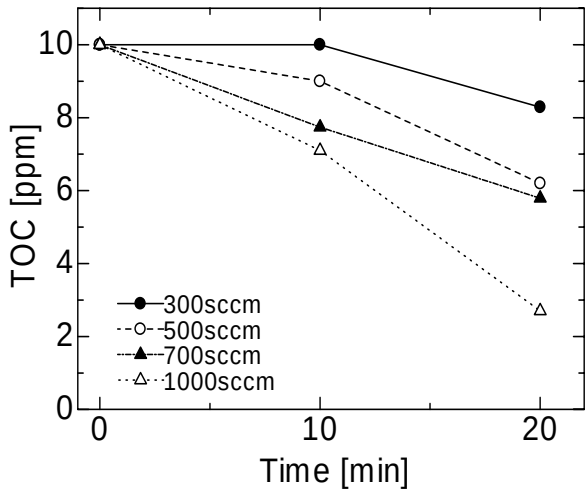

(b)ϕ300 μm

Fig. 6 Decomposition of TOC with various gas flow rate when the hole diameters were (a)200 μm, and (b)300 μm.

Fig. 6 shows the results of the process with various gas flow rates and fixed discharge current (=40mA), and hole diameters are (a)200 μm and (b)300 μm respectively. Fig. 7 shows the energy efficiency which was calculated by the same method as Fig. 5. From Fig. 7, it is found that the energy efficiency became higher with increased gas flow rate. It can be assumed that this was caused by the injection of more gas. But considering that the efficiencies of ϕ300 μm were lower than those of ϕ200 μm, the gas flow rate is not a critical parameter.

The lifetime of O radicals, which were generated in the plasma, was very short, so it is important to inject radicals into water within the lifetime of O radical. The gas flow velocity at the hole was calculated with the gas flow rate, the hole diameter and the gas pressure. However, accurate values couldn't be calculated and the converted gas flow velocities were unrealistic values. Fig. 8 shows the results when x-axis has been converted to gas flow velocity from Fig. 7. It is found that the efficiency largely depended on the gas flow

velocity. O radicals seem to exist only within very short distance from the electrode because they disappear within several millimeters if the lifetime is several tens microseconds and the gas flow velocity is 100 m/s. That indicates that quick injection of radical was important.

It can be also considered that the effect was caused by the difference of the size of bubbles. In any case, the gas flow velocity is important parameter because the size of bubbles is affected with gas flow velocity.

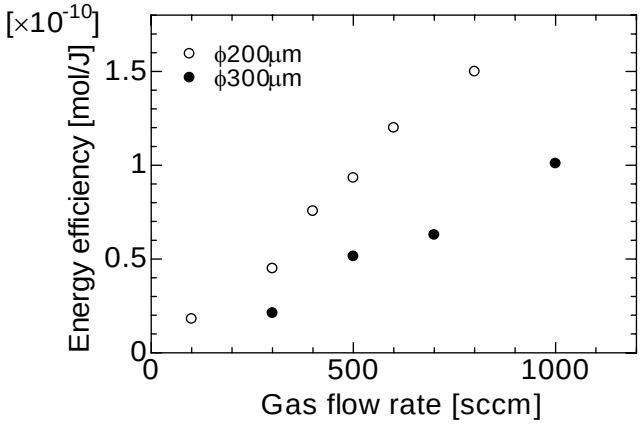

Fig. 7 Energy efficiency of decomposition with various gas flow rate.

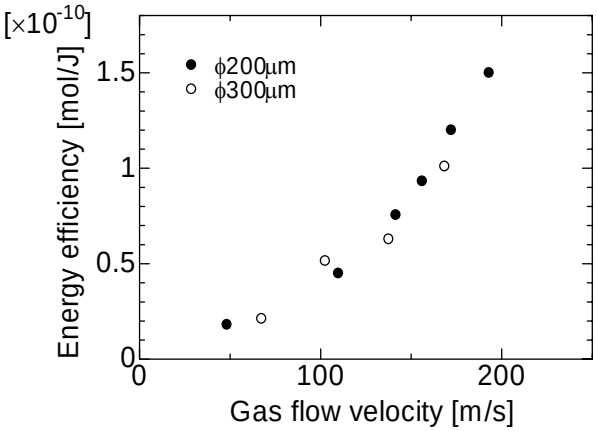

Fig. 8 Energy efficiency of decomposition with gas flow velocity converted from gas flow rate and so on.

4. Conclusion

Direct water treatment by radical injection with DC driven micro plasma and oxygen was achieved, and decomposition of acetic acid in water was measured by analyzing TOC concentration.

- Acetic acid couldn't be decomposed by injecting ozone and oxygen bubbles.
- Decomposition rate became high when increasing the discharge current.
- Energy efficiency of decomposition became high with increasing the gas flow rate.
- Energy efficiency in the case of the hole diameter of 300 μm was lower than that in case of 200 μm. The most important parameter was the gas flow velocity, and not the gas flow rate.

References

[1] K.H.Schoenbach - Plasma Sources Sci. Technol, **6**, 468-477 (1997)

[2] Yasunobu Endo, Koichi Yasuoka, Shozo Ishii - T. IEE Japan, **123-A**, 364-369 (2003)

[3] Atsushi Yamatake, Koichi Yasuoka, Shozo Ishii - Jpn. J. Appl. Phys., **43**, 6381-6384 (2004)

[4] Noriaki Sano, Daisuke Yamamoto, Tatsuo Kanki and Atsushi Toyoda - Ind. Eng. Chem. Res., **42**, 5423-5428 (2003)

Pulsed Corona Discharge in Supercritical Carbon Dioxide

E.H. Lock[1], A.V. Saveliev[1], L.A. Kennedy[1]

[1]*Department of Mechanical and Industrial Engineering, University of Illinois at Chicago, Chicago, USA*

Abstract
The initiation of a pulsed corona discharge in supercritical CO_2 is studied experimentally. The corona discharge was successfully generated using wire-to-cylinder and point-to-plane configurations. In the wire-to-cylinder configuration plasma was produced in the vicinity of the critical point. In the point-to-plane geometry plasma was observed in a wide range of temperatures and pressures. Possible applications of plasmas generated in supercritical CO_2 are discussed.
Keywords: pulsed corona, supercritical fluid, breakdown

1. Introduction

Although the ability of the supercritical fluids (SCFs) to dissolve non-volatile solids has been well known for more than a century, interest in their commercial applications has risen dramatically in the past twenty years. Supercritical fluid extraction for the decaffeination of coffee with supercritical CO_2 and the ROSE process for separating the components of heavy fraction of petroleum using supercritical pentane are well established large scale applications. Recent developments in supercritical CO_2 research include several different areas such as polymerization and polymer processing, cleaning and degreasing of parts in microelectronics, metal and low-k film deposition, organic and inorganic chemistry, fine particles formation, bacteria inactivation and drug delivery. Such intensive research is driven by the unique physical and chemical properties of supercritical fluids, which are in an intermediate between the gas and liquid states.

In SCFs, the large effective mass transfer is realized by their low viscosity and high diffusivity while the high heat transfer is achieved by large thermal conductivity. The solvent properties of the SCF can be tuned by simply varying their pressure and temperature. SCFs are often referred to as "cluster fluids" [1], which means that regions of strong density inhomogeneities are observed. This provides a unique chemical reaction medium. Molecular association via intermolecular interactions or the formation of solvation structure of solute molecules is local and short-lived, and does not inhibit the transport of the reactants and products as in the case of liquid phase. Concurrently, the molecular clusters formed in SCF are responsible for reaction mechanisms typical for liquids. In these conditions reactants are usually surrounded by a number of supercritical molecules, which accelerates the reaction rates relative to the gas phase.

In this study we chose supercritical CO_2 as a medium for plasma generation because it is nontoxic, not corrosive, inflammable and not explosive. Its critical temperature of 304 K is close to the ambient temperature. Supercritical CO_2 solvent properties such as diffusivity, viscosity, and thermal conductivity can be tuned by simply varying the pressure and temperature. The solvation power of the SC CO_2 is directly proportional to its density [2]. Another important property of SC CO_2 is its zero surface tension, which allows the carbon dioxide to penetrate into small cracks, cavities, and cell walls. This is very important for medical waste treatment and for microelectronic industry, where size reduction of chips and other components is a critical issue. Furthermore, supercritical CO_2 is characterized by solvent-free reactions, which means that by simply reducing the pressure gaseous carbon dioxide leaves the system due to phase transformation.

Supercritical plasma is a new emerging area in plasma research. In 2002, Terashima and co-workers demonstrated the generation of plasma in 1 and 2 μm gaps between planar electrodes [3]. The further efforts of several research groups were directed toward pulsed discharges with large interelectrode distances. Non-thermal pulsed corona discharge under supercritical fluid conditions was generated in two discharge configurations: wire-to-cylinder and point-to-plane [4-6]. In the present work we studied development of corona discharges in a wide range of supercritical pressures and temperatures. The basic feature of non-thermal plasma technologies involves the generation of plasma where the majority of the electrical energy goes into the production of energetic electrons. These energetic electrons produce excited species (free radicals and ions), which under supercritical fluid conditions are expected to increase the rate of cluster formation while supercritical fluid will provide a chemical environment for their effective chemical

utilization. The unique combination of gas phase discharge and heterogeneous chemistry defines several potential applications of supercritical plasmas. This includes material synthesis and processing, plasma chemical reactions and pollution control. Several developed applications of supercritical fluids include extraction and removal of toxic components, e.g. in medical and pharmaceutical fields and in chip manufacturing. The application of SCF discharge plasmas is an innovative approach to the development of pollution control technologies.

2. Experimental Setup

The experimental setup is presented in Fig. 1. Liquid carbon dioxide is compressed to the desired pressure by high-pressure pump (Thar Technology, P-50) and supplied in the supercritical fluid cell, which is 10 ml cylindrical stainless steel optical chamber. The high-pressure windows (Pressure Products, Co.) are made from quartz. A thyratron-based variable-voltage, variable-frequency power source is used for plasma generation. The delivered power can be varied from 0.2 to 12 W by controlling the high voltage pulse amplitude and the pulse repetition rate. Pulses of about 100 ns duration and 10 ns rise time are transmitted to the corona electrode inside the supercritical cell by means of the electrical high-pressure high voltage feedthrough (Conax, Inc.). The thickness of the used wire was 80 μm. Additional breakdown experiments were conducted using point-to-plane geometry. The radius of the curvature at the top of the needle electrode was 90 μm and the interelectrode distance 84 μm.

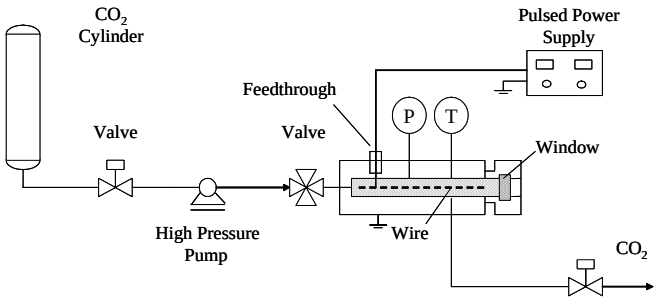

Fig. 1. Experimental setup for generation of pulsed corona discharge in supercritical CO_2.

3. Results and Discussion

The experiments on plasma generation in supercritical fluids were first performed using the wire-to-cylinder configuration. Picture of the resulted discharge is shown in Fig. 2. The experimental conditions were close to the critical point with temperature of 310 K and pressure of 80 bar and the required voltage was only 6 kV. This voltage was much lower than the one predicted by the Paschen's law [4]. The generation of non-thermal plasma at elevated pressures usually requires high voltages or small interelectrode distances. In gases, the Paschen's law is usually applied to estimate breakdown voltage required to initiate discharge between coplanar electrodes. This law states that the breakdown is a function of the product Pd, where P is the pressure and d is the interelectrode distance. This defines the breakdown region with the boundary usually referred to as a Paschen curve. The region of high pressure corresponds to the linear right-hand branch of the Paschen curve where the breakdown voltage increases linearly with Pd. This suggests that extremely high voltage will be required for breakdown of supercritical CO_2 at pressures approximately 74 times higher than atmospheric. Even more challenging will be a plasma generation in supercritical water due to the much higher critical point temperature and pressure equal to 647 K and 221 bar, respectively.

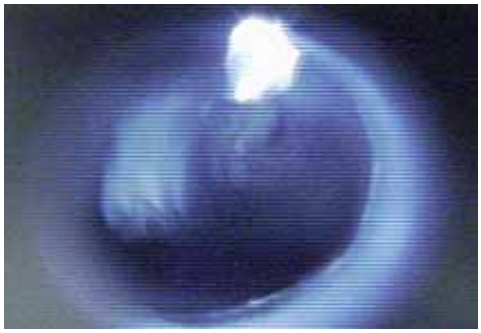

Fig. 2. Pulsed corona discharge in supercritical CO_2, wire-in-cylinder configuration.

Due to the extensive cluster formation in supercritical fluids, the breakdown mechanism significantly differs from the known mechanisms for gas and liquid phase. The clusters affect all elementary processes involving electrons. These include ionization, collisional energy losses, and loss of electrons via recombination and attachment. The clusters in supercritical fluids typically have low ionization potentials, which, in turn, reduce required breakdown voltages. Concurrently, the losses due to recombination and attachment can be increased by the cluster presence. Additionally, a high heat capacity of the fluid near the critical point affects development of the streamer channels and slows the development of thermal instabilities.

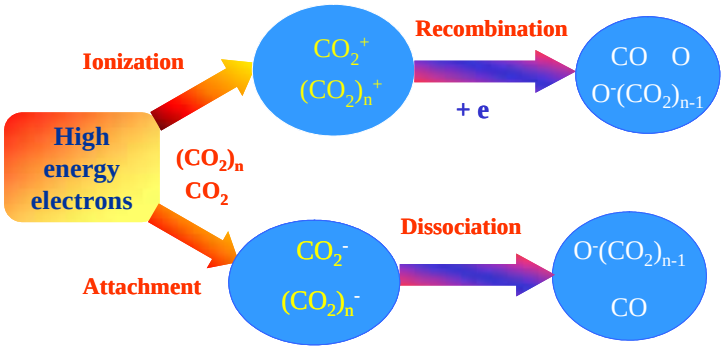

Fig. 3. Electron kinetics in supercritical CO_2.

Possible explanation of the electrical discharge initiation in supercritical CO_2 with sufficiently low voltage involves the presence of clusters and density inhomogeneities. The energetic electrons are formed in the regions of supercritical fluid, where the density is low. These electrons ionize clusters in the high density regions additionally forming ion and radical clusters. The important aspect of supercritical plasma studies is to understand the effect of the neutral SCF clusters and plasma-generated radicals and ions on discharge characteristics. As shown in Fig. 3, the high energy electrons ionize the CO_2 molecules and clusters to produce CO_2^+. The electron losses occur via recombination (charge neutralization) and electron attachment. The electron attachment reactions are important for the electrical breakdown and can occur either dissociative via the reactions

$$e + (CO_2)_n \rightarrow O^-(CO_2)_{n-1} + CO \quad (1)$$

$$O^-(CO_2)_{n-1} \rightarrow CO_3^-(CO_2)_{n-2}^* \quad (2)$$

or nondissociative depending on the electron energy [7]. Other important reactions that need to be considered involve electron transfer between the clusters. As some studies suggest this process could be caused either by their reorganization or by core switching [8]. Further research is needed for development of electron kinetic mechanisms governing the breakdown in supercritical fluids.

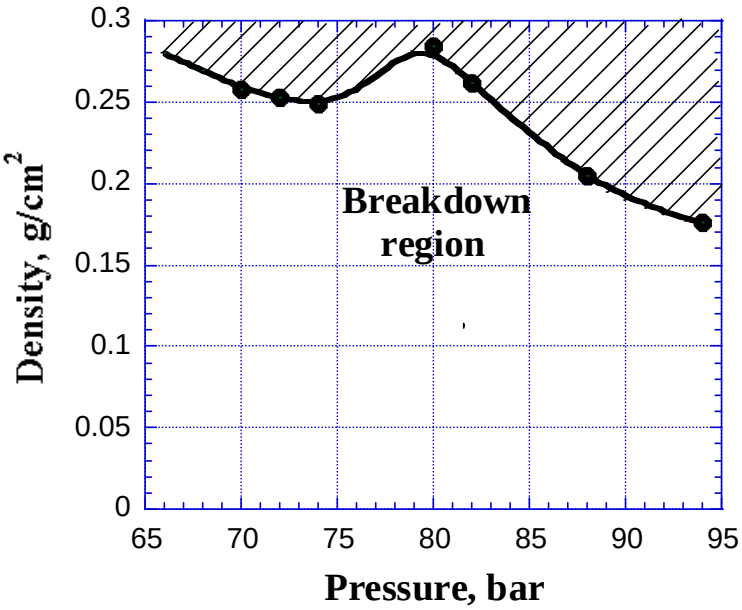

Fig. 4. Pressure-density diagram depicting the breakdown region in supercritical CO_2: point-to-plane configuration, breakdown voltage 10 kV.

The results for point-to plane-configuration (Fig. 4) suggest that another critical parameter affecting the electrical breakdown is the density of the supercritical CO_2. The breakdown was initiated using peak pulse voltage of 10 kV. Electrical breakdown was observed even at pressures as high as 100 bar and temperature as high as 373 K due to the relatively low density. However, in the vicinity of the critical point plasma was not produced due to the high critical density of the SC CO_2. The Pashen's law would represent constant density line in Fig. 4. In the supercritical state, the non-linear dependence of breakdown voltage from the density is observed with pronounced maximum effect in the region close to the critical point. Further research is needed for complete understanding of the breakdown in supercritical conditions.

As mentioned in the introduction, supercritical plasmas offer a novel approach for effective cleaning and waste treatment technologies. This original method also provides opportunity for material synthesis and surface modification. Supercritical plasma can be used as a unique process combining the advantages of supercritical fluids such as penetration in small cracks, liquid free processing, and low operational cost with the advantages of plasma treatment. Supercritical plasma cleaning will be compatible with most metals, ceramics and plastics, because supercritical CO_2 does not corrode their surfaces. The pressures and temperatures sufficient for effective processing are easily attainable with the modern pressure pumps. By-product vapors will not require scrubbing and can be vented into the atmosphere. Application of supercritical CO_2 plasma will be beneficial when there is a need for CO_2 cleaning so that the solvent can be reused. If in some applications chlorofluorocarbons still have to be employed, and the supercritical plasma offers a solution for cleaning the residues of these processes.

Non-thermal supercritical fluid plasma will allow environmentally friendly synthesis of novel materials eliminating the problem of recycling and reuse of residue solvents. Plasma polymerization under supercritical conditions may not result in a crosslinked polymer, which is typically produced by plasma. This would extend the variety of polymers that can be produced by plasma treatment. Plasma produced thin film are extensively used in chip manufacturing industry. Chemical fluid deposition (CFD) as alternative to chemical vapor deposition (CVD) was recently implemented in thin film production. Including plasma in the CFD process may increase its efficiency in analogy with the well-known plasma enhanced chemical vapor deposition (PECVD).

5. Conclusions

In this paper generation and possible applications of supercritical CO_2 plasma are discussed. The initiation of pulsed corona discharge is studied using wire-to-plane and point-to-plane configurations. It is found that a relatively large area exists where plasma generation is possible with relatively low breakdown voltages.

Pressure, temperature, and density in the SCF region are the important parameters controlling abnormal behavior of breakdown voltages in this region. From practical point of view supercritical plasma offers interesting potential applications that include waste treatment, polymer synthesis, and surface processing.

References

[1] K. Nishikawa, I. Tanaka - J. Phys. Chem. **100**, 418 (1996).
[2] L. Taylor, Supercritical Fluid Extraction - John Wiley & Sons (1996).
[3] T. Ito, K. Terashima - Appl. Phys. Lett. **80**, 2854 (2002).
[4] E. Lock, A. Saveliev, L. Kennedy - Proceedings of AIChE Annual Meeting, San Francisco, November 16-21, (2003).
[5] E. Lock, A. Saveliev, L. Kennedy - 15th International Conference on Gas Discharge, Toulouse, France, September 5-10, (2004).
[6] E. Lock, A. Saveliev, L. Kennedy - IEEE Trans. Plasma Sci. **33**, 850 (2005)
[7] C.E. Klots, R.N. Compton - J. Chem. Phys. **69**, 1636 (1978).
[8] I. Shkrob - J. Phys. Chem. A **106**, 11855 (2002).

Comparison of the Efficiency of Nanosecond Gas Discharge and Laser Flash-Photolysis in Initiation of Combustion

I.N. Kosarev[1] , E.N. Kukaev[1] , S.M. Starikovskaia[1] , A.Yu. Starikovskii[1]

[1] *Physics of Nonequilibrium Systems Laboratory, Moscow Institute of Physics and Technology, Institutskii lane,9, Dolgoprudny 141700 Russia*

Abstract

Measurements of ignition delay time for combustible gas mixtures with N_2O as an oxidant in a case of autoignition, ignition by high-voltage nanosecond gas discharge and ignition by excimer laser flash-photolysis have been performed. Experimental data for temperature range 1100-1700 K and pressure range 0.3–0.9 atm are represented and analyzed.

1 Introduction

The problem of the uniform fast ignition of combustible mixtures is of great importance. The question of the efficiency of using nonequilibrium plasmas for initiation of combustion still remains open. In a case when high-voltage nanosecond discharge us used for artificial initiation of ignition, it is possible to excite gas mixture homogeneously in a large volume and to produce ionized, dissociated and excited species practically instantly in comparison with typical time of ignition. The relative role of different species in initiation of combustion is under discussion now. To check the role of excited and dissociated species we organized special set of experiments with excitation by laser flash-photolysis with dissociation of molecules of the mixture at wavelength of 193 nm.

2 Experiment

The diagnostic system used for ignition by the discharge, described in details elsewhere ([1], [2]) was modified to control ignition by laser flash-photolysis. A scheme of experimental setup is represented in Fig. 1. gas mixture was heated by the shock wave. A flash of UV-radiation of ArF excimer laser ("Center of Physical Devices" production, Troitsk, $\lambda = 193$ nm) was organized behind the reflected shock wave. The laser radiation was supplied to the dielectric section of the shock tube through the MgF_2 optical window perpendicularly to the shock tube axis in the same cross-section were we performed measurements in a case of the ignition by nanosecond discharge. Laser spot had approximately rectangular shape with 5×21 mm dimensions and was controlled by special sensible paper. The synchropulse to trigger the laser was produced at the instant the reflected shock wave arrived at measurement cross-section. The time delay between the synchropulse and laser flash was a few μs. The schlieren system consisted of three He-Ne lasers mounted at different points along the shock tube and three photodiodes (PD). The gas density (ρ_5), pressure (P_5), and temperature (T_5) behind the reflected shock wave were determined from the known initial gas mixture composition, the initial pressure, and the velocity of the incident shock wave, using conservation laws and assuming that relaxation was complete and chemical reactions frozen. Thermodynamic data were taken from [3].

A piroelectric detector (PEM21) with 21 mm diameter of receiving site was used to determine energy input from laser radiation into the gas. Signal from PEM21 was controlled every time before the experiment, when the system was pumped up to 10^{-2} Torr and then during the experiment. Knowing spectral transmission of MgF_2 windows in this spectral range (were controlled by Varian Cary50 Spectrophotometer) we calculated energy input into a gas. We organized experiment so, that energy input in the discharge and energy input from a laser were within one order of magnitude. We controlled initial

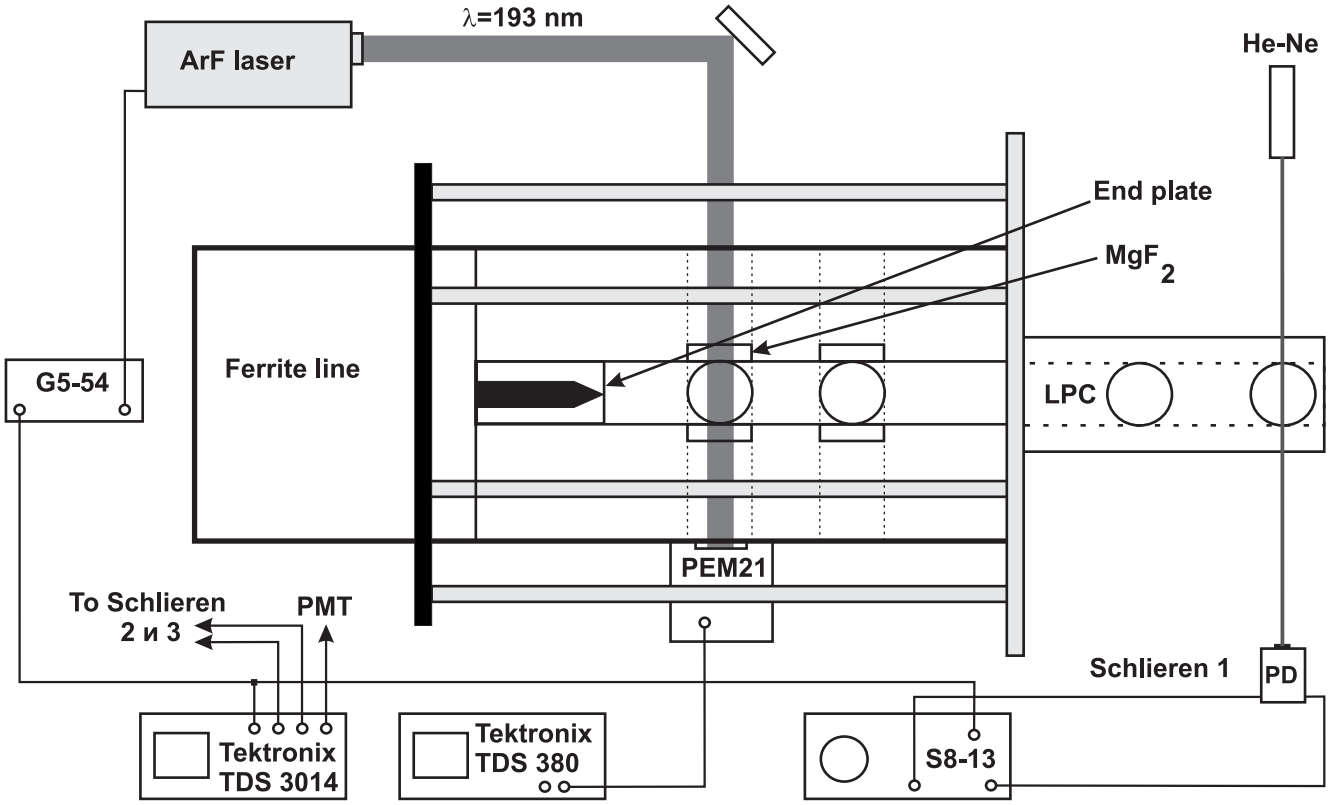

Figure 1: Scheme of the experimental setup: LPC - low pressure cell of a shock tube; PM - photomultiplier; PEM21 - energy meter; G5-54 - pulse generator.

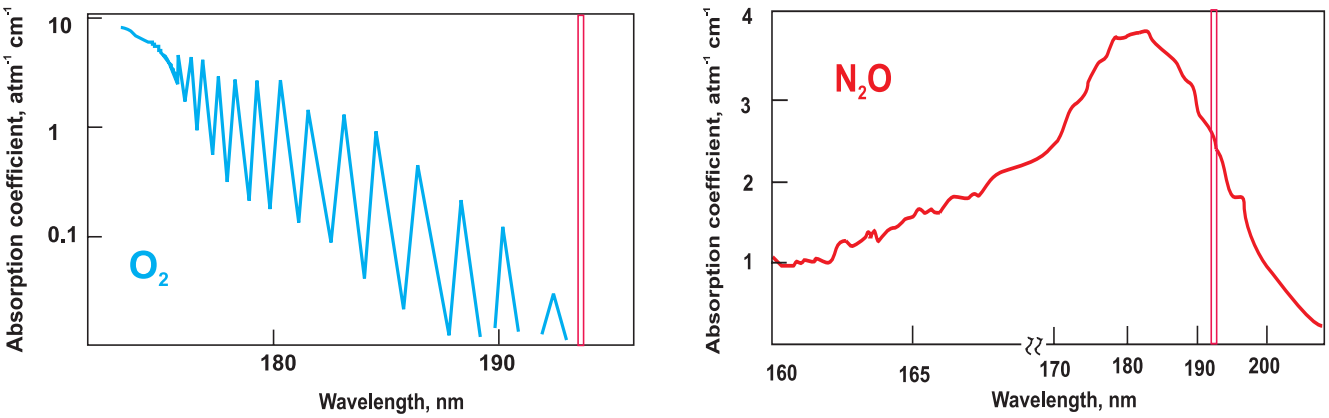

Figure 2: Cross-sections of absorption for oxygen and N_2O in UV-range of spectrum [4].

gas pressure and shock wave velocity, and parameters behind the reflected shock wave were calculated as in the previous case. Ignition delay time was calculated from the OH emission at 306 nm.

The combustion process was investigated using emission spectroscopy. Emission generated in the course of combustion was monitored in the direction perpendicular to the shock tube's axis at a distance of 55 mm from the end plate with the help of an MDR-23 monochromator (1.2 nm/mm, 1.2-m focal length, 1200 groove/mm, manufactured by LOMO), an FEU-100 photomultiplier (PMT) manufactured by MELZ, and a Tektronix TDS 3014 oscilloscope. Ignition time delay was determined from OH emission at 306.4 nm.

To compare action of the discharge and of flash-photolysis, we have repeated discharge experiments for investigated mixture. Simultaneously with OH emission in nanosecond time scale, we controlled nanosecond discharge parameters. The system for monitoring the electric parameters of the nanosecond discharge included a magnetic current gauge measuring the discharge current and capacitance gauges, located at two different points along the discharge section, and measuring the shape and amplitude of

the high-voltage pulse. The gauges were calibrated with a high-voltage signal of known amplitude and duration. The power deposited in the discharge was determined from the simultaneous measurements of the discharge current and voltage.

The experiments were repeated with the same mixture for autoignition, nanosecond discharge initiation of ignition and ArF flash-photolysis. Ignition delay times were compared for all cases. To make these experiments, we chosen N_2O as a main absorbing component. Really, N_2O is known to be very efficient as an oxidant. On the other hand, it absorbs radiation at 193 nm better than molecular oxygen. To demonstrate this, cross-sections of molecular oxygen and N_2O molecule at gas temperature 300 K are represented in the Fig. 2. With temperature increase, cross-section of molecular oxygen increases significantly, while cross-section of N_2O remains practically constant [5]. Nevertheless, at 1300 K cross-section of N_2O (approximately $3 \cdot 10^{-19}$ cm^2) is still by an order of magnitude higher than cross-section of O_2. So, the experiments were performed in gas mixtures N_2O:H_2:Ar = 1:1:8 and N_2O:H_2:Ar = 1:4:5. In part of our experiments 1% of CO_2 was added to a gas mixture for control of a gas temperature using emission in IR range of spectrum.

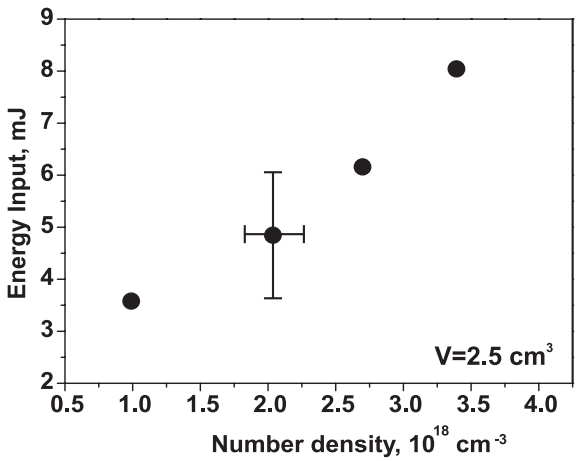

Figure 3: Energy input into a gas in experiments with flash-photolysis. N_2O:H_2:Ar = 1:1:8 mixture

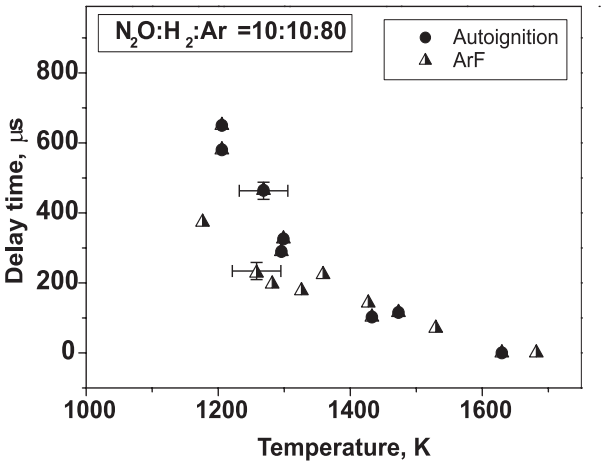

Figure 4: Ignition delay dependence upon gas temperature for gas mixture without additive of carbon dioxide.

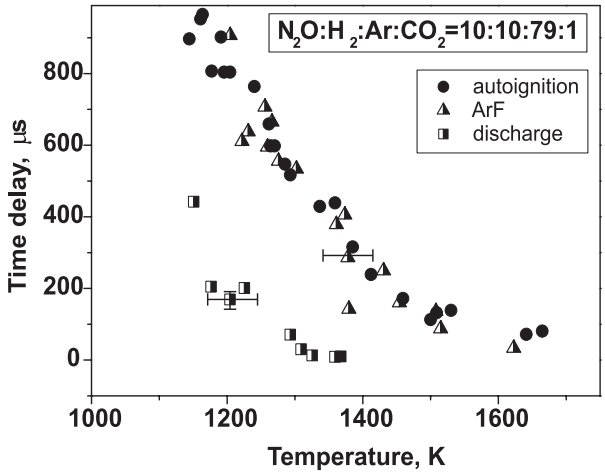

Figure 5: Ignition time delay dependence upon gas temperature for gas mixture with additive of carbon dioxide. Autoignition, ignition by ArF laser and ignition by the discharge (U=-110 kV). 10% N_2O in the mixture; gas pressure is 0.3-0.6 atm

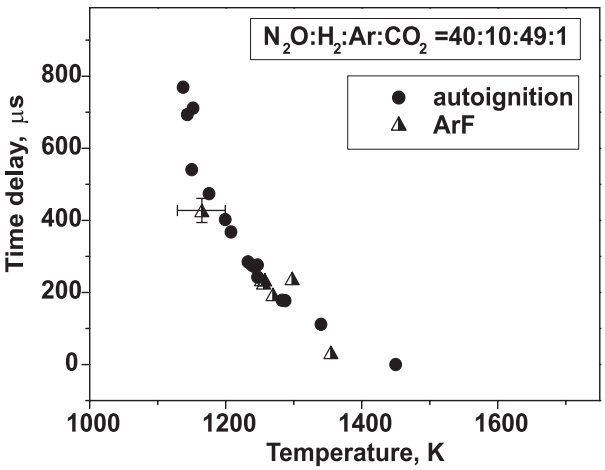

Figure 6: Ignition time delay dependence upon gas temperature for gas mixture with additive of carbon dioxide. 40% N_2O in the mixture; gas pressure is 0.7-0.9 atm

3 Results and Discussion

Typical energy input in a gas in experiments with flash-photolysis is demonstrated by Fig. 3. To obtain energy input per cubic centimeter, the energy value obtained by piroelectric gauge was divided by volume 5x20x25 mm^3, where 25 mm is a transverse size of a shock tube channel.

It is known that N_2O photolysis takes place via the reactions:

$$N_2O + h\nu = N_2 + O(^1D), \tag{1}$$

$$N_2O + h\nu = N_2 + O(^4S), \tag{2}$$

at the weight of reaction (1) is 99%. $O(^1D)$ is a metastable atom, its life time is 150 s, and usually it loses excitation in collisions with other species. It may destruct N_2O via the reactions

$$N_2O + O(^1D) = N_2 + O_2, \tag{3}$$

$$N_2O + O(^1D) = NO + NO. \tag{4}$$

On the other hand, $O(^1D)$ has to be active in chain initiation:

$$H_2 + O(^1D) = OH + H. \tag{5}$$

Reaction rates for reactions (3) and (4) are $4.9 \cdot 10^{-11}$ cm^{-3} and $6.7 \cdot 10^{-11}$ cm^{-3}, respectively [3]. Reaction rate for process (5) is $1.1 \cdot 10^{-10}$ cm^{-3}, that is for gas mixture were N_2O:H_2= 1:4, $O(^1D)$ losses due to reactions with N_2O may be significant. In gas mixture N_2O:H_2:Ar = 1:1:8 without CO_2 additives we were able to obtain a few distinct points, which is represented in the Fig. 4. Unfortunately, we were not able to reproduce these points systematically. The nanosecond discharge shifts the threshold by hundreds of K, which is typical for this discharge in different gas mixtures. Behavior of mixture with 1% CO_2 additive is illustrated by Fig. 5. Energy input into a gas under the action of nanosecond gas discharge in these experiments was within a range of $(3-5) \cdot 10^{-3}$ J/cm^3, which is in a good correlation with energy input in experiments with laser flash-photolysis. We performed experiments with gas mixture N_2O:H_2:Ar = 1:4:5 (also with 1% CO_2) to enhance N_2O fraction (Fig. 6) and focused laser radiation, but we obtained zero shift in the ignition delay under the action of flash-photolysis.

Preliminary calculations made by N.A.Popov [7] demonstrate that autoignition correlates quite well with our experimental data, while significant shift of ignition delay time can be reached only when $O(^1D)$ exceeds 10^{15} cm^{-3}. Estimations of possible density of $O(^1D)$ atoms based on energy input (Fig.3) give values in a range $(1-3) \cdot 10^{15}$ cm^{-3}, that exceeds a little bit the boundary of possible effect. We believe that it is possible to obtain delay time shift by ArF flash-photolysis analyzing gas mixture composition and relative role of reactions (3) and (4), which are responsible for $O(^1D)$ quenching.

4 Conclusion

So, autoignition, ignition by nanosecond discharge and ignition by laser flash-photolysis were investigated for N_2O-containing mixture. Shift of the ignition by nanosecond discharge has been obtained. Absence of shift for a case of laser flash-photolysis can be explained by reactions of excited atomic oxygen with N_2O molecule.

Acknowledgments

This work was partially supported under Grants by PR0-1349-MO-02 EOARD/CRDF, 05-02-17323- and 05-03-32975- of Russian Foundation for Basic Research; Project 1440 by ISTC; Award MO-011-0 of the CRDF. The authors are grateful to Dr.N.A.Popov for helpful discussions.

References

[1] S.A. Bozhenkov, S.M. Starikovskaia and A.Yu. Starikovskii, Combust. Flame, **133**, 2003, 133–146.

[2] 5. S.M. Starikovskaia, I.N. Kosarev, A.Yu. Starikovskii. 15th International Conference on MHD Energy Conversion and 6th Workshop on Magnetoplasma Aerodynamics for Aerospace Applications, 2005.

[3] V.P. Glushko (Ed.), Thermodynamical properties of individual species, Moscow: Nauka, 1978.

[4] E.-P.Roeth, R. Runke, G.Moortgat, R.Meller, W.Schneider. UV/VIS Absorption Cross sections and Quantum Yields for Use in Photochemistry and Atmospheric Modelling. Part 1. Inst. fur Chemie und Dynamik der Geosphare: Stratospharishe Chemie. Forschungszentrum Julich. **Jul-3341**, 1997.

[5] A.P.Zuev, A.Yu.Starikovskii, Russ. Journal of Applied Spectroscopy, **52**, 1990, 455.

[6] W. B. DeMore, C. J. Howard, et al., JPL Publication 97-4, "Chemical Kinetics and Photochemical Data for Use in Stratospheric Modeling Evaluation" N 12, Jan 15, 1997.

[7] N.A.Popov, private communication, 2005.

VUV Wavelength-Dependent Surface Modification of Polyolefins

F. Truica-Marasescu, M. R. Wertheimer

Groupe de Couches Minces (GCM), Department of Engineering Physics,
Ecole Polytechnique, Montreal, QC, H3C 3A7, Canada

Abstract

We report λ-dependent VUV photolysis of polyolefins under high vacuum and in a low-pressure ammonia gas. LDPE and BOPP samples have been exposed to the radiation generated by four different VUV sources. We use in-situ quartz crystal microbalance (QCM) measurements to monitor material ablation, while the near-surface chemical composition and the formation of unsaturation during photolysis is characterized by attenuated total reflectance infrared spectroscopy (ATR-FTIR) and X-ray photoelectron spectroscopy (XPS).

1. Introduction

The surface treatment of organic polymers for adhesion enhancement, for example, is now routinely performed with the help of electrical discharges [1]. Plasmas comprise a wide variety of different components like energetic particles, both charged (electrons, ions) and neutral (excited molecules, radicals, metastables), which react with a polymer in the outermost molecular layers, and photons that can penetrate much deeper into the material. Due to its complex nature, an understanding of interactions between the plasma and the surface can only be achieved by appropriately separating the contributions of each component type to the overall observed modification. Since the pioneering work of Hudis [2], it is known that vacuum ultraviolet (VUV) photons can give rise to an important photochemical contribution during plasma treatments of polymers. Hydrocarbon polymers display a very strong absorption band below 160 nm that originates from electronic excitation of carbon-carbon and carbon-hydrogen σ bonds [3]. The absorption of radiation with $\lambda < 200$ nm leads to homolytic scission of C-C, and C-H bonds, followed by the formation of radicals [4] on the polymer surface that can evidently undergo further reactions. In the outermost surface region (a few nm) these can react with other free radicals, including ones in the neighbouring gas phase, thereby incorporating new functional groups which are chemically bonded to the polymer. In the region where gas molecules have little or no access, for example in the "subsurface" (typically a few tens of nm), radicals can recombine among one another to form a linkage, or a radical can split a hydrogen atom from a neighbouring carbon atom to form a double bond (C=C) [4]. The present work is intended to investigate the interaction mechanisms of VUV radiation with polymer surfaces. For this purpose, samples of low-density polyethylene, LDPE and biaxially oriented polypropylene, BOPP have been exposed to the radiation generated by four different VUV sources, and the wavelength-dependent effects of the VUV radiation on their physico-chemical properties have been investigated under two different circumstances: (i) for the case of exposure in vacuum, and (ii) when specimens were irradiated in a reactive low-pressure ammonia atmosphere.

2. Experimental Methodology

The experimental set-up used for the VUV treatments is presented in detail elsewhere [5]. Briefly, it consists of a stainless steel "cross" chamber evacuated to a base pressure of about 5×10^{-6} torr ($\sim 7 \times 10^{-4}$ Pa), and then filled (when necessary) with pure ammonia, NH_3 at low pressure (p = 300 mtorr, or 40 Pa). The VUV sources used for this study are commercial resonant or excimer lamps with MgF_2 windows (cut-off wavelength, $\lambda_c = 112$ nm, all from Resonance Ltd., Barrie ON, Canada), based on radiofrequency (r.f.) discharges in noble gases. Their main characteristics are shown in Figure 1.

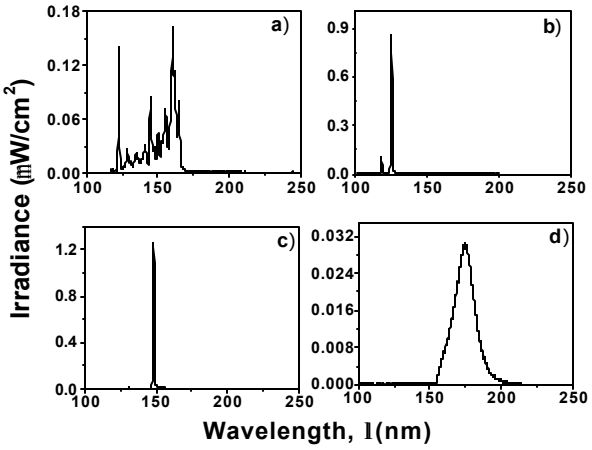

Figure 1 Intensities, I and spectral distributions of the VUV radiation emitted by the a) D_2Ar (I_{tot} = 1.8 mW/cm^2); b) resonant Kr, KrL (I_{tot} = 1.2 mW/cm^2) ; c) resonant Xe, XeL (I_{tot} = 1.8 mW/cm^2) ; and d) Xe excimer, XeE (I_{tot} = 0.6 mW/cm^2) lamps, measured at d = 4.0 cm.

For the case of treatment (i), in-situ mass change measurements during irradiations were carried out using a QCM (Phelps Electronics Inc.) placed perpendicularly to the impinging photon flux, at a frontal distance of d = 4.0 cm. Real mass changes result in frequency shifts which are recorded using a Philips PM 6669 universal frequency counter connected to a personal computer through a GPIB interface. Thin polymer films were prepared on quartz crystals (Xinix, 5 MHz, with gold electrodes from Phelps Electronics Inc.) by dip coating using solutions of LDPE (Chevron Phillips Company, 2% w/w in xylene, 80°C), and BOPP (3M Company, 2% w/w in xylene, 100°C). The irradiation dose, D, has been calculated using the following formula:

$$D = \Phi \times t \qquad (ph/cm^2) \qquad (1)$$

where Φ is the photon flux impinging on the polymer surface (ph/cm^2/s), and t is the treatment duration (up to 4200 seconds).

For the case of treatment (ii), the polymer samples (4x4 cm squares of commercial films) were mounted on a stainless steel sample holder, which can move axially within the treatment chamber, over a maximal distance of 10 cm. This allowed us to vary the sample distance, d, with respect to the lamp window, and thereby also the VUV power density arriving at the polymer surface, according to the Beer-Lambert law:

$$I_s = \int_{\lambda} \frac{I_0(\lambda)}{d^2} \exp\left(-\alpha(\lambda) \cdot p \cdot d\right) d\lambda \qquad (W/cm^2) \qquad (2)$$

where I_0 and I_s are the intensities at the MgF_2 window and at the polymer surface, respectively; α is the absorption coefficient of ammonia (NH_3) [6] (in cm^{-1}atm^{-1}); p (atm) is the NH_3 pressure, and d (cm) is the distance between sample and the MgF_2 window.

Following the same protocol presented in ref. 5 and 6, we investigated the physico-chemical effects produced by the treatments using a combination of surface analytical techniques. These methods included X-ray Photoelectron Spectroscopy (XPS), and Fourier Transform Infrared Spectroscopy in the Attenuated Total Reflectance configuration (ATR-FTIR), using a germanium prism.

3. Results and Discussion

3.1 VUV Irradiation in Vacuum

The mass variations, Δm for LDPE and BOPP during irradiation in vacuum with all four VUV sources are presented in Fig. 2, as a function of irradiation dose, D.

Values of the etch rate, R_0 (ng/photon), defined as the initial slope of the Δm versus D curve, are summarized in Table 1.

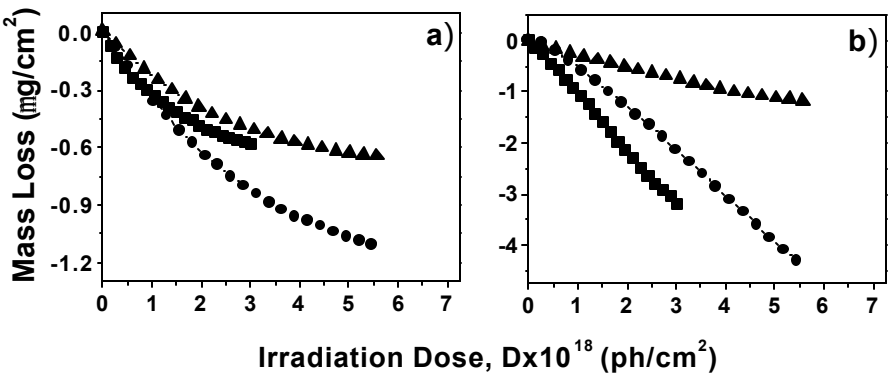

Figure 2 Mass losses for a) LDPE; and b) BOPP during irradiation with the KrL ( ), XeL ( ), and D_2Ar ( ) VUV sources as a function of the irradiation dose, D.

Table 1: Initial etch rate, R_0 for the investigated polymers.

Polymer	Lamp	R_0 x 10^{-15} (ng/ph)
LDPE	KrL	0.42±0.02
	XeL	0.34±0.02
	D_2 Ar	0.24±0.01
	XeE	Very small
BOPP	KrL	0.98±0.03
	XeL	0.50±0.07
	D_2 Ar	0.29±0.04
	XeE	Very small

Since the absorption coefficient, α of both polyolefins increases with decreasing λ, α (KrL) > α (XeL) > α (D_2Ar) > α (XeE) [3], it is not surprising to observe the same trend for R_0 values: R_0 (KrL) > R_0 (XeL) > R_0 (D_2Ar) (see Table 1). Note that R_0 was immeasurably small under irradiation with the XeE lamp, most probably due to the fact that very little VUV radiation with λ > 160 nm is absorbed by both LDPE and BOPP samples [3, 6]. However, we observed that the etch rates, R(D), continuously decreased with increasing D values (see Fig. 2). The explanation resides in structural changes (formation of double bonds and crosslinking) within the polymer near-surface layer [2, 4, 7]. Since C=C bonds absorb at λ = 180-190 nm [4], a region where our VUV sources emit very little, the formation of unsaturation tends to lower α, and hence also the value of R(D). We investigated this hypothesis by means of ATR-FTIR. Figures 3 a) and b) show the difference spectra of LDPE and BOPP, respectively, following 60 min of KrL irradiation. Regardless of λ of the source, VUV irradiation of LDPE gives rise to three new absorption bands at 965, 909, and 888 cm^{-1}, which can be assigned to *trans* vinylene -CH=CH-, vinyl -CH=CH_2, and vinylidene >C=CH_2 groups, respectively, and to a shoulder at 3050 cm^{-1} assigned to =CH_x (x = 1,2) stretch vibrations in unsaturated hydrocarbons (see Figure 3 a). VUV irradiation of BOPP with the KrL, XeL and D_2Ar lamps produces only chain-end double bonds, as proven by the two new IR bands at 909 and 888 cm^{-1}, and the shoulder near 3000 cm^{-1}. Although the type of alkene groups seems to be a function only of the nature of the polymer, their concentrations was found to depend strongly on λ used for irradiation [5]. In agreement with the previously presented QCM results, irradiation with XeE lamp produced no measurable structural changes at the surface of both polyolefins.

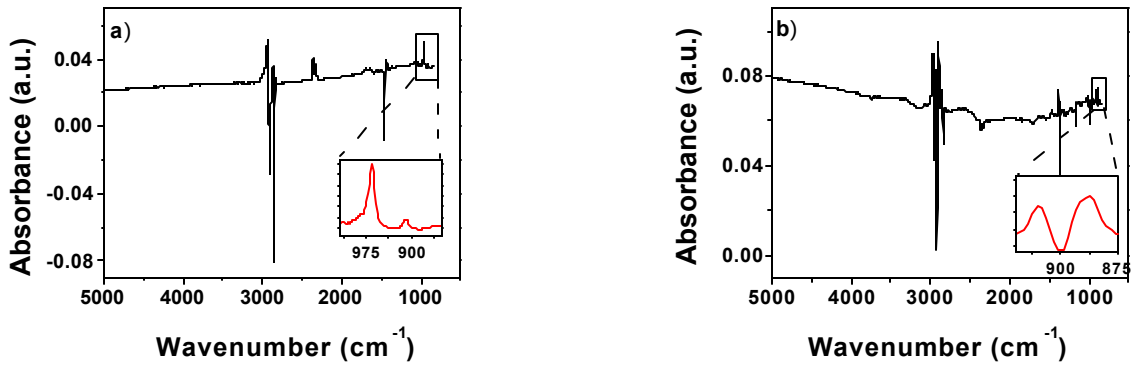

Figure 3 FTIR-ATR difference spectra between irradiated and pristine a) LDPE and b) BOPP; irradiated samples were treated for 60 min with a) KrL (D = 2.88 x10^{18} ph/cm^2). The inserts show the newly- formed bands; in all cases 200 spectra were accumulated, resolution 4 cm^{-1}.

3.2 VUV Irradiation in Low Pressure Ammonia

The results presented in section 3.1 suggest that KrL and D_2Ar lamps efficiently activated the polyolefins' surfaces, while the XeE lamp was found to produce no measurable effect. Gaseous ammonia absorbs in the 112-220 nm spectral range; since its bond energy is approximately D_0 (H-NH_2) = 4.4 eV, the absorption of energetic VUV photons ($h\nu$ > 6.2 eV) will lead to photo-dissociation of the NH_3 molecule, to produce amino ($NH_2^{\bullet}$) and imino ($NH^{\bullet}$) radicals in various excited states [6]. Using emissions from the three above-mentioned sources for polymer irradiation in low-pressure NH_3 gas, three types of irradiation experiments have been carried out:
(1) Kr (resonant), radiation which efficiently activates both ammonia molecules and the polymer surface, (2) D_2Ar, radiation which efficiently activates the polymer surface, but not the gas phase; and finally(3) Xe (excimer), radiation which is absorbed only by NH_3 molecules, producing NH and NH_2 radicals that may possibly react with the unactivated polymer surface.
Therefore, it is possible to investigate the relative importance of surface and/or gas phase activation to the overall reaction using this set of experiments. In Figures 4 a) and b) the evolutions of nitrogen, [N], and oxygen, [O], surface concentrations (determined by XPS) are plotted versus I_s for VUV treated LDPE using the Kr and the D_2Ar lamps, respectively, both for total durations of 60 min. Using the KrL lamp (Fig. 4 a) we can obtain high [N] values (up to 25%), roughly proportional to I_s, until saturation is reached near 3 mW/cm^2. The presence of some oxygen ([O] ≤ 5%) can be attributed to reactions between long-lived radicals or unstable functional groups created during the VUV irradiation with molecular oxygen or water vapor when the samples are subsequently exposed to ambient atmosphere [5, 7]. Regarding Fig. 4 b, corresponding to D_2Ar irradiation, the situation is seen to be very different: while only 1.5 % [N] is incorporated into the LDPE surface, [O] is seen to rise to nearly 8%. This can be attributed to the relatively high degree of surface activation of the polymer, accompanied by inefficient photo-dissociation of NH_3 in the gas phase [6]. Finally, regarding treatment (3), XeE radiation, no measurable nitrogen incorporation was detected by XPS on LDPE. Based on these results, we believe that although simultaneous activation of gas and solid phase might not always be necessary, it can greatly enhance the degree of surface modification for engineering the physico-chemical properties of polymers.

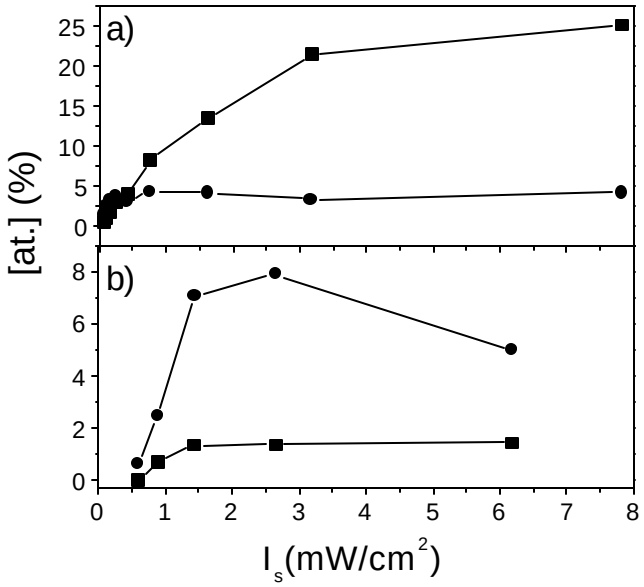

Figure 4 Surface concentrations (in at. %) of nitrogen, [N] ( ), and oxygen, [O] ( ), incorporated during irradiation of LDPE for 60 min in flowing NH_3 (p = 300 mtorr) with the Kr lamp a), and the D2Ar lamp b), as a function of I_s.

4. Conclusions

We show that during the initial stages of photolysis in vacuum, the etch rate, R (in ng/ph), of the investigated polyolefins rises with decreasing λ, which correlates very well with their λ-dependence of VUV absorption coefficients, α. However, with increasing irradiation dose, D, R tends to gradually decrease, due to near-surface structural changes, namely the creation of C=C bonds and crosslinks. For irradiation in low-pressure NH_3 gas, XPS measurements of nitrogen up-take at the surface have proven that the mechanism involves simultaneous, synergetic activation (formation of free radicals) of both the solid and gas phases, followed by heterogeneous reaction of these chemically activated species.
The data presented here, based on complementary experimental techniques, provide a coherent, self-consistent picture of the VUV photolysis of polyolefins both in vacuum and in a reactive gas, along with valuable new information about the mechanisms in the photochemical/plasma surface modification of polymers.

Acknowledgement:
This work is supported by grants from the Natural Sciences and Engineering Research Council of Canada (NSERC)

References:

[1]: M. R. Wertheimer, L. Martinu, J. E. Klemberg-Sapieha, G. Czeremuszkin, in Adhesion Promotion Techniques: Technological Aplications (K. L. Mittal, A. Pizzi Eds.) Marcel Dekker Inc., New York, pp 139-173 (1999)
[2] M. Hudis, J. Appl. Polym. Sci **16**, 2397 (1972)
[3] S. Onari, J. Phys. Soc. Jap. **26**, 500 (1969)
[4] V.E. Skurat, Y. Dorofeev, Die Angewandte Makromolekulare Chemie **216**, 205 (1994)
[5] F. Truica-Marasescu, M. R. Wertheimer, Macromolecular Chemistry and Physics **206**, 744 (2005)
[6] H. Okabe, *Photochemistry of Small Molecules*, John Wiley & Sons, New York 1978
[7] F. Truica-Marasescu, M.R. Wertheimer, Journal of Applied Polymer Science **91**, 3886 (2004)

Microstructural investigation of YSZ thermal barrier coatings fabricated by hybrid plasma spraying

J.Q. Li, H. Huang, M. Kambara, K. Eguchi, T. Yoshida

Department of Materials Engineering, The University of Tokyo, Tokyo, Japan

Abstract

Zirconia-yttria thermal barrier coatings fabricated by hybrid plasma spraying have fine and sophisticated microstructure. For a comprehensive analysis on the microstructure over the whole coatings, chemical etching method using HF acid was attempted. After being etched, the splat structure and columnar grains within splats were observed clearly in thermal plasma sprayed coatings. The etching procedure further revealed a nano-sized structure of twin variant of t' phase in the spraying PVD coatings. These results clearly show an effectiveness of this technique for an investigation of the microstructures of both the sprayed and PVD coatings.

Keywords: TBCs, Microstructure, Etching, Plasma spraying

Introduction

Yttria-stabilized Zirconia (YSZ) is the top candidate material for thermal barrier coating due to its high melting temperature, low thermal conductivity, relative high thermal expansion coefficient matching with that of metallic substrates and other superior physical properties. Plasma spraying (PS) and Electron beam-physical vapor deposition (EB-PVD) are well-developed techniques to fabricate YSZ coatings with characteristic structures [1]. In plasma spraying, molten droplets of a desired materials impact on substrate and undergo rapid spreading and solidification. The solidified droplets called splats, are the basic building units of PS coatings. Splats are usually composed of columnar grains with the width often less than 100 nanometers due to high cooling rate [2]. EB-PVD coating, on the other hand, is characterized by its structure in which feather-like columns with diameter at a micron scale, intercolumnar pores, subcolumns, and nanopores were present [3,4]. In contrast, Hybrid Plasma Spraying (HYPS) is a novel and promising technique which enables deposition of the coatings with plasma powder sprayed and/or spraying PVD columnar structures [5,6]. Such HYPS coatings exhibit in general more sophisticated microstructure compared to that produced by PS and EB-PVD.

Structural knowledge such as grain size, growth direction on YSZ coatings is obtained by TEM and SEM. Such structural information is important to understand the coating formation and the resultant high temperature performance. However, it is practically difficult to evaluate the variations of the microstructure over a wide area of the coating [7]. Chemical etching may be the one of the effective techniques to facilitate this.

Only a few papers were reported on the chemical etching of YSZ coatings [8]. This is probably because zirconia is chemically inert against most of the corrosive chemicals. In the present paper, therefore, the etching with HF acid at ambient condition was attempted to show the characteristic structures of the HYPS processed YSZ coatings.

Experimental

The YSZ coatings were deposited by a novel Twin Hybrid Plasma Spraying System, which is equipped

with two hybrid plasma torches and is capable of the combination of plasma PVD, CVD and/or spraying techniques. The splat, columnar, and their composite structures have been achieved through precise control of powder size, powder feeding rate, RF input power, etc. The detail of processing conditions can be found elsewhere [5,6].

Table 1 The processing conditions of HYPS

Parameters	**Powder spraying**	**Spraying PVD**
Powder size	63-88μm	5-15μm
Substrate holder	Rotated	Stationary, water cooled
DC/RF power	8/100 KW	8/70 KW
Plasma gas (slm)	DC: 10Ar RF: 170Ar, 30H_2	DC: 10Ar RF: 85Ar, 15H_2
Powder carrier gas	4 slm, Ar	4 slm, Ar
Feeding rate	15 g/min	2 g/min
Deposition time	7min	3.5min
Coating thickness	870μm	550μm

In the present study, two typical specimens were prepared. One is plasma sprayed coating and the other is spraying PVD coating. The general processing conditions are listed in Table 1. The coatings were deposited on the graphite block so that only the top coat was removed easily from the substrate for observation. The removed coating segments were embedded in resin, sliced and polished up to 0.1μm in surface roughness. The whole specimens were dipped into HF acid (mass 50%) for various durations, and rinsed in water with supersonic facility and dried afterwards.

The microstructure of the coatings was analyzed using a laser microscope (KEYENCE, VK-8510) and a field-emission scanning electron microscope (FE-SEM, JEOL, JSM-6340F). The phase was identified by X-ray diffraction (XRD, MAC Science Co. Ltd., MXP18XHF).

Results and Discussion

I. Microstructure of plasma sprayed coating

Figure. 1 shows the optical micrographs of the cross-section of the plasma sprayed coating which was etched in HF acid for different soaking durations. From the un-etched sample (Fig. 1a), we can not observe clear boundaries between splats except some macro cracks and pores. In contrast, after being etched for 5min (Fig. 1b), splat form appeared clearly and exhibited well-flattened, wavy structure with a thickness of about 2-3 μm. It also indicates that the splat boundary was etched more easily than the splat body due to its higher reaction rate with HF acid. Figure 1 (d) shows the morphology of the specimen etched for 15min. The splats boundary was etched heavily and exhibited the huge gaps between the splats with a width up to 1μm. Some big holes were also observed within the splat body, indicating the over-etching by HF acid. As a result, 5-10 min etching are found to be an appropriate condition for etching the plasma powder sprayed coatings.

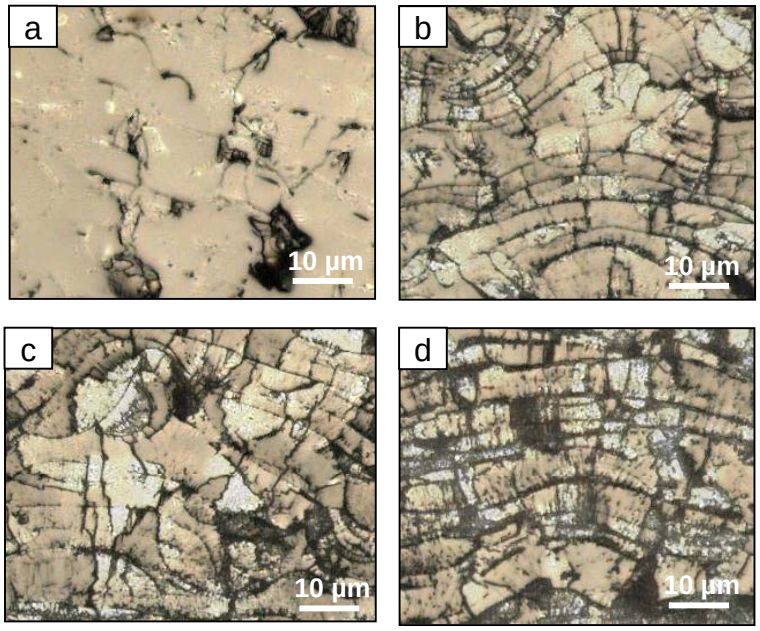

Fig.1 Optical micrographs of a sprayed coating etched for (a) 0min (b) 5min (c) 10min (d) 15min.

Figure 2 is a magnified SEM micrograph of the etched section. Not only splat boundaries (arrow A) but also columnar grain boundaries (arrow B) within the splats were observed clearly. The columns in a single

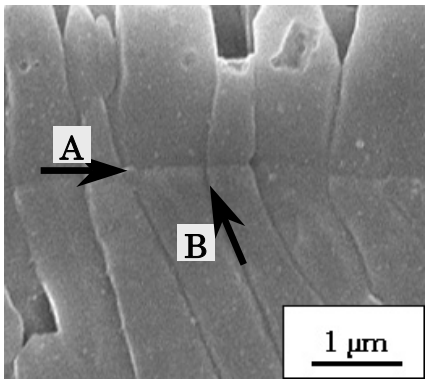

Fig. 2 SEM micrograph of cross-section of plasma sprayed coating after etching for 10min

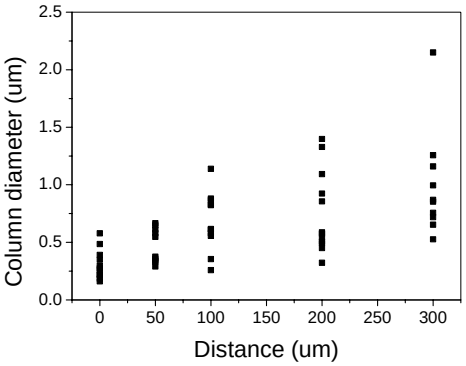

Fig. 3 Average column diameters of splats with different distances from the bottom of the coating

splat are approximately parallel each other. Grain size has a large distribution within a splat from 100 nm to 1μm. Furthermore, the width of each column is not uniform from its bottom to top. The columnar crystals above and below the splat boundary contact well and have the approximately same diameter and grain shape. It is similar to the columnar grains grown continuously within two splats reported by others [9].

The above results show that the nano structures appeared by an etching with HF acid. As a result, the structural information over the whole coating, such as the flattening degree of molten droplet, columnar grain size, can be evaluated. The variation of average column diameter of splats through the coating thickness is analyzed in Fig. 3, as a function of distance from the bottom of the coating. The distance ranges from 0 to 300 μm. Although the rather scatters, at least the average column diameters increase with the distance. This tendency is an indication that the grains growth rate reduced during deposition as a result of thermal insulting effect of the underlying grains.

II. Microstructure of plasma spraying PVD coating

PVD coatings normally have finer structure than plasma powder sprayed coatings. No structural information was obtained from the un-etched cross-section of the spraying PVD coating, as shown in Fig. 4a. However, after etched for 3min, fine cross-bracing columnar grains became visible and showed wider column width compared to that of the columns in EB-PVD coating, as observed in Fig. 4b. The width of the cross-bracing structure is less than 1.5 μm on average. Figure 4c demonstrates the morphology of the coating cross-section etched for 10min. In this case, finer cross-bracing grains were destroyed by HF acid. In PVD case, therefore, an appropriate etching time was considered to be 3 min.

Figure 5a shows the TEM morphology of the same specimen shown in Fig. 4. Large PVD grains were observed clearly and cross-bracing structure was also found inside the grains. In comparison Fig. 5a with SEM image shown in Fig. 5b, it was found that both TEM and SEM images showed the nearly identical microstructure. That is, the size and shape of the fine cross-bracing grains were preserved after the etching. This result, therefore, confirms that the etching is a powerful technique to observe the fine and complicated structure of YSZ coatings produced by HYPS.

Only the *t'* phase was identified in the sprayed PVD coating by X-ray diffraction. In addition, the TEM diffraction pattern (shown in the inset of Fig. 5a) confirmed that no *m*- and *c*- phases in the coating. Also, the TEM structural analysis revealed that the twin variant in *t'* phase grain and antiphase domain boundaries were present in the variant. Therefore, it is possible that such complicated microstructure was formed through the *c*-*t'* phase transformation during rapid cooling after deposition [10]. It is notified that there is no report on the finding of such a cross-bracing structure in PVD YSZ coating. Therefore, more detailed analysis is

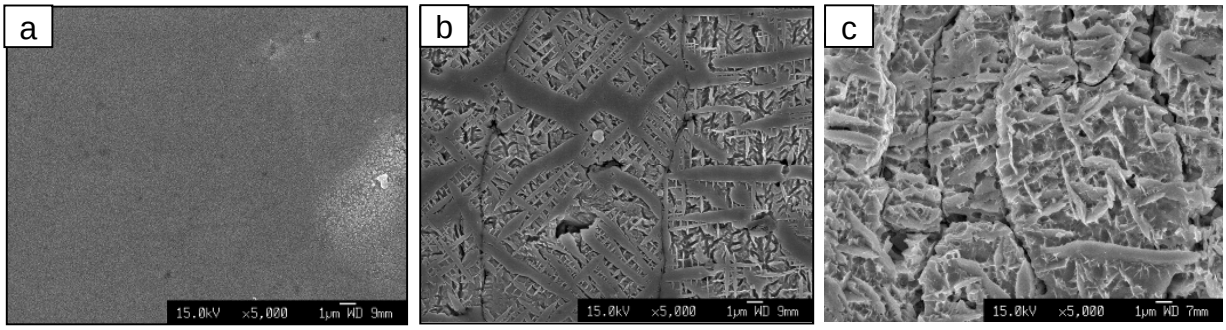

Fig. 4 SEM micrographs of plasma PVD coating etched for (a) 0min (b) 3min (c) 10min.

required to identify the formation of such a structure. Nevertheless, this structure has shown an enhanced reflectance for light in the infrared wavelength [11]. A real novel coating as TBC is expected to control this *t'* phase formation.

Conclusion

The chemical etching by HF acid was found effective to investigate the microstructure of YSZ thermal barrier coatings. After etching, the structural characteristics of plasma sprayed coating were observed at micron and nanometer scales by optical microscopy and SEM. A novel twin variant structure of *t'* phase was demonstrated in spraying PVD coating by HF etching, which was confirmed by TEM characterization.

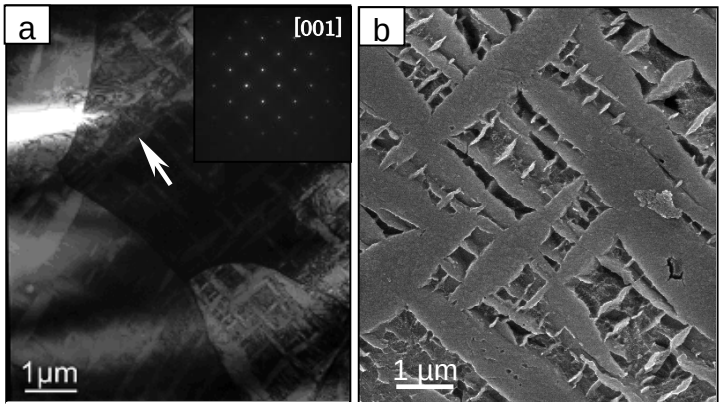

Fig. 5 Micrographs of plasma PVD coating (a) TEM, the white arrow shows diffraction position, (b) SEM, etched cross-section.

Acknowledgements

The authors acknowledge Prof. Ikuhara and his group for their efforts in the PVD sample observation by TEM. This work was surpported by NEDO as the Nano-coating Project.

Reference

[1] N.P. Padture, M. Gell, E.H. Jordan, Science. 296 (2002) 280.
[2] T. Chraska, A.H. King, Thin Solid Films 397 (2001) 30
[3] Y. Jung, T. Sasaki, T. Tomimatsu, Science and Technology of Advanced Materials, 4 (2003) 571
[4] N. Yamaguchi, K Wada, K. Kimura, etc., Journal of the Ceramic Society of Japan, 111-12 (2003) 883
[5] H. Huang, K.Eguchi, T.Yoshida, Sci. Technol. Adv. Mater. 4 (2003) 617.
[6] H. Huang, K.Eguchi, M. Kambara, T.Yoshida, Mater. Sci. Forum 475-479 (2005) 2883
[7] P.D. Harmsworth, R. Stevens, Journal of Materials Science, 27 (1992) 616
[8] K.R. Mikeska, S.J. Bennison, S.L. Grise, J. Am. Ceram. Soc. 83-5 (2000) 1160
[9] T. Chraska, A.H. King, Thin Solid Films 397 (2001) 40
[10] A.H. Heuer, R. Chaim, V. Lanteri, Acta metal. 35-3 (1987) 661
[11] T. Ma, M. Kambara, K. Eguchi, T. Yoshida, ISPC-17 (submitted)

On the Two-Temperature Modeling of Thermal Plasma Systems

Xi Chen [1] and He-Ping Li [2]

[1] *Department of Engineering Mechanics, Tsinghua University, Beijing 100084, China*

[2] *Department of Engineering Physics, Tsinghua University, Beijing 100084, China*

Abstract

In previous modeling studies for non-equilibrium thermal plasmas, different forms of energy conservation equations for electrons and heavy particles were employed by different authors. In this paper, the energy equations for electron and heavy-particle subsystems, which can be used for the modeling of kinetic and/or chemical non-equilibrium plasma systems, are derived in detail. For the LTE case, the energy conservation equations presented here can be reduced to the form being extensively employed for LTE plasma modeling.

Keywords Thermal plasmas, Non-equilibrium, Energy conservation equation, Theoretical derivation

1. Introduction

Non-Equilibrium phenomena often exist in thermal plasma systems, such as in the plasma regions near the arc electrodes, near a cold wall, near the outer edge of a plasma jet, etc. (e.g., [1, 2]). Since the electron mass is much less than the heavy-particle (atom or ion) mass, the energy coupling between electrons and heavy particles is rather weak, and thus at lower electron number densities, electrons might not transfer promptly their excess energy gained from an external electric field to heavy particles. The electron temperature may thus be different appreciably from the heavy-particle temperature and the plasma deviates from local thermodynamic equilibrium (LTE) state for many cases. Two-temperature (2-T), local chemical equilibrium (LCE) or non-LCE models are often employed to study the non-equilibrium plasma characteristics [3-20]. Numerous 2-T modeling results have been reported in past decades, such as those for arc plasmas [3-7, 10-13, 16-19], for plasma jets [8, 9, 15, 20], for radio-frequency (RF) and microwave (MW) plasmas, etc. However, so far there still exists some confusion in the available 2-T plasma modeling approaches, mainly in the formulations of the energy equations for the electron subsystem and for the heavy-particle subsystem. In the papers previously published [3-20], different forms of the energy conservation equations for electrons and heavy-particles were employed by different authors. And most of the employed equations even cannot be reduced to that for the LTE model if the plasma is assumed to be in the LTE state. Hence, it is worthy to re-examine the formulation of the energy equations suitable for the 2-T plasma modeling. In this paper, a theoretical derivation on the energy conservation equations of electrons and heavy particles used for modeling of kinetic and/or chemical non-equilibrium plasmas is presented with 2-T argon plasma as an example. The forms of the derived energy conservation equations are also examined for the limiting case of LTE plasmas.

2. Theoretical derivations

2.1. Assumptions

For simplicity, an argon plasma is considered in this study for deriving the energy conservation equations of electrons and heavy-particles with the following assumptions:

(1) The argon plasma system consists of four species, i.e., electrons *e*, atoms *Ar*, singly-ionized ions Ar^{+}, and doubly-ionized ions Ar^{++}.
(2) The argon plasma system is divided into two subsystems, i.e., electron subsystem, including free electrons and electrons in the excited energy levels of atoms and ions, and heavy-particle subsystem, including all of the translational degrees of freedom of atoms and ions. The electron and heavy-particle subsystems are characterized by electron temperature T_e and heavy-particle temperature T_h, respectively, and separate Maxwellian distributions of electrons and heavy particles are satisfied, respectively, with T_e and T_h as the characteristic temperatures.
(3) The species number densities have been calculated. For the 2-T LCE case, the four particle number densities can be calculated from the state equation, the quasi-neutrality condition and two 2-T Saha equations [21], respectively, for single and double ionizations. For the 2-T non-LCE case, two species conservation equations (e.g., for atoms and for doubly-ionized ions) are used to replace the two 2-T Saha equations, but for this case the related kinetic constants must be known.
(4) The forms of the continuity equation, mass-averaged momentum equation and electromagnetic field equations are the same as those used for LTE plasmas.
(5) The plasma flow is quasi-steady and in laminar regime.
(6) The thermodynamic and transport properties of argon plasmas are functions of the species number densities (n_j) and the temperatures (T_e and T_h).

2.2. Theoretical derivations

Based on the foregoing assumptions, the energy conservation equations for electron subsystem and for heavy-particle subsystem can be derived in a finite control volume by using energy balance, i.e., under steady state, the energy leaving the control volume should be balanced by the energy entering the control volume and the energy produced inside the control volume for each of the subsystems. Due to the paper space limit, only the final forms of the energy equations are presented in this paper as follows.

Electron energy conservation equation:

$$\nabla\cdot\left(\frac{5}{2}n_e k_B T_e \vec{v}\right)=\nabla\cdot\left(k_e\nabla T_e\right)-\nabla\cdot\left(\frac{5}{2}k_B T_e\vec{\psi}_e\right)+\vec{j}\cdot\vec{E}+\vec{v}\cdot\left(\nabla p_e\right)-U_{r,e}+\frac{5}{2}\frac{k_B}{e}\left(\vec{j}\cdot\nabla T_e\right)-\dot{E}_{el}-\dot{E}_{ex}-\dot{E}_{ion\text{-}rec} \tag{1}$$

Heavy-particle energy conservation equation:

$$\begin{aligned}\nabla\cdot\left\{\left[\frac{5}{2}\left(n_a+n_i+n_d\right)k_B T_h+\left(n_i E_{i,i}+n_d E_{i,d}\right)\right]\vec{v}\right\}=&\nabla\cdot\left[\left(k_a+k_i+k_d\right)\nabla T_h\right]-\nabla\cdot\left[\frac{5}{2}k_B T_h\left(\vec{\psi}_a+\vec{\psi}_i+\vec{\psi}_d\right)\right]-\nabla\cdot\left(\vec{\psi}_a E_{ex,a}\right)\\&-\nabla\cdot\left[\vec{\psi}_i\left(E_{ex,i}+E_{i,i}\right)\right]-\nabla\cdot\left[\vec{\psi}_d\left(E_{ex,d}+E_{i,d}\right)\right]+\vec{v}\cdot\nabla p_h+\vec{\tau}:\nabla\vec{v}-U_{r,h}+\dot{E}_{el}+\dot{E}_{ex}+\dot{E}_{ion\text{-}rec}\end{aligned} \tag{2}$$

In Equations (1) and (2), the subscripts *h*, *e*, *a*, *i* and *d* express heavy-particle, electron, atom, singly-ionized ion and doubly-ionized ion, respectively. *p*, *n* and *T* are pressure, particle number density and temperature; $\vec{\tau}$ viscous stress tensor; *e* and k_B elementary charge and Boltzmann's constant; *k* and U_r thermal conductivity and radiation power per unit volume; E_{ex} and E_i internal excitation energy and ionization energy; and $\vec{v}$, $\vec{\psi}$, $\vec{j}$

and $\vec{E}$ are velocity, particle diffusion flux, electric current density and electric-field intensity vectors, respectively.

The terms on the left-hand side of Equations (1) and (2) represent the convective energy transfer, while the first terms on the right-hand side of these two equations express the conductive heat transfer. $\dot{E}_{el}$ is the energy transferred in elastic collisions between electrons and heavy particles. $\dot{E}_{ex}$ is the energy loss (or gain, if negative) of the electron subsystem in excitation collisions between electrons and heavy-particles, whereas $\dot{E}_{ion-rec}$ is the energy loss (or gain, if negative) of the electron subsystem in ionization-recombination collisions between electrons and heavy-particles. The radiation energy loss for electrons and atoms can be calculated from experimental data or using a three-level collision-radiation model [22].

The terms related with diffusion flux of species *j* (*j*=*a*, *i*, *d* and *e*) on the right-hand side of Equations (1) and (2) represent the energy transfer due to diffusion process in the argon plasma system. Here there are two points should be emphasized for the calculation of the diffusion flux of species *j*: (i) The number flux of species *j* can be calculated by using Equation (19) in Ref. [23] without including the term related with externally applied electric field. The influence of the external electric filed on the energy transfer due to diffusion process is represented by the electron enthalpy transport term appearing on the right-hand side of Equation (1). (ii) In Equations (1) and (2), only two particle diffusion fluxes have to be calculated from pertinent concentration and temperature gradients, since the other two diffusion fluxes can be obtained using the relations $\vec{\psi}_e = \vec{\psi}_i + 2\vec{\psi}_d$ and $\vec{\psi}_a = -(\vec{\psi}_i + \vec{\psi}_d)$ [24].

2.3. Simplification of the energy conservation equations

In many previous studies (e.g., [5-7, 17-19]), the following additional assumptions were used:

(1) Double ionization can be neglected (i.e., argon plasma temperatures are lower).
(2) There is no change in excitation energy of atoms or ions.
(3) Only electron impact ionization and three-body collision recombination with electron as the third body are treated as the ionization-recombination mechanism.
(4) Pertinent Mach number is small so that the pressure work and viscous dissipation in the energy equations can be ignored.

Based on those additional assumptions, Equations (1) and (2) reduce to the following forms:

$$\nabla\cdot\left(\frac{5}{2}n_e k_B T_e \vec{v}\right) = \nabla\cdot\left(k_e \nabla T_e\right) - \nabla\cdot\left(\frac{5}{2}k_B T_e \vec{\psi}_e\right) + \vec{j}\cdot\vec{E} + \frac{5}{2}\frac{k_B}{e}\left(\vec{j}\cdot\nabla T_e\right) - U_{r,e} - \dot{E}_{el} - \dot{E}_{ion-rec} \tag{3}$$

$$\nabla\cdot\left\{\left[\frac{5}{2}\left(n_a + n_i\right)k_B T_h + n_i E_{i,i}\right]\vec{v}\right\} = \nabla\cdot\left[\left(k_a + k_i\right)\nabla T_h\right] - \nabla\cdot\left[\frac{5}{2}k_B T_h\left(\vec{\psi}_a + \vec{\psi}_i\right)\right] - \nabla\cdot\left(\vec{\psi}_i E_{i,i}\right) - U_{r,h} + \dot{E}_{el} + \dot{E}_{ion-rec} \tag{4}$$

In Equations (3) and (4), the energy loss related with ionization-recombination process can be expressed as

$$\dot{E}_{ion-rec} = k_{ion} n_e n_a E_{i,i} - \alpha k_{rec}\, n_e^2 n_i E_{i,i} \tag{5}$$

in which α is a factor introduced to account for such a fact that a part of the atoms formed in the recombination processes are initially in their excited state (*p*-level instead of *s*-level), and thus, the energy carried away by the third body (electron) will be less than $E_{i,i}$. The energy released in the transition from the excited level (*p*-level) to the ground level (*s*-level) has been included in the radiation power loss $U_{r,h}$. The energy exchange between electrons and heavy particles due to elastic collisions can be expressed as

$$\dot{E}_{el} = (2m_e / m_h)(\bar{\nu}_{ea} + \bar{\nu}_{ei}) n_e [(3/2) k_B (T_e - T_h)] \tag{6}$$

where $\bar{\nu}_{ei}$ and $\bar{\nu}_{ea}$ are the average collision frequency between electrons and ions [25], and between electrons and atoms [26], respectively.

Equations (3) and (4) can be used for non-equilibrium modeling of DC arc plasmas in subsonic, laminar regime. It can be seen that Equations (3) and (4) are somewhat different from their counterparts used in previous modeling studies for non-LCE case (e.g., [3, 7-11, 15, 17-20]), and even for the LCE case with $k_{ion} n_e n_a = k_{rec}\, n_e^2 n_i$ (e.g., [4-6, 16]) if α is not equal to 1.

In addition, for the case of RF and MW thermal plasmas, the term $(5/2)(k_B / e)(\vec{j} \cdot \nabla T)$ in Equations (1) and (3) will disappear since the electric current is alternative. For the plasma jets, all the terms containing the current density $\vec{j}$ will disappear.

2.4. Energy conservation equation for LTE plasmas

Although different forms of energy conservation equations of electrons and heavy particles for non-equilibrium modeling of thermal plasmas have been employed in previous references, not all of these energy equations can be reduced to the commonly used form of the energy equation for the limiting case of LTE plasmas. In our opinion, as one of the necessary conditions, the correct, self-consistent energy conservation equations of electrons and heavy particles, after combined, should be reduced to the energy equation extensively used for modeling of LTE plasmas if the plasma system is in kinetic and chemical equilibrium state.

For the limiting case of LTE plasmas, the electron temperature is equal to heavy particle temperature, and no net production of electrons occurs, i.e., $T_e = T_h = T$ and $k_{ion} n_e n_a = k_{rec}\, n_e^2 n_i$. By combining Equations (1) and (2) together, one can obtain

$$\begin{aligned} \nabla \cdot \left\{ \left[\frac{5}{2} (n_e + n_a + n_i + n_d) k_B T + (n_i E_{i,i} + n_d E_{i,d}) \right] \vec{v} \right\} &= \nabla \cdot [(k_e + k_a + k_i + k_d) \nabla T] + \vec{v} \cdot \nabla (p_e + p_h) + \vec{\tau} : \nabla \vec{v} - (U_{r,e} + U_{r,h}) \\ &- \nabla \cdot \left[\frac{5}{2} k_B T (\bar{\psi}_e + \bar{\psi}_a + \bar{\psi}_i + \bar{\psi}_d) + \bar{\psi}_a E_{ex,a} + \bar{\psi}_i (E_{ex,i} + E_{i,i}) + \bar{\psi}_d (E_{ex,d} + E_{i,d}) \right] + \vec{j} \cdot \vec{E} + \frac{5}{2} \frac{k_B}{e} (\vec{j} \cdot \nabla T) \end{aligned} \tag{7}$$

The total specific enthalpy of argon plasmas (h) is defined as

$$\rho h \approx \frac{5}{2}\left(n_e + n_a + n_i + n_d\right)k_B T + \left(n_i E_{i,i} + n_d E_{i,d}\right) \tag{8}$$

in which ρ is the mass density of argon plasmas.

According to the definition of reactive thermal conductivity for reacting gas mixtures in chemical equilibrium [24, 27], the term containing diffusion flux of species j (j = e, a, i, d) on the right-hand side of Equation (7) can be expressed as

$$-\nabla\cdot\left[\frac{5}{2}k_B T\left(\vec{\psi}_e + \vec{\psi}_a + \vec{\psi}_i + \vec{\psi}_d\right) + \vec{\psi}_a E_{ex,a} + \vec{\psi}_i\left(E_{ex,i} + E_{i,i}\right) + \vec{\psi}_d\left(E_{ex,d} + E_{i,d}\right)\right] = \nabla\cdot\left(k_r \nabla T\right) \tag{9}$$

where k_r is the so-called reactive thermal conductivity of argon plasmas [27].

In addition, the total pressure and radiation loss per unit volume of plasmas can be expressed as

$$p = p_e + p_h;\ \ U_r = U_{r,e} + U_{r,h} \tag{10}$$

Thus, the final form of Equation (7) can be written as

$$\nabla\cdot\left(\rho\vec{v}h\right) = \nabla\cdot\left(k\nabla T\right) + \vec{v}\cdot\nabla p + \vec{\tau}:\nabla\vec{v} - U_r + \vec{j}\cdot\vec{E} + \frac{5}{2}\frac{k_B}{e}\left(\vec{j}\cdot\nabla T\right) \tag{11}$$

where $k = k_e + k_a + k_i + k_d + k_r$ is the total thermal conductivity of argon plasmas. Equation (11) is the energy equation used extensively for the modeling studies of LTE plasmas. Particularly for the subsonic flow simulations, the pressure work and viscous dissipation in the energy equation can be ignored, i.e.,

$$\nabla\cdot\left(\rho\vec{v}h\right) = \nabla\cdot\left(k\nabla T\right) + \vec{j}\cdot\vec{E} + \frac{5}{2}\frac{k_B}{e}\left(\vec{j}\cdot\nabla T\right) - U_r \tag{12}$$

3. Conclusions

In this paper, the energy conservation equations for electron subsystem and heavy-particle subsystem used for non-equilibrium (including kinetic and/or chemical non-equilibrium) modeling of thermal plasmas are derived based on the energy balance in a finite control volume. The physical meanings of the terms appearing in the energy equations for electron subsystem and heavy-particle subsystem are discussed. The simplified form of the energy equation for the limiting case of LTE plasmas is consistent with that extensively employed in the literature. For investigating the characteristics of non-equilibrium plasmas, the following research work need to be conducted based on this primary study:

(1) The influences of the source terms related with elastic/inelastic collision processes and radiation processes on the non-equilibrium characteristics of plasmas should be clarified.

(2) The correct calculation of the thermodynamic and transport properties of non-equilibrium plasmas is one of the prerequisites for non-equilibrium modeling of thermal plasmas.

(3) The energy equations for electrons and heavy particles derived here can be extended for simulating the non-equilibrium characteristics of other gases, such as helium, nitrogen, oxygen, etc., with the similar derivation method. Perhaps, the source terms in the energy conservation equations need to be modified.

(4) For simulating the non-equilibrium plasma flow patterns in turbulent regime, the turbulent kinetic energy and its dissipation rate equations should be solved simultaneously with the continuity, momentum, energy and species conservation equations modified for the turbulent case.

Acknowledgment

This work was supported by the National Natural Science Foundation of China (Nos. 50336010, 10405015).

References

[1] J. F. Bott - The Physics of Fluids. 9, 1540 (1966).
[2] R. J. Giannaris, and F. P. Incropera - J. Quant. Spectrosc. Radiat. Transfer. 11, 291 (1971).
[3] H. A. Dinulescu, and E. Pfender - Journal of Applied Physics. 51, 3149 (1980).
[4] D. M. Chen, and E. Pfender - IEEE Transactions on Plasma Science. PS-9, 265 (1981).
[5] D. M. Chen, K. C. Hsu, and E. Pfender - Plasma Chemistry and Plasma Processing. 1, 295 (1981).
[6] K. C. Hsu, and E. Pfender - Journal of Applied Physics. 54, 4359 (1983).
[7] C. Delalondre, and O. Simonin - Colloque de Physique. 51, C5-199 (1990).
[8] C. H. Chang, and E. Pfender - Plasma Chemistry and Plasma Processing. 10, 473 (1990).
[9] C. H. Chang, and E. Pfender - Plasma Chemistry and Plasma Processing. 10, 493 (1990).
[10] J. J. Beulens, D. Milojevic, D. C. Schram, and P. M. Vallinga - The Physics of Fluids B. 3, 2548 (1991).
[11] O. Simonin, C. Delalondre, and P.-L. Viollet - Pure & Applied Chemistry. 64, 623 (1992).
[12] E. Meeks, and M. A. Cappelli - IEEE Transactions on Plasma Science. 21, 768 (1993).
[13] E. Meeks, and M. A. Cappelli - J. Appl. Phys. 73, 3172 (1993).
[14] M. I. Boulos, P. Fauchais, and E. Pfender - Thermal Plasmas: Fundamentals and Applications. Vol. 1, New York: Plenum Press. (1994).
[15] T. Kunugi, K. Ezato, T. Yokomine, and A. Shimizu - Fusion Engineering and Design. 28, 63 (1995).
[16] K. Charrada, G. Zissis, and M. Aubes - Journal of Physics D: Applied Physics. 29, 2432 (1996).
[17] J. Jenista, J. V. R. Heberlein, and E. Pfender - IEEE Transactions on Plasma Science. 25, 883 (1997).
[18] T. Amakawa, J. Jenista, J. Heberlein, and E. Pfender - Journal of Physics D: Applied Physics. 31, 2826 (1998).
[19] C. S. Wu, M. Ushio, and T. Tanaka - Computational Materials Science. 15, 302 (1999).
[20] Y. Bartosiewicz, P. Proulx, and Y. Mercadier - J. Phys. D: Appl. Phys. 35, 2139 (2002).
[21] Xi Chen, and Peng Han - J. Phys. D: Appl. Phys. 32, 1711 (1999)
[22] C. G. Braun and J. A. Kunc - Phys. Fluids. 30, 499 (1987).
[23] He-Ping Li, and Xi Chen - Chinese Physics Letters. 18, 547 (2001).
[24] J. N. Butler, and R. S. Brokaw - The Journal of Chemical Physics. 26, 1636 (1957).
[25] M. Mitchner, and C. H. Kruger, Jr. - Partially Ionized Gases. John Wiley and Sons, New York. (1973).
[26] R. S. Devoto - The Physics of Fluids. 16, 616 (1973).
[27] Xi Chen, and He-Ping Li - Int. J. Heat Mass Transfer. 46, 1443 (2003).

Atmospheric-pressure SiO_2 deposition using remote plasma source of integrated microdischarges

O. Sakai and K. Tachibana

Department of Electronic Science and Engineering, Kyoto University, Kyoto, Japan

Abstract

A new plasma-enhanced chemical vapor deposition (PE-CVD) scheme working at the atmospheric pressure was presented with experimental and numerical results. Dielectric barrier microdischarges were integrated on one plane by low driving voltage (~ 2 kV) in N_2 and O_2 mixture with their hollow structures leading to activation of O_2. Created O and O_3 coalesced with N_2 flow including tetraethoxysilane and gave rise to precursors. Deposition rate of SiO_2 significantly depended on the laminar flow rate due to change of diffusion flux to a substrate.

1. Introduction

One of the conventional schemes of thin-film deposition of high-quality semiconductor and dielectric layers has been plasma-enhanced chemical vapor deposition (PE-CVD) under low pressure less than 1 kPa in a vacuum chamber [1]. If the working gas pressure is shifted up to the atmospheric pressure, vacuum equipment can be removed, which leads to simple and low-cost reactor system for semiconductor and flat-panel-display industry.

Several methods of non-thermal plasma production at atmospheric pressure have been proposed so far, such as plasma jets, microwave discharges, radiofrequency discharges, and dielectric barrier discharges (DBDs) [2]. If we aim at replacing low-pressure PE-CVD with atmospheric-pressure PE-CVD, a stable discharge which is uniform over large area (or at least a stable line discharge with one-dimensional uniformity) is required, hopefully using low-cost gases like N_2. However, almost every method contains some problems against this goal. Most of the problems are attributed to high pd condition, where p is the discharge gas pressure and d is the discharge gap. The plasma source we used here is integrated microdischarges to reduce the value of pd by decreasing d by one or two orders of magnitude and to realize a stable palsma source for N_2 and O_2 by low discharge voltage.

In terms of application of these schemes to PE-CVD, there have been several reports on thin-film deposition using atmospheric-pressure glow discharges (APGDs) so far [3-6], and such studies are now limited to phenomenological understanding of the gas phase at the atmospheric pressure. Sawada *et al.* [3] set substrates in an APGD of a parallel-plate DBD, and gas mixture of tetraethoxysilane (TEOS), O_2, and He was introduced into the discharge region to deposit SiO_2 films. That is, He plays a role of both reducing discharge voltage and sustaining discharge uniformity. Babayan *et al.* [4] and Nowling *et al.* [5] used APGD sources driven by radio-frequency power supply to deposit SiO_2 and silicon nitride films using TEOS and SiH_4. Their plasma source was remote type, but they also used He for plasma production at atmospheric pressure. Yuasa [6] utilized N_2 and O_2 gases without He, but the operation voltage for plasma production would be so high since their APGD was produced in a parallel-plate DBD.

Here we propose a new scheme for thin-film deposition at the atmospheric pressure using the integrated microdischarges [7] without He gas, which is widely used as an APGD working gas but is quite expensive. In our scheme, the microdischarges take place in small holes penetrating through two electrode platescovered with dielectric layers, and enable the gas flowing in the holes dissolve into reactive species. These reactive species coalesce N_2 including TEOS and produce precursors of deposition of SiO_2 films. These combined gas flow gets into deposition space which is separated from the plasma source. That is, the deposition process is affected by several key parameters in the gas phase. The goals of this study are realization of lower driving voltage for an atmospheric-pressure plasma source despite of no use of He, optimization of thickness and flow rate of the laminar flow in the deposition space, and understanding of the gas-phase reactions and the transports of reactive gases.

We show first the experimental setup in Section 2, and demonstrate the experimental results in both terms of

discharge properties and deposition film features in Section 3. In Section 4, the gas flow regime in the reactor is numerically analyzed and it is compared with the experimental results of deposition rate dependence on the gas flow rate. Finally we summarize this study in Section 5.

2. Experimental Setup

Integration of microdischarges for atmospheric-pressure plasma processes has realized a sheet-like plasma source with 50 mm diameter and perpendicular gas-flow structure [7]. A coaxial microhollow electrode structure was covered with dielectric layer, and the opening of the unit hole became 200 μm x 1700 μm. A dielectric barrier discharge generated in this small hole between the stacked electrodes, and such microdischarges were assembled on one plane. Inlet gases flew through the holes where discharges took place. The equivalent discharge path *d* between the two electrodes was several hundred μm in length, and relatively low discharge voltage is possible in such a low *pd* condition even at the atmospheric pressure.

Using this plasma source, we developed a remote-plasma-enhanced chemical vapor deposition reactor, shown in Fig. 1 (a). TEOS was vaporized at 170 ℃ in a liquid delivery system (PD-0-1, Japan Pionics), and its laminar flow carried by N_2 was combined with the gas flow dissociated by the plasma source. The predominant dissociation of TEOS is by electrons, O atoms, and O_3 molecules [1, 8]. The main deposition area, which was located under the combined gas flow with the thickness of 2 mm, was separated from the plasma source region. Gas flow rate was not so high (less than 10 litter per minutes (SLM)), leading to condition of the atmospheric pressure along all gas-flow paths including the plasma source region and the deposition area. In the cases of film deposition, the typical gas flowing through the microdischarges was O_2, and the gas of the laminar flow carrying TEOS was N_2. The applied voltage on the powered electrode was 2.1 kV_{0p} with 1-20 kHz bipolar square pulses, and discharge current was 2.2 A as a peak value. Used substrates for deposition rate estimation by thin-film step-height standard method (XP-2, Ambious Technology) were plates of Fe and Ni alloy, and Si wafers were used for film bonding analysis by Fourier transform infrared (FT-IR) spectroscopy (WINSPEC100, JEOL). The substrate temperature was set to be 150 ℃.

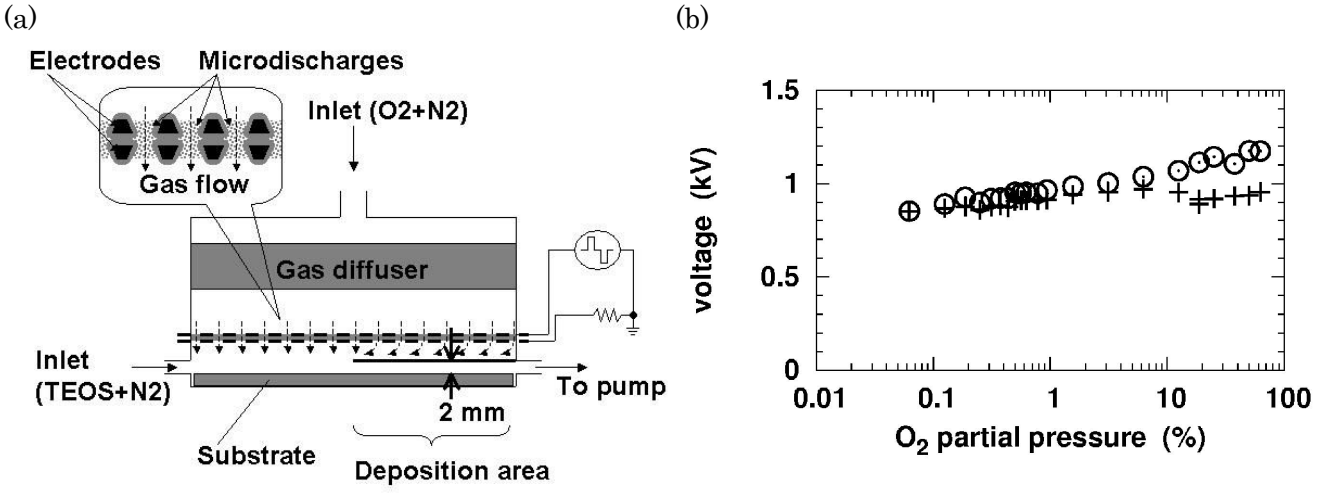

FIG. 1. (a) Schematic view of deposition reactor using remote plasma source of integrated microdischarges. (b) Firing voltage as a function of O_2 partial pressure in N_2 and O_2 mixture gas. Crosses and open circles indicate the partial ignition and the whole-area ignition voltages, respectively.

3. Experimental results

Mixture gas of N_2 and O_2 flew through the plasma source region, and homogeneous discharge emission was observed in the aperture of a square of 50 x 50 mm. Figure 1 (b) shows firing voltage as a function of O_2 partial pressure. Although the voltage increases up to 40 % as the O_2 partial pressure is raised, the discharge voltage is

quite low in comparison with that in usual dielectric barrier discharges [9].

In the measurement of the FT-IR spectroscopy, the deposited films showed the usual properties of SiO_2 films without C-H peaks. To characterize precursor's transport in the gas phase, the total gas flow rate was varied with the same fraction of N_2, O_2, and TEOS flow rates. Simultaneously, the frequency of the power supply was also changed linearly to the total flow rate, which means that power dissipation density in a unit mass flow is kept constant. The standard condition was as follows: the N_2 gas flow rate was 3.0 SLM with TEOS flow rate 0.25 g/min, and the O_2 gas flow rate was 3.6 SLM, and the power supply frequency was 14 kHz. Since the TEOS flow was by 2 orders lower than the N_2 and O_2 flows, the total flow rate of this standard condition was 6.6 SLM.

Figure 2 shows the film deposition rate as a function of the total flow rate. As the total gas flow rate was increased with the same partial flow rate of each gas, the deposition rate decreased significantly. Figure 2 also shows estimated gas residence time in the deposition area. The tendency is similar to the deposition rate, which indicates that diffusion of the precursors across the combined laminar flow is important for the deposition process. If we keep the similar residence time to that in a low pressure case, the gas flow rate should be raised in a high pressure case. However, diffusion flux toward the substrate, which decreases as the pressure increases due to reduction of diffusion coefficient, becomes smaller in comparison with convective flux in the laminar flow. One solution to overcome this discrepancy about the gas flow rate is to decrease thickness of the laminar flow, which enhances the diffusion flux by increasing gradient of precursor density near the substrate. In our experimental setup, the laminar flow thickness was 2 mm, which is by one order smaller than the electrode-to-substrate gap in a conventional parallel plate PE-CVD used in low pressure operation.The relation between the flow rate and the deposition rate in our experiment will be reexamined in Section 4 by fluid dynamics analysis.

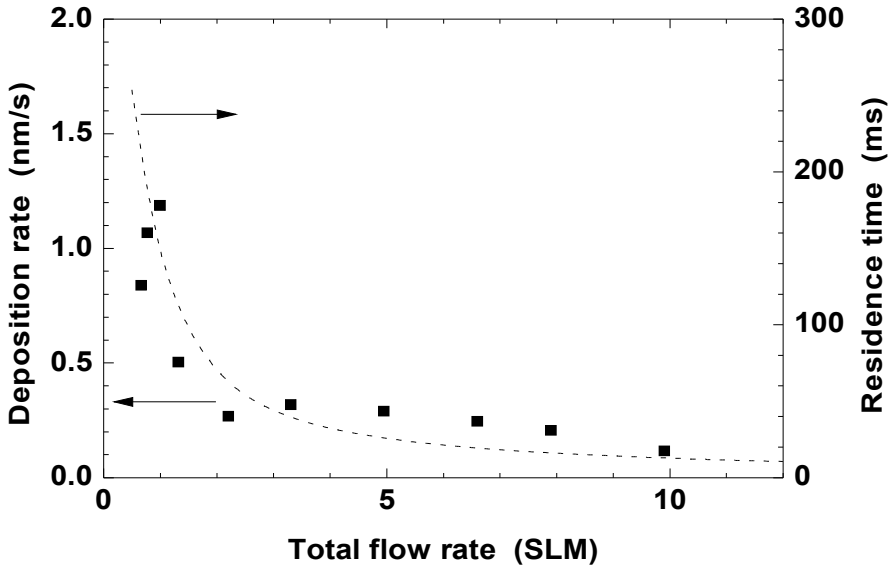

FIG. 2. Deposition rate (closed squares) as a function of total gas flow rate. The film thickness for the deposition rate estimation is measured 7 mm inside from the outlet point. The inset dashed line indicates estimated residence time of gases in the deposition area.

When the total gas flow rate was decreased down to 1 SLM, the deposition rate reached its maximum value. As the total flow rate was decreased further, the deposition rate became lower. This is due to the powder formation resulting from gas-phase polymerization of deposition precursors, since white particles were attached on the surface of the substrate after the deposition process in the case of the lowest total flow rate (0.66 SLM). In general, shorter residence time enhances both precursor diffusion flux to the substrate and particle growth in

the gas phase. If the collision rate is so high and the precursor particles encounter each other so frequently, they will get together before they arrive on the substrate surface and cannot contribute to form the film. The low substrate temperature (150 ℃) is another enhancement factor for powder growth. The other mechanism of enhancement of the powder formation will be mentioned in Section 4.

4. Discussion

Numerical analysis of gas flow distribution was performed by a solver for computational fluid dynamics (PHOENICS version 3.5.1, Concentration Heat & Momentum Limited) [10]. In brief, the general conservation equations of mass, momentum and energy are numerically solved using the finite volume method. It is capable of analyzing three dimensional gas flows, although we calculated two dimensional distribution in a cross section from the gas inlets to the outlet shown in Fig. 1 (a). Figure 3 displays the model configuration used for numerical analysis which will be compared to the experimental results. From the inlet on the left wall, N_2 gas at 170 ℃ flows into the analysis space, and O_2 at 27 ℃ flows down from the inlet on the upper wall. Rigorously, N_2 flux carries TEOS particles, and O_2 flux includes O and O_3 fractions, but they are simplified into pure N_2 and pure O_2 flows, respectively. They are combined in the left part in Fig. 3, which we can denote "mixing region" here, and the mixture flows through the deposition area under the insert plate and goes out from the outlet on the right wall. To distinguish a fraction of O_2 from N_2, each continuum equation is written as, using the total mass density as ρ and the average velocity as $\boldsymbol{u}$,

$$\frac{\partial (C_\alpha \rho)}{\partial t} + \nabla \cdot (C_\alpha \rho \boldsymbol{u}_\alpha - D_\alpha \rho \nabla C_\alpha) = 0, \qquad (1)$$

where C_α represents a fraction of α species in the mixture at each position, and $\alpha = N_2$ or O_2 with $C_{N2} + C_{O2} = 1$. Each D_a represents diffusion coefficient of α species at 27 ℃. In the specific calculation, Eq. (1) for O_2 species is solved and N_2 concentration is determined from the rest part of ρ. The lower wall can be considered as a substrate. Gas flow is assumed to be laminar one, and the boundary condition on the walls is no-slip wall boundaries. The unit calculation cell is 1.0 mm x 0.25 mm, and the fluid dynamics parameters in each cell depends on the local composition of the gas species.

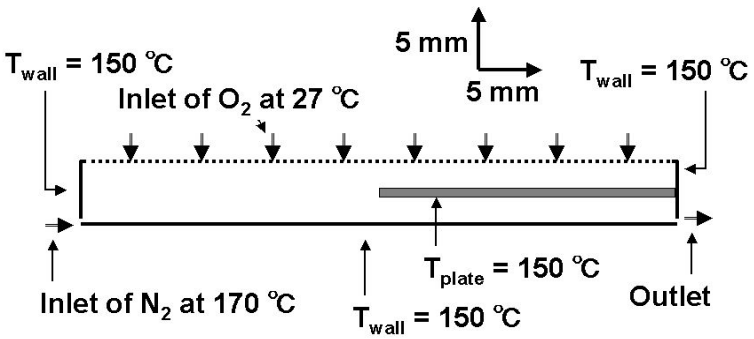

FIG. 3. Model configuration of the reactor. The experimental parameters are adapted to the boundary condition of the numerical analysis.

Figures 4 and 5 show the typical numerical results obtained using this model, where the flow rates are adjusted to the experimental values shown in Fig. 2. When the total gas flow rate is high, shown in Fig. 4, the N_2 flux from the left inlet expands in a limited region on the substrate and goes almost directly to the deposition area, and so no contact of N_2 including TEOS with the microdischarges occurs. The O_2 flux cannot diffuse in the N_2 flux layer so much, and so the mixing rate is very small. When the fluxes get into the deposition area, the large vertical gradient of the O_2 concentration is kept throughout this region, which indicates that dissociation above the substrate cannot be expected so much. On the other hand, when the total gas flow rate is low, as

shown in Fig. 5, the N_2 flow expands the mixing region up to the upper inlet where the microdischarges take place. The O_2 flow, including O_3 in the experiments, also expands downward in the mixing region, and so the well-mixed flux is formed before it enters the deposition area. In the deposition area, the flux is almost homogeneous vertically and the flux with high O_2 concentration gets contact with the whole substrate surface.

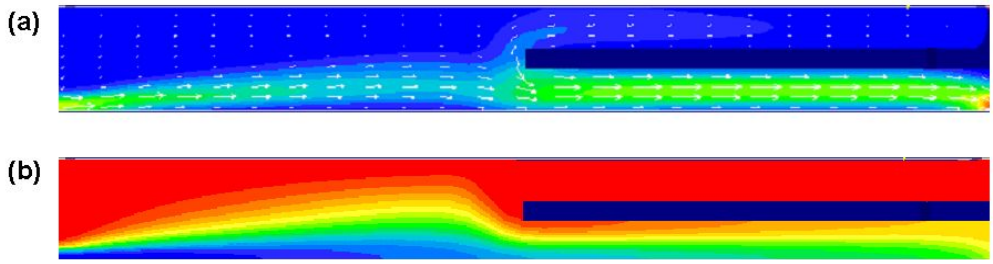

FIG. 4. (a) Velocity distribution calculated in the cross section shown in Fig. 3 in the case with the total gas flow 6.6 SLM. The contours and the white arrows indicate the velocity values and its vectors, respectively In the region in bright red the velocity becomes maximum (3.2 m/s), and the dark blue represents the minimum velocity region (~0.0 m/s). (b) O_2 concentration distribution calculated in the similar condition to (a). The bright red region is the area where only O_2 is present, whereas there is no O_2 in the dark blue area.

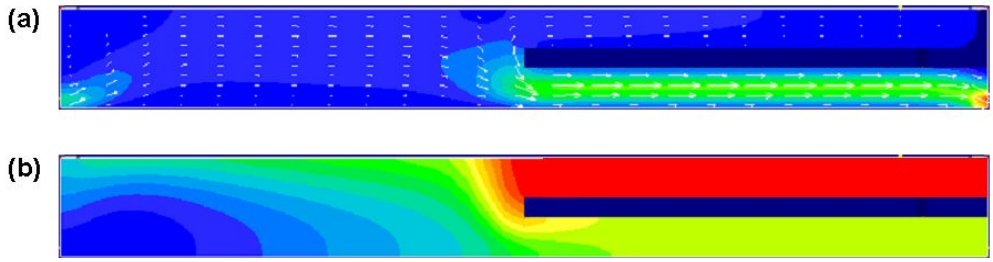

FIG. 5. (a) Velocity distribution in the cross section shown in Fig. 3 in the case with the total gas flow 0.66 SLM. The maximum velocity is 0.35 m/s on the outlet. (b) O_2 concentration distribution in the case similar to (a). The contours and the arrows are used in the similar way as in Fig. 4.

Figure 6 shows the O_2 concentration on the surface of the substrate. As indicated in Figs. 4 and 5, the O_2 concentration is low on the substrate surface when the total flow rate is high. As the total flow rate decreases, the O_2 concentration increases, which would enhance precursor production near the substrate and oxidation of the grown film surface. This tendency coincides the change of the deposition rate for the total flow rate more than 2 SLM in Fig. 2, but this result cannot explain the deposition rate increase as the total flow rate is decreased in the range less than 2 SLM.

As mentioned in Section 3, the diffusion flux of the precursors towards the substrate would be enhanced when the gas flow rate is decreased. That is, the decrease of the total gas flow rate affects two important factors in the deposition process; one is the increase of precursor production in the collisions between O_3 and TEOS, and another is the precursor transport to the substrate surface. These two factors would create a larger effect than that expressed by a simple consideration of residence time of the gas species, and could be related to the drastic change of the deposition rate in the range less than 2 SLM. Another possibility for this drastic change can be attributed to the direct dissociation of TEOS by the microdischarges in the low-flow-rate region. In the case of Fig. 5 (b), the TEOS molecules have a chance to encounter the microdischarges which play a major role in dissociation of O_2 throughout the whole flow-rate range. The attachment with the microdischarges might also enhance powder formation in the gas phase due to excessive decomposition of TEOS. Further clarification of this complicated feature of this deposition process is beyond the scope of this study, but the aspects revealed in

this study on the combined laminar flows and the diffusion flux across them can be lead to more understanding and development of atmospheric-pressure plasma processes.

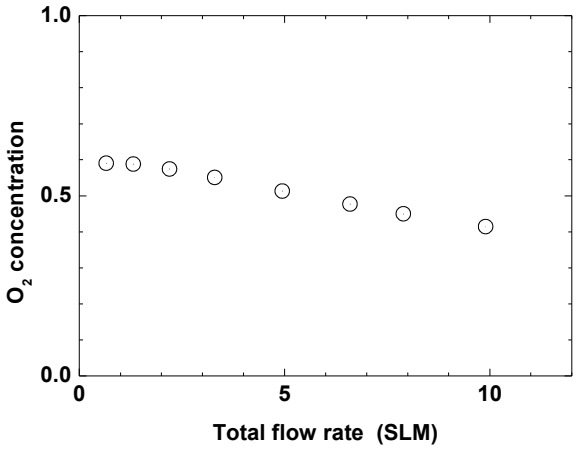

FIG. 6. Calculated result of O_2 concentration on the surface of the substrate 7 mm apart from the outlet, as a function of the total gas flow rate.

5. Conclusion

A new plasma-enhanced chemical vapor deposition (PE-CVD) scheme working at atmospheric pressure was presented, and the deposition process was investigated as a dependence of the total gas flow rate experimentally and numerically. Dielectric barrier microdischarges were integrated on one plane with their hollow structures leading to activation of gases O_2 flowing through them. Created O atoms (and O_3 molecules) coalesced with N_2 flow including TEOS and gave rise to precursors. Deposition rate strongly depended on their laminar flow rate, and gas-phase transports of active species were examined using the computational fluid dynamics solver. The gas flow rate affects the mixture rate of the O_2 and the N_2 fluxes, the precursor diffusion fluxes, and the direct dissociation rate of TEOS. The revealed experimental and numerical results in this study indicated quite different features from the cases of low-pressure PE-CVD.

Acknowledgments

This work was supported partially by a Grant-in-Aid for Scientific Research from the Japanese Ministry of Education, Culture, Sports, Science and Technology and by an entrustment from the New Energy and Industrial Technology Development Organization.

References

[1] M. A. Lieberman, A. J. Lichtenberg, *Principles of Plasma Discharges and Materials Processing* (New York, John Wiley & Sons, 1994) p. 518.
[2] E. E. Kunhardt - IEEE Trans. Plasma Sci. **28**, 189 (2000).
[3] Y. Sawada, S. Ogawa, M. Kogoma - J. Phys. D: Appl. Phys. **28**, 1661 (1995).
[4] S. E. Babayan, J. Y. Jeong, A. Schutze, V. J. Tu, M. Moravej, G. S. Selwyn, R. F. Hicks - Plasma Sources Sci. Technol. **10**, 573 (2001).
[5] G. R. Nowling, S. E. Babayan, V. Jankovic, R. F. Hicks - Plasma Sources Sci. Technol. **11**, 97 (2002).
[6] M. Yuasa, *Proc. 7th Asia Pacific Conference on Plasma Science and Technology and Symposium on Plasma Science for Materials*, p. 231.
[7] O. Sakai, Y. Kishimoto, K. Tachibana - J. Phys. D: Appl. Phys. **38**, 431 (2005).
[8] S. Romet, M. F. Couturier, T. K. Whidden - J. Electrochem. Soc. **148**, G82 (2001).
[9] Z. Falkenstein, Z. Z. Coogan - J. Phys. D: Appl. Phys. **30**, 817 (1997).
[10] S. V. Patankar, D. B. Spalding - Int. J. Heat Mass Transfer **15**, 1878 (1972).

Chemical and physical Characterization of Thin Films Deposited by Inductive RF Plasma Polymerisation of the Methyl 2-Methyl Propanoic Ester

F. Renaux[1], L. Denis[1], R. Gouttebaron[2], V.Carlier[3], M. Hecq[1]

1 Laboratoire de Chimie Inorganique et Analytique, Université de Mons Hainaut, Parc Initialis, 1 Avenue Copernic, 7000 Mons, Belgique
2 Materia Nova, Parc Initialis, 1 Avenue Copernic, 7000 Mons, Belgique
3 CoRI – Coatings Research Institute, 21 Avenue P.Holoffe, 1342 Limelette, Belgique

Abstract

Through an experimental design method, we have investigated the influence of working pressure, of organic precursor flow and of r.f. power on plasma polymer films properties synthesized through PECVD. The organic precursor is the methyl 2-methyl propanoic ester, a saturated counterpart of the widely studied methyl methacrylate. Surface stoechiometry and chemical functions are determined by means of XPS measurements and the deposition rates are evaluated through height step profilometry.

Keywords: Aluminum, Corrosion, Experimental Design, PECVD, Plasma Polymer, Ester, XPS.

1. Introduction

New European environmental protection laws require industries to eliminate as much as possible potentially dangerous treatments, reagents or by-products from their industrial processes. To date, the corrosion protection of aluminium alloys has been extensively based on chromate conversion treatments. Unfortunately, these processes use dangerous reactants and produce toxic waste. Moreover, the chromium VI, a capital element for the conversion coating properties, is proved to be carcinogenic. Its release into the ground waters by lixiviation or because of industrial bath cleanings must be avoided [1, 2, 3]. Among the numerous alternatives, the deposition of a functionalized plasma polymer through PECVD is an attractive approach to solve the problem. From a mechanical point of view, the plasma polymers are dense, quite hard material, highly cross-linked and free of structural defects like pinholes [4, 5]. Moreover, good adhesion of the plasma layer on the substrate could also be achieved through plasma processes. For example, the substrate pre-treatment can be performed by plasma cleaning using the same reactor [6, 7]. Finally, the adhesion of a topcoat could be highly enhanced by grafting specific chemical organic functions at the plasma polymer surface.
In the present work, we synthesize a plasma polymer from the methyl 2-methyl propanoic ester, a saturated counterpart of the widely studied methyl methacrylate. Any possible implementation problems because of using unsaturated compounds are avoided. Indeed, drastic conditions of temperature, pressure, purity or light must be kept to prevent uncontrolled polymerization of such unsaturated monomers in the precursor source or vacuum system. The influence of discharge parameters on adhesion and on protective properties of functionalized plasma polymers has to be studied. The adhesion with aluminium and with subsequent primer layer can be enhanced by the presence of carboxylic functions. Therefore, equilibrium between preserving the carboxylic functions at the film surface and synthesizing a truly highly cross-linked plasma polymer is to be found. The fragmentation rate of monomer in the r.f. inductive plasma must be controlled.

2. Experimental

The plasma polymers are deposited by inductively coupled r.f. plasma in a PECVD vacuum chamber. The precursor is methyl 2-methyl propanoic ester. The chamber is a cylinder of 300 mm diameter and of 450 mm length. High vacuum is maintained through a mechanical and turbo molecular system (Pfeiffer TPU 621) with a total pumping speed of 440 l/s. A throttle valve (MKS 653 B) placed upstream the pumping system is regulating the pressure in the chamber. A load and lock system allows transferring the substrate inside the

reactor without any venting of the main chamber. Eventually, a Baratron gauge and a Pfeiffer Full range Gauge measure the pressure in the PECVD reactor. A water-cooled coil placed inside the reactor produces the r.f. (13.56 MHz) induction field by which the plasma is powered. The r.f. generator is a Restler Caesar with a maximal delivering power of 1000 W. The copper coil has a diameter of 150 mm and is placed in front of the substrate at a distance of 50 mm. No copper pollution has been detected on polymer film because of capacitive discharges appearance. We assumed that the plasma polymer quickly covers the r.f. coil as all the plasma-exposed surfaces. The different substrates are aluminium "2024" foils of 360 mm^2 for ageing tests, floated glass for contact angle measurements and thickness determination, and silicon wafers of about 10 mm^2 for XPS measurements. The substrate holder could be earthed, kept at floating potential or independently biased up to 600 volts by an r.f. generator (ATX 600 Advanced Energy). The samples are strongly clamped to provide good electrical contact. The substrate holder is entirely mounted on the linear drive of the load and lock system. The distance between the coil and the sample can be varied from 50 mm to 300 mm. The organic precursor is introduced into the chamber through a needle valve. The boiling point of methyl 2-methyl propanoic ester is quite low (57 °C). Therefore, evaporation is simply performed under low vacuum to feed the reactor; no carrier gas is used. Measuring the pressure inside the chamber allows controlling and calibrating the precursor flow. The deposition rates are determined by step height profilometry (Dektak).

The surface chemical composition of the polymer films is obtained by means of XPS measurements (VG-ESCALAB 220iXL spectrometer). The pressure inside XPS analysis chamber is about 1.3×10^{-10} mbar. The excitation radiation is an Al Kα mono chromatised x-ray beam and the irradiated surface is about 1 mm^2. As the plasma polymers are insulating, an electrical compensation is always applied through an electron flood gun. The carbon and oxygen atomic compositions are deduced from the photoelectron peak areas corrected by photo ionization cross-sections calculated by Scofield. The escape depth dependence on the kinetic energy of the electrons (assumed to have the form $\lambda = KE_{kin}^{\ 0.6}$) and the analyser transmission function are taken into account. An evaluation of the organic functions present at the film surface is deduced by means of envelope fitting of the C1s photoelectron peaks. The samples are exposed to air for one day before being transferred to the XPS load and lock system. Contamination of the surface is expected during this period.

3. Results and discussions

The surface chemical composition has been studied in function of working pressure (mbar), of organic precursor flow (ml/min) and of r.f. power (W). To outline our domain of investigation, we use an experimental design program called Design-Expert from Stat-ease. The software sets the studied discharges parameters (factors) through a Box-Bhenken type design. In this experimental design, two parameters vary simultaneously to investigate possible factor interactions. Moreover, the central domain experiment is duplicated five times to evaluate experimental errors. Finally, a response surface is calculated as a function of the three previously selected discharge parameters. The responses are constituted of the film surface oxygen contents determined through XPS, of deposition rate evaluations and of water contact angle measurements. The response surface adequacy is checked by means of different statistical diagnosis. Eventually, the so-called experimental design is an efficient and complete method of process diagnosis and results treatment. However, a full explanation is beyond the scope of the article [8,9].

The experimental domain boundaries results from technical limitations or experimental observations. The applied r.f. power range lies between 50 W and 120 W. Below 50 W there is no film deposition. The working pressure varies from 2×10^{-2} mbar to 8×10^{-2} mbar and the monomer flow from 0.04 ml/min to 0.08 ml/min. For each experiment, the deposition duration is 15 minutes and the substrate coil distance is set to 50 mm. Seventeen films were deposited according to the established experimental design. Eight additional samples were prepared to confirm (or not) predicted values. Determination of film deposition rate, measurements of water contact angles, MEB photography and XPS surface characterization were performed. Here we will discuss XPS results obtained with the experimental design program.

Substrates are cleaned in capacitive coupled argon oxygen plasma. The r.f. power (50 W) is applied on the substrate holder and the resulting bias is about – 650 V. A pre treatment of 10 minutes is realized and less than 1 carbon at% of residual organic pollution is detected through further XPS measurements. The film

thickness varies from 20 nm up to 1000 nm depending on the studied discharge parameters. The deposition rate is about 1 nm/min at 50 W r.f. power and rises up to 60 nm/min at 120 W r.f. power values. Water contact angle changes from 75° down to 55° while the applied r.f. power rises from 50 W to 120 W. The working pressure is of 4 x 10^{-4} mbar and the monomer flow is set at 0.06 ml/min.

3.1 Dependence of the surface chemical composition on applied r.f. power, precursor flow and working pressure

The carbon/oxygen surface ratio is determined through XPS on plasma polymer coated silicon wafers substrates. The influence of the discharge parameters on the surface composition is studied by means of the experimental design response surfaces. Afterwards, the C1s photoelectron peak is fitted to identify the grafted organic functions at the film surface. To avoid over or under estimation of the surface oxygen responses due to the program fitting, Y'"logit" values of the oxygen at% are introduced as responses into the experimental design [9, 10].

$$y' = \ln\left(\frac{y - \text{lower}}{\text{upper} - y}\right)$$

This mathematical transformation allows outlining the predicted values. As the organic precursor is the methyl 2-methyl propanoic ester ($C_5H_{10}O_2$) and hydrogen atoms are not detected through XPS measurements, the oxygen maximal value is set up to 30 at% and the minimal oxygen content is of course set to 0 at%. The response equation is expressed in coded factors to reflect the statistical weight of the studied parameters. The equation of oxygen content response surface is expressed as follows:

$$Ln\left(\frac{O-0}{(30-O)}\right) = -0.11 + 0.017P - 0.48W - 0.09P^2 + 0.13W^2 \quad (a)$$

Where O is the oxygen at%, F the monomer flow, P the pressure and W the applied r.f. power.

Equation (a) indicates that the pressure has a lower influence on the film oxygen content compared to r.f. power. Moreover, the monomer flow is not taken into consideration. It has probably no influence on the oxygen content within our experimental limits. The lack of interaction between the discharges parameters is expressed by the absence of mixed term in equation (a). The standard deviation error is about 6 % and there are no outliers in the predicted values. Finally, the model adequacy is verified through residuals analysis on a normal probability plot.

Increasing the applied r.f. power reduces the surface oxygen content from 18 at% (50W) to approximately 10 at% (120W). At higher r.f. power (120 W), the plasma probably produces more volatile non-reactive species (like CO_2 as detected with MS measurements) since the collision cross section increases [9]. These oxygen-containing fragments do not polymerize at the substrate and are evacuated by the pumping system. Moreover, it is assumed that the monomer fragmentation is already significant at 50 W. Indeed, the oxygen content reaches a maximum of 18 at% while the organic precursor contains 28 at%.

Each surface response graph presented below is expressed in actual values and illustrates the general behavior of the equation (a).

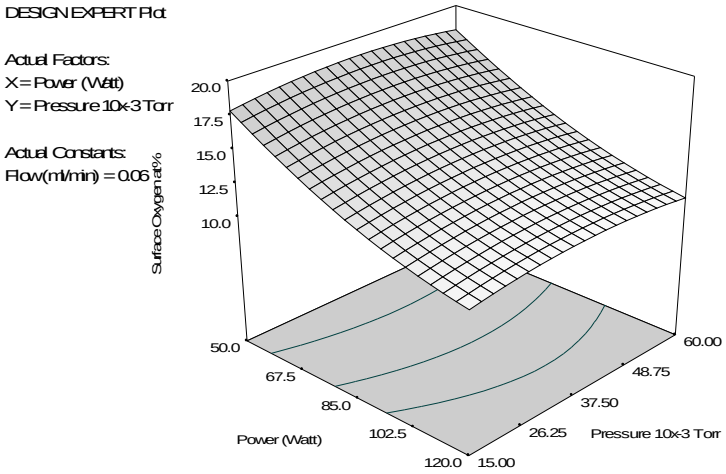

Figure 1: O at% in function of pressure (torr) and r.f. power (W)

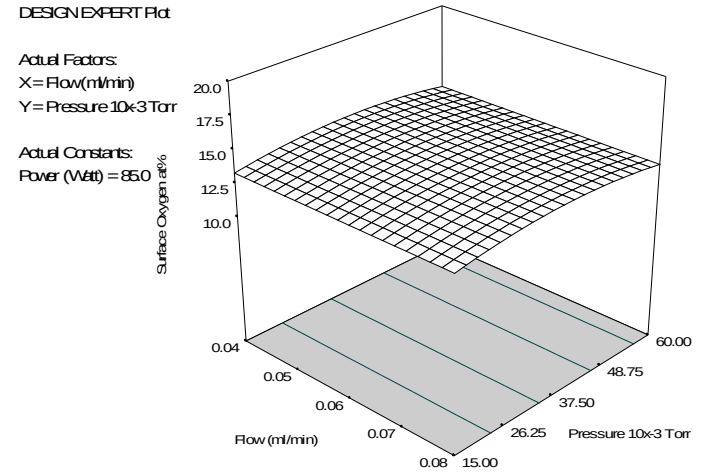

Figure 2: O at% in function of pressure (Torr) and monomer flow (ml/min)

As already noted on equation (a), the figure 1 illustrates perfectly the expected r.f. power influence on film surface oxygen contents. Regardless of any pressure variation, the oxygen rate decreases by a factor two when the applied r.f. power doubles. Figure 2 shows the lack of influence of monomer flow and of pressure on the surface oxygen content the plasma polymer. According to literature [11, 12], this behavior was not truly expected but could be explained owing to our very low working pressure and monomer flow.

3.2 Determination of the plasma polymer surface chemical functions deduced from the C1s XPS peak fitting.

The plasma polymers exhibit quite complex C1s peaks that allow fitting. The discriminated components give us information about the chemical surface composition of the films. Indeed, prior to any polymerization, the organic precursors are first decomposed by the plasma into various reactive fragments. Only a part of the primary monomer chemical functions is remaining at the polymer surface but new ones may appear. Moreover, the samples are exposed to air before XPS analyses and chemical surface reactions like oxidation may occur during the delay.

Eventually, six components are discriminated in the C1s peak that depends on the carbons atoms chemical environment. An example of a C1s peak fitting spectra is presented in figure 4. Some fitting constraints were

applied to avoid impracticable ratio intensities, abnormal peak widths and binding energy inconsistencies. The peaks binding energies of the ^{2}C,^{3}C,^{4}C,^{5}C,^{6}C carbons are imposed regards to ^{1}C carbon position and to the hypothetical surface functions. The fitting peak width (FWHM) is set to 1.5±0.1 eV. Finally, α carbon peak areas (^{2}C and ^{3}C) are linked to peak areas of their corresponding functions (^{6}C and ^{5}C respectively). Four components are directly resulting from the organic precursor structure: carbon-carbon bond -C-^{1}C (285 eV), α carbon of carboxyl ^{2}C-COO (285.5 eV), methyl carbon of ester -O-^{4}C (286.5 eV), and carboxylic carbon O-^{6}C=O(289 eV). Two additional components are resulting from the plasma processing: α carbon of carbonyl ^{3}C-C=O, and carbonyl carbon ^{5}C=O. Accordingly, the films surface compositions are supposed mainly formed of carboxyl, carbonyls, ether and hydroxyl organic functions. This assumption has to be confirmed by future FT-IR measurements. The carbon peak ^{4}C is related to the ester monomer function but also to plasma born ether and hydroxyl functions. However, chemical shifts are too close for allowing peak discrimination. The peaks assignments and component ratios are summarized in table 1 for two different powers (50 W and 120 W, p = 4 x 10^{-2} mbar, monomer flow = 0.06 ml/min).

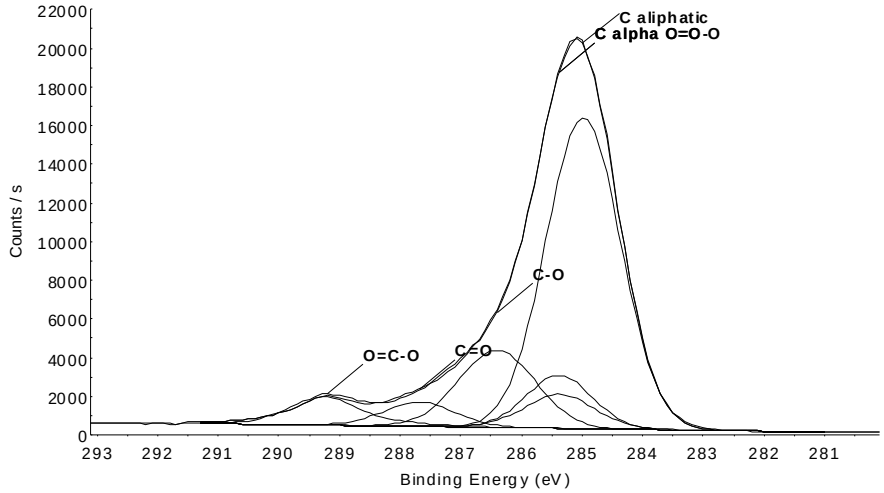

Figure 3: C1s peak fitting spectra example (85 W, 0.06 ml/min and 5x10^{-2} mbar)

Table 1.Plasma polymers atomic ratios measured through XPS by fitting the carbon peak Area

Bonding energy (eV)	%at ratio r.f. 120W	%at r.f. 50W
285 (^{1}C-C)	} 84	} 71
285.5 (^{2}C-COO)		
285.5 (^{3}C-C=O)		
286.5 (^{4}C-O)	9.7	18.1
288 (^{5}C=O)	2.4	5.2
289 (^{6}COO)	4.1	5.7

Table 1: C1s peak fitting assignments and ratios

According to table 1, the surface functions are mainly composed of ester/ether/hydroxyl (^{4}C), and to a lesser extend of carbonyl (^{5}C) and of carboxyl (^{6}C). Concerning the origin of these organic functions, one may notice that the plasma generates the majority. First, the carbonyl functions are entirely generated by the plasma as it does not appeared in the initial monomer. Secondly, the ester contribution to the ^{4}C component is linked to the carboxyl function and may not exceed it. As the esters represent less than 50% of the ^{4}C component intensity, it is mainly composed by plasma-born hydroxyl and ether functions. This behavior has

to be related to the significant fragmentation rate occurring since 50 W and that is resulting in a low-content carboxyl plasma layer. Another important feature is the seemingly lack of power influence on the ^{6}C peak intensity that could be explained through monomer adsorption occurring at the very end of the process. As mentioned earlier, total oxygen content decreases with a rising of the applied r.f. power. This oxygen ratio evolution seems mainly related to the variation of the ^{4}C and ^{5}C plasma-born components intensities. This observation is in agreement with the assumption that more volatiles oxygenated species are produced while the applied r.f. is increased.

4. Conclusions

Plasma polymer films have been synthesized from methyl 2-methyl propanoic ester through PECVD process. Experimental design technique has been used to study the influence of discharge parameters on film formation. More particularly, surface atomic and chemical composition of the films were deduced from XPS spectra. The most significant discharge parameter is the r.f. power applied at the coil. An increase of the r.f. power decreased the surface oxygen content. This behavior was explained through the production of non-reactive volatile oxygenated compounds in the plasma. Finally, the plasma polymer surface is mainly composed of plasma born carbonyl and ether/hydroxyl functions.

5. Acknowledgements

This work is financially supported by Walloon Region in the framework of a collective research project "ECOPO" in collaboration with "Facultés universitaires Notre-Dame de la Paix" and "Coatings Research Institute"

6. References

(1) "Chromate Treatment Alternatives"; G. Stefano, E. Paquay, D. Roosens, A. T. Serstevens and F. Ghigny; Edited by Promosurf (2003).
(2) "Application of Plasma Deposited Organosilicon Thin Films for the Corrosion Protection of Metals"; F. Fracassi, R. D'Agostino, F. Palumbo, E. Angelini, S. Grassini, F. Rosalbino; Surface and Coatings Technology 174-175 (2003) 107-111.
(3) "Plasma Polymerization For Industrial Production"; S. Gaur and G. Vergason; Society of Vacuum Coaters; 44th Annual Technical Conference Proceedings (2001).
(4) "Deposition and properties of carbon-based amorphous protective coatings"; C.-P. Klages, A. Dietz, T. Höing, R. Thyen, A. Weber and P. Willich ; Surface and Coating Technology 80 (1996) 121-128.
(5) "Plasma Deposition, Treatment, and Etching of Polymers"; R. D'Agostino; Academic Press (1990)
(6) "Corrosion Protection of Cold-rolled Steel by Low Temperature Plasma Interface Engineering"; T.F. Wang, T.J. Lin, D.J. Wang, J.A. Antonelli and H.K. Yasuda; Progress in Organic Coatings 21 (1996) 291-297.
(7) "Plasma Treatment of Automotive Steel for Corrosion Protection- a Dry Energetic Process for Coatings"; T.J. Lin, J.A. Antonelli, D.J. Yang, T.F. Wang and H.K. Yasuda; Progress in Organic Coatings 31 (1997) 351-361.
(8) "Characterisation of a Magnetron Radiofrequency Glow Discharge with a Glass Cathode Using Experimental Design and Mass Spectrometry"; C. Molle, M. Wautelet, J.P. Dauchot and M. Hecq; JAAS 1039- 1045 vol.10 (1995).
(9) "Pratiquer les plans d'expérience" J.Goupy; Ed Dunod (2005).
(10) "Design Expert Software 5.0 User's Guide"; Stat-ease Inc (1997).
(11) "Plasma Polymerization Processes"; H. Biderman and Y. Osada; Elsevier (1992).
(12) "Plasma Surface Modification and Plasma Polymerization"; N. Inagaki; Technomic Publishing CO (1996).

Deposition of hexafluoropropene on polyethylene glycol-coated PET film using dielectric barrier discharge reactor at atmospheric pressure: - Application to release coatings on pressure-sensitive tape -

Kunihito Tanaka, Yoshihisa Yanagawa and Masuhiro Kogoma

Department of Chemistry, Faculty of Science and Technology, Sophia University
7-1 Kioi-cho, Chiyoda-ku, Tokyo 102-8554, Japan

Abstract

Plasma-polymerized hexafluoropropene (PPHFP) film had adhesive strength that was low enough for use as a release coating, but the bond strength between PPHFP film and a poly (ethylene terephthalate) (PET) base substrate film was slightly weak. The insertion of a soft and elastic polymer, polyethylene glycol, between the two films hindered the peeling off of PPHFP from PET. The results also suggested that the polymerization degree of PPHFP was low and that this caused the weak bond strength.

1. Introduction

Pressure-sensitive adhesive (PSA) tapes are kept in rolls until use. To peel them out smoothly when we use them, PSA tape surfaces, which are in contact with their own glue, are generally coated with some low adhesiveness matter (*the release coating*). Some silicone polymers have frequently been used as a release coating because of their quite low surface energy. However, since those silicone polymers can become a serious impurity especially for the semiconductor industry, the development of a silicon-free PSA is strongly desired.

Generally, the adhesive strength between PSA tapes and solids strongly depends on the surface morphology and the surface energy of the solid: an extra smooth or a moderately rough solid surface and a lower surface energy will make the adhesive strength weaker [1]. Thus, it is clear that any material with sufficiently low surface energy is suitable for depositing release coatings. According to references 1 and 2, some fluorinated polymers such as polytetrafluoroethylene (PTFE) and polyhexafluoropropene have lower critical surface tensions, from which the surface energies can be estimated, than the values of some silicone polymers. However, they are rarely used as release coatings since there is currently no solvent suitable for applying the fluorinated polymers onto PSA tape films.

We have already reported that atmospheric pressure glow (APG) plasma can polymerize some fluorinated plasma-polymers [3-5]. In those studies, we found that a plasma-polymerized hexafluoropropene (PPHFP) film deposited using a dielectric barrier discharge (DBD) reactor had adhesive strength low enough for use as the release coating. These studies also showed that the adhesiveness of PPHFP film was lower than that of plasma-polymerized trifluoroethylene (CF_2CFH) film; this result agreed with the general propensity that a fluorinated polymer with a trifluoromethyl functional group (CF_3) has a lower critical surface tension (surface energy) than one without CF_3 [1, 6].

However, a small amount of PPHFP did peel from the PET film during the peel force measurement. This phenomenon could not be solved completely only by making the bond between PPHFP and PET stronger; for example, by insertion of some intermediate plasma-polymer layers between them or by introduction of radical sites on the PET surface. We supposed that this phenomenon occurred due to the high hardness and low elasticity of PPHFP. Thus, in this study, we examined the effect of the insertion of a soft and elastic polymer, polyethylene glycol (PEG), between PPHFP and PET as a solution of the problem.

2. Experimental

The DBD reactor shown in figure 1 was used for the PPHFP deposition. The reactor body was made of a Pyrex glass tube whose inner diameter was 46 mm. The inner stainless tube whose diameter was 44 mm was the ground electrode and the copper mesh electrode, whose height was 110 mm, wrapped around the Pyrex tube was the high voltage electrode. A PEG-coated PET film whose height was 130 mm was wrapped around the inner stainless electrode. Another (non-PEG-coated) PET film was used for preventing PPHFP deposition on the inner surface of the reactor.

First, the pressure in the reactor was lowered with a rotary pump to 3 Pa to remove any impurity gas. Then He gas was introduced into the reactor and the reactor pressure was restored to atmospheric

pressure. Finally, the PET film was treated with He plasma for 30 s to introduce some radical sites on the PET or PEG surface. Continuously (while we maintained the discharge), hexafluoropropene (HFP, C_3F_6) was added into the He gas to deposit PPHFP. The PPHFP deposition conditions are shown in table 1.

PEG coating was performed as follows: 1 wt% PEG - 33 wt% H_2O - 66 wt% ethanol solution was dropped on a PET film and was spread with a Mayer bar, which is a grooved rod. Then this film was dried in the atmosphere at 100 ºC for 1 min. The PEG thickness could be varied, if one used a Mayer bar with a different groove depth. In this study, the PEG thickness was fixed at about 200 nm.

The peel force was measured with a 180º peel test: No.31B PSA tape (Nitto Denko Co., Ltd) of 20 mm width was pressed onto the deposited film and then peeled off at a speed of 300 or 30 mm·min^{-1}. Although peel force was formerly presented in units of grams (force) per 20mm, the SI unit, Nm^{-1}, is used in this article, the relationship between these units is 1.0 gf(20mm)$^{-1}$ ≈ 4.9×10^{-1} Nm^{-1}. The chemical state of the deposited films was determined by XPS (ULVAC-Phi Co., Ltd., ESCA-5800ci). The XPS spectrum binding energy was corrected by shifting the hydrocarbon component (CHx, x=0 to 3) peak in the C_{1s} spectrum to 284.6 eV in most cases. Then we carried out curve fitting with the XPS program of ULVAC-Phi by reference to the interval energies between each chemical group observed from references 7 and 8. If the CHx peak in the C_{1s} spectrum was not identified clearly, for example in the PPHFP film, we set the peak position of F_{1s} spectrum at 689 eV; this value is the F_{1s} peak energy of an ordinary Teflon sample [9]. Then, the same process as mentioned above was followed.

3. Results and Discussion

Figure 2 shows peel forces of PET substrate, Teflon sheet as a control and PPHFP on PET without or with PEG coating. And Figure 3 shows atomic ratios F/C obtained from XPS measurements of adhesive tape glue side surfaces, which were used for the peel force measurement of the same samples as in Figure 2. If we compare among the white bars in Figure 2, the peel force of the PPHFP on the PET without PEG coating (#3) was low enough, but the F/C ratio was quite high. This result indicated that some PPHFP flakes had moved to the adhesive tape glue side. On the other hand, the peel force of the PPHFP deposited on PEG coated PET (#4) became slightly bigger than those of the #3 sample and the Teflon sheet (#2), but was low enough to use for the release coating. However, the F/C of #4 showed a much lower value than that of #3: it was almost the same as the value of the Teflon sheet; since the fluorine atoms on the Teflon surface are easily transcribed to a contacted surface, the F/C of the Teflon sheet was not zero. These result indicated that a soft and elastic polymer such as PEG inhibited the peeling off the PPHFP from the PET film by decreasing the stress on the PPHFP.

Since the F/C of #3 was slightly bigger than that of Teflon, we tried to use several times thicker PEG coats. However, there was no dependence between the PEG thickness and the inhibitory effect. We supposed that the PPHFP was essentially fragile: in other words, the polymerization degree of the PPHFP was quite low. Then, we measured the peel force of those samples with low peel speed, 30 mm·min^{-1} again.

The peel force obtained from the 180º peel test generally becomes smaller with slower peel speed because the adhesive glue of a test PSA tape becomes extended like a rubber band: the

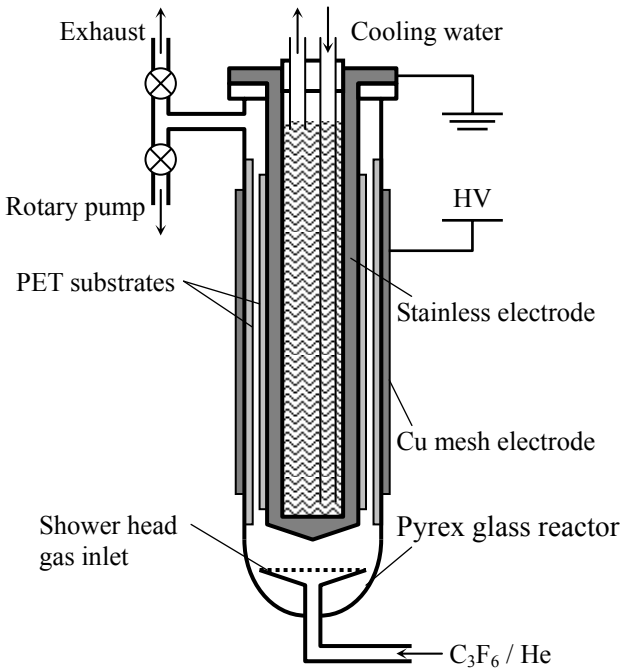

Fig. 1 Schematic diagram of dielectric barrier discharge reactor.

Table 1 Deposition conditions.

Discharge Frequency / kHz	100
Discharge Power / W	100
Deposition time / min	3
HFP Flow Rate / sccm	20
He Flow Rate / slm	5
Pressure	atmospheric pressure
PEG thickness / nm	200-500

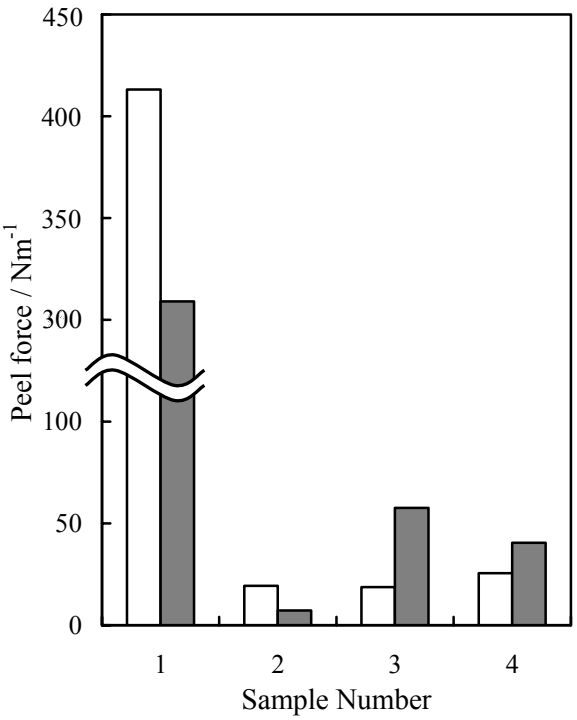

Fig. 2 Peel forces of 1) PET film, 2) Teflon sheet, 3) PPHFP on PET without PEG coating and 4) PPHFP on PEG-coated PET. The peel speeds of white and gray bars were 300 and 30 mm·min^{-1}, respectively.

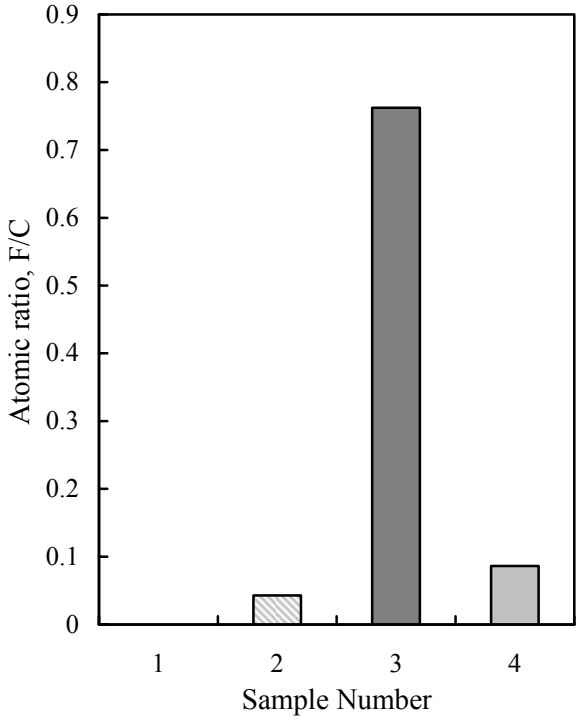

Fig. 3 Atomic ratios, F/C of adhesive tape glue side surfaces which were used for peel force measurement of the same samples as those in Fig. 2.

stress on a sample surface will decrease as a result of this phenomenon.

While the peel force of the PET film (#1) and the Teflon sheet (#2) shown with gray bars in figure 2 became smaller as mentioned above, those of PPHFPs (#3 and 4) became bigger. Moreover the PPHFPs (#3 and 4) were not peeled off from the PET film with slow peel speed. This result suggested that the peel forces under high peel speed condition indicated seemingly low values, since some PPHFP flakes peeled off, and that the peel forces of the PPHFPs under slow peel speed condition were the true values. If this assumption was true, the peel forces of PPHFPs (#3 and 4) were not as low as that of Teflon.

One well-known fact is that the cross-linking in a plasma polymerized polymer becomes less as one decreases the discharge frequency. Thus, we supposed that the polymerization degree of PPHFP would be made higher with a low frequency discharge, so we tried to deposit a PPHFP with 3 kHz power generator.

Figure 4 show the peel forces of PET substrate, Teflon sheet and PPHFP deposited on PEG coated PET under conditions of 100 and 3 kHz discharge frequency. And Figure 5 shows atomic ratios F/C of adhesive tape glue side surfaces, which were used for the peel force measurement of the same samples as in Figure 4. The deposition time of the PPHFP deposited with 3 kHz generator (#5) was 60 min. The #5 sample showed almost the same peel force as #4: according to their C_{1s} XPS spectra shown in Figure 6, the reason of this peel force result was considered that their chemical compositions and structures were not so different. On the other hand, the fact that the F/C of #5 was lower than that of #4 suggested that our assumption was probably true. And the slightly sharper C_{1s} spectrum of #5 shown in Figure 6-(b) than that of #4 suggested that the PPHFP deposited with 3 kHz generator had a more homogeneous chemical structure. We thought that this result also supported our assumption. However, the #5 peel force of slow peel speed shown with gray bar was even bigger than that of high peel speed. This indicates that the PPHFP was peeled off from the PET substrate.

4. Conclusion

The insertion of the soft and elastic polymer, polyethylene glycol (PEG), between PPHFP and PET inhibited the PPHFP peeling off from the PET substrate. However, since the PPHFP was essentially fragile, we considered that the peeling off problem would be not solved only by improvement the bond strength

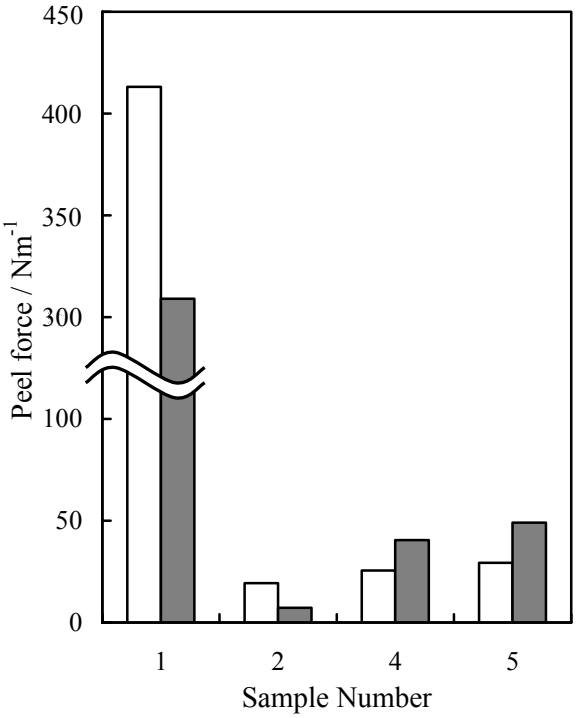

Fig. 4 Peel forces of 1) PET film, 2) Teflon sheet, 4), 5) PPHFP deposited on PEG-coated PET under conditions of 100 and 3 kHz discharge frequency. The peel speeds of white and gray bars were 300 and 30 mm·min^{-1}, respectively.

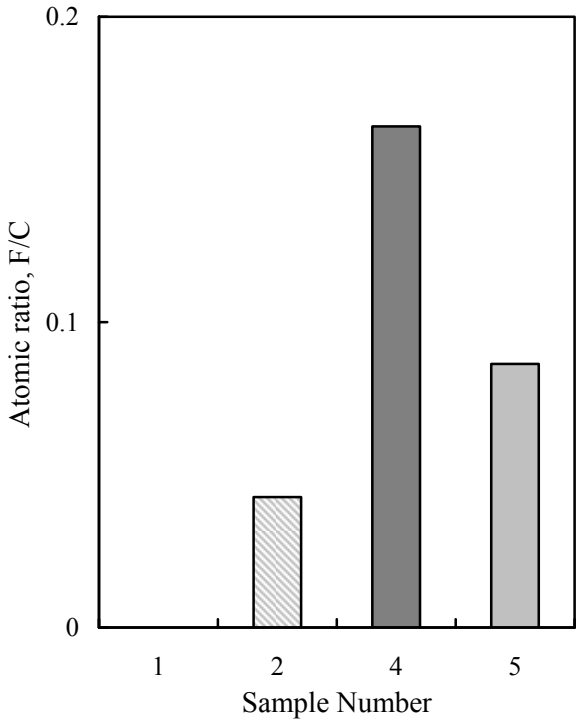

Fig. 5 Atomic ratios, F/C of adhesive tape glue side surfaces which were used for peel force measurement of the same samples as those in Fig. 4.

between PPHFP and PET. One of the solutions was that one would use a low frequency generator or pulse-controlled high frequency generator with low duty ratio.

Acknowledgments

The authors wish to express their gratitude to Professor Frank Scott Howell S. J. for his valuable comments.

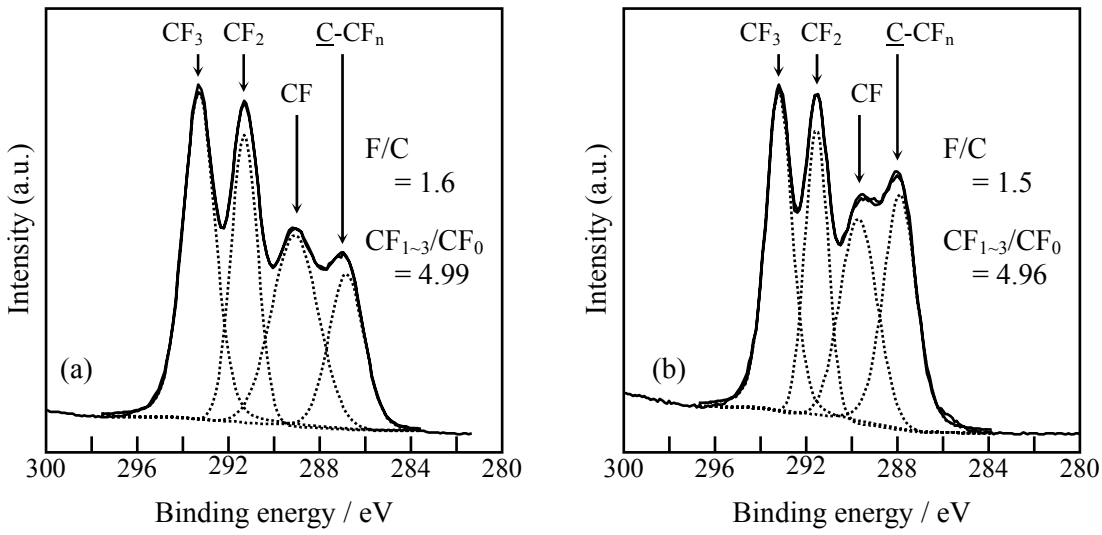

Fig. 6 C_{1s} XPS spectra of the same samples as (a) #4 (100 kHz) and (b) #5 (3 kHz) of Fig. 4.

References

[1] W. Karmann and A. B. Kummer, Adhesive Tapes, in *Adhesives and Adhesive Tapes*. G. Gierenz and W. Karmann, ed., WILEY-VCH, Weinheim (2001), p. 97.

[2] W. A. Zisman, *Ind. Eng. Chem.* ***55***, 19 (1963).

[3] T. Yokoyama, M. Kogoma, S. Kanazawa, T. Moriwaki and S. Okazaki, *J. Phys. D 23*, 374 (1990).

[4] K. Tanaka, T. Inomata and M. Kogoma, *Proc. HAKONE VII* ***2***, 422 (2000).

[5] K. Tanaka and M. Kogoma, Plasma and Polymers, **8**, 3, 199-208 (2003).

[6] A. Carre and J. Vital, Surface Free Energy Caliculation for Polymers by a Group Contribution Method, in *Adhesion*, Vol. 13, K. W. Allen, ed., ELSEVIER APPLIED SCIENCE, London (1989), p. 23.

[7] U. Gelius, P. F. Heden, J. Hedman, B. J. Lindberg, R. Manne, R. Nordberg, C. Nordling and K. Siegbahn, *Phys. Scr.* ***2***, 70 (1970).

[8] D. T. Clark, W. J. Feast, D. Kilcast, and W. K. R. Musgrave, *J. Polym. Sci.* ***11***, 389 (1973).

[9] C. D. Wagner, Chapter 7, in *Handbook of X-ray and Ultraviolet Photoelectron Spectroscopy*, D. Briggs, ed, Heyden and Sons, London (1977).

Iron doped TiO_2 Nano Powder Treatments in Atmospheric Pressure

M. Kogoma[1], K. Tanaka[1] and A. Takeda[2]

[1] Department of Chemistry, Faculty of Science and Technology, Sophia University
7-1, Kioi-cho,Chiyoda-ku,Tokyo 102-8554, Japan
[2] ISI corporation, 5-40-6, Motobuto, saitama-shi, Saitama,330-0052, Japan

Abstract

Fe ion doped TiO_2 particles for coametics were atained by means of atmospheric pressure glow discharge using IAA and TEOS. The ion doped particles were coated by a silica protection layer. To examine the UV catalytic ability of ion doped TiO_2, a squalene that contained the powders after being irradiated by a Xe lamp for one hour, were measured by GCMS for the gas products. Using of silica coated ion doped TiO_2, we have no signal assigned as harmful organic oxides in the GC-MS spectra of the UV irradiated squalene.

1. Introduction

Some kinds of pigments that are used for cosmetics give rise to a skin irritation problem when they contact the skin directly. TiO_2 is an UV reflective white pigment powder for cosmetics. But naked TiO_2 is a kind of photosensitive catalyst, so the powder easily attacks a human skin surface and oxidizes oil in the sweat as a squalene. Oxidized squalene molecules will produce many kinds of peroxy-organic compounds that may cause an allergy or cancer. So we need to avoid such effects caused by the catalytic ability of TiO_2 particles.

Some previous studies reported the possibility of powder handling with atmospheric pressure glow discharge [1-5]. Then, at the first stage in this experiment, we will try to develop some SiO_2 coating on the TiO_2 powder pigments by means of atmospheric pressure glow discharge using TEOS adsorbing and plasma oxidation to prevent the oxidation of squalene oil in the UV irradiation.

On the other hand the SiO_2-coated TiO_2 powders will not have only a very high refractive index for the UV region but also high transparency for visible and IR regions. For such reasons, silica-treated powders will have too white a tint to use for the cosmetics and cannot prevent IR penetration through the powder, which is also a cause of human skin irritation. We can expect that some metal ion doping can achieve wide band light absorption in TiO_2. At the second stage, we will try to obtain a thin deposition layer of iron between the TiO_2 surface and the silica layer to eliminate the photo-catalytic ability and to suppress the wide band light transparency of bulk TiO_2.

Finally, we measure the catalytic effect and light absorption of the new material iron doped silica- coated TiO_2.

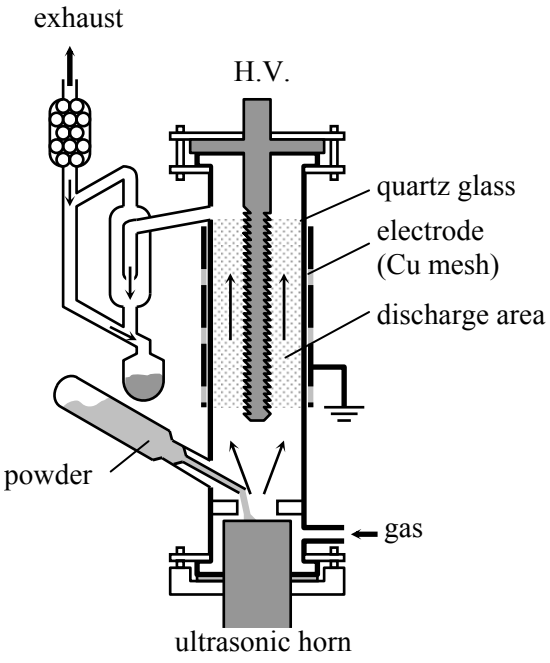

Fig. 1 Schematic of discharge apparatus.

2. Experimental

The mean diameter of TiO_2 particles is two hundred nm; they contain 80% of anatase and 20% of rutile (Toho Titanium Corporation, HT-170R). For iron doping, we used tris (2, 4-pentanedionato) iron (IAA). In this study, we employed the Adsorb and Dry method to achieve the coated surface [5]. The schematics of the discharge reactor is shown in Figure 1. The discharge conditions are as follows: discharge frequency, 13.56 MHz; power, 1.5 - 2.5 kW; O_2/He gas flow rate, 100 ml min^{-1}/10 l min^{-1}. Treating rate is about 2 g min^{-1} for the powder.

To examine the photo catalyst ability of the powders, we irradiated the squalene oil
(2, 6, 10, 15, 19, 23-hexamethyl-2, 6, 10, 14, 18, 22-tetracosahexaene) that contained the powder samples by UV in a Pyrex glass bottle. After 1 hour UV-irradiation by Xe lamp, the gas products were measured by GC-MS (Shimazu QP5050).

Process 1) Silica coating on TiO_2

At first we tried to make sure of the possibility of the Adsorb and Dry method with TEOS to coat SiO_2 on the bulk TiO_2. In this treatment, adsorbed TEOS is partly reacted with naturally adsorbed water on the TiO_2 surfaces to deposit SiO_2. The percentages of SiO_2 on the sample TiO_2 powders are calculated using the next equation:

$$Y=Xa/100\times W/M \qquad (1)$$

Y, SiO_2 wt% on TiO_2 powders
X, sample powder weight/g
a, wt % of SiO_2 on the sample powder
W, Molecular weight of SiO_2 (60)
M, Molecular weight of TEOS (208)

Weighed TEOS is diluted in ethanol (lower than 10%); then the powder is dried in air ambience. Adsorbed powder is treated in the atmospheric pressure glow plasma in He-O_2 system to eliminate the organic part from the adsorbed TEOS molecules.

Process 2) Iron ion doping

TiO_2 powders were pre-treated with IAA-ethanol mixture to adsorb organic metal molecules on the surfaces of the particles. The amount of IAA in ethanol are calculated using same equation(1) as in TEOS adsorption. After the evaporation of the ethanol, the IAA adsorbed powders are treated to have iron ion doped TiO_2 using atmospheric pressure glow plasma in He-O_2 system to eliminate the organic part from the adsorbed IAA molecules.

Process 3) Silica-Iron-TiO_2 multi coating.

After process 2, the iron-doped TiO_2 powders were pre-treated with TEOS (tetraethoxysilane) - ethanol mixture aero - sol to adsorb TEOS on the surfaces of the particles. After the ethanol evaporation, the powders are oxidized in atmospheric pressure glow plasma. Using the plasma treatment, SiO_2 was deposited on the iron-doped TiO_2 surface as an inorganic fine layer. The thickness of SiO_2 deposited can be controlled by the concentration of TEOS in the solvent ethanol during the adsorbing process.

3. Results and discussion

Process 1)

From the XPS analysis, we found Si2p and Ti2p spectra for TiO_2 that adsorbed TEOS (b), and for TiO_2 that adsorbed TEOS and then was oxidized in the He-O_2 plasma (c), as shown in figure 2. After plasma oxidation (c), Si atomic concentration is increased because the naked TiO_2 surfaces are completely covered by an inorganic SiO_2 thin layer.

In figure 3, sharp peaks of O_{1s} were obtained in the spectra of (a), (b) and (c). In the spectrum of (a) only one

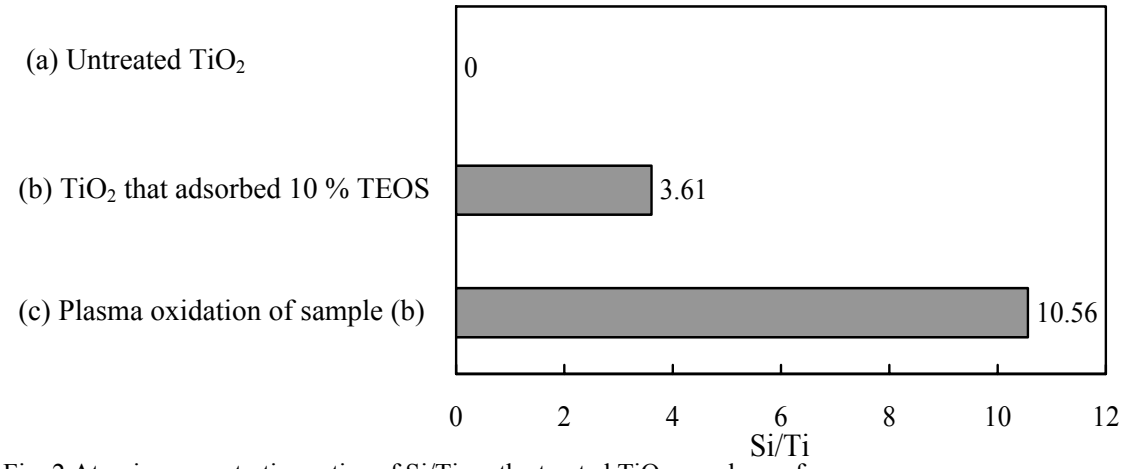

Fig. 2 Atomic concentration ratios of Si/Ti on the treated TiO_2 powder surfaces.

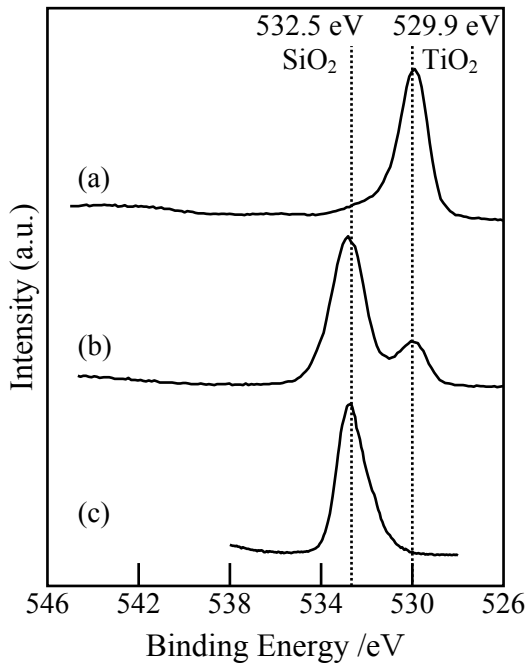

Fig. 3 O_{1s} spectra of XPS: a) untreated TiO_2,b) TiO_2 that adsorbed 10wt%TEOS c) Plasma oxidation of TiO_2 that adsorbed 10wt%TEOS.

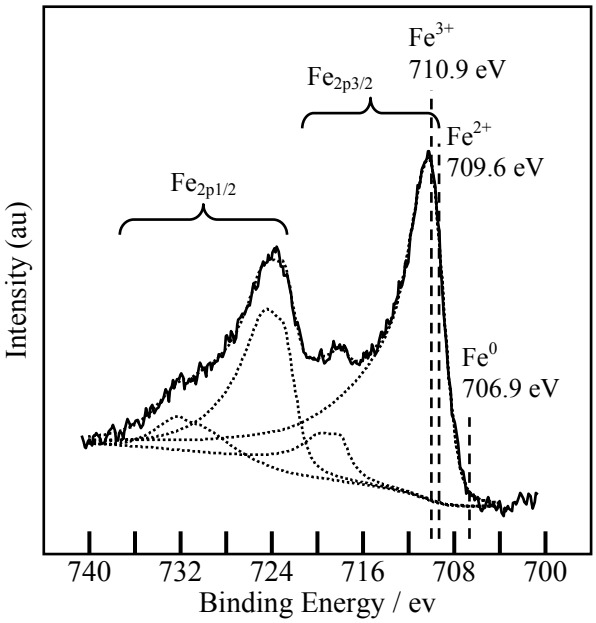

Fig. 4 XPS Fe_{2p} spectra of IAA-treated TiO_2 particles oxidized in the O_2/He plasma.

peak (529.9 eV) assigned to TiO_2 existed. On the other hand, in the spectrum of (b) the peak (532.5 eV) assigned to SiO_2 newly appeared while the peak assigned to TiO_2 decreased. Therefore, we concluded that the surface of (b) was coated with SiO_2 but the coating was not enough. The surface of TiO2 is still partly covered by half-dissociated TEOS molecules that are reacted with adsorbed water on the surface of TiO_2. In the spectrum of (c), the peak assigned to TiO_2 has almost disappeared and the shape of the peak looked like that of pure SiO_2. So, we could confirm that the surface of (c) was almost completly coated with an inorganic SiO_2 layer without any organic contamination.

A TEM photo of silica-coated TiO_2 particles is shown in photo 1. In the photo, homogineous SiO_2 thin layer(1-2nm in thickness) is found on the particles. So we attained a very homogeneous SiO_2 layer with the TEOS Adsorb and Dry method.

Process 2)

Figure 4 shows the XPS Fe_{2p} spectra of IAA-treated TiO_2 particles oxidized in the O_2/He plasma. In the figure, we can find $Fe_{2p1/2}$ and $Fe_{2p3/2}$ peaks assigned as Fe ion, but the binding energies of Fe^{2+} and Fe^{3+} ions are very close to each other. So it is difficult to define which ion is on the TiO_2. The amount of deposited Fe ion can be controlled by the concentration of IAA in the solvent ethanol at the adsorbing process. Figure 5 show the UV-VIS reflection spectra of naked TiO_2, IAA 1% adsorbed TiO_2; adsorbed, then plasma -treated TiO_2; and pure IAA powder. Naked TiO_2 show a high and flat reflectivity from near IR region to UV region. Light incident to the surface partly penetrates into the bulk and is absorbed in the solid, then it reflects to the surface boundary, so the reflection spectra contain the absorption characteristics. IAA-adsorbed TiO_2 shows small peaks attributed to adsorbed IAA on the TiO_2 but such a peak is lost in the plasma-irradiated IAA itself. It

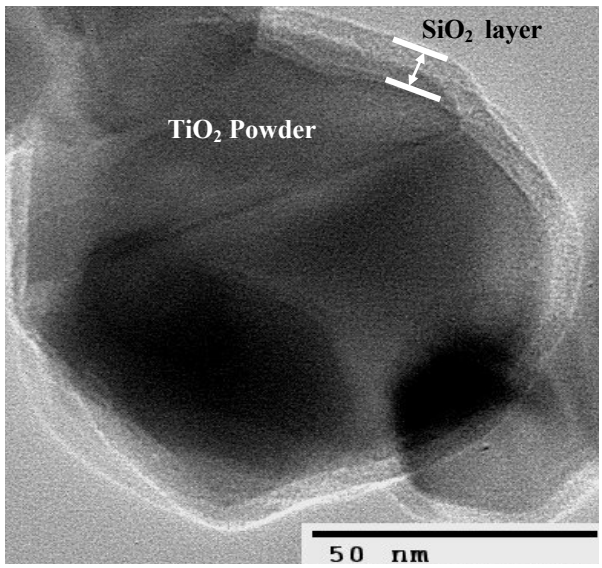

Photo 1 TEM photography of TiO_2 treated by SiO_2 in plasma oxidation

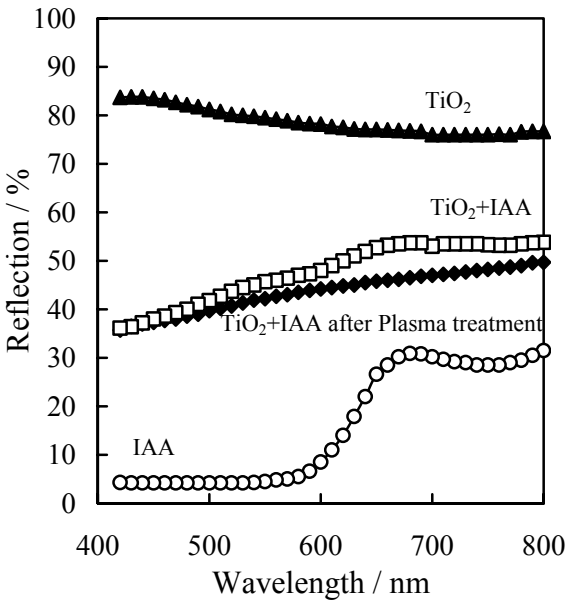

Fig. 5 Reflection spectra of TiO_2; IAA adsorbed TiO_2; adsorbed, then plasma-treated TiO_2; and pure IAA powder.

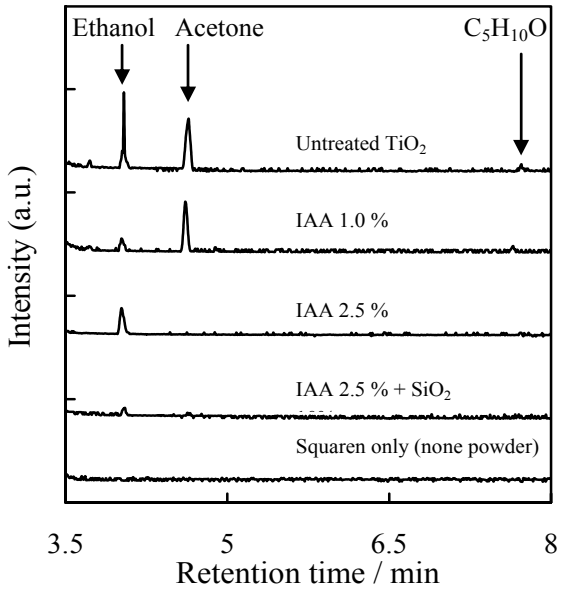

Fig. 6 GCMS spectra of gas products in squalene which contained the powders after one hour irradiated by Xe lamp.

seemed that plasma-treated IAA on the TiO_2 were completely oxidized to inorganic Fe ion.

Figure 6 show the GCMS spectra of gas products in squalene which contained the powders after being irradiated by an Xe lamp for one hour.

Untreated TiO_2 produces many kinds of organic oxides such as ethanol, acetone and long chain oxidant compounds that should be harmful materials for human skin. Also, the oil emits a foul odor. The product concentrations decreased with increasing of the concentration of the doped iron. However even for 2.5% iron-doped TiO_2, we still have a small amount of alcohol in the spectrum. But using silica-coated iron-doped TiO_2 which is produced in process 3), we have almost no signal assigned as an organic oxide in the GC-MS spectra of the UV irradiated squalene, except for a very small amount of ethanol signal. Normally the anatase-type TiO_2 crystals have small rectangular open spaces, such a few angstroms in size, in the structure. It seemed that the iron ions are partly inserted into the open spaces of the TiO_2 latice. However, the crystal lattice of iron-doped TiO_2 is the same as that of untreated one measured by XRD. So we could not infer whether the iron ion is in solid solution in TiO_2.

The treated powder shows fine and flesh colour with pearl-like glowing, that should be caused from a multi-reflection effect from the thin layer boundaries of silica-iron-TiO_2. Especially, the powder can cover the skin furrows and prevent easy drop-off of the powder from the skin surface by sweat, because of the high reflection for the incident light in the skin furrow and the strong absorbing ability of the nano powder to absorb the skin oil.

4.Conclusion

We attained Fe ion doped TiO_2 particles by means of atmospheric pressure glow discharge using IAA, TEOS adsorbing and plasma oxidation method. The particles were coated by a silica protection layer to avoid the UV catalytic ability of TiO_2. The plasma -treated TiO_2 powders will provide many functional contributions for the future cosmetics.

5. Reference

[1] S. Kanazawa, M. Kogoma. T. Moriwaki, S. Okazaki, J. Phys. D: Appl. Phys. 21 (1988) 838.
[2] T. Yokoyama, M. Kogoma, S. Kanazawa, T. Moriwaki, S. Okazaki, J. Phys. D: Appl. Phys. 23 (1990) 374.
[3] T. Yokoyama, M. Kogoma. T. Moriwaki, S. Okazaki, J. Phys. D: Appl. Phys. 23 (1990) 1125.
[4] T. Mori, K. Tanaka, T. Inomata, A. Takeda, M. Kogoma, Thin Solid Films 316 (1998) 89.
[5] S. Ogawa, K. Kiuchi, K. Tanaka, M. Kogoma, Proc. 18th Symp. Plasma Process., 449(2001).

Modeling of Plasma Chemistry and Particle Growth Mechanisms in Dusty Plasmas

Kathleen De Bleecker[1], Annemie Bogaerts[1], and Wim Goedheer[2]

[1]*PLASMANT, Department of Chemistry, University of Antwerp (UA), Wilrijk, Belgium*
[2] *FOM Institute for Plasma Physics "Rijnhuizen", Nieuwegein, The Netherlands*

Abstract
The initial mechanisms of dust formation in radiofrequency acetylene (C_2H_2) plasmas are investigated by means of a self-consistent 1D fluid model. Possible routes for particle growth are discussed and a comparison with particle formation in silane (SiH_4) discharges is made. The model considers a set of 39 species, including neutrals, radicals, ions and electrons, describing hydrocarbons (C_nH_m) containing up to 12 carbon atoms. Both successive anion/cation – molecule reactions seem to lead to a fast build up of the carbon skeleton.

1. Introduction

Dust particles, from a few nanometers up to several micrometers, have been observed in many processing plasmas used for etching, sputtering or deposition of thin surface films. Until recently, the presence of dust was solely considered as a potential hazard, especially in the microelectronic and other surface processing technologies, as particles provide a significant source of film defects redeeming them as 'killer' particles. Therefore, early investigations mainly attempted at suppressing the particle growth or tried to avoid interference with the wafer surface. Currently, it seems that small particles can also have very interesting and useful properties, mainly due to their very small sizes (e.g. nanometer range), chemical composition or uniform size distribution [1,2]. In the photovoltaic cell production, for example, the creation and inclusion of nanocrystalline silicon particles in the intrinsic layer of amorphous hydrogenated silicon (a-Si:H), can result in a significant increase of the product quality [3]. The newly formed material shows improved transport properties and stability against the light induced effect, also known as the Staebler-Wronski effect. In order to obtain a controlled growth and deposition of these particles on the substrate material, we obviously must understand the mechanisms behind their origin and their behavior, including their transport, in the plasma. Comprehension of these aspects will help to advance the existent and future technological applications.

In chemically active plasmas, such as silane (SiH_4) and acetylene (C_2H_2), it is generally believed that particle formation proceeds through a series of chemical reactions in the gas phase, better known as gas phase polymerization, whereby parent gas monomers are gradually transformed to macromolecules. Although the behavior of particles in the micrometer-sized regime is relatively well understood, the transition of gas species to particles remains a complex process, which is still open for investigation. These earlier stages, known as nucleation and coagulation, are of specific interest in current research. Besides investigations of the plasma chemistry, the dust particles will also acquire a negative charge due to the collection of plasma ions and electrons. The magnitude of the charge on a particle will greatly depend on the particle size and the plasma conditions. This negative charge will also be responsible for the confinement and consequently longer lifetimes of such particles in the plasma. Once the particles reach a certain size (i.e. several nanometers), other forces, besides the electric force and diffusion, will dominate their transport (e.g. the ion drag, the thermophoretic, and the neutral drag force). The competition between these different forces ultimately leads to the confinement of the particles in well-defined regions of the discharge [4,5]. In the end, particles will continue to grow until gravity drags them out of the discharge.

In this paper we will mainly discuss the chemical processes through which larger particles can be formed in a capacitively coupled acetylene (C_2H_2) RF discharge and try to identify the precursors of the dust formation with the use of a self-consistent one-dimensional (1D) fluid model. The gas phase discharge chemistry is investigated and the similarities and differences with particle formation in silane discharges are discussed.

2. Plasma chemical kinetics

Particles in chemically active plasmas emerge as a result of numerous chemical processes in the ionized gas phase. In silane plasmas, anion-induced chain reactions are considered to be the main pathway leading to powder

formation. Negative ions are generally believed to play a very important role in the dust formation, as they are confined by the sheath electric fields in the plasma bulk [6]. The long residence time of the anions in the plasma favors their further growth and makes them good candidates to trigger particle formation. Previously we have developed a detailed chemical kinetics model for gas phase nucleation of hydrogenated silicon particles [7,8]. In that model dust is primarily formed by successive reactions of anions with silane molecules,

$$Si_nH^-_{2n+1} + SiH_4^{(*)} \rightarrow Si_{n+1}H^-_{2n+3} + H_2 \quad (1a)$$

$$Si_nH^-_{2n} + SiH_4^{(*)} \rightarrow Si_{n+1}H^-_{2n+2} + H_2\,. \quad (1b)$$

In addition to ground state SiH_4 molecules, reactions with vibrationally excited SiH_4 ($SiH_4^{(1\text{-}3)}$ and $SiH_4^{(2\text{-}4)}$) are also taken into account, as these species have sufficient internal energy to overcome probable energy barriers in some of the endothermic chain reactions [9]. The mechanism starts primarily from SiH_3^- and SiH_2^- anions, and includes silicon hydrides containing up to twelve silicon atoms. Other pathways involving e.g. positive ions can be excluded as a kinetic bottleneck is already formed at particles having relatively low numbers of silicon atoms, preventing the formation of positive ions having more than five or six silicon atoms [10].

Discharges in hydrocarbon mixtures also tend to produce dust, especially when a sufficient amount of acetylene is present [11]. In contrast to silane plasmas, the dust formation mechanisms in hydrocarbon discharges are much less understood and only a limited amount of data for hydrocarbon molecules is available. Therefore, various mechanisms have been proposed. Presumably both positive and negative ions play a role in the initial phase of the dust forming process, as mass spectrometry measurements reveal the same features in both the anion and cation mass spectra [12, 13].

In this paper acetylene is considered as an example of the hydrocarbon discharge chemistry, as it yields more highly polymerized ions than methane (CH_4) and also has a much stronger and faster tendency to form dust. Table 1 gives an overview of the 39 different species considered in the acetylene model, besides the electrons. Starting from C_2H_2 a series of chemical reactions has been gradually incorporated in the 1D fluid model that leads to the formation of larger hydrocarbons (C_nH_m) containing up to a maximum of 12 carbon atoms. The absence of hydrocarbon molecules with an odd number of carbon atoms is a distinct feature of acetylene discharges. The typical spectral pattern in mass spectrometric measurements shows clear sequences of ions with even numbers of carbon atoms indicating that the strong carbon bond structure ($H-C \equiv C-H$) of the initial acetylene molecule persists upon successive insertion of acetylene in the hydrocarbon species.

Table 1. Different species taken into account in the hydrocarbon model, besides the electrons

Molecules	Ions	Radicals
C_2H_2	$C_2H_2^+$, C_2H^+, CH^+, C_2^+, C^+	CH, CH_2
C_4H_2, C_6H_2, C_8H_2	$C_4H_2^+$, $C_6H_2^+$, $C_6H_4^+$, $C_8H_6^+$	
$C_{10}H_2$, $C_{12}H_2$	$C_{10}H_6^+$, $C_{12}H_6^+$	
		C_2H_3, C_4H_3, C_6H_3
	C_2H^-, C_4H^-, C_6H^-, C_8H^-	C_2H, C_4H, C_6H, C_8H
	$C_{10}H^-$, $C_{12}H^-$	$C_{10}H$, $C_{12}H$
H_2	H_2^+, H^+	H

While in our model for silane plasmas the positive ions could be limited to three different species, i.e. SiH_3^+, $Si_2H_4^+$ and H_2^+ [8], both the positive and negative ions in the acetylene model are extended up to hydrocarbons containing 12 carbon atoms, as the role of both pathways in the first step of particle formation can not be excluded. In the model we account for a total of 78 volume reactions comprising 22 electron impact reactions with acetylene and hydrogen, 35 ion-neutral reactions (anion or cation – acetylene reactions and mutual anion-cation neutralization reactions) and 21 neutral-neutral reactions (hydrogen abstraction, C_2H insertion). Since detailed data on many processes in an acetylene discharge is still lacking, some assumptions have to be made which are tested against the data known from the experimentally obtained mass spectra. Below a comprehensive summary is given of the most important part of the reaction mechanism.

2.1 Reactions involving anions

Usually negative ions are not considered in the modeling of 'standard' acetylene discharges, i.e. without the inclusion of dust formation [14,15]. However, the primary C_2H^- ion, formed through the dissociative attachment of C_2H_2, can be incorporated in neutral species, thereby creating larger negative ions which can eventually grow to nanometer and micrometer sized particles that remain trapped in the plasma due to their large negative charge. In spite of the difficulty of adding an electron to the filled valence shell of acetylene, the electron affinity of the C_2H radical seems to be sufficiently large to produce a stable C_2H^- anion,

$$e^- + C_2H_2 \rightarrow C_2H^- + H\,. \tag{2}$$

This dominant anion is the first species of the particle formation and can in turn undergo the following anion-molecule chain reactions:

$$C_2H^- + C_2H_2 \rightarrow C_4H^- + H_2 \tag{3a}$$

$$C_4H^- + C_2H_2 \rightarrow C_6H^- + H_2 \tag{3b}$$

$$\cdots$$

$$C_{2n}H^- + C_2H_2 \rightarrow C_{2n+2}H^- + H_2\,. \tag{3c}$$

High resolution mass spectra [12] show that the majority of the anions in C_2H_2 plasmas are nearly pure carbon anions, hence, in accordance with the analogous path in silane discharges, molecular hydrogen is lost in every polymerization reaction. Only anions with an even carbon atom number are included in the model, as the triple carbon bond of acetylene is preserved.

No precise rate coefficients for anion chain reactions can be found in literature, but a theoretical upper limit for ion-molecule reactions can be predicted by the Langevin collision rate constant k_L [16]:

$$k_L = e\left(\frac{\pi}{\varepsilon_0}\right)^{1/2}\left(\frac{\alpha}{m_r}\right)^{1/2} \tag{4}$$

where α is the neutral atom or molecule polarizability (in $Å^3$) and m_r is the reduced mass (in amu) of the two reacting species. Inserting the polarizability of 3.49 $Å^3$ for acetylene [17] results in a Langevin rate of the order of 10^{-15} m^3 s^{-1}. However, since these rate constants represent an upper bound for the actual reaction rates, we have used, according to experimental data in [18], Langevin rate constants reduced by three orders of magnitude in our modeling study, i.e. values of the order of 10^{-18} m^3 s^{-1}. Taking larger reaction rates would result in an increase in concentration with rising carbon atom number, which is not in agreement with the observed high resolution mass spectra [12].

2.2 Cation-molecule reactions

In contrast to silane plasmas, the hydrocarbon positive ions polymerize to the same extent as the negative ions and, hence, can not be excluded as a possible route of powder formation. Positive ions are formed from acetylene by electron impact ionization, creating mostly $C_2H_2^+$. Starting from $C_2H_2^+$ rapid condensation reactions with acetylene yield the production of higher mass hydrocarbon cations with or without subsequent loss of molecular or atomic hydrogen. The principal reaction sequence can be summarized by:

$$C_2H_2^+ \xrightarrow{C_2H_2} \underset{(+H_2)}{C_4H_2^+} \xrightarrow{C_2H_2} C_6H_4^+ \xrightarrow{C_2H_2} C_8H_6^+ \xrightarrow{C_2H_2} \underset{(+H_2)}{C_{10}H_6^+} \xrightarrow{C_2H_2} etc. \tag{5}$$

The specific ionic product obtained from any given ion-acetylene reaction, and thus the degree of hydrogenation, depends upon the extent of stabilization achieved by the chemical intermediate [19, 20]. The primary reaction between $C_2H_2^+$ and C_2H_2 can for example lead to $C_4H_2^+$ and $C_4H_3^+$ production. $C_4H_3^+$ is not considered as a separate species in the model; however its production is intrinsically incorporated in $C_4H_2^+$ by using the overall reaction rate constant of both reaction channels, i.e. 1.2 x 10^{-15} m^3 s^{-1} [21]. Another fragment ion generated from acetylene ionization, i.e. C_2H^+, also reacts with C_2H_2 to give $C_4H_2^+$,

$$C_2H^+ + C_2H_2 \rightarrow C_4H_2^+ + H \tag{6}$$

with the fast rate constant of 1.7 x 10^{-15} m^3 s^{-1} [20]. C^+, C_2^+ and CH^+ ions are also formed through dissociative ionization of acetylene, and can in principle react with C_2H_2 via condensation with loss of H or H_2. Although all

these reactions are rapid with rate constants close to the collision limit, these reactions are not taken into account in the model, since the initial formation of these species is too low to make these reactions efficient.
Besides fast polymerization reactions, mutual ion-ion neutralization represents another loss process for both the anion and cation molecules. The rate constant for neutralization is taken from [22] and is only weakly dependent on the nature of the molecule, resulting in our case in a reaction rate constant of 8.7 x 10^{-14} m^3 s^{-1}.

2.3 Neutral chemistry

Breakage of a C-H bond in acetylene by electron impact dissociation produces the C_2H radical that can in turn be inserted into hydrocarbons to produce larger $C_{2n}H_2$ molecules,

$$C_2H + C_{2n}H_2 \rightarrow C_{2n+2}H_2 + H\ . \qquad (7)$$

The reaction chain is initiated by the insertion of C_2H into acetylene leading to the formation of diacetylene (C_4H_2) and atomic hydrogen. A corresponding $C_{2n}H$ radical can be formed by electron induced dissociation of the $C_{2n}H_2$ molecule and can play a role in the deposited layer. The deposition process itself is described by a sticking model that ensures that the loss of species due to plasma-wall interactions is taken into account.

3. Results and discussion

A typical parallel-plate PECVD reactor has been modeled with an inter-electrode spacing of 3 cm at a discharge frequency of 13.56 MHz. The capacitively coupled RF plasma is operated at a total gas pressure of 40 Pa, a power of 5 W and a gas temperature of 400 K, with a gas flow of 20 sccm of pure acetylene or silane. Figure 1 presents the calculated densities of the electrons and the most abundant positive and negative ions in a pure acetylene (a) and a pure silane discharge (b) as a function of position in the plasma. Near the sheaths a slight time variation of the ion profiles can occur, hence, time-averaged electron and ion densities have been plotted.

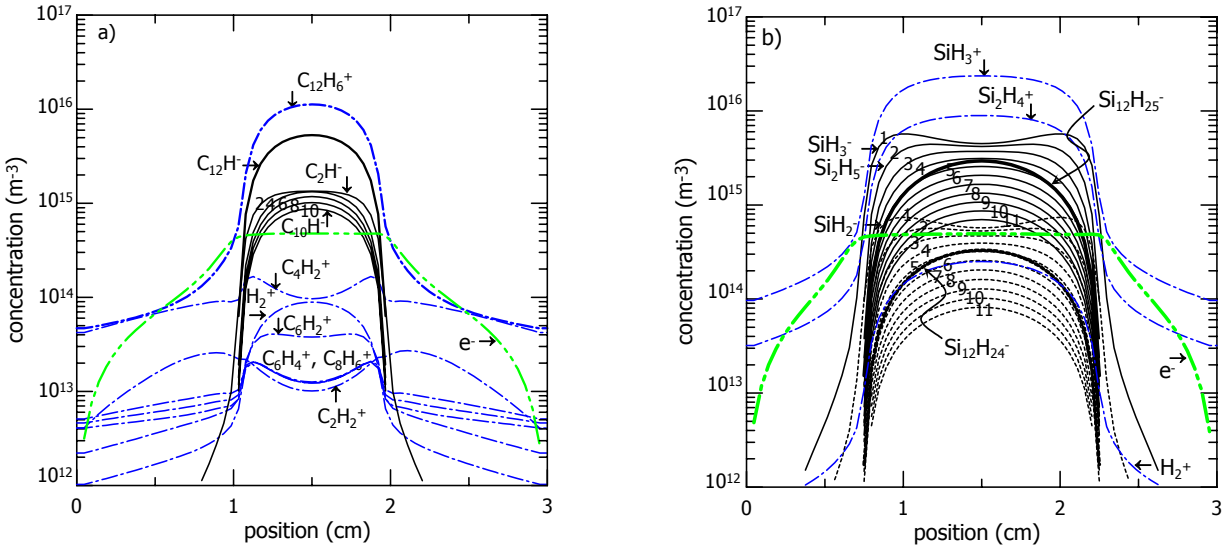

Fig. 1. Density profiles of ions in an acetylene (C_2H_2) discharge (a); and a silane (SiH_4) discharge (b); at a pressure of 40 Pa, a power of 5 W and 13.56 MHz.

In the acetylene plasma (Fig. 1a) two different pathways involving positive or negative ions, respectively, can be distinguished. The number indicated on every anion plot specifies the number of carbon atoms. In each pathway a gradually decreasing trend can be observed with increasing number of carbon atoms. This is in good agreement with the observed mass spectra in [12] where the same trend can be detected. In the model both chains are stopped at hydrocarbon ions containing 12 carbon atoms. Therefore, $C_{12}H_6^+$ and $C_{12}H^-$ appear to be the most prominent species formed in the plasma which represent the final accumulating stage and thus symbolize the sum of all larger cations or anions, respectively. Since most cation-acetylene reactions proceed at a rate close to the collision limit (see above) lower concentrations of the intermediate hydrocarbon positive ions are produced in comparison to the intermediates in the anion chain, where the reactions proceed at a rate constant close to

10^{-18} m^3 s^{-1}. The cation density profiles exhibit a lower density in the plasma bulk which is probably a direct consequence of the fast loss processes, i.e. association reactions with C_2H_2, which can not be entirely compensated by the slow movement of the positive ions towards the plasma center. In the figure only the most dominant positive hydrocarbons are shown. Other positive ions formed through the dissociative ionization of acetylene, i.e. C^+, C_2^+ and CH^+, reach a concentration of approximately 10^{10} m^{-3} (not shown). $C_4H_2^+$ appears to be the most abundant positive ion followed by $C_6H_2^+$ and $C_6H_4^+$. This is also seen in mass spectra which peak at ions containing 4 and 6 carbon atoms.

For comparison the electron and ion profiles in a silane plasma are shown in Fig. 1(b). The major positive ion appears to be SiH_3^+ with a density of about 2 x 10^{16} m^{-3} in the center of the discharge. In experimental data no cation powder route can be observed, hence, only two other positive ions are considered in the model, i.e. $Si_2H_4^+$ and H_2^+. For the anions, however, two different routes can be discerned, starting from either SiH_3^- or SiH_2^- [see Eqs. 1(a) and 1(b) above]. Similar to the acetylene plasma, the anions are mostly confined to the bulk of the discharge since they are repelled by the high electric fields in the plasma sheaths, and they show a general decreasing trend towards larger numbers of silicon atoms (apart from the final $Si_{12}H_{25}^-$ and $Si_{12}H_{24}^-$ stages which represent the sum of all larger anions). The rate coefficient for the anion reactions (~10^{-18} m^3 s^{-1}) is similar to the one used in the acetylene anion chemistry. It is clear from Fig. 1(b) that mainly the SiH_3^- pathway, represented by solid lines, will create higher mass silicon hydrides and less than 10% of the particle formation proceeds through the SiH_2^- pathway, depicted by dashed lines.

In Fig. 2 the calculated concentrations of the various hydrocarbon molecules (a) and radicals (b) in the acetylene discharge are shown at the same conditions as discussed above. The densities of the background neutrals are homogeneously distributed over the entire reactor and are produced in larger amounts compared to their corresponding radicals. Similar to the ion density profiles higher mass hydrocarbon molecules show a decreasing trend with increasing number of carbon atoms.

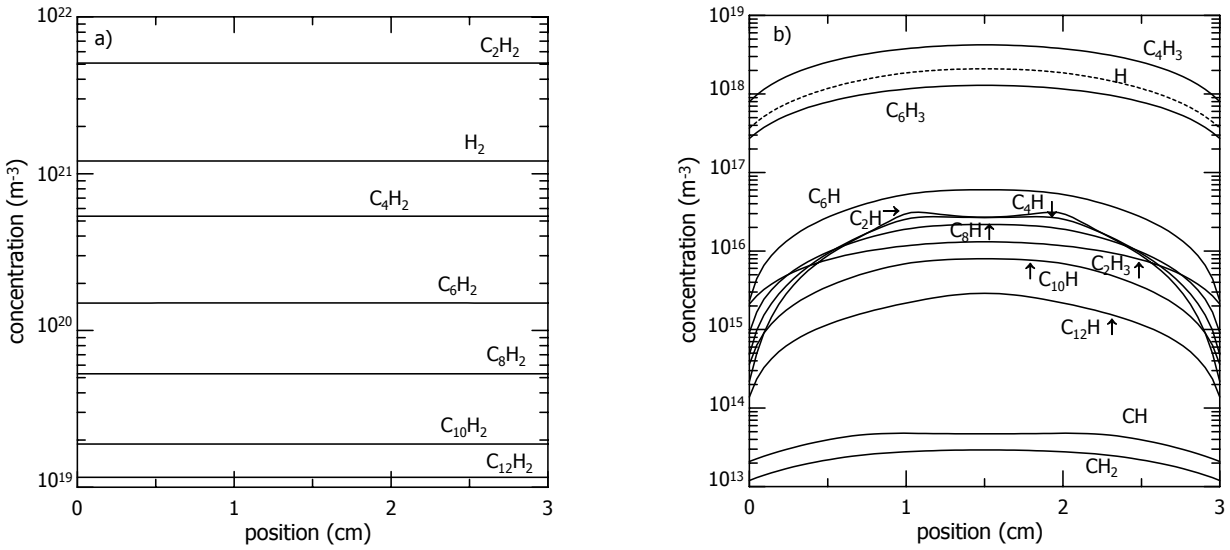

Fig. 2. Density profiles of the various hydrocarbon molecules (a); and radicals (b) in an acetylene discharge; at a pressure of 40 Pa, 5 W and 13.56 MHz.

The acetylene background gas is present at the highest density and takes a value of 4 x 10^{21} m^{-3}. Other non-ionic gaseous products that can be found at high concentrations in the acetylene discharge are diacetylene (C_4H_2) and molecular hydrogen. The high H_2 concentration comes from the many chemical reactions that produce molecular hydrogen as a side product (see above).

All twelve radicals are depicted in Fig. 2(b) and mostly encompass carbon rich species C_nH_m (with n > m). The radicals are typically characterized by their decreasing density towards the electrodes, representing their reactivity at the walls. A large amount of atomic hydrogen is present with a density of ~ 1 x 10^{18} m^{-3}.

From our results we can conclude that more pathways towards dust formation exist for acetylene plasmas. Indeed, both positive ions, starting from $C_2H_2^+$, and negative ions, starting from C_2H^-, derived from acetylene may participate as precursors to dust formation, while in silane processing discharges the anions, and more specifically SiH_3^-, are the likely precursors of powder formation. Once the particles reach the nanometer size the negative ions will however probably again persist as the most important dust precursors, since they remain trapped in the discharge due to their large negative charge, while the positive ions will likely be extracted from the discharge before they can grow any further.

4. Acknowledgments
This research was financed by the Institute for Promotion of Innovation through Science and Technology in Flanders (IWT-Vlaanderen).

References
[1] A. Bouchoule, in Dusty Plasmas: Physics, Chemistry and Technological Impacts in Plasma Processing, edited by A. Bouchoule (Wiley, Chichester, UK, 1999).
[2] S. V. Vladimirov, and K. Ostrikov, Phys. Reports **393**, 175 (2004).
[3] Y. Poissant, P. Chatterjee, and P. Roca i Cabarrocas, J. Appl. Phys. **94**, 7305 (2003).
[4] K. De Bleecker, A. Bogaerts, and W. Goedheer, Phys. Rev. E **70**, 056407 (2004).
[5] K. De Bleecker, A. Bogaerts, and W. Goedheer, *Role of the thermophoretic force on the transport of nanoparticles in dusty silane plasmas*, Journal of Applied Physics, submitted (2005).
[6] A. A. Howling, L. Sansonnens, J-L. Dorier, and Ch. Hollenstein, J. Phys. D: Appl. Phys. **26**, 1003 (1993).
[7] K. De Bleecker, A. Bogaerts, W. Goedheer, and R. Gijbels, IEEE Trans. Plasma Sci. **32**, 691 (2004).
[8] K. De Bleecker, A. Bogaerts, R. Gijbels, and W. Goedheer, Phys. Rev. E **69**, 056409 (2004).
[9] A. A. Fridman, L. Boufendi, T. Hbid, B. V. Potapkin, and A. Bouchoule, J. Appl. **79**, 1303 (1996).
[10] M. L. Mandich, W. D. Reents, Jr., and K. D. Kolenbrander, J. Chem. Phys. **92**, 437 (1990).
[11] S. Hong, J. Berndt, and J. Winter, J. Phys. D: Appl. Phys. **12**, 46 (2003).
[12] Ch. Deschenaux, A. Affolter, D. Magni, Ch. Hollenstein, and P. Fayet, J. Phys. D: Appl. Phys. **32**, 1876 (1999).
[13] Ch. Hollenstein, W. Schwarzenbach, A. A. Howling, C. Courteille, J.-L. Dorier, and L. Sansonnens, J. Vac. Sci. Technol. A **14**, 535 (1996).
[14] J. R. Doyle, J. Appl. Phys. **82**, 4763 (1997).
[15] D. Herrebout, A. Bogaerts, R. Gijbels, W. J. Goedheer, and A. Vanhulsel, IEEE Trans. Plasma Sci. **31**, 659 (2003).
[16] J. Perrin, O. Leroy, and M. C. Bordage, Contrib. Plasma Physics **36**, 3 (1996).
[17] C. J. F. Böttcher, and P. Borderwijk, *Theory of electric polarization*, Elsevier, Amsterdam (1978).
[18] J. Perrin, C. Böhm, R. Etemadi, and A. Lloret, Plasma Sources Sci. Technol. **3**, 252 (1994).
[19] M. J. Vasile, and G. Smolinsky, Int. J. Mass Spectrom. Ion Phys. **24**, 11 (1977).
[20] V. G. Anicich, W. T. Huntress, Jr., and M. J. McEwan, J. Phys. Chem. **90**, 2446 (1986).
[21] J. S. Knight, C. G. Freeman, M. J. McEwan, V. G. Anicich, and W. T. Huntress, Jr., J. Phys. Chem. **91**, 3898 (1987).
[22] S. Stoykov, C. Eggs, and U. Kortshagen, J. Phys D: Appl. Phys. **34**, 2160 (2001).

Chemical Processes in Water Solutions During the Diaphragm Discharge

Z. Stará[1], F. Krčma[1], P. Slavíček[2]

[1]*Institute of Physical and Applied Chemistry, Faculty of Chemistry, Brno University of Technology, Brno, Czech Republic*
[2]*Faculty of Science, Masaryk University, Brno, Czech Republic*

Abstract
The work is focused on investigation of chemical processes occurring during the diaphragm discharge in water solutions, especially on production of various chemical active species (hydrogen peroxide, hydroxyl radicals) and on degradation of organic compounds (dyes) dissolved in water. All processes are investigated for various discharge conditions (applied voltage, initial conductivity of the solution, used electrolyte, diaphragm parameters, electrode material etc.). Chemical analyses are complemented with electrical measurements.

Keywords: discharge in water, degradation of organic compounds, hydrogen peroxide

1. Introduction

Discharges generated in liquids have a special position among the plasma sources. Various active chemical species such as hydroxyl radicals, hydrogen and oxygen atoms, hydrogen peroxide etc. are produced by this kind of discharge [1]. These active species initiate many further chemical reactions. Therefore the processes taking place in such discharges can be applied in fields of water treatment, surface treatment etc. Especially the destruction of various organic pollutants or organic dyes dissolved in water and specific reactions in liquid phase are currently the main research fields of discharges in liquids [1, 2].

The most common discharge configurations used for the discharge creation in previous works of many authors are point-to-plane [1] and coaxial [3], several experiments were done in diaphragm (electrode-less) configuration [4, 5]. During almost all of these experiments, a pulsed high voltage in range from about 10 to 20 kV was used to create the discharge.

This work focuses on the diaphragm discharge created using the non-pulsed DC high voltage with the tension of about 2 kV only. Such discharge is also called "electrode-less" [4] because it is created in a small pinhole in the centre of the dielectric diaphragm in a relatively great distance from the high voltage electrodes (2 cm). The dielectric diaphragm is placed between two plane electrodes [6]. When the DC voltage is used, different plasma channels (so-called streamers) are created in both parts of the reactor (Fig. 1). These streamers have converse polarity and differ in their structure, shape, velocity of propagation and energy of electrons [4].

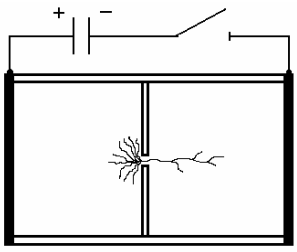

Fig. 1: Scheme of the diaphragm discharge principle with different plasma channels in the parts of the reactor.

2. Experimental setup

A special batch discharge reactor was used in experiments. Its simplified scheme is shown in Fig. 2 and it was described in details in [7]. It consisted of two chambers divided by a dielectric diaphragm (PET). A small pinhole (initially with the diameter of 0.25 mm) was localised in the centre of this diaphragm. During the discharge the pinhole slightly enlarged its diameter and the edges became corroded. In the case of some tested diaphragm materials, the increase in the diameter was too rapid, therefore it was not convenient to create the discharge. Each chamber contained a planar electrode (stainless steel or platinum), a cooling box with a mixture of ice and water, a defined volume of electrolyte (1500 ml) and a mixing system that ensured homogenous conditions. The electrodes were arranged in the distance of 4 cm symmetrically with respect to the dielectric diaphragm. To generate high voltage and to create the discharge, a non-pulsed DC high voltage source (1-3 kV) was applied.

In experiments where production of hydrogen peroxide by the discharge was studied, it was important to ensure the liquid temperature of about 15°C in the whole volume because in the case of the temperature close to 30°C and higher, hydrogen peroxide was thermally decomposed to hydroxyl radicals.

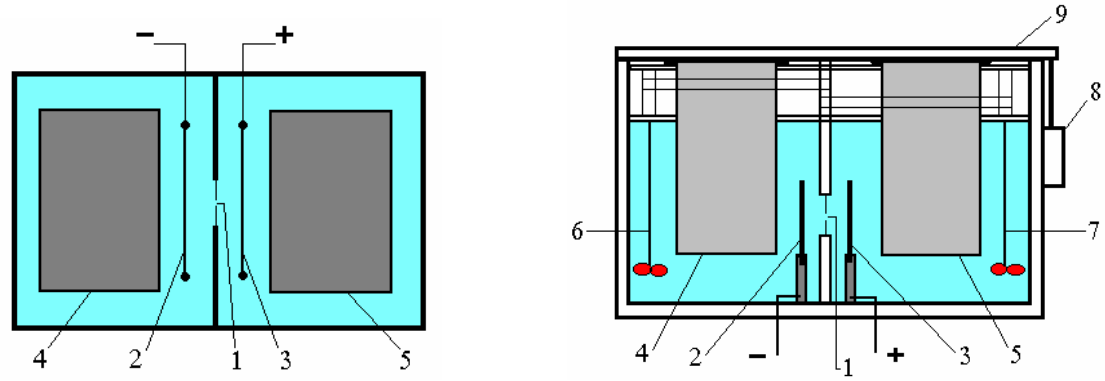

Fig. 2: A simplified scheme of the discharge reactor – a platform (left) and a side view (right): 1 – diaphragm with pinhole, 2 – cathode, 3 – anode, 4, 5 – cooling boxes, 6, 7 – stirrers, 8 – security pin, 9 – security top.

Demineralised water containing electrolyte of defined concentration (NaCl, Na_2HPO_4) was used to obtain the solution of defined initial conductivity (optimum 300-700 $\mu S \cdot cm^{-1}$). Various organic dyes dissolved in water and of various structure, colour, origin and purpose of use were used in experiments. The concentration of the used dyes varied from 1 to 20 $mg \cdot l^{-1}$. As most of the organic dyes were not electrolytes, it was necessary to add extra electrolyte of a defined amount to the solution.
Concentration of hydrogen peroxide produced by the discharge was determined by colorimetric method using a specific reaction between H_2O_2 and titanium reagent [8]:

$$Ti^{4+} + H_2O_2 + 2H_2O \rightarrow TiO_2 \cdot H_2O_2 + 4H^+ \qquad (1)$$

The yellow-coloured peroxotitanyl complex was determined by UV-VIS spectroscopy at 407 nm, hydrogen peroxide concentration in this complex was directly proportional to its absorption intensity. Concentration of organic dyes in the solution was also determined by photometry. Generation of hydroxyl radicals was observed by the optical emission spectroscopy. Electric measurements using the oscilloscope were carried out to ascertain the character of the discharge.

3. Results and Discussion

A series of electric investigations, done by two probes installed in the circuit and measured a discharge current, had ascertained the real discharge character. Figure 3 shows the real evaluation of the discharge current, voltage and resistance in time. Although the continuous DC high voltage was used to create the discharge, the evaluation of electric characteristics is not completely non-pulsed and we have estimated it as quasi-pulsed. This phenomenon is probably caused by the mechanism of creation of the diaphragm discharge (i.e. creation in the pinhole) and it can be explained by the thermal (bubbles) theory [8]. This theory is based on the fact that liquid in the region of a high electric field (it means in the pinhole) is heated and starts to boil, the bubbles appear and the breakdown is created in these bubbles of evaporated liquid. So the discharge is in fact generated in the gas phase. A very important phenomenon is that the bubble is expanding and in quite a short time it is disappearing along with the discharge. But immediately, a new bubble is created and a new breakdown appears. When the bubble (with the discharge) exists, the discharge current is high and resistance very low. But if the bubble vanishes and the discharge is switched off, the discharge current decreases and, on the other hand, the resistance rapidly increases, all with high repetition. Therefore the discharge character is quasi-pulsed.

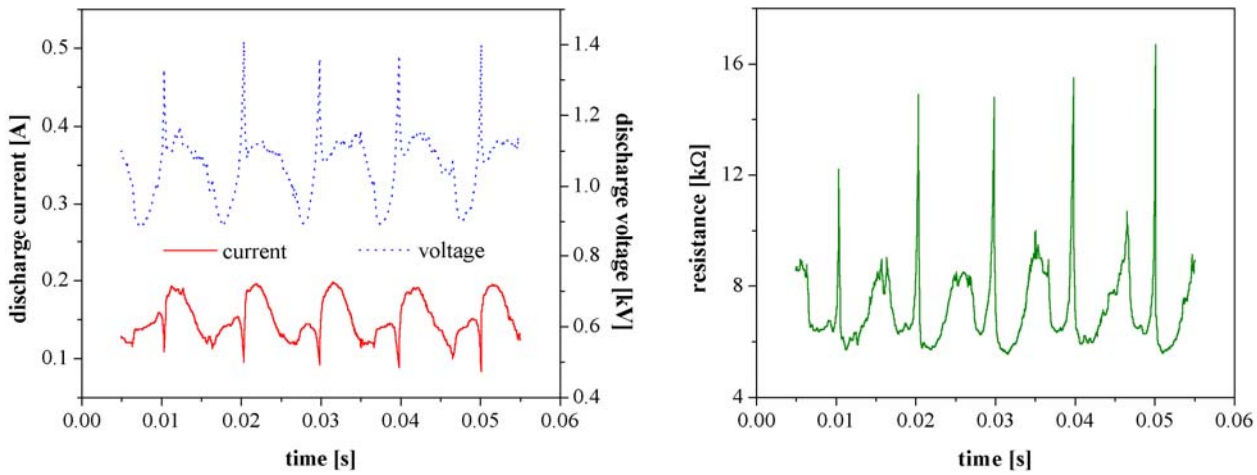

Fig. 3: Evaluation of the discharge current and voltage (left) and discharge resistance (right) in time (3,7 mM Na_2HPO_4, the initial conductivity of 700 $\mu S \cdot cm^{-1}$).

The investigation of hydrogen peroxide generation by the DC diaphragm discharge in water solutions has already been an object of our study in some previous works [6, 7]. This contribution extends the dependencies of hydrogen peroxide concentration on the initial discharge conditions. A special view is focused on the material of the dielectric diaphragm. Several kinds of materials were used in experiments, varied in their chemical structure and thickness. The rate constants of H_2O_2 creation were calculated as a quantitative parameter characterising each process. They are compared in Table 1. The most convenient material for the hydrogen peroxide generation was PET or PES with the thickness about 0.20 mm. For example PTFE (Teflon®) was not suitable, because this material became very soon mechanically degraded by the discharge and it was not possible to create the discharge.

Table 1: Rate constants of hydrogen peroxide production for various types of the dielectric diaphragm (1.75 kV, 5 mM NaCl, the initial conductivity of 500 $\mu S \cdot cm^{-1}$).

Material	Thickness [mm]	Rate constant [$mol \cdot l^{-1} \cdot s^{-1}$]
PET	0.25	$3.750 \cdot 10^{-7}$
PES	0.05	$1.167 \cdot 10^{-7}$
PES	0.19	$3.600 \cdot 10^{-7}$
PTFE	0.50	unmeasurable
PTFE	1.00	unmeasurable
POM-C	1.00	$4.667 \cdot 10^{-8}$

Generally, production of hydrogen peroxide by the discharge in water solution was almost linear in time as it can be seen in Figure 4 (right). The generation of H_2O_2 was also highly dependent on the discharge polarity. In the case of the one-hour positive discharge treatment (i.e. in the part of the reactor with the cathode!), the final concentration of H_2O_2 was approximately 1.8 $mmol \cdot l^{-1}$ (about 60 $g \cdot l^{-1}$), in the opposite polarity, the amount of hydrogen peroxide was only about 0.3 $mmol \cdot l^{-1}$ (about 10 $g \cdot l^{-1}$), i.e. six times lower. The comparison with another process, a degradation of organic compounds by the discharge, is described below.

At present, our work is focused on the investigation of the degradation force of the electric discharge in water, which is caused mainly by the active species (especially hydroxyl radicals and hydrogen peroxide). One of these processes is decolorisation and degradation of organic dyes dissolved in water [9]. This process is, of course, dependent on initial discharge conditions, for example on the discharge polarity, applied high voltage etc.

Several organic dyes differed in chemical structure, colour and purpose of used (for textile dying, in food industry etc.) were used. Water solutions of each dye (the initial concentration from 6 to 20 $mg \cdot l^{-1}$) were carried out with a defined amount of electrolyte (NaCl, Na_2HPO_4) to obtain the required solution conductivity. A typical evaluation of the dye concentration during the discharge treatment is shown in Figure 4 (left). This figure shows the relative concentration decrease of the dye Evans Blue. The degradation was dependent on the discharge polarity because the decolorisation process was more significant in the negative discharge treatment than in the positive one. The concentration of Evans Blue became less than 10% after 30 minutes in the negative discharge. In the positive discharge, the concentration was about 30% after 100 minutes.
The comparison with hydrogen peroxide generation (Fig. 4 right) gives very interesting results. In the case of the positive discharge treatment, the production of H_2O_2 was higher than in the negative one and therefore we had expected more significant decolorisation in the positive discharge. But the experiments gave opposite results! This phenomenon is an object of our contemporary study and we hope it will be solved soon.

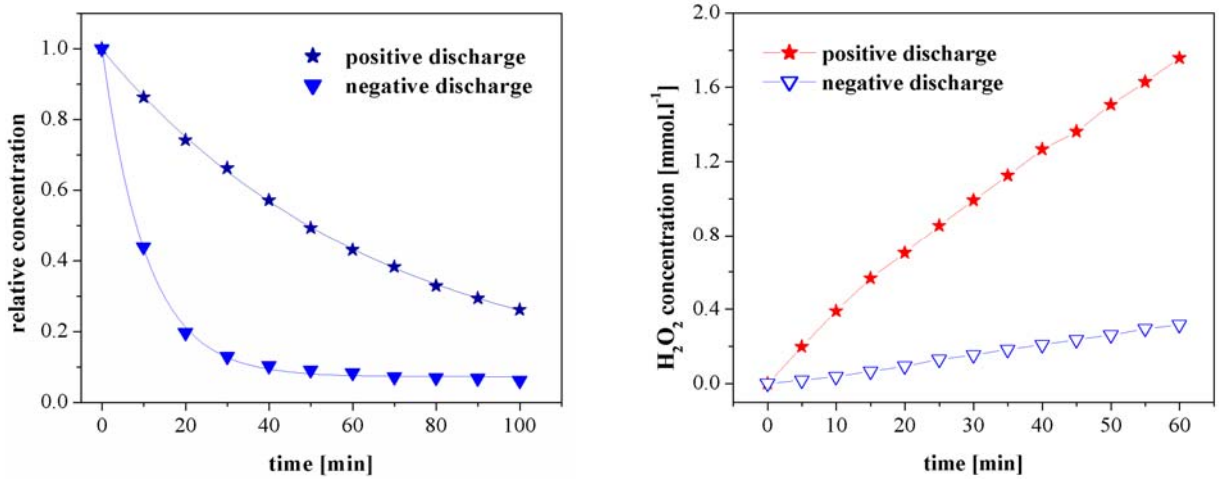

Fig. 4: Evans Blue dye decolorisation (left) and hydrogen peroxide generation (right) in time as a function of applied voltage polarity (2.45 kV, 5 mM NaCl, 500 $\mu S \cdot cm^{-1}$).

The process of organic dye degradation was investigated as a function of various parameters. One of them was a chemical structure of used dyes. Five different compounds were treated by the discharge and their concentration decreases during the discharge treatment are shown in Figure 5.

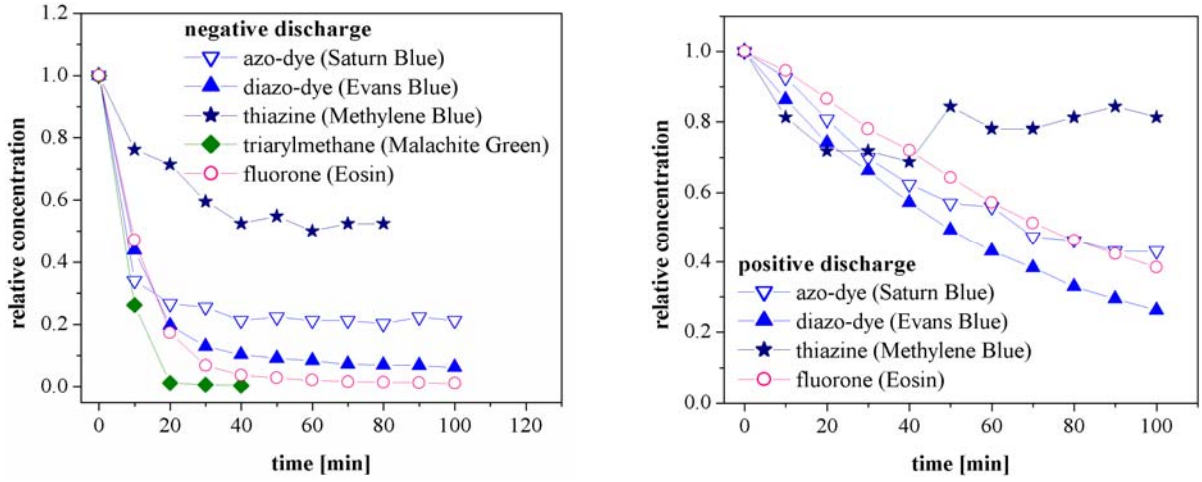

Fig. 5: Comparison of the concentration decrease for various organic dyes solutions treated by the negative (left) and positive (right) discharge (2.45 kV, 5 mM NaCl, 500 $\mu S \cdot cm^{-1}$).

The comparison is given for both negative (left) and positive (right) discharge polarity. The fastest decrease of concentration was observed in the case of Malachite Green that was ranked among triarylmethane dyes. Its concentration became nearly zero in the first twenty minutes of the discharge. All investigated dyes except Methylene Blue had more or less similar evaluation of the degradation process. Generally, it started with a quite fast decolorisation in the negative discharge but after twenty minutes of the experiment, the concentration decrease was not very significant. The final concentration of the studied dyes became lower than 20% of the initial dye concentration after 100 minutes of the experiment. In the case of Methylene Blue, a thiazine, the process of decolorisation was much slower and the final concentration did not even reach 50%.

Another parameter investigated in our experiments was the applied high voltage. The dependence of the processes in the discharge on the voltage polarity is discussed above, the influence of the voltage magnitude on investigated processes is given in Figure 6. The dependence of hydrogen peroxide concentration after one-hour discharge treatment (Fig. 6a) was increasing with the increasing applied voltage and it was also almost linear. The production of hydroxyl radicals by the discharge was proportional to the high voltage (Fig. 6b). The OH emission intensity was also dependt on the electrolyte and on the initial solution conductivity. The most significant dependence was observed in the case of NaCl solution with the initial conductivity of 400 $\mu S \cdot cm^{-1}$.

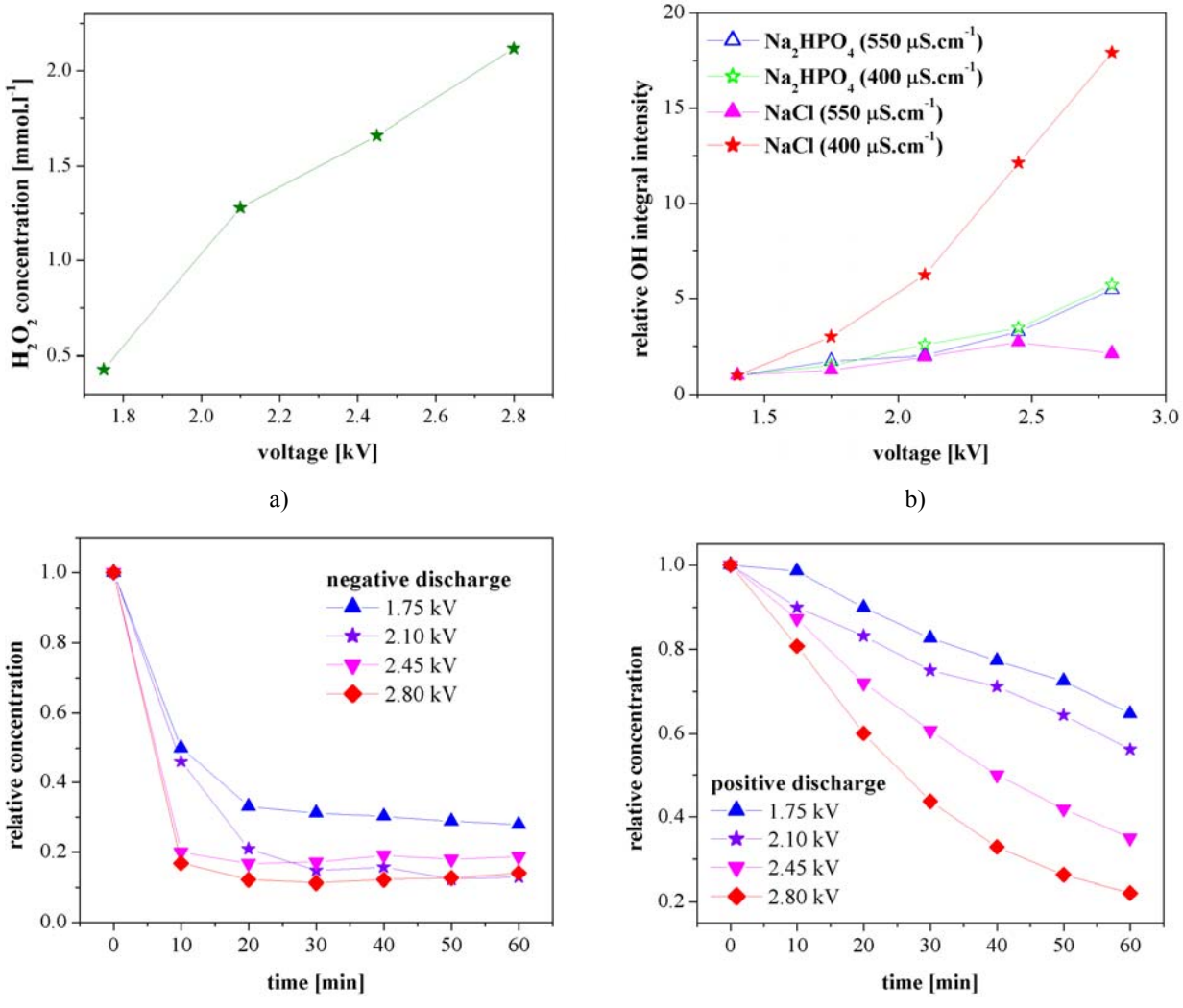

Fig. 6: Influence of the applied high voltage on the production of a) hydrogen peroxide, b) hydroxyl radicals and c) on degradation of the organic dye Saturn Red (5 mM NaCl, the initial conductivity of 500 $\mu S \cdot cm^{-1}$).

The time evaluation of the relative dyes concentration as a function of the applied voltage is shown in Figure 6c. The comparison is given for both negative (left) and positive (right) discharge treatment of the water solution of Saturn Red dye. While in the case of the lower applied positive voltage (1.75 kV) the dye was decomposed to only 65% of the initial concentration, in the case of the higher positive voltage magnitude (2.80 kV), the concentration became about 25% of the initial concentration. The voltage dependence did not cause a significant difference in the negative discharge polarity. Generally, the investigated processes, such as production of reactive species (hydrogen peroxide, hydroxyl radicals) and degradation of organic compounds (organic dyes) in the diaphragm discharge were highly dependent on the applied voltage.

4. Conclusion

This contribution has described selected chemical processes occurring during the diaphragm discharge in water solutions, namely the production of chemical active species (hydrogen peroxide, hydroxyl radicals) and the degradation of organic compounds (dyes) dissolved in water. The processes were investigated for various discharge conditions (applied voltage, initial conductivity of the solution, used electrolyte, diaphragm parameters). Chemical analyses were completed with electric and optical measurements.

The series of electric measurements ascertained the real character of the diaphragm discharge. It was estimated as quasi-pulsed. This character was probably caused by the discharge creation mechanism in the pinhole.

Hydrogen peroxide was produced by the diaphragm discharge in water solutions. Its concentration increase in time was almost linear and was influenced by the applied voltage and by parameters of the dielectric diaphragm (its material and thickness). The most suitable diaphragm was made of PET or PES with the thickness of about 0.2 mm. The production of hydrogen peroxide was more significant in the positive discharge polarity, its concentration became about 60 $g \cdot l^{-1}$ after one-hour experiment. The dependence on the voltage magnitude was proportional and almost linear. A similar evaluation of the dependence of the process on the high voltage was also observed in the production of hydroxyl radicals. The OH emission intensity increased with the increasing voltage and it was influenced by the used electrolyte and also by the initial conductivity of the solution.

The degradation of organic compounds by the diaphragm discharge was studied in water solutions of selected organic dyes. The decrease of the dye concentration was observed in the both discharge polarities but in the negative discharge the decolorisation was more evident. This was the opposite phenomenon than in the production of hydrogen peroxide. In most of the experiments, the dye decomposition had decreased to the final concentration of less than 20% of initial dyes concentration after 100 minutes of the discharge treatment. Five organic dyes differing in their chemical structure, colour and its purpose of use were compared. A fast decomposition was observed in the solution of Malachite Green. The influence of the magnitude of the applied high voltage was studied, too. The degradation increased with the increasing applied voltage in both discharge polarities.

Acknowledgements

This work was supported by the Czech Science Foundation, contract No. 202/03/H162 and by the Grant of the Czech Ministry of Education number 2003/0894.

References

[1] A. A. Joshi, B. R. Locke, P. Arce, W. C. Finney – J. Hazard. Mater. **41**, 3 (1995).
[2] S. C. Goheen, D. E. Durham, M. McCulloch, W. O. Heath – Proc. 2nd Int. Symp. Chem. Oxid., 356 (1992).
[3] P. Šunka, V. Babický, M. Člupek, P. Lukeš, M. Šimek, J. Schmidt, M. Černák – Plasma Source Sci. Tech. **8**, 258 (1999).
[4] I. P. Kuzhekin – Proc. 9th Int. Symp. High Voltage Eng., Graz, 8073-1 (1995).
[5] M. Monte, F. De Baerdemaeker, C. Leys, A. I. Maximov – Czechoslovak J. Phys. **52**, D724 (2002).
[6] Z. Stará, F. Krčma – Czechoslovak J. Phys. **54**, C1050 (2004).
[7] F. Krčma, Z. Stará – Chemical Papers **96**, S82 (2002).
[8] P. Lukeš – Water Treatment by Pulsed Streamer Corona Discharge, Ph.D. Thesis, Prague (2002).
[9] F. Krčma, Z. Stará – Proc. 22nd SPIG, Bajina Bašta, 601 (2004).

Applied Plasma Chemistry – New Practical Exercises

F. Krčma[1], Z. Stará[1], P. Sťahel[2]

[1]*Institute of Physical and Applied Chemistry, Brno University of Technology, Brno, Czech Republic*
[2]*Faculty of Science, Masaryk University, Brno, Czech Republic*

Abstract
Three new practical exercises oriented on the application of plasma chemical processes are presented. Two exercises for the special practical course are focused on the study of processes in the DC diaphragm discharge in a water solution. The first measurement is the hydrogen peroxide generation, the second part of the task studies destruction of the chosen organic dyes. The third exercise is focused on the plasma treatment of polymers by the surface discharge. The treated and untreated samples are characterised by the surface energy evaluation from the contact angles of 3 different testing liquids with the measured sample. Each of these works can be completed within a relatively short period of 150 minutes.

Keywords: discharge in liquids, diaphragm discharge, practical exercises, surface discharge, plasma treatment, surface energy, contact angle.

1. Introduction

Plasma chemistry is a comparatively new scientific discipline that has became a part of university curricula relatively recently. The discipline can be studied from two rather different points of view. The plasmachemistry courses for physicists are naturally focused on the basic phenomena in plasmas, the courses for chemists focus more on the use of plasma as an instrument for demonstrating various processes. In both of these conceptions, the problem of modern plasmachemical technologies plays only a minor role, although a huge increase of plasmachemical technologies has been observed during the last years. Practical exercises complementing the lectures at universities are normally focused on the basic processes and basic phenomena (studies of DC glow discharge etc.) and on some plasma diagnostic methods. At technical universities, practical exercises are usually in the form of plasma technology demonstrations without an active participation of students.
The curricula at our university include a course in applied low temperature plasma physics and chemistry, where students can obtain the basic information about a theoretical description of plasmas and later about some plasmachemical technologies. Four years ago we prepared a special practical course focused on the applications of low temperature plasma processes [1]. This contribution presents two new practical exercises. Both of them share the main characteristics of the other exercises, the expenses connected with them are reasonable and the degree of their safety gives students a possibility to carry them on. Finally, the experimental plasma devices used in the practical course are simultaneously used also during the work on the students' master and doctoral theses. This in return makes possible the continual enlargement and improvement of the exercises.

2. Diaphragm discharge in liquids

Experimental

A special batch discharge reactor is used in the experiments [2]. It consists of two chambers with one planar electrode in each part. Electrodes are arranged in the distance of 2 cm from the diaphragm. A small pinhole (initially of 0.25 mm) is located in the centre of the dielectric diaphragm. Processes investigated in this discharge are influenced by the material of the dielectric diaphragm and the high voltage electrodes, too. The most convenient material for the diaphragm is PET with the thickness of about 0.2 mm, stainless steel electrodes are suitable for the experiments [3]. The DC non-pulsed voltage source (from 1.3 kV to 1.6 kV) is used to create the discharge [2]. To ensure the homogeneous conditions in the whole volume of liquid, a mixing system is placed in the reactor. Due to the considerable heating of the reactor by the discharge and to prevent the hydrogen peroxide from destruction, two cooling boxes with ice are installed in both parts of the reactor. In the case of organic dyes, the cooling system is not necessary.

Results and Discussion

The experimental studies showed that hydrogen peroxide molecules are one of the main active species for the other processes in the liquid phase [4]. Therefore they are measured also in this practical exercise as a quantitative parameter of the discharge.

The demineralised water containing suitable electrolyte (NaCl, Na_2HPO_4) was used to obtain the defined initial conductivity of the solution (optimal 300-700 $\mu S \cdot cm^{-1}$).

The mechanism of hydrogen peroxide generation by the electric discharge in water is not simple, because the process is a series of subsequent chemical reactions. Partially it was described in [3]. The active species (especially radicals) are produced by the discharge, they can react together to create molecules or they can react with other compounds present in the liquid medium and cause their decomposition. However, we can express the overall reaction of hydrogen peroxide creation by the following equation [5]:

$$2\ H_2O \xrightarrow{disch.} H_2O_2 + H_2. \quad (1)$$

The rate constant of this reaction is $k_{per.}$. Due to the constant water concentration, the reaction is regarded as a zero-order reaction. Thus the final expression for the peroxide concentration is:

$$c_{per.,\,t} = k_{per.} \cdot t, \quad (2)$$

so it increases linearly in time.

The colorimetrical method was used for the hydrogen peroxide determination. The selective titanium reagent in sulphuric acid reacted with H_2O_2 and gave a yellow complex with the maximum absorbance at 407 nm. The hydrogen peroxide concentration in the sample was directly proportional to the absorbance value. This exercise was more suitable for students of chemistry due to the special chemical reagent used in experiments.

The second exercise focused on the organic dyes decomposition by the discharge could be more suitable for students of physics. Different organic dyes in solid phase, varied in colour and structure, and of the defined quantity were solved in demineralised water. The list of suitable dyes with their absorbance maximum is shown in Table 1. These dyes were quite fast decomposed by the discharge and thus this effect was also clearly seen visually. For example, the dye Methylene Blue was not convenient for this experiment because its degradation took more time and its decolorisation was not visible without a photometer.

Table 1: List of organic dyes suitable for the experiment.

Organic dye	**Type**	**Colour**	**Absorbance maximum**
Fluorescein	fluorone	yellow	484 nm
Saturn Red L4B	azo-dye	red	506 nm
Azorubin	azo-dye	red	516 nm
Evans Blue	disazo-dye	blue	592 nm
Malachite Green	triarylmethane	green	621 nm

Chemical active species (especially radicals) produced by the discharge caused the decomposition of organic dyes dissolved in water. This process was visible directly through the decolourisation of the dye [6]. Therefore the degradation can be clearly and simply observed by photometry. The main absorption peaks of these dyes are relatively broad and no significant peaks of the discharge products were observed around the absorbance maxima listed in the Table 1. Due to this fact, the photometer can be replaced by a simple photodiode detector equipped with an interference filter transparent around the absorbance maximum of the selected dye.

Figure 1 shows the H_2O_2 concentration increase during the discharge in water. The production of hydrogen peroxide had almost a linear character in time and it was highly dependent on the discharge polarity. The generation was more significant in the positive discharge. The hydrogen peroxide amount became about 1 $mmol \cdot l^{-1}$, i.e. approximately 34 $g \cdot l^{-1}$. The second process, degradation of organic dye dissolved in water, is presented in Fig. 2. Water solution of the dye Azorubin was treated for 100 minutes by the discharge. The concentration decrease was more significant in the negative polarity, when the concentration became nearly zero already after 40 minutes of the experiment. Therefore the experimental time for the practical exercises can be

shorter, e.g. about only half an hour. The evaluation of the dye decrease was approximately exponential in both discharge polarities. In the case of positive discharge, the final concentration became about 30 % after 100 minutes.

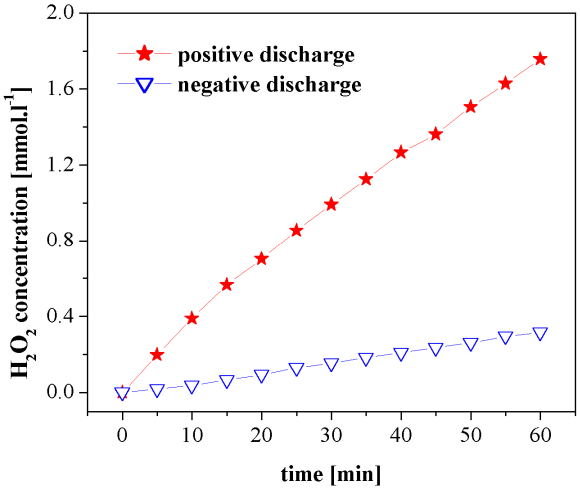

Fig. 1: Production of hydrogen peroxide by the diaphragm discharge in a water solution (146 W, 5 mM NaCl, 500 μS·cm^{-1}).

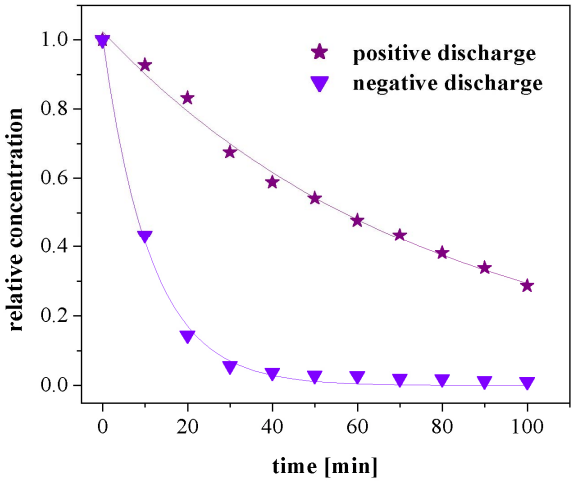

Fig. 2: Concentration decrease of the dye Azorubin during the discharge treatment (146 W, 5 mM NaCl, 500 μS·cm^{-1}).

During the experiments, the changes in both conductivity and pH were observed. Results of these measurements are given in Figs. 3 and 4. The solution conductivity increased in both discharge polarities (Fig. 3). A higher enhancement was observed in the negative discharge (i.e. in the part of the reactor with the anode). This effect can be explained by the production of chemical species by the discharge and by metallic traces involved NEROZUMÍM from electrodes by the electrolysis. Fig. 3 also compares two water solutions – electrolyte NaCl (left) and Saturn Red dye with NaCl (right). The relative increase in conductivity was higher in the pure electrolyte and the difference between the two polarities was also more significant in this solution.

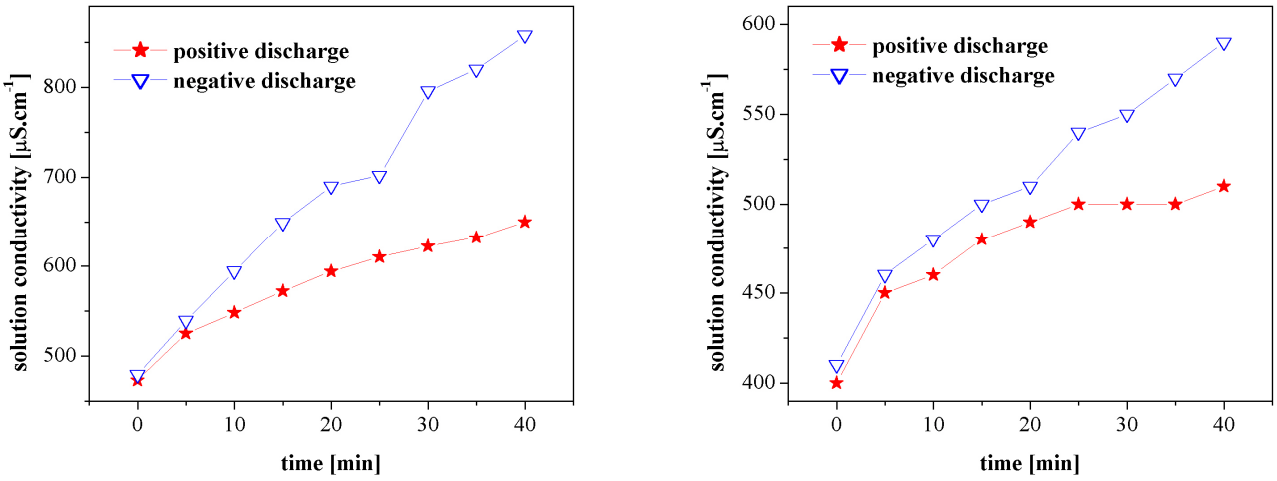

Fig. 3: Change in conductivity during the discharge treatment in a water solution of the electrolyte NaCl (left) and in a water solution of the same electrolyte with the dissolved organic dye (right); 117 W, 4 mM NaCl, Saturn Red dye (12 mg l^{-1}).

Fig. 4 demonstrates the obtained results of pH measurements in both solutions, pure electrolyte (left) and Saturn Red dye with NaCl (right). The time evaluation had similar character in both experiments. While in the positive discharge the pH increased from approximately 6 to almost 10, in the opposite polarity, it had a decreasing tendency (from 6 to less than 4). In the solution with the dissolved dye, the difference in pH was more significant.

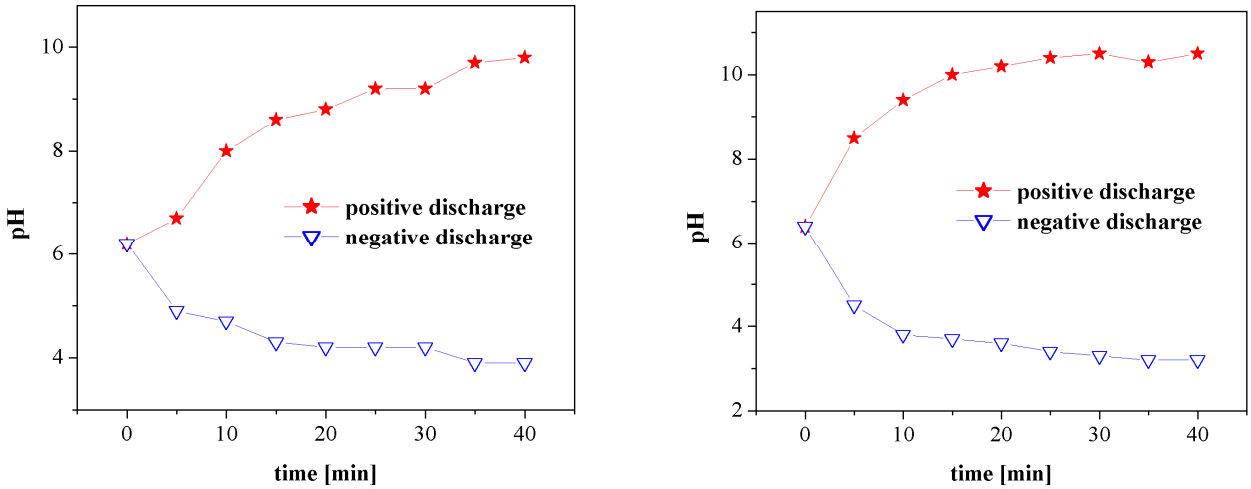

Fig. 4: Change in pH during the discharge treatment in a water solution of the electrolyte NaCl (left) and in a water solution of the same electrolyte with the dissolved organic dye (right); 117 W, 4 mM NaCl, Saturn Red dye (12 mg l^{-1}).

3. Treatment of polymers by the surface discharge

Experimental

The surface modification of the polymers is at present one of the most emerging plasma technologies. Industrial applications prefer the treatment in low temperature plasma at an atmospheric pressure. The surface barrier discharge and diffuse coplanar discharge are very suitable for this purpose.

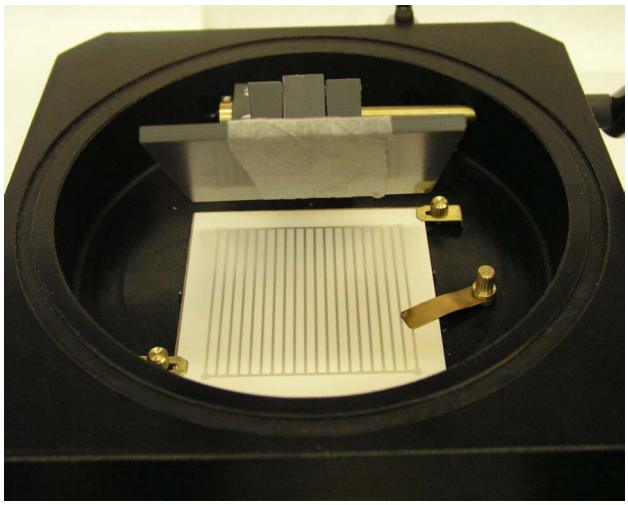

Fig. 5: a) An universal plasma reactor UPS100W. *b) A detail of the discharge electrode.*

A special plasma reactor based on the surface barrier discharge [7] was developed for this application (see Fig. 5). The surface discharge is the non-equilibrium plasma supplied by the high DC voltage with the operation frequency of 7 kHz. The reactor was constructed in order to prevent students from being injured by the high

voltage, therefore the plasma chamber is mounted with a power supply and the electrode is placed under a glass cylinder. Moreover, the device is portable (30x30x35cm). The discharge chamber can be evacuated before the plasma treatment and then filled with pure gases or various gas mixtures. The reactor is constructed only for laboratory tests therefore the treated samples are restricted to the maximal dimensions of 10x10cm. In the real industrial application it is possible to shape the treating unit for a continuous treatment of materials with the width of even more than 1 m. The treatment time can vary from a few seconds up to 20 min, but the electrode and power supply need cooling. The treatment time longer than one minute is not necessary during the exercises (see below) therefore the supplementary cooling is not integrated in the reactor.
Students investigate the effect of treatment time on the surface properties of samples (polyethylene and polyester plates). Smooth materials are used for easier characterisation of the surface energy. The discharge is burning in separate rows parallel with the electrodes and thus the treatment is not homogeneous over the whole sample, if the sample is not moved through the reactor. The width of the treated rows is about 3 mm and it is sufficient for the treatment characterisation. The treatment time of both used materials is up to 60 s, a longer treatment is not recommended due to a thermal deformation of the samples that significantly decreases the treatment homogeneity.
The treated and untreated samples are characterised by the surface energy evaluation from the contact angles of 3 different testing liquids with measured sample. Surface energy evaluation is provided by the means of Surface Energy Evaluation System (SEE System) [8]. Inexpensive and fully computer-controlled setup allows to measure contact angles of various testing liquids with the sample surface and to calculate the surface energy using different models. The acid-base model was applied in our case [9, 10]. The setup is also equipped with a complete analysis of errors.

Results and discussion

The experimental results are shown in Fig. 7. It can be seen that the contact angles of the selected liquids decrease with the increase of the plasma treatment time. This effect is most remarkable in the case of distilled water, i.e. the hydrophylity of both materials increases. The main changes can be observed during the first 30 seconds, later the changes are not so high. Both figures clearly demonstrate also the problem with the surface energy estimation. The contact angles at longer treatment times are similar for the used liquids. The contact angles also have significant experimental errors that result from the inhomogeneity of the static plasma treatment. This causes the high errors in the calculated surface energies (see Table 2 below).

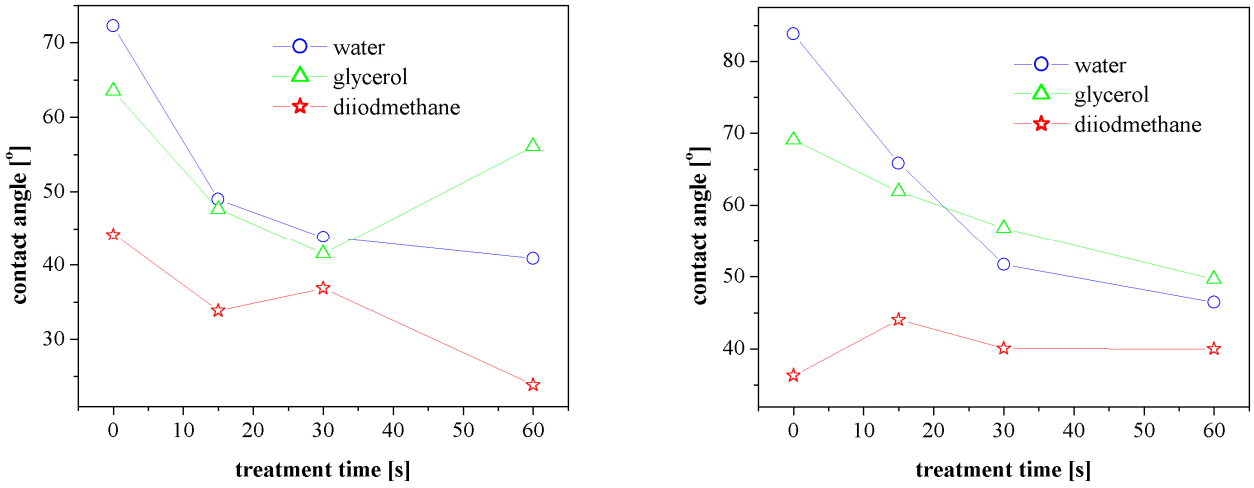

Fig. 7: Dependencies of the contact angle for various liquids as a function of the treatment time; left – polyethylene, right – polyester.

Table 2: Calculated surface energies of plasma treated polyethylene and polyester samples.

Material	treatment time [s]	Total surf. energy [mJ·m^{-2}]	Disperse component [mJ·m^{-2}]	Polar component [mJ·m^{-2}]	Acid component [mJ·m^{-2}]	Basic component [mJ·m^{-2}]
PE	0	42.28	41.06	1.21	0.13	2.92
PE	15	45.15	41.26	3.89	0.30	12.61
PE	30	47.16	42.34	4.82	0.26	22.61
PE	60	49.57	42.74	6.82	0.48	24.34
PES	0	42.55	41.41	1.14	0.11	2.90
PES	15	41.09	37.52	3.56	0.19	16.44
PES	30	42.10	39.57	2.53	0.05	31.74
PES	60	46.66	39.60	7.06	0.38	32.96

4. Conclusions

The practical exercises described in this contribution are a part of a special practical course focused on applied low temperature plasma-physical and plasma-chemical processes. The first exercise consists of two parts investigating the processes in the DC diaphragm discharge – hydrogen peroxide generation and organic dyes degradation. The experimental basis of this exercise is mostly very cheap, and thus the device can easily be installed anywhere. The diagnostic methods presented above are based on the apparatus available to us and they can be replaced by other methods as it was proposed.

The second exercise is focused on the treatment of polyethylene and polyester by the surface discharge. The contact angles of the selected liquids are measured as a function of treatment time up to one minute. On this basis the changes of the polymer surface energy are calculated. The whole experimental equipment is inexpensive and as safe as possible, and thus it can easily be used anywhere.

Each of the presented practical exercises can be completed within 150 minutes without any significant problems. These practical exercises show students new directions in the plasma-chemical processes and technologies. They are fully interdisciplinary, a good knowledge of both physic and chemistry is necessary. A further extension of our course is planed in the near future.

Acknowledgements

This work was supported by the Grant of the Czech Ministry of Education number 2003/0894 and by the Czech Science Foundation, contracts No. 202/03/H162 and 202/02/D097.

References

[1] F. Krčma, J. Pryčková, H. Grossmannová, J. Janča, P. Slavíček, V. Kudrle, L. Sodomka – Proc. ISPC XV, Orleans, 1143 (2001).

[2] Z. Stará, Z. Rašková, F. Krčma, P. Slavíček – Proc. Symp. Phys. Switch. Arc XV, Brno, 182 (2003).

[3] Z. Stará, F. Krčma – Czechoslovak J. Phys. 54, C1050 (2004).

[4] P. Šunka, V. Babický, M. Člupek, P. Lukeš, M. Šimek, J. Schmidt, M. Černák – Plasma Sources Sci. Technol. 8, 258 (1999).

[5] P. Lukeš – Water Treatment by Pulsed Corona Discharge, Ph.D. Thesis, Charles University, Prague (2002).

[6] Z. Stará, F. Krčma, P. Slavíček – Proc. ISPC XVII, Toronto, submitted (2005).

[7] www.pst-systems.cz.

[8] www.seesytems.wz.cz.

[9] K. L. Mittal – Contact Angle Wettability and Adhesion, V.S.P. Intl. Science 1993.

[10] V. Buršíková, P. Sťahel, Z. Navrátil, J. Buršík, J. Janča – Surface Energy Evaluation of Plasma Treated Materials by Contact Angle Measurement, Masaryk University Brno, 2004.

THERMAL PROPERTIES OF GRAVITY-FREE ARC DISCHARGE AND ITS APPLICATION TO PRODUCTION OF CARBON CLUSTERS

T. Mieno, D. Kato, A. Yamashiro

Department of Physics, Shizuoka University, 836 Ooya, Shizuoka-shi, 422-8529, Japan

Abstract

Diffusion properties and gas temperature around a DC arc discharge are analyzed related with the carbon-cluster production. By means of parabolic flight of a jet plane, the gravity-free arc discharge is carried out. The point symmetric temperature distribution and slow diffusion of carbon clusters are clearly observed under the gravity-free condition.

Keywords: gravity-free arc discharge, production of carbon clusters, thermal property, nanotubes, fullerenes, heat convection, cooling process

1. Introduction

Carbon clusters are produced by the arc discharge method, where strong heat convection flows up sublimated carbon atoms immediately, and the reaction time is restricted. The cooling and cohesion process of carbon clusters is important for the production of fullerenes and carbon nanotubes. In order to examine the effect of gravity and heat convection for the arc production, a 12-m-high vertical-swing-tower was constructed, and endohedral metallo-fullerenes and single walled carbon nanotubes (SWNTs) [1, 2] were produced under repetitive gravity-free condition. From this experiment dramatic increase of production efficiencies of metallo-fullerenes and SWNTs was obtained.

In order to make clear this gravity effect [3], gas temperature distribution under the gravity-free condition is investigated by use of parabolic flight of a jet plane, and the result is compared with that of the normal gravity condition [4]. Production place and diffusion characteristics of carbon clusters around the arc are measured by the Mie scattering method.

2. Theory

When carbon particles are produced at the center of the spherical coordinate and they diffuse isotropically without reaction with diffusion coefficient D_C, the equation of continuity is written as,

$$\frac{\partial n_c}{\partial t} = D_c \frac{1}{r}\frac{\partial}{\partial r}\left(r \frac{\partial n_c}{\partial r}\right) \quad , \tag{1}$$

where n_C is density of carbon molecules. In the steady state condition, the density profile and the particle flux J_C are written as

$$n_c = C_1 \ln(r) + C_2 \quad , \tag{2}$$

$$J_c = -\frac{C_3 D_c}{r} \quad , \tag{3}$$

where C_i shows some constant value. When the carbon clusters diffuse in He gas, their diffusion coefficient D_{cHe} is written as,

$$D_{cHe} = C_4 \frac{T^{3/2}}{\sqrt{m_c}\, d_c^2\, p_{He}} \quad , \tag{4}$$

where T is the gas temperature, m_C is the averaged cluster mass, d_C is the averaged cluster diameter and

p_{He} is He pressure. From this equation, radial diffusion velocity of carbon clusters can be estimated. Figure 1 shows the calculation results of diffusion velocities of C_2 and C_{60} molecules versus He pressure (where T_{He}= 5000 k and r= 3 cm and the chamber size is same as the experimental chamber). The natural convection velocity of He, by which all the carbon clusters are brought up, is calculated by the fluid simulation program (SMAC method) using a UNIX computer and the result is shown in the same graph. From these calculations it can be predicted that heavier and larger carbon clusters much more slowly diffuse under the gravity-free condition. As the gas temperature monotonically decreases at the edge of the plasma flame, big carbon clusters cool down much more slowly under the gravity-free condition.

From the fluid simulation, time evolution of temperature contour of He gas around the arc flame can be calculated. Figure 2(a) shows the temperature contour under the gravity-free condition at t= 1.0 s after the arc start, where p= 40 kPa and the region of T=500-5000 k is shown. Under this gravity condition the hot gas reagion monotonical expands isotropically, and it takes much time to be a steady state. Meanwhile, under the normal gavity condition, temperature contour is calculated as Fig. 2(b), where t= 0.6 s, p= 40 kPa and the region of T=500-5000 k is shown. Under this gravity condition, the temperature contour immediately becomes a steady state, and thereafter there is almost no change. The particles and the thermal energy are continuously brought to the upper- end boundary.

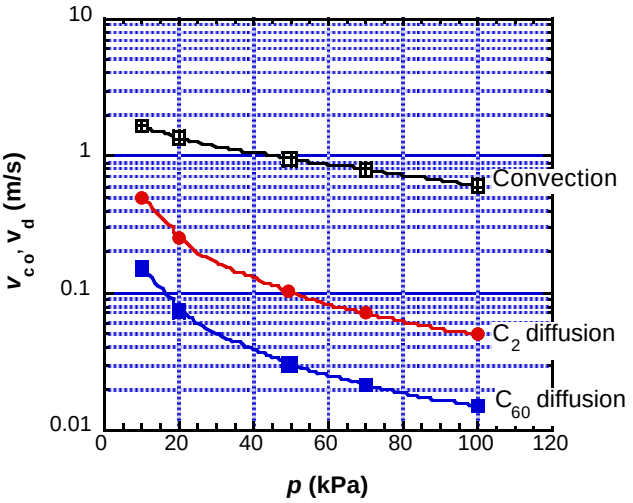

Fig. 1 He pressure dependence of thermal difusion velocities and heat convectino velocity. Calculation for T= 5000 k and r= 3 cm.

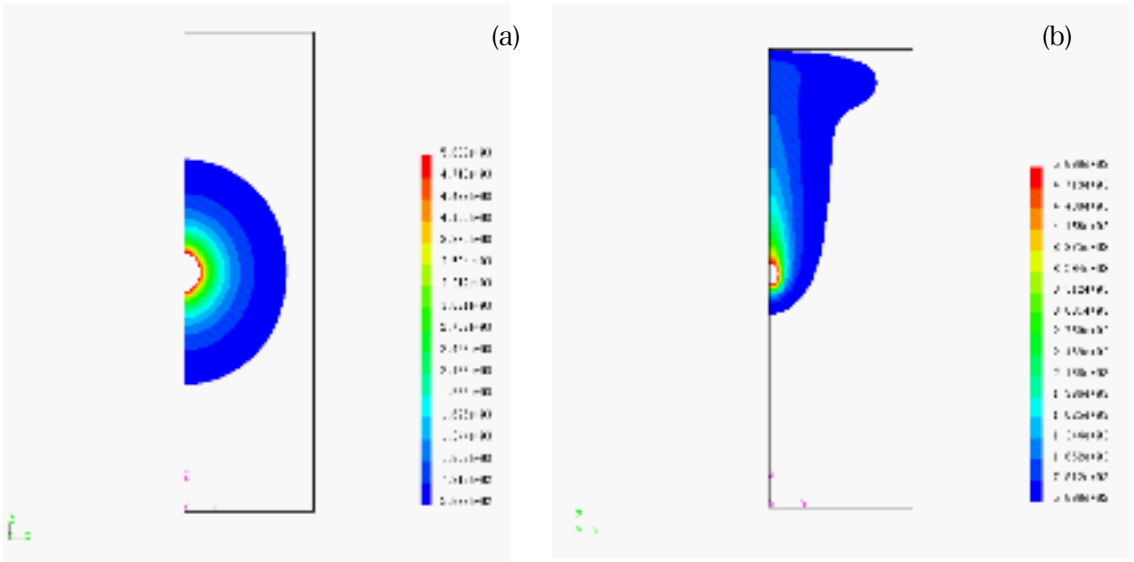

Fig.2. Simulation results of temperature contours (T= 500-5000 k) for the two gravity conditions. (a) G= 0, t= 1.0 s, p(He)= 40kPa. (b) G= 1g_0, t= 0.6 s, p(He)= 40 kPa.

3. Experimental setup and method

All the experimental setup is installed in one aluminum rack as shown in Fig. 3, which is specially prepared for a jet plane (Grumman G-II operated by Diamond Air Service, Japan). A pumping system, a gas-feeding system, a DC power supply, a video camera, an array of thermocouples and a recording system are installed. In a cylinder-type arc reactor of 11.5 cm***f***, 19.4 cm high, two carbon electrodes are set. After evacuation, He gas is introduced and the reactor is closed.

When the jet plane starts parabolic flight and the gravity becomes zero, the arc is turned on by an operator and kept for about 40 s (20 s of the gravity-free time, $G = 0$, and 20 s of $G = 1.5\ g_0$), where time dependence of the vertical distribution of gas temperature over and under the arc is measured by 11 thermocouples. The analog data are digitized by a special AD converter and stored in a computer. At the right upper side of Fig. 3, a typical arc flame (side view) is shown.

In order to make clear the production place of carbon clusters and their diffusion speed, the passive-type Mie scattering method is utilized. By using a metal-obstacle plate, the direct light from the arc flame is cut and scattered light from the produced carbon clusters is recorded by a video camera, by which a vertical profile of the produced carbon clusters and their diffusion can be observed.

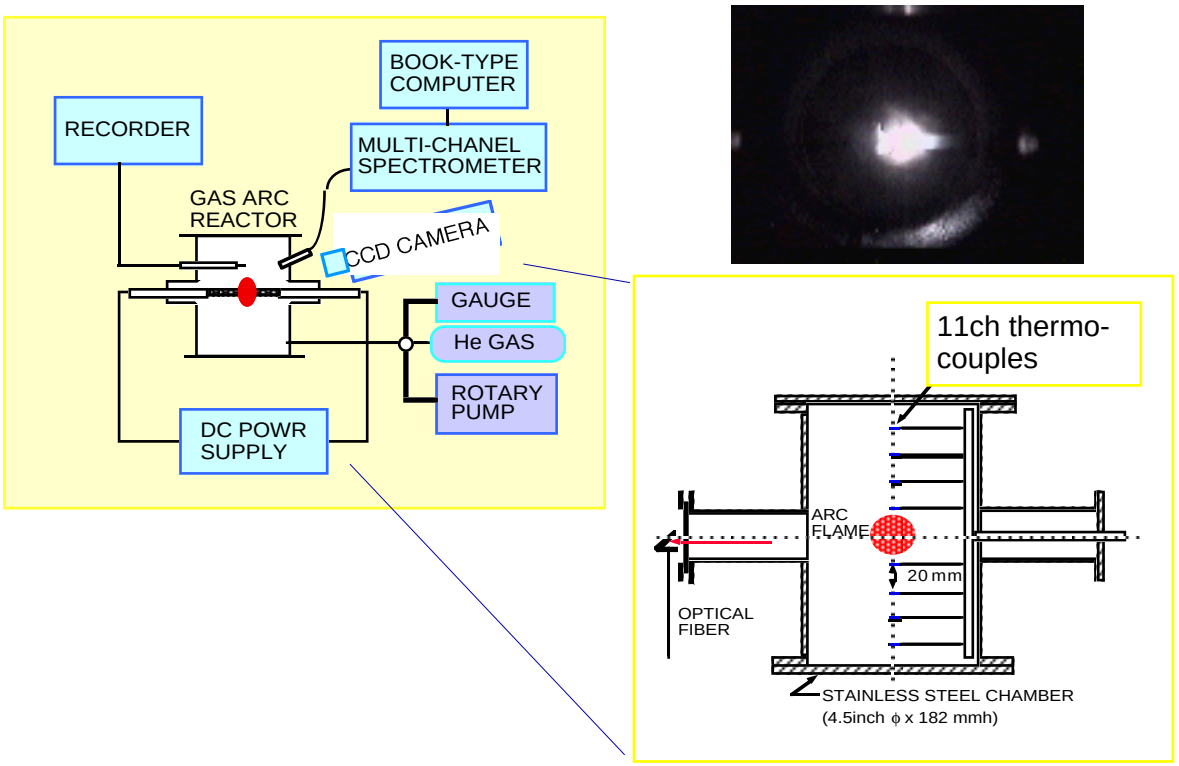

Fig. 3 Schematic of experimental setup set in a jet plane. A typical photo of the arc is shown at the upper right side.

4. Experimental results and discussion

Typical time variation of gas temperatures over and under the arc are shown in Fig. 4, where $p = 40$ kPa, and $I_d = 40$ A. When the gravity becomes zero from 2 g_0, the arc is turned on. After about 45 s, the arc is turned off (20 s of 0 g_0 and 25 s of 2 g_0). The clear gravity effect is recorded.

Figure 5 shows gas temperature distributions under the gravities $G = 0\ g_0$ and $1.5\ g_0$, where He pressure $p = 40$ kPa and discharge current $I_d = 40$A. When the gravity becomes 0, the arc is turned on, and hot gas region monotonically and symmetrically expands with the arc time Dt. It is conjectured that the heat flow is suppressed under the convection-free condition and the generated ohmic heat tends

to be accumulated, which makes spherical large-volume hot-gas region. The model of the temperature contours is shown on an upper inset, which is consistent with the simulation result. It is confirmed that the steady-state, spherical hot-gas region with large volume can be generated under the longer gravity-free condition, which can be realized by longer gravity-free time than 20 s. Figure 6 shows typical expansion speed of temperature contour of T= 500 k as a function of He pressure. The expansion speed is very slow and it does not become zero within 20 s. Under the normal gravity condition, the steady-state convection flow is immediately formed and the thermal energy continuously diffuse to the upper region. Therefore, the hot gas region is not symmetrical and has small volume, which is also consistent with the simulation result.

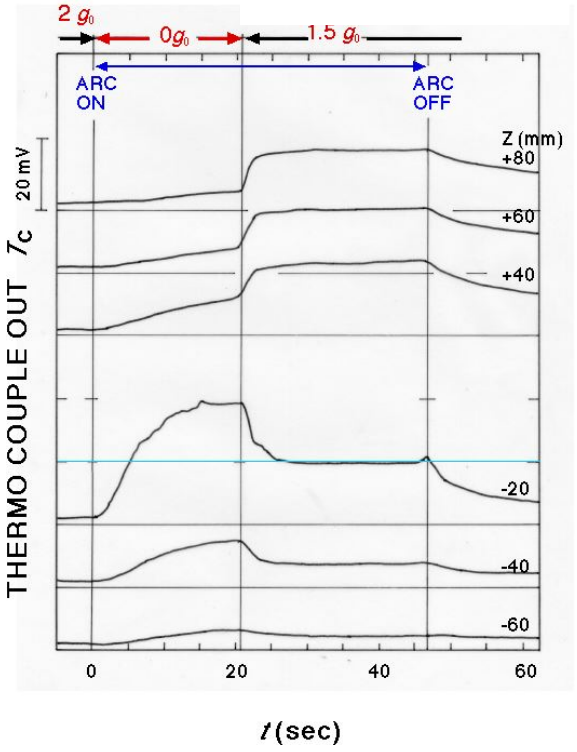

Fig. 4 Typical time variation of thermo-couple outputs at 6 postion over and under the arc. p(He)= 84 kPa and I_d= 40 A.

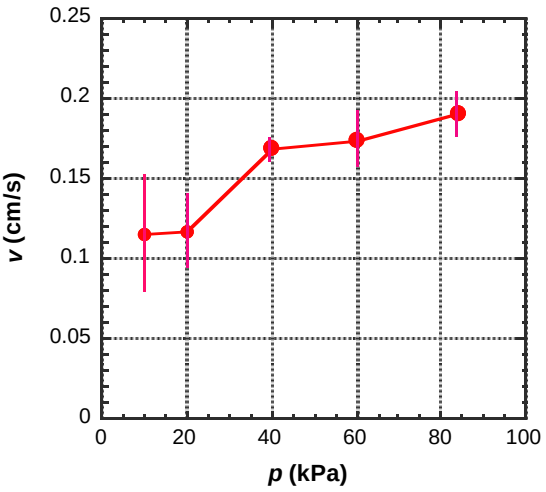

(a)

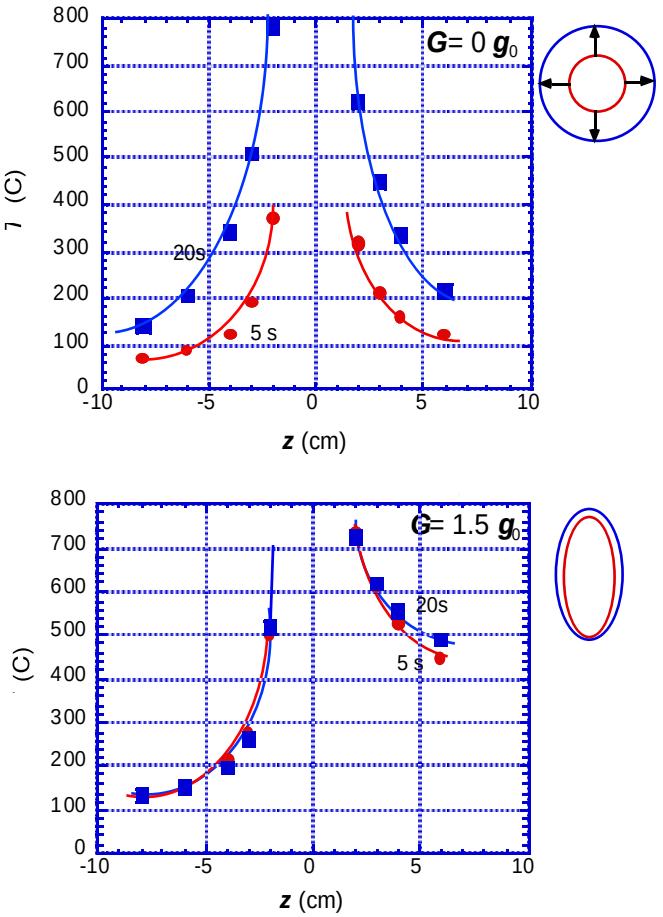

(b)

Fig. 5 Vertical temperature distributions over and under the arc at Δt= 5 s and 20 s after gravity becomes 0 (a) and after gravity becomes 1.5 g_0 (b). p(He)= 40 kPa and I_d= 40 A.

Fig. 6 Typical expansion speed of temperature contour of T= 500 k versus He pressure, when the gravity-free arc is turned on. I_d= 40 A.

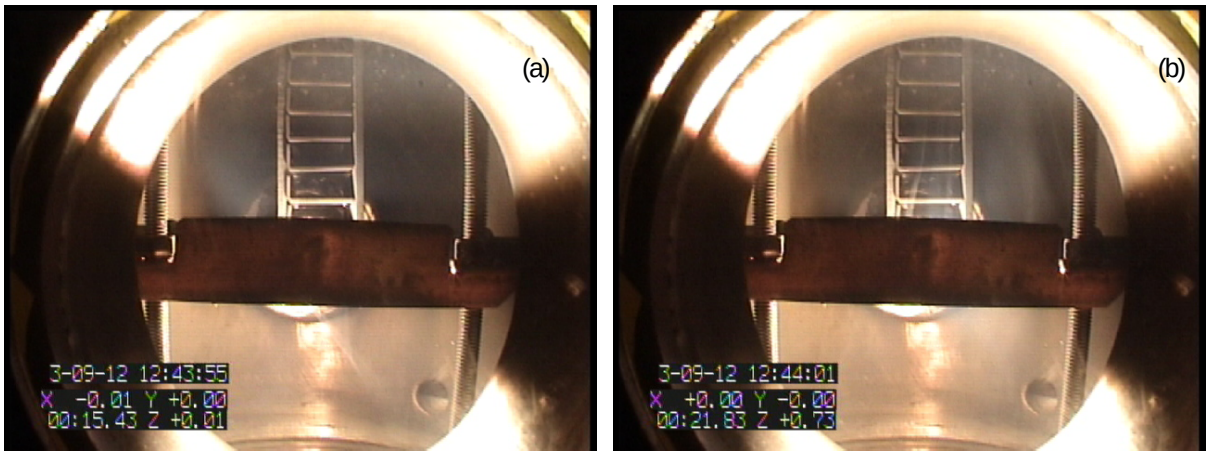

Fig. 7 Photos of scattered light by the Mie scattering taken from a side port. SWNTs are synthesized around the arc flame. p(He)= 40 kPa, I_d~ 50 A. (a) under 0 g_0 and (b) under 1.5 g_0.

By using an obstacle plate, the passive style Mie scattering from the carbon clusters is measured. Two shots of the video images under the two gravity conditions are shown in Fig. 7. Under the gravity-free condition, the carbon clusters diffuse isotropically and its speed is very slow (less than 1 cm/s with random motion). The carbon clouds move very slowly and randomly and their density is rather homogeneous. When the scattering is measured under the normal gravity condition (1 g_0), strong heat convection (about 1 m/s) is measured. The continuous particle flow to upward direction is clearly observed. From these measurements, the production place of the clusters is regarded as the narrow region around the arc flame for the both gravity conditions, where the gas temperature drops from 10000 k to less than 1000k. Only in the narrow region around the arc flame, carbon clusters are synthesized.

SWNTs are produced by using a catalyst-mixture carbon anode under the two gravity conditions. Produced samples are observed by a TEM and analyzed by a Raman spectrometer. It is confirmed that fatter bundles of SWNTs tend to be efficiently produced under the gravity-free condition.

5. Summary

The thermal properties of the arc discharge are measured by use of a jet plane and the clear expansion of the hot gas region is observed under the gravity-free condition, where the lower temperature gradient and the slow expansion of the hot gas region are expected. From the Mie scattering method, the production place and the diffusion properties of carbon clusters are observed, which is consistent with the theoretical prediction.

Acknowledgments

This study was supported by the Japan Space Forum. We thank Diamond Air Service for the operation of jet planes.

References

[1] T. Mieno, Jpn. J. Appl. Phys., **37** (1998) L761.
[2] M. Kanai ***et al***., Appl. Phys. Lett. **79** (2001) 2967.
[3] T. Mieno, Plasma Phys. Control. Fusion **46** (2004) 211.
[4] T. Mieno, Jpn. J. Appl. Phys. **42** (2003) L960.

Influence of the applied voltage type on the removal of gaseous acetaldehyde by DBD

A. S. Chiper[1], N. Blin-Simiand[2], F. Jorand[2], S. Pasquiers[2], G. Popa[1], C. Postel[2]

[1]*Plasma Physics Department, Faculty of Physics, "Al. I. Cuza" University, Bd. Carol I, No. 11, 700506 Iasi, Romania, alina.chiper@uaic.ro*
[2]*Laboratoire de Physique des Gaz et des Plasmas, Université Paris XI, Bât. 210, 91405 Orsay Cedex, France, stephane.pasquiers@pgp.u-psud.fr*

Abstract
A dielectric barrier discharge (DBD), in a cylindrical geometry, has been used for acetaldehyde removal in air at atmospheric pressure. Efficiency of the DBD for the VOC molecule decomposition has been measured, by chromatographic and electrical measurements, for different types of applied voltage (AC and pulsed) to the DBD reactor and for various values of the initial concentration of acetaldehyde. It has been shown that the AC energized DBD is much less efficient than the pulsed one.
Keywords - Dielectric barrier discharge - VOC abatement - Acetaldehyde

1. Introduction

A large interest is still growing for Dielectric Barrier Discharges (DBDs) due to their large area of applications like pollutant destruction, ozone generation, surface treatment, excimer UV lamps, CO_2 lasers and plasma display panels. The DBD generates a non-equilibrium plasma at atmospheric pressure following application of a high voltage, of AC or pulsed type, to special system of electrodes [1, 2]. Quickly described, the DBD consists of plasma microfilaments which are established following the propagation of ionization fronts, usually called streamers, in multiple places in the gas volume. These filaments have a very short lifetime, of the order of a few tens of nanoseconds. Each one is a narrow cylindrical channel (radius of the order of 100 μm). The exchange of energy between electrons and molecules takes place mainly during the phase of discharge development, namely during the propagation of the streamers. Electrons (average energy of some eV) excite the molecules and then transform a share of their kinetic energy into energy stored by excited species and free radicals (by dissociation of molecules). Therefore, like other type of transient discharges, non-thermal plasmas of DBDs have the advantage of decreasing the energy necessary for the elimination of the pollutants in air compared to more traditional techniques like thermal decomposition.
The capacities of a DBD to break up Volatile Organic Compounds (VOCs) were already shown [3-5], but much of work remains to be made to achieve a full understanding of the physico-chemical mechanisms responsible for this decomposition. For some VOCs like aliphatic hydrocarbons, alcohols, or aldehydes, it seems clear that production of oxygen atoms and hydroxyl radicals in the plasma leads to the removal of the undesirable molecule through oxidation processes. The higher the specific electrical energy deposited in the gas mixture (in Joule/litre), the higher radical productions and removal efficiency of those molecules. However, following recently published investigations on the removal of NO in air [6], one can expect that the removal efficiency of the above mentioned VOCs should not only depend upon the specific energy value, but also should depend upon other discharge parameters such as the number of streamers per unit volume and the energy deposited in each micro-discharges. In other words, the electrical excitation type of the DBD, AC mode or pulsed mode, as well as the discharge geometrical characteristics (which perhaps could have an influence on the reduced electric field value in the streamer head), should play a role. As a first step to study this problem in our laboratories, the aim of this paper is to determine the effect of the electrical excitation on the elimination of acetaldehyde, and to understand the implied kinetic mechanisms.

2. Experimental set-up and experimental conditions

The whole experimental set-up (Fig.1), which was constructed for evaluating the removal of acetaldehyde from air, is composed of three different parts: (i) a continuous gas flow generating system, (ii) a DBD reactor, and (iii) a gas sampling analysis and detection system.
The gaseous acetaldehyde was generated by passing part of the air (2.5 sccm) above liquid acetaldehyde, kept at a constant temperature (-35°C±0,5°C) in a cooled alcohol - liquid nitrogen mixture. The gas flow rates of each component, in air with acetaldehyde and air with or without water vapour, were kept constant

using mass flow controllers. The value of the total gas flow rate was 602.5 sccm and the residence time in the DBD was 0.97 s. All experiments were performed at atmospheric pressure and room temperature.
The DBD reactor was made of a pyrex tube (relative permittivity ε_r=4.6). The inner diameter of this tube was 11 mm and the wall thickness was 1.6 mm. The high voltage electrode was the central electrode, which was made of stainless steel screw rod with 3 mm diameter. The grounded outer electrode was made of stainless steel wire mesh and covered up the outside of the dielectric. This electrode was 10.7 cm long, while the inner one and the pyrex tube were 40 cm long.

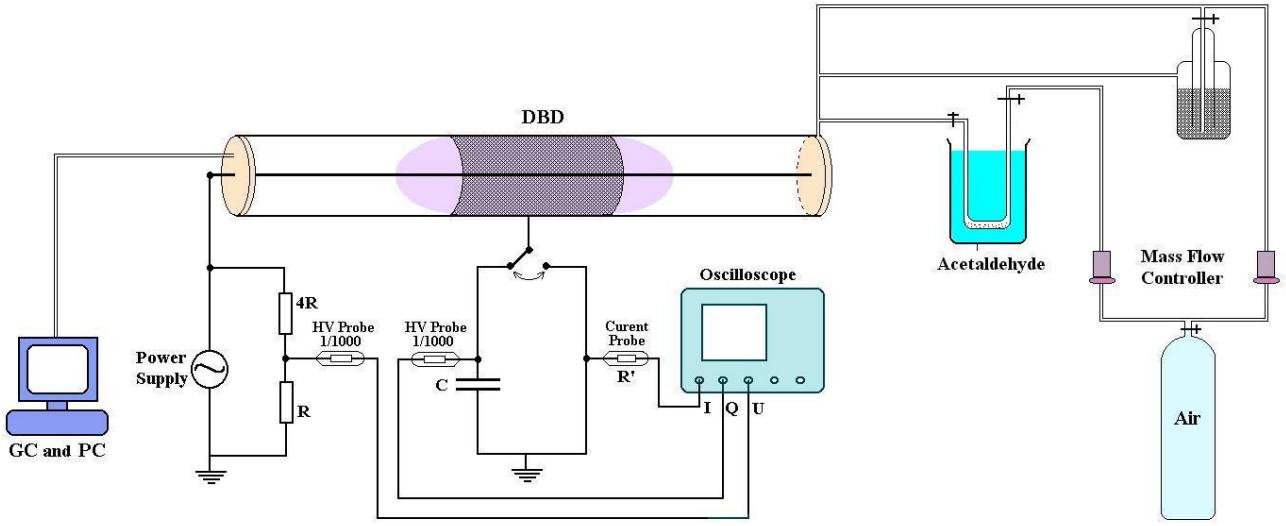

Fig. 1 - Experimental set-up

The electrical energy was supplied either by a high voltage AC generator (peak voltage value up to 30 kV, working at a frequency of 50 Hz), or by a pulsed high voltage generator (peak voltage value up to 30 kV, voltage pulse duration 2 µs, working at a frequency between 10 Hz and 10 kHz). Electrical characterization was made by measurements of the applied voltage across the electrodes (Ua), the electrical charge (Q) flowing through the system or the discharge current (I_d). The applied voltage was measured using a resistance divider and a high voltage 1:1000 probe (Tektronix P6015A) coupled to a 200 MHz digital oscilloscope (LeCroy 9304AM) (Fig.1). The electrical charge was determined using another high voltage 1:1000 probe (LeCroy PHV-1308) in order to measure the voltage across a capacitance C. The current intensity was measured via a current probe as in Fig. 1. Typical waveforms of the applied voltage, electrical charge flowing through the system and electrical current for the AC DBD discharge and the pulsed DBD discharge are displayed in figures 1 and 3.

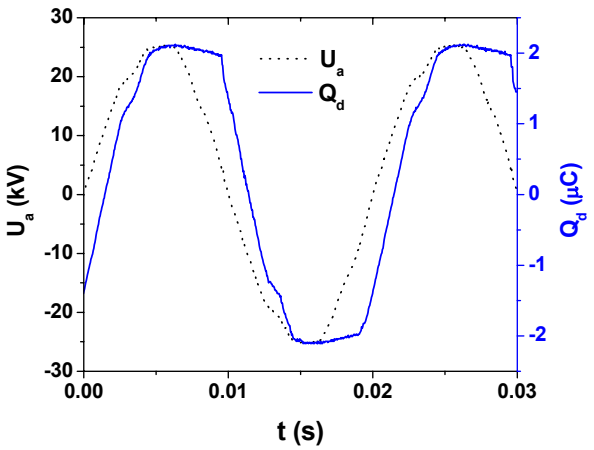

Fig. 2 - Example of electrical discharge characteristics in case of the AC excitation.

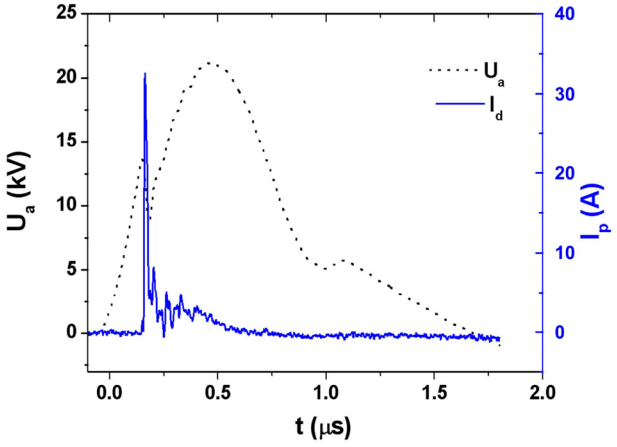

Fig. 3 - Example of electrical discharge characteristics in case of the pulsed excitation.

For the AC DBD discharge, the electrical power was determined using the well-known Manley's method of Lissajous figures [7]. The maximum value is 600 J/l at 30 kV peak voltage. As shown in figure 4, the specific energy increases linearly when the peak voltage value increases from 14 kV up to 30 kV. For the pulsed high voltage generator, the electrical energy per pulse is almost constant for a frequency varying between 20 Hz and 200 Hz. Therefore the energy increases linearly when the frequency increases, as shown in figure 5.

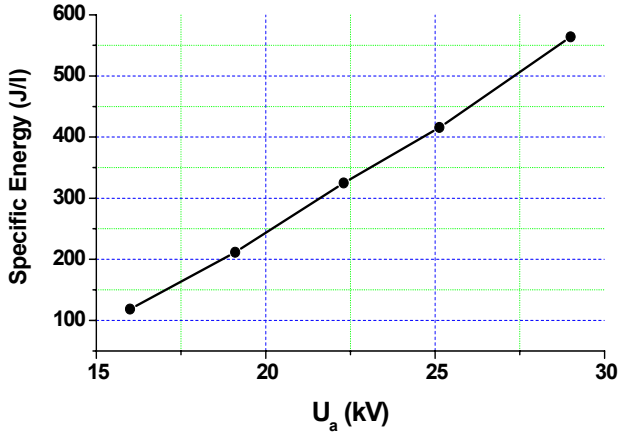

Fig. 4 - Specific energy versus applied voltage, for AC generator, in dry air and humid air.

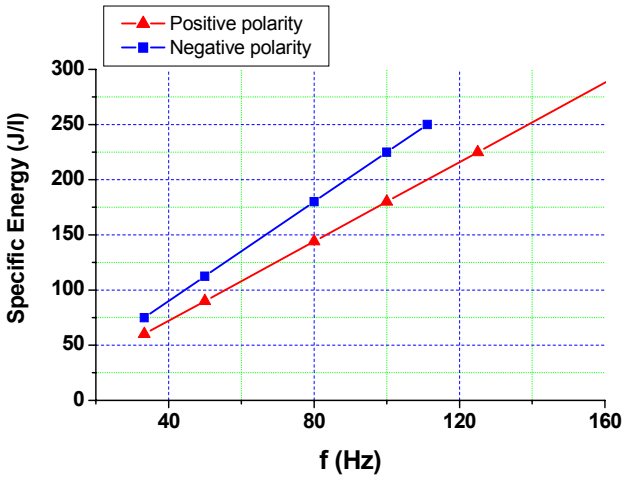

Fig. 5 - Specific energy versus frequency, for pulsed generator, in dry air.

The treated gas mixture was flowing from the DBD reactor to the gas analysis apparatus (Micro Gas Cromatography CP-4900) equipped with a thermal conductivity detector. The Micro GC has three columns. Two of them are identical, molsieve, but with different carrier gases (He and N_2 respectively). The third chromatographic column is a CP-PoraPLOT Q and the carrier gas is He. Using the Micro GC, by-products such as CO, CO_2, H_2O, and HCHO have benn identified. Concentrations of carbon oxides have been measured after appropriate calibration of the apparatus. Three compounds have not been yet identified, at retention times equal to 72.7, 72.8 and 157 seconds.

3. Results and discussions

The acetaldehyde removal has been studied as a function of the specific energy and of the initial acetaldehyde concentration, $[CH_3CHO]_{initial}$. These results are plotted in figure 6.

Acetaldehyde removal efficiency was calculated as follows,

$$\mathrm{CH_3CHO\ Removal}\,(\%) = \frac{[CH_3CHO]_{initial} - [CH_3CHO]_{afterDBD}}{[CH_3CHO]_{initial}} * 100 \qquad (1)$$

where $[CH_3CHO]_{aftef\,DBD}$ is the acetaldehyde concentration at the exit of the reactor.

It was found that the CH_3CHO removal increases with the increase of the specific energy, both for AC and pulsed voltages. The CH_3CHO removal decreases slightly with increasing initial concentration of acetaldehyde, for the case of pulsed voltage, but for AC voltage this effect is more accentuated. For the same value of specific energy (such as, 200 J/l) and the same value of initial acetaldehyde concentration (such as, 195 ppm), it was observed that the removal of acetaldehyde is more efficient when the DBD is energized using a negative or positive pulsed generator by comparison with the case of an AC power supply.

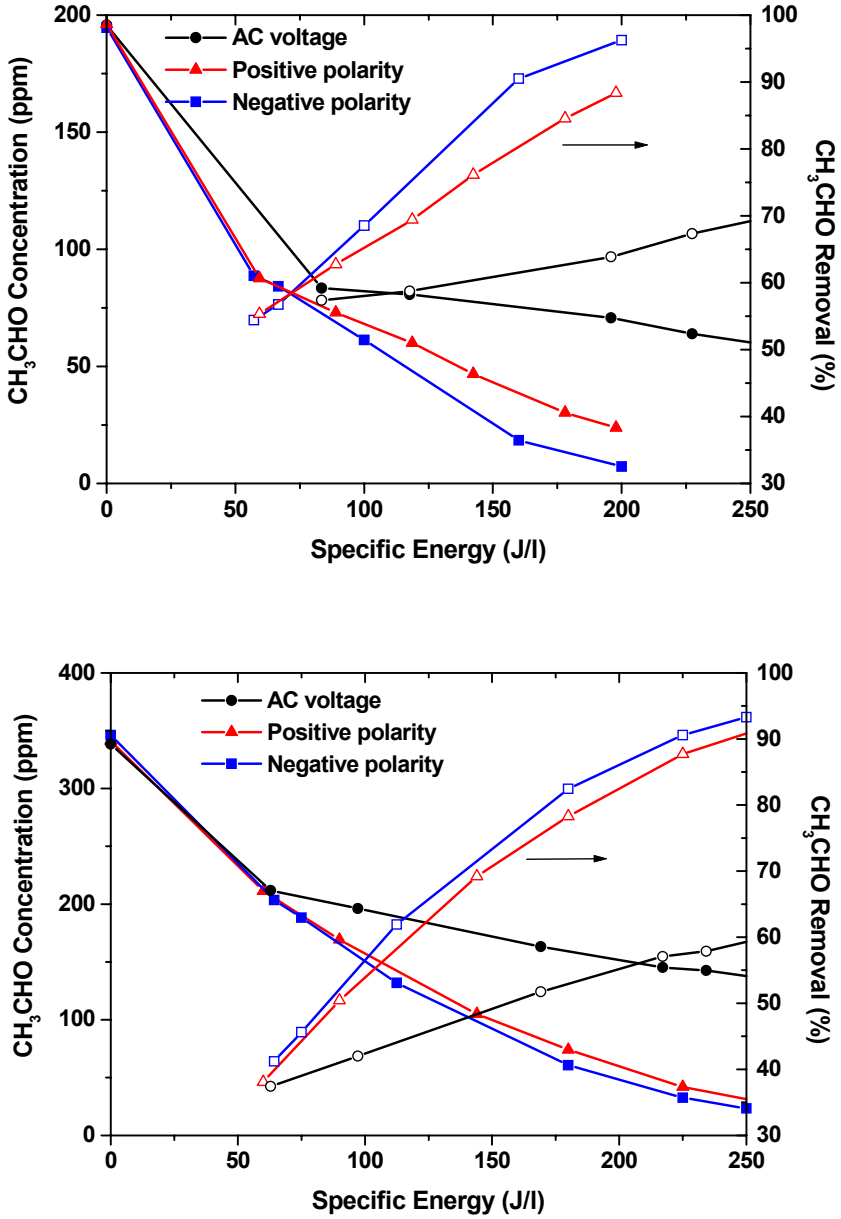

Fig. 6 - CH_3CHO concentration and CH_3CHO removal at the exit of the DBD reactor in dry air, energized by different type of generators, for various values of initial concentration of CH_3CHO: 195 ppm (upper diagram) and 343 ppm (lower diagram).

Figure 6 clearly emphasizes that the removal of acetaldehyde is more efficient when the DBD is energized with the pulsed generator by comparison with the case of the AC power supply. This should be related to the fact that the discharge current pulses are very different, i.e. one very short intense current in the pulsed case, and a great number of much less intense current pulses in the AC case. Streamers are probably more intense in the pulsed case, or more numerous per unit volume, leading to a higher production of oxygen atoms which leads to a higher oxidation rate of acetaldehyde for a given value of the specific deposited electrical energy. This result is similar with those obtained for other VOCs [8, 9].

Amongst by-products following the VOC oxidation, only concentrations of CO_2 and CO are significant, see figures 7 and 8.

For same values of the specific energy and of the initial acetaldehyde concentration, it was observed that the concentrations of carbon oxides are doubled, or even tripled, when the DBD is energized with a negative or positive pulsed generator as compared to the AC one.

The ratio between CO_2 and CO concentrations is approximately 1:1 for the pulsed excitation, whereas it is 1.5: 1 in the AC case (see Table 1). Therefore the overall oxidation of the CH_3CHO molecule is more important in the pulsed DBD than in the AC DBD.

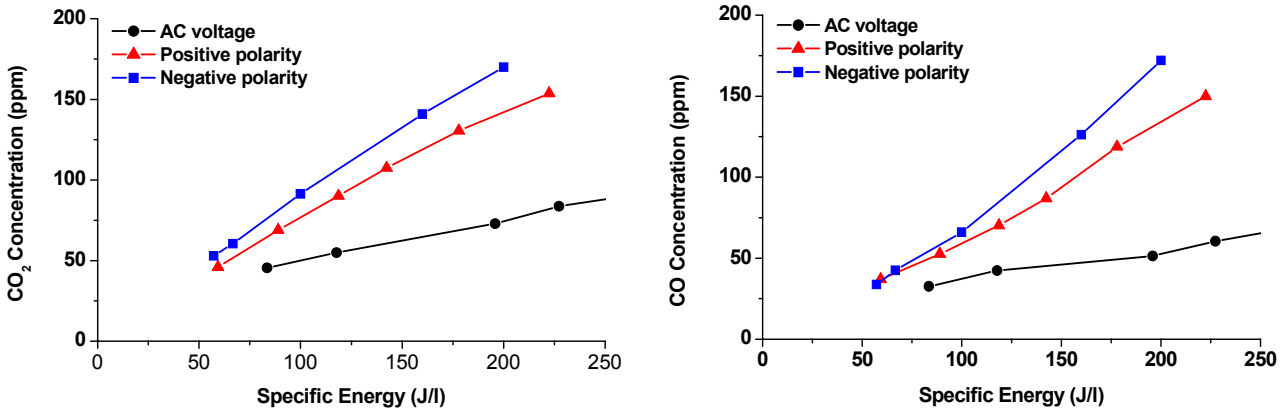

Fig. 7 - CO_2 and CO concentrations at the exit of the DBD reactor, for an initial CH_3CHO concentration of 195 ppm

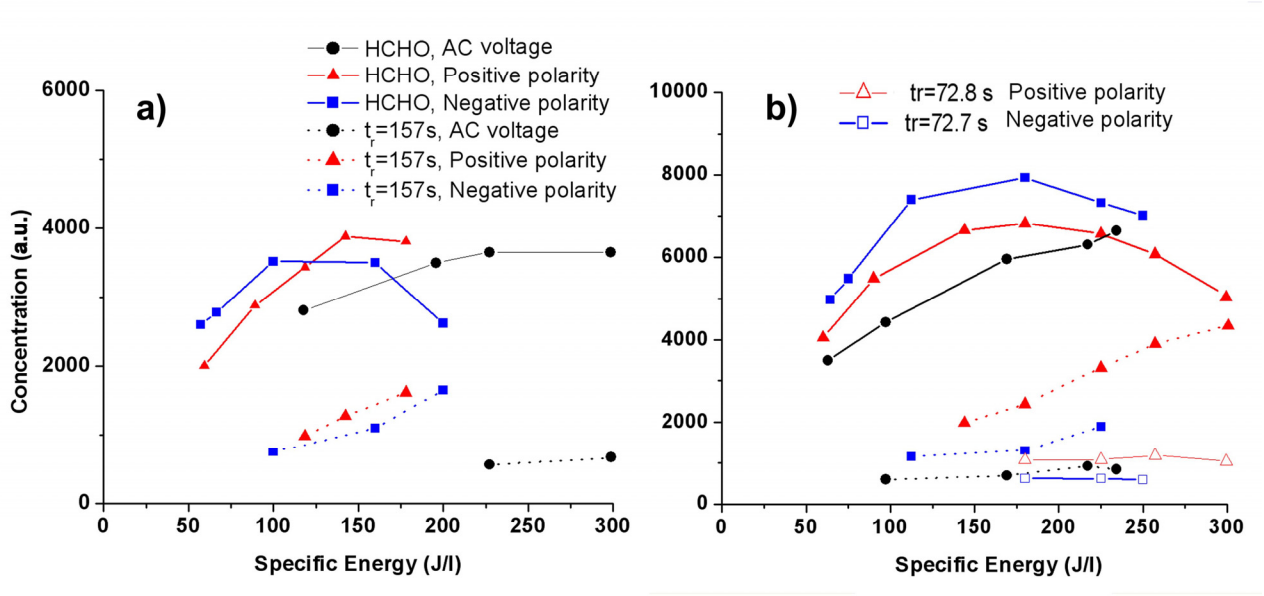

Fig. 8 - Concentration of other by-products at the exit of the DBD reactor, for an initial concentration of : a) 195 ppm and b) 343 ppm. Unidentified products are refereed by their respective retention time values.

Between 70 % to 92 % carbons of acetaldehyde are going to CO_2 and CO, for an initial acetaldehyde concentration value of 195 ppm. This percentage decreases slightly with an increase of the initial acetaldehyde concentration. In Table 1 are given the CO and CO_2 concentration values and carbon balance at the exit of the DBD reactor for the two initial concentration of acetaldehyde studied and for three types of electrical excitation at a fixed deposited electrical energy of 200 J/l : (i) AC, (ii) pulsed with a positive polarity and (iii) pulsed with a negative polarity. The carbon balance is determined as follows,

$$\%C = \frac{[CO_2] + [CO] + 2*[CH_3CHO]_{afterDBD}}{2*[CH_3CHO]_{initial}} * 100 \qquad (2)$$

Table 1- Typical CO and CO_2 concentrations and C balance at the exit of the DBD reactor.

Type of excitation, (E_S=200 J/l=const.)	$[CH_3CHO]_{initial}$ **(ppm)**	$[CO_2]$ **(ppm)**	$[CO]$ **(ppm)**	$CO_2 : CO$	$[CH_3CHO]_{afterDBD}$ **(ppm)**	$\%C$	**Removal (%)**
AC generator	195	75	53	1.41 :1	70	68.5	**64**
Positive polarity		144	132	1.08 :1	23	82.5	**88**
Negative Polarity		170	173	0.98 :1	**8**	**92.2**	**96**
AC generator	343	105	66	1.6 :1	151	69.1	**56**
Positive polarity		191	170	1.13:1	60	70.0	**83**
Negative Polarity		212	170	1.25 :1	**48**	69.7	**86**

5. Conclusions

The removal of acetaldehyde by a DBD reactor, in dry air at atmospheric pressure, has been investigated for two different types of electrical excitations, an AC voltage waveform or a pulsed voltage waveform. It has been found that the removal of acetaldehyde is more efficient when the DBD is energized with the pulsed generator by comparison with the case of the AC power supply. Studies on the spatial distribution of the electrical energy deposition (number of micro-discharges per unit volume and energy deposited in each micro-discharge) are probably necessary to explain these results.

Acknowledgement

The first author acknowledges the *Laboratoire de Physique des Gaz et des Plasmas (Orsay, France)* for the opportunity of work in this laboratory and for financial support, together with the *SOCRATES Scholarship*.

References

[1] U. Kogelschatz, B. Eliasson, W. Egli - Pure Appl. Chem. **71**, 10 (1999).
[2] U. Kogelschatz, B. Eliasson, W. Egli - ICPIG XXIII, Toulouse, France, vol.1, July 1997.
[3] *Non-Thermal Plasma Techniques for Pollution Control*. Penetrante B and Schultheis S (eds) 1993 NATO ASI Series Vol.G34, parts A and B, (Berlin : Springer-Verlag).
[4] *Electrical discharges for environmental purposes. Fundamentals and applications.* Van Veldhuizen E-M (ed) 2000 NOVA Science Publishers.
[5] K. Yan, E. van Heesch, A. Pemen, P. Huijbrechts - Plasma Chem. Plasma Proc. **21**, 107 (2001).
[6] A. Khacef, J-M. Cormier, J-M. Pouvesle - XVIth International Symposium on Plasma Chemistry, Taormina, Italy (22-27/06/2003).
[7] Z. Falkenstein, J. Coogan - J. Phys. D **30**, 817 (1997).
[8] R. Hackam, H. Akiyama - IEEE Trans. Dielect. Elect. Insul. **7**, 5 (2000).
[9] J. Jarrige, N. Blin-Simiand, F. Jorand, L. Magne, S. Pasquiers, C. Postel - This conference.

Automotive toxic gases removal by non thermal plasma

M. Pacheco[1], H. Moreno[2], J.Pacheco[1, 2]
[1] *Instituto Nacional de Investigaciones Nucleares, México*
[2] *Instituto Tecnológico de Toluca, México.*

Abstract
This study provides a simple technique to treat automotive toxic gases, particularly nitrogen and sulfur oxides, by using an inexpensive and small sized reactor. The reactor proposed combines a dielectric discharge barrier (DBD) with a corona discharge. Theoretical results obtained from kinetics of different species present in the plasma reinforce and explain experimental results effectuated. Spectroscopic analysis giving information about some species in plasma was also reported.
Keywords: NO_x removal, SO_x removal, non-thermal plasma.

1. Introduction

Air pollutants like nitrogen and sulfur oxides (SOx, NOx), carbon monoxide (CO), unburned hydrocarbons (HC) and particulate matter (PM) have been released into the atmosphere over the last decades. These pollutants are the main cause of acid rain, urban smog, and respiratory organ disease. Mexico City is an alarming example of these huge emanations; mobile sources are responsible for the generation of more than 80% of atmospheric contaminants. In relation with an inventory of 1998, for year 2010 an increase of air pollutants is expected (i.e. 48% in SO_2, 37% in NO_x and 30% in CO emissions) [1].

The exhausts of gasoline engines are cleaned efficiently with the three-way-catalyst, but for diesel and lean burn engines, these technique does not operate because the high oxygen content in these exhaust gases prevents the reduction of NO [2]. Non thermal plasma technologies can solve such problems [3].

The plasma process, here proposed, is particularly attractive for this purpose, because it can be operated stably at atmospheric pressure, besides, the reactor dimensions are small. Particular conditions of the plasma induce the formation of active chemical radicals which lead to the destruction of gaseous pollutants.

This paper is focused in a dielectric barrier discharge technique (DBD) combined with the Corona effect, and their consecutive application in treatment of flue gases, particularly SO_x and NO_x. A theoretical and experimental analysis of removal of these gases will be presented.

2. Plasma Model

In a DBD-Corona process energetic electrons can interact with molecules, like O_2, H_2O, N_2, to produce active chemical radicals which contribute to the subsequent chemical reactions responsible of the De-NOx/SOx process. These radicals could be OH, N, O, H, $O(^1D)$. Another way to produce radicals as OH and O is by rapid quenching of excited oxygen atoms ($O(^1D)$) .

We consider a uniform electric field for uniform plasma. The proposed model consists in two main steps:

1) Electrons generation by discharge and formation of radicals by direct electron dissociation impact and quenching of $O(^1D)$
2) NO_X and SO_X removal by radicals formed in 1)

In order to simulate the streamer head (high field) we start with 1 electron/cm^3 in a uniform field corresponding to an E/N of 100Td. For the streamer channel the E/N was 40Td.

A total of 18 species were taken into account in the model for de-SOx process (e-, O, OH, $O(^1D)$, O_2, O_2^-, O^-, H^-, H, $O_2(a^1\Delta g)$, O_2^+, O_3, H_2O, N_2, SO_3, SO_2, H_2SO_4, HSO_3). For de-NOx process 23 species were used (e-, O_2, O_2^-, O^-, $O_2(a^1\Delta g)$, O, O_2^+, H_2O, H^-, OH, H, O_3, NO, NO_2, NO_3, N_2O_5, N, N_2O, O('D), N_2, $N_2(A_3\Sigma_u^+)$, HNO_3, HNO_2). Rate coefficients as well as the main reactions most likely responsibly for NOx and SOx removal were taken from [4-6].

3. Experimental

The non-thermal plasma reactor uses a barrier discharge, which prevents large current intensities because of the use of glass as a dielectric, quenching the current and distributing the discharge over the whole surface.
A pyrex glass tube of 27 mm of diameter and 175 mm of length is used as reactor; outside the glass tube, a grounded mesh electrode is wrapped. A stainless steel central electrode of 2.1mm of diameter is used to establish a radial discharge homogenously distributed along the reactor (figure 1).

This reactor is connected to different voltage sources and different operating frequencies (60 Hz to 70 kHz) and atmospheric pressure. The voltage required to produce a high frequency discharge was supplied by a series-parallel resonant converter described in [7].

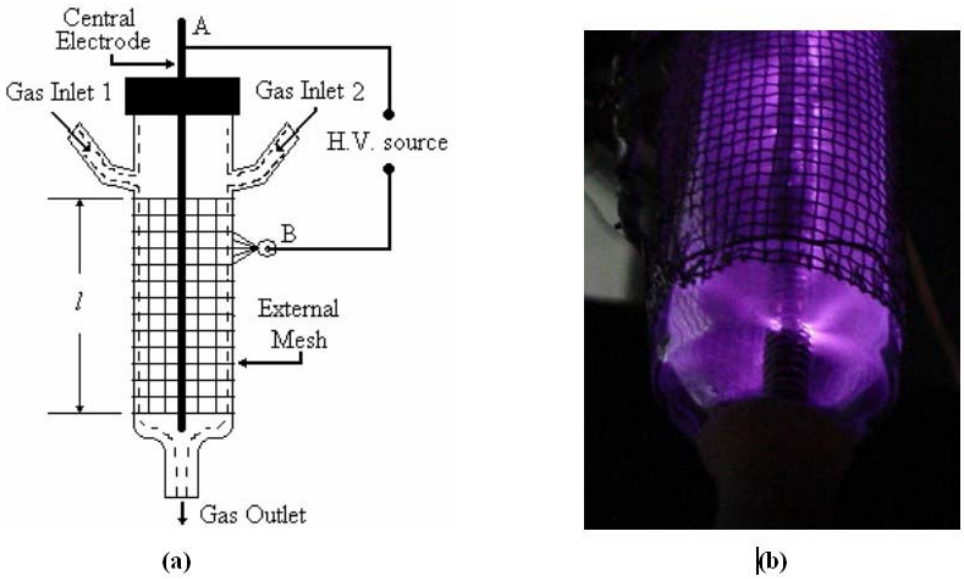

Figure 1. DBD-Corona reactor. (a) Reactor scheme. (b) Plasma discharge with an air-He-NOx mixture.

During each test, exhaust gases are characterized by gas chromatography (Varian Star 3400CX) and a gas analyzer (SENSONIC 2000) to obtain the degree of pollution abatement.
The plasma reactor was also provided with a special port for OES measures. The radiation emitted by the plasma discharge was focused by a convergent lens towards the entry slit of the monochromator, endowed with a 1800 grooves/mm holographic grating, and a CCD detector (122 x 1024 pixels) with a spatial resolution of 0.6nm. The optical signal of the plasma discharge was guided by an optic fiber mounted in a XY electromechanical system so to achieve a vertical and horizontal scanning of the plasma discharge with very precise incremental steps (0.1mm).

4. Results

- **Plasma model.**

Preliminary results obtained shown the importance of different radical in de-SOx process. In general the O radical have a major role in the oxidation of SO_2 to SO_3. The excited oxygen atoms ($O(^1D)$) formed have a significant effect in producing OH radicals. These radicals are the most important in removing SO_2 contributing to acid formation

In figure 2 we observe particle densities per cubic centimeter taking into account mixtures of 50 ppm of NOx-air and SOx-air respectively considering 1.5% of water vapor. From figure 2a a rapid diminution of NO and its conversion to NO_2 is observed; for the SOx-air mixture, SO_2 and radicals [OH] diminishes rapidly generating acids.

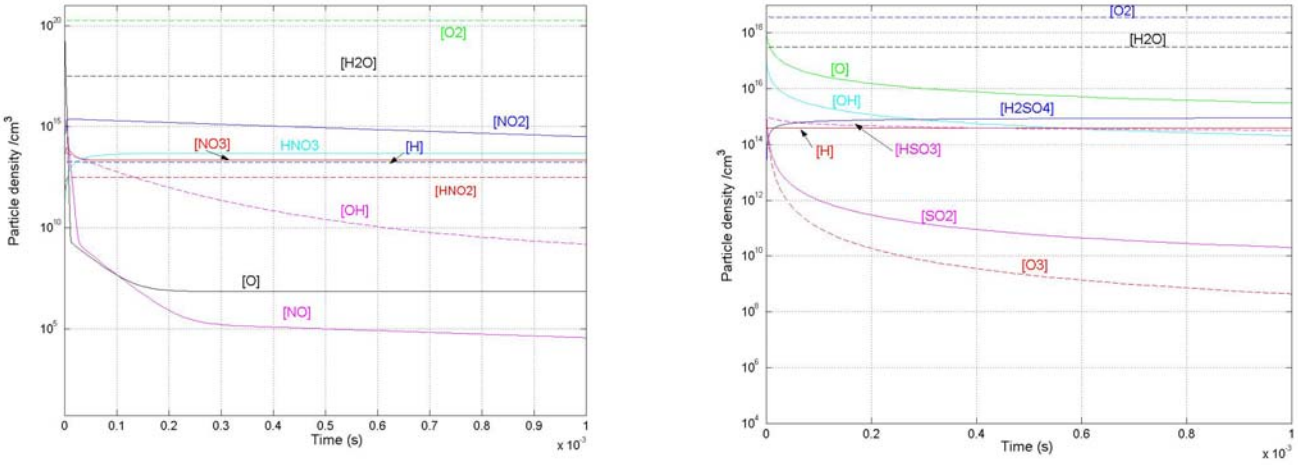

a)NOx-air b)SOx-air

Figure 2. Calculated species concentrations

In figure 3 we appreciate the de-NOx and de-SOx in parts per million (ppm). We observe NO_x ($NO+NO_2$) removal being slower than SO_2 removal (figure 3a); OH radicals play a more important role in de-SOx process than de-NOx process, turning SO_2 in H_2SO_4 almost immediately (figure 3b).

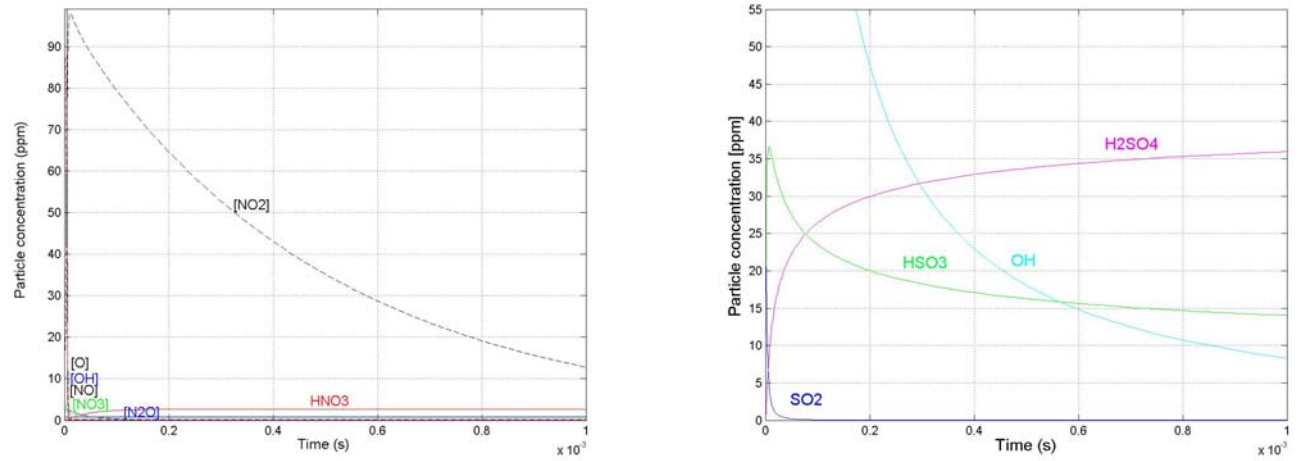

a)NOx-air b)SOx-air

Figure 3. Calculated species concentrations in ppm.

From results of our calculations, considering mixture of NO_x-air, we observe that the principal channel for the removal of NO_x is through reduction by N atoms. Some reverse reactions oxidize the nitrogen atoms and produce NO, however the effect of these oxidation reactions is small compared with the reduction reactions.

For de-SO_x and de-NO_x processes, the radical OH has the major role in removing SO_2 and a minor effect in removing NO_x.

OH radicals are mainly produced from the dissociative attachment of electrons to water vapor and from the reaction of $O(^1D)$ atoms with water vapor. Therefore several tests, with different concentrations of vapor water, were done in order to observe the influence of OH radicals in the de-NOx and de-SOx processes.
In table 1, NO, NO_2 and SO_2 concentrations obtained at 1ms in function of water percentage added are summarized.

Products (ppm)	**H_2O % added**					
Air-NO_x	**0**	**1**	**5**	**10**	**50**	**80**
NO	0	0	0	0	0	0
NO_2	12.5	12.5	5	1	0	1
Air-SO_x						
SO_2	50	0	0	0	0	15

Table 1. NO_x and SO_2 concentrations obtained in function of water vapor concentration.

For de-NOx process a conversion of NO to NO_2 is observed with no addition of water; when a percentage of water is added, OH radicals lead to reactions which produce nitric acid (figure 3a).
Influence of OH radicals in SO_2 removal is more marked than in NO_x removal. From the table we can appreciate that small amounts of water vapor are sufficient to remove SO_X.

However if percentage of water vapor is about 80% we observe an incomplete SOx and NOx removal, it could be explained by a disappearance of OH radicals. O. Motret et al [8] explain this effect in argon-water plasma following three main mechanisms: two collisional processes with argon atoms and with water molecules and the radiative de-excitation.

The collisional de-excitation with water molecules becomes dominant at higher water vapor concentrations. For example, at water vapor saturation the decay term of OH by water molecules collisions is about 100 times larger than those observed through the two other ways. Consequently the increase of the water vapour ratio strongly accelerates the decay kinetic of OH.

- **Experimental results**

To identify the various chemical species present in the discharge, OES is applied. OES allows the analysis of the radiation emitted by the atoms, ions, molecules, and radicals when they are excited by the field or by collisions with other particles. Figure 4 shows the emission bands from the He-air discharge in the wavelength range of 300–700 nm. The spectra are dominated by N_2, OII and HeI transitions. Note that the emission bands above 600 nm are due to second-order light (no filters were used in front of the entrance slit of the monochromator).
When NO_x or SO_x are introduced (without vapor water, therefore no OH bands are present) same spectral lines appear but with a lower intensity.

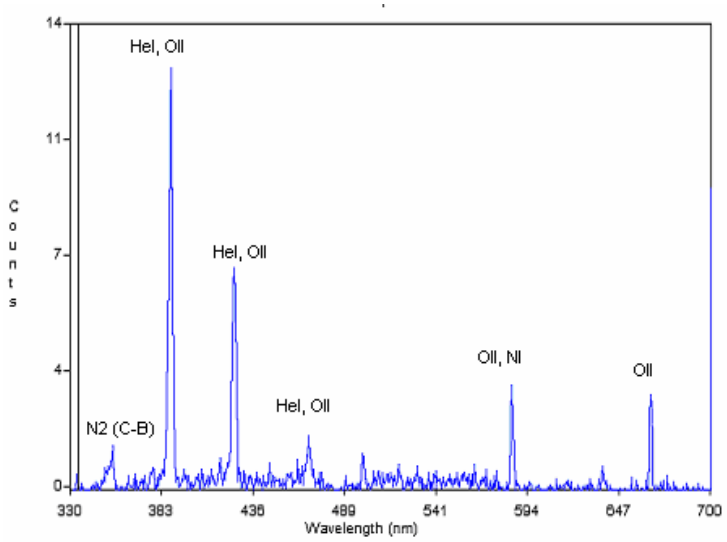

Figure 4. Emission spectra in the 300-700 range of a He-air plasma

Removal experiments were only done with a He-SO_2-air mixture with 50ppm of SO_2, 67kHz, and 150mA peak to peak. From figure 2 we observe a slow removal of this gas arriving approximately to 98% in 40 seconds. In this case no water vapor was added. If we compare with theoretical results it seems to be a contradiction, however we thought that a small amount of humid air penetrates the reactor during the discharge. More experiments must be done in order to verify the presence of OH radicals.

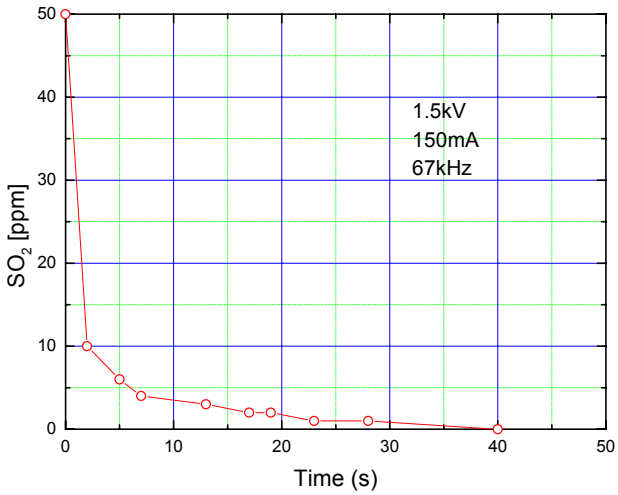

Figure 5. SO_2 removal.

5.Conclusions

Experimental results obtained shown a 98% of SO_2 removal in 40 seconds, OH radicals necessary to its removal were probably generated by humid air.

Results obtained shown the major role of OH radical in removing SO_2, whereas radicals N remove NO_x. The importance of including vapor water is also discussed.

Removal of SO_2 in dry air is zero; then, it will be absolutely necessary to add water vapor (production OH by the dissociative attachment of electrons to water) for its removal, as we will see in our theoretical results. More experiments will be done in order to study the influence of OH radicals in the de-NOx-SOx processes.

Acknowledgements
The authors are very indebted to M. A. Cruz, M. A. Duran, F. Ramos and R. Valdivia for the experimental support. This work was effectuated under the project FOSEMARNAT-2004-01-104.

References
[1] "Programa para mejorar la calidad del aire de la zona metropolitana del Valle de México 2002-2010", Secretaria de ecología del Estado de México, Secretaria del Medio Ambiente, Secretaria del medio ambiente y recursos naturales, Secretaria de Salud, Comisión Ambiental Metropolitana (2002).
[2] S. Broer, T. Hammer, T. Kishimato, "NO-removal in hydrocarbon containing gas mixtures induced by dielectric barrier discharges," in Proc. 12th Int. Conf. Gas Discharge and Their Applications, **I**, 188–191, (1997).
[3] G. Lepperhoff, K. Hentschel, P. Wolters, W. Neff, K. Pochner, F. Trompeter, "Lean-combustion spark-ignition engine exhaust aftertreatment using non thermal plasma," SAE Paper 982 512, (1998)
[4] J.J Lowke, R. Morrow, "Theory of electric corona including the role of plasma chemistry", Pure Appl. Chem. **66**, 1287 - 1294 (1994).
[5] N.A. Guntoro, "Modélisation de la dynamique des neutres et de la cinétique chimique dans les réacteurs plasmas de dépollution des gaz d'échappement" Thèse Université Paul Sabatier, Toulouse, France (2001).
[6] Y. S. Mok, W. Ham "Conversion of NO to NO_2 in air by a pulsed Corona discharge process", Chem.Eng. Science, **53**, 9, 1667-1678, (1998).
[7] J.O. Pacheco, R. Valdivia, M. Pacheco, J.F. Ramos, M.A. Durán, J.S. Benitez, R. Peña, R. López "A Universal Resonant Converter for Equilibrium and Nonequilibrium Plasma Discharges" IEEE Transactions on Plasma Science, **32**, 2105-2112, (2004).
[8] O. Motret, C. Hibert, S. Pellerin, J. M. Pouvesle, "Rotational temperature measurements in atmospheric pulsed dielectric barrier discharge—gas temperature and molecular fraction effects", J. Phys. D: Appl. Phys. **33,** 1493–1498 (2000).

Fluid Model for dc Glidarc Discharge Plasma[1]

WU Bin, LIN Lie, YANG Chi, WU Cheng-Kang

Institute of Mechanics, Chinese Academy of Sciences, Beijing 100080, China

Abstract

A fluid model for dc gliding arc plasma is presented to describe the arc and to understand the arc property in detail. It can give the velocity and temperature field of the plasma reactor. This model is based on steady-state analysis and some experimental data. The numerical results at ignition stage show that the arc boundary is sharp on the upstream side, whereas it is relatively blurred on the down stream side at this stage.

Key words: Glidarc, Fluid Model, Plasma

1. Introduction

Interest in Glidarc plasma reactor has been continuing in recent ten years for its simplicity, easy operation and high efficiency [1], [2].

Some models have been proposed to describe the arc [3]-[5]. Most of them assume the arc as string or column. However, the arc boundary properties on the upstream side and the downstream side are different. The nature of the velocity and temperature in the reactor and the flow downstream of the arc is also important. The objective of the present paper is to give a fluid model of gliding arc plasma generator. It can describe the arc property of the arc to understand the arc in detail. Special attention is given to the arc shape described by the model.

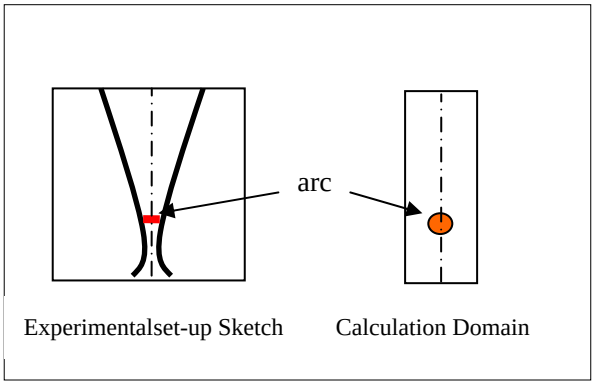

Fig 1 Experimental set-up sketch and calculation domain

2. Gliding arc plasma generator

Figure 1 gives the experimental set-up sketch and corresponding calculation domain.

The experimental set-up consists of two electrodes and two dc power supply. Two copper rod electrodes are formed into a horn-like shape with 30^0 included angle and 1mm minimum electrode separation distance. The power source combines a main supply (600V, 20A) with one for ignition (10000V, 0.1A).

The modeled air plasma is generated by a dc gliding arc working at one atmosphere. The gas flow was inlet from the down side. The arc was ignited at the narrowest position and then moves to the upward by the gas flow.

[1]This work is supported by National Natural Science Foundation of China projects 10375083, 90205026.

Figure 2 showed the voltage and current measured during eight consecutive ignition and extinction cycles. The current and the voltage are all saw tooth-like signals. From the result, we can know that the current and voltage of the arc at different time.

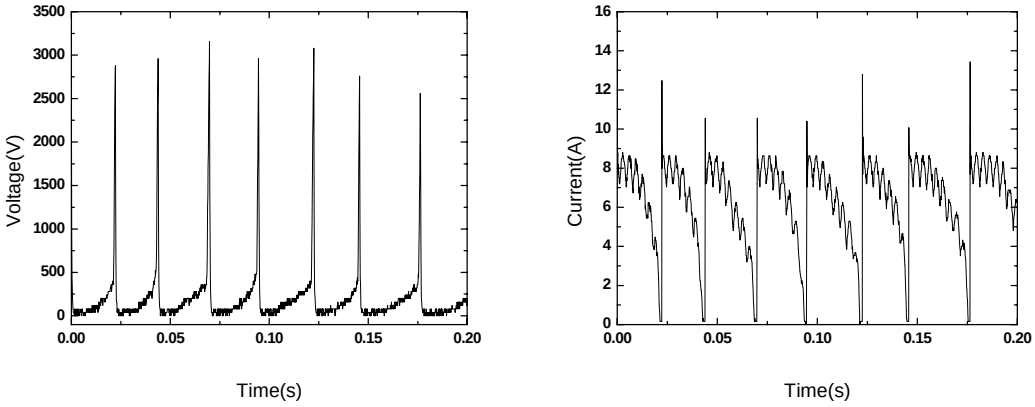

Fig.2 Voltage and current as functions of time

The four stages of the gliding arc from arc ignition to break are shown in figure 3. It includes four stages. Figure 4(a) is the ignition stage, in which the arc just starts. The arc becomes bigger, pushed by the gas flow in Fig 4(b). Then the arc is the longest in Fig 4(c). Finally, the arc breaks in Figure 4(d). From the sequence of the photo and the time interval, we can decide the arc velocity.

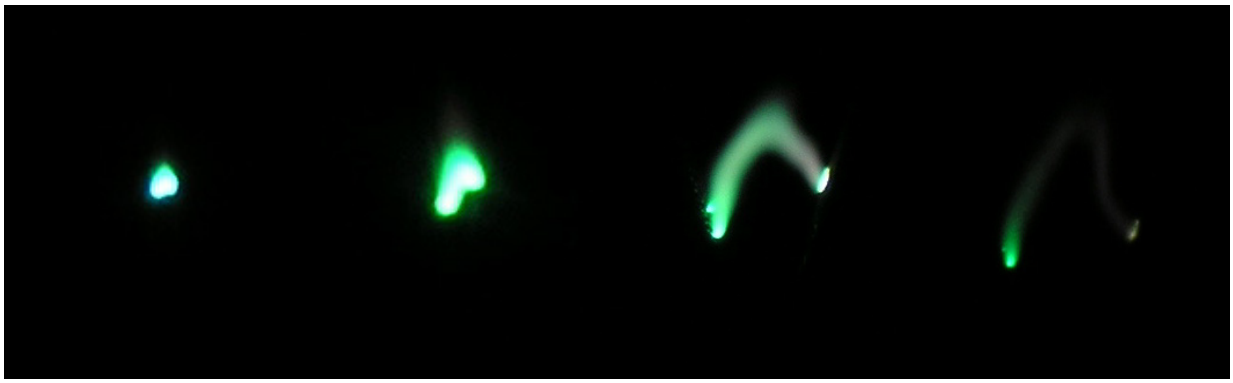

(a) ignition (b)bigness (c)elongation (d) break

Fig.3 Four stages of the gliding arc from arc ignition to break

3. Theoretical model

The model is based on steady-state analysis and some experimental data. We focus on the temperature and flow field at specific time. The arc root and the arc itself are complex physical phenomena. To form a simplified model for use in flow field analysis, the arc position and arc velocity are recorded by a CCD camera in the experiment. The arc properties are measured by oscillograph, and the measured parameters are used as known conditions in this model.

3.1 General governing equation

The mathematical model is based on the k-ε two-equation turbulence model. In order to introduce the

governing equations, the following assumptions are made.

(1) The plasma is an optically thin.

(2) The displacement current, viscous dissipation and pressure work in the energy equation are negligible.

(3)The magnetic effect of the arc is not considered.

Under this given assumptions, the governing equations of a turbulent arc and its surrounding flow are presented as follows.

$$\nabla \cdot (\rho \vec{V}) = 0 \tag{1}$$

$$\nabla \cdot (\rho \vec{V} \phi) = \nabla \cdot (\Gamma_\phi \nabla \phi) + S_\phi \tag{2}$$

ϕ represents *u, v, w, k, ε,* T_i, T_e respectively. $\vec{V}$ is the velocity of the gas. The meaning of ϕ, Γ_ϕ and S_ϕ are shown in Table 1, where μ is the laminar viscosity, μ_t is the turbulent viscosity, $\lambda_{eff\text{-}i}$ and $\lambda_{eff\text{-}e}$ are the effective thermal conductivity for i and e, respectively.

Table 1. Definitions of parameter in governing equations

equations	ϕ	Γ_ϕ	S_ϕ
continuity	1	0	0
X-momentum	u	$\mu+\mu_t$	S_u
Y-momentum	v	$\mu+\mu_t$	S_v
Y-momentum	w	$\mu+\mu_t$	S_w
Turbulent kinetic	k	$(\mu+\mu_t)/\sigma_k$	S_k
Turbulent dissipation	ε	$(\mu+\mu_t)/\sigma_\varepsilon$	S_ε
Energy for i	T_i	$\lambda_{eff\text{-}i}$	S_i
Energy for e	T_e	$\lambda_{eff\text{-}e}$	S_e

Where ρ is the gas density, σ_k and σ_ε are the constant in turbulent model.

3.2 The governing equation for the ignition stage

At ignition stage of the gliding arc generator shown in figure 2(a), the general governing equation can be simplified into two-dimension. We set the 2-D domain vertically to the arc length direction, as shown on the right of Fig 1.

The two dimensional governing equations should be as the following:

$$\frac{\partial(\rho u)}{\partial x} + \frac{\partial(\rho v)}{\partial y} = 0 \tag{3}$$

$$\frac{\partial(\rho u \phi)}{\partial x} + \frac{\partial(\rho v \phi)}{\partial y} = \frac{\partial}{\partial x}\left(\Gamma_\phi \frac{\partial \phi}{\partial x}\right) + \frac{\partial}{\partial y}\left(\Gamma_\phi \frac{\partial \phi}{\partial y}\right) + S_\phi \tag{4}$$

ϕ represent u, v, k, ε, T respectively. At the ignition stage the plasma is in the equilibrium state [6]. Then, we have $T_i=T_e=T$.

3.3 Calculation procedure

To obtain flow and temperature field at a given time instant during the cycle, Equations (3) and (4) were solved using an iterative finite difference scheme with appropriate boundary conditions. The numerical procedure used is based on vorticity and stream function equations [10].

The boundary conditions are as follows. On the walls, the non-slip condition was assumed and the temperature was given as 350K. On the axis of symmetry, symmetrical conditions were imposed. At the inlet, base on the given flow rates, uniform velocity profiles were assumed. At the exit, axial gradients were set equal to zero. The thermal conductivity, electrical conductivity, total radiation and velocity of air were obtained from ref. [8] and [9].

The calculation was performed for a 30×100 grid system in the x and y direction, respectively. As a general rule, more grid points were introduced in areas where a steep temperature of vorticity gradient existed. Parameter relaxation was also applied to stabilize the solutions. The relaxation factors varied between 0.5 and 0.7. The auxiliary relations and the transport properties were evaluated in every iteration cycle.

4. Numerical results and discussion

Calculations were made for air plasma at atmospheric pressure. The plasma operating conditions were as follows:

A total plasma gas flow rate of Q=140Scm^3/s.

The current was 8A, as shown in figure 2.

The Joule heat

$$Q=I^2R \qquad (5)$$

Where, R is resistance of the arc, determined by the electrical conductivity corresponding to the temperature.

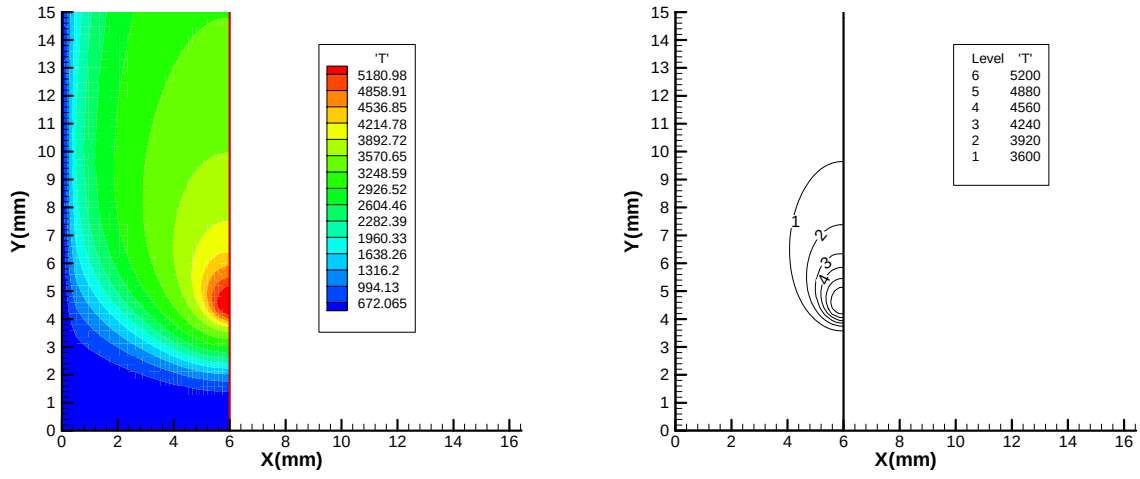

(a) Whole zone (the temperature in K) (b) Arc zone (the temperature in K)

Fig. 4 Temperature field of Glidarc at ignition

Typical results are shown in Fig. 4. This temperature field is vertical to the arc and only half of the field was shown. The red circle corresponds to the half arc area. The gas was inlet from the down edge. The

left side was the solid and the right side is the axis of symmetry of the field. The upper side is the outlet of the generator. Figure 4(a) gives the temperature field in the whole area. The 4(b) shows the temperature field near the arc. From the result, we can see that the temperature near the arc is not as a perfect column, but an egg-like shape. The gradient of temperature up stream side is much greater than down stream side. The figure 2(a) has shown the similar shape in experiment.

5. Conclusion

In order to understand the arc in the gliding-arc plasma generator in detail, we simulated the arc in a fluid model. The results are summarized as follows:

1) The fluid model is helpful for the description of arc in detail.
2) The simplified 2-D numerical results show that the arc in the ignition stage of glidarc is not exactly column. The arc boundary is sharp on the up stream side, whereas it is relatively blurred on the down stream side at this stage.
3) In order for it to be more useful, the model needs to be further developed, especially in the arc root behavior.

References

[1] J. B. Blaisot, L. Delair, J. L. Brisset, and B. G. cheron, “Experimental analysis of a 50 Hz air gliding arc: lighting and development, ISPC-15, 1441-1446

[2] Lin Lie, Wu Chengkang, “Study on characteristics of Rotating glidarc discharge at atmospheric pressure”, ISPC-13, 807-812

[3] S. Pellerin, F. Richard, J. Chapelle, J. M. Cormier, and K Musiol, “Heat string model of bi-dimensional dc glidarc”, J. phys. D: Appl. Phys. 33(2000) 2407-2419.

[4] INga kuznetsova, Nikolay Kalashnikov, Alexander Gutsol, Alexander Fridman and Lawrence A. Kennedy, “Theoretical consideration of gliding arc discharge” ISPC-15, 1509-1514.

[5] S. Pellerin, J. M. Cormier, F. Richard, K. Musiol and J. Chapelle, “Determination of the electrical parameters of a bi-dimensional d. c. Glidarc, J. phys. D: Appl. Phys. 32 (1999) 891-897.

[6] A. Fridman, S. Nester, L. A. Kennedy, A. Saveliev, O. Mutaf-Yardimci, “Gliding arc gas discharge”, Progress in Energy and Combustion Science 25 (1999) 211-231.

[7] F. Richard, J. M. Cormier, S. Pellerin, and J. Chapelle, “Physical study of a gliding arc discharge”, J. Appl. Phys., Vol. 79, No. 5, 2245-2250(1996)

[8] M. I. Boulos, P. fauchais, and E. Phender, Thermal plasma, Fundamentals and Application. 1. New York and London Plenum. 1994.

[9] Chen Xi, Heat transfer and flow in high temperature ionization gas, Science pressure, Beijing 1993 (in Chinese)

[10] Peyret, R. and Tayler, T. D., Computational Methods for Fluid Flow, Springev-Verlag, New York (1983).

A novel organosilicon precursor for low temperature plasma deposition of silicon nitride-like thin films.

R. Di Mundo[1], R. d'Agostino[1], F. Fracassi[1], F. Palumbo[2]

[1]*Department of Chemistry, University of Bari and* [2]*Istituto di Metodologie Inorganiche e Plasmi (IMIP)- CNR, via Orabona 4, 70126, 21Bari, Italy*

Abstract
Silicon nitride-like films have been deposited at low temperature in radiofrequency inductively coupled plasmas fed with bis(dimethylamino)dimethylsilane (BisDMADMS)-Ar mixtures. The effect of input power and of BisDMADMS-to-Ar ratio on the chemical composition of the coating has been investigated by means of FT-IR and XPS analysis. The results indicate that at high input power and low monomer-to-Ar ratio stable silicon nitride-like films, with a refractive index as high as 1.87, can be obtained.

Keywords: PECVD, silicon nitride-like, organosilicon, FT-IR, XPS.

1. Introduction

Silicon nitride-like films (SiN_x) have high density, hardness and refractory character which make them suitable for silicon device technology (IC passivation, diffusion and oxidation barriers, interlevel isolation) as well as for wear and corrosion protection applications. Highly stoichiometric SiN_x films with a very low hydrogen content are generally deposited by HT (High-Temperature, 700-800°C) CVD techniques which, of course, cannot be utilized for processing temperature-sensitive substrates such as plastics or low-melting-point metals [1,2]. For such applications Plasma Enhanced Chemical Vapor Deposition (PECVD) is more appropriate, since it allows to obtain good deposits at lower temperatures. PECVD processes are commonly based on SiH_4 and NH_3 (or N_2) feeds and result in films which tend to be non stoichiometric and to contain appreciable amount of hydrogen (known to be detrimental to the barrier properties) usually in the form of Si-H and N-H groups [2-9]. The refractive index of the coating represents a useful control parameter for nitride deposition (2.0 is the value reported for the thermal films); for plasma deposited SiN_x it can vary from about 1.8 to 2.2 and it increases by increasing the Si/N ratio and by decreasing the H content of the coating [2,3,4,7,9].
Nowadays, other precursors for SiN_x deposition less hazardous than SiH_4, which is toxic and explosive, are under study. So far many organosilicon compounds, already largely used for plasma deposition of SiO_2-like films, have been tested as feed sources in PECVD of silicon nitride, but, from an extended survey of published results, it seems that high quality films, i.e. with low hydrogen and negligible organic carbon content, are very hardly obtained [12-21].
Hexamethyldisilazane (HMDSN), reported in many papers, results in $SiC_xN_yH_z$ films with a high content of organic carbon (i.e. CH_x and $Si(CH_3)_x$ groups, as detected by IR analysis), which is seen to decrease only with high addition of NH_3 and/or by heating the substrate at high temperature; NH_3 addition, however, leads to a higher H content, as Si-H or N-H groups, while highly inorganic SiO_xN_y can be easily achieved by adding small amounts of oxygen to the feed gas [13,15,17,19]. Also tetramethyldisilazane (TMDSN), due to the lower number of methyl groups in its structure, has been utilized for nitride deposition in H_2-N_2 remote plasmas. By increasing the N_2-to-H_2 ratio in the upstream feed gas the SiN character increases, even though a not negligible amount of $Si(CH_3)_x$, SiH and NH is detected [14].
Dimethylbis(2,2-dimethylhydrazil)silane, an organosilicon compound with a high N-to-Si ratio, has also been investigated, in mixture with H_2 and He, for nitride plasma deposition; a substrate temperature higher than 400°C was necessary to obtain inorganic silicon nitride films [12]. High electrode temperature is also reported to reduce the organic character of films deposited from 1,1,3,3,5,5hexamethylcyclotrisilazane (HMCTSN) plasmas, at high input power and NH_3 concentrations [18].
In this work, Bis(dimethylamino)dimethylsilane (figure 1) has been utilized as precursor for silicon nitride-like coatings at low substrate temperature. BisDMADMS is a low cost compound at our knowledge not tested before for this application; it is characterized by two N-atoms and one Si-atom and a fairly low boiling point (128°C). We report the results of FT-IR and XPS investigation for films obtained at low substrate temperature

in RF inductive coupled plasmas (ICP) fed with BisDMADMS-Ar mixtures, without N_2 or NH_3 addition; the effect of feed composition and input power on the chemical characteristics of the films and their stability towards ageing are presented.

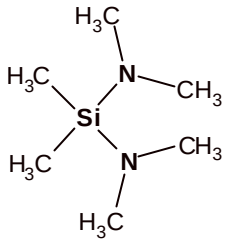

Figure1.Molecular structure of Bis(dimethylamino)dimethylsilane.

2. Experimental details

The utilized Inductive Coupled Plasma reactor consists of a RF (13.56 MHz) powered planar coil (two turns) placed on the top of a quartz plate covering a cylindrical stainless steel plasma chamber. The coil is surrounded by a high magnetic permeability ferrite which concentrates the magnetic field below the quartz plate. The feed gas is admitted through a shower ring positioned close to this plate. The gas flow rates are controlled by MKS mass flow controllers, while the BisDMADMS vapor flow rate is controlled by means of a MKS vapor source controller and all the system is pumped by a turbomolecular-rotary pumping system. The substrates, c-Silicon (100) slabs, were placed on the electrically grounded and thermally controlled bottom electrode. Electrode temperature was never found to exceed 80°C.

Glow discharges were fed with mixtures of BisDMADMS (ABCR, 97% purity) and Ar, with a total flow rate of 22 sccm, at a constant pressure of 9 mTorr. The BisDMADMS-to-Ar flow rate ratio was varied from 0.05 to 0.6, while the input power was changed in the range 150-700 W. In the same power range, a set of experiments was performed using HMDSN (ABCR, 98 % purity) instead of BisDMADMS as film precursor, for comparison. Some experiments were also carried out replacing Ar with He to study the role of the inert gas.

FT-IR Absorption analysis have been performed, within one hour after the deposition, in transmission mode using an Equinox 55 (Bruker) apparatus, by N_2 purging the analysis chamber, in the wavenumber range 500-4000 cm^{-1} (4 cm^{-1} resolution); all the spectra acquired have been normalized to film thickness.

XPS analyses have been performed by means of a PHI 5300 ESCA instrument with a non-monochromatized MgKα radiation. Wide scan, in the Binding Energy range 0-1000 eV, and high-resolution (Si2p, N1s, C1s, O1s) spectra were acquired at an electron take-off angle of 45°, within one hour after the deposition. The atomic percentages reported have been calculated, using the sensitivity factors of the instrument, from the high resolution peaks, acquired after ten minutes of surface cleaning by means of a 4 KeV Ar ion sputtering. Some FT-IR and XPS results have also been compared with those obtained with a 160 nm thick HT-CVD Si_3N_4 film (HT-SiN) on silicon substrate.

Deposition rate have been evaluated from thickness measurements carried out by means of a a-step 500 profilometer (Tencor Instruments) on samples partially masked during the deposition. Refractive index (at 632.9 nm) has been measured with a Jobin Yvon-Sofie single wavelength ellipsometer.

3. Results and Discussion

In figure 2 the FT-IR absorption spectrum of BisDMADMS in the gas phase (a) is compared with those of films deposited at 300 W with different gas feeds: 100% BisDMADMS (b), He-BisDMADMS (c), and Ar-BisDMADMS (d). The details of the bands detected (assignments and positions) are reported in Table 1 [11-20]. It can be observed that the coating obtained in pure monomer is highly organic since strong absorption of CH_x and $Si(CH_3)_x$ features are present. Furthermore, since SiH, NH, and reasonably C=N and NH_2 groups can be detected, a poorly crosslinked structure with a general stoichiometry $SiC_xN_yH_z$ is expected. He addition does not affect appreciably the FT-IR spectrum, while, if Ar is utilized as buffer gas, a more inorganic coating is obtained, since the intensity of CH_x, $Si(CH_3)_x$ and SiH absorptions are markedly reduced.

The FT-IR spectra of films deposited as a function of input power (150 - 700 W) at BisDMADMS-to-Ar ratio of 0.1 are reported in figure 3. As the input power is increased, the organic features as well as those of SiH and NH decrease and the main absorption band shifts towards lower wavenumbers. By integrating the areas of

the absorption peaks at 3380 cm^{-1}(NH), 2960 cm^{-1} (CH_x) and 2180 cm^{-1} (SiH), it can be appreciated the strongest effect of input power on CH_x and SiH absorptions, which are reduced of about 95 % when input power is increased from 150 to 700 W, while the reduction of NH absorption is 70%. Thus, at higher power values the FT-IR spectrum becomes close to that of a silicon nitride, as it can be appreciated by the comparison of the spectrum at 700 W (d), where the SiN stretching is peaked at 850 cm^{-1}, with spectrum (e) corresponding to thermal nitride film (SiN stretching peaked at 835 cm^{-1}).

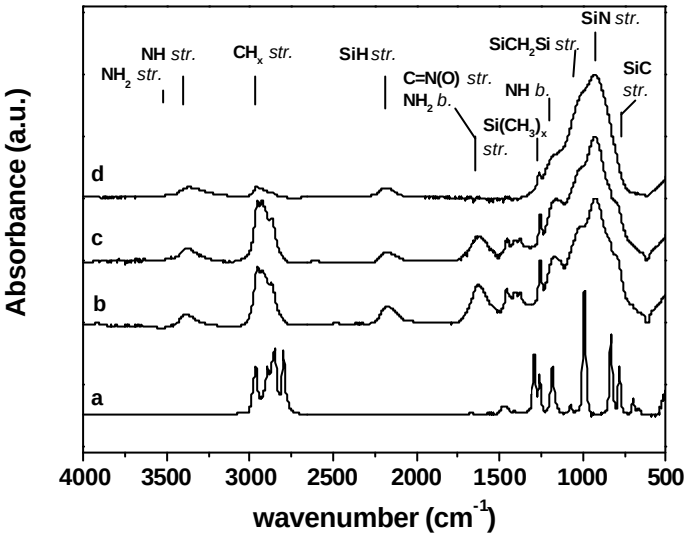

Figure 2. Normalized FT-IR absorption spectra of BisDMADMS (gas phase) (a) and of films deposited at 300W from plasmas fed with: 100% BisDMADMS (2 sccm) (b); BisDMADMS – He (2 sccm-20 sccm) (c); BisDMADMS - Ar (2 sccm - 20 sccm) (d). Band assignements are in table 1.

Table 1. Positions and assignments of the FT-IR features.

Wavenumber (cm^{-1})	Assignements
3480	NH_2 *stretch.*
3380	NH *stretch.*
2960	CH_x *stretch.*
2180	SiH *stretch.*
1630	C=N (O) *stretch.*
1550	NH_2 *bend.*
1460	CH_x *bend.*
1260	$Si(CH_3)_x$ *stretch.*
1165	NH *bend.*
1040	$SiCH_2Si$ *stretch.*.(SiOSi *stretch.*)
925-850	SiN *stretch.*
835	SiN *stretch.* **in HT-SiN**
800	$Si(CH_3)_x$, SiC *stretch.*

XPS analysis confirms the significant change of chemical composition *vs.* input power revealed by FT-IR spectra. As the input power is raised the carbon content decreases from 60 % at 150 W to 10% at 700 W, while the nitrogen and silicon percentages increase from 11 to 32% and from 18 to 43 %, respectively. A N-to-Si ratio of 0.74 is obtained at 700 W. XPS peak position, after charge correction, has been found almost constant at 398.9 eV for N1s, while for Si2p a shift from 102.0 eV (150W) to 102.8 eV (700W), consistent with a more nitrogen rich chemical surrounding, has been detected. A certain amount of oxygen (about 9 %) has been always detected and it is believed to be due to moisture or oxygen uptake during air exposition after the deposition or released from the reactor walls during the process, as it is usually reported also for other plasma processes as well as for the deposition of thermal silicon nitride films [2,6,12,17]. In fact, about 5% of oxygen has been found in the HT-SiN reference sample which is characterized by a N-to-Si ratio of 0.99 (and by a B.E. of 398.8 eV for N1s and 102.7 eV for Si2p). However, it should be pointed out that the atomic

percentages found may be affected by the sputter cleaning procedure (i.e. differential sputtering and/or ion bombardment induced surface remixing phenomenon).

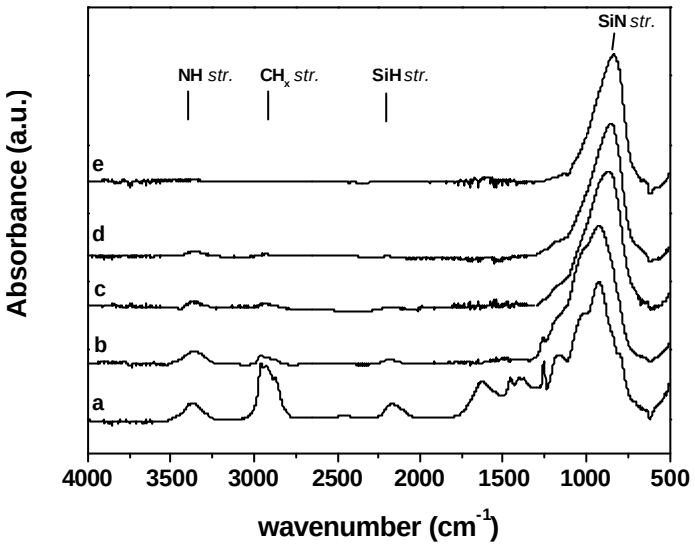

Figure 3. Normalized FT-IR absorption spectra of films deposited in plasmas fed with BisDMADMS-Ar (ratio=0.1) at 150 W (a), 300 W (b), 500 W (c), 700 W(d). The spectrum of a thermal SiN_x film (HT-SiN) is also reported for comparison (e).

Due to their similarity in terms of XPS peak position, N-to-Si ratio and IR absorption, a curve-fitting of the SiN stretching FT-IR absorption band was performed for the HT-SiN film and for the sample deposited at 700 W. The results for the plasma coating are shown in figure 4 and the details are reported in table 2. The SiN signal is typically asymmetric and even though the Si-N bond in a nitride network gives origin to four vibrational modes, in both cases six peaks have been utilized for the fitting [6,9]. In fact, in agreement with published data, in addition to the four gaussian curves due to the nitride network vibrations, two further small peaks have been introduced at 1075 and 1154 cm^{-1}, assigned to SiOSi stretching and NH bending, respectively. In the plasma coating the intensity of SiOSi stretching and NH bending are higher and the SiN features are shifted to higher wavenumbers but with the same relative intensity ratio as in HT-SiN.

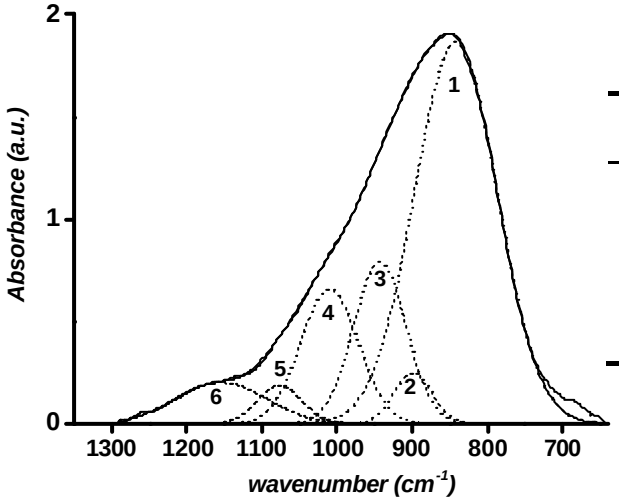

Table 2. Best-fitting of the FT-IR SiN absorption band.

curve	*Vibrational mode*	*Position (cm^{-1})*	*FWHM (cm^{-1})*
1	SiN *stretch.*	842	130
2	SiN *stretch.*	899	60
3	SiN *stretch.*	943	82
4	SiN *stretch.*	1010	90
5	SiOSi *stretch.*	1075	70
6	NH *bend.*	1154	142

Figure 4. Best fitting of the SiN stretching FT-IR absorption band for the coating deposited in a BisDMADMS-Ar fed discharge at 700 W and monomer-to-Ar ratio of 0.1. Peak assignmets, positions and FWHM's are reported in table 2.

The effect of BisDMADMS dilution in Ar has been investigated at the input power of 300 and 700 W in the monomer-to-Ar ratio range of 0.05 - 0.6. By increasing the BisDMADMS-to-Ar ratio the coating becomes more organic and less cross-linked. In particular at 700 W the SiN moves from 850 cm^{-1}, at the ratio of 0.05 (very close to SiN stretching in HT-SiN), to 895 cm^{-1} at a ratio of 0.6, indicating a higher organic character; moreover, an increase of the absorption of CH_x, SiH and NH bands has been revealed. A similar trend, but more marked, has been observed at 300 W where, for the monomer-to-Ar ratio of 0.6, a coating very close to that deposited from pure BisDMADMS (figure 2) has been obtained.
Summarizing, it can be concluded that when BisDMADMS is utilized as film precursor, high input power and low monomer-to-Ar ratio are required to produce silicon nitride-like films. Under the experimental condition utilized, at 700 W and BisDMADMS-to-Ar ratio of 0.1 the deposition rate was 20 nm/min and the refractive index of deposited films was found to be 1.87 ± 0.02.
Figure 5 shows the FT-IR spectra of films obtained at the BisDMADMS-to-Ar ratio of 0.1, at 300 and 700 W, recorded as deposited and at one month after the deposition. It is clear that while the chemical composition of the coating deposited at 300 W changes, the film obtained at 700 W does not show any ageing since the FT-IR spectrum appears unmodified. Coating (b) of figure 5, in fact, shows an evident oxygen uptake since the intensity of the OH stretching at 3100-3500 cm^{-1} and of Si-O-Si stretching at 1050 cm^{-1} increase after one month, while the intensity of SiH bands decreases suggesting that reactive SiH may undergo oxidation and hydrolysis reactions with oxygen and water molecules diffused through the film network, in agreement with the reported mechanism of ageing for highly organic and poorly crosslinked coatings (i.e. $SiC_xN_yH_z$ films) [11, 17, 18].

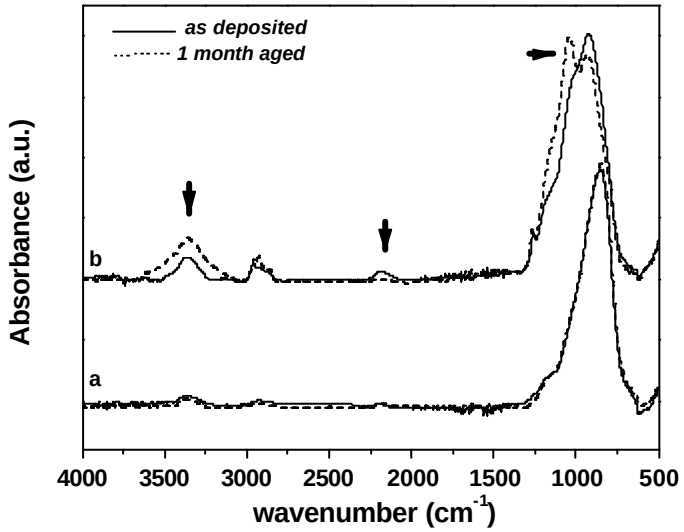

Figure 5. FT-IR spectra of coatings obtained in bisDMADMS-Ar (ratio = 0.1) fed plasmas at 700 W (a) and 300 W (b) acquired within 1 hour after the deposition and after 1 month of air exposure. The arrows indicate the variations occurred in the spectra.

The importance played by the BisDMADMS with respect to other organosilicon compounds for nitride deposition, has been defined by performing a set of experiments under the same conditions utilizing hexamethyldisilazane (HMDSN) as film precursor. XPS analysis of films obtained by HMDSN reveal a carbon content higher than 40 % and a nitrogen content not lower than 10 %; their FT-IR spectra show the main band always peaked at 800 cm^{-1}, assigned to Si-C bonds. Therefore BisDMADMS is more suitable to obtain SiN-like coatings while HMDSN produces silicon carbonitrides films. This could be a consequence of the higher bond energy of Si-C (92 Kcal/mol) with respect to C-N (73 Kcal/mol); in fact, the HMDSN molecule has six carbon atoms all strongly bonded to silicon, while in the molecule of BisDMADMS there are four C-N bonds and two Si-C bonds and therefore in the plasma phase BisDMADMS is expected to undergo a higher fragmentation with a more effective reduction of its organic fraction.

4. Conclusions

In this work FT-IR and XPS investigations of the chemical composition of silicon nitride-like thin films deposited in IC plasmas fed with BisDMADMS-Ar mixtures have been performed. The results show that this novel organosilicon compound is particularly suitable to produce silicon nitride-like film, also at low substrate temperature and without the addition of reactant gases; at high input power and low BisDMADMS-to-Ar ratio the nitrogen content is maximized and the carbon concentration in the film is low. Stable quite inorganic films with good optical properties (refractive index of 1.87) have been obtained under the best experimental conditions.

Acknowledgements

We gratefully acknowledge Prof. A. Valentini (Physics Department, University of Bari) for the ellipsometric measurements and Gianvito Caputo for the scientific contribution. The financial support of the European Community VI Framework Programme (MATECO- Contract No NMP3-CT-2003-505928) is also acknowledged.

References

[1] C. E. Morosanu - Thin Solid Films, **65**, 171 (1980).
[2] K. K. Schuegraf - "Handbook of thin films deposition processes and techniques", Noyes Publ. (1988).
[3] E. A. Taft - Journal of Electrochemical Society, **118**, 1341 (1971).
[4] M. J. Hernandez, J. Garrido, J. Martinez, J. Piqueras - Journal of Electrochemical Society, **141**, 3234 (1994).
[5] G. N. Parsons, J. H. Souk, J. Batey - Journal of Applied Physics, **70**, 1553 (1991).
[6] B. R. Zhang, Z. Yu, G. J. Collins - Journal of Vacuum Science and Technology A, **7**, 176 (1989).
[7] L. Da Silva Zambom, R. D. Mansano, R. Furlan - Vacuum, **65**, 213 (2002).
[8] B. F. Hanyaloglu, E. S. Aydil - Journal of Vacuum Science and Technology A, **16**, 2794 (1998).
[9] S. Han, B. Jun, K. No, B. Bae - Journal of Electrochemical Society, **145**, 652 (1998).
[10] M. L. Naiman, C. T. Kirk, R.J. Aucoin, F. L. Terry, P. W. Wyatt, S. D. Senturia - Journal of Electrochemical Society, **131**, 637 (1984).
[11] A. M. Wrobel, M. R. Wertheimer - "Plasma-polymerized Organosilicones and Organometallics", in: Plasma deposition, Treatment and Etching of Polymers, R. d'Agostino, Academic Press Boston, 163 (1990).
[12] T. P. Smirnova , A. M. Badalyan, V.O. Borisov, L.V. Yakovkina, V.V. Kaichev, A. N. Shmakov, A.V. Nartova, V.I. Rakhlin, A.N. Fomina - High Energy Chemistry, **37**, 303 (2003).
[13] N. I. Fainer, Yu. M. rumyantsev, M. L. Kosinova, G. S. Yurjev, E. A. Maximovskii, F. A. Kuznetsov - Applied Surface Science, **113/114**, 614 (1997).
[14] A. M. Wrobel, I. Blaszezyk, A. Walkiewicz-Pietrzykowska, A. Traez, J. E. Klemberg-Sapieha, T. Aoki, Y. Hatanaka - Journal of Material Chemistry, **13**, 731 (2003) .
[15] R. Gonzalez-Luna, M. T. Rodrigo, C. Jimenez, J. M. Martinez-Duart - Thin Solid Films, **317**, 347 (1998).
[16] N. C. Da Cruz, S. F. Durrant, M. Bica de Moraes - Journal of Polymer Science, B, **36**, 1873 (1998).
[17] F. Fracassi, R. d'Agostino, G. Bruno - Plasmas and Polymers, **1**, 3 (1996).
[18] T. A. Brooks, D. W. Hess - Thin Solid Films, **153**, 521 (1987).
[19] M.T. Kim, J. Lee - Thin Solid Films, **303**, 173 (1997) .
[20] M.R. Yang, S.K. Wu - Surface and Coatings technology, **127**, 274 (2000).
[21] T. Aoki, T. Ogishima, A. M. Wrobel, Y. Nakanishi, Y. Hatanaka - Vacuum, **51**, 747 (1998).

Time-Resolved Mass and Energy Spectral Measurements in an Acrylic Acid Pulsed Plasma

S.A. Voronin[1], M. Alexander[2] and J.W. Bradley[1]

1 Dept of Electronic Engineering, University of Liverpool, Liverpool, UK
2 Dept of Pharmacy, University of Nottingham, Nottingham, UK

Abstract
We present a technique for obtaining time-resolved mass spectra and ion energy distribution functions (IEDFs) using a commercial quadrupole mass energy analyser. The measurements were carried out in a 1.3 Pa pressure acrylic acid RF discharge, pulsed at a frequency of 1 kHz. Both the extractor and detector of the analyser were triggered independently which allowed *time-of-flight (mass) independent* measurements.

Keywords: acrylic acid, mass spectrometry, time-resolved, ion energy distribution, plasma diagnostics, pulsed RF plasma.

Introduction

Pulse-modulated processing plasmas are extensively used for a number of material processing applications such as reactive ion etching, reactive magnetron sputtering, plasma enhanced chemical vapour deposition and plasma polymerization. Modulating the applied power, typically through variation of the pulse frequency and duty ratio has advantages in terms of enhancing consumed electrical power efficiency and greater control over the plasma properties, particularly the ion energy distribution function at a work piece of substrate [1]. Making accurate time-resolved energy and mass spectra measurements at the plasma-material interface is important for obtaining better understanding of pulsed plasma particle dynamics, ion bombardment energy, sheath structure and plasma chemistry.

A number of commercially available mass spectrometers are capable of making mass- and energy-resolved measurements of positive and negative ions, neutrals, excited species and electrons extracted from a plasma discharge. Time-resolved mass spectra and IEDFs measurements were done either in inner gases plasmas and chemically active plasmas [2-4], by gating the digital ion counting pulse on the analyser detector. This common technique is reliable and simple in use. However, it has some disadvantages.

First of all, time-of-flight (TOF) of the ions through the optics is rather long (dozens-hundreds microseconds). Measurements made at one time point (connected to the spectrometer detector triggering signal) are "delayed" with respect to the TOF to the time point where the ions originally came. Hence, the transit time required for an ion to transit from the entrance orifice to the secondary electron multiplier (SEM) must be taken into account when referring the IEDFs to the modulation pulse front. Ion transit times τ_t are mass-dependent ($\tau_t \sim (M_i)^{-1/2}$) which makes it impossible to obtain a mass spectra and IEDFs for ions of different masses at one selected time point at once. Another problem, that occurs by using this method – is an increase in IEDFs uncertainty when two energy groups of ions exist in a discharge. Typically this can happen when ions with higher energies from "on" time and ions with lower energies from "off" time exist simultaneously. This may cause deviations of the IEDFs (obtained in afterglow) from the expected single low-energy peak, namely, a simultaneous contribution from the second high-energy peak [2].

Moreover, ion transit time to the detector must be smaller than the period of modulation of pulsed plasma. Otherwise ions from an earlier pulse periods will corrupt the data measured in the subsequent pulse period.

Karkari et al [5] used a simple technique of electrostatic gating the ions at the entrance of the spectrometer for ion spectral measurements in a high-frequency pulsed Ar discharge. A high positive retarding potential was applied to the grid mounted in front of the extraction orifice. The potential of this grid was rapidly lowered to zero for a chosen duration, which provided a window for the ions to enter the spectrometer. At other times, a large repulsive bias is applied, electrostatically shuttering the ions. We base our system on this method, to examine the fundamental characteristics of an RF discharge in an acrylic acid plasma, which is an important monomer compound used for plasma film polymerisation [6].

Several significant steps have been made to improve this technique for complex measurements in a multicomponent chemically reactive pulsed RF plasma. (i) An extractor was located inside of the barrel of the mass spectrometer (behind an orifice) and directly triggered from the external circuit. This prevented possible film deposition on it and no "parasitic" discharge could happen between an extractor and orifice due to the high vacuum inside the barrel (~10^{-1}-10^{-2} Pa near the orifice). (ii) Within the gating time the potential of the extractor was rapidly lowered to an adjusted value between -20 V and +20 V instead of zero what gave more control of the ion extraction. (iii) SEM was also triggered with a prescribed delay with respect to extractor gating window. This allowed us to increase the counts response (compare to situation if the SEM was constantly enabled) and at the same time to detect ions of different masses at one investigated time point for one scan.

Experimental setup

The plasma used in this study was maintained inside a glass cruciform by the application of RF excitation (13.56 MHz) from a four-turn coil copper strip, wound around one axis of the vessel. The system, pumped by a rotary pump and its electrical part are described elsewhere [7]. A needle valve was used to control acrylic acid flow and pressure, while a Baratron gauge was used to monitor the pressure. Schematic diagram of the discharge geometry and electrical arrangement is shown in figure 1a.

The RF power and data acquisition signals are synchronized by a pulse-width generator (figure 1a,b). The exciting RF voltage U_{rf} (applied to the driving coil) is generated by an Advanced Energy RFG-150 power supply triggered from pulse U_{pulse}. It is coupled to the coil electrode via a separate matching unit. Power input is measured using the built-in meter and the reflected power never exceeded 3%.

The positive ion energy distribution functions with respect to the earth potential were measured by a Hiden EQP 300 energy-resolved mass spectrometer. Its input orifice (diameter of 100 μm) was located close to the centre of the vessel (figure 1a). The ions from the plasma enter the spectrometer through the orifice of the end cap. In a new electrode configuration by Hiden Analytical the extractor was mounted in the vacuum inside the barrel behind the orifice (figure 2c). This excluded the possibility of unwanted discharge between an extractor (at high voltage) and other electrodes which could occur if the extractor was immersed into the gas medium as in [5].

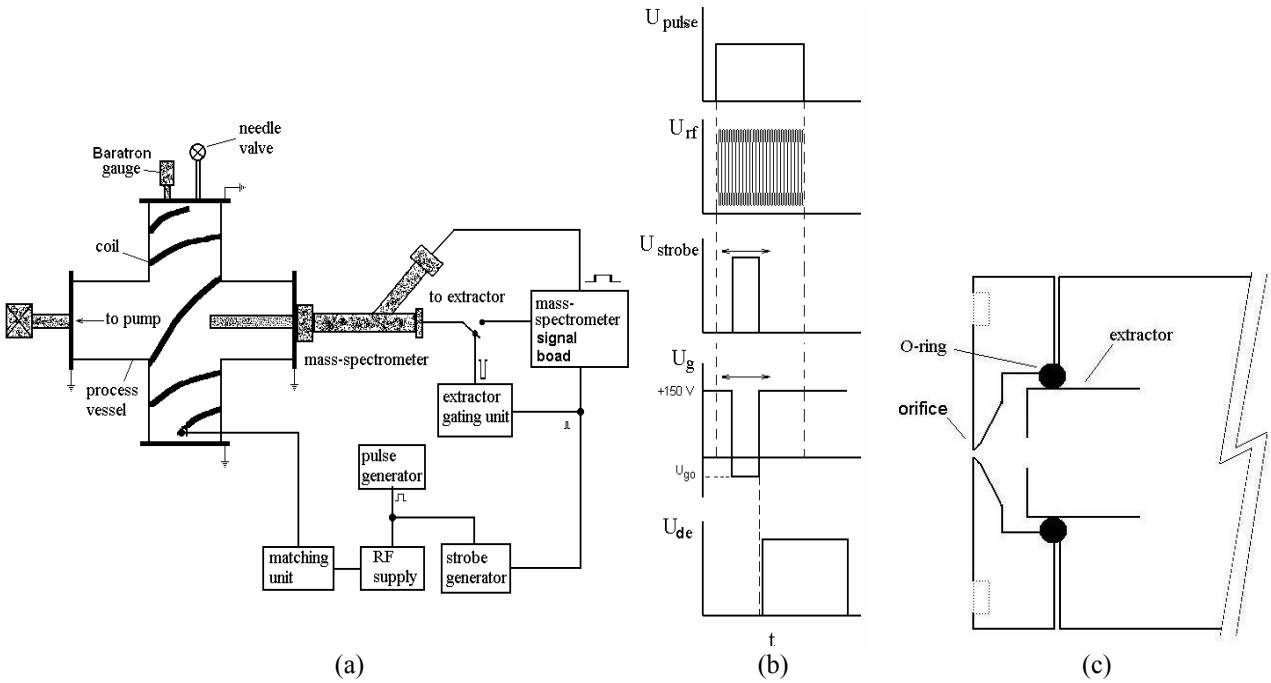

Figure 1. (a) Schematic diagram of experimental set-up and (b) signal diagram. (c) Extractor location inside the barrel

Both an extractor gating unit and mass spectrometer circuit board were connected to the extractor through the electric switch (figure 1a) to get an opportunity to supply the extractor externally (from pulsing generator) or internally from EQP 300 signal board.

In the periods of the pulse when ions were not to be selected for measurement, the extractor was held at a constant positive voltage U_g = +150 V to repel all positive ions from the plasma (figure 1b). A 10 μs pulse U_{strobe} was launched from the generator with a prescribed delay with reference to the leading edge of the pulse U_{pulse}. At the measured time point with respect to the strobe signal U_{strobe} the potential of extractor U_g was rapidly reduced to the adjusted potential level U_{go} (between -20 V and +20 V) allowing the ions to achieve the spectrometer optics and SEM. In that way the ion energy distribution functions and mass spectra could be obtained at the same instant of time. By using a gating switch based on a MOSFET transistor the fall and rise times of the extractor bias were as short as 0.02 μs and 0.1 μs respectively. These times were much shorter than the gating window width (10 μs), thus a number of "false" ions (accelerated or decelerated ions in the gaps orifice-extractor-focusing lens within these transient time periods) was relatively insignificant. Hence, possible distortion of IEDFs causing those "transient" ions was minimized. Within a short time (~2 μs) after an extractor gating pulse was over, a detector enabling pulse U_{de} of 250 μs duration was generated by an EQP internal signal board allowing the digital ion counting pulses to be counted (figure 1b). To proceed from transit time for Ar^+ (m/z=40) is 80 μs, time-off-flight of ions with masses between 2 amu and 300 amu will assuredly lie in the limit of 250 μs. To assure adequate signal-to-noise ratio counts were accumulated over a period of 30 ms.

Results and discussion

The experimental data are presented for a fixed acrylic acid pressure of 1.3 Pa and RF power 10W. The modulation frequency is 1 kHz and 50% duty cycle (500 μs "on" time and 500 μs "off" time). The analyser was originally tuned for ion mass m/z = 73.

The time-averaged IEDFs for m/z = 19 (H_2OH^+), m/z = 55 (CH_2CHCO^+) and m/z = 73 ($[M+H]^+$) are shown in figure 3. Two energy peaks are observed of those three described by Charles and Boswell [8].

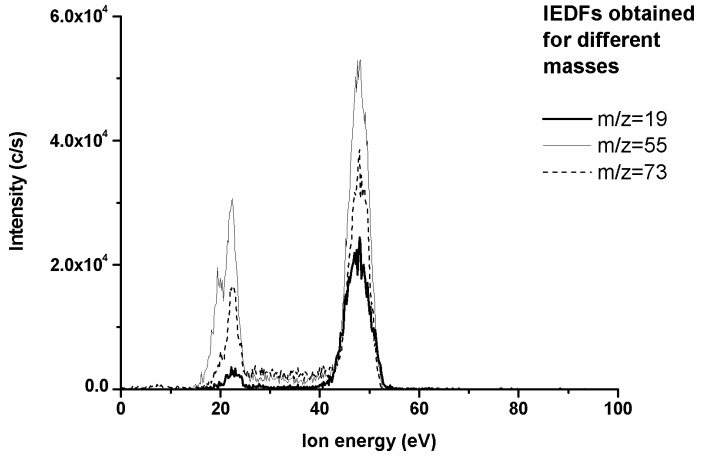

Figure 3. Time-averaged IEDFs of different ion masses obtained with the spectrometer for a pulsed RF acrylic acid plasma.

The low-energy peaks (~20 eV) correspond to ions extracted to the earthed analyser in the post-discharge. The dominant higher-energy peaks (~48 eV) are associated with the IEDFs for continuous wave when the plasma is on. In [9] it was experimentally found, for the same discharge conditions, that transient periods between "off" and "on" times (when the plasma potential jumps up) were about 20 μs. This time is much shorter than the modulation pulse period (1 ms). Hence the high-energy ions contribution to the IEDFs are negligible. This explains why the high-energy peaks above 50 eV are not recognisable in the figure.

Figure 4 shows the time-resolved IEFDs obtained for different ion masses using the shuttering method. Each of the IEDFs shown represents a measurement with a particular time delay from the leading edge of the pulse in steps of 10 μs. For closer examination the IEDFs obtained during "on" and "off" periods are shown in different energy scales (plots 4a,c,e and 4b,d,f respectively). Figure 5 represents the time-resolved positive ion mass spectrums, obtained at the same time points with the IEDFs.

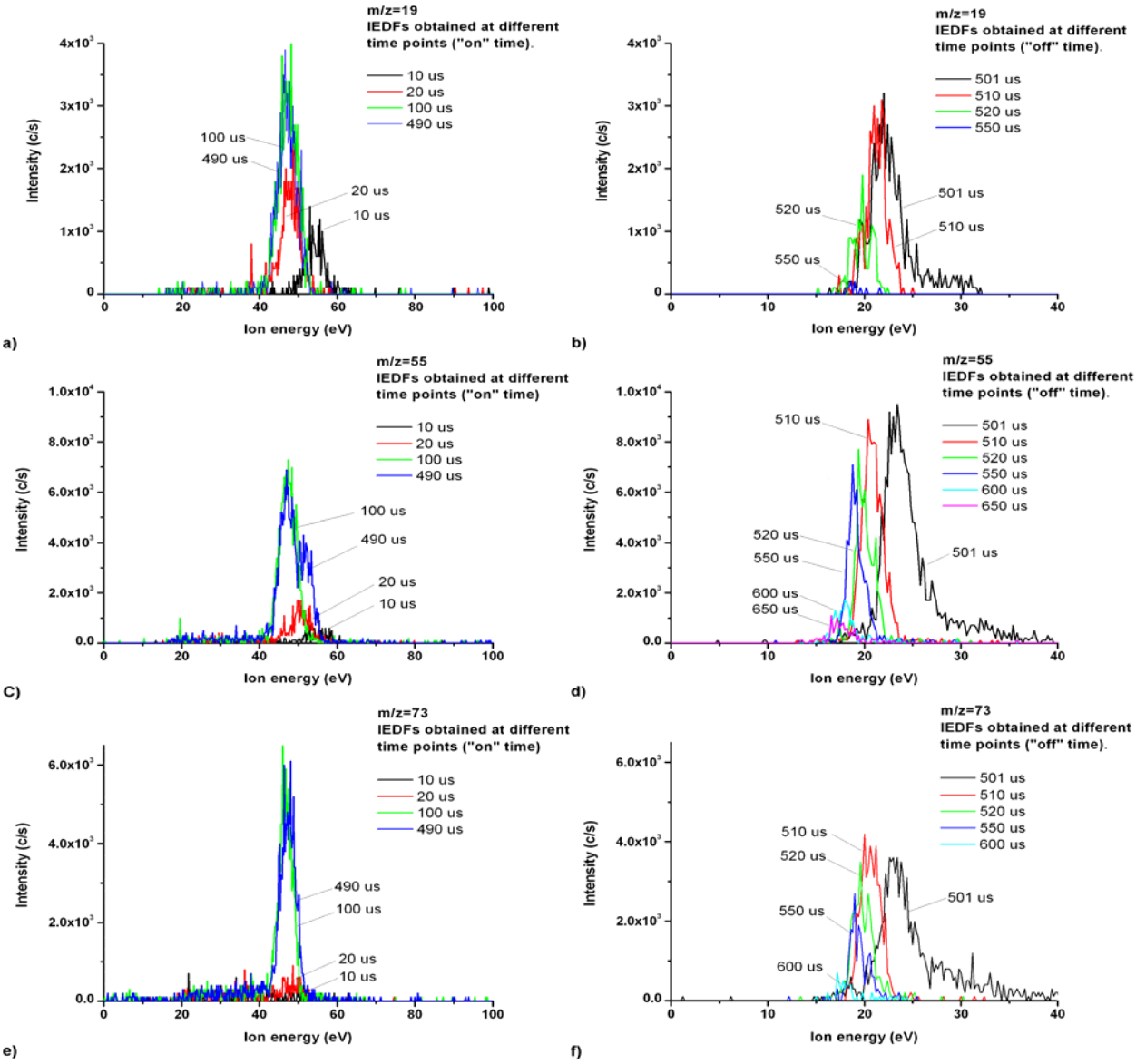

Figure 4. Time-resolved IEDFs of the different ion groups obtained at the different time points.

At the beginning of a pulse the plasma potential rises sharply to peak values greater than those for the case of a continuous wave [9]. This causes an initial spike of the ion energies (t = 10 μs and 20 μs in figure 4). The peak intensities are small due to the low plasma density at the beginning of the "on" period. It must be admitted that the peak intensities for m/z = 19 in this transient time period (figure 4a) are relatively much bigger than those for heavier ions of masses 55 and 73 (figures 4c and 4e). The same tendency is observed on the mass scans (figures 5a and 5b). Due to their high energies and as a result of high velocities the ions must cross the plasma sheath and arrive at the analyser much earlier than for 20 μs. Slower time response of the heavier masses shows that their ionization happens in a deep bulk, not near the sheath, and once created, they drift toward the EQP.

After a period of 20 μs the discharge approaches its steady state and the IEDFs obtained at t = 100 μs and t = 490 μs have a single peak with a mean ion energy of 48 eV which is similar to high-energy area of the time-averaged IEDFs (figure 3). The corresponding mass spectra are shown in figures 5c and 5d. At the end of "on" time the mean ion energies drop sharply to about 23 eV and then slowly decrease together with the peak intensities (figures 4b,d,f). Here is an opposite situation to that at the beginning of the pulse. The heavier ions stay longer in the chamber while lighter ones reach the chamber walls and recombine earlier due to their higher mobility. As a result their peak intensities decay quickly (figure 4b and figures 5e – 5i).

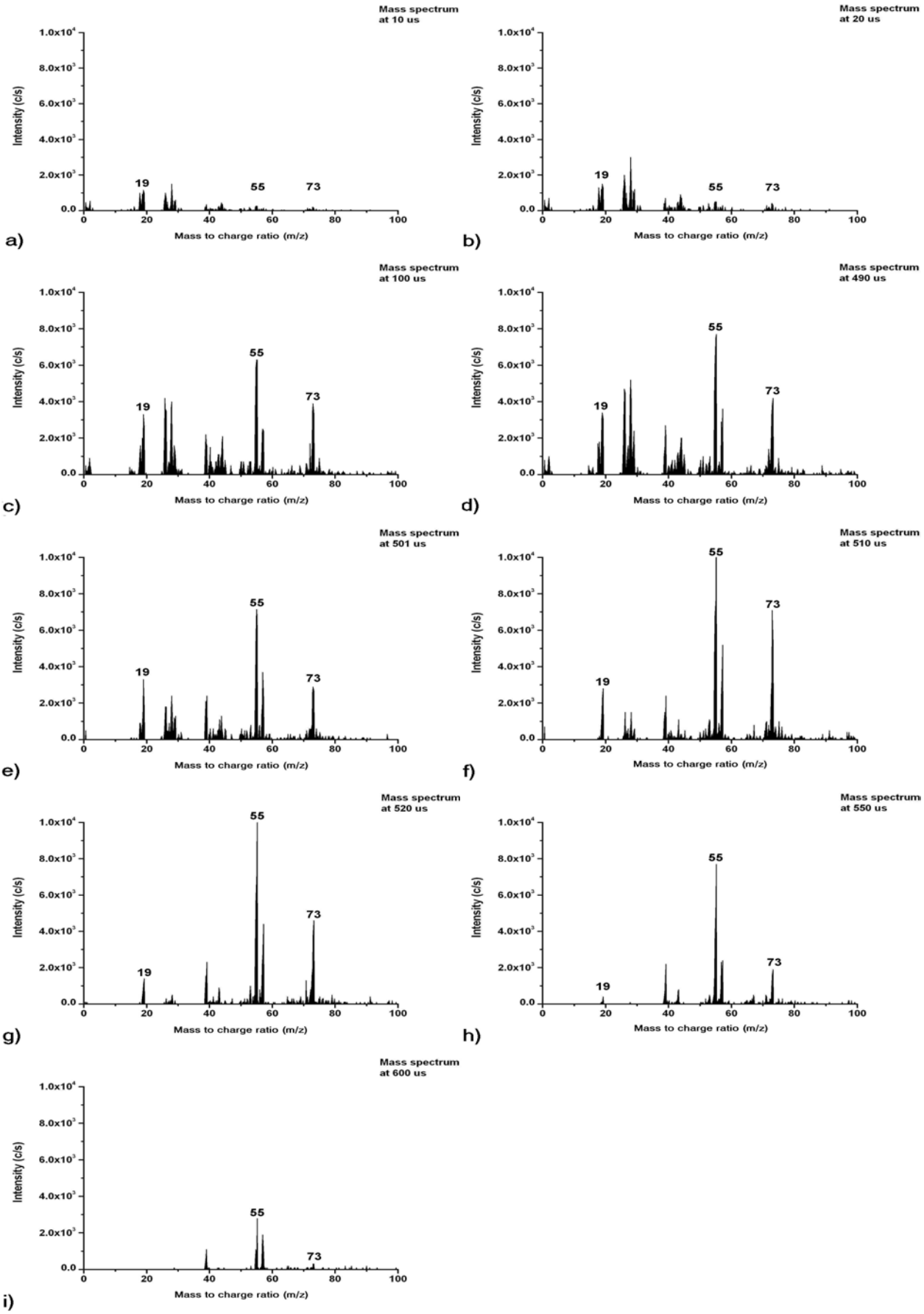

Figure 5. Time-resolved mass spectrums obtained at the different time points. (a) – (d) "on" period, (e) - (i) "off" period.

This impacts the time-averaged ion energy distributions (figure 3). The low-energy peak intensity to higher-energy peak intensity ratios for the case of large ion masses are greater than those for the ion m/z = 19. Furthermore, the low-energy peaks of masses 55 and 73 are slightly shifted to the left with respect to the lighter ion peak. Higher intensities at the beginning of afterglow than those for the "on" time (figures 4c and 4d) might be explained by a higher fragmentation of heavier components when the plasma is "on".

One should note that the mass scans were done with respect to the peak energies of m/z = 73. As it is seen from figure 4 the energy peaks for different ion masses at the same measurement points are slightly different. This means that unlike IEDFs, the mass spectra, obtained this way are not completely accurate. However, they do show the short-term and long-term variations of the mass to change.

Conclusions

Using a technique of electrostatic gating the ions the time-resolved IEDFs and mass spectra were obtained independently of the ion time-of-flight in an acrylic acid RF pulse discharge. Time dependences of the mean ion energy values of different ion masses were determined. Analysis of the obtained IEDFs and mass spectra showed that ionization took place in the bulk plasma. At the beginning of an RF pulse the lighter ions could almost immediately reach a potential target, but heavier ones incurred a delay. In the afterglow heavier ions stayed longer, while lighter fractions were evanescent. This effects on the time-averaged IEDFs: low-energy peak of the heavier ion is bigger than and shifted to the left with respect to that for the lighter ion.

Acknowledgements

This work was supported by the EPSRC through grant GR/S55026.

References

[1] S.B. Wang and A.E. Wendt - J. Appl. Phys **88,** 643 (2000)

[2] O. Zabeida, A. Hallil, M.R. Wertheimer and L. Martinu - J. Appl. Phys. **88**, 635 (2000)

[3] Y. Wang, E.C. Benck, M. Misakian, M. Edamura and J.K. Olthoff - J. Appl. Phys. **87**, 2114 (1999)

[4] C. Pan and F.L. King - Anal. Chem. **65**, 3187 (1993).

[5] S.K. Karkari, H. Backer, D. Forder and J.W. Bradley - Meas. Sci. Technol. **13**, 1431 (2002)

[6] D. Barton, A.G. Shard, R.D. Short and J.W. Bradley - J. Phys. Chem. B **109**, 3207 (2005)

[7] D. Barton, J.W. Bradley, D.A. Steele and R.D. Short - J. Phys. Chem. B **103** 4423 (1999)

[8] C. Charles and R.W. Boswell - J. Appl. Phys. **78**, 766 (1995)

[9] S. Voronin, M. Alexander and J.W. Bradley - Meas. Sci. Technol. **15** 2375 (2004)

Study of a dusty CH_4/N_2 plasma by optical emission spectroscopy.

Jeremy Pereira, Véronique Massereau-Guilbaud, Isabelle Géraud-Grenier,
André Plain and Charles De Izarra.
LASEP, Faculté des Sciences, Université d'Orléans, Site de Bourges,
rue G. Berger, BP 4043, 18028 BOURGES CEDEX, France.

Abstract

In this work, we have more particularly investigated the particle formation in a CH_4/N_2 discharge in order to understand the effect of the nitrogen addition on the particle structure and behaviour. Optical emission spectroscopy has been used to characterize the plasma bulk in order to evidence the formation of various excited species. Nitrogen incorporation leads to a better decomposition of CH_4 and enhances the formation of CH and CN radicals contained in the plasma. Changes in the particle growth appear for nitrogen content up to 50 %. Moreover, infrared analyses evidence, both in the particles and in the coatings, the emergence of nitrogen related bond absorption bands [C-N, C=N, C≡N and N-H] whereas the CH ones seem to vanish for a nitrogen ratio up to 50%. A good correlation has been established between OES results and IR analyses.

Keywords : Carbon nitride particles, dusty plasmas, optical emission spectroscopy, CH and CN radicals.

Introduction

Amorphous hydrogenated carbon thin films (a-C:H) have been widely studied. Indeed, carbonated thin films are of big interest because of their physical and chemical properties [1] : great hardness, good thermal conductivity, great electric resistivity… Their mechanical and electronic applications are numerous. These coatings are used to impart particular properties to unspecified surfaces. One way to depose a-C:H thin films is to use Plasma Enhanced Chemical Vapour Deposition (PECVD).

Some works have evidenced the appearance of particles in the plasma bulk, in addition to coating formation on the electrodes. Langmuir et al. [2] first observed the formation of dusty particles in reactive plasmas. Most recently and for over a decade, some works have been made in silane plasmas [3,4,5] and only a few papers deal with the particle formation in pure methane plasmas [6,7,8].

Particle formation in a plasma takes a particular interest because they fundamentally alter plasma properties such as the dielectric response of the background plasmas or the distributions of plasma potential and density [9]. Thus, the presence of dusts leads to inhomogeneities in the coatings and are responsible of surface contamination. They can alter the quality of deposited thin films and etching works in microelectronics devices (etching, sputtering or deposition processes). Moreover, particles that appear in methane plasmas are of interest in astrophysics to study nebulae or comet tails.

In order to understand the particle formation and growth within the plasma, the effect of nitrogen addition in methane is studied. Nitrogen is preferentially chosen because different effects can be produced on diamond-like carbon, such as the formation of the hypothetical super hard compound β-C_3N_4 or the creation of fullerene-like bonding structures [10]. In this paper, investigation is focused on the effect of nitrogen addition on the particle and thin films structure, and on the emission line intensity of excited species in the plasma.

Experimental set-up

The experiments are performed in a classical capacitively coupled parallel plate radio-frequency stainless steel reactor. The dimensions of rf and grounded electrodes are respectively 13.5 cm and 20 cm in diameter with a space of 2.5 cm. A gas pumping, achieved by two separate pumping systems permits to reach a residual pressure lower than 10^{-3} Pa in the reactor. Gas flow rates were typically 5.6 sccm (9.45 10^{-3} $Pa.m^3.s^{-1}$) for all the CH_4/N_2 mixtures and pumping using a primary pump system is used in order to maintain a constant pressure of 120 Pa within the reactor's enclosure. A 13.56 MHz radio frequency power is delivered by a rf generator (Hüttinger PRG 300) and an output power of 80W is applied. The generator is capacitively coupled with the powered electrode inducing a negative dc self bias voltage (V_{dc}) on the cathode. Experimental time is 30 min.

In order to study the effect of nitrogen partial pressure on the plasma composition, and on the thin film and the particle formation, different gas mixtures are used with a nitrogen ratio in the range 0-90%. For each experiment, particles are collected and a stainless steel substrate is put onto the grounded electrode in order to analyse the amorphous hydrogenated nitride carbonated film. Particle generation and growth are observed and evidenced using an Argon ion laser light scattering (λ=514.5nm). Particles and films are analysed by Scanning Electron Microscopy (SEM) and Fourier Transformed Infra-Red spectroscopy (FTIR) using a Nicolet Spectrometer. Optical Emission Spectroscopy (OES) is used to obtain a qualitative study of excited species contained in a CH_4/N_2 rf plasma at the boundary between the cathodic sheath and the plasma bulk. Previous works [11] evidenced that the values of the emission line intensities are maximum at the cathodic sheath boundary. OES analyses are made using a lens focusing the light onto an optical fiber connected to a spectrometer (Chromex 500i) and coupled with a multichannel analyzer (CCD Pl 330×1100, Princeton Instruments).

Results and Discussion

1. Optical emission spectroscopy analyses.

The optical emission spectrum of a CH_4/N_2 plasma shows the typical species of a pure methane plasma (CH, H_α, H_β, H_2, C_2…) associated to the excited species corresponding to a nitrogen gas (CN, NH, N_2, N_2^+…). In order to understand the various contributions of radicals on the chemical growth of particles and coatings created in the reactor, we are especially interested in the following species :

- CH ($A^2\Delta$; v'=0 → $X^2\Pi$; v''=0) system at 431 nm,
- CN ($B^2\Sigma$; v'=0 → $X^2\Sigma$; v''=0) system at 388.1 nm,
- NH ($A^3\Pi_i$; v'=0 → $X^3\Sigma^-$; v''=0) system at 336 nm,

The figure 1 respectively presents the temporal evolutions of CH (fig. 1-a) and CN (fig. 1-b) radicals for different nitrogen percentages in the gas mixture. We can observe for CN radicals an increase of the emission line intensity during the first minutes after the discharge is on. This increase is improved with the nitrogen ratio in the plasma. In the same time, at the beginning of the experiment, the CH emission line intensity decreases for poor-nitrogen plasmas whereas the nitrogen addition leads to a slope inversion. The CH intensity presents the same temporal evolution than the CN ones for rich-nitrogen plasmas. Then, we can observe a stabilisation of the emission lines for these radicals after about 8-10 minutes of experiment in accordance with the different experimental conditions. The analysis of the dc self bias voltage Vdc permits to understand these temporal evolutions as can be seen in the figure 2. According to previous works in a pure methane plasma [11], the decrease of the absolute value of the Vdc is correlated with the particle formation within the gas discharge. The particle growth leads to a diminution of the |Vdc| which tends to a minimum value about 3-5 minutes of experiment corresponding to a maximum of particle generation, and recover it initial value at the end of the particle perturbation correlated with the stabilisation of the CH and CN

emission lines. Thanks to the CH and CN emission line evolution during the first ten minutes, we can assume a chemical perturbation of the excited species containing in the plasma due to the particle formation.

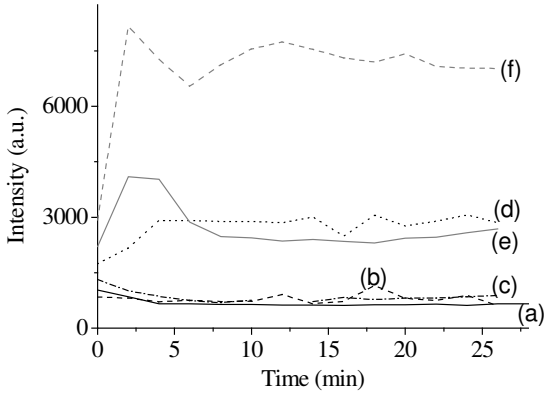

Fig. 1-a

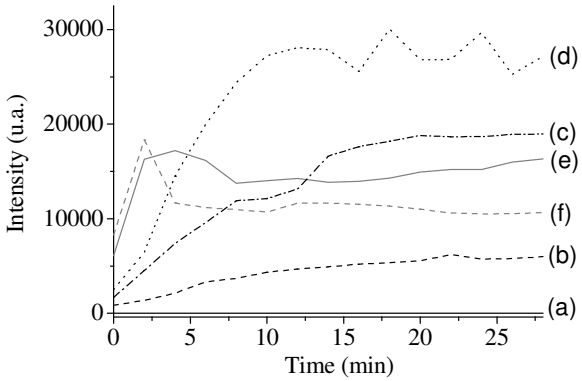

Fig. 1-b

Figure 1 : Temporal evolution of the CH radical emission line at 431 nm (fig. 1-a) and of the CN radical emission line at 388.1 nm (fig. 1-b) .

(a) 100% CH_4, (b) 90% CH_4 / 10% N_2, (c) 75% CH_4 / 25% N_2, (d) 50% CH_4 / 50% N_2, (e) 25% CH_4 / 75% N_2, (f) 10% CH_4 / 90% N_2.

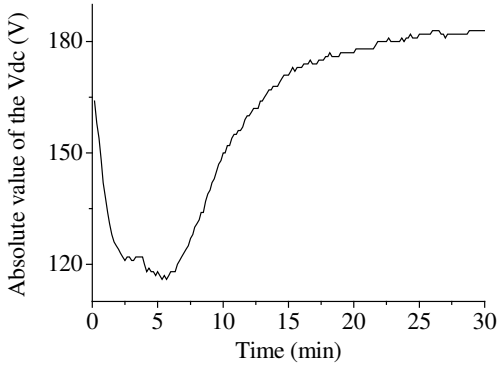

Figure 2 : Temporal evolution of the absolute value of self bias voltage for a 75% CH_4 / 25% N_2.

The influence of the nitrogen ratio in the plasma on the CH and CN radicals is quite different. For a nitrogen-poor gas mixture (from 0 to 25% of N_2), whereas the CN emission regularly increases, the CH one stays almost constant. For nitrogen ratio varying from 25% to 50%, both the CH and CN emission increases. Nevertheless, whereas the CN emission begins to decrease for nitrogen ratio up to 50%, the CH one keeps constant values until 75% and then strongly increases for nitrogen-rich gas mixture (10% CH_4 / 90%N_2).

According to T. Vandevelde et al. [12], in a high pressure micro-wave reactor, the nitrogen ratio increase furthers the CH_4 precursors dissociation. We can suppose, in our process, that the nitrogen addition in the methane gas discharge leads to a better decomposition of CH_4 precursors and enhances the formation of CH and CN radicals contained in the plasma. Indeed, until a nitrogen percentage equal to 50%, the CH and CN emissions increase. But, up to 50% of N_2, the CN emission line decrease probably results from a diminution of the CH_4 precursors in the reactor and a CN radical consumption for the particle and coating growth. In the same time, in the range [50%-75% N_2], the CH emission stagnation is due to a compensation between the higher CH_4 dissociation, the CH participation in the particle and deposition formation and the lack of methane ratio in the gas mixture. The huge increase of the CH radical emission for nitrogen-rich plasmas (10% CH_4 / 90% N_2) seems to confirm the CN radical participation in the thin film and the dust growth instead of the CH ones.

Concerning the NH radicals, the temporal evolution of the NH emission line is more difficult to study. Indeed, the N_2C emission line at 337.1 nm is close of the NH ones at 336 nm. NH emission line is almost completely obscured by the N_2C ones. Figure 3 presents the shape of the N_2C emission line for different nitrogen ratio. Whereas none NH emission line appears for nitrogen ratios less than 50%, we can notice for rich-nitrogen plasmas, the appearance of a small peak attributed to the NH radicals. Intensity measurement seems to indicate an increase of the NH emission line following the N_2C ones for nitrogen ratio up to 50%.

The NH formation comes from the recombination phenomena between the nitrogen species and the hydrogen ones both released during the particle and coating formation and exit of the methane precursor dissociation. It's quite difficult to predict a possible correlation between the NH radicals and the thin film and the particle growth.

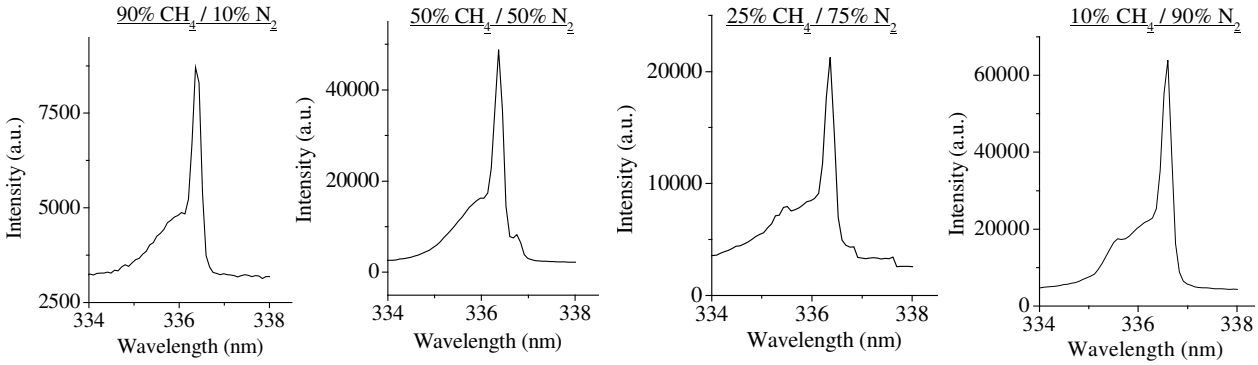

Figure 3 : Analysis of NH and N_2C emission line for different CH_4/N_2 ratios.

In order to support the optical emission spectroscopic results and to confirm the role played by the CH, CN and NH radicals containing in the plasma, particles and coatings are analysed using infrared spectroscopy.

2. Infrared analysis.

The infrared absorption spectra of the amorphous hydrogenated carbon nitride particles and coatings, obtained for different CH_4/N_2 gas mixtures, are performed and reported in figure 4. Even if structural differences seem to exist between the thin films and the analysed dusts, the two spectra show the presence of four typical absorption bands for the a-CN_x:H compounds, as observed by Mutsukura in amorphous carbon nitride deposited films [13].

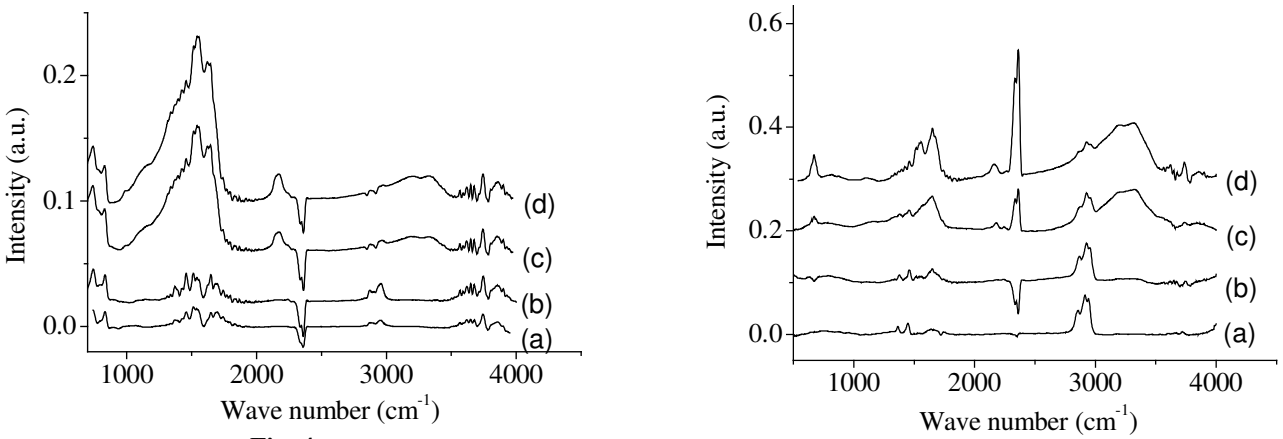

Fig. 4-a **Fig. 4-b**

Figure 4 : Infrared absorption spectrum of a-CN_x:H particles (fig. 4-a) and thin films (fig. 4-b) obtained in CH_4/N_2 plasmas.

(a) 100% CH_4, (b) 90% CH_4 / 10% N_2, (c) 50% CH_4 / 50% N_2, (d) 10% CH_4 / 90% N_2.

1- The absorption region in the range 3200-3500 cm^{-1} is consistent with modes involving N-H and/or OH stretching vibrations [14]. The increase of this band by addition of nitrogen content in the reactor suggests for the particles as for the coatings an incorporation of NH bonds. The NH absorption band appears for nitrogen ratios up to 50%.

2- The 2800-3100 cm^{-1} absorption region is related to CH stretching vibrations [sp^3 CH_3 in symmetric (2875 cm^{-1}) and asymmetric (2960 cm^{-1}) vibrational modes, sp^3 CH_2 and sp^3 CH (2920 cm^{-1})] [15]. Whereas CH related band regularly decreases in the coating with addition of nitrogen in the gas mixture, CH incorporation in the particles seems to increase until 50% of N_2 ratio, then vanishes for nitrogen-rich plasmas.

3- The third band in the range 2000-2300 cm^{-1} is related to the triple-bonded –C≡N nitrile (2109-2178 cm^{-1}) and C≡N- isonitrile (2225-2275 cm^{-1}) structures [16]. The emergence of nitrile and isonitrile structures appears for nitrogen ratio up to 50% and the shape of this band suggests an important conjugation with various structures (aromatic rings, aliphatic chains….).

4- The 1000-1800 cm^{-1} broad absorption band decomposition is more difficult. This band is often associated to various bond vibrations such as C-N (1100-1300 cm^{-1}), and C=N (1617 cm^{-1}) stretching modes or NH bending modes (1620 cm^{-1}) [17]. But peaks attribution is not clear because of the activation of the Raman active G (graphite-like sp^2 carbon at 1570 cm^{-1}) and D (disordered sp^2 carbon network at 1370 cm^{-1}) peaks due to nitrogen inclusion in the carbon matrix. Moreover, for Ferrari et al. [18], the absorption band in this range is mainly due to skeletal C=C vibrations. Nitrogen effect in amorphous carbon can be assimilated to doping or photo-excitation in conjugated polymers. Nitrogen doping leads to a breakdown of the electrical symmetry (removal or injection of charges). The band around 1300-1800 cm^{-1} should be only due to the C=C sp^2 phase.

Even if the meaning of this band is quite obscured, we can deduce that the increase of this broad band with the nitrogen addition is due to nitrogen incorporation in the carbon matrix and C-N, C=N and NH incorporation seems evident for the particles as for the coating.

Conclusion :

IR results confirms the optical emission spectroscopy. The N_2 rise in the reactor leads both in the particles and in the coating to an increase of nitrogen related bands (that is to say an increase of C-N, C=N, C≡N and NH bonds). Whereas the CH links regularly decrease in the coating resulting from an incorporation of the CN and NH species containing in the plasma, the increase of the methane dissociation thanks to the nitrogen flow is confirmed in the particles by an increase of CH bonds in the particles for nitrogen percentage less than 50%. But for nitrogen rate up to 50%, the CH bonds in the particles decrease and vanish for nitrogen-rich plasmas.

The CN and NH radicals seem to be incorporated either in the coating or in the particles in order to produce N-H, C-N, C=N and C≡N bonds substituting for C-H bonds present in a-C:H coatings and particles. These results confirm the OES assumptions. Indeed, the nitrogen increase leads to a decrease of the CN radicals in the reactor which are incorporated both in the particles and in the coatings, leading to an increase of nitrogen related peaks. On the other hand, the CH related band vanishes for nitrogen rich plasmas leading to a rise in the reactor of the CH radicals which do not take part in the formation of coating and particles.

References :

[1] A. Richardt, A.M. Durand - Le Vide, 444-452 (1997).

[2] I. Langmuir, G. Found and A.F. Dittmer - Sci. NewYork **60**, 392 (1924).

[3] A. Bouchoule, A. Plain, L. Boufendi, J.P. Blondeau, C. Laure - J. Appl. Phys. **70**, 1991-2000 (1991).

[4] Y. Watanabe, M. Shiratani, H. Kawasaki, S. Singh, T. Fukusawa, Y. Ueda, H. Ohkura - J. Vac. Sci. Technol. **14**, 540 (1996).

[5] A. Gallagher, G. Bano and K. Rozsa - Sol. Energy Mat. Sol. Cells **78**, Issues 1-4, 27-40 (2003).

[6] I. Géraud-Grenier, V. Massereau-Guilbaud and A. Plain - Eur. Phys. J. AP **14**, 187-192 (2001).

[7] V. Massereau-Guilbaud, I. Géraud-Grenier and A. Plain - Eur. Phys. J. AP **11**, 71-76 (2000).

[8] Ch. Hollenstein - Plasma Phys. Control. Fusion **42**, R93-R104 (2000).

[9] G.S. Selwyn, J. Sing and R.S. Benett - J. Vac. Sci. Technol. **A7**, 2758 (1989).

[10] B. Kleinsorge, A. C. Ferrari, J. Robertson, W. I. Milne, S. Waidmann and S. Hearne - Diam. rel. Mat. **9**, 643-648 (2000).

[11] I. Géraud-Grenier, V. Massereau-Guilbaud and A. Plain - Eur. Phys. J. AP **8**, 53-59 (1999).

[12] . Vandevelde, T.D. Wu, C. Quaeyhaegens, J. Vlekken, M. D'Olieslaeger, L. Stals - Thin Sol. Films **340** 159-163 (1999).

[13] N. Mutsukura and Ken-ichi Akita - Thin Sol. Films **349**, 115-119 (1999).

[14] G.-Q. Yu, S.-H. Lee, D.-G. Lee, H.-D. Na, H.-S. Park and J.-J. Lee - Surf. Coat. Technol. **154**, 68-74 (2002).

[15] A.P. Mousinho, R.D. Mansano and P. Verdonck - Diamond Relat. Mater. **13**, 311-315 (2004).

[16] N. Mutsukura - Diamond Relat. Mater. **10**, 1152-1155 (2001).

[17] M. Lejeune, O. Durand-Drouhin, K. Zellama and M. Benlahsen - Solid State Communications **120**, 337-342 (2001).

[18] A.C. Ferrari, S.E. Rodil and J. Robertson, Phys. Rev. - **B 67**, 155306-1 (2003).

LASER PLASMA EUV SOURCE BASED ON A GAS PUFF TARGET FOR METROLOGY OF MULTILAYER (MO/SI) MIRRORS FOR THE MICROELECTRONICS PROCESSING TECHNOLOGY

R. Rakowski[1], A. Bartnik[1], H. Fiedorowicz[1], R. Jarocki[1], J. Kostecki[1], J. Krzywiński[2], J. Mikołajczyk[1], L. Ryć[3], M. Szczurek[1], P. Wachulak[1]

[1]*Institute of Optoelectronics, Military University of Technology, Warsaw, Poland*
[2]*Institute of Physics, Polish Academy of Sciences, Warsaw, Poland*
[3]*Institute of Plasma Physics and Laser Microfusion, Warsaw, Poland*

Abstract
In this paper an application of a recently developed laser plasma source of extreme ultraviolet (EUV) for optical measurements is presented. The source is based on a double-stream gas puff target. The xenon-helium target was irradiated with laser pulses from a Nd:YAG laser system (E = 0.55 J, t = 3.9 ns, f = 10 Hz, M^2 = 2.5). A laser-plasma created this way is an efficient and debris free source of EUV radiation and is useful for EUV lithography technologies as a processing and metrology tool in the semiconductor industry.

1. Introduction

Probably laser produced plasmas (LPPs) will be able to meet the technical and operational requirements of sources for EUV lithography (EUVL) [1]. There are no transparent optics below 100 nm of wavelength, therefore collective and imaging optics for the future lithographic tools are based on multi-layer mirrors (MLMs) [2]. The spectral window of Mo/Si mirrors is a common consensus for all considered materials of EUVL: Sn, Xe and Li [1]. A development of proper EUV sources dedicated to metrology of EUV optics should follow the progress during multi-layer fabrication. This paper directly addresses this problem. One can produce a stack of Mo/Si layers that satisfy demands of a 2 % bandwidth (BW) with a peak reflection of about 70 % at 13.5 nm, measured near to normal. A double stream Xe/He gas puff laser-plasma EUV source was proposed [3,4] and recently applied successfully to the optical measurements of the Mo/Si multi-layer mirrors. The source has been developed in the frame of the EUV sources development project under the European MEDEA+ programme, dedicated for EUV lithography technologies (metrology of EUV optics such as mirrors or masks, EUV resists and EUV processes). The sources for EUV metrology do not have the same specifications as sources for EUV lithography exposure tools (Conversion efficiencies (CEs) of 3 % within 2 % BW per 2π steradians, high repetition rate, pulse to pulse repeatability). The characterization research of the source, including CE, spectral, spatial and temporal measurements of EUV emission have been carried out. The diagnostic tools such as grazing incidence spectrograph, a pinhole camera and absolutely calibrated semiconductor detecting systems in order to characterize properties of the source were utylized. The optimization of the source has enabled the optimum parameters to be identified. A gas puff target approach EUV source made it possible to measure the reflectivity of the Mo/Si mirrors at a selected grazing angle and after one laser shot.

2. Experimental arrangement

A Schematic diagram of the experimental set-up is presented in Fig.1. An electromagnetic valve to control gas puff target was located in the center of the source chamber. A Nd:YAG Laser (E = 0.558 J, t_{FWHM} = 3.9 ns, M^2 = 2.5, f_{max} = 10 Hz) was located inside a cylindrical pipe that was tightly connected to the source chamber. Between the chamber and the laser a lens of focal length 50 mm was positioned. This solution simplifies the set-up and prevents users from laser exposures. Since it was found in previous experiments that EUV emission is very sensitive on changes of laser focus position in a region of the gas puff target, a micromanipulator to move the valve perpendicularly to the laser beam axis was employed. Experiments have been performed using a specially prepared chamber that coupled to the source chamber, and which were motorized stages inside for alignment of the mirrors. In this chamber a Mo/Si multi-layer mirror (Fraunhofer Insitute, Jena, Germany) was located and enabled the selection of radiation from the plasma. The mirror was set at 45º thus allowing a 33 % reflectivity for 13.5 ± 0.5 nm. Moreover Mo/Si mirrors fabricated by Reflex s.r.o., Prague, Czech Republic were installed inside the chamber on motorized translation and rotation stages in order to measure angular distribution of reflectivity. Three mirrors were used, two of which were

previously etched with a stream of argon for 6 and 12 minutes respectively. In addition this chamber enabled the connection of various diagnostics such as spectrograph, pinhole camera and silicon photodiodes and is shown schematically in Fig.1. A flat field grazing incidence spectrograph with the varied grooves period grating (Hitachi, average 1200 grooves/mm) equipped with a CCD back illuminated camera (Roper) was used. Spectra with one laser shot were recorded. A spectral resolution of this spectrograph was of the order of 0.1 Å. For spatial imaging of the plasma emitting at 13.5 nm (radiation from plasma reflected from selective Mo/Si mirror was investigated) a platinum pinhole of 20 μm in diameter was applied. A pinhole was located at 54 cm from the plasma and covered with a Zr filter of 200 nm thickness, deposited on Si_3N_4 filter of the same thickness giving a transmission of 15.4 % at 13.5 nm. Because of low contrast a magnification of about 0.4 was employed. Spatial images were recorded during 60 laser shots. Absolute measurements of energy at 13.5 nm with a detection system of a silicon photodiode AXUV 100 Si/Zr (IRD) were performed. This detector equipped with a diaphragm of 8 mm in diameter and to two different flanges marked '1' or '2' in Fig. 1 dependently on measurements was coupled. Then in order to measure the time duration of EUV pulses fast HS1 photodiode (IRD) with mentioned above a stack of Zr/Si_3N_4 filters connected to '1' flange was applied. Both photodiodes recorded radiation reflected from the Mo/Si mirror (Jena).

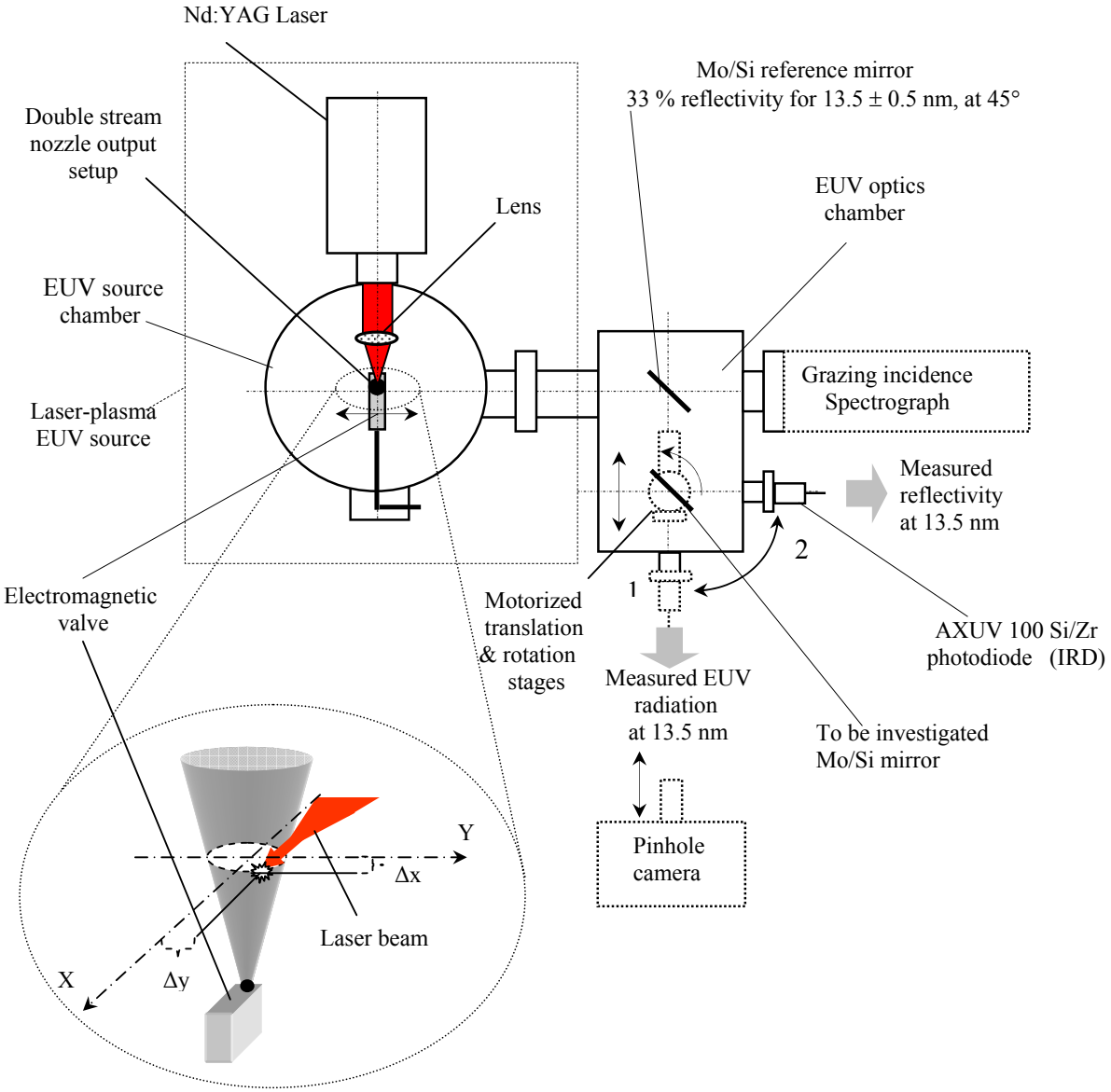

Fig. 1. Scheme of the experimental setup used to investigate EUV optics.

3. Results

3.1. Optimum source parameters

A variety of characteristics of the source were measured in series of experiments in order to obtain the input parameters of the source that lead to the optimum CE. The following input parameters that have meaningful influence on EUV emission can be distinguished: time delay between laser pulse and opening valves, position of laser spot in space in reference to the gas puff target and the backing pressure of the gas in the valves. Time delays: Δt_{Xe} = 800 μs and Δt_{He} = 350 μs for which the emission at 13.5 nm is the highest were chosen. The laser focus spot should be positioned at least H = 1 mm from the nozzle output in order to prevent its thermal degradation. A vertical distance H = 1.2 mm was selected in experiments. A 35 μm diameter laser focus was calculated using the OSLO program and support for this was experimentally confirmed. It was found that the best position of the laser spot, in order to assure the most efficient EUV production at 13.5 nm was located at Δx = 2 mm beyond the axis of the nozzle output of the valve. While the laser focus spot was located at the axis, efficient emission was shifted to the shorter wavelength, but when was at Δx = 2.5 mm condition was not corresponded to enough for xenon ionization and plasma creation. A strong EUV emission dependence on a shift of the laser spot in the gas target perpendicularly to the laser beam axis direction was observed. This shift Δy from the axis of the nozzle output was measured. It was found that the laser focus should be located at the edge of the gas target to obtain the highest EUV emission because of strong absorption of low ionized xe and of neutral xe in the surrounding plasma region. Positioning laser spots at the edge of the gas target causes production of the plasma of relatively large sizes if it is compared to the case when the spot is inside the gas target, but EUV emission observed from this side of the gas target where plasma is created is the highest. Using a AXUV 100 Si/Zr photodiode the highest emission for Δy = 900 μm was measured. Results of this investigation are presented in Fig. 2.

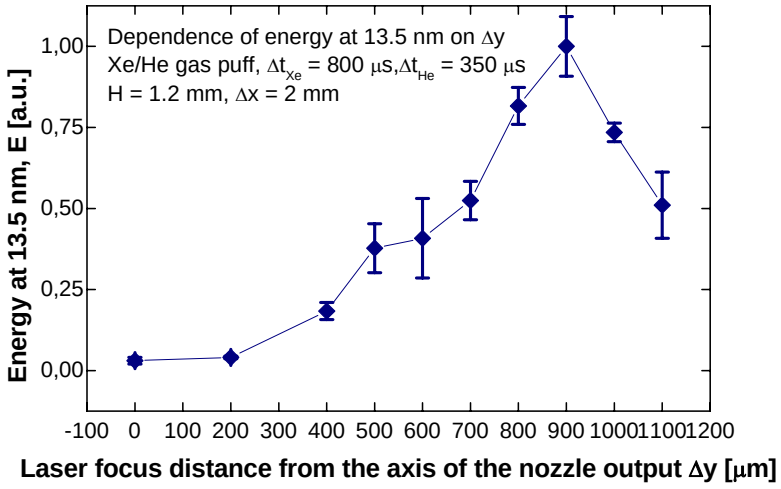

Fig. 2. EUV energy dependence on Δy.

For fixed optimum parameters mentioned previously ($\Delta t_{Xe,He}$, H, Δx and Δy), EUV emission dependence on various backing pressure in the valves was investigated. From this, optimum pressures of P_{Xe} = 1.5 MPa and P_{He} = 0.2 MPa were found. The maximum attainable energy of 1.6 mJ/sr at 13.5 ± 0.5 nm was calculated for optimum parameters and leads to CE of 0.54 % within 2 % BW per 2π sr. In Fig. 3 a pinhole image of the plasma for this case is presented. The plasma is relatively large with its dimensions of the order of 1 mm in comparison to other LPPs. A typical spectrum recorded for the optimum parameters is shown in Fig. 4. The strongest feature belongs to an unresolved transition array (UTA) [5] and for xenon is centered at about 10.85 nm. The spectral distributions for the most interesting Δy, from the significant emission point of view, are presented in Fig. 5. From spectral measurements it is clear that for Δy = 800 μm a feature at 13.5 nm was higher than in the case of Δy = 900 μm and was the strongest feature emission attainable. The Following description can account for this behaviour. Increasing the Δy parameter significantly increases the sizes of the plasma. Moreover in the case of the spectral measurements photons were collected only from the hottest region of the plasma, limited by a slit, while using the photodiodes photons were summed from the whole

plasma surface. For comparison a spectrum for H = 1.1 mm with frozen rest parameters is shown. It is discernible that the peak of the UTA is unaltered while the profile width increases with Δy. Increase of Δy follows growth of plasma dimensions and the decrease of electron temperature. A similar effect for mass limited target was observed when the emission dependence on Sn concentration in tin reach targets was investigated [6]. An explanation of this can be found in [7]. A feature at 13.5 nm which origin is from Xe XI ion stage is marked in Fig. 5 within 2 % BW. It is known that the time duration of the EUV emission corresponds to the laser pulse duration. Measured with the fast photodiode HS1 (τ_{rise} = 0.25 ns), the EUV pulse had a FWHM in the range of 3.7-3.8 ns while a FWHM the laser pulse had a 3.9 ns FWHM.

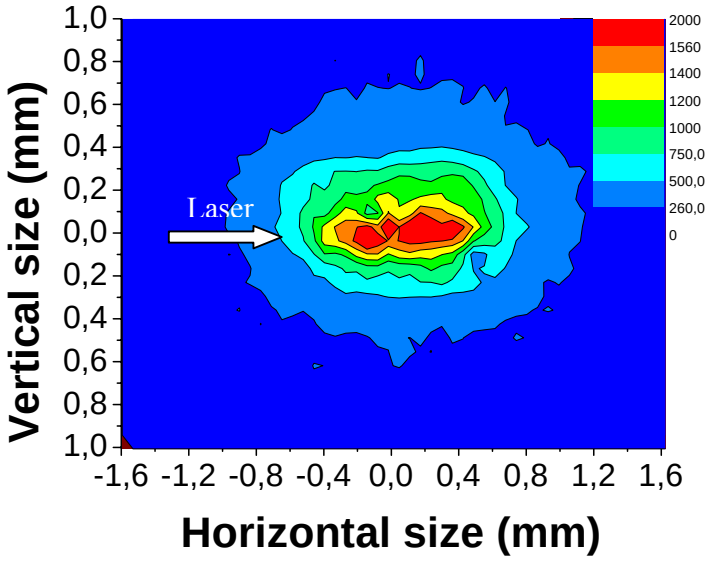

Fig. 3. Pinhole image of plasma emitting at 13.5 nm for optimum condition.

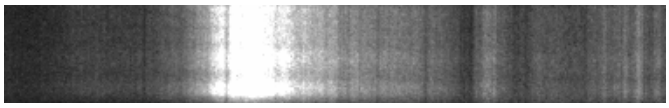

Fig. 4. Spectrum for Xe/He plasma: P_{Xe} = 1.5 Mpa, P_{He} = 0.2 Mpa, H = 1.2 mm, Δx = 2 mm and Δy = 800 μm.

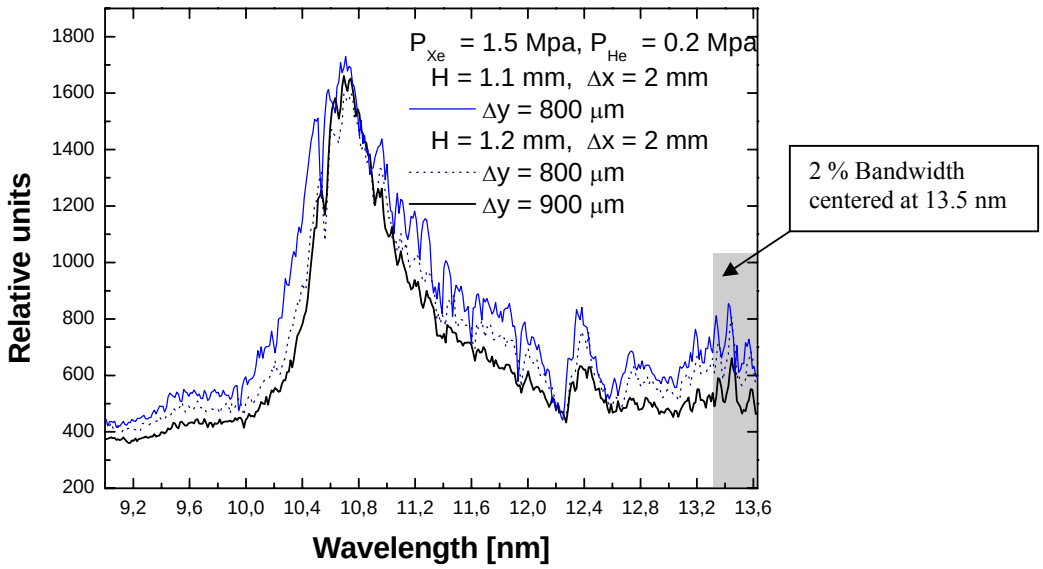

Fig. 5. Spectral distribution for optimum conditions.

3.2. Mo/Si mirrors investigation

An optimised EUV source based on a Xe/He gas puff target in reflectivity measurements of Mo/Si mirrors, was employed. Firstly an EUV average energy for the optimum parameters at 13.5 ± 0.5 nm, with the use of the calibrated photodiode AXUV 100 Si/Zr from 1 flange side, was measured. This yield was used as a reference energy for reflectivity calculations. Next the motorized stages with a mirror to be investigated were located inside the optics chamber. The photodiode from the '1' flange to the '2' flange side (see Fig. 1) was replaced. For each the Mo/Si mirror, for selected grazing angles, after one laser shot, reflected energies have been measured. For each angle position at least 10 independent measurements were performed and averaged with the reflectivity being then obtained. As a result the reflectivity distribution versus grazing incidence angle are presented in Fig. 6a-6c. In the previous experiment the maximum reflectivity at 12.7 nm at 45º in the EUV region for these mirrors was found out. But the maximum was expected for 13.5 nm, because there were so optimised. Thus a peak reflectivity was not expected for the 45º grazing angle. One can see that the peak reflectivity for 52º grazing angle in the case of no etched and for 6 min. etched mirrors and for 49º in the case when mirror was etched for 12 minutes. The maximum reflectivity only at the level of half that is theoretically attainable [8] for no etched mirror was reached. Moreover it is evident that diagrams are not symmetrical. Probably reasoning of all this may dates back to that parameters of the mirror processing such as the layer and the inter-diffusion thickness were not successfully controlled during the deposition process.

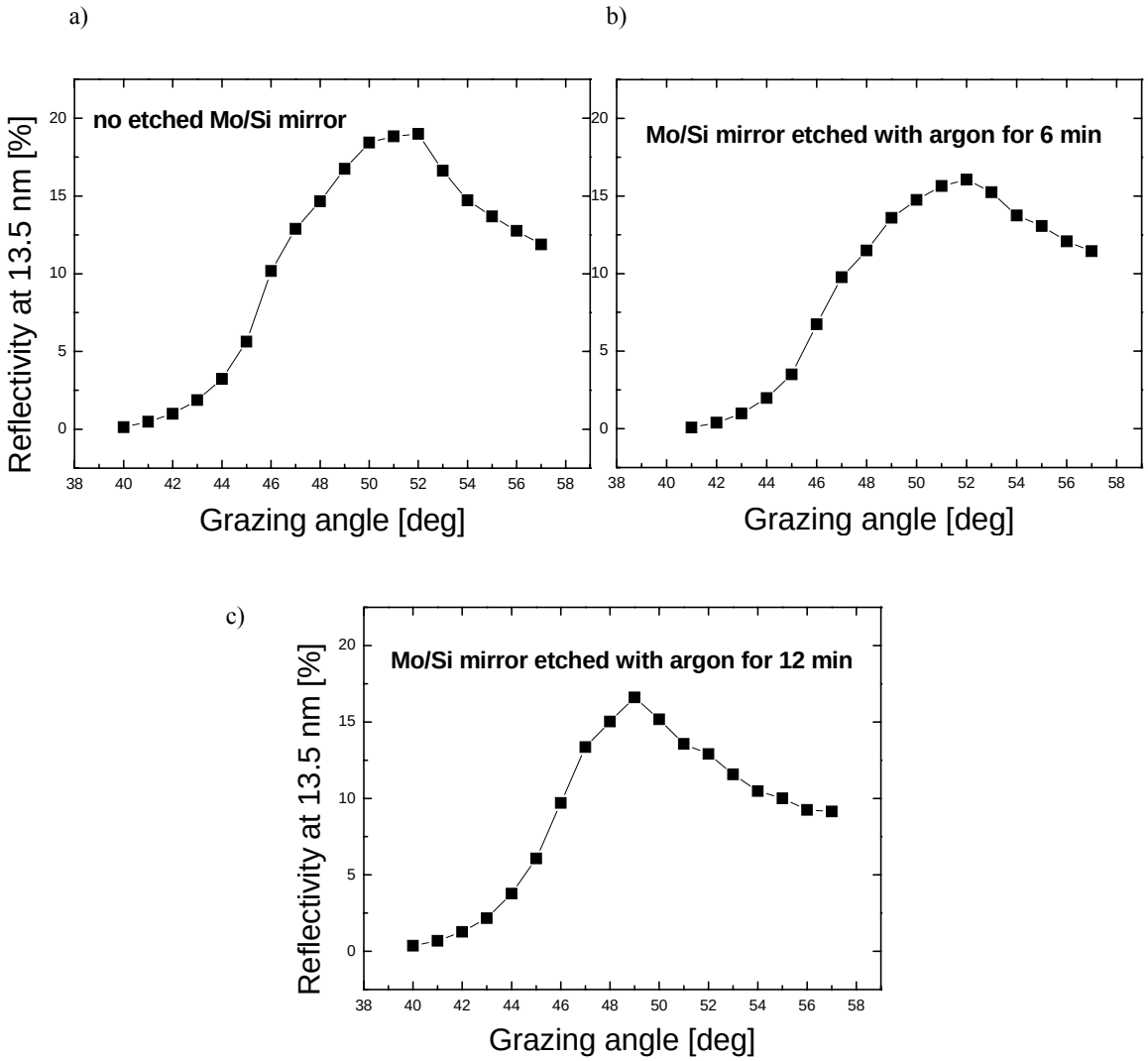

Fig. 6. Spectral distribution for optimum conditions.
a) for no etched mirror, b) for etched for 6 min., c) for etched for 12 min.

4. Conclusion

A significant feature at 13.5 nm up to half of the UTA peak, centered at about 11 nm, was attained. The CE of the laser energy into the EUV for 13.5 nm (2 % BW in 2π sr) up to 0.54 % for the xenon-helium gas puff target, has been reached. The growth of CE should be possible if opacity effects are minimised (by controlling a profitable absorption/emission ratio in plasma) [9]. The Angular distributions of the Mo/Si multi-layer mirrors fabricated by Reflex s.r.o., were performed successfully. The results have proved a usefulness of the source for EUV metrology applications having an effect on a further development of next generation of the EUV technologies.

References

[1] V. Banine and R. Moors, Plasma sources for EUV lithography exposure tools. J. Phys. D: Appl. Phys. **37**, p. 3207 (2004).

[2] R. Stuik, E. Louis, A. E. Yakshin, P. C. Gorts, E. L. G. Maas, F. Bijkerk, D. Schmitz, F. Scholze, G. Ulm, and M. Haidl, Peak and integrated reflectivity, wavelength and gamma optimization of Mo/Si, and Mo/Be multilayer, multielement optics for extreme ultraviolet lithography. J. Vac. Sci. Technol. B **17**(6), p. 2998 (1999).

[3] R. Rakowski, A. Bartnik, H. Fiedorowicz, R. Jarocki, J. Kostecki, J. Mikołajczyk, A. Szczurek, and M. Szczurek, Laser plasma soft x-ray and EUV source based on a laser-irradiated double-stream gas puff target. In the Proc. 16 International Symposium on Plasma Chemistry, Taormina, Italy (2003).

[4] H. Fiedorowicz, A. Bartnik, R. Jarocki, R. Rakowski, and M. Szczurek, Appl. Phys. B **70**, p. 305 (2000).

[5] G. O'Sullivan and R. Faulkner, Tunable narrowband soft x-ray source for projection lithography. Opt. Eng. **33**(12), p. 3978 (1994).

[6] M. Nakai, H. Nishimura, K. Shigemori, N. Miyanaga, T. Norimatsu, K. Nagai, R. Matsui, T. Hibino, T. Okuno, F. S. Sohbatzadeh, Y. Tao, K. Hashimoto, M. Yamaura, S. Fujioka, H. Nagatomo, V. Zhakhovckii, K. Nishihara, S. Uchida, Y. Shimada, H. Furukawa, M. Nakatsuka, and Y. Izawa, Study on EUV emission properties of laser-produced plasma at ILE, Osaka. Laser-Generated and Other Lab. X-ray and EUV Sources, Optics, Apps., Proceeding. of SPIE **5196**, p. 289 (2004).

[7] G. O'Sullivan, A. Cummings, P. Dunne, P. Hayden, L. McKinney, N. Murphy, and J. White, EUV sources for EUVL lithography SPIE chapter 2.2 Ed V Bakshi to be published (2005).

[8] http://www-cxro.lbl.gov.

[9] R. de Bruijn, K. Koshelev, G. Kooijman, E. S. Toma, and F. Bijkerk, Absorption of EUV laser plasmas generated on xenon gas jets. J. Q. S. R. T. **81**, p. 97 (2003).

Reduction of NO_x by plasma-assisted methods

A. Fateev[1], F. Leipold[1], Y. Kusano[1], B. Stenum[1], H. Egsgaard[2], H. Bindslev[1]

[1] *Risoe National Laboratory, OPL, Building 128, P.O. Box 49, Frederiksborgvej 399, DK-4000 Roskilde, Denmark*
[2] *Risoe National Laboratory, BIO, Building 313, P.O. Box 49, Frederiksborgvej 399, DK-4000 Roskilde, Denmark*

Abstract
Combustion causes formation of NO_x, which in turn causes acid rain and ozone production when it is released into the air. Reduction of NO_x in the exhaust gas of power plants is therefore of high interest. In our paper we have considered different plasma-assisted techniques for NO_x-reduction: direct treatment of exhaust gases by plasma, injection of N atoms and injection of (stable) reactive species (N_2H_4, O_3). Advantages and disadvantages of these techniques are discussed.
Keywords
$DeNO_x$; ozone; hydrazine; dielectric barrier discharges (DBD); absorption and emission spectroscopy

1. Introduction

The NO_x emission into the atmosphere leads to serious environmental problems. Although the problem of NO_x reduction is quite old, up to now there is no efficient and economical method of NO_x reduction. Non-plasma techniques for NO_x-reduction require ammonia injection and are operated either at a narrow temperature window, 900-1100°C (Thermal $DeNO_x$) [1] or over a catalytic surface at temperatures around 400-500°C (selective catalytic reduction) [2]. Both methods are quite expensive to operate. Non-thermal and thermal plasmas at atmospheric pressure have been widely studied for reduction of NO_x in flue gases. However, non-thermal plasmas seem to be very promising in terms of operation time and costs compared to thermal ones. For instance, a dielectric barrier discharge (DBD) is one of the most attractive plasma sources for this application due to its compactness, low costs, efficiency, and ability to operate in a stable mode at atmospheric pressure at high average power. Combination of a DBD with a catalyst improves the efficiency of NO_x reduction [3], but increases the costs. In general, direct treatment of exhaust gases reduces NO_x, but produces other undesired products [4] which also affect the environment. Therefore, selective NO_x reduction is desirable. Selective NO reduction can be achieved by injection of highly reactive species (atoms, radicals or short-lived molecules) produced by a DBD into the exhaust gas stream. Although sufficient amount of highly reactive species can be produced in DBD plasma, short lifetimes of species cause a limitation of the injection methods. In the paper we consider different plasma-assisted techniques for NO_x-reduction: direct treatment by plasma, injection of N atoms and injection of reactive and stable species (N_2H_4, O_3) into the exhaust gas. Advantages and disadvantages of these techniques are discussed.

2. Experimental set ups

The experimental set up was described in details in our previous work [5]. The DBD reactor consists of two parallel plate metal electrodes. Two alumina (Al_2O_3) discs in contact with each electrode serve as dielectric barriers. The discharge gap between the two alumina discs was 3 mm. The outlet of the plasma reactor is connected to a stainless steel exhaust chamber with a connection to the gas cell of an IR-spectrometer. Both the plasma reactor and the exhaust chamber are equipped with windows for UV- emission/absorption measurements. The DBD is driven by an AC power generator at 15 kHz. Optical emission and absorption measurements were performed by a UV-VIS spectrometer equipped with a CCD-camera and an IR-spectrometer equipped with a multiple-pass absorption cell. A deuterium lamp was used as a light source for UV-absorption measurements in the exhaust chamber. The gas flows were controlled by means of mass flow controllers. In our experiments, the total pressure in the plasma reactor was kept at approximately one atmosphere.
In the experiments with ozone injection, thermal ammonia and hydrazine decomposition stainless steel and quartz reactors placed in a split-oven were used. The temperature in the oven was varied from room temperature to 1000°C. In these experiments the outlet from the reactors was connected to the exhaust chamber and subsequently to the gas cell of the IR-spectrometer.

3. Results and discussion

We performed experiments with different synthetic exhaust gas mixtures and experimental set ups: direct plasma treatment of exhaust gases, treatment of exhaust gases by injection of N-atoms, ozone and hydrazine. These different methods are discussed in this chapter.

3.1 Direct treatment of exhaust gases by plasma

We investigated direct plasma treatment of synthetic flue gases (N_2+O_2(<10%)+NO(<500ppm)+H_2O(<3.5%)+CO_2(<10%)+CH_4(<3%)). Methane is a major constitute of unburned hydrocarbons (UHC) in the exhaust gases from methane fuelled gas engines. The low ionization and dissociation energies of methane compared to those of nitrogen lead to an efficient production of methyl (CH_3) and methylene (CH_2) radicals in the plasmas. These radicals can also be formed by reaction of nitrogen metastable molecules (N_2(A)) with methane [6]. Important radical reactions are:

$$CH_2 + H \rightarrow CH + H_2, \qquad k^{300K} = 4.9\text{x}10^{-10}\ cm^3s^{-1}$$
$$CH + N \rightarrow CN + H, \qquad k^{300K} = 1.7\text{x}10^{-10}\ cm^3s^{-1}$$
$$CN + H \rightarrow HCN, \qquad k^{300K} = 8.9\text{x}10^{-31}\ cm^6s^{-1}$$
$$CH_3 + N \rightarrow HCN + 2H, \qquad k^{300K} = 3.3\text{x}10^{-13}\ cm^3s^{-1}$$
$$CH_3 + CH_3 \rightarrow C_2H_6, \qquad k^{300K} = 2.2\text{x}10^{-26}\ cm^6s^{-1}$$
$$CN + C_2H_6 \rightarrow HCN + C_2H_5, \qquad k^{300K} = 3.0\text{x}10^{-11}\ cm^3s^{-1}$$

All these reactions have high rate constants [7] and even a concentration of hydrocarbons about 2000 ppm leads to a formation of cyanogens in significant amounts on a time scale less than 1 μs. Emission spectra in a N_2/CH_4 DBD show intensive CN emission between 382 nm and 389 nm, Figure 1 (Left panel). The presence of oxygen and water reduces the CN emission intensity due to consumption of CH_2 and CH_3 radicals in competitive reactions, Figure 1:

$$CH_3 + O \rightarrow H_2CO, \qquad k^{300K} = 1.4\text{x}10^{-10}\ cm^3s^{-1}$$
$$CH_3 + OH \rightarrow CH_3OH \qquad k^{300K} = 2.6\text{x}10^{-27}\ cm^6s^{-1}$$
$$CH_2 + OH \rightarrow H_2CO + H \qquad k^{300K} = 3.0\text{x}10^{-11}\ cm^3s^{-1}$$
$$CH_2 + O \rightarrow \text{products (CO, } H_2) \qquad k^{300K} = 1.3\text{x}10^{-10}\ cm^3s^{-1}$$

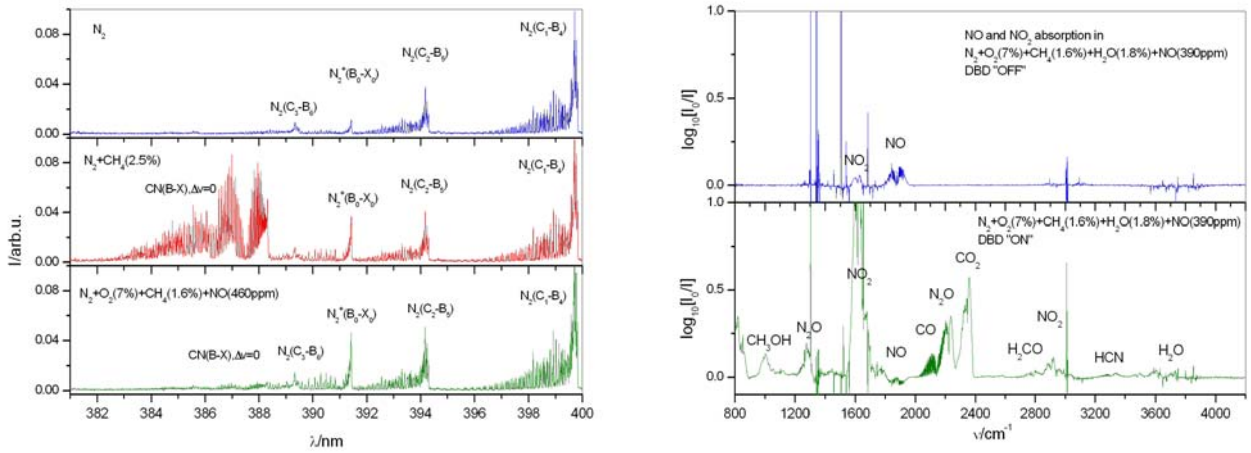

Figure 1.
Left panel: UV-emission spectra from N_2(blue), N_2/CH_4(2.5%)(red) and N_2/O_2(7%)/CH_4(1.6%)/NO(460 ppm)(green) atmospheric pressure DBD.
Right panel: Reference IR-absorption spectrum of NO and NO_2 before plasma treatment (DBD "OFF")(blue) in the mixture N_2/O_2(7%)/CH_4(1.6%)/H_2O(1.8%)/NO(390 ppm) and IR-absorption spectrum of plasma exhaust (DBD "ON")(green).

Water vapors change the plasma chemistry. We have observed an additional production of NO in an N_2+O_2(7%)+NO(400ppm)+H_2O(2.5%) DBD. Addition of ammonia (< 1%) to the mixture inhibits formation of

NO. However, reduction of NO was only achieved with methane addition. When only traces of water vapor are present in the exhaust, nitric acid (HNO_3) is efficiently produced:

$$OH + NO_2 \rightarrow HNO_3, \qquad k^{300K} = 3.4x10^{-30}\ cm^6s^{-1}$$

On the other hand, at a certain water content, nitric acid is consumed by reacting with OH and formation of dinitrogen pentoxide (N_2O_5) as observed in our experiments:

$$OH + HNO_3 \rightarrow H_2O + NO_3, \qquad k^{300K} = 1.5x10^{-13}\ cm^3s^{-1}$$

$$NO_3 + NO_2 \rightarrow N_2O_5, \qquad k^{300K} = 2.1x10^{-30}\ cm^6s^{-1}$$

Direct treatment of exhaust gases causes also formation N_2O, which is difficult to decompose.

$$N_2(A) + O_2 \rightarrow N_2O + O, \qquad k^{300K} = 7.8x10^{-14}\ cm^3s^{-1} \qquad (1)$$

$$NO_2 + N \rightarrow N_2O + O, \qquad k^{300K} = 1.2x10^{-11}\ cm^3s^{-1} \qquad (1a),$$

3.2 Injection of N-atoms produced in DBD plasma

To prevent generation of acids and cyanogens in the discharge, treatment of the flue gases by injection of reactive radicals or molecules is preferable. Injection of nitrogen atoms into the exhaust gas can reduce NO according to the reaction

$$N + NO \rightarrow N_2 + O, \qquad k^{300K} = 2.9x10^{-11}\ cm^3s^{-1} \qquad (2)$$

A typical emission spectrum of an N_2 DBD is shown in Figure 2 (Left panel). Traces of O_2 in the discharge cause the formation of oxygen atoms. Due to recombination of N and O atoms in the afterglow,

$$N + O \rightarrow NO, \qquad k^{300K} = 1.0x10^{-32}\ cm^6s^{-1} \qquad (3)$$

a variety of electronically excited states of NO is expected. In particular, the *B*- and *c*- states of NO are populated. The spectrum in Figure 2 (Left panel) shows emission bands of the β-system of NO in an N_2 afterglow.

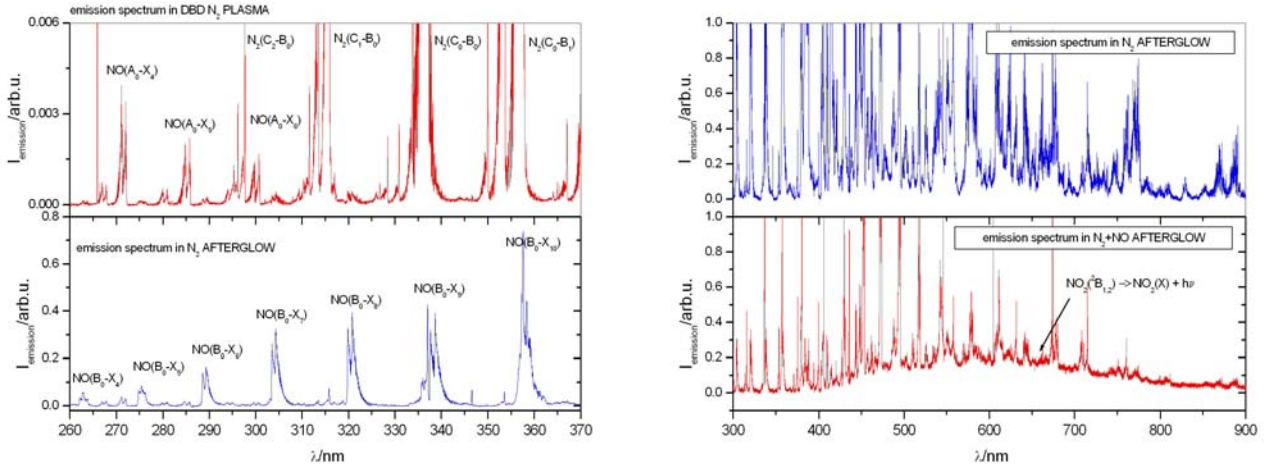

Figure 2.
Left panel: UV-emission spectrum in an N_2 DBD with traces of O_2(red) and its afterglow (blue) at a distance of 10 cm from plasma zone. The flow rate is 40 l_n/min.
Right panel: VIS-emission spectrum in the N_2 afterglow (blue) and in N_2 afterglow in presence of NO(100 ppm) (red).

If the concentration of injected nitrogen atoms is less than the NO concentration, oxygen atoms produced according to (2) will react with NO to form NO_2 in an excited state:

$$O + NO \rightarrow NO_2^* \rightarrow NO_2 + h\nu, \qquad k^{300K} = 8.9x10^{-32}\ cm^6s^{-1}$$

The broad continuum emission in the visible (Figure 2, Right panel) is caused by the decay of excited NO_2 molecules.

When the concentration of nitrogen atoms is larger than the NO concentration, NO is also formed again according to the reaction (3). If the concentration of N-atoms is equal to that of NO, all NO molecules can be consumed and only molecular oxygen will be formed at the end as a product of recombination of oxygen atoms.

The time for transportation of N-atoms into the exhaust gas must be short compared to its lifetime. Nitrogen atoms are consumed in the recombination reaction.

$$N + N \rightarrow N_2 \qquad k^{300K} = 1.3x10^{-32}\ cm^6s^{-1} \qquad (4)$$

Recombination of N-atoms in the afterglow (4) produces mostly $N_2(A)$. The presence of $N_2(A)$ in the exhaust can cause formation of N_2O according to reaction (1).

3.3 Treatment of exhaust gases by injection of hydrazine

A DBD of Ar/NH_3 or N_2/NH_3 can produce NH_2 radicals, which can be used for efficient reduction of NO according to the reaction

$$NH_2 + NO \rightarrow N_2 + H_2O, \qquad k^{300K} = 1.69x10^{-11}\ cm^3s^{-1}.$$

However, at atmospheric pressure, the NH_2 lifetime is short (about a few microseconds) and the final products of ammonia decomposition in a DBD are hydrazine (N_2H_4), N_2 and H_2 [5].

Hydrazine may be decomposed at high temperatures back into NH_2 due to the surface and gas-phase reactions in the exhaust. NH and NH_2 radicals can be also produced by thermal decomposition of ammonia. According to our experiments, ammonia decomposition requires temperatures above 600 ºC and 800 ºC in the heated stainless steel reactor and quartz reactor, respectively. The walls of the stainless steel reactor play the role of a catalyst. Therefore hydrazine decomposition was investigated in the quartz reactor in order to reduce the catalytic effect on the walls. Nitrogen was passed through a hydrazine hydrate, and thus hydrazine vapors were introduced into the quartz reactor where they were mixed with the exhaust gas. It was found that thermal decomposition of hydrazine requires temperature around 300°C. The presence of oxygen accelerates the hydrazine decomposition, but does not reduce NO, Figure 3 (Left panel). It is noted that the UV-absorption spectrum of hydrazine decomposition products is the same as UV-absorption spectrum of ammonia, Figure 3 (Left panel, orange and black lines, respectively) and that the NO reduction starts only at temperatures above 500°C (green line). These observations are in an agreement with previous works [8-10]. If methane is also present in the mixture, NO decomposition becomes more efficient at temperatures around 700°C, Figure 3 (Right panel, red line). However, a complete NO reduction could not be achieved, Figure 3 (Right panel, black line).

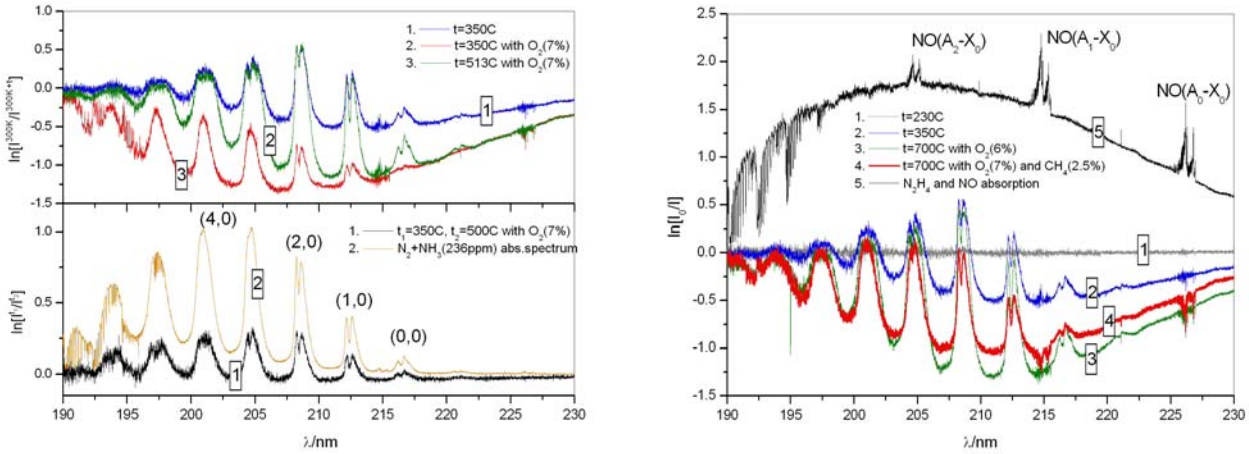

Figure 3.

Left panel: UV-absorption spectra in $N_2/N_2H_4/NO$(190 ppm)(blue) and $N_2/N_2H_4/O_2(7\%)/NO$(180 ppm)(green, red) mixtures at various temperatures in the oven (350°C and 513°C); UV-absorption spectrum of NH_3(orange) and UV-absorption spectrum in $N_2/N_2H_4/O_2(7\%)/NO$(180 ppm) mixture at 500°C with reference spectrum measured at 350°C (black).

Right panel: UV-absorption spectra in $N_2/N_2H_4/NO$(190 ppm)(gray, blue), $N_2/N_2H_4/O_2(6\%)/NO$(190 ppm)(green) and $N_2/N_2H_4/CH_4(2.5\%)/O_2(7\%)/NO$(170 ppm)(red) at various temperatures in the oven. A reference absorption spectrum corresponding to UV-absorption of NO (190 ppm) and N_2H_4 is also shown (black).

3.4 Injection of ozone generated in a plasma

A DBD operated in an oxygen containing gas can serve as ozone generator. Ozone has a typical decay time of 20 minutes at room temperature and therefore it can be easily produced in a cooled DBD and transported into the exhaust. Ozone initiates oxidation of NO to N_2O_5:

$$\begin{aligned} NO + O_3 &\rightarrow NO_2 + O_2, & k^{300K} &= 1.8\text{x}10^{-14}\ cm^3s^{-1} \\ NO_2 + O_3 &\rightarrow O_2 + NO_3, & k^{300K} &= 3.7\text{x}10^{-17}\ cm^3s^{-1} \qquad (5) \\ NO_3 + NO_2 &\rightarrow N_2O_5, & k^{300K} &= 2.1\text{x}10^{-30}\ cm^6s^{-1} \end{aligned}$$

The N_2O_5 can be efficiently trapped by water in a scrubber or bubbler system:

$$N_2O_5(g) + H_2O(aq) \rightarrow 2HNO_3(aq),$$

Oxidation of NO_2 to NO_3 takes typically a few seconds, whereas all other reactions occur fast. Thus a relatively long residence time of the exhaust gases is needed in the reaction volume where NO oxidation takes place.

The other limitation is due to a temperature effect. Exhaust gases usually have high temperatures (> 300°C) which are sufficient for thermal decomposition of ozone. Ozone decomposition leads to inhibition of the NO_x reduction and to formation of N_2O:

$$\begin{aligned} O_3 &\rightarrow O + O_2, & k^{600K} &= 5.6\text{x}10^{-18}\ cm^3s^{-1} \\ O + N_2 &\rightarrow N_2O, & k^{300...568K} &= 5.0\text{x}10^{-38}\ cm^6s^{-1} \end{aligned}$$

Moreover, at high temperatures thermal decomposition of N_2O_5 and NO_3 to NO_2 and NO starts. Therefore low temperatures (< 200°C) of exhaust gases are needed for the NO reduction process.

If ozone is produced from air, N_2O is formed according to reactions (1, 1a) and cannot be trapped by scrubber or bubbler system. The use of pure oxygen overcomes this problem.

We investigated ozone oxidation of $NO \rightarrow NO_2 \rightarrow NO_3 \rightarrow N_2O_5$ and subsequent removal of N_2O_5 by a bubbler system. Ozone produced in an O_2 DBD was injected in the exhaust chamber where the oxidation took place. When the ozone concentration is too low for a complete oxidation of NO to N_2O_5, intermediates will remain in the exhaust, Figure 4 (Left panel, black line). On the other hand, if O_3 concentration exceeds the amount needed, the N_2O_5 and unused O_3 will be detected after NO oxidation, Figure 4 (Left panel, red line). Due to N_2 impurities in O_2 DBD plasma faint admixture of N_2O can be also observed. The bubbler system will remove completely N_2O_5 and mostly all O_3, Figure 4 (Left panel, blue line).

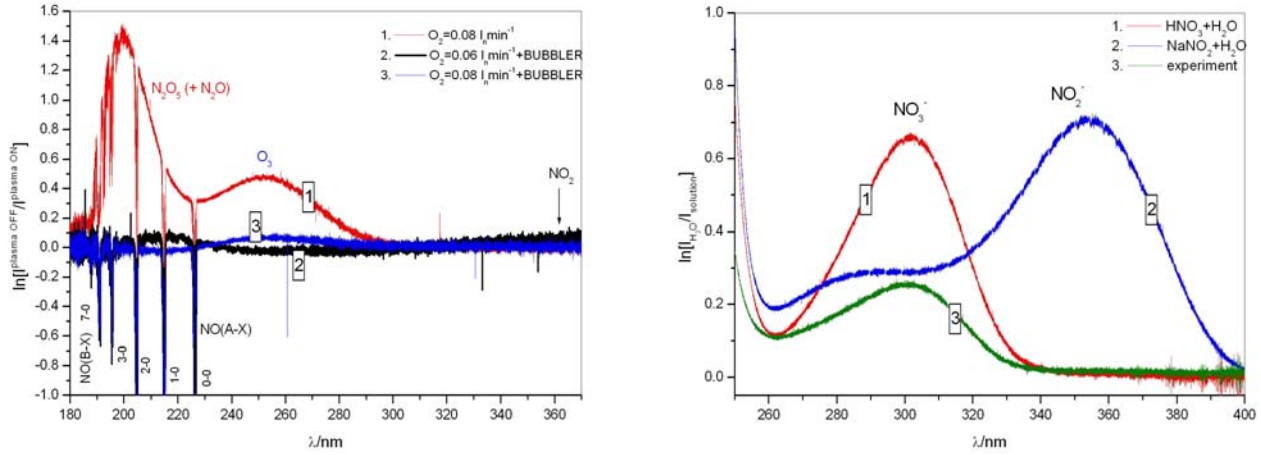

Figure 4

Left panel: UV-absorption spectra in the $O_3/N_2/O_2(6\%)/NO(470\ ppm)$ mixtures at various ozone concentrations with and without bubbler.

Right panel: UV-absorption spectra of aqueous solutions of nitrite (NO_2^-)(blue) and nitrate (NO_3^-)(red) ions in comparison with the UV-absorption spectrum of the water from the bubbler after ozone treatment of a $N_2/O_2(6\%)/NO(470\ ppm)$ mixture (green).

The UV-absorption spectra of water from the bubbler clearly show absorption at 300 nm indicating the presence of NO_3^- ions (HNO_3) in water solution and no absorption at 360 nm indicating absence of NO_2^- ions (nitrous acid, HNO_2). Nitrous acid can be formed in the net reaction [11]

$$2NO_2 + H_2O \rightarrow HNO_3 + HNO_2,$$

However HNO_2 reacts with NO_3 to form HNO_3

$$HNO_2 + NO_3 \rightarrow HNO_3 + NO_2, \qquad k^{300K} < 2x10^{-15}\ cm^3s^{-1}$$

4. Summary and conclusions

Different plasma-assisted techniques for NO_x-reduction, namely: direct treatment of exhaust gases by plasma, injection of N atoms and injection of (stable) reactive species (N_2H_4, O_3) into the exhaust gas have been considered.

- Direct treatment of exhaust gases by plasma oxidizes NO to NO_2 and later to N_2O_5. However, the presence of UHC in exhaust makes the process more complicated and lead to a production of undesirable hydrocarbons and cyanogens whose negative impact into the environment is known. The use of a catalyst in combination with direct treatment will improve the situation, but will increase the costs. Moreover, this method has low selectivity, because a lot of energy is consumed by other processes.
- Injection of N-atoms increases the selectivity in NO reduction. However, high N_2 consumption due to the short lifetime of N-atoms and a possible formation of N_2O makes this technique impractical.
- Hydrazine produced in DBD can be used for reduction of NO in hot exhaust gases. However, the products of thermal N_2H_4 decomposition are NH_3, H_2 and N_2. Therefore, this method is close to the Thermal $DeNO_x$ process which advantages and disadvantages are well established.
- Ozone treatment of exhaust gases seems to be the most promising way for NO reduction. It has a high selectivity for NO reduction, but the oxidation process requires a relatively long reaction time (a few seconds). This limits its applicability when exhaust gases with high flow rates need to be treated. Low reaction temperatures for NO oxidation and oxygen consumption can also be limiting factors for economically reasonable applications.

Acknowledgement

This work is supported by Elkraft Systems (Grant number 103159).

References

[1] J. Warnatz, U. Maas and R.W. Dibble "*Combustion: Physical and Chemical Fundamentals, Modeling and Simulation, Experiments, Pollutant Formation"*, Springer Verlag 2001.

[2] N-Yu Topsoe "*Infrared Spectroscopic Investigations on Environmental $DeNO_x$ and Hydrotreating Catalysts"*, PhD Thesis, The Haldor Topsoe Research Laboratories 1998, Lyngby, Denmark.

[3]M.S. Cha, Y-H Song, J-O Lee and S.J. Kim, "NO_x and soot reduction using dielectric barrier discharge and selective catalytic reduction in diesel exhaust", in: *Proceedings of the 16th International Symposium on Plasma Chemistry*, R. d'Agostino, P. Favia, F. Fracassi, F. Palumbo, Eds., Taormina 2003, University of Bary, Italy.

[4] A. Knasef, J.M. Cormier and J.M. Pouvesle "Investigation of nanosecond pulsed dielectric barrier discharges in various gas mixtures", in : *Proceedings of the 16th International Symposium on Plasma Chemistry*, R. d'Agostino, P. Favia, F. Fracassi, F. Palumbo, Eds., Taormina 2003, University of Bary, Italy.

[5] A. Fateev, F. Leipold, Y. Kusano, B. Stenum, E. Tsakadze and H. Bindslev *Plasma Process. Polym.* **2**, 193 (2005).

[6] J.L. Jauberteau, I. Jauberteau, M.J. Cinelli and J. Aubreton *New J. Phys.* **4,** 39 (2002)

[7] NIST Chemical Kinetics Data Base, http://www.nist.gov

[8] C. Lim and C.H. Choi *J. Chem. Phys.* **120**, 979 (2004)

[9] J.B. Lee and S.D. Kim *Chem. Eng. J.* **69**, 99 (1998)

[10] S. Azuhata, H. Akimoto and Y. Hishinuma *AIChE Journal* **31**, 1223 (1985)

[11] J. Notholt, J. Hjorth and F. Raes *Atm. Environm.* **26A**, 211 (1992)

Immobilization of sodium tungstate on plasma treated PVDF membranes: catalytic membranes for the oxidation of secondary amines

L.C. Lopez[1], M.G. Buonomenna[2], G. Iacoviello[1], P. Favia[1,3], G. Licini[4], E. Drioli[2], R. d'Agostino[1,3]

[1] *Department of Chemistry, University of Bari, via Orabona 4, 70126, Bari, Italy*

[3]*Institute on Membrane Technology, National Research Council of Italy, ITM-CNR, c/o University of Calabria, via P. Bucci cubo 17/C, 87030 Rende (CS), Italy*

[2]*Institute of Inorganic Methodologies and Plasmas IMIP-CNR, c/o University of Bari, via Orabona 4, 70126, Bari, Italy*

[4]*Department of Chemical Sciences, Università of Padova, via Marzolo 1, I- 35131, Padova, Italy*

Abstract

The oxidative conversion of secondary amines to nitrones has been investigated on novel plasma-processed catalytic active membranes. Sodium tungstate, the catalyst, has been immobilized on plasma treated Polyvinylidenefluoride (PVDF) membranes. In particular, the membranes have been modified by means of Ar plasma pre-treatment followed by an NH_3 plasma treatment to produce a surface rich of amino functionalities, active sites for a stable chemical immobilization of the catalyst. Very promising results have been obtained in terms of amine-nitrone conversion in catalytic membrane reactors (CRMs) equipped with the plasma modified PVDF membranes.

Introduction

Low temperature plasma modification techniques appear very attractive in several scientific fields to modify in a controlled way surface chemistry and properties of a wide range of materials [1-5]. Main advantages of plasma techniques are the possibility of modifying only the few topmost layers of materials leaving the bulk totally unaltered, the possibility of functionalization, the negligible environmental impact, and the versatility for industrial processes and substrates. In particular, among plasma techniques, plasma grafting allows to produce surfaces characterized by a tuneable density of functional groups (i.e. –COH; OH; NH_2, etc.) [6-8] which can be conveniently used for the immobilization of various molecules. The grafting process of N-containing groups in NH_3-based RF glow discharge has been described in refs. [7, 8].

The entrapment of homogeneous catalysts in polymer membranes by means of "Van der Waals wrapping" is a rather easy way to heterogenise the catalyst obtaining, in some cases, results comparable to the analogue homogeneous systems [9-13]. However, the absence of strong interaction forces between the complexes and the polymer could represent a failure of this method; in particular, with low molecular weight homogeneous catalysts like sodium tungstate, leaching represents a major lack of the technique. This problem may be avoided by the generation of a stable chemical bond (covalent, ionic, coordinative) between the catalyst and the membrane surface.

In this work we report on the immobilization of sodium tungstate on plasma treated PVDF flat membranes prepared via the inversion phase technique. Modified membranes have been used in CRMs to activate H_2O_2 for the synthesis of nitrones from secondary amines.

Nitrones are versatile synthetic intermediates for the synthesis of heterocycles and natural products and can be synthesized by oxidation of secondary amines or the corresponding hydroxylamines. Enzymes are involved in the metabolic oxidation of amines: mitochondrial monoamine oxidases transforms secondary amines to imines; flavin monooxygenase oxidizes secondary amines to nitrones via hydroxylamines [14,15]. Therefore, the simulation of the activity of such oxidation enzymes, using metal complexes immobilized in polymeric membranes provides mimetic method for catalytic oxidation of amines.

Very promising results have been obtained, in this work, in terms of amine-nitrone conversion in CRMs employing plasma modified membranes loaded with sodium tungstate in presence of H_2O_2. No reaction occurred when plasma modified membranes, not loaded with catalyst, have been employed.

Results and discussion

Flat PVDF membranes have been first plasma treated in a RF (13.56 MHz) glow discharge fed with Ar (20 sccm, 800 mTorr of pressure, 30 W, 1 min), in order to cross-link the surface of the substrate by means of CASING (Cross-linking of Activated Species by Inert Gases) process [16]. The cross-linked top most surface layer becomes much more stable to accommodate the N-groups to be grafted in the following plasma process, and much less sensible to restructuring ageing processes of the fluorinated substrate. This process provided a surface much less prone to ageing. Such approach has been successfully followed for obtaining a permanently wettable polytetrafluoroethylene surface [6] in NH_3 glow discharges. Ar treated membranes have been then plasma treated in a NH_3 RF glow discharge (20 sccm, 800 mTorr of pressure, 20 W, 5 min) to graft N-containing groups grafted on a stable surface. Plasma treatments have been performed in a tubular glass pyrex RF plasma reactor, with internal steel electrodes, in the parallel plate configuration. The chemical composition of modified and native PVDF membranes was determined by X-ray photoelectron spectroscopy (XPS) and Water Contact Angle (WCA) analysis. XPS analysis were performed using a PHI ESCA 5300 spectrometer equipped with non-monochromatic MgK_α rays (1253.6 eV, 300 W). Evidence of the immobilization of the W-based catalysts on plasma treated surfaces (PVDF/Ar/NH3/sodium tungstate) have been obtained via XPS performed after each modification step. Ar pre-treatments caused a severe defluorination of the surface evidenced in the C1s spectrum by a strong reduction of the CF_2 peak component at 294,3 eV and confirmed by the F1s/C1s elemental ratio which decreases drastically from 0.92 to 0.38, attesting a massive fluorine loss.

Soon after the treatment modified PVDF membranes have been immersed in acid solutions of sodium tungstate to allow a chemical interaction between the acid catalyst and the basic sites grafted at the plasma modified membrane.

After sodium tungstate immobilization the presence of W4f peak, in XPS spectra, appeared (C: 61,4%, 13,2%, W4f: 2,9, F: 17,5%, N: 5,0 %). Ageing of modified membranes has been measured over a long period and cross-linking of membranes with Ar appears an effective way to reduce ageing of ammonia treated membranes. The immobilization of sodium tungstate affected also the WCA values. A reduction from 93 ± 2 (unmodified membrane) to 72 ± 2 (PVDF/Ar/NH3) to 64 ± 2 (PVDF/Ar/NH3/sodium tungstate) was recorded.

Catalyst modified membranes have been employed in CRMs and the conversion of dibenzylamine to nitrones has been observed trough the formation of N, N-Dibenzyl hydroxylamine, a reaction intermediate according to the scheme 1.

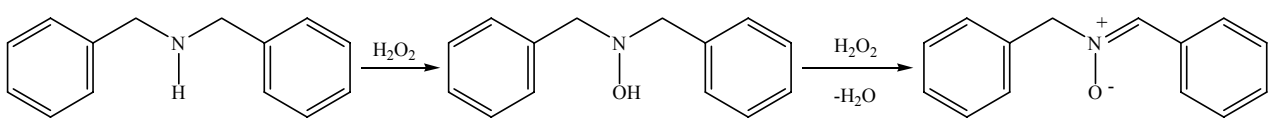

Scheme 1. Conversion of dibenzylamine to nitrones in presence of H_2O_2, trough the formation of N, N-Dibenzyl hydroxylamine

Stable chemical immobilization of sodium tungstate has been achieved on plasma treated PVDF membranes and this represents a novel efficient catalytically active system for the oxidation of secondary amines. The catalytic membranes have been tested in the experimental apparatus schematically shown in figure 1. Both permeate and retentate have been recyrculated in the system in order to increase the contact time between the unreacted reagent and the catalytic membrane surface. UV-Vis measurements confirmed no leaching of the W-based catalyst confirming that a stable chemical bond occurred trough the basic active sites of the membrane and the catalyst.

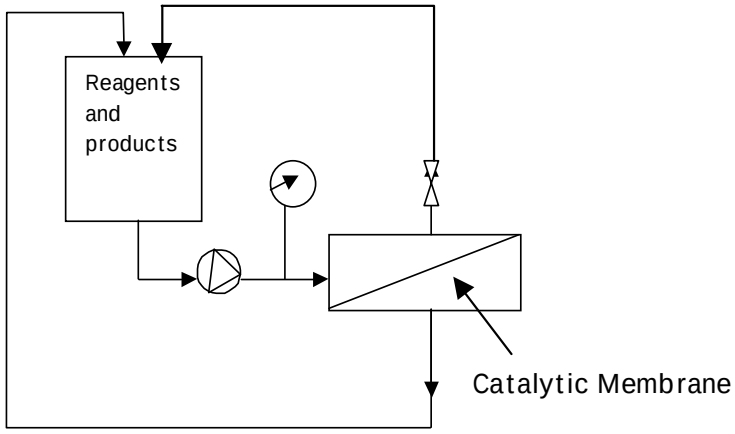

Figure 1-Scheme of the catalytic membrane reactor

The conversion % from dibenzylamine to nitrone and the selectivity of the reaction to nitrone with respect to N, N-Dibenzyl hydroxylamine are shown in Figure 2. Data obtained at 0 and 1 bar of transmembrane pressure in the CRM are reported when plasma modified catalytic PVDF membranes are used. The system efficiently catalyses the oxidation affording the nitrone in good yields (70%) operating at transmembrane $\Delta P=0$ bar in reasonable reaction times, almost comparable to the ones of the homogeneous system [17]. At $\Delta P=1$ the reagent conversion decreased to 60% while the selectivity trend remains almost unvaried.

Future studies will address aspects related to the contact time between the reagent and the catalyst immobilized at the membrane surface. A deeper surface characterization of the plasma modified membranes is also in progress, with the aim of optimizing the combined plasma process and improve the immobilization reaction.

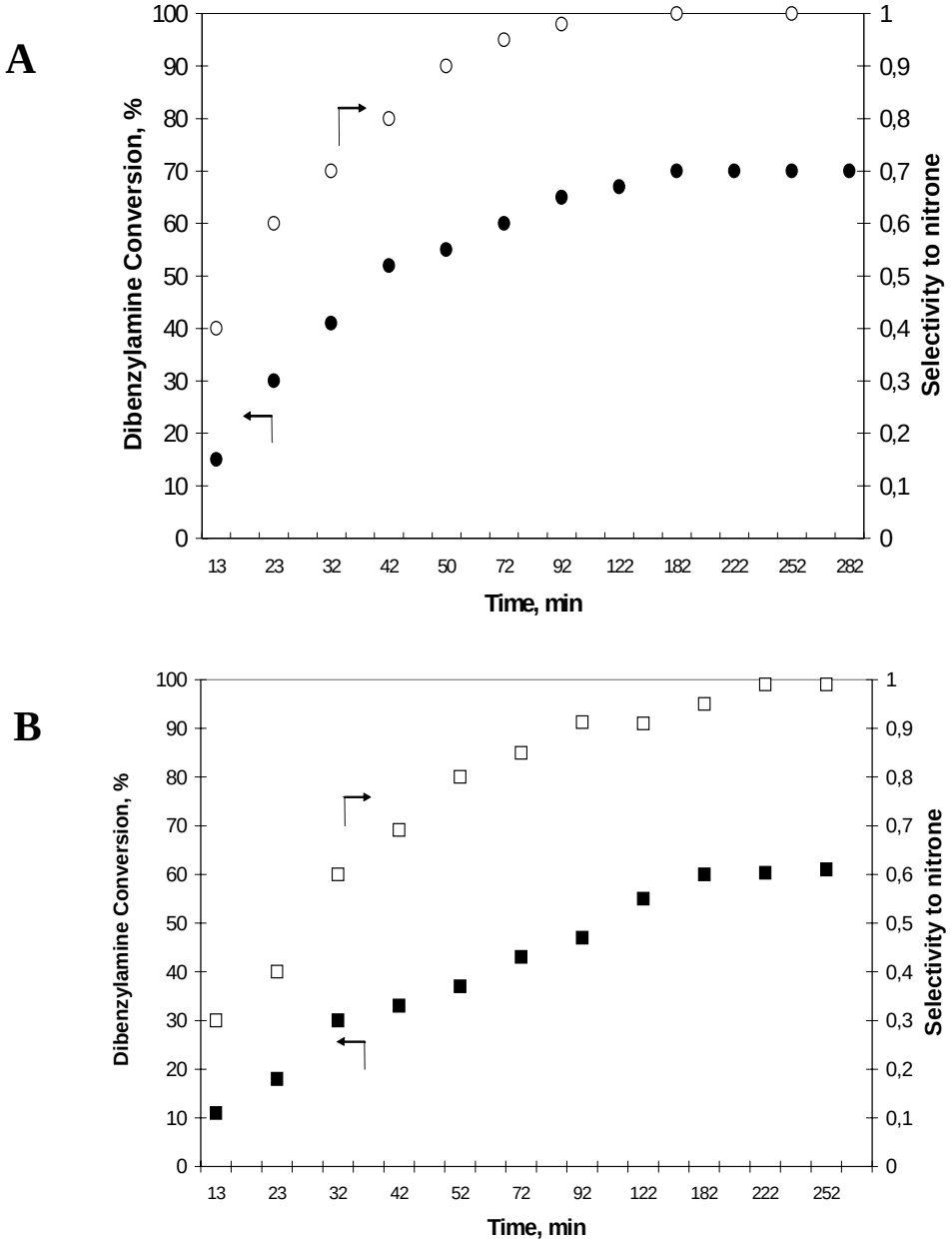

Figure 2 Dibenzylamine conversion % and selectivity to nitrone vs. time at two different transmembrane pressures: (**A**) ΔP=0; (**B**) ΔP=1 bar

.

Conclusions

In this work we have reported for the first time, at the authors knowledge, about the surface immobilization (heterogeneization) of a W-based catalyst on N-grafted PVDF membranes for CRMs. Polymeric catalytic membranes consisting of Na_2WO_4 immobilized on plasma functionalised PVDF are active systems for the oxidation of dibenzylamine to nitrone. The reactivity screening allowed us to select modified PVDF catalytic membrane as the best system in terms of dibenzylamine conversion (operating at low transmembrane pressures) and selectivity to nitrone and exclude the occurrence of competing homogeneous pathways.

Acknowledgments

We kindly acknowledge the Italian Ministry of University and Research for funding this research trough the Cofin 2002; 2002033184_001 project.

References

[1] R. d'Agostino (Ed.), "Plasma Deposition, Treatment and Etching of Polymers", Plasma-Materials Interaction, Academic Press, San Diego, CA, (1990).
[2] D.J. Wilson, R.L. Williams, R.C. Pond, Surface and Interface Analysis, **31**, 385 (2001).
[3] B.D. Ratner, A. Chilkoti, G.P. Lopez in: Plasma Deposition, Treatment and Etching of Polymers, R. d'Agostino ed., Acad. Press, (1990).
[4] B.D. Ratner in: "Plasma Processing of Polymers", R. d'Agostino, P. Favia, F. Fracassi ed., Kluwer Acad. Publ., NATO ASI Series, E: Appl. Sci., Vol. **346**, (1997).
[5] R. d'Agostino, P. Favia, C. Oehr, M. Wertheimer, Plasma Processes and Polymers, **2**, 7, (2005).
[6] P. Favia, A. Milella, L. Iacobelli, R. d'Agostino, "Plasma Processes and Polymers", R. d'Agostino, P. Favia, C. Oehr, M. Wertheimer Eds. Wiley VCH, pp 271-280, (2004).
[7] P. Favia, M.V. Stendardo, R. d'Agostino, Plasmas and Polymers, **1**, 2, (1996).
[8] P. Favia, R. d'Agostino, F. Palumbo, J. De Physique IV, **7**, 199, (1997).
[9] R.F. Parton, I.F.J. Vankelecom, D. Tas, B.M. Janssen, P.P. Knops-Gerrits, P.A. Jacobs, J. Molecular Catalysis A: Chemical **113**, 283 (1996).
[10] G. Langhendries, G.V. Baron, I.F.J. Vankelecom, R.F. Parton, P.A. Jacobs, Catalysis Today **56**, 131 (2000).
[11] P.P Knops-Gerrits, I.F.J. Vankelecom, E. Beatse, P.A. Jacobs, Catalysis Today **32**, 63.(1996).
[12] M.G. Buonomenna, E. Drioli, W.A. Nugent, L. Prins , P. Scrimin, G. Licini, Tetrahedron Letters **45**, 7515 (2004).
[13] M. Bonchio, M. Carraro, G. Scorrano, E. Fontananova, E. Drioli, Advanc. Synthesis and Catalysis **345**, 1119 (2003).
[14] F. P. Ballistreri, Chiacchio, U.; Rescina, A.; Tomaselli, G.; Toscano, R.M. Tetrahedron **48**, 8677 (1992)**.**
[15] Ballistreri, F. P.; Bianchini, R.; Pinzino, C.; Tomaselli, G.; Toscano, R.M., J.Physis.Chem.A, **104**, 2710 (2000).
[16] D.T. Clark, A. Dilks, J. Polym. Sci. Polym. Chem. Ed. **15**, 2321 (1977).
[17] S.I. Murahashi, H.Mitsui, T.Shiota, T. Tsuda and S. Watanabe J.Org. Chem. **55**, 1736 (1990).

VOC Destruction in Atmospheric Pressure Plasma Discharge

H.Grossmannová, F. Krčma, K. Slánská

Faculty of Chemistry, Brno University of Technology, Purkyňova 118, 612 00 Brno, Czech Republic

Abstract
This work is focused on the studies of gliding arc discharge with respect to its use in the decomposition of volatile organic compounds (VOC). The products of decomposition were sampled by Solid Phase Microextraction, which is an innovative, solvent free and economical sampling technique, and analyzed by Gas Chromatography linked to Mass Spectroscopy (GC-MS). During our work, we tried to check up appropriateness of the SPME technique for the destruction products analyzes. The Carbowax/divinylbenzene coated SPME fiber was founded as the best for detection of the highest number of discharge products.

Keywords
Solid Phase Microextraction (SPME), Volatile organic compounds (VOC), atmospheric plasma discharge, gliding arc discharge.

Introduction

The gliding arc reactor is a widely exploited plasma source in many industrial chemical applications, because it is a simple and inexpensive way to generate the non-thermal plasma [1, 2]. The high energy efficiency, reaction selectivity or production of specific species may be achieved in this kind of plasma, and thus for various chemical processes it can be much more effective then in common technologies [3]. The excitation energy can be transported to specific molecules in the reacting gas mixture. Recent studies showed that the reaction stimulation efficiency by the gliding arc discharge plasma is very high [1]. This plasma can be applied in many industrial branches, especially in the surface treatment [4]. One of the applications that are at present widely studied is the emission control of Volatile Organic Compounds (VOC) in the combustion exhaust gas (so called exhaust treatment [5]). Various non-thermal discharge kinds (DC and AC corona discharge or Gliding Arc) were used in several studies on dilute air-pollution control [6]. In these experiments, various aliphatic and aromatic pollutants were presented in order of several hundreds of volume ppm [6].
The in-situ gas chromatography with a simple detector (usually a flame detector) or the active coal sorption tubes were used for the discharge exhaust gas analysis. These techniques have a serious disadvantage in their limited selectivity. The chromatograms contain many different peaks. Their identification is not easy then a flame detector is installed. The use of mass spectrometer as a detector (GC-MS) is more sensitive and selective, and thus many discharge products can be clearly identified even from a complicated exhaust gas mixture. The Solid Phase Microextraction (SPME) technique is a relatively new method (used since 1996) for a sampling Gas Chromatography analysis. It is a very sensitive method for the higher molecular products and it offers a partial selectivity for some kinds of molecules depending on the extraction fiber solid coating (see below). This work is focused on the SPME technique suitability for the discharge exhaust gas analyses.

Experiment

Gliding arc discharge combines the advantages of the thermal and the non-equilibrium plasmas. Most of the plasma in Glidarc exit in the non-equilibrium condition (80%) [2]. The experimental device is schematically shown in Fig. 1. The reactor consists of a single pair of diverging knife-shaped copper electrodes (thickness 1 mm, size 60 mm x 40 mm each), whose minimal distance is 0.6 mm. A pair of ceramic plates was used to limit a gas flow into the active discharge for a higher efficiency of the selected VOCs decomposition. The carrier gas did not scatter the whole reactor area, but the maximum of it was passing through the discharge and the decomposition could be more efficient as it was presented recently [7]. Gliding arc discharge was created in various gas mixtures of nitrogen, oxygen, and argon at the atmospheric pressure. The carrier gas passes through

the mass flow controller and mixes just before entering the reactor with an auxiliary nitrogen flow enriched by toluene or cyclohexane, which were chosen as the model VOCs. The total gas mixture flow rate was typically 1000–1300 ml·min^{-1}. The applied DC voltage was from 3.5 kV up to 4 kV with the discharge current of 35 mA. The exhaust gas leaves the reactor through a special device arranged for the sampling by Solid Phase Microextraction (see Fig. 2).

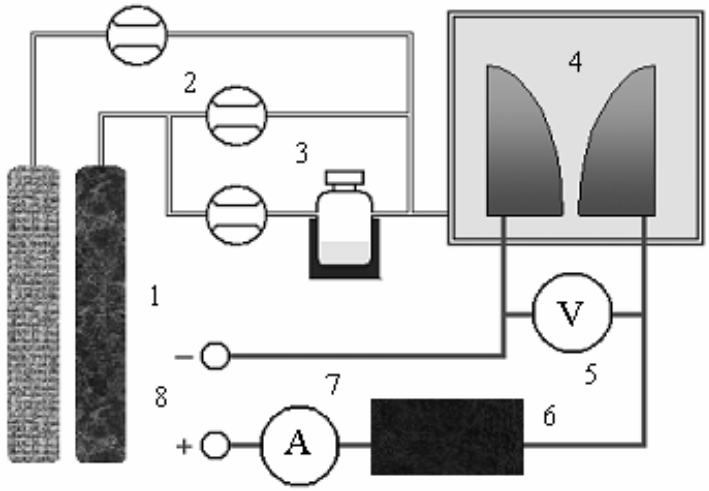

Fig. 1: Experimental setup: 1 – gas bottles, 2 – mass flow controllers, 3 – VOC reservoir, 4 – discharge reactor, 5 – voltmeter, 6 – resistance, 7 – ampere meter, 8 – HV power supply.

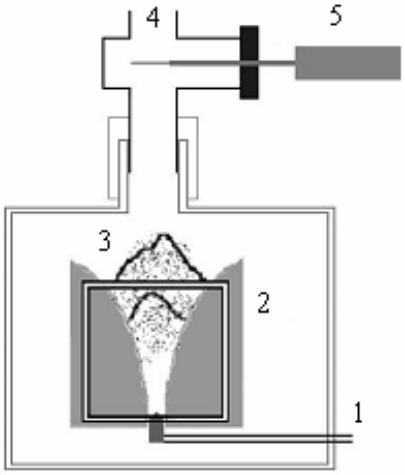

Fig. 2: Discharge reactor: 1 – gases input, 2 – electrodes, 3 – discharge area, 4 – product outlet, 5 – sample collection by SPME.

SPME technique

The solid-phase microextraction is a solvent-free equilibrium extraction method which, with the due calibration, can allow also the quantitative determinations of organic compounds. The sensitivity is very good and usually reaches up to low-to-mid parts per trillion [8] without the use of any organic solvents not only at sampling, but also during the analysis. This technique uses a short thin solid rod of fused silica, coated with a polymeric absorbent for the extraction of volatile compounds. The fiber coating removes the compounds from the gas or liquid sample by absorption or adsorption. The whole analysis using the SPME sampling technique requires only 30 minutes for the sample preparation and analytical separations. It can be easily automated and it is ideally suited for use in the terrain. Although the method was originally developed for the analysis of water samples, now SPME has gained a wide spread acceptance as the technique of preference for many applications including flavours and fragrances, forensics and toxicology, environmental and biological matrices, and product testing, to name a few [9].

The principle of SPME is an equilibrium partitioning of the analyte between the coating fiber and the solution or the headspace. The extraction should be carried out by two methods: direct sampling (the fiber is plunged in the liquid sample) or headspace (sample is collected above the liquid sample from the gas; it is better for volatile compounds). The absorbed (in the case of liquid coatings) or adsorbed (in the case of solid coatings) compounds in (at) the fiber coating are in the thermodynamic equilibrium with the same compounds in the sample [9]. After the extraction, the SPME fiber is inserted directly into the Gas Chromatograph for desorption and analysis.

For the quantitative analysis, it is very important to explore the dependence of the analyte mass in the fiber as a function of the extraction time (see Fig. 3). It is clear the selection of an appropriate SPME fiber is a very important task for obtaining optimal results. There are many important factors which should be considered: polarity of the analyte, volatility and molecular size and shape of the analyte, the effects of analyte size on SPME fibers, capacity of SPME fiber, minimum detection limits or fiber extraction mechanism. Polar analytes are attracted to polar phases (e.g., polyacrylate and Carbowax coatings). Fibers with a thicker coating film (100μm) are better volatile liquids, but also can be used for semi-volatile compound when longer extraction times are recommended.

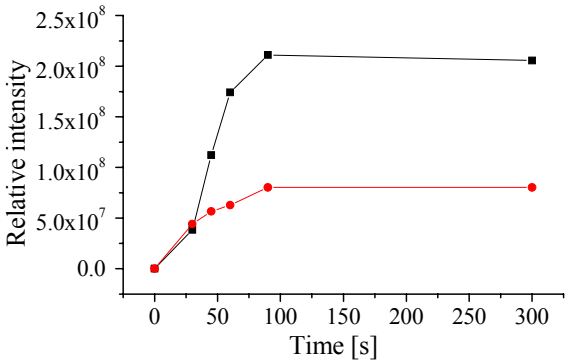

Fig. 3: Time dependence of the relative intensities of cyclohexane and toluene using the sampling by Carbowax/ divinylbenzene SPME fiber.

Porous fibers (Carboxen or divinylbenzene coating) can also retain small analytes as C2 – C6. Thinner coating films (7µm and 30µm polydimethylsiloxane - PDMS) are better for larger molecules. To collect volatile analytes, the Carboxen/ polydimethylsiloxane (CAR/PDMS) fiber is ideal for the extraction of volatile compounds. Adsorption type fibers are also better for extracting analytes presented in low concentrations. The sample heating slightly increases the volatility of the analytes. To ensure reproducibility, the sample must be stabilized at the extraction temperature before inserting the fiber and starting the sample extraction. The absorptive fiber coatings such as PDMS or polyacrylate are recommended for the extraction of semi-volatile compounds in the headspace. Even analytes with high boiling points can be extracted from the headspace, if they have sufficient vapor pressure. Excessive headspace volume reduces the analyte concentration in the headspace and reduces the extraction efficiency [9].

Results

Tree different types of SPME fibers were used for the experiments, namely polydimethylsiloxane (PDMS), Carboxen/polydimethylsiloxane/divinylbenzene (CAR/PDMS/DVB), Carbowax/divinylbenzene (CW/DVB). The toluene and cyclohexane were used as VOC samples for the selection of an appropriate fiber coating for the discharge product analyses.

Fig. 4 shows the chromatographic spectra of toluene destruction products extracted using all three tested SPME fibers. Besides the traces of various compounds generated from the fiber material, the real discharge products were identified. The most abundant higher molecular products of the toluene destruction in the nitrogen – oxygen gas mixture are shown in Table 1.

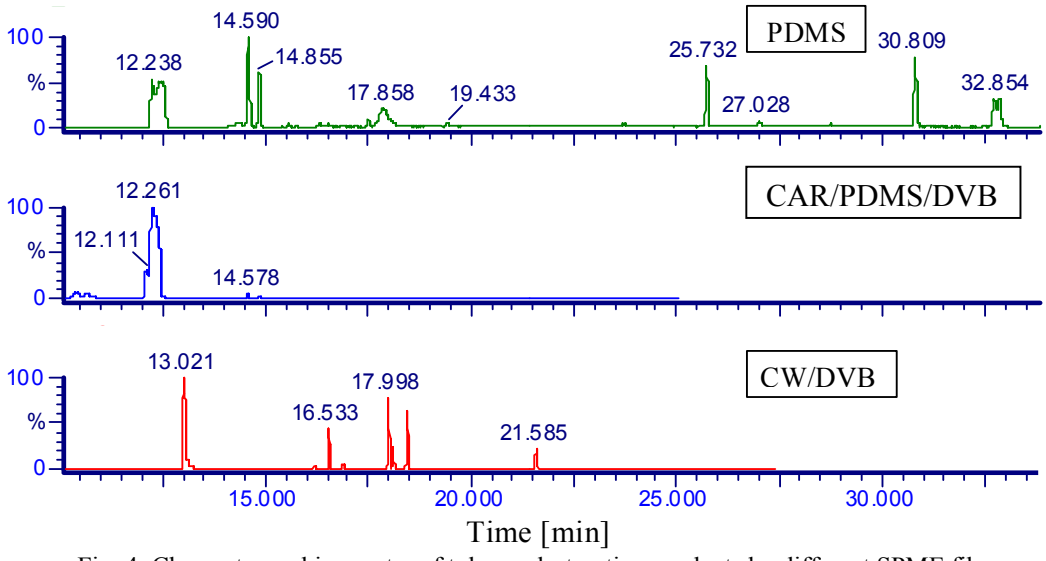

Fig. 4: Chromatographic spectra of toluene destruction products by different SPME fibers.

CW/DVB	PDMS	CAR/PDMS/DVB
toluene	toluene	toluene
methylbenzene	trimethylsilanol (fiber)	2,3-dihydrofuranone
phenol	2,3-dihydrofuranone	benzaldehyde
benzaldehyde	octamethylcyclotetrasiloxane (fiber)	benzenemethanol
benzenemethanol	Benzaldehyde	--------
4-methylphenol	2,4-dimethylimidazol	--------
4-(phenylmethoxy)benzaldehyde	--------	--------
2-methylphenol	--------	--------

Tab. 1: Analysis of toluene destruction products.

Fig. 5 presents the chromatographic spectra of cyclohexane destruction products extracted by the CAR/PDMS and CW/DVB SPME fibers. In the case of PDMS fiber, only cyclohexane and compounds released form fiber material or chromatographic column were observed and thus this spectrum is not presented. The main high molecular products of cyclohexane decomposition are presented in Table 2.

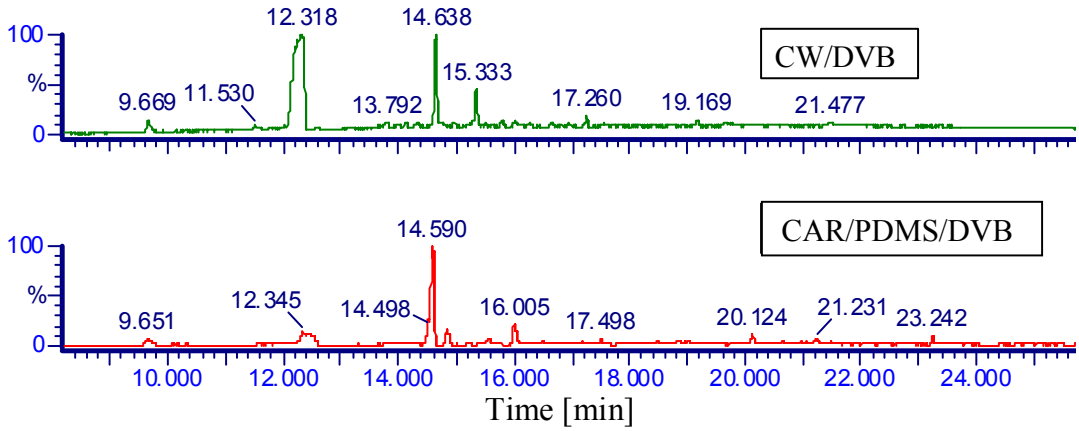

Fig. 5: Chromatographic spectra of cyclohexane destruction products extracted by different SPME fibers.

CW/DVB	CW/DVB	CAR/PDMS/DVB
cyclohexane	2,4-dimethylpentane-3-one	cyclohexane
cyclopenta-1,2-diol	3-methylbutan-2-ol	2,3-dihydrofuranone
benzaldehyde	4-methylcyclohexa-2-en-1-ol	2-ethylhexan-1-ol
heptanale	3-undecene-1-yne	4-phenoxybutanoic acid
2,4-dihydrofuran-2-one	4-decen	2-phenoxyethanol
2-methylcyklohexanol	-------	phenol acetate
2,3-dihydrofuranone	-------	benzenemethanol
3,5-dimethylhexan-3-ol	-------	tetradecane

Tab. 2: Identified cyclohexane destruction products.

These results show that the fiber coated by CW/DVB can extract the highest number of destruction products, the CAR/PDMS coating can be used for the extraction of some other compounds such as phenol acetate or benzenemethanol (C_2 – C_{12} carbons), and the PDMS coating could not be applied for the discharge exhaust gas analysis.

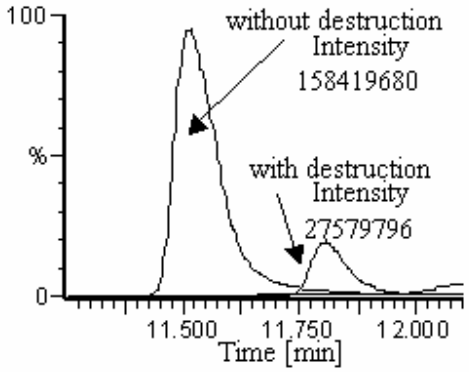

Fig. 6: Chromatographic peak of toluene destruction by CW/DVB SPME fiber.

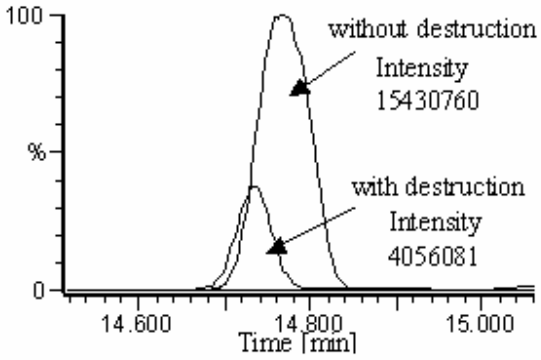

Fig. 7: Chromatographic peak of cyclohexane destruction by CW/DVB SPME fiber.

The total destruction efficiency was studied at the initial concentration of VOC in the range of 100 – 300 $\mu g \cdot l^{-1}$ in the ambient air as a carrier gas. The chromatographic peaks of both studied VOC represents are shown in Figs. 6 and 7. The highest destruction efficiency under the optimal conditions (the power supply of 3,5 kV) was 86 % for toluene and 79 % for cyclohexane.

The destruction efficiency depends of course on the reacting gas mixture composition. The influence of the oxygen and argon admixture in the carrier air based gas mixture was studied in conditions when the best decomposition in ambient air was observed. The increase of the oxygen content in the gas mixture plays a relatively small role, the destruction efficiency increases only by about 20 % when the oxygen content is increased from 20 % up to 60 % (see Fig. 8). The role of the argon admixture is negative because the argon adding rapidly decreases the efficiency down to 8 % at about 12.5 % of argon in the gas mixture [7].

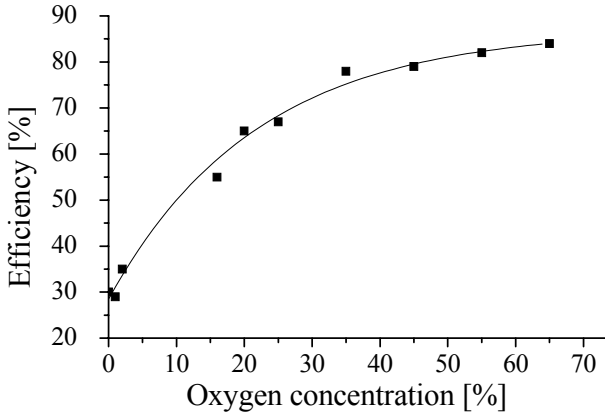

Fig. 8: Dependence of toluene decomposition on the oxygen concentration in nitrogen carrying gas.

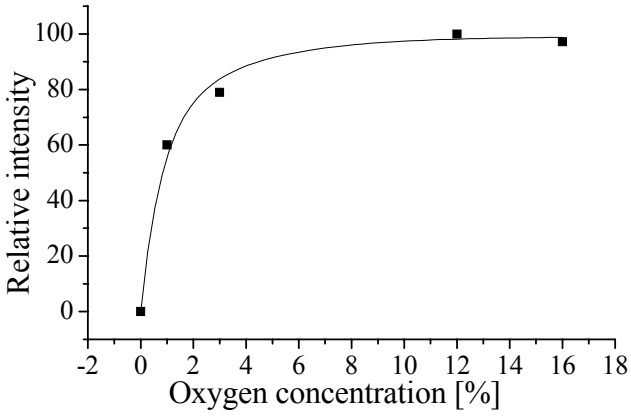

Fig. 9: Dependence of the benzaldehyde concentration on the oxygen concentration in nitrogen carrying gas (the maximum value was chosen as a reference).

The concentrations of various extracted compounds are also dependent on the gas mixture composition. The dependence of benzaldehyde was chosen as an example. Fig. 9 demonstrates the significant production of this compound even in oxygen pure gas mixture (about 3 % only) and it is not too dependent on further increase of oxygen presence. On the other hand, the concentration of benzene decreses with the increase of oxygen presence. The exact study of these dependencies for more or less all discharge products will be the subject of further studies that will be extended by the measuring of the carbon conversion into its inorganic form.

Conclusion

The presented work gives the first results about applicability of the Solid Phase Microextraction in the analysis of Volatile Organic Compounds destruction in the non-thermal plasma. Using this technique, better results can be obtained in comparison with the classical Solid Phase Extraction (sorption tubes with an active coal). Three different SPME sorption fibers were tested, the Carbowax/divinylbenzene coated fiber was found as sensitive to main part of discharge products, the Carboxen/polydimethylsiloxane can be used as an additional extraction medium. On the other hand, the polydimethylsiloxane fibers cannot be used for the discharge exhaust gas analyses due to their negligible sensitivity to products. The analysis using Carbowax/divinylbenzene fibers showed that the total destruction efficiency of toluene and cyclohexane reach up to 86 %, resp. 79 %. Many different higher molecular weight products were analyzed by the GC-MS analysis. Their concentrations as well as the total destruction efficiency are dependent on the discharge conditions, mainly on the oxygen content. The destruction is more effective than oxygen presence in the carrying gas mixture increases and concentrations of the more oxidized products increases, too.

The following experiments will be focused on the estimation of concentration dependencies for more or less all discharge products on the discharge conditions. The organic carbon conversion measurements with CH-meter and low molecular products analysis will be completed, too.

Acknowledgements

This work was supported by Czech Ministry of Education, project No. 3218/2005 and by the Czech Science Foundation, contract No. 202/03/H162.

References

[1] A. Czernichowski, A. Ranaivosoloerimanana – Chem. Tech. **26**, 45 (1996).
[2] A. Czernichowski – Pure and Appl. Chem. **66**, 1301 (1994).
[3] O. Mutaf-Yardimci, A. Saveliev, A. Fridman, L. Kennedy – J. Appl. Phys. **87**, 1632 (2000).
[4] J. Janča, A. Czernichowski – Surf. Coat. Tech. **98**, 1112 (1998)
[5] A. Fridman, S. Nester, L.A. Kennedy, A. Saveliev, O. Mutaf-Yardimci – Progress in Energy and Combust. Sci. **25**, 211 (1999).
[6] H.-H. Kim, – Plasma Processes and Polymers **1**, 91 (2004).
[7] H. Grossmannová, K. Slánská, F. Krčma – Proc. 22nd SPIG, Bajina Bašta, 597 (2004).
[8] *http://www.eerc.und.nodak.edu/rnd/analyticallabs/EnvironmentalChemistry/solid.asp* (22 March 2005).
[9] *http://www.sigmaaldrich.com/Brands/Supelco_Home/Spotlights/SPME_central.html* (20 March 2005).

The Parameters and Conditions of Appearance of Branching Streamer

A.V. Krasnochub, M.M. Nudnova, A.Yu. Starikovskii.
Physics of Nonequilibrium Systems Laboratory (NEQ-Lab),
Moscow Institute of Physics and Technology, Dolgoprudnyi, Russia, krasnochub@neq.mipt.ru

Abstract
In this paper the experimental results of research of a branching streamer discharge in an mixture (N_2:O_2 4:1) both cathode-directed and anode-directed streamer in plane – plane gap at 26 – 42 kV and pressure 300 - 1200 torr are shown. Experimental data are supplemented with results of numerical modeling of solitary cathode-directed streamer. The method of measuring of electro-dynamical diameter of the streamer's head is offered. The pattern of radiation of the streamer's head is observationally restored.

1. Introduction

Plasma of pulsed discharges is widely used in different applications [1] - from radiation sources to plasma chemical reactors - due to the main advantage in comparison with stationary and quasistationary discharges, namely - minimal rate of thermal heat. This leads to a high efficiency of the energy input to the channels with high energy thresholds [2]. Another important characteristic of plasma generator is a large bulk which could be filled with of plasma. The branching streamer gives such possibility. The comprehension of mechanism of branching and knowledge of parameters and conditions which influence on bifurcation of streamer allow us to predict optimal characteristics of plasma chemical reactors.
The aim of the paper is the investigation of conditions of appearance of branches both for cathode and anode streamer.

2. Experimental setup.

On fig. 1 the block scheme of the experimental installation is shown. Investigations were carried out in cubic discharge chamber with an edge of 220 mm. The construction of the chamber allowed us to carry out investigation both at the reduced (300 torr) and at increased (1200 torr) pressure. In the present research we analyzed distribution of a streamer in synthetic air (mixture N_2:O_2 4:1) in a plane - plane gap with distance between electrode of 30 mm. During experiment we controlled electro-dynamical and optical parameters of a streamer. Optical diagnostics was carried out through windows with diameter of 100 mm, made of quartz QU-1. The high-voltage electrode is made of brass as a disk with diameter of 80 mm, the earthed electrode is made of an aluminum disk with diameter of 100 mm. For initiation of streamer at the centre of the earthed electrode is set a needle with diameter of 0.8 mm, with height of 8 mm. Current of streamer's flash was measured by means of the current shunt which was built in between a needle and the earthed electrode.

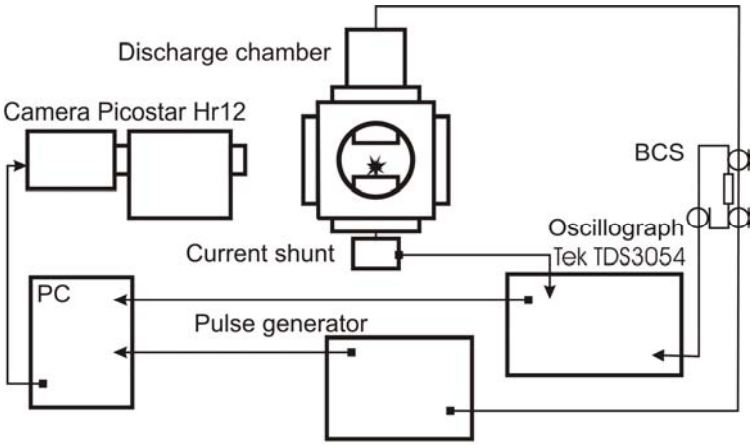

Fig. 1. The block scheme of the experimental installation.

For getting of the discharge pulses both of positive, and negative polarities with amplitude in a cable line from 12 up to 24 kV (24-48 kV on a discharge gap) with front of increase 5 ns, duration on half-height of 20 ns were given. Frequency of following pulses was 40 Hz. Parameters of the incident pulse were measured using a back-current shunt placed in a break in the cable braiding such as to make possible the separation of the incident pulse from generator and the pulse reflected from the chamber. During the experiment were carried out [3] the experimental measuring of parameters of a streamer at pressure in the discharge camera 300÷740 torr and voltages in a cable of 12 kV. In this paper the range of pressures is dilated up to 1200 torr, voltages up to 22 kV.
For definition of spatial and temporal characteristics the camera PicoStar HR12 of company LaVision with a spectral range of sensitivity 300÷700 nm and temporal exposure up to 200 ps was used. The camera ICCD was focused on the needle of the low-voltage electrode thus, so the upper and lower electrodes could hit in the picture. Photos of a streamer discharge were received in two modes of work of the high-speed camera: an integral and stroboscopic mode. By working in an integral mode the amplifier of the high-speed camera was switching on simultaneously with coming of a high-voltage pulse on an electrode. Time of exposure was 50 ns and included the duration of a high-voltage impulse. For working in a stroboscopic mode, on the amplifier of the camera is set a starting sine signal with frequency of 300 MHz, time of exposure of the camera's amplifier is set by the program and in our experiments it was 300 ps.

3. The experimental results and discussion.

During the work photos of a streamer were received at voltages on electrodes 26÷48 kV and pressure 300÷1200 torr for both polarities. For the specified voltages within a range of pressures 300÷740 torr 200 photos of anode-direct streamer were analyzed, typical Fig. 2a, 2c, 5c. In pictures it is visible, that the single streamer channel or some channels, starting from an initiating needle can be observed. From 200 images of anode-directed streamer we received, only in one picture (fig 2b), was obtained the image which can be interpreted as branching anode-directed streamer, thus in our opinion indeterminacy is maintained: there was a branching or channels will start from the needle of the cathode. The statistical weight of this image is very small. Also we concluded that branching is not typical for anode-directed streamer in the explored range of pressures and voltages. This result should be especially underlined because in articles [4,5] devoted to numerical model operation of the anode-directed streamer, it was drawn a conclusion that there is an opportunity of branching of the anode-directed streamer. Such results, as we have shown, contradicts with experimental data.

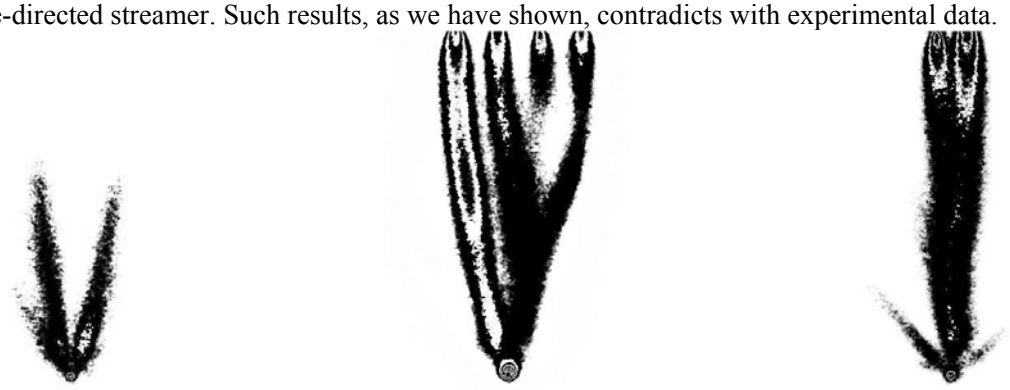

a) – 30 kV b) – 36 kV c) – 42 kV

Fig.2 Images of anode-directed streamer in an integral mode at pressure of 740 torr

To determine how the parameters (P, U) influence on occurrence of branches of cathode-direct streamer, the following procedure was done. For each applied voltage and for each pressure it was received not less than 20 pictures. For each picture the amount of apparent branches of a streamer was counted and then the received data were statistically handled. The results of this processing are shown in Fig. 3

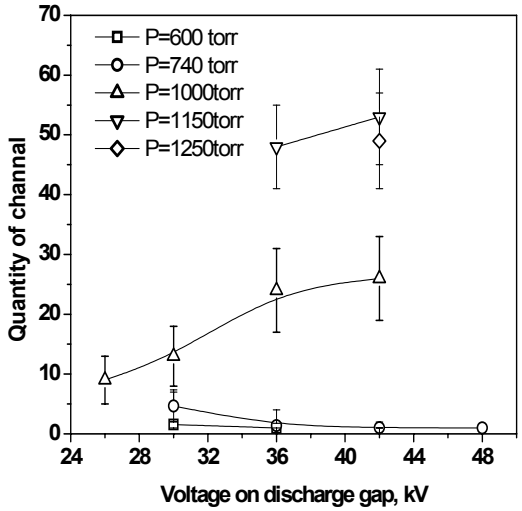

Fig.3. Dependence of branches on value of pressure and voltage on a discharge gap.

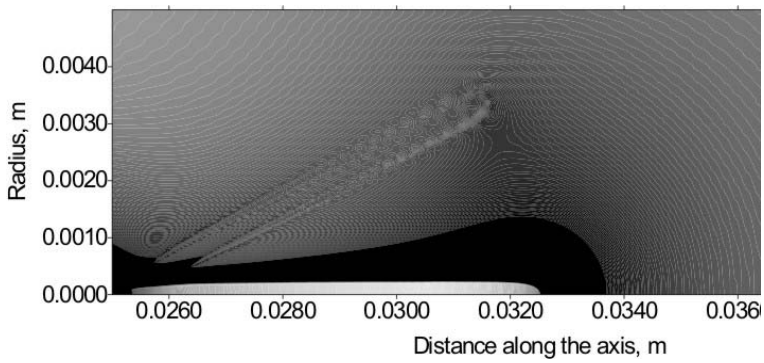

Fig.4. Electric field distribution in the gap ($\log_{10}(E/n)$). One additional "conical branch" is added.

We developed a numerical model, which allowed us to calculate the influence of branches on each other. We have performed the calculations for two different regimes: single channel propagation, and simultaneous propagation of two "branches". In the axially symmetric geometry this means that we add charge, equal to the charge of the main channel, into the cone with the deviation angle α =0.5 rad (Fig.4). For initial configuration we have observed streamer channel with radius $R_{streamer}$=0.282 mm, current I =14 mA, total charge in the discharge gap Q =$7.4 \cdot 10^{-10}$ Cl, streamer velocity V =5.06 10^5m/s. For simultaneous propagation of two streamer branches we have I =10 mA, Q =$5.5 \cdot 10^{-10}$ Cl, V =$4.85 \cdot 10^5$m/s. So, strong influence of the streamer branching on the channel parameters is shown. It follows from the received numerical data, first, that at the given pressures and voltages velocity of a streamer hardly depends on presence or lack of branching, second, that the branching influences most of all on a current of a streamer.

Thus, for more detailed studying of mechanisms leading to the branching of streamer, it is necessary to synchronize the moment of a streamer start, with the beginning of shooting of its spreading and with the moment of recording of a current and the voltage enclosed to a discharge gap. To start with we have investigated spreading of a streamer in stroboscopic mode, without synchronization with a current of a streamer. Photos in a stroboscopic mode for various pressures are shown in fig. 5

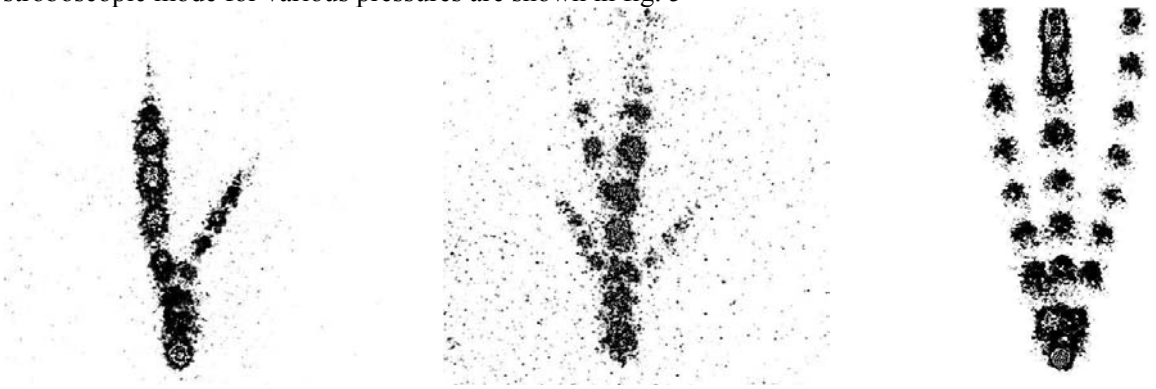

a) – cathode-direct streamer at a voltage of 30 kV and pressure of 600 torr

b) – cathode-direct streamer at a voltage of 30 kV and pressure of 740 torr

c) – anode-direct 30 kV 740 torr

Fig. 5 Image of development of a streamer received in a stroboscopic mode.

Velocity of cathode-directed streamer were measured in a wide range of pressures and voltages. Velocity was

determined, as the ratio of a distance between two positions of the streamer's head to the time interval between the exposures. The distance between positions of the streamer's head was determined by the maximum or minimum of intensity of a side view of radiation. On fig. 6 the diagram of dependence of streamer's velocity on a voltage is shown. At pressures 740 and 600 torr, where the experimental points are added with the diagram received by results of numerical modeling of solitary cathode-directed streamer in a hydrodynamic approximation in a two-dimensional formulation, description of model see [6]. The results of modeling of velocity must transmit the tendency of rising of velocity with the raising of voltage at the fixed pressure.

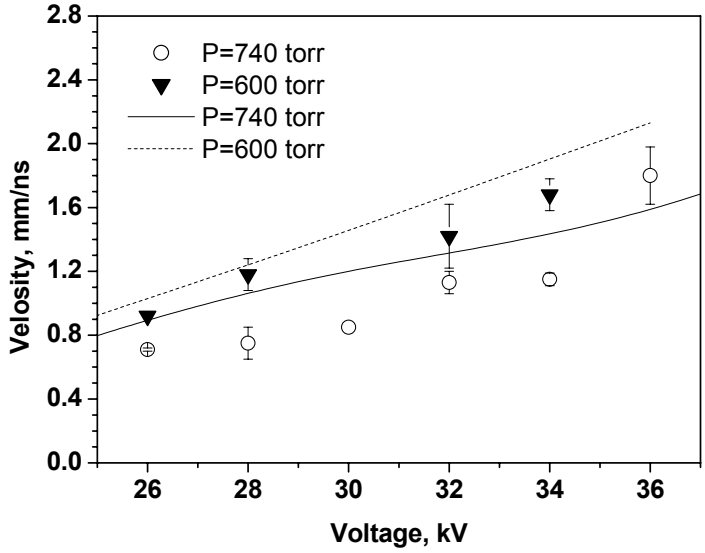

Fig. 6 Diagram of velocity's dependence of a streamer on voltage between electrodes for pressure 740 and 600 torr. The experimental points and the relevant to them diagrams re-constructed by means of numerical model [6]

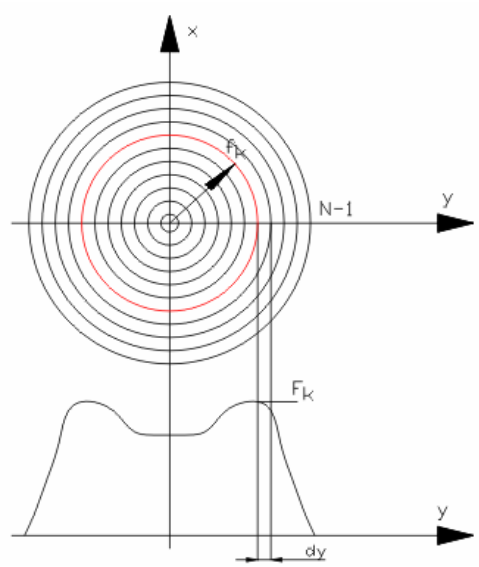

Fig. 7 Scheme of transformation of two-dimensional section of the streamer's head in the one-dimensional profile view of emission

In article [7] we supposed that the accumulation time of the active particles happens exclusively at the head of a streamer. In a spectrum of radiation N_2-O_2 under one influence of nanosecond discharge in a visible range the basic contribution imports emission of the second positive system of nitrogen in transition $N_2(C^3\Pi_u \rightarrow B^3\Pi_g)$.
On fig. 8 the profile view of radiation of the streamer's head P=740 torr, U=30 kV is shown, which is removed with exposure interval of 300 ps (curved line 1), 2 shows a lateral view after FFT-transformation. This two-dimensional lateral view is gained by summation of radiation of three-dimensional cylindrical rotationally symmetric object on fig. 7. To restore a picture of distribution of radiation along the radius of the streamer's head, we have used the inverse transformation of Abel:

$$f_k = \left[\frac{F_k}{2} - \sum_{j=2}^{N-k} f_{k+j-1} \times \Delta y \left(\sqrt{(k+j)-k} - \sqrt{(k+j-1)-k} \right) \right] \times \frac{1}{\Delta y \sqrt{2k}},$$

where f_k - required emission along radius of object, F_k - apparent emission after summation on chords.
The curved line 3 on fig. 8 shows distribution of emission on radius of a streamer which is received by means of transformation of Abel. The distance between maximums of radiation is required diameter of a streamer. The radius of the streamer's head, which is received by means of photos with picosecond's endurance, counted on maximums of radiation, makes 0.3÷0.4 mm, that approximately is twice less, than the lateral view which has been removed on half-height. On fig. 9 typical profiles of radiation after inverse transformation of Abel are shown, which were removed in different parts of the head (by virtue of axial symmetry of the head only half of lateral view of radiation is given).Actually, the profile 2 has the peak of intensity on an axis of the streamer's head while the profile 3 which is removed apart of 0.2 mm from a profile 2 on axis of the head aside the anode, has two peaks of radiation. The profile 1 is removed apart 0.2 mm from a profile 2 aside the cathode where with reduce of a field intensity of radiation decreases. On fig.9 the picture of emission of the streamer's head is

shown, which is restored on profiles of radiation in different sections of the streamer's head.

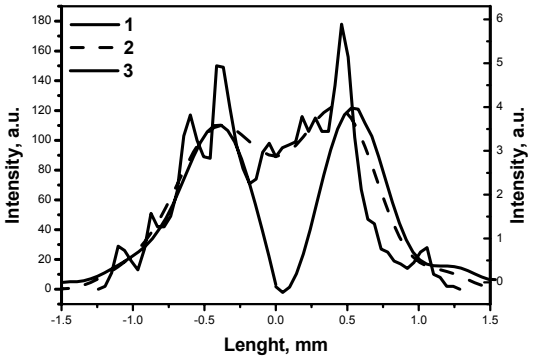

Fig. 8. 1-profile of radiation of the streamer's head P=740 torr U=30 kV, 2-profile after transformation Fourier, 3-profile after inverse transformation of Abel.

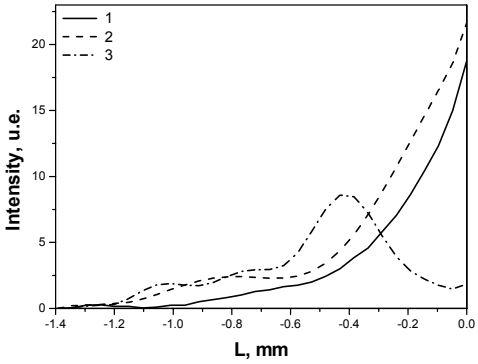

Fig. 9. Profiles of radiation on section of the head of a streamer: 2- a pique of radiation of the head, 1-on distance 0.2 mm from 2 aside the cathode, 3-apart 0.2 mm from 2 aside the anode.

Observationally filed radiation with the ICCD camera is proportionally to concentration of emissive transition $N_2(C^3\Pi_u)$. On fig. 11 it is shown the instantaneous image of concentration of excited states $N_2(C^3\Pi_u)$ for pressure P=740 torr U=30 kV, received by means of numerical model [6]. Whereas the concentration of the excited particles is proportional to quantity of a field on the streamer's head, diameter of the streamer's head is determined on a location of maximums of radiation

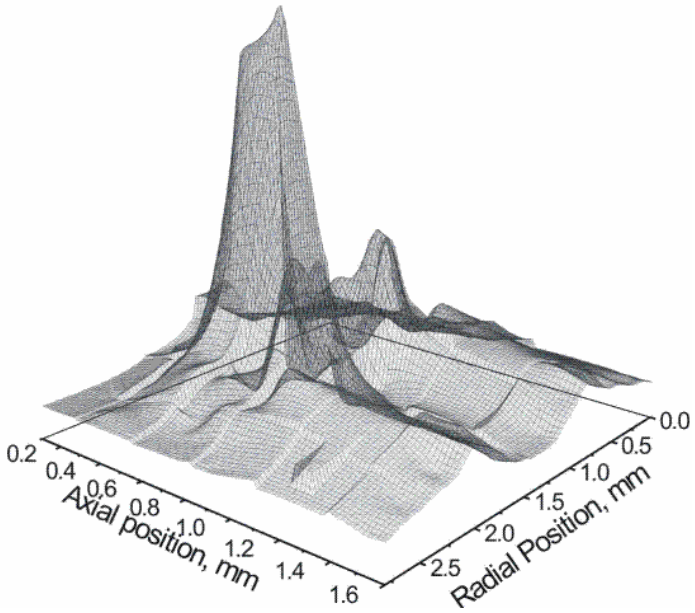

Fig. 10. A picture of radiation of the streamer's head, restored on lateral views of radiation in different sections of the streamer's head. P=740 torr U=30 kV

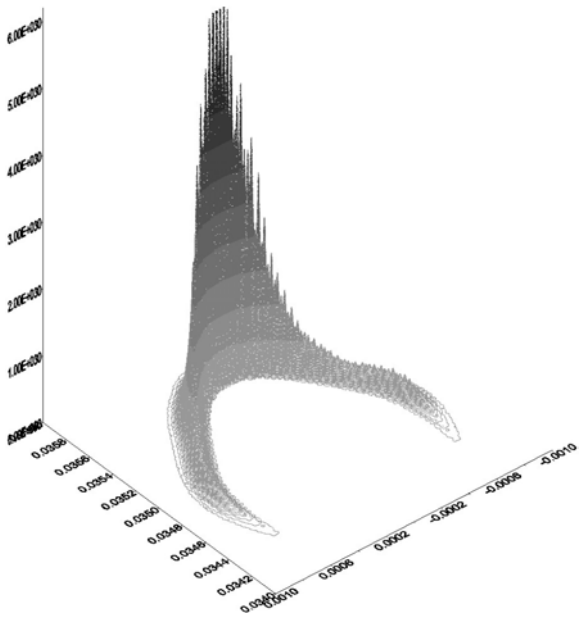

Fig. 11. The instantaneous image of concentration of excited states $N_2(C^3\Pi_u)$ for pressure P=740 torr U=30 kV, constructed by means of numerical model [6].

Conclusions.

In this work the data on branching of a streamer are received at voltages on electrodes 26÷42 kV and pressure 300÷1200 torr for both polarities. It is shown, that anode-directed streamer does not branch. Comparison of the experimental values of velocity's distribution, diameter of a streamer with results of numerical modeling [6] is carried out. It is shown, that the numerical model may predict velocity (radius, diameter) of a streamer in a wide range of pressures and voltages.
Profiles of emission of the streamer's head, received in a stroboscopic mode of operation of the high-speed camera, prove the guess that in basic points the operating time of the active particles occurs on a surface of the streamer's head. Also it is shown, that the numerical model offered before, also allows to predicting correctly the structure of the streamer's head.

Acknowledgments
The work is supported in part by grants of Netherlands Organization for Scientific Research/RFBR "Pulsed Corona Discharges for Plasma Chemical Treatment of Gases" (03SRF08), CRDF/GE GRC "Flow Regimes and Boundary Layer Separation Plasma Control Using Low-Temperature Non-equilibrium Plasma of Gas Discharge" (RP1-5002-MO-03), and EOARD/CRDF "Plasma Assisted Combustion" Project (PR0-1349-MO-02).

References

[1] E.I. Mintoussov, S.V. Pancheshnyi, A.Yu. Starikovskii Propane-Air Flame Control by Non-Equilibrium Low-Temperature Pulsed Nanosecond Barrier Discharge Plasma//42nd AIAA Aerospace Sciences Meeting and Exhibit, 2004, AIAA paper 2004-1013.
[2] E.M. van Veldhuizen Electrical discharges for environmental purposes: fundamentals and applications // (New York: Nova Science) (ed) 2000 ISBN 1-56072-743-8
[3] S V Pancheshnyi, M M Nudnova, A Yu Starikovskii // Development of a cathode-directed streamer discharge in air at different pressures: experiment and comparison with direct numerical simulation. Phys. Rev. E 71, 016407 (2005)
[4] O. A. Sinkevich // Anode Streamer Branching, High Temperature. Volume 41, Issue 5, September - October 2003, Pages 609 – 618
[5] M. Arrayás, U. Ebert, W. Hundsdorfer // Spontaneous Branching of Anode-Directed Streamers between Planar Electrodes, Phys. Rev. Lett. 88, 174502 (2002)
[6] S V Pancheshnyi and A Yu Starikovskii //Two-Dimensional Numerical Modeling of the Cathode-Directed Streamer Development in a Long Gap at High Voltage. Journal Physics D: Applied Physics, 2003. V. 36 (2003) pp.2683-2691
[7] S. V. Pancheshnyi, S. V. Sobakin, S. M. Starikovskaya, A. Yu. Starikovskii //Discharge Dynamics and the Production of Active Particles in a Cathode-Directed Streamer. Plasma Physics Reports, 2000. V.26. N.12. P.1054.

Modelling for Characteristics of Dielectric Barrier Discharge Lamp

Yoshio Watanabe, Hideto Kurimoto and Takayuki Nitta
Dept. of Electrical, Electronics and Information Engineering, Kanagawa University, Yokohama, Japan

Abstract

The model for the barrier discharge lamp has been studied. First, the coefficients in the model are estimated. Good agreements between the calculated and measured waveforms are obtained by this model. Next, the distribution of electron density, ion density, electric field and ionization amount per second are calculated at each current phase. Then, ionization mechanism in the barrier discharge lamp is investigated.

Keywords: barrier discharge, numerical model

1. Introduction

Dielectric barrier discharge (**DBD**) is employed in various fields, such as LASER, ozonizer, plasma display panel and so on. Recently, **DBD** lamp filled with xenon gas has been investigated as a mercury free light source. **DBD** lamp also has advantages of full light output from the start of operation and independence of ambient temperature because of mercury absent. It has been known that **DBD** shows unique voltage-current characteristics due to the electrification on the discharge tube wall and its efficacy is strongly depend on the applied voltage waveform [1]. To analyse this unique characteristics, the numerical model for **DBD** lamp has been studied in this study [2].

2. Objective DBD Lamp

The objective **DBD** lamp is as follows. The cylindrical discharge tube with diameter of 10 mm and length of 345 mm is filled with gas mixture of Xe (30%) and Ne (70%) at 4.4×10^4 Pa. Phosphor is not coated inside the tube. A pair of stripe electrodes is printed on the outside of the tube. The lamp is operated at 50 kHz. The waveforms of the discharge current, I, and output light, Φ, are measured at various waveforms of applied voltage, V, and compared with the calculated waveforms by the model.

3. Model

The discharge tube configuration assumed in the model is shown in Fig.1. The model is one-dimensional model with infinite length in the axial direction. The continuity equations for electron density, n_e, and ion density, N_i, are given as follows,

$$\frac{\partial}{\partial t} n_e = -\mathrm{div}(\mu_e n_e E - D_e \mathrm{grad} n_e) + \nu_i n_e - \frac{D_a}{\lambda^2} n_e \quad (1)$$

$$\frac{\partial}{\partial t} N_i = \mathrm{div}(\mu_i N_i E) + \nu_i n_e - \frac{D_a}{\lambda^2} n_e \quad (2)$$

where μ_e: electron mobility, E: electric field, D_e: diffusion coefficient for electron, D_a: ambipolar diffusion coefficient, λ: characteristic diffusion length, and μ_i: ion mobility. Ionisation frequency, ν_i, is given by using the Townsend coefficient of primary ionisation.

$$\nu_i = \mu_e E A p \exp(-\frac{Bp}{E}) \quad (3)$$

where p: filling gas pressure, A and B: coefficients determined by gas condition.
The continuity equation for current density, i, is given as follows,

$$i = q(n_e \mu_e E - D_e \mathrm{grad} n_e) + q N_i \mu_i E + \varepsilon_0 \frac{\partial}{\partial t} E \quad (4)$$

where q: electron charge and ε_0: dielectric constant.

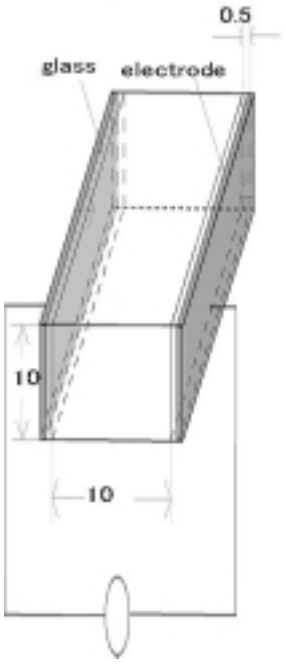

Fig.1 Assumed discharge tube configuration

The boundary condition on the wall during cathode cycle is given as follows,

$$i = (1+\gamma)qN_{i0}\mu_i E_0 + \varepsilon_0 \frac{\partial}{\partial t} E_0 \qquad (5)$$

where γ: the secondary coefficient of the glass wall.

4. Calculation Result

The values of the coefficients are estimated by the try-and-error method. The coefficients, μ_e, μ_i and *Bp,* are sensitive to the characteristics while D_a/λ^2 and γ are insensitive. The values for trapezoid waveform of applied voltage by which the most similar waveform of *I* is obtained are shown in Table 1. The calculated waveforms of discharge current, *I*, and ionisation amount per second, $\nu_i n_e$, by these values are shown in Fig.2 together with the measured waveforms. Since output light from plasma is produced by electron impact as well as ionization, the calculated $\nu_i n_e$ waveform and the measured output light waveform should be somewhat resemble to each other.

Table.1 Selected coefficient values for *the* applied voltage with trapezoid waveform

μ_e	6.0×10^{-2}m^{2}V^{-1}s^{-1}	μ_i	4.0×10^{-5}m^{2}V^{-1}s^{-1}
D_e	3.6×10^{-2}m^{2}s^{-1}	D_a/λ^2	10^2s^{-1}
Ap	6.0×10^{8}m^{-1}	*Bp*	11.4×10^{6}m^{-1}V
γ	10^{-4}		

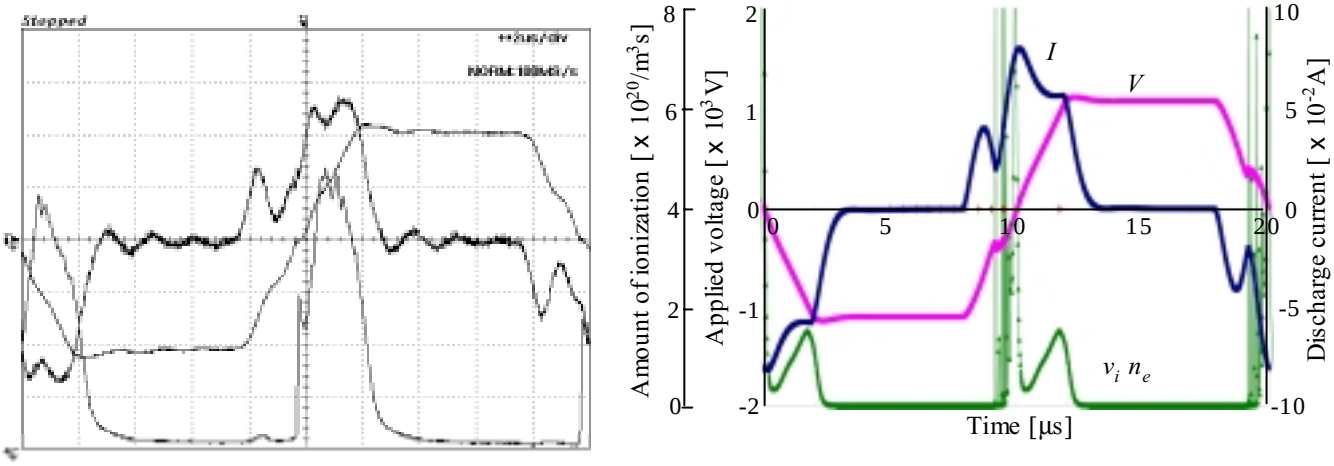

(a) measurement (b) calculation

Fig.2 Waveforms obtained under trapezoid waveform of applied voltage

The result shows good agreement between the calculated and the measured waveforms. The calculated characteristics depend on μ_e are also agree with those shown in the reference [3].

Calculations are continued for the case of sinusoidal and triangle applied voltage waveforms. The agreement between the calculated and the measured current waveforms for sinusoidal and triangle applied voltage waveforms were not so good when the values in Table 1 were employed. Thus, the coefficient values are modified for sinusoidal and triangle waveforms. The modified coefficient values for sinusoidal and triangle waveforms are shown in Table 2. The calculated waveforms by these coefficients are shown in Figs.3 and 4, respectively. Good agreement between the measurement and the calculation are obtained by these coefficient values.

Table.2 Selected coefficient values for *sinusoidal* and triangle applied voltage waveform.

μ_e	3.0×10^{-2}m^{2}V^{-1}s^{-1}	μ_i	6.5×10^{-5}m^{2}V^{-1}s^{-1}
D_e	3.6×10^{-2}m^{2}s^{-1}	D_a/λ^2	10^2s^{-1}
Ap	6.0×10^{8}m^{-1}	*Bp*	6.8×10^{6}m^{-1}V
γ	10^{-4}		

The case of triangle waveform of applied voltage with absent period at zero-cross phase is calculated using the values shown in Table 2. The calculation results are shown in Fig.5 together with the measured waveforms. The agreement between the calculation and the measurement are fairly good.

Up to now, the reason why the appropriate coefficient values are a little bit different between trapezoid waveform and sinusoidal/ triangle waveform is not clear yet. The problem might be existed in the

assumption that the plasma coefficients are taken as constant in this study.

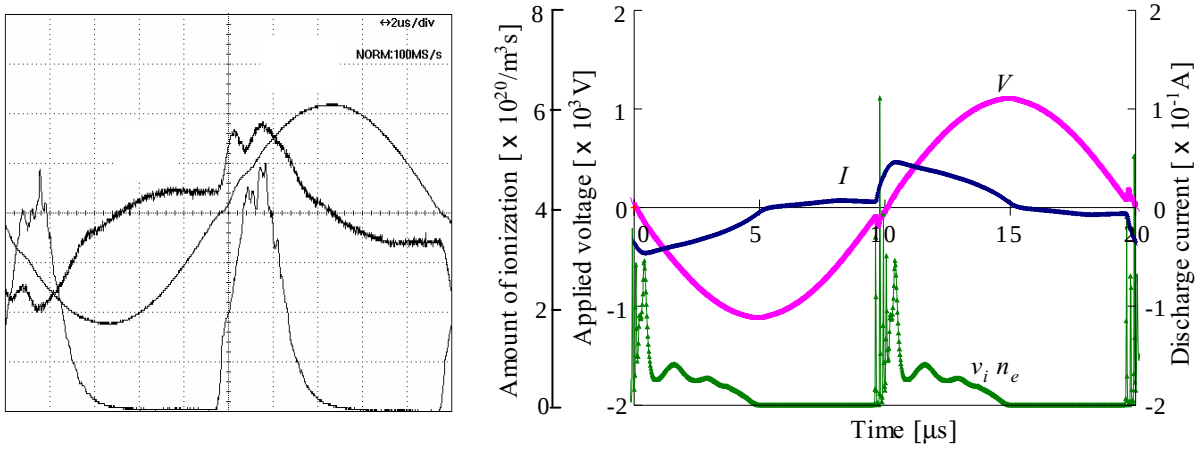

(a) measurement (b) calculation

Fig.3 Waveforms obtained under sinusoidal waveform of applied voltage

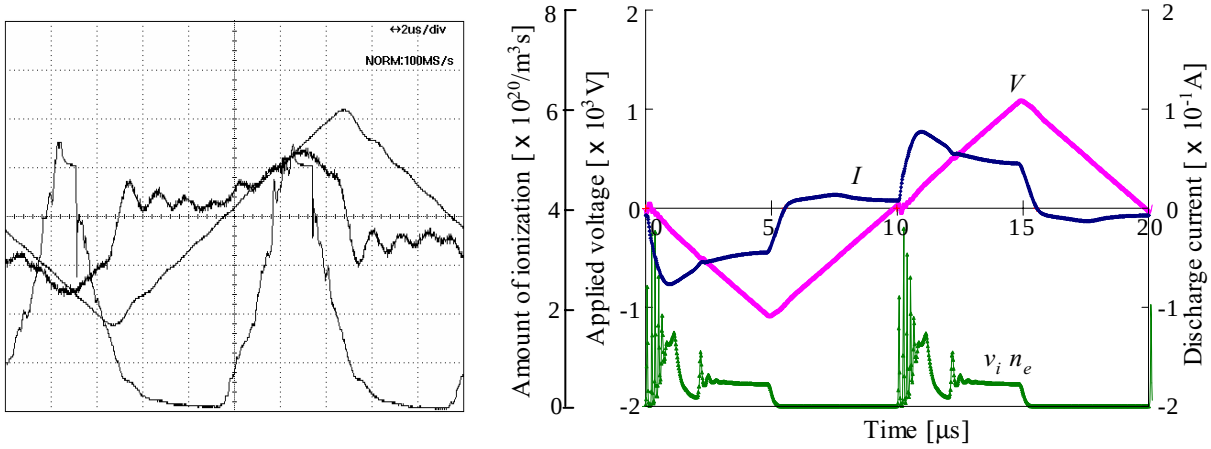

(a) measurement (b) calculation

Fig.4 Waveforms obtained under triangle waveform of applied voltage

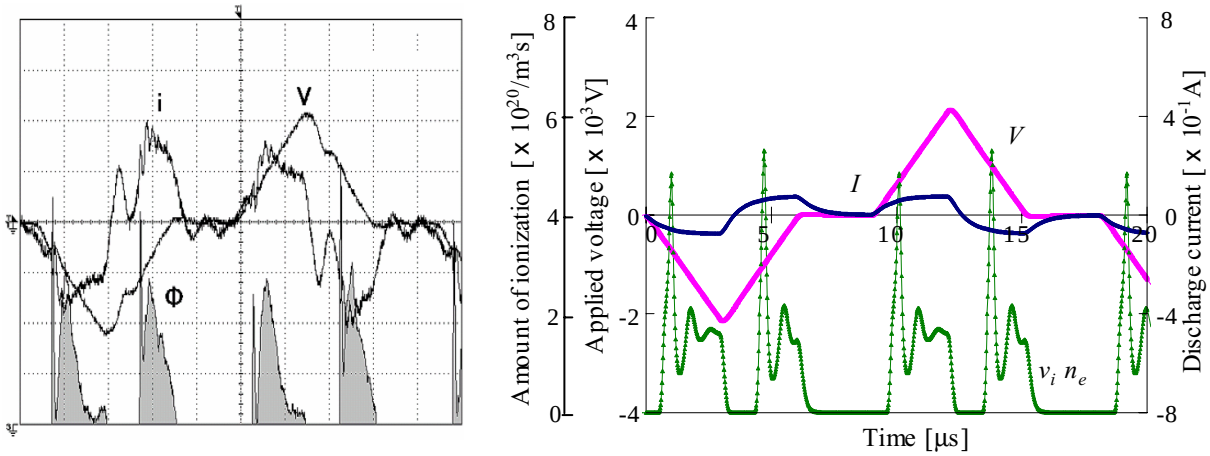

(a) measurement (b) calculation

Fig.5 Waveforms obtained under triangle waveform of applied voltage with absent period

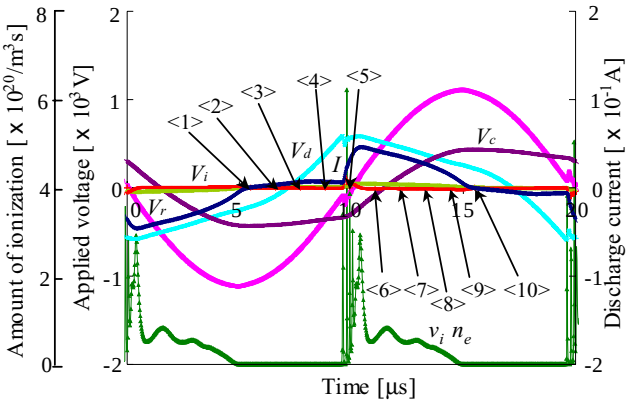

Fig.6 Calculated waveforms by sinusoidal waveform of the applied voltage. The number in the figure indicates the phase when the figures in Fig.7 are calculated.

Next, the distributions of electric field, E, electron density, n_e, ion density, N_i, and ionization amount per second, $\nu_i n_e$, at each phase designated in Fig.6 are calculated and shown in Fig.7. The calculated voltage across the plasma, V_d, and the voltage across the glass wall (barrier), V_c, are also shown in Fig.6.,

Electron density n_e in the central part which is almost equal to ion density N_i is nearly constant during the cycle. Thus electric field E in the central part changes proportionally with discharge current I. Even though electron density in the central part is high, the electric field there is low to produce intense ionization, while ionization mostly takes place in the space charge layers formed on the glass walls.

Fig.7<1> shows the distribution of E, n_e, N_i and $\nu_i n_e$ at t=5.5μs. At this phase, discharge current takes zero cross as shown in Fig.6. The most part of discharge voltage V_d is the voltage across the space charge layer formed on the right side glass wall. At t=6.6μs shown in Fig.7<2>, the discharge current is increasing while discharge voltage remains at negative polarity. This condition indicates that the space charge layer acts as a capacitor and its impedance is much larger than the impedance at the central part of the plasma at this phase. At t=7.7μs shown in Fig.7<3>, the discharge voltage polarity turns to inverse in accordance with the formation of space charge layer on the left side. At t=8.8μs shown in Fig.7<4>, the space charge on the left side becomes to grow rapidly, since electrons are enforced to move to right direction by electric field. At t=9.9μs shown in Fig.7<5>, intense ionization takes place in the space charge layer. Since electrons and ions are enormously produced in the space charge at the phase, the impedance of discharge plasma sharply decreases. Then discharge current becomes to increase abruptly.

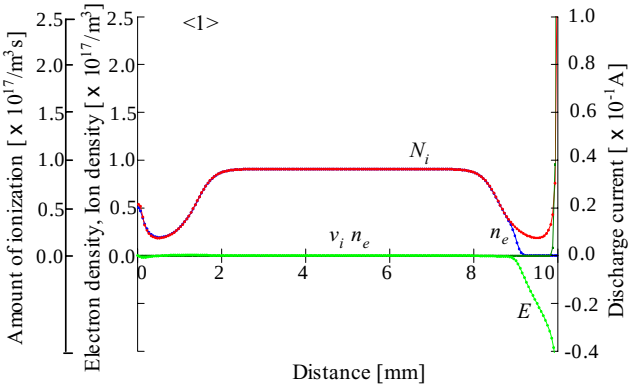

<1> t=5.5μs

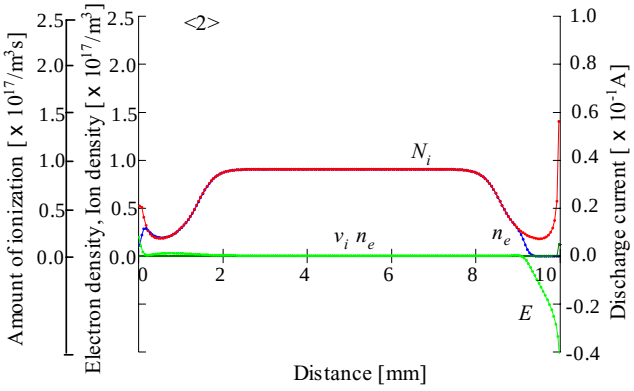

<2> t=6.6μs

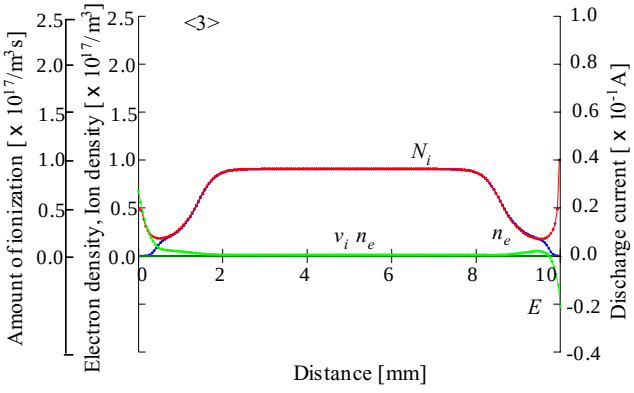

<3> t=7.7μs

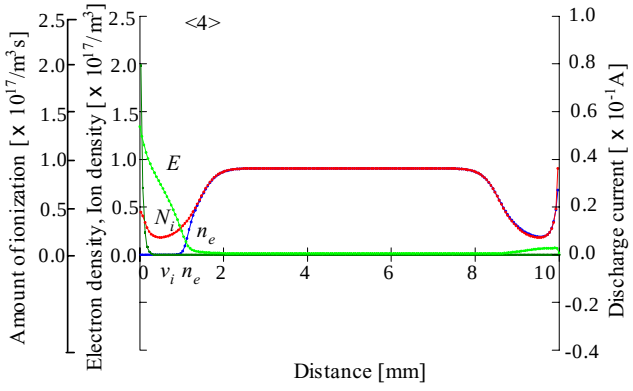

<4> t=8.8μs

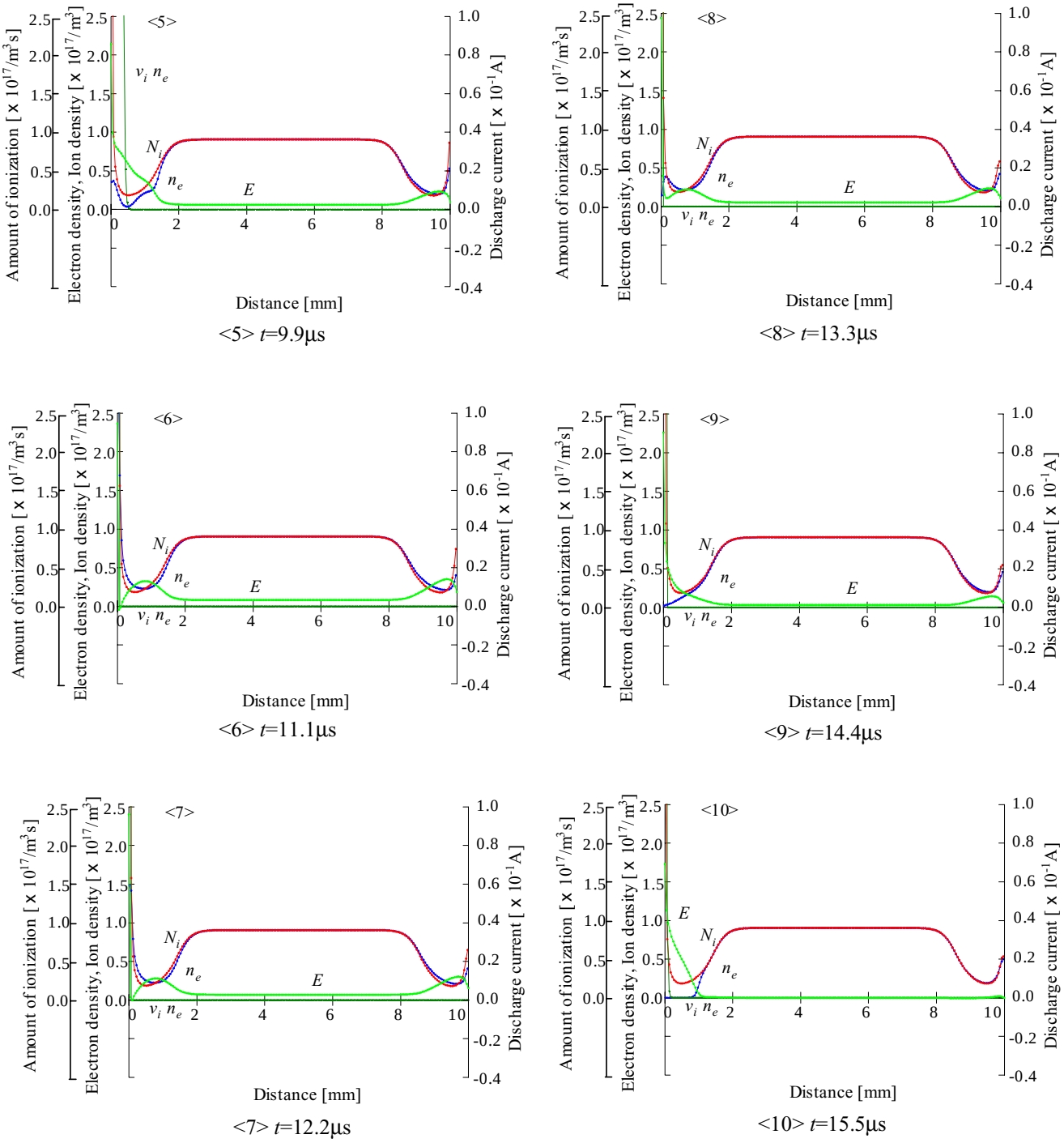

Fig.7 Distribution of electric field, E, electron density, n_e, ion density, N_i, and ionization amount per second, $\nu_i n_e$, at each phase designated in Fig.6.

At t=11.1μs shown in Fig.7<6>, the space charge on the left side is almost banished since the electron produced by the intense ionization neutralizes the space charge. Then the electric field in the space charge almost is vanished and intense ionization will cease. At t=15.5μs shown in Fig.7<10>, the space charge becomes to form again on the left side wall. Since electron density on the left side is nearly zero at this phase, intense ionization will not produce due to the lack of electron. However, if the applied voltage has absent period at zero cross phase, electron can diffuse into the space charge layer from near plasma region during the absent period. Then intense ionization might be produced when the applied voltage begins to increase

again. This mechanism may explain the phenomena shown in Fig.5.

5. Conclusion

Good agreements between the calculation by the model and the measurement are obtained for **DBD** lamp. The appropriate coefficient values for the model should be modified for each applied voltage waveform up to now. The reason is not clear yet. The distributions of electron density, ion density, electric field and ionization amount per second at each phase are calculated by the model. It is shown that ionization in **DBD** lamp mainly takes place in the space charge layer on the glass wall and it strongly depends on the applied voltage waveform.

6. References

[1] Y.Watanabe, *Proc. 15th Int. Symp. Plasma Chemistry*, Vol.IV, Orléans (2001) p.1649.

[2] Y.Watanabe, H.Kurimoto, N.Takizawa, *Proc. 10th Int. Symp. Science & Technology of Light Sources*, Toulouse (2004) p.271

[3] F.Massines, P.Ségur, et. al. *Proc. 16th Int. Symp. Plasma Chemistry*, Taormina (2003) p.774.

PRODUCTION OF HYDROGEN GAS AND CARBON BLACK BY DECOMPOSITION OF HYDROCARBON USING THERMAL PLASMA

Sun-Hee Park and Dong-Wha Park

Department of Chemical Engineering and RRC- ETTP(Regional Research center for Environmental Technology of Thermal Plasma) , Inha University, 253 Yonghyun-dong, Nam-gu, Incheon 402-751, Korea

Abstract

On the basis of the thermodynamic equilibrium calculations, the optimum condition of methane decomposition by thermal plasma was investigated. Methane was found to be decomposed mainly into hydrogen and solid carbon in the temperature range between 1000 and 2000 K. The amount of hydrogen produced increased with increasing the methane flow rate. Methane conversion was higher than 90% and decomposed carbon was solidified to amorphous carbon black. The particle size of carbon black was observed to be strongly dependent on methane flow rate.

Keywords

Thermal Plasma, Methane decomposition, Thermodynamic equilibrium calculations, Hydrogen, Carbon black

1. Introduction

Hydrogen has long been considered as an alternative, renewable, and clean energy source to replace fossil fuels [1]. A hydrogen energy based fuel economy is fast becoming interesting and it is certain that automobiles and electrical energy generation facilities will begin to use hydrogen in the very near future. Hydrogen has been produced mainly through steam reforming or partial oxidation of natural gas. Because the hydrogen produced by these processes inevitably contains CO and CO_2 beyond a tolerable range, the removal of CO is required. An alternative for hydrogen production is water electrolysis using renewable energy, which is not presently cost competitive. Methane, which is the main component of natural gas, is being used in a variety of fields. Direct thermal decomposition of methane can produce high purity of hydrogen without CO_2 and other pollutants (SOx, NOx, etc)[2], although it requires quite a high temperature (1500−2000℃) in order to obtain a reasonable hydrogen yield. Thermal plasmas have been suggested and considered as a promising heat and radical source for the direct decomposition of methane, because of its high temperature property and flexibility. Besides the high purity of hydrogen produced, carbon can be recovered as carbon black without emission of CO_2 [3]. When methane is heated to high temperature, the methane is decomposed or cracked into carbon and hydrogen:

$$CH_4 \rightarrow C + 2H_2 \qquad \triangle H^{o}_{298} = 76 \text{ kJ/mol}$$

Decomposition of methane is endothermic reaction and 38 kJ/mol H_2 produced is required, which is considerably lower than that for the steam reforming process (63 kJ/mol H_2). Compared with methane combustion, it can save 10% of energy required to operate the process [4-6].

Carbon produced by thermal decomposition can be either sequestered or used as a law material and it is much easier to be separated, handled, transported, and stored.

2. Experimental

Thermal plasma system has been developed for the decomposition of methane. The experimental system consists of D.C plasma torch, plasma reactor and filter assembly, as shown in Fig 1. All the experiments were carried out at atmospheric pressure with 6 kW electric powers. The feed gas (CH_4) flow rate was varied from 3 ～15 l/min depending on the operating conditions. All gaseous products were analyzed by gas chromatography equipped with TCD and molecular sieve 13X column.

Table 1 Experimental conditions

Plasma formation gas		Nitrogen(7~12 l/min)
Reforming source gas		Methane(99.9%, 3~15 l/min)
Plasma input power		6kW
Analysis	Gas composition	Gas chromatography (TCD, molecular 13X)
	Carbon black	SEM (S-4200, Hitachi Co.)
		BET (ASAP 2010, Micromeritics)
		PSA (LS230, COULTER Co.)

The specific surface areas of carbon produced were measured by the BET method (ASAP 2010, Micromeritics). Morphology and particle size of the formed carbon were investigated by the scanning electron microscopy (SEM: S-4200, Hitachi Co.) and particle size analyzer (PSA: LS230, COULTER Co.). The experimental conditions are summarized in Table 1.

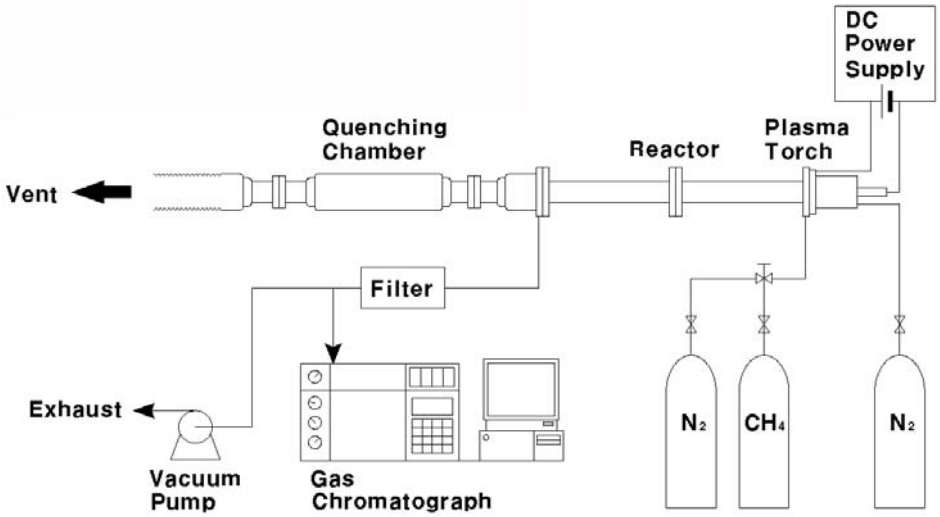

Fig. 1 Schematic diagram of experimental equipment

3. Results and Discussion

For comparison, thermodynamic equilibrium concentrations of reactant and products for both steam reforming and thermal decomposition were calculated using Fact sage (Version 5.3.1, GTT-TECHNOLOGIES) and the results are shown in Fig 2. This calculation was based on the Gibbs free energy minimization.

In the case of steam reforming, as expected, major products were H_2, CO and CO_2 at above 500℃ (Fig. 2-(a)). In thermal decomposition, major products were H_2 and solidified carbon at the similar temperature range, which can be easily separated from each other. These calculations imply that high purity of hydrogen can be easily achieved by thermal decomposition without separation process.

The feed gas (CH_4) and all gaseous products were analyzed by gas chromatography (GC) and the methane conversion and hydrogen yield were calculated from the area of each peak. The results with respect to methane flow rate are shown in Fig 3. The methane conversion was defined as:

$$\text{Decomposition of } CH_4\ (\%) = \frac{\text{In } CH_4 - \text{Out } CH_4}{\text{In } CH_4} \times 100$$

Where In CH_4: Amount of the methane gas before the plasma reaction

Out CH_4: Amount of the methane gas after the plasma reaction

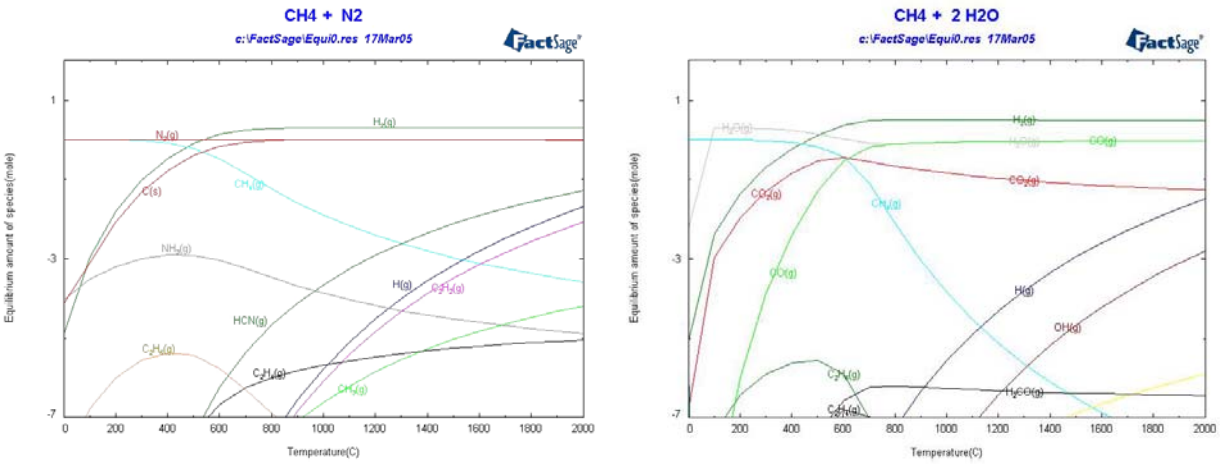

(a) (b)

Fig. 2 Calculations of equilibrium chemical composition
(a) in steam reforming process (b) in thermal decomposition of methane

As shown, methane conversion was very high (above 90%) all over the ranges investigated. At very high methane flow rate (when the flow rate was 15 l/min), the conversion slightly decreased, probably due to the decrease of residence time. Because the hydrogen selectivity is very high, as evidenced from Fig 2, the hydrogen yield was very close to the methane conversion all over the ranges. No other gaseous product was detected even by FT-IR analysis, which means all the products from methane decomposition by thermal plasma are hydrogen and solidified carbon.

The morphology of the carbon was characterized by SEM and particle size was determined by particle size analyzer. For comparison, carbon was taken from several parts, reactor, quencher, and filter. Fig. 4 shows SEM photographs of the carbon blacks formed at different locations of the process. As shown, all carbons from three places under the same flow rate of methane have the similar particle size, although they form aggregates rather than isolated form. For accurate determination of particle size, particle size analyzer was used and particle sizes of carbons synthesized are compared with commercially used carbon black (N700 and N800, KCB) in Table 2.

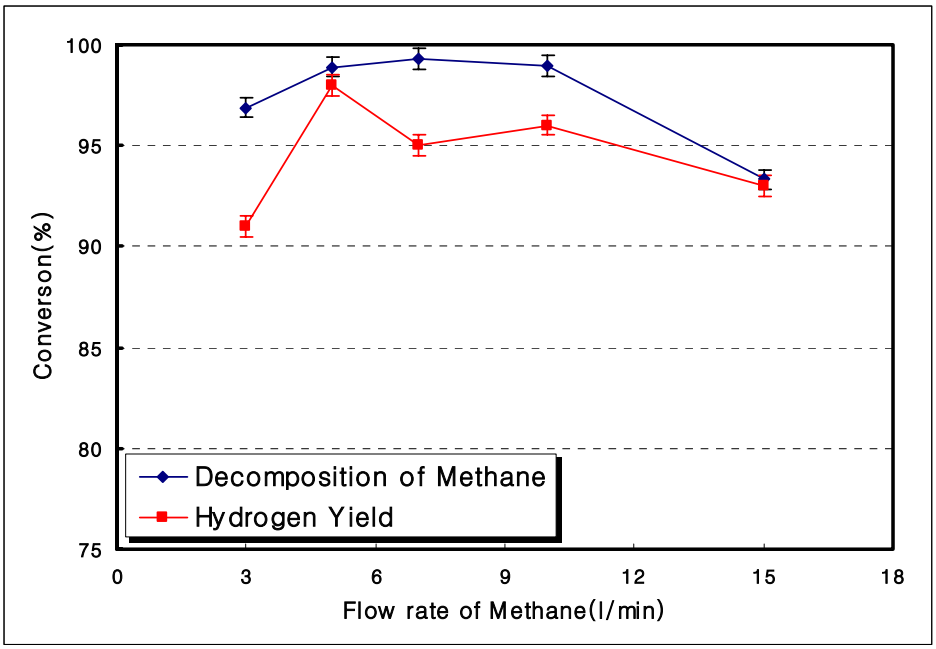

Fig. 3 Methane conversion and hydrogen yield as a function of methane flow rate

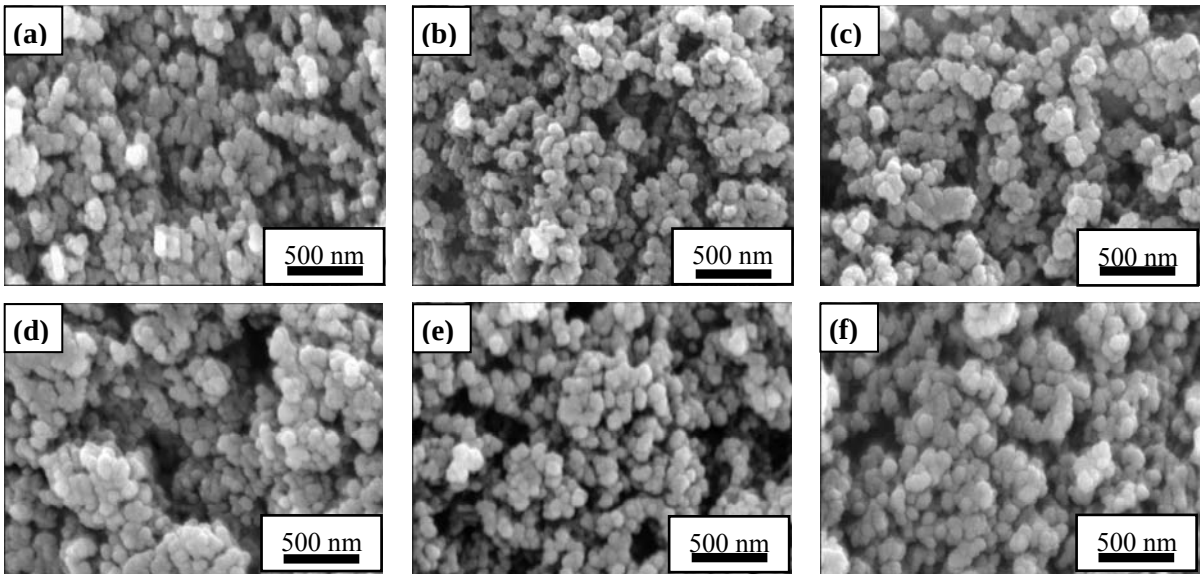

Fig. 4 SEM images of the carbon black
(a) Reactor part under CH_4 3 l/min (b) reactor part under CH_4 5 l/min (c) reactor part under CH_4 7 l/min
(d) Reactor part under CH_4 10 l/min (e) filtering part under CH_4 5 l/min (f) quenching chamber under CH_4 7 l/min

Table 2 Size of carbon black by particle size analyzer

Flow rate of methane (l/min)	N700(SRF)	N800(FT)	3	5	7	10
Particle diameter(nm)	61~100	101~200	84	109	113	116

N700(SRF) : Semi Reinforcing Furnace
N800(FT) : Medium Thermal

It was confirmed from particle size analysis that particle size of carbon increased with increase of methane flow rate, as also evidenced from SEM analysis. The particle size increase with methane flow rate can be explained by the increase of the number of carbon in the reactor for unit time with increase of flow rate. These results imply that particle size can be easily controlled by the methane flow rate. It varied from 80 to 120 nm. BET surface areas of carbon as a function of methane flow rate were compared with those of commercially used carbon blacks in Table 3. BET surface area ranges from 58 to 100 m^2 /g with methane flow rate and this decrease is due to the increase of particle size. Carbon black which has lower surface area (30~100 m^2 /g) can be used in rubber industry, while high surface area (> 700 m^2 /g) carbon black is like activated carbon.

Table 3 Nitrogen Surface Area of carbon blacks by CH_4 flow rate

	Corax® Hard Grade	Corax® Soft Grade	Exp.1	Exp.2	Exp.3	Exp.4
Feed gas (l/min)	Natural gas, Tar, Oil Pyrolysis	Natural gas, Tar, Oil Pyrolysis	CH_4 3	CH_4 5	CH_4 7	CH_4 10
Nitrogen Surface Area (m^2/g)	100±10	50±10	193	191	100	81

Corax® Hard Grade , Corax® Soft Grade : Used to rubber industry

4. Conclusion

Thermal plasma system has been developed and direct thermal decomposition of methane was carried out, which is an environmentally favorable process. For comparison, thermodynamic equilibrium concentrations were calculated by Fact sage software for both steam reforming and thermal decomposition. In case of thermal decomposition, high purity of hydrogen and solidified carbon can be achieved without any contaminant.

Methane conversion and hydrogen yield were investigated with respect to methane flow rate and both of the two was very high (above 90%) Particle size and surface area of synthesized carbon were strongly dependent on methane flow rate and it was observed that particle size decreased with increasing methane flow rate. Hydrogen produced from thermal plasma can be applied to fuel cell due to its high purity and carbon black can be applied for the synthesis of rubber industry.
It could be concluded that thermal plasma process for methane decomposition is very effective in terms of production of high purity of hydrogen as well as synthesis of carbon black.

5. Acknowledgment
The authors gratefully acknowledge the financial support of the Ministry of Commerce, Industry and Energy RRC- ETTP (Regional Research center for Environmental Technology of Thermal Plasma).

References

[1] S.Takenaka, S.Kobayashi, H.Ogihara, K.Otsuka - J. Catal. **217**, 468 (2003).
[2] N.Z. Muradov - Int. J. Hydrogen. Energy. **18**, 211 (1993).
[3] L. Fulcheri, Y. Schwob - Int. J. Hydrogen. Energy. **20**, 197 (1995).
[4] N. Muradov - Int. J. Hydrogen. Energy. **26**, 166 (2001).
[5] M. Steinberg - Int. J. Hydrogen. Energy **24**, 771 (1999).
[6] E. Shpilrain, V. Shterenberg, V. Zaichenko - Int. J. Hydrogen. Energy. **24**, 613 (1999).
[7] Z.W. Liu, K.W. Jun, H.S. Roh, S.E. Park - J. Power. Sources **111**, 283-287 (2002).

Carbon-Copper-Sulfide Film by Cooperation Process of Plasma CVD and Sputtering

Masanori Mizuno, Shinya Kato, and Shinzo Morita

Department of Electronic Information System, School of Engineering, Nagoya University
Furo-cho, Chikusa-ku, Nagoya 464-8603 JAPAN
morita@nuee.nagoya-u.ac.jp

Abstract

Cu dispersed C-S dielectric thin film was fabricated by simultaneous process of plasma CVD of CH_4, SF_6, and Ar mixture gas, and sputtering of Cu plate discharge electrode. The C-S film was supposed to be formed by HF dissociation reaction in the plasma CVD process. Effect of substrate holder temperature on the deposition was studied. With increasing the temperature, sulfur content was decreased and oxygen content was very large for all samples. At 400℃, the sulfur content became negligibly small. Atomically distribution of Cu in the dielectrics was expected from no X-ray diffraction peak for the Cu dispersed C-S dielectric thin film. The large oxygen content was referred to oxidization of atomically dispersed Cu atom in the film in the air.

Keywords: plasma CVD, sputtering, HF dissociation, C-Cu-S, X-ray diffraction

1. Introduction

Metal containing dielectric is studying variously as an optical memory [1], large refractive index material [2], large non-linear electro-optic effect [3, 4] and semi-conductive film [5]. For the metal containing dielectric film formation, there are wet and dry processes [4, 6]. For the dry process, co-evaporation method of metal and dielectric and co-operation method of plasma CVD and sputtering.

We are forming gold (Au) atom containing C (carbon)-S (sulfur) film by co-operation process with plasma CVD of CH_4, SF_6, and Ar mixture gas and sputtering of discharge electrode with gold plate on graphite plate electrode [2,5]. The gold atom was observed to be distributed atomically in the C-S dielectric film caused on chemical bond between gold atom and sulfur atom [7]. Therefore the co-operation method of plasma CVD and sputtering is unique and useful method, because the large refractive index more than 3.5 and other interesting properties were realized [2].

However there is a question that other metal can also be distributed uniformly in the C-S dielectrics like as the gold atom.

In the plasma CVD that used the CH_4-SF_6-Ar mixed gas, chemical reaction between C and S atom was realized by dissociating H and F atom from CH_4 and SF_6 and by forming HF molecule if the stoichiometrical condition is maintained [5]. Under the self-bias condition, the sputtering of metal atom from upper metal plate discharge electrode is performed, and it mixes into the C-S dielectrics.

Pyrite-type CuS_2 is known to show superconductivity with T_S = 1.5 K, which is formed by synthesis under high pressure [8-11]. For the Cu dispersed C-S (C-Cu-S) by plasma processes, it is interesting to know the chemistry on C-Cu-S synthesis. In this work, the effect of substrate temperature was studied. In order to study the effect of substrate holder temperature on the deposition, a new substrate holder was prepared which can heat the substrate up to 1000℃.

2. Experiments

The reactor for the co-operation process of plasma CVD and sputtering are shown in Fig. 1, which was used for our C-Au-S film formation. However the reactor was changed like as Fig. 2 for the study of substrate temperature effect on the deposition. But the gap between the parallel plate electrodes was extended from 15 mm to 22 mm in order to insert the substrate heating system. The metal target for the sputtering was a Cu plate electrode (200 mm diameter), which has numerous small holes in order to introduce the reaction gases in the discharge plasma space between the parallel plate electrodes.

The deposition was performed at a constant discharge power of 100 W for 30 min discharge period at 13.56 MHz. The substrate temperature was controlled to be 66 (no heating), 200, 300 and 400℃. For the characterization of the films, ESCA spectrum and X-ray diffraction pattern measurement were performed.

3. Results

When the gas flow rates of CH_4, SF_6 and Ar were 5, 3, and 20 sccm respectively at 0.07 Torr, the atomic composition was measured as shown in Table 1 by ESCA measurement. The result was obtained after Ar plasma sputtering of the surface layer. By the Ar plasma sputtering for 3 min, the surface atomic layer was supposed to be taken off. Fluorine and oxygen atom content were negligibly small. Copper, carbon, and sulfur content were almost same as 30 %.

For the substrate temperature effect on the deposition, the deposition was performed with using the reactor as shown in Fig. 2. The flow rate of CH_4, SF_6 and Ar were 10, 6, and 10 sccm, respectively. The discharge power and the pressure were set as 100 W and 0.07 Torr, respectively. The atomic composition of the film was measured as shown in Table 2, which surfaces were not cleaned by Ar sputtering.

Fluorine atom content was negligibly small for all samples. This fact means that the stoichiometrical condition was maintained during the deposition. With increasing the substrate temperature, sulfur atom content was decreased. For all samples oxygen atom content was significantly large. The sulfur atom content was not observed at 400℃. Oxygen was not mixed with the reaction gas, whereas the oxygen content was referred to oxidization of the film while the sample was keeping in the air.

The x-ray diffraction pattern of the film was measured as shown in Fig. 3. The observed single peak was referred Si wafer. Whereas, the Cu dispersed C-S dielectric film did not show any X-ray diffraction peak. This fact means Cu is expected to be distributed uniformly in the film same as the gold atom in the C-Au-S film.

It is concluded that the large oxygen content in the film will be referred the atomically distributed Cu in the film because the atomic Cu will be oxidized easily in the air.

The sulfur content was decreased with substrate temperature and the sulfur was disappear from the film formed at 400℃. This fact means that plasma process has some possibility to synthesize sulfide compounds in the evacuated system. However substrate temperature is negatively affected on the sulfide.

These experimental results are important, because the proposed process has a possibility to realize atomically distribution of metal atom in the dielectrics.

4. Conclusion

With using the co-operation process of plasma CVD of CH_4, SF_6, and Ar mixture gas and sputtering of copper discharge electrode, Cu dispersed C-S dielectrics film was formed. The Cu atom was expected to distribute uniformly in the film because the X-ray diffraction peak on the Cu cluster was not observed.

The sulfur atom content was decreased with increasing the substrate temperature and the sulfur was not observed at 400℃.

Acknowledgements

Part of this work was performed at the Center of Co-operation Research in Advanced Science and Technology, Nagoya University.

References

[1] Yoshihiro Asano, Hiroki Yamazaki, and Akira Morinaka, Jpn. J. Appl. Phys., Part 1 **22**, (1983) 480.

[2] Mohammad Abul Kashem, Masaki Matsushita and Shinzo Morita, Jpn. J. Appl. Phys., **43**, 3A (2004) L.355.

[3] F. Hache, D. Ricard, and C. Flytzanis, J. Opt. Soc. Am. **B3** (1986) 1647.

[4] Y. Hamanaka, A. Nakamura, S. Omi, N. Del Fatti, F. Vallee, and C. Flytzanis, Appl. Phys. Lett., **75**, (1999) 1712.

[5] Kazuaki Omura and Shinzo Morita, Jpn. J. Appl. Phys. **43**, 5B (2004) L.689.

[6] R. d'Agostino, Ed.; *Plasma Deposition, Treatment, and Etching of Polymers*, Academic Press, Boston, (1990).

[7] Md. Abul Kashem and Shinzo Morita, Phys. Rev. **B69** (2004) 193406.

[8] T.A. Bitter, C.T. Prewitt, J.L. Gillson, P.E. Bierstedt, R.B. Flippen, and H.S. Young, Solid State Commun., **4** (1966) 533.

[9] T.A. Bitter, R.J. Bouchard, W.H. Cloud, P.C. Donohue, and W.J. Siemons, Inorg. Chem., **7** (1968) 2208.

[10] R.A. Munson, W. Desorbo, and J.S. Kouvel, J. Chem. Phys. 47 (1967) 1769.

[11] M. Kontani, T. Tutui, T. Moriwaka and T. Mizukoshi, Physica B, 284-288 (2000) 675-676.

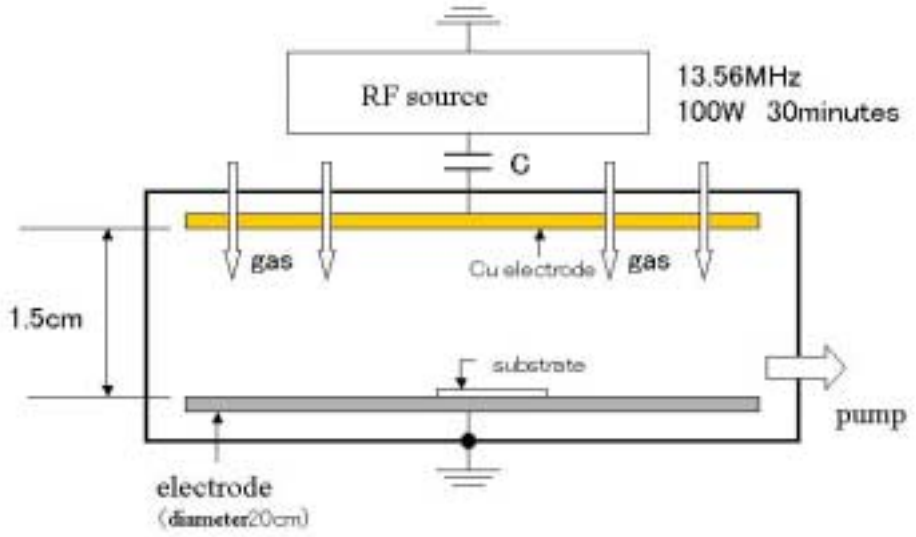

Fig. 1. Original reactor for plasma CVD and sputtering.

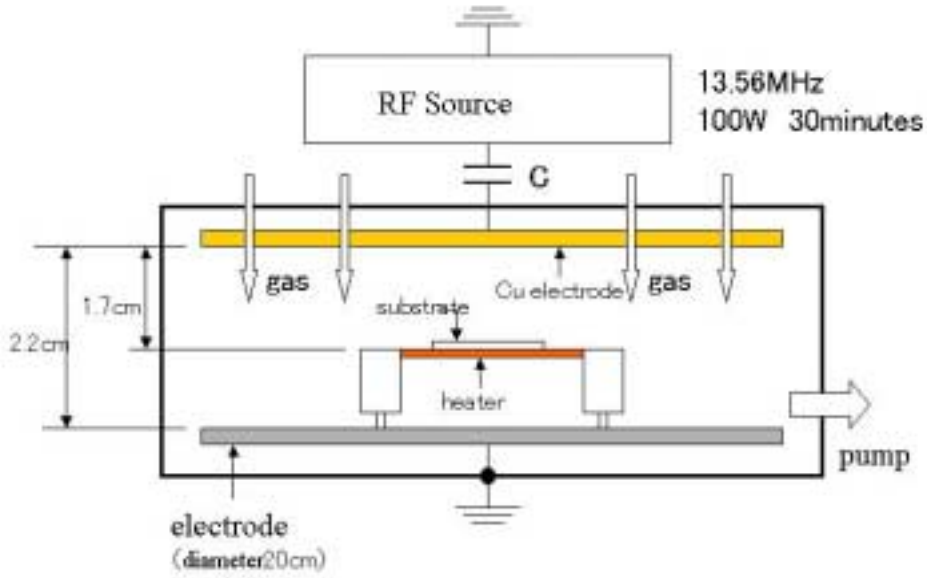

Fig. 2. Modified reactor for the plasma CVD and sputtering

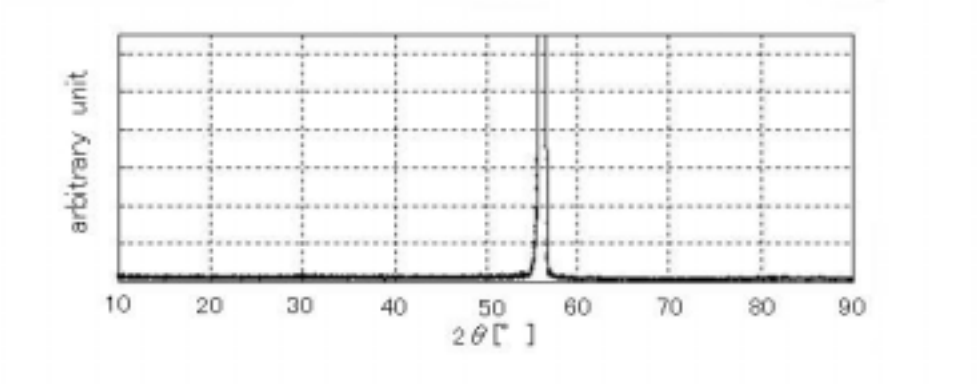

Fig. 3. X-ray diffraction pattern of Cu dispersed C-S dielectric Thin Film

Table 1：Atomic composition of the film formed at the condition:
CH_4-：5 sccm ,SF_6：3 sccm, Ar：20 sccm, gas pressure 0.07Torr

Cu	C	S	O	F
35.3%	34.3%	29.2%	1.2%	0.0%

Table 2：Effect of substrate temperature on the atomic composition of film
CH_4-：10 sccm ,SF_6：6 sccm, Ar：10 sccm, gas pressure 0.07Torr

Temperature	Cu	C	S	O	F
65	9.55	64.35	13.6	12.55	0
200	17.25	48.9	14.35	19.5	0
300	24.75	35	3.2	33.8	3.25
400	22.1	44.3	0	33.6	0

Transferred-arc in flight evaporation of Al for the production of AlN nanosize powder

O.W. Bender, A.C. Doring, H. Toku and A.C. da Cruz

Institute for Technological Research (IPT), São Paulo- SP, Brazil

Abstract

A thermal plasma synthesis reactor aimed at nanosize metal and ceramics synthesis has been studied at our lab at IPT in the past years. Applied to the vapour phase synthesis of aluminum nitride (AlN), the results presently reported refer to the study of gas flow at nozzle and a sequence of modifications introduced in the anode assembly intended to increase energy and productivity efficiencies.

1. Introduction

Thermal plasma vapor-phase synthesis of ceramics of many different compositions has been demonstrated on the lab scale in the past years. Although thermal plasmas present many important features needed in this field (e.g. suitability to carrying out high temperature reactions, promotion of fast quenching which invariably conducts to the production of finely dispersed particles, and provision of easy means to control process atmosphere, all of which are of the interest of production of high purity materials), scaling up of plasma reactors still meets major problems. In particular, the availability of gas phase metal precursors is a major technical barrier. Although the use of metal halides is possible in most cases, these are expensive and one has to deal with the inconvenient production of undesirable contaminants and non-environment-friendly by-products. Transferred-arc evaporation of pure metal precursors is an interesting alternative which has been studied [1].

The work we carry out is focused on the development of a plasma reactor concept for the vapor-phase synthesis of fine particles, of both pure metal and ceramic compositions. For most of the development work, aluminum nitride (AlN) has been adopted as a study case.

Previous work on transferred-arc evaporation of aluminum (Al) from a molten anode [2] showed that only about 7% of the aluminum vapor (Al(v)) produced (anode mass balance) came out the evaporation chamber (sampling probe measurement). The remaining 97% condensed on the plasma chamber walls. Also it was observed that because of the anode high temperatures, reaction between metal and anode material was a major practical problem to be solved.

With the main objective to produce greater amounts of final product powder, in order to overcome the difficulties pointed out, a modification of the initially proposed reactor concept was introduced [3]. Instead of using a molten precursor metal anode from which its vapor phase is produced, the material is introduced in the form of a powder directly into the arc at the cathode assembly. In the electrical configuration, an annular anode is used to transfer the arc. Previous report on this work also includes the theoretical study of particles nucleation and growth in the reaction section [4-6].

The presently reported results refer to a study of gas flow at nozzle and a sequence of modifications introduced in the anode assembly intended to increase energy and productivity efficiencies.

2. Experimental

Fig. 1(a) shows a schematic drawing of the experimental setup. A general description of the whole assembly was given elsewhere [3]. Fig. 1(b) physically shows the arc circuit, which includes a multi-gas and powder injection cathode assembly and a hollow anode.

Compared to the previously reported experiments [3], a main modification to be noted is the simplification of reactor assembly introduced by mounting the reaction section right below the plasma chamber (intermediate hot gas chamber removed).

Metal vapor is produced in the upper section, under inert (argon) atmosphere by injecting atomized Al powder into the arc [Fig. 1(b)], through the cathode assembly, using a SULTZER-METCO Dual Powder Feeder 4MP 800. Vapor phase reaction takes place at the outlet of the evaporation section as the hot metal vapor carrier gas is cooled by NH_3/N_2 gas jets. Powder is collected at the reactor walls, heat exchanger, and on a bag house

filter. Pressure drop in the filter is compensated by a vacuum pump in order to control reactor internal pressure.

Commercial atomized Al powder (Höganäs MG-300) was used as metal precursor. Tab. I shows the general plasma operating conditions used. Three different anode assemblies were tested to verify the effect of increasing degree of anode insulation (referred as Steps A, B, and C) on reactor performance, evaluated in terms of Al conversion to AlN: A) a single water cooled cooper ring, 100 mm i.d. (Exp. #32 - #38); B) a graphite tube, 80 mm i.d. x 115 mm long, supported by a water cooled cooper ring (Exp. #39 and #40); and C) a graphite tube, 90 mm i.d. x 120 mm long (no cooling water, Exp. #41).

After each experiment, the reactor was carefully cleaned and all the powder produced and condensates collected for the purpose of mass balance. The powder collected in the bag house filter was characterized for composition using x-ray diffraction and for average particle size using BET specific surface area (SSA) and transmission electron microscopy (TEM). Carbon content was analyzed by direct combustion using infrared detection.

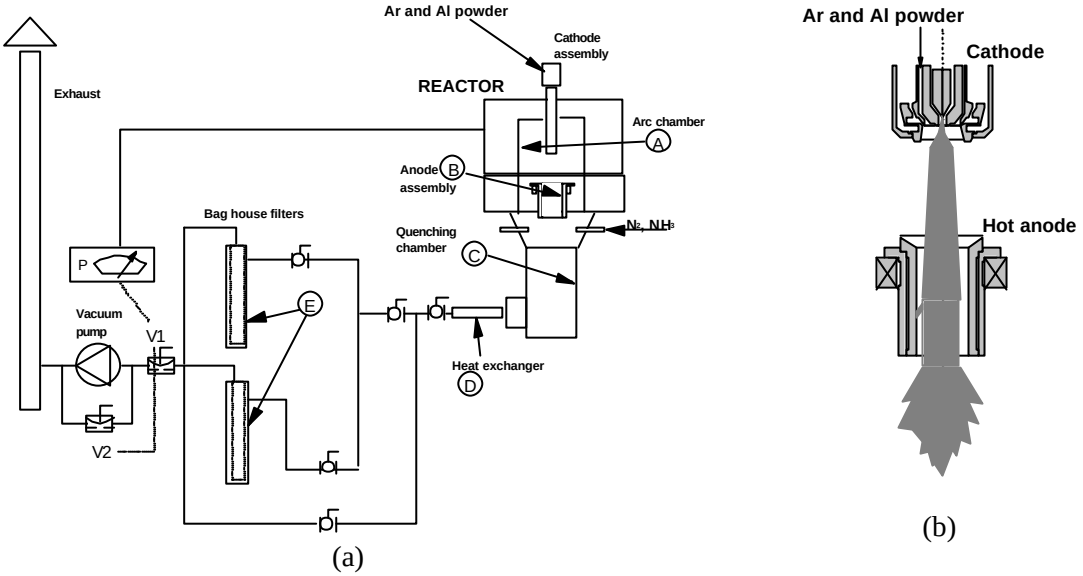

Fig. 1 – Schematic diagram of the synthesis reactor: a) hot anode assembly with bag house powder collection; letters indicate powder collection points for mass balance purpose; and b) illustration of the transferred-arc, showing the cathode and anode assemblies.

Tab. I – General plasma operating conditions used for reported experiments.

Gas flow rates	
Cathode gas (Q_1)	33 lpm
Powder carrier gas (Q_2)	33 lpm
Sheath gas (Q_3)	33 lpm
Arc conditions	
Voltage	100 ~ 160 V
Current	200 ~300 A
Arc length[1)]	10 cm
Total cooling gas flow rate (Ar/15%NH_3)	115 lpm

1) Arc length referred to the top of anode.

3. Results and discussion

Fig. 2 shows nozzle details, computational and experimental results for the near nozzle and evaporation chamber gas flow pattern. Given the nozzle design [Fig. 2(a)], the theoretical study focused on determining the most appropriate operating conditions in order to avoid as much as possible gas recirculation in the

vicinity of the water cooled nozzle. In practice, gas recirculation brings metal vapor laden hot gas into contact with cold, water cooled walls, which ultimately results in metal condensation in this region. A strong recirculation will result in the blockage of powder injection ports and interruption of metal powder supply.
The schematic drawing of Fig. 2(a) indicates the different gas injection ports: central hole (Q1); annular aperture around the cathode through which powder is injected using carrier gas (Q2); and a second annular aperture forming a gas sheath around the arc (Q3). The computational study using CFX shows the velocity vectors inside the nozzle [Fig. 2(b)].

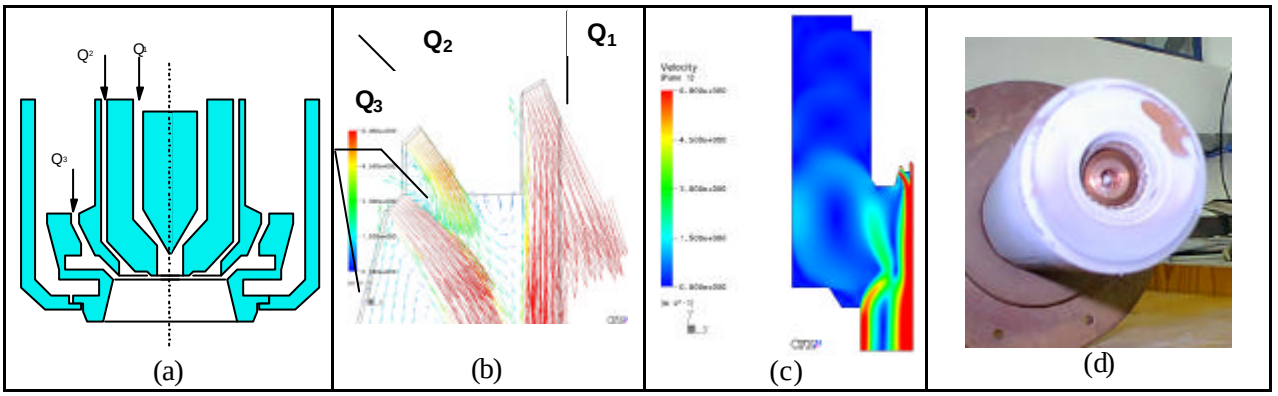

Fig. 2 – Schematics of the gas injection ports in the nozzle (a); velocity fields in the nozzle vicinity (b); and in the evaporation chamber (c); photograph of nozzle after experiment (d). Modeling results refer to: Q1 = 30 lpm (17.7 m/s); Q2 = 40 lpm (5.2 m/s); and Q3 = 30 lpm (11.8 m/s).

Tab. II – Operating data, mass balance considering the material collected in different regions of reactor according to Fig. 1(a), and powder specific surface area (SSA) of AlN powder produced.

Operating data and powder collecting place		Experiment Nr.						
		#32	#33	#37	#38	#39	#40	#41
Operating time - ?t (min)		105	76	90	114	60	42	21
Al powder feed rate (g/min)		3.5	5.8	2	3	3.7	4.9	5.4
Mass (%)	A (Al)	0.0	3.6	0.0	0.0	0.0	0.0	0.0
	B (Al)	76.4	59.9	76.8	55.0	38.1	7.3	57.5
	C (AlN)	25.3	22.0	22.1	44.4	43.5	18.5	26.5
	D (AlN)	8.4	8.6	9.4	19.5	67.3	22.4	5.3
	E (AlN)	5.2	4.1	6.6	7.1	6.7	5.4	7.1
Al converted (%)		25.4	22.8	25.1	47.0	77.4	30.5	25.6
xAl(plasma chamber) [1)]		0.031	0.050	0.018	0.027	0.033	0.043	0.047
xAl(reaction chamber) [2)]		0.008	0.012	0.005	0.013	0.025	0.013	0.012

SSA (BET) (m^2/g)	68	82	90	75	65	64	110
Average particle size BET (nm)	27	22	20	24	28	29	17

1) xAl(plasma chamber)=gas mole fraction inside arc chamber, before condensation at anode;
2) xAl(reaction chamber)=gas mole fraction that enters reaction chamber;
3) Material collected above reaction chamber (A and B): predominantly condensed Al; reaction chamber and below: predominantly AlN (C, D, and E);
4) BET analysis refers to the powder collectedin the bag house (E).

Different flow conditions where simulated. Only the one with flow rates closer to the ones adopted for all the experiments reported is shown [Fig. 2(b)]. At the vicinity of nozzle cold wall the model indicates little gas recirculation. The cold flow pattern inside the plasma chamber indicates a strong central flow, directed

towards the tubular anode; and a lower intensity recirculation inside the chamber that brings hot gas into contact with the external wall of the cathode assembly [Fig. 2(c)]. Although plasma flow and temperature effects were neglected, the visual observation after the experiments indicates that little material deposition is observed inside the nozzle, and some deposition is verified on the external wall of the cathode assembly. These observations demonstrate a good agreement between modeling predicted results and practice [Fig. 2(d)], at about same gas flow rates. For the stated analysis purpose, the cold reactor simplification is considered to underestimate the potential of the present nozzle design (the results seen from the theoretical analysis are to the safety side). The plasma arc will in principle enhance both the flow outward the nozzle and in the plasma chamber due to cathode jet and gas expansion effects.

Data on operating variables for each experiment, the resulting mass balance considering the material collected in different regions of reactor according to Fig. 1(a), the evaluation of amount of converted Al, and powder specific surface area (SSA) of AlN powder produced are all shown in Tab. II. The operating time shown in this table refers only to the period during which AlN production is carried out. The total experiment time includes up to 1 h operation without powder and NH_3 injection, until steady state condition monitored by gas and water temperature measurement is reached. Converted aluminum percentage was determined as the ratio between total AlN collected and the total amount of Al feed into the reactor. The aluminum mole fraction (xAl) in the vapor phase shown was determined for the plasma chamber (before anode condensation), and reaction chamber (aluminum which in fact is brought to react), considering the total amount of gas fed through the cathode assembly and, respectively, the total amount of Al introduced and amount of AlN collected. The Al powder feed rate shown is the average figure determined from the given operating time and mass balance of aluminum in the powder feeder vessel before and after each experiment. The feed rates thus determined is in very good agreement with the value adjusted and made constant during each experiment.

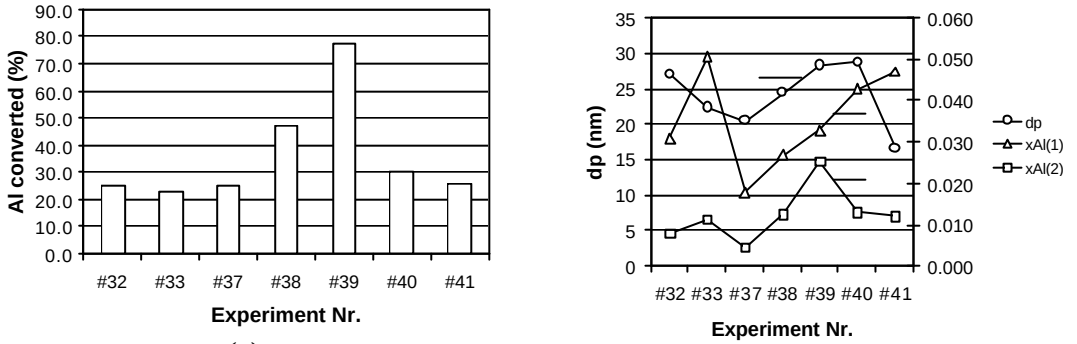

(a) (b)

Fig. 3 – a) amount of aluminum converted in aluminum nitride for each of the experiments considered; b) specific surface area average particle size and aluminum mole fraction in the plasma [xAl(1)] and reaction [xAl(2)] chambers.

The bar plot shown in Fig. 3(a) indicates that Al conversion first increased with a more intense anode insulation (increase of anode temperature), from Step A to B, but decreased when the anode was even better insulated (from Step B to C). This decrease of conversion might be possibly result from intensified reaction between anode material and metal vapor as a consequence of a higher anode temperature. Average BET particle size and metal vapor concentrations of each experiment are shown in Fig. 3(b). For the set of experiments carried out with the Step A anode preparation, it is observed that the changes of Al concentration inside the plasma chamber [a direct consequence of the range of powder feeding ratio (2 to 5.8 g/min) tested] reflects on the Al(v) concentration determined for the reaction section. Because of a more intense Al(v) condensation on the anode, and eventually in the plasma chamber walls with greater feeding rates, a narrower correspondent range of change is verified in case of the reaction chamber Al mole fraction. Also, because of the interdependence of effects of both temperature and metal vapor concentration on supersaturation, and consequently on the definition of particle diameter, the data plotted in Fig. 3(b) do not allow any dear conclusion on this aspect.

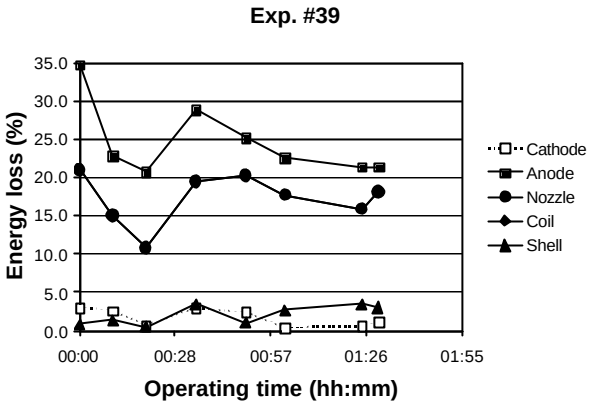

Fig. 4 - Energy loss to each of the water cooled parts of reactor (Exp. #39 shown as a typical case), expressed in percentage of total plasma arc power.

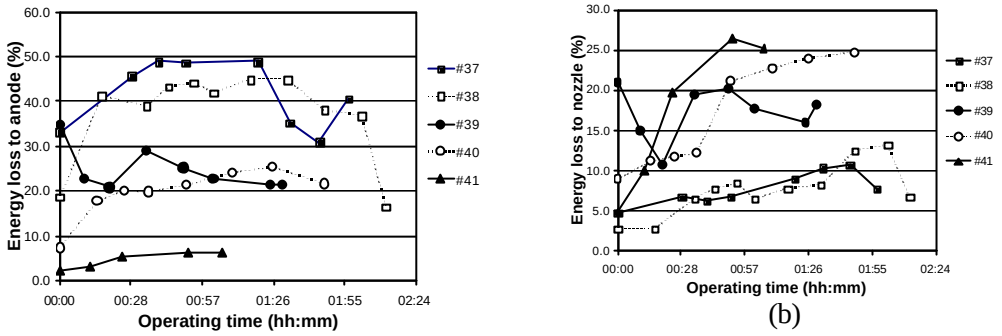

Fig. 5 – Energy losses for different degrees of anode insulation, shown as a function of operating time; Exps. #37 and #38 refer to insulation Step A; Exp. #39 and #40 to Step B, and Exp. #41 to Step C: (a) energy loss to anode; and (b) energy loss to the nozzle assembly.

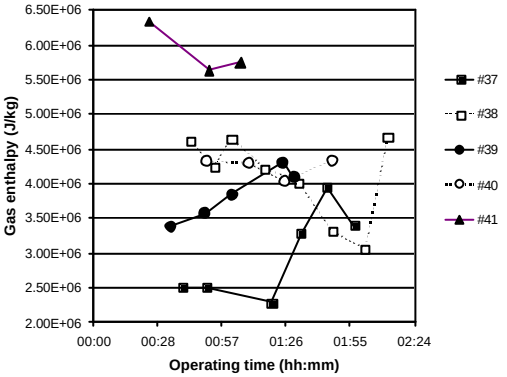

Fig. 6 – Gás enthalpy at the entrance of reaction section, evaluated base on calorimetric measurements.

As a typical example, heat losses determined based on calorimetric measurements for Exp. #39 are shown in Fig. 4. The most import losses are verified in the anode and nozzle assemblies. Considering experiments under different anode insulation levels as discussed before, energy losses to anode and nozzle assemblies are shown in Fig. 5 (a) and (b), respectively. Because of the progressive better insulation, energy loss to anode decreases from 30%-50% in Step A to 20%-30% and under 10%, Step B and C, respectively. Because a hotter anode results in more radiation loss, its heat losses to the water cooled nozzle assembly increases going inversely from Step C to Step A. The gas enthalpy evaluation based on calorimetric measurement is shown in Fig. 6.

A TEM micrograph and a x-ray diffraction pattern from a typical AlN produced is shown in Fig. 7. Samples of powders collected at the filter for Exp. #39 e #41 were analyzed for carbon: 0.38±0.1 %C (#39) and 0.61±0.02 %C (#41). Compared with Exp. #38, the greater C content observed for Exp. #41 possibly results from a greater amount of C sublimation.

4. Conclusion

A study including theoretical and experimental work focused on the development of a plasma reactor concept for the vapor-phase synthesis of fine particles was carried out. The theoretical study aimed to predict gas flow inside the cathode assembly nozzle in order to identify conditions which would led to metal vapor condensation and consequent blockage of gas and metal injection ports well agreed with experiment. Although plasma flow and temperature effects were neglected, the visual observation after the experiments indicates that little material deposition is observed inside the nozzle, and some deposition is verified on the external wall of the cathode assembly.

For three different anode cooling conditions tested, Al conversion was observed to reach a maximum with the increase of anode insulation. The decrease in conversion with higher anode insulation might be a possible consequence of increased reaction between anode material and the metal present in the gas phase resulting from a higher anode temperature.

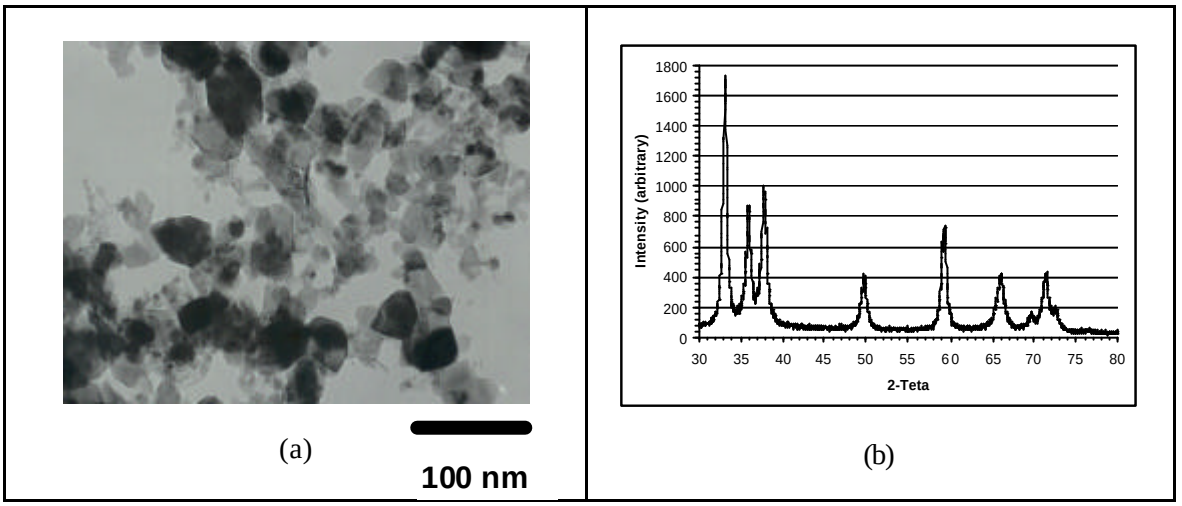

Fig. 7 – TEM micrograph (a) and x-ray diffraction pattern (b) of one of the AlN powder produced.

Acknowledgements

The financial support of the Fundação de Amparo à Pesquisa do Estado de São Paulo – FAPESP, Brazil (Process Nr. 98/14864-5) to the present research is gratefully acknowledged.

References

[1] Munz, R.J., Da Cruz, A.C., e Addona, T., Applications of transferred arcs to the production of nanoparticles, Pure and Appl. Chem., 71(20), 2000.

[2] Da Cruz, Experimental and Modelling study of the plasma vapour-phase synthesis of ultrafine aluminum nitride powders, PhD Thesis, McGill University, 1997.

[3] Da Cruz, A.C., Bender, O.W. , Thomaz, O., Yoshimura, H.N., and Kiyohara, P.K., ISPC 15, Orléans, pp. 2723-2728, 2001.

[4] Da Cruz, A.C. and Munz, R.J., Aerosol Science and Technology, 34:499-511 (2001).

[5] Da Cruz, A.C., Bender, O.W., Thomaz, O., Yoshimura, H.N., and Kiyohara, P.K., ISPC 15, Orléans, pp. 2729-2734 (2001).

[6] Da Cruz, A.C. and Munz, R.J., Inter. Congress for Particle Technology (PARTEC), Nuremberg, P126 (2004).

Effect of ammonia plasma on the structure and properties of poly(ethylene terephthalate) track membranes

S. Dmitriev[1], L. Kravets[1], A. Lazea[2], G. Dinescu[2]

[1]*Joint Institute for Nuclear Research, Flerov Laboratory of Nuclear Reactions, Dubna, Russia*
[2]*National Institute for Lasers, Plasma and Radiation Physics, Bucharest, Romania*

Abstract

Poly(ethylene terephthalate) track membranes were exposed to radiofrequency plasma generated in ammonia gas for different power and pressure values. The influence of the plasma treatment conditions on the surface topography, thickness, chemical composition, contact angle is studied. The transport properties (water permeability) of the plasma modified track membranes are presented and discussed in relation with the mechanisms affecting the chemical composition and structure of the membranes.

Keywords: Poly(ethylene terephthalate) track membrane, Plasma treatment of polymers, Water permeability;

1. Introduction

Among the technologies for separation of complex mixtures of liquids and gases that based on filtration through membranes are the most promising. The nuclear track membranes, obtained by irradiation of polymer films with high-energy ions and subsequent chemical etching of ions trajectories, play a key role in the separation processes [1]. Owing to certain properties, such as small thickness and high uniformity of pores, track membranes are responsible for their wide use in medicine, biotechnology, microelectronics and other engineering areas. The manufacturing technology of track membranes has recently developed in a new direction, the surface modification of membranes: the change in composition and structure of the surface layer, aiming to improve the filtration properties. There are various methods for surface modification of polymer materials by physical and chemical means. Plasma treatment is superior to other methods, as it allows a wide variety of compounds to be used. The new properties of the membranes produced in this way depend mainly on the chemical compound used. Related to that, a number of studies published recently were devoted to understanding of the plasma discharge effects on polymeric membranes [2-4], including the nuclear track ones [5-10]. These previous studies showed that the low temperature plasma of both non-polymerizing and polymerizing gases in various discharge conditions lead to modification of the membrane surface layer accompanied by the change of a number of properties, namely the adsorption, selectivity and the transport ones. Therefore the studying of these processes which depend on the plasma discharge parameters and the composition of the plasma-forming gas, aiming to the membrane properties improvement, is dictated by practical and scientific challenges.

In this paper the properties of poly(ethylene terephthalate) track membranes (PET TM) exposed to ammonia plasma were investigated. The influence of plasma treatment the conditions on the basic characteristics of the membranes, namely surface topography, chemical composition, thickness, water permeability, is reported and discussed.

2. Experimental

PET TM obtained by a standard procedure [1] with the thickness of 9.5 μm and the effective pores diameter of 0.220 μm (pore density $2 \cdot 10^8$ cm^{-2}) were under study. The plasma treatments were performed in a discharge chamber with two plan parallel electrodes, the upper electrode being RF powered (13.56 MHz, max. 500 W) and the lower being grounded. The electrodes were situated in a grounded stainless steel chamber (60 cm diameter, 30 cm height) provided with quartz windows allowing visual and spectral inspection. The gas (ammonia) was admitted through the perforated RF electrode (acting as a gas shower) via a mass flow controller. A mechanical pump, insuring a background pressure of 10^{-2} torr, pumped down the system. Membrane samples shaped as disks with area of 5.6 cm^2 were positioned on the grounded electrode, at 3 cm distance from the powered electrode. The schematic view of the experimental set-up can be found in reference [11]. The discharge parameters (gas

pressure in the vacuum chamber, discharge power) and the duration of the plasma action were varied. Only one side of the membrane was exposed to plasma.

The characteristics of the initial and modified membranes were determined through a series of complementary methods described in more detail in [8, 9]. The topography of the membranes was characterized by Atomic Force Microscopy (AFM, Q-Scope^{TM} Nomad^{TM}). The membranes thickness was determined with an electronic meter for thickness measurements (Unit Tesa, Austria). The contact angle was measured by the goniometric method. The ESCA spectra were recorded with the spectrometer Riber SIA-100 with MAC-2 analyzer (MgK_a, 100 W, 15 kV, 20 mA). The position of peaks (the binding energy values) was calibrated against the C_{1s} standard peak (284.6 eV). The permeability of water solutions was measured with a standard filtration installation FMO-2 (Russia) at a pressure drop $7 \cdot 10^4$ Pa on samples having an area of 254 mm^2.

3. Results and discussion

Surface topography

The modification of the membranes surface due to the plasma exposure was studied by AFM. Images of untreated (a) and ammonia plasma treated (b) PET track membranes are presented in Figure 1. The ammonia plasma exposure leads to a moderate increase of the surface roughness. The pores shape is modified as well, but not in a significant manner. These results can be compared with the results obtained in the case of similar treatments in air [11]. In that case the appearance of numerous craters on the originally smooth polymeric surface was revealed, the occurrence of which was explained by the difference in the etching rates of the amorphous and crystalline areas of the polymer [9]. The membrane surface got rough. The crater sizes varied with treatment conditions and increased with treatment duration. The comparative results indicate that the ammonia plasma is much less aggressive as compared to the plasma containing oxygen, and conserves better the surface topography.

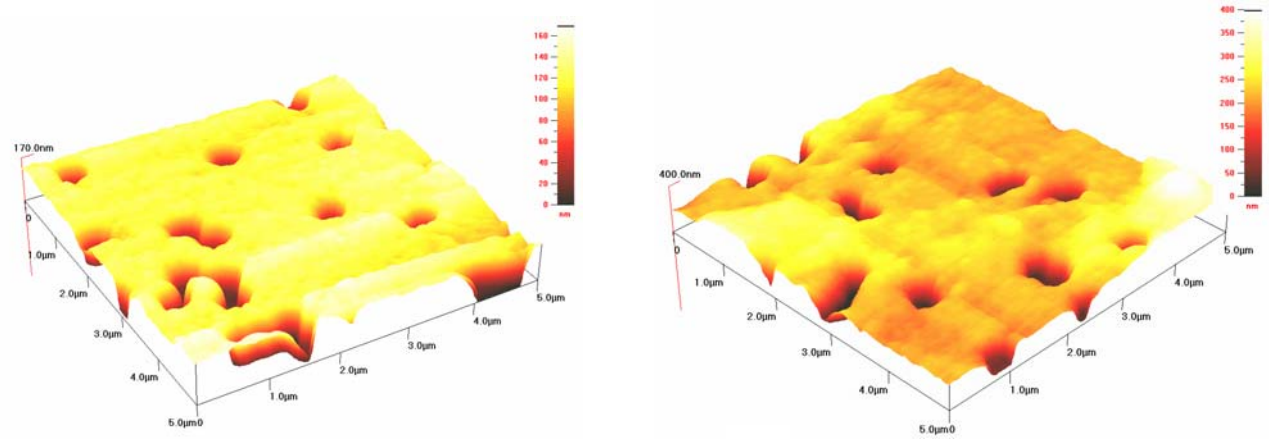

a) b)

Fig. 1. AFM images of PET TM of 0.4 µm pore diameter for a) untreated membrane, b) treated in ammonia plasma at the discharge power 60 W , 10 min treatment time; gas pressure is 13.3 Pa.

Dependence of the membrane characteristics on the process parameters

The results of the measurements of the membranes thickness, effective pores diameter, and porosity for membranes treated for different time values and different power values are presented in Table I. Here, each value represents an average of at least three measurements. One can observe a slight increase of the effective pore diameters for the samples subjected to plasma. It testifies that during the plasma treatment there is an etching at the surface inside the pores. From the data represented in the table, it follows that the etching rate depends on the values of the discharge power: increase of the discharge power leads to an increase in the etching rate. Similar studies showed that the etching rate depends also on the pressure of plasma-forming gas. Increase of pressure

results in increase of the etching rate. More detailed analysis of the etching process in the ammonia plasma showed that the process develops in two stages: a first stage (short treatment time) when the etching rate is high and a second stage with lower etching rate [11].

Table I. Parameters of PET TM subjected to the ammonia plasma treatment at gas pressure 13.3 Pa

Discharge power, W	Plasma treatment time, min	Thickness, μm	Effective pore diameter, μm	Porosity, %	Water contact angle, deg
–	–	9.5	0.220	7.6	65
20	5	9.5	0.230	8.3	50
20	10	9.4	0.235	8.7	75
40	5	9.6	0.230	8.3	80
40	10	9.7	0.230	8.3	90
60	5	9.7	0.235	8.7	100
60	10	9.8	0.240	9.1	95
80	5	9.7	0.230	8.3	95
80	10	9.8	0.240	9.1	100

The process of PET TM etching by plasma containing oxygen was investigated in detail previously. In the previous studies of the effect of air [6] and oxygen [10] plasma on PET TM an increase in the diameter of the membrane pores was observed, as well. In those studies has been also shown that the plasma generated in these gases causes the etching of the polymer surface that leads to a reduction of the PET TM thickness. The data from the present experiments show that the effect of ammonia plasma on track membranes leads to a more complex dependence. In this case two competing processes are indicated by the results: etching of the polymeric matrix and re-deposition of a polymeric layer on their surface. At small treatment durations and low values of the discharge power the process of plasma etching is basically observed – a reduction of the membrane thickness testifies it (Fig. 2, curve 1). This is related to a rapid removal from the surface of the low weight material, which is formed on surface during the membrane fabrication by caustic etching and probably of the amorphous PET materials. At longer plasma treatments and a higher discharge power, a process of deposition of a polymeric film gets appearing. Increasing of the thickness of the membranes (Fig. 2, curve 2) and changing their color proves it. Reduction of the growth rate of the effective pore diameter at longer plasma treatment can be then, at least partially, connected to the re-deposition of a cross-linked polymeric film on the pore surface, whose formation is caused by polymerization of the products of etching the membrane matrix.

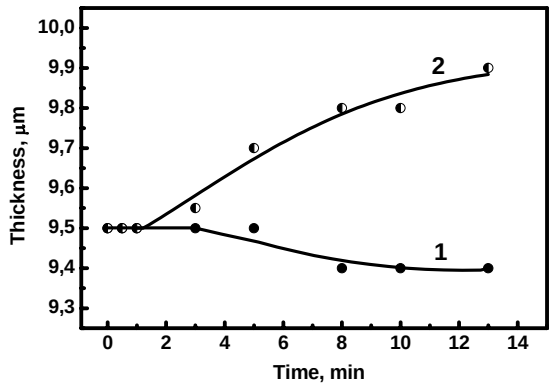

Fig. 2. Dependence of the thickness of PET TM on the treatment time in ammonia plasma at the discharge power 20 W (1) and 60 W (2); gas pressure is 13.3 Pa.

Chemical composition

The analysis of the ESCA spectra of the modified membranes shows the change of the chemical composition of their surface. The O_{1s}, N_{1s} and C_{1s} peaks belonging to the respective species were identified in the spectra. The presence of O_{1s} peak testifies that the oxidation of the polymer surface occurs. Most likely the oxidation appears when carrying the samples out on air.

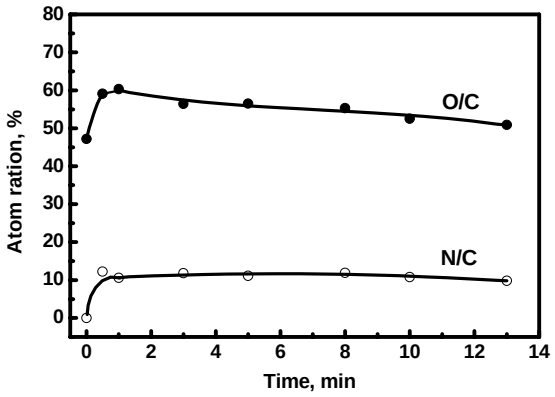

Fig. 3. The dependence of the relative content of atoms on the treatment time in ammonia plasma at the discharge power 40 W and gas pressure is 13.3 Pa.

In Figure 3 one can observe the behavior of the intensity of O_{1s} /C_{1s} and N_{1s}/C_{1s} ratios with the treatment time. At long times the ratios decrease somewhat with the plasma treatment duration. The abstraction of oxygen from the surface at long plasma treatment can be made due to ammonia plasma species, for example H atoms and NH radicals. The presence of N_{1s} peak proves that in the process of PET TM treatment in ammonia plasma, a fixing of nitrogen with formation of nitrogen-carbon bonds takes place. For long treatments the content of nitrogen, practically does not change with the treatment time. Thus, the treatment of PET TM in ammonia plasma leads to membrane functionalization.

Water permeability

The experiments showed that the water permeability usually decreases during the filtration process, with final values after 30 minutes in the range of 16 to 40% from the initial values. Both the initial values and the decrease rate are depending on the treatment conditions, as follows.

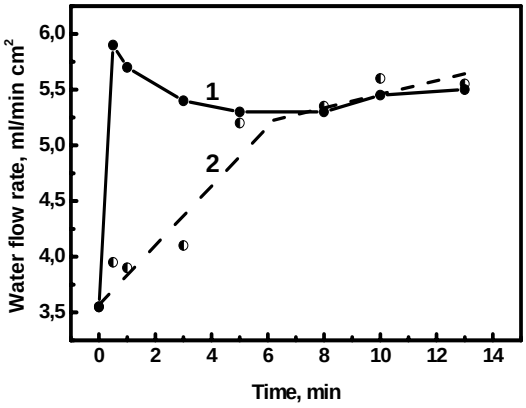

Fig. 4. Dependence of the water flow rate of PET TM on the treatment time, for discharge power 20 W (1) and 60 W (2); gas pressure is 13.3 Pa.

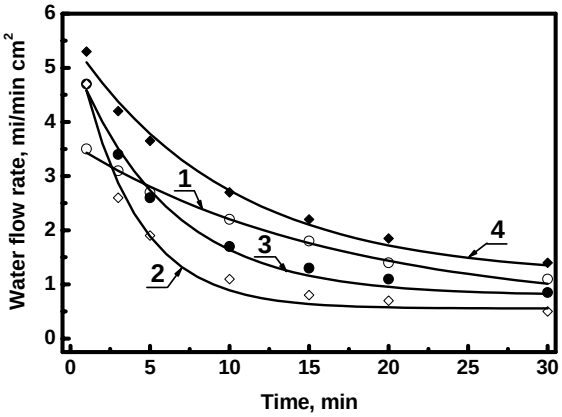

Fig. 5. Dependence of the water flow rate in time for initial PET TM (1) and membranes treated in ammonia plasma during 5 min at gas pressure is 13.3 Pa and the discharge power 20 W (2), 40 W (3) and 60

The initial water permeability dependence upon the treatment time exhibits a rapid growth at low discharge power (20 W) and short treatment times (Figure 4, curve 1), which is correlated with the increase of the pores size (Table I). This growth is followed by a slight decrease at longer treatment time which relates to the change of the hydrodynamic properties owing to the decrease of the membrane wettability [11]. At higher discharge power (60 W) one observes a gradual growth of the water permeability, reaching a plateau toward the long

treatment time region.
The curves describing the behavior of the water permeability during the filtration time, for membranes treated 5 minutes at different power values, are shown in Figure 5. The curves profiles depend strongly on the surface properties. A drastic decrease (to 16 % from the initial value) of the water flow rate in time (30 min) is observed in case of the membranes for which a reduction of the contact angle was produced by the treatment (power 20 W, Figure 5, curve 2). The decrease is slower for the membranes treated at higher power (Figure 5, curves 3 and 4), for which the increase of the contact angle was obtained by treatment, reaching up to 40% from the initial permeability value in case of membranes treated at 60 W. It results that the decrease of the hydrophilicity (reduction of the concentration of polar functional groups) in the surface layer leads to a higher filtrate volume in the course of filtration process. Thus, the results show that improved filtration performances as compared to the untreated samples are obtained for membranes containing smaller numbers of polar groups after the plasma treatment (Figure 5, curve 4).

4. Conclusion

Radiofrequency ammonia plasma treatments of PET TM were performed with various power levels and exposure times. The AFM investigations proved that ammonia plasma produces a moderate roughening of surface and a slight pore size modification. The ammonia plasma is less aggressive as compared to the plasma containing oxygen (air plasma), and conserves better the surface topography. The chemical analyses proved that functional groups are attached to the surface, mostly containing O and N atoms. These functional groups and the surface topography play a determinant role in changing membrane wettability, leading to surfaces which can be more or less hydrophylic in comparison to the initial ones.

The modification of surface properties entails the changing of the transport characteristics. In particular conditions of treatment the water permeability raises above that of the untreated samples. The use of such type of membranes can lead to considerable increase of the filtration processes efficiency.

References

[1] G.N. Flerov - Vestnik Academii Nauk SSSR - **4**, 35 (1984).
[2] Y.J. Wang, C.H. Chen, M.L. Yeh, G.H. Hsiue, B.C. Yu - J. Membr. Sci. **53**, 275 (1990).
[3] M.S. Kang, B. Chun, S.S. Kim - J. Appl. Polym. Sci. **81**, 1555 (2001).
[4] M. Bryjak, G. Pozniak, I. Gancarz, W. Tylus - Desalination. **163**, 231 (2004).
[5] A.I. Vilenskii, V.V. Berezkin, B.V. Mchedlishvili - Kolloidnyj Zhurnal. **53**, 117 (1991).
[6] S.N. Dmitriev, L.I. Kravets, V.V. Sleptsov - Nucl. Instr. and Meth. **142B**, 43 (1998).
[7] S.N. Dmitriev, L.I. Kravets, V.V. Sleptsov et. al. - High Energy Chemistry. **32**, 310 (1998).
[8] L.I. Kravets, S.N. Dmitriev, V.V. Sleptsov, V.M. Elinson - Desalination. **144**, 27 (2002).
[9] S.N. Dmitriev, L.I. Kravets, V.V. Sleptsov, V.M. Elinson - Desalination. **146**, 279 (2002).
[10] L.I. Kravets, S.N. Dmitriev, V.V. Sleptsov, V.M. Elinson - Surf. Coat. Technol. **174-175**, 821 (2003).
[11] A. Lazea, L.I. Kravets, B. Albu, C. Ghica, G. Dinescu - Surf. Coat. Technol. In press. (2005).

Design and optimization of a miniature He-O_2 atmospheric pressure glow discharge torch for bio-applications

V. Léveillé, S. Coulombe and S. Yonson
Department of Chemical Engineering, McGill University, Montréal, Canada

Abstract
We report on the design and optimization of a novel miniature atmospheric pressure glow discharge torch (APGD-*t*) aimed at bio-applications. The APGD-*t* produces a 500 μm-diameter plasma jet which is ~3 mm-long with a gas temperature of ~45-55 ºC when operated at ≈1 W with 1-1.5 SLM He as the plasma-forming gas. We demonstrate that the use of a central capillary electrode to inject the source of reactive species in the He plasma afterglow is a more efficient way to produce the excited reactive species (O from O_2). Our optimization study reveals that the optimum O_2/He flow rate ratio is 0.3 v/v%.

1. Introduction

The interest in atmospheric pressure non-thermal plasma sources for bio-applications has grown considerably over the last decade (sterilization [1,2], surface functionalization [3], cell removal [4], and microcontact printing of protein on polymers [5]). In the field of local bio-applications, Stoffels *et al* [4,6,7] developed an atmospheric pressure unipolar RF "plasma needle", operating at power levels ranging from 10 to 100 mW. The plasma needle involves electrical coupling of the plasma source with the surface, and relies on diffusion to transport the reactive species to the substrate. To inhibit the electrical coupling between the plasma source and the surface under treatment, and to facilitate the transport of reactive species, we designed a miniature atmospheric pressure glow discharge torch (APGD-*t*). The design challenges associated with the APGD-*t* were the need to maintain a non-thermal equilibrium state in the plasma to minimize the thermal load to the substrates while maintaining a high degree of chemical reactivity, and to limit the rapid recombination of the reactive species in the plasma afterglow. The principal design characteristics of the APGD-*t* are: 1) the use of an amplitude-modulated high-frequency excitation source (RF), 2) the use of helium as the plasma-forming gas, 3) the injection of the source of reactive species through a central capillary electrode downstream of the plasma-forming region, and 4) the use of a torch configuration permitting the rapid transport of reactive species to the remote substrate. In this proceeding, we present the torch design, reveal the advantage of adding O_2 separately from the plasma-forming gas, and present the results of an optimization study aimed at enhancing the production of atomic oxygen.

2. Torch construction

A schematic of the APGD-*t* is presented in Fig. 1. The torch is made of two concentric electrodes; the central powered electrode is a stainless steel capillary tube while a silver epoxy painted on the plasma confinement quartz tube serves as the grounded electrode. The quartz tube also acts as a dielectric barrier in this DBD configuration. The outside and inside diameters of the quartz tube are 4 mm and 2 mm, respectively. The capillary electrode is 0.3556 mm-outside diameter by 0.1778 mm-inside diameter. The entire torch is approximately 10 cm long and held together with a Swagelok® tee. The downstream end of the quartz tube is shaped into a converging nozzle with an exit diameter of 500 μm. The plasma-forming gas, helium, is injected through the side arm of the tee and O_2, the source of reactive species used in this study, can be injected either in the capillary electrode or with the plasma-forming gas. This torch design allows easy translation of the capillary electrode by sliding it inside the lower Teflon fittings.

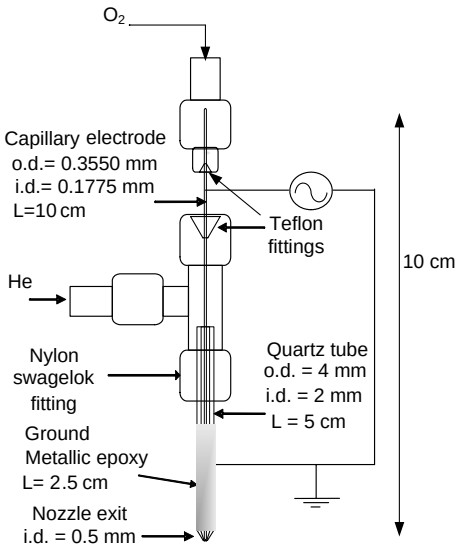

Figure 1: Schematic of the APGD-*t*

Under a typical configuration, the capillary electrode tip is recessed by a few 100's µm from the nozzle exit plane (see Fig. 2 - left). Fig. 2 (right) shows the beveled capillary electrode tip as well as some degree of melting at the capillary tip due to local heating (the capillary electrode was translated to the left for clarity). The position of the capillary electrode along the torch axis is crucial for the formation of a relatively long and straight jet, and for the efficient generation of O atoms. If the capillary electrode is located outside of the nozzle, the strong electrical field created at the capillary electrode tip favors the excitation of air molecules at the expense of dissociating O_2 into O, freeing electrons, and exciting He atoms to metastable states (i.e. excited radicals are formed by electron-impact dissociation and excitation, and by other collisional processes involving He metastables). When the tip of the capillary electrode is slightly recessed inside the nozzle exit, the gap delimited by this electrode and the inside surface of the quartz confinement tube becomes very small (72 µm when perfectly aligned in the middle of the nozzle exit) thus favoring the acceleration of the plasma flow and the excitation of the plasma-forming gas. This position also favors the mixing of the reactive species injected through the capillary electrode with the flowing plasma-forming gas and thus, with the plasma electrons and He metastables. Finally, since most of the plasma volume is occupied by the main plasma-forming gas (He), the electrical characteristics and stability of the plasma torch are not significantly affected by the nature of the gas used as the source of reactive species. The breakdown voltage of the APGD-*t* is relatively low due to the geometrical amplification of the electric field (~ 220 $V_{peak\text{-}to\text{-}0}$ in He [8]).

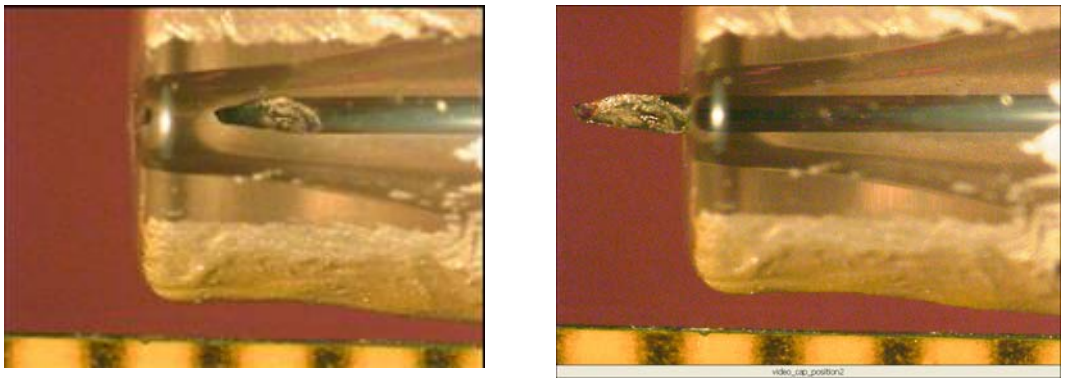

Figure 2: Left - Picture of the nozzle end of the APGD-*t* with the capillary electrode ending ~600 µm upstream of the nozzle exit plane. Right - Same picture but with the capillary electrode translated outside the nozzle. Scale is in mm.

3. Experimental considerations

The APGD-*t* is powered by a RF signal generated using an arbitrary waveform generator (HP 33120A, 15 MHz bandwidth) set at a carrier waveform frequency of 13.56 MHz, and amplitude-modulated (10-50% duty cycle) by a variable duty-cycle square wave generator (Racal-Dana model F64 AM-FM-sweep-trig/pulse-function generator). The use of a 10-50% duty cycle allows a continuous modulation of the APGD-*t* power over the ~1-5 W[8] range. A 10% duty cycle is used in the present study. The signal is amplified with a broadband RF amplifier (Amplifier Research 75A250, 75W, 10 kHz-250 MHz, 50 Ω input/output impedances). A homemade series inductor is used as matching network and provides near-resonance circuit conditions. The electrical power delivered to the APGD-*t* is deduced from measurements [8] of the torch voltage, circuit current and phase angle between both signals using a fast digitizing oscilloscope equipped of two probes (Passive voltage probe: Tektronix P6139A, 10X, 500 MHz, 10 MΩ, 8 pF; Current probe: Tektronix CT-2 current transmitter, 1mV/1mA into 50 Ω, with a Tektronix P6041 probe, 1X; Digital oscilloscope: Tektronix TDS3054B, 500 MHz, 5 GS/s). The voltage and current measurements are transferred to a PC through a GPIB interface and displayed on a LabView™ interface. A PID control loop is used in order to regulate the torch power and monitor the operating parameters. Helium (99.998 % purity) or a certified mixture of He + 1 v/v% O_2 (±5 %) is used as a plasma-forming gas. Extra dry oxygen (99.6 %, 5 ppm impurities) can also be injected through the capillary electrode as

a source of reactive species. The gas flow rates are regulated using thermal mass flow controllers (Qualiflow, AFC 80 MD). The plasma jet temperature is measured using a 0.5 mm-OD, ungrounded and shielded type K thermocouple. Pictures and optical emission spectra of the plasma jet were captured with a telemicroscope (Edmund Optics, 16X) and a low-resolution UV-VIS spectrometer (Ocean Optics USB2000). A bi-convex lens (50 mm-diameter, 15 cm focal length) was used to collect the plasma emission and to focus it onto a 400 μm optical fiber attached to the spectrometer.

4. Results and discussion

4.1. Telescopic images of the plasma jet

In figure 3, pictures of the jet are presented for three different flow rates of helium and a torch power of ≈1W (no O_2 added). Under typical operating conditions, the plasma jet is approximately 2 to 4 mm-long (the jet diameter at the nozzle is 500 μm). One can distinguish a bright (whitish) plasma core surrounded by a blue plume. The whitish plasma core is characteristic of the He plasma emission while the bluish afterglow is attributable to the optical emission from species produced from the N_2 and O_2 molecules present in the ambient air and entrained in the plasma afterglow. The pictures reveal that an increase of the He flow rate elongates the jet. Higher axial plasma flows are beneficial to the transport of excited reactive species to a remote substrate since the ratio of the recombination time scales over the convective transport time scale is higher. On the other hand, larger flow rates involve higher He consumption and more momentum transfer to the substrates which, in the case of bio-applications, might not be mechanically strong (ex. cells attached on a petri dish). The picture of the plasma jet on Fig. 3a best reveals a structure near the nozzle exit that might originate from sonic flow conditions. To verify this hypothesis, we used the one-dimensional adiabatic flow approximation (assuming a local isentropic flow, no friction) to determine the flow conditions prevailing at the nozzle exit. We found that a 0.5 SLM He annular flow passing through the nozzle exit with a gas temperature up to 315°C gives Mach numbers < 0.06, thus discarding, *a priori*, the sonic flow hypothesis. Additional STP flow calculations revealed that an annular flow rate of 6 SLM He at the nozzle exit is required to reach a Mach number of 1. It is not clear at this point if other mechanisms such as the thermal expansion of the gas or some sort of EHD or MHD pumping can contribute to the flow acceleration. Future work will focus on a more detailed analysis of the plasma jet hydrodynamics. Nevertheless, it is important to note that supersonic flow conditions would be beneficial in the context of the applications sought: the excited reactive species would be transported further downstream than under subsonic conditions.

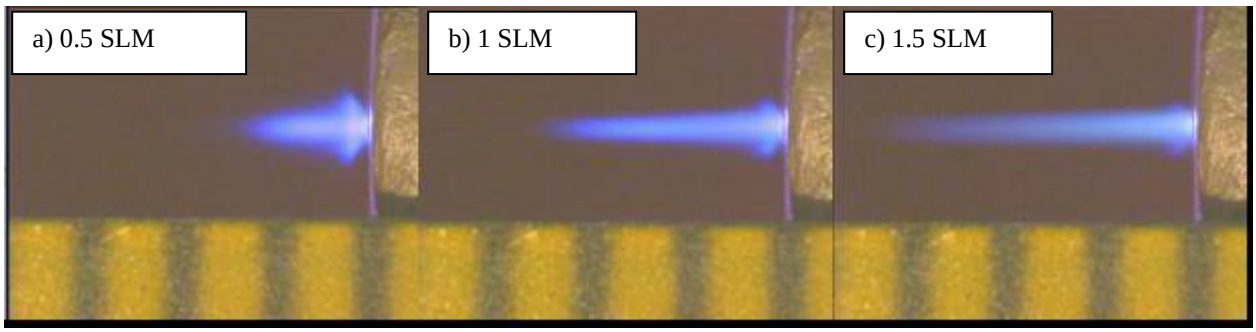

Figure 3: Pictures of the plasma jet produced by the APGD-*t* operating at ≈1 W for different He flow rates.

Fig. 4 presents a comparison of the visual appearance of the plasma jet when O_2 is injected in the capillary electrode (10 SCCM O_2, Fig. 4b) or added to the plasma-forming gas (1v/v% of O_2 in He is equivalent to 10 SCCM in the capillary electrode, Fig. 4c) with an helium flow of 1 SLM (He only, Fig. 4a). The injection of 10 SCCM O_2 in the capillary electrode leads to a slight reduction of the plasma jet length, while the injection of an equivalent amount to the plasma-forming gas leads to a drastic reduction of the length. Such decrease in optical emission implies a decrease in the density of excited atomic and molecular species having radiative transitions in the visible range. Since several excitation channels involve collisions with electrons and He metastables, the

decrease of the optical emission can be seen as a reduction in the density of those populations. The actual situation is slightly more complex though. Our preliminary investigation of the jet using optical emission spectroscopy [8] revealed that the emission from excited atomic O increased with O_2 injection through the capillary electrode and collapsed with the injection of O_2 with the plasma-forming gas. We infer from this that the electrons and He metastables are used to dissociate and excite the O_2 injected through the capillary electrode at the expense of N_2 (ambient air) dissociation/excitation. With O_2 injected with the He flow, a drastic overall reduction of the optical emission is observed suggesting that the plasma in the plasma-forming region is quenched.

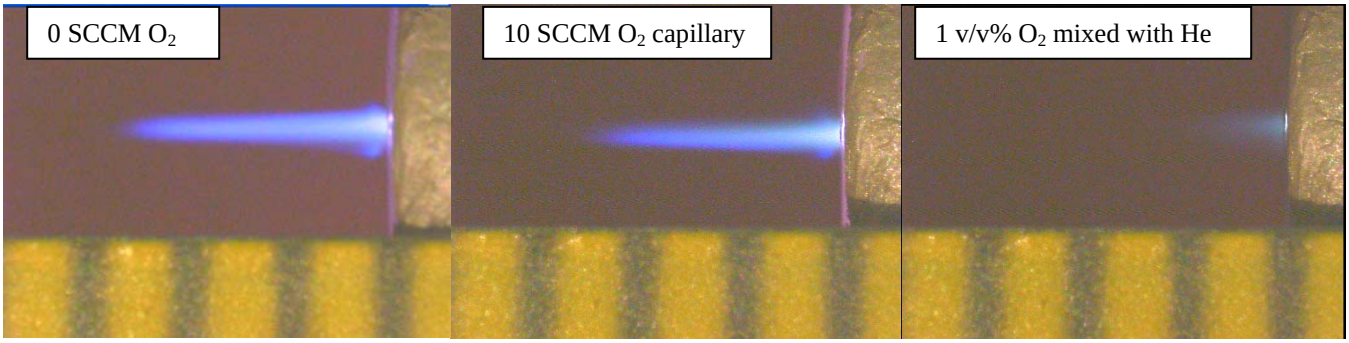

Figure 4: Pictures of the plasma jet at ≈1 W and 1 SLM He (left) with 10 SCCM O_2 injected through the capillary electrode (center) or with 1 v/v% O_2 added to the plasma-forming gas (right).

4.2. Optical emission spectroscopy analysis

From the telescopic image analysis and the preliminary spectroscopic investigation [8], we found that adding O_2 through the capillary electrode was more efficient than adding it with the plasma-forming gas. We then optimized the amount of O_2 added in the capillary electrode in order to get the maximum generation of O atoms. We used as a measure of the atomic O production the peak intensity of the excited O line at 777 nm, measured in the nozzle exit plane along the jet axis. Figure 5 shows the relative intensity profiles of the O (777 nm) line along with some other monitor lines of He and N_2. All emission intensities are normalized with respect to the maximum emission intensity of the O (777 nm) line. As can be seen in Fig. 5a (1 SLM He at ≈1 W), 3 SCCM of O_2 injected in the capillary electrode produced an emission maximum from the O (777 nm) line. This flow rate corresponds to a O_2/He volumetric ratio of 0.3%. The gas temperature under those conditions is ~55°C. (Note that this gas temperature can be slightly too elevated for bio-applications - i.e. skin and cells treatments - and thus, a continuous movement of the torch over the surface of interest might be required in order to reduce the local thermal load).

The He gas flow rate too was optimized to reach the maximum emission from the excited O atoms. During this series of experiments, the O_2/He volumetric flow rate ratio of 0.3% was kept constant independently of the He flow rate and torch power. As can be seen in Fig. 5b, the increase in He flow rate causes an increase of the excited O emission (777 nm line) at the nozzle exit. One can attribute this phenomenon to a more significant axial transport: the isolines for the particle densities are stretched further downstream with the increase of the plasma gas flow. At 1.5 SLM He, the production of excited O atoms is highest and the gas temperature is slightly lower than at 1.0 SLM due to the increased convective cooling (~45 °C versus ~55 °C). It is interesting to note that the intensity of the He (706 nm) line seems to saturate around 1.5 SLM while the O (777 nm) line does not. This phenomenon can be attributed to the fact that the upper energy level of the He (706 nm) transition is much larger than the O (777 nm) transition (22.72 eV versus 10.74 eV). By optimizing the production of excited He atoms we, in turn, optimize the production of metastable He atoms (upper energy levels ~20 eV). Since the metastable states have much longer lifetimes, those species will be found even further downstream the plasma jet and potentially, contributing too to the formation of excited O. The increase of the He flow rate has another positive effect: the reduction of air entrainment in the plasma jet (see Fig. 5d). At a flow rate of 0.5 SLM

He, the spectral emission of one of the strong emission lines of air, N_2 at 357 nm, is as strong as the spectral emission lines of He (706 nm) and O (777 nm) reported in Fig. 5b and Fig. 5c, respectively. However, for He flow rates of 0.75 SLM and higher, the emission from the N_2 line becomes much less significant than for the He and O lines.

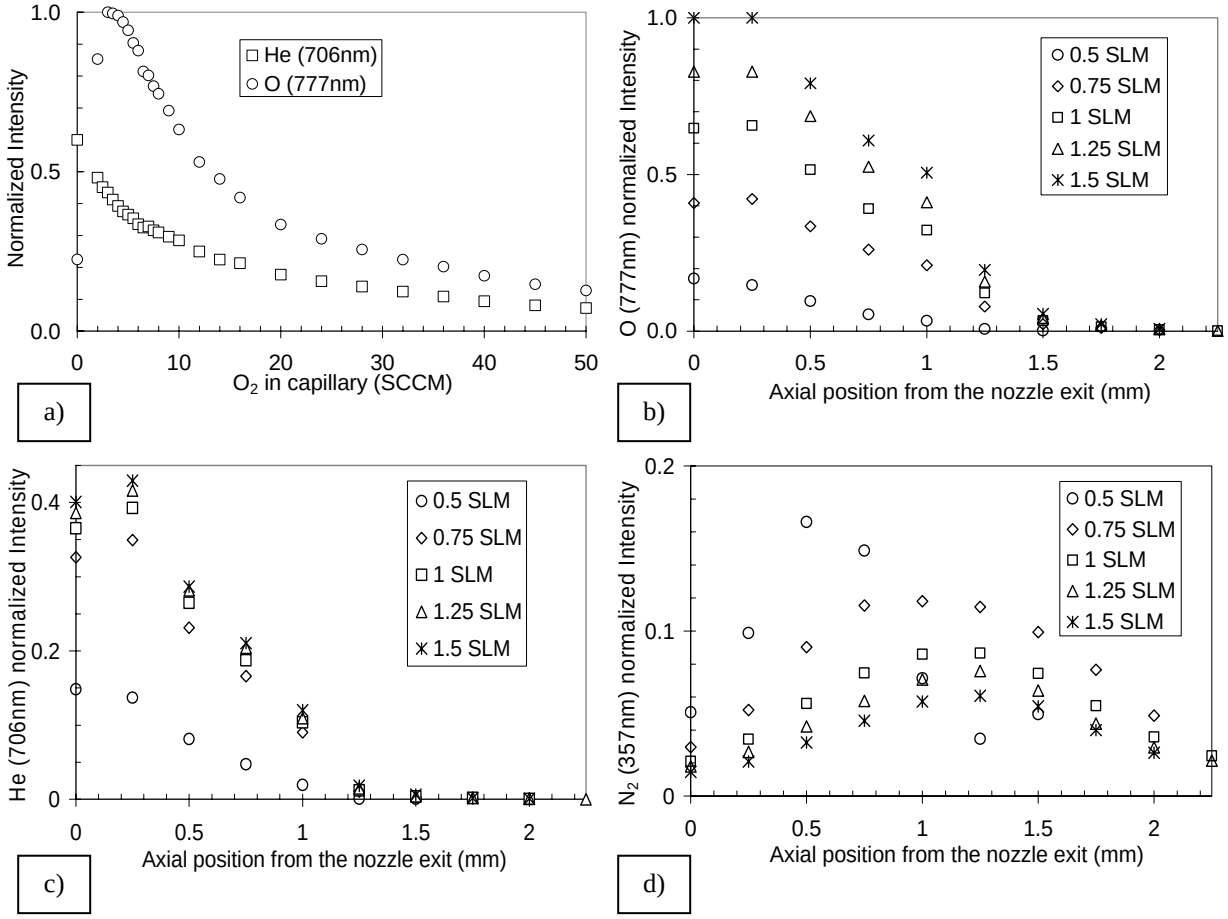

Figure 5: Normalized peak line emission intensity of a) O (777 nm) and He (706 nm) at the nozzle exit for different flow rates of O_2 in the capillary electrode. Axial distribution of the normalized peak line emission intensity of b) O (777 nm), c) He (706nm) and d) N_2 (357 nm) for different He flow rates.

5. Concluding remarks

The main goals of this report were to present the design of a novel atmospheric pressure glow discharge torch (APGD-*t*) specifically designed for bio-applications, and to reveal the advantages of injecting the source of reactive species (O_2) downstream of the plasma-forming region (He) and the operating conditions which optimize the production of O atoms (reactive species). The APGD-*t* operating at ≈1 W in a 1.5 SLM flow of He produced a small-scale plasma jet (~3 mm long by 500 μm diameter at the nozzle exit) with a gas temperature of ~45 ºC, which is suitable for bio-applications. A volumetric O_2/He ratio of 0.3% gave rise to the maximum production of excited O atoms. In future work, He metastable and ground state O atoms will be monitored by laser-induced fluorescence spectroscopy in order to validate/invalidate the assumption that He metastable atoms participate in the production of ground state O atoms, and to see if the highly reactive O atoms reach the bio-surface of interest.

Acknowledgments
The authors wish to thank Luciano Cusmich, Frank Caporuscio, and Alain Gagnon for their technical assistance. The project was funded by the National Sciences and Engineering Research Council of Canada (NSERC), through the Discovery and Canada Research Chairs programs, the Fonds québécois de la recherche sur la nature et les technologies (FQRNT), and McGill University.

References

[1]M. Laroussi, D.A. Mendis and M. Rosenberg - New J. Phys. **5**, 41.1 (2003).
[2] J.R. Roth, D.M. Sherman, R. Ben Gadri, F. Karakaya, Z. Chen, T.C. Montie, K. Kelly-Wintenberg and P.P-Y. Tsai - IEEE Trans. Plasma Sci. **28**, 56 (2000).
[3] A. Bruil, L.M. Brenneisen, J.G.A. Terlingen, T. Beugeling, W.G. Van Aken and J. Feijen - J. Colloid Interface Sci. **165**, 72 (1994).
[4] E. Stoffels, I.E. Kieft, R.E.J. Sladek - J. Phys. D: Appl. Phys. **36**, 2908 (2003).
[5] K.E. Schmalenberg, H.M. Buettner and K.E. Uhrich - Biomaterials **25**, 1851 (2004).
[6] E. Stoffels, A.J. Flikweert, W.W. Stoffels and G.M.W. Kroesen - Plasma Sources Sci. Technol. **11**, 383 (2002).
[7] I.E. Kieft, E.P. v d Laan and E. Stoffels - New J. Phys. **6**, 1 (2004).
[8] V. Léveillé, S. Coulombe - article submitted for publication in Plasma Sources Sci. Technol. (2005).

Plasma-Assisted Synthesis of Pre-Coated C_{60} Nanopowders from a Mixed Fullerenes Source

S. Coulombe, A. Tariq and J. –L. Meunier

Department of Chemical Engineering, McGill University, Montreal (QC), Canada

Astract
C_{60} nanopowders were produced by in-flight exposition of C_{60} molecules sublimed from a C_{60}-rich mixed fullerenes source to a continuous flow ethane plasma sustained by RF capacitive coupling. TEM et SEM micrographs of the deposits reveal nanopowders of size ranging from 30 to 50 nm, and agglomerates of those nanopowders. Conversely, micrographs of powders produced in an inert argon plasma show large μm-sized crystallites.

1. Introduction

There is a growing interest for the development of synthesis techniques for the production of coated nanoparticles. The driving force for such development activities lies in the inherent difficulties associated with the high surface energy of nanoparticles. Examples of application of such new production techniques include the passivation of metal nanoparticles for safer and easier handling considerations, to the enhancement of dispersion properties and compatibility of nanoparticles with host materials in nanocomposites. Examples of emerging applications are found in biosensors, heat and electrically conducting polymer films, and strengthened polymers. Nanofluids and ferrofluids, which constitute a relatively new class of liquid composite materials, emerge as advanced materials also taking advantage of the unique properties associated with metal nanopowders suspended in an organic medium. The key challenges one faces when processing nanocomposite materials are associated with the compatibility of the nanopowders with the host material, the stability of the suspension, the control of the mutual agglomeration, and the handling of the nanopowders.

Two general processing routes leading to the synthesis of polymer nanocomposites are commonly reported in the literature ([1] and references therein). The *in-situ* approach whereby nanoparticles are synthesized in a solution (wet chemistry) and then the polymer is formed around the nanoparticles. A second, *ex-situ* approach whereby the nanoparticles are first synthesized and stabilized, and then introduced into the polymer matrix through mechanical means. The first approach is based on chemical precipitation and generally involves numerous wet-chemical steps. The second approach involves the use of nanoparticles pre-coated with a thin layer of a material compatible with the host matrix, as precursor materials for nanocomposite fabrication. An interesting aspect of this approach is that the nanoparticle synthesis and nanocomposite formation processes can be isolated and thus, developed and optimized independently. Vollath and Szabó [2] developed a sequential microwave plasma-assisted process whereby nanoparticles coated with ceramic or polymeric materials are synthesized. This process development led to the present work where the synthesis of pre-coated C_{60} nanopowders is considered. Such powders represent potential candidates for nanocomposite and nanofluid applications due the high thermal and electrical conductivities, optical properties as well as physico-chemical stability of C_{60} [3].

2. Experimental details

In this study, pre-coated C_{60} nanopowders are produced from a commercially available C_{60}-rich mixed fullerenes source. The process is sequential and consists in three steps: i) the selective sublimation of C_{60} molecules from the mixed fullerenes extract; ii) the synthesis of nanopowders by gas phase nucleation and growth; iii) the coating of the nanopowders through in-flight plasma polymerization. The rationale that led to the development of this process consists of four aspects: i) Fullerenes C_{60}, have a significant

vapor pressure at modest temperatures [4]. ii) Fullerenes C_{60} are inclined towards polymerization through the formation of covalent bonds between cages but also tend to readily react with functional organic groups [5]. Thus, C_{60} nanopowders of desired size can potentially be synthesized by controlling the residence time of the fullerenes C_{60} in a nanopowder formation zone prior to their exposure to a surface stabilization process. iii) When injected into a weakly-ionized plasma and exposed to the electron gas, nanoparticles develop a negative floating potential due to the build-up of surface charges [6]. The repulsive electrostatic force that develops amongst nanoparticles is expected to play a role in the control of the mutual agglomeration process caused by van der Waal interactions. iv) Plasma polymerization reactions involving a foreign monomer gas and the growing C_{60} nanopowders will terminate their growth by encapsulation. It has been shown recently that the conditions leading to plasma polymerization onto nanoparticles are readily achieved using a monomer gas which produces the methyl radical upon dissociation in the plasma environment [7].

A schematic diagram of the plasma system is shown in Fig. 1A. It consists of three sequential units: (i) the C_{60} sublimation unit, (ii) the nanopowder synthesis tube, and (iii) the tubular plasma polymerization reactor where an optional substrate can be inserted. The C_{60} sublimation unit consists of a quartz piece fabricated to hold mixed fullerenes samples in powder form and to allow inlet for gases (Fig. 1B). Four cartridge heaters uniformly distributed inside a brass furnace are used to bring the powders to the desired temperature (typical range: 500-700 ^{o}C). The sublimed C_{60} molecules and growing nanoparticles are introduced in the plasma reactor along with the carrier/plasma polymerization gas through a narrow quartz tube. The plasma polymerization reactor consists of a 60 cm-long x 4 cm-ID quartz tube with two electrodes mounted externally, whereby a 13.56 MHz RF capacitively-coupled plasma is maintained. The chamber is evacuated with a mechanical pump to a base pressure of approximately 8 mTorr. The pressure during operation with a gas flow is regulated using a manual flow valve. Substrate discs can be placed normal to the flow of gases/nanopowders in order to collect plasma polymerized films and nanopowders.

The raw material used was a refined mixed fullerenes extract purchased from MER Corporation (USA) and having a composition of 75% C_{60}, 22% C_{70} and 3% higher fullerenes. Approximately 10 mg of mixed fullerenes were used every run. Prior to the initiation of the plasma surface treatment, the chamber was evacuated to the base pressure while the temperature of the fullerene extract was brought 50 ^{o}C under the desired process temperature. In order to avoid significant deposition of C_{60} nanoparticles on the substrate before the plasma treatment, the substrate was pushed forward to its desired location just before the treatment started (1 cm to the right of the electrodes' edge). The extract temperature was then ramped to 50 ^{o}C above the desired value over the 10 min plasma treatment time, such that the average temperature during the treatment was near the desired value (550 ^{o}C). The other process conditions were: a 0.025 slm flow of either argon or the monomer gas; a chamber pressure of 133 Pa; and a plasma power of 30 W. Ethane, C_2H_6, a commonly used organic monomer gas was used for the in-flight plasma polymerization onto the growing nanopowders. The same gas was used with success for the in-flight coating of amorphous SiO_2 nanoparticles [7]. The nanopowders were collected from the reactor walls and from Si substrates following treatment in first, an inert argon plasma and then, in the reactive C_2H_6 plasma. The morphology of the nanopowders collected from the reactor walls in the inter-electrode region were analyzed using transmission electron microscopy (TEM) while the morphology of the granular deposits (nanopowders) and organic films formed on the substrate was analyzed using scanning electron microscopy (SEM). A FTIR-ATR analysis of the films obtained in both cases was performed in order to determine their chemical composition.

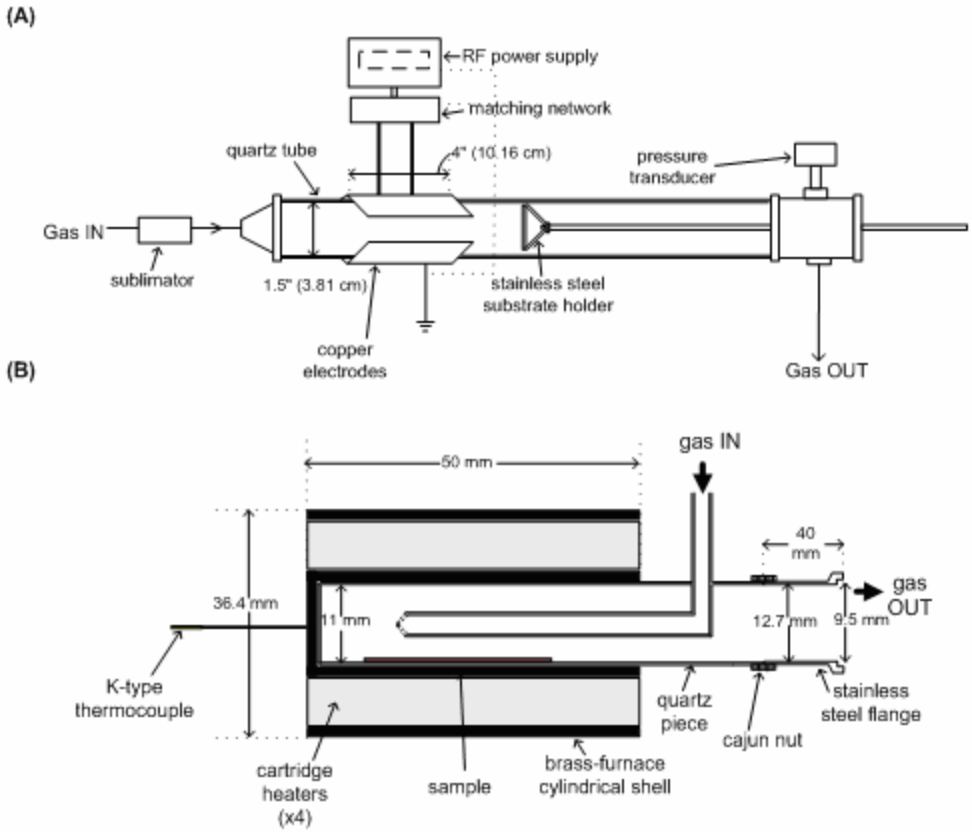

Fig. 1. (A) Schematic diagram of the equipment. (B) Lateral view of particle injector.

3. Results and discussion

Figure 2 shows the contrasting morphological differences between a sample of the as-received mixed fullerenes extract and the nanopowders deposited on the reactor walls during treatment with ethane. The as-received samples (Fig. 2(A-C)) show a significant agglomeration of the particles with no distinct features, resulting in plate-like structures. In contrast, the micrographs of Fig. 2(D-F) reveal fullerene nanopowders of size ranging from 30 to 50 nm and glued together with a translucent coating.

The images on Fig. 3 show the morphology of the deposits obtained on a Si substrate via sublimation and transport of the fullerenes in argon (Fig. 3(A)) and in ethane (Fig. 3(B)), followed by in-flight exposure to the RF plasma of the same gas. In this geometry, the growing nanopowders have a longer residence time in the plasma while the substrate benefits from a higher mass transfer rate due to its perpendicular exposure to the flow. While the treatment of the fullerenes in an inert atmosphere leads to the formation of crystallite-like structures (> 1 μm in size) and several μm-large aggregates, the treatment using ethane gives rise to the formation of 100 to 200 nm-diameter aggregates dispersed over the substrate. The aggregates appear to be made of smaller nanopowders, comparable in size to the ones observed on the reactor walls. A careful look at the nanopowders of Fig. 3(B) reveals that the morphology of the coating on their surface is very similar to the coating on the adjacent Si substrate (Fig. 3(C) & 3(D)). In fact, the individual nanopowders appear to be encapsulated and isolated from each other by a film, and glued altogether into a larger aggregate by the same film. Unfortunately, it was not possible to study the chemical composition of the coating deposited onto the nanopowders.

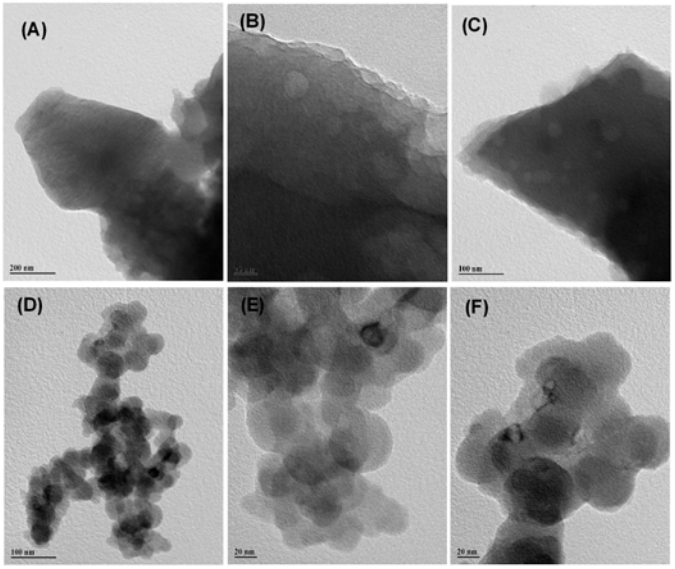

Fig. 2. (A-C) TEM images of untreated fullerene samples. (D-F) TEM images of pre-coated fullerene nanopowders produced with the ethane plasma.

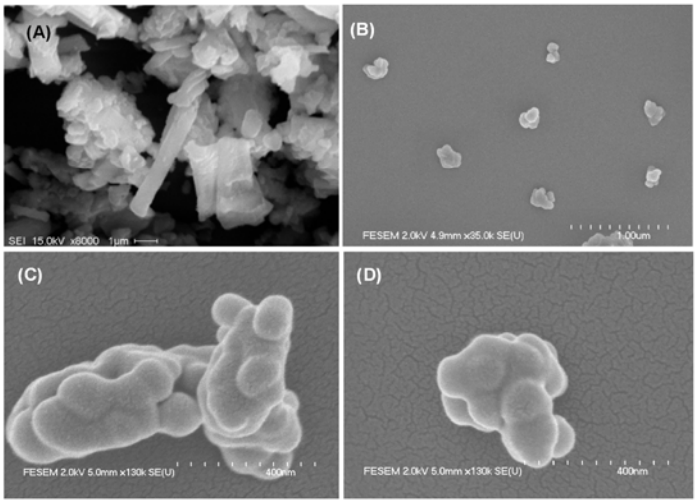

Fig.3. SEM images of the deposits obtained via C_{60} sublimation and transport in argon (A) and ethane (B) followed by exposure to the plasma of the same gas. (C-D) Close-up views of nanopowders obtained in (B).

Figure 4 presents the ATR-FTIR absorbance spectra of the films and granular deposits obtained. Fig. 4(a) shows the spectrum of a pure polyethylene (PE) film manufactured by 3M. Fig. 4(b) shows the spectrum of the polymer film deposited on a substrate under typical experimental conditions but without fullerene sublimation. Peaks of interest that match the pure PE spectrum correspond to the C-H rock and bend excitations around 2900 and 1470 cm^{-1}, respectively, thus confirming the organic nature of the film. The absence of the C-H stretch bands beyond 3000 cm^{-1} indicates lack of unsaturation. Fig. 4(c) shows a spectrum obtained with the granular fullerene films deposited via sublimation and condensation in the inert argon plasma. This spectrum features strong absorbance peaks near 1429 and 1183 cm^{-1}, two characteristic peaks of fullerene C_{60}. It is worth noting that, while monitoring the optical emission from the argon plasma seeded with the fullerenes using a low-resolution spectrometer (Ocean-Optics

USB2000) equipped with an optical fiber, no significant optical emission from the C_2 Swan band around 516 nm was recorded. One would expect to observe C_2 molecular emission from the plasma if fragmentation of the C_{60} occurred.

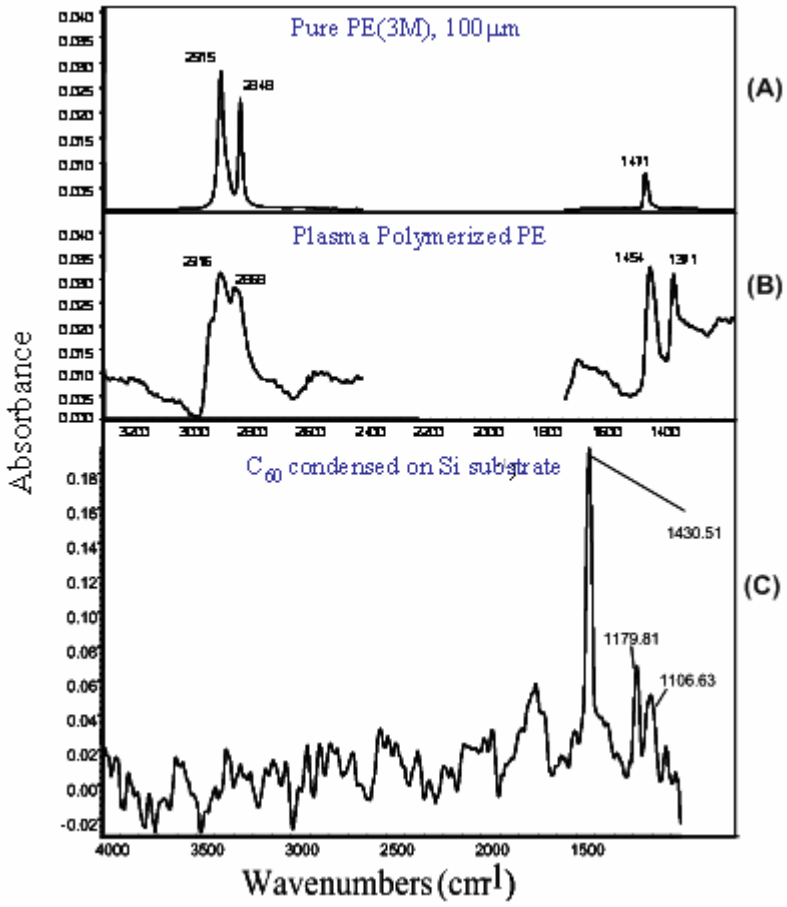

Fig. 4 (A) FTIR-ATR spectrum of a pure polyethylene (PE) film. (B) Spectrum of plasma polymerized PE film (no fullerenes added). (C) Spectrum of fullerene nanopowders film.

4. Conclusions

Under the light of the preliminary observations reported, we propose the following mechanism for the formation of the C_{60} nanopowders from the mixed fullerenes source. During the short duration of the experiments (10 minutes), the fullerenes C_{60} were selectively sublimed from the mixed fullerenes source. Once exposed to a carrier gas, the C_{60} molecules polymerized and agglomerated to form C_{60} nanopowders. With the ethane plasma, a competition between the growth of the C_{60} nanopowders by polymerization and agglomeration, and the encapsulation by the build-up of an organic film set in. Due to the dilution of the fullerenes C_{60} gas by the organic monomer gas, the encapsulation process eventually took over. Otherwise, polymerization of the fullerene C_{60} into large structures, as observed with the inert gas, would have occurred. Much remains to be done after this preliminary investigation. On the other hand, the present process is versatile enough to vary the sublimed fullerene vapor density, the residence time of the fullerene C_{60} in the nanopowder formation zone, and the plasma polymerization conditions (plasma density, pressure and nature of monomer gas).

Acknowledgments

This work was supported by the National Sciences and Engineering Research Council of Canada

(NSERC) through the Discovery and Canada Research Chairs programs, the Fonds québecois de la recherche sur la nature et les technologies (FQRNT), and McGill University.

References

[1] M.K. Corbierre, N.S. Cameron, M. Sutton, S.G.J. Mochrie, L.B. Lurio, A. Rühm, R.B. Lennox - J. Am. Chem. Soc. **123**, 10411 (2001).
[2] D. Vollath, D.V. Szabó - J. Nanoparticle Res. **1**, 235 (1999).
[3] H.W. Kroto, A.W. Allaf, S.P. Balm - Chem. Rev. **91**, 1213 (1999).
[4] M.V. Korobov, E.V. Skokan, D.Y. Borisova, L.M. Khomich - Russian J. Phys. Chem. **70**, 926 (1996).
[5] C. Giusca, M. Baibarac, S. Lefrant, O. Chauvet, I. Baltog, A. Devenyi, R. Manaila - Carbon **40**, 1565 (2002).
[6] H. Kersten, H. Deutsch, M. Otte, G.H.P.M. Swinkels, G.M.W. Kroesen - Thin Solid Films **377-378**, 530 (2000).
[7] A. Kouprine, F. Gitzhofer, M. I. Boulos, A. Fridman - Plasma Chem. Plasma Process. **24**, 189 (2004).

Development of a Dual-Plasma Process for the Synthesis of Coated Metal Nanoparticles from a Solid Source

C. Qin and S. Coulombe

Department of Chemical Engineering, McGill University, Montreal (QC), Canada

Abstract

A novel process for the synthesis of pre-coated metal nanoparticles is presented. The metal nanoparticles are produced in an inert (Ar) low-pressure pulsed metal vapor arc system which uses the metal of interest as the cathode, and subsequently exposed to a continuous flow C_2H_6 polymerization plasma for in-flight coating. Typical nanoparticle size ranges from 10 to 30 nm while the thickness of the film deposited onto the nanoparticles is ~10 nm. The effect of operating parameters on the nanoparticles' properties and stability of the dual-plasma system are discussed.

Keywords

Coated metal nanoparticles, metal vapor arc, pulsed arc, capacitively-coupled RF plasma, plasma polymerization.

1. Introduction

Due to their unique thermal, electronic, magnetic, and optical properties, metal nanoparticles find numerous applications in various fields either as individual entities (e.g. catalysts, solid additives to propellants [1], raw materials for plasma spraying) or as dispersed phases into host materials (e.g. optoelectronic nanodevices, magnetic ferrofluids [2], nanofluids [3], and polymer nanocomposites). In many of these applications, it is desirable to use metal nanoparticles pre-coated with ultrathin organic layers to reduce their surface energy (i.e. for safe handling and/or to control agglomeration), to enhance their compatibilities with host materials or simply, to avoid contamination (ex. oxidation). Coated metal nanoparticles can be produced by wet chemistry methods, which generally involve numerous chemical steps, or by "dry" plasma-based methods. Vollath and Szabo [4] developed a continuous dual-plasma process whereby finely dispersed coated nanoparticles are produced from gaseous precursors injected into a microwave plasma. Though versatile and applicable to the direct synthesis of metal nanoparticles pre-coated with organic layers, this process involves the use of harmful and unwieldy metal precursors, such as ferrocenes and organometallics. More recently, Kouprine *et al* [5] developed a similar continuous process using a capacitively-coupled RF plasma source. In this report, we present our progress made toward the development of a continuous dual-plasma process whereby metal nanoparticles coated with thin organic layers are produced from a solid source.

2. Overview of the Dual-Plasma Process

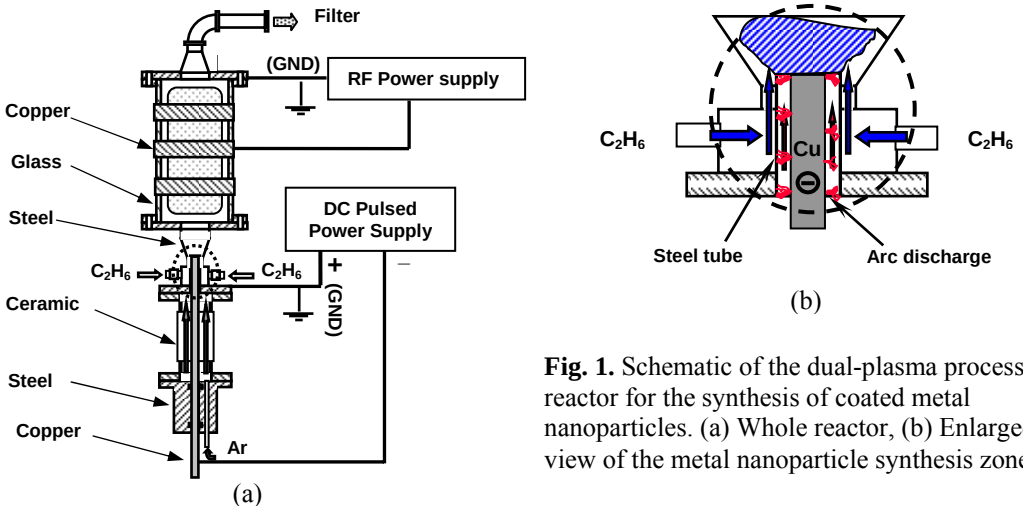

Fig. 1. Schematic of the dual-plasma processing reactor for the synthesis of coated metal nanoparticles. (a) Whole reactor, (b) Enlarged view of the metal nanoparticle synthesis zone.

The process consists of two sub-steps: the metal nanoparticle synthesis followed by the in-flight plasma polymerization onto the nanoparticle surface. A flow-through reactor configuration is used (see Fig. 1 for the detailed schematic of the entire plasma reactor). Both sub-steps have unique requirements and thus, required the development of two different plasma sources within the constraint of a common pressure (1-100 torr). In the synthesis stage, metal vapors are produced from the erosion of the cathode of a low-pressure pulsed metal vapor arc system. The use of pulsed arcs limits the heating of the cathode bulk while maintaining erosion conditions. The cloud of metal vapors released from the cathode surface is transported away and quenched by an inert gas to favor homogeneous nucleation and nanoparticle growth. Further downstream, the nanoparticles are exposed to a capacitively-coupled RF plasma sustained in a mixture of the inert gas and a monomer gas in order to form organic deposits on their surface. The produced nanoparticles are collected over various packings (polymer and paper filters or silica wool) placed inside the vacuum line. The entire reactor is evacuated between each run to a base pressure lower than 10^{-3} torr in order to control the contamination.

Pulsed Metal Vapor Arc Source & Metal Nanoparticle Synthesis

The metal vapor arc system uses as the cathode, a 1/4" rod made of the metal of interest. A stainless steel tube, concentric with the cathode rod, acts as the grounded anode. In the current geometry, the gap between the cathode rod and the inside of the anode is ~1 mm. In order to produce pulsed arcs, we designed and built a self-oscillatory (i.e. not triggered by external means) pulsed DC power supply capable of generating current pulses of amplitude >30 A; A high-voltage capacitor (General Atomics, 336 μF) is charged by a 1.5 kW capacitor charging power supply (Analog Modules, model 5723-1000N) until the voltage across the gap reaches the gas breakdown level. At this point, the capacitor rapidly discharges through the gap, forming a current pulse. A severe erosion of the cathode surface occurs due to the ignition of cathode spots. The process self-regulates itself and a periodic pulsation of arcs is observed. Fig. 2 shows typical arc voltage and current waveforms measured with a digital oscilloscope (Tektronix, TDS2024) equipped with a high-voltage probe (Tektronix, P6015A). A 330 Ω resistor is used to limit the charging current and pulsation rate to ~3 Hz, while the arc discharge current is limited by a ballast resistor (5-20 Ω). The current pulse duration is typically ~3 ms. We recently undertook a systematic study of the effect of the system pressure (1-100 torr), inert gas flow rate (50-2000 sccm Ar), pulse frequency (0.5-10 Hz), and pulsed arc peak current (~30-200 A) on the stability of the self-oscillatory power supply, and the properties of the bare copper powders produced. Preliminary results are presented in section 3.1.

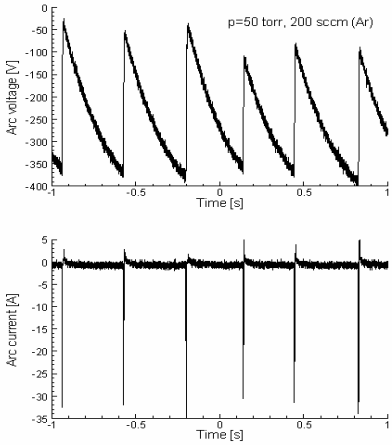

Fig. 2. Charging capacitor voltage (top) and arc current (bottom) waveforms.

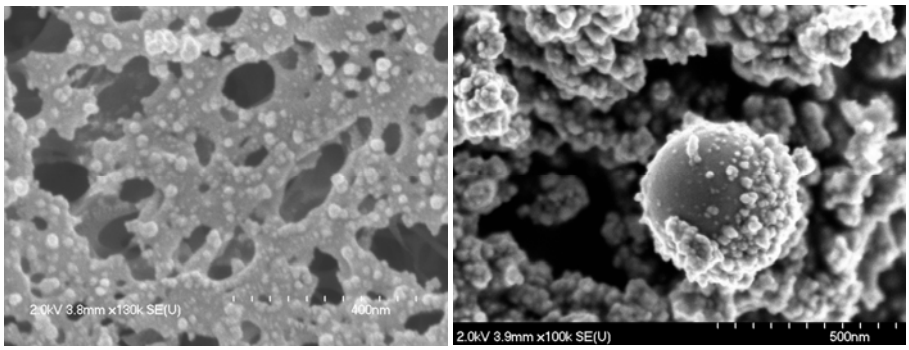

Fig. 3. FE-SEM images of copper powders produced with the pulsed metal vapor arc source (200 sccm Ar, p=50 torr). Left: nanoparticles collected on a polymer filter. Right: particles collected inside the pulsed metal vapor arc reactor.

Plasma Polymerization Reactor

The produced copper particles and inert carrier/quench gas are transported through an expanding nozzle, where a monomer gas is added, and subsequently into a cylindrical reactor made of a Pyrex tube (114 mm I. D. by 305 mm height). The residence time of the gas in this reactor can be adjusted over the 12-120 sec range by varying

the Ar flow rate from 1000 to 100 sccm at 50 torr. Several copper sheets (38 mm-wide), wrapped around the Pyrex tube, are used as RF electrodes: the live and grounded electrodes alternate (starting with a live electrode on the mid-plane of the reactor) to ensure the plasma fills the entire volume available, and to increase the capacitance value of the assembly (better impedance matching with the RF power supply). The current assembly uses three sheets of live electrodes separated by two sheets of grounded electrodes. The spacing between the borders of the live and grounded electrodes is approximately 12 mm. The bottom and top flanges of the reactor are grounded. The electrodes are capacitively-coupled to an amplitude-modulated (square wave) 13.56 MHz RF generator (Dressler, Cesar 1312) through an automatic L-type matching network (Dressler, VM 1000 A). C_2H_6 is used as the source of organic monomers since the methyl radical (CH_3) is regarded as the main precursor in the formation of ultrathin C:H coatings [5]. The effect of the C_2H_6 gas flow rate (5 to 15 sccm) and RF power (40 to 100 W) were considered in this preliminary study (Section 3.2).

3. Results and Discussion

3.1 Synthesis of copper nanoparticles

3.1.1 Pressure

The preliminary experiments revealed that, when the system pressure was lower than 30 torr, the stability of the pulsed arc system was intermittent: the system would sometimes evolve into a stable DC glow discharge where essentially no vapor was produced. At higher pressure, the pulsed arc system was consistently stable and led to the production of a significant amount of powders. Fig. 3 shows FE-SEM (Field Emission Scanning Electron Microscope) images of the copper powders produced under low quench rate conditions (200 sccm Ar) and moderate pressure (50 torr). The powders were collected on a polymer filter located downstream the plasma polymerization reactor (left) and on the anode of the pulsed metal vapor arc system (right). The images clearly reveal two size distributions: nanoparticles whose size ranges from 10 to 30 nm, and much bigger ones whose size can be as large as 1 μm ("macroparticles"). We also observe agglomerates of nanoparticles. The nanoparticles transported downstream to the polymer filter tend to form small agglomerates. In fact, the deposit formed on the anode surface seems to result from the pilling up of several nanoparticles. We suspect that macroparticles are produced as a result of the solidification of liquid droplets ejected from cathode spots upon extinction [6]. In order to control the formation of these macroparticles, the peak current and duration of the pulses can be reduced. The pressure also influences the mean diameter of the produced copper nanoparticles. Fig. 4 shows that the mean diameter of the copper nanoparticles is in the range of 10-30 nm when the pressure is ~60 torr, while this range shifts to 30-50 nm above 100 torr. At higher pressure, the metal vapor cloud produced at the cathode spot does not expand as much [7, 8]. This phenomenon gives rise to a more significant supersaturation of the vapor and to higher rates of collisions, both processes enhancing homogeneous nucleation and particle growth. Larger agglomerates too are observed at higher reactor pressure.

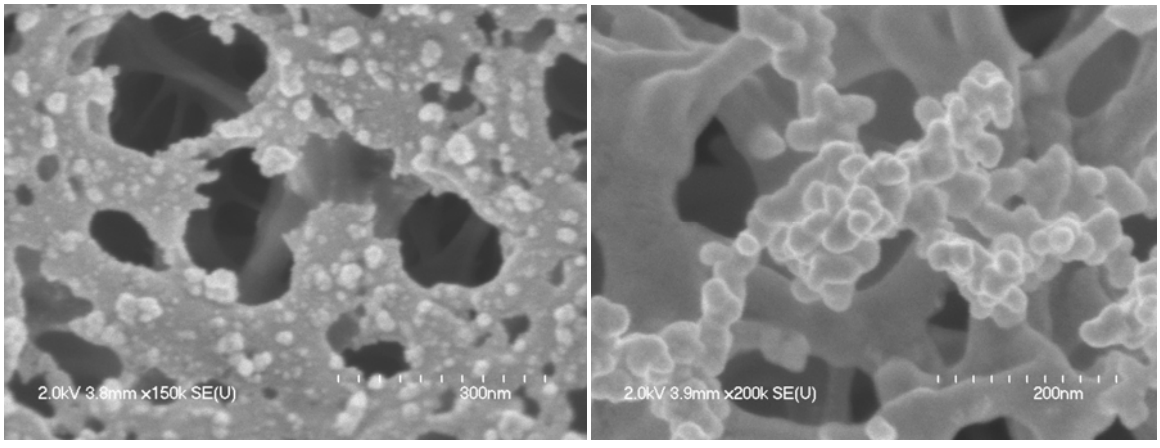

Fig. 4. FE-SEM images of copper nanoparticles produced under different reactor pressures with an argon flow rate of 400 sccm. Left: p = 60 torr; Right: p = 500 torr.

3.1.2 Inert gas flow rate

The FE-SEM images also show that when the gas flow rate is raised above 200 sccm, little effect is seen on the mean diameter of the produced copper nanoparticles. Fig. 5 compares copper nanoparticles produced at a reactor pressure of ~40 torr with 200 (left) and 1000 sccm Ar (right). The nanoparticles in both images are in the range 10~30 nm. The number of nanoparticles collected on the filter is more significant at 200 sccm than at 1000 sccm, since a higher fraction of the nanoparticles are swept through the filter at higher gas flow rate.

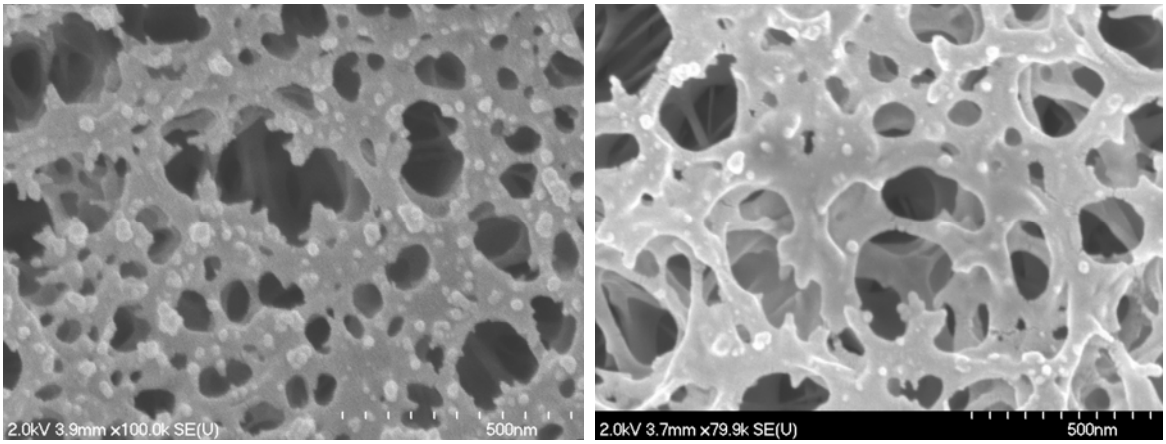

Fig. 5. FE-SEM images of copper nanoparticles produced under different gas flow rates at a reactor pressure of 40 torr. Left: 200 sccm Ar. Right: 1000 sccm Ar.

3.1.3 Frequency and amplitude of current pulses

We found that the arc pulsation frequency and current per pulse both affect the nanoparticle and microparticle production yields, but both seem to have little effect on the mean size of the nanoparticles. When increasing the pulse frequency, more copper vapors are produced per unit of time and consequently, more nanoparticles are produced. On the other hand, a higher pulse frequency increases the heat load on the copper rod to the point of bulk melting. Operation at higher current enhances the cathode erosion rate but at the same time, leads to an increase of the macroparticle yield; the increased erosion rate is mainly caused by the ejection of more liquid droplets from the cathode spots. Our preliminary process optimization study revealed that the use of a pulsation frequency of 3-5 Hz, and a current per pulse of 40-60 A, leads to the best compromise. Additional metal vapor source development efforts are currently under progress. An interesting avenue is to use magnetic confinement of the cathode spots in order to increase the metal vapor pressure within the cathode spots and in turn, reduce the fraction of the heat load dissipated by heat conduction to the cathode [9] (i.e. control the formation of macroscale liquid volumes).

3.2 Plasma polymerization

Fig. 6 shows FE-SEM images of coated copper nanoparticles collected on the polymer filter. Due to limitations of the working conditions of the FE-SEM, the images of coated particles are not as clear as the ones with bare metal particles. Nevertheless, one can distinguish a thin film (~10 nm) covering the individual copper nanoparticle. It is also interesting to notice the small-size nanoparticle agglomerates (~100 nm): most of these agglomerates show Cu nanoparticles isolated from each other by the coating and some others, showing small agglomerates of Cu nanoparticles that formed before the surface coating took place. We infer from these images that the current reactor configuration and operating conditions favor the formation of the coating before the metal nanoparticles get a change to agglomerate. Furthermore, despite the size distribution of the nanoparticles, the thickness of the deposited film seems to be relatively uniform. This result seems to indicate a uniform distribution of active radicals in the plasma polymerization chamber [10] and a narrow distribution of residence

times. The images also show that the individual coated copper nanoparticles tend to scatter more on the polymer filter, suggesting that the surface energy of the nanoparticles is reduced due to the presence of the film.

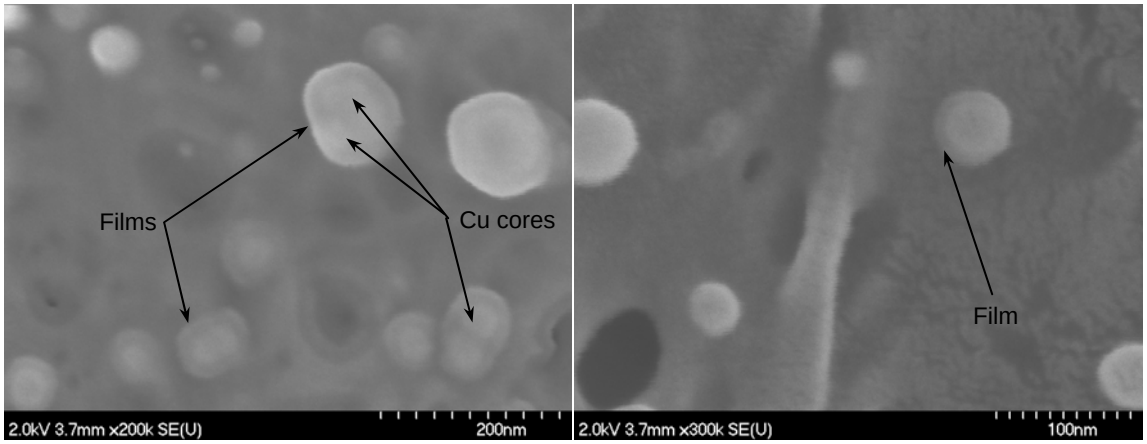

Fig. 6. FE-SEM images of coated copper nanoparticles (CW rf plasma power: 40 W; Ar flow rate: 300 sccm; C_2H_6: 10 sccm; Pressure: 65 torr)

4. Preliminary conclusions

We demonstrated that copper nanoparticles, ranging in size from 10 to 30 nm and coated with a ~10 nm-thin film, can be synthesized in a single-step by combining a cathodic arc evaporation/condensation process, with an in-flight plasma polymerization process. It has been demonstrated that the reactor pressure, the peak current and frequency of the pulsed arcs, and the flow rate of the carrier/quench gas, play important roles in the control of the nanoparticles' properties and yield, and in the stability of the pulsed arcs. Our preliminary optimization study led to the adoption of the following conditions for the nanoparticle synthesis stage: chamber pressure: 30 - 60 torr; inert carrier/quench gas flow rate: 400 - 800 sccm; arc pulsation frequency: 3 - 5 Hz; and peak arc discharge current: 40 - 60 A. Further research activities aimed at mitigating the formation of macroparticles and optimizing the in-flight plasma polymerization process are currently under progress.

Acknowledgments

The authors wish to thank L. Cusmich, A. Gagnon and W. Greenland for their technical assistance. The project was funded by the National Sciences and Engineering Research Council of Canada (NSERC), through the Discovery and Canada Research Chairs programs, the Fonds Québecois de la Recherche sur la Nature et les Technologies (FQRNT), and McGill University.

References

[1] A. Ermoline, M. Schoenitz, E. Dreizin, N. Yao - Nanotechnology **13**, 638 (2002).
[2] F.E. Kruis, H. Fissan, A. Peled – J. Aerosol Sci. **29**, 511 (1998).
[3] P. Keblinski, S.R. Phillpot, S.U.-S. Choi, J.A. Eastman - Int. J. Heat Mass Transfer. **45**, 855 (2002).
[4] D. Vollath, D.V. Szabo - J. Nanoparticle Res. **1**, 235 (1999).
[5] A. Kouprine, F. Gitzhofer, M.I. Boulos, A. Fridman - Plasma Chem. Plasma Process. **24**, 189 (2004).
[6] D.T. Tuma, C.L. Chen, D.K.J. Davies - J. Appl. Phys. **49**, 3821 (1978).
[7] M.G. Drouet, J.-L. Meunier - IEEE Trans. Plasma Sci. **13**, 285 (1985).
[8] R.L. Boxman, D.M. Sanders, P.J. Martin, J.M. Lafferty - Handbook of vacuum arc science and technology: fundamentals and applications. 1995.
[9] S. Coulombe, J.-L. Meunier – Plasma Sources Sci. Technol. **9**, 239 (2000).
[10] D. Shi, S.X. Wang, W.J. van Ooij, L.M. Wang, J. Zhao, Z. Yu - App. Phys. Lett. **78**, 1243 (2001).

Collection of Nano-powders Generated by Radio Frequency (RF) Plasma Spray Synthesis (PSS) Processing, Using a Sampling Probe

L. Jia, F. Gitzhofer

Energy, Plasma and Electrochemistry Research Centre (CREPE)
Université de Sherbrooke, Canada

Abstract
A particle-sampling probe has been designed and constructed for the continuous collection of nano-powders produced by the plasma spray synthesis (PSS) process. The probe comprises a powder sampling line (inner tube), a quench gas line (outer tube) and a water-cooling jacket surrounding the outer tube. The results obtained to date indicate that the sampling probe location in the plasma reactor and the quenching gas flow rate employed are the most important parameters involved in the satisfactory operation of the sampling probe.

1. Introduction

Recently, the Radiofrequency (RF) Plasma Spray Synthesis (PSS), based on using solution precursors as the process feedstock, has become a mature and advanced materials processing technique for nano-particles synthesis. In this process, the liquid phase precursor is atomized and injected into the high temperature plasma flame, the plasma synthesized particles being collected by a series of filters downstream. As the atomized droplets enter the high temperature flame and are accelerated towards the collecting surface, various step-wise occur [1-4]. As shown in Fig.1 [5], the first step is the evaporation of the solvent, which is followed by "condensation" of the solid precursor materials. Chemical reactions are initiated next, followed by grains nucleation and growth, resulting in the formation of dense solid particles. Interactions among these highly reactive particles lead to the formation of either larger particles/crystals, agglomerates or aggregates.

In order to characterize the freshly synthesized powders, the conventional method is to scrape the powders from the chamber walls and the filters, prepare the specimen for transmission electron microscopy (TEM) or field emission scanning electron microscopy (FESEM), obtain and analyze the images. There are several drawbacks in this method, for example, it is necessary to clean the chambers and the filters perfectly after completing the experiment. During the plasma synthesizing process, the nano-powders adhere to internal walls of the plasma chamber and the filters. If the clean-up is not performed well, undesirable particle contamination would be caused to future process products, resulting in inaccurate powders characterization. However, in practice, this cleaning work takes more than two hours according to the previous experiences.

The conventional product recovery methods do not recover the plasma produced powders at the desired chamber positions. This may cause uncertainty in the experimental results. Furthermore, the conventional method is vulnerable to contamination, because it is necessary to separate the activities of powder collecting and specimen preparation.

Accordingly, there exists a strong need for a sampling probe that has a quick but complete clean–up characteristic, a reduced risk of cross-contamination, yet be capable of withdrawing powder samples from all desired chamber positions.

2. Experimental

2.1. Experimental setup and procedure

The experimental setup, as used in this study, is illustrated by the schematic diagram of Fig.2, and consisted of three major parts: (1) an induction plasma torch (model PL – 50, from Tekna Plasma System Inc. Canada) connected to a radio frequency (RF) power supply; (2) a water cooled cylindrical reactor attached to a filter assembly; and (3) a sampling probe system connected to a vacuum pump. A water cooled atomization probe penetrates the plasma along the torch axis, thereby permitting the injection of the cerium nitrate solution into the plasma. The probe tip is "axially" located in the centre of the torch [6].

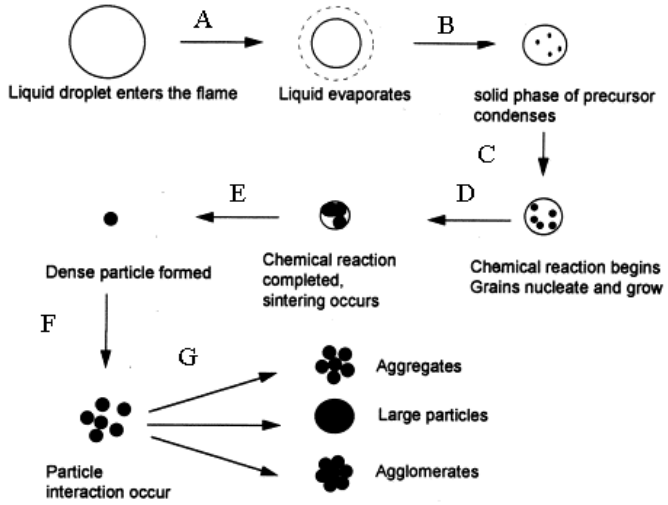

Fig.1. Schematic of the Plasma Spray Synthesis process

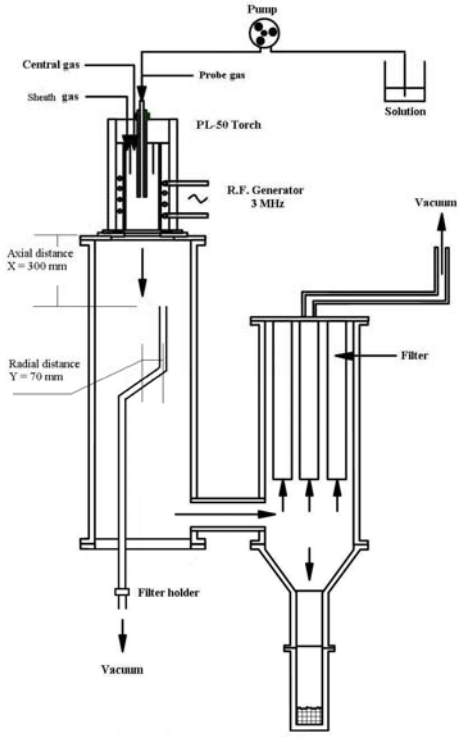

Fig.2. RF plasma installation for PSS

The plasma spray synthesis of nano-powders with consistent properties requires control of both the size and the size distribution of atomized feed liquid droplet droplets and optimization of the spray parameters. Hence, a series of experiments were carried out by varying the gap size of the atomization probe, the pressure and flow rate of the atomizing gas and the flow rate of the liquid feedstock, and recording the variations in the droplet size distribution of the aerosols using a Malvern RTsizer. Based on the results of these experiments, atomization and spray parameters were optimized to obtain droplets with 12 μm mean size [7].
In this work, the pressure in the plasma reactor chamber and the torch plate power were considered as the variable parameters in order to obtain more experimental data towards the end of the sampling probe evaluation. The experimental conditions for these tests are summarized in Table 1.

2.2. Sampling probe system

The sampling probe is described in detail by reference to Fig. 3 which shows a schematic view of the sampling probe. It comprises a perforated cup that is made from molybdenum because of its very high melting point (2896 K), a powder sampling line (inner tube), a cleaning liquid and drying gas line (outer tube) and a water-cooled jacket surrounding the outer tube. The sampling probe has an outer diameter of 13 mm, a median diameter of 10 mm and an inner diameter of 5 mm. It is constructed from four concentric thin wall stainless steel tubes. The median tube (inside water – cooling jacket) guides the cooling water to and from the perforated cup. A pump is connected to the outlet of the inner tube and draws a flow of gas into the inner tube through the perforated cup. A standard 3.08 mm TEM copper grid is disposed within the sample holder, and used to withdraw the sample powders. Quench gas is introduced to the probe, via the outer tube, to quench and entrain the as-synthesised powder clusters. After each sample collection, the inner tube is cleaned by the injection of the cleanser liquid (water) and then dried using a compressed gas flow. In our application, helium (He) is used as the quench gas because of its higher thermal conductivity compared to that of other inert gases [8].
In order to evaluate the utility of the sampling probe, it was located at various positions within the reactor chamber and performance comparison experiments were carried out. Initially, the sampling probe was located on the axis of the reactor chamber, the axial distance between the torch exit and the probe perforated cup (denoted

as X) was 500 mm (X = 500 mm). In a second position, by rotating the sampling probe symmetrically, the probe perforated cup was able to traverse the reactor chamber cross-section circularly. The radial distances between the axis of the reactor chamber and the perforated probe cup of the sampling probe (denoted as Y) were 70 mm (Y = 70 mm). Finally, the sampling probe was relocated at X = 300 and 400 mm and Y = 0 and 70 mm, respectively, and the sampling evaluation experiments repeated. In order to compare the two sampling methods, synthesized powders were also collected from the wall of the reactor chamber at the same sampling probe collecting position after each experiment.

The powder samples so collected were examined by TEM or FESEM to observe their surface morphology and subsequently, to measure their size by using a software which was developed specially to address agglomerated powders diameter measurement based on fractal dimensions, to be published soon by the same authors.

Table.1. PSS experimental parameters

Plasma torch	PL - 50
Central plasma gas [slpm]	27 (Ar)
Sheath plasma gases [slpm]	90 (Ar) 80 (O_2)
Power [kW]	35 and 50
Chamber pressure [kPa]	8 and 12
Atomization gas pressure [kPa]	345
Atomization gas [slpm]	21 (Ar)
Solution concentration [mol/L]	1
Solution injection flow rate [mL/min]	10

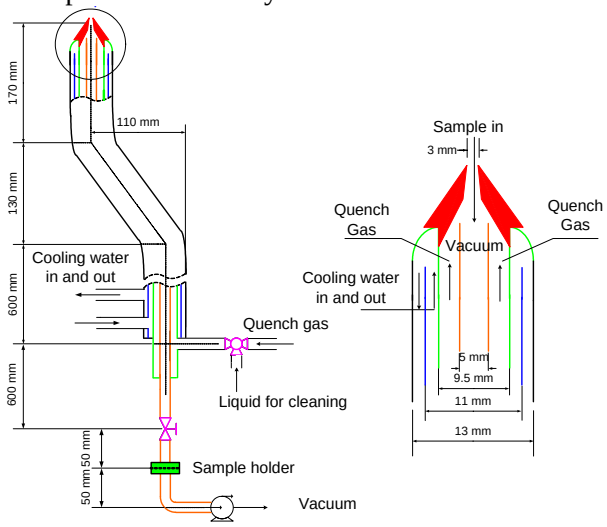

Fig.3. Schematic of the sampling probe

3. Results and Discussions

3.1. Determination of quench gas flow rate

The quench gas introduced into the sampling probe is used to quench and entrain the freshly "as-synthesized" nano-powders. Fig.4 (a) is a graphical presentation of the quench gas flow rate's influence of the synthesized powders' average particle size. It can be observed that smaller helium flow rates, up to 21.5 slpm, do not greatly affect the synthesized powder particle size. A major difference is observed when the helium flow rate is raised to 29 slpm, the powder particle size then is falling to below 20 nm. However, this does not mean that the quench gas flow rate can be increased without limit to continually reduce the size of the synthesized powder particles. Fig.4 (b**)** shows that, if the helium flow rate is raised to 36.5 slpm, not all of the helium flow can be extracted by the vacuum pump, part of the helium input would by-pass the sampling probe, and it may cause the plasma characteristics to be affected.

Additionally, in order to determine the optimum quench gas flow rate Q_1, the sampling gas flow rate Q_2 is calculated. The sampling gas, which should contain all of the quench gas, passes through the inner tube of the sampling probe, due to the imposed pressure difference (vacuum). According to the Hagen-Poiseuille equation, the sampling gas flow rate Q_2 through the inner tube is the product of its cross section area and the average gas velocity. The average velocity is calculated by summing all of the gas velocities over the suction probe section and then dividing the result by the probe cross section area [9]:

$$\langle v_z \rangle = \frac{\int_0^{2\pi}\int_{kR}^{R} v_z r dr d\theta}{\int_0^{2\pi}\int_{kR}^{R} r dr d\theta} = \frac{(p_0 - p_L)R^2}{8\mu L} \qquad (1)$$

Thus, the total volume flow rate through the inner tube can be calculated by (2),

$$Q_2 = \pi R^2 \langle v_z \rangle = \frac{\pi (p_0 - p_L) R^4}{8 \mu L} \qquad (2)$$

where $p_0 - p_L$ is the pressure difference between the sampling probe inlet and exit (Pa); R is radius of the inner tube (m); L is length of the tube (m); and μ is the viscosity of the gas ($Pa \cdot s$).

The calculated value of Q_2 (from (2)) for our experimental conditions is 41.2 slpm, which is much higher than the experimental result (between 29 and 36.5 slpm). The difference between the calculated and the measured sampling gas flow rate can be explained as follows:

- The actual flow rate difference may be attributed to the value of the fluid parameter (viscosity), used in (2), were developed for gases only, whereas our input materials is biphasic (i.e. as nano-dispersed solids and gases).
- In the previous calculation (2), no bending of the sampling probe is considered. However, the resistance caused by probe bending is unavoidable during the sampling process.

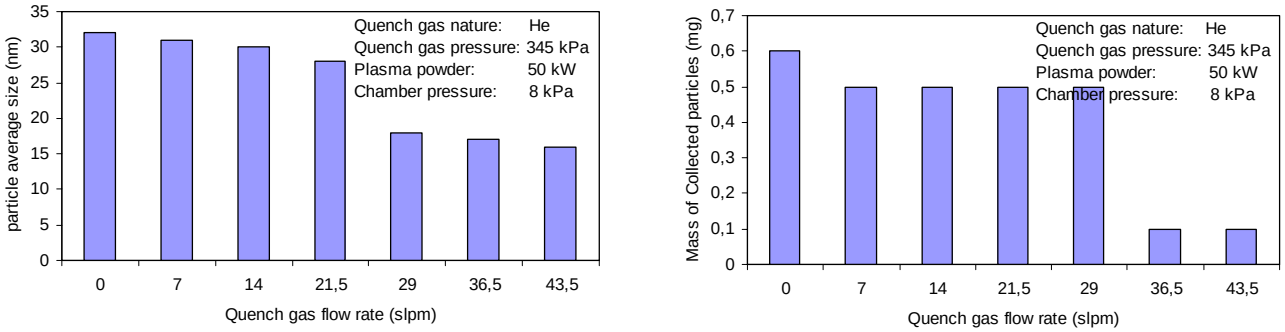

Fig.4. Influence of quench gas flow rate on (a) the synthesized particle average size and (b) the mass of synthesized powder at axial position 300 mm

Consequently, in considering the provision of the highest possible cooling rate to the suspended particles within the sampling probe, the quench gas flow rate of 29 slpm is fixed as the optimum value in the following experimental tests.

3.2. Effects of sampling method and position

Fig.5 illustrates the effect of the sampling methods on the synthesized powder size. It is observed that when the sampling probe is located at an axial position of 300 and 400 mm from the torch exit plane (X = 300 and 400 mm, Y = 0 mm), the sizes of powders that are collected by the sampling probe are reduced by about 30% and 20%, respectively, compared to those powders collected using the conventional method. This finding was expected since, as illustrated in Fig.1, it is supposed that the "grains" are nucleated and then "grown" in the plasma flame between the axial locations of X = 300 and 400 mm. The "grains" are drawn into the sampling probe at the point where the quench gas is introduced. These grains are rapidly cooled to cause the production of smaller sized grains. Furthermore, the micrographs shown in Fig.6**,** produced by TEM for the revelation of powder morphology, indicate that the high cooling rate also reduces the rate of particle aggregation and leads to decreased agglomeration levels in the powder [10]. Fig.5 also shows that the average particles size, collected within the sampling probe, is almost same as that collected from the reactor wall at the 500 mm axial location (X = 500 mm), because particle interaction has occurred (step G) and aggregated powders are formed at this region. Thus, the quench gas has no influence on the powder grain size.

Fig.7 shows the effect of sampling position on the synthesized powder size. The presence of the large powder size at the radial location of 70 mm can be explained by incomplete evaporation of the injected evaporation. The plasma flame is characterized by a certain temperature distribution in the radial and axial directions. When the radial location is 70 mm, the gas temperature is now too low for complete evaporation of the solvent and

condensation of the precursor materials at the outer layer of the plasma flame and the product particle size is consequently increased.

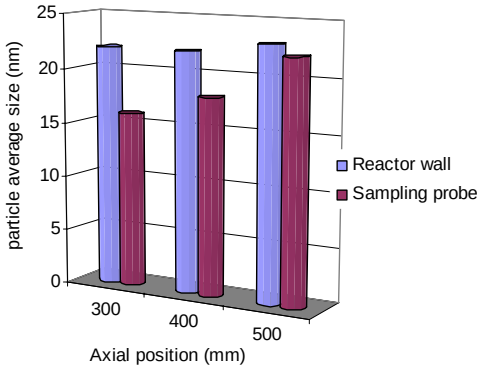

Fig.5. Effect of the sampling method on the synthesized

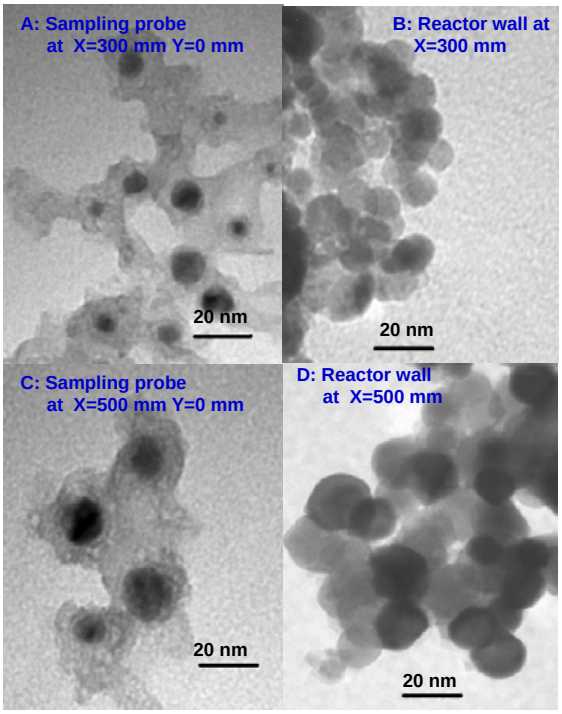

Fig.6. TEM micrographs illustrating the effect of sampling method on the degree of powder agglomeration.

3.3. Effects of chamber pressure and plasma power

The influence of the chamber pressure as well as that of the plate power on the size of powder (collected by the sampling probe) can be clearly recognized by reference to Fig.8. Fig. 8 shows the influence of plasma power and chamber pressure on the synthesized powder size that was collected using the sampling probe.

For a given plasma power, decreased powder size is observed when the chamber pressure decreases. Powders follow the “free molecular regime” in the condensation zone. Consequently, “Brownian coagulation mechanism” can occur and powders grow by the process of collisions and fusions. Thus, as the chamber pressure increases, the rate of collisions increases, providing for the particle size continuing growth.

On the other hand, for a given pressure, large variations in the powder size are noticed when the plasma power level (Fig.8) is changed. Initially, as the plate power is raised, the plasma to particles heat transfers increases. Evaporation is thereby favoured, and particle velocities are increased. This results in diminished residence times in the plasma for the particles and leads to shorter growth times and decreased particle diameters.

All the experimental results on the influence of plasma power and chamber pressure on the synthesized powder size, collected using sampling probe, are in good agreement with the previous published results [8], obtained using a conventional powder collecting method. This agreement also validates the successful application of the sampling probe.

3.4. Sampling probe clean–up

As mentioned before, during the sampling process, nano-powders adhere to the internal wall of the sampling probe, leading to contamination of future processing products. This is unacceptable for the proper operation of the sampling probe. Thus, the probe should be cleaned by water and dried by compressed gas after completion of every experimental use. In order to identify satisfactory completion of the clean-up process, experimental tests were conducted to evaluate the clean-up achieved. All previous plasma operating parameters were employed,

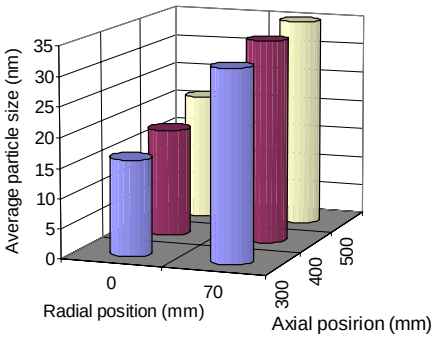

Fig.7. Effect of sampling position on the synthesized

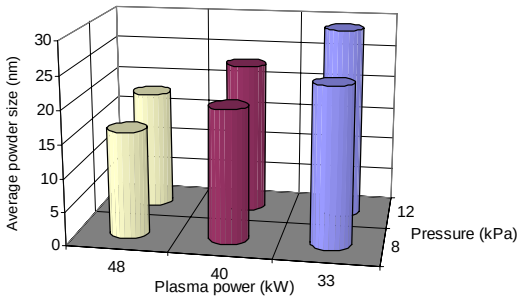

Fig. 8. Influence of plasma power and chamber pressure on the synthesized powder size collected using sampling probe

with the exception of the solution injection. Observation of the now empty TEM grid confirms that the clean-up task is successful.

4. Conclusions

A particle-sampling probe has been demonstrated to successfully collect nano-powders that are produced by plasma spray synthesis (PSS) processing. Compared to the conventional sample collection method, this technique has more advantages, i.e. quick clean-up, reduction in the risk of contamination and withdrawal of powders at the desired internal plasma chamber position. The quench gas is introduced into the sampling probe at a flow rate of 29 slpm. This benefits the reduction of grain size and the degree of agglomeration of the synthesized powder. The optimum sampling position has been found at the axial position X = 300 mm inside the reactor chamber, which also coincides with the position for optimum product particle size generation. This approach is compatible with the combinatorial approach which will be used extensively in the Energy Plasma and Electrochemistry Research Centre.

Acknowledgement

The authors would like to acknowledge the support of NSERC through a strategic grant # 257902 – 02.

References

[1] J.L. Katz, P.F. Miquel “Synthesis and applications of oxides and mixed oxides poduced by a flame process” Nanostruct. Mater. 4 (5) (1994) 551–557.

[2] A. Gurav, T. Kodas, T. Pluym, Y. Xiong “Aerosol processing of materials” Aerosol Sci. Technol. 19 (1993) 411–452.

[3] C. Roger, T. Corbitt, C. Xu, D. Zeng, Q. Powell, M. Nyman,M.J. Hampden-Smith, T. T Kodas “Principles of molecular precursor selection for aerosol synthesis of materials” Nanostruct.Mater. 4 (5) (1994) 529–535.

[4] S. K. Friedlander, R. S. Windeler, A. P. Weber “Ultrafine particles formation in turbulent jets: mechanisms and scale-up” Nanostruct. Mater. 4 (5) (1994) 521–528.

[5] I. Wiedemann, K. L. Choy, B. Derby “Flame-assisted deposition of lead titanate-based thin films; correlation of deposition process, microstructure and electrical properties” in: F.R. Sale (Ed.), Novel Synthesis and Processing of Ceramics. The Institute of Materials, London, 1994, pp. 133–142.

[6] M. I. Boulos ”The inductively coupled R.F. (radio-frequency) plasma” Pure Appl. Chem, vol. 57, no. 9,1985

[7] L. Jia, C. Dossou-Yovo, C. Gahlert, F. Gitzhofer “Induction Plasma Spraying of Samaria doped Ceria as Electrolyte for Solid Oxide Fuel Cells” ITSC 2004 (conference), Japan

[8] R. William, J. Dwyer “Experiences with nitrogen, argon, and helium as quench gasses” Proceedings of the Conference, 21st, Indianapolis, IN, United States, Nov. 5-8, 2001, 236-239

[9] R. Byron Bird, Warren E. Stewart, Edwin N. Lightfoot “Transport phenomena” (1976), 42-48

[10] S.Y. Kim, J.H. Yu, Ji Hun, J.S. Lee; J.R. Kim “Synthesis of nanosized TiO2 powder by chemical vapor condensation process (1)” Yoop Hakhoechi (1999), 36(7), 742-750.

Permeation barrier coatings for flexible electronics and polymer/inorganic layer interphase development in an expanding thermal plasma

M. Creatore[1], V.I.T.A. Lohmann[1], C. G. Klaasse Bos[1], A.C.M. Hamelinck[1],
M. M. Koetse[2], H.F.M. Schoo[2], M.C.M. van de Sanden[1]

[1]*Department of Applied Physics, Eindhoven University of Technology*
5600 MB Eindhoven, the Netherlands

[2] *TNO Science and Industry, 5612 AP Eindhoven, the Netherlands*

Abstract

The multi-layer system of alternated inorganic and organic layers is considered to be the winning technology for ultra-barrier permeation layers for flexible electronics. Here we present our first studies concerning the moisture permeation barrier properties of inorganic films achieved by means of the expanding thermal plasma. Moreover, we report on the interphase development between the polymer and the barrier layer, as investigated by means of *in situ* and real time diagnostics, i.e., spectroscopic ellipsometry.

Keywords

Plasma Enhanced-CVD; permeation barrier coatings; in situ real time diagnostics.

1. Introduction

In the last three-four decades polymers have rapidly spread in several and diverse technological fields due to their benefits, i.e., lightweight, transparency, printability, sealability, safety, flexibility, mouldability. Next to the "allure" of plastics, polymer- based technologies started to face also their major and inherent deficiencies, i.e., their low surface energy/ poor reactivity and high gas/vapor permeation. Consequently, plasmas became widely acknowledged in modifying and tailoring the polymer surface chemistry (e.g., for improving polymer/metal adhesion), as well as in providing thin (≈ 100 nm) gas/vapor permeation barrier film deposition on the polymer substrates [1,2]. Literature on plasma deposition of inorganic barrier layers (mostly SiO_2, Si_3N_4) flourished: plasma- deposited films performed better than evaporated and sputtered counterparts in terms of barrier properties and adhesion to the polymer substrates; the ultimate barrier layer performance (O_2 transmission rates in the range of 0.1-0.5 $cm^3/m^2 \cdot day \cdot atm$) was found to be governed by defects density in the deposited layer [3].
Nowadays, the interest in polymeric substrates grows in fields where long- term stability devices are required, such as flexible solar cells and OLEDs (electronics integrated into textile, rollable displays). Here, the film barrier technology needs to achieve moisture permeation as low as 10^{-6} $g/m^2 \cdot day$, in order to guarantee, for example, a 10 years- lifetime for a flexible OLED device. Due to the limits reached by single plasma-deposited barrier layers, a few μm-thick multi-layer system consisting of alternated inorganic and organic layers appears to be the winning technology in flexible electronics, reaching moisture permeation values as low as 10^{-5} $g/m^2 \cdot day$ [4]. Plasma technology, however, has not been yet explored (with a few exceptions, [5]) in the deposition of multi-layer barrier systems, since sputtering/ evaporation (of the inorganic barrier layer) and vacuum deposition + UV curing (of the organic interlayer) are mostly preferred. Though successful results in terms of moisture permeation barrier are achieved, the role of the organic interlayer is still under debate and not fully developed: smoothening of the inorganic surface roughness [4], decoupling of the defects present in the inorganic layer [6], infiltration of the organic (liquid) precursor in the defects of the underlying inorganic films [7], are the most plausible hypotheses. The presence of the interlayer, therefore, can affect the growth of the inorganic layer (and vice versa), as well as the final mechanical performance of the multi-layer system (e.g., adhesion between the polymer and the inorganic layer and between the inorganic layer and organic interlayer). In this framework, plasma deposition can certainly contribute to the improvement of a multi-layer system design: the development (and, ultimately, the control) of an interphase between the polymer and the inorganic layer (as well as between the inorganic and the organic interlayer), due to the synergic effects of radicals, ions

and UV light [8], may affect the barrier and mechanical properties of the system. Moreover, the possibility of an entirely plasma-deposited multi-layer system may simplify the roll-to-roll or batch production line because a single chamber for barrier deposition would be required. This contribution aims:

- to describe our recent results on SiN_x and SiO_2-like barrier layers deposited by means of the expanding thermal plasma (ETP), a remote plasma where ion bombardment towards the substrate is negligible (E_i< 2V);
- to report on the development of an interphase region between the inorganic layer and the polymeric substrate, as followed by means of in situ and real time diagnostics, i.e. spectroscopic ellipsometry.

2. Experimental

The ETP set-up, already described in detail in [9], is depicted in Figure 1. Briefly, the ETP is a remote plasma where an Ar (Φ_{Ar}) plasma is ignited at a variable arc current (I_{arc}) in a wall-stabilized dc cascaded arc in a pressure (P_{arc}) range of 0.1-0.4 bar. The arc consists of three cathodes, four cascade plates and an anode in which a nozzle is present. The thermal plasma expands supersonically through the nozzle into the deposition chamber kept in the pressure ($P_{chamber}$) range of 0.1-0.3 mbar. The Ar ion and electron fluence (Ar^+, e^-) expanding from the arc are fully controlled by the plasma parameters, i.e., Φ_{Ar} and I_{arc}, and measured by means of Langmuir Probe [10]. Co-precursors for SiO_2-like film deposition are O_2 and hexamethyldisiloxane ($(CH_3)_3SiOSi(CH_3)_3$, HMDSO), injected via the nozzle and via a ring placed at 5 cm from the nozzle, respectively. Co-precursors for SiN_x film deposition are NH_3 (via the nozzle) and SiH_4 (via the ring). Table 1 summarizes the deposition parameters. The depositions were carried out on (100) Si substrates and 100 μm-thick poly(ethylene 2,6 naphtalate) substrates placed on a substrate holder 60 cm (in the case of SiO_2-like films) and 40 cm (in the case of SiN_x films) distant from the nozzle. The deposition temperature was fixed at 100°C (the glass transition temperature of PEN is 128°C) and a He backflow was used for thermal contact between the polymer and the substrate holder. An active $N_{2(l)}$/ water cooling system guaranteed a constant substrate temperature (± 10°C) during plasma processing (determined to be ± 10°C in the case of deposition on c-Si).

Table 1. ETP deposition parameters for SiO_2-like and SiN_x films.

Parameters	**SiO_2-like**	**SiN_x**
Φ_{Ar}	30 sccs	40 sccs
I_{arc}	75 A	40 A
Φ_{O2}; Φ_{NH3}	16.6 sccs	16.6 sccs
Φ_{hMDSO}; Φ_{SiH4}	0.4 sccs	0.4 sccs
$P_{chamber}$	0.11 mbar	0.14 mbar

As already commented in the previous section, in the ETP the growth of films occurs in the absence of ion bombardment: this is due to the low electron temperature (≈ 0.3 eV) in the downstream region, which, consequently, allows developing a very low bias voltage at the substrate (E_i < 2 V). Therefore, dedicated studies on the effects of ion bombardment on the film growth were performed by means of an external rf substrate bias: the substrate holder was connected to a 13.56 MHz RF power supply; the substrate voltage and peak-to-peak voltage were monitored using a high voltage probe and an oscilloscope operating in DC mode.

The deposited layers were characterized by means of IR spectroscopy and in situ spectroscopic ellipsometry in the 245-1000 nm range at an angle of 68°. In situ real time ellipsometric studies, with a time resolution of 2 s, were performed on the PEN substrates during the SiO_2-like film growth. The optical properties of the PEN substrate were obtained by fitting the ψ and Δ angles in the range of 300-1000 nm with the Cauchy model, a dispersion relationship often used for transparent films. Below λ= 300 nm, the optical properties of the polymer were obtained by a point-by-point fit. The SiO_2-like and SiN_x film bulk were also modeled by means of the Cauchy formula.

The water vapor barrier properties of the SiO_2-like (data not reported here) and SiN_x films on PEN were evaluated by means of the Ca test; the SiN_x layers were also tested in a multi-stack system consisting of PEN/SiN_x(130 nm)/P(400 nm)/SiN_x(130 nm), where P is a sprayed/UV cured acrylate-based interlayer.

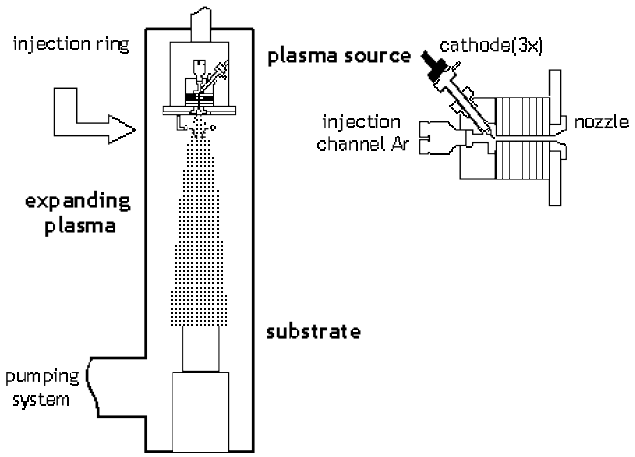

Figure 1. Expanding thermal plasma setup.

3. Results and Discussion

3.1 ETP deposition of inorganic moisture barrier layers

Figure 2a shows the SiN_x film refractive index (λ = 633 nm) increase (corresponding to an increase in film density and/or N-to-Si ratio) as a function of the rf power delivered to the substrate, confirming the results already presented on ETP- deposited SiN_x densification by means of ion bombardment [11].

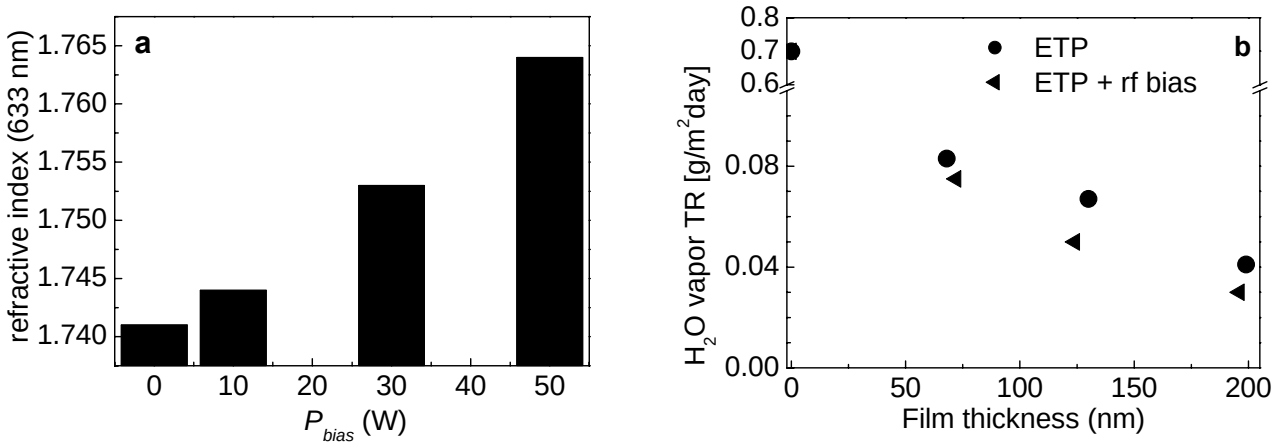

Figure 2. a) Refractive index (=633 nm) as a function of the biasing power externally applied to the substrate. b) Water vapor permeation of PEN/SiN_x, the SiN_x layer being deposited in the presence and absence of subtrate bias (P_{bias}= 50 W; V_{bias}= -160 V).

The moisture barrier permeation of SiN_x layers grown in the presence and absence of ion bombardment was tested and reported in Figure 2b: it appears that the substrate biasing allows to deposit efficient single SiN_x barrier films ≈ 50 nm thinner than SiN_x layers obtained in the absence of ion bombardment. These results agree with what reported in literature: a critical barrier layer thickness in the 50-100 nm range [12], when the films are deposited by means of rf plasmas (i.e., ion bombardment is present). Evidently, the ion bombardment- induced film matrix densification does not contribute to an improvement in the film barrier properties (the water vapor transmission rate of a 200 nm- thick layer hardly decreases); instead, the data in Figure 2b are indicative of conductance-limited permeant transport (e.g., via defects) across the barrier layer. The SiN_x layer deposited in the presence of an external substrate bias (P_{bias}= 50 W) has been tested in a two dyads barrier system, as described in the Experimental section. Figure 3 highlights the beneficial effect of an interlayer between two

SiN_x layers: the water permeation decreases of a factor 100 compared to the pristine PEN. At this rate, three additional dyads (P/SiN_x) could be sufficient to meet the requirements for OLEDs encapsulation.

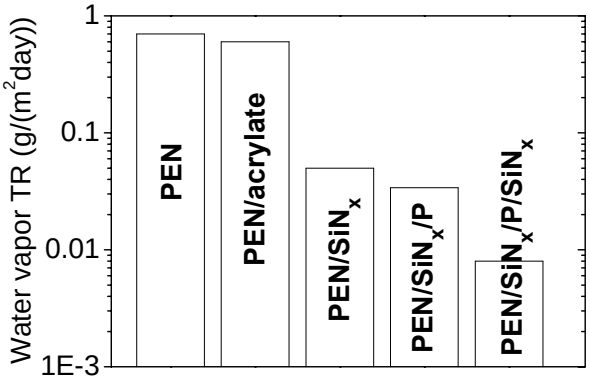

Figure 3. Water vapor transmission rate of a two dyads system, PEN/PEN/SiN_x(130nm)/P(400 m)/SiN_x(130nm).

3.2 Interphase development during the deposition of an inorganic layer on a polymer substrate

Literature studies on plasma deposition of inorganic layers on polymer substrate have shown the presence of an interphase region between the polymer bulk and the deposited layer bulk [8]. This region has been only investigated by means of ex situ diagnostic tools, such as x-ray photoelectron spectroscopy (coupled to Ar^+ sputtering), IR spectroscopy and Rutherford backscattering spectroscopy [8, 13]. On the contrary, in situ real time studies during the interphase evolution and inorganic film growth have not been reported; moreover, the optical (e.g., via spectroscopic ellipsometry) detection of an interphase developed between a polymer substrate (polycarbonate) and SiO_2 was reported to be difficult to attain [14]. The formation of this interphase region is hypothesized to develop during the early stage of interaction between the plasma and the polymer surface: UV light, non-depositing radicals (e.g., O, OH, N, NH_x), ion bombardment may, in fact, affect the polymer surface before appreciable deposition occurs. The presence of the interphase can strongly influence the adhesion of a barrier layer/polymer system, as well as the inorganic layer critical thickness.

Here, initial studies devoted to the detection of the interphase have been carried out first on plasma- deposited SiN_x layers on PEN substrates by means of *ex situ* spectroscopic ellipsometry. Figure 4a shows the experimental ψ data of a SiN_x layer deposited on PEN fitted with two models. It can be observed that a *homogeneous layer* model, which assumes constant optical properties for the deposited SiN_x layer, does not properly fit the experimental data. On the contrary, including an interphase region before the bulk growth occurs, improves the fitting. Figure 4b shows the evolution of the refractive index *n* (at 633 nm) as a function of the film depth: a graded interphase of ≈ 25 nm appears to be present before the SiN_x bulk layer develops. Also a surface roughness modeled according to the Bruggeman effective medium approximation was included. Thin SiN_x film depositions (up to 50 nm) have been also carried out: Figure 4b shows that their refractive index values align with the evolution of the refractive index observed for the thick SiN_x layer, therefore, confirming the adopted optical model. The thin film *n* values are, however, lower compared to those describing the interphase region: this can be explained by post-deposition oxidation due to the porosity of the layers. Although the interphase region is optically modeled by linearly mixing the dielectric function of the SiN_x bulk layer with different percentages of voids, the interphase region may be differently interpreted. A (sub)-surface polymer modification by means of NH_x radicals and UV light, resulting in a decrease of the polymer refractive index (*n*= 1.77 at 633 nm) could occur before appreciable deposition takes place.

These initial *ex situ* studies have been followed up by an *in situ* real time investigation on the growth of SiO_2-like films on PEN in order to monitor the development, if present, of the interphase region. The SiO_2-like films were deposited at a deposition rate of 3.5 nm/s (as derived from the growth of a 150 nm thick film on Si).

Figure 5a shows the refractive index development (at 633 nm) as obtained by modeling the deposited layer on PEN (*static measurement*) and by modeling the same layer during its growth (*dynamic measurement*).

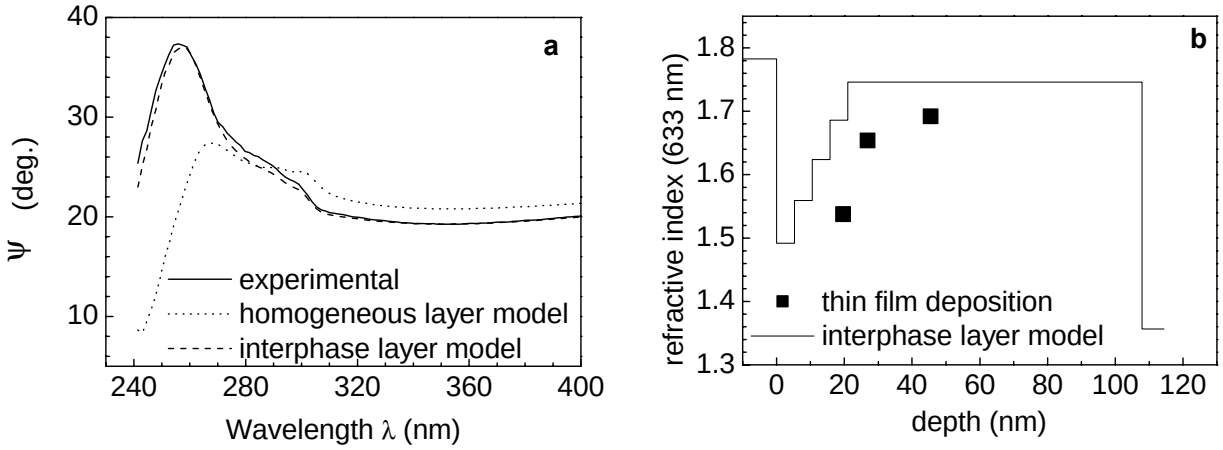

Figure 4. a) Experimental ψ data for a SiN_x film deposited on PEN, fitted with two different models. b) Refractive index evolution as a function of the SiN_x film depth for the interphase layer model. The refractive index and thickness of three thin SiN_x layers deposited on PEN are also shown.

The optical model built up for the SiO_2-like layer grown on PEN includes a graded composition- interphase region, interpreted as a linear combination of the (complex) dielectric functions of the polymer substrate and the SiO_2-like film bulk. The *in situ* real time ellipsometric data confirms the presence of an interphase characterized by optical properties, which are intermediate between the polymer and the inorganic layer bulk. This interphase region, which extends for ≈ 30 nm, can be interpreted as it follows. During the initial growth of the SiO_2-like layer a polymer (sub-) surface modification via atomic oxygen (and UV light) occurs, most certainly, increasing its porosity. More in detail, the refractive index values in the 10-30 nm-depth region are too high to be attributed to SiO_2-like layers; instead, they suggest the presence of carbon. Literature studies [8] document the presence of a carbon-rich interphase which formation is attributed to the initial interaction of ions and photons with the polymer surface. Its partial ablation would generate volatile hydrocarbon fragments which, mixed with the plasma chemistry typical of a SiO_2 deposition, lead to the formation of an "organosilicon"-like interphase. In the expanding thermal plasma, however, the ion bombardment effect can be definitely neglected and, although Ar metastables could play a role in surface processes, their density is about a factor 10 lower than the ion density [15]. Also, if the considerably high deposition rate is taken into account (3.5 nm/s), a high radical flux towards the substrate can be estimated around $2\text{-}5\cdot10^{19}/m^2\cdot s$. In conclusion, the observed interphase region developed during the expanding thermal plasma deposition of SiO_2-like films can be attributed to a polymer modification due to a non- depositing radical (O, OH) flux competitive with the depositing radical (Si, SiO) flux. In this framework, initial growth of the SiO_2-like layer via island formation cannot be excluded. Moreover, when short depositions (≤ 10 s) are performed on both Si and PEN substrates, different deposition rates are observed, as shown in Figure 5b. The higher deposition rate in the case of PEN appears to point out towards an initial growth of a porous layer; moreover, the presence of an intercept ≠ 0 in the case of PEN, seems to suggest the physical contribution of the (modified) polymer sub-surface to the interphase region observed in Figure 5a.

4. Conclusion

We have addressed the deposition of inorganic permeation barrier layers on PEN substrates by means of the expanding thermal plasma with and without an external substrate bias. The ion bombardment does hardly affect the water vapor permeation rate; however, it allows depositing efficient (barrier improvement factor of 23) single SiN_x barrier films ≈ 50 nm thinner than SiN_x layers obtained in the absence of ion bombardment. The SiN_x layer was tested in a two dyads barrier system, with a water permeation decrease of a factor 100 compared to the pristine PEN. In the absence of ion bombardment towards the substrate, an interphase development between the polymer bulk and the inorganic film bulk is observed. At this moment it is hypothesized that non-depositing radicals (O, OH in the case of SiO_2 deposition) may be responsible for polymer sub-surface modification during the initial layer growth.

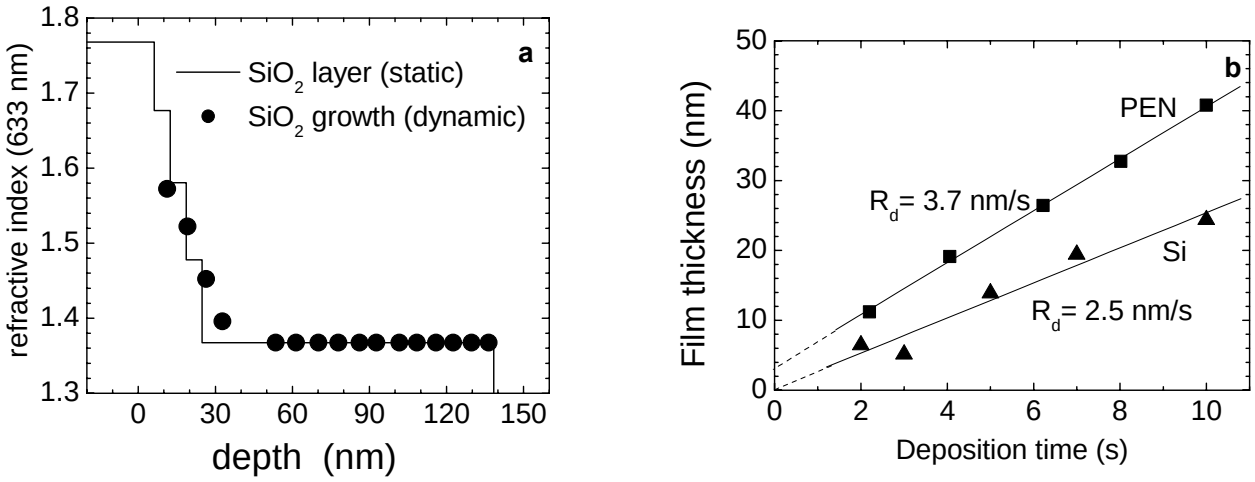

Figure 5. a) Refractive index evolution as a function of the SiO_2–like film depth, as obtained by modelling the deposited layer on PEN (static measurement) and the same layer during its growth (dynamic measurement). b) Growth rate of SiO_2-like films on Si and PEN substrates for short deposition times.

Acknowledgments

The authors would like to thank M.J.F. van de Sande, J. Jansen, H. de Jong, B. Hüsken for their skilful technical assistance, as well as M.A. Blauw for the useful discussion on the external substrate biasing. One of the authors (M.C.) acknowledges the Techno Technology Foundation (STW), applied science division of NWO and the technology programme of the Ministry of Economic Affairs, for supporting this research.

References

1. *Plasma deposition and treatment of polymers*, Materials Research Society Proc. 544, (1999).
2. *Plasma processes and polymers*, R. d'Agostino, C. Oehr, M.R. Wertheimer, P. Favia eds., Wiley-VCH, (2005).
3. A.S. da Silva Sobrinho, M. Latrèche, G. Czeremuszkin, J.E. Klemberg-Sapieha, M.R. Wertheimer, *J. Vac. Sci. Technol.* A16, 3190, (1998).
4. P.E. Burrows, G.L. Graff, M.E. Gross, P.M. Martin, M.K. Shi, M. Hall, E. Mast, C. Bonham, W. Bennett, M.B. Sullivan, *Displays* 22, 65, (2001).
5. M. Schaepkens, T.W. Kim, A.G. Erlat, M. Yan, K.W. Flanagan, C.M. Heller, P.A. McConnellee, *J. Vac. Sci. Technol.* A22, 1716, (2004).
6. G.L. Graff, R.E. Williford, P.E. Burrows, *J. Appl. Phys.* 96, 1840, (2004).
7. J. Affinito, D. Hilliard, *47th Annual Technical Conference Society of Vacuum Coaters Proc*., 563, (2004).
8. A.S. da Silva Sobrinho, N. Schuhler, J.E. Klemberg-Sapieha, M.R. Wertheimer, M. Andrews, S.C. Gujrathi, *J. Vac. Sci. Technol.* A16, 2021, (1998).
9. M. Creatore, J.-C. Cigal, G.M.W. Kroesen, M.C.M. van de Sanden, *Thin Solid Films*, available on line 13 April 2005, in press.
10. M.F.A.M. van Hest, J.R. Haartsen, M.H.M. van Weert, D.C. Schram, M.C.M. van de Sanden, *Plasma Sources Sci. Technol.* 12,539, (2003).
11. F.J.H. van Assche, W.M.M. Kessels, R. Vangheluwe, W.S. Mischke, M. Evers, M.C.M. van de Sanden, *Thin Solid Films*, available on line 19 March 2005, in press.
12. H. Chatam, *Surf. Coat. Technol.* 78, 1, (1996).
13. G. Dennler, A. Houdayer, P. Raynaud, I. Séguy, Y. Ségui, M.R. Wertheimer, *Nuclear Instrum. Meth. Phys. Res.* B 208, 176, (2003).
14. A. Bergeron, J.E. Klemberg-Sapieha, L. Martinu, *J. Vac. Sci. Technol*. A16, 3227, (1998).
15. A.J.M. Buuron, D.K. Otorbaev, M.C.M. van de Sanden, D.C. Schram, *Phys. Rev.* E 50, 1383, (1994).

Bio-decontamination by Gliding arc discharges : Application to the treatment of Erwinia carotovora atroseptica 1526

M. Moreau[1,2,4], M.G.J. Feuillolley[2], T. Meylheuc[3], S. Chevalier[2], N. Orange[2], J .L. Brisset [1]

1 Université de Rouen -Laboratoire d'Electrochimie (LEICA), Mont-Saint-Aignan, France
2 Université de Rouen- Laboratoire de Microbiologie du Froid (LMDF), Evreux, France
3 INRA-Unité de recherche en bio-adhésion et hygiène des matériaux (UBHM), Massy,France
4 GIE Comité Nord, Paris, France

Abstract

Decontamination of a phytopathogenic strain of agricultural interest *Erwinia carotovora atroseptica* (Eca) is achieved by means of gliding arc discharges in humid air in specially adapted devices. Cultures of Eca exposed to the plasma in two different gliding arc reactors prototypes were inactivated by ten logarithm units. The destruction kinetics of the bacteria with the two prototypes are compared and the involved mechanisms discussed.

Keywords

Gliding arc discharges, decontamination, viability, sterilisation

Introduction

Among the emerging decontamination techniques, the electrical discharges are probably the most promising methods for getting efficient plasma techniques. The gliding arc discharges (or glidarc) draw industrial attention because of their low cost in equipment and working conditions, since they are operated at atmospheric pressure and low temperature. Moreover their efficiency for the destruction of micro-organisms have been already established on *Escherichia coli* [1], *Erwinia* spp. [2] and *Staphylococcus epidermidis* [3] .

Several techniques give rise to non-thermal plasmas at atmospheric pressure and low temperature, i.e., pulse and/or dielectric barrier discharges, glow, microwave and gliding arc discharges. Most of them were recently tested for pollution abatement of liquid effluents. The literature also reports attempts to use non-thermal plasmas for bio-decontamination [4]. However, the mechanisms responsible for bacterial destruction are poorly known and the effect of this technique on pathogen bacteria has never been investigated.

We have selected a strain of Erwinia which is a major potato pathogens [5]: *Erwinia carotovora atroseptica* (Eca), Indeed, many countries encounter serious problems with pectinolic Erwinia which cause the loss of entire crops and financial damages estimated to 100 billions dollars a year for potatoes producers. In temperate regions, *Erwinia carotovora atroseptica* is frequently responsible for potato diseases and the producers are seeking for rapid and efficient decontamination techniques that could be applied for the treatment of both water and solid surfaces. This bacteria was selected to test the efficiency and the reproducibility of the glidarc quenched plasma treatment.

Two generations of glidarc reactor prototypes were used for this study, and the relevant destruction kinetics of Eca are compared. These results are discussed in regard of the mechanisms potentially involved in the decontamination process.

Materiel and method

Gliding arc reactors

Two prototype reactors were used for this study: both derive from the gliding arc device previously described by Lesueur *et al.* [6]. The simplest reactor (Reactor I) is sketched in figure 1.

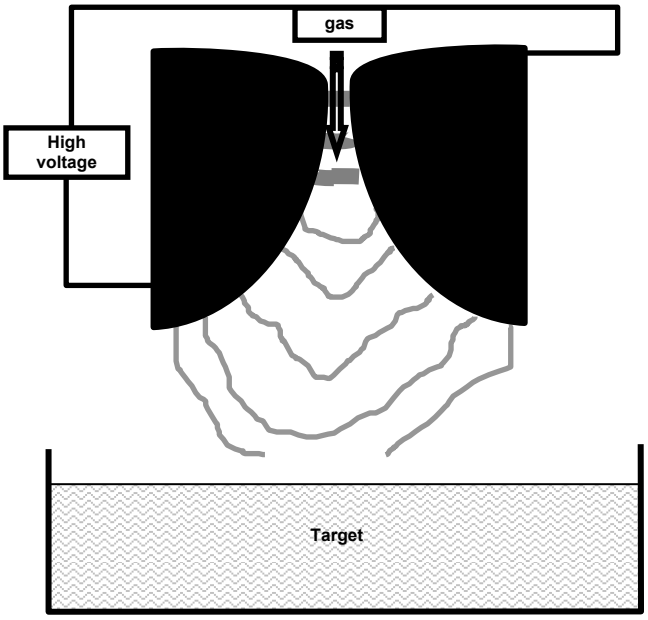

Figure 1: Scheme of the gliding arc reactor I.

It consists in two metallic diverging electrodes raised to a high voltage fall (9kV, 100mA in open conditions) fitted with a feeding gas nozzle disposed along the axis of the reactor. An arc forms at the electrode minimum gap and moves along the electrodes as it is pushed by the gas flow, until it breaks in a plasma plume and a new arc forms. The plasma plume then makes contact with the target and the plasma activated species react at the liquid-gas interface.

The plasma is a mixture of N_2 and O_2 supplied by an air compressor. The feeding gas gets water saturated by passing through a bubbling flask filled with distilled water in order to create more reactive species. The working parameters of the reactor, such as the gas flow rate ($L.min^{-1}$), the electrode gap and the distance between the electrode tips and the target are controlled.

The reactor of the second generation (Reactor II) is a development of the former one. The general scheme of the reactors is similar but the improved reactor II involves electronic improvements that provide a more energetic plasma which occupies a larger volume and allows to treat a more important liquid surface.

Bacterial strain and culture conditions

Erwinia carotovora atroseptica 1526 was provided by the French Collection of Phytopathogenic Bacteria (CFBP, Angers).

The bacteria were maintained as glycerol stocks and stored at – 80°C for further use. 5ml precultures were grown on LB medium at 28°C for 24 hours. An aliquot of them were used to inoculate 100ml of sterile LB medium, grown in the same conditions, to allow bacteria to be in statinary growth phase. 25 ml of these cultures were used as samples and exposed to the plasma.

Before and after each plasma treatment, counts of surviving cells were determined by the standard platting technique. The CFU (Colonies Forming Units) were counted after 48h at 28°C.

Viability of bacteria

The viability, i.e, the growing faculty for of the bacteria, was assessed with the LIVE/DEAD *backlight* viability kit (Molecular Probes, Eugen, OR) based on the use of SYTO 9® and propidium iodide nucleic acid probes. Whereas SYTO 9® can easily enter a bacteria and labels all the living population, propidium iodide only penetrates cells with damaged membranes. The SYTO 9® green labelled bacteria are thus considered as living cells while the red stained bacteria obtained with propidium iodide are actually dead cells.

Untreated and gliding arc treated cultures of Eca were observed by Scanning Electron Microscopy. Photomicrographs were realised with a S4500, Hitachi camera.

Results and discussion

The effect of the gliding arc technique was studied over a 15 minutes period, which is long enough to inactivate the whole bacterial population. The plots reported in figure 2 illustrate the kinetics of the treatment on the growth potential of *Erwinia caratovora atroseptica* relevant to the two reactor prototypes.

The kinetics evolutions of the bacterial population (Log N) with the treatment time (min) presents three steps: *i)* the initial plateau accounting for a lag phase, during which the number of growing cells remains almost steady, *ii)* a rapid decrease in the bacterial population accounting for an overall first order kinetic law with the inactivation rate $k \approx 3.33\ s^{-1}$ (the relevant rate of which reaches 10 logarithm units of the bacterial population within 30 seconds) and *iii)* a steady state characterised by a number close to zero number of bacteria able to generate colonies on Petri dishes at the end of this second phase.

As evidenced in figure 2, the gliding arc reactor II is more efficient for bacterial destruction than reactor I in our working conditions since the total destruction of the bacterial culture is obtained for 8 min with reactor I and for less than 5 min with the matching reactor II. This difference is assigned to a more energetic discharge available in reactor II than in reactor I, which thus induces a faster reaction due to an increased production of activated species.

During the plasma treatments, no variation of the suspension temperature is observed: the target temperature never gets higher than 25°C (reactor I) or 35°C (rector II) and prevents from considering any direct thermal effect [2].

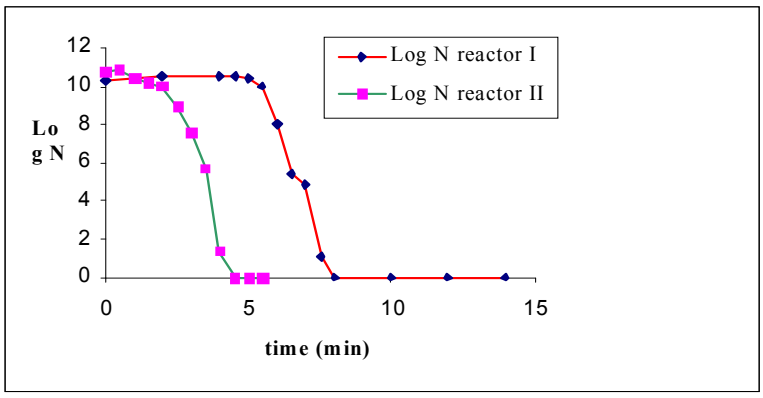

Figure 2: Destruction plots of *Erwinia carotovora atroseptica 1526* (Eca) vs. exposure time t(min) relevant to the couple of two gliding arc reactors.

The effects of the electric discharges and those of the plasma species on bacteria are still poorly known and specially those concerning the gliding arc.

Different degradation mechanisms are proposed in the literature to explain the bacteria death:
* Pelletier [7] and Lerouge *et al.* [8] suggest that the alteration of the integrity of the membranes is followed by irreparable damages of DNA and RNAs.

* The UV light was proposed as the main component of the plasma responsible for the lethal effect. Moisan *et al*. [4] demonstrated that the UV energy transferred by the discharge to the surrounding gas in low pressure discharges corresponds to the absorption band of nucleic acids. However, the number of UV photons emitted by a gliding arc discharge is limited [9], so the effect observed for such treatments probably involves other determining factors.
* We have thus to develop the main valuable assumption to account for the action of the glidarc discharges on bacteria which is based on the chemical processes induced by the discharges in humid air. Benstaali *et al.* [10] evidenced oxidising and acid effects in aqueous solutions of organic compounds exposed to the discharge. These changes are respectively attributed to the occurrence of the $HO^{\bullet}$ and $NO^{\bullet}$ radicals formed in the humid air plasma [11]. Our measurements confirm that $NO^{\bullet}$ is responsible for acid effects and for a steep pH lowering of the medium by means of the formation of HNO_2/HNO_3 derivatives in solution. The relevant rapid pH fall from 6.87 to 3.55 [2] can provoke a stress so violent that the bacteria have no time to adapt and die.
The matching radical involved in the discharge, $OH^{\bullet}$, is a strong oxidising agent which is probably associated with the rapid degradation of organic matter [12]. In addition, it combines to yield H_2O_2, in aqueous medium, and hydrogen peroxide is well known for its very high sterilisation activity. Indeed, this reactive species can induce alterations of enzymatic activities, hyperoxydation of lipids, protein degradation and DNA alterations.

The results of bacterial destruction obtained by direct counting are consistent with those obtained by epifluorescence observations [2]. The bacteria exposed to glidarc plasma were not stained by the matching fluorescent probes and the untreated bacteria were effectively green-fluorescent. Since the SYTO 9 ® and propidium iodide dyes bind to the nucleic acids, the lack of fluorescence of the treated bacteria can be explained by the denaturation and/or fragmentation of DNA and RNAs. The total absence of green labelled bacteria after the exposure to glidarc indicates that this technique do not generate viable but non cultivable forms of *Erwinia.* This result reinforces the interest of the glidarc decontamination process for industrial applications.

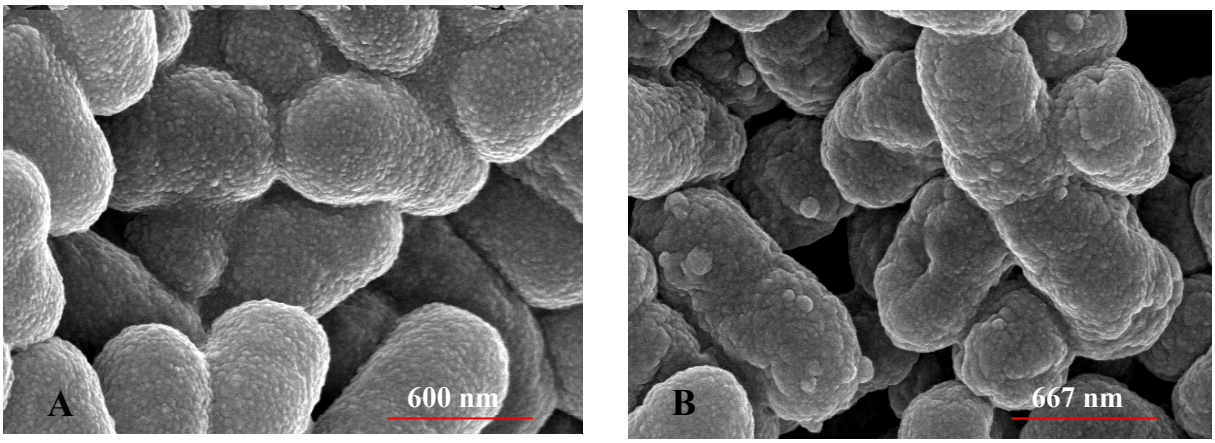

Figures 3 A and B: SEM photomicrographs of *Erwinia carotovora atroseptica* 1526. A) Eca untreated, x 50 000, B) Eca treated for t = 2.5 min, x 45000

The epifluorescence technique demonstrates that exposure to the plasma for a few minutes causes very important damages to the bacteria and suggests a loss of integrity of the bacterial membranes. This assumption is confirmed by SEM observations that show ruptures and/or disorganisation of the membrane (figures 3 A and B).

Conclusion

The presented study reports the effects of a new decontamination technique, i.e., the use of the gliding arc discharge at atmospheric pressure, on closely related bacterial pathogens of industrial interest. Simple improvements in the reactor prototype first qualitatively confirms the former results on bacterial inactivation and additionally shorten the treatment time by a ratio close to 2. The absence of formation of resistant forms of *Erwinia* after exposure to the discharge is also demonstrated. These features strongly suggest that the decontamination process is related to the occurrence of the plasma formed reactive species and is affected by changes in the composition of the culture medium and very important impact on the bacterial structure.
Work in progress is intended to precise the impacts of the gliding arc discharges on the bacterial structure.

References

[1] H. Vitrac, J. Guespin-Michel, J.L. Brisset - International symposium on high pressure low temperature plasma chemistry. Proc. Hakone VII. **2** (Greifswald, Ge) 393-397 (2000).
[2] M. Moreau, M.G.J. Feuilloley, N. Orange, J.L. Brisset - J. Appl. Microbiol. **98**, 1039-1046 (2005).
[3] R. Briandet, J.O. Kamgang, Y. Ruttery, J.M. Herry, M-N. Bellon-Fontaine, J.L. Brisset. - Biofilms in medecine (Elsinore, Danemark) (2003).
[4] M.Moisan, J.Barbeau, S.Moreau, J.Pelletier, M.Tabrizian, L'H.Yahia – Int. J. Pharmac. **226**, 1-21(2001).
[5] M.C.M.Pérombelon Plant Path. **51**, 1-12 (2002).
[6] H. Lesueur, A. Czernichowski, J. Chapelle - Fr. Pat. 2639172 (1988).
[7] J. Pelletier - Agressologie. **33**, 105-110 (1993).
[8] S. Lerouge, M.R. Wertheimer, R. Marchand, M. Tabrizian, L'Y. Yahia – J. Biomed. Mat. Res. **51** , 128-135 (2000).
[9] A.I. Kuzmichev, I.A. Soloshenko, V.V. Tsiolko, V.I. Kryzhanovsky, V.Y. Bazhenov, I.L. Mikhno, V.A. Khomomich – Proc. Hakone VII. **2** (Greifswald, Ge) 402-406 (2000).
[10] B. Benstaali, D. Moussa, A. Addou, J.L. Brisset – Europ. Phys. J. Appl. Phys. **4**, 171-179 (1998).
[11] M. Laroussi, F. Leipold – Int. J. Mass Spectrometry **233,** 81-86 (2004).
[12] D. Moussa, J.L. Brisset - J. Haz. Mat.. **B102**, 189-200 (2003).

Influence of Electric Fields on Methane Combustion: Interaction of Electrostatic Forces with the Gas Flow of a Low-Pressure 1-Dimensional Laminar Flame

Th. Hammer[1], L. Sun[2], G. Lins[1]

[1] *Siemens AG, Corporate Technology Department CT PS 5, Erlangen, Germany*

[2] *On leave from Siemens AG, Corporate Technology Department CT PS 5, Erlangen, Germany*

Abstract

The influence of weak electric fields on burner-stabilized, premixed CH_4-air flames was investigated at a flat flame burner at pressures down to 60 mbar. From temperature profiles evaluated from the CH $A^2\Delta$-$X^2\Pi$ (0,0) emission band at 431.42 nm and from chemo-luminescence intensity profiles a shift of the reaction zone of the flame in direction of the E-field increasing with the applied voltage was obtained. At high reduced electric fields E/n ionization and the excitation of N_2-emission bands were observed.

Keywords: premix combustion; reaction zone; electro-hydrodynamics; ionic wind; temperature profile; ionization; glow discharge

1. Introduction

The influence of electric fields on flames has often been investigated in the past. Calcote and Pease e.g. attributed the increase of the stability limit of an n-butane air flame on a Bunsen burner to an ionic wind induced by the interaction of the electric field with chemi-ions present in the flame [1]. Noorani and Holmes [2] obtained an extension of 83 % of the blow-off limit of a laminar premixed methane-air flame. A systematic experimental study of electric-field effects on flame stability was presented by Calcote and Berman [3] who found effects on flame stability for laminar as well as turbulent flow. A comprehensive treatment of theoretical aspects of the interaction of electric fields with flames was given in [4] and [5] by Lawton, Weinberg and Mayo. They showed that the body force transferred is proportional to the current density induced by the electric field and that the attainable ion wind velocity is limited by the current density corresponding to the breakdown field strength of the electrode-flame system. However, corona discharges can also be utilized for combustion control [6, 7]. Presently a growing number of publications are devoted to plasma-chemical control of combustion processes [8]. Nevertheless, a clear picture of electric field combustion control under conditions where plasma-chemical effects are unlikely to occur is still missing.

Thus the objective of the investigations reported here is to give experimental evidence of ionic wind effects on the reaction zone of a CH_4-air premix flame at reduced electric fields E/n lower than those required for electrical gas breakdown and in a transitional region of E/n values, were combustion-assisted gas discharge effects can be observed. All experiments were performed on a McKenna flat flame burner [9] because in this case the burner-stabilized, laminar flow, premix combustion can be described by 1-dimensional simulation using e.g. Chemkin. At atmospheric pressure a spatial resolution of around 10 μm would be required in order to observe electric field effects on position and thickness of the reaction zone. Since with decreasing pressure both the gap between burner surface and reaction zone and the thickness of the reaction zone increase [10], the investigations were performed at pressures between 60 mbar and 200 mbar.

2. One-Dimensional Model of Electro-Hydrodynamic Effects on Premix Combustion

Since a simple 1-dimensional model of electro-hydrodynamic effects on premix combustion has been published in [4] only a short review will be given here. Electrons and ions are generated by chemo-ionization

$$CH + O \rightarrow HCO^+ + e^- \qquad (1)$$

in the reaction zone of the flame. They are removed from the reaction zone by the convective flow of the flame, undergo charge exchange reactions, and finally recombine. Because negative oxygen ions are not

very stable at high temperature electrons are the dominating negative charge carriers. When an electric field is applied, charge separation occurs on scales larger than the Debye length. The following assumptions are made: (i) Generation of charge carriers outside the reaction zone can be neglected. (ii) Due to charge separation the only charge carriers are electrons between anode and reaction zone, and positive ions between cathode and reaction zone. Therefore outside the reaction zone recombination does not take place. (iii) The ion current density between cathode and reaction zone equals the electron current density between anode and reaction zone. This is a consequence of the continuity of current density at the reaction zone.

Because of the small electron mass only the ions are able to transfer momentum to the gas flow, which results in an ionic wind directed towards the cathode. Neglecting viscous losses, the stationary, one-dimensional momentum balance equation reads

$$\rho \cdot u \cdot \frac{\mathrm{d}\,u}{\mathrm{d}\,z} + \frac{\mathrm{d}\,p}{\mathrm{d}\,z} = f_{es} \tag{2}$$

where u, ρ, and p are the flow velocity, mass density, and pressure, respectively, and z gives the height above the burner surface. If other external forces can be neglected the force density f_{es} is determined by the electric field acting on the ions

$$f_{es} = e_0 \cdot n_i \cdot E \tag{3}$$

where e_0 denotes the elementary charge. Using the approximation

$$v_{di} = \mu_i n \cdot E / n \tag{4}$$

for the ion drift velocity with the reduced mobility $\mu_i n$ being independent of the gas density n, and the definition of the ion current density

$$j = e_0 \cdot n_i \cdot v_{di}, \tag{5}$$

the force density is found to be proportional to the current density:

$$f_{es} = j \cdot n / \mu_i n \tag{6}$$

Two extreme cases can be considered in solving (2): If the pressure gradient dp/dz is neglected an ionic wind velocity

$$u = \sqrt{f_{es} \cdot d_{cr} / \rho} = \sqrt{j \cdot d_{cr} / \mu_i n \cdot n / \rho} \tag{7}$$

results at the cathode, where d_{cr} is the distance between reaction zone and cathode. In the other case a pressure gradient proportional to the force density is generated.

If electron collision ionization occurs, which due to the high temperature (and low gas density) is more likely between reaction zone and anode, assumption (ii) is no longer valid, and ions may contribute to the current density thus inducing electro-hydrodynamic effects in this region, too. At sufficiently high electric field strength even gas discharge breakdown can take place. Then electrons contribute to the current density between reaction zone and cathode, such that (6) and (7) are no longer valid. As a consequence a reduced ionic wind velocity results.

3. Experimental Set-up and Procedure

A McKenna flat flame burner was mounted inside the lower vertical arm of a CF six-way cross with a nominal inner diameter of 150 mm (Figure 1). It consisted of a water cooled porous bronze plate with a diameter of 60 mm, through which the methane–air mixture was passed. A water-cooled exhaust gas pipe connected the upper vertical arm of the six-way cross to a water ring pump via a throttle valve by which pressures down to 60 mbar could be controlled. Three view ports equipped with fused silica windows provided optical access to the flame.

A ring electrode 90 mm in diameter made of stainless steel wire (∅ 4 mm) was placed 60 mm above the burner plate and connected to a DC high voltage power supply. The burner plate was connected to ground. To measure the current a 2 MOhm resistor was inserted between the HV supply and the ring electrode. Short rise time square wave pulses were generated by means of a fast high-voltage transistor switch HTS controlled by a wave generator. Voltages were measured using two HV-probes; the current was

evaluated from the voltage drop at the 2 MOhm resistor.

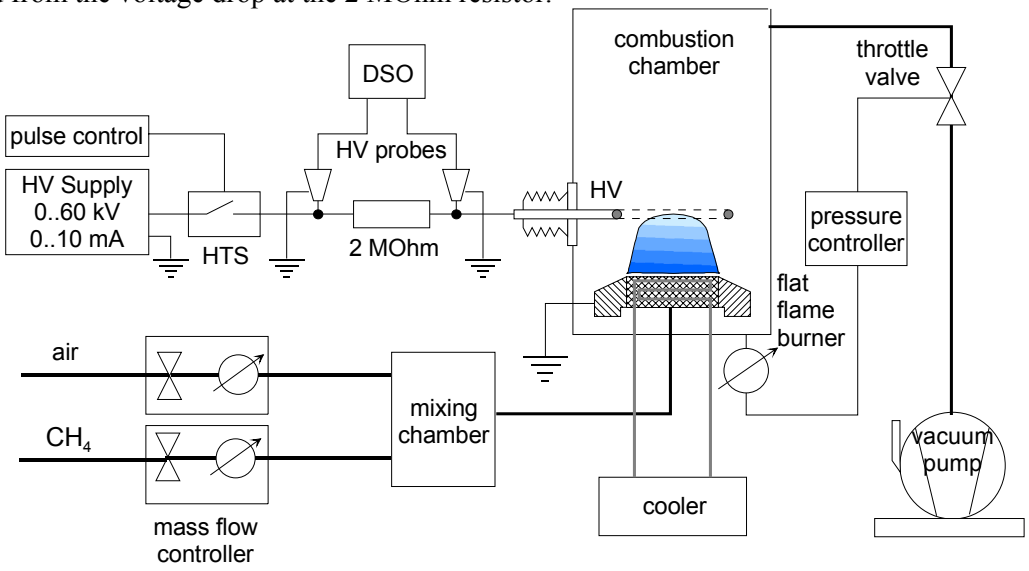

Figure 1. Set-up of the low pressure combustor

For spectroscopic investigations an image of the flame (magnified by a factor 1.43) was focused on the entrance slit of an imaging spectrometer of 500 mm focal length, equipped with a 1200 lines/mm grating blazed at 300 nm using two quartz lenses. Spectra were recorded by an intensified CCD camera with 1024 x 1024 pixels on a square of 13.3 x 13.3 mm^2. 10 (and in some cases 20) rows of the CCD-chip were „binned" to obtain a sufficient signal-to-noise ratio. Thus the spatial resolution of 90 (or 180 μm) was lower by a factor of 10 (or 20) than the theoretical limit.

For temperature measurements emission spectra were appropriately corrected for sensitivity variations and background and normalized to their peak intensity. The normalized spectra were fitted to spectra simulated with the temperature as a parameter [11,12] using a least-square-fit algorithm. Without an electric field this procedure can be applied to the CH $A^2\Delta$-$X^2\Pi$ (0,0) emission band at 431.42 nm and to the OH-band at 308 nm. For the CH-band good agreement between the maximum temperature obtained this way and the adiabatic flame temperature was achieved. From the OH-band, however, unreasonably high temperatures were derived. When sufficiently strong electric fields were applied, the N_2-bands of the second positive system $C^3\Pi_u$-$B^3\Pi_g$(0,0) at 337.13 nm, and $C^3\Pi_u$-$B^3\Pi_g$(0,1) at 357.69 nm could also be observed.

4. Experimental results

Temperature profiles

Temperature profiles with and without electric field were taken at pressures of 60, 80, and 200 mbar (Figure 2). The operating conditions of the flat flame burner are shown in Table 1. For a quantitative assessment of the temperature profiles a representation of the temperature data as a function of z similar to that of Berg et al. [16] was chosen:

$$T(z) = A + B\left\{1 - \exp\left[C(z - z_0)^D\right]\right\} + F(z - z_0)^2 \qquad (8)$$

From these profiles minimum and maximum temperature, maximum temperature gradient $(dT/dz)_{max}$, thermal thickness δ_L^T, (defined as $(T_{max}\text{-}T_{min})/(dT/dz)_{max}$), and displacement of the flame-front (defined as $z(T_{1/2},0)$-$z(T_{1/2},U)$ where $T_{1/2}$ is the average of minimum and maximum temperature) due to the applied voltage U were evaluated (Table 2).

As expected the thermal thickness of the flame increased with decreasing pressure. At 200 mbar it amounted to 0.2 mm and rose to 1.7 mm at 60 mbar. While at 200 mbar the application of an electric field did not result in effects on the temperature profile observable with the available spatial resolution, conspicuous changes occurred at 60 mbar. The CH temperature profile was displaced towards the burner by

1.3 mm. At the same time the flame front was flattened while the maximum temperature of about 2200 K did practically not change. The thermal thickness increased and reached values from 2.3 to 2.5 mm. These effects were measured both with DC and pulsed electric fields.

The displacement of the flame front as a function of applied voltage was evaluated from axial intensity profiles of the total visible emission, which peaked near the maximum of the temperature profiles. For 60 mbar and a DC voltage of 2.5 kV good agreement between the displacement of the temperature profile (Table 2) and that of the intensity profile was achieved. Up to this value the displacement increased linearly with the applied voltage.

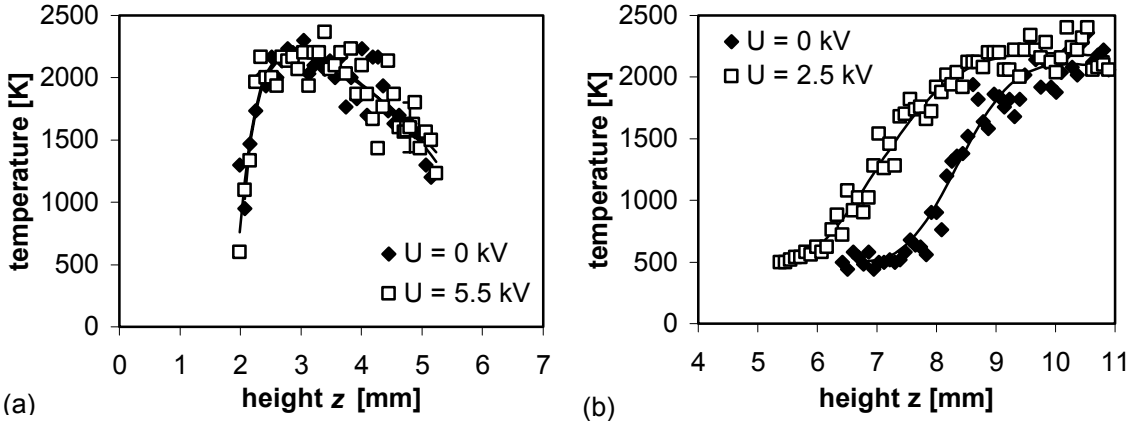

Figure 2. Influence of the electric field on the temperature profile evaluated from the CH $A^2\Delta$-$X^2\Pi$ (0,0) emission band (a) at a pressure of 200 mbar; (b) at a pressure of 60 mbar.

Table 1. Operating conditions of the McKenna flat flame burner.

p [hPa]	Q(CH4) [slm]	Q(air) [slm]	Q(Ar) [slm]	Φ	v [m/s]
60	0.49	4.8	1	0.97	0.52
80	0.51	5.5	0	0.89	0.44
200	0.70	7.0	0	0.95	0.23

Table 2. Influence of the electric field on the temperature profile.

p [mbar]	U [kV]	T_{min} [K]	T_{max} [K]	$(dT/dz)_{max}$ [K/mm]	δ_L^T [mm]	Δz [mm]
200	0	*800* [b]	2192	*7166* [b]	*0.2* [b]	
200	5.5	*600* [b]	2189	*4315* [b]	*0.4* [b]	0.0
80	0	800	1648	622	1.4	
80	2.5	783	1708	567	1.6	0.4
60	0	504	2104	923	1.7	
60	2.5	492	2193	743	2.3	1.3
60	0	503	2243	968	1.8	
60	2.9 [a]	492	2264	720	2.5	1.3

a) Unipolar square wave excitation; pulse rise time 100 µs, duration 1 ms, repetition frequency 500 Hz.
b) Rough estimates only. Minimum temperature could not be determined exactly.

Electrical characteristics

From the voltage-current characteristics of the flame taken at p = 60 mbar (Figure 3) several conclusions can be drawn: At low voltage electrons and ions generated due to chemo-ionization are partly separated and drawn to the electrodes before they can recombine. Thus the current increases with increasing voltage. Application of the model described above using a reduced ion mobility of $2.7 \cdot 10^{21}$/Vms results in an

ionic wind velocity at the cathode of about 1.8 m/s for a voltage of 2.5 kV (Figure 2b), which exceeds the feed flow velocity of 0.52 m/s substantially. Thus it appears likely that near the cathode a pressure gradient is generated due to the applied electric field.
At a DC-voltage of 800 V, when all charge carriers are extracted from the reaction zone before they can recombine, the current saturates. The increase of current at voltages larger than 1.7 kV can be attributed to ionization by electron collisions. The presence of the flame is considered to be essential for this effect. However, from the present experiment no conclusion about the transition from a non-self-sustained to a self-sustained glow discharge can be drawn. The different slope of the characteristics at negative electrode polarity can be attributed to the ratio of the electron mobility in the cold feed gas to that in the product gas of the combustion process being roughly equal to the inverse ratio of the respective temperatures 500 K/2200 K ~ 0.15.
Under pulsed excitation the current increases substantially slower as a function of the applied voltage amplitude. As will be seen more clearly below this indicates, that the relaxation of the space charge distribution between the reaction zone and the electrodes takes much more than 1 ms.

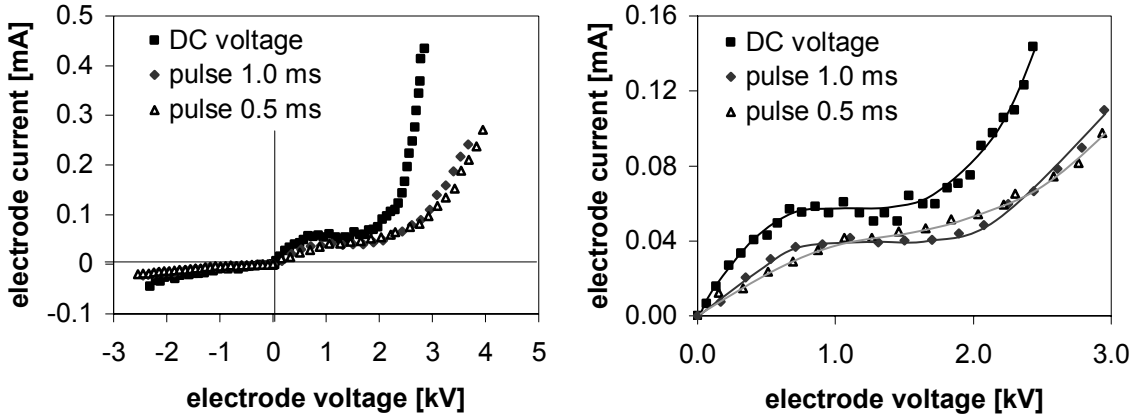

Figure 3. Voltage-current characteristics of the flame for DC and pulsed voltage (rhs shows a magnified view)

Relaxation of the reaction zone on application of electric fields
The temporal behaviour of the reaction zone was investigated by applying voltage pulses with an amplitude of U = 2.6 kV, rise time less than 0.1 ms and duration exceeding 100 ms. Photographs of the luminous zone of the flame were taken with an intensified CCD camera at preset times after the beginning of the high-voltage pulses. The displacement of the reaction zone required about 36 ms, which can only partly be understood in terms of the ionic wind propagating towards the cathode. However, according to [14] the time required to transfer momentum to the unburned gas by collisions between ions and neutral molecules may be several 10 ms.

N_2-emission bands
The appearance of N_2 bands is attributed to the onset of gas discharge effects that are responsible for the population of the high-lying upper level $C^3\Pi_u$. Thus it indicates the presence of electrons and of sufficiently strong reduced electric fields. Because of the inhomogeneous electric field due to the electron space charge near the ring electrode an increase of the N_2 band emission both in axial and in radial direction can be observed (Figure 4a). Therefore the conclusion can be drawn that the highest ionization rates occur near the ring electrodes. A few mm upstream of the ring electrode the profile measured at the axis shows substantially higher intensity values than that measured outside of the combustion zone having a radius of 30 mm, only. This indicates that due to the higher temperature and the ensuing lower density in the axial region higher reduced electric fields predominate.
Finally the temperature profiles evaluated from the N_2 spectra deviate from the CH temperature profiles (Figure 4b): Evaluation of the CH band results in a temperature of 500 K near the burner surface increas-

ing to its maximum value of 2200 K in a 3 mm wide zone. Evaluation of the N_2 $C^3\Pi u$-$B^3\Pi g$ (0,0) band resulted in the same maximum temperature, but even 6 mm upstream of the maximum a temperature of 1400 K is observed. This indicates that excitation and quenching mechanisms must be different for both species.

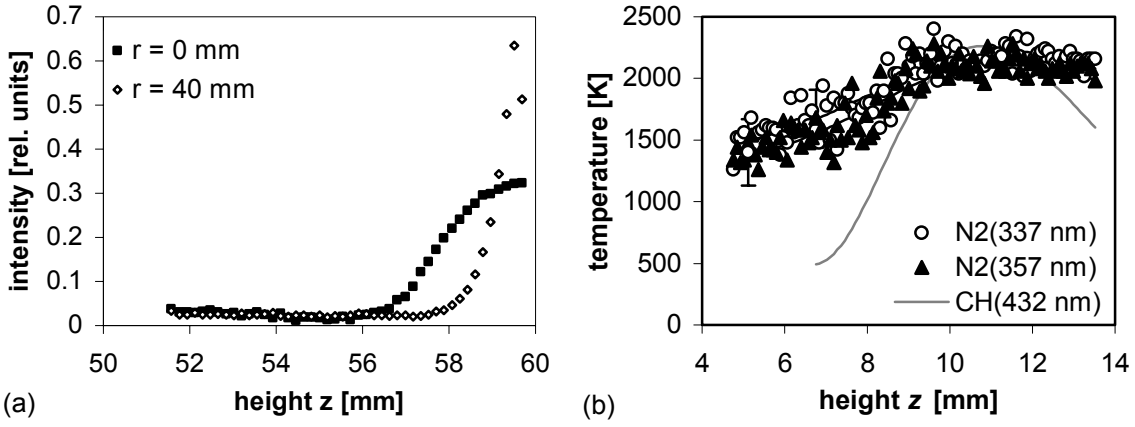

Figure 4. Intensity profiles of the N_2 $C^3\Pi_u$-$B^3\Pi_g$(0,0) band emission (a) and temperature profiles evaluated from N_2-emission bands (b) (pulsed excitation; temperature profile evaluated from CH emission shown for reference).

5. Conclusions

The displacement of the reaction zone of a low pressure burner stabilized flat flame is roughly proportional to the applied electric field in a wide range covering charge separation, current saturation and onset of gas discharge effects. The peak temperature is not influenced by application of an E-field. On application of square wave pulses the relaxation of the reaction zone takes several 10 ms. From the N_2 $C^3\Pi u$-$B^3\Pi g$ (0,0) band emission intensity profiles information about the reduced electric field can be obtained. High intensities are found in regions around electrode structures with small radius of curvature or in regions of high temperature. The temperatures upstream the reaction zone of the flame evaluated from the N_2-bands of the second positive system are unrealistically high indicating a non-thermal excitation mechanism of the upper molecular levels.

References (Times 11, bold)

[1] H.F. Calcote, R.N. Pease - Industrial and Engineering Chemistry **43**, 2726 (1951)
[2] R.I. Noorani, R.E. Holmes - AIAA Journal **23**, 1452-1454 (1985)
[3] H.F. Calcote, C.H. Berman - Proc. ASME Fossil Fuels Combustion **PD-25**, 25-31 (1989)
[4] J. Lawton, F.J. Weinberg - Proc. Roy. Soc. London **227**, 468-497 (1964)
[5] J. Lawton, P.J. Mayo, F.J. Weinberg - Proc. Roy. Soc. **A 303**, 275-298 (1968)
[6] D. Bradley, S.H. Nasser - Combustion and Flame **55**, 53-58 (1984)
[7] H. Ohisa, I. Kimura, H. Horisawa - Combustion and Flame **116**, 653-661 (1999)
[8] L. A. Rosocha, D. M. Coates, D. Platts, S. Stange - Physics of Plasmas **11**(5), 2950-2956 (2004)
[9] S. Prucker, W. Meier, W. Stricker - Rev. Sci. Instrum. **65**, 2908-11 (1994)
[10] J. Warnatz, U. Maas, R.W. Dibble – Combustion, 3rd edition, Springer-Verlag, Berlin, Heidelberg, New York, 2001
[11] J. Luque, D.R. Crosley - "LIFBASE: Database and spectral simulation program (version 1.5)" SRI International Report MP 99-009 (1999)
[12] K. Behringer - Plasma Phys. Contr. Fusion **33**, 997-1028 (1991)
[13] P.A. Berg, D.A. Hill, A.R. Noble, G.P. Smith, J.B. Jeffries, D.R. Crosley – Combustion and Flame, **121**, 223-235 (2000)
[14] M. Kono, F.B. Carleton, A.R. Jones, F.J. Weinberg – Combustion and Flame **78**, 357-364 (1989)

Group V metal oxides (V, Nb and Ta) doping of titania coatings by means of suspension plasma spraying

Igor Burlacov[1*], Robert B. Heimann[1#], Matthias Müller[2]

1 Dept. of Mineralogy, Technische Universität Bergakademie Freiberg, Brennhausgasse 14, 09596 Freiberg, Germany
2 Institute of Technical Thermodynamics, German Aerospace Center, Pfaffenwaldring 38-40, D-70569 Stuttgart, Germany
** Present affiliation: Infineon Technologies Dresden, Königsbrücker Strasse 189, D-01099 Dresden, Germany*
 # Present affiliation: Oceangate Consulting, Questenbergweg 48, D-34346 Hann.Münden, Germany

Abstract
TiO_2 coatings doped with varying amounts of V, Nb or Ta oxides were deposited by suspension plasma spraying (SPS). The dopants were incorporated *in situ* by plasma spraying of aqueous suspensions of fine oxide powders. Microstructural properties were studied by X-ray diffraction (XRD) and micro-Raman spectroscopy. The photocatalytic activities of coatings doped with 4 at.% of either Nb or Ta exceeded those of standard Degussa P-25 sol-gel coatings.

Keywords
Titania coatings, anatase, rutile, group V elements, photocatalytic activity, suspension plasma spraying

1. Introduction

The 4th International Symposium on Group Five Compounds has proclaimed these compounds key elements in solid-state chemistry, material science, catalysis, and engineering of functional materials [1]. In particular, V, Nb and Ta demonstrate great potential for various research and industrial applications, both as a main component or a dopant. Doping is a very effective way to improve the electronic performance of different semiconductor systems including titanium dioxide. TiO_2 is of particular interest as an outstanding photocatalyst for environmental applications such as water or air purification by degradation of organic pollutants [2]. Also, in recent years a rapid increase occurred of research interest into TiO_2 in the field of gas sensors [3-6]. Its high sensitivity, improved selectivity and fast response make it particularly suitable for automotive applications.
Improvement of photocatalytic and sensory properties of TiO_2 can be achieved by doping with different elements [7,8]. Among them, V, Nb and Ta show unique features: they are pentavalent, have ionic radii close to Ti^{4+}(61 pm) and thus demonstrate higher solubility of their oxides in the TiO_2 lattice. It has been found that (i) small amounts of Nb_2O_5 added to TiO_2 powder significantly increase surface acidity and photocatalytic activity [9], (ii) TiO_2–Nb_2O_5 sensors show higher sensitivity and shorter response time than pure TiO_2 [3-6, 10, 11], and (iii) low doping levels of Nb and Ta efficiently suppress the anatase-to-rutile phase transition below 1000°C [12, 13]. Addition of vanadium oxide can reduce the band gap of TiO_2, by a downward shift of the conduction band [14, 15] suggesting effective utilization of the visible part of the spectrum of the sun in photocatalysis.
Research into and development of mechanically stable TiO_2 coatings without reduction of their photocatalytic activity is being pursued worldwide. A variety of deposition techniques have been applied to achieve well-adhering, porous coatings with high photocatalytic activity. They include, among others, sol-gel processing [16], chemical vapor deposition [14] and rf sputtering [5]. However, thermal spraying also appears to be an appropriate process to produce coatings demonstrating such improved properties with additional promising economic prospects for industrial scale-up.

2. Experimental

2.1. Suspension plasma spraying

Thermally sprayed TiO_2 powder frequently decomposes at elevated temperature to form oxygen-deficient, non-stoichiometric Magnèli phases Ti_nO_{2n-1}. To counteract this effect and to deposit coatings with stoichiometric composition the oxygen containing atmosphere of an induction plasma torch was selected.

The suspension plasma spraying (SPS) process was introduced about 10 years ago and has been applied to the deposition of a variety of metallic and ceramic materials [17-20]. Also, *in situ* synthesis of ceramic coatings by reactive SPS was successfully achieved [21].

In the present work, (V, Nb, Ta)-doped TiO_2 coatings were deposited by reactive suspension plasma spraying with a wide range of dopant concentrations (0–16 at.%). The dopants were incorporated *in situ* by plasma spraying of aqueous suspensions of fine oxide powder mixtures in given proportions. Figure 1 shows the plasma reactor used for the experiments. The plasma source is a PL50 induction plasma torch from Tekna Plasma System Inc., Sherbrooke, Québec, Canada. The rf power is supplied by a 500 kHz rf generator from Himmelwerk GmbH, Tübingen, Germany, delivering a maximum power of 60 kW. The plasma expands into a water-cooled vacuum reactor. The substrate can be scanned in two orthogonal horizontal directions to coat larger surface areas.

Although in previous experiments it was found that oxygen must be added to the plasma gas to maintain the TiO_2 stoichiometry, the amount of oxygen had no significant influence on the stoichiometry of the titania coatings obtained. Therefore, all experiments were performed with low oxygen content (85 slpm Ar, 3 slpm O_2). The reactor pressure was kept constant at 20 kPa. The rf power was 24 kW. The precursor was fed with a rate of 3 ml/min and atomized with 5 slpm Ar using an air-blast atomizer, shown enlarged in Fig. 1, left bottom corner.

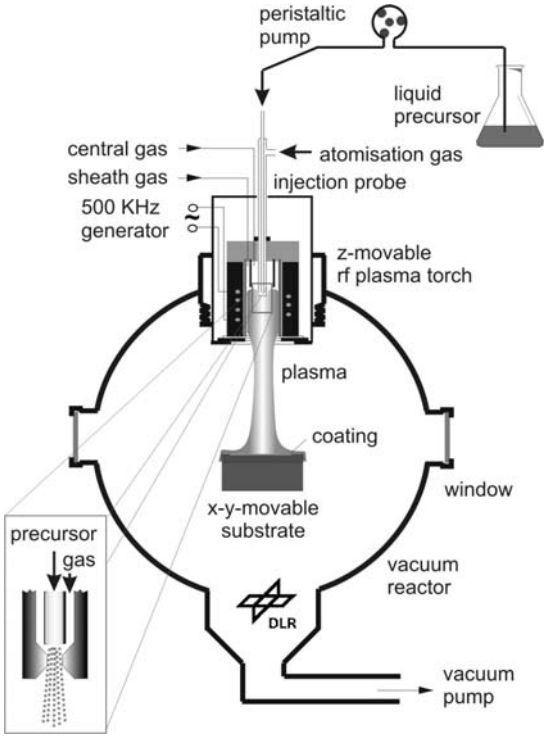

Fig. 1. Induction plasma reaction chamber.

2.2. Materials

Suspensions were prepared from 67 mass% deionised water and 33 mass% anatase powder with a crystallite size <10 nm and an average agglomerated particle size of 0.2 μm. The specific surface area (BET) was >250 m^2/g. Nb and Ta doping was performed by adding appropriate amounts of V_2O_5, Nb_2O_5 or Ta_2O_5 powder of identical particle size to the suspension. The precursor suspensions applied contained the following doping concentrations (in at. % of TiO_2): 0.5, 1.0, 2.0, and 4.0 % V, Nb and Ta, respectively. Furthermore, suspensions containing 8, 12, and 16 % of Nb resp. Ta were applied.

Titanium (cp-Ti) metal sheets and vitreous silica plates with dimensions of 8.5 x 12.5 x 1 mm^3 were used as substrates. Prior to spraying the Ti substrates were grit-blasted with fine alumina powder (-120+60μm) and ultrasonically cleaned in alcohol for 15 min. The vitreous silica plates were sized to fit a mini-photoreactor designed at the J. Heyrovský Institute of Physical Chemistry, Academy of Sciences, Prague, Czech Republic.

2.3. Coating characterization

The microstructure of the as-sprayed TiO_2 coatings was characterized by Raman spectroscopy using a Dilor XY double spectrometer equipped with a liquid nitrogen cooled CCD detector. The Spectra-Physics 2016 Ar+ ion laser line at 514.5 nm wavelength with an output power of 5 mW was used for excitation. Raman spectra were collected at 5, 10 and 50 times magnifications in backscatter geometry at room temperature. The spot size of the laser probe was between 1 and 10 μm. The spectral resolution was 1 cm^{-1}.

Information on the crystalline structure of coatings was obtained on an X-ray $\vartheta/2\vartheta$ Bragg-Brentano diffractometer (40kV/25mA) with CoK_α radiation at a scan rate of 0.04° 2Θ s^{-1}.

Coating surface roughness was measured using a Hommel Tester T8000 profilometer according to DIN EN ISO 4287. The parameters Ra, Rz and Rmax were found to be 3.6, 24.0 and 29.2 μm, respectively. Typical coating thickness was between 10 and 12 μm.

The photocatalytic activity of doped TiO_2 plasma-sprayed coatings was tested in a special mini-photoreactor designed from a standard spectroscopic cell using the decomposition of 0.01M 4-chlorophenol in aqueous solution with 0.01M $NaClO_4$. The sample was irradiated by polychromatic UV light (> 320 nm) from an Hg-lamp (Narva HBO 200, 26 V, 2 A). The UV radiation was filtered with an IR liquid filter and with a solid WG-3 UV cut-off filter. The pH change following a release of hydrochloric acid was continuously monitored by a glass electrode positioned above the sample coating. The initial reaction rate of the HCl formation is supposed to be proportional to the photocatalytic activity of the coating. The pH changes of the solutions were measured in both, in the dark and under UV irradiation. The kinetic parameter was determined from a slope of dependence (pH vs. time). The rates of pH changes obtained were compared with those of standard Degussa P-25 coatings under the same test conditions.

3. Results and Discussion

3.1. Phase content of the coatings

Figure 2 shows XRD patterns of the precursor anatase powder (top) as well as of a typical SP-sprayed coating (bottom). Anatase and rutile contents were estimated from the ratio of the intensities of anatase (101) ($2\theta = 29.4^o$), I_A and rutile (110) ($2\theta = 31.9^o$), I_R by the equation [22]

$$Rutile(\%) = 0{,}679 \cdot \frac{I_R}{I_R + I_A} + 0{,}312 \cdot \left(\frac{I_R}{I_R + I_A} \right)^2 \qquad (1)$$

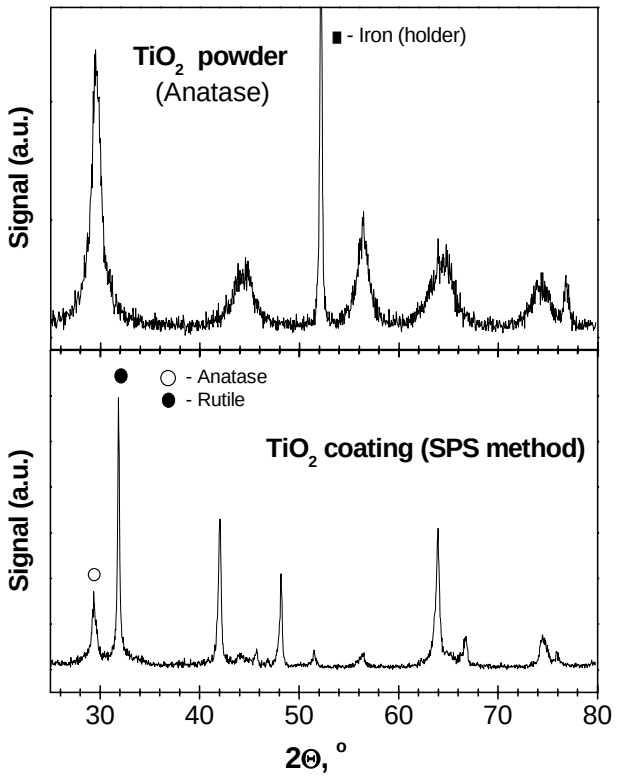

Fig. 2. XRD pattern of precursor anatase powder (top) and a typical SP-sprayed titania coating (bottom). The circles indicate, respectively the most intense interplanar spacings of rutile (110) and anatase (101).

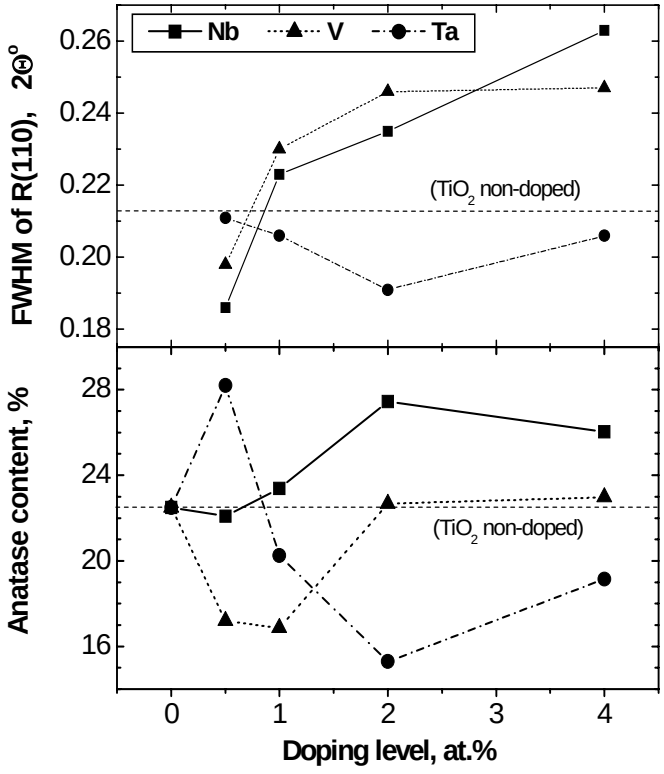

Fig: 3. FWHM of rutile (110) (top) and calculated anatase contents (bottom) of SPS titania coatings as functions of the doping concentration. The dotted lines refer to non-doped SPS titania coatings.

Undoped SPS titania coatings show anatase contents around 22% (Fig. 3, dotted line). Doping with 2 to 4at% Nb increases the anatase content to about 28%. Evidently Nb_2O_5 and V_2O_5 dissolve well in the TiO_2 structure as confirmed by a shift of the (110) spacing of rutile towards lower diffraction angles as well as by an increase in FWHM of the (110) spacing of rutile (Fig. 3, top).
Photoelectron spectroscopic (XPS) measurements of the $Nb3d_{5/2}$ line showed Nb^{5+} atomic concentrations in TiO_2 coatings ranging from 1 to 3 at%, approximately corresponding to the Nb contents in the precursor powders. Contrariwise, doping with Ta beyond a concentration of 1at% showed reduced anatase contents, presumably owing to only limited solubility of the Ta ion in the structure of anatase (Fig. 3, top).

3.2. Raman micro-probe analysis

Anatase is known to undergo irreversible transformation to the thermodynamically stable rutile structure during thermal spraying. Furthermore, the photocatalytic efficiency of titania coatings depends not only on their anatase content but also on their surface microstructure*, e.g.*, the distribution of spatial and structural inhomogeneities. Since Raman scattering is a useful tool to characterize thin films and coatings, in particular to detect and quantify spatially inhomogeneous surface states, micro-Raman spectroscopy was used to analyse and classify the phase structure and surface quality of SPS coatings.
Compared to XRD data, Raman spectroscopy provides information on the structure of submicron surface regions, *i.e*. regions essential to UV light penetration and hence the photocatalytic process. The micro-probe Raman method associated with the scanning mode of the laser beam allows collecting a huge amount of statistical information (10^3-10^4 points/cm^2 coating surface) on the TiO_2 phase content through so-called phase mapping. Intensities, peak positions, and widths of Raman bands of both anatase and rutile phases provide unique information on the crystalline quality of the coatings. The micron-scale spatial resolution of the Raman method coupled with the visual monitoring technique gives a more realistic and relevant picture than conventional x-ray diffraction.

Optical microscopy of the coating surfaces shows three different surface features tentatively denoted as (i) "bulk" coating as main background matrix, (ii) "exploded" splats, and (iii) glassy splats. The contrast image analyses of the coating surfaces showed about 80% of the surface area belonging to type (i) with the remainder approximately equally represented by types (ii) and (iii).The microstructure of these typical objects was analysed by the Raman micro-probe technique to yield the spectra shown in Fig. 4.

(i) The microstructure of the "bulk" coatings consists of a porous skeleton-like matrix of rutile filled with fine anatase particles. Consequently, the vibrational spectra of this phase (Figs. 4b to d) show additional Raman bands at 238(comb), 447(E_g) and 611(A_{1g}) cm^{-1}, suggesting the coexistence of rutile and anatase.
(ii) The "exploded" splats consist of agglomerates of anatase particles that have reached the coating surface without thermal transformation. Their origin is probably related to the formation of bigger suspension droplets that did not disintegrate in the plasma but were spray-dried to form hollow spheres that exploded upon impact. The Raman spectrum (Fig. 4a) is composed of five from six characteristic Raman bands at 147(E_g), 197(E_g), 396(A_{1g}), 515(B_{1g}) and 638(E_g) cm^{-1}, corresponding to different vibrational modes

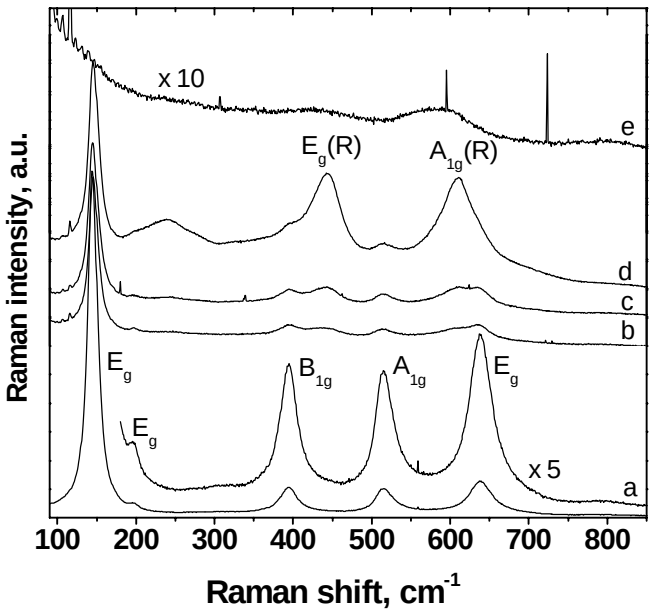

Fig. 4. Raman spectra of (a) "exploded" splats (type (ii)), (b to d) "bulk" coating (type (i)), and (e) glassy splats (type (iii)) of SPS titania coatings. For details see text.

of the anatase structure. The first one is the most intensive band, serving as a "finger-print" for the anatase structure during phase mapping.
(iii) The Raman spectra of the glassy splats (Fig. 4e) show the more or less amorphous structure of titania particles also originating from single bigger suspension droplets that did, in comparison to type (ii), completely melt after spray drying, either due to their limited size or due to their residence closer to the hot central axis of the plasma jet. The spatial distribution of these molten particles at the coating surface is comparable to that of the spray-dried agglomerates of anatase particles of type (ii). No additional Raman modes were found in the doped samples. For a more precise estimation of the anatase-rutile ratio the Raman micro-probe method is insufficient. Hence, a calibration with quantitative XRD of the near-surface coating layer is required. Nevertheless, from the intensity ratios of the two characteristic Raman bands of anatase (147 cm^{-1}) and rutile (447 cm^{-1}) a rough estimate could be obtained, yielding average values around 40-50% anatase in the "bulk" coating of type (i).

3.3. Photocatalytic performance

The rates of pH changes (d(pH)/dt) during photocatalytic degradation of 4-chlorophenol in aqueous solution in contact with doped titania coatings irradiated with UV light are shown in Figure 5. The Nb resp. Ta doped coatings demonstrate quite similar degradation rates with the maximum activity at 4at.% of doping, which exceeds that of standard Degussa P-25 sol-gel coatings. Doping with V appears to quench the photocatalytic performance of the coatings (low values not shown in Fig. 5). A compelling reason for this unexpected behaviour is still missing.

As pointed out by Sobczynski and White [23] the solubility of Ta in TiO_2 is very low. While it increases with temperature, at 1400°C it is still three times lower than that of Nb. The fact that in the present study the photocatalytic activities of Ta- and Nb-doped TiO_2 coatings are comparable suggests that additional electronic effects pertaining to Ta must be considered. Such effects could, for example, be related to a more strongly reduced coating surface in the presence of Ta ions, forming oxygen vacancies and leaving OH groups connected to the resulting Ti^{3+} ions [24].

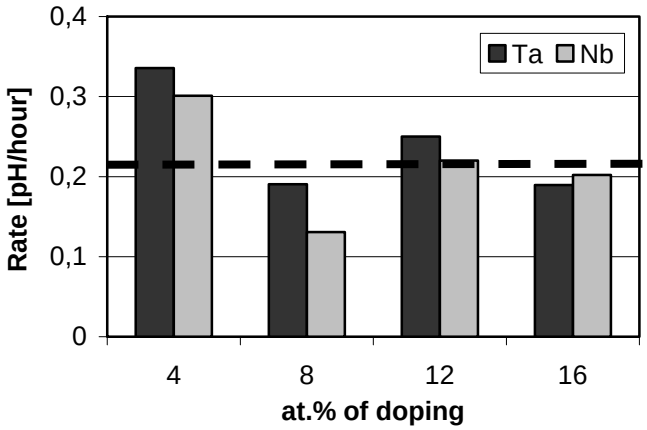

Fig. 5. Rates of pH changes during degradation of 4-chlorophenol on contact with doped TiO_2 coatings under UV radiation. The dashed line indicates the rate of a standard Degussa P25 sol-gel coatings.

4. Conclusions

(V, Nb, Ta)-doped TiO_2 coatings were deposited by suspension plasma spraying. The dopants were incorporated *in situ* by plasma spraying of aqueous suspensions of fine oxide powders. Microstructural properties were studied by X-ray diffraction (XRD) and micro-Raman spectroscopy. Special attention has been paid to the inhibition of the thermally induced anatase-to-rutile transformation by the dopants and the associated improvement of the photocatalytic activity of the sprayed coatings.

The plasma-sprayed coatings were about 10-12 μm thick with a deep blue-grey colour, indicating (i) the introduction of new electronic states into the band gap of the TiO_2 host, and (ii) an oxygen loss of the original TiO_2 powder due to the thermal treatment in the plasma. The surface morphology of the coated samples was rough and inhomogeneous due to the different size of droplets formed in the suspension spray. Larger "spray-dried" particles adhering to the surface of the samples contained higher amounts of anatase and were thought to constitute unmelted remnants of larger anatase precursor particles. By micro-Raman technique it was possible to identify the phase content and the crystalline quality of these microscopic objects. The XRD results obtained revealed a high solubility of V_2O_5 and Nb_2O_5 in TiO_2 and a more limited one for Ta_2O_5. The incorporation of dopant atoms into the TiO_2 lattice leads to broadening and shifting to lower diffraction angles of the TiO_2 XRD

peaks. The estimated anatase content of the coatings reached the maximum value of 28% for moderate doping levels, substantially higher than for non-doped TiO_2 coating.
Coatings doped with 4 at% of either Ta or Nb demonstrate a photocatalytic activity of about 0.33 pH/h and 0.30 pH/h, respectively, 40 to 50% better than that of a standard Degussa P25 sol-gel coating (0.22 pH/h).In spite of the quite low anatase content in the coatings the results of the photocatalytic performance of the coatings are quite encouraging for large-scale applications of group V element-doped TiO_2 SPS coatings.

Acknowledgements
The work was supported by the EC FP5 "Growth" Programme CRAFT Project on 'Innovative Thin –Film UV-Reactor (UVREC)', contract EVKI-2002-30025. The authors are indebted to Prof. Ladislav Kavan and Dr. Jaromir Jirkovsky, J.Heyrovský Institute of Physical Chemistry, The Czech Academy of Sciences, Prague, Czech Republic for the photocatalytic measurements.

References
[1] 4th International Symposium on Group Five Compounds Bicentennial, Catalyst Today 78, 1 (2003).
[2] A. Fujishima, and K. Honda, Nature 238, 37 (1972).
[3] R.K. Sharma and M.C. Bhatnagar, Sensors and Actuators B 56, 215 (1999).
[4] Y. Yamada, Y. Seno, Y. Masuoka, T. Nakamura, and K. Yamashita, Sensors and Actuators B 66, 164 (2000).
[5] K. Zakrewska, Vacuum 74, 335 (2004).
[6] Ruiz, G. Dezanneau, J. Arbiol, A. Cornet, and J.R. Morante, Thin Solid Films 436, 90 (2003).
[7] W. Li, S. I. Shah, C.P. Huang, O. Jung and C. Ni, Mater. Sci.Eng. B96, 247 (2002).
[8] S.E. Park, H. Joo, and J.W. Kang, Solar Energy Materials & Solar Cells 83, 39 (2004).
[9] H. Cui, K. Dwight, S. Soled, and A. Wold , J. Solid State Chem. 115, 187 (1995).
[10] R.K. Sharma, M.C. Bhatnagar, and G.L. Sharma, Sensors and Actuators B 46, 194 (1998).
[11] M. Ferroni, M.C. Carotta, V. Guidi, G. Martinelli, F. Ronconi, O. Richard, D. Van Dyck, and J. Van Landuyt, Sensors and Actuators B 68, 140 (2000).
[12] B.M. Reddy, I. Ganesh, and V.R. Reddy, J. Mater. Sci. Lett. 17, 1913 (1998).
[13] D. Morris, Y. Dou, J. Rebane, C.E.J. Mitchell, R.G. Egdell, D.S.L. Law, A. Vittadini, and M. Casain , Phys. Rev. B 61, 13445 (2000).
[14] Y. Gao, S. Thevuthasan, D.E. McCready, and M. Engelhard, J. Cryst. Growth 212, 178 (2000).
[15] A. Fuerte, M.D. Hernandez-Alonso, A.J. Maria, A. Martinez-Arias, M. Fernandez-Garcia, J.C. Conesa and J. Soria , Chem. Commun. 2718 (2001).
[16] C.B. Rodela and V.R. Mastelaro, J.Phys. Chem.Solids 64, 833 (2003).
[17] E. Bouyer, F. Gitzhofer, M.I. Boulos, Proc. 9th Nat. Thermal Spray Conf., Oct. 1996, Cincinnati, OH, USA, Eds. C.C. Berndt & S. Sampath, ASM International, Materials Park, Ohio, 683 (1996)
[18] E. Bouyer, M. Müller, N. Dignard, F. Gitzhofer, M.I. Boulos, Progress in Plasma Processing of Materials 1997: Proc. 4th Int. Thermal Spray Conf., 1996, Athens, Greece; Begell House, Inc., New York, 751 (1997)
[19] M. Müller, G. Schiller, F.Gitzhofer, M. Boulos, R.B. Heimann , Thermal Spray: A United Forum for Scientific and Technological Advances, Proc. 1st United Thermal Spray Conference, Indianapolis, Indiana, USA, Sept. 1997, ASM International, Materials Park, Ohio, 343 (1998)
[20] M. Müller, E. Bouyer, M. v. Bradke, D.W. Branston, R.B. Heimann, R. Henne, G. Lins, G. Schiller, Materialwiss. u. Werkstofftech., 33(6), 322 (2002)
[21] G. Schiller, M. Müller, F. Gitzhofer, J. Thermal Spray Technol., 8(3), 389 (1999)
[22] J. Arbiol, J.Cerdà, G. Dezanneau, A. Cirera, F. Peiró, A. Cornet, J.R. Morante, J. Appl. Physics 92(2), 853 (2002)
[23] A. Sobczynski and J.M. White, J.Molec.Catalys. 29 (1985) 379-391
[24] E. Serwicka, R.N. Schindler and R. Schumacher, Ber. Bunsenges.Phys.Chem. 85(1981) 192.

Au nano-wiring process by plasma processes

Mikinori Suzuki and Shinzo Morita

Department of Electronic Information System, Nagoya University, Nagoya, 464-8603, Japan

Abstract

Au nano-wiring process with using plasma processes was proposed because metal wiring circuit fabrication is almost impossible to process by a conventional lithography. The processes are nano-insulation bed fabrication, C-Au-S semi-conductive layer formation and electroplating of Au. Au plating was confirmed by ESCA measurement, which was formed on n-type Si wafer in $NaAuCl_4$ solved ethanol at 0.5 atom%. Au nano-wiring circuit was processed on the n-type Si with a resist trench pattern of 100 nm L&S, but circuit wiring pattern was broken lines. In order to form continuing wire line, Au plating is trying to performed with using C-Au-S semi-conductive layer which is formed by co-operation process of plasma CVD and sputtering, because the C-Au-S layer with Au content more than 10 atom% has sub-nanometer conductive grain. Au nano-wiring process will be completed forming the circuit on nano-insulation bed.

Keywords: nano-wiring, electroplating, $NaAuCl_4$ solved ethanol, C-Au-S semi-conductive layer, nano-insulation bed

1. Introduction

Nano-lithography for a single electron transistor (SET) working at a room temperature is the most interesting target in the study of lithography after Likharev and others [1]. However there are many problems to be solved. We expected quantum dots in C-Au-S film formed by cooperation process of plasma CVD and sputtering by several experimental results of refractive index [2], ESCA [3], X-ray diffraction [3], AFM/STM [4] and spectroscopic ellipsometry [5]. In order to evaluated the quantum properties, nano-wiring circuit must be fabricated. Au nano-wiring process was proposed to realize the nano-wiring circuit because nano-metal wiring fabrication by a conventional lithography process is almost impossible to realize. The proposed nano-wiring process is performed by an electro-plating method. The processes are composed by nano-insulation bed fabrication, C-Au-S semi-conductive layer formation and electroplating of Au

The nano-insulation bed fabrication process is performed as following, nanometer size polls or walls are formed on n-type Si wafer by a lithography, the polls and walls on Si wafer are oxidized, then the polls and walls are etched off to flat the surface. Therefore the Si wafer surface is composed with insulating and semi-conducting area [6].

The C-Au-S semi-conductive layer formation is realized by cooperation process of plasma CVD and sputtering [2].

The electro-plating of Au wires is realized by using $NaAuCl_4$ because $NaAuCl_4$ can be solved in ethanol. The Au atom can be electro plated under the electric field in the liquid.

In this work, the Au nano-wiring circuit is aimed to fabricate by using plasma processes.

2. Experiments

In order to confirm the electro-plating on n-type Si wafer, the two parrel Si wafers with 1 cm distance were immersed in $NaAuCl_4$ solved ethanol at 0.5 atom% as shown in Fig. 1 and the 9V battery was connected

to them. Then the surface of n type Si wafer was served to ESCA measurement to confirm the plated materials. The ESCA measurement was performed with using ESCALAB 210 (VG. SCIENTIFIC LIMITED).

The nano-wires were tried to form on the n-type Si by the electroplating after a resist pattern fabrication using the $NaAuCl_4$ solved ethanol. The resist pattern was fabricated by an electron-beam patterning system (JEOL, JBX-6000SG). The fabricated pattern was observed by SEM.

Where the n-type Si wafer doped by Sb shows a resistance less than 0.02 Ωcm. The pattern delineation was performed by an electron-beam patterning system (JEOL, JBX-6000SG) at an acceleration voltage of 50 KV and electron-beam current of 100 pA.

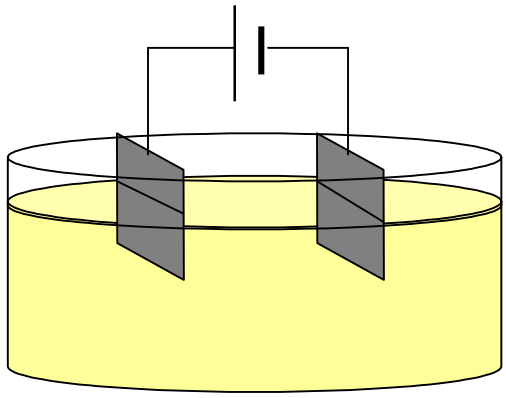

Fig.1. Reactor for an electroplating with $NaAuCl_4$ solved ethanol

3. Experiment Results and Discussion

Au plated Si wafer was examined by ESCA measurement. The Au atom layer was detected, but there are no Au atom peak at the anode electrode. Whereas the Au was plated only on the cathode electrode.

Resist pattern was formed on Si wafer by an electron-beam delineation. The 100 nm L&S resist pattern was filled by Au on n type Si wafer as shown in Fig. 2. Au wiring pattern was not continuous. The reason why the dots pattern was formed on linear trench structure in the resist film was formed. There are two reason, one is that the resist was not developed completely and other is that oxidized part inhibited the Au plating. Presently the most possible one is oxidized area in the trench bottom.

Therefore some additional process was proposed to realize uniform plating of Au film on the n-type Si wafer. Then the C-Au-S semi-conductive layer formation was proposed here, because the film will contain sub nm C-Au-S dots and the Au continuous wire will be realized by the electro plating of Au film at about 1nm thickness.

About 100 nm width Au electroplated lines on the C-Au-S film in the trench array was observed by SEM as shown in Fig. 2. Au plated line was not continuous. Possible reason will be referred to the C-Au-S film because the Au content was not large as expected.

4. Future work

The cross section model pattern of nano-insulation bed and electro-plated nanometer size wire are shown in Fig. 3. The nano-insulation bed will be formed as following; nanometer size polls or walls are formed on n-type Si wafer by a lithography. At the next step, the polls and the walls on the Si wafer are oxidized, then the polls and walls are etched off to realize uniform flat surface but the positions of polls and walls are remained without oxidize. On the un-oxidized area which is n-type Si, semi-conductive C-Au-S

layer is coated by cooperation process of plasma CVD and sputtering, then Au layer will be electro plated on the C-Au-S layer on the area the polls and the walls had been fabricated.

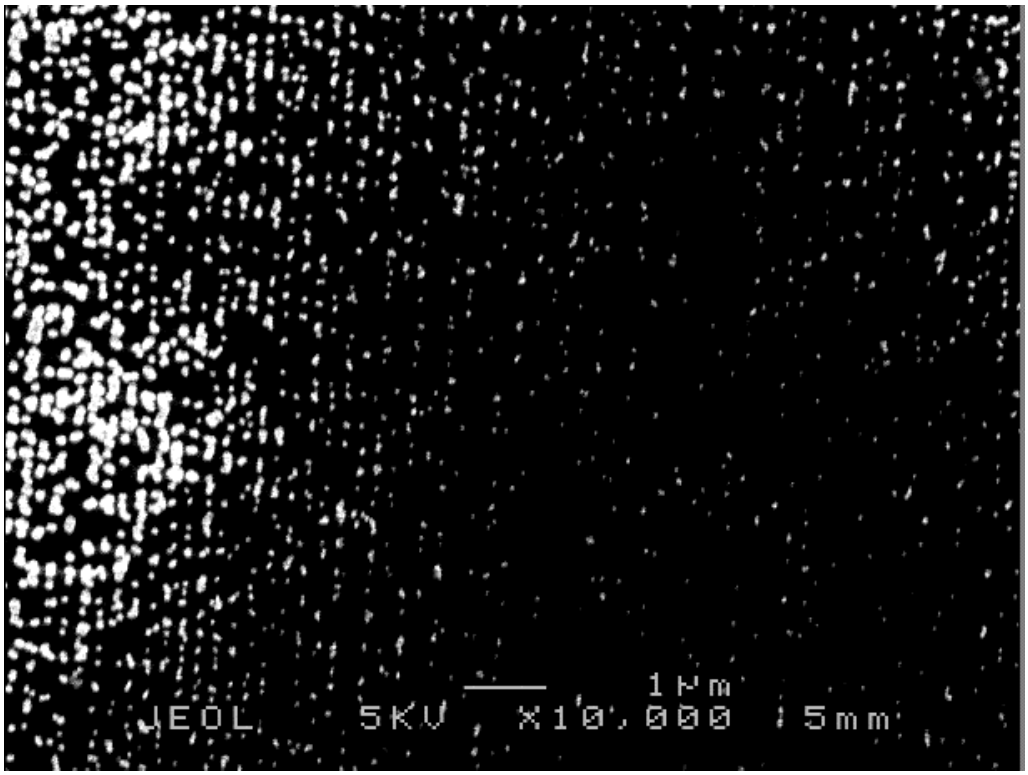

Fig.2. Electroplated Au nano-wires through resist pattern at 100 nm L&S after O_2 plasma ashing of resist.

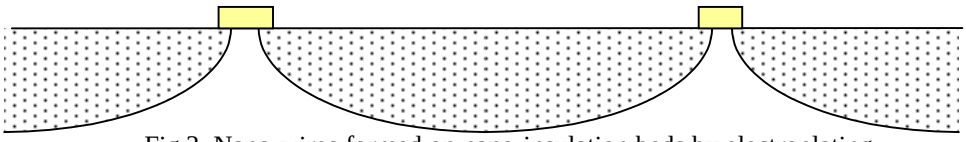

Fig.3. Nano-wires formed on nano-insulation beds by electroplating using $AuNaCl_4$ solved in ethanol.

5. Conclusion

The nano-wiring process was proposed by an electroplating with using $NaAuCl_4$ solved ethanol on the C-Au-S film formed by cooperation process of plasma CVD and sputtering. However continuous line pattern was not formed. The electro-plating process must be optimized.

Acknoweledgement

A part of this experiments were carried out at the Center for Co-operation Research in Advanced Science and Technology, Nagoya University. We express our gratitude to all who contributed to this study.

References

[1] K. K. Likharev; Single Electronics in Granular Nanoelectronics. NATO ASI Series B, Physics Vol. 251. Edited by David K. Ferry et al. Plenum Press, 1991.

[2] Md. Abul Kashem, M. Matushta and S. Morita, JJAP,**43** No.3A (2004) pp.355-357
[3] Md. Abul Kashem and S. Morita, Phys. Rev.,B.69.1934606(2004)
[4] M. Suzuki, Md. Abul Kashem and S. Morita, IEICE, Trans. Electron., E87-C, No.2 Feb. (2004) pp179-182
[5] M. Suzuki, S. Morita, O. Zabeida and L. Multinu, Abstract, 7th APCPST & 17th SPSM, Fukuoka Int. Cong. Center, June 29-July 2, 30P-31 (2004) p.271.
[6] M. Suzuki and S. Morita, 16th Int. Symp. on Plasma Chem., Po6.38, Taormina, Italy, June 22-27, (2003).

Modification of poly(ethylene terephthalate) track membrane properties by plasma of dimethylaniline

L. Kravets[1], S. Dmitriev[1], A. Gilman[2], A. Drachev[2], G. Dinescu[3]

[1]*Joint Institute for Nuclear Research, Flerov Laboratory of Nuclear Reactions, Dubna, Russia*
[2]*Enikolopov Institute of Synthetic Polymeric Materials, Russian Academy of Sciences, Moscow, Russia*
[3]*National Institute for Laser, Plasma and Radiation Physics, Bucharest, Romania*

Abstract
Deposition of plasma polymer thin films on poly(ethylene terephthalate) track membranes was realized in a direct current parallel plate discharge generated in dimethylaniline vapors, leading to formation of composite porous structures. The change induced by the plasma polymerization deposition on the basic characteristics of the composite membranes (pore size, wettability, surface charge, water permeability) is presented. The study of the water permeability through the composite structure formed revels that it depends nonlinearly on pressure at different PH values of the filtrate. This is interpreted in the frame of a model in which the molecular interactions in aqueous media change the conformational state of the molecules deposited by plasma polymerization inside the pores.

Keywords: Plasma polymerization, Poly(ethylene terephthalate) track membrane, Conformational changes, Controlled permeability;

1. Introduction

The development of responsive functional devices, in which the basic properties can be controlled by changing external parameter values are of high applicative interest and gained considerable attention in the last period. Among them the design and preparation of filtration membranes with controllable transport properties, whose permeability can be regulated by changing environmental conditions such as temperature [1], solution pH [2, 3], electrical [4] and magnetic [5] fields, solvent composition [6], pressure [7] were recently discussed. A way to create membranes with controlled transport properties is to exploit the ability of macromolecules at the surface layer of pores to perform reversible conformational transitions. The research in this direction is related to approaching methods leading to formation of polymeric layers with predefined chemical structure at the surface of membranes. To this aim various techniques are employed: chemical [1], radiation-induced graft polymerization of monomers [2], preliminary activation of the surface by plasma with a subsequent grafting of polymers from the solution [3], deposition on the surface of membrane thin polymeric layers obtained with the help of plasma polymerization [7]. These investigations are of major practical and scientific importance as they allow not only gaining of a wide spectrum of membranes with unique properties, but also to discover opportunities of synthesis of membranes with new functionalities, as example imitating the biological ones.

In this paper the water permeability of composite membranes obtained by deposition of a polymeric layer formed by plasma polymerization of the dimethylaniline vapours (DMA) onto a porous substrate consisting of poly(ethylene terephthalate) track membranes (PET TM is studied. A direct-current (DC) discharge was selected for polymer deposition because it is very effective in creating high concentration of functional groups; it is known that such groups play a key role in the processes of mass transfer. Dimethylaniline was chosen as monomer, since nitrogen-containing polymers are capable of forming cationic units in an acidic medium, which can influence the conformational state of macromolecules. In addition, experiments of doping the composite membranes with iodine were performed because it is also known that iodine has a high electron affinity and doping with iodine increases the concentration of positively charged units in a polymeric layer. The dependencies of water permeability on pressure at various pH values of the filtrate solution, obtained for the membranes prepared in the above conditions, are presented and discussed.

2. Experimental

The technique of producing track membranes consisted of two steps. First the irradiation of PET thin foils with

positively ionized atoms of krypton accelerated up to an energy of ~ 3 Mev/nucleon was realized at the cyclotron U-400 (Flerov Laboratory of Nuclear Reactions, Dubna). Subsequently, the irradiated foils were subjected to physico-chemical treatments in a caustic solution [8], leading to the removal of the material along the ions trajectory. Poly(ethylene terephthalate) (PET) track membranes of thickness of 10.0 μm with pore density of $2 \cdot 10^8$ cm^{-2}), and effective pore diameters of 0.215 μm were obtained in this way.

As substance for membrane modification by plasma polymerization, *N*,*N*-dimethylaniline (Fisher Scientific Co, USA) with T_{boil} = 193 °C was used. No additional purification has been applied. Deposition of the plasma polymer was realized at a pressure of DMA vapours 26.6 Pa and a discharge current density 0.1 mA/cm^2 . The deposition time was varied in the range of 20-180 s. Only one side of the membranes was subjected to the plasma treatment. Details on the treatment procedure and the schematic of the plasma reactor set-up can be found in reference [9].

The doping with iodine was realized by introduction of the plasma deposited track membrane in a desiccator containing saturated iodine vapour at 20 C for 30 minutes.

The characteristics (pore size, thickness, contact angle, chemical composition, morphology) of the initial and modified membranes were determined through a series of complementary procedures and techniques, as described in detail in [10].

The thickness of the membranes was measured by using an electronic meter of thickness (Unit Tesa, Austria). The effective pore size was calculated from the air flow rate, taking into account the gas flow regime in the pores. The surface morphology and the pore structure of the initial PET TM and that modified by plasma were investigated with a scanning electron microscope JSM-840 (JEOL). The water contact angle was determined by the goniometrical method. Fresh distilled water was used for the measurements. The permeability of membranes to water solutions with various pH values was measured with a standard filtration installation (FMO-2). The effective membrane area subjected to permeability investigations was 254 mm^2. Solutions of hydrochloric acid of various concentrations were used as working solutions.

a)

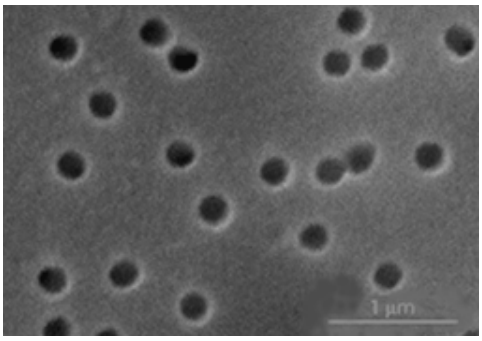

b)

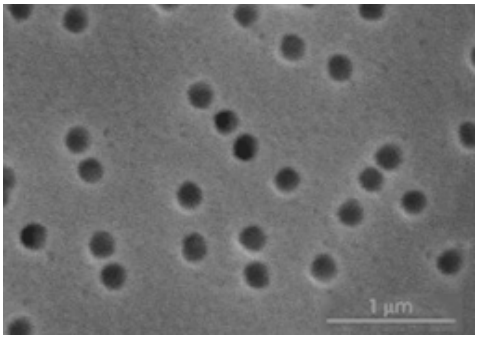

Fig. 1. SEM photographs of the initial PET TM (a) and PET TM treated by plasma for 180 s (b).

The chemical composition of the membranes modified by plasma and the DMA polymer was studied by ESCA and FTIR spectroscopy. The ESCA spectra were recorded with a Riber SIA-100 spectrometer (MgK_α, 100 W, 15 kV, 20 A) provided with a MAC-2 electron energy analyzer. The position of peaks (the binding energy values) was calibrated against the C_{1S} standard peak (284.6 eV). FTIR-spectra were recorded with a Bruker Equinox 50S spectrometer in the range of 400-4000 cm^{-1}, working with 500-fold accumulation of data and a scanning step of 2 cm^{-1}.

3. Results and discussion

Scanning Electron Microscopy images of membranes surface, before and after the plasma deposition are shown in Figure 1. As it is seen, the plasma does not have destroying effects on the surface and the pore contours are not changed. This is different as comparing with the treatment of PET TM membranes in oxygen containing radiofrequency plasmas. Moreover, at a closer look, a slighter decrease of the pore diameters can be observed, which suggest that the deposition inside the pores occurred.

The results concerning the modification of the mass, thickness, effective pore diameters, and contact angles of membranes subjected to treatment with various duration in the DC plasma generated in DMA vapours are presented in Table 1. An increase of the mass of membranes is observed, which can be explained by the deposition of the polymeric layer on its surface. As expected, the thickness of the mem-

branes increases too, while the effective diameter of pores decreases. These results strongly confirm that the deposition of the polymer took place both on the surface of the membrane and on the walls of its pores.

Table I. Change of the membrane characteristics during plasma treatment

Plasma treatment time, s	Relative increase in the mass, %	Thickness, μm	Effective pore diameter, μm	Water contact angle, deg
Control	–	10.0	0.215	65
20	9.5	10.3	0.210	45
60	11.5	10.5	0.205	45
180	13.5	10.7	0.200	45

The PPDMA deposition in pores is sustained by the ESCA data as well. According to the ESCA data, nitrogen atoms were detected both on the treated and on the untreated sides of the membrane. This is the proof that plasma species responsible for deposition penetrate inside the pores and the polymer layer reaches the reverse side of the sample. The analysis of PPDMA ESCA spectrum shows the presence of peaks related to carbon and nitrogen atoms, and notifies on small content of oxygen. The ratio of nitrogen atoms to carbon atoms in the plasma polymer and the initial DMA is practically the same. These results indicate that the chemical structure of the deposited polymer is much closed to the chemical structure of the initial DMA. These results are confirmed by the FTIR spectroscopy. In the FTIR spectra of the deposited membranes the vibration of bonds specific to the structural units of the DMA, like that of the aromatic rings is prominent. A small amount of oxygen in PPDMA can be explained by the presence of residual oxygen in the plasma-forming gas and also by subsequent oxidizing of PPDMA in the ambient air, after plasma treatment, which is characteristic for polymers synthesized by plasma polymerization technique.

Plasma treatments lead to the modification of the contact angle, and the wettability of the surface increases. After deposition the contact angle values (Θ) were not more than 45°, irrespective of the plasma treatment time, which can be compared with the initial contact angle value of 65°. The wettability improving can be connected with the formation of additional hydrophilic groups on the surface; as example PPDMA absorption spectrum contains the absorption bands connected with stretching vibrations of CN groups in tertiary amines.

The above mentioned results prove that in all cases, irrespective to the treatment duration, there is a complete coating of the membrane surface by a layer of the deposited polymer. SEM observations say about the absence of erosion of the membrane surface under plasma treatment, mass and pore size measurements proves the deposition of a layer on membrane and inside the pores, the ESCA and FTIR analyses testify that the composition of the deposited film is closed to that of the initial DMA monomer.

The dependence of water permeability, in acidic medium corresponding to pH=1.2, upon the applied pressure is presented in Figure 2. The curve 1, corresponding to the initial PET TM, reveals a linear dependence that is typical for membranes with a hard structure at a viscous character of the filtrate flow (when the pore diameter is much larger than the size of water molecules [11]). For the plasma modified membranes with DMA the dependence of water permeability upon pressure, with the same filtrate, is not linear (Figure 2, curves 2 and 3). Apparently, this effect is caused by the decreasing of the pore diameters which may be explained by the changing of PPDMA macromolecules conformation state. Indeed, at low pH values the protonation of the nitrogen atoms will occur, due to the high concentration of the H^+ ions in solution. The segments of the macromolecules of the plasma deposited polymer acquire a positive charge, as is pictured in Figure 4. This causes the swelling of the molecular chains and formation of a gel [12], which lead to a decrease of the pore size (pore contraction). The PPDMA macromolecules in this case are disposed like a loose "glomus". Such a conformational state of macromolecules results from the electrostatic interaction of charged segments with water molecules and is steady. One may observe that the curves behaviour depends on the relative mass increase during the plasma treatment. Higher is the mass increase, lower is the permeability and higher is the departure from the linear dependence exhibited by the untreated membrane. This correlates with the thickness of PPDMA layer. The departure from

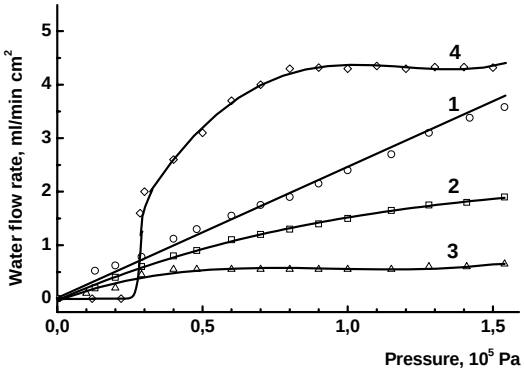

Fig. 2.

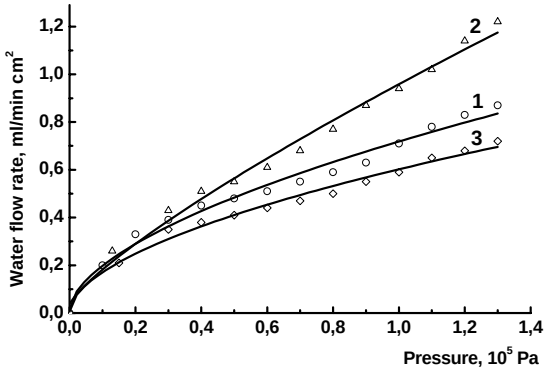

Fig. 3.

Fig. 2. Dependence of water flow rate on the value of applied pressure if filtering a solution with pH = 1.2 for initial PET TM (1), PET TM treated by plasma during 20 s (2), PET TM treated by plasma during 60 s (3), and PET TM treated by plasma during 60 s and doped by iodine (4).

Fig. 3. Dependence of water flow rate on the value of applied pressure when filtrating a solution with pH = 4.6 for initial PET TM (1), PET TM treated by plasma during 60 s (2), and PET TM treated by plasma during 60 s and doped by iodine (3).

the linear behaviour of the treated membranes indicates that the degree of swelling of plasma deposited polymer is significant in comparison with the swelling of the initial polymeric matrix.

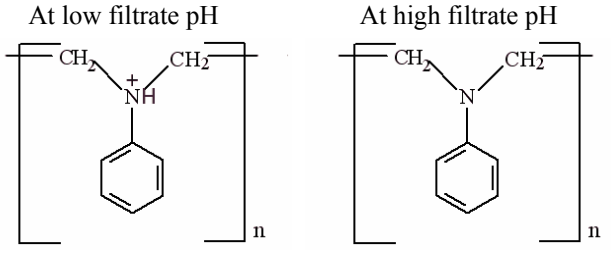

Fig. 4. Chemical structures PPDMA in various mediums.

The dependence of water permeability, in a medium corresponding to pH=4.6, upon the applied pressure is presented in Figure 3. For the initial membrane (curve 1) the increase of the filtrate pH (the reduction of ion concentration H^+ in the solution) changes in non-linear, as comparing with curve 1 in Figure 2, the dependence of water permeability on the applied pressure. At pH = 4.6 the dissociation of carboxylic groups increases – pK_{COOH} in PET TM is abut 3.6-3.7 [10]. This leads to formation of a negative charge on PET TM macromolecules which changes, due to the coulombian repulsion, the conformational state. The lower values of the permeability and the nonlinear character of the dependence, as comparing with Figure 2, curve 1 points out at the decrease of the pore diameters. Moreover, for the modified PPDMA membrane (Fig. 3, curve 2) an increase of the water permeability is observed which relates to the reduction of the protons concentration in the filtrate. In the medium with higher pH the content of positively charged atoms nitrogen in PPDMA decreases, therefore the electrostatic interaction gets weaker. With decreasing Coulomb's interaction, the nonelectrostatic interaction of hydrophobic groups, in this case, of non-polar CH_2-groups increases [12]. That results in a collapse of the gel and to the transition of macromolecules in a compact conformational state of "globule" type. This state does not cause appreciable decreasing of the pore diameters. Consequently for modified membranes used at this pH values one can still observe a viscous character of the filtrate flow: the dependence of the water permeability upon the the applied pressure has an almost linear character (Fig. 3, curve 2). It is interesting to mark that despite a lower effective diameter, the values of the flow for the modified membrane are higher than for the initial PET TM. Probably, this aspect is related to the changing of the structure and chemical composition of the surface layer of the membrane.

The treatment of the DMA plasma modified membranes in iodine vapours leads to diffusion of the latter into the surface layers of the membrane and of the pores, as proved by ESCA and FTIR investigations. From Fig. 2 (curve 4) it is seen that in an aqueous medium with low value pH = 1.2 such a membrane is not permeable up to $2.8 \cdot 10^4$ Pa. This is caused by a large swelling of the plasma deposited polymer and the gel formation, whose volume closes completely the pores (Fig. 5a). The increase of pressure over $2.8 \cdot 10^4$ Pa causes a collapse of the gel, and the membrane pores pass into an "open" state (Fig. 5b). The membrane in such state is characterized by high water permeability values. This phenomenon is related to the conformational transformation of PPDMA macromolecules from the loose "glomus" to the compact "globule", which is characteristic for polymers containing charged monomeric segments [12]. The pressure growth results in the decrease of the distance between the

fragments of macromolecules that, in turn, change the balance of hydrophobic and electrostatic forces, the forces of intermolecular attraction becoming dominant resulting in pores opening. A similar effect can occur not only at the pressure and pH solution increase, but also at the change of the solution temperature or quality of the solvent. Increase of pH value (at 4.6) causes partial loss of the charge fixed on nitrogen atoms; therefore, sharp weakening of intramolecular electrostatic interaction is observed and formation of a gel does not occur in this case. Thus, the macromolecules of the deposited polymer, having compact conformation, do not block the penetration of solution into pores. As a result the dependence of the flow through the membrane upon the value of applied pressure is of viscous character, similar to the case of modified TM not containing iodine (Figure 3, curve 3).

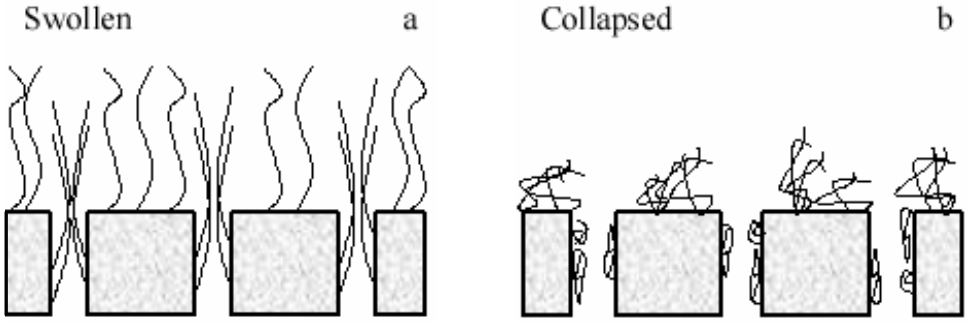

Fig. 5. Schematic illustration of the change in permeability of the track membrane with PPDMA layer: a – medium with low pH value; b – medium with high pH value.

4. Conclusion

The results presented in the paper prove that the plasma polymerization in a discharge configuration with the membrane at anode leads to deposition both at the surface and inside the pores. The polymer obtained from DMA plasma has swelling capabilities when introduced in water solutions with low pH values. The swelling of the PPDMA layer deposited onto the pore surface causes the decrease of the pores diameters, accompanied by a decrease of the water permeability. The introduction of iodine in the PPDMA layer results in formation of a polyelectrolyte, whose swelling in media with low pH value causes a complete contraction of pores in a specific range of pressure. Consequently, the PET track membranes, modified by DMA plasma, are capable of a reversibly change of water permeability depending on the pH of solution and the applied pressure.

References

[1] L. Liang, X. Feng, L. Peurrung, V. Viswanathan - J. Membr. Sci., **162,** 235 (1999).
[2] H. Omichi, M. Yoshida, M. Asano et al. - Nucl. Instr. And Meth. **131B**, 350 (1997).
[3] Y. Ito, S. Kotera, M. Inaba et al. - Polymer. **31**, 2157 (1990)
[4] S.J. Kim, S.G. Yoon, S.M. Lee, S.H. Lee, S.I. Kim - J. Appl. Polym. Sci. **91**, 3613 (2004).
[5] J.P. Gang, J. Kawakami, V.G. Sergeyev, Y. Osada - Macromolecules. **24**, 5246 (1991).
[6] W. Cai, R.B. Gupta. - J. Appl. Polym. Sci. **88**, 2032 (2003).
[7] Y. Osada, M. Takase - J. Polym. Sci.: Polym. Chem. Ed. **23**, 2445 (1985).
[8] G.N. Flerov - Vestnik Akademii Nauk SSSR. **4**, 35 (1984).
[9] A.I. Drachev, A.B. Gilman, E.S. Obolonkova, A.A. Kuznetsov - Synthetic Metals. **142**, 35 (2004).
[10] S.N. Dmitriev, L.I. Kravets, V.V. Sleptsov, V.M. Elinson - Desalination. **146**, 279 (2002).
[11] M. Katz, T.J. Wydeven - Appl. Polym. Sci. **26**, 2935 (1981).
[12] A.R. Khokhlov, E.E. Dormidontova - Uspekhi Fizicheskikh Nauk. **167**, 113 (1997).

Q-MACS – a new diagnostic tool for on-line process monitoring in plasma chemical applications

S. Glitsch, F. Hempel, N. Lang, U. Macherius, J. Röpcke, S. Saß, H. Zimmermann

[1] *INP-Greifswald, F.-L.-Jahnstr. 19, D-17489 Greifswald, Germany*

Abstract

A compact quantum cascade laser measurement and control system (Q-MACS) based on infrared absorption spectroscopy has been developed for time-resolved plasma diagnostics, process control and trace gas monitoring. The Q-MAC system contains a tuneable quantum cascade laser which can be directed through a plasma or into a multipass cell for exhaust or trace gas detection. Rapid scan software with real-time line shape fitting provides a time resolution up to 1 μs to study kinetic processes of infrared active compounds in plasmas or gases. The capabilities of the Q-MAC system have been demonstrated for trace gas detection and in plasmas.

Keywords:

Plasma diagnostics. Process monitoring, Absorption spectroscopy, Quantum Cascade Laser

1. Introduction

Plasmas containing molecular precursors are used in a variety of plasma enhanced chemical vapour deposition and etching systems to deposit or remove thin films. For reasons of enhanced efficiency, increased stability and product quality the direct control of such plasma applications is a challenging subject for plasma technology. The key to an improved understanding and control of chemical active discharges is the analysis of the fragmentation of the precursor and the monitoring of transient or stable plasma reaction products, in particular the measurement of their ground state concentrations. Therefore appropriate diagnostic tools are necessary allowing an on-line process monitoring in such applications.

Tuneable infrared diode laser absorption spectroscopy (TDLAS) in the mid infrared spectral region between 3 and 20 μm, using lead salt lasers, is a well known non-invasive technique for the detection and the measurement of stable and radical molecular species not only in the gas phase but in gas discharges as well [1,2]. It can also be used to determine neutral gas temperatures and to investigate dissociation processes in a wide range of molecular discharge plasmas. The TDLAS method also allows time resolved measurements.

The main disadvantage of TDLAS systems, based upon lead salt diode lasers, is the necessary cryogenic cooling of the lasers and even of the detectors, because they operate at temperatures below 100 K. Systems based upon lead salt diode lasers are typically large in size and require closed cycle refrigerators and/or consumables like liquid nitrogen.

The recent development and commercial availability of quantum cascade lasers with distributed feedback (DFB-QCL) based on sophisticated band structure engineering offers an attractive new option for infrared absorption spectroscopy. Pulsed DFB-QCL are able to emit mid-IR radiation near to room temperature. Compared to lead salt lasers, QCLs allow the realization of very compact mid-infrared sources characterized by narrow line width combining single-frequency operation and considerably higher power values of tens of mW. The output power is sufficient to combine them with thermoelectrically cooled infrared detectors, which permits a decrease of the apparatus size and gives a unique opportunity to design compact liquid nitrogen-free mid-IR spectroscopic systems. Such a quantum cascade laser absorption spectroscopic (QCLAS) system of decreased instrument size and weight would lead to a reduced transport logistics. “Turn-Key” operation and unattended remote monitoring and control at an improved safety level and at a low level of maintenance could be ensured. These positive features of QCLAS systems can open up new fields of application in research and industry, including studies of gases in atmospheric, environmental and plasma chemistry but also for in-situ control of industrial plasma processes.

This article describes a compact quantum cascade laser measurement and control system (Q-MACS) which has been developed for time-resolved plasma diagnostics, process control and trace gas monitoring [3]. The Q-MAC system contains a tuneable quantum cascade laser which can be directed through a plasma or into a multi-pass cell for exhaust gas detection. With examples of trace gas detection and of phenomena in plasmas the capabilities of the Q-MAC system is demonstrated.

2. The Q-Macs-Basic

As platform for various applications of QCLAS the Q-MACS-Basic, has been designed. It consists

1. of a laser head, which serves as the mount for commercially available QCL-chips and has the complete associated electronics to drive the laser in,
2. of a supply unit, which delivers the supply voltages needed in the laser head of Q-MACS and where the user can read and set the working parameters of the QCL, and
3. of a connection cable between the two parts.

Figure 1 shows a photograph of the three parts of this system, the Q-MACS-Basic. In Table 1 the main technical features of the Q-MACS-Basic are given. The supply unit allows in addition the remote controlling

Figure 1. Q-MACS-Basic system with laser head, supply unit and connection cable.

of the Q-MACS via a commercial PC and the software "TDLWintel". TDLWintel is a Windows based software package of Aerodyne Research Inc., which is used to tune the QCL, to remote control the operating parameters of the Q-MACS as well as to analyse and display the measurement results [4,5]. TDLWintel allows an easy integration of the system into experiments. The software sweeps the laser frequency over the full infrared transition or group of transitions using a small bias dc ramp and returns absolute species concentrations from non-linear least squares fits of the transitions. For time resolved measurements the stream mode of data acquisition can be applied. Fig. 2 shows the block diagram of the electronics of the laser head of Q-MACS-Basic capable of operating at high power, voltage up to 30 V and current up to 15 A, and high duty cycle. An efficient, highly stable peltier cooling enables temperatures in the range between – 35°C and 40 °C to be attained. Variable pulse length from 8 ns to 255 ns allow the laser to be operated in true pulsed or near to CW regimes, the "Intrapulse Mode". In addition the laser can be tuned via a bias current ramp of up to 1 A, the "Interpulse Mode".

Width of single pulses:	8 … 255ns
Pulse frequency:	up to 1 MHz
Working modes:	Intrapulse (Single pulse) Interpulse (Bias DC-Ramp)
Temperature range for the QCL:	-35 … + 40 °C
QCL Provider	Alpes Lasers Laser Components

Table 1: Technical features of the Q-MACS-Basic.

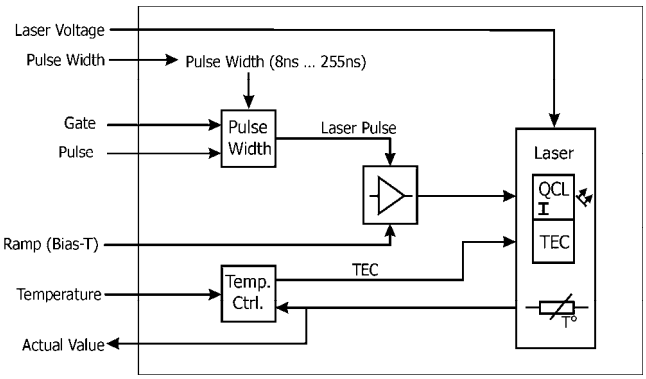

Figure 2: Block diagram of the electronics of Q-MACS-Basic

3. Examples of Applications

Measurements with the Q-MACS-Basic were performed in an industrial pulsed dc plasma reactor to deposit borone based hard coatings. Figure 3 shows an absorption spectrum of diborane near 1613 cm^{-1} recorded with 5 % admixture of this molecular precursor gas in hydrogen and argon. Using TDLWintel it was possible to monitor permanently the concentration change of diborane while driving a process plasma. The measurement results are not only displayed but can be transferred via hardware interfaces to other systems, e.g. for the use in automated process monitoring and controlling. These measurements proof that QCLAS can be useful to improve the reliability and effectiveness of industrial plasma processes.

The scan through an infrared spectrum can not only be done by a bias dc ramp, in the interpulse mode. Another option is the scanning in single, longer pulses, the intrapulse mode. Recently new routines were developed to control the Q-MACS in this mode via TDLWintel. An example of a 1.7 cm^{-1} long scan in this mode is shown in figure 4. Since the duty cycle of QCL is about 1 percent the temporal resolution can be in this mode as good as some µs. Therefore it fits very well measurements of rapidly changing chemical processes.

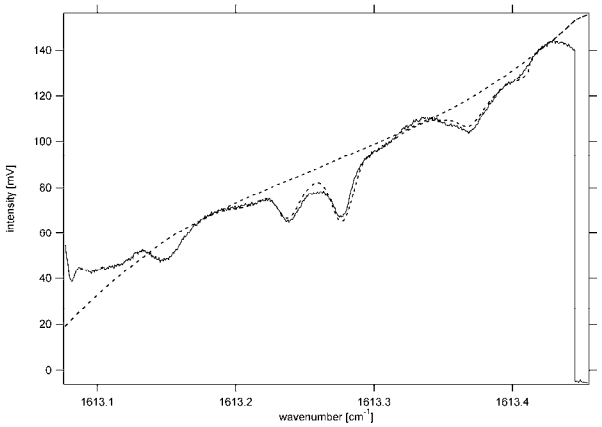

Figure 3: Absorption spectrum and fit of diborane at 1613 cm^{-1} measured in an industrial pulsed DC reactor with 5 % diborane in the gas inlet (p= 200 Pa).

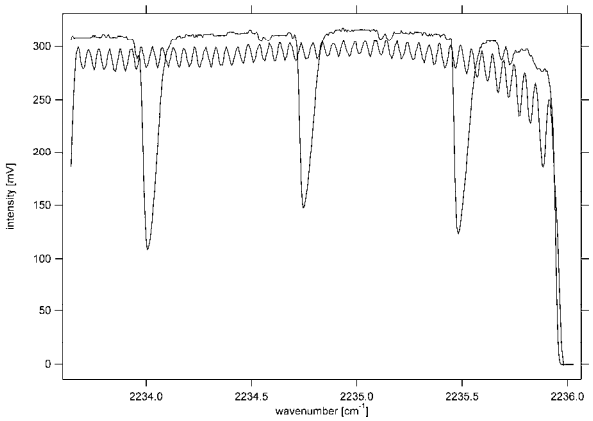

Figure 4: Absorption spectrum of a N_2O reference gas cell (l= 15 cm, p= 6.6 mbar) at 2235 cm^{-1} and the etalon pattern of known fringe spacing (fsr = 0.049 cm^{-1}) in a single QCL pulse (t= 100 ns).

4. Q-MACS-Trace

For high sensitive trace gas measurements a compact and transportable measurement system, the Q-MACS-Trace was developed. It combines the Q-MACS-Basic with an 50 m astigmatic multi-pass absorption cell of the Herriot type [6], a compact optical system and a computer system. The sensitivity of the Q-MACS-Trace was as high as a few ppb (parts per billion – $1/10^9$). Fig. 5 shows a photograph of the Q-MACS-Trace with optical arrangement and laptop for analysis. The Q-MACS-Trace optical system is designed around the QCL laser head.

Figure 5: Photograph of the Q-MACS-Trace with optical arrangement and laptop for analysis.

5. Summary

The Q-MAC-System was used to study dissociation processes of several precursor gases, as e.g. hydrocarbons or boron containing species, in industrial reactors. The applicability of Q-MACS and of QCLAS for high sensitive trace gas analysis and for on-line process monitoring under industrial-near conditions has been proofed.

Acknowledgments
This work was partly supported by the Deutsche Forschungsgemeinschaft, Transferbereich 36.

References

[1] J. Röpcke, L. Mechold, M. Käning, W.Y. Fan, and P.B. Davies, *Plasma Chem. Plasma Process*., **19**, 395, 1999.
[2] F. Hempel, P.B. Davies, D. Loffhagen, L. Mechold, and J. Röpcke, *Plasma Sources Sci. Technol.* **12**, 98, 2003.
[3] http://www.q-macs.de
[4] M.S. Zahniser, D.D. Nelson, and C.E. Kolb, C.E. In Applied Combustion Diagnostics, Kohse-Hoinghaus K and Jeffries J (eds), Tallor and Francis, New York, 648, 2002.
[5] D.D. Nelson, J.H. Shorter,. J.B McManus, and M.S Zahniser, *Appl. Phys. B,* **75**, 343, 2002.
[6] J.B. McManus, P.L. Kebabian, and M.S. Zahniser, *Appl. Opt.,* **34**, 3336, 1995.

Numerical Simulation and Experimental Evaluation of Solidification Behavior of Vacuum Plasma Sprayed Ti-6Al-4V Alloy

H.R. Salimijazi, M. Raessi, T.W. Coyle, and J. Mostaghimi
Centre for Advanced Coating Technologies, University of Toronto, Canada

Abstract
In the present study, the solidification behavior and morphology of a single splat of Ti-6Al-4V alloy deposited under Vacuum Plasma Spray (VPS) conditions were investigated using both numerical simulation and experimental observations. A three-dimensional model of droplet impact has been employed to investigate the solidification behavior of a single particle of Ti-6Al-4V alloy under vacuum plasma spray conditions. The numerical results were compared to the experimental observations of the behavior of droplets with the same in-flight droplet characteristics such as droplet temperature, velocity, and size. The behavior of a 50 μm diameter Ti-6Al-4V alloy droplet at an initial temperature of 1600°*C* impinging with an impact velocity of 500 *m/s* onto the surface of a Ti-6Al-4V alloy substrate at 800°*C* was simulated numerically. The average cooling rate and solidification front velocity were estimated to be 6×10^8 °*C/sec* and 63 *cm/sec*, respectively. Numerical results showed that approximately 30% of the droplet material is lost due to splashing. The thickness of the simulated splat, calculated from the cross-section of the solidified droplet, was approximately 4 μm in the central region of the splat. The splat thickness and diameter found by numerical simulation was in good agreement with the experimental results.

Keywords
Vacuum plasma spray, Numerical simulation, Droplet impact, Solidification behavior, Ti-6Al-4V alloy

Introduction

Ti-6Al-4V alloys have been widely used in the aerospace industry for more than three decades due to their superior properties. These properties have also increased demand for the alloy in other applications such as biomedical, automotive, and power generation industries. Due to the high reactivity with oxygen, poor weldability and low thermal conductivity, these alloys are difficult to process and form using conventional techniques, especially for complex shaped components. Near-net-shape forming of the alloy by Vacuum Plasma Spraying (VPS) is a promising new alternative to conventional manufacturing processes. In a VPS process, Ti-6Al-4V powders are fed into the high gas velocity and temperature environment generated by a dc arc in a plasma torch inside an evacuated chamber. The powders are melted and accelerated toward the substrate which is located approximately 20 cm from the torch. The powder particles impact the substrate or prior deposit, spread out and finally solidify to form splats. Thus, the as-sprayed microstructure consists of individual splats connected to each other by mechanical inter-locking and chemical bonding across the splat boundaries. A significant density of microcracks and pores are found at the inter-lamellae boundaries. Therefore, the properties of thermal spray deposits depend on the solidification history and morphology of individual splats and the strength of the inter-lamellae contacts [1-4].

Computational Modeling of a Single Ti-6Al-4V Molten Metal Droplet

Thermal spray deposit properties mainly depend on the solidification and morphology of individual splats after solidification on the substance or prior deposit. The form of splats after solidification is a function of droplet characteristics, such as in-flight particle size, velocity, and temperature distributions and also substrate temperature, surface roughness, and material. A three-dimensional model of free-surface fluid flow of droplet impact and solidification developed by Bussmann *et al.* [5] and Pasandideh-Fard *et al.* [6] has been employed. The model has been discussed in detail in previous publications [5-9].

Only a quarter segment of the droplet was simulated and the entire droplet reconstructed by reflecting the results about planes of symmetry. The contact resistance was assumed to be zero which means maximum heat transfer of the droplet to the substrate. Thermophysical properties of the molten Ti-6Al-4V alloy and substrate used in calculations are given in Table 1.

Table 1: Data used for the numerical simulation of a Ti-6Al-4V molten droplet.

Physical property	Value	Reference
Initial splat temperature (K)	1873[a]	
Substrate temperature (K)	1073[a]	
Melting point temperature (K)	1873	[10]
Latent heat of fusion ($kJkg^{-1}$)	440[b]	[10]
Viscosity of liquid ($s^{-1}m^{-2}$)	3×10^{-7} [b]	[10]
Thermal conductivity of liquid ($Jm^{-1}s^{-1}K^{-1}$)	30[b]	
Thermal conductivity of solid ($Jm^{-1}s^{-1}K^{-1}$)	33.1	[10]
Thermal conductivity of substrate ($Jm^{-1}s^{-1}K^{-1}$)	33.1	[10]
Specific heat of solid ($Jkg^{-1}K^{-1}$)	854.1	[10]
Specific heat of liquid ($Jkg^{-1}K^{-1}$)	989.2[b]	
Specific heat of substrate ($Jkg^{-1}K^{-1}$)	854.1	[10]
Density of liquid metal (kgm^{-3})	4120[b]	
Density of solid metal (kgm^{-3})	4500	[10]
Surface tension (Nm^{-1})	1.2[b]	[10]
Velocity of particle (ms^{-1})	500[a]	
Diameter of particle (μm)	50[a]	

[a] Measured values from experiments were used.
[b] Values for commercially pure titanium were used.

Figure 1 shows a sequence of the numerical simulation of a 50 μm diameter Ti-6Al-4V alloy droplet, initially at 1600°C, impinging with an impact velocity of 500 m/s onto a smooth surface of Ti-6Al-4V alloy substrate at 800°C. Column (a) shows the droplet during successive stages of impact on the surface. Column (b) illustrates half of the A-A cross section of the spreading of the droplet at the corresponding times.

Immediately after impact, the droplet flattens and spreads in the radial direction. Since melts always wet their own solids, a small contact angle would be expected between the droplet and the substrate or prior deposit layer. Thermal contact resistance between the substrate and droplet is neglected in the numerical simulation. The temperature of the flattened splat is uniform and there is a large temperature gradient between liquid and substrate. With such a high cooling rate, the liquid layer quickly cools down to below the melting point, T_m=1600°C, solidification starts, and further spreading is arrested. The points of contact between the substrate and flattened droplet act as heterogeneous nucleation sites. Crystals nucleated by both homogenous and heterogeneous mechanisms grow into the melt at a growth rate which is not controlled by the heat transfer rate. A small portion of the drop which is in contact with the substrate solidifies during spreading (see Fig. 1(b) at 0.1 μs). The residual liquid jets out over the periphery of the solidified bottom layer. This radial flow of liquid becomes unstable and disintegrates into fingers at the edge of the drop (see Fig. 1(a) at 0.1 and 0.22 μs). Some of these fingers finally detach to form satellite droplets; called “splashing”. These small droplets solidify during splashing and/or after impacting on the substrate or prior deposit. The low heat content, velocity, and temperature of the satellite droplets during impact result in formation of weakly adherent solidified fine droplets around the bulk of the splat. The splashed particles reduce adhesion of splats and can be seen in the fracture surface of the as-sprayed structure. Figure 2 shows SEM micrographs of (a) a fracture surface of the as-sprayed Ti-6Al-4V alloy

showing splashed particles, and (b) the morphology of a single splat of Ti-6Al-4V which impacted onto the ground surface of the titanium alloy substrate initially at 800°*C*.]

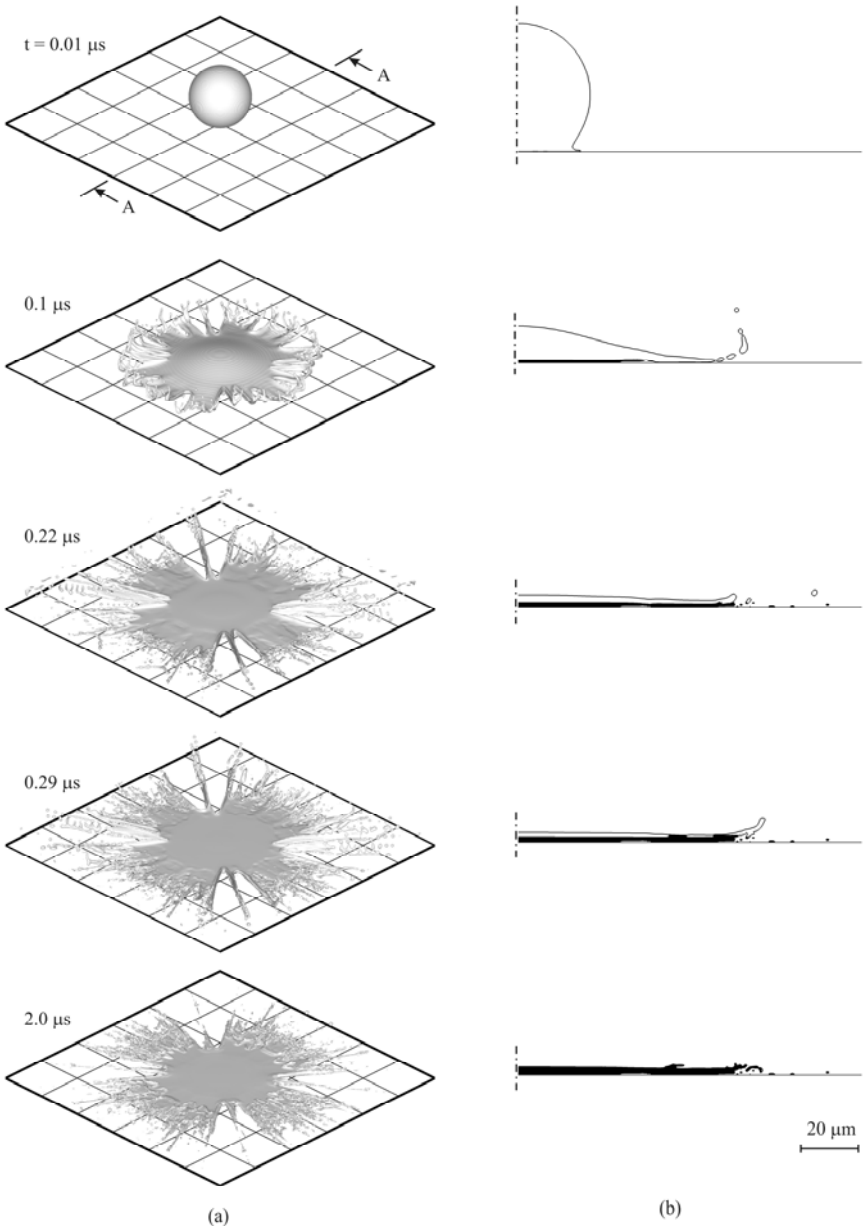

Figure 1: (a) Computer generated images of a 50 *μm* diameter Ti-6Al-4V alloy droplet at 1600°*C* impacting with a velocity of 500 *m/s* onto a titanium substrate at 800°*C*. (b) A-A cross section of the droplet at the corresponding times. Solid phase is shown in black.

The heat of fusion released from solidification increases the temperature of the residual liquid. When the growth rate becomes limited by heat transfer, further nucleation would be suppressed, and columnar crystal growth from the interface into the droplet would occur with a planar front morphology. After solidification, the splat cools down through the β phase region ands enters the α plus β region (at the beta transus temperature) of the phase diagram at a very high cooling rate; see Figure 3. Because of the high cooling rate, the β transus temperature would be shifted down towards the α + β region compared to

equilibrium cooling conditions. Hence, the martensitic formation of α' within the columnar β gains is expected.

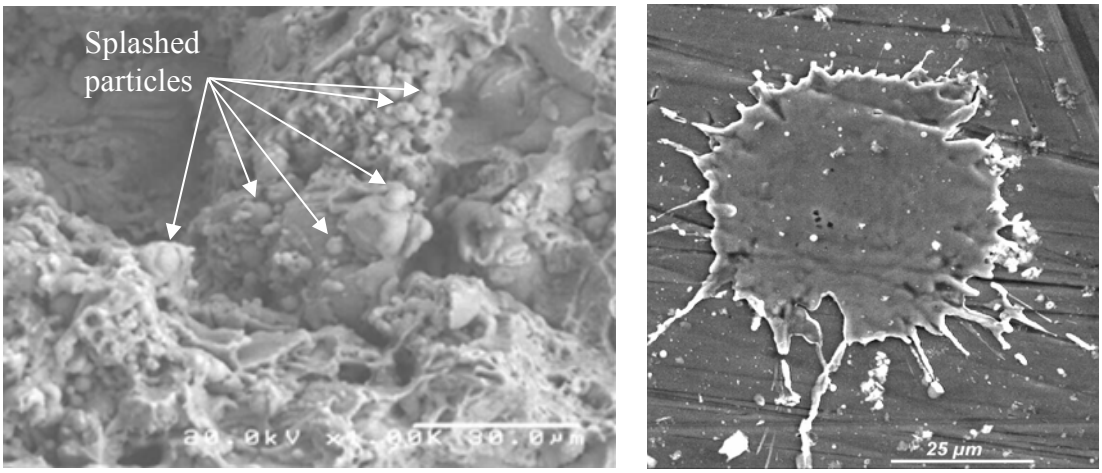

Figure 2: SEM images of (a) fracture surface of the as-sprayed Ti-6Al-4V alloy showing splashed particles and (b) morphology of a single splat of Ti-6Al-4V alloy.

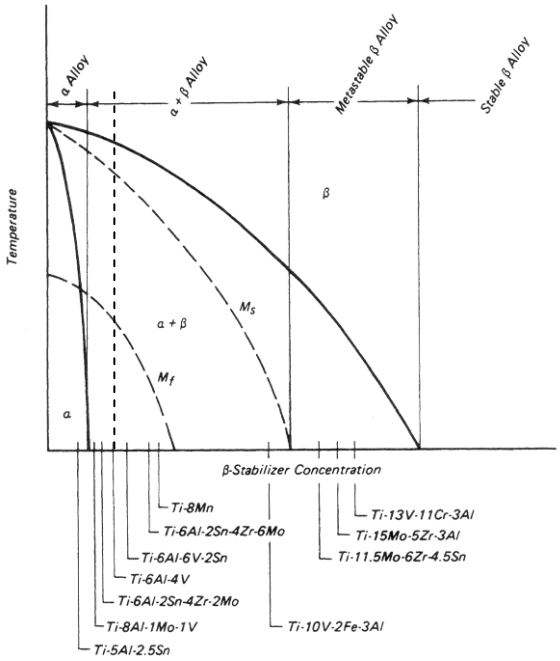

Figure 3: Pseudo titanium phase diagram.

Figure 4 illustrates the normalized volume of the droplet and the volumes of liquid and solid phases as a function of time. About 30% of the droplet material is lost due to splashing starting approximately 0.18 μs after the impact. The solidification rate reduces at approximately 0.08 μs after the impact because of the latent heat released by the thin solid formed at the interface. The thickness of the simulated splat is estimated from the cross section of the solidified droplet after impact (see Fig. 1b at 2 μs) to be approximately 4 μm in the central region of the splat.

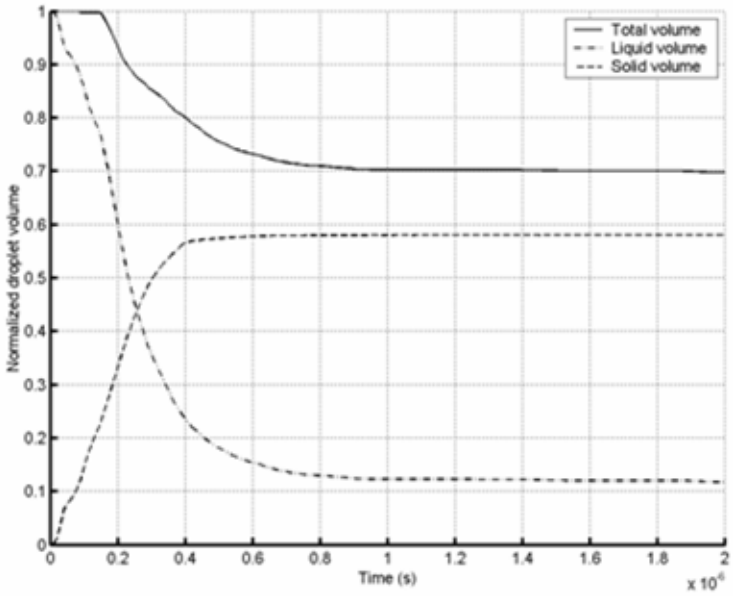

Figure 4: Calculated total volume of the droplet and the volumes of liquid and solid phases, all normalized by the initial droplet volume, versus time.

Figure 5 presents the calculated droplet temperature as a function of time at various positions within the splat, such as the centre of impact near the splat-substrate interface (point 1), middle of splat thickness (point 2), and close to the top surface of splat (point 3). The average temperature of the splat is also depicted in this figure. As expected, point 1 experiences a sharp temperature decrease immediately after impact. The cooling rate can be derived from the curves. Since the solid-liquid interface acts as a planar heat source while moving through the splat, the cooling rates change discontinuously at the solidification point. The inversion which occurs at 0.08 μs on the near substrate-splat interface curve is due to formation of a thin layer of solid on the substrate. Because of the latent heat released by solidification, the cooling rate of point 1 after 0.08 μs decreased. The solid-liquid interface has passed through the region near the mid point of the splat at around 0.23 μs and finally it has reached the outer surface of the splat at 0.4 μs and solidification is complete. At this time, the solidified splat cools down to the substrate temperature, which it reaches at 2 μs. The calculated average cooling rate is approximately 6×10^8 $^\circ C/sec$.

Discussion and Conclusion

The solidification behavior and morphology of a single droplet of Ti-6Al-4V alloy under vacuum plasma spray conditions were successfully simulated. The average cooling rate was estimated to be 6×10^8 $^\circ C/sec$ under interface-controlled heat transfer circumstances. The contact resistance at the droplet/substrate interface was assumed to be zero. Under real conditions, because of the existence of inclusions and roughness and the formation of micro-gaps within the splat/substrate interface, there is a contact resistance at the interface and therefore, actual the cooling rate is lower than the estimated value. The experimentally measured cooling rate under vacuum plasma spray conditions for nickel was reported [4] to be of the order of 10^7 $^\circ C/sec$, which is slightly lower than that obtained from the numerical results. Simulated results showed that solidification of a single splat was complete after 0.4 μs and approximately 30% of the initial droplet was splashed after solidification. While the solidification front morphology was assumed to be planar in this study, both planar and dendrite front morphology under vacuum plasma spray conditions have been reported in the literature [4]. Thus, the three-dimensional numerical model has to be developed to predict the solidification morphology and the transition conditions from dendrite to planar growth. The cooling rate and solidification behavior may change using dendrite front morphology

growth. Despite differences in the assumed substrate roughness and contact resistance between the numerical model and experiments, the estimated splat thickness and diameter by numerical simulation exhibited good agreement with the experiments.

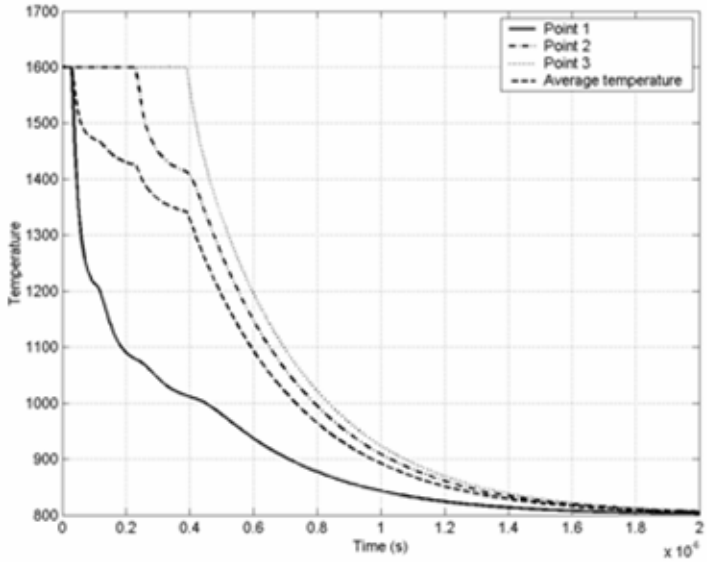

Figure 6: Calculated droplet temperature at the centre of impact (point 1), mid-point of the splat (point 2), top surface of the splat (point 3), and the average temperature of the splat.

References

1. S. Safai and F. Herman, "Microstructural Investigation of Plasma Sprayed Al-Coatings", Thin Solid Films, Vol. 45, pp. 295-307, 1977.
2. M. Cohen, B.H. Kear, and R. Mehrabian, "Rapid Solidification Processing – An Outlook", Rapid Solidification Processing: Principles and Technologies, Vol. II, R. Mehrabian, B.H. Kear, and M. Cohen, (Eds.), Louisiana, USA, pp. 1-24, 1980.
3. M. Cohen and R. Mehrabian, "Some Fundamental Aspects of Rapid Solidification Processing: Principles and Technologies, Vol. III, R. Mehrabian (Ed.), National Bureau of Standards, pp. 1-26, 1980.
4. S. Sampath and H. Herman: "Rapid Solidification and Microstructure Development during Plasma Spray Deposition," J. Thermal Spray Tech., 5(4), pp. 445-456, 1996.
5. M. Bussmann, J. Mostaghimi, S. Chandra, On a Three-Dimensional Volume Tracking Model of Droplet Impact, Physics of Fluids**,** 11, pp. 1406-1417, 1999.
6. M. Pasandideh-Fard, S. Chandra, and J. Mostaghimi, "A Three-Dimensional Model of Droplet Impact and Solidification", Int. J. Heat and Mass Transfer, Vol. 45, pp. 2229-2242, 2002.
7. M. Bussmann, S. Chandra , J. Mostaghimi, Modeling the Splash of a Droplet Impacting a Solid Surface, Physics of Fluids**,** 12, pp. 3121-3132,2000.
8. M. Pasandideh-Fard, R. Bhola, S. Chandra, and J. Mostaghimi, Deposition of Tin Droplets on a Steel Plate: Simulations and Experiments, International Journal of Heat and Mass Transfer**,** 41**,** pp. 2929-2945, 1998.
9. M. Pasandideh-Fard, V. Pershin, S. Chandra, and J. Mostaghimi, "Splat Shape in a Thermal Spray Coating Process: Simulations and Experiments", J. Thermal Spray Tech., Vol. 11(2), pp. 206-217, 2002.
10. R. Boyer, G. Welsch, and E.W. Collings (Eds.), "Materials Properties Handbook: Titanium Alloys", 2nd Ed., ASM International, Materials Park, OH, USA, pp. 483-636, 1998.

ARGES: RADIAL SEGREGATION AND HELICAL INSTABILITIES IN METAL HALIDE LAMPS STUDIED UNDER MICROGRAVITY CONDITIONS IN THE INTERNATIONAL SPACE STATION

Gerrit Kroesen[1], Marco Haverlag[2], Erwin Dekkers[1], Jovita Moerel[1], Rob de Kluijver[1], Peter Brinkgreve[1], Charlotte Groothuis[1], Joost van der Mullen[1], Winfred Stoffels[1], Rob Keijser[2], Mark Bax[1], Danny van den Akker[1], Guido Schiffelers[1], Pim Kemps[1], Frank van den Hout[1], André Kuipers[3]

[1] : Eindhoven University of Technology, Faculty of Applied Physics, P.O. Box 513, 5600 MB Eindhoven, the Netherlands

[2] : Philips Lighting, Central Development Lamps, Eindhoven, the Netherlands

[3] : European Astronaut Corps, European Space Agency ESA

ABSTRACT

HID lamps (High-Intensity Discharge) are gaining ground in the lighting industry because of their very high energy efficiency (up to 40%). In these lamps, which are operated in the arc regime and which are contained in a ceramic balloon, filled with argon or xenon, mercury, and salts of various rare earth metals and iodine), de-mixing occurs. This de-mixing is driven by differences in diffusion velocities of molecules and atoms. Furthermore, helical instabilities might occur in the lamp. Both phenomena are severely modified under 1 G conditions: convection will bend a horizontally burning arc channel upwards, and a vertically burning arc channel will exhibit convective cells. This makes it impossible to study these phenomena on the ground. If a proper understanding of these phenomena is to be gained, experiments under microgravity are necessary.

The main objectives of the experiment are: (1) determination of the critical factors for the onset of helical instabilities in HID lamps and (2) characterisation of the radial de-mixing processes by radially resolved high-resolution emission spectroscopy.

To this end, special hardware has been designed and built which houses a very compact high-resolution spectrometer, a video camera and a caroussel with 20 lamps in it. The lamps are measured consecutively.

The experiments have been performed successfully by the Dutch astronaut André Kuipers on board the International Space Station during the Dutch Soyuz Mission "DELTA" on 24 and 25 April 2004. Especially the helical instabilities part yielded immediate and surprising results: the arc channel does bend, but does not rotate under microgravity. This fact is very important in improving the performance of the lamps, especially since the instabilities occur mainly in the most efficient lamps.

INTRODUCTION

The name of the experiment is "ARGES". This is an acronym for: **A**tomic densities measured **R**adially in metal halide lamps under micro-**G**ravity conditions with **E**mission and absorption **S**pectroscopy. The lamp geometry is quite simple: a burner made of quartz or sintered aluminum oxide contains the gas mixture (see figure 1a). The burners are contained in a second envelope made of quartz. Between the electrode in the burners, a discharge is struck in the background gas (argon) by a high voltage pulse. After ignition, the discharge quickly moves from the glow regime to the arc regime, and then the mercury rapidly evaporates. Due to this evaporation, the total gas pressure increases to several tens of Bars. The metal salts start to evaporate also. In the central arc channel the temperature can get as high as 5000 K. At these temperatures, the salt molecules dissociate into atoms, and the metal atoms even ionize to a substantial degree. Differences in diffusion velocity of atoms and molecules cause radial segregation, which in combination with convection results in axial segregation or axial de-mixing, which is apparent from the colour distribution in the lamp (see figure 1b)[1]. Probably driven by self-generated magnetic fields, the discharge channel starts forming a helix, which rotates around its axis (figure 1c).

EXPERIMENTAL

The discharge is studied with high-resolution spectroscopy and video imaging (helical instabilities). The optical emission spectrocopy has two goals: analysis of the self-inversion of the spectral lines of mercury for temperature determination and determination of the intensities of various of the very numerous spectral lines of the rare earth metal additives atoms and ions for the study of the radial de-mixing processes[2]. All measurements have to be done as a function of the radius in the lamp.

In the flight hardware, 20 lamps are combined in a caroussel. At any one time, only one lamp is in the measurement position, where it can be analysed by the two diagnostics.

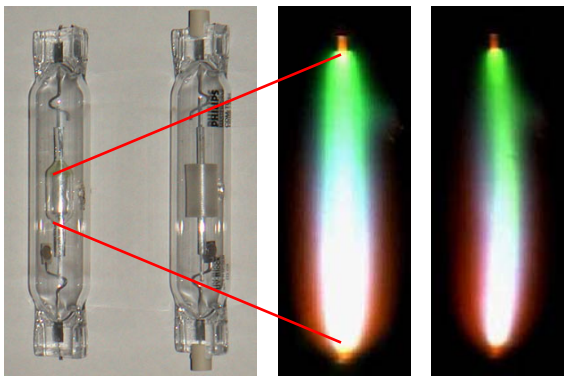

(a) (b) (c)

Figure 1: HID lamps. (a): geometry of the burners inside the outer balloon. (b): axial and radial de-mixing illustrated. (c): frame of a lamp which shows helical instabilities.

The spectrometer had to be small, light weighted, and robust. The requirement for compactness is solved by using an Echelle grating with a high blaze angle (74^{o}). Because of the high dispersion, due to the high angle of incidence and the high orders used, the focal length of the main lens can be relatively small, and consequently the spectrometer can be very compact. A disadvantage of Echelle-type spectrometers is however that they have a small free spectral range (FSR), which results in wavelength overlapping of adjacent orders. By installing an interference filter in the optical system for selecting a small wavelength interval, the problem of overlapping orders can be avoided. When several interference filters can be selected, these filters can be used for wavelength selection, and the angle of the grating can remain fixed.

All hardware is integrated on one frame, which is enclosed by an aluminum dome structure. The frame holds the spectrometer, the video camera which is used to observe the Helical Instabilities (a stripped Philips Toucam webcam), and it also supports the lamp caroussel in which 20 lamps can be mounted. Figure 4 shows the flight hardware, just before the aluminium dome is mounted on the bottom plate which holds the frame.

The astronaut operates the experiment using a Human Machine Interface (HMI). The experiments have operated in the ESA Microgravity Science Glovebox (MSG), in the US Destiny lab. Figure 5 shows a picture of one of the authors (A. Kuipers) installing the Arges hardware into the MSG on board of the ISS during the Delta Soyuz Mission..

RESULTS

A modified version of the Arges hardware has participated in the 34th and 35th ESA parabolic Flight Campaigns. During parabolic flights, only 20 seconds of microgravity is available. This is largely insufficient in view of the long stabilisation times of the plasma in the lamps, which is of the order of 10 minutes, but still one can get a good impression of the proper operation of the hardware and of the phenomena to be expected during the experiments in the ISS.

A demonstration of the performance of the high-resolution spectrometer is give in figure 6, where a part of the emission spectrum of dysprosium is given. Two lines, which are seperated by only 0.5 nm, can clearly be distinguished. The line integrated measurements of the spectrometer represent lateral profiles.

They have to be converted to radial profiles by Abel inversion. This has been done for a number of experiment conditions. An extreme example of the differences to be observed for 0g and 2g can be found in figure 7. Under 2 g conditions, it is obvious that the radial de-mixing, which is strongly occuring (see the 0g measurement), is almost totally suppressed by convective mixing or “stirring”.

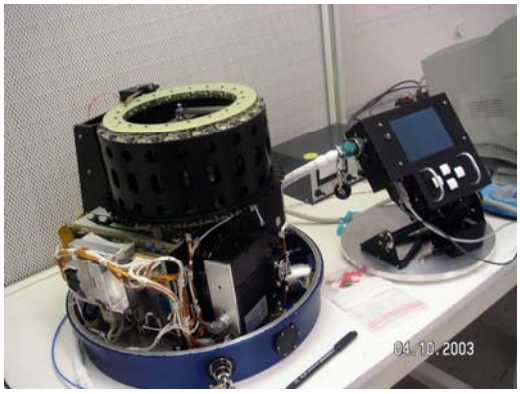

Figure 4: The interior of the Arges container, together with the HMI, prior to closure of the container with the aluminium dome.

Fig. 5: One of the authors (Anré Kuipers) installing the Arges hardware in the MSG aboard ISS. Photo: ESA

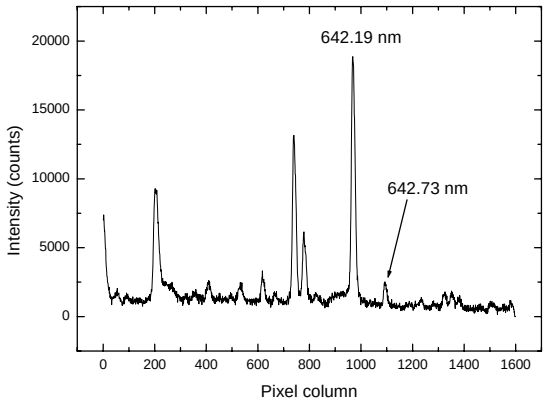

Figure 6: Measured spectrum of a Dy lamp at a certain lateral position during microgravity phase. .

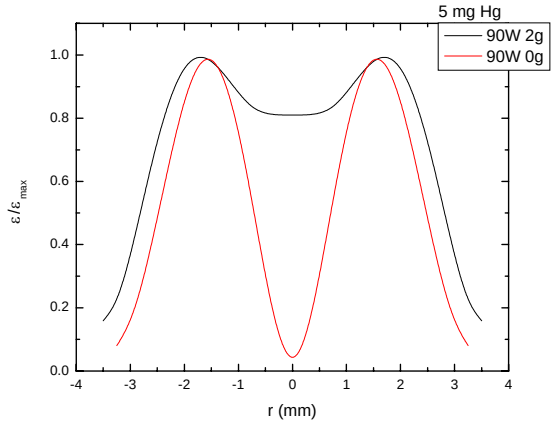

Figure 7:Radial profile of the dysprosium line emission for microgravity and hypergravity conditions..

The experiments in the ISS were a 100 % success. All foreseen measurements have been taken and all data was transported back to the experimenters. Already during the experiment operations, the results proved to be very surprising. Whereas the instabilities in the lamp were expected to be shaped as a rotating helix, they appeared to be a singly bent curve which is not rotating. Analysis afterwards has indicated that the rotation is caused by convection solely and that the curving is caused by self-generated magnetic fields. For one condition, residual gravity caused a very slow rotation.
As expected, the axial de-mixing did not occur during the Delta mission experiments, so the radial de-mixing can indeed be studied undisturbed. The analysis of the spectra is well underway.

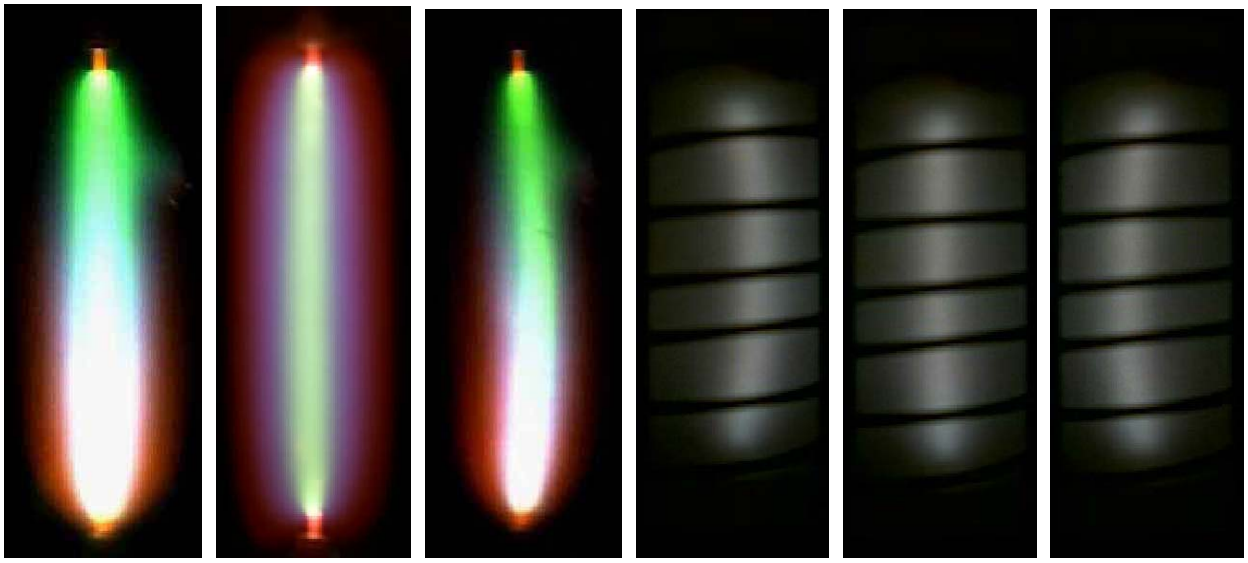

(a) (b) (c) (d) (e) (f)

Figure 8: pictures of the plasma in the lamp. (a): on the ground, axial demixing is vlearly visible; (b): same lamp in space: only radial demixing is observed, no axial demixing; (c): helical instability on the ground; (d), (e) and (f): helical instability in space, with suppressed axial demixing and with very slow rotation due to residual gravity of 0.001 g.

ACKNOWLEDGEMENT

This research is sponsored by the Space Research Organisation Netherlands (SRON), the Eindhoven University of Technology, Philips Lighting, the Netherlands Ministries for Education and Research and for Economic Affairs, NOVEM, and SENTER. We acknowledge the support of ESA for the participation in the 34th , 35th and 37th ESA parabolic Flight Campaigns.

REFERENCES

1: Fischer, E., *Axial segregation of additives in mercury-metal-halide arcs*, J. Appl. Phys. **47** 2954-2960 (1976)

2: Thorne, A.P., *Spectrophysics*, Chapman and Hall & Science Paperbacks, London, 1970.

Combustion of Mixtures, Electronically-Vibrationally Excited by Nanosecond Barrier Discharge

E.I. Mintoussov, A.V. Krasnochub, A.Yu. Starikovskii

Physics of Nonequilibrium Systems Laboratory, me@neq.mipt.ru
Moscow Institute of Physics and Technology, Moscow, Russia

Abstract

The study of nanosecond barrier discharge influence on flame propagation and flame blow-off velocity was carried out. The study shows that, besides proper form of energy input, proper organization of discharge is of great importance. Streamer development under different parameters was experimentally investigated. It was found that active particles (O and OH), which are produced in the discharge under its action, play the most significant role in the effect of combustion acceleration.

Keywords: plasma-assisted combustion, streamer, nanosecond non-equilibrium discharge, active particles conversion.

1. Introduction

The effect of an electric field (or electric discharge) on a flame's behavior has been studied widely and extensively since Brande has published his work in 1814. Most of these studies apply electric fields or discharges for stabilization of flames, reducing carbon formation, increasing flame velocity and extending flammability limits. Faster burning means the possibility to practice combustion of mixtures with low fuel content followed by reducing the formation of NOx oxides. Another application is SCRAMJET engines, where it's necessary to provide fast stable combustion of lean mixtures at high flow speeds. Therefore, the problem of an effective control of flame stability is actual nowadays.

The combustion of a fuel proceeds via a chain mechanism, and the rate of these processes grows according to exponential law. The delay time of ignition is limited by the rate at which active centers are produced, usually by thermal dissociation [1]. So we can accelerate the rate of combustion if we produce a number of additional active particles artificially, e.g. in gas discharge.

For discharges resulting in the formation of an equilibrium (or nearly equilibrium) plasma (e.g., sparks and arcs), the main factor of influence is local heating of gas (with dissociation rate increase) followed by ignition and flame propagation to unburned mixture. On the contrary, in the case of non-equilibrium plasma, the main mechanism of initiating chain reactions is dissociation and excitation of molecules by electron-impact. Theoretical estimations tell us that even relatively small amount of atoms and radicals (10^{-5}–10^{-3} of the total number of the gas particles) can shift equilibrium in the system and initiate a chain reaction [1]. So it's seem to be promising nowadays to use such discharges, (e.g. streamer discharge), which allow to perform volume (or nearly volume) ignition, which is of greatest interest for applications with a high rate of energy release.

The acceleration of combustion by means of non-equilibrium excitation of gas mixture components was studied in [2]. Short (nanosecond) pulses were used to provide high values of reduced electric field E/p (up to 600-800 Td) and high-performance electronic excitation. Pulsed barrier discharge was selected to avoid the transition of the streamer discharge to the spark form (dielectric barrier limits the maximum current). The form of discharge is non-equilibrium – electron's temperature is quite high (about 4-5 eV), whereas temperature of heavy particles is near to room temperature. Thus there is no gas heating by the discharge, and energy is put into the vibrational and electronic degrees of freedom of the mixture.

In this paper we analyze plasma-assisted combustion of premixed fuel – air mixtures at atmospheric conditions. The goal is to study the influence of kinetic of excited states, which takes place under a nanosecond discharge action, on combustion acceleration, and determine main factors (required type of radicals, optimal discharge parameters, optimal place for radicals injection into the flame etc.), which are responsible for combustion rate increase.

2. Experimental Setup

Detailed description of the setup you can find in [2]. Three different quartz nozzles with rectangular cross-section, with 2.2, 2.5 and 4.3 mm in width and the same length of 30 mm, were used. Stainless steel 0.8 mm thick high-voltage electrode was placed inside the nozzle (the length of the electrode is 28 mm) and the grounded electrodes were set tightly into quartz tubes and placed near the nozzle edges, parallel to them.

To fix the point of streamer's start and the number of streamers as well, the high-voltage electrode has a number of pins on its upper edge. Three electrodes were used - with 8, 15 or 28 pins, so the number of streamers could change. The nozzle and images of discharge and flame are presented in fig.1, as well as the set-up for streamers development investigations

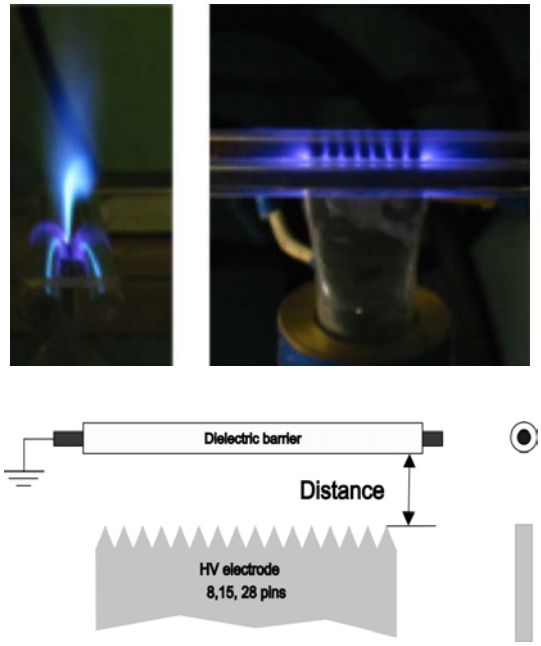

Fig.1. Overall view of the nozzle with discharge and the set-up for streamer development study.

In the present work we used three different types of nanosecond pulses: with FWHM 7, 19 and 24 ns. The voltage on the discharge gap could be 14 kV or 22 kV, pulse polarity was negative. Pulse repetition rate could be varied within the range of 400-1000Hz.

For determining of spatial and temporal characteristics of a streamer the PicoStar HR12 camera (LaVision) with a spectral range of sensitivity 300÷700 nm and time resolution up to 200 ps was used. Photos of streamer discharge were received in two modes of operation of the high-speed camera: integral and stroboscopic mode. When working in integral mode the amplifier of the high-speed camera was switching on simultaneously with coming of high-voltage pulse on electrode. Time of exposure was 50 ns and was longer than the duration of a high-voltage impulse. For working in stroboscopic mode, on the amplifier of the camera a triggering sine signal is set with frequency of 300 MHz.

The investigations of active particles and measurements of the combustion rate increase were performed by emission spectroscopy methods. The recording facility consisted of CCD-line (spectral range 200–800nm) and MDR-41 monochromator (with an operating range of 190—600 nm and a linear dispersion of 0,96 nm/mm). The optical system was calibrated using a standard emission source (a calibrated DDS-30 deuterium arc lamp emitting in the range 190–500 nm).

3. Results and Discussion

In the paper [2] mechanisms for the interaction of non-equilibrium pulse-periodical discharges with premixed propane-air flames have been investigated. A comparative analysis of dc and pulsed discharge of both polarities and their effect on the blow-off velocity was performed and presented in fig.2. From the standpoint of increasing the flame propagation velocity, a positive-polarity pulsed barrier discharge is the most efficient. The higher efficiency of this discharge in comparison with negative-polarity barrier discharge stems from the fact that, at the same pulse voltages, a cathode-directed streamer produces a larger number of active particles than an anode-directed one because of the difference in mechanisms of their propagation. In the case of a dc discharge, the situation

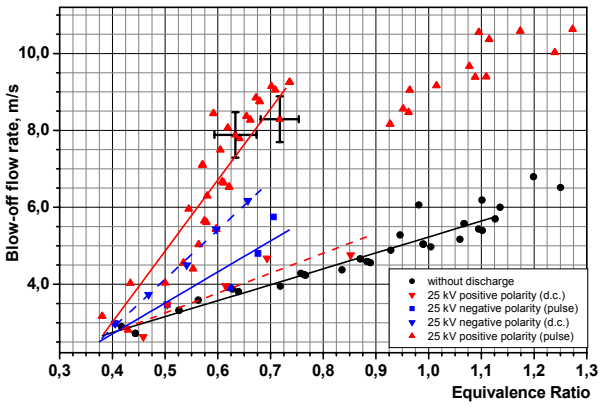

Fig.2. Flame blow-off velocity increase under the influence of different types of discharges.

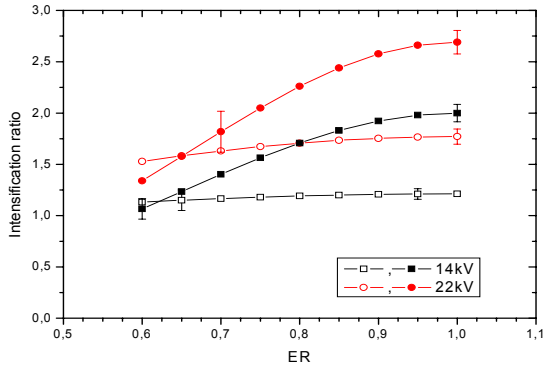

Fig.3. The comparison of the effectiveness of discharge influence. 8-pin versus 15-pin HV electrode.

Fig 4a. Photos of cathode directed streamer, 28 pins

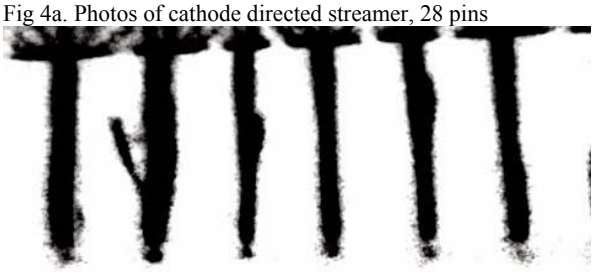

Fig 4b. Photos of cathode directed streamer, 8 pins

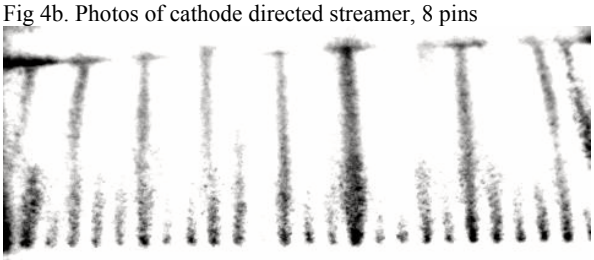

Fig 4c. Photos of anode directed streamer, 28 pins

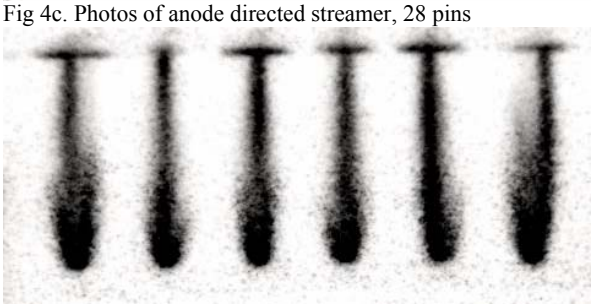

Fig 4d. Photos of anode directed streamer, 8 pins

is opposite. At a negative polarity, the tapered electrode efficiently emits electrons, which leads to the formation of a dc corona with a high current density near the points. In the given geometry, a positive dc voltage only slightly affects the flame propagation velocity. At positive polarity of a pulsed nanosecond barrier discharge, more than twofold increase in the combustion rate was achieved at the same fuel content in the mixtures. The energy input in the mixture from the discharge was less than 1% of the burner chemical power

To check a statement about possible thermal effect, in this work two different high-voltage electrodes were used - with 8 and 15 pins. It was found that both types of electrodes lead to flame acceleration for the cases of 14 kV and 22kV. The velocity increase is proportional to the pulse amplitude and energy input. We used parameter called “intensification ratio” for more convenient comparison of results in different geometries. Intensification ratio (IR) is a ratio between propane-air flame blow-off velocity with discharge and without discharge at the same equivalence ratio (ER). The results for both types of electrodes are presented in Fig.3. It’s seen quite well that the effectiveness of such influence is different - the effect is greater for 15-pin electrode, because of the larger quantity of streamers and active particles, produced by them. So, the flame stabilization occurs due to the plasma action and hardly depends on the local overheating near the steel plate pins, because estimations shows that overheating is greater in case of 8-pin electrode. The energy input in both cases was the same and was equal approximately to 2-5 mJ per pulse (2-5 W of total power). This value corresponds to 0,5% of the chemical power of the burner. The equivalent value of gas heating by this energy is 10-20 K. This fact confirms the thesis about the importance of the way we put energy in the mixture.

Here a comparison of emission intensity, which is proportional to electronically-excited nitrogen, was performed. As it was mentioned above, we explained higher effectiveness of positive streamer by larger number of active particles. Using the images from CCD, it was found that positive streamer has greater intensity (fig.4), and this confirms experimental data. It’s also shown that, beginning from a number of pins, further pin’s number increase doesn’t increase number of streamers and total amount of active nitrogen production. Streamers begin interact with each other and their velocity decreases, and this confirms theory suggested in [3].

The main area, where active particles are produced in the case of weak external electric field in comparison with streamer own field, is the streamer head, which is quite small (0.05 cm for typical voltages of 20 kV [4]), but has high values of reduced electric fields (up to 600-800 Td). If the gap is quite short, the reduced fields are high (higher than the breakdown fields in the atmospheric air), and active particles could be produced in the streamer channel as well. But in both cases it's important to have pulse duration long enough to overlap the gap, otherwise active particles are produced only in the part of the flow. The streamer velocity, measured in this work, is equal to 0.5±0.2 mm/ns under the voltage of 22 kV. In the regimes near blow-off point streamer prefers go through the weakly ionized zone just below the flame instead of the shorter way [2]. Calculations were made for the time of the gap overlapping, and the result is approx. 5 ns in the case of 2 mm nozzle, and greater in the case of 4.3 mm nozzle.

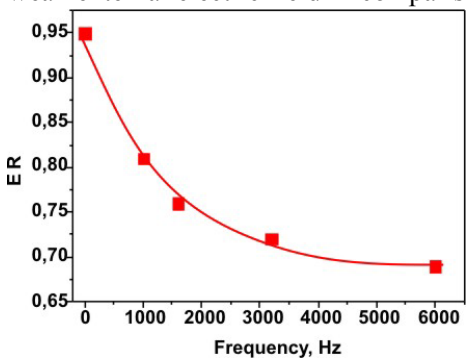

Fig.5. ER shift at different frequencies at same burner power.

Experiments with different pulses showed that with pulse length increase flame blow-off velocity increases too. Two types of additional line pieces were used to provide different pulse duration (FWHM 7 ns and 19 ns). It was found that at frequency 500 Hz and ER=0.8 19 ns pulse is much more efficient than 7 ns one for all three nozzles, and the advantage of using 19 ns pulse grows with nozzle widening [5]. So, we can draw a conclusion that we should produce plasma with sufficient electron energy longer to increase effect.

Another way to raise effectiveness is to produce larger areas filled with plasma to provide uniform discharge influence followed by flame acceleration. We increased pulse repetition rate frequency, and the flame blow-off

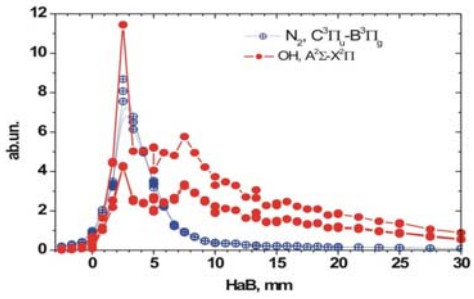

Fig.6. OH* profile along the HaB in methane-air flame.

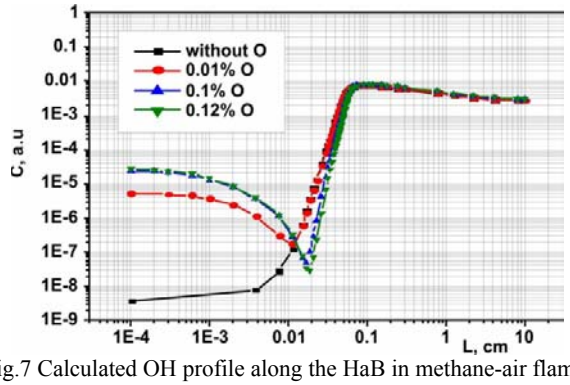

Fig.7 Calculated OH profile along the HaB in methane-air flame.

velocity increased too, because greater number of active particles per second had produced. These results are presented in fig.5 [2]. Based on this result a conclusion could be drawn that with frequency increase it's necessary to input larger amount of discharge energy to provide the same burner chemical power. We think that this fact could be explained by OH recombination rate.

On the other hand, dielectric barrier discharge with 50 Hz frequency and up to 20 kV amplitude was examined. It was found that such type of discharge does not affect on burning efficiency and flame blow-off velocity. One of the reasons is that the discharge power is two orders of magnitude smaller than in the case with 1,2 kHz discharge, and the reduced electric field in the gap is also weaker. But this power cannot be increased by voltage increase, because low frequency principally restricts maximum energy input. When the voltage was increased up to 21 kV, the canalization of the discharge took place. These effects result in quartz dielectric breakdown and development of arc discharge with high current value. These results are confirmed by ICCD-camera images.

Based on the results mentioned above, we can conclude that proper organization of discharge is important for effective power input. Depending on the gap length, mean reduced electric field in the gap could change as well as number of active particles and area where they are produced, which are responsible – directly or indirectly – for combustion intensification.

It worth mention that geometry of burner and discharge cell are of great importance. Electrodes, if placed near or inside the burner, serve as additional stabilizers and allow to increase blow-off velocity even without discharge. The way of influence in this case is changes in flow pattern and heat-transfer processes. Another mechanism for flame stabilization is creation of zones with near-zero flow rate, where ignition occurs, and than flame moves upward the stream. So, there are two types of discharge application in combustion tasks. The first is to ignite mixture in areas with low flow speed with combustion rate remaining constant, i.e., by heating, as in [6], and the second is to increase combustion rate by uniform treatment of mixture in the discharge. We think that the second way is more perspective and that's why one should use relative flame velocity increase as the main parameter of discharge effectiveness, instead of absolute values of flow speed. We should compare the discharge power to relative burner power increase, taking into account that completeness of combustion could change.

Now we'll try to describe physical processes, taking place in the flow and flame under discharge action. We'll consider 1D stationary task as an approach. In this case kinetics of plasmochemical process taking place in the pre-combustion zone in the presence of discharge can be divided into three spatially-separated parts: excitation of molecules by electron impact in the barrier discharge, kinetics of excited states and combustion processes.

On the first stage formation of excited particles by the electron impact takes place. The main processes taking place as given below:

- Elastic collisions of electrons with molecules;
- Vibrational and electronic excitation of molecules;
- Dissociation;
- Ionization.

The analysis of high-voltage pulse energy branching to the processes given above was performed using a Boltzmann approximation. The main part of energy is put into the electronic excitation of molecules (especially N_2) as well as dissociation, and into the nitrogen ionization in the case of strong fields. On the second stage that lasts tens of microseconds, processes with participation of formed excited particles take place. Let's consider the main of them:

- Quenching of electronically excited states of nitrogen molecules. We treat this channel as the main source of active radicals (O, OH) production:
$$N_2^*(A,B,C,a') + O_2 \rightarrow N_2 + O + O. \quad (1)$$
- Dissociation of oxygen molecule through its electronically-excited states.
$$O_2^* \rightarrow O(^3P) + O(^3P) \quad (2)$$
$$O_2^* \rightarrow O(^3P) + O(^1D) \quad (3)$$
According to energy levels diagram, reaction (3) goes trough $O_2(B^3\Sigma^-)$ state, and reaction(2) goes through $O_2(A^3\Sigma^+)$ state. The number of O atoms formed in reaction (3) is three times greater than that in (2), so about a half of all atoms are in $O(^1D)$ state. This fact explains appearance of electronically-vibrationally excited OH in the presence of barrier discharge on wavelength which equals 294.5 nm
- Ionization of mixture's components (N_2 mainly). The main ions – N_2^+ and O_2^+ – quite quickly transform into the N_2 and O_2 molecule through N_4^+ and O_4^+ ions
- Translational relaxation of vibrationally excited states of reagents. This is the way the gas heating occurs.

Authors draw a conclusion that at the mentioned times electronic and vibration excitation relaxes into translational movement as well as oxygen dissociation. Thus, the third stage can be treated as combustion of new mixture formed at the burner exit as a result of barrier discharge influence with non-equilibrium atomic oxygen concentration. One-dimensional numerical simulations of the propagation of a premixed flame with allowance for additional gas excitation in a discharge have been performed.

So, it is shown that the main mechanism through which the discharge plasma affects the flame parameters is the change in the initial mixture composition, which results in the onset of thermal chain reactions in the pre-flame zone. Applying a non-equilibrium discharge leads to the electronic excitation of the gas components, the production of active particles (in particular, atomic oxygen), and the acceleration of the processes governing the combustion rate and the flame propagation velocity. An advantage of employing a strongly non-equilibrium

plasma of a nanosecond discharge is that, in this case, the efficiency of energy deposition is higher as compared to other methods for flame control.

A series of additional experiments were made to prove the correctness of the model of flame acceleration and kinetic scheme. Spectroscopic investigations of the flame itself and the flame under discharge action were performed. The profile of OH radical along the height above burner in propane-air flame is presented in fig.6. The blow-off flow rate for methane-air flame has been measured and obtained results are similar to previous for propane-air mixture. This fact should be treated as the conformation of the same kinetic mechanism for flame acceleration for both cases. The simulation results (the density profiles of atoms and radicals, as well as the profiles of the flame temperature and velocity) were in qualitative agreement with the experimental data (fig.7.).

An additional proof to the suggested theory and the model of radical influence lies in the results of experiments with $Ar/O_2/C_3H_8$ mixture. We have changed the nitrogen in the mixture to argon in order to remove main channel of active particles production by quenching of electronically-excited nitrogen. This substitute was considered to reduce the atomic oxygen formation and decelerate flame in comparison with $N_2/O_2/C_3H_8$ mixture. Indeed, the results showed that the phenomenon in argon mixture is much more weaker. This is an evidence for our flame acceleration model.

Now our efforts aimed at finding the exact mechanism of excited mixture combustion and building maximally full kinetic scheme. Laser system, based on dye laser TDL-50 “Quantel”, is adjusting now to perform LIF-diagnostic of OH radical and obtain 2D picture of OH distribution in a flame and in a discharge.

4. Conclusions

The study of nanosecond barrier discharge influence on a flame propagation and flame blow-off velocity was carried out. The following conclusions could be made:

- With energy input negligible in comparison with burner's chemical power, a double propane-air flame blow-off velocity increase was obtained. It was shown experimentally that the results for methane-air flame are similar with propane-air one.
- Besides proper form of energy input, proper organization of discharge is of great importance. It was found that the effectiveness of plasma-assisted combustion depends on type of discharge, pulse duration, pulse repetition rate and other parameters, which are responsible for active particles production. One should use the discharge power ratio to relative burner power increase as the main parameter of discharge effectiveness, instead of absolute values of flow speed.
- It was found that active particles (H, O and OH primarily), which are produced in the streamer head under its action, play the most significant role in the effect of combustion acceleration. The model of flame acceleration, based on nitrogen quenching on oxygen molecules, with production of O and OH radicals, was confirmed by the new spectroscopic investigations and experiments with $Ar/O_2/C_3H_8$ mixture, where discharge influence is small because of the absence of mechanism of active particles production.

4. Acknowledgments

This work was partially supported Grants by PR0-1349-MO-02 EOARD/CRDF, 02-03-33376, 02-15-99305, A~01-02-17785 of Russian Foundation for Basic Research; Project 1474 by ISTC; Award MO-011-0 of the CRDF; and Grant E02-3.2-97 by Ministry for Higher Education of Russian Federation.

References

[1] N.N. Semenov, Nobel Lecture, December 11, 1956.
[2] E.I. Mintoussov, S.V. Pancheshnyi, A.Yu. Starikovskii**.** AIAA paper 2004-1013, 2004.
[3] G.V. Naidis. J.Phys.D: Appl. Phys., 29(1996) 779-783.
[4] M.M. Nudnova, S.V. Pancheshnyi, A.Yu. Starikovskii. Phys.Rev.E, 2014. 71, 2005.
[5] S.M. Starikovskaia, I.N. Kosarev, A.V. Krasnochub, E.I. Mintoussov, A.Yu. Starikovskii**.** AIAA paper 2005-1195, 2005.
[6] D. Galley, G. Pilla, D. Lacoste, S. Ducruix, F. Lacas, D. Veynante and C.O. Laux. AIAA paper 2005-1195.

What Do We Know about Long Laminar Plasma Jets?

Xi Chen[2], Wenxia Pan[1], Xian Meng[1], Kai Cheng[2], Dong-Yan Xu[2], Chengkang Wu[1]

[1] *Institute of Mechanics, Chinese Academy of Sciences, Beijing 100080, China*

[2] *Department of Engineering Mechanics, Tsinghua University, Beijing 100084, China*

As is well known, laminar gas jets at room temperatures are unstable even at comparatively low Reynolds numbers. They can only maintain their laminar flow regime within a short distance from the exit of jet nozzle. Linear stability analysis showed that the laminar jet even becomes more unstable when the density of the gas jet is less than that of the ambient gas [1]. Since the density of a plasma jet is much less than that of the ambient air, one might consider it is not easy to generate a stable laminar plasma jet in atmospheric air. However, stable long laminar plasma jets have been successfully generated recently using a non-transferred DC arc plasma torch at atmospheric pressure [2,3]. Preliminary experimental studies [2,3] indicated that the long laminar plasma jets are characterized by stable flow state, reduced entrainment of surrounding air into the jet leading to a rather long high-temperature region length (jet length / diameter ratio may be as great as 70 or even more as shown in photographs), adjustable jet lengths, etc. So far it is still puzzling why such a stable long laminar plasma jet can be generated and maintained. Since there exists no complexity caused by turbulent effects and due to its adjustable flow field parameters, the long laminar plasma jet can become a rather ideal object for the fundamental study of the plasma flow characteristics. Preliminary attempts using the laminar plasma jets in the preparation of thermal barrier coatings, in the re-melting hardening of cast iron and in the stainless-steel surface cladding have shown encouraging results, including the fine microstructure, low surface roughness and small porosity of the prepared coatings, the good re-melting process controllability and surface morphologies, as well as the metallurgically bonded clad layer. Hence, more detailed studies of the long laminar plasma jet characteristics are highly desirable.

In our experiments, photographs of the plasma jet are taken to determine the visible high-temperature-region length of the jet (called jet length hereafter). Spectral-line intensity method is employed to measure the plasma temperature distributions over the jet cross-section at different axial distances from the plasma torch exit. A small-size, taper-head and water-cooled Pitot probe is used to measure the local stagnation pressure to deduce the jet axial-velocity. Rapid-response sensors are used to analyze the fluctuations of arc voltage, jet radiation intensity and stagnation pressure.

Experiments show that, depending on process parameters (arc current, working-gas flow rate, etc.), long laminar plasma jets or short turbulent plasma jets can all be generated with the same DC arc plasma torch. The interior configuration of the plasma torch has some effects on the plasma jet characteristics. For a given torch configuration and for a fixed arc current, there exist two different critical values of the working-gas (argon) flow-rate, i.e. G_1 and G_2 ($G_1 < G_2$), demarcating the jet flow regimes. When the gas flow-rate is less than the lower critical value G_1, the plasma jet assumes the silent laminar flow state, and the jet length increases appreciably with increasing gas flow-rate. When the working-gas flow-rate is larger than the higher critical value G_2, the plasma jet assumes the noisy turbulent flow state, and the jet length is short and almost does not depend on the working-gas flow-rate. Between the stable laminar and turbulent flow regimes (i.e. with flow-rate less than G_2 but larger than G_1) there exists an unstable transitional regime,

showing an alternative change from a silent long jet to a noisy short jet. The average jet length in the transitional regime decreases with the increase of gas flow-rate, as shown in Fig. 1.

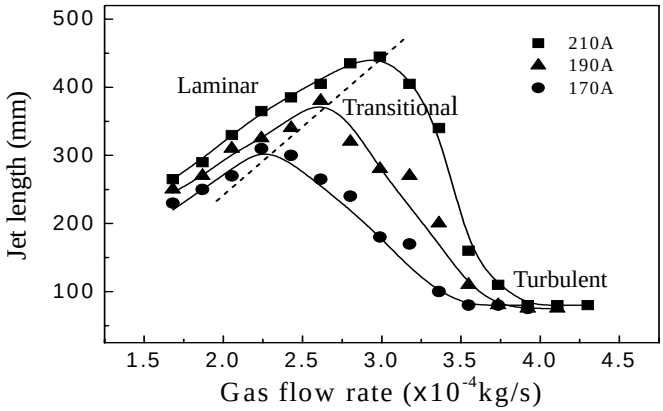

Fig. 1: Jet length vs. gas flow rate

Modeling results show that the jet length of laminar plasma jet increases appreciably with increasing plasma-jet inlet axial-velocity or temperature, while much less change in jet length is found for the turbulent jets. The axial gradients of plasma temperature and axial velocity in the laminar plasma jet are much less than those in the turbulent plasma jet. Although a temperature difference as great as 10^4 K is involved in the plasma-jet / ambient-air system, the effect of natural convection on the laminar plasma jet is negligible, in consistence with experimental observation, as shown in Fig. 2. The long laminar plasma jet has good enough stiffness to endure the impact of the lateral injection of powders and their carrier gas. The laminar plasma jet assumes only a small deflection (a few degrees) from its geometrical axis due to the carrier-gas impact [4]. Particulate matter can be injected into the jet high-temperature region with suitable injection parameters.

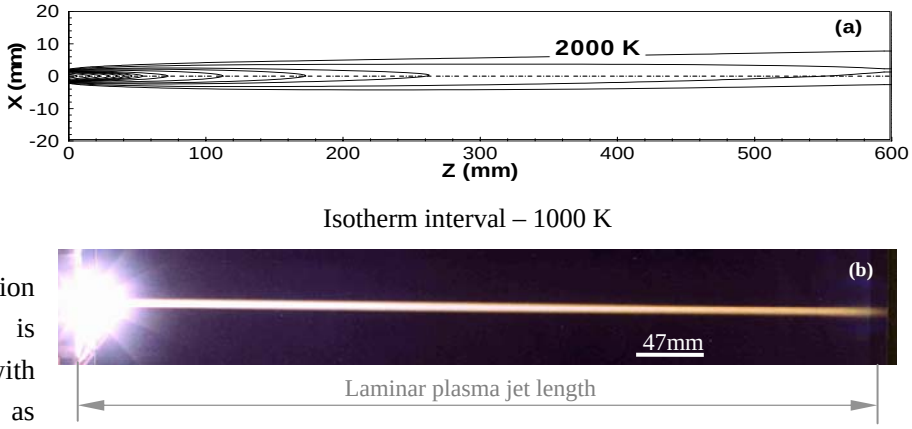

Fig. 2: 3-D modeling results of isotherms with natural convection (a) and jet photo (b)

It is found that the long laminar plasma jet can be generated in a rather wide range of plasma torch parameters (working-gas flow-rate, arc current, etc.) and rather high exit axial-velocity (~800 m/s) and temperature (~16000 K) can be achieved. Regular fluctuations often appear in arc voltage, jet stagnant pressure and optical emission intensity due to the existence of AC components in the DC power supply with the main fluctuation frequency of 300 Hz. The measured fluctuations of the arc voltage, jet stagnant pressure and optical emission intensity are almost in phase.

Acknowledgment: This work was supported by the National Natural Science Foundation of China (Nos. 50336010, 50276065, 50176024).

References

[1] S. Jendoubi and P. J. Strykowski, Phys. Fluids 6, 3000 (1994).
[2] W.-X. Pan, W.-H. Zhang, W.-H. Zhang, and C.-K. Wu, Plasma Chem. Plasma Process. 21, 23 (2001).
[3] W.-X. Pan, W.-H. Zhang, W. Ma, and C.-K. Wu, Plasma Chem. Plasma Process. 22, 271 (2002).
[4] D. –Y. Xu, X. Chen, and K. Cheng, J. Phys. D: Appl. Phys. 36, 1583 (2003).

Nanocomposite Ti/hydrocarbon plasma polymers for biomedical applications

A. Grinevich[1], A. Choukourov[1], H. Koshelyev[2], H. Biederman[1], D. Slavínská[1], ,
H. Boldyryeva[3], L. Bačaková[4], J. Pešička[5]

[1]*Department of Macromolecular Physics, Charles University, 18000 Prague, Czech Republic*

[2] Department of Physics, Faculty of Electrical Engineering, Czech Technical University in Prague, Czech Republic

[3] *Departement of Neutron Physics, Academy of Science of the Czech Republic, Nuclear Physics Institute, Rez near Prague 250 68 Rez, Czech Republic*

[4] *Institute of Physiology, Academy of Sciences of the Czech Republic,14000 Prague, Czech Republic*

[5] *Faculty of Mathematics and Physics, Department,of Metal Physics, Charles University 12116 Prague, Czech Republic*

Abstract

Deposition of composite Ti/hydrocarbon plasma polymer films is performed by DC magnetron sputtering of Ti target in Ar/n-hexane mixture. Heterogeneous film structure is confirmed. Adhesion, proliferation and maturation of vascular endothelial cells in cultures derived from the bovine pulmonary artery (line CPAE) are studied. The cells are similarly or more active in adhesion, proliferation and maturation than those on glass or pure hydrocarbon plasma polymer.

Keywords: composites, magnetron sputtering, vascular cells.

1. Introduction

Composite metal/plasma polymer thin films have been studied for several decades now [1-4]. The benefits of composites arise from the combination of materials with very different properties, e. g. hardness, flexibility or weight, to produce structural or functional properties not present in any individual component. Methods involving sputtering and plasma polymerization have been applied to produce hydrocarbon based composites, mainly metal/hard carbon plasma polymer thin films (Me/C:H) (Biederman). The deposition of silver, molybdenum, nickel, germanium/C:H films by magnetron sputtering in Ar/n-hexane working mixture was studied in detail. It was shown that optical, electrical, mechanical properties of these composites varied in a wide range depending on metal volume fraction.

Hydrocarbon plasma polymers have been shown to increase wear resistance, smoothness, hydrophobia and blood compatibility of various polymer- or metal-based biomaterials [5-9]. For example, they have been employed for coating of femoral heads of metallic hip prostheses in order to prevent the release of metal ions and wear particles [5] or deposited on various blood-contacting devices, e.g., blood pumps, in order to enhance their resistance to protein adsorption and thrombus formation [6-8].

Titanium is widely used material for construction of bone, joint or dental implants, and it has been reported to support adhesion and growth of osteogenic and vascular smooth muscle cells [10, 11]. The aim of this study is to evaluate the physicochemical properties of these films as well as adhesion, growth and maturation of vascular endothelial cells in cultures on Ti/hydrocarbon plasma polymer films.

2. Experimental

Ti/hydrocarbon plasma polymer films were deposited using unbalanced magnetron with Ti target operated in the DC mode in a working gas mixture of Ar/n-hexane. The depositions were performed at a working mixture pressure of 2 Pa. The flow rate of argon was automatically adjusted by a flow-controller (MKS instruments) and set to the constant value of 20 sccm. The flow rate of n-hexane was manually controlled by a needle-valve to the value of 0.4 sccm. The depositions in pure Ar and n-hexane were also performed. The substrate holder was placed opposite to the magnetron at a distance of 50 mm from the target. Direct current generator MDX 1.5K (Advanced Energy) powered the magnetron in a constant current mode (0.2 A).

The elemental composition of the Ti/hydrocarbon plasma polymer films was determined by Rutherford back-scattering spectrometry (RBS) and elastic recoil detection (ERD) methods using a Van de Graaf accelerator. The α-particles at kinetic energiy of 2.68 MeV have been used. RBS spectra were evaluated by computer code GISA 3, whereas ERD spectra by the SIMNRA code, both using cross-section values from SigmaBase.

Optical Emission Spectroscopy was applied using a self-built OES apparatus consisting of an optical fiber, an ARC SpectraPro-300i monochromator with a grid, and a Hamamatsu photomultiplier R928.

Transmission Electron Microscopy (Jeol FX 2000) was performed on the films deposited on carbon foil supported with copper mesh grids (S160, Elektronenmikroskopie, Austria).
Surface morphology of composite Ti/hydrocarbon plasma polymer films was studied by means of Atomic Force Microscopy (AFM) (Q-Scope^{TM} 850, Quesant). The measurements were performed in intermittent contact mode in air immediately after depositions. AFM was also used for thickness measurements.
A set of different substrates was treated. Silicon was used for RBS/ERDA and AFM analysis. Glass substrates were used for water contact angle measurements and for biological tests. The samples (size 8 x 8 mm) were sterilized by UV irradiation, inserted into Nunclon Multidishes (NUNC, Denmark; 24 wells, diameter 15 mm) and seeded with bovine pulmonary artery endothelial cells (line CPAE, ATCC CCL 209, 17 000 cells per cm^2). The cells were incubated in 1.5 ml of Dulbecco's Modified Eagle Minimum Essential Medium supplemented with 20% of fetal bovine serum for 1, 3 or 7 days at 37^{o}C in air atmosphere with 5% CO_2.
Adhesion of endothelial cells on the Ti/hydrocarbon plasma polymer films were evaluated by the number of initially adhering cells on day 1 after seeding, cell-material contact area (i.e., cell spreading area) and formation of focal adhesion plaques, detected by immunofluorescence staining of vinculin [12]. Cell proliferation was estimated by the percentage of cells newly synthesizing DNA. The nuclei of these cells were visualized by 30-min-incubation of cells with bromodeoxyuridine (BrdU), followed by anti-BrdU immunoperoxidase staining [12]. Markers of endothelial cell maturation, used in this study, were represented by formation of confluent cobblestone-like cell layer, content of von Willebrand factor and formation of distinct beta-actin cables. The latter two parameters were evaluated by immunofluorescence staining [12].

3. Results and discussion

The deposition process was monitored by OES (Fig. 1). A considerable decrease in Ti emission intensity when sputtering in Ar is observed when adding n-hexane. In this case, two concurrent processes contribute to the film formation: sputtering of titanium and plasma polymerization of hydrocarbon precursor leading to partial or complete poisoning of the Ti target.

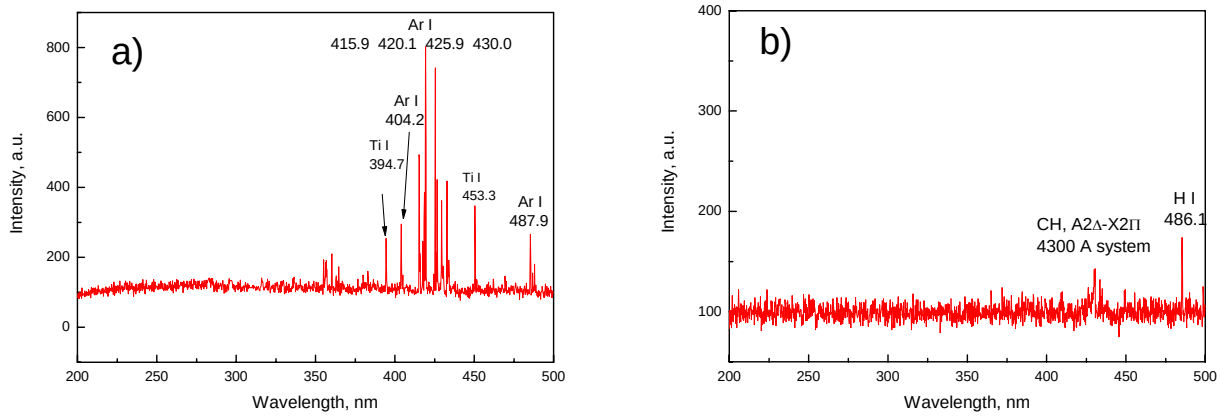

Fig.1. The OES spectra taken in discharge of: a) pure Ar, b) mixture of Ar and n-hexane and c) pure n-hexane.

A ratio of Ti line [363.5 nm] and Ar line [420.1 nm] served as an indication of the amount of Ti built in the depositing composite film.
Table 1 gives the elemental composition RBS/ERDA of the films deposited in n-hexane and Ar/n-hexane mixture. Both films contain 3-4 at. % of oxygen, which is believed to appear as a result of post-deposition oxidation reactions. The films are deficient with hydrogen as is typical for plasma polymers as such. The C/H ratio is 2.3 for the n-hexane monomer. However, it reaches only 1 for the plasma polymer and is even lower (C/H=0.7) for the composite film. This let us assume that polymeric part of the films is highly cross-linked. Film prepared with n-hexane only resulted in plasma polymer with negligible amount of Ti. Using Ar/n-henxane

mixture we prepared maximum up to 3 at. % Ti. We selected these two cases for cell experiments (deposition conditions, please, see Table 1).

Table 1 The elemental composition determined by RBS/ERDA.

Film	Flow rate	Elemental composition			
		C, at. %	H, at. %	Ti, at. %	O, at. %
Ti/hydrocarbon plasma polymer	Ar 20 sccm hexane 0.4 sccm	54	40	3	3
hydrocarbon plasma polymer	hexane 5.5 sccm	48	48	-	4

TEM image (Fig. 2) demonstrates that the film deposited by magnetron sputtering in Ar/n-hexane mixture is a composite hydrocarbon plasma polymer with the embedded titanium aggregates (dark regions).

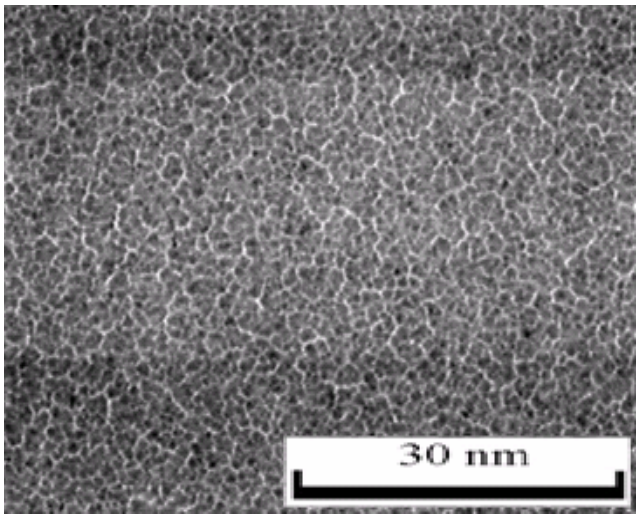

Fig. 2. TEM image of composite Ti/hydrocarbon plasma polymer film with 3 at. % Ti.

Biological tests showed that the endothelial cells adhered in higher initial numbers and by a large cell-material contact area on Ti/hydrocarbon plasma polymer layers than on pure hydrocarbon plasma polymer (Figs. 3A, B). Similar results were obtained earlier on vascular smooth muscle cells, osteoblast-like MG-63 cells or bone marrow cells cultured on carbon-fibre reinforced carbon composites (CFRC) or titanium discs coated with Ti-containing a-C:H [10, 11]. The synthesis of DNA in cells on Ti/hydrocarbon plasma polymer samples, measured by BrdU incorporation, tended to be lower than on pure hydrocarbon plasma polymer, although these differences were not significant (Fig. 3C). The latter result is consistent with the findings that the proliferation activity is the highest at the intermediate strength of cell adhesion. When the adhesion is very high, the cells skip the proliferation phase and enter sooner the differentiation program [12].

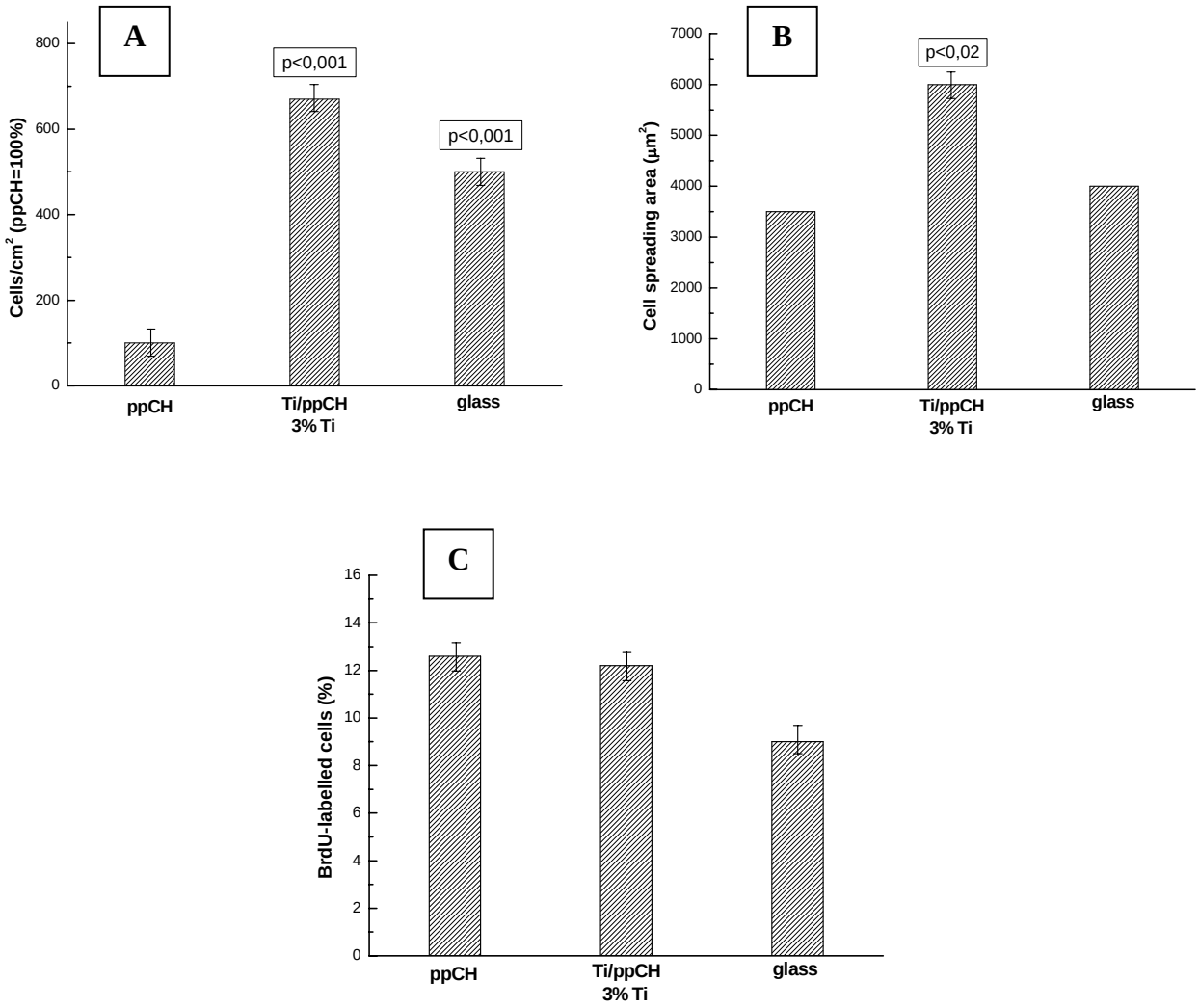

Fig. 3. Number (in % of values obtained on pure ppCH; A), cell-material contact area (B) and percentage of DNA synthesizing endothelial cells (C) on Ti/ppCH layers with low concentration of titanium on day 1 (A, B) or day 3 (C) after seeding. Average ± SEM from 9-38 measurements, Student's t-test for unpaired data, statistical significance: $p<0.02$, $p<0.001$ in comparison with values obtained on pure ppHC.

Ti/hydrocarbon plasma polymer films allowed formation of continuous layers of cobblestone-like endothelial cells (Fig. 4). Thus, the Ti/hydrocarbon plasma polymer films showed a good compatibility with endothelial cells, so that these materials could be used for cardiovascular applications, such as coating of vascular prostheses or heart valves in order to improve their lining with endothelial cells. Another possible application is surface coating of bone implants.

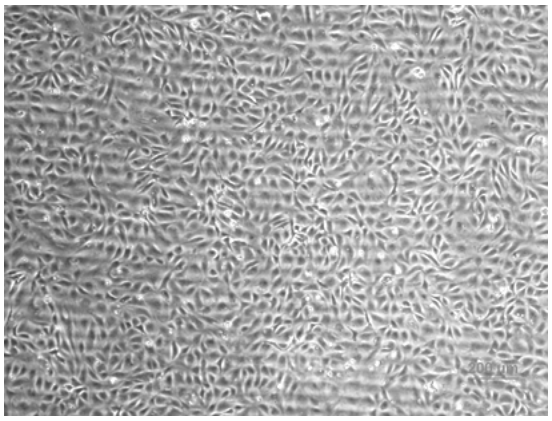

Fig. 4. Formation of a confluent cell layer on Ti/ppCH with low concentration of Ti. Day 7 after seeding, bar=100 μm.

4. Conclusions

DC magnetron sputerring of titanium in Ar/n-hexane mixture deposits composite films with Ti aggregates randomly dispersed in a hydrocarbon plasma polymer matrix. Ti/hydrocarbon plasma polymer films support adhesion, growth and maturation of vascular endothelial cells in cell culture conditions. These films could be used for construction of long-term artificial implants into human body, e.g. for coating of the inner surface of vascular prostheses or surface modification of bone implants.

Acknowledgements

This work is a part of the research plan MSM 0021620834 that is financed by the Ministry of Education of the Czech Republic.

References

[1] H. Biederman, P. Kudrna, D. Slavinska- Hard plasma polymers, composites and plasma polymer films prepard eby rf sputtering of conventional polymers, In: Plasma Polymer Films, ed. H. Biederman, London, Imperial College Press (2004).

[2] D. Monaghan, D.G. Teer, P.A. Logan, I. Efeoglu and R.D. Arnell- Surf. and Coat. Tech. **60,** 525 (1993).

[3] S.Kvasnica, W. Fallmann, H. Biederman, H. Boldyreva, D. Slavínská, in 15th Int. Symp. On Plasma Chemistry, Symp Proceedings Vol. VI, Eds. Bouchoule A., Pouvesle J. M., Thomann A.L., Bauchire J.M. and Robert E., (GREMI, CNRS/University of Orleans, Orleans, France 2001) 2403.

[4] R. Hauert, L. Knoblauch-Meyer, G. Franz, A. Schroeder, E. Wintermantel, Surf.Coat.Technol. **120-121**, 291 (1999).

[5] J. Fisher, X. Q. Hu, J. L. Tipper, T. D. Stewart, S. Williams, M. H. Stone, C. Davies, P. Hatto, J. Bolton, M. Riley, C. Hardaker, G. H. Isaac, G. Berry, E. Ingham- Proc. Inst. Mech. Eng. [H] **216,** 219 (2002).

[6] K. Yamazaki, P. Litwak, O. Tagusari, T. Mori, K. Kono, M. Kameneva, M. Watach, L. Gordon, M. Miyagishima, J. Tomioka, M. Umezu, E. Outa, J. F. Antaki, R. L. Kormos, H. Koyanagi, B. P. Griffith- Artif. Organs **22**, 466 (1998).

[7] M. I. Jones, I. R. McColl, D. M. Grant, K. G. Parker, T. L. Parker- J. Biomed. Mater. Res. **52**, 413 (2000).

[8] R. D. Schaub, M. V. Kameneva, H. S. Borovetz, W. R. Wagner- J. Biomed. Mater. Res. **49**, 460 (2000).

[9] L. K. Krishnan, N. Varghese, C. V. Muraleedharan, G. S. Bhuvaneshwar, F. Derangere, Y. Sampeur, R. Suryanarayanan- Biomol. Eng. **19**, 251 (2002).

[10] A. Schroeder, G. Francz, A. Bruinink, R. Hauert, J. Mayer, E. Wintermantel- Biomaterials **21**, 449 (2000).

[11] L. Bačáková, V. Starý, O. Kofroňová, V. Lisá- J. Biomed. Mater. Res. **54**, 567 (2001).

[12] L. Bačáková, V. Lisá, L. Kubínová, J. Wilhelm, J. Novotná, A. Eckhart, J. Herget- Virchow's Archiv **440**, 50 (2002).

Syngas production from organic aqueous waste by underwater electrical arc

N. Boudesocque[1], C. Vandensteendam[2], J. Fazilleau[2], C. Lafon[1], C. Girold[1] and J.M. Baronnet[2]

[1]CEA Marcoule, BP 17171, 30207 Bagnols sur Cèze Cedex, France
[2]Laboratory of Plasma Chemistry, University of Limoges,123 avenue Albert Thomas, 87060, France

Abstract
We exposed the preliminary results and interpretations concerning a new method of organic aqueous waste treatment by underwater electrical arc. First experimentations permit to produce a combustible gas corresponding to syngas (50 % vol. H_2 and 35 % vol. CO) from a diluted glucose aqueous solution. High temperature due to electrical arc decomposes organic material into simple molecules. Development and process potential applications are also detailed.

Keywords : Syngas, organic liquid waste, underwater electrical arc, gasification

1.Introduction

Primary energy consumption reached ten billions of tons of oil equivalent petrol (toe) in 2000. After being decupled during the last century, it increases now with a rate of 3% each year. Development is linked to the access at cheap energy. Global warming due to greenhouse effect gas emissions shows us the limits of fossil fuel use. The use of hydrogen as energetic vector can be a good perspective with the decrease of fuel cell cost. Hydrogen gas is not a native species, its production consumes energy. Nowadays, 90 % of production is issued of natural gas reforming with an harmful effect on carbon dioxide balance. Electrolysis produces clean hydrogen if electrical power is produced by a process without carbon dioxide emission.

Waste treatment is also a problem now for industrialized society and on the future for emerging countries. Yet, the source of carbon and hydrogen included in waste is not totally used. Waste gasification is another way to treat waste and to recover energy [1]. So, for an industrial country, waste can be a real resource of energy with a good effect on carbon dioxide balance.

Plasma gasification processes have been developed for specific applications such as naval waste incineration, municipal solid waste or toxic waste [2], [3], [4], [5]. Units are in operation and permit to eliminate waste without harmful emission. But, some waste can not be eliminated with such a process, in particular, waste issued from agribusiness industries. The main reason is the high moisture content of this kind of waste. So, drying stage needs much energy to permit the valorization of this material. Sewage sludge and wet waste are eliminated by co-firing or spread on fields. Co-firing is the combustion of two combustibles, in this case, sewage sludge and high calorific value combustible such as natural gas or heavy fuel oil. Most of energy is used to evaporate waste water content.
Besides, different patents claim the feasibility of syngas production from water by use of an electrical arc between graphite electrodes [6], [7]. The global reaction seems to be steam reforming of electrode carbon.
The work, reported here, deals with a syngas synthesis process where a DC arc is stricken between two electrodes inside an aqueous waste, carbon oxides being formed mainly from organic content.

2. Process basis

Water decomposition study is one of the fundamental works of modern chemistry. Water decomposition is actually made by alkaline electrolysis to produce pure hydrogen and oxygen. But, water thermal decomposition is also a possible way to produce hydrogen. This process needing a large thermal energy source, the use of concentrated solar energy is a possible solution. In the process presented in this work, an electrical arc provides high temperature gradients within the aqueous solution. Water and organic molecules are decomposed. Atomic hydrogen, oxygen, carbon are quenched by solution whose temperature is maintained under water boiling temperature, and recombination of atoms leads to simple molecules such as gaseous hydrogen, carbon monoxide and carbon dioxide.

Our hypothesis is that thermal energy is the main actor for gas production but photochem ical and electrochemical phenomena can also take place in our process.
Benefits of this process are numerous :

- no preliminary drying,
- soot washing in reactor without filter,
- thermal quench preventing dioxin formation,
- pure syngas production (H_2, CO, CO_2), no NOx formation,
- no incombustible gases (except carbon dioxide).

3. Experimental

In order to simulate organic liquid waste, a mix of glucose and fructose diluted in drinking water is used. The choice of these molecules is due to its chemical formula $C_6H_{12}O_6$ which is proposed for an phantom of agribusiness waste (sugar industry liquid waste, milk waste, blood from animals). It is soluble in water and easy to prepare.

3.1 Experimental setup

An electrical arc is produced between two graphite electrodes connec ted to a DC power supply (Intensity: 100 - 400 A, DC Voltage: 10 - 100 V). Two reactors are used to treat aqueous solution: they are different by volume, electrode motion and electrode fitting. The reactor 1 in Figure 1 has been designed to allow experiments with a long duration (few hours). The anode is a rotating graphite disk (for these experiments: ω = 150 rad.s^{-1}, v_t = 10 m.s^{-1}) to move the anodic spot on a larger surface. A graphite cathode has a translation motion to control inter-electrode space, and so to compensate anode erosion. Reactor 1 volume is about 60 litres. Reactor 2, on Figure 2, uses two graphite electrodes. The anode is fixed and the cathode has a translation motion. Reactor 2 volume is about 8 litres. This confers to reactor 2 a lower thermal inertia than reactor 1 and an easier utilization.

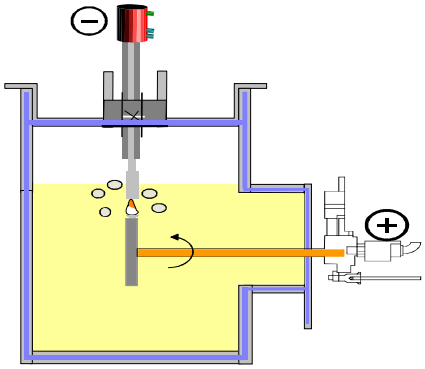

Figure 1: Reactor 1 with rotating disk and translating cathode

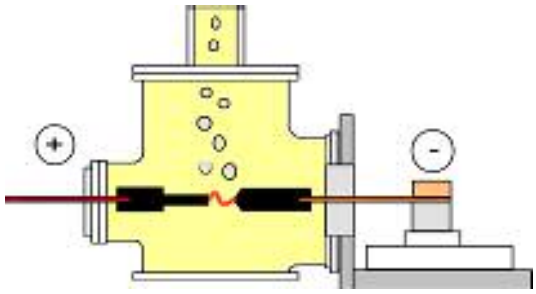

Figure 2: Reactor with coaxial electrodes

Exhaust gas flow rate is measured by a FURNESS CONTROLS volumetric flow meter (0 - 30 NL/min). Gas composition analysis is realized by mass spectroscopy (Gaslab 300 FISONS) with Ar as inner standard gas after calibration. The process full block diagram is represented on Figure 3.

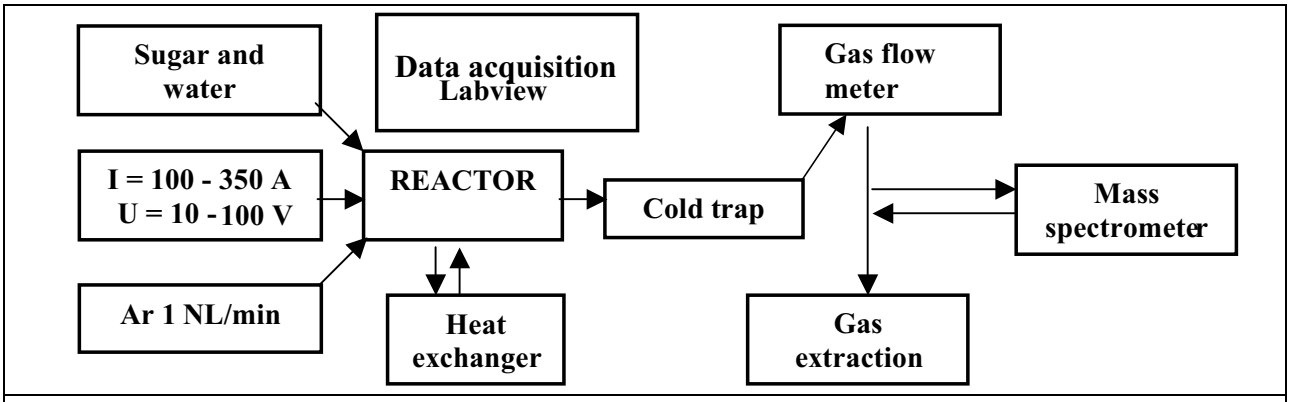

Figure 3: Process block diagram

3.2 Experiments

3.2.1 Electrical arc and electrode observations

Initially, the reactor is filled with sugar solution (sugar concentration between 100g/L and 650g/L) and the electrodes are brought closer at zero voltage. Then, voltage is applied and a small gas production is observed, corresponding to water electrolysis. When inter-electrode space is set closer, the electrical arc is stricken. Intensity is controlled by the DC supply regulator; voltage, function of the arc length is self adjusted. To increase voltage, the arc is drawn by moving the cathode. To observe the location of gas formation, a high speed camera (1000 pictures/s) is used. Gas bubbles and electrical arc have been observed. Photos of experiments in reactor 1 are exposed on Figure 4:

Figure 4: Immerged electrical arc in sugar solution

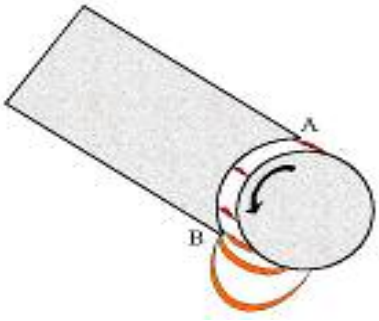

Figure 5: Electrical arc motion

On Figure 5, we can see the extension of the arc due to the anode rotation. The arc begins at A point a nd extends to B point until it cuts off and strikes again at point A. According to anode velocity and voltage, arc lifetime is very short. The high speed camera observation has confirmed that lifetime is shorter than 10 ms. Pink flashes are observed at each experiments and could be due to H_α emission line (656,3 nm) (cf. Figure 6).

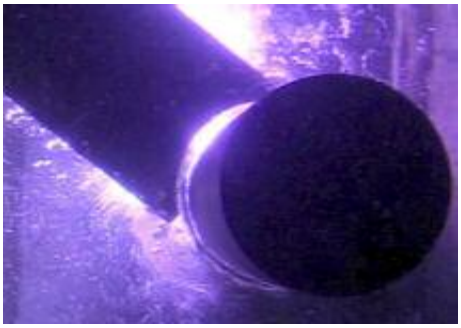

Figure 6: Pink flashes in reactor 1

Experiments on anode rotation velocity showed that erosion is both chemical and mechanical, perhaps sublimation. Oxygen and hydrogen recombination induces shock waves which erode electrodes (in reactor 1, the inversion of rotation moves cathode erosion area). Micrometric carbon particles are produced darkening quickly the solution. If, at the moment, the characteristics of produced carbon are not known, some studies indicate that fullerens and nanotubes can be obtained with this type of process [8], [9]. In reactor 1, with drinking water, with I = 200 A and V ~ 30 V, the erosion of the electrodes is of about 30 g/h for the anode and 10 g/h for the cathode. In reactor 2, the consumption is similar for the anode but there is no erosion of the cathode. During sugar solution treatment, a graphite deposit was noticed which could be an electro-deposition due to electrical field and presence of carbon cations in the electrical arc (cf. Figure 7) [9].

Considering that when treating drinking water, there is no deposit: it can be deduced that carbon comes from sugar.

Figure 7: Graphite deposit

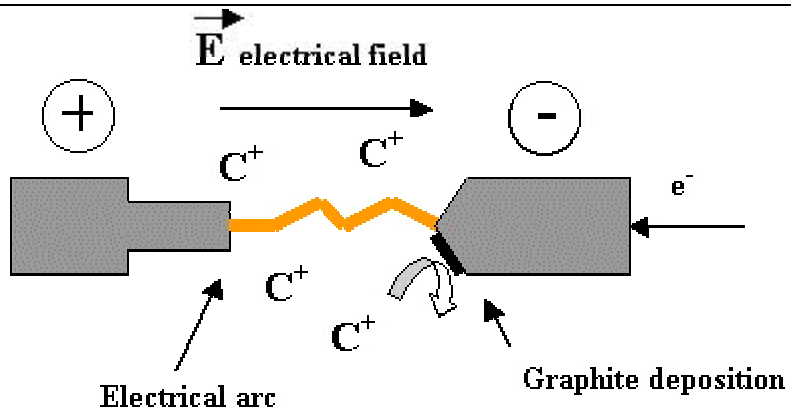

Figure 8: Graphite electro-deposition on cathode in sugar solution

3.2.2 Gas composition versus time

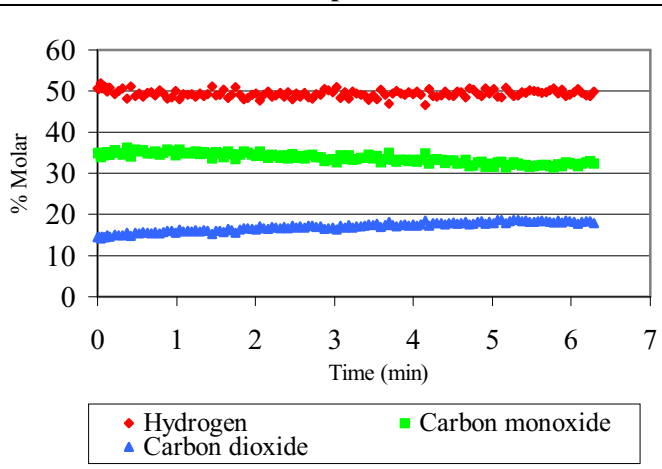

Figure 9: Major gas contents versus time

During treatment of aqueous sugar solutions, mass spectroscopy showed that the exhaust gas mixture is mainly composed of H_2, CO and CO_2 with very small amounts of light hydrocarbons (CH_4 and C_2H_2). On Figure 9 is presented versus time, the evolution of the major gases for a sugar solution. Considering that thermodynamic equilibrium is quickly reached at high temperature, no significant evolution in gas composition should be expected. However, if the percentage of H_2 is constant since the beginning, about 5 minutes are necessary to reach a quasi steady state for CO and CO_2. We can notice that the global amount ($CO+CO_2$) is constant. The evolution observed for the ratio CO/CO_2 could be due to dissolution of CO_2 until saturation.

According to this gas analysis, the high calorific value is about 8 MJ/Nm^3, (~10 MJ/Nm3 for pure H_2 or pure CO).

3.2.3 Gas flow rate versus intensity and electrical power

In order to quantify produced gas, efficiency of the process and sugar behavior in r eactions, we have measured gas flow rate while parameters are changed (type of solution, intensity, inter electrode space). Results for drinking water are shown on Figure 10. The electrical arc is very erratic in drinking water and does not allow to work easily at constant power. On Figure 11, results for sugar solution treatment are exposed and we can see that, for the same power, the gas flow rate for the sugar solution is widely higher than for drinking water. Sugar addition increases the gas flow rate.

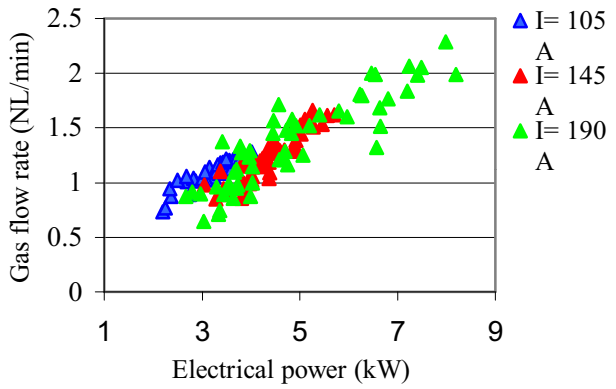

Figure 10: Gas flow rate versus electrical power for drinking water in reactor 1

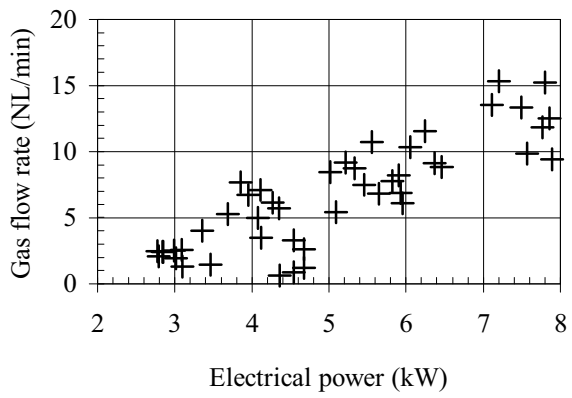

Figure 11: Gas flow rate versus electrical power for a sugar solution (550 g/L) in reactor 2

It has also been noticed that longer is the arc, higher is the gas production. This indicates that chemical reactions are not only taking place at graphite electrode edges. Yet, experiments with dr inking water and graphite electrodes produce carbon monoxide due to reactions with graphite electrodes and a chemical consumption of electrodes. Nevertheless, gas flow rate with drinking water is very low compared to gas flow rate with sugar solution (magnitude order between 5 – 10).

3.2.4 Gas composition versus sugar concentration

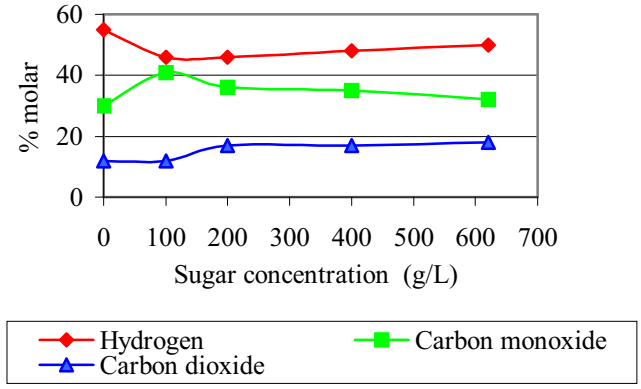

Figure 12: Gas composition versus sugar concentration

Reactor	Intensity (A)	Time average voltage (V)	Sugar concentration (g/L)
2	150	40	0
1	150	40	100
2	100 - 250	40	200
2	150	45	400
1	100	25	620

Figure 13: Operating parameters

Results are exposed on Figure 12 obtained with different parameters (cf. Figure 13). Power control is quite difficult because of arc motion. We may observe that hydrogen ratio is higher for drinking water than for sugar solution.

We suppose that after water thermolysis due to high electrical arc tempera ture, hydrogen gas and oxygen gas are recombined to water. Studies on water thermolysis by concentrated solar energy showed that hydrogen gas flow rate is a function of thermal quench [8]. In our process, quench is not fast enough to inhibit this reaction.

But carbon presence at sublimation temperature and oxygen gas permit the production of carbon monoxide. Hydrogen and oxygen consumption exposed in equations (2) and (3) assists water (steam) decomposition (equation 1).

$$H_2O_{(g)} \rightleftharpoons H_{2(g)} + O_{2(g)} \quad (1)$$

$$C_{(g)} + \tfrac{1}{2} O_{2(g)} \rightleftharpoons CO_{(g)} \quad (2)$$

$$CO_{(g)} + \tfrac{1}{2} O_{2(g)} \rightleftharpoons CO_{2(g)} \quad (3)$$

$$H_2O_{(g)} + CO_{(g)} \rightleftharpoons CO_{2(g)} + H_{2(g)} \quad (4)$$

According to gas analysis, there is very few oxygen (< 1 %) in produced gas. Equations (2) and (3) are almost quantitative and reaction (4) must be considered despite low pressure and low temperature conditions in solution.

4. Perspectives

Organic molecule gasification in aqueous solution is feasible: an hydrogen rich gas is obtained from aqueous sugar solution (about 50 % H_2, 35 % CO, 15 % CO_2). Experiments with tracker elements (deuterium via heavy water, ^{13}C via sugar) could about carbon and hydrogen origins in gas. Works on electrode material and shapes could improve the process and reduce electrode erosion. Concerning fundamentals phenomena, spectroscopy emission measurements may provide some information about reactive species such as H, O and C. Our further experiences will concern aqueous suspensions of organic material in order to show or not the feasibility for insoluble materials such as sewage sludge.

This process aims to propose an alternative way to co-firing process. Several applications are conceivable such as reduction of sewage sludge volume or treatment of milk or wine industry residues with high moisture contents.

It appears that our process eliminates some problems of usual gasification processes and can find its place in aqueous waste treatment. Ratio between hydrogen and carbon monoxide indicates that produced gas can be used in liquid fuel making processes like Fischer-Tropsch or Mobil. With a high calorific value (8 MJ/Nm^3), cogeneration units can use it to produce electrical and thermal energy.

References

[1] W. Kaiser, U. Drost, "Thermoselect-an advanced field proven high temperature recycling process", IT3'04 Conference, May 10-14, 2004 Phoenix, Arizona.

[2] T. Watanabe, "Recent development of waste treatment by reactive thermal plasmas in Japan", ISPC 16, June 22-27, 2003, Taormina (Italy).

[3] P. Carabin, E. Palumbo, T. Alexakis, "Two stage plasma gasification of waste", IT3'04 Conference, May 10-14, 2004 Phoenix, Arizona.

[4] S.V. Dighe, D. E. Lazzara, "Westinghouse plasma gasification technology for application to coal gasification and co-fired coal/biomass gasification", Coal Conference September 15-19, 2003, Pittsburgh, Pennsylvania.

[5] T. Toda, M. Deguchi, R. Itatani, "Abatement of global warming gases with an arc plasma of new type at at atmospheric pressure", XVth International Conference on gas discharge and their applications, September 5-10, 2003, Toulouse (France).

[6] H. Eldridge, D. Clark, S. Blum, US Patent 603,058, (1898).

[7] C. Y. Lee, S. K. Chen, N. H. Tai, US patent 6,217,713 (2001)

[8] H. Lange, A. Huczko, M. Sioda, M. Bystrzejewski, "Arc discharge in water as a source of carbon nanostrucutures", ISPC 16, June 22-27, 2003, Taormina (Italy).

[9] N. Sano, M. Chhowalla, H. Wang, K. Iimura, G. Amaratunga, T. Kanki, "Synthesis of fullerene-like particles and nanotubes by arc discharge in cold liquid", ISPC 16, June 22-27, 2003, Taormina (Italy).

[10] F. Lapicque, J. Lede, P. Tironneau, J. Villermaux, Solar Energy. **35**, 2 (1983).

Remarkable Enhancement in the Dispersion and Stability of Catalysts Using Novel Plasma Treatment

Chang-jun Liu

Key Laboratory for Green Chemical Technology and School of Chemical Engineering, Tianjin University, Tianjin 300072, China

The supported metal catalysts have been extensively employed in chemical industries. The catalytic performance of these supported catalysts is mostly dependent upon the preparation of the catalyst, which determines the acidity, dispersion, activity and stability of the catalyst. A sufficiently high dispersion of metal active species is normally required. To improve the dispersion and thereby to improve the catalytic performance, various promoter elements have usually been applied. However, the addition of promoter elements may not work well with those catalysts for high-temperature reactions, for example, oxidations. Many groups have also attempted to use some innovative catalyst preparations to improve the catalytic performance of the supported metal catalysts. These preparations include applications of plasmas, sonic treatment and microwave.

We previously reported a novel plasma catalyst preparation, with which the catalyst is first treated by a glow discharge and then the plasma treated catalyst is thermally calcined [1-3]. During the plasma treatment, the metal ions loaded will be normally reduced. A plasma reduction is thereby occurred. And, during calcination thermally after plasma treatment (no plasma employed in this step), the metal particles will be oxidized again. We nominated this preparation as Plasma Reduction and Calcination (PR&C) method. This PR&C preparation can lead to a better catalyst preparation with a high dispersion of metal active species, a significantly enhanced acidity, an improved low-temperature activity and a remarkable promotion of catalyst stability, which will be summarized in this paper.

The catalyst preparation using PR&C method has been reported in detailed elsewhere [10-18]. The procedure for this method includes: the conventional incipient wetness impregnation, drying (sometimes no drying needed), plasma treatment and calcination thermally. For the plasma treatment, several plasma phenomena, e.g., glow discharge, dielectric-barrier discharge and microwave discharge, can be employed. The different discharge plasma treatment would induce a very different catalytic performance. In this work, we focus on the discussion of PR&C method with glow discharge plasma treatment. Glow discharge is a kind of plasma that is created by inserting two electrodes in a cell filled with gas at low pressure (e.g.,1 Torr). During the glow discharge plasma treatment, the catalyst was hold in a quartz container and placed in a glow discharge tube. A high-voltage (DC or AC) generator is used to generate the glow discharge plasma. The catalyst powder or particles are usually placed in the “positive column” of glow discharge where it was characterized with highly energetic electrons at low gas temperature. To confirm the low gas temperature process, we have applied IR thermal imaging to measure the gas temperature during the glow discharge treatment of catalysts. The gas temperature is normally below 50 °C during the plasma treatment of all catalysts we investigated by far. We can therefore ignore the possible thermal effect during the glow discharge plasma catalyst treatment. After the plasma treatment, the catalyst is then calcined thermally.

As mentioned above, during plasma treatment, the catalyst is normally reduced. Evidently, some metal species present after the plasma treatment. A plasma reduction is thereby addressed. XPS analysis of the plasma treated catalysts gives us further evidences of the plasma reduction.

The reduced metal species would play an important role in the plasma-enhanced dispersion. During the oxidation of the reduced metal species in calcinations thermally, the new-formed metal oxide will induce an intense electric field. The metal species with the same electric properties will therefore exclude each other, which induces a highly dispersion. For example, the Ni-supported catalysts prepared via PR&C method exhibit an unusual dispersion characteristic. From hydrogen chemisorption, XRD characterization and TEM analysis, no metal particles can be identified. The metal species is ultra-highly dispersed over the support. Moreover, the calcination temperature has a significant effect on the dispersion of the catalysts prepared via PR&C method. From the results of palladium dispersion of PR&C prepared Pd/HZSM-5 catalysts, the palladium dispersion of the catalyst calcined at 673 K exhibits the highest palladium dispersion, 13.4%. With the increasing of calcination temperature, the palladium dispersion reduces because of the agglomeration of palladium particles at higher temperatures. The palladium dispersion of the catalysts calcined at 773 K and 873 K is 10.95% and 9.89%, respectively. To achieve a high dispersion, the calcination temperature of 673 K or 773 K would be the best.

All the catalysts prepared by PR&C method and tested by far for methane conversion show a better low-temperature activity. We take methane combustion here as an illustration, the methane conversion over the PR&C prepared catalyst is close to 100% at 450 °C, but it is only 50% at the same temperature over the conventional catalyst. The alumina supported Pd catalysts exhibit a similar plasma-enhanced low-temperature activity. The light-off temperature of the PR&C prepared catalyst is 370 °C, 50 °C lower than that obtained from the conventional catalyst. A remarkable enhanced stability for methane combustion from the PR&C preparation has also been achieved.

The principal procedure of the catalyst preparation using PR&C method can be summarized: 1) impregnation conventionally; 2) drying or no drying needed; 3) plasma treatment; and 4) calcination thermally. The PR&C preparation will normally induce significantly plasma-enhanced acidity and dispersion, which further leads to a low-temperature catalytic activity, upon the experimental investigations on methane conversion (including partial oxidation of methane, methane combustion, CO_2 reforming of methane and NO reduction by methane). A remarkable improved in the stability of catalysts has also achieved with the PR&C catalyst preparation. This improved stability is achieved principally thanks to the plasma-enhanced acidity and the improvement in the interaction between metal species and the support. Further improvement in the PR&C preparation is leading to a development of a novel and practical catalyst preparation technology.

Reference:

[1] J.G. Wang, C.-J. Liu, Y.P. Zhang, X.L. Zhu, J.J. Zou, K.L. Yu and B. Eliasson, Chem. Lett. 1068 (2002).

[2] C.-J. Liu, K.L. Yu, X.L. Zhu, Y.P. Zhang, F. He and B. Eliasson, Appl. Catal. B. 47, 95 (2004)

[3] K.L. Yu, C.-J. Liu, Y.P. Zhang, F. He, X.L. Zhu and B. Eliasson, Plasma Chem. Plasma Processing, 24, 393 (2004).

Diagnostics of a Supersonic Plasma Jet CVD System with Secondary Discharge

J. McLaren[1], L. Zajickova[2], J.V.R. Heberlein[1]
1 Department of Mechanical Engineering, University of Minnesota, Minneapolis, MN
2 Department of Physical Electronics, Masaryk University, Brno, Czech Republic

Abstract

We have examined how various deposition conditions affect plasma parameters important for superhard thin film deposition in a supersonic thermal plasma jet chemical vapor deposition system through Langmuir probe measurements. These measurements have revealed that the plasma floating potential is affected by a positive substrate bias, ion density is increased most effectively by increasing the torch power, and introduction of hydrogen decreases both electron temperature and electron density.

Keywords: Langmuir probe, superhard coatings, B-C-N composites, substrate bias

1. Introduction

Thermal plasmas have various advantages for materials deposition applications. Their high energy densities allow for the rapid dissociation of a wide variety of precursors, facilitating rapid deposition over large areas. Also, the rapid quench rates and high flow velocities inherent in thermal plasma deposition methods lead to strong temperature and reactant species gradients near the substrate, enhancing the potential for nanostructured materials deposition. Further advantages of thermal plasma deposition methods may be realized when the plasma is expanded into a low pressure environment and a low-power secondary discharge is superimposed over the plasma, as such expansions may lead to supersonic flows and lower heat fluxes to the substrate compared to deposition at higher pressure, while secondary discharges may lead to higher degrees of species dissociation, increased film growth rates, and film composition modification [1-2].

We are currently studying a supersonic thermal plasma jet chemical vapor deposition process with secondary discharge for the deposition of nanostructured B-C-N composites. Materials from the B-C-N ternary system hold particular advantages and potential for use in superhard coatings ($H > \sim 40$ GPa) for machine tools, as such coatings could potentially reduce the cost of high speed machining applications by up to 40% [3] by eliminating costs associated with the use and disposal of environmentally hazardous coolants. While two materials from the B-C-N system, diamond and cubic boron nitride (cBN), are respectively the hardest and second hardest known materials, both materials have notable limitations. Specifically, diamond dissolves with ferrous materials at temperatures greater than $\sim 1000^{o}$C, and cubic boron nitride films have limited thicknesses due to residual stress caused by the ion bombardment necessary for their deposition. As a potential solution to these limitations, it has been proposed that B-C-N materials could possess intermediate properties between those of diamond and cBN, namely superhardness, low residual film stress, and chemical stability at high temperatures [4]. Various deposition methods have been employed for diamond [7], cBN [8-9], and B-C-N deposition [4-6]. However, relatively few B-C-N deposition methods have involved thermal plasmas. Similarly, while there exist a few publications of diagnostic measurements of operative deposition parameters in cBN [9-10] and diamond deposition [7], measurements of such parameters for B-C-N film deposition are also quite rare. Such measurements in a thermal plasma B-C-N deposition system could potentially enhance the understanding of a superior superhard coating deposition process.

Our current research is focused on understanding how various processing conditions such as torch power, plasma chemistry, and substrate bias affect plasma parameters such as ion density, electron temperature, and precursor distributions in the plasma, which are assumed to play important roles in deposited film qualities. Substrate bias is of particular interest as ion bombardment of the substrate, facilitated through negative substrate bias, has been widely accepted as necessary for cBN deposition. For example, it has been shown that the cBN content scales with the total amount of momentum transferred to the substrate and growing film due to ion bombardment rather than the momentum transferred in a single binary ion collision [11]. Therefore, a higher total ion flux to the substrate is preferable for cBN deposition. Negative substrate bias also increases boron carbide film density [1], and potentially plays an important role in B-C-N film composition [4]. Positive substrate bias has been shown to increase boron carbide deposition rates by an order of magnitude and greatly increase optical emission from the plasma [1]. Diagnostic measurements of the previously mentioned plasma

parameters under various substrate bias conditions could provide insight towards the origins of these film enhancements. Values of these parameters may be obtained from Langmuir probe measurements.

2. Experiment

The supersonic plasma jet deposition system (SPJR) is shown schematically in Figure 1. Mixtures of argon and, depending on the material being deposited, hydrogen or nitrogen flow through the torch. A bias is applied to the cathode and an arc strikes between the cathode and grounded anode nozzle. The gases are heated by the arc, form a thermal plasma, and accelerated towards the substrate at supersonic speeds. Reactants such as boron trifluoride, methane, hydrogen, and mixtures thereof are injected in the expanding portion of the nozzle, dissociated in the plasma jet, and transported to the substrate where they react to form a film. To enhance the deposition process a secondary discharge is superimposed over the plasma jet by applying a positive or negative bias to the substrate with respect to the grounded anode. The distance from the substrate to the nozzle exit for all results reported here is approximately 6 cm, and the pressure is approximately 2.7 to 3 torr.

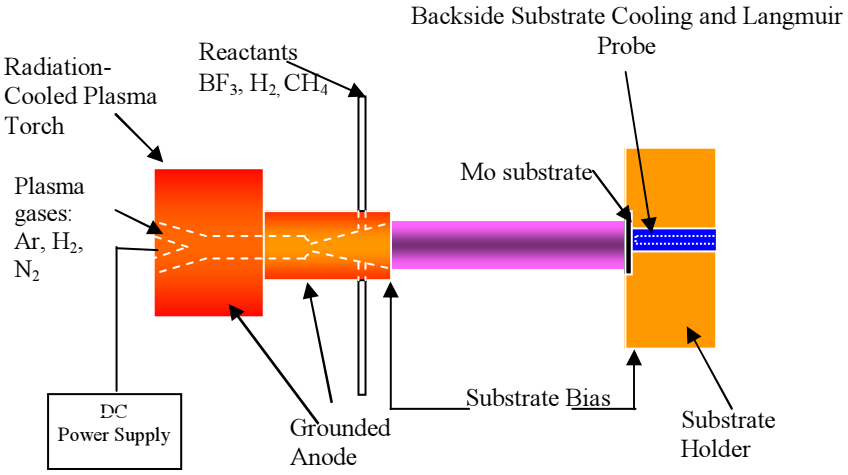

Figure 1: Schematic of the supersonic plasma jet deposition system

To enhance our understanding of the film deposition process in the SPJR we are using a Langmuir probe to measure the effects of deposition conditions such as torch power, plasma chemistry, and substrate bias on plasma parameters such as plasma potential, electron temperature, and electron density, which are assumed operative in the deposition of B-C-N materials. These measurements are carried out by inserting a 0.023-inch diameter tungsten wire through the back of the molybdenum substrate. The probe tip is flush with the substrate surface and insulated from the substrate by an alumina sleeve. The electrical circuit used to obtain probe characteristics is shown in Figure 2. A bias is applied to the probe with respect to the grounded torch anode and amplified by a Kepco bipolar power amplifier. The probe current is calculated by measuring the voltage drop across two resistors with two Lecroy differential amplifiers. The floating potential and ion saturation current, typically on the order of 100 microamps, are measured across R_2 with a resolution of 2 microamps. The retardation region and electron current, which may be measured up to 0.25 A with this circuit, are measured across R_1 with a resolution of 100 microamps. The diode configuration shown in Figure 2, adapted from [12], allows us to take both high and low resolution measurements simultaneously. Each current-voltage probe characteristic consists of one thousand points. Each of these points consists of the average current of one thousand voltage pulses at a given voltage obtained at a frequency of 59.96 Hz in order to filter out electrical noise from the torch power supply. Between each data point the probe is cleaned by applying one thousand pulses of the highest probe voltage for the given characteristic. All probe biasing and measurement is automated using National Instruments LabWindows software.

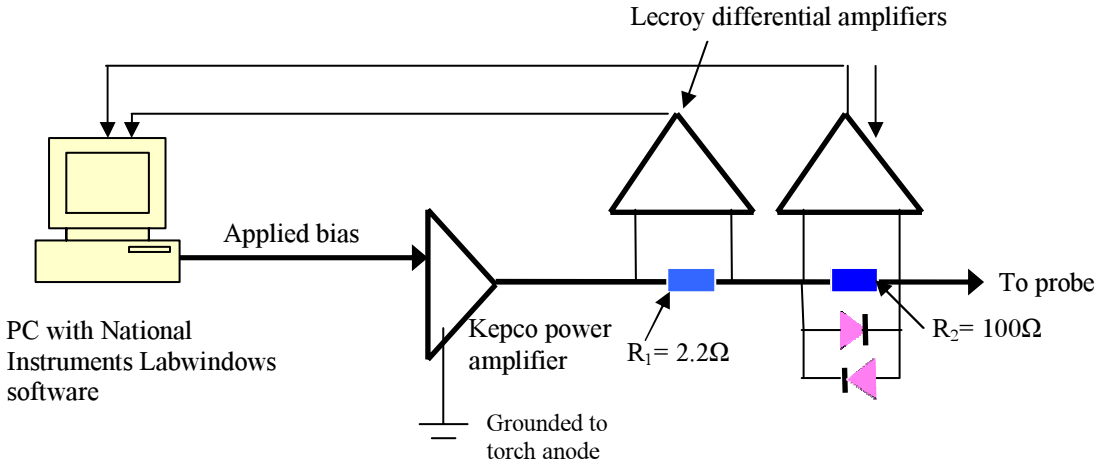

Figure 2: Schematic of electrical setup used for Langmuir probe measurements

Values of the plasma parameters of interest are obtained as follows. The floating potential is simply identified as the probe potential where no current flows between the probe and the plasma. The saturation ion current density for each condition is determined by taking the average current over the ion saturation region. The electron temperature is obtained, assuming a Maxwellian electron velocity distribution, from the electron retardation region of the probe characteristic using equation (1):

$$T_e = \frac{e}{k_B}\frac{1}{\tan\alpha} \tag{1}$$

where T_e is the electron temperature in Kelvin, e is the electron charge, k_B is Boltzmann's constant, and α is the slope of the natural log of the current density as a function of probe bias. This slope is corrected for the possibility of a non-constant ion saturation current by fitting the ion current with a polynomial and subtracting this from the current in the electron retardation region. The plasma ion density, assumed equal to the electron density, is calculated from the Bohm criterion shown in equation (2):

$$n_i = \frac{j_i}{e}\cdot\left(\frac{k_B T_e}{M}\right)^{-1/2} \tag{2}$$

where n_i is the ion density per cubic meter, j_i is the saturation ion current density, and M is the ion mass in kg. It should be noted that equation (2) assumes a collisionless sheath in front of the probe, or that the plasma Debye length is much smaller than the ion mean free path. Estimations of these parameters for the SPJR using the elastic collision momentum transfer cross-section [15] indicate that the mean free path for ion-neutral collisions in argon is approximately ten to fifteen times larger than the Debye length, indicating that the assumption of a collisionless sheath is reasonable.

3. Results and Discussion

Langmuir probe measurements have been completed in plasma compositions consisting of pure argon and argon with 0 to 30 sccm of hydrogen added through the reactant portion of the nozzle under various substrate biases and torch powers. Substrate bias as been varied from -15V to +15V with torch powers ranging from 1.6 to 3.3 kW. Parameter measurements from these conditions are presented in the following section.

3.1. Floating Potential Measurements

Considering the previously mentioned phenomenon that cBN deposition scales with the momentum transferred to the substrate and growing film by bombarding ions, as well as other results showing the enhancement of deposited film properties resulting from ion bombardment, determining how the degree of ion

bombardment is affected in the SPJR is quite important. One way to gain such insight is to measure the change in plasma potential as a function of various parameters. If we assume our probe does not thermionically emit electrons during measurement, it is reasonable to assume that changes in the plasma potential scale proportionally with changes in the floating potential. Figure 3 shows a plot of plasma floating potential as a function of the applied substrate bias in a pure argon plasma. The plotted points represent averages of three to five measurements at each bias condition while the error bars represent two standard deviations of the data. Conditions such as torch power and hydrogen addition had a negligible effect on the floating potential.

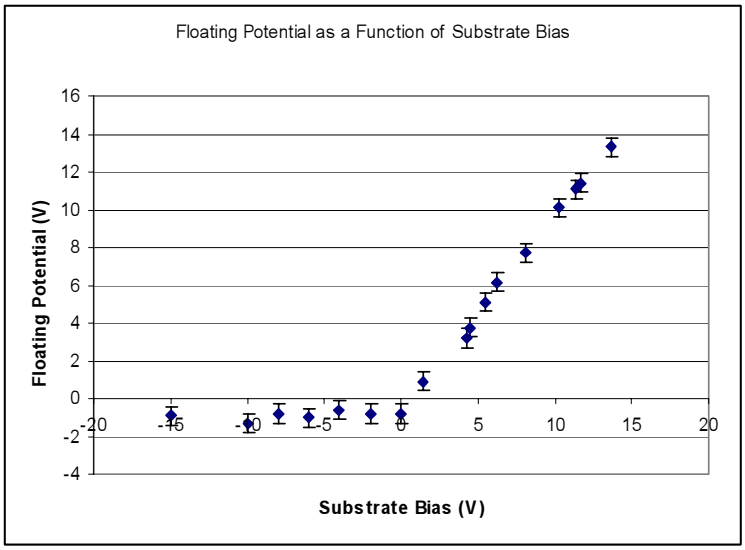

Figure 3: Plot of floating potential as a function of substrate bias

From Figure 3 it is evident that a negative substrate bias has little effect on the floating potential, while the floating potential increases linearly with positive substrate bias. Since negative substrate bias is the instrumental parameter in changing the degree of ion bombardment, the result presented in Figure 3 reveals that, since the plasma potential is assumed to remain relatively constant as a function of negative substrate bias, the bombarding ion energy is not affected by the plasma potential as negative bias is increased. Therefore, the bombarding ion energy scales with the ion mass and substrate bias, and effects of the plasma potential are negligible. This result is consistent with assumptions made by Berns et al [13] in estimating bombarding ion energy in cBN deposition via Monte Carlo simulations.

3.2. Electron Temperature Measurements

Electron temperatures were calculated using equation (1) for various conditions. Figure 4a shows a plot of electron temperature at different torch powers, showing a very slight increase in electron temperature with torch power. Figure 4b shows the electron temperature as a function of the hydrogen flow rate, showing a decrease in electron temperature with the introduction of 10 sccm of hydrogen to the plasma, and a much more modest decrease as hydrogen flow is increased further. These results are significant for film deposition if we consider that higher electron temperatures will affect the amounts of dissociated precursors in the plasma through promoting dissociation through bond-breaking collisions of free electrons with reactant species. Therefore, Figure 4a indicates that higher torch powers could promote slightly higher concentrations of dissociated precursors, while Figure 4b indicates addition of hydrogen may inhibit precursor dissociation. However, Figure 4b also indicates that the electron temperature decreases with addition of 10 sccm of hydrogen, but remains relatively constant with increasing amounts of added hydrogen. Substrate bias had a negligible effect on electron temperature.

3.3. Electron Density Measurements

Electron densities were calculated using equation (2) for various conditions as well. The measured electron densities as a function of substrate bias at three different torch powers in a pure argon plasma are shown in Figure 5. Figure 5 shows that the density increases

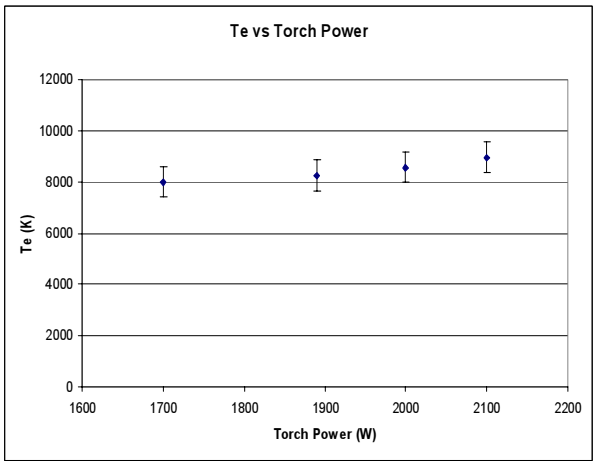

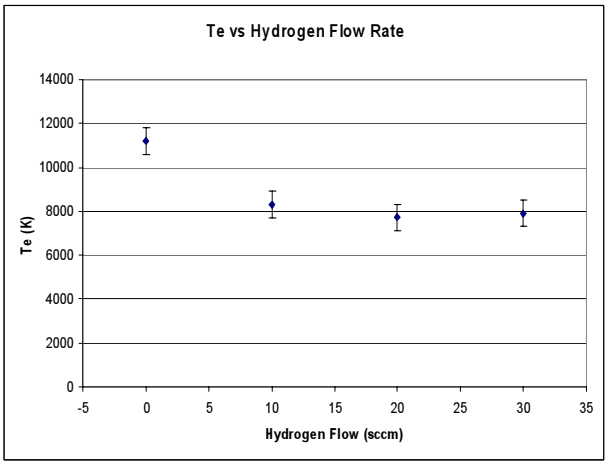

Figures 4a (left) and 4b (right): Measured electron temperatures as functions of torch power (4a) and hydrogen flow (4b)

most drastically with torch power, increasing by approximately 60% to 80% with a torch power increase from 1738 W to 2200 W at a given substrate bias. The density also increases with a positive substrate bias by approximately 30% at a given torch power. Addition of hydrogen decreased the density by approximately 30%, regardless of the amount of hydrogen added. These results are significant when considering the effects of ion bombardment in film deposition. According to the Bohm criterion, the flux of ions to the substrate follows the relationship in equation (3):

$$F_{ion} \alpha n_i \left(\frac{k_B T_e}{M} \right)^{1/2} \tag{3}$$

where F_{ion} is the ion flux to the substrate and n_i is the ion density at the sheath edge [10]. Therefore, if one considers the total amount of momentum transferred to the film from bombarding ions to be instrumental in cBN deposition, and important in B-C-N deposition, a higher ion flux is desirable. However, one must also consider that large degrees of compressive film stress, which limit attainable deposited film thickness, are a result of high degrees of momentum transfer due to ion bombardment [1]. With knowledge of these effects of ion density, the results shown in Figure 5 could allow one to select appropriate operating conditions with regard to the desired degree of ion bombardment.

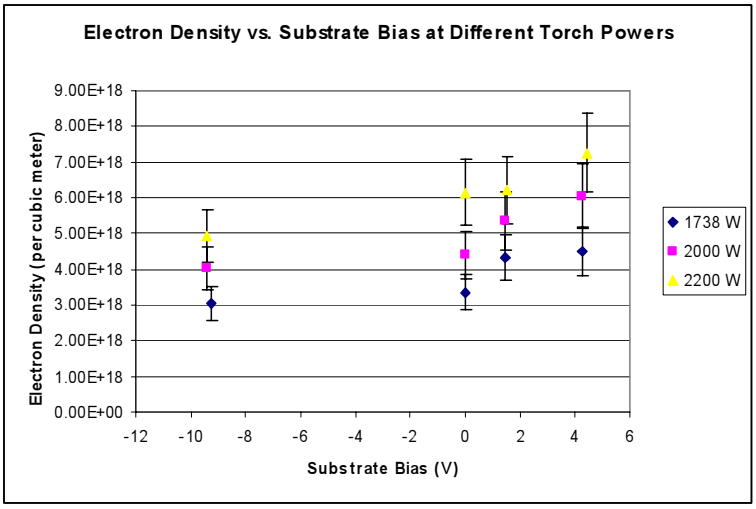

Figure 5: Measured electron /ion density as a function of substrate bias at 3 different torch powers

4. Conclusion

We have presented Langmuir probe measurements of plasma parameters under different conditions in the SPJR. These measurements have shown that the floating potential, assumed to scale with the plasma potential, is unaffected by a negative substrate bias and increases linearly with positive substrate bias, that electron temperature decreases slightly with increasing torch power and more drastically with addition of hydrogen, and that the ion/electron density increases with positive substrate bias, and more drastically with increasing torch power. These results are potentially useful in thin film deposition when one considers the importance of ion bombardment and potential for precursor dissociation. Work planned for the immediate future includes examining the effects of nitrogen and hydrogen incorporation as plasma gases on the parameters discussed above, as well as integrating optical emission spectroscopy measurements of precursor distribution in the plasma under different deposition conditions. Spectroscopic measurements of electron densities via Stark broadening will also be implemented. Ultimately, the data obtained from these plasma diagnostic techniques will enhance our understanding of the B-C-N film deposition process in the SPJR.

Acknowledgments

We would like to acknowledge support from NSF IGERT grant 0114372 and NSF-NATO postdoctoral fellowship grant DGE0312210.

References

[1] O. Postel. Ph.D. Thesis. University of Minnesota (1998).
[2] O. Postel, J. Heberlein. *Surface and Coatings Technology*, **108-109**, 247 (1998).
[3] S. Veprek. *J. Vac. Sci. Tech. A*, **17** (5), 2401 (1999).
[4] D. Hegemann, R.Riedel, C.Oehr. *Thin Solid Films,* **339,** 154, (1999).
[5] A. Stanishevsky, H. Li, A. Badzian, T. Badzian, W. Drawl, L. Khriachtchev, E. McDaniel. *Thin Solid Films* **398-399**, 270 (2001).
[6] M.P. Johansson, I. Ivanov, L. Hultman, E.P. Munger, A. Schutze. *J. Vac. Sci Tech.A*, **14** (6), 3100 (1996).
[7] M. Asmann, A. Wank, H. Kim, J. Heberlein, E. Pfender. *Plasma Chemistry and Plasma Processing*, **21** (1), 37 (2001).
[8] S. Matsumoto, W.J. Zhang, *Jpn J Appl Phys part 2,* **39**, L442 (2000).
[9] O. Tsuda, Y. Tatebayashi, Y. Yamada-Takamura, T. Yoshida. *J. Vac. Sci. Tech. A* **15** (6), 2859 (1997).
[10] A. Lousa, S. Gimeno. *Diamond and Related Materials* **10**, 1347 (2001).
[11] T. Ichiki, S. Amagi, T. Yoshida. *Journal of Applied Physics*. **79** (8), 4381 (1996).
[12] J. Luhmann, S. Lichtenberg, O. Oangenscheidt, M.S. Benilov, J. Mentel. *Journal of Physics D: Applied Physics* **35**, 1631 (2002).
[13] D.H. Berns, M.A. Capelli. *Journal of Materials Research* **12** (8), 2014 (1997).
[14] P.B. Mikarimi, K.F. McCarty, T. Friedmann. *Journal of Materials Research* **9**, 2125 (1994).
[15] A.V. Phelps. *Journal of Physical Chemical Reference Data* **20**, 557 (1991).

Spectral Emission of Ar_2^* in the 300 - 650 nm region: Effect of O_2 Addition

Abdulaziz Al-Jalal and Mohammad Aslam Khan

Department of Physics
King Fahd University of Petroleum and Minerals
Dhahran 31261, Saudi Arabia

Abstract

We have recently reported a significant enhancement in the atomization of O_2 in an Ar-O_2 glow discharge. During our investigations of energy transfer between Ar and O_2, we have observed a strong emission from Ar_2^* dimer in the 300-650 nm spectral region in pure Ar discharge. However, addition of a small amount of O_2 to Ar virtually wiped out this emission. This provides direct evidence of a strong channel of energy transfer between Ar and O_2 in a glow discharge under our experimental conditions.

1. Introduction

Atomic oxygen (O) is highly useful in many chemical and material processing applications [1]. However, production of a large number of O atoms for these applications in sources such as glow discharges has been difficult due to several reasons. On the other hand, the intriguing result of adding a small amount of O_2 in Ar discharge leading to a manifold increase in the creation of O atoms has attracted considerable interest in recent years [2,3,4].It is believed that the energy transfer between Ar and O_2 does not proceed in a simple collisional process. Instead, this involves formation of Ar_2* dimer followed by resonant collisional energy transfer to O_2, possibly through appropriate potential energy curve-crossings. These excited O_2 molecules subsequently dissociate into oxygen atoms.

The main collisional processes between O_2 and Ar atoms exited by energetic electrons in the discharge may be outlined as below.

$$e + Ar \rightarrow Ar^* + e \quad (1)$$

$$Ar^* + O_2 \rightarrow 2O + Ar \quad (2)$$

$$Ar^* + Ar^* \rightarrow Ar_2^* \quad (3)$$

$$2Ar^* + O_2 \rightarrow 2O + 2Ar \quad (4)$$

Spectral emissions attributed to Ar_2* dimer in a pure Ar gas discharge have been reported in several spectral regions below 250 nm [5,6,7]. In particular, strong emission bands were reported in the regions around 130, 155 190, and 213 nm. In some studies, production of highly excited Ar_2 states was monitored indirectly by recording peak intensity of Ar lines at 811.5 and 810.4 nm assuming that these states are partly a result of predissociation of Ar_2*[8].

We have observed a considerably strong emission in the spectral region 300-650 nm from a pure Ar glow discharge that is attributed to Ar_2* dimer spectra. To the best of our information, this is the first observation of spectral emission from Ar_2* in this region. More importantly, however, we observed that the addition of a small amount of O_2 to Ar virtually wiped out this emission. This is in line with the report of Moselhy et. Al. [4] and provides further evidence of energy transfer between Ar and O_2 in a glow discharge.

2.Experimental detail

We used a DC glow discharge to study the energy transfer between Ar and O_2 at low pressures, up to a few mbar.

The experimental set up has been described in a previous paper [2]. Briefly, it consisted of a cross-shaped discharge cell with an adjustable gap between the electrodes. The light emitted by the discharge could be collected through one of the two side ports of the cell for the purpose of monitoring and analysis. The cell was first evacuated to pressures of the order of 10^{-3} mbar and then filled to the appropriate pressure of O_2 or Ar-O_2 gas mixture under carefully controlled conditions. A constant current mode of the discharge was used with 150 mA current.

The population densities of O atoms were monitored through spectrally resolved light emitted by the discharge using a scanning monochromator coupled to a thermoelectrically cooled photomultiplier. A compudrive unit provided precise scanning of the monochromator in the selected wavelength region. The signal from the photomultiplier was transferred to a boxcar averager and signal processing system linked to a PC.

Two modes of data acquisition were used. In the wavelength scanning mode, emission in the 250-850 nm region was recorded. Typical scan times were 15 minutes. On the other hand, for the time evolution of different atomic and molecular species present in the discharge, spectral emission on a particular wavelength belonging to a particular species was recorded as a function of time.

3.Results and discussion

Our main interest was in maximizing the atomization of O_2 in low pressure glow discharges where the main control parameters are gas pressure, gas composition, and discharge current.

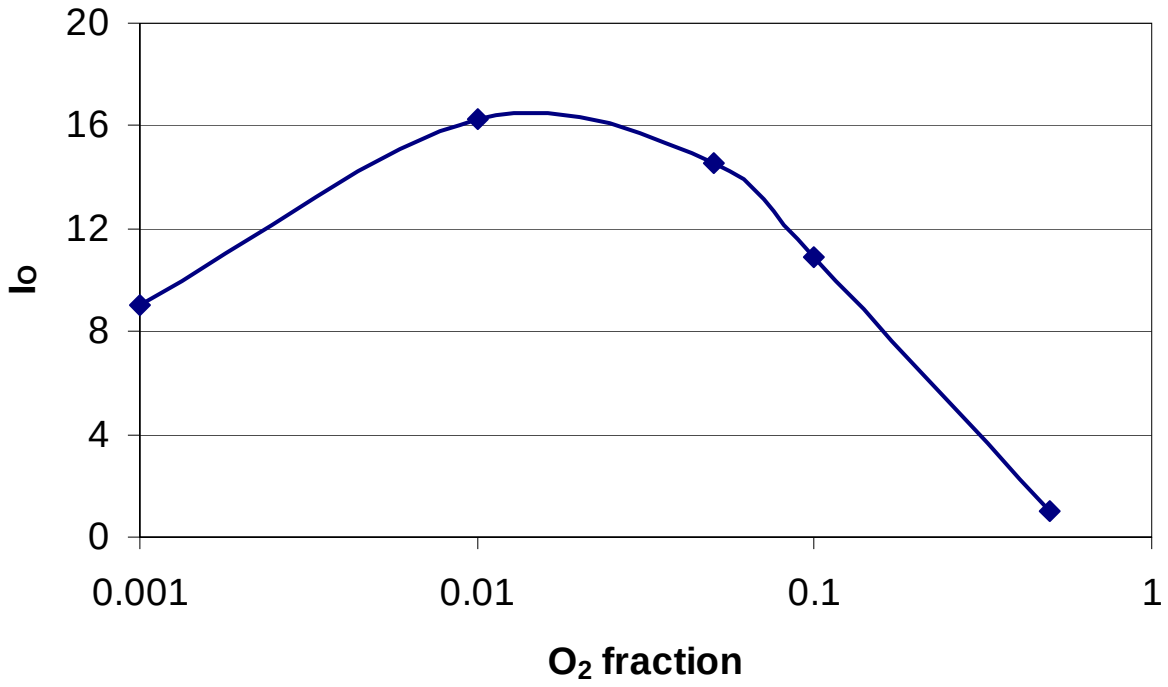

Figure 1. O atom yield as a function of O_2 fraction in Ar-O_2 mixture.

We carried out a detailed study of the effect of gas composition in the Ar-O_2 gas mixture on the overall yield of O atoms. Figure 1 shows a large enhancement of O atoms as seen from the spectral emission on 777.4 nm

transition (3s ^{5}S – 3p ^{5}P) of O atoms in the Ar-O_2 gas mixtures as a function of O_2 fraction. The total pressure was 0.5 mbar.

We note that with a decreasing fraction of O_2 in the mixture, the atomization increases significantly. In particular, for O_2 component around 1 %, the number of O atoms increases manifolds. However, below 1% O_2, the O atom yield decreases, understandably due to a smaller number of available O_2 molecules.

We investigated possible channels of energy transfer between excited Ar atoms and O_2 molecules leading to enhanced O atom yields by comparing the intensities of Ar transitions at 750.4, 715.4, and 763.5 nm with the 777.4 nm transition of O atoms. Figure 2 shows the behavior of intensity ratios as a function of O_2 fraction.

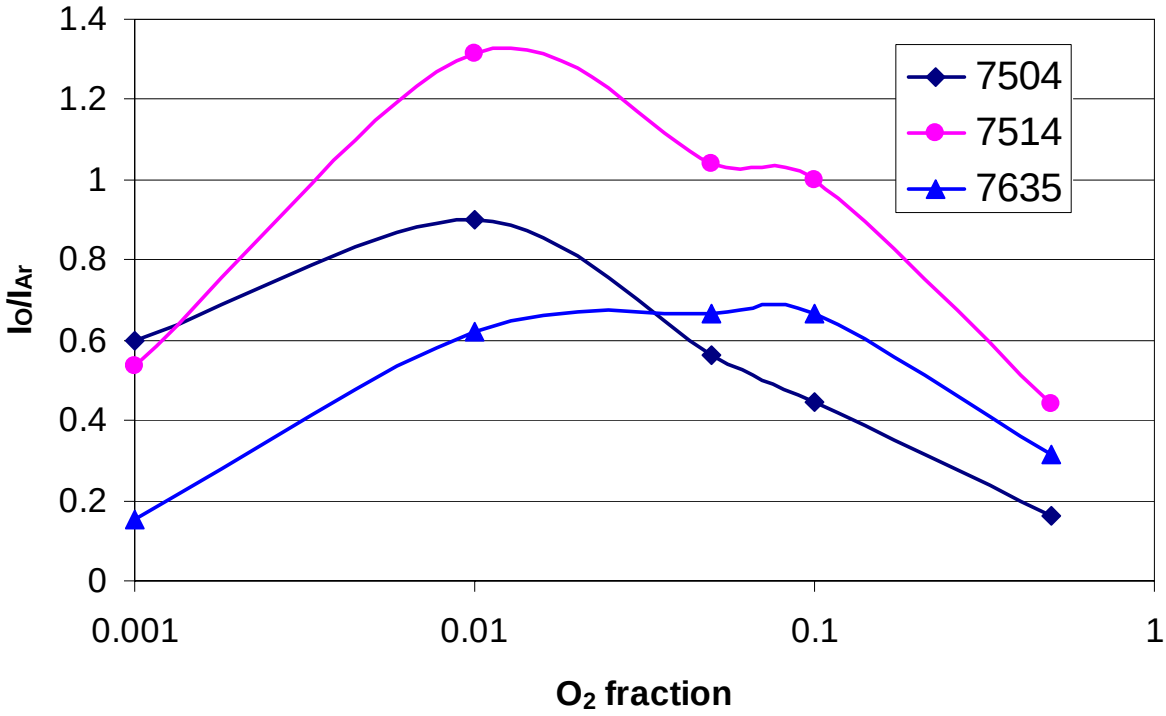

Figure 2. Line intensity ratios of O atom transition at 777.4 nm and Ar transitions at 750.4, 751.4, and 763.5 nm as a function of O_2 fraction in Ar-O_2 gas mixtures.

Apparently there is a maximum around 1% O_2 component. However, this alone can not explain the large enhancement in atomization of O_2.

We tried to explore other possible channels of energy transfer between Ar and O_2. For this, we recorded the spectra covering the range 250-850 nm. We investigated emission from pure Ar, pure O_2 and Ar-O_2 gas mixtures. An important observation is a strong continuum emission in the spectrum of Ar in the 350-650 nm region. More interesting, however, is the fact that this continuum totally disappeared when O_2 was added to Ar. Figure 3 compares the spectra in the three cases.

Several recent reports have suggested the presence of Ar_2^* dimer in the gas discharges containing Ar [5-8]. However, no reports of emission from Ar_2^* in the above-noted region have so far appeared. The total disappearance of Ar emission accompanied by a large enhancement in O atom yields is a strong evidence of energy transfer between Ar_2^* dimer and O_2 molecule.

To further investigate the continuum emission from Ar_2^* dimers, we investigated the spectral emission as a function of O_2 fraction for a constant total pressure of 0.5 mbar. We observed that the continuum emission decreases in intensity with increasing fraction of O_2, and completely disappears when the O_2 fraction reaches about 10% as in Figure 4. This is consistent with our understanding that a reasonable number of O_2 molecules are needed to affect the energy transfer.

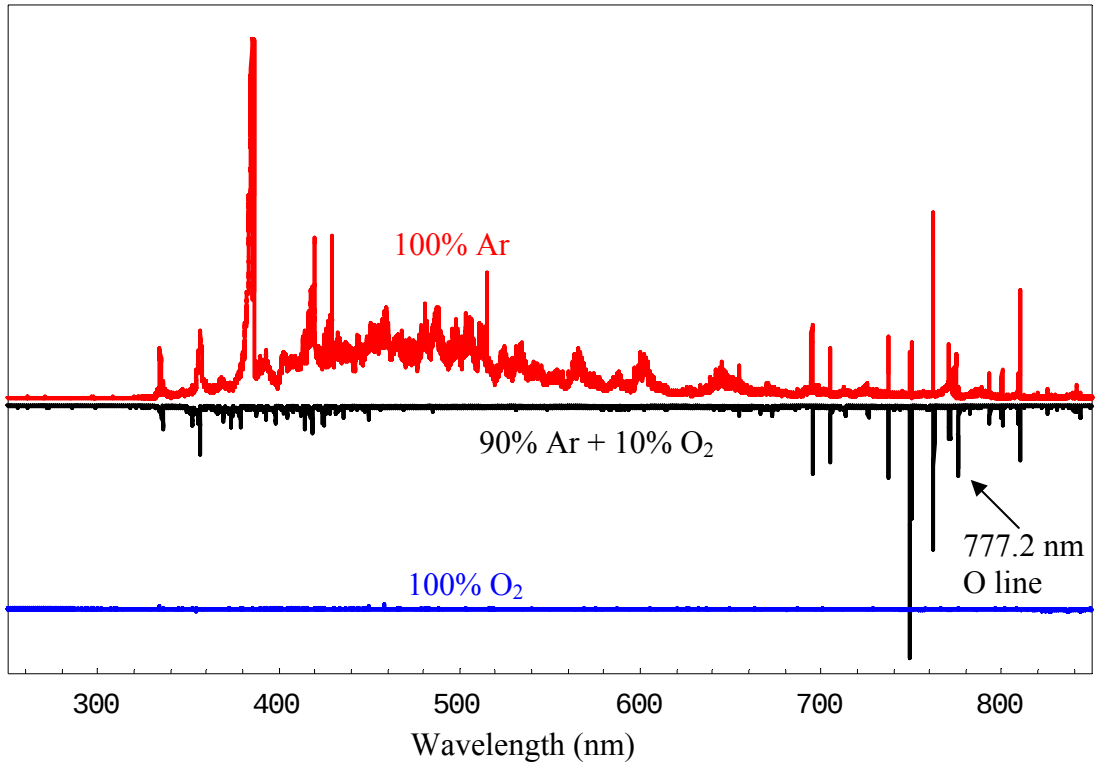

Fig. 3. Spectral emission from glow discharges in pure Ar, Ar+O_2 (9:1), and pure O_2 under identical pressures of 0.5 mbar and 100 mA discharge current. The spectrum of Ar+O_2 mixture is inverted and shifted to facilitate visual comparison. The spectrum of pure O_2 is also shifted downwards and shows weak emission. The intensity scale is the same for the three cases.

4.Conclusion

We have recorded a strong emission in the 300-650 nm spectral region from Ar_2^* dimers in glow discharges in Ar. Interestingly, addition of O_2 to Ar virtually wiped out this emission. This suggests that the formation Ar_2^* in an Ar discharge plays a critical rule in the energy transfer between Ar and O_2 leading to large enhancement in O atoms yields.

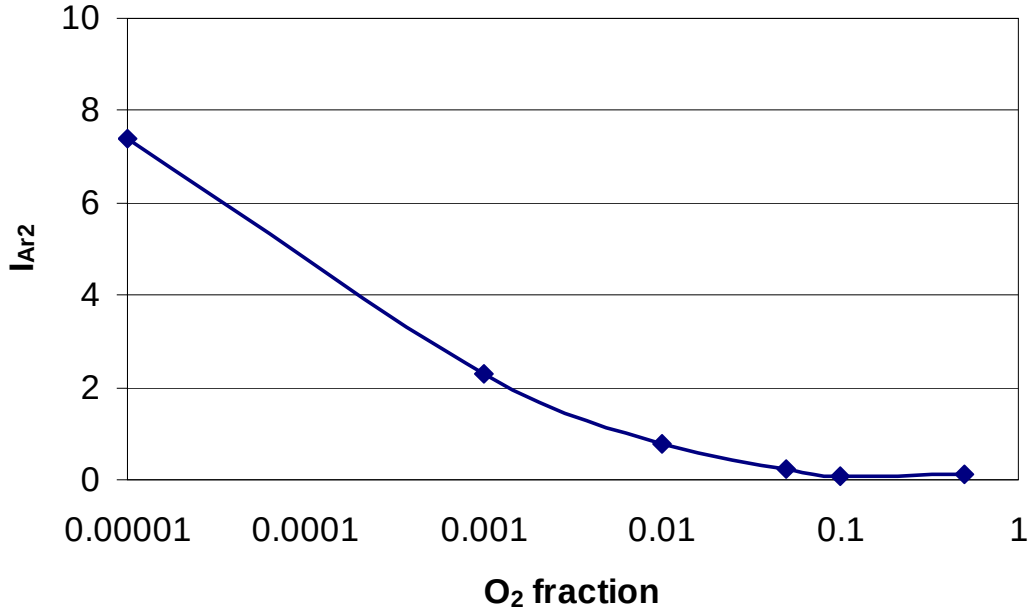

Figure 4. Variation of Ar_2^* continuum intensity as a function of O_2 fraction in Ar-O_2 gas mixture.

References

[1] J. R. Hollahan, A. T. Bell (Eds.), Techniques and Applications of Plasma Chemistry, John Wiley and Sons, New York (1974).

[2] M. A. Khan, A. A. Aljalal, Applied Catalysis A, 272,141 (2004).

[3] M. A. Khan, A. A. Aljalal, I. A. Bakhtiari, Anal. Bioanal. Chem., 377, 89 (2003).

[4] M. Moselhy et al, Appl. Phys. Lett., 78, 880 (2001).

[5] T. Griegel et al, J. Chem. Phys., 93, 4581 (1990).

[6] H. Langhoff, J. Phys. B., 27, L709 (1994).

[7] P. Dube, M. J. Kiik, B. P. Stoicheff, J. Chem. Phys., 103, 7708 (1995)

[8] C. M. Herring, et al, J. Chem. Phys., **101**, 4561 (1994).

Diagnostics of plasma polymerization process in RF magnetron sputtering and evaporation of polymers

J. Kousal[1], J. Hanus[1], A. Choukourov[1], A. Grinevich[1], Y. Pihosh[1], P. Hlidek[2], P. Zemek[3], H. Biederman[1], D. Slavinska[1]

[1] *Department of Macromolecular Physics, Charles University, Prague, Czech Republic*
[2] *Institute of Physics, Charles University, Prague, Czech Republic*
[3] *Institute of Physics, Academy of Sciences, Prague, Czech Republic*

Abstract
RF magnetron sputtering, sputtering induced evaporation, and thermal evaporation of polyimide with and without simultaneous activation by glow discharge were studied. Deposition rate in the case of evaporation is an order(s) of magnitude faster than in sputtering. Evaporated films are similar in chemical composition to the orginal material. Application of glow discharge results in formation of cross-linked plasma polymers.

Keywords: evaporation, polyimide, plasma polymers

1. Introduction

Thin polymeric films can be deposited by several methods utilizing bulk polymer as the source of material. In particular, RF magnetron sputtering can be used for preparation of films from a broad range of conventional polymers [1-4]. However, the molecular structure of such films usually does not match well the molecular structure of the source bulk polymer due to inevitable fragmentation and crosslinking of the target material. If vapours of melted polymer are used for physical-vapour deposition [5] a resulting film has more similar molecular structure. However, such films are composed of low molecular weight fragments and often reveal poor adhesion and mechanical properties.
Both methods can be combined either by inducing evaporation of a polymer or its precursors by heating from plasma [6, 7] or by activating the vapours of the heated polymer with independently generated plasma [8]. The study is focused on studying these processes on polyimide.

2. Experimental

Polyimide sheet 1 mm thick was used as a source material (Fig. 1, Cirlex CL-HN, Goodfellow, pyromellitic dianhydride – oxydianiline (PMDA-ODA) type) for both sputtering and evaporation experiments.

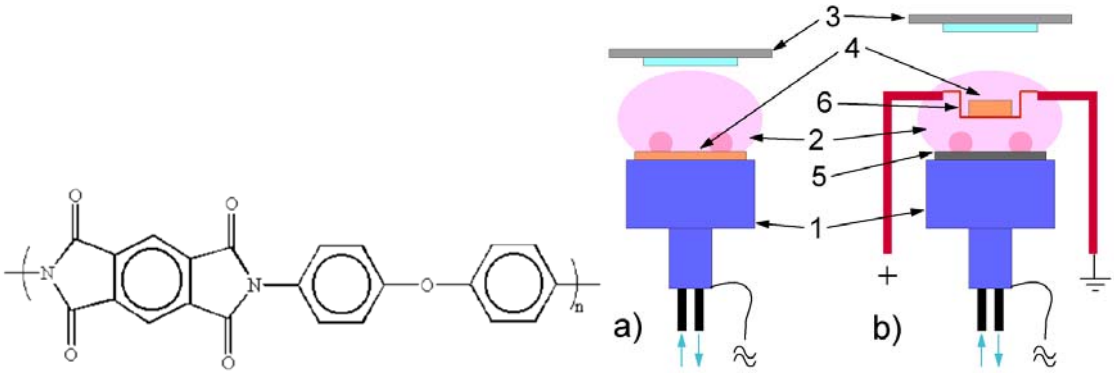

Fig. 1 Chemical formula of polyimide and the scheme of the experimental setup.a) RF magnetron sputtering b) evaporation with activation by plasma (1 - water-cooled magnetron, 2 - plasma, 3 - substrate, 4 - polyimide, 5 - graphite, 6 - heating boat)

In the case of RF (13.56MHz) magnetron sputtering (Fig.1a), a steel bell-jar reactor was used (volume 50 l, diameter 40 cm, pumped by a diffusion pump with liquid nutrogen trap backed by oil rotary pump, base pressure $<10^{-3}$ Pa). Sputtering was performed using a planar magnetron with 80 mm diameter. Substrates

were placed 4 cm above the magnetron. Argon was used as a working gas (pressure 2 Pa, flow rate 8.5 cm^3(STP)/min).
In the case of polyimide evaporation (Fig. 1b), another steel bell-jar chamber was utilized (volume 50 l, diameter 30 cm, pumped by the diffusion pump backed by oil rotary pump, base pressure 1×10^{-3} Pa). A planar magnetron covered by 5 mm thick graphite target was used as a plasma source. Graphite known for the low sputtering yield was chosen to minimize the contribution from sputtering to evaporation process. Argon pressure 0.5 Pa and flow rate 33 cm^3(STP)/min were used in this case. Polyimide was heated in a molybdenum heating boat, which was mounted 4 cm above the magnetron and 11 cm below the substrates. The temperature of the heating boat and substrates was measured by a thermocouple. It was found that during the deposition the temperature of samples was only slightly higher than the room temperature. Approximately 100 mg of polyimide was placed into the heating boat before each experiment.
Volatile species were monitored by means of neutral species mass spectroscopy (Hiden HAL 301 RC) and optical emission spectroscopy (Acton Research SpectraPro 300i). The deposition rate was measured by 5 MHz quartz-crystal microbalance sensor.
Glass, silicon and silver-coated glass were used as substrates. Deposited films were characterised by means of Fourier-transform infrared spectroscopy (Bruker Equinox 55) in reflection-absorption arrangement (FTIR-RAS), both in- and ex-situ. AFM topography (Quesant Q-Scope 850) and water contact angle measurements were performed to characterize surface of prepared films.

3. Results and discussion

a) RF magnetron sputtering

The initial stages of sputtering are characterized by an increase of deposition rate (Fig. 2). This is typical for polymer sputtering processes. At extended times of sputtering with lower powers (<40 W) deposition rate slightly decreases to reach a constant value. However, the sputtering at 75 W leads to drastic increase of the deposition rate. We attribute this effect to sublimation of lower molecular weight polymeric chains. The polyimide target rests on the water-cooled electrode, but because of poor thermal conductivity of the polymer surface exposed to plasma is at elevated temperature. When a certain plasma power is applied the local surface temperature in the erosion zone can reach the values sufficient for thermal degradation of polymeric chains and emitting of lower molecular weight fragments. Hence, both sputtered and evaporated fragments of the target material can contribute to the deposition process. In the particular system used, the effect started at magnetron power about 75W with the deposition rate reaching 30 nm/min after 15 minutes of discharge operation (compare with 2-5 nm/min without evaporation).

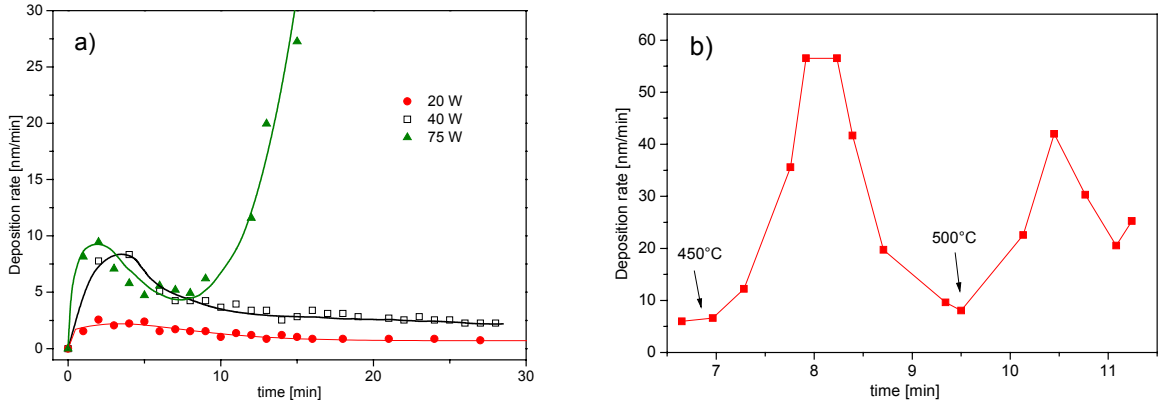

Fig. 2 Time dependence of the deposition rate. a) RF magnetron sputtering with various magnetron powers b) evaporation with activation by plasma.

The effect of sputtering with co-evaporation was observed also by mass spectroscopy (Fig. 3a) and optical emission spectroscopy of the plasma. At low power, weak signal of water trapped in the target and the fragments of polyimide molecule ($C_{1\text{-}3}H_x$, CN and especially CO) were detected. The onset of evaporation is visible as a significant increase of the mentioned polyimide fragments signal. The CO proved to be an

especially good indicator, since it is detected both by mass spectroscopy and optical emission spectroscopy and partly by in-situ FTIR.

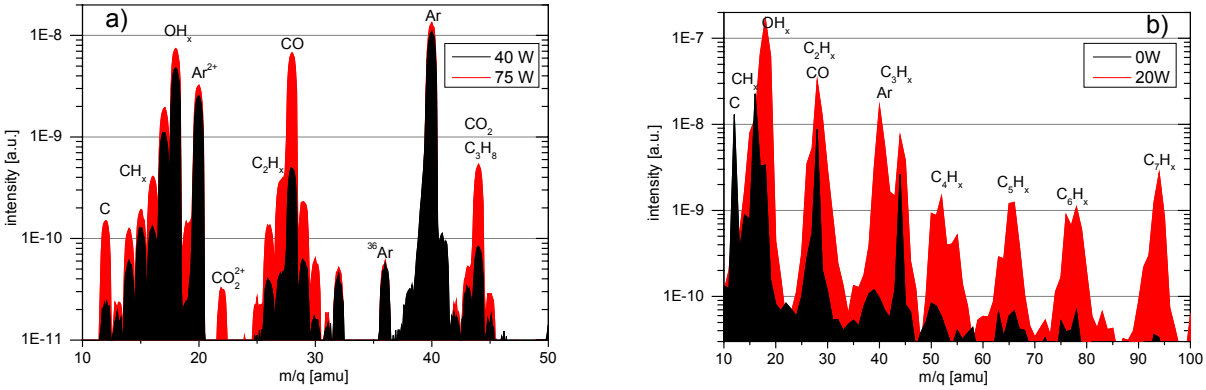

Fig. 3 Neutral species mass spectra. a) RF magnetron sputtering b) evaporation with activation by plasma, spectrum obtained without plasma was without Ar as well.

Only limited structural information can be obtained from the infrared spectra of films prepared by RF magnetron sputtering (Fig. 4). Broad peak centered near 3350 cm^{-1} can be assigned to the OH and NH stretching vibrations. Peak at 3000-2800 cm^{-1} shows aliphatic CH_2 and CH_3 groups stretching vibrations. The C≡C and C≡N stretching vibrations are present around 2200 cm^{-1}. The peak at 1700 cm^{-1} can be assigned to C=O stretching vibrations with some contribution of C=C and C=N stretching vibrations (1650 cm^{-1}). The peaks at 1450 cm^{-1} and 1375cm^{-1} are attributed to absorbtion of the CH_2 and CH_3 groups (deformation vibrations). In general, no signs of aromatic structures are present. Structure of the film is probably highly disordered and cross-linked, what is a typical feature of plasma polymers. With increasing power an increase in the NH/OH peak to aliphatic CH peaks ratio can be observed, the amount of triple bonds decreases and amount of C=O bonds increases.
AFM topography gives roughness of the films about 1-3 nm and water contact angle is 40°-55°.

b) plasma polymerized vapour deposition
When heated, polyimide started to emit volatile species at the temperature around 450°C. Polyimide was sublimating in a step-like manner without going through a liquid state. At a particular temperature only a part of the source material was transferred to the gas phase. The deposition almost stopped unless the temperature was raised again (Fig. 2b). The evaporation process was effective up to approximately 650°C. By this point, an extreme degradation of polymer chains probably occured. During evaporation, the peak deposition rate reached almost 60nm/min regardless with or without the plasma. However, due to surface decompostion of the material at higher temperatures (which probably prevents evaporation from the bulk of the sample), utilization of polyimide was never complete. Approximately 70-80 wt.% of partly decomposed polyimide remained in the heating boat. The material consumption increased to 40% by grinding the source material prior to experiment.
Evaporation of the material was clearly observable in the mass spectra (Fig. 3b). The start of the heating is characterized by increase of intensity of the species with m/q 17-19 (the spectrum not shown), which is attributed to trapped water emerging from the material. As the evaporation temperature is reached the hydrocarbon fragments appear. Most of them can be assigned to various C_xH_y species. Another visible specie is CO. During evaporation without a discharge the signal was rather weak. On the contrary, it increased considerably when the discharge was applied. This can be probably explained by the fragmentation effect of the discharge. As expected, during evaporation various fragments with a wide distribution of molecular weights are emitted from polyimide. The maximal mass detectable by the spectrometer used was 300 amu and its sensitivity to masses beyond 100 was low. The discharge can fragment higher molecular weight fragments (not detectable in our case) to lighter species, which are within the detection limit of the spectrometer. Such fragments as CO and CN were detected in the plasma by optical emission spectroscopy.
The infrared spectrum of the film deposited without discharge is remarkably similar regarding the positions of individual peaks to those reported for polyimide prepared by solution formation [9], vapor deposition

polymerization [10], cluster beam deposition [11] and by glow discharge vapor deposition polymerization [12]. The region below 1800 cm^{-1} is of major importance because the imide structure absorbs here: 1780 and 1730 cm^{-1} bands belong to imide C=O symmetric and asymmetric stretching, and imide C-N stretches at 1380 cm^{-1}. Furthermore, the aromatic ring exhibits stretching vibrations at 1500 cm^{-1} and deformation vibrations at 1120 and 830 cm^{-1}. The peak at 1240 cm^{-1} is assigned to aromatic ether stretching [12]. A broad band at the wavelengths higher 3000 cm^{-1} is attributed to OH and NH stretching vibrations. A lack of significant peaks at 3000-2800 cm^{-1} indicates a deficiency in aliphatic CH_2 and CH_3 groups stretching vibrations. However, at lower discharge powers some CH on double or aromatic bond stretching vibrations are present around 3050 cm^{-1}. This reflects well the structure of the source molecule.

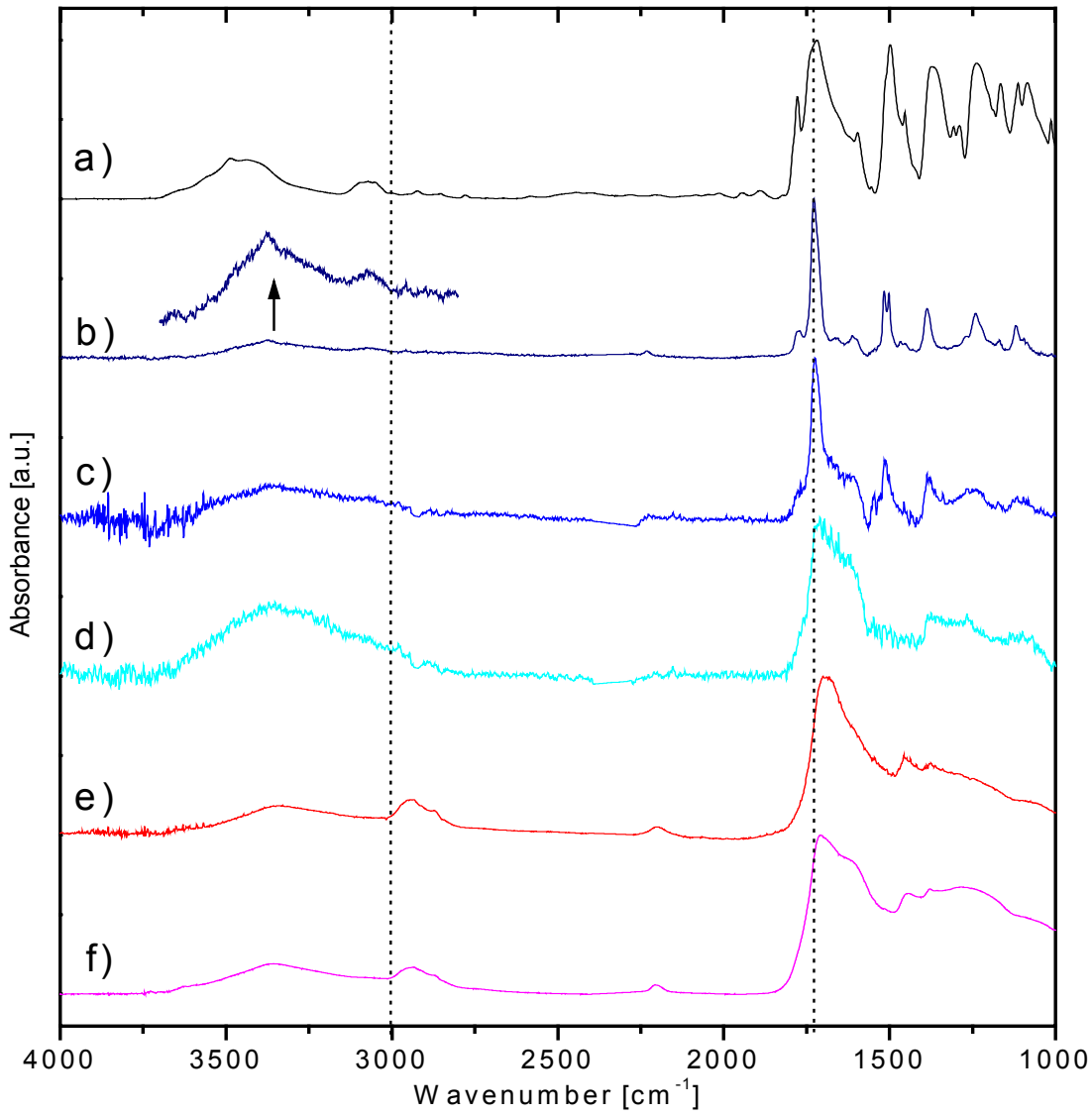

Fig. 4 Infrared spectra of source and deposited material. Spectra are normalised on the highest peak.
a) source material (powder form)
b) evaporation without plasma (part of the spectra magnified in intensity for clarity)
c) evaporation with activation by plasma (magnetron power 40W)
d) evaporation with activation by plasma (magnetron power 160W)
e) RF magnetron sputtering (magnetron power 20W)
f) RF magnetron sputtering induced evaporation (magnetron power 75W).

For the deposition with the discharge, the structure of the fingerprint region becomes less distinct with increasing power. The individual peaks degrade in intensity and broaden into the wide bands. The C=O peak at 1730 cm^{-1} remains dominating. However, it shows a developing shoulder at 1620 cm^{-1}, which is attributed to the contribution from various C=C and C=N species. Stretching of C=O bound in amide structure may also contribute to the shoulder and this is consistent with a considerable increase of the NH_x peak at 3400 cm^{-1}. At 160W power, the spectrum becomes unresolved and more similar to the films prepared by the magnetron sputtering. The mentioned changes of FTIR spectra suggest that the application of plasma leads to the loss of imide and aromatic structures and to the formation of cross-linked plasma polymer.
AFM shows rather flat surface of the films (roughness several angstrom at 1 micron scan size). Water contact angle decreases from 82° without plasma to 53° at 80W power with a small increase at higher powers.

4. Conclusions

Polyimide starts to thermally emit volatile species during RF magnetron sputtering at higher powers applied. This leads to significant increase of the deposition rate and changes in the plasma and film composition. One of the most important specie in the discharge is CO fragment of the polyimide molecule.
When polyimide is heated sufficiently the vapour phase produced by emitted fragments can be used as a working medium for plasma polymerization. In this case, the high deposition rate is achieved, although the deposition is limited in duration. The films deposited without plasma are similar in chemical composition to the original material. Plasma polymerization induces some fragmentation and crosslinking within the film structure. At high discharge powers such films are similar to plasma polymers prepared by RF magnetron sputtering.

Acknowledgements

This work was financed by the Ministry of Education of the Czech Republic as a part of the research plan MSM 0021620834. The authors would like to thank Dr. Miroslava Trchova for FTIR measurements of source polyimide.

References

[1] I. Kholodkov, H. Biederman, D. Slavinska, A. Choukourov, M. Trchova, Vacuum **70**, 505 (2003).
[2] V. Stelmashuk, H. Biederman, D. Slavinska, M. Trchova, P. Hlidek, Vacuum **75**, 207 (2004).
[3] M. Kitoh, Y. Honda, Thin Solid Films **271**, 92 (1995).
[4] A. Kinbara, T. Hayashi, K. Wakahara, N. Kikuchi, E. Kusano, H. Nanto, Thin Solid Films **433**, 274 (2003).
[5] P. P. Luff, M. White, Thin Solid Films **6**, 175 (1970).
[6] G. Maggioni, A. Quaranta, S. Carturan, A. Patelli, M. Tonezzer, R. Ceccato, G. Della Mea, submitted to Surface and Coatings Technology (2004)
[7] G. Maggioni, A. Quaranta, E. Negro, S. Carturan, G. Della Mea, Chem. Mater. **16**, 2394 (2004).
[8] H. Usui, Thin Solid Films **365**, 22 (2000).
[9] M.C.Buncick, D. D. Denton, J.Vac.Sci.Technol. **A 9 (2)**, 350 (1991).
[10] I. Karamancheva, V. Stefov, B. Soptrajanov, G. Danev, E. Spasova, J. Assa, Vibrational Spectroscopy **19**, 369 (1999).
[11] K. W. Kim, C. E. Hong, S. C. Choi, S. J. Cho, C. N. Whang, T. E. Shim, D. H. Lee, J. Vac. Sci. Technol., **A 12 (6)**, 3180 (1994).
[12] G. Maggioni, S. Carturan, V. Rigato, G. Della Mea, Surface and Coatings Technology **142-144**, 156 (2001).

Continuous and pulsed PECVD of ultralow-*k* dielectrics from various olefinic silane and siloxane discharges

A. Milella[1], J. L. Delattre[2], F. Fracassi[1], R. d'Agostino[1]

[1] *Department of Chemistry, University of Bari, Istituto di Metodologie Inorganiche e Plasmi - CNR, Bari, Italy*

[2] *NanoHorizons Inc., 200 Innovation Blvd., State College, PA 16803, USA*

Abstract

Continuous and modulated discharges fed with divyniltetramethyldisiloxane (DVTMDSO) and allyltrimethylsilane (ATMS) mixed with oxygen and argon carrier gas, were used to deposit ultralow-*k* films. The effect of various process parameters on the dielectric constant of films as well as on their chemical composition were investigated. For both monomers, lowering the oxygen content in the discharge allowed for a continuous decrease in *k* values down to 2.3 for DVTMDSO and 2.2 for ATMS.

1. Introduction

Enhancements in integrated circuit performance over the past four decades stem mainly from the periodic scaling down of device features, however interconnect cross-talk (RC delay) limits performance as feature sizes are reduced below 1 micron. Efforts to minimize delay through new materials introductions are well underway. With respect to wire materials, the migration from Al to Cu metallization reduced line resistance by ~30% and it is expected to remain the interconnect of choice for the near future. Further reduction of RC delay can also be achieved with low-permittivity dielectrics [1].

Intense research efforts have focused on developing inorganic and organic low-*k* materials that meet the stringent requirements for successful integration, but few exhibit the proper combination of low-permittivity plus thermal, chemical and mechanical stability. Current estimates suggest that ultralow-*k* dielectrics with *k*=2.1-2.4 will be needed for 2007-2012 [2]. To achieve *k* values below 2.5 in the next generation of dielectrics, pores must be introduced into the network, as air, with *k*~1, reduces the total dielectric constant in accordance with Lichtenecker`s law of mixed dielectric materials. Two synthetic approaches have emerged as the likely candidates for the first generation of porous dielectrics; spin-on and PECVD [1]. Porous spin-on dielectrics are typically prepared by spin coating the substrate material with a dual phase gel/porogen mixture which is annealed to give a rigid glass-like matrix. Annealing at higher temperatures removes the labile porogen phase, leaving pores within the organosilicate glass (OSG) matrix. While this strategy to produce low-*k* dielectrics has made extraordinary progress, commercialization has been slowed because of integration issues as well as the additional cost of new equipment.

Over the next decade PECVD solutions are preferable because they have shorter integration cycles and don't require new equipment. PECVD methods for depositing porous OSG have only recently become available. Basically, two approaches for the synthesis of porous dielectrics are currently under investigation: (1) codeposition of a porogen and an organosilane or organosiloxane precursor [3, 4], (2) deposition of an organosilane or organosiloxane precursor with a labile side-group [5]. In both cases, an annealing step is then required to generate pores. It is still unclear whether the pore formation mechanism is driven by –OH group elimination, through condensation reactions, or by C_xH_y loss.

In this contribution we report our latest results on the deposition of ultralow-*k* films from continuous and pulsed glow discharges fed with divyniltetramethyldisiloxane (DVTMDSO) and allyltrimethylsilane (ATMS) mixed with oxygen and argon carrier gas. The effect of process

parameters such as feed mixture composition and RF input power onto dielectric constant and chemical composition of films are reported.

2. Experimental

Organosilicate films were deposited using a capacitively coupled parallel plate reactor. The upper electrode is driven by a 13.56 MHz power supply (RF POWER PRODUCTS, model RF5). Impedance matching was accomplished with a LC network. The lower electrode was grounded and can be heated up to 600 °C through a heating element. RF input power can be modulated by a pulse generator implemented into the RF generator. An oscilloscope (TEKTRONIX, model TDS 200) was used to check pulse duration and amplitude. The flow rates of the gases (O_2, Ar) and of the monomer vapor (DVTMDSO, ATMS) were controlled by MKS flow meters, and the pressure was monitored with a MKS capacitive gauge. The reactor was pumped by a turbomolecular and a rotary pump. For continuous mode deposition, the discharges were sustained at various feed mixture compositions and power values, keeping constant all the other process parameters. Finally, the effect of modulating the RF power, by changing the duty cycle (DC) at a fixed period (T=320 ms), was evaluated on the discharge leading to the film with the lowest *k*. Table I summarizes the deposition parameters.

Table I: Experimental Conditions

Process Parameters	
Monomer	DVTMDSO, ATMS
RF Power	30-100 W
Pressure	750 mTorr
O_2 flow rate	0-16 sccm
Ar flow rate	270 sccm
Monomer flow rate	3 sccm
Deposition temperature	150 °C
Annealing temperature	400 °C

Films were deposited at 150 °C and then annealed in vacuum at 400 °C for 30 min. Dielectric constants of films were determined before and after annealing using a mercury probe (MDC). For dielectric measurements films were deposited onto *n*-type Si (100). Film chemical composition was investigated through FT-IR and X-ray photoelectron spectroscopy (XPS). FT-IR spectra were recorded using a Bruker Equinox 55 spectrometer at 4 cm^{-1} resolution. In order to minimize effects of water vapor and carbon dioxide, the spectrometer was purged with nitrogen for 15 min between each measurement. XPS spectra were acquired with a PHI ESCA 5300 with a non-monochromatic Mg K_α radiation (1253.6 eV).

3. Results and discussion

Figure 1 shows the trends of the dielectric constants, before and after annealing, for films deposited from continuous plasmas fed with mixtures of Ar, DVTMDSO and increasing amounts of O_2. The effect of varying the RF power delivered to the discharge is also reported. Data clearly show that the annealing is always responsible for a decreasing in the dielectric constant values and this effect becomes more pronounced as RF power gets lower. Lowering the oxygen flow rate in the feed allows for a continuous decrease in *k* values. Finally, for both as deposited and annealed films, higher RF power inputs lead to higher dielectric constant. All results for ATMS are similar to those presented for DVTMDSO, unless specified otherwise. For the sets of conditions investigated, the lowest *k* values after annealing at 400 °C, are 2.3 for DVTMDSO and 2.2 for ATMS.

Another key consideration is the reduction in film thickness upon annealing. Figure 2 shows the loss in thickness as a function of oxygen flow rate, at various RF powers. At 30 and 60 W the decay of the thickness loss is nearly exponential with oxygen flow rate, while it is pretty reduced

when 100 W is considered. The lowest dielectric constant of 2.3 for DVTMDSO corresponds to a shrinkage of 11%. The best result for ATMS is accomplished by adding a very small amount of oxygen to the discharge which yields films with a shrinkage of 10%.

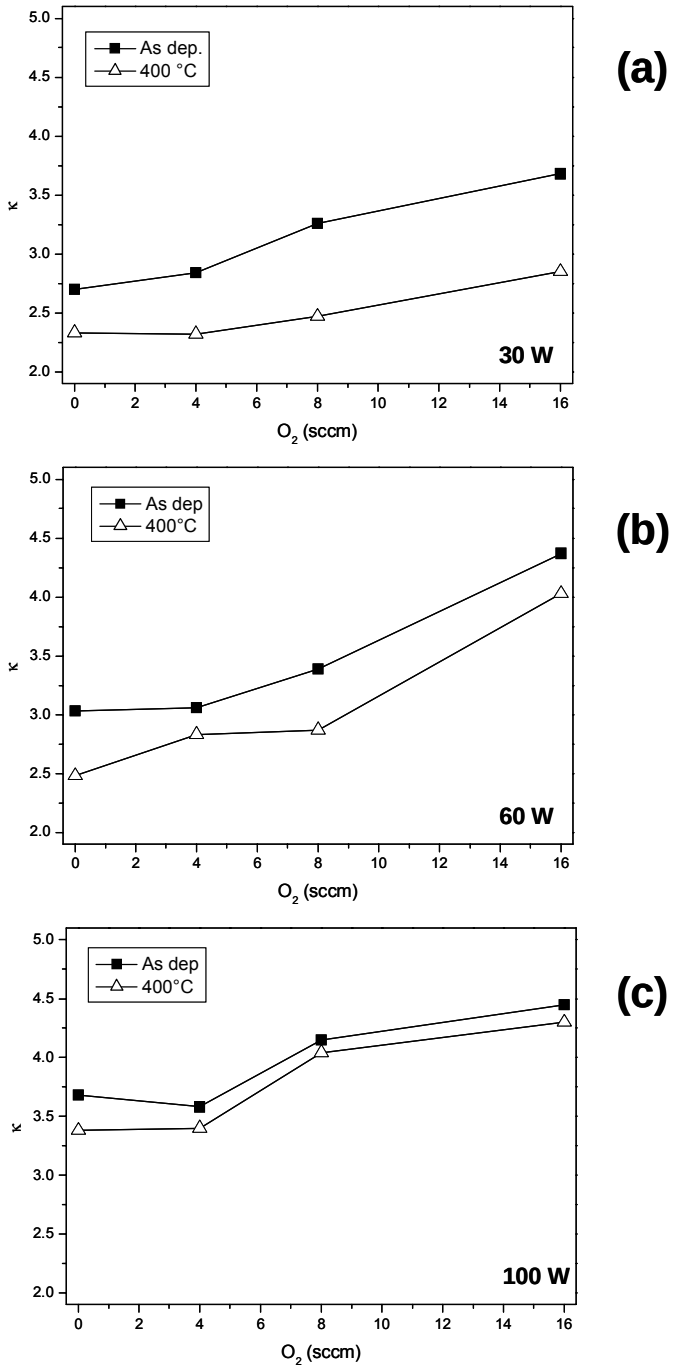

Figure 1: Trends of dielectric constants for films deposited from DVTDSO as a function of oxygen flow rate in the gas feed, at different RF powers: (a) 30 W, (b) 60 W, (c) 100 W.

In order to understand if a less extent in monomer fragmentation could allow for a further reduction in *k* values, modulation of RF input power was introduced in the discharge resulting in the films with the lowest dielectric constant. In this set of experiments , the duty cycle was varied in the range 10-60% while keeping the period fixed at 320 ms. Neither film electrical properties nor shrinkages improve by using pulsed plasmas.

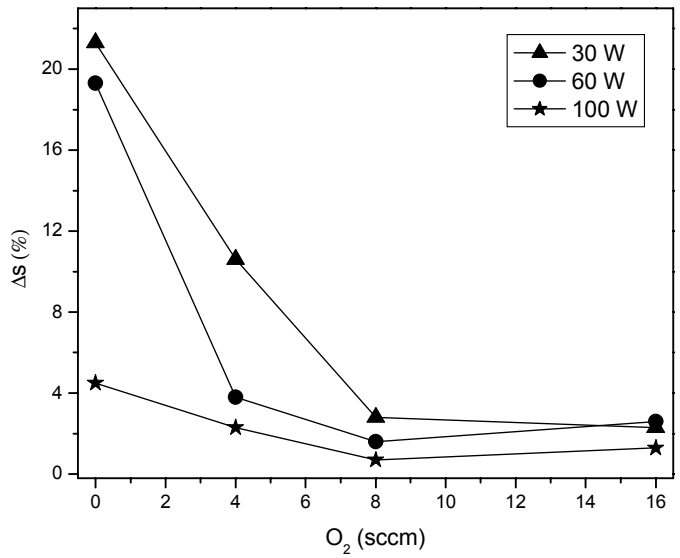

Figure 2: Loss in thickness during annealing as a function of the oxygen flow rate in the gas feed, at three RF powers.

Figure 3 shows normalized FT-IR spectra of films deposited from DVTMDSO/Ar/O_2 with the lowest and highest dielectric constant to highlight major differences in chemical composition of the films. Switching from the discharge sustained at 30 W and 4 sccm of oxygen content in the feed to the one at 100 W and 16 sccm of oxygen, an organic to inorganic crossover in deposited films is observed.

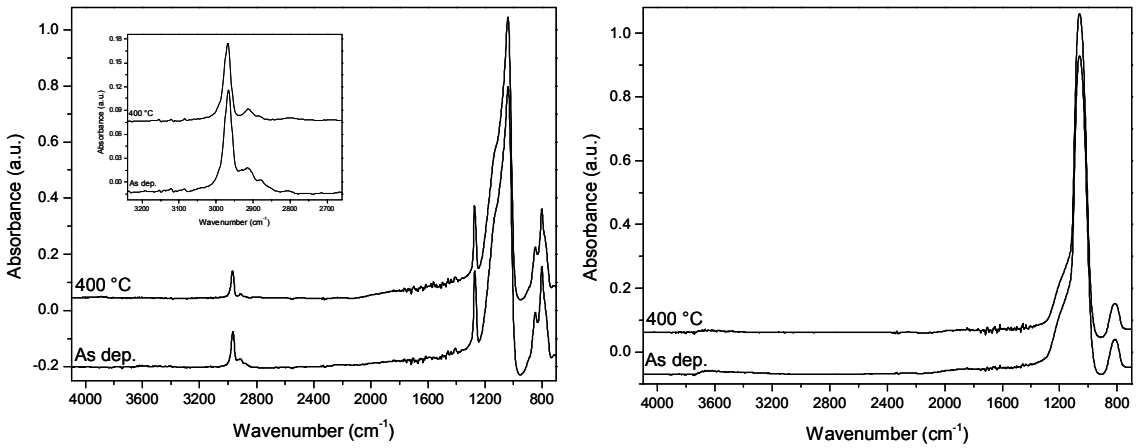

Figure 3. FT-IR spectra of films deposited from DVTMDSO with very different k values after annealing. (a) k= 2.3, (b) k= 4.3. The inset in figure 3(a) shows the change in CH_x absorption after annealing.

The spectra in figure 3b display the absorption bands typical of SiO_2 network: stretching and bending at about1060 and 800 cm-^{1}, respectively and a weak absorption band at 3650 cm^{-1} due to isolated SiOH groups. As oxygen flow rate is reduced and the RF power is decreased from 100 to 30 W, some carbon related bands appear: the CH symmetric and asymmetric stretching in CH_x (x=1-3) around 2915 and 2970 cm^{-1}. Moreover the absorption due to $SiCH_3$ is observed at 1275 cm^{-1}. The

band around 800 cm-1 in this case can be assigned to $Si(CH_3)_2$ and $Si(CH_3)_3$, overlapping the one due to SiO bending mode. The marked organic content of this films leads to a shift of the most intense band from 1060 cm^{-1} to 1037 cm^{-1}. Spectra of figure 3b does not reveal any change upon annealing while the one in figure 3a basically shows a reduction in CH_x and $SiCH_3$ absorptions. Thus, the larger reduction in the k value of this film is correlated to the loss of CH_x fragments. The latter may lead, in turn, to a rearrangement of the network resulting in the formation of nanopores in the films, as suggested by other researchers [4-5].

4. Conclusions

Low-k films were deposited from continuous and modulated discharges using DVTMDSO and ATMS as precursors, in mixture with Ar and variable oxygen flow rate. The effect of varying RF power delivered to the discharge was also evaluated. Results presented so far can be summarized as follows.

For both monomers, lowering the oxygen content in the discharge allowed for a continuous decrease in *k* values down to 2.3 for DVTMDSO and 2.2 for ATMS. The corresponding reduction in film thickness upon annealing are 11% and 10%, respectively. Comparison of FT-IR spectra before and after annealing for these samples clearly revealed a reduction in the CH absorption upon annealing. The reduction in carbon content was confirmed quantitatively by XPS analysis. Lowest dielectric constants are achieved by introduction of porosity in the films through the removal of organic fragments upon annealing. Finally, no further improvement was observed by using pulsed plasmas.

References

[1] K. Maex, M.R. Baklanov, D. Shamiryan, F. Iacopi, S.H. Brongersma and Z.S. Yanovitskaya - Journal of Applied Physics 93, 11 (2003).
[2] International Technology Roadmap for Semiconductors (2003).
[3] D.D. Burkey, K.K. Gleason – Journal of Vacuum Science and Technology A 22, 1 (2004).
[4] A. Grill, V. Patel – Applied Physics Letters 79, 6 (2001).
[5] S.K. Kwak, K.H. Jeong, S.W. Rhee - Journal of the Electrochemical Society 151, 2 (2004).

PLASMA-DEPOSITED NANOPATTERNED AND NANOCOMPOSITE COATINGS FOR BIOMEDICAL APPLICATIONS

E. Sardella[1], R.Gristina[2], D. Gilliland[3], G. Ceccone[3],
G.S. Senesi[2], F. Rossi[3], R. d'Agostino[1,3], P.Favia[1,3],

[1]*Department of Chemistry, University of Bari, Italy*
[2]*Institute for inorganic methodologies and plasmas (IMIP); CNR, Bari, Italy*
[3]*Joint Research Center, European Commission, Institute for Health and Consumer Protection, Ispra (Va), Italy*

Abstract

Surfaces containing nanofeatures have become recently of paramount importance in many areas of the modern Material Science, for very diverse applications. Recent advances in biomedical materials and biomaterials engineering, for example, have shown the possibility to use random and geometrically micro- and nano-patterned surfaces as effective tools to address specific interactions between cells (and/or proteins) and materials to be applied in fundamental and applied studies on cell physiology, cell engineering, tissue engineering, micro-fluidic systems, bioreactors, bioMicroElectroMechanical Systems (bio-MEMS), and sensors.

This contribution will provide an overview of various methodologies to modify surfaces at micro- and nano-metric scale in which RF (13.56MHz) Glow Discharges are involved. In particular, the attention will be focused on two aspects of this matter, which are under scrutiny in our laboratory for different projects, namely: nanopatterning procedures and synthesis of nanocomposite coatings.

Different lithographic methods, including colloidal lithography and soft lithography in genera[1,2] and the deposition of nano-patterned polymers [3,4] make use of non-equilibrium, low temperature plasma processes (deposition of thin films, grafting of chemical groups, etching) in several approaches, with the aim of producing nano-patterned surfaces on large areas. This is possible because of the many advantages ("cold" processes, no change of bulk properties) and of the cost effectiveness of plasma processes. In lithography plasma processes can be involved either in the patterning procedure, to obtain differently shaped nanofeatures [5], either, in a final step, to custom-tailor the chemical composition of the patterned surfaces [6]. Another approach, that uses "physical masks", allows to produce geometrical micro-domains with different chemical composition and properties at the same surface [7,8]. With all these approaches it is possible to disentangle the effects of surface chemical composition and surface topography/morphology on cell-material adhesion and interactions.

Plasma chemistry could be also involved in producing nano-composite films; in these cases the nanofeatures are represented by metal nanoclusters embedded in an organic matrix. Such nano-composite coatings could be used for controlled drug-release systems in which, for example, a controlled delivery of antibiotics or antimicrobial agents could exert a tight control on adhesion and growth of bacteria at the surface of materials of biomedical interest. For its broad antimicrobial activity [9], silver and related compounds, as well as other antimicrobial agents, are often directly applied at the surface of biomedical devices. It has been shown that silver-based coatings exert a remarkable toxic effect against a wide range of bacteria including, among others, *Escerichia Coli* and *Psaeudomona Aeruginosa* [10]. Silver-containing coatings are widely used, nowadays, as a antimicrobial barrier layers for partial and full-thickness healing of wounds, such as leg ulcers, as well as for coating catheters. Nevertheless, especially for long periods of contact with physiological fluids, like blood, a non controlled release of silver from the device could promote pathologies. Plasma-deposited nano-composite films with silver clusters embedded, therefore, could be preferred because by carefully tuning the structure of the coating (density/dimensions of the clusters; composition/crosslinking of the matrix) it is possible to control the quantity of silver released as a function of time. A combined procedure, where the plasma deposition of an organic

coating occurs while a sputtering process takes place from a metal target will be discussed in this contribution as a method to embed metal clusters into the organic matrix, resulting in nano-composite films with interesting tailored physical and chemical properties [11,12]. Results about the release of silver during the time and about the antibacterial effect of plasma deposited nano-composite films will be discussed.

Acknowlegdements
This research has been developed in the framework of the MIUR-FIRB RBNE01458S_006 and "NANOMED" QLKE-CT-2000 projects, whose financial contribution is gratefully acknowledged.

References

[1] M.Geissler, Y. Xia; Advanced Materials; 16, 1249 (2004)
[2] P. Hanarp, D. Sutherland, J. Gold, B. Kasemo, Journal of Colloidal and Interface Science, 241, 26 (2001)
[3] P.Favia, Plasma depositino of fluoropolymer films in different glow discharge regimes in: Plasma Polymer Films, H. Biederman Ed. Imperial College Press, London UK (2004)
[4] A. Milella, F. Palumbo, P. Favia, G. Cicala, R. d'Agostino; Plasma Processes and Polymers, 1, 87-90, 2004
[5] M.J. Dalby, M. O. Riehle, D. S. Sutherlandb, H. Agheli, A. S.G. Curtis. Biomaterials 25, 5415 (2004)
[6] L. Detomaso, R.Gristina, G.S. Senesi, L.C. Lopez, P.Favia, R.d'Agostino in : Plasma Processes and Polymers Wiley-VCH; R. d'Agostino, P. Favia, M.R. Wertheimer, C. Oehr eds. VCH-Wiley (2005), in press
[7] A. Valsesia, P. Colpo, M. M. Silvan, T. Meziani, G. Ceccone, F. Rossi, Nanoletters. 4,6, 1047 (2004)
[8] E. Sardella, R. Gristina, G.S. Senesi, R. d'Agostino, P. Favia; Plasma Processes and Polymers, 1, 63-72, 2004
[9] H. Liedberg, T. Lundeberg, Urol. Res. 17, 357 (1989)
[10] S.S. Block in: Disinfection, Sterilization and Preservation, 3rd edition, Philadelphia, PA: Lea &Febiger, 375 (1983)
[11] P. Favia, M. Vulpio, R. Marino, R. d'Agostino, R. Pinto Mota, M. Catalano, Plasmas and Polymers 5, 1 (2000)
[12] H. Biederman, Y. Osada in: Plasma technology 3, Plasma Polymerisation Processes. Elsevier Science Publishers, 5, 127 (1992)

Destruction of ethylene by pulsed dielectric barrier discharge in dry and wet air – parametrical study

O. Motret, O. Aubry, C. Thuillier, M. Lascaud, C. Met and J-M. Cormier

GREMI - Polytech'Orléans, 14 rue d'Issoudun, B.P. 6744, 45067 Orléans cedex 2, France
olivier.motret@univ-orleans.fr

Abstract
We realized a parametrical study concerning the conversion of ethylene by atmospheric cold plasma. The electric parameters such as the frequency, the high voltage applied to the reactor and the value of capacitors of the pulsed generator were studied. The influence of the water vapour on the rate of conversion was also studied.

Keywords: Non thermal plasma, VOCs, DBD

1. Introduction

Among the emergent techniques envisaged to treat the polluting and harmful emissions of the human activities, cold atmospheric plasmas took a considerable development these last ten years. Energy speed deposition and voltage rise time are fundamental parameters of a dielectric barrier discharge reactor.
At constant energy rate, weak variations of these parameters could modify the conversion efficiency and also by-products. In numerous applications the pulsed generators showed their superiority compared to AC conventional generators. Strong energetic electrons and chemical active species can be easily produced using a pulsed generator. Active species such as hydroxyl radicals ($^{\bullet}OH$) and [1,2] oxygen atoms initiate the chemical processes of the pollutant conversion. The efficiency of the conversion process depends too strongly on electric parameters of the pulsed generator. The parametric study presented here allows defining adjustments of electric parameters leading to an optimal efficiency of conversion.

2. Experimental set-up

The gas mixture used in this study was composed of dry or water saturated air with 460 ppm of ethylene at ambient temperature, see figure 1. The gas mixture flow at atmospheric pressure was regulated at 830 $cm^3.mn^{-1}$ by mass-flow controllers. Chemical analyses were made by a Fourier Transform Infra-Red spectrometer (FTIR) equipped with a 10 m absorbing chamber heated at 110°C. The reactor cell has a tubular shape with a 12 mm inner diameter and a 16 cm^3 active volume. The dielectric wall is made of a quartz tube (thickness : 1 mm). The inner electrode is a 2 mm diameter tungsten centred on the tube axis, an aluminium outer electrode covers the dielectric layer.

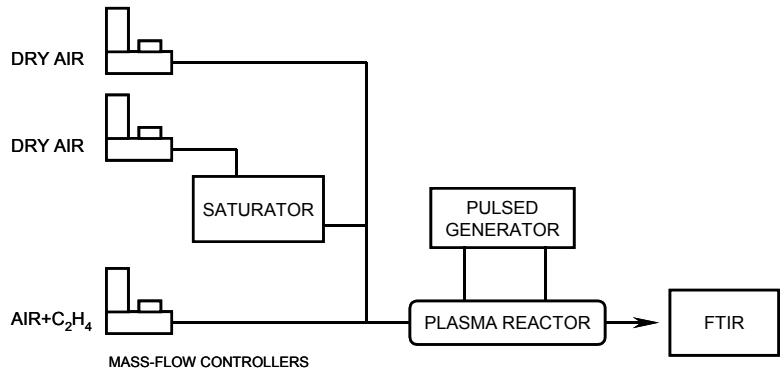

Figure 1: Experimental arrangement.

The reactor was powered by a triggered pulsed high voltage generator (working frequency: from 1 to 300 Hz, applied voltage: from 4 to 30 kV). This generator [3] is able to produce short voltage pulses (FWHM = 30 ns) with very steep front voltages $dV/dt > 10^{12}$ $V.s^{-1}$. Figures 2a and 2b show time evolutions of voltage and current respectively.

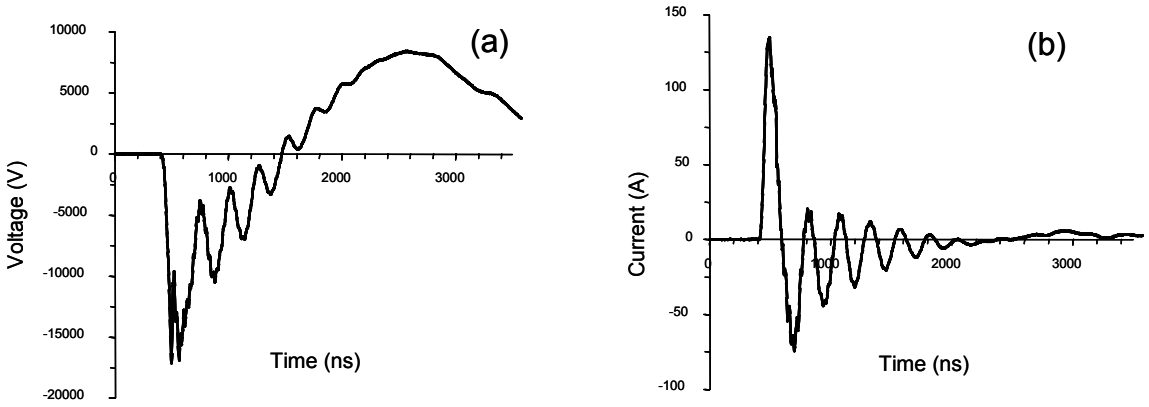

Figure 2: (a) Breakdown voltage, (b) current, at the reactor cell for 10 kV applied voltage.

3. Experimental results

Electrical parameters were adjusted in the following range : frequency from 1 to 10 Hz, high voltage from 10 to 14 kV and capacitors 2, 4 or 6 nF. These values correspond to an energy domain of injected energy from 20 to 150 $J.l^{-1}$. The flow-rate of the gas mixture was maintained at a fixed value of 830 $cm^3.mn^{-1}$ and the frequency was varied, in order to modify the pulse number that the gas undergoes during the reactor cell crossing.

3.1. Dry gas mixtures

Frequency effect

For dry gas mixtures, the increase of the frequency shows a linear increase of the conversion rate for all the tested combinations (capacitor/high voltage), figure 3 illustrates this behaviour. It suggests that in our experimental conditions, the increase of the frequency corresponds to an increase of the number of sites of destruction of the ethylene without appearance of saturation phenomenon.

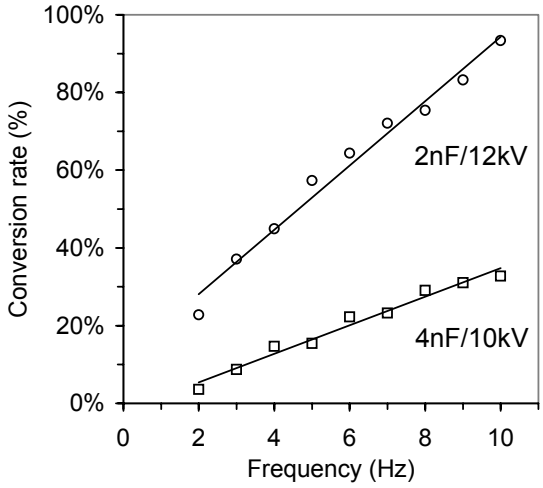

Figure 3: Frequency effect for two sets of parameters (2nF/12kV and 4nF/10kV).

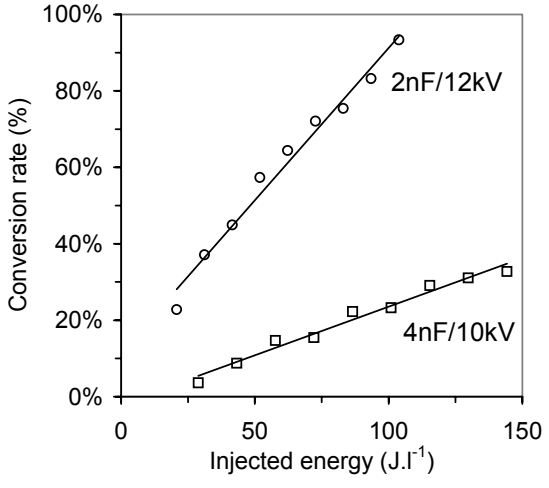

Figure 4: Frequency effect in term of injected energy for two sets of parameters (2nF/12kV and 4nF/10kV).

In term of energy consumption, it is more interesting to consider the injected energy than the frequency, see figure 4. We note that for the same consumption, we obtain widely different rates of conversion according to the choice of electrical parameters. For our experimental conditions, in particular for our geometry of reactor

(inter-electrode gap, inner electrode diameter, nature and thickness of the dielectric), it seems preferable to work on the weakest values of capacitor and on the strongest applied voltage.

Applied voltage effect

Figure 3 shows the effect of capacitors according to the applied voltage at a fixed frequency. It appears a phenomenon of saturation which occurs when almost totality of ethylene molecules are destroyed in the neighbourhood of streamers, see figure 5. As previously it is not necessary to work with too strong values of capacitor, as we can see it on the figure 6.

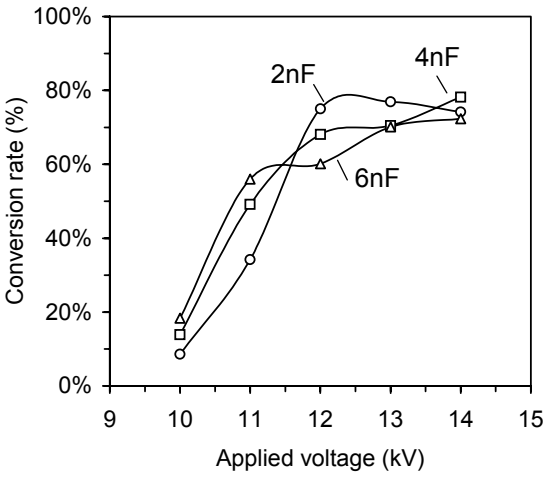

Figure 5: Applied voltage effect for N = 5 Hz and for various capacitors.

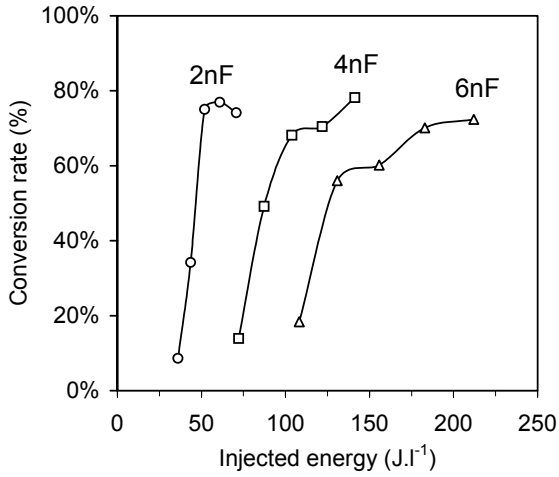

Figure 6: Applied voltage effect in term of injected energy for N = 5 Hz and for various capacitors.

The representation in term of energy cost informs us about the selectivity of the process, as we can observe it on the figure 7. It seems that it's better to work with the combination 2nF / 12 kV to minimize the energy cost.

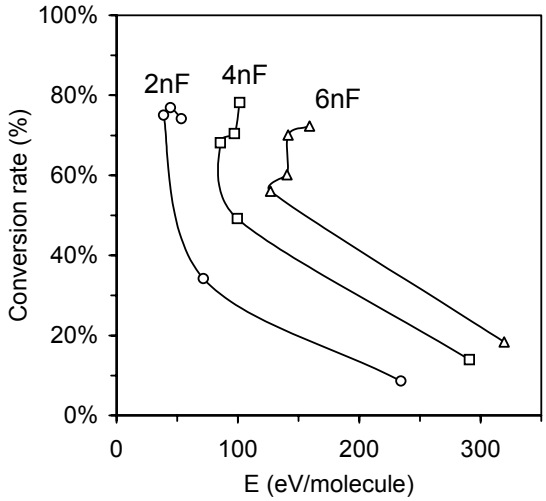

Figure 7: Applied voltage effect in term of energy cost for N = 5 Hz and for various capacitors.

3.2. Humid gas mixtures

Similar parametrical study on water vapour saturated mixtures at ambient temperature was performed, see figures 8 and 9. On the other hand the rate of conversion remains widely lower in the majority of the cases, this divergence which can reach 40 % at most. On the figure 10 we can compare, for the same discharge conditions, the conversion rate in dry and humid mixtures.

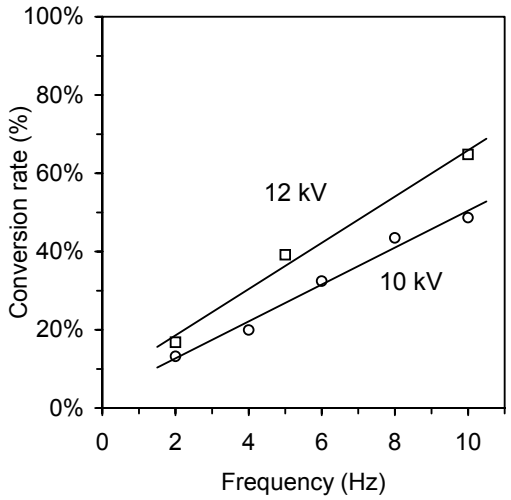

Figure 8: Frequency effect for two sets of parameters (○ 4nF/10kV, □ 4nF/12kV).

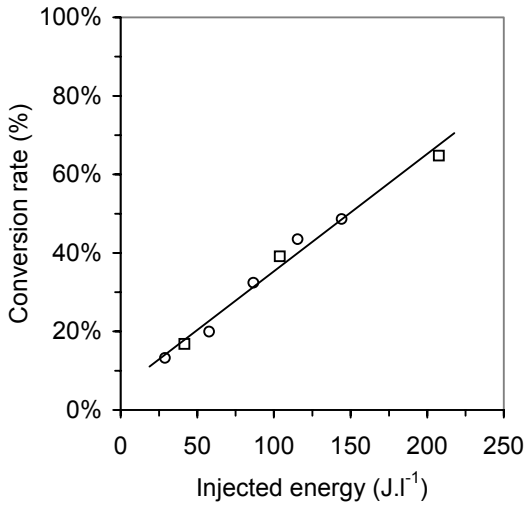

Figure 9: Frequency effect in term of injected energy for two sets of parameters (○ 4nF/10kV, □ 4nF/12kV).

Only for the lower value of applied voltage (10 kV), this tendency was inverted. This behaviour was confirmed by a frequency study at 10 kV, see figure 11.

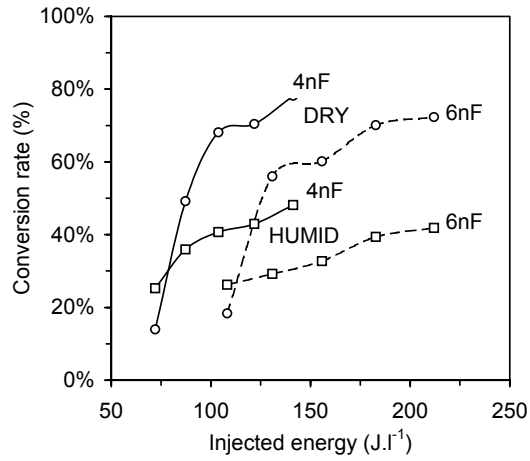

Figure 10: Comparison between dry and humid mixtures versus applied voltage in term of injected energy (○ dry mixtures, □ humid mixtures, continuous line 4nF/5Hz, dashed line 6nF/5Hz).

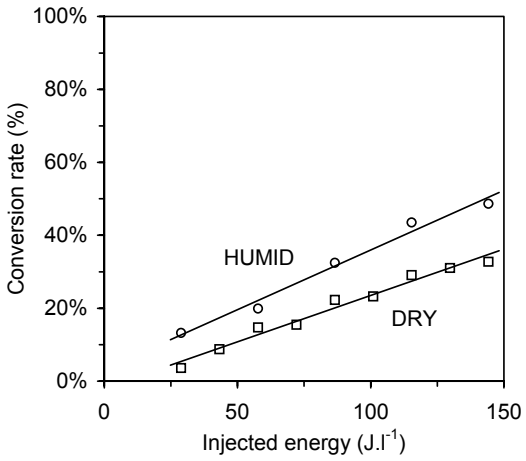

Figure 11: Frequency study at 4nF/10 kV, in dry and humid mixtures.

This behaviour could be explained by a consumption of oxygen atoms, responsible for the first step of ethylene molecules destruction, by hydroxyl radicals produced by the decomposition of water molecules. For low applied voltages, the water dissociation stays at a moderate level and affects slowly ethylene conversion.

4. Conclusion

A constant specific energy supplying can be easily obtained by adjustment of peak voltage value, frequency or capacitors but do not produce a constant effect. Our results show that the specific energy is not the only parameter to determine the conversion rate and products. Rise time of applied voltages is considerably effective on the dynamics of the excitation as well as the radical's initiators production. According to the choice of electric parameters, strong variations of the conversion rate can be observed.

Using the following combination of electric parameters: 2nF/12 kV, good results are obtained with our experimental device. In the future, correlations could be achieved with a 0D model in order to explain the specific behaviour of humid mixtures.

Acknowledgments
The authors gratefully acknowledge the financial support of the *"Action Concertée NPD29 – non-pollution, dépollution, deCOV plasma (CNRS)"*.

References
[1] A. Khacef, J.M.Cormier, J.M.Pouvelle, Proc. ISPC 16, 2003.
[2] O Martinie, J.M.Cormier, A.Khacef, Proc. ISPC 16, 2003.
[3] A Khacef, J. M Cormier, J. M Pouvesle, J. PHYS D : APPL. PHYS, 35,1491 (2004).

Model of a Dielectric Barrier Discharge in a cylindrical reactor and experimental validation

R. Valdivia-Barrientos[1], J. Pacheco-Sotelo[1,2], M. Pacheco-Pacheco[2],
J S. Benitez-Read[1,2]A. Cruz-Azocar[2]
[1] *Instituto Tecnológico de Toluca, México*
[2] *Instituto Nacional de Investigaciones Nucleares, México*

Abstract
A Dielectric Barrier Discharge (DBD) model is here proposed based on theoretical analysis and experimental signals obtained at different ionization frequencies and captured from a cylindrical reactor with Helium gas flow. The physical dimensions and configuration of the reactor are also considered in this model. All the signals occurring inside the reactor are measured and the power consumption of the micro discharge is evaluated as a function of the operating frequency.
Keywords: Dielectric Barrier Discharge, resonant converter, DBD Model, ionization frequency

1. Introduction

Dielectric Barrier Discharges (DBD) occurs generally in a filamentary form because they are created as a number of individual breakdown channels (microdischarges) with short period of time The approach the accumulation of charges on the dielectric barrier to reduce the electrical field in the gap and finally to quench the discharge. This kind of discharges has several applications such as materials surface treatment, toxic gases decontamination, and lighting, among others. DBD prevents large current intensities because of the use of glass as a dielectric, quenching the current and distributing the discharge over the whole surface [1-3]. In this work a cylindrical DBD reactor is used. It is composed of a Pyrex glass tube of 24.6mm of external radius $d+x$, 1.2mm of thickness x and 175mm of length is used as reactor; outside the glass tube, a grounded mesh electrode is wrapped covering 82.2mm length l. A stainless steel central electrode of 2.54mm of radius r_0 is used to establish a radial discharge homogenously distributed along the reactor. Due to its physical characteristics and the material employed, the electrical behavior is associated by two capacitors connected in series, one of them, C_g, has dielectric permittivity of air (Helium in this case) and the other, C_d , has the dielectric permittivity of glass (Pyrex) [4, 5]. The microdischarges occur in the region limited by the central electrode and the dielectric barrier, this region is denominated gap and its radial distance is 20.86mm. Considering these conditions the model was designed and employed to estimate the microdischarges power in function of the ionization frequency.

2. Description

The configuration and equivalent electrical model of the DBD reactor above mentioned are presented in figure 1. Being C_d the equivalent capacitance of the dielectric barrier and C_g the equivalent capacitance of the gap where the microdischarges occur. The voltage $v_a(t)$ is applied to the reactor and was supplied by a voltage source with variable operating frequency (from 10kHz to 100kHz) produced by a series-parallel resonant converter, specially designed for this purpose [6].

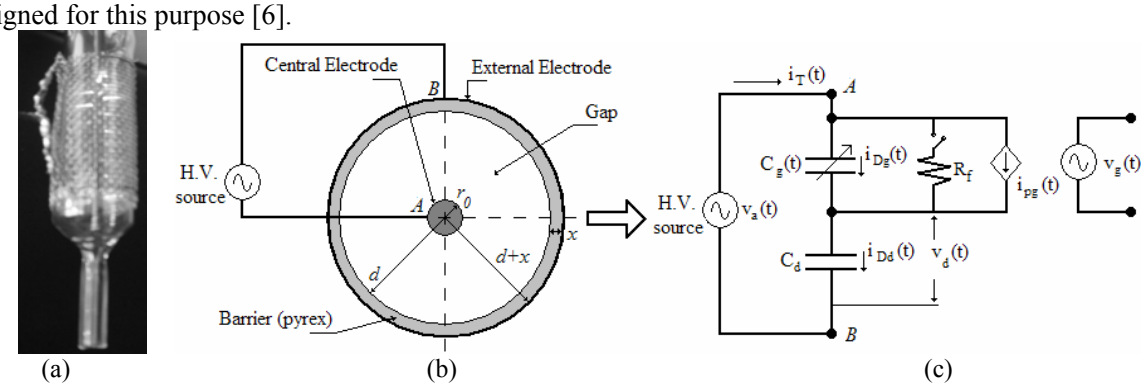

(a) (b) (c)

Figure 1. (a) DBD reactor, (b) transversal section of DBD reactor, and (c) electrical model of a DBD reactor.

The cylindrical geometry allows a homogeneous distribution of the discharge along the whole reactor, avoiding undesirable effects in edges and corners. A second advantage of this geometry consists in the possibility of mixing the effect corona with DBD discharge obtaining remarkable electrical field strength in the gap. When a tension of 1.2kV is applied, the electrical field distribution depicted in figure 2 is obtained, according to the next equation [7]:

$$E(r) = \frac{v_a}{r \ln\left(\frac{d}{r_0}\right)} \tag{1}$$

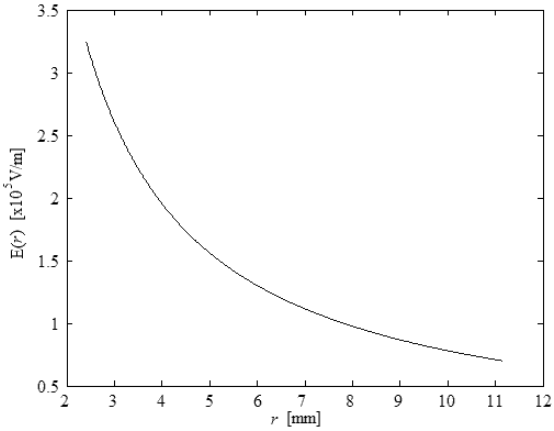

Figure 2. Distribution of the electrical field E(*r*) along the gap.

The equivalent capacitances of the cylindrical reactor are:

Table 1. Equivalent capacitances of the reactor.

Gap equivalent capacitance C_g	Dielectric equivalent capacitance C_d
$C_g = \frac{2\pi\varepsilon_0\varepsilon_{r_1} l}{\ln\left(\frac{d}{r_0}\right)}$ (2)	$C_d = \frac{2\pi\varepsilon_0\varepsilon_{r_2} l}{\ln\left(\frac{d+x}{d}\right)}$ (3)

where ε_0 is the permittivity of vacuum, ε_{r_1} is the relative permittivity of Helium (1.000065) [8], and ε_{r_2} is the relative permittivity (4.5) of the Pyrex glass. By substituting these values in equations (2) and (3), the obtained equivalent capacitances in off state (without discharge) are 3.1pF and 200.37pF respectively. The total capacitance of the whole reactor is:

$$C_T = \frac{C_d C_g}{C_d + C_g} \approx C_g \tag{4}$$

Being $C_g << C_d$ the total capacitance C_T is strongly dependent of the gas capacitance C_g which cannot be considered to have a constant value, because the ionization degree is different when the microdischarge are occurring and when there are not. That's why, it's better to decompose this gap capacitance into two different values.

The analysis aimed to diagnose the internal parameters begins with the Kirchhoff's theorem obtained from figure 1(c):

$$\frac{dv_d(t)}{dt} = \frac{1}{C_d} i_T(t) = \frac{1}{C_d} i_{Dd}(t) \tag{5}$$

$$\frac{dv_g(t)}{dt} = \frac{i_{Dg}(t)}{C_g} = \frac{1}{C_g}\left[i_T(t) - i_{pg}(t)\right] \tag{6}$$

$$v_a(t) = v_d(t) + v_g(t) \tag{7}$$

By differentiating equation (7) with respect to time and substituting equations (5) and (6) into equation (7), the following equation is obtained:

$$\frac{dv_a(t)}{dt} = \frac{i_T(t)}{C_d} + \frac{1}{C_g}\left[i_T(t) - i_{pg}(t)\right] \tag{8}$$

Rearranging equation (8), the expression to diagnostic the current of the discharge is

$$i_{pg}(t) = \left(1 + \frac{C_g}{C_d}\right) i_T(t) - C_g \frac{dv_a(t)}{dt} \tag{9}$$

Finally, by integrating equation (5) respect to time, the voltage of the dielectric equivalent capacitance C_d is determined by

$$v_d(t) = \frac{1}{C_d}\int_0^t i_T(\tau)d\tau + V_d(0) \tag{10}$$

From equation (7) and by substituting equation (10) the voltage of the gap equivalent capacitance C_g is:

$$v_g(t) = v_a(t) - \frac{1}{C_d}\int_0^t i_T(\tau)d\tau - V_d(0) \tag{11}$$

With equation (9) and (11) it is possible to determinate internal parameters from external ones. This is the fundamental part for the model developing here proposed.

Respect to the breakdown condition, when $v_a(t)$ reaches the breakdown voltage (V_{bd}) amplitude, the occurrence of microdischarges begins, and their magnitude is added to the displacement current intensity. This magnitude is decreasing by an effect caused by $dv_a(t)/dt$ modulation. The microdischarges occurrence ends when $v_a(t)$ is maximum ($dv_a(t)/dt=0$). Figure 3 shows the waveforms of the total current ($i_T(t)$) and the applied voltage $v_a(t)$ for the DBD generation.

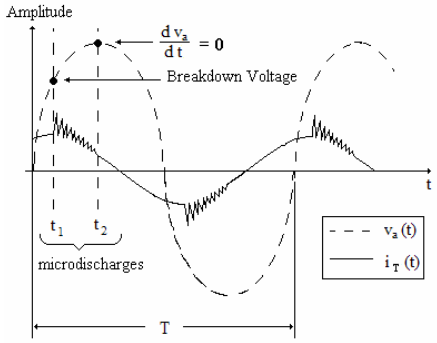

Figure 3. Wave forms of the applied voltage and the total current of a DBD.

The resultant model is depicted in figure 4 by using Simulink blocks of Matlab ® software. The two values assumed by Cg are implemented by two capacitors in a parallel connection, Cg1 and Cg2. At the time t_1, (refereed to Fig. 3) Cg2 is disconnected and only Cg1 participates in the microdischarges. Its equivalent value corresponds to the value of about $0.7C_g$ (in off state) according with electronic densities (10^{13} cm-3) obtained from references [3, 5], with the value of the ionization frequency and the constants established. Consequently, Cg2 needs to be $0.3C_g$, to give a C_g value when both capacitance (Cg1 and Cg2) are connected in parallel. When the microdischarges cease, the capacitor Cg2 is reconnected in parallel and C_g returns to its off state value at t_2. This sequence is repeated for each semi period. Simultaneously to this, a resistance Rf is also connected as

indicated in figure 4(a), to simulate the equivalent impedance of the filamentary microdischarge. A controlled current source (CCS) is connected, to provide the microdischarges impulsions flowing through C_g and the signal designated to control it consists of a high-frequency sinusoidal source (with period of nanoseconds order) which is modulated by the corresponding value $dv_a(t)/dt$.

Inside of MCB subsystem (Fig 4b), the Pulse1 and Pulse2 blocks switch ON and OFF the elements Cg2 and Rf respectively, which are designated to modify the C_g value during the microdischarges. They have a high logic state (1) when the conditions of breakdown are valid (from t_1 to t_2), and a low logic state (0) in the rest of the semi period. At the same time, these pulses are also used to allow or deny the microdischarges flow by controlling the controlled current source block (CCS).

A resistor called Rw is included to simulate the resistance of the wires from the voltage source to the reactor and because of the good performance during the simulation calculations. The model designed and the corresponding subsystem that controls the current source are shown in the figure 4.

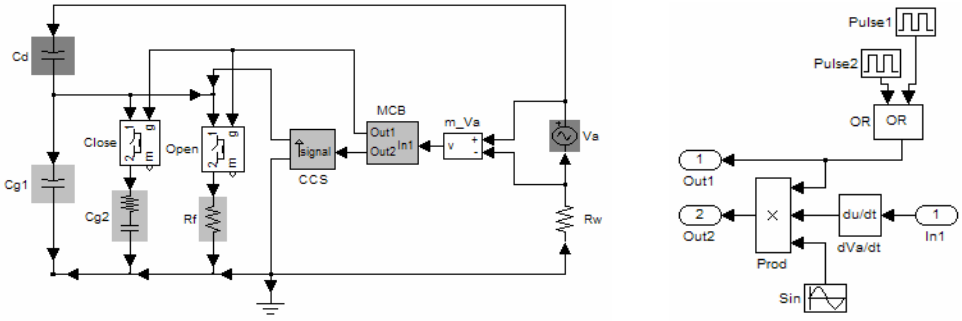

(a) (b)

Figure 4. (a) Simulation model, (b) subsystem of the microdischarges conditions (MCB block).

The model can work with any value of frequency and amplitude in the Va block which represents the high voltage source applied to the reactor. All the measurement blocks are not exhibited in Figure 4 for best appreciation of the DBD model.

3. Results

The Helium gas flow (1LPM) passing through the reactor was ionized at different operating frequencies (19kHz, 46kHz and 66kHz). The external parameters ($v_a(t)$ and $i_T(t)$) which were captured with a digital scope Tektronix® Model THS710A are presented in figure 6 for all these frequencies. The displacement current is 90° dephased respect to the applied voltage. The microdischarges are present when the applied voltage reaches the breakdown voltage value. It is clear that the microdischarges magnitude is diminished conforms the applied voltage reaches the maximum level. With respect to the displacement current intensity, the experimental results obtained shows that its magnitude increases with frequency.

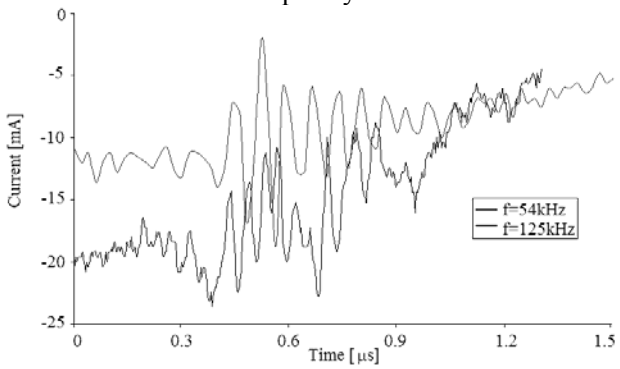

Figure 5. Zoom of microdischarges

It was also observed by zooming at the microdischarges registered at 54kHz and 125 kHz in figure 5, that the microdischarge signal has almost the same period independent of the ionization frequency.

Simulation test where realized at different frequencies (19kHz, 46kHz and 66kHz). These results are shown in figure 7.

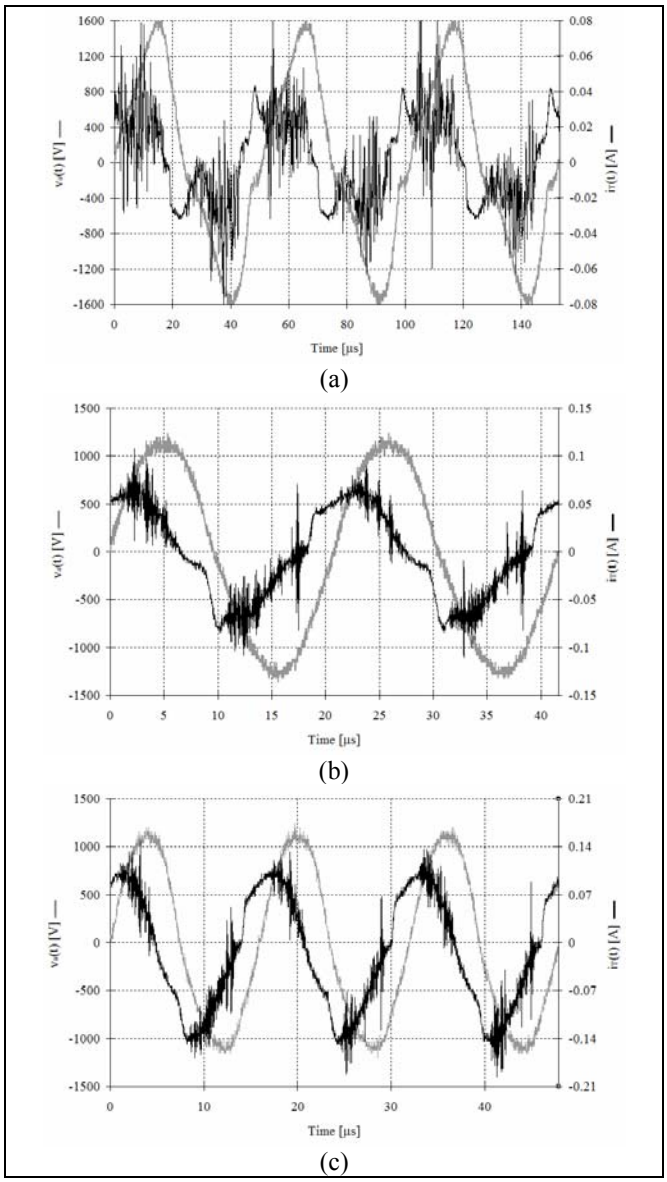

Figure 6. Experimental $v_a(t)$ and $i_T(t)$ at: (a) 19kHz, (b) 46kHz, and (c) 66kHz.

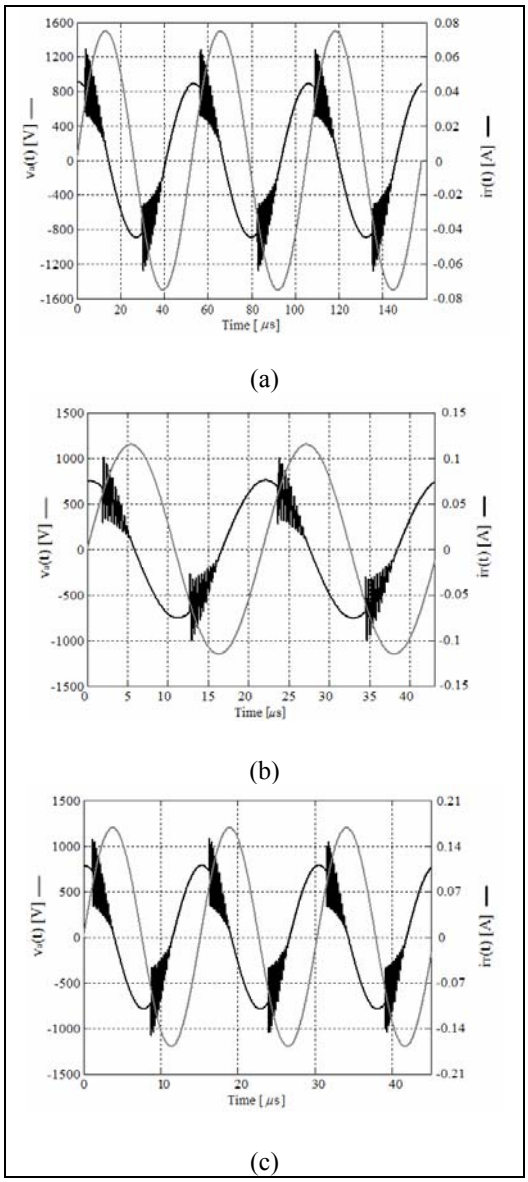

Figure 7. Theoretical $v_a(t)$ and $i_T(t)$ at: (a) 19kHz, (b) 46kHz, and (c) 66kHz.

The comparison of experimental signals in figure 5 with theoretical ones in figure 6 shows that the amplitude values of current, consequence of the applied voltage, are of the same order. The distortion that exists in the experimental signals of current is not presented in the theoretical model because the simulation model contains ideal components. This is the reason of clean signals. Due the correspondence in the magnitude and basic behavior of both signals (experimental and theoretical), the model can be applied to study different parameters such as the power of the discharge generated respect to the ionization frequency. By running the model and

sweeping the frequency from hundreds of hertz to hundreds of kilohertz, and maintaining the amplitude in the applied voltage, the RMS applied power to the reactor had the following behavior.

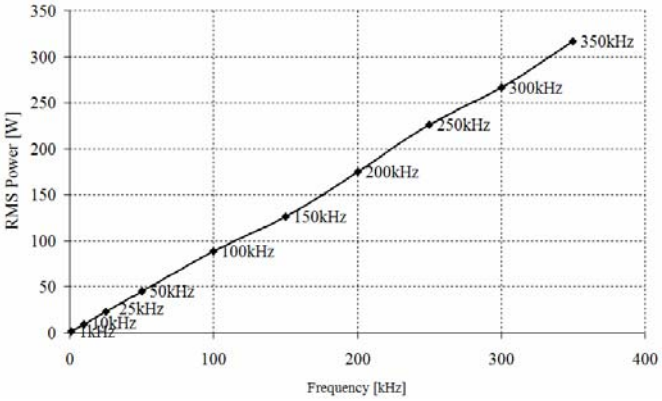

Figure 8. Variation of RMS power respect to ionization frequency ($v_a(t)$=1.25kV)

This figure obeys to well known equation of Manley [10] used for calculate the power consumed by dielectric discharges. The formula establishes that power depends directly on ionization frequency

4. Conclusion

According to the experimental results, the electrical simulation model of a DBD was developed and validated. After validation, the model was examined to acquire knowledge of the effect that the ionization frequency produces directly on the discharge. It is clear that by increasing the frequency, the power will also increase. It means that if the reactor is operated at low frequency, then it is necessary more amplitude of the applied voltage to produce the same intensity of the discharges than at high frequency. This result gives the option to construct high voltage sources with high operating frequency in order to feed DBD reactors with the purpose of generating discharges with greater intensity and small electrical devices. On the other hand, the model can be useful to determine the best conditions of the reactor by modifying its physical dimensions and composing materials.

6. References

[1] G. Nersisyan and W. G. Graham. Characterization of a dielectric barrier discharge operating in an open reactor with flowing helium. *Plasma Sources Science and Technology*. No. 13. pp 582-587.(2004).

[2] I. Radu, R. Bartnikas, and M. R. Wertheimer. Frequency and Voltage Dependence of Glow and Pseudoglow Discharges in Helium under atmospheric pressure. *IEEE Trans. Plasma Sci.*, Vol.**31**, No. 6. pp 1363-1378. (2003).

[3] Y. Kim, W. S. Kang, J. M. Park, S. H. Hong, Y. H. Song, and S. J. Kim. Experimental and numerical analysis of streamers in pulsed corona and Dielectric Barrier Discharges. *IEEE IEEE Trans. Plasma Sci.*, Vol. **32**, No. 1. pp 18-24. (2004).

[4] Shuhai Liu, Manfred Neiger. Electrical modeling of homogeneous dielectric barrier discharge under an arbitrary excitation voltage. *J. Phys. D: Appl. Phys.*, Vol. **36**. pp 3144-3150. (2003).

[5] U. Kogelschatz. Dielectric-barrier Discharges: Their History, Discharge Physics, and Industrial Applications. *Plasma Chemistry and Plasma Processing*. Vol. **23**, No. 1. (March 2003).

[6] J. Pacheco-Sotelo, R. Valdivia, M. Pacheco-Pacheco, F. Ramos, M. Durán, J. Benitez-Read, R. Peña-Eguiluz, and R. López-Callejas. A Universal resonant converter for equilibrium and non-equilibrium plasma discharges. *IEEE Trans. Plasma Sci.*, Vol. **32**, No. 5. pp 2105-2112. (2004).

[7] J. R. Roth, Industrial Plasma Engineering. Bristol, UK: IOP. Vol. **1**, Principles. Sec. 12.5.2. (1995).

[8] R. Lide David. Handbook of Chemistry and Physics. 82nd Edition. CRC Press LLC. (2001).

[9] Y. P. Raizer, Gas Discharge Physics. Springer. Sec. 3.4. (1997).

[10] T. C. Manley, Trans. Electrochem. Soc. **84**, 83 (1943).

Formation of soot particles in Ar/H2/CH4 microwave discharges during nanocrystalline diamond deposition : a modelling approach

F. Mohasseb, K. Hassouni, F. Bénédic, G. Lombardi, A. Gicquel
LIMHP, Université Paris Nord – CNRS UPR 1311 – 99 Avenue J.B. Clément – 93430 Villetaneuse (France)
E-mail:hassouni@limhp.univ-paris13.fr

This work deals with the modeling of $Ar/H_2/CH_4$ discharges ignited in microwave cavity systems and used for nanocrystalline diamond film deposition. These discharges are characterized by a strong thermal and chemical non-equilibrium, and the gas mixture is typically composed of an argon amount greater than 90% and a CH_4 concentration of around 1 %. As far as chemistry is concerned, the plasmas obtained exhibit H/C ratio ranging between 8 and 18 so as heavy hydrocarbons and soot particles may form in some discharge conditions. Soot formation also depends on pressure and input power values. Thus, in order to investigate the plasma chemistry various thermochemical models were developed and used under quasi-homogeneous plasma assumption.

To probe the soot particle sources a numerical model, previously developed for conditions where the formation of heavy hydrocarbons and soot particles may be neglected [1], was extended to take into account Poly-Aromatic Hydrocarbons (PAHs) growth, following several mechanisms. The first one took into account large neutral PAHs up to 4 aromatic rings (A4 model) from which the particle nucleation was assumed to take place. This study was performed in such a way to investigate the whole temperature domain that characterize both the plasma bulk, the plasma-substrate boundary layer and the regions outside the discharge (plasma edges and post-discharge regions). This was achieved by exploring a large domain of input microwave power which includes conditions that do not correspond to those used for NCD deposition. The variation of the gas temperature with the input microwave power at a pressure of 200 mbar is shown in figure 1. The gas temperature varies between 1000 K and 4000 K when the input power is increase from 10 to 600 W. The A4 model indicate that soot formation with a nucleation rate as high as 10^8 part./cm^3/h takes place for gas temperature values below 1500 K (figure 2). Such low gas temperature are found in two regions : the boundary layer between the plasma and the substrate surface and the post-discharge region between the discharge-plasma and the reactor walls.

The second mechanism that was considered in this work, take into account the formation of PAH compounds with up to 9 aromatic rings (A9 model). The soot is assumed to nucleate from an A9—A9 complex. The purpose was to investigate how the assumption on the size of the PAH-species that lead to soot nucleation affects the nucleation rate predicted by the model. Results showed that the values found for this rate by the A4 and A9 models are quite similar (see figure 3) and therefore that the A4 model is adequate for studying PAHs formation and soot nucleation in $Ar/H_2/CH_4$ microwave discharges.

The chemical model was then extended to take into account the formation of large hydrocarbon ions. Ions with up to four aromatic rings were considered (A4+ model). Results showed that the growth of PAHs and the nucleation of soot through this ionic mechanism is significant especially at high temperatures (>1500K). Note however that the nucleation rate at temperatures greater than 2000K is two orders of magnitude lower that the values obtained around 1000-1200 K. Note also that although nucleation seems to be possible in the bulk of the plasma at very high temperature (>2500 K) the predicted rate would be very small and almost 5 orders of magnitude smaller than the values obtained at 1000-1200 K.

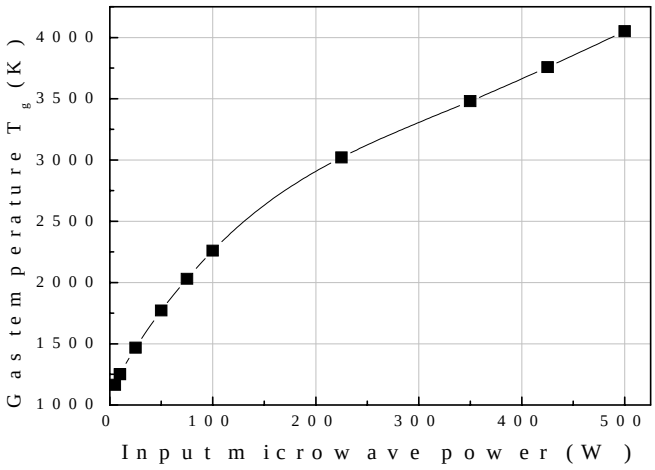

Figure 1 : Variation of gas temperature as a function of the microwave power absorbed by the discharge

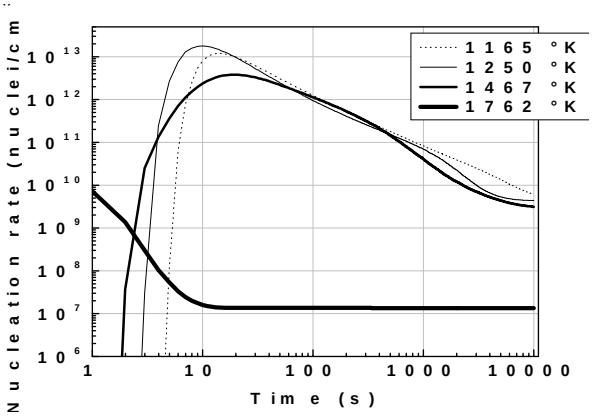

Figure 2 : Time-variation of the soot nucleation rate for different gas temperature values corresponding to several microwave power absorbed in the plasma (see figure 1)

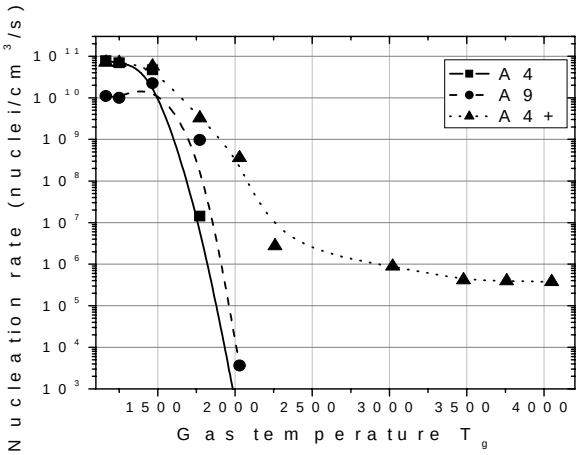

Figure 3 : Variation of the soot nucleation rates predicted from the A9, A4 and A4+ models as function of the gas temperature in plasma

References

[1] G. Lombardi, K. Hassouni, F. Bénédic, F. Mohasseb, J. Röpcke, and A. Gicquel, J. Appl. Phys **96**, 6739-6751 (2004).

Thermal Spray: Past, Present and Future

Richard Knight, Ph.D., FASM*
Department of Materials Science and Engineering, Drexel University,
3141 Chestnut Street, Philadelphia, PA 19104, USA

*2004-2006 President ASM International Thermal Spray Society.

Thermal spray is a family of versatile particulate/droplet consolidation processes which deposit overlay coatings onto surfaces to provide improved wear, corrosion and/or thermal protection to the underlying substrate. This group of 5 or 6 processes is capable of forming metals, ceramics, intermetallics, composites and polymers into coatings or freestanding structures. During processing, powders, wires, rods and/or sol-gel suspensions are introduced into combustion, DC arc, DC or RF plasma heated gas jets, where they are heated, melted or softened, accelerated and directed towards the surface being coated.

This talk will trace the evolution of the technology from the first processes developed almost a century ago to today's current state of the art, together with example applications. Recent process, process-control, materials, and applications will also be presented, together with some "crystal ball" speculations on what lies ahead in the future.

Biography

Dr. Richard Knight, FASM received his Ph.D. in Electronic and Electrical Engineering from Loughborough University in the UK in 1985, having previously completed his M.Sc. in Electroheat and Industrial Process Heating, also at Loughborough University, in 1978. Dr. Knight was a Postdoctoral Fellow at the University of Minnesota, Minneapolis, MN, from 1985 to 1989, prior to joining Drexel University in 1989, and since 1997 he has directed the Center for the Plasma Processing of Materials.

Dr. Knight has over 20 years of experience in the design, development and use of electric arc and thermal plasma systems for materials processing, including electrodes and torches, furnaces/reactors, and DC power supplies. Dr. Knight has more than 15 years experience in the development of parameters and techniques for the thermal spraying of materials, including metals, ceramics, composites, polymers and polymer-ceramic nano-composite coatings. His current research interests include thermal spray technology and education, thermal spraying of polymers, plasma recycling and treatment of waste and plasma synthesis of materials. His research has been funded by NSF, DoE, NASA and a number of industrial sponsors.

Dr. Knight was elected as a Fellow of ASM International in 2003 and is currently President of ASM International's Thermal Spray Society (TSS). He previously chaired the TSS Program and Training Committees and served as Secretary/Treasurer of TSS. He has published over 60 papers related to plasma, arc and thermal spray coating technology, has given ~60 presentations at National and International Conferences, holds 3 Patents and has co-organized several technical sessions at conferences. Dr. Knight serves as proposal reviewer for NSF, DoE, EPA and CRDF, and is a member of the editorial boards of the *Journal of Thermal Spray Technology* and *Plasma Chemistry and Plasma Processing*.

Production of reactive species by atmospheric-pressure streamers in N_2-O_2 mixtures

M.Šimek, M.Člupek, V.Babický, and P.Šunka

Department of Pulse Plasma Systems, Institute of Plasma Physics, Academy of Sciences of the Czech Republic, Za Slovankou 3, 18221 Prague, Czech Republic

A filamentary streamer is a rather frequent form of a high-pressure transient discharge usually occurring between metallic electrodes in high-voltage pulse systems. It may also develop between electrodes fully or partially covered with a dielectric barrier or on the interface between gaseous and liquid phases. Streamer discharges in atmospheric gases are currently receiving increasing attention in connection with environmental issues (*e.g.*, air pollution control, atmospheric chemistry, ozone synthesis) or material treatment technologies (*e.g.*, surface modification). The main reasons for the current interest in these topics are the low efficiency of conventional pollution control technologies, such as carbon adsorption and catalytic/thermal oxidation, and the incompatibility of vacuum-based low-pressure plasma treatment techniques, such as surface modification of polymers or surface hardening of ferrous metals, with industrial process lines. A non-equilibrium low-temperature high-pressure plasma produced by filamentary streamers is an interesting option to tackle the above-mentioned challenges in an economical way.

The reactivity of "streamer plasma" is a critical parameter for most application areas. Depending on electrode configuration, electrical power supply and gas composition, streamer discharges can produce a variety of transient species (e.g., vibrationally and electronically excited molecules, atomic species, molecular positive and negative ions), as well as many post discharge products (e.g. nitrogen oxides or ozone). The most important issue for applied plasma technology research today is the necessity to optimize efficiency and to scale-up laboratory plasma reactors so as to achieve maximum performance at minimal cost. To this end, advanced physical and chemical modeling of streamer discharges are often necessary so as to predict the performance of a streamer discharge for a selected application. As the physics of streamers has not been completely understood to date, numerical codes currently-used are based, because of the lack of knowledge, on many assumptions and estimates. Therefore any new or improved experimental measurements of streamer properties might always be of fundamental importance.

The diagnostics that have been used up to now (*e.g.*, cloud chamber tracks, streak pictures, fast photography, Schlieren photography, emission spectroscopy and electrical measurements) provided useful information on some streamer fundamentals (*e.g.*, avalanche-streamer formation, streamer propagation and branching, gas and electron temperatures). Detailed information on many other important physical and chemical processes "responsible" for streamer properties (*e.g.*, photo-ionization and recombination processes, diffusion processes, vibrational relaxation, streamer channel heating and expansion, production and quenching of atoms, molecular metastable species and radicals) is, however, strongly limited.

In an attempt to get further insight into the streamer discharge physics and chemistry, several diagnostic approaches based on optical techniques have been applied recently and their further development may help to investigate streamer basics. Especially promising are methods capable of characterizing several key reactive species, such as, *e.g.*, free electrons, $N_2(A^3\Sigma)$ metastables, N^I and O^I atoms, and vibrationally-excited $N_2(X^1\Sigma, v)$ species. In the case of $N_2(A^3\Sigma)$ metastables, a new method based on the pooling and resonant energy transfer was recently developed and tested to investigate streamers in pure nitrogen [1-3]. Essentially, the method of "normalised HIR curves" tracks the evolution of $N_2(A^3\Sigma^+_u)$ species through the square root of the $N_2(C''^5\Pi_u \rightarrow A'^5\Sigma^+_g)$ Herman infrared (HIR) emission intensity. Relative $N_2(A^3\Sigma^+_u)$ time-course is then placed on an absolute scale by applying proper normalisation procedure. Considering that HIR has been observed only in connection with the pooling, the HIR provides an interesting tool whenever the pooling mechanism becomes a predominant $N_2(A^3\Sigma_u^+)$ (self)quenching process.

The objective of this lecture is to give an overview of current research in the field of streamer discharges in IPP labs and to discuss basic characteristics of streamers generated in atmospheric gases. Various optical

diagnostic techniques suitable for investigating streamer discharges will be reviewed and their potential use in quantifying important reactive species will be examined. Finally, the latest results in the field obtained by various research groups will be compared.

This work was supported by Grant Agency of the Academy of Sciences of the Czech Republic under contract No. A1043403.

References

[1] M. Šimek, V. Babický, M. Člupek and P. Šunka - J.Phys.D:Appl.Phys. 34**,** 3185 (2001).
[2] M. Šimek - Plasma Sources Sci.Technol. 12, 421 (2003).
[3] M. Šimek - Plasma Sources Sci.Technol. 12, 454 (2003).

Electrical diagnostic and control of dust particle forming radio-frequency plasma.

M. Ch. Jouanny, L. Boufendi, M. Cavarroc, and M. Mikikian
GREMI, Ecole Polytechnique de l'Université d'Orléans, 14, rue d'Issoudun BP 6744,45067 Orléans cedex2

Abstract
The plasma chemistry of a radio-frequency silane based dust forming plasma is analyzed thanks to an electrical diagnostic. This diagnostic gives the possibility to follow and control the particle nucleation and growth from the negative ion formation stage. A correlation with the evolution of the electrical parameters of the plasma is performed.

1. Introduction

Physics and chemistry of dusty plasma are considered now as one of the important branches of science and technology. Besides its importance for laboratory plasmas and applications for environment control, electronics, powder chemistry and metallurgy, dust in plasma also plays an important role in many extraterrestrial situations, from planetary science to interstellar clouds. The presence of dust particles in industrial reactors can lead to the production of defects in the deposited thin layers. However, Recently, it has been shown that nanocrystallites embedded in an amorphous matrix give very interesting opto-electronic and mechanical properties to these thin layers and open the way to many potential applications of these nanostructured thin films such as polymorphous silicon based solar cells with high and stable efficiency. They can be used as quantum dots in a wide range of new generation of microelectronic devices such as memories for tera bit storage, single electron devices, cold electron emitters, etc…

It is well known now, for silane based low-pressure plasma, that the dust particle formation is a four-step process. The first one corresponds to the chemical reactions involving negative ions and vibrationaly excited silane molecules.

$$Si_nH_{2n+1}^- + SiH_4^* \rightarrow Si_{n+1}H_{2(n+1)+1}^- + 2H$$

This phase ends with the formation of 2-3 nm in size nanocrystallites that accumulate in the gas phase. When their number density reaches a critical value of about 10^{12} cm^{-3}, they start to coagulate to form big particles. Thus, the most interesting and important phenomena take place in the early beginning of the process. To understand and control this phenomenon needs to control the formation of the nanocrystallites. Also, the small deviation in plasma and gas parameters in this period (gas temperature, pressure, electron concentration etc.) could change completely the law of cluster growth, particle formation and following discharge behavior [1]. For example, the first phase is strongly slowed down when the gas temperature is increased.

In this contribution we will focus on the study of the physical and chemical characterization of the earlier phase of the dust particle formation.

2. In situ particle detection

An electrical diagnostic has been developed and used. It is based on the measurements of the modifications induced by the occurrence of the nanoparticles in the electrical characteristics of the discharge. Indeed, their presence affects the electrical conductivity of the plasma [2]. The electrical measurements have been correlated to the time evolution of the electron density measured by means of a microwave resonant cavity method. By increasing the time resolution up to 100 µs we can detect the formation of the negative ions which are the first nuclei of the particle formation. This allows the

understanding of the effects of the most sensitive plasma parameters, which is the gas temperature that has a drastic effect on the earlier chemical reactions.

3. Results and discussion

Figure 1 shows the time evolution of the electron density during the nanocrystallites formation and accumulation in the plasma for different gas temperatures. The drastic decrease observed around 200 ms for room temperature curve (green one) corresponds to the agglomeration phase of the nanoparticles. In the first few milliseconds of this curve one can observe a peak (inserted figure) which corresponds to the formation of the negative ions. These ions are formed by dissociative attachment of the silane molecules. As it can be seen, the gas temperature as reported in previous works [3] does not affect this process. However the growth of the nanocrystallites is strongly affected. Two raisons can explain this phenomenon. The first one [4] is related to the temperature induced vibrational -translational relaxation of the vibrationaly excited silane molecules involved in the growth chemical reaction. The second one [5] is related to the radical loss at high gas temperatures. This behavior is well correlated to the evolution of the electrical characteristics of the discharge.

4. References

[1] L. Boufendi, J. Hermann, A. Bouchoule, B. Dubreuil, E. Stoffels, W.W. Stoffels, and M.L. de Giorgi, "Study of initial dust formation in an Ar-SiH4 discharge by laser induced explosive evaporation." J. Appl. Phys. **76**, 148 (1994).

[2] L. Boufendi, J. Gaudin, S. Huet, G. Viera and M. Dudemaine, « Detection of particles of less than 5 nm in diameter formed in an Argon – Silane PECVD plasma », Appl. Phys. Lett.79, 4301 (2001).

[3] J. Perrin et al, Plasma sources Sci. and Technol. **3**, 252 (1994).

[4] A. Fridman, L. Boufendi, T. Hbid, B. Potapkin, and A. Bouchoule, "Dusty plasma formation : Physics and critical phenomena theoritical approach." J. Appl. Phys.**79**, 1303 (1996).

[5] U. Bhanarkar, U. Kortshagen and S.L. Girshick, J. Phys. D: Appl. Phys. **36**, 1399, (2003).

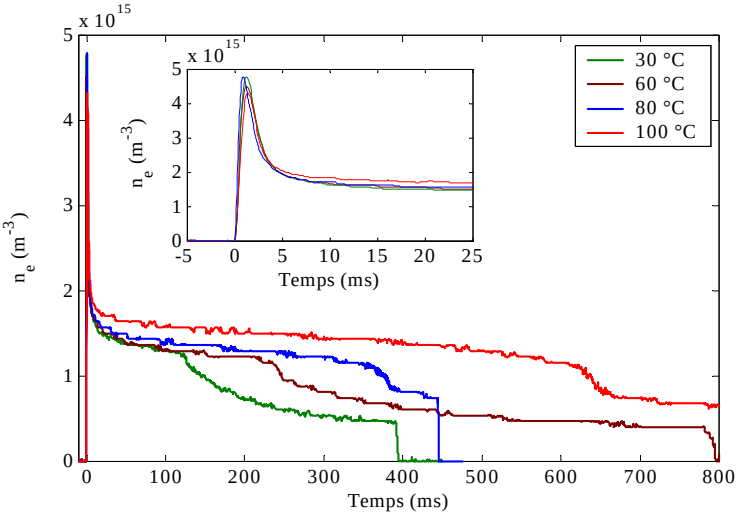

Fig.1: Time evolution of the electron density during the dust formation for different gas temperatures.

Deposition of hard coatings in a high vacuum ambient

Jochen M. Schneider[1], Johanna Rosén[1], Stanislav Mráz[1], and Adil Atiser[1]

[1]Materials Chemistry, RWTH Aachen University, D-52056 Aachen, Germany

ABSTRACT

In this topical review the effect of the presence of residual gas on the plasma chemistry and the composition and properties of hard coatings grown by physical vapour deposition is discussed. Furthermore, the effect of magnetic fields on the plasma composition for low pressure discharges is reviewed.

The synthesis of hard coatings in industry takes place in high vacuum growth systems. The residual gas in such systems is dominated by water. Cathodic arc deposition and magnetron sputtering are often used for the industrial synthesis of hard coatings. The chemistry of cathodic arc plasmas is investigated by time-of-flight mass spectrometry as well as by energy resolved mass spectrometry. We describe the hydrogen incorporation from residual gas during cathodic arc and magnetron sputtering and discuss the implications for the elastic and plastic properties of the coatings. The temporal development of the plasma composition of a pulsed aluminium plasma stream in the presence of oxygen as well as the charge state resolved plasma composition of a pulsed zirconium arc in a nitrogen atmosphere is reviewed. Furthermore, the charge state resolved ion energy distributions of aluminium ions in a cathodic arc plasma are measured and analyzed.

These results are of importance for the understanding of the evolution of the hard coatings composition and structure evolution during deposition.

Biological Applications of Plasma Polymers

R. D. Short
Department of Engineering Materials, University of Sheffield, Mappin Street, Sheffield S1 3JD, United Kingdom

Radio frequency glow discharge (rfgd) or plasma polymers have been applied to biomaterials and biomedical devices since the 1960's [1]. In the process of plasma deposition, an electric field (usually radio frequency) is applied across a vapour or gas filled chamber of a suitably "polymerisable" compound (termed "monomer"). This ionises a fraction of the molecules and generates electrons, ions, free radicals, photons and molecules in both ground and excited states within the gas plasma. Polymer film growth then occurs within this environment [2]. The deposition of polymer films from plasma for biomedical applications, has a number of specific advantages over alternative surface modification techniques, including the deposition of sterile, pinhole-free conformal films onto objects of complex geometries and different materials.

By judicious choice of monomer and control over the deposition environment, films retaining the original chemistry of the monomer compound (e.g. carboxylic acid from acrylic acid) can be obtained [3,4]. This paper reviews the application of plasma deposited films (plasma polymers) in biological applications. The uses of plasma-deposited films are now so widespread that a comprehensive review is beyond the scope of a single paper, and, therefore, the author will concentrate on the more typical applications of plasma-deposited films and trends in the field.

Perhaps naively, the view some 30 or more years ago was that the provision of a synthetic polymeric coating (on a traditional engineering material) would elicit a specific biological response *in vivo* (in the patient) and could improve the long term implantability of the material. However, experience has taught that this is not generally the case – with a few notable exceptions - and the rapid progress that has been made in the past decade in understanding the material-biological interface has helped explain why. Simple ideas that "biocompatibility" may correlate with a single surface property have rarely been supported by the data from animal or patient trials. Commonly observed reactions to implanted biomaterials include those associated with the adsorption of biomolecules e.g. protein adsorption/retention and lipid absorption, those associated with normal/abnormal wound healing e.g. platelet activation, macrophage adhesion, phagocytosis, macrophage release, neutrophil attachment and angiogenesis; and unwanted events such as bacterial adhesion, platelet adhesion and fibrous encapsulation.

Notable successes for plasma-deposited films include surface coatings to reduce the discomfort of wearing non-permeable contact lenses, leads for pace maker devices, surgical instruments and a cell transport vehicle for the delivery of cells to a wound bed. Better correlation between a single material property and biological utility is seen in *ex-vivo* devices e.g. in a study of baboon A-V shunts, it was shown that platelet consumption increased with the water content of hydrogel-coatings on the shunts [5].

The knowledge and materials developed thus far are finding applications elsewhere, in new, emerging technologies, such as microarray analysis and microfluidics, where the problems encountered are similar to implantable devices but coating performance is required only for a short period of time (minutes to hours). In these technologies the biological complexity is significantly reduced (cf. *in-vivo*), and, in general, on the solid-phase support (e.g. glass slide) only one single specific biological event is being controlled (e.g. hybridization of a nucleic acid).

1.B.D Ratner, A. Chilkoti, G.P Lopez in "Plasma deposition, treatment, and etching of polymers" R d'Agostino, ed; Academic Press: San Diego, (1990)
2. H. Yasuda, "Plasma polymerisation" Academic Press: London, (1985)
3. V. Panchalingam, et al., Biomater. Sci. 5, (1993)
4. S. Fraser, R. D. Short, D. Barton, J. W. Bradley, J.Phys.Chem.B. 106, (2002)
5.B D Ratner and A S Hoffman in "Biomaterial Science: An Introduction to Materials in Medicine", Edited by B D Ratner, A S Hoffman, F J Schoen and J E Lemons, Academic Press, (1996)

Abatement of greenhouse gases using surface-wave microwave discharges sustained at atmospheric pressure

Y. Kabouzi[*], M. Nantel-Valiquette, M. Moisan and J. C. Rostaing[†]

Groupe de physique des plasmas, Université de Montréal, Montréal, Québec.

[†]Air Liquide, Recherche et développement, Les Loges-en-Josas, France.

Reducing perfluorinated compound (PFC) emission from chamber cleaning and dielectric etch tools continues to be an important challenge for the semiconductor industry. In some cases, there are advantages to the use of abatement techniques using plasmas at atmospheric pressure. To date, this approach has received less attention than plasma abatement at low pressure. Microwave surface-wave plasmas can be operated at atmospheric pressure and have been successfully used to eliminate PFCs gases. As an example, we present results from the abatement of SF_6/CF_4 diluted in nitrogen gas with concentration ranging from 0.1 to 2.4% of the total flow rate. Oxygen or water vapor is added to the gas mixture to ensure efficient oxidation of PFC fragments and to provide scrubbable byproducts (acid-like byproducts). The destruction and removal efficiency (DRE) of SF_6/CF_4 is investigated as functions of microwave power, field frequency, nitrogen flow rate and PFCs concentration. The DRE is found to increase with increasing microwave power (as a result of increasing electron density and residence time) and decreasing field frequency. Reformation of the PFC molecules form their fragments is found to be the main mechanism limiting the abatement efficiency. Reformation increases with decreasing gas temperature and increasing initial concentration of PFC molecules. Comparison between measurements and thermodynamic calculations shows good agreement. The residual PFC flow rate (or mass flow), for a given concentration of PFC in the gas mixture, is found to depend only on the specific energy, i.e. the energy deposited per PFC molecule expressed as the total microwave power divided by the PFC flow rate. This is illustrated in figure 1 for a fixed concentration of 0.75% of SF_6 in the gas mixture at three different nitrogen flow rates. It shows that a specific energy of 1.05 kJ/cm^3 is required to achieve an almost complete abatement of SF_6. We will show that the energy efficiency of this plasma process increases with increasing the concentration of PFC. A method for improving the energy efficiency of our plasma reactor will also be presented.

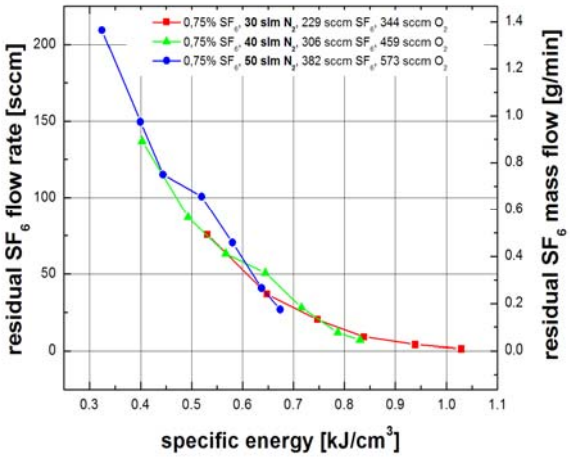

Fig 1: Residual SF_6 flow rate as a function of the specific energy, for different set of experimental conditions

*Present address: Department of Chemical Engineering, University of California, Berkeley, California 94720.

Swift chemical sputtering of covalently bonded materials

K. Nordlund, E. Salonen and A. V. Krasheninnikov
Accelerator Laboratory, P.O.Box 43, 00014 University of Helsinki, Finland

When energetic atoms or ions escape from a plasma and hit a wall material, they can cause the material to erode. The erosion is well understood if the ion energy is high enough that the erosion is caused by physical sputtering, *i.e.* when the ion collides with a sample atom and directly kicks it out of the sample. Alternatively ions with thermal energies can also cause erosion if a chemical etching reaction can
take place.

In the particular case of hydrogen escaping from a fusion reactor plasma and hitting a carbon-based wall material, high carbon erosion has been observed for hydrogen ion energies which are so low (10-30 eV) that physical sputtering is impossible. On the other hand no chemical etching reaction has been able to explain the erosion either. Using classical and quantum mechanical atomistic simulations of the ion-sample collision dynamics, we have shown that the observed erosion can be explained by a chemical sputtering mechanism, where the incoming ion attacks a chemical bond between two carbon atoms, and causes the bond to break [1,2,3]. This mechanism requires an ion energy of only about 3 eV, and occurs on femtosecond time scales, whence we call it swift chemical sputtering.

In my talk I will present the swift chemical sputtering mechanism in detail, and discuss why it is neither a previously known physical or chemical sputtering mechanism, nor chemical etching. I will also present our results on how this mechanism can explain many of the observed features of carbon erosion in fusion reactors, and finally show that it can also be important in mixed materials like tungsten carbide.

[1] E. Salonen, K. Nordlund, J. Keinonen, and C. H. Wu, *Bond-breaking mechanism of sputtering*, Europhysics Letters **52**, 504 (2000).

[2] E. Salonen, K. Nordlund, J. Keinonen, and C. H. Wu, S*wift chemical sputtering of amorphous hydrogenated carbon*, Phys. Rev. B **63**, 195415 (2001).

[3] A. V. Krasheninnikov, K. Nordlund, E. Salonen, J. Keinonen, and C. H. Wu, *Sputtering of amorphous hydrogenated carbon by hyperthermal ions as studied by tight-binding molecular dynamics*, Comput. Mater. Sci **25**, 427 (2002).

Reactive deposition of ruthenium oxide by RF-assisted Ionized Physical Vapor Deposition magnetron sputtering.

D. Benzeggouta, M.C. Hugon, O. Voldoire, J. Bretagne, M. Touzeau, and B. Agius
Lab. de Physique des Gaz et des Plasmas, Université Paris-Sud, 91405 Orsay Cedex, France

Abstract
High permittivity (***k***) oxides are actively studied for highly integrated microelectonic devices in order to replace silicon oxide. In MOSFET devices, the gate electrode have to be compatible with high ***k*** oxide. In this work we chose ruthenium oxide which presents a weak resistivity (35μΩ.cm for the bulk material), a good thermal stability. To improve the RuO_2 film quality compatible with a low thermal budget on the substrate we study a new process, called Ionized Physical Vapor Deposition (IPVD).
Keywords: Reactive IPVD magnetron sputtering, High k thin film deposition

Introduction

As silicon CMOS devices are scaled below the 100 nm gate length node, advanced high-k gate dielectrics will be required to obtain equivalent oxide thickness (EOT) < 1.0 nm, EOT being the equivalent silicon oxide thickness deduced by quantum correction. New high permittivity (***k***) oxides are actively studied for highly integrated microelectonic devices in order to replace silicon oxide.
Thin films of transition conducting metal oxides such as ruthenium oxide, RuO_2, and iridium oxide, IrO_2, are attractive gate electrodes, since they have large work functions (~ 5 eV), low resistivity (35μΩ.cm for the RuO_2 bulk material), and excellent thermal stability. In this work, we evaluate the electrical and thermal stability of ruthenium oxide which presents good diffusion barrier properties to oxygen [1] and a good compatibility with the etching standard process.

Reactive magnetron sputter deposition is currently studied to deposit RuO_x from a metallic target. The composition of the deposited films is related to the oxygen/argon flow ratio. The classical transition between a "metallic" and an "oxide" regime is observed when the oxygen partial pressure is increased [2]. In classical magnetron discharges, sputtered species are emitted as neutral particles which have relatively low energy (~ 3-10 eV). The deposition regime depends on the working pressure, for a given distance between the substrate and the target: it varies from a ballistic one for which the film density is high to a thermalized one where deposited films present poor qualities in particular in terms of density and resistivity.
In order to improve the film quality compatible with a low thermal budget on the substrate, we explore the capabilities of the RF-assisted IPVD technique for the deposition of thin films mainly when working in reactive conditions. This last process is made more complex since an additional transition (inductive to capacitive [3]) is associated to the classical one (metallic to oxide) observed when the oxygen partial pressure is increased. In this process, we use a classical magnetron reactor equipped with a RF coil [4] placed in the region between the target and the substrate, coil which induces an additional plasma for vapor ionization. The goal of the present work is to study the discharge behavior versus various parameters and its correlation with deposited film properties in order to optimize the process.

Experimental procedure

RuO_x thin films were deposited using reactive magnetron IPVD with a Ru metallic target in an Ar/O_2 buffer gas discharge (Table 1). The IPVD reactor is a prototype developed by Alliance Concept. The reactor is a 45 cm diameter and 30 cm height cylinder, and contains a planar circular magnetron cathode (10 cm diameter). The process was designed to produce an additional inductively coupled plasma by using a RF coil to ionize the sputtered vapor and the buffer gas and to dissociate the reactive gas. The target to substrate distance was approximately 10 cm. In order to understand the oxygen role during the RuO_x film formation, we studied the plasma properties through the current and voltage characteristics of the discharge and by optical emission spectroscopy [5] according to the O_2 flow rate, DC target power, RF coil power and the total gas pressure.
Optical emission spectroscopy was used to detect and follow typical species emitted by the plasma. Emission spectra were recorded with a Jobin Yvon monochromator (HR 640) in the spectral range 180-850 nm with a resolution of 0.3nm.

The as-deposited thin films were characterized using profilometry for film thickness, and 4-point probe to obtain film sheet resistance. The films were analyzed by ion beam analysis (IBA) performed with a 2.5 MeV linear Van de Graff accelerator to determine the composition of thin films: Rutherford Backscattering Spectroscopy (RBS) allows the detection of the heavier elements such as ruthenium while Nuclear Reaction Analysis (NRA) allows to analyze light elements such as oxygen.

Table 1: *Deposition conditions.*

Target composition	*Ru*
Substrate to target distance	*10 cm*
DC power density	*80-130 W*
RF coil power	*0-200 W*
Coil/substrate distance	*2 cm*
Pressure	*0.5-5 Pa*
Deposition temperature	*Floating temperature*
Ar flow	*15-37 sccm*
O_2 flow	*0-15 sccm*

By analyzing simultaneously the plasma and the deposited films, it will possible to optimise the plasma conditions in order to obtain the best quality of films.

Results and interpretation.

In this IPVD concept, relatively high pressure (a few Pa) is necessary to optimize the sputtered vapor ionization fraction [5]. Indeed, sputtered neutral particles must be thermalized when they reach the RF coil discharge region in order to increase their residence time and consequently, their ionization rate. Figure 1 shows the variations of the magnetron discharge voltage (V_{Dis}) and current (I_{Dis}) versus O_2 flow rate, for 4 values of the RF coil power, P_{RF}=0W; P_{RF}=100W; P_{RF}=150W and P_{RF}=200W.

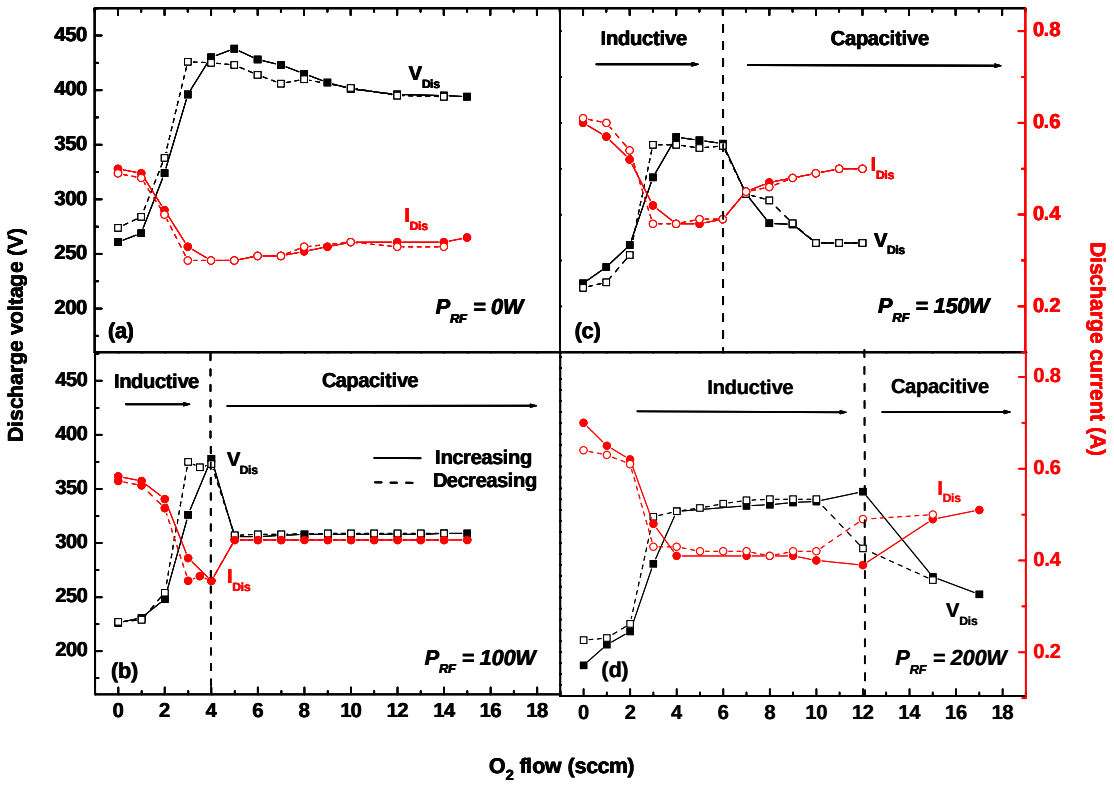

Fig. 1: *Variation of the magnetron discharge voltage and current versus O_2 flow rate for P_{DC}=130W, p=5Pa and an Ar flow rate of 37 sccm. The transition from inductive to capacitive modes is indicated by arrows for the different RF coil powers applied (P_{RF} = 100W, 150W, 200W).*

In addition to the well known metallic-oxidized target transition, another phenomenon, which consists in a transition from an inductive coupling mode to a capacitive one, is observed: this phenomenon modifies strongly the discharge and possibly the film properties. For a DC power (P_{DC}) of 130W, the first transition (V_{Dis} increases while I_{Dis} decreases) occurring around 4 sccm oxygen flow rate, corresponds to the transition from metallic to the oxide regime (fig. 1). This behavior can also be observed on the emission of the Ru I, O I and Ar I lines emitted by the magnetron plasma (fig. 2).

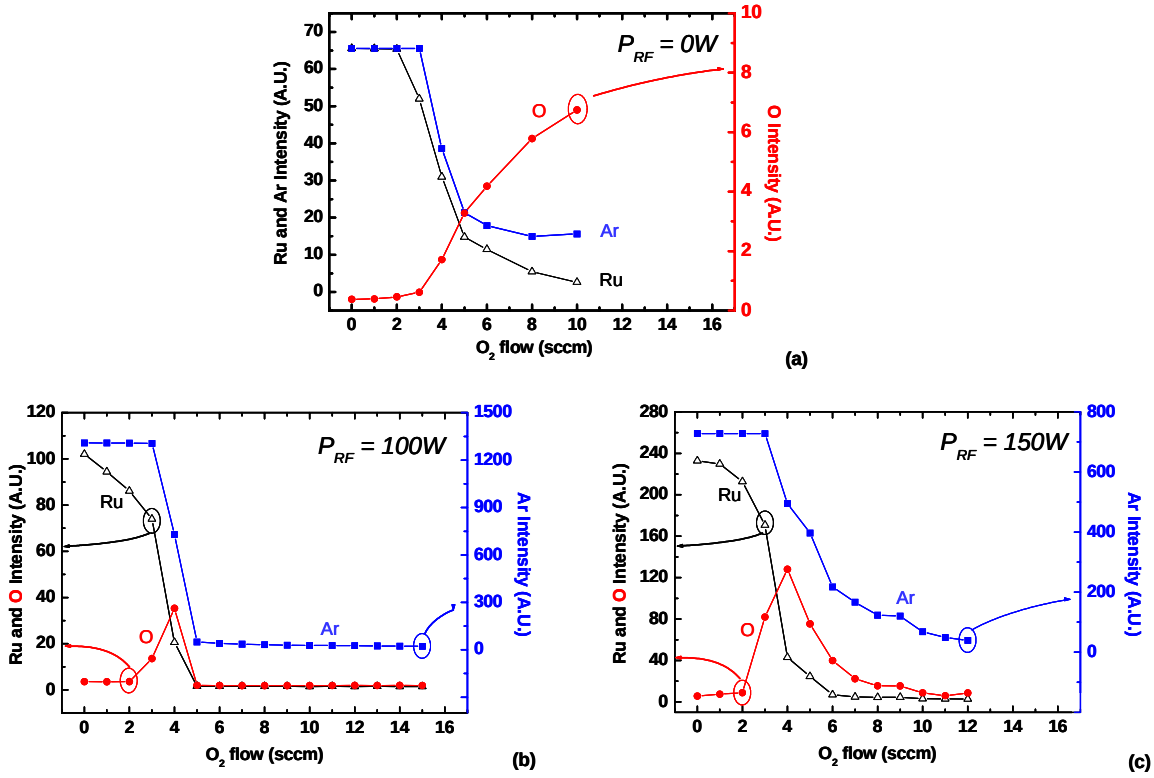

Fig. 2: *Variation of the 777 nm O I (●), 349.8 nm Ru I (Δ) and 811.4 Ar I (■) line intensity versus O_2 flow rate for conditions of fig. 1.*

The second transition (inductive to capacitive) appears in the voltage current plot (V_{Dis} decreases while I_{Dis} increases); this transition shifts to higher oxygen flow rate when the RF power applied to the coil increases (fig. 1.b.c.d). This effect is explained by the fact that the RF power is not sufficient to maintain the coupling of the coil in the inductive regime when the composition of the gas contains a larger proportion of oxygen. We can also see on OES spectra the same effect (fig. 2.b and c): in the oxide regime discharge (O_2 flow rate $\geq$ 4 sccm in our experimental conditions), the intensity of all the lines emitted in the RF plasma (Ru I but also O I and Ar I) decreases. This last result confirms a reduction of electron density and probably electron temperature in the RF plasma during the inductive-capacitive transition inducing a weak excitation of Ar, Ru and O atoms.

Figure 3 shows the variation of the magnetron discharge voltage and current versus O_2 flow rate for P_{RF} = 200W and two values of P_{DC} (80W and 130W). For larger DC power, the sputtering rate increases, consequently, oxygen target saturation occurs at large O_2 partial pressure. This effect also shifts the inductive to capacitive coupling transition (arrows of fig. 3) towards higher O_2 flows. This second transition, which is correlated to the cooling of electrons, is directly connected to the O_2 partial pressure in the plasma chamber.

In the inductive coupling regime, a high ionization of the gas is achieved in the coil centre and in the target-substrate region which produces a gas heating and a gas rarefaction. When the O_2 partial pressure is increased, due to a greater influence of e - O_2 low-threshold inelastic processes, the overall ionization efficiency decreases, producing new spatial ionization equilibrium and a transition to

capacitive regime. Effects of electron losses due to dissociative attachment on O_2 molecules can also be invoked for the reduction of the electron density. In this regime, a greater part of RF power is deposited in sheaths around the coil and near the walls. In the coil area, the gas temperature is lowered and the gas density is increased. The consequence is that the current-voltage characteristics of the DC magnetron discharge is modified: indeed, the increase of the gas density makes more efficient the ionization in the magnetized region leading to a decrease of the voltage necessary to sustain the DC magnetron discharge and then an increase of the current discharge.

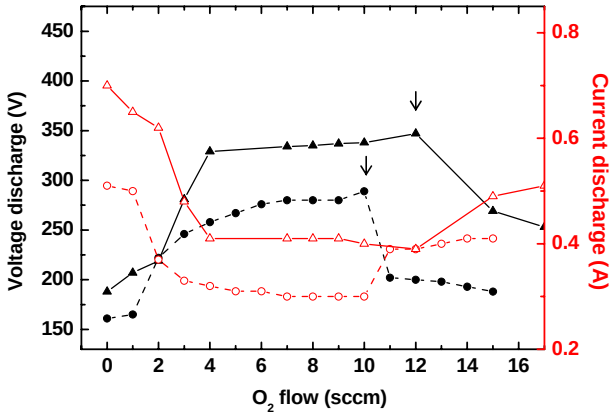

Fig. 3: *Variation of the magnetron discharge voltage and current versus O_2 flow rate for P_{RF} = 200W, two different P_{DC}, a pressure of 5 Pa and Ar flow rate of 37 sccm. The transition from inductive to capacitive modes is indicated by arrows.* ●*: V_{Dis}, P_{DC}=80W,* ○*: I_{Dis}, P_{DC}=80W,* ▲*: V_{Dis}, P_{DC}=130W,* Δ *: I_{Dis}, P_{DC}=130W.*

Film properties are reported on Figures 4 and 5, as a function of the O_2 flow rate, for two pressures (5Pa and 0.5Pa) and a RF coil power of 100W. For the two pressures, the deposition rate decreases when the RF coil power (P_{RF}) increases (fig. 4). The two parameters, pressure and RF power, do not seem to have any effect on stoichiometry (fig. 4) and density (fig. 5).

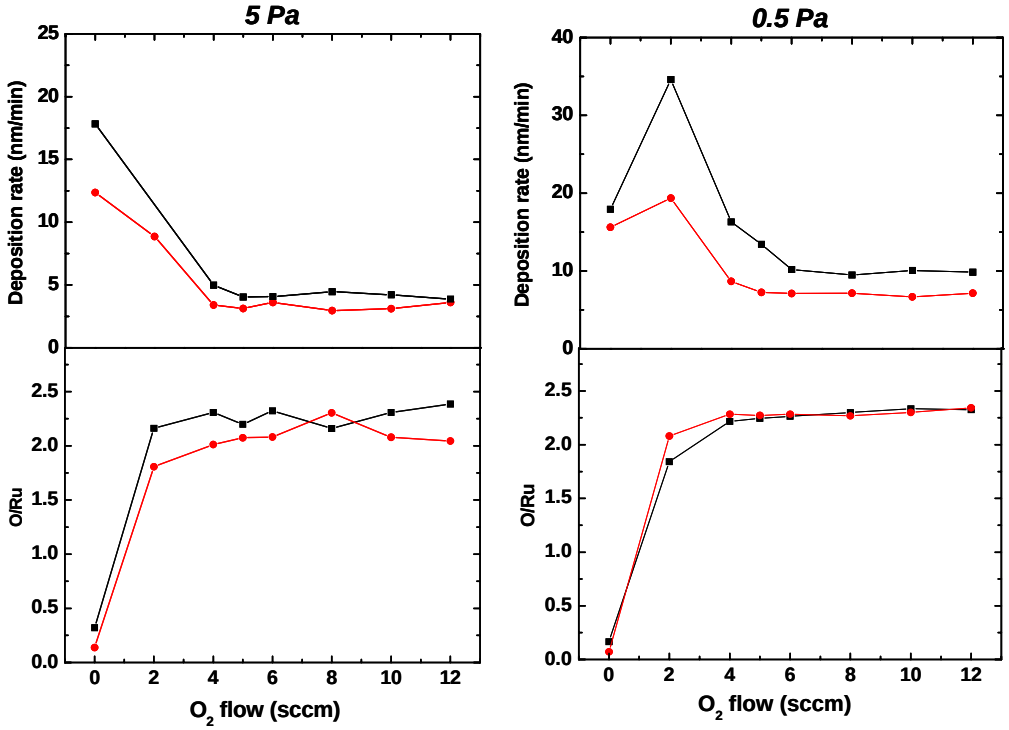

Fig. 4: *Variation of RuO_x thin film properties: deposition rate, stoichiometry* ***O/Ru****, versus O_2 flow, for two deposition pressures (0.5 and 5Pa) and two RF coil powers* ***P_{RF}*** *(■: P_{RF}=0 W,* ●*: P_{RF}=100W) - P_{DC}=80W.*

For usual PVD magnetron sputter deposition, the best quality of deposited films are usually obtained at low working pressure. In the present work we are mainly interested in dense and low resistivity oxide films, performed without any intentional heating or any post deposition annealing. The comparison of the first results reported in figs. 4 and 5 permits to draw some conclusions on the interest in using RF-assisted IPVD process when working in reactive conditions for deposition of conductive films. From these figures, we first observe that the presence of the RF plasma does not modify significantly the film density. Second, it appears, from fig. 4, that film stochiometry O/Ru reaches a value of about 2 (within the accuracy of the determination of composition by IBA) for O_2 flow rate higher than 2 sccm which corresponds to the beginning of the metal/oxide transition. But a too high O_2 flow rate produces a transition from inductive to capacitive discharge regime which is less effective for ionization, and then for the physical properties of thin film. So, for conditions of figures 4 and 5 and respective values of P_{DC}= 80W and P_{RF}=100W used here, the most interesting conditions in terms of O_2 flow rate are achieved between 2 and 4 sccm. In this range, we clearly observe an important improvement of the film resistivity when the additional RF plasma is used, particularly for a pressure of 5 Pa for which we get better results that for a pressure of 0.5 Pa.

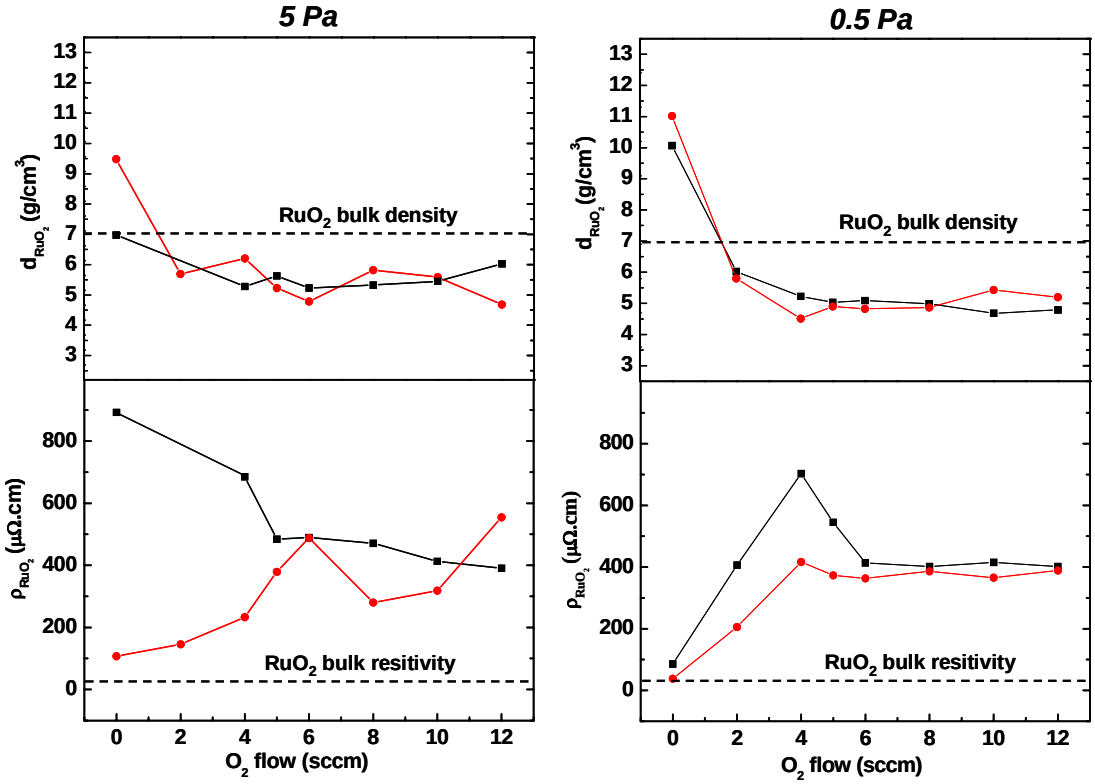

Fig. 5: *Variation of RuO_x thin film properties: density and resistivity, versus O_2 flow, for different pressures, RF coil power* $\mathbf{P_{RF}}$ *(■: P_{RF}=0 W, ●: P_{RF}=100W) - P_{DC}=80W.*

These results are very promising and can be probably improved by exploring some ways: *1)* by working with a higher ratio of P_{RF}/P_{DC} (see from fig. 1) we have the possibility to extend the range of O_2 flow rate for which we can work in simultaneous oxide and inductive regimes, *2)* the use of voltage bias on the substrate could permit to deliver a higher energy to the film, to increase the film density and to improve its morphology in term of a better crystallinity, *3)* by optimizing the geometry of the reactor, in particular for the position of the RF loop.

Conclusion

In this paper, we have studied the RF-assisted IPVD technique for the deposition of RuO_2 thin film. This technique associates a classical magnetron discharge to a RF plasma generated by a coil placed

between the magnetron and the substrate. We followed the effect of three parameters (O_2 flow rate, RF coil power and DC magnetron power) on the plasma and film properties.
We observed that in addition of the well known transition from metallic to oxide mode, in reactive PVD, it appears another phenomenon which consists of a transition from an inductive to a capacitive coupling when we apply a RF coil power. This effect depends at the same time on the oxygen presence in plasma, the RF coil power and DC magnetron power. Results clearly show an improvement of the film resistivity for conditions corresponding to simultaneous oxide and inductive regimes. Work is in progress to confirm, extend and control the potentialities of RF-assisted IPVD process for reactive conditions.

REFERENCES

[1] W. T. Lim, K. R. Cho, C. H. Lee, Thin Solid Films, 348 (1999) 56-62
[2] G. Contoux, F. Cosset, A. Célérier, J. Machet, Thin Solid Films 292 (1997) 75-84
[3] K. Suzuki,, K. Nakamura, H. Ohkubo, and H. Sugai, Plasma Sources Sci. Technol. 7 (1998) 13-20
[4] T. Nakamura, K. Okimura, Vacuum, 74 (2004) 391.
[5] M.Touzeau, D.Pagnon, and J.Bretagne, Vacuum 52, 33-40 (1999).
[6] M. Dickson, G. Zhong and J. Hopwood, J. Vac. Sci. Technol. B16(2), 523 (1998).

Vacuum Beam Studies of Radical Enhanced Atomic Layer Deposition of TiN Thin Films

Frank Greer

As microelectronics devices shrink and as their aspect ratios increase, it has become increasingly difficult to deposit thin films with sufficient conformality and control for many different practical applications. For example, the deposition of Cu diffusion barrier layers has been traditionally accomplished by advanced Physical Vapor Deposition (PVD) methods. However, as the step coverage required for the barrier layer approaches 100%, and as the barrier thickness required shrinks below 100A, PVD methods may not be able to meet these demands. To address these concerns, Atomic Layer Deposition (ALD) has been proposed as an alternative to PVD. In thermal ALD, a metallic precursor (*e.g.* Titanium Tetrachloride TiCl4) and a reactive species (*e.g.* NH3) are alternately introduced in isolated pulses into a deposition chamber. Repeating these pulses in a cyclical fashion, results in the growth of a film (*e.g.* TiN). Because the pulses of precursor and reactive species do not overlap, the film growth proceeds entirely through a series of surface reactions. This ensures that the film grows one layer at a time, allowing for precise thickness control, and yielding conformal step coverage in high aspect ratio features.

One problem with thermal ALD is that the deposition temperatures required to achieve practical growth rates and acceptable film properties can be relatively high (400C or greater). [1] Unfortunately, deposition temperatures in excess of 300C, may be incompatible with the temperature-sensitive films and structures in microelectronics processing. However, by using a more reactive species like a radical as the second reactant, atomic layer film deposition at much lower temperatures is possible. [2]

In this work, fundamental studies of Radical Enhanced Atomic Layer Deposition (RE-ALD) of TiN were performed in an ultra-high vacuum beam system.[3] By directing independent, calibrated beams of $TiCl_4$ precursor molecules, hydrogen radicals, and nitrogen radicals at different surfaces (inc. TiN, W, Cu, Si, and SiO_2), the individual steps of this RE-ALD process were characterized as a function of temperature (see Figures 1-3). With these data, phenomenological models were developed to calculate deposition rate parameters such as sticking and reaction rate probabilities (see Figure 4). These models were verified using modulated beam mass spectrometry to measure surface reaction products evolved during the RE-ALD process. XPS analysis and sheet resistance measurements for the deposited films will also be presented to illustrate that conductive TiN films with low residual Cl content can be grown at temperatures below 450K with the RE-ALD process.

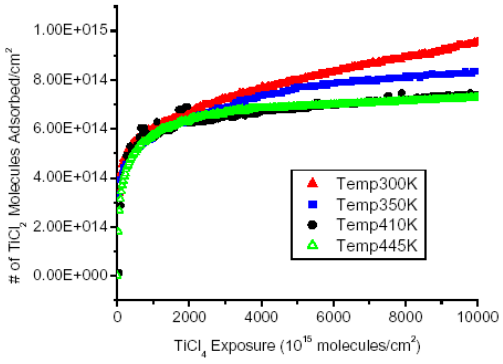

Fig 1: TiCl4 adsorption as a function of substrate temperature

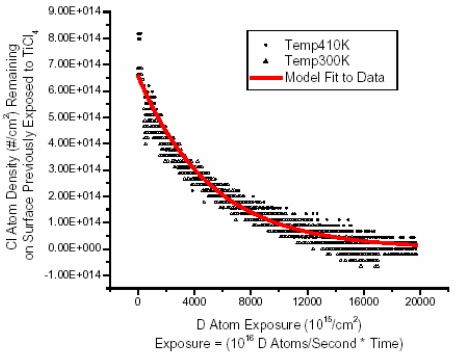

Fig 2: Cl abstraction as a function of substrate temperature

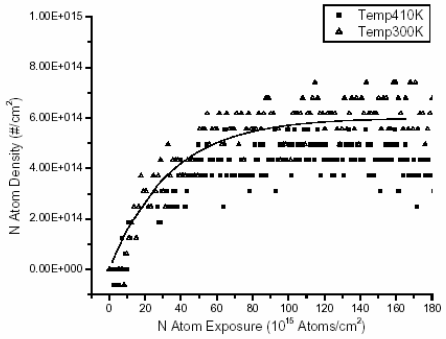

Fig 3: N radical reaction as a function of temperature

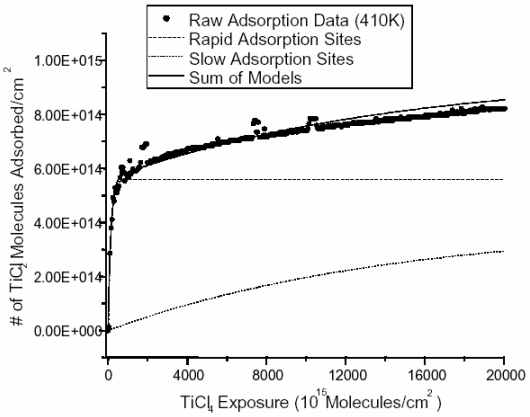

Fig 4: Phenomenological model fit to TiCl4 adsorption

[1]A. Satta et al. Spring MRS Meeting 2000 D6.5
[2]A. Sherman US Patent 5916365.
[3]F.Greer, D.Fraser, J.W. Coburn, and D.B. Graves, *JVST A.* Jan/Feb 2003.

Plasma - surface interaction in a free burning electric arc in air between composition electrodes

A.N. Veklich[1], I.L. Babich[1], V.Ye. Osidach[1], L.A. Kryachko[2], R.V. Minakova[2]

[1]Taras Shevchenko Kyiv National University, Kyiv, Ukraine
[2]Institute of Materials Technology Problems NAS of Ukraine, Kyiv, Ukraine

Abstract
In this paper the processes occurred in a free burning electric arc in air between electrodes from composition materials on the base of cooper *(Cu, Cu-W, Cu-Mo, Cu-Mo-LaB$_6$)* and silver *(Ag, Ag - CdO)* were studied. By methods of optical spectroscopy radial profiles of plasma temperature are determined. The structural changes in a working layer of electrodes are investigated by metallographic techniques.
Keywords: electric arc, plasma, consumable electrodes, composition material.

1. Introduction

A problem of developing of reliable interrupting devices, where ignition of electric arc often is realised, can not be resolved without careful analysis of processes which take place in the arc and its electrodes. Furthermore, an electric arc, being generated at contact disconnection, results in considerable material erosion of contacts. We investigated plasma of the free burning electric arc in air between electrodes from composition materials. Such arc is model of arcs arising between contacts of current releases of electric circuits.

2. Experimental Set-up

The arc was ignited between the end surfaces of the non-cooled electrodes. The discharge gap l_{ak} was of 2, 4, 6 or 8 mm. The diameter of the rod electrodes was of 6 mm. To avoid the metal droplets appearing a pulsing mode was used: the current pulse up to 30 A was put on the "duty" weak-current (3.5 A) discharge. The pulse duration ranged up to 30 ms. The quasi-steady mode was investigated.

Because of the discharge spatial and temporal instability the method of the single tomographic recording of the spectral line emission was used. A 3000-pixel CCD linear image sensor (B/W) Sony ILX526A accomplished fast scanning of spatial distributions of radiation intensity. It allows the recording of the radial distributions of unsteady-state arc radiation intensity in arbitrary spatial sections simultaneously.

3. Results and Discussions

3.1 Electric arc between electrodes from composition materials on the base of cooper *(Cu, Cu-W, Cu-Mo, Cu-Mo-LaB$_6$)*

The radial profiles of temperature are determined in the average cross section of the discharge gap l_{ak} = 2, 4, 6 and 8 mm in air at arc currents 3.5 and 30 A. The temperature profiles are obtained from relative intensities of copper spectral lines 510.5 and 521.8 nm. Because of the discharge spatial and temporal instability the statistical treatment of obtained data was carried out. The spectral sensitivity of the experimental set-up was taken into account.

As recently was found the some secondary structure on a surface of electrodes can be realised during the discharge operation [1]. Therefore we studied our plasma in a two different modes. In the first mode the measurements of radial distributions of spectral line intensities were carried out as a statistical average value during the series of current pulses (30A) putted on the "duty" weak-current discharge (3.5 A). In this case the secondary structure on a surface of electrodes was realised. To avoid the influence of such secondary structure during the discharge operation in an another mode we measured the radial distribution of spectral line intensities as a statistical average value of single current pulses of an electric arc between smoothed surface of electrodes.

The radial temperature profiles of the arc between Cu-Mo-LaB_6 electrodes in two different modes are measured. In the first mode of the arc operation we investigated plasma of the discharge between smoothed surfaces of

electrodes. The next mode corresponds to the case of electrode surfaces covered by a secondary structure, which is realised under the arc activity.

From the comparison of obtained results the key role of the condition of the surface electrode follows. Really the presence of the secondary structure must decrease the erosion of the electrode material. As a result the amount of lightly ionised metal vapours in a discharge gap must be decreased. Therefore at the same arc currents the temperature in plasma column must be higher in case of secondary structure on a surface of electrodes.

It was interesting to compare the influence of composition of the electrodes on the plasma parameters. Additionally investigations of radial profiles of temperature in the arc discharge between pure copper electrodes were carried out. The plasma of an electric arc between Cu-Mo and Cu-W electrodes in the first mode of the arc operation was investigated in a similar way as well.

We can compare obtained radial temperature profiles of the arcs between Cu-Mo-LaB_6 electrode surfaces with a secondary structure and between copper electrodes. From these results follows that in arcs with discharge gaps 4, 6 and 8 mm at the arc current 30 A the axial temperatures are higher in case of Cu-Mo-LaB_6 electrodes. This phenomenon can be cased by both the additions of the Mo-LaB_6 to copper in such composition and a secondary structure of electrode surfaces. In case of discharge gap 2 mm such behaviour of axial temperatures are not observed. It is natural because the plasma of such arc probably is not in a local thermodynamic equilibrium. Such effect was observed in plasma of a short free-burning electric arc between copper electrodes [2].

The increasing of both the temperature and the efficiency of the plasma torch as a tool in the electrical erosion cutting is probably one of the factors, which determine the productivity of the dimensional treatment in the presence of the boron-containing compounds.

We compared radial temperature profiles of the arc between Cu, Cu-Mo, Cu-Mo-LaB_6 and Cu-W electrodes also. The arcs between composition electrode surfaces with a secondary structure were investigated in this case. The essential influence of the additions to the electrode materials on the arc plasma temperature is found [3].

3.2 Electric arc between electrodes from composition materials on the base of silver *(Ag, Ag-CdO)*

To realize spectroscopic techniques of plasma diagnostic of electrical arc discharges between composition electrodes on the silver base the reliable data on spectroscopic constants of silver and/or impurity atoms spectral lines are necessary.

Unfortunately, we have no information about discharge plasma investigation with usage of silver spectral lines. In the literature there are very negligible data on silver spectroscopic constants. The arrangement of energy levels of this atom does not give optimism for usage of silver lines in experiments on temperature determination by relative intensities technique with adequate accuracy. Nevertheless, we for the first time attempted to realize a spectroscopic technique of plasma diagnostic of electrical arc discharges between silver electrodes.

For this purpose, despite of a small difference of excitation energies of upper levels (~ 0.8 eV), the lines AgI 520.9, 768.7, 827.3 nm are selected.

The atomic spectroscopic data for these lines are taken from Ref. [4,5,6] and are listed in Table 1. Unfortunately, in the database NIST (National Institute of Standards and Technology, USA) the atomic spectroscopic data for lines AgI 768.7 and 827.3 nm are absent.

Table 1. Silver atomic spectroscopic data

λ,nm	E_m,eV	g_n	g_m	Ref.[4]		Ref.[5]			Ref.[6]
				g_mA*10^8	$g_mA/(g_mA)_{520.9}$	f	$A*10^8$	g_mA*10^8	$g_mA/(g_mA)_{520.9}$
827.7	5.256	4	2	2.3	0.153	0.166	0.323	0.646	0.107
768.7	5.256	2	2	1.4	0.093	0.157	0.177	0.354	0.069
520.9	6.015	2	4	15	1	0.565	0.694	2.77	1

The radial profiles of temperature are determined in the average cross section of the discharge gap l_{ak} = 6 mm in air at arc current 3.5 A. The temperature profiles are obtained from relative intensities of two pair's chosen silver spectral lines. In Fig. 1, as an example, the results of measurements are shown. The temperatures are determined with usage of atomic spectroscopic data fromRef. [4] and Ref. [5] for two independent serials of experiments (1 and 2). As the data from Ref. [4] and from Ref. [6] are practically coincide the temperatures by using data from Ref. [6] were not calculated.

The registration accuracy of spectral lines intensities does not exceed 10 % in our experiments. As the difference in upper levels energies of these lines are not significant, the final accuracy in determination of temperature is about 30%. The measurement results obtained by two pairs of spectral lines and in different serials of experiments practically coincide. We can conclude, that the chosen lines AgI 520.9, 768.7, 827.3 nm can be able to use in the temperature measurements in plasma contaminating the silver vapors with above mentioned accuracy.

One can note that we obtained the rather low temperature in the investigated plasma. Really, temperature on the arc axis in our case does not exceed 4200 K. But in plasma of free burning in air electric arc between copper electrodes in the same mode of discharge it is about 7000 K at the contents of cooper vapors of some percents in plasma [7, 8].

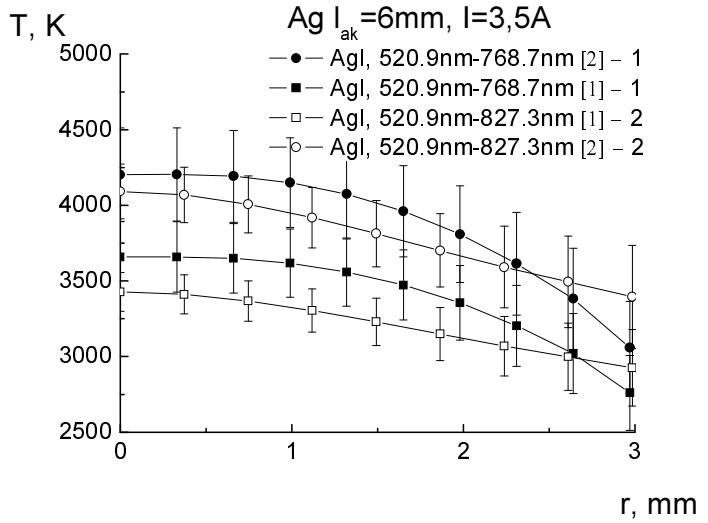

Fig 1. Radial profiles of temperature of arc plasma between silver electrodes (l_{ak} = 6 mm)

The simple estimation of equilibrium composition of a plasma mixture Ag-N_2 indicates, that at the contents of silver 1 % and temperature 4000 K the electron density is about $7*10^{13}$ $см^{-3}$. Apparently, such electron density is sufficient for maintenance of an arc current 3.5 A in a discharge.

In spectroscopy measurements of radial temperature profiles in plasma of an electric arc discharge between Ag-CdO electrodes to increase the reliability of obtained results were used both line of silver, and line CdI 479.9, 508.5 and 643.8 nm. The atomic spectroscopic data for these lines CdI are taken from Ref. [4,5,9,10] and are listed in Table 2. From the table the essential differences of these data from each other are visible.

Table 2. Cadmium atomic spectroscopic data

λ,nm	g_n	g_m	Ref.[4]		Ref.[9]		Ref.[10]		Ref.[5]		
			g_nf	$g_nf/(g_nf)_{643.8}$	g_nf	$g_nf/(g_nf)_{643.8}$	$A*10^8$	$g_nf/(g_nf)_{643.8}$	gnf	$A*10^8$	$g_nf/(g_nf)_{643.8}$
479.9	3	3	4.9	1.02	0.42	0.23	0.41	0.23	0.41	0.4	0.3
508.5	5	3	12	2.5	0.65	0.38	0.56	0.44	0.72	0.62	0.52
643.8	3	5	4.8	1	1.8	1	0.59	1	1.38	0.45	1

The temperatures at the discharge axis calculated by intensities of cadmium spectral lines with usage of spectroscopic data from Ref. [4] twice and more exceed temperatures obtained with usage of data from other references. Therefore in further these data were not taken into account.

In Fg. 2 the radial distributions of temperatures in the average cross section of the discharge gap l_{ak} = 6 mm in air at arc current 3.5 A obtained by spectral lines of silver and cadmium are shown. It is visible, that the temperatures obtained by AgI and CdI spectral lines are in close agreement.

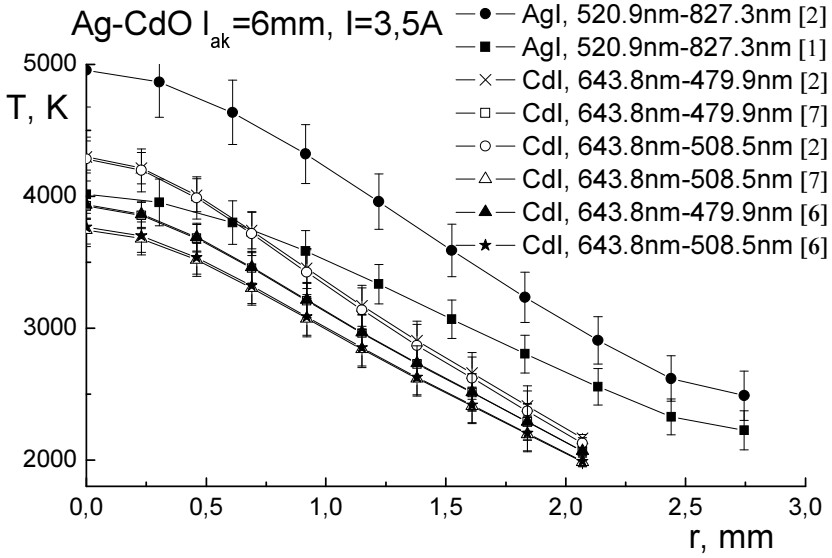

Fig 2. Radial profiles of temperature of arc plasma between composition Ag-CdO electrodes (l_{ak} = 6 mm)

The structural changes in a working layer of electrode take place during the electric current switching. These changes were studied metallographicly (Neophot-2) by a raster microscopy and X-ray spectral analysis of microvolumes of a working layer (JSM Super Probe-733, JEOL). A surface of a working layer and its perpendicular section were investigated.

It was found, that under effect of electric discharge the relief of a surface changes first of all because of melting away of a contact material. The cracks initiation is observed in a working layer on cooling caused by the arc extinction. Some of cracks on the surface «are healed» by a melt on the basis of silver. There is upbuilding of these defects observed metallographicly in a volume of a contacts working layer as the switching cycles number increases. The temperature increasing of a working layer results in a segregation of a composition. The oxide of cadmium is stored in a near-surface layer in defects and in crack edges (see Fig. 3).

Quite often the increasing of this phase concentration is observed because of segregation phenomena near crack face. Lengthy areas of material enriched by silver structurally associated with enriched by oxide composition. At segregation, apparently, there is dissociation oxide of cadmium. It is known that the dissociation temperature of oxide is lowered with a decreasing of the contents of oxygen in a material. However, most probably, these processes are intensified during the melting of component on the silver base or at pre-melting temperatures. The segregation enrichment of crack faces by cadmium or by phase on its base takes place in the solid-phase of the composition.

The structure change of a working layer can exert influence on the mass transfer in an arc discharge gap. The decrease of electrical and thermal conductivity of areas enriched by oxide and fixation of an arc discharge on these parts of surface [11] can promote an overheating of areas of a material enriched by silver and their ejection into a discharge gap. This mechanism of erosion can promote a decrease of temperature of an arc discharge caused by the intensive silver ejection. In this case the electrical erosion of contacts accompanied also by

dissociation oxide of cadmium is increased. The probability of welding together of contacts is increased too. These results do not contradict by the authors of paper [12].

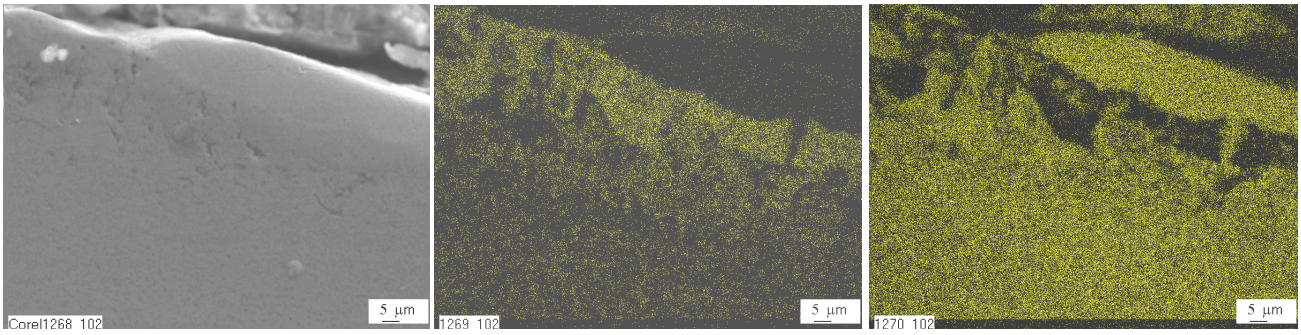

REM (second. electrones) RX Cd Kα RX Ag Rα

Fig 3. Cadmium and silver distribution in working layer of composition Ag-CdO electrodes

Conclusions made on the base of obtained results of metallographic investigations can be compared with results of spectroscopy measurements. In Fig. 4 radial distributions of silver and cadmium spectral line emissions are shown.

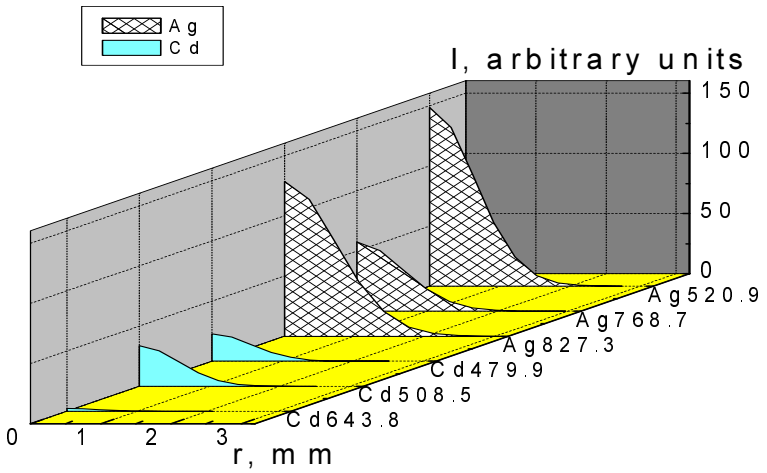

Fig 4. Radial distributions of silver and cadmium spectral line emissions

From such radial profiles the ratio of these atoms in plasma is possible to calculate on the base of obtained temperature profiles. In the assumption of the equilibrium of the energy level population we calculated radial profile of atom concentration ratio of silver and cadmium in the average cross section of the discharge gap l_{ak} = 6 mm in air at arc current 3.5 A. We used relative intensities of spectral lines AgI 768.7nm and CdI 479.9nm. Calculations carried out in such manner indicated that in plasma at the discharge axis the atom concentrations of silver and cadmium approximately equal (see Fig.5).

The next explanation of this parameter behaviour can be suggested.

The mass content of the cadmium oxide in the electrode material is about 10 percents. The approximately equal amount of the atom concentrations of silver and cadmium at the discharge axis can be formed due to the pressure of saturated vapors of cadmium above the electrode surface some orders exceeds the pressure of silver vapors (see Fig.6). The decreasing of the silver fraction at the discharge periphery can be simple explained by geometrical factor.

However, as the ionization potential of cadmium atom (8.99 eV) exceeds this potential of silver atom (7.58 eV), the ionization processes in the channel of investigated arc are determined for the most part by silver atoms.

About that indicates the temperature established in plasma of such arc discharge, which correlates with the plasma temperature of arc between silver electrodes (see Fig.1 and Fig.2). Based on the foregoing analysis of the secondary structure at the surface of the composition Ag-CdO electrodes this results can be quite expected.

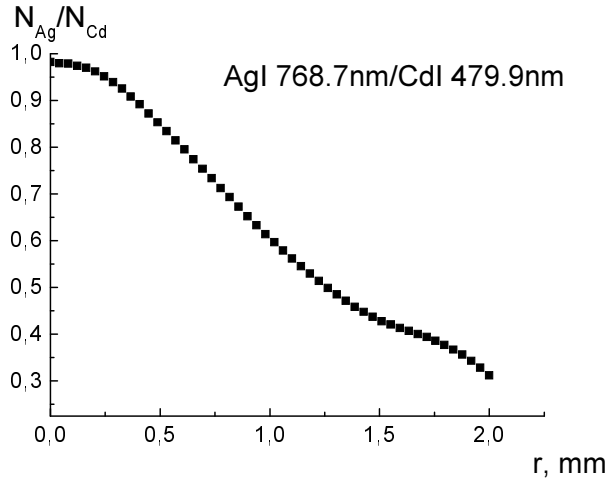

Fig 5. Radial distributions of atom concentration ratio of silver and cadmium

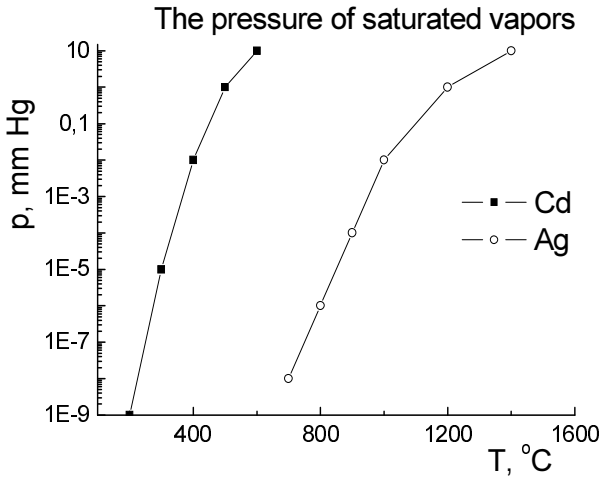

Fig 6. The temperature decencies of the saturated vapors pressure of cadmium and silver

4. Conclusions

Tthe processes occurred in the discharge gap are determined by erosion of the electrode material and condition of its surface. The obtained results allow to make some conclusions concerning of processes of the electrode material erosion in arc. The spectroscopy techniques yield results, which are not at variance with another metallographic technique results.

We for the first time attempted to realize a spectroscopic technique of plasma diagnostic of electrical arc discharges between silver electrodes and composition electrodes on the silver base.

References

[1] I.L. Babich, A.N. Veklich, V.Ye. Osidach et al. - 15th Int. Symp. on Plasma Chemistry. Orleans, France. 1003, **III** (2001).

[2] A.N. Veklich - PhD Thesis, Taras Shevchenko Kyiv University (1997) (in Russian).

[3] I.L. Babich, V.Ye. Osidach, V.I. Sobovoy, A.N. Veklich - Czechoslovak Journ. of Phys. **52**, **Suppl. D**, D731 (2002).

[4] C.H.Corliss, W.R.Bozman - Experimental transition probabilities for spectral lines of seventy elements. NBS (1962).

[5] A.G.Zhiglinsky - Handbook of data of elementary processes with participation of atoms, ions, electrons, photons. St.-Petersburg University (1994) /in Russian/.

[6] J.Terpstra, J.A.Smit - Physica. **24**, 937 (1958).

[7] I.L.Babich, A.N.Veklich, V.A.Zhovtyansky, A.I.Cheredarchuk - J. of Engineering Physics and Thermophysics. **71**, 127 (1998).

[8] A.M.Rahal, B.Rahhaoui, and S.Vacquie - J. Phys. D: Appl. Phys. **17**, 1807 (1984).

[9] A.A.Radzig, B.M.Smirnov - Parameters of atoms and atom's ions. Nauka (1986) /in Russian/.

[10] http://physics.nist.gov/cgi-bin/AtData.

[11] N.L.Pravoverov - Electrotechnology. **No9**, 42 (1979) /in Russian/.

[12] Yuan Shon Shen, R.H.A.Kroch - Proc. of the 7th Int. Conf. on Electr. Cont. Phenom. Paris. 31(1974).

HIGH PRESSURE NON-EQUILIBRIUM RF PLASMA REACTOR

George Paskalov

The Polymet Company, LLC, Los Angeles, California, USA

1. INTRODUCTION

Different plasma technology applications use a variety of plasma reactors and torches. A capacitive discharge has been shown to generate non-equilibrium plasma at atmospheric pressure [1]. In the present study we developed several co-axial plasma reactors with different electrode configurations in order to produce large volume, uniform, non-thermal plasma. Coaxial type reactors have been developed for pollution control applications [2]. Alternating voltages at frequencies up to 100 kHz generated electric field and gap discharges. These discharges spread widely in a fine pattern.

2. EXPERIMENTAL SET-UP

The experimental set-up shown in fig.1 includes an RF generator, plasma reactor, enthalpy probe, spectrum analyzer, gas analyzer, temperature/micro-pressure controller and a data acquisition system. The RF generator was developed with two potential outputs (push-pool schematic diagram), 160 kW RF power at 13.56 MHz working frequency and variable RF output voltage between 0 and 20 kV. Two different types of plasma reactors were tested: planar and co-axial geometry. The cross section of the co-axial plasma reactor is shown in fig.1. The parameters of the reactor are presented in the following table:

Number, i	1	2	3	4	5	6
R_i ,mm	3	9	10	18	20	25
ε_t	80	4	1	4	80	-

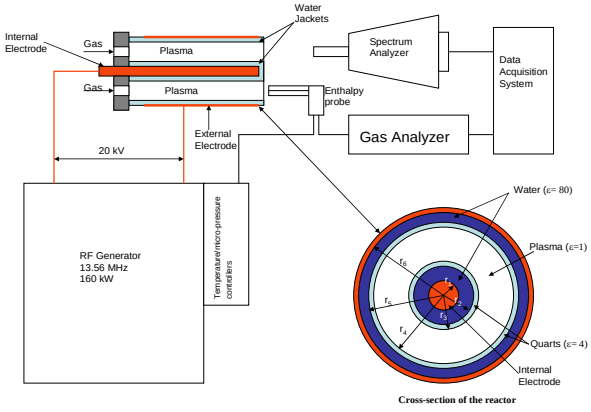

Fig. 1 Experimental Setup

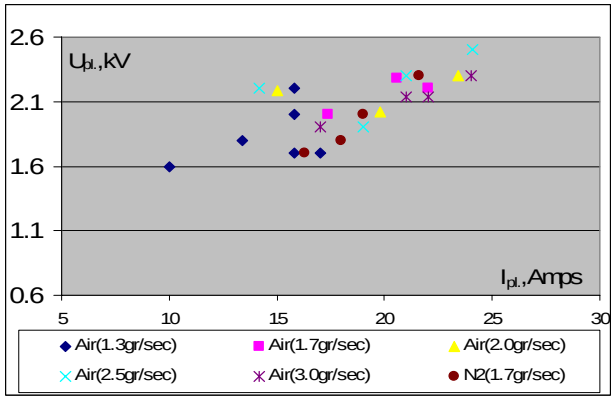

Fig.2. U-I characteristics

Argon, Helium, Nitrogen and small quantities of methane are used as the plasma gas. The gas flow rate was measured by mass-flow controllers. Plasma discharge is self-ignited. An emission spectroscope was used to study the spectrum of plasma radiation and to measure the electron and vibration temperatures. The chemical composition of the plasma gas was analyzed by a residual gas analyzer RGA-500. The gas temperature was measured using the enthalpy probe.

3. Results and Discussion

3.1 Electrical parameters. The equivalent electrical parameters were calculated based on a multi-coaxial capacitor analogy. The electrical field in each layer can be written as: $E_i = U_e/(\varepsilon_i r_i A)$, where U_e –

voltage, ε_i – dielectric penetrability for layer i; r_i – the radius for the layer i; i – is the number of layers; $A = \Sigma_i (\ln(r_{i+1}/r_i)/\varepsilon_i)$. Parameter A was constant and depended only on torch geometry. The radial distribution of the electric field intensity was non-uniform and varied from 48 V/cm to 7620 V/cm. For example, for water cooled reactor and U_e = 5000 Volts the electric field in the plasma gap ($r_3 – r_4$) is about E_3 = 7620 V/cm and E_1 = 317 V/cm. In case of air cooling: $E_1 \sim 25$ kV/cm and could cause sparking in the gap between the internal electrode and the quartz.

The loading impedance was calculated for two regimes: with and without plasma. The equivalent capacitance of the plasma reactor was calculated using the following formula: $C_{pl.} = 2\pi\varepsilon_0\lambda/\Sigma_i ((\ln(r_{i+1}/r_i)/\varepsilon_i)$. The typical reactor's capacitance without plasma is between 5 and 10 pF. After plasma ignition the the plasma reactor's total capacitance changed to approximately 75 pF. The voltage – current characteristics of the plasma reactors is shown in fig.2. As we can see, the influence of the plasma gas flow rate is negligible. U-I characteristics are different for different plasma reactors, but they always have a positive slope ($\Delta U_{pl.}/\Delta I_{pl.} > 0$). The U-I characteristics are similar to those for the positive column of a DC discharge. For non-uniform plasma discharges the U-I characteristics typically have a negative slope ($\Delta U_{pl.}/\Delta I_{pl.} < 0$). Over a wide range of plasma power ($P_{pl.}$) the discharge ($R_{pl.}$) active resistance varies from 50 to 200 Ohms. The ionization and recombination processes define the balance of electrons in the plasma gap. The current density was evaluated by following formula [3]: $j_e = E\,\mu_e\,e\,n_e$, where μ_e – is the electron mobility, n_e – electron density, e – electron charge. Typical experimental j_e were in range of 120 – 400 Amps/cm^2.

The dynamics of atmospheric pressure capacitive discharge was studied for different plasma reactor configuration and gas compositions. The stability of the plasma depends of the plasma gas flow rate and electric field profile. Electric field profile can be change by changing the geometry of the electrodes. Compared to the planar capacitive plasma reactor [1], the plasma, produced by coaxial reactor is much more stable. The stability of co-axial plasma is higher for smaller ratios of R/r, where R and r – are the radius of the external and internal electrodes respectively.

The structure of the plasma discharges depended on the power, torch geometry and plasma gas flow rate. Analysis of the electrical characteristics and visual observations showed that the discharge has a uniform structure at atmospheric pressure. The stability of plasma depended on the plasma gas flow rate and the electric field profile. The velocity and partial pressure profiles (see fig. 3) were asymmetric and depended on the plasma gas injection method: axial or tangential. The most effective condition was found at the ratio: $G_{axial}/G_{tang.} = 4 – 6$. Power losses into electrodes are high, but decrease with plasma gas flow. For example, at $G_{pl.} = 0$ gr./sec, the thermal efficiency of the reactor, $\eta_{pl.}$, is only 30 %. However, at $G_{pl.} > 1.3$ gr./sec the $\eta_{pl.}$ increases up to 60%. The maximum efficiency of the co-axial reactor was 65%.

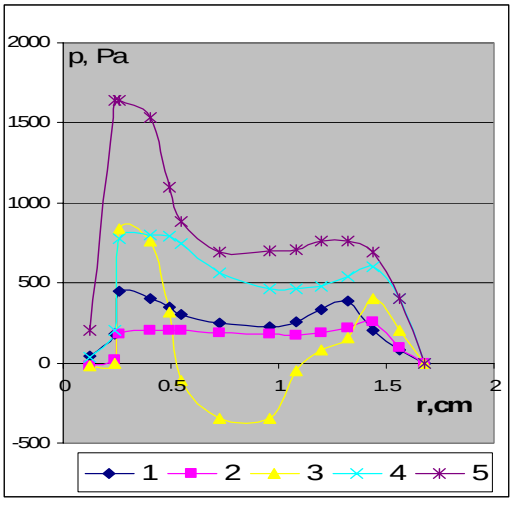

Fig.3 Radial distribution of the partial pressure

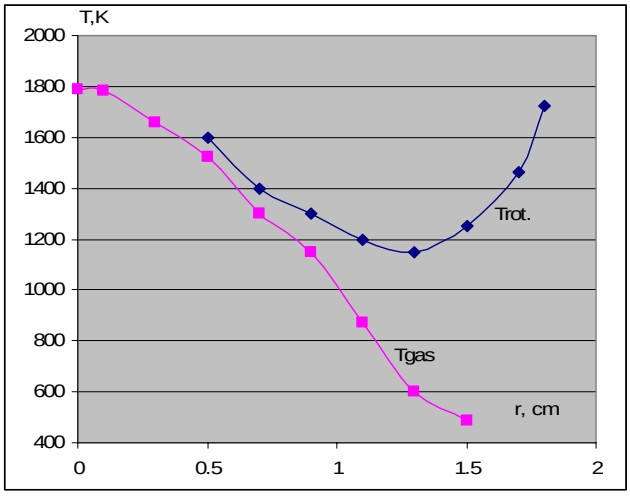

Fig.4 Radial distribution of rotational and gas temperature at plasma discharge power of 28 kW.

In Fig.3 the following curves are shown: 1 – G_{axial} =19 gr/sec + G_{tg} = 8.2 gr/sec; 2.- G_{axial}=11 gr/sec; 3.- G_{tg}=12 gr/sec; G_{axial} = 11 gr/sec + $G_{rad.}$= 8.2 gr/sec; 5. $G_{axial.}$ = 19 gr/sec + G_{tg}= 8.2 gr/sec; 1 – 3 no discharge; 4,5 – discharge.

3.2 Optical characteristics.

Visually the discharge has a volumetric form. At lower power the discharge is located only at the end of the torch. Increasing the power allowed, increased the volume of the discharge making the discharge very uniform. At the same time the sheet space (~ 1mm thickness) became much brighter. The uniformity of the discharge is very sensitive to the plasma gas flow. At higher gas flows the discharge is less uniform. By increasing the power, the stability and uniformity of the discharge can be restored. The plasma energy was 4.5 kJ/gr at the specific plasma flow rate of 0.31 gr./(cm^2 sec).

In order to investigate the influence of discharge parameters on plasma temperature we measured the rotational, vibrational and electron temperatures using spectroscopic methods. We studied the plasma spectrum in the interval of $5000A^0$ – $6700A^0$. Emission intensity was measured by monochromator SPM-2. Analysis of the emission spectra showed that the plasma spectrum content dominantly vibrational-rotational bands of Nitrogen molecules - N_2, Nitrogen Oxide -NO and the radical - OH. The most intensive spectrum is $(+2)N_2$ – second positive system for $C^3\Pi$ and $B^3\Pi$. High level $C^3\Pi$ is at the level of 11 eV compared to the base of $N_2(X'\Sigma^+)$. We did not observed the radiation spectrum of the first positive Nitrogen $(+1)N_2$ (transfer $B^3\Pi$ ---$A^3\Sigma^+$). The above spectrum was intensive for linear capacitive discharge [1]. The evaluation of the rotational temperature $T_{rot.}$ was made based on OH and $(+2)N_2$ spectrum bands. To increase the intensity of the emission spectrum of the OH A-X transition we added a small amount of water vapor to the plasma gas [2]. The radial distribution of the rotational and gas temperatures is shown on fig.4 and 6.

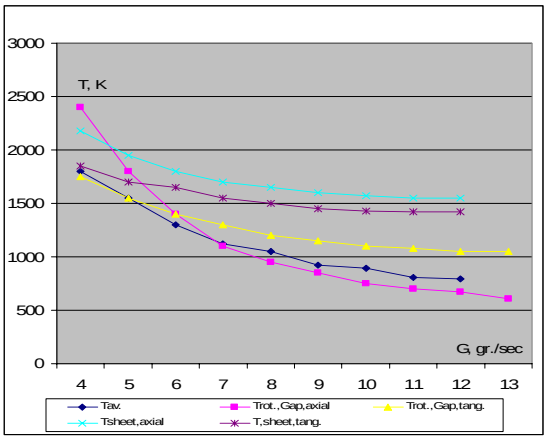

Fig. 5 Plasma temperature vs. plasma gas flow

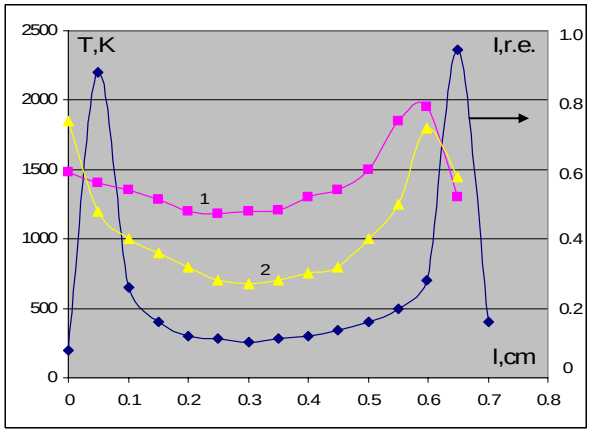

Fig.6 Radial temperature and plasma intensity distribution

The rotational temperature $T_{rot.}$ was determined by analysis of the line sequences intensities $(+2)N_2(\nu' = 0; \nu''=0)$. Rotational temperature was calculated on intensity of band $\Delta\nu = -2$ of the rotational-vibrational plasma spectrum of the system $(+2)N_2$. In the region of the middle of the plasma gap $T_{rot.}$ = 1200K at $G_{pl.}$=2.15 l/min and $P_{pl.}$ = 12 kW. $T_{rot.}$ (See fig 6, curve 1) does not depend on the power, $P_{pl.}$. Increasing $P_{pl.}$ allows a higher intensity of the rotational-vibrational spectrum. At constant plasma power, increasing the plasma gas flow rate, decreases the gas temperature in the middle of the gap up to 900K (Fig.6, curve 2), but does not change in the area under electrodes. The length of the plasma jet was 110 mm at $P_{pl.}$ = 14.3 kW and $G_{pl.}$ = 3 gr./sec. The radial distribution of the gas temperature T_{gas} at the end of the plasma torch is shown in fig. 4. In the interval of power 10 kW < $P_{pl.}$ < 14.3 kW and $G_{pl.}$ = 2.15 gr./sec, the maximum gas temperature is approximately1700 K and decreases if we increase the gas flow. The characters of the $T_{gas}(r)$ and $T_{rot.}(r)$ show that the plasma gas is well mixed at the exit of the torch and there is no significant influence of the

electrical field on the temperature profile. The very narrow high intensity layer is located near the internal electrode. The intensity of the spectrum in the positive column and close to the electrodes is very different.

The radiation profile is practically constant up to $G_{pl.}$= 18 gr/sec and does not depend on the gas plasma input method. The plasma is more uniform for the tangential plasma gas input, but $T_{rot.}$in the plasma column is much higher compared to the axial gas input because the axial velocity of plasma is much lower and residence time for the gas is higher.

Vibrational temperatures around 0.35 eV, were independent of power. In non-equilibrium plasma the spectroscopic techniques couldn't give us reliable data about gas temperature. Gas temperature was measured by an enthalpy probe. In the middle of the region between internal and external electrodes T_{gas} was about 0.1 eV at $G_{pl.}$= 1.3 gr./sec. Changing the power from 5 to 45 kW didn't affect the absolute value of T_{gas}, but significantly changed the emission intensity of the rotational spectrum. The gas temperature in the sheath region was approximately 0.15 eV and was less sensitive to plasma gas flow.

The parameters of the non-equilibrium plasma depend of the electric field, E, cyclotron frequency, ω, electron-molecule collision frequency ν_{e-m} and change of quantity, δ. The effect of the electric field on the energy of electrons is negligible, if $E << E_p$, where $E_p = 4.5x10^{-8}(\delta T_g(\omega^2+\nu_{e-m}^2)^{0.5}$, V/cm. In case of Nitrogen plasma $\delta = \sim 10^{-3}$, T_g = 4000 K, $\nu_{e-m}=\sim 10^{11}$ c^{-1} and $E_p \sim$ 180 V/cm. In our experiments $E =\sim E_p$. Thus, electric fields could have a substantial effect. In simple case δ does not depend on the average electron energy ε, and $\omega >> \nu_{e-m}$: $T_e = T_g(1+0.75E/E_p)$. At $E = E_p$, $T_e =\sim 1.75\ T_g$. Thus, the electron temperature could be very close to the gas temperature. For typical experimental conditions (Nitrogen plasma and high frequency electric field: $\Delta T = T_e - T_g = e^2E_0^2(1 + 0.2\cos\omega t+0.4\sin\omega t)$. Thus, during one period of the electric field, the ΔT is changed from $1.4A^*$ to $1.2A^*$, where $A^* = e^2E_0^2/(3m\ \delta\nu_{e-m}^2)$. Note that $A^*=0.5\Delta T_{dc}$, where ΔT_{dc} is the temperature change in constant electric field ($E = E_0$, $\omega = 0$). At $\omega = 8.5x10^7$ (sec^{-1}), $\nu_{e-m} = 2x10^{11}$ (sec^{-1}), $\delta = 10^{-3}$ and E_0 = 200 V/cm we have $\Delta T =\sim 0.8$ eV. Thus, if $T_g =\sim 0.31$ eV , the T_e will be $=\sim 1.1$ eV. In the above calculations we use the value of ν_{e-m} at $T_e \sim 1$ eV, and assume that $\omega \sim = \delta\nu_{e-m}$. In reality ω is less than $\delta\nu_{e-m}$. Also, ν_{e-m} depends of the T_e. In order to get better results we calculated the T_e using the iteration method and the following formulas:

$\nu_{e-m} = 2.9x10^{-7}[N_2]xT_e(1+T_e^{0.5})^{-0.5}$ and

$T_e = T_g + (e^2E_0^2/(3m\delta(T_e)\nu_{e-m}^2(T_e))x(1 + (1-2\omega^2/\delta\nu_{e-m}^2)\cos2\omega t/(1+4(\omega/\delta\nu_{e-m})^2 + \sin2\omega t/(2\omega/\delta\nu_{e-m} +0.5\delta\nu_{e-m}/\omega)$.

The solution of the above system for our experimental data give us $T_e =\sim 0.8$ eV.

We have tried to evaluate the electron density, n_e , by analyzing of Hydrogen lines (Balmer series), but the intensity of H_β line was very weak. In order to increase the intensity of the Hydrogen lines, we added to plasma gas a small quantity of Hydrogen (less than 0.02% vol). The n_e in the area close to the internal electrode was around 3×10^{19} (m^{-3}) and was much higher than in the area under external electrode, $n_e \sim 2x10^{18}$ It was direct correlation with the electrical field profile.

The coaxial reactor was tested for two applications, such as: laser excitation and water treatment. Plasma water treatment system was developed to decontaminate drinking water and waste water.

Conclusion

Electrical and spectroscopic measurements were conducted to understand the structure and effectiveness of the co-axial plasma reactor. The plasma was thermodynamically non-equilibrium. The difference between electron and gas temperature was around 0.8 eV. Plasma discharge was uniform and stable in the wide range of the plasma gas flow. However, it was no difference between electron, vibrational and rotational temperature at the end of the reactor in the plasma jet.

References

[1] Low temperature Plasma (RF and UHF Plasmatrons) Nauka, Novosibirsk, **6** (1992).
[2] C.O.Laux et al. Plasma Sources Science Technology, 125-138, **12** (2003)
[3] Thermal Plasmas: fundamentals and applications, Plenum Press, New York, **1** (1994).

Self-trapping effect of fast electrons in pulsed non-local plasma sources

C. A. DeJoseph, Jr.[1], V. I. Demidov[2], and A. A. Kudryavtsev[3]

[1]*Air Force Research Laboratory, Wright-Patterson AFB, OH 45433*
[2]*UES, INC., 4401 Dayton-Xenia Rd., Dayton, OH 45432*
[3]*St. Petersburg State University, St. Petersburg 198904, Russia*

Low pressure (<1 Torr) plasma sources utilizing time-modulated power, where the plasma properties of the post-discharge phase are important [1], have recently attracted the attention of a number of researchers. It has been shown that the characteristics of the afterglow plasma, where the electron temperature, T_e, is small, greatly depend on an additional group of fast electrons with large initial energy $\varepsilon_f >> T_e$. These electrons can lead to a dramatic increase in the potential drop between plasma and wall in post-discharge plasma or similar plasmas with external sources of fast electrons [2-4].

It is well known, that the electrons escape the plasma much more faster than ions and charge the wall surface negatively. To maintain the plasma quasi-neutrality, the layer of positive space charge in the vicinity of the boundary surface is formed and it is equalizing the electron and ion fluxes ($j_e = j_i$) to the wall.

In traditional local approximation, the EDF is factorized as $f_0(w,\vec{r}) = n_e(\vec{r})\, f_0^0(w, E/p)$, so the electron distribution over the kinetic energy *w* at a fixed point *r* depends on the local values of the reduced longitudinal field *E p* and other parameters (the gas temperature, the density of excited particles, etc.). In this approach the electron density profile at retarding (negative) potentials $\varphi(\vec{r},t)$ for the Maxwellian EDF is Boltzmann distribution

$$n_e(\vec{r},t) = n_0 \exp\left(-e\varphi(\vec{r},t)/T_e\right), \qquad (1)$$

n_0 corresponds to the plasma density at $\varphi = 0$. Electron flux to the wall is equal to

$$j_{eb} = j_{eT} \exp\left(-e\Delta\Phi/T_e\right), \qquad (2)$$

where the chaotic flux at the plasma-sheath edge $j_{eT} = n_s \bar{v}_e = n_s\sqrt{T_e/2\pi m}$, n_s is the plasma density and, $\Delta\Phi = (\varphi_w - \varphi_s)$ is the potential drop in the sheath. In the surface vicinity the electrons are repelled, and the Boltzmann distribution (1) is invariant with respect to choice of the reference point, where $\varphi = 0$, $n_e = n_0$. It means that in (2) it is possible to replace n_s by n_0 and $\Delta\Phi$ by φ.

The ion flux is formed in quasi-neutral plasma with $n_e \approx n_i = n$. So, it does not depend on the negative $\Delta\Phi$ value, and is referred as the ion saturation current. This flux corresponds to the sum of the diffusion and conductivity fluxes, and at uniform partial temperatures equals to ambipolar flux:

$$j_i(\vec{r},t) = -D_i dn/dr + b_i E_a n = -D_a dn/dr \qquad (3)$$

The normal to the boundary density gradient is to be calculated in the region where plasma is quasi-neutral and collisional, but not too far from the wall in order to consider the particle fluxes as conserving.

The near-wall sheath, which width is determined by the local Debye radius r_D, is collisionless in low-pressure plasmas, i.e. thin with respect to ion mean free path λ_i. The separation into plasma and sheath is, of course, conventional and at distance order λ_i from the boundary surface the charge separation (and the field strength) smoothly increases towards the surface; this region is often referred to, as presheath. The directed ion velocity u_i continuously increases towards the wall up to the sound velocity c_s ($u_i = c_s$) in some distance from the wall. For $r_D < \lambda_i$ it means that the quasi-neutral approximation ($n_e = n_i$) becomes invalid in the vicinity of this point and in the quasi-neutral approximation the electric field diverges here. The transition to the sheath

occurs, and n_e decreases fast toward the wall. This point is adopted usually as a position of the plasma-sheath boundary, and the condition is known also as the Bohm criterion (see, f.e. [5] for details). For electron temperature $T_e >> T_i$ it has simple form

$$u_i = \sqrt{T_e / M} \qquad (4)$$

The plasma density decreases by the factor $\sqrt{e}$ over the last ion mean free path, and according to (1), the potential difference over the presheath is $\approx T_e / 2$. [5]. Therefore, sometimes they say that in a collisionless plasma only voltage of a half of T_e can be applied.

The potential drop in the near-wall sheath, which corresponds to the absence of the net current through the surface, from (2) and (4) is equal to

$$\Delta\Phi_b = \frac{T_e}{e}\ln\left(\frac{\sqrt{T_e/(2\pi m)}}{c_s}\right) = \frac{T_e}{2e}\ln\left(\frac{M}{2\pi m}\right) \approx (3-6)\frac{T_e}{e} \qquad (5)$$

Estimation (5) is widely used in practices (see, f.e. [5]). However, the EDF in the partially ionized plasma is, as a rule, non-Maxwellian. For such EDF in [6] it was proposed to use the Bohm criterion (4) the "screening" temperature

$$T_{sc} = -\left(\partial\left(\ln(f_0)/\partial\varepsilon\right)\right|_{e\varphi_b}^{-1}, \qquad (6)$$

i.e. reduction scale EDF at the energy equal to the potential drop in the sheath $e\varphi_b$. Naturally, for the Maxwellian EDF $T_{sc} = T_e$. In reality the inelastic collisions with frequency ν^* result in the EDF tail depletion with respect to the Maxwellian, so that EDF tail temperature $T_e^* = \sqrt{D_\varepsilon / \nu^*}$ is markedly less then T_e [7] (D_ε is the electron coefficient of diffusion along the energy). Therefore "screening" temperature (6) can be very small even when T_e is large.

The escape of the fast electrons to the wall enhances this EDF decrease. The EDF tail depletion due to the fast electrons escape is efficient only at the distances less than the electron energy relaxation length λ_ε. At low pressure, when the plasma scale L is less than λ_ε, the EDF is non-local (see [7] for details), and the EDF tail is depleted throughout the whole plasma volume. Appropriate "temperature", which can be estimated as $T_{ew} = \sqrt{D_\varepsilon \tau_{df}}$, is also small ($\tau_{df} = \Lambda^2 / D_{ef}$ - time of free electron diffusion to the walls). Thus, the EDF in this case is additionally depleted and "screening" temperature (6) and the potential drop (5) can be very small. That fact that due to these kinetic effects, the wall potential $\Delta\Phi_b$ is considerably reduced, and even can eventually disappear was marked in [8].

For atomic gases in the energy range $\varepsilon < \varepsilon^*$, in which most electrons are concentrated, length $\lambda_\varepsilon = \lambda\sqrt{M/m} > 100\lambda$ (ε^* is the threshold energy for inelastic processes). Therefore the inequality $\lambda_\varepsilon > L$ holds up to relatively high pressures pL<5–10 cm Torr. The electron current density j_w to the negatively biased wall surface is transported only by the high energy part of electron population. The principal distinction with the results of the fluid approach is caused by the fact, that at distances less than the EDF relaxation length λ_ε, the concept of mean directed velocity fails and we cannot represent electric current as the sum of the diffusion and conductivity fluxes like the expression (3) [7]. Electrons with total energy $\varepsilon = w + e\varphi(\vec{r})$ (kinetic plus potential in electric field) lower than eΔΦ are trapped and at these distances do not contribute to electron current. The current in the vicinity of a surface is transported in the form of free diffusive flux of fast untrapped electrons with ε >eΔΦ at constant value of ε. This mechanism can not be taken into account by fluid theory.

The ratio of density of trapped electrons (n_{et}), to density of free (n_{ew}) electrons, can be, in general, be estimated from the condition that the ambipolar flux of ions must equal the free diffusion flux of fast electrons ($n_i D_a / L \sim n_{ew} D_{ew} / L$). Therefore the number of higher energy free electrons is always small ($n_{ew} < 10^{-3} n_{et}$, so that $n_i = n_{ew} + n_{et} \approx n_{et}$). In such a situation, the addition even of a small number of fast electrons with energies $\varepsilon_f >> T_e$ can dramatically change the characteristics of plasma with non-local EDF. This statement is the main point of this paper and presented here results differ significantly from obtained in the framework fluid model with beam electrons [9] and for plasma with bi-Maxwellian EDF [10].

These additional fast electrons can be created by various plasma-chemical volume processes with participation of long-living excited states of atoms and molecules, negative ions, photoionization, etc., or externally injected. Examples of volume processes are Penning ionization of metastable atoms and molecules

$$A^* + A^* \rightarrow A^+ + A + \vec{e}\,, \qquad (7)$$

superelastic collisions of slow bulk electrons with metastable atoms and molecules

$$A^* + e \rightarrow A + \vec{e}\,, \qquad (8)$$

or associative detachment of electrons from negative ions

$$A^- + A \rightarrow A_2 + e_f\,. \qquad (9)$$

Excessive energy in reactions (7-9) is passing to fast electrons e_f and can considerably exceed average energy of electrons and the potential drop (5). For example for Ar metastables (with energy $\varepsilon^* = 11.55\ eV$), the energy of fast electrons $\varepsilon_f \approx 7.3\ eV$ for (7) and $\varepsilon_f \approx 11.55\ eV$ for (8); for O_2 molecules $\varepsilon_f \approx 3.6\ eV$ for (9).

Non-local fast electrons with $\varepsilon_f > e\varphi_b$ are produced in the volume by results from reactions (7-9) and they are lost to the walls due to their free diffusion, i.e. kinetic equation for their EDF $f_{of}(\varepsilon, \vec{r})$ is

$$\nabla D_f \nabla f_{of}(\varepsilon, \vec{r}) = \nabla \cdot j_{ef}(\varepsilon, \vec{r}) = \sum I_j(\vec{r}) R_j(\varepsilon) \qquad (10)$$

In the source terms in (10) $I_j(r)$ are the source intensities and $R_j(\varepsilon)$ are the energy spectra of the reactions (7-9). Because $R_j(\varepsilon)$ is a narrow (like δ-function) peak in energy region of their origin [2-4], then at $\varepsilon_f > e\varphi_b$ density of fast electrons is

$$n_{ef} = I_j \tau_{df} \qquad (11)$$

where $\tau_{df} = \Lambda^2 / D_{ef}$ - time of free electron diffusion to the walls. The physical meaning of these is evident: fast electrons escape on the wall faster then they can relax and loss their energy by collisions in the discharge volume.

The fast electrons flux to plasma boundary with area S can be found via their birth from (10) as

$$j_{ef} = \int_V \sum I_j dV / S\,. \qquad (12)$$

As source term I_j may be determined enough accurately, the balance equation (12) lets easy to find the flux j_{ef}. For example, for reaction (7), $I_p = \beta_p N_m^2$, where $\beta_p \approx 10^{-9}\ cm^3/s$ is the rate of (7) and N_m is density of metastable atoms.

In the presence of additional fast electrons (7-9), the zero current condition is of the form

$$j_i = j_{eb} + j_{ef} \qquad (13)$$

where j_{eb}, j_i and j_{ef} are defined according to Eqs. (2,3,12).

The Eq. (13) determines the potential drop in the sheath as a function of the fast electron flux j_{ef}

$$\Delta\Phi = \Delta\Phi_b + \frac{T_e}{e} \ln\left(\frac{j_i}{j_i - j_{ef}}\right) \qquad (14)$$

The near wall potential jump increases in comparison with the value $\Delta\Phi_b$ (5), calculated at the assumption only bulk electrons, i.e. when j_{ef} is negligible.

In stationary plasma of self-sustained glow discharges the wall potential $e\Phi > \varepsilon^*$ [5], so created in reactions (7-9) fast electrons are usually trapped in the volume and so not contribute in flux on the wall.

In contrast, in the post-discharge plasma T_e falls rapidly so the potential jump (5) decrease also rapidly and it is low with respect to the energy ε_f of additional fast electrons (7-9) . As the densities of long-lived excited states, which determine sources I_j in (10-12), are decreasing slowly, at some time afterglow the flux (12) will equal the ambipolar ion flux (3). The relation (14) become incorrect if j_{ef} is close to j_i and if $j_{ef} > j_i$, in order to maintain quasi-neutrality, part $j_{ef} - j_i$ of the flux of fast electrons must be self-trapped, i.e., the walls will acquire a potential of the order of ε_f / e [2-4]. When this occurs the wall potential, $\Delta\Phi$, will increase from $\Delta\Phi_b \approx 0.1-0.3\ V$ to anomalous large $\Delta\Phi_f = \varepsilon_f / e \approx 3-10\ V$. In this case the trapped electrons with $\varepsilon < \Delta\Phi_f$ cannot escape to the wall and are cooled in the plasma volume by collisions with atoms and bulk electrons (heating the latter) forming a step-like EDF in low energy direction (see [3] for detail). The physical meaning of these is evident: this part of appearing fast electrons trapped in the volume and can not escape to the wall. They relax by electron-electron and elastic electron-atom collisions, e.g. by processes with small energy losses, creating a continuos electron spectra in the region $\varepsilon < \varepsilon_f$.

The fast trapped electrons can lead to excitation from metastable levels and significantly increase the intensity of spectral line emission in afterglow [3,4]. These effects have been experimentally investigated in pulsed rf ICP discharge in Ar. The plasma excitation experiment has been described in detail in [4]. To show the effect of gradual increase in the wall potential, measurements of the time dependence of the plasma potential have been made for different gas pressures (see Fig.1). The transition between regimes of free-flight and partial

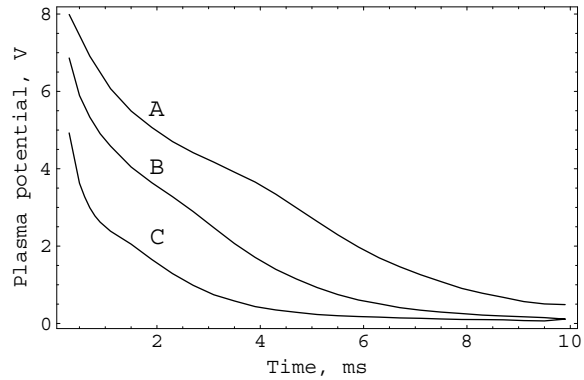

Fig. 1 Time dependence of the plasma potential for different pressure after termination of rf power. Average power is 250 W and rf pulse duration is 100 μs. A – 20 mtorr, B – 10 mtorr, and C – 5 mtorr.

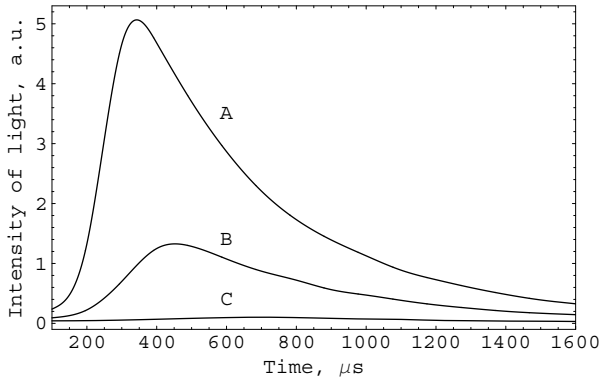

Fig. 2 Intensity of the Ar spectral line 420.1 nm in the afrerglow. Argon pressure is 20 mtorr. (100mks,500 Hz) A – 20 mtorr, B – 15 mtorr, and C – 10 mtorr.

trapping has been observed over a pressure range of 3 to 20 mTorr. During this transition, the wall potential increases from a few tenths of a volt to several volts. We also observe a significant increase in the intensity of spectral lines corresponding to transitions between the argon $3p^5 4p$ and $3p^5 4s$ levels, which is consistent with stepwise excitation (see Fig.2). These experiments demonstrate the presence of self-trapping of fast electrons and the existence of large near-wall potentials in afterglow.

This work was supported by the Air Force Office of Scientific Research. AAK is grateful for the support of CRDF grant RP-1-567-ST-03.

References

[1] M.A. Lieberman, S.Ashida, Plasma Sources Sci.Technol., 5, 145 (1996).
[2] V.I.Demidov, N.B.Kolokolov, Sov.Phys.Tech.Phys., 25, 338 (1980).
[3] N.B. Kolokolov, A.A. Kudrjavtsev, A.B. Blagoev, Physica Scripta, 50, 371 (1994).
[4] V.I.Demidov, C.A.DeJoseph, A.A.Kudryavtsev, Phys.Plasmas, 11, 5250 (2004).
[5] M. A. Lieberman and A. J. Lichtenberg. Principles of Plasma Discharges and Materials Processing. John Wiley & Sons, New York, (1994).
[6] K.-U. Riemann, IEEE Trans. PS-23: 709 (1995).
[7] L.D. Tsendin, Plasma Sourse Sci.Technol., 4, 200 (1995).
[8] A.P. Zhilinsky, I.F.Liventseva, L.D.Tsendin. Sov.Phys.-Techn.Phys., 22, 177 (1977).
[9] J.W. Bradley. J.Phys.D:Appl.Phys., 29, 706 (1995).
[10] V.A. Godyak, V.P. Meytlis, H.R. Strauss. IEEE Trans. Plasma Phys., 23, 728 (1995).

DEGRADATION OF ETHYL ACETATE AND TOLUENE BY MEANS OF AN ELECTRIC DISCHARGE IN HUMID AIR

E.B.Tsagou-Sobze[1,2], D. Moussa[2], A. Doubla[1], E. Hnatiuc[3], J.L.Brisset[2]

1 Department of inorganic Chemistry, Laboratory of mineral chemistry, University of Yaoundé-1, (Cameroon)
2 Department of chemistry ,Laboratory of electrochemical (L.E.I.C.A),University of Rouen (France)
3 technical University "Gheorghe Asachi" lASI, Romania

ABSTRACT:

The plasma treatments of two typical volatile organic hydrocarbons (i.e., liquid ethyl acetate and toluene) taken as liquid targets were examined with a particular device consisting of two gliding arc reactors in humid air operated in series.

The strongly oxidising species generated by the discharge and present in the plasma (i.e., the radicals °OH and °ON) are responsible for the degradation of ethyl acetate and toluene with an excellent efficiency. Analysis of the out going gases show that approximately 90% of the total organic carbon disappeared from the system are converted into CO_2 and CO.

Keywords:

non thermal plasma; gliding arc electric discharge; pollution abatement; oxidation ; degradation of toluene; ethyl acetate.

1-Introduction

The occurrence of oxidation phenomena in the natural world is largely identified as it occurs in biological or industrial processes. Among the later ones, the phenomena are largely involved to solve the endemic problems of the wastes treatments [1]. The quantity of mankind provided wastes drastically increases, so that a major question now concerns national and even international authorities: how to control the pollution, and also how to favour its abatement.

Traditional techniques were improved, and new ones were proposed. Among the most promising emerging technique for pollution abatement, the use of on-thermal plasma appears as a side technique close to the Advanced Oxidation Processes. It occupies a special situation which is related to its low cost and high efficiency.

We report here on using electric discharges and in particular, a new "Duplex" system involving two coupled gliding arc discharges for the treatment of Ethyl acetate and Toluene. These organic compounds are generally used as solvents in the industry of painting, inks and varnishes, of the pickling solutions, of the plastics and pharmaceutical. Both Volatile Organic Compounds (VOCs) are hazardous for human health, so that their throwing out is strictly regulated and they must be degraded, in agreement with the local regulations.

The particular plasma technique used is known to be well adapted for removing organic solutes dispersed in aqueous solutions [2-5], because it works at atmospheric pressure and quasi-ambient temperature. It also enables us to degrade non aqueous liquid media, such as spent extraction solvents [6].

2-Experimental data

The selected plasma device retained for the degradation of Ethyl acetate and Toluene involves two closed pyrex reactors (volume: 500 mL), connected by a pipe approximately 5mm in diameter. These matching reactors are intended to degrade respectively the VOCs in aqueous solution (R_1 reactor) and the organic vapours (R_2 reactor) presents in exhaust gases from R_1. The plasma reactors were built on the basis of Czernichowski's work [7] and involved a discharge between two diverging electrodes. An arc forms at the neck between the electrodes and moves along them, as a gas flow is directed along the axis of the reactor. When the feet of the arc reach the tips of the electrodes, the breaks into a plasma plume and a new arc resumes.

The target aqueous solutions were prepared by dissolving 225.05 mgL^{-1} and 228.02 mgL^{-1} of industrial grade VOCs, respectively Ethyl acetate and Toluene.

Analysis of the plasma treated solutions were performed by Total Organic Carbon (TOC) Shimadzu VOC-VE analyser. CO and CO_2 were evidenced at the output of each reactor by means of Dräger disposable test tubes.

3-Experimental Results and discussions

3-1 Kinetics

For the treatment of aqueous VOCs solutions, a problem related to evaporation takes place. In switched off discharge conditions, the amount of organic compound dispersed in R_1 decreases rapidly as it is carried out by the feeding gas flow. Elimination by 50% of toluene and acetate respectively need 7 and 9 mins (Figs.1 and 2).

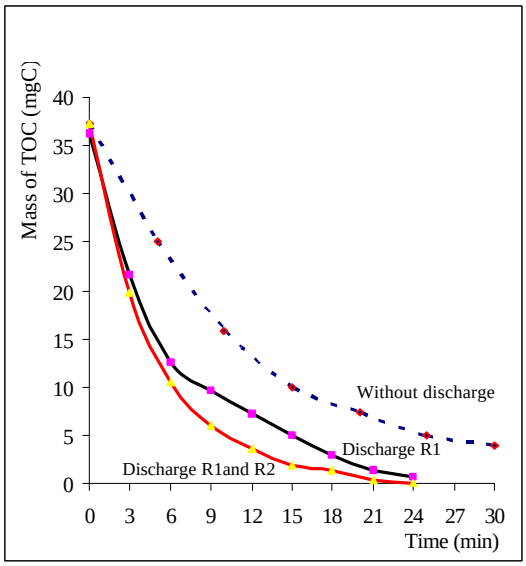

Figure 1: Decrease in the TOC with the treatment time of Toluene

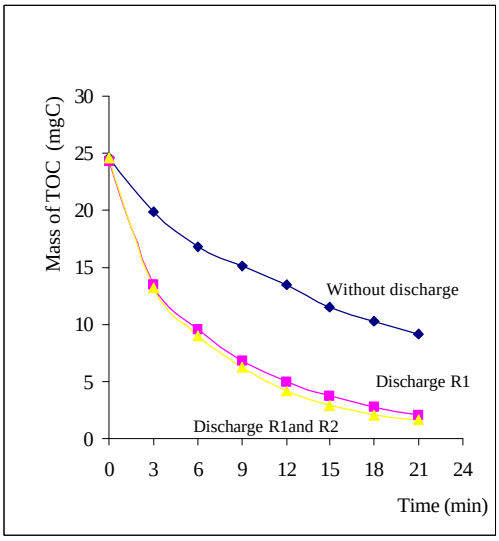

Figure 2: Decrease in the TOC with the treatment time of Ethyl acetate

However, the same pollutant abatement requires around only 3 mins for both VOCs when operating in the simplex mode with the single discharge reactor R_1 (Figs 1 and 2). This feature illustrates the fact that the interaction between the plasma species and the liquid target takes place at the liquid/gas interface. The degradation of the target probably results from the action of the oxidising OH radicals present in the plasma plume.

The exhaust gases of the system were identified by means of specific Dräger reagents. The relevant analysis show that approximately 90% of the total organic carbon disappeared from the system are converted into CO_2 and CO (Figs 3 and 4).

Operation of the reactors R_1 and R_2 in series to improves the effectiveness of the treatment. The contribution of the Duplex system is explained by the rejected CO_x rate (i.e.,90% of ethyl acetate and 80% of toluene) higher than for simplex [i.e., 60% of (Ethyl acetate) and 55% of (Toluene)], and by degradation rate which increases for simplex [i.e., V_1 = 0.1011mgC/min (ethyl acetate) and $V_{1'}$= 0.279 mgC/min (toluene)] to [i.e., V_2= 0.1241mgC/min (ethyl acetate) and $V_{2'}$ = 0.4016mgC/min (toluene)] in Duplex (tab 1). The desired effect of the second discharge is less significant, but not negligible.

Parameters of degradation	Simplex	Duplex
Kinetics constant (mgC/min) (O – 18 min)	Ethyl acetate V_1= 0.1011	Ethyl acetate V_2= 0.1241
	Toluene $V_{1'}$= 0.279	Toluene $V_{2'}$= 0.4016
Pourcentage CO_x	Ethyl acetate 60%	Ethyl Acetate 90%
	Toluene 55%	Toluene 80%

Tableau1: Comparative study enters Simplex and Duplex

Detailed measurements also show that the elimination of VOCs obeys an overall 1st order kinetics, as evidenced by the linear ln C% vs t. plots (Figs.5 and 6).

This feature agrees with diffusion phenomena of the solutes to the liquid surface.

Additionally, the plasma treatment induces a strong and rapid acid effect, so that the pH of unbuffered aqueous solutions is lowered by about 4 pH units within 1-2 minute [8]. This is related to the occurrence of NO radicals formed in the discharge.

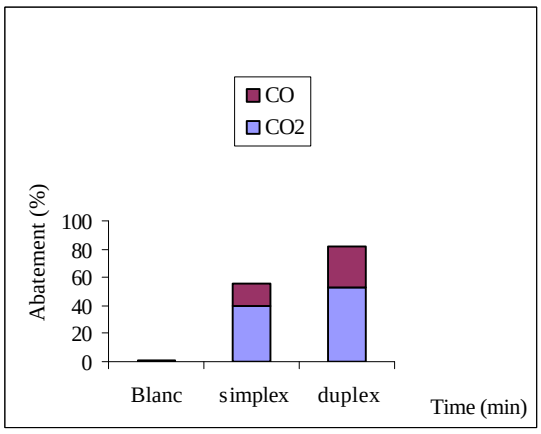

Figure 3: Conversion rate of Toluene into CO and CO_2

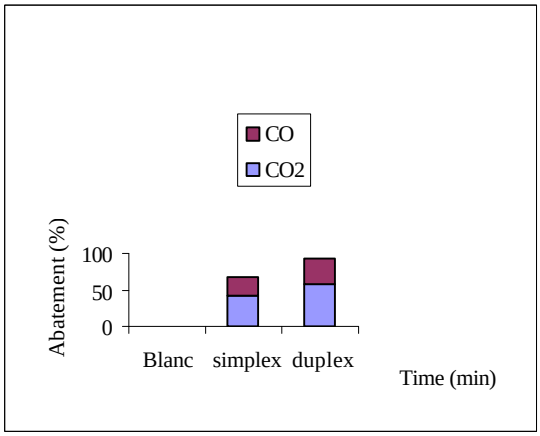

Figure 4: Conversion rate of Ethyl acetate into CO and CO_2

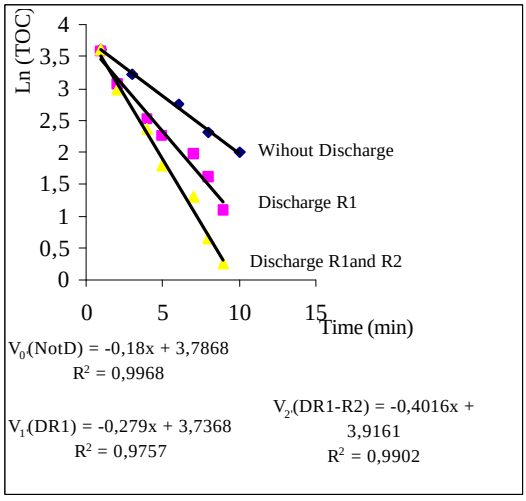

Figure 5: Kinetics of Toluene degradation

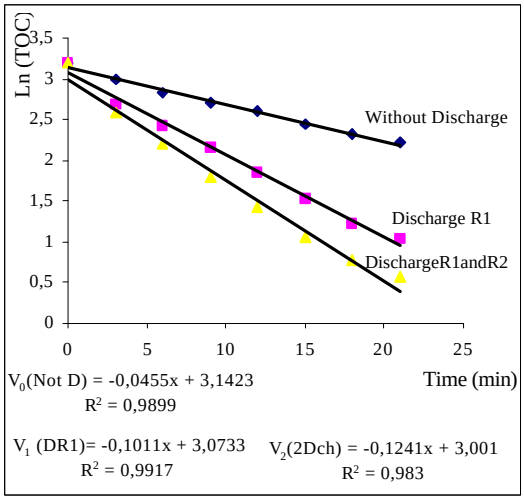

Figure 6: Kinetic of Ethyl acetate degradation

3-2 Suggested degradation mechanisms

The gas selected for this study is humid air. The electric discharge generates radicals, such as °OH, NO°, etc. which are present in the plasma and able to react at the liquid surface with the target molecules. The °OH radicals are the more suitable oxidising agents due to their high potential : E(°OH/H_2O) = 2.85V. OH reacts with the ethyl acetate or the toluene molecules by first removing an hydrogen atom from a C-H group in connection with an initiation step. This phenomenon propagates by a file of oxidation reactions which lead to the formation of intermediate acid compounds (i.e., acetic acid for ethyl acetate or benzoic acid for toluene). These acids then decarboxylate and release carbon oxides.

The Hydroxyl radicals will add to the aromatic ring of toluene before opening the ring and leading to intermediate species also able to decarboxylate.

Assumed degradation mechanism for toluene

Step I

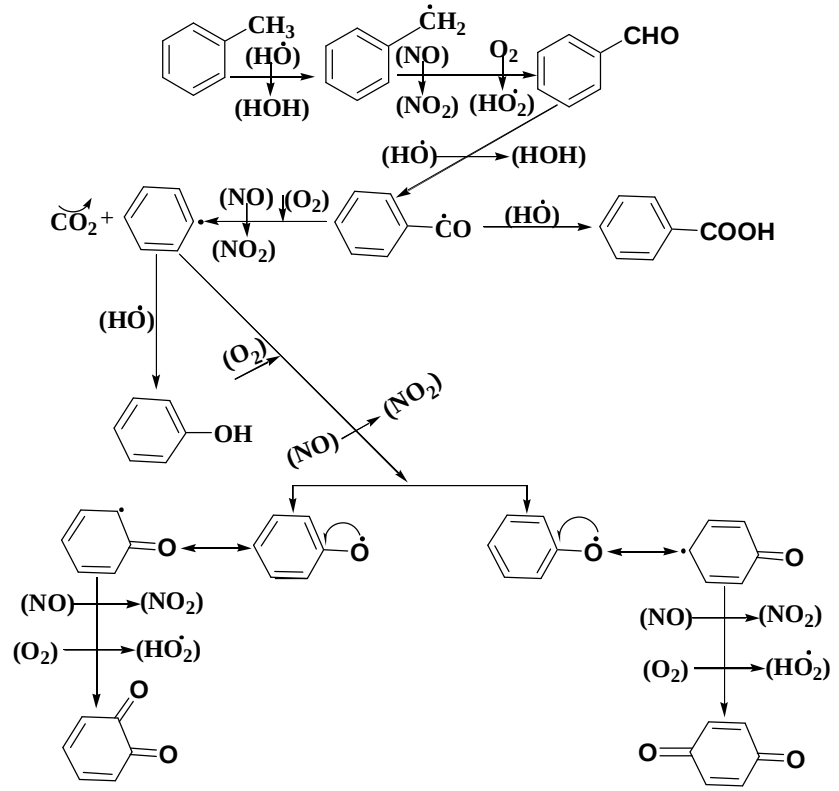

Step II

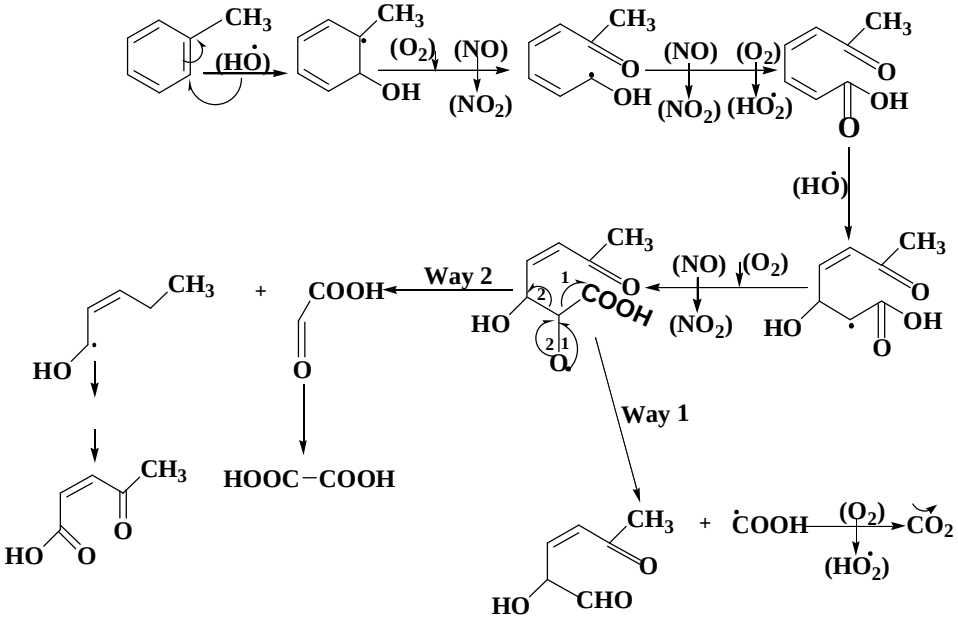

Assumed degradation mechanism for Ethyl acetate

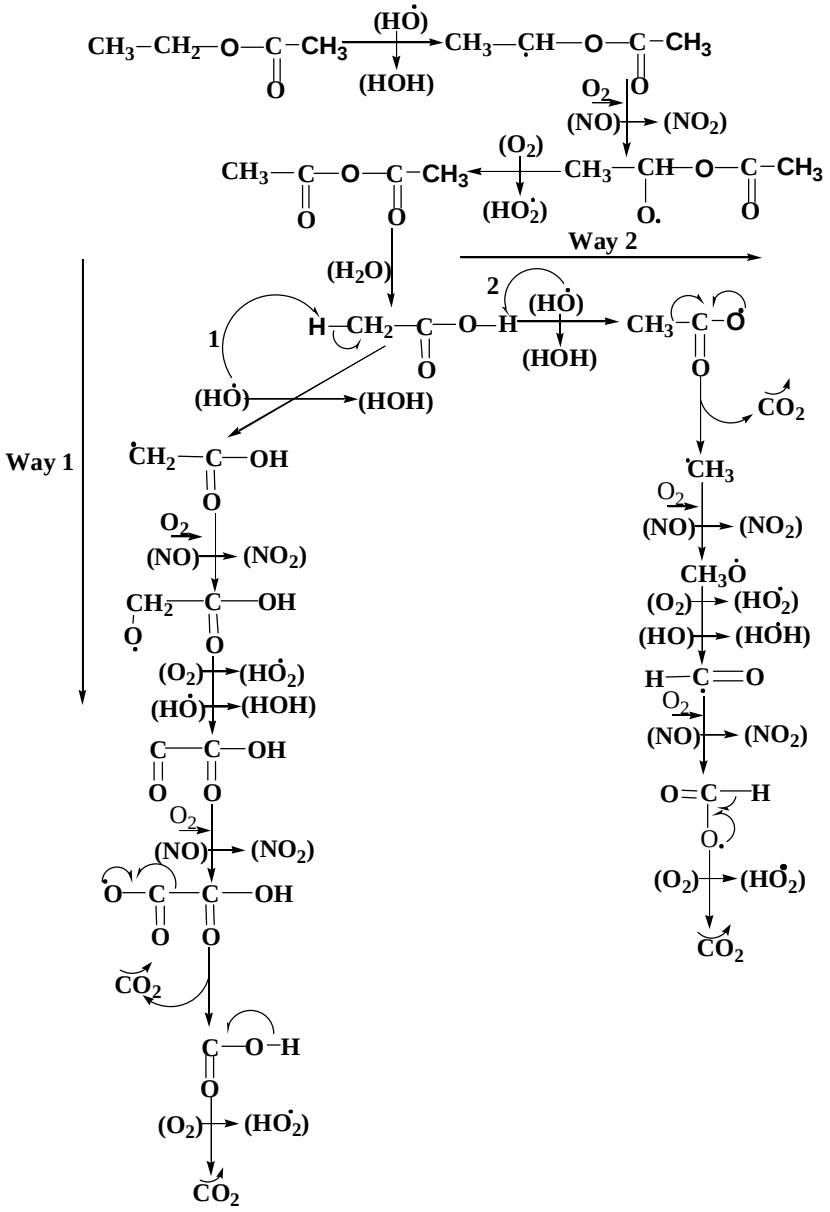

4-CONCLUSION

The pollution abatement of aqueous solutions of dissolved VOCs exposed to non-thermal plasma treatments confirms the efficiency of this technique which is evidenced by the short time needed to remove 50% of the solutes. A mechanism involved may be related to the active species present in the plasma, (i.e., °OH and NO°).

This work was intended to limit the quantity of untreated pollutant thrown away in the open. When limited to CO_x degradation parameter, the simplex system alone allows a 60% abatement (i.e., Ethyl acetate), while it reaches 8O% with the duplex system (i.e., an increase by 25%). This increase shows that our Duplex device actually improves the effectiveness of the treatment.

REFERENCES.

[1] E.HNATIUC "*Procédés électriques de mesure et de traitement des polluants*? Tec&Doc Ed., Paris, (2002).
[2] N.BELLAKHAL, F. MORAS, S.BOULAY, C.DESANAUX, J-L.BRISSET ;*Water, Wastes Env.Res.* 2 (2002) 59-68
[3] F.ABDELMALEK, S.GHARBI, B.BENSTAALI, A.ADDOU, J-L.BRISSET, *Wat.Res.*38(2004)2339-2347.
[4] F.MORAS, J.-L. BRISSET, *PROC.14th GRUTTEE(Limoges, France*, 2001) 227-230.
[5] J.FANMOE, J.KAMGANG, D.MOUSSA, J.-L.BRISSET, *Phys. Chem. News* 14(2003)1-4
[6] D.MOUSSA, J.-L.BRISSET, *J. Hazard. Mat.B102*(2003) 189-200 .
[7] H.LESUEUR, A. CZERNICHOWSKI, J.CHAPELLE, *Fr.Pat*.(1988) 2639172.
[8] B.BENSTAALI, D.MOUSSA, A.ADDOU, J-L.BRISSET, Europ.Phys.*J.- A.P.*(1998),171-179.

Production of Broad Arc by Alternating Magnetic Field

T. Yamamoto[1], K.Takeda[1],T.Toh[2] and J.Tanaka[2]
[1]*Department of Machine Intelligence and System Engineering,*
Akita Prefectural University, Japan
[2] *Steelmaking R&D Division, Environment & Process Development center,*
Nippon Steel Corporation, Japan

Abstract

Interaction of a transferred arc with an external magnetic field is investigated experimentally. By applying an alternating magnetic field perpendicularly to the arc, the arc root oscillates on the anode in the direction of **IxB**.

The movement of the oscillating arc is observed by a stroboscopic technique. The arc responds to the time varying field up to a frequency 100Hz in the same manner as a static field. Beyond 100Hz, the oscillation amplitude of the arc reduces with the increase of the frequency.

Gas injection to the cathode region with swirling velocity results in the increase of the stiffness of the arc.

The amplitude of the arc oscillation increases proportionally with the increase of the magnetic field. It is confirmed that various pattern of heat flux on the anode can be obtained by changing the strength and the wave form of the applied magnetic field.

1. INTRODUCTION

Various types of plasma torches have been developed to generate a concentrated heat flux. Plasma arcs in a transferred mode are widely used as convenient means to weld or cut metals. However, soft and broad plasma arcs are often required for some material processing such as surface conditioning or heat treatment over a large area[1)].

By applying an alternating magnetic field perpendicular to the arc, the authors developed a system to drive an arc root on a anode back and forth at a frequency of several tens Hz. Schematic illustration for driving plasma arc is shown in Fig.1[2)]. Such an oscillating plasma arc can be regarded as a broad heat source having a width of the oscillation amplitude. By changing the field strength and the wave form, it may be easy to control the heat pattern on the anode. However few studies have been done on the distribution of the heat flux and the arc pressure.

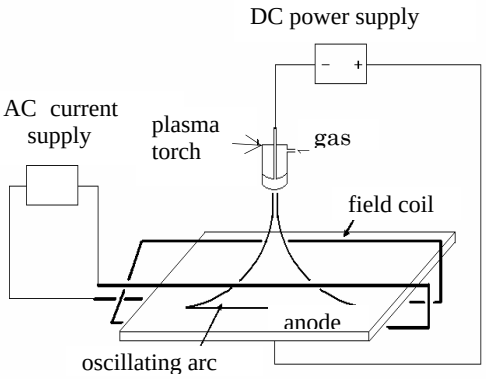

Fig.1 Schematic arrangement to generate the broad arc.

By using a simplified momentum equation, it is known that the displacement of the arc root on an anode is expressed as [1)]

$$X = (1/\beta) - \{(1/\beta)^2 - L^2\}^{1/2}, \qquad (1)$$

where L represents the distance between nozzle exit of a plasma torch and an anode, and

$$\beta = I_a B / \rho_o Q_o u. \qquad (2)$$

In Eq.(2), I_a, B, ρ, Q and u express an arc current, magnetic flux density, plasma gas density, its volumetric flow rate and plasma jet velocity at the outlet of the torch, respectively. Suffix o represents a standard state. If $(1/\beta) >> L$, the displacement of the arc root is proportional to the magnetic field as

$$X = I_a B L^2 / 2 \rho_o Q_o u. \qquad (3)$$

When the applied magnetic field varies with time as $B = B_o \sin \omega t$, it is expected for small ω that

$$X = (I_a B_o L^2 / 2 \rho_o Q_o u) \sin \omega t. \qquad (4)$$

If $(1/\beta) < L$, the second term in the right hand side of equation (1) becomes imaginary. It means that the

arc motion becomes unstable under too much strong magnetic field.

The objectives of the present work are to investigate the arc movement and the heat flow distribution on the anode under various types of alternating magnetic fields.

2. EXPERIMENT

2.1 Plasma torch and power supply for arc

A transferred arc torch with a tungsten cathode is used to generate an oscillating arc. The torch cathode is connected to a DC power supply, which is operated in a constant current mode. The arc current is adjustable up to 120A. Open circuit voltage of the power supply is 280V. Argon gas is used as a plasma forming gas in this experiment. A transferred arc is produced in the open air between the torch and a water cooled copper anode. Typical stand off distance between the torch orifice and the anode is 70mm. The arc is ignited by applying high voltage radio frequency between the cathode and orifice of the torch outlet.

The authors investigate effect of gas injection into the cathode region on the oscillating amplitude. Two types of gas feeders are used for this study. One of them shown in Fig.2 (a) produces swirling flow and the other shown in Fig 2 (b) does straight flow.

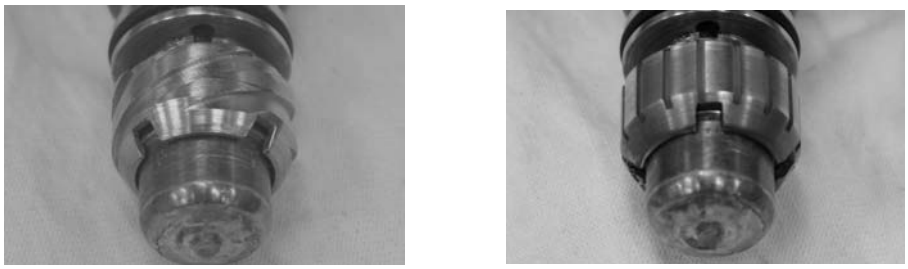

(a) **(b)**

Fig.2 Plasma gas feeding guide (a) for swirling flow and (b) for straight flow.

2.2 Magnetic field coil and current supply to the coil

As shown in Fig.3, a two-turns coil with rectangular form is designed to generate a magnetic field perpendicular to the arc.

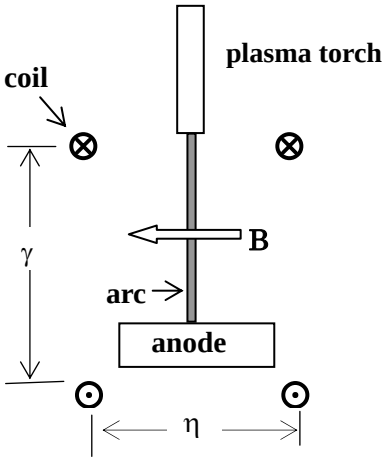

Fig.3 Arrangement of a magnetic coil.

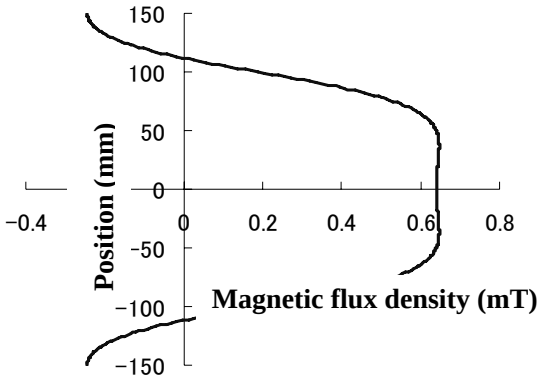

Fig.4 Magnetic flux density along vertical center line

The coil is connected to the current source, which can supply various types of alternating currents such as sinusoidal, triangular and rectangular ones with different amplitude and different frequency. The coil current and its frequency can be changed up to 300A, and up to 1kHz, respectively. One of the examples of the magnetic field strength obtained along the vertical line at the center is shown in Fig. 4 for the coil of γ=200mm and η=100mm, at an electric current of 100A.

2.3 Observation of arc motion

In order to observe the high speed oscillating movement of the plasma arc, the authors used a stroboscopic technique as shown in Fig 2. The arc is observed through the holes of the disk which rotates at a constant angular velocity. In this case, the arc is exposed at a certain time interval τ and an observation frequency, f is expressed as $f = 1/\tau$. If the frequency (f) satisfies the following relation with the frequency of the alternating magnetic field (f_o) as

$$f = f_o / N \text{ , (N; an integer)} \qquad (5)$$

the observer finds the arc in the same position. If the observation frequency is slightly different from Eq.(5) as

$$f = (1 - \alpha) f_o / N, \qquad (6)$$

the arc is observed as if it moves at a frequency of αf_o.

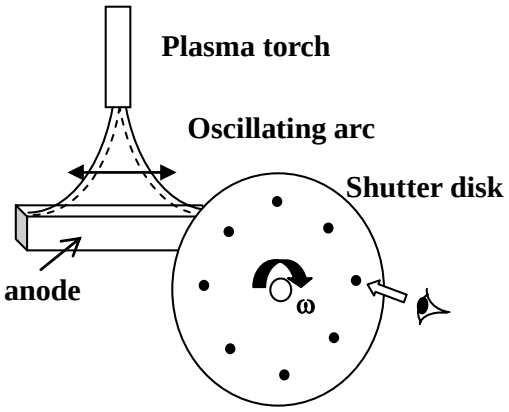

Fig.5 Schematic illustration on the stroboscopic observation of the arc.

If the observation frequency is adjusted to 1% shift from that written in Eq.(5) by controlling the disk speed, the arc movement can be observed as if it moves at a frequency a hundred times smaller than the real one.

2.4 Measurement of heat flux distribution on the anode;

The distribution of the heat flux along the arc motion is investigated by using specially designed copper anode as shown in Fig.6. Its dimension is 200mm (L) and 100mm (W). The anode is divided into several sections through which a cooling water channel passes. Thermocouples are inserted into the water channel at the inlet and the outlet of each section.

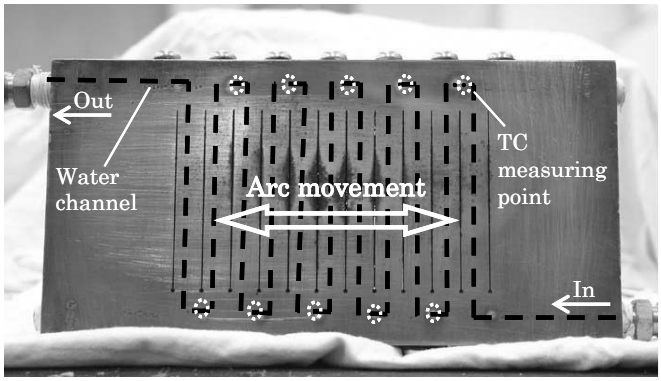

Fig. 6 Water cooled copper anode for the measurement of heat flux distribution.

Heat flow from the arc root into each section is evaluated by measuring the temperature increase of the cooling water.

3. RESULTS

3.1 Effect of swirling flow

A stable long arc is obtained under no external magnetic field as shown in Fig. 7 (a). Under the alternating magnetic field perpendicular to the torch axis, the arc oscillates in a plane perpendicular both to the magnetic field and to the torch axis as shown in Fig.7 (b) and Fig 7 (c). The effect of the swirling velocity on the amplitude of the oscillating arc motion is studied by using two different types of the gas feeding guides as shown in Fig. 2. Fig. 7 (b) and Fig.7 (c) illustrate the arc movements with and without swirling velocity, respectively. As is evident from these figures, swirling gas injection leads to the increase of the stiffness of the arc.

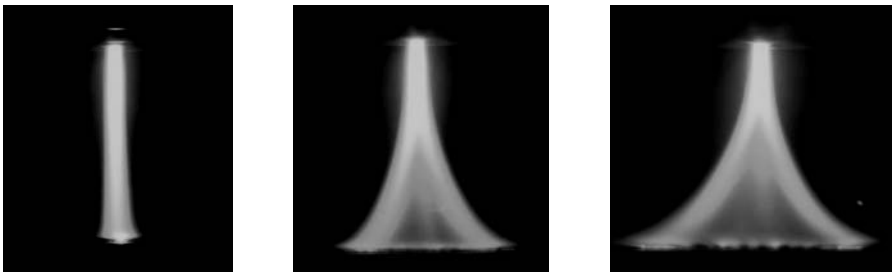

(a) **(b)** **(c)**

Fig.7 Plasma arcs: (a) without magnetic field, (b) oscillating arc with swirling gas flow and (c) oscillating arc without swirling gas flow. Plasma gas flow rate is 15NL/min. Arc current is 130A. In the case of (b) and (c), the wave form of the applied magnetic field is rectangular and its amplitude Bo is $3x10^{-3}$ T. The oscillating frequency is 60Hz.

3.2 Variation of oscillation amplitude with magnetic field

Experimental observation reveals that the time response of the arc motion is considerably good. Up to 100 Hz of the magnetic field frequency, the displacement of the arc is not different from that under the static field. When the field changed with time at 200Hz, 10% reduction is observed in the arc amplitude.

The oscillating amplitude of the arc motion increases with the increase of the applied field strength, as shown in Fig. 8. The proportional relationship between the arc amplitude and the magnetic flux density is quite reasonable as the arc movement is caused by the electromagnetic force of (**I** x **B**). However, proportional relation is not obtained between the arc amplitude and arc current.

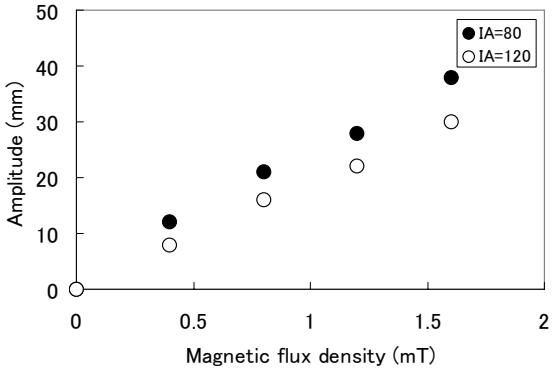

Fig.8 Variation of arc oscillation amplitude with the applied magnetic field .at a frequency of 60 Hz. The flow rate of plasma gas is 7.5 NL/min argon.

It should be noticed that, as is written in Eqs.3 and 4, the arc amplitude is not only proportional to I but also inverse proportional to u. The increase of the arc current, I surely results in the increase of the arc jet velocity, u due to the expansion of the gas volume inside the torch. Therefore the increase in arc gas velocity has negative effects on the deformation of the arc by the electro magnetic force.

3.3 Distribution of the heat flux on the anode

Heat flow patterns on the anode without and with external magnetic field are illustrated in Fig. 9 (a) and Fig. 9 (b), respectively. The flow rate of plasma gas is 15 NL/min in both cases. Applied magnetic field is in the form of triangle with the frequency of 60 Hz. The amplitude of the alternating magnetic field is 20 mT. The arc current is 120A. If the stationary arc is assumed an uniform heat source with the width of 2cm as shown by dashed line in Fig.9 (a), and the arc is driven by an alternating magnetic field with a triangle wave form , expected heat flow pattern should be as shown by dashed line in Fig.9 (b), which is similar to the experimental result.

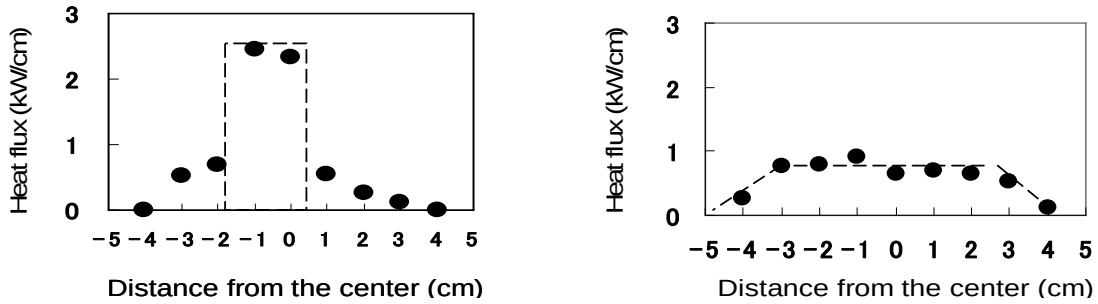

Fig.9 Heat flux distribution along the oscillating arc movement on the anode.

Heat flow pattern can be modified easily by changing the amplitude of the magnetic field and changing the wave form of the electric current supplied to the field coil.

4. Conclusions

Interaction of a transferred arc with an external magnetic field is investigated experimentally. By applying an alternating magnetic field perpendicularly to the arc, the arc root oscillates on the anode in the direction of **IxB**.

The movement of the oscillating arc is observed by a stroboscopic technique. The arc responds to the time varying field up to a frequency 100Hz in the same manner as a static field. Beyond 100Hz, the oscillation amplitude of the arc reduces with the increase of the frequency.

Gas injection to the cathode region with swirling velocity results in the increase of the stiffness of the arc.

The amplitude of the arc oscillation increases proportionally with the increase of the magnetic field. It is confirmed that various pattern of heat flux on the anode can be obtained by changing the strength and the wave form of the applied magnetic field.

Acknowledgements

Major part of this report provides the results of the energy saving projects of Nippon Steel Corporation, financially supported by the Ministry of Economy, Trade and Industry of Japan. The

authors thank Prof. O. Solonenko for designing and manufacturing a plasma torch.

Refereces

(1) J.E.Harry and D. Goodwin; Surfaceheat treatment using a plasma torch with a magnetically traversed arc, Proceedings of 4th Int. Conf. on Advance in Welding processes, England, (1978), 181

(2) K.Takeda; Generation of magnetically oscillating plasma arc and its properties, Ko-on gakkaisi (Japanese) vol.16 (1990), 357-367

QUANTIFICATION OF HYDROXYL RADICALS PRODUCED IN AQUEOUS PHASE PULSED ELECTRICAL DISCHARGE REACTORS

Mayank Sahni, Wright C. Finney, and Bruce R. Locke

Department of Chemical and Biomedical Engineering, FAMU-FSU College of Engineering, Tallahassee, U.S.A.

Abstract

High voltage aqueous phase pulsed corona discharges is an emerging technique in environmental pollutant degradation that is characterized by the production of hydroxyl radicals as the primary degradation species. This paper focuses on quantification of hydroxyl radicals using chemical probes (dimethylsulfoxide (DMSO) and disodium salt of terephthalic acid (NaTA)) that have been extensively used in several other advanced oxidation studies.

1. Introduction

High voltage pulsed electrical discharges in liquids and in gas phases over or near gas-liquid interfaces have been shown to produce highly reactive radicals ($OH\cdot$, $H\cdot$) and molecular species (H_2O_2, H_2, O_2, O_3). Through utilization of these reactive species, primarily the non-selective highly reactive hydroxyl radical and the more selective oxidant ozone, these electrical discharge reactors have been shown to also effectively degrade various organic contaminants such as phenol, nitro and chloro substituted phenol, polychlorinated biphenyls, and trichloroethylene ([1], [2], [3], [4]). The study of the physical and chemical processes that arise due to discharge initiation and investigation of how the bulk chemical reactions are affected by the discharge parameters have resulted in quantification of several reactive species (e.g., H_2O_2, H_2, O_3, O_2) and in increased knowledge of the impact of various parameters (e.g, peak voltage, solution conductivity, pH, type of salt, salt concentration, and presences of additives) on contaminant degradation ([1], [4], [5]). The presence of hydroxyl radicals in electrical discharges in water has been demonstrated by emissions spectroscopy ([6].[7]). To develop knowledge of the fundamental chemical and physical processes occurring in these electrical discharge reactors and to develop quantitative predictive mathematical models of reactor performance it is necessary to obtain accurate quantitative estimates of hydroxyl radical generation by the pulsed electrical discharge.

There have been earlier attempts to quantify hydroxyl radicals generated in water by pulsed corona discharges ([8], [9]). Joshi et al. [8] determined the rate of formation of hydroxyl radicals by using a pseudo steady-state approach utilizing a probe (phenol) and scavenger (carbonate ions) in combination. Varying concentrations of carbonate ions led to different initial conductivity of the solution and this can impact the hydroxyl radical formation. Hoeben et al. [9] tried to quantify the concentration of hydroxyl radicals using electron spin resonance (ESR) and fluorescence spectroscopy. The spin trap 5,5-dimethyl-1-pyrroline N-oxide (DMPO) was used in ESR studies but the authors didn't detect any DMPO-OH adduct due to pulsed corona discharges. Coumarin-3-carboxylic acid (CCA) was used as the probe in the fluorescence experiments but the high background signal in water compared to the fluorescent standards led to hydroxyl radical quantification problems.

In this study we use two different chemical probes to obtain independent and accurate quantitative estimates of hydroxyl radicals generated by the pulsed corona discharges. The probes selected react with hydroxyl radicals with a high rate constant of reaction to generate products that can be detected easily with techniques such as fluorescence spectroscopy and UV detection. The first method to quantify hydroxyl radical uses dimethylsulfoxide (DMSO) that reacts with hydroxyl radical to yield methanesulfinic acid and methyl radical. Several hydroxyl radical quantification techniques focus on the quantification of methane sulfinic acid or the subsequent products methane sulfonic acid and sulfate anions. Another approach is the quantification of the methyl radical or its subsequent oxidation product formaldehyde. Quantification of formaldehyde is achieved by fluorescence detection utilizing Hantzch reaction or by derivatization with 2,4

dinitrophenylhydrazine and subsequent analysis of the hydrazone by HPLC-UV detection. The later approach was followed in this study utilizing a derivatization procedure developed by Tai et al.[10] that was slightly modified for the current application. The probe selected for the fluorescence experiments is the disodium salt of terephthalic acid (NaTA). NaTA react with hydroxyl radicals to form 2-hydroxyterephthalic acid (HTA), that gives a bright stable fluorescence ($\lambda_{analyzing}$ = 425 nm, $\lambda_{excitation}$ = 315 nm)[11]. Terephthalic acid and its disodium salt are extensively used in radiation and sonochemical studies.

2. Experimental

Methods and Materials:

The compounds dimethyl sulfoxide, acetonitrile, sodium dihydrogen phosphate, acetic acid, hydrogen peroxide, potassium chloride, platinum wire (Fisher Scientific), phosphoric acid (Kodak Chemicals), reticulated vitreous carbon (RVC) disk of 1 cm thickness (Ultramet, Pomoma, CA) were used as received from the manufacturers. 2,4-dinitrophenyl hydrazine (Aldrich) was purified by a standard U.S. EPA stipulated method [12]. Desired amounts of DMSO were dissolved in the reactor (concentration = 28.16mM) and oxygen was bubbled for 30 minutes prior to the start and during the experiments. Solutions of NaTA (concentration = 0.5mM) were prepared by stirring in a flask overnight and experiments were conducted by bubbling 400 ml/min of oxygen 30 minutes prior to and during the experiment. The solution conductivity was adjusted to a desired value using potassium chloride before the experiments.

Formaldehyde quantification using HPLC:

Derivatization of formaldehyde was performed with a saturated solution of purified DNPH in acetonitrile. The derivitization procedure featured a reaction of 5 ml of the aqueous solution from the reactor, 5 ml of pH 4 buffer (NaH_2PO_4 + H_3PO_4) and 1 ml of saturated solution of DNPH at 40 ºC for an hour. The hydrazone thus formed was equilibrated to room temperature for 30 minutes and then analyzed on the HPLC-UV at 360 nm. The analysis was performed on a Perkin Elmer reverse phase HPLC unit with Supelcosil LC-18 column using acetonitrile and 0.5% acetic acid solution.

Quantification of 2-hydroxyterephthalic acid (HTA):

5 ml of samples from the reactor were analyzed within 8 hours of performing the experiments on a Shimadzu fluorescence spectrophotometer. The excitation wavelength was set at 315 nm and the fluoresence spectra of the sample was collected from 340 to 625 nm. The peak area was quantified for various samples.

Reactor Configuration:

Two different reactors with a volume of 1 liter were used in this work. The reactor setup has been extensively described in previous publications [1,2,13]. Cooling water at 15°C flowed through the jacket to maintain isothermal conditions in the reactor. The reactor was operated in batch mode in both reference and hybrid-series configurations.

3. Results and Discussion

The quantification of hydroxyl radicals in Advanced Oxidation Processes and biological systems using DMSO as the probe compound is popular due to its high solubility, low volatility and large rate constant of reaction with hydroxyl radicals ($k = 4.5*10^9\ M^{-1}s^{-1}$). The pathway of degradation of DMSO upon reaction with hydroxyl radicals has been extensively studied and results in the formation of methyl radical and methane sulfinic acid as the primary intermediate products. Reaction stoichiometry and experimental evidence indicate that 2 moles of hydroxyl radical yield 1 mol of formaldehyde [10].

$$(CH3)_2SO_3 + OH\cdot \longrightarrow CH_3SOOH + \cdot CH_3 \quad \ldots\ldots\ldots\ldots \tag{1}$$

$$\cdot CH_3 + O_2 \longrightarrow CH_3OO\cdot \quad \ldots\ldots\ldots\ldots \tag{2}$$

$$2\ CH_3OO\cdot \longrightarrow HCHO + CH_3OH + O_2 \ldots\ldots\ldots\ldots \tag{3}$$

$$\cdot CH_3 + RH \longrightarrow CH_4 + R\cdot \quad \ldots\ldots\ldots\ldots \tag{4}$$

Experiments were performed to analyze the effect of oxygen gas flowing into the reactor on the production of formaldehyde at an applied voltage of 45 kV and an initial conductivity of 150μS/cm. The methyl radical formed by the reaction of DMSO and hydroxyl radical react with oxygen to form formaldehyde (Reactions 2 and 3) or can abstract a hydrogen atom from organics to yield methane (Reaction 4). It has been previously determined that the reaction 4 consumes only 0.3 to 0.5 % of the methyl radicals [10].

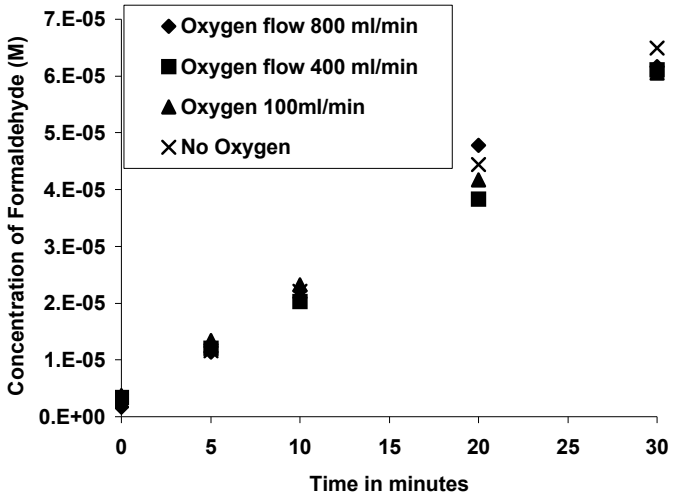

Figure 1. Formaldehyde production as a function of pulsed corona discharge time for different oxygen flow rates through the reactor. (Reference configuration, Applied voltage = 45 kV, Initial conductivity = 150 μS/cm)

Figure 1 shows that there was no change in formaldehyde production by varying oxygen flow rates. The pulsed corona discharge is a source of radical species that can recombine to give various gases (H_2 and O_2). The rate of production of oxygen at an applied voltage of 45 kV is ~$24*10^{-8}$ Ms^{-1}[5]. This result shows that the quantity of the oxygen generated by the discharge that dissolves into the solution is sufficient to quantitatively convert methyl radical into formaldehyde.

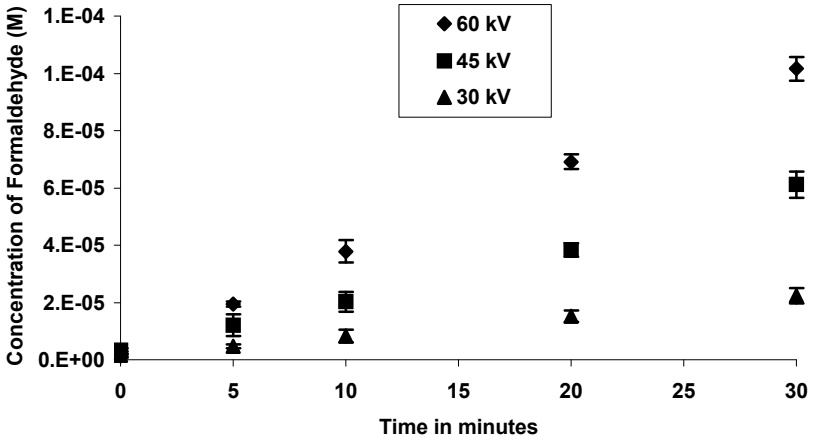

Figure 2. Formaldehyde production as a function of pulsed corona discharge time at different applied voltages (Initial conductivity = 150 μS/cm; Reference Reactor)

The applied voltage of the pulsed corona discharge was varied to test the effect of input power on the generation of hydroxyl radicals. The slope of the production of formaldehyde with time (Figure 2) is utilized to calculate the rate of production of hydroxyl radical as a function of the applied voltage. The input power into the reactor (by calculating the area under the curve obtained by multiplying the current and voltage waveforms) at an applied voltage of 45 kV is 66 J/second.. Figure 3 shows that the rate of production of hydroxyl radicals increases linearly with applied voltage and is qualitatively similar to results in literature [8]. However, the rate of production of hydroxyl radical (at 45 kV applied voltage = $6.70*10^{-8}$ Ms^{-1}) is higher than reported by Joshi et al.[8] (at 45 kV applied voltage (extrapolated from data) = $9.25*10^{-10}$ Ms^{-1}). This difference in hydroxyl radical production can be attributed to various modifications made to the reactor (reactor dimensions, electrode materials and configurations) as well as differences in methodology of measurement. The rate of production of hydrogen peroxide for similar discharge conditions without DMSO in solution is $55.6*10^{-8}$ Ms^{-1}[5]. The probe compounds should act as scavengers of hydroxyl radical thereby preventing the recombination of hydroxyl radicals to form hydrogen peroxide. However, considerable peroxide is still produced when DMSO is used as a probe compound ($42.83*10^{-8}$ Ms^{-1} (this work; data not shown)) thereby leading to the conclusion that either hydrogen peroxide is produced directly from water by the discharge or that hydroxyl radical recombination to produce hydrogen peroxide takes place inside the streamer where the non-volatile probe can't prevent it.

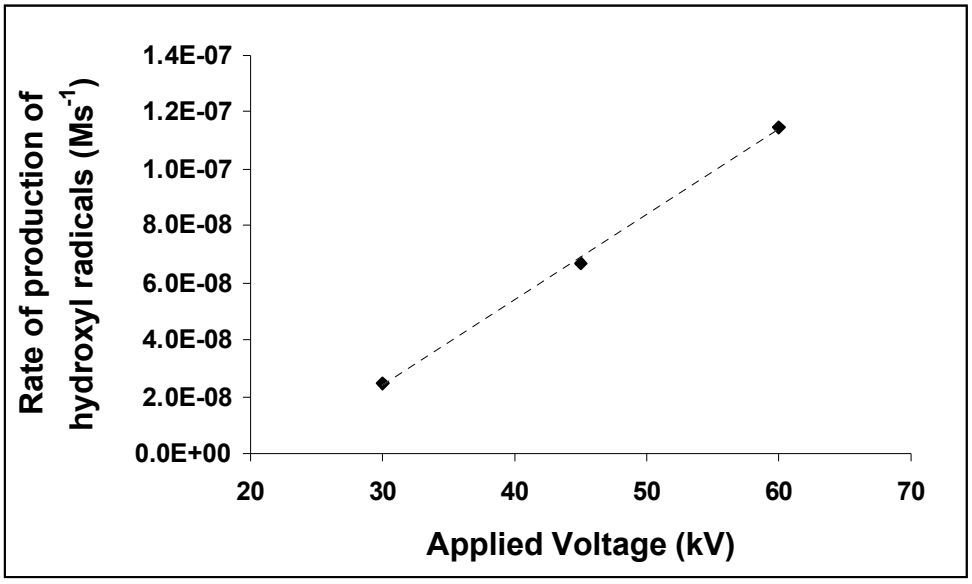

Figure 3. Rate of production of hydroxyl radical as a function of applied voltage.

Reactor modifications have also resulted in the development of hybrid reactor systems. The hybrid reactors employ an additional gas phase discharge that produces ozone and other reactive species. These species can dissolve in the liquid phase and react to produce hydroxyl radicals. Preliminary studies have shown the same amount of hydrogen peroxide generation in the hybrid and reference reactors, however, the degradation of certain organics (phenol and substituted phenols) is considerably faster in the hybrid reactors [4].

To qualitatively demonstrate the difference in hydroxyl radical production in the reference and hybrid reactors the probe compound shouldn't react with ozone. Therefore, DMSO can't be used as the probe compound. The probe compound selected for these experiments is the disodium salt of terephthalic acid that reacts selectively with hydroxyl radicals. Experiments performed in the reference and the hybrid-series reactor at the same applied voltage and initial conductivity show that a considerably higher production of the fluorescent byproduct 2-hydroxy terephthalic acid in the hybrid-series configuration (Figure 4). This implies a larger rate of production of hydroxyl radicals. The additional hydroxyl radicals in the hybrid series reactor can potentially arise from two sources; directly from the discharge at the interface of the liquid and gas surfaces and

from reactive species (such as ozone) formed in the gas phase that dissolve in the liquid phase and subsequently react to form hydroxyl radicals. However, the reaction of dissolved ozone with hydrogen peroxide to produce hydroxyl radical is pH dependent can be ruled out at the pH (~5.5) of these experiments [10].

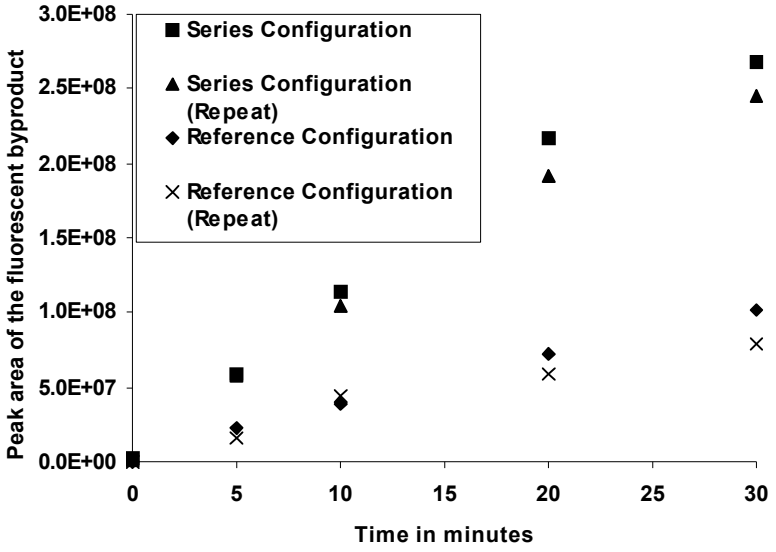

Figure 4. Fluorescent by-product formation in the hybrid-series and reference configurations (Applied voltage = 45 kV, Initial conductivity = 150 μS/cm)

4. Conclusions

The production of hydroxyl radicals by the liquid phase pulsed corona discharges has been quantified using a chemical probe compound DMSO. A linear increase in the rate of production of hydroxyl radicals is observed by increasing the applied voltage. The hybrid-series reactor results in greater production of hydroxyl radical as compared to the reference configuration as seen from the results of the NaTA experiments. This result can partly explain the greater degradation of organics seen in the hybrid reactors.

Acknowledgements

The authors acknowledge Dr Igor Alabugin (Florida State University, Chemistry) for use of his fluorescence spectrophotometer, Dr Louis J. Kirschenbaum (University of Rhode Island, Chemistry) for supplying 2-hydroxyterephthalic acid standards, and the Florida State University Fellowship Program.

References

[1] D. R. Grymonpré, A. K. Sharma, W. C. Finney and B. R. Locke, "The role of Fenton's reaction in aqueous phase pulsed streamer corona reactors" Chemical Engineering Journal, 82, 1-3, 15 (2001).

[2] M. Sahni, W. C Finney, and B. R. Locke, "Degradation of Aqueous Phase Polychlorinated biphenyls (PCB) Using Pulsed Corona Discharges", Journal of Advanced Oxidation Technologies, 8,1 (2005).

[3] M. Sahni, W. C. Finney, R. J. Clark, W. Landing, and B. R. Locke,: "Degradation of aqueous phase trichloroethlyene using pulsed corona discharge", presented at HAKONE VIII, International Symposium on High Pressure, Low Temperature Plasma Chemistry, Puhajarve, Estonia, 2002.

[4] Lukes, P; Locke, B.R., “Degradation of substituted phenols in hybrid gas-liquid electrical discharge reactor”, submitted to Industrial and Engineering Chemistry Research.
[5] M.J. Kirkpartick, and B.R. Locke, “Hydrogen, Oxygen, and Hydrogen Peroxide Formation in Electrohydraulic Discharge”, submitted to Industrial and Engineering Chemistry Research.
[6] Sun, B., M. Sato, et al. (1997). "Optical Study of Active Species Produced by a Pulsed Streamer Corona Discharge in Water." Journal of Electrostatics 39: 189-202.
[7] Sunka, P., V. Babicky, et al. (1999). "Generation of Chemically Active Species by Electrical Discharges in Water." Plasma Sources Science and Technology 8: 258-265.
[8] Joshi, A.A., Locke, B.R., Arce, P., and Finney, W.C., “Formation of Hydroxyl Radicals, Hydrogen Peroxide and Aqueous Electron by Pulsed Streamer Corona Discharge in Aqueous Solution”, Journal of. Hazardous Materials, 41, 1, 3 (1995).
[9] W F L M Hoeben, E M van Veldhuizen, W R Rutgers and G M W Kroesen J., “Gas phase corona discharges for oxidation of phenol in an aqueous solution”, J. Phys. D: Appl. Phys., 32, No 24, L133 (1999).
[10] C. Tai, J-F Peng, J-F Liu, G-B Jiang, and H. Zou, “Determination of hydroxyl radicals in advanced oxidation processes with dimethyl sulfoxide trapping and liquid chromatography”, Analytica Chimica Acta, 527, 73–80, (2004).
[11] X. Fang, G. Mark, C. von Sonntag, “OH radical formation by ultrasound in aqueous solutions Part I: the chemistry underlying theterephthalate dosimeter”, Ultrasonics Sonochemistry, 3, 53 (1999).
[12] U.S. EPA Method 8315A, “Determination of Carbonyl Compounds by High Performance Liquid Chromatography (HPLC)”.
[13] Lukes, P., Appleton, A.T., and Locke, B.R., **“**Hydrogen Peroxide and Ozone Formation in Hybrid Gas–Liquid Electrical Discharge Reactors”, IEEE Trans. Ind. Appl., 40, 1(2004).

LOW AND ATMOSPHERIC PLASMA MODIFICATION OF CARBON BLACK: A COMPARISON

[1)] N. Tricás, [1)] J. Herranz [2)] R.H. Schuster [1)]S. Borrós

1) Institut Químic de Sarrià, Av. Sarrià 390, 08017 Barcelona, Spain. s.borros@iqs.url.edu
2) Deutsches Institut für Kautschuktechnologie e.V., Eupener Straβe 33, 30519 Hannover, Germany.
Robert.Schuster@DIKautschuk.de

Abstract

In this work two different plasma techniques have been used to modify chemically the surface of carbon black. In some cases HOPG was used as a model material. Both, low pressure plasma as well as atmospheric plasma, have been proved to be successful to achieve this goal. To characterize the final material specific surface area, pH and acid titrations as well as XPS analysis were carried out. Although cold plasma has some advantages due to a better control of the reaction medium, atmospheric plasma has shown very good results both at oxidation and nitration of the carbonaceous surface.

1. Introduction

Plasma is a very well known technique in order to modify the surface of materials without changing the bulk properties. This is a very interesting possibility as many materials present good performance properties but should improve the interaction with the surroundings. Quite a lot of work has been done on flat surfaces both at low and atmospheric pressure, for example in the case of carbonaceous materials HOPG has been widely used [1,2]. On the other hand, concerning powder materials this technique has not been so extendedly developed.

In the present case the modification is focused on carbon black (CB). This material is known for being the most wide used reinforcement filler in the rubber industry, but it also presents other very interesting applications such as catalyst support or pigment in jet inks [3, 4]. In each of this applications CB is used in different mediums, which present a very wide range of polarity. It should be pointed out that one of the essential characteristics for a successful performance of CB in all of these cases is a good interaction with the surrounding molecules. Some attempts have already been described in literature in order to modify the surface to obtain similar compositions of the surroundings for rubber applications [5,6], oxidation reactions can also be found [7]. In most cases cold plasma was used to modify the material, which was placed on a shacking tray in a bell-jar type reactor.

Cold plasma presents some advantages such low temperatures and higher composition control; however atmospheric plasma is much more attractive to industrial processes due to the lack of vacuum and for being a continuous process. Nevertheless, the difficulty to handle powder materials through such a system does not favour the research work on this field. In the present work both a down-stream reactor as well as an atmospheric plasma torch were adapted to modify CB in O_2, N_2, NH_3 plasma environments.

2. Experimental

The modified CB was a N-134 as described by the ASTM, provided by Sid Richardson Carbon Co. Also HOPG was treated as a model for carbon black surface graphitic domains.

2.1 Treatment Description

The first step is to describe the set-up of the reactors. The cold plasma reactor is made of a glass cylindrical body which ends in two spherical vessels. The plasma is created by means of a copper coil which is coupled to the RF generator (13,56 MHz) through a capacitive impedance adaptor. In the lower vessel carbon black is placed and stirred in order to have homogeneous modification. The vacuum connection is placed at the upper part of the reactor and two cold traps are used in order to protect the vacuum pump and helping to perform a good vacuum. The pressure without modification gas was 10^{-3} mbar while during modification it was kept at 0,4 mbar. Batches of 10 grams were obtained in each experiment.

For the atmospheric treatment an Openair system from Plasmatreat Gmbh, was used. A high voltage discharge is used between two nozzles to create the plasma. A flow of gas (air or nitrogen) goes along the discharge route taking part of the plasma and transporting it to the surface of the material being treated. The plasma torch is usually active up to 20mm long and can reach a treatment width of 15mm. The torch was adapted to a reactor in which the carbon black was introduced by means of a flow of a carrier gas (nitrogen). The CB was introduced 10 mm from the torch origin, this region being described as the most active by the supplier. After the modification, the plasma gas together with the carrier gas brought the modified CB into the collection system. 95% of the powder was recovered and a treatment rate of 1 g/min was achieved. In some cases NH_3 was introduced after the plasma treatment as post-modification gas.

2.2 Specific Surface Area

Specific surface area was measured by using the BET nitrogen isotherm (N_2SA), representing the total surface area. Also the statistical thickness surface area STSA, known as external surface area measurements were carried out in order to study porosity modifications.

2.3 pH and Acidic Titration

The pH from aqueous suspensions of CB was determined as described by ASTM procedures [8]. The acidic groups were quantified and classified by using the Bohem's titration method [9] using NaOH and $NaHCO_3$.

2.5 XPS

XPS measurements were performed both at the surface of CB and HOPG. XPS experiments were performed in a PHI 5500 Multitechnique System (from Physical Electronics) with a monochromatic X-ray source (Aluminium Kalfa line of 1486.6 eV energy and 350 W), placed perpendicular to the analyzer axis and calibrated using the 3d5/2 line of Ag with a full width at half maximum (FWHM) of 0.8 eV. The analyzed area was a circle of 0.8 mm diameter, and the selected resolution for the general spectra was 187.85 of Pass Energy and 0.8 eV/step, and for the fitted (multiplex) spectra was 23.5 of Pass Energy and 0.1 eV/step. Measurements after a light surface cleaning were performed by sputtering the surface with an Ar+ ion source (4 keV energy). These measurements were made in a ultra high vacuum (UHV) chamber pressure between 4x10-8 and 1x10-8 torr.

3. Results and Discussion

Table 1 and 2 show a description of the treatments that were carried out by means of atmospheric and low pressure plasma respectively. Although many other experiments were performed only the most interesting are presented.

Table 1. Atmospheric plasma treatments

Name	Plasma gas	Post-treatment
A-N_2	N_2	No
A-Air	Air	No
A-N_2/NH_3	N_2	Yes (90 L/h NH_3, 10mm)
A-N_2/NH_3	N_2	Yes (90 L/h NH_3, 40mm)
A-HOPG	N_2	No

The post-treatment was done by introducing a flow of ammonia at the given position in table 1, after the CB inlet.

Table 2. Cold plasma treatments

Name	Plasma Gas	Power (W)	Time (min)
C-O_2	O_2	80	30
C-N_2	N_2	80	30
C-NH_3	NH_3,Ar	60	30
C-HOPG/NH_3	NH_3, Ar	60	40
C-HOPG/N_2	N2	60	40

Background reached pressure was 5·10-3 mbar, while working pressure was 0,4mbar.

One of the main concerns about the chemical modification of CB is not to alter any other parameter that may have an influence on its properties. One of the most important parameter to characterize CB is specific surface area, in other words, the amount of surface that is exposed to the surroundings. Obviously if there is a variation in this parameter the activity of CB will also probably change. Another important point is the CB porosity. The porous may have the ability to locate certain compounds or molecules, therefore a change in their size could lead to a different interaction process. Both parameters were studied and in any of the cases the changes were not large enough in order to attribute a variation in CB performance. Table 1, presents the values for the studied parameters. As it can be seen, samples treated in rich oxygen plasma environments present a larger modification of these parameters. This is due to the oxidation process which increases not only the surface area but also the porosity of the carbon black, that is the reason why the external surface area is decreased slightly. However all this parameters still fit in the N-134 ASTM classification, and therefore the effect of this variations is negligible.

Table 3. N_2SA and STSA measurements for original and treated CB

Sample	N_2SA (m^2/g)	STSA (m^2/g)
Original CB N-134	141	131,5
A-N_2	141,4	129,8
A-Air	143,4	126,7
A-NH_3	141,4	129,8
C-N_2	140,3	124,8
C-O_2	143,5	125,5
C-NH_3	141	125

When the pH was measured the presence of other groups was already likable. Table 3 presents the value for the different treatments. As it can be seen in table 3 the CB treated with O containing plasma (air or pure O_2) are highly acidic. The most acidic pH values are obtained by using atmospheric plasma, being this system highly effective for this kind of modification. For the N_2 treatment the decrease of the pH is attributed to the residual oxygen in the plasma reactor.

Table. 3 pH and acidic values for original and treated CB

Sample	pH	Total acidic groups (meq/g)	Strong acid groups
Original CB N-134	9,8	0,02	-----
A-N_2	7,8	0,146	0,02
A-Air	3,2	0,438	0,12
A-NH_3	9,2	-----	-----
C-N_2	8,5	0,051	-----
C-O_2	4,5	0,330	0,08
C-NH_3	9,8	------	------

The pH results are highly related to the acidic titration values. In this case both the total as well as only carboxylic acidic groups were determined. It should be remarked that the presence of ammonia both during the reaction in cold plasma or as post-treatment in the atmospheric system diminishes de oxidation and higher pH are found.

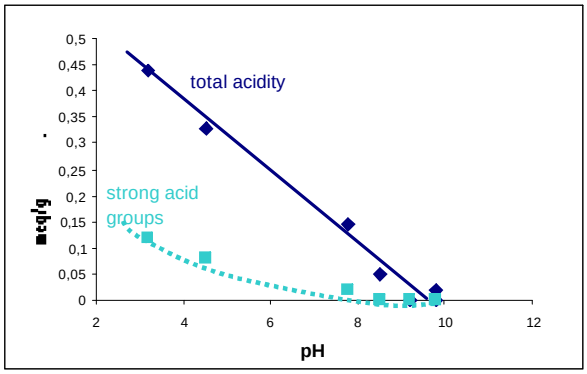

Fig. 1 pH vs. total and strong acid groups

As it can be seen in fig.1, there is a close relation between the amount of acidic groups on the surface and the measured pH. However is it also important to notice that there are not only carboxylic groups but also all other kind of weak acids, as the figure shows is the total acidity value which presents a linear relation between these two parameters.

All the previous described changes have been attributed to a variation in the chemistry composition of CB surface. To confirm this hypothesis, XPS analysis were performed on the most interesting samples. The surface atomic composition was determined (fig. 2,3), the main functionalities for O were also obtained by doing the deconvolution of the respective peaks (table 5), N signal had not enough resolution to make the corresponding deconvolution.

Fig 2,3 show the atomic composition of the CB surface before and after treatment (C,O,N,S) respectively.

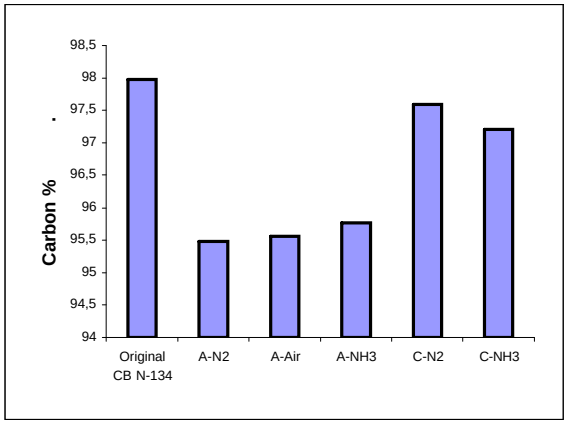

Fig. 2 % atomic C on CB

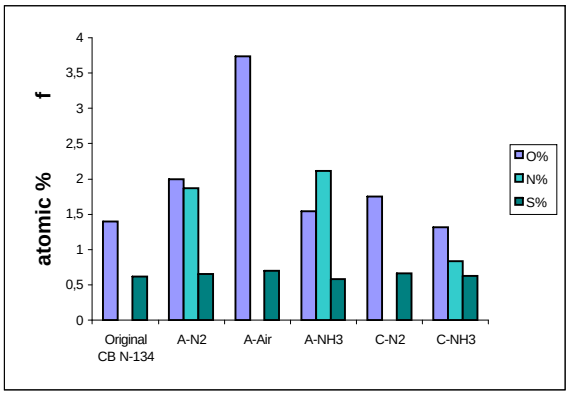

Fig. 3 % O,N,S on CB

Table 5. % of main Oxygen functionalities on the surface of CB

O groups	**N-134 orig.**	**A-N_2**	**A-AIR**	**A-NH_3**	**C-N_2**	**C-NH_3**
C=O	4	21	16	22	16	35
C-O	70	15	17	32	59	43
C-OOH, C-O-C	26	64	67	46	28	23

The peaks were assigned as following C=O 531-531,8eV C-O 532-533eV C-OOH, C-O-C 533-534eV as found in literature [10,11,12]

For this experiments also some HOPG samples were analyzed as shown in table X. When modifying HOPG with N_2 atmospheric plasma (A-HOPG/N_2), no N was detected on the surface. Probably because being in the open air oxidation is a predominant reaction. On the other hand, when modifying HOPG in the down-Stream reactor at different positions, a dramatic increase of the N functionalization was observed when using NH_3 as plasma gas. It has to be said though, that pure N_2 plasma did not modify the chemical composition of HOPG at all. The higher functionalization compared to CB is attributed to the position of the sample which was placed 2 cm below and above as well as in the cooper coil, while the CB is placed 7 cm. Different positions of HOPG did not show any relevant changes in this domain.

The result shows that it is possible using plasma treatments, not only to functionalize the edges of the crystallites, as it happens with the wet treatments, but the whole CB surface. Fig. 5 shows the surface atomic

composition for both samples while table 7 and 8 presents the major O and N functionalities for the cold plasma modified HOPG respectively.

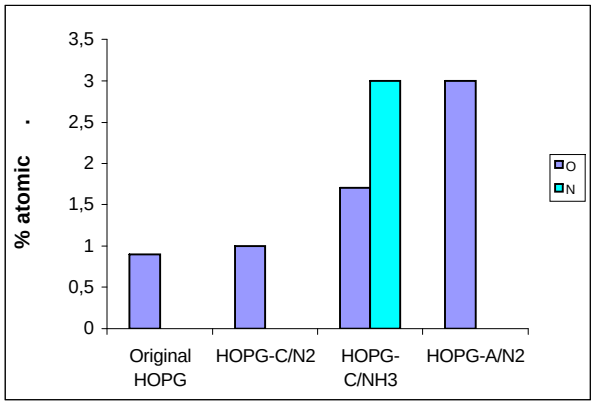

Fig. 5 HOPG atomic surface composition

Table 7. % of main Oxygen functionalities on HOPG

O groups	**HOPG**	**HOPGC/N_2**	**HOPGC/NH_3**	**HOPGA/N_2**
C=O	1,5	1,3	8,6	10
C-O	53	49,5	38	19,5
C-OOH, C-O-C	43,5	49,2	53,4	70,5

Table. 8 % of main Nitrogen functionalities after HOPG treatment with ammonia cold plasma

Sample	**Pyridine**	**Nitrile**	**Pyrrole**	**Graphitic**	**Noxide**
HOPG-NH_3	42	34	13	7	2

The peaks were assigned as following pyridine 398-399 eV, nitrile 400-4005 eV, pyrrole 400,2-400,9 eV, grphitic 4001-402, N oxyde 402-405 as found in literature [13,14,15]

4. Conclusions

CB and HOPG have been shown to be susceptible to surface chemical modification when treated both with cold plasma and atmospheric plasma. This modification has not altered other important parameters such specific surface area or porosity. The chemical modification not only concern oxidation, but also the introduction of various N functions. The treatment could be improved by modifying the position of CB in the cold plasma reactor as well as the gas composition in the case of atmospheric plasma.

Aknowledgements.

We would like to thank Dr. Michel Gerspacher and Dr. Jean-Pol Dodelet for their helpful advices and interesting discussions.

References

[1] J. I. Paredes, A. Martínez-Alonso, and J. M. D. Tascón Langmuir 2002, 18, 4314-4323
[2]S. O'Kell, S. Pringle and C. Jones, J. Adhesion, 56, 261.273
[3] Gerspacher, M.; O'Farrell, C.P.; Yang, H. H. Elastomerics 1990, 122(11), 23-30.

[4] Villers, Dominique; Jacques-Bedard, Xavier; Dodelet, Jean-Pol. Journal of the Electrochemical Society (2004), 151(9),
[5] Akovali, G.; Ulkem, I. Polymer , 1999, 40(26), 7417-7422.
[6] N. Tricás, E. Vidal-Escales, S. Borrós, M.Gerspacher, "Influence of plasma polymerized carbon black in the in-rubber properties of filled compounds" IRC Nurnberg, June 2003.
[7] CB-Jin Park, Ki-Sook Cho, Seung-Kon Ryu, Carbon 2003, 41, 1437-1442.
[8] Carbon Black slurry pH as proceeded by the ASTM D1512-95(2000)
[9] P. Bohem, E. Diehl, W. Heck and S. Sappok, Angew. Chem. 1964, 76, 742-751.
[10] Hontorialucas, C.; Lopezpeinado, A. J.; Lopezgonzalez, J. D. D.; Rojascervantes, M. L.; Martinaranda, R. M. Carbon 1995, 33, 1585
[11] Estrade-Szwarckopf, H. Carbon 2004, 42, 1713.
[12] Cagniant, D.; Magri, P.; Gruber, R.; Berlozecki, S.; Salbut, P. D.; Bimer, J.; Nanse, G. Journal of Analytical and Applied Pyrolysis 2002, 65, 1
[13] Jansen, R. J. J.; Vanbekkum, H. Carbon 1995, 33, 1021.
[14] M. Barber, J.A. Connor, M.F. Guest, I.H. Hillier, M. Schwartz and M. Stacey. J. Chem. Sco., Faraday Trans., 1973, 69,551.
[15] Cagniant, D.; Gruber, R.; Boudou, J. P.; Bilem, C.; Bimer, J.; Salbut, P. D. Energy & Fuels 1998, 12, 672.

Atmospheric pressure microwave H_2O plasma source

Y. Matsuo, M. Unno, S. Ono
Department of Electrical Engineering, Musashi Institute of Technology, Tokyo, Japan

Abstract
We have developed a microwave H_2O plasma source that operates at atmospheric pressure. The basic characteristics of the plasma have been measured by the spectroscopic method. Electron temperature was about 6100K at the tip of plasma torch. The electron temperature decreases in downstream region, on the other hand, the rotational temperature increases with increasing distance from the torch exit, and these temperatures coincide at downstream region of the plasma.
Keywords:H_2O, Electron temperature, Rotational temperature, OH radical

1. Introduction

Atmospheric pressure microwave induced plasmas have been used for years as means of exciting and ionizing species for elemental analysis, plasma chemistry, plasma surface treatment and electro thermal propulsion[1]. Microwave plasma differs significantly from other plasmas, showing many interesting properties. For example, the electron density is higher in microwave plasma than in radio-frequency (RF) or direct current (DC) plasma, so its reactivity is expected to be very high. However, the pressure range of microwave plasma is very narrow, or the volume of the plasma is very small at high pressure. This is why the microwave plasma has not been utilized in the new materials synthesis in the industry [2].

In the present work in our laboratory, the study of the decomposition of the waste plastics by H_2O plasma at low pressure is carried out, and we have found that the H, O, and OH radicals play an important role in the decomposition of plastics [3]. The cost of the treatment becomes expensive because of need of a vacuum system and complex devices at low-pressure operation. Moreover these apparatus has demerit that can't treat in large enough quantities at once. Therefore we have attempted to generate big volume plasma at atmospheric pressure and to apply it to decomposition of plastics.

In this paper, an atmospheric pressure microwave plasma apparatus that was designed for H_2O plasma source is presented and the experimental results concerning the basic characteristics are shown.

2. Experimental

2.1 Experimental set-up

Microwave power generator is consisting of a magnetron, an isolator, a power monitor and three stub tuners. Microwave power (0～1.5kW) was generated by the magnetron and supplied to the coaxial type electrode through the rectangular wave guide.

A schematic diagram of plasma source we designed is shown in figure 1. The plasma source consists of a rectangular wave guide, a microwave mode converter and a coaxial waveguide. The mode converter connects the rectangular waveguide to the coaxial waveguide with a small reflected wave. The TE_{10} mode microwave which is propagated through the rectangular waveguide from the microwave power generator is converted into the TEM mode at mode converter. The diameters of the center and outer conductor of the coaxial waveguide are 6 and 16mm, the conductors taper off and play roles as electrodes for plasma generation. The microwave plasma jet is generated at atmospheric pressure at the tip of a center electrode and blown into the air by the gas pressure inside the waveguide. Argon-H_2O mixture gas was employed as plasma gas.

A schematic diagram of the spectroscopic system is shown in figure 2. The emission of the plasma is carried through an optical fiber to the multi channel spectroscope (Hamamatsu Photonics PMA-50) equipped with electrically cooled CCD detection head.

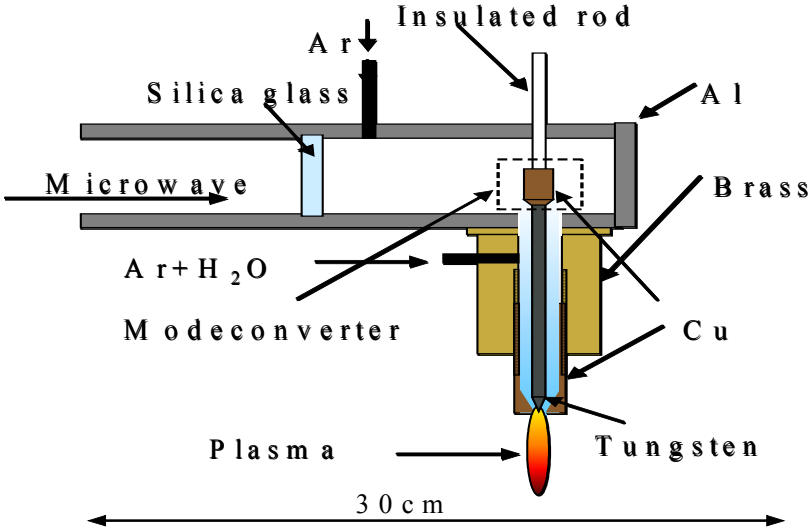

Figure 1. Atmospheric pressure microwave H_2O plasma source

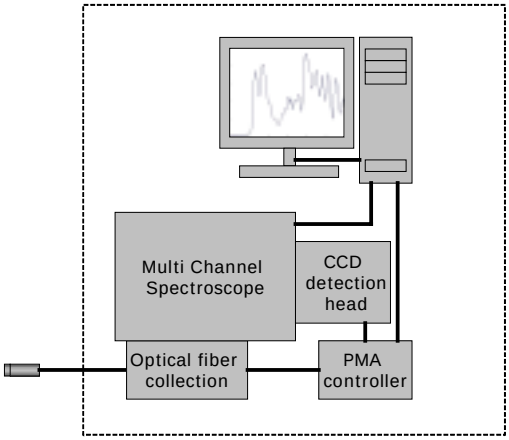

PMA-50 CCD system
Figure 2. Spectroscope system

2.2 Experimental method

2.2.1 Gas temperature measurements [4][5]

Gas temperature is generally close to the rotational temperature of a diatomic gas. Therefore we measure a rotational temperature of OH radicals by spectroscopic method. OH rotational temperature was estimated by using OH[$A^2\sum^+ - X^2\Pi^-$(v', v'') = (0, 0)] emission of the plasma. The experimental spectrum are compared with synthetic spectrum calculated from accurate experimental data of lines intensity $I_{J'J''}$(3000) of Lyman and by Dieke and Crosswhite obtained at 3000K for the rotational band OH. Using their results and equation (1), we can calculate the relative intensity of each rotational line $I_{J'J''}$ *(Trot)* through the following expression:

$$I_{J'J''}(T_{rot}) = I_{J'J''}(3000)\exp\left(-\frac{F_{v'}(J')(3000-T_{rot})}{3000T_{rot}}\right) \times \frac{Q_{rot,v'}(3000)}{Q_{rot,v'}(T_{rot})} \qquad (1)$$

Where $F_{v'}(J')$ is the energy of the upper rotational level J' and $Q_{rot,v'}(T_{rot})$ is the rotational partition function of the upper vibrational level v'. It should be noted that only the shape of different rotational spectra as a function of T_{rot} is relevant for this work. The term $Q_{rot,v'}(3000)/Q_{rot,v'}(T_{rot})$ is the same for all rotational lines issued to the upper vibrational level v'. From that point of view, this term is normalized to 1 in the evaluation of expression (1). The shape of the synthetic OH spectra varies as a function of rotational temperature due to variation of population density of concerning energy levels.

2.2.2 Electron temperature measurements [6][7]

Electron temperature was measured by LTE based measurement of high lying levels of recombining plasma because this plasma is a flowing afterglow, typical recombining plasma. Relative electron populations in excited states are generally described by the Boltzmann distribution. Therefore we can obtain the electron temperature from Boltzmann plot by using optical emission of argon (the parameters of these lines are shown in table 1).

Table 1. Argon spectrum line parameter

λ [nm]	E_k[cm^{-1}]	g_k	A_{kj} [$\times 10^8$s^{-1}]
425.9	118871	1	0.0415
426.6	117184	5	0.0033
427.2	117151	3	0.0084
430	116999	5	0.0039

3. Results and discussion

3.1 Axial position dependence of gas temperature Tg and electron temperature Te

The results for T_g and T_e are show in figure 3 at four axial locations of 1, 5, 10, 15 mm from the top of the touch. The electron temperature decreases toward downstream region, on the other hand, the rotational temperature increases with increasing distance from the torch exit, and these temperature shows coincide at downstream region of the plasma. This phenomenon can be attributed to the electron collision with heavy particles that results in energy transfer.

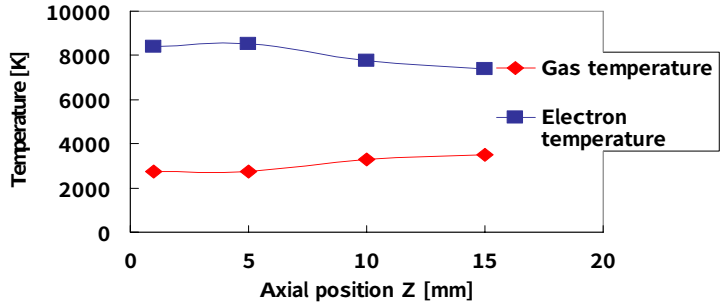

Figure 3. Axial position dependence of temperature (Ar 10 l/min, H_2O 1.2 l/min, Power 150W)

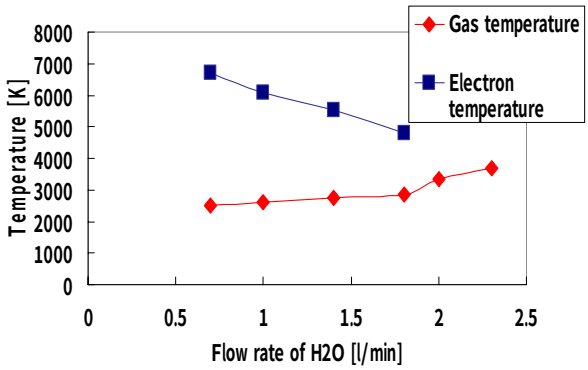

Figure 4. H_2O flow rate dependence of temperature (Ar 10 l/min, Z=10, Power 150W)

3.2 H_2O flow rate dependence

T_g and T_e dependence of H_2O flow rate are shown in figure 4. We observed, when the H_2O flow rate increases, that the electron temperature drastically decreases. It is thought that this phenomenon originates in the increase in the inelastic collision of electrons and the molecules of water. On the other hand, the gas temperature slightly increases with increasing H_2O flow rate. Since the percentage of water molecule increased, this tendency is considered to be the result from which electronic energy was efficiently transformed into the energy of translational motion of the molecule.

3.3 Microwave power dependence

T_g and T_e dependence of microwave power is shown in figure 5. We observed that gas temperature and electron temperature were not change with increasing microwave power. Dependence of the optical emission intensity of Ar, H, O, OH are shown in figure 6. These intensities increase with increasing microwave power. It is thought that the increased microwave power causes the increasing of

electron density from this result.

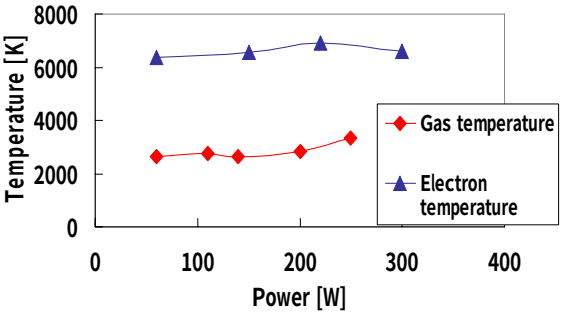

Figure 5. Power dependence of temperature (Ar 10 l/min H_2O 1.4 l/min Z=10mm)

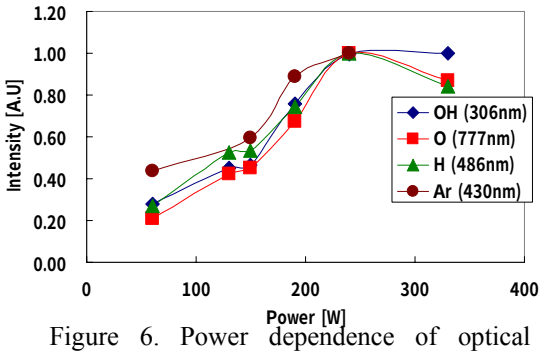

Figure 6. Power dependence of optical emission intensity of OH, O, H and Ar (Ar 10 l/min, H_2O 1.4 l/min Z=10mm)

4. Summary

Development of the source of water plasma that operates with an atmospheric pressure was performed. The fundamental characteristic of the generated plasma was clarified by the spectroscopic measurement. To use this plasma for recycling of a waste plastic is desired.

References

[1]M Moisant, Plasma Sources Sci. Techonol. 3, 584 (1994)
[2] Y Mitsuda, Rev. Sci. Instrum. 60(2), Feb (1989)
[3]T.Yamazaki et al., IEEJ Annual meeting report, 2004, 67 (2004)
[4] G H Dieke, H M Crosswhite, J. Quant. Spectro. Radiat. Transfer 2, 97 (1961)
[5] Charles de Izarra, J. Phys. D: Appl. Phys. 33 1697 (2000)
[6] T.Tandai et al., Spectroscopic Research, 49, 72(2000)
[7] M. D. Calzada, A. Rodero, A. Sola and A. Gamero, J. Phys. Soc. Japan 65, 948(1996)

MAGNETIC FIELD AS A TOOL FOR CONTROLLING THE GROWTH OF MICROCRYSTALLINE SILICON THIN FILMS

H. Stuchlíková, J. Stuchlík, T. Mates, M. Ledinský, A. Fejfar, J. Kočka
Institute of Physics, Academy of Sciences of the Czech Republic,
Cukrovarnická 10, 162 53 Prague 6, Czech Republic

Abstract

Magnetic field of permanent magnet placed directly under the substrate can locally change the growth of hydrogenated silicon during the low deposition temperatures PECVD. A small permanent magnet with poles parallel to the substrate led to microcrystalline spot formation in otherwise amorphous film. Perpendicular placed magnet led to a microcrystalline ring formed at the magnet edges.

Keywords

plasma enhanced chemical vapor deposition - PE CVD, magnetic field, hydrogenated microcrystalline silicon (μc-Si:H), hydrogenated amorphous silicon (a-Si:H), growth, deposition process

1. Introduction

Attempts to modify silane plasma between electrodes by magnetic field to improve the quality of deposited films were reported already in 1980 [1]. Unlike the previous work [2] where the magnetic field was applied at RF powered cathode, we placed a small magnet on the opposite electrode, directly under substrates. Magnetic field influences distribution of charged particles in the silane plasma above the substrate and thus also the Si film growth. Magnetic field effects depend on the magnet orientation (parallel or perpendicular to the substrates, see insets of the Fig. 1).

2. Experimental arrangement

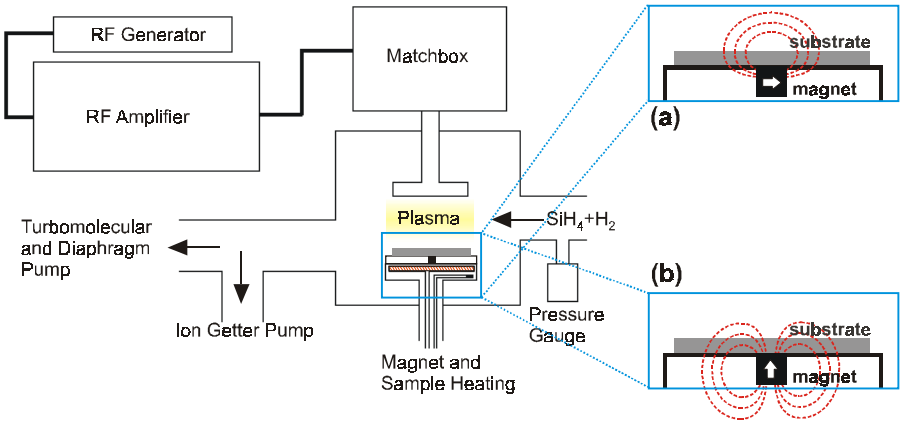

Fig. 1. PECVD deposition set-up. Insets show the detail of the magnet placement in the substrate holder.

We used standard PECVD technique of hydrogenated silicon films in an UHV chamber pumped by turbomolecular and diaphragm pumps (see Fig. 1). The glow discharge between two electrodes (diameter 80 mm, separated by 18 mm) was excited by RF generator at 13.56 MHz frequency and power 9 W. The mixture of H_2 and SiH_4 with 3 % SiH_4 and total flow rate about 52 sccm was led via the chamber at pressure 70 Pa. Films were deposited on Corning C7059 substrates with 0.9 mm thickness. Substrates were placed on the floating electrode kept at 100 °C. Magnetic field was induced by permanent magnet with dimensions 4 x 4 x 4 mm and field strength 0.4 T at the pole and 0.1 T at the side. We used an atomic force microscope (AFM – Veeco Dimension 3100) to study surface morphology of the films. Local crystallinity of the films was measured by the microscopic Raman scattering spectra excited by CW argon ion laser at 514.5 nm wavelength.

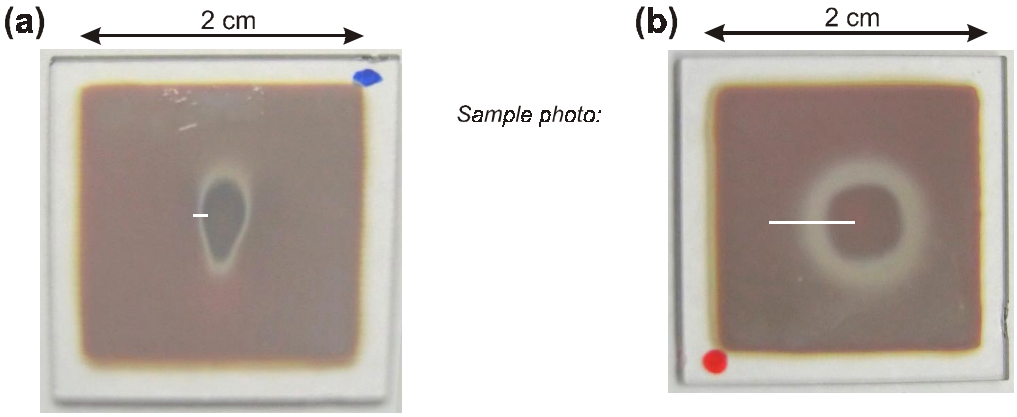

Fig. 2 Two samples of Si thin films. Films grew amorphous except in the region above the magnet. In case of magnetic field parallel with the substrate microcrystalline spot was formed (a). In case of magnetic field perpendicular to the substrate (b) microcrystalline ring with amorphous center was formed.

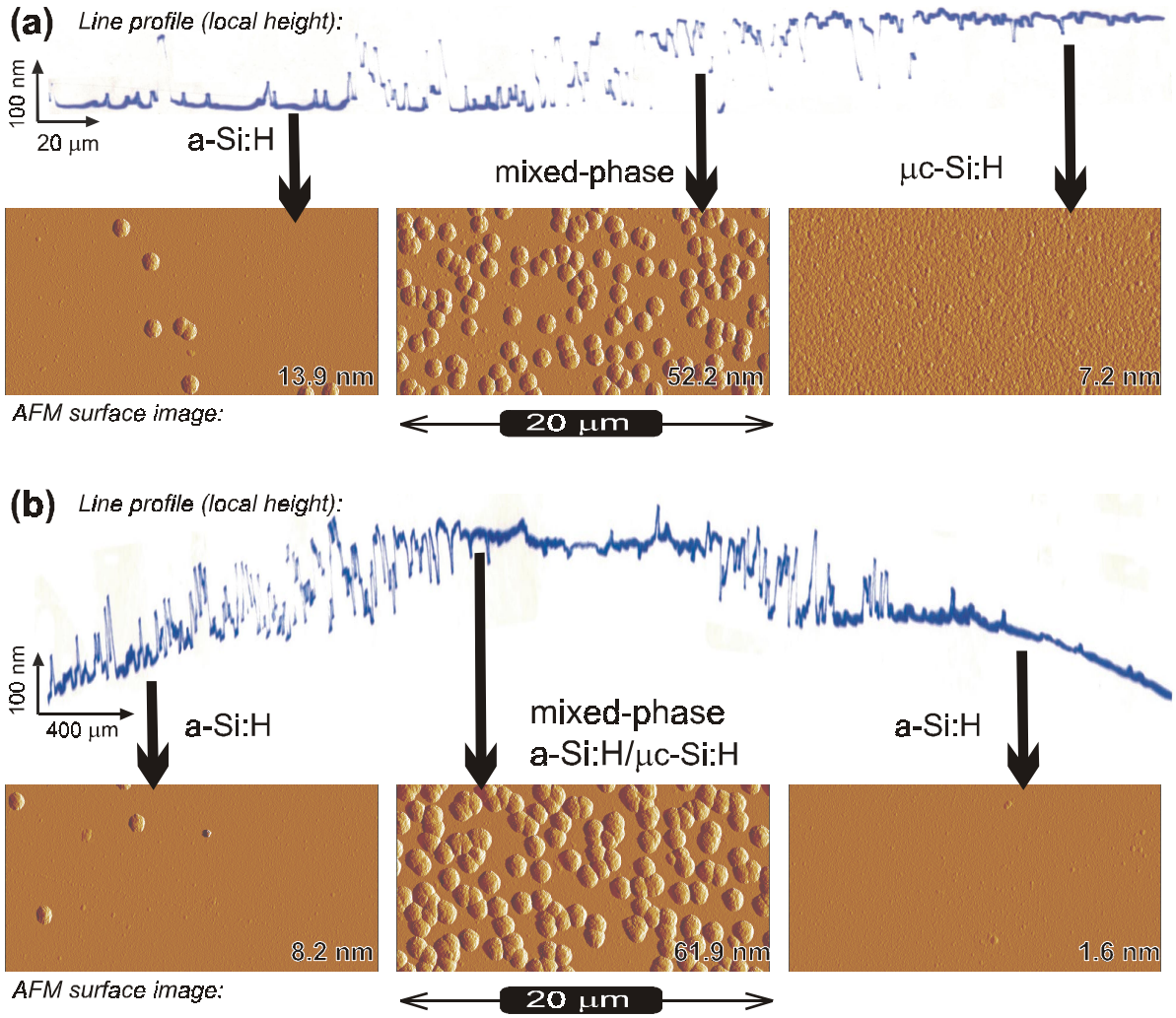

Fig. 3 Surface profiles and morphologies of the Si films. Positions of the surface profiles are shown in the Fig. 2 by white horizontal lines. The profiles show that the microcrystalline and amorphous areas of the film differ not only by their structure, but also by their thickness. AFM morphologies at selected positions of the profile show the different densities of the microcrystalline grains.

3. Experimental results

Deposition at the selected conditions normally leads to amorphous films, however, presence of the magnet locally changes the plasma and results in formation of microcrystalline regions, as evidenced by Raman spectra [3]. The changes of film structure are visible by naked eye (see also Fig. 2). The most conspicuous is the matt boundary between the area above the magnet and the rest of the film. The boundary between amorphous and microcrystalline regions scatters light due to the large surface roughness of the mixed phase film [4, 5].

Structure of the films depends on the orientation of the magnet with respect to the substrate surface. In case of magnet parallel with the substrate, the film above it grew fully microcrystalline, see Fig.2a. When the magnet was perpendicular to the substrate, the film directly above it was amorphous, but a microcrystalline ring along the edge of the magnet appeared. Transitions between the two phases are illustrated by AFM micrographs in Fig. 3.

Fig. 3 shows also the surface height profiles measured by stylus method for both cases. The thickness of the surrounding amorphous film after 2 hour of deposition was 1 μm, but the microcrystalline regions were on average 16 % thicker. About the same difference in thickness was observed between the microcrystalline and amorphous parts for both magnet orientations. Note that the amorphous center of the spot in Figs. 2b and 3b is less thick then the μc-Si:H ring around it and has approximately the same thickness as the surrounding a-Si:H.

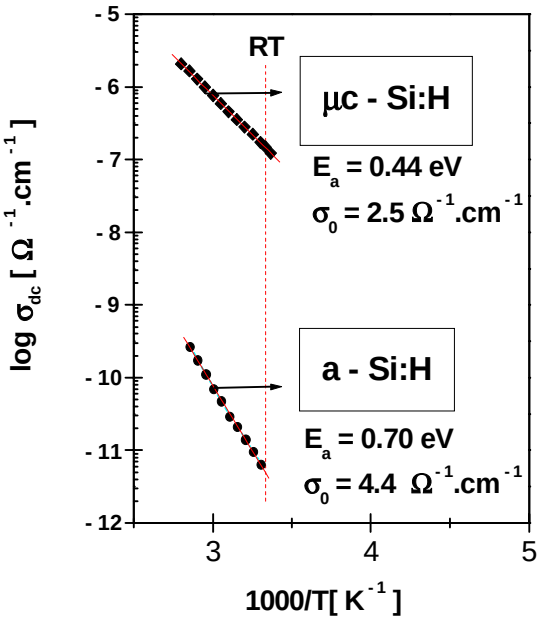

Fig. 4. Arrhenius plot of the temperature dependence of the dark conductivity for μc-Si:H spot grown above the magnet parallel to the substrate (see Fig. 2a) and for surrounding a-Si:H.

The difference in structure leads also to corresponding changes of material properties, illustrated here by the difference in the dark conductivity between the μc-Si:H spot and surrounding

a-Si:H, shown in the Arrhenius plot in Fig. 4. Conductivity of the a-Si:H at room temperature was about $7x10^{-12}$ $\Omega^{-1}cm^{-1}$ and its activation energy E_a = 0.7 eV, corresponding to standard device quality material. However, the microcrystalline spot above the magnet exhibited dark conductivity $2x10^{-7}$ $\Omega^{-1}cm^{-1}$ and activation energy E_a = 0.44 eV.

4. Discussion

The above described phenomenon may lead to important technological applications. Reduction of the deposition temperature of silicon films would enable industry to deposit microcrystalline hydrogenated silicon on flexible organic substrates such as PET. However, lowering the deposition temperature also leads to crossing the border between μc-Si:H and a-Si:H growth [5, 6]. Parallel magnetic field could make it possible to maintain the growth of μc-Si:H even at low temperatures.

Finally, our findings suggest an experimentally simple method for studying both the silane plasma and the nucleation of μc-Si:H in the early growth stages by applying a magnetic field to the substrates and using the growth of the grains as a developing process for making the nucleation density observable.

5. Conclusions

We have demonstrated new simple and effective way for influencing the growth of hydrogenated silicon thin films by magnetic field at the substrates. Magnetic field locally changes the growth conditions and at proper conditions leads to crossing of the amorphous – microcrystalline growth boundary. Properly arranged magnets could be used for reproducible deposition of microcrystalline pattern in otherwise amorphous films.

Acknowledgements

This research was supported by AV0Z 10100521, VaV/300/01/03, VaV SN/172/05, GAAV IAA1010316, IAA1010413 and GA ČR 202/05/H003 projects.

References

[1] M. Taniguchi, M. Hirose, T. Hamasaki, Y. Osaka, Appl. Phys. Lett. 37 (1980) 787.

[2] M. Ohnishi, H. Nishiwaki, K. Uchihashi, K. Yoshida, M. Tanaka, K. Ninomiya, M. Nishikuni, N. Nakamura, S. Tsuda, S. Nakano, T. Yazaki and Y. Kuwano. Jpn. J. Appl. Phys. 27 (1988) 40-46.

[3] A. Fejfar, J. Stuchlík, T. Mates, M. Ledinský, S. Honda, J. Kočka, submitted to Appl. Phys. Lett.

[4] T. Mates, A. Fejfar, I. Drbohlav, B, Rezek, P. Fojtik, K. Luterova, J. Kočka, Ch. Koch, M.B.Schubert, M. Ito, K. Ro, H. Uyama, J. Non-Crystaline Solids 299-302 (2002) 767 - 771.

[5] A. Fejfar, T. Mates, P. Fojtík, M. Ledinský, K. Luterová, I. Drbohlav, I. Pelant, H. Stuchlíková, J. Kočka, V. Baumruk, A. Macková, M. Ito, K. Ro, H. Uyama, Japanese Journal of Applied Physics, 42 (2003) L987

[6] J. Kočka, T. Mates, H. Stuchlíková, J. Stuchlík, A. Fejfar, Proceedings of the 3rd International Conference on Hot-Wire CVD (Cat-CVD) Process, Utrecht (The Netherlands), 23.-27. 8. 2004, to be published in Thin Solid Films.

Multi-Component Modeling for Co-Condensation Systems of Silicon-Based Intermetallic Nanoparticle Synthesis Using Induction Thermal Plasmas

Masaya Shigeta and Takayuki Watanabe

Department of Environmental Chemistry and Engineering, Tokyo Institute of Technology, Yokohama, Japan

Abstract

A multi-component co-condensation model was proposed to clarify the formation mechanisms of silicide nanoparticles in induction thermal plasmas. In Cr-Si and Co-Si systems, Si nuclei are produced and they grow, subsequently the metal vapor condenses on the Si particles. In Mo-Si system, Si condenses on the Mo particles produced earlier. Their composition shows a wide range. In Ti-Si system, both vapors of Si and Ti simultaneously condense on the Si nuclei. The silicon content shows a narrow range.

1. Introduction

Induction thermal plasmas (ITPs) have been utilized for material processes such as nanoparticle synthesis since they have several advantages such as high enthalpy, high chemical reactivity, variable properties, large plasma volume, long residence/reaction time, and high quenching rate [1, 2]. Nowadays, nanoparticles of disilicides are required in industrial fields because they provide high electrical conductivity and heat/oxidation resistance. They are, therefore, expected to be applied for electromagnetic shielding, solar control windows, VLSI electrodes, and so on.

The process of the synthesis is, however, a complicated phenomenon with many controlled parameters, and it includes a co-condensation process with large or small vapor pressure differences of prepared species. Although only a few studies and researches have been conducted concerning the synthesis of silicide nanoparticles using ITPs up to the present [3], the formation mechanism of silicide nanoparticles in ITPs is still poorly understood. Therefore, investigation of the formation mechanism of silicide nanoparticles is intensively important for the precise control of the particle size distributions and stoichiometric compositions.

In the present study, numerical analysis is conducted for the synthesis of silicide nanoparticles in an induction thermal plasma to clarify the formation mechanisms especially for chromium-silicon system, cobalt-silicon system, molybdenum-silicon system, and titanium-silicon system. A multi-component co-condensation model is proposed for the co-condensation processes in silicide nanoparticle formation.

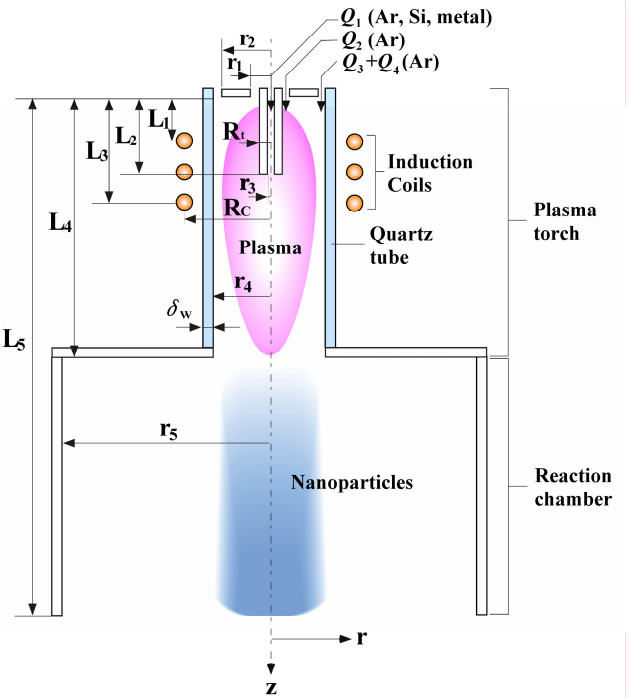

Fig. 1 Nanoparticle synthesis systems.

Table 1 Torch geometry and operating condition.

Torch Power	5 kW
Work Frequency	4 MHz
Reactor Pressure	101.3 kPa
Coil Radius	32 mm
Coil turn number	3
Wall thickness of quartz tube	1.5 mm
Distance to frontal end of coil (L_1)	19 mm
Distance to rear end of coil (L_3)	65 mm
Insertion length of probe (L_2)	45 mm
Torch length (L_4)	190 mm
Outer radius of inner slot (r_1)	6.5 mm
Outer radius of outer slot (r_2)	21 mm
Inner radius of injection tube (r_3)	1 mm
Inner radius of quartz tube (r_4)	22.5 mm
Outer radius of injection tube (R_t)	4.5 mm
Flow rate of carrier gas (Q_1)	0 Sl min^{-1}
Flow rate of plasma gas (Q_2)	3 Sl min^{-1}
Flow rate of plasma gas (Q_3)	10 Sl min^{-1}
Flow rate of sheath gas (Q_4)	20 Sl min^{-1}
Powder feed rate	0.1 g min^{-1}
Silicon content of feed powders	66.7 at%

2. Numerical formulation

Figure 1 shows a schematic illustration of nanoparticle synthesis systems consisting of a plasma torch and a reaction chamber. A summary of the geometry and operating conditions is given in Table 1. Powders of metals and silicon are supplied as the raw materials for silicides with the carrier gas from the central nozzle. The supplied powders are assumed to be vaporized completely due to the high enthalpy of the thermal plasma [3, 4]. The vapors of the metals and silicon are transported with the plasma flow to the reaction chamber and become supersaturated due to the rapid temperature decrease there, which leads to homogeneous nucleation. After homogeneous nucleation, the vapors of metals and silicon co-condense on the nuclei. Silicide nanoparticles are consequently synthesized from the gas phase. The silicon content of the feed powder is chosen to be 66.7 at% considered as the stoichiometric composition of disilicides.

2-1 ITP model

The calculation are based on the following assumptions to derive the governing equations: (a) steady-state laminar flow; (b) axial symmetry; (c) optically thin; (d) negligible viscous dissipation in energy equation; (e) negligible displacement current in comparison with the conductive current; (f) negligible flow-induced electric field; (g) identical temperature of heavy particles and electrons; (h) negligible effects of metals and silicon on thermofluid fields or properties of a plasma.

The fields of flow, temperature and concentration in the induction thermal plasma flow were calculated by solving the two-dimensional continuity, momentum, energy and species conservation equations coupled with the Maxwell's equations. The non-equilibrium effects by the ionization and recombination were taken into account.

Continuity:

$$\nabla \cdot (\rho \boldsymbol{u}) = 0 \tag{1}$$

Momentum:

$$\rho \boldsymbol{u} \cdot \nabla \boldsymbol{u} = -\nabla p + \nabla \tau + \boldsymbol{J} \times \boldsymbol{B} \tag{2}$$

Energy:

$$\rho \boldsymbol{u} \cdot \nabla h = \nabla \cdot \left(\frac{\lambda}{C_p} \nabla h \right) + \boldsymbol{J} \cdot \boldsymbol{E} - q_r \tag{3}$$

Species:

$$\rho \boldsymbol{u} \cdot \nabla Y = \nabla \cdot (\rho D \nabla Y) + R_r \tag{4}$$

Electromagnetic:

$$\nabla^2 \boldsymbol{E} - \xi \sigma_e \frac{\partial \boldsymbol{E}}{\partial t} = 0 \tag{5}$$

The boundary conditions along the centerline were set to insure axial symmetry. At the wall of the plasma torch, no slip conditions are maintained for the velocity, and the concentrations have zero gradient. The temperature at the inside wall of the plasma torch was calculated assuming that the outside wall was maintained at 300 K by water cooling. The injection tube was assumed to be at 500 K. The outflow boundary conditions at the torch were assumed that the gradient of the variables are zero. The sheath gas has swirl velocity component. Each gas stream has constant axial velocity with zero radial velocity having temperature at 300 K. Reaction kinetic rates of the dissociation and recombination as well as the ionization were taken into account. The transport properties were estimated using higher-order approximation of Chapman-Enskog method [5].

The governing conservation equations were solved using SIMPLER (Semi-Implicit Method for Pressure Linked Equation Revised) algorithm [6]. The governing equations and the electric field intensity equation with the associated boundary conditions were discretized into finite difference form using control-volume technique. Non-uniform grid points 30 by 30 were used for radial and axial directions, respectively. Grids were made finer close to the center and the coil region. Thermodynamic and transport properties were calculated from the temperature and compositions at each position in the calculation domain at each iteration step.

2-2 Multi-component co-condensation model

A one-dimensional multi-component model is proposed to clarify the formation mechanism of silicide nanoparticles with the following assumptions: (a) spherical particles; (b) negligible particle inertia due to the small size; (c) the same velocity of the condensing phase and the condensed phase as that of the plasma gas; (d) the same temperature of the nanoparticles as that of the plasma gas; (e) negligible heat generation caused by condensation; (f) the vapors of the metal and silicon considered as ideal gases; (g) negligible agglomeration among the nanoparticles; (h) atmospheric pressure in the systems.

Supersaturated vapor creates nuclei with the critical diameter by homogeneous nucleation [7], subsequently vapors condense heterogeneously on the nuclei [8], which results in nanoparticle growth.

Homogeneous nucleation rate of the species *i*:

$$J_i = \frac{(\beta_{11})_i n_{si}^2 S_i}{12}\sqrt{\frac{\Theta_i}{2\pi}}\exp\left(\Theta_i - \frac{4\Theta_i^3}{27(\ln S_i)^2}\right) \tag{6}$$

Critical diameter:

$$d_{pcri} = \frac{4\sigma_i v_{mi}}{k_B T \ln S_i} \tag{7}$$

Particle growth rate by heterogeneous condensation:

$$\frac{d(d_{pi})}{dt} = \sum_j \alpha_{ij}\frac{4\rho_g}{d_{pi}\rho_{cj}} D_j (X_j - X_j^s)\left\{\frac{1+Kn_i}{1+1.7Kn_i+1.333Kn_i^2}\right\} \tag{8}$$

In Eq. (6), the normalized surface tension Θ and the collision frequency function between a-mer and b-mer β_{ab} can be written as

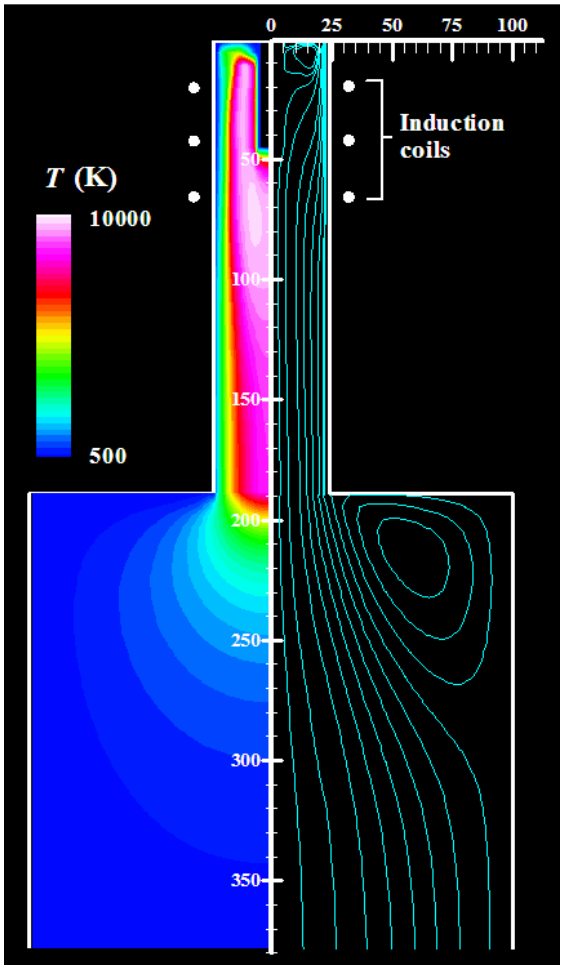

Fig. 2 Temperature (left), streamlines (right).

$$\Theta_i = \frac{\sigma_i s_{1i}}{k_B T} \tag{9}$$

$$\beta_{ab} = \left(\frac{3v_1}{4\pi}\right)^{1/6}\sqrt{\frac{6k_B T}{\rho}\left(\frac{1}{a}+\frac{1}{b}\right)}\left(a^{1/3}+b^{1/3}\right)^2 \tag{10}$$

The concentration of the metal and silicon vapors in the reaction chamber is obtained from the conservation equation written as

$$\rho u\frac{\partial c_i}{\partial z} = -G_i \tag{11}$$

The very fine computation grids are required for the nanoparticle synthesis since the nucleation and condensation processes have much smaller characteristic times than the plasma flow. Thus the grids of the reaction chamber (z=190-380 mm) are divided in 5,000 uniform grids in z-direction for the nanoparticle synthesis. The data obtained by the computation of the plasma such as the temperature and the velocity are modified for the fine grid system to calculate the rates of nucleation and condensation.

3. Results and discussion

Figure 2 shows the thermofluid fields in the plasma torch and the reaction chamber. The Joule heating by the applied electromagnetic power generates the remarkably high temperature zone (higher than 9,500 K) in and below the coil region. The high enthalpy of the plasma is

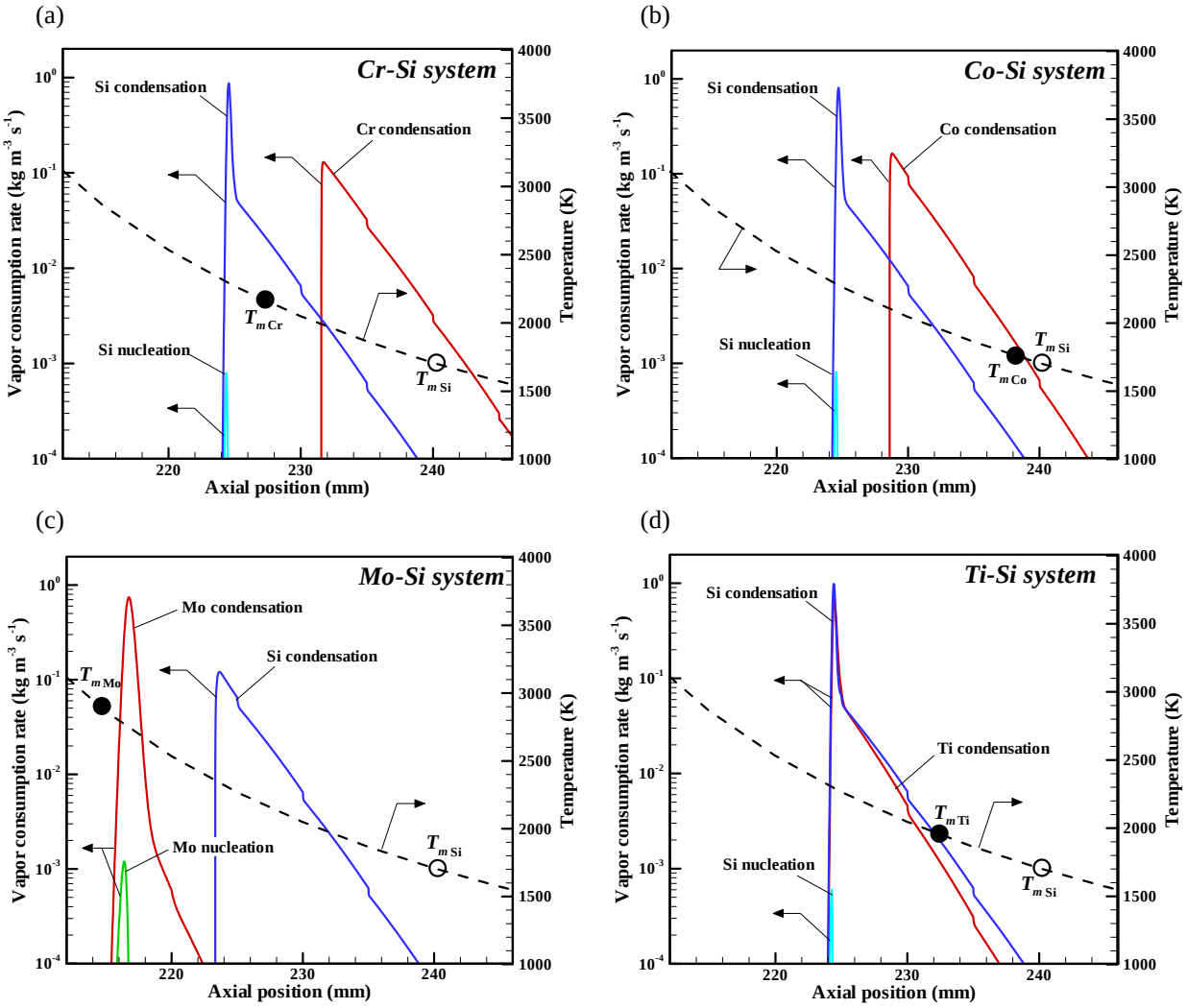

Fig. 3 Axial evolution of vapor consumption rate:
(a) Cr-Si system, (b) Co-Si system, (c) Mo-Si system, and (d) Ti-Si system

transported to the downstream region by the convection. The characteristic recirculation flow exists above the coil region since the radial Lorentz force induced in the plasma pinches the flow. In the reaction chamber, the temperature decreases drastically to below 500 K. As the result, the high quenching rate (10^4-10^5 K s^{-1}) is obtained, which leads to considerable promotion of particle nucleation.

Figures 3 (a)-(d) show the axial evolutions of the vapor consumption rate. In Cr-Si system, silicon vapor is consumed by the particle growth with homogeneous nucleation and heterogeneous condensation at the more upstream position than chromium vapor. At the downstream position, the chromium vapor consumption occurs by heterogeneous condensation on silicon particles. When chromium vapor condenses on the silicon particles, chromium is considered to be well-mixed in the liquid silicon particles with the particle growth since the temperature is higher than the melting temperature of silicon. Therefore, the nanoparticles of chromium-silicides are well-synthesized. In Co-Si system, it shows the same tendency as Cr-Si system. The cobalt vapor consumption by condensation occurs at the more upstream position compared with Cr-Si system as shown in Fig. 3 (a) since the saturation pressure of cobalt is smaller than that of chromium.

In Mo-Si system, molybdenum particles grow by homogeneous nucleation and heterogeneous condensation, subsequently silicon vapor condenses on the molybdenum particles. The temperature of the nanoparticle growth region is lower than the melting point of molybdenum. This indicates poor synthesis of silicides, because molybdenum and silicon should be well-mixed to form silicides in the condensation process. However, the stoichiometric compounds of molybdenum-silicides were observed in the experimental study [3]. The nanoparticles are, therefore, considered to grow in a super-cooled liquid state as the mixture of molybdenum and silicon even at the lower temperature than the melting point of

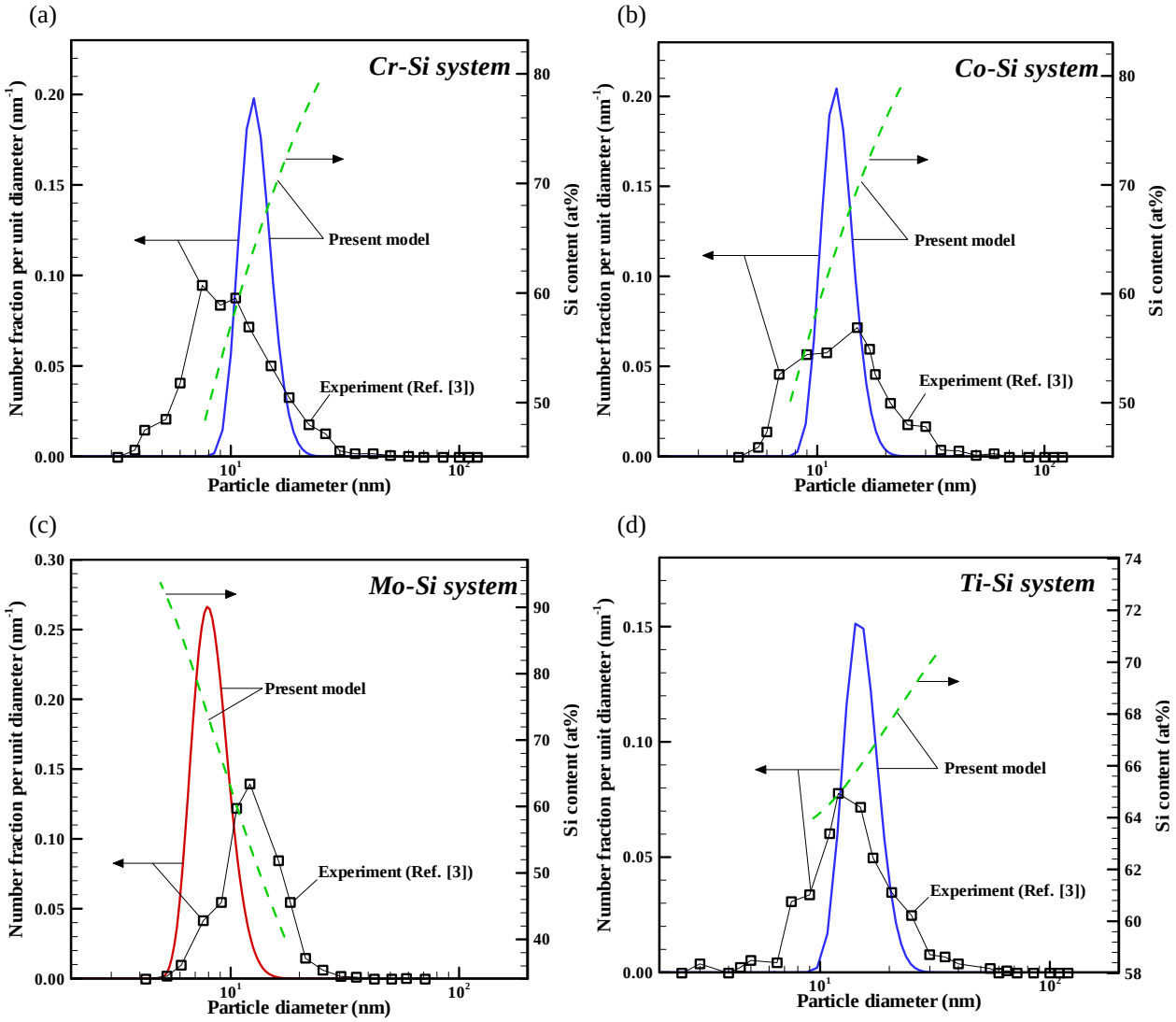

Fig. 4 Particle size distribution and silicon content:
(a) Cr-Si system, (b) Co-Si system, (c) Mo-Si system, and (d) Ti-Si system

molybdenum by the high quenching rate at the tail of the induction thermal plasma.

In Ti-Si system, silicon nucleates earlier than titanium. Immediately after the nucleation of silicon, the vapors of silicon and titanium are simultaneously consumed by heterogeneous condensation. Silicon and titanium are considered to be well-mixed in a liquid state in this co-condensation process since the particles grow at the temperature higher than the melting points of titanium and silicon, which results in the better synthesis of titanium-silicides.

Figures 4 (a)-(d) show the particle size distributions and the silicon contents finally obtained by the present model for four systems. The number mean diameters are 13.3 nm in Cr-Si system, 12.8 nm in Co-Si system, 8.5 nm in Mo-Si system, and 15.8 nm in Ti-Si system. Mo-Si system produces smaller nanoparticles than the other systems due to the difference of the nucleus size. Molybdenum nucleates with the smaller critical diameters from 0.59 to 1.94 nm, while the critical diameters of the silicon nuclei in other systems show from 0.83 to 2.65 nm. Since a larger number of the smaller nuclei are produced in Mo-Si system, a smaller amount of the vapors is consumed per one nucleus for the particle growth. As the result, the obtained particle diameters in Mo-Si system show smaller than those in the other systems. In all systems, the particle size distributions agree well with the experimental results [3].

The silicon contents show some ranges along with the particle diameters. Cr-Si system and Co-Si system have a range 48.1-79.4 at% and 49.5-79.3 at%, respectively. Mo-Si system particularly has a wide range 40-94 at%. Only Ti-Si system has a narrow range 64-70 at%, which results in the more homogeneous synthesis of the disilicide. These are determined by the balance of the contents of the formerly produced

Table 2 Compositions estimated from Ref. [9]

System	Main product	Sub-product
Cr-Si	$CrSi_2$	Cr_5Si_3, CrSi, Si
Co-Si	$CoSi_2$	CoSi, Si
Mo-Si	$MoSi_2$	Mo_5Si_3, Si
Ti-Si	$TiSi_2$	TiSi, Si

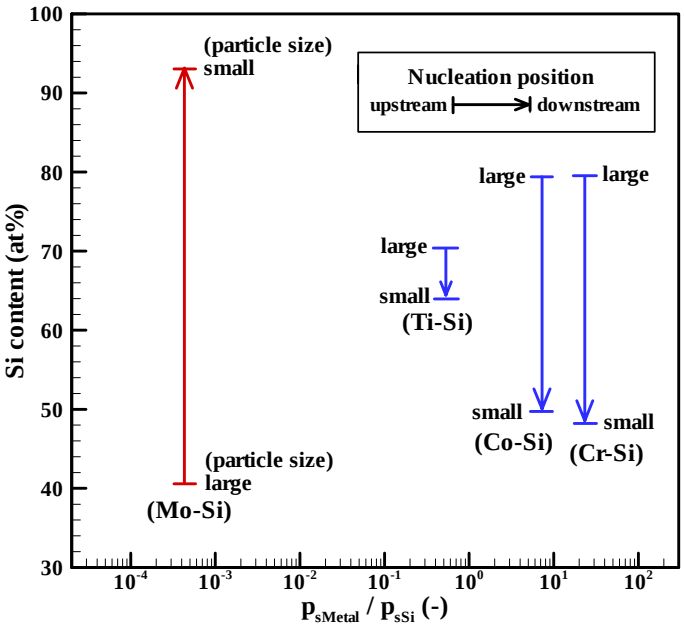

Fig. 5 Correlation chart between saturation pressure ratio and silicon content.

nuclei and the following condensing vapor. This indicates that the silicide nanoparticles synthesized in the induction thermal plasma provide diverse compositions. The compositions of the products can be estimated from the obtained silicon contents by comparing with the phase diagrams of silicides [9] and summarized in Table 2. In all systems, the required disilicides are synthesized as the main products, while the sub-products are synthesized as well, even though the powders of the raw materials are supplied with the stoichiometric compositions of the disilicides. This is because the condensation positions are different due to the different vapor pressures of the materials. However, induction thermal plasmas with the high enthalpy and the high quenching rate are notably effective even for the difficult co-condensation processes with the large vapor pressure differences. These results about the composition of the synthesized silicide nanoparticles obtained from the present model also show good agreements with the experiment [3].

Figure 5 is the correlation chart between the saturation pressure ratios and the silicon contents at the nucleation positions obtained from the present study. The larger particles with silicon nuclei generated at the upstream positions provide the larger silicon contents in Cr-Si system, Co-Si system, and Ti-Si system, while the smaller particles with molybdenum nuclei generated at the downstream positions provide the larger silicon contents in Mo-Si system. Furthermore, the silicon contents show the wide ranges when condensations of metal and silicon occur at the different positions due to the largely different vapor pressures as shown in Cr-Si system, Co-Si system, and Mo-Si system. The silicon content shows the particularly narrow range when condensations of metal and silicon occur simultaneously as shown in Ti-Si system.

This chart indicates that processes including large difference of the saturation pressures between the metal and silicon tend to produce silicide nanoparticles with wide range of composition. Conversely, the composition of the nanoparticles can be evaluated from the ratio of the saturation pressures between the metal and silicon. This chart can be used for prediction of composition in the co-condensation process.

References

[1] T. Watanabe, A. Nezu, Y. Abe, Y. Ishii, K. Adachi - Thin Solid Films 435, 27 (2003).
[2] M. Shigeta, T. Watanabe, H. Nishiyama - Thin Solid Films 457, 192 (2004).
[3] T. Watanabe, H. Okumiya - Sci. and Tech. of Advanced Materials 5, 639 (2004).
[4] M. Shigeta, T. Sato, H. Nishiyama - Int. J. Heat and Mass Transfer 47, 707 (2004).
[5] J. O. Hirschfelder, C. F. Curtiss, R. B. Bird - Molecular Theory of Gases and Liquids (John Wiley, New York, 1964).
[6] S.V. Patankar - Numerical Fluid Flow and Heat Transfer, 138 (Hemisphere, New York, 1980).
[7] S.L. Girshick, C.P. Chiu, P.H. McMurry - Aerosol Sci. and Tech. 13, 465 (1990).
[8] S.V. Joshi, Q. Liang, J.Y. Park, J.A. Batdorf - Plasma Chem. Plasma Proc. 10-2, 339 (1990).
[9] T.B. Massalski - Binary Alloy Phase Diagrams. 2nd Ed. 3, 2664 (American Society for Metals, Materials Park, 1990).

Effect of adding O_2 or CO_2 on the formation of NH_3 and NO in an N_2/H_2 plasma

R.A.B. Zijlmans[1], G. Lombardi[2], G. Stancu[2], J. Röpcke[2], R. Engeln[1] and D.C. Schram[1]

[1]*Department of Applied Physics, Eindhoven University of Technology, P.O. Box 513, 5600 MB Eindhoven, The Netherlands*

[2] *INP-Greifswald, Friedrich-Ludwig-Jahn-Str. 19, D-17489 Greifswald, Germany*

Abstract

We have shown that it is in principle possible to make selectively specific molecules by means of an expanding thermal plasma. An NH_3 mole fraction of 6 % in the plasma is observed in a N_2/H_2 plasma. After adding O_2, the density of the formed NH_3 is decreased strongly and instead mainly H_2O and some NO is formed. The effect of adding CO_2 instead of O_2 shows the same qualitative and quantitative behavior.

Keywords: molecule formation, recombining plasma, cascaded arc, NH_3, NO

1. Introduction

Lately, the topic of molecule formation in plasmas receives a revived interest. Understanding the fundamental processes leading to the formation of molecules in plasmas used for deposition and etching, will result in the optimization of these production steps in the semiconductor industry. Also for understanding molecular abundances in the interstellar medium it is important to know how certain types of molecules are formed. We expect that we can obtain relevant information about these processes by studying the general behavior of the formation of specific molecules in recombining plasmas containing mixtures of $N_2/H_2/O_2$. Ultimately, this research could lead to a new methodology for producing selectively specific molecules by adjusting the plasma parameters.

Hempel et al. [1] studied the abundance of different types of stable molecules and radicals in a microwave plasma reactor to obtain information about the kinetics of the plasma. Only a complicated model in which all the reactions of interest take place in the gas-phase of the plasma could explain their measurements. The formation of NH_3 molecules has been observed by Vankan et al. [2] in a N_2/H_2 containing expanding thermal plasma, produced by a cascaded arc. This research pointed to the importance of molecule formation as a result of the interaction between plasma produced radicals and the walls of the plasma vessel. Also reference [3] and [4] observe the formation of NH_3 in a microwave plasma and a dielectric barrier discharge respectively. Further research on N_2/H_2 containing recombining plasmas has been conducted by van Helden et al. [5]. In this contribution we concentrate on the effect of adding O-containing species (O_2 or CO_2) to the N_2/H_2 plasma in order to investigate the tuning possibilities of the system and to find a way to predict the abundances of the molecular end products in the plasma.

By means of a dedicated tunable infrared diode laser system and mass spectrometry, we measured the mole fractions of several species in the background of the plasma vessel. We here report on the measured mole fractions of NH_3, NO and CO_2.

2. Theory

In a non-plasma environment, practically all the reactions leading to the formation of a certain type of molecule, exhibit an activation energy. This results in very specific equilibrium states of a system containing various species, strongly dependent on the exact parameters of the complete system.

By starting with a high flux of radicals, produced by plasma, radical chemistry with small or no activation energy dominates in first order the resulting equilibrium state of the system. Therefore species with the highest relative binding energies are expected to be the most abundant species. The binding energies of several species in the gas phase can be obtained from [6, 7]. A complicating factor can be that the effective binding energy of certain molecules adsorbed at a surface, is different from the binding energy in the gas phase. To get a first estimate of the end products in the gas phase, we consider only the binding energies in the gas phase.

The cascaded arc is able to produce a high flux of radicals. These active species interact with the gases injected into the background of the plasma vessel. When N_2 and H_2 are directed via the cascaded arc into the plasma

vessel, the active species N, H, N^+ and H^+ , produced in the plasma source, will interact with the molecules injected into the plasma vessel. In case molecular oxygen is injected in the plasma vessel, a fraction of the O_2 is dissociated mainly by the N^+ ions in a charge exchange reaction, followed by dissociative attachement:

$$N^+ + O_2 \rightarrow N + O_2^+ \quad (1)$$

$$O_2^+ + e \rightarrow O + O \quad (2)$$

Also the 'neutral' gas-phase reaction:

$$N + O_2 \rightarrow NO + O, \quad (3)$$

can lead to atomic oxygen radicals. These two mechanisms result in a high flux of O radicals towards the walls of the vessel.

Based on this simple consideration, the formation of H_2O compared to H_2 and O_2 is expected to be favorable, because the total binding energy of $2H_2O$ is equal to 19.0 eV and of $2H_2 + O_2$ only 14.1 eV. Therefore a high abundance of H_2O is expected compared to H_2 and O_2 in an H_2/O_2 containing plasma. The same comparison for 2NO (13.0 eV) and $N_2 + O_2$ (14.9 eV) suggests a strong tendency of a N_2/O_2 containing plasma to form mainly N_2 and O_2. It appears that in the N_2/H_2 case, dominantly N_2 and H_2 and only for 10% NH_3 is formed. This does not correspond directly to the binding energies of $N_2 + 3H_2$ versus $2NH_3$ (23.2 and 23.2 eV respectively), so apparently other factors play also a role: e.g. which species are adsorbed at the surface.

3. Setup

A sketch of the experimental setup is given in figure 1. On the left the cascaded arc plasma source is shown. The cascaded arc consists of a stack of copper plates with a central bore of 4 mm in diameter, forming a channel. PVC spacers to keep them electrically insulated. The plates stabilize the discharge, which is sustained between cathode and anode. A current of 55 - 60 A is fed through the arc channel. A substantial flow of argon and/or N2 and H2 is fed through the arc channel, producing atoms and ions. O_2 can only be directed into the background of the plasma vessel. Also N_2 and H_2 can be injected into the background of the plasma vessel.

The plasma created in the cascaded arc expands into the plasma vessel, which is kept at a pressure of 20 Pa. Also a mass spectrometer has been installed to analyze the stable species present in the background of the plasma vessel.

The laser beam from the tunable diode laser system (IRMA, [8]) is directed through the vessel. The IRMA system is composed of four different diode lasers, which can be used subsequently without changing much on the alignment of the system. So in principle four different species can be monitored relatively easy. Here we report on measurements on NO, NH_3 and CO_2.

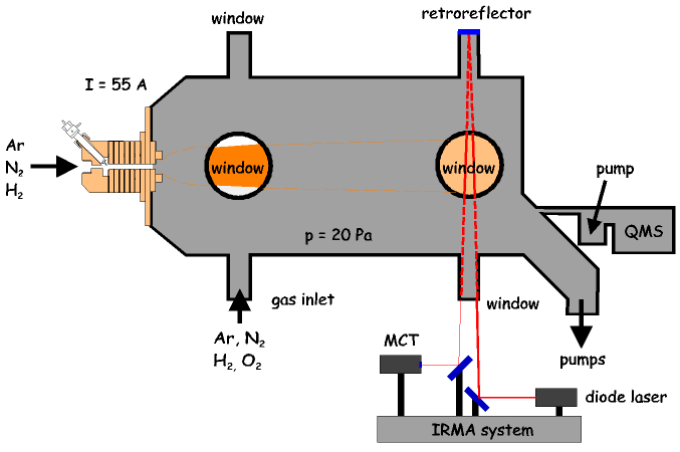

Figure 1. Sketch of the experimental setup

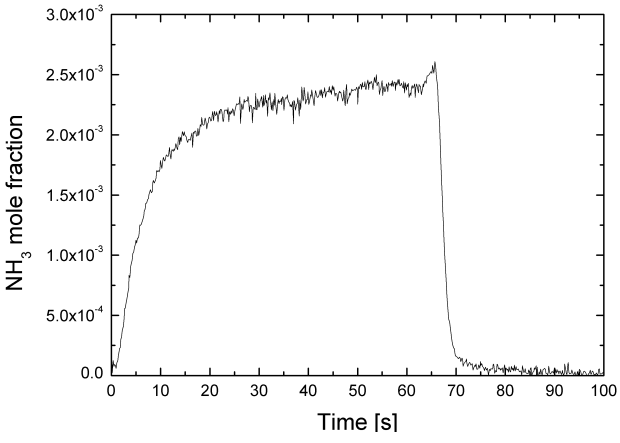

Figure 2. Time dependence of the destruction and formation of NH_3 in a $N_2/H_2/O_2$ plasma. See the text for details.

3. Results

3.1. Time dependent destruction and formation of NH_3

Figure 2 shows the time–dependence of the NH_3 concentration in an argon plasma (3.0 SLM Ar directed via the cascaded arc, operated at 60 A) with N_2 (0.28 SLM) and H_2 (0.02 SLM) added in the background of the vessel. During the admixture of 0.1 SLM O_2 in the background of the vessel, no NH_3 is observed (at time < 0 s and time > 70 s). Apparently the presence of O_2 hampers the net production of NH_3 significantly.

After closing the oxygen flow at t = 0 s, it takes 30 s for the NH_3 mole fraction to reach its maximum value of 2.3×10^{-3}. Ar^+ ions created in the cascaded arc dissociate N_2 and H_2, leading to N and H atoms, which associate at the surface to NH_3. The transit time of particles in the plasma beam is around 0.03 s and the residence time in the vessel around 0.73 s. Both these time scales are significantly shorter than the observed time constants in figure 2 of the formation of NH_3. This suggests that the formation of NH_3 is hampered by oxygen and/or oxygen containing compounds that desorb from the vessel walls. Another possibility is that the density of H atoms necessary for the formation of NH_3 takes time to build up, which is only possible when the H atoms are not bound into H_2O anymore.

3.2. N_2/H_2 plasma with O_2 in the background

In figure 3 and 4 the NH_3 and NO mole fraction in the plasma vessel are given as a function of the O_2 flow. We observe that at $\Phi(O_2) = 0$ sccm, a significant fraction of the initial gases N_2 and H_2, both directed through the cascaded arc, is converted into NH_3. Depending on the ratio of the flows of these gases, a maximum mole fraction of 6 % is obtained, as can be seen in figure 3. This implies that 7.9 % of the total N_2 flow and 15 % of the total H_2 flow is converted into NH_3. Decreasing the relative amount of H_2 results in a lower maximum observed mole fraction of 3.2 % as is shown in figure 4. The optimal ratio of $\Phi(N_2)$ / $\Phi(H_2)$ is determined to be 0.45 / 1.0 from a more detailed study on the NH_3 formation in this type of plasma.

When O_2 is added to the plasma, especially at a relatively low H_2 flow, the net production of NH_3 is stopped very efficiently, already at a low O_2 flow.

In the same experiments, we also monitored the mole fraction of NO, which is displayed in figure 3 and 4. We conclude that especially at high O_2 flows, mainly H_2O (determined by mass spectrometry) and a small fraction NO is formed. A remarkable fact is a threshold value of $\Phi(O_2) = 0.1$ SLM for the formation of NO.

3.2. N_2/H_2 plasma with CO_2 in the background

When we add another type of molecule containing O or O_2, in this case CO_2, the effect on the net production of NH_3 is qualitatively the same, which is shown in figure 5. We do observe that especially for relatively low H_2

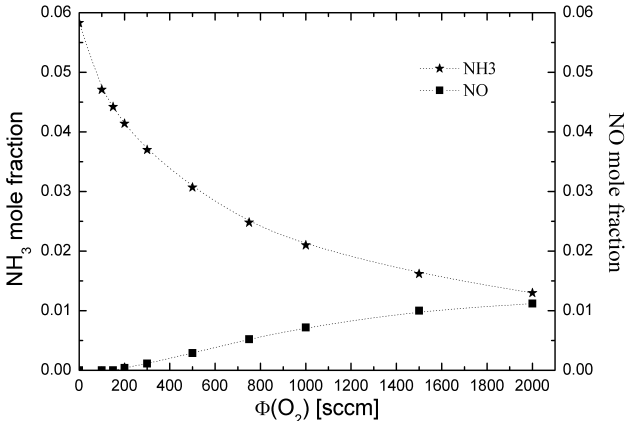

Figure 3. NH_3 and NO formation in a N_2/H_2 plasma to which O_2 is added. Gases directed through the cascaded arc: $\Phi(N_2)$ = 800 sccm, $\Phi(H_2)$ = 1200 sccm. Oxygen is injected in the background of the plasma vessel.

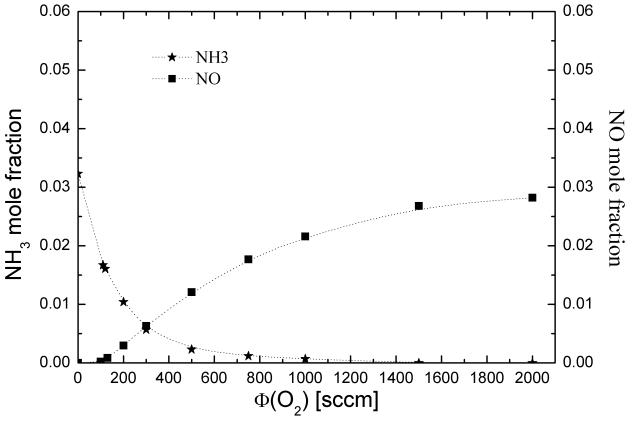

Figure 4. NH_3 and NO formation in a N_2/H_2 plasma to which O_2 is added. Gases directed through the cascaded arc: $\Phi(N_2)$ = 1700 sccm, $\Phi(H_2)$ = 300 sccm. Oxygen is injected in the background of the plasma vessel.

fractions, the effect of CO_2 is less pronounced. The depletion of CO_2 in plasmas with different N_2/H_2-ratios is displayed in figure 6 and turns out to be around 30 %. Together with the fact that dissociation of CO_2 gives only one O atom (and the stable molecule CO) and the dissociation of O_2 gives two O atoms, this suggests the competitive formation of mainly H_2O at low O_2 or CO_2 flows. The effect of adding O_2 is more pronounced because of the greater abundance of O atoms.

4. Discussion

4.1. N_2/H_2 plasma with O_2 in the background

Based on the binding energies given in section 2, we expect that in the presence of (dissociated) O_2 primarily H_2O is formed at the expense of NH_3. This is consistent with figure 3 and 4: adding O_2 to the system results in a significant decrease of the NH_3 density. Also a large fraction of H_2O was observed by mass spectrometry. A smaller abundance of NO compared to N_2 and O_2 can also be expected from the binding energies given in section 2, which is supported by figure 3 and 4 as well.

4.2. N_2/H_2 plasma with CO_2 in the background

When CO_2 is added to the plasma, instead of O_2, the same effects are observed, as is displayed in figure 5. Especially at low H_2 fractions, the effect of adding CO_2 to the plasma on the production of NH_3 is not as big as when pure O_2 is added. This is caused by the number of O atoms (the active species) that can be delivered by O_2 and CO_2. The abstraction energy of an O atom from O_2 and CO_2 is roughly the same: 5.17 eV and 5.51 eV for O_2 and CO_2 respectively. Each dissociation of O_2 delivers two O atoms for the plasma, where CO_2 only delivers one O atom.

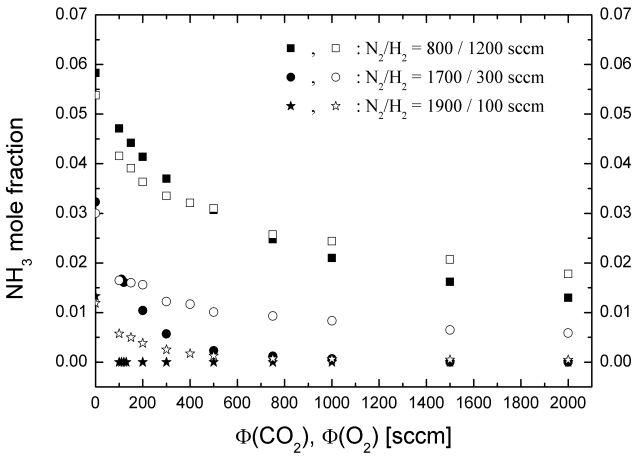

Figure 5. NH_3 mole fraction after adding O_2 (solid points) or CO_2 (open points).

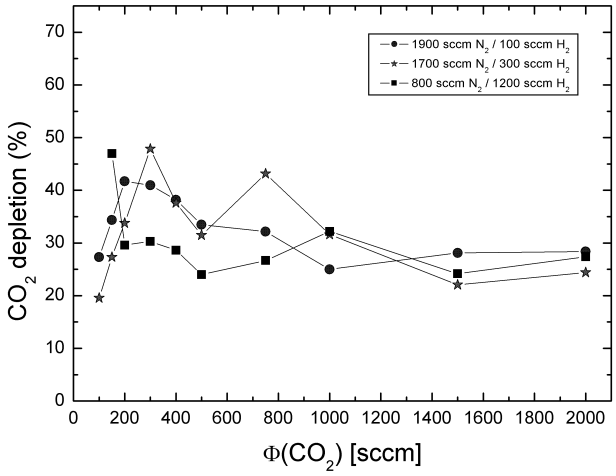

Figure 6. CO_2 depletion as a function of the CO_2 flow.

5. Conclusions

We conclude that based on an analysis of the binding energy of the species present in the plasma, an estimate of the abundance of the various species in the plasma can be obtained. Furthermore, we have shown that it is possible to selectively form specific molecules, by tuning the plasma parameters. In this case a low fraction of O_2 or CO_2 added to the plasma results in a significant mole fraction of NH_3. A high fraction of O_2 or CO_2 added results mainly in NO, H_2O and CO.

References

[1] F. Hempel, PhD thesis, Ernst-Moritz-Arndt-Universität Greifswald (2003).
[2] P. Vankan et al. – APL **83**(3):418-420 (2002).
[3] J.L. Jauberteau et al. – J. Phys. D: Appl. Phys **35**: 665-674 (2002).
[4] M. Bai et al. – IEEE Tranactions on plasma science **31**(6): 1285-1291 (2003).

[5] J.H. van Helden et al. – Proceedings of the 16th International Symposium on Plasma Chemistry, June 22-27, Taomina, Italy (2003).
[6] M. Capitelli et al. – *Plasma kinetics in atmospheric gases*, Springer, (2000).
[7] P.W. Atkins - *Physical Chemistry*. Oxford University Press, 6th edition (1998).
[8] J. Röpcke et al. - Rev. Sci. Instrum. **71**: 3706-3710 (2000).

MICROWAVE PLASMA CATALYST

D. Hitchen[1], M. Houghton[1], A.I. Al-Shamma'a[1], J. Lucas[1]

[1]*Dept. of Electrical Engineering & Electronics, University of Liverpool, Liverpool, UK*

Abstract

As the internal combustion engine does not burn with 100 % efficiency, some of the, non-burnt fuel causes the release of hydrocarbons (HC) and due to inadequate mixing with the air molecules exit the engine as carbon monoxide (CO). Additionally the combustion combines nitrogen with oxygen to form oxides of nitrogen (NOx). This paper presents the microwave plasma catalyst and its effective use against vehicles against gases and particulates.

1. Introduction

The emissions from transport vehicles have dramatically increased over the last 30 years and huge sums of money are being invested in the reduction of vehicle pollution. The current method for treating these gasses is using a catalytic converter. A catalytic converter has a honeycomb of porous ceramic. This honeycomb structure is used to maximise surface area and to reduce the amounts of palladium, platinum and rhodium that are embedded in the ceramic. Once the catalyst has been heated to over 300 ^{0}C the unwanted molecules are ripped from their compounds and stick to the catalyst where they bind with other similar atoms and are then released into the atmosphere. In engines, emission control of CO, HC and NO_x is obtained by using the three-way catalyst. This is the only technique, which is presently available to the transport industry.

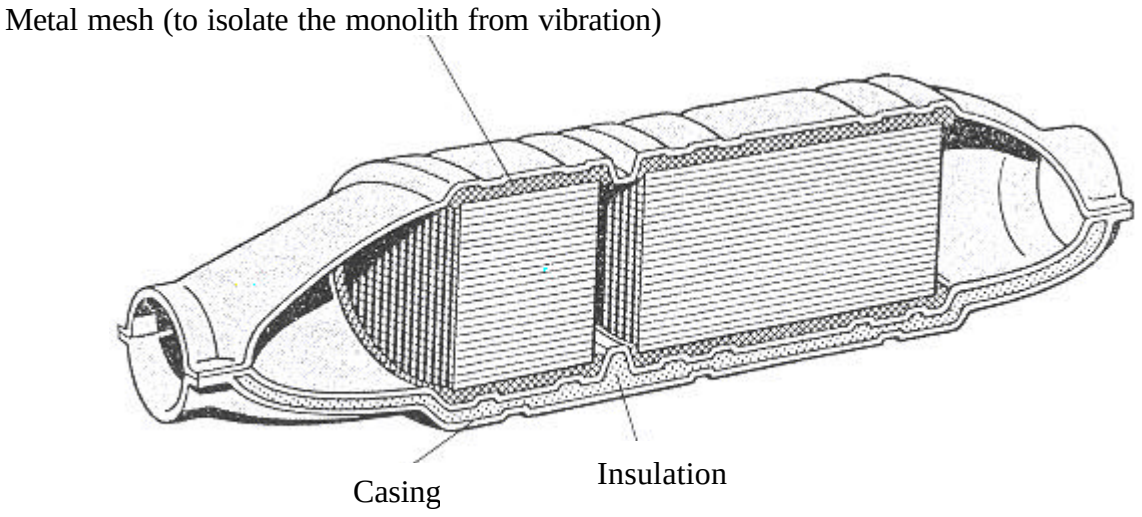

Figure 1: The three-way catalyst

The construction of the three-way catalyst is shown in figure 1. It is supported on an alumina substrate. The need to operate the air/fuel around the stoichiometric mixture means that the catalytic system reduces the fuel economy by as much as 10%. Other disadvantages are:

1. Deterioration by poisoning of the catalyst by deposits, mechanical failure of the substrate and sintering which reduces the effective interaction area giving an average lifetime of 3 years.
2. Do not start working until a minimum substrate temperature of 300^{o}C is attained.
3. The high cost of precious metals and the worldwide scarcity of sources.
4. Less efficient operation with hydrocarbon and black smoke particulate emissions.

The converter will only run at a specific air to fuel ratio, the stoichiometric ratio, of 14.7:1 [1]. The ratio is maintained by fuel injection. If there is an increase in the fuel level for example from a misfiring spark plug, overly rich fuel mixture, a leaky exhaust valve or head gasket, the temperature of the catalyst can rise dramatically causing it to melt and block up. In addition the catalytic converters have become a cause of pollution in their own right with pollution studies of the icecaps in central Greenland show that palladium

and rhodium levels have risen by 40 to 80 times since 1976 [2]. The ratio of platinum/palladium to rhodium in the snow compares closely to the ratio of use in the exhaust systems from another study [3,4]. The use of a combined catalyst and engine management system adds considerably to the cost of the engine. Present catalyst costs are €1800 for a three-litre engine reducing to €600 for a 1-litre engine.

2. Microwave Plasma Catalyst

A new form of catalyst, which has the same attributes as the three-way catalyst, has been researched, which uses plasma chemistry to clean up the exhaust gas. It has shown that microwave plasma readily satisfies the EURO IV standards for emissions but has the added advantages as follows:

1. It does not obstruct the exhaust gas flow, hence gives 10% fuel saving.
2. Only uses 2% of engine power to provide microwave power.
3. Lower cost than the three-way catalyst, it could be as low as 50%.
4. Able to efficiently oxidise HC and carbon particles especially the micro-particles that are giving the main health concern.
5. Microwave catalyst works immediately the engine is started and does not require a warm up period.
6. It does not use expensive rare earth materials (platinum, rhodium and palladium).

In plasma chemistry, the reactions that occur can differ vastly from the reactions expected at the temperatures involved. For example, even in low temperature plasma, the noble gasses become reactive and will readily oxidise in the presence of oxygen. Additionally the oxidisation of CO to CO_2 in an electric discharge, at relatively low current densities, the concentration ratios at room temperature can be shown to correspond to the ratios of reactants and products obtained in a purely thermal reactor at 3000 °K. The reason for this is that if an electron collides with a neutral atom it can throw a tightly bound local electron into an unpopulated shell; the atom is then no longer in such a strongly localised bound state and is free to form chemical bonds with other atoms.

Table 1. Ions Produced by Electron Induced Reactions in Plasmas [5].

Plasma	Ions
H_2	H^+, H_2^+
He	He^+, He_2^+
O_2	O^+, O^-, O^{2+}, O_2^{2+}
N_2	N^+, N_2^+
Cl_2	Cl^-, Cl_2^-
Br_2	Br^-, Br_2^-
I_2	I^+, I^-, I_2^-
CO	C^+, O^+, O^-, CO^+

In a microwave discharge, electrons gain energy from the applied microwave field and lose energy by elastic and inelastic collisions. The constant ionisation of the gas molecules creates new electrons, which flow to the walls due to density and space charge potential gradients. To produce free radicals at the relatively low temperatures involved, the electron temperature to gas temperature must be at least 10:1. For a microwave discharge to occur the electric field strength, which is proportional to the square root of the input power, must be increased until at some point the field will reach a strength at which a breakdown of the gas can occur. The average power transferred to a unit of gas in a microwave discharge can be given [6]: -

$$\overline{P} = \frac{e^2 e^2 n}{2m} \frac{V_c}{V_c + w^2} \qquad (1)$$

Where: (e) the maximum field strength, (n) electron concentration, (m) the electron mass, (V_c) elastic collision frequency and (?) angular frequency of the applied field.

Due to their higher electron temperatures ranging from 5 to 15eV compared to 1 or 2eV for D.C., low frequency or R.F. discharges, a higher degree of ionisation is possible using a microwave discharge.

3. System Setup

The microwave plasma laboratory systems consists of a power supply, magnetron, operating at powers up to 1000W at 2.45GHz, circulator, E-H tuner and the interaction cavity as shown in figure 1 [7,8]. However, the industrial prototype system will only contain the magnetron and the plasma cavity. The microwave power can be coupled effectively to the plasma cavity by either a flexible cable of a waveguide based up on the vehicle type and requirements.

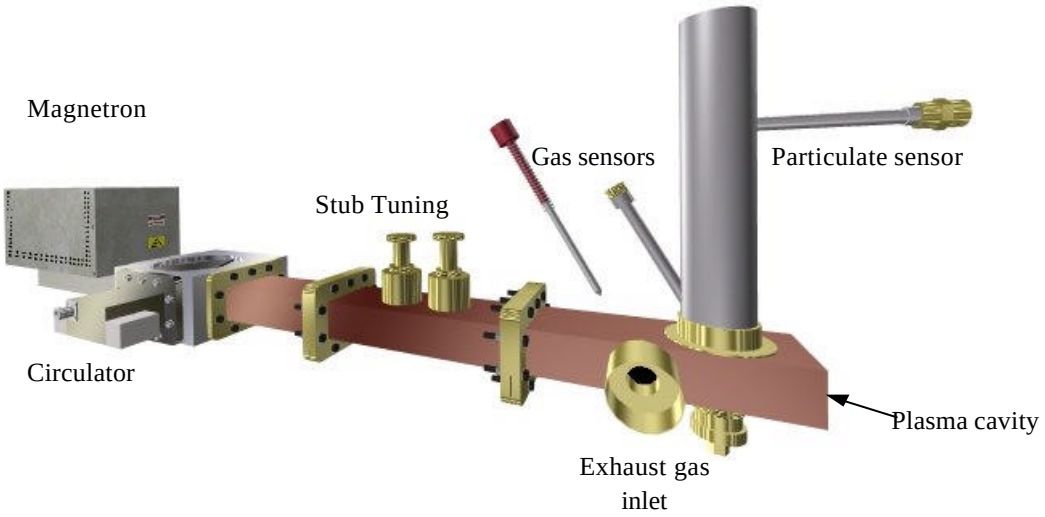

Figure 1: Microwave plasma catalyst laboratory arrangements

The microwave plasma is generated between two electrodes within the plasma cavity as shown in figures 2 and 3.This arrangement provides a uniform microwave plasma between the electrodes of the top and bottom plates. The top electrode is covered by a fine mesh, which acts as the first particulate trap. It also requires an operating power of at least 500W for a duration of at least 10 microseconds. To maintain a good plasma at reduced power, it is necessary to modulate the input microwave power so that it is alternatively turned on and off. In order to avoid any problems of re-striking the arc then the off time must be no longer than 1 millisecond. Typical powers, which will be required to keep the mesh carbon free, are expected to be of the order of 200W average. So far only two course metallic meshes have been used having 75µm holes and 25µm.

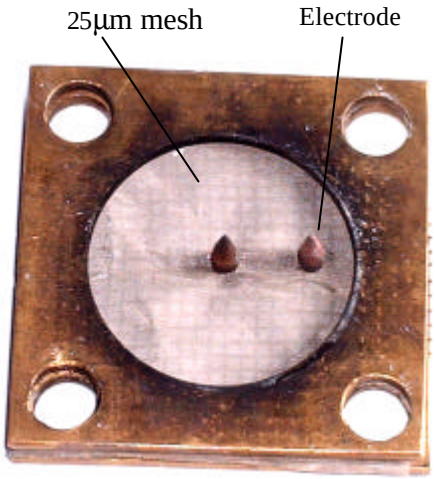

Figure 2: The Electrodes Plus 25µm Mesh

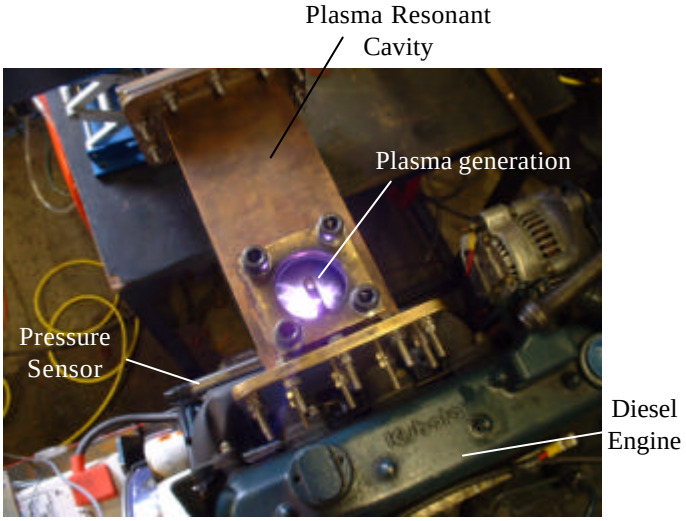

Figure 3: The Microwave Plasma – Top View

In order to maximise the electrical field within the plasma cavity resonator, various shapes of electrodes have been simulated, designed and constructed using the High Frequency Structure Simulator (HFSS). Figure 4 shows a sample of one type of electrode with strong e-field being generated to breakdown the gases and reduce particulates. When the field strength reaches a value of about 20kV/cm then automatic breakdown occurs. This has been designed to occur when the microwave power is in excess of 500W, however a pulsed power modulator is used to operate at lower average powers.

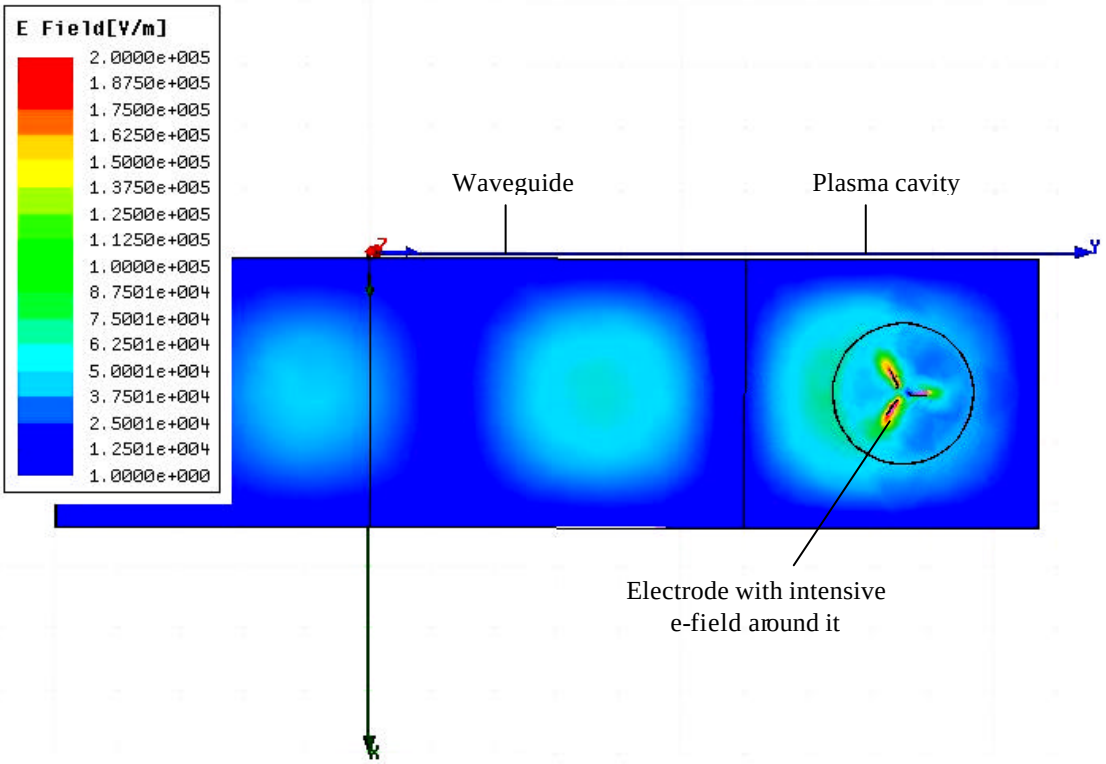

Figure 4: Top view of the microwave plasma cavity, e-field analysis using HFSS, including a trio-structure of electrodes

4. Cleaning Action of Microwave Plasma

The carbon particulates collected at the first filter having 25µm holes is shown in figures 5 and 6 with and without the plasma. The results show the effect of running the engine for 10 minutes both with and without the microwave plasma respectively. During this 10 minute period the plasma was only operated for about 2 minutes and this was sufficient to keep the mesh totally clean. Figure 7, shows the effects of the plasma on HC when the system power varied between 0 to 1kW. A reduction of 60% is achieved with this configuration, however further 30% reduction was obtained with alternative setup, the details are subject to patent pending.

Figure 5: 25µm mesh without plasma

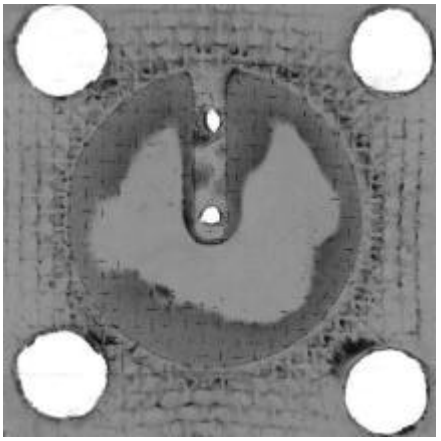

Figure 6: 5µm mesh with plasma

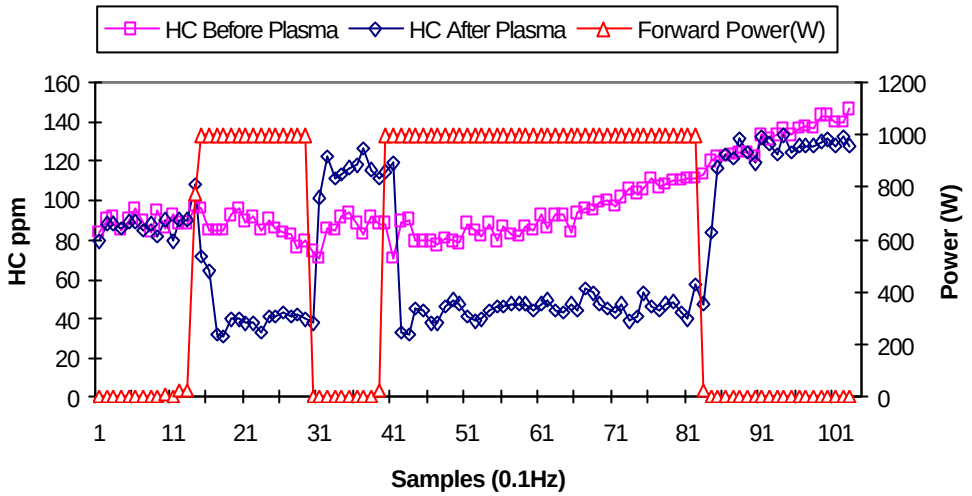

Figure 7. Hydrocarbon levels before and after plasma

Figure 8 shows the results when the exhaust emissions from a 1.8 litre petrol engine. The engine was periodically revved and on alternate accelerations, the plasma was switched on. It can be seen that the CO output peaked at 2% without the plasma on yet whilst the plasma was active, the maximum-recorded level was around 0.3%. The data were logged at 10sec using Quintox gas analyser [9].

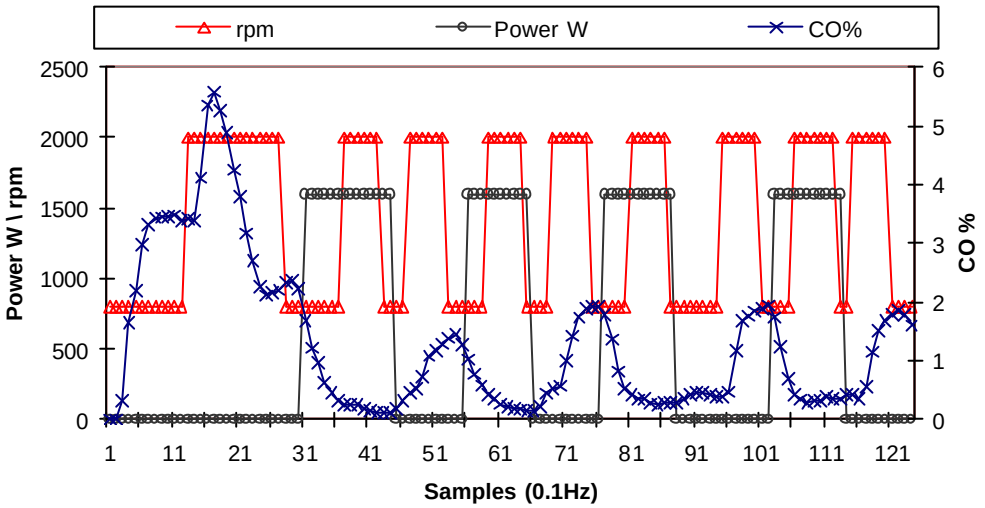

Figure 8: Carbon monoxide levels with and without plasma

It is also worth mentioning that with the plasma having an extremely high temperature, >600^{o}C any ultra fine particles passing through it will be incinerated. It has been found that the larger carbon particulates do not remain in the plasma for longer time. Comprehensive investigations have been carried out using meshes to hold up the particles long enough for the plasma to burn them proved unsuccessful as meshes with a small enough apertures, below 5 microns, and with a sufficient transmission were not available. However, initial trials conducted using a ceramic filter to remove the larger solids from vehicle exhaust have proved successful, see figure 9, and future work will be carried out to asses the effect of the plasma on the ultra fine particulates. Although earlier tests had shown that it was possible to reduce NOx with a plasma these tests where done without an abundance of oxygen. Unfortunately the intense heat of the plasma and the availability of nitrogen and oxygen ions the plasma also generates NO and NO_2 in quantities greater than that of the disassociation. Future work will also involve investigation into the reduction of the NO emissions and the possibilities of using the NO_2 as an oxidising agent to reduce particulate levels.

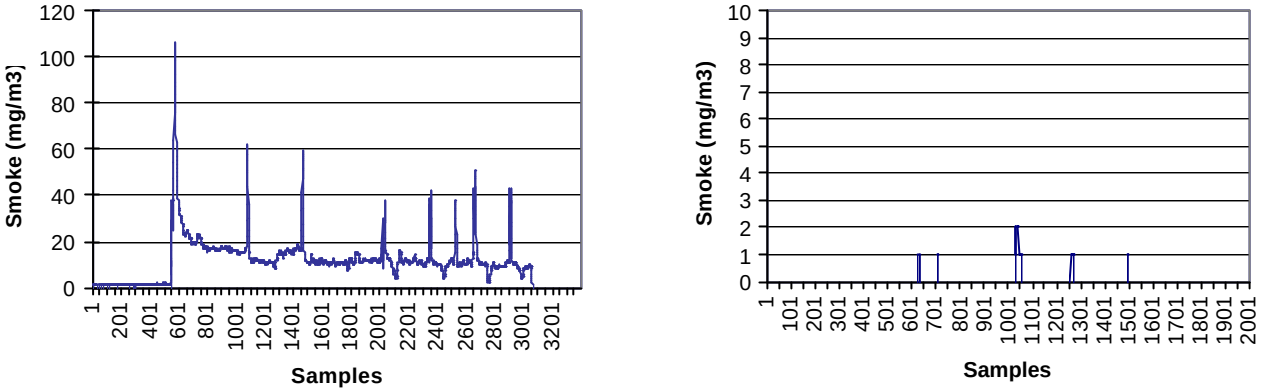

Figure 9: Smoke levels with and without filtration treatment

5. Conclusions

The microwave plasma device has been adapted for use in reducing harmful exhaust emissions from petrol, diesel and LPG engines. This system uses an electromagnetic field to cause an electrical discharge in the exhaust gasses. This breakdown causes the carbon monoxide, hydrocarbons and particulates to oxidise. The system is currently under vigorous industrial trials on diesel and LPG engines.

Acknowledgements

The authors would like to thanks the EU community for their kind support.

References

[1] J. Dale Long, Sensors, http://et.nmsu.edu/~etti/winter99/manufacturing/long/long.html.
[2] C. Barbante et al., Environment Science Technology, **35**, 835, (2001).
[3] Helmers E et al, J. Anal. Chem., **6**, 522, (1998).
[4] D. J. Hitchen, S. R. Wylie, A.I. Al-Shamma'a, A. Shaw, VAFSEP2004, 92, (2004).
[5] M. Venugopalan, Reactions Under Plasma Conditions, **2**, 13, (1970).
[6] R. Baddour et al, "Applications of Plasmas to Chemical Processing", (1967).
[7] S.R. Wylie, A.I. Al-Shamma'a, J. Lucas, GD2002, **2**, 32, (2002).
[8] J. Lucas, A.I. Al-Shamma'a, "Exhaust Gas Reactor", British Patent, P 407724 GB, (2003).
[9] Kieson Products, http://www.keison.co.uk/kane/kane1.htm.

MICROWAVE PLASMA SOURCE AS AN OZONE GENERATOR

I. Panditha s[1], A.I. Al-Shamma'a[1], A. Shaw[1], J. Lucas[1]

[1]*Dept. of Electrical Engineering & Electronics, University of Liverpool, Liverpool, UK*

Abstract

Ozone is one of the strongest oxidising agents known. Its germicidal action having been recognised for nearly a century and it is used in drinking water sterilisation and wastewater management and more recently for killing bacteria during food packaging and cleaning food preparation areas. With the development of such applications in these industries, the efficiency and cost of ozone production has become more and more important and industry is interested in having very efficient with high ozone yield system operating at 10kWs of power.

1. Introduction

Presently, two methods are used for generating ozone namely corona discharge and ultraviolet radiation [1,2]. The Corona Discharge (CD) system is produced by passing air through a strong electric field, which is close to the ignition voltage required for electrical breakdown. Typical operating conditions range from 5000 volts for a high frequency of 1000Hz to 16000 volts for a low frequency of 50Hz (mains frequency). Air (containing approximately 21% oxygen) or concentrated oxygen (up to 95% pure oxygen) dried to a minimum of –60°C dew point passes through the corona which contains free electrons (e) which causes the oxygen (O2) bond to split allowing two atomic (O) atoms to collide with other O2 molecules to create ozone (O3):

$$O_2 + e = 2O + e, \qquad O_2 + O = O_3 \qquad (1)$$

This method suffers from the presence of moisture in the feed-gas, which causes two serious problems. First, moistures (humidity) will cause a significant drop in ozone production and a waste of applied electrical energy. Second, a small amount of nitrogen in the air converts to oxides, which then dissolve in moisture to form nitric acid, which is corrosive to the CD system construction materials causing increased maintenance. As indicated in figure 1, the production of ozone with un-dried air (-10°C) is less than half of that at the dew point of –60°C. The figure alone shows the increase in the production of nitrogen oxides increases exponentially above –40°C dew point. The overall efficiency of the CD and associated silence discharges is 1-2%.

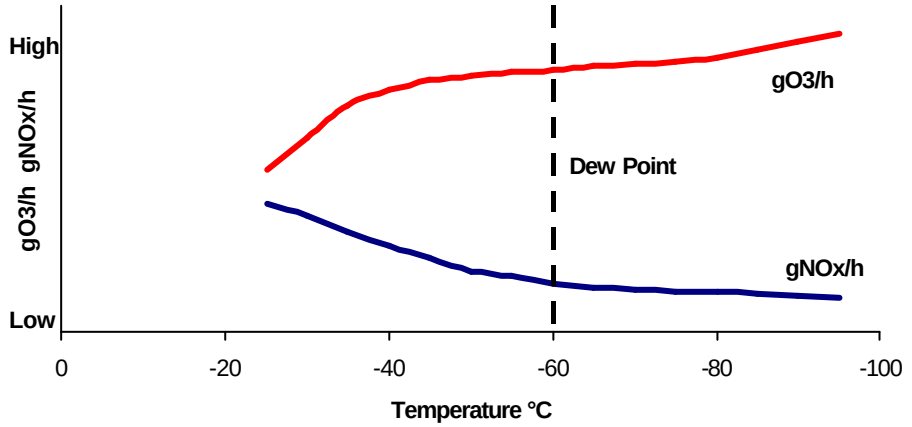

Figure 1: Corona Discharge Ozone Production

In conventional UV generation of Ozone, Ozone is produced by irradiating ambient air with UV, using low-pressure mercury vapour lamps, having wavelengths below 200nm. Longer wavelengths, around 250nm, are more efficient at destroying ozone rather than producing it. The energy of the UV splits some of the O2 molecules into two O atoms, which collide, with other O2 molecules to produce ozone (O3). Because UV light sources are not monochromatic both long and short wavelengths are generated therefore in UV systems ozone is simultaneously produced and destroyed. The concentration of ozone from the UV generator depends on the UV energy output of the lamp used, the enclosure surrounding the lamp, the

temperature, humidity and oxygen content of the air and the volume of air flowing through the generator. The UV excited ozone has an efficiency of 0.5-1.5%. UV process designers are therefore looking to develop lamps with constant improvements in the lamp characteristics including the increased power per lamp, increased UVC output per lamp (efficiency), longer lamp life, instant start and stop and no efficiency losses due to temperature.

2. Microwave Plasma Lamp

Microwaves are high frequency electromagnetic waves, generated by magnetrons, which can be stored in a resonance cavity made of metal or dielectric material. The principle is illustrated in figure 2 in which microwaves are launched into the lamp via a metal cavity resonator [3,4]. The electric field ionises the mercury vapour in the lamp to produce the UV emission, see figure 3. The design specification for the resonant cavity are summarised in table 1. The microwave frequency is 2.45GHz and is the same as that used in a microwave oven. This allows low cost magnetrons to be used. The lamps differ significantly from conventional UV lamps because they have no warm up time, do not deteriorate with age, do not have electrodes, have adaptable shapes and can be used in pulsed mode. Also the lamp does not suffer from nitric acid or moisture and does not use the expensive oxygen-enriched air as the corona discharge systems.

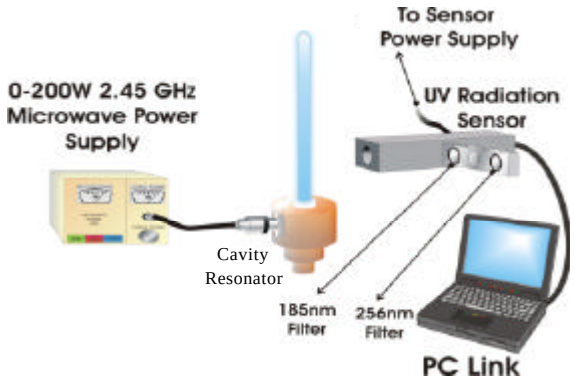

Figure 2: The Microwave UV lamp set up

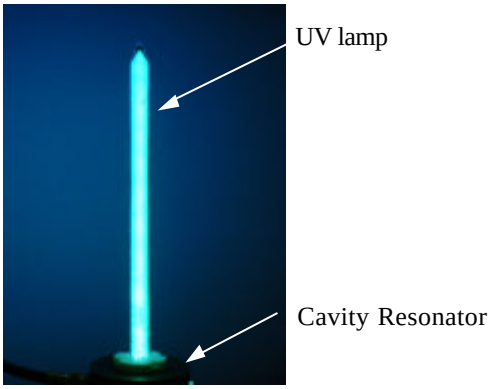

Figure 3: Microwave UV lamp in operation

Table 1: Calculation Characteristics for the resonant cavity [5]

Resonator	Mode	Resonance Wavelength (?)	Q × d	Shunt Resistance R (ohm)
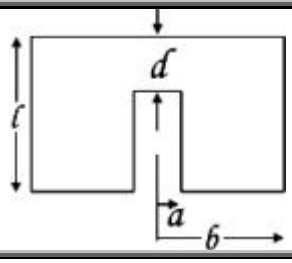	TE_{010}	$2\pi a\left(\frac{l}{2d}\log_e\frac{b}{a}\right)^{1/2}$	$\left\{\frac{1}{l}+\frac{1}{2\log_e(b/a)}\left(\frac{1}{a}+\frac{1}{b}\right)\right\}^{-1}$	$120\pi Q\frac{l}{l}\log_e\frac{b}{a}$

The lamp tube material is usually in fused silica (quartz). The choice of the suitable glass type is entirely dependent upon the emission range achievable and the application. In order to produce radiation at 185nm and 254nm, there is a limited choice of glass materials where General Electric and Heraeus usually classify this as “GE214” or “214”. Silica has the advantage of being quite transparent to a very wide spectrum of UV light and the transmittance characteristic is fairly high. For deep-UV emissions however, it is preferred to use synthetic fused silica [6]. Figure 4 shows the transmission characteristics for such quartz tubing. It has to be noted that the choice of the envelope material is important, as well as the choice of the tube wall thickness and finally, the lamp diameter.

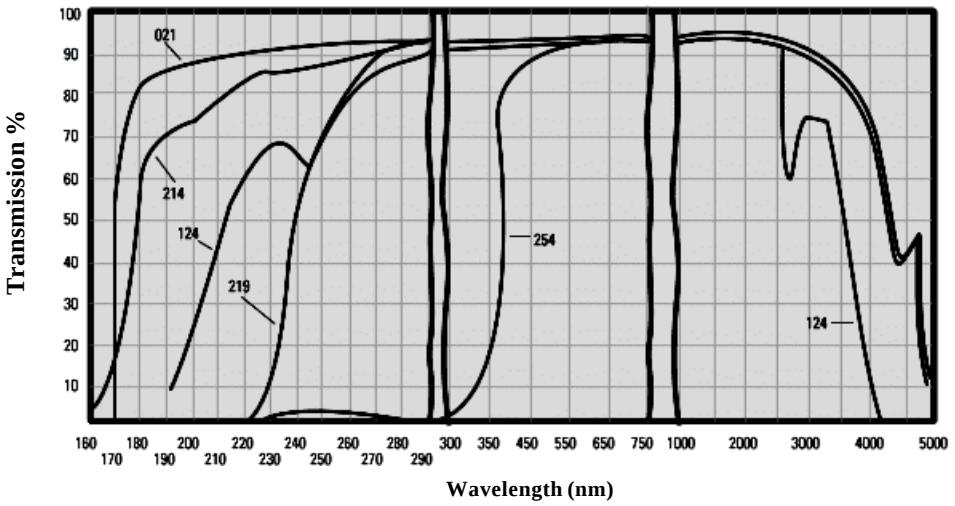

Figure 4: Transmission characteristics for different quartz tubing types [6].

3. Microwave Ozone Generator

The microwave plasma system has the benefit of being converted to an ozone generator by mounting a specially designed cylinder on top of the resonant cavity. The material used for the ozone chamber fitting was machineable grade nylon, which is a cost effective material and needs few man-hours to derive its desirable form. The PTFE ring positioning screws, allow for fine positioning and tuning of the lamp, whilst being converted to an ozone generator. The Ozone generation setup is illustrated in figure 5.

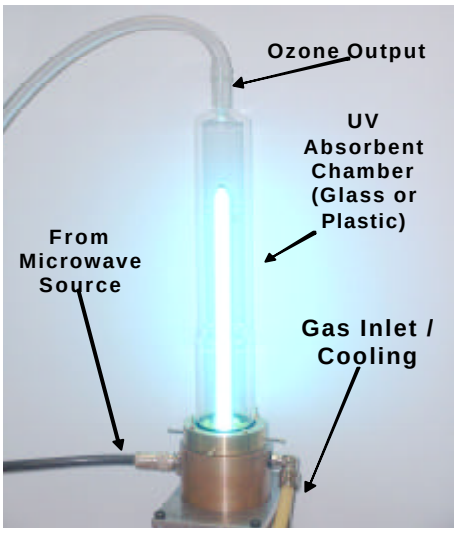

Figure 5: Schematic representation of the microwave Ozone generator

The main concept behind the ozone generator setup takes advantage of the fact that the resonant cavity allows gas flow which can be directed longitudinal to the lamp. As the gas flows alongside the lamp it gets irradiated by the 185nm line emitted and the oxygen content of the gas is converted to Ozone. Because this process is not static, the 254nm lines emitted do not severely interact with the ozone. Furthermore, whilst the gas flows through the ozone generator setup, it has already cooled the lamp and consequently resulting a high productivity rate. The inlet gas has no needs to be specially prepared for the process, i.e. a compressed air and not enriched oxygen as in the case of the conventional ozone production systems [7]. The concept of the ozone generator is shown schematically in figure 6. Ozone measurements were carried out using electrochemical transducers. The rated ambient temperatures are between -25^{o}C to $+50^{o}$C. The ranges can vary between 0 and 10ppm with a sensitivity of 0.1ppm up to a range between 0 and 100ppm. The output signal can be transmitted on a 4 – 20 mA current loop to remote displays or data logger. The device normally operates off mains power but hand held sets operating off 12V dc batteries are also used [8]. Various

experimental measurements were carried out in order to optimise the performance of the system. Figure 7, shows results of ozone concentration in ppm at various gas flow rates and microwave power ranging from 70-150W. Whilst figure 8 shows the overall ozone production rate using microwave power of only 70W .

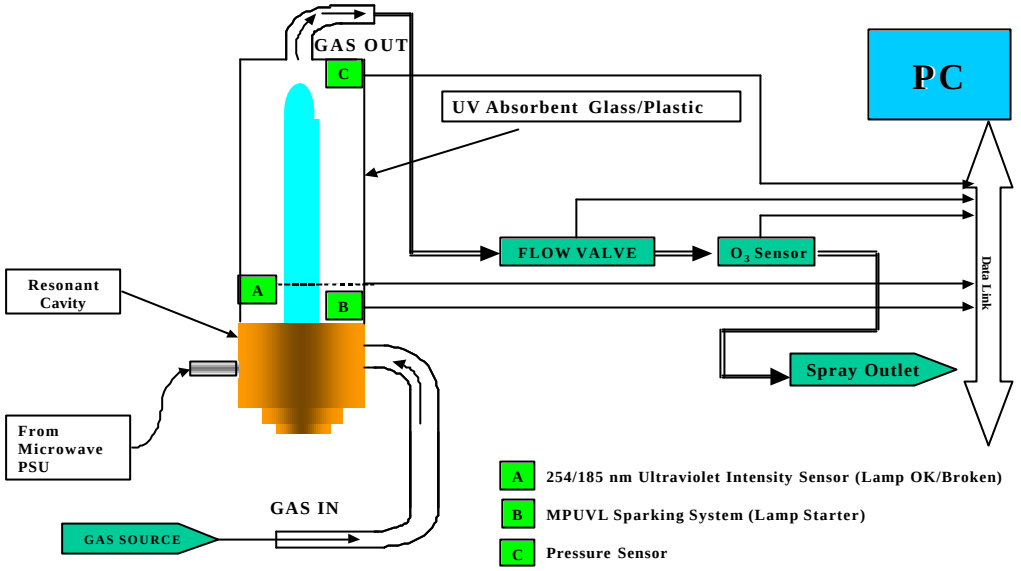

Figure 6: Experimental setup for Ozone production measurements

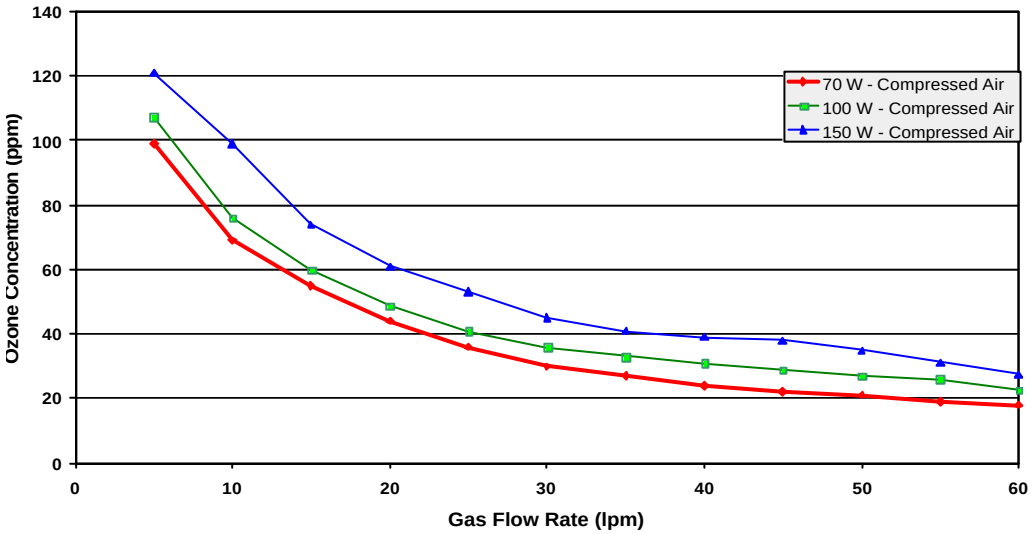

Figure 7: The performance of the ozone generator for compressed air for different net microwave power settings and different gas flow rates

This figure shows that when a fast gas flow is established, the ozone production rate is higher whilst the absolute ozone concentration is low and vice versa. Other investigations were conducted to study the effects of the microwave ozone source on various bacteria in comparison with the corona system. The both system parameters were similar in order to achieve a fair conclusions. The testing medium were varied from Petri dish to stainless metal surface. Figure 9a shows the effects of ozone on Pseudomonas Aeruginosa. The right-hand side Petri dish with agar cultivated bacteria shows the untreated Pseudomonas Aeruginosa stain and the left-hand side Petri dish shows the effect of ozone, where almost no bacteria colonies are visible. The results of the test are shown in figure 9b. As can be seen that in using agar Petri dish a reduction of more than 5 logs has been achieved within 10min operation with microwave ozone production of 70ppm. Similar results were achieved on reduction of Staphylococcus Aureus bacteria species.

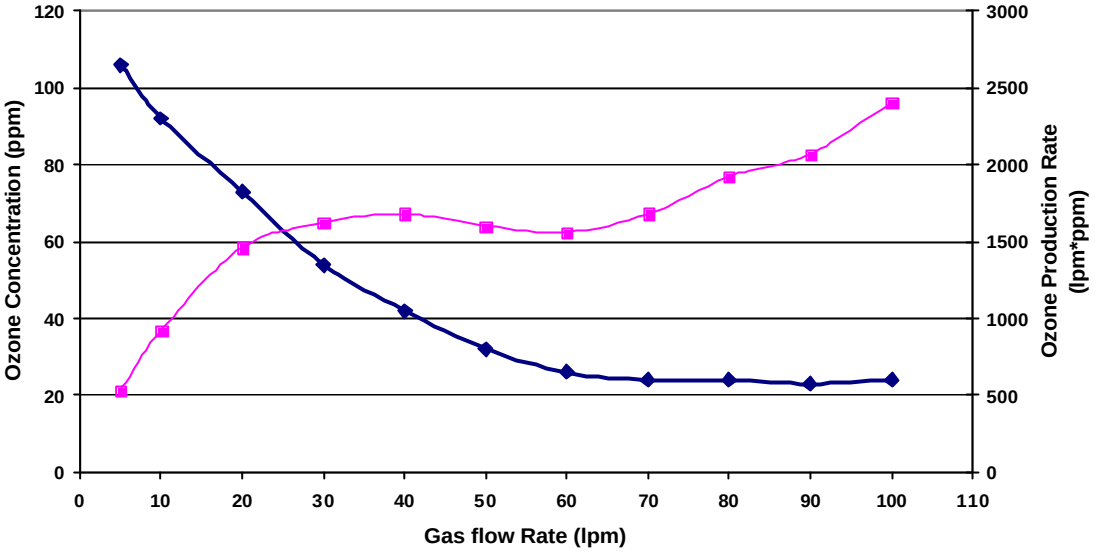

Figure 8: Ozone production rate using microwave power of 70W

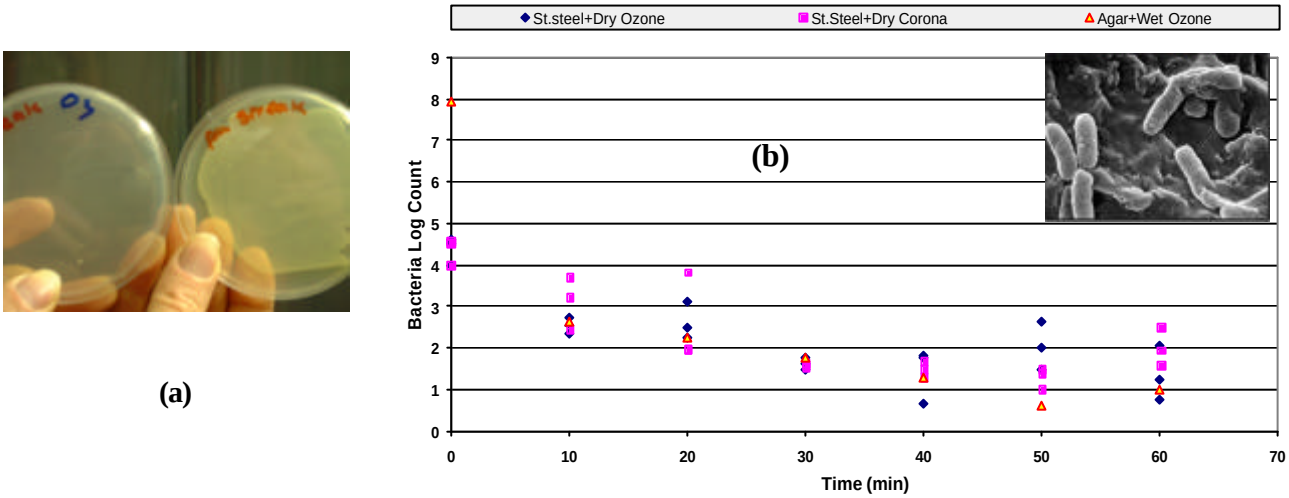

(a)

Figure 9: (a) Pseudomonas Aeruginosa before (right) and after (left) ozone irradiation, (b) Destruction of Pseudomonas Aeruginosa by Ozone

4. High Frequency Simulations Using Mote Carlo Algorithm

The simulation obtains certain information concerning the number of gasses or (gaseous elements) involved, and their cross-sections for all their elastic, inelastic and ionisation collisions. The cross-sections are inserted into a special text file with a specified index, so that all processes and entries are accounted for. The software obtains information about the microwave field frequency and strength and the gas pressure. Having obtained all the necessary data, the electron trajectory can be calculated. Let Q be the collision between the electron and the gas atoms, N the number of these atoms and n the number of the collision processes. The mean free path of the electron (L) is then given by [9,10]:

$$L = \frac{1}{\sum_{j=1}^{n} NQ_j} \qquad (2)$$

The type of collision, K, is decided upon the comparison with a random number, with $RN \in \{1, n\}$:

$$K = \frac{\sum_{j=1}^{k} NQ_k}{\sum_{j=1}^{n} NQ_j} \succeq RN \qquad (3)$$

Where, n is the process with the highest electron energy demands. For the majority of the ionised gasses, process one is considered the elastic collisions and process n, the ionisation collisions. Between one and n reside the inelastic collisions in terms of energy requirements. RN is the pseudo-random number that the process is correlated and the compared with. The simulation requires some input from the user, such as, the frequency of the microwaves (GHz), the strength of the electric field (V/m), the gas pressure (torr) and finally, the number of collisions. The outputs of such a simulation include the time the electron expended after the simulation alongside with its energy. Figure 10 shows the simulation run for the Hg plasma as a function of the power fraction and the strength of the microwave field, for a frequency of 2.45GHz.

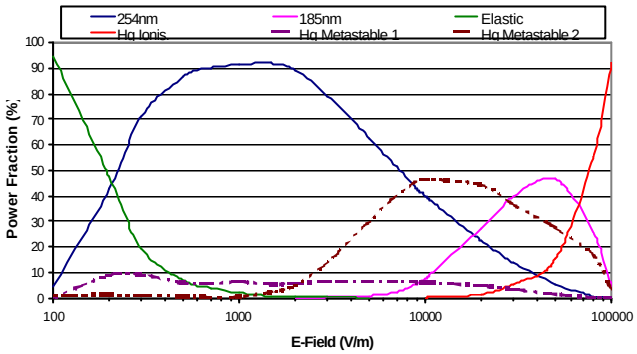

Figure 10: Monte Carlo Simulation of microwave plasma at 2.45GHz

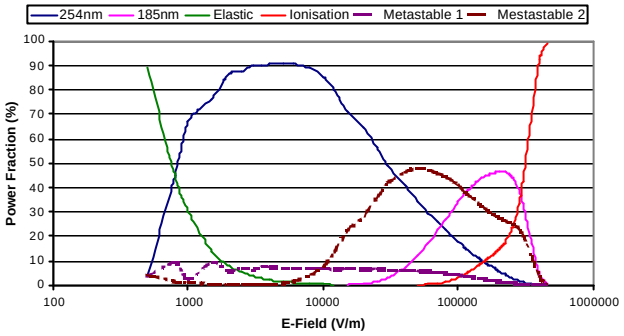

Figure 11: Monte Carlo simulation of microwave plasma at 10GHz

As the field strength increases, the 254nm line emission rises, along with some metastable processes, which is then followed by the 185nm line. At the depletion of this line, the energy the microwave field is high enough to cause ionisation. This is the highest limit reachable that can cause an effect to the gas. Figure 11 shows the simulation results for 10GHz microwave plasma. Even though the efficiencies of 254nm and the 185nm wavelengths are not severely affected, but it can be observed that the E-field required to drive the plasma has to be higher as the frequency increases. This observation is very important in the microwave plasma system development to operates at very high microwave power conditions, and produce high absolute UV/Ozone intensity.

6. Conclusions

The results have shown that a controlled low-pressure microwave discharge is able to produce higher yields of ozone than by the corona discharge for the same input energy. Currently a low power lamp (200W per meter) has been developed using a low-pressure mercury microwave discharge lamp. This system is able to develop ozone at the rate of 38 gm/kWh compared with the corona system which produces ozone at the rate of 15 gm/kWh. Furthermore a Monte Carlo theoretical model on gaseous simulation has indicated that the microwave lamp can be scaled up to produce an output of 1kW/m by using higher frequency >2.45GHz and operating under pulse mode. This level of efficiency cannot be achieved by other technologies.

References

[1] J.F. Waymouth, “Electric Discharge Lamps”, MIT Press, (1971).
[2] L.R. Koller, “Ultraviolet Radiation”, (1965).
[3] A.I. Al-Shamma’a, I. Pandithas, J. Lucas, J. Phys D: Appl. Phys., **34**, 14, 2775, (2001).
[4] M Moisan and Z Zakrzewski, Plasma Sources Science and Technology, **4**, 3, 379, (1995).
[5] E.V.D. Glazier, H.R.L Lamont,“Transmission and Propagation”, (1958).
[6] General Electric Quartz Inc., www.gequartz.com, Heraeus Ltd., www.heraeus-noblelight.com.
[7] Reference Manual by the Water Quality Association Ozone Task Force, 65, (1997).
[8] ATi (Analytical Technologies Incorporated), www.analyticaltechnology.com
[9] H.T. Saelee, J. Lucas, J. Phys. D: Appl. Phys., **10**, 343, (1977).
[10] I. Pandithas, A.I. Al-Shamma’a, A. Shaw, GD2004, 793, (2004).

THERMAL SPRAY TECHNOLOGY USING MICROWAVES

P. Mavromatidis[1], M. Houghton[1], A.I. Al-Shamma'a[1], J. Lucas[1], H. Al-Badiary[2]

[1]*Dept. of Electrical Engineering & Electronics, University of Liverpool, Liverpool, UK*
[2]*Dept. of Engineering, University of Liverpool, Liverpool, UK*

Abstract

Thermal spraying is a generic name for the process of projecting molten particles at high velocity to form a surface coating on a component to give a superb mechanical bond. In this way the surface of a component can be rebuilt, if worn or damaged, or given a wide range of attributes. This paper describes the key advances using microwave thermal spray compared with current techniques including plasma spraying and high velocity oxy-fuel (HVOF). Furthermore, the system setup, electromagnetic wave simulations using High frequency Structure Simulator (HFSS) package and calculation of gas velocity is also presented.

1. Introduction

Thermal spraying is a continuous, directed melt spray process in which particles (10 to 50μm diameter) of virtually any material are simultaneously melted and accelerated to high velocities through either a combustion flame or a non-transferred thermal-plasma arc [1-3]. Combustion flame spraying uses compressed air or oxygen mixed with a fuel (e.g. acetylene, propylene, propane, hydrogen). The process yields low performance coatings due to the low flame velocity (~50m/s) and low temperature achieved within the combustion flame. In addition the combustion products, which include HC, CO, NOx, are both dangerous and contribute to air pollution, whose standards are becoming more stringent. HVOF spraying is a novel variation on combustion spraying. The compressed flame undergoes free expansion upon exiting the torch nozzle thereby experiencing high gas acceleration generating high velocities up to 800m/s. Figure 1 shows the main principal of this process. The powder particles, injected at the rear of the torch, attain these high velocities so that upon impact on to the substrate, the particles spread out very thinly and bonds tenaciously to the substrate and to all other splats in its vicinity. This yields a well-bonded, dense deposit. Alternatively high velocity methods alone can be used.

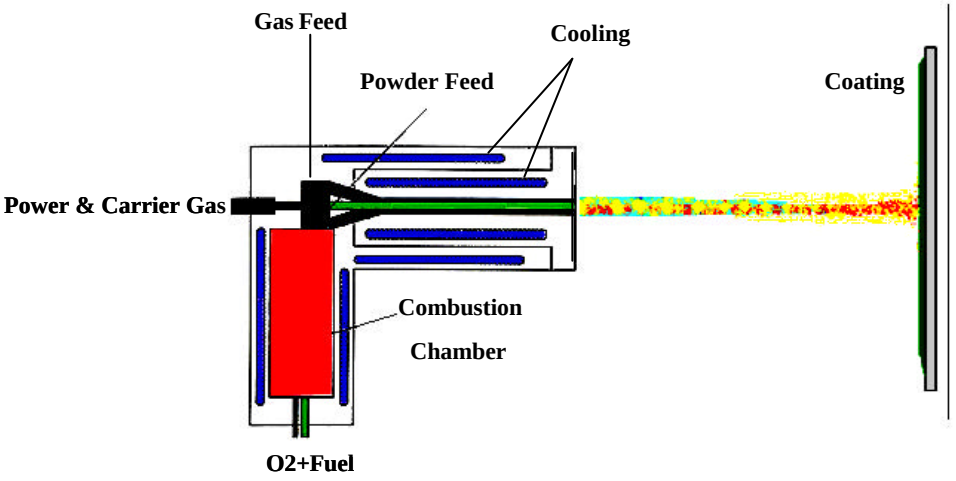

Figure 1: High Velocity Oxy -Fuel process

In plasma spraying [4], as shown in figure 2, the plasma is created by an electric arc burning within the nozzle of a plasma gun and the argon arc gas is formed into a plasma jet as it emerges from the nozzle. Powder particles are injected into the jet where they melt and the strike the surface at high velocity to produce a strongly adherent coating. Almost any material can be sprayed including metals, ceramics and plastics. The workpiece remains cool because the plasma is localised in the gun. Antolli Papyrin and colleagues at the Russian Academy of Sciences were the first to demonstrate the cold spray process in the mid-1980s [5]. The basis of the cold spray, as shown in figure 3, process is the gas-dynamic acceleration of

particulates to supersonic velocities (300-1000 m/sec), and hence high kinetic energies, so that solid-state plastic deformation and fusion occur on impact to produce dense coatings without the powder material being significantly heated. This is achieved using convergent-divergent, de Laval nozzles, high pressures (up to 500 psi [3.5 MPa]) and flow rates (up to 90 m^3/hr) of gases such as helium. The spray pattern is roughly 20 to 60 mm^2; spray rates - 3-5 kg/hr, with build-ups of about 250 µm (10 mils) per pass. Powder particle sizes are typically of the order of 1-50 µm. Obvious disadvantages to the cold spray process include the use of high gas flows, increased gas costs, especially in the case of helium. Also, this spraying process is only suitable for low temperature melting powders (e.g. copper and plastic). Furthermore, solid materials travelling at high velocities are abrasive, so the lifetime and dimensional stability of key components such as nozzle lifetimes should meet the industrial requirements in excess of 200 hours.

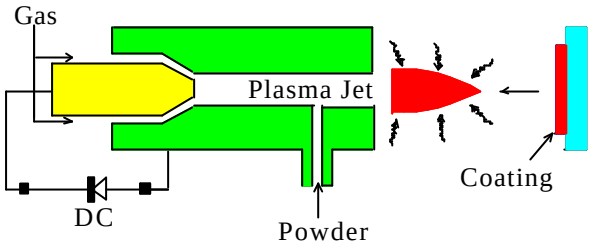

Figure 2: Plasma spraying process

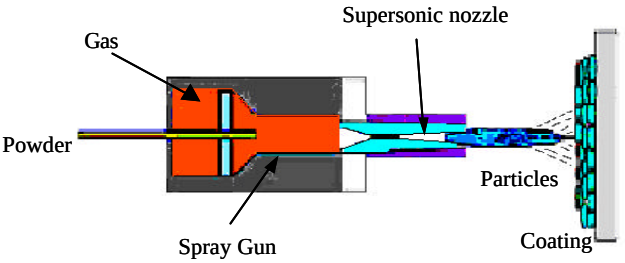

Figure 3: Cold spraying process

Thermally sprayed coatings have, in recent years, gained wide spread acceptance for a variety of industrial applications - the global market for thermal sprayed coatings is currently about £1.35 billion. This growth has been primarily technology led, and high value plasma coatings hold the lion's share of the market. A vast majority of these applications involve wear resistance, although the use of thermal sprayed coatings in combating high temperature corrosion also continues to receive considerable industrial and academic interest. These sprayed coatings are applied in order to achieve predeterminable life periods under severe operating conditions. Table 1, shows the automotive coating applications according to industry served.

Table 1: Automotive coating applications

	Wear							**Electrical**
Industry	Abrasive	Adhesive	Fretting	Erosion	Impact	Restoration	Corrosion Oxidation.	Resistance
Automotive engines	X	X	X	X	X	X	X	X
Diesel engines	X	X		X	X	X	X	
Automotive parts (non engines)	X	X				X	X	X
Rubber and plastic parts	X			X	X	X	X	
Electrical parts	X	X		X	X	X	X	

2. Key Advances

Presently the role of plasma coating within automobiles is relatively small at about £335M p.a. Such activities are concerned with engines and transmission, which represent about 10 to 20% of the car cost. Coatings are presently only 6% of this cost but are expected to rise to 8% by 2005 due to the expected increase in the use of 16 valve engines and catalytic converters for clean air emission. This low uptake of coating technology is because the two most popular commercial spray techniques, namely plasma spraying and HVOF have limitations when used with automotive applications. Plasma spraying uses expensive inert gases and has an inefficient heating process (<5%) whilst HVOF produces heating of the substrate and oxygen contamination. In addition, recently developed Cold spray technique requires high-pressure helium to give the powders sufficient kinetic energy, which is converted into thermal energy on impact with the

substrate. Cold spraying is only suitable for low temperature melting powders (e.g. copper and plastic). The spraying technique used in this research, is a continuous melting spray using a different approach on performing the bond between the injected particle and the surface. It uses a long and high thermal interaction path to gradually and uniformly heat the particles above melting temperature and only then use the extra kinetic energy to project them onto the substrate surface creating a weld-bonded coat. It uses microwave thermal heating (60% efficient) to preheat the nitrogen gas/powder so that the energy producing the forging actions is a combination of kinetic and thermal energy. This technique can be used with all coating powders including high temperature ceramics (e.g. silica, alumina). The fine control obtainable with this technique, which is a combination of cold and thermal spraying, will now open up a much wider range of coating activities within automotive manufacture.

3. Methodology

The background technology to this project is to demonstrate the use of "cold" microwave thermal heating by using to preheat the mixture of high-pressure gas and powder to produce a new arrangement for surface coating of substrates. The microwave thermal spraying system consists of a standard microwave waveguide cavity resonators operating at 2.45GHz, with the magnetron (2-6 kW) as a power source, circulator, matched load, stub tuner and the interaction cavity as shown in figure 4 (a and b). This microwave process heats up dielectric materials within the interactive cavity in a uniform distribution and then transfers the heat by convection/conduction to the carrier gas. Industrial heating in general remains one of the most difficult processes to control, due to the slow and imprecise nature of the convection, conduction and radiation process. Even when a uniform distribution of temperature is achieved, the heating time is limited by the physical properties of the heating material, such as specific heat, heat capacity and thermal conductivity. Thus in conventional heating all the heat energy is generated externally and transferred through the surface of the heating material. The microwave heating is a volumetric process and is generated internally within a dielectric material. The microwave energy is applied with a special mode distribution of the electrical (E) and magnetic field (M) profile inside the interaction cavity. The optimum arrangement has been modelled and realised by using Agilent HFSS "High Frequency Structure Simulator" software package. The electromagnetic field is distributed along and around the helix tube and throughout the silicon carbide (SiC) rod within the cavity resonator as shown in figure 5 (a and b). Thus to insure, that the rate of heating is relatively faster and accurately controlled. Once the microwaves are converted into heat in the dielectric material consisting of a SiC rod, the heat is then transferred through a helix stainless steel tube to the nitrogen carrier gas, as shown in figure 4b. Nitrogen is selected as the carrier gas, as it will prevent oxidation of the powder particles and at the same time provide a cost effective solution.

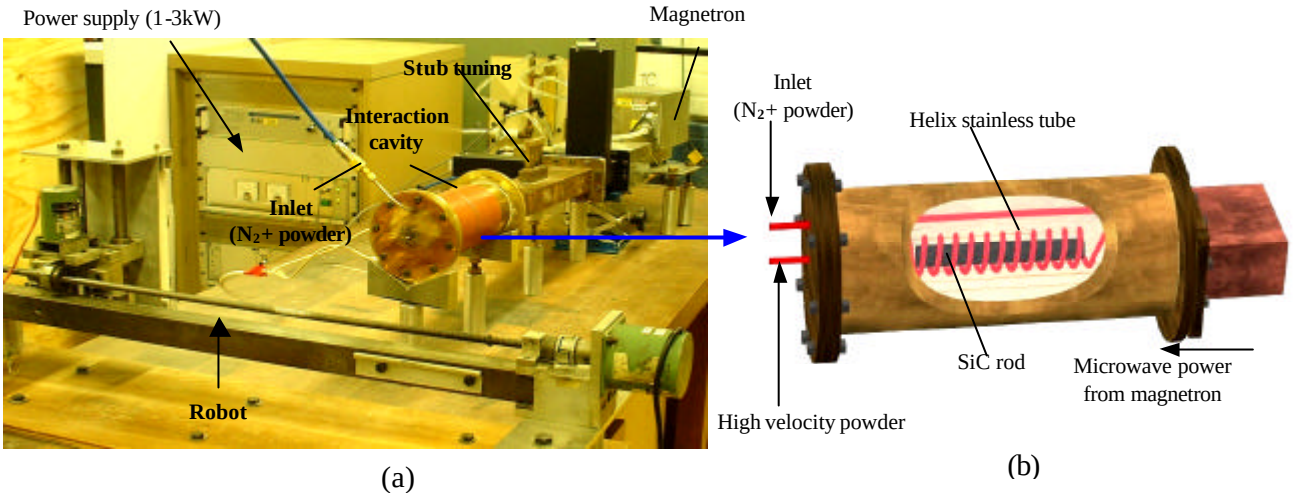

Figure 4: (a) The completed microwave system, (b) The interaction cavity

The nitrogen gas is passed longitudinally through the interactive cavity via an inner helix tube so that it has a long path interaction with the walls of the tubes. The microwaves are able to directly or indirectly heat the silicon carbide at all temperatures because it has an electrical resistance.

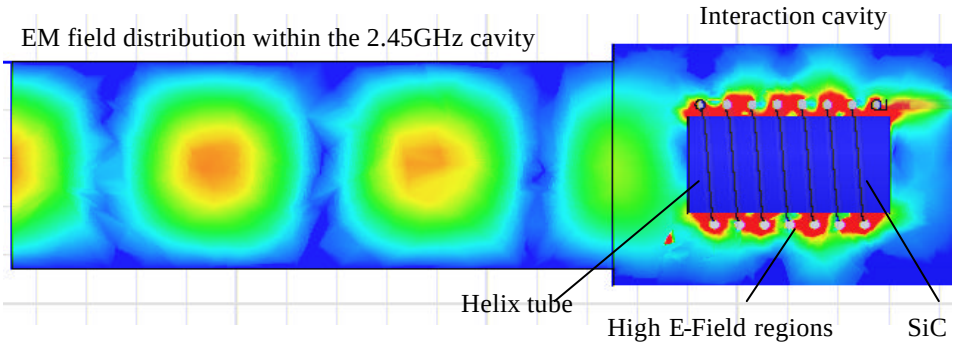

Figure 5: (a) HFSS modelling of the microwave thermal spray system

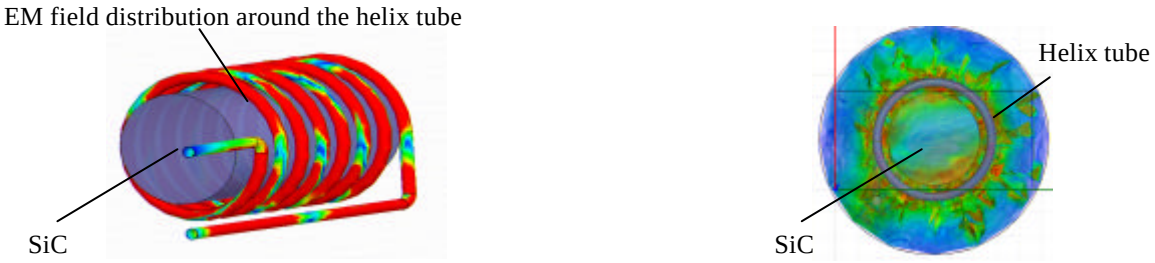

(b) (c)

Figure 5: (b) close look up into the interaction cavity resonator, (c) End view: E-field distribution within the interaction cavity

Thus the gas heating has been achieved by combining the direct and conduction heating of the silicon carbide rod and the helix tube. The hot gas and metal powder leave the helix tube via an accelerating nozzle of various designs. For each technique a model of the flow field, full 3D CFD analysis, computational temperature analysis and multiple phase supersonic flow was modelled [6]. This analysis has been carried out using a specialist CFD software package. Based upon these analyses, the optimum technique has been chosen to allow the microwaves to interface efficiently inside the interactive cavity. As the SiC warm up, the microwaves are able to use direct dielectric heating of the SiC because their electrical resistance dramatically reduces with increasing temperature (>200^{o}C). This allows the pre-heating of the nitrogen gas to be controlled by varying the cavity length (L) and microwave power (W). The calculations have shown that the nitrogen gas pressure varies between 15 and 25 bars with 76 to 152gm/min of coating powder. The input power (W_H) to pre-heat to $T_1{}^{o}$C from T_o is related to the mass flow rates of the gas (F_{gas}) and powder (F_{powder}) and their specific heats (C_g and C_p).

$$W_H = (F_{gas}\, C_g + F_{powder}\, C_p)\,(T_1 - T_o) + \text{Thermal Losses} \qquad (1)$$

Specifically for the powder we have, $W_H = R_{powder}\, C_p\, (T_1 - T_o)$

To attain the cold process supersonic flow conditions, it is necessary to either taper the helix tube or design a special nozzle to meet this requirements for various materials including copper and aluminium. Upon impact with the substrate the kinetic energy is converted into thermal energy and at the substrate surface, the temperature of the coating momentarily rises to $T_2{}^{o}$C. The relationship is given below,

$$W = C_p\,(T_1 - T_0) + \nu_p^2/2 = C_p\,(T_2 - T_0) + L \quad . \qquad (2)$$

Where L is the latent heat and ν_p is the powders velocity.

Table 2, shows how the powder temperature and velocity are related for soda glass. When T=1400 ^{o}C the powder is at its melting point. At 600^{o}C, the powder velocity has to be 1022m/s, which is the maximum nitrogen gas velocity (Mach 1.33) achievable without the need of excessive gas pressure (less than 10 bar) in order to achieve the melting condition. Hence a coating of glass ceramic is achievable within our experimental range of temperature of 800 to 1000^{o}C. The long microwave-heating path ensures efficient transfer of energy to the powder and up to 60% thermal efficiency was achieved. This independent control of

the thermal energy will allow the powder to be pre-heated to a fixed temperature below the melting temperature so that the 'cold forging' coating techniques can be used upon impact.

Table 2: Deposition of ceramic (soda glass)

T_o °C	T_1-T_o °C	$W_H = C_p (T_1 - T_o)$ Watts	ν m/sec	W_{KE} Watts	$(W_H + W_{KE})$ Watts
20	600	401	1022	522	923
20	800	535	880	388	923
20	1000	669	712	254	923
20	1380	923	-	-	923

The advantage of microwave thermal heating is that the temperature of the dielectric material continues to rise as long as power is applied. Furthermore the relationship of gas temperature with microwave power is proven to be linear, as shown in figure 7. This allows us to use a wide range of industrial relevant metals as summarised in table 3.

Table 3: Thermal and velocity spray parameters

Material	T (°C)	L (J/gm)	Sp ht (J/gm °C)	Mach 1.33 Velocity (m/s)
Tin	232	59	0.226	597
Lead	327	25	0.127	650
Zinc	420	117	0.389	699
Aluminium	660	393	0.907	811
Copper	1083	175	0.389	978
Glass	1400	0	0.669	1086

4. Coatings

The quality of coatings produced from the microwave thermal spraying system can be varied within a fully controlled environment to achieve the industrial desired conditions. In general, when coating a material, it is important that the powder is spherical and has uniformly sized particles thus easing the melting and deposition of the powder particles. The structure and phase of each coat depends on the cooling and solidification rates experienced during solidification [7]. The cooling rate, in turn, depends on material properties such as the melting point, density and specific heat. In addition, the gas conditions also affect the particle size that can be sprayed and processed economically. The substrate surface has to be adhered to the industrial standard practice of grid blasted then cleaned to remove grids, oil or other impurities. It is important that the right amount of powder is mixed in the gas at a uniform rate to ensure the melting of the deposit and create a smooth surface. The combination of the above parameters will ensure a strong bond between the surface and the particles with the minimum amount of impurities and contamination. Figure 8 shows the industrial Praxair powder spray unit used in this project. Microstructures of coatings are shown in figures 9 (a and b) and 10 (a and b) using scanning electron microscope (SEM) imaging for aluminium and copper respectively. On microscopic observation of cross section of the coating, such "splash like" morphology can be observed. The presence of entrapped gases as well as unmelted particles, determines the coating properties because they create points of stress concentration during in service loading. Larger particles do not melt down to their core, and thus do not spread on impact, which lead into a porous coating with irregular signs of cracks running through it especially for brittle materials. The porosity adversely affects the wear property, higher porosity coating resulting in a failure by oxidation whilst a low porosity level reduces the ability of coating to accommodate stress. However, for the case of the aluminium and copper powders, the particles are non-uniformly shaped with sharp edges and variable particle sizes. Pre-treatment of the surface was limited only to its cleaning with ethanol. These powders are fed in a nitrogen gas stream with velocity of only 70 m/s at various temperatures and the SEM magnifications of 1:500, which clearly shows that particles have fully melted and adhered onto one another as shown in figures 9b and 10b. The coating process applied with this microwave thermal spray system is for a range of materials including tin, aluminium, copper, zinc, lead and ceramic (soda glass) powder on steel surface and plastics. Using this technique will allow a new concept of wiring harness, where the electrical conductors are integrated into the

vehicle body shell by using a spray technique. This reduces the weight and eliminates the expensive manual fabrication and installation of the wiring harness. Thus leading towards fully automated vehicle manufacture.

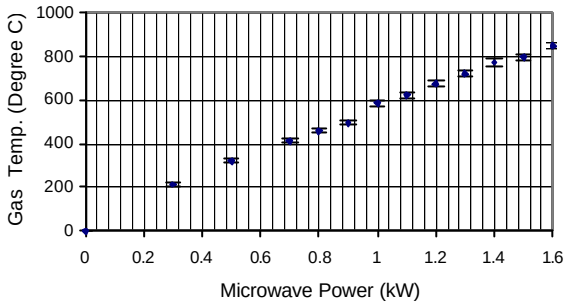

Figure 7: Temperature response with N_2=30ltr/mm or 0.62 gm/s

Figure 8: Praxair powder spray unit

Figure 9a: Aluminium coating on steel metal

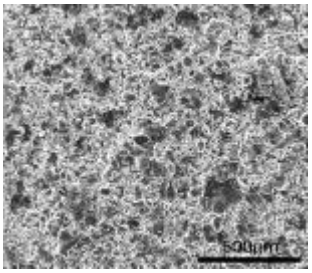

Figure 9b: SEM scan for aluminium coated steel metal

Figure 10a: Copper coating on steel metal

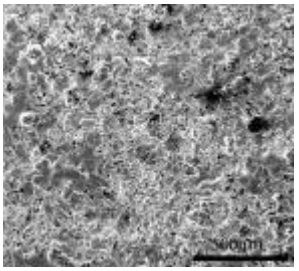

Figure 10b: SEM scan for copper coated steel metal

6. Conclusions

The microwave thermal spray technique will provide a low cost, energy efficient system having superior control facilities. By the use of nitrogen gas, the operating costs are low and as well as higher temperature ceramics can now be sprayed. It is expected that these properties will allow new application areas to be undertaken. As a specific result of this research, the automotive industry will be provided with a more flexible mode of BIW production which will allow vehicles to be produced more cheaply and with a lighter weight, higher fuel efficiency and better protection during collisions. The choice of manufacturing materials will be increased so that designs using aluminium and composites can be used. The results of this project will allow a higher degree of robotic automation to be used in the manufacture of the vehicle and will lead to better quality control.

Acknowledgement

The authors would like to thank the Engineering and Physical Sciences Research Council (EPSRC) and the Department of Trade and Industry for their kind support.

References

[1] R. Knight and R.W. Smith, Powder Metal Tech. and Applications, **7**, 408, (1998).
[2] P. Mavromatidis, A. Shaw, A.I. Al-Shamma'a, J. Lucas, J. Mat. Proc. Tech., **153/154**, 294, (2004).
[3] R.C. Tucker, Surface Engineering, **5**, 497, (1994).
[4] R. F. Smart and J. A. Catherall, "Plasma spraying", Mills & Boon Limited, (1972).
[5] www.gordonengland.co.uk/coldspray.htm.
[6] A.I. Al-Shamma'a and J. Lucas and , EPSRC/DTI Link project, 2004.
[7] S. Das et al, Metallurgical and Materials Transactions A, **34A**, 1909, (2003).

TUNEABLE MICROWAVE INDUCED PLASMA SOURCE FOR BIOLOGICAL AND ENVIRONMENTAL APPLICATIONS

C.C. Wright[1], M. Houghton[1], A.I. Al-Shamma'a[1], R.A. Stuart[1], J. Lucas[1]

[1]*Dept. of Electrical Engineering & Electronics, University of Liverpool, Liverpool, UK*

Abstract

There is increasing interest in the use of microwave power for industrial applications. A pulsed tuneable microwave source is beneficial as it allows the high electromagnetic field of a high power to be applied to a target without excessive heating. The Free Electron Maser (FEM) is the tuneable source with ability to operate across a wide range of frequencies from 8 to 20 GHz. Using higher frequencies than the common 2.45 magnetron, increases the fields obtained and also beneficial scaling effects on some applications, such as microwave induced plasmas. The paper presents the basic principles of the FEM system as well as the applications of UV, Ozone and chemistry.

1. Introduction

A research project assessing the use of microwave radiation for industrial applications at higher frequencies than the standard 2.45GHz produced by most magnetrons is being undertaken as part of the European Community Competitive and Sustainable Growth programme. The basic principals of the FEM system is that as electrons passing through the Industrial Free Electron Maser (IFEM) resonant cavity oscillate from side to side due to the static magnetic field produced by the wiggler magnet array [1-3]. These oscillating electrons emit electromagnetic energy, which forms what is referred to as a radiation field. The radiation field combines with the wiggler field to produce a pondermotive or beat wave. This pondermotive wave then promotes axial bunching of the electrons in the electron beam allowing a more coherent radiation output from the electrons. To allow such an interaction to take place, and energy to be extracted from electrons in the electron beam, the electron velocity must be matched to the phase velocity of the electromagnetic field in the cavity. This condition is often referred to as beam wave synchronism. For the synchronism case, equation 1 shows one form of the basic FEL resonance equation. This equation describes the wavelength output from a FEL, and has been reported previously many times.

$$\lambda_r = \lambda_w \frac{(1-\beta_e)}{\beta_e} \qquad (1)$$

where, λ_r : Electron output radiation wavelength, λ_w : is the wiggler magnet period, $\beta_e = v_e/c$, which is the ratio of the electron beam velocity, v_e to the speed of light, c. Apart from the electron velocity, another factor which is used to describe the energy of an electron in an electron beam is the relativistic mass factor γ. This quantity relates an electrons rest mass to the effective mass of the electron when it has been accelerated to a particular energy, $\gamma=1+E/511$, where, γ : is the electron relativistic mass factor; E: is the electron energy in kilovolts and 511 : is a factor relating to the rest mass of an electron (mc^2). As the relativistic mass factor may also be defined as $\gamma = (1-\beta_e^2)^{-1/2}$ then for highly relativistic electrons with a large value of γ, then $\beta_e \approx 1$. For this case equation 1 may be approximated as:

$$\lambda_r \approx \frac{\lambda_w}{2\gamma^2} \qquad (2)$$

What is significant about equation (2) is that the radiation output wavelength from an FEM varies in proportion to the wiggler period, and inversely with the electron energy. Although equation (2) is the standard relation in most FEMs work, equation 1 is more suitable for FEM, where $\beta_e << 1$.

The FEM is operated in an oscillator configuration. The FEM interaction region is a rectangular waveguide resonant cavity terminated by copper irises. It has a frequency tuneability between 8-12.4GHz. This cavity is placed in the centre of an NdFeB permanent magnet undulator with 33 periods [4]. The electron beam source is a travelling wave tube (TWT) type dispenser cathode electron gun. After passing through the interaction region the electron beam is recovered using a single-stage depressed collector. The FEM system set up is shown in figure 1.

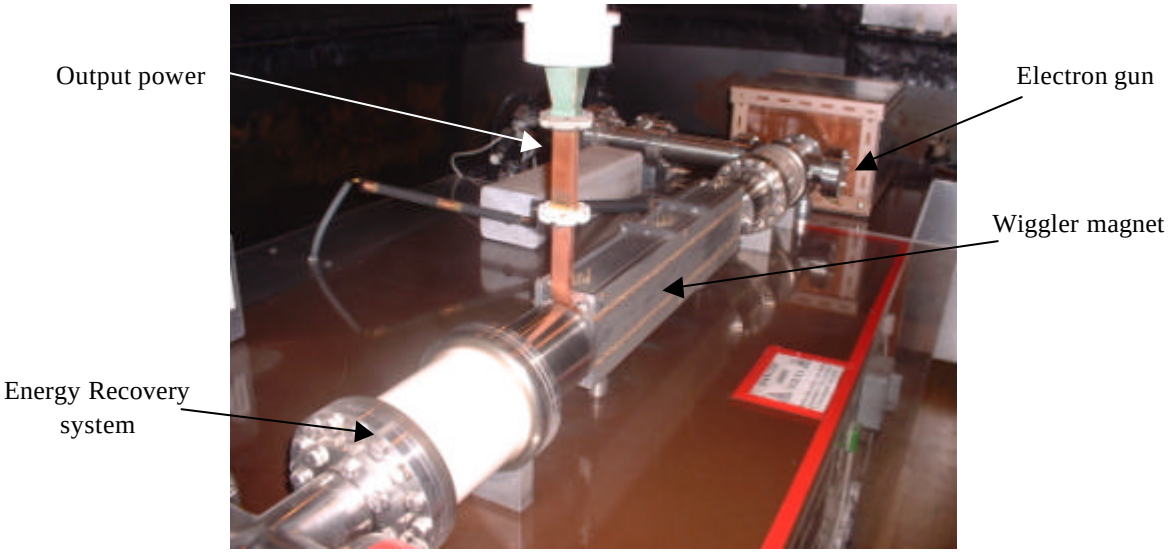

Figure 1: X-band FEM System setup seen from the collector end

The FEM characteristics is governed by the behaviour and capabilities of various components. The pulse length is limited to about 200µs by droop of the cathode supply voltage. The output power is limited to 1kW by the beam current. The pulse repetition frequency (PRF) is limited to 2kHz by the pulse generator. Average power is limited to 50W by vacuum degradation considerations because the electron beam trip level on the vacuum gauge has been set at a conservative $1x10^{-6}$ mbar to avoid any risk of poisoning the gun cathode. Various experiments in the following areas have been performed including Microwave UV/ozone chemistry, Focussed microwave heating, Microwave thermal chemistry, Microwave plasma chemistry and Microwave plasma material processing.

2. Microwave UV/ozone chemistry

The purpose of this experiment was to assess whether there is any benefit to be gained using higher frequency microwave radiation as the power source for UV fluorescent tubes [5,6]. Microwave driven fluorescent tubes can operate at much higher power per unit length than conventional mains driven tubes because there is no need for electrodes, which wear out at high currents. For the initial experiments, commercially available 16mm diameter UV tubes were used. The waveguide used at the workstation is WR90 (22.86mm x 10.16mm). This is 23mm across, so it was possible to simply drill a 16mm hole through the centre of the broad faces of the waveguide and push the tube through. Unfortunately the measured reflected power was as highest 60% of the forward power. Widening the waveguide around the tube to give the 8GHz microwaves a more "square" field distribution increased the efficiency, but reflected power was 30%. For this reason we changed to a waveguide surfatron [7], to launch surface waves along the inner surface of the quartz tube. Using the surfatron, see figure 2, it was possible to achieve almost 100% transmission of microwave power into the UV tube. The waveguide surfatron is a microwave structure for launching surface waves within a plasma column. Microwave power is supplied via a rectangular waveguide the coaxial section with tuning short circuit enables optimised the microwave power launching.

Figure 2: The 8-12GHz waveguide Surfatron

For 2.45GHz operation, the variable power magnetron was coupled to a WG9A (86mm x 43mm) waveguide. A small antenna coupling on the next wave-guide section enabled forward power to be monitored via crystal

microwave detector diode [HP423B]. The microwaves next pass through a circulator onto the tuning section. This section consists of a waveguide surfatron mounted on the wide section of the waveguide, this part of the waveguide is tuned by a stub tuner and movable short circuit, see figures 3 and 4. Any reflected power from this section goes back into the circulator and is dissipated in a dummy load mounted on the circulator's third port. A small antenna coupling mounted on this port provides reverse power measurement via crystal detector. The waveguide surfatron is it's self tuned for minimum reflected power and maximum plasma column length by correct positioning of the coaxial short circuit plunger.

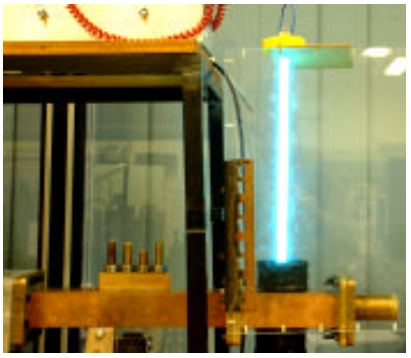

Figure 3: The 2.45GHz Microwave UV lamp demonstrator system

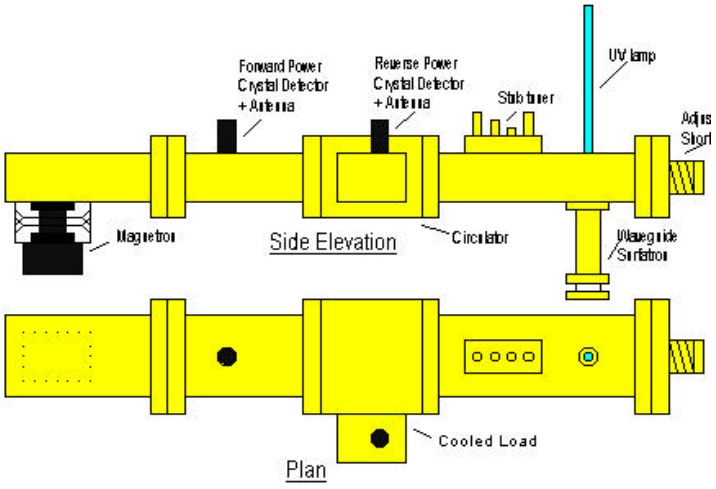

Figure 4: A Block diagram of the 2.45GHz microwave UV lamp

3. Theoretical and Experimental Considerations

A Monte Carlo algorithms [8] have been used to simulate the effect of microwaves on gases discharges at frequencies ranging from 2-10GHz. Figure 5 shows simulation results for the 2.45GHz using conventional microwave oven (magnetron) system. It can be clearly seen that as the microwave electric field increases, at 10kV/cm region that the 185nm radiation increases as the 254nm line decreases. This theoretical result is confirmed in the experimental measurements shown in figure 6 which indicated that as the microwave power increases, i.e. the electric field, so does the 185nm to 254nm radiation ratio. The FEM system was set up to generate a 100µs pulse required for the plasma column to reach the ends of a 30cm UV tube, as in figure 7. Figure 8 confirms the trend shown by this theoretical model. High power (high E field), narrow pulses yield more ozone than low power, wide pulses.

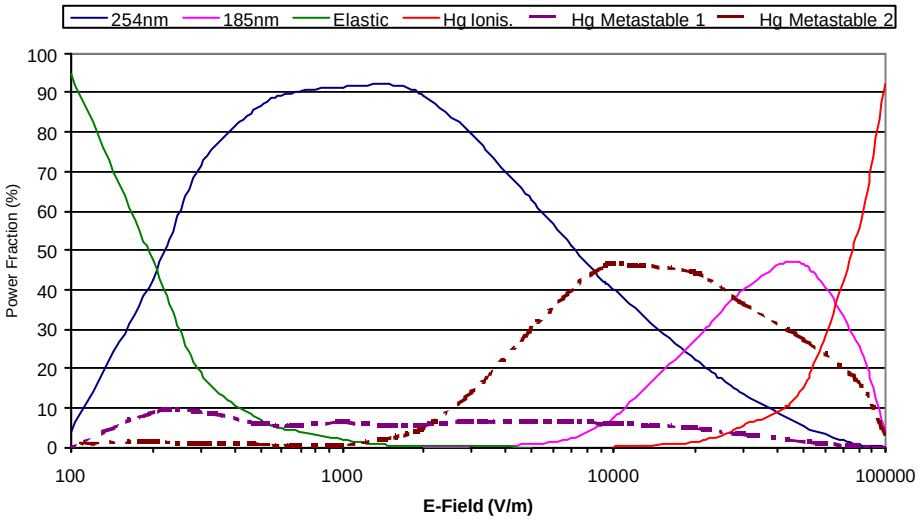

Figure 6: The 2.45GHz microwave discharge simulation

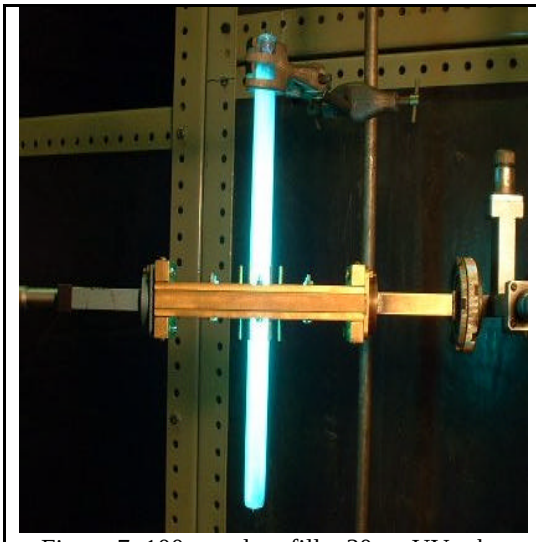

Figure 7: 100µs pulses fill a 30cm UV tube (shown with the waveguide surfatron assembly removed).

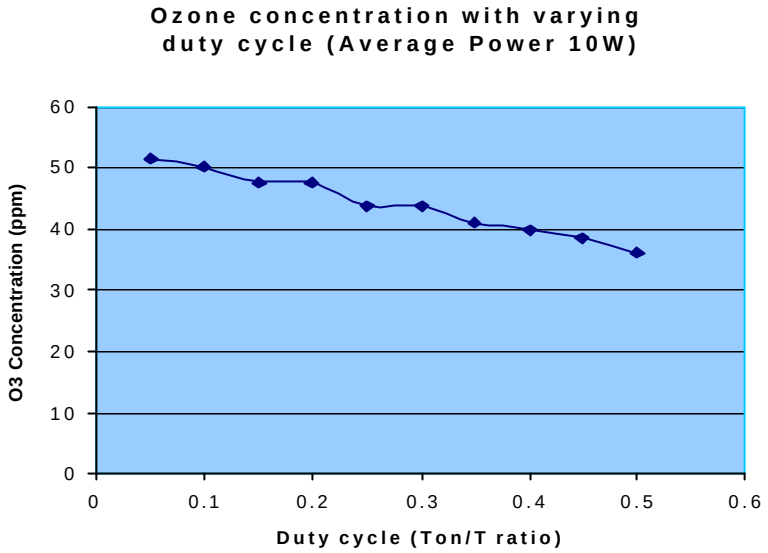

Figure 8: Experimental measurements to investigate the effect of duty – cycle on Ozone production

If high UV power density required, for example at 254nm, one can increase the microwave power but a point is reached where the power fraction, at 254nm, decreases as shown in figure 6. The theoretical model indicates the solution to obtain high power densities is to increase microwave frequency [8]. Figure 9 shows the Monte Carlo simulation for microwaves at 10GHz. It can be seen the fractional power curves have shifted right. The maximum 254nm radiation curve has now moved from 1000 v/m to approximately 10,000 v/m. This is a very important point in order to maintain the germicidal efficiency at high power densities, i.e. higher output power per unit length.

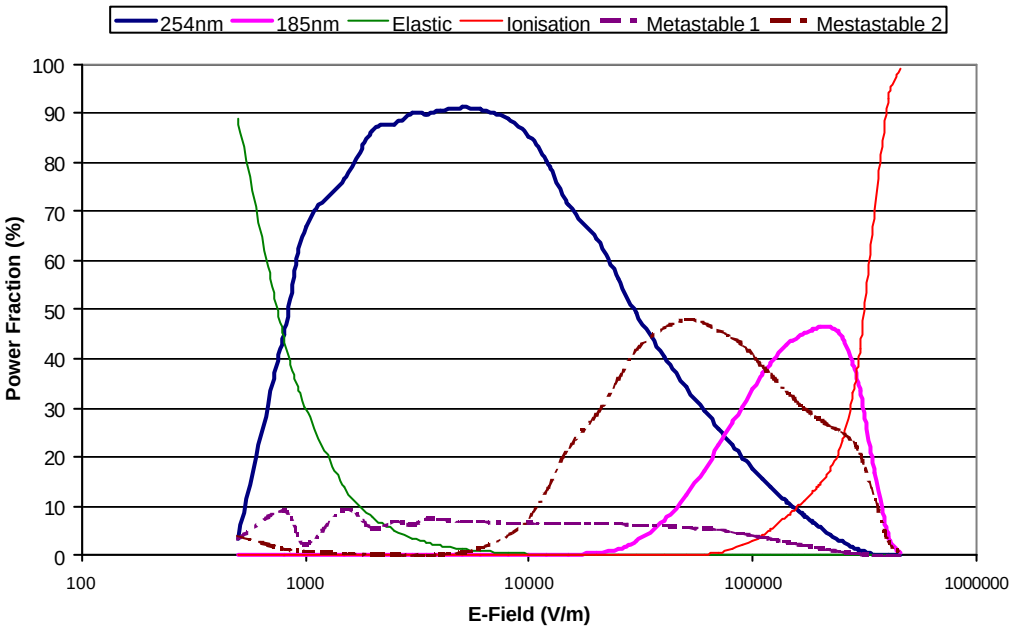

Figure 9: The 10GHz microwave discharge simulation

In addition, figures 10 and 11 agree with the theoretical model that 2.45GHz produces more UV at 254nm than 8GHz at lower microwave powers. Also in agreement with theory is the fact that at higher powers the 2.45GHz powered UV gradient levels off while the 8GHz powered UV is relatively steeper. It is estimated that the IFEM operating at 8GHz will become more efficient, than the 2.45GHz system, at producing UV at 254nm and Ozone at approximately 400 Watts. As the microwave frequency increases so does the UV power

density. However, there are limits to the theoretical model as electric field can only be increased so far before die lectric breakdown and arcing occurs. Wavelengths higher than 254nm has not been included in this simulation.

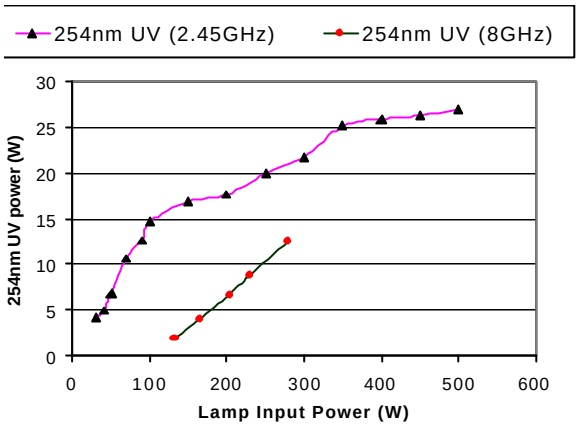

Figure 10: UV Output at 254nm for 2.45 GHz and 8GHz

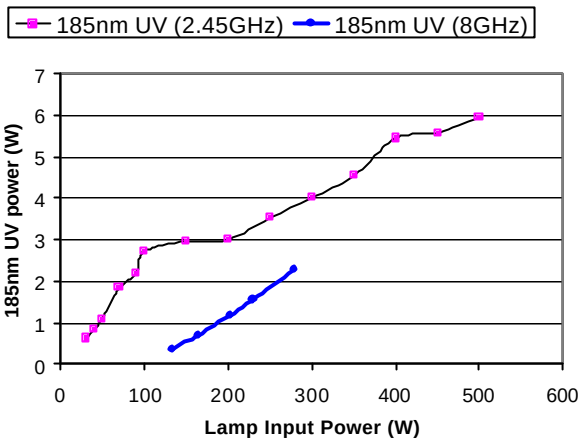

Figure 11: UV Output at 254nm for 2.45 GHz and 8GHz

4. Microwave Thermal Chemistry

This experiment involved the acceleration of chemical synthesis by microwave irradiation. Small samples of dissolved chemical were placed in a sample vessel as shown in figures 12. This was placed in an irradiating chamber mounted in X-band waveguide, figure 13. The waveguide section was terminated in a tuneable short circuit and reflected power minimised using a matching transformer. The procedure used was to tune the transformer and short circuit with a measured quantity of the solvent in the sample tube prior to irradiating the chemical product. During the heating process, an infrared probe at the base of the sample tube monitored the temperature.

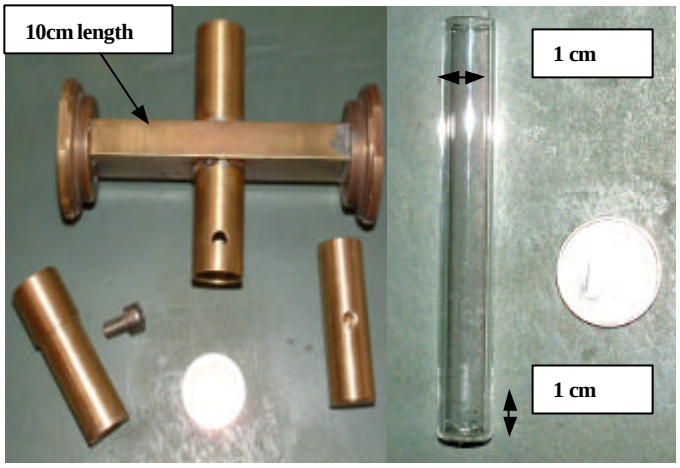

Figure 12: X-Band chemical synthesis reactor

Figure 13: FEM chemistry experimental setup

A selection of three sets of model synthesis have been investigated including the synthesis of cyclohexenes starting from imine and methyl cyanoacetate, see figure 14.

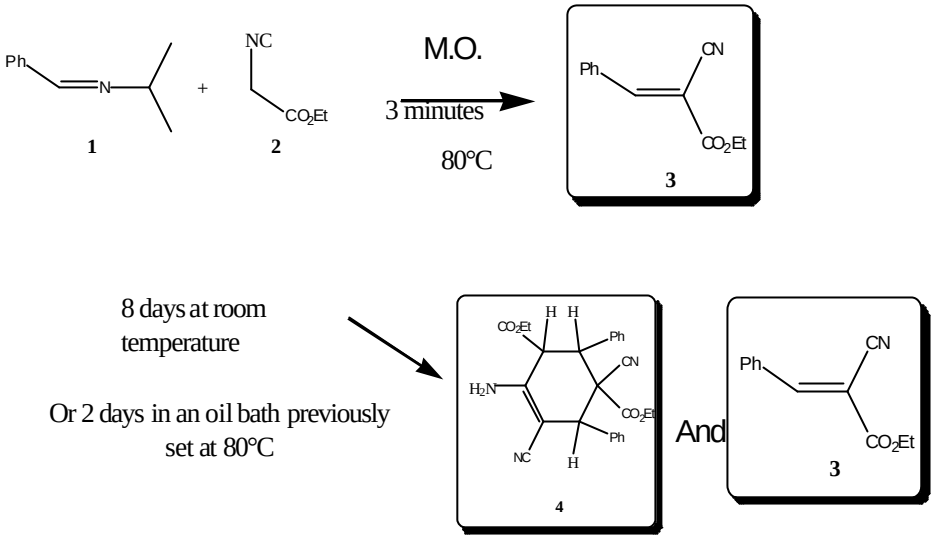

Figure 14: Types of chemicals have been used in FEM system

This model is particularly suitable owing to the fact that according to the conditions, the results are different. At room temperature (8days) or under conventional heating (2 days in an oil bath at 80°C) cyclohexene **4** and alkene **3** are formed, but under microwaves (2.45 GHz) only the alkene **3** is observed at 80°C (3 minutes). The mechanism of the formation of the cyclohexene has been established, the first step being the formation of the alkene **3** (Scheme 4).The FEM experiments led to the synthesis of products that have not been seen using a conventional laboratory microwave oven as the heat source [9,10]. Previously these products have only been seen after eight days at room temperature or five days in an 80° oil bath. In the FEM experiment the production took three minutes, this may be due to the use of higher frequency radiation but it could also be due to the fact that the FEM power is applied in a "pseudo continuous" manner, the "off" periods are around a millisecond, whereas the oven cycles on and off over several seconds just like a domestic oven.

Acknowledgements

The authors would like to thanks the EU community for their kind support.

References

[1] A. Shaw, A.I. Al-Shamma'a, R.A. Stuart, J. Lucas, Nucl. Instr. and Meth. In Phys. Res., **A375**, 245, (1996).
[2] A.I. Al-Shamma'a, R.A. Stuart, J. Lucas, Nucl. Instr. And Meth. In Phys. Res., **A375**, 424, (1996).
[3] C.C. Wright, R.A. Stuart, J. Lucas, A. Al-Shamma'a, C. Petichakis, Vacuum, **44**, 4, 527, (2005).
[4] C.C. Wright, R.A. Stuart, A.I. Al-Shamma'a, J. Lucas, Optics Communications, **185**, 387, (2000).
[5] A.I. Al-Shamma'a, I. Pandithas, J. Lucas, J. Phys D: Appl. Phys., **34**, 14, 2775, (2001).
[6] I. Pandithas, A.I. Al-Shamma'a, J. Lucas, Proc.of the 14th IEEE Int. Pulsed Power Conf., 1112, (2003).
[7] M Moisan, Z Zakrzewski, Plasma Sources Science and Technology, **4**, 3, 379, (1995).
[8] I. Pandithas, A.I. Al-Shamma'a, A. Shaw, GD2004, 793, (2004).
[9] J. Hamelin et al, Tetrahedron, **58**, 5865, (2002).
[10] J. Hamelin et al, Catalysis communications, 185, (2002).

Diagnostics of high power pulsed microwave discharge

M. Meško, P. Vašina, A. Tálský, V. Kudrle, Z. Bonaventura, D. Trunec, J. Janča

Department of Physical Electronics, Masaryk University, Kotlářská 2, CZ-61137 Brno, Czech Republic

Introduction

There is growing interest in using of the pulsed discharges in both research studies and industrial plasmachemical processes. The main advantage of using pulsed discharges is the possibility of promoting complex chemical reactions with rather low average thermal power. Although there are many studies on the plasmachemistry of pulsed discharges, they have mostly used common supplies (dc, radiofrequency, microwave), with relatively low peak power (10^2–10^3 W). However, our work deals with pulse peak powers of the order of 10^5 W.

When studying the volume plasmachemical reactions, the surface reactions are often a complication. Therefore, we used an experimental device in which the role of the plasma – wall interactions is suppressed. We achieved this by separating the plasma and the walls. The discharge is produced only at the vicinity of a focal point of the microwave beam, which is 25 cm from the nearest wall.

In this paper we present the experimental results of microwave and optical diagnostics of low pressure, high power microwave pulsed discharge in nitrogen. We recorded intensities of important emission bands as well as temporal evolution of electron concentration and microwave power transmitted through the plasma.

Experimental

A schematic drawing of experimental apparatus is presented in Fig.1. The plasma is produced in a spherical glass vessel with an inner diameter of 0.5 m. From one side the vessel is irradiated by a horn antenna. On the opposite side wall, an aluminium foil is placed to reflect and focus the microwaves. Microwaves (X-band) are generated by refurbished radar (100 kW peak power, 2.5 μs duration, 400 Hz repetition). The field has a maximum in the centre of the glass vessel and therefore a plasma ball is formed there. It does not touch the walls which suppresses influence of surface reactions.

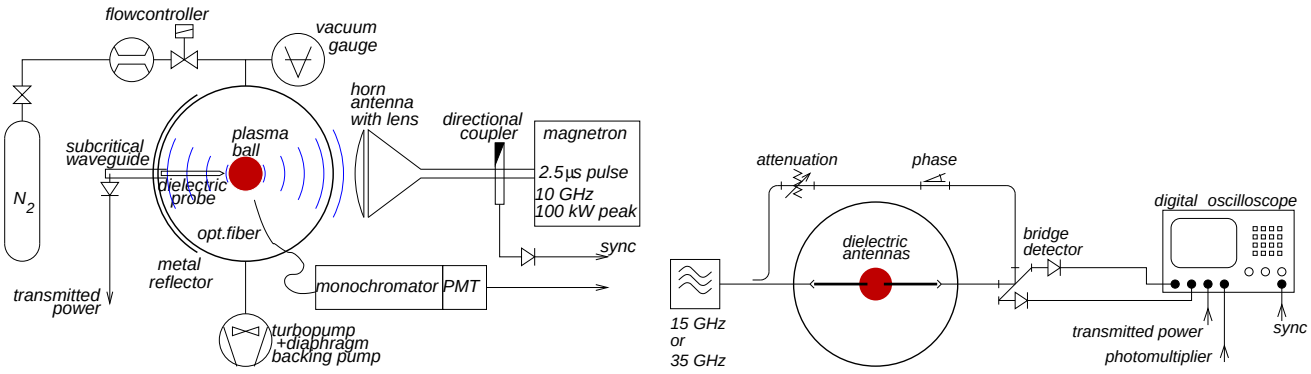

Figure 1: Experimental setup.

The experiment was carried out in a flow regime. The pressure was measured using a capacitance diaphragm gauge and maintained by a gas flow controller. The operating pressure was in the range 20–2000 Pa.

Microwave interferometers operating at 15 and 35 GHz were used to measure the plasma density. They were coupled to the plasma by means of dielectric (PTFE) rod antennae. This configuration permits rather localised measurements, as the dielectric waveguides/antennae were separated by 40 mm. Diameter of the waveguides was selected large enough to achieve propagation of microwaves inside of them without perturbation by outer

plasma. Detailed description and discussion is in [1]. The output signal from the interferometer was detected using diodes and then measured using an HP Infinium 500 MHz digital oscilloscope.

We recorded time resolved intensities of selected spectral lines and bands by means of monochromator (Zeiss SPM2) with photomultiplier (EMI 6255B). The transmitted part of exciting microwave power was measured by dielectric probe, attenuating subcritical waveguide and diode detector.

Results and discussion

The evolution of the important quantities (electron density, transmitted power, intensity of second positive (N_2 $C^3\Pi_u \rightarrow B^3\Pi_g$) and first negative ($N_2^+$ $B^2\Sigma^+ \rightarrow X^2\Sigma^+$) systems of nitrogen is presented in the left part of Fig.2 together with the shape of exciting microwave pulse. It is seen, that microwaves are efficiently absorbed even sooner than electron density reaches our detection limit. The overshoot in emission intensities is caused by combination of rising electron density and falling of electron temperature (see theoretical article [2]).

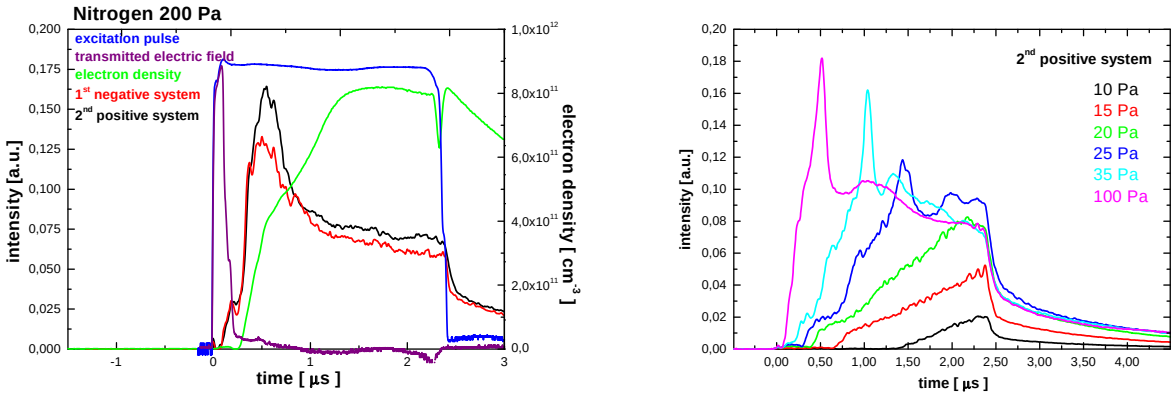

Figure 2: Results of time resolved diagnostics of high power pulsed microwave plasma. Left side: time resolved electron density, incident and transmitted microwave power, intensities of $2^{nd}+$ and $1^{st}-$ systems of nitrogen. Right side: influence of pressure on temporal evolution of intensity of $2^{nd}+$ system of nitrogen.

The right side of Fig.2 shows the dependence of temporal evolution of 2^{nd} positive system on pressure. For optimal pressures (around 100-200 Pa) the discharge develops quickly, but for lower pressures the reaching of steady state is much slower. The same behaviour can be observed in electron density curves.

Conclusion

We performed complex diagnostics of high power pulsed microwave discharge in nitrogen using microwave interferometry, optical emission spectroscopy and microwave power measurements. The results are compared to model.

Acknowledgements

This work was partially supported by the projects GAČR 202/03/H162 and COST 527.20.

References

[1] M. Mesko et al: Plasma Sources Sci. Technol. **13** (2004) 562
[2] Z. Bonaventura et al: Modelling of high power pulsed microwave discharge, in Proceedings of ISPC 17 (Toronto, Canada) (2005)

Characterisation of nitrogen–oxygen flowing afterglow

V. Kudrle, M. Mrázková, P. Vašina, A. Tálský, J. Janča

Department of Physical Electronics, Masaryk University, Kotlářská 2, CZ-61137 Brno, Czech Republic

Introduction

Plasmachemical reactions occurring in N_2–O_2 mixtures are of great interest to many fields of the research. One of promising directions in applied plasmachemistry is a use of the plasma for a low temperature sterilisation, which is needed if e.g. polymer objects are to be sterilised. Generally, as the main agents responsible for killing bacteria are considered [1] atoms, radicals and UV radiation. To maximise the efficiency of the process the optimal operating conditions (mixture, power, CW/pulsed regime, etc.) should be found.

In our experiment in flowing afterglow configuration we measured the concentration of N, O, electrons together with radiation intensity of NOβ and NOγ systems. The measurements were carried out at various flow rates of oxygen and nitrogen. Moreover we investigated the influence of the afterglow position on the measured quantities.

Experimental

A schematic drawing of experimental apparatus is presented in Fig.1. A microwave discharge is produced in a quartz discharge tube with inner diameter of 13 mm by means of surfatron cavity, powered by 20 W microwaves (2.45 GHz). Our experiments being carried out in a flowing regime, afterglow is observed downstream in 1 m long quartz tube with inner diameter of 8 mm. Small amount of oxygen admixture may be added to the nitrogen gas before its passing through the discharge.

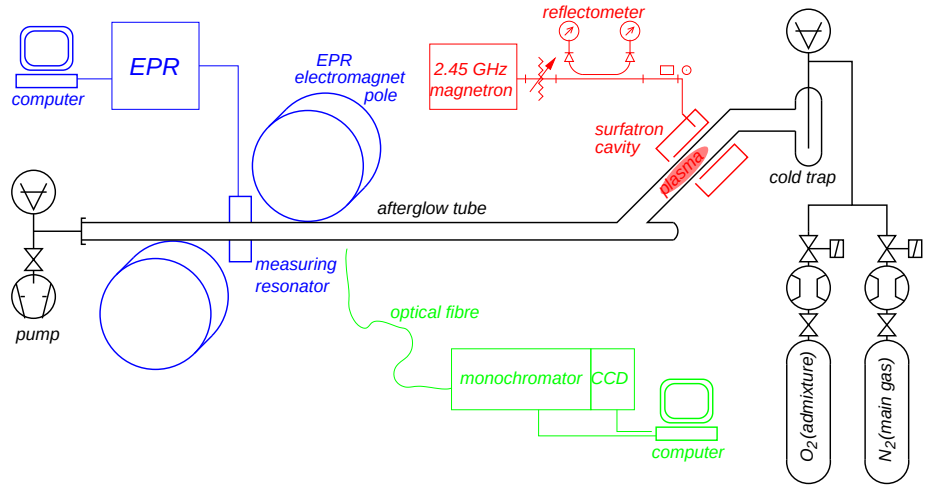

Figure 1: Experimental setup.

The gases are led from gas cylinders through the mass flow controllers to a LN_2 cold trap, which removes traces of unwanted impurities, like a water or hydrocarbons. The purities of all used gases were better than 99.995% according to manufacturers' certificates. Flow rate of oxygen was varied between 0 and 10 sccm and the flow rate of main gas was between 25–200 sccm. The pressure in the discharge was independently set at value between 300 Pa and 700 Pa by throttling the pump.

We employed electron paramagnetic resonance (EPR) spectrometer JEOL JES-3B operating in X-band to measure the concentration of atomic species. This method is based on resonance absorption of microwave energy

by the transitions between Zeeman split levels. After a calibration of the EPR device by molecular oxygen the absolute concentration was obtained. For details of use of EPR spectroscopy in plasma afterglow, see [2].

Optical emission spectroscopy was carried out using Jobin-Yvon TRIAX 330 spectrometer.

Results and discussion

We observed that N concentration reaches a visible maximum[3] for certain oxygen admixture. The evolution of [N] along the afterglow tube is relatively flat for pure N_2 plasma but the losses along the tube are increasing with oxygen admixture.

Oxygen atom density is rising when small amount molecular oxygen is added. For higher O_2 percentages it remains nearly constant. Evolution of [O] along the tube is rather independent of N concentration.

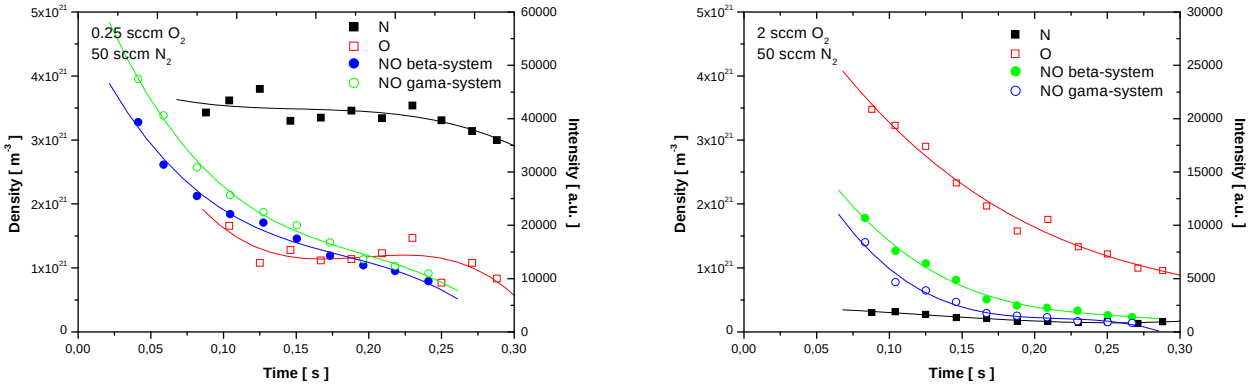

Figure 2: Influence of afterglow position on concentrations of oxygen and nitrogen atoms and intensities of NOβ and NOγ systems. The measurements were carried out at pressure 760Pa.

Two spectral systems of nitric oxide are produced by different reactions. The NOβ system is produced by reaction $N+O(+M) \rightarrow NO^*(+M)$ and NOγ by $N_2(A)+NO \rightarrow NO^*+N_2(X)$. Their recorded intensities give us deeper insight into the processes involved.

In Fig.2 there is presented the temporal evolution of concentrations of oxygen and nitrogen atoms and intensities of NOβ and NOγ systems for two flow rates of oxygen admixture.

Conclusion

Certain mixture of oxygen and nitrogen can be found which maximises the production of UV radiation from excited NO along the whole afterglow tube. In a similar manner there exist another N_2/O_2 ratio for maximal production of N and another one for maximising O production. By varying the amount of oxygen admixture we can therefore optimise the production of wanted species.

Acknowledgements

This work was partially supported by the projects GAČR 202/03/H162 and COST 527.20.

References

[1] S. Moreau et al: J. Appl. Phys. **88** (2000) 1166
[2] A. A. Westenberg: Prog. React. Kinet. **7** (1973) 23
[3] V. Kudrle et al: Acta Phys. Slovaca **53** 5 (2003) 397

REFRACTORY METAL FILM DEPOSITION BY THERMIONIC VACUUM ARC METHOD

G. Musa[1, 2], I. Mustata[1], C. P. Lungu[1], C. Surdu Bob[1], A. M. Lungu[1], R.Vladoiu[2], V. Ciupina[2], V. Bursikova[3]

[1]*Low Temperature Plasma Physics Laboratory, National Institute for Lasers, Plasma and Radiation Physics, Bucharest, Romania*
[2]*Department of Physics, Ovidius University, Constanta, Romania*
[3]*Department of Physical Electronics, Faculty of Science, Masaryk University, Czech Republic*

Abstract

Despite of the highest melting point and lowest vapor pressure of all metals, tungsten thin film can be obtained with the Thermionic Vacuum Arc (TVA) method. For the characterization of hardness we used depth sensing indentation tester Fischerscope H100 Xyp and the results have indicated a high value for plastic hardness. Also, the AFM measurements have proved the smoothness of the deposition. The structure of the deposited W films was studied using TEM electronic microscope PHYLIPS CM 120 with a magnification of 1.4 M and a resolution of 1.4 Å. The samples of tungsten films deposited on small size NaCl or KCl monocrystals have been submitted to TEM examination (after solving the monocrystal supports in water). HRTEM image confirms the cubic structure of W. (SG: Im3m, a = 3.158 nm).

Keywords: Thermionic Vacuum Arc, tungsten thin film, AFM, HRTEM, nanointendation

Introduction

Coating of carbon fiber composite (CFC) and turbine blades used in the energy applications (future fusion devices, respectively classical thermal power generators) with refractory metal as tungsten is highly desired as thermal barrier in order to increase operation temperature and lifetime of the devices. Tungsten, with the highest melting point and lowest vapor pressure of all metals, has – at temperature over 1923 K - the highest tensile strength. It has excellent corrosion resistance and is attacked only by most mineral acids.

In this work is reported deposition of tungsten films on graphite substrates of 30 x 30 x 8 mm^3 by Thermionic Vacuum Arc (TVA) method. This type of arc ignites in high vacuum conditions in the vapors of the anode material, continuously generated by the electron bombardment of the anode[1]. The electrons, emitted from a heated tungsten cathode, are accelerated towards the anode, by a d.c. high voltage applied across the electrodes.

Experimental set-up

The TVA method [1-4] is characterized by producing plasma in the pure vapors of the metal to be deposited (W) without using any buffer gas. The evaporation of the metal takes place in high vacuum conditions (10^{-3} Pa and less). An external heated cathode (W + 0.2%Th filament) produces thermally emitted electrons of about 100 mA. These electrons are accelerated and focused by a Whenelt cylinder to the anode which is biased to high voltage (1 – 6kV). The electron bombardment creates space tungsten atoms above the anode at a local pressure of about 133 Pa.

The thermoelectrons produced by the heated cathode are able to build up plasma by electron-tungsten atoms collisions. The new electrons generated in the plasma together with the original ones emitted by cathode enhance once more the anode evaporation and produce high quantity of ions. Usually the cathode potential fall is in the range of 200-300 V and therefore the plasma potential in comparison with ground ensure generation of the high energy ions which collide the substrate.

Because this system can heat any material at elevated temperature, it is one of the most adequate methods for the evaporation of high melting point materials. In the case of such materials, instead of a crucible containing the material to be evaporated, a rod of refractory metals is used directly as anode. Moreover, the discharge can be ignited in high vacuum condition, ensuring high purity of the deposition. In Fig 1 is shown the photograph of the TVA arrangement. Such an arrangement has been used for the deposition of Re or Nb [5].

The anode, a W rod of 8-10 mm in diameter and 80 mm in length (20 tungsten wires of 1 mm diameter) was sustained by a Mo support, which could be rotated during deposition by an electrical motor. The ignited thermionic vacuum arc parameters were: cathode filament current - 150 A, arc current; 2 – 3 A, the arc voltage drop on the arc; 1000 - 1200V d.c.

The obtained films were characterized by nanoindentation and atomic force microscopy (AFM). Also a HRTEM was used for information concerning the structure of the tungsten thin films.

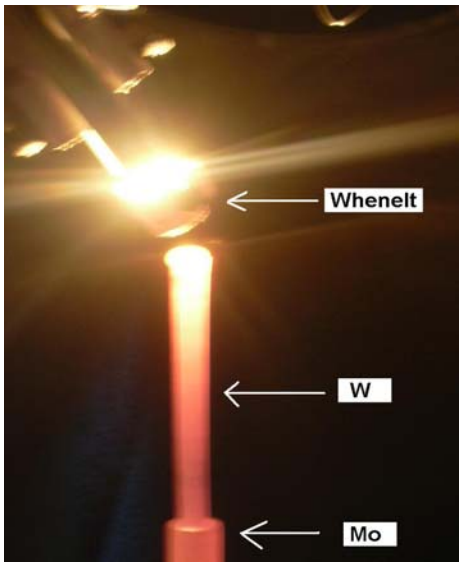

Fig. 1 Photograph of the TVA arrangement.

Results and discussion

The samples (graphite substrates 30 mm x 30 mm x 8 mm coated with W) were tested using depth sensing indentation tester Fischerscope H100 Xyp. We can notice from the Fig. 2 that the tungsten film had significantly higher resistance against indentation.

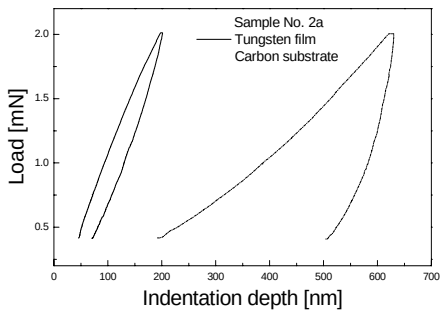

Fig. 2 Comparison of loading / unloading curves for maximum indentation load of 3 mN.

The material parameters obtained on the graphite substrate and the tungsten films are listed below in Table 1, where: - HU- universal hardness (resistance against elastic and plastic deformation)

- W_e/W_{tot} – ratio of the elastic indentation work to the total indentation work
- HU_{pl} – plastic hardness (resistance against plastic deformation – equivalent of the so called Vickers hardness
- h_{max} – maximum depth at given maximum load- $Y = E/(1-\nu^2)$, where E is the Young's modulus and ν is the Poisson's ratio.

Table 1. Results of the nanoindentation test

Sample	HU [N/mm^2]	We/Wtot [%]	HUpl [N/mm^2]	Hmax [μm]	Y [GPa]
Substrate	158	24.81	205	0.692	6.0
tungsten film	30	0.23	5700	0.250	80.0

The AFM measurements have proved the smoothness of the deposited films (however with some droplets as can be seen in Fig. 3) with peak to valley roughness in the range of 20-30 nm.

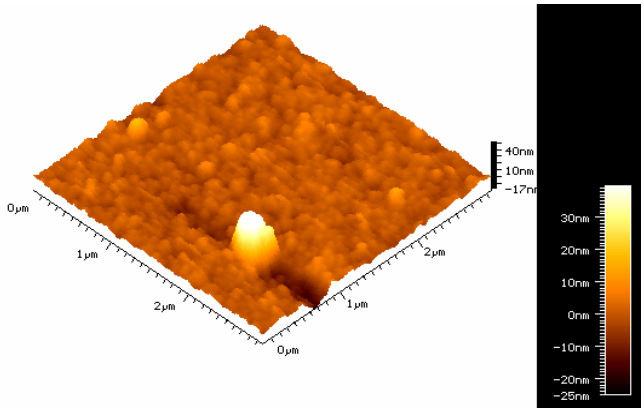

Fig. 3 AFM image of the W film.

The structure of the deposited W films were studied using TEM electronic microscopy with a magnification of 1.4 M and a resolution of 1.4 Å. The samples of tungsten films deposited on small size NaCl or KCl monocrystals have been submitted to TEM examination (after solving the monocrystal supports in water). TEM analysis of thin layers (10-20 nm thickness) revealed the nanostructured tungsten film with grain size in the range of 10 nm (Fig. 4 and Fig. 5).

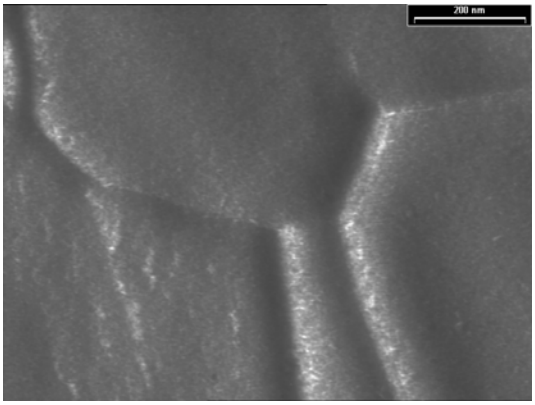

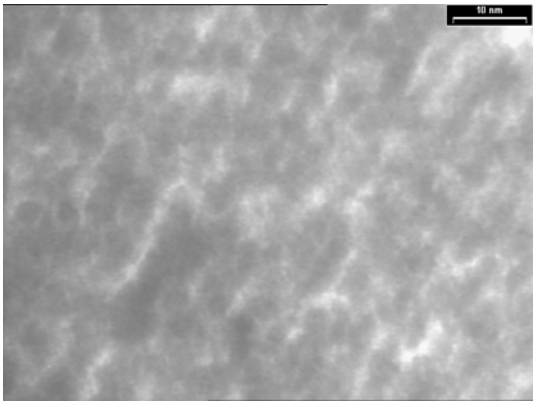

Fig. 4. BF-TEM image of W film**.**

Fig.5 Detail image of W film at 10 nm scale.

Also in Fig. 5 one can see clustered tungsten nanoparticles with mean diameters bellow 10 nm.

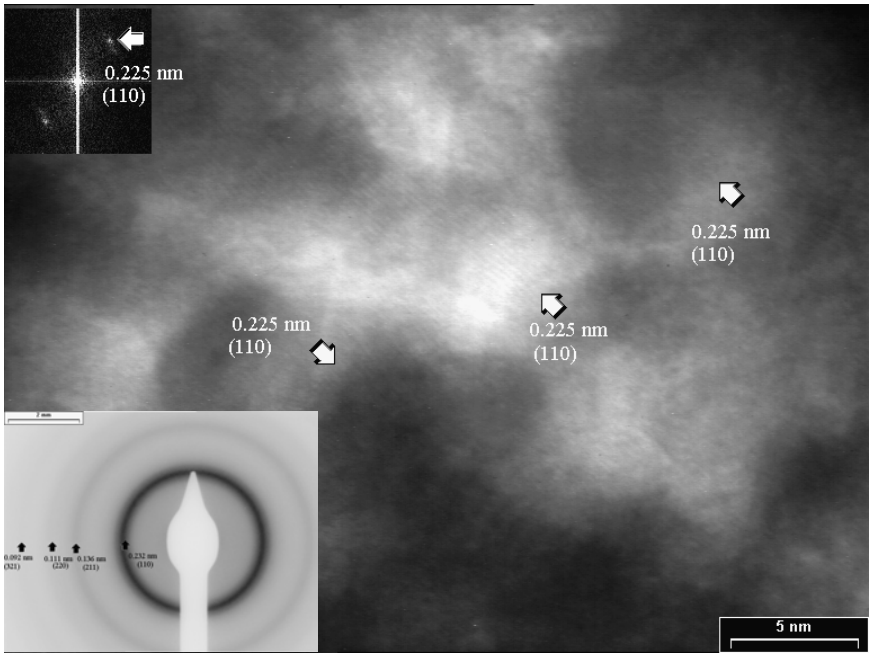

Fig. 6 HRTEM image of the deposited thin tungsten film with FFT (left up inset image) and SAED (left inset down image)

Figure 6 shows HRTEM image of W nanoparticles that exhibits (110) planes. Left inset shows FFT (Fast Fourier Transmission) representation of selected zone. SAED (Selected Area Electron Diffraction) image confirms the cubic structure of W. (SG: Im3m, a = 3.158 nm

Conclusion

The obtained results prove the possibility to use TVA for high quality, pure tungsten film deposition with nanohardness in the range of 5700 N/mm^2 and peak to valley roughness in the range of 20-30 nm. Tungsten film deposition is now considered in fusion programs to be used to cover the wall of the divertors and also as thermal barrier coating on the Nb based superalloys for gas turbine blades.

References

[1] G. Musa, H. Ehrich, M. Mausbac, J Vac Sci and Techn., A12, 2887-2895 (1994).
[2] G.Musa, I. Mustata, A.Popescu, H.Ehrich, J.Schumann, Thin Solid Films, 333, 95-102 (1998).
[3] H. Ehrich, J. Schuhmann, G.Musa, A.Popescu, I,Mustata, Adhesive metal films obtained by thermionic vacuum arc (TVA) deposition, Thin Solid films, vol.333, p.95-102 (1998).
[4] G. Musa, I. Mustata, V. Ciupina, R. Vladoiu, G. Prodan, E. Vasile and H. Ehrich, Diamond and Related Materials, 13(4-8), 1398-1401 (2004).
[5] C. P. Lungu, I. Mustata, G. Musa, A. M. Lungu, V. Zaroschi, K. Iwasaki, Y. Matsumura, R. Tanaka, I. Iwanaga, H. Tanaka, T. Oi, K. Fujita, Proceedings of PSE2004, Germany, 1-5 Sept 2004, p. 33 (2004).

Power Supply Design for Pulsed Power Plasma Applications

Maciej A. Noras, William A. Maryniak

Trek, Inc., 11601 Maple Ridge Rd., Medina, N.Y., U.S.A.

Abstract: A design of the solid state power supply for pulsed power plasma applications is described and explained. This particular design was created for the PACT (plasma and catalyst integrated technologies) reactor, with current, voltage, shape and frequency of pulses adjusted to requirements of the PACT system. Non-thermal plasma systems frequently utilize a short pulse-width, fast rising time and high repetition rate of the electrical pulses generated by the power supply. The proposed solution allows for adjustment of these parameters. This, in turn, permits optimization of removal rates of volatile organic compounds (VOC), NO_x and other agents. In addition, the output current and voltage monitors provide possibility of discharge energy observations.

1. Introduction

In recent years, non-thermal plasma technologies have been widely researched, and the range of their applications has rapidly expanded. Non-thermal plasmas are also known as non-LTE ("local thermal equilibrium") or as low-temperature plasmas. These definitions come from the fact that during the plasma generation process electrons become highly energized while much heavier ions and neutral particles remain at low energy level. Typical applications of non-LTE plasmas include etching, ion implantation, thin films deposition, chemical neutralization and/or decomposition of pollutants. Low temperature plasma are most frequently created from electronic excitation using DC and pulsed DC or AC coronas, dielectric barrier discharges (DBD), and radio-frequency (RF) discharges. The choice of a particular plasma generation technology depends on the application. Non-thermal plasmas utilized in the air pollution control and VOC removal usually are generated by the pulsed DC or AC corona methods. The DC corona technique and RF discharge plasma create undesirable electrode etching, and, in addition, DC plasma tends to be very non-uniform when applied to relatively large volumes of contaminated air. Therefore, pulsed DC and AC, as well as DBD plasmas, became preferred methods for contaminant gases and VOC removal. DBD technique uses either AC or pulsed DC electric field to create plasma. Regardless of the plasma generation technique, a power supply is a critical component of every plasma generator. A properly designed power source for plasma has to be reliable, efficient, and be able to provide suitable energy coupling between the power supply and the plasma. It should also deliver adequate homogeneity of the plasma and control over plasma parameters. Safety, cost and size of the power supply are also very important issues. Specific parameters required from the power supply, such as voltage amplitude and shape, current, frequency etc., depend on the particular design of the plasma generation system. During the preliminary development stage it is often practical and convenient to use AC power supplies or high voltage amplifiers that permit a certain range of adjustments of the aforementioned parameters. Linear AB class high voltage amplifiers are able to provide precise control of the output voltage waveform: amplitude, frequency, rise and fall time, duty cycle, etc. Once the operating parameters are optimized, the next step is to design the power supply that is small and efficient with respect to performance and cost, as required by most of industrial applications. Figure 1 presents an example, simplified circuit diagram of an output stage of a class AB amplifier. It consists of transistors Q_1 and Q_2 and the resistive load R_L. For the sinusoidal voltage signal V_{IN}, the current drawn from the power supplies is:

$$I_{supply} = \frac{1}{T}\int_0^T i_Q dt \tag{1}$$

$$I_{supply} = \frac{1}{2\pi}\int_0^T i_{output}\sin(\theta)d\theta \quad (2)$$

$$I_{supply} = \frac{1}{\pi} i_{output} = \frac{1}{\pi}\frac{V_{OUT}}{R_L} \quad (3)$$

The input power therefore is:

$$P_{supply} = 2 \cdot V_{CC} \cdot I_{supply} = \frac{2 \cdot V_{CC} V_{OUT}}{\pi \cdot R_L} \quad (4)$$

The power delivered to the load is:

$$P_{load} = \frac{1}{2}\frac{V_{OUT}^2}{R_L} \quad (5)$$

The efficiency is:

$$\eta = \frac{P_{load}}{Psupply} = \frac{\pi}{4}\frac{V_{OUT}}{V_{CC}} \approx 78\% \quad (6)$$

This is the maximum achievable efficiency of the class AB amplifier. Once the desired parameters of

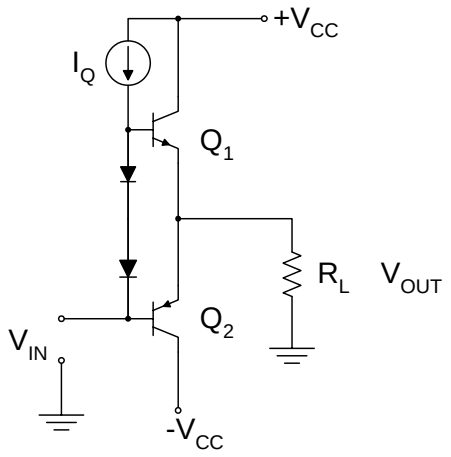

Figure 1: Example circuit diagram of a class AB amplifier output stage.

the power supply for a specific plasma generator are determined, the pulsed DC power supply can be developed. With a proper design, efficiency of a pulsed DC power supply can reach 96% level [1]. In addition, while high voltage amplifiers provide flexibility of plasma parameters adjustment, it may be difficult to meet the size and cost requirements using class AB topology. The power supply presented in this paper is an all-solid-state high voltage pulse generator, designed and built for the PACT reactor - a new type of technology using plasma and catalyst integrated approach for VOC and other contaminants removal. Solid state switching devices usually have larger lifetimes than gaseous discharge elements used in some applications and they also provide much faster and more reliable switching.

2. Power supply design

2..1 Design requirements for "no load" condition

1. Output Voltage Range adjustable from 0 to 12 [kV] peak-to-peak AC.
2. Output Current Range 0 to ± 240 [mA] peak AC.

3. Output Waveform trapezoidal.

4. Output Frequency 10 [kHz].

2..2 Design description

The all-solid-state design was developed basing on the commercially available pulse width modulator (PWM) TL598. A pulsed power supply block diagram is shown in Figure 2.

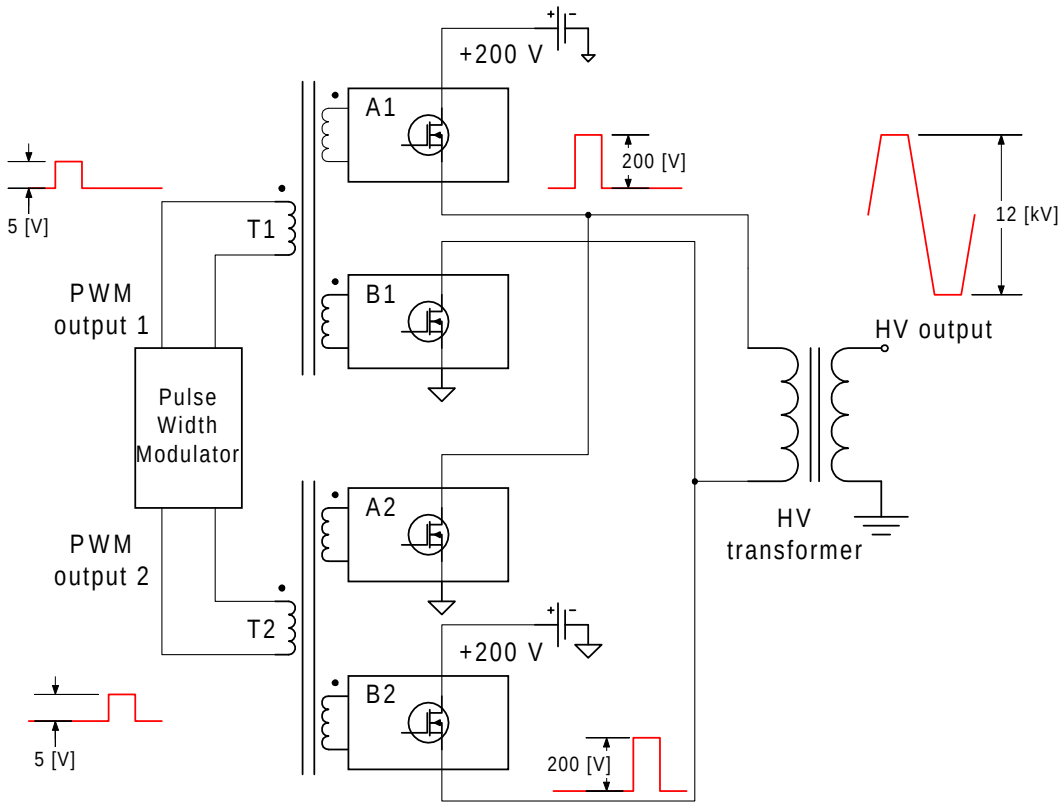

Figure 2: Block diagram of the pulsed power supply.

The TL598 control circuit is capable of directly driving MOSFET switches [2]. The control circuitry is separated from the high voltage driven transistors by transformers T1 and T2. The PWM provides 5 [V] square wave pulses with a positive polarity at the one-half oscillator frequency rate on each of the outputs (Figure 3). The dead time control comparator prevents overlapping of the pulses from the outputs 1 and 2 during push-pull operation. The PWM also prohibits the possibility of either output being pulsed twice during one cycle of operation.

A pulse P1 from the PWM output 1 is supplied to the transformer T1. This pulse, after being transformed, turns the MOSFET amplifying blocks A1 and B1 on. The square pulse of 200 [V] (positive polarity) appears across the high voltage (HV) transformer, resulting in high voltage 6 [kV] peak square signal of the positive polarity at the high voltage output of the power supply. The duration of the high voltage pulse is controlled by the duration of the PWM signal. After the dead time a voltage square pulse P2 is supplied by the PWM output 2 to the transformer T2. It turns the blocks A2 and B2 on, and the 200 [V] square signal appears on the primary winding of the HV transformer. The polarity of this pulse is inverted, so the negative 6 [kV] peak square signal is present at the high voltage output. The frequency and the amplitude of the HV signal can be easily adjusted.

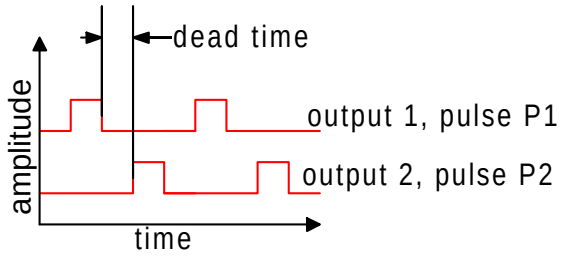

Figure 3: Square wave pulses supplied by the PWM.

2..3 Design verification

The validity of the power supply design was verified by extensive testing. First, the no load parameters of the power supply were confirmed. Figure 4 presents an example of an oscillogram taken with a 1000:1 HV Tektronix P6015A divider along with a TDS402A Tektronix oscilloscope. The square wave signal becomes distorted after reaching 14 [kHz] frequency.

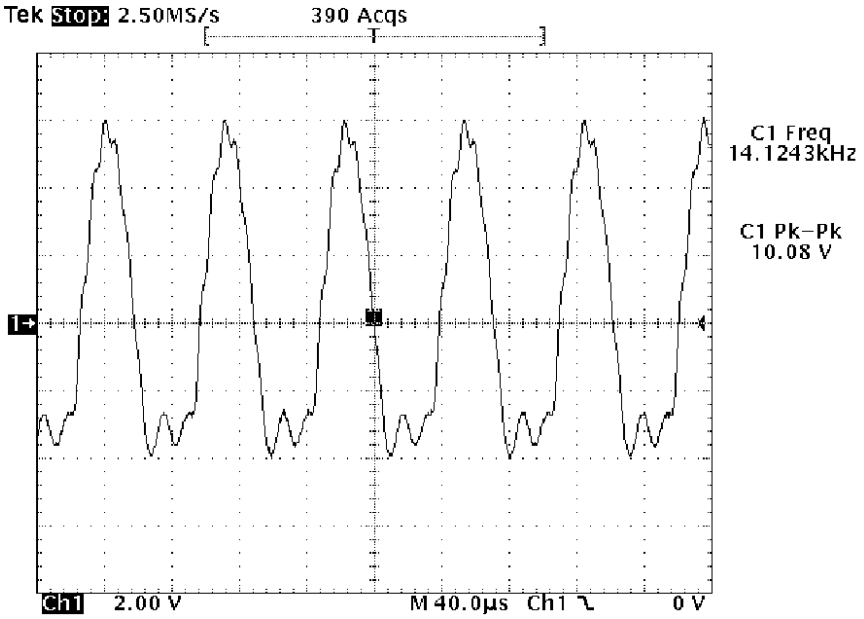

Figure 4: High voltage output waveform under no load condition. The limiting frequency of operation is 14 [kHz].

The power supply was also tested with various capacitive and resistive loads. The PACT system, for which the power supply was designed, represents a 28.2 [pF] capacitive load. Tests of the system with the PACT tube were conducted in the configuration shown in Figure 5.

Figure 6 shows voltage and current waveforms recorded for the PACT reactor:

The very fast and relatively high initial current peaks correspond to charging processes occurring in the PACT system. The current ripple after the initial current surge is due to discharge phenomena occurring inside the reactor. Variations in the current values result in disturbance of the voltage waveform, therefore the voltage is not of ideal square-wave shape. The power supply circuitry has ability of correcting such disturbance with certain, limited speed of response. The power supply has a built-in current limit block protecting from the possible shorted output current damages. Another feature of the PS design is a

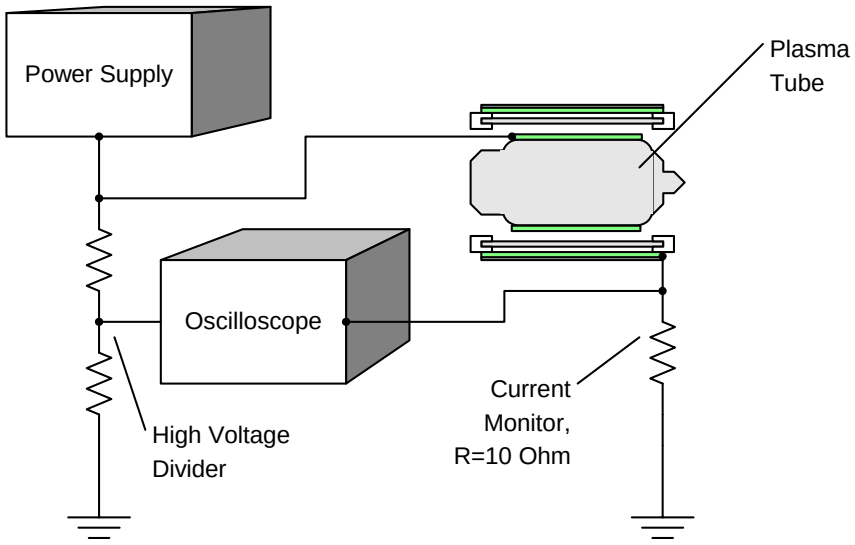

Figure 5: Test setup.

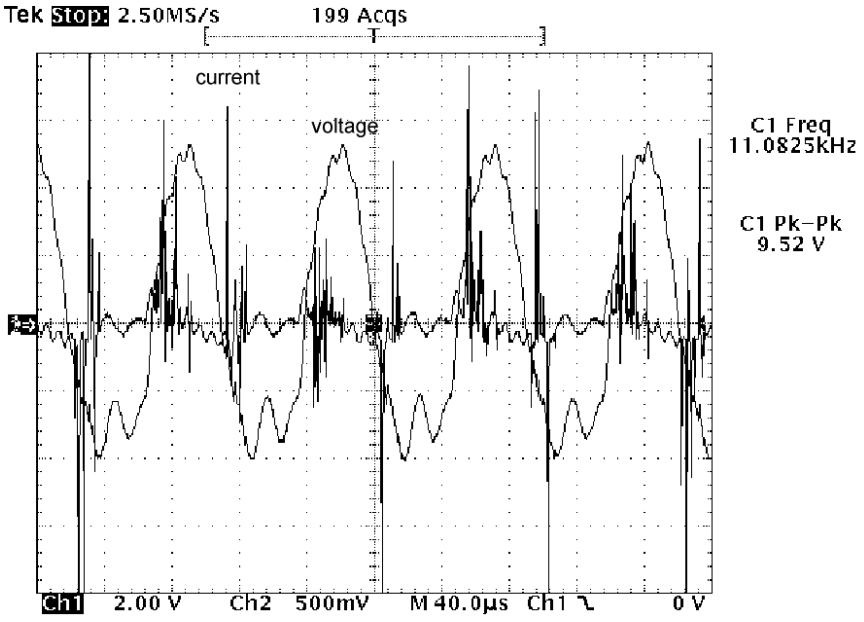

Figure 6: Voltage and current waveforms, voltage signal scale is 1 [kV]/div, current signal scale is 20 [mA]/div.

remote on/off switch.

3. Summary

The power supply described in this paper was designed for driving the PACT reactor. Therefore the capability of the driving system can be judged by the performance of the PACT tube. As reported in [3], the PACT system working with the power supply designed in Trek is very effective in perfluoro-compounds (PFC) decomposition (Figure 7). PFCs are widely used in semiconductor device fabrication processes, especially during etching and cleaning. These compounds are long-lasting agents that are believed to be contributors to the "greenhouse effect". For example, the maximum decomposition rate of $c - C_4F_8$, as shown in Figure 7, was 40%. Voltage and frequency adjustments allow for optimization of the plasma environment inside the reactor. In this way the decomposition rate of pollutants and contaminants can be also optimized. Other parameters of the power supply designed for the PACT tube can be also conveniently altered, if needed, to drive broad variety of pulsed plasma reactors. The efficiency of the plasma power supply described in this work was found to be around 90%.

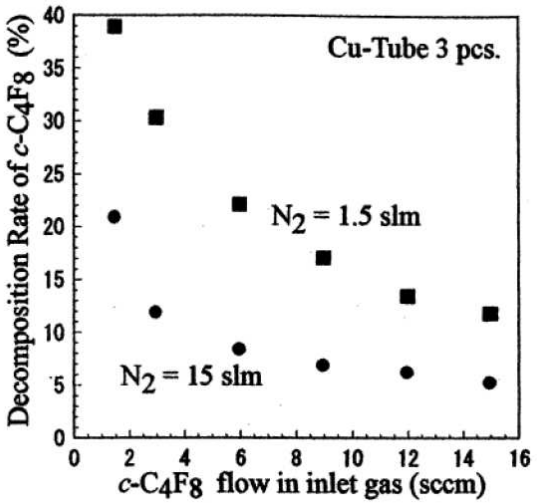

Figure 7: Decomposition rate dependence on $c - C_4F_8$ flow rate at $N_2 = 1.5$ slm or 15 slm [3].

Acknowledgment

Authors would like to thank Dr. Yuji Hayashi for supplying results of the PACT reactor tests.

References

[1] H. Conrads, M. Schmidt,"Plasma Generation and Plasma Sources", Plasma Sources Sci. Technol., **9**,(200), pp. 441-454.

[2] TL598C, TL598Q, TL598M, TL598Y pulse-width-modulation control circuits, Texas Instruments datasheet, 1995.

[3] A. Egami, Y. Hayashi, T. Kikuchi, K. Ishikawa and M. Nakamura, "Decomposition mechanism of $c - C_4F_8$ in plasma assisted catalytic technology (PACT)", Proceedings of the 2002 Dry Process International Symposium, Tokyo University, Tokyo, Japan, October 10-11, (2002), pp. 243-248.

Investigations of Plasma-sprayed hydroxyapatite coating on titanium alloy Reinforced by ZrO_2

Yung-chin Yang

Department of Materials and Mineral Resources Engineering,
National Taipei University of Technology, Taipei 106, Taiwan, R. O. C.

Abstract

The cohesive and adhesive strengths of plasma-sprayed hydroxyapatite coatings (HAC) were strengthened by respectively, adding ZrO_2 particles as a reinforcing second phase (HA+ZrO_2 composite coating), and using an intermediate ZrO_2 layer between the HA coating and the Ti alloy substrate as a bond coat (two-layer HA/ZrO_2 coating). Results indicate that the bond strength of the HA coatings increases from 28.6±3.2 MPa for HA coating to 32.5±4.2 MPa and 36.2±3.0 MPa for HA+ZrO_2 and two-layer HA/ZrO_2 coatings, respectively.

1. Introduction

Among the methods of fabricating HA coatings on metallic implants, plasma-spraying technique appears to be most favorable [1]. It has been well documented that plasma-sprayed coatings suffers from the low adhesion between coating and substrate, as well as the low cohesion within the coating [2]. Failure of the HA-coated Ti alloy implants during in vivo testing can happen (1) at the HA/bone interface, (2) inside the lamellar splat layer of coatings, or (3) at the HA/Ti alloy substrate interface. In evaluating the performance and stability of HA coating in the load-bearing situation after long-term follow-up, researchers suggested the presence of a potentially weak HA/substrate interface or cohesive failure within the coating, rather than at the HA/bone interface [3,4]. One method to improve the weak lamellar splat layer of the coating is to strengthen the microstructure of HA through plasma spray processing, but a second phase can also be added as reinforcement for the same purpose. The improved coating microstructure should be conducive to the enhancement of the cohesive strength, i.e., the strength of the intra- and inter-lamellar bonding of the HA coating. The increase of cohesive strength may also contribute to the strength of the adhesion of the plasma-sprayed HA to titanium. Alternatively, an intermediate bonding layer can be placed between the brittle HA and the substrate to promote their adhesive bonding to the HA/Ti alloy interface. This study aims to elucidate the dominant mechanical weakness in plasma-sprayed HA coating: the adhesion between coating and substrate, or the cohesion within the coating.

2. Experiments

2.1. Specimen fabrication

Powders with compositions of (1) hydroxyapatite (HA powder), (2) zirconia (TZ8Y powder), and (3) mixed 90 wt% hydroxyapatite + 10 wt% zirconia (HA+ZrO_2 powder) were used in the current study. As-sintered HA+ZrO_2 powder suitable for plasma spraying with particle size 74~125 μm was produced using the following

procedure. HA and TZ8Y powders were mixed in a zirconia ball mill using ethyl alcohol as medium. The resulting slurry was vacuum dried, crushed, and ground by pestle and mortar. The mixed powders were then granulated with 10 wt% of aqueous PVA solution (conc. at 5 wt%), and sieved to the desired particle size. Finally, the granulated powders were heated at 600°C for 1h to volatilize the PVA binder and sintered at 1000°C for 4h to consolidate the particles. As-sintered HA and TZ8Y powders were agglomerated and sintered similarly to yield a particle size of 125~177 μm.

As-sintered HA+ZrO_2 powder was plasma sprayed onto the Ti-6Al-4V titanium alloy. Accordingly, plasma-sprayed HA+ZrO_2 composite coatings (abbr. HA+ZrO_2 coating) were fabricated on Ti-6Al-4V substrates with a thickness of 150 μm. Another coating system studied here was the introduction of a plasma-sprayed ZrO_2 bond coat on Ti-6Al-4V substrate prior to the deposition of HA. The thickness of ZrO_2 bond coat was 15 μm and the total thickness of two-layer HA/ZrO_2 coating (abbr. HA/ZrO_2 coating) was 150 μm. The detailed spray parameters are listed in Table 1. Slightly higher power was used for the HA+ ZrO_2 coating and the ZrO_2 bond coat compared to the HA coating since the former coatings exhibit higher melting points.

2.2. Materials characterization

The HA+ZrO_2 coating (nominal thickness: 150 μm) was removed mechanically from the Ti-6Al-4V substrate and pulverized. The powders, mixed with pure silicon as external standard, were subjected to X-ray diffraction analysis (XRD) for phase identification (Rigaku D/MAX III.V, CuKa radiation). The morphology of the coating surface, the cross-sectional microstructure and the chemical composition were examined by scanning electron microscopy (SEM) (Philips XL-40 FEG) in conjunction with an energy dispersive X-ray spectrometer (EDS) system.The XRD analyses for phase identification of ZrO_2 bond coat and HA top coat of the HA/ZrO_2 coating were carried out as in the case of HA+ZrO_2 coating, and so were the SEM investigation. Moreover, the surface roughness of the grit-blasted Ti-6Al-4V alloy and the ZrO_2 bond coat were evaluated by Surfcorder SE-40D, Kosaka Laboratory Ltd.

2.3. Bond strength testing and fracture surface investigation

Bond strength was measured using a tensile test (ASTM C633-79) especially designed for plasma-sprayed coatings. Each test specimen was comprised of a substrate rod, to which the HA+ZrO_2, HA/ZrO_2, and HA coatings were applied, and a loading rod. The facing of the loading rods were then grit-blasted and attached to the surfaces of coatings using a special adhesive-bonding glue (METCO EP-15). The segments were held perpendicularly and put into an oven at 180°C for 2h. The couples were then subjected to tensile tests at a constant cross-head speed of 0.02 mm/s until failure. For each testing material, ten specimens were used, and the bond strength data were reported as the average values. To characterize the fractography, the optical pictures of the fracture surfaces for bond strength specimens from HA, HA+ZrO_2 and HA/ZrO_2 coatings on the Ti-6Al-4V substrates were analyzed by the OPTIMAS 6.0 software.

3. Results

3.1. Coating characterization

Fig. 1(a) shows the X-ray diffraction spectrum of as-sintered HA+ZrO_2 powder pre-mixed with pure silicon. The XRD pattern is characteristic of hydroxyapatite in accordance with the standard XRD spectrum (JCPD 9-432). In addition, peaks of cubic ZrO_2 are present as indicated by the symbol F (JCPD 30-1468). The result of the XRD analysis of the pulverized plasma-sprayed HA+ZrO_2 coating on the Ti-6Al-4V substrate is shown in Fig. 1(b). The XRD pattern of Fig. 1(b) retains the characteristics of Fig. 1(a) except that a few extra small peaks occur at approximately 30.71° and 37.52° (2θ). These extra peaks belong presumably to α-tricalcium phosphate (α-TCP, JCPD 9-348) and calcium oxide (CaO, JCPD 37-1497), respectively.

Fig. 2 shows the XRD spectra of as-sintered ZrO_2 powder (Fig. 2(a)) and as-sprayed ZrO_2 bond coat on the Ti alloy substrate (Fig. 2(b)). No phase change occurred in the cubic ZrO_2 during the plasma-spraying process (JCPD 30-1468). The appearance of Ti (101) and Ti (002) peaks in the Fig. 2(b) is caused by the penetrating X-ray beam. Fig. 3 shows the XRD spectra of as-sintered HA powder (Fig. 3(a)) and as-sprayed HA top coat deposited upon the bond coat (Fig. 3(b)). From Fig. 3(a), it is obvious that a well-crystallized HA powder suitable for plasma spraying was obtained after the sintering and consolidating processes, in which the decomposition of HA was not observed. However, similar to the case of spraying HA+ZrO_2 coatings, traces of α-TCP, tetracalcium phosphate (TP) and CaO are present in the HA top coat as shown in Fig. 3(b).

The surface roughness of the ZrO_2 bond coat is 5.7 ±0.2 μm, while that of grit-blasted Ti-6Al-4V substrate is 3.6±0.1 μm only. Hence the ZrO_2 bond coat provides a rougher surface than that provided by grit-blasted Ti-6Al-4V for the deposition of HA in the HA/ZrO_2 coating.

Typical SEM surface morphologies of the plasma-sprayed HA/ZrO_2 coating and the HA+ZrO_2 coating are shown in Fig. 4. Comparison of the surface morphology shows that the ZrO_2 containing HA+ZrO_2 coating exhibits more unmelted small particles than does the HA top coat in the HA/ZrO_2 coating. It reveals that the melting conditions in HA+ZrO_2 coating are poorer than that of the HA coating using the present plasma-spraying parameters. SEM cross-sectional views with EDS analysis of the HA/ZrO_2 and HA+ZrO_2 coatings on Ti-6Al-4V substrates are shown in Figs. 5, and 6, respectively. From the result of EDS Zr mapping in Fig. 6(b), it reveals that the ZrO_2 particles are distributed in the HA+ZrO_2 coating.

3.2. Bond strength measurements and fracture surface investigation

The bond strength data measured by the adhesion test according to ASTM C633-79 are listed in Table 2, where each value in the table represents the average of ten data. It is found that the bond strength increases from 28.6±3.2 MPa for the HA coating to 36.2±3.0 MPa for the HA/ZrO_2 coating, whereas the value for the HA+ZrO_2 coating is intermediate at 32.5±4.2 MPa. The results verified by a statistical *t-test* reveal that the bond strength obtained in each coating is significantly different from the others ($p < 0.005$).

The morphology of the fracture surfaces of the bond strength specimens after the ASTM C633-79 test is shown

in Fig. 7. Figs. 7(a), (b) and (c) represent the typical failure morphology of HA, HA+ZrO_2 and HA/ZrO_2 coatings on the Ti-6Al-4V substrate, respectively. The site that is characteristic of adhesive failure (ad) is indicated by an arrow as shown in Fig. 7(c), and so is the site of cohesive failure (co). The area percentage of adhesive failure in each coating was calculated according to the image analysis and reported as the average of data from ten specimens (Table 2).

Addressing the potential weakness of the HA/Ti alloy interface [3,4], some researchers have suggested to introduce a bond coat between the HA coating and the Ti alloy substrate to improve the adhesion [5,6]. In our present study, the bond strength of the HA coating was increased from 28.6±3.2 MPa to 36.2±3.0 MPa by application of a ZrO_2 bond coat (Table 2). The area percentage of adhesive failure in a HA/ZrO_2 coated Ti-6Al-4V substrate was estimated to be 15.8±3.8 %. The reduction of adhesive failure in HA/ZrO_2 coatings as compared to that in HA coatings (26.8±5.2 %) indicates that the adhesive strength of a HA coating is reinforced by the introduction of a ZrO_2 bond coat. Furthermore, higher bond strengths obtained in the HA/ZrO_2 coatings than in the HA+ZrO_2 coatings indicate that the enhancement of the adhesion between the HA coating and the Ti alloy substrate is more important than the strengthening of the HA coating per se. Namely, the HA coating/Ti alloy interface is a site of critical weakness when compared to the cohesive strengths of the inter- and intra-lamellar structure of HA coating. However, it should be noted that both cohesive strength, i.e. the strength of intra- and inter-lamellar bonds of the HA coating, and the adhesive strength of the HA coating to the substrate will influence the bond strength of the HA coating on the titanium implant.

The strengthening effect of the HA/ZrO_2 coating is believed to arise from the following mechanisms: (1) the promotion of mechanical interlocking between the coating and the metal substrate. It is obvious from Table 2 that a rougher surface morphology was provided by the ZrO_2 bond coat for the deposition of the HA top coat. (2) the elemental interdiffusion between HA top coat and ZrO_2 bond coat [7], which might also promote the bonding.

4. Conclusions

The bond strength of HA coatings on Ti alloy substrates can be improved from 28.6±3.2 MPa to 32.5±4.2 MPa with ZrO_2 particles added as a reinforcing second phase, to 36.2±3.0 MPa with a ZrO_2 intermediate layer applied as a bond coat. A possible strengthening mechanism of the two-layer HA/ZrO_2 coating is the rougher surface provided by the ZrO_2 bond coat, which promotes a better mechanical interlocking between the HA top coat and the ZrO_2 bond coat. The cohesive strength of HA coatings can be reinforced by ZrO_2 particles and hence the improved cohesive strength will contribute to the bond strength of the HA coating on Ti-substrate. However, other mechanism of a reduction of the CTE mismatch stress between the HA+ZrO_2 coating and the Ti-6Al-4V substrate can not be excluded. The interface of the HA coating/Ti alloy substrate is a site of critical weakness when compared to the cohesive strength of the inter- and intra-lamellar structure of HA coating.

5. References

[1] F. Brossa, A. Cigada, R. Chiesa, L. Paracchini, C. Consonni, Biomed. Mater. Eng. 3 (1993) 127-136.

[2] Ö. Ünal, D. J. Sordelet, Scripta Materialia 42 (2000) 631-636.

[3] K. Hayashi, T. Inadome, T. Mashima, Y. Sugioka, J. Biomed. Mater. Res. 27 (1993) 557-563.

[4] B. C. Wang, T. M. Lee, E. Chang, C. Y. Yang, J. Biomed. Mater. Res. 27 (1993) 1315-1327.

[5] Y. C. Tsui, C. Doyle, T. W. Clyne, Biomaterials 19 (1998) 2031-2043.

[6] D. Lamy, A. C. Pierre, R. B. Heimann, J. Mater. Res. 11 (3) (1996) 680-686.

[7] B. Y. Chou, E. Chang, Interface investigation of plasma-sprayed hydroxyapatite coating on titanium alloy with ZrO_2 intermediate layer as bond coat, Scripta Materialia 2001, accepted.

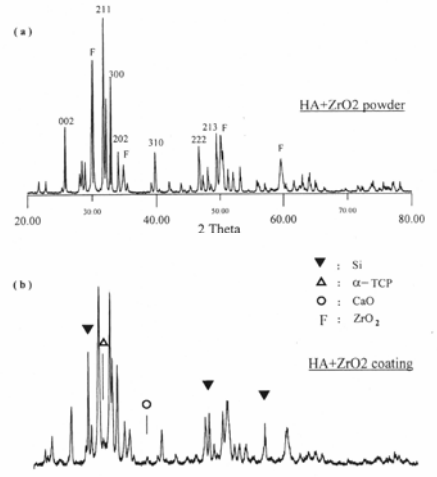

Fig. 1 X-ray diffraction patterns of (a) as-sintered $HA+ZrO_2$ powder, and (b) $HA+ZrO_2$ coating.

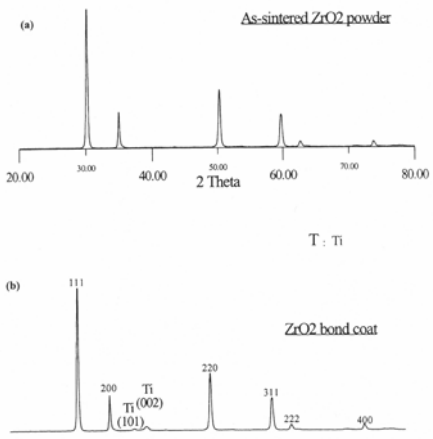

Fig. 2 X-ray diffraction pattern of (a) as-sintered ZrO_2 powder, and (b) as-sprayed ZrO_2 bond coat of the HA/ZrO_2 coating.

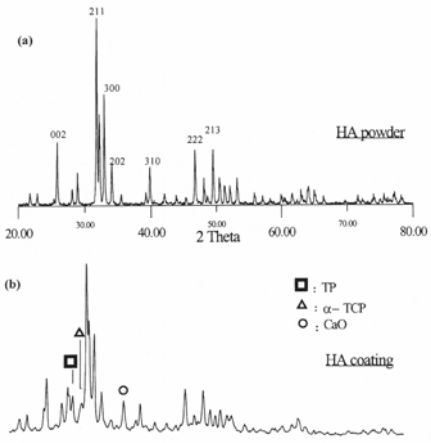

Fig. 3 X-ray diffraction patterns of (a) as-sintered HA powder, and (b) as-sprayed HA top coat of the HA/ZrO_2 coating.

Table 1 Plasma-spraying parameters employed for preparation of the coatings in the present study

	Coatings	
Parameters	HA	$HA+ZrO_2$
Primary gas, flow rate (l/min)	Ar, 41	Ar, 41
Secondary gas, flow rate (l/min)	H_2, 8	H_2, 10
Powder carrier gas, flow rate (l/min)	**Ar, 3**	Ar, 3
Powder feed rate (g/min)	33	33
Power (kW)	40.2	42
Stand-off distance (cm)	7.5	7.5
Surface speed (cm min^{-1})	8000	8000
Traverse speed (cm min^{-1})	60	60

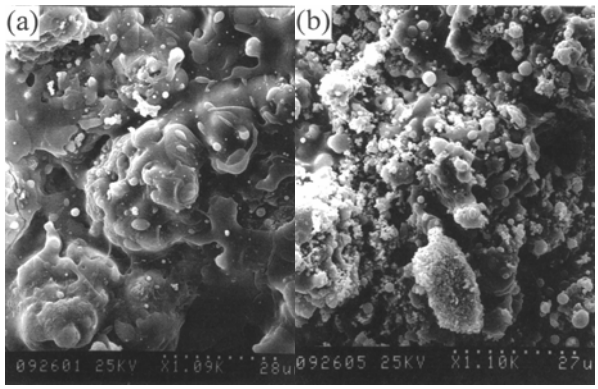

Fig. 4 SEM surface morphologies of plasma-sprayed (a) HA/ZrO_2 coating, and (b) $HA+ZrO_2$ coating.

Table 2 Results of bond strength measurements and corresponding area percentage of adhesive (ad) failure

Coatings	Bond strength (MPa)	Ad failure(%)
HA coating	28.6 ± 3.2	26.8 ± 5.2
HA+ZrO_2 coating	32.5 ± 4.2	36.2 ± 4.3
HA/ZrO_2 coating	36.2 ± 3.0	15.8 ± 3.8

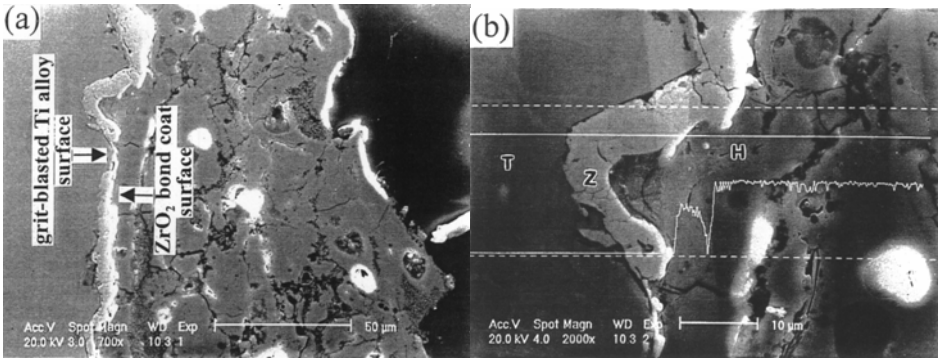

Fig. 5 SEM cross sectional microstructure of plasma-sprayed (a) HA/ZrO_2 coating, and (b) high magnification of (a) with EDS line scan of Ca distribution. T, Z and H denote grit-blasted Ti alloy, ZrO_2 and HA, respectively.

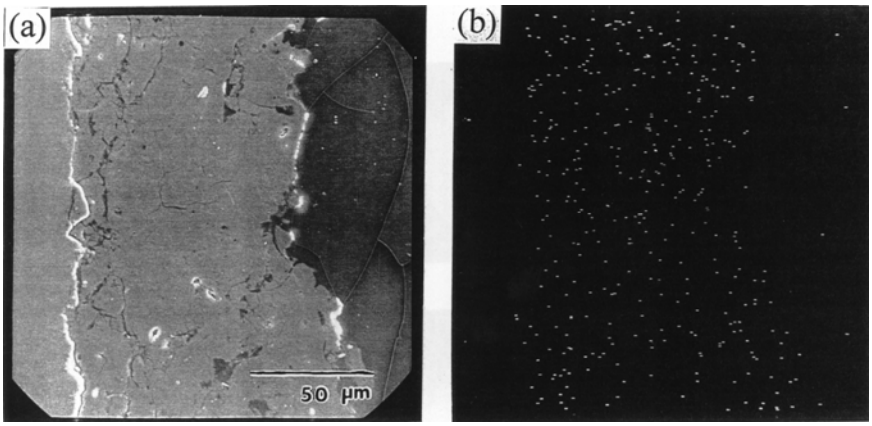

Fig. 6 SEM cross sectional microstructure of plasma-sprayed (a) HA+ZrO_2 coating, (b) EDS mapping of Zr distribution in (a).

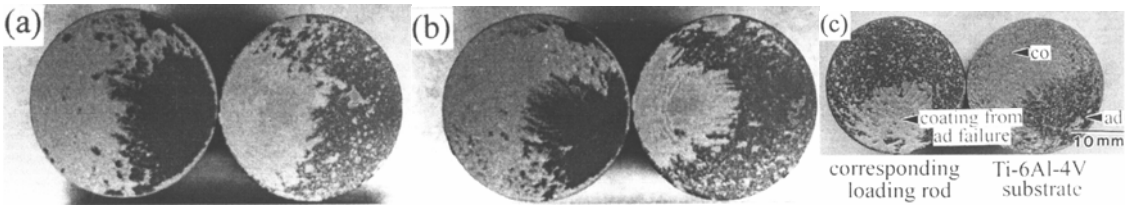

Fig. 7 Morphology of fracture surfaces of coatings on Ti-6Al-4V substrates after the ASTM C633-79 test: (a) HA coating, (b) HA+ZrO_2 coating and (c) HA/ZrO_2 coating.

Deposition of TiC Film on Ti Substrate by Ion-Enhanced Triode Plasma CVD Using $TiCl_4+CH_4+H_2$

M.Shimozuma[1], YH.Zhu[2], H.Date[1], M.Yoshino[3] and F.Watari[2]

[1]*Department of Health Sciences, School of Medicine, Hokkaido University, Sapporo, Japan*
[2]*Graduate School of Dental Medicine, Hokkaido University, Sapporo, Japan*
[3]*Hokkaido Polytechnic College, Otaru, Japan*

Abstract

Deposition of Titanium Carbide (TiC) layer on Ti surface has been demonstrated by means of an ion-enhanced triode plasma chemical vapor deposition (CVD) method using a $TiCl_4+CH_4+H_2$ gas mixture. The plasma reactor used was equipped with a triode system, in which a substrate bias circuit with two diodes is employed to accelerate the deposition through ion bombardment processes. The deposition rate of the TiC film was 2.5 μm/h at T_{sub} = 750 ℃ with the bias voltage V_b = -400 V. The Vickers hardness of the film was about 5500 Hv. The X-ray diffraction pattern suggested that the deposited TiC film is in a state of TiC crystal with (111) , (200) and (220) orientations.

Keywords Titanium Carbide (TiC), Plasma CVD, Hard coating, Ion-enhanced triode plasma CVD, Biomedical instruments

1. Introduction

Titanium Carbide (TiC) is a useful material for biomedical instruments, such as an abrasion resistant implant material, and surface hardening of cutting tools because of its properties which include high surface hardness, good corrosion resistance and low friction coefficient. Usually, TiC films are produced by the techniques of physical vapor deposition (PVD), thermal chemical vapor deposition (CVD) and plasma vapor deposition (PCVD). However, these methods need the substrates for deposition to be high-temperature (>1000℃) , which sometimes causes thermal damage to the deposited films. Therefore, it is desirable to develop a deposition technique using low-temperature (<800℃) substrates preventing the films from the thermal damage.

In this study, we demonstrate TiC film deposition on titanium (Ti) substrate at about 750℃ by an ion-enhanced triode plasma CVD method using a $TiCl_4+CH_4+H_2$ gas mixture. The production characteristics of the TiC films are investigated in the low frequency of power from 50 to 200Hz and the bias voltage (V_b) ranging from -100 to -400V with the triode technique. We have observed the Vickers hardness and the X-ray diffraction pattern of the TiC films. In addition, the optical emission spectra of the plasmas near the heated substrate (T_{sub} = 750 ℃) have been measured to make clear the state of the dissociated atoms and molecules in the $TiCl_4$ (5%) + CH_4 (10%) + H_2 (85%) mixture plasmas.

2. Experimental details

The experimental apparatus is similar to that of Ref.[1] and shown schematically in Fig.1. The cylindrical plasma reactor is 40 cm in diameter and 40 cm in height. Before the deposition, the reactor is evacuated to

about 1×10^{-5} Torr by a diffusion pump subsidized by a rotary pump. While the deposition is in progress, the evacuation is made by the rotary pump only, and the total pressure in the reactor is monitored by a Baratron pressure gauge. A pair of plane electrodes is made of 10 cm-diameter stainless steel and the gap length between the electrodes is 5 cm. The low frequency (50 to 200 Hz) power is supplied to the upper electrode, while the lower electrode is grounded. The stainless steel rod connected with the heater is inserted into the middle of the inter-electrode gap. The rod is electrically insulated from the grounded reactor and is negatively biased (about both the electrodes) by the diode circuit connected to it. The cubical substrate of stainless steel [2] which mounts Ti tips is attached to the rod heater. The Ti tips are in size of about 10 × 10 mm and 1mm thickness. The tips are cleaned beforehand by the ultrasonic cleaner using acetone and alcohol.

The plasmas between the upper electrode and the center rod and between the lower electrode and the center rod are driven alternately by the diode circuit, and these are generated symmetrically with respect to the substrate rod. Various negative bias voltages are applied to the substrate rod, and the potential energy of positive ions in the plasmas can be controlled by the bias voltage.

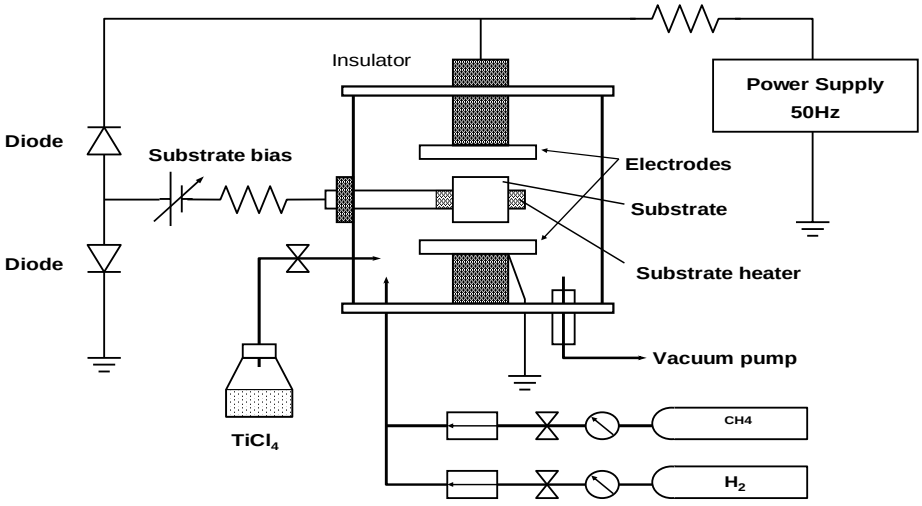

Fig. 1 Schematic diagram of the ion-enhanced triode plasma CVD apparatus.

The substrate temperature T_{sub} is measured by the thermocouple in the rod heater. The gases used are $TiCl_4$ (99.9 %), CH_4 (99.9 %) and H_2 (99.999 %), and these are introduced into the reactor at flow rates of 10-15 sccm, 25 sccm and 250 sccm, respectively. Before the deposition, Ti substrate is heated to a temperature around 750 ℃ by the rod heater, and the $TiCl_4 + CH_4 + H_2$ mixture gas is put into the reactor. The substrate temperature is kept 750 ℃ constantly throughout the entire course of the work. Deposition parameters for TiC films in this work are listed in Table 1.

We estimate the deposition rate of the TiC film by using a surface profile recorder. The Vickers hardness of the deposited TiC films is measured by a micro-Vickers hardness tester. The preferred orientation of the deposited film is evaluated by the X-ray diffraction (XRD) method. Optical emissions from the plasmas are observed using a Photonic Multi-Channel Analyzer (PMA, Hamamatsu C7473) connected to the plasma reactor. The PMA has an adequate sensitivity in the wavelength from 200 nm to 800 nm. The light guide window is made of quartz plate.

Table 1. Deposition conditions

Plasma power	20 - 50W
Power frequency	50 - 200 Hz
Plasma current	50 - 100 mA
Gap length	5 cm
Pressure	1Torr
Substrate temperature T_{sub}	700-800℃
Gas flow rate: $TiCl_4$	10 – 15 sccm
CH_4	25 sccm
H_2	250 sccm
Bias V_b	-200 - 400 V
Substrate	Ti

3. Results and discussion

3.1 Photo-emission from the $TiCl_4$+CH_4+H_2 mixture plasma

In order to investigate the composition of the dissociated atoms and molecules in the $TiCl_4$+CH_4+H_2 plasmas, optical emissions from the plasma near the heated substrate (T_{sub} = 750) were observed. Figure 2 shows a typical emission spectrum from the $TiCl_4$ (5%) + CH_4 (10%) + H_2 (85%) mixture plasma. Emissions from Ti^+, CH and H were clearly identified, and this indicates that $TiCl_4$, CH_4 and H_2 were decomposed into those particles. The $TiCl_4$ molecules are possible to be decomposed into a variety of other particle species such as TiCl, $TiCl_2$, $TiCl_3$, and Cl, but the emissions from these species were not observed. The emission from C atom might have occurred below 200 nm wavelength (100 to 150 nm) [9].

It is expected that the ions are accelerated to reach the substrate surface and to collide with it by the negative bias during a relatively long term of the low frequency cycle, which must be difficult in rf plasma reactors.

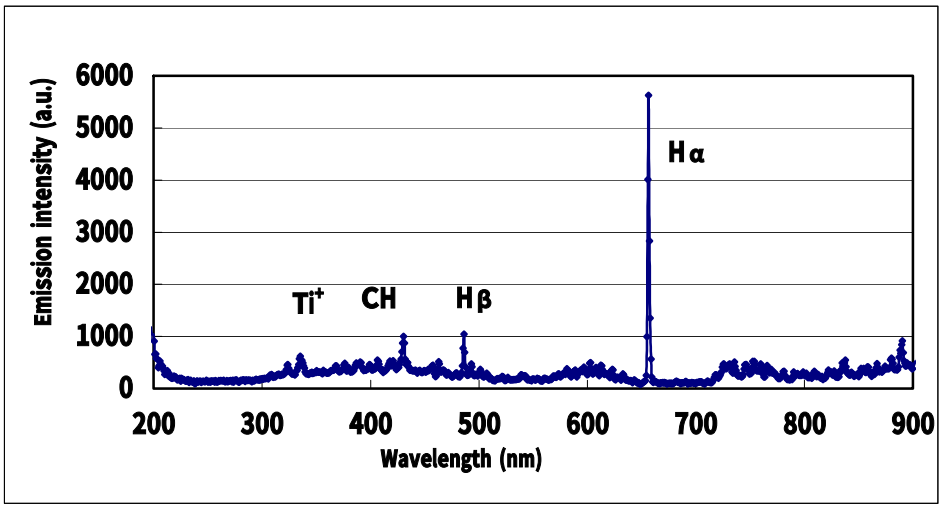

Fig. 2 Emission spectrum from the $TiCl_4$ (5%) + CH_4 (10%) + H_2 (85%) mixture plasma.

3.2. Deposition rate of the TiC

The deposition rate of the TiC film was measured by a surface profile recorder. Figure 3 shows the deposition rate on the substrate bias voltage V_b. The deposition rate of the TiC film increases from 0.2 μm/h to 1.7 μm/h as decreasing V_b from -100 to -400V with a condition of the plasma current 50mA (input power is about 25W). The thickness of deposited TiC film at the plasma current 100mA with V_b = -400V was about 5μm

for two hours deposition period of time. The TiC film around 5μm thickness can be used for surface hard coating of biomedical instruments and cutting tools. The deposition rate of TiC films in this method is greater than that of the pulsed laser deposition method (0.22μm/h) [3].

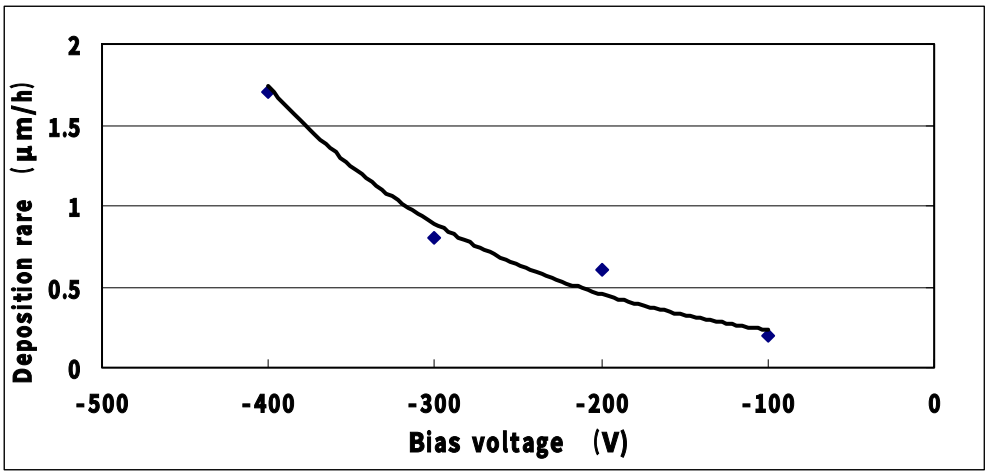

Fig. 3 Deposition rate of the TiC film against bias voltage at plasma current 50mA.

3.3. Vickers hardness of TiC

The Vickers hardness of the deposited TiC films on Ti tips was measured by a micro-Vickers hardness tester with a load of 10-200gf (gram-force). As shown in Fig .4, the Vickers hardness of the TiC film increases up to the value of about 5000 Hv (at V_b = -400 V and 25gf) as V_b decreases. The present value of the Vickers hardness for TiC is higher than that produced by thermal CVD or PVD method. Figure 5 shows that the Vickers hardness value of the film at 5μm thickness decreases with an increase in the lord. The TiC film on Ti was cracked by a load of more than 300gf. The Vickers hardness of the deposited TiC films at 750 ℃ with bias voltage V_b =–400V was above 3500Hv with a lord of 100gf, which is equivalent to the value of stoichiometric TiC's. This high value of the hardness may be attributed to the present unique plasma process in which the substrate potential is always lower than that of both (upper and lower) electrodes at every half cycle, causing the positive ions in the plasma to hit the substrate of the negative potential. We suppose that the bombardment energy of ions is consumed by the migration for giving rise to rearrange the atoms deposited on the substrate surface leading to a denser material layer.

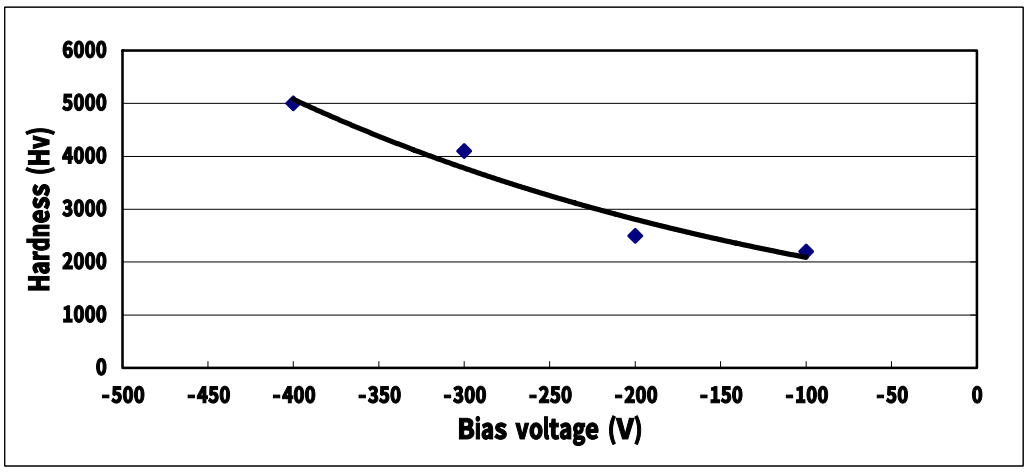

Fig. 4 Vickers hardness of the TiC film against bias voltage at plasma current 50mA.

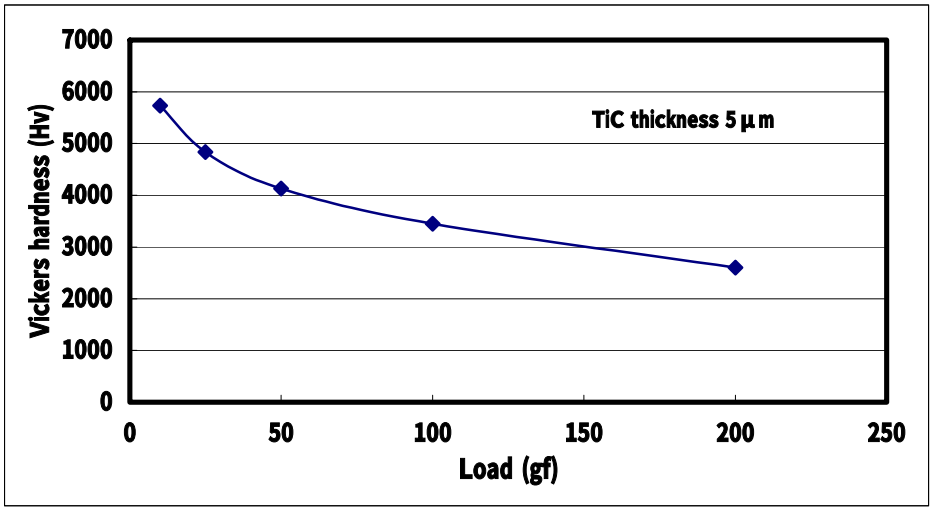

Fig. 5 Vickers hardness of the TiC film against load.

3.4. Crystal structure

The crystal structure of the deposited TiC films was determined by the X-ray diffraction (XRD) method. The XRD pattern originating from the deposited TiC on Ti substrate is shown in Fig.6. Peaks of Ti from bulk Ti substrate and of TiC from deposited TiC film appear in the XRD pattern. The pattern for TiC suggests that the film contains TiC crystal with TiC(111), TiC(200) and TiC(220) orientations. The peaks representing these orientations are in about 2.0 degrees of FWHM, while the peaks for Ti are sticking out sharply. The diffraction peak pattern for C atom was not observed, suggesting that the TiC film has a good crystal structure. From the observation of a SEM micrograph, it was confirmed that the deposited TiC film possesses a very flat surface.

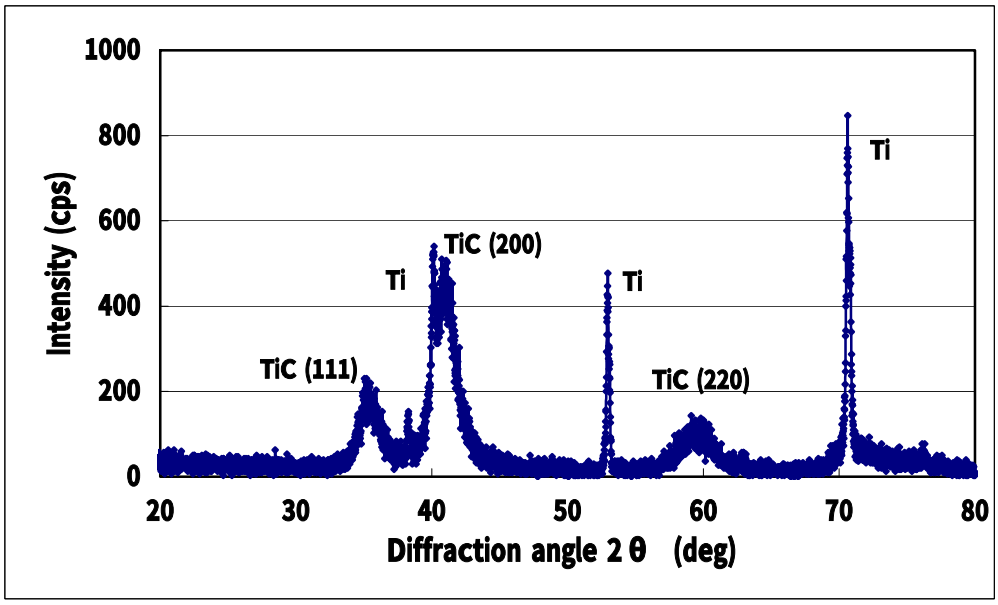

Fig. 6 X-ray diffraction pattern of deposited TiC film on Ti substrate.

4. Conclusion

In this study, the deposition of TiC films on Ti substrate was demonstrated by the triode low frequency plasma technique with the gas mixture of $TiCl_4$+CH_4+H_2. The deposition rate and the Vickers hardness of the

deposited TiC were 2.5 μm/h and 5000 Hv, respectively, at a substrate temperature of T_{sub} = 750 ℃ with a bias voltage V_b = -400 V and a plasma current 100mA

X-ray diffraction (XRD) spectra suggested that the deposited TiC film contains the preferred orientations of TiC (111), TiC(200) and TiC(220). It was confirmed from observation of the SEM micrograph that the deposited TiC film has a very flat surface.

We reached the conclusion that the Vickers hardness above 5000Hv can be achieved even under a relatively low–temperature condition by taking advantage of the negative-bias circuit with two diodes. In this system, the substrate potential is always lower than those of the upper and lower electrodes at every half cycle, which enables the substrate to attract positive ions by the negative potential enhancing the deposition process. It was conjectured that the bombarding energy of the ions to the substrate is consumed by the deposited atoms for rearranging the state of the surface structure.

Acknowledgements

The authors wish to thank Dr. K. Satoh for many helpful discussions and useful suggestions.

References

[1] M. Yoshino, M.Shimozuma, H.Date, A.Rodrigo and H.Tagashira: Jpn. J. Appl. Phys., 39, 1299 (2000)

[2] M. Shimozuma, H. Date, T.Iwasaki, H. Tagashira, M. Yoshino, and K.Yoshida: J. Vacuum Science & Tech. A, 15, 1897 (1997)

[3] Y.Suda, H.Kawasaki, C.Cho, A.Grishin and V.rao: Jpn. J. Appl. Phys., 39, 4575 (2000)

Wetchemical surface modification of medical PVC by remote argon plasma

Li Ru [a,c] Li ke[b] Chen Jie-rong [a]

[a] *Environment &Chemical Engineering institute, Xi'an Ji aotong University, Xi'an 710049, China*

[b] *Peking University Health Science Center, Beijing 100083, China*

[c] *College of environmental and chemical engineering, Xi'an University of Engineer Science Technology, Xi'an ,710048 ,China*

Abstract

The paper study surface modification of medical PVC by remote argon plasma and analyze surface structure, performance of treated material by contact angle measurement, SEM and XPS. Relative concentration of free radicals of treated material analyzed by ESR. The result shows, The surface wettability and anticoagulant property of PVC film can be improved by remote argon plasma, it is advantaged to improved biocompatibility of medical PVC. Remote argon plasma can inhibit the ion and electron etching reactions and enhance free radicals reaction.

Keywords Remote Argon plasma; PVC; Surface modification; ESR

1.Introduction

Plasticized PVC films are used in biological and medical applications in storing of substances (e.g. blood and blood products, drugs and injectables), for catheters with antithrombogenic activity[1]. In these applications it is necessary to use materials having a morphology, a chemical composition, and a polarity of the surface which do not affect the biological environment.

Plasma treatment is a useful technique to study and develop biomedicine materials for its many merits, such as speediness, simplicity, sterilization, and ability to treat complex shape surface[2,3]. However, So far, researches about plasma surface modification have merely been limited to a mixed atmosphere constituted by all active species. The main reactions occurring on polymer surface in plasma are etching, cleaning, crosslinking, grafting and other chemical reactions dependent on the presence of active species in plasma[4]. How much do the different active species contribute to surface modification? Such perplexities occurred at plasma chemistry basic theory research and the key techniques in application haven't been seen whether in native or foreign reports yet.

Plasma contains highly activated species such as electron, ions, and radicals. Radicals can be isolated from the plasma because of their longer life-spans than electrons and ions (the rate constants of electron-positive ion recombination and radicals recombination are $10^{-7}cm^3/s$, and $10^{-33}cm^6/s$, respectively)[5]. High-concentration of radicals can be obtained at certain position away from the plasma source. When materials are positioned at a remote zone, uncontrolled rupture of large molecular chain caused by direct attack can be avoided, activated species interacted with samples are reduced, and the complexity of interface reactions between solid and gas are reduced. All of these make the surface modifying reaction (radical

reactions) dominant, while electron and ionic etching reactions are inhibited. Therefore, the control of a plasma reaction can be realized to a certain extent, and more desirable surface modification effect can be obtained, in contrast with conventional plasma treatment. The paper studied surface modification of medical PVC by remote argon plasma to obtain favorable surface performance.

2. Experimental part

2.1. Materials

Medical PVC film(20μm thickness, made by Blood Center of Shanghai) was cut into pieces of dimensions 20mm×10mm. Prior to the experiment, the sheet was washed with distilled water and dried naturally at room temperature.

2. 2. Remote plasma treatment

A self-designed reactor was used. In Fig. 1, we show the "Remote plasma" reactive system. The reactor includes four parts-gas inlet, reaction chamber, gas exhaust, power supply and matching network (SY-500W power supply and SP-Ⅱ matcher which are made in Chinese Academy of Science Micro-electronics Center). The reaction chamber is hard glass tube (length 1000mm, diameter 45mm), where inductance-coupling discharge is applied.

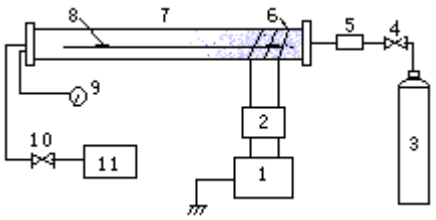

Fig. 1. Schematic structure of remote plasma reactor.

1.RF generator 2.Matching system 3.Gas bottle 4.Valve 5.Mass flowmeter 6.Inductance coil 7.Reaction chamber 8.Sample 9.Vacuum gauge 10.Electromagnetism valve 11.Vacuum pump

The PVC films were positioned on the carrier at a constant distance of 0, 20, 40, 60, and 80cm from the center of the inductance coil to distinguish remote plasma treatment from conventional plasma treatment (discharge zone). The purity of argon was more than 99.99%.

2.3 Contact Angle Measurement

The contact angle was measured by a contact angle meter (JY-82) made in Chengde, China. To lessen the effect of gravity, the volume of each drop was regulated to about 0.2cc by a micro syringe. The measurement was carried out at a 20℃ and humidity of 45% RH; the averaged value of the angles of the both sides of each drop was counted as one measurement. Each sample was measured at different points more than 10 times, and the contact angle was determined by their average values. The measurements were carried out immediately after plasma treatment.

2.4 X-ray photoelectron spectroscopy

X-ray photoelectron spectroscopy (XPS) (PHI5400ESCA, Perkin-Elmer USA) was used to analyze chemical compositions of surface layers of the PVC film at a pressure lower than 5×10^{-8}Pa; MgK_{α}(1256.6eV) X-ray was used as the source.

2.5 scanning electron microscopy (SEM)

The surface morphology of the PVC film was examined using scanning electron microscopy (SEM) in a JEOL instrument (Model JSM－5800, Japan) after vacuum coating the specimens with gold.

2.6 Electron spin resonance (ESR)

Crude wool washed is used as the trapping agent of free radicals in remote plasma field [6]. The wool is positioned on the carrier at a constant distance of 0, 20, 40, 60, and 80cm from the center of the inductance coil to be treated by remote argon plasma. Concentration of free radicals of surface layers is measured by Electron spin resonance (ESR) after 24h storage.

ESR spectra were recorded at room temperature (22-24℃) on a Bruker ESP-500E spectrometer Operating at 9.8GHz，x-band with 100kHz field modulation. The following instrumental settings were employed; microwave power 3.177mw; modulation amplitude 0.08G.

3. Results and discussion

3.1 concentration distribution of free radicals in remote argon plasma

The long life-span free radicals are formed at the polymer surface by the interaction between the polymer surface and the free radicals. When the power is 90W，treatment time is 3min，Ar flux is 20 sccm，figure 2 shows the ESR spectrum of wool of various remote distance.

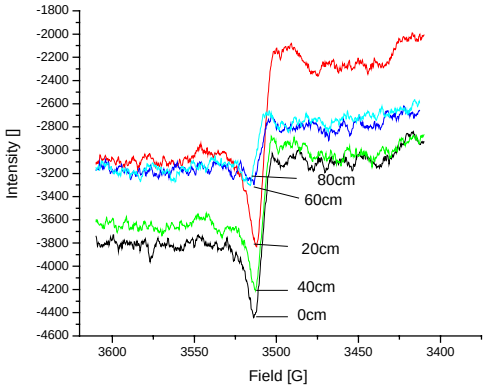

Fig.2 The ESR spectrum of wool of various remote distance (power: 90W; Ar flux: 20 sccm; treatment time:3min)

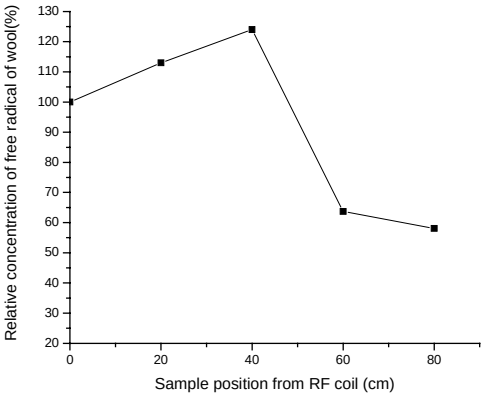

Fig. 3 Relative concentration of free radicals (c/c_0) on remote distance

As shown in figure 2, the samples at different remote distances appear absorb peak value of the same figures

but different intensity at the value of 3413.3g. It shows that all samples are the same kind of free radicals, but the remote distance effects the concentration of free radicals. As to a same kind of free radicals, the hight of absorb peak value can be used as its intensity, the rate(C/C_0) of the content of free radicals of samples(C) and of samples at a distance of zero(C_0) is used as the relative concentration. Relative concentration of free radicals (C/C_0) on remote distance is shown in fig.3. As it shows, with the increase of the remote distance, relative concentration of free radicals increases slowly at first and forms a zone of high concentration of free radicals and then decreases and tends to be stable at the remote distance of 80cm when the relative concentration of free radicals is still 58%. Therefore, there is a zone of comparative high concentration of free radicals in remote argon plasma which can enhance free radicals reaction.

3.2 etching of the surface of medical PVC by remote argon plasma

When plasma power is 60W, treatment time is 3 min, Ar flux is 20sccm, the SEM of plasma-treated PVC films are showed in fig.4. It can be known that compared with untreated samples the degree of etching of medical PVC film surface at discharge zone is very high. As the remote distance increases, the degree of etching of medical PVC film surface is weaken. There is only slight etching at the distance of 40cm and no etching at 60cm. It shows that in remote argon plasma, electrons and ions produced in discharge zone have strong etching action. But with the increase of the distance from discharge zone, electrons and ions annihilate quickly. Therefore, etching actions are inhibited in remote zone. As the distribution of concentration of free radicals in remote argon plasma shown above, Remote argon plasma can inhibit the ion and electron etching reactions and enhance free radicals reaction.

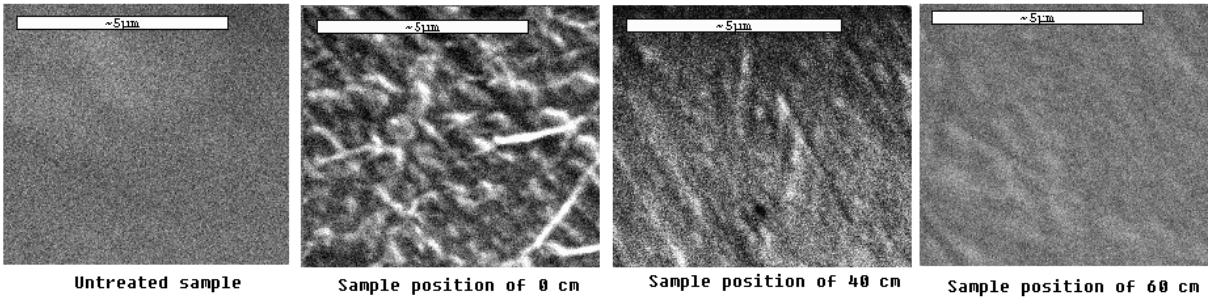

Fig. 4. Scanning electron micrograph of plasma-treated PVC film
(power:60W;treatment time:3min; Ar flux: 20 sccm)

3.3 Effect of plasma treatment conditions on the surface wettability of medical PVC

The research shows that if the surface of polymer is made to have strong wettability, the polymer will have good anticoagulant property and biocompatibility. We use contact angles to express the wettability of PVC surface to evaluate the biocompatibility of medical PVC surface modified by remote argon plasma.

When the treatment time is 3min and Ar flux is 20sccm, the effect of RF power and remote distance on the contact angles to water of PVC is shown in fig.5. Fig.5 shows that with the increase of discharge power , the contact angles of every sample all decreased rapidly from the untreated 109° （-20cm）. After it reaches

150W, it increases slightly, but the range of decrease is different in different distances. These curves implied that a quantity of argon molecule acquired more energy resulted from the increase of discharge power, so ionicity of argon and the average energy of active particles increased, and the reaction chance and intensity of active particles with PVC are further enhanced. so that the effect of surface modification is improved. However, after the power reaches 150W, ionicity of argon and the average energy of active particles increased, and the collision and recombination between activated species are accelerated. Therefore, the contact angles increased. The effect of discharge power on contact angles is similar to the result studied by Cooper and his colleagues [7].

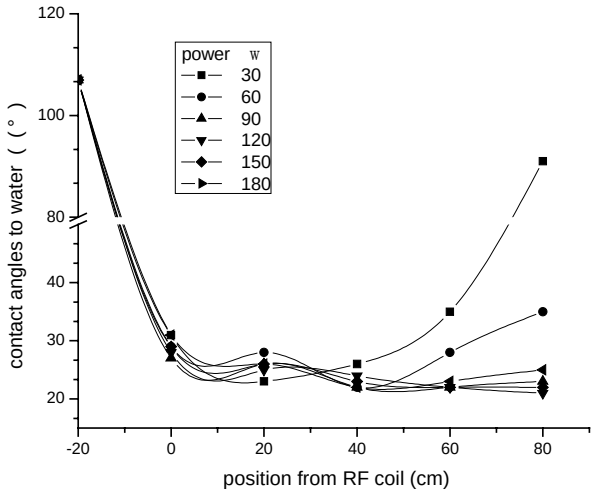

Fig.5 Effect of RF power on the contact angles to water of PVC
(treatment time 3min; Ar flux:20sccm)

3.4 chemical composition of the Surface of PVC

Table 1 The Atom concentration plasma modified PVC film

Sample	C_{1s}(%)	N_{1s}(%)	O_{1s}(%)	O+N/C
Untreated	82.66	0.39	5.55	0.072
Sample position of 0 cm	81.49	0.91	10.96	0.14
Sample position of 40 cm	79.17	2.99	14.69	0.223

The content of each group and O/C ratio are given in Table 1. The O/C ratio increases remarkably after treatment, especially in the remote area. That oxygen content increases shows that oxygen-containing and nitrogen-containing groups are introduced into the material surface, especially in the remote position. The oxygen content of samples is much higher than that of the discharge area. Thus, in the remote area, polarity and hydrophilicity of the surface increase more due to the intensified radicals reactions in the remote area.

Form the above, it can be seen that to enhance surface hydrophilicity of PVC, remote plasma treatment is more desirable than conventional plasma treatment.

4. Conclusions

Experimental results are summarized as follows:

(1) Both remote and conventional plasma can improve the surface of PVC film hydrophilic, but the increase of oxygen and nitrogen polar functional group on the surface of treated PVC by remote plasma is higher than conventional plasma. It shows that remote plasma treatment is more effective in surface modification.

(2) Surface modification effects depend on remote distance, discharge power, exposure time and argon flux. The optimal results was achieved when plasma treatment parameters were set, that was treatment time 3min, Ar flux at 20 sccm , power at 60W, Sample position of 40cm.

(3) Remote plasma treatment can enhance radicals reaction and inhibit electrons and ions etching reaction

Acknowledgements

The authors thank the financial support of the National Natural & Science Foundation Council of China, the specialized research Fund for the Doctoral Program of Higher Education, the Scientific Research Star Fund for the Study Abroad Returnee and the key Scientific Technique item of Shaanxi province. We are also grateful to every professor and assistant in the Microbiology Laboratory. We finally thank all the colleagues in Air Pollution Control Laboratory in Environmental & Chemical Engineering Institute of Xian Jiaotong University for their assistance in the preparation of the article.

References

[1] Chen K.-S.,Yang M.-R., He J.-L. The interaction between blood and the surface characteristics of plasma polymerized films. Materials Chemistry and Physics [J]. 48(1):71－75 (1997)

[2] Chung Yun M., Jung Min J. et al. Surface modification effects on film growth with atmospheric Ar/Ar+O_2 plasma. Surface and Coatings Technology [J]. 174-175:1038－1042 (2003)

[3] Kaczmarek Halina, Kowalonek Jolanta et al. Surface modification of thin polymeric films by air-plasma or UV-irradiation. Surface Science[J]. 507-510:883－888 (2002)

[4] L.Pekker . plasma chemistry model of DC magnetron reactive sputtering in Ar-O_2 gas mixtures. Thin Solid Films [J]. 312:341－347(1998)

[5] Chen Jierong, Yan Jingliang, Zhang Yunze. Surface modification of medical PVC by remote oxygen plasma Composite Interfaces. 11(2):123-130(2004)

[6] Chen Jie-rong， Study on Free Radicals of Cotton And Wool Fibers Treated with Low Temperature Plasma J.Appl.Polym.Sci. [J]. 62：1325-1329(1996)

[7] KoTM,Cooper S.L. Surface properties and platelet adesion characteristics of acrylicacid and allylamine plasma treated polyethylene. J Appl.Polym.Sci. [J]. (47):1601～1619 (1993)

Study of non-thermal plasma on the efficacy and mechanisms of indoor air sterilization

Li Ke[a], Chen Jie-rong[b] , Mo Xiao-yan[b], Li Ru[b,c] ,Li Ying[b]

[a] *Peking University Health Science Center, Beijing 100083, China*

[b] *Xian Jiaotong University, Xian 710049, China*

[c] *Xi'an University of Engineer Science Technology, Xi'an ,710048 ,China*

Abstract

The paper investigated the possibility and several possible influencing factors of the "on-line" indoor air sterilization utilizing non-thermal plasma. We also analyzed the mechanisms and evaluated further the role of all kinds of active species such as electrons, ions and free radicals involved in plasma sterilization at a "remote plasma" field. The results showed that air-based non-thermal plasma could control the total number of bacteria continuously and efficiently even when people were in the room. The inactivation rate of microorganisms could reach about 95%.

Keywords Air; Sterilization; Non-thermal plasma; Inactivation rate

1. Introduction

Plasma is usually considered the forth state of matter being free of the solid, liquid and gaseous state [1]. According to the research, the active species in plasma can destroy a broad spectrum of microorganisms or disturb their organism functions through the reaction with the inner protein and nucleic acid [2]. When the glow discharge takes place in the gas, the UV radiation produced simultaneously will eliminate microorganisms cooperatively [3]. Non-thermal plasma technique makes it possible that the air-born pathogenic bacteria are killed in the room temperature, and once the discharge is terminated, those active species are no longer present in a few milliseconds, so this sterilization method has little danger for the personnel due to no leakage radiation. And it has other prominent advantages including convenient operation, short sterilization time and no toxicity [4].

So far, researches about plasma sterilization have merely been limited to a mixed atmosphere constituted by all active species, which are produced in some special discharge gases such as N_2, O_2, Ar and so on[5]. However, how much do the different active species contribute to sterilizing the workpieces or the air? And how to achieve "on-line" air sterilization on the working circumstance, such perplexities occurred at plasma chemistry basic theory research and the key techniques in application haven't been seen whether in native or foreign reports yet.

Supported by National Natural & Science Foundation Council of China, we put forward an innovative idea – remote plasma, that is, taking advantage of the different life-spans of various active particles such as electrons, ions and free radicals (Rate constants of recombination and dissociation reactions between electrons and ions, free radicals and free radicals are orders of $10^{-7}cm^3/s$ and $10^{-33}cm^3/s$ respectively) to make them separated at a special plasma field and attain super pure and high free radicals concentration at a distance from the plasma discharge region. In the presentation, we studied the possibility of the "on-line" indoor air sterilization utilizing non-thermal plasma at a high-voltage pulse corona discharge plasma field. In addition, we analyzed the mechanisms involved in air plasma sterilization and evaluated further contributions of the electrons, ions and free radicals to air sterilization at a "remote plasma" field.

2. Materials and methods

2.1 Plasma reactive system

2.1.1 “On-line” plasma reactive system and sterilization experiment

The “on-line” plasma reactive system (high-voltage pulse corona discharge plasma reactor) is shown in Fig.1. The airflow is forced into the reaction chamber through mass flowmeter, then purified and expelled from ventilating fan fit at the bottom of the chamber. The plasma reactor consists of chamber, electrodes and high voltage pulse power supply. The reaction chamber is made of the organic glass, on the right side of which, there is a gate for sending the sample into the chamber. The electrodes include comb type electrodes and plane-parallel plates used simultaneously for the sterilization-bed. And the pins number of the comb type electrodes, the space between the pins and the plates is adjustable. A self-made pulse power supply is employed in the reactor, which can range from 12V to 24V. When the signal is transmitted into the amplifier, the peak pulse voltage will exceed 20kV, and the discharge power will reach 50W at one atmosphere pressure. To test the “on-line” air sterilization, we change the plasma treatment parameters (discharge power, treatment time, peak value voltage, space between electrode pins and plane-parallel plates and pins number) and make the airflow pass through the reactor at constant flow rate.

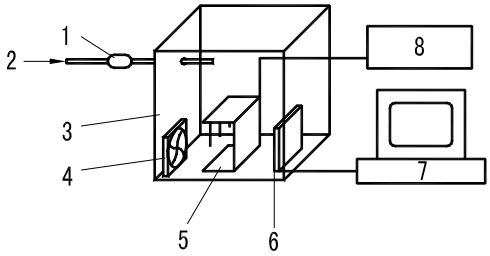

Fig.1. Schematic of high-voltage pulse corona discharge plasma reactor

1.Mass flowmeter 2.Inlet of air 3.Reaction chamber 4.Ventilating fan 5. Electrode pins and plane-parallel plates 6.Sensor 7.Personal Computer 8. High-voltage pulse power supply

2.1.2 “Remote plasma” reactive system and sterilization mechanism experiment

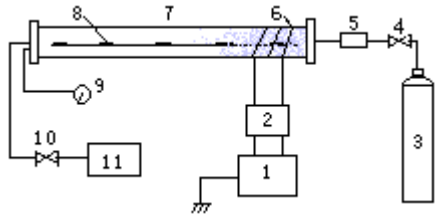

Fig.2. Schematic structure of remote plasma reactor

1.RF generator 2.Matching system 3.Gas bottle 4.Valve 5.Mass flowmeter 6.Inductance coil 7.Reaction chamber 8.Sample 9.Vacuum gauge 10.Electromagnetism valve 11.Vacuum pump

In Fig. 2, we show the “Remote plasma” reactive system. The reactor includes four parts -- gas inlet, reaction chamber, gas exhaust, power supply and matching network (SY-500W power supply and SP-Ⅱ matcher are made in Chinese Academy of Science Micro-electronics Center). The reaction chamber is hard glass tube

(length 1000mm, diameter 45mm), where inductance-coupling discharge is applied.

To compare the characteristic and effect of the remote plasma with that of the routine plasma on sterilization, we fix the microorganisms, which are captured from the air and deposited on the filter membrane, on different distances (0, 10, 20, 30cm separately) from inductance coil on the carrier, then evaluate the sterilization efficacy by changing the plasma treatment parameters (Also see 2.1.1).

2.2 Sample preparation

According to conventional air sampling method[6], when sampling, we set the cellulose acetate ester millipore membrane(diameter 55mm, aperture 0.45μm) disinfected in advance (boiled in distilled water for 15 to 30 minutes and repeated three times) on the tray of the sampler, and make the rough surface upward, then cover the cylinder and fasten it and tray with the special clip. The airflow rates on both inlet and outlet can be controlled through the rotameter between the vacuum pump and sampler.

The sample (millipore membrane) containing the microorganism was placed into plasma reaction chamber where discharge parameters were controlled. After treatment for a time, the sample was taken out. And the sampling surface was wiped with the aseptic cotton swab as soon as possible, which was immersed in the sterile physiological saline solution before. When operating, we must wipe the millipore membrane evenly five times toward both horizontal and vertical direction, and rotate the cotton swab simultaneously. Then the cotton swab was cut off the part that hands held first, and added to 10ml of sterile saline in a test tube and blended for 30 seconds in the shaker. After proper dilution, 0.2ml of the above suspension was inoculated on nutrient agar media including 3g beef extract, 10g peptone, 5g sodium chloride, 15g agar and 1000g distilled water [6], and incubated for 24h at 37℃ in a constant temperature incubator. The millipore membrane not subjected to plasma treatment served as the controls, other operations were as same as the above.

2.3 Statistical analysis of the inactivation rate

The initial colony formation units and the survivors after plasma treatment were counted after incubation for 24h at 37℃, further the inactivation rate could be calculated. All the experiments were repeated at least three times.

3. Results and discussion

3.1 Effect of discharge power

Effect of discharge power and remote distance on inactivation rate is shown in Fig. 3, and the discharge operating conditions are given in it. As shown in Fig. 4, with the increase in the discharge power, inactivation rate accordingly was raised no matter how far the samples were to plasma region, but its increase speed was obviously different in the different distances. When the millipore membranes were placed at sample positions of 0 and 20cm from discharge center, the inactivation rate increased rapidly with the increase of discharge power. Conversely, it increased slowly at the distance of 20cm and 30cm at the lower discharge power than 30W. Once exceeding the power, the inactivation rate was raised sharply. These curves implied that a quantity of air molecule acquired more energy resulted from the increase of discharge power, so ionicity of air and the average energy of active particles increased, and the reaction chance and intensity of active particles with bacteria was further enhanced. Therefore, the inactivation rate increased.

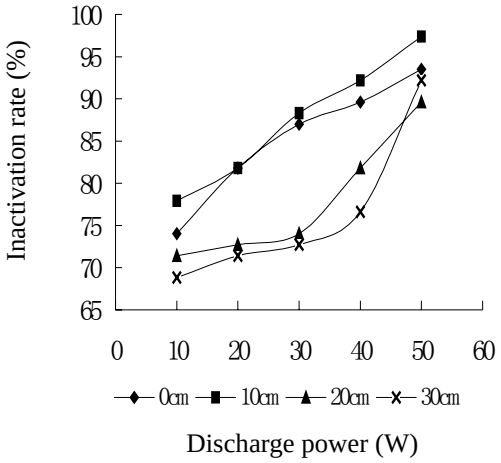

Fig. 3. Effect of discharge power and remote distance on inactivation rate of bacteria (discharge operating conditions: 60s, peak value voltage at 20kV, 40 electrode pins, space between electrode pins and plane-parallel

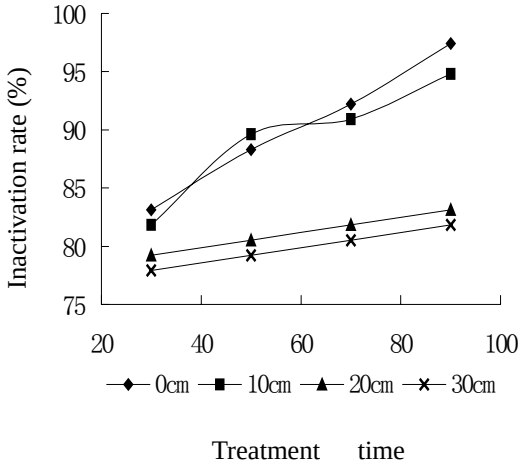

Fig. 4. Effect of treatment time and remote distance on inactivation rate of bacteria (discharge operating conditions: power at 40W, peak value voltage at 20kV, 40 electrode pins, space between electrode pins and plane-parallel

3.2 Effect of treatment time

Fig. 4 shows effect of treatment time and remote distance on inactivation rate as well as discharge conditions. As can be seen from Fig. 5, the inactivation rate increased along with the treatment time despite the remote distance, for the absolute dead bacterial count was accumulated with the increase in treatment time. But it increased at the completely different speed at different positions located in the remote region. For example, inactivation rate in the discharge region (within10cm) increased sharply, but it increased slowly in the remote region (20cm, 30cm), and at the same treatment condition, inactivation rate decreased with the increase of the remote distance. The above results demonstrated that it was the electrons and the ions that contributed to sterilization. As for the mechanisms of the free radicals reacting with microorganisms, which maybe include killing, inhibiting and variating processes, we will discuss in detail in later paper.

3.3 Effect of peak value voltage

The curve in Fig. 5 expresses the relation between the inactivation rate and the peak value voltage. Adjusting the peak value voltage that ranges from 5 to 28 kV and setting the discharge conditions as Fig.6, we can notice that the inactivation rate increased rapidly when the peak value voltage was boosted. And the trend didn’t reduce gradually until the inactivation rate reached 90%. The reason for this was that the boost in peak value voltage resulted in the intensification of electric intensity in the discharge region and correspondingly the active particles acquired more energy, and finally led to the increasing inactivation rate. However, once the voltage was more than 20kV, the inactivation rate would remain around 90% without evidently rise, because the energy of active particles was saturated in a quantity of air, and the further rise of the peak value voltage made the electric field energy superfluous. Consequently, taking both energy consumption and inactivation rate into account, we can select an optimal voltage (it was 20kV at our experiments).

3.4 Effect of space between electrode pins and plane-parallel plates

The relation between the space (within electrode pins and plane-parallel plates) and the inactivation rate is

shown in Fig. 6. Discharge conditions are also given in it. Fig. 6 shows that the inactivation rate changed little when the space between electrode pins and plane-parallel plates varied from 15 to 25mm, but it declined sharply along with the increase of the space, This is because that at certain power and voltage, the electric intension changed in inverse proportion to the space, with the rise of the space, the electric intension weakened which resulted in the decrease of the inactivation rate.

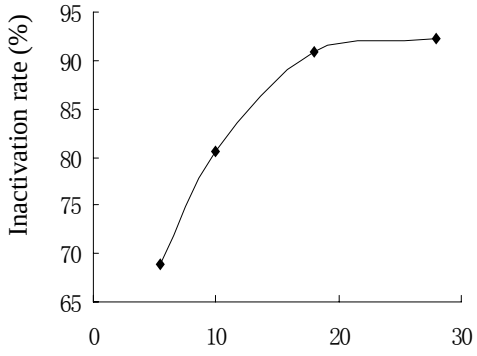

Fig. 5. Effect of peak value voltage on inactivation rate of bacteria (discharge operating conditions: 60s, power at 40W, 40 electrode pins, space between electrode pins and

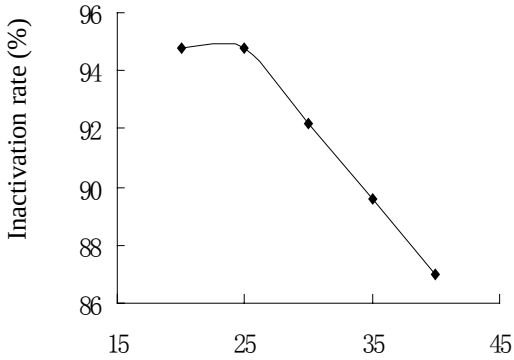

Fig. 6. Effect of space between electrode pins and plane-parallel plates on inactivation rate of bacteria (discharge operating conditions: 60s, power at 40W, peak value voltage at 20kV, 40

3.5 Effect of pins number

In the part of experiment, pins number varies from 25 to 60, and other discharge conditions are listed in the Fig. 7, which illustrates the relation between pins number and the inactivation rate.

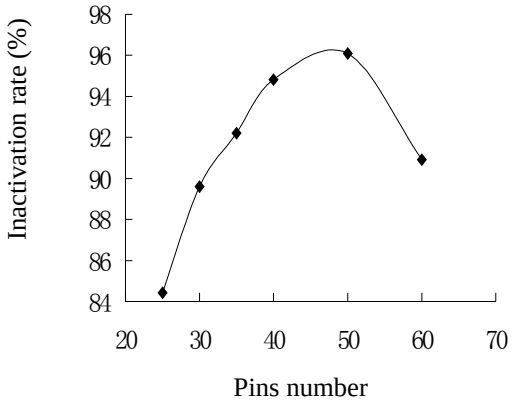

Fig. 7. Effect of pins number on inactivation rate of bacteria (discharge operating conditions: 60s, power at 40W, peak value voltage at 20kV, space between electrode pins and plane-parallel plates at 20mm)

As shown in Fig. 7, the inactivation rate increased sharply until the comb type electrode was added to 50 pins, instead, it decreased with the rise of pins number when the pins exceeded 50 pins. Because the density of active particles produced in gas discharge was raised with the increase of pins number, which expressed directly the increase of inactivation rate. But the internal energy of active particles decreased due to a constant discharge power when there were too many pins, so some active particles had no enough energy to

kill the bacteria, despite its increasing density, the inactivation rate decreased yet.

4. Conclusions

(1) We realized the “on-line” air sterilization on the working circumstance at a high-voltage pulse corona discharge plasma field. At a certain condition, the inactivation rate could reach 95% in tens of seconds. This demonstrated non-thermal plasma could kill a broad spectrum of microorganisms, and it was a concurrent, rapid and safe sterilization method.

(2) Discharge operating conditions including discharge power, treatment time, peak value voltage, and the structure of plasma reactor could affect biocidal effects. The change of inactivation rate obeyed the following rules, with the increase in the discharge power, the treatment time, and the peak value voltage, inactivation rate accordingly was raised. Conversely, Inactivation rate decreased along with the increase of the space between the electrode pins and the plane-parallel plates. With the change of the pins number, inactivation rate increased first, reaching a maximum, then decreased. The optimal results was achieved when plasma treatment parameters were set: 80s, power at 45W, 45 electrode pins, peak value voltage at 25kV, space between the electrode pins and the plane-parallel plates at 20mm.

(3) At a “remote plasma” field, sterilization efficacy in discharge region (within 10cm) was far superior to that in remote region (beyond 20cm). This further demonstrated that it was mainly the attack of the electrons and ions on the microorganisms that played the most important role in plasma air sterilization, and the high active free radicals had little influence on the microorganisms. The mechanisms that the free radicals react with the microorganisms are in investigation from molecule biology.

Acknowledgements

The authors thank the financial support of the National Natural & Science Foundation Council of China, the specialized research Fund for the Doctoral Program of Higher Education, the Scientific Research Star Fund for the Study Abroad Returnee and the key Scientific Technique item of Shaanxi province. We are also grateful to every professor and assistant in the Microbiology Laboratory. We finally thank all the colleagues in Air Pollution Control Laboratory in Environmental & Chemical Engineering Institute of Xian Jiaotong University for their assistance in the preparation of the article.

References

[1] Chen Jie-rong Low-Temperature Plasma Chemistry and Application [M]. Beijing: Science Press, 2000:
[2] Pelletier J. Sterilization by the plasma procedure [J]. Agressologie, 1992, 33(S2): 105.
[3] Gu Chun-ying, Xue Guang-bo. Disinfection and sterilization using plasma [J]. Shanghai Preventive Medicine, 1999, 11(11): 486-491.
[4] Cao Jin-xiang. Sterilization techniques and characteristics of low-temperature plasma [J]. Modern Physics Knowledge, 1999, 11(1): 11-12.
[5] Dambadarjaa Purevdorj, Noriyuki Igura, Isao Hayakawa et al. Inactivation of *Escherichia coli* by microwave induced low temperature argon plasma treatments [J]. Journal of Food Engineering, 2002, 53: 341-346.
[6] Yu Xi-hua. Modern Air Microbiology [M]. Beijing: People’s Military Medical Press, 2002

PLASMA PROCESSES AS NEW CONSERVATION TREATMENTS FOR WORKS OF ARTS: THE CASE OF PRECIOUS METAL ARTEFACTS

E. Angelini[1], R. d'Agostino[2], F. Fracassi[2], S. Grassini[1], S. Laera[2], F. Palumbo[3], F. Rosalbino[1]

[1]*Department of Materials Science and Chemical Engineering, Polytechnic of Turin, Turin, Italy*
[2]*Department of Chemistry, University of Bari, Bari, Italy*
[3]*Institute for Inorganic Methodologies and Plasmas, CNR, Bari, Italy*

Abstract
PECVD technology has been proposed for protection of silver-based alloy artefacts from tarnishing by SiO_2-*like* coatings. The deposition performed in RF plasma fed with tetraetoxysilane/oxygen/argon mixture, by increasing both O_2/monomer ratio in the feeding gas and input power produces layers with excellent barrier effects against diffusion of water and gaseous aggressive agents from the environment towards the metal surface; the coating adhesion increases if the deposition process is performed after hydrogen plasma treatment.

Keywords
PECVD, Silver alloys, SiO_2-*like* coatings, Tarnishing, Cultural Heritage

1. Introduction

This research has been developed in the framework of a European Project, named PROMET [1], devoted to find innovative conservation approaches for monitoring and protecting ancient and historic metals collections from the Mediterranean basin. Museums and historical sites in the Mediterranean region exhibit collections of Phoenician, Hellenistic, Roman, and Islamic metallic works of art that are witnesses of mankind past. Unfortunately, these artefacts often suffer of serious problems of conservation due to the corrosion and degradation phenomena that may, for example, take place during burial and/or after their excavation during storage and exhibition. The high relative humidity and aggressive agents in the atmosphere may accelerate these corrosion attacks.

In order to decrease the kinetic of the degradation phenomena, it is difficult to protect the metal collections by placing them in strict environmentally controlled areas or by treating them on a regular basis, due to the large number of objects and the heavy cost of repeated maintenance, so the development of a protective layer with good aesthetic appearance and excellent barrier properties against atmospheric pollution has to be preferred.

Among the ancient artefacts, the precious noble metals objects are characterized by a wide chemical composition range (Cu, Ag and Au-based alloys, Ag and Au coated artefacts) and have been produced via different complex manufacturing techniques that have greatly influenced their chemical and metallurgical stability. Dealing with the degradation state, ancient precious artefacts are often fragile and subjected to various alteration and corrosion processes, Fig. 1.

Indeed, even though the chemical nobility and the good ability to resist to corrosion is one of the properties of silver and silver-based alloys, the well-know tarnishing phenomenon takes place if silver is exposed to sulphur compounds present in the environment.

The gold-based or nearly pure gold artefacts are more stable with respect to the silver objects but the presence of less noble metals as traces or alloying elements, such as Pb and Cu, could play a detrimental effects on the chemical and physical stability of the object due to the formation of separated metal islands or secondary precipitated phases. The resulting alloy, whose equilibrium state is not a single phase, is less resistant to long-term corrosion.

Furthermore, on the Ag or Au-based surface of ancient artefacts, a thin *patina* is formed where relicts of metal and insoluble corrosion products (Ag_2S, AgCl, CuS, CuO, Cu_2O, etc.) are mixed to form a complex composite structure.

Fig. 1 – Roman coins of the 1st century B.C.: Suberatae coin, constituted by a core of copper coated with a silver layer, corrosion attacks are evident on the surface of the artefact due to the corrosion of the copper interior with the formation of copper corrosion product as malachite (left); Serratus, silver coin characterized by a notched edge, in dependence on the conservation conditions tarnishing may appear on the surface of the artefact darkened in some areas (right)

The removal of tarnished film on silver-based alloys usually requires the use of chemicals to convert the silver sulphide into soluble compounds, or abrasives, which use mechanical action. These methods may cause loss of silver from the artefact, because in addition to removal of the silver combined as silver sulphide some of the metallic silver is abraded. Moreover the freshly cleaned surface is very reactive and will quickly retarnishes again, so repeated cleaning may increase the damage.
At present there is not a satisfactory methodology for the overcoming of the never-ending problem of cleaning, protecting and preventing further damages of restored artefacts.
As said before a possible solution may be to coat the surface of metal precious artefacts with a protective layer. In this context the high chemical stability, the low gas and vapour permeability and the optical transparency of thin films deposited in organosilicon containing plasma render them particularly promising for the protection of precious metal artifacts [2, 3].
In this paper the description is limited to the deposition of SiO_2-*like* thin films on Ag-Cu alloys of chemical composition and microstructure similar to the ancient artefacts. This study will help archaeologists and curators to preserve, restore and protect the artefacts in order to display them in museums without causing further damaging

2. Experimental

The deposition of SiO_2-*like* coatings has been carried out on mirror polished samples (20x20x2 mm) of Ag-Cu alloys of different composition (from 10 to 90 atomic % of Ag). The Ag-based alloys have been melted in a graphite crucible under a reducing atmosphere in order to reduce surface oxidation, nevertheless noticeable amount of oxygen has always been detected on the silver alloy surfaces. The capacitively coupled apparatus used is a home-made parallel-plate-reactor with an asymmetric electrode configuration. It consists of a stainless steel vacuum chamber with a upper powered electrode connected to a 13.56 MHz RF power supply through an impedance matching unit, and a bottom grounded electrode [4].
The samples were processed on the grounded electrode at the floating temperature reached by the plasma (T<70°C), by applying the RF power, 50-250W, to a gas mixture containing tetraetoxysilane (TEOS), oxygen and argon (feed composition: TEOS 2 sccm, O_2 0÷45 sccm, Ar 22÷67sccm; total flow rate: 69 sccm), at a pressure of 100 mTorr. A pre-treatment step in H_2-containing plasma has been performed, by applying the RF power of 15 W to hydrogen, 20 sccm, at P = 1000 mTorr.
The chemical characterization of the coating has been performed by means of Fourier Transform Infrared Absorption Spectroscopy in transmission mode (EQUINOX 55 BRUKER FT-IR) on coatings deposited onto polished silicon, and X-ray Photoelectron Spectroscopy (XPS). XPS spectra have been obtained with an ESCA PHI5300 spectrometer by means of non-monochromatic MgKα X-ray source. The acquisitions were performed at a take off angle of 45° within 2h from the deposition. Coated samples were also analyzed during continuous sputtering of the surface by means of an *in situ* 3 KeV Ar-ion beam (depth profile mode), this allowed to evaluate the effect of feed gas composition and RF power value on the film chemistry as well as to investigate the substrate-coating interface with and without pre-treatment. Quantitative analysis has been performed with C1s, O1s, Si2p, Ag3d, Cu2p high resolution peaks, while for a better comprehension of the oxidation state of Ag and Cu the Auger signals Cu L_3VV and Ag M_4VV were investigated [5]. Depth

profile analysis was also carried out on the Ag-based alloys and on freshly polished pure silver and copper, for comparison.
Tarnishing tests have been performed in 0.1 M Na_2S aerated solution at room temperature by intermittent immersions in the solution (24h immersion, 24h air exposure, 48h immersion, 24h air exposure and finally 72h immersion). Tarnishing has been evaluated quantitatively by means of CIE L*a*b* colorimetric measurements (Chroma-Meter CR-400, Minolta).
The protective effectiveness of the coatings has been also assessed by means of Electrochemical Impedance Spectroscopy (EIS). Impedance measurements have been performed at room temperature in aerated 0.1 M NaCl solution, in the frequency range 100 kHz -10 mHz. The experimental data have been interpreted on the basis of a suitable equivalent circuit model [4, 6] in order to evaluate, the charge transfer resistance, R_{ct}, which can be directly related to the protective properties of the coatings.
Morphological characterisation of the coatings has been performed by means of Scanning Electron Microscopy (SEM-EDS, Philips 515 SEM and EDAX 9900 energy dispersion microprobe, equipped with a W filament and a Robinson back scattered electron detector) and by means of an Atomic Force Microscope (AFM, Thermomicroscope Auto CP). The film thickness has been evaluated by means of an α-step Tencor Profilometer.

3. Results and discussion

3.1 Chemistry and morphology of SiO_2-like layers

The identification and the correlation between the chemical composition and the barrier properties of the coatings have been carried out by means of FT-IR investigations, Fig.2.

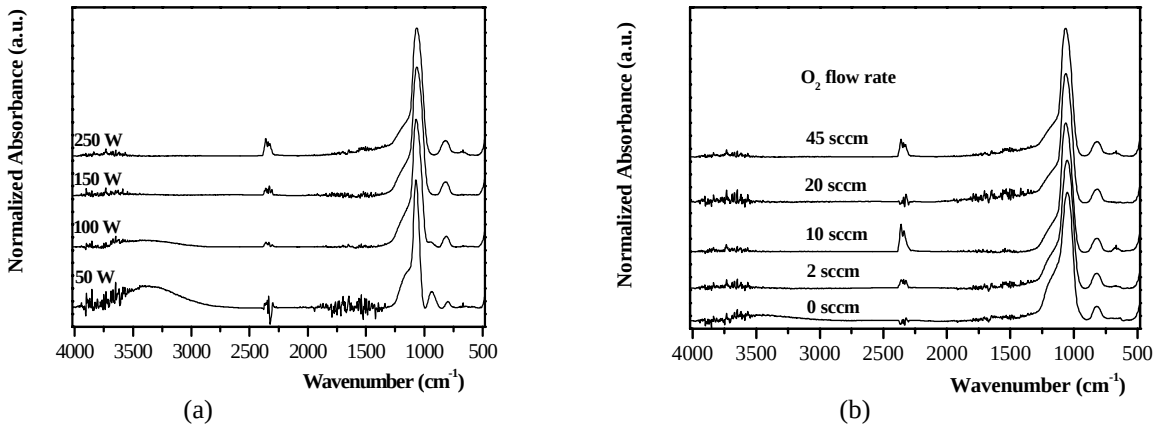

Figure 2 - IR absorption spectra of SiO_2-*like* coatings deposited at: (a) different RF Power values (100 mTorr, TEOS=2 sccm, O_2= 45 sccm, Ar=22 sccm) and (b) different O_2 flow rate in the feed gas (250 W, 100 mTorr, TEOS=2 sccm). The Ar flow rate is changed to keep the total flow rate at 69 sccm

In agreement with our previous results obtained on SiO_x films deposited in hexamethyldisiloxane (HMDSO)/O_2 fed plasmas [7], the RF power largely influences the chemistry of the layer. As a matter of facts, for coatings deposited at a fixed O_2-to-monomer ratio (22.5) with increasing RF power (Fig. 2a), the absorption features are consistent with an inorganic SiO_2-*like* matrix: the Si-O-Si stretching and bending absorption bands (at 1068 cm^{-1} and 820 cm^{-1}) and the features of silanols (Si-OH) at 935 cm^{-1} (bending) and 3450 cm^{-1} (stretching) may be detected. Moreover, the FTIR spectra highlight also the decrease of the silanol groups content by increasing the input power; SiOH absorption peaks completely disappear at input power higher than 100 W, because of the higher ion bombardment energy and dose, which are expected to enhance the OH groups abstraction. The presence of silanols decreases the barrier effects of coatings because of the higher porosity of the films and of their intrinsic reactivity. The effect of feed gas composition, in terms of O_2/TEOS flow rate ratio, on the chemistry of the film has been studied at 250 W of input power (Fig. 2b). It is important to underline that any absorption can be ascribed to organic moieties even when the feed gas does not contain oxygen. The coating obtained with pure TEOS (without oxygen) shows a light absorption of OH groups at 3450 cm^{-1}, indicating that input power plays an important role also in the removal of the organic fraction of the coating. The morphology of the SiO_2-*like* film has been investigated by means of AFM and

SEM observations. AFM images highlights that the layers uniformly cover the surface; they are also characterized by good adaptability to the underlying substrate independently from the different surface roughness (Fig.3).

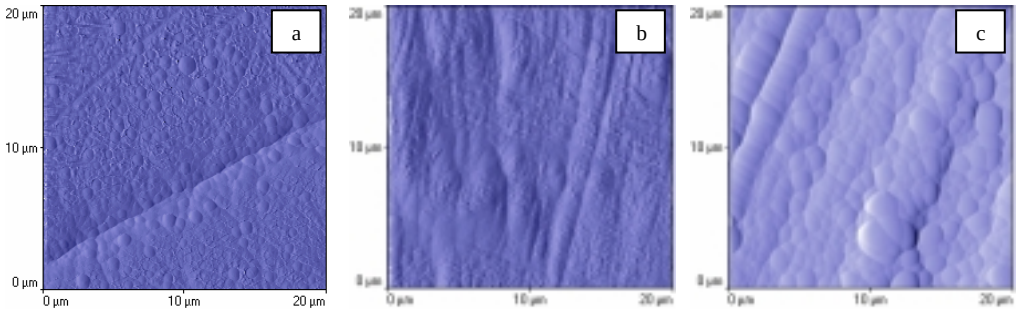

Fig. 3 – AFM images of SiO_2-*like* film (TEOS=2 sccm, O_2= 45 sccm, Ar=22 sccm, 250W, 100mTorr) deposited on Ag90Cu10 alloy samples with different surface roughness; the medium square roughness is: a) 24 nm, b) 78 nm, c) 224 nm

The good conformability of these layers to the metal surface has been also confirmed by the SEM observation of the cross-section of a patterned Si wafer coated with SiO_2-*like* film (Fig. 4). This high degree of adaptability to any kind of surface is a key factor in order to meet the requirements of curators involved in the conservation of historical and archaeological artefacts that are usually characterised by very complex shapes and decorations.

The substrate/coating interface, essential for good adhesion of the coating and a consequent good barrier effect, has been studied by means of XPS depth profile analysis. An important parameter affecting the quality of the substrate/coating interface is the pre-treatment step, in the case of silver-alloys performed in hydrogen.

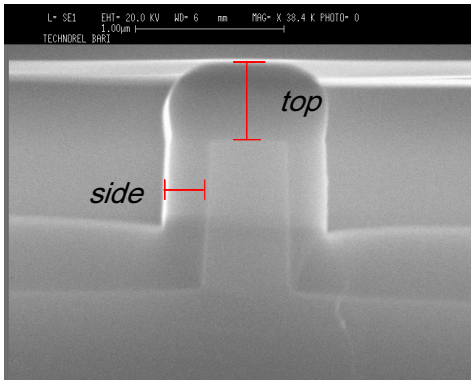

Fig. 4 – SEM image of the cross-section of a patterned Si wafer coated with SiO_2-*like* film (TEOS=2 sccm, O_2= 45 sccm, Ar=22 sccm, 250W, 100mTorr)

The XPS profiles recorded on as polished Ag after SiO_2-*like* film deposition are shown in Figure 5. With and without H_2 pre-treatment, the oxygen profile is close to that of silicon, and the average O/Si ratio in the bulk of the coating is slightly higher than 2, as is usually observed on inorganic PECVD coatings deposited at low temperature. Furthermore the carbon content at the metal-coating interface is lower in the pre-treated sample. When the depth profile analysis is performed on Ag samples polished and exposed to the atmosphere for few days, the modified Auger parameter for silver passes from 724.4 eV for the untreated sample (a typical value for Ag_2O) to 725.2 eV for H_2 plasma pre-treated samples, which corresponds to the unoxidized state [9]. Moreover the Cu 2p signal of the untreated alloy is broad because it includes the features of not oxidised and oxidized copper. After H_2 plasma pre-treatment the intensity of the shake up, typical of Cu^{2+}, drastically decreases and the Cu2p signal features become sharper. These results highlight that on oxidized alloys the H_2 plasma pre-treatment leads to a surface chemical reduction of Ag and Cu.

Summarizing, the H_2 pre-treatment improves the coating adhesion and, as shown below, the tarnishing resistance of silver-based alloys, mainly for two reasons: i) removal of organic contaminants from the metal surface, ii) reduction of silver and copper oxides on the surface.

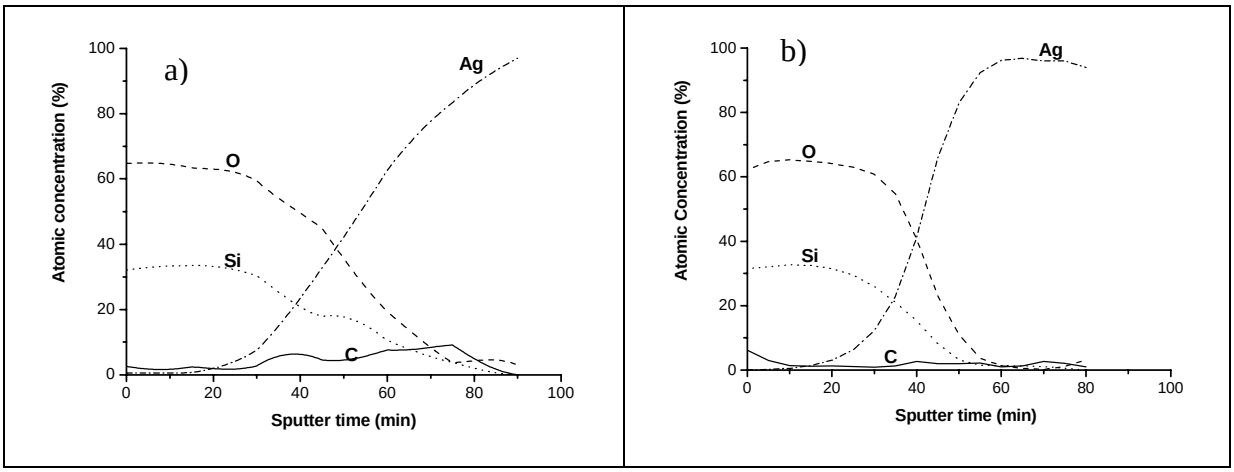

Figure 5 - XPS depth profiles of Ag samples coated with SiO_2-*like* film (a) without H_2-plasma pre-treatment and (b) after pre-treatment. The profile concentrations of C, O, Si and Ag are reported

3.2 Tarnishing Test

Usually, silver-based alloys tarnishing very quickly if exposed to sulphide containing environment. Notwithstanding the low thickness, the deposition of a SiO_2-*like* layer increases noticeably the tarnishing resistance of these substrates, as evidenced by the colorimetric measurements. The tarnishing susceptibility has been evaluated by taking into account the trend of the colour vector ΔE ($\Delta E=(\Delta L^{*2}+\Delta a^{*2}+\Delta b^{*2})^{1/2}$) as a function of the immersion time in the 0.1M Na_2S solution.

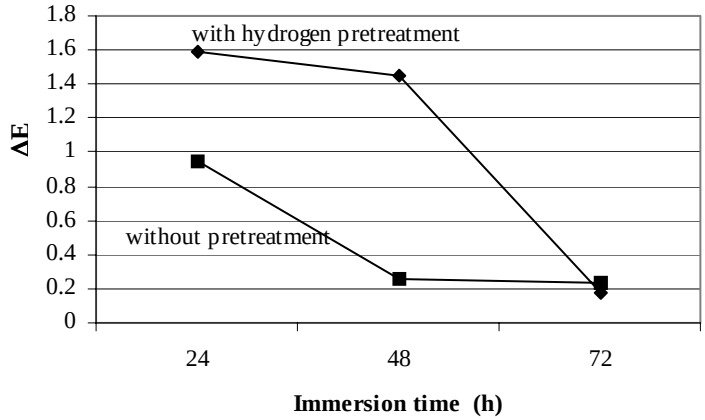

Fig.6 – Colorimetric measurements carried out as a function of the immersion time in 0.1M Na_2S solution on Ag90Cu10 alloy samples coated with 900 nm SiO_2-*like* film (TEOS=2 sccm, O_2=45 sccm, Ar=22 sccm, 250W, 100mTorr) with and without H_2-plasma pre-treatment

As evidenced in Fig.6, surface pre-treatment is a fundamental step in order to achieve high protective coatings. As a matter of fact, on Ag90Cu10 alloy treated in H_2-plasma before the deposition process, more than 48h of exposure are necessary for identifying an appreciable darkening of the surface; tarnishing becomes noticeable after 72h of immersion. On the contrary, a serious tarnishing occurs quickly (after 24h of immersion) on sample coated without any plasma pre-treatment. In this case, the high tarnishing susceptibility can be correlated to the poor adhesion of the SiO_2-*like* film on the metal surface. Consequently, the detachment of the layer takes place, starting from the coatings defects, which allow the penetration of the electrolyte, as evidenced by SEM observations not reported for brevity [5].

3.3 Electrochemical characterisation

The impedance measurements confirm the good protective effectiveness of the SiO_2-*like* films deposited after H_2-plasma treatment, as evidenced by the trend of the charge transfer resistance, R_{ct}, as a function of the immersion time in the 0.1M NaCl solution (Fig.7). For film deposited on the coated alloy the R_{ct}, decreases rapidly after 240h, while a constant trend is observed in the case of pre-treated and coated sample thereby indicating that the electrochemically active area increases to a lesser extent upon prolonged exposure, which points out to the better barrier effect and longer maintenance of protective properties.

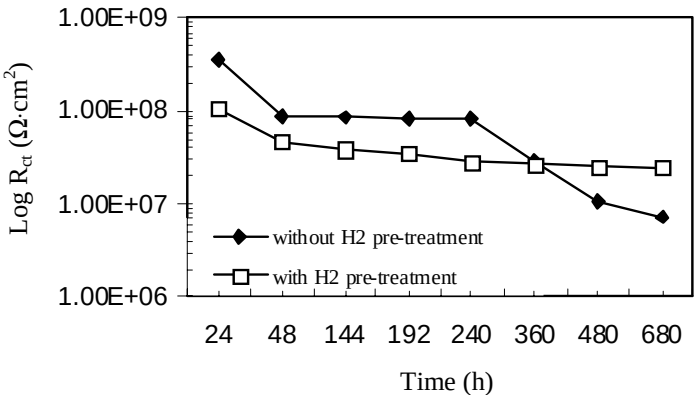

Fig.7 – Colorimetric measurements carried out as a function of the immersion time in 0.1M Na_2S solution on Ag90Cu10 alloy samples coated with 1500nm SiO_2-*like* film (TEOS=2 sccm, O_2= 45 sccm, Ar=22 sccm, 250W, 100mTorr) with and without H_2-plasma treatment

4. Concluding remarks

The conservation field of Cultural Heritage requires a multidisciplinary approach in developing new tailored strategies for protecting artefacts, which are based on science and technology as well as must be adapted to meet the conservation problems and needs of archaeologist and curators.

SiO_2-*like* coatings deposited by PECVD are proposed for protection of silver-based alloy artefacts from tarnishing; these coatings are effective in the protection of the artefacts: serious tarnishing has been observed on coated samples only after 72h of immersion in the sodium sulphide solution. The optimization of the deposition conditions lead to the identification of the influence of different process parameters. The protective effectiveness is higher for coatings deposited in oxygen rich plasmas at high input power, because under these experimental conditions the coatings have low defect density and no silanol groups. Moreover, protection against tarnishing increases if the deposition is performed after a pre-treatment in hydrogen plasma since better adhesion is obtained.

5. References

[1] Incomed –Project Contract n°: 509126-2004 Title: *Innovative conservation approaches for monitoring and protecting ancient and historic metals collections from the Mediterranean basin, Acronym: Promet*

[2] F. Fracassi, R. d'Agostino, F. Palumbo, E. Angelini, S. Grassini, F. Rosalbino, *Surface and Coating Technology* **174-175**, 107-111 (2003)

[3] L. Favre-Quattropani, P. Groening, D. Ramseyer, L. Dchalpbach, *Surface and Coating Technology*, **125**, 377-380 (2000)

[4] E. Angelini, F. Fracassi, R. d'Agostino, S. Grassini, F. Rosalbino, *Trends in Electrochemistry and Corrosion at the Beginning of the 21st Century*, I. Costa J.M. II. Brillas Enric ed. III. Cabot, Pere-Lluìs ed. IV. Collecciò, ISBN: 84-475-2639-9, 979-999 (2004)

[5] R. d'Agostino, F. Fracassi, F. Palumbo, E. Angelici, S. Grassini, F. Rosalbino, *Plasma Processes and Polymers* **2**, 91-96 (2005)

[6] E. Angelini, S. Grassini, F. Rosalbino, F. Fracassi, R. d'Agostino, *Progress in Organic Coatings* **46**, 107-111 (2003)

[7] M. Creatore, F. Palumbo, R. d'Agostino, *Plasmas and Polymers* **7**, 291-310 (2002)

TRIBOLOGICAL AND ELECTROCHEMICAL CHARACTERISATION OF PECVD COATINGS

E. Angelini[1], R. d'Agostino[2], R. Di Mundo[2], F. Fracassi[2], S. Grassini[1], S. Laera[2], F. Palumbo[3], F. Rosalbino[1]

[1]*Department of Materials Science and Chemical Engineering, Polytechnic of Turin, Turin, Italy*
[2]*Department of Chemistry, University of Bari, Bari, Italy*
[3]*Institute for Inorganic Metodologies and Plasmas, CNR, Bari, Italy*

Abstract
In this study a systematical investigation of the tribological and electrochemical behaviour of SiOx and SiNx thin films has been undertaken. Moreover, the deposition of multilayers, such as Ti/TiN/SiOx and Cr/CrN/SiOx has been investigated, too.
Corrosion tests carried out by means of EIS has shown that when SiOx or SiNx coatings are deposited by means of plasma at low temperature, a marked increase of the protective properties is detected, if the process is preceded by a suitable plasma treatment, which depends on the particular metal under study.
Moreover, a huge increase of the corrosion behaviour, without affecting their mechanical properties, has been observed for Ti/TiN/SiOx and Cr/CrN/SiOx coated steel in comparison to magnetron sputtered ones.

Keywords
PECVD, SiO_x, SiN_x, corrosion, tribological properties

1. Introduction

Among main objectives of surface engineering are the applications of thin films and modification treatments in order to improve the surface properties without affecting the characteristics of the base materials.
In this context, it is particularly interesting from the scientific and technological point of view to develop coatings with different chemical composition and properties in order to increase the wear, sliding and corrosion characteristics of metallic materials.
Plasma Enhanced Chemical Vapour Deposition (PECVD) using silicon containing organic compounds emerged as a viable technique for depositing SiO_x thin films that, notwithstanding the low thickness, can improve the corrosion resistance of metals in different aggressive environments.
Silicon based materials including more or less C, O, N and H show high potential for corrosion protection essentially because they are dense (low permeability to water and gases), amorphous, chemically inert and show a low electrical conductivity or can be insulator depending on their composition. Moreover, the coating promotes no galvanic coupling deleterious to the uncoated metallic surfaces.
As a matter of facts, some interesting results have been obtained by these authors showing the increase of corrosion protection of low carbon steel and Mg alloys when coated with SiO_x thin films [1-2].
However, from the mechanical point of view, SiO_x coatings can be rather brittle. Therefore, the substitution of oxygen by nitrogen and/or carbon should allow getting higher tribological properties keeping the insulating nature, that is one of the parameters responsible for corrosion protection [3, 4].
Nowadays, Physical Vapour Deposition and magnetron sputtering processes are usually employed to deposit hard and wear resistant coatings for many industrial applications. These films make a significant impact also in many application areas, such as decorative coatings and coatings with specific optical or electrical properties. Unfortunately, most of these coatings often exhibit growth related defects (pores, pinholes) that are detrimental to the corrosion resistance in environments containing corrosive agents; defects are deleterious as they provide direct paths for corrosive electrolytes to reach the coating/substrate interface, where the localised corrosion attack takes place [5, 6].

The improvement of the corrosion performances of metal substrates coated with hard PVD coatings is of importance as increasingly demand for corrosion resistance from these coatings are required to enhance their tribological lifetime in aggressive working environments.
In this context, the high versatility of plasma processes allows also the deposition of multifunctional layers by combining PECVD and sputtering processes in order to increase both the corrosion and tribological behaviour of coated systems.
Aim of this study is to discuss the preliminary results concerning a comparison between the corrosion behaviour of SiO_x and SiN_x films deposited in RF plasmas with emphasis on the correlation of deposition parameters and their corrosion and tribological behaviour.
Moreover the use of amorphous SiO_x to interrupt the growth of TiN and CrN, deposited by magnetron sputtering in order to suppress their columnar structure, has been investigated, too.

2. Experimental

Low carbon and stainless steel substrates have been chosen for this study. Substrates were polished and cleaned with ethanol in ultrasonic cleaner for 15 min.
The coatings have been deposited in plasmas fed with different organosilicon precursors in mixture with argon and/or oxygen in different experimental conditions: SiO_x films have been obtained starting from hexamethyldisiloxane (HMDSO), tetraethoxysilane (TEOS), tetramethoxysilane (TMOS), hexamethyldixylazane (HMDSN), while SiN_x coatings have been deposited from bis(dimethylamino)dimethylsilane (BIS). SiOx coatings have been deposited by feeding the plasma with the monomer in mixture with O_2 and Ar with a O_2/monomer flow rate ratio higher than 10. On the other hand SiNx-like films have been deposited by addition of Ar.
Experiments have been carried out in two reactors with two different configurations: a capacitive coupled (CC) parallel-plate reactor and an inductively coupled reactor (IC). The capacitive coupled reactor has been extensively described elsewhere [7]. The IC reactor is a home made reactor consisting of a 20 cm diameter copper coil separated from the plasma by a quartz window 5 mm thick. The source is mounted over a stainless steel chamber of 30 cm in diameter. Both reactors are pumped down by a turbomolecular apparatus and pressure and gas flow rates are controlled by means of MKS baratron and mass flow meters.
Before the deposition a O_2-plasma treatment (500 mTorr, 50 W, 12 sccm O_2) has been performed. The pre-treatment increases the oxidation degree of the metal surface, reduces the porosity of the coating and improves its adhesion to the substrate [8].
TiN and CrN films have been deposited by magnetron sputtering, using Ti and Cr targets at 200°C, $3{,}0 \cdot 10^{-2}$ Torr and input power ranging from 150 to 300W; N_2 and Ar gases were used as a reactive source and a sputtering gas, respectively in an apparatus describe elsewhere [9].
The chemical and morphological characterisation of the coatings has been carried out by means of Infrared Spectroscopy (FT-IR) and Scanning Electron Microscopy (SEM).
The corrosion protective properties of deposited films have been assessed by means of Electrochemical Impedance Spectroscopy (EIS). The measurements are performed by applying an alternating potential of 10 mV amplitude in the frequency range 100 kHz -10 mHz to the coated substrate exposed to an aerated 0.1 M NaCl solution at room temperature. Impedance spectra recorded at the open circuit potential have been interpreted on the basis of a suitable equivalent circuit model [10, 11] in order to evaluate the value of the charge transfer resistance, R_{ct}, which can be directly related to the protective properties of the coatings.
Vickers microhardness measurements (ASTM E 384 Standard Method) and sliding wear resistance tests (pin-on-disc) have been also carried out in order to evaluate the mechanical and tribological behaviour of the layers. The film thickness has been evaluated by means of an α-step Tencor Profilometer.

3. Results and discussion

3.1 Corrosion and tribological behaviour of SiO_x and SiN_x coatings

The values of the charge transfer resistance, R_{ct}, obtained on low carbon steel samples coated with SiO_x and SiN_x films deposited starting from the monomers under study are shown in the plot of Fig. 1a.

Among the various monomers tested it has been shown that TMOS is not suitable to deposit SiO_x coatings characterised by a good protective effectiveness against corrosion, as confirmed by the R_{ct} value of about 2800 $\Omega \cdot cm^2$. On the contrary, high protective effectiveness has been observed for SiO_x and SiN_x coatings deposited in plasma fed with TEOS/O_2/Ar and BIS/Ar mixtures: the highest impedance modulus obtained are $7.5 \cdot 10^6$ $\Omega \cdot cm^2$ and $2.3 \cdot 10^7$ $\Omega \cdot cm^2$ for SiO_x and SiN_x films, respectively.

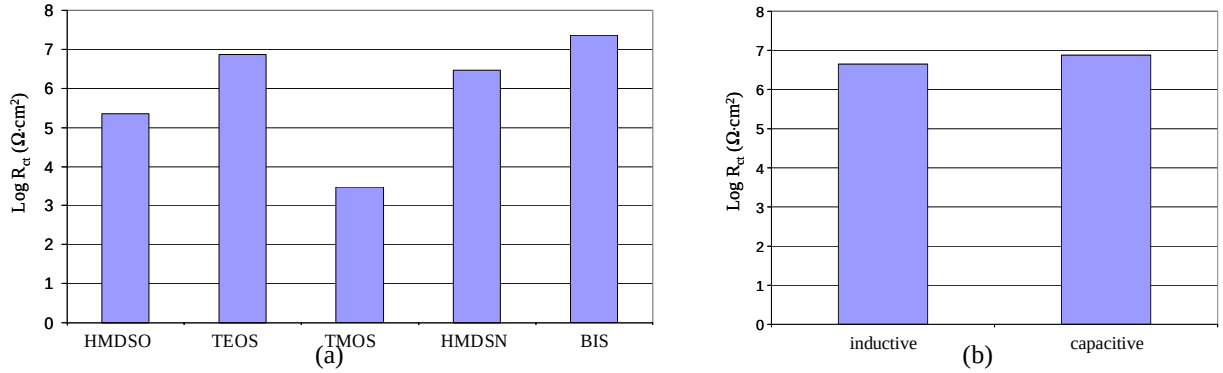

Fig. 1 – R_{ct} values obtained after 24h immersion in 0.1M NaCl solution on low carbon steel substrates coated with: SiO_x and SiN_x films deposited from different organosilicon precursors (a); SiO_x film deposited from TEOS in the capacitive and inductive coupled reactor (b). Coatings thickness is 2 μm.

The poor corrosion properties of coatings deposited in plasma fed with TMOS can be correlated to the low compactness of the film (Fig. 2a), while coatings deposited from TEOS and BIS precursors show a very low defects density and a good adhesion to the metal substrate (Fig. 2b, 2c).

(a) (b) (c)

Fig. 2 – SEM images of: SiO_x films deposited from TMOS (a) and TEOS precursor (b); SiN_x film deposited from BIS (c).

Moreover, the comparison of the R_{ct} values obtained for coatings deposited in the experimental conditions optimised for the two reactors, the capacitive and the inductively coupled one, shows that independently from the reactor geometry utilised, if the experimental conditions are adjusted in the proper way it is possible to deposit coatings with the same corrosion performances (Fig. 1b).

It this context, it is important to take into account that one of the experimental parameter that mainly affects the coating chemistry and, consequently, its corrosion and mechanical properties is the RF power. Best corrosion performances have been obtained for SiO_x and SiN_x thin films deposited on low carbon and stainless steel substrates by increasing the input power (Fig. 3). On the contrary, in the case of SiN_x films high Vickers micro-hardness values, about 1100-1150 Hv (kgf/mm^2), have been obtained for coatings deposited at 100W of input power. From the chemical point of view it has been shown [1, 2, 7] that the SiOx coatings deposited at high input power and at high O_2/monomer ratio are carbon and silanol free. FTIR has been used to analyse the chemistry of SiNx coatings and an absorption spectrum is reported in fig 4. The absorption band characteristic of

SiN stretching can be observed. However NH, CH and SiH bands can be easily recognised. These bands highlight that in the investigated conditions the coating is not a stoichiometric Si_3N_4.

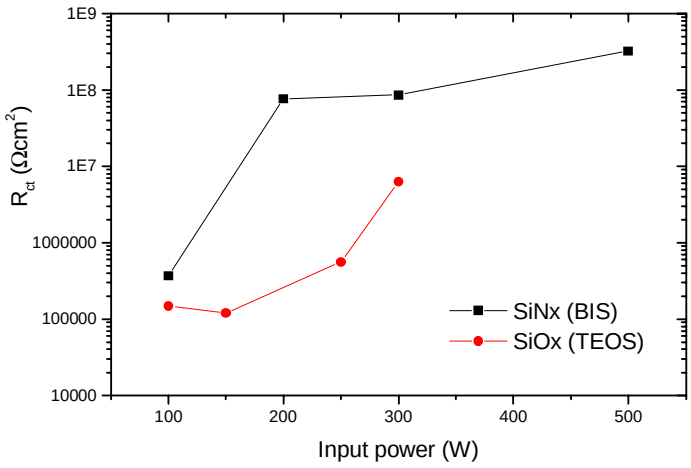

Fig. 3 – R_{ct} values as a function of the RF power for SiO_x film deposited on low carbon steel and SiN_x films deposited on stainless steel substrates. The R_{ct} values have been obtained after 24h of immersion in the 0.1M NaCl solution.

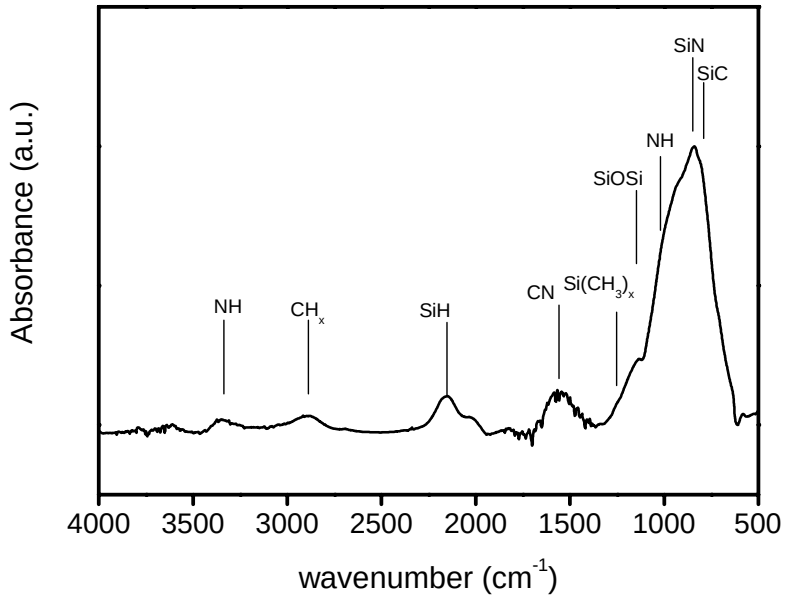

Fig. 4 – FT-IR spectrum of a coating deposited from a BIS/Ar gas feed at 300W in the CC reactor.

3.2 Corrosion behaviour of TiN/SiO_x and CrN/SiO_x multilayers

The good barrier properties against corrosive electrolytes and the amorphous structure of SiO_x thin films deposited from TEOS at high input power allow also to increase the corrosion behaviour of TiN and CrN hard coatings deposited by magnetron sputtering.

Table 1 - R_{ct} values obtained on low carbon steel substrate coated with TiN/SiO_x and CrN/SiO_x after 24h of immersion in 0.1M NaCl solution

Coating	**R_{ct} ($\Omega \cdot cm^2$)**
TiN	$1.5 \cdot 10^4$
CrN	$3.0 \cdot 10^3$
TiN/SiO_x	$1.5 \cdot 10^8$
CrN/SiO_x	$1.7 \cdot 10^7$

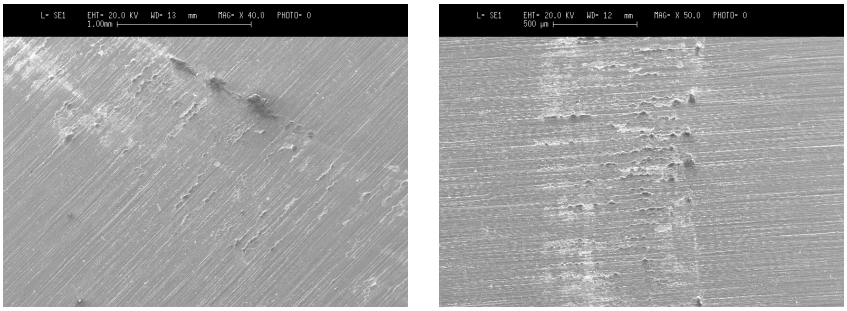

(a) (b)

Fig. 5 – SEM images of the surface of low carbon steel substrates coated with: TiN/SiO_x (a) and CrN/SiO_x after the sliding wear resistance test

Sliding wear resistance tests allow to confirm that the presence of the SiO_x layers doesn't affect the tribological behaviour of the coated systems as it is possible to observe in SEM images of Fig. 5. As a matter of facts, non significative weight lost has been determined after the pin-on-disc tests.

4. Conclusions

It can be concluded that coatings plasma deposited from organosilicon sources can be effectively used for protecting metals from corrosion. Furthermore coatings have not detrimental effects onto the tribological properties of the samples.

5. Acknowledgements

The authors would like to thank the European Community (MATECO Project) for the financial support to this reseach. Gianvito Caputo is kindly acknowledged for his scientific support. Authors would thank Savino Cosmai and Vincenzo Colaprico for their technical expertise.

6. References

[1] F. Fracassi, R. d'Agostino, F. Palumbo, E. Angelini, S. Grassini, F. Rosalbino - Surf. Coat. Technol. 174-175, 107 (2003)
[2] E. Angelini, S. Grassini, F. Rosalbino, F. Fracassi, R. d'Agostino - Prog. Org. Coat. 46, 107 (2003)
[3] P. Jedrzejowski, J. Cizek, A. Amassian, J.E. Klemberg-Sapieha, J. Vlcek, L. Martinu – Thin Solid Films 447-448, 201 (2004)
[4] D. Rats, L. Martinu, J. von Stebut – Surf. Coat. Technol. 123, 36 (2000)
[5] C. Liu, Q. Bi, A. Leyland, A. Matthews – Corr. Sci. **45**, 1243 (2003)

[6] C. Liu, Q. Bi, A. Leyland, A. Matthews – Corr. Sci. 45, 1257 (2003)
[7] R. d'Agostino, F. Fracassi, F. Palumbo, E. Angelini, S. Grassini, F. Rosalbino, Plasma Process. Polym. 2005, 2, 91–96
[8] F. Fracassi, R. d'Agostino, A. Buccolieri, V. Colaprico, E. Angelini, S. Grassini, F. Rosalbino, in Proc. of 15th International Symposium on Plasma Chemistry, Orleans, July 2001; paper OR817
[9] S. Grassini, PhD Thesis in Metallurgical Engineering (XVI Cycle), Politecnico di Torino (2004)
[10] J.R. Macdonald - Impedance Spectroscopy, John Wiley & Sons, New York (1987)
[11] G.L. Kahanda, M. Tomkiewicz - J. Electrochem. Soc. 137, 3423 (1990)

Nitric oxide decomposition by hollow-needle to plate atmospheric discharge in N_2-NO mixtures

S. Pekárek[1] and M. Šimek[2]

[1]*Czech Technical University, Faculty of Electrical Engineering, Technická 2, 166 27 Prague 6, Czech Republic, pekarek@feld.cvut.cz*
[2] *Department of Pulse Plasma Systems, Institute of Plasma Physics, Academy of Sciences of the Czech Republic, Za Slovankou 3, 182 21 Prague, Czech Republic, simek@ipp.cas.cz*

Abstract
We performed an experimental study of nitric oxide decomposition by an atmospheric-pressure DC hollow-needle to plate electrical discharge in N_2-NO mixtures. A needle electrode was biased negatively, mass flow through the needle and energy density ranged between 2.5-10 l/min and 0-250 kJ/m^3, respectively. Decomposition of NO and production of NO_2 species was monitored for several initial NO concentrations (20-200 ppm). We conclude that the transformation of NO is controlled by the production of atomic nitrogen.
Keywords: nitric oxide, DC discharge, atmospheric pressure

1. Introduction

Nitrogen oxides are formed when fuel is burned in combustion processes. They are toxic and cause serious health problems. The development of the NO_x control technologies is therefore an important challenge. Non-thermal plasma produced by electrical discharges is an efficient means for NO decomposition [1,2,3]. The principle of non-thermal plasma de-NO_x technologies is to produce an environment in which a majority of energy supplied to the discharge goes into the production of free energetic electrons rather than into gas heating. Even though these free electrons are short-lived under atmospheric pressure conditions and rarely collide with pollutant molecules, they undergo many collisions with dominant background gas molecules, thereby producing reactive species through electron impact excitation, dissociation and ionization processes. Chemically active species can, in turn, reduce and/or oxidize NO_x molecules.

In connection with N_2 + NO mixtures and for NO concentrations that do not exceed a few hundreds parts per million (ppm), the NO conversion is primarily controlled by ground state nitrogen atoms N(^{4}S). Molecular nitrogen N_2 is dissociated due to the presence of free electrons either through the direct electron impact or through the sequence of e-V, V-V and V-D processes [4]. Nitric oxide is then reduced by nitrogen atoms via a very fast process ($k_1 = 3.1\times10^{-11}$ cm^{3}s^{-1} [2]) with a subsequent formation of oxygen atoms:

$$N + NO \rightarrow N_2 + O. \qquad (1)$$

Additionally, free oxygen radicals created by (1) can react further with remaining NO species through an oxidative process ($k_2 = 9\times10^{-32}$ cm^{6}s^{-1} [5]) producing NO_2:

$$O + NO + N_2 \rightarrow NO_2 + N_2. \qquad (2)$$

Therefore, any removal of NO in the N_2+NO mixture which is induced by N(^{4}S) atoms created by electrical discharge should in general, be accompanied by formation of NO_2 species. The rate of NO removal and NO_2 formation then gives an indirect measure of N(^{4}S) production by a given type of discharge. In this connection we performed an experimental study of nitric oxide decomposition by a DC hollow-needle to plate electrical discharge in N_2-NO mixtures of a dilute amount of NO. All presented results were obtained with a needle electrode biased negatively.

An advantage of the hollow-needle to plate electrode arrangement with a supply of the mixture through the needle electrode is that all the mixture passes through the discharge zone and therefore is affected by plasma chemical processes. This idea was recently confirmed in a study of volatile organic compounds

decomposition [6]. We compared two different ways of the mixture supply to the discharge region. In the first case the mixture of air with VOC was supplied externally perpendicular to the needle electrode and in the second case the mixture was supplied through the needle electrode. The decomposition efficiency was about four times higher if the mixture of VOC with air had been supplied through the needle electrode.
Chemical reactivity of the same type of the discharge with the supply of dry synthetic air through the needle electrode was investigated through a comparative evaluation of ozone production efficiency [7]. Subsequently, it was discovered that the interaction of an ultrasound field with hollow needle to plate discharge substantially increases ozone production [8].

2. Experimental arrangement

Non-thermal plasma chemical decomposition of nitric oxide was studied in a DC-driven atmospheric pressure negative corona discharge. The experimental set-up is shown schematically in Fig. 1. A stainless steel needle *N*, (Terumo, Belgium) having an outer diameter of 1.2 mm and inner diameter of 0.7 mm was placed in a stainless steel discharge chamber. The needle was used as a cathode. A stainless steel disc anode was situated

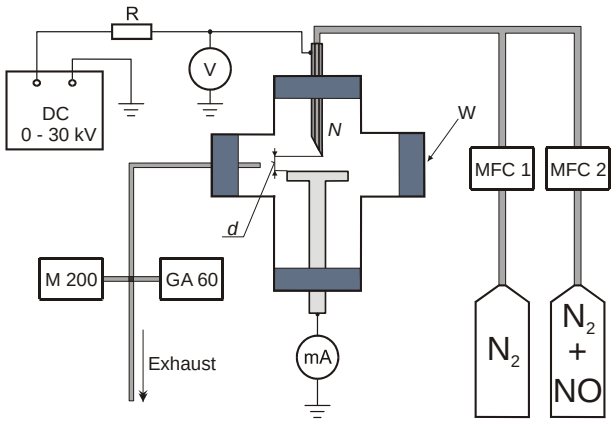

Figure 1. Experimental arrangement

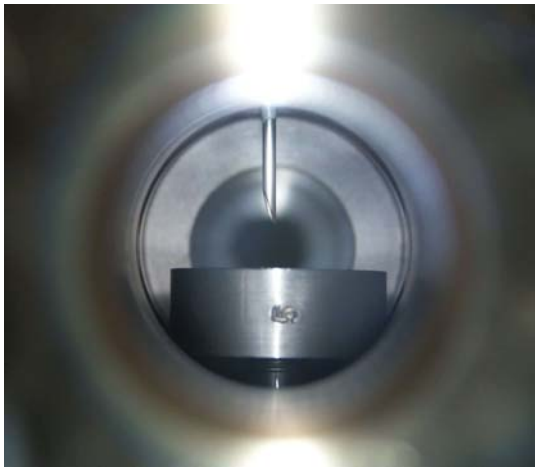

Figure 2. Photograph of the electrode system taken through the diagnostic window W.

perpendicular to the needle. The distance between the tip of the needle and the anode surface was *d*=4 mm. A digital photograph of the electrode arrangement is shown in Fig. 2.
The DC high voltage power supply, Technix, provided voltage up to 30 kV. The needle cathode was ballasted by a resistor R=0.889 MΩ. A stable flow of high-purity nitrogen with a defined quantity of NO was

maintained through the reactor. The gas pressure in the discharge chamber was fixed at 1.01×10^5 Pa and controlled by a pressure gauge. Nitrogen (99.9999) (Messer Austria, with certified impurities H_2O<0.5 ppm, O_2<0.5 ppm, CO/CO_2<0.1 ppm, HC<0.1 ppm and Ar<1 ppm) was delivered through Bronkhorst HI-TEC model mass flow controllers MFC. Quantified traces of NO (20, 100, 200 ppm) were added by the controlled flux of N_2+NO mixture (Pulmonix® forte, Messer Austria, 900 ppm NO in N_2, with main impurities H_2O< 3 ppm, O_2<1 ppm and NO_2<1 ppm). The GA-60 flue gas analyzer (Madur Electronics) equipped with electrochemical cells (O_2, CO, SO_2, NO, NO_2) and chemiluminiscence NO_x analyzer API 200EM (Teledyne Instruments) were used to monitor volumetric concentration of nitrogen oxides. Both instruments were used to verify a gas feed composition (N_2+NO) prepared by mass flow controllers and to analyze the discharge products ($NO+NO_2$) as well.

For a given electrode arrangement, stable discharge occurs for a wide range of the two most important external parameters: a) mass flow through the needle >2 l/min and b) DC driving high voltage >2.5 kV. We explored various combinations of the mass flow and DC driving voltage; however we observed only two basic discharge modes (shown in Fig. 3). At low energy dissipated between electrodes (usually obtained by combining a high

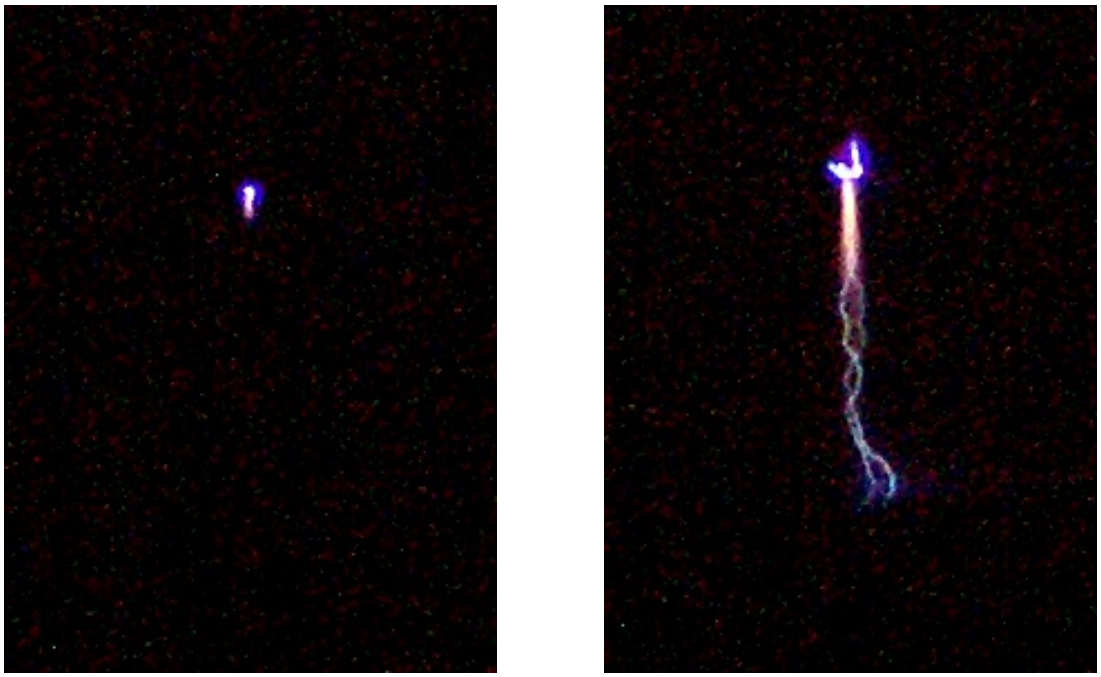

Figure 3. Two basic discharge regimes observed at low energy (left photo) and high energy (right photo) dissipated between electrodes.

mass flow with low driving DC voltage), the discharge is restricted to the small area surrounding the needle cathode. It takes the shape of a short luminous continuous jet, which is directed towards anode (see left photograph in Fig. 3). At higher energy dissipated between electrodes (usually obtained by combining a low-intermediate mass flow with a high driving DC voltage), the discharge is much more complex. The luminous jet directed towards the anode becomes longer (by 1-2 mm) and, simultaneously, the gap between the tip of the jet and the anode surface is frequently bridged by very thin filamentary discharges (see right photograph in Fig. 3). Our experimental results are presented as functions of energy density, which is defined as a ratio of power delivered to the discharge and flow of the mixture through the needle electrode. It is well known that depending on the nature of the feeding gas and polarity of the coronating electrode, the corona discharges

sometimes operate in the form of periodic pulses of different frequencies even at constant voltage conditions. For the purpose of this paper we determined the power delivered to the discharge as a product of discharge voltage and current. The discharge current was measured by milliamp-meter with a magnetoelectric system.

3. Experimental results

The experimental results concerning nitric monoxide transformation as a function of energy density for various initial NO concentrations obtained for constant flow rates through the needle 2.5, 5 and 10 slm are summarized in Figs. 4 - 6. The dependence of nitric monoxide concentration versus energy density delivered to the discharge for three different initial concentrations of nitrogen monoxide $[NO]_{in}$ = 20, 100 and 200 ppm is shown in Figs. labeled *a*. Equivalent dependence in the case of nitrogen dioxide is shown in Figs. *b*. Resulting NO removal rate is shown in Figs. *c* and, finally, the ratio of NO/NO_x concentration is shown in Figs. labeled *d*.

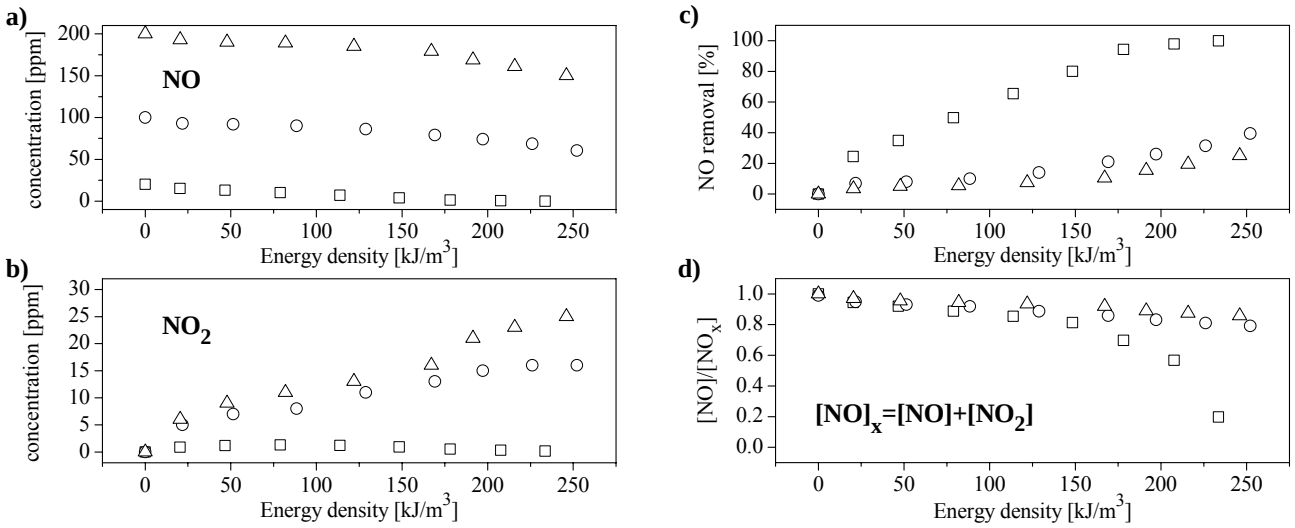

Figure 4. Nitric monoxide transformation as a function of energy density for various initial NO concentrations (□ =20 ppm O =100 ppm and Δ =200 ppm) and for a constant flow rate through the needle 2.5 slm.

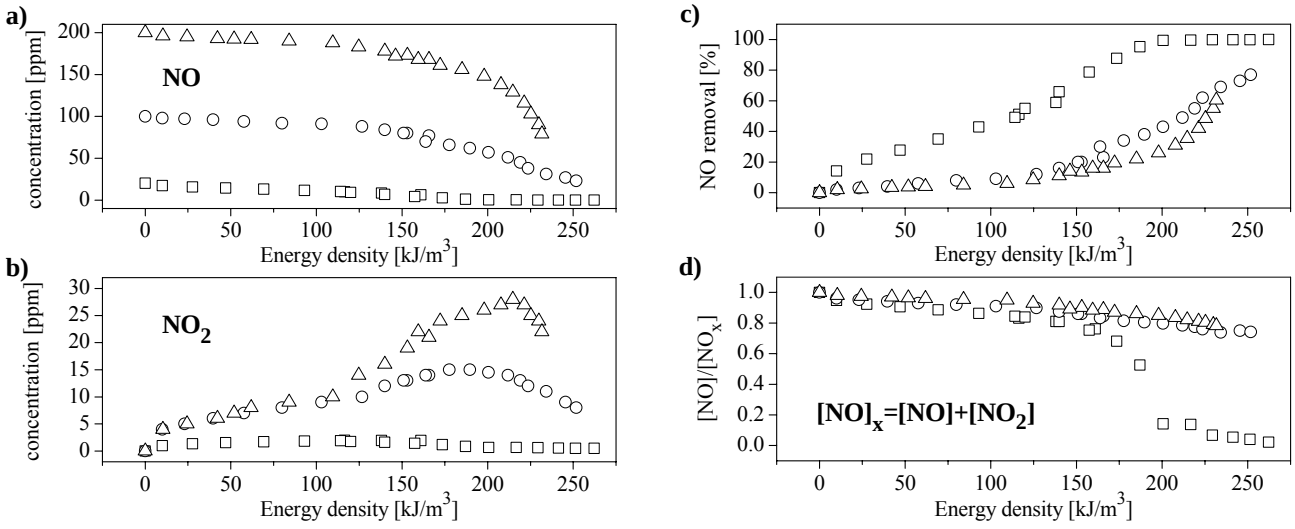

Figure 5. Nitric monoxide transformation as a function of energy density for various initial NO concentrations (□ =20 ppm O =100 ppm and Δ =200 ppm) and for a constant flow rate through the needle 5 slm.

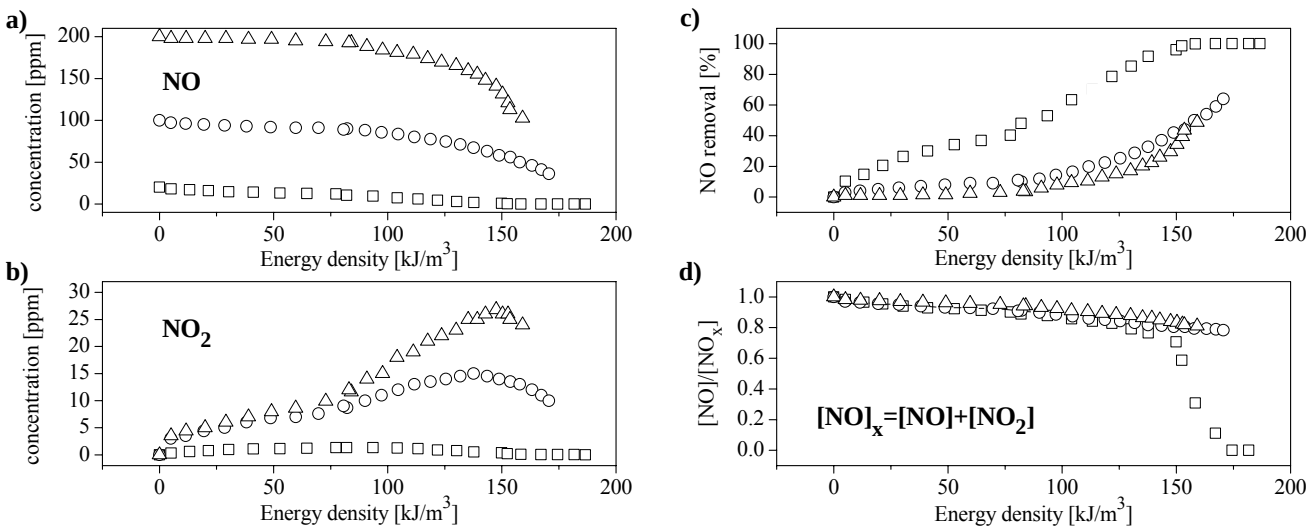

Figure 6. Nitric monoxide transformation as a function of energy density for various initial NO concentrations (□ =20 ppm O =100 ppm and Δ =200 ppm) for a constant flow rate through the needle 10 slm.

4. Discussion and conclusions

We have conducted experiments using the diluted mixtures of NO in N_2 to examine rigorously how various parameters affect the efficiency of N_2 dissociation and subsequent reduction of NO by N radicals. In our experimental arrangement the electric, energetic, hydrodynamic and chemical processes occurring in the discharge are strongly coupled. The mixture leaving the needle electrode expands and consequently the chemical kinetics is necessarily affected by this expansion. Furthermore a fraction of input energy in the discharge relaxes into thermal energy. The resulting change in the temperature induces perturbation on the chemical kinetics. The NO decomposition is therefore a result of many processes, which in a complex way depend on many factors such as:

- Reduced electric field - *E/N*
- Gas heating
- Polarity of the needle electrode
- Mixture composition
- Energy density
- Flow of the mixture through the needle electrode.

In our experiments we focused namely on the role of the last three parameters on NO decomposition. To summarize experimental results, the following findings can be highlighted:

- The NO decomposition in the discharge strongly depends on energy density for all three investigated initial NO concentrations.
- Complete NO removal can be more easily achieved for lower initial NO concentrations.
- The production of NO_2 increases with increasing the removal of NO. This result is in agreement with previous findings published in [9]. However we found that the production of nitrogen dioxide versus energy density exhibits a certain maximum. The position of this maximum depends on initial NO concentration and with increasing initial NO concentration is shifted towards higher energy densities.
- NO removal efficiency depends on initial NO concentration; complete NO removal is obtained for lower initial NO concentrations with lower energy density.

- The ratio of nitric oxide to the sum of nitric oxide and nitrogen dioxide decreases with increasing energy density. The sharp decrease of this ratio for initial NO concentration $[NO]_{in}$=20 ppm depends on the energy density and on the flow of the mixture through the needle electrode.

In conclusion, all experimental findings indicate that the transformation of nitric oxide in a negative hollow needle to plane HV discharge is controlled by the production of atomic nitrogen. The production of atomic nitrogen probably increases monotonously with increasing energy density as reflected by increasing NO removal efficiency (throughout all the 0-250 kJ/m^3 range inspected in this study) and by increasing NO_2 production as well (to a certain energy density level). In a low energy density range certainly both (1) and (2) processes strongly influence the NO removal. When the production of atomic nitrogen reaches a certain level, then subsequent production of atomic oxygen through (1) allows efficient production of NO_2 through (2) which is reflected by a peak NO_2 value. With a further increase of N^I production, the majority of NO species are removed in (1) and, consequently, the NO_2 concentration curve shows a declining trend.

Acknowledgement
This work has been supported by Grant Agency of the Academy of Sciences of the Czech Republic under contract No. A1043403.

References
[1] J.S.Chang, P.A.Lawless, and T.Yamamoto - *IEEE Trans. Plasma Sci.* **19**, 1152 (1991).
[2] B.M.Penetrante *et al.* - *IEEE Trans. Plasma Sci.* **23**, 679 (1995).
[3] H. Lin, X. Gao, Z.Y. Luo - *Fuel* **83**,1251 (2004).
[4] M.Šimek - *J. Phys.D: Appl.Phys.* **35**, 1967 (2002).
[5] J.L. Lowke, R. Morrow - *IEEE Trans. Plasma Sci.* **23**, 661 (1995).
[6] S.Pekárek, V.Kříha and M.Pospíšil - *J. Phys.D: Appl. Phys.* **34**, L117 (2001).
[7] M. Šimek, M.Člupek, S. Pekárek, J.Rahel, M. Šimor and M.Černák - *Proceedings of ISPC 16.*, Abstracts and full-papers CD, ISPC-327.PDF, June 22-27, Taormina, Italy (2003).
[8] S.Pekárek, R.Bálek - *J. Phys.D: Appl. Phys.* **37**, 1214 (2004).
[9] K.Takaki, M.A. Jani and T.Fujiwara - *IEEE Trans. Plasma Sci.* **27**, 1137 (1999).

STUDY ON THE ATMOSPHERIC-PRESSURE NON-THERMAL SURFACE-DISCHARGE PLASMA TORCH

Shin-ichi Kuroda, Kazuyuki Tamura, Tomoe Goto, Wataru Tobe and Hitoshi Kubota

Department of Chemistry, Faculty of Engineering, Gunma University, Tenjin-cho 1-5-1, Kiryu, Gunma 376-8515, Japan

Abstract

A cylindrical plasma torch composed of a stainless steel tube, a silicone tube and an aluminum ring belt was developed to generate an atmospheric-pressure non-thermal plasma jet. The plasma jet was obtained by applying pulse-modulated power under He gas flow. The electric current and the plasma jet length were found to depend on the input power frequency leading to the variation of active species concentration in the jet. Polymer films were effectively treated in the plasma jet resulting in the hydrophilic surfaces.

1. INTRODUCTION

There has been lately growing interests in low-temperature plasma sources working at atmospheric pressure[(1)]. Corona and dielectric barrier discharges (DBD) are traditional sources of atmospheric-pressure plasma that produce non-equilibrium plasmas with gas temperatures between 5-400 °C. However, since these discharges take place non-uniformly in a narrow gap of electrodes, their use in material processing is limited.

Recently, several plasma torch systems employing low-temperature flowing plasma jets have been developed, which seem promising for the surface treatment of large substrates with complex shape on the surface[(2-5)]. If a plasma jet with an adequate length is generated expanding out of the torch, more various and useful chemical reactions would be expected. In the previous study, we have developed a double cylindrical barrier discharge plasma torch and examined the effects of positioning of inner and outer electrodes on the generated plasma jet[(6)]. It was found that a stable He plasma jet was generated when the inner electrode was earthed and withdrawn back into the outer electrode.

In this paper, we developed another type of non-thermal plasma torch working at an atmospheric pressure. The torch consists with two coaxial cylindrical electrodes with different length and the plasma is generated by the surface discharge along the silicone tube that is inserted between the electrodes. The effects of applied voltage and helium gas flow rate on the plasma jet length are examined. The surface treatment of polypropylene film is carried out and the results are discussed in relation to the emission spectra observed for the plasma jet.

2. EXPERIMENTAL

The plasma torch used in this paper is illustrated in Fig.1. A stainless steel cylindrical tube of 6 mm diameter was used as the inner electrode and 20 mm length aluminum ring was located at the distance 5 mm from the tip of inner electrode. Silicone tube of 10 mm diameter was inserted coaxially between the electrodes for insulation. Helium gas was supplied to flow in the inner electrode at various rates. The input power was pulse-modulated bipolar sine wave with a pulse width of ca. 5 μs and applied by an impulse source (Haiden Laboratory, PHF-2K). The excitation frequency

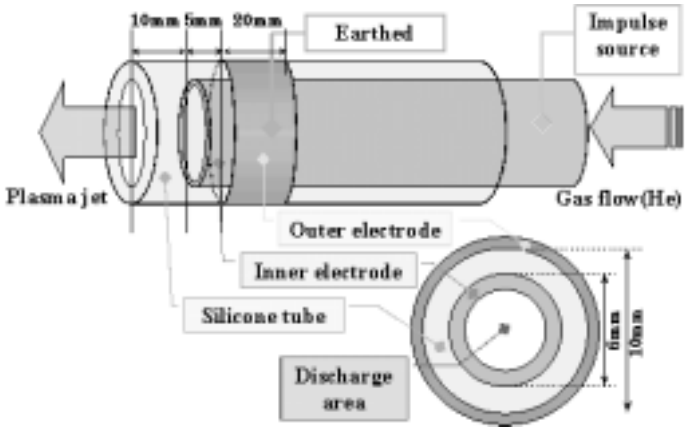

Fig.1 Scheme of plasma torch.

of discharge was varied from 2 to 100 kHz. The plasma was generated by applying the power to the inner electrode (A connection) or the outer electrode (B connection).

The plasma jet generated by the plasma torch was monitored by a CCD camera (SONY, DCR-TRV7) and recorded on a digital tape. The plasma jet length was evaluated on the recorded picture. In order to estimate the active species in the plasma jet, emission spectra were observed by using a plasma process monitor (Hamamatsu Photonics, C7460). The spectra were collected through an optical fiber for the plasma jet region out of the torch.

Polystyrene (PS) films were treated by the plasma torch for 10 s at the positions of 5-40 mm away from the torch end. XPS measurements were carried out after the treatment on the film surface by using Perkin Elmer ESCA 5600.

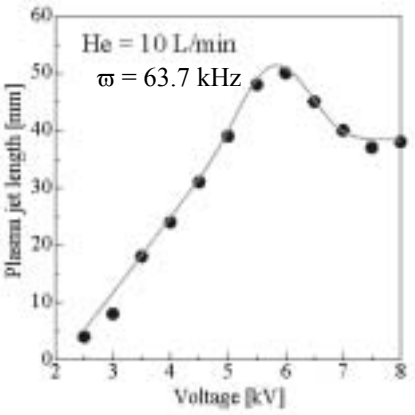

Fig.2 Effect of applied voltage on plasma jet length.

3. RESULTS AND DISCUSSION

The plasma jet was successfully generated both in the A connection and B connection.

The applied voltage and the flow rate of helium had a big influence on the length of plasma jet generated. The dependency of plasma jet length on the applied voltage and the helium flow rate is shown in Fig.2 and Fig.3, respectively for the case of A connection i.e. the outer electrode was earthed. The plasma jet length increases with the applied voltage up to 6 kV, which seems reasonable as the length should correspond to the amount of charged particles generated by the applied field. On the other hands, as the flow rate of helium increases, the plasma jet length increases till the flow rate of 30 L/min then turns into decrease. Too high fluid velocity seems to reduce the contact time of helium gas and inner electrode leading to the less generation of charged particles.

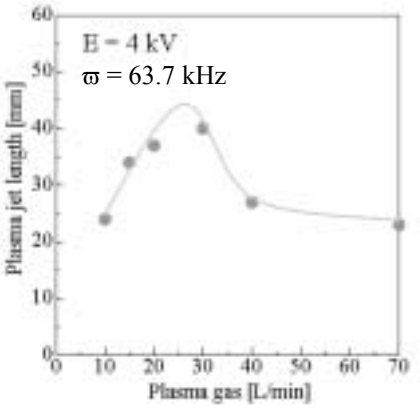

Fig.3 Effect of He gas flow rate on plasma jet length.

The input power frequency also affected the plasma generateon behavior. The electric current and plasma jet length were monitored with changing the frequency and plotted in Fig. 4 for the A connection as well as B connection. A similar dependency of current on the frequency is observed both in A and B connections, however that of plasma jet length is very different from each other in those two connections. The A connection leads to the consistent dependency of electric current and plasma jet length. On the contrary, the B connection shows almost opposite dependency. It is thus clear that the plasma jet length is not determined only by the electric current.

The raw emission spectra from the plasma jet region out of the torch are shown in Fig. 5. They were collected at 10 mm away from the torch end for the plasma jet generated under the frequency of 40 kHz. They exhibited prominent two nitrogen molecular band systems, i.e., N_2 second positive system (N_2 2+ ; 296, 316, 337, 358, 380 and 406 nm) and N_2^+ first negative system (N_2^+ 1– ; 391, 428 and 471 nm). The relatively weak bands due to oxygen neutral atoms (777 and 845 nm) and helium neutrals (588, 668, 706 and 728 nm) were also observed. It is considered that the energy transfer from the metastable helium species to the molecular nitrogen and oxygen take place very rapidly in the plasma jet. It is should be noted that the N_2

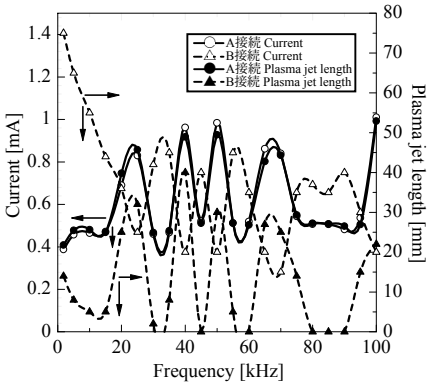

Fig.4 Effect of input power frequency on electric current and plasma jet length.

2+ emission is emphasized in A connection while the emission is weak in B connection though the emission intensity of N_2^+ 1– is close to the intensity in the A connection. In the similar manner, the intensity of O emission is about four times stronger in A connection than that in B connection while those of He are similar in A ad B connections.

The surface treatment of PS films was performed as one of applications of the present plasma torch. No fusion of polymer films was observed during the treatment indicating the gas temperature of the plasma jet was adequately low. The surface atomic concentrations of oxygen on the PS films estimated by XPS measurements are shown in Fig.4. It is obvious that the PS films are oxidized by the treatment. The O/C ratio keeps over 0.3 and changes little while the distance is less than 30 mm, i.e. the films are set in the plasma jet. On the other hand, the concentration drops down rapidly with increasing the distance when the films are treated at the outside of plasma jet. It is clear that the larger effect can be achieved when treated in the plasma jet than in the afterglow region.

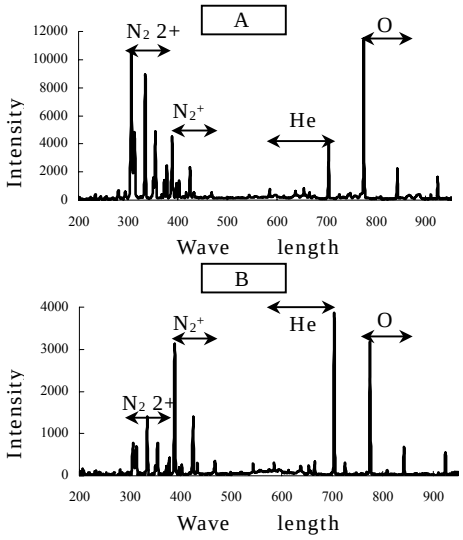

Fig.5 Emission spectra of plasma jet observed in A and B connections. . (Discharge conditions: E = 8.0 kV, ϖ = 63.7 kHz, He gas flow rate 10 L/min.)

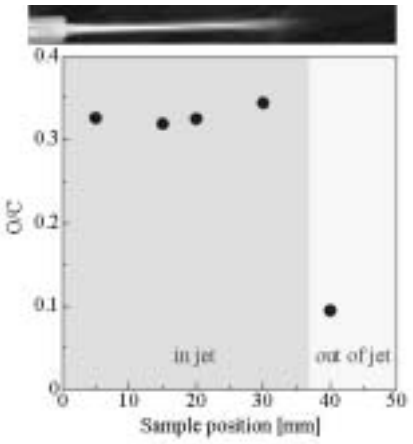

Fig.6 Surface atomic concentration of oxygen on polystyrene film treated for 10 s by plasma torch. (Discharge conditions: E = 8.0 kV, ϖ = 63.7 kHz. He gas flow rate 10 L/min.)

References

1. A. P.Napartovich, *Plasmas and Polym.*, **6**, 1 (2001).
2. A. Schütze, J. Y. Jeong, S. E. Babayan, J. Park, G. S. Selwyn, and R. F. Hicks, *IEEE Trans. Plasma Sci.*, **26**, 1685 (1998) .
3. K. Tanaka, T. Inomata, and M. Kogoma, *Plasmas and Polym.*, **4**, 269 (1999) .
4. J. Janča, L. Zajíčková, M. Klíma, and P. Slavíček, *Plasma Chem. Plasma Proc.* **21**, 565 (2001).
5. Z. Hubička, M. Čada, M. Šícha, A. Churpita, P. Pokorný, L. Soukup, and L. Jastrabík, *Plasma Sources Sci. Tech.*, **11**, 195 (2002).
6. A. Kuwobara, S. Kuroda, and H. Kubota, *Plasma Chem. Plasma Proc.* , submitted.

TIME-DEPENDENT D.C. PLASMA FLOW MODELING

E. Meillot, D. Guenadou, A. Saget

C.E.A. LE RIPAULT, B.P. 16, 37260 MONTS, France
Erick.Meillot@cea.fr

Abstract: The main problem in D.C. plasma flow modeling concerns the taking-into-account of the time-dependent arc root movements in the anode. These movements are responsible of high fluctuations of the flow outside the torch. From a simple numerical model based on the gas acceleration and heating by JOULE effect in the anode, realistic flow behavior is reproduced, in particular, the mechanisms of air engulfment into the plasma plume, such as it was described by PFENDER and al [1]. Moreover, the centerline velocities and temperatures of the gas are compared with experimental values: the comparison shows good agreement.

1. Introduction. D.C. plasma torches are commonly used in industrial fields such as plasma spraying, waste destruction and so on. These guns based on electrical energy transformation to kinetic and thermal energies need high electrode cooling and rapid arc root movements on the anode wall on pain of destruction. These movements are responsible of high fluctuations of the plasma plume outside the torch and so of air engulfment in the flow. These interactions are not without consequence in the particle treatment in the case of plasma spraying. Depending on the in-flight time of the particles in the jet, their thermo-kinetic state at impact varies in a large range and so the coating structure can present different morphologies. This paper, first step of the global plasma spraying process modeling, is devoted to a simple time-dependent numerical model based on the gas heating and acceleration by JOULE effect inside the torch. The aim is to reproduce the behavior of the plasma flow outside the torch interacting with the air atmosphere from the only main operating parameters opened by the operators. The problem of the D.C. arc generation is not new. Literature is rich of simulation models but not yet including time instabilities. PFENDER et al. [1] have proposed a steady 3 D. model including the LORENTZ forces and the JOULE heating. CHEN et al. [2] have implemented a 3-D no-time-dependent model including LORENTZ and JOULE heating.

2. CFD code. The governing equations, the Reynolds average NAVIER-STOKES and heat equations, are solved using FLUENT commercial code. The turbulent model is the REYNOLDS STRESS MODEL (RSM) provided by FLUENT without any modification. In [3], k-ε model has been used for turbulence simulating. The results have showed that the plasma jet length was too short outside the torch. That is why RSM tests are performed in this paper. The mass, momentum conservative equations are standard provided by FLUENT. The only heat equation is modified by integrating a source term SE representing the electric power inside the torch. The conduction and radiation losses are also considered. The FLUENT Code is in its commercial way. No MAXWELL equations and no electromagnetic phenomena in relation with the electric arc (LORENTZ forces, electrode phenomena…) are implemented in it. The code has been only adapted to plasma spraying conditions by the way of user-defined-functions (plasma gas and atmosphere transport and thermodynamic properties, calculation of mixed gas properties, simple JOULE effect model).

3. Basic assumptions. The plasma, considered like a Newtonian mono-fluid, is supposed to be in the local thermodynamic equilibrium, optically thin and chemically inert; the mono-fluid assumption integrates, at high temperature, the interactions between ionic and electronic species through global transport coefficients and thermodynamic properties. The properties of the mixture between plasma gas and surrounding atmosphere at lower temperatures are calculated by the formula of WILKE and MASSON [4], [5] from the data of pure gases or the plasma mono fluid [6]. The enthalpy temperature tabulation is also introduced. No magnetic or electric effects are taken into account.

4. Simple model. The gas heating and acceleration are simulated by introducing an energy source in the torch (Fig. 1). This zone, which spreads from the cathode tip to the anode, is divided in two volumes V1 and V2. The area V_1 near the cathode tip depends on the radius r(x) with a constant length l_1. The volume V_2 inside the anode has a length l_2 depending on the movement of the electric arc root on the anode wall and so

is a function of time t. In these two volumes, the electric power transferred to the fluid is defined respectively by: $P_1 = P_m/L_m * l_1$ (Eq. 1) $P_2 = P_m/L_m * l_2(t)$ (Eq. 2)

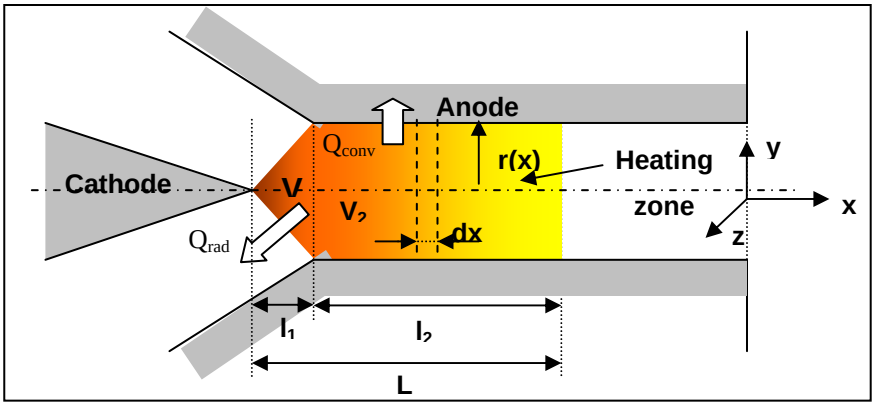

Figure 1: Different heating zones inside the gun.

where P_m is the time-average input power, P_m = U.I. (U and I are the mean arc voltage and intensity) and L_m is the plasma column length corresponding to P_m. l_1 is always constant while l_2 (t) is linked to the fluctuation of the arc voltage due to the arc root movement. The local volume energy density ∅(x) can be defined by:

$$\varnothing(x) = \frac{P_m}{r_{(x)}^2 . \pi . L_m} \qquad \text{(Eq. 3)}$$

with $r(x) = a.x^n + r_0$ (r0 is the cathode radius)

And so the electric power fluctuations depending on time can be written as:

$$P(t) = U(t).I = \int_o^l \varnothing(x)\, dx \qquad \text{(Eq. 4)}$$

With conduction and radiation losses, respectively written Q_{conv} and Q_{rad}, the thermal efficiency η is calculated as:

$$\eta = 1 - \left(\frac{Qconv + Qrad,}{P_m}\right) \quad \text{(Eq. 5)}$$

The first step of the model validation procedure consists in getting the stationary-state thermal efficiency by adjusting the function r(x) and the length l_2.

5. Operating plasma conditions. SULZER-METCO F4VB plasma gun, working with Argon/Hydrogen (75/25 %vol.) mixture flowing in standard air atmosphere, has been simulated with a 6 mm diameter anode. The other parameters are in Table 1. These conditions lead to voltage-vs- time evolution (Fig. 2).

Table 1: Operating parameters

Total gas flow rate	60 slpm
Total input power	32.5 kW
Arc intensity	500 A
Average arc voltage	65 V
Thermal efficiency	50 %

Figure 2 shows the fitted fluctuations of arc voltage from oscilloscope measurements. The arc voltage fluctuates from 55 V to nearly 90 V at the frequency of 4.3 kHz, which is in accordance with [7].

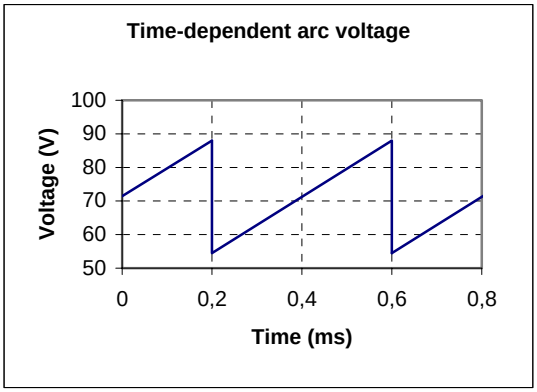

Figure 2: Time-dependent fitted arc voltage fluctuations.

6. Grid and boundary conditions.

A 2-D axis-symmetry grid has been performed. Near the wall and in the first millimeters outside the torch, the grid presents highest mesh number because of the high temperature and velocity gradients. The boundary conditions for turbulence input data are the turbulence intensity, the hydraulic diameter or the length scale. The engaged values are those proposed by FLUENT user guide [8].

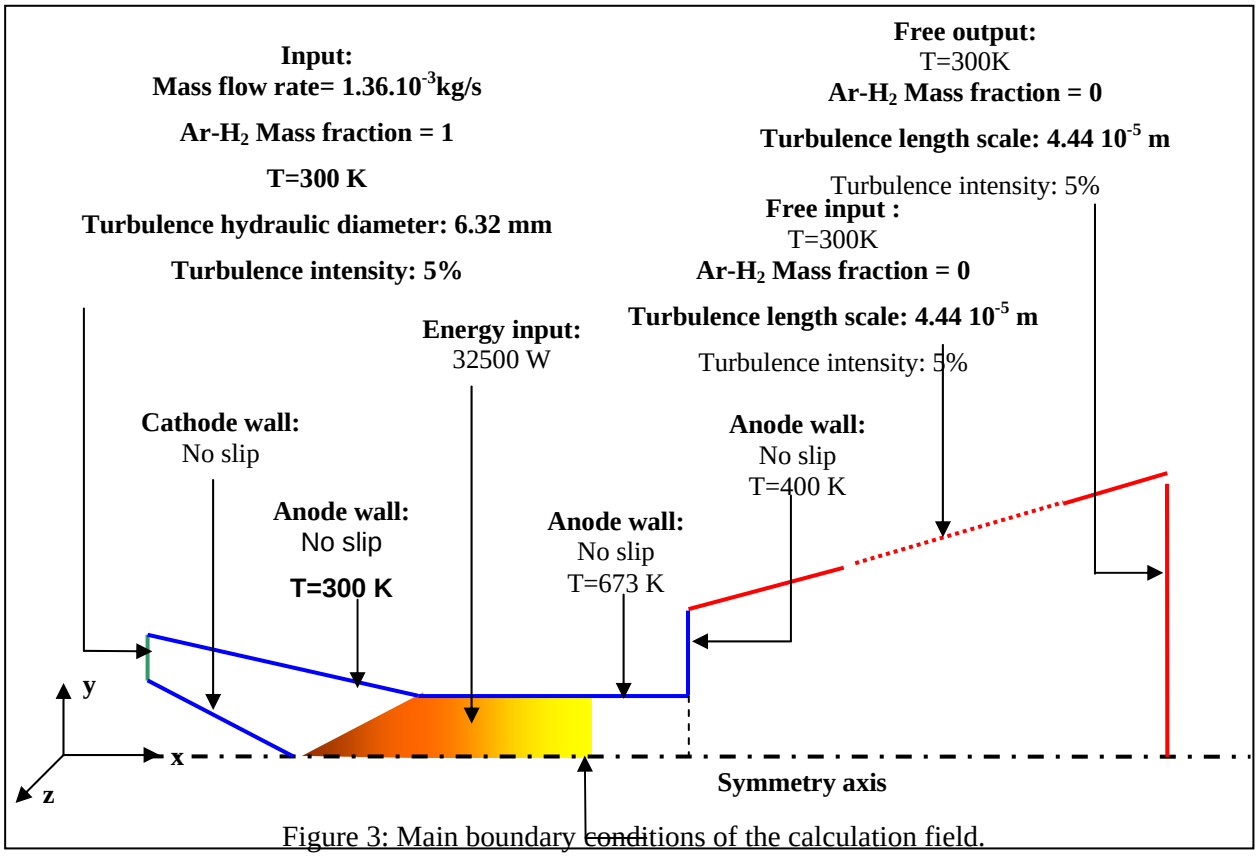

Figure 3: Main boundary conditions of the calculation field.

7. Results.

7.1 Stationary case. First of all, in no-dependent-time state, the two areas V_1 and V_2 have to be defined to get correct thermal efficiency. The V_1-defined-function is assumed such as $r(x) = a.x^n + r_0$ where r_0 is the cathode arc root radius. According to [9], [10], r_0 is fixed at 0.5 mm. x moves from 0 to l_1 = 7 mm. Three values (n=1, n=4, n= 12) have been tested. The V_2 area is defined by l_2 varying from 7 to 21 mm (torch exit position) while r_2 is constant at the anode radius 3 mm. Adjustment of thermal efficiency presents rather good correlation when n=1, l_2=15 mm (global volume= 487 mm^3) as shown in Figure 4.

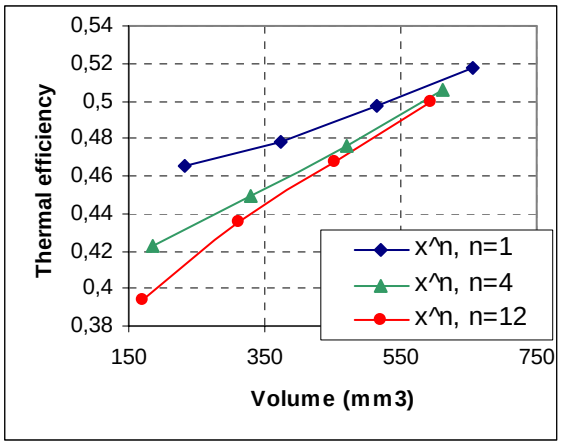

Figure 4: Thermal efficiency versus global heating zone volume.

The thermal efficiency η results from radiation and convection loss contributions. In V_1, convection is null due to no-direct contact between this zone and the walls. Radiation loss contribution ranks 90% in V_1 zone and 10% in V_2 due to different temperatures. On one side, expecting longest V_2 zone will tend to increasing in η (cf. Figure 4): the electrical power is diluted in a largest volume with lowest temperature and so conduction losses are diminished. On the other side, n modification leads to changing the constriction of V1 and so, mainly, the radiation loss level due to higher temperature near the cathode. That is why η decreasing when n increasing. Figure 5 shows the evolutions of velocity, temperature and molar air fraction on x centerline axis. Velocity values have been multiplied by 10 and air molar fraction by 10 000 to visualization in the same scale then that of temperature, point 0 corresponding to the torch exit.

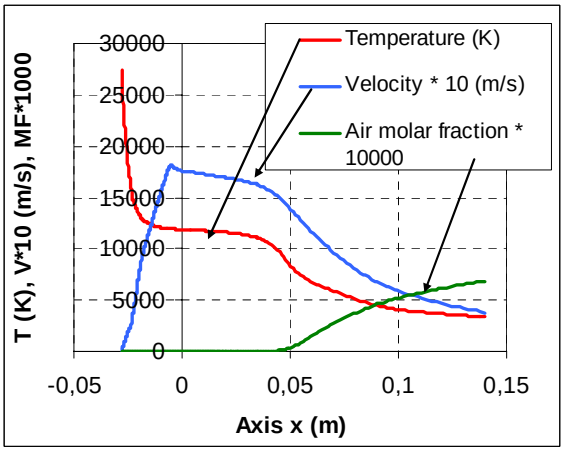

Figure 5: Evolution of temperature, velocity and molar air fraction on the x centreline axis.

First comments can be advanced about the general evolution of the velocity and temperature curves. If they are quite different inside the anode, they follow the same look after the anode exit, decreasing together faster and faster in a similar way when moving away from the torch. In particular, the two curves decrease strongly around 40 mm when turbulence becomes principal. If temperature values are in similar range than measurements near the torch exit [11], velocity gets 200 m/s too high at the torch exit [12]. Assumptions can be done about the theoretical arc root position which could be too near the torch exit. Previous works [3] have shown that the velocity increases when the electrical arc root comes near the front torch. As no cathode cooling has been taken into account, this could be the reason of this discrepancy. The same reason could be assumed for the delay of the air introduction which implies a too low molar air fraction at 80 mm (40% in place of 70% [13]). The cold atmosphere dilution absence leads to a too high temperature far from the front gun. Turbulence model can be charged: first tests with k ε model have shown similar behavior.

7.2 Time-dependent case. In figures 6 to 11, the mixing of the two fluids (air and plasma) is represented by their density at different times. In spite of the axis symmetry, air engulfment is well visualized with high constrictions and swirl developments of the plasma plume. Because of starting with stationary initial

conditions, the surface instability generation presents a delay as seen in figure 6. At time=0.84 ms (figure 6), the interactions between the two fluids become visualizing from the plasma surface which deteriorates to form arrows (figure 7). Then, acceleration of plasma gas, due to longer electrical arc in the anode, tends to develop again the plasma plume (figures 8 and 9): the arrows are smaller and smaller and a big puff of gas flows into the atmosphere. Then the cycle starts again (figure 10) with a lower constriction of the plasma and again generation of the arrows (figure 11). The surface instabilities are typically KELVIN HELMOLTZ. Unfortunately, their generation is not strong enough: as seen before, the air molar fraction is lower than the experiment measured one. Several reasons could be proposed to explain that phenomenon.

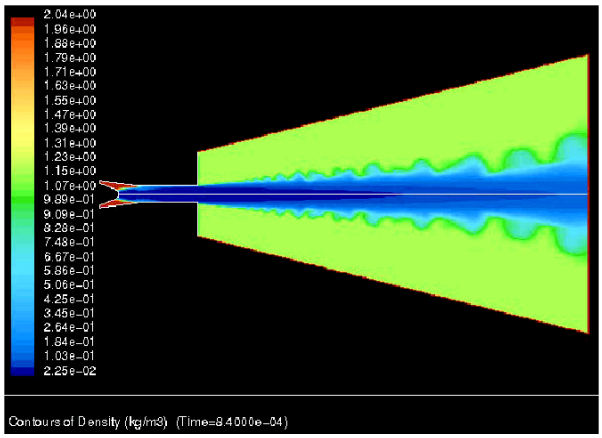

Figure 6: density of the two fluids at t=0.84 ms.

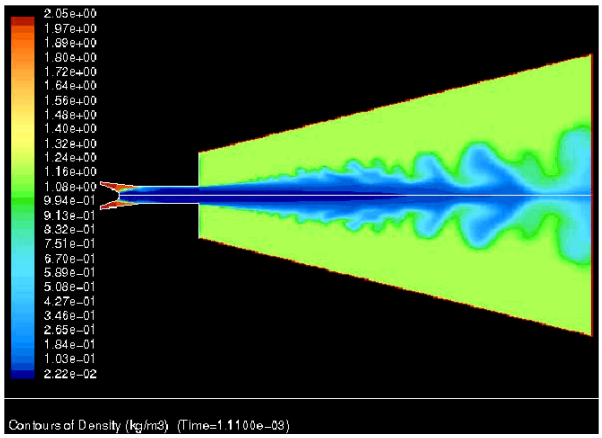

Figure 7: density of the two fluids at t=1.11 ms.

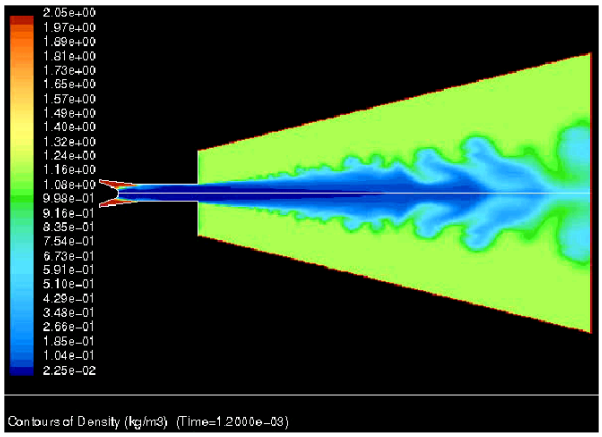

Figure 8: density of the two fluids at t=1.20 ms.

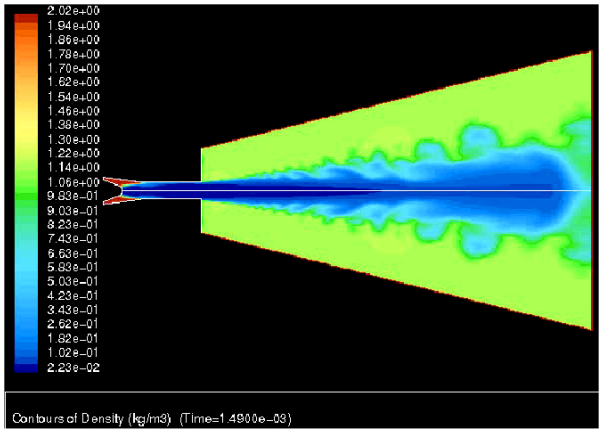

Figure 9: density of the two fluids at t=1.49 ms.

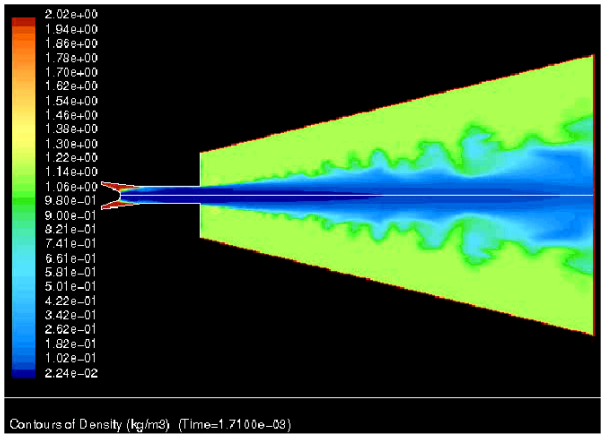

Figure 10: density pf the two fluids at t=1.71 ms.

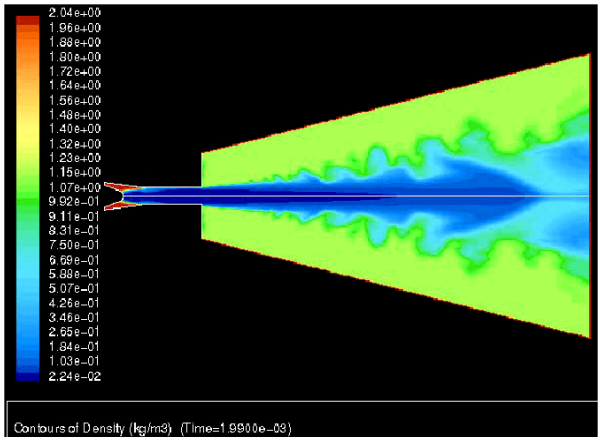

Figure 11: density of the two fluids at t=1.99 ms.

Due to convergence problem, mainly at the initial state, calculations have not been performed in 3-D but in 2-D axis-symmetry design: yet, electrical arc movement fluctuations are typically 3-D phenomena. Moreover, the preliminary initial conditions of the time-dependent case are from the average stationary solution. So, the complete development of air engulfment needs perhaps more time than 2.7 ms to forget the initial conditions and to penetrate completely the plume (stand-off position is on the centerline).

8. Conclusion. From a simple model based mainly upon JOULE effect, the operating parameters and the torch design, the plasma flow behavior outside the plasma spraying torch has been reproduced in time dependent simulations. The average results, temperature velocity and air fraction engulfment, in steady state, are a lit bit too high in comparison with experiments. Nevertheless, in dynamic simulation, plasma constrictions and puffs are well observed. Several correcting assumptions will be integrated in further works: the first one will improve the heating model by adding cathode cooling and modifying the heating zone with a casual and fast movement of the arc root all along the anode wall perimeter, the second one concerns the turbulence model to advance the laminar-turbulence transition. This movement will simulate the taking-into-account of the anode wall surface state but will imply 3-D simulations. The third proposes to start the calculation without stationary solution but, for the moment, this was unsuccessful due to convergence problem.

References

[1] E. PFENDER, W.L.T. CHEN, R. SPORES, Proceedings of 3rd National Thermal Spray Conference, Ed. T.F. BERNEEKI, LONG BEACH, CA, USA, 20 – 25 May 1990.

[2] X.CHEN, H.P. LI, Three-dimensional flow and Heat Transfer in Thermal Plasma Systems, Surface and Coatings Technology, 171, 2003, pp. 124-133.

[3] E. MEILLOT, D. GUENADOU, Thermal Plasma Flow Modelling: a Simple Model for Gas Heating and Acceleration, Plasma Chemistry and Plasma Processing, 24, 2, 2004.

[4] C.R. WILKE, A Viscosity Equation for a Gas Mixture, Journal of Chemical Physics, 18, 4, 1950, pp. 517-519.

[5] E.A. MASON, S.C. SAXENA, Approximate Formula for the Thermal Conductivity of Gas Mixture, The Physics of Fluid, 1, 5, 1958, pp. 361-369.

[6] M. BOULOS, P. FAUCHAIS, E. PFENDER, Thermal Plasmas Fundamentals and Applications, Vol. 1, Ed. Plenum Press, New York, 1995.

[7] J.F. COUDERT, M.P. PLANCHE, P. FAUCHAIS, Characterization of D.C. Plasma Torch Voltage Fluctuations, Plasma Chemistry and Plasma Processing, 16, 1, 1996, suppl., pp. 2115-2275.

[8] FLUENT users' guide, V 6.1, 2000.

[9] X. ZHOU, J. HEBERLEIN, Analysis of the Arc-Cathode Interactions of Free-Burning Arcs, Plasma Source Science Technology, 3, 1994, pp 564-574.

[10] C. BAUDRY, A VARDELLE, G MARIAUX, C DELAFONDRE, E MEILLOT, Three-Dimensional and Time-Dependent Model of the Dynamic Behaviour of the Arc in a Plasma Torch, Proceedings of ISTC 2004, OSAKA, JAPAN, May 2004.

[11] O. BETOULE, M. MELLALI, J.F. COUDERT, M. VARDELLE, P. FAUCHAIS, M. DUCOS, Thermal spraying Diagnostics from Plasma Jet to Coatings Properties, Proceedings of the International Conference on Surface Modification Technologies, NICE, Sept 26-28, 1994, Published by Institute of LONDON, pp. 721-733.

[12] M.P. PLANCHE, Ph. D. Thesis in French, University of LIMOGES, N° 37-1995, 1995.

[13] O. LAGNOUX, Ph. D. Thesis in French, University of LIMOGES, FRANCE, 1999.

Three-Dimensional Modeling of Non-Equilibrium Effects in a Transferred DC Arc Plasma with Lateral Gas Blowing

He-Ping Li[1, 2], J. Heberlein[1], and E. Pfender[1]

[1] *Department of Mechanical Engineering, University of Minnesota, Minneapolis, MN 55455, USA*

[2] *Present address: Department of Engineering Physics, Tsinghua University, Beijing 100084, P. R. China*

Abstract

In this paper, three-dimensional, non-equilibrium physical/mathematical models of transferred DC arc plasmas with lateral cold gas blowing are described, and the modeling results under typical operation conditions are presented. The predicted deflections of the anode arc-root attachments in the direction of the lateral cold gas flow for different lateral gas flow rates are in reasonable agreement with measurements.

Keywords Three-dimensional modeling, Non-equilibrium effects, Arc plasmas

1. Introduction

Thermal plasmas have been widely used in industrial applications, such as plasma spraying, welding, cutting, etc., because they can provide high fluxes of charged species and other useful radicals, usually coupled with high heat fluxes. However, the high heat fluxes also lead to erosion of electrodes, and such plasmas are not suitable for processing of low melting point and/or thin film materials. In many applications, large plasma volumes, with high electron densities and higher electron temperatures compared to heavy-particle temperatures, and operation at relatively high pressures ($p \geq 0.1$ atm) are desirable as an ideal plasma processing environment.

Previous numerical [1-3] and experimental [4, 5] investigations on plasma arcs showed that the non-equilibrium effects were pronounced near the electrodes, near cold walls or in the fringes of arc plasmas, even though deviations from local thermodynamic equilibrium (LTE) in the arc core were insignificant for high-intensity arcs. However, these non-equilibrium regions are very small, and in general, not suitable for plasma processing applications. Recently, experimental studies on arc-anode attachment instabilities in this laboratory have shown that a stable form of an arc attachment with a relatively large non-equilibrium region in front of the anode can exist when a cold gas is injected laterally along the anode surface [6, 7]. A schematic diagram of the experimental setup of a transferred DC arc plasma with lateral cold gas flow, used in the experimental studies [6, 7], is shown in Figure 1.

Associated with the combinations of different arc currents, working gas flow rates and lateral gas flow rates, different anode attachment modes, including a steady deflected anode root, a randomly fluctuating attachment, and a periodically fluctuating attachment, have been observed in experiments [7]. But up to now, the understanding to this non-equilibrium effect is still very limited. Few papers [8, 9] were published describing this three-dimensional (3D), non-equilibrium effect numerically and comparing it with measurements. In this paper, a 3D, non-equilibrium model of transferred DC arc plasmas with lateral cold gas flow, as shown in Figure 1, is described. The 3D modeling results with constant plasma working gas flow rate, arc current and variable lateral cold gas flow rates are presented and compared with experimental measurements. The predicted arc

deflections in the direction of the lateral gas flow for different cold gas flow rates are in reasonable agreement with experimental data.

2. Descriptions of the 3D, non-equilibrium model

A schematic diagram of the calculation domain (indicated by the dashed lines in Figure 1), as a simplification of the real apparatus, is shown in Figure 2 with geometrical dimensions. Because the actual flow patterns and heat transfer in the region outside the constrictor tube are symmetrical about the plane passing through the constrictor tube axis and perpendicular to the injection frontal plane (plane ABCD as shown in Figure 2, which is called injection plane hereafter), only half of the 3D space is adopted as the calculation domain (formed by the points ABCDEFGH) in this modeling work. The inner diameter of the constrictor tube is 10 mm. In this paper, a part of the constrictor tube (10 mm in length) is included in the calculation domain, because the flow patterns at the exit of the nozzle are not completely axi-symmetrical due to the 3D behavior of the deflected arc with larger lateral cold gas blowing. And this non-axi-symmetrical behavior will, to some extent, influence the local characteristics of the deflected arc near the exit of the nozzle. In addition, the solid anode region with the thickness of 5 mm is also considered in this study, which is convenient for specifying the boundary conditions for heavy-particle temperatures [10, 11].

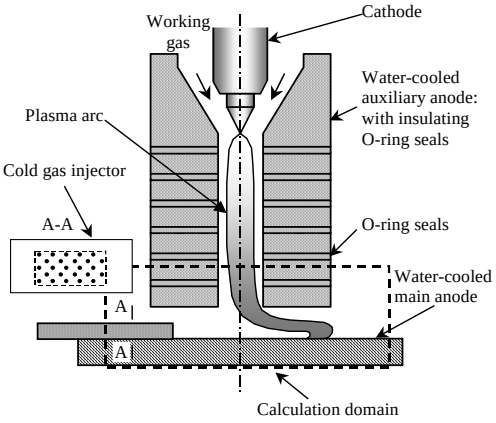

Figure 1. Schematic diagram of a transferred arc

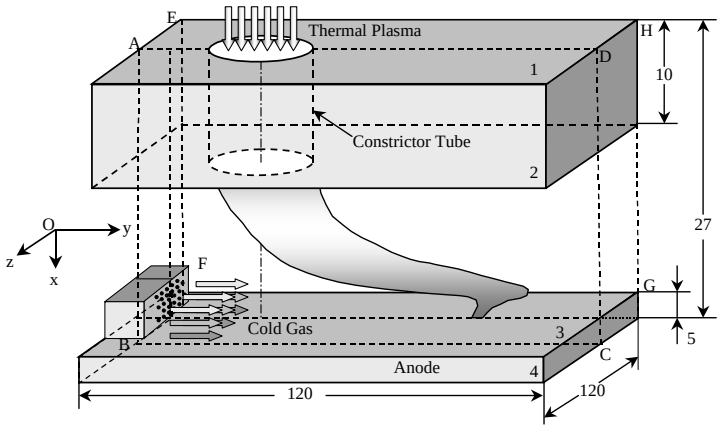

Figure 2. The schematic diagram of the computational domain

In this paper, we assume that: (1) the plasma flow is 3D, quasi-steady and laminar; (2) the plasma is in kinetic and chemical non-equilibrium state, i.e., the electron temperature is very different from the heavy-particle temperature, indicated with T_e and T_h, respectively, and separate Maxwellian distributions of electrons and heavy particles are postulated; (3) the plasma is optically thin; (4) argon is used as the plasma working gas and the transversely injected cold gas; (5) the plasma system is composed of three components, i.e., atoms (Ar), singly-ionized ions (Ar^+) and electrons (e), with only one ionization-recombination reaction as $Ar + e \Leftrightarrow Ar^+ + e + e$, with charge neutrality sustained in this system; (6) the thermodynamic and transport properties of the argon plasmas are a function of the species number densities (n_e) and the temperatures (T_e and T_h); (7) the gravity, viscous dissipation and the pressure work terms are neglected in the momentum equation and energy equations, respectively.

Based on the foregoing assumptions, the governing equations for the 3D, quasi-steady numerical simulations can be written in Cartesian coordinates as follows:

Species Continuity Equation:

$$\nabla \cdot \left(n_e \vec{v} \right) = -\nabla \cdot \vec{\psi}_e + \dot{S}_e^c \tag{1}$$

where n_e and $\vec{\psi}_e$ are the number density and number flux of electrons, respectively. $\vec{v}$ is the mass-averaged velocity of plasmas. $\dot{S}_e^c$ is the source term of chemical reactions for electrons, and can be calculated as [12a]

$$\dot{S}_e^c = \alpha n_a \left[S(T_e) - \frac{{n_e}^2}{n_a} \right] \tag{2}$$

where α is recombination coefficient ($\alpha = 8.72 \times 10^{-22} n_e T_e^{-9/2}$ is used in this study [13]). In Equation (2), $S(T_e) = \left({n_e}^2 / n_a \right)^*$ is the ratio of number densities for chemical equilibrium [14].

Mass-Averaged Momentum Conservation Equation:

$$\nabla \cdot \left(\rho \vec{v} \vec{v} \right) = -\nabla p - \nabla \cdot \vec{\vec{\tau}} + \vec{j} \times \vec{B} \tag{3}$$

where $\vec{\vec{\tau}}$ is the shear stress tensor, $\vec{j}$ and $\vec{B}$ are the total current density vector and the self-induced magnetic induction.

Electron Energy Conservation Equation:

$$\nabla \cdot \left(\frac{5}{2} n_e k_B \vec{v} T_e \right) = \nabla \cdot \left(k_e \nabla T_e \right) - \nabla \cdot \left(\rho_e h_e \vec{V}_e \right) + \vec{j} \cdot \vec{E} + \dot{Q}_{eh}^{el} + \dot{Q}_{e,ch} - \dot{Q}_r \tag{4}$$

Total Heavy-Particle Energy Conservation Equation:

$$\nabla \cdot \left[\left(\frac{5}{2} n_h k_B + \frac{n_i E_i}{T_h} \right) \cdot \vec{v} T_h \right] = \nabla \cdot \left(k_h \nabla T_h \right) - \nabla \cdot \left(\rho_a h_a \vec{V}_a \right) - \nabla \cdot \left(\rho_i h_i \vec{V}_i \right) - \dot{Q}_{eh}^{el} - \dot{Q}_{e,ch} \tag{5}$$

In Equations (4) and (5), n_j, ρ_j, h_j and k_j are the number density, mass density, specific enthalpy and thermal conductivity of species j, while $\vec{V}_j$ is the diffusion velocity of species j, which can be calculated using the formulas presented in Ref. [15]. The subscripts a, i, e and h represent atoms, ions, electrons and heavy particles, respectively. k_B and E_i are the Boltzmann constant and the ionization energy of argon atoms. $\vec{E}$ is the total electric field. $\dot{Q}_r$ is radiation power per unit volume. The rate of energy exchange per unit volume during elastic collisions between electrons and heavy particles can be calculated as

$$\dot{Q}_{eh}^{el} = -\frac{3 m_e}{m_i} n_e \left(\bar{\nu}_{ei} + \bar{\nu}_{ea} \right) k_B \left(T_e - T_h \right) \tag{6}$$

where $\bar{\nu}_{ei}$ and $\bar{\nu}_{ea}$ are the average collision frequency between electrons and ions [12b], and between electrons and atoms [16], respectively. The chemical energy source term $\dot{Q}_{e,ch}$ is calculated by

$$\dot{Q}_{e,ch} = -\dot{S}_e^c E_i \tag{7}$$

Electric Potential Equation:

$$\nabla \cdot \left(\sigma \nabla \phi_{eff} \right) = 0 \tag{8}$$

where σ is the electric conductivity of argon plasmas, ϕ_{eff} is the effective electric potential written as

$$\vec{E}_{eff} = -\nabla \phi_{eff} \tag{9}$$

where $\vec{E}_{eff}$ is the effective electric field, which relates to the total electric field $\vec{E}$ as $\vec{E}_{eff} \cong \left(\vec{E} + \nabla p_e / e n_e \right)$.

And thus, the current density $\vec{j}$ can be calculated by $\vec{j} = \sigma \vec{E}^e$.

Magnetic Vector Potential Equation:

$$\nabla^2 \vec{A} = -\mu_0 \vec{j} \tag{10}$$

where μ_0 is the permeability in vacuum. The three-dimensional, self-induced magnetic induction $\vec{B}$ is defined as $\vec{B} = \nabla \times \vec{A}$.

For obtaining converged solutions, appropriate boundary conditions for the foregoing dependent variables are necessary. On the injection plane (ABCD), symmetry conditions are employed. At the outer edges of the calculation domain (Plane ABFE, DCGH, EFGH), free boundary conditions are used. Two-dimensional modeling results are employed as the boundary conditions of the variables to be solved in the 3D case at the inlet of the calculation domain. At the rear surface of the anode, a uniform temperature (T=300 K) and electric potential (ϕ=0) are specified. The modeling results are very sensitive to the boundary conditions of electron temperature and electron number density along the inner surface of the anode. In this study, the (2^3-1) extrapolation rule [17] is employed to specify the values of the electron number density and electron temperature along the anode inner surface. In the actual experimental setup, the injector is composed of 25 1 mm-in-diameter circular holes as shown in Figure 1. For simplicity in this study, these circular holes are replaced by the 1×1 mm^2 rectangular holes because the rectangular mesh is employed in this modeling work. The velocity of the injected cold gas issued from each injection port is calculated based on the actual lateral gas flow rate and injection port cross-sectional area. The boundary conditions for the magnetic vector potential are specified using the analytical solutions of Equation (10) [11].

3. Modeling results and discussion

3.1. Discussion on the typical modeling results

In this study, the foregoing 3D governing equations are solved simultaneously with appropriate boundary conditions. For a typical experimental operation condition (arc current I=100 A, working gas flow rate Q_1=5 slpm, lateral gas flow rate Q_2=18 slpm, and the distance between the frontal surface of the constrictor tube and the anode inner surface L=12 mm), the calculated distributions of heavy-particle temperature, electron temperature and number density, and velocity vectors in the injection plane are shown in Figures 3(a)~(d), respectively. It can be seen that the anode arc-root attachment moves downstream in the direction of the cold gas flow due to the blowing of the lateral cold gas along the anode inner surface. The calculated heavy-particle temperature and velocity distributions in the plane parallel to the anode surface and located 0.05 mm away from the anode inner surface are shown in Figure 4. It can be seen that a large part of the injected cold gas flows around the core region of the arc instead of passing through it, and the center of the anode arc root also deviates from the constrictor tube geometrical axis.

3.2. Comparisons with measurements

Under the same operation condition as those discussed in Section 3.1, the experimental charged-coupled device (CCD) image of the deflected arc is shown in Figure 5 [7]. By comparing Figures 3 and 5, the predicted deflection of the anode arc attachment in the direction of the lateral gas flow is ~6.7 mm, which is almost the same as the value derived from the experimentally obtained image (Figure 5) [7]. By varying the flow rate of the lateral gas from 0.0~20.0 slpm, the predicted deflections of the anode arc root attachments in the direction of the lateral cold gas flow are shown in Figure 6, compared with the corresponding derived values from the experimental images [7]. It can be seen that the calculated locations of the anode arc root attachments are in reasonable agreement with the experimental observations for different lateral cold gas flow rates. The maximum

relative discrepancy between the calculated and measured arc deflection length is ~25% at Q_2=17 slpm.

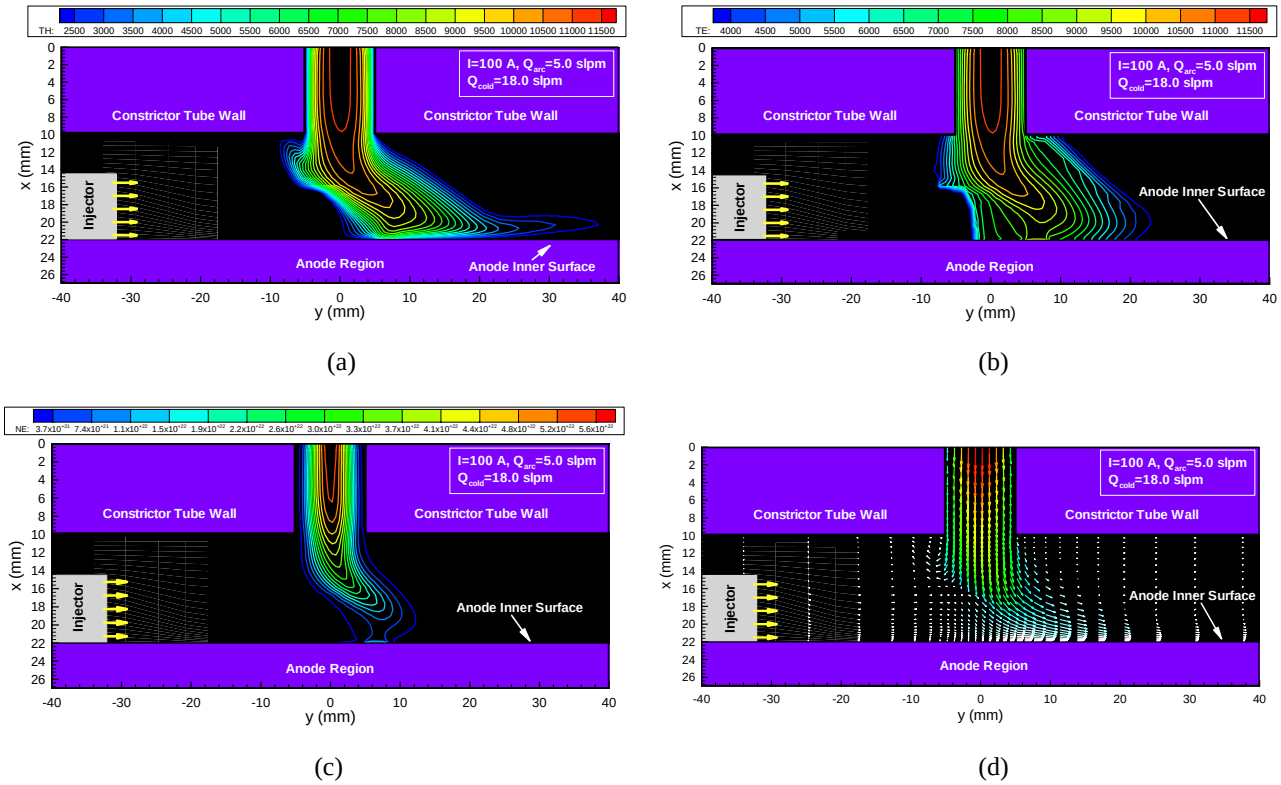

Figure 3. Distributions of heavy-particle temperature (a), electron temperature (b) and number density (c), and velocity vectors (d) in the injection plane

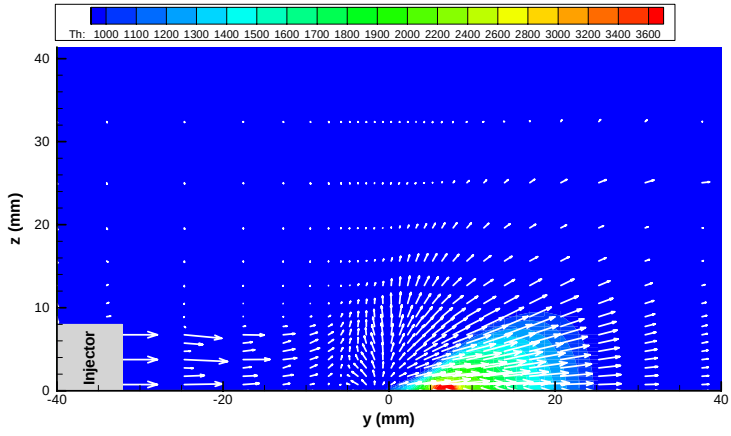

Figure 4. Distributions of the heavy-particle temperature and velocity in a plane 0.05 mm away from the anode inner surface

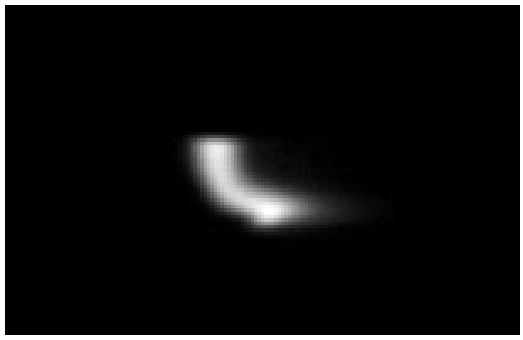

Figure 5. Picture of a deflected argon arc [7]

4. Conclusions

In this paper, the 3D, non-equilibrium effects of transferred DC arc plasmas with lateral cold gas blowing along the

anode inner surface are simulated. The physical/mathematical models are described and the modeling results are presented for typical operation conditions. The predicted arc deflection lengths are in reasonable agreement with experimental observations for different lateral cold gas flow rates.

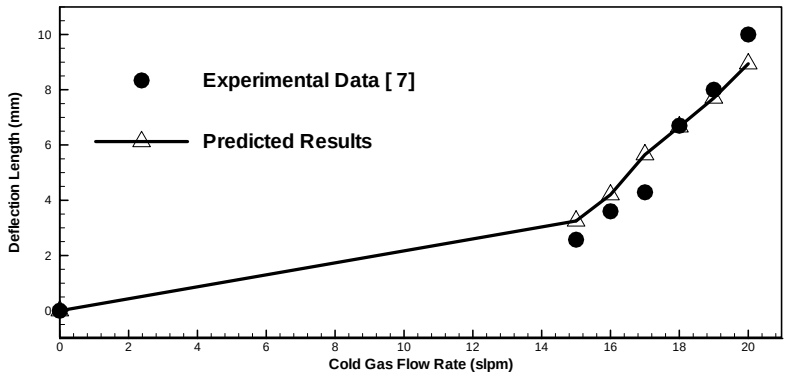

Figure 6. Comparisons of the predicted deflections of the anode arc root with measurements [7]

Acknowledgement

This work has been supported through NSF of USA (Grant # CTS-0225962) and the National Natural Science Foundation of China (Grant # 10405015). The first author has been supported through a postdoctoral fellowship by the Department of Mechanical Engineering, University of Minnesota. The support through a supercomputer grant by the University of Minnesota Supercomputing Institute is gratefully acknowledged.

References

[1] K. C. Hsu, and E. Pfender - Journal of Applied Physics. 54, 4359 (1983).

[2] D. M. Chen, and E. Pfender - IEEE Transactions on Plasma Science. PS-9, 265 (1981).

[3] J. Jenista, J. V. R. Heberlein, and E. Pfender - IEEE Transactions on Plasma Science. 25, 883 (1997).

[4] J. F. Bott - The Physics of Fluids. 9, 1540 (1966).

[5] R. J. Giannaris, and F. P. Incropera - J. Quant. Spectrosc. Radiat. Transfer. 11, 291 (1971).

[6] R. M. Hartmann, and J. V. Heberlein - Proc. of the 15th Int. Symp. Plasma Chemistry, France. 497 (2001).

[7] T. Iwao, P. Cronin, D. Bendix, and J. Heberlein - Proc. of the 16th Int. Symp. Plasma Chemistry, Italy. (2003).

[8] J. Park - Ph. D. Thesis, University of Minnesota. (2003).

[9] He-Ping Li, J. Heberlein, and E. Pfender - IEEE Transactions on Plasma Science, 2005 (in press).

[10] He-Ping Li, and Xi Chen - Journal of Physics D: Applied Physics. 34, L99 (2001).

[11] He-Ping Li, E. Pfender, and Xi Chen - Journal of Physics D: Applied Physics. 36, 1084 (2003).

[12] M. Mitchner, and C. H. Kruger, Jr. - Partially Ionized Gases, John Wiley and Sons, New York. a: 461; b: 58 (1973).

[13] E. Hinnov, and J. G. Hirschberg - Physical Review. 125, 795 (1962).

[14] Xi Chen, and Peng Han - Journal of Physics D: Applied Physics. 32, 1711 (1999).

[15] He-Ping Li, and Xi Chen - Chinese Physics Letters. 18, 547 (2001).

[16] R. S. Devoto - The Physics of Fluids. 16, 616 (1973).

[17] L. Rade, and B. Westergren - Mathematics Handbook for Science and Engineering, 4th Ed., Springer, New York. (1999).

Continuous Optical Discharge in Gas Flow

E.B. Kulumbaev[1], V.M. Lelevkin[1]

[1]*Kyrgyz-Russian Slavic University, Bishkek, Kyrgyz Republic*

Abstract

Theoretical model of continuous optical discharge burning in air at atmospheric pressure is used to carry out numerical analysis of optical radiation power input, wind speed at optical discharge localization in Earth's gravitation field, influencing the characteristics of optical discharge.

Introduction

The continuous optical discharge (COP) obtained a series of unique features in comparison with other electric discharge sources [1]: high temperature (~18000 K in atmospheric air), spectral purity of plasma (maintenance in free space), small spatial sizes (sizes of the discharge in a cross direction toward a laser beam ~ 1 mm), a possibility of re-localization in space et al. The COP, realized in practice, differs by length of the wave and focus of the laser radiation, by structure and exterior gas flows direction.

In experimental COP researches the discharge burning special temperature distributions in the atmospheric air free space, in a channel with forced gas pumping (in laser plasmatron regime) depending on gas flow were measured; the area of steady burning depending on a type and pressure of plasma-generating gas, wave length and a laser beam intensity, velocity and direction of blowing flow, focal distance and available target was established [2-4].

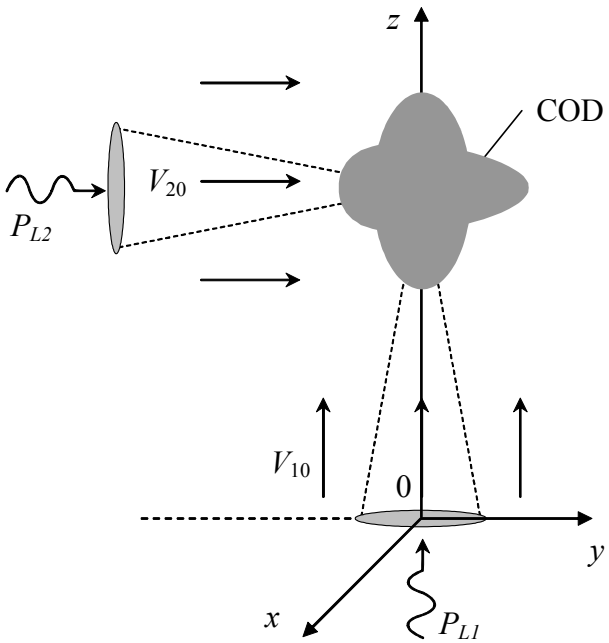

Figure 1. Schematic of a COD: P_{L1}, P_{L2} – intensities of vertical and respective horizontal laser beams; V_{10}, V_{20} – velocities of external gas flows.

Model

We consider a continuous optical discharge burning maintained by adsorption of power, supplied by CO_2-laser beams in airflow at atmospheric pressure. (fig.1). We guess that the flow is laminar, subsonic; plasma is balanced; the refraction of laser light is negligible; laser beams are Gaussian in shape.

Characteristics of the COD are found by solving a set of continuity equations, Navies-Stokes equation, energy balance equation, equation for selective radiation transport in multi-group diffusion approximation, and transport equation for laser radiation along optical beams axes:

$$\frac{\partial\rho}{\partial t}+\nabla\cdot\left(\rho\vec{V}\right)=0;\qquad \rho\left[\frac{\partial\vec{V}}{\partial t}+\left(\vec{V}\cdot\nabla\right)\vec{V}\right]=-\nabla\left(p+\frac{2}{3}\eta\nabla\cdot\vec{V}\right)+2\nabla\cdot\left(\eta\dot{S}\right)-\left(\rho_0-\rho\right)\vec{g};$$

$$\rho C_p\left[\frac{\partial T}{\partial t}+\left(\vec{V}\cdot\nabla\right)T\right]=\nabla\cdot\left(\lambda\nabla T\right)+Q_L-Q_R+\vec{V}\cdot\nabla p+2\eta\dot{S}^2-\frac{2}{3}\eta\left(\nabla\cdot\vec{V}\right)^2;$$

$$\nabla\cdot\left(\frac{1}{3\chi_k}\nabla U_k\right)=\chi_k\left(U_k-U_{kp}\right),\quad k=1,2,...,N_k;\qquad Q_R\approx\sum_{k=1}^{N_k}c\chi_k\left(U_{kp}-U_k\right);$$

$$Q_L=\frac{\mu P_{L1}}{\pi R_{L1}^2}\exp\left(-\frac{x^2+y^2}{R_{L1}^2}\right)\exp\left(-\int_{z_0}^{z}\mu dz\right)+\frac{\mu P_{L2}}{\pi R_{L2}^2}\exp\left(-\frac{x^2+\left(z-z_1\right)^2}{R_{L2}^2}\right)\exp\left(-\int_{y_0}^{y}\mu dy\right).$$

Notation: $\vec{V}$ - average-mass velocity; p - the pressure difference relative to the atmospheric pressure $p_0 = 10^5$ Pa; T - temperature; $\dot{S}$ - the tensor of velocities deformations; $\rho, C_p, \eta, \lambda, \mu$ - density, thermal capacity, viscosity, heat conductivity, the laser radiation absorption factor; χ_k, U_k, U_{kp} - group values of the absorption factor, density of the radiation of ambience and black body, averaged in each N_k spectral intervals; c -velocity of light; ρ_0 - density of a cold gas; $\vec{g}(0, 0, g_z = -g)$ - gravity acceleration; P_{L1}, P_{L2} - laser beams power with the radius $R_{L1}(z)$ and $R_{L2}(y)$; x, y, z - Cartesian coordinates; the optical laser beams axes are in parallel with the axes z and y (fig.1).

A numerical solution of a set of equations in physical variables is carried out by the method SIMPLE [5] in air at atmospheric pressure with thermal-physic, transport and optical (N_k =10) properties on data [6].

Results

It was found (fig. 2) that the COD high temperature core is located near the focus of a single laser beam or in area of crossed laser beams [7].

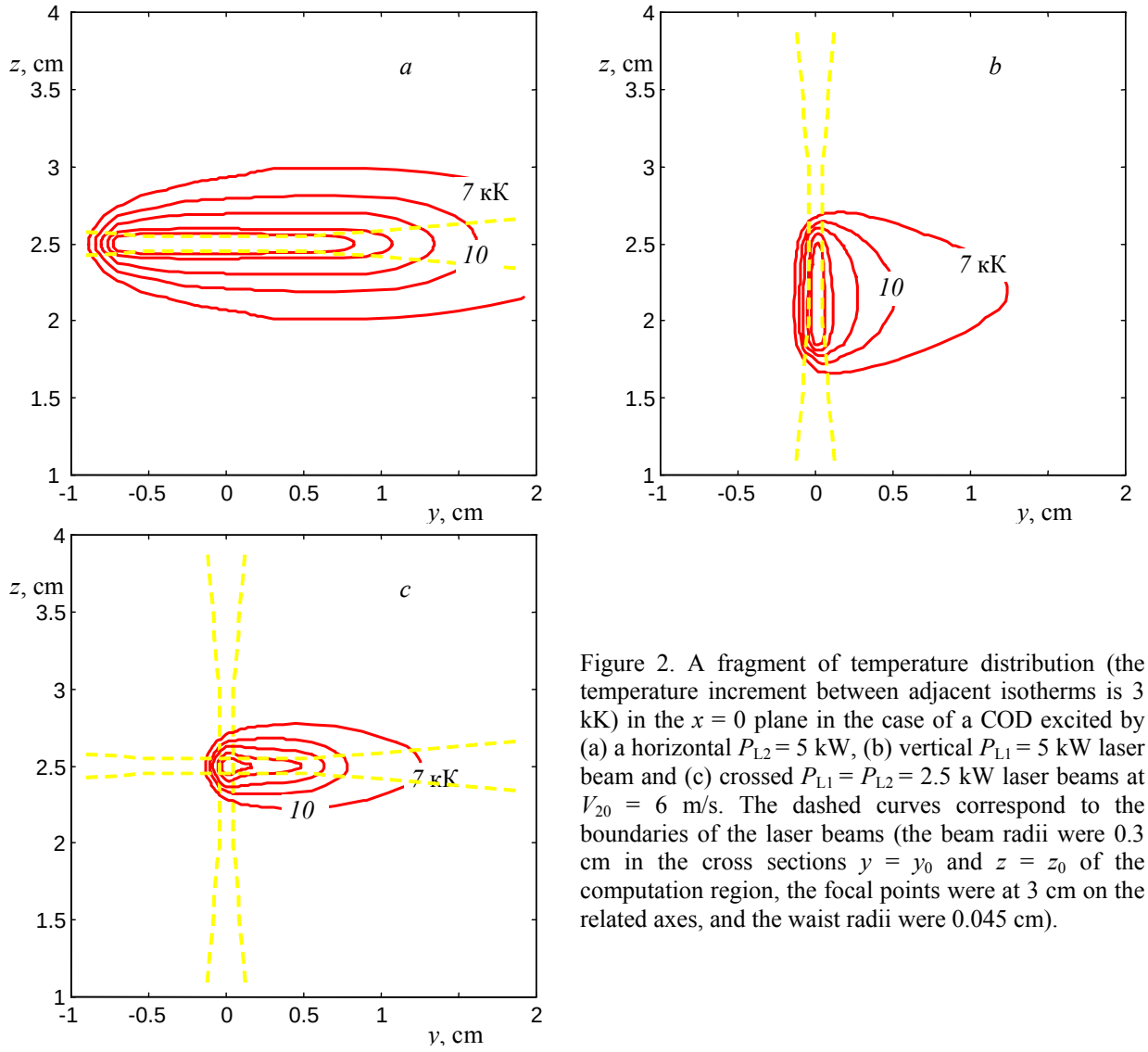

Figure 2. A fragment of temperature distribution (the temperature increment between adjacent isotherms is 3 kK) in the x = 0 plane in the case of a COD excited by (a) a horizontal P_{L2} = 5 kW, (b) vertical P_{L1} = 5 kW laser beam and (c) crossed $P_{L1} = P_{L2}$ = 2.5 kW laser beams at V_{20} = 6 m/s. The dashed curves correspond to the boundaries of the laser beams (the beam radii were 0.3 cm in the cross sections $y = y_0$ and $z = z_0$ of the computation region, the focal points were at 3 cm on the related axes, and the waist radii were 0.045 cm).

Independently of the direction of exterior gas flow, the gas deceleration is observed on the directed to it front of discharge, where a zone of increased pressure is formed and preferential gas flow around the high-temperature area of COD without vortex structures formation is realized (fig.3).

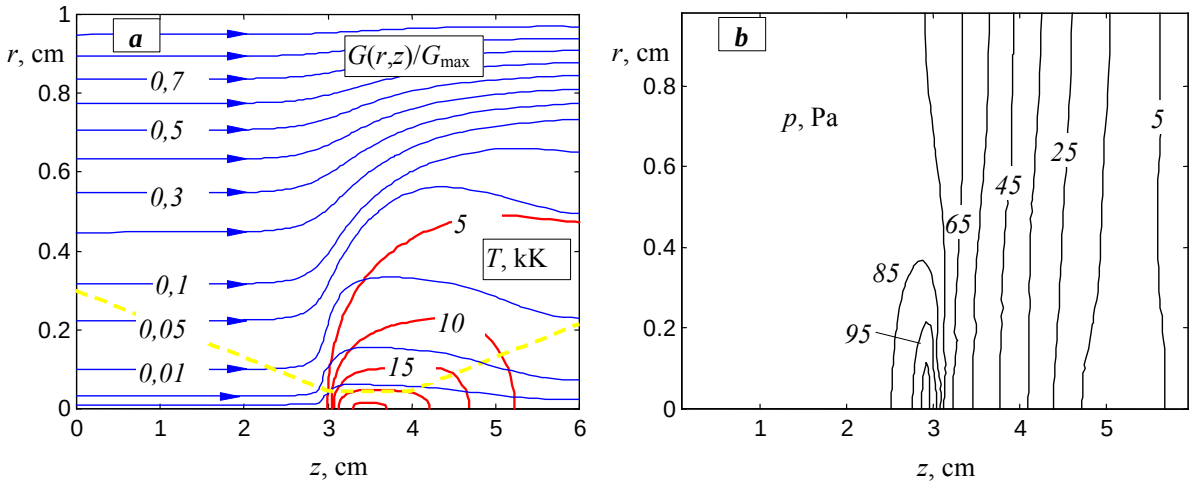

Figure 3. (a) Temperature distribution and the lines of the gas flow and (b) the distribution of the excessive gas pressure for P_L =5 кW, V_{20}=8 m/s, G_{max}=2.9 g/s (the dashed curve corresponds to the conditional boundary of the laser beam).

In variables "laser power – flow rate" the area of existed continuous optical discharge in the cross gas flow (relative to direction of the laser radiation propagation) an amount of gas is less than in the longitudinal flow.

As a result of calculation the optical discharge steady burning in area of the laser beams crossing, where power of each beam is insufficient to maintain the discharge, was established.

A possibility to run a shape and sizes of the discharge depending on flow rate, power and direction of laser beams is shown.

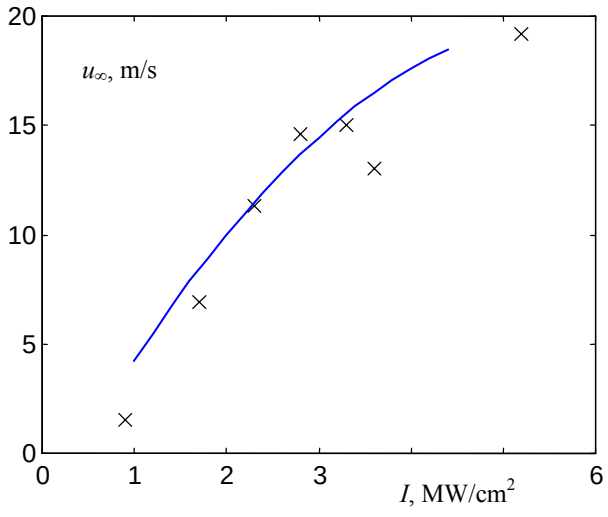

Figure 4. Front velocity of the discharge versus the laser intensity (crosses correspond to the experimental values).

The outcomes are in accord with experimental data (fig.4). The optical gas-dynamic structure of the discharge is interpreted in frames of a model problem of motion of a slow burning front. [8] We write down the Bernoulli equation in accordance with computation results along a normal to the front (zero) line of the gas flow: $u_1^2 + 2\delta p_1 / \rho_\infty = u_\infty^2$. The index "1" marks parameters before the discharge front; δp_1 - pressure excess, arising as a result of the velocity drop at a motion toward the front. After the flow passes through the discharge front, the gas is heated, and the gas flow becomes quasi-uniform and is characterized by a temperature close to maximum value T_0 and a density ρ_0, the viscosity forces and pressure gradients being insignificant. The thickness of hot and gas dynamic layers are small compared to the cross dimensions of the region in which the gas flow is quasi-uniform and the layers themselves are similar to gas-dynamic discontinuity surfaces on which the flow structure changes. At the front of the discharge the conditions of the mass fluxes density and impulse are conserved: $\rho_\infty u_1 = \rho_0 u_0$; $\rho_\infty u_1^2 + \delta p_1 = \rho_0 u_0^2$. The above equations allow us to determine the gas–dynamic characteristics of the discharge plasma from prescribed parameters of the incident flow of a cold gas:

$$u_0 = \frac{\rho_\infty / \rho_0}{\sqrt{2\rho_\infty / \rho_0 - 1}} u_\infty, \quad u_1 = \frac{1}{\sqrt{2\rho_\infty / \rho_0 - 1}} u_\infty, \quad \delta p_1 = \frac{2(\rho_\infty / \rho_0 - 1)}{2\rho_\infty / \rho_0 - 1} \frac{\rho_\infty u_\infty^2}{2}.$$

If the parameters of the gas state on both side of the front and the velocity u_1 with which a cold gas enters the front (this velocity has the meaning of the normal velocity of burning) are known, then we arrive to classical statement of a gas-dynamic problem of slow burning. In this case at $\rho_0 << \rho_\infty$, yields the following expression for the propagation velocity of the discharge: $u_\infty \approx u_1\sqrt{2\rho_\infty / \rho_0}$. The parameters of the problem are weakly sensitive to the properties of the cold gas flow around the discharge because a hot discharge region is filled by gas from a narrow paraxial tube of current. The gas parameters in the tube and both sides of the front determine main discharge characteristics.

The rotary gas flow results in pressure reduction around the axis, the COD as though rises along the lines of symmetry axis, influencing qualitative change of the pressure propagation versus the non-swirling flow and reducing of a value around the axis near the discharge front (fig.5). The area of increased pressure shifts toward the laser beam. A cold flow deceleration begins long before its flowing on COD. A dynamic gas pressure impacting the discharge front reduces, and an amount of gas in the discharge high-temperature region (isotherm ~10 kK) remains practically constant. The COD shifts noticeably toward the gas flow. Maximum temperature is realized near the laser beam focusing as in a case without gas swirling. Near the discharge front a region of vortex toroid gas flow appears, promoting heat transference on axes from the discharge region toward incident flow. With increase of the gas swirling we observe pulsations or crushing of a vortex cell, gas current lines and absence of stationary COD burning regimes.

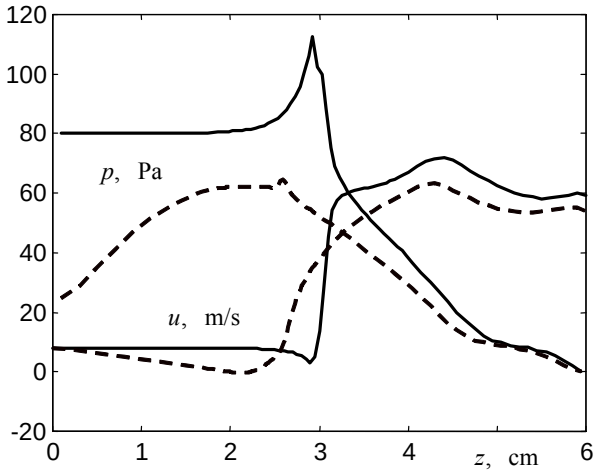

Figure 5. Longitudinal profiles of the velocity and pressure at the discharge axis for P_{L1} = 5 kW, V_{10} = 8 m/s, ω = 0 (solid curves), and ω = 1800 s^{-1} (dashed curves).

By decreasing the laser power the axis parameters, core temperature, and dissipated in COD power of the laser radiation (P_d = 4; 1.6; 0.9 kWt for P_{L1}=5; 3; 2.4 kWt accordingly) decrease, the pressure variation (surplus) on the front and gas, flowing through the front, increase (fig.6). The pressure and mass velocity in the core practically do not change. The constant is a negative depressed pressure behind the front, which ″ensures″ a reverse gas motion of the same gas quantity from a zone of the laser radiation dissipation toward trailing edge of the discharge. Both fronts shift toward each another. The fronts as though come together in beam-convergence cross section (z = 4 cm) at the supplied power 2.4 kWt. It is minimum (threshold) value of the laser radiation power, when the iteration came to a non-trivial solution. At power of 2.3 kWt and less the discharge in iterations “went out”.

The available power threshold and two stationary regimes of burning are observed in accounts (fig.5b) in a shape of two branches (with a “low” and a “high” temperatures) of maximum temperature $T_m(P_L)$ depending on the supplied laser radiation power. When the supplied power is higher than the threshold power, two stationary burning regimes are realized: with a low and a high temperature (fig.6). The low-temperature state is unsteady regard to temperature fluctuations, and any small temperature growth results in increase of the actual power value, necessary for maintaining a regime with a new temperature. As a consequence, the plasma heats up to reaching a steady high temperature state.

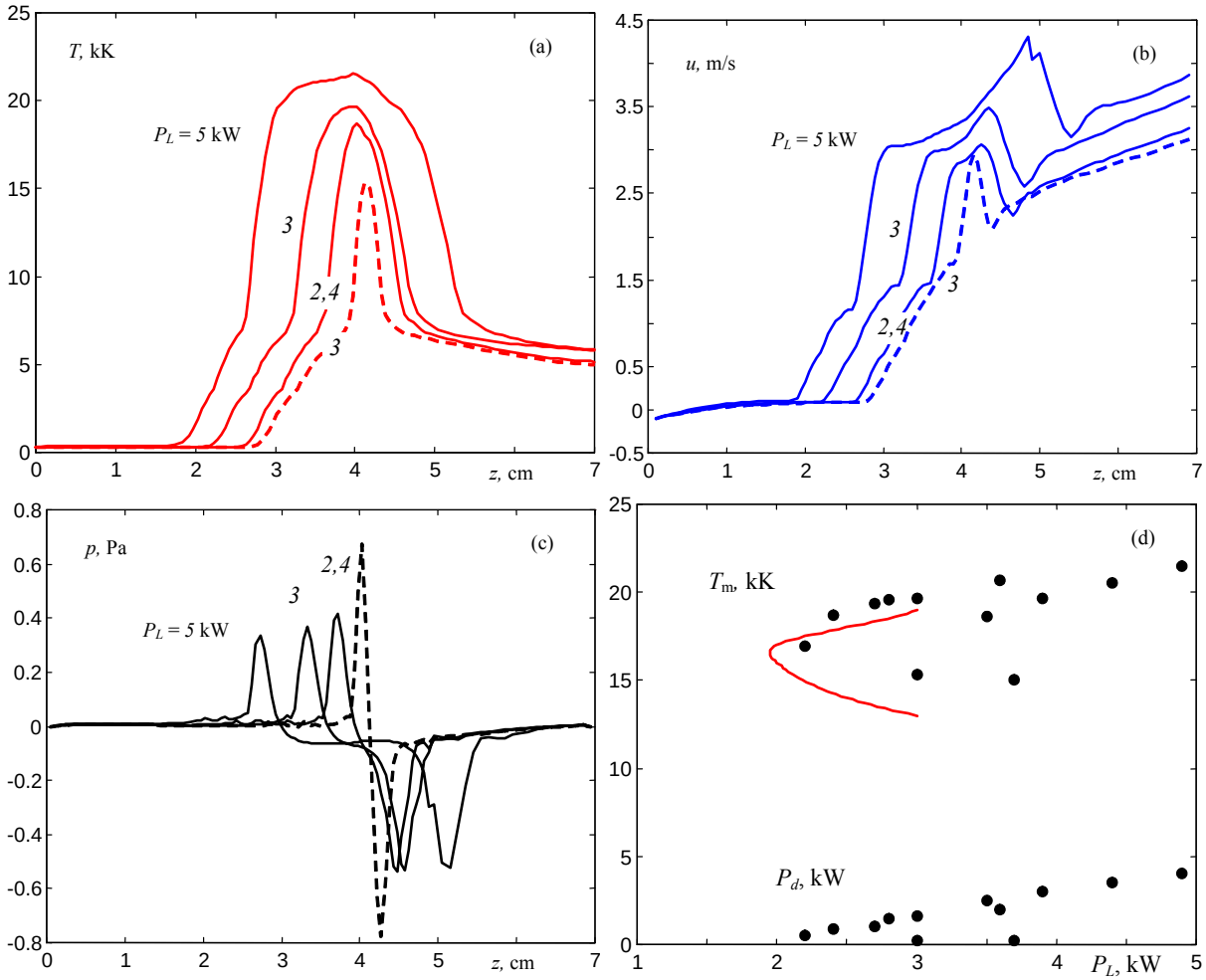

Figure 6. Distributions of the (a) temperature, (b) velocity, (c) pressure along the COD-axis at different laser power (the dashed curves correspond to the unstable regime) and (d) the maximum temperature and the fraction of the laser power dissipated in the discharge plasma as functions of the laser power (the solid curves illustrate the results of calculations based on the analytical model of a spherical COD).

Literature

1. Yu.P. RaÏzer, *Gas Discharge Physics* (Nauka, Moscow, 1987; Springer-Verlag, Berlin, 1991).
2. A.A. Vvedenov and G.G. Gladush, *Physical Processes in Laser Treatment of Materials* (Energoatomizdat, Moscow: 1985).
3. D.R. Keefer, B.B. Henriksen, W.F. Braerman, J. Appl. phys. **46**, 1080 (1975).
4. N. A. Generalov, A. M. Zakharov, V. D. Kosynkin, and M. Yu. Yakimov, Fiz. Goreniya Vzryva **22** (2), 91 (1986).
5. S. Patankar, *Numeral Heat Transfer and Fluid Flow* (McGraw-Hill, New York, 1980).
6. S. Predvoditelev, E. V. Stupochenko, A. S. Pleshanov, *et al.*, *Tables of Thermodynamic Functions of Air* (Vych.Tsentr Akad. Nauk SSSR, Moscow, 1959); A. S. Predvoditelev, E. V. Stupochenko, V. P. Ionov, *et al.*, *Thermodynamic Functions of Air* (Akad. Nauk SSSR, Moscow, 1960).
7. E.B. Kulumbaev, V.M. Lelevkin. Plasma Physics Report, **26**, 658 (2000).
8. V.Ts Gurovich, E.B. Kulumbaev, V.M. Lelevkin. Plasma Physics Report, **24**, 943 (1998).

Ultra-dispersed silicon powder combustion activation by corona discharge plasma

Lelevkin V.M.[1], Kanygina O.N.[1], Petrenko N.L.[1], Tokarev A.V.[1]

[1] *Kyrgyz-Russian Slavic University, Bishkek, Kyrgyz Republic*

Abstract

Self-distributed high-temperature synthesis of silicon powder in air at high pressures was studied. A new method of obtaining ultra-low-dense structure by creation of ultra-dispersed silicon powder suspension at electrical deposition on the base plate was developed. The content of silicon nitride in combustion products, dependences of increase in mass and combustion rate on air pressure were defined.

Introduction

The synthesis by combustion is one of the most modern directions in science of materials [1]. To control a process of silicon synthesis by combustion chemical reactions between powder mixture particles and gaseous environment are needed. At self-distributed high-temperature synthesis (SHS) complex phenomena connected with mass-transport (diffusion component, exothermal reaction energy liberation and distribution, temperature variation etc.) occur.

When burning silicon with use of gaseous nitrogen, one obtain nitride ceramic materials, and when burning in oxygen or air - obtained is oxide ceramics. The combustion of ultra-dispersed silicon powder in air or nitrogen at normal conditions does not occur because of insufficient oxidizing agent. In order to conduct similar reaction, high pressures of reacting gas are needed. One of the ways for reaching the ignition limit at normal pressures is a reaction realized in liquid nitrogen, or SHS realized with silicon powders of ultra-low density. Pursuant to assessments, the necessary relative density of silicon powder should be around 4% that corresponds to bulk density of 100 kg/m^3.

The purpose of this work is to obtain silicon nitride by realization of self-distributed high-temperature synthesis, occurred in ultra-dispersed silicon powder in air at different pressures.

Experiment

Experiments on combustion of silicon powder in air are carried out as follows:

- Feedstock is washed by hydrochloric acid solution for removing iron admixtures;
- Monocrystalline silicon is grinded in a ball mill;
- From obtained silicon powder the ultra-dispersed powder of ultra-low density forms with use of electrostatic method;
- With help of electric discharge at different pressures initiated was SHS, the results of which were compositions of silicon oxide, dioxide and nitride;
- Silicon nitride selection from compositions mixture realized by chemical leaching.

Air suspensions of ultra-dispersed silicon powder creation

Silicon powder after grinding represents a dense conglomerate. It is very difficult to organize SHS in air at normal conditions because of densely inter-linked silicon powder particles. Therefore a preliminary turbulent air current with suspended silicon particles is provoked. At supply of air through the tangential integrated fitting, a turbulent gas movement entraining silicon powder arises in camera. At rotating, the large conglomerates of the powder strike on the camera walls and split into the smaller ones. As a result of friction on walls the particles are charged and due to coulomb (electrostatic) forces push off the basic mass, forming a homogenous two-phase medium (silicon-air).

Silicon powder deposition on base plate

Ultra-dispersed low-dense silicon powder is obtained with help of a process installation (fig.1). The installation consists of camera 1 inside of which there are corona-forming electrodes 2, base plate 3 on the camera floor is the cathode. At high positive polarity voltage supply the corona discharge appears between corona electrode and the base plate. Silicon powder particles are supplied into the camera together with air current, get in the field of corona discharge and are charged positively due to positive ions sticking on them. Positive silicon particles drift under coulomb forces towards the base plate and deposit on it. A bit later rather a thick layer of low-dense silicon powder forms on the base plate.

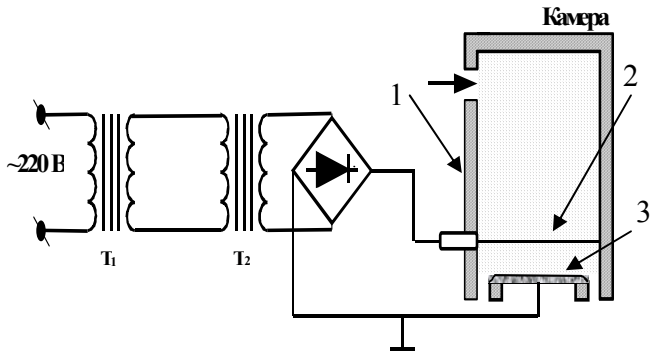

Figure 1. Scheme of silicon powder deposition:
1 – camera; 2 – corona electrodes;
3 – base plate (cathode); T_1 – autotransformer;
T_2 – high-voltage transformer.

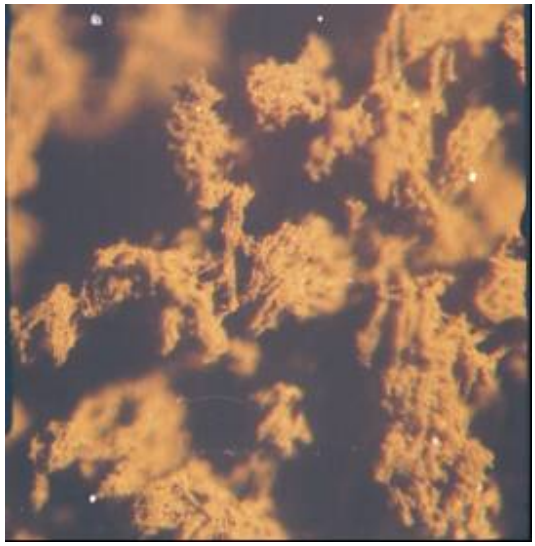

Figure 2. Deposited silicon structure (image magnification in 56 times)

The layer structure is loose with a large amount of pores and spasmodic thread-like silicon particles (fig.2). Similar structure contains a lot of reacting gas and easily lets oxidizers into deposited silicon powder and promotes SHS occurring. By measuring a volume of deposited layer and its mass one define a density of silicon powder, which is equal to ~100 kg/m^3 (by one order less than [2]).

Initiating of a process of deposited powders burning

The installation given in fig. 3 is proposed for silicon combustion. Base plate with deposited silicon 2 is placed in camera 1 with a given air pressure. The electrode is introduces in the camera above base plate through insulator. The second electrode is the camera itself and base plate. The electrode system connects to the high-voltage transformer T. The voltage of 2kV is supplied in the electrode system; the electric discharge is ignited between electrode and base plate, as a result of that the surface of deposited silicon heats up to the temperature sufficient for SHS progress.

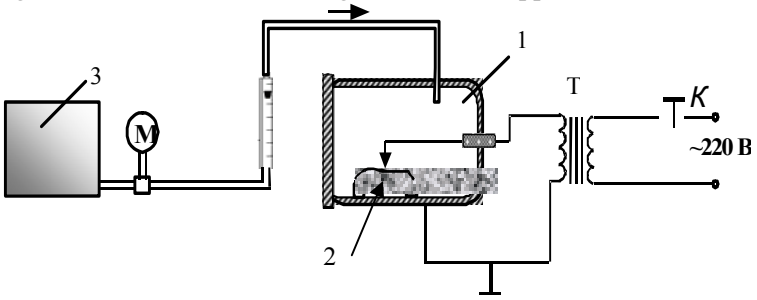

Figure 3. Scheme of the installation for silicon powder combustion:
1 – camera; 2 – base plate; 3 – compressor; M – manometer;
T – transformer; K – key.

After the ignition a zone of preliminary heating forms in ultra-dispersed silicon powder; the zone defines a character of burning wave (astable mode of burning) [3,4]. Combustion temperature in a volume of the ultra-dispersed powder occasionally varies, consequently a

typical “spasmodic” astable mode of layer-by-layer combustion of silicon happens. The heat, emitted in a zone of reaction comes in a zone of preliminary heating that ensures the process’s high rate. If the material diffusion progresses slower then the thermo-diffusion, then in a zone of reaction more surplus energy is emitted than in stationary wave of combustion [5].

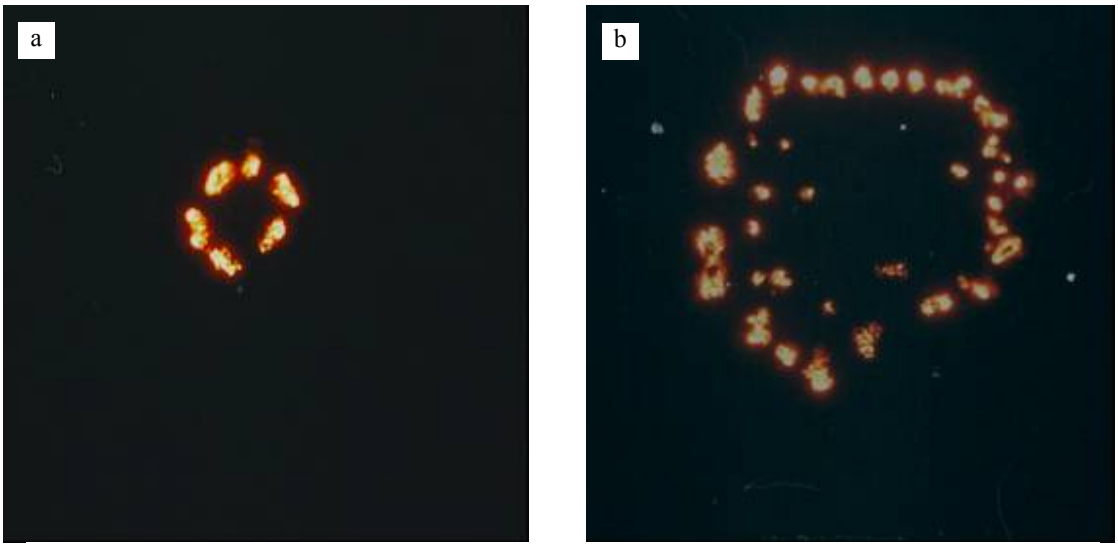

Figure 4. Ultra-dispersed silicon powder combustion in air (image magnification in 1.5 times):
a) combustion time - 5 sec. b) combustion time – 60 sec.

In the course of the study it was established that ultra-low-dense silicon powder burns both in an astable and a spin mode. The mode of spin burning is characterized by available large quantity of burning fronts inside of the pattern and on its surface. From figure 4a it is viewed that after SHS forming high-temperature local areas of combustion waves in a shape of bright luminous spots, which migrate on the pattern, appear. Due to heterogeneity of heat losses the front of combustion wave distorts (fig. 4b). With the mixture density growth

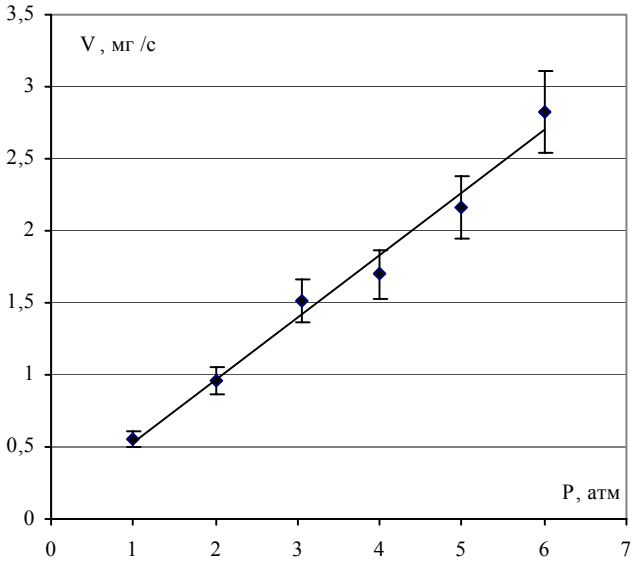

Figure 5. Dependence of silicon combustion rate on pressure

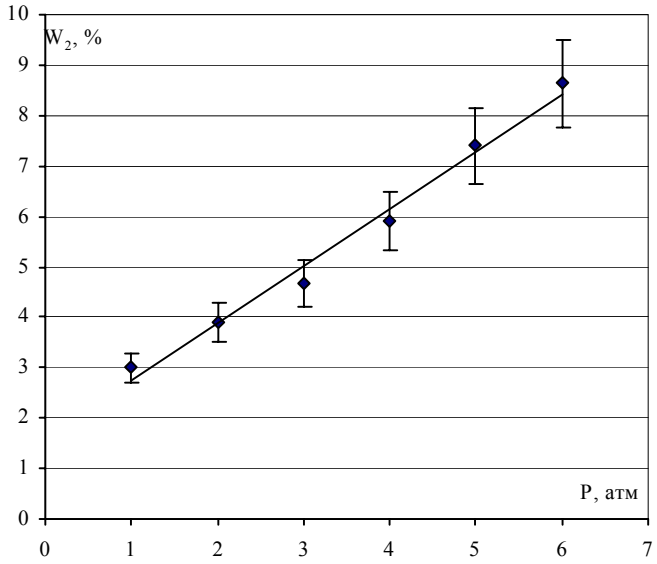

Figure 6. Dependence of output of silicon nitride on pressure

the distribution of combustion wave decelerates, relative share of heat losses from the surface decreases, and the front of combustion wave becomes flat. The time of existed high-temperature area over combustion wave increases that ensure greater degree of the initial silicon transformation.

At combustion of silicon powder the structured, laminated materials of SiO, SiO_2, Si_3O_4 as well as residuals of the burnt silicon are formed. With increase of pressure the rate of combustion front linearly grows (fig.5). At pressure increase from 1 to 6 atm. combustion rate increases from 0.5 to 2.7 mg/s that is connected with air concentration increase in the system's pores, and because of oxidized silicon mass increase a higher temperature develops, that promotes chemical reactions accelerated progressing. The mass of obtained compositions grows. The conditions for greater junction of O_2 and N_2 molecules with molecules of Si appear depending on pressure.

Output of silicon nitride

With pressure growth from 1 to 6 atm the pattern's increase in weight grows from 47 to 68%. Maximum increase in weight of silicon nitride at pressure 6 atm makes around 70% that corresponds to increase of the pattern mass in 1.7 times.

For quantitative determination of silicon nitride a chemical method of treatment by alkaline solution was applied:

$$SiO_2 + H_2O + 2NaOH \rightarrow Na_2SiO_3 + 2H_2O,$$

$$SiO + 2NaOH \rightarrow Na_2SiO_3 + H_2,$$

$$Si + 4NaOH \rightarrow Na_4SiO_4 + 2H_2$$

Silicon nitride (Si_3N_4) does not interact with alkaline at temperature close to normal and precipitates as gray sediment. X-ray structural analysis shows that the obtained material is a coarse-grained silicon nitride of β-structure.

It is visible from fig.6 that with pressure growth a percentage of silicon nitride linearly grows towards the initial pattern in the product of reaction. Minimum concentration of silicon nitride makes 3.1% at pressure of 1 atm. At pressure of 6 atm. the percentage increases up to 8.5% that is explained by increase of reacting components concentration in porous space between silicon particles. At SHS wave passage a greater mass of the material chemically reacts, emitting energy. A high temperature develops in SHS wave, which enhance the chemical reactions rate.

The initial material reacts in several reaction channels, but the reaction, which has lowest activation energy, prevails: it begins at lower temperatures accompanied by great energy liberation and has greater dependence of the reaction rate on temperature. If end product of any reactions channel results from several intermediate ones, then the channel with minimum intermediate reactions and maximum rate of each reaction prevails. For obtaining Si_3N_4 atomic nitrogen is needed which concentration in SHS grows pro rata to temperature. Besides, the SHS is a fast process, therefore slow reactions have no time for termination. That is why a higher temperature emerged at silicon combustion with high pressures results in slow cooling of a system and promotes full course of slow reactions with Si_3N_4 formation. On the basis of the analysis of end products enthalpy formation a channel with energy-liberation process can be determined.

$$Si + O_2 \rightarrow SiO_2 + 912\ \ kJ/mol = 32{,}571\ \ MJ/kg$$

$$2Si + O_2 \rightarrow 2SiO + 100\ \ kJ/mol = 1{,}786\ \ MJ/kg$$

$$Si + N_2 \rightarrow Si_3N_4 + 759\ \ kJ/mol = 9{,}378\ \ MJ/kg$$

It is viewed that the most favorable reaction will be in a channel of SiO_2 formation, then Si_3N_4, and SiO forms most weakly.

Conclusions

1. The method of ultra-dispersed silicon powder obtaining is developed;
2. A new way of ultra-low-dense structure of ultra-dispersed silicon powder creation by electrostatic deposition on base plate in corona discharge plasma is offered;
3. The conditions of SHS synthesis course in the system silicon-air at high pressures are determined;
4. Linear growth of silicon combustion rate in air, and silicon nitride output with pressure growing are defined.

Literature

1. A.G. Merzhanov, V.M. Shkiro, I.P. Borovinskaya. Patent of the USSR # 255221 (1971), Patent of the USA # 3726643 (1973), Patent of Japan # 1098839 (1982).
2. O. Kubavara. Publishing collection of materials processing study. University C&co, 1991.
3. M. Koidzumi. Chemistry of synthesis by burning. M., 1998.
4. K.G. Shkadinsky, B.I. Khaikin, A.G. Merzhanov. Physics of combustion and blast, – 7, 19 (1971).
5. V.M. Shkiro, I.P. Borovinskaya, G.A. Nersisyan. Physics of combustion and blast, - 14, 58 (1978).

Surface barrier discharge with a plasma electrode

V.M. Lelevkin [1], A.V. Tokarev[1].

[1] *Kyrgyz-Russian Slavic university, 44 Kievskaya str., Bishkek, the Kyrgyz Republic*

Abstract

The researches of statistical and dynamic volt-ampere and volt-coulomb characteristics of the surface barrier discharge (SBD) with a plasma inductive electrode were carried out. The dependences of current on gas pressure in a discharge electrode, of a corona electrode coil pitch and power factor on voltage, supplied to the discharge node are determined.

Introduction.

The surface barrier discharge (SBD) of alternating current with frequency less than 100 kHz is ignited between gas condenser plates, where both electrodes touch a dielectric. Corona forming electrodes are made in a shape of strip and in case of a flat configuration lay on the dielectric surface. An inductive (flat) electrode is located on the dielectric adverse side. The electrodes are supplied with alternating voltage of 10 kV. The discharge appears as a continuous luminous band, covering an end strip of the corona forming electrodes. The band consists of multiple luminous micro-discharges, which appear in every half a period of input voltage and are directed perpendicular to the electrode [1]. The micro-discharges number increases with the increase of voltage, promoting the luminescence intensity strengthening.

The surface barrier discharge (SBD) differs from the barrier discharge by dynamic capacitance, caused by the dielectric covered with plasma of the discharge [2-4]. It is possible to obtain record ozone concentrations in SBD (more than 200 g/m^3) at minimum power inputs (around 15 kV*h/kg) [5–6].

Here the SBD was carried out by substitution a plasma electrode for the metal inductive one [7]. By supplying power to a dielectric barrier with help of a plasma electrode it is possible to reduce power inputs for the ozone synthesis compared to the classical surface barrier discharge. The available two electric discharges located consequently on the electric circuit are an essential distinction of a surface barrier discharge with plasma inductive electrode (SDPE) against standard surface discharge.

Purpose of the work is to study features of the surface barrier discharge with a plasma inductive electrode: investigation of static and dynamic volt-ampere and volt-coulomb characteristics of the discharge; determination of pressure of plasma-generating gas inside the tube and the corona electrode coil pitch, influencing electric characteristics of SDPE.

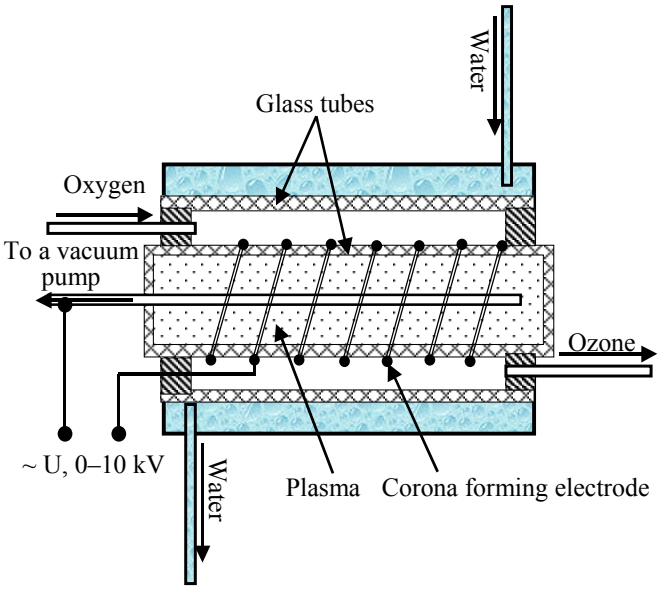

Fig. 1 The gas-discharge node

Experiment.

The experimental installation consists of a gas-discharge node (fig. 1) made of two glass tubes. Exterior diameter of the first (exterior) tube is 25 mm and interior diameter of this tube is 23 mm; exterior diameter of the second (interior) tube is 21 mm and interior diameter of this tube is 19 mm. A co-axial gap between two tubes is 1 mm, through which a dried by silicagel oxygen is pumped. A nichrome wire of diameter 250 mcm (corona electrode) is coiled with a certain specified pitch on exterior surface of the interior tube in 16 cm long. A metallic tube with exterior diameter 4 mm is a grounded electrode, which is hermetically introduced into

interior glass tube and serves for air exhaust and letting-to-air. The installation comprises a fore-vacuum pump for air exhausting from the tube to reaching pressure of 10^{-3} Torr, a device for vacuum registration, a tap for letting-to-air from atmosphere, a device for oxygen drying, and a rotameter for registration of oxygen consumption, flowing through the discharge node. Cooling of the discharge node is realized with help of water jacket, being on exterior glass tube. In order to prevent the ignition of a barrier discharge, in interval between glass tubes the installation is fixed on dielectrics, and the discharge node cooling system is equipped with input and output drop dielectric discontinuities. Alternating voltage under 10 kV and frequency 50 Hz is supplied to the corona electrode and metal tube.

The electric scheme contains the instruments for measuring average values of electric current (I_{avg}), voltage (U_{avg}), and devices for registering dynamic characteristics of electric discharge. According to instantaneous current, voltage, and discharge, flowing through the discharge gap, the parameters of SDPE are calculated: average current and voltage; full active and reactive power; power factor of the installation.

Output.

At critical voltage a volume barrier discharge is ignited on the discharge contour inside the tube. When pressure inside the tube is 10^{-3} Torr, the discharge burns, when glass dielectric is available, due to bias currents. The barrier discharge ignition is registered according to volt-ampere characteristics modification and weak lilac luminescence inside the tube. When increasing voltage, a surface barrier discharge is ignited between nichrome wire coils. For alternating current the SDPE first looks like a weak corona around the wire. With voltage increase the micro-discharges begin to appear and propagate from the wire. Their length increases with voltage growth. When the electric current increases, luminescence increases too, the discharge passes in a creepage form. Pulses – surges of active current appear on oscillograms of current as in case of a barrier discharge. On exterior luminescence it is viewed that the electric discharge snuggles up to the surface. According to data [1], an active form of the electric current is developed as micro-discharges, lasting ~ 10 ns, and following the magnitude order corresponds to the time needed for forming of channel in a barrier discharge.

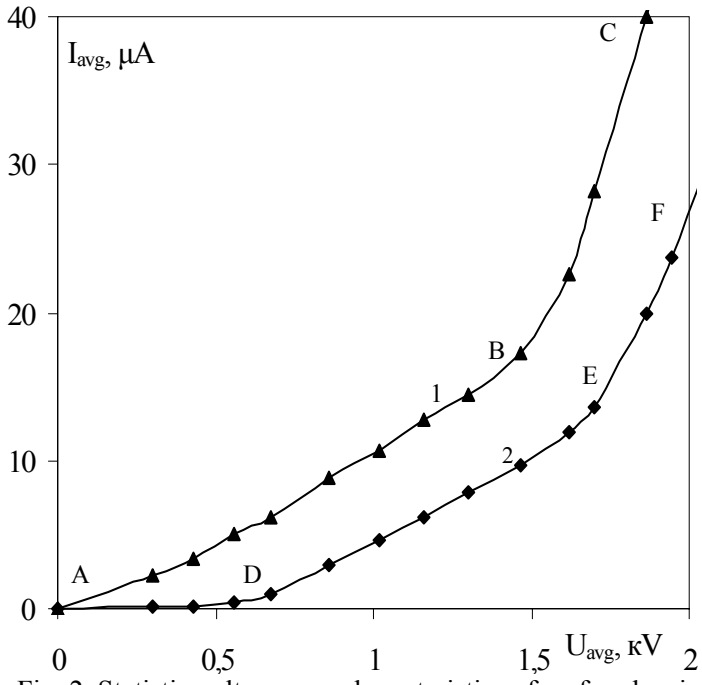

Fig. 2. Statistic volt-ampere characteristics of surface barrier discharges with a classical (1) and plasma (2) inductive electrodes.

Statistic and volt-ampere characteristics. The SBD's volt-ampere characteristics are similar to characteristics of the barrier discharge (BD) [8]. Traditional volt-ampere characteristics of the surface discharge were obtained on a discharge cell of similar construction (fig. 1.), but with a metallic internal electrode instead of plasma electrode. The area AB (fig.2. 1): corresponds to average electric current depending on effective stress at absence of electric discharge on the tube's surface. The slopping of this area is defined by general capacity of the discharge cell. At the SBD ignition and development a slope modifies (area BC), that is connected with increase of the discharge cell capacity. The continuation of the area BC is in a shape of a straight line up to the voltage on a discharge cell 10 kV.

Unlike SBD the volt-ampere characteristics for SDPE consists of three segments, each segment practically represents a straight line (fig.2): 1 – In interval to 500 V (segment AD) passes a current of

displacement, stipulated by a small capacity of electrodes of discharge; 2 – At voltage more than 500 V (segment DE) the current increases at the expense of the discharge gap general capacity growth at ignition of a volume barrier discharge; 3 – At voltage 2.7 kV (segment EF) a fracture of volt-ampere characteristics, connected with development of a surface barrier discharge with plasma inductive electrode is considered.

Dynamic characteristics of the discharge. Volt-coulomb characteristics of a barrier discharge have a shape of parallelogram [9]. The parallelogram's parallel sides point to that, that the barrier discharge burning voltage at steady ozone concentration in a discharge gap is constant during a half-period of current [10].

Volt-coulomb characteristics of SDPE for U_{avg} on the discharge contour 3 kV and 6 kV differ from characteristics of a barrier discharge (BD) (fig. 3). At U_{avg} on the discharge cell equal to 3 kV the cycle pattern is of a shape of ellipse, which is transformed in parallelogram at voltage growth to 6 kV. This can be explained that

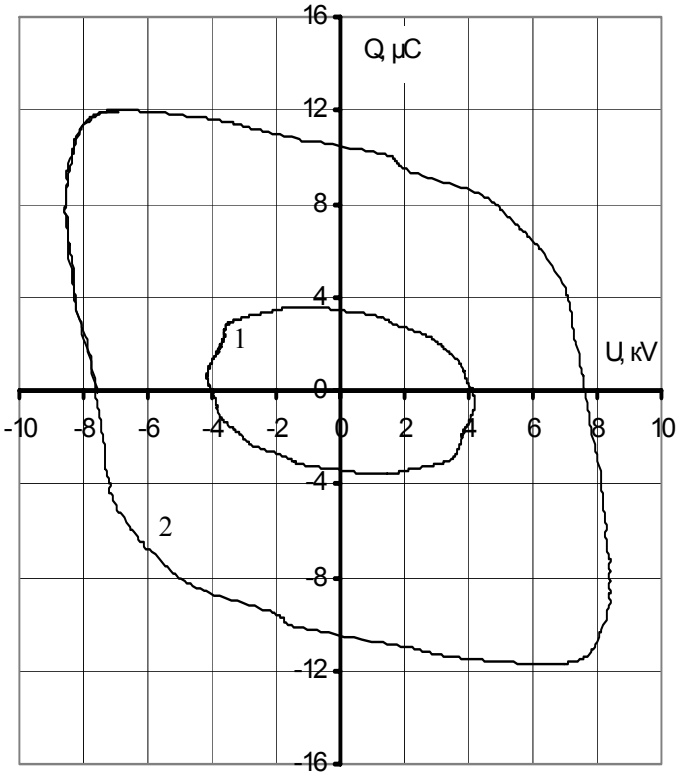

Fig. 3. Volt-coulomb characteristics of SDPE for effective voltages 3 (1) and 6 (2) kV.

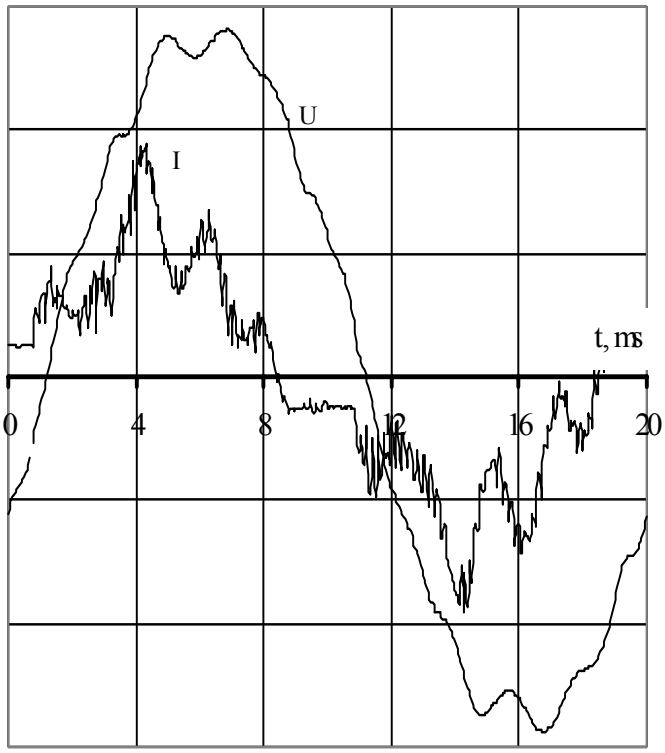

Fig.4.Oscilograms of the SDPE current and voltage. Amplitude values of current 3.1 mA, voltage 14 kV.

at voltage 3 kV a dynamic capacity, arising at plasma spreading on the dielectric surface by order of magnitude is comparable with electrodes own capacity. When increasing voltage, plasma fills a dielectric gap between wire coils, a dynamic capacitance stops to grow, and a cycle pattern gains a shape close to parallelogram.

Voltage of the discharge burning is a constant for classical BD. In case of SDPE volt-coulomb characteristics it follows, that voltage of burning depends not only on U_{avg}, but also on air consumption. When U_{avg} is higher than 8 kV, a burning voltage stops to change, because plasma of the surface discharge covers completely a free area of the dielectric. Influence of air consumption on voltage of burning is explained by ozone generation in the discharge.

Oscillograms of current and voltage on ozonizer are symmetrical for axis of abscissas (fig. 4.) with a cycle of vibration T=0.02 s. A lagging phase is insignificant between current and voltage, that is stipulated by

influence of the SDPE active capacity load. The forms of current and voltage differ from the sinusoid. Modification of a voltage form is defined by grand output resistance of the transformer. Distortion of an electric current form depends on the discharge ignition points and on appeared active component of current, that signifies a presence of an ohmic resistance in a chain of the barrier discharge [10]. A high-frequency component of electric current (separate pulses are hardly distinguished) are observed on oscillograms that is connected with forming of micro-discharges, sliding on the dielectric surface.

Parameters of a discharge contour and characteristics of the discharge. It was established (fig. 5, 6), that dependences of the electric current's discharge on pressure inside the inductive electrode tube and on the corona electrode coil pitch are of complex nonlinear nature. For the coil pitch d=1.1 mm and 2.2 mm at P=50 Torr minimum current is considered (fig. 5). At pressures 150 – 200 Torr and the same d there is an area of a small increase of current. At increasing d this area is gradually smoothed and for d=40÷80 mm the dependence is practically linear. The appeared minimums and maximums of current can be explained by modification of structure of both volume barrier and exterior (surface) discharges. This is well viewed at observation of a volume barrier discharge. At low pressures it fills all volume of a discharge tube, at increased pressures the

discharge structure modifies depending on a form of the wire coiled on a glass tube. Hereupon the discharge dynamic capacity changes, a resistance of the discharge node grows, and the electric current reduces.

Depending on a corona electrode coil pitch (fig.6), the area with sharply increased electric current is realized, that is explained by screening of the corona electrode neighboring coils. At a small pitch of coiling, neighboring coils of the corona electrode screen a horizontal component of the electric field strength, and the discharge cannot be distributed throughout a free surface of the tube. This brings about that the dynamic capacity and electric current reduce. When increasing d the screening reduces between coils, and at d=4–5 mm plasma of

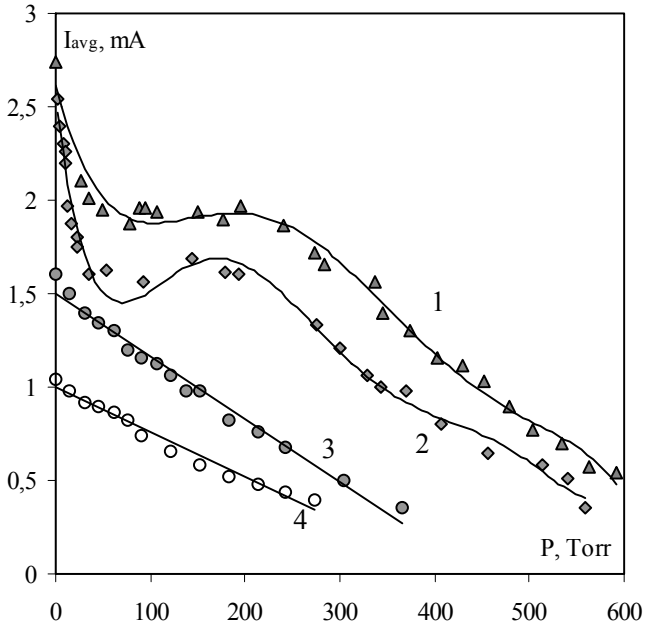

Fig. 5. Dependences of the discharge mid current on gas pressure in plasma electrode for the corona electrode coil pitch 1.1 (1), 2.2 (2), 25 (3) and 80 mm at voltage 10 kV.

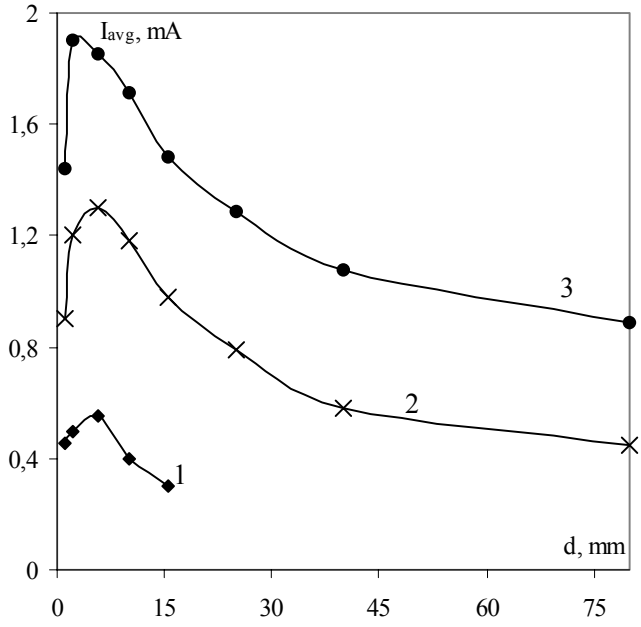

Fig. 6. Dependencies of mid SDPE current on the corona electrode coil pitch for the voltage effective values 5 (1), 8 (2) and 10 (3) kV.

the surface discharge covers in full the tube's area, that corresponds to maximum current. At further increase of d a value of horizontal component of the electric field strength reduces, and plasma cannot fill all space between

neighboring coils of the corona electrode. Therefore a dynamic capacity of the discharge node diminishes, a resistance increases and the discharge current reduces.

At increasing voltage on a discharge cell from 3 kV to 10 kV, power factor reduces linearly from 0.7 to 0.54. This means that with increase of U_{avg} the discharge active power decreases and reactive power increases. Therefore, for economic reason, the SDPE is effective in a range of voltages 3 – 5 kV, at further increase of voltage, power factor drops due to logging phases between amplitudes of current and voltage, and due to increase of the discharge node dynamic capacity.

Conclusions.

1. Volt-ampere characteristics of SDPE differ from a similar dependence for barrier and surface discharges because another fracture appears in region of 600 – 700 V, which corresponds to ignition of a volume barrier discharge in a vacuum tube. At voltage around 1.8 – 1.9 kV the investigated SDPE is ignited.
2. From dynamic characteristics follows, that around 70% of the discharge current accounts for a high-frequency component.
3. The power factor of SDPE is higher than at classical barrier and surface discharges due to a grand contribution of a high-frequency current in active power;
4. Complex dependences of current on pressure and on a corona electrode coil pitch are defined by the discharge basic adjustment depending on pressure and mutual screening of neighboring coils of a corona forming wire.

Literature

1. Kozlov M.V. Investigation of a high-frequency surface discharge in order to increase electromagnetic installations effectiveness: Abstract…cand. tech. sc. M. , 1993.
2. Masuda S. et al. A ceramic-based ozoniser using high frequency discharge //“IEEE Trans. Ind. Appl.”-1988.- 24. №2 –PP/. 223-231.
3. Engelsht V.S. The ozonizer. Patent of Russia # 17544647, 15.04.92. Bul. #30, 15.08.92. Relog 20.05.93.
4. Masuda S., Kiss E. On streamer discharges in ceramic based ozoniser using high frequency Surface discharge. /Electrostatics / 87, Oxford, 8-10/April, 1987. - P. 243-248.
5. Samoilovich V.T., Gibalov V.I., Kozlov K.V. Physical chemistry of the barrier discharge. M.: MSU, 1989, - p. 176.
6. Lunin V.V., Popovich M.P., Tkachenko S.N. Physical chemistry of ozone. – M.: MSU, 1998. – p. 5.
7. Tokarev A.V., Yudanov V.A., Kel O.P., Alemsky I.N., Nikulicheva T.B., // Bulletin of Kyrgyz-Russian Slavic University. 2003. V. 3, # 5. P. 23.
8. Filippov Yu.V., Emelianov Yu.M.// J. of physical chemistry. - Pub. 2., 1958. - #12. - P.1217-1823.
9. Borombaev M.K., Sharshembiev K., Engelsht V.S.// Bulletin of Kyrgyz-Russian Slavic University. Bishkek, 2002. V. 2. # 2. P. 53.
10. Filippov Yu.V., Emelianov Yu.M. // J. of physical chemistry. Pub. 33. – 1959. - # 5. P. 1042 –1046.

Two-dimensional Actinometric Study of Fluorine and Oxygen Atom Densities in the CVM Plasma Gap and the Temperature Estimation with Electronic Spectra of Diatomic Molecules

Yasushi Oshikane[1], Akihiko Nagao[1], Akinori Oda[2], Colin M. Western[3], Kazuya Yamamura[1], Katsuyoshi Endo[1]

[1]*Osaka University, 2-1 Yamada-oka, Suita, Osaka 565-0871, Japan*
[2]*Nagoya Insitute of Technology, Gokiso-cho, Showa-ku, Nagoya, Aichi 466-8555, Japan*
[3]*University of Bristol, Bristol BS8 1TS, United Kingdom*

Abstract

A stable plasma can be generated in a sub-mm gap by using both VHF electric power and a cylindrical electrode at 10^5 Pa. The chemical vaporization machining (CVM) plasma uses a mixture of He, CF_4 and O_2 for an ultra precise polishing of silicon wafer. The plasma is diagnosed by an optical emission spectroscopy. Both fluorine and oxygen atom densities are measured by an actinometry technique. The gas temperature is estimated with electronic spectra of diatomic molecules. The results are compared with the etched patterns.

Keywords: atmospheric plasma, capacitively coupled plasma, chemical vaporization machining, actinometry, optical emission spectroscopy, molecular spectrum, rotational spectrum, rotational temperature

1. Introduction

A stable capacitively coupled plasma in a narrow gap (~500 μm) at one atmosphere can be generated with both VHF (150 MHz) electric power and a rotating cylindrical electrode (ϕ160 mm) coated with alumina. When we use a diluted fluorocarbon gas, a mixture of He, CF_4 and O_2, for the plasma generation, this system is named the "Chemical Vaporization Machining; CVM [1-3]." The CVM process can polish a silicon wafer and glass surface very softly by a kind of plasma etching mechanism coupled with a high-speed shear flow in the plasma gap. Purpose of this paper is to diagnose an atomic density of both oxygen and fluorine by an optical emission spectroscopy (OES) [4-6]. For the plasma etching of silicon, both fluorine and oxygen atoms play important roles. Therefore we have tried to realize a visualization for spatial density distribution of both fluorine and oxygen atoms. The spatial distribution is observed by a simple technique based on an actinometry technique [7-9]. This major technique could determine a "relative density" by calculating a line emission intensity ratio between target atom and argon. The resultant density map is compared with a etched pattern on silicon wafer in four conditions for plasma generation. The CVM plasma is a kind of glow discharge at low gas temperature (T_{gas}). In such plasmas, chemical reactions in the gas may govern the etching mechanism. Therefore we concentrate on molecular spectra observed by OES to estimate rotational temperatures (T_{rot}) and vibrational temperatures (T_{vib}) [10-12]. T_{rot} normally relaxes to equilibrium much faster than T_{vib} (of the order of one collison as compared to 1000 collisions). T_{rot} of several diatomic molecules (CO [13], SiF [14], He_2 [15,16], O_2^+ [17], C_2 [18]) are determined by fitting calculated relative intensities to those observed experimentally. T_{vib} is estimated with a rotational spectrum of C_2. An Excitation temperature of the plasma is also estimated by rare gas OES technique [18].

2. Experiments and results

2-1 Two dimensional argon actinometry

Experimental setup for two dimensional argon actinometry is shown in figure 1 (a). In this study, a cooled CCD camera (C4880-10-12AU, 1018x1000 pixels; Hamamatsu) coupled with both a macro camera lens (180 mm F3.5 APO MACRO; SIGMA) and a 2x teleconverter (TELEPLUS PRO300; Kenko) was covered with an interference filter (Optical Coatings Japan) of very narrow bandpass (~1.5 nm FWHM) to record monochromatic images of each line emission. Magnification of the plasma image was unity on the CCD chip. The OES spectrum of plasma confirmed that the interference filter was enough to record monochromatic images with O. D. values of more than four at Ar I 750.4 nm (E_{th}; 13.48 eV), F I 739.9 nm (E_{th}; 14.37 eV), and O I 844.6 nm (E_{th}; 10.99 eV), respectively. We brought a center of the plasma into focus. Spatial resolution of the image was determined by a CCD pixel size of 12 μm. Ten consecutive frames were recorded and accumulated to produce the averaged

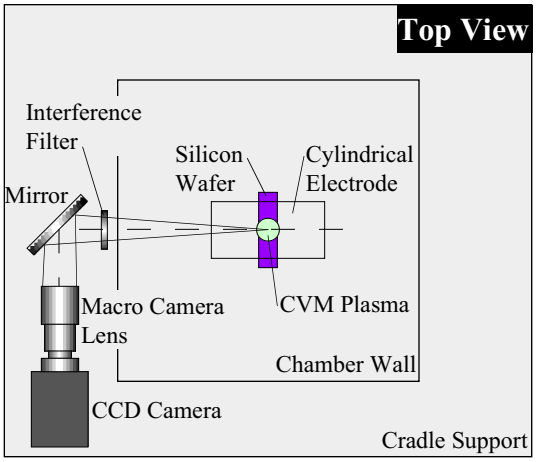

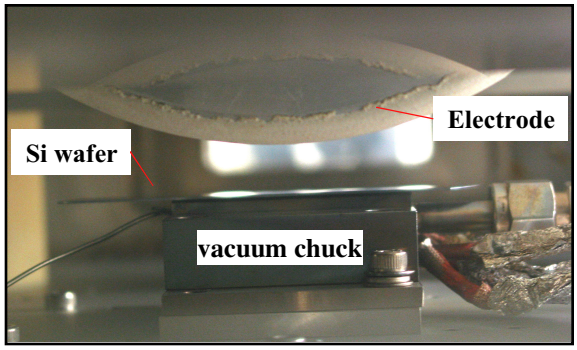

(b) Sideview of plasma gap w/o discharge.

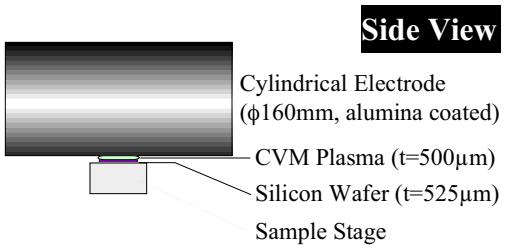

(a) Setup for actinometric measurment

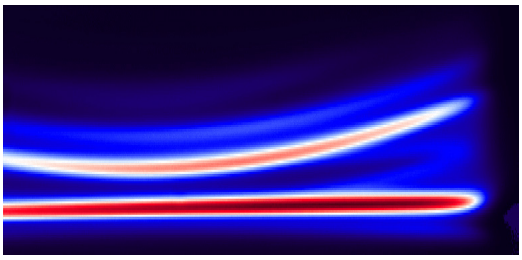

(c) Typical monochromatic image.

Figure 1. (a) Experimental setup for actinometric measurement, (b) configuration of plasma gap, and (c) typical monochromatic image of plasma gap taken by CCD camera.

image of 14bit. Two dimensional density maps of both fluorine and oxygen were constructed by dividing each pixel value of the monochromatic images by corresponding each pixel value of the plasma image of argon. Dependence of the density maps on both VHF power (50, 100 W) and rotation speed of electrode (250, 1000 rpm) was studied. The plasma gas mixing ratio was fixed at $He/CF_4/O_2/Ar=99.89/0.1/0.01/0.05$. Specimen for the process was prepared by cutting off a 90*15 mm^2 strip from p-type, mirror-polished silicon wafer. Figure 1 (b) shows a widened plasma gap between electrode and wafer, and fig. 1 (c) is a typical monochromatic image of the plasma at 750.4 nm with the interference filter. The both of plasma sheaths are clearly resolved. Figure 2 shows a dependence of the monochromatic plasma image at 750.4 nm on both VHF electric power and rotation speed of the electrode. These images act as references of two dimensional distribution of fluorine and oxygen atom densities. Figure 3 shows a dependence of the plasma image at 844.6 nm (left) and 739.9 nm (right) on the condition of plasma generation, respectively. The emission patterns differ considerably between oxygen and fluorine. Two dimensional density maps of both fluorine and oxygen were finally constructed by dividing each pixel value of the monochromatic

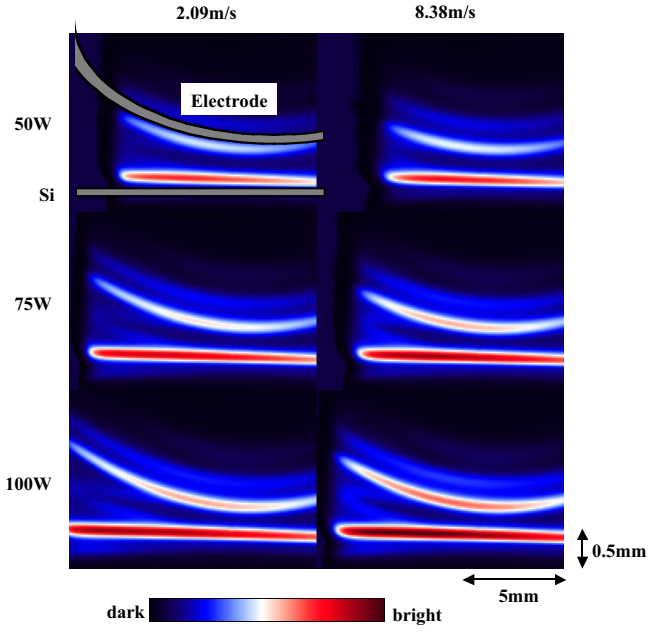

Figure 2. Dependence of argon monochromatic image on both VHF power and gas flow rate. The gas flows from left to right.

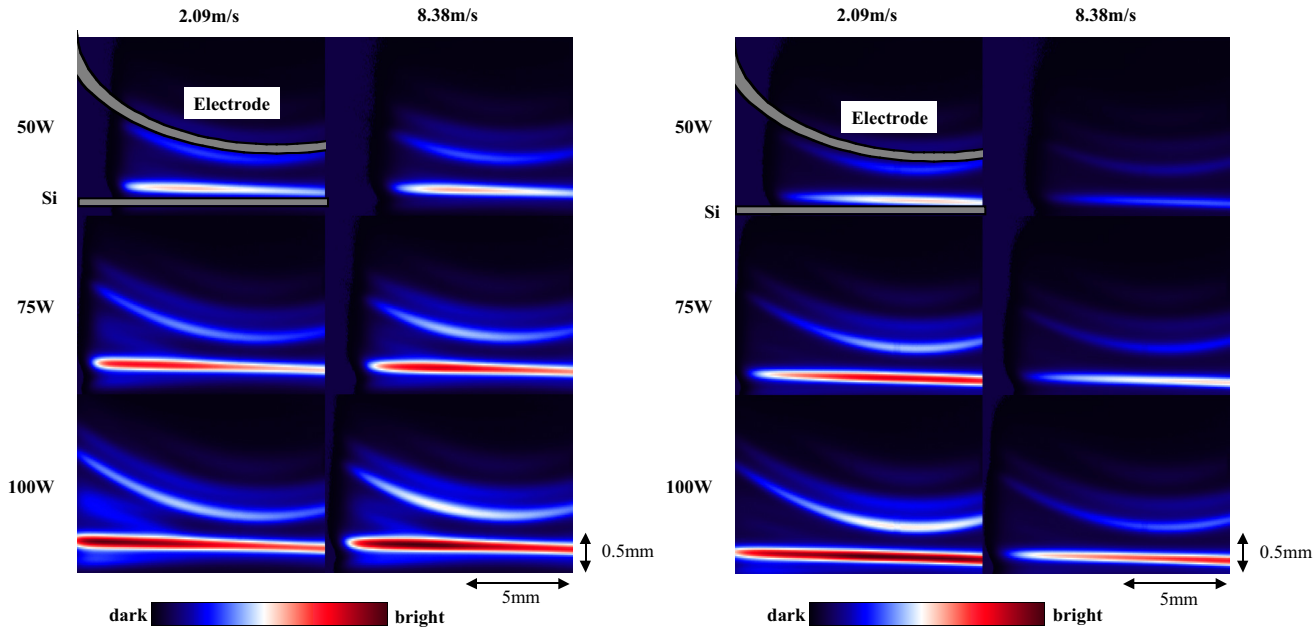

Figure 3. Dependence of oxygen (left) and fluorine (right) monochromatic images on both VHF power and gas flow rate. The emission patterns differ considerably between oxygen and fluorine. The gas flows from left to right.

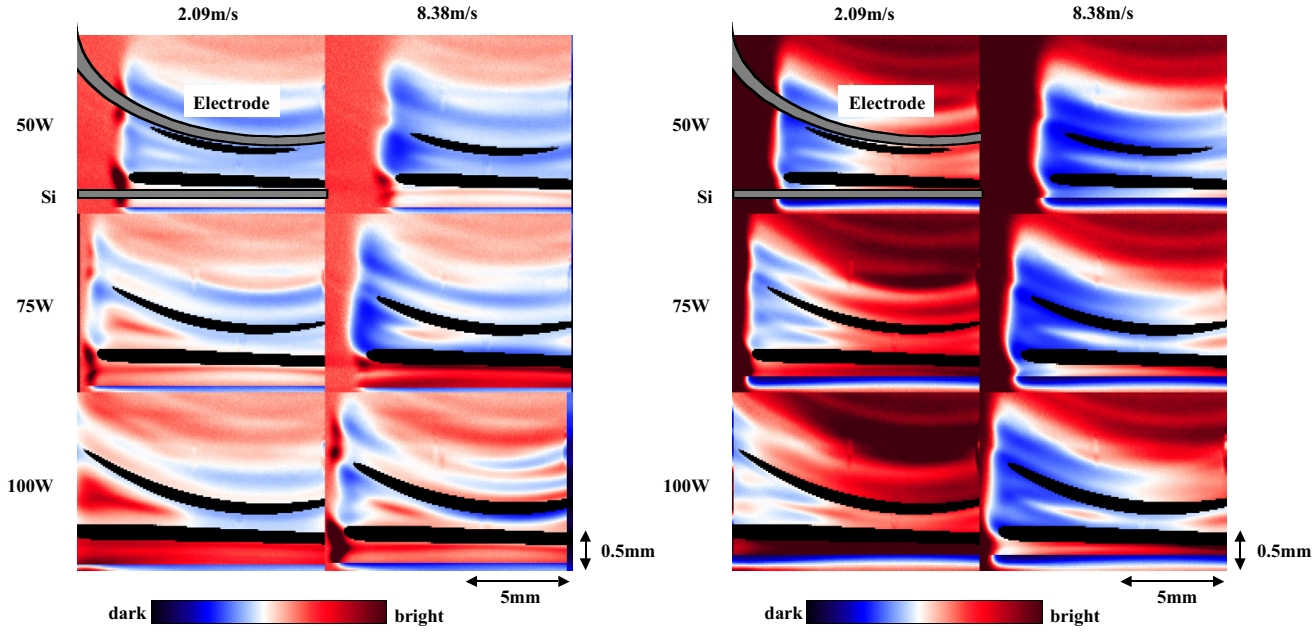

Figure 4. Dependence of oxygen (left) and fluorine (right) atom density maps on both VHF power and gas flow rate calculated with fig. 2 and fig. 3. The density maps differ considerbly.

images by corresponding each pixel value of argon image. The result is shown in figure 4. The density maps differ considerbly by changing both VHF power and gas flow rate, and the maps are quite different from fig. 3. These differences are reflected to the etched patterns on silicon specimens. Figure 5 summarizes the results of CVM process by changing both VHF power and rotation speed of electrode. As with the actinometric results differ, the etched patterns differ greatly.

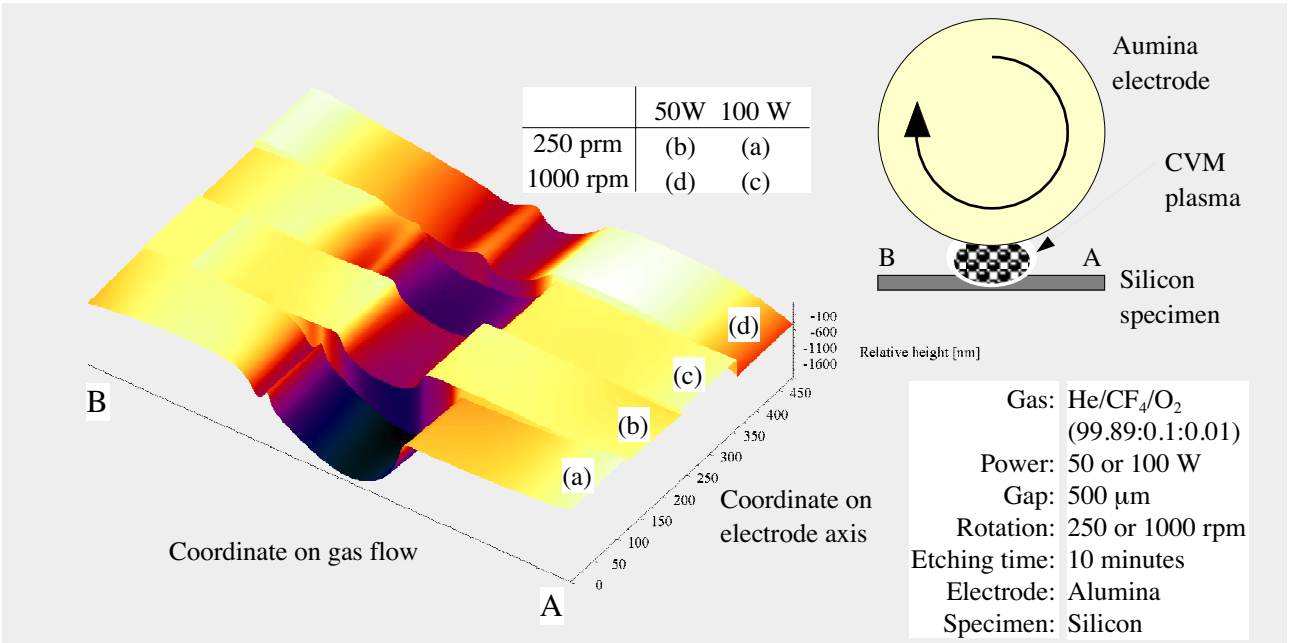

Figure 5. Dependence of the CVM plasma etching process on VHF power and rotation speed of electrode. Length and width of the plasma is about 15 mm, respectively. Specimen is made from Cz P-type Si (100) wafer. Etching condition is 250 rpm with (a) 100 W and (b) 50 W, 1000 rpm with (c) 100 W and (d) 50 W, respectively. The surface profile is measured with Zygo NewView.

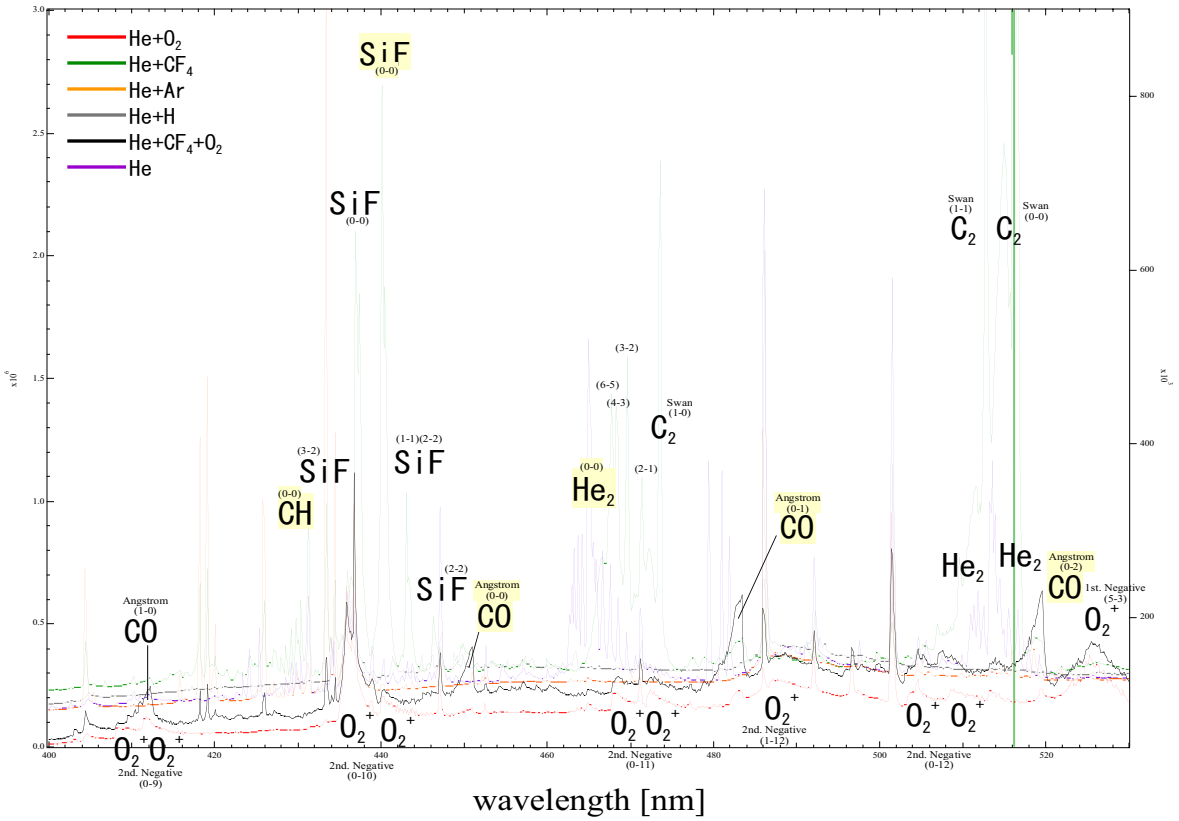

Figure 6. Electronic band spectra of diatomic molecules observed with several gas compositions based on an atmospheric helium. CH spectra appeared in several compositions because the chamber cleaning was not enough after the other CVD experiments. Pure helium plasma shows band spectra of He_2 excimers.

2-2 Electronic spectra of diatomic molecules in the CVM plasma

The electronic spectra of diatomic molecules as the plasma products were recorded with the MS257 spectrograph (ORIEL) coupled with the CCD camera used in the actinometry measurement. The MS257 is an F/3.9 instrument with a focal length of 257.4 mm, usable as a monochromator or true flat field imaging spectrograph because aspheric mirrors are installed. This instrument has three gratings of 300, 600 and 1200 lp/mm. For exmple, we can obtain spectral range of 38 nm on the CCD chip with 1200 lp/mm grating. An optical emission from the plasma was collected and focused onto the entrance slit of the spectrograph through L39 and L40 short cut filters (HOYA). Hence the OES spectrum was recorded at the wavelengths longer than 400 nm. The slit width was 10 μm. Ten consecutive images of spectrum were recorded and accumulated to produce the averaged spectrum of 14bit. A total spectral response of the spectrograph and the CCD camera was calibrated with a calibrated tungsten halogen light source LS-1-CAL (Ocean Optics). To understand roles of each gas component, OES spectrum was recorded with He, He/CF_4, He/O_2 and He/CF_4/O_2 plasma from 400 nm to 530 nm with both high and low resolution. The resultant spectra are superimposed in figure 6. Of couse, each gas composition emits different spectrum, but the spectra of both He atom and He_2 molecule were profoundly affected or suppressed by minor constituents. Sharp two peaks of C_2 (0-0) and (1-1) bands were saturated to record week tails of the bands. These electronic band spectra were numerically simulated, and one of the simulation parameters, T_{rot}, were estimated by a spectral simulation program "Pgopher" with NIST database [19]. The estimated rotational temperatures were from 400 to 600 K. On the other hand, the vibrational temperature of C_2 was estimated to be 10000 K with (0-0) and (1-1) bands.

2-3 Estimation of excitation temperature by OES of rare gases

We have taken a OES approach to determining electron excitation temperature in the CVM plasma. Emission is detected from multiple rare gases (Ar/Ne/Kr/Xe) that are added to a plasma at such low levels that they cause minimal perturbation to the plasma. Furthermore, their partial pressures are sufficiently low for their emissions to be under optically thin conditions. This trace rare gases OES (TRG-OES) method has been used to measure T_e and EEDF in several types of plasmas, and Donnelly recently reviewed the TRG-OES method and provided an updated model and recommendations for electron impact cross sections [20]. In our experiment, line emission spectra of the rare gases were recorded with MS257. After a spectral calibration of the spectroscopic system, the excitation temperature was estimated by drawing Boltzmann plot.

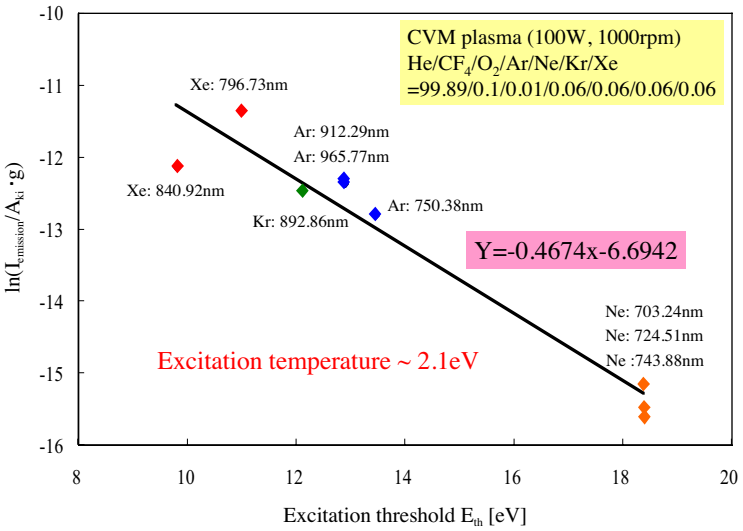

Figure 7. Excitation temperature estimated from rare gas OES spectrum of atomic line emissions.

3. Discussion

The sheath on sample is much brighter in all images in fig. 2and 3 because the sample is metal. Since sheaths in the images of fig. 2 are relatively homogeneous, the CVM plasma is basically uniform in the direction of gas flow, and only the height or the thickness of bulk plasma region changed. However in fig. 2, an interesting feature is observed in the left hand side or wider part of bulk plasma region. A weak emission bump in the bulk region seems to be splitted into two parts, and they seems to be drawn into the sheaths. This pattern might arise from a gradual decline in the plasma gap rather than an injection of laminar gas flow along the electrode surface. Narrawing of the plasma gap might changes a penetration of electric field into plasma bulk region. This bulk emission might be caused by a kind of stochastic heating beacuse of supplying VHF field at 150 MHz. In parallel plate CCP experiments, the same emission in bulk region has been observed more than one atmosphere. The resultant actinometric data are different from the plasma images. The actinometric data in fig. 4 emphasize a density maximum in the central region. In fig. 4, density maps of fluorine (right) has three density maxima

which might reflect an opposite pattern of argon emission. It is caused by that in fig. 3 (right), despite a threshold energy is almost same as the values of oxygen and argon, the bulk emission of fluorine is weak and nearly homogeneous. The position of density maximum is same as that of oxygen. Hence oxygen atoms might increase a dissociation of CF_X molecules. The whole bulk plasma region might contains both fluorine atoms and CF_X molecules homogeneously, and a small amount of oxygen atoms distributes inhomogeneously reflecting the bulk field and results in fluctuation of fluorine distribution.

The OES spectra shown in fig. 6 confirm that (1) CF_4 molecules are basically dissociated enough to couple with Si and O, (2) Si is etched with F atoms, (3) suppression of He_2 spectra may caused by reduction of He(2P) atom density because the excited states of He_2 are generated by He(2P) + 2He [16]. The rotational temperature or gas tempeature was very low because the room-temperature gas cools the plasma by its high speed shear flow. But the vibrational temperature was very high because the relaxation time long, and there may be a lot of population at higher vibrational level. Hence the dissociation of molecules may be governed by vibrational excitation in the CVM plasma.

The electron excitation temperature as shown in fig. 7 has reproducebility. But the temperature may not be a key parameter for the CVM proccess monitoring. Further discussion will presented in the conference.

References

[1] K. Yamamura, et al., *Fabrication of elliptical mirror at nanometer-level accuracy for hard x-ray focusing by numerically controlled plasma chemical vaporization machining*, Rev. Sci. Instrum. **74** (10), 4549-4553 (2003).

[2] K. Yamauchi et al., *Two-dimensional submicron focusing of hard x-rays by two elliptical mirrors fabricated by plasma chemical vaporization machining and elastic emission machining*, Jpn. J. Appl. Phys. **Part 1. 42** (11), 7129-7134 (2003).

[3] Y. Mori et al., *Thinning of silicon-on-insulator wafer by numerically controlled plasma chemical vaporization machining*, Rev. Sci. Instrum. **75** (4), 942-946 (2004).

[4] Y. Oshikane et al., *Two-dimensional density mapping of oxygen and fluorine atoms by argon actinometry with narrow bandpass filters*, Proc. of Plasma Science Symposium 2005 and the 22nd Symposium on Plasma Processing (PPS-2005/SPP-22, Nagoya, Japan), P3-040 (2005).

[5] Y. Oshikane et al., *Fluorine and oxygen monitoring in plasma CVM etching process for silicon wafer by argon actinometry technique*, Program of the 57th Annual Gaseous Electronics Conference (GEC04, Bunratty, Ireland), DS1-003 (2004).

[6] Y. Oshikane et al., *Fluorine and oxygen density monitoring in plasma cvm process by argon actinometry technique*, Abstracts of 7th APCPST & 17th SPSM (Fukuoka, Japan), 29P-99 (2004).

[7] V. M. Donnelly et al., *Anisotropic etching of SiO_2 in low-frequency CF_4/O_2 and NF_3/Ar plasmas*, J. Appl. Phys. **55** (1), 242-252 (1984).

[8] H. M. Katsch et al., *Detection of atomic oxygen: Improvement of actinometry and comparison with laser spectroscopy*, J. Appl. Phys. **88** (11), 6232-6238 (2000).

[9] M. Seman et al., *Investigation of the role of plasma conditions on the deposition rate and electrochromic performance of tungsten oxide thin films*, J. Vac. Sci. Technol. **A21** (6), 1927-1933 (2003).

[10] R.W.B. Pearse et al., *The identification of molecular spectra (Chapman and Hall)* (1976).

[11] W.G. Mallard, *NIST Chemistry WebBook (NIST Homepage)*, http://webbook.nist.gov/chemistry/ (2003).

[12] G. Herzberg, *Molecular spectra and molecular structure Volume I - Spectra of diatomic molecules (Van Nostrand Reinhold)* (1950).

[13] A. C. Le Floch et al., *Fourier transform spectroscopy of the CO Angstrom bands*, Chem. Phys. **97**, 379-389 (1985).

[14] M.N.R. Ashfold et al., *Resonance enhanced multiphoton ionisation of the SiF radical: a reinvestigation*, Chem. Phys. Lett. **263**, 138-144 (1996).

[15] A.Treshchalov et al., *The role of He_2 molecules in plasma kinetics of high pressure helium fast discharges*, *Proc. of the 23rd. Int. Conf. on Phenomena in Ionized Gases (Toulouse, France)*, 110-111, (1997).

[16] F. Emmert et al., *Reaction kinetics of the He(2P) and the He_2*(a,v) states in high-density helium*, J. Phys. D: Appl. Phys. **21**, 667-674 (1998).

[17] S. P. Sharma et al., *Analysis of emission data from O_2 plasmas used for microbe sterilization*, J. Appl. Phys. **95** (7), 3324-3333 (2004).

[18] L. L. Danylewych et al., *Intensity measurements on the C_2 ($d^3\Pi_g$-$a^3\Pi_u$) Swan band system. I. Intercept and partial band methods*, Proc. R. Soc. London **A339**, 197-212 (1974).

[19] C. M. Western, spectral simulation program "Pgopher", http://www.tlchm.bris.ac.uk/pt/western/pgopher/simulate.htm.

[20] V. M. Donnelly, *Plasma electron temperatures and electron energy distributions measured by trace rare gases optical emission spectroscopy*, J. Phys. D: Appl. Phys. **37,** R217–R236 (2004).

Diagnostics of grid-assisted magnetron sputtering using energy-resolved mass spectroscopy

P. Kudlacek[1], J. Vlcek[1], J. Houska[1], Jeon G. Han[2], Min J. Jung[2], and Yong M. Kim[2]
[1]Department of Physics, University of West Bohemia, Univerzitni 22, 306 14 Plzen, Czech Republic
[2]Center for Advanced Plasma Surface Technology (CAPST),
Sungkyunkwan University, 300 Chunchun-dong, Jangan-gu, Suwon 440-746, Korea
e-mail: kudla@kfy.zcu.cz

Abstract

Energy-resolved mass spectroscopy was used to study differences in ion bombardment characteristics during conventional reactive magnetron sputtering and a grid-assisted magnetron sputtering proposed for deposition of films with a dense microstructure and smooth surface. An effect of the ion extraction grid potential, the total pressure and the argon-nitrogen gas mixture composition on energy distributions and integral fluxes of ions bombarding the growing Ti and TiN films was also investigated.

Keywords

Magnetron sputtering
Mass spectroscopy
Grid-assisted system
Ion bombardment effects

1. Introduction

It is well known that ion bombardment of growing films is of key importance for their structure and properties [1,2]. Recently, a novel grid-assisted magnetron sputtering system was developed in the CAPST laboratories at the Sungkyunkwan University in Suwon (Korea) making it possible to form high-quality films with a dense microstructure and smooth surface [3,4]. The main aim of this paper is to characterize energy and flux of ions bombarding growing films during their deposition using the grid-assisted magnetron sputtering. Reactive deposition of TiN films has served as a model system to illustrate differences between a conventional magnetron sputtering and the grid-assisted magnetron sputtering.

2. Experimental details

Figure 1 shows the new magnetron system with two mesh type Ti grids and a circular anode, electrically isolated from a chamber wall. A cylindrical vacuum chamber (diameter 160mm, length 220mm) was pumped down to a base pressure of 5×10^{-3}Pa by a diffusion pump backed with a rotary pump. An unbalanced

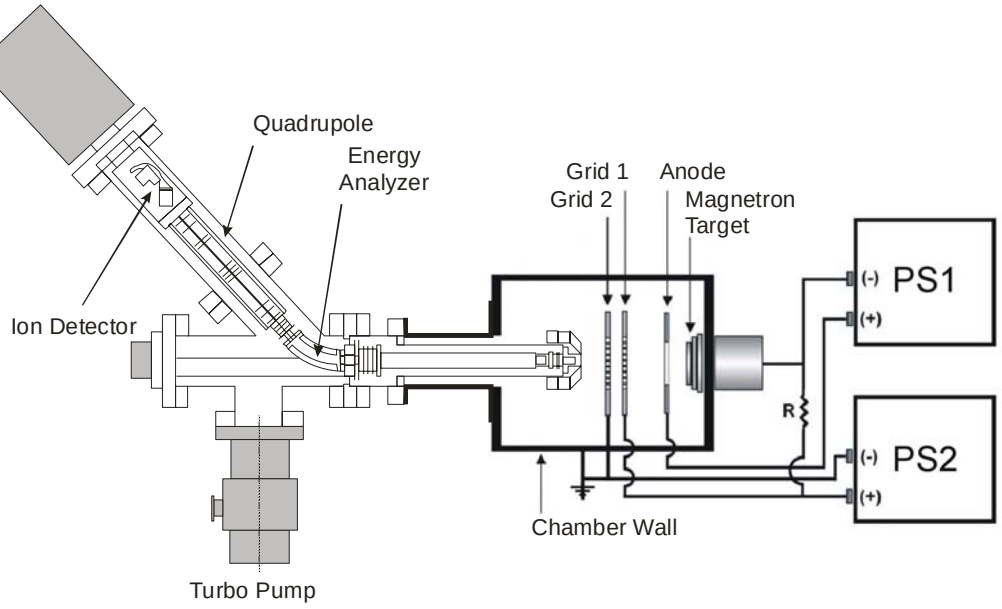

Fig. 1. Schematic illustration of the experimental set-up.

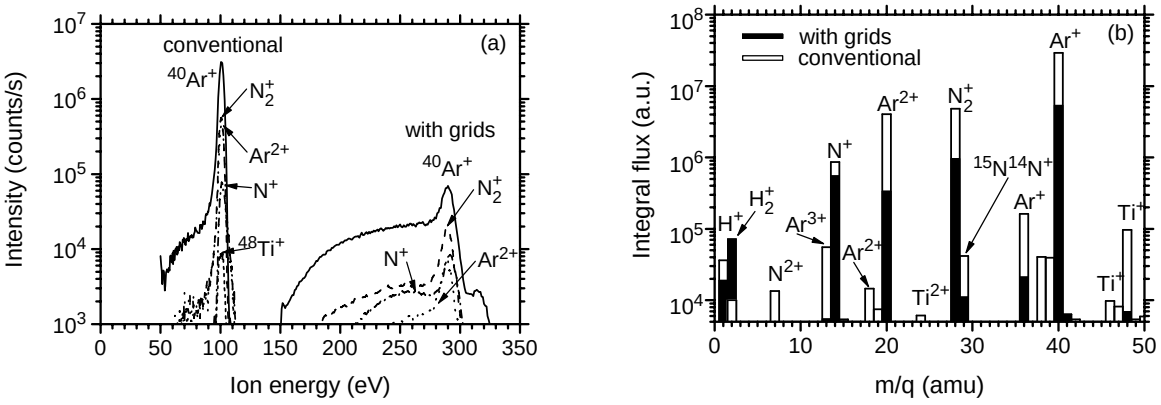

Fig. 2. Energy distributions (a) and integral fluxes (b) of the ions incident at a biased substrate (V_b=-100V) during conventional magnetron sputtering and at a grounded substrate during grid-assisted (V_g=+100V) magnetron sputtering.

circular planar magnetron equipped with a 45mm diameter Ti target was connected to the power supply PS1. An ion extraction potential V_g at the first grid was established by the power supply PS2. The films were deposited on silicon substrates located at the distance of 65mm from the target. The total pressures of argon-nitrogen gas mixtures were p=0.5 and 1Pa at the argon fraction ranging from 40 to 100%. The discharge current on the magnetron target was held constant at 0.9A. Microstructure and surface morphology of the as-deposited TiN films were investigated by FESEM (Philips XL30 ESEM-FEG) and AFM CP Research (Thermo-Microscope).

The energy-resolved mass spectrometer (EQP 300 Hiden Analytical) was placed at the substrate position in the center line of the discharge (see Fig. 1). We used a configuration, in which an extraction electrode with a 0.1mm diameter orifice in the center was located 5mm behind a grounded front electrode of the spectrometer with a central input aperture of 5mm in diameter. A negative extraction potential V_b=-100V, relative to ground potential of the chamber walls, was applied to simulate the same negative substrate bias used in the conventional magnetron sputtering. A low extraction potential of -10V, compensated at the output, was applied in measurements of the energy distributions of ions arriving at the grounded substrate during the grid-assisted magnetron sputtering with the first grid at a positive potential V_g in the range from 0 to 150V and the second grid at ground potential. The integral fluxes of individual ionic species were determined by a direct integration of the respective energy distributions.

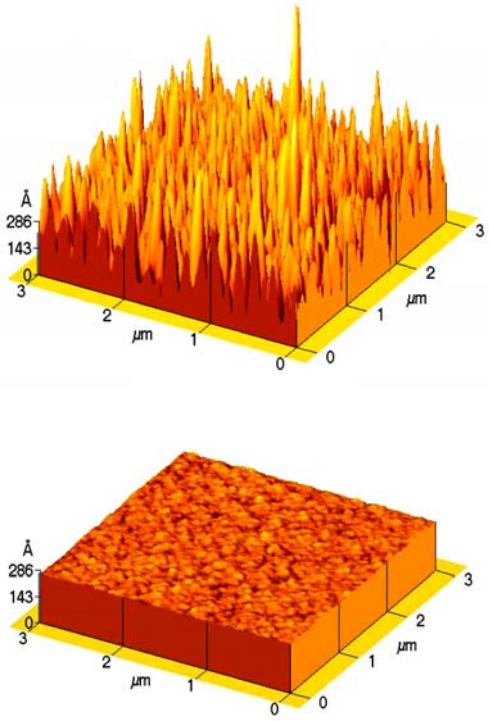

Fig. 3. AFM images of the TiN films deposited using conventional magnetron sputtering at V_b=-100V (top) and grid-assisted magnetron sputtering at V_g=+100V (bottom).

3. Results and discussion

3.1. Comparison of conventional and grid-assisted magnetron sputtering of TiN films

Figure 2 provides information on energy distributions and integral fluxes of ions bombarding the growing TiN films during their conventional magnetron deposition on a biased substrate

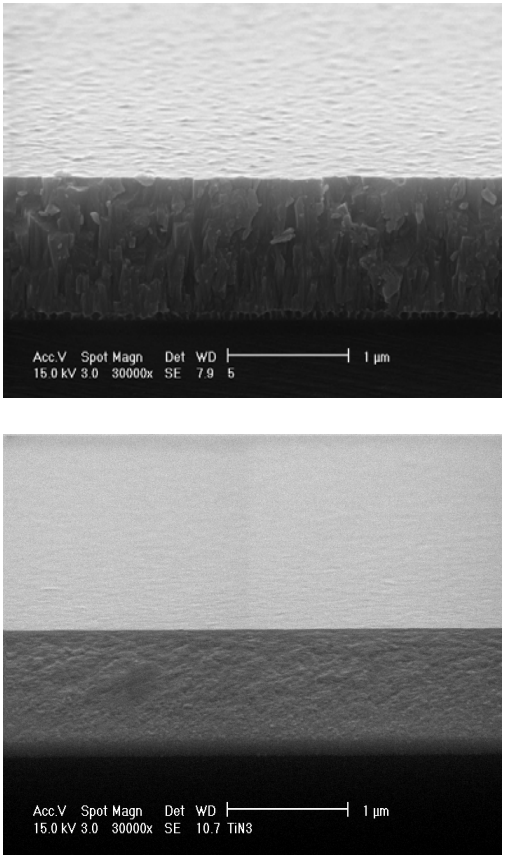

Fig. 4. Tilted cross-sectional SEM photographs of the TiN films deposited using conventional magnetron sputtering at V_b=-100V (top) and grid-assisted magnetron sputtering at V_g=+100V (bottom).

(V_b=-100V) and grid-assisted (V_g=+100V) magnetron deposition on a grounded substrate in an 80%Ar+20%N_2 gas mixture at the total pressure p=0.5Pa. The sputtered Ti target was at a cathode potential V_C=-445V with respect to the grounded chamber walls in the used conventional magnetron system. This value is in good agreement with a difference between the respective anode potential V_A=+318V and cathode potential V_C=-101V in the grid-assisted magnetron system with V_g=+100V. Figure 2(a) shows a progressive rise in the kinetic energy of ions bombarding the substrate in the grid-assisted magnetron system. This is mainly due to the high positive value of the anode potential resulting in a strong increase in the plasma potential V_p in the discharge, where ionization processes are realized (see the ion energies close to eV_A corresponding to maxima of the energy distributions). In addition, the used two-grid configuration is important for extraction and acceleration of the ions towards the grounded substrate. As expected, relatively narrow spectra with the maxima corresponding to the ion energy $e(V_p-V_b)$, where $V_p \approx 1$V, were obtained in the conventional magnetron discharge. As can be seen in Figs. 2(a) and 2(b), the ion flux to the substrate substantially decreases in the grid-assisted magnetron system under practically the same magnetron power. The main reason are large losses of the charged particles at grounded chamber walls. A total ion flux to the substrate decreases 5.4 times in the grid-assisted system compared to the conventional system at almost the same fractions of predominant Ar^+ (73 and 74%, respectively) and N_2^+ (13 and 12%, respectively) ions and the increased fraction of the N^+ ions from 2 to 7% [see Fig. 2(b)]. The enlarged dissociation degree of nitrogen ion flux towards the substrate, which could reflect an increase in the dissociation degree of neutral nitrogen molecules, might be caused by a substantial rise in the electron temperatures measured in the grid-assisted magnetron discharges [5]. As expected, the contributions of the Ti^+ and particularly the TiN^+ ions were very low in both the systems investigated. The respective fractions were 0.2 and 0.005% in the conventional system, whereas they decreased 2 and 5 times, respectively, in the grid-assisted system.

The AFM images proved a very smooth surface morphology of the TiN films (RMS=0.7nm) deposited using the grid-assisted magnetron sputtering at V_g=+100V, see Fig. 3. This can be explained by an increasing role of ion-induced effects (such as ion-induced knock-on subplantation of the film-forming particles leading to densification of the films, and resputtering) in film growth processes at the enlarged ion energies and low ion fluxes to the substrate. In Fig. 4, a significant increase in the density of the film deposited by grid-assisted magnetron sputtering is shown. It should be noted that the deposition rate of 67nm/min achieved for TiN films in the conventional magnetron system at V_b=-100V decreased to 25nm/min in the grid-assisted system at V_g=+100V [5], mainly due to resputtering of growing films at the enlarged ion energies.

Table 1. The cathode and anode potentials in the grid-assisted magnetron system during depositions in an 80%Ar+20%N_2 gas mixture at various values of the extraction potential V_g, and p=0.5Pa and V_b=0V.

Grid 1 potential V_g (V)	0	50	100	150
Cathode potential V_C (V)	-170	-130	-101	-67
Anode potential V_A (V)	254	290	318	348

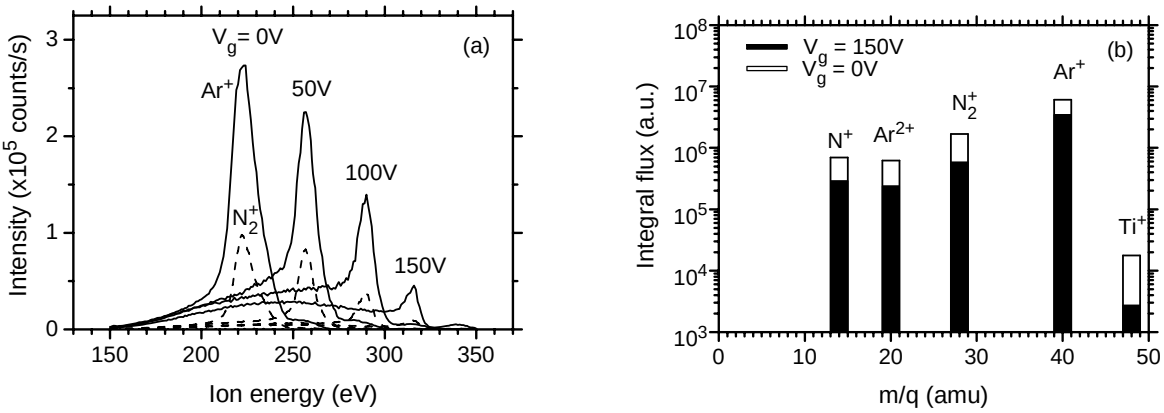

Fig. 5. Energy distributions (a) and integral fluxes (b) of the predominant ions incident at a grounded substrate during grid-assisted magnetron sputtering for various potentials V_g.

3.2. Effect of the process parameters on ion bombardment characteristics during grid-assisted sputtering

As can be seen in Figs. 5(a) and 5(b), an increase in the values of the potential V_g from 0 to 150V leads to a rise in the kinetic energy of ions and to the corresponding decrease of the ion fluxes to the substrate. These effects are natural consequences of a substantial increase in the plasma potential in the discharge due to the respective rise in the anode potential V_A from 254 to 348V (see Table 1). Let us recall that the V_A values increase as a result of the raising values of the cathode potential V_C from -170 to -67V (see Table 1 and a direct electrical connection between the cathode and the grid1 electrode in Fig. 1), as the potential difference V_A-V_C, keeping constant the discharge current on the magnetron target I=0.9A, is only slightly decreasing from 424 to 415V with the increase in the V_g values from 0 to 150V. This rise in the extraction potential V_g leads to almost 2 times lower total ion flux to the substrate at increasing fraction of Ar^+ ions (from 67 to 76%) and decreasing fractions of the N_2^+ ions (from 18 to 13%) and N^+ ions (from 8 to 6%). The N^+/N_2^+ ion flux ratio was in the range from 0.42 to 0.58. The corresponding deposition rate of films decreased from 46 to 20nm/min.

Figure 6 shows the effect of the total pressure and the argon-nitrogen gas mixture composition on ion bombardment characteristics during grid-assisted magnetron sputtering at a fixed extraction potential V_g=+100V. The obtained results can be explained on the basis of the data given in Table 2 if one takes into account that the values of the cathode potential V_C and the potential difference V_A-V_C are affected by a plasma conductivity determined by the total pressure and the gas mixture composition.

4. Conclusions

Energy-resolved mass spectroscopy was used to study differences in ion bombardment characteristics during conventional reactive magnetron sputtering and the grid-assisted magnetron sputtering proposed for deposition of films with a dense microstructure and smooth surface. It was found that the grid-assisted magnetron system makes it possible to increase substantially the values of the plasma potential in the discharge. As a result, the role of ion-induced effects (such as knock-on subplantation of the film-forming particles leading to densification of the films, and resputtering) is enhanced in film growth processes at the enlarged ion energies and low ion fluxes to the substrate. The effect of the ion extraction grid potential, the total pressure and the argon-nitrogen gas mixture composition on energy distributions and integral fluxes of ions bombarding the growing Ti and TiN films was shown.

Table 2. The cathode and anode potentials in the grid-assisted magnetron system during depositions in various argon-nitrogen gas mixtures at two total pressures, and V_g=+100V and V_b=0V.

Total pressure p (Pa)	0.5	0.5	1.0	1.0
Ar fraction (%)	80	100	40	100
Cathode potential V_C (V)	-101	-89	-105	-67
Anode potential V_A (V)	318	294	320	279

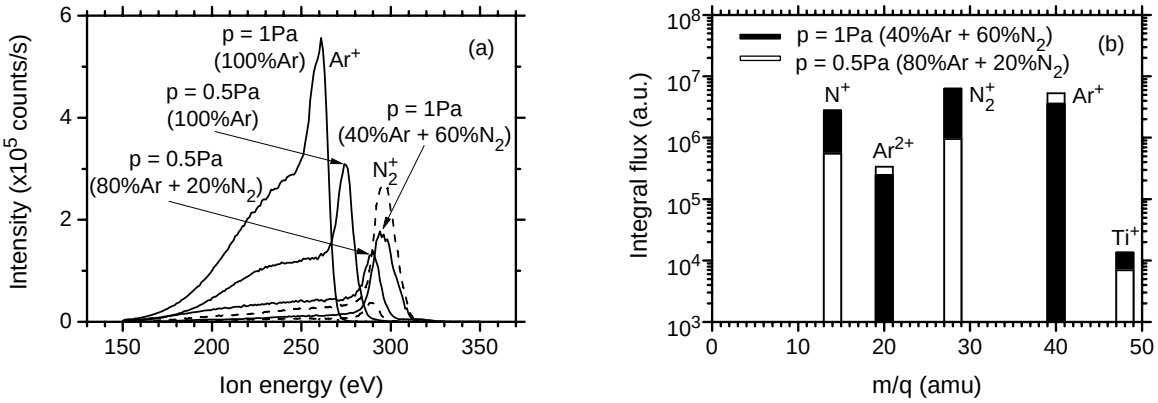

Fig. 6. Energy distributions (a) and integral fluxes (b) of the predominant ions incident at a grounded substrate during grid-assisted magnetron sputtering for various gas mixtures and total pressures.

Acknowledgement

This work was supported by the Ministry of Education of the Czech Republic (Projects No. MSM 4977751302 and ME 673) and by the Korea Science and Engineering Foundation through the CAPST at the Sungkyunkwan University.

References

[1] J. Musil, Surf. Coat. Technol. 100-101 (1998) 280.
[2] I. Petrov, P. B. Barna, L. Hultman, J. E. Greene, J. Vac. Sci. Technol. A 21 (2003) S 117.
[3] Kyung H. Nam, Min J. Jung, Jeon G. Han, T. Kopte, U. Hartung, C. Peters: Synthesis of high-density MgO films by a novel magnetron sputtering system, Vacuum 75 (2004) 1.
[4] Min J. Jung, Kyung H. Nam, Jeon G. Han, J. Vlcek, J. Houska, and P. Kudlacek: Grid-assisted magnetron sputtering of high-quality TiN films, J. Vac. Sci. Technol. A, submitted.
[5] Min J. Jung, CAPST, Sungkyunkwan University, Korea (unpublished).

Synthesis of carbon nanostructures by arc discharge in liquid

Shenli Jia, Gang Xing, Pu Yang, Zongqian Shi

Department of Electrical Engineering, Xi'an Jiaotong University, Xi'an China

Abstract

In this paper, we conducted serial experiments on synthesis of nanomaterials by arc discharge both in water and liquid nitrogen. The parameters of arc discharges such as arc current and electrodes size have been optimized, the products were analyzed and compared. In order to understand the mechanism of the formation of nanomaterials during the arc discharges, the cross magnetic field was introduced to disturb the arc plasma. The interesting result was got and tentative explanation was given.

1.Introduction

After the discovery of carbon nanotubes in 1991 [1], the synthetic methods of nanomaterials have been widely studied. At present, there are three kinds common methods to fabricate nanomaterials. They are arc discharges in protection gases [2-5], laser ablation [6-9] and chemical vapor deposition [10-13]. Most of those methods need complex vacuum system and the arc discharge in protection gas needs additional cooling for cathode and reaction container wall. So the cost is high and the nanomaterials yield is relatively low. Ishigami *et al* [14] proposed a method for fabrication multi-walled carbon nanotubes by arc discharge in liquid nitrogen. After that, due to its simple implementation, potential for high yield and low cost , synthesis nanomaterials by arc discharge in liquid has been studied more widely. Sano et al obtained nano-onions by arc discharge in water [15] and single wall nanohorns (SWNHs) in liquid nitrogen [16].

Although a lot of experimental research have been conducted on this field, the mechanism of nanomaterials formation in arc discharge in liquid is still not clear. Such as, the effects of different liquid medium on the products, why the nanotubes formed on the cathode surface but nanoparticles got from the liquid surface. In this paper, a tentative physical model was proposed to explain the nanomaterials synthesis process in liquid arc discharge. In order to study the effect of stability of arc discharge on the characteristics of products, a low frequency cross magnetic field was used to make the arc column swinging.

2.Experiments and results

DC arc discharge was used for the experiments. Two pure graphite electrodes were submerged in liquid, the arc was initiated by slowly detaching the moveable anode from the cathode. The arc gap should keep at the value that the continuous arc discharge can be obtained. Arc current scope is 30~100A.

For arc discharge in water, the cathode size is 20mm in diameter and anode 6mm in diameter. The arc current was selected from 30A to 100A. The anode was eroded during the arc discharge, most of carbon come from anode was reacted with water under the high temperature and turn into gases, part of carbon flow to cathode and deposit on cathode surface, some products float on the water surface and some products deposit at the bottom of liquid container. When the arc current was 60A, reaction gases production rate was 225cm^3 min-1. Analysis by chromatograph showed that the major content of gases produced during the arc discharge in water was CO and others were H2, CO2, C2H2, C2H4, C2H6 and CH4.The percentage of carbon coming from anode went to gases was about 79.66%, and deposition at container bottom was 10.85%, cathode deposition 9.377% and floating products 0.1145%. TEM investigation showed that multi-wall carbon nanotubes were the major content of cathode deposition and carbon-onion found in the floating product. The

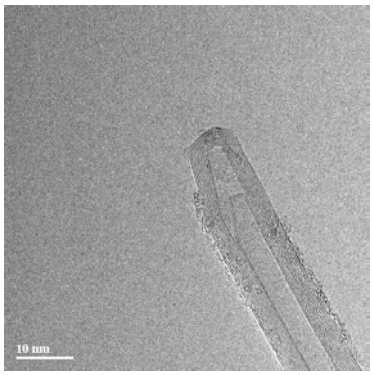

Figure 1. TEM image of multi-wall carbon nanotubes from the cathode deposition of arc discharge in water.

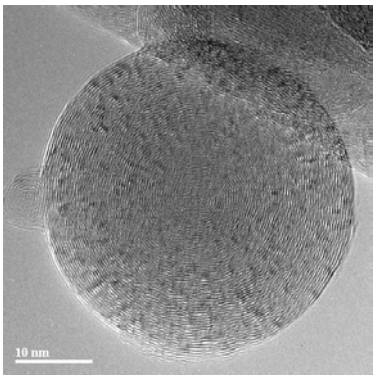

Figure 2. TEM image of carbon onion from floating products of arc discharge in water.

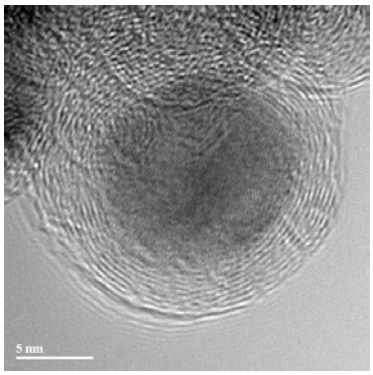

Figure 3. TEM image of cobalt encapsule carbon onion of arc discharge in water.

deposition at container bottom was amorphous carbon. The TEM images are shown in figure 1. and figure 2. The TEM was performed using a H-9000NAR microscope operated at 300 kV. The samples of TEM were prepared by decentralizing the dried powder in ethanol by supersonic, then drop the solution on copper grid.

The effect of catalyst metal was also tested. A hole of 2mm in diameter is drilled in the anode and filled with the mixed powder of cobalt and graphite. Then the arc discharge was conducted in water also. Comparing with pure graphite anode, the cobalt encapsule carbon onions was got from floating products as shown in figure 3.

When the liquid changed to liquid nitrogen, the arc discharge will be more “quiet” compared with that in water and the anode vaporization rate was also lower. If the arc discharge parameters do not change, no nanoparticles could be found in the surface floating products such as carbon onions produced in water. It could be expained that since liquid nitrogen could provide a much stronger cooling effect to the graphite electrodes than water, which made the anode temperature keeping lower and the anode vaporization rate decreased, the nanoparticles could not be formed around the arc column if the density of carbon species were low. So we decreased the anode to 3mm in diameter as the arc current maintained at 60A. The floating products were collected by adding water into the liquid nitrogen after arcing and then collected the floating materials on the water surface after liquid nitrogen completely vaporized. The major content of cathode deposition was multi-wall nanotubes same as arc discharge in water. But the major content of floating product were not carbon onion like in water, it was carbon nanohorns, spherical agglomerate composed of single- wall graphene sheets. The TEM images of carbon nanohorns produced by arc discharge in liquid nitrogen were shown in figure 4.

Besides the temperature gradient, the density of carbon species (carbon atoms or ions) is also the very important parameter for the carbon nanoparticles formation. In order to disturb the carbon species flow come from the anode, the cross magnetic field was introduced for the arc discharges in water, the direction of magnetic field were arranged perpendicular to the arc column and alternate at 5 Hz. The magnetic strength was chosen to get maximum arc swing but not blow out the arc. The density of carbon species from arc plasma became unstable at a certain place out of arc column where the carbon onions being produced. Under this condition, the major products formed in the bubble were some 2 or 3 layers defective carbon nanostuctures as shown in figure 5. The formation of this new structure may be caused by the carbon species (carbon atoms and ions) diffusing out of the arc column become unstable due to the disturb of magnetic field, and the disturb of the magnetic field and the disturb is fast than the carbon-onions formation time.

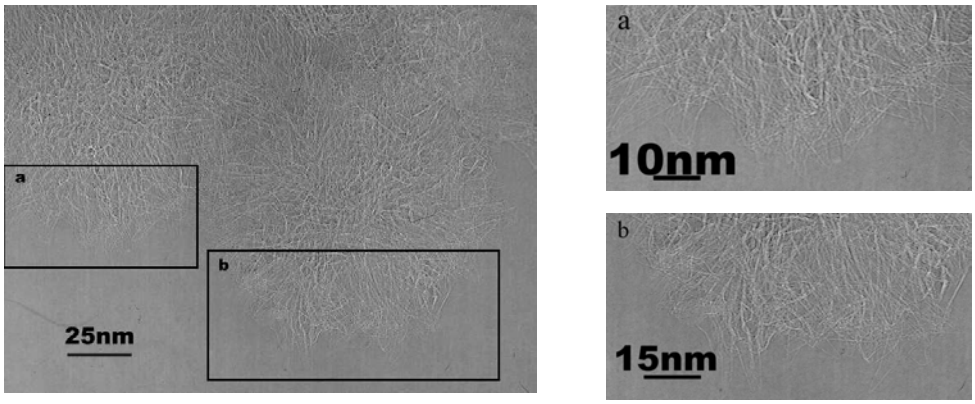

Figure 4. Carbon nanohorns produced by arc discharge in liquid nitrogen

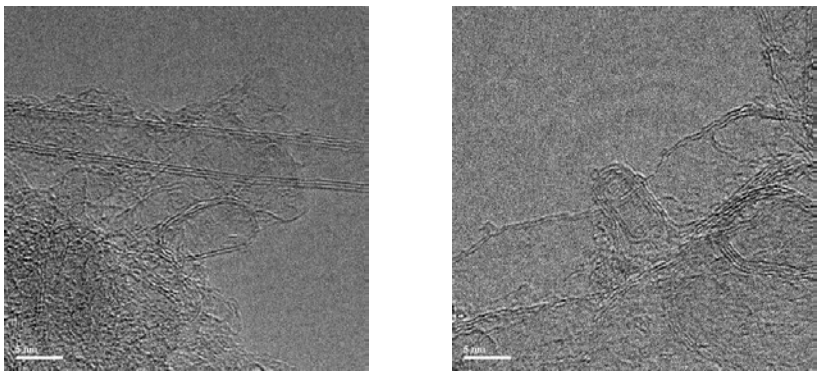

Figure 5. The defective carbon nanostructures produced by magnetic disturb arc discharge in water

3.Tentative Physical Model

After analyzing and summarizing above experimental results and relevant investigations by other researchers, we proposed that the formation of the nanomaterials should be determined by following parameters: directionality of carbon species (carbon ions, atoms and dimers), density of carbon species and quenching effect (temperature gradient).

In most cases, it was the cooling wall where the seeds of nanotubes or nuclei of carbon onions products formed and then growth. The cooling wall provides a relative high temperature gradient that is favourable for seeds or nuclei formation. The pressure of atmosphere gas, if used, may affect the temperature gradient and the moving speed of carbon species.

The carbon vapor density plays an important role in the growing process. Low carbon vapor density will lead only nuclei formation but no further growth. The experiment of the discovery of C_{60} is a good example. The carbon vapor density is not high enough at the large reaction chamber wall, that's why C_{60} formed rather than carbon onions. Certainly, the growth nanotubes also needs a sufficient density. Otherwise, the open end of nanotubes will come to close.

The aforementioned mechanism should be applicable to arc discharge in liquid (water, liquid nitrogen) for the nanomaterials fabrication. The tentative physical model is shown in figure 6. It was assumed that the reaction between carbon and the liquid material does not participate the nanomaterials formation. The major difference between arc discharge in liquid and in gases is that the liquid provides both the cooling for electrodes and an ideal quenching wall (bubble wall). High temperature gradient and high carbon species density near the bubble wall contributed to the small bubble size. As shown in Figure 6, the carbon ions and atoms come from anode and arc

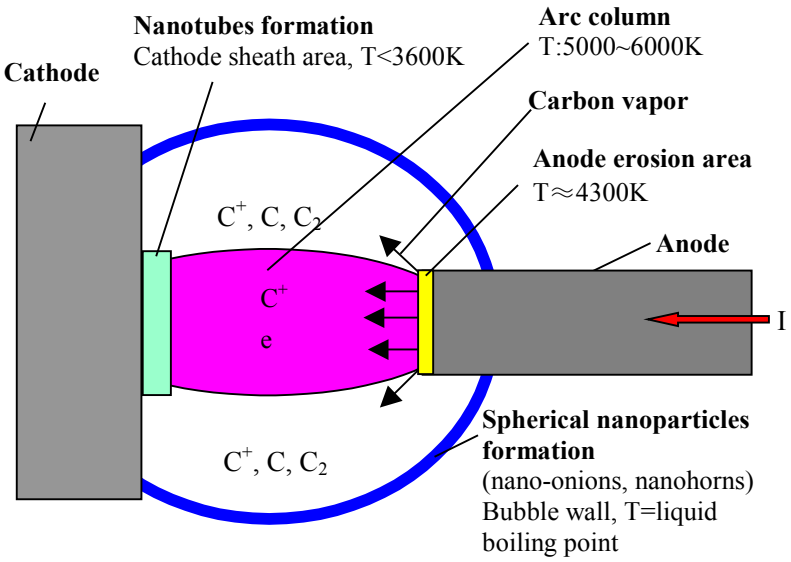

Figure 6. Schematic of physical model arc discharge in liquid

column gradually formed C_2 and further bonded into small fragments as the temperature decreasing when they move toward to cold bubble wall. The cooling sheath near the bubble wall provides a sufficient temperature gradient that is the critical parameter for fullerene and related structures to nucleate and growth. The temperature of liquid nitrogen was much lower than water. So the temperature gradient in the cooling sheath near the bubble wall of liquid nitrogen was higher than that in water. When the fragments move into cooling sheath of liquid nitrogen, they intend to bend due to strong quenching effect and formed single- wall graphene sheets, which finally agglomerate to carbon nanohorns. But in water, the fragments can grow to perfect spherical carbon onions due to the weaker quenching effect. The carbon species flow from anode to cathode formed nanotubes contributed to their directional movement.

4.Conclusion

We experimentally investigated fabrication of carbon nanomaterials by arc discharge in water and liquid nitrogen, carbon onions and carbon nanohorns were produced respectively besides multi-wall nanotubes, and 2 or 3 layers defective carbon nanostructures were produced when cross magnetic field added to arc discharge in water. A tentative model to explain the experiments phenomena was proposed. The major parameters for nanomaterials fabrication should be temperature gradient and the density of carbon species.

5.Acknowledgement

This work was supported by the National Natural Science Foundation of China under project 50377030.

References:

[1] S. Iijima, “Helical microtubules of graphitic carbon”, Nature, 1991;354:56

[2] H. W. Kroto, J. R. Heath, S. C. O’Brien, R. F. Curl and R. E. Smally, Buckyminister-Fullerene, Nature, 1985;318:162

[3] Ebbesen T W and Ajayan P M, Large scale synthesis of carbon nanotubes, *Nature* 1992;358: 220–2

[4] Journet C, MaserW K, Bernier P, Loiseau A, de la ChapelleM L, Lefrant S, Deniard P, Lee R and Fischer

J E, Large-scale production of single-walled carbon nanotubes by the electric-arc technique, Nature 1997; 388:756–8

[5] Wang X K, Lin X W, Dravid V P, Ketterson J B, and Changa R P H, Carbon nanotubes synthesized in a hydrogen arc discharge, Appl. Phys. Lett., 1995;66:2430-2

[6] Thess A, Lee R, Nikolaev P, Dai H J, Petit P, Robert J, Xu C H, Lee Y H, Kim S G, Rinzler A G, Colbert D T, Scuseria G E, Tomanek D, Fischer J E and Smalley R E, Crystalline ropes of metallic carbon nanotubes, Science 1996; 273: 483–7

[7]Guo T, Nikolaev P, Rinzler A G, Tomanek D, Colbert D T, Smallry R E. Self-assembly of tubular fullerenes. J. Phys. Chem.,1995:99(27):10694-7

[8] Scott C D, Arepalli S, Nikolaev P and Smalley R E, Growth mechanisms for single-wall carbon nanotubes in a laser-ablation process, Appl. Phys. A 2001; 72 573–80

[9] Geohegan D B, Schittenhelm H, Fan X, Pennycook S J, Puretzky A A, GuillornM A, Blom D A and Joy D C, Condensed phase growth of single-wall carbon nanotubes from laser annealed nanoparticulates Appl. Phys. Lett. 2001;78:3307–9

[10] Yacaman M J, Yoshida M M, Rendon L, Catalytic growth of carbon microtubes with fullerene structure, Appl. Phys. Lett., 1993;62:657-9

[11]Dai H J, Rinzler A G, Nikolaev P, et al. Single-wall nanotubes produced by metal-catalyzed disproportionation of carbon monoxide. Chem. Phys. Lett., 1996;260:471-5

[12] Zhang R Y, Amlani L, Baker J, Tresek J and Tsui R K , Chemical vapor deposition of single-walled carbon nanotubes using ultrathin Ni/Al film as catalyst, Nano Lett., 2003;3:731–5

[13] Cui H, Eres G, Howe J Y, Puretkzy A, Varela M, Geohegan D B and Lowndes D H, Growth behavior of carbon nanotubes on multilayered metal catalyst film in chemical vapor deposition, Chem. Phys. Lett., 2003;374: 222–8

[14] IshigamiM, Cumings J, Zettl A and Chen S**,** A simple method for the continuous production of carbon nanotubes**,** Chem. Phys. Lett., 2000; 319:457-9

[15] Sano N, Wang H, Chhowalla M, Alexandrou I and Amaratunga G A J, Nanotechnology—synthesis of carbon ‘onions’ in water Nature 2001;414: 506–7

[16] Wang H, Chhowalla N, Sano N, Jia S and Amaratunga G A J ，Large-scale synthesis of single-walled carbon nanohorns by submerged arc，Nanotechnology 15 (2004) 546–550

Diffusion and reaction of deposition precursor molecules in expanding thermal plasmas

M. A. Blauw, T. Miebach*, M. Creatore, D. C. Schram, and, M. C. M. van de Sanden

Department of Applied Physics, Eindhoven University of Technology, Eindhoven, The Netherlands
**Polymer & Specialty Chemical Technology, GE Global Research, Niskayuna NY, USA*

Abstract
The diffusion and reaction of oxygen molecules in the expanding thermal plasma (ETP) leads to reduction of the ion density and creation of oxygen atoms. The reduction of the ion density was investigated with a Langmuir probe. An analytical model shows that the ratio of the reaction and diffusion rate governs the mixing behavior. It can at least qualitatively reproduce the experimental results. A computational fluid dynamics (CFD) simulation shows that the assumptions made in the analytical model are justified.

Keywords:
Plasma chemistry, expanding thermal plasma, diffusion, reaction, modeling, computational fluid dynamics.

1. Introduction

Expanding thermal plasmas are outstanding in the deposition of a wide variety of materials such as amorphous silicon, diamond-like carbon and carbon-doped silicondioxide [1-3]. Adiabatic expansion of a nearly atmospheric argon plasma into a low-pressure reaction chamber leads to the formation of a stationary, normal shock wave. The deposition precursor is often injected through a ring downstream of the shock. The deposition process can be perfectly controlled because of the strong, spatial separation between the argon plasma generation and the background plasma containing the deposition precursor. Charge transfer between argon ions and precursor molecules, which is followed by dissociative recombination, is an important source of radicals. Therefore, the mixing of argon ions and precursor molecules is an important issue in the deposition of uniform, high-quality thin films.

The influence of oxygen injection on the radial ion density profile was investigated in order to clarify the exact nature of the mixing. Experiments were performed with oxygen because oxygen has a single dissociation path whereas other deposition precursors often have highly complicated dissociation patterns, for example, hexamethyldisiloxane (HMDSO). Besides, oxygen is an important reactant in the deposition of silicon oxides. For example, oxygen is used together with HMDSO to deposit abrasion-resistant, carbon-doped silicondioxide layers on polycarbonate substrates. The dissociation path of oxygen is shown in scheme 1.

Charge Transfer
$Ar^+ + O_2 \quad \Rightarrow \quad Ar + O_2^+$

Dissociative Recombination
$O_2^+ + e^- \quad \Rightarrow \quad 2O$

Scheme 1. The charge transfer and dissociative recombination mechanism of argon and oxygen.

Both the results of experimental work and numerical modeling are presented the next three sections of this paper. First, the ion density in the ETP was measured with a Langmuir probe. The amount of charge transfer followed by dissociative recombination was derived from the difference of the ion density before and after oxygen injection. The measured ion density is thus an indirect measure of the mixing. Second, a numerical model was developed to investigate the diffusion-reaction mechanism. The experimental data were used to validate the results obtained for a 3-dimensional, cylindrical reactor geometry assuming a uniform flow velocity. Third, the full flow pattern was simulated with a commercially available CFD code to investigate all details of the mixing in the reactor and to verify the assumptions of the model.

2. Experiment

The plasma is generated in a cascade arc, which ionizes the argon efficiently at near atmospheric pressure. The plasma flows through a 2.5 mm wide and 30 mm long cylindrical channel after which it expands supersonically through a nozzle into the low-pressure reactor chamber. The reactor set-up was described extensively by other authors [4,5]. Oxygen is injected downstream in the reactor chamber. Good separation of the plasma generation and the plasma chemistry is achieved due to the remote plasma generation. The argon flow was in the range of 500 sccm to 2000 sccm, the oxygen flow in the range of 0 sccm to 200 sccm, the arc pressure in the range of 262 mbar to 714 mbar, and, the reactor pressure in the range of 20 Pa to 200 Pa. The arc current was fixed at 70 A.

The influence of downstream oxygen injection on the plasma properties was investigated with a double Langmuir probe. Radial ion density and electron temperature profiles were measured at a distance of 200 mm from the nozzle. The radial ion density profile is both reduced in height and width after oxygen injection, which is shown in figure 1a. The reduction of the height is exponential as a function of the oxygen density. The reaction is of first order if oxygen is abundantly available. The reduction of the width can only be caused by a higher concentration of oxygen molecules at the sides of the plasma jet. It indicates that the diffusion of oxygen molecules is considerably limited, which is directly related to the short residence time in the plasma jet because of the high flow speed (subsonic). The measurements also show that the injection ring position only has a small influence on the radial ion density profile. It can be explained if it is assumed that the background plasma is well mixed.

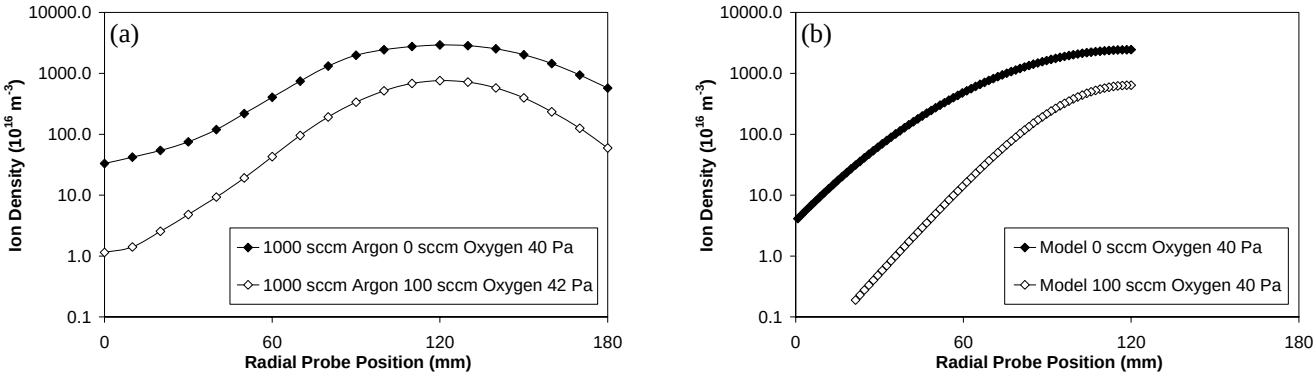

Figure 1. The height and the width of the radial ion density profile decrease if oxygen is injected (a). The calculated radial ion density profiles resemble the experimental results for radial probe positions between 60 mm and 120 mm (b).

The ion density profiles with and without oxygen are approximately Gaussian. The Gaussian form is preserved if the oxygen density profile has a parabolic form. Since the simplest approximation of an arbitrary oxygen density profile is a constant plus a quadratic term, the profile remains approximately Gaussian with oxygen injection. The width and the amplitude that were obtained by curve fitting were used to calculate the ion flow assuming a constant flow velocity of 600 m·s^{-1}. It was found that the ionization degree is approximately 0.1 in pure argon plasmas. Exact analysis of the flow-diffusion-reaction problem is very complicated because radial diffusion of both argon ions and oxygen molecules and their reactions need to be considered. Moreover the axial flow speed is non-uniform requiring a 3-dimensional model. The results of a numerical model describing the basics of process are presented in the next section.

3. Analytical modeling of diffusion and reaction

The flow-diffusion-reaction process was modeled analytically by a set of differential equations each representing one plasma species. Cylindrical reactor geometry is used. The model is a simplified representation of reality yet the main physical processes are included. It is assumed that diffusion from the background plasma into the plasma jet starts after the shock. The residence time before the shock is very short so that little oxygen diffuses into the plasma jet during this period. Further assumptions are: uniform flow velocity (plug flow), no axial diffusion, good mixing of oxygen with the background plasma, and, immediate dissociation after charge

transfer. With these assumptions the transport in the radial direction is governed by diffusion only and the transport in the axial direction is governed by flow only. The plasma jet diameter is constant because the pressure and the flow velocity are constant. The boundary conditions are: zero gradient for all species in the centre of the plasma jet, full recombination of argon ions and oxygen atoms at the reactor walls, and, no recombination of oxygen molecules. The initial argon ion density profile is a Gaussian centered on the middle of the plasma jet. The plasma jet is surrounded by a background plasma containing oxygen with a uniform density. It has been shown that strong recirculation exists, which makes it possible to distribute oxygen throughout the whole reactor. In spite of this, the model does not include recirculation but it assumes that the background plasma is initially well mixed. The experiments show that the reduction of the argon ions does not depend on the injection position, which can be understood if the background plasma is well mixed. The set of differential equations was solved with the Mathematica 5.0 software package. The physical quantities were: uniform flow velocity of 600 $m \cdot s^{-1}$, plasma jet diameter of 29 mm (reactor pressure of 40 Pa), reactor diameter of 159 mm, argon ion diffusion constant of 1.683 $m^2 \cdot s^{-1}$, oxygen diffusion constant of 0.858 $m^2 \cdot s^{-1}$, and, background oxygen density of $1 \cdot 10^{20}$ m^{-3} (partial pressure of 4 Pa). The species profiles are given for distances from 50 mm to 200 mm from the nozzle.

For comparison with the experimental results, the radial ion density profile at the Langmuir probe position before and after oxygen injection are shown in figure 1b. With a rate constant for charge transfer of $2.5 \cdot 10^{-16}$ $m^3 \cdot s^{-1}$, the decrease of the argon ion density is in line with the experiments. The rate constant is in reasonable agreement with the rate constant of $1.5 \cdot 10^{-16}$ $m^3 \cdot s^{-1}$ that is calculated using a reaction cross-section from literature [6]. The radial density profiles of argon ions, oxygen atoms, and, oxygen molecules are given in figure 2. Oxygen atoms are first produced at the edges of the plasma jet. The production in the middle of the plasma jet only starts when oxygen molecules have arrived here. Note that the oxygen atom density profile is fairly flat in the centre.

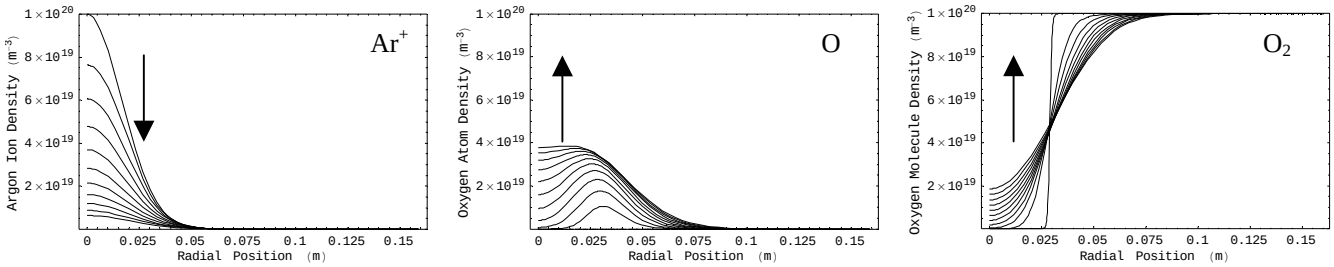

Figure 2. The behavior of the argon ion, oxygen atom and oxygen molecule densities in the downstream region of the reactor. Radial density profiles are given between 50 mm and 200 mm from the nozzle where the arrow shows the direction of the successive curves. The argon ion flux is strongly reduced due to reaction with oxygen molecules. Initially, oxygen atoms are only produced at the sides of the plasma jet. When oxygen molecules have reached the centre, reactions also take place over there. In the end, the oxygen atom density is fairly constant in the plasma jet.

The diffusion of argon ions from the centre of the plasma jet can be observed well when the density profiles are normalized. The narrowing of the profiles as a result of reaction can be observed in figure 3. Depletion of oxygen increases as a function of pressure, which is shown in figure 4. Without reactions the oxygen density in the centre is equal for all pressures. The higher ion density due to compression of the plasma jet leads to a higher reaction rate and more depletion. The relative reduction of the ion density in the centre of the plasma jet decreases.

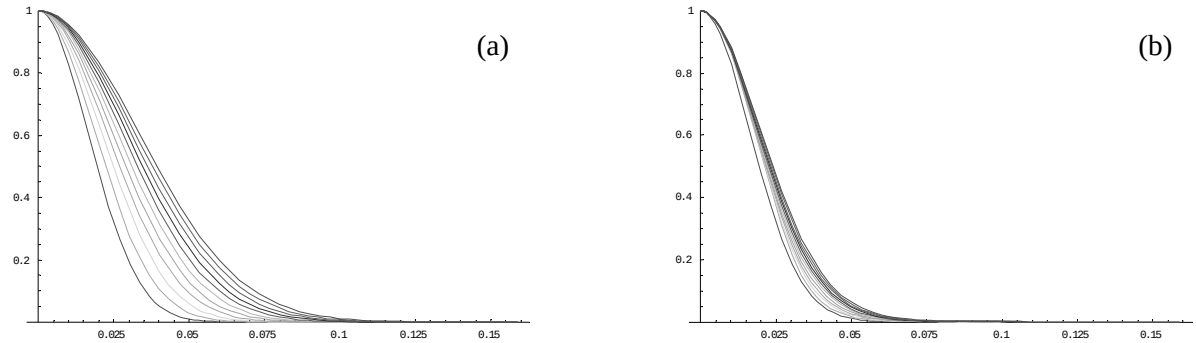

Figure 3. Normalized argon ion density profiles show widening by diffusion if no reactions take place (a). Widening of the argon ion density profiles is reduced as a result of the plasma chemistry, which is in line with the experiments (b).

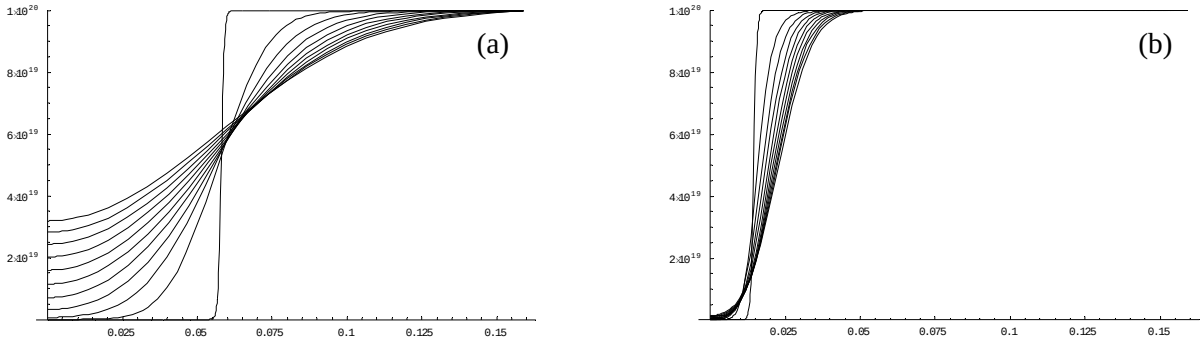

Figure 4. Depletion of oxygen in the centre of the plasma jet increase as a function of pressure. Oxygen density profiles for a pressure of 10 Pa (a). Oxygen density profiles for a pressure of 160 Pa (b).

Depletion of oxygen is a major effect if the reaction rate is larger than the diffusion rate. The balance between reaction and diffusion is given by the second Damkohler number

$$\text{Da II} = \frac{\kappa \cdot n_{Ar^+}}{\frac{D}{d_J^2}}$$

where κ is the rate constant, n_{Ar+} the argon ion density in the plasma jet, D the oxygen diffusion constant and d_J the plasma jet diameter. Note that the oxygen density does not appear in this expression. For a constant argon flow, the characteristic diffusion time, D/d_J^2, does not depend on the reactor pressure because both the plasma jet diameter and the diffusion length are inversely proportional to the square root of the pressure.

Depletion plays a role if the reaction rate is much larger than the diffusion rate. If the ion density is much lower than the oxygen density, all ions are swept by the oxygen diffusion front. On the contrary, if the ion to oxygen density ratio is much larger than one, all oxygen disappears at the edge of the ion density profile. In the situation that the reaction rate is much smaller than the diffusion rate, oxygen will distribute uniformly before significant reaction takes place. In this situation, no narrowing of the ion density profile is observed. In the model, the reaction rate and the diffusion rate are approximately equal. Only a fraction of the oxygen molecules reaches the centre of the plasma jet, which leads to narrowing of the ion density profile because of the higher oxygen density at the edges of the plasma jet. If sufficient oxygen is available, the ion density decreases significantly downstream.

The influence of the reaction rate on the oxygen density profile was investigated. Modeling results are shown in figure 5a, 5b, and, 5c for a reaction rate of 0 $m^3 \cdot s^{-1}$ (no reaction), $2.5 \cdot 10^{-16}$ $m^3 \cdot s^{-1}$ and $10 \cdot 10^{-16}$ $m^3 \cdot s^{-1}$, respectively. The background oxygen density is $1 \cdot 10^{20}$ m^{-3}. For figure 5d, the reaction rate is $10 \cdot 10^{-16}$ $m^3 \cdot s^{-1}$ and the background oxygen density is $1 \cdot 10^{19}$ m^{-3}. The depletion of the oxygen is larger for a higher rate constant, as expected. The reduction of the argon ion density (not shown) is also larger. If the background oxygen density is

reduced by a factor of 10, there is not enough oxygen available to significantly reduce the ion density. The second Damkohler number remains invariably high and oxygen depletion is large.

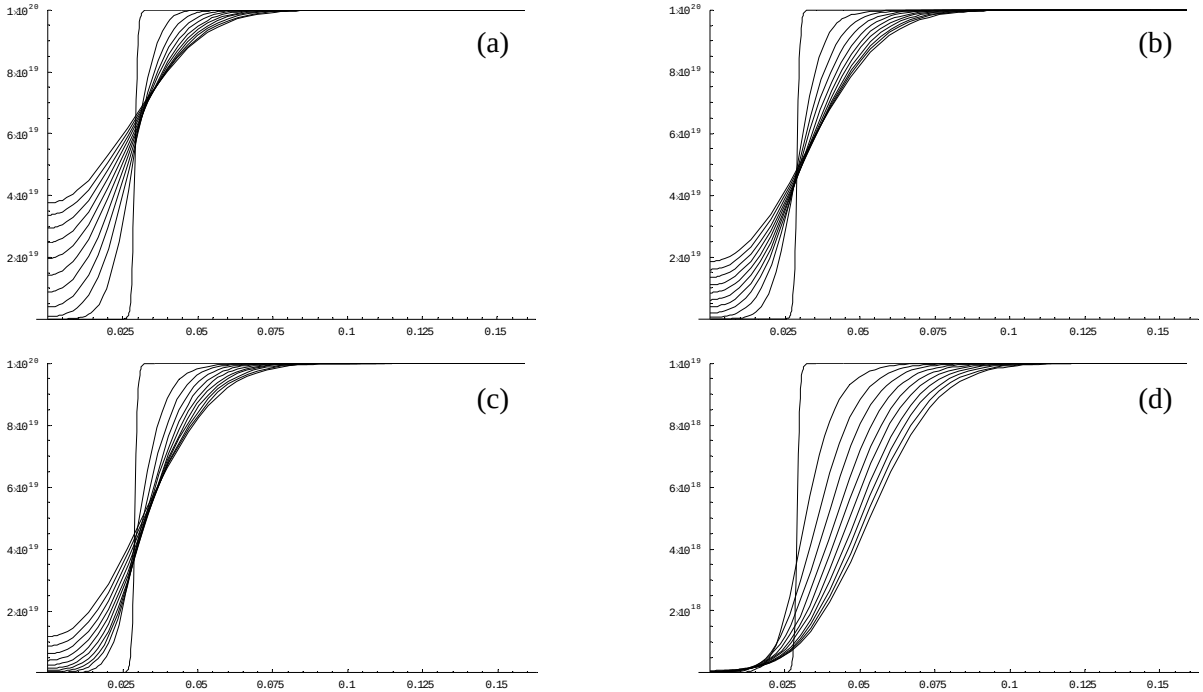

Figure 5. Influence of the reaction rate on the oxygen density profile. The oxygen density profiles if no reactions take place (a). The oxygen density profiles for a rate constant of $2.5 \cdot 10^{-16}$ $m^3 \cdot s^{-1}$ (b). The oxygen density profiles for a rate constant of $10 \cdot 10^{-16}$ $m^3 \cdot s^{-1}$ (c). The oxygen density profiles for a rate constant of $10 \cdot 10^{-16}$ $m^3 \cdot s^{-1}$ and a background oxygen density of $1 \cdot 10^{19}$ m^{-3} (d).

4. Computational fluid dynamics simulation

The supersonic expansion and the subsonic flow in the reactor were simulated using the commercially available CFD code FLUENT 6.0. Simulations of pure argon plasmas have been reported in literature [7]. Nearly the same reactor geometry and physical properties were used in this work. A new element is the oxygen ring injection 50 mm downstream of the nozzle. Ions were not taken into account since they do not influence the flow properties of the plasma much. An argon flow of 3000 sccm is forced into the nozzle at a temperature near 12000 K, and, an oxygen flow of 300 sccm is forced into the reactor at a temperature of 600 K. The reactor wall temperature is set to 300 K. The pressure is fixed at 40 Pa in the pumping region.

The temperature along the symmetry axis of the cylindrical reactor has been plotted in figure 6a. The temperature contours near the nozzle are shown in figure 6b. The shock is clearly visible. However, the temperature jump is only a factor of 2.3 whereas a factor of about 10 is expected on theoretical grounds. The shock thickness is significant compared to the distance from the nozzle to the Mach disk location, which is approximately 42 mm in this case. The shock is thus transparent. As a result, dissipative effects such as viscosity and heat conductivity reduce the temperature jump.

The oxygen mole fraction contours in the entire reactor are shown in figure 7a. The oxygen mole fraction contours near the nozzle are shown in figure 7b. In the background plasma, oxygen has a fairly constant density. Mixing is thus described by diffusion of oxygen from the background plasma into the plasma jet, which was assumed in the previous section. Oxygen can also be found before the maximum of temperature, which indicates that the shock is transparent for molecular transport. In the previous section it was assumed that diffusion starts after the shock. However, the results are still qualitatively correct because the origin of the model is only shifted towards the nozzle.

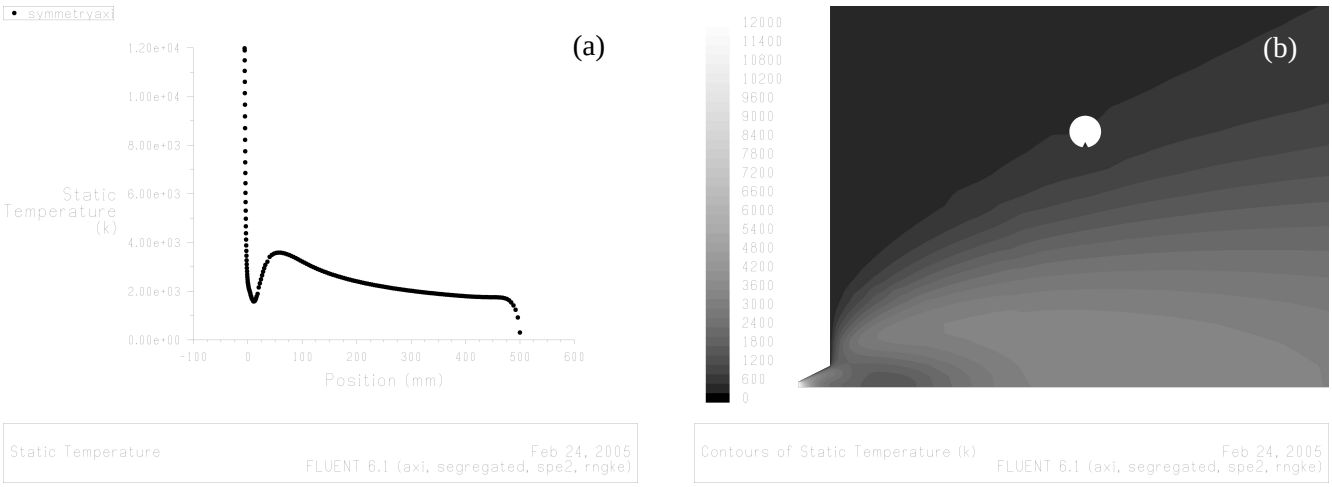

Figure 6. The temperature along the symmetry axis of the reactor shows a clear jump at the shock (a). Temperature contours near the nozzle (b).

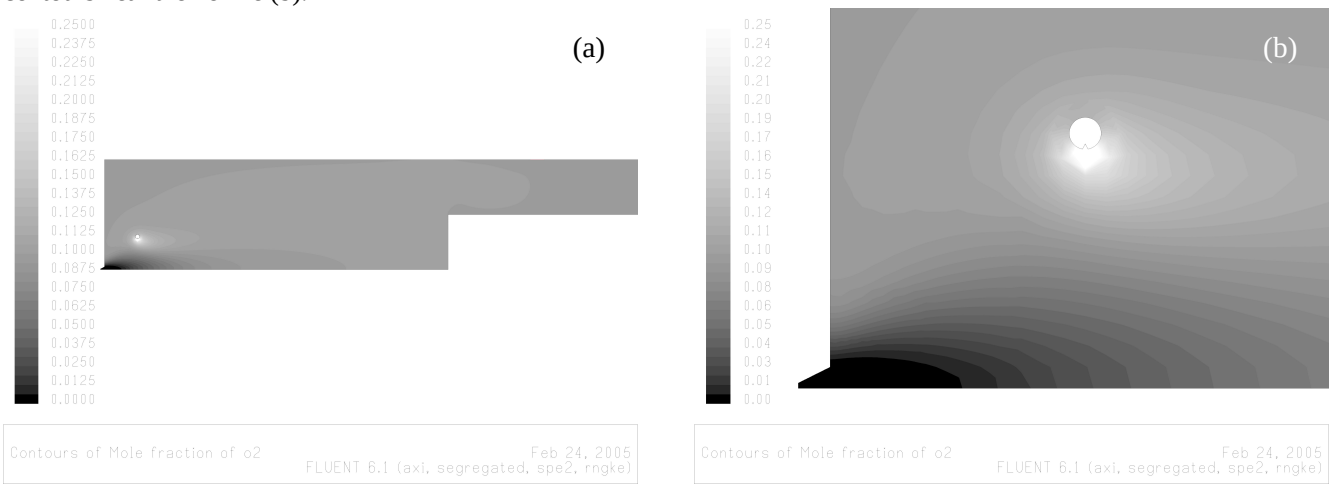

Figure 7. Oxygen mole fraction contours in the entire reactor (a). Oxygen mole fraction contours near the nozzle (b).

5. Conclusion

Both the height and the width of the ion density profiles are influenced by oxygen injection as a result of charge transfer and dissociative recombination. Diffusion of oxygen molecules from the background plasma into plasma jet is a limiting factor. The width is reduced because the oxygen density is higher at the edges of the plasma jet. An analytical model of the flow-diffusion-reaction process describes the main properties of the process well. The numerically calculated reduction of the ion density is in line with the experiments. Depletion of oxygen molecules is observed if the reaction rate is larger than the diffusion rate, which is quantified by the second Damkohler number. More detailed CFD simulations show that oxygen mixes well in the background plasma, which is assumed in the analytical model. However, they also show that oxygen diffuses into the plasma jet before the shock. As a result, the origin of the analytical model should be shifted towards the nozzle.

References

[1] W.M.M. Kessels *et al.*, J. Appl. Phys. **89**, 2404 (2001).
[2] J. Benedikt *et al.*, Diamond and Related Materials **11**, 989 (2002).
[3] M. Creatore *et al.*, Thin Solid Films **427**, 137 (2003).
[4] J.W.A.M. Gielen *et al.*, J. Appl. Phys. **82**, 2643 (1997).
[5] M.C.M. van de Sanden *et al.*, J. Appl. Phys. **84**, 2426 (1998).
[6] G.D. Flesch *et al.*, J. Chem. Phys. **92**, 3590 (1990).
[7] S.E. Selezneva *et al.*, J. Phys. D **35**, 1362 (2002).

Ambient Plasma in Decontamination of Microorganisms

Sridevi Bankupalli[1], Shirshak Dhali[1], and Michael Madigan[2]

[1]*Department of Electrical Engineering, Southern Illinois University, Carbondale, IL 62901*
[2]*Department Microbiology, Southern Illinois University, Carbondale, IL 62901*

Abstract

Here we report the results of killing of different bacteria using ambient non-thermal plasma. We have developed a radio frequency driven non-thermal plasma source, which has been shown to be very effective in killing bacteria under controlled conditions. The studies were done for gram negative bacteria *E.coli*, and endospores *B. cereus* and *B.megaterium.* The effect of RF power, exposure time and oxygen concentration on the destruction of these bacteria are discussed.

1. Introduction

Relatively large volume low temperature plasmas are traditionally generated at reduced pressures. However, for practical sterilization/decontamination purposes, to have a vacuum system-based device would be inconvenient and expensive. Today, cold plasmas at atmospheric pressure can be generated by various methods. Amongst these, the Dielectric barrier discharge (DBD) [1] and the Atmospheric Pressure Plasma Jet (APPJ) [2] have been especially researched in the past few years. These devices can generate relatively large volumes of non-equilibrium, low temperature plasmas at or near atmospheric pressure. Air or other gas mixtures can be used. The plasmas produced by these devices have typically electron densities in 10^9 cm^{-3} - 10^{11} cm^{-3} range, plasma power densities in the 10 – 300 mW/cm3, and gas temperatures generally below 100 ^oF. They are sources of UV, visible, and IR radiation, and free radicals such as O and OH, which play important roles in the destruction of microorganisms.

Historically, Siemens used atmospheric pressure plasma (corona discharge) to generate ozone to disinfect water. Later, Menashi [3] used a corona discharge to sterilize the surface of materials. In the mid-nineties Laroussi [1] used a DBD – based diffuse discharge at atmospheric pressure to decontaminate biological media. Other experiments soon followed using various discharge configurations to destroy both gram-negative and gram-positive bacteria, as well as other microorganisms such as viruses.

UV affects the cells of bacteria by inducing the formation of thymine dimers in the DNA [1]. This inhibits the bacteria's ability to replicate properly. By comparing the killing kinetics of UV radiation from a low-pressure mercury vapor lamp and that of atmospheric pressure cold plasma, Laroussi [1] concluded that UV does not play the prominent inactivation role in atmospheric pressure plasmas. This claim was later supported by the work of Herrmann et al. [4] and others.

It has always been recognized that the reactive species, generated in a high-pressure non-equilibrium discharge through electron impact excitation and dissociation, play an important role in its germicidal characteristics. Several investigators showed that discharges containing Oxygen have a strong germicidal effect: The D-value (the time for a one log 10 reduction) decreases if a certain amount of Oxygen is added. This is due to the presence, in such discharges, of Oxygen-based active species such as atomic Oxygen and ozone. Other radicals such as OH have also been found to play an important role in the inactivation process.

Mendis et al. [5] suggested that charged particles might play a very significant role in the rupture of the outer membrane of bacterial cells. They showed that the electrostatic force caused by charge accumulation on the outer surface of the cells' membrane could overcome the tensile strength of the membrane and cause its rupture. They claim that this scenario is more likely to occur for gram-negative bacteria, the membrane of which possesses an irregular surface.

Several reports have been published on the interaction of plasmas with chemical and biological agents, in particular in context of sterilization and decontamination has received much attention in recent years. Particular emphasis has been on the utilization of atmospheric-pressure plasmas as they do not require operation in costly vacuum enclosures and thus facilitate the convenient and low-cost treatment of large surface areas. However, atmospheric-pressure discharge plasmas are highly susceptible to instabilities and the generation and reliable maintenance of uniform, large-volume discharge plasmas at or near atmospheric pressure remain formidable Challenges.

Spore-forming bacteria, in particular bacteria of the genera *Bacillus*, are believed to be among the most resistant microorganisms. The species *Bacillus subtilis* has received particular attention, as these bacteria are easy to grow in a reproducible fashion under chemically well-defined conditions. As a result, *Bacillus subtilis* has been the species of choice in many sterilization experiments in the past (see e.g. Refs. [6], [7], and references therein to earlier work. Reliable and reproducible experimental data on sterilization rates have been obtained by different investigators using a variety of methods and can readily be compared.

First experiments aimed at the quantitative determination of the destruction of spore-forming bacteria, which are believed to be among the most resistant microorganisms, using a novel atmospheric-pressure plasma shower reactor whose design utilizes patented atmospheric-pressure dielectric capillary electrode discharge plasma [8]. In those experiments, N.S.Panikov established a straightforward protocol to prepare and characterize various bacteria including *Bacillus subtilis* on either glass or aluminum surface supports and analyze the samples after treatment by atmospheric-pressure plasma jets emanating from the plasma reactor using either in He or in air (N2 /O2mixture) as a carrier gas at varying power levels and exposure times. They found significant reductions in colony-forming units ranging from 104 (He plasma) to 108(air plasma) for plasma exposure times of less than 10 minutes [4].

2. Results and Discussions

Shown in Fig. 1 is the picture of the plasma source. In the configuration shown, the discharge is "struck" in the noble gas (Argon) and the reactive gas is added to the afterglow. The centered electrode is bored to allow the reactive gases to flow into the afterglow. This is critical for the

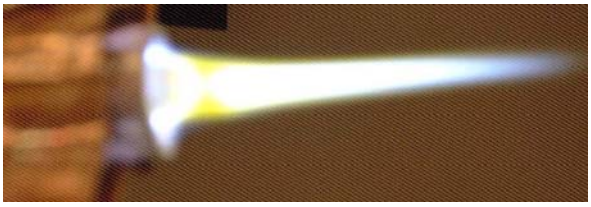

Figure 1: The picture of an atmospheric afterglow in a radio frequency Argon discharge.

stability of the discharge: Gases like H_2 and O_2 are attaching and change the physical characteristics of the discharge. Due to increase in breakdown voltage, even for concentration of reactive gases in few percentages, it is difficult to strike a discharge using radio frequency (RF). RF is the most suitable power source because it can be tuned to the load easily compared to low

frequencies: Low frequency discharges have very high capacitive current, which is difficult to correct. Similar discharges at radio frequency are being investigated [3]. The discharges by Park et al. produce a narrow plasma jet and are stabilized by very high flow of helium at 600 Torr. Our approach does not depend on high gas flow, but uses a dielectric to stabilize the discharge. The dielectric is alumina with an outer diameter of 6.4 mm and an inner diameter of 2.4 mm. The inner electrode is 1.6 mm in diameter, and the active discharge length is 30 mm.

The mechanism of destruction of microorganism by nonthermal plasma is not very well understood. However, we have shown that the UV in the atmospheric pressure plasma does not play an important role. This was done by allowing the UV from the plasma to pass through a quartz window without the direct contact of the bacteria to plasma. Therefore it may be concluded that plasma chemical reactions are important in the destruction of microorganisms.

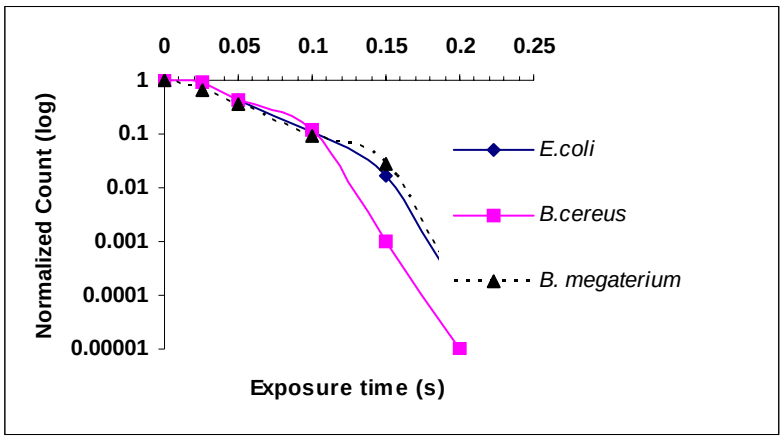

Figure 2: Fractional surviving colonies after treatment with RF plasma.

The OH radicals are strong oxidizing agents. In an Argon/Oxygen plasma the following

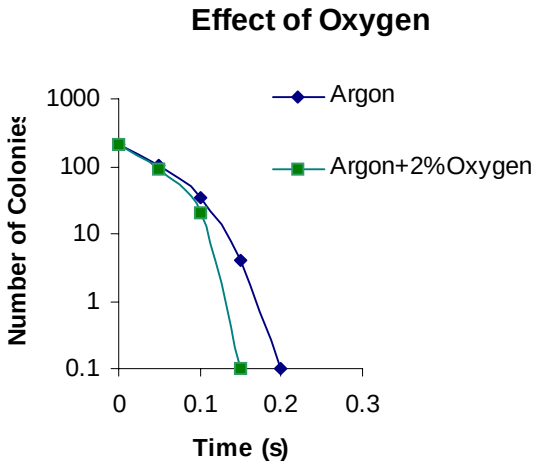

Figure 3: The killing of bacteria for an Argon and Argon/Oxygen plasma.

additional electron impact reaction is present

$$O_2 + e \rightarrow O + O^* + e$$

$$H_2O + O^* \rightarrow 2OH$$

Therefore addition of oxygen to Argon plasma produces additional oxidizing radicals and is more effective as an oxidizer. However, when the oxygen concentration is above 2-3% of the total gas, it starts to affect the discharge negatively. Since oxygen is an electronegative gas, it scavenges electrons in the plasma to form negative ions. The depletion of the electrons in the plasma leads to instabilities.

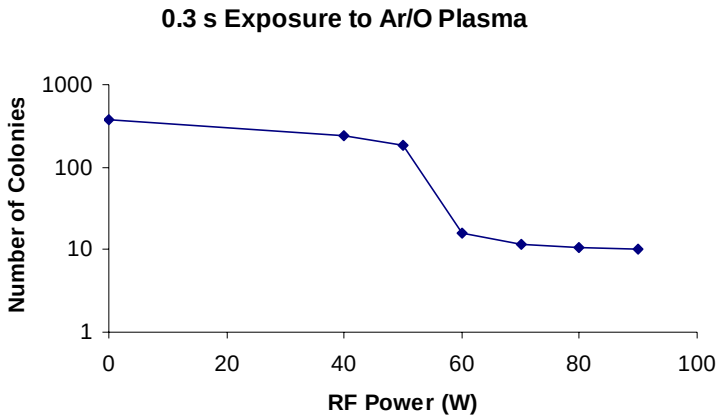

Figure 4: Number of surviving colonies as a function of applied power for an exposure time of 0.3 s of RF plasma.

We used several Bacillus subtilis strains such as Bacillus subtilis in its colonial morphologies, prototypical examples of spore-forming bacteria. We also used non-spore-forming bacteria (*E.coli*) for selected experiments for comparison. The bacteria were sub-cultured on agar plates. The spore suspensions were obtained from homogeneous batch cultures grown on chemically defined media.

Experiments aimed at the quantitative determination of the destruction of all kinds of bacteria especially spore-forming bacteria, which are believed to be among the most resistant microorganisms, were carried out using an atmospheric-pressure plasma. Various well-characterized cultures of Ecoli, Bacillus Cereous, Bacillus Magaterium were prepared, placed in petri dish, subjected to atmospheric-pressure plasma jets emanating from dielectric barrier discharge, RF plasma generator using either in Ar or Oxygen (Ar/O2 mixture) as a carried gas at

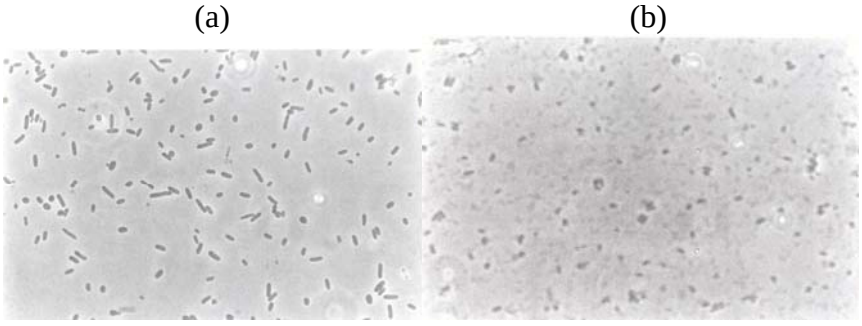

Figure 5: (a) Unexposed *Bacillus megaterium* 1000x photomicrograph, (b) *Bacillus megaterium* 1000x photomicrograph, exposed to RF plasma for 0.25 s.

varying power levels and exposure times, and analyzed after plasma treatment. A reduction in colony-forming units by exposure of the bacteria to ambient afterglow plasma is shown in Fugure 2. All three type of bacteria show rapid reduction of colonies with increasing exposure time. Within 0.25 s exposure time, all three bacteria show a reduction by an order of 4. The maximum cell kill rate was found in the presence of oxygen. The results of surviving colonies for argon and argon/oxygen mixture are shown in Fig. 3. Due to the presence fo Oxygen in the Ar/O_2 mixture, radicals such as O and OH are formed which are very effective in destroying the bacteria. Figure 4 shows the kill rate as a function of power for exposure time of 0.3 s. There seems to be optimum power at which maximum killing is achieved. Increasing power produces diminishing returns because at high power a large fraction of the energy goes into heating.

Figure 5 shows microscopic observations of unexposed *Bacillus megaterium* samples with 1000x magnification. Figure 4.11 shows microscopic observations of exposed *Bacillus megaterium* samples with 1000x magnification. In Figure 4.11 you can see debris and lice of dead *Bacillus megaterium* cells caused by exposure to plasma. Montie and coworkers have shown that non-thermal plasma is capable of sterilizing both porous and nonporous surfaces at standard pressure and temperatures [1]. They have shown that plasma kills different types of microorganisms including bacterial vegetative cells, bacterial endospores, viruses, and fungi (yeast). Their data suggests that membrane lipids are the most vulnerable macromolecule of the cell to atomic oxygen attack.

3. Conclusions

Non-thermal Dielectric barrier discharge and radio frequency plasmas have been shown to be effective in destroying different types of bacteria. Since the RF plasma has more power density, it is more effective in destroying the microorganisms. *Escherichia coli,* which is a most common bacterium, is easily destroyable when compared to *Bacillus cereus* and *Bacillus megaterium*. *Bacillus cereus* and *Bacillus megaterium* are spore-forming bacteria and so it is hard to destroy them. *Escherichia coli,* when treated with Dielectric barrier discharge took lot of time to get the same killing rate as that of when treated with RF discharge. So, using RF discharge is much more effective when compared with Dielectric barrier discharge for destruction of bacteria.

References

[1] M. Laroussi, I. Alexeff, J. P. Richardson, and F. F. Dyer, IEEE Trans. Plasma Sci., Vol. 30 (2002).

[2] A. Scutze, J. Y. Jeong, S. E. Babyan, J. park, G. S.Selwyn, and R. F. Hicks, IEEE Trans. Plasma Sci. Vol. 26 1685 (1998).

[3] W. P. Menashi, U. S. Patent No. 3,383,163, 1(968).

[4] H. W. Herrmann, I. Henins, J. Park, and G. S. Selwyn, Phys. Plasma,*s* Vol.6, 2284 (1999).

[5] D. A. Mendis, M. Rosenberg, and F. Azam, IEEE Trans. Plasma Sci. Vol. 28, 1304(2000).

[6] S. Moreau, M. Moisan, M. Tabrizian, J. Barbeau, J. Pwlletier, AS. Ricard, and L'H. Yahia, J. Appl. Phys.88, 1166 (2000).

[7] C.L. Nelson and T.J. Berger, "Inactivation of Micro-organisms by Oxygen Gas Plasma", Curr. Microbiology, Vol. 18, 275(1989).

[8] E.E. Kunhardt, "Generation of Large-Volume, Atmospheric-Pressure Non-Equilibrium Plasmas", IEEE Trans. Plasma Sci Vol.28, 189(2000)

[9] T. C. Montie, K. Kelly-Wintenberg, and J. R. Roth, J.R. An overview of research using the one atmosphere uniform glowdischarge plasma (OAUGDP) for sterilization of surfaces and materials IEEE Transactions on Plasma Science, Volume: 28, 41-50 (2000)

Ambient Afterglow Plasma

Shariff Shakir[1], Sandhya Mynampati[1], Bijan Pashaie[2], and Shirshak Dhali[1]

[1]*Department of Electrical Engineering, Southern Illinois University, Carbondale, IL 62901*
[2]*Department of Engineering Physics, Southeast Missouri State University, Cape Girardeau, MO63701*

Abstract

A radio frequency driven atmospheric-pressure afterglow plasma source is discussed. The light intensity measurement shows that the discharge is continuous in time unlike low frequency dielectric-barrier discharges, which are intermittent in nature. The discharge, under ambient conditions, can be generated in Argon, Helium and Nitrogen. Trace amounts of N_2 or O_2 in Ar or He produce dissociated N and O respectively.

1. Introduction

At atmospheric pressures, there are two popular methods for producing non-thermal plasmas; (1) a corona discharge and (2) a barrier-type ac discharge. Although corona discharges have found numerous applications, they are not particularly suitable for large surface or volume gas phase plasma processing [1]. The dielectric-barrier discharge, also known as a silent discharge or a partial discharge, is widely used in industry for ozone synthesis. These discharges are best characterized by streamers, which are a result of space charge dominated transport at high electric fields [2] A disadvantage of existing plasma sources is that the specific energy (energy per unit volume of the processing gas) is low. This is a major shortcoming for adaptability to manufacturing processes. We have taken a different approach for the generation of plasma under ambient conditions.

2. Results and Discussions

Shown in Fig. 1 is the picture of the plasma source. In the configuration shown, the discharge is "struck" in the noble gas (Argon) and the reactive gas is added to the afterglow. The centered electrode is bored to allow the reactive gases to flow into the afterglow. This is critical for the stability of the discharge: Gases like H_2 and O_2 are attaching and change the physical characteristics of the discharge. Due to increase in breakdown voltage, even for concentration of reactive gases in few percentages, it is difficult to strike a discharge using radio frequency (RF). RF is the most suitable power source because it can be tuned to the load easily compared to low frequencies: Low frequency discharges have very high capacitive current, which is difficult to correct. Similar discharges at radio frequency are being investigated [3]. The discharges by Park et al. produce a narrow plasma jet and are stabilized by very high flow of helium at 600 Torr. Our approach does not depend on high gas flow, but uses a dielectric to stabilize the discharge. The dielectric is alumina with an outer diameter of 6.4 mm and an inner diameter of 2.4 mm. The inner electrode is 1.6 mm in

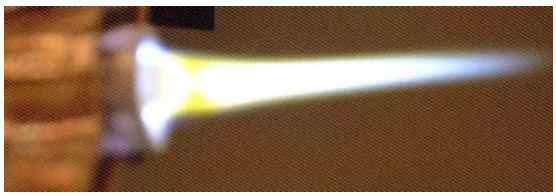

Figure 1: The picture of an atmospheric afterglow in a radio frequency Argon discharge.

diameter, and the active discharge length is 30 mm. For the RF discharge discussed in this paper, the air gap capacitance, c_g= 4.1 pF and the dielectric capacitance, c_d=9.2 pf, and the excitation frequency is 13.56 MHz. The electric field (E_m) is the highest on the surface of the inner electrode and is given by

$$E_m = \frac{c_d}{c_d + c_g} \frac{V}{a \ln(b/a)} \quad (1)$$

Where V is the applied voltage and a and b are the inner and outer radius of the air gap respectively. In the RF discharge the argon breakdown occurs around 575 V, which corresponds to a peak field of 12 kV/cm, which is less than the static breakdown voltage of argon of 15 kV/cm at atmospheric pressure [4]. This is expected for frequencies, f, greater than the critical frequency, $f_c = v_+ / (\pi d)$ where v_+ is the argon ion mobility, and d the typical dimension of the air gap [4]. In atmospheric pressure argon discharge, the positive ion mobility at a field of 12 kV/cm is approximately 1.5 cm^2/Vs [5]. For our discharge with an air gap of about 0.4 mm, we estimate the critical frequency to be 145 kHz. The discharge is in the mobility-controlled region as the frequency (13.56 MHz) is lower than the second critical frequency, $f_{c0} = v_e / (\pi d)$ for diffusion-controlled discharge [5]. For an electric field of 12 kV/cm, the electron drift velocity, $v_e = 5\times10^6$cm/s at atmospheric pressure and the f_{c0} is about 40 MHz [6]. The discharge electrodes do not play any significant role at these pressures and the DC bias on the powered electrode is measured to be near zero.

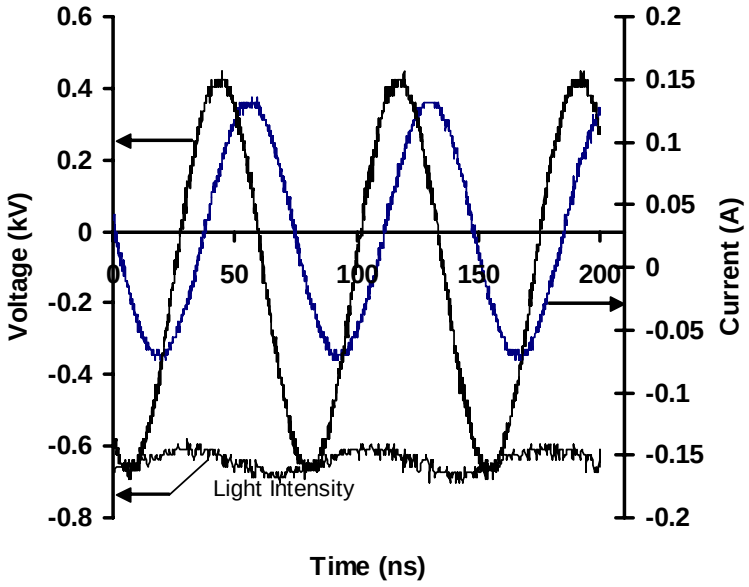

Figure 2: The waveforms for current, voltage, and the integrated light output for the RF discharge.

Figure 2 shows the RF current through the discharge and the voltage across the discharge. The RF current was measured with IPC CM-10-M (0.1 V/A into 50Ω) current monitor. The current waveform is sinusoidal indicating a temporally uniform discharge. Also shown in Figure 2 is the total light intensity. Again, the light is uniform in time therefore the discharge at 13.56 MHZ is temporally uniform. Low frequency dielectric barrier discharge is intermittent and show spikes in the current waveform [3].

The discharge power, P, in a dielectric-barrier type discharge is given by [3]

$$P = 4 f V_c' [c_d V_p - (c_g + c_d) V_c] = 4 f V_c' c_d [V_p - \frac{(c_g + c_d)}{c_d} V_c] \quad (2)$$

where f is the power frequency, c_g and c_d are the gap and dielectric capacitance respectively, v_p, v_c', and v_c are the peak to peak applied voltage, the critical gap voltage required to sustain a discharge, and the critical voltage at which the gap breaks down, respectively. The voltages v_c and v_c' are nearly equal, however we have observed that v_c' tends to be lower than v_c [5]. This equation shows that the power input to a dielectric type discharge has a linear dependence on voltage. At low frequencies, dielectric-barrier discharges show these characteristics for all gases [4, 8]. However for a discharge continuous in time, the power absorbed per unit volume, Vol, in a field $E=E_0 \cos(\omega t)$ is given by [9]

$$\frac{P}{Vol}=\frac{1}{2}\frac{e^2 n_e}{m_e \nu}\frac{\nu^2}{\nu^2+\omega^2}E_0^2 \qquad (3)$$

This shows a square dependence on the applied field. The power versus voltage plot of the RF discharge shown in Fig. 3 is consistent with Eq. 3. The dependence of discharge power is faster than linear as expected for a continuous discharge. Therefore the RF discharge at atmospheric pressure is continuous unlike low frequency dielectric-barrier discharges.

The light intensity measurement shows that the discharge is continuous in time unlike low frequency discharges, which are intermittent in nature. The gas temperatures are near ambient and the afterglow temperatures do not exceed 85°C. Spectroscopic measurements show that He and Ar metastables in the discharge produce excited Nitrogen and Oxygen atoms.

In plasma chemical devices, the aim is to produce desired radicals to carry out a particular reaction. The main thrust for atmospheric pressure plasma for our application is the production of H and O radicals and Ar ions. For efficient cleaning the production of radicals rather than gas heating is important. The ambient afterglow discharge is a cold discharge with most of its energy being utilized for the production of excited species. In He/Air plasma the following electron impact processes will be present

$$He + e \rightarrow He^+ + 2e \text{ and } He^* + e$$
$$He^* + N_2/O_2 \rightarrow \text{excited species}$$

Figure 4 shows a typical spectrum of the afterglow Helium plasma in ambient air. The ambient afterglow discharge is a cold discharge with most of its energy being utilized for the production of excited species. The afterglow interacts with the ambient gas and a typical optical emission spectrum of the helium afterglow is shown in Figure 4. The highest peak in the spectrum is the transition $O^*(3p \rightarrow 3s)$ at 777.2. Clearly the He metastables excite the oxygen molecules to produce excited

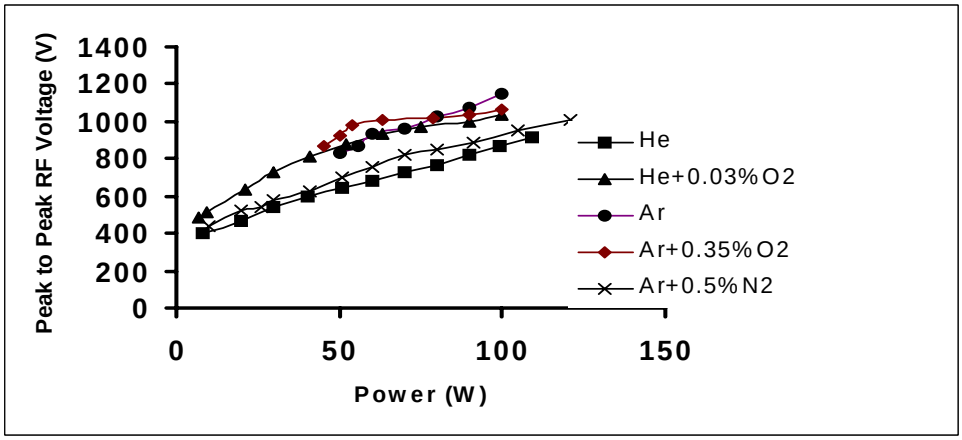

Figure 3: The RF peak voltage versus power for different gases.

oxygen atoms.

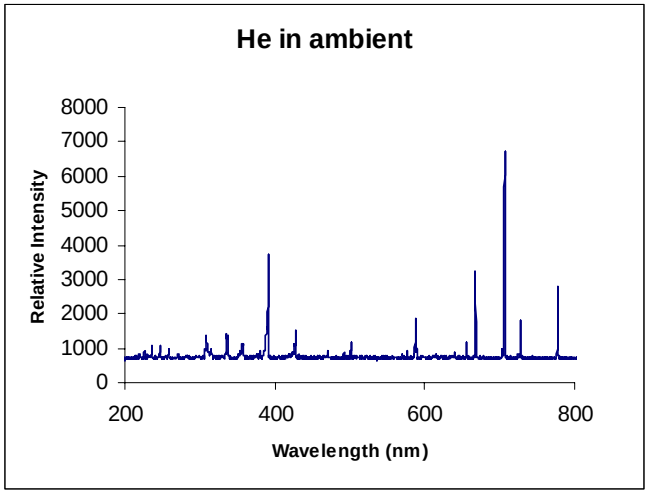

Figure 4: Optical emission spectra of He afterglow in ambient air.

In metal surface cleaning experiments, the afterglow plasma with a 1% hydrogen additive was very effective in cleaning metal surfaces. Figure 5 shows the XPS analysis of a stainless steel surface treated with and without plasma. Both the He and Ar afterglow plasmas are very effective in removing organic contaminants.

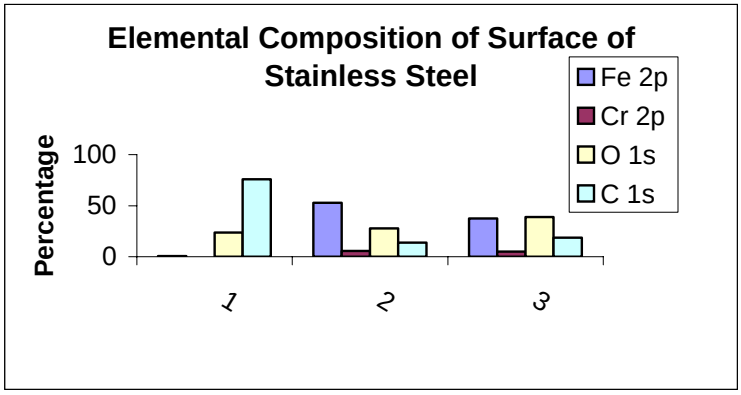

Figure 5: XPS analysis of stainless steel surface. The blank sample of steel has a coating of adhesive on it. (1) The surface composition of the blank. (2) The surface after 30 seconds of Ar/H_2 plasma treatment. (3) The surface composition after 30 seconds of He/H_2 plasma.

3. Conclusions

In conclusion, an ambient afterglow plasma source driven by RF power source has been demonstrated, which is continuous in time and behaves like a glow discharge. The discharge is stable for non-attaching gases and small concentration of additives. The afterglow has excited species that can be used for plasma chemical reactions.

This research work was partially supported by a grant from the National Science Foundation.

References

[1] B. Eliason and U. Kogelschatz. Nonequilibrium Volume Plasma Chemical Processing. IEEE Tran. On Plasma Science. Vol. 19, pp1063(1991).

[2] S. K. Dhali and A. K. Pal. Numerical simulation of streamers in SF_6, Journal of Applied Physics. 63:1355(1988).

[3] J. Park, I Hennis, W. H. Herman, G. S. Selwyn, J. Y. Jeong, R. F. Hicks. Discharge phenomena of an atmospheric pressure radio-frequency capacitive discharge source, J. Appl. Physics, vol. 89, 20(2001).

[4] R. Sankaranarayan, B. Pashaie, and S. K. Dhali. Characteristics of Barrier Discharge in monatomic and molecular gases, App. Phys. Let. Vol. 74, pp3199, (1999).

[5] E. Nasser, Fundamentals of Gaseous ionization and Plasma Electronics, Wiley Interscience, New York, 363(1971)

[6] S. Brown, Basic data of plasma physics, MIT and John Wiley, New York, 55(1959)

[7] J. Park, I Hennis, W. H. Herman, G. S. Selwyn, J. Y. Jeong, R. F. Hicks. Discharge phenomena of an atmospheric pressure radio-frequency capacitive discharge source, J. Appl. Physics, vol. 89, 20(2001).

[8] H. D. Park and S. K. Dhali. Generation of Atmospheric Pressure Plasma with Duel-Chamber Discharge, App. Phys. Lett. Vol. 77, pp2112 (2000).

[9] M Schmidt and H. Conrads, Low temperature Plasma Physics, Eds. R. Hippler, S. Pfau, M. Schmidt, K. H. Schoenbach, Wiley-VCH, p285(201).

Study of anode phenomena in dc arc plasma torch by electric probes

O. Chumak, M. Hrabovský, T. Kavka, V. Kopecký

Thermal Plasma Department, Institute of Plasma Physics, Prague, Czech Republic

Abstract
Currents on electric probes connected to an anode via biasing resistances were measured in an anode region of arc in dc plasma torch. Existence of conductive layer near an arc column and flowing of the diffuse currents onto the anode surface upstream of constricted anode attachment position is showed. This current is assumed to be controlled by distributed resistance of the intermediate layer between highly conductive arc core and an anode surface. Importance of anode surface roughness and shape for the diffuse current distribution is discussed.
Keywords: anode attachment, plasma torch, arc fringe

1. Introduction

Anode processes have strong influence on plasma properties and flow character of a plasma jet generated by dc arc plasma torch. Arc attachment to an anode surface, which is parallel to arc column in typical plasma torch is commonly represented by bright constricted current channel. Dc arc torches usually works in so called restrike mode that is characterized by periodical movement of the anode attachment in stream-wise direction followed by ignition of new anode attachment in an upstream position and accompanied with sudden decrease of arc voltage and shortening of the arc [1]. This phenomenon causes fluctuations of arc power as position of the arc root determines arc voltage [2, 3]. Downstream movement of arc root is caused by gas dynamic drag acting on arc attachment in gas flow in the arc fringes and by action of self-magnetic field on current loop in the anode region. The mechanism of sudden restrike in the upstream position is not fully understood and often is referred as breakdown. Another hypothesis assumes existence of diffuse current flowing through conductive intermediate layer between the arc column and the anode surface and thermal building of the new attachment [4].
Our previous measurements with electric probes reveal significant currents flowing to the probes in the fringes of arc column in positions close to the anode [5]. However, these measurements were made in a free boundary of arc, where physical conditions could be substantially different from conditions in a gap between conductive arc column and the anode surface. Therefore in present experiments the probe measurements were made in a situation, which better simulates conditions in an anode region of dc arc plasma torches. Electric probes were housed into steel cube, which was connected to anode via ballast resistor to simulate anode surface around the probes.

2. Experimental set-up

Anode region of dc arc plasma torch WSP-500H with hybrid argon-water stabilization of arc [6] was investigated. The torch has an external anode and thus observation and investigation of the anode region is possible. The anode is created by water cooled rotating copper disc. The Active surface of the electrode is parallel to plasma jet axis as in common plasma torches, as it is shown in Fig. 1a. The anode was positioned 12 mm from the exit nozzle in order to create long stable free arc for measurements of current and potential distributions along it. Plasma torch working parameters were not changed during experimentation: arc current was 300 A, argon (secondary plasma forming gas) flow rate was 12.5 slm, nozzle with diameter 5.6 mm was used. These parameters correspond to plasma torch power 75 kW, plasma jet axial temperature at the nozzle exit 17000 K and diameter of the high radiative plasma jet core about 4 mm.
For simulation of the anode the stainless steel cube connected to the anode via ballast resistor was used. Resistance 0.5 Ω was chosen for limitation of current to the cube in order to prevent formation of constricted attachment of arc. To avoid overheating the cube was driven transversally to the jet through boundary layer with the speed of about 1 m/s. The cube movement was considered to have no influence on plasma jet as plasma has

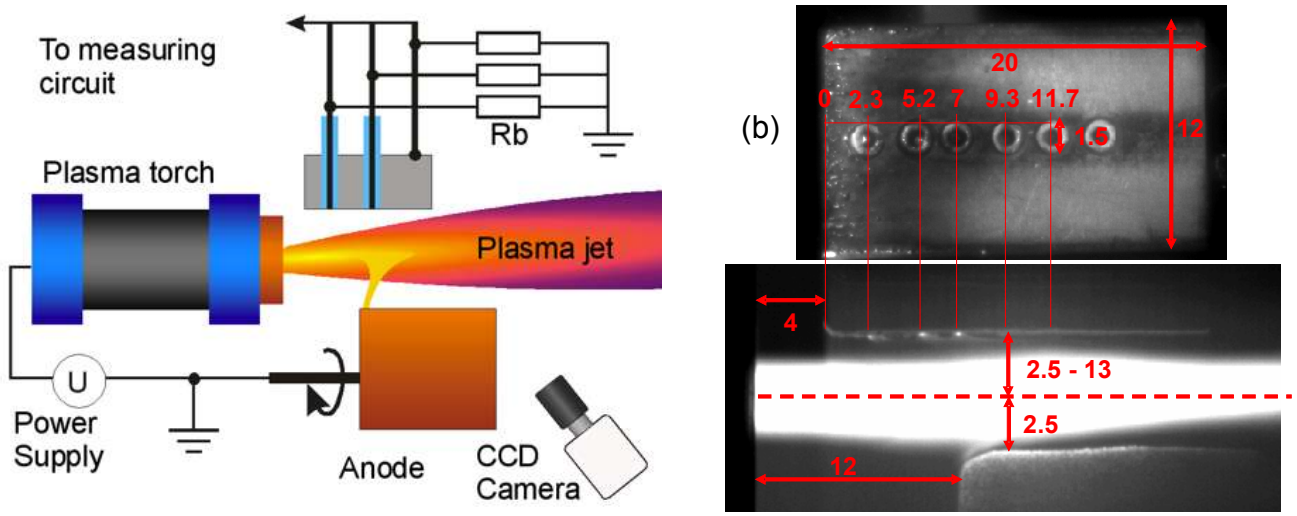

Fig. 1. Schematic picture of experimental setup (a), photo of the cube with the probes e from the bottom(b) and photo of anode region(c). All dimensions are in mm.

velocity three orders higher than cube speed. The anode region and the cube passing the jet fringes were photographed by fast shutter CCD camera with exposure time 10 μs.

Five molybdenum wires (probes) insulated by ceramic tubes were housed into the cube (Fig. 2b, 2c) for measurement of the current distribution. The probes had plain end surface and were 0.6 mm in diameter. Insulator tubes were made of alumina, and had inner diameter 1 mm and outer diameter – 1.5 mm. As the wires had smaller diameter than insulator tubes, it was difficult to determine their active surface gathering the current. But since all probes had the same dimensions, it can be assumed that they had the same area of active surface. The probes and ceramic tubes ends were aligned with bar surface. The alignment accuracy was estimated to be ±0.2 mm. Probes were connected to the anode via biasing resistances with values varying in the range of 0.53-8.3 Ω. The probes and cube potentials were recorded by oscilloscope with time resolution of 1 μs.

3. Results and Discussion

An example of an oscilloscope record of signals from the five probes and from the cube is shown in Fig. 2a. An accompanying photo (Fig. 2b) of the anode region was taken at the time corresponding to 15 ms in the oscilloscope record. The increase of the probe current due to movement of the probe towards the jet is followed by the current decrease when the probe moves from the jet. It is evident that a layer between the cube surface

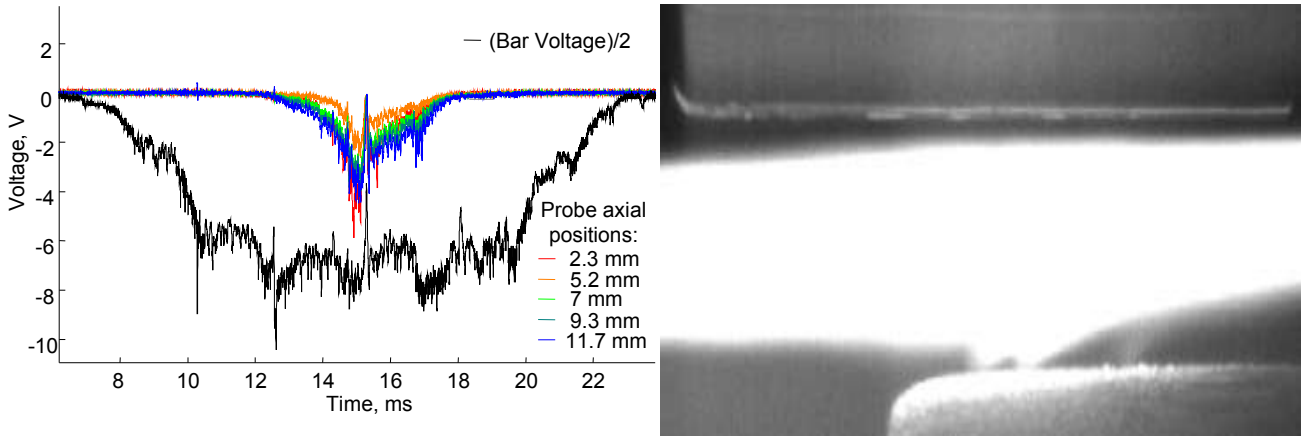

Fig. 2. Signals of the probes in different axial positions (a) and accompanying photo (b) of anode region. Probe biasing resistance is 4.7 Ω, bar – 0.56 Ω. Distance of the bar from the arc axis is 3 mm.

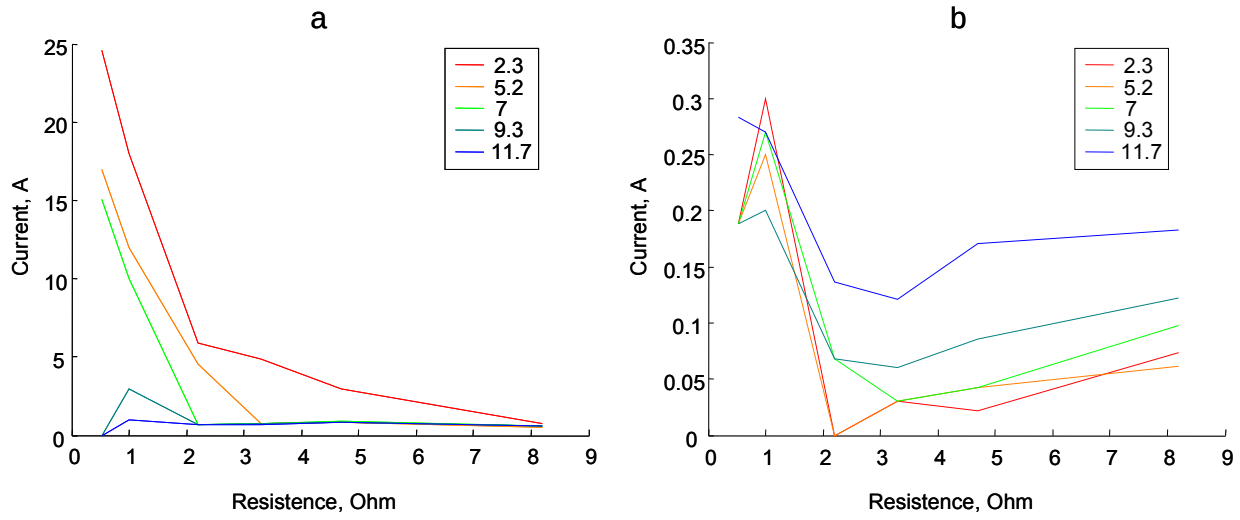

Fig. 3. Dependence of probe current on biasing resistance for different axial positions along the (in mm) jet at radial distances 2.5 mm (a) and 4 mm(b) from the plasma jet axis.

and the arc core is conductive. The signal of the cube current has similar rise and decrease, but it has steady maximum because of cube width. The current to the cube was about 28 A during the passage of the cube above the arc. Although this current is relatively high, no spot on the cube surface was found on the images of the cube. It seems that the current is distributed over the cube surface without constriction of current carrying channel.

In Fig. 3 the probe current at two distances from the arc axis and for different axial positions is shown in dependence on biasing resistance. At the distance 3 mm from the axis (Fig. 3 a) low biasing resistance allowed flowing of currents high enough to establish a thermal current channel. Evaporation from the probe surface is observed in these cases on the images of the probes. For biasing resistance 3.3 Ω and higher at both radial distances the probe currents were much lower and no constricted current channels were observed on photos. Moreover for biasing resistances 8.2, 4.7, 3.3 Ω and sometimes for 2.2 Ω the probe current almost did not depend on biasing resistance, which implies an independence on the voltage difference probe-plasma.

In Fig. 4a an axial distribution of probe currents for different radial distances from the arc column axis is shown in the form of contours of the same current. This type of visualization is chosen for better demonstration of development of the intermediate layer along the jet. The current contours were evaluated from repeated measurements of probe currents at different radial distances of the cube. Diffuse currents were considerably

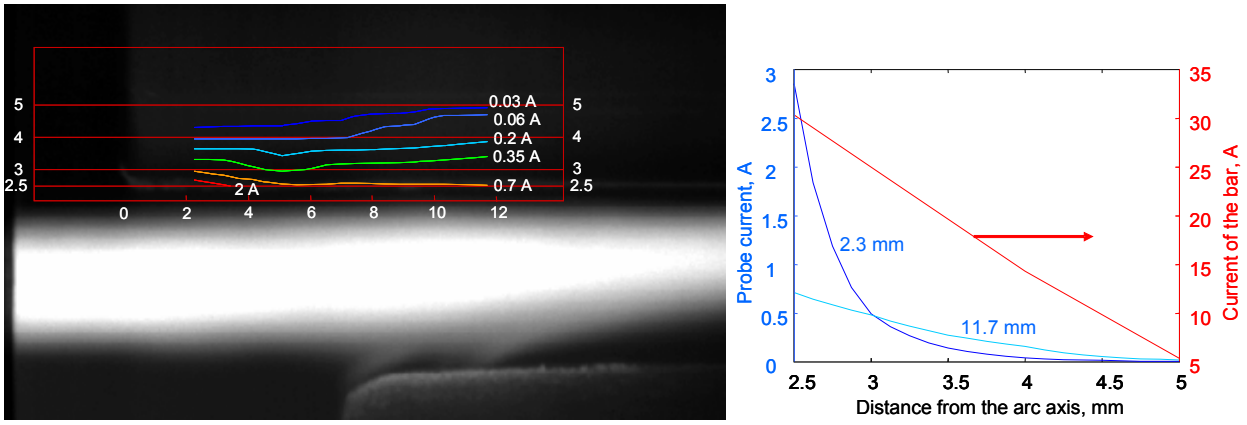

(a) (b)

Fig. 5. Distribution of probe current (axes are in mm), and dependence of bar current and probe current for two axial positions on radial distance.

lower for higher distances of the cube from the arc axis. The shape of the counters changes with increasing distance from the jet axis, which represents the changes of axial distribution of current. For distances closer than 3 mm the current decreases stream-wise of the jet, while for distances higher than 4 mm the current increases. At the distance 3.5 mm the current was almost constant. Probe currents for two axial positions and cube current are shown in Fig. 4b. For the upstream position 2.3 mm the dependence of the current on radial distance from the arc is much steeper. It can be expected that for distance of anode surface in range 2.5-3 mm from the axis most current flows in the part closest to a nozzle. Bar current decreases linearly with increase of distance from the axis, and almost disappears at 5 mm.
Changes of diffuse current axial distribution can be caused by two effects. The first effect is broadening of the conductive core downstream the plasma jet, caused probably by heating of intermediate layer, convection and developing of instabilities. Second effect concerns magnetic interaction of anode attachment with plasma jet causing deflection of plasma jet opposite to the attachment and toward the cube, as can be seen on the photos (Fig. 2b). Both effects seem to be much weaker for the cube position closer to the jet.

4. Summary

Electric probes measurements were provided in anode region of plasma generated by dc arc plasma torch. Anode surface was parallel to arc column axis, like in common plasma torches. Probes were housed into the steel cube, which simulated anode.
Currents flowing on probes in the fringes of the arc column prove existence of conductive layer between the arc column and the anode surface. The currents had diffuse character. It was confirmed by absence of bright constricted channel at a current of 28 A flowing onto the cube surface. Diffuse current axial distribution was found to depend strongly on distance from the arc axis As strong dependence of probe current on distance from the arc axis was found it can be concluded that shape and relief of anode surface can strongly influence diffuse current distribution on anode surface.

References

[1] Wutzke S.A., Pfender E., Eckert E.R.G., AIAA J. 6, 1474 (1968).
[2] Brilhac, J.F. et al. 1995. Study of dynamic and static behavior of dc vortex plasma torches: Part I: Button type cathode. Plasma Chem. and Plasma Process. 15: 231-277.
[3] P. Fauchais, Understanding plasma spraying . J. Phys. D: Appl. Phys. 37 (2004) 86–108.
[4] O. Chumak, M. Hrabovský, V. Kopecký Investigation of Anode Attachment in dc Arc Plasma Spraying Torch with External Anode Proc. of 16th Int. Symp. on Plasma Chemistry, on CD.
[5] M. Hrabovský, O. Chumak, T. Kavka, V. Kopecký, Study of anode restrike processes in dc arc plasma torch, Proc. of 12th Workshop on Plasma Technology, September 2004. TU Ilmenau, 15-22.
[6] V. Brezina, M. Hrabovsky, M. Konrad, V. Kopecky and V. Sember, Proc. of 15th Int. Symp. on Plasma Chemistry (ed. A. Bouchoule et al.), Vol. III, 9-13 July 2001, Orleans, 1021 – 1026.

Modification of plastic into a superhydrophilic surface with pure CF_4 plasma

Miao-Ju Chuang[1,*], Chun-Hsiang Wen[2] ，Hsiao-Feng Huang[2] and Ging-Ho Hsiue[3]

[1] *Department of electronic Engineering, Chienkuo Technology University, Changhua City, Taiwan, 500, R.O.C.*

[2] *Materials Research Laboratories, Industrial Technology Research Institute, Hsinchu, Taiwan, 310, R.O.C.*

[3]*Department of Chemical Engineering, National Tsing Hua University Hsinchu, Taiwan, 300, ROC.*

Abstract

We used low-pressure microwave plasma to treat plastic substrate in pure CF_4. The plastic surface has changed into very high wettability. The super-hydrophilic surface is made by using a mask and controls the gap between the mask and substrate.

1. Introduction

Low-pressure plasma is widely used for the surface modification of various materials, such as increasing the adhesion between the polymers and the metal and changing the wettability of materials [1-3]. In general, oxygen-containing plasma can be used to enhance the wettability of polymers, whilst CF_4 plasma treatment can improve its hydrophobicity. In our study, it is a little against to the general concept. We used low-pressure microwave plasma to treat plastic in pure CF_4. The plastic surface has changed into very high wettability. The super-hydrophilic surface is made by using a mask and controls the gap between the mask and substrate. The contact angle measurement, atomic force microscopy (AFM) and x-ray photoelectron spectroscopy (XPS) are using for characterizing the surface properties.

2. Experiment

In these experimental, plasma treatments were performed on DuPont Kapton® HN polyimide films with a thickness of 25 μm. The Kapton films, cut in a sample size of 5 cm× 5 cm and mounted on a sample frame, were plasma treated using a commercial installation of Plasma Systems 400 from PVA Tepla .The microwaves of 2.45 GHz are applied through a window in the wall of the vacuum chamber producing an extended plasma.

The chemical natures of the treated films were measured by X-ray photoelectron spectroscopy (XPS). The XPS measurements were carried out in a Thermo-VG- Scientific Escalab 250 system using a monochromatized Al Kα (1486.6 eV) x-ray .Photoelectrons were collected at a take-off angle of 90^o with respect to the sample plane. The reference binding energy was set at 284.6 eV for the C-C component of C 1s peak.

The surface roughness and morphology of the Kapton films before and after plasma- treated was measured with an Atomic Force Microscope (AFM). AFM measurements were performed with a scanning probe microscope SPA 300HV (Seiko Instrument Incorporation, Japan) in air at room temperature, operated in the contact mode and using a silicon nitride tip.

The contact angles of water on Kapton surface were measured at room temperature by the sessile drop technique with VCA 2500XE surface analysis equipment (AST Products Incorporation, USA). For each sample, the contact angle value reported here was the mean of five locations where uniformly distributed on each sample was measured.

To obtain patterned metal copper by first patterning plastic substrate by using a mask in glow-discharge plasma treatment, then performing electroless copper plating to obtain metal copper within the regions of mask shielded, that is, hydrophilic area.

3. Results and discussion

Table 1 shows the water contact angle and relative peak areas of curve-fitted spectra for C (1s) .TyKaptoncal C (1s) spectrum for the CF_4 treated Kapton films and untreated Kapton film are shown in Fig.1. The C (1s) spectrum for untreated Kapton film [Fig. 1(a)] is fitted with four peaks. The carbon atoms in Phenyl ring at 284.6 eV, the carbon atoms singly bond to oxygen or nitrogen at 285.7 eV, the carbonyl carbons appear at 288.6 eV, and the π-π* shake up peak at 290.6 eV. The C (1s) spectra of plasma treatment on shielded and nonshielded surface are shown in Figure 1(b) and 1(c). CF_4 plasma treatments of Kapton films result in an enormous amount of fluorine incorporation at the surface. There is a dramatic change in the C (1s) XPS envelope, which can be attributed to formation of fluorinate carbon functionalities: $\underline{C}FH\text{-}CF_2$ at ～286.9 eV, $\underline{C}F_2\text{-}CH_2$ at ～290.5 eV, and $\underline{C}F_2\text{-}CF_2$ at 292.2 eV [4-6]. From table 1, there is abundant fluorine atoms incorporated to the non-shielded Kapton surface. The water contact angle raises to 108 deg is its appearance. F/C ratio increases to 1.51 and O/C ratio is only 0.17 at non-shielded Kapton surface. On the contrary, the shielded Kapton surface after plasma treatment is exhibiting super hydrophilic property, that is, lower than 5 deg. The F/C ratio is only 0.21 and O/C ratio rises from 0.18 to 0.36.

Glow discharge plasmas generally consist of energetic particles (e.g., positive ions, electrons, free radicals, metastable species and photons). The plastic surface with the energetic particles breaks the covalent bonds on the surface of the bombarded polymer and leads to the formation of the surface radicals on the treated polymer. These surface radicals interact with the active plasma species to form various functional groups on the surface of polymer. Furthermore, the predominant reactive components of CF_4 plasma are reported to be F atoms and relatively low concentrations of CF_n (n = 1, 2, 3) radicals [7-8]. With a low CF_n/F ratio, CF_4 does not polymerize in plasma, it can produces fluorination through a direct grafting of F atoms onto polymer surface [9-12]. Therefore, the fluorine atoms in the CF_4 plasma undergo hydrogen abstraction and substitution reaction at the Kapton surface yield $\underline{C}FH\text{-}CF_2$, $\underline{C}F_2\text{-}CH_2$, and $\underline{C}F_2\text{-}CF_2$ functionalities.

Table 1: The water contact angle data and relative areas for cure-fitted XPS data for CF_4 plasma treated Kapton

Treatment		Untreated Kapton	Shielded substrate	Nonshielded substrate
Water Contact Angle (degree)		76.08 ± 1.211	< 5	108.275 ± 0.657
	F/C	0.00	0.21	1.54
	O/C	0.18	0.36	0.17
% C (1s)	C-C/C-H	40.18	26.47	11.67
	C-O/C-N	45.99	36.76	0.00
	O=C/$\underline{C}$FH-CF_2	13.83	25.73	32.50
	$\underline{C}F_2$ -CH_2	-	5.15	41.67
	$\underline{C}F_2$ -CF_2	-	5.88	14.17

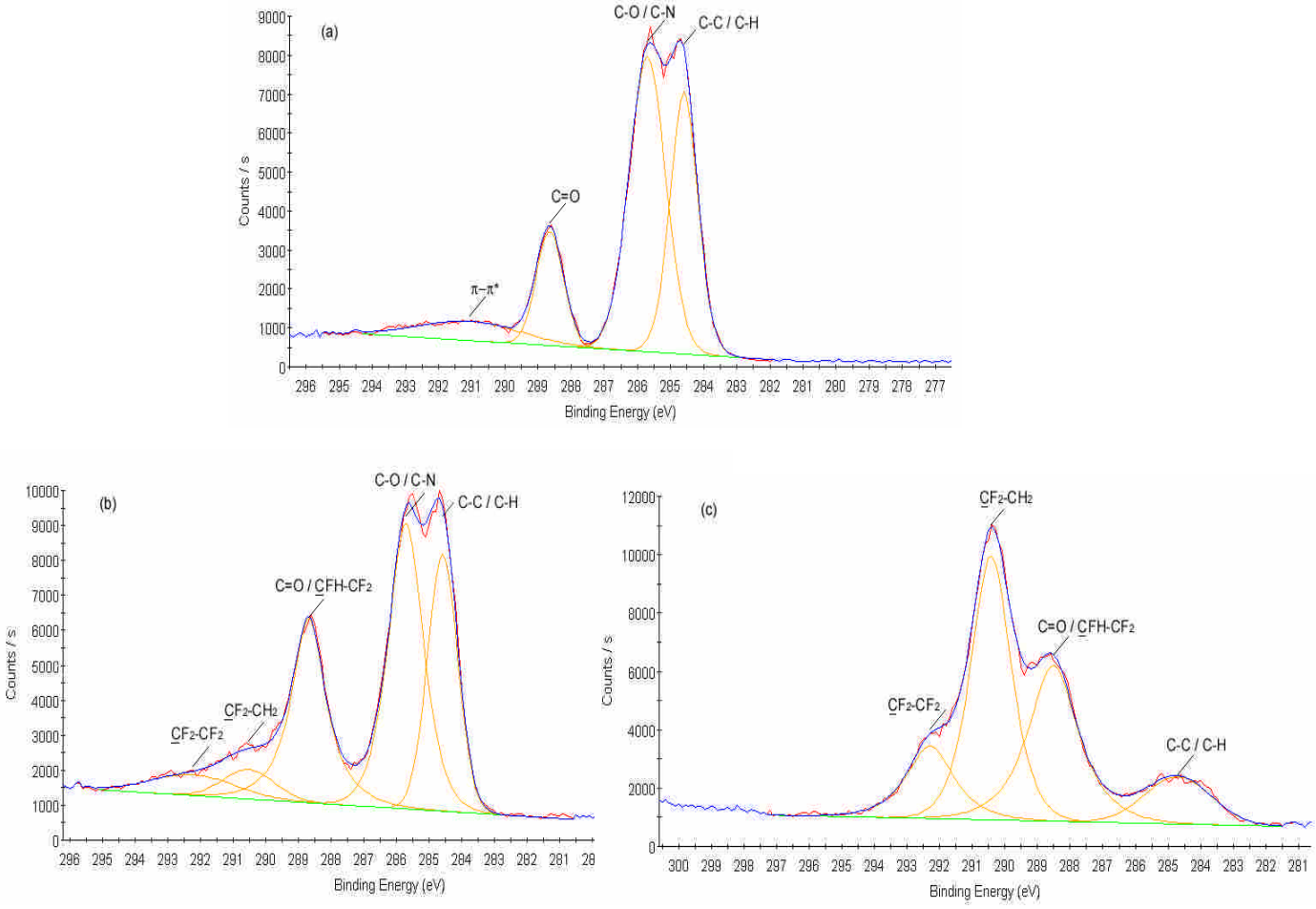

Fig. 1. XPS C(1s) spectra for untreated Kapton film (a), an CF_4 plasma treated shielded substrate (b), and an CF_4 plasma treated nonshielded substrate.

To evaluate the influence of plasma treatment upon surface physical nature, AFM analysis was performed with both the untreated Kapton and plasma treated Kapton. The results are shown in table 2. The difference of RMS value for the non-shielded surface (0.50 nm) is much larger then those for the shielded surface (0.23 nm). This is the case that the non-shielded surface with the more energetic particles bombarded than shielded surface and therefore the reactions on both surfaces were dissimilar.

Table 2: The surface roughness of CF4 plasma treated Kapton films

Treatment	RMS (nm)	ΔRMS (nm)
Untreated Kapton	0.59	-
Shielded area	0.82	0.23
Nonshielded area	1.09	0.50

RMS : Root-mean-square height
ΔRMS : Difference of RMS

Figure 2 is the optical microscopy image that is finished patterning hydrophilic and hydrophobic surface by plasma surface modification then fabricating a metallic pattern on plastic substrate. The Metal Cu is only growth at hydrophilic area and its shortest line width is 180μm.

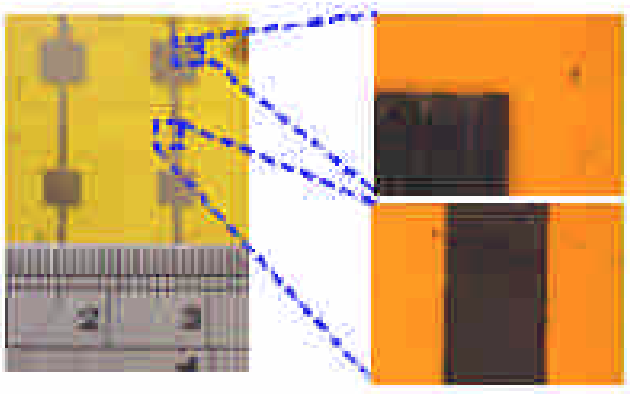

Fig. 2: Optical microscopy image of a copper pattern onto a Kapton surface.

4. Conclusions

In the conclusion, we succeed in getting super-hydrophilic surface on plastic substrate, by using microwave plasma with pure CF_4 and a mask with certain distance to the substrate. The contact angle measurement and XPS analysis result indicate the non-shielded surface, water contact angle is 108 degree and the O/C and F/C ratios are 0.17 and 1.54, respectively. On the other hand, the shielded surface is less than 5 degree, the O/C and F/C

ratios are 0.36 and 0.21, respectively. Furthermore, we have also success in fabricating a metallic pattern on plastic substrate patterning metal on plastic substrate without photo lithography process. The Metal Cu is only growth at hydrophilic area and its shortest line width is 180μm.

References

[1] M. K. Shi, A. Semani, L. Martinu, E. Sacher, M. R. Wertheimer and A. Yelon, J. Adhesion Sci. Technol. 8 , 1129 (1994).

[2] M. D. Duca, C. L. Plosceanu and T. Pop, Polym. Degrad. Stabil., 61 ,65 (1998).

[3] S. Marais, M. Métayer, M. Labbé, J. M. Valleto, S. Alexandre, J. M. Saiter, F. Poncin-Epaillard, Surf. Coat. Technol. 122, 247 (1999).

[4] J. F. Moulder, W. F. Stickle, P. E. Sobol and K. D. Bomben, In Handbook of X-ray Photoelectron Spectroscopy; Jill Chastain Ed.; Perkin-Elmer Corporation, Physical Electronics Devision, Minnesota ,1992.

[5] F .D. Egitto, F. Emmi , R. S. Horwath and V. Vukanovic, J. Vac. Sci. Technol. B3 (3) 893 (1985)

[6] T. R. Gengenbach and H. J. Griesser, Surf. Interface. Anal. 26, 498 (1998)

[7] M. Strobel, P. A. Thoms, and C. S. Lyons, J. Polym. Sci.: Part A Polym. Chem., 25 (1987) 3343.

[8] J. Hopkins and J. P. S. Badyal, J. Phys. Chem., 99 (1995) 4261.

[9] J. W. Coburn and H. F. Winters, J. Vac. Sci. Technol., 16 (1979) 391.

[10] J. Wang, D. Feng, H. Wanf, M. Rembold, and F. Thommen, J. Appl. Polym. Sci., 50 (1993) 585.

[11] M. Strobel, S. Corn, C. S. Lyons, and G. A. Korba, J. Polym. Sci. Polym. Chem Ed., 23 (1985) 1125.

[12] Y. Iriyama and H. Yasuda, J. Polym. Sci. Part A Polym. Chem., 30 (1992) 1731.

Photocatalyst activation in a pulsed low pressure discharge

O. Guaitella[1], A. Rousseau[1], L.V. Gatilova[1], F. Thevenet[2], C. Guillard[2], J. Röpcke[3], G.D. Stancu[3]

[1]*LPTP, GdR CATAPLASME, Ecole Polytechnique, Route de Saclay 91 128 Palaiseau Cedex, France*
(Antoine.Rousseau@lptp.polytechnique.fr)

[2]*LACE, Université Lyon1, 69 100 Villeurbanne, France*
[3]*INP-Greifswald, F.-L.-Jahn-Str. 19, 17489 Greifswald, Germany*

Abstract

The synergy of the plasma-photocatalyst combination for Volatile Organic Compounds (VOC) removal is investigated using a pulsed DC discharge at low pressure (210 Pa). The photocatalyst is TiO_2 and the VOC is acetylene 1000 ppm in dry air. Time resolved Tuneable Diode Laser Absorption Spectroscopy (TDLAS) in the mid infrared region is performed in-situ the discharge tube to measure the decrease of C_2H_2 during 1 s plasma pulse duration. The respective influence of external ultraviolet radiation and of the plasma exposure, with and without photocatalyst is checked. It is shown that the combination of plasma and ultraviolet radiation in presence of TiO_2 pellets leads to a strong increase of the C_2H_2 oxidation efficiency.

1. Introduction

Indoor air cleaning has become a new technological challenge for odours or diluted pollutant removal. Photocatalysis is based on the oxidation of molecules on the surface of a porous semiconductor material illuminated with ultraviolet radiation; the main advantage of this technique is that it leads to complete oxidation of Volatile Organic Compounds (VOC) to CO_2 and salts [1]. It was recently shown that the combination of photocatalytic material with a non-thermal plasma activates the oxidation process [2-7]. The synergy between the plasma and the photocatalytic material leads to a higher CO_2/CO ratio (selectivity) [2,7], as well as a better oxidation efficiency [3,7]. Up to now there is no clear explanation concerning the reason of such a synergy of the photocatalyst by the non-thermal plasma. When TiO_2 is located inside the discharge region, it is bombarded by ultraviolet radiation generated by excited nitrogen molecules, by charged particles, by metastable states of molecules and atoms, and by ground states O and N atoms. However, atmospheric pressure plasmas such as Dielectric Barrier Discharges (DBD) are strongly non-uniform and direct in-situ measurements are not possible. In the present study, to avoid this major difficulty, time resolved and in-situ absorption spectroscopy measurements are performed in the positive column of a low pressure pulsed DC discharge, which is approximately spatially homogenous. This gives a practical way to study the plasma-photocatalyst interaction by Tuneable Diode Laser Absorption Spectroscopy (TDLAS) in the infrared region. Moreover such DC discharges have been extensively studied in continuous current by two groups, Gordiets et al. [8] and Smirnov et al. [9]. Therefore, plasma parameters such as reduced electric field, plasma density and temperature are known for various set of experimental conditions. We report the time evolution of C_2H_2 under plasma exposure, with or without TiO_2 pellets, with or without additional ultraviolet irradiation.

The pulsed discharge is ignited in a 47 cm long (59 cm optical length) and 2,1 cm inner diameter pyrex tube (Figure 1).

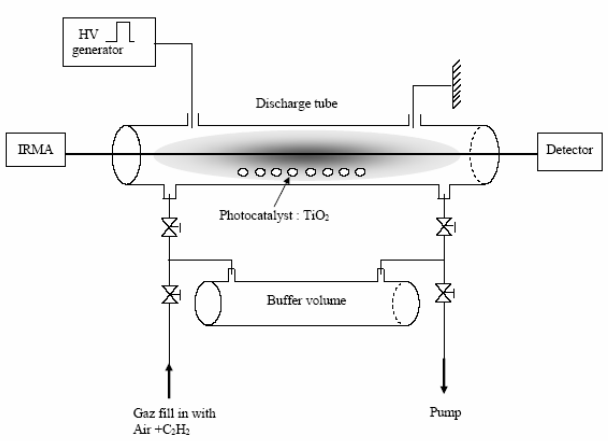

Figure 1. Experimental set-up showing the pulsed DC discharge containing TiO_2 pellets and the in situ laser absorption spectroscopy

2. Experiment

The pulsed DC generator delivers a current of 3 mA, with a pulse duration of 1 s. Commercially available TiO_2 pellets (20g of pure anatase, Alfa Aesar #43828, size specific surface 37 m^2/g) may be introduced inside the tube. Experiments are performed under static conditions: dry synthetic air N_2/O_2 = 80/20 % (< 3 ppm of H2O and 0,5ppm of hydrocarbons) is first pre-mixed to reach 900 ppm C_2H_2 in a buffer volume, the discharge tube being pumped out to a base vacuum of less than 5 Pa. The pre-mixed gas is injected in the discharge tube, which is then closed, the pressure being equal to 210 Pa. When TiO_2 pellets are present inside the discharge tube, part of the injected C_2H_2 molecules are adsorbed until a steady state is reached (Figure 2); following this, pulsed TDLAS measurements are performed starting from the steady state conditions shown in Fig. 2.

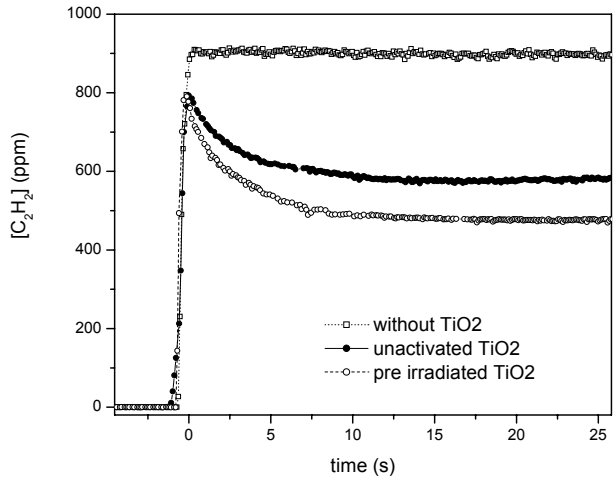

Figure 2. Filling of the discharge tube showing adsorption of C_2H_2 on TiO_2 pellets: time evolution of the C_2H_2 concentration, without pellets, with TiO_2 pellets, with TiO_2 pellets after UV irradiation. Pressure 210 Pa.

In order to check the influence of external ultraviolet radiation, two mercury lamps (Philips PL-L 24W/10/4P) were mounted parallel to the discharge tube axis.

In-situ laser absorption spectroscopy is performed on C_2H_2 molecule by single path through the discharge tube (Figure 1). The infrared diode laser is a helium cooled IRMA, described in Röpcke et al.10, which may be externally triggered and provides a pulse resolution of 0.46 ms. C_2H_2 density is deduced from the Beer's law:

$$I(\nu) = I_0(\nu)\exp[-k(\nu)L] \quad (1)$$

where I(ν) is the transmitted radiation intensity, $I_0(\nu)$ is the incident intensity on the sample, k(ν) is the absorption coefficient per unit length and L is the total absorption path length. The integrated absorption coefficient over frequency, Kν, for a homogeneous sample is

$$K_\nu = \int_\nu k(\nu)d\nu = \frac{1}{L}\int_\nu \ln\left(\frac{I_0}{I}\right)d\nu = N\,S(T) \quad (2)$$

where N is the total density of the absorbing species; S(T) is the line strength of the rovibronic transition used for species measurement. The temperature increase during the plasma pulse was estimated to be less than 50°C from thermal diffusion equation; hence, the temperature dependency of S(T) was neglected. At room temperature (296 K) the line strength value was taken from Rothman et al. 11 to be 3.65 x 10^{-19} cm molecule-1. In the present work a strong line of C_2H_2 which is located at 771,40482 cm^{-1} has been used. The IRMA system measured the integrated absorption coefficients, then by using the line strength value, absolute concentrations were obtained.

3. Results

The steady state density of C_2H_2 is about 900 ppm, without TiO_2 pellets inserted inside the discharge tube. On the contrary, when the discharge tube is filled with the pre-mixed gas in the presence of TiO_2 pellets, its steady state density is only 580 ppm. This means that about 36 % of the injected C_2H_2 is adsorbed on the TiO_2 pellets with a characteristic adsorption time of about 3.5 s (Figure 2). Let us notice that N_2/O_2 molecules are not adsorbed since no measurable pressure drop is observed during C_2H_2 adsorption. Figure 2 also shows the time evolution of C_2H_2 density when the discharge tube contains TiO_2 pellets, which have been irradiated by UV lamp just before filling. At the steady state about 47 % have disappeared from the gas phase, which is notably higher than without UV pre-irradiation. We have no evidence whether this is due to an increase of the adsorption efficiency or if it is partly due to an oxidation of C_2H_2 on the pre-irradiated photocatalyst. It is worthwhile to notice that such a pre-irradiation effect last for more than 20s (time between pre-irradiation and filling of the discharge tube).

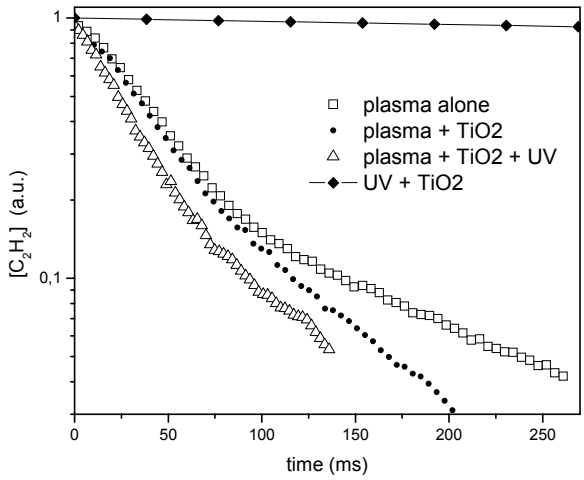

Figure 3 shows the time evolution of C_2H_2 (for first 250 ms) during a 1 s pulse duration for different experimental conditions.

Most of the curves show a bi-exponential decay of C_2H_2 and the corresponding characteristic frequency are presented in Table 1.

case	Conditions	1st decay frequency (s^{-1})	2nd decay frequency (s^{-1})
a	UV + TiO_2	0.33	-
b	Plasma only	20.8	7
c	Plasma + TiO_2	22.2	14
d	Plasma + TiO_2 + UV	30.3	14

Table 1: Decay frequencies for different experimental conditions. 1st and 2nd decay frequency refer to the biexponential function of C_2H_2 time evolution.

For case b (plasma only), the decay frequency is reduced by a factor 3 (from 20.8 to 7 s^{-1}) about 100 ms after the beginning of the pulse. The electron density and reduced electric field being about constant during the pulse duration, such an effect must be attributed to gas phase kinetics between neutrals. When some photocatalytic surface is inserted inside the plasma region, the decay decreases only by 37 % (from 22.2 to 14 s^{-1}). This may be due either to surface oxidation of C_2H_2 and/or to a modification density of oxidative radicals and molecules in the gas phase.

The presence of photocatalytic pellets lead to a very small increase of the first decay frequency from 20.8 to 22.2 s^{-1} (case b, c). This shows that, for low pressure conditions, plasma only is not able to activate efficiently TiO_2. More over, it was recently shown, under similar experimental conditions that the reduced electric field E/N increases from 80 to 92 Td [12]. From Fig. 3 we conclude that C_2H_2 destruction in the gas phase is not controlled by electron impact dissociation since an increase of electron energy does has no definite influence on the C_2H_2 destruction frequency.

The most interesting result is the strong synergetic effect obtained when the plasma is combined with TiO_2 pellets with external UV irradiation (case d). The 1st decay frequency is increased from 22.2 s^{-1} in the case of plasma / TiO_2 combination (case c) to 30.3 s^{-1} when external UV irradiation is added (case d); this represents a 36 % increase of the C_2H_2 decay frequency. Hence the photocatalytic effect of TiO_2 irradiated with UV is strongly enhanced when non-thermal plasma is added: the decay frequency increases from 0.33 s^{-1} (case a), to 30.3-22.2 = 8.1 s^{-1} (case d). Hence, TiO_2 is much more effectively activated by UV when exposed to the plasma and the photocatalytic activity is increased by a factor of 25. The reason of such a synergy may be due a priori to : i) enhancement of electron-hole pair formation; ii) promotion of oxidative radicals in the gas phase, which are activated by photocatalysis onto the TiO_2 surface, iii) desorption of adsorbed C_2H_2 or intermediate oxidative products.

First, there is no clear evidence as to why exposure of TiO_2 to the plasma should lead to an increase of electron-hole formation (hypothesis (i)); it is well known that the plasma generates UV in the 330–390 nm region (2nd positive system of nitrogen molecules), which are, in principle, suitable for photocatalysis; however, comparing cases b and c shows that UV produced by the plasma itself do not lead to appreciable photoactivation of TiO_2 (22.2 s^{-1} vs 20.8 s^{-1}), because the UV flux produced by the plasma is much weaker than the one produced by the UV lamps.

Second, plasma produces active species such as O atoms, O_2 (1Δ) molecules as well charged particles; this species may be adsorbed on the TiO_2 surface. It was recently shown by Roland et al [13] that a porous surface, such as silica or alumina located inside the plasma region increases oxidation processes of pollutants, because of the presence of physi- or chemisorbed species on the surface of the pores. O atoms created by the plasma may be adsorbed on the TiO_2 surface and react with adsorbed C_2H_2. This could also contribute to the small increase of the decay frequency from case b to case c. However, when external UV irradiation is applied to the TiO_2 surface, electron-hole pairs may activate these adsorbed species and increase the oxidation rate of C_2H_2.

Third, it is more likely that, in the present study, plasma bombardment increases the number of adsorption sites as shown by Cartry et al. [14] under similar experimental conditions; it was also shown by Futamura et al. [2] , under atmospheric pressure conditions, that the cleaning effect of plasma bombardment prevents deactivation of TiO_2 catalyst.

Conclusions

Time resolved laser absorption measurements have been performed in the gas phase of a pulse d plasma exposed to a photocatalytic material (TiO_2 anatase). It was shown that:

i) the combination of a non thermal plasma with photocatalysis leads to a strong increase of photocatalytic activity by a factor 25.

ii) Under our experimental conditions, UVs generated by the plasma itself are insufficient to ensure such a synergetic effect.

Therefore the observed synergetic effect is due to an increase of the photocatalysis efficiency when the photocatalytic material is exposed to species produced by the plasma such as radicals, excited molecules, ions… Additional work is needed to understand the mechanisms of plasma-photocatalysis synergy and to characterize the oxidation products: activation of adsorbed species by electron-hole pair or an increase of the number of adsorption sites.

References

1 R. M. Alberici and W. F. Jardim Applied Catalysis B: Environmental, 14, 55, (1997)

2 S. Futamura, H. Einaga, H. Kabashima, L.Y. Hwan, Catal. Today 89, 89 (2004)

3 M. Kang, B.-J. Kim, S.M. Cho, C.-H. Chung, B.-W. Kim, G.Y. Han, K.J. Yoon, J. of Molecular Catalysis A : Chemical 180, 125 (2002)

4 A. Mizuno, Y. Kisanuki, M. Noguchi, S. Katsura, S.H. Lee, Y.K. Hong, S.Y. Shin, J.H. Kang, IEEE trans. Ind. Appl. 35, 1284 (1999)

5 D. Li, D. Yakushiji, S. Kanazawa, T. Ohkubo, Y. Nomoto, J. Electrostatics 55, 311 (2002)

6 H.-H. Kim, Y.-H. Lee, A. Ogata, S. Futamura, Cat. Commun. 4, 347 (2003)

7 B.-Y. Lee, S.-H. Park, S.-C. Lee, M. Kang, S.-J. Choung, Cat. Today 93, 769 (2004)

8 B.F. Gordiets, C.M. Ferreira, V.L. Guerra, J.M.A.H. Loureiro, J. Nahorny, D. Pagnon, M Touzeau, M. Vialle, IEEE trans. Plasma Science 23, 750 (1995)

9 S.A.Smirnov,V.V.Rybkin, I.V.Kholodov. High Temp. 2002, 40, No.2.

10 Röpcke J, Mechold L, Käning M, Anders J, Wienhold F G, Nelson D and Zahniser M. , Rev. Sci. Instr. 71, 3706 (2000)

11 L.S. Rothman, C.P. Rinsland, A. Goldman, S.T. Massie, D.P. Edwards, J.-M. Flaud, A. Perrin, C. Camy-Peyret, V. Dana, J.-Y. Mandin, J. Schroeder, A. McCann, R.R. Gamache, R.B. Wattson, K. Yoshino, K.V. Chance, K.W. Jucks, L.R. Brown, V. Nemtchinov and P. Varanasi, J. Quant. Spectrosc. Radiat. Transfer, 60 (5), 665 (1998)

12 O. Guaitella, L. Gatilova, A. Rousseau, Appl. Phys. Lett. 86, 151502 (2005)

13 U. Roland, F. Holzer, F.-D. Kopinke, Cat. Today 73, 315 (2002)

14 G. Cartry, L.Magne, G. Cernogora, J. Phys. D: Appl. Phys. 33, 1303 (2000)

Dispersion study of TiO_2 nanoparticles modified by pulsed RF plasma polymer coating

Ying Wang[1,4], Jing Zhang[2,4,*], Xinyuan Shen[1,4], Changnian Shi[3], Ping Ji[3], Zhan Cheng[3], Jiajun Wu[2], Li Sun[2]

[1]*College of Material Science and Engineering, Donghua University, Shanghai, P.R. China*

[2] *College of Sciences, Donghua University, Shanghai, P.R. China*

[3] *Yizheng Chemical Fibre Co.,Ltd., Yangzhou, Jiangsu Province, P.R. China*

[4]*State Key Laboratory for Modification of Chemical Fibers and Polymer Materials, Donghua University, Shanghai, P.R. China*

Abstract: The dispersion of TiO_2 nanoparticles after acrylic acid plasma coating was measured by ultraviolet absorbency measurements. The results showed that the absorbency of TiO_2-glycol suspensions reached an optimal value at certain discharge power. The EDLVO theory of colloid stability was applied to simulate the potential energy of TiO_2 nanoparticles in glycol according to the surface energy measured. It was found that the potential maxima in the EDLVO curves matched well with the optimal dispersion values.

1.Introduction

Functional organic/inorganic composites are attracting more and more attention and interest these years. In these kinds of materials, the properties of composites directly depend on the aggregation state of nanofillers. Only when the inorganic phase is dispersed at a nanoscale level in the matrix phase [1-5], some composites with special functionality can be formed. However, nanoparticles are difficult to well disperse in the background media due to severe agglomeration and high ratio of surface area to volume. Hence, dispersion is the "bottleneck" problem to hinder the applications of nanoparticles.

TiO_2 nanoparticle is one of the most studied transition metal oxide for various applications ranging from pigment, ultraviolet light absorber, visible light photo catalyst, gas sensors, etc. A lot of novel composites and fibers with good functions are prepared based on its special properties and the dispersion state in the medium. Many studies have been reported about the surface modification of TiO_2 nanoparticles [5] to obtain well-dispersed composites by chemical methods. But the rare is done on surface coating of TiO_2 nanoparticles by pulsed plasma polymerization. It is not only a simple, dry state and environmental-friendly process operating at room temperature but also suitable to all kinds of inorganic, organic, solvable and insolvable nanoparticles.

In our previous study [6], a plasma polymer coating of acrylic acid (AA) has been successfully applied to the surface modification of TiO_2 nanoparticles. This allows us to effectively control the desired chemical components, physical morphology and thickness of the coating on particle surface by adjusting discharge parameters. So in the present study the surface energy of TiO_2 nanoparticles is measured and calculated through a custom-built measurement system and Lifshitz-van der Waals/acid-base (LW-AB) approach. The dispersion investigation of AA-coated TiO_2 nanoparticles in glycol solution is carried out by ultraviolet absorbency measurement experimentally and potential simulation between particles through the extended DLVO (EDLVO) theory (A further application of this project is to obtain TiO_2-polyester composite, then glycol is selected as the dispersion medium). The aim of this work is to correlate the ultraviolet absorbency results of TiO_2-glycol suspensions with the discharge parameters, the surface properties as well as the surface energy of nanopowders to investigate the dispersion behaviors and even explain the dispersion modifications of surface-coated TiO_2 nanoparticles in glycol solution.

*To whom correspondence should be addressed. Email: jingzh@dhu.edu.cn

2.Experimental

2.1 Surface coating

TiO_2 nanoparticles (rutile) were coated in a custom-built fluidized bed reactor [6] through exposing to AA plasma. At first TiO_2 nanoparticles with a primary mean size of 35nm were put into the reactor. Then a base pressure in the reactor was pumped down to less than 3 Pa. The mixture of monomer and carrier gas (argon) in a certain ratio was introduced into the reactor to fluidize the nanoparticles through a porous plate and mass flow controllers. Finally the RF plasma generator (13.56 MHz) was turned on at gas pressure of 150 Pa, gas flow rate of 15 sccm, pulsed rate of 15% and coating time of 4 hours. To obtain desired surface coating on nanoparticles, the discharge power was changed in turn.

An amorphous thin film about 3-5 nanometers was tightly bound to the nanoparticle surface according to the HRTEM and EDS tests in our previous study [6].

2.2 Surface energy calculation

The contact angle measurement system was specially designed based on the Washburn's equation [7]. The measurement process was illustrated as follows. At first a piece of cotton cloth was stuck at one end of a cleaned glass tube. Then the powders were put into the tube and vibrated until no further change of the powder column height was observed. The packed tube was hung under an electronic balance vertically and the tube bottom was made to contact with the liquid surface by carefully moving up the liquid container on a platform. Thus the weight of liquid penetrating into the packed powders was automatically transmitted to the computer and recorded as a function of time.

In the contact angle measurement of TiO_2 nanoparticles, Methanol is considered as a liquid that may perfectly wet the sample. Water, glycol and dimethyl sulfoxide are selected as tested liquids. The surface energy of powder is calculated by LW-AB approach [8].

2.3 Ultraviolet absorbency measurement

Some nanopowders were put into glycol solution and a dilute suspension was made. After dispersed the suspension for 15 minutes by ultrasonic, it was poured into the rectangular cell of quartz and the absorbency measurement was carried out through UV-3000 ultraviolet spectrophotometer (Shimadzu Cor., Japan).

3.Results and discussion

3.1 Surface energy of TiO_2 nanoparticles

The experimental results of contact angles and surface energy of TiO_2 nanopowders are reported as Tab.1. It displays that the surface energy (γ_S^{Total}) as well as the nonpolar (γ_S^{LW}) and the polar component parts (γ_S^{AB}) of any AA-plasma-coated nanoparticles is much lower than that of the uncoated TiO_2. But the surface energy and its parts do not decrease linearly with the discharge power.

Tab.1. Surface energy and it parts of TiO_2 nanoparticles coated under different power

Monomer	Power (W)	Contact angle (cosθ)			Surface energy (mJ/m^2)				
		Water	Glycol	Dimethyl sulfoxide	γ_S^{Total}	γ_S^{LW}	γ_S^{+}	γ_S^{-}	γ_S^{AB}
Uncoated		0.113	0.903	0.129	35.31	16.64	2.22	39.26	18.67
AA	5	0.209	0.517	0.671	7.70	6.81	2.79	0.07	0.88
AA	20	0.133	0.292	0.484	8.58	7.63	3.24	0.07	0.95
AA	25	0.058	0.151	0.315	7.12	6.09	3.31	0.08	1.03
AA	40	0.044	0.193	0.256	4.34	3.11	3.17	0.12	1.23

* γ_S^{+} and γ_S^{-} are the electron accepting part and the electron giving part in the polar part of the surface energy, respectively.

3.2 Dispersion of TiO_2 nanoparticles

The measured absorbency may yield the most significant information about the particle-particle

conglomeration because the diameters of TiO_2 nanoparticles play an important role in the ultraviolet shielding effect of TiO_2. The less the conglomeration of nanoparticles in solution, the higher the absorbency value. Fig.1(A) displays the ultraviolet absorbency curves of TiO_2-glycol (in Tab.1) suspensions at the ultraviolet-visible bands. It is clearly seen that all the absorbency curves move upwards from the baseline of untreated TiO_2 particle and there exists a maximum at about 310nm. Then the ultraviolet absorbency maximum (UAM for short) is recorded and plotted as a function of plasma discharge power to correlate the dispersion behaviors of nanoparticles and the discharge parameters. Note how the UAM in Fig.1(B) progressively increases with the power until reaching a maximum close to 25W. A further increase in the discharge power yields a significant decrease of the slope. From these absorbency tests, it is indicated that the dispersion of any AA-plasma-polymer coated TiO_2 nanoparticles is greatly improved in 200-400nm ultraviolet bands. The optimum dispersion of TiO_2-glycol suspensions takes place at the discharge power of 25W. Such a dispersion improvement of nanoparticles is mainly caused by the change of the surface properties of nanoparticle through plasma polymer coating. The particular reason for this will be discussed later.

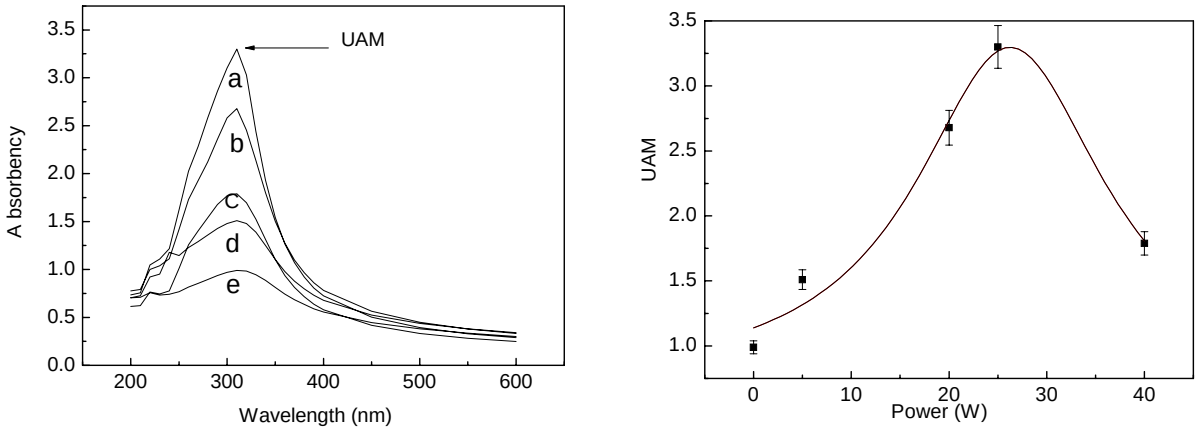

Fig.1. (A) Ultraviolet absorbency curves and (B) UAM curve of TiO_2-glycos suspensions coated under different power (a) 25W (b) 20W (c) 40W (d) 5W (e) uncoated TiO_2

3.3 Potential energy of interaction between nanoparticles

Until now the surface energy of TiO_2 nanoparticles and their dispersion behaviors in glycol solution have been carefully investigated. Here, we will try to simulate the potential energy of interaction between nanoparticles according to the EDLVO theory and measured surface energy to explain the dispersion behaviors of nanoparticles in glycol suspension. The AA-plasma-polymer coated TiO_2 is assumed to be a spherical particle covered with a concentric, continuous layer as show in Fig.2, where R is the particle radius, h is the surface-to-surface distance between the particles and d is the thickness of the coating layer.

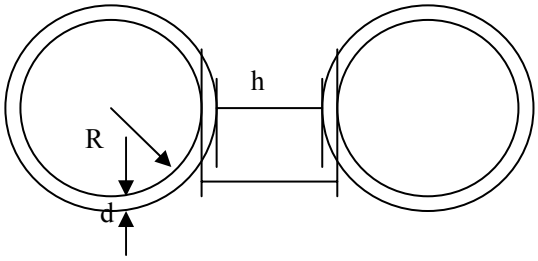

Fig.2. Schematic diagram of coated particulate

The total potential energy of interaction is the sum of three contributions, namely, electrostatic double-layer repulsion (V^{EL}), Van der Waals attraction (V^{LW}) and Lewis AB (electron-acceptor /electron-donor) interaction (V^{AB}). The following equation is used for V^{EL}:

$$V^{EL} = \frac{\varepsilon_o \varepsilon_r R \ \varphi_0^2}{2} \exp(-\kappa h) \tag{1}$$

where $\varepsilon_0\varepsilon_r$ is the dielectric constant of the solution, κ is the inverse Debye length and φ_0 is the zeta potential.

The Van der Waals attraction has been calculated according to the following expression [9]:

$$V^{LW} = -\frac{1}{12}\left[\left(A_p^{\frac{1}{2}} - A_i^{\frac{1}{2}}\right)^2 H_p + \left(A_i^{\frac{1}{2}} - A_m^{\frac{1}{2}}\right)^2 H_i + 2\left(A_i^{\frac{1}{2}} - A_m^{\frac{1}{2}}\right)\left(A_p^{\frac{1}{2}} - A_i^{\frac{1}{2}}\right)H_{ip}\right] \quad (2)$$

where subscript 'p' refers to the central part of the particles, subscript 'i' refers to the coating layer , subscript 'm' refers to the intervening continuous medium between particles, and A is the Hamaker constant of material (liquid or solid). Because the Hamaker constant (A) is unknown for the materials, it is estimated from the nonpolar part of the surface energy, which may be given by [10]:

$$A = 24\pi l_0^2\ \gamma^{LW} \quad (3)$$

where l_0 is the so-called equilibrium separation distance between the interfaces and a good estimation of it is l_0=0.157nm.

The H functions are defined in the equations displayed below. For various situations:

$$H(X,Y) = \frac{Y}{X^2 + XY + X} + \frac{Y}{X^2 + XY + X + Y} + 2Ln\left(\frac{X^2 + XY + X}{X^2 + XY + X + Y}\right) \quad (4)$$

$$H_p : X = \frac{(h+2d)}{2R}, Y = 1 \qquad H_i : X = \frac{h}{2(R+d)}, Y = 1 \qquad H_{ip} : X = \frac{(h+d)}{2R}, Y = \frac{(R+d)}{R}$$

The Lewis AB interaction between two spherical surfaces, immersed in a solution, is presented by [11]:

$$V^{AB} = \pi R \cdot \lambda \cdot \Delta G_{l_0}^{AB} \cdot \exp\left[(l_0 - h)/\lambda\right] \quad (5)$$

where λ is the characteristic length, for hydrophilic system λ=1.0 nm, and $\Delta G_{l_0}^{AB}$ is expressed as a function of the electron accepting part and the electron giving part of the polar surface energy of solid and liquid.

$$\Delta G_{l_0}^{AB} = -4\left(\sqrt{r_l^+\gamma_l^-} + \sqrt{\gamma_s^+\gamma_s^-} - \sqrt{\gamma_s^+\gamma_l^-} - \sqrt{\gamma_l^+\gamma_s^-}\right) \quad (6)$$

The total potential energy of interaction (V) between particles is formulated by:

$$V £½ V^{EL} £« V^{LW} + V^{AB} \quad (7)$$

In many cases, a small amount of water exists in the polar organic solution. Although it is difficult to develop surface charges on particles in nonaqueous liquids, the contribution of water ionization to V^{EL} should not be neglected. So in this simulation model the inverse Debye length and the zeta potential of nanoparticles coated under any discharge parameters in glycol are supposed similar of κ=0 and φ_0=20mV, respectively. The diameter of uncoated TiO_2 nanoparticles is taken as a constant of 35nm. Then the diameter of the coated TiO_2 nanoparticle is 41nm according to the average coating thickness of 3nm measured by HRTEM [6].

Using the surface energy data shown in Tab.1 and Eq.(1-7), the potential energy curves of EDLVO are plotted in Fig.3, which express the relationship between the total potential energy and the distance h between nanoparticles. It is notable that the relative tendencies of simulated curves V(h) are almost the same when TiO_2 nanoparticles is coated under different discharge parameters. A potential maximum, which expresses the maximal long-range repulsion between two particles, observes at distance within 0-5nm for any nanoparticles. This potential maximum among particles governs the conglomeration/dispersion behaviors of ultra-fine

nanoparticle in suspension. The larger the potential maximum in the EDLVO curves, the greater the stability of the nanoparticles suspension since that two particles must surpass such a potential maximum at a critical distance prior to encounter and aggregate together.

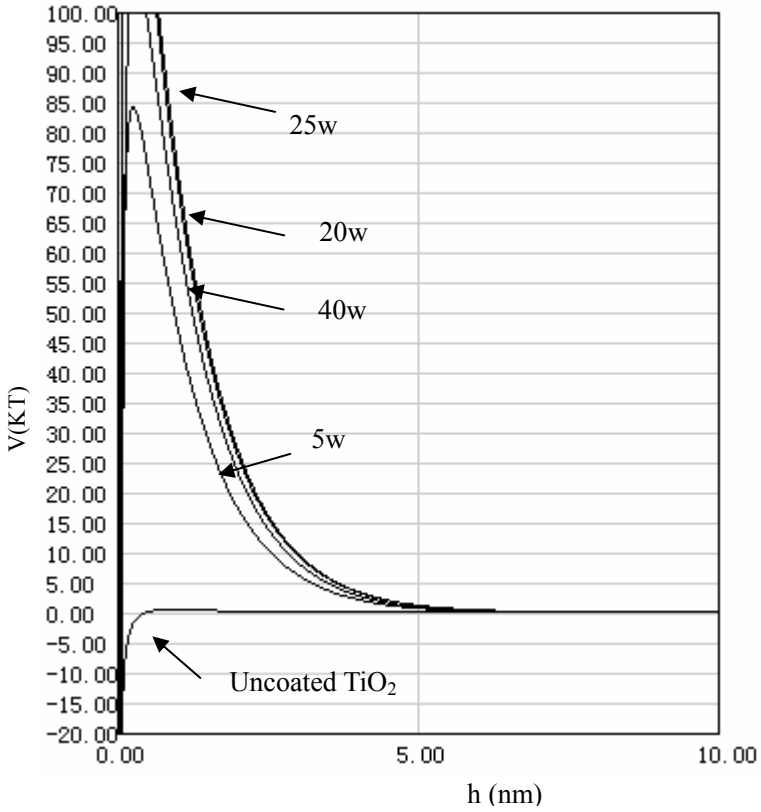

Fig.3. Potential energy curves of TiO_2- glycol suspensions coated under different power
(The potential maximum at 25W (139.74KT) is a little higher than that at 20W (138.74KT).)

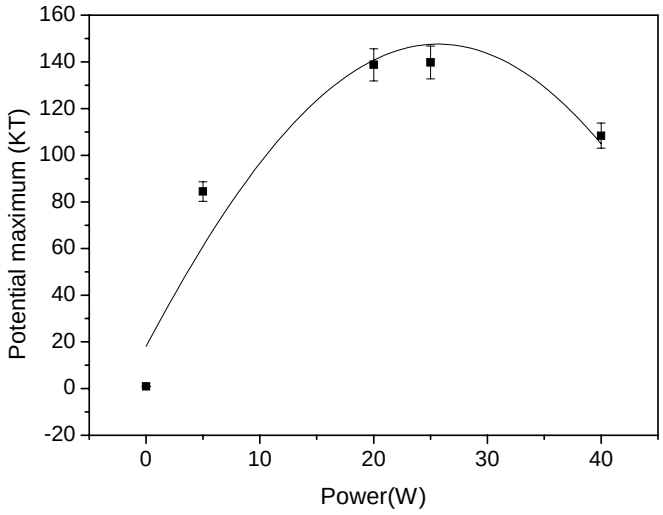

Fig.4. Potential maximum curve of TiO_2-glycol suspensions coated under different power

To character and compare the dispersion of colloidal suspensions, the potential maximum in Fig.3 are plotted in Fig.4 as a function of discharge power. Note how the experimental data in Fig.1 are explained in view of the potential maximum curve as discharge parameters increase. It is distinctly shown that there is a large difference in the simulated potential maximum between the uncoated and the coated TiO_2 nanoparticles.

The uncoated TiO_2 yields a very small potential maximum of repulsive interaction, while this repulsive interaction becomes larger for any AA-plasma-coated nanoparticles. The increasing tendency of simulated maxima in the EDLVO theory corresponds to the UAM values in the ultraviolet absorbency experiment very well. The higher the UAM, the larger the potential maximum.

Although the simulated curves in the Fig.4 does not match well with the surface energy data in Tab.1, the potential maxima in the EDLVO theory verify the experimental results of ultraviolet dispersion in Fig.1 (B) quite well by using the surface energy of nanopraticles as a main entrance. It is therefore demonstrated that such an increase in the potential maximum between nanoparticles, which is caused by the surface energy tailoring of nanoparticles through plasma polymer coating, is the reason of the great dispersion improvement of nanoparticles suspensions. It is also indicates that the surface energy of TiO_2 nanoparticles governs the overall dispersion process of nanoparticles in organic solution.

4.Conclusions

In this study, the dispersion behaviors of AA-plasma-polymer coated TiO_2 nanoparticles in glycol solution is evaluated through the ultraviolet absorbency measurements. From the measured absorbency data, it is clearly seen that the dispersion of TiO_2-glycol suspensions is effectively improved after plasma polymer coating. The optimum dispersion of TiO_2-glycol suspensions takes place at the discharge power of 25W. It is therefore concluded that pulsed RF plasma polymerization is a useful surface coating way to make well-dispersed nanoparticles in the background medium through controlling discharge parameters.

The EDLVO theory is used to simulate the dispersion of nanoparticles in glycol solution through the calculation of V^{EL}, V^{LW} and V^{AB} potential energy, which are the function of the measured surface energy of TiO_2 nanoparticles and glycol solution. It is displayed that the potential maxima in the simulated EDLVO curves correspond with the experimental phenomena very well. It is also indicated that the dispersion results of nanoparticles in organic solution are explained by the classical EDLVO theory after estimation the surface energy of TiO_2 nanoparticles. This simulation method is applicable to estimate the dispersion behaviors of other nanoparticles systems.

Acknowledgements

The author would like to acknowledge the support from the “Dawn” program of Shanghai Education Commission-01SG31, the Foundation of Shanghai Science and Technology Commission-015207004.

References

[1] C.Saujanya, Y.Imai, H.Tateyama - Polym.Bull. **49**, 69(2002).

[2] T.Corrales, C.Peinado, N.S.Allen, M.Edge, G.Sandoval, F.Gatalina - Photoch.Photobio.A. **156,**151(2003).

[3] M.Frounchi, R.P.Burford, R.P.Chaplin - Polym.Polym.Compos. **2,**77(1994).

[4] J.Zhang, A.W.Charles- Polym.Degrad.Stabil. **80,** 163(2003).

[5] M.Zhu, Q.Xing, H.He, Y. Zhang, Y.Chen, P. Pötschke, H. A. dler-Mcromol.Symp. **210**,251 (2004).

[6] J.Zhang, F.Zhu, C.Shi, L.Sun, Y.Wang, Z.Chen, J.Ping, Q.Yang, Y.Guo, R.Zhou, H.Xie, W.J.Van Ooij, J.Liang, D.Shi - The 16th International Symposium on Plasma Chemistry. Taormina, Italy, (2003).

[7] E.W.Washburn - Phys.Rev. **273,**17(1921).

[8] P.K.Sharma, K.Hanumantha Rao - Adv. Colloid. Interfac. **98,**341(2002).

[9]J.Gregory, In The Scientific Basis of Flocculation, (K.J.Ives Ed.), Sijthoff and Noordhoff, Nehterlands, (1978).

[10] R.C.Plaza, A.Quirantes, A.V.Delgado - J.Colloid.Interf.Sci. **252**,102(2002).

[11] C.J. van Oss- J.Mol.Recognit. **16,**177(2003).

PLASMA CHEMICAL ACTIVATION OF COAL GASIFICATION AND COMBUSTION

A.S.Askarova[1], E.I. Karpenko[2], V.E. Messerle[3] and A.B. Ustimenko[3]*
[1] *Department of Physics, al-Farabi Kazakh National University, Kazakhstan;*
[2] *Branch Centre of Plasma-Power Technologies of Russian J.S.Co. "United Power System of Russia", Russia;*
[3] *The Combustion Problems Institute, Kazakhstan; * ust@ntsc.kz*

Abstract
Plasma activation promotes more effective and environmental friendly low-rank coal incineration. The work presents new plasma-fuel systems improving the efficiency of coal combustion, numerical modelling results of plasma ignition, gasification and thermochemical preparation of a pulverized coal for incineration at power boilers. Comprehensive image of plasma activated coal combustion processes in a combustion chamber of pulverised coal fired boiler was obtained.

Introduction
Coal is one of the main energy resources of the 21 century. To improve efficiency of coal gasification and incineration new plasma-energy technologies are developing. The main element of these technologies realization is plasma-fuel systems (PFS). Plasma chemical activation using PFS promotes more effective and environmental friendly low-rank coals incineration and gasification increasing reactivity of solid fuels. PFS have been tested for boilers starting up by plasma ignition of pulverized coal and flame stabilization in different countries at 26 power boilers steam-productivity 75 to 670 t/h equipped with different type of pulverized coal burners (direct flow, muffle and swirl burners) [1]. At PFS testing power coals of all ranks (brown, stone, anthracite and their mixtures) were incinerated. Volatile content of them was from 4 to 50%, ash varied from 15 to 48% and heat of combustion was from 1600 to 6000 kcal/kg.

For wide dissemination of the plasma technology there is necessity to show their advantages before conventional technologies of coal combustion. Experimental investigation on full-scale boilers is expensive and laborious and some times practically impossible. In this connection numerical experiment with full-scale boiler is the most realized method. Numerical investigation of plasma ignition, gasification and thermochemical preparation of a pulverized coal for incineration at a power boiler was fulfilled. Three reliable codes were used for the research [2]. Thermodynamic code TERRA allows calculating products species and thermal physics coefficients of plasma activated pulverized coal depended on temperature, pressure and plasma source power. 1D kinetic code PLASMA-COAL with an emphasis on complex chemistry calculates concentrations of species (CO, CO_2, H_2, CH_4, C_6H_6, N_2, H_2O), temperatures and velocities of treated coal-air mixture along the chamber with plasmatron. It gives initial data for 3D-modeling of power boiler furnace by FLOREAN code. The computer simulation experiments were conducted for low-rank bituminous coal with ash content 44% incinerated at the boiler of steam productivity 475 ton per hour. Twelve swirl burners are mounted on the furnace of the boiler; in accordance with our presumption all of them are equipped with plasmatrons.

1. Realization of the Plasma-Fuel Systems at Coal-Fired Thermal Power Plants
Plasmatron (Fig.1) is a main element of the PFS. Plasma forming gas is air blown through the electrodes. Plasmatron power is varied from 100 to 350 kW and geometrical sizes are as follows: the height is 0.4-0.5 m, diameter is 0.2-0.25 m and the weight is 25-30 kg. Mass averaged temperature of the plasma-air flame on plasmatron outlet is varied from 5000 to 6000 K. The technology encloses in air-fuel mixture plasma heating up to the temperature of coal volatile release and char carbon partial gasification. Thus no matter whether the initial coal is high or low rank from air-coal mixture highly reactive two-component fuel is obtained. When mixed with secondary air at a furnace it can be ignited and burn stably without using of additional fuels (fuel oil or natural gas) traditionally applied for starting up the boilers and low-rank power coals flame stabilization.

Fig.2 illustrates a diagram of arrangement of BKZ-420 boiler burners with PFS at Ulan-Bator TPP-4. 12 burners are placed in three layers in the corners of the boiler. Two PFS were mounted on the low layer opposite each other. In 2-3 seconds from start of PFS the temperature of both pulverised coal flames achieved 1100 to 1150 ^{O}C. In an hour the flames temperature which were 7 to 8 meters in length was 1260-1290 ^{O}C. In

accordance with operating instruction duration of the boiler starting up was 4 hours. All eight boilers of the power plant were equipped with PFS for fuel oil free boiler starting up.

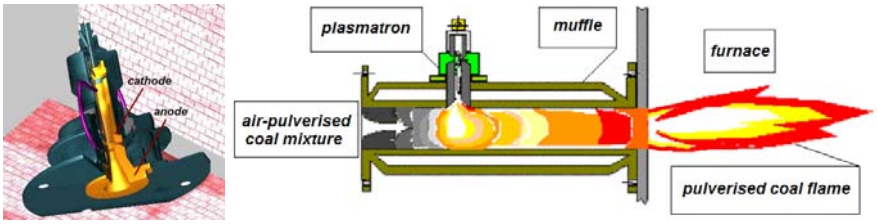

Figure 1. Plasmatron and Scheme of its Mounting onto Direct Flow Pulverized Coal Burner.

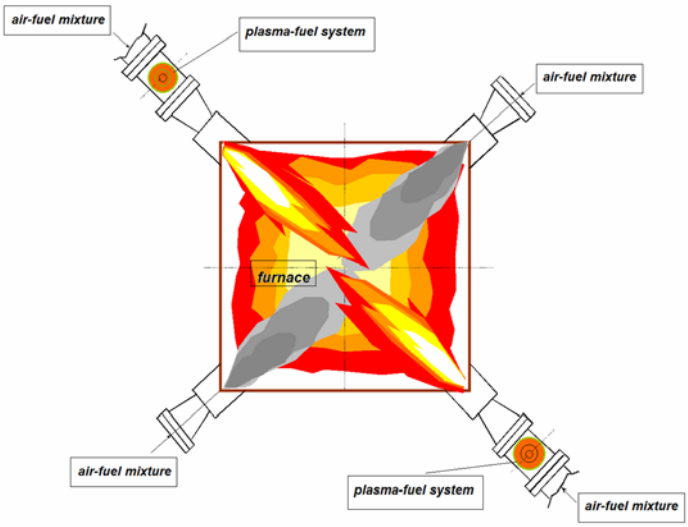

Figure 2. Diagram of Mounting Equipped with Plasma-Fuel Systems for Pulverised Coal Ignition Burners onto the Boiler of 420 t/h Steam Productivity at Ulan-Bator Thermal Power Plant - 4 (Mongolia).

Fig.3 (*a*) presents results of experiments on NO_X reduction and decrease of unburned carbon at plasma ignition of coals on the outlet of a furnace [1]. When a plasmatron operates (in a regime of plasma stabilization of a flame), NO_X concentration is reduced twice, amount of unburned carbon is reduced 4 times. NO_X is reduced owing to two-stage pulverised coal combustion. The first one is PFS where ignition and partial gasification of coal in primary air is realised.

1 – Northern Korea; 2, 12 – Ukraine; 3 – China; 4, 5, 8, 10, 11, 15 – Russia; 6 – Kazakhstan; 7 – USA; 13 – Mongolia; 14 – Kirghizia; 15 – Estonia, 16 – Slovakia.
P – plasmatron electric power; Q – heat of coal combustion; G – coal consumption through a plasma-fuel system.

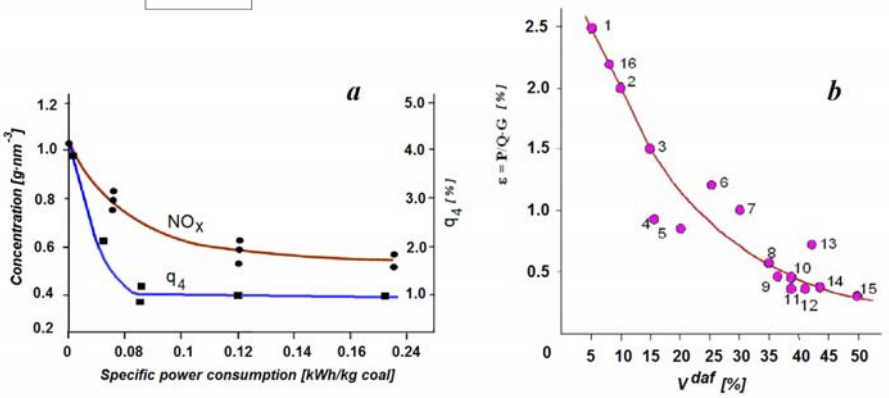

Figure 3. Specific Power Consumption Influence onto NO_X and Unburned Carbon (q_4) Reduction at Plasma Activation of a Pulverised Coal Flame (*a*) and Relative Power Consumption of a Plasmatron versus Coal Volatiles Content for Different Thermal Power Plants (*b*).

The second stage is a furnace of a boiler where combustion of the products after the first stage in the secondary air is taken place. Fuel nitrogen is released with coal volatile inside PFS. It forms molecular nitrogen due to deficit of oxygen in air-fuel mixture treated in PFS. In the second stage mainly thermal NO_X are formed. As known [3] fuel nitrogen is a main source of nitrogen oxide emission from furnace. But thermal NO_X can reach 10-15% of all NO_X emission in a furnace at temperature more than 1700 ^{O}C. As regards unburned carbon (q_4), its decrease can be explained by the fuel reaction ability increase. It happens due to formation of two-component high-reactive fuel from pulverised coal and heat explosion of coal particles at their interaction with arc plasma. Coal particles of 50-100 μm initial size in PFS undergo heat shock. As a result they are crushed into fragments. Each fragment is of a size of 5-10 μm. This leads to intensive devolatilization (CO, CO_2, H_2, N_2, CH_4, C_6H_6 and

others) and 3-4 times accelerates the process fuel combustible matter oxidation. An experimental dependence of specific electric power consumptions on a plasmatron versus coal volatiles content (Fig.3 (*b*)) was gotten during PFS tests at different thermal power plants. We can see the specific power consumption for PFS decrease with coal volatile content increase, i.e. when coal reactivity rises. Mark, power consumption for plasmatron is within 2.5 % from heat capacity of the pulverised coal burner, even for the anthracite coal with minimal reactivity. For example own needs of electric power for a boiler are 8-10 %.

2. Numerical Experiment for PFS and a Power Boiler Furnace

TERRA code [4] was used for thermodynamic modelling. It was created for high temperature processes computation. The program is based on the principle of entropy maximum for isolated thermodynamic systems in equilibrium. It has its own database of thermo chemical properties for more than 3500 chemical agents over a temperature interval from 300 to 6000K.

Computation of thermochemical preparation of the Ekibastuz bituminous coal of Kazakhstan with ash content 44%, heat of combustion 16750 kJ/kg, moisture content 7% and volatile matter 24% was fulfilled. The calculations were performed over a range of temperatures from 600 to 4000K and pressure 0.1 MPa. Thermochemical preparation of coal-air mixture for incineration is realised in the space of PFS, at dust concentration in air-coal mixture about 0.4 kg of coal per kg of air. It corresponds to 0.44 of air theoretically necessary for complete combustion of the coal. Calculations showed that big part of gaseous phase is synthesis gas. At 1200K CO concentration is 28.5 % and H_2 concentration is 11 %. Concentrations of oxidants CO_2 and H_2O are less than 6 % all over the temperature range. Nitrogen-containing compounds are basically molecular nitrogen. Concentration of it is 71 % at the temperature 600 K and decreases linearly to 44.6 % by the temperature 4000 K. NO_X concentration is less than 0.006 % (60 ppm) at the temperature below 2800K and increases to 0.8% (8000 ppm) by the temperature 4000 K. There are no sulphur oxides and fuel sulphur is represented as oxygen-free species such as H_2S, SH, SiS and S. At the temperatures more than 2000K species of coal mineral mass appeared in the gaseous phase. They are silicon monoxide (SiO), aluminium monoxide (AlO), aluminium (Al) etc.

For modelling thermochemical preparation of coal for combustion by “Plasma-coal” code described below the main thermo-physical constants for the gas phase were determined and polynomial approximated.

The calculations of the coal thermo chemical plasma preparation processes at the PFS are performed with the help of the code PLASMA-COAL [5]. The code accounts two-phase (coal particles and gas-oxidiser), chemically reacting flow, with an internal heat source (electric arc, plasma flame or chemical reactions) [5-7]. Detailed kinetics of chemical reactions is used. Its general scheme, along with the reactions of devolatilization and char carbon gasification, takes into account the reactions of their products further transformations. The temperature dependence of rate constants is governed by the Arrhenius equation. The list of the chemical reactions used in the model consists of 116 reactions. The starting chemical stage of coal conversion in the PFS is volatile matter evolution (CO, CO_2, CH_4, H_2, H_2O, C_6H_6, C_5H_5N, C_4H_5N, CH_3SH, C_4H_4S). Then there are two more stages. They are char carbon gasification including fuel nitrogen oxidation (seven reactions with H_2O, CO_2, CO, O_2, NO, H_2S) and conversation of evolved volatile products in the gas phase. For NO formation a model of fuel NO, thermal NO and prompt NO is considered. The model comprises 36 chemical reactions [3]. Among them there are reactions of C_5H_5N and C_4H_5N emission from coal, char-N oxidation, the following transformation of them through HCN and NH_3 to NO. Experimental validation of the one dimensional model was performed for different coal–oxygen rates, power of plasma source and processes (steam gasification, combustion and air gasification) and showed satisfied results [2, 5].

Calculations were performed for the cylindrical direct-flow burner equipped with plasmatron of 100 kW power. The diameter of the burner is 0.73 m, wall temperature is accepted as 700 K. Mean diameter of coal particles is 60 μm. Temperature of the air-coal mixture on the inlet of the burner is 423 K. Coal consumption through the burner was 7.3 t/h. This PFS efficiency was taken as 90%.

The results of the numerical simulations are presented in Table 1 for the PFS outlet. These data were taken as initial parameters for 3D simulation of the furnace equipped with PFS.

Table 1. 1D calculations of the coal plasma preparation for combustion results

CO	**H_2**	**CH_4**	**CO_2**	**H_2O**	**N_2**	**O_2**	**NO** *ppm*	**X_C** *%*	**V_g** *m/s*	**T_g** *K*	**t_g** *s*
Volume %											
11.04	2.17	0.22	13.53	1.93	70.55	0.13	3.67	67.6	42.1	1076	0.016

For 3D-modeling of power boiler of steam productivity 475 ton per hour FLOREAN code [8] was used. This code is based on the solution of the conservative equations of the flue gas mixture by finite volume method. It includes a submodel of momentum and energy balances, SIMPLE-method for pressure corrections, k-ε turbulence model, six-flow model for radiation heat transfer calculations and balance equation for the components of substance. This computer code allows to extract the velocity components {u,v,w}, the temperature T, the pressure P, the concentration of combustion products and other characteristics of the process. Two-fluid model is considered. For description of chemistry simplified models were used. They account only chemical reactions of the main components and integral reactions of fuel components oxidizing up to stable end-products of the reactions. At that intermediate reactions are not considered. For NOx formation global mechanism is used [9]. The code FLOREAN has been validated in details for a lot of experiments in laboratory and industrial furnaces [2, 8].

The computer simulation experiments were conducted for the boiler with steam productivity 475 ton per hour. The boiler is installed on Ermakovsk Thermal Power Plant in Kazakhstan. The furnace size is as follows: 30 m height, 10 m in width and 7 m depth. Twelve swirl burners are mounted on the furnace of the boiler. They are placed in two layers by six ones in every layer on the opposed walls. In accordance with our presumption six of the burners are equipped with plasmatrons. They are placed in the lower layer. The furnace grid of 25x47x58 size, this comprises 68150 control volumes, was used for numerical simulation. The numerical results for combustion of the pulverised coal in the furnace are presented in the following figures. All the results are presented for plasma activated coal combustion in comparison with conventional regime of coal incineration.

Fig. 4 shows temperatures and NO concentrations along the furnace with account of plasmatrons and without it. One can see in general the temperatures along the furnace for plasma-activated coal combustion are less than ones for conventional incineration of coal. But there is a zone where the temperature of coal combustion with plasma activation is more than one without it. This zone is lower part of the furnace. It extends till the level of the upper tier of the burners. It can be explained by influence of plasma-fuel systems. They cause earlier heating and ignition of air mixture and subsequent front of combustion displacement to the PFS orifice. NO concentration along the furnace relatively less for plasma activated combustion for mean, maximal and minimal values. Fig. 5 illustrates the oxygen and carbon dioxide concentration distribution along the furnace height. Mean level of oxygen (curves 3 and 4) along the full height of the furnace is lower for the plasma activated coal combustion, but as consequence mean values of carbon dioxide is higher. These data confirm more complete coal incineration and unburned carbon decrease when plasma-fuel systems assist combustion process.

Fig. 6 visually demonstrates the difference between traditional and plasma activated coal incineration in the furnace by the example of NO formation. PFS influence is developed in forming of NO_X in wall area on the outlet of plasma-fuel systems. On the contrary at conventional coal combustion NO_X is formed in the centre area of the furnace on the level of the burners. Said above is confirmed by NO curves behaviour in Fig. 4. For instance curve 1 has two and curve 2 has one pronounced peaks on the level of the burners. Plasma-fuel systems influence on NO formation can be seen along the full height of the furnace. Interesting, plasma-fuel systems decrease NO concentration even in the lower part of the furnace (below the level of PFS allocation). That is explained by phenomena of suppression of fuel NO_X formation inside the PFS. Fuel nitrogen is released with coal volatile inside PFS. It forms molecular nitrogen due to deficit of oxygen in air-fuel mixture treated by plasma that is confirmed by low NO concentration (3.67 ppm) on the outlet of plasma-fuel system (see Table 1), but as known [3] fuel nitrogen is a main source of NOx at coal combustion.

Table 2 gives a comparison of the two calculated variants (conventional and plasma activated coal combustion). Comparison of the numerical and experimental data for traditional coal incineration [10] showed satisfactory

agreement. The difference in experimental and calculated parameters is within 17%. Influence of plasma-fuel systems onto coal combustion in the furnace is developed in decrease of mean level of temperature (9%), NO_X (11.5%) and O_2 (14%) concentration and increase of CO_2 (7%) concentration. These values show an improvement of the main characteristics of the process at plasma supported coal combustion.

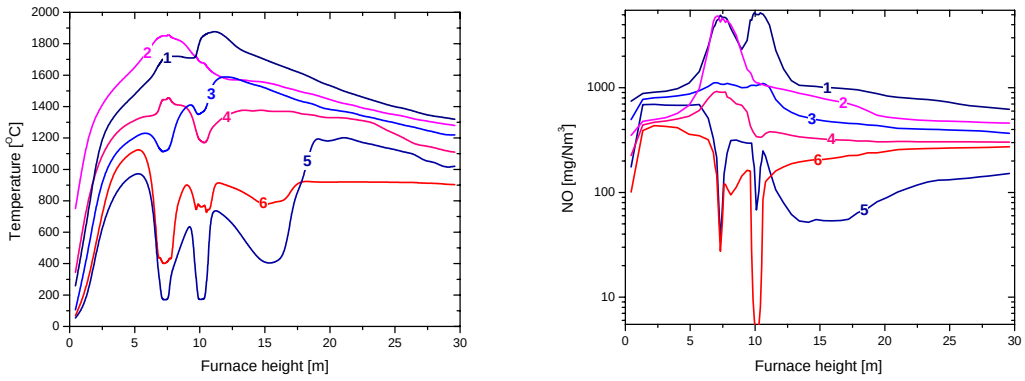

Figure 4. Temperature (on the Left) and NO Concentration (on the Right) Variation along the Furnace.
1, 3, 5 – traditional regime of coal incineration, maximal, mean and minimal values correspondingly; 2, 4, 6 – regime of coal incineration with six plasma-fuel systems, maximal, mean and minimal values correspondingly.

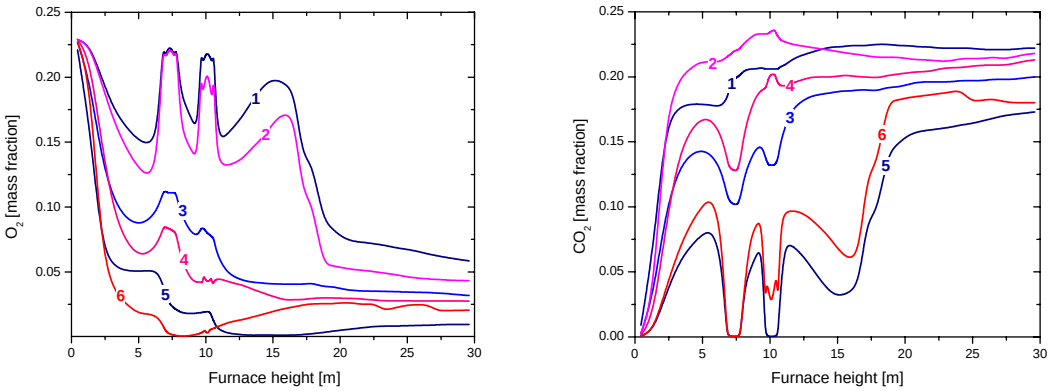

Figure 5. Oxygen (on the Left) and Carbon Dioxide Concentration (on the Right) Variation along the Furnace.
1, 2, 3, 4, 5, 6 – See Fig.4.

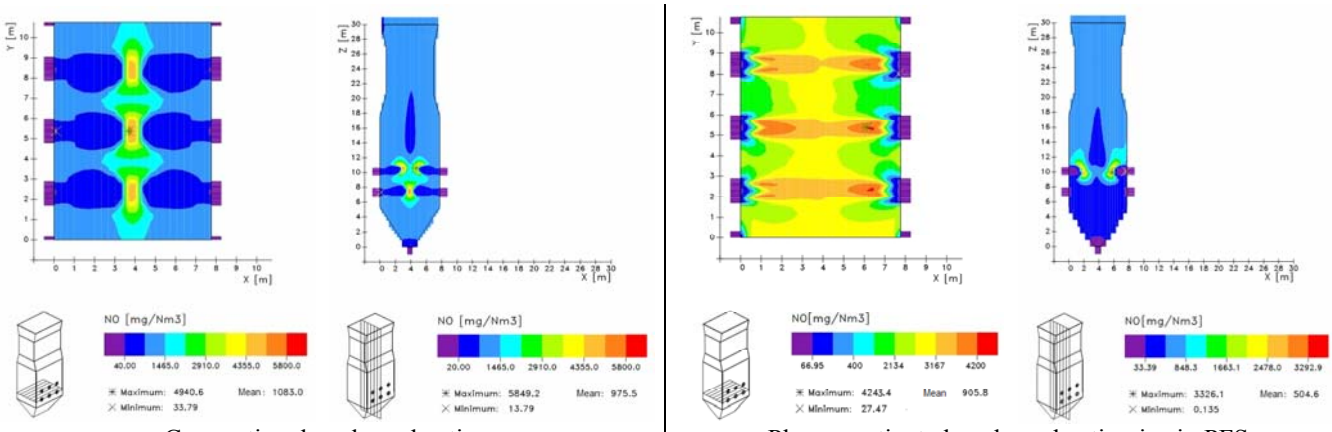

Conventional coal combustion | Plasma-activated coal combustion in six PFS

Figure 6. Nitrogen Oxide Distribution in Cross Section of the Furnace on the Level of PFS and along the Furnace Height.

Table 2. Comparison of flue gas characteristics on the outlet of the furnace.

	Conventional incineration (experiment)	*Plasma activated incineration*
T, ^{O}C	1220 (1180)	1110
NO, ppm	180	137
CO_2, kg/kg	0.185 (0.17)	0.188
O_2, kg/kg	$3.18\ 10^{-2}$ ($3.5\ 10^{-2}$)	$1.74\ 10^{-2}$

Conclusion

Thermodynamic and two fluid dynamics kinetic models were used for the research. Computer simulation of pulverised coal combustion with use of plasma-fuel systems was fulfilled from the burner's inlet to the furnace outlet. Analysis of the numerical experiment and experience of PFS industrial use showed ecological efficiency of the plasma technology. The most familiar advantages of PFS include decrease in NO_X emission through the suppression of their formation in PFS and increase in efficiency of solid fuel incineration by reducing unburned carbon. Thus when 1 kWh of electric power or 1Gcal of heat power is generated with the help of PFS a lesser quantity of fuel is burnt and a lesser quantity of CO_2 is produced. In other words, specific emissions of greenhouse gases on generating the unit of electric or heat power decrease by 2%.

Acknowledgments

The authors would like to gratefully acknowledge the European Commission for this work funding through the Copernicus Program (Contracts No IC15-CT98-0516 and No ICA2-CT-2001-10006) and ISTC (Project K-746) and personally Professor F. Lockwood for his support and coordination of these collaborative research projects.

References

[1]. E.I.Karpenko, V.E.Messerle, A.B.Ustimenko. Plasma-Fuel Systems for Enhancement Coal Gasification and Combustion // Presentations Abstracts of 30th International Symposium on Combustion //University of Illinois at Chicago, July 25-30, – 1I5-19; – P. 110, (2004).

[2]. A.S.Askarova, E.I.Karpenko, V.E.Messerle, A.B.Ustimenko. Modeling of Coal Combustion Activated by Plasma Flame // Presentations Abstracts of 30th International Symposium on Combustion //University of Illinois at Chicago, July 25-30, – 5F4-03; – P. 423, (2004).

[3]. D.H. Tike, S.M. Slater, A.F. Sarofim, J.C. Williams. Nitrogen in Coal as a Sourse of Nitrogen Oxide Emission from Furnace // Fuel, Vol.53, P. 120-125, (1974).

[4]. E.I.Karpenko, V.E.Messerle, B.G.Trusov, S.S.Tutebaev, A.B.Ustimenko. Modelling of Plasmochemical Processing of Solid Fuels // Combustion and Plasmochemistry, V.1, N4, P. 291-310 (2003).

[5]. E.I. Karpenko, V.E. Messerle, A.B. Ustimenko. Mathematical Model of the Processes of Ignition, Combustion, and Gasification of the Pulverized Coal Fuel in the Electric Arc Devices. Thermophysics and Aeromechanics, Vol.2, N 2, pp 151-165, (1995).

[6]. A.Goal, D.Gidaspow. Modelling of Entrained Flow in Coal Hydrolysis Reactors. 1. Mathematical Formulation and Experimental Verification. 2. Reactor design. // Ind. and Eng. Chem. Process Des. and Develop., Vol.21, P. 611-632, (1982).

[7]. R.A.Kalinenko, A.P.Kuznetsov, A.A.Levitsky, V.E.Messerle, Yu.A.Mirokhin, L.S.Polak, Z.B.Sakipov, A.B.Ustimenko. Pulverized Coal Plasma Gasification // Plasma Chemistry & Plasma Processing, Vol. 13, N 1, P. 141-167, (1993).

[8]. J. Müller. Dreidimensionale Simulation der NO-Kinetik und SO2-Einbindung bei der Kohleverbrennung in Zirkulierenden Atmosphärischen Wirbelschichtfeuerungen. Fortschr.-Ber. VDI Reihe 6 Nr.323. Düsseldorf: VDI-Verlag, 200s, (1995).

[9]. J.W. Mitchell, J.M. Tarbell. A kinetic model of nitric oxide formation during pulverized coal combustion. AIChE Journal. Vol.28 p 302, (1982).

[10]. A.S. Askarova, V.E. Messerle, I.V. Loktionova, A.B. Ustimenko. 3D Modelling of the Two-Stage Combustion of Ekibastuz Coal in the Furnace Chamber of a PK-39 boiler at the Ermakovo District Power Station // Thermal Engineering. Vol.50, N 8, pp 633-638, (2003).

Droplet Impact during the Plasma Spray Coating Process- Effect of Surface Roughness on Splat Shapes

M. Raessi, J. Mostaghimi and M. Bussmann

Department of Mechanical and Industrial Engineering, University of Toronto, Canada

Abstract
We used a three-dimensional model of droplet impact and solidification to simulate the effect of surface roughness on the impact dynamics and the splat shape of an alumina droplet impinging onto a substrate. The substrate surface was patterned by a regular array of cubes spaced at an interval twice their size. Three different cube sizes were considered, and the results were compared to the case of droplet impact onto a smooth substrate. To understand the effect of solidification on the droplet impact dynamics and splat morphology, the simulations were run with and without considering solidification. Comparing the results, we have concluded that solidification plays a major role in determining splat shape on a rough surface. We also present results of the distribution of voids between the splat and the substrate.

Keywords: Surface roughness, droplet impact, numerical model, solidification

1. Introduction

Thermal sprayed coatings are applied to protect substrates against wear, corrosion, and thermal shock. In thermal spray processes a hot gaseous jet is used to melt and accelerate the powder of a metallic or ceramic coating material. The hot jet draws energy from either a plasma or a combustion source. During these processes, a spray of molten (or partially-molten) droplets, or particles is directed at a substrate. As the droplets impact the substrate, they spread and solidify, each forming a so-called *splat*. A coating forms as a result of the accumulation of many such splats.

Among many experimental and numerical studies that have been done on droplet impact and solidification, only a few have considered the effect of surface roughness. For instance, Ahmed and Rangel [1] numerically studied the impingement and solidification of an aluminum droplet on uneven substrates, using a two-dimensional axi-symmetric model. Their results show that droplet impact onto an uneven substrate is almost always accompanied by splashing. However, the degree of splashing decreases with the increase in surface roughness height. Fukanuma [2] presented a formula which describes the flattening process of a droplet onto a rough surface, and concluded that the flattening ratio and the flattening time decreases with increasing roughness. Liu et al. [3] numerically studied the impact of a droplet onto substrates with wavy surfaces; however, their two-dimensional axi-symmetric model did not include solidification. They found that for wavelengths of the surface larger than the droplet diameter, droplet spreading ended with breakup.

This paper then, presents the results of three-dimensional numerical simulations of droplet impact and solidification onto substrates with rough surfaces. The effect of surface roughness on splat morphology and the bonding between the splat and the substrate are studied.

2. Numerical Method

The three-dimensional numerical model of droplet impact and solidification which is used in this study was developed by Bussmann et al. [4] and Pasandideh-Fard et al. [5]. Detailed discussion of the model is in [4, 5] and is not repeated here.

Equations of conservation of mass and momentum governing the liquid phase in the presence of a solid phase are

$$\vec{\nabla} \cdot (\Theta \vec{V}) = 0$$

$$\frac{\partial(\Theta \vec{V})}{\partial t} + (\Theta \vec{V} \cdot \vec{\nabla})\vec{V} = \frac{-\Theta}{\rho}\vec{\nabla} p + \Theta \upsilon \nabla^2 \vec{V} + \frac{\Theta}{\rho}\overrightarrow{F_b}$$

where $\vec{V}$ represents the velocity vector, p the pressure, ρ the density, υ the kinematic viscosity, and $\overrightarrow{F_b}$ any body forces acting on the fluid. In these equations, Θ denotes the liquid-solid fraction, and it is equal to one within the liquid phase and zero within the solid phase. The free surface of the liquid is defined by using the "Volume of Fluid" (VOF) method, in which a scalar function f is defined equal to one within the droplet material (liquid or solid) and equal to zero without. Since f is passively advected with the flow, it satisfies the advection equation which in the presence of the solid phase is

$$\frac{\partial f}{\partial t} + (\Theta \vec{V} \cdot \vec{\nabla}) f = 0$$

The energy equation which is solved for heat transfer and phase change is [5]

$$\rho \frac{\partial h}{\partial t} + \rho(\vec{V} \cdot \vec{\nabla})h = \vec{\nabla} \cdot (k \vec{\nabla} T)$$

where h represents the enthalpy, k the conductivity, and T the temperature. To solve the energy equation, the enthalpy transforming model [6] is used to convert the energy equation to one with a single dependent variable: the enthalpy. The main advantage of this method is that it represents the energy equation for both phases simultaneously.

These governing equations are solved using a finite volume technique on a three-dimensional Cartesian structured grid. According to the problem geometry, symmetry boundaries are utilized to reduce the problem size and therefore to save computational time. Along symmetry boundaries, fluid flow obeys free slip and no-penetration conditions, and an adiabatic thermal boundary condition is applied. Numerical computations were performed on an AMD Athlon 1.4 GHz PC; the average CPU time was 36 hours.

3. Results and Discussion

Fig. 1 shows simulated images of 40 μm diameter alumina droplets, initially at 2055ºC, impinging with an impact velocity of 65 m/s onto smooth and rough alumina substrates. Each column shows a droplet during successive stages of impact. For the rough substrates, the surface is patterned by cubes which are regularly spaced at an interval twice their size. Three different cube sizes, of 1, 2, and 3 μm, were considered. In Fig. 1(a) to (d), the fluid flow, heat transfer and phase change are modeled. The splat shape on the smooth substrate (Fig. 1(a)) differs little from the shape on the 1 μm rough substrate (Fig. 1(b)). But as the roughness size increases further to 2 and 3 μm, the splat shape changes substantially. In particular, on the 3 μm rough substrate, the droplet is blocked at t = 0.8 μs from spreading along the 45º diagonal and effectively the liquid flow is channeled in two directions. To understand the effect of solidification, Fig. 1(e) presents results of fluid flow without solidification for the case of 3 μm roughness.

In Fig. 2, a quarter of the final shape of the alumina splats is depicted for different substrate surface conditions. It clearly depicts the effect of roughness size on the splat morphology. As it is shown in Fig. 3(a), as the size of the surface roughness increases from zero (smooth) to 1 and 2 μm, the splat radius also increases. However, on the 3 μm rough substrate, the extent of spreading along the horizontal and vertical axes is approximately equal to that on the smooth substrate.

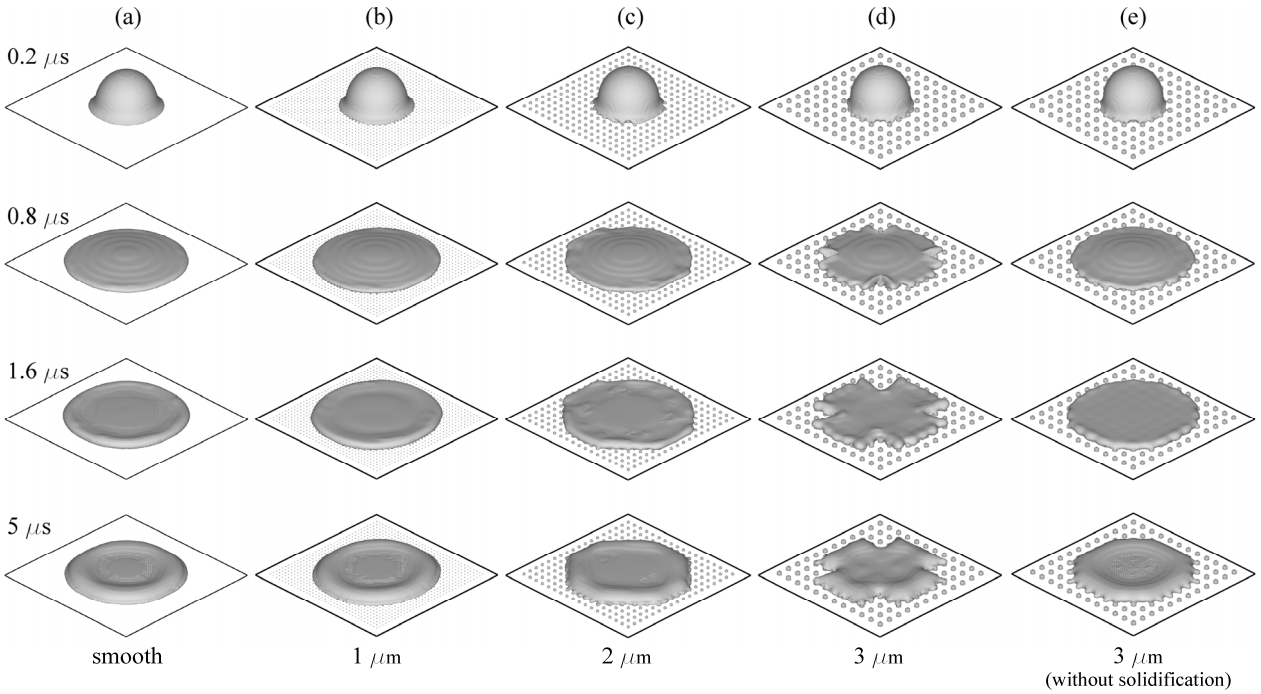

Fig. 1. Computer generated images of 40 μm diameter alumina droplets at 2055 °C impacting with a velocity of 65 m/s onto alumina substrates initially at 25 °C, characterized by different values of surface roughness.

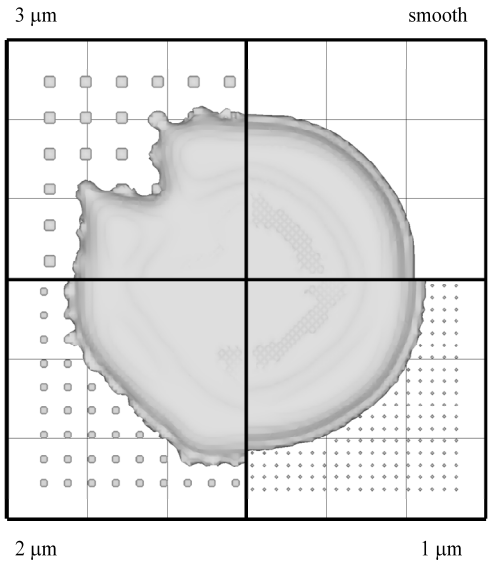

Fig. 2. Comparison of alumina splats on different surface conditions in the presence of solidification.

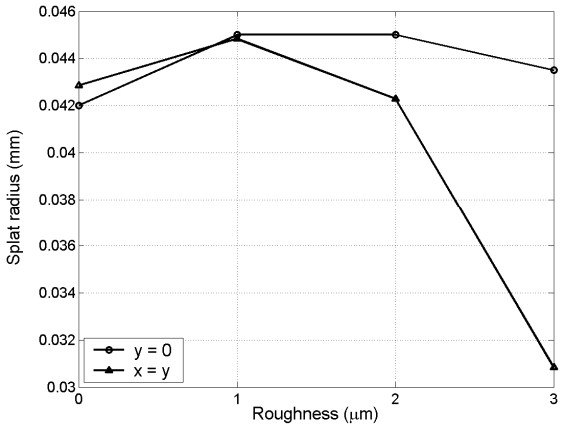

Fig. 3. Splat radius versus surface roughness.

The maximum spreading radii along y=0 and x=y axes are plotted for different surface conditions in Fig. 4. As the surface roughness changes from zero to 1 μm, maximum spreading radii along two axes increase, similar to splat radius. As the roughness size is increased to 2 μm, the radius along y=0 axis remain almost unchanged; however, the maximum spreading radius along x=y axis decreases. Further increase in roughness size to 3 μm decreases both radii along both axes.

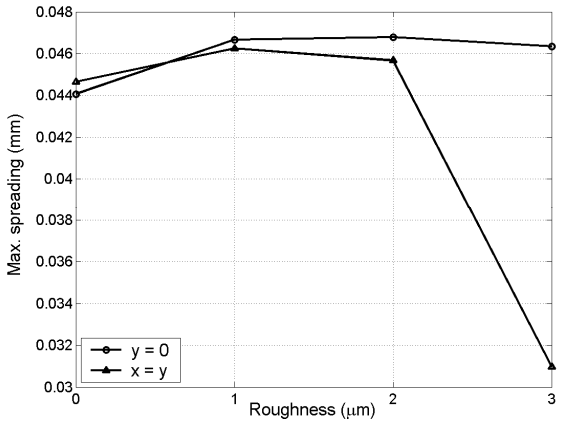

Fig. 4. Maximum spreading raidus versus surface roughness.

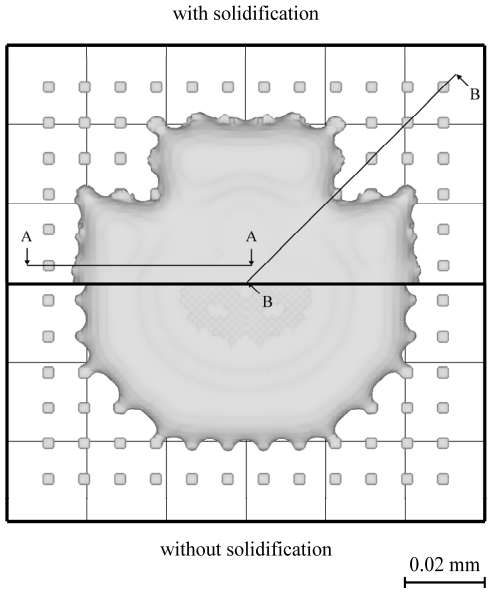

Fig. 5. Comparison of splat shape on a substrate with 3 μm roughness with and without solidification.

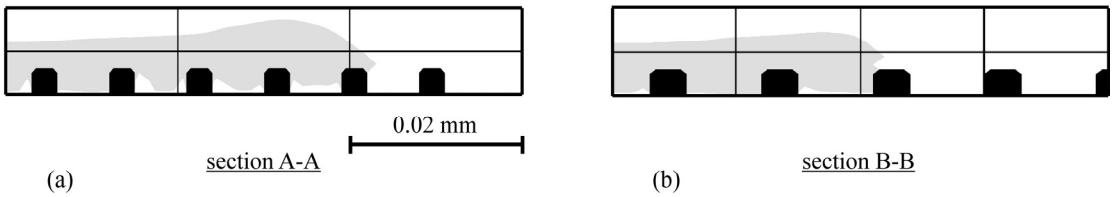

Fig. 3 Cross section of an alumina splat on a substrate with 3 μm roughness in the directions shown in Fig 2(b). The cubes on the substrate and the splat are shown in black and gray, respectively.

The upper half of Fig. 5 shows an alumina splat on the substrate of 3 μm roughness at t = 5 μs, for the case when solidification is modeled. For comparison, the lower half of Fig. 5 shows the droplet shape on the same substrate and at the same time, but without solidification. Comparing the two cases, the effect of solidification on the splat shape is very well seen. It must be mentioned that without solidification, the droplet recoils further until it reaches to its equilibrium configuration which is not shown here.

Finally, Fig. 6 shows the cross sections of the alumina splat on the 3 μm rough substrate, along directions A-A (horizontal) and B-B (45º diagonal) shown in Fig 5. The cubes on the substrate and the splat are shown in black and gray, respectively. The splat appears to bond more completely with the substrate along the diagonals, as the voids beneath the splat are smaller along section B-B than along section A-A. Hence, heat transfer and consequently solidification rate are larger along the diagonals than along section A-A. Therefore, the droplet spreads less along B-B section due to faster solidificiation in this direction.

4. Conclusion

The effect of substrate roughness on an alumina splat shape was studied. We concluded that droplet solidification is the main mechanism responsible for changing the splat shape. An increase in roughness size up to a certain value increases the splat diameter. For the case of a splat on a substrate of 3 μm roughness, voids between the splat and the substrate are seen to be smaller along the 45 º diagonal than along the horizontal

direction. This causes faster solidification along the diagonal and stops the droplet from further spreading earlier than in other regions.

References:

[1] A.M. Ahmed and R.H. Rangel, Int. J. Heat Mass Transfer 45 (2002) 1077.
[2] H. Fukanuma, in: C.C. Berndt (Ed.), Thermal Spray: Practical Solutions for Engineering Problems, Cincinnati, U.S.A., October 7-11, 1996, 9th National Thermal Spray Conference Proceeding, Published by ASM International (1996) 647.
[3] H. Liu, E.J. Lavernia, and R.H. Rangel, Acta Metal. Mater. 43 (1995) 2053.
[4] M. Bussmann, J. Mostaghimi, and S. Chandra, Phys. Fluids 11 (1999) 1406.
[5] M. Pasandideh-Fard, S. Chandra, and J. Mostaghimi, Int. J. Heat Mass Transfer 45 (2002) 2229.
[6] Y. Cao, A. Faghri, W.S. Chang, Int. J. Heat Mass Transfer 32 (1989) 1289.

Hydrogen Creation in a Water-Plasma Non-Self Sustained Discharge.

A.S. Galov, V.A. Gostev, A.A. Fomkin.

Department of physics engineering, Petrozavodsk state university, Petrozavodsk, Russia.

Abstract.
There are results of the research on non-self-sustain discharge initiated by plasma jet from a liquid water electrode in this paper. The experimental devise consists of a two-stage plasma generator with non-self-sustain discharge. The water is supplied in the plasmatron as the working substance. The atomic and molecular hydrogen is generated in the non-self-sustain discharge.

Introduction.
The problems of natural resources exhaustion such as petroleum, natural gas, high-grade coal are the essential problems of our civilization. Prepared fuel obtaining such as obtaining hydrogen from water is issue of the day.
Plasma jet generation from water surface is sufficiently new effect, whereas the use of discharge initiation from the gas phase is prevailing. The research on the discharge generation when one of the electrodes is placed into water is very interesting for some application.
The high rating of the nonequilibrium plasma systems and high gas flow rate through the discharge determine high specific capacity of plasmachemical reactors. From this point of view the plasmachemical methods of hydrogen creation are especially interesting according to the atomic-hydrogen power engineering. From the point of effectiveness, these methods similar to the other electrical methods of hydrogen creation, but the plasmachemical methods exceed other methods in the specific capacity.
The hydrogen obtaining in non-self-sustain discharge, generated by plasma get from water surface, is the essentially new method of hydrogen producing. The hydrogen synthesis is based on the use of water dissociation in non-self-sustain discharge onto the atoms of hydrogen and oxygen with the subsequent partial ionization up to the ions of hydrogen and oxygen. The obtained hydrogen can be use as effective fuel and for other application.

The experimental device.
The experimental device consists of a two-stage plasma generator with a non-self-maintained discharge (figure 1). The photo of the non-self sustained discharge is shown on the figure 2.

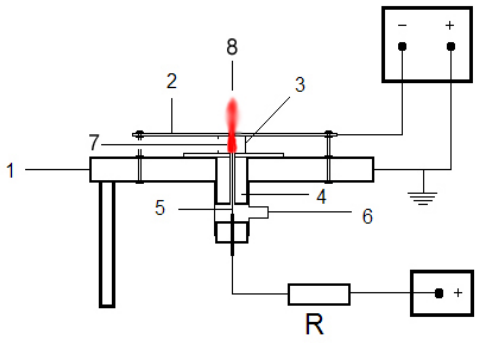

Figure 1. Scheme of a plasma generator.

Figure 2. Photo of the non-self sustained discharge.

Working substance – water – flows through the tube (6) and the ceramic tube (4). The anode – a nichrome needle (5) – is placed into water. When high voltage is put between the anode (5) and the flat ground cathode (1), the disruption of discharge gap occurs. The basic discharge gap is made with two flat electrodes (1) and (2). These electrodes are separated by the ceramic tube (3). The plasma jet (7), which is generated in the first

stage, is injected through the hole in the first electrode. The diameter of plasma jet is 2mm and the length is 30mm. Plasma (8) which permeated through the second electrode is a subject of the research.

Breakdown voltage in the first stage was 1500V. Voltage of stable jet burning was 300V in the first stage, current was 500mA. Voltage value was 600V in the second stage. Current value was 0.2A. Water flow was 0.03 milliliter per second. The temperature of plasma jet was 2000K. The first stage is a plasma source for discharge generation in the second discharge gap.

The water decomposes at the heating in the non-self-sustain discharge:
$H_2O \rightarrow OH + H \rightarrow O + H + H$
There is the ionization of atomic oxygen and atomic hydrogen in the plasma jet. There is the possibility of formation of molecular hydrogen and molecular oxygen.

Working conditions.
The working conditions of plasma jet burning depend on many factors. The output of obtained hydrogen depends on field density between flat electrodes. When the distance between electrodes was changed from 1cm to 0.5cm, the radiation power in ultraviolet area (which was conditioned by $(^2\Sigma_g \rightarrow ^1\Sigma_u)$ energy jump) increased by order. The plasma jet burning conditions are summarized in Table 1.

Table 1. Working conditions of plasma jet burning.

Working conditions.	Voltage	Current	Water flow ml/sec	Temperature of plasma jet.	Characteristics of plasma jet.
There is no voltage in the second stage	300V in the first stage	0,5A in the first stage	0.03	1000-1200C	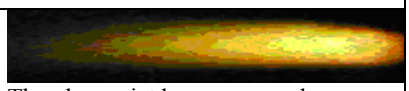 The plasma jet has orange color. There is the intensive molecular band in 590-600 nm spectral domain.
There is no voltage in the second stage	300V in the first stage	0,5A in the first stage	0.06	1500-1700C	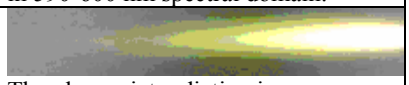 The plasma jet radiation is more intensive. The jet has green color. There is the intensive molecular band in 500-560 nm spectral domain.
There is high voltage between the flat electrodes. The distance between the electrodes is 1cm	300V in the first stage and 400V in the second stage.	0,5A in the first stage and 0,6A in the second satge.	0.03	2000C	 The plasma jet changes the color and the shape. There are intensive lines of atomic hydrogen (H_α and H_β) in the plasma jet spectrum.
There is high voltage between the flat electrodes. The distance between the electrodes is 0.5cm	300V in the first stage and 400V in the second stage.	0,5A in the first stage and 0,6A in the second satge.	0.03	1500C	 There are intensive lines of atomic hydrogen (H_α and H_β) and bands of triplet molecular hydrogen $(^2\Sigma_g \rightarrow ^1\Sigma_u)$ in the ultraviolet area in the plasma jet spectrum.

Measurements.
Energy and spectrometric characteristics of auxiliary plasma jet were measured. These characteristics showed that working substance (water steam) and active plasma particles are very effective for the formation of the non-self-sustained discharge.
The discharge radiation spectrum was registered using diffraction MUM-1 monochromator in a spectral interval 200-700 nm. The spectrum of auxiliary plasma jet was characterized by molecular bands in 500-560

nm spectral domains (N_2, O_2, NO, NO_2). The hydrogen lines were registered only on the plasmatrone output. The situation changed when we put a potential on the second electrode. The analysis of non-self-sustain discharge radiation spectrum showed that there were intensive Balmer lines of atomic hydrogen (H_α, H_β) in the non-self sustained discharge. Spectrum was also characterized by bands of triplet molecular hydrogen ($^2\Sigma_g \rightarrow {}^1\Sigma_u$) in the ultraviolet area, lines of atomic and molecular oxygen, and bands of OH group.

Energy characteristics of plasma jet.

The power of the plasma jet was measured using IKT-1M calorimeter. Mean heat power, which was generated by the plasma jet was 90W when the electric power was 150W. Efficiency factor was 60%. There is the integral distribution of the auxiliary plasma jet intensity in the figure 3 and the integral distribution of non-self-sustain discharge intensity in the figure 4.

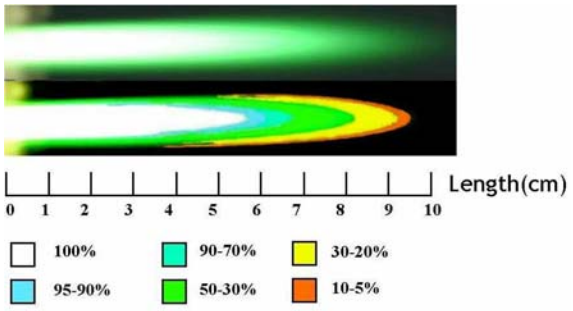

Figure 3. Distribution of the auxiliary plasma jet intensity.

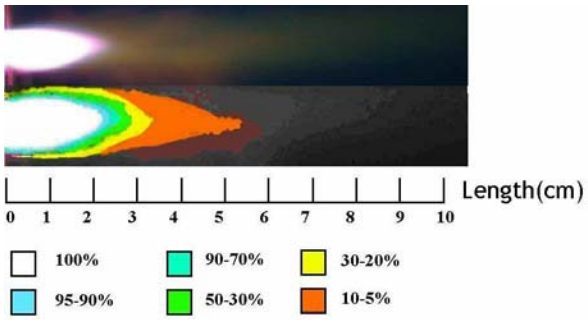

Figure 4. Distribution of the plasma jet intensity

As we can see, when we did not put a potential on the second electrode, the long plasma jet was generated. The intensity of the plasma jet zones changed fluently. When we put a potential on the second electrode, the length of plasma jet became shorter. The area of maximal intensity occupied the most part of plasma jet.

Conclusion.

The conducted research of the non-self-sustained discharge revealed some characteristics of plasmachemical processes in the jet. They account for technological applications of this plasmatron. In particular, this devise can be used as the injector of active plasma for a plasmachemical reactor, because of hydrogen creation in plasma jet. This devise also can be used for plasma spray obtaining.

Acknowledgement.

The research described in this publication was made possible in part by Award No. PZ-013-02 of the U.S. Civilian Research & Development Foundation for the Independent States of the Former Soviet Union (CRDF) and of Ministry of Education of Russian Federation.

References.

[1]. Rusanov V.D., Fridman A.A. Physics of chemical-active plasma. Moscow. (1984). [In Russian]
[2]. Gerzberg G. Electronic spectra and structure of multinuclear molecules. Moscow. (1969). [In Russian]
[3]. Son E.E., Gaisin F.M., Shakirov Y. Glow discharge with liquid electrodes. Massachusetts Institute of technology, USA, (1993).
[4]. Striganov A.R., Sventitsky N.S., The tables of spectral lines. Moscow. (1966). [In Russian]

Atmospheric pressure radio-frequency capacitive plasma jet operated with argon

J. Laimer, S. Haslinger, W. Meissl, J. Hell, H. Störi

Institut für Allgemeine Physik, Vienna University of Technology, Vienna, Austria

Abstract

We developed an atmospheric pressure RF capacitive plasma jet having planar electrodes und investigated its performance when operated with argon. A stable uniform glow-like discharge (α-mode of an RF discharge) can be sustained within a wide power range. However, a non-uniform discharge (coexisting α- and γ-mode) was observed immediately after ignition. A transition to the pure α-mode occurred at a very low RF power. Contrary, a transition from the pure α-mode to the coexisting α- and γ-mode took place at a high RF power.

Keywords: RF discharge, α-discharge, γ-discharge, atmospheric pressure, argon

1. Introduction

Today, non-equilibrium atmospheric pressure plasmas attract more and more attention. They can be realized by a variety of techniques, one of them is the atmospheric pressure plasma jet (APPJ), which was introduced a few years ago [1-4]. The APPJ operates in a capacitive mode using RF power and produces a stable glow-like discharge without dielectric material between the electrodes. Usually, it is operated with a high gas flow of pure helium or helium with addition of reactive gases in the range of a few percent. The gas flow out of the discharge has a relatively low gas kinetic temperature. Due to recombination the effluent consists only of neutral species, including metastable species and radicals (in case of reactive gas addition). Some applications in materials processing and decontamination have been already investigated [6-10]. Recently, Wang et al. claimed that they are able to operate an APPJ with argon as well [11]. However, they used a configuration with concentric electrodes.

Very recently we developed an APPJ with planar electrodes featuring a rectangular cross section of the effluent [12]. Tests with contaminated helium showed that the APPJ can be operated in a rather uniform glow-like mode within certain limits. This mode was identified as the α-mode of an RF discharge. However, at the upper limit of this mode a transition to the γ-mode occurred. This high current density mode covered the electrodes only partially. This type of transition is well known for capacitive RF discharges at moderate pressures [13], however, for APPJs the transition at the high power limit of the α-mode was often attributed to arcing.

2. Experimental details

The homemade APPJ with the lifted grounded counter electrode is shown in Fig. 1. A scheme of the discharge and the experimental setup is exhibited in Fig. 2. An RF generator with a frequency of 13.56 MHz and a manually adjustable matching network was used to supply the RF power for the APPJ. Forward as well as reflected power was measured. The discharge was produced between two planar copper electrodes; one is RF powered the other one is grounded. The reflected power was minimized by adjustment of the capacitances of the matching

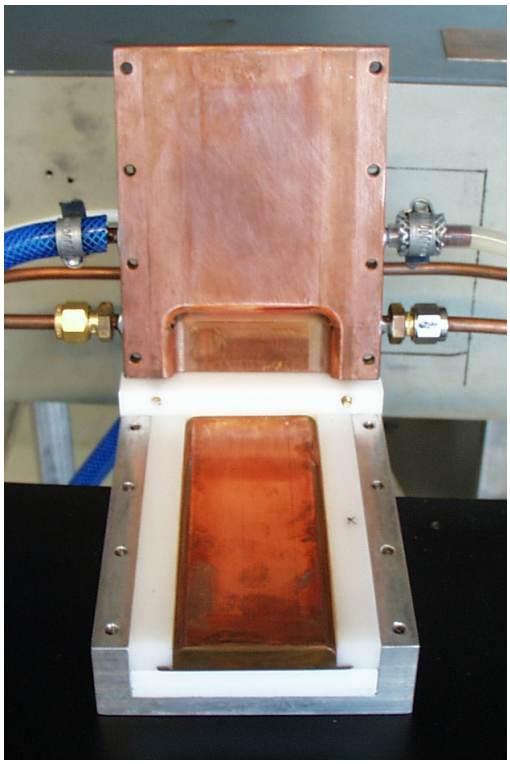

Fig. 1: Picture of the APPJ. RF electrode is in centre, grounded counter electrode is lifted.

network. The electrodes were cooled with water. The effective surface area was approximately 38 cm^2. The exit of the used APPJ has a width of approximately 50 mm and a gap spacing, which can be adjusted with PTFE spacers between 0.5 and 2.5 mm in steps of 0.5 mm. However, a gap spacing of 2.5 mm was used throughout the experiments. The APPJ was operated with argon (purity 99.999%) at a gas flow rate of 2 standard litres per minute (slm). The plasma was exhausted directly into ambient air. Ambient pressure in Vienna is in average roughly 960 hPa.

The electric properties of the APPJ were studied by measuring voltage and current simultaneously by using a high voltage probe (Tektronix P5100), a current probe (Tektronix P6021) and a digital oscilloscope (Tektronix TDS 3052B). Additionally, pictures showing the front view of the discharge were taken with a digital camera (Minolta Dimage Xt), while the APPJ was illuminated with a 500 W halogen lamp. Pictures with higher magnification were taken with the same digital camera in combination with an optical microscope (Zeiss OpMi-1) of 0.3 m focal length.

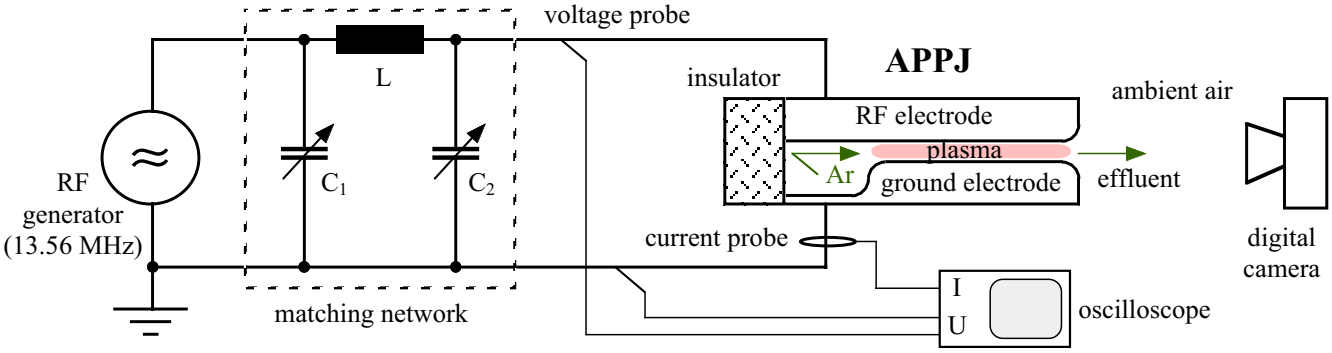

Fig. 2. Schematic illustration of the experimental setup.

3. Results and discussion

It turned out that the argon discharge is more difficult to ignite than the helium discharge. The current-voltage curves shown in Fig. 3 demonstrate the behaviour. An ignition was only accomplished by an increase of the forward power up to 200 W, whereby before ignition all power is reflected. Therefore, the “no discharge” operation mode shows a pure capacitive behaviour. The current leads the voltage by 90°. Both waveforms are purely sinusoidal. From the slope of the curve a capacitance of 57.8 pF was determined, consisting of a parallel plate capacitance of 13.5 pF and a parasitic capacitance of 44.3 pF.

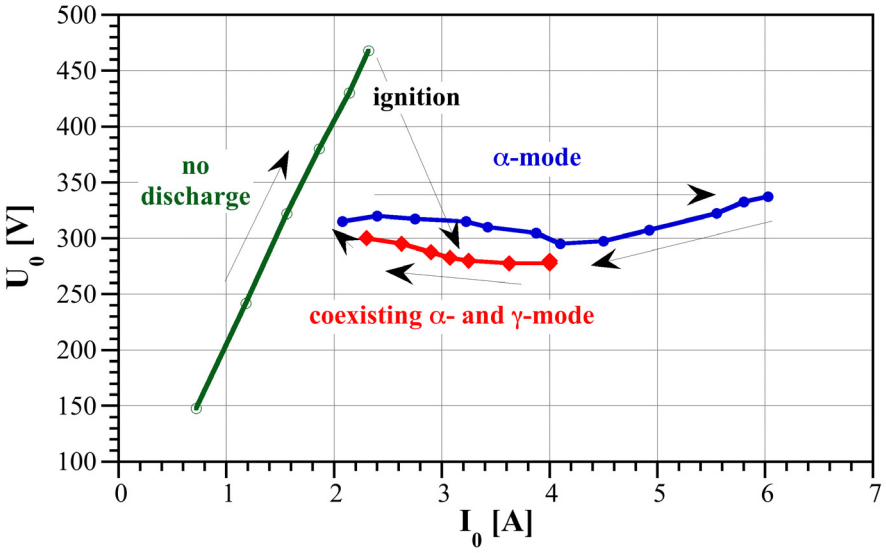

Fig. 3. Current and voltage characteristics of the APPJ. Peak-amplitudes are given. Different types of operating modes as well as transitions between them are indicated. Gap spacing is 2.5 mm.

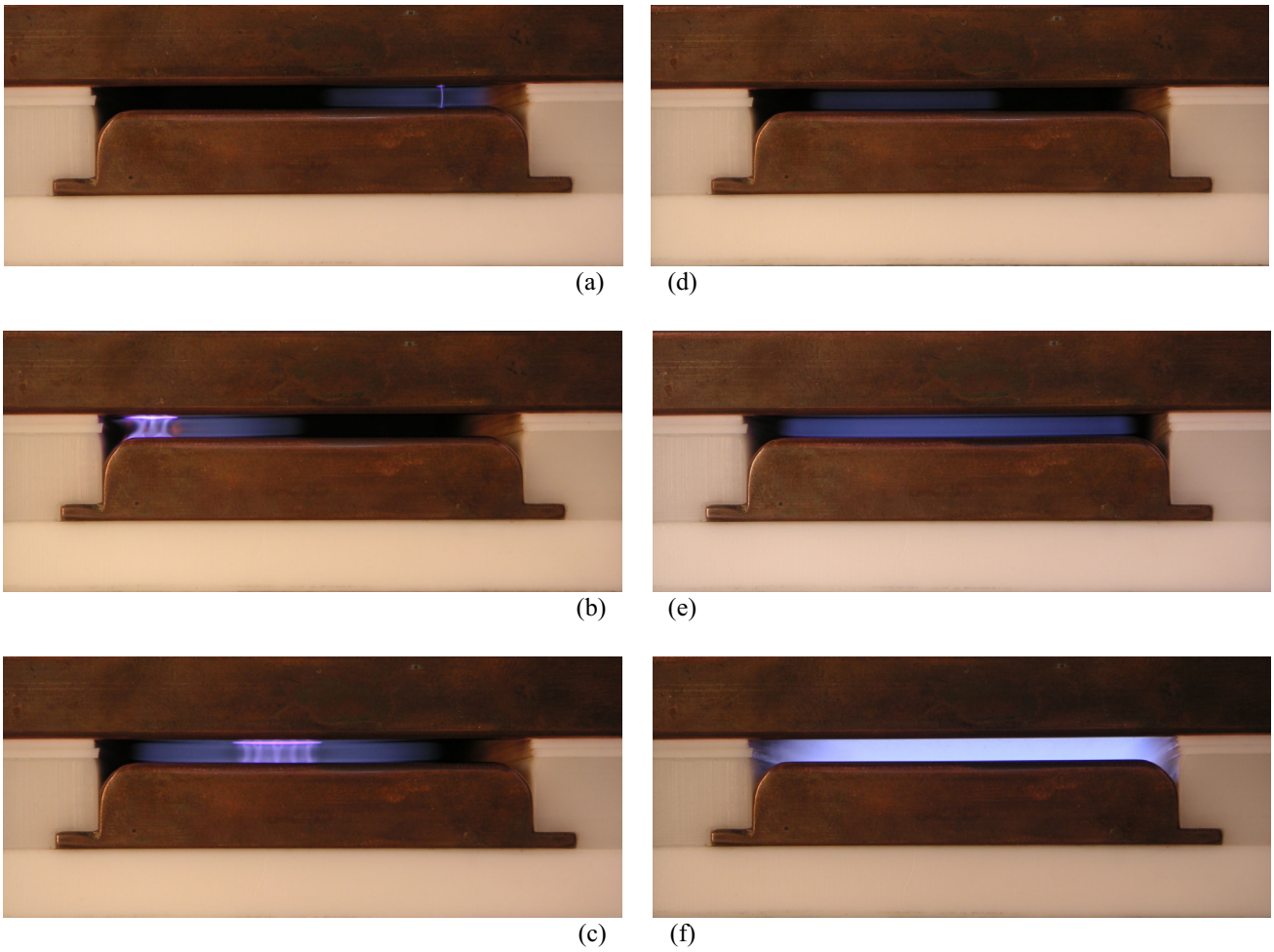

Fig. 4: Front view of the RF discharge for various operating conditions. Gap spacing is 2.5 mm. RF electrode is in centre and grounded electrode is on top. On the left side are the coexisting α- and γ-modes. On the right side are the pure α-modes.
(a) P = 20 W, lower power limit of the coexisting α- and γ-mode
(b) P = 200W, immediately after ignition
(c) P = 260 W, highest RF power investigated
(d) P ≤ 20 W, lower power limit of the pure α-.mode, partial coverage of the electrodes
(e) P = 20W, low power limit of the pure α-mode, full coverage of the electrodes
(f) P = 220 W, upper power limit of the pure α-mode

Fig. 4 shows all discharge patterns observed. Immediately after ignition the electrodes are only partially covered with a glow (Fig. 4b), which moves around between the left and the right electrode edge. Within this discharge two different regions can be distinguished. In the centre of the discharge there is a bright negative glow very close to both electrodes connected with a few filament-like contracted positive columns. It is surrounded by a region of reduced brightness (halo) featuring a much wider dark space. A comparison with [13] leads to the conclusion that a γ-discharge is present, which is surrounded by an α-discharge. Both discharge modes seem to coexist. An increase in RF power up to 260 W showed that the coexisting α- and γ-mode is present throughout this power rage. However, the coverage of the electrodes with the γ-mode as well as the number of filament-like positive columns increased (Fig. 4c). By reducing the RF power the discharge becomes weaker, whereby the number of filament-like positive columns is decreased. Fig. 4a shows the lower power limit of this type of discharge with a barely visible γ-mode. By reducing the RF power even further until the last filament-like

positive column is gone the discharge changes drastically. A transition to a pure α-discharge occurs (Fig. 4d). However, this takes place at very low RF powers (≤20 W). If one reduces the RF power to quickly the discharge extinguishes. At this very low power level the pure α-mode only partially covers the electrodes. However, an only slight increase in RF power (20 W) leads to a spreading of the α-discharge across the electrodes causing an already full coverage (Fig. 4e). It has to be mentioned that the power measurements at this very low power levels are not very accurate. By increasing the RF power the discharge becomes brighter and brighter (Fig. 4f). When the RF power exceeds approximately 220W a transition to the coexisting α- and γ-mode takes place.
We repeated the experiments several times, but we never accomplished a direct ignition of the α-discharge. On the other hand we also never observed arcing at the upper power limit of the α-discharge.
Pictures of the discharges taken with higher magnification show clearly visible dark spaces close to the electrodes in regions where the α-mode is present (Fig. 5). The sheath thickness estimated from the pictures is in the order of a few tens of a millimetre. Only in pure α-discharges at high power levels the dark space is less visible due to the high brightness of the discharge (Fig. 5d). In the region of the γ-discharge a very intense negative glow is visible close to the electrodes indicating a much higher current density. An increase in RF power leads to an increase of the surface covered by this high current negative glow. The sheath thickness of the γ-discharge is much smaller; it cannot be estimated from the pictures taken. The negative glows on both electrodes are connected with a bright positive column (e.g. Fig. 5a). At low RF powers the positive column is contracted and exhibits one plasma filament. With increasing RF power, first, branching of the plasma filament occurs, than the number of the plasma filaments increases, whereby branching might still occur (Fig. 5b). Each plasma filament seems to need a minimum on current and is able to carry only a limited amount of current. As such type of structural non-uniformity might transform a γ-discharge into an arc [13], we did not explore the stability of the coexisting α- and γ-mode at RF powers beyond 260 W.

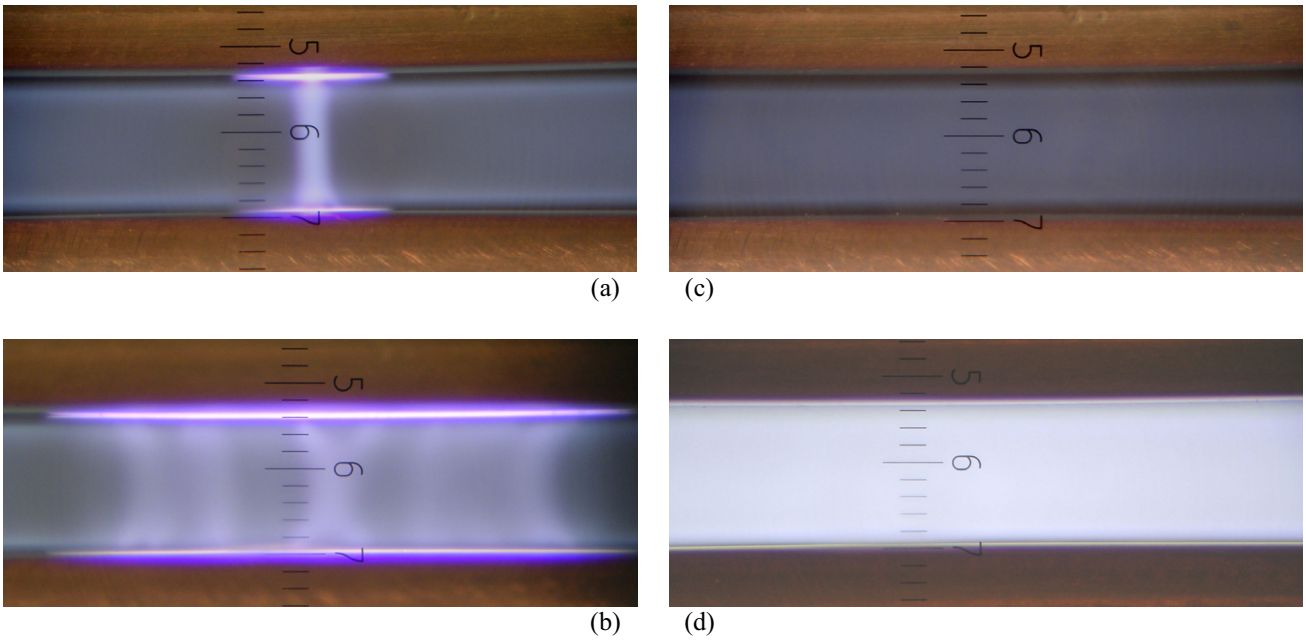

Fig. 5: Pictures of the RF discharge for various operating conditions taken with higher magnification. Gap spacing is 2.5 mm. RF electrode is on bottom and grounded electrode is on top. On the left side are the coexisting α- and γ-modes. On the right side are the pure α-modes: (a) P = 40 W, (b) P = 240W, (c) P = 20 W and (d) P = 220 W.

The current and voltage waveforms of both modes show a distinct behaviour with increasing RF power. At the low power limit of the α-mode both the current and voltage exhibit sinusoidal waveforms, whereby the current leads the voltage by more than 85°. With increasing RF power the phase difference between current and voltage

decreases. The current shows only a very small contribution of the third harmonic, even at a high RF power. At the low power limit of the coexisting α- and γ-mode the current leads the voltage by more than 80°. However, the current already shows a small contribution of the third harmonic. With increasing RF power the phase difference between current and voltage decreases much more than in the case of the pure α-mode. At the highest RF power investigated (260 W) the third harmonic makes up to 20% of the fundamental of the current. Even the voltage waveform exhibits a small distortion due to a contribution of a third harmonic.

4. Conclusions

A stable uniform glow-like discharge can be sustained in an APPJ operated with argon in a power range of 20 to 220 W. The uniform glow-like discharge was identified as the α-mode of an RF discharge. As the upper power limit of stability of the α-mode is due to a transition to a coexisting α- and γ-mode and not due to arcing, damaging of the electrodes is not a problem.

Besides the pure α-mode a non-uniform RF discharge, which was identified as a coexisting α- and γ-mode, was observed as well. It occurred at RF powers ranging from 20 W to at least 260 W. At even higher RF powers a transition to an arc might occur, which was, however, not investigated.

It was not possible to ignite the pure α-discharge directly. The breakdown always led to a coexisting α-and γ-mode. However, at very low RF powers a transition to the α-mode took place.

The APPJ operated with argon in the α-mode is surely an interesting tool for future plasma applications. Maybe, the high current density γ-mode can be used in a differently designed APPJ.

References

[1] A. Schütze, J.Y. Jeong, S.E. Babayan, J. Park, G.S. Selwyn, R.F. Hicks - IEEE Trans. Plasma Sci. **26**,1685 (1998).

[2] J. Park, I. Henins, H.W. Herrmann, G.S. Selwyn, J.Y. Jeong, R.F. Hicks, D. Shim, C.S. Chang - Appl. Phys. Lett. **76**, 288 (2000).

[3] J. Park, I. Henins, H.W. Herrmann, G.S. Selwyn - J. Appl. Phys. **89**, 15 (2001).

[4] J. Park, I. Henins, H.W. Herrmann, G.S. Selwyn - J. Appl. Phys. **89**, 20 (2001).

[5] J.Y. Jeong, S.E. Babayan, V.J. Tu, J. Park, R.F. Hicks, G.S. Selwyn - Plasma Sources Sci. Technol. **7**, 282 (1998).

[6] S.E.Babayan, J.Y. Jeong, V.J. Tu, J. Park, G.S. Selwyn, R.F. Hicks - Plasma Sources Sci. Technol. **7**, 286 (1998).

[7] H.W. Herrmann, I. Henins, J. Park, G.S. Selwyn - Phys. Plasmas **6**, 2284 (1999).

[8] J.Y. Jeong, J. Park, I. Henins, S.E. Babayan, V.J. Tu, G.S. Selwyn, G. Ding, R.F. Hicks - J. Phys. Chem. A **104**, 8027 (2000).

[9] V.J. Tu, J.Y. Jeong, A. Schütze, S.E. Babayan, G. Ding, G.S. Selwyn, R.F. Hicks - J. Vac. Sci. Technol A **18**, 2799 (2000).

[10] G.S. Selwyn, H.W. Herrmann, J. Park, I. Henins - Contrib. Plasma Phys. **6**, 610 (2001).

[11] S. Wang, V. Schultz-von der Gathen, H.F. Dobele - Appl. Phys. Lett. **83**, 3272 (2003).

[12] J. Laimer, S. Haslinger, W. Meissl, J. Hell, H. Störi - Vacuum (accepted).

[13] Y.P. Raizer, M.N. Shneider, N.A. Yatsenko - Radio-Frequency Capacitive Discharge, Boca Raton, CRC (1995).

TGA study of the thermal decomposition of aqueous cerium nitrate solutions as liquid precursors for thermal plasma synthesis of cerium oxide particles.

M. J. Desroches, I. Castillo[1], R. J. Munz[1]

[1]*Plasma Technology Research Center (CRTP), McGill University, Montreal, Canada*

Abstract
The effect of fuel addition in the thermal decomposition of water soluble cerium nitrate salts was studied. The fuels investigated were glycine and alanine based on their low molecular weight and high energy of combustion. The results showed that both alanine and glycine effectively lowered the calcination temperature of the solution and that alanine is the preferred fuel based on its higher energy of combustion.

Keywords
Cerium oxide, SOFC, TGA, thermal decomposition, solution plasma synthesis.

1. Introduction

The synthesis of CeO_2 (cerium oxide) powders doped with controlled and precise compositions of gadolinium, yttrium and samarium has been recently investigated using a rf inductive coupled plasma reactor [1]. Cerium oxide doped powders are regarded as one of the most promising materials to substitute YSZ (yttria stabilized zirconia) as the preferred electrolyte in SOFCs (solid oxide fuel cells) operation. Cerium oxide doped powders were synthesized from solutions of cerium and dopants nitrate salts dissolved in water, which were injected as a fine mist into the plasma torch using an air-blast type atomizer. As the fine droplets come in contact with the plasma (mixture of argon-oxygen), a portion of the plasma's energy is employed in the evaporation of the solution's excess water; rather than in the direct calcination of the nitrate salts to form the oxide powders. Recent work done by Chung [2] and Wang [3] has shown that the addition of glycine or alanine to the nitrate precursor solution could serve as fuel. By providing additional energy, the combustion of the fuel could promote the thermal decomposition of the nitrates into the desired oxides at lower temperatures. Decreasing the calcination temperature is important to promote an *earlier* synthesis due to the very short residence times that the droplets are in contact with the plasma core. To corroborate this hypothesis, an analysis of the thermal decomposition of mixtures of cerium nitrate, fuels and water was conducted using thermogravimetric techniques, i.e. TGA. Selected combustion-synthesized powders were then characterized by X-ray diffraction and their morphology examined by SEM micrographs.

2. Thermal decomposition of cerium nitrate hexahydrate and associated fuel reactions

The thermal decomposition of hydrated rare earth nitrates in air into their corresponding oxides has been reported by Wendlandt [4,5]. It was found that CeO_2 was produced as follows:

$$Ce(NO_3)_3.6H_2O \rightarrow Ce(NO_3)_3 \rightarrow CeO_2$$

The hydrate begins to gradually lose its water of hydration at 80°C and the final metal oxide is formed beginning at ~350°C.

The fuels investigated were glycine (H_2NCH_2COOH) and alanine ($CH_3CH(H_2N)COOH$). These aminoacids are small molecules that posses large energies of combustion and that are unlikely to interfere with the thermolysis of the nitrate salts. The combustion energy of glycine (MW=75.07) is 13,000 J/g and that of alanine (MW=89.09) is 18,000 J/g [6]. Their respective combustion reactions assuming complete fuel decomposition are:

$$Ce(NO_3)_3 \cdot 6H_2O + \frac{15}{9} NH_2CH_2COOH + \frac{1}{4} O_2 \rightarrow CeO_2 + \frac{7}{3} N_2 + \frac{10}{3} CO_2 + \frac{61}{6} H_2O$$ ……..for glycine

$$Ce(NO_3)_3 \cdot 6H_2O + CH_3CH(NH_2)COOH + \frac{1}{4} O_2 \rightarrow CeO_2 + 2N_2 + 3CO_2 + \frac{19}{2} H_2O$$ …for alanine

3. Precursor mixtures investigated and experimental techniques

It was determined experimentally that a saturated solution at 25° C of hexahydrated cerium nitrate in water had the following proportions: 1.8g of salt per g of water [1] (base case). Three different amounts of fuel, either glycine or alanine, were added to the base case taking the nitrate salt as the basis of calculation, i.e. a stoichiometric amount, fuel-deficient (less than stoichiometric) and fuel-rich (more than stoichiometric).

Table 1 Summary of precursor mixtures

	Glycine				**Alanine**		
Mixture	A1	A2	A3	A4	C1	C2	C3
Description	No fuel	Stoichiometric	Fuel lean	Fuel rich	Stoichiometric	Fuel lean	Fuel rich
Molar ratio (Salt/Fuel)	-	1:1.67	1:1	1:2	1:1	1:0.60	1:1.2

Once the best two mixtures of each fuel were determined, two more precursors were prepared. The aim was to retain the optimal fuel to salt proportions but now with a minimal amount of water. The saturated solutions prepared in this fashion were about twice as concentrated as the previously used ratio of 1.8 g salt/g of water (B2 for glycine and D2 for alanine), i.e. 3.9 g salt/g of water.

The thermal decomposition analyses were done using the Pyris Thermogravimetric Analyzer from PerkinElmer in air. A small drop of the precursor sample was placed within the crucible. Two different heating rates were investigated: 5°C/min and 10°C/min. The X-Ray diffraction analysis on the residue was done using a PHILIPS PW1710 powder X-ray diffraction system equipped with a copper X-ray source operated at 800 W. Finally, the synthesized powders were analyzed using a Hitachi 4700 Field Emission Scanning Electron Microscope (FE-SEM).

4. Results

4.a) Thermal decomposition and optimum ratio of nitrates, fuel and water

The A and C series were analyzed using a heating rate of 10°C/min on the TGA. It was found that complete nitrate decomposition was obtained at different temperatures depending on the amount of glycine added. The fuel deficient and the stoichiometric fuel mixtures formed the oxides at ~225 °C, whereas the fuel rich and no-fuel mixtures formed the oxides at temperatures close to ~350 °C (Fig. 1a). It was observed that there was an *auto-ignition* of the samples forming oxides at lower temperatures. Auto-ignition effectively decreases the temperature of oxide formation as previously reported [7].

For the C series, auto-ignition occurred for all mixtures regardless of the amount of alanine added. Complete decomposition of the salt into cerium oxide was found to be at ~225 °C (Fig. 1b). Both glycine and alanine decreased the temperature at which the oxides are formed by approximately 125 °C and the most favorable case was when stoichiometric amounts were added. Less fuel per salt is needed to produce the same effect in the case of alanine, and thus it is a more efficient fuel source.

For the twice as concentrated solutions (B2 and D2) of stoichiometric alanine and glycine; it was found that *only* the concentrated alanine mixture further reduced the oxide formation temperature (~200 °C) (Fig. 2). This could be attributed to the higher combustion energy of alanine (5,000 J/g more than glycine), which is sufficiently large to promote auto-ignition at a lower temperature.

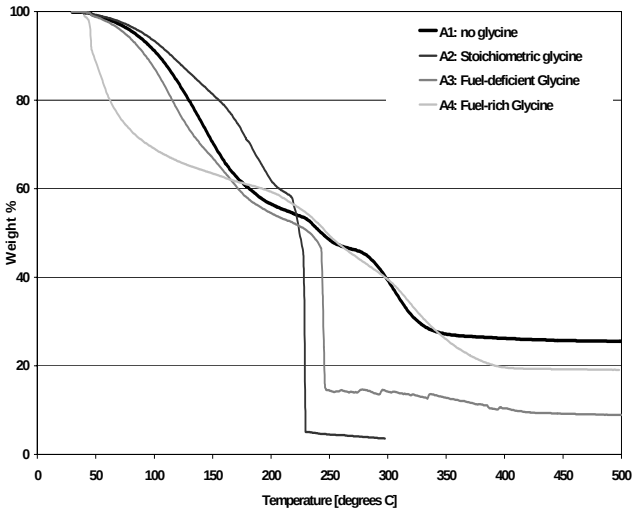

a. glycine

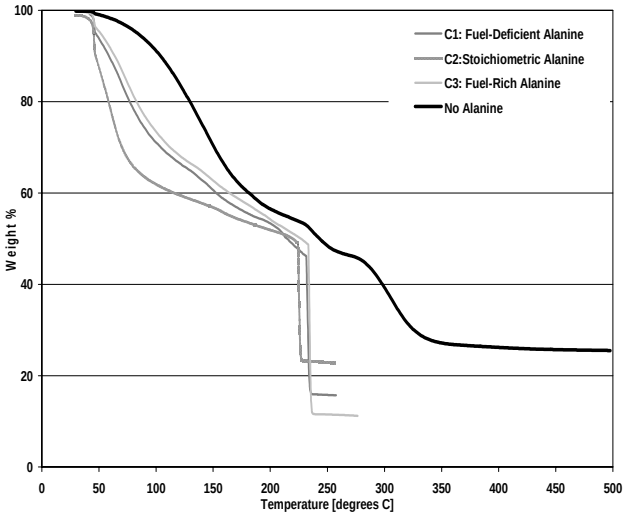

b. alanine

Figure 1. Thermal decomposition of the Series A and C mixtures obtained using TGA (heating rate: 10°C/min).

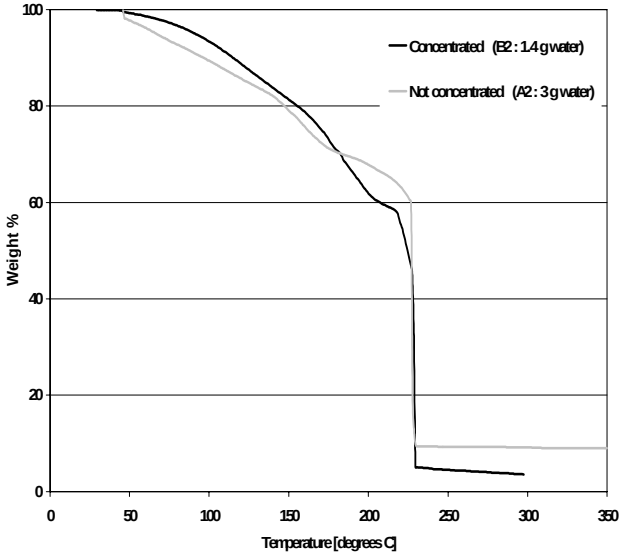

a. glycine

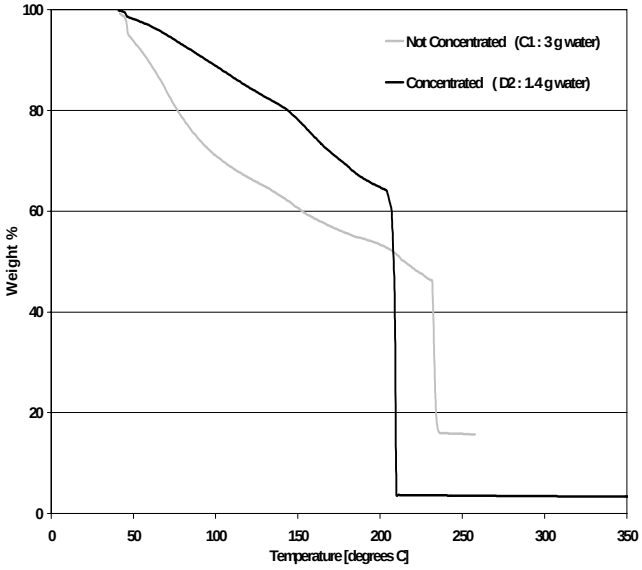

b. alanine

Figure 2. Effect of concentrating the mixture containing cerium nitrate and stoichiometric

The A and C series were re-analyzed at a lower heating rate of 5°C/min. It was found that there was *no* auto-ignition in *any* of the glycine-containing mixtures. Conversely, auto-ignition was encountered in all of the alanine-containing mixtures (Fig. 3a and 3b). This shows that the higher combustion energy of alanine is sufficient to promote auto-ignition of the nitrates even at a lower heating rate.

Based on the TGA results where the heating rate was fixed at 10°C/min, there appears to be an optimum ratio of nitrates, water and fuel that results in the formation of the CeO_2 powders at the lowest temperature. This optimum composition corresponds to the mixture D2 containing stoichiometric amounts of alanine. On a mass basis, this mixture is composed of 68% $Ce(NO_3)_3 \cdot 6H_2O$, 14% alanine and 18% water.

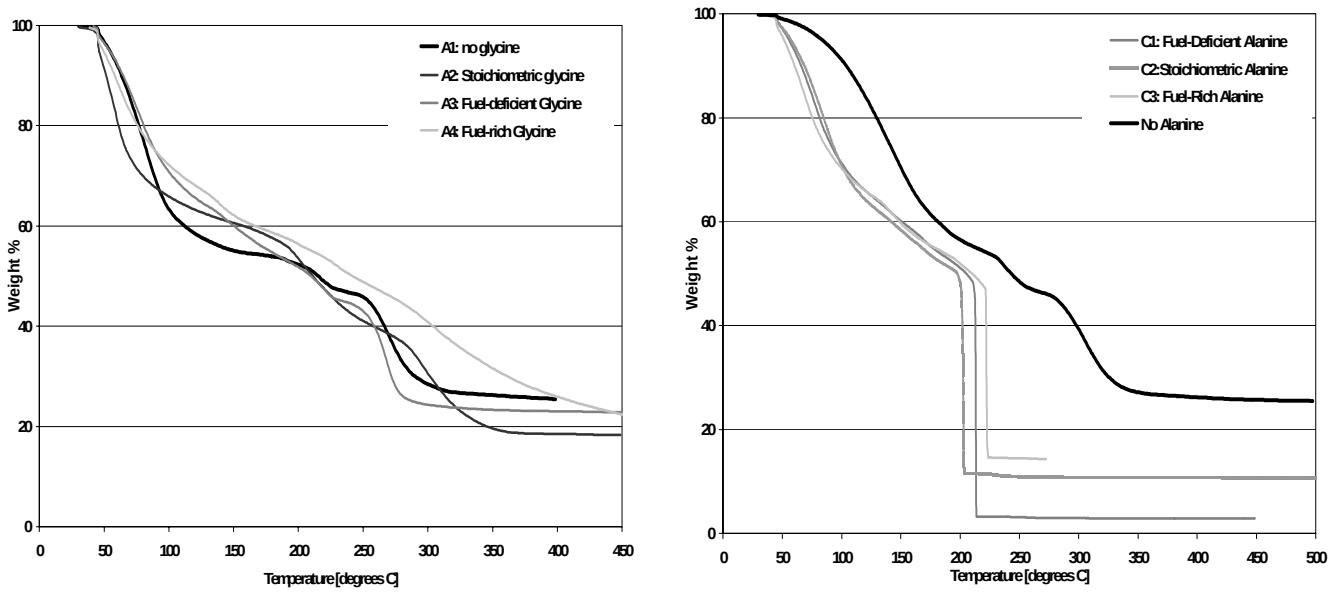

a. glycine b. alanine

Fig. 3. Thermal decomposition of the Series A and C mixtures obtained using TGA (heating rate: 5°C/min)

4. b) Crystallinity and purity of the oxides

The X-ray diffraction patterns of selected oxides powders produced from the TGA experiments showed that pure cerium oxide was produced. Also, the choice of glycine and alanine did not impact the crystallinity nor the purity of the oxides. However, the addition of fuel seemed to produce oxides with larger crystals judging from the narrower peaks observed when autoignition occurred.

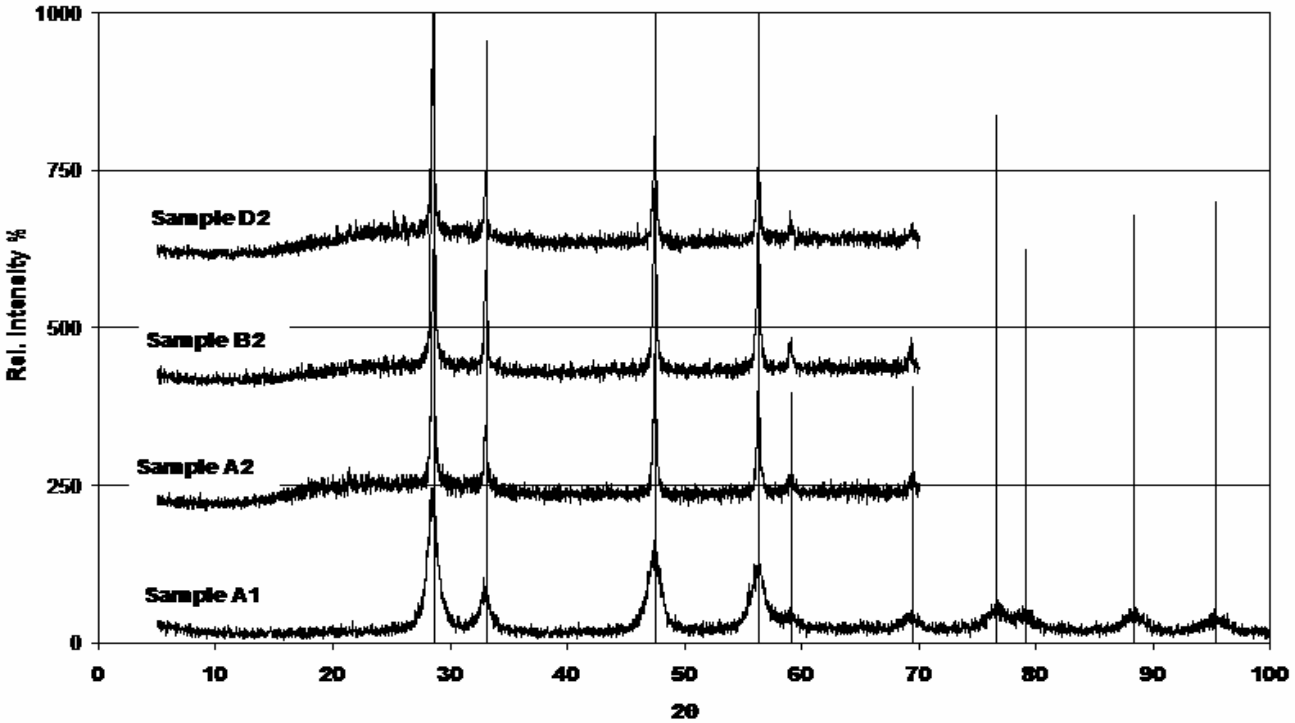

Figure 4. X-ray diffraction patterns of four CeO_2 powders synthesized from the TGA experiments. SD2=Stoich. conc. alanine, SB2=Stoich. conc. glycine; SA2=Stoich. glycine, SA1=No fuel

4. c) Powder morphology

Two different types of powder morphologies were observed from SEM micrographs. Porous-coral-like structures when auto auto-ignition was present, and dense-paste-like morphologies in its absence. This confirms the results obtained from the X-ray diffraction patterns which showed a difference in crystal size between mixtures that auto-ignite and those which do not. The foamy-coral-like structure is due to the evolution of gaseous materials during ignition.

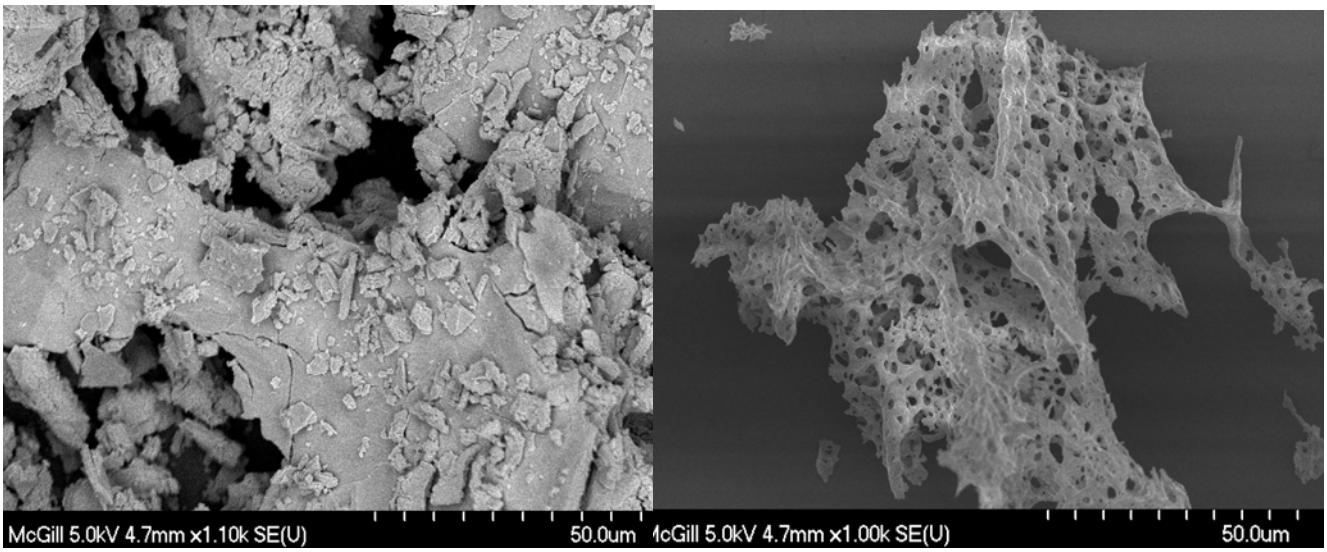

Figure 5. (a) SEM micrograph of powder produced from a mixture containing only $Ce(NO_3)_3 \cdot 6H_2O$ and water (no auto-ignition observed) (b) SEM micrograph of a powder produced from a mixture containing $Ce(NO_3)_3 \cdot 6H_2O$, water and stoichiometric alanine (auto-ignition observed)

5. Conclusions

The effect of adding glycine and alanine as fuel sources to precursor solutions of salt and water was investigated. Alanine is the preferred fuel based on the thermal decomposition results of the prepared mixtures. A smaller mass of alanine is required to achieve a similar reduction of the calcination temperature of cerium nitrate salts. Furthermore, concentrating the precursor mixture by removing water leads to an additional drop in the temperature at which the oxides are formed. The optimum composition of the precursor mixture has been found to be 68% $Ce(NO_3)_3 \cdot 6H_2O$, 14% alanine and 18% water (by mass). Auto-ignition of this mixture led to the production of the oxides at approximately 200°C (as opposed to ~350°C when no fuel is present).

The X-ray diffraction analysis results determined that the powders produced in the TGA were in fact the desired CeO_2. Lastly, the morphology of a few selected powders was characterized using SEM. Powders where auto-ignition had not occurred were found to be dense and of flaky appearance. The oxide powders obtained following auto-ignition were found to be porous and of foamy texture. This morphology can be attributed to the large amount of gases evolved during auto-ignition

6. Acknowledgements

The financial assistance of the Natural Sciences and Engineering Council of Canada via scholarships for M.J. Desroches and I. Castillo and les Fond Québequoise de la Recherché sur la Nature et les Technologies is gratefully acknowledge.

7. References

[1] I. Castillo, R. J. Munz. *Plasma Chemistry and Plasma Processing*, **25**(5), 87-107 (2005)
[2] D. Y. Chung, E. H. Lee. *Journal of Alloys and Compounds*, **374**(1-2), 69-73 (2004)
[3] H. B. Wang, J. F. Gao, D. K. Peng, G. Y. Meng. *Materials Chemistry and Physics*, **72**, 297-300 (2001)
[4] W. W. Wendlandt, L. J. Bear. *Journal of Inorganic and Nuclear Chemistry*, **12**, 276-280 (1960)
[5] W. W. Wendlandt, *Analytica Chimica Acta*, **15**, 435-439 (1956)
[6] X. W. Yang, et al, *Thermochimica Acta*, **329**, 109-115 (1999)
[7] R. D. Purohit, B. P. Sharma, K. T. Pillai, A. K. Tyagi. *Materials Research Bulletin*, **36**, 2711-2121 (2001)

Growth Behaviors and Properties of Transparent Conducting ZnO films by Pulsed Laser Deposition

Sang-Moo Park[1], Kenji Ebihara[1], Tomoaki Ikegami[1] and Paik-Kyun Shin[2]

[1] *Graduate School of Science and Technology, Kumamoto University, Kurokami 2-39-1, Kumamoto 860-8555, Japan*

[2] *School of Electrical Engineering, Inha University, 253 Yonghyun-Dong Nam-Gu, Incheon 402-751, Korea*

Abstract

High quality transparent conductive ZnO thin films were deposited on quartz glass substrates using pulsed laser deposition (PLD). We varied the growth conditions such as the substrate temperature and oxygen pressure. Crystallographic structures, electrical and optical properties of the as-grown doped ZnO films were mainly investigated. In general, the study indicates that doped ZnO films show electrical and optical properties comparable with that of ITO films and emerging as a potential good challenger to ITO films.

1. Introduction

Zinc oxide (ZnO) is a Ⅱ-Ⅵ semiconductor, highly transparent in the visible region with a wide and direct band gap of about 3.37 eV at room temperature and a high exciton binding energy of 60 meV [1]. This material is very attractive because it has many applications such as transparent conductive contacts, solar cells, laser diodes, ultraviolet lasers, thin films transistors and other [2,3]. Generally, undoped ZnO thin films typically exhibit *n*-type conduction with a background electron concentration as high as 10^{21} cm^{-3}. ZnO is an oxide that can be grown as a thin film by many deposition techniques including chemical vapor deposition, radio frequency sputtering, magnetron sputtering, sol–gel, ion-beam-assisted, molecular-beam epitaxy, and pulsed laser deposition [4, 5]. Among the several fabrication techniques, pulsed laser deposition (PLD) has attracted much attention because the fabrication process is quite suitable for optoelectronic devices using the ZnO transparent electrode. The composition of films grown by PLD is quite close to that of the target, even for a multi component target. PLD films may be crystallized at lower deposition temperatures relative to other physical vapor deposition techniques due to the high kinetic energies of the ionized and ejected species in the laser plumes [6]. However, it is difficult to make the transparent layer on the optoelectronic devices because the electrical and optical properties of doped ZnO films very drastically depending on the PLD condition. In this work we report results obtained from nominally undoped ZnO, Al doped ZnO (AZO) and Ga doped ZnO (GZO) films grown by KrF excimer (λ=248 nm, 25 ns pulse width) pulsed laser deposition (PLD) at different substrate temperatures and background pressure of oxygen gas. The crystallographic structure and the electrical and optical properties of the films prepared at different growth parameters will be discussed.

2. Experimental

Fig.1 shows a schematic diagram of the PLD system. Transparent conductive ZnO films were prepared by pulsed laser deposition on quartz glass substrates. The pulsed laser was the KrF excimer laser (λ=248 nm, 25

ns pulse width) and energy fluence of 2 J/cm^2. The nominally undoped ZnO films were deposited by ablating a 99.99% pure ZnO target. The AZO and GZO films were produced by ablating ZnO targets containing 2 wt. % Al_2O_3 and 5 wt. % Ga_2O_3, respectively. A substrate was placed at 40mm away from the target and could be heated up to 1000°C. The typical grown run consisted of 9,000 laser shots with a repetition rate of 10 Hz. All of the films were also deposited on quartz glass cleaned in an ultrasonic bath acetone and then ethanol for 5 min. The deposition chamber was initially evacuated to 4×10^{-5} Torr and during deposition, oxygen gas was introduced into the growth chamber and the pressure was controlled to be 1~100 mTorr by using a conductance valve and a turbo molecular pump. The as-grown doped ZnO films were characterized by X-ray diffraction (XRD: Rigaku, RINT 2100/PC). The surface morphology was observed by atomic force microscopy (AFM: Seiko Instrument, SPI 3800N). The growth rate and the thickness of the sample were determined by cross-sectional scanning electron microscopy (SEM: JEOL JSM-T200). The transmission through the films was measured using UV-visible spectrophotometer in the wavelength range from 200~800 nm. Electrical properties of the AZO films were measured by van der Pauw method at room temperature.

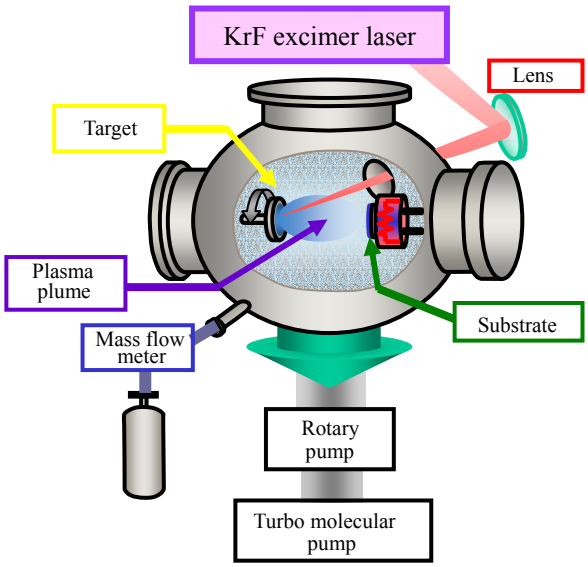

Fig. 1 Schematic diagram of PLD system

3. Results and discussion

Fig. 2a shows effect of oxygen pressure (pO_2) on the crystallinity of the AZO films. The ambient oxygen pressure was changed from 1 mTorr to 100 mTorr at substrate temperature of 500°C. XRD 2θ scans in the vicinity of the ZnO (002) reflection were performed on these films. The strong peak signal of the (002) diffraction was observed for the 5 mTorr film, while the film prepared at 1 mTorr shows fine evidence of crystallinity. Similar sets of samples were deposited using the Ga containing targets and XRD 2θ scans were carried out on these films, also. These results are not presented here but showed the same trend with pO_2 as the Al doped ZnO films. Table 1 show that the crystal size of the AZO films increases from 10.15 nm at 1 mTorr to 34.02 nm at 5 mTorr and then decreases gradually for samples prepared up to 100 mTorr. The facts suggest that the crystalline quality of the AZO films degraded from single-oriented crystal to polycrystalline with the increase of the oxygen content. The excess oxygen might induce defects in the films, which influenced the nucleation and growth of the films, and resulting in the degradation of the crystalline quality (see also Table 1). These results also confirm that a pressure of 5 mTorr will give the better epitaxy (as seen from 2θ scan), better texture, and larger crystal size (34 nm using Scherrer's formula) of the AZO films. Fig. 2b shows effect of substrate temperature on the crystallinity of the GZO films. Two diffraction peaks corresponding to (002) and (004) reflections are predominant and indicate that the film has a c-axis direction with an out-of-plane lattice parameter around 5.2 Å. At higher substrate temperatures the intensity of (002) peaks increased. The FWHM values decreased from 0.36 to 0.198º as the growth temperature increased from

100 to 500ºC.

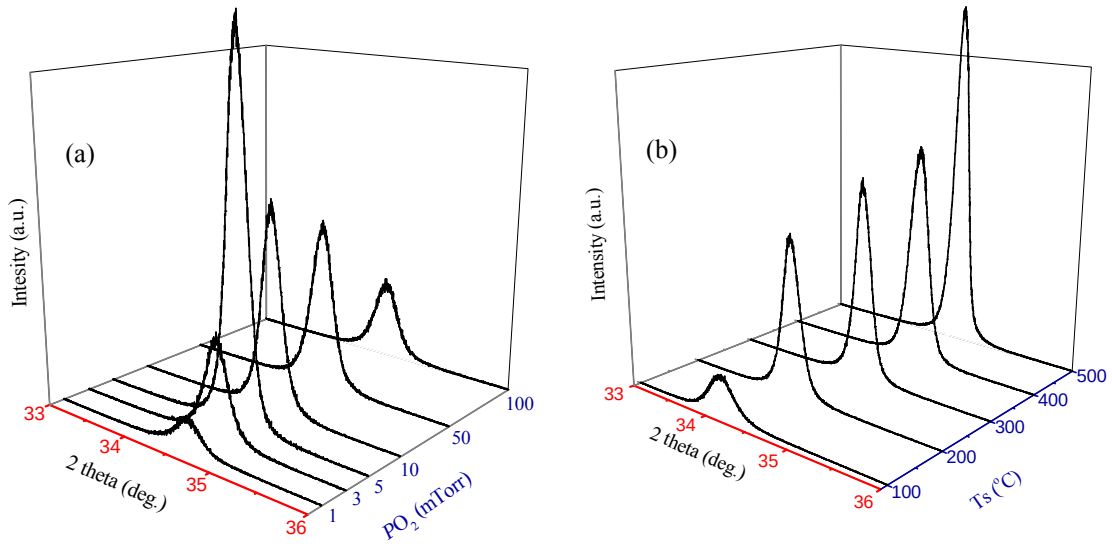

Fig. 2 XRD 2 theta scans of ZnO films grown on quartz substrates in the vicinity of ZnO (002) peaks. (a) AZO films as a function of pO_2. (b) GZO films as a function of Ts.

Table 1

Properties of AZO films on quartz glass substrates at 500°C as a function of oxygen pressure.

pO_2 (mTorr)	Crystal size (nm)	c-axis length (Å)	Roughness (nm)	T (%) (400-800 nm)	Band gap (eV)	Resistivity (Ωcm)	Carrier concentration (cm^{-3})	Carrier mobility (cm^2/Vsec)
1	10.15	5.178	7.062	88.66	3.36	5.14×10^{-4}	1.25×10^{21}	9.74
3	22.8	5.173	7.142	90.97	3.36	4.97×10^{-4}	1.16×10^{21}	10.87
5	34.02	5.176	7.97	93.37	3.35	3.92×10^{-4}	1.14×10^{21}	14.03
10	25.3	5.182	7.354	95.46	3.34	7.5×10^{-4}	1.04×10^{21}	8.01
50	23.5	5.187	7.227	94.63	3.32	1.78×10^{-3}	9.92×10^{20}	3.55
100	21.3	5.185	6.834	95.14	3.26	5.22	1.25×10^{19}	0.1

The morphology and the surface roughness determined by AFM measurement are shown in Fig. 3. The roughness seems to increase with the increase of substrate temperature and in the same time, the grain size on the surface is varied. For the film grown at low temperature (100°C), the grain size is around 90 nm. Furthermore, the roughness of this film is about 9 nm. On the contrary, the film grown at higher temperature (300°C) the grain size of around 115 nm and the roughness of the film slightly decrease to about 8 nm. Sample prepared at up to 500°C shows the grain size of around 230 nm and the roughness of about 8 nm.

Fig. 4 shows optical transmittance of the ZnO, AZO and GZO thin films prepared at a substrate temperature of 500°C and at an oxygen pressure of 5 mTorr. The transmittances obtained are around 90% at the wavelength from 400 to 800 nm. We also find the transmission edge shift around 350-390 nm toward lower energies either by doped material. This shift is confirmed by representing absorbance squared versus the excitation energy *hv*. The optical absorption coefficient α is related to the threshold absorption energy (Eg) by $\alpha = A\bullet (hv - Eg)^{1/2}$ (A is a constant). The band gap energy Eg can be determined by extrapolation of the

linear part of the plot of α^2 versus, *hv*. The band gap of ZnO, AZO and GZO films are 3.23, 3.36 and 3.51 eV, respectively. The high-energy shift of the optical band gap of GZO and AZO films compared to the ZnO films are due to the much higher carrier concentration of these doped films and filling of electronic states of the conduction band (Burstein-Moss-Shift) [7]. According to this Burstein-Moss-Shift, the band gap would increase with increasing carrier concentration.

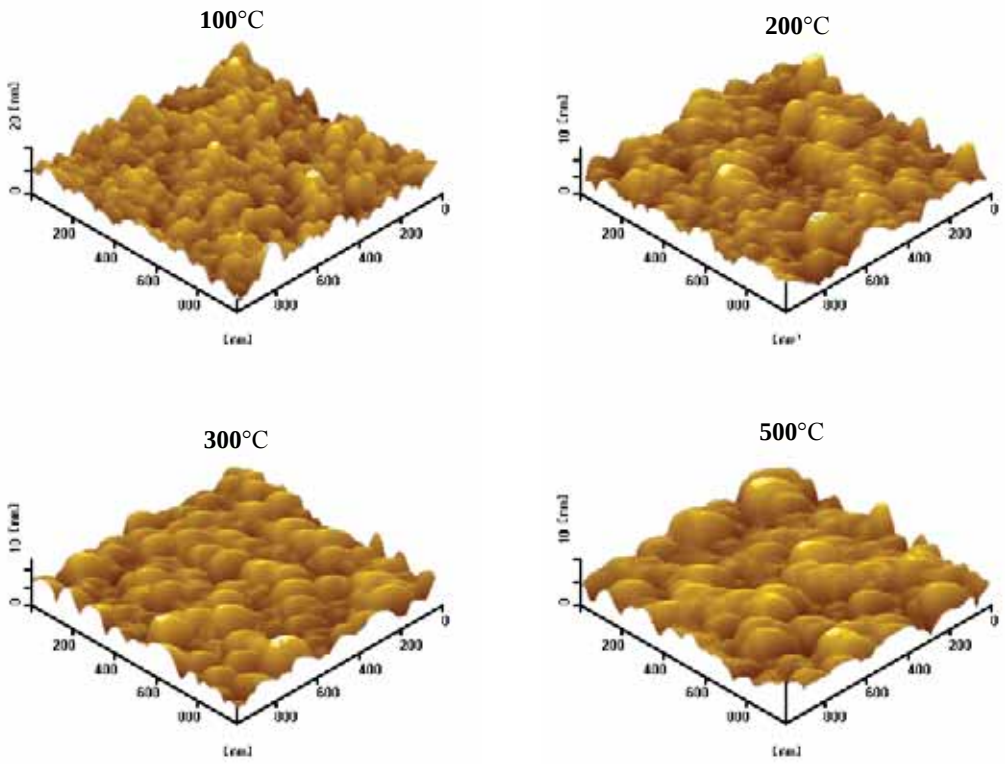

Fig. 3 AFM images of GZO films over 1μ×1μ area grown under 5 mTorr of O_2 at various substrate temperatures.

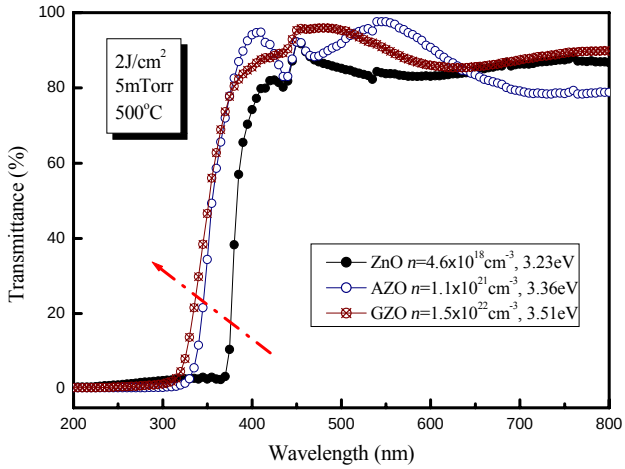

Fig. 4 Optical transmittance of the ZnO, AZO and GZO thin films prepared at a substrate temperature of 500°C and at an oxygen pressure of 5 mTorr.

The carrier concentration in the AZO films was observed to gradually decrease from 1.36×10^{21} to

9.92×10^{20} cm^{-3} as the oxygen pressure was increased (see also Table 1). A maximum in the carrier mobility was observed for an oxygen pressure of 5 mTorr. For the lower ratio O and Zn (oxygen flow rates of 1-5 mTorr) incorporation of interstitial Zn lead to a worsening of crystalline quality and creation of electron scattering centers. Consistent with this, the carrier mobility was found to increase with increasing oxygen flow rate below the optimum oxygen pressure of 5 mTorr. For ratios O and Zn higher than the optimum oxygen pressure of 5 mTorr, excess oxygen on the growth surface presumably induces changes in growth mode and crystal quality, resulting in increased carrier scattering and lower mobility. Carrier mobility thus decreases with increasing oxygen pressure of 5 mTorr.

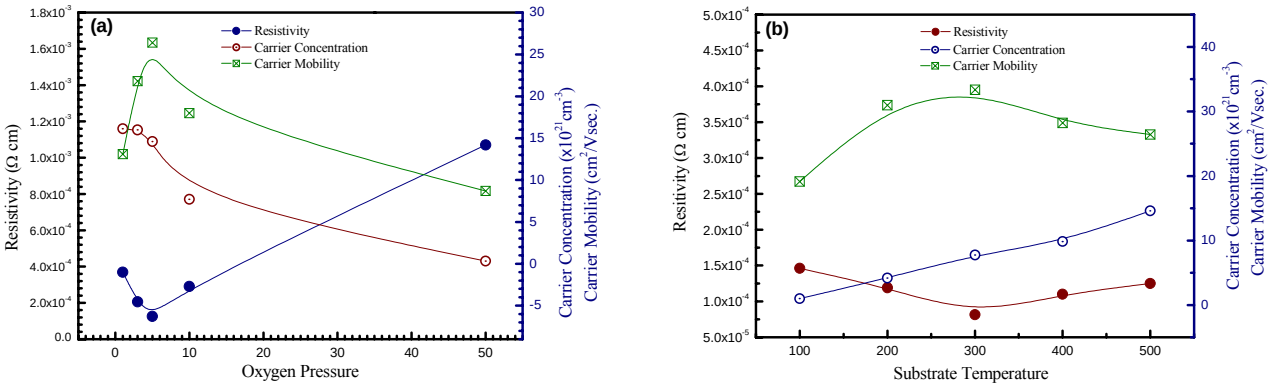

Fig. 5 Variation of the resistivity, the carrier concentration, and the carrier mobility as a function of the pO_2 for the GZO films deposited at the deposition temperature of 500°C (a) and as a function of the Ts for the GZO films deposited under the oxygen pressure of 5mTorr (b).

Fig. 5 (a) shows the variation of resistivity, carrier concentration and carrier mobility as a function of the oxygen pressure of the GZO films grown at the deposition temperature of 500°C. Films thickness was about 2000Å for all films. The resistivity of the GZO films decreases from 3.69×10^{-4} to 1.25×10^{-4} Ωcm as the pO_2 was increased from 1 mTorr to 5 mTorr. A drastically increases in the resistivity is observed as the pO_2 is further increased from 5 mTorr to 100 mTorr. Electrical property of GZO films has close relationship to oxygen content in the film. GZO is an oxide semiconductor having *n*-type conduction. High conductivity of the GZO might be resulted from Ga-doped effect. Since electrons in the AZO films are supplied from oxygen vacancy and aluminum atoms in the film, it can be though that increase of oxygen content might cause decrease of the oxygen vacancy, resulting in increase of resistivity. Fig. 5 (b) shows the variation of the resistivity, carrier concentration, and carrier mobility as a function of the deposition temperature of the GZO films grown at an oxygen pressure of 5mTorr. As the substrate temperature increases from 100°C to 300°C, the resistivity decreases from 1.46×10^{-4} to 8.12×10^{-5} Ωcm and then increases again. The decrease of the resistivity is due to the increase of both carrier concentration and carrier mobility. As the substrate temperature increases to 500°C, the corresponding resistivity becomes 1.25×10^{-4} Ωcm. The slight increase in resistivity of the films grown at higher substrate temperature from 300°C to 500°C may be due to contamination of the alkali ions from quartz glass substrates [8]. The carrier concentration in the GZO films was observed to gradually increase as the deposition temperature was increased. This increase in carrier concentration may be due to an increase in diffusion of Ga atoms from interstitial locations and grain

boundaries into the Zn cation sites [9]. The carrier mobility increases from 19.12 cm^2/Vsec at 100°C to 33.36 cm^2/Vs at substrate temperature 300°C, then decreases to 26.42 cm^2/Vsec. Moreover, the finding that the 1.46×10^{-4} Ωcm at 100°C suggests that film deposition into the semiconductor devices is possible.

4. Conclusion

High quality transparent conductive doped ZnO thin films were grown using the PLD technique on quartz glass substrates starting from ZnO target containing 2 wt.% of Al_2O_3 and 5wt.% of Ga_2O_3, respectively. The growth was performed under wide oxygen pressure range of 1-100 mTorr in the different substrate temperature range 100-500°C. We have studied the influence of the growth conditions (oxygen pressure, substrate temperature) on the structural properties that are directly related to essence of films, such as out of plane alignments, in plane epitaxy, crystal size, grain size, and so on. The resistivity and the carrier concentration of the films were decreased due to the decrease of the oxygen vacancy with increasing the oxygen pressure. With increasing the deposition temperature, the resistivity of the films was decreased and the carrier concentration was increased due to the grain growth and the enhancement of the impurity diffusion. The GZO films formed at a substrate temperature of 300°C showed low electrical resistivity of 8.12×10^{-5} Ωcm, carrier concentration of 7.73×10^{21} cm^{-3} and carrier mobility of 33.36 cm^2/Vsec at an oxygen pressure of 5 mTorr. In general, the study indicates that AZO and GZO films show comparable electrical and optical properties comparable with that of ITO films and emerging as a potential good challenger to ITO films. We suggest that, although Al is a better dopant for producing high quality n-type ZnO, Ga maybe economically viable as lower process temperatures can be used and the conductivity of the films can be expected to be more reproducible.

Acknowledgment

This work is supported in part by a Grant-in-Aid for Scientific Research (2003-2006, No. 15360171) by the Ministry of Education, Science, Sports and Culture of Japan.

References

[1] D. G. Thomas, J. Phys. Chem. Solids, 15, 86 (1960).

[2] M. Joseph, H. Tabata, T. Kawai, Appl. Phys, Lett. 74, 2534 (1999).

[3] W. W. Wenas, A. Yamada, K. Takahashi, J. Appl. Phys. 70, 7119 (1991).

[4] B. P. Zhang, K. Wakatsuki, N. T. Binh, N. Usami, Y. Segawa, Thin solid Films 449, 12 (2004).

[5] S. Suzuki, T. Miyata, M. Ishii, T. Minami, Thin Solid Film 434,14 (2003).

[6] D. B. Chrisey, G. K. Hubler, Pulsed Laser Deposition of Thin Films, Wiley, New York, 327 (1994).

[7] T. Makino, K. Tamura, C. H. Chia, Y. Segawa, M. Kawasaki, A. Ohtomo, H. Koinuma, Phys. Rev. B 65, 121201 (R) (2002).

[8] J. C. Manifacier, Thin Solid Films 90, 297 (1982).

[9] H. Kim, C.M. Gilmore, A. Pique, J.S. Horwitz, H. Mattoussi, H. Murata, Z.H. Kafai, D.B. Chrisey, J. Appl. Phys. 86,6452 (1999).

CO_2 Reforming of Methane with Nonthermal Plasma

S. Futamura and G. Annadurai

National Institute of Advanced Industrial Science and Technology, Tsukuba, Japan

Abstract
Reaction behavior of CH_4 and CO_2 in nonthermal plasma was investigated with a ferroelectric packed-bed reactor at 298 to 433K. CH_4 conversion increased with reaction temperature, while CO_2 reactivity was not affected by temperature. No chemical interaction was observed between these substrates. The composition of synthesis gas was affected by the molar ratio of CO_2 to CH_4 and reaction temperature.

Keywords Nonthermal plasma, CO_2, reforming, CH_4, temperature, mechanism

1. Introduction

It is estimated that CO_2 contributes to ca. 64 % of global warming according to the 2nd Assessment Report of Intergovernmental Panel of Climate Change in 1997. Recognition of CO_2 as the major culprit in the global warming stimulated researches relevant to the development of environmentally friendly technologies for CO_2 utilization: photochemical CO_2 reduction, catalytic CO_2 hydrogenation, and CO_2 reforming. Application of the former two processes will be limited because of the low efficiency and the high cost of H_2, respectively. Catalytic CO_2 reforming of natural gas also has drawbacks such as high reaction temperature and clogging caused by coke formation.

On the other hand, CO_2 can act as an oxidant in nonthermal plasma because its deoxygenation proceeds rapidly in the absence of O_2 [1]. CO_2 reforming of CH_4 is a significant reaction because this process contributes to the co-processing of ubiquitous global warming compounds such as CO_2 and CH_4. From the chemical viewpoint, the in situ concentrations and reaction behavior of the radical species such as H and O released from CH_4 and CO_2 determine the substrate conversions and the yields of H_2 and CO. Reaction temperature is one of the important parameters because the downstream reactions would not be accelerated by nonthermal plasma.

Hitherto, dielectric barrier discharge reactors have been applied to fuel reforming reactions, and the effects of reactor type [2], feed gas composition [3], [4], gas pressure [3], specific energy density [4], reaction temperature [3], and energy efficiency [5] have been investigated. The authors have been exploring the potential of nonthermal plasma in the processes of H_2 production from water, CH_4, and CH_3OH [6], CH_3OH reforming [7], steam reforming of CH_4 [8], [9], and reforming of H_2O-CO_2 [10]. Compared to catalytic processes, similar compositions of synthesis gas have been obtained from the corresponding reaction systems in nonthermal plasma.

This paper presents the reaction behavior of CH_4 and CO_2 with different compositions, product distribution, temperature effect, and reaction mechanism relevant to CH_4 conversion, H_2 formation, and the role of CO_2 as an oxidant.

2. Experimental

In this research, a ferroelectric packed-bed reactor (**FPR**) was used because **FPR** worked much better than a silent discharge plasma reactor in the reforming reactions under the same conditions with 50 Hz ac and a neon transformer [8]-[10]. **FPR** was a coaxial reactor whose reaction length and gap distance were 127 mm and 15.4 mm, respectively. $BaTiO_3$ pellets (ε = 5000 at ambient temperature, 1 mm in diameter) were packed between the two concentric electrodes in **FPR**.

CH_4 and CO_2 balanced with N_2 in standard gas cylinders were introduced to **FPR** in an oven through a Teflon tube by adjusting their concentrations and flow rates with sets of mass flow controllers and a gas mixer. All the reactions were carried out in N_2 in the temperature range of 298K to 433K. The oven temperature was controlled within ± 2K. After each run, O_2 was passed through **FPR** at 7.6 kV for 20 min. With this operation, the concentrations of CO and CO_2 were correctly determined because the carbonaceous materials deposited on the inner reactor walls and on the $BaTiO_3$ surface were oxidatively removed as CO and CO_2 after reforming reactions.

Plug-in power consumptions and applied voltages for **FPR** were measured with a digital powermeter and a digital wavemeter, respectively. The volatile byproducts were identified by GC-MS. The substrates and the major products were quantified by gas chromatographs equipped with FID and TCD. The conversions of CH_4 and CO_2 and the yields of H_2, CO, and C_2 hydrocarbons (C_2H_x, x = 2, 4, 6) are defined according to eqs. (1) to (5), respectively.

CH_4 conversion (mol%) = 100 X {1 – [CH_4 concentration (%)] / [Initial CH_4 concentration (%)] } (1)

CO_2 conversion (mol%) = 100 X {1 – [CO_2 concentration (%)] / [Initial CO_2 concentration (%)] } (2)

H_2 yield (mol%) = 100 X [H_2 concentration (%)] / [2 X Initial concentration of CH_4 (%)] (3)

CO yield (mol%) = 100 X [CO concentration (%)] / [Initial concentration of CO_2 (%)] (4)

C_2H_x Yield (mol%) = 100 X [C_2H_x concentration (%)] / [0.5 X Initial concentration of CH_4 (%)] (5)

3. Results and Discussion

Increase of CO_2 concentration from 0 to 2.0 % at the fixed CH_4 concentration of 1.0 % decreased CH_4 conversion at 298K (Fig. 1). These facts suggest that the kinetic energies of high-energy electrons in nonthermal plasma are partitioned to CH_4 and CO_2 in proportion to their initial concentrations. CO_2 conversion was also decreased with an increase in the initial CH_4 concentration. No chemical interaction was observed between CH_4 and CO_2 even at elevated temperatures.

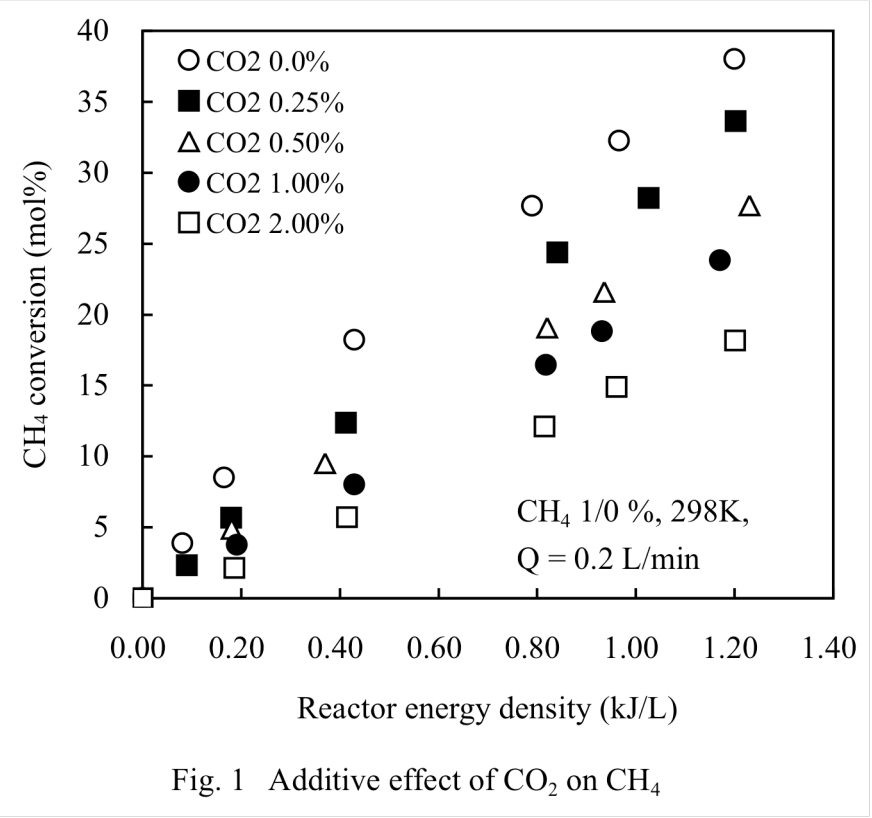

Fig. 1 Additive effect of CO_2 on CH_4

The temperature effect on CH_4 conversion (Fig. 2) suggests that CH_4 decomposition is promoted by some species at elevated temperatures. On the other hand, CO_2 conversion increased proportional to reactor energy density (RED, kJ/L) irrespective of reaction temperature. Fig. 3 shows the effects of temperature and CH_4 addition on CO_2 conversion. At 298K, CO_2 conversion was not affected by the presence of CH_4. At 433K, CO_2 conversion tended to be lower at higher REDs in the presence of CH_4. It is suggested that CO is oxidized back to CO_2 under hydrogen-deficient conditions.

H_2 and CO were obtained as the major products in the CO_2 reforming of CH_4. In the absence of CH_4, CO_2 deoxygenation was a clean reaction, and CO was almost quantitatively produced from CO_2. Since CO is stable in nonthermal plasma, further cleavage of carbon to oxygen bond in CO is unlikely under the reaction conditions. At 298K, no C_2 hydrocarbons were detected by GC in the range of 0.125% to 1.0 % of initial CH_4 concentration. At 433K at 1.0 % of CH_4, C_2 hydrocarbons were obtained, but their yields were approximately 1/20 of H_2 yields and 1/30 to 1/100 of CO yields, respectively. It is unlikely that recombination of methyl radicals occurs under the reaction conditions.

Fig. 4 shows a temperature effect on H_2 yield. At fixed REDs, higher H_2 yields are obtained at lower temperatures. At 298K, the maximum H_2 selectivity was 26 % (Figs. 2 and 4). At higher temperatures, H_2

would be consumed in the reactions with oxygen atoms from CO_2 because the yields of C_2 hydrocarbons are much lower and poor carbon recoveries are obtained.

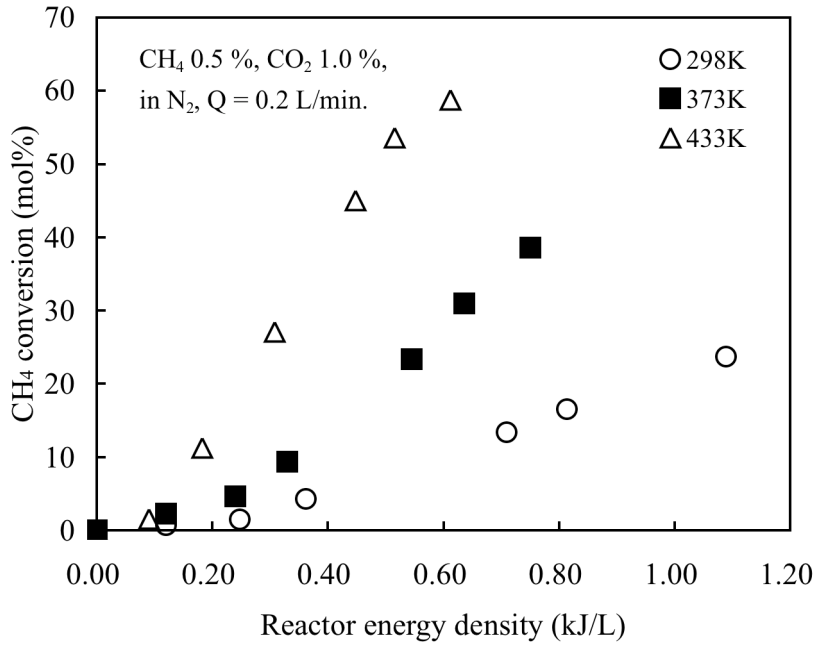

Fig. 2 Temperature effect on methane conversion

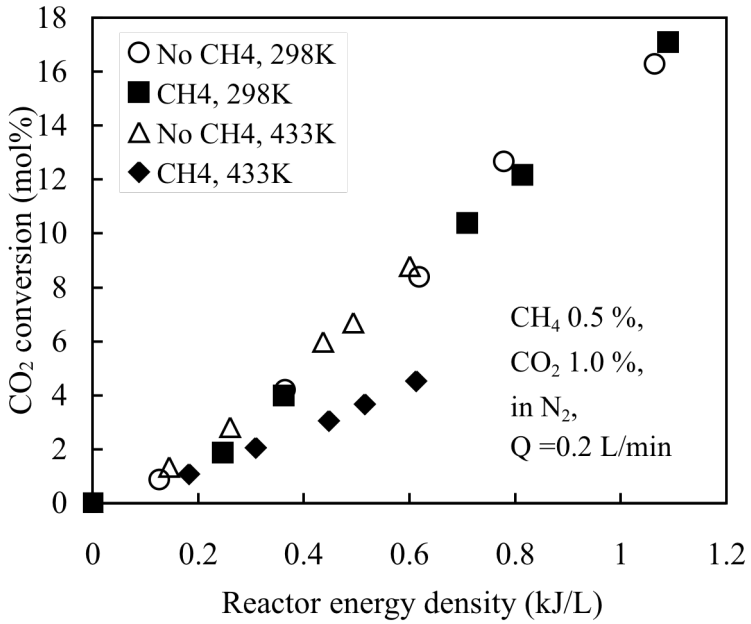

Fig. 3 Effects of temperature and CH_4 addition CO_2 conversion

Fig. 5 shows a temperature effect on the composition of synthesis gas. The molar ratio of H_2 to CO {[H_2] / [CO]} is lower than unity, and it decreases with an increase in temperature at fixed REDs. [H_2] / [CO] tended to decrease with an increase in RED and level off at higher REDs. This ratio can be flexibly controlled by changing the molar ratio of CH_4 to CO_2.

Fig. 6 shows a temperature effect on the carbon balance in the CO_2 reforming of CH_4. The x-axis stands for the total concentration of the carbon atoms consumed in CH_4 and CO_2. Data points are on the dotted line if all the carbon atoms in consumed CH_4 and CO_2 are recovered as CO. As discussed above, CO_2 deoxygenation is a clean reaction (Fig. 3), missing carbon atoms are ascribed to those in consumed CH_4. At

298K, a fairly good carbon balance is obtained, but carbon recovery decreases with an increase in reaction temperature. As in the case of synthesis gas composition, carbon balance can be improved by decreasing the molar ratio of CH_4 to CO_2. Thus, reaction conditions should be optimized depending on compositions of target synthesis gases.

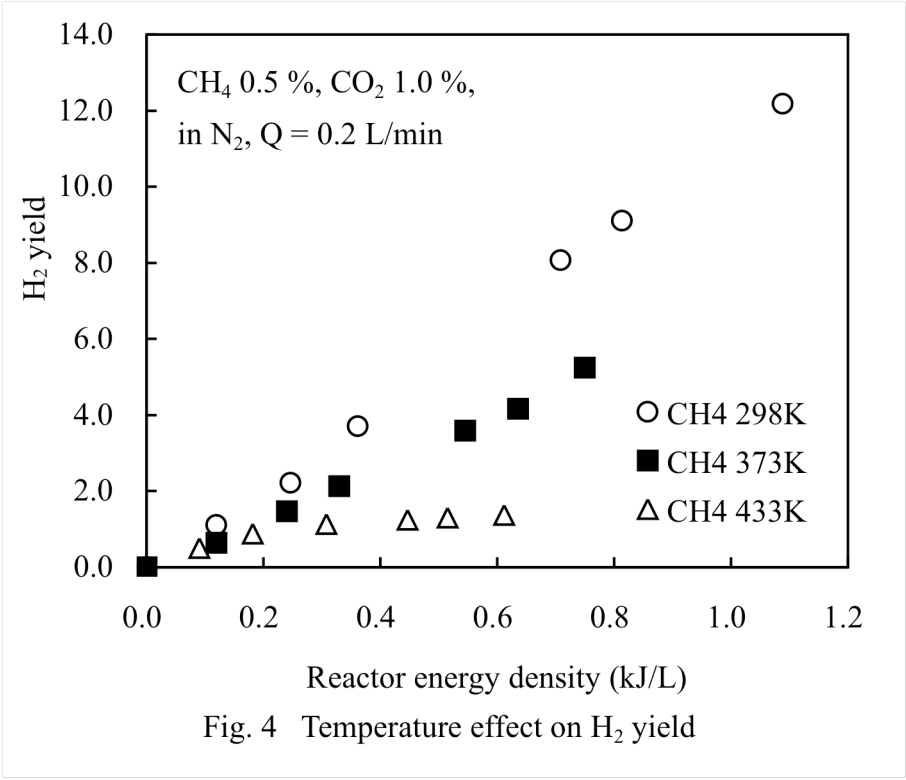

Fig. 4 Temperature effect on H_2 yield

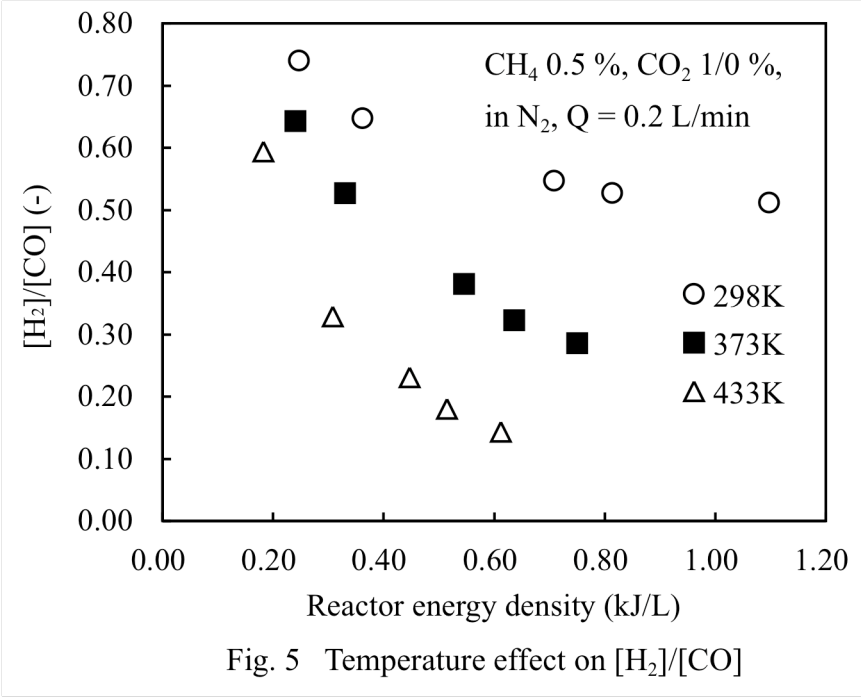

Fig. 5 Temperature effect on $[H_2]/[CO]$

Fig. 7 shows plausible pathways for the CO_2 reforming of CH_4. Eqs. (1) and (2) are the initial reactions occurring between high-energy electrons and the substrates. A hydrogen atom and a methyl radical is produced from CH_4, and CO and an oxygen atom is produced from CO_2. H_2 is produced from the hydrogen atom abstraction from CH_4 by the hydrogen atom [eq. (3)]. The reaction of the oxygen atom and CO is slow in nonthermal plasma, and the major pathway for this species should be the reaction with CH_4, giving OH and methyl radicals [eq. (4)]. OH radical also reacts with CH_4 to give water and a methyl radical [eq. (5)].

Due to the low concentrations of the substrates, recombination of methyl radicals can be neglected under our reaction conditions. This radical further undergoes oxygenation and dehydrogenation to give CO [eq. (6)]. At lower temperatures, cleavage of the C-H bond in CH_4 is rate-limiting. The temperature effect observed in this research suggests that secondary decomposition of only CH_4 is accelerated at elevated temperatures according to eqs. (4) and (5).

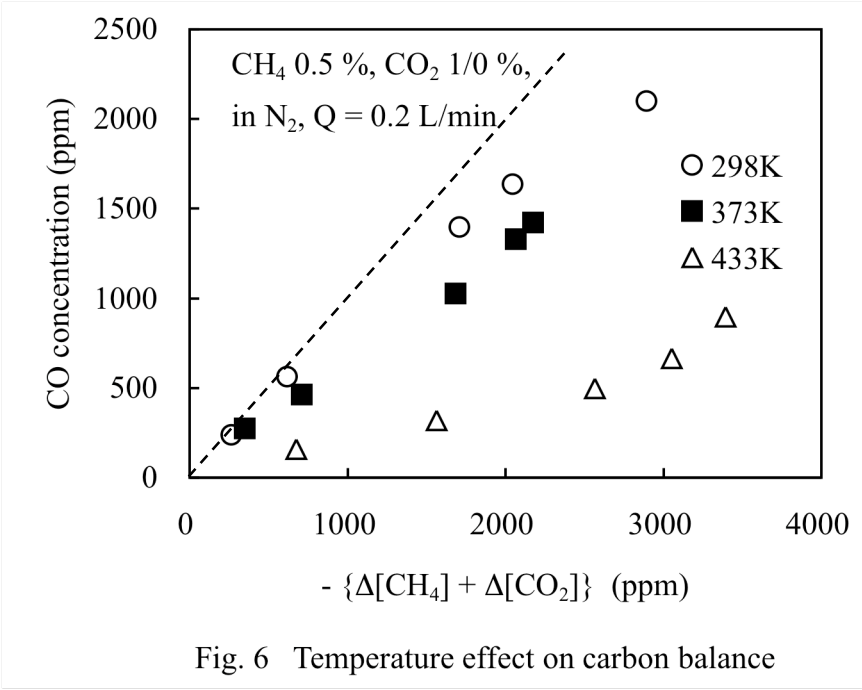

Fig. 6 Temperature effect on carbon balance

$$CH_4 + e^* \longrightarrow \bullet CH_3 + H\bullet + e \quad (1)$$

$$CO_2 + e^* \longrightarrow CO + O\bullet + e \quad (2)$$

$$H\bullet + CH_4 \longrightarrow H_2 + \bullet CH_3 \quad (3)$$

$$O\bullet + CH_4 \longrightarrow \bullet OH + \bullet CH_3 \quad (4)$$

$$\bullet OH + CH_4 \longrightarrow H_2O + \bullet CH_3 \quad (5)$$

$$\bullet CH_3 \xrightarrow{O} \xrightarrow{-H} CO \quad (6)$$

Fig. 7 Plausible pathways for CO_2 reforming of CH_4

4.Summuary

Temperature affects CH_4 conversion, but not that of CO_2 in the CO_2 reforming of CH_4. H_2 yield and the molar ratio of H_2 to CO are flexibly varied by controlling initial gas composition and temperature. Better carbon balances are obtained at lower temperatures.

References

[1] S. Futamura, A. Zhang, T. Yamamoto - IEEE Trans. Ind. Applicat., **35**, 760 (1999).
[2] S. L. Yao, M. Okumoto, A. Nakayama, E. Suzuki – Energy Fuels, **15**, 1295 (2001).
[3] L. M. Zhou, B. Xue, U. Kogelschatz, B. Eliasson – Energy Fuels, **12**, 1191 (1998).
[4] S. Kado, K. Urasaki, Y. Sekine, K. Fujimoto – Chem. Commun., 415 (2001).
[5] A. Huang, G.-G. Xia, J.-Y. Wang, S. L. Suib, Y. Hayashi, H. Matsumoto, J. Catal., **189**, 349 (2000).
[6] H. Kabashima, H. Einaga, S. Futamura – IEEE Trans. Ind. Applicat., **39**, 340 (2003).
[7] S. Futamura, H. Kabashima – IEEE Trans. Ind. Applicat.,**40**, 1459 (2004).
[8] H. Kabashima, S. Futamura – Chem. Lett., 1108 (2002).
[9] S. Futamura, H. Kabashima, H. Einaga – IEEE Trans. Ind. Applicat.,**40**, 1476 (2004).
[10] S. Futamura, H. Kabashima – Stud. Surf. Sci. Catal., **153**, 119 (2004).

Covalent immobilization of biological molecules on various plasma modified polymers

L. C. Lopez[1], R. Gristina[2], P. Favia[1,2], R. d'Agostino[1,2]

[1] *Department of Chemistry, University of Bari, Bari, Italy*
[2]*Institute of Inorganic Methodologies and Plasmas IMIP-CNR,, Bari, Italy*

Abstract

Different polymeric substrates were modified by means of plasma deposited coatings in order to functionalise the surfaces with tuneable density of functional groups (i.e. –COOH; C-O-C; etc.) to be used as anchor groups for biomolecules immobilization. Modified surfaces were employed in cell culture experiments to verify the effect of biomolecules immobilization in improving the biological response of Polyethylene terephthalate, in terms of adhesion, growth and metabolic function of different cell types.

Keywords: plasma deposition, functional groups, RGD, carbohydrates, cell behaviour.

1. Introduction

The ability of any biomaterial to regulate cell behaviour requires control over bulk and surface chemistry, topography and properties in general. Among the principles driving the development of biomaterials reducing to a minimum the immune response from the organism to the foreign biomaterial body and to increase their capacity in providing specific functionality to the desired target tissue/organ can be considered of paramount importance. Most of the existing biomaterials are limited because they represent a clear compromise. For instance, living tissues normally respond to changing physiological loads and biochemical stimuli providing the basic factors of the homeostasis; synthetic materials instead, cannot have control of such biological activities. This limits development and lifetime of biomedical materials used to replace body parts or promote tissue repair and regeneration. The engineering of polymeric materials tailored to activate cell proliferation and differentiation represent a shift toward a more biologically based method for the repairing and regeneration of tissues.

One promising strategy to control the interaction between biomaterials and cells involves covalent grafting of biological molecules to polymers that hardly support cell adhesion and growth. To provide a stable linking those molecules should be covalently attached to the polymer surface, e.g. via functional groups like hydroxyl-, amino-, or carboxyl groups or others. Since many polymers do not present such groups on their surface, these have to be introduced with a chemical or physical treatment. Plasma surface modification of polymers represents one of the more versatile process to functionalize material surfaces without interfering with its bulk properties. PE-CVD (plasma enhanced chemical vapour deposition), Plasma Etching, and Plasma Treatment processes are nowadays extensively used to tailor the surface of materials to be utilized in contact with biological systems, *in vitro*, *ex vivo*, and *in vivo*, in a wide number of biomedical applications.

Surface properties like free energy, wettability, electric charge, surface chemistry and morphology, that might all affect cell attachment and behaviour either indirectly, e.g., by controlling protein adsorption, or directly, e.g., by guiding cell spreading with surface topography, can all be easily tuned by means of surface modifications in plasma processes [1, 2]. Modification of polymeric surface by plasmas, alone or followed by immobilisation of proper biomolecules, could be particularly advantageous because surface modified polymers offer the advantage to have a material with selective properties, defined geometry and stability with intelligence to activate specifically a given metabolic cell pathway.

More advanced and recent plasma-based surface modifications deal with the immobilization of biomolecules (i.e., heparine, heparine-like, peptides, enzymes, antibodies, etc.) on biomedical surfaces, to induce the growth of primary cells, or to act as sensors in immunodiagnostics, or to exhibit blood compatibility [3]. PE-CVD and Plasma Treatments are utilized as patterning techniques to develop biomedical surfaces characterized by cell-adhesive micro-domains alternated with cell repulsive ones. Such an approach is devoted to drive the

behaviour of cells on biomedical surfaces (e.g., on biodegradable scaffolds) to be utilized in Tissue Engineering [4].

In this work different plasma-processed surfaces were utilized for cell growth experiments as it, or functionalized with RGD peptides or with carbohydrate-based molecules. Galactose, in particular, was shown to selectively bind hepatocytes via the asialoglycoprotein receptor when immobilised to polymer surfaces. The immobilization was performed through wet chemical reactions, in order to develop surfaces more suitable to support the growth of primary cells. The biomolecules were immobilized through proper hydrophilic "spacer arm" molecules, that leave the highest conformational freedom to the immobilized molecules, or directly to the surface. Modified surfaces were investigated by means of WCA (Water Contact Angle) and XPS (X-ray Photoelectron Spectroscopy) analysis after each step of modification. Hepatocyte and fibroblast cell lines were used to verify the cell behaviour on modified substrates with respect to unmodified polymers.

2. Materials and Methods

2.1 Materials

Polyethylene terephthalate (PET, Goodfellow UK) (10 to 14 mm dia disks) were used as substrates. Acrylic acid (AA), RGD (Arginine- Glycine- Aspartic acid), morpholine ethane sulfonate (MES) and 1-Ethyl-3-(3-dimethylamino-propyl) carbodiimide (EDC) were supplied by Sigma-Aldrich. O,O'-bis-(2-aminopropyl)-polyethylene glycol 500 (bNH_2PEG) was supplied by Fluka. Ar was supplied by Air Liquid. All reagents were used without further purification.

2.2 Surface plasma modification

Plasma deposited acrylic acid (pdAA) coatings were deposited in a stainless-steel parallel plate plasma reactor (internal steel electrodes), with the upper electrode shielded and connected, through a matching network, to a 13.56 MHz RF generator. The bottom electrode, grounded, was used as substrate holder. Two different type of pdAA coated samples were prepared by regulating the AA vapour flux rate (3 or 6 sccm). RF power was supplied for 5 min in continuous wave mode (CW) with 100% duty cycle (DC) at 100, thus leading to a high AA fragmentation. All discharges were fed with AA vapours (3 sccm or 6 sccm) and Ar (20 sccm). AA degassed with freeze-thaw cycles, was fed through a needle valve from a liquid reservoir and a steel line. Pressure was kept at 150 mTorr. Very thin pdAA coatings (< 30 nm) were always deposited; the thickness of the coatings was measured with an Alpha-Step® 500 KLA TENCOR Surface Profiler.

2.3 Biomolecules covalent immobilization

To covalently immobilise RGD on both pdAA films, PET coated substrates were first immersed in 7,5 ml of a EDC solution in MES buffer (100 mg EDC; pH 5.5; 1h at 4°C; mild stirring) to activate -COOH groups. After activation, samples were rinsed and sonicated three times in distilled water. After achieving the formation of an amide bond between the COOH groups and a NH_2 group of the RGD molecule, the substrates were reacted in 7,5 ml of MES (pH 5.5; 24h at 4°C; mild stirring) with 20 µl of a 1,44 $x10^{-2}$ M RGD solution and 100mg of EDC. RGD modified substrates were rinsed three times in distilled water.

The immobilization of galactose units on the surface of pdAA coatings, was accomplished on pdAA 6 sccm coating. Galactose was oxidized to galactonic acid according to ref [5] then it was immobilized at the surface of pdAA coatings by following the same step described for RGD. The oxidation to galactonic acid was necessary to create COOH groups available on the molecule for the immobilization.

2.4 Surface diagnostic

XPS analyses were carried out with a PHI ESCA 5300 equipped with a non-monochromatized MgK_α X-ray source (1253.6 eV). Survey (0-1150 eV Binding Energy (BE)) and high resolution spectra (C1s, O1s, N1s)

were recorded at pass energy of 160eV and 20eV, respectively. All spectra were recorded at a take off angle of 45°. Sample charging was corrected by positioning the hydrocarbon peak component of the C1s signal at 285.0 eV of BE. Chemical composition value were obtained from high resolution spectra after a linear background subtraction, using sensitivity factors provided by the software.
Static WCA measurements were carried out soon after each plasma process with a Ramé-Hart NRL 100 goniometer, using 2 µl drops of bidistilled water (five measures per sample, in triplicate).
XPS and WCA were performed also after at least one week of water soaking at 37°C. After the immersion period, samples were air dried for 12 hours and analysed.

2.5 Cell culture experiments

3T3 fibroblast and HepG2 hepatocyte cell lines were utilized for cell culture experiments, obtained from stocks routinely grown in Dulbecco's Modified Eagle Medium (DMEM), supplemented with 10% fetal bovine serum, 50 IU/ml penicillin, 50 IU/ml streptomycin and 200 mM glutamine, under 5% CO_2/ 95% air atmosphere at 37°C.
PET and TCPS (tissue culture polystirene) were used as control substrates. Plasma-processed, biomolecules modified and control samples were placed, modified side up, in Iwaki 24 well culture plates. Cells, obtained after trypsinization of confluent or near-confluent culture, were seeded at $2x10^4$ cells/well in 1 ml of DMEM and incubated at 37°C under 5%CO_2 atmosphere. Cell attachment and morphology were determined (at least 10 areas of 0.8 mm^2 per sample) at various time intervals acquired with a phase contrast microscope (Leica DM IL). Unpaired Student's t-test was used to evaluate statistical significant differences among tests (four repeated samples per experiment). Data were considered significant when $p<0.01$ was obtained.

3. Results and Discussion

Two different pdAA films were deposited on PET from different feeds of AA (3 and 6 sccm) and Ar in order to obtain functionalised surfaces with different density of COOH groups. XPS C1s signals and WCA analysis (Fig. 1) show that pdAA 6 coating resulted more hydrophilic and with an higher COOH/R density than pdAA 3 films.

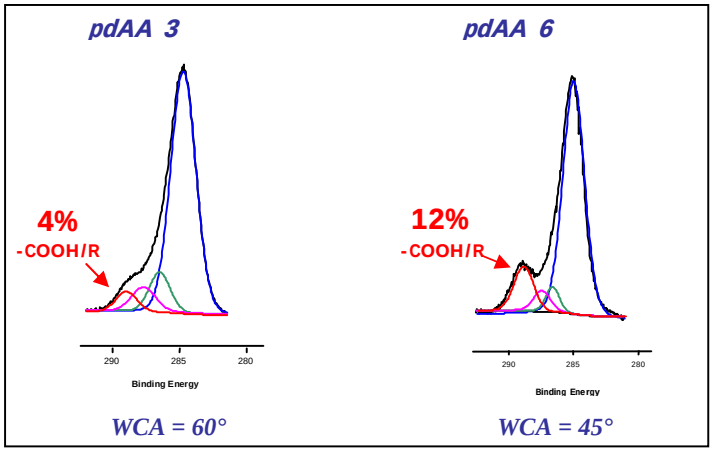

Figure 1: C1s XPS signals and WCA values of pdAA3 and pdAA6 coatings.

Particular care was devoted to investigate the stability of the coatings in water after at least 1 week of soaking. It was already known that pdAA 3 coatings are very stable in water [6]. PdAA 6 coatings presented an higher amount of COOH groups but were found less stable after water soaking as shown in Figure 2.

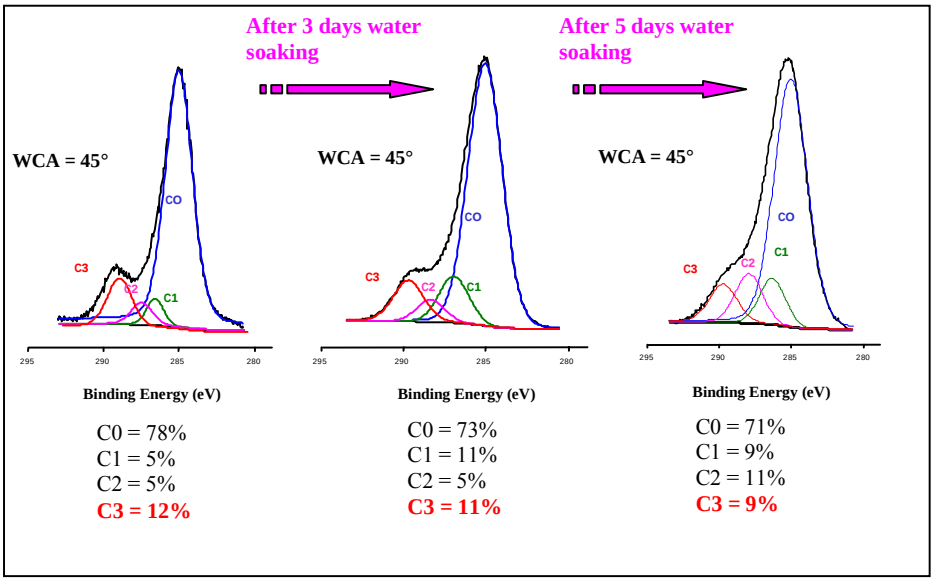

Figure 2: C1s XPS peaks of pdAA 6 coatings and best fittings after 3 and 5 days of water soaking.

PET samples coated with pdAA 3 and pdAA 6 were used for immobilization of the RGD peptide. Interestingly, pdAA 6 coatings, unstable to water soaking, resulted stabilized after the covalent immobilization of RGD involving surface COOH anchor groups and this is shown by the XPS analysis in Figure 3. This very interesting result suggests that the instability of the coatings, mainly due to surface groups, can be overwhelmed when surface groups are involved in stable bond with molecules.

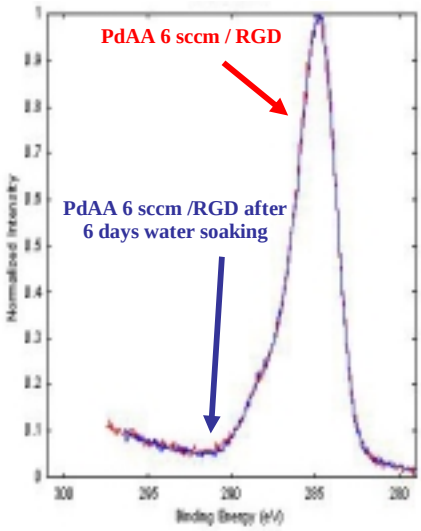

Figure 3: C1s XPS peaks of pdAA 6sccm coated PET samples after RGD immobilization before (blue) and after (red) six days of water soaking.

Plasma modified surfaces with and without immobilised RGD were tested in cell adhesion and growth experiments with 3T3 fibroblasts. After 7 hours of cell culture cell adhesion was dramatically increased on pdAA 6-RGD samples as shown in Figure 4, with respect to the other substrates. It was also seen that the adhesion is higher respect to pdAA 3-RGD surface, probably due to the higher density of surface RGD on the first kind of surfaces. Surface analysis are being performed to confirm this hypotheses.

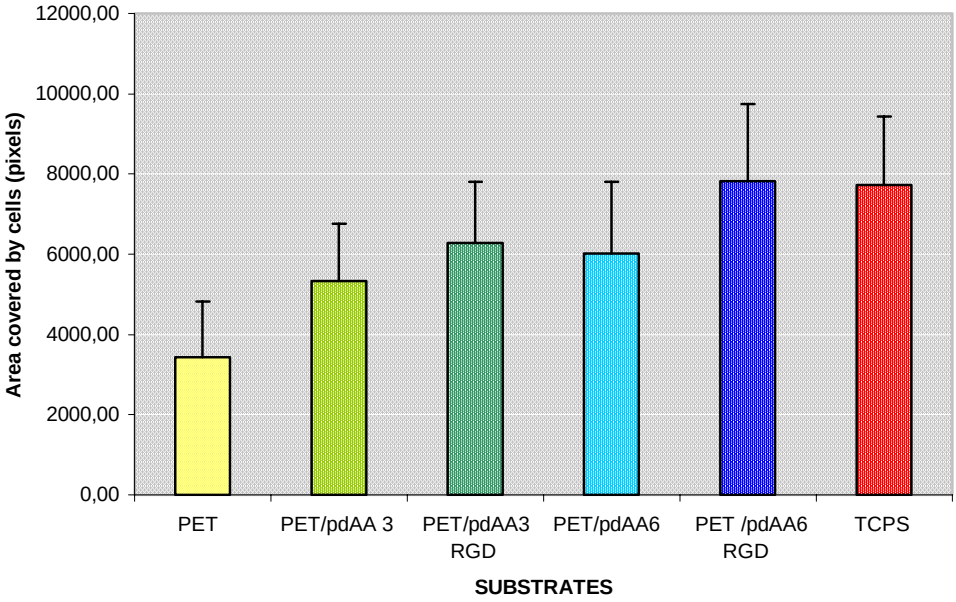

Figure. 4: Means (+ SD) of the area covered by 3T3 on different substrates after 7 hours of cell culture.
TCPS: Tissue Culture Polystyrene; **PET**; **PET/pdAA3**: pdAA 3 coating on PET; **PET/pdAA3 RGD:** RGD immobilised on pdAA 3; **PET/pdAA6:** pdAA 6 coating on PET **PET/pdAA6 RGD:** RGD immobilised on pdAA 6.

In another set of experiments PET substrates coated with the pdAA 3 sccm, were used to immobilize galactose moieties for cell adhesion experiments with HepG2 hepatocyte cell line. XPS spectra [7] showed the occurred immobilization. When HepG2 cells were seeded on galactose immobilised substrates a very different cell behaviour was found with respect to cells seeded on the other substrates. As it is shown in figure 5 an higher aggregation of Hep G2 cells was present on galactose immobilised on PET with respect to the other substrates.

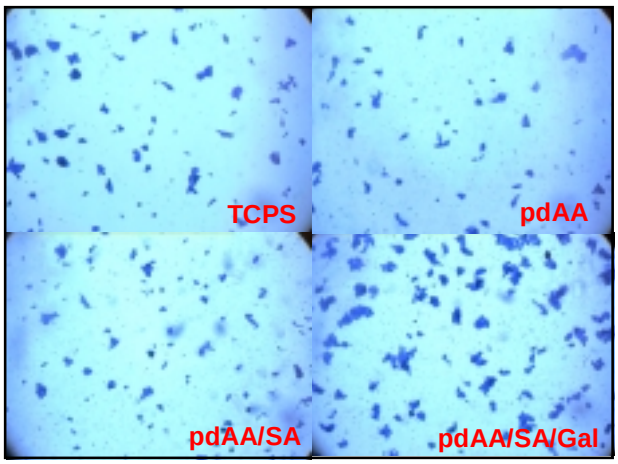

Figure 5: Coomassie blu stained HepG2 cells on different substrates after 24 hours of cell culture. **TCPS**: Tissue Culture Polystyrene; **pdAA**: pdAA 3sccm coating on PET ; **pdAA/SA :** pdAA 3sccm coating plus spacer arm on PET; **pdAA/SA/Gal:** Galactose immobilised via spacer arm on pdAA 3sccm coated PET

4. Conclusions

In this paper cell adhesion and spreading in the first hour of cell culture was increased on different pdAA coated PET that were used as substrates for biomolecules immobilization. Those results show that the presence of biomolecules further increases cell adhesion and spreading on coatings that were already shown to be cell adhesive [6]. It is very important to note that coupling the capacity of plasma processing of tuning the chemical composition of surfaces with the specificity of immobilized biomolecules offers formidable tools for the study of cell substrates interaction.

.

5. References

[1] B.D. Ratner in: Plasma Processing of Polymers, R. d'Agostino, P. Favia, F. Fracassi ed., Kluwer Acad. Publ., NATO ASI Series, E: Appl. Sci., Vol. **346**, 1997.

[2] P. Favia, R. d'Agostino Le Vide **203-1/4**, 1 (2002).

[3] P. Favia, F. Palumbo, R. d'Agostino, S. Lamponi, A. Magnani, R. Barbucci Plasmas and Polymers **3(2)**, 77-96 (1998).

[4] E. Sardella, R. Gristina, G.S. Senesi, R. d'Agostino, P. Favia Plasma Processes and Polymers, Wiley- VCH, **1(1)**, 63–72, (2004).

[5] S. Moore, K. P. Link, *J. Biol. Chem.,* **133**, 293, 1940.

[6] L. Detomaso, R. Gristina, G.S. Senesi, R. d'Agostino, P. Favia Biomaterials **26**, 3831-3841, (2005).

[7] L.C. Lopez, R. Gristina, L. De Bartolo, S. Morelli, P. Favia, R. d'Agostino Journal of Applied Biomaterials and Biomechanics **2**, 211, (2004).

[8] L. De Bartolo, S. Morelli, L.C. Lopez, L. Giorno, C. Campana, S. Salerno, M. Rende, P. Favia, L. Detomaso, R. Gristina, R. d'Agostino, E. Drioli Biomaterials **26**, 4432-4441, (2005).

Frequency analysis of arc voltage, light intensity and stagnation pressure fluctuations of DC laminar/turbulent plasma jets

Xian Meng, Wenxia Pan, Teng Li, Chengkang Wu

Institute of Mechanics, Chinese Academy of Sciences, Beijing, China

Abstract
The time-resolved arc voltage in plasma generation, related responses of light intensity and local stagnation pressure of DC pure argon laminar/turbulent plasma jets have been measured, and the frequency distributions have been obtained by using Fast Fourier Transform method to treat the measured signals. Results show that these parameters fluctuate with the similar oscillatory characteristics as the power supply, while there exists a high frequency component in turbulent state, indicating different arc-flow interactions.

Keywords DC plasma jet, fluctuation characteristics, frequency, laminar flow, turbulent flow

1. Introduction

Thermal plasma jets are widely used to heat materials difficult to melt by ordinary heating sources [1] because of their high temperature and high power density. Commonly used non-transferred DC plasma jets at atmospheric pressure operate in turbulent flow state, characterized by strong fluctuations with sharp noise. Up to now, the turbulent plasma jets have been widely used in plasma spray technology [1,2], but its inherent fluctuating characteristics cause difficulties in process control, and limit its application to low precision and less reproducible processing. The fluctuation characteristics of electric arc and turbulent jets have been much discussed these years [3-7]. Z. Duan etc. identified three different arc operating modes in a DC plasma torch, i.e., the restrike mode, the takeover mode and the steady mode, through arc voltage measurements; and suggested that the thickness of the cold gas boundary layer between the arc column and the anode surface was the most important variable influencing the arc mode occurrence and transition [3]; J. -L. Dorier etc. investigated the fluctuating behavior of a commercial DC plasma spraying torch at various working conditions, and found that the time dependence voltage signals for pure argon operation fluctuated with weak amplitude, which suggested the arc experienced the so-called “take-over mode”, while the voltage signals for the H_2/Ar mixture showed a clear sawtooth pattern, which was typical of “restrike mode” [4]; W. H. Zhao etc. presented three main factors for the jet fluctuation, i. e., the fluctuation of the power supply output, the arc root motion on the anode and the fluid dynamic process of the jet，and considered that the power supply characteristic was the dominant fluctuation source for the argon plasma jet [5].
There are several reports about the generation of laminar plasma jets [8-11]. Long laminar plasma jets have the characteristics of stable flow condition, reduced entrainment of surrounding gas, low temperature and velocity gradients along the jet axis and low working noise, and preliminary work shows favorite reproducibility for re-melting hardening of cast iron surfaces and in the stainless-steel surface cladding using laminar plasma jets, while turbulent jets are difficult to use in these material processing for their violent fluctuation and high stagnation pressure [8]. There are no detailed reports on fluctuating characteristics of laminar plasma generation and jet flow, and on comparisons between laminar and turbulent jets. So it is meaningful to compare laminar and turbulent plasma jet characteristics, for a better understanding of laminar jets and for developing novel material processing methods using them.
Both laminar and turbulent jets can be generated with the same plasma torch by changing the working parameters [9]. In this paper, the time-resolved arc voltages in plasma generation have been measured directly by using an oscilloscope, and related responses of light intensity and local stagnation pressure of the DC pure argon laminar and turbulent plasma jets have been measured by using a spectrometric system and a pressure probe respectively; the frequency distributions of these parameters have been obtained by using Fast Fourier Transform method (FFT) to treat the measured signals.

2. Experimental details

The plasma torch is the same as used in our former work [8, 9]. Both laminar and turbulent jets can be

generated with the same plasma torch by changing the working parameters, such as the gas flow rate and arc current. Plasma jets were generated with pure argon gas at gas flow rate of 2.2×10^{-4} kg/s to 5.5×10^{-4} kg/s and arc currents of 160 A to 200 A, and issued into the atmosphere after leaving the torch nozzle.

Fig. 1 shows the schematic diagram of experimental setup. Three parts are included in this experimental setup, i.e., the oscilloscope is used to measure directly the time-resolved arc voltage signals in generating plasma jets, with sampling rate of 125 kHz, and each group of signal contains 5000 points, which can be transferred to a computer at the same time; the pressure probe is used to measure the local stagnation pressure in laminar and turbulent jets; and the spectrometric system is applied to measure the spectral line intensity of ArI 750.4 nm in laminar and turbulent jets; the oscilloscope is also applied to collect the signals of light and pressure.

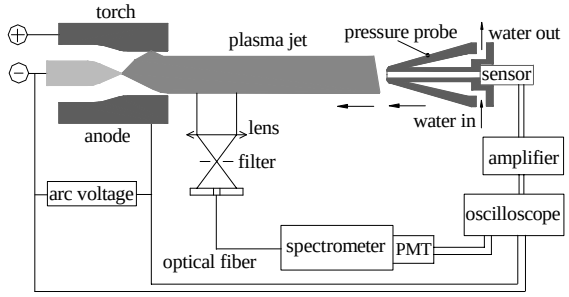

Fig. 1 The schematic diagram of experimental setup.

A tapered small size water-cooled probe is designed to connect a pressure sensor of 40 kHz in response ability. In order to get the actual fluctuation amplitude values and high system response frequency, a 0.6 mm hole is opened in the tip center of the probe, and the tip size is 3 mm. The pressure sensor can transfer the pressure signals into milli-voltage signals, and an amplifier without frequency loss is employed to enlarge the original signal values to 100 times, and then the signals are recorded by the oscilloscope with the same sampling rate as the arc voltage.

The spectrometric system consists of a lens with focal length of 120 mm, a line-type optical fiber of 10mm×1mm in dimension which can receive the whole light signals of a jet cross section, a spectrometer with focal length of 550 mm, a photo-multiplier tube (PMT) and the oscilloscope. The 1:1 image of plasma jet is formed on one side of the optical fiber through the lens, and light signals at the jet cross section are transferred to the slit of the spectrometer by the fiber. Spectral line of ArI 750.4 nm is selected by the spectrometer and transferred to the PMT by which the spectral line intensity can be detected and outputted as voltage signals. Similarly, the outputted voltage signals are collected by the oscilloscope with the same sampling rate as the arc voltage.

Fast Fourier Transform method (FFT) is applied to treat the measured signals, and then to find out the frequency distributions of laminar and turbulent plasma jets.

3. Results and discussions

Fig. 2(a) shows the voltage signals across a fixed resistance at current of 180 A, and Fig. 2(b) shows the FFT result of the voltage. It can be seen that the output of the rectified DC power supply includes obviously alternating components. The amplitude spectrum shows that 300 Hz is the prominent frequency, which is the characteristic frequency of the three-phase full-wave rectified power supply. The 100 Hz peak is due to the imbalance of the commutating circuit for three-phase AC input.

Fig. 3(a) plots the time-resolved arc voltages in generating laminar and turbulent plasma jets at arc current of 180 A and gas flow rate of 2.2×10^{-4} kg/s for laminar jet and 5.5×10^{-4} kg/s for turbulent jet, and the related local stagnation pressures of laminar and turbulent jets at the distance of 20 mm from the torch exit are presented in Fig. 3(b). The signals of arc voltage and local stagnation pressure for laminar jet and turbulent one are sampled at the same time respectively. One can see from Fig. 3(a) that the alternating components are included in the voltage signals in generating the laminar and turbulent jets, which could suggest that the characteristic of the power

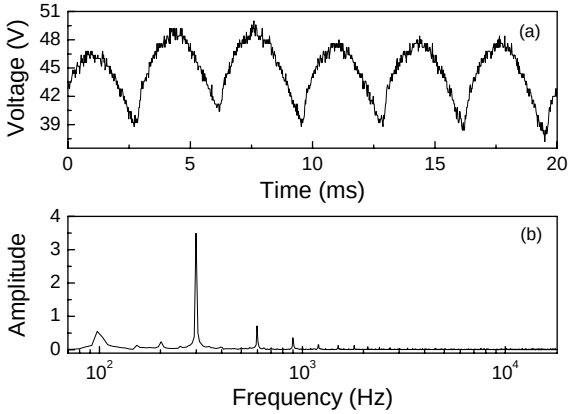

Fig. 2 Measured time-resolved voltages on resistance (a) at current of 180 A and the FFT result of the voltages (b).

supply affects the arc voltages in generating the laminar and turbulent jets in almost the same way. There is an apparent high frequency component added to the low frequency wave affected by the power supply in the case of turbulent plasma generating. The local stagnation pressures for laminar jet and turbulent one plotted in Fig. 3(b) show the similar fluctuating characteristics as the arc voltages. It is clearly seen that there are high frequency fluctuations of stagnation pressure in turbulent jet. The measured pressure is related to the gas density and flow velocity at the measuring point according to the Bernoulli's equation, where gas density value is a function of the gas temperature. At the same working parameters, the maximum stagnation pressure P_{max} can reach 28000 Pa, while the minimum pressure P_{min} is just over 8000 Pa within the time interval of 20 ms. The pressure change of laminar jet at the same measurement point is just 1500 Pa. Though the mean stagnation pressure of turbulent jet (about 19200 Pa) is larger than that of laminar jet (about 4300 Pa), where "mean stagnation pressure" is defined as the averaged time-resolved pressure signals, the ratio of the variation of stagnation pressure (P_{max} - P_{min}) to the mean pressure of turbulent jet (about 104.2%) is also larger than laminar jet (about 34.9%), which suggests the much more stable flow filed characteristics in the laminar jet. The fluctuation characteristics of spectral line intensity of ArI 750.4 nm have been studied. A high frequency component also exists in the waveform of turbulent jet. The fluctuations of stagnation pressure and spectral line intensity could represent the flow filed fluctuations of the plasma jet. This unstable property is related to the arc power fluctuation in generating plasma jets. For the convenience of later description and discussion, the word "fluctuation" is defined as the varying component added to the low frequency wave and the word "mean" refers to the average value of the related parameters, which is averaged out from time-resolved total signal data.

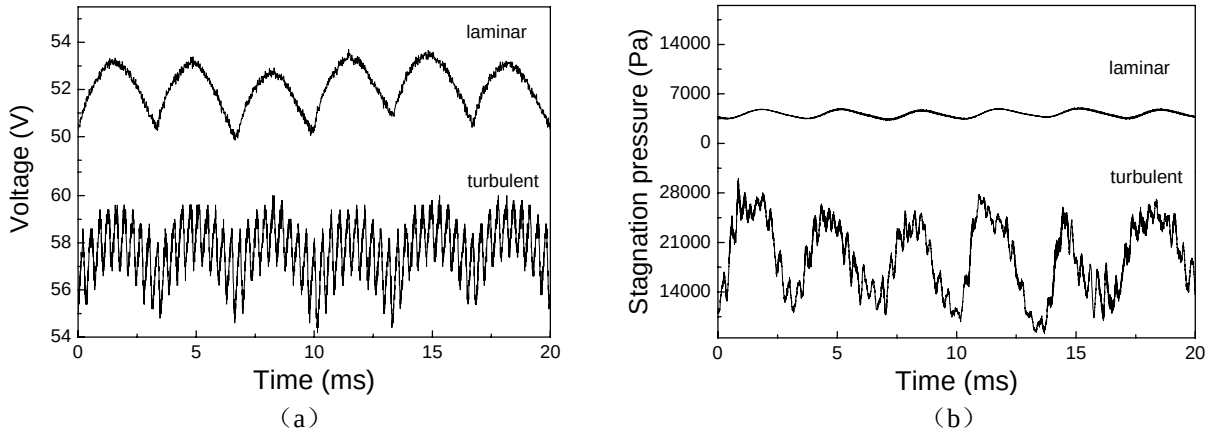

Fig. 3 Measured time-resolved arc voltages (a) in generating plasma jets and stagnation pressures (b) at the distance of 20 mm from the torch exit at arc current of 180 A and gas flow rate of 2.2×10^{-4} kg/s for laminar jet and 5.5×10^{-4} kg/s for turbulent jet.

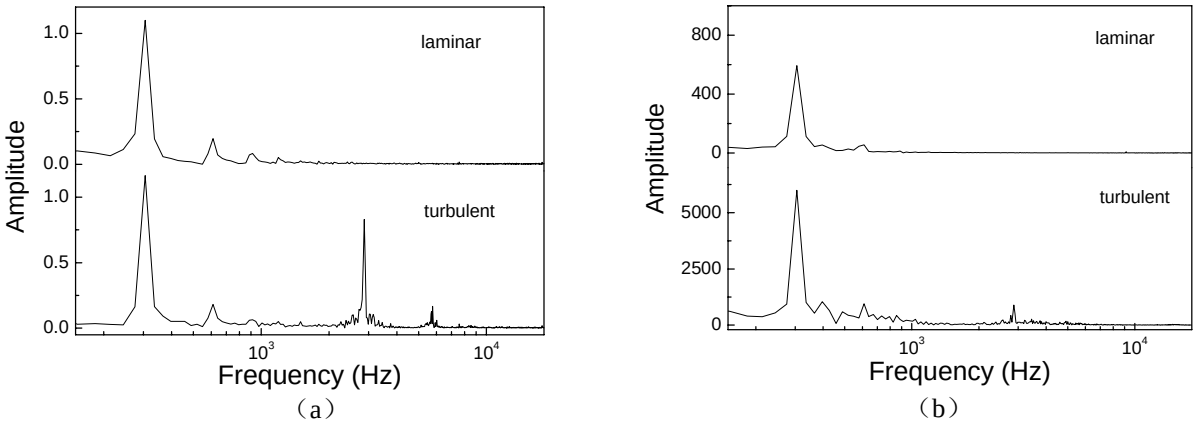

Fig. 4 FFT results for arc voltages (a) in generating plasma jets and stagnation pressures (b) at the distance of 20 mm from the torch exit at arc current of 180 A and gas flow rate of 2.2×10^{-4} kg/s for laminar jet and 5.5×10^{-4} kg/s for turbulent jet.

By using the FFT method, the amplitude spectra of the arc voltages and local stagnation pressures of Fig. 3(a) and 3(b) can be obtained, the results are shown in Fig. 4(a) and 4(b) separately. One can see that the peak of 300 Hz appears in all these spectra, similar to the spectrum of the voltage across the fixed resistance, which could prove that the characteristics of the power supply have apparent influence on the arc voltage and plasma jet flow. The amplitude spectrum of arc voltage also shows that there exists a high frequency peak close to 3 kHz in the turbulent state, which could indicate the rapid movement of the arc root on the anode surface in the generation of the turbulent plasma jet. And the value of the high frequency peak in the stagnation pressure spectrum is the same as that of the arc voltage, which indicates that the motion of the anode arc root attachment can affect the fluctuation characteristics of plasma jet. From the waveforms of Fig. 3(a) and the FFT results of Fig. 4(a), it could suggest the different moving behaviour of arc root attachment spot on the anode surface for laminar and turbulent jets generation. The arc motion in generating turbulent plasma jets seems to be similar to the “takeover mode”, since the scale of the voltage fluctuation is relatively low compared with the situation of conventional “restrike mode” [3].

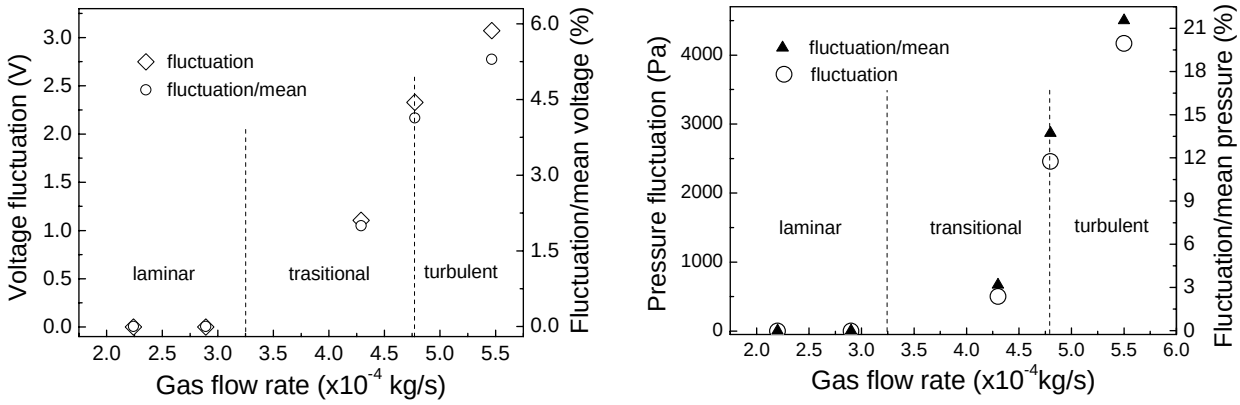

(a) (b)

Fig. 5 Voltage fluctuation and fluctuation/mean voltage (a), pressure fluctuation and fluctuation/mean pressure (b) change with gas flow rate at arc current of 180A. The words “laminar”, “transitional” and “turbulent” represent different jet flow regime.

Fig. 5(a) and 5(b) show the voltage fluctuation and the ratio of voltage fluctuation to mean voltage, and local stagnation pressure fluctuation at 20 mm from the torch nozzle and the ratio of pressure fluctuation to mean pressure at arc current of 180A and with the increase of gas flow rate from 2.2×10^{-4} kg/s to 5.5×10^{-4} kg/s separately. The words “laminar”, “transitional” and “turbulent” in these figures represent three different jet flow regimes, i.e., in the laminar flow regime, jet length increases apparently with gas flow rate and arc current; at a certain arc current, there exists a maximum gas flow rate where the jet length shows its maximum value and keeps the laminar flow state; and then the jet flow changes into the transitional regime, the jet length fluctuates heavily, and the mean jet length decreases with the increase of gas flow rate; while in the turbulent regime, the jet length is very short and almost independent of gas flow rate and arc current [12]. The values of voltage fluctuation and the ratio of voltage fluctuation to mean voltage for laminar jet are zero, for there is no high frequency fluctuation from the FFT results. It is clearly seen from these figures, the arc voltage fluctuations and the ratio of fluctuation to the mean voltage increase with the increase of gas flow rate, and the stagnation pressure has the similar characteristics, which could indicate that the flow regime of the plasma jet is directly corresponding to the arc voltage fluctuation characteristics. The ratio of the voltage fluctuation to mean voltage at the gas flow rate of 5.5×10^{-4} kg/s is about 5.3%, while that of the stagnation pressure fluctuation to mean stagnation pressure is about 20.8%, it could caused by the strong fluctuations of temperature and velocity of the turbulent plasma jet.

Similarly, the voltage fluctuation and the ratio of voltage fluctuation to mean voltage change with the increase of arc current are plotted in Fig. 6, at gas flow rate of 2.2×10^{-4} kg/s for laminar plasma jet and 5.5×10^{-4} kg/s for turbulent one. The voltage fluctuations increase a little from 3 V to 3.2 V with the increase of arc current from 170 A to 200 A for the turbulent jet, and the ratios of voltage fluctuation to mean voltage decrease a little with the increase of arc current. The increase of arc current can lead to the increase of arc voltage, though the voltage fluctuation increases a little, the net effect may lead to the decrease of the ratio.

The stagnation pressure and the ratio of pressure fluctuation to mean pressure with the increase of arc current have the same trend as that of the arc voltage, which is shown in Fig. 7. The decrease of the ratio could suggest that there is a stabilizing effect on the turbulent jet as the arc current increases.

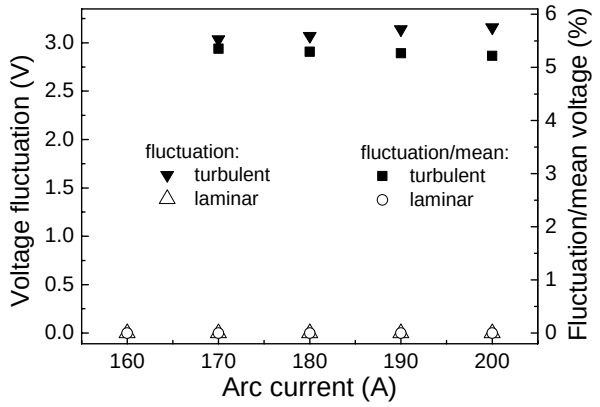

Fig.6 Voltage fluctuation and fluctuation/mean voltage change with the increase of arc current at gas flow rate of 2.2×10^{-4} kg/s for laminar plasma jet and 5.5×10^{-4} kg/s for turbulent jet.

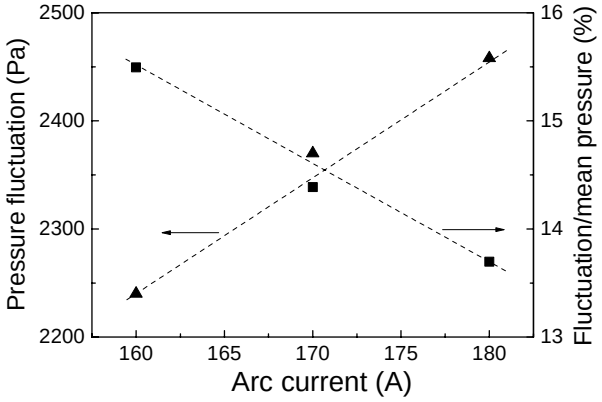

Fig. 7 Stagnation pressure fluctuation at 20mm from the torch exit and fluctuation/mean pressure change with the increase of arc current at gas flow rate of 4.8×10^{-4} kg/s for turbulent jet.

4. Conclusions

Experimental results show that the fluctuations of arc voltage in generating plasma jet, and related spectral line intensity and local stagnation pressure in a plasma jet have similar characteristics. The power supply affects the arc voltages in generating the laminar and turbulent jets in almost the same way; A high frequency component, close to 3 kHz, exists in the arc voltage in generating turbulent jet and in the corresponding stagnation pressure signals. At the same working parameters, the ratio of stagnation pressure fluctuation to the mean pressure is much larger than that of the arc voltage. Both the ratios of arc voltage fluctuation to mean voltage and the stagnation pressure fluctuation to the mean pressure decrease with the increase of arc current.

Acknowledgements

Work supported by the National Natural Science Foundation of China (Project Nos. 50336010 and 50276065).

References

[1] E. Pfender – Plasma Chem. Plasma Process. 19, 1(1999)
[2] P. Fauchais – J. Phys. D: Appl. Phys. 37**,** R86(2004)
[3] Z. Duan, K. Wittmann, F. Coudert, J. Heberlein, P. Fauchais – Proc. 14th Int. Symp. Plasma Chem. Prague, Aug. 2-6, 233(1999).
[7] E. Pfender, R. Spores, W. L. T. Chen – Int. J. Materials Product Tech. 10, 548 (1995).
[5] W. H. Zhao, K. Tian, H. Z. Tang, D. Liu, G. Z. Zhang – J. Phys. D: Appl. Phys. 35, 2815 (2003).
[6] E. Pfender – Thin Solid Films, 238, 228 (1994).
[4] J. -L. Dorier, Ch. Hollenstein, A. Salito, M. Loch, G. Barbezat – Proc. 14th Int. Symp. Plasma Chem. Prague, Aug. 2-6, 331(1999).
[8] W. X. Pan, W. H. Zhang, W. Ma, C. K. Wu – Plasma Chem. Plasma Process. 22, 271(2002).
[9] W. X. Pan, W. H. Zhang, W. H. Zhang, C. K. Wu – Plasma Chem. Plasma Process. 21, 23 (2001).
[10] V. Kuz'min, O. Solonenko, M. Zhukov – Proc. 8th National Thermal Spray Conf., Houston, Sep. 11-15, 83 (1995).
[11] K. Osaki, O. Fukumasa, A. Kobayashi –Vacuum 59, 47(2000).
[12] W. X. Pan, X. Meng, K. Cheng, D. Y. Xu, X. Chen, C. K. Wu – Proc. 7th Asia Pacific Conf. Plasma Sci. Tech. Fukuoka, Jun. 29-Jul. 2, 67 (2004).

MATHEMATICAL MODELING OF ARGON PLASMA IN ICP TORCH BY NON-EQUILIBRIUM MODEL

S. Dresvin[1], J. Amouroux[2], D. Ivanov[1]

[1] *SPb State Polytechnical University, 29 Polytechnicheskaya Str., 195251 Saint-Petersburg, Russia*
[2] *LGPPTS, EMSCP, 11 rue P. & M. Curie, 75005 Paris, France*

ABSTRACT

A calculation of plasma parameters in RF ICP torch was made using a non-equilibrium model. The RF ICP torch for spectrochemical analysis works at a frequency of 27.12 MHz; the plasma power is 2 kW; the inner diameter of the torch is 24 mm and the plasma gas is argon. The plasma torch has three axial gas flows: the transport gas flow is G_1=3.0 l/min, the plasma gas flow is G_2=2.5 l/min, the sheath gas flow is G_3=20 l/min.

Two cases were calculated: without and with the transport gas flow. The results calculated using the Saha and Potapov equations were compared. The results of calculation using an equilibrium (LTE) model are also given for comparison.

1. INTRODUCTION

The features of plasma in RF ICP torches such as a high purity due to the absence of electrode and large volumes of plasma have resulted in a wide range of applications. Main technologies based on RF ICP torch application are the following: powder spheroidization, synthesis of ultra-fine powder, plasmachemical technologies, material treatment at reduced pressures etc. One of the most widespread applications of ICP torches is a spectrum source for spectrochemical analysis.

The particularity of spectrochemical ICP torch is the feeding of the investigated material into the axial plasma zone through a central tube by a transport gas flow. This material evaporates and the elements contained in this material emit spectra. These spectra are recorded and analyzed by spectral instruments. The transport gas flow leads to the formation of a cold channel in the axial zone of the plasma.

The numerical modeling of plasma parameters in RF ICP torches is widely used to analyze the plasma processes and to select the optimal operating conditions of the torch. A review of early articles on RF ICP torch modeling was carried out in the book of S. Dresvin [1]. Reviews of recent articles on this topic are contained in articles of M. Boulos, R. Barnes and J. Mostaghimi [2, 3].

The first two dimensional (2D) models of plasma were developed assuming equilibrium, see for example [4]. Non-equilibrium effects in Ar atmospheric plasma were showed in the sixties [5], but the first 2D model of a non-equilibrium Ar plasma only appeared in 1987 [6].

To calculate non-equilibrium plasma parameters in RF ICP torch, it is necessary to use data on thermodynamic and transport properties of non-equilibrium argon plasma. The calculation of non-equilibrium plasma composition is the basis of thermodynamic and transport properties calculation.

At present time, in most of works, non-equilibrium plasma composition is calculated using either non-equilibrium Saha equation [7, 6] or Potapov equation [8, 9]. The present work is devoted to the calculation of non-equilibrium Ar plasma parameters in ICP torch for spectrochemical analysis and the comparison of the results obtained using Saha and Potapov equations.

2. MATHEMATICAL MODEL OF NON-EQUILIBRIUM AR PLASMA

The model is based on the following assumptions:

- plasma is axisymmetric, fields of temperature, velocity and electromagnetic values are two dimensional;
- gas flow is laminar, stationary, at atmospheric pressure;
- plasma is optically thin;
- only the following species are present in plasma: Ar atoms, Ar+ positive ions and e electrons;
- temperatures of heavy species (Ar atoms and Ar+ ions) are equal;
- electron temperature T_e can differ from temperature of heavy species T_h (thermal non-equilibrium);
- the ionization equilibrium is present in the plasma;

- viscous dissipation and pressure work in the energy equation, gravity force and displacement current are neglected.

The non-equilibrium model of plasma involves the following equations:

- equation of energy balance for electrons:

$$\mathrm{div}\left(\left(\frac{5}{2}kT_e + E_i\right)n_e\vec{v}\right) = \mathrm{div}\left(\lambda_e \mathrm{grad}T_e\right) + \sigma_e E_\varphi^2 - u_{rad} - b_{eh}\cdot\left(T_e - T_h\right), \quad (1)$$

- equation of energy balance for heavy species:

$$\mathrm{div}\left(\frac{5}{2}kT_h\left(n_i + n_a\right)\vec{v}\right) = \mathrm{div}\left(\lambda_h \mathrm{grad}T_h\right) + b_{eh}\cdot\left(T_e - T_h\right), \quad (2)$$

- continuity equation:

$$\mathrm{div}\left(\rho\vec{v}\right) = 0, \quad (3)$$

- momentum transfer equations for axial and radial components of velocity:

$$\mathrm{div}\left(\rho\vec{v}v_z\right) = -\frac{\partial p}{\partial z} + \frac{\partial}{\partial z}\left(2\mu_h\frac{\partial v_z}{\partial z}\right) + \frac{1}{r}\frac{\partial}{\partial r}\left[r\mu_h\left(\frac{\partial v_r}{\partial z} + \frac{\partial v_z}{\partial r}\right)\right] + F_z, \quad (4)$$

$$\mathrm{div}\left(\rho\vec{v}v_r\right) = -\frac{\partial p}{\partial r} + \frac{\partial}{\partial z}\left[\mu_h\left(\frac{\partial v_r}{\partial z} + \frac{\partial v_z}{\partial r}\right)\right] + \frac{1}{r}\frac{\partial}{\partial r}\left(2r\mu_h\frac{\partial v_r}{\partial r}\right) - 2\mu_h\frac{v_r}{r^2} + F_r, \quad (5)$$

- equation of electromagnetic problem:

$$\frac{\partial^2\dot{E}_\varphi}{\partial z^2} + \frac{1}{r}\frac{\partial}{\partial r}\left(r\frac{\partial\dot{E}_\varphi}{\partial r}\right) - \left(\frac{1}{r^2} + j\mu_0\omega\sigma_e\right)\dot{E}_\varphi = 0. \quad (6)$$

It is necessary to notice that the 2D electromagnetic problem was developed and solved for the vector potential $\dot{A}_\varphi$ [10, 11]. But in the articles [12, 13], it has been showed that this problem can be solved for electric field intensity $\dot{E}_\varphi$ with the exception of intermediate value – vector potential $\dot{A}_\varphi$ (see (6)). Moreover, contrary to most of the works, the complex equation (6) was not decomposed into two real ones but was solved in complex numbers [14]. This system of non-linear differential equations (1) – (6) was solved using the SIMPLER algorithm [15].

To solve the system (1) – (6) it is necessary to calculate the thermodynamic and transport properties of non-equilibrium Ar plasma which depend on two temperatures: electron temperature T_e and temperature T_h of heavy species.

The following system of equations was used for the calculation of plasma composition:

- quasi-neutrality equation:

$$n_e = n_{Ar+}, \quad (7)$$

- Dalton's law of partial pressures:

$$p = n_e kT_e + \left(n_{Ar} + n_{Ar+}\right)kT_h, \quad (8)$$

- Potapov equation:

$$n_e\left(\frac{n_{Ar+}}{n_{Ar}}\right)^{T_h/T_e} = g_e\frac{Z_{Ar+}\left(T_e\right)}{Z_{Ar}\left(T_e\right)}\left(\frac{2\pi m_e kT}{h^2}\right)^{3/2}\exp\left(-\frac{E_i}{kT_e}\right), \quad (9a)$$

or non-equilibrium Saha equation:

$$n_e\frac{n_{Ar+}}{n_{Ar}} = g_e\frac{Z_{Ar+}\left(T_e\right)}{Z_{Ar}\left(T_e\right)}\left(\frac{2\pi m_e kT}{h^2}\right)^{3/2}\exp\left(-\frac{E_i}{kT_e}\right). \quad (9b)$$

Data from reference [16] were used to calculate the partition functions $Z_{Ar}\left(T_e\right)$, $Z_{Ar+}\left(T_e\right)$. The calculation of plasma composition using Potapov equation (solving of system of equations (7), (8) and (9a)) and Saha equation (solving of system of equations (7), (8) and (9b)) was carried out by Newton method for increment of logarithm of unknown values [17].

As the plasma composition is known, its thermodynamic properties can be calculated using simple formulas [1]. The transport properties of plasma were calculated by the Chapman-Enskog method [18, 19]. In this calculation, the data for collision integrals recommended in works [20, 21] were used.

3. DATA FOR CALCULATIONS

The plasma torch for spectrochemical analysis operated at a frequency of 27.12 MHz, the electrical power in plasma was 2 kW and the gas was argon. The plasma torch had three axial gas flows: transport gas flow G_1, plasma gas flow G_2, sheath gas flow G_3. The torch geometry is given in Fig. 1.

Two cases were calculated:

- without the injection of transport gas: G_1=0;
- with the injection of transport gas: G_1=3.0 l/min.

The plasma gas flow rate was G_2=2.5 l/min and the sheath gas flow rate was G_3=20 l/min. A non-uniform grid system of (r,z)=(40,50) points was used for the calculation.

Both cases were calculated using 3 different models:

- non-equilibrium model using Potapov equation;
- non-equilibrium model using Saha equation;
- equilibrium model.

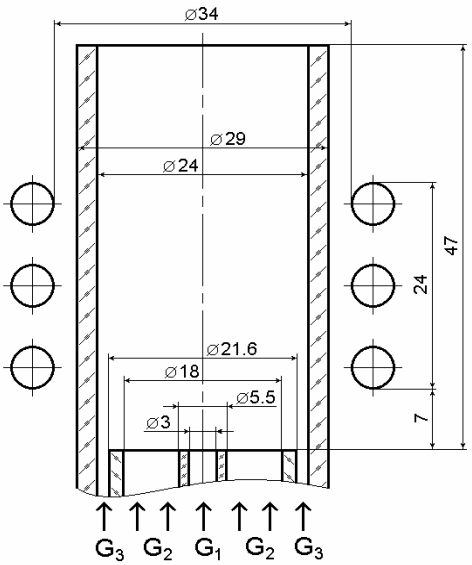

Figure 1. The torch geometry (dimensions are given in mm)

4. RESULTS AND DISCUSSION

The results of the calculations are shown in Figs. 2 – 4.

Comparing the results from the different models, one can notice the following:

1. The electron temperature T_e in the model using Potapov equation is higher by about 1000 K than the electron temperature predicted with the model using Saha equation.

2. In the case of two gas flows the heavy species temperatures T_h of concerned non-equilibrium models are equal near the torch wall but in the axis zone the heavy species temperature of the model using Potapov equation is higher by 1000 K and more. The transport gas flow G_1 (the case with three gas flows) leads to the formation of a cold channel in which the heavy species temperatures T_h predicted by the both models are equal.

3. In the case of the two gas flow a substantial deviation from LTE is observed near the wall of the torch (the difference between T_e and T_h can reach 6000 K) but near the axis, plasma is close to LTE. The deviation from LTE is observed also near the inlet of the torch. The transport gas flow leads to a substantial deviation from LTE on the torch axis.

4. The comparison of the equilibrium temperature with the heavy species temperature T_h shows that the equilibrium temperature is lower near the wall. This fact can be explained as follows: the heavy species have an additional source of energy resulting from the energy exchange with electrons due to the high electron temperature in this region. This source of energy can not be taken into account in the equilibrium model.

The equilibrium temperature is higher than the heavy species temperature near the axis of the torch. This fact can be explained as follows: the zone of power dissipation is smaller for the equilibrium model; therefore, the plasma temperature has to be higher in the equilibrium model to dissipate the same electrical power as for non-equilibrium plasma [3].

a) non-eq, Potapov, T_e (left) and T_h (right)

b) non-eq, Saha, T_e (left) and T_h (right)

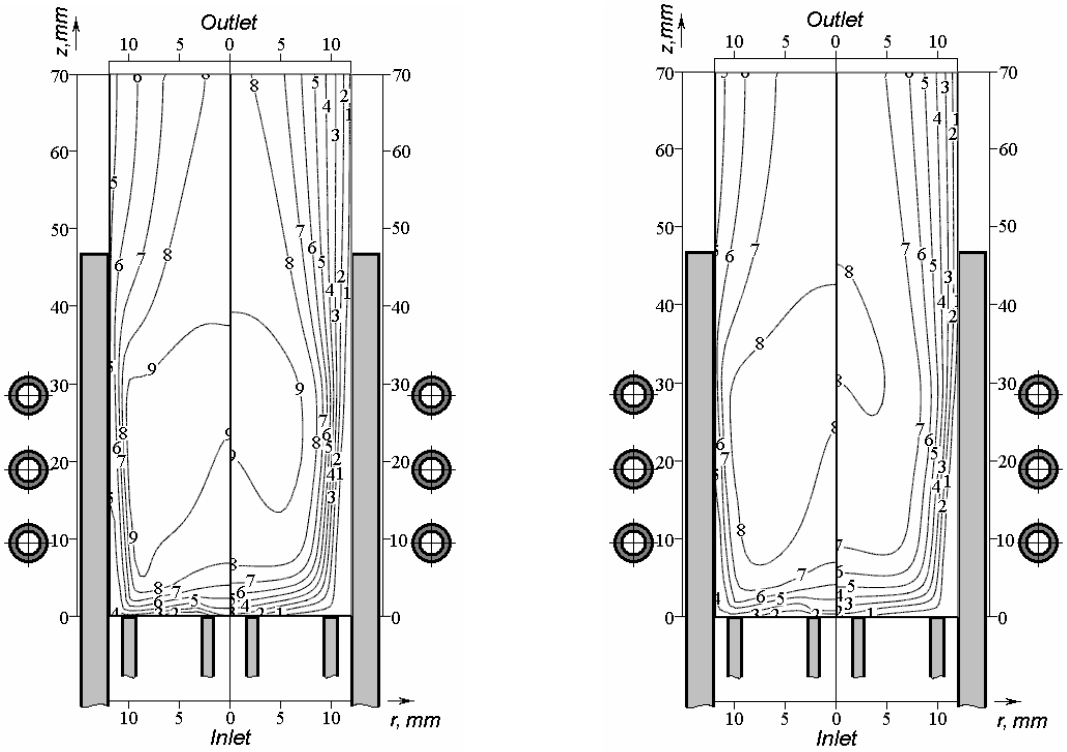

c) non-eq, ψ, Potapov(left) and Saha(right)

d) equilibrium, T (left) and ψ (right)

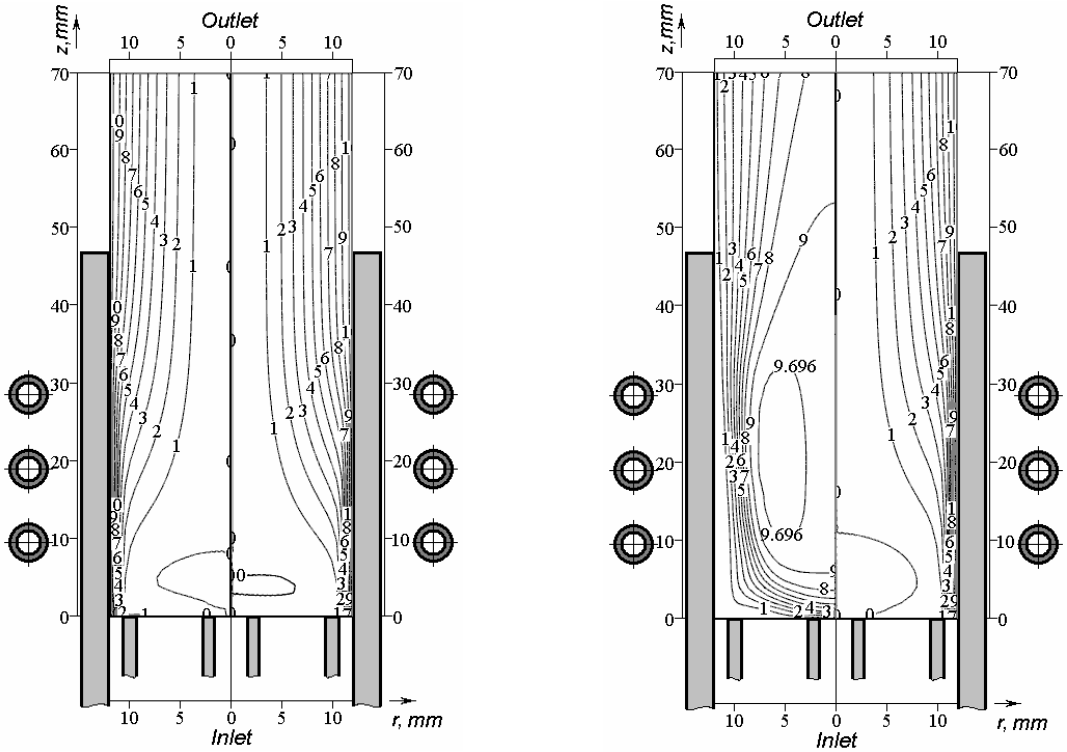

Figure 2. Temperature (in 10^3 K) and flow (in 10^{-5} kg/s) fields for concerned models in case of two gas flows

a) non-eq, Potapov, T_e (left) and T_h (right)

b) non-eq, Saha, T_e (left) and T_h (right)

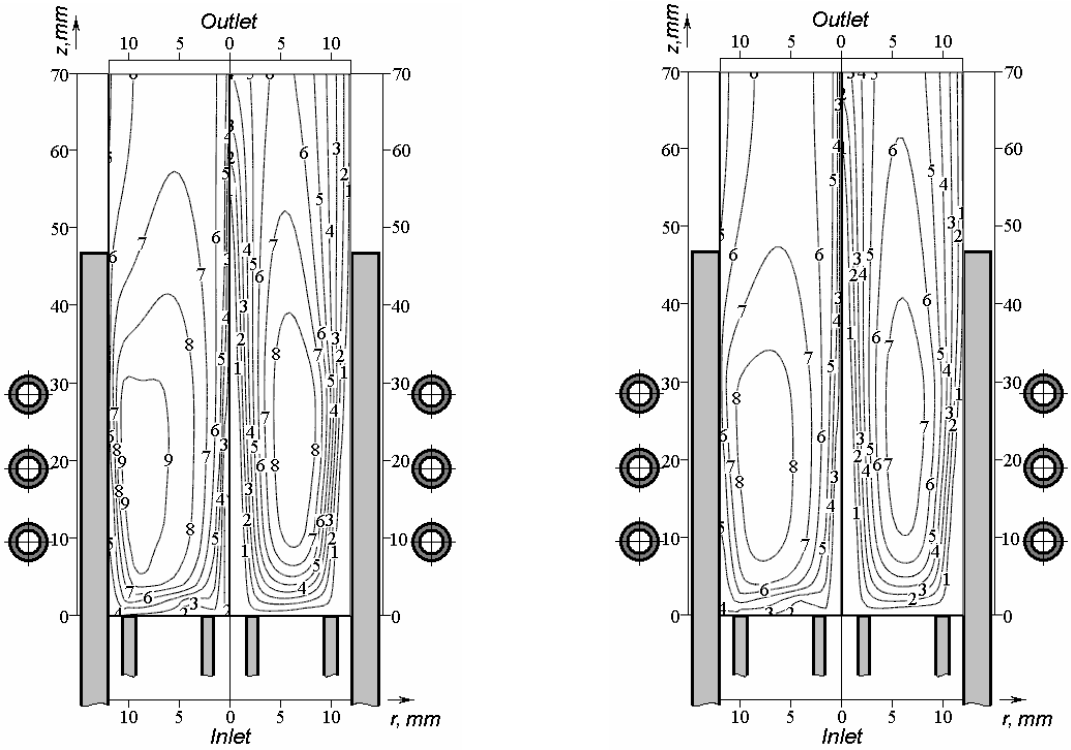

c) non-eq, ψ, Potapov(left) and Saha(right)

d) equilibrium, T (left) and ψ (right)

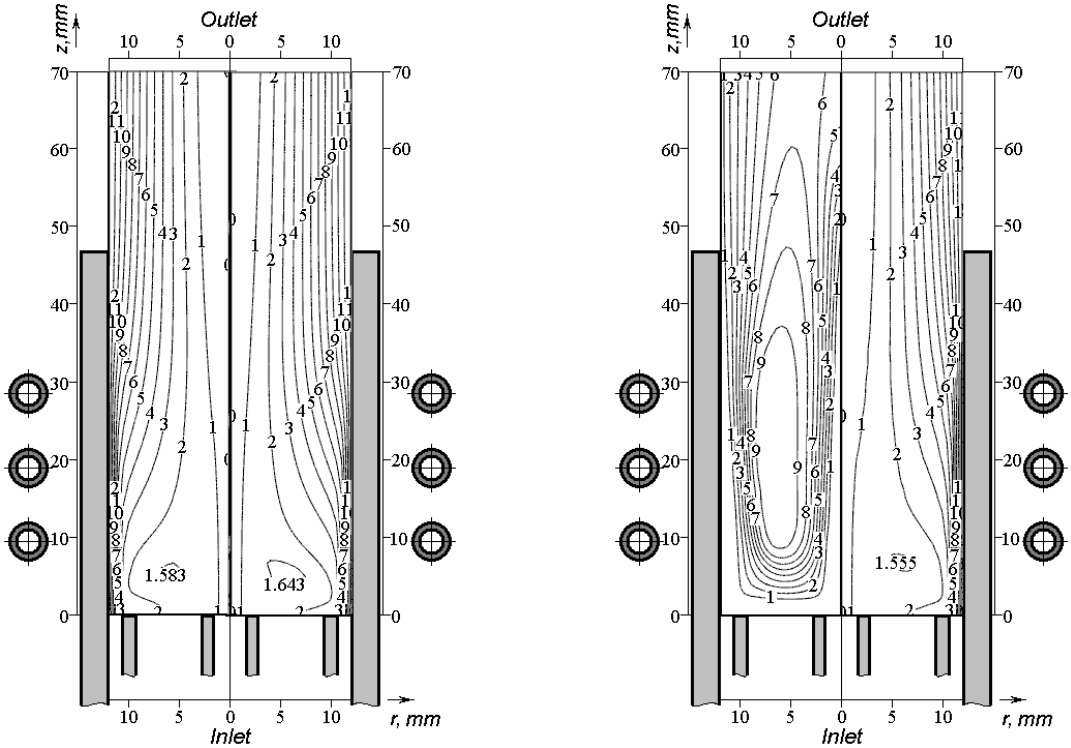

Figure 3. Temperature (in 10^3 K) and flow (in 10^{-5} kg/s) fields for concerned models in case of three gas flows

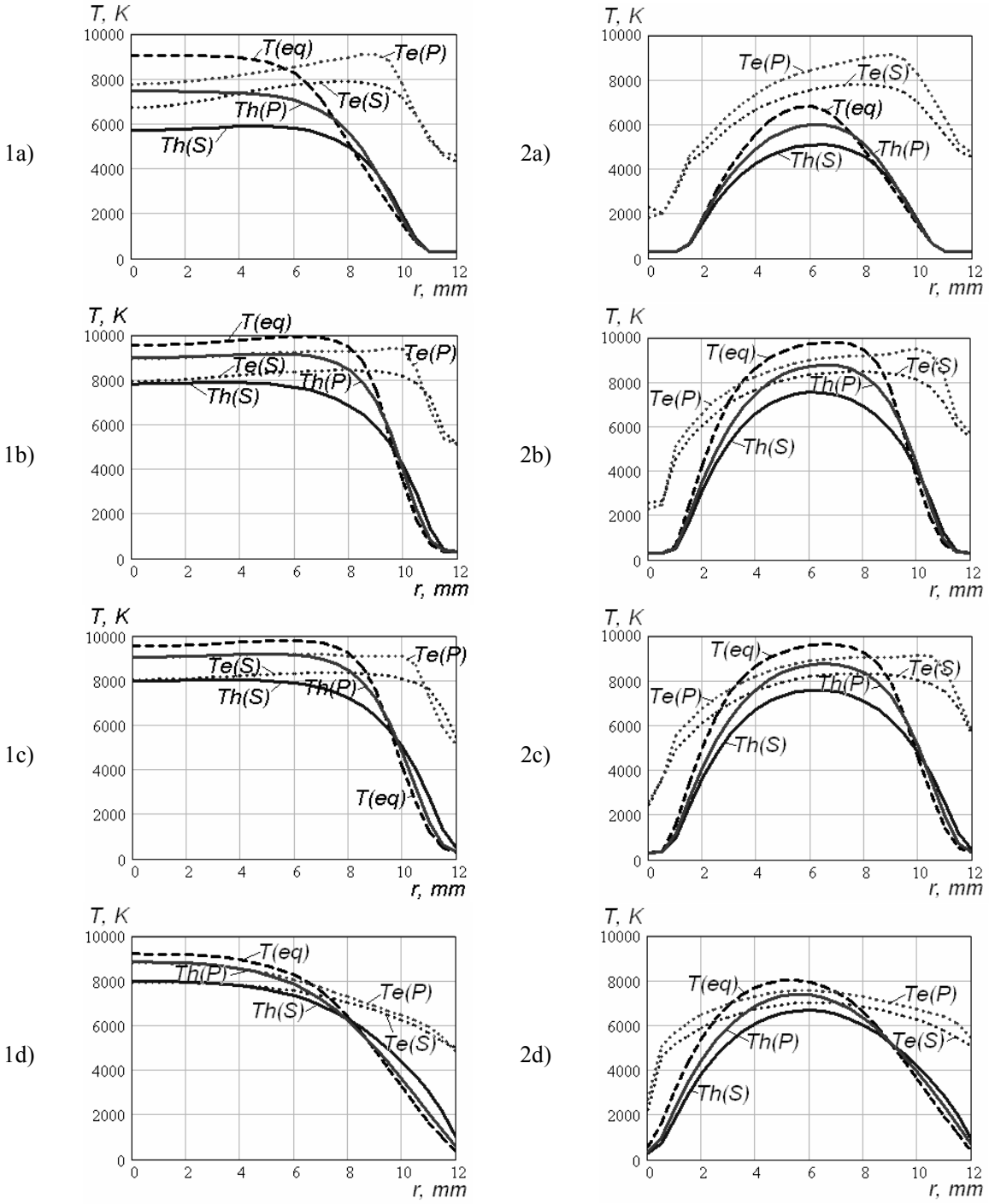

Figure 4. Radial distributions of electron temperature T_e, temperature T_h of heavy species and equilibrium temperature in various cross sections: a - z =6 mm, b - z =20 mm, c - z =30 mm, d - z =47 mm; 1 (left) – case of two gas flows, 2 (right) – case of three gas flows. Symbols in the graphs: T(eq) – equilibrium temperature, Te(P) and Th(P) – electron and heavy species temperatures in model with Potapov equation, Te(S) and Th(S) – the same with Saha equation

5. The peak of temperature is located near the axis according to the equilibrium model. Meanwhile plasma has an obvious skin effect at a frequency of 27.12 MHz. Therefore, the results of the non-equilibrium

models are closer to the reality because the peak of electron temperature is located noticeably closer to the wall of the torch.

It is necessary to notice that the transport gas does not change the position of the peak of electron temperature.

6. The plasma flows predicted with the two non-equilibrium models are the same. The comparison of the plasma flows obtained using equilibrium and non-equilibrium models shows that the gas penetrates faster into the plasma core in the case of the non-equilibrium model.

5. CONCLUSIONS

The results of the calculations have shown that the non-equilibrium model is closer to experimental data comparing to the equilibrium one when mathematical modeling of RF ICP torch for spectrochemical analysis. The basic features of the plasma torches of this kind are the following ones: small size, small plasma power, high frequency – not lower than 27 MHz, feeding of material into the axial zone of plasma.

The non-equilibrium models have shown that most part of plasma in the ICP torch is far from LTE. In the case of two gas flows, the substantial deviation from LTE is observed near the wall and inlet of the torch but near the axis of the torch plasma is close to LTE. Feeding of the transport gas flow leads to a substantial deviation from LTE on the axis.

Differences between the non-equilibrium model with Potapov equation and the one with Saha equation were shown. The final choice between these two models can be done only on the basis of experimental data.

SYMBOL LIST

b_{eh}, W/(m^3·K) - coefficient of energy exchange from the electrons to the heavy species

E_i, J - ionization potential of Ar atom

$\dot{E}_\varphi$, V/m - electric field intensity

F_z, F_r, N/m^3 - axial and radial components of the Lorentz force

f, Hz - frequency

$g_e = 2$ - statistical weight of electron

h, J·s – Plank's constant

k, J/K – Boltzmann's constant

$n_a = n_{Ar}$, m^{-3} - Ar atom density

n_e, m^{-3} - electron density

$n_i = n_{Ar+}$, m^{-3} - Ar ion density

p, Pa - pressure

T_e, K - electron temperature

T_h, K - temperature of the heavy species

u_{rad}, W/m^3 - radiation power

$\vec{v}$, m/s - vector of plasma velocity

v_z, v_r, m/s - axial and radial components of velocity

$Z_{Ar}(T_e)$, $Z_{Ar+}(T_e)$ - partition functions of Ar atom and Ar ion

λ_e, W/(m·K) - electron heat conductivity

λ_h, W/(m·K) - heat conductivity of the heavy species

μ_0, h/m - permeability of the free space

μ_h, kg/(m·s) - viscosity of the heavy species

ρ, kg/m^3 - mass density of plasma

σ_e, mho/m - electron electrical conductivity

$\omega = 2\pi f$, radian/s - pulsation

ψ, kg/s - plasma flow

REFERENCES

[1] S. Dresvin, *The Fundamental of Theory and Design of H.F. Plasma Generators*, 1991. Translation from Russia in 1993.

[2] M. Boulos and R. Barnes, "Plasma Modeling and Computer Simulation" in *Inductively Coupled Plasma Emission Spectroscopy*, P. W. J. Boumans, Ed. (Wiley, New York, 1987.) – Part II. – pp. 289-352.

[3] J. Mostaghimi and M. Boulos, "Mathematical Modeling of the Inductively Coupled Plasmas", in *Inductively Coupled Plasmas in Analytical Atomic Spectrometry*, A. Montaser and D. W. Golightly, Eds. (VCH, New York, 1992). – p. 949-984.

[4] M. I. Boulos, "Flow Temperature Field in the Fire Ball of an Inductively Coupled Plasma", *IEEE Trans.on Plasma Sci.,* **PS-4**, 28 (1976).

[5] S. Dresvin, *Physics and technology of low temperature plasmas*. Edited by A. V. Donskoy, V. M. Goldfarb and V. S. Klubnikin, English edition translated by T. Checon and edited by H. U. Eckert, Iowa State University Press, 1977.
[6] J. Mostaghimi, P. Proulx, M. Boulos, "A Two-Temperature Model of the Inductively Coupled RF Plasma" *J. Appl. Phys.*, **61 (5)**, 1753 (1987).
[7] E. Richley and D. T. Tuma, "On the determination of particle concentrations in multitemperature plasmas", *J. Appl. Phys.*, **53 (12)**, 8537 (1982).
[8] A. V. Potapov, "Chemical Equilibrium of Multitemperature Systems", *High Temp.*, **4**, 18 (1966).
[9] S. Dresvin, Nguyen Kuok Shi, D. Ivanov, J. Amouroux, "Calculation of RF Plasma Torch Parameters by means of Non-Equilibrium Model of Ar Plasma", Proc. TPP-6 (2001), P. Fauchais, ed., Begell House, New York, p. 257.
[10] J. W. McKelliget, N. El-Caddah, "The effect of coil design on material synthesis in an inductively coupled plasma torch", *J. Appl. Phys.*, **64 (6)**, 2948 (1988).
[11] J. Mostaghimi, M. I. Boulos, "Two-dimensional Electromagnetic Field Effects in Induction Plasma Modeling", *Plasma Chem. Plasma Process.*, **9 (1)**, 25 (1989).
[12] Xi Chen and E. Pfender, "Modeling of RF Plasma Torch with a Metallic Tube Inserted for Reactant Injection", *Plasma Chem. Plasma Process.*, **11 (1)**, 103 (1991).
[13] B. W. Yu and S. L. Girshick, "Modeling inductively coupled plasmas: The coil current boundary condition", *J. Appl. Phys.*, **69 (3)**, 656 (1991).
[14] Nguyen Kuok Shi, *Investigation of RF and Arc Plasma Torches*, Science Doctor Dissertation, SPb, 2002 (in Russian).
[15] S. Patankar, *Numerical Heat Transfer and Fluid Flow*, Mc Graw Hill, New York, 1980.
[16] E. V. Stupochenko, I. P. Stahanov et al., "Termodinamicheskie svoystva vozduha v intervale temperatur ot 1000 do 12000 K i intervale davleniy ot 0.001 do 1000 atm" in *Fizicheskaya Gazodinamica*, A. S. Predvoditelev, Ed., Izd-vo AN SSSR, Moskva, 1959, p. 3-38 (in Russian).
[17] A. L. Suris, *Termodynamica vysocotemperaturnych processov*, Metallurgia, Moskva, 1985 (in Russian).
[18] J. O. Hirschfelder, C. F. Curtiss, and R. B. Bird, Molecular Theory of Gases and Liquids, 2nd ed., Wiley, New York, 1964.
[19] M. I. Boulos, P. Fauchais, E. Pfender, *Thermal Plasmas: Fundamentals and Applications, Vol. 1*, New York: Plenum Press, 1994. – 452 p.
[20] J. Aubreton, C. Bonnefoi, J. M. Mexmain, "Calcul de propriétés thermodynamiques et des coefficients de transport dans un plasma Ar-O_2 en non-équilibre thermodynamique et à la pression atmosphérique", *Revue Phys. Appl.*, **21**, 365 (1986).
[21] A. B. Murphy and C. J. Arundell, "Transport Coefficients of Argon, Nitrogen, Oxygen, Argon-Nitrogen and Argon-Oxygen Plasmas", *Plasma Chem. Plasma Process.*, **14 (4)**, 451 (1994).

Heat transfer of particles in thermal plasmas

S. Dresvin[1], J. Amouroux[2], S. Zverev[1]

[1] *SPb State Polytechnical University, 29 Polytechnicheskaya Str., 195251 Saint-Petersburg, Russia;*
[2] *LGPPTS, EMSCP, 11 rue P. & M. Curie, 75005 Paris, France*

Abstract

One of the most widespread areas of plasma technology is a treatment of fine-dispersed materials in plasma jets. Complexity of an experimental research of system «plasma flow – particles» has caused the creation of the mathematical models describing movement, heat transfer and physical and chemical transformations of dispersed materials in plasma. Researches of heat transfer in high-temperature flows are of significant interest as heat transfer from plasma to particles of powder is the determining factor.

A number of studies of particle heat transfer in thermal plasmas give the following expression for Nusselt number: $Nu=2+A\cdot Re^{0.5}\cdot Pr^{0.33}$, where A is constant. However, this expression overestimates Nu in comparison with experimental data. In this connection authors offer the criterial expression for calculation of particle heat transfer in plasma taking into account the correction for conductive term: $Nu=2\cdot(V_s/V_p)+A\cdot Re^{0.5}\cdot Pr^{0.33}$. Introduction of correction namely V_s/V_p obviously explains mechanism of influence of heat transfer conductive component on particle conductive-convective heat transfer in thermal plasma and result in sufficiently good agreement of calculations with numerous experimental data.

Key words

Plasma, solid particle, calculation, heat transfer, experimental data.

Symbol list

«p»	Plasma index	Pr	Prandtl number
«s»	Solid particle index	Re	Reynolds number
«f»	Boundary layer average value index	Nu	Nusselt number
T	Temperature	d	Diameter
H	Enthalpy	μ	Viscosity
V	Velocity	ρ	Density
α	Heat transfer coefficient	q	Specific power
c_p	Specific heat at constant pressure	λ	Heat conductivity

1. Introduction

In most cases a heating of fine-dispersed materials is determined by intensity of particles heat transfer in thermal plasmas. So depending on sizes, one of particles are have time to heat up to a certain temperature, others are melt and super-dispersed particles are evaporate completely. Therefore particles and thermal plasmas heat transfer investigation is necessary for understanding of plasma technologies of dispersed materials treatment.

2. Investigation of criterial dependences of heat transfer

A body placed into a flow of ionized gas is received a heat by a heat conductivity, a convection and a radiation. Here it is meant that the heat transfer is carried out by the all kind of processes: atomic, molecular, electron, recombinational, dissociational and chemical processes.

An analytic solution of differential equations can not be obtained for complex conditions of heat transfer in plasma. Therefore to understand complex physical phenomena in plasma a method of modeling is used. That method is based on the theory of similarity. The Newton model of the heat transfer underlies of the method:

$$q = \alpha \cdot \Delta T . \qquad (1)$$

A heat transfer coefficient α is a complex function. It depends on different parameters and both the body and plasma properties.

A relationship between the heat transfer coefficient and the mentioned parameters is usually defined by a criterial dependence:

$$\mathrm{Nu} = \alpha \cdot \frac{d_s}{\lambda_p} = f(\mathrm{Re}, \mathrm{Pr}) . \qquad (2)$$

There are a big number of semi-empirical criterial dependences that differ considerably from each other for the same conditions of a streamline of the spherical model [1–3].

By now a lot of coefficients and corrective modifications for Reynolds and Prandtl numbers were proposed by a series of authors on the basis of an analysis of experimental data of small bodies heat transfer in plasma [4–16].

In most cases they use the following formula [17]:

$$\mathrm{Nu} = \underbrace{2}_{\text{conduction}} + \underbrace{0.6 \cdot \mathrm{Re}^{0.5} \cdot \mathrm{Pr}^{0.33}}_{\text{convection}}, \qquad (3)$$

where the first item «2» characterizes the process of heat transfer by a thermal conductivity through the boundary layer and the second one «$0.6 \cdot \mathrm{Re}^{0.5} \cdot \mathrm{Pr}^{0.33}$» expresses a convective heat transfer from an incident plasma flow.

It is necessary to notice important features in a point of view of different authors to a taking into account of a strong temperature change in a thermal boundary layer of a streamlined body. For example, as the defining temperature to calculate plasma properties in the papers [11, 12, 18] they use the temperature of an incident flow, in the papers [6, 7] – mass averaged temperature, in the paper [10] they recommend to use the averaging temperature of the boundary layer. The authors of the paper [12] calculate a flow viscosity using the temperature $T_s + 0.19 \cdot (T_p - T_s)$, but a heat conductivity – using the temperature of the particle surface T_s, in the paper [9] they calculate properties using the temperature of the particle surface T_s. Different points of view also exist to a calculation of heat fluxes, in the papers [7, 10–12, 18] they use the temperature difference $\Delta T = T_p - T_s$, but in the papers [4, 5, 9] – the enthalpy one $\Delta T = (H_p - H_s)/c_p$. Some authors suppose that as the defining temperature it is necessary to use a temperature that was found experimentally.

Thus, the differences between the criterial dependences of different authors lie in a choice of the defining temperature to calculate plasma properties – the flow temperature (T_p), the particle surface temperature (T_s) or the average value of the flow and particle surface temperatures (T_f), and in a using of different temperature corrections. In addition each of authors introduces the correction in a form of an additional item in one's own way on the basis of one or another reason [18]. That fact makes difficulties for the heat transfer analysis.

3. Heat transfer experimental data

A big number of formulas to calculate the Nusselt number exist. Those criterial dependences are correct for narrow ranges of temperatures and conditions at which they were obtained. Therefore their using often leads to errors that are difficult to evaluate (an error of the heat flux calculation may exceed a hundred per cent). In this connection it seems to be important to compare the most generally used formulas with existing experimental data in a wide range of the temperature.

To have a total notion of the process of heat transfer it is necessary to measure at the same time the following values: the heat flux to a model, the plasma temperature and velocity in a local point. Such investigation is complex to realize; therefore data does not exist in large quantities. Figs. 1 and 2 present practically all well-known experimental data of a heat transfer research in high temperature flows and plasma jets for models of metal water-cooled spheres with a diameter of 25.4 mm and for moving ceramic particles with diameters of 330-820 μm.

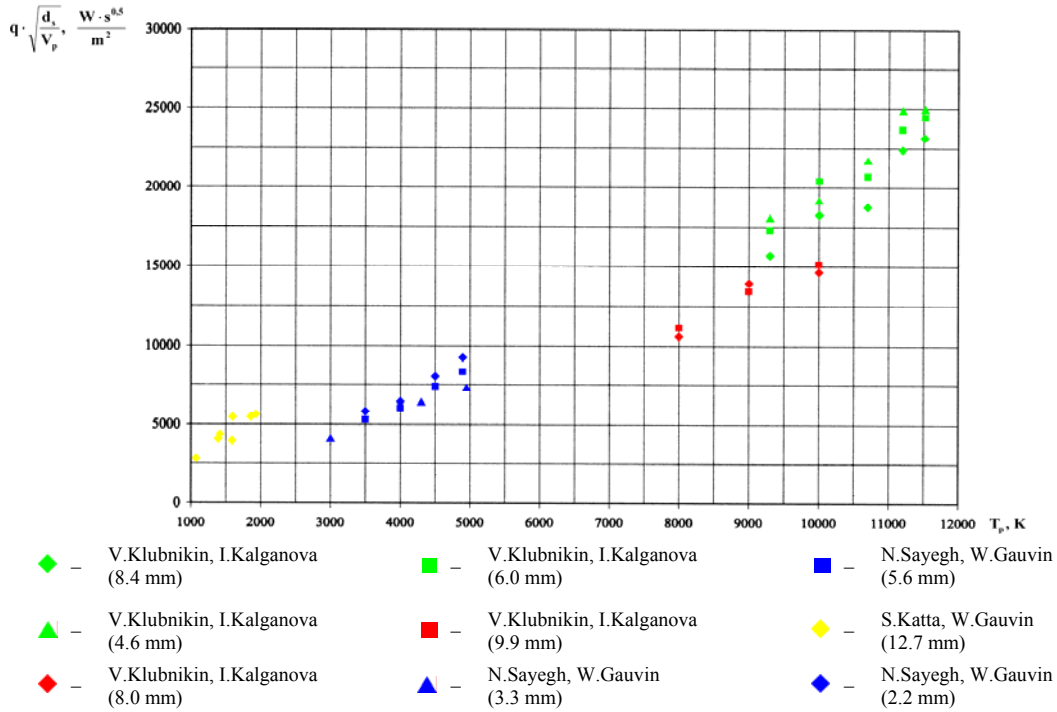

Fig. 1. Experimental data of a heat transfer research in argon plasma jets for copper models

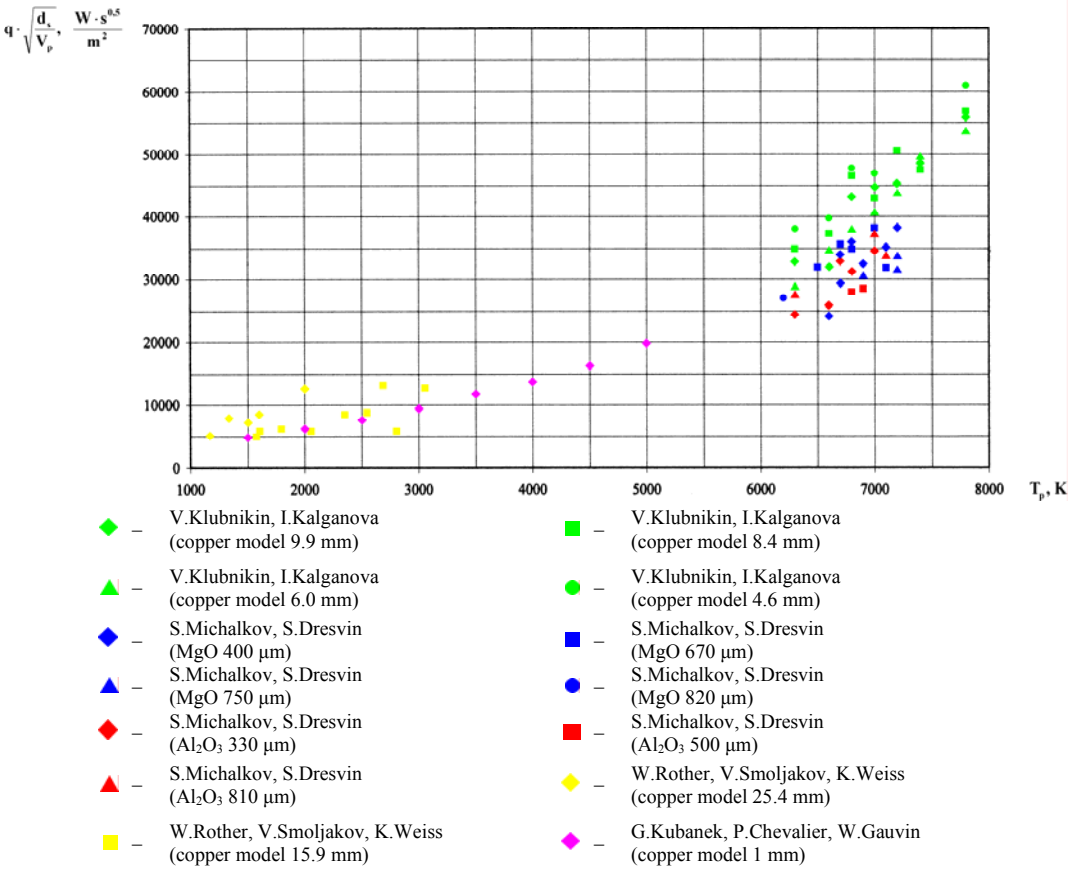

Fig. 2. Experimental data of a heat transfer research in air plasma jets for different models

On the basis of that experimental data the authors of the paper [19] made temperature dependences of heat flux for argon and air plasma, here those dependences had been calculated using the different criterial formulas and reduced to the same conditions: d_s = 6 mm, V_p = 25 m/s, T_s = 300 K. There was shown that all dependences of the heat flux in argon plasma on the temperature have a monotonic character. A character of those dependences in a case of air plasma is more complex. That difference for argon and air plasma connects to the dependence on temperature of the plasma heat conductivity (see Fig. 3).

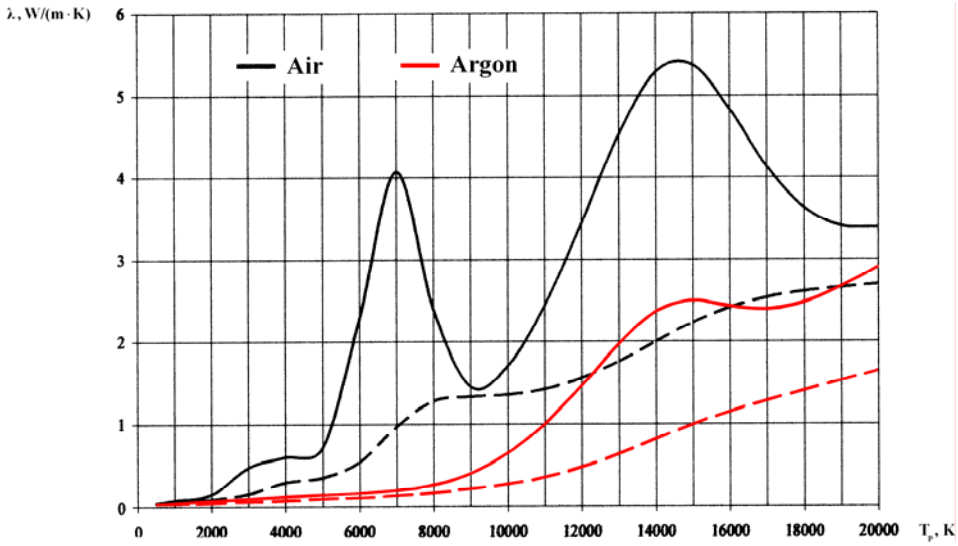

– Plasma heat conductivity from the paper [20];

– Plasma heat conductivity averaged through the particle boundary layer

Fig. 3. Dependence on temperature of the heat conductivity for air and argon plasma

If they use the temperature of the plasma flow to calculate the heat conductivity of air plasma that is necessary to estimate a heat flux, it leads to a disturbance of dependence on temperature monotonicity for high temperatures (higher than plasma dissociation takes place) and to an appearance of sharp decreasing of heat fluxes. Some doubts are cast upon it because an experimental confirmation of that fact has not been obtained up to now. Dependences on temperature of the heat flux have a smooth increasing character when using the heat conductivity averaged through the boundary layer:

$$\overline{\lambda}_p = \frac{1}{T_p - T_s} \cdot \int_{T_s}^{T_p} \lambda_p \cdot dt . \qquad (4)$$

A comparison of different criterial dependences given in the paper [19] shows a considerable variation of heat flux values for argon plasma and especially for air one. For example, the heat flux has values from 0.7 to 2 MW/m^2 for argon plasma at the temperature of 8000 K, and for air plasma at the same conditions – from 2 to 14 MW/m^2. Therefore a recommendation to use some of them can be made only as a result of a comparison of that criterial dependence with experimental data given in the paper [19].

However the direct comparison of experimental data with calculated curves is not possible as different experimental data were obtained for different model spheres (fixed copper water-cooled models or ceramic particles moving in a plasma flow) at different conditions that vary by the velocity and the temperature of plasma flows.

4. Method of D-function

To compare experimental data that had been received at different values of an incident flow velocity, a model sphere diameter and its temperature, it is convenient to use a method of D-function considering only the convective part of heat transfer.

That method allows to compare experimental data received at different conditions and to connect parameters of plasma itself with values of a heat flux to a spherical model [4].

The method of D-function is realized by the following way: the equation of the heat flux

$$q_s = Nu \cdot \frac{\lambda_p}{d_s} \cdot \left(T_p - T_s\right) = \left[A \cdot Re^{0.5} \cdot Pr^{0.33}\right] \cdot \frac{\lambda_p}{d_s} \cdot \left(T_p - T_s\right) \qquad (5)$$

is rearranged so that the right side of that equation consists of items that are dependent on the temperature only, the other items are carried to the left side.

By substituting of the formulas of definition of Reynolds and Prandtl numbers into the expression (5) of heat flux, we have:

$$q_p = A \cdot \sqrt{\frac{\rho_p \cdot V_p \cdot d_s}{\mu_p}} \cdot \sqrt[3]{\frac{\mu_p \cdot c_p}{\lambda_p}} \cdot \frac{\lambda_p}{d_s} \cdot \left(T_p - T_s\right). \qquad (6)$$

Let the equation (6) is rearranged by the following way: the left side consists of items that were measured during experiments, and the right side – ones that are dependent on the plasma temperature only:

$$\underbrace{q_p \cdot \sqrt{\frac{d_s}{V_p}}}_{\text{Experimental data}} = \underbrace{A \cdot \sqrt{\frac{\rho_p}{\mu_p}} \cdot \sqrt[3]{\frac{\mu_p \cdot c_p}{\lambda_p}} \cdot \lambda_p \cdot \left(T_p - T_s\right)}_{\text{D-function}}. \qquad (7)$$

Then the right side of the equation (7) that is dependent on the temperature only can be denoted as D-function:

$$D(T) = A \cdot \sqrt{\frac{\rho_p}{\mu_p}} \cdot \sqrt[3]{\frac{\mu_p \cdot c_p}{\lambda_p}} \cdot \lambda_p \cdot \left(T_p - T_s\right). \qquad (8)$$

Thus, the D-function connects a value of the heat flux q_p to the spherical model with the values of the sphere diameter d_s, the plasma temperature T_p and velocity V_p by the following way:

$$q_p \cdot \sqrt{\frac{d_s}{V_p}} = D(T). \qquad (9)$$

Using the D-function, it is very convenient to make a criterial treatment of results of different experiments. Then it is possible to present practically all experimental data in an only graph. Figs. 4 and 5 present dependences on temperature of the D-function for argon and air plasma correspondingly that had been created for different values of the semi-empirical coefficient A and with using of the plasma heat conductivity averaged through the boundary layer. Experimental data of different authors expressed by a universal complex $q_p \cdot \sqrt{\frac{d_s}{V_p}}$ are shown in the same figures.

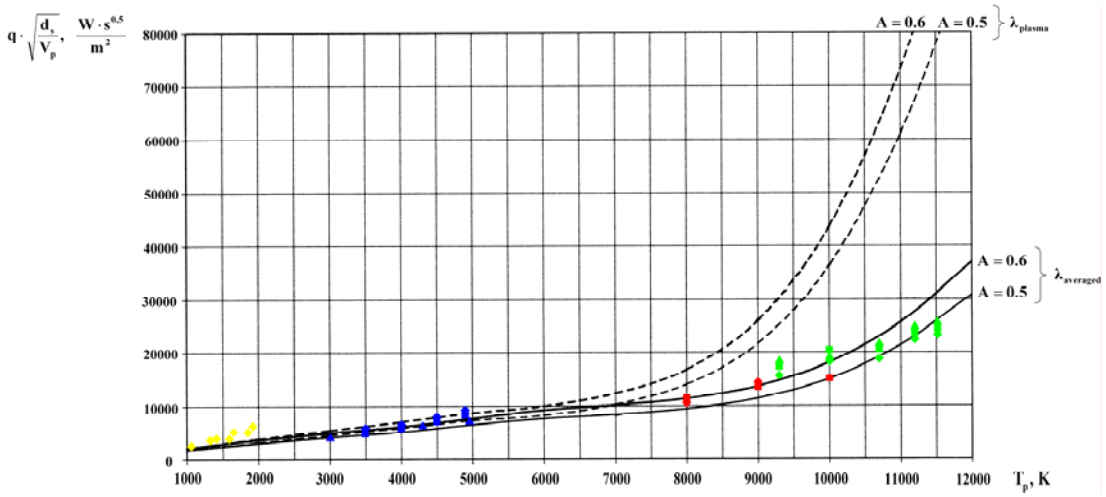

Fig. 4. Dependence on temperature of the D-function and experimental data for argon plasma

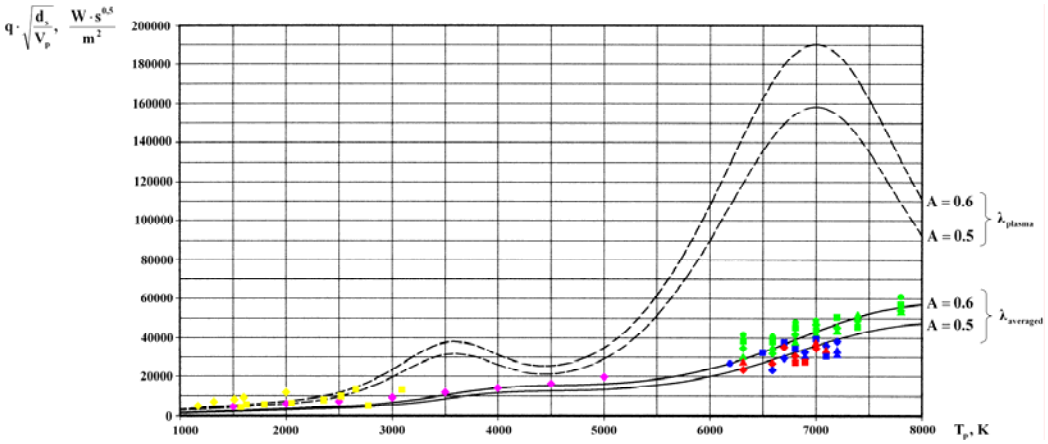

Fig. 5. Dependence on temperature of the D-function and experimental data for air plasma

A comparison by the D-function of different experimental data with the convective part of the heat transfer has shown a good agreement for the both argon and air plasma when the coefficient A is in the range of 0.5-0.6 – for metal particles, and 0.4-0.5 – for ceramic particles.

Thus, an analysis and a comparison of different experimental data with a big number of criterial formulas of spherical model heat transfer in plasma flows as well as a quantity of calculations of dynamics and heat transfer of particles of different powdered materials in plasma jets of RF plasma torches [21] let make the following conclusions:

1) When the plasma flow velocity is much more than the particle velocity – $V_p > V_s$, the conductive part does not play a noticeable role in the heat transfer;

2) When a particle is accelerated and its velocity becomes comparable with a plasma jet velocity – $V_p \approx V_s$, that is typical for small particles (less than 50 μm) and especially for fine-dispersed ones, the convective part of the heat transfer becomes equal zero $0.6 \cdot Re^{0.5} \cdot Pr^{0.33} \to 0$ because the Reynolds number becomes equal zero $Re = \frac{\rho_p \cdot \left|\vec{V}_p - \vec{V}_s\right| \cdot d_s}{\mu_p} \to 0$, and the conductive part becomes the main part of the heat transfer.

5. Correction proposal

A using of the criterial formula that takes into account the both conductive part and convective one (5) of the heat transfer under the condition that $V_p > V_s$ leads to an overestimation of the heat flux value in 2-3 times and to considerable errors in results due to the conductive part $Nu = 2$ presence. That fact is confirmed as well as calculations that had been carried out in the paper [19].

Thus, there are the following types of the criterial formulas of the particle heat transfer in plasma for different proportions of their velocities:

$$Nu = A \cdot Re^{0.5} \cdot Pr^{0.33}, \qquad \text{if} \qquad V_p > V_s;$$

$$Nu = 2, \qquad \text{if} \qquad V_p \approx V_s.$$

The goal is to find a universal criterial formula that is agreed in a satisfactory degree of accuracy with experimental data of heat fluxes from plasma to particles (Figs. 1 and 2) as well as takes into account the feature of a calculation of dynamics and heat transfer of different particles in plasma jets when the heat transfer may be changed from the convective nature to the conductive one.

As shown above, a dominance of the conductive part ($Nu = 2$) or the convective one ($Nu = A \cdot Re^{0.5} \cdot Pr^{0.33}$) of the heat transfer is determined by a proportion between the particle velocity and plasma one. That fact let us to propose a correction to the conductive part of the heat transfer ($Nu = 2$) that is a ratio $\frac{V_s}{V_p}$ of the particle velocity to the plasma one (in the current point of time). Then for heat flux calculations we recommend the following criterial formula that takes into account the features of the heating of different particles in plasma:

$$\mathrm{Nu} = 2 \cdot \frac{V_s}{V_p} + 0.6 \cdot \mathrm{Re}^{0.5} \cdot \mathrm{Pr}^{0.33}. \qquad (10)$$

Here the classical formula without any other corrections is taken as the basis because different correction factors of other authors result in correction of the heat flux of no more than 15 %. The simplest expression (3) is the most reasonable for the heat transfer analysis especially because an investigation of the convective part of that expression with using of D-function and taking into account the heat conductivity averaged through the boundary layer has shown a good agreement with experimental data (see Figs. 4 and 5). And the formula to an estimation of the heat flux from plasma to the particle has the following form:

$$q_p = \mathrm{Nu} \cdot \frac{\overline{\lambda}_p}{d_s} \cdot \left(T_p - T_s\right). \qquad (11)$$

Here as the plasma heat conductivity $\overline{\lambda}_p$ we recommend to use that one averaged through the boundary layer, but to calculate other plasma properties, using the temperature of the incident plasma flow (at the external border of the boundary layer).

The formula (10) takes automatically into account above mentioned disadvantages that take place when changing of the nature of the heat transfer from plasma to the particle. If the plasma velocity is higher than treated particles velocities $V_p > V_s$ then the formula (10) takes into account only convective part of the heat transfer, it is transformed into the following form:

$$\mathrm{Nu} = 0.6 \cdot \mathrm{Re}^{0.5} \cdot \mathrm{Pr}^{0.33}, \qquad \left(2 \cdot \frac{V_s}{V_p}\right) \to 0.$$

If treated particles velocities are comparable with the plasma velocity $V_p \approx V_s$ then the formula (10) takes into account only the conductive part of the heat transfer, it is transformed into the following form:

$$\mathrm{Nu} = 2, \qquad \left(0.6 \cdot \mathrm{Re}^{0.5} \cdot \mathrm{Pr}^{0.33}\right) \to 0.$$

Thus, there is the following universality of the formula (10) that provides changing of the nature of the heat transfer depending on the ratio of the particle velocity V_s to the plasma one V_p:

$$\mathrm{Nu} = 2 \cdot \frac{V_s}{V_p} + 0.6 \cdot \mathrm{Re}^{0.5} \cdot \mathrm{Pr}^{0.33}, \quad \begin{cases} \mathrm{Nu} = 0.6 \cdot \mathrm{Re}^{0.5} \cdot \mathrm{Pr}^{0.33} & \text{if } V_p > V_s \\ \mathrm{Nu} = 2 & \text{if } V_p \approx V_s \end{cases}$$

Conclusions

A result of a treatment of numerous experimental data on the particle heat transfer in plasma as well as the analysis of numerous criterial formulas described the heat transfer let to make the following conclusions:

1. A using of the enthalpy difference ΔH in the formula (11) for a calculation of the heat flux q leads to an overestimation of the last one in 3-5 times. Therefore the temperature difference $\Delta T = T_p - T_s$ is recommended to use for a calculation of the heat flux.

2. A calculation of the heat flux q with a using of the heat conductivity of the incident plasma flow (at the external border of the boundary layer) leads to an overestimation of the heat flux in comparison with experimental data in 2-3 times. Therefore the heat flux is recommended to calculate with a using of the heat conductivity averaged through the boundary layer (4). But the other plasma properties such as a specific heat c_p, a density ρ_p, a viscosity μ_p should be calculated with a using of the temperature of the incident plasma flow.

3. We propose to use the correction coefficient depending on the particle velocity and the plasma one in the criterial formula of the particle heat transfer in plasma jet. That coefficient regulates the value of a conductive part of the heat transfer according on the ratio of the particle velocity to the plasma one.

Reference

[1] Y.C.Lee, Y.P.Chyou, E.Pfender. Particle Dynamics and Particle Heat and Mass Transfer in Thermal Plasmas. Part II. Particle Heat and Mass Transfer in Thermal Plasmas. Plasma Chem. Plasma Process., 1985, vol. 5 (4). – pp. 391-414.

[2] R.M.Young, E.Pfender. Nusselt Number Correlations for Heat Transfer to Small Spheres in Thermal

Plasma Flows. // Plasma Chemistry and Plasma Processing. – V. 7. – № 2. – 1987. – pp. 211-229.
[3] Xi Chen. Particle Heating in a Thermal Plasma. // Appl. Chem. – V. 60. – № 5. – 1988. – pp. 651-662.
[4] S.V.Dresvin, S.M.Mikhalkov. Heat Exchange of Spherical Stationary Model and Small Particles Moving in a Plasma Jet. // Heat and Mass Transfer under Plasma Conditions: Proceedings of International Symposium on Heat and Mass Transfer under Plasma Conditions / Ed. P.Faushais. Begell House, New York – Wallington (UK), 1995. – pp. 209-222.
[5] I.V.Kalganova, V.S.Klubnikin. Investigation of Model Sphere Heat Transfer in Argon Plasma Flow. High Temperature Thermal Physic Journal, V.10, №2, 1976. – pp. 408-410 (in Russian).
[6] G.R.Kubanek, P.Chevalier, W.H.Gauvin. Heat Transfer to Spheres in a Confined Plasma Jet. // Canad. J. Chem. Eng. – V.46, № 2. – 1968. – pp. 101-107.
[7] S.Katta, W.H.Gauvin. The Effect of Local Gas Velocity and Temperature on Local Heat Transfer to a Sphere in a High-Temperature Jet. //Can. Chem. Eng. – V.51. – 1973. – pp. 307-311.
[8] W.Romer, V.Smoljakov, K.-H.Weiss. Konvektive Wanneubertragung in Einem Laminaren Stickstoff - Plasmastrahl I. // Beitr. Plasrnaphys. – 1968, V.8, № 3. – pp. 145-155.
[9] J.Fay, F.Riddell. Theory of Stagnation Point Heat Transfer in Dissociated Air. Journal of the Aeronautical Sciences, 1958, v.25, №2, pp. 73-85.
[10] J.A.Lewis, W.H.Gauvin. Motion of Particles Entrained in a Plasma Jet. // AIChE J., 1973, V.19, № 5. – P. 982.
[11] Y.C.Lee, K.C.Hsu, E.Pfender. Modeling of Particles Injected into a D. C. Plasma Jet. // V Int. Symposium on Plasma Chemistry, Edinburgh, Scotland, – 1981, V.2. – P. 795.
[12] N.N.Sayegh, W.H.Gauvin. Heat Transfer to a Stationary Sphere in a Plasma Flames. // AIChE J. – V. 25, № 6. – 1979. – pp. 1057-1064.
[13] P.Rose, W.Stark. Stagnation Point Heat Transfer Measurement in Dissociated Air. Journal of the Aeronautical Sciences, 1958, v.25, №2, pp. 86-97.
[14] M.I.Boulos. Heating of Powders in the Fire Ball of on Induction Plasma // IEE TPS. – PS. 6, № 2. – 1978. – pp. 93-106.
[15] M.Abu-Romia, B.Bhatia. Heat Pipe Calorimetry for Plasma Stagnation-Point Heat Transfer. AIAA Journal, 1972, v.10, №3, pp. 313-316.
[16] A.V.Donskoy, S.V.Dresvin, M.A.Orlova. Flat and Sphere Models Heat Transfer in Thermal Plasma. Proc. of the 6-th Conference on Low Temperature Plasma Generators, Frunze, 1974. – P. 428 (in Russian).
[17] W.E.Ranz, W.R.Marshall. Chem. Eng. Progr., 1952, V.48, № 2. – P. 173.
[18] Physics and Technology of Low Temperature Plasmas. Edited by S.V.Dresvin. Iowa State University Press, 1977.
[19] S.Zverev. Engineering and Investigation of Radio-Frequency Plasma-Plant for Dispersed Refractory Materials Treatment. Ph.D. Thesis, Department of Electrical Engineering, Saint-Petersburg Polytechnic University, 2002 (in Russian).
[20] M.I.Boulos, P.Fauchais, E.Pfender Thermal Plasmas: Fundamentals and Applications. V.I. New York: Plenum Press, 1994.
[21] J.Amouroux, S.Dresvin, D.Morvan, L.Ouvrelle, D.Ivanov, S.Zverev, O.Feygenson, A.Balashov. Calculation of Silicon Particle Dynamics and Heat and Mass Transfer in Thermal Plasmas. Effect of Particle Vaporization. / Proc. of the 7-th European Conference on Thermal Plasma Processes, Strasburg. – 2002.

CHEMICAL REACTIONS IN HEAT AND MASS TRANSFER BETWEEN SMALL PARTICLES AND PLASMA

J.Amouroux[1], S.Dresvin[2], D.Ivanov[2]

[1] *LGPPTS, EMSCP, 11 rue P. & M. Curie, 75005 Paris, France*
[2] *SPb State Polytechnical University, 29 Polytechnicheskaya Str., 195251 Saint-Petersburg, Russia*

ABSTRACT

Our goal is to qualify the chemical reaction mechanisms which take place during the interaction between a RF air plasma and silicon particles.

The energy and mass transfer in the usual model take into account heat transfer from plasma by conduction and convection on the surface of the particle, radiation effect, melting, heating of vapor cloud and vaporization. So that heat and mass balance give us the possibility of modeling these processes. However exothermic reactions are able to appear between oxygen atoms and silicon which give SiO gas and strong enthalpy effect.

These mechanisms of chemical reactions between the air plasma and the silicon particles depend mainly of the plasma temperature and of the gas flow velocity. We propose to discuss the main results of this model in order to take into account the chemical mechanisms which appear on the surface plasma–powder.

1. INTRODUCTION

One of the main difficulties of plasma treatment of particles is to take into account the chemical mechanisms which appear during the heat and mass transfer phenomena.

Nevertheless the main applications are for plasma spraying, and because the usual material are oxides such as Al_2O_3, S, O_2, MgO, ZrO_2 … usual works don't take into account the stoechiometric modifications of the oxides. As we know for mixtures of oxides for examples perovskites of lanthanium manganese LaMnOx few works point out that manganese oxide is vaporized during the plasma spraying of such kind of material.

So in that work our goal is to qualify the mechanisms of heat and mass transfer in an air plasma of silicon particles of diameters between 100 to 300 μm. The main aspect is to point out the role of oxygen-silicon interaction during the residence time of the particle in the plasma and to identify the heat transfer which appear during the exothermic reaction between silicon and oxygen.

2. GENERAL PRESENTATION OF THE PROBLEM

Silicon powder is mainly characterized by its melting temperature 1712 K and its boiling temperature 3505 K, while its density in the liquid phase 2570 kg/m^3 is higher than in the solid phase 2340 kg/m^3, at last we have to remember that at high temperature 2500 K its viscosity is the same than the viscosity of water, while its reaction with oxygen is a strong exothermic one. From all the data we are able to summarize the main phenomena which are able to be taken into account for the simulation of heat and mass transfer between silicon particle and air plasma.

The heating of one particle is supposed to follow 4 sequential steps (Fig. 1).

1 – Heating of the solid particle up to the melting temperature T_{melt}
2 – Melting of the particle at constant temperature T_{melt}
3 – Heating of the liquid droplet up to the boiling temperature T_{boil}
4 – Boiling of the particle at constant temperature T_{boil}

These phenomena are correlated with the size of the spherical particle, we can said that its main evolution appears during the evaporation process (Fig. 1b).

Neglecting the heat propagation phenomenon within the particle, the energy balance in the boundary layer surrounding the particle can be written :

$$m_s c_{ps} \frac{dT_s}{dt} = \sum_i P_i \,, \qquad (1)$$

where $\sum_i P_i$ is the sum of the different heat fluxes corresponding to the steps presented in Fig. 1, each of them being expressed by a power P_i.

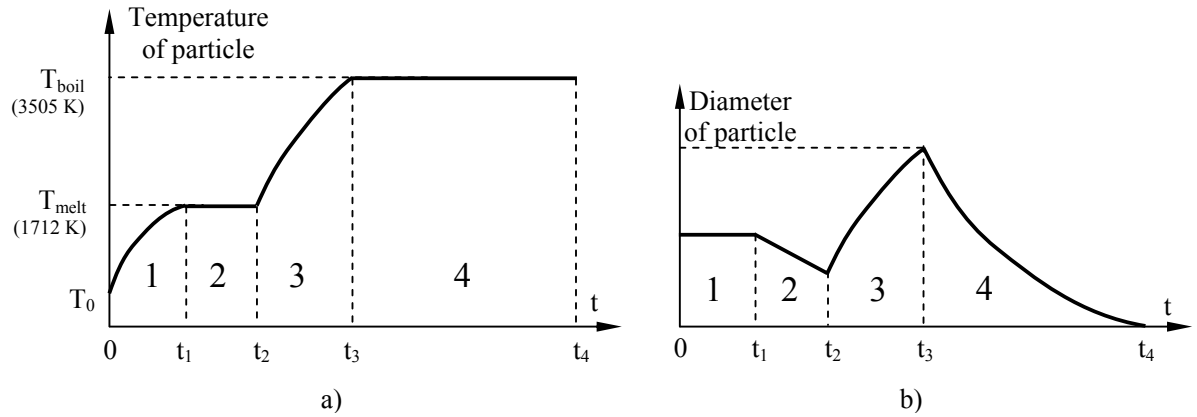

Figure 1. Steps of particle heating: a – change of particle temperature, b – change of particle diameter

These steps of particle heating by the plasma and the different mechanisms of heat and mass transfer were already described in details [1]. In the present paper, the different formulae allowing calculating those values are recalled in Tables 1 and 2.

Table 1. Equation for particle heating

Heating of the solid particle up to the melting temperature	$m_s c_{p_s} \frac{dT_s}{dt} = P_{pl} - P_{rad}$	(2)
Melting of the particle	$m_s c_{p_s} \frac{dT_s}{dt} = 0 = P_{pl} - P_{rad} - P_{melt}$	(3)
Heating of the liquid droplet up to boiling temperature	$m_s c_{p_s} \frac{dT_s}{dt} = P_{pl} - P_{rad} - P_{vap} - P_{cloud}$	(4)
Boiling of the droplet	$m_s c_{p_s} \frac{dT_s}{dt} = 0 = P_{pl} - P_{rad} - P_{boil} - P_{cloud}$	(5)

Table 2. Heat and mass transfer mechanisms

Conductive-convective heat transfer from plasma	$P_{pl} = \left(2 + 0.6 \cdot Re^{0.5} \cdot Pr^{0.33}\right) \cdot \frac{\lambda_p}{d_s} \cdot \left(T_p - T_s\right) \cdot S_{surface}$	(6)
Radiation of the particle	$P_{rad} = \varepsilon \cdot \sigma \cdot T_s^4 \cdot S_{surface}$	(7)
Melting of the particle	$P_{melt} = \Delta H_{melt} \cdot \dot{m}_{melt}$	(8)
Vaporization of the particle	$P_{vap} = \Delta H_{boil} \cdot \dot{m}_{vap}$	(9)
Boiling of the particle	$P_{boil} = \Delta H_{boil} \cdot \dot{m}_{boil}$	(10)
Heating of the vapor cloud	$P_{cloud} = \dot{m}_{\substack{vap \\ (boil)}} \cdot \bar{c}_{p_{vapor}} \cdot \left(T_p - T_{boil}\right)$	(11)
Mass losses by boiling	$\dot{m}_{boil} = \frac{P_{pl} - P_{rad}}{\Delta H_{boil} + \bar{c}_{p_{vapor}}\left(T_p\right) \cdot \left(T_p - T_{boil}\right)}$	(12)
Mass losses by vaporization	$\dot{m}_{vap} = h_m \cdot S_{surface} \cdot p_{pl} \cdot \ln\left(\frac{p_{pl}}{p_{pl} - p_v\left(T_s\right)}\right)$	(13)

3. CHEMICAL INTERACTION BETWEEN PLASMA GAS AND SILICON PARTICLES

If the silicon particle is heated in a reactive gas such as air we have to take into account the chemical reactions between silicon atoms and atoms or molecules of oxygen. These mechanisms can appear in the boundary layer between silicon vapor and oxygen atoms of the plasma, or on the surface of the silicon

melted particle and oxygen atoms. We consider that the thermal conduction in the particle is higher than the heat transfer by convection at the surface of the particle ; that mean that the temperature of the particle is constant during the melting phenomena. The boundary layer around the particle is not deformed by the plasma gas flow (no turbulence effect).

During heating of the liquid droplet up to its boiling temperature and the boiling of the droplet, the silicon is evaporated from the particle surface, resulting in a cloud of silicon vapor surrounding the particle. When the silicon vapor is oxidized in the air plasma with the formation of silicon oxide (SiO), energy is released through the reaction :

$$\text{Si (gas)} + \text{O (gas)} \leftrightarrow \text{SiO (gas)} - \Delta_r H_{SiO}(T), \tag{14}$$

where $\Delta_r H_{SiO}(T)$ is the enthalpy of the chemical reaction.

The heat flux P_{chem} due to the chemical reaction can be calculated using the following equation:

$$P_{chem} = \Delta_r H_{SiO}(T_{b.l.}) \cdot \dot{m}_{Si_{react}}. \tag{15}$$

This heat flux shall be subtracted from the right side of equation (1) when the third and fourth steps of particle hating are considered.

The model assumes that the speed of the chemical reaction is very high, much higher than the considered time intervals of heating (chemical kinetics is not taken into account). Also it is supposed that the whole energy released by the chemical reaction is absorbed by the particle.

The mass flow rate $\dot{m}_{Si_{react}}$ of silicon reacting with oxygen is defined by the following formula:

$$\dot{m}_{Si_{react}} = \frac{M_{Si}}{N_A} \cdot \frac{N_{Si_{react}}}{\Delta t}. \tag{16}$$

The quantity of silicon atoms that react with atomic oxygen during the time Δt can be defined using the law of action mass:

$$K_{SiO}(T_{b.l.}) = \frac{p^*_{SiO_{eq}}}{p^*_{Si_{eq}} \cdot p^*_{O_{eq}}}.$$

Here $p^*_{SiO_{eq}}$, $p^*_{Si_{eq}}$, $p^*_{O_{eq}}$ are the ratios of the partial pressures $p_{SiO_{eq}}$, $p_{Si_{eq}}$, $p_{O_{eq}}$ of species at thermodynamic equilibrium to the atmospheric pressure p_{atm}. These values can be expressed using the atom quantities $N_{SiO_{eq}}$, $N_{Si_{eq}}$, $N_{O_{eq}}$. For example :

$$p^*_{Si_{eq}} = \frac{p_{Si_{eq}}}{p_{atm}} = \frac{n_{Si_{eq}} \cdot k_B \cdot T_{b.l.}}{p_{atm}} = \frac{N_{Si_{eq}}}{V_{b.l.}} \cdot \frac{k_B \cdot T_{b.l.}}{p_{atm}}.$$

Taking into account the last expression, the law of action mass can be written in the following form :

$$\frac{K_{SiO}(T_{b.l.}) \cdot k_B \cdot T_{b.l.}}{V_{b.l.} \cdot p_{atm}} = \frac{N_{SiO_{eq}}}{N_{Si_{eq}} \cdot N_{O_{eq}}}. \tag{17}$$

It should be noted that $N_{Si_{eq}}$ is the quantity of silicon atoms at thermodynamic equilibrium. It means that during the time Δt, the quantity $N_{Si_{ini}}$ of silicon atoms was evaporated from the particle surface while a part $N_{Si_{react}}$ of those atoms have reacted with the atomic oxygen.

The initial quantity $N_{Si_{ini}}$ of silicon atoms, i.e. the quantity of atoms evaporated from the silicon droplet surface during the time Δt, is defined by:

$$N_{Si_{ini}} = m_{Si} \cdot N_A / M_{mol_{Si}}. \tag{18}$$

The partial pressure of oxygen atoms in the particle boundary layer is usually very low in comparison to that of evaporated silicon atoms, so that if we calculate the heat flux P_{chem} due to the chemical reaction, then the value obtained will be lower by several orders of magnitude than the heat transfer P_{pl} from

the plasma [2, 3]. However, the difference velocity between the plasma and the particle give blowing gas through the particle boundary layer (see Fig. 2).

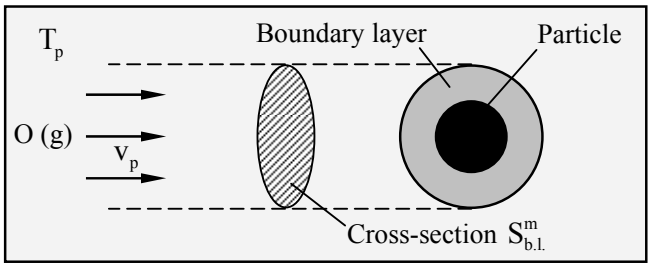

Figure 2. Evaluation of the number of oxygen atoms that takes part in the reaction

Therefore the quantity $N_{O_{ini}}$ of oxygen atoms in the particle boundary layer over Δt is defined using the following formula [3]:

$$N_{O_{ini}} = n_O \cdot \left|\vec{v}_p - \vec{v}_s\right| \cdot S^m_{b.l.} \cdot \Delta t \,. \tag{19}$$

To perform this calculation, it is the necessary to define the volume $V_{b.l.}$ and the middle cross section $S^m_{b.l.}$ of the boundary layer around the particle. For the sake of simplicity it has been assumed that the diameter of the boundary layer is twin the diameter of the particle: $d_{b.l.} = 2 \cdot d_s$.

4. DATA FOR CALCULATIONS

We first consider the reaction between silicon and molecular oxygen gases, to form SiO(g) (14). This can be taken into account for temperatures greater than melting temperature, for which we have some silicon gas either from evaporation or boiling.

We can either consider this reaction as a total reaction or as an equilibrium. Because oxygen is present in a very low concentration compared to the silicon one, the results will be similar. Nonetheless, if we want to be able to study the influence of oxygen concentration in that case where it is similar to the silicon one, it is better to consider an equilibrium.

We can calculate the thermodynamic parameters of this reaction bases on the enthalpy and entropy molar data available in [5] for the three compounds. These values are interpolated so that we can work at any temperature.

The dependence of the number density of atomic oxygen on temperature T in air plasma was drawn from reference [6]. Reference data of particle material are given in reference [1]. The thermo physical properties of air plasma were taken from reference [4].

5. RESULTS AND DISCUSSION

We start the simulation of heat transfer between air plasma (T = 5000 K) and a particle of silicon of 200 µm for a low difference of velocity between gas and plasma (Δv =1 m/s).

Fig. 3,a shows the different contributions of the heat transfer to the particle. It can be seen that the conductive-convective heat transfer P_{pl} from plasma to particle decreases with time, over the time interval 0 to about 25 ms the decrease is rather drastic, and then relatively smooth. That character can be explained by the fact that the particle temperature increases sharply over the time interval 0 to about 25 ms (see Fig. 3,b) resulting in a decrease in P_{pl} (see eq. (6)). After that, the particle temperature reaches the boiling point and ceases to change, while the lowering of P_{pl} takes place by the decreasing of the particle diameter (see Fig. 3,c).

Fig. 3, a shows that the main energy loss is the particle radiation P_{rad} (it is necessary to note that for particles of smaller diameter [1], the part of radiation in the energy balance decreases because of the reduction in the particle surface area – see eq. (7)), more over an important part of energy is lost because of vaporization and boiling. At last (Fig. 3,a) the heat flux P_{chem} due to the chemical reaction is small when the particle velocity relative to plasma is Δv =1 m/s.

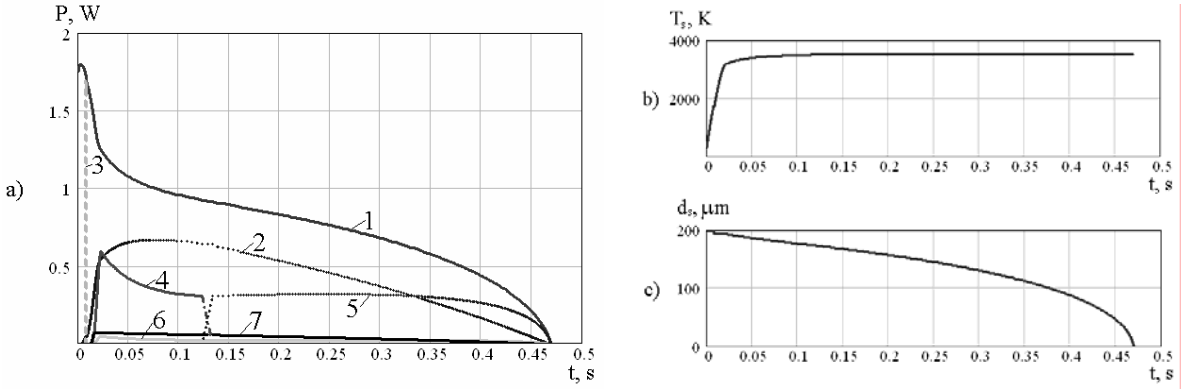

Figure 3. Evolution versus the heating time of the different energies received by the particle (a), the particle temperature (b) and its diameter (c) (particle velocity relative to plasma Δv=1m/s, particle diameter d_s =200 μm, and plasma temperature T_p = 5000 K). In Fig. 3a : 1 – P_{pl}, conductive-convective heat transfer from plasma 2 – P_{rad}, particle radiation 3 – P_{melt}, heat rate of melting 4 – P_{vap}, heat rate of vaporization 5 – P_{boil}, heat rate of boiling 6 – P_{cloud}, vapor cloud heating 7 – P_{chem}, heat flux due to the chemical reaction

The calculation showed that the number density of silicon atoms in the boundary layer during the particle evaporation exceeds considerably the number density of oxygen atoms. Therefore the quantity of oxygen atoms that react with silicon atoms in the particle boundary layer is a limiting factor. That quantity increases with Δv.

Fig. 4 presents the energy balance for the particle in the cases when the particle relative velocity is equal respectively to Δv=20 m/s (a) and Δv=100 m/s (b), all other conditions being the same.

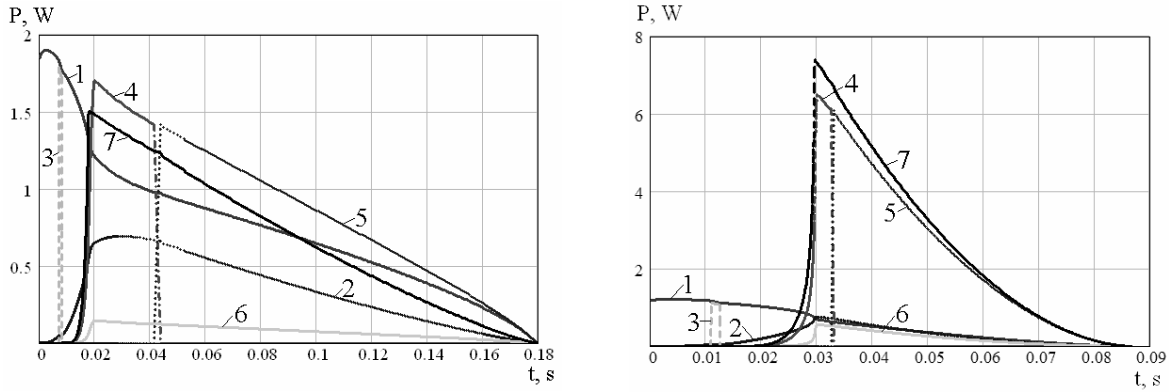

a) b)

Figure 4. Evolution with the heating time of the different energies of the particle for a particle velocity relative to plasma respectively of Δv=20 m/s (a) and Δv=100 m/s (b). The particle diameter is d_s =200 μm, the plasma temperature is T_p =5000 K. Different heat transfer : 1 – P_{pl}, conductive-convective heat transfer from plasma 2 – P_{rad}, particle radiation 3 – P_{melt}, heat rate of melting 4 – P_{vap}, heat rate of vaporization 5 – P_{boil}, heat rate of boiling 6 – P_{cloud}, vapor cloud heating 7 – P_{chem}, heat flux due to the chemical reaction

It can be seen that with high velocities the heat flux P_{chem} due to the chemical reaction plays an important role in the energy balance for the particle: P_{chem} is approximately equal to the heat transfer P_{pl} from the plasma when Δv=20 m/s, and P_{chem} is higher by several orders of magnitude than P_{pl} when Δv=100 m/s !

Thus, the heat flux due to the chemical reaction may be very important during the process of heating of a 200 μm silicon particle in a reactive plasma.

Therefore, we need to evaluate the effect of the different conditions on the power of the chemical reaction. For that purpose we propose to determine the integral value of energy received by the particle during the residence time at constant temperature : conductive-convective heat transfer from plasma and due to the chemical reaction :

$$E_{pl} = \int_0^{t_{total}} P_{pl} dt, \qquad E_{chem} = \int_0^{t_{total}} P_{chem} dt .$$

A ratio of the chemical energy E_{chem} to the plasma energy E_{pl} can also be defined :

$$\delta_{chem} = \frac{E_{chem}}{E_{pl}} .$$

The parameter δ_{chem} is used for the definition of the conditions at which the chemical reaction plays an important role in the process of particle heating. Fig. 5,a shows the dependence of this parameter δ_{chem} on the relative particle velocity for two plasma temperature: T_p=5000 K and T_p=7000 K. It can be seen that δ_{chem} increases with Δv. At the plasma temperature T_p=5000 K, the parameter δ_{chem} is equal to 1 at $\Delta v \approx 25$ m/s. It means the energy received by the particle due to the chemical reaction is equal to that one received by the particle due to heat transfer from the plasma.

Fig. 5,a also shows that an increase of the plasma temperature T_p leads to a decrease of the parameter δ_{chem}, i.e. the effect of the chemical reaction onto the energy balance for the particle decreases. The dependence of the parameter δ_{chem} on the plasma temperature T_p is shown in Fig. 5,b in detail.

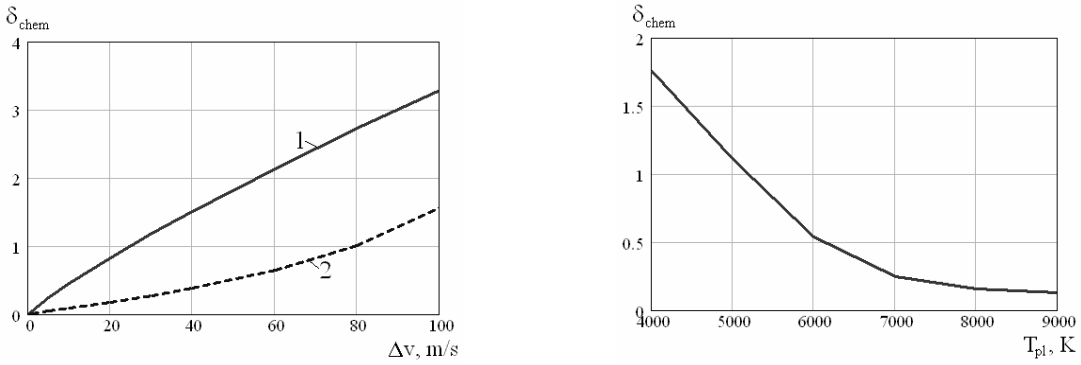

a) b)

Figure 5. Dependence of the parameter δ_{chem} on different parameters for the particle with diameter of 200 μm: a – dependence on the relative particle velocity Δv for different plasma temperatures : 1 – T_p= 5000 K ; 2 – T_p=7000 K; b – dependence on the plasma temperature T_p when the relative particle velocity is Δv=20 m/s

Fig. 6 shows the dependence of the parameter δ_{chem} on the particle diameter d_s. It can be seen that the parameter δ_{chem} increases when increasing d_s. It is due to the increase of the volume and correlatively of the midle cross section of the particle boundary layer. That fact in turn leads to an increase of the number of oxygen atoms that react with silicon atoms in the particle boundary layer.

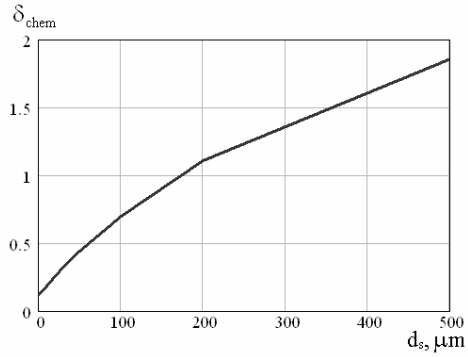

Figure 6. Dependence of the parameter δ_{chem} on the particle diameter d_s for the plasma temperature T_p = 5000 K and the relative particle velocity Δv=20 m/s

6. CONCLUSIONS

The heat and mass transfer between plasma gas (air) and spherical particles (d < 500 μm) of silicon were simulated with a model which take into account the evaporation of the silicon from the surface and its reaction with the oxygen atom.

The exothermic reaction of SiO oxide formation was taken into account in order to qualify the competitive phenomena which appear between thermal transfer and chemical heat transfer : under special condition the heat flux P_{chem} due to chemical reaction is several time higher than the conductive-convection heat transfer from the plasma gas.

To evaluate the effect of the chemical reaction onto the energy balance to the particle, the parameter δ_{chem} (characterizing the part of the power of the chemical reaction in the energy balance to the particle) was proposed. It increases under the following conditions : increase of the relative particle velocity Δv, decrease of the plasma temperature T_p, increase of the particle diameter d_s.

At last our experimental study[1] which was realized in an inductive RF plasma torch of 30 kW with a counter current injection of silicon powder of 200 μm gives a strong cloud of SiO/SiO_2 vapor with a strong deposition of SiO_2 amorphous powder on the wall of the reactor. The final diameter of the silicon particles was 159 μm (or 44 % of mass evaporation) for a residence time of 56 ms. In a second experimental study[2] we have a cocurrent axial injection of the Si particles (60 μm) in a RF plasma torch. On line Anemometric Doppler laser and optical measurement give a final diameter of 56 μm that mean an evaporation rate of 20 % for a 20 μs of residence time. Optical emission spectroscopy permits to control the evaporation zone from the injection point along the axial trajectory in the RF plasma torch.

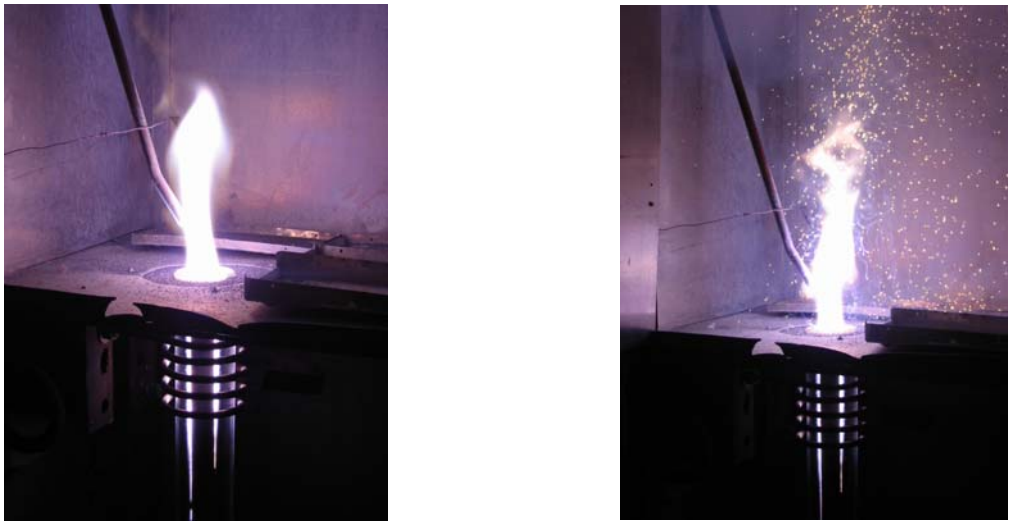

a) b)

Figure 7. Photos of inductive RF plasma torch of 30 kW with a counter current injection of silicon powder: a – without injection of particles, b – with injection of particles

SYMBOL LIST

$\bar{c}_{p\,vapor}$ – specific heat of vapor, averaged on the boundary layer (J/kg.K)

d_s – diameter of the particle (m)

$d_{b.l.}$ – diameter of the particle boundary layer (m)

h_m – mass transfer coefficient (W/m^2)

$K_{SiO}(T)$ – equilibrium constant of the reaction (-)

k_B – Boltzmann's constant (J/K)

M – molecular weight (kg/mol)

m_s – mass of the particle (kg)

$\dot{m}_{melt} = -\left(dm_{\substack{solid \\ core}} / dt \right)_{melt}$ – melting rate (kg/s)

$\dot{m}_{vap} = -\left(dm_s / dt \right)_{vap}$ – vaporization rate (kg/s)

[1] Experimental study was carried out together with S. Zverev in Electrotechnical and Electrothermal Laboratory for Plasma Applications, Saint Petersburg State Polythechnical University (Russia)

[2] Experimental study was carried out together with D. Morvan in Laboratoire de Genie des Procedes Plasmas et Traitements de Surfaces, Universite Pierre et Marie Curie Paris VI (France)

$\dot{m}_{boil} = -(dm_s/dt)_{boil}$ – boiling rate (kg/s)

N_A – Avogadro constant ($6.023.10^{23}$part/mol)

$N_{SiO_{react}}$, $N_{Si_{react}}$, $N_{O_{react}}$ – number of atoms (molecules) of species which react during a time interval Δt (-)

$N_{SiO_{eq}}$, $N_{Si_{eq}}$, $N_{O_{eq}}$ – number of atoms (molecules) of species at thermodynamic equilibrium (-)

$N_{Si_{ini}}$, $N_{O_{ini}}$ – initial number of species (-)

n_O – number density of oxygen atoms (m^{-3})

P_{pl} – conductive-convective heat transfer from plasma to particle (W)

P_{rad} – radiation from the particle (W)

P_{melt} – heat rate of particle melting (W)

P_{vap} – heat rate of particle vaporization (W)

P_{cloud} – heating of the vapor cloud (W)

P_{boil} – heat rate of particle boiling (W)

P_{chem} – heat flux due to chemical reactions (W)

p_{atm} – atmospheric pressure (p_{atm} =101325Pa)

p_{pl} – total pressure of plasma (Pa)

$p_{SiO_{eq}}$, $p_{Si_{eq}}$, $p_{O_{eq}}$ – the partial pressures of species at thermodynamic equilibrium (Pa)

$p^*_{SiO_{eq}}$, $p^*_{Si_{eq}}$, $p^*_{O_{eq}}$ – ratios of the partial pressures of species at thermodynamic equilibrium to the atmospheric pressure (-)

$p_v(T_s)$ – partial pressure of saturated vapor for the particle temperature (Pa)

$Pr = \mu_p \cdot c_{Pp}/\lambda_p$ – Prandtl number (-)

R – universal gas constant (8.32 J/mol.K)

$Re = \rho_p \cdot |\vec{v}_s - \vec{v}_p| \cdot d_s/\mu_p$ – Reynolds number (-)

$S_{surface} = \pi d_s^2$ – surface area of the particle (m^2)

$S^m_{b.l.} = \pi d^2_{b.l.}/4$ – middle area of the particle boundary layer (m^2)

T_{melt} – melting temperature (K)

T_{boil} – boiling temperature (K)

T_p – temperature of plasma (K)

T_s – temperature of the particle (K)

$T_{b.l.} = (T_s + T_p)/2$ – average temperature of the boundary layer (K)

t – time (s)

t_{total} – total time from the start of heating to full particle evaporation (s)

$V_{b.l.}$ – volume of the particle boundary layer (m^3)

$\vec{v}_p$ – velocity of plasma (m/s)

$\vec{v}_s$ – velocity of the particle (m/s)

ΔH_{melt} – heat of fusion of the particle material (J/kg)

ΔH_{boil} – heat of evaporation of the particle material (J/kg)

$\Delta_r H_{SiO}(T)$ – enthalpy of reaction of SiO formation (J/kg)

Δv – particle velocity relative to plasma (m/s)

δ_{chem} – parameter that characterizes the fraction of the power of the chemical reaction in the energy balance of the particle (-)

ε – emissitivity factor of the particle material (-)

K_p – thermal conductivity of plasma (W/m.K)

σ_s– Stephan-Boltzmann constant

($\sigma_s = 5.67.10^{-8}$ W/m^2.K^4)

REFERENCES

[1] J. Amouroux, S. Dresvin, D. Morvan, L. Ouvrelle, D. Ivanov, S. Zverev, O. Feigenson, A. Balashov, "Calculation of silicon particles dynamics, heat and mass transfers in thermal plasmas. Effect of particles vaporization" in *Progress in Plasma Processing of Materials 2003*. P. Fauchais, Ed. – Begell House, N.Y., Walling Ford (U.K.), 2003. – pp. 299 – 311.

[2] Cartier C. *Modeling and simulation of a radio frequency plasma torch. Calculation of motion and heating of a silicon particle : effect of a chemical reaction*, Master Thesis, Ecole Nationale Superieure de Chimie de Paris, St. Petersburg State Technical University, 2002.

[3] Jannes J. *Modeling and simulation of silicon particle behavior in a radio frequency plasma torch : Influence of chemical reactions and oxygen content*, Master Thesis, Ecole Nationale Superieure de Chimie de Paris, St. Petersburg State Technical University, 2003.

[4] V. S. Engelsht et al., *Teoriya stolba electricheskoy dugi*, Novosibirsk, Nauka, 1990 (in Russian).

[5] L. V. Gurvich, I. V. Veyts, V. I. Medvedev etc., *Thermodynamic properties of individual substances.* A reference book: In 4 volumes, Moskva, Nauka, 1978 (in Russian).

[6] S. Dresvin, *Physics and technology of low temperature plasmas.* Edited by A. V. Donskoy, V. M. Goldfarb and V. S. Klubnikin, English edition translated by T. Checon and edited by H. U. Eckert, Iowa State University Press, 1977.

Time-dependent modeling of a pulse-current-operated EUV radiation source

K. C. Paul[1], T. Takemura[1], G. Niimi[2], Y. Teramoto[2], H. Sato[2], T. Shirai[2], K. Bessho[2], D. Yamatani[2], T. Yokota[1], M. Yoshioka[1], T. Igarashi[1], K. Hotta[1], T. Hiramoto[1], and F. Dawson[3]

[1] *R&D Center, Lamp Company, Ushio Inc., 1-90 Komakado, Gotenba City, Shizuoka 412-0038, Japan.*
[2] *Extreme Ultraviolet Lithography System Development Association, Hiratsuka R&D Center / Gotenba Branch, Japan.*
[3] *Department of Electrical & Computer Engineering, University of Toronto, Canada.*

Abstract

Optical lithography has been the key technology for manufacturing microprocessors or integrated circuits (ICs). To meet future manufacturing demands for smaller feature sizes, today's conventional optolithography will have to be replaced by a new system that operates in the extreme ultraviolet (EUV). In such a system, an efficient and reliable radiation source of adequate in-band power (〜115 W) is one of the major issues. This paper presents a numerical model that is qualitatively helpful in designing a pulsed current discharge-based radiation source.

1. Introduction

Over the last few decades, optical lithography has been the key technology for manufacturing microchips in semiconductor industries. The advances in this technology have been crucial in helping the semiconductor industries develop and market fast integrated circuits (ICs). The speed and performance of integrated circuits or the final product, for instance computer systems, are dictated by the lithographic minimum feature printing capability. With the miniaturization of feature size, lithographic systems have been required to work with light of shorter wavelength.

Today's state-of-the-art optolithographic tools use deep ultraviolet (DUV) light with a wavelength of 193 nm to allow the printing of a 90 nm minimum feature size. There are indications that light of 193 nm may be able to print features as small as 45 nm, however this limit will ultimately spell the end for the conventional approach to optolithography. According to the SIA (Semiconductor Industry Association) roadmap of 2000, the feature size will decrease to 30 nm at the middle of the next decade at which time a new lithographic system will become a must. Foreseeing the physical limits of current lithographic systems, the global semiconductor industries have made enormous efforts to develop a new system, which has been dubbed as the next generation lithography (NGL) system. Among several candidates for NGL, extreme ultraviolet lithography (EUVL) is the most prominent one. In EUVL, extreme ultraviolet (EUV) light with a wavelength band of 2%, centering at 13.5 nm, will be used.

In commercial EUVL systems, the generation of EUV light with adequate power at the intermediate focus point (~115 W) is one of many key issues. Plasma of very high temperature is necessary in order to obtain the desired EUV light. There are two possible approaches for generating the high-temperature plasma: either by laser or by

an electrical discharge. Currently, discharge produced plasma (DPP) for EUVL is in the lead in terms of radiation output power. Generation of DPP has been tried using several engineering techniques by different industrial and/or research and development organizations. Reported discharges include the conventional capillary discharge, hollow-cathode triggered capillary discharge, dense plasma focus and Z-pinch [1].

Mathematical simulations and computer-aided engineering (CAE) have been gaining significant importance in industries because they are a vital tool in expediting the development of new products and/or improving the performance of existing products. Modeling and CAE have also been shown to reduce the development cost and the time to launch new products. Likewise, the benefits of CAE in designing reliable and efficient EUV discharge source have been progressing [2].

We are working to simulate the discharge dynamics for the purpose of extracting phenomenological concepts that will allow the efficient and rapid development of new designs. In this paper, we discuss the details of a newly developed model that can predict the plasma dynamics of an EUV discharge generated using the combined scheme of capillary and Z-pinch discharges. Calculations are done for a discharge medium of xenon gas with mass flow-rates of 40 and 100 sccm. The discharge is heated using a 23.7 kA peak current with a pulse duration of 275 ns. The flow is considered as compressible and the P-1 radiation method is used to predict the radiative energy.

2. Model description

A time-dependent axisymmetric model consisting of the complete set of magnetohydrodynamic equations (MHD) assuming compressibility has been solved. Expressions for the MHD equation set are given below.

Mass continuity:

$$\frac{\partial \rho}{\partial t}+\frac{\partial}{\partial z}(\rho u)+\frac{1}{r}\frac{\partial}{\partial r}(r\rho v)=0\,. \tag{1}$$

Momentum conservation:

$$\frac{\partial}{\partial t}(\rho u)+\frac{1}{r}\frac{\partial}{\partial z}(r\rho uu)+\frac{1}{r}\frac{\partial}{\partial r}(r\rho uv)=-\frac{\partial p}{\partial z}+\frac{1}{r}\frac{\partial}{\partial r}\left[r\mu\left(\frac{\partial u}{\partial r}+\frac{\partial v}{\partial z}\right)\right]+\frac{1}{r}\frac{\partial}{\partial r}\left[r\mu\left\{2\frac{\partial u}{\partial z}-\frac{2}{3}(\nabla\cdot\mathbf{u})\right\}\right]+\mathbf{J}\times\mathbf{B}\big|_z \tag{2-a}$$

$$\begin{aligned}\frac{\partial}{\partial t}(\rho v)+\frac{1}{r}\frac{\partial}{\partial z}(r\rho uv)+\frac{1}{r}\frac{\partial}{\partial r}(r\rho vv)=&-\frac{\partial p}{\partial r}+\frac{1}{r}\frac{\partial}{\partial z}\left[r\mu\left(\frac{\partial v}{\partial z}+\frac{\partial u}{\partial r}\right)\right]+\frac{1}{r}\frac{\partial}{\partial r}\left[r\mu\left\{2\frac{\partial v}{\partial r}-\frac{2}{3}(\nabla\cdot\mathbf{u})\right\}\right]-\frac{2\mu v}{r^2}\\&+\frac{2}{3}\frac{\mu}{r}(\nabla\cdot\mathbf{u})+\mathbf{J}\times\mathbf{B}\big|_r\end{aligned} \tag{2-b}$$

where, $\nabla\cdot\mathbf{u}=\frac{\partial u}{\partial z}+\frac{1}{r}\frac{\partial}{\partial r}(rv)$.

Energy conservation:

$$\frac{\partial}{\partial t}\left[\rho\left(H-\frac{p}{\rho}+\frac{1}{2}|\mathbf{u}|^2\right)\right]+\frac{\partial}{\partial z}\left[u\rho\left(H+\frac{1}{2}|\mathbf{u}|^2\right)\right]+\frac{1}{r}\frac{\partial}{\partial r}\left[r\rho v\left(H+\frac{1}{2}|\mathbf{u}|^2\right)\right]=\frac{\partial}{\partial z}\left(\frac{\kappa}{C_p}\frac{\partial H}{\partial z}\right)+\frac{1}{r}\frac{\partial}{\partial r}\left[\frac{\kappa}{C_p}\frac{\partial}{\partial}(rH)\right]+\phi$$
$$+\frac{5}{2}\frac{k}{e}\left(\frac{J_z}{C_p}\frac{\partial H}{\partial z}+\frac{J_r}{C_p}\frac{\partial H}{\partial r}\right)+\sigma E^2-R \qquad (3)$$

where, energy due to viscous dissipation is $\phi=\vec{\tau}\cdot\nabla\mathbf{u}=2\mu\left[\left(\frac{\partial u}{\partial z}\right)^2+\left\{\frac{1}{r}\frac{\partial}{\partial r}(rv)\right\}^2+\frac{1}{2}\left(\frac{\partial u}{\partial r}+\frac{\partial v}{\partial z}\right)^2\right]-\frac{2}{3}\mu\left[\frac{\partial u}{\partial z}+\frac{1}{r}\frac{\partial}{\partial r}(rv)\right]$.

Laplace equation:

$$\frac{\partial V}{\partial t}+\frac{\partial}{\partial z}(\sigma\frac{\partial V}{\partial z})+\frac{1}{r}\frac{\partial}{\partial r}(r\sigma\frac{\partial V}{\partial r})=0. \qquad (4)$$

Curl of Ampere's law:

$$\frac{\partial B_\theta}{\partial t}+\frac{\partial}{\partial z}(\frac{\partial B_\theta}{\partial z})+\frac{1}{r}\frac{\partial}{\partial r}(r\frac{\partial B_\theta}{\partial r})=\frac{B_\theta}{r^2}+\mu_0\frac{Jz}{\sigma}\frac{\partial\sigma}{\partial r}-\mu_0\frac{Jr}{\sigma}\frac{\partial\sigma}{\partial z}. \qquad (5)$$

Here, ρ is mass density; u and v are the axial (z-direction) and radial (r-direction) velocities; μ is the dynamic viscosity; σ and κ are electrical and thermal conductivities; C_p and H are specific heat at constant pressure and enthalpy; **u** is the velocity vector with u and v components; **J** is the current density vector with J_r and J_z components; **B** is the B_θ component of the magnetic field vector; p is the static pressure; V and E are electrostatic potential and electric field respectively; k is the Boltzmann constant; e is the electronic charge; R is the volumetric radiative loss; $\vec{\tau}$: is the stress tensor; and μ_0 is the free-space permeability.

The energy balance equation accounts for the pressure work and kinetic energy since these two effects can be significant in a compressible flow, especially when magnetic pumping is large. The model, however, does not include the gravitational effect. This effect would not play a role for a system with very high electromagnetic forces. For calculating the radiative energy, the P-1 radiation method [3] is employed. The radiation spectrum is divided into the following 5 bands between 2 and 20,000 nm: 2-13.365 nm, 13.365-13.635 nm, 13.635-100 nm, 100-400 nm, and 400-20000 nm. The radiation energy of band 2 (13.365-13.635 nm) is the in-band (2% centering 13.5 nm) EUV radiation energy that is useful for EUVL. The P-1 radiation method involves the solution of a Helmholtz-type equation of the following form for band i:

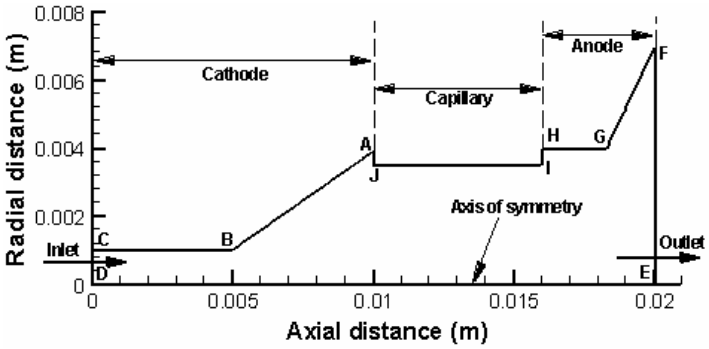

Figure 1 Schematic of the modeled discharge domain.

$$\frac{\partial G_i}{\partial t}+\frac{\partial}{\partial z}(\frac{1}{3\alpha_i}\frac{\partial G_i}{\partial z})+\frac{1}{r}\frac{\partial}{\partial r}(r\frac{1}{3\alpha_i}\frac{\partial G_i}{\partial r})=-\alpha_i(4\pi B_i-G_i) \qquad (7)$$

and the radiative energy R is calculated using the expression $R=\sum_i \alpha_i(4\pi B_i-G_i)$.

Here, G_i, B_i and α_i are the mean incident radiation, weighted Planck function and mean absorption coefficient of band *i* respectively.

3. Assumptions, boundary conditions, material and optical properties

The assumptions adopted for the model include: axisymmetric geometry with compressible flow and local thermodynamic equilibrium (LTE). The LTE assumption is likely critical for this discharge where temperature, density and pressure gradients are very high. However, information necessary for the very complicated non-LTE modeling of high-stage ionization species (viz. for Z between 4 and 10) is not available yet. The well-known numerical approach [2] is also based on the LTE assumption.

Figure 1 shows the schematic of the geometry used for the simulation. An arbitrary profile for the current density, at the cathode surface, with a known total current total has been chosen. The pulse current waveform and the assumed current density profile for peak current (23.7 kA at t = 137.5 ns) are shown in Figure 2. At the anode surface (HGF), a constant and reference potential of zero is specified. At the inlet and exit, current densities are set to zero. In an axisymmetric geometry, the azimuthal component of the magnetic field intensity is of interest and contributes to the Lorentz forces. Eqn. (5) is derived from Ampere's Law assuming an azimuthal magnetic field. In solving this equation, the following boundary conditions are used.

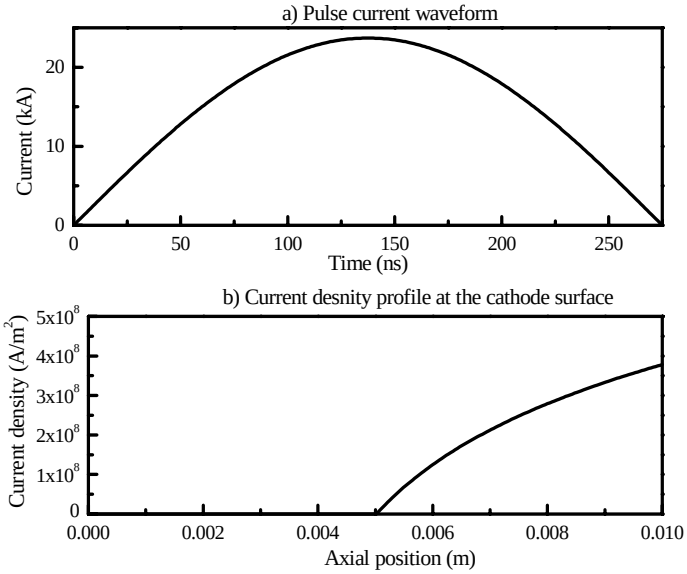

Figure 2 a) Waveform of the pulse current and b) the applied current density profile at the cathode surface

$$B_\theta\big|_w = \begin{cases} \sum_0^r \dfrac{\mu_0 I(r)}{2\pi r} & \text{on ABC} \\ \dfrac{\mu_0 I}{2\pi r} & \text{on AJIH and HGF} \end{cases} . \qquad (8)$$

Here subscript *w* is used to interpret the wall. At the inlet and outlet, B_θ is set to zero.

The following boundary conditions are used for the energy equation: 500 K at the inlet (CD), 1000 K at the outlet (EF), 3500 K at the cathode surface (ABC), 3000 K at the anode surface (HGF) and 1800 K at the capillary surface (AJIH). All of these conditions are chosen arbitrarily and are not likely to affect the plasma fields except energy conservation at the boundaries. For the P-1 radiation method, Marshak's boundary condition

in the following form is used to specify the boundary flux for the mean incident radiation of band *i*:

$$\Gamma_i \frac{\partial Gi}{\partial \vec{n}} = \frac{\varepsilon_{wi}}{2(2-\varepsilon_{wi})}(4\pi B_{wi} - G_{wi}). \tag{9}$$

Here, Γ_i and ε_{wi} are the diffusion coefficient and mean hemispherical emissivity of the boundary wall respectively for spectral band *i*. $\vec{n}$ is the outward normal vector to the boundary.

Other boundary conditions are: 1 Pa pressure at outlet, 40 or 100 sccm mass flow-rate at the inlet, no-slip at the walls (electrodes and capillary surface), and a zero axial gradient for all variables on the axis of symmetry (DE).

The calculation procedure for determining the material properties (σ, κ, μ, π and C_p) and optical properties (α_i) are the same as described in Ref. 4. Xenon species up to the 11th-stage ionization of xenon are considered; the spectroscopic data required for calculating the material and optical properties are taken from Ref. 5.

Calculations are performed by using a vendor-supplied software package, called Fluent, where most physical models are introduced through customized modules. The domain of Fig. 1 is divided into 23,000 quadrilateral meshes in order to calculate the dynamics of the discharge.

4. Results

Figure 3 shows the isotherms at two instants in time during the current pulse. Isocontours in the lower-half and upper half are for the time of 160 ns and 200 ns respectively. Although the peak current is at 137.5 ns, the plasma continues to be heated after that instant. In fact, the plasma temperature is found to be at its highest level just a few tens of nanoseconds prior to the current reaching zero. For instance, the maximum temperature of the discharge for a 100 sccm flow-rate is found to be 18 eV at 209 ns after the pulse has been initiated. Indeed, the spatial position of the highest-temperature changes with time. The plasma is mainly heated by extremely large magnetic compression. The distribution of magnetic field intensity and in-band mean incident radiation are presented in Figure 4. Although the P-1 radiation model can not give the directional radiation distribution, it helps in realizing the qualitative nature of radiation from a radiation source. Figure 5 illustrates the flow-rate effect on the plasma temperature. As was seen experimentally, the model also predicts an axial advancement of the hot-plasma or radiation core. The high flow-rate pushes the gas in the axial direction and the axial Lorentz force pushes the

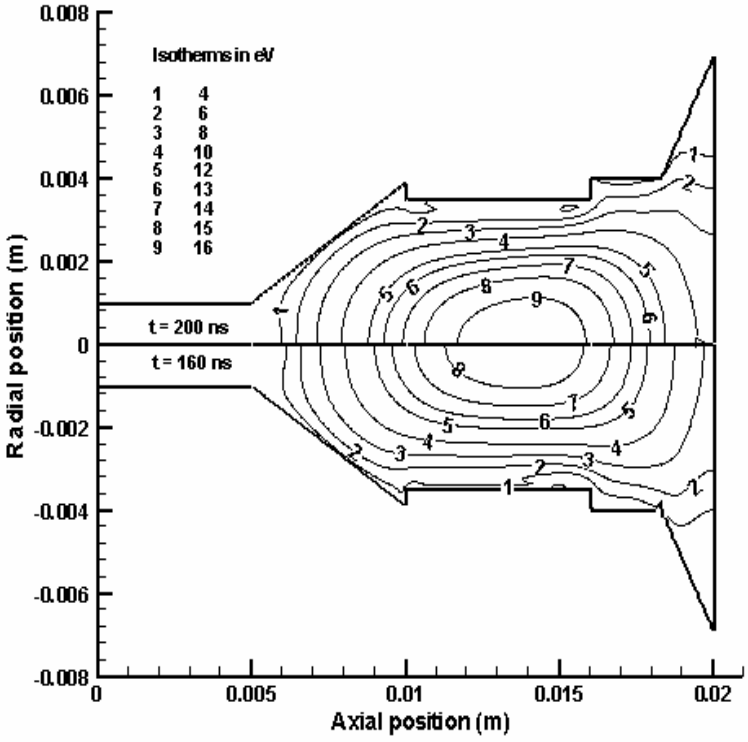

Figure 3 Temperature isocontours: upper-half is for t = 200 ns and lower-half for t = 160 ns

hot gas further in an axial direction.

5. Conclusions

In this paper, we have presented a time-dependent numerical model that solves the complete set of magnetohydrodynamics (MHD) assuming axisymmetry and compressibility. The model has been applied to calculate the dynamics of a capillary and Z-pinch discharge source. This source is expected to produce EUV radiation energy from a 2% spectral band, centering at 13.5 nm, for an EUVL application. The model predicts most physical phenomena and is helpful as a first principle design-approach.

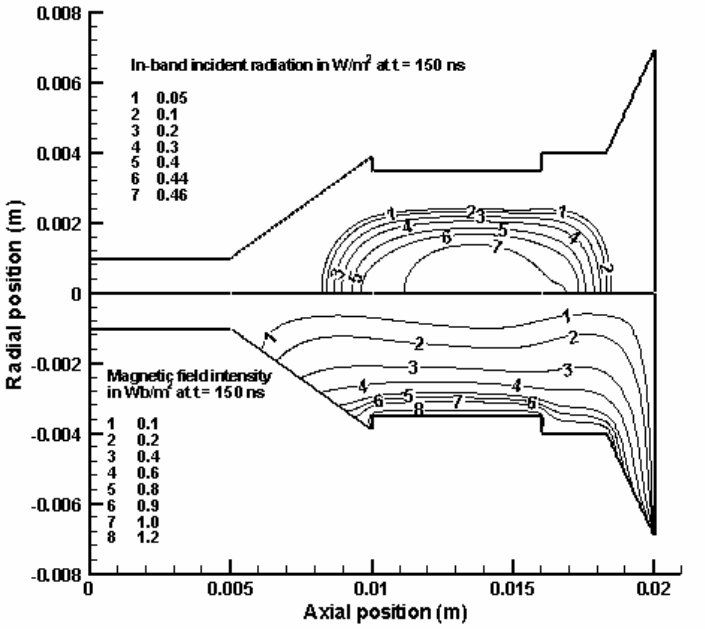

Figure 4 Isocontours of in-band radiation energy (upper-half) and magnetic field intensity (lower-half) at t = 150 ns

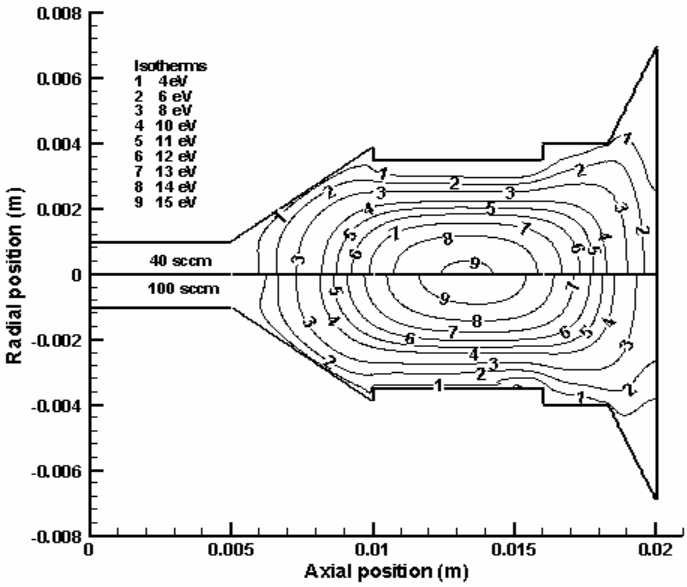

Figure 5 Isotherms for a flow-rate of 40 sccm (upper-half) and 100 sccm (lower-half) at t = 150 ns

Acknowledgements

This work has been partly supported by NEDO.

References

[1] Y. Teramoto, H. Sato, K. Bessho, T. Shirai, D. Yamatani, T. Takemura, T. Yokota, K. C. Paul, K. Kabuki, M. Miyauchi, M. Ikeuchi, K. Okubo, K. Hotta, M. Yoshioka and K. Toyoda, Emerging Lithographic Technologies VIII, Proce. of SPIE, 5374, 935 (2004)

[2] A Hassanein, V. Sizyuk, V. Tolkach, V. Morozov and B. Rice, Emerging Lithographic Technologies VII, Proce. Of SPIE, 5037, 714 (2003)

[3] M. F. Modest *Radiative heat transfer*, (New York: McGraw-Hill) ch. 14 (1999).

[4] K.C. Paul, T. Takemura, H. Matsuno, T. Hiramoto, F. Dawson, J.J. Gonzalez, A. Gleizes, G. Zissis, A. Erraki and J. D. Lavers, *IEEE Trans. Plasma Science*, 32, 118 (2004).

[5] E. B. Saloman, *J. Phys. Chem. Ref. Data*, 33, 765 (2004).

Comparaison between plasma and ionic treatment of PTFE and PVDF with oxygen.

N. Vandencasteele[1], D.H. Fairbrother[2], F. Reniers[1]

[1] *Chimie Analytique et Chimie des Interfaces C.P. 255, Faculté des Sciences Université Libre de Bruxelles, Bld du triomphe, B-1050 Bruxelles Belgique*

[2] *Department of Chemistry, Johns Hopkins University, 3400 North Charles Street, Baltimore, MD 21218, USA*

Abstract

Polytetrafluoroethylene (PTFE) and poly(vinylidene fluoride) (PVDF) surfaces were treated by oxygen species generated either in a remote (filtered) RF plasma or in an ion gun. In the first case the majority of the species reaching the surface are neutral molecules, whereas in the second case, ions are the reactive agent. In this paper, we show that PTFE and PVDF exhibit a completely different behaviour versus oxygen species.

Keywords PTFE, PVDF, oxygen plasma, XPS, contact angle

Introduction

The modification of polymer surfaces is of enormous importance in today's chemical industry. Compared to traditional wet chemistry, plasma treatments are surface sensitive and environmental friendly. However due to the variety of species created in the plasma (ions, neutrals, electrons, UV), the understanding of the chemical mechanisms involved in the plasma treatment of polymer is not trivial.

This paper presents the result of a NSF-funded collaboration [1]. PTFE and PVDF samples were modified by the various constituents of a oxygen plasma: oxygen ions and a filtered plasma. The polymer was exposed to an ion gun or a modified RF plasma. In previous studies we've already shown the differences between the ionic and the plasma treatment of PE and PTFE with nitrogen [2,3]. The plasma was characterized by optical emission spectroscopy (OES). The samples were characterized by X—Ray photoelectron spectroscopy (XPS) and water contact angle (WCA).

Experimental

Sample preparation:
PTFE and PVDF samples were from Goodfellow. After having been cut to size, they were cleaned with methanol and then with pure isooctane. Once cleaned, they were introduced into the plasma chamber or into a UHV chamber equipped with an ion gun and a XPS analyser.

Plasma treatment:
The plasma chamber consisted of a stainless steel based vessel surmounted by a pyrex bell jar. Isolation was realised by a viton O-ring. The pumping system consisted in an Edwards primary pump (up to 1.33 Pa) and a turbomolecular pump (Balzers 230 l/s) coupled to a membrane pump. Pure oxygen from Alphagaz was used (Alphagaz 2). Before introduction of oxygen, the chamber was pumped down to a pressure of $2.67\ 10^{-4}$ Pa, and then backfilled to the working pressure. In order to avoid contamination, the chamber was continuously pumped during the experiments (dynamic regime). The RF plasma was initiated using a Huttinger PFG300RF generator,

coupled to a PFM 1500 A matchbox. The samples were positioned outside the plasma region, above the anode grid, which could be either grounded or biased. A schematic of the experimental setup has already been published [2]. As in a RF plasma the cations remain mostly close to the cathode and, as we put the sample out of the plasma (remote mode), and above the anode, we expect that the majority of the plasma – polymer interactions will be due to neutrals and electrons. This was already show in our previous studies dedicated to the N_2 plasma – PE, PTFE surface interaction [2,3].
The plasma chamber is also equipped with a multiple (up to 8) fiber optic probe in order to detect simultaneously the excited species generated into the plasma at different locations : close to the cathode, middle of the plasma, close to the anode and close to the sample. The plasma was characterized using a Acton SpectralPro 2500i (Acton Research) optical emission spectrometer (OES) capable of a resolution of 0.06 nm and operating in the 200 nm – 900 nm region. The detector consisted in a Princeton Instrument Digital Camera type EEV, 400x1340 pixels.
After treatment the chamber is backfilled to atmospheric pressure using liquid nitrogen, and the sample is transferred either to the XPS chamber or to the contact angle room.
XPS analysis was carried out in a UHV chamber (originally PHI AES 590 system) equipped with a VG clam II analyser. Spectra were acquired using the Mg anode (1253.6 eV), operating at 300 W. Wide surveys were acquired at 100 eV pass energy. Spectra of the C1s, O1s and F1s regions were acquired with a pass energy of 30 eV. The average surface concentrations were determined with the usual formula, with the following sensitivity coefficients: C = 0.296; F = 1; O = 0.711
Water contact angle (WCA) measurements were performed in the static mode, in a climatized room, with controlled humidity. Milli-Q water was used. 10 drops were deposited statistically on the modified surfaces, and the angle was measured on both sides of the drop. The results presented here are therefore an average of 20 measurements.

Ion treatment
PTFE or PVDF samples were introduced into a PHI 5400 UHV chamber equipped with a Physical Electronics (PHI) 04-303 ion gun, aligned at 45° with respect to the sample normal, a PHI 04-500 Dual anode X-ray Source (Mg Kα anode (1253.6 eV)) and a PHI 10-360 Semi-Hemispherical Analyzer. The typical base pressure of the system during analysis was 6.67 10^{-6} Pa. During O_2^+/O^+ ion beam treatment of the PTFE and PVDF surfaces, a typical chamber base pressure of 1.33^{-5} Pa was maintained, while a pressure of 1.5 10^{-2} Pa of oxygen was established in the ion gun. The emission current was set to 10 mA, while the accelerating voltage could be varied from 0.5 to 4 keV. As the only effect of the ion energy observed was on the duration of the experiment (faster at 4 keV), only the 4 keV results will be presented here. After exposure to the O_2^+/O^+ ion beam, PTFE and PVDF samples were analyzed in situ using XPS. All XPS spectra were acquired using 15 kV voltage and 300W power. Elemental scans employed a pass energy of 44.75 eV and 0.125 eV/step and the binding energy scale calibrated on the F1s peak of native PTFE (689.7 eV) and PVDF (688.2) [5].

Results

Ionic treatment:
The samples were exposed to oxygen ions for different times and then analyzed in-situ by XPS. The XPS results for PTFE shows that there is almost no oxygen (0.8%) grafted on the PTFE sample after 3 hours of treatment (Fig1a). There is a strong decrease of the fluorine content at the surface. This is probably due to a sputtering of the surface by the ions. Fig1b indicates that untreated PVDF contains already 3.5 at% of oxygen. This residual contamination could not be removed by the usual washing procedures. However this contamination decreases very rapidly (to 1.5 at%) during the first minute of the treatment probably because of the sputtering effect. The at% of oxygen increase then again to reach a final value of 3 at%.

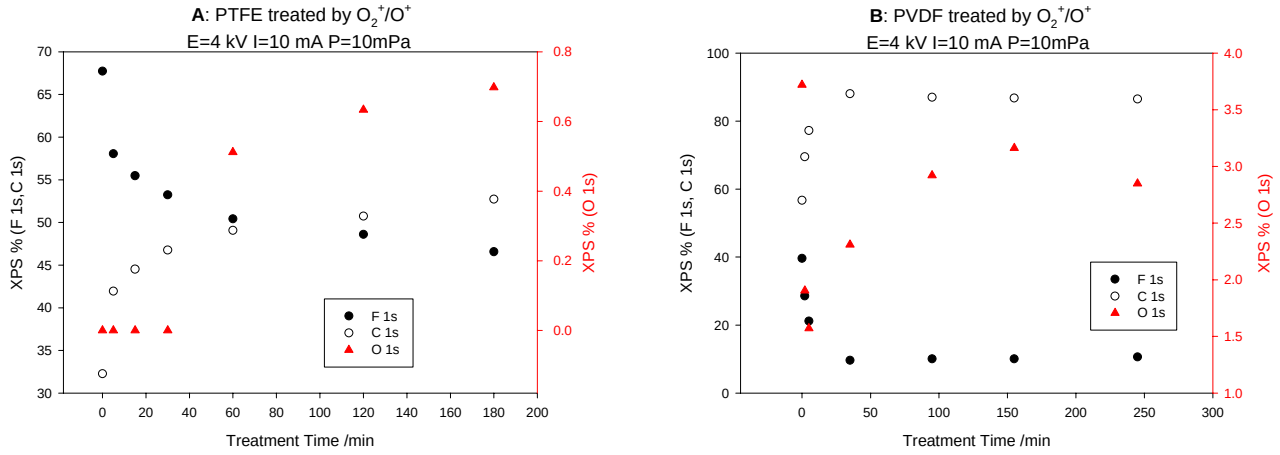

Fig1: XPS composition of PTFE (left) and PVDF (right) samples treated by oxygen ions.

Plasma treatment:

For PTFE, the ex-situ XPS results show that the oxygen content increases rapidly during the first 5 minutes and reaches a steady state value after 10 minutes at around 4.5% of oxygen on the surface (Fig2a). The same trend was observed for PVDF (Fig 2b) but with major differences in the time scale and in the amount grafted. Indeed, for PVDF, the oxygen content increases very rapidly during the first 2 minutes of treatment and the steady state value is around 25 at%.

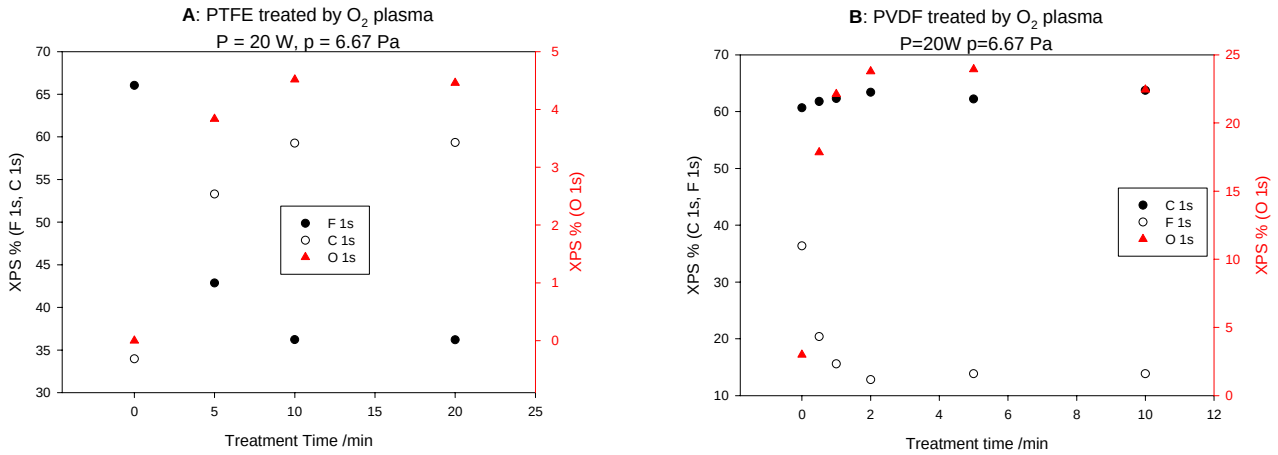

Fig2: XPS composition of PTFE (left) and PVDF (right) samples treated by oxygen plasma. Plasma power=20 W, O_2 pressure=6.67 Pa.

Water contact angle (WCA) measurements show that PTFE and PVDF exhibit a very different behavior upon the plasma treatment. PTFE becomes more hydrophobic (Fig3) but PVDF become very hydrophilic.

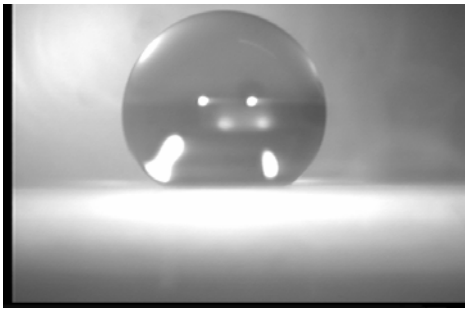

Fig3: Drop of milliQ water on a PTFE sample modified by an oxygen plasma.

For the PTFE no relation could be established between the surface composition and the surface free energy. As there is almost no oxygen grafted onto the sample and that the C1s peak shape doesn't change (Fig4). We suggest that the increase of WCA (i.e. decrease in surface energy) arise from an increase in the surface roughness due to a chemical etching (oxidation) of the polymer. The increase in roughness is therefore the only explanation left for the decrease in surface free energy. Figure 4 shows the evolution of the spectral envelope of the C1s peak for PTFE (A,C) and PVDF (B,D) during plasma treatment (A,B) and ion treatment (C,D). Whereas the ion treatment seems to suggest that there is mostly a defluorination of the surface leading as a final result to C-H type carbon (at 285 eV), the plasma treatment on PTFE shows no change of the C1s peak (indicating chemical etching) and shows that for PVDF, a lot of polar oxygenated functions are grafted (high energy components in the C1s peak). It seems that the presence of C-H bond in the PVDF allow to graft much more oxygen functionalities onto the samples surfaces. The formation of HF could be the driving force of the grafting reaction of oxygen functionalities onto PVDF surfaces.

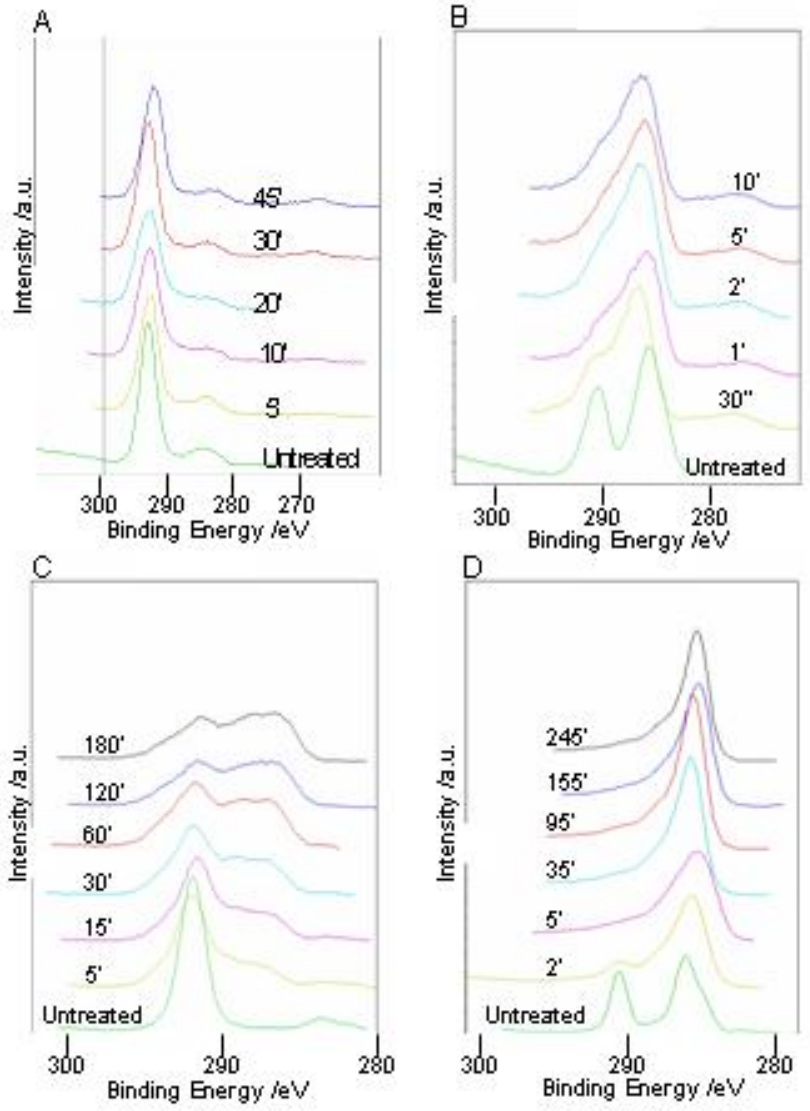

Fig4: C1s photoelectron peak of PTFE and PVDF exposed to an oxygen plasma or to an ion treatment.

A very clear relation between the amounts of these oxygenated polar groups grafted and the change in surface free energy is revealed in Figure 5.

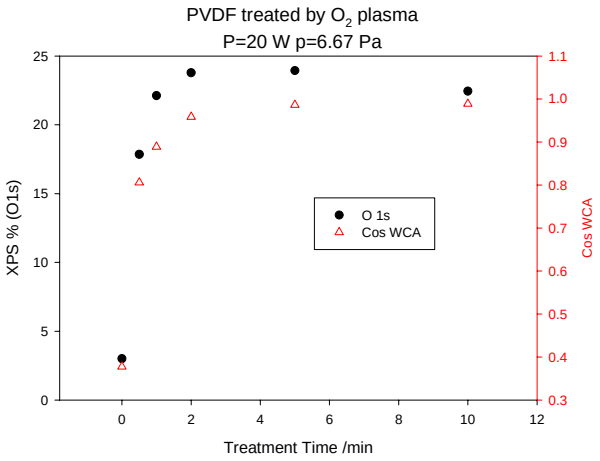

Fig5: Oxygen RF plasma treatment of PVDF surfaces, no bias was applied at the anode grid. The surface composition (at%) was determined by XPS. The working pressure is 6.67 Pa.

OES results show that during plasma treatment of PTFE, beside the O line at 777.39nm, F lines (685.63 nm and 703.84 nm), CO line (313.99 nm) and CO_2^+ line (289.83 nm) could also been observed. These results are in good agreement with the etching theory discussed above. This etching seems to be the only modification of the polymer as the C1s peak shape doesn't change.

Conclusions

Plasma treatment seems to be much more efficient than ionic treatment for the grafting of oxygen functionalities on the PVDF surfaces. For the PTFE there is a strong difference in the C1s peak shape between the ionic and the plasma treatment. The ionic treatment leads to a much wider peak than the plasma treatment in the case of PTFE. However in either case these treatments are not very efficient for grafting oxygen species onto PTFE surfaces. This is probably because oxygen treatments of PTFE lead mainly to an etching of the sample. This is confirmed in the case of the oxygen plasma by the contact angle measurement and the OES measurements. The contact angle increases after the plasma treatment. An increase in the surface roughness will increase the contact angle as stated by the Wenzel equation (1) were θ is the Young angle and r is the roughness:

$$\cos \theta^* = r \cos \theta \qquad (1)$$

For the PVDF the ionic treatment graft about 3 at% of oxygen functionalities on the surface but the plasma treatment are much more efficient. Indeed the oxygen content of the surface reached almost 25 at%. XPS results also shows that the fluorine content of the PVDF decreases very quickly with the treatment time for both ionic and plasma treatment. The contact angle of treated PVDF decreased dramatically after the plasma treatment, from 67° for an untreated sample to less than 10° after a 5 minutes plasma treatment at 20W.
For both PTFE and PVDF it seems that plasma treatment is more efficient for grafting oxygen functionalities. It also seems that the presence of C-H bond in the PVDF allow to graft much more oxygen functionalities onto the samples surfaces. The formation of HF could be the driving force of the grafting reaction of oxygen functionalities onto PVDF surfaces.

Acknowledgements

This work is supported by the Belgian National Fund for Scientific Research (FNRS, grant 2.4543.04)

References

[1] International Supplement to NSF award (#9985372)
[2] A.J. Wagner, D.H. Fairbrother, F. Reniers *Plasma Polym*. 2003; **8**:119
[3] N. Vandencasteele, F. Reniers *Plasma Processes and Polymers.* 2005 *Under press*
[4] N. Vandencasteele, F. Reniers *Surf. Interface Anal*. 2004; **36**: 1027-1031
[5] D. Briggs, *Surface Analysis of polymers by XPS and static SIMS*; (Cambridge University Press, Cambridge, UK, 1998).

Atmospheric DBD plasma remediation of hexachloropropene

C. Pierard[1], E. Silberberg[2] and F. Reniers[1]

[1] *Université Libre de Bruxelles, Service de Chimie Analytique et Chimie des Interfaces, Brussels, Belgium (contact : freniers@ulb.ac.be)*
[2] *Arcelor Group, RDCS, Liège, Belgium*

Abstract
Liquid hexachloropropene (HCP) was treated by a He/O_2 (5%) plasma and an O_2 plasma at, respectively, atmospheric and nearly atmospheric pressure. We show that the efficiency of the degradation depends on the number of electrons injected in the reaction, the oxygen pressure, and the presence of water in the plasma. After analysis of all the products obtained as a function of the experimental parameters, a tentative reaction path with as first step a successive dechlorination of HCP is proposed, followed by oxidation.

Keywords : hexachloropropene, organic pollutant remediation, dielectric barrier discharge, He/O_2 discharge, O_2 discharge

Introduction

Persistent organic pollutants such as polychlorinated molecules represent an environmental issue. Due to their hydrophobicity these molecules accumulate in fat tissues and some of them are suspected to be carcinogenic [1]. Such molecules were extensively used as pesticides and solvents during the past decades and consequently a large degree of contamination is observed in ground water, in soils and in the atmosphere.
Plasma techniques could represent a good alternative to incineration. Indeed, burning these molecules at high temperature requires a huge energy consumption, and undesired by-products such as dioxins can be formed. Since a few years, plasma techniques have been successfully used to degrade volatile organic compounds (VOC) in the gaseous phase [2], but few researches have been done regarding the destruction of halogenated molecules in the liquid or the solid phase. The purpose of this work is to study the degradation of hexachloropropene (HCP), which is liquid at room temperature, by means of a dielectric barrier discharge (DBD) at nearly or at atmospheric pressure. The expected overall degradation reaction can be summarized by:

$$C_3Cl_6 + a\ O_2 + b\ H_2O \rightarrow 3\ CO_2 + x\ HCl + y\ Cl_2 \qquad (1)$$

The left side of the expression contains all the oxygenated species which are brought into the plasma by O_2 (alone or mixed with He) and the liquid water (used in some experiments).

Experimental

Experiments were carried out in a home made steel – pyrex plasma chamber. A schematic of the experimental set up is presented in Fig. 1. More details can be found in the literature [3]. The plasma is initiated between two electrodes covered with alumina. The inter electrode spacing is set to 5 mm. The upper electrode is connected to the high voltage – low frequency generator (Solar Electronics, model 8850-1) which can deliver up to 4 kV at a frequency up to 100 kHz. The current delivered into the system is measured with a 23,5 Ω resistor. 200 or 2480 mg of HCP (Merck, 96%) and 2 ml of water, if needed, are placed on the alumina cover of the cold electrode, which is grounded. The gases used are O_2 (Air Liquide, N45), He (Air Liquide N45), CO_2 (Air Liquide N48). The gas mixture and the gas flow are realized using a mass flow controller (Brooks 5850s). Prior to any experiment, the chamber is isolated and pumped down to 50 mbar using a Edwards EDM2 rotary pump. For the He/O_2 set of experiments, a 150 ml/min gas flow at atmospheric pressure is applied during the plasma treatment, the gaseous products of the degradation being trapped in the liquid nitrogen trap. After the experiments, the flow is maintained during 1 hour to capture the residual products of the reaction.
For pure O_2 plasma experiments, the treatment is realized without flow, in static conditions. After the plasma, a He gas flow is introduced in the chamber to push products to the trap (cooled with liquid nitrogen).

After all the experiments, the trap is heated to temperatures higher than 373 K to release the gases and bring them under flow to the mass spectrometer.
An atmospheric pressure mass spectrometer (Pfeiffer Omnistar GSD 301, 0-300 amu) is used to analyze the gases released from the nitrogen cooling trap (see Fig. 1). The quantification of the degradation is realized on the CO_2^{2+} m/z signal at 22, therefore the spectrometer was calibrated using a CO_2 flow. The major gaseous by-products of the reaction were analysed using MS. The electrical characteristics of the discharge are recorded using a computer based oscilloscope (National Instruments, NI 5102).

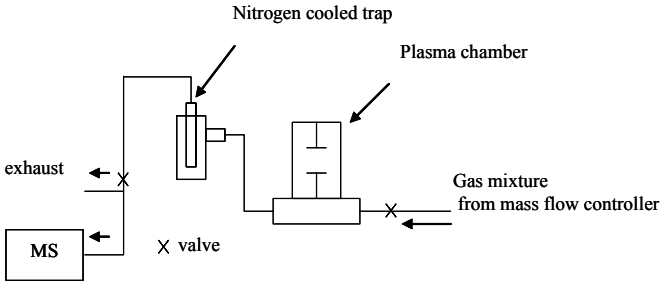

Fig. 1: Schematic of the plasma chamber used for the degradation of organohalides [3].

Two different sets of experiments were carried out : atmospheric pressure He-O_2 (5%) degradation of HCP, and pure oxygen plasma degradation of HCP at reduced pressure. The effect of the gas pressure, the plasma time, the water content and the discharge current were followed in this particular study. The other parameters (gas flow, He/O_2 composition, discharge voltage, frequency and inter electrode spacing) were optimized for the best degradation efficiency in a previous study [3]

Results and Discussion

Degradation by an He/O_2 plasma

A mixture of He/O_2 has been chosen to proceed with this set of experiments because the goal was to degrade HCP in a homogeneous way at atmospheric pressure (eventually under flow). Helium is known to stabilize glow discharges thanks to high a energy metastable state undergoes penning ionization without any influence of the electric field [4]. It also allows the initiation of an atmospheric pressure plasma at far lower voltages (around 1000 V) than other gases due to an favourable effective ionization coefficient [5].
The oxydation of the molecule is assumed to be performed by oxygen atoms and by all the others oxygenated species present in the plasma. The percentage of O_2 in the mixture is set to 5% (see Ref. 3).
In the results shown in Fig. 2, 200 mg of HCP, mixed with 2 ml of water (full circles), or alone (open circles) is treated by an He/O_2 (5%) plasma under atmospheric pressure and a 150 ml/min flow at a discharge current of 29 mA and reaction time from 1 to 40 min. In addition, to emphasize the importance of the electrical charge density applied, experiments at variable discharge current (20 and 25 mA) and constant reaction time of 10 min were performed. The charge density is obtained by integrating the discharge current over time and per unit area of the electrode, it can be expressed by the following equation:

$$\frac{Q}{A} = \frac{\int I_d dt}{A} \qquad (2)$$

Where Q/A is the electrical charge density (C/cm^2), I_d is the discharge current (mA) integrated over the reaction time t (s) and A is the electrode area (cm^2).
Figure 2 presents the evolution of the CO_2 amount produced at different discharge current and reaction time, with or without water. Increasing amount of CO_2 is released if the reaction time is increased, the dependence being quite linear. If the experiment is performed in anhydrous conditions the amount of CO_2 produced is between 30 and 50 % lower than the experiment with a mixture of 2 ml of water and HCP.

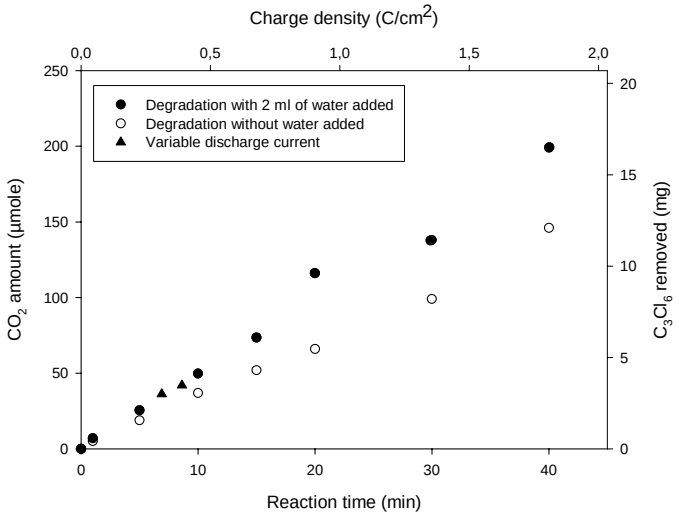

Fig. 2: Degradation of 200 mg HCP by an He/O_2 (5%) atmospheric pressure plasma (under a 150 ml/min flow). The discharge current is 29 mA and reaction time is going from 1 to 40 min. Full triangles represent experiments performed at other discharge currents (20 and 25 mA) for 10 min of reaction time.

Fig. 2 also shows that if the electrical charge density is kept constant by varying either the discharge current or the reaction time the CO_2 production will remain the same. Indeed, the triangles in fig. 2 are in good agreement with the linear dependence of the full circles, showing that the electrical charge is important for the degradation but not the way it is applied (in our experimental conditions.

The difference between the results obtained with and without water could be explained by the different active species present in each case. The creation processes of the main active species in the absence of water are:

$$He + e^- \rightarrow He^* + e^- \quad (3)$$

Where He^* is a metastable state with energy ranging from 18,8 to 20,6 eV,

$$O_2 + e^- \rightarrow 2\,O + e^- \quad (4)$$

$$He^* + O_2 \rightarrow 2\,O + He \quad (5)$$

The latest equations are the synthesis of complex processes involving inelastic collision and formation of ionic species which finally lead to O formation (O (^{3}P) or O (^{1}D)).

In absence of water the main active species, without taking into account the free electrons, is O (^{3}P)

When water is added, the following processes occur:

$$H_2O + e^- \rightarrow H + OH + e^- \quad (6)$$

$$He^* + H_2O \rightarrow H + OH + e^- \quad (7)$$

$$H_2O + O(^1D) \rightarrow 2\,OH \quad (8)$$

In presence of water, the reactive species are O and OH in addition to free electrons and a part of the O produced are used to dissociate water, therefore OH becomes the main actor in the formation of CO_2 process [6,7].

The analysis of the by-products obtained by MS shows that the main chlorinated products are HCl, $COCl_2$ and Cl_2. Traces of C_3H_5Cl have been detected and allow us to propose a reaction mechanism. Figure 3 represents the variation of the reduced area (RA) of the chlorinated by-products over the range of reaction time for the HCP + 2 ml of water degradation (same conditions as full circles on Fig. 2). The RA is the ratio between the MS signal area of the chlorinated product (HCl, $COCl_2$, Cl_2) and the MS signal area of CO_2, as shown in the following equation:

$$RA = \frac{\int MS\,signal\,X}{\int MS\,signal\,CO_2} \quad (9)$$

In this figure, the reduced area follows an exponential decay with time, suggesting that the first step of the degradation is the release of chlorinated molecules and then progressively production of CO_2.

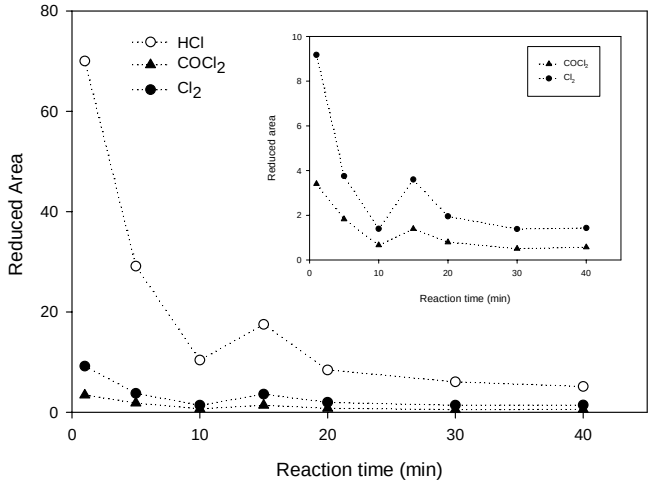

Fig. 3: Evolution of the relative amount of the main chlorinated by-products of the HCP degradation in an He/O_2 (5%) atmospheric pressure plasma (under a 150 ml/min flow). These results are extracted from the set of experiment in a aqueous medium (2 ml of water). The insert is a zoom on the regions of $COCl_2$ and Cl_2 contributions.

In absence of water, the exponential decay of the by-products formation is also observed. HCl seems to be the most abundant independently of the presence of water. HCl would normally not be produced in absence of water but it seems that the atmosphere contains small amount of water and this is enough to generate important amount (regarding the $COCl_2$ and Cl_2 quantities produced). The anhydrous set of degradation leads to the formation of twice more Cl_2 than in the aqueous set of degradation. This is normal if we consider that there is a lack of H atoms to form HCl and thus Cl atoms recombine to form preferentially Cl_2 in absence of water. Surprisingly the amount of $COCl_2$ produced seems to be identical in aqueous or anhydrous conditions. Although it is known that $COCl_2$ decompose in presence of water to give HCl and CO_2, as shown in Eqn. 10 [8]:

$$COCl_2 + H_2O \rightarrow CO_2 + 2\ HCl \qquad (10)$$

No clear explanation has been found yet. This kind of information in addition with the detection of C_3H_5Cl, which is the product of nearly complete dechlorination, allows us to suggest that this process is the starting point of the degradation.

A degradation experiment of 200 mg of HCP in anhydrous conditions by a pure He plasma at atmospheric pressure was done to confirm the dechlorination process as a possible step in the degradation mechanism (results on Table 1). He plasma interacts with the pollutant mainly by electronic collision and the result is the dissociation of HCP as shown in the Eqn. 11 :

$$R\text{-}Cl + e^- \rightarrow R + Cl^- \text{ or } R + Cl + e^- \qquad (11)$$

The formation of Cl^- instead of Cl depends on the electron energy. Table 1 shows the comparison between pure He degradation and He/O_2 degradation for 200 mg of HCP in anhydrous conditions. For both experiments, the plasma was at atmospheric pressure, the discharge current set at 29 mA and the reaction time at 10 min. In pure He plasma, no CO_2 (at m/z 22) was found but large quantities of chlorinated products were detected (HCl, $COCl_2$, Cl_2). There is more Cl_2 formed in respect with the He/O_2 experiment and a few $COCl_2$ is formed and his presence is due to a water contamination. Thus it seems that dechlorination by electronic collision is occurring.

Table 1 : Comparison between the products obtained for the degradation of HCP (200 mg) in a pure He plasma and a mix of He/O_2 (5%) both at atmospheric pressure. The discharge current is set at 29 mA and the reaction time at 10 min. No water was added is these experiments.

	MS normalized area			
	CO_2	HCl	$COCl_2$	Cl_2
He	NA	$1{,}11\ 10^{-9}$	$1{,}07\ 10^{-10}$	$2{,}15\ 10^{-10}$
He/O_2 (5%)	$1{,}46\ 10^{-10}$	$1{,}11\ 10^{-9}$	$9{,}45\ 10^{-10}$	$1{,}28\ 10^{-10}$

Degradation by an O_2 plasma

The degradation of HCP in a He/O_2 plasma has however some limitations. First, the O_2 percentage in the mixture is limited because large quantities of O_2 destabilize the discharge, which induces a decrease of the effeciency. The second issue is the expensive cost of He which is, thus, not suitable for industrial applications.

To get round of these problems a pure O_2 discharge seems to be the solution, but discharges in O_2 require very high voltages to be run at atmospheric pressure (10 000 V) and in our experimental conditions the maximum voltage allowed is 4 000 V. This set of experiment will be done at reduced total pressure (50 to 200 mbar O_2) to allow the initiation of the plasma.

As in the previous section we will work in aqueous (2 ml of water) or in anhydrous conditions. The degradation experiments are now conducted in static conditions (without flow) and for reaction time going from 5 to 15 min. We expect a greater efficiency in pure O_2 discharge because the amount available is larger. The results obtained for the degradation of HCP in an O_2 discharge (at various oxygen pressure, with and whitout water) are presented in the Fig. 4.

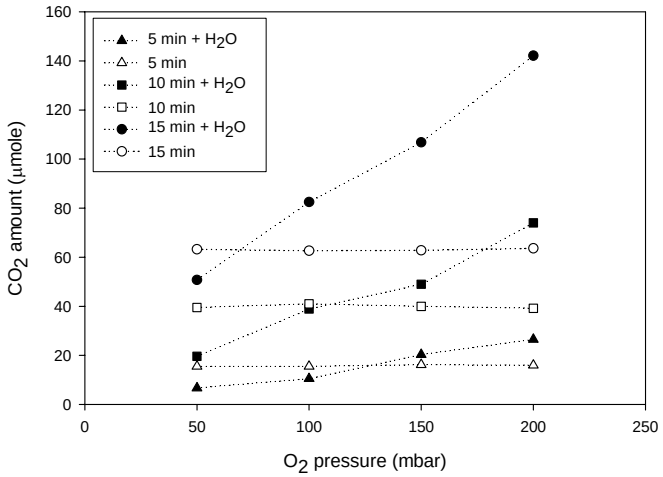

Fig. 4 : Degradation of HCP in an O_2 plasma at reduced pressure (50 to 200 mbar).For experiments at 5 and 10 min, 200 mg of HCP was used, and for experiments at 15 min, 2 480 mg of HCP was used.

In Fig. 4, the amount of CO_2 produced is constant over all the pressure range if the degradation is performed without water added (open circles). This means that the process is not dependent on the O_2 amount. However, as the quantity of CO_2 released is increasing with the charge density, in this case the number of electrons are the limiting reactant. If O (^{3}P or ^{1}D) is the active species for the degradation and is created by the processes described by the Eqn. 4, it is clear that the reaction will be limited by the amount of free electrons.

In presence of water, the CO_2 amount produced is dependent on the O_2 pressure and on the charge density applied. The lack of free electrons is no more restricting the reaction. If water is added to the medium, reactions 4, 6 and 8 will occur. Free electrons collide either with O_2 or H_2O to give O, OH and H (Eqn. 4 and 6) and subsequently O (^{1}D) can do inelastic collision with H_2O to produce more OH (Eqn. 8). This set of reactions can explain why the process is more efficient in the presence of water but not the O_2 dependence. The latter one can be explained by the following reactions:

$$H + O_2 \rightarrow HO_2 \quad (12)$$

$$H + HO_2 \rightarrow 2\ OH \quad (13)$$

H atoms coming from water dissociation react with O_2 to give the hydroperoxyl radical which in turn reacts again with an H to give two hydroxyl radicals. The first reaction is O_2 pressure dependent and the whole process explains the better results obtained with higher a O_2 pressure. The CO_2 amount depends also on the electrical charge density applied. For longer treatment times (thus higher charge density, see Eqn. 2) the CO_2 amount increases for all the pressures investigated (see Fig. 4) and the relation is always linear whether water is added or not. The chlorinated by-products obtained by the treatment of HCP in an O_2 discharge are the same as in a He/O_2 discharge, HCl, $COCl_2$, Cl_2 and C_3H_5Cl. Table 2 shows the reduced area of chlorinated products, the influence of

water and reaction time. For a short treatment time (1 min), mainly chlorinated products are detected (their reduced area is large). This supports our idea of a successive dechlorination mechanism prior to the oxidation of the carbon content. The presence of water increases the amount of HCl and C_3H_5Cl produced, while there is more Cl_2 when no water is present. The H atom is very important at this stage to control the recombination of Cl atoms.

Table 2: Chlorinated by-products obtained for the degradation of HCP in an O_2 plasma at 200 mbar and a discharge current of 27 mA. The experiment with 1 min of reaction time was performed with 200 mg of HCP, the other two with 2480 mg of HCP.

	Reduced Area		
	Reaction time : 15 min No water	Reaction time : 15 min 2 ml of water	Reaction time : 1 min 2 ml of water
HCl	30,8	173,6	1102
$COCl_2$	32,5	32,2	30,2
Cl_2	19,4	3,06	104,2
C_3H_5Cl	1,98	5,61	603

Conclusions

The tentative reaction mechanism for HCP degradation is presented in Fig 5. Based on the different chlorinated by-products found and their relative importance compared to CO_2 we attribute the first step of the degradation process to a successive dechlorination ending with the chloropropene. After this step the oxygenated species react with the molecules formed to lead to CO_2.

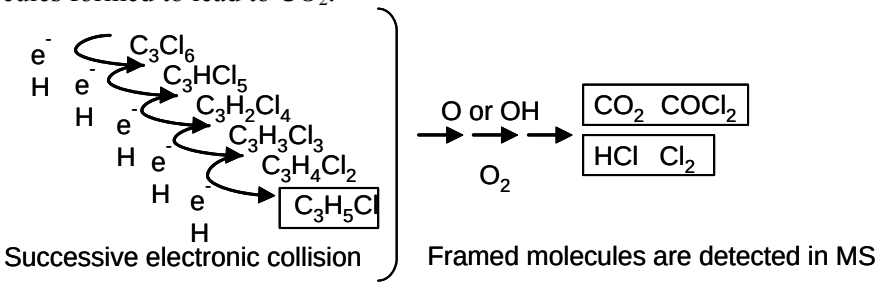

Fig 5: Reaction mechanism based on the experimental results obtained in He/O_2 and O_2 plasma degradation of HCP. Framed molecules have been detected in MS.

References

[1] K.C. Jones, P. de Voogt - Environ. Poll. **100** 209-221 (1999).

[2] M. Koch, D.R. Cohn, R.M. Patrick, M.P. Schuetze, L. Bromberg, D. Reilly, P. Thomas – Phys. Lett. A **184** 109-113 1993

[3] C. Pierard, and F. Reniers - Patent n°FR-04.00981 (2004).

[4] A. Ricard , Ph. Decomps, F. Massines - Surf. Coat. Technol.**112** 1-4 (1999).

[5] B. Eliasson, W. Egli, U. Kogelschatz - Pure & Applied Chemistry **6** 1275-1286 (1994).

[6] L. Prager, R. Mehnert, A. Sobottka, H. Langguth, W. Baumann, H. Mätzing, H-R. Paur, J. Schubert, R. Rashid, K.M. Taba, H-P. Schuchmann and C. von Sonntag - J. Adv. Oxid. Technol. **3** 87-97 (1998).

[7] R. Atkinson - *Chem. Rev.* **85** 69-201 (1985)

[8] A.J. Wagner, C. Vecitis and D.H. Fairbrother - J. Phys. Chem. B **106** 4432-4440 (2002).

Acknowledgements

C. Pierard would like to thank Solvay s.a., l'Université Libre de Bruxelles and le Fond David et Alice Van Buuren for financial support.

Reduction of surface oxides on steel using a DBD H_2 plasma

E.Michel[1], E. Silberberg[2] and F. Reniers[1]

[1] *Université Libre de Bruxelles, Service de Chimie Analytique et Chimie des Interfaces, Brussels, Belgium*
[2] *Arcelor Group, NCT Industry Centre Liège, Belgium*

Abstract

An hydrogen DBD plasma was used to reduce surface oxides on steel substrates. We show that the reduction efficiency (analysed by XPS) increases with the discharge current, and decreases when the hydrogen pressure increases. The density of atomic hydrogen created in the discharge was studied by OES. We show that the reduction efficiency is directly correlated to the density of atomic hydrogen in the discharge.

Keywords: Hydrogen plasma; Discharge cleaning; Surface treatment; Steel products; Optical emission spectroscopy.

1. Introduction

The reduction of surface oxides on steel is of great importance in an industrial process, as they can influence the adhesion properties of the further coatings. Reduction of these oxides is often realized using wet chemistry (electrolysis in acid solution), but plasma techniques can lead to similar results, with a better respect for the environment. An hydrogen plasma is particularly suitable in this respect, as the active hydrogen atoms created in the discharge can react with surface oxide to produce water that desorbs and is pumped away. The overall reaction can be written as:

$$Fe_2O_3\ (s) + 6H \rightarrow 2Fe\ (s) + 3\ H_2O\ (g) \quad (1.1)$$

2. Experimental

Dielectric barrier discharges DBD are obtained between two parallel metallic electrodes, one of which being covered by a dielectric (Al_2O_3, thickness 1 mm). The second electrode on which the sample is located (steel substrate), is connected to the ground.
Steel plates either covered with their native oxide layer, or having been submitted to oxygen plasma, are introduced in a DBD plasma reactor. Hydrogen is injected in the chamber at a pressure varying from 2 to 200 mbar. In some experiments, helium was added. Typical plasma conditions were V = 1000 to 2000 V, frequency = 10 to 20 kHz.

2.1. Discharge characterisation

Figure 1 presents the oscillograms obtained in a hydrogen discharge. The applied voltage is measured with a high voltage probe (Lecroy, attenuation factor: 1000). The oscilloscope (Lecroy LT264) used for those experiments has a bandwidth of 350 MHz and its sampling rate is 1 GS/s. The total current delivered in the system was obtained by measuring the terminal voltage of the resistance.

To estimate the efficiency of the process from these data (applied voltage, current in the system), the discharge parameters (voltage and current) are calculated using an electrical model [1-3].

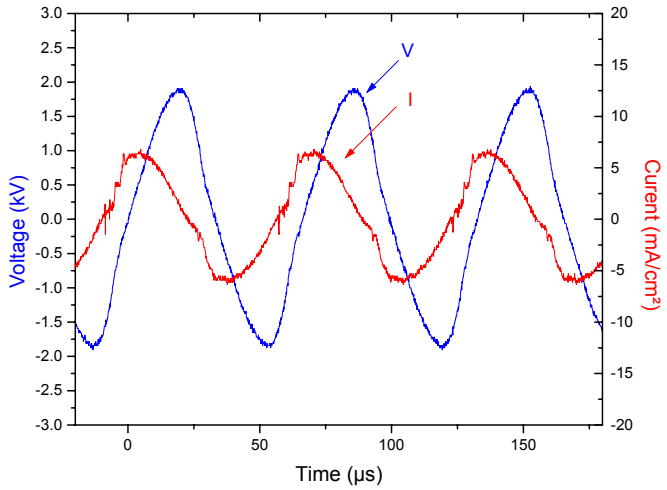

Fig 1 : Oscillograms obtained in a hydrogen discharge (5 mbar, V = 1700 V, 15 kHz).

The discharges are also characterized by OES (Optical Emission Spectroscopy, Digisem Sofie SCM 350 mm, 1800 g/mm, resolution of 0,14 nm) between 200 and 900 nm. Figure 2 presents an OES spectrum of hydrogen discharge. Molecular and atomic hydrogen emission lines are detected.

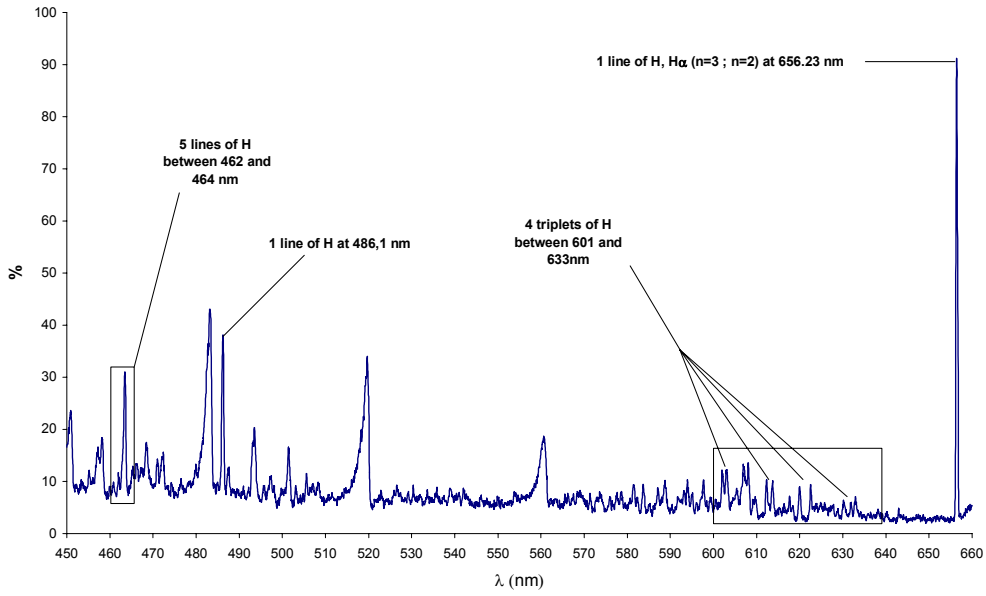

Fig 2: OES spectrum of a hydrogen discharge.

In this study, the intensity of the hydrogen line noted H_α (656,23 nm) was used as an indirect probe for the density of atomic hydrogen. The production and consumption of the excited atomic states are described by reactions 2.1 (electronic impact) and 2.2 (direct excitation).

$$H + e^- \rightarrow H^* + e^- \qquad (2.1)$$

$$H_2 + e^- \rightarrow H^* + H + e^- \qquad (2.2)$$

The processes of loss (de-excitation) can be radiative according to the reaction (2.3) and non radiative according to reactions (2.4) to (2.6). It should be noted that for a pressure higher than 5 mbar [4], the de-excitation by ionization is negligible.

$$H^* \rightarrow H + h\nu \qquad (2.3)$$

$$H^* + e^- \rightarrow H^+ + 2\,e^- \qquad (2.4)$$

$$H^* + H_2 \rightarrow H + H_2 \qquad (2.5)$$

$$H^* + H \rightarrow H + H \qquad (2.6)$$

According to Figure 3, the hydrogen signal increases with the discharge current (this can be realised either by increasing the frequency and/or by increasing the voltage). It should also be noted that the hydrogen signal is reversely proportional to the pressure.

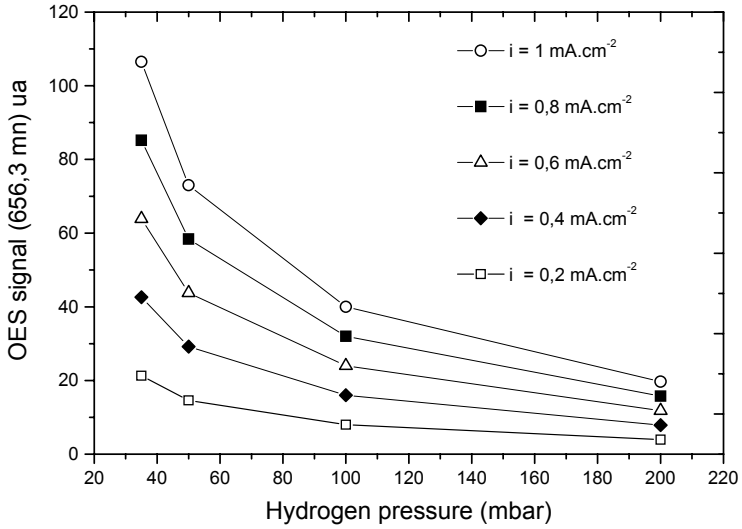

Figure 3: Evolution of hydrogen signal (656,23 nm) versus pressure, for different values of discharge current.

2.2. Surface analysis

The surface was analyzed by XPS in order to determine the oxidation and the contamination levels. We followed the O(1s)/Fe(2p3/2) and C(1s)/Fe(2p3/2) ratio respectively. The efficiency ε can be evaluated according to the equation (2.7):

$$\varepsilon = \frac{\dfrac{A_{XPS}^{Ref}O(1s)}{A_{XPS}^{Ref}Fe(2p3/2)} - \dfrac{A_{XPS}^{x}O(1s)}{A_{XPS}^{x}Fe(2p3/2)}}{\dfrac{A_{XPS}^{Ref}O(1s)}{A_{XPS}^{Ref}Fe(2p3/2)}} \qquad (2.7)$$

Where A is the peak area, *ref.* indicates the oxidized reference and X the sample treated by hydrogen plasma. This equation, which represents the reduced fraction, will be used to correlate the discharge parameters (current, pressure...) and the process efficiency.

Figure 4 presents the XPS spectrum of a steel plate surface. The binding energies are calculated using the carbon at 284,6 eV as a reference [5]. The iron oxide present at the surface is hematite (Fe_2O_3), as confirmed in the literature [6-8].

For steel plates covered with their native oxide layer, the O/Fe and C/Fe ratios are respectively equal at 2,1 ± 0,1 and 0,6 ± 0,1. For steel plates submitted to an oxygen plasma, the O/Fe and C/Fe ratios respectively worth 2,3 ± 0,1 and 0,3 ± 0,1.

To limit the oxidation after treatment, the DBD reactor is directly coupled to the XPS chamber. The residual pressure reached before the injection of hydrogen is about 10^{-6} mbar.

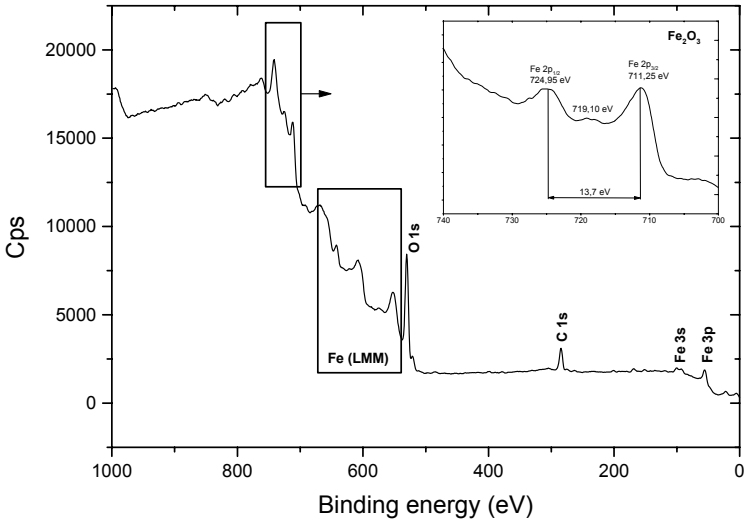

Fig 4: XPS spectrum of steel plate showing the presence of iron oxide.

3. Results and discussion

The effects of the hydrogen partial and total pressure and of the discharge current have been studied. Figure 5 presents the effect of the hydrogen pressure on the O/Fe ratio. By decreasing the hydrogen pressure, the $H \rightarrow H_2$ recombination reaction is disadvantaged and the reduction efficiency increases (the O/Fe ratio decreases). The number of active species (H) being more significant at low pressure (for an equal current), this result is in good agreement with the reaction (1.1).

On the other hand, an increase of the discharge current, leads to a better reduction efficiency, as shown in Figure 6. An increase in the discharge current leads to an increase of the hydrogen dissociation. Consequently, the number of active species is higher, as is the reduction efficiency (O/Fe decreases). This result is also in agreement with the reaction (1.1).

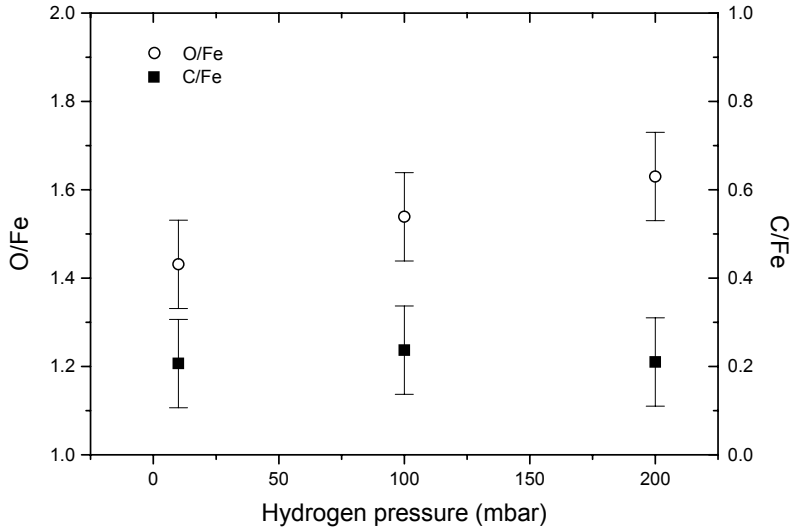

Fig 5: O(1s)/Fe(2p3/2) XPS ratio as a function of the total hydrogen pressure, the charge density is 0,8 mA/cm^2 and the treatment time is 3 min.

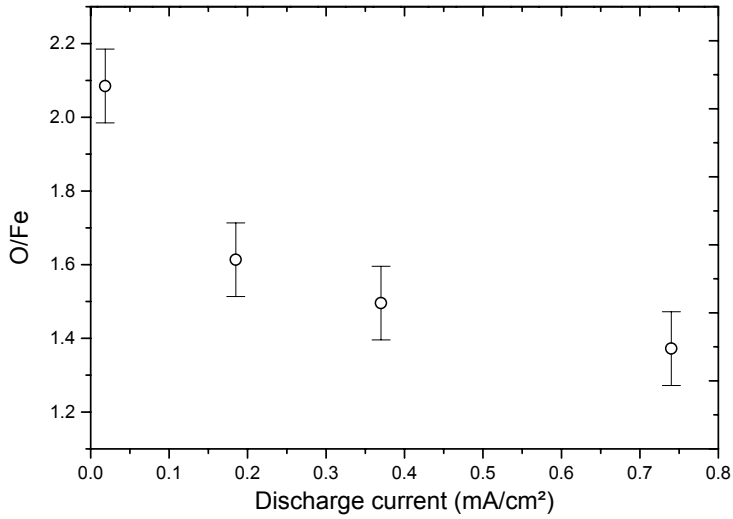

Fig 6: O(1s)/Fe(2p3/2) XPS ratio as a function of the discharge current for a fixed hydrogen pressure (35 mbar), and the treatment time is 10 min.

The reduction efficiency can be directly correlated to the intensity of the OES emission line of atomic hydrogen (Figure 7). This intensity decreases when the hydrogen pressure increases, indicating that recombination occurs in the gas phase. A complex kinetic process occurs in which atomic hydrogen is produced in the plasma by molecular hydrogen dissociation under the effect of electrons, and can either recombine in the gas phase, or react at the oxide surface to form OH or H_2O, both able to desorb and to be pumped away. The effective mean free path of hydrogen in the gas phase is the critical parameter. Helium was therefore introduced in the gas phase to raise the total pressure but, without being able to react with hydrogen, no decrease in the reduction efficiency was observed in such conditions.

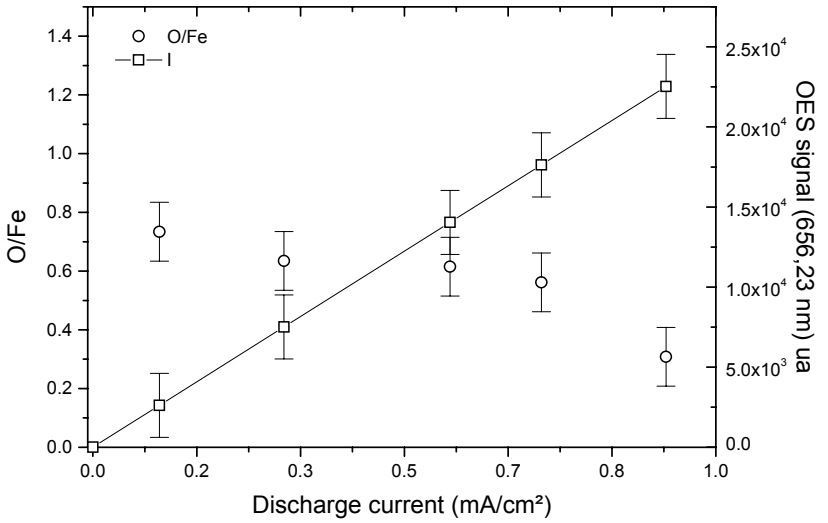

Fig 7: Correlation between the O(1s)/Fe(2p3/2) XPS ratio, the charge density, and the intensity of the H emission line at 656.23 nm (the H_2 pressure is 5 mbar, treatment time : 10 min).

4. Conclusions

A DBD H_2 plasma can successfully remove the surface oxide layer on steel substrates. The kinetics of reduction depends mostly on the amount of hydrogen atoms able to reach the surface.
The electrons of high energy (on average 10 eV) are able to dissociate molecular hydrogen by inelastic collisions. The oxide is reduced under the action of atomic hydrogen. The treatment time will depend on the H density. Consequently, for a greater efficiency, it is necessary to obtain a high dissociation degree. This can be reached by increasing the discharge current and/or by decreasing the total pressure.
In conclusion, this "dry" process respects the environment and gives good results for the reduction of metallic oxides. Under the best experimental conditions, approximately 90 % of the oxide initially present on the steel surface can be removed. It should be noted that the reduction efficiency by "wet" treatment tested in laboratory, reaches approximately 60 %.

Acknowledgements

The authors acknowledge the Arcelor group for technical and financial supports.

References

[1] U.Kogelschatz, *Plasma Chem. and Plasma Proc.* **23**, 1-45 (2003).
[2] M.Petit, *Rev. Sci. Instruments.* **73**, 2705-2712 (2002).
[3] G.Bauville, P.Choquet, B.Lacour, E.Michel, V.Puech and E.Silberberg, in *ISPC* (Taormina, 2003).
[4] A.Giquel, M.Chenevier, Kh.Hassouni, A.Tserepi and M.Dubus, *J.Phys. D: Appl. Phys.* **83**, 7504-7521 (1998).
[5] *Handbook of X-Ray photoelectron spectroscopy* (CRC press, 1993).
[6] Usinor, in *Le livre de l'acier*, edited by Usinor (1997).
[7] L.Lefèvre, T.Belmonte, T.Czerwiec, A.Ricard and H.Michel, Appl. surf. Sci 153, 85-95 (2000).
[8] J.M.Thiébaut, T.Belmonte, D.Chaleix, P.Choquet, G.Baravian, V.Puech and H.Michel, Surf. and Coat. Tech. 169-170, 186-189 (2003).

Plasma deposition of silicon nitride thin films

A. Batan[1], J. Vereecken[2] , F. Reniers[1]

[1]*Université Libre de Bruxelles, Faculty of Sciences, Analytical and Interfacial Chemistry, CP 255, Bd Triomphe, B-1050 Brussels, Belgium*.

[2]*Vrije Universiteit Brussel,Faculty of Applied Sciences, META, pleinlaan 2, B-1050 Brussels, Belgium.*

Abstract

Silicon nitride thin films were deposited by DC magnetron sputtering. The sputtering was performed from a silicon target in a (Ar, H_2, N_2) atmosphere. Deposition rates of about 33.6 Å/s for pure Si and 13.5 Å/s for Si_3N_4 were obtained. The XPS spectra indicated that Si_3N_4 stoeichiometric was obtained for a molar fraction of nitrogen in the gas phase of 0.2 and above and also indicated that the sputtered silicon nitride films were uncontaminated. The process was stable and the structure of the films was amorphous.

Keywords

Silicon nitride; Magnetron sputtering.

Introduction

Silicon nitride thin films have numerous applications in the semiconductor industry. They are used in very large scale integrated circuits, thin film transistors, alkali-ion diffusion barrier, oxidation mask and solar cell applications. Silicon nitride can be prepared by various methods such as chemical vapour deposition (CVD), plasma-enhanced CVD, inductively coupled plasma (CVD) and sputtering. Among those methods, the sputtering technique is a low temperature method like plasma-enhanced CVD. Various sputtering techniques, including sputtering and reactive sputtering in different systems such as direct current (DC), radio frequency (RF), and S-gun, were used to prepare the silicon nitride. In this study we deposited SiN_x films using the plasma DC reactive magnetron technique.

Experimental

Silicon nitride thin films were deposited by DC magnetron sputtering on stainless steel substrates in a planar DC sputtering home apparatus. The sputtering was performed from a silicon target in a sputtering atmosphere of (Ar, H_2, N_2) mixture. The gas composition could be varied from 0 to 100% for Ar and N_2 and from 0 to 10% for H_2.

The deposition rate, the composition, structure and purity of the coatings have been investigated as a function of the process parameters, such as the composition of the sputtering atmosphere, the total pressure, and the plasma power. The plasma was characterized by the current – voltage curves. The deposited films were characterized by optical interferometry (thickness measurement) and XPS.

Results

Due to the high affinity of Si for oxygen, the deposition of silicon films is not trivial. Any trace of water vapour, or remaining oxygen contain molecule in the chamber usually induces the formation of a silicon oxide layer. Figure 1 shows that the use of pure Argon for sputtering leads to the formation of a SiO_2 film. In order to avoid this effect, we added hydrogen to the plasma. For our setup, pure silicon films can be obtained if the plasma gas contains at least 10% H_2. This gas mixture will therefore be the starting gas for the reactive sputter deposition of silicon nitride, through the addition of nitrogen.

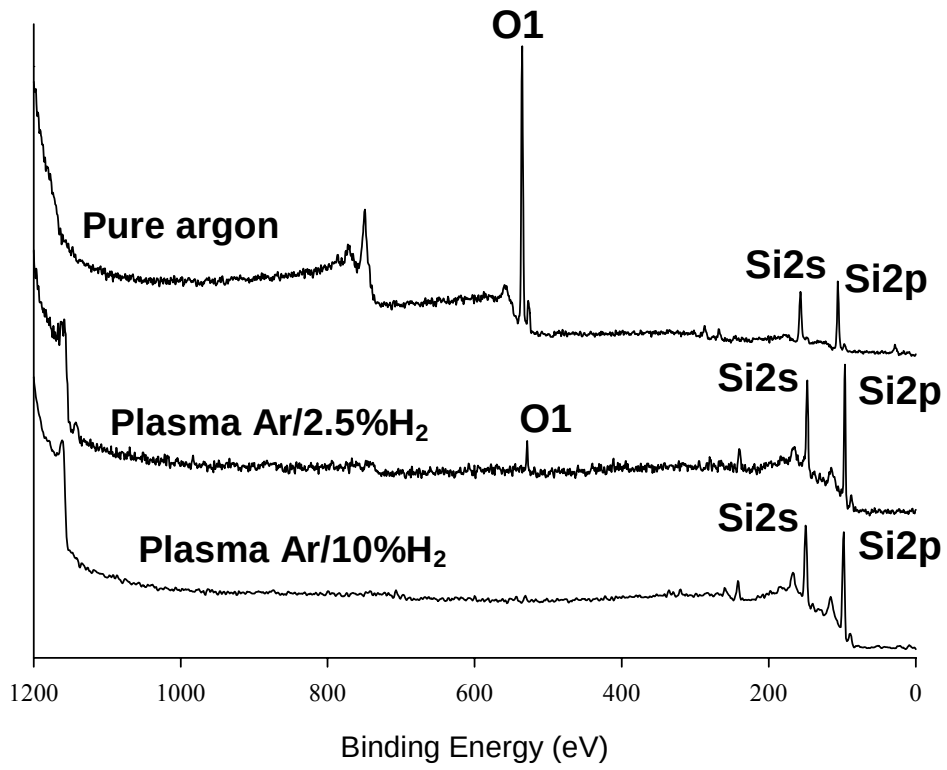

Figure 1: Effect of the hydrogen percentage in the sputtering gas on the purity of silicon films obtained.

When nitrogen is added to the plasma gas, pure silicon nitrides of various stoeichiometry (depending on the molar fraction of nitrogen in the plasma) are formed. Figure 2 shows a typical XPS survey of a Si_3N_4 film obtained with 50% nitrogen in the plasma. After a short cleaning of the film surface into the XPS chamber by Ar^+ bombardment, no contaminations (C, O) are detected.

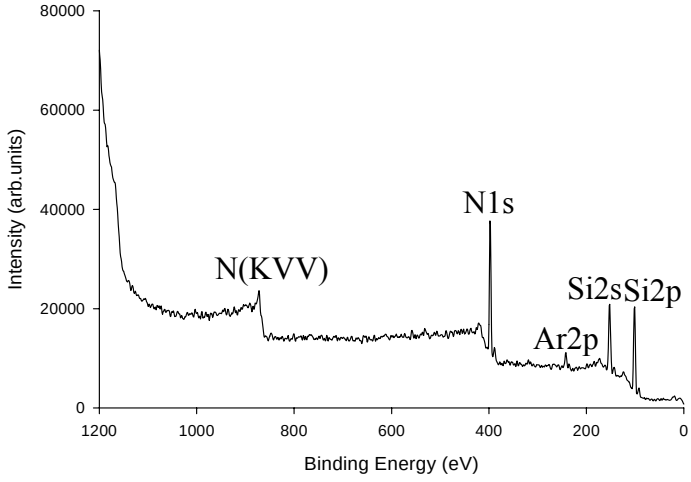

Figure 2: XPS survey spectra of a Si_3N_4 film obtained using a $((Ar/10\%H_2)/50\%N_2)$ plasma.

The XPS spectra indicated that Si_3N_4 stoeichiometric was obtained for a molar fraction of nitrogen in the plasma of 0.2 and above and also indicated that the sputtered silicon nitride films were uncontaminated with oxygen and carbon. Figure 3 illustrates the evolution of the Si XPS peak as a function of the nitrogen concentration. X-ray diffraction analysis indicates that the structure of all the films was amorphous.

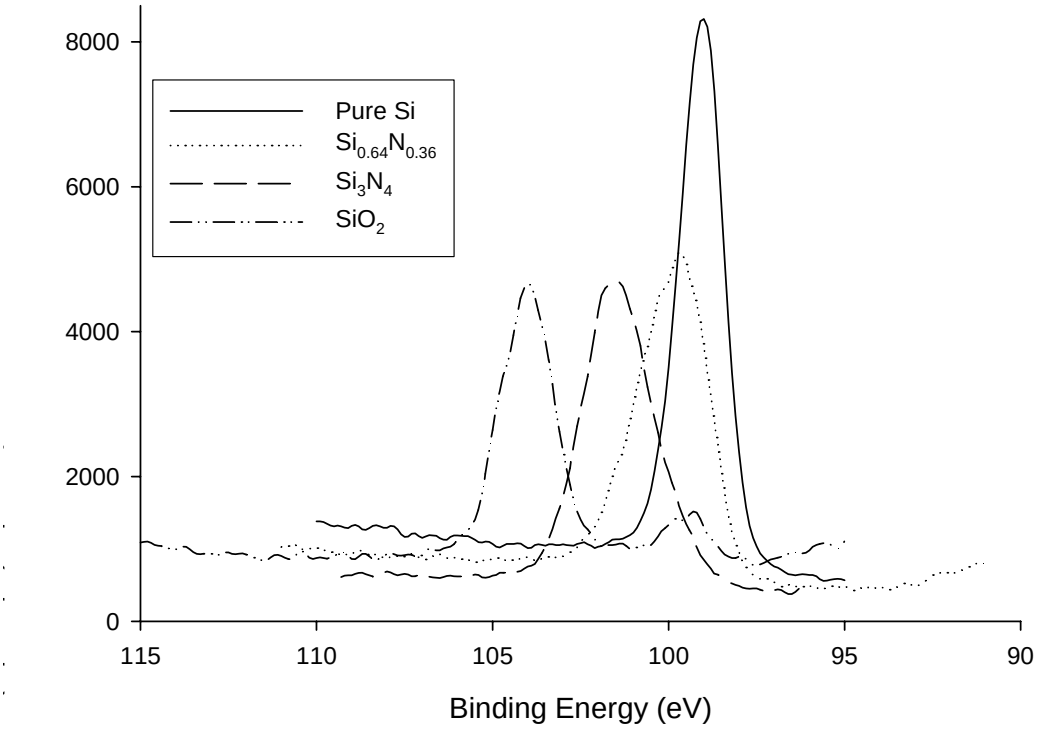

Figure 3: XPS Si 2p peak for pure silicon, silicon nitride under-stoichiometric, Si_3N_4 and SiO_2.

Study of the deposition rate

Figure 4 shows the average deposition rate as a function of the nitrogen mole fraction in the plasma gas for a fixed total pressure. Deposition rates of 33.6 Å/s for pure Si using a $Ar/10\%H_2$ are obtained. The deposition rate decreases rapidly when nitrogen replaces argon, due mainly to a strong difference in the sputtering yield of the two gases.

The behavior is different if nitrogen is added to a fixed Ar/H_2 pressure in the plasma gas. Figure 5 shows that the deposition rate decreases also, but with a different slope. This decrease is not due in this case to a decrease of the Argon amount available, but to a pressure effect. When the total pressure increases, the mean free path in the gas phase decreases, lowering therefore the deposition rate. Similarly, a pressure increase leads to a decrease of the target voltage (at same current). This induces lower energies for the sputtering ions, and consequently a smaller sputtering yield, and a lower deposition rate. A deposition rate of 13.5 Å/s for pure Si_3N_4 could be reached (see Fig.5)

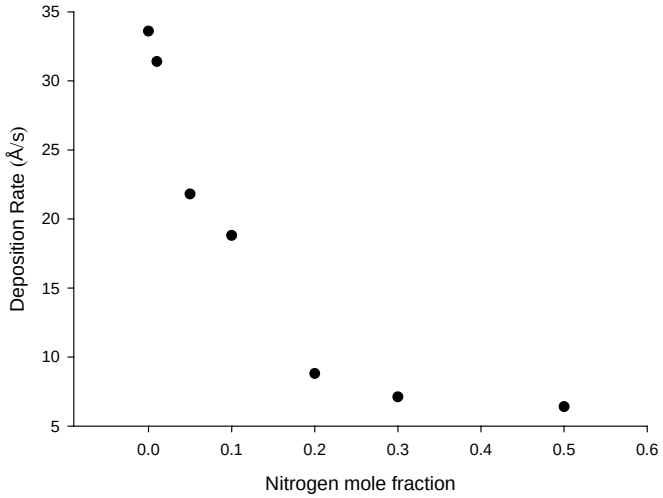

Figure 4. Deposition rate vs nitrogen mole fraction (sputtering current and total pressure are 0.35A and 10^{-2}Torr respectively)

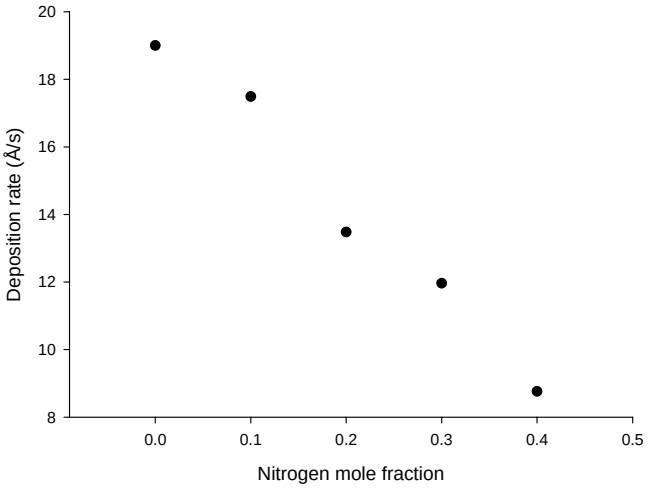

Figure 5. Deposition rate vs nitrogen mole fraction (sputtering current: 0.3 A and ($Ar/10\%H_2$) partial pressure: 910^{-3}Torr)

Stability of the plasma process

The influence of the nitrogen addition to the ($Ar/10\%H_2$) gas on the stability of the plasma process is shown in Figure 6. The mole fraction of nitrogen was increased stepwise with 2 min between two consequent additions. After reaching a nitrogen mole fraction of 0.8, the nitrogen flow was reduced stepwise with again 2 min between two points. The increase of the nitrogen mole fraction leads to a decrease of the target voltage. This

well-known effect can be attributed to more volume ionisation resulting in a current increase and, at constant power, a target voltage decrease. Switching off the nitrogen flow resulted in a reverse behaviour with a small increase in the target voltage compared to the one obtained in the forward process. This increase is due to the implantation of reactive ions in the target surface [1-4]. No hysteresis effect was observed.

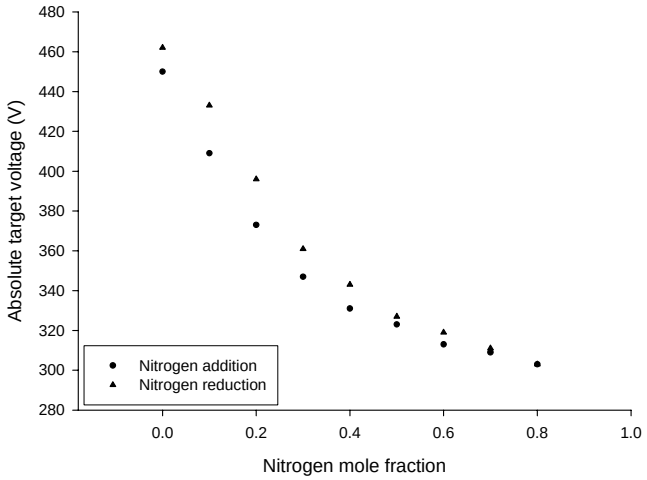

Figure 6. Target voltage vs the nitrogen mole fraction (Ar/10%H_2 partial pressure: 9 10^{-3} Torr; time between points: 120s; pumping speed of 230 l/s).

The addition of nitrogen to the plasma gas was repeated at a lower pumping speed (23 L/s instead of 230 L/s). As shown in Figure 7, the transition from the metallic state to the 'poisoned' state occurs at a critical nitrogen mole fraction of x = 0.5, where a sudden change of the target voltage behaviour as a function of the nitrogen content is observed. This indicates a change in the surface state of the target. This instability is due to an insufficient pumping speed of the reactive gas. We also noted, for nitrogen mole fractions larger than 0.3, a small decrease in the target voltage when we diminished the nitrogen flow. This decrease of the target voltage is probably due to the formation of silicon nitride layer, which is characterized by a high secondary electron emission coefficient compared to the metal and leads to a decrease in the target voltage.

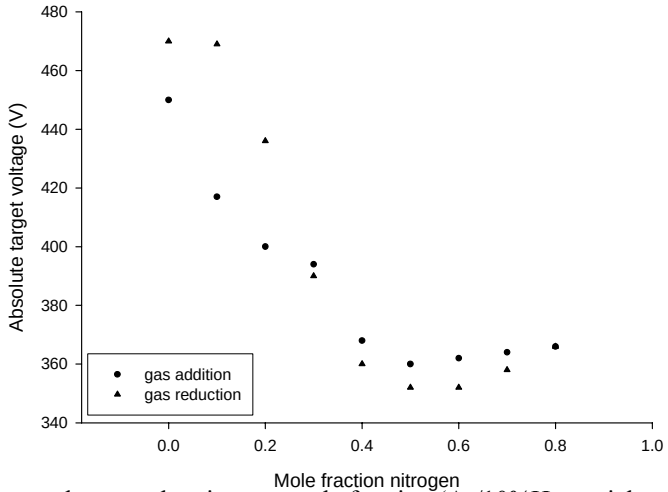

Figure 7. Target voltage vs the nitrogen mole fraction (Ar/10%H_2 partial pressure: 9 10^{-3} Torr; time between points: 120s; pumping speed of 23 l/s).

For pumping speeds of 230 L/s, Figure 8 reveals that no hysteresis effect is detected in the current-voltage curves indicating that the reactive sputtering proceeds in the metallic mode and the process is stable.

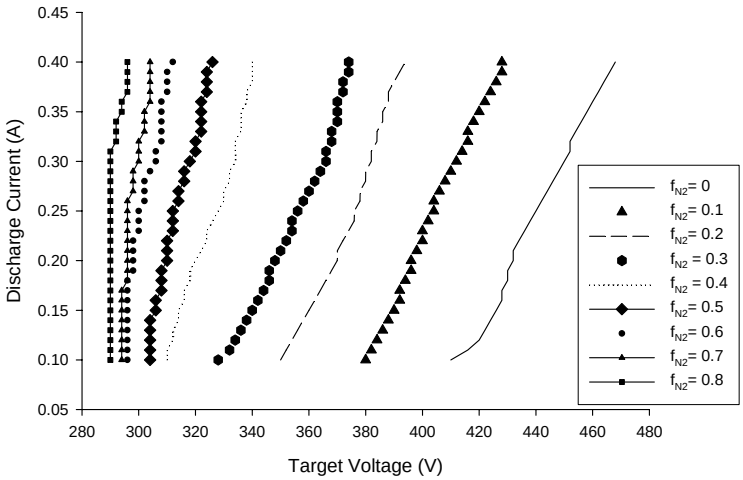

Figure 8: I-U characteristics of the discharge vs nitrogen mole fraction (Ar/10%H_2 partial pressure fixed: 9 10^{-3} Torr, variable total pressure).

Conclusions

High purity SiN_x films could be deposited at a high speed by DC planar magnetron sputtering. The sputtering is operating in the metallic mode, and no hysteresis effect is observed in our deposition conditions. A high pumping speed is needed to avoid a contamination of the target. The deposition rate decreases when the fraction of nitrogen in the plasma gas increases. The reasons identified are synergetic: lowering in the sputtering yield, lowering of the target voltage, decrease of the mean free path. Therefore, a compromise has to be found between high speed and efficient nitridation.

Acknowledgments

Abdelkrim Batan would like to thank "ULB FUNDS" for financial support. We are grateful to A. Franquet (VUB) for the XPS analysis.

References

[1] D. Depla, R De Gryse, Vacuum 529-536, 69(4) (2003).
[2] D. Depla, A. Colpaert, K. Eufinger, A. Segers, J. Haemers, R. De Gryse, Vacuum 9-17, 66(1) (2002).
[3] D. Depla, J. Haemers, R. De Gryse, Plasma Sources Science & Technology 91-96, 11(1) (2002).
[4] D. Depla, R. De Gryse, Journal of Vacuum Science & Technology, A: Vacuum, Surfaces, and Films 521-525, 20(2) (2002).

Fabrication of Self-Assembled Carbon Nanowalls Using Plasma Enhanced Chemical Vapor Deposition with Hydrogen Radical Injection

M. Hori[1] and M. Hiramatsu[2]

[1]*Department of Electrical Engineering and Computer Science, Graduate School of Engineering, Nagoya University, Chikusa, Nagoya 464-8603, Japan*
[2]*Department of Electrical and Electronic Engineering, Meijo University, Tempaku, Nagoya 468-8502, Japan*

Abstract
Carbon nanowalls, two-dimensional carbon nanostructures, were fabricated using fluorocarbon plasma-enhanced chemical vapor deposition assisted by H radical injection. The correlation between carbon nanowall growth and the fabrication conditions was investigated. The morphologies and growth rate of carbon nanowalls were dependent on the types of carbon source gases and the amount of H radicals injected. In addition, straight, aligned carbon nanowalls with regular spacing were fabricated by controlling the radical flow configuration.
Keywords: Carbon nanowalls, PECVD, Field emission

1. Introduction

Self-assembled carbon nanostructures such as carbon nanotubes have attracted much attention for several applications, including field emitter arrays, gas storage, and membranes for electrochemical energy storage [1-4]. Recently, two-dimensional carbon nanostructures have also been grown. Shang *et al*. [5] prepared carbon nanoflake films using hot filament chemical vapor deposition (CVD). Wu *et al*. [6] reported the fabrication of two-dimensional carbon nanostructures (carbon nanowalls) standing vertically on a catalyzed substrate using microwave plasma-enhanced chemical vapor deposition (CVD). Very recently, the authors have fabricated carbon nanowalls without catalysts, using radio-frequency (rf) plasma-enhanced CVD (PECVD), assisted by a hydrogen (H) radical injection [7,8]. Carbon nanowalls, two-dimensional carbon nanostructures consisting of plane graphene layers standing on the substrate, have been grown recently. The large surface area of carbon nanowalls may provide opportunities for various applications. In view of their practical application, further investigations should be performed in order to enable control over the structure and electronic properties and understand their growth mechanism.

In this work, carbon nanowalls were fabricated on a Si substrate without catalysts, using rf-PECVD assisted by H radical injection. The correlation between carbon nanowall growth and the fabrication conditions, such as the carbon source gases used, was investigated. As one of applications of carbon nanowalls, field electron emission characteristics were investigated for the carbon nanowall film.

2. Experiments

The experimental setup used in this study is shown in Figs. 1(a) and 1(b). Figure 1(a) shows a schematic of the rf-PECVD assisted by a remote radical source, which consists of a parallel-plate rf (13.56 MHz) capacitively coupled plasma (CCP) region and a remote radical source which uses an inductively coupled H_2 plasma (H_2 ICP). The main reaction chamber was equipped with circular parallel-plate electrodes separated by 5 cm. Carbon source gas (C_2F_6, CH_4, CF_4, CHF_3 and C_4F_8) was introduced into the rf-CCP region. H_2 was fed through a quartz tube of 26 mm inner diameter and 20 cm in length. A five-turn rf coil was mounted on the quartz tube. The rf coil was connected to the rf power generator operating at 13.56 MHz. The flow rates of carbon source gas and H_2 were kept at 15 and 30 sccm, respectively, and the total gas pressure was 100 mTorr. Typical rf powers of CCP and ICP were 100 W and 400 W, respectively, and the substrate temperature was 500 °C, which was the maximum temperature in the present system.

Figure 1(b) shows a schematic of the experimental arrangement for measuring the absolute H radical density by the VUVAS system employing a microdischarge hollow-cathode lamp (MHCL). The VUVAS technique has been described in detail elsewhere [9,10]. The MHCL was used as a vacuum ultraviolet (VUV)

light source for absorption spectroscopy. The absorption path length was restricted to be 15 cm by using two stainless steel pipes and the capillary plates in order to prevent the saturation of absorption. The VUV light passed once through the chamber at 2 cm above the substrate, and was focused on the slit of a VUV monochromator (Acton Research Corp., ARC VM-520) by MgF_2 lens and detected by a photomultipliar tube (PMT). The transition line used for the absorption measurement was Lyman alpha at 121.6 nm for the H radical density.

Scanning electron microscopy (SEM) was used to evaluate the surface morphology of the deposits grown under various conditions. In addition, the field electron emission characteristics of the carbon nanowall films were measured with a spherical stainless steel anode of 2-mm diameter in a vacuum of 10^{-6} Torr. The distance between anode and cathode (carbon nanowall film) was kept at 80 μm.

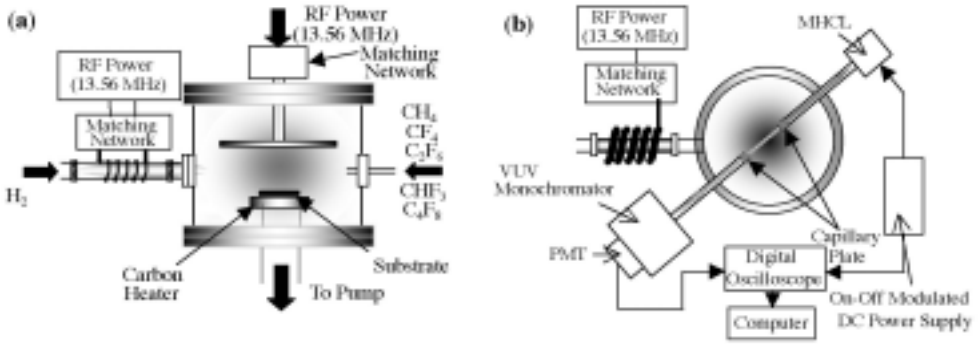

Fig. 1. (a) Schematic of the rf-PECVD assisted by a remote H radical source used for the growth of carbon nanowalls. (b) Schematic diagram of the experimental arrangement for measuring absolute H radical density using VUVAS technique.

3. Results and discussion

Typical SEM image of the carbon nanowalls grown on Si substrate using a C_2F_6/H_2 system for 8 hours are shown in Figs. 2(a) and 2(b). These pictures show that two-dimensional carbon sheets were grown vertically on the substrate, forming a unique nanostructure like a maze. The thickness of carbon nanowalls was 40-60 nm, and their height was about 1.5 μm. Figure 2(c) shows a SEM image of 8-hour-grown carbon nanowall mat scratched out from substrate, which implies that free-standing aligned carbon nanowall filter will be fabricated using the present system.

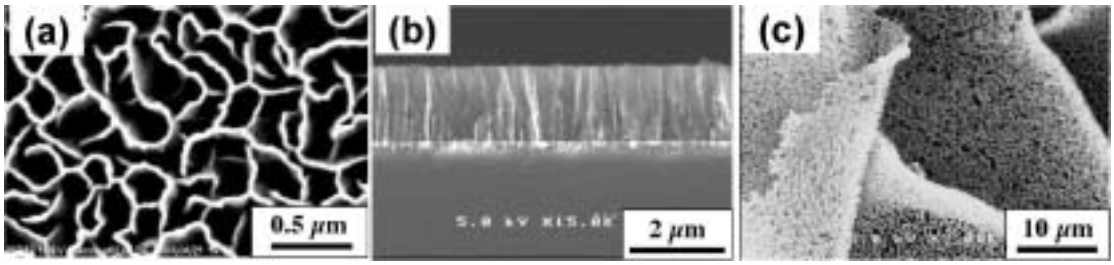

Fig. 2. SEM images of carbon nanowalls using C_2F_6/H_2 system for 8 hours; (a) top view, (b) cross-sectional view, and (c) carbon nanowall filter which was scratched out from Si substrate.

Figures 3(a) - 3(c) show SEM images of carbon nanowalls grown for 15 min, 30 min, and 1 hour, respectively. As shown in Fig. 3(a), at the nucleation stage of growth, nano-islands with size of 3-10 nm were formed on the substrate, followed by the formation of disordered carbon nanoflakes of smaller sizes (Fig. 3(b)) and subsequent growth of isolated nanowalls with semicircular shape standing vertically on the substrate in the next stage of growth as shown in Fig. 3(c).

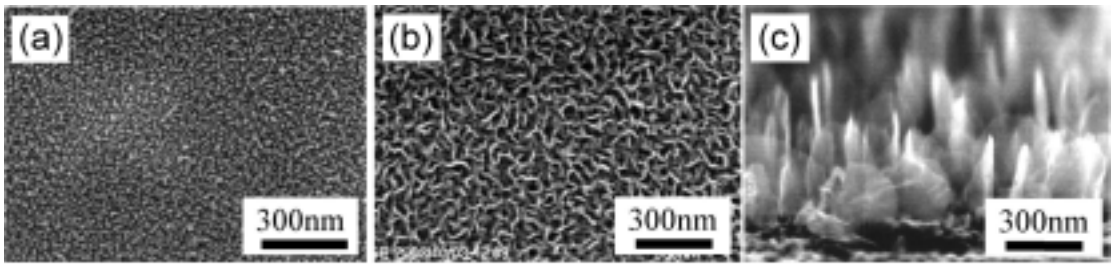

Fig. 3. SEM images of carbon naowalls grown for (a) 15 min, (b) 30 min, and (c) 1 hour.

The mechanism responsible for the nanowall growth was speculated as follows. At the nucleation stage, carbon species would condense to form nano-islands with dangling bonds as shown in Fig. 3(a). At these dangling bonds, disordered carbon nanoflakes of smaller sizes would be nucleated, followed by the two-dimensional growth and subsequent formation of graphene sheets. Among nucleated graphene sheets with random orientations, those standing almost vertically on the substrate continued preferably to grow up faster to aligned nanowalls, as shown in Fig. 3(c), due to the difference of the growth rates in the direction of parallel and perpendicular to the graphene layer. Here, parallel growth indicates that reactive carbon species arrive at the edge of graphene layer and this plane graphene layer expands, while perpendicular growth indicates that reactive carbon species arriving at the surface of graphene layer form another layer on the surface. On the other hand, low-lying inclined graphene sheets were shadowed by the high-grown vertical graphene sheets. As a result, amounts of reactive carbon species arriving at the low-lying inclined graphene sheets decreased, resulting in the termination of growth for the inclined smaller nanowalls. Sifting vertical nanowalls from nucleated graphene sheets with random orientations at the early stage of growth would occur, resulting in the increase of spacing between nanowalls. As the growth time increased, spread vertical nanowalls met with one another, eventually resulting in the formation of linked nanowalls like a maze. With the further increase of growth time, it became more difficult for the reactive carbon species to reach the sidewall, resulting in the saturation of increase in the wall thickness.

Growth experiments were carried out using CH_4, CF_4, CHF_3 or C_4F_8 as a carbon source gas under similar conditions as those for the case using the C_2F_6/H_2 system. Carbon nanowalls were successfully fabricated using CH_4/H_2, CF_4/H_2 and CHF_3/H_2 systems. The morphology of the carbon nanowalls grown using CF_4/H_2 and CHF_3/H_2 systems was similar to that using the C_2F_6/H_2 system shown in Fig. 2(a), except that the spacing between nanowalls was a little larger than that of nanowalls grown using C_2F_6/H_2 system. Carbon nanowalls grown using CH_4 were rather wavy and very thin, and their thickness was less than 10 nm. When using C_4F_8/H_2 system, on the other hand, definite nanowalls were not grown.

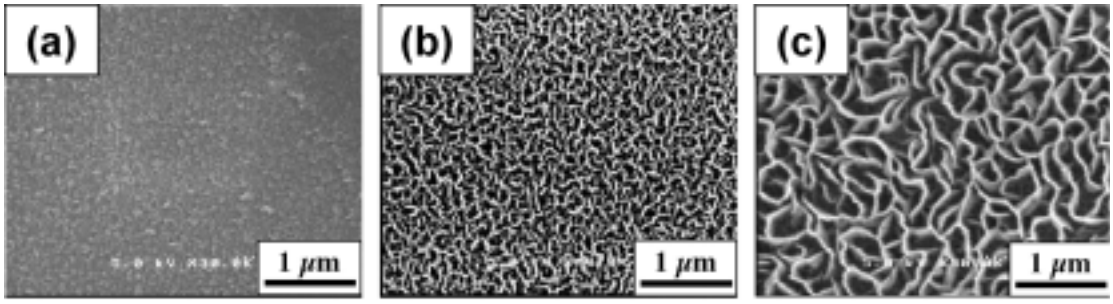

Fig. 4. SEM images of carbon nanowalls grown at the rf power of remote H_2 ICP of (a) 0 W, (b) 100 W and (c) 400 W.

The effect of H atom injection into the CCP region on the morphology of deposits was investigated by changing the rf power of the H_2 ICP. It was observed that the morphologies were dependent on the rf power of the remote H_2 ICP. Figs. 4(a) - 4(c) show SEM images of deposits grown using the C_2F_6/H_2 system for 3 hours at

various rf powers of the H_2 ICP. In the case of deposition without the H_2 ICP, where a C_2F_6/H_2 mixture was excited only by the rf-CCP, carbon nanowalls were not fabricated, but fluorocarbon polymers with a cauliflower shape were deposited, as shown in Fig. 4(a). At a low power of 100 W, however, carbon nanowalls were grown as shown in Fig. 4(b), although the carbon nanowalls grown at the ICP power of 100 W were not so clear, as compared with the carbon nanowalls grown at 400 W, as shown in Fig. 4(c).

We have measured H radical density in the plasma by the VUVAS technique. Absorption measurements were carried out with varying the rf power of the H_2 ICP. Figure 5 shows the H radical density in the CCP region as a function of rf power of remote H_2 ICP. The H radical density in the CCP region without H radical injection, where C_2F_6/H_2 mixture was excited by rf-CCP only, was $1.7x10^{11}$ cm^{-3}. As the rf power of remote H_2 ICP increased, the amount of H radicals produced in the ICP increased, resulting in the increase of the H radical density in the CCP region. The H radical density was $3.1x10^{11}$ cm^{-3} at the rf ICP power of 400 W, where definite typical carbon nanowalls were fabricated as shown in Fig. 2. The H radical density in the CCP region increased by about two times as a result of the H radical injection under the typical growth condition for the carbon nanowalls.

The morphologies and growth rate of carbon nanowalls were found to depend on the type of carbon source gas. Of the variety of fluorocarbon gases investigated in this study, C_2F_6 is expected to yield CF_3 radicals most effectively. CF_3 radicals could also be generated in the CF_4 or CHF_3 plasma to some extent. Meanwhile, the CF_3 radical density in the C_4F_8 plasma is considered to be low, although large amounts of CF_2 radicals would be generated in the C_4F_8 plasma, due to the cyclic structure of C_4F_8. Therefore, it is suggested that the CF_3 radicals are important species responsible for the formation of carbon nanowalls from fluorocarbon/hydrogen systems.

Injected H atoms would react effectively with fluorocarbon radicals in the gas phase as well as at the surface by the reaction of F abstraction. At a substrate temperature of 500 °C, H atoms play an important role for producing sp^2-bonded carbons at the surface to form a continuous sp^2 network, eventually resulting in the formation of carbon nanowalls. However, the H atom density in the CCP region measured using vacuum ultraviolet absorption spectroscopy (VUVAS) increased by two times at most, as a result of H atom injection using the remote H_2 ICP, in spite of the fact that the surface morphology of the carbon films was drastically influenced by the H radical injection. It is possible that the ratio of CF_x (x=1-3) radicals to H atoms could be an important factor in the formation of carbon nanowalls. Measurement of the CF_x radical density in the plasma is currently being performed using appearance mass spectrometry.

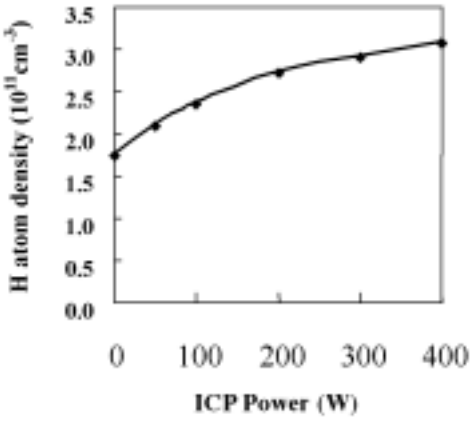

Fig. 5. H atom density of in the CCP region measured using VUVAS technique as a function of rf power of remote H_2 ICP.

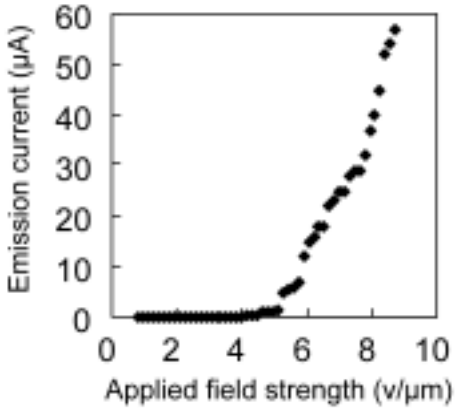

Fig. 6. Field emission characteristic of the vertically aligned carbon nanowall film.

As one of applications of carbon nanowalls, field electron emission characteristics were investigated for the carbon nanowall film. Figure 6 shows the characteristic curve of the electron emission current as a function of the field strength for the carbon nanowall film. The onset electric field for the electron field emission was 5

V/μm.

The aggregation of carbon nanowalls would be useful as templates for the fabrication of other types of nanostructured materials, supporting materials for nano-particles of catalysts, and would certainly find application in gas sensors, bio-sensors, energy storage devices and electrodes for fuel cells, due to their large surface areas.

4. Conclusions

We have presented a fabrication of vertically aligned carbon nanowalls using capacitively coupled, rf-PECVD assisted by H radical injection. The morphologies and growth rate of carbon nanowalls were dependent on the kinds of carbon source gases and the rf power of remote H_2 ICP. Without H radical injection, carbon nanowalls were not fabricated. H radicals were found to play an important role for forming nanowalls. In addition, H radical density in the plasma was measured using a VUVAS. The H radical density in the CCP region increased by about two times as a result of H radical injection using remote H_2 ICP. Furthermore, The field electron emission from carbon nanowalls was clearly observed.

Acknowledgement

This work was supported in part by Research Foundation for the Electrotechnology of Chubu.

References

[1] A. G. Rinzler, J. H. Hafner, P. Nikolaev, L. Lou, S. G. Kim, D. Tomanek, P. Nordlander, D. T. Cobert, R. E. Smalley, *Science* **269**, 1550 (1995).
[2] A. C. Dillon, K. M. Jones, T. A. Bekkedahl, C. H. Kiang, D. S. Bethune, M. J. Heben, *Nature* (London) **386**, 377 (1997).
[3] G. Che, B. B. Lakshmi, E. R. Fisher, C. R. Martin, *Nature* (London) **393**, 346 (1998).
[4] W. A. de Heer, A. Chatelain, D. Ugarrte, *Science* **270**, 1179 (1995).
[5] N.G. Shang, F.C.K. Au, X.M. Meng, C.S. Lee, I. Bello, S.T. Lee, Chem. Phys. Lett. **358**, 187 (2002).
[6] Y. H. Wu, P. W. Qiao, T. C. Chong, Z. X. Shen, Adv. Mater. **14**, 64 (2002).
[7] M. Hiramatsu, K. Shiji, H. Amano, M. Hori, Appl. Phys. Lett. **23**, 4708 (2004).
[8] K. Shiji, M. Hiramatsu, A. Enomoto, M. Nakamura, H. Amano, M. Hori, *Diamond & Related Materials*, in press.
[9] S. Takashima, M. Hori, T. Goto, A. Kono and K. Yoneda, *Appl. Phys. Lett.* **90**, 5497 (2001).
[10] S. Takashima, M. Hori, T. Goto, A. Kono, M. Ito and K. Yoneda, *Appl. Phys. Lett.* **75**, 3929 (1999).

High-Rate Growth of Dense, Aligned Carbon Nanotube Film Using Microwave Plasma Enhanced Chemical Vapor Deposition

M. Hiramatsu[1] and M. Hori[2]

1Department of Electrical and Electronic Engineering, Meijo University, Tempaku, Nagoya 468-8502, Japan
2Department of Electrical Engineering and Computer Science, Graduate School of Engineering, Nagoya University, Chikusa, Nagoya 464-8603, Japan

Abstract
Carbon nanotube (CNT) films were grown using microwave plasma-enhanced chemical vapor deposition. Catalytic Co nanoparticles were prepared on a Si substrate using the pulsed arc deposition. Titanium nitride (TiN) thin film was used as a buffer layer in order to prevent the formation of Co silicide. Dense, vertically aligned, CNT film was grown rapidly on the Co-catalyzed Si substrate. The CNTs grew at an extremely high rate of 600 nm/s during the first 10 min. Dense films with thickness over 500 μm could be obtained in 20 min.
Keywords: carbon nanotube, microwave plasma-enhanced chemical vapor deposition, Co catalyst

1. Introduction

Carbon nanotubes (CNTs) have attracted much attention for several applications, such as electron field emitter arrays and multi-level interconnection of ultra-large scale next generation integrated circuits [1,2]. Many of the proposed applications for CNTs require aligned nanotubes grown on a substrate. Of the variety of methods used for growing CNTs, plasma-enhanced chemical vapor deposition (PCVD) has gained considerable importance for industrial application compared to other methods, due to its feasibility and potential for large-area production with reasonable growth rates at relatively low temperatures.

When using PCVD to synthesize CNTs on a substrate with a catalytic metal thin film, the substrate is preheated. This is done in order to form catalytic nano-islands in the range of 10-100 nm, prior to the CNT growth. The size of the catalyst islands depends on the initial thickness of the catalytic metal thin film. In other words, thicker catalyst films yield larger catalyst islands, whereas thinner films result in the formation of smaller catalyst islands. When using a Si substrate, the formation of metal-silicide, as a result of the heat pre-treatment, will complicate the synthesis process. At present, it is difficult to simultaneously control both the size of the catalyst particles and their density on the substrate surface. Considering the practical applications of CNTs, further investigations should be performed in order to enable control over the structure and electronic properties, and to understand the growth mechanism. In particular, the control over the preparation of catalytic metal nanoparticles on the substrate would be essential to realize the potential of CNTs. In this work, CNTs were synthesized on a Si substrate using microwave plasma-enhanced CVD (MWPCVD). Co nanoparticles were prepared on the substrate using the pulsed arc plasma deposition. Titanium nitride (TiN) thin film was used as a buffer layer in order to prevent the formation of Co silicide. A film of dense, aligned CNTs was grown on the Co-catalyzed Si substrate.

2. Experiments

CNT films were grown by conventional MWPCVD with a 2.45 GHz, 1.5 kW microwave generator [3-5], as shown in Fig. 1. The reactor consists of a cylindrical-stainless steel chamber of 11 cm inner diameter and a molybdenum substrate stage with a graphite heater that allows control of the substrate temperature independent of the input microwave power. This MWPCVD system is usually used to grow diamond films [3]. A mixture of CH_4 and H_2 was used as a source gas. The flow rates of CH_4 and H_2 were 50 and 70 sccm, respectively. The microwave power and total pressure were 900 W and 70 Torr, respectively. The growth experiments were carried out for 0.5-20 min at a substrate temperature ranging from 600 to 800˚C, which was measured using an optical pyrometer. The substrate used for the growth experiments was Si (100).

Substrate treatment was performed as follows. Firstly, a thin TiN layer, with thickness of 20 nm, was prepared on the Si substrate. The TiN thin layer has an important role as a buffer layer, in order to prevent the

formation of Co silicide during the increase of substrate temperature, just before introducing CH_4 gas into the reaction chamber. Secondly, Co particles were deposited on the TiN buffer layer using pulsed arc plasma deposition (Arc plasma gun, ULVAC, Inc.) in vacuum, at a pressure of 10^{-4} Torr at room temperature. The Arc plasma gun was operated intermittently (pulse operation). No heat pre-treatment was performed for the catalyst prior to the CNT growth process. We have found that the pulsed arc evaporation using the Arc plasma gun yielded Co nanoparticles of about 4 nm in size, according to the preliminary experiment. However, Co nanoparticles deposited on the TiN buffer layer have not been recognized yet, although we tried to observe using scanning electron microscopy (SEM) and atomic force microscopy (AFM). The density of Co nanoparticles on the substrate was controlled by varying the number of pulses in the range from 50 to 250 shots.

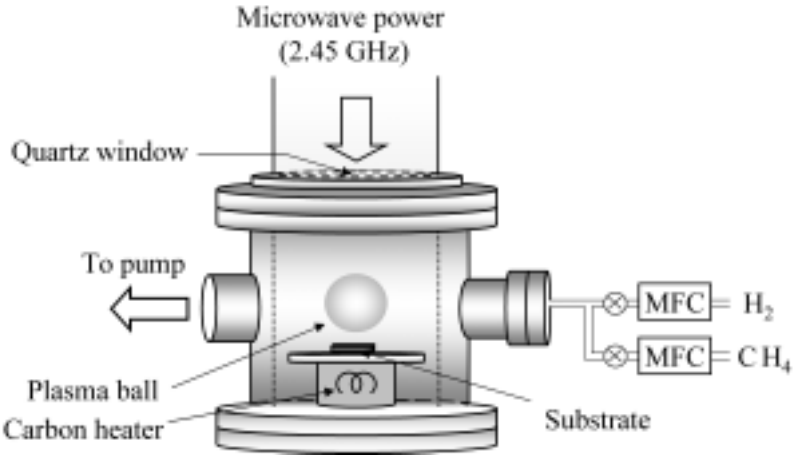

Fig. 1. Schematic of microwave plasma-enhanced CVD reactor used for formation of carbon nanotube films.

3. Results and discussion

CNTs were grown on the Co-catalyzed Si substrates at a substrate temperature of 700 °C. Figures 2(a) and 2(b) show typical SEM images of CNT films. Dense CNTs were grown on the Co-catalyzed substrate with a TiN buffer layer. From consideration of the morphology observed in Fig. 2(b), it was found that individual CNTs were not straight, but grown almost vertically, via a self-support mechanism, due to the extremely high density of the CNTs. It was noted that there was a tangled appearance of some CNT bundles, as seen in the cross-sectional SEM image of Fig. 2(b), and this was presumed to have originated from the cleaving of the substrate.

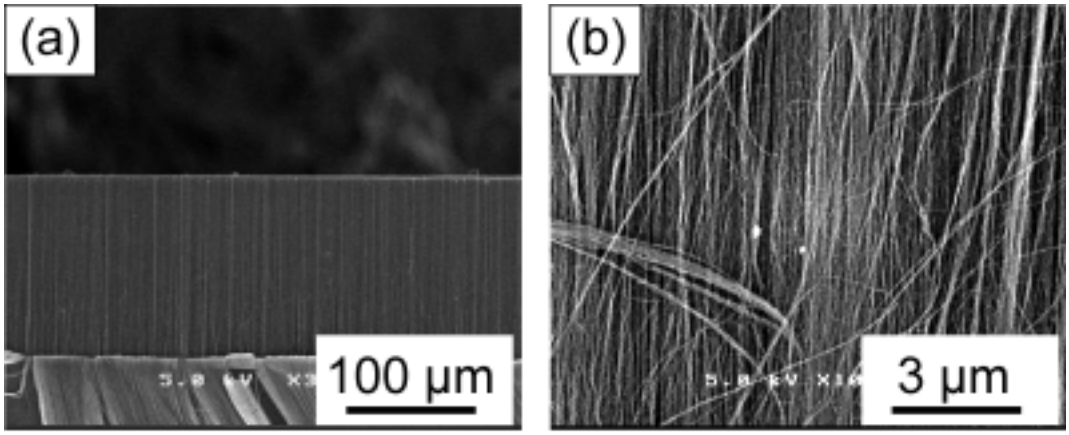

Fig. 2. SEM images of CNT films grown on a Co-catalyzed Si substrate with TiN buffer layer. Co particles were prepared using pulsed arc plasma deposition by 250 pulses. (a) Cross-sectional SEM image of dense CNT film. (b) Close-up image of cleaved CNT film showing aligned growth of nanotubes.

A growth rate curve for the CNT film was obtained by measuring the thickness of the CNT films at different growth times. CNT films were grown from Co nanoparticles deposited by 250 shots using pulsed arc plasma, which were nearly optimum conditions for the extremely dense nucleation of CNTs. The thickness of the CNT

film increased linearly up to 10 min of growth. The CNTs grew at an extremely high rate of 600 nm/s during the first 10 min. Dense CNT films with thickness over 500 μm could be obtained in 20 min.

Figure 3(a) shows a low-magnification transmission electron microscopy (TEM) image of typical CNTs grown under the same condition as that in Figs. 1(a) and 1(b). TEM specimen shown in Fig. 3(a) was scraped away from the substrate. CNTs are hollow and have small average diameter of approximately 4.5 nm. Note that no Co particles were observed at the nanotube tips with TEM. Figure 3(b) shows a typical magnified TEM image of the same CNTs, revealing that most of CNTs have the double-walled structure, which contains a clear inner channel with an inner diameter of about 4 nm. Single-walled nanotubes were also found in the CNTs grown, as shown in Fig. 3(c). It is noted that no Co particles were observed at the nanotube tips in the TEM images. The fact that no Co particles were observed at the nanotube tips, suggests that our process could be explained by the base-growth mechanism.

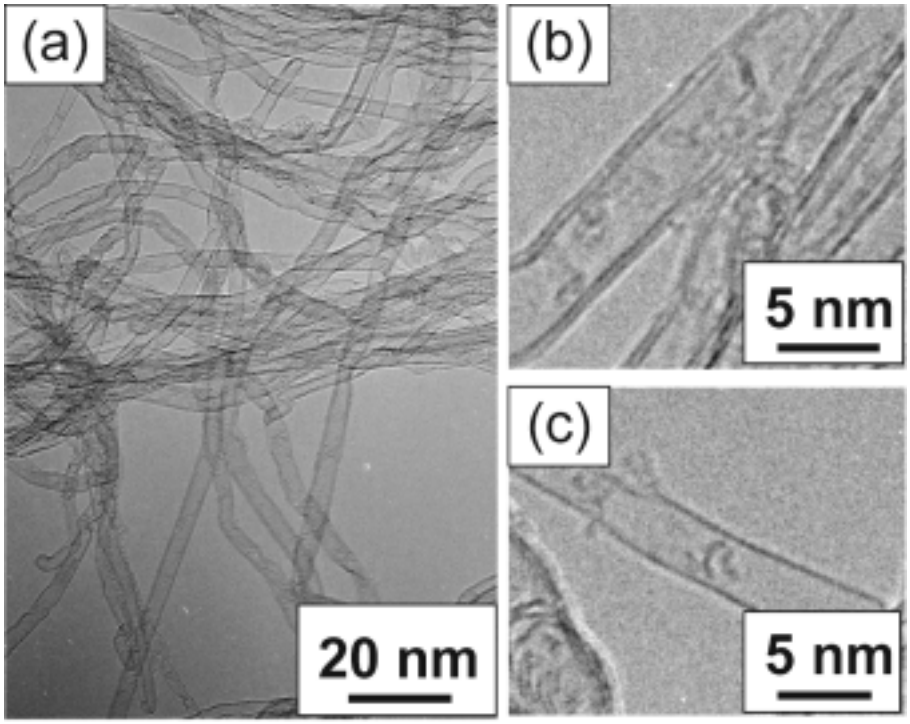

Fig. 3 TEM images of CNTs scraped from the substrate. CNTs were grown on the Co-catalyzed Si substrates at a substrate temperature of 700 °C. (a) A low-magnification TEM image of CNTs. (b)(c) Magnified images of the CNTs shown in (a).

The most significant difference from previous reports is that the catalyst was prepared originally in the form of nanoparticles in our case. It was reported that the nanotube growth rate was inversely proportional to the nanotube diameter [6]. Namely, the smaller diameter nanotubes would grow at a faster rate in their height. In our case, the size of Co particles formed by pulsed arc deposition was relatively small. The density of isolated Co nanoparticles on the Si substrate was found to be of the order of 10^{13} cm^{-2} after 50 shots of pulsed arc deposition at room temperature. In our system, it takes about 10 minutes to increase the substrate temperature from room temperature to 700 ˚C. Many of nanoparticles would remain nearly unchanged in increasing substrate temperature just before CNT growth, due to the existence of TiN buffer layer prepared to prevent the formation of Co silicide, although the overlapped or closely adjacent particles would join together during the increase of substrate temperature up to 700 ˚C in the case of high density of Co particles after 250 shots of pulsed arc deposition. Deposited Co nanoparticles would play an important role as a template for the CNT growth, resulting in the determination of nanotube diameters as small as 4.5 nm and consequently, a fast rate of growth could be attained for the CNTs.

Unlike the PCVD-grown, well-aligned, isolated CNTs reported by Bower *et al.* [6,7] and Hirata *et al.* [8], individual nanotubes in our case were not so isolated, and aligned nanotube forests were composed of nanotube bundles supporting one another. Bower *et al.* have explained that the alignment was induced by the electrical self-bias field imposed on the substrate surface from the plasma environment. On the other hand, in our case, the substrate was not exposed to a plasma ball, and the contribution of the self-bias to the alignment was low. The 'remote' plasma mainly produces important radicals for the CNT growth and heats the substrate to some extent in our case. In the case of CNT growth without the electrical field, CNTs would grow in a curly fashion. If the density of catalytic particles with small size on the substrate is low, CNTs would grow in random orientation or in less aligned manner, resulting in the low growth rate of CNT film. The density of Co nanoparticles on the substrate was changed by varying the shot numbers of pulsed arc discharges in the range from 50 to 250. Figure 4(a) shows a cross-sectional SEM image of CNT film grown from Co nanoparticles deposited by 250 shots using pulsed arc plasma, which were nearly optimum conditions for the extremely dense nucleation of CNTs. As shown in Fig. 4(a), nanotube bundles grew almost straight due to the high density of CNTs, corresponding to the high growth rate of 600 nm/s for the growth of 5 minutes. On the other hand, in the case of the growth using a substrate with low-density Co nanoparticles, the growth rate of CNT film decreased. Figure 4(b) shows a cross-sectional SEM image of CNT film grown from Co nanoparticles deposited by 50 shots using pulsed arc plasma. As shown in Fig. 4(b), the CNTs grew in a curly fashion because individual nanotubes had more space to grow, resulting in the decrease of CNT film growth rate (150 nm/s for the growth of 5 minutes).

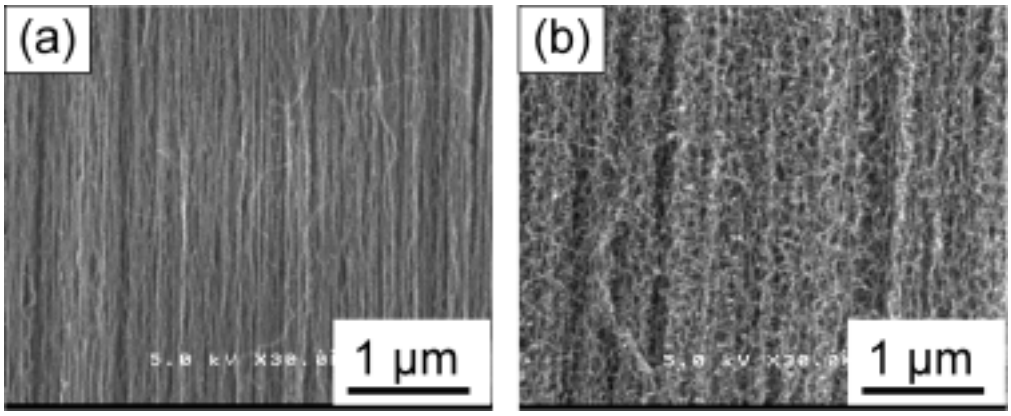

Fig. 4. Cross-sectional SEM images of CNT films grown from Co nanoparticles prepared using pulsed arc plasma by (a) 250 shots and (b) 50 shots.

In summary, we have presented a fabrication of dense, vertically aligned, double-walled carbon nanotube films at an extremely high rate. The film growth rate of 600 nm/s was attained by controlling the size and density of catalytic nanoparticles on the substrate.

References

[1] A. G. Rinzler, J. H. Hafner, P. Nikolaev, L. Lou, S. G. Kim, D. Tomanek, P. Nordlander, D. T. Cobert, R. E. Smalley, Science **269**, 1550 (1995).
[2] M. Nihei, A. Kawabata, Y. Awano, Jpn. J. Appl. Phys. **42**, L721 (2003).
[3] M. Hiramatsu, K, Ito, C. H. Lau, J. S. Foord, M. Hori, Diamond Relat. Mater. **12**, 365 (2003).
[4] M. Hiramatsu, M. Taniguchi, H. Nagao, Y. Ando, M. Hori, Jpn. J. Appl. Phys. **44**, 1150 (2004).
[5] M. Taniguchi, H. Nagao, M. Hiramatsu, Y. Ando, M. Hori, Diamond Relat. Mater. in press.
[6] C. Bower, W. Zhu, S. Jin, and O. Zhou, Appl. Phys. Lett. **77**, 830 (2000).
[7] C. Bower, O. Zhou, Appl. Phys. Lett. **77**, 2767 (2000).
[8] T. Hirata, N. Satake, G.-H. Jeong, T. Kato, R. Hatakeyama, K. Motomiya, K. Tohji, Appl. Phys. Lett. **83**, 1119 (2003).

Effect of Oxygen Injection into Argon Induction Plasmas on Chemically Non-Equilibrium Conditions

Nobuhiko Atsuchi[1], Masaya Shigeta[2], and Takayuki Watanabe[2]

[1] *Department of Nuclear Engineering, Tokyo Institute of Technology, Tokyo, Japan*
[2] *Department of Environmental Chemistry and Engineering, Tokyo Institute of Technology, Yokohama, Japan*

Abstract
Effective generation of chemical reactive species in thermal plasmas has been required in the field of material processing and waste treatment. The effect of oxygen injection into argon induction plasmas was investigated by numerical analysis without chemical equilibrium assumptions for the dissociation and ionization. Oxygen dissociation and heat flux to torch wall can be controlled by oxygen injection location. Therefore, suitable oxygen injection needs to be chosen according to the application requirement.

1. Introduction

Thermal plasmas have been used for a number of applications of material processing and waste treatment. In these applications, effective generation of chemical reactive species is required. The modeling of induction thermal plasmas with several injection methods of nitrogen or hydrogen was performed previously [1]. The purpose of this work is to investigate the effect of oxygen injection into argon induction plasmas on chemically non-equilibrium (CNE) conditions by numerical analysis. Reaction kinetics rates of the dissociation and recombination of oxygen as well as the ionization were taken into account in this modeling. The transport properties were estimated using higher-order approximation of Chapman-Enskog method [2].

2. Numerical formulation

2-1 Thermodynamic and transport properties

Higher-order approximation of the Chapman-Enskog method is used according to the required accuracy for transport properties. Modeling of induction thermal plasmas has been performed with the first-order approximation because higher-order of Sonine polynomial expansion requires many kinds of collision integrals resulting in the complex formula. The first-order approximation may cause errors especially for electrical conductivity and thermal conductivity of electron translational contribution over 10000 K [3]. The collision integrals were taken from Ref. [4-11] which provide intermolecular potential and fitting data. Detailed descriptions of the calculation method of viscosity, thermal conductivity and electrical conductivity are given by Watanabe and Sugimoto [3]. In CNE model, the transport and thermodynamic properties are related to the temperature and the composition of plasmas. Therefore, the transport and thermodynamic properties should be estimated considering the diffusion of species in plasmas at each calculation step until the convergence.

The thermodynamic properties, enthalpy and specific heat at constant pressure, were obtained from the equilibrium properties. This would be oversimplification, however, the exact estimation of the non-equilibrium thermodynamics properties is very complex to satisfy the self-consistent conditions. The radiative intensity of argon and oxygen was taken from Ref. [12-13].

2-2 Kinetic rate constants

The equilibrium composition was estimated by FACT (Center for Research in Computational Thermochemistry), considering six species of Ar, Ar^+, O_2, O, O^+, and e^-. Table 1 summarizes the reactions of Ar-O_2 mixture considered in this study. Twelve reactions comprising 6 forward reactions in Table 1 and their backward reactions were taken into account. The reaction rates for forward direction are given by Arrhenius equation.

Table 1 Chemical reactions in argon-oxygen mixtures.

Reaction	a_l	b_l	c_l
$O_2 + O_2 \rightarrow O + O + O_2$	2.0×10^{21}	-1.5	59500
$O_2 + O \rightarrow O + O + O$	1.0×10^{22}	-1.5	59500
$O_2 + Ar \rightarrow O + O + Ar$	1.0×10^{22}	-1.5	59500
$O_2 + e^- \rightarrow O + O + e^-$	9.68×10^{22}	-2.0	59500
$O + e^- \rightarrow O^+ + e^- + e^-$	3.91×10^{33}	-3.78	158500
$Ar + e^- \rightarrow Ar^+ + e^- + e^-$	k_l^f was calculated by Eq. (2)		

$$k_l^f = a_l T^{b_l} \exp(-c_l / T) \qquad (1)$$

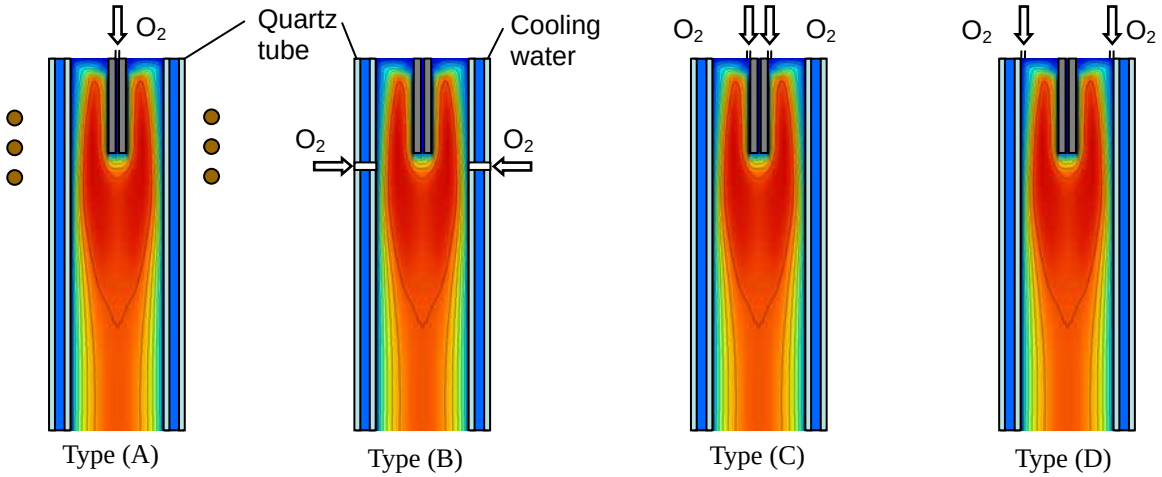

Fig. 1 Schematic diagram of oxygen injection location types.

For Ar ionization reaction, the reaction rate can be calculated by Eq. (2) [14].

$$k_l^f = 1.68\times10^{-20}T^{1.5}(135300/T+2)\exp(-135300/T) \quad (2)$$

2-4 Calculation model

Four injection locations of oxygen were considered in the modeling as illustrated in Fig. 1; (A) center injection; (B) radial injection at the center of the coil; (C) inner injection from the top; (D) sheath gas injection.

The geometry of calculation domain of induction plasma torch is shown in Fig. 2 and the operating conditions are summarized in Table 2. Gas flow rate of each oxygen injection type was shown in Table 3. The plasma torch consists of a water-cooled quartz tube, and is surrounded by a water-cooled induction coil. The coil consists of three turns and applies the induction frequency at 4 MHz to the plasma. The actual power level was assumed to be 5 kW.

The calculation are based on the following assumptions to derive the governing equations: (a) steady-state laminar flow; (b) axial symmetry; (c) optically thin; (d) negligible viscous dissipation in energy equation; (e) negligible displacement current in comparison with the conductive current; (f) negligible flow-induced electric field; (g) same temperature of heavy particles and electrons.

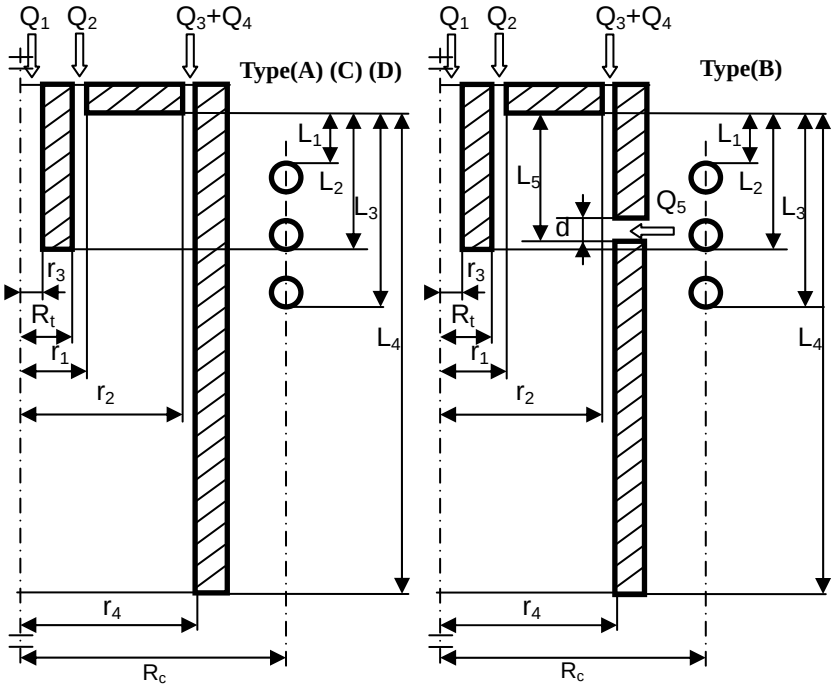

Fig. 2 Geometry of calculation domain of induction plasma torch.

Table 2 Torch characteristic dimensions and operational condition.

Torch Power	5 kW
Work Frequency	4 MHz
Reactor Pressure	101.3 kPa
Coil Radius	32 mm
Coil turn number	3
Wall thickness	1.5 mm
L_1	19 mm
L_2	45 mm
L_3	65 mm
L_4	190 mm
L_5	40 mm
r_1	6.5mm
r_2	21 mm
r_3	1 mm
r_4	22.5 mm
R_t	4.5 mm
d	0.1 mm

The effect of turbulence has been reported by Chen and Boulos [15]. They reported that most of the flow field in induction plasmas was laminar at the Reynolds number 625 at the gas inlet, while the turbulence effect is large at the Reynolds number 3125. The flow field of the present induction plasmas can be considered as laminar, because the inlet Reynolds number is 350 in this study.

Table 3 Flow rate of each injection type.

(L/min)	Type (A)	Type (B)	Type (C)	Type (D)
Q1	**O_2: 0.1**	0	0	0
Q2	3	3	3 (**O_2: 0.1**)	3
Q3 + Q4	26.9	24	27	27(**O_2: 1**)
Q5	-	**O_2: 3**	-	-
Total	30	30	30	30

2-5 Governing equations and boundary conditions

The field of flow, temperature and concentration in induction thermal plasmas were calculated by solving the two-dimensional continuity, momentum, energy, and species conservation equations coupled with the Maxwell's equations. Reactions of the dissociation and recombination as well as the ionization were taken into account in this modeling.

Continuity:

$$\nabla \cdot (\rho \mathbf{u}) = 0 \tag{3}$$

Momentum:

$$\rho \mathbf{u} \cdot \nabla \mathbf{u} = -\nabla p + \nabla \tau + \mathbf{J} \times \mathbf{B} \tag{4}$$

Energy:

$$\rho \mathbf{u} \cdot \nabla h = \nabla \cdot \left(\frac{\lambda}{C_p} \nabla h \right) + \mathbf{J} \cdot \mathbf{E} - q_r \tag{5}$$

Species:

$$\rho \mathbf{u} \cdot \nabla Y_i = \nabla \cdot (\rho D \nabla Y_i) + R_{ri} \tag{7}$$

Electromagnetic:

$$\nabla^2 \mathbf{E} - \xi \sigma \frac{\partial \mathbf{E}}{\partial t} = 0 \tag{8}$$

The boundary conditions along the centerline were set to insure axial symmetry. At the wall of the plasma torch, no slip conditions are maintained for the velocity, and the concentrations have zero gradient. The temperature at the inside wall of the plasma torch was calculated assuming that the outside wall was maintained at 300 K by water cooling. The injection tube was assumed to be at 500 K. The outflow boundary conditions at the torch were assumed that the gradient of the variables are zero. The sheath gas has swirl velocity component. Each gas stream has constant axial velocity with zero radial velocity having temperature at 300 K.

2-5 Calculation procedure

The governing conservation equations were solved using SIMPLER (Semi-Implicit Method for Pressure Linked Equation Revised) algorithm [16]. The governing equations and the electric field intensity equation with the associated boundary conditions were discretized into finite difference from using control-volume technique. In oxygen injection types (A), (C), and (D), non-uniform grid points 30 by 30 were used for radial and axial directions, respectively. In oxygen injection type (B), non-uniform grid points 30 by 54 were used for radial and axial directions, respectively. Grids are made finer close to the center and the coil region. Thermodynamic and transport properties were calculated from the temperature and compositions at each position in the calculation domain at each iteration step.

3. Result and discussion

The effect of oxygen injection of type (A: center injection) on plasma characteristics is presented in Fig. 3. At the oxygen injection region, the temperature decreases due to oxygen dissociation as shown in Fig. 3 (a). Higher heat capacity including oxygen dissociation approximately 4000 K leads to a decrease in the plasma temperature. The flow field in Fig. 3 (b) exhibits the characteristic recirculation caused by the radial Lorentz force above the coil region. The corresponding concentration profiles of oxygen atoms and molecules are illustrated in Fig. 3 (c) and (d), respectively. Injected oxygen molecules are dissociated quickly because oxygen is injected directly into the high-temperature region. Therefore, dissociated oxygen

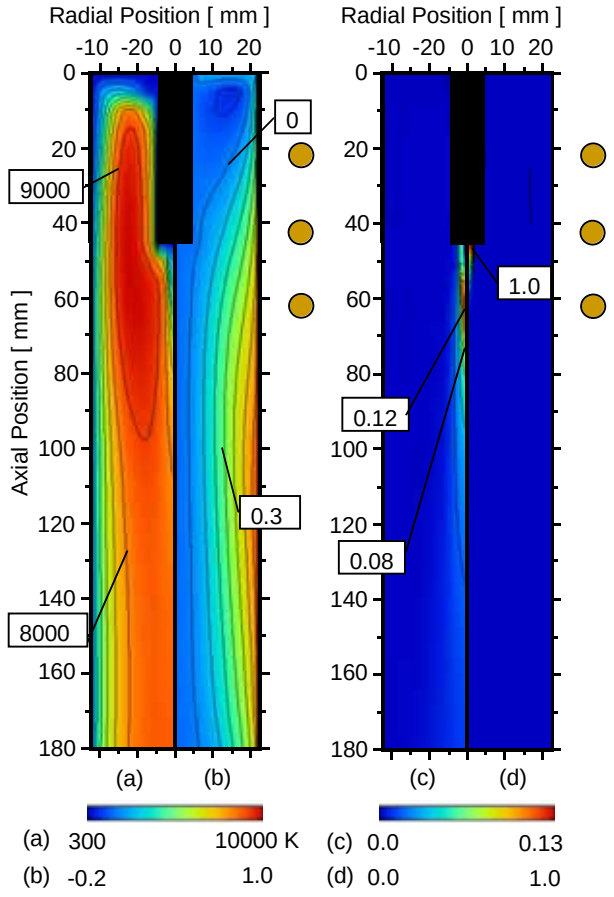

Fig. 3 (a) Isotherms, (b) streamlines, (c) O atom concentration, and (d) O_2 concentration distributions in an Ar-O_2 plasma; Type (A): center injection at 0.1 L/min.

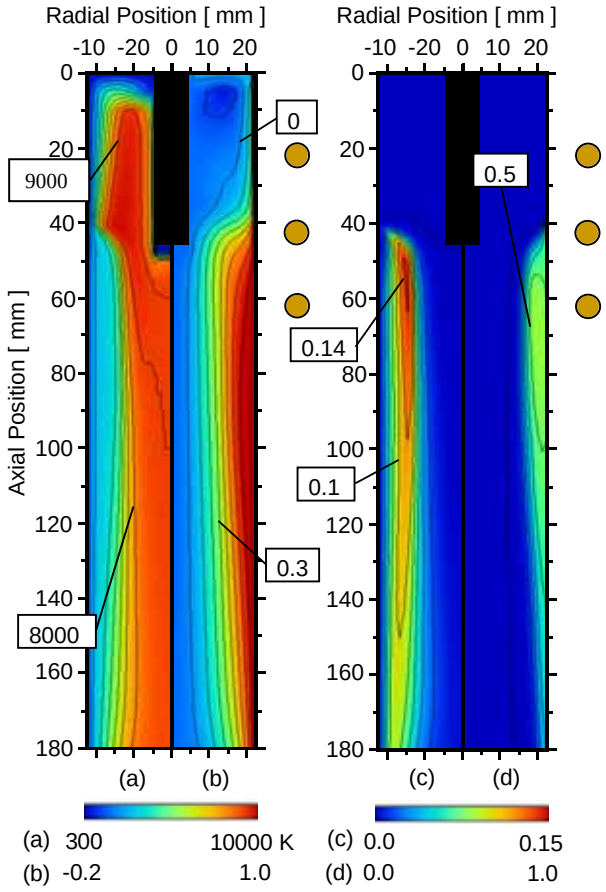

Fig. 4 (a) Isotherms, (b) streamlines, (c) O atom concentration, and (d) O_2 concentration distributions in an Ar-O_2 plasma; Type (B): radial injection at 3 L/min.

atoms can be found near the center of the torch.

Numerical results of oxygen injection type (B: radial injection) is shown in Fig. 4. The calculated temperature field in Fig. 4 (a) shows the severe decrease in temperature at the oxygen injection region along the torch wall due to oxygen dissociation. The streamlines shown in Fig. 4 (b) demonstrate the modified flow field from other injection types in the coil region because of the radial injection toward the high-temperature region. The concentration profiles of oxygen atoms and molecules are presented in Fig. 4 (c) and (d), respectively. Oxygen molecules and dissociated oxygen atoms exist locally near the torch wall owing to the negligible diffusion of dissociated oxygen atoms toward the torch center.

The temperature field in Fig. 5 (a) and the flow field in Fig. 5 (b) in the case of oxygen injection type (C: inner injection) are comparable to types (A) and (D). Thus, the effect of inner injection from the top is weak on the plasma characteristics. The corresponding concentration profiles of oxygen atoms in Fig. 5 (c) and molecules in Fig. 5 (d) indicate that injected oxygen molecules are dissociated quickly above the coil region. Dissociated oxygen atoms exist broadly except the low-temperature region near the torch wall. The widespread mixing of oxygen is due to the recirculation caused by the Lorentz force in the coil region.

The effect of oxygen injection type (D: sheath gas injection) is presented in Fig. 6. High-temperature region above 8000 K is almost the same with an argon plasma, while the temperature decreases slightly near the torch wall region as shown in Fig. 6 (a). The concentration profiles of oxygen atoms and molecules are shown in Fig. 6 (c) and (d), respectively. Injected oxygen molecules exist near the torch wall through the downstream region. The dissociated oxygen atoms exist broadly to the torch center owing to the recirculation. Oxygen injection from the top of the torch results in the broad distribution of dissociated oxygen atoms.

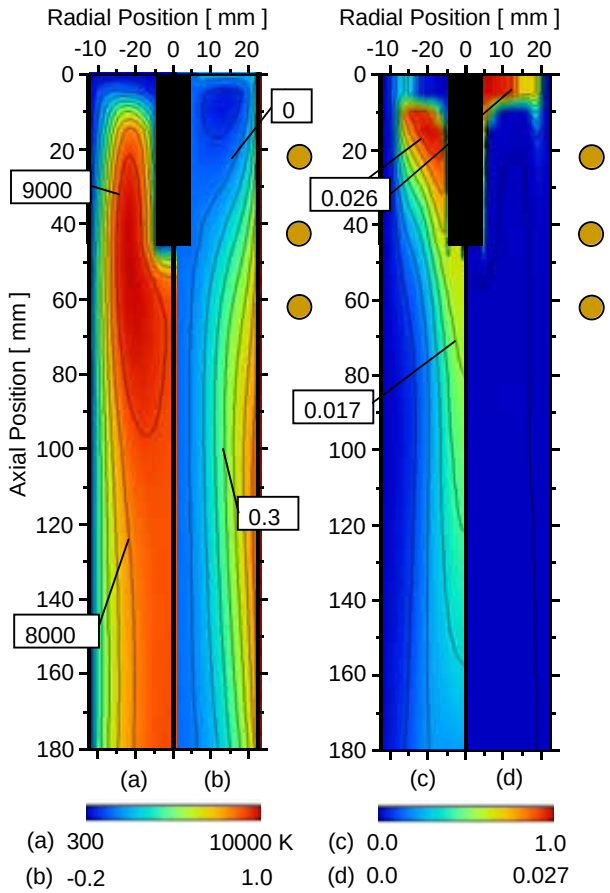

Fig. 5 (a) Isotherms, (b) streamlines, (c) O atom concentration, and (d) O_2 concentration distributions in an Ar-O_2 plasma; Type (C): inner injection at 0.1 L/min.

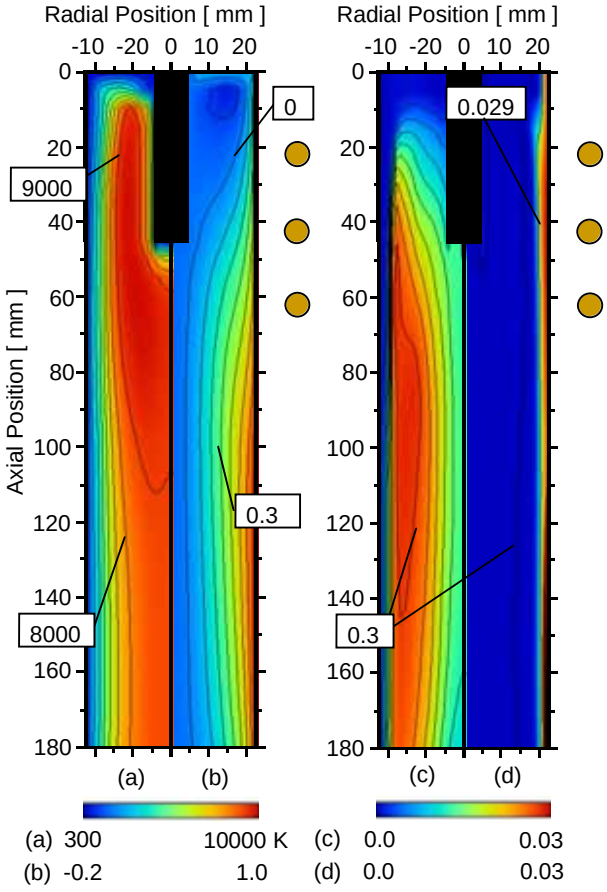

Fig. 6 (a) Isotherms, (b) streamlines, (c) O atom concentration, and (d) O_2 concentration distributions in an Ar-O_2 plasma; Type (D): sheath gas injection at 1 L/min.

Degree of CNE, δ, was introduced to evaluate chemical non-equilibrium of plasmas.

$$\text{Degree of CNE for dissociation: } \delta^{d}_{O_2} = \frac{[O]^2}{[O_2]K_d} \tag{9}$$

$$\text{Degree of CNE for ionization: } \delta^{i}_{O} = \frac{[O^+][e^-]}{[O]K_i} \tag{10}$$

In these definitions, value of $\delta = 1$ represents complete equilibrium. In non-equilibrium, $\delta > 1$ represents overpopulation of products and underpopulation of reactants for $\delta < 1$.

Fig. 7 presents the radial profiles of the degree of CNE due to dissociation of injected oxygen with type (B) at the center of the coil. The degree of CNE deviates strongly from the equilibrium value at the oxygen injection region. This indicates that the chemical non-equilibrium occurs at the injection region due to the effect of diffusion and finite reaction rate. In the downstream region, the chemical non-equilibrium occurs near the torch wall. In all injection types, the strong chemical non-equilibrium was found at the oxygen injection region and near the torch wall where the concentration gradient is high.

Fig. 8 shows the effect of oxygen injection on axial profiles of the degree of dissociation. High degree of dissociation is obtained by oxygen injection types (A) and (C). The high degree of dissociation in types (A) and (C) is attributed to the direct oxygen injection into the high-temperature region of plasmas. While, the degree of dissociation is low in the case of types (B) and (D), because oxygen molecules exist locally near the torch wall. Oxygen injection type (B) which is direct radial injection from the torch wall provides the lowest degree of dissociation. The lowest degree of dissociation results from the insufficient penetration of

injected oxygen into the high-temperature region of plasmas, therefore higher injection velocity is required to obtain higher degree of dissociation of oxygen.

Fig. 9 presents the effect of oxygen injection on axial profiles of heat flux to the torch wall. The low heat flux in the coil region in type (B) and (D) is due to the large amount oxygen flow along the torch wall, resulting in the severe decrease in the temperature. In contrast, the heat flux to the torch wall in type (A) and (C) is high. The contribution of the center or inner oxygen injection is small for lowering the heat flux to the torch wall by the oxygen injection.

Non-equilibrium modeling with finite reaction rates for various oxygen injection locations demonstrates the following results; chemical non-equilibrium exists at the region of high-concentration gradient such as oxygen injection region and near the torch wall. The degree of dissociation of oxygen and the heat flux to torch wall can be controlled by oxygen injection location. Therefore, suitable oxygen injection location needs to be chosen according to the application requirements. The present modeling would give the guidance for the rational design of new material processing with effective reactive gas injection into plasmas.

4. References

[1] T. Watanabe, T. Honda, and A. Kanzawa Proc. ISPC-10, 1.1-31, Bochum (1991)

[2] J. O. Hirschfelder, C. F. Curtiss, and R. B. Bird, Molecular Theory of Gases and Liquids, John Wiley, New York, (1964)

[3] T. Watanabe and N. Sugimoto, Thin Solid Films, **457**, 201 (2004)

[4] E. Mason, J. Chem. Phys., **22**,169 (1954)

[5] L. Monchick, Phys. Fluids, **2**, 695 (1959)

[6] T. Kihara, et al., Phys. Fluids, **3**, 715 (1960)

[7] F. Smith, et al., J. Chem. Phys., **41**, 3560 (1964)

[8] R. Devoto, Phys. Fluids, **10**, 354 (1967)

[9] H. Milloy, Aust. J. Phys., **30**, 61 (1977)

[10] M. Capitelli, et al., J. Thermophys., **14**, 259 (2000)

[11] J. Aubreton, C. Bonnefoi, and J. M. Mexmain, Rev. Phys Appl., **21**, 365 (1986)

[12] R. Krey and J. Morris, Phys. Fluids, **13**, 1483 (1970)

[13] R. Miller and R. Ayen, J. Appl. Phys., **40**, 5260 (1969)

[14] M. I. Hoffert and H. Lien, Phys. Fluids, **10**, 1769 (1967)

[15] K. Chen and M. I. Boulos, J. Phys. D: Appl. Phys. **27**, 946 (1994)

[16] S. V. Patanker, Numerical Heat and Fluid Flow, McGraw-Hill, New York, (1980)

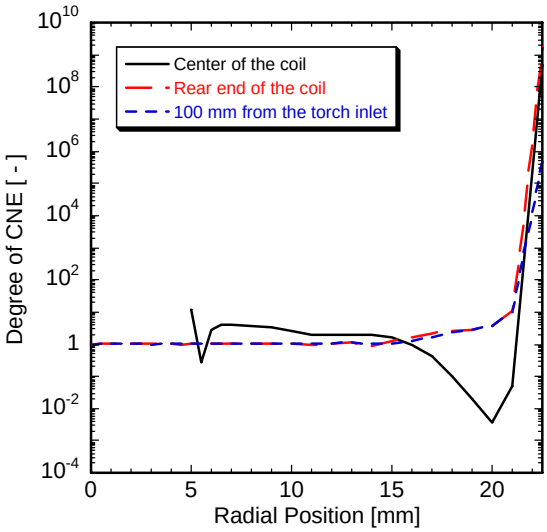

Fig. 7 Radial profiles of degree of CNE due to dissociation; (B) radial injection.

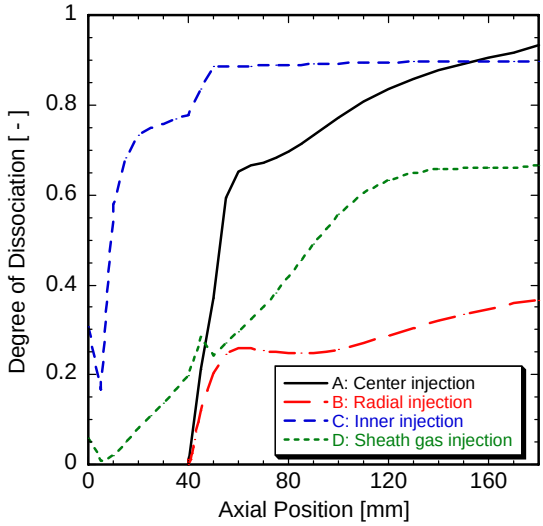

Fig. 8 Effect of oxygen injection on axial profiles of degree of dissociation.

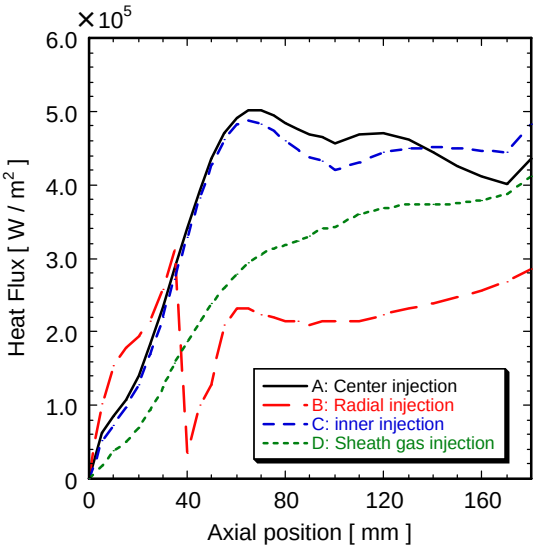

Fig. 9 Effect of oxygen injection on axial profiles of heat flux to torch wall.

Effect of Metal-Wire Catalyst on Non-Thermal Plasma NO Decomposition

Nobuyuki Kikukawa, Yoshiaki Kintaichi, and Hideaki Hamada

National Institute of Advanced Industrial Science and Technology (AIST), Tsukuba 305-8569, Japan

Abstract

We investigated NO decomposition reactions over metal-wire (Pd, Fe, Ni, SUS) catalysts in a DBD plasma. The catalysts were found to improve remarkably the NO*x* decomposition rate. The metal-wire was concluded to play a role of not redox reagent but catalyst. The catalytic active points were found to consist in the both end of metal-wire. The metal-wire catalyst also promoted N_2O formation rate depending on metal materials.

Moreover, the present work clearly indicates the importance of the catalytic effects of the electrode metals.

Keywords *nitrogen oxides, atmospheric pressure low temperature plasma, metal wire catalyst, DBD*

1. Introduction

Air pollution caused by nitrogen oxides (NO*x*) emitted from combustors and automotive engines is a serious environmental problem. Although catalytic NO reduction processes have already been put to practical use such as in three-way catalysts for gasolinefueled vehicles and in the ammonia SCR process for large-scale boilers, the development of effective abatement technique for such as diesel exhaust is still a subject to be solved.

There have been many attempts applying non-thermal plasmas (NTP) for de-NO*x* reaction [1]. But a few works have considered the catalytic effects of electrode metal [2-4]. *Takaki et al.* have examined NO*x* decomposition using several types of multipoint-to-plane geometry and found that this geometry effectively lowered the operation voltage. However, they used brass as an electrode material only and did not consider the effects of materials. *Hayashi et al.* developed a plasma chemical reactor using plasma-assisted catalytic technology (PACT) [3]. Using this concept, *Suib et al.* compared the de-NO*x* reactions using metal (Rh or Fe)-electrode reactors with that using all-glass reactors, and they observed much higher initial NO conversion and gradual deactivation with both metal electrodes [4], which clearly indicates the influence of the existence of metal substances in the plasma zone.

We have investigated plasma-assisted catalytic decomposition of NO using a dielectric barrier discharge (DBD) plasma reactor. In this presentation, we report the results of NO decomposition over metal-wire catalysts settled in the plasma zone.

2. Experimental

The DBD reactor used was parallel plane type, and was originally designed by Kodama and Sekiguchi [5]. The schematic of experimental setup was shown in Fig. 1. Both electrodes (80ϕ alunimum discs) were covered with quartz plates (1 mm thick). The chamber wall was made of polymethylmethacrylate (PMMA). Therefore, the

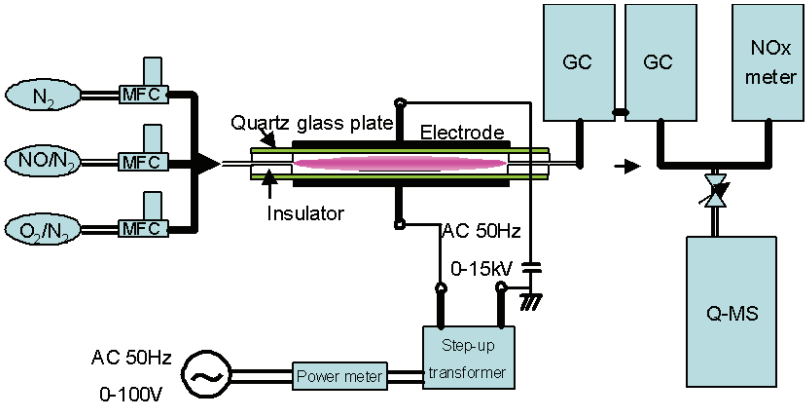

Fig.1 Schematic of experimental setup.

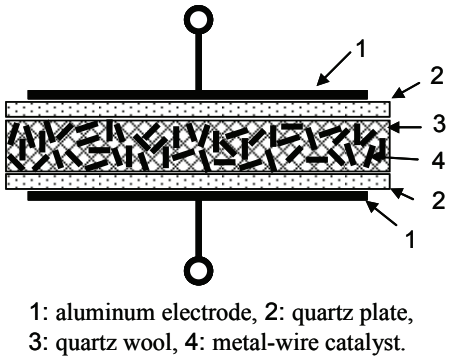

Fig.2 Schematic of plasma chamber.

generated plasma does not contact with any metal parts. The gap between electrodes was 10 mm.

The metal-wire catalysts used were Pd, Fe, Ni, SUS. Each wire or mesh was cut into short chips (2-3 mm). For comparison, a commercial Pd/Al_2O_3 powder catalyst (Pd: 5%, Wako Pure Chemical Ind., Ltd.) was also used. These catalysts were dispersed in quartz wool and put into the plasma chamber, as shown schematically in Fig. 2.

The reaction gas containing 1000 ppm NO, 0-10% O_2, and N_2 as the balance, was fed. The total flow rate was 20 ml/min. Some experiments were carried out with He as the balance gas. The effluent gas was monitored by a quadrapole mass spectrometer and was analyzed using a chemiluminescent-type NO*x* analyzer (Shimadzu MOA-305A) and two gas chromatographs with a Molecular Sieve 5A column (for the analysis of O_2, N_2, CO and NO) and a Porapak Q column (for that of N_2O and CO_2).

High voltage was supplied through a step-up transformer and the frequency was 50 Hz. The power was measured in two ways. One is input power to step-up transformer measured by a power meter (Hioki 3332)("gross power"). The other is power consumed in plasma which was calculated from *V-Q* Lissajous figure ("net power").

3. Results and Discussion

3.1 NO decomposition with/without metal-wire catalyst and with powder catalyst

Figure 3 shows the results of NO*x* decomposition rate, deduced from NO*x* analyser, in the presence of stainless steel (SUS) mesh chip catalyst compared with that in the absence of any catalyst. From the figure, it is clearly seen that the SUS catalyst improved the NO decomposition reaction. All metal-wire catalysts examined showed improving effects and lowered the minimum operating voltage.

Figure 4 shows the dependency of the NO*x* decomposition rate on O_2 concentration in reactant. The catalysts used were Pd wire chips (0.05ϕ, total length of 2 m, 0.045g) and Pd/Al_2O_3 (Pd: 5%, 0.94 g). Although the Pd weights of both Pd catalysts were almost same, powder-shaped Pd did not improve the NO*x* decomposition. This result implies that the catalytic effect should be attributed to the shape of the catalyst.

These metal-wire catalysts did not show any deactivation after long time experiments, indicated in Fig. 5. Moreover, according to a gas chromatogram shown in Fig. 6, the ratio of the amounts of product oxygen and nitrogen was nearly 1:1. From these results we can conclude that metal-wire plays a role of not redox reagent but catalyst.

Next, we examined the effect of the number of chips, that is, we cut a piece of Pd wire of 2 m long into 8, 32, and about 600 chips, and then we investigated the NO*x* decomposition. The result is shown in Fig.7, which clearly shows that the active points exist in both end of each Pd segment.

The fact that these metal-wires showed catalytic behaviours even in the case of oxygen-sensitive Fe implies that the "self-cleaning mechanism" found in vacuum arcs [6] might occur at the both end of metal catalyst chips. The detailed mechanism will be the subject to be solved.

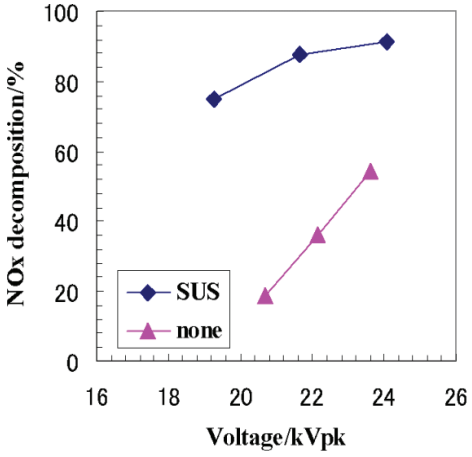

Fig.3 NOx decomposition rate as a function of voltage.
NO : 1000ppm, O_2 : 2.7%, base: N_2, 20ml/min.

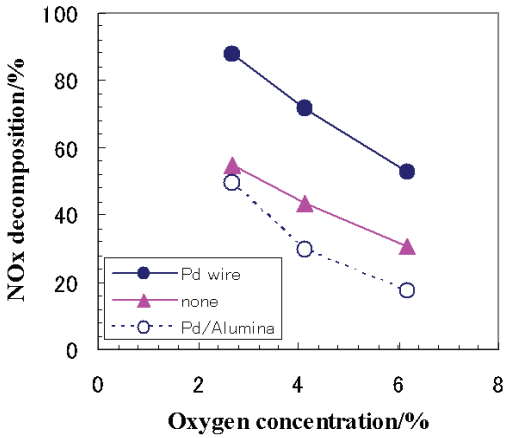

Fig.4 NOx decomposition rate as a function of O_2 concentration.
NO : 1000ppm, base: N_2, 20ml/min, 22-24 kVpk.

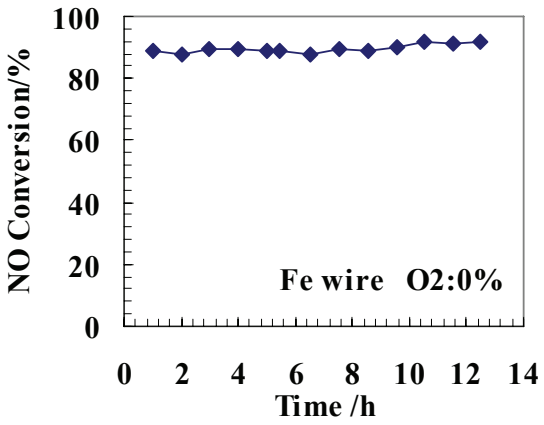

Fig.5 Variation of NO conversion with time.
NO: 1000ppm, base N2 20ml/min, 23kVpk.

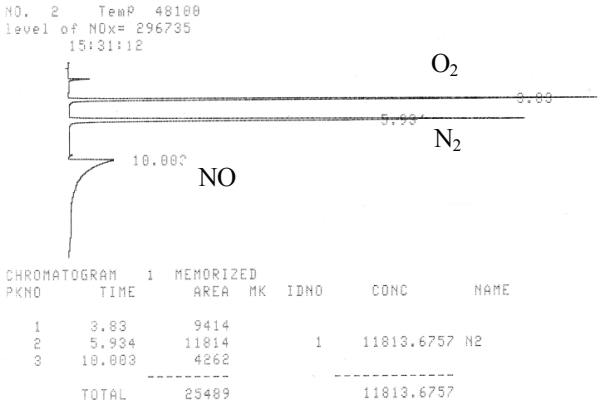

Fig.6 Example of gas chromatogram.
NO: 1060ppm, base He 60 ml/min, 10kVpk, Pd catalyst.

3.2 Effect of metal materials on product gas composition

In N_2-O_2-NO system, we also found that these metal-wire catalysts promoted a side reaction, N_2O formation. Figure 8 shows the N_2O concentrations in the presence of various metal-wire catalysts as a function of oxygen concentration in the reactant. The amounts of the catalysts were chosen so that the improvement of NO*x* decomposition was almost the same. From the figure, there are some differences of N_2O formation rates between metal materials. From the experiments of He-O_2-NO system, we found that the amount of the decomposed NO was equal to the amount of the generated N_2 and that negligible amount of N_2O was formed. Therefore, N_2O might be formed through the catalytic reaction of N_2 and O_2.

This effects is clearly shown in the experiments of N_2- O_2 system without NO (Fig. 9). Fe wire catalyst much more promoted the formation of NO and NO_2 as well as N_2O. Although the comparison among various metal materials is still inadequate, these results at least indicate that metal parts in plasma zone may substantially affect NO decomposition reaction.

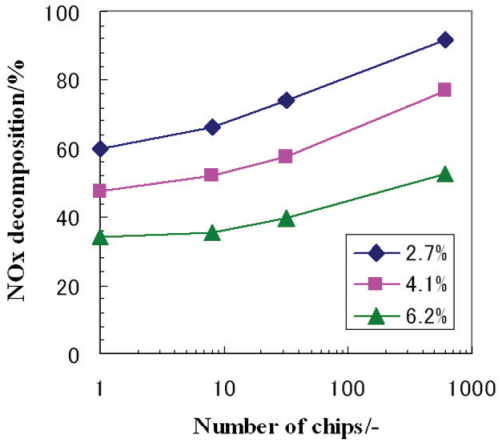

Fig.7 Relationship between NO*x* decomposition rate and the number of Pd wire chips with a parameter of O_2 concentration. Total length was 2 m.
NO : 1000ppm, base : N_2 20ml/min, 22-24 kVpk.

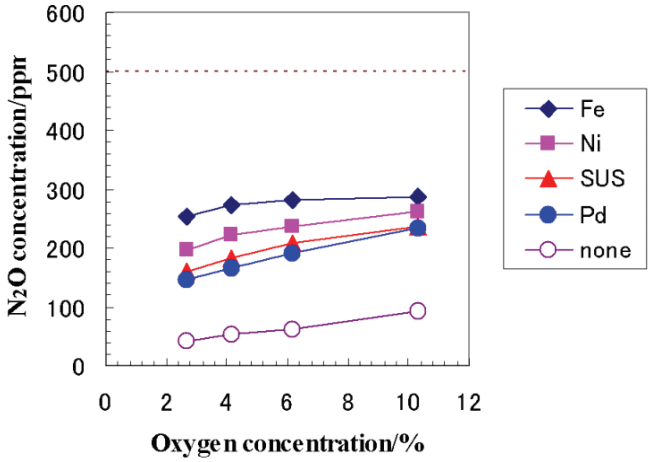

Fig. 8 N_2O concentration as a function of O_2 concentration.
NO : 1000ppm, base: N_2, 20ml/min, 22-24 kVpk.

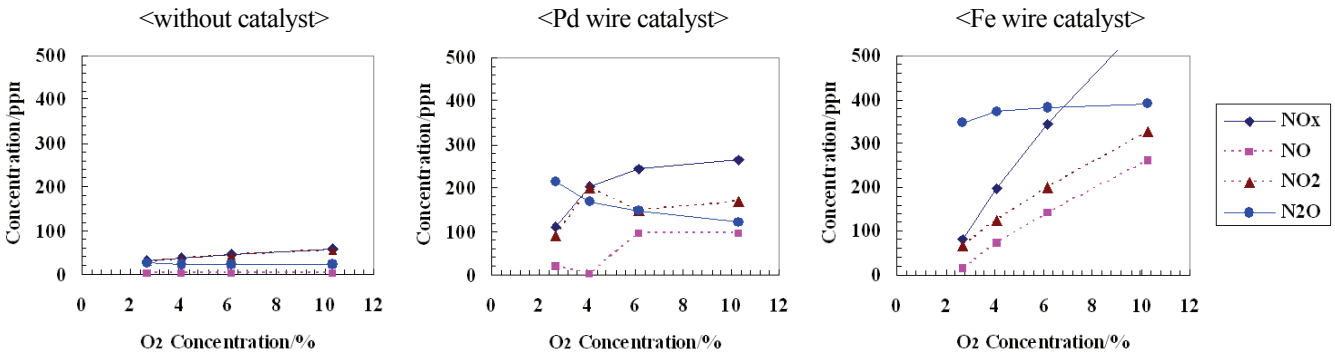

Fig.9 Product gas concentrations as a function of O_2 concentration in reactant gas.
[NOx]=[NO]+[NO_2], Initial NO : 0ppm, base : N_2 20ml/min, 22-24 kVpk.

3.3 Comparison of "gross power" and "net power"

Figure 10 shows the relationships between gross power and applied voltage (Fig.10a) and between net power and applied voltage (Fig.10b) in the N_2-O_2-NO system with several catalysts. From the figure, one can see the net power depends on the amount of metal-wire catalysts, while gross power is a simple function of applied voltage. The power dependency of NO decomposition with/without Pd-wire catalysts as functions of gross power (a) and net power (b) are shown in Fig. 11. From Fig.11b, the amount of Pd does not affect the NO decomposition rate. Therefore, the amount of Pd-wire catalyst affects the energy efficiency that means how much energy was absorbed in plasma from input energy. Since the gross power directly affects electric energy consumption, this improving effect of metal-wire would lead to a new energy saving plasma reactor. Moreover in Fig.11b, the difference of NO decomposition rates between with Pd-wire catalyst and without catalyst should be regarded as the net catalytic effect.

4. Conclusion

Through the experiments on the plasma-assisted catalytic NO decomposition in DBD reactor, we found that the NO*x* decomposition rate remarkably increased in the presence of metal-wire catalysts and that N_2O formation rate also increased. The metal-wire was found to play a role of not redox reagent but catalyst. The catalytic active points are concluded to consist in the both end of metal-wire.

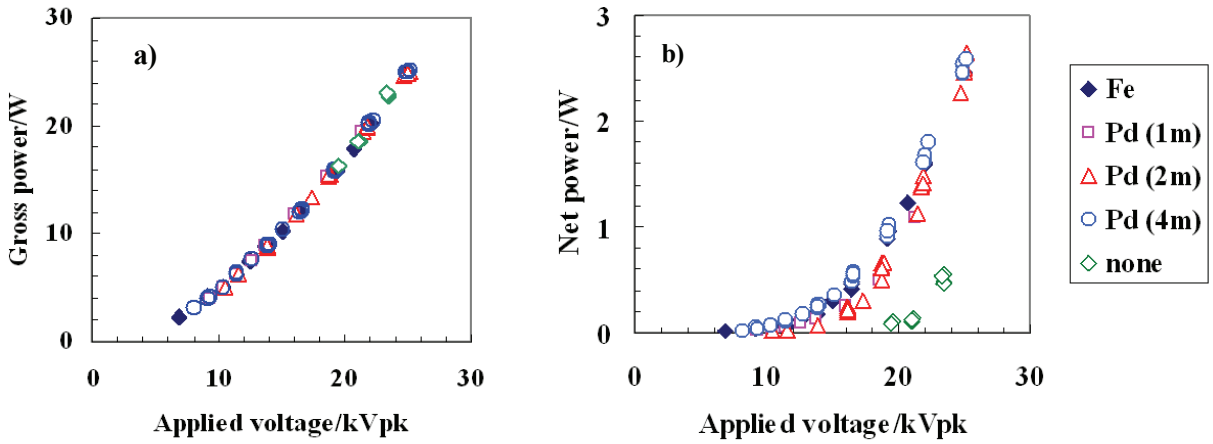

Fig.10 Relationships between applied voltage and gross power (a) net power (b) in N_2-(O_2) plasma with/without several metal-wire catalyst.
Pd (1m), Pd (2m), Pd (4m) : total Pd wire length were 1m, 2m, 4m, respectively.

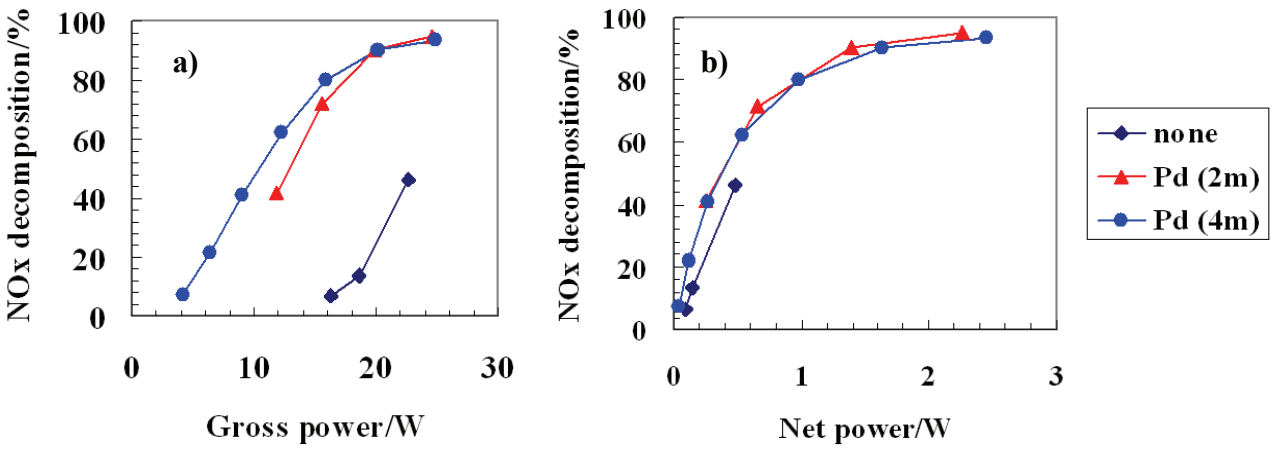

Fig.11 NOx decomposition rate with Pd-wire catalysts as functions of gross power (a) and net power(b).
NO : 1000ppm, O_2 : 2.7%, base : N_2 20 ml/min.

Finally, the primary effect of metal-wire catalyst probably consists in improving the energy efficiency, and depending on the metal materials, there appear somewhat the differences of product gas composition as the secondary effect.

Moreover, the present work clearly indicates the importance of the catalytic effects of the electrode metals.

References

[1] for example, A. Fridman, Proc. 16th Int. Symp. Plasma Chem., ISPC-867 (Taormina, Italy, 2003.6).
[2] K. Takaki, M.A. Jani, and T. Fujiwara, IEEE trans. Plasma Sci. **27** (1999) 1137; M.A. Jani, K. Takaki, and T. Fujiwara, Rev. Sci. Instr., **69** (1998) 1847.
[3] Y. Hayashi, N. Wakatsuki, Japan Patent 2111722; USA Patent US5474747.
[4] J. Luo, S.L. Suib, M. Marquez, Y. Hayashi, and H. Matsumoto, J. Phys. Chem. A **102** (1998) 7954; J. Luo, S.L. Suib, Y. Hayashi, and H. Matsumoto, J. Phys. Chem. A **103** (1999) 6151; Y. Hayashi, O. Ueda and H. Fukuda, Fujitsu **52** (2001) 169.
[5] S. Kodama, H. Habaki, H. Sekiguchi, and J. Kawasaki, Thin Solid Films **407** (2002) 151.
[6] K. Takeda and S. Takeuchi, Thin Solid Films **407** (2002) 163.

Diagnostics of Dielectric Barrier Discharges Operating at Atmospheric Pressure with Two Different Electrode Structures

K. Tachibana[1], T. Kishimoto[1], T. Sakaguchi[1], O. Sakai[1], and T. Shirafuji[2]

[1] *Department of Electronic Science and Engineering, Kyoto University, Kyoto 615-8510, Japan*
[2] *International Innovation Center, Kyoto University, Kyoto 615-8510, Japan*

Abstract

The densities of metastable He*(2^3S_1) atoms and electrons were measured in two-types of DBD plasma sources operated at atmospheric pressure in He containing a small amount of impurities, depending on the gas flow. It was found that the Penning ionization of He*(2^3S_1) atoms with impurities contributes considerably to the production of electrons. Both densities are larger in a mesh-type system than in a conventional parallel-plate system by about five to ten times in accordance with the input power densities.

1. Introduction

Dielectric barrier discharge (DBD) has been enthusiastically investigated for the generation of glow discharge at atmospheric pressure range (APGD) [1]. Specific conditions for realizing APGD have been found, which depend on the electrode structure, gas species, flow rate and power-source in each experimental situation. In order to find out generalized conditions based on physical parameters, plasma diagnostics in DBDs must be performed systematically. In the first step towards the purpose, we have performed the measurement of metastable He*(2^3S_1) atoms with diode laser absorption spectroscopy as well as the measurement of electron density with mm-wave transmission experiment in two different types of DBDs as described below. The obtained results in those two types of plasma sources are compared with each other and argued on the production and loss processes of metastable atoms and electrons.

2. Experimental

We have been using two types of electrode structures with the DBD scheme. One is a conventional parallel plate system with electrodes of 60 mm diameter covered by ceramic (Al_2O_3) insulating plates of 1 mm thickness at a gas gap of 3 mm [2]. A unique pulsed power supply was used, in which the primary square-wave bipolar-pulse train was amplified by a high-voltage transformer, so that the output waveform had a high-voltage impulse followed with a ringing tail as shown below. The other is an integrated type of coaxial-hollow microdischarges with metal mesh electrodes covered by thick Al_2O_3 films [3]. The latter structure is shown in **Fig. 1** together with the driving pulse waveform and the discharge image in N_2. The firing voltage with this structure is as low as 500 V in He gas and 1.2 kV in pure N_2 gas at atmospheric pressure.

We measured the absolute density of He metastable atoms in the 2^3S_1 state by a laser absorption spectroscopy (LAS) technique using a tunable diode laser operated at around 1083 nm. The absolute density of He*(2^3S_1) atoms was derived from the integrated area of the absorption line profile [4]. The plasma density in these DBDs was estimated from the transmission of mm-waves in the frequency

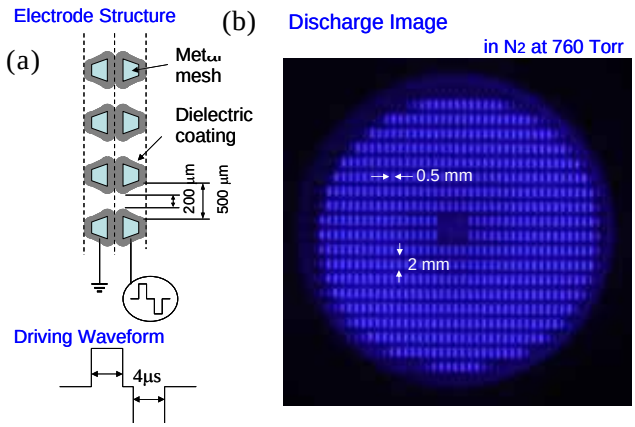

Fig. 1 (a) Structure of mesh-type system and driving waveform, and (b) discharge image in N_2.

range from 50 to 75 GHz.

3. Results and Discussion

3. 1. Discharge characteristics

The driving waveform in the parallel plate system is shown in **Fig. 2 (a)** and the operating regimes are classified in **Fig.2 (b)** by eye observation in the parameter ranges characterizing the waveform. To investigate the underlying physics, we analyzed the transferred charge to each electrode by the conduction current as shown in **Fig. 3**. From the result it is seen that the glow-like (uniformly looking) discharge is realized when the accumulated charge by the impulse current is almost erased by the following ringing current. This suggests that even if a non-uniform charge distribution is formed at first, the following current sweep out the source of the positive feedback which leads to the filamentation of the discharge. In the microdischarge integrated type (mesh-type) system, there observed is no current constriction in each cell and the discharge looks glow-like. Uniformity was also good over the whole electrode area of 50 mm diameter.

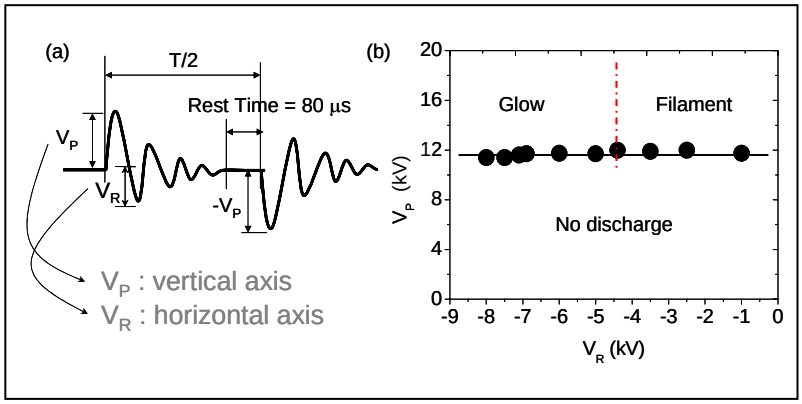

Fig. 2 (a) Driving waveform of parallel plate system and (b) operating regimes in the parameter plane of waveform characteristics.

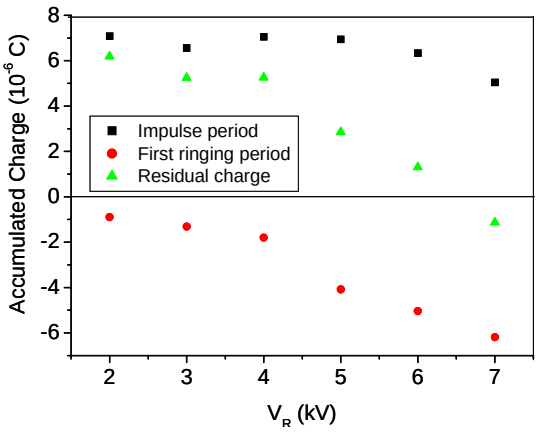

Fig.3 Accumulated charge in the first and second periods and the residual charge.

3. 2. Measurement of metastable atom density

The results on the density of metastable He*(2^3S_1) atoms N_m measured by the LAS method in the two configurations are shown in **Fig. 4**. It is seen that the density in the parallel plate system is smaller by about an order of magnitude than the mesh-type system in the active plasma region. The reason will be attributed to the difference in the electron density as argued below. The density of He*(2^3S_1) atoms depends strongly on the gas flow rate. It suggests that the impurity concentration decreases as the gas flow rate increases.

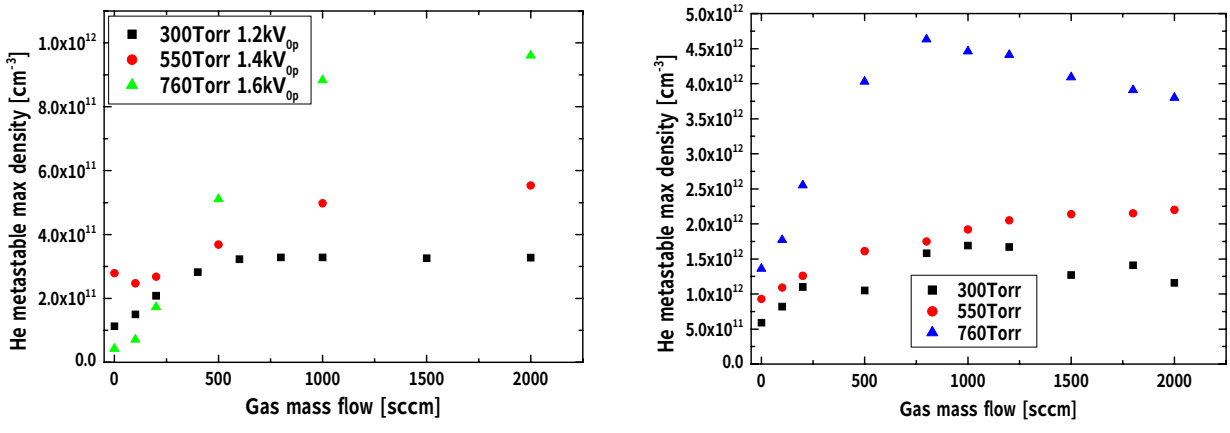

Fig. 4 Density of He* metastable atoms measured in (a) parallel plate system and (b) mesh-type system at several pressures as a function of the gas flow rate.

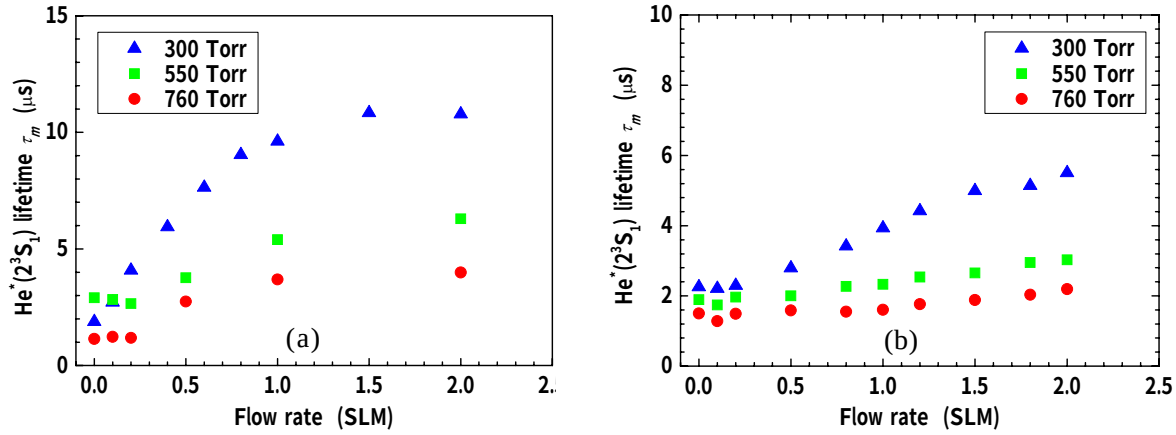

Fig. 5 Lifetime of He*(2^3S_1) atoms measured in (a) parallel plate system and (b) mesh-type system under situations corresponding to those given in Fig. 4

Figure 5 shows the lifetime of He*(2^3S_1) atoms τ_m measured under the same experimental conditions as in those given in Fig. 4. From the comparison of Fig. 4(a) and Fig. 5(a), it is seen that both the He*(2^3S_1) atom density and the lifetime behave similarly in the parallel-plate system. It suggests that the impurity level is decreasing with the gas flow rate. However, the absolute values of the lifetime are still smaller than those estimated from the rate constant of the three-body collisional process; He*(2^3S_1) + 2He → He_2 + He. If the difference is attributed to quenching by the Penning ionization with N_2, the major impurity species, the impurity concentration is estimated to be about 100 ppm at the flow rate more than 1 SLM. On the other hand, in the mesh-type system the measured lifetime keeps increasing gradually with the flow rate, but the absolute values are smaller than those in the parallel plate system. It is due to the smaller dimension of the mesh-type system with larger surface losses. The saturating tendency of the He*(2^3S_1) atom density observed in this system at the higher flow rate may be attributed to the effect of blowing-out loss of plasma species which leads to the decrease of plasma density.

3. 3. Measurement of electron density

The temporal transmittance characteristics of mm-waves were analyzed for the derivation of electron density [5]. The results are shown in Figs. 6(a) and 6(b) for the absolute density of electrons n_e and the corresponding lifetime τ_e measured in the parallel plate system. For the data at 1 atm, both n_e and τ_e behave

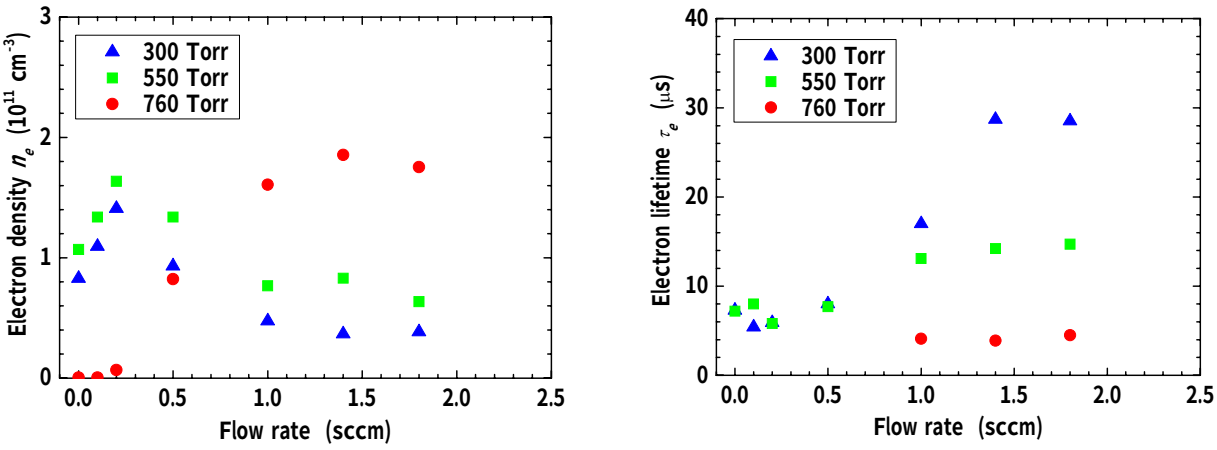

Fig. 6 (a) Electron density and (b) the lifetime measured in parallel-plate system as a function of the gas flow rate

similarly to the pressures probably due to the change in the contribution of the Penning ionization process to the production metastable atom density N_m and the lifetime τ_m, respectively. Noticeable differences are seen at lower of electrons, depending on the impurity level. However, the fairly large values of lifetime at those low pressure cases remain unexplained at the moment. At the atmospheric pressure, a comparison of waveforms of the mm-transmission and the laser absorption signal suggests that in the early period of rising current the direct ionization process is predominant, but in the afterglow period the contribution of the Penning ionization becomes important for the production of electrons.

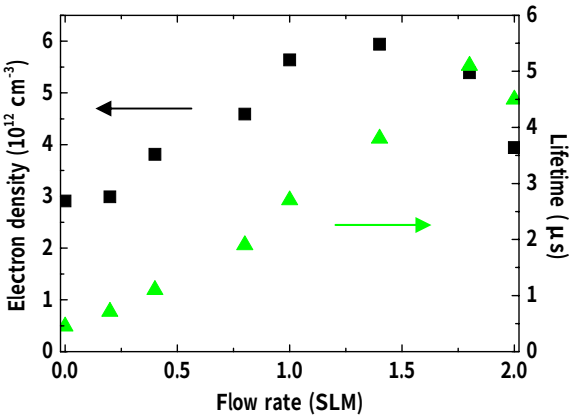

Fig. 7 Electron density and the lifetime measured in mesh-type system as a function of the flow rate.

The results of n_e and τ_e measured in the mesh-type system at 1 atm are shown in **Fig. 7**. It is seen that n_e increases with the gas flow rate and then saturates similarly to the density of He*(2^3S_1) atoms. However, the behavior of τ_e is somewhat different, showing a larger increasing tendency at higher flow rates. The reason for this discrepancy should also be answered later. We are now working on the measurement in the mixture of He with N_2 by varying the mixing ratio up to 100%. As a preliminary result, the measured values of n_e take a peak at a N_2 concentration of 1%, showing the maximum contribution of the Penning effects to the production of electrons. The full results will be shown at the time of the symposium.

4. Concluding Remarks

The density of He*(2^3S_1) atoms in the metastable state was successfully measured in two different types of DBD systems in pure He gas containing a trace of impurities. The densities measured in the mesh-type system were larger than those in the parallel plate system by five to ten times. The electron density estimated by the mm-wave attenuation in the mesh-type ranged on the order of 10^{12} cm^{-3}, which was also larger than the values obtained in the parallel plate system. However, by considering the difference in the active volume of those systems, the production efficiency of the metastable atoms and electrons per input electric power is equivalent in both systems. Experiments in N_2 are going on, in which the density of N_2^+ ions is also going to be measured by a laser induced fluorescence (LIF) technique as well as the mm-wave transmission technique.

References

[1] See, e.g., a cluster issue edited by F. Massines: J. Phys. D: Appl. Phys. **38**(4), 505-575 (2005).
[2] T. Somekawa, T. Shirafuji, O. Sakai, and K. Tachibana: J. Phys. D: Appl. Phys. 38 (2005) to be published.
[3] O. Sakai, Y. Kishimoto and K. Tachibana: J. Phys. D: Appl. Phys. **38**, 431-441 (2005).
[4] K. Tachibana, Y. Kishimoto and O. Sakai: J. Appl. Phys. **97** (2005) to be published.
[5] K. Tachibana, Y. Kishimoto, S. kawai, T. Sakaguchi and O. Sakai: Plasma Phys. Control. Fusion, **47** (2005) in press.

Effective Plasma Chemical Reactions in Micro Channel

M. Suzuki[1], M. Kadowaki[1], A. Yamamoto[2], H. Yoshizawa[1] and S. Mori[1]

[1]*Department of Chemical Engineering, Tokyo Institute of Technology, Tokyo, Japan*
[2]*The Research Association of Micro Chemical Process Technology (MCPT), Japan*

Abstract
We pick up two typical plasma reactions, which we have tried recently, and discuss about the effectiveness of micro channel for plasma reaction. One is the plasma CVD in the inner surface of micro channel and another is the plasma decomposition reaction of CO_2 in a micro channel. From these demonstration, we can conclude that the plasma reaction in a micro channel can be achieved with high effectiveness and efficiency, if the reaction is selected properly, considering the reaction time and the diffusion time which characterize the phenomena in the plasma in a micro channel.
Keywords: micro plasma, micro channel, plasma CVD, CO_2 decomposition**.**

1. Introduction

Various micro plasmas have been developed and many basic and application studies have been done since the concept of micro plasmas was proposed[1-5]. In particular, application studies of micro plasmas in the fields of micro total analysis system (μ-TAS) and micro electro mechanical system (MEMS) have been developed extensively.

Generally, the advantage of plasma chemistry is to promote selective reactions effectively among active species generated by electron impacts in the plasma. A micro channel reactor has enough wide area to deactivate the active species and it is not suitable to the plasma chemistry, in this point of view. A micro plasma reactor can be useful sometimes, however, if the inner surface area is utilized positively.

In the past studies, for example, it has been recognized that, in the steady-state of electrical discharge of CO_2, a significant amount of CO_2 equilibrates with CO even if the input energy and gas residence time are increased and it is difficult to decompose CO_2 completely into CO and O_2 by the conventional plasma reactors[6]. As shown in this paper, the micro channel reaction has a potential to complete such a decomposition reaction.

In the heterogeneous reaction such a micro channel reaction with having wide surface area, we can determine whether the dominant reaction takes place in bulk or at surface by comparing characteristic diffusion time (τ_d) and characteristic gas phase reaction time (τ_r). For example, we consider the following dissociation reaction of molecule (*AB*) in plasma phase.

$$e + AB \rightarrow A + B + e$$

In the heterogeneous system, which contains the surface, usually it works as a catalytic wall and reactive species, either *A* or *B*, which diffuses to surface is lost at surface immediately. In this situation characteristic diffusion time (τ_d) is expressed, for example, such as b/V by using diffusion velocity V of species and micro channel gap b. And also V is evaluated such as D/b by diffusion coefficient. On the other hand characteristic gas phase reaction time (τ_r) can be expressed such as $1/kC_i$ by using species concentration C_i and recombination reaction rate k. By using these parameters we can select the effective plasma reaction in the micro channel reactor configuration.

In this paper, We pick up two typical plasma reactions, which we have tried recently, and discuss about the effectiveness of micro channel for plasma reaction. One is the plasma CVD in the inner surface of micro channel and another is the plasma decomposition reaction of CO_2 in a micro channel.

2. Plasma CVD Reaction on Inner Surface of Micro Channel.

Plasma CVD reaction on inner surface of micro channel is effective. Especially, it is effective when using unstable chemical compound as a precursor. We tried uniform plasma chemical vapor deposition (P-CVD)

process on inner surface of a micro capillary and a micro channel generating plasma inside a micro channel[2]. This process has an advantage to be able to coat the inner surface of a micro channel after graving a micro channel on a glass plate and fabricating glass plates by fusing, instead of using lithography technique.

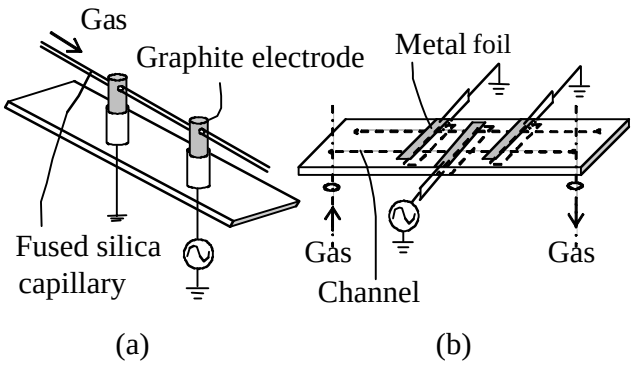

Fig.1 Electrode arrangements for palasma CVD in microchannel.

2.1 Micro channel plasma CVD method[7].

We tried uniform plasma chemical vapor deposition (P-CVD) process on inner surface of a micro capillary and a micro channel generating plasma inside a micro channel[2]. Figure 1 shows schematics of the electrode layouts of the micro capillary plasma and of the micro channel plasma in a Pyrex chip. The micro capillary plasma was generated by dielectric barrier discharge between cylindrical graphite electrodes (ϕ4mm) pierced by a capillary as shown in Fig. 1(a). The distance between the centers of the electrodes was defined as the electrode gap (20mm). A fused silica capillary of 450 m o.d., 320 m i.d., and 150mm length (Shimadzu) was used. For the micro channel (100 m×40 m×60mm) fabricated in a Pyrex chip (Institute of Micro chemical Technology), micro channel plasma was generated by the discharge between metal foil electrodes attached to the outer surface of the Pyrex chip as shown in Fig. 1(b). We chose the platinum film for CVD demonstration, which is used widely as catalyst, electrode, sensor, etc. For this purpose, we used platinum (II) bisacetylacetonate ($Pt(C_5H_7O_2)_2$) as a precursor, which was diluted by Ar, He, or O_2. Micro plasmas can be generated in a micro capillary (450μm o.d., 320μm i.d.), and a micro channel (100μm) fabricated in a chip by applying a few kilo volts by using outer electrodes at a few Torr. After P-CVD processing, the capillary with deposited film is cut in some parts and dissolved into hydrogen fluoride acid to measure the platinum quantity in each part by inductively coupled plasma mass spectrometry (ICP-MS). Also, effects of changing plasma power on distribution of platinum quantity deposited on inner surface of the micro capillary are investigated. Also the cross sectional view of deposited samples was observed with a scanning electron microscope.

Table 1 Experimental conditions of plasma CVD in micro channel.

No.	Run 1	Run 2	Run 3	Run 4	Run 5	Run 6
Frequency (kHz)	2	5	10	5	5	5
Current density (mA/cm2)	21	65	150	59	69	69
Power(mW)	25	59	130	53	63	63
Deposition time (sec)	30 Completion	150 Completion	375 Completion	50	120	160 Completion
Tt (℃)	170					
Tf (℃)	200					
Flow rate (sccm)	0.06					
Pressure (kPa)	1.0					
Peak voltage (kV)	2.6					

2.3 Characteristics of microchannel CVD

In our demonstration, if the voltage is properly controlled, for example at 2.6 kV as is indicated in Table 1, the film is almost evenly deposited between the electrodes. During the deposition of electrically conductive materials such as platinum, the plasma discharge has a peculiar behavior. When film deposition between electrodes is completed, the plasma in the capillary is extinguished. Deposition time for runs 1-3 and run 6 in Table 1 is the time in which film deposition is completed. After complete film deposition, surface discharge takes place at the outer capillary surface around the electrodes. This change of discharge is attributed to the electrical conductivity of the deposited film. Hence there is a fair possibility that the deposited film mostly consists in metal platinum.

Figure. 2 shows the profiles of the platinum amount deposited on inner surface of a fused silica capillary in runs 1-3. These results were obtained by varying the frequency. An increase in frequency corresponds to an increase in input power. The upstream and downstream electrode positions are located between –12~–8 mm and 8~12 mm, respectively. The results indicate that as input power is increased, the time required for film deposition completion is longer, and the amount deposited is larger. Although it is assumed that these results have a strong connection with the concentration gradient of a precursor generated at upstream range in the plasma, an accurate explanation to this phenomenon has not yet been found. Figure. 3 shows the profiles of the platinum amount deposited on inner surface of a fused silica capillary in runs 4-6. These three runs indicate the progression of the deposition profile in time for similar experimental conditions. The figure shows that little platinum is deposited around the point of the downstream electrode in runs 2 and 3. In these conditions, the decomposition of the precursor and film deposition mostly takes place at the upstream range in the plasma and the precursor is no longer transported to the range around the downstream electrode. In addition, judging from little deposition in the range of –20~–4 mm after 50 sec, it is clear that the plasma discharge region is shortened as film deposition proceeds. Therefore, it seems reasonable to conclude that film deposition starts locally at the inner surface attached with an upstream electrode, and is completed at a downstream electrode. Also SEM micrographs showed that the average deposition rate between electrodes is evaluated roughly at 16-22 nm/min, based on the film thickness of approximately 110-150 nm measured with some SEM micrographs.

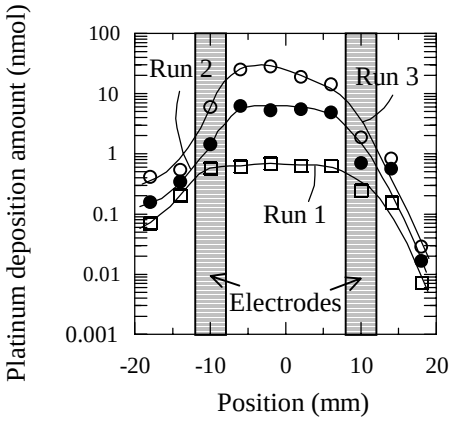

Fig. 2 Experimental results of plasma CVD for experiments for run 1 ~ run3

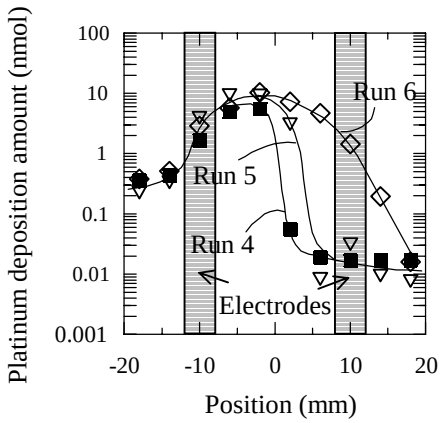

Fig. 3 Experimental results of plasma CVD for experiments for run 5 ~ run6

3. Dissociation Reaction of Carbon Dioxide[8].

We tried to carry out plasma decomposition experiments of carbon dioxide in a micro channel. This reaction is the typical one, whose heterogeneous effect is required very much. Because the recombination reaction takes place in the gas phase and the dissociation reaction of carbon dioxide can not completed only in gas phase plasma reaction.

3.1 Experimental Setup

The micro plasma reactor is a Pyrex glass tube of 48-mm length, 6-mm outer diameter, and 500, 1000, 1500-μm inner diameter, which is connected to the gas inlet and outlet line by 1/4" stainless steel union tee. In order to create the uniform glow discharge plasma in the capillary tube, the stainless steel union tees are used as hollow electrodes and a 50 Hz AC voltage (Max. 15kV) is applied between those two electrodes. Helium gas is used as carrier gas to stabilize the micro plasma. The conditions for discharge were as follows: discharge pressure was about 10–300 Torr, discharge voltage was 3.7 to 12.3 kV, discharge current was 0.8 to 19.8 mA, the mole ratio of helium to CO_2 was 1 to 4, and total gas flow rate was 6.8 to 60.8 cm^3/min (at 101.3 kPa, 293.15K). Composition of decomposed gas was measured by gas chromatography.

3.2 Numerical Simulation

The CO_2 decomposition in a micro plasma reactor have been studied experimentally and decomposition degree over 90% of initial CO_2 have been obtained without scavenger species that avoid recombination of O and CO. Similar studies, not in microscale reactors, are reported and low CO_2 decomposition degree are obtained in a case without scavenger species [1]. Therefore, downscaling effect in a plasma rector is conceivable. Since reactions of the CO_2 decomposition is very fast and flow rate through a reactor decreases as reactor size decreases, it is very hard to investigate precisely in experiments. In this study, we developed a model for describing the kinetics of the CO_2 decomposition in a micro plasma rector and carried out simulations to obtain characteristics of the CO_2 decomposition.

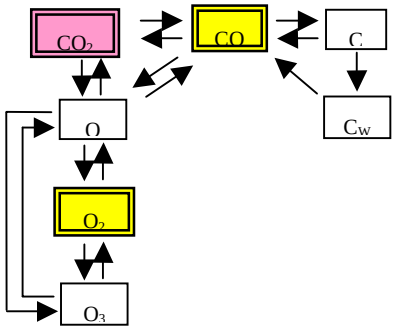

Fig. 4 Dominant channels of the CO_2 decomposition reaction in a micro plasma reactor.

Three types of reactions are considered: i) plasma reaction, ii) homogeneous reaction, and iii) heterogeneous reaction. Dominant reaction channels are shown in Fig. 1. Data of reactions and their rate coefficients are obtained from reports of CO_2 laser, O_2 glow discharge, and ozone generator, mainly. Heterogeneous reactions at a reactor wall is one of the most important process in effect of downscaling, and rate coefficients for those reactions are represented by $k=\gamma u/d$, where γ is the recombination probability, u is the mean molecular velocity, and d is the reactor diameter. The reactor in this study is a simple tube type reactor (Fig. 2). We carried out computer simulations for reactions about the CO_2 decomposition in a micro plasma rector and time evolutions of number density of each species were obtained. Conditions used in simulations are listed in Table 1 and simulated results are shown in Fig. 3.

3.3 Results

In these experiments we measured decomposition degree of CO_2 in each size of micro channel changing input energy, flow rate and pressure. The smaller size of reactor and the higher input power give the higher decomposition degree as we expected. Figures 4 show that the decomposition degree of CO_2 increases and saturates as current density increases. In these figures, all of data obtained in the channel diameter, 0.5mm and 3mm are plotted simultaneously. And it can be seen that their data have the same tendency and they can be fit on one curve line. This is the reason why each experiment for different diameter was carried out under the same residence time by changing each flow rate properly. Of course these results show that the data in the lower pressure saturate in the earlier period and gives the higher decomposed degree of CO_2 decomposition up to over 95%. Although it is not impossible to make the difference of the saturated values among micro channel diameters clear, because of difficulty of plasma experiments under the same flow rate, simulation results, whose data are virtual ones, can make them clear as shown in Figures 5. These figures include the numerical results calculated for large diameter, 10mm and infinity adding to the same channel diameter, 0.5mm 1mm and 3mm as experiments. Although the decomposition degree looks like being saturated, the decomposition reaction may be completed at last at infinity current density, which is not realistic..

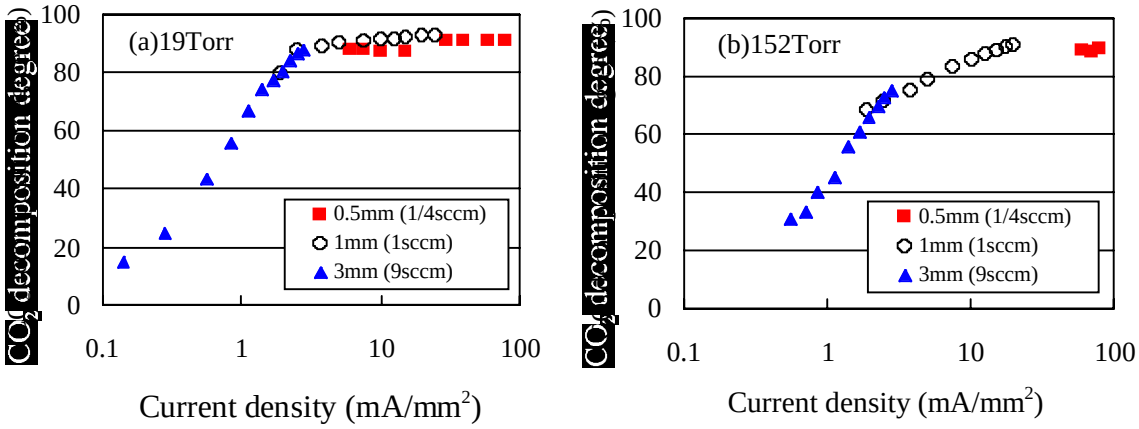

Fig.5 CO_2 decomposition result in experiments under the same

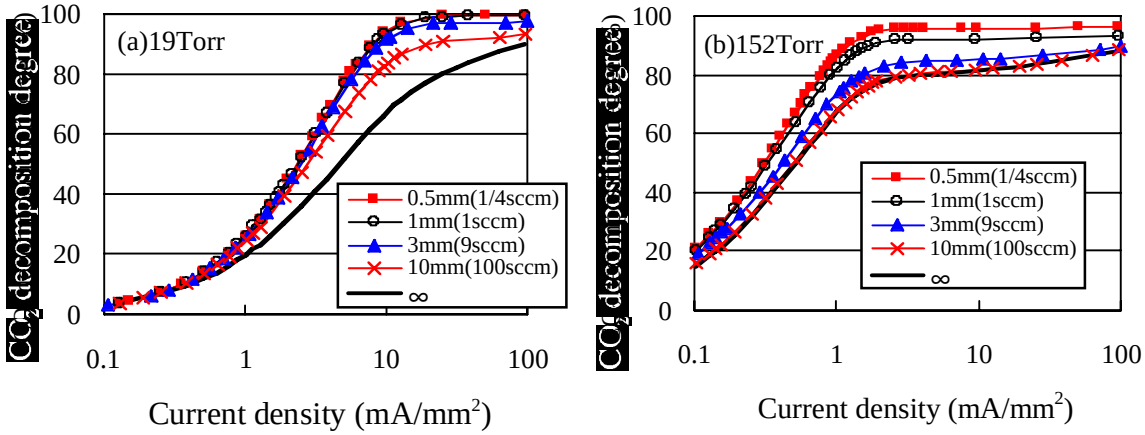

Fig.6 Dependenth of decomposition degree on microchannel diameter by simyulation. (t=0.0455s, E/p=5V/cm/Torr)

4. Discussion

In these typical reactions, the surface, which is the most important characteristic in a micro channel, works effectively.

In plasma CVD experiments, it can be reasonable to conclude that film deposition starts locally at the inner surface attached with an upstream electrode, and is completed at a downstream electrode. Hence, we can suggest the model picture as following. When the plasma discharge in a capillary is maintained between a downstream electrode and the end of a deposited film instead of an upstream electrode, it is reduced in length as film deposition proceeds. After completion of film deposition, surface discharge at the outer surface around electrodes takes place and the inside discharge quits no longer and film deposition completed automatically. Fujiyama [9] reported such a behavior of discharge as “the extended anode effect” in plasma sputtering. This phenomenon works effectively to create uniform films in the P-CVD process even if the concentration gradient of the precursor in the micro channel is steep. In the usual plasma CVD reaction, it is very scarce that all of reactants dissociate and all of dissociated species deposit on the surface wall. This means that the micro plasma CVD complete with high efficiency, utilizing the characteristics of micro channel.

Also in the dissociation of CO_2, we can see that the heterogeneous reaction works effectively in such a

reaction as CO_2 dissociation. Plasma decomposition of CO_2 in gas phase has been tried by other researchers and they reported[6] that the decomposition degree could be improved up to 75% by using the reaction quenching technique. This means the upper limit of CO_2 decomposition in gas phase reaction. Although high temperature plasma can decompose CO_2 to CO and O very much, recombination reaction occurs simultaneously and consequently it gives low decomposition degree. In heterogeneous micro channel reaction, however, the micro channel wall works to promote consumption of O by O-O reaction and it can give such a high decomposition degree. We demonstrated the decomposition reaction to show the effectiveness of heterogeneous plasma reaction in a micro channel. In this point of view, the demonstration is successful, but the example is not proper as an application because of low pressure operation. It is very important to search more effective reactions to be applied, judging from the reaction time and the diffusion time, which we mentioned in above introduction of this paper.

These two examples which are the typical heterogeneous reaction suggest us how to use a micro reactor. We can conclude that the micro channel plasma reactor can be useful, if the suitable chemical reaction is selected.

5. Conclusion.

We mentioned two typical plasma reactions, which we have tried recently. One is the plasma CVD in the inner surface of micro channel and another is the plasma decomposition reaction of CO_2 in a micro channel. From these demonstrations, we can conclude that the plasma reaction in a micro channel can be achieved with high effectiveness and efficiency, if the reaction is selected properly, considering the reaction time and the diffusion time which characterize the phenomena in the plasma in a micro channel. We can also conclude that excellent ideas can lead the fruitful applications for the micro plasma reactor.

References.

[1] J. C. T. Eijkel, H. Stoeri, A. Manz, Anal. Chem. 72 (2000) 2547.
[2] H. Yoshiki, K. Taniguchi, H. Ogawa, Y. Horiike, J. Vac. Soc. Jpn., 45 (2002) 433.
[3] M. Miclea, K. Kunze, G. Musa, J. Franzke, K. Niemax, Spectrochim. Acta Part B 56 (2001) 37.
[4] H, Qiu, K. Martus, W. Y. Lee, K. Becker, Int. J. Mass Spectrom. 233 (2004) 19.
[5] M. Bilgic, U. Engel, E. Voges, M. Kückelheim, J. A. C. Broekaert, Plasma Sources Sci. Technol. 9 (2000)
[6] H. Sekiguchi, A. Kanzawa, T. Honda, Ko-on Gakkai-shi, 15[3], 102-108 (1989)
[7] Kadowaki, H. Yoshizawa, S. Mori, M. Suzuki, to be published in Thin Solid Films
[8] S. Mori, A. Yamamoto. and M. Suzuki, Proc. 8th International Conference on Microreaction Technology (IMRET8), Atlanta, U.S.A., April 11-14, 2005.
[9] H. Fujiyama, Surf. Coat. Technol. 131 (2000) 278.

Hydrogen enrichment of low-calorie gas using DBD enhanced Ni/γ-Al_2O_3 catalyst reactor: Low-temperature reforming due to radical injection.

Hiroyuki Tsukijihara, Ken Okazaki, and Tomohiro Nozaki*

Department of Mechanical and Control Engineering, Tokyo Institute of Technology
**Corresponding author: tnozaki@mech.titech.ac.jp*

Abstract

Authors have developed a barrier discharge/catalyst hybrid reactor for the reforming of low-calorie fuels such as biogas (main component is methane) at low temperature (300°C~600°C). This technique allows utilizing low temperature thermal energy wasted from various industries, which eventually provides variety of energy utility options. The idea behind the project is that radicals produced by non-thermal plasma can be decomposed at much lower temperature than normal reforming condition. However, situation becomes even more complicated since barrier discharge enhances chemical reaction in many different ways: (1) Excited species, radicals, and ions decompose on catalyst at lower temperature than stable molecule. Life time of radical species has remarkable effect on synergistic effects. (2) Secondary products such as acetylene and ethane decompose at lower temperature than methane. Life time of those products is long enough so that they reach catalyst surface to decompose. (3) Heat generated by barrier discharge also enhances regular catalytic reforming. Relationship between discharge energy (J) and endothermic enthalpy (J) has remarkable effect on the increase in reaction temperature. In order to distinguish each contribution, steam reforming in regular catalytic reactor, barrier discharge reactor, and combination of these two has been demonstrated in detail. In addition, infrared camera was used to measure temperature distribution of catalyst bed for the best understanding of given hybrid system.

1. Introduction

Renewable energy from bio-resources such as organic wastes, landfill gas, and agricultural residues is attracting considerable attention with growing concern of energy saving and environmental protection. Since bio-resource is carbon neutral and potentially minimizes both consumption of fossil fuel and CO_2 emission. However, efficient use of bio-resource has major challenges. First of all, heating value of bio-resource is generally 20% to 80% of natural gas and many of them are flame-resistant. Diversity of composition and both moisture an energy content of bio-resource makes the situation even more difficult. Those “poor” resources are primarily upgraded for desired purpose; however, reforming reaction generally requires high temperature heat source (~800°C) where large part of initial fuel must be burned out, losing initial enthalpy of the fuel or resulting in much lower calorie fuel than it is before. Even though conventional catalytic reforming is a promising option, further development of existing process is being claimed with increasing demand of bio-resources.

More recently, atmospheric pressure non-thermal plasmas such as Plasmatron [1-2] and Glidarc [3-5] are recognized as economically competitive plasma fuel converters. Electrical energy consumption of those plasma reactors is normally less than 10% of heating value of the initial fuel when combined with partial oxidation. Because driving force of reforming reaction essentially depends on heat released by partial oxidation, while the plasma preliminary enhances the combustion process of low-calorie poor fuels. Unfortunately, heating value of resulting upgraded fuel is inherently low because air is used as oxidant that introduce large amount of nitrogen into the fuel.

From these aspects, authors have proposed combustion-free, low-temperature (300°C~600°C) steam reforming of low-calorie fuels using DBD/catalyst hybrid reactor [4-5]. The idea behind the project is that radicals produced by non-thermal plasma can be decomposed at much lower temperature than normal reforming conditions, and thus low temperature wasted thermal energy could be utilized in the process: reforming reaction is completely free from combustion of initial fuel. It does not necessarily mean that initial fuel is fully reformed since partially hydrogen enriched fuel remarkably improves combustibility and enables to drive an internal combustion engine. On the contrary, polymer electrolyte fuel cells, for instance, might not be an economically

compatible partner since the temperature of exhaust is too much low to drive hybrid reactor. Not only plasma reactor, but also appropriate energy utility system must be well considered so that a small amount of electrical energy input improves the entire energy system. Otherwise, consumption of electricity may become large and proposed plasma process will not be economically competitive. Up to now, authors have demonstrated that existence of non-thermal plasma in catalyst bed reactor enhances the hydrogen production rate. Radical injection due to non-thermal plasma is essential in order to derive synergistic effect between catalyst and plasma; however, situation becomes even more complicated in hybrid reactor since barrier discharge enhances chemical reaction in many different ways:

(1) Excited species, radicals, and ions are decomposed on catalyst at lower temperature than ground state molecules. Lifetime of radical species has remarkable effect on lowering reaction temperature.
(2) Secondary products such as acetylene and ethane also decompose at lower temperature than methane. Lifetime of secondary products is long enough so that they reach catalyst surface to decompose.
(3) Heat generated by barrier discharge also enhances regular catalytic reaction. Relationship between discharge energy (J) and endothermic enthalpy (J) has remarkable effect on the increase in reaction temperature.

In order to distinguish each contribution, steam reforming in regular catalytic reactor, non-thermal plasma reactor, and combination of those two has been investigated in detail. In addition, infrared camera was used to measure temperature distribution of catalyst bed for the best understanding of given hybrid system.

2. Experimental system

Figure 1 schematically shows experimental setup and Fig. 2 illustrates the configuration of barrier discharge/catalyst hybrid reactor. The rod-to-tube (ϕ_r 3 mm × ϕ_i 20 mm) reactor was located in a constant temperature bath where ambient temperature was 150°C to avoid liquid condensation. Catalyst pellets of 12wt%/γ-Al_2O_3 (3 mm) was packed in the volume of ϕ_i 20 mm × 50 mm. Bipolar pulsed voltage (+/- 20 kV at 1-5 kpps) was applied between center and external electrode. The discharge is ignited at pellet contacts, and then propagates covering pellet surface. We used simulated biogas which includes 60% methane and 40% nitrogen (CH_4:N_2 = 6:4). Steam and methane ratio (S/C) was set to one (S/C = H_2O/CH_4 = 1). S/C is normally set to between 2 and 3 in order to prevent carbon precipitation. We do not have to supply excess amount of water vapor since our purpose is partial steam reforming of initial methane, that is,

Initial composition: CH_4: N_2: H_2O = 6: 4: 6 ; where S/C = 1.
Steam reforming: $CH_4 + 2H_2O = CO_2 + 4H_2$; low temperature reforming does not yield CO.
Gas composition after 20% of methane converted (dry base) ; CH_4: N_2: CO_2: H_2 = 4.8: 4: 1.2: 4.8.

When methane conversion is 20%, hydrogen in the resulting gas is enriched by 32vol%. Initial S/C ratio (= 1) is large enough for converted methane to prevent carbon precipitation. Total gas flow (including CH_4, H_2O, and N_2) was selected so that space velocity (SV) becomes 10000 hr^{-1}. The reaction temperature increased up to 600°C with external electric heater, and discharge power was carefully selected so as not to exceed endothermic

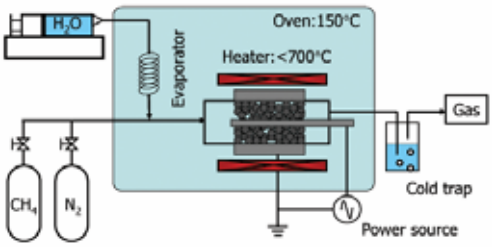

Fig. 1 Experimental setup of reactor.

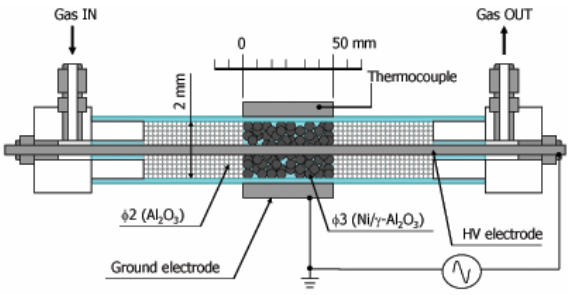

Fig. 2 Plasma/catalyst hybrid reactor.

enthalpy due to steam reforming of methane. Part of reaction gas was sampled after cold trap. H_2 and N_2 were analyzed by gas chromatograph equipped with TCD detector. Methane, CO, and CO_2 were measured by GC (FID) after methanation.

3. Enhancement of methane conversion in plasma/catalyst hybrid reactor

Figure 3 shows methane conversion with respect to electrode temperature in both hybrid and normal catalyst reactor. It is no doubt that methane conversion in hybrid reactor is larger than those in regular catalyst reactor. It is interesting why such high rate could be resulted from combined reactor. This question has not been understood well, and it is important to investigate reaction mechanisms for further improvement of given hybrid reactor. From next section, we will investigate the reaction mechanism in plasma/catalyst hybrid reactor. First of all, we will measure catalyst bed temperature distribution during reaction and see how electrode temperature could be different from catalyst bed temperature that directly influences reforming reaction.

4. Catalyst bed temperature measurement

We used infrared camera to measure catalyst bed temperature. Figure 4 shows temperature measurement setup. The external electrode has a square window that allows infrared signal coming out of the bed medium. The reactor is made of sapphire in this measurement so that infrared signal transmits the reactor wall. The infrared camera made a focus to 10 mm × 50 mm square window and detected signals. The camera was calibrated in advance. The advantage of

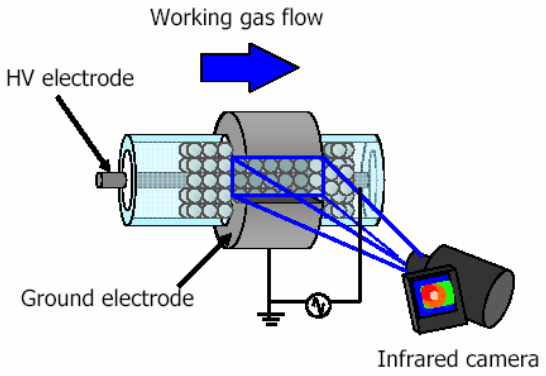

Fig. 4 Temperature measurement setup.

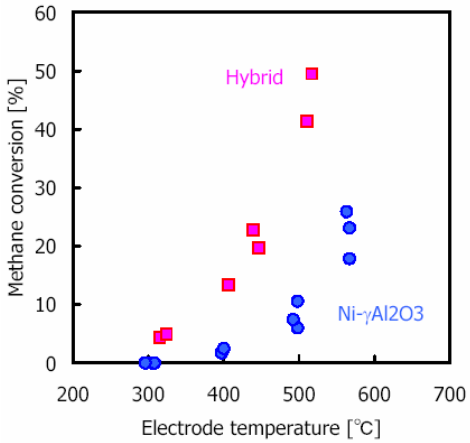

Fig. 3 Methane conversion vs. electrode temperature. SV = 10000 hr^{-1}, $CH_4/N_2/H_2O$ = 1100/733/1100 sccm (S/C = 1). Discharge power = 25-220 $kJ/mol_{\_CH4}$

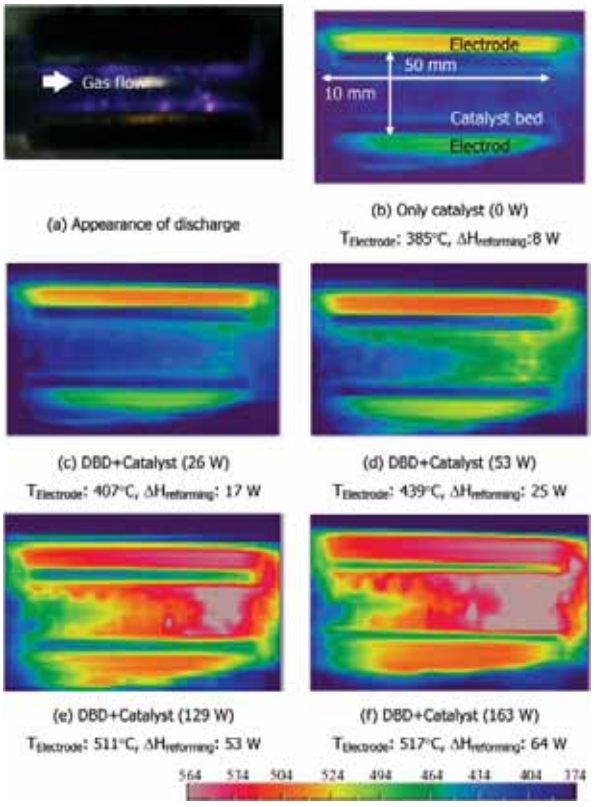

Fig. 5 Temperature distribution of catalyst bed. P: Discharge power, Q: Endothermic enthalpy, SV = 10000hr^{-1}, $CH_4/N_2/H_2O$ = 1100/733/1100 sccm (S/C = 1).

using infrared camera is that temperature distribution in bed medium is obtained by in situ and results are not disturbed by either electrical noise or visible light emission from plasma.

Figure 5 (a) shows actual picture of reactor during plasma operation. Figure 5 (b) shows an infrared image of catalyst bed without plasma, and (c) through (f) corresponds to the bed temperature with plasma. A caption of each image shows discharge power, endothermic enthalpy of steam reforming, and temperature of ground electrode which was measured by thermocouple. In the case of (b), temperature of the bed is almost uniform. In the case of (c) where discharge power (P) and endothermic enthalpy of methane steam reforming (Q) is the same level, temperature distribution is still uniform. And these temperatures were almost same level as electrode temperature. However, in the case of P > Q, i.e. from (d) to (f), we observed that bed temperature in downstream was 200°C higher than inlet. It suggests that both feed gas and catalyst bed were heated by plasma, and bed temperature is not uniform and increases much higher than electrode temperature. Reaction mechanisms must be analyzed on the basis of catalyst bed temperature.

5. Contribution of secondary products to the synergistic effect

Three different conditions were investigated in the hybrid reactor shown in Fig. 2: (1) Ni/γ-Al_2O_3 (without plasma), (2) hybrid (plasma and Ni/γ-Al_2O_3), and (3) plasma with α-Al_2O_3 (without catalyst). Figure 6 compares methane conversion obtained by three different conditions. The results clearly show that methane is hardly decomposed by barrier discharge since discharge power was limited in order to avoid excess gas heating, i.e. input power was carefully adjusted so as not to exceed endothermic enthalpy. Input power density with respect to methane flow rate was smaller than 120 kJ/mol$_{_CH4}$. According to Fig. 6, Ni/γ-Al_2O_3 catalyst is more effective than barrier discharge, but result does not reach equilibrium because the space velocity is high (SV = 10000 hr^{-1}). On the other hand, combined result reached equilibrium all the way through the temperature tested. Plasma produces secondary products such as acetylene and ethane. Those products also contribute to low temperature catalysis of methane since they decompose at lower temperature; however, yield of secondary products is obviously negligible small. Thus contribution of those products to the synergistic effect can be reasonably neglected.

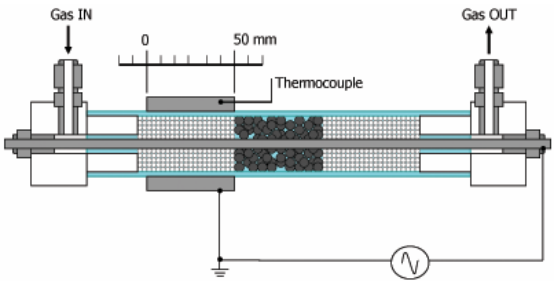

Fig. 7 Plasma pre-processing reactor.

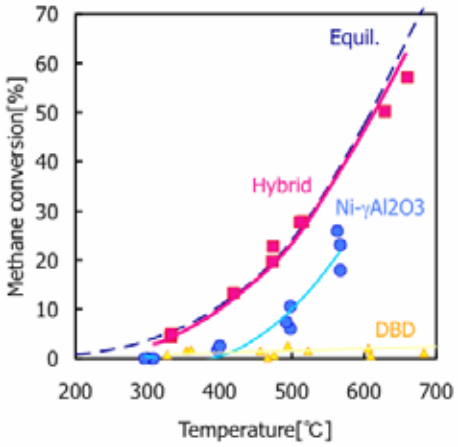

Fig. 6 Methane conversion between DBD and Ni-γAl_2O_3 catalyst. SV = 10000hr^{-1}, $CH_4/N_2/H_2O$ = 1100/733/2200 sccm (S/C = 1). Power = 25-120 kJ/mol$_{_CH4}$.

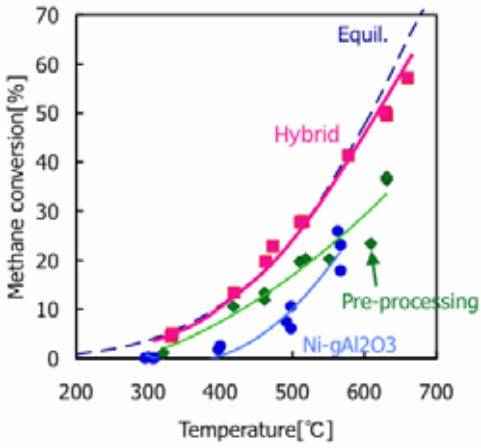

Fig. 8 Methane conversion between hybrid reactor and plasma pre-processing reactor. SV = 10000 hr^{-1}, $CH_4/N_2/H_2O$ = 1100/733/1100 sccm (S/C = 1). Discharge power = 25-120kJ/mol$_{_CH4}$.

6. Contribution of radical injection to the synergistic effect

In this experiment, we used plasma pre-processing reactor in order to separate the effect of heat produced by barrier discharge. Figure 7 describes schematic diagram of plasma pre-processing reactor. All radicals are most likely to be deactivated before flowing into the catalyst bed. On the other hand, the feed gas is heated up by plasma and flows into the catalyst bed. Plasma zone must be placed right in front of the catalyst bed in order to minimize heat loss thorough reactor wall. The results obtained by pre-processing reactor are shown in Fig. 8, comparing (1) Ni/γ-Al_2O_3 (without plasma), (2) hybrid (plasma and Ni/γ-Al_2O_3), and (3) plasma pre-processing reactor. The pre-processing reactor adds only thermal energy and methane conversion increases up to equilibrium when bed temperature is lower than 450°C. The hybrid reactor supplies both radicals and thermal energy, and methane conversion in hybrid reactor is larger than those obtained in pre-processing reactor: the differecen between those result corresponds to the effect of radical injection. Non-thermal plasma mainly produces heat and radicals. The heat produced by non-thermal plasma maintains bed temperature at desired level, while radical injection promotes chemical conversion process at given temperature. However, contribution of radical injection become remarkable when bed temperature is higher than 450°C.

7. Conclusion

We developed combustion-free, low-temperature steam reforming of low-calorie fuels using barrier discharge and catalyst hybrid reactor. Some of the important aspects are as follows:

[1] Synergistic effect between barrier discharge and Ni/γ-Al_2O_3 catalyst was observed. Methane conversion is enhanced at lower temperature than normal reforming condition. The chemical conversion process can be enhanced by both radical injection and heat generated by plasma. On the other hand, contribution of secondary products such as C_2H_2 and C_2H_6 is negligible small.

[2] Non-thermal plasma also works as an excellent heat source. It has remarkable effect between 300°C and 450°C of bed temperature. Heat is released uniformly through reactor volume. Unlike auto-thermal reforming, non-thermal plasma does not require additional oxygen to burn out a part of feed gas. Therefore it is free from catalyst oxidation and additional CO_2 which may be a cause of coking problem.

[3] Radical injection has remarkable effect when the bed temperature exceeds 450°C. Although radical species can be decomposed at lower temperature, it still requires at least 450°C of bed temperature.

[4] When $P \approx Q$, where Q is endothermic enthalpy and P is discharge power, temperature of catalyst bed is maintained uniform. If $P >> Q$, temperature of the bed increases significantly from the downstream of catalyst bed.

Acknowledgement

This project is partly granted by New Energy and Industrial Technology Development Organization of Japan (NEDO), Strategic Development of Technology for Efficient Energy Utilization (P03033). Authors also would like to thank Dr. Shigeru Kado of Tokyo Institute of Technology for intensive discussion.

References

[1] L Bromberg, D R Cohn, A Rabinovich, J Heywood, Int. J. of Hydrogen Energy, **26**(10) (2001) 1115-1121.

[2] L Bromberg, D R Cohn, A Rabinovich, N Alexeev, A Samokhin, R Ramprasad, S Tamhankar, Int. J. of Hydrogen Energy, **25**(12) (2000) 1157-1161.

[3] http://www.glidarc-tech.com/

[4] A Czernichowski, Oil and Gas Science and Technology, **56**(2) (2001) 181-198.

[5] Mutaf-Yardimci, A V Saveliev, A A Fridman, L A Kennedy, J. of Appl. Phys., **87**(4) (2000) 1632-1641.

[6] T Nozaki, N Muto, S Kado, K Okazaki, Catalysis Today, **89** (2004) 57-56.

[7] T Nozaki, N Muto, S Kado, K Okazaki, Catalysis Today, **89** (2004) 57-56.

Two-Temperature Chemically Non-Equilibrium Modeling of Argon Induction Plasmas with Diatomic Gas

Takayuki Watanabe[1], Nobuhiko Atsuchi[2], and Masaya Shigeta[1]

[1] *Department of Environmental Chemistry and Engineering, Tokyo Institute of Technology, Yokohama, Japan*
[2] *Department of Nuclear Engineering, Tokyo Institute of Technology, Tokyo, Japan*

Abstract
A non-equilibrium modeling of argon-oxygen and argon-hydrogen induction thermal plasmas was performed without thermal and chemical equilibrium assumptions. Reaction rates of dissociation and recombination of diatomic gas and ionization were taken into account. A substantial deviation from LTE exists near the torch wall in argon-oxygen induction plasmas under atmospheric pressure, while small deviation in argon-hydrogen plasmas results from the large collision frequency electrons and hydrogen atoms.

1. Introduction

Induction thermal plasma approach has been applied for many fields. Attractive recent applications are treatment of harmful materials and recovery of useful material from wastes [1]. Another important application is production of high-quality and high-performance materials, such as synthesis of nanoparticles, deposition of thin films, and plasma spraying. In these applications, thermal plasmas with adding reactive gas are desirable to enhance the chemical reactivity of the plasmas.

Sophisticated modeling considering chemical reaction has been required for industrial applications. However, thermal plasmas have been mainly treated with equilibrium conditions. The purpose of this work is to develop two-temperature chemically non-equilibrium (2T-CNE) modeling of induction plasmas, comprising argon-oxygen and argon-hydrogen mixtures. This formulation including finite-rates of the dissociation and ionization is presented using higher-order approximation of the Chapman-Enskog method [2] for the estimation of the transport properties.

2. Numerical formulation

2-1 Thermodynamic and transport properties

Up to now, modeling of induction thermal plasmas has been performed with the first-order approximation of the Chapman-Enskog method because higher-order of Sonine polynomial expansion requires many kinds of collision integrals resulting in the complex formula. The first-order approximation may cause errors especially for electrical conductivity and thermal conductivity of electron translational contribution over

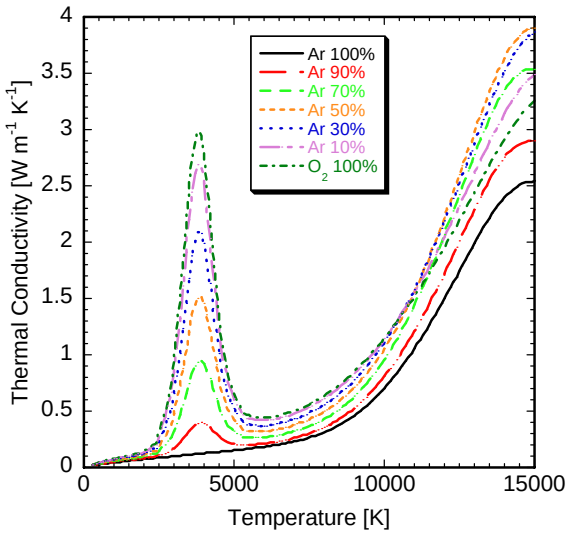

Fig. 1 Thermal conductivity of mixtures of argon and oxygen.

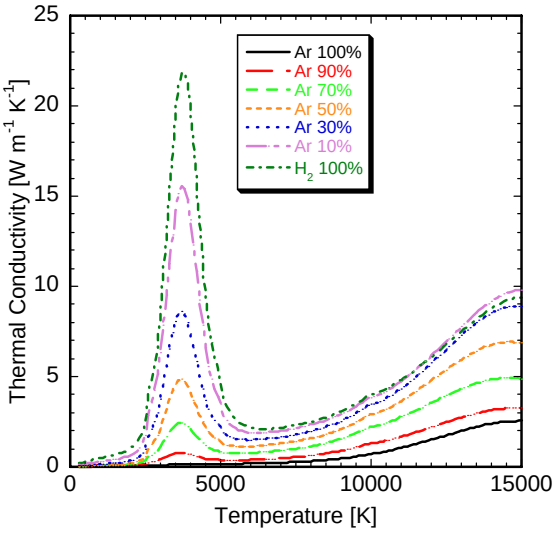

Fig. 2 Thermal conductivity of mixtures of argon and hydrogen.

10000 K [3]. Therefore, higher-order approximation is used according to the required accuracy in this study. The collision integrals were taken from the reference data which provide inter molecular potential and fitting data. Detailed descriptions of the estimation method of viscosity, thermal conductivity and electrical conductivity are given by Watanabe and Sugimoto [3].

Thermal conductivity of mixtures of argon-oxygen and argon-hydrogen are shown in **Figs. 1** and **2**, respectively. Thermal conductivity has high value where the dissociation and ionization occur. In mixture of argon and oxygen or hydrogen, thermal conductivity is proportional to the composition of their mixture. Viscosity of mixtures of argon-oxygen and argon-hydrogen are presented in **Figs. 3** and **4**. Viscosity has the maximum at 10000 K where the ionization begins to play important roles. In mixture of argon and hydrogen, viscosity decreases with hydrogen addition due to small mass of hydrogen.

In CNE model, the transport and thermodynamic properties are strongly related to the temperature and the composition of plasmas. Therefore, the transport and thermodynamic properties should be estimated considering the diffusion of species in plasmas at each calculation step until the convergence.

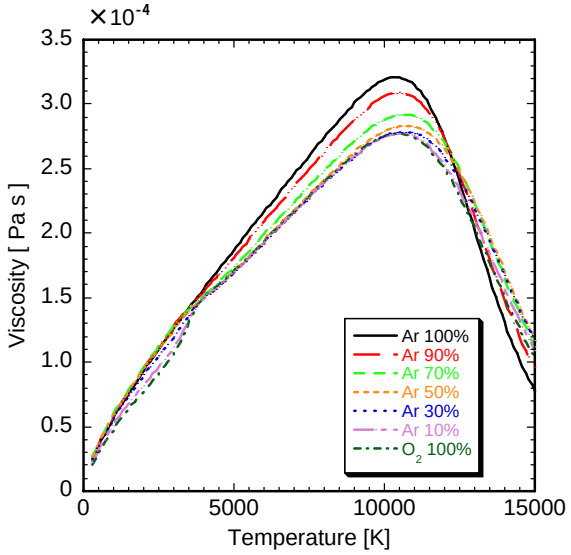

Fig. 3 Viscosity of mixtures of argon and oxygen.

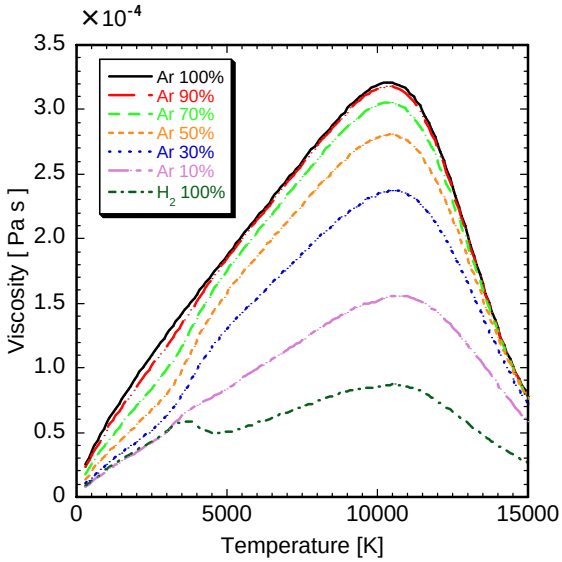

Fig. 4 Viscosity of mixtures of argon and hydrogen.

2-2 Kinetic rate constants

The equilibrium composition was estimated by FACT (Center for Research in Computational Thermochemistry), considering six species of Ar, Ar^+, O_2, O, O^+, and e^- in argon-oxygen plasmas and six species of Ar, Ar^+, H_2, H, H^+, and e^- in argon-hydrogen plasmas in this study. **Tables 1** and **2** summarize Ar-O_2, Ar-H_2 plasma reactions considered in this study, respectively. Twelve reactions comprising 6 forward reactions for each plasma and their backward reactions were taken into account. The reaction rates for the forward direction are given by Arrhenius equation.

$$k_l^f = a_l T^{b_l} \exp(-c_l / T) \tag{1}$$

For Ar ionization reaction, the reaction rate can be calculated with Eq. (2) [4].

$$k_l^f = 1.68\times10^{-20} T^{1.5} (135300/T + 2) \exp(-135300/T) \tag{2}$$

Table 1 Chemical reactions in argon-oxygen plasmas.

Reaction	a_l	b_l	c_l
$O_2 + O_2 \rightarrow O + O + O_2$	2.0×10^{21}	-1.5	59500
$O_2 + O \rightarrow O + O + O$	1.0×10^{22}	-1.5	59500
$O_2 + Ar \rightarrow O + O + Ar$	1.0×10^{22}	-1.5	59500
$O_2 + e^- \rightarrow O + O + e^-$	9.68×10^{22}	-2.0	59500
$O + e^- \rightarrow O^+ + e^- + e^-$	3.91×10^{33}	-3.78	158500
$Ar + e^- \rightarrow Ar^+ + e^- + e^-$	k_l^f was calculated by Eq.(2)		

Table 2 Chemical reactions in argon-hydrogen plasmas.

Reaction	a_l	b_l	c_l
$H_2 + H_2 \rightarrow H + H + H_2$	2.23×10^{12}	0.5	46600
$H_2 + H \rightarrow H + H + H$	2.23×10^{12}	0.5	46600
$H_2 + Ar \rightarrow H + H + Ar$	2.23×10^{12}	0.5	46600
$H_2 + e^- \rightarrow H + H + e^-$	2.23×10^{12}	0.5	46600
$H + e^- \rightarrow H^+ + e^- + e^-$	1.51×10^{31}	-3.0	158000
$Ar + e^- \rightarrow Ar^+ + e^- + e^-$	k_l^f was calculated by Eq.(2)		

2-3 Calculation model and assumptions

The geometry of calculation domain of the induction plasma torch is shown in **Fig. 5** and operating conditions are summarized in **Table 3**. Plasma gas and sheath gas composition were mixtures of argon and oxygen (3%) or argon and hydrogen (3%). The plasma torch consists of a water-cooled quartz tube, and is surrounded by a water-cooled induction coil. The coil consists of three turns and applies the induction frequency at 4 MHz to the plasma. The actual power level was assumed to be 5 kW.

The calculations are based on the following assumptions to derive the governing equations: (a) steady-state laminar flow; (b) axial symmetry; (c) optically thin; (d) negligible viscous dissipation in energy equation; (e) negligible displacement current in comparison with the conductive current; (f) negligible flow-induced electric field.

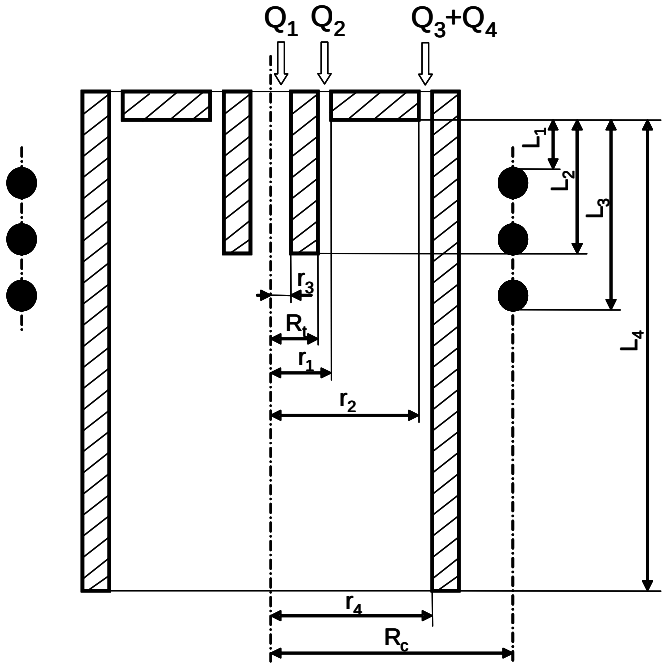

Fig. 5 Geometry of calculation domain of induction plasma torch.

Table 3 Torch characteristic dimensions and operational condition.

Torch Power	5 kW
Work Frequency	4 MHz
Reactor Pressure	101.3 kPa
Coil Radius	32 mm
Coil turn number	3
Wall thickness of quartz tube	1.5 mm
Distance to frontal end of coil (L_1)	19 mm
Distance to rear end of coil (L_3)	65 mm
Insertion length of probe (L_2)	45 mm
Torch length (L_4)	190 mm
Outer radius of inner slot (r_1)	6.5mm
Outer radius of outer slot (r_2)	21 mm
Inner radius of injection tube (r_3)	1 mm
Inner radius of quartz tube (r_4)	22.5 mm
Outer radius of injection tube (R_t)	4.5 mm
Flow rate of carrier gas (Q_1)	0 l/min
Flow rate of plasma gas (Q_2)	3 l/min
Flow rate of plasma gas (Q_3)	10l/min
Flow rate of sheath gas (Q_4)	20 l/min

2-4 Governing equations and boundary conditions

The field of flow, temperature and concentration in induction thermal plasmas were calculated by solving the two-dimensional continuity, momentum, energy (heavy particle and electron), and species conservation equations coupled with the Maxwell's equations. Reactions of the dissociation and recombination as well as the ionization were taken into account in this modeling.

Continuity:

$$\nabla \cdot (\rho \mathbf{u}) = 0 \tag{3}$$

Momentum:

$$\rho \mathbf{u} \cdot \nabla \mathbf{u} = -\nabla p + \nabla \tau + \mathbf{J} \times \mathbf{B} \tag{4}$$

Energy (heavy particle):

$$\rho \mathbf{u} \cdot \nabla h = \nabla \cdot \left(\lambda_h^{tr} \nabla T_h\right) + \sum_{i(i \neq e)}^{N} \nabla \cdot \left(\rho D_i h_i \nabla Y_i\right) - \sum_{l(\beta_{el}^f \cdot \beta_{el}^r)}^{L} \Delta Q_l + E_{eh} \tag{5}$$

Energy (electron):

$$\frac{5}{2} k \nabla (\mathbf{u} n_e T_e) = \nabla \cdot \left(\lambda_e^{tr} \nabla T_e\right) - \frac{5}{2m_e} k \nabla (T_e \Gamma_e) - \sum_{l(\beta_{el}^f \cdot \beta_{el}^r \neq 0)}^{L} \Delta Q_l + \mathbf{J} \cdot \mathbf{E} - q_r - E_{eh} \tag{6}$$

Species:

$$\rho \mathbf{u} \cdot \nabla Y_i = \nabla \cdot \left(\rho D \nabla Y_i\right) + R_{ri} \tag{7}$$

Electromagnetic:

$$\nabla^2 \mathbf{E} - \xi\sigma\frac{\partial \mathbf{E}}{\partial t} = 0 \qquad (8)$$

The boundary conditions along the centerline were set to insure the axial symmetry. At the wall of the plasma torch, no slip conditions are maintained for the velocity, and the concentrations have zero gradient.

2-5 Calculation procedure

The governing conservation equations were solved using SIMPLER (Semi-Implicit Method for Pressure Linked Equation Revised) algorithm [5]. The governing equations and the electric field intensity equation with the associated boundary conditions were discretized into finite difference form using control-volume technique. Non-uniform grid points 30 by 30 were used for radial and axial directions, respectively. Grids were made finer close to the center and the coil region. Thermodynamic and transport properties were calculated from the temperature and compositions at each position in the calculation domain at each iteration step.

3. Result and discussion

The calculated temperature fields with the 2T-CNE model were presented in **Fig. 6 (a)**. The left is the heavy particle temperature (T_h), and the right is the electron temperature (T_e). The electron temperature near the torch wall of coil region is higher than the heavy particle temperature, although $T_e = T_h$ at the high-temperature region near the torch center. Radial temperature distributions by three models (LTE, 1T-CNE, 2T-CNE) in an argon plasma at the center of the coil are shown in **Fig. 7**. The electron temperature is 4000 K higher than the heavy particle temperature at r = 20 [mm]. In contrast, the distributions of the heavy particle temperature estimated from the three models are almost the same. These results reveal that substantial thermal non-equilibrium exists near the torch wall of the coil region in an argon plasma. The calculated streamlines were presented in **Fig. 6 (b)**. The left is the 2T-CNE result, and the right is the LTE result. The streamlines are almost the same between the results by the 2T-CNE and the LTE model.

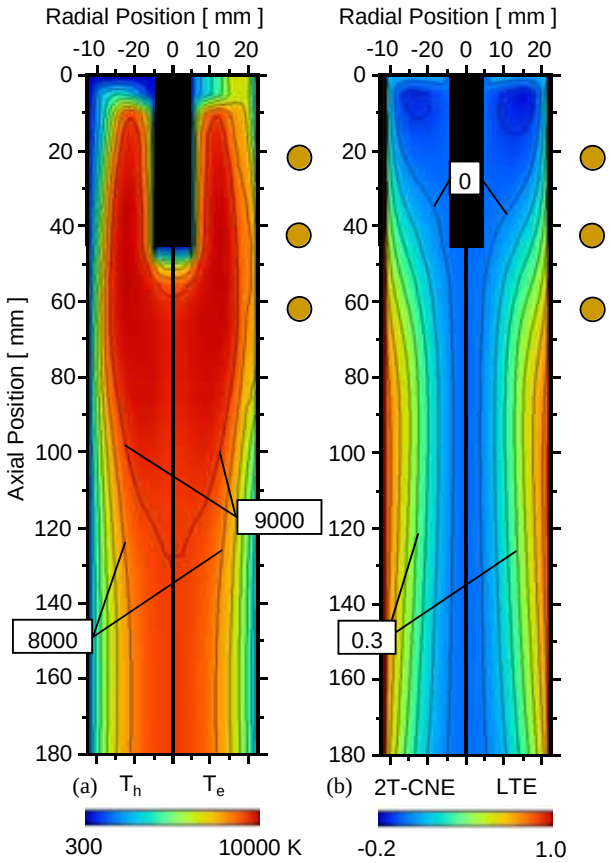

Fig. 6 (a) Heavy particle (left) and electron temperature (right), (b) streamlines by 2T-CNE (left) and LTE (right) model in an argon plasma.

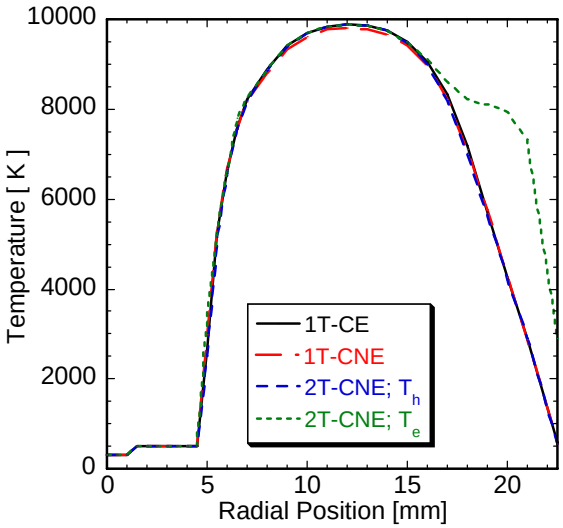

Fig. 7 Radial temperature distributions by three models in argon plasma at the center of the coil.

The calculated temperature (a), streamlines (b), and concentration contours of oxygen atom (c) in an argon-oxygen plasma are shown in **Fig. 8**. The electron temperature near the torch wall of the coil region is higher than the heavy particle temperature, indicating the same trend in an argon plasma. Oxygen atoms distribute broadly in the torch due to the low dissociation energy of O_2. Comparison of the number densities estimated by the 2T-CNE and the LTE model in an argon-oxygen plasma at the center of the coil are shown in **Fig. 9**. Deviation from the equilibrium composition exists near the torch wall, because the diffusion rate is larger than the recombination rate in this region.

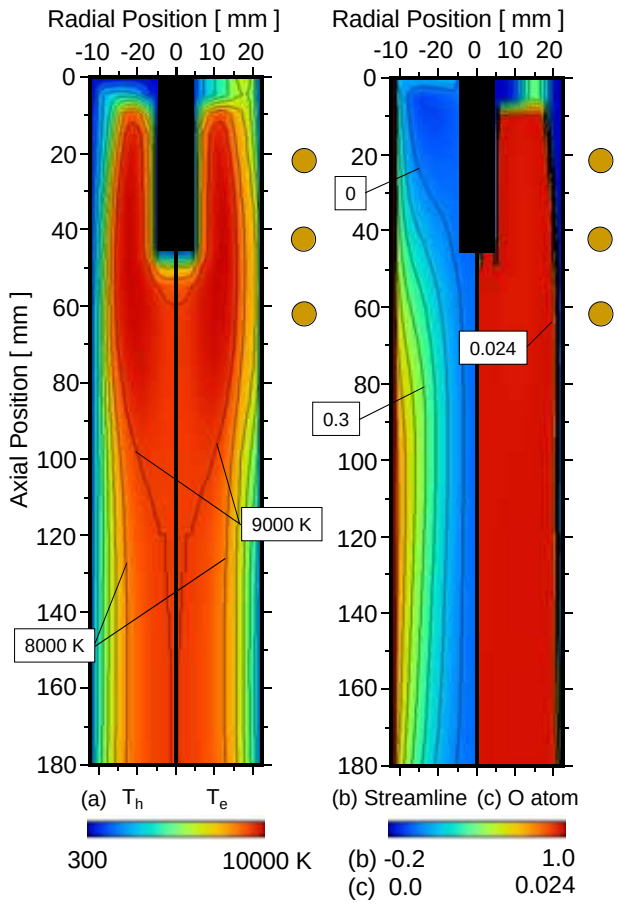

Fig. 8 (a) Heavy particle (left) and electron temperature (right), (b) streamlines (left) and oxygen atom distribution (right) in an argon-oxygen plasma.

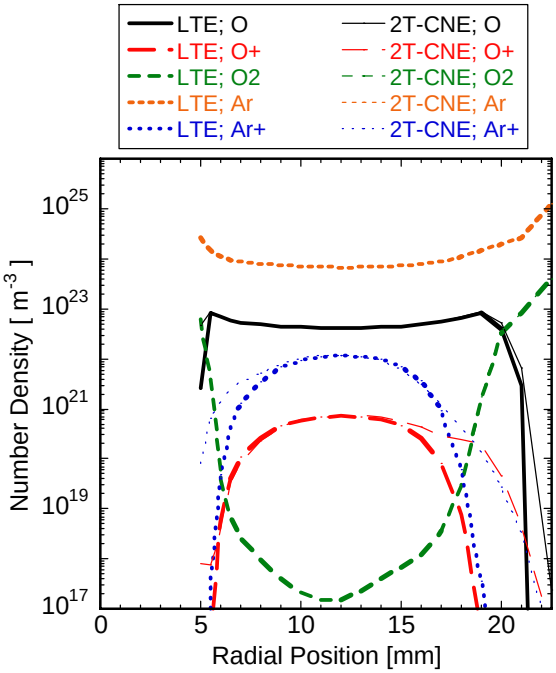

Fig. 9 Comparison of number densities between LTE and 2T-CNE model in an argon-oxygen plasma.

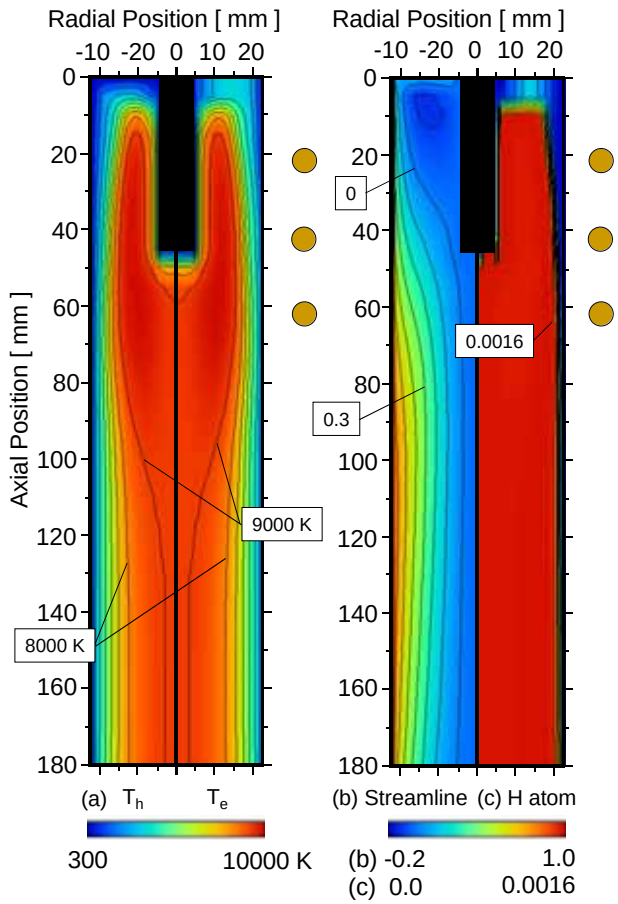

Fig. 10 (a) Heavy particle (left) and electron temperature (right), (b) streamlines (left) and hydrogen atom distribution (right) in an argon-hydrogen plasma.

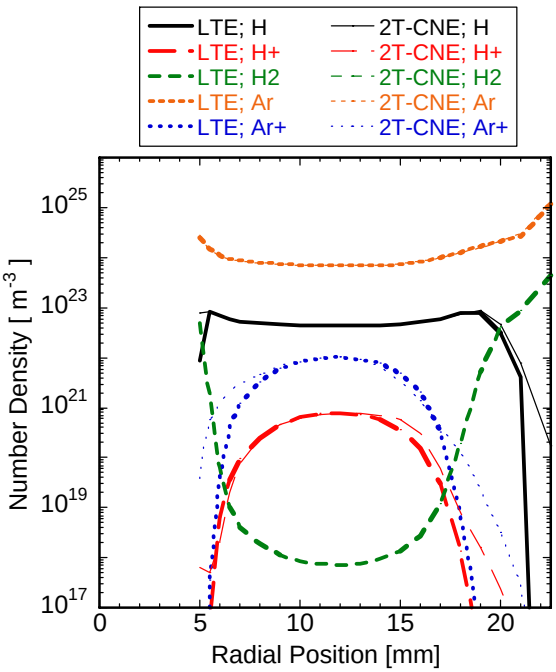

Fig. 11 Comparison of number densities between LTE and 2T-CNE model in an argon-hydrogen plasma.

The calculated temperature (a), streamlines (b), and concentration contours of hydrogen atom (c) in an argon-hydrogen plasma are illustrated in **Fig. 10**. Deviation between the electron temperature and the heavy particle temperature is small near the torch wall. The streamlines are almost the same with an argon and an argon-oxygen plasma. Hydrogen atoms distribute broadly in the torch due to the low dissociation energy of H_2. Comparison of number densities by the LTE with the 2T-CNE model in an argon-hydrogen plasma at the center of the coil are shown in **Fig. 11**. The deviation from the equilibrium composition exists near the torch wall, resulting in the similar characteristics in an argon-oxygen plasma.

Thermal non-equilibrium presented by the calculated results can be explained from the electron energy balance. The energy exchange from electrons to heavy particles is balanced to Joule heating rate in the region of $T_h \neq T_e$.

$$\sum_{i \neq e} \frac{3}{2} k(T_e - T_h) \frac{2 m_i m_e}{(m_i + m_e)^2} \nu_{ei} = \mathbf{J} \cdot \mathbf{E} \qquad (9)$$

In an argon-hydrogen plasma, the collision frequency (ν_{ei}) between electrons and heavy particles is higher than that of an argon and an argon-oxygen plasma near the torch wall due to larger collision integral between electrons and hydrogen atoms. Therefore, thermal non-equilibrium is weak in an argon-hydrogen plasma.

The degree of CNE (chemical non-equilibrium), δ, and Damkohler number, ζ, were introduced to evaluate chemical non-equilibrium in plasmas,

Degree of dissociation: $\delta^d_{O_2} = \dfrac{[O]^2}{[O_2]K_d}$ (10), Degree of ionization: $\delta^i_O = \dfrac{[O^+][e^-]}{[O]K_i}$ (11),

Damkohler number: $\varsigma = \dfrac{\delta_d}{\delta_r}$ (12).

where τ_d and τ_r are the characteristic times of diffusion and reaction, respectively. In these definition, $\delta = 1$, $\zeta \to \infty$ express equilibrium, $\delta \neq 1$, $\zeta \to 0$ indicates non-equilibrium.

The Damkohler number and the degree of CNE due to dissociation at the center of the coil region are shown in **Fig. 12**. The result of an argon-nitrogen plasma was taken from Ref. [6]. Near the torch wall, the degree of dissociation is high, then the corresponding Damkohler number is small. Consequently, the Damkohler number is strongly related to the degree of CNE. In an argon-nitrogen plasma, chemical non-equilibrium is more noticeable near the torch wall than that in an argon-oxygen and an argon-hydrogen plasma due to high dissociation energy of N_2. The corresponding Damkohler number is smaller in an argon-nitrogen plasma. Therefore, Damkohler number can be used as the indication to evaluate the degree of chemical non-equilibrium.

As a result, the present modeling reveals that thermal non-equilibrium and chemical non-equilibrium exist near the torch wall. Furthermore, Damkohler number is useful indication to evaluate the degree of chemical non-equilibrium in plasmas.

4. References

[1] M. Sakano, M. Tanaka, and T. Watanabe, Thin Solid Films, **386**, 189 (2000)

[2] J. O. Hirschfelder, C. F. Curtiss, R. B. Bird, Molecular Theory of Gases and Liquids, John Wiley, New York, (1964)

[3] T. Watanabe and N. Sugimoto, Thin Solid Films, **457**, 201 (2004)

[4] M. I. Hoffert and H. Lien, Phys. Fluids, **10**, 1769 (1967)

[5] S. V. Patanker, Numerical Heat and Fluid Flow, McGraw-Hill, New York, (1980).

[6] Y. Tanaka, J. Phys. D: Appl. Phys., **37**, 1190 (2004)

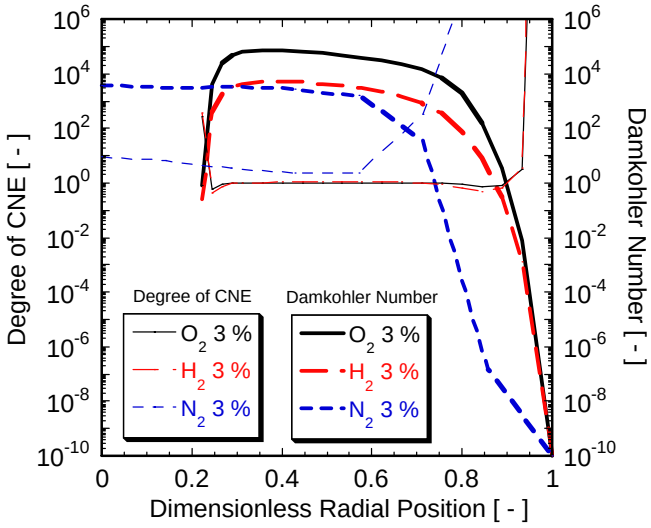

Fig. 12 Relationship between Damkohler number and degree of CNE due to dissociation.

CFC Destruction by Steam Plasmas Generated by Atmospheric DC Discharge

Takayuki Watanabe[1], Taira Tsuru[1], and Akihiro Takeuchi[2]

[1] *Department of Environmental Chemistry and Engineering, Tokyo Institute of Technology, Yokohama 226-8502, Japan*
[2] *Chubu Electric Power Co., Inc., Nagoya 459-8522, Japan*

Abstract
Characteristics of 100%-steam plasma with DC discharge were investigated for the application of halogenated hydrocarbon decomposition. The presented steam plasma system is portable light-weight plasma generation system that does not require gas supply unit. The system has high-energy efficiency resulting from the unnecessity of water-cooling. The decomposition efficiency of 99.9% was obtained up to 0.43 mmol/kJ of the ratio of HFC-134a feed rate to the arc power.

1. Introduction

Halogenated hydrocarbons have been used widely as refrigerant, working fluid, foaming agent for plastics and insulating material, solvent, because of inflammability, no toxicity, and chemical stability. However, chlorofluorocarbons (CFCs) are revealed to be the matter of global warming and ozone depleting. Therefore, manufactures of CFCs have been prohibited by Montreal Protocol since 1987. Destruction of CFCs as well as research for the alternatives has been required.

CFCs can be effectively decomposed by reaction with hydrogen and oxygen; hydrogen combine with halogen to form halogenated hydrogen, oxygen combine with carbon to form CO and CO_2 to prevent reformation of by-products. Thus, destruction of CFCs with hydrogen and oxygen was demonstrated by argon plasmas [1]. However, hydrogen has disadvantage of high cost and explosibility, therefore steam plasmas that produce hydrogen and oxygen at high temperature are more favorable for industrial application of waste treatment. Radio frequency (RF) steam plasmas have performed high level destruction with ppm range concentration of destructed CFCs or halon in the exhaust gas [2]. Besides, small microwave steam plasmas for CFCs destruction have been used commercially [3].

Direct current (DC) plasma can be generated efficiently with simpler configuration than RF and microwave plasmas. Applications of DC argon plasma for CFCs destruction have already been operated with injection of oxidizing gas such as steam and oxygen [4-6]. DC steam plasma process was also applied to various waste treatments such as decomposition of PCB [7]. Nevertheless, the electrodes require protection from erosion derived from high reactivity of steam plasmas. In the PCB decomposition, tungsten cathode is protected by nitrogen or argon. In the steam plasma generation with several plasma gases, thoriated tungsten cathode is protected by using hydrogen [8].

Plasma generation system generally requires complex sub-equipments such as gas supply unit or cooling system. Especially steam plasma system requires sub-equipments such as heater to prevent condensation of steam through the reactor. Thus, efficient steam plasma generation system has been required for industrial application. The purpose of this paper is to generate stable steam plasma using portable light-weight DC plasma system without water-cooling and gas supply unit. Another purpose is to investigate decomposition mechanism of hydrofluoroethylene (HFC-134a) by the steam plasma.

2. Thermodynamic consideration

Thermodynamic equilibrium was calculated from the minimization of Gibbs free energy of the system with assumption that complete thermodynamic equilibrium is achieved. The chemical composition obtained from the calculation is probably not practical, however the thermodynamic equilibrium is useful to assess the important species in CFC decomposition. Thermodynamic equilibrium was calculated by FACT (Centre for Research in Computational Thermochemistry, Canada) to determine the species in plasma. FACT is database software for searching chemical equilibrium composition in which Gibbs free energy is the lowest.

Thermal equilibrium composition of pyrolised HFC-134a is shown in **Fig. 1**. CF_4 is the stable by-product under 2500 K, while HFC-134a does not exist. In the destruction of HFC-134a, suppresion of CF_4 production is strongly required, because the global warming potential (GWP) of CF_4 is 6500 times higher than that of CO_2. Chemical composition of water is shown in **Fig. 2** as function of temperature. H_2O dissociates to O and H at 3500 K. These dissociated O and H play important roles in the reformation control of undesirable

by-products.

Thermal equilibrium composition of HFC-134a decomposition with steam is presented in **Fig. 3**. The ratio of HFC-134a to steam is decided from the stoichiometric coefficient of following reaction.

$$C_2H_2F_4 + 4H_2O \rightarrow 4HF + 3H_2 + 2CO_2$$

Hydrofluorine is the most stable fluoride under 3800 K without undesirable by-products. Therefore, steam plasmas are suitable for decomposition of HFC-134a. HFC-134a with steam produces H_2 and CO from 800 K to 3500 K, resulting in reduction atmosphere.

Thermal equilibrium composition of HFC-134a decomposition is shown in **Fig. 4** in the case of low supply of steam:

$$C_2H_2F_4 + 2H_2O \rightarrow 4HF + H_2 + 2CO.$$

Hydrofluorine is the most stable fluoride under 4400 K without undesirable by-products.

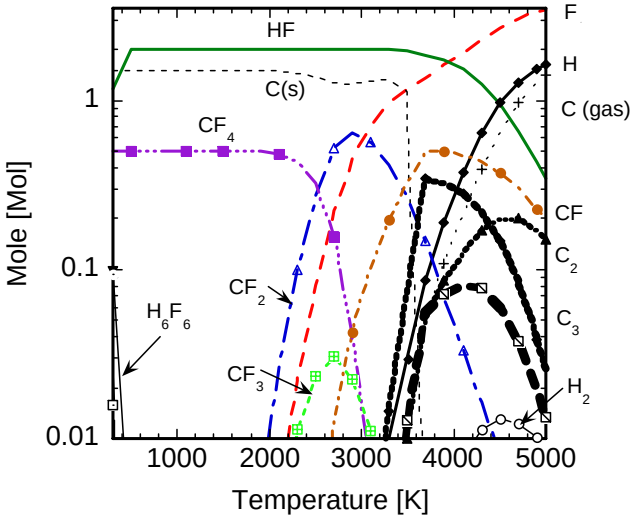

Fig. 1 Equilibrium composition of pyrolized HFC-134a.

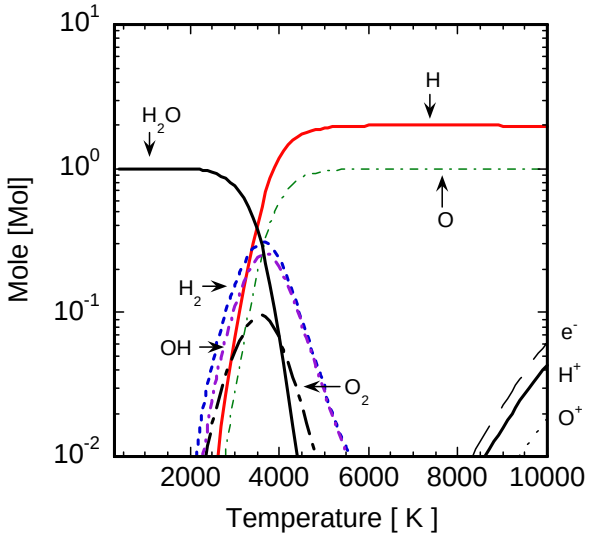

Fig. 2 Equilibrium composition of H_2O

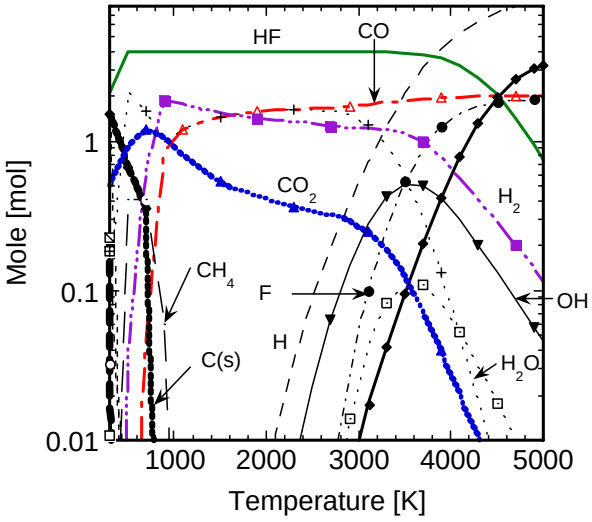

Fig. 3 Equilibrium composition of 20mol% HFC-134a and 80mol% steam.

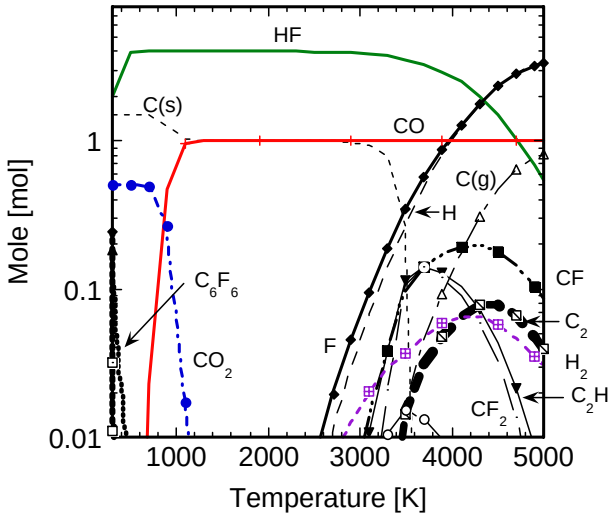

Fig. 4 Equilibrium composition of 33mol% HFC-134a and 67mol% steam.

3. Steam Plasma Generation

The steam plasma torch is a DC thermal plasma generator of coaxial design with a cathode of hafnium embedded into the copper rod and a nozzle-type copper anode. When steam plasmas are applied to waste treatment, the use of additional steam generator is unsuitable, because the steam generator requires larger and complicated system including the heating-up of the water feeding line preventing steam from condensation. The presented plasma torch can generate 100%-steam plasma without commercially available steam generator.

The configuration of the DC steam plasma torch is presented in **Fig. 5**. The advantage of the presented steam plasma torch is generation of 100%-steam plasma by DC discharge. The features of the torch result from the simple steam generation; water from the reservoir is heated up and evaporated at the anode region to form the plasma supporting gas. Simultaneously, anode is cooled by the water evaporation, therefore the electrodes do not require additional water-cooling. The distinctive steam generation method provides the portable light-weight plasma generation system that does not require the gas supply unit, as well as the high energy efficiency resulting from the unnecessity of the additional water-cooling.

The arc power was 0.65-1.47 kW with the arc current of 4.0-7.0 A. During the arc discharge, water feed rate is set at 325 mmol/min.

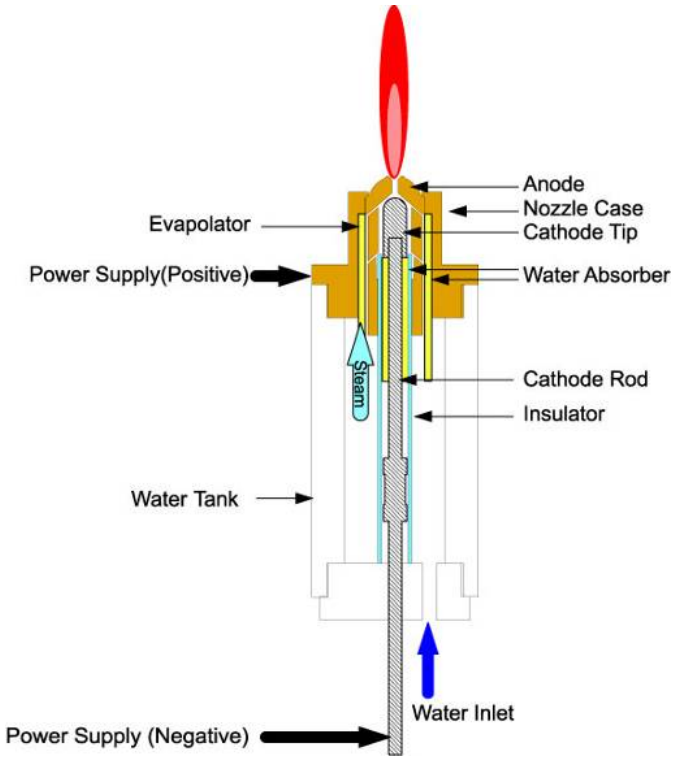

Fig. 5 Schematic diagram of steam plasma torch with DC discharge.

4. CFC Destruction System

Reaction tube and neutralization vessel are presented in **Fig. 6**. Reaction tube is water-cooled Inconel C-276 tube with inside diameter of 14 mm. Inconel C-276 is used as corrosion resistance material. HFC-134a was injected from the water-cooled tube at 8 mm upper from the nozzle exit of the steam plasma and at 7 mm outer from the center. Neutralization vessel is combined to the reaction tube to absorb F_2 and HF generated from the HFC-134a decomposition. Neutralization vessel is filled with pure-water monitored with pH meter. The destruction was performed with changing the feed rate of HFC-134a up to 185 mmol/min. The gas chromatography for monitoring of the exhaust gas indicated that productions of by-product such as CF_4 were not found. After the decomposition of HFC-134a, total organic compounds (TOC) and organic compound (OC) were measured to estimate the by-product concentration in the water with the pH measurements by

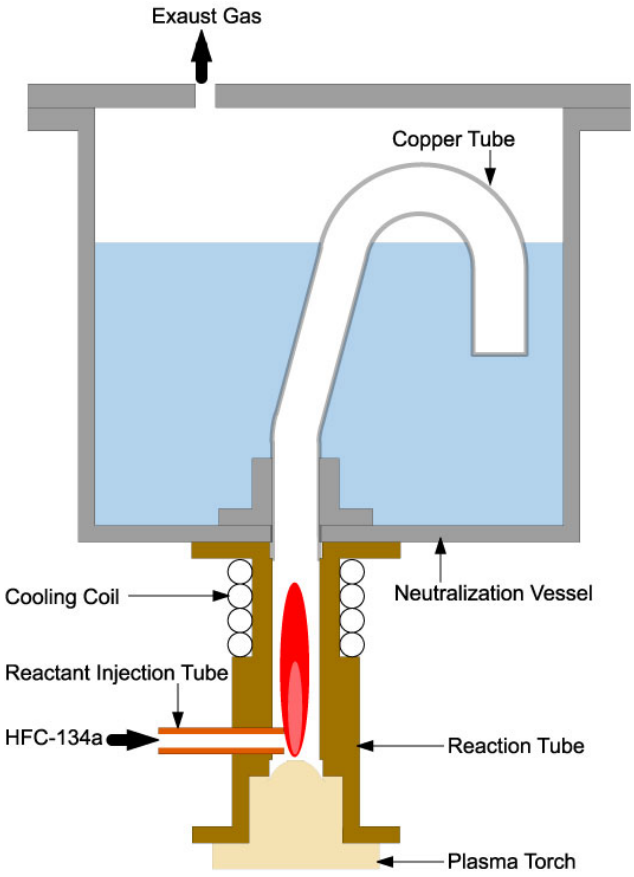

Fig. 6 Schematic diagram of CFC destruction system with steam plasma generator and neutralization vessel.

neutralization titration.

5. CFC Decomposition Results

The decomposition efficiency of HFC-134a can be evaluated from the recovery of the fluorine which is produced from the decomposition. Fluorine in the decomposition gas easily dissolves in water, therefore the recovery of fluorine is a good indication of the HFC-134a decomposition. The exhaust gas composition also provides the decomposition efficiency, however the estimation of the decomposition efficiency is complicated owing to the unknown peaks of the gas chromatographs and to the calibration of all peaks.

The decomposition results of HFC-134a with different injection locations are presented in **Fig. 7**. The recovery of fluorine was estimated from the pH measurements by neutralization titration of the water for the exhaust gas treatment after the HFC-134a decomposition. The injection of HFC-134a at the 8 mm from the nozzle exit of the steam plasma gives the complete recovery of fluorine, indicating the complete decomposition of HFC-134a. More downstream injection of HFC-134a leads to a decrease in the recovery of fluorine, because the plasma temperature decreases with the distance form the nozzle exit.

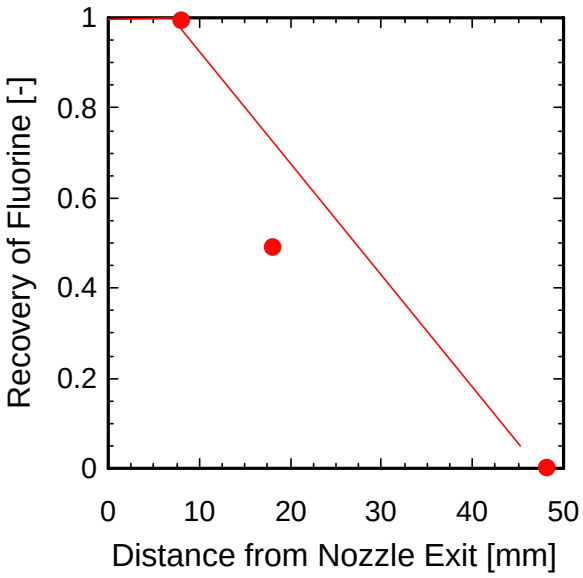

Fig. 7 Effect of HFC-134a injection location on recovery of fluorine. Arc power: 1.10 kW.

The effect of injection location of HFC-134a on the exhaust gas composition is shown in **Fig. 8**. HFC-134a injection at shorter distance from the nozzle exit leads to larger production of CO and CO_2. These results indicate the enhanced decomposition can be obtained from the HFC-134a injection at higher temperature. Besides, the selectivity of CO decreases with the distance, because the selectivity of CO decreases with a decrease in the decomposition temperature. This trend can be also expected from the equilibrium composition as shown in Figs. 3 and 4.

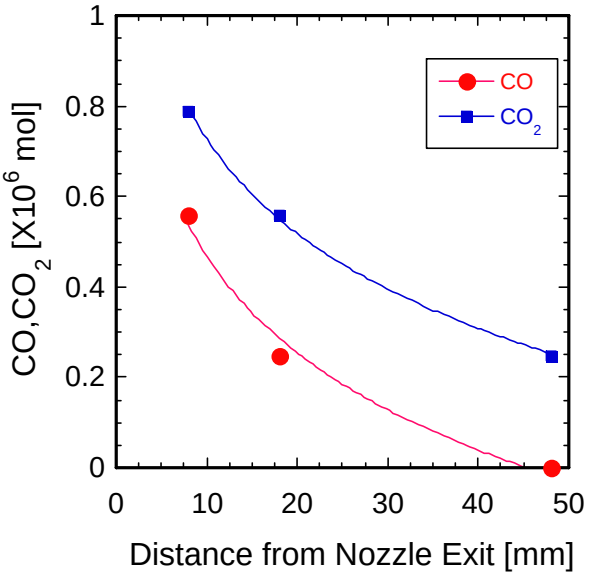

Fig. 8 Effect of HFC-134a injection location on CO and CO_2 production. Arc power: 1.10 kW.

The feed rate of HFC-134a into the high-temperature region has critical effect on the decomposition, because the maximum feed rate of HFC-134a depends on the enthalpy of the plasma. The effect of the feed rate on the recovery of fluorine is presented in **Fig. 9**. The recovery of fluorine at 99.9% can be obtained at 23 mmol/min of HFC-134a feed rate and at 1.47 kW of the arc power. The feed rate of HFC-134a over the threshold brings about the sudden decrease in the recovery of fluorine.

The effective decomposition is related to the feed rate of HFC-134a as well as the arc power, therefore the ratio of the feed rate to the arc power was calculated to estimate the decomposition efficiency. The effect of the ratio of the feed rate to the arc power on the recovery of fluorine is shown in **Fig. 10**, showing the comparable decomposition efficiency of the presented system with other CFC destruction systems. The recovery of fluorine with 99.9% can be obtained up to 0.43 mmol/kJ, hence the maximum feed rate is estimated to be 160 g/h at 1 kW of the arc power.

Effect of the feed rate of HFC-134a on CO_2 and CO production in the exhaust gas is shown in **Figs. 11** and **12**, respectively. Larger feed rate of HFC-134a leads to decreasing of CO_2 and CO production. This is

due to the temperature decrease owing to the larger feed rate of HFC-134a and to the insufficient mixing of HFC-134a at the high-temperature region of the steam plasma. Moreover, larger amount of CO is produced at higher arc power, resulting from the enhanced decomposition.

Fig. 13 presents the effect of feed rate of HFC-134a on the selectivity of CO in the exhaust gas. The selectivity of CO decreases with increasing of the feed rate of HFC-134a and with decreasing of the arc power, because CO is more stable than CO_2 at higher temperature. The temperature decrease in the plasma resulting from larger feed rate of HFC-134a is predictable from Fig. 13.

Analysis of by-product from the HFC-134a decomposition is presented in **Fig. 14**. Total organic carbon (TOC) in the water for the exhaust gas treatment was measured after the decomposition. There is a tendency of a decrease in TOC with increasing of the feed rate of HFC-134a, but the TOC can be negligible compared with the solubility of HFC-134a in water (1.5×10^{-2} mol/L). The measured organic carbon (OC), which is not shown, is also negligible in the water. Therefore, the main component in the water is HF after the HFC-134a decomposition.

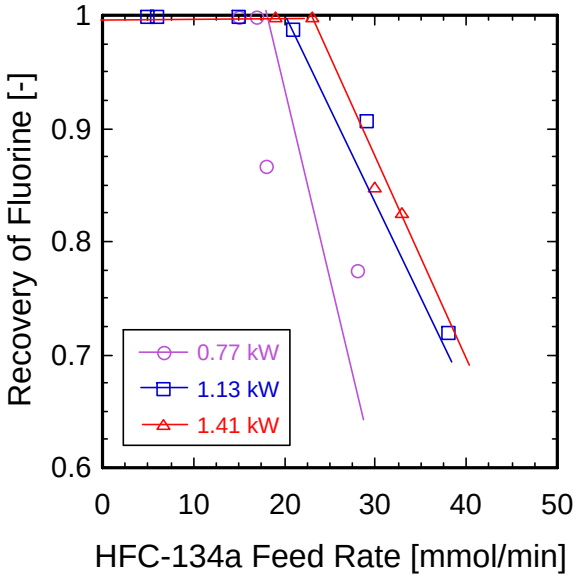

Fig. 9 Effect of HFC-134a feed rate on recovery of fluorine.

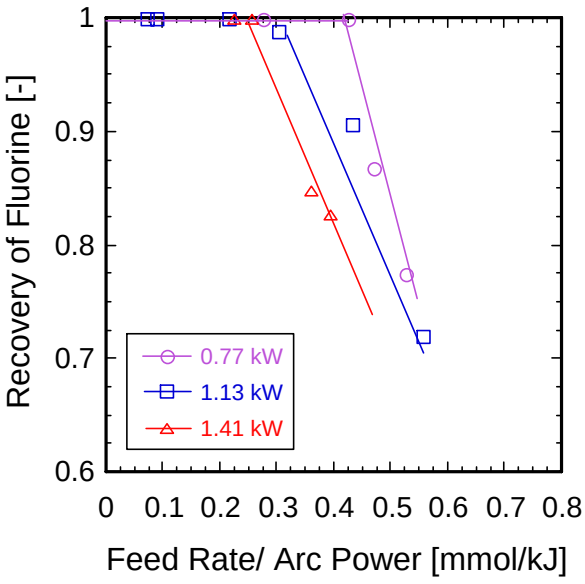

Fig. 10 Recovery of fluorine as a function of the feed rate normalized to the arc power.

6. Conclusions

Stable DC 100%-steam plasma generation under atmospheric pressure was developed for CFC decomposition.

Decomposition of HFC-134a produces CO, CO_2, and H_2 in the exhaust gas, and HF which can be recovered in the water of the neutralization vessel. The total organic carbon as the by-products after the decomposition can be negligible in the water. The decomposition efficiency of 99.9% can be obtained up to 0.43 mmol/kJ of the ratio of HFC-134a feed rate to the arc power, hence the maximum feed rate is estimated to be 160 g/h at 1 kW of the arc power. More detailed investigation is required to optimize the plasma system for industrial application.

Thermal plasmas such as steam would provide more capability for waste treatments, if thermal plasmas are utilized effectively as chemically reactive gas. Application of plasma systems for waste treatment is expected to downsize the system, reduce hazardous substances in exhaust gas, finally low cost of waste treatment.

4. References

[1] H. Sekiguchi, T. Honda, A. Kanzawa, Plasma Chem. Plasma Processing, **13**, 463-478 (1993)

[2] S. Takeuchi, K. Takeda, N. Uematsu, H. Komaki, K. Mizuno, and T. Yoshida, Proc. 12th Int. Symp. Plasma Chem., **2**, 1021-1026 (1995)

[3] M. Bessho, M. Danno, T. Hattori, T. Ikeda, and Y. Okada, Mitsubishi Heavy Industries Technical Review, **37**, 90-93 (2000)

[4] A. B. Murphy, T. McAllister, Applied Physics Letters, **73**, 459-461 (1998)

[5] A. B. Murphy, Proc. 16th Int. Symp. Plasma Chem., ISPC-492 (2003)
[6] A. B. Murphy, A. J. D. Farmer, E. C. Horrigan, and T. McAllister, Plasma Chem Plasma Processing, **22**, 371 (2002).
[7] S. W. Kim, H. S. Park, H. J. Kim, Vacuum, **70**, 59-66 (2003)
[8] B. Glocker, G. Nentwig, E. Messerschmid, Vacuum, **59**, 35-46 (2000)

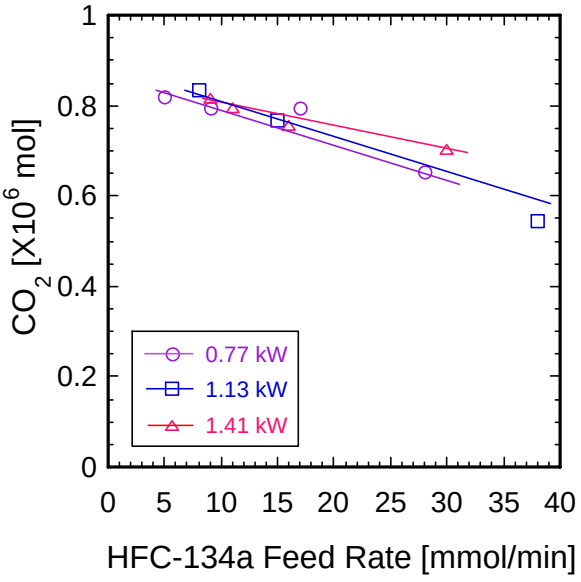

Fig. 11 Effect of f HFC-134a feed rate on CO_2 production in exhaust gas.

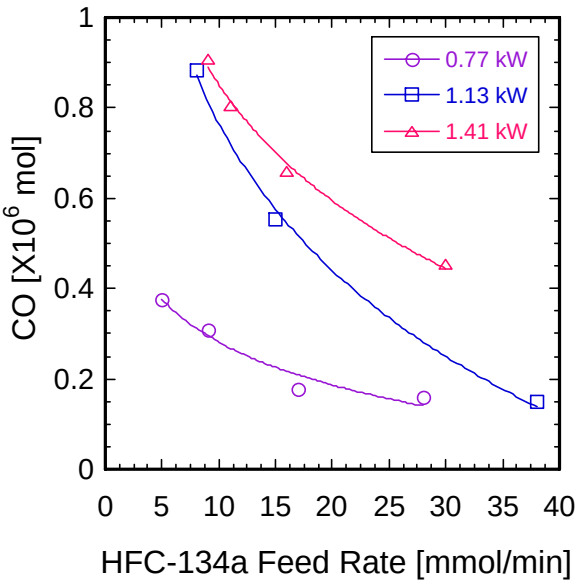

Fig. 12 Effect of HFC-134a feed rate on CO production in exhaust gas.

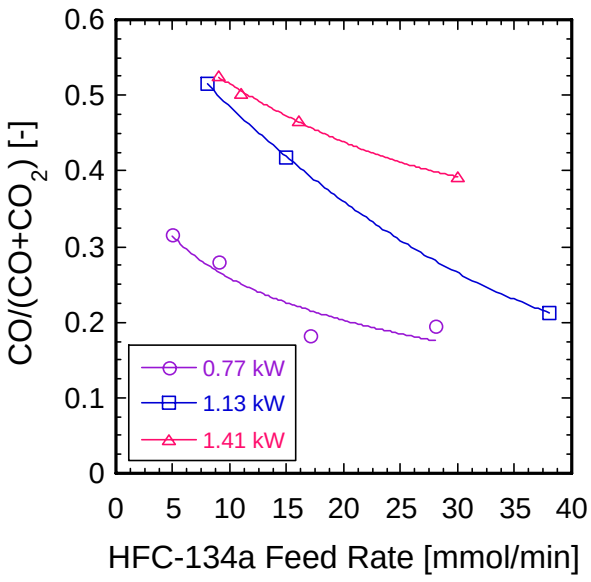

Fig. 13 Effect of HFC-134a feed rate on selectivity of CO in exhaust gas.

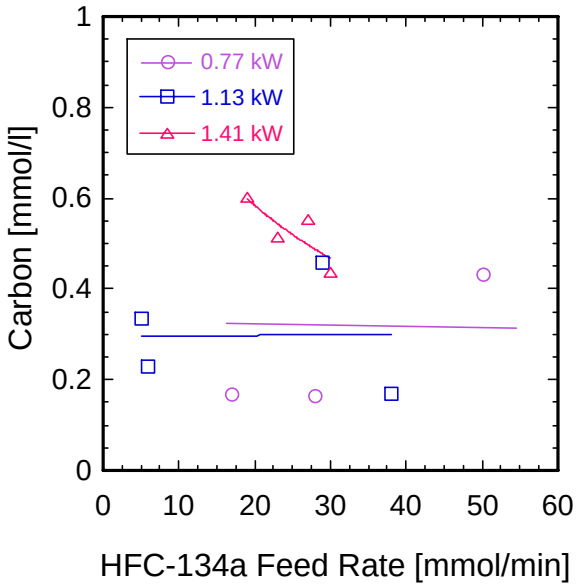

Fig. 14 Total organic carbon in water of neutralization vessel after decomposition.

Optical Dynamics Measurement in Laser Ablation TiO_2 Plasma Plume

T. Ohshima[1], S. Nakashima[1], Y. Matsunaga[1], H. Kawasaki[1], Y. Suda[1] and K. Ebihara[2]

[1]*Department of Electrical Engineering, Sasebo National College of Technology, Nagasaki, Japan*
[2]*Department of Electrical and Computer Engineering, Kumamoto University, Kumamoto, Japan*

Abstract

We have investigated the temporal and spatial resolved optical emission properties of the TiO_2 plasma plume generated by laser ablation using Nd:YAG laser. Emissions are dominated at neutral and ionic Ti (Ti I, Ti II) or neutral O (O I), and there are no emission species such as molecular TiO, TiO_2 and ionized molecular O_2. Ti I and Ti II species move with high speed of 1×10^4 m/s at the distance of 0.5 mm from the target. 2-dimentional ICCD images of plume emission indicated that spatial distributions of Ti I and Ti II species were different to each other.

Keywords: Laser ablation; Plasma plume; Titanium dioxide; Optical emission spectroscopy

1. Introduction

Pulsed laser ablation (PLA) has been used to prepare functional thin films. In order to fabricate high quality functional thin films and nano-structure materials, it is required to investigate the properties of pulsed laser ablation plumes. Especially, it is important to know the correlation between the plasma properties and characteristic of the deposited films. Optical emission spectroscopic (OES) analysis has been used to measure the plasma plume. OES measurement can monitor the in-situ ablation process without the external affect [1].

Titanium dioxide (TiO_2) has attracted much attention for its photocatalytic applications in the field of environmental sanitation. In previous research, we prepared TiO_2 thin films at various deposition parameters (ambient gas, substrate temperature, target materials, post-annealing) by using PLD technique and reported on the relationship between the deposition parameters and film properties such as crystalline structure, morphology, chemical composition and decolorization ability [2]. Recently, the development of photocatalysts shows a high activity under visible and/or solar light irradiation. Visible light photoactivity has been introduced to TiO_2 by doping of nitrogen or transition metals such as Cr and Pt. We have also attempted to synthesize nitrogen doped $TiO_{2-x}N_x$ thin films using TiN target in a nitrogen/oxygen gas mixture by PLD [3]. In photocatalytic test using methylene blue solution, the deposited $TiO_{2-x}N_x$ thin film was energized by visible light irradiation as well as UV light irradiation. However the correlation between the properties of the deposited films and the plasma characteristics has not been found.

This paper demonstrates a detailed spectroscopic investigation of plasma plume produced during the film deposition in order to estimate the processing plasma state and prepare high quality TiO_2 or $TiO_{2-x}N_x$ thin films. The temporal and spatial distributions and the optical emission species of plasma plume at various states using target materials and ambient gases were observed through a spectrometer and an ICCD camera.

2. Experimental

Experimental setup for measuring laser-ablated plasma plumes is shown in Fig. 1. A Nd:YAG laser (Continuum SureliteIII; wavelength of 532 nm, pulse duration of 3.5 ns, maximum output energy of 340 mJ) with a laser fluence of 4 J/cm^2 and a repetition rate of 10 Hz was used for ablating Ti (purity 99.99 %), TiN (purity 99.9 %) and TiO_2 (purity 99.99 %) targets. The vacuum chamber was evacuated to a base pressure of 5×10^{-4} Pa by a turbomolecular pump, and then filled with O_2 gas or N_2 gas or a mixed (O_2+N_2) gas of 10Pa at a flow rate of 20 sccm. Optical emission spectra were recorded through a spectrometer (Hamamatsu Photonics PMA-11) in the range of 200-800 nm at time delays (τ_d) varying from 50 to 1500 ns and distances (d) of 0.5-10 mm from the target surface. Two-dimensional plasma emission images were observed through an ICCD camera (Hamamatsu Photonics PMA-11). The gate width of 20 ns was kept fixed for the optical emission spectra and ICCD images measurements.

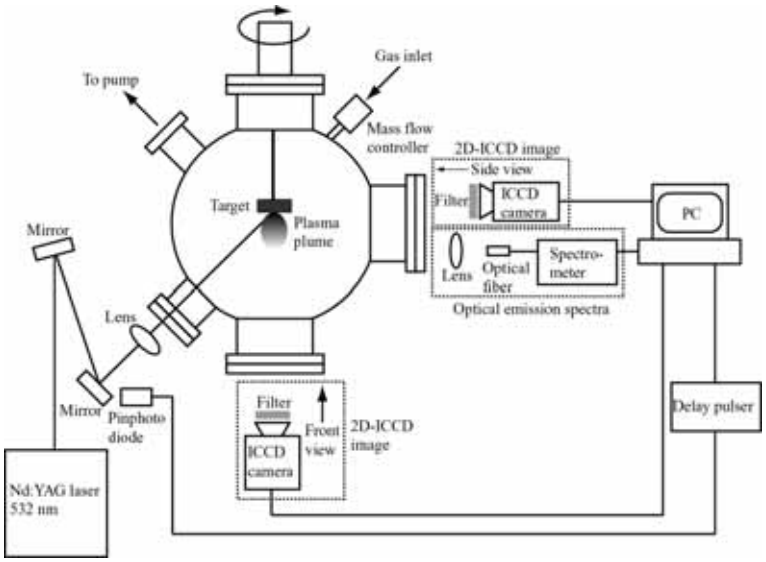

Fig.1 Schematic diagram of the experimental setup.

3. Results and discussions

The optical emission spectra of the plume produced by ablating Ti, TiN and TiO_2 targets in O_2 gas of 10 Pa are shown in Fig. 2. These spectra were measured at the distances (d) of 1-10 mm away from the target with the delay times (τ_d) varying 100-1000 ns after the laser irradiation. Mainly the neutral/ionized titanium species and the neutral oxygen species are seen. However, the molecular species such as TiO, TiO_2, O_2 or molecular oxygen ions were not detected. This worked well with the optical spectroscopic results of the plume emission during a KrF excimer laser (wavelength of 248 nm) ablation process with supplied radio frequency power [4]. Many series of TiO molecule in the range of 550-750 nm were obtained by ablating the Ti target using an ArF excimer laser (wavelength of 193 nm) in accordance with Ref. [5]. However, the emission intensity of the spectra from these molecular species was very weak as compared with other monoatomic species. At d=0.5 mm in Fig. 2 (a), (d) and (g), the strong emission spectrum is observed at τ_d=100 ns, although it becomes weak rapidly after 200 ns. The peak intensity at d=5 mm in Fig. 2 (b), (e) and (h) is maximum at τ_d =200 ns, and it delays further at

d=10 mm of (c), (f) and (i). It was found that the emission plasma plume moved forward from the target.

Figure 3 shows the time delay (τ_d) differences of emission spectral lines of Ti atoms (Ti I, λ=430 nm), Ti ions (Ti II, λ=323 nm), and O atoms (O I, λ=777 nm) at peak intensity as a function of the distance (*d*) from the target. The spectra in the plume generated by ablating TiO_2 targets in O_2 gas of 10 Pa were observed. At near the target surface (*d*=0.5~3 mm), the emission species have high velocities because the peak rises sharply. The velocities of

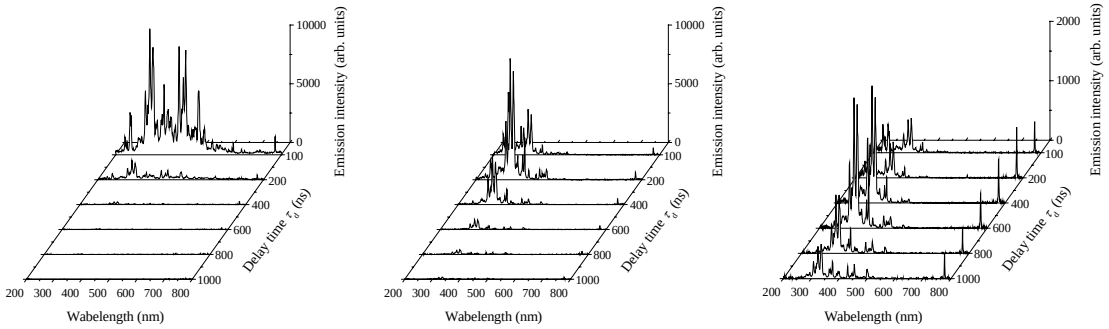

(a) TiO_2 target, *d*=0.5 mm (b) TiO_2 target, *d* =5 mm (c) TiO_2 target, *d* =10 mm

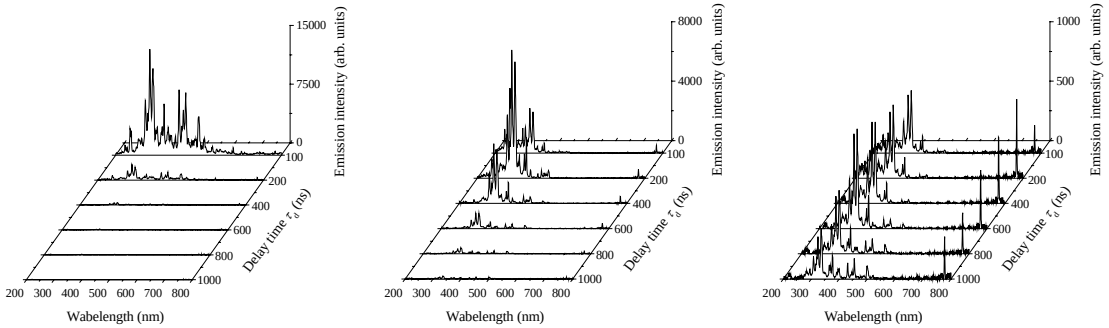

(d) TiN target, *d* =0.5 mm (e) TiN target, *d* =5 mm (f) TiN target, *d* =10 mm

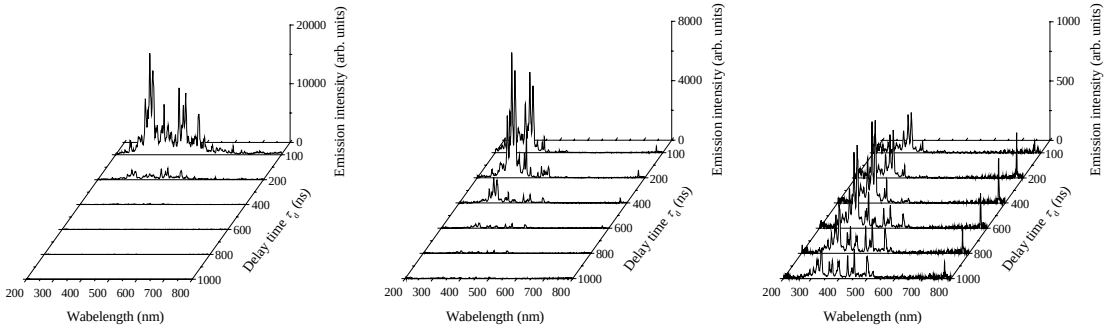

(g) Ti target, *d* =0.5 mm (h) Ti target, *d* =5 mm (i) Ti target, *d* =10 mm

Fig.2 Optical emission spectra of the plasma plume generated by ablating TiO_2, TiN and Ti targets in oxygen gas of 10Pa. Distances *d* from the target surface were varied from 0.5 to 10 mm. Delay times τ_d after the laser irradiation were changed from 100 to 1000 ns.

Ti atoms and ions at d=0.5 mm are 1×10^4 m/s and the kinetic energies are estimated about 50 eV. At further away from the target surface (d=5~10 mm), the peak rises steadily. It was considered that the emission species in the plasma plume lost the kinetic energy by collisions to the ambient gas, so that these species moved with various velocities. The emission intensity of O atoms was very weak compared with Ti atoms and ions over d=1 mm, and there was no dissociation reaction to the ambient O_2 gas.

Figure 4 shows the relationship between the distances (d) and time delays (τ_d) when the intensities of Ti I, Ti II emission lines are at a maximum. The species of Ti atoms and Ti ions reach high velocities immediately after the laser irradiation and later become saturated at τ_d due to collision of excited species and ambient gas. This behavior can be demonstrated with a drag model, which is used to analyze optical emission spectroscopy in the plume during the PLD process of ambient gas [6]. The velocities of Ti ions ablated from TiO_2, TiN and Ti targets are almost same, but the velocities of Ti atoms are different depending on the target.

In order to investigate the distribution of Ti atoms or ions in the plasma plume, the band path filters (Ti I: λ=323 nm, FWHM=10 nm; Ti II: λ=430 nm, FWHM=10 nm) which pass Ti atoms or ions emission from the spontaneous plasma plume emission were mounted in front of the ICCD camera as shown in Fig. 1. Figure 4 shows the side of the plasma plume images ablated from TiO_2, TiN and Ti targets in O_2 gas of 10 Pa at τ_d=100ns. It is found that the distributions of Ti atoms are divided between the tip of the plume and the point near the target although those of Ti ions exist near the tip of the plasma plume. It seems that Ti ions are emitted from the target with the separated velocities. The distribution difference of the Ti atoms or ions depending on the target is observed due to the difference of the ablation process.

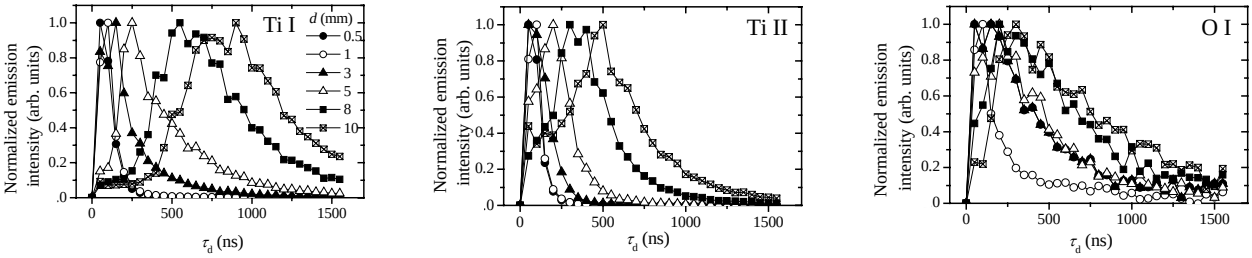

Fig.3 Delay times (τ_d) dependence of the normalized emission intensity of Ti I, Ti II and O I peaks at different distances (d) from the target.

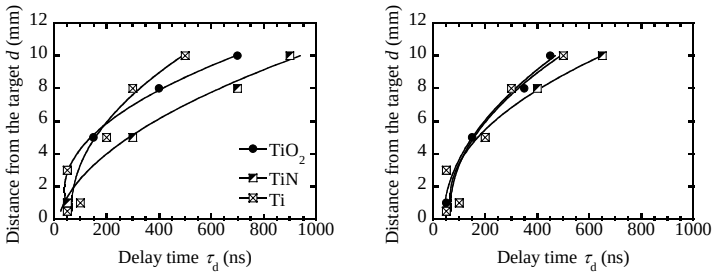

Fig.4 Relation between distances (d) and delay times (τ_d) of Ti I and Ti II emission lines in the plasma plume generated by ablating TiO_2, TiN and Ti targets.

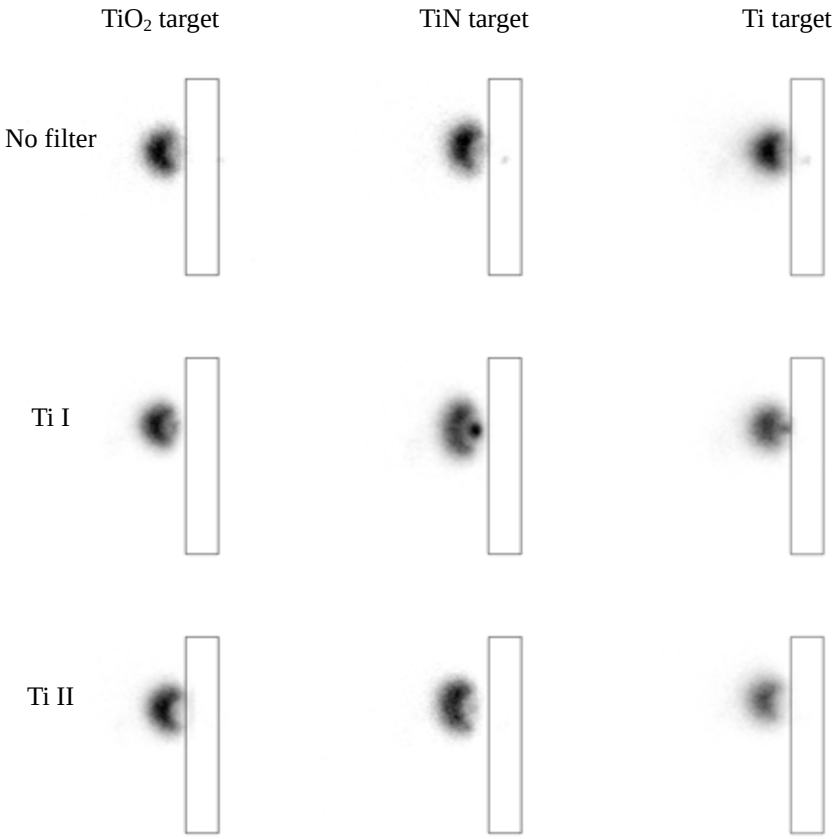

Fig.5 2-dimentional ICCD images of the plasma plume generated by ablating different targets of TiO_2, TiN and Ti using the band path filter.

4. Conclusions

Optical emission spectra of the plume generated by ablating TiO_2, TiN and Ti targets in various ambient gases were predominantly observed Ti atoms and ions. It is revealed that the behavior of Ti atoms and ions in the plume is different by both optical emission spectroscopy and ICCD images.

References

[1] C. Cal, R. Macaluso, and M. Mosca, SpectrochimActa Part B, 56, 743 (2001)
[2] T. Sasaki, K.M. Beck, N. Koshizakai, Appl. Surf. Sci. 197-198, 619 (2004).
[3] Y. Suda, H. Kawasaki, T. Ueda, T. Ohshima, Thin Solid Films 453-454, 162 (2004).
[4] A.De. Gioacomo, V.A. Shakhatov, G.S. Semesi, S. Olando, Spectrochimica ACT A, PART B, 1459 (2001).
[5] S. Kitazawa, Y. Choi, S. Yamamoto, Vacuum 74, 637 (2004).
[6] J.Gonzalo, C.N. Afonso, I. Madariaga, J. Appl. Phys. 81, 951 (1997).

Particles and thin film growth in a dielectric barrier Townsend discharge and in a dielectric barrier filamentary discharge

F. Massines, N. Gherardi, C. Jimenez, S. Martin, A. Fornelli, I. Enache, H. Caquineau, B. Despax

Laboratoire de Génie Electrique de Toulouse, Université Paul Sabatier, 118 route de Narbonne, 31062 Toulouse cedex, France. Email : massines@lget.ups-tlse.fr

Abstract
In this work, thin silicon oxide films obtained in dielectric barrier discharges fed with nitrogen (N_2), nitrous oxide (N_2O) as oxidizer gas, and small admixtures of silane (SiH_4) or hexamethyldisiloxane vapor (HMDSO) as deposit precursor, have been investigated. The aim is to evaluate the importance of the reactivity of the precursor on the deposit properties in order to contribute to a better understanding of the reactive transport taking place in such process.
Keywords
Dielectric barrier discharge (DBD), Atmospheric Pressure Townsend Discharge (APTD), coating, silane, hexamethyldisiloxane (HMDSO), heterogeneous and homogeneous growth, ellipsometry, FT-IR

1. Introduction

The development of a PECVD process working at atmospheric pressure and allowing an easy on-line treatment of films, fibbers and plates is a challenge of great interest. The successful solution will avoid batch treatments and significantly reduce the cost of the coating, allowing an expansion of the use of plasma technologies outside microelectronics. The main questions to be solved are how to get a well controlled thin film in terms of chemical composition, structure and thickness? How to get a high growth rate? Previous to the process development, the main difficulties concern the plasma homogeneity, the gas injection over large dimensions, the control of the atmosphere in the plasma area while the substrate is moving at speed up to 800m/min and the efficiency of the transfer of the reactive species to the surface taking into account the very low diffusion of the neutral radicals.
In case of two dimensional materials like roll of thin polymer films, metal foils or glass plates, dielectric barrier discharge (DBD) appears like the more suitable discharge because it is cold, robust and not disturbed by the movement of the substrate. Furthermore, roll to roll process allowing a very good control of the atmosphere in the DBD is already commercialised. This solution is in competition with remote plasmas but knowing that the quenching of excited state drastically increases with the pressure, as far as the substrate can be moved inside the discharge without inducing perturbation, remote plasmas have to be avoided.
Today, DBDs can be separated in two families: the filamentary one and the homogeneous one which are atmospheric pressure glow discharge (APGD) in noble gases and atmospheric pressure Townsend discharge (APTD) in nitrogen [1]. The reactive gas used for the coating formation is diluted in a main gas which is usually helium, argon or nitrogen. The content of reactive gases or vapours is in the range of 1 to 1000 ppm. In such conditions, several authors obtained uniform coatings [2, 3, 4] but the question of the control of the reactive transport is still open. The aim of this paper is to contribute to answer to that question.
The approach consists in a comparison of silicon oxide thin film obtained with a very reactive gas, the silane (SiH_4) and a more stable vapour, the hexamethydilsiloxane (HMDSO).

2. Experimental

The experimental set-up has been previously described [5]. The discharge being realised between two parallel plates and the gas injection being a longitudinal one, the study is done as a function of the gas residence time in the discharge. The main gas is N_2 and N_2O is the oxidant one. The gas flow, the precursor rate and Si/O ratio as well as the discharge power are the other main parameters. Thin films have been mainly characterised by FT-IR spectroscopy, ellipsometry, SEM and thickness profile.

3. Results and discussion

3.1. Effect of the discharge regime

Attention has been first paid on the effect of the discharge regime on the deposit homogeneity. Usually the DBD consists in microdischarges i.e. different channels of local plasma with mean radius up to 100 µm, but in N_2 a Townsend breakdown leading to a Townsend transient homogeneous discharge (APTD) is obtained in specific conditions:

- If the voltage variation with time is slow enough i.e. for a sinusoidal excitation if the voltage amplitude and frequency are limited. This limitation depends on the power supply and solid dielectric characteristics as well as on the intrinsic cathode secondary emission coefficient of the material in contact with the discharge [1]. More precisely, during Townsend discharge development, the gas impedance drastically changes and then the load connected to the power supply changes from the capacitance due to the solid dielectrics and the gas before breakdown to the capacitance due to the solid dielectric after breakdown. If this variation is too quick, power supply oscillations and then transition to filamentary discharge occur. Moreover, when the Townsend regime is reached, for a given configuration of the discharge cell, the current amplitude is determined by the slope of the applied voltage. If it is too high the streamer development can occur when the cathode secondary emission coefficient decreases due to the removal of the electrons trapped in shallow traps during the previous discharge.

- If an opportune choice of the gas chemical composition is done, which determines the lifetime of the N_2 metastables. This life time has to be long enough to induce a continuous emission of electrons from the cathode during the time between two consecutive discharge pulses. This is an essential condition to get a Townsend breakdown before the electrical field is high enough to have a streamer development.

For these reasons, in the conditions of this study, APTD is obtained for power up to about 2 W/cm^2 (20 W/cm^3), due to a limit frequency of 6 kHz, and for HMDSO or SiH_4 rate lower than about 50 ppm.

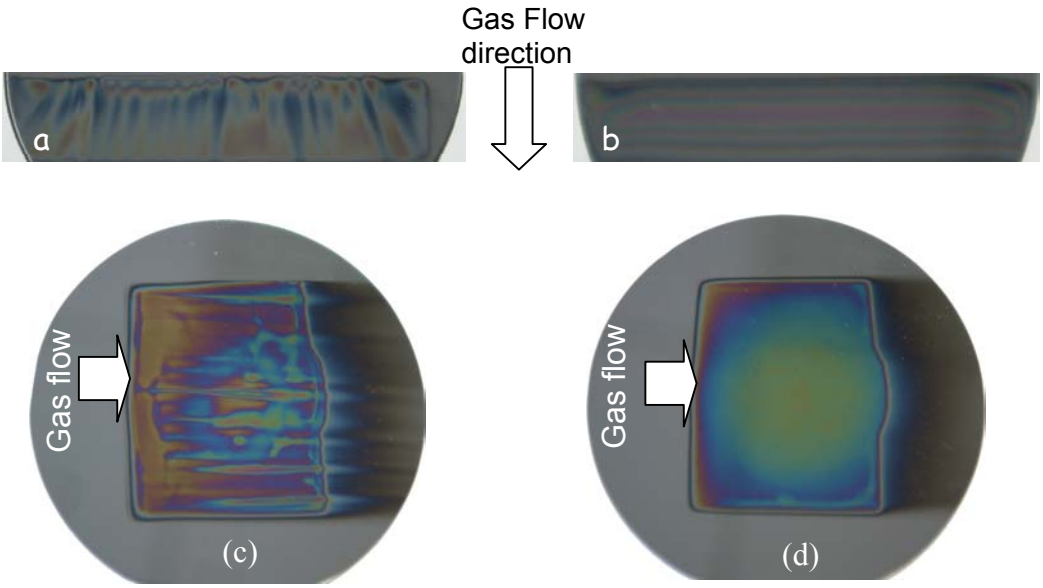

Figure 1: Comparison of silicon oxide coatings made on a silicon wafer with **a)** a $SiH_4/N_2O/N_2$ filamentary DBD, **b)** $SiH_4/N_2O/N_2$ Townsend DBD **c)** a HMDSO/ N_2O/N_2 filamentary DBD **d)** HMDSO/N_2O/N_2 Townsend DBD. The colour is proportional to the thickness showing that whatever the coating precursor, the APTD leads to thin layer uniform in one direction, then if the substrate is moved perpendicularly to this direction, the coating will be uniform.

Photos of the coatings obtained in the two different discharge regimes are reported on the figure 1 for HMDSO and SiH_4. The transition from Townsend to filamentary DBD has been obtained by increasing the HMDSO rate and by increasing the power in case of SiH_4 coating. On the pictures, the color is proportional to the thickness. The coatings thickness appears completely different. In case of filamentary discharge the coating thickness is a fair reflection of the number and localization of the micro-discharges. This is explained by the high density of electrons in a micro-discharge: typically 10^{14}/cm^3, which efficiently dissociates the HMDSO or SiH_4 inducing a local increase of the coating growth. The distribution of the micro-discharge is not uniform enough to ensure a uniform coating. In case of Townsend discharge, the coating is rather

uniform in the direction perpendicular to the gas flow. There is only a small decrease of the thickness close to the wall which is explained by the decrease of the gas flow. This effect is more pronounced with HMDSO than with SiH_4. Obviously, in the direction of the gas flow, the deposit is not homogeneous because of the precursor consumption which is quicker for SiH_4.
The important point to realize a homogeneous coating on a large and flat substrate that can be moved is to be able to make a coating uniform in one direction which will be the direction perpendicular to the substrate displacement. According to our results this is only possible with the APTD. However, some authors report about uniform coatings obtained with a filamentary discharge [6]. Such a result supposes a uniform and reproducible distribution of the micro-discharges which is not so easy to get. Then, the conclusion is that it is easier to get uniform coatings with an APTD than with a filamentary discharge. Consequently, only results concerning deposits obtained using an APTD are further discussed in this work.

3.2. Properties of the deposit using an APTD in standard conditions

The coating properties have been first studied has a function of the position in the gas gap along the direction of the gas flow for given conditions. HMDSO coating is made with 4 ppm of HMDSO, a N_2 gas flow of 5 l/min and 96 ppm of N_2O in order to have a $[N_2O]/[HMDSO]$ equal to 24 which is the stoichiometric ratio for obtaining SiO_2. A dissipated power in the discharge is equal to 0.5 W/cm^2 and the deposition time is 20 minutes. SiH_4 coating is made in similar conditions: 5ppm of SiH_4, a N_2 gas flow of 5 l/min, a SiH_4/N_2O ratio equal to 20, a dissipated power in the discharge equal to 0.35 W/cm^2 and a deposition time of 20 minutes. The length of the electrode in the direction of the gas flow is slightly different: 32 mm for SiH_4 and 25 mm for HMDSO.

Physical properties

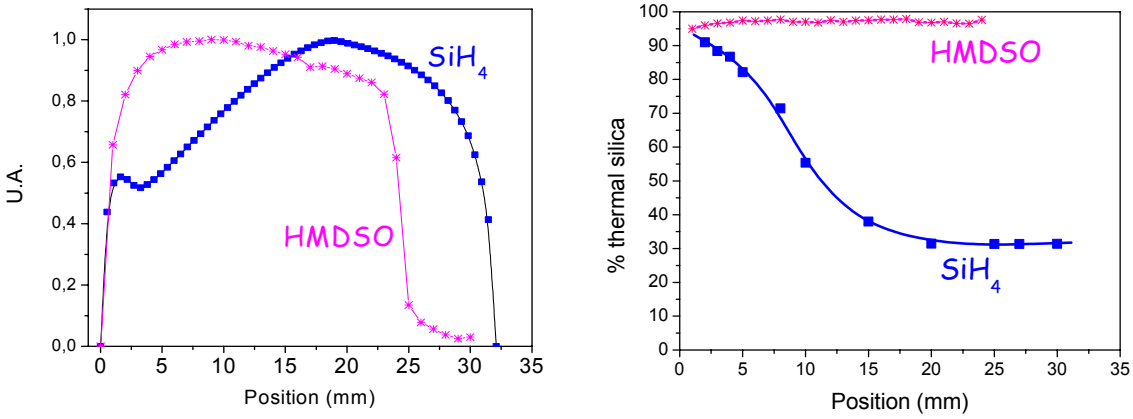

Figure 2: Normalised thickness and percentage of thermal silica deduced from ellipsometry measurements for coating realised with SiH_4 or HMDSO mixed with N_2 and N_2O in the following conditions. HMDSO: 4ppm, N_2O/HMDSO=24, power: 0.5W/cm^2, t=20min ; SiH_4: 5ppm, N_2O/SiH_4=80 , power: 0.34W/cm^2, t=20min. The electrode length is 25 mm for HMDSO and 32 mm for SiH_4. The substrate is not heated and the maximum thickness is about 200nm in the two cases.

The thickness profile is measured with a profiler and is also deduced from ellipsometry assuming the Bruggeman approximation (Figure 2). The deposited layer is generally considered as a mixture of SiO_2 and voids. It clearly shows a very different behaviour for the two precursors. The 2 maxima observed in the case of SiH_4 are no more present in the case of HMDSO while the theoretical percentage of thermal silica largely varies with SiH_4 and not with HMDSO. This large variation has been attributed to the relative contribution of homogeneous and heterogeneous growth [5]. In the SiH_4 case, the thin layer at the gas entrance is due to radicals while for longer gas residence time in the discharge, the contribution of particles becomes dominant. The particle accumulation at the surface forms a very porous layer which explains the small percentage of silica. In HMDSO particles are not formed, and only the radicals participate to the growth. This large difference is due to the reactivity of the precursor in the gas phase. When silane radical is created, it can react

with the surface or with silane in the gas bulk. The competition between these two possibilities limits the contribution of radicals to the thin film growth.
These results are similar to those obtained in low pressure plasma but what is amazing is that the distribution of the particles size is very thin, the mean diameter being around 30nm, and this whatever the discharge regime. The detailed study of the formation and the transport of these particles (through SEM, TEM and laser diffusion) shows that they are constituted of clusters of 10nm in diameter which can grow up to the point where their size is large enough to support a fixed electrical charge. Then, the electrostatic force becomes the most important and pushes them to the surface, as long as the frequency excitation is low enough. In the APTD, even for high power discharges, the time needed to reach the critical size is of some ms and this is why it is possible to get a dense layer without any particles at the entrance of the discharge. Our results show that this is not possible with a filamentary discharge, even for lower power, because the local energy density is so high that the high radicals density induces a quasi-instantaneous particles growth.
The study of the particles shows that the transport to the surface of all the charged species, including of course the ions, is efficient as far as the frequency is maintained to a low value. But the case of the neutral radicals is different as the diffusion is limited. According to the numerical modelling of the reactive transport, under the conditions of this study, using a longitudinal injection, only the SiH_3 created in a boundary layer of about 30µm reach the surface before leading to the particle formation. Then a more efficient injection system has to be found in order to increase the radical contribution to the deposit.

Chemical properties

Whatever the precursor, the same infrared absorptions are observed through FT-IR spectroscopy. The highest absorption at 1070 cm^{-1} is due to stretching vibrational mode of Si-O-Si group that mainly characterizes the film, but not negligible absorption is also attributed to Si-OH group, H-bounded and free, respectively at 3450 cm^{-1} and 3650 cm^{-1}. The film is completely inorganic and there is no nitrogen.

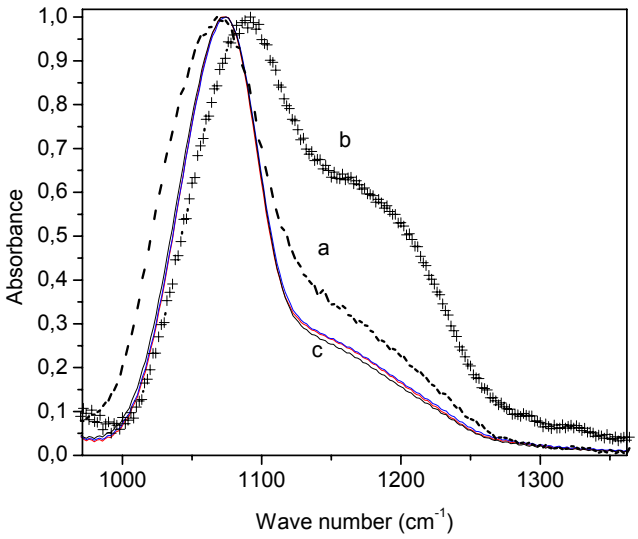

Figure 3: Normalized FT-IR Si-O-Si stretching peak of **a)** SiH_4 coating at the first maximum **b)** SiH_4 coating at the second maximum **c)** HMDSO coating at different positions

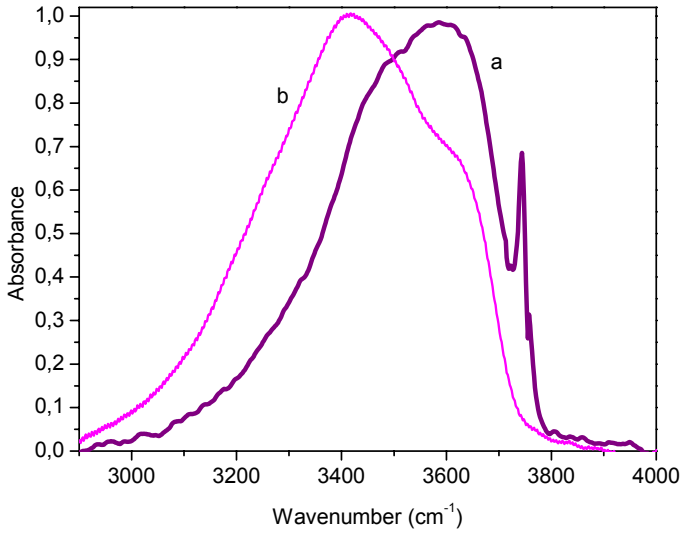

Figure 4: Normalized FT-IR OH band between 3000 and 3800 cm^{-1} of **a)** SiH_4 coating at the second maximum **b)** HMDSO coating at the maximum thickness

With the increase of residence time, from the beginning to the end of the discharge area, a slight increase of Si-OH groups absorption is observed for HMDSO coating. This variation is more significant for SiH_4 coating. However, the main differences concern the shape and the position of the maximum absorption peak attributed to Si-O-Si stretching mode (figure 3). The shape of this peak is characterized by the ratio of the peak shoulder intensity, due to AS2 mode and the main peak intensity, due to the AS1 mode. The position of this peak is related to the angle of the Si-O-Si bonds [7]. Lower is the wave number smaller is the angle and higher is the stress of the Si-O-Si bonds. In coatings obtained in SiH_4 containing plasmas, the

constraint is lower in the particles coming from the homogeneous radical recombination processes than in the thin film grown on substrate thanks to the heterogeneous reactions. The value of 1070 cm^{-1} found for coatings obtained in case of HMDSO-N_2O-N_2, whatever the position in the discharge area is the typical one of thermal silica. Concerning the ratio AS2/AS1, higher is this ratio higher is the disorder of the silica network [8]. In film obtained in SiH_4 containing APTD, this ratio increases with the gas residence time and the consequent contribution of the particles to the film growth. Because of the corresponding higher absorption of Si-OH peak absorption in FT-IR spectra, it is possible to conclude that powders are richer in silanol groups than the dense film. In comparison, coatings obtained using HMDSO have demonstrated to be more similar to thermal silica though a discrete absorption due to silanol groups is observed.

The OH absorption between 3000 and 3800 cm^{-1} also presents some differences (Figure 4). The concentration of non-bounded Si-OH between 3560 and 3800 cm^{-1} is higher in case of porous layer (2nd maximum of SiH_4 coating) and even the surface non-bounded Si-OH are observed at 3750 cm^{-1}, while in HMDSO coatings (due to a radical growth) the bounded Si-OH absorption around 3450 cm^{-1} dominates.

3.3. Influence of process parameters

Among the different process parameters, the precursor concentration and the power have been studied because they usually largely influence the growth rate.

Effect of precursor concentration in the discharge

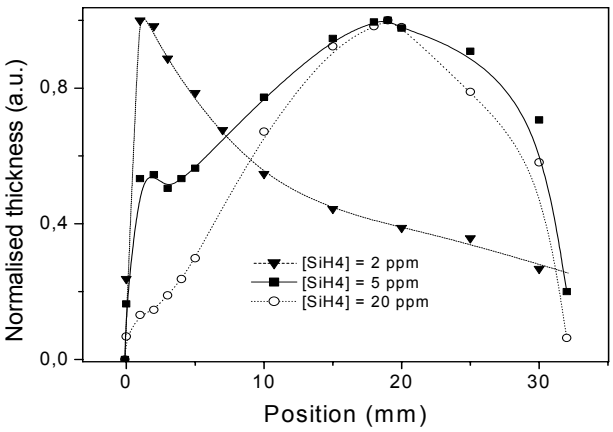

Figure 5: SiH_4 coating thickness profile normalized on their maximum as a function of the distance from the gas inlet for different SiH_4 concentrations all the other conditions being the standard one.

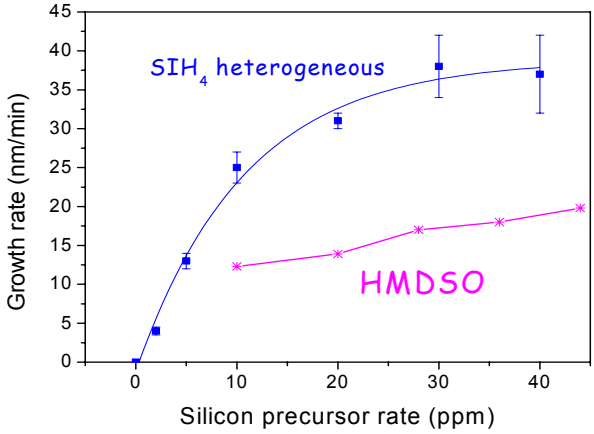

Figure 6: Evolution of the maximum of the heterogeneous growth rate of SiH_4 and HMDSO coating with the precursor concentration all the other conditions being the standard one.

Keeping the N_2O rate equal to 400 ppm, the SiH_4 rate has been increased up to 40ppm. The chemical composition of the layer is not significantly affected. As shown in figure 5, the two maxima position does not changed even if the growth kinetic significantly increases, from 15 to 35 nm/min for the first maximum (figure 5) and from 26 to 800nm/min for the second one. When the SiH_4 partial pressure becomes very low (0.2 Pa for 2ppm) the homogeneous growth i.e. the formation of particles is drastically reduced compared to the heterogeneous growth: this is explained by the decrease of the probability of interaction of a SiH_4 radical and an other silicon compound in the gas phase. This competition between gas and surface reactions also explains the saturation of the increase of the heterogeneous growth rate with the SiH_4 concentration.

The effect of HMDSO content on the discharge and film properties has been studied for [N_2O]/[HMDSO] ratio equal to 24 and a fixed power of 0.5 W/cm^2. Increasing the HMDSO concentration from 4 ppm up to 44 ppm, (partial pressure from 0.4 up to 4.4 Pa) a Townsend discharge is always obtained and no modification is observed on the film chemical composition. The maximum growth rate increases almost linearly as a function of HMDSO concentration (figure 6), with a slope of 0.2 nm/min per HMDSO concentration unit (ppm). This variation is very slow compared to that observed in case of SiH_4. A possible explanation of this behaviour is that the growth rate is limited by the HMDSO activation, the slowest step of

the overall deposition process. An easy way to check this hypothesis consists in increasing the power i.e. the density of energetic species like electrons and nitrogen metastables.

Effect of discharge power

For a given rate of precursor (4ppm of HMDSO, 5ppm of SiH_4), the power has been varied by a factor close to ten: from 0.166 W/cm^2 to 1.45 W/cm^2 in SiH_4 case and from 0.2 up to 2 W/cm^2 (2 to 20 W/cm^3) in HMDSO case. In SiH_4, higher is the power, quickest is the formation of powder but also of the radicals and the separation between the two mechanisms becomes clearer and clearer. This can be attributed to a larger dissociation of SiH_4 molecules. In the same time, the growth rates at both maxima increases (Figure 7). However, the rate of the heterogeneous growth saturates for high power values while the homogeneous growth rate increases linearly. This can be explained taking into account the fact that radicals leading to the heterogeneous growth have to be created in a boundary layer close to the surface. The thickness of this boundary layer is defined (i) by the diffusion coefficient of the radicals and the gas flow which determines the radicals trajectory and (ii) by the volume reactivity of the radicals which determines the radicals lifetime. Then, the power does not directly affect it. Then the results observed in figure 6 suggest that the SiH_4 contained in this layer is entirely decomposed and transferred to the surface when the power is increased.
In HMDSO, the maximum growth rate increases almost with a linear trend when the power increases from 0.2 up to 2 W/cm^2 (2 to 20 W/cm^3) and a value of 36 nm/min is reached for a discharge power of 1.9 W/cm^2. There is no saturation. Even if the HMDSO rate is lower than the SiH_4 one, more silicon radicals reach the surface showing that the boundary layer is larger. This is in agreement with lower volume reactivity. This linear dependency on the power also confirms that HMDSO dissociation is the slowest step of the overall deposition process.

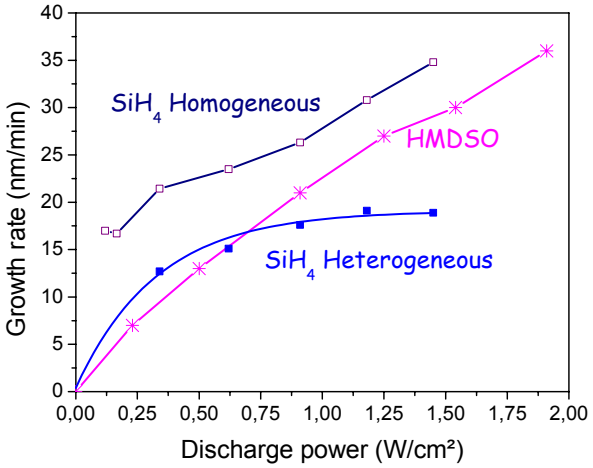

Figure 7: Maximum growth rate as a function of the discharge power at the first (heterogeneous) and second (homogeneous) maximum for SiH_4 coating and for HMDSO

4. Conclusion

The comparison of the properties of thin film coatings obtained with SiH_4 and HMDSO clearly shows that the reactivity of the precursor in the gas phase largely defined the properties of the coating and the ability to get a homogeneous layer. It also largely influences the boundary layer thickness from which radicals can reach the surface. Lower is the reactivity of the precursor in the gas phase, larger is this boundary layer and longer should be the discharge length to allow the radicals to reach the surface.

[1] F. Massines, P. Ségur, N. Gherardi and A. Ricard - Surface and Coatings Technology. 174-175, 8 (2003)
[2] Y. Sawada, S. Ogawa and M. Kogoma - J. Phys. D: Appl. Phys. 28, 1661 (1995)
[3] R. Foest, F. Adler, F. Sigeneger, M. Schmidt - Surface and Coatings Technology. 163-164, 323 (2003)
[4] D. Trunec,Z.Navrátil,P.Stahel,L.Zajícková,V.Bursíková,J.Cech - J. Phys. D: Appl. Phys. 37, 2112 (2004)
[5] S. Martin, F. Massines, N. Gherardi, C. Jimenez, Surface and Coatings Technology, 177 –178 (2004) 693
[6] R. Thien, A Weber and C. P. Klages, Surface and Coatings Technology 97 (1997) 426
[7] P. N. Sen, M. F. Thorpe, Phys. Rev B, 15 (1977) 4030
[8] C.T. Kirk, Phys. Rev. B, 38 (1988) 1255

Investigation of interaction of polymer-Coated chamber wall and oxygen plasma in an ICP discharge by time resolved visible and VUV spectroscopy

Zhi-Gang Guo, Zhen-Dong Yu and Yi-Kang Pu
Department of Engineering Physics, Tsinghua University, Beijing 100084, China

Abstract:

The process of cleaning nitrogen-containing hydrocarbon polymer films on chamber wall employing O_2/N_2 discharge is investigated using vacuum ultraviolet (VUV) and optical emission spectroscopy. Electron temperature and relative concentration of various atomic species are measured as a function of process time. The measurement results suggest that the ion loss rate is highest on polymer surface, lower on quartz and lowest on stainless steel.

Keywords: plasma cleaning, chamber wall condition, polymer coating, electron temperature, ion loss rate

I. Introduction

Organic polymers often deposits on chamber wall in plasma etching of silicon dioxide and plasma enhanced chemical vapor deposition (PECVD) when fluorocarbon or hydrocarbon compound is employed as an etchant or precursor. Concentration of active species is greatly influenced by polymer coating on chamber wall [1, 2]. This may lead to fluctuation in etching or deposition rate and poor process reproducibility [3, 4]. Therefore, oxygen or oxygen-containing compound is commonly used for polymer removal from chamber wall or their formation control in gas phase [5, 6].

In the present work, a nitrogen-containing hydrocarbon polymer thin film, deposited on stainless steel cylinder wall during a CH_4/N_2 discharge, is being removed by an O_2/N_2 plasma. Relative concentrations of various species in cleaning process are monitored by VUV and optical emission spectroscopy (OES) as function of cleaning time. Time resolved electron temperature is obtained by line ratio technique through molecular nitrogen emissions. Three phases in the polymer removal process are identified and variation of these parameters during these phases is analyzed.

II. Experiment

Figure 1 is a schematic diagram of our MPS2000 ICP reactor and optical diagnostic apparatuses used in this experiment. The reactor consists of a quartz tube (with inner diameter 17 cm and height of 40 cm) and stainless steel chamber (inner diameter 60 cm and height of 40 cm) with many ports. An rf power supply (13.56 MHz, 0-1000 W) is coupled to the plasma in the quartz tube through an induction coil (4.5 turns). A Faraday shield is mounted outside of the quartz tube to reduce the effect of capacitive coupling. A small stainless steel cylinder (inner diameter 15 cm and height 35 cm) is placed in the center of stainless steel vacuum chamber to confine the plasma and polymer film is deposited on its inner surface. A rectangle window (15mm width and 40 mm height) on the small cylinder wall allows VUV emission entering the slit

of the spectrometer through one of the ports on the large vacuum chamber. With a 500 l/s turbo pump, a base pressure of 10^{-7} Torr is achieved without baking. The operating pressure is monitored by a capacitance diaphragm gauge (CMR264, Balzers Inc.).

The VUV emission intensity is measured by a grazing incidence monochromator (Model 248, McPherson Instrument Inc.). A gold-coated 300 grooves/mm grating allows a wavelength range of 30 to 180 nm with a spectral resolution of 0.3 nm when the slit width is 150 μm. The detector system consists of a sodium salicylate-coated window and a photomultiplier tube operating in photon counting mode (Model 76915, Oriel Inc.). A two-stage differential pumping system is used so that the pressure inside the VUV monochromator is less than 10^{-5} Torr. Intensities of O 130 nm ($3s\ ^3S—2p^4\ ^3P$), H 121 nm ($2p\ ^2P—1s\ ^2S$), N 120 nm ($3s\ ^4P—2p^3\ ^4S$) and C 115 nm ($2p^3\ ^3D—2p^2\ ^3P$) resonance lines are measured.

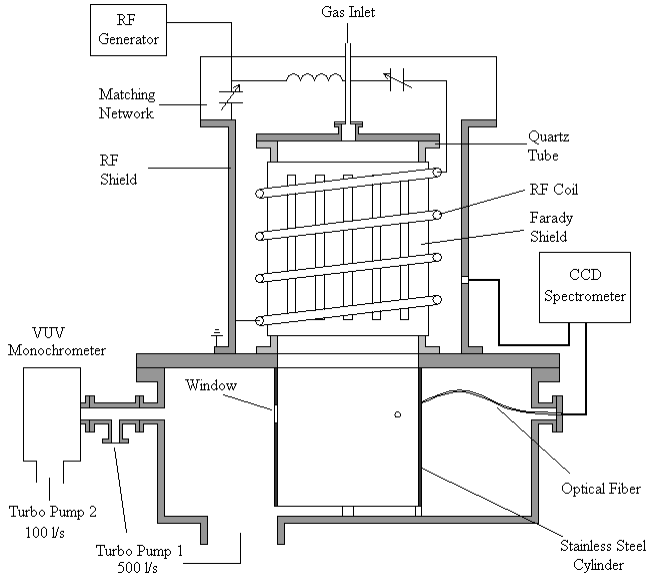

Figure 1. Schematic diagram of experimental setup and diagnostics apparatus.

Optical emission from both the source and downstream regions is monitored by a four-channel CCD spectrometer (SQ2000, Ocean Optics Inc.) through an optical fiber probe mounted inside the vacuum chamber and another fiber mounted outside of the quartz tube, as shown in figure 1. An optical collimator (with a hole of 1 mm diameter and collimation length of 4 cm) is used to prevent polymer coating on the optical fiber probe. The collimator, the optical fiber and the spectrometer are intensity-calibrated all together by a tungsten filament lamp within its wavelength range of 350 nm to 900 nm.

The nitrogen-containing hydrocarbon polymer thin film is deposited by using a CH_4/N_2 discharge under the following condition: total flow rate is 30 sccm, volume percentage of CH_4 is 42%, gas pressure is 10 mTorr, rf power is 200 W and deposition time is 1 hour. The deposited film is removed by O_2/N_2 plasma under the following condition: total flow rate is 30 sccm, O_2 volume percentage is 80%, gas pressure is 10 mTorr, rf power is 200 W and process time is 50 minutes. The VUV emission intensities at four resonance lines of O, H, N and C are recorded in every three minutes in cleaning process. Optical emission intensity is recorded every 30 seconds. The emission intensity ratio between molecular nitrogen first positive series of 762.5 nm and first negative series of 391.4 nm is used to calculate the electron temperature along the line of sight in the downstream and source regions.

III. Results and discussion

1. Time resolved VUV emission spectroscopy

VUV emission in wavelength range of 90~150 nm in O_2/N_2 plasma is shown in figure 2. The atomic resonance lines of O (130.4 nm), H (121.6 nm), N (120.0 nm and 113.4 nm) and C (115.8 nm) can be identified. Time resolved relative intensity of these lines (except N 113.4 nm) is shown in figure 3 as a function of process time. As can be seen from figure 3, the cleaning process can be considered as a combination of three different phases: a cleaning phase, a transition phase and a finish phase, separated by two dashed lines located at about 18 minutes and 30 minutes respectively. The emission intensity of O 130 nm increases rapidly in cleaning phase, and then slowly increases in transition phase and remains a constant in finish phase. Correspondingly, the emission intensity of H 121 nm decreases throughout the cleaning and transition phase (except a small peak at the cleaning/transition boundary) and stabilizes in finish phase. The emission intensity of C 115 nm stays constant in the cleaning phase and decreases continuously in transition phase and finish phase. The boundary of the three phases is best marked by the change of emission intensity of N 120 nm, whose values are highest in the transition phase.

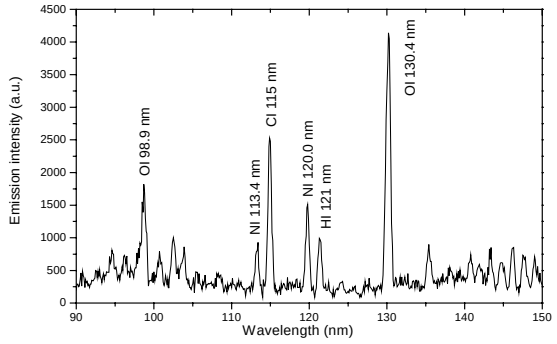

Figure 2. Main VUV emission lines in O_2/N_2 plasma.

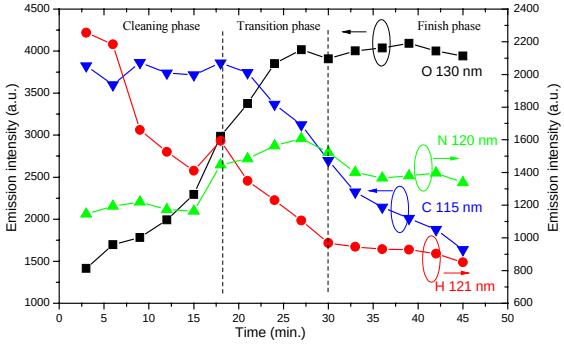

Figure 3. The time resolved relative intensity of VUV emissions of atomic O, H, N and C.

Variations of intensities of the four VUV lines with cleaning time suggest the possible existence of transition phase in the cleaning process. This may be caused by the non-uniformity of polymer-coating layer or etching rate along axial direction of the stainless steel cylinder due to variation of species concentration in downstream region. At the beginning of transition phase, polymer film on the top part of cylinder wall will be removed out first due to higher oxygen atom density. Density of atomic H and C will decrease in gas phase because of the chemical reaction involved and their source (polymer film) being depleted. This results in the rapid decrease of their VUV emission intensities. This trend will last until the polymer film is removed from the entire inner surface of the cylinder and this marks the end of the transition phase. In this phase, the stainless steel wall is covered partially by an electrically insulating polymer. The total area of stainless steel that is in direct contact with the plasma increases with time as a result of etching. Plasma parameters like electron temperature will change continuously due to the change of loss rate of charged species on the wall, as indicated by the measurement of electron temperature using line-ratio technique (described in the next section). Furthermore, this may be the reason why there is a peak in emission intensity of N in transition phase, even though more detailed study is required to verify this argument.

2. Time resolved electron temperature and relative atomic concentration in downstream and source area by OES

Time resolved OES from both downstream and source regions is employed to monitor relative species' density and electron temperature. Species' density is derived from optical actinometry by emission intensity ratio between interested species and argon (volume percentage less than 5%) used as an actinometer. Emissions of O at 844 nm ($3p\ ^3P—3s\ ^3S$), H at 486 nm (Balmer series, β) and Ar at 811 nm ($2p_9—1s_5$) are selected to determine actinometry signal because their peaks are strong and are away from other emission lines. The excitation thresholds of O and H lines (11 eV and 12.75 eV) approximates to that of Ar line (13.08 eV), which is a necessary condition to apply actinometry [7].

Relative concentration of O and H in downstream region is shown in figure 4 as a function of cleaning time. The concentration of H has the same trend as its VUV intensity. But the oxygen concentration has a different trend from its VUV emission by showing a high peak in cleaning phase and slowly increasing in transition and finish phases. At this time, we do not know how to interpret this measured result.

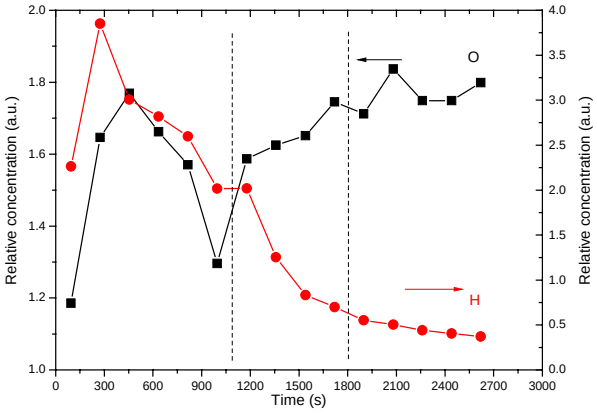

Figure 4. Relative concentration of O and H by optical actinometry in O_2/N_2 plasma with cleaning time (downstream region).

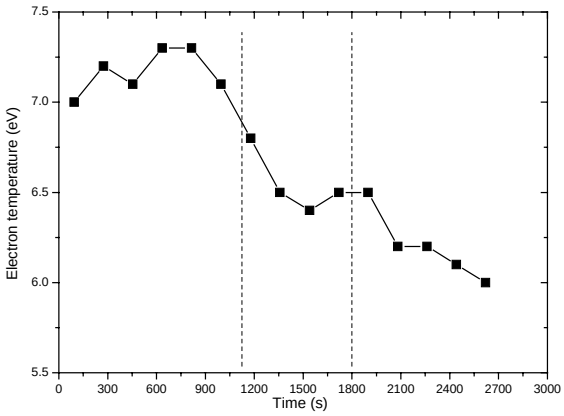

Figure 5. Electron temperatures in O_2/N_2 plasma in downstream region as a function of cleaning time.

The electron temperature of O_2/N_2 plasma in downstream region is shown in figure 5 as a function of cleaning time. Electron temperature is highest in cleaning phase. It decreases in both transition and finish phases, even though its rate of decrease is somewhat lower in finish phase. The higher electron temperature in cleaning phase than in finish phase indicates a higher loss rate of ions when polymer is coated on the chamber wall, according to Global Model [8].

Similar measurements are performed in source area of our ICP device. Results of atomic concentration and electron temperature with cleaning time are shown in figure 6 and figure 7 respectively. The concentration of O shows stable low value in cleaning phase, rapid increase in transition phase and saturation in finish phase. This transition can be simply explained as more loss of O in cleaning phase due to reaction with organic polymer film. It also indicates two stable states of plasma with and without the polymer film on the cylinder wall and there is a transition region between them. The increasing electron temperature in cleaning phase in figure 7 is attributed to measurement error using line ratio technique and is caused by continuous thickness reduction of polymer film, whose absorption of plasma emissions depends on wavelength. Taking this into

account, the true electron temperature should be along the dotted line in the figure. As mentioned before, higher electron temperature when polymer coating is present suggests a higher ions loss rate on polymer surface than on quartz surface. Notice that, in the source region, the difference in electron temperature between the two cases (polymer coated wall and quartz wall) is small (about 0.8 eV). While in the downstream region the difference is larger (about 1.2 eV) when the wall changes from a polymer coated one to its original stainless steel wall. This may suggest that stainless steel wall has the smallest ion loss rate, followed by quartz and polymer.

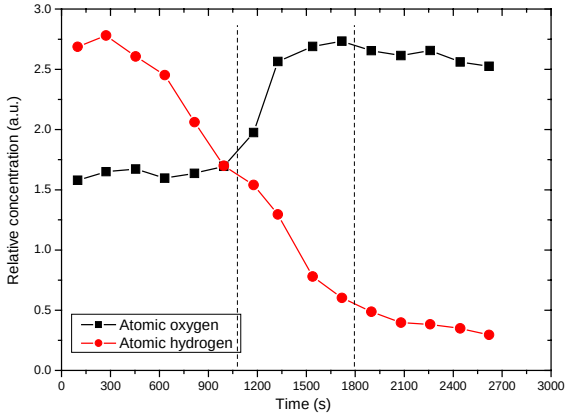

Figure 6. Relative concentration of O and H by optical actinometry in O_2/N_2 plasma with cleaning time (source region).

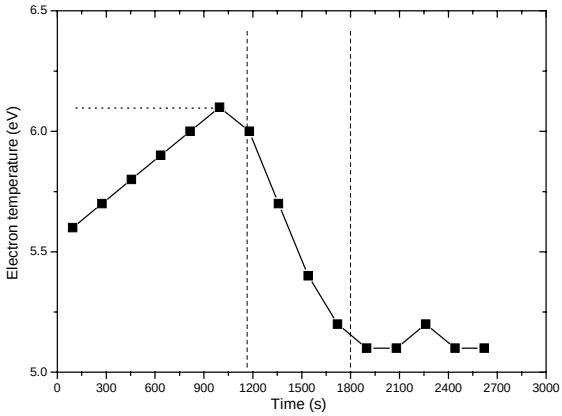

Figure 7. Electron temperatures in O_2/N_2 plasma in source region as a function of cleaning time.

IV. Conclusion

The process of cleaning nitrogen-containing hydrocarbon polymer films on chamber wall employing O_2/N_2 discharge is monitored and investigated using VUV and optical emission spectroscopy. Electron temperature and relative concentration of H and O are obtained by line ratio technique and optical actinometry, respectively. Three phases during the polymer removing process are identified: a cleaning phase, a transition phase and a finish phase. Experimental results show that polymer coating has a strong effect on electron temperature and concentration of different species in the plasma. The preliminary results also imply ion loss rate is the highest on polymer surface, followed by quartz and stainless steel has the lowest loss rate.

Acknowledgement

We wish to thank Prof. Wang Long of Institute of Physics, Chinese Academy of Sciences for lending us the VUV spectrometer. This work is supported by National Science Foundation of China under Grant Nos. 10105006 and 10275040.

References

[1] Tachibana K., Kamisugi H. and Kawasaki T., Behavior of F atoms and CF_2 radicals in fluorocarbon plasmas for SiO_2/Si etching, *Japanese Journal of Applied Physics, Part 1*, **38**(7B): 4367-4372, 1999.
[2] Cunge G., Joubert O. and Sadeghi N., Enhancement of the recombination rate of Br atoms by CF_4 addition and resist etching in $HBr/Cl_2/O_2$ plasmas, *Journal of Applied Physics*, **94**(10): 6285-6290, 2003.

[3] Lee S., Tien Y.C. and Hsu C.F., Direct spectroscopic evidence of the influence of chamber wall condition on oxide etch rate, *Plasma Chemistry and Plasma Processing*, **19**(2): 285-298, 1999.
[4] Yasuda H.K., Yu Q.S., Reddy C.M., Moffitt C.E. and Wieliczka D.M., Effects of wall contamination on consecutive plasma processes, *Journal of Vacuum Science & Technology A*, **19**(5): 2074-2082, 2001.
[5] Xu S.L., Sun Z.W., Chen A., Qian X.Y. and Podlesnik D., Fluorocarbon polymer formation, characterization, and reduction in polycrystalline-silicon etching with CF_4-added plasma, *Journal of Vacuum Science & Technology A*, **19**(3): 871-877, 2001.
[6] Ullal S.J., Singh H., Daugherty J., Vahedi V. and Aydil E.S., Formation and removal of composite halogenated silicon oxide and fluorocarbon films deposited on chamber walls during plasma etching of multiple film stacks, *Journal of Vacuum Science & Technology B*, **20** (5): 1939-1946, 2002.
[7] Coburn J.W. and Chen M., Optical emission spectroscopy of reactive plasmas: a method for correlating emission intensities to reactive particle density, *Journal of Applied Physics*, **51**(6): 3134-3136, 1980.
[8] Lieberman M.A. and Lichtenberg A.J., "Principles of Plasma Discharges and Materials Processing", John Wiley & Sons Inc., New York, 1994.

NUMERICAL MODELING AND SPECTROSCOPIC DIAGNOSTICS OF A PULSE-MODULATED INDUCTIVELY COUPLED PLASMA

R. Ye[1], H. Taguchi[1,2], H. Lange[3], N. Kobayashi[1,4], S. Ito[2], T. Watanabe[5] and T. Ishigaki[1]

[1] *Advanced Materials Laboratory, National Institute for Materials Science, 1-1 Namiki, Tsukuba, Ibaraki 305-0044, Japan*
[2] *Department of Pure and Applied Chemistry, Tokyo University of Science, Noda, Japan*
[3] *Department of Chemistry, Warsaw University, Poland*
[4] *Department of Nuclear Engineering, Tokyo Institute of Technology*
[5] *Department of Environmental Chemistry and Engineering Chemistry, Tokyo Institute of Technology*

Numerical modeling and spectroscopic diagnostics of an Ar-H_2 inductively coupled plasma under pulse-modulated power conditions were carried out. It was found that the predicted and measured electron number densities were in good agreement in the central region of the torch; while the observed discrepancies between them in the fringes of the plasma suggested the presence of departure form local thermodynamic equilibrium in those regions. The nonequilibrium effect became more appreciable in the plasma operated under the pulsed power conditions.

1. Introduction

Pulse-modulated inductively coupled plasmas (PM-ICPs) are characterized by their nonequilibrity and relatively high concentrations of chemically reactive radical species. Under pulsed power conditions, their enthalpies can be easily controlled by adjusting the high-low power ratio and the duty factor of pulsation, and their radiation losses can also be considerably reduced, compared with those of continuous plasmas [1-5]. These features are crucial to avoiding the overheating of specimen when processed in such environments with high heat fluxes. The PM-ICPs have shown some prominent advantages in materials processing, such as the doping of hydrogen into functional ceramics [6, 7].

In the past few years, a number of theoretical and experimental studies on induction plasmas operated under pulsed power conditions have been carried out [4, 8-10]. Most of those researches were concentrated on the dynamic behavior of PM-ICPs. The nonequilibrium phenomena in those plasmas were interpreted in terms of the temporal behavior of line emission intensities. However, work involving direct comparisons between experimentally and theoretically obtained results for pulsed power plasmas is likely lagging behind. In the present study, numerical modeling and spectroscopic diagnostics of an Ar-H_2 pulse-modulated inductively coupled plasma were carried out. The numerical modeling was performed using a renormalization group (RNG) *k-e* turbulence model with the local thermodynamic equilibrium (LTE) assumption [11]. The electron number densities were measured by using Stark broadening. Since the experimentally detected electron population densities were independent of the equilibrium conditions in the plasma, a comparison between the predicted LTE profiles of the plasma temperatures and the electron number densities and the measured ones should reveal more conceivable information on the nonequilibrium situations in such thermal plasma generators operated under pulsed power conditions.

2. Experimental set-up

The plasma torch and spectroscopic diagnostics systems for the present work are schematically shown in Figure 1. A voltage-control-type solid state amplifier (MP-22CY, Denki Kogyo Co., Ltd.) was used in the generation of pulsed power plasmas. An invert-type power source supplied an electric power of 22 kW continuously at a nominal frequency of 1 MHz. The power source and the load were electrically matched by using a phase-locked loop (PLL) with variable frequencies and an LC matching circuit. The radio frequency (RF) power was pulse-modulated by using an external pulsed signal generated by a pulse generator (HP-8116A)

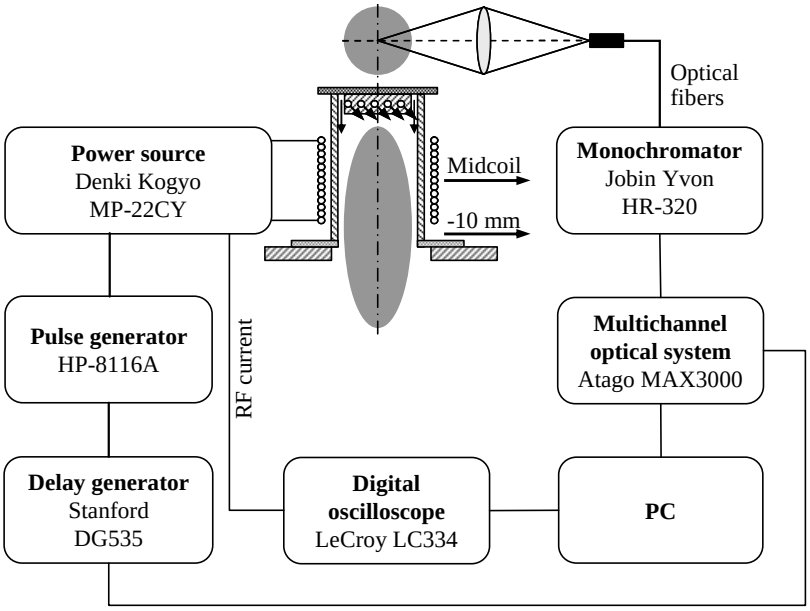

Figure 1. Schematic of the plasma generation and optical diagnostics systems.

to switch a static induction transistor in the power source. The rise time of the power source was less than 1 μs. The plasma was firstly generated at continuous power level of 13 kW and chamber pressure of 200 Torr. Then, the external pulse signal was imposed to switch the plate power from the continuous operating mode to the pulse-modulated one with pulse-on and pulse-off times of 10 and 5 ms, and high and low power levels of 13 and 4 kW, respectively.

The plasma line emissions were monitored at the middle of the RF coil and 10 mm below the last coil in the downstream direction. The optical systems for the measurements of the emission intensities were calibrated using a halogen lamp. The lights emitted from the plasma were focused by an optical system with a spatial resolution of 0.5 mm, and were transmitted to the monochromators through optical fibers. In order to obtain the radial profiles of the plasma emissions, the optical system was mounted on a displacement frame driven by a step motor. For the measurement of the electron temperature, the focused plasma radiations were monochromated using a JOBIN YVON HR-320, and the light signals for two hydrogen atomic lines (H_α: 656 nm and H_β: 486 nm) and were processed in a multichannel detection system (Atago MAX-3000). The time-resolved measurement was performed with a gate period of 10 μs, in which the delayed signal was given by a delay generator (Stanford DG535). The net emission intensities for the two spectral lines were obtained by subtracting the continuum component from the measured line intensities, and the temperature was then calculated using the two-line method. For the measurement of electron number density, the signal of the H_β line at 486 nm were processed. The coil current signals were stored in a PC through a digital oscilloscope (LeCroy LC334). The electron number density was determined using Stark broadening, and the coefficients used in the calculation were taken from Hill [12]. Abel inversion was performed to obtain the radial profiles of the plasma temperature and the electron number density.

3. Mathematical model

The plasma is considered axisymmetrical and in local thermodynamical equilibrium. The two-dimensional, time-dependent governing equations consist of the conservation of mass, energy, momentum, electromagnetic field, as well as those of the turbulent kinetic energy and the dissipation rate of the turbulent kinetic energy, which are based on the renormalization group (RNG) *k-e* turbulence model. The model equations are written into a general form:

$$\frac{\partial}{\partial t}(rf)+\frac{\partial}{\partial z}(ruf)+\frac{1}{r}\frac{\partial}{\partial r}(rrvf)=\frac{\partial}{\partial z}\left(\Gamma_f\frac{\partial f}{\partial z}\right)+\frac{1}{r}\frac{\partial}{\partial r}\left(r\Gamma_f\frac{\partial f}{\partial r}\right)+S_f\,. \tag{1}$$

Table I. Variables, coefficients and source terms for the conservation equations.

f	Γ_Φ	S_Φ
1	0	0
u	m_e	$-\frac{\partial p}{\partial z}+\frac{\partial}{\partial z}\left(m_e\frac{\partial u}{\partial z}\right)+\frac{1}{r}\frac{\partial}{\partial r}\left(rm_e\frac{\partial v}{\partial z}\right)+F_z$
v	m_e	$-\frac{\partial p}{\partial z}+\frac{\partial}{\partial z}\left(m_e\frac{\partial u}{\partial r}\right)+\frac{1}{r}\frac{\partial}{\partial r}\left(rm_e\frac{\partial v}{\partial r}\right)-\frac{2m_e v}{r^2}+\frac{rw^2}{r}+F_r$
w	m_e	$-\frac{w}{r}\left(rv+\frac{m_e}{r}+\frac{\partial m_e}{\partial r}\right)$
h	$k/C_p+m_t/\mathrm{Pr}_t$	P_0-P_R
k	$a_k m_e$	$G-re$ *
e	$a_e m_e$	$\frac{e}{k}(C_{e1}G-C_{e2}re)-R$ **

* $G=m_t\left\{2\left[\left(\frac{\partial u}{\partial z}\right)^2+\left(\frac{\partial v}{\partial r}\right)^2+\left(\frac{v}{r}\right)^2\right]+\left(\frac{\partial w}{\partial r}-\frac{w}{r}\right)^2+\left(\frac{\partial w}{\partial z}\right)^2+\left(\frac{\partial v}{\partial r}+\frac{\partial u}{\partial r}\right)^2\right\}$

** $R=\frac{C_m r h^3(1-h/h_0)}{1+bh^3}\frac{e^2}{k}$

$h\equiv Sk/e$, $S^2=G/m_t$, $m_e=m_m+m_t$, $m_t=rC_m k^2/e$, $h_0=4.38$, $b=0.012$,

$\mathrm{Pr}_t=0.7$, $C_m=0.0845$, $C_{e1}=1.42$, $C_{e2}=1.68$, $a_k=a_e=1.39$

Table II. Torch dimensions and operating conditions.

Inner radius of central tube (R_1)	1.0 mm	Central gas flow rate (Q_1)	0 slpm
Outer radius of central tube (R_2)	2.0 mm	Plasma gas flow rate (Q_2)	0 slpm
Radius of sheath tube (R_3)	27.0 mm	Sheath gas flow rate (Q_3)	98 slpm (Ar)
Inner radius of torch (R_0)	27.5 mm		6 slpm (H_2)
Radius of RF coil (R_c)	44.0 mm	Plasma power (P_0)	4–13 kW
Position of first RF coil (L_1)	60.0 mm	Pressure (p)	27 kPa
Position of last RF coil (L_2)	145.0 mm	Numer of RF coil (N_c)	13 turn
Length of torch (L_3)	170.0 mm	Operating frequency (f)	1 MHz
Thickness of torch wall (d_w)	7.5 mm		

The dependent variables, the transport coefficients and the source terms are summarized in Table I, and detailed descriptions of the model and the solution method are found in Ref. 11.

4. Results and discussion

Computations were performed for the PM-ICP under the operating conditions given in Table II. In Figure 2, the left-hand side depicts the predicted isotherms under the continuous power condition (13 kW), and another side presents the time-averaged ones over one pulse cycle (15 ms) under the pulsed power condition. Compared to the continuous plasma, the high temperature zone was much smaller in the pulsed power plasma, and the

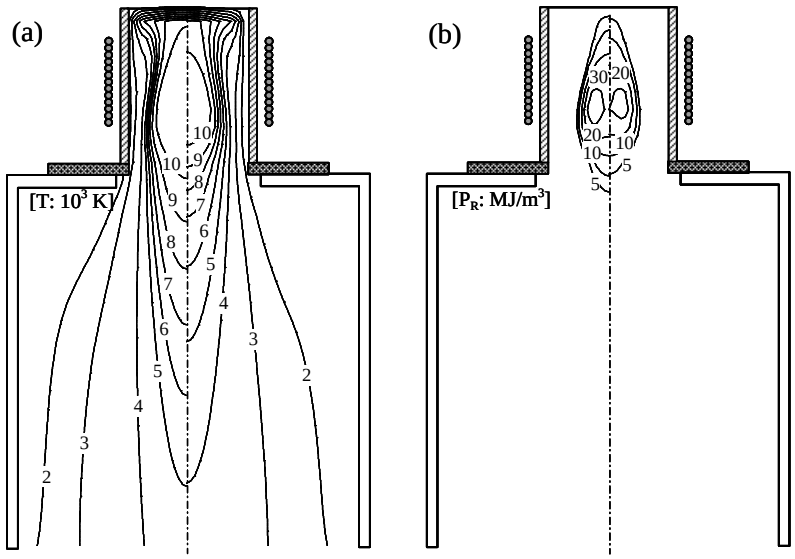

Figure 2. Predicted temperature fields (a) and volumetric radiation power (b) for the continuous plasma (left-hand side) and the pulse-modulated plasma (right-hand side).

plume length of the time-averaged plasma was also much shorter. Along the axis, in the downstream of the torch the time-averaged temperatures were 1000–1500 K lower than those of the steady-state at the same axial position. The volumetric radiation power was also reduced considerably in the pulsed power plasma. Consequently a specimen can be put closer to the discharge zone of the pulse-modulated plasma and better irradiation effects may be achieved.

Figure 3 illustrates the predicted and measured profiles of plasma temperatures at 10 mm below the end of the coil (z=155 mm). Although the measured plasma temperatures were found scattered around, most of them were about 1000–2000 K higher than the predicted ones. This phenomenon could be attributed to the fact that the measured temperatures were actually the excitation temperatures which were closer to those of the electrons, and therefore were higher than the heavy particle temperatures. In addition, under the pulsed power condition, the radial temperature gradients became less steep, and more uniform plasma temperature profiles could be obtained.

The electron number densities under given pressure and temperature conditions were calculated using a chemical reaction kinetics model [12]. In Figure 4, the predicted and measured time-averaged electron number densities were very close to each other in the central region of the torch (r<12 mm), but the differences between these two densities increased with the radial position. The measured electron number densities only had slight decreases at the boundaries of the plasma where the emission signals could be detected. However, the predicted ones dropped significantly in the fringes of the plasma. The differences between the predicted and measured results were beyond the ranges of experimental errors, and could be ascribed to the presence of nonequilibrium phenomena in these regions. Taken into account the radial diffusion of species, the electron temperatures and number densities at the boundaries under nonequilibrium conditions should be much higher than those values under equilibrium conditions owing to the high mobility of electrons [13]. Consequently, rather than using the LTE temperature, the electron number densities should be evaluated using nonequilibrium models that could include the effects of temperatures for different species. In Figures 4 and 5, we may find that the departure from LTE became more significant as the plasma flowed downward and cooled down.

Moreover, the results indicated that the deviation from equilibrium became more noticeable under the pulse-modulated operating condition. The nonequilibrium regions even extended into the central region where the plasma was normally in equilibrium under the continuous operating condition, see Figure 5. For example, at

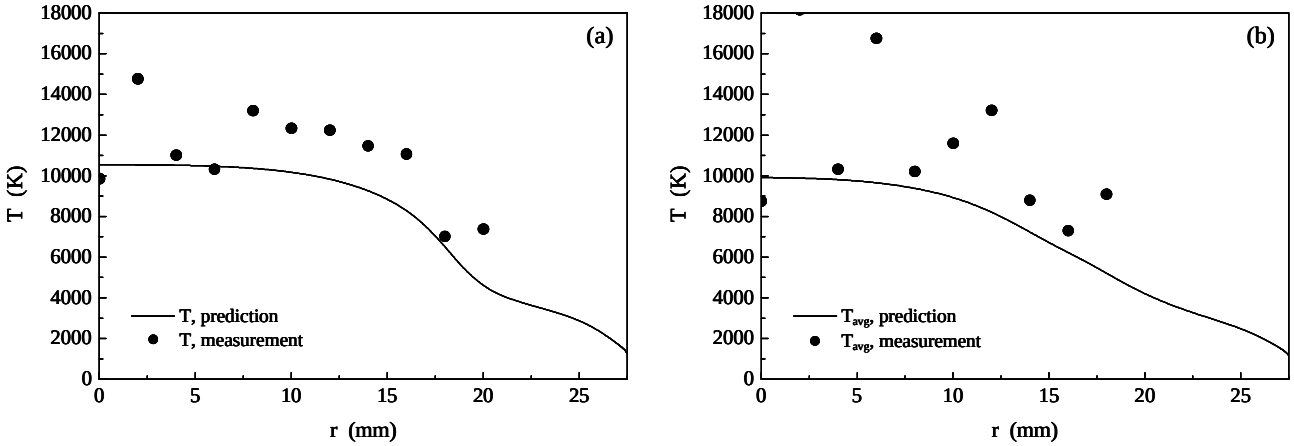

Figure 3. Predicted and measured temperatures at 10 mm below the end of the coil (z=155 mm): (a) steady-state, and (b) time-averaged.

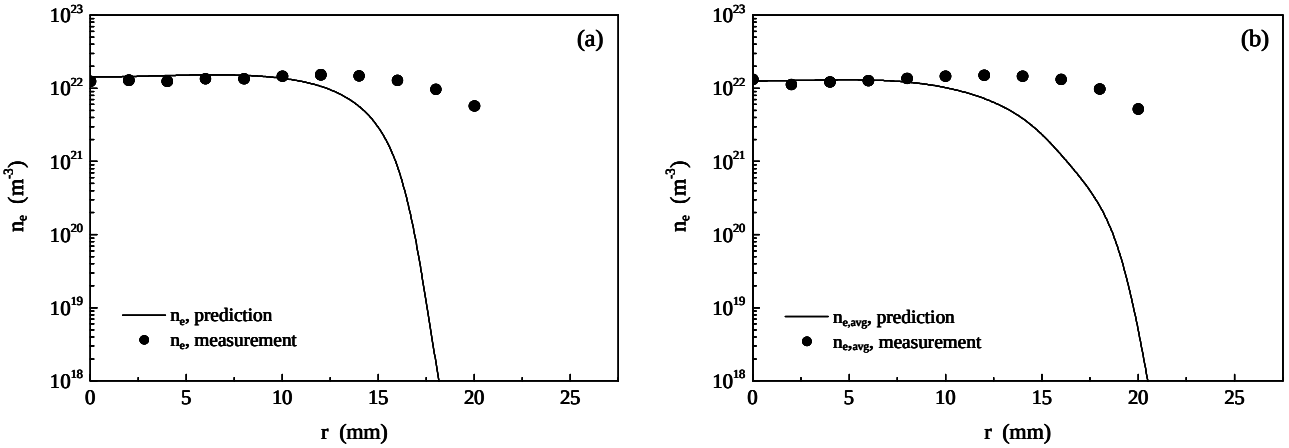

Figure 4. Predicted and measured electron number density at the midcoil (z=102.5 mm): (a) steady-state, and (b) time-averaged.

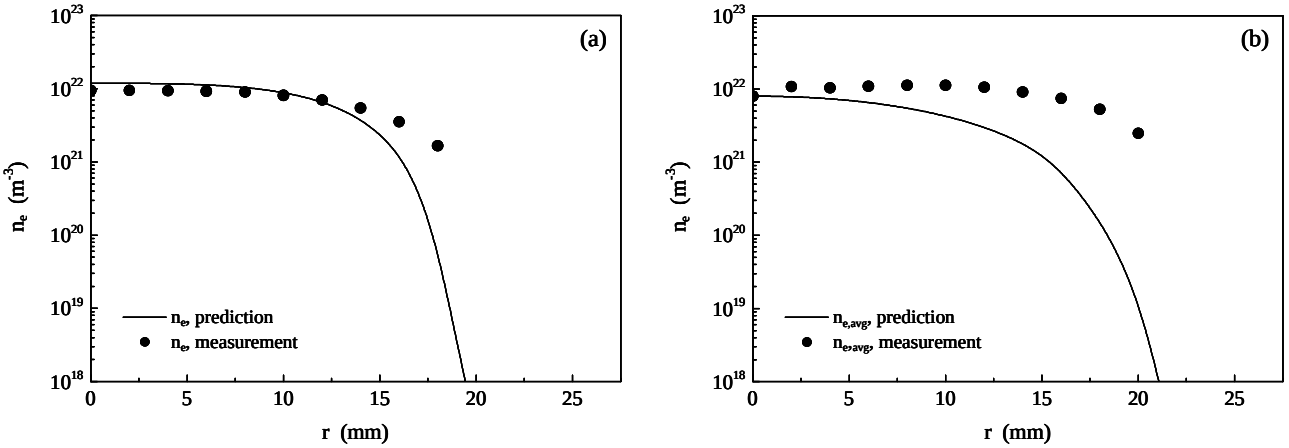

Figure 5. Predicted and measured electron number density at 10 mm below end of the coil (z=155 mm): (a) steady-state, and (b) time-averaged.

r=10 mm, the measured and predicted electron number densities were respectively 1.1×10^{22} and 4.1×10^{21} m^{-3}, the former was 2.7 times as high as the latter. This difference was due to the fact that the electrons reacted to the changes in the input power much faster than the heavy particles did, the electron temperature had a quick increase at the stage of pulse-on, and the degree of departure from LTE was enhanced under the pulsed power condition. However, the effect of electron temperature on the plasma properties was not considered in the LTE model, and the plasma composition was estimated based on the equilibrium temperature. As a result, the electron number densities might be underestimated when the plasma deviated from equilibrium.

5. Conclusion

In summary, the predicted results showed that the time-averaged temperature of the PM-ICP was much smaller than that of the continuous plasma. The measured plasma temperatures had similar radial profiles to the predicted ones, although the former were a bit higher. The agreement between the theoretical and experimental electron number densities was satisfactory in the central region of the torch, but the discrepancies became larger in the fringes of the plasma where the deviation from LTE was the most pronounced. It was suggested that the LTE model might not be accurate enough to adequately describe the behavior of plasmas under such pulsed power conditions. Our work involving the development of non-LTE models for PM-ICPs is on-going.

Acknowledgement

The Japan Society for the Promotion of Science (JSPS) is greatly acknowledged for providing a JSPS research fellowship to R. Ye.

References

[1] T. Ishigaki, X. Fan, T. Sakuta, T. Banjo, and Y. Shibuya, Appl. Phys. Lett. **71**, 3787 (1997).
[2] T. Sakuta, K. C. Paul, M. Katsuki, and T. Ishigaki, J. Appl. Phys. **85**, 1372 (1999).
[3] T. Sakuta and T. Ishigaki, Pure Appl. Chem. **71**, 1845 (1999).
[4] Y. Tanaka and T. Sakuta, Plasma Source Sci. Technol. **12**, 69 (2003).
[5] T. Ishigaki, N. Okada, N. Ohashi, H. Haneda, and T. Sakuta, Pure Appl. Chem. **74**, 435 (2002).
[6] N. Ohashi, T. Ishigaki, N. Okada, T. Sekiguchi, I. Sakaguchi, and H. Haneda, Appl. Phys. Lett. **80**, 2869 (2002).
[7] N. Ohashi, T. Ishigaki, N. Okada, H. Taguchi, I. Sakaguchi, S. Hishita, T. Sekiguchi, and H. Haneda, J. Appl. Phys. **93**, 6386 (2003).
[8] J. Mostaghimi, K. C. Paul, and T. Sakuta, J. Appl. Phys. **83**, 1898 (1998).
[9] M. M. Hossain, Y. Hashimoto, Y. Tanaka, K. C. Paul, and T. Sakuta, IEEE Trans. Plasma Sci. **30**, 327 (2002).
[10] K. C. Paul, T. Ishigaki, J. Mostaghimi, and T. Sakuta, J. Appl. Phys. **93**, 8867 (2003).
[11] R. Ye, T. Ishigaki, and M. I. Boulos, J. Appl. Phys. **96**, 118 (2004).
[12] E. Richley and D. T. Tuma, J. Appl. Phys. **53**, 8537 (1982).
[13] J. Mostaghimi, P. Proulx, and M. I. Boulos, J. Appl. Phys. **61**, 1753 (1987).

Methane conversion with sol-gel-derived catalyst in a dielectric-barrier discharge

Seung-Soo Kim† , Hwaung Lee[1], Hyung Keun Song[1]
† *Department of Environmental Engineering, Donghae University, Korea*
[1]*Clean Technology Research Center, Korea Institute of Science and Technology, Korea*

Abstract
Plasmacatalytic reaction for methane conversion was carried out in a dielectric-barrier discharge (DBD) reactor at atmospheric pressure. Pt catalysts supported on the Al_2O_3 and TiO_2 were tested, and the catalysts were prepared by sol-gel-derived synthesis. Plasma-assisted reduction (PAR) was applied to reduce the prepared metal catalysts in DBD reactor. Plasma assisted reduction (PAR) was applied to the prepared metal catalysts as a method of catalyst reduction, which is novel method to reduce metal oxide catalyst in DBD reactor. Prepared metal oxide catalysts are reduced using plasma energy, and Pt/TiO_2 and Pt/Al_2O_3 catalysts were successively reduced by PAR. The main products of methane conversion were the light alkanes such as C_2H_6, C_3H_8 and C_4H_{10} when the catalytic plasma reaction was carried out with catalyst. Methane conversion reached 53% depending on Pt loading and calcination temperature.

1. Itroduction

Natural gas is one of the most useful resources in the world due to the greatness of the amount and wideness of its distributions. As fossil fuels such as oil and coal are depleting, the value of natural gas as an alternative fuel is becoming greater and greater[1-3]. This is the reason why many researchers have been trying to convert methane, the main component of natural gas, to liquid fuels or more useful chemicals. But, there are a lot of difficulties in doing so because of the stability of methane. Natural gas can be indirectly converted to liquid fuels or other chemicals by way of synthesis gas, or directly transformed to C_2 hydrocarbon or methanol. Most of commercial natural gas converting processes convert methane to synthesis gas by steam reforming, and then synthesize methanol or gasoline using this synthesis gas as an intermediate. Since the process producing synthesis gas by steam reforming of natural gas requires much endothermic heat, it needs lots of energies and high temperature over 800 ℃. To overcome these problems, there have been lots of studies on the direct conversion method. Oxidative coupling[4-8], thermal coupling[9], plasma[1,7,10-13] and so on have been tried for direct methane conversion.

Methane conversion with plasma has been widely researched nowadays as an alternative method. Especially, methane conversion and methane reforming with CO_2 were extensively studied[2-3,8,14-17]. Methane activation with non-thermal plasma is very effective not only in that methyl radicals could be easily made by the high energy of plasma, but also in that various kinds of chemical reactions could be induced through the high energy [14,16-18]. The methyl radicals produced from plasma make C_2, C_3 and C_4 hydrocarbons by coupling with other methyl radicals[1,14]. However, the conversion was limited by the plasma power and the plasma reaction produced various kinds of by-product. Recently, to solve these problems, heterogeneous catalysts were introduced into the plasma reaction.

Liu et al.[14,15,18] investigated the effect of Zeolite on the plasma methane conversion. Also, metal oxide catalysts were widely used for producing high value-added compounds from methane[13,19-21]. Moreover, preparation of catalyst and surface treatment of catalyst have been attempting using plasma energy[22-23]. Li et al.[22] reported that conversion of methane was increased 5-10% by plasma treatment of Ni catalyst, maintaining the same selectivity of synthesis gas. Liu et al.[23] also reported that Pd/HZSM-5 catalyst treated by glow discharge showed high catalytic activity and durability. In their work, the conversion of methane was almost 100% at 450 ^oC while the conversion was 50% without plasma treatment at the same conditions. In our previous work[24-26], the plasma-assisted reduction (PAR) of novel metal catalyst was proposed using dielectric-barrier discharge (DBD). The reduction of catalyst was completed rapidly in the plasma, and the selectivity of alkane such as ethane and propane was highly increased.

Although the above mentioned plasma-catalytic reactions showed improved results, the catalysts used are in powder forms. For practical applications in large scale, spherical catalysts having the desired pore structures are preferred. In this study, Plasmacatalytic reaction for methane conversion was carried out in a dielectric-barrier

discharge (DBD) reactor at atmospheric pressure[1-3]. Pt catalysts supported on the Al_2O_3 and TiO_2 were tested, and the catalysts were prepared by sol-gel-derived synthesis[4]. Plasma-assisted reduction (PAR) was applied to reduce the prepared metal catalysts in DBD reactor. Plasma assisted reduction (PAR) was applied to the prepared metal catalysts as a method of catalyst reduction, which is novel method to reduce metal oxide catalyst in DBD reactor. Prepared metal oxide catalysts[5-7] are reduced using plasma energy. The effect of catalyst on methane conversion and product selectivities was studied.

2. Experimental

A schematic diagram of the experimental apparatus is shown in Figure 1. Quartz tube with an i.d. of 8mm and the length of 270mm was used for Dielectric-Barrier Discharge (DBD) reactor. Two stainless steel wires with a diameter of 0.45mm were installed in the quartz tube as an inner electrode. The outer surface of quartz tube was coated with silver paste as another electrode, and the length of coated silver paste was 200mm. An AC pulse power supply (ITM) with [0-10kV, 10-40kHz, 2-5μs] was used in this experiment. The flowrate of methane was controlled by the mass flow controller (Bronkhorst, B-5534-FA). The reaction products of hydrocarbons were analysed with the gas chromatograph (HP 5890 equipped with a Haysep Q packed column and FID detector). Gas chromatograph (Younglin M600D) equipped with TCD was used to analyse the produced hydrogen. The peaks were identified when the retention times compared with those of standard gases (CH_4, C_2H_2, C_2H_4, C_2H_6, C_3H_4, C_3H_6, C_3H_8 and C_4H_{10}) with a purity above 99.5%.

For preparation of Al_2O_3 and TiO_2 xerogel, sec-butanol, aluminium tri-sec-butoxide (ATB; $Al[O(CH_3)C_2H_5CH]$), and titanium tetraisopropoxide(TTIP; $Ti(OC_3H_7)_4$) were used as precursor. $H_2PtCl_6 \cdot 6H_2O$ was used as a metal precursor. Catalysts were prepared with sol-gel method, and prepared sol was drying at 120℃ for 24hr.

Prepared catalyst was sieved 20~42mesh and then calcined between 400℃ and 600℃ for 2hr with oxygen flowrate of 100ml/min. The catalyst of 0.3g was packed with the lower part of DBD reactor for catalytic plasma reaction, while the upper part remained blank. Below the catalyst-packed volume, i.e. at the lower non-plasma zone, glass beads were packed. All experiments were carried out under atmospheric pressure.

The catalyst of 0.3g was packed with the lower part of DBD reactor for catalytic plasma reaction, while the upper part remained blank. Below the catalyst-packed volume, i.e. at the lower non-plasma zone, glass beads were packed. All experiments were carried out under atmospheric pressure.

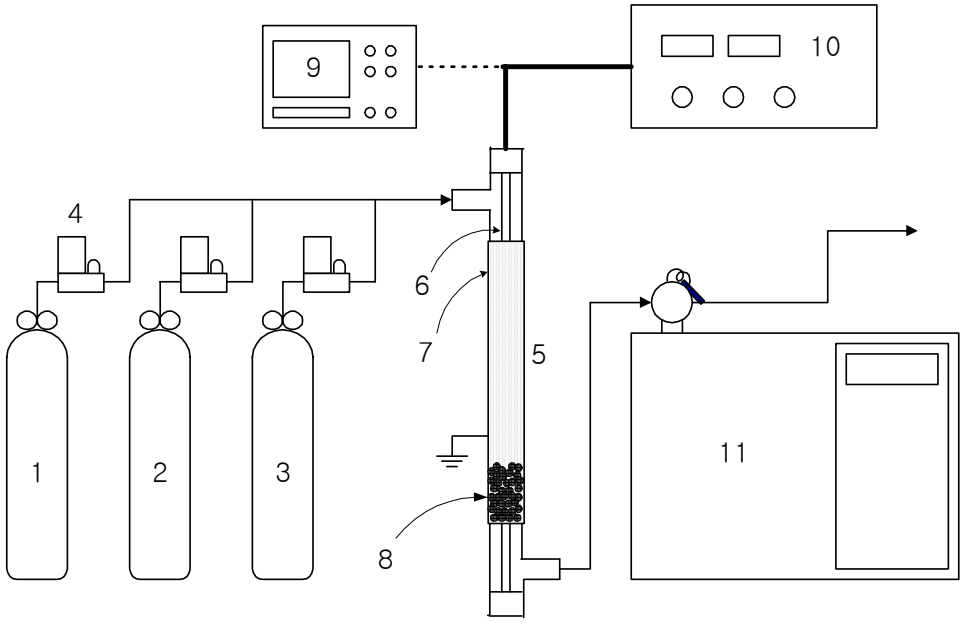

Figure 1. Schematic diagram of experimental apparatus.

The methane conversion is defined as:

$$\text{CH}_4 \text{ conversion} = \frac{\text{moles of CH}_4 \text{ consumed}}{\text{moles of CH}_4 \text{ introduced}} \times 100 .$$

The selectivities and yields of C_2, C_3 and C_4 hydrocarbons are:

$$\text{Selectivity of } C_xH_y = x \cdot \frac{C_xH_y}{\text{moles of CH}_4 \text{ consumed}} \times 100 .$$

The selectivity of hydrogen is:

$$\text{Selectivity of H}_2 = 0.5 \times \frac{\text{moles of H}_2 \text{ formed}}{\text{moles of CH}_4 \text{ consumed}} \times 100 .$$

The yields of hydrocarbons are:

$$\text{Yields of } C_xH_y = \text{Conversion of CH}_4 \times \text{Selectivity of } C_xH_y .$$

3. Results and Discussion

Plasma treatment is one of novel methods for preparation and reduction of catalysts. Non-thermal plasma makes large amount of free electrons which have high energy. Produced high energy electrons are used to activate other molecules. In a plasma state, hydrogen can be easily activated due to high-energy electron, which can lead to reduce metal oxide catalyst. Generally, metal oxide catalysts are reduced at high temperature in the hydrogen atmosphere. The catalyst surface (metal oxide) in contact with the highly activated hydrogen can be reduced. In this work, plasma was applied to reduce prepared Pt/γ-Al_2O_3 catalysts in dielectric-barrier discharge reactor.

Plasma assisted reduction was applied to reduce Pt-based catalyst at the flow rate of 10 ml/min of 20 vol% H_2 in N_2. The rate of hydrogen consumption was monitored by a thermal conductivity detector. The applied voltage was fixed at 3.0 kV, and then the power input was in the range of 37-39 W with the variations of experimental conditions. The prepared catalyst was successively reduced by PAR. PAR was an effective method to reduce metal oxide catalyst in DBD reactor. Plasma catalytic reaction was carried out after PAR. Typical PAR pattern of Pt/Al_2O_3 was shown in Figure 2. The selectivity of C_2H_6, C_2H_4 and C_2H_2 was higher among the produced hydrocarbons when the methane conversion was carried out in the absence of catalyst. In the presence of a Pt catalyst, the main products of plasma catalytic reaction were the light alkanes such as C_2H_6, C_3H_8 and C_4H_{10}.

The effects of metal loading and calcination temperature on methane conversion and product selectivity were examined. Prepared catalysts were reduced by PAR at 3.0 kV for 2h with reduction gases. After reduction, the plasma catalytic reaction of methane was carried out *in situ* with flow rate of 30 ml/min at the applied voltage of 3.0 kV. All experiments were carried out with 0.3 g catalyst. In order to verify the effect of catalysts, blank experiment was carried out without catalysts. Methane conversion was not much difference depending on calcination temperature and metal loading when the Pt/TiO_2 catalyst was used, but product selectivity was slightly changed with calcination temperatures (Table 1, Table 2). Methane conversion and product selectivity was highly changed depending on calcination temperature and metal loading when sol-gel-derived Ru/TiO_2 catalyst was applied to DBD. The highest methane conversion was 47.35% when 5 wt% Ru/TiO_2 catalyst was calcined at 400 ℃. Anatase phase showed positive effect methane conversion in DBD.

XRD patterns of the Pt/TiO_2 and Pt/Al_2O_3 catalysts were shown in Figure 3 and 4. Pt peaks appeared after 600℃ calcined for 3wt% and 5wt% Pt//γ-Al_2O_3. It is assumed that metal particles migrated to the alumina surface during the calcination, and then sintering occurred. TiO_2 phase was changed from anatase to rutile with the calcination temperature increasing.

References

[1] C.J. Liu, A. Marafee, B. Hill, G. Xu, R. Mallinson, L. Lobban, *Ind. Eng. Chem. Res.*, **35**, 3295 (1996).

[2] C.J. Liu, B. Xue, B. Eliasson, F. He, Y. Li, G.H. Xu, *Plasma Chem. Plasma Proc.*, **21**, 301 (2001).

[3] D.W. Larkin, L.L Lobban, R.G. Mallinson, *Ind. Eng. Chem. Res.*, **40**, 1594 (2001).

[4] J.A. Sofrank, J.J. Leonard, C.A. Jones, *J. Catal.*, **103**, 302 (1987).

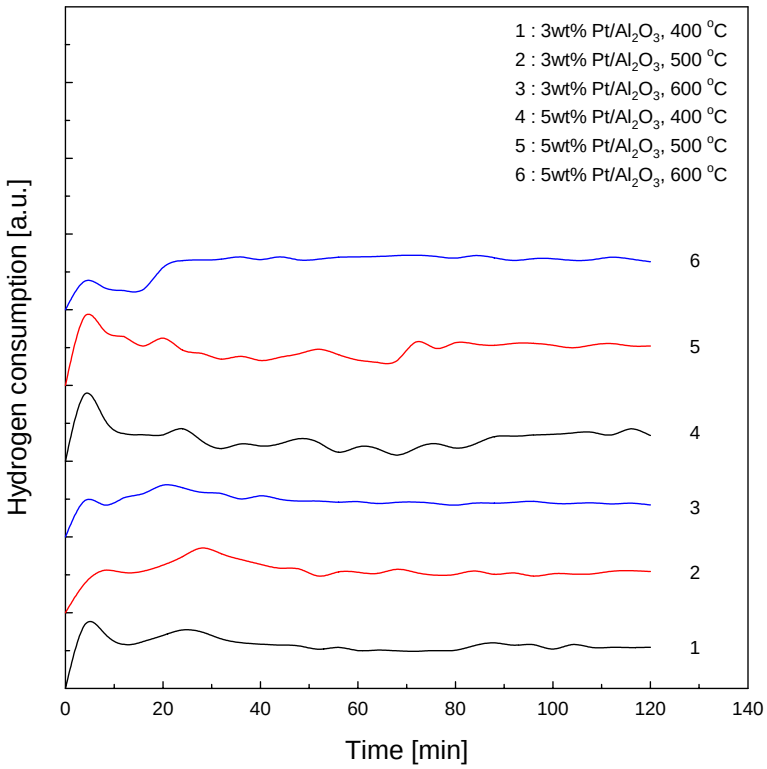

Figure 2. PAR profile of prepared catalysts (Pt/γ-Al_2O_3); hydrogen and nitrogen flowrate = 10ml/min (20vol.% H_2 in N_2).

Table 1. Effect of the calcinations temperature for Pt on alumina(Al_2O_3) catalyst on methane conversion and selectivity. (methane flowrate : 30 ml/min)

Reduction conditions		Methane conversion (%)	Selectivities (%)						
			C_2H_6	C_2H_4	C_2H_2	C_3H_8	C_3H_6	C_4H_{10}	H_2
Without catalyst		36.71	15.42	9.74	12.71	3.74	1.90	2.00	47.45
γ-Al_2O_3	400℃ calcined	34.19	19.17	5.92	-	7.97	0.15	7.00	9.38
3wt% Pt/γ-Al_2O_3	400℃ calcined	37.73	28.83	1.91	-	7.77	0.34	2.61	12.97
	500℃ calcined	42.31	33.13	2.20	-	13.46	0.56	6.05	9.03
	600℃ calcined	53.17	30.35	1.22	-	11.67	0.17	6.28	11.06
5wt% Pt/ γ-Al_2O_3	400℃ calcined	33.01	37.37	0.25	-	11.50	0.20	7.45	10.48
	500℃ calcined	28.97	39.57	0.35	-	11.72	0.63	5.02	10.06
	600℃ calcined	28.18	39.01	0.37	-	13.18	1.61	8.85	9.33

Table 2. Effect of the calcinations temperature for Pt on titania(TiO_2) catalyst on methane conversion and selectivity. (methane flowrate : 30 ml/min)

Reduction conditions		Methane conversion (%)	Selectivities (%)						
			C_2H_6	C_2H_4	C_2H_2	C_3H_8	C_3H_6	C_4H_{10}	H_2
Without catalyst		36.71	15.42	9.74	12.71	3.74	1.90	2.00	47.45
TiO_2	400℃ calcined	37.73	17.97	3.20	-	9.12	1.15	6.61	9.88
3wt% Pt/TiO_2	400℃ calcined	38.06	24.82	0.56	-	11.82	0.24	9.25	10.00
	500℃ calcined	37.56	25.07	0.59	-	11.89	0.26	12.31	9.97
	600℃ calcined	39.55	22.74	0.75	-	10.91	0.83	8.88	10.62
5wt% Pt/TiO_2	400℃ calcined	38.84	27.99	0.09	-	8.78	0.07	7.63	11.10
	500℃ calcined	38.15	33.21	0.37	-	6.13	-	4.80	10.74
	600℃ calcined	39.87	23.60	0.27	-	10.97	0.32	6.84	9.77

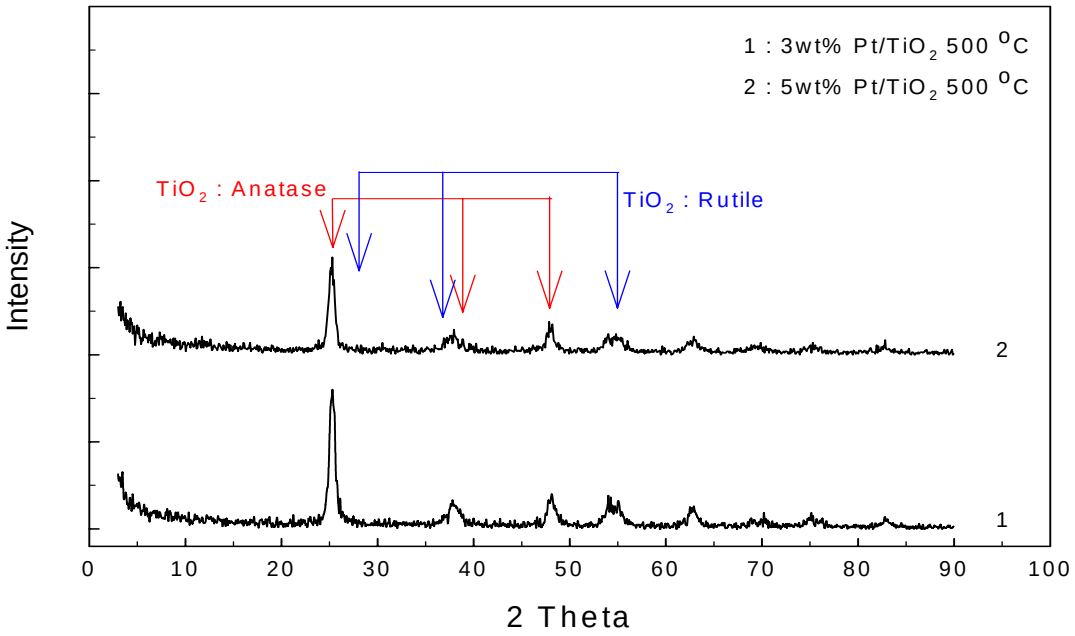

Figure 3. XRD patterns for the Pt/TiO_2 catalysts

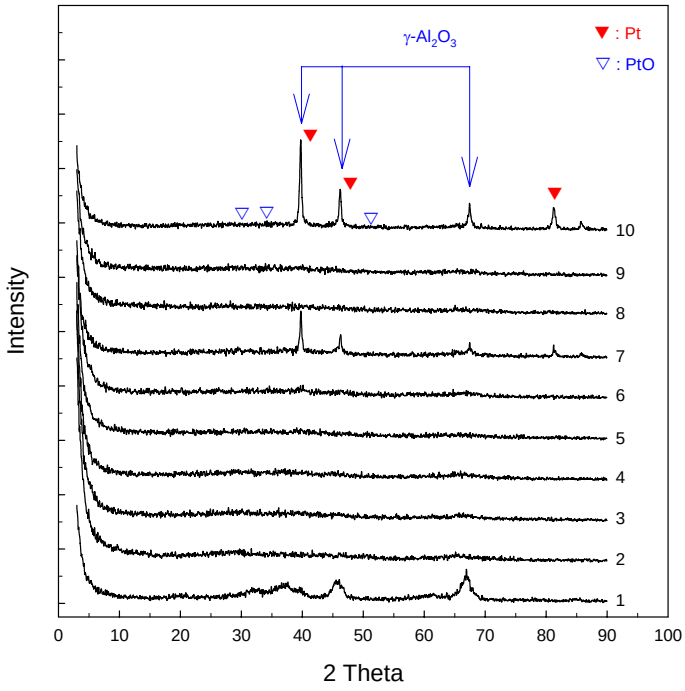

(1) γ-Al_2O_3, (2) γ-Al_2O_3, 400℃ calcination, (3) γ-Al_2O_3, 420℃ calcinations, (4) γ-Al_2O_3, 440℃ calcinations, (5) 3wt% Pt/γ-Al_2O_3, 400℃ calcination, (6) 3wt% Pt/γ-Al_2O_3, 500℃ calcination, (7) 3wt% Pt/γ-Al_2O_3, 600℃ calcination, (8) 5wt% Pt/γ-Al_2O_3, 400℃ calcination, (9) 5wt% Pt/γ-Al_2O_3, 500℃ calcination, (10) 5wt% Pt/γ-Al_2O_3, 600℃ calcination

Figure 4. XRD patterns for the Pt/TiO_2 catalysts

[5] H.S. Zhang, J.X. Wang, D.J. Driscoll, J.H. Lunsford, *Journal of Catalysis*, **112**, 366 (1988).
[6] C.H. Lin, J.X. Wang, J.H. Lunsford, *Journal of Catalysis*, **111**, 302 (1988).
[7] C.J. Liu, A. Marafee, R. Mallinson, L. Lobban, *Applied Catalysis A: General*, **164**, 21 (1997).
[8] Y. Zhang, K.J Smith, *Catalysis Today*, **77**, 257 (2002).
[9] A. Holmen, O. Olsvik, O.A. Rokstad, *Fuel Processing Technology*, **42**, 249 (1995).
[10] J.S. Chang, P.A. Lawless, T. Yamamoto, *IEEE Trans. Plasma Sci.*, **19**, 1152 (1991).
[11] A. Marafee, C. Liu, G. Xu, R. Mallinson, L. Lobban, *Ind. Eng. Chem. Res.*, **36**, 632 (1997).
[12] S.Y. Savinov, H. Lee, H.K. Song, B.K. Na, *Ind. Eng. Chem. Res.*, **38,** 2540 (1999).
[13] H.K. Jeong, S.C. Kim, C. Han, H. Lee, H.K. Song, B.K. Na, *Korean J. Chem. Eng.*, **18**, 196 (2001).
[14] C.J. Liu, R. Mallinson, L. Lobban, *Journal of Catalysis*, **179**, 326 (1998).
[15] C.J. Liu, G.H Xu, T. Wang, *Fuel Processing Technology*, **58**, 119 (1999a).
[16] B. Eliasson, C.J. Liu, U. Kogelschatz, *Ind. Eng. Chem. Res.*, **39**, 1221 (2000).
[17] K. Thanyachotpaiboon, S. Chavades, T.A.Caldwell, L.L Lobban, R.G.Mallinson, *AIChE J.*, **44**, 2252 (1998).
[18] C.J. Liu, R. Mallinson, L. Lobban, *Applied Catalysis A: General*, **178** 17 (1999b).
[19] L. Chen, J. Lin, H.C. Zeng, K.L. Tan, *Catalysis Communication*, **2**, 201 (2001).
[20]S.S. Kim, H. Lee, B.K. Na, H.K. Song, *Korean J. Chem. Eng.*, **20**, 869 (2003a).
[21]S.S. Kim, H. Lee, J.W. Choi, B.K. Na, H.K. Song, *J. Ind. Eng. Chem.*, **9**, 787 (2003b).
[22] Z.H. Li, S.X. Tian, H.T. Wang, H.B. Tian, *J of Molec. Catalysis A: Chemical*, **211**, 149 (2004).
[23] C.J. Liu, K. Yu, Y.P Zhang, X. Zhu, F. He, B. Eliasson, *Applied Catalysis B: Environmental*, **47**, 37 (2004)
[24] S.S. Kim, H. Lee, B.K. Na, H.K. Song, *Catalysis Today*, **89**, 193 (2004a).
[25] S.S. Kim, H. Lee, B.K. Na, H.K. Song, *J. of Chem. Eng. Japan, in press* (2004b).
[26] S. S. Kim, H. Lee, H. K. Song, *proceeding of 226th APCChE Congress*, Hukuoka, 352 (2004)

CO_2 Reforming of Methane in a Gliding Arc Discharge Reactor

H. K. Song, J.-W. Choi and H. Lee

Clean Technology Research Center, Korea Institute of Science & Technology, Seoul, Korea

Abstract

Experiments for CO_2 reforming of methane using gliding arc discharge were performed. A mixture gas of methane was introduced into gliding arc discharge region to produce more valuable hydrocarbons or synthesis gas. The main products of reactions were synthesis gas and acetylene, and small amounts of other C2 hydrocarbons were observed. The methane conversion rate in a gliding arc discharge reactor was calculated and compared with that of other low temperature plasma reactors. The experimental results showed that gliding arc discharge could be an effective tool for methane conversion reaction.

Keywords

Methane, Carbon Dioxide, Reforming, Conversion, Gliding Arc Discharge

1. Introduction

Natural gas is one of the most useful resources in the world due to the greatness of its amount and wideness of its distributions. As reserves of oil are depleting, the value of natural gas as an alternative fuel is becoming greater and greater. Natural gas can be indirectly converted to liquid fuels or other chemicals by way of synthesis gas, or directly transformed to C2 hydrocarbon or methanol. Most of commercial natural gas converting processes convert methane to synthesis gas with steam reforming, and then synthesize methanol or gasoline using this synthesis gas as an intermediate. However, these processes require extreme reaction conditions of high temperature and pressure, and suffer from the rapid deactivation of catalyst and the carbon deposition on the surface of catalyst. So, many studies on the methane conversion using plasma processes are being performed as a promising tool to overcome these problems [1-6]. In plasma processes, the electrical input energy is transferred to energetic electrons rather than heating gas. Through electron impact ionization, dissociation and excitation, generated are excited atomic and molecular species such as electrons, ions and radicals, which in turn enhance the chemical reaction.

In this study, the performance of methane conversion was investigated in a gliding arc discharge reactor. The gliding arc discharge easily generated between two or more diverging electrodes placed in a fast gas flow is a new interesting subject in the area of the chemical reactive conversion for its power effectiveness and its treatment volume [7-8]. The effects of applied frequency, total flowrate, and methane concentration in feed mixture on the conversion and product selectivities were investigated. The chemical reaction performance of the gliding arc discharge was compared with that of other low temperature plasma reactors.

2. Experiments

Experimental setup for CO_2 reforming of methane using gliding arc discharge was shown in Fig. 1. The gliding arc discharge reactor was made of a quartz tube of inner diameter 45 mm and length 300 mm. The upper and bottom part of the reactor was sealed with Teflon and two electrodes were set up inside the reactor. The electrode made of stainless steel had a triangular form with the height of 100 mm. The narrowest gap distance between two electrodes was about 1.5 mm. The gas mixture was introduced between the electrodes through a capillary tube of inner diameter 0.8 mm. A high frequency AC power supply with a maximum voltage of 10 kV, a frequency of 10~20 kHz and a current of 0~100mA was connected to a gliding arc reactor to generate discharge. The waveforms of input voltage and current were measured with a digital oscilloscope (Agilent 54641A) having analog bandwidth of 350 MHz through a high voltage probe (Tektronics 6145A) and current monitor (Pearson 4997).

Methane with a purity of 99% and carbon dioxide with a purity of 99% were used as feed gas, and the flowrate of each gas was controlled with mass flow controllers. Total flowrate of feed gas was fixed at 1

l/min and the concentration of methane was varied from 20 vol% to 90 vol%. Gaseous products were analyzed with two gas chromatographs. A gas chromatograph (HP5890) equipped with flame ionization detector containing Haysep Q column was used to analyze the light hydrocarbon products. Another gas chromatograph (Younglin 600D) equipped with thermal conductivity detector containing molecular sieve 5A and mixture of Porapak Q and R column was also used to detect hydrogen, carbon monoxide and carbon dioxide.

In all experiments, the performance of a gliding arc discharge reactor was evaluated by conversion and selectivities. The conversion and selectivities are defined as bellows.

$$\text{CH}_4 \text{ conversion} = \frac{\text{moles of } \text{CH}_4 \text{ converted}}{\text{moles of } \text{CH}_4 \text{ in feed}} \times 100$$

$$\text{CO}_2 \text{ conversion} = \frac{\text{moles of } \text{CO}_2 \text{ converted}}{\text{moles of } \text{CO}_2 \text{ in feed}} \times 100$$

$$\text{Selectivity of CxHy} = \frac{x \times \text{moles of } \text{C}_\text{X}\text{H}_\text{y} \text{ produced}}{\text{moles of } \text{CH}_4 \text{ converted} + \text{moles of } \text{CO}_2 \text{ converted}} \times 100$$

$$\text{Selectivity of } \text{H}_2 = \frac{\text{moles of } \text{H}_2 \text{ produced}}{2 \times \text{moles of } \text{CH}_4 \text{ converted}} \times 100$$

$$\text{Selectivity of CO} = \frac{\text{moles of CO produced}}{\text{moles of } \text{CH}_4 \text{ converted} + \text{moles of } \text{CO}_2 \text{ converted}} \times 100$$

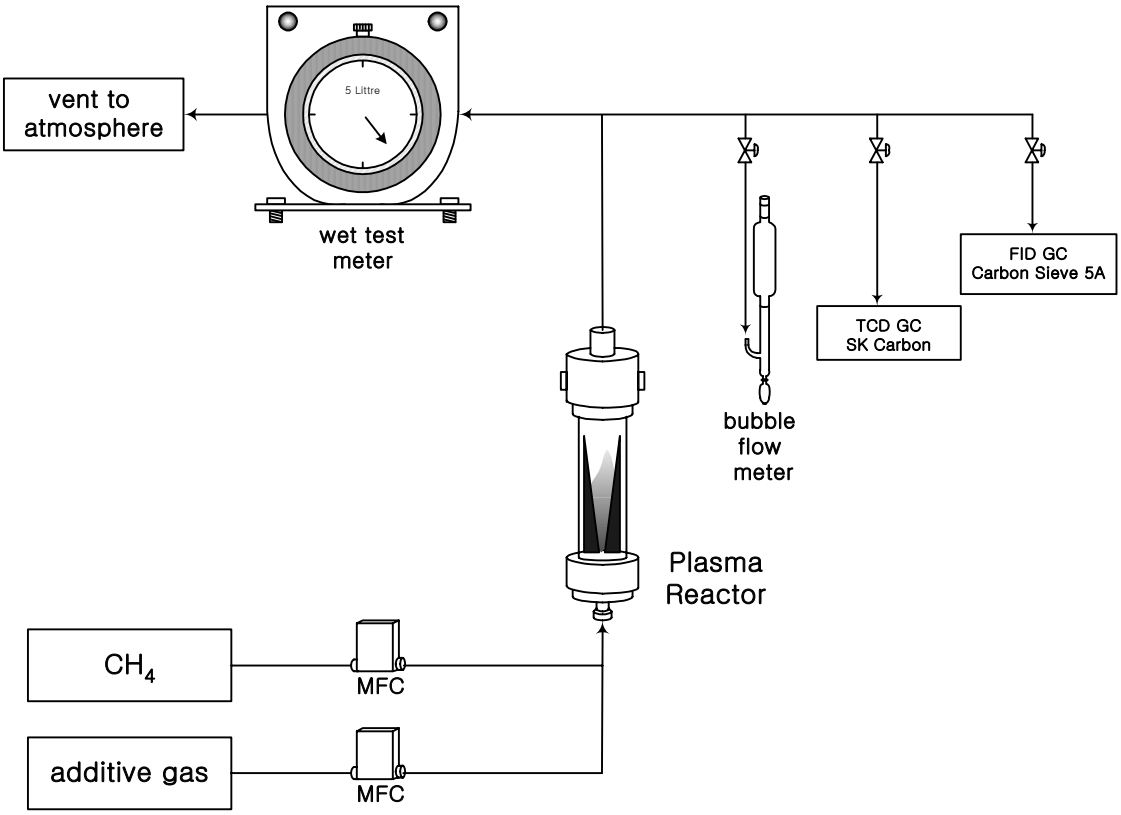

Fig. 1. Experimental setup for methane conversion using gliding arc discharge.

3. Results and Discussion

To investigate the performance of conversion of methane and carbon dioxide in a gliding arc discharge reactor, laboratory experiments were carried out under various experimental conditions. The experimental variables were the input power and the concentration of methane in a feed mixture. Hydrogen, carbon monoxide and acetylene were the main products in a gliding arc discharge reactor and other light hydrocarbons such ethylene and ethane were not observed. Carbon solid material was formed when the concentration of methane was over 50 vol%.

The effect of concentration of methane on conversion was shown in Figure 2. The methane conversion was increased from 35% to 47% although the number of methane molecule was increased. This is mainly due to the introduction of carbon dioxide. In the plasma region, carbon dioxide was decomposed to carbon monoxide, oxygen and atomic oxygen, and this was helpful to destruct the carbon-hydrogen bond of methane molecule. The carbon dioxide conversion was also increased from 26% to 36% with the increase of methane concentration since the total number of carbon dioxide molecule was decreased.

Figure 3 showed the selectivity of plasma products with concentration of methane. The selectivity was strongly dependent on the concentration of methane. The selectivity of hydrogen was decreased from 62% to 37%, and the selectivity of carbon monoxide was rapidly decreased from 93% to 5% when the concentration of methane was increased from 20 vol% to 90 vol%. The selectivity of acetylene showed a maximum value at the methane concentration of 80 vol%. From these results, it was found that the concentration of methane determined the product selectivity and the lower concentration of methane produced more hydrogen and carbon monoxide

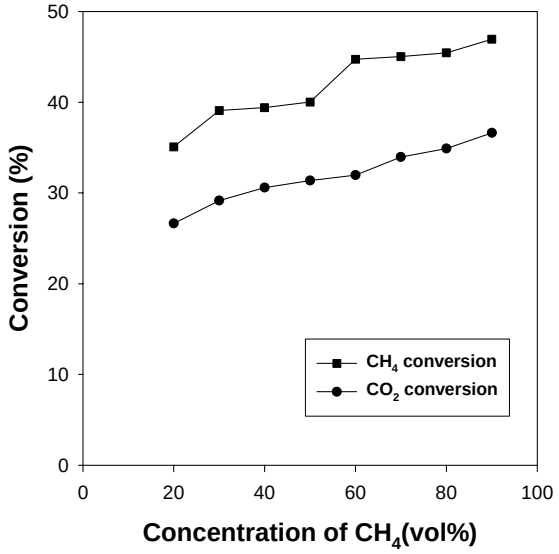

Fig. 2. Effect of CH_4 concentration on conversion.

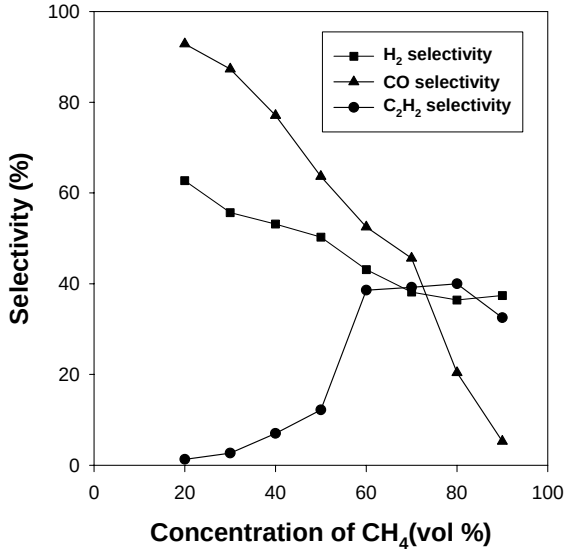

Fig. 3. Effect of CH_4 concentration on selectivity.

To evaluate the reaction efficiency of different plasma source, we calculated the methane conversion rate. Figure 4 showed the consumed power inside a gliding arc discharge reactor with the concentration of methane. The consumed power was decreased from 262W to 162W although the conversion of methane was increased with methane concentration. So, the higher methane concentration was favorable from a viewpoint of energy cost. Figure 5 showed methane conversion rate with some other kinds of plasma sources. The result of microwave was obtained from the literature [9], and those of dielectric barrier discharge were calculated in our previous works [5]. Methane conversion rate obtained in a gliding arc discharge reactor was much higher than those of DBD and microwave discharge. From results, it can be considered that the gliding arc discharge could be an alternative tool for methane conversion reaction.

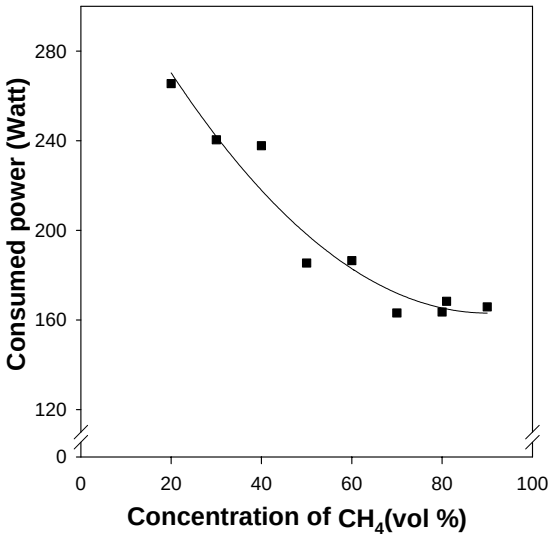

Fig. 4. Consumed power.

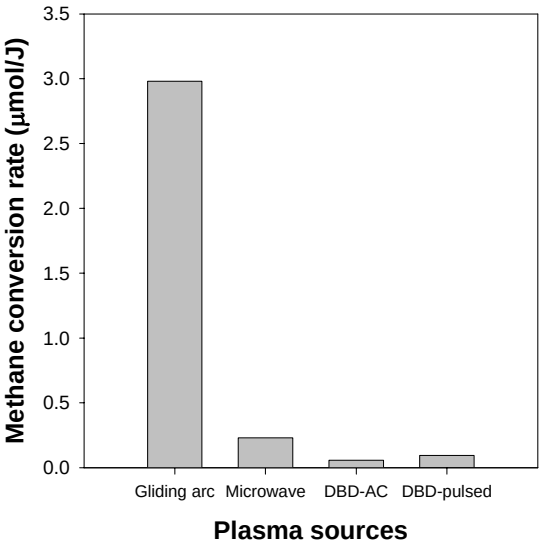

Fig. 5. Comparison of methane conversion rate.

4. Conclusions

Gliding arc discharge is a new interesting subject in the area of the chemical reactive conversion for its high specific throughputs in the reaction zone, and its power effectiveness. In this study, the performance of CO_2 reforming of methane in a gliding arc discharge reactor was experimentally examined and compared with that of other low temperature plasma reactors.

Hydrogen, carbon monoxide and acetylene were the main products in a gliding arc discharge reactor and carbon solid soot were observed when the methane concentration was over 50%. The methane concentration was the key factor to determine the conversion of methane and product selectivities. The lower methane concentration was more favorable to obtain the synthesis gas. The methane conversion rate obtained in this study was much higher than those of dielectric barrier discharge and microwave plasmas.

From these results, it can be considered that the gliding arc discharge could be an alternative tool for methane conversion.

Acknowledgement

This study has been supported by National Research Program of Korean Ministry of Science and Technology.

References

[1] S. L. Yao et. al., Energy & Fuels **14**, 910 (2000).
[2] C. J. Liu et. al., Plasma Chemistry Plasma Processing **21**, 301 (2001).
[3] D. W. Larkin, L. Zhou, L. L. Lobban, and R. G. Mallinson, Ind. Eng. Chem. Res. **40**, 5496 (2001).
[4] M. Heintze, and M. Magureanu, J. Catal. **206**, 91 (2002).
[5] H. K. Song, H. Lee, J. W. Choi, and B. K. Na, Plasma Chemistry Plasma Processing **24**, 57 (2004).
[6] I. Rusu, and J. M. Cormier, Chem. Eng. J. **91**, 23 (2003).
[7] A. Fridman et. al., Progress in Energy & Combustion Science **25**, 211 (1999).
[8] F. Richard, J. M. Cormier, S. Pellerin, and J. Chapelle, J. Appl. Phys. **79**, 2245 (1996).
[9] S. L. Suib, and R. P. Zerger, J. Catal. **139**, 383 (1993).

Low Temperature Synthesis of Carbon Nanofiber in Vibrationally Nonequilibrium CO Plasma and Its Carbon Isotopic Contents

S. Mori, M. Fukuya, and M. Suzuki

Department of Chemical Engineering, Tokyo Institute of Technology, Tokyo, Japan

1. Introduction

In glow discharge of diatomic molecules with translational mode cooling and moderate electric field, one can create vibrationally excited plasma. In the moderate electric fields, plasma free electrons excite the vibrational mode of diatomic molecules preferentially and a decrease of translational temperature strongly decreases the vibration-to-translation energy transfer rates, having only minor effect on vibration-to-vibration energy exchange ones [1]. Such vibrationally nonequilibrium plasma have been studied for being applied to an isotope separation method because vibrational states of heavier isotopic species are overpopulated due to the smaller oscillation frequency for the heavier isotopic species [1-3]. Chemical reactions occurring among vibrationally excited molecules are also attractive for some chemical synthesis processes because the activation energy for the reaction is provided by the vibrational energy mode and the gas kinetic temperature can be kept at a value suitable for those processes [4]. In the previous study, we demonstrated the formation of carbon thin film materials enriched in heavier carbon isotopes in the liquid nitrogen cooled CO plasma, which is enriched in heavier carbon isotopes [5, 6].In the subsequent analysis of wall deposits, we have found the formation of microstructured and nanostructured carbons, notably aligned carbon fibers, in the presence of metal catalysts. Here, we present the structure, morphology, and carbon isotopic contents of that carbon thin film materials formed in the liquid nitrogen cooled CO plasma.

2. Experimental

Figure 1 shows the schematic diagram of experimental apparatus. The central component of our experimental apparatus is the U-shaped discharge tube, which consists of 7.0 mm inner diameter Pyrex tube, with liquid nitrogen cooling bath. In the U-shaped discharge tube, there are two electrodes which are connected to the DC power supply; one of them is stainless steel rod with a diameter of 6 mm and located in the lower part of U-tube and the other is nickel rod with a diameter of 1.5 mm and placed in the upper part of U-tube.

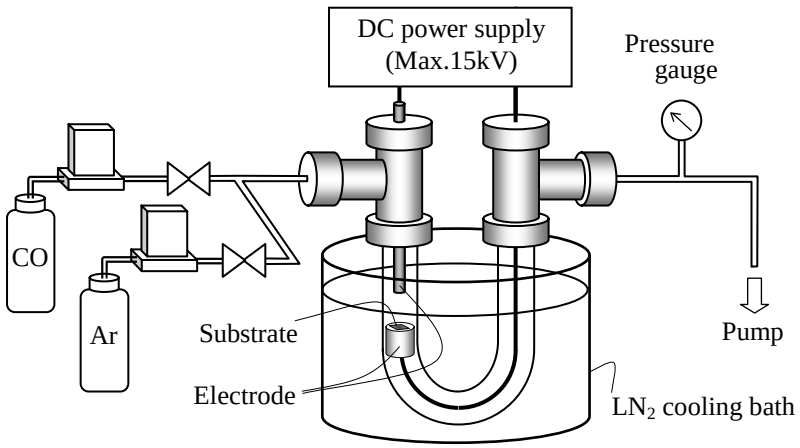

Fig. 1 Schematic diagram of experimental apparatus.

In this study, silicon and glass with a thin nickel catalyst layer were used as substrates. The nickel layer was prepared using DC sputtering process. In the sputtering process, substrates are placed on the lower electrodes (anode) and DC voltage is applied between electrodes spaced 5 mm apart. The detailed parameters for the deposition process are as follows: Ar flow rate: 2.0 sccm, pressure: 100 mTorr, sputtering time: 10-120 seconds. After obtaining Ni thin layer, discharge tube is cooled by liquid nitrogen and the distance and the polarity of electrodes are replaced; in the deposition process lower electrode is the cathode and the distance between two electrodes is set to 20 cm. Then the CO glow discharge plasma is generated between two electrodes. The detailed parameters for the deposition process are as follows: CO flow rate: 10 sccm, Ar flow rate: 10 sccm, total pressure: 6 Torr, deposition time: 10-180 min. Carbon deposits grown on the substrates were observed by scanning electron microscopy and transmission electron microscopy, and analyzed by Raman spectroscopy and Fourier transform infrared spectroscopy. To analyze the isotopic contents of the carbon materials, deposited materials were oxidized to CO_2 and carbon isotopic contents of converted CO_2 were measured by quadru-pole mass spectrometer.

3. Results and discussion

Figure 2 shows the SEM images of carbon nanofibers (CNFs) synthesized on the borosilicate glass substrates after 120-180 minutes deposition time. Aligned carbon nanofibers were synthesized under both room temperature and liquid-nitrogen cooled temperature conditions and the diameter of fibers are several hundreds nanometers and those length are about 10 microns. Figure 3 shows a typical Raman spectrum of the carbon materials formed on the glass substrates. The spectrum for the sample R3 presents two peaks of the graphite structures: the strong G-line peak at approximately 1590 cm^{-1} which indicates crystalline graphene layers and the broad D-line peak at 1350 cm^{-1} which indicates the existence of defective graphene layers such as amorphous carbon layers. However, for liquid nitrogen cooled samples (R1 and R2), both of intensities become very weak. Figure 4 shows a typical FT-IR spectrum of carbon thin film materials deposited on the CaF_2 substrates. There are strong carbonyl band peaks around 1750 and 3400 cm^{-1} for the liquid nitrogen cooled samples (F1 and F2). On the other hand, without liquid nitrogen cooling (F3), carbonyl peaks are weak and aromatic C=C vibration band around 1600 cm^{-1} appears instead. The morphology and structure of the film depend strongly on the metal catalysts, substrate material, substrate temperature, and discharge conditions.

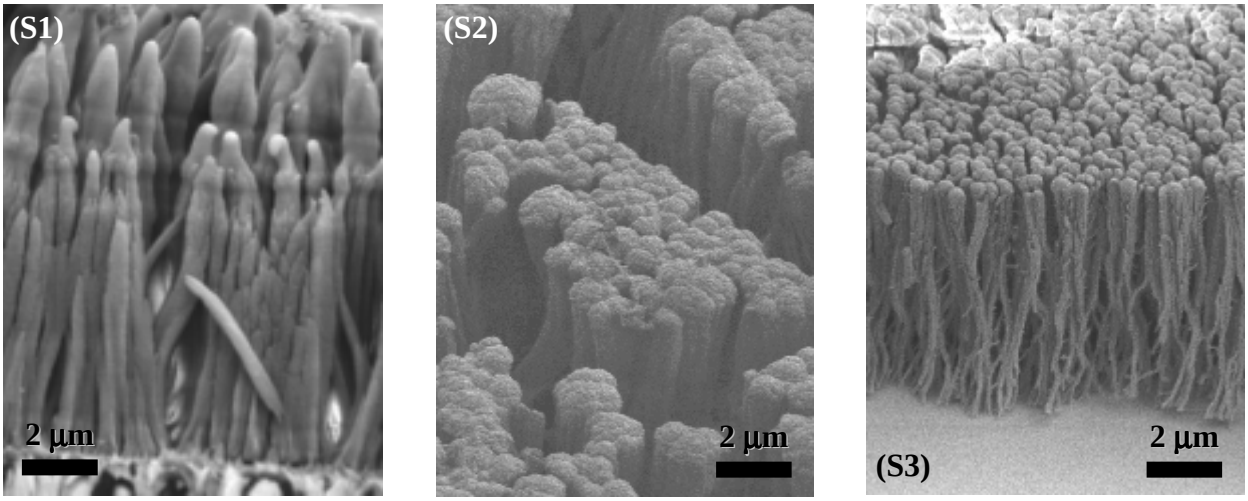

Fig. 2 SEM images of CNFs grown on the glass substrates (S1) with LN_2 cooling and Ni catalyst, (S2) with LN_2 cooling and without Ni catalyst, and (S3) with Ni catalyst and without LN_2 cooling.

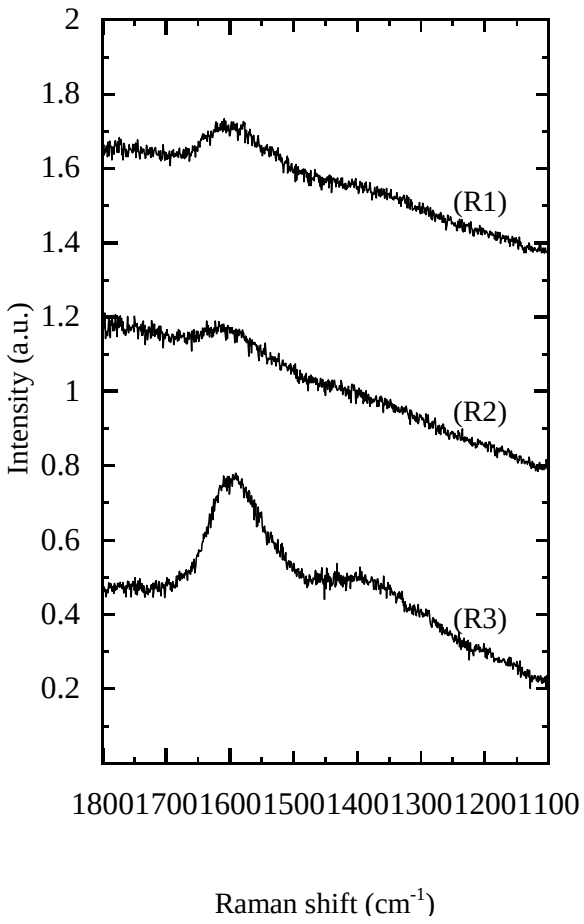

Fig. 3 Raman spectrum: (R1) with LN_2 cooling and Ni catalyst, (R2) with LN_2 cooling and without Ni catalyst, (R3) without LN_2 cooling and Ni catalyst.

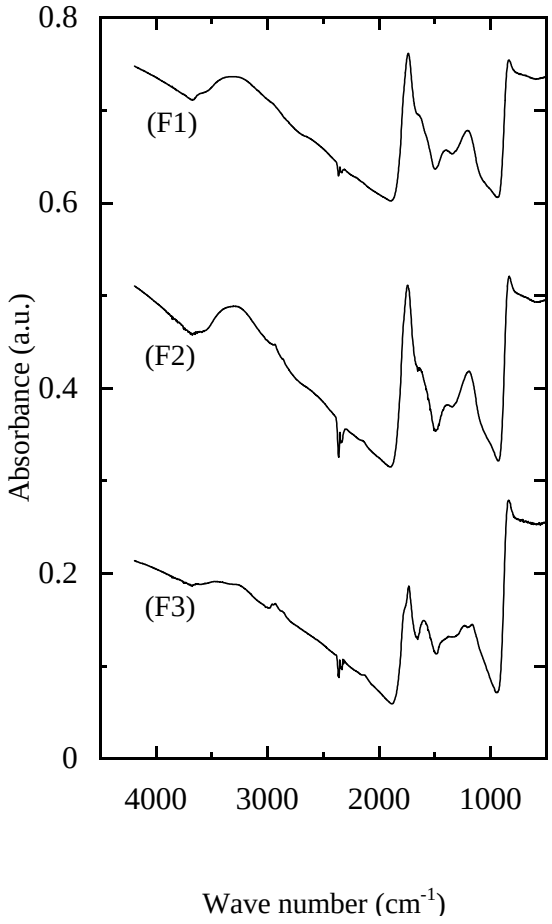

Fig. 4 FTIR spectrum: (F1) with LN_2 cooling and Ni catalyst, (F2) with LN_2 cooling and without Ni catalyst, (F3) without LN_2 cooling and Ni catalyst.

To verify the relation between reaction of vibrationally excited CO molecules and formation of CNFs, carbon isotopic contents in carbon deposits were also analyzed. This is due to the fact that carbon-13 isotope enrichment in carbon deposits results from reactions among vibrationally excited CO molecules [1]. In this study, the isotope enrichment of ^{13}C in the deposits is presented as isotope enrichment coefficient defined as:

$$^{13}\beta_C = (^{13}C/^{12}C)_{deposit} / (^{13}C/^{12}C)_{reactant} , \quad (1)$$

where $^{13}\beta_C$ is the ^{13}C enrichment coefficient in carbon deposit. The relative abundance of ^{13}C in carbon deposit, $(^{13}C/^{12}C)_{deposit}$, is determined by the mass spectrometric peak height at m/e = 44 and 45 of CO_2 converted from the deposit. The relative isotopic abundances in reactant, $(^{13}C/^{12}C)_{reactant}$ is calculated from the mass spectra for ^{13}C at m/e = 44, 45 of natural isotopic abundance CO_2. And only the natural isotopic composition CO was used as a reactant in this study. The carbon isotope enrichment coefficient for CNFs synthesized at room temperature is almost 1, that is, the isotope enrichment is not observed. However, the carbon isotope enrichment coefficient for the CNFs synthesized under the condition of liquid nitrogen cooling is 1.05. From this result, it was suggested that the vibrationally excited molecule perform the key role in this CNFs synthesis process.

4. Conclusion

We have performed the experimental study of low temperature synthesis of carbon nanofibers in nonequilibrium CO plasma. Nanostructured carbon thin film materials, notably well aligned nanofibers, were obtained on the glass substrate at room temperature and liquid-nitrogen cooled conditions in the presence of Ni catalysts. The film contains not only carbon but also oxygen in the structures. Diameter of fibers are several hundreds nanometers. The morphology and structure of the film depend strongly on the metal catalysts, substrate material, substrate temperature, and discharge conditions. To verify the relation between reaction of vibrationally excited CO molecules and formation of CNFs, we have also perfomed the analysis of carbon isotopic contents in carbon deposits. The isotope enrichment is not observed for CNFs synthesized at room temperature. However, the carbon-13 is slightly enriched in CNFs synthesized under the condition of liquid nitrogen cooling. From this result, it was suggested that the vibrationally excited molecules perform the key role in this low temperature CNFs synthesis process.

Acknowledgement

This work was partially supported by Grant-in-Aid from the Ministry of Education, Culture, Sports, Science and Technology of Japan.

References

[1] M. Capitelli, *Nonequilibrium Vibrational Kinetics*, Springer, Berlin (1986).
[2] E.M. Belenov, E.P. Markin, A.N. Oraevskii, V.I. Romanenko, *JETP Lett.* **18**, 118 (1973).
[3] E. Ploenjes, I. Adamovich, V.V. Subramaniam, J.W. Rich, *AIAA Paper* 98-0993, Jan. (1998).
[4] E. Ploenjes et al., *Chem. Phys. Lett.* **352** (2002) 342-347.
[5] S. Mori, H. Akatsuka, M Suzuki, *Proc. 15th Int. Symp. on Plasma Chem.* (Orleans, France), 647-652 (2001).
[6] S. Mori, H. Akatsuka, M Suzuki, *J. Nucl. Sci. Technol.* **38**, 850-858, (2002).

Modeling Study of Heat Transfer from a Laminar Argon Plasma Jet Impinging upon a Workpiece in Ambient Air

Kai Cheng [1], Hai-Xing Wang [1], Xi Chen [1], Wenxia Pan [2]

[1] *Department of Engineering Mechanics, Tsinghua University, Beijing 100084, China*
[2] *Institute of Mechanics, Chinese Academy of Sciences, Beijing 100080, China*

Abstract

Modeling is performed to study the heat transfer for a laminar argon plasma jet impinging upon a workpiece in ambient air. The heat flux density distribution on the workpiece surface obtained from this modeling is then used for predicting the re-melting of the cast-iron workpiece. The effects of workpiece moving speed, Marangoni convection et al on the workpiece heating are included in the workpiece heating study. The predicted width and depth of the molten pool in the workpiece agree reasonably with experimental data.

1. Introduction

Stable and silent long laminar plasma jets have been successfully generated recently with elaborately designed DC arc plasma torches (e.g. see [1]). Since only molecular diffusion mechanism is involved for the laminar case, the entrainment of ambient air into the laminar jet is appreciably reduced, and thus its high-temperature region length is much longer than that for the conventional turbulent plasma jet. The axial gradients of plasma temperature and axial-velocity in the laminar plasma jet are also much smaller. In addition, the laminar plasma-jet length can be easily adjusted by changing the arc current and/or the working-gas flow rate. These merits of the long laminar plasma jet make it very attractive from the viewpoint of materials processing, since it provides a new possibility to achieve low-noise working surroundings, better process repeatability and controllability, and reduced oxidation degree of metallic materials processed in air surroundings. Preliminary attempts [2,3] to use the laminar plasma jet in the preparation of thermal barrier coatings and in the re-melting hardening of cast iron and the stainless-steel surface cladding have shown encouraging results including the fine microstructure, low surface roughness and small porosity of the prepared coatings, the good re-melting process controllability and surface morphologies, as well as the preferable metallurgically bonded clad layer.

With the laminar plasma-jet hardening of cast iron surface [2,3] as the main research background, modeling study is conducted in this paper concerning heat transfer from a laminar argon plasma jet impinging normally upon a workpiece located in ambient air. Typical computed distributions of temperature, axial velocity, argon mass fraction distributions are presented and then a numerical modeling is also conducted to study the heating of the workpiece by the laminar plasma jet. In order to reveal the effects of the workpiece moving speed on the molten pool, three-dimensional modeling approach is used here to study the workpiece heating.

2. Modeling Approach

2.1 Laminar impinging plasma jet

Main assumptions used in the jet modeling study include steady, laminar and axi-symmetrical flow with negligible swirling velocity component; local thermodynamic equilibrium (LTE) and optically thin plasma; the diffusion of ambient air into the plasma jet can be handled by use of the combined-diffusion-coefficient method [4]. The governing equations including the mass, momentum, energy, and gas species conservation

equations in the cylindrical coordinate system are the same as those used in [5] as follows.

$$\frac{\partial}{\partial x}(\rho u)+\frac{1}{r}\frac{\partial}{\partial r}(r\rho v)=0 \tag{1}$$

$$\frac{\partial(\rho uu)}{\partial x}+\frac{1}{r}\frac{\partial(r\rho uv)}{\partial r}=-\frac{\partial p}{\partial x}+2\frac{\partial}{\partial x}\left[\mu\frac{\partial u}{\partial x}\right]+\frac{1}{r}\frac{\partial}{\partial r}\left[r\mu\left(\frac{\partial u}{\partial r}+\frac{\partial v}{\partial x}\right)\right] \tag{2}$$

$$\frac{\partial(\rho uv)}{\partial x}+\frac{1}{r}\frac{\partial(r\rho vv)}{\partial r}=-\frac{\partial p}{\partial r}+\frac{2}{r}\frac{\partial}{\partial r}\left[r\mu\frac{\partial v}{\partial r}\right]+\frac{\partial}{\partial x}\left[\mu\left(\frac{\partial v}{\partial x}+\frac{\partial u}{\partial r}\right)\right]-2\mu\frac{v}{r^2} \tag{3}$$

$$\frac{\partial(\rho uh)}{\partial x}+\frac{1}{r}\frac{\partial(r\rho vh)}{\partial r}=\frac{\partial}{\partial x}\left[\frac{k}{c_p}\frac{\partial h}{\partial x}\right]+\frac{1}{r}\frac{\partial}{\partial r}\left[r\frac{k}{c_p}\frac{\partial h}{\partial r}\right]-U_r-\frac{\partial}{\partial x}\left[(h_A-h_B)J_x\right]-\frac{1}{r}\frac{\partial}{\partial r}\left[r(h_A-h_B)J_r\right]$$

$$-\frac{\partial}{\partial x}\left[\frac{k}{c_P}(h_A-h_B)\frac{\partial f_A}{\partial x}\right]-\frac{1}{r}\frac{\partial}{\partial r}\left[r\frac{k}{c_P}(h_A-h_B)\frac{\partial f_A}{\partial r}\right] \tag{4}$$

$$\frac{\partial(\rho uf_A)}{\partial x}+\frac{1}{r}\frac{\partial(r\rho vf_A)}{\partial r}=\frac{\partial}{\partial x}\left[\Gamma_f\frac{\partial f_A}{\partial x}\right]+\frac{1}{r}\frac{\partial}{\partial r}\left[r\Gamma_f\frac{\partial f_A}{\partial r}\right]+S_f \tag{5}$$

Here u and v are the axial (x-) and radial (r-) velocity components, ρ, μ, k, c_p, h and U_r are temperature- and composition-dependent plasma density, viscosity, thermal conductivity, specific heat at constant pressure, specific enthalpy and radiation power per unit volume of plasma, respectively, p and f_A are the pressure and the argon mass fraction in the argon-air mixture. In Eq. (4), h_A and h_B are the specific enthalpies of gases A (argon) and B (air), respectively, whereas J_x and J_r are the axial (x-) and radial (r-) components of the argon diffusion mass flux vector $\vec{J}_A=-\left(n^2/\rho\right)\overline{m}_A\overline{m}_B\overline{D}_{AB}^{x}\nabla X_A-\overline{D}_{AB}^{T}\nabla\ln T$. Here n is the total gas-particle number density, $\overline{m}_A$ and $\overline{m}_B$ are the averaged particle masses for all the *heavy* gas particles (excluding electrons) coming from argon and those from air, X_A is the mole fraction of argon in the argon-air mixture, whereas $\overline{D}_{AB}^{x}$ and $\overline{D}_{AB}^{T}$ are the combined ordinary diffusion coefficient associated with the argon mole fraction gradient ∇X_A and the combined thermal diffusion coefficient associated with the temperature gradient ∇T, respectively [4]. The transport coefficient in Eq. (5) is expressed by $\Gamma_f=[\overline{m}_A\overline{m}_B/(\overline{MM}_A)]\rho\,\overline{D}_{AB}^{x}$, in which $\overline{M}$ and $\overline{M}_A$ are the averaged gas-particle mass for *all* the gas particles (including electrons) of the gas mixture and that for *all* the gas particles coming from argon, respectively, whereas the source term S_f is [4,5]

$$S_f=\frac{\partial}{\partial x}\left(\Gamma_f\frac{f_A}{\overline{M}}\frac{\partial\overline{M}}{\partial x}\right)-\frac{\partial}{\partial x}\left(\Gamma_f\frac{f_A}{\overline{M}_A}\frac{\partial\overline{M}_A}{\partial x}\right)+\frac{1}{r}\frac{\partial}{\partial r}\left(r\Gamma_f\frac{f_A}{\overline{M}}\frac{\partial\overline{M}}{\partial r}\right)-\frac{1}{r}\frac{\partial}{\partial r}\left(r\Gamma_f\frac{f_A}{\overline{M}_A}\frac{\partial\overline{M}_A}{\partial r}\right)$$
$$+\frac{\partial}{\partial x}\left(\overline{D}_{AB}^{T}\frac{\partial\ln T}{\partial x}\right)+\frac{1}{r}\frac{\partial}{\partial r}\left(r\overline{D}_{AB}^{T}\frac{\partial\ln T}{\partial r}\right) \tag{6}$$

The computational domain employed in this study is the region A-J-I-H-A shown in Fig. 1, i.e. only a semi-plane of the axi-symmetrical impinging jet. The left-hand side of plane K-D-E is the plasma torch with A-B being the plasma flow inlet. B-C-D is a backward-step region, whereas K-D is the torch outlet. E-F is the annular slot used for the shrouding gas (argon) injection, if a shrouding gas is desirable to be used. I-J is the workpiece surface, whereas G-H and H-I are the free boundaries, respectively.

In the computation, the radial size (AH) of the computational domain is set to be 50 mm, whereas axial size (AJ) is 18 mm. Other sizes adopted are as follows: Inner radius of plasma flow inlet (AB) is 2 mm, torch exit inner radius (KD) 4 mm, wall thickness (BG) 33 mm, backward-step length (CD) 8 mm. SIMPLE algorithm and a non-uniform 92 (x-) × 187 (r-) mesh are employed in the computation with finer mesh spacing near the

jet axis.

The boundary conditions used in the jet modeling include that at the jet inlet A-B, zero radial velocity, argon mass fraction $f_A = 1.0$ and the power-law profiles of axial velocity and temperature are used. The inlet maximum axial velocity and temperature at the jet inlet are 400 m/s and ~14500 K, respectively. Axi-symmetrical conditions are employed along the jet axis A-J; free boundary conditions are employed along G-H and H-I; and zero velocity, fixed temperature and zero diffusion flux are used at the solid surfaces.

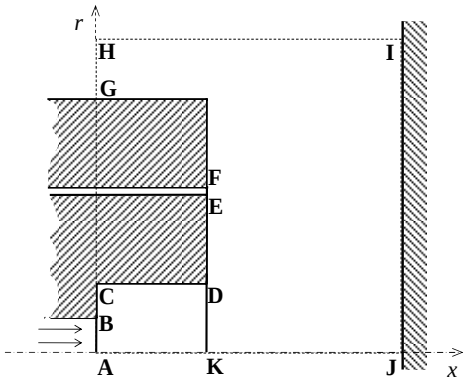

Fig. 1 Computational domain

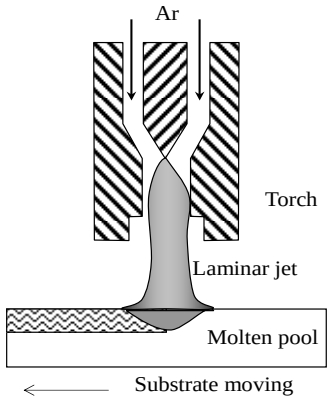

Fig. 2 Schematic diagram of plasma heating system

2.2 Heating of the workpiece by the plasma jet

The schematic diagram for the laminar plasma-jet re-melting hardening of cast iron surface is shown in Fig. 2. The plasma jet impinges normally upon the workpiece with a constant transverse velocity U_s moving relative to the workpiece. In the following computational study of workpiece heating, the coordinate system fixed with respect to the plasma jet is employed.

Main assumptions employed in this study include that the melting process is steady in the coordinate system fixed with the plasma jet; there is no deformation on the top surface of the molten pool. Based on these assumptions, the governing equations in the Cartesian coordinate system (x, y, z) (*x* is in the negative direction of workpiece motion, whereas *z* in the vertical direction) to describe the melt flow and heat transfer in the workpiece are as follows [6,7]:

$$\frac{\partial(\rho u)}{\partial x}+\frac{\partial(\rho v)}{\partial y}+\frac{\partial(\rho w)}{\partial z}=0 \tag{7}$$

$$\rho\left(u\frac{\partial u}{\partial x}+v\frac{\partial u}{\partial y}+w\frac{\partial u}{\partial z}\right)=\frac{\partial}{\partial x}\left[2\mu\left(\frac{\partial u}{\partial x}\right)\right]+\frac{\partial}{\partial y}\left[\mu\left(\frac{\partial u}{\partial y}+\frac{\partial v}{\partial x}\right)\right]+\frac{\partial}{\partial z}\left[\mu\left(\frac{\partial u}{\partial z}+\frac{\partial w}{\partial x}\right)\right]-\frac{\partial p}{\partial x}+S_u \tag{8}$$

$$\rho\left(u\frac{\partial v}{\partial x}+v\frac{\partial v}{\partial y}+w\frac{\partial v}{\partial z}\right)=\frac{\partial}{\partial x}\left[\mu\left(\frac{\partial v}{\partial x}+\frac{\partial u}{\partial y}\right)\right]+\frac{\partial}{\partial y}\left[2\mu\left(\frac{\partial v}{\partial y}\right)\right]+\frac{\partial}{\partial z}\left[\mu\left(\frac{\partial v}{\partial z}+\frac{\partial w}{\partial y}\right)\right]-\frac{\partial p}{\partial y}+S_v \tag{9}$$

$$\rho\left(u\frac{\partial w}{\partial x}+v\frac{\partial w}{\partial y}+w\frac{\partial w}{\partial z}\right)=\frac{\partial}{\partial x}\left[\mu\left(\frac{\partial w}{\partial x}+\frac{\partial u}{\partial z}\right)\right]+\frac{\partial}{\partial y}\left[\mu\left(\frac{\partial w}{\partial y}+\frac{\partial v}{\partial z}\right)\right]+\frac{\partial}{\partial z}\left[2\mu\left(\frac{\partial w}{\partial z}\right)\right]-\frac{\partial p}{\partial z}+S_w+S_b \tag{10}$$

$$\rho c\left(u\frac{\partial T}{\partial x}+v\frac{\partial T}{\partial y}+w\frac{\partial T}{\partial z}\right)=\frac{\partial}{\partial x}\left(k\frac{\partial T}{\partial x}\right)+\frac{\partial}{\partial y}\left(k\frac{\partial T}{\partial y}\right)+\frac{\partial}{\partial z}\left(k\frac{\partial T}{\partial z}\right)+S_h \tag{11}$$

Here *u*, *v* and *w* are velocity components in *x*-, *y*- and *z*-directions, *T* and *p* are temperature and pressure,

whereas ρ, μ and k are density, viscosity and thermal conductivity, respectively. In order to account for the solid-liquid phase change in the workpiece, the fixed-grid method suggested by Voller and Swaminathan [8] has been employed. Namely, the heat and momentum transfer on the solid-liquid phase interface are incorporated into the governing equations through introducing suitable volume source terms. The source terms S_u, S_v and S_w introduced in the momentum equations (8) – (10) take the following forms [6,7]:

$$S_u = A(u - U_s), \quad S_v = Av, \quad S_v = Aw, \tag{12}$$

where parameter A depends on material and the liquid-phase fraction f, and $A = -C(1-f)^2/(f^3+q)$ for the materials in which phase change takes place with a mushy region, where q is merely a very small computational constant introduced to avoid division by zero and C is a large constant (e.g. 10^{10}). The liquid mass fraction f is in the range of $0 \le f \le 1$. S_h in Eq. (11) is introduced to account for the latent heat release, and takes the following form:

$$S_h = -\rho L\left(u\frac{\partial f}{\partial x} + v\frac{\partial f}{\partial y} + w\frac{\partial f}{\partial z}\right) \tag{13}$$

in which L is the melting latent heat of cast iron. The additional source term S_b in the momentum equation (10) in the vertical direction is introduced to account for the natural convection in the molten pool, and

$$S_b = \rho_m g\beta(T - T_m) \qquad (\text{for } T > T_m), \tag{14}$$

where Boussinesq approximation has been used. In Eq. (14), β is the volume expansion coefficient, g the gravity acceleration, whereas T_m is the melting point of the workpiece material.

Boundary conditions employed in the study of workpiece heating are as follows: At the upstream boundary, $u = U_s$, $v = 0$, $w = 0$ and $T = T_a$ (T_a is the ambient temperature). At the downstream boundary, $u = U_s$, $v = 0$, $w = 0$ and $\partial T/\partial x = 0$. At the symmetrical plane ($y = 0$): $\partial u/\partial y = 0$, $v = 0$, $\partial w/\partial y = 0$ and $\partial T/\partial y = 0$. At the top surface of molten pool, *i. e.* at $z = h$ (h is plate thickness), since the melt temperature may be high and the melt temperature distribution is often non-uniform, the effects of surface heat loss and surface tension gradient on melt flow are included in the present study. Namely, we employ the conditions $\mu\partial u/\partial z = f(\partial\sigma/\partial T)(\partial T/\partial x)$, $\mu\partial v/\partial z = f(\partial\sigma/\partial T)(\partial T/\partial y)$, $w = 0$ and $k(\partial T/\partial z) = q_j - \varepsilon\Sigma T^4$ at the top surface. Here σ is the surface tension coefficient, ε and Σ are the emissivity and the Stefan-Boltzmann constant, whereas q_j is the local heat flux density from the plasma jet to the workpiece surface. At the bottom surface of workpiece (*i. e.* at $z = 0$), $u = U_s$, $v = 0$, $w = 0$ and $\partial T/\partial z = 0$ are used.

Actual computational domain used in the modeling of workpiece heating is the cylindrical region with sizes $0 \le r \le 15$ mm, $0 \le \theta \le \pi$ and $0 \le z \le 10$ mm. Altogether 36 (r-direction) × 12 (θ-direction) × 36 (z-direction) grid points are employed in the modeling. For this case, at the geometrical axis of the computational domain (r = 0), the averaged values of ϕ_i (i = 1, 2, …, N) at all the N grid points in the θ-direction and on the small circle nearest to the axis in the mesh are employed for the variable ϕ.

SIMPLE-like algorithm is also used to solve the governing equation for the workpiece regions.

3. Modeling results and discussions

3.1 Modeling results of laminar impinging plasma jet

Typical computed results of the temperature, argon mass fraction and axial velocity distributions in the impinging jet are shown in Fig. 3. The distributions of impact pressure, radial velocity gradient (or viscous stress) and temperature gradient (or heat flux density) on the workpiece surface are also obtained. In the

calculation of surface heat fluxes, the contribution to the heat fluxes of electron-ion recombination at the metallic surface is included besides the convective heat transfer. The heat flux profiles are shown in Fig. 4.

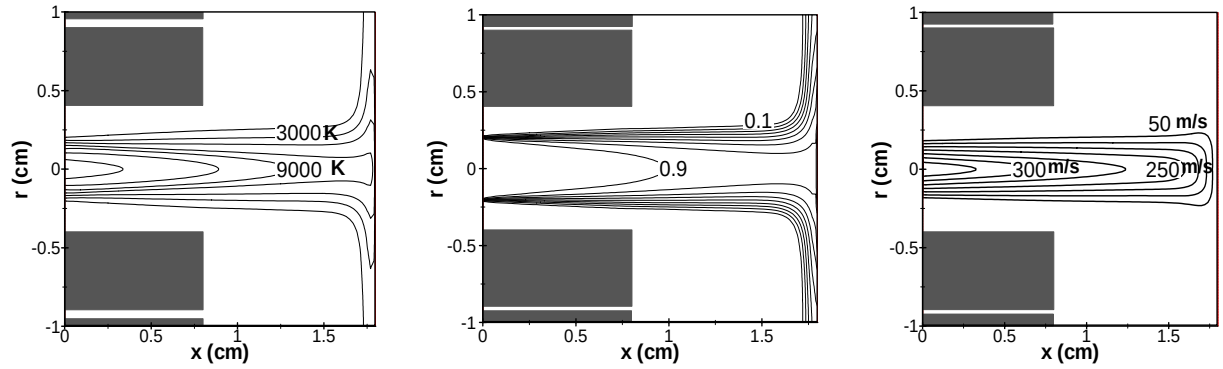

(a) (b) (c)

Figure 3 Computed isotherms (a), Ar mass fraction (b) and axial-velocity distributions. (T_0=13900 K, U_0=400 m/s)

3.2 Modeling results of workpiece melting process

It is expected that the power absorbed by the workpiece of the plasma jet will be used to the solid-phase heating, melting and liquid-phase heating as well as the surface radiation loss of the workpiece material.

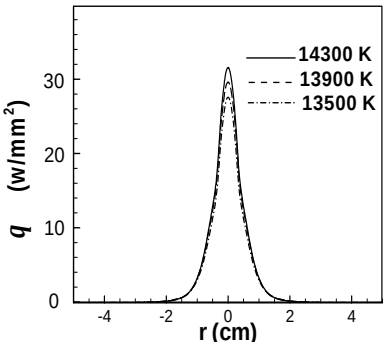

Fig. 4 Heat flux profiles on workpiece surface

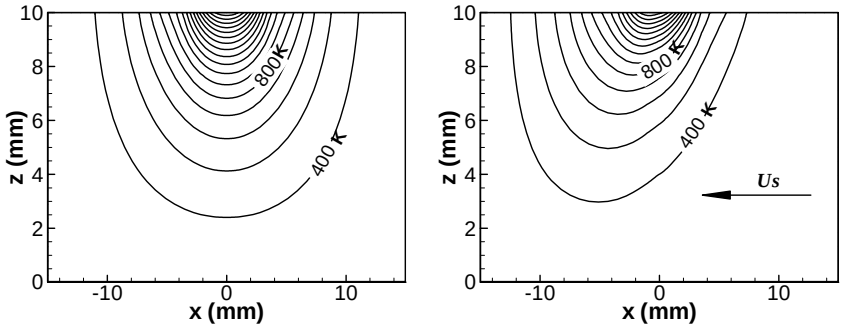

(a) workpiece speed 0 mm/s (b) workpiece speed 5.0 mm/s

Fig. 5 Computed isotherms on the x-z section

Figures 5(a) and 5(b) show the computed isotherms on the x-z section for the workpiece moving speeds of 0 and 5 mm/s. The computed isotherms on the x-y section are shown in and Fig. 6 for 5 mm/s moving speed. All these results are for the case with the maximum axial velocity and temperature at the jet inlet being 400 m/s and 14300 K. From Fig. 5(a) it is seen that the isotherms are symmetrical for this case without workpiece moving, as expected. Non-symmetrical isotherms are obtained when the workpiece is moving, cf. Fig. 5(b) and Fig. 6. The moving speed affects significantly the temperature distribution in the workpiece.

The computed molten pool shapes on x-z plane of the workpiece are compared in Fig. 7 for the cases with the same U_0 (400 m/s) and T_0 (14300 K) but different U_S (workpiece moving speeds), and in Fig. 8 for the cases with the same U_0 (400 m/s) and U_S (1.7 mm/s) but different T_0. It is seen from Fig. 7 that with the increase of the workpiece moving speed, narrower, shallower and more asymmetrical molten pools are obtained. Fig. 8 shows that deeper and wider molten pools are obtained at high jet temperatures (T_0).

We can compare our modeling results with some available experiment data. The plasma torch and associate operating conditions employed in this modeling study are similar to those for the experiment of Pan et al [2]. In their experiment, non-transferred DC laminar plasma jet was used to heat the cast iron for re-melting

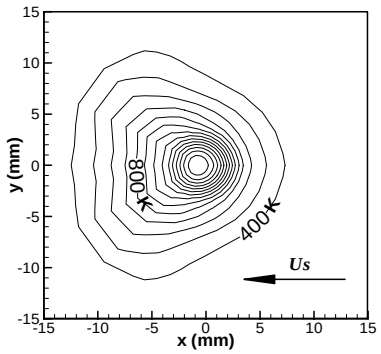

Fig. 6 Isotherms on the x-y section For workpice speed 5 mm/s

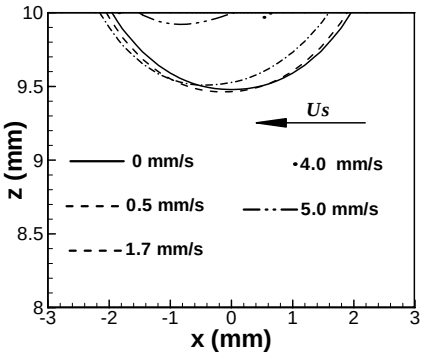

Fig. 7 Molten pool shapes for different workpiece speed U_s

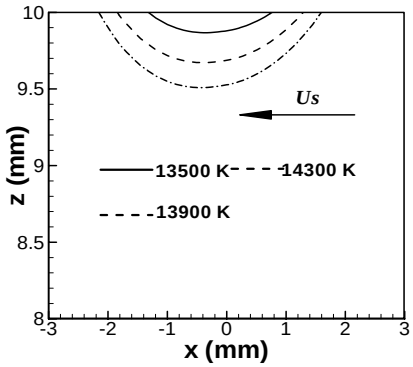

Fig. 8 Molten pool shapes for different jet temaperatures

hardening. The surface treatment conditions were fixed with the distance 9 mm from the torch nozzle exit to the workpiece surface, the workpiece moving speed 0.5~5 mm/s, the gas flow rate 75~220 cm^3/s and the arc current 180~200 A. The molten pool widths observed in their experiment are in the range of 2.0 – 4.0 mm, whereas the thickness of the hardened layer is the range of 0.6~1.7 mm. Because the thickness of the hardening layer is the sum of the molten pool depth and the thickness for the solid phase-change region (about 0.6 mm). So the actual molten pool depth range is 0~1.1 mm, these experimental results agree reasonably with the present modeling predictions.

4. Conclusions

Modeling results are presented in this paper concerning the heat transfer from a laminar argon plasma jet impinging normally upon a workpiece located in air surroundings and concerning the workpiece melting process. The modeling results show that the workpiece moving speed and the maximum temperature at the jet inlet affect significantly the temperature distributions and the molten pool shapes in the workpiece. The predicted sizes of molten pool are reasonably consistent with available experimental data.

Acknowledgement

This study was supported by the National Natural Science Foundation of China (Nos. 50336010, 50276065 and 10405015) and the Chinese Postdoctoral Science Foundation (No. 20040350044).

References

[1] W. X. Pan, W. H. Zhang, W. H. Zhang, C. K. Wu, *Plasma Chem. Plasma Process.* **21**, 23 (2001)
[2] W. X. Pan, X. Meng, G. Li, Q. X. Fei, C. K. Wu, *Surf. Coat. Technol*. (in press, 2005)
[3] W. X. Pan, W. Ma, C. K. Wu, in *Mechanics and Material Engineering for Science and Experiments, eds.* Y.-C. Zhou et al (eds.), Science Press, Beijing, 427 (2003)
[4] A.D. Murphy, *Physical Review* **48**, 3594 (1993)
[5] D.-Y. Xu, X. Chen, K. Cheng, *J. Phys. D: Appl. Phys*. **36**, 1583 (2003)
[6] X.-H. Ye, X. Chen, *J. Phys. D: Appl. Phys*. **35**, 1049 (2003)
[7] H.-X. Wang, X. Chen, *J. Phys. D: Appl. Phys*. **36**, 628 (2003)
[8] V. R. Voller, C. R. Swaminathan, B. G. Thomas, *Int. J. Numer. Methods Eng*. **30**, 875 (1990)

Comparison of microwave, radio frequency, and dual mode plasmas: Deposition of SiO_x films from oxygen and hexamethyldisiloxane

A. Bieder, A. Sonnenfeld, Ph. Rudolf von Rohr

Swiss Federal Institute of Technology Zurich, Institute of Process Engineering, CH-8092 Zurich, Switzerland

Abstract

A reactor equipped with a remote 2.45 GHz slot antenna plasma source and a 13.56 MHz-biased substrate holder was used to conduct deposition experiments. This study focuses on the dependence of the gas phase emission on the oxygen-to-HMDSO flow rate ratio, radio frequency and microwave power. The influence of different gas phase species on the barrier performance of SiO_x films is investigated. It was found that the gas phase is dominated by the microwave discharge, but the gas barrier mainly by the substrate self-bias.

Key words: PECVD, silicon oxide, OES, water vapor transmission rate

1. Introduction

In food packaging, medical device, and electronic industries the interest in silicon oxide films has increased [1]. SiO_x thin films are transparent, recyclable, and suitable for the microwave oven. Their chemical and mechanical properties can be varied in a wide range by applying different process conditions [2, 3]. To get an insight into the gas phase, optical diagnostics are often used since they are selective, non-intrusive, and allow time/spacial resolution [4]. For a better understanding of the plasma processes and the influence of the gas phase on the water vapor barrier performance of the deposited silicon oxide film, investigations with optical emission spectroscopy were conducted in this study. The effect of the oxygen-to-monomer flow rate ratio, radio frequency and microwave power input was analyzed and the important factors on the film properties evaluated. As former studies showed, the discharge parameters strongly influence the barrier performance of thin SiO_x films [2, 3].

2. Experimental

All experiments were conducted in a 20 liter batch reactor. The reactor is equipped with a remote microwave (MW) and a direct radio frequency (RF) plasma sources. The 2.45 GHz slot antenna plasma source (Slan I, Plasma Consult) and a 13.56 MHz-biased substrate holder can be ignited separately or simultaneously in so called dual mode. During the experiments, oxygen and argon are fed at the top of the reactor and the monomer hexamethyldisiloxane (HMDSO) is injected through a ring shower in the afterglow of the MW plasma source. The range of variation of process parameters and the default values can be seen in Tab.1. In this study the oxygen-to-HMDSO flow rate ratio, RF, and MW power input were varied. The default settings were deduced from preliminary experiments and correspond to a good oxygen and water vapor barrier performance of the silicon oxide films. In each series one process parameter was varied in the mentioned range, the other parameters were kept constant at the default value. In all experiments the HMDSO flow rate was set 10 sccm. The substrate self-bias depends strongly on the RF power input as shown in Fig.1. Due to different stages of SiO_x coverage of the reactor walls the self-bias was varying by +/- 10 %. Further details are described elsewhere [2, 3].

Table 1: Process parameters with range of variation and default values.

Parameter	Variation range	Default value
Oxygen-to-HMDSO flow rate ratio	1 – 40	15
RF power (substrate holder)	50 – 300 W	200 W
MW power	600 – 3000 W	1500 W
Reactor pressure	0.2 mbar	0.2 mbar
Temperature (substrate holder)	20 °C	20 °C
Temperature (reactor walls)	50 °C	50 °C
Deposition time (film thickness resp.) for permeation measurements	60 s	60 s

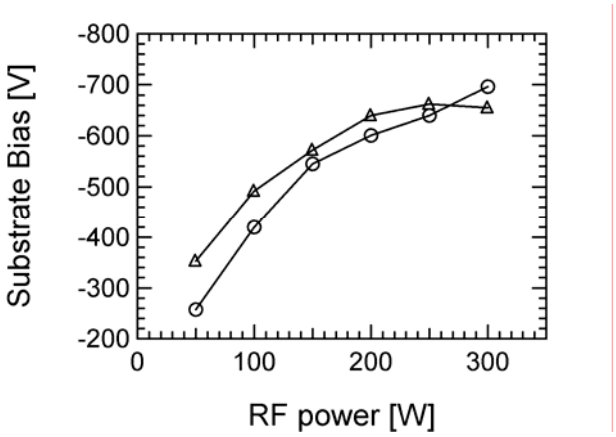

Figure 1: Substrate bias vs. RF power input. RF mode: circles, dual mode: triangles.

The barrier coatings were deposited on 12 µm PET films (Dupont, Mylar Typ A) with deposition rates of approximately 500 nm per minute. For the water vapor transmission rate (WVTR) measurements a Lyssy water vapor permeation tester L 80-5000 (Lyssy AG, Zollikon, CH) was used. The accuracy of the results is +/- 15 %. The quality of the coated PET films was, prior to the WVTR measurements, tested with an Oxtran-100 (Mocon, Modern Controls INC., Minneapolis, USA). This was done, because it is much harder to achieve good barrier coatings against water vapor than against oxygen. The influence of the process parameters on the oxygen transmission rate was studied elsewhere [3]. Unlike WVTR measurements, it is assumed that oxygen permeation measurements do not affect the coating properties and are non-destructive [5].

Plasma analyses were done by optical emission spectroscopy (OES). The emitted light was analyzed with an optical emission spectrometer (Jobin Yvon, Triax 320) equipped with an UV-coated 1024 x 128 CCD and an exit slit with photomultiplier (Hamamatsu, R928). The emitted light analyzed through a quartz window situated 5 cm above the substrate holder. The quartz window is transparent for 200 – 1100 nm. The measurements were conducted with the 1200 mm^{-1} grating for 200 – 350 nm and with the 1800 mm^{-1} grating for 350 – 1000 nm. For all spectroscopic measurements 10 sccm argon was added to the process gas. The emission lines are normalized to the intensity of the 750 nm Ar* line.

3. Results and discussion

3.1. Power variation

By OES the Ar* (750 nm), O (777 nm), O_2^+ (559 nm), SiO (239 nm), and H_α (656 nm) intensity lines were investigated. For pure RF plasmas the noise-to-peak intensity ratio was higher than for MW and dual mode plasmas. As can be seen in Fig. 2, with increasing RF power input the argon emission was increased. Similar tendencies were found for dual mode at constant MW power (1500 W) and varied RF power input (50 – 300 W) and for the variation of MW power (600 – 3000 W) at constant RF power input (200 W).

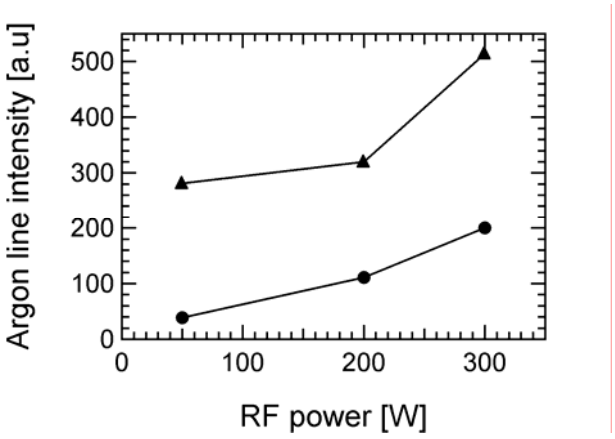

Figure 2: Dependence of the 750 nm Ar* line intensity on the RF power input. For dual mode the MW power was set to 1500W. Similar tendencies were found for dual mode at constant MW power (1500 W) and varied RF power (50 – 300 W) and for the variation of MW power (600 – 3000 W) at constant RF power (200 W). RF mode: circles, dual mode: triangles.

An increase in RF power leads to a decrease of the O_2^+ and SiO intensities and to an increase of the O and H_α line as demonstrated in Fig. 3. This is due to an enhanced fragmentation due to an increased energy input. For dual mode the influence of the RF power variation on the gas phase emission is small since all investigated line intensities varied only slightly. This findings for constant MW power (1500 W) and varied RF power input (50 – 300 W) are in contrast to the results at constant RF power input (200 W) and a variation of MW power (600 – 3000 W). As shown in Fig. 4, an increase was detected for the O and H_α line intensities. Comparing these results with the WVTR measurements, only little similarities could be found. Films deposited from RF or dual mode (constant MW power, varied RF power) plasmas exhibit similar tendencies for WVTR as can be seen in Fig. 5 and OTR (WVTR: factor 150 and OTR: factor 200, resp. improvement). By varying the MW input power at a constant RF power level, it was shown that the deposition is dominated by the substrate bias since no influence on the barrier performance was detected. Despite the stronger influence of the MW than the RF power on the gas phase composition is the substrate self-bias essential for the deposition of an effective gas barrier. This is due to a network densification and an additional energy input. The necessity of substrate self-bias was also shown from preliminary experiments with remote MW plasmas. Films deposited by pure MW plasma led to an improvement of the oxygen barrier (factor 20) but not to an effective barrier against water vapor despite the low organic content in the film [3]. This is due to the missing substrate bias and thus lack of ion bombardment onto the substrate.

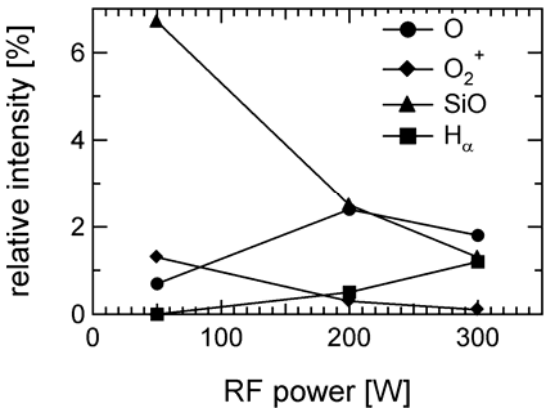

Figure 3: Dependence of the relative emission intensities in a pure RF discharge on the RF power input.

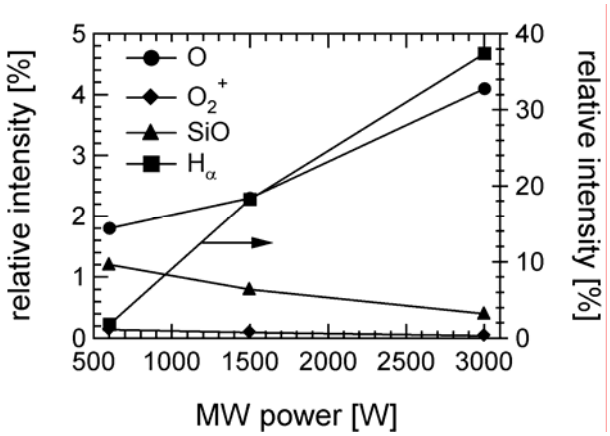

Figure 4: Dependence of the relative emission intensities in a dual mode plasma on MW power input.

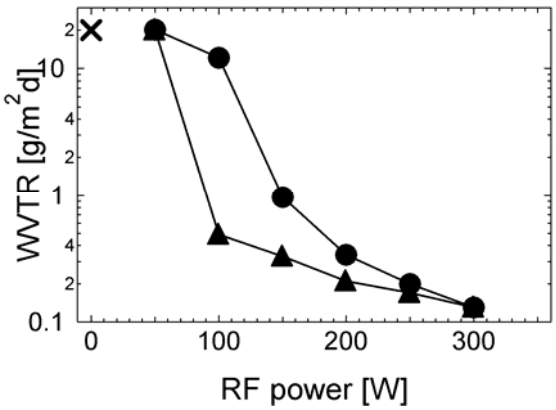

Figure 5: Influence of RF power input on the WVTR for pure RF and dual mode plasmas. RF mode: circles, dual mode: triangles, uncoated PET (reference value): cross.

3.1. Oxygen-to-HMDSO flow rate ratio variation

An increase of the oxygen content in the process gas leads to a decrease of the argon emission intensity for dual mode, whereas no influence could be detected for pure RF plasmas (Fig. 6). This is due to a higher gas flux and thus a reduced exposure time in the MW plasma source with increasing oxygen flow. The pressure was kept constant thus no loss due to enhanced recombination occurred.

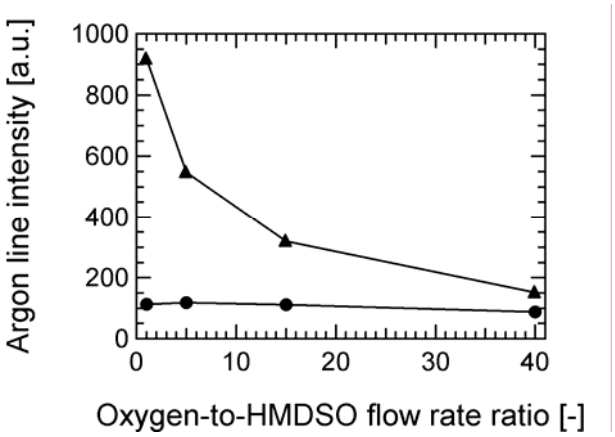

Figure 6: Dependence of the argon line intensity on the oxygen-to-HMDSO flow rate ratio. RF mode: circles, dual mode: triangles.

With increasing oxygen-to-monomer flow rate ratio for RF mode a pronounced increase of the O and SiO line intensities was found. Similar tendencies were found for dual mode but not as strong for the SiO line intensity. For RF mode the O_2^+ and H_α intensities increased only slightly. In contrast, for dual mode an increase up to 150 sccm and then a decrease of the H_α intensity was detected (Fig. 7). The increase of the oxygen line intensities can be explained by the surplus of oxygen. As a result of the decreased activation of the process gas with increasing oxygen-to-HMDSO flow rate ratio the SiO line is increased. The H_α intensity first increases due to an enhanced fragmentation because of the rising oxygen flow and thus energy transport from the microwave to the deposition chamber. After a peak value the decrease is an effect of the reduced activation of the process gases. Compared with the WVTR measurement it is visible that an increase of the oxygen-to-monomer flow rate ratio leads to an enhanced water vapor barrier performance for pure RF mode, whereas for dual mode an increase of the oxygen flow rate above 200 sccm results again in permeable films as can be seen in Fig. 8.

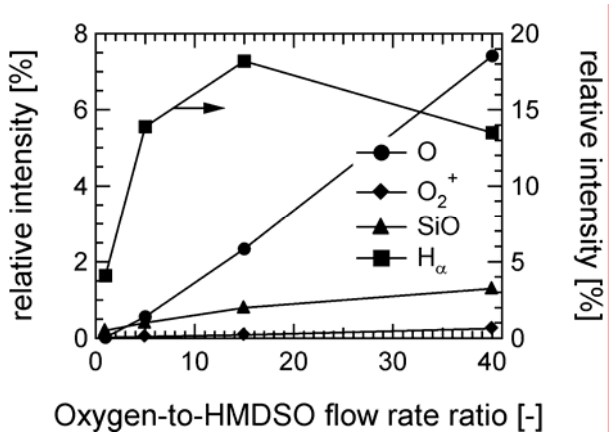

Figure 7: Oxygen-to-HMDSO flow rate ratio vs. relative emission intensities for dual mode plasmas.

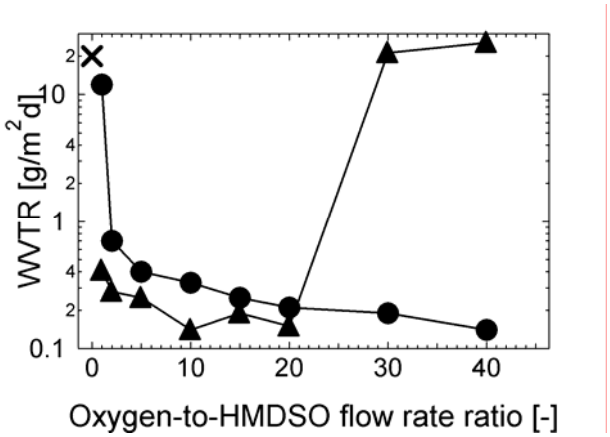

Figure 8: Influence of the RF power input on the WVTR for pure RF and dual mode plasmas. RF mode: circles, dual mode: triangles, uncoated PET (reference value): cross.

4. Conclusions

For a better understanding of the plasma processes and the influence of the gas phase on the barrier performance of the deposited silicon oxide film, investigations with optical emission spectroscopy were conducted. The influence of the oxygen-to-monomer flow rate ratio, radio frequency and microwave power input was investigated.

With increasing RF power input the 750 nm Ar* line emission increased. Similar tendencies were found for dual mode as were for the variation of MW power (600 – 3000 W) at constant RF power input (200 W). An increase in RF power leads to a decrease of the O_2^+ and SiO intensities and to an increase of the O and H_α line. This is due to an enhanced fragmentation because of an increased energy input. From WVTR measurements it can be seen that despite the stronger influence of the MW than of the RF power on the gas phase composition, the substrate bias is essential for the deposition of an effective gas barrier. This is due to a network densification and an additional energy input [3].

An increase of the oxygen content in the process gas leads to a decrease of the argon emission intensity for dual mode whereas no influence could be detected for pure RF plasmas. With increasing oxygen-to-monomer flow rate ratio an increase of the O and SiO line intensities was found. For dual mode an increase up to 150 sccm and then a decrease of the H_α intensity was detected. Compared with the WVTR measurement it was shown that an increase of the oxygen-to-monomer flow rate ratio leads to an enhanced water vapor barrier performance for pure RF mode, whereas for dual mode an increase of the oxygen flow rate above 200 sccm results again in permeable films.

5. References

[1] G.L. Czeremuszkin, et al., Plasmas and Polymers, 2001. 6(1/2): p. 107-120.
[2] A. Bieder, A. Gruniger, Ph. Rudolf von Rohr, Surf. Coat. Tech., (2005). in press.
[3] A. Gruniger, Deposition of SiOx diffusion barriers by PECVD. PhD Thesis No. 15684, 2004. Swiss Federal Institute of Technology Zurich.
[4] M.F. Creatore, et al., Plasmas and Polymers, 2002. 7(3): p. 291-310.
[5] A.G. Erlat, et al., J. Phys. Chem. B, 1999. 103(29): p. 6047-6055.

Optical and Electrical Diagnostics of a Miniature Microwave-Excited Plasma Source for an Ultra Small Thruster

Y. Takao, K. Takahashi, K. Ono

Department of Aeronautics and Astronautics, Graduate School of Engineering, Kyoto University, Kyoto, Japan

Abstract
A miniature microwave-excited plasma source for an ultra small thruster has been investigated by optical emission spectroscopy and an electrostatic probe. Experimental results and a numerical analysis have shown that the microplasma source is useful for the miniature thruster, having the electron density of 10^{16}–10^{19} m^{-3}, the rotational temperature of 400–1200 K, and the specific impulse of 60–71 s, in the microwave power range from 2 to 11 W.
Keywords: microthruster, microplasma, microwave, micronozzle, electric propulsion

1. Introduction

In recent years, microplasma sources have attracted increasing attention, aimed at applications in a number of microsystems. Such microplasma sources are obtained by dc [1], capacitively coupled [2], inductively coupled [3], and microwave excited [4, 5] plasma discharges. For space systems, there is an ongoing trend toward miniaturization of spacecraft to reduce the mission costs and risk [6]. Such microspacecraft concept has supported a new approach to develop accurate, reliable, and low-power-consumption micropropulsion systems for high-precision station keeping (requiring a thrust of ~ mN) and attitude control (~ μN).

For such a great interest in both microplasma and micropropulsion, we propose an application of a miniature plasma source excited by microwaves to an ultra small thruster on microspacecraft. Figure 1 shows a schematic diagram of a microplasma thruster, which consists of a microplasma source and a micronozzle. The plasma source is composed of a cylindrical dielectric tube, the outside of which is covered with a metal grounded. The inner radius and the length of the tube are about 1 mm and 10 mm, respectively. Microwaves are injected through a coaxial cable into the plasma chamber, where the propellant gas, argon in this study, is ionized and heated up in the pressure range from 10 kPa to 100 kPa. Such high thermal energy is converted into the kinetic energy through the micronozzle, which has a converging and diverging section, to produce the thrust required. On the basis of this concept, we developed a numerical model for design consideration and estimated the thrust performance [7–10].

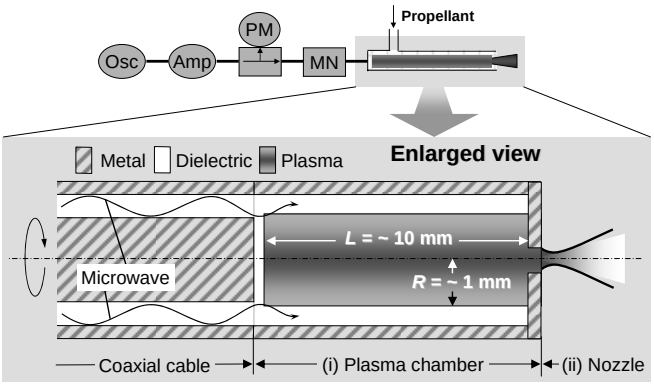

Fig. 1. Schematic of the microplasma thruster using microwave-excited plasmas, consisting of an azimuthally symmetric microplasma source and a converging-diverging (Laval) micronozzle. The working gas is Ar in this study.

In this paper, we present a microplasma source fabricated and the plasma characteristics observed by optical emission spectroscopy (OES) and an electrostatic probe. The OES analysis of the microplasma source indicates that the plasma source is useful for the microthruster in view of the distribution of the rotational temperature inside the plasma chamber. The electrical diagnostics show that the electron density achieved is in the range of 10^{16}–10^{19} m^{-3} at microwave powers of 2–11 W.

2. Experimental

Figure 2 shows a schematic diagram of the experimental setup and a cross-sectional view of the microplasma source. Microwave signals of 2 and 4 GHz generated by an oscillator (Agilent Technologies, 8648D) are amplified through a 4-stage semiconductor amplifier, and then fed through a semi-rigid coaxial cable

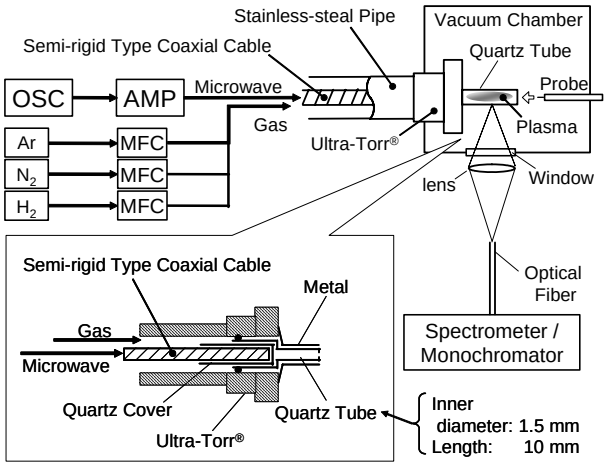

Fig. 2. Schematic of the experimental setup and the cross section of the microplasma source developed (bottom).

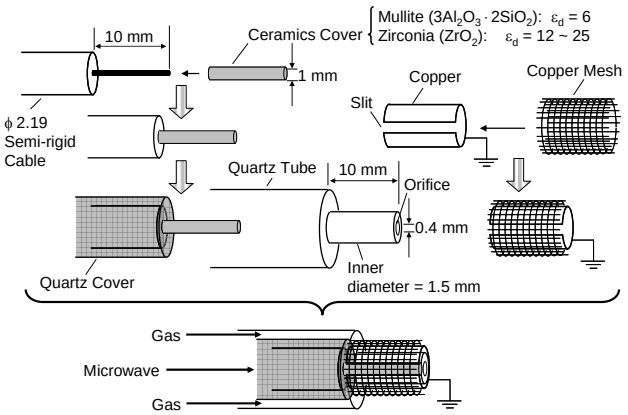

Fig. 3. Assembly of the microplasma source presently developed, which has an orifice at the exit to vacuum. The slit of the copper envelope is for optical diagnostics.

(RG-405/U) into the plasma chamber made of a straight quartz tube, to generate and sustain the plasma discharges therein. Here, the reflection of microwaves power is suppressed by adjusting the cable length. The quartz tube, connected to the stainless-steel pipe through which the working gas is introduced, is inserted into a stainless-steal chamber evacuated by a dry and mechanical booster pump. A pressure gauge, equipped with the stainless-steal pipe before the plasma chamber, is used for measurement of the feed gas pressure, which is assumed to be the pressure inside the plasma chamber.

Figure 3 shows an assembly of the microplasma source presently developed. The center conductor of the semi-rigid coaxial cable, protruding 10 mm beyond the insulator and outer conductor, is covered with a ceramic tube; two types of ceramics, mullite (relative permittivity ε_d = 6) and zirconia (ε_d = 12–25), are employed to investigate the dependence on dielectric constants. The outer conductor is also covered with a quartz tube for the protection against erosion of electrodes. The plasma chamber, made of a quartz tube 10 mm in length and 1.5 mm in inner diameter, has an orifice 0.4 mm in diameter at the exit to vacuum. This structure results in a small conductance to keep the pressure inside the plasma chamber much higher than that in the vacuum chamber. The outside of the plasma chamber is covered with a copper grounded which has a single slit for optical diagnostics. Moreover, a copper mesh prevents microwaves from leaking through the slit.

Emission intensities are measured with a spectrometer (Ocean Optics, HR2000CG-UV-NIR) through a quartz optical fiber, the head of which is directly connected to a window of the vacuum chamber without a lens. In the case of precise diagnostics, the emissions are collected by a lens and transmitted to a 25-cm focal length monochromator (Nikon, P250) with a 1200 grooves/mm grating plate. The light emerging from the fiber is focused onto an entrance slit of the monochromator and detected by a photomultiplier (Hamamatsu, R1509). For electrical diagnostics, a cylindrical Langmuir probe, with the probe tip made of a tungsten wire 0.05 mm in diameter and 0.5 mm long, is positioned at an immediate downstream of the orifice to determine the electron density thereat.

3. Results and Discussion

3.1. Power Dependence of Intensity

Experiments were performed at an Ar flow rate of 50 sccm, a feed gas pressure of 10 kPa, and a vacuum chamber pressure of 9 Pa. Figure 4 shows photograph images of the emission of microplasma discharges, taken for total microwave power P_t = (a) 3.5, (b) 5.0, and (c) 7.0 W with a microwave frequency f = 4 GHz and a mullite tube (ε_d = 6). The plasma was maintained only inside the microplasma chamber at P_t > 0.3 W [Fig. 4(a)], the plasma at P_t > 4 W was found to flow out into vacuum through the orifice at the end of the plasma chamber, forming a supersonic free jet in vacuum [Fig. 4(b)], and at P_t > 6 W the exhausted plasma was sustained around the end of the plasma source [Fig. 4(c)].

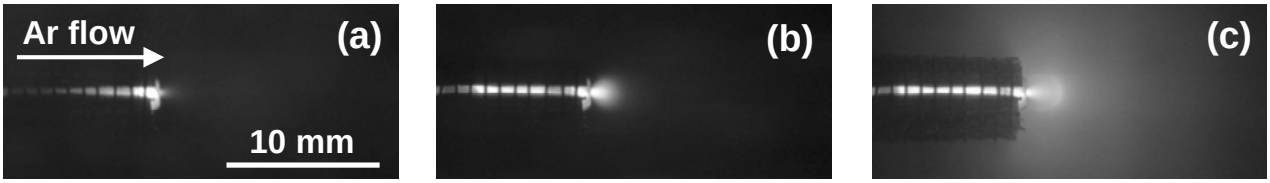

Fig. 4. Photograph images of the emission of microplasma discharges, taken for total microwave power P_t = (a) 3.5, (b) 5.0, and (c) 7.0 W with a microwave frequency f = 4 GHz and a mullite tube (ε_d = 6), measured at an Ar flow rate of 50 sccm, a feed gas pressure of 10 kPa, and a vacuum chamber pressure of 9 Pa.

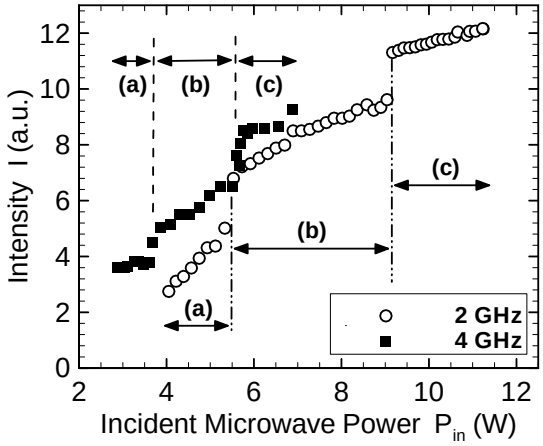

Fig. 5. Emission intensity (Ar I 763.5 nm) as a function of incident microwave power $P_{in} = P_t - P_{rf}$ for different microwave frequencies f = 2 and 4 GHz, otherwise measured under the same conditions as in Fig. 4.

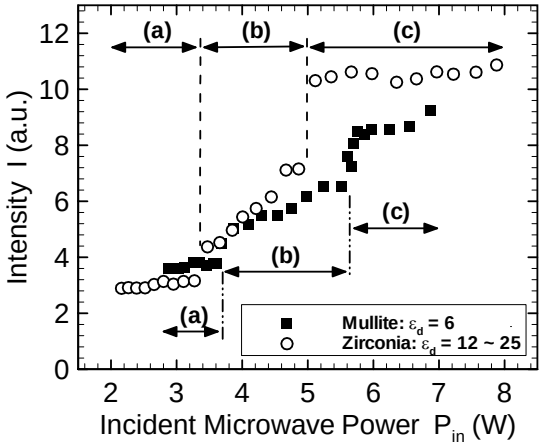

Fig. 6. Emission intensity (Ar I 763.5 nm) as a function of incident microwave power $P_{in} = P_t - P_{rf}$ for different ceramic tubes of ε_d = 6 and 12–25, otherwise measured under the same conditions as in Fig. 4.

Figure 5 shows the emission intensity (Ar I 763.5 nm) as a function of incident microwave power $P_{in} = P_t - P_{rf}$ for different f = 2 and 4 GHz, where P_{rf} is a reflected microwave power, so that P_{in} is assumed to be a net power absorbed in the plasma. Other experimental conditions are the same as in Fig. 4. The emission intensity increases with increasing P_{in}, involving sudden jumps among the regions labeled (a), (b), and (c) in the figure, where these labels correspond to those in Fig. 4. As shown in the figure, higher intensities are observed for the higher microwave frequency at the same incident microwave power; more incident microwave power is required to yield intensity jumps for f = 2 GHz.

Figure 6 shows the emission intensity (Ar I 763.5 nm) as a function of incident microwave power P_{in} for different ceramic tubes of ε_d = 6 and 12–25, where other experimental conditions are the same as in Fig. 4. The emission intensity increases with increasing P_{in}, involving sudden jumps among the regions labeled (a), (b), and (c), like the result in Fig. 5. Higher intensities are observed for ε_d = 12–25 at the same incident microwave power. From the results in Figs. 5 and 6, higher microwave frequencies and dielectric constants are found to be desirable to maintain the plasma discharges in the microplasma source developed. Note that the emission intensities were measured with the spectrometer without light condensing here.

3.2. Electron Density

Figure 7 shows the electron density n_e as a function of incident microwave power P_{in} for different f = 2 and 4 GHz and different ε_d = 6 and 12–25, otherwise measured under the same conditions as in Fig. 4. The electron density increases as P_{in} increases, and higher microwave frequencies and dielectric constants result in higher electron densities at P_{in} > 6 W, although the electron density for f = 2 GHz and ε_d = 6 does not decrease with decreasing P_{in} at lower P_{in} compared to that for f = 4 GHz. This result derived from disturbance due to the probe measurement at f = 2 GHz, whereas there seemed to be less perturbation at f = 4 GHz. Taking the disturbance into account, we could conclude that the electron density tends to become higher at higher microwave frequencies and dielectric constants.

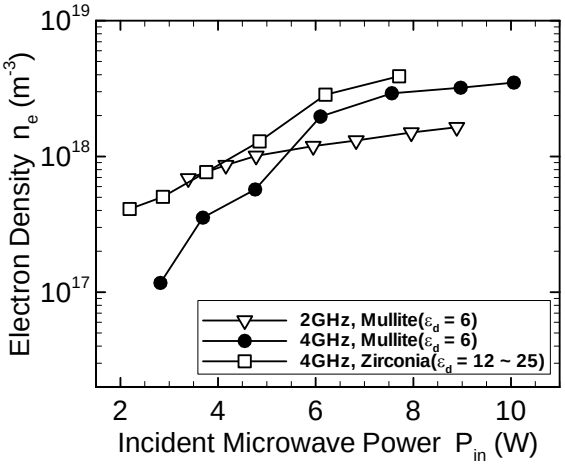

Fig. 7. Electron density n_e as a function of incident microwave power $P_{in} = P_t - P_{rf}$ for different f = 2 and 4 GHz and different ε_d = 6 and 12–25, otherwise measured under the same conditions as in Fig. 4. Here, the Langmuir probe was located at downstream from the orifice as in Fig. 2.

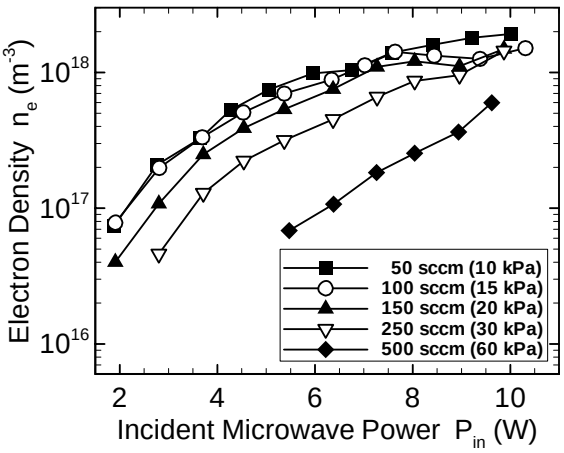

Fig. 8. Electron density n_e as a function of incident microwave power $P_{in} = P_t - P_{rf}$ for different Ar flow rates of 50, 100, 150, 250, and 500 sccm, where corresponding feed gas pressures are 10, 15, 20, 30, and 60 kPa, measured at f = 4 GHz and ε_d = 6.

Figure 8 shows the electron density n_e as a function of incident microwave power P_{in} for different Ar flow rates of 50, 100, 150, 250, and 500 sccm, measured at f = 4 GHz and ε_d = 6. The electron density decreases with increasing Ar flow rates, while the density increases with increasing P_{in} for all flow rates. High flow rates, leading to high feed gas pressures in the plasma chamber, affect the plasma discharges; more microwave power seems to be required to sustain high-density plasmas at high flow rates.

3.3. Rotational Temperature

Since the monochromator employed in this paper does not resolve the rotational structure, we have fitted the experimental data with theoretical calculations by using the transition band of N_2 $C^3\Pi_u$–$B^3\Pi_g$ at 380.49 nm (second positive band), in order to calculate the rotational temperature.

Figure 9 shows the rotational temperature T_{rot} as a function of position of the plasma discharge with a photograph image of the emission taken for incident microwave power P_{in} = 7 W at a microwave frequency f = 4 GHz and a zirconia tube (ε_d = 12–25), measured at an Ar flow rate of 50 sccm, a N_2 flow rate of 0.2 sccm, a feed gas pressure of 10 kPa, and a vacuum chamber pressure of 9 Pa. The rotational temperature increases from

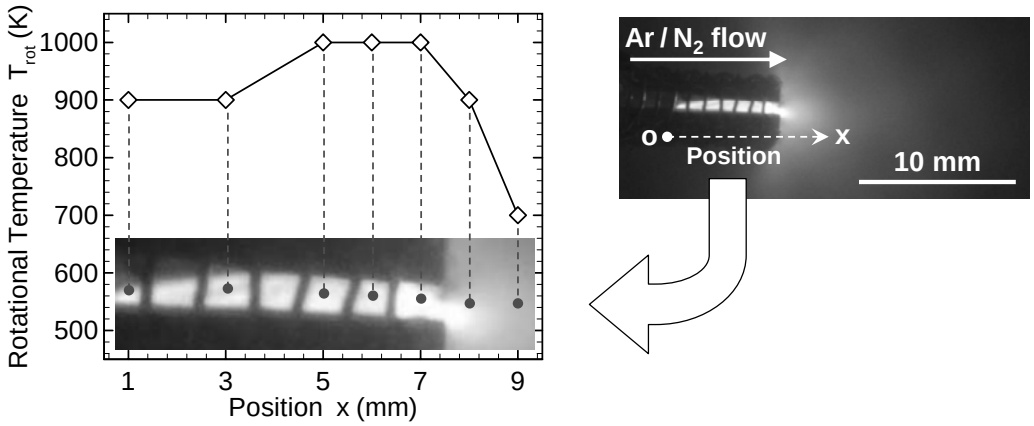

Fig. 9. Rotational temperature T_{rot} (N_2) as a function of position of the plasma discharge (left) and a photograph image of the emission (right), taken for incident microwave power P_{in} = 7 W with a microwave frequency f = 4 GHz and a zirconia tube (ε_d = 12–25), measured at an Ar flow rate of 50 sccm, a N_2 flow rate of 0.2 sccm, a feed gas pressure of 10 kPa, and a vacuum chamber pressure of 9 Pa.

upstream to downstream before the exit of the plasma chamber (x = 7 mm), decreasing at downstream after the orifice. Notice that it is important to increase the temperature at the exit of the plasma chamber where a micronozzle will be equipped, because the thermal energy should be effectively converted into the kinetic energy without any undesirable energy loss in the plasma chamber before the micronozzle. Thus, the temperature distribution obtained indicates that the microplasma source is highly desirable to the miniature thruster presented here.

Figure 10 shows the rotational temperature T_{rot} at the exit of the plasma chamber (x = 7 mm) as a function of incident microwave power P_{in} for different f = 2 and 4 GHz and different ε_d = 6 and 12–25, otherwise measured under the same conditions as in Fig. 9. The rotational temperature increases with increasing P_{in}, where the temperature tends to be higher at higher microwave frequencies and dielectric constants as in the case of the emission intensity and electron density.

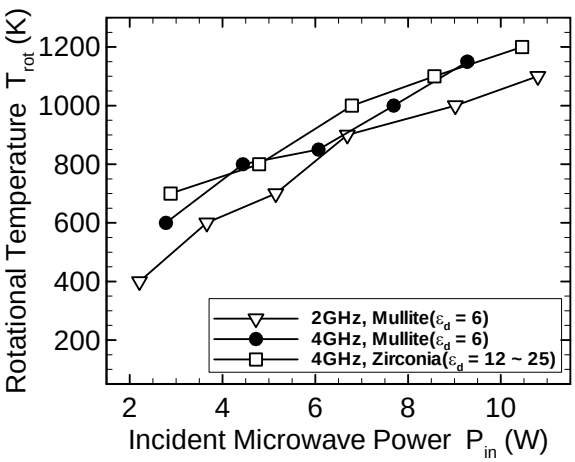

Fig. 10. Rotational temperature T_{rot} (N_2) at a position of 7 mm in Fig. 9 as a function of incident microwave power $P_{in} = P_t - P_{rf}$ for different f = 2 and 4 GHz and different ε_d = 6 and 12–25, otherwise measured under the same conditions as in Fig. 9.

3.4. Specific Impulse

Finally, assuming that the rotational temperature T_{rot} equals the gas temperature T_{gas}, we have estimated the specific impulse by using the results of plasma diagnostics obtained above and the model analysis in [7–10]. Since the plasma source has the orifice 0.4 mm in diameter at the exit to vacuum, a micronozzle with a throat 0.4 mm in diameter is assumed to be equipped with the plasma chamber, in order to calculate the thrust performance. A cross-sectional view and computational grid for the micronozzle are shown in Fig. 11. Moreover, the specific impulse I_{sp}, meaning how much thrust the thruster produces per unit propellant weight per one second, is defined as

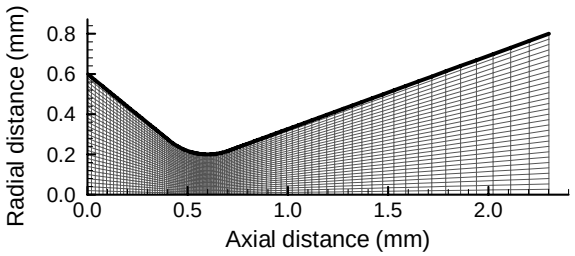

Fig. 11. Cross-sectional view and computational grid for a micronozzle with a 20°-half-cone-angle isothermal wall (T_{wall} = 300 K). The radii of the nozzle inlet, throat, and exit are set at 0.6, 0.2, and 0.8 mm, respectively. The computational domain is divided into 100 cells in the axial direction and 30 cells in the radial direction.

$$I_{sp} = 2\pi \int_0^{r_{ex}} (\rho u^2 + p) r dr / \dot{m} g \ , \tag{1}$$

where r_{ex} is the exit radius of the nozzle, ρ is the mass density, u is the velocity in the axial direction, p is the pressure, $\dot{m}$ is the mass flow rate, and g is the gravitational constant. Thus, the specific impulse is a measure of the fuel efficiency of a thruster; the higher the value is, the more efficient the thruster is.

Figure 12 shows the specific impulse I_{sp} as a function of incident microwave power P_{in} for f = 4 GHz and ε_d = 12–25 with the rotational temperature T_{rot} plotted in Fig. 10, otherwise measured under the same conditions as in Fig. 9. The specific impulse increases with increasing T_{rot} in the range from 60 to 65 s. In the case of a cold gas thruster (T_{gas} = 300 K) under the same conditions, the specific impulse is determined to be 53 s, so that the increasing rate of the specific impulse is 13 to 23 % by generating the plasma.

Figure 13 shows the rotational temperature T_{rot} at the exit of the plasma chamber (x = 7 mm) and the specific impulse I_{sp} as a function of Ar gas flow rate for P_{in} = 7 W, f = 4 GHz, and ε_d = 12–25, at a N_2 flow rate of 0.2 sccm. The specific impulse has the maximum value at a gas flow rate of 250 sccm, decreasing as the gas flow rate increases, because the rotational temperature decreases with increasing gas flow rate owing to the low electron density and the cooling effect of gas flows. Higher specific impulse would be expected by increasing the gas temperature at high gas flow rates.

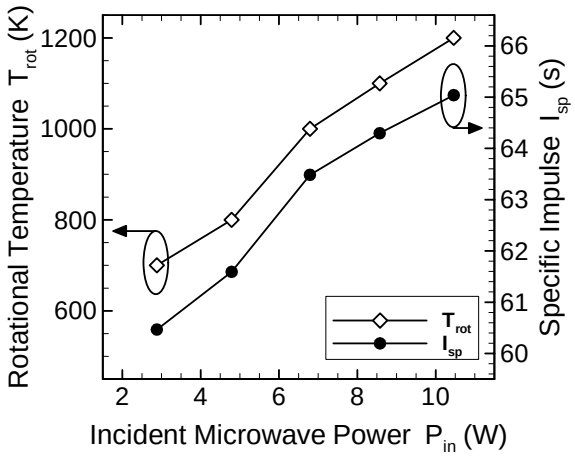

Fig. 12. Rotational temperature T_{rot} at a position of 7 mm in Fig. 9 and specific impulse I_{sp} as a function of incident microwave power P_{in} for f = 4 GHz, and ε_d = 12–25, otherwise measured under the same conditions as in Fig. 9. Here, the specific impulse is estimated from the measured temperature $T_{gas} = T_{rot}$ and the model analysis in [7–10].

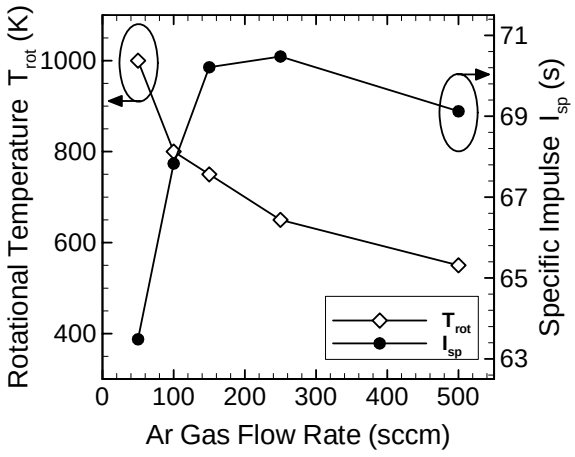

Fig. 13. Rotational temperature T_{rot} at a position of 7 mm in Fig. 9 and specific impulse I_{sp} as a function of Ar gas flow rate for P_{in} = 7 W, f = 4 GHz, and ε_d = 12–25, with a N_2 flow rate of 0.2 sccm.

4. Conclusions

A miniature microwave-excited plasma source for an ultra small thruster has been investigated by optical emission spectroscopy and an electrostatic probe. Experimental results have shown that the emission intensity, electron density, and rotational temperature increase with increasing incident microwave power, microwave frequency, and dielectric constant; whereas the electron density and rotational temperature decreases with increasing Ar gas flow rate. The distribution of the rotational temperature inside the microplasma chamber indicates that the microplasma source presented here is desirable to the microthruster, because the temperature increases at the exit of the plasma chamber where a micronozzle will be equipped. In estimation of the thrust performance, the specific impulse increases with increasing incident microwave power, while it has the maximum value depending on gas flow rates. In the range of microwave powers 2–11 W and of gas flow rates 50–500 sccm, the electron density is 10^{16}–10^{19} m^{-3}, the rotational temperature is 400–1200 K, and the specific impulse is 60–71 s. Fabricating a micronozzle and measuring the thrust performance will be a future work.

Acknowledgments

This work was supported by a Grant-in-Aid for Scientific Research from Ministry of Education, Culture, Sports, Science and Technology, Japan, and by Research Fellowships of the Japan Society for the Promotion of Science for Young Scientists.

References

[1] K. Terashima, L. Howald, H. Haefke, H. Guntherodt - Thin Solid Films **281**-**282**, 634 (1996).
[2] H. Yoshiki, Y. Horiike - Jpn. J. Appl. Phys. **40**, L360 (2001).
[3] J. Hopwood, O. Minayeva, Y. Yin - J. Vac. Sci. Technol. B **18**, 2446 (2000).
[4] A.M. Bilgic, U. Engel, E. Voges, M. Kuckelheim, J.A.C. Broekaert - Plasma Sources Sci. Technol. **9**, 1 (2000).
[5] F. Iza, J.A. Hopwood - IEEE Trans. Plasma Sci. **31**, 782 (2003).
[6] J. Mueller - *Micropropulsion for Small Spacecraft*, ed. M.M. Micci and A.D. Ketsdever (AIAA, Reston, 2000), Chap. 3.
[7] Y. Takao, K. Ono - AIAA Paper 2004-3621 (AIAA, Reston, 2004).
[8] Y. Takao, K. Ono - ISTS Paper 2004-o-1-08v (JSAAS, Tokyo, 2004).
[9] Y. Takao, K. Ono, K. Takahashi, Y. Setsuhara - to be published in Thin Solid Films (2005).
[10] Y. Takao, K. Ono - submitted to Plasma Sources Sci. Technol.

Observations of Ar and Ar/H_2 DC Arc Plasma Jets Generated at Reduced Pressures

Wenxia Pan[1], Xi Chen[2], Xian Meng[1], Teng Li[1], Chengkang Wu[1]

[1] *Institute of Mechanics, Chinese Academy of Sciences, Beijing 100080, China*
[2] *Department of Engineering Mechanics, Tsinghua University, Beijing 100084, China*

Abstract

Experimental observations are conducted for the DC arc plasma jets generated at reduced pressures without or with an applied magnetic field. It is shown that the laminar plasma jets are quite stable, while turbulent plasma jets are unstable and non-axisymmetrical. Arc-root attachment on the anode surface is diffusive for argon arc, while the attachment becomes constrictive when hydrogen is added to the plasma-forming gas and the arc-root rotates quickly around the anode surface under the action of external magnetic field.

Keywords DC plasma jet, flow stability, arc-root attachment, external magnetic field

1. Introduction

Numerous studies have been performed in recent decades concerning the characteristics of DC non-transferred arc plasma jets due to their widespread applications in industries and in labs. Although a wealth of experimental and modeling results have been accumulated in the literature, our understanding on DC non-transferred arc plasma jet characteristics is still incomplete, especially for the plasma jets generated at reduced pressures and for the relationship between the plasma jet characteristics and the arc-root attachment at the anode surface of the DC arc plasma torch used for generating the plasma jet.

In this work, non-transferred DC arc plasma jets are generated at reduced pressures with argon or argon-hydrogen mixture as the plasma-forming gas. The generated plasma jet is studied when it flows as a free jet or as a jet impinging normally upon a substrate. Different gas flow rates are employed in the study in order to obtain laminar and turbulent flow regimes. An external magnetic field is applied if the effect of magnetic field on the arc plasma jet is to be studied. The plasma jets are observed using an ordinary camera to show the jet appearance and using an ICCD camera with much shorter exposure time to obtain the instantaneous plasma jet images in the visible range. Using a specially designed copper mirror, the arc-root behavior on the anode surface of the plasma torch is also observed with the ICCD camera.

2. Experimental details

The non-transferred DC arc plasma torch used for generating the plasma jets at reduced pressures contains a three-piece inter-electrode insert and a co-axial DC magnetic-field coil encircling the torch. Fig. 1 shows the schematic drawing of the torch configuration. The inner diameter of torch anode-nozzle exit is 60 mm, whereas the distance from the cathode tip to the frontal end of anode is 105 mm. Pure argon or argon-hydrogen mixture (with volumetric fraction of hydrogen 0~18% in the Ar-H_2 mixture) has been used as the plasma-forming gas. The total volumetric flow rate of the working gas can be changed in the range of 40~470 STP cm^3/s, and thus both laminar and turbulent plasma flow regimes can be achieved in the experiment. As in Ref. [1], the working gas is introduced axially and tangentially into the plasma torch. The

working chamber pressure can be regulated in the range of (0.05~3.0)×10^4 Pa. Arc current is 80~130 A, whereas the input electric power is 5.5~18 kW, depending on the gas type and pressure and on whether an external magnetic field is applied. The plasma jet is issuing freely into the vacuum chamber or impinging normally upon the substrate (electrically floating) with diameter of 60~120 mm and located 20~300 mm below the torch anode-nozzle exit.

The plasma jets are observed using two different imaging techniques. Namely, photographs of the plasma jet are taken using an ordinary camera to show the jet appearance, and an ICCD camera with much shorter exposure time (may be as short as 5 ns) is used to obtain the instantaneous plasma jet images in the visible range. A copper mirror with good thermal conductance is installed on the water-cooled substrate holder beneath the torch exit and co-axial with the plasma torch. The mirror surface is set to be 45° inclination with respect to the torch axis so that the mirror can reflect the image of the torch exit (with certain depth of field) into the ICCD camera, which is located outside the vacuum chamber, normally to the torch axis and with the same horizontal level as the mirror center. A boron nitride film is coated on the central region of the mirror surface with a size a little larger than the diameter of the central hole-channel of the inter-electrode insert. It is found that in this way the reflection at the mirror surface of the strong light emitted from the central arc column can be greatly weakened and thus the interference caused by the arc column radiation upon the detailed observation of the arc root attachment on the anode surface can be effectively avoided. With this new experimental design, the arc root behaviors in the non-transferred arc Ar and Ar-H_2 plasma torches have been successfully observed.

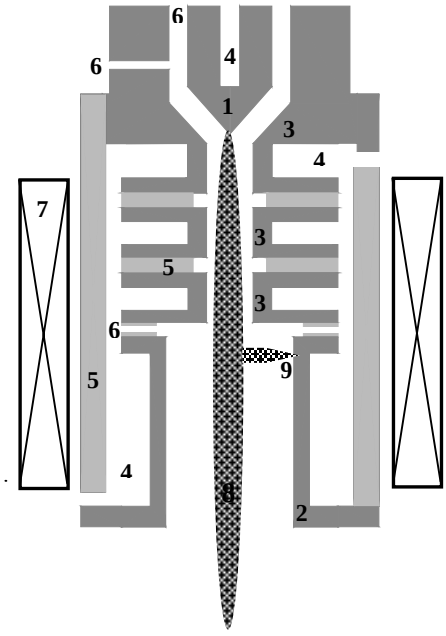

Fig. 1 Schematic diagram of the plasma torch. 1 cathode, 2 anode, 3 inter-electrode inserts, 4 cooling water, 5 electric insulator, 6 gas inlets, 7 magnetic field coil, 8 plasma jet, 9 arc root attachment.

3. Results and discussions

Figures 2(a) and 2(b) show the photographs of Ar and Ar-H_2 plasma jets, respectively, in the laminar flow regime, while Figs. 3(a) and 3(b) show their counterparts for the turbulent regime. The arc current is kept to be 80 A for all the four plasma jets shown in Fig 2 and Fig. 3. The argon flow rate is 290 cm^3/s and the chamber pressure is 3.8×10^3 Pa for Fig. 2(a), whereas they are 320 cm^3/s and 2.2×10^4 Pa for Fig. 3(a). On the other hand, the flow rate is 120 cm^3/s argon plus 7 cm^3/s hydrogen and the chamber pressure is 1.6×10^3 Pa for Fig. 2(b), whereas they are 320 cm^3/s argon plus 17 cm^3/s hydrogen and 2.5×10^4 Pa for Fig. 3(b). It is found that increasing the gas flow rate and increasing the chamber pressure may promote the transition of the plasma jet from the laminar flow regime into the turbulent flow regime, since higher Reynolds number will be involved at higher gas flow rate and at higher gas pressure. Visual observation and the photographs shown in Fig. 2 demonstrate that the laminar Ar and Ar-H_2 plasma jets are stable, axisymmetrical and with longer high-temperature length, but visual observation shows that turbulent plasma jets are not stable and with shorter high-temperature length.

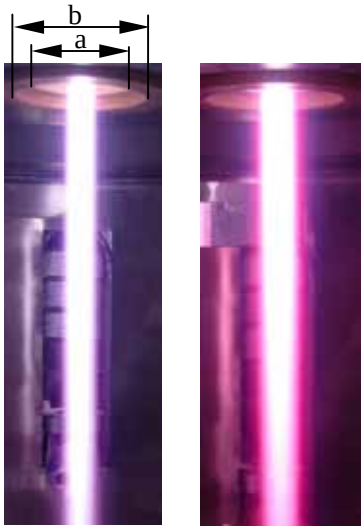

(a) (b)

Fig. 2 Photographs showing the appearance of the pure argon (a) and Ar-H_2 (b) laminar plasma jets. Sizes a and b are 60 and 76 mm, respectively, representing the inner and outer diameters of anode flange plate.

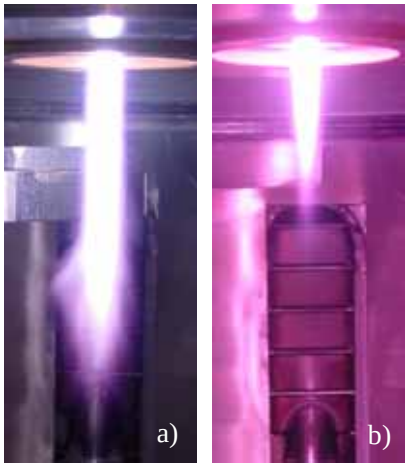

Fig. 3 Photographs showing the appearance of the turbulent argon (a) and Ar+H_2 (b) plasma jets.

Figure 4 gives four luminous-region images of the plasma jets taken by the ICCD camera with two different exposure times, i.e. 5 μs and 10 μs, corresponding jet appearances have been shown in Fig. 2 for the laminar plasma jets and shown in Fig. 3 for the turbulent plasma jets. It is found that the laminar jets are highly stable, and both the two images as shown in Fig. 4(a) and 4(b) do demonstrate that the luminous regions of the laminar Ar and Ar-H_2 plasma jets are well axi-symmetrical and co-axial with the plasma torch even as the exposure time is as short as 10 μs. These observation results for the laminar plasma jets are different from those obtained for the turbulent plasma jets shown in Fig. 4(c) and 4(d), and quite different from those obtained previously [2,3] for the turbulent plasma jets. For a turbulent argon plasma jet issuing into ambient air at atmospheric pressure, Refs. [2,3] reported that the photographs with exposure times of 100 μs and 1 ms showed that the studied turbulent plasma jet was unsteady and thus the forms and sizes of the jet visible-region varied at all time. The turbulent plasma jet images taken at reduced pressures in this study, as shown in Figs. 4(c) and 4(d), reveal almost the same phenomenon as reported in [2,3] for the atmospheric-pressure turbulent plasma jet. Namely, the luminous regions of the turbulent plasma jets shown in Figs. 4(c) and 4(d) are non-axisymmetrical, implying that the turbulent Ar or Ar-H_2 plasma jet generated at the reduced pressure is unstable.

Although the laminar Ar and Ar-H_2 plasma jets all assume axi-symmetrical appearances, as seen in Fig. 4(a) and 4(b), it is difficult to identify correspondent arc-root behaviors only based on their appearances. Fig. 5 gives some additional observation results concerning the arc root attachment with help of the specially designed copper mirror mentioned above and the ICCD camera. In order to show the related dimensions of the plasma torch, Fig. 5(a) gives a rear-view photograph of the torch channel configuration for the cold-state case (without plasma production) using a ruler across the torch exit and using a lamp to illuminate the

observed object. The inter-electrode insert channel cannot be seen in Fig. 5(a) since it is just covered up by the ruler. It is noted that the bright spots seen in Fig. 5(a) are not the arc roots and are formed only due to the reflection of lamp light at the end wall of the torch anode. Fig. 5(b) shows the rear-view image of the argon arc at the chamber pressure of 3.2×10^3 Pa taken by using the ICCD camera with an exposure time of 10 μs. From Fig. 5(b) we only see some low-intensity luminous region on the anode surface, and cannot see any sign of a constricted arc-root formation in the pure argon plasma jet generation. Fig. 5(c) is the correspondent rear-view image of the Ar-9%H_2 plasma jet at the chamber pressure of 2.4×10^4 Pa and with a camera exposure time of 80 μs. It is clearly seen from Fig. 5(c) that constricted arc root attachment appears in the Ar-H_2 plasma generation. It is found that when pure argon is used as the plasma-forming gas, almost completely diffuse attachment of the arc root always appears at the anode surface, no mater whether the plasma jet is in laminar or turbulent flow regime. Such a diffuse arc-root attachment is obviously favorable for reducing the anode erosion and prolonging the service period of the torch anode. The arc root attachment becomes sharply concentrated, as shown in Fig. 5(c), when hydrogen is added into argon for generating the plasma jet even as the content of hydrogen in the mixture is small, and the arc root generally attaches at the anode end-wall with a particular angular-direction. The arc root shows no apparent movement within the observation time of a few minutes if the jet-generating conditions are unchanged. This special feature of Ar-H_2 plasma will lead to relatively serious anode erosion when hydrogen is added into argon to generate the plasma jet. This phenomenon is well known in the DC non-transferred arc plasma generation at atmospheric pressure.

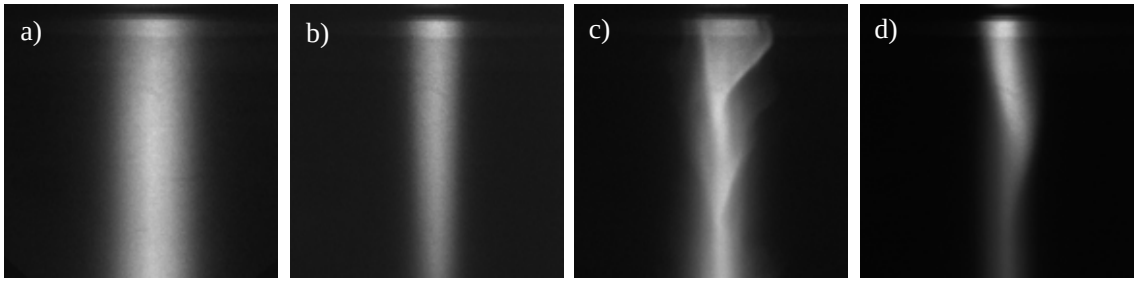

Fig.4 Luminous images of the laminar (a) and turbulent (c) argon plasma jets and the laminar (b) and turbulent (d) Ar-H_2 plasma jets. The exposure time of ICCD camera is 5 μs for (c) and 10 μs for others.

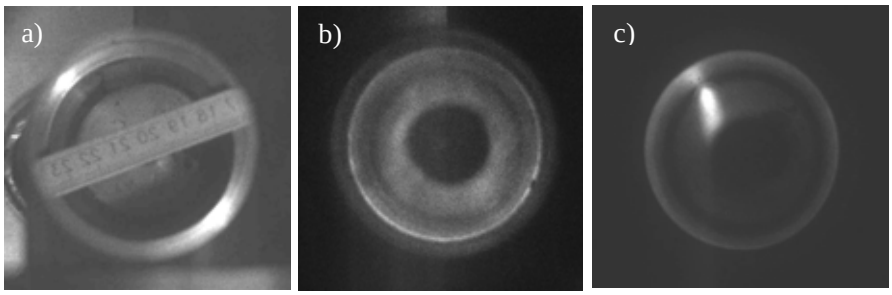

Fig. 5 (a) Rear-view photograph of the torch channel configuration with a ruler across the anode exit section but without plasma; (b) photograph of the Ar plasma at chamber pressure of 3.2×10^3 Pa; and (c) photograph of Ar- 9%H_2 plasma at 2.4×10^4 Pa. The exposure time is 10 μs for (b) and 80 μs for (c).

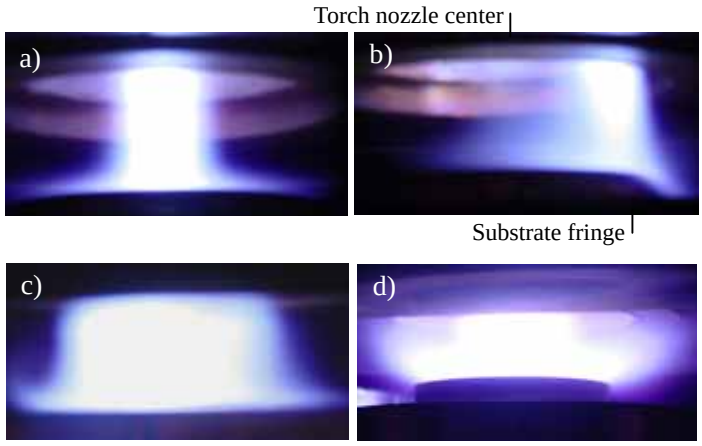

Fig. 6 Appearance of the pure argon plasma jets. (a) - (c) at chamber pressure of 1.7×10^4 Pa and (d) at 6.5×10^2 Pa. External magnetic field is applied for the case (b) and (c).

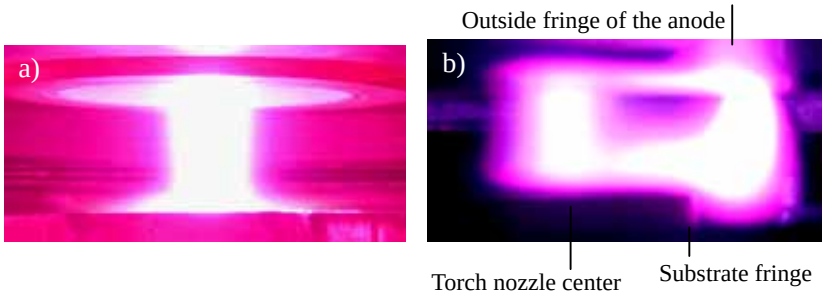

Fig. 7 Appearance of the Ar+H_2 plasma jets. (a) taken at chamber pressure of 1.6×10^3 Pa and 4%H_2 , and (b) at 1.8×10^4 Pa and 15%H_2.

Figure 6 shows the appearance of the pure argon plasma jet generated at 6 kW input power and impinging on the water-cooled substrate. The photographs are taken using the digital camera. Figs. 6(a) - 6(c) are with chamber pressure of 1.7×10^4 Pa, whereas 6(d) is with pressure 6.5×10^2 Pa. Figs. 6(a) and 6(d) are for the case without external magnetic field, whereas Fig. 6(b) and 6(c) are for the case with an applied external magnetic field of about 0.03 T. It is seen that the argon plasma jet is well axi-symmetrical for the case without the external magnetic field, as shown in Fig. 6(a) and 6(d). At the higher pressure, i.e. at 1.7×10^4 Pa, the radial size of high-temperature regions of the argon plasma jet including its impinging zone at the substrate surface are somewhat concentrated, whereas at the lower pressure, i.e. at 6.5×10^2 Pa, the high-temperature regions are more diffusive and can cover up the whole substrate with diameter of 60 mm. The appearance of the argon plasma jet under the action of external magnetic field (Fig. 6(b)) is quite different from that shown in Fig. 6(a) for the case without external magnetic field effect. As seen from Fig. 6(b), the high-temperature region of the plasma jet is no longer axi-symmetrical and is not steady when an external magnetic field is applied to drive the arc root moving along the inner surface of the torch anode-nozzle. The high-temperature region rotates around the torch axis, and thus approximately axi-symmetrical picture can be obtained if the exposure time of the digital camera is long enough, as seen in

Fig. 6(c). With the rotation driven by the external magnetic field, the argon plasma jet can cover up the whole substrate surface with 60 mm diameter. This situation is favorable for getting more uniform heating of the substrate with a relatively large surface area.

When hydrogen is added into argon to generating the plasma jet, the arc voltage increases with the increase of hydrogen content in the Ar-H_2 mixture. Fig. 7 shows two photographs taken by the ordinary camera for the argon-hydrogen plasma jet (a) and arc column (b) without the external magnetic field. When the hydrogen content in the Ar-H_2 mixture is relatively low (about 4%), Fig. 7(a) shows a similar impinging jet characteristics as for the pure argon plasma jet shown in Fig. 6(a). It is found that when the argon-hydrogen mixture is used as the plasma-forming gas, arc column can be blown out from the torch exit for certain parameter combinations. For the case shown in Fig. 7(b), a straight arc column goes down along the torch axis until it reaches the region near the water-cooled substrate surface and then bends up to the anode-nozzle exit with a constricted arc-root attachment at the outer fringe of the anode-nozzle. When the external magnetic field is applied, it is found that the argon-hydrogen arc root rotates quickly along the outer fringe of anode-nozzle, and the arc root attachment location tends to retreat back inside the torch nozzle as the magnetic induction intensity of applied magnetic field increases when the plasma-generating conditions are kept unchanged.

The present observation results suggest that the attachment mode of the arc root in the plasma generator, i.e. as a diffused- or constricted-type arc-root, is mainly determined by the working gas type; and the axial position of arc root and the arc root movement are essentially controlled by the balance between the gas flow action and the magnetic field driving.

4. Conclusions

The present observation results show that the laminar argon or argon-hydrogen plasma jet is very stable, while the turbulent plasma jet is obviously unstable and non-axisymmetrical. Arc attachment on the anode surface is almost completely diffusive when pure argon is used as the plasma-forming gas, while the arc root attachment becomes sharply concentrated when hydrogen is added into argon as the plasma-forming gas even for the case with a rather low content of hydrogen in the Ar-H_2 mixture. When the chamber pressure is reduced, the high-temperature region of argon plasma jet becomes more diffused with a larger cover-area as it impinges on the substrate. When the argon-hydrogen mixture is used as the plasma-forming gas, the arc column is easily blown out from the torch nozzle exit until it reaches the region near the water-cooled substrate surface and then bends up to attach at the outer fringe of the anode-nozzle. When an external magnetic field is applied, the argon-hydrogen arc-root rotates quickly along the anode surface, and the arc-root attachment location tends to retreat back inside the torch nozzle as the magnetic induction intensity of the external magnetic-field is enhanced.

Acknowledgment: This work is supported by the National Natural Science Foundation of China (Nos. 50336010, 50276065).

References

[1] W.X. Pan, W.H. Zhang, W.H. Zhang, and C.K. Wu, *Plasma Chem. Plasma Process.* **21**, 23 (2001).

[2] E. Pfender, Thin Solid Films **238**, 228 (1994).

[3] S. Russ, E. Pfender, and P. J. Strykowski, *Plasma Chem. Plasma Process.* **14**, 425 (1994).

Thermodynamic Properties of Fluorocarbons

M. K. VanOtterloo[1], S. L. Girshick[1], and J. T. Roberts[2]
1 Department of Mechanical Engineering, University of Minnesota, Minneapolis, United States
2 Department of Chemistry, University of Minnesota, Minneapolis, United States

Abstract
A group additivity method was developed to estimate heats of formation for linear and branched radical and closed-shell, gaseous fluorocarbon neutrals containing four or more carbon atoms. These groups are derived from *ab initio* calculations by Bauschlicher and Ricca [1,2]. Heats of formation and other thermochemical properties determined by a group additivity approach will be utilized in the development of a computational model to simulate gas-phase nucleation in an octafluorocyclobutane (*c*-C_4F_8) plasma.
Keywords: Fluorocarbon plasmas; Heats of formation; Group additivity; Radicals

1. Introduction

Fluorocarbon plasmas are commonly used as etchants in integrated circuit fabrication due to selectivity and anisotropic capabilities. Nanoparticles have been observed in these systems [3] but little is known about how the particles form. We have begun developing a computational model to simulate gas-phase nucleation in an octafluorocyclobutane (*c*-C_4F_8) etching plasma, accounting for particle production via chemical reactions, and particle growth by coagulation and surface reactions.

Many important reactions leading to particle formation may be reversible, requiring knowledge of reaction free energies, and hence, knowledge of the standard enthalpies of formation (Δ_fH^o) and entropies of the chemical species involved. Experimental data are available for only a few fluorocarbon species containing more than two carbon atoms. More extensive work has been done by means of *ab initio* computational studies, including a study by Zachariah et al. [4] that reported thermochemical data for around 100 hydrofluorocarbon species. Computational chemistry calculations become more expensive as the size and complexity of the molecule grows, making studies of this sort impractical for our exploration of large fluorocarbon clusters.

In order to provide enough thermodynamic data to proceed with modeling of fluorocarbon cluster formation, we have developed a group additivity method, an empirical method that has been successfully used for hydrocarbons, partially halogenated hydrocarbons [5], and silicon hydrides [6]. In general, group additivity allows for estimation of a molecule's Δ_fH^o by summing the Δ_fH^o values of contributing groups, e.g., group additivity values (GAVs). Yamada and Bozzelli [7,8] and Zhang and Pollard [9] conducted group additivity studies on partially fluorinated systems: hydrofluorocarbons and chlorofluorocarbons, respectively. While these GAVs could be applied to fully fluorinated systems, GAVs for fluorocarbon radicals are lacking in both studies. Yamada and Bozzelli reported no radical groups while Zhang and Pollard reported two radical groups. In the case of plasma chemistry, radicals can be very important to the kinetics and therefore the lack of radical thermochemistry could be a problem. This paper describes the methodology used in determining new GAVs for fluorocarbon molecules, including radicals, and compares results to those previously reported in other studies.

2. Methodology, Results, and Discussion

The accuracy of GAVs depends on the precision of the data used in their estimation and on the size of the database. Bauschlicher and Ricca computationally determined Δ_fH^o for C_xF_y (x=1-3) [1] and cyclic C_4F_n (n=4-8) [2] on the G3MP2 level and found their calculations to be accurate to within ± 2 kcal/mol. We chose to base our group additivity analysis on these values because there is no experimental study, to our knowledge, that could provide us with as large or as accurate a database. The heats of formation from the Bauschlicher and Ricca study are listed in Table 1 along with the generalized molecular structures of the studied species for illustrative purposes. We utilized data for two single-bonded molecules, C_2F_6 and C_3F_8; three single-bonded radicals, C_2F_5, C_3F_7A ($F_3C(CF)CF_3$), and C_3F_7B ($F_2C(CF_2)CF_3$); three double-bonded molecules, C_2F_4, C_3F_4, and C_3F_6; three

double-bonded radicals, C_2F_3, C_3F_2, and C_3F_3; one triple-bonded molecule, C_2F_2; and one cyclic molecule, *c*-C_4F_8. From these data, eighteen groups were defined, including one ring correction, as shown in Table 2.

Table 1. Heats of formation and general geometries from Bauschlicher and Ricca [1,2] used in determination of group additivity values. Data includes five single-bond species, six species containing double bonds, one specie with a triple bond, and *c*-C_4F_8, which requires a four-carbon ring correction.

Single Bonded Species		$\Delta_f H°(298K)$ kcal/mol
C_2F_5	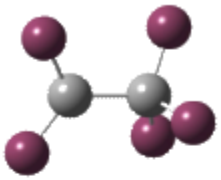	-215.29
C_2F_6	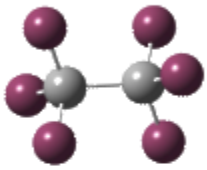	-322.34
C_3F_7 A	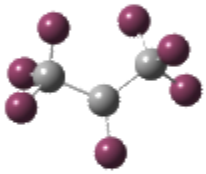	-322.41
C_3F_7 B	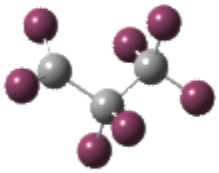	-315.64
C_3F_8	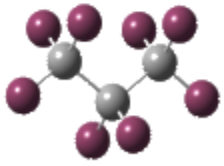	-422.00

Other Species		$\Delta_f H°(298K)$ kcal/mol
C_2F_2	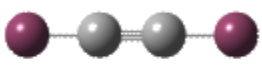	0.03
c-C_4F_8	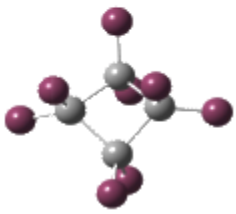	-375.60

Double Bonded Species		$\Delta_f H°(298K)$ kcal/mol
C_2F_3	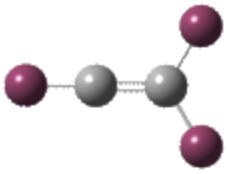	-53.57
C_2F_4	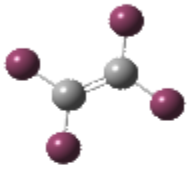	-161.69
C_3F_2		55.19
C_3F_3	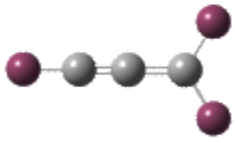	-31.94
C_3F_4	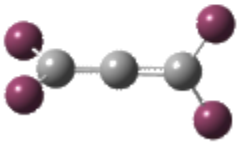	-132.34
C_3F_6	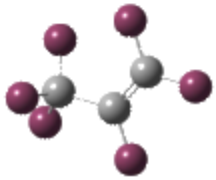	-276.04

Table 2. Definition of groups, group additivity values for fluorocarbon compounds, and comparison of GAVs from Yamada and Bozzelli [7].

	Group	$\Delta_f H^o$(298K) kcal/mol	
		Previous work [7]	This work
1	C-[F]$_3$[C]	-168.2	-168.9
2	C-[F]$_3$[Ċ][b]		-168.9[a]
3	C-[F]$_3$[C$_d$][c]		-168.9[a]
4	C-[F]$_2$[C]$_2$	-104.9	-111.8
5	C-[F]$_2$[C][Ċ]		-110.2
6	Ċ-[F]$_2$[C]		-60.2
7	Ċ-[F][C]$_2$		-0.2
8	C$_d$-[F]$_2$[C]	-86.8	-88.9
9	C$_d$-[F]$_2$[C$_d$]		-83.2
10	C$_d$-[F]$_2$[Ċ]		-88.9[a]
11	C$_d$-[F][C]$_2$		-34.9
12	Ċ$_d$-[F][C]		26.4
13	Ċ$_d$-[F][C$_d$]		26.4[a]
14	[C]-C$_a$-[C][d]		34.0[a]
15	[C]-C$_a$-[Ċ]		24.8
16	[Ċ]-C$_a$-[Ċ]		2.3
17	C$_t$-[F][C][e]	2.8	0.3
18	R4[f]		32.2

[a] Assumed value. [b] Ċ: carbon radical. [c] C$_d$: double-bonded carbon. [d] C$_a$: allyl-like carbon ([C]=C=[C]). [e] C$_t$: triple-bonded carbon. [f] R4: four-carbon ring correction.

Fluorocarbons are not a good candidate for the traditional group additivity method introduced by O'Neal and Benson [10], because average errors exceed 10 kcal/mol, as reported by Yamada and Bozzelli [7]. To reduce errors, Yamada and Bozzelli included a correction for interactions between fluorine atoms located on adjacent carbon atoms, determined by studying hydrofluorocarbons. Unfortunately, the Bauschlicher and Ricca study does not produce a large enough database so that both group values and interaction values can be determined. Therefore, we utilized the interaction terms determined by Yamada and Bozzelli, shown in Table 3, for all of our GAV calculations. The groups and fluorine interactions contained in each of the molecules studied by Bauschlicher and Ricca are listed in Table 4.

Given that heat of formation data are available for only thirteen molecules, while eighteen groups are defined in Table 2, five further assumptions are required to determine the set of GAVs. First, we assumed that C-[F]$_3$[Ċ] is equivalent to C-[F]$_3$[C]. The analog to this assumption in the hydrocarbon system, namely that C-[H]$_3$[Ċ] is equivalent to C-[H]$_3$[C], is commonly made, and Marsi et al. [11] determined that on average it affected GAVs

by only 0.5 kcal/mol in an alkyl radical system. Therefore, we supposed that setting GAV for C-[F]$_3$[Ċ] equal to that of C-[F]$_3$[C] would have only a small effect on the fluorocarbon results as well. Similarly, we assigned the GAV of C_d-[F]$_2$[Ċ] to be equal to that of C_d-[F]$_2$[C]. We also assumed that the GAV of C-[F]$_3$[C_d] was equal to that of C-[F]$_3$[C], which was supported by Cohen and Benson [12] in the hydrocarbon system, for which they found that the GAV of C-[H]$_3$[C_d] equaled that of C-[H]$_3$[C]. We also assumed that the GAV of Ċ$_d$-[F][C_d] equaled that of Ċ$_d$-[F][C], based on the same logic. Finally, we assigned the GAV of [C]-C_a-[C] to be equal to Cohen and Benson's [12] value of 34.0 kcal/mol for the same group.

Table 3. Correction values to heats of formation due to interaction between fluorine atoms on adjacent carbon atoms. Values are from Yamada and Bozzelli [7].

Fluorine Correction Terms[a]	$\Delta_f H^o$(298K) kcal/mol
F/3F	7.8
2F/2F	9.8
2F/3F	13.8
3F/3F	15.5
F//2F	8.9
2F//2F	16.1
F///F	-0.50

[a] /, //, /// indicates interaction across a single, double, and triple bond, respectively.

From these assumptions, a step-by-step approach was used in determining the group additivity values from the available database. Though this is not as accurate as performing a least-squares-fit over a large database of molecules, Cohen and Benson [12] found that GAVs determined from accurate data for single molecules were within experimental error. Recall that all fluorocarbon-fluorocarbon interaction values were assumed from Yamada and Bozzelli [7], therefore C-[F]$_3$[C], C_d-[F]$_2$[C], and C_t-[F][C] were determined directly from C_2F_6, C_2F_4, and C_2F_2, respectively. With these values, C-[F]$_2$[C]$_2$ could be determined from C_3F_8. Next, Ċ-[F]$_2$[C], Ċ-[F][C]$_2$, and C-[F]$_2$[C][Ċ] could be derived from C_2F_5, C_3F_7A, and C_3F_7B, respectively, once C-[F]$_3$[Ċ] = C-[F]$_3$[C] was assumed. After C_d-[F]$_2$[Ċ] = C_d-[F]$_2$[C] was assumed, Ċ$_d$-[F][C] was found from C_2F_3. Then, after [C]-C_a-[C] is assigned a value of 34.0 kcal/mol and Ċ$_d$-[F][C_d] = Ċ$_d$-[F][C], C_d-[F]$_2$[C_d], [C]-C_a-[Ċ], and [Ċ]-C_a-[Ċ] were determined from C_3F_4, C_3F_3, and C_3F_2, respectively. Finally, since C-[F]$_3$[C_d] = C-[F]$_3$[C], C_d-[F][C]$_2$ was found from C_3F_6. To determine the ring correction, *c*-C_4F_8 is assumed to be composed of four C-[F]$_2$[C]$_2$ groups and four 2F/2F interactions plus the R4 correction. The resulting group additivity values are listed in Table 2.

Any direct comparison between our group additivity values and those from other studies is only relevant to the extent that the other studies also included fluorine-fluorine interaction corrections. Therefore, GAVs of this work could only be judged against those determined by Yamada and Bozzelli [7]. Comparison of the GAVs of the four groups coincident in both studies, shown in Table 2, resulted in an average difference of 3.1 kcal/mol.

3. Conclusions and Future Work

Group additivity values were developed to determine heats of formation for gaseous fluorocarbon species. GAVs previously defined by Yamada and Bozzelli [7] for four of the groups defined herein are on average within ± 3.1 kcal/mol of the GAVs of this study, lending support that our other GAV estimations are reasonable. These GAVs can be used to estimate the $\Delta_f H^o$ for linear and branched radical and closed-shell, gaseous fluorocarbon neutrals containing four or more carbon atoms.

In the future, this group additivity scheme will be extended to estimate entropies. Also, further ring corrections will be estimated, probably by reference to available experimental work.

Table 4. Groups, interactions and ring corrections in gaseous fluorocarbons species from Bauschlicher and Ricca [1,2] studies.

Species	1	2	4	5	6	7	17	F///F	F/3F	2F/2F	2F/3F	3F/3F	18
C_2F_5		x			x						x		
C_2F_6	x											x	
C_3F_7 A		x				x			x				
C_3F_7 B	x			x	x					x	x		
C_3F_8	x		x								x		
c-C_4F_8			x							x			x
C_2F_2							x	x					

Species	3	8	9	10	11	12	13	14	15	16	F/3F	F//2F	2F//2F
C_2F_3				x		x						x	
C_2F_4		x											x
C_3F_2							x			x			
C_3F_3			x				x		x				
C_3F_4			x					x					
C_3F_6	x	x			x						x	x	

Acknowledgements
This work was partially supported by NSF IGERT grant DGE-0114372 and by the Minnesota Supercomputing Institute.

References
[1] C.W. Bauschlicher, Jr. and A. Ricca – J. Phys. Chem. A **104**, 4581 (2000).
[2] C.W. Bauschlicher, Jr. and A. Ricca – J. Phys. Chem. A **104**, 9026 (2000).
[3] W.W. Stoffels, E. Stoffels, and K Tachibana – J. Vac. Sci. Tech. A **16**, 87 (1998).
[4] M.R. Zachariah, P.R. Westmoreland, D.R. Burgess, W. Tsang, and C.F. Mellius – J. Phys. Chem. **98**, 1100 (1996).
[5] S.W. Benson, Thermochemical Kinetics; Wiley-Interscience: New York, 1976.
[6] M.T. Swihart and S.L Girshick – J. Phys. Chem. B **103**, 64 (1999).
[7] T. Yamada and J.W. Bozzelli – J. Phys. Chem. A **103**, 7373 (1999).
[8] T. Yamada, T. Lay, and J Bozzelli – J. Phys. Chem. A **102**, 7286 (1998).
[9] Z. Zhang and R. Pollard – Thermochim. Acta **257**, 21 (1995).
[10] H.E. O'Neal and S.W. Benson – Int. J. Chem. Kinet. **1**, 221 (1969).
[11] I. Marsi, B Viskolcz, and L. Seres – J. Phys. Chem. A **104**, 4497 (2000).
[12] N. Cohen and S.W. Benson – Chem. Rev. **93**, 2419 (1993).

Atmospheric plasma for thin film deposition

M. Thomachot[1], E. Jouvet[1], T. Sindzingre[1], B. Parbhoo[2], G. Ravel[3]

1 AcXys Technologies, 148 rue des vingt toises, 38950 Saint Martin le Vinoux, France
www.acxys.com
2 Surface Chemical Performance, 1, Weston Avenue, Sully, Wales, CF64 5SW, United Kingdom
bhukan@tiscali.co.uk
3 CEA-DRT-LETI/DOPT CEA/GRE, 17 rue des Martyrs, 38054 Grenoble CEDEX 9, France

Abstract
We report on the deposition of thin film coatings produced at atmospheric pressure by mixing plasma with sprayed chemicals phases. SiO_2 and TiO2 like coating were homogeneously deposited on a variety of materials. Surface analyses show the formation of a very dense layer, comparable to those made with other deposition techniques. Furthermore, deposition temperature can be as low as 50°C for SiO2 and 300°C for TiO2. The whole process can be completed on existing continuous production lines.

Keywords
Atmospheric plasma. Thin film deposition. Silica.

Introduction
Film deposition has a wide range of industrial applications such as protective and abrasion resistant coatings, optical layers, diffusion barriers, hydrophilic / hydrophobic layers, super-hydrophilic and super-hydrophobic surfaces, low-k, high-k, food packaging, etc. Plasma processes are being used for film depositions. They offer important advantages such as: avoidance of wet and hazardous chemical processes, enhancement of chemical reactions, and excellent performance in terms of adhesion and homogeneity. In recent years, plasma technology has evolved considerably and new technological possibilities have emerged. A new post-discharge plasma system has been developed by AcXys Technologies producing low temperature plasma at atmospheric pressure, away from electrodes confinement, and using low cost nitrogen or nitrogen/gases mixtures. This plasma technology is ideally suited to deposit inorganic and organo-inorganic thin films.

1. Atmospheric plasma technology

AcXys Technologies provides equipment and turn-key processes based on a unique atmospheric pressure plasma technology (Figure 1).

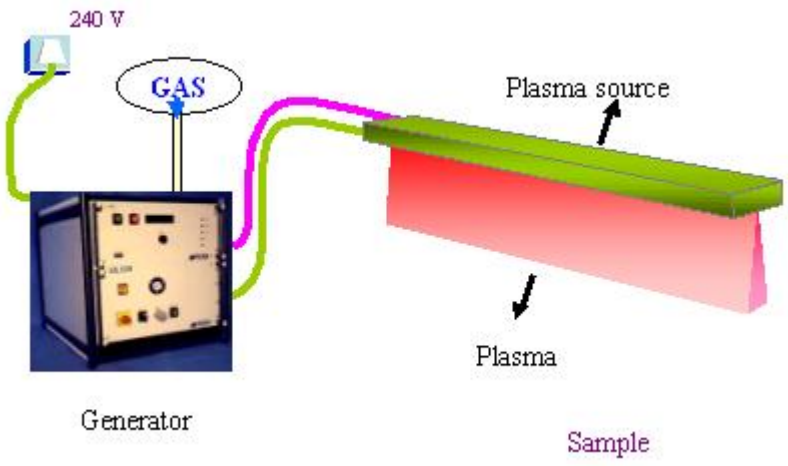

Figure 1: Schematic description of the AcXys Plasma system. The plasma source can vary in lengths.

The AcXys system produces a low temperature reactive atmosphere (Figure 2) capable of treating almost any materials in any size or shape. Examples of materials are: polymers, metals, glass, optics, electronics devices and products, rubbers, textile or webs.

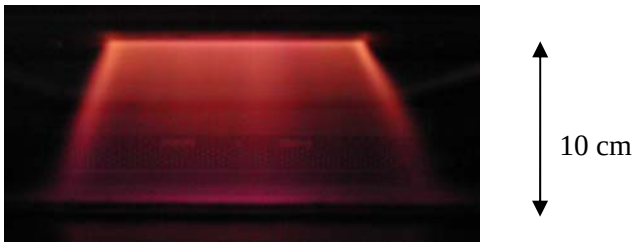

Figure 2 : Nitrogen plasma phase ejected from the plasma source at atmospheric pressure.

This plasma technology is being used in a variety of applications across many industries using nitrogen, nitrogen/gas mixtures or purified air. The technology can be used to clean surfaces, to chemically activate them, to perform oxido-reduction chemistry at surfaces, and to surface engineer materials. Properties like wettability, spreading rates, adhesion and thin film cohesion can be considerably improved. In addition, new concept of adhesion called dry-adhesion have been invented by avoiding the use of wet adhesives.

AcXys Technologies' equipment generate a blade-shaped plasma, which length can be adjusted depending on customer's needs (Figure 3). When used in controlled atmosphere, the plasma phase can be large enough to enable treatment of 3D objects. This makes AcXys the only technology that offers atmospheric plasma treatment for any shape and any size.

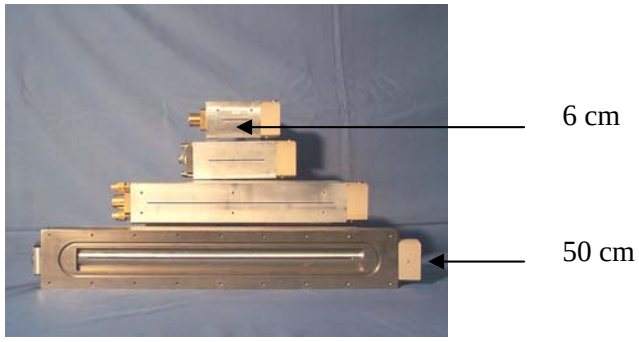

Figure 3 : Plasma sources of varying lengths.

When treatment is required over a precise area or when there is a confinement space from the source, the plasma can be directed through a tube and delivered where and when needed (Figure 4).

Figure 4 : Delivering of a plasma phase for local treatment.

Several kinds of equipment have been designed and proposed for specific needs. For instance, Miniweb equipment is used for web material and films (Figure 5), 3D-Box is used for small objects and ideally replaces low pressure glow discharge plasma systems (Figure 6) and ultra-light is easy to adapt on existing continuous production lines or custom reactors (Figure 7).

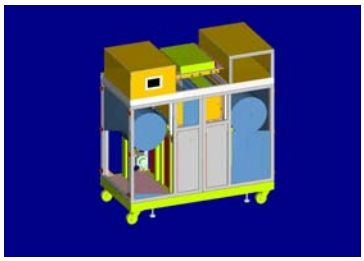

Figure 5 : Web material treatment system incorporating a plasma system.

Figure 6 : Bench-top plasma system for batch treatment of small objects.

Figure 7 : Ultra-light equipment (UL) series for customized applications.

2. Experimental setup

An atmospheric plasma is created in a confined tunnel, then mixed with a sprayed liquid precursor. A substrate holder is conveyed near the mixing zone, so as to realize deposition (Figure 8).

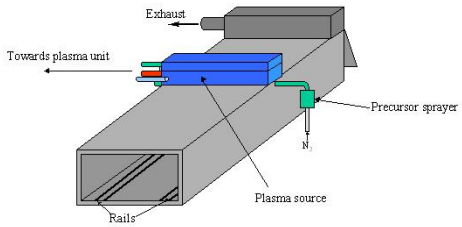

Figure 8 : Schematic of the experimental setup.

Substrate can be conveyed under the plasma with a robot, at a precise speed, thus enabling a precise and homogeneous film deposit (Figure 9).

Figure 9 : Picture of the overall experimental setup.

We used several precursors, such as hexamethyldisiloxane (HMDSO or MM), octamethylcyclotetrasiloxane (OMCTS or D_4) to deposit SiO_2 like films on silicon wafer. We chose silicon because it is easier to analyze and to compare with existing deposition techniques. However, we have been able to deposit other materials on many other substrates like plastics, glass, fabrics, leather.

3. Results

We compared our film deposits to those made with traditional deposition methods with the following means: Scanning Electron Microscopy (SEM), FTIR, and Variable Angle Spectrocopic Ellipspometry (VASE).
SEM views (Figure 10) show a very dense layer, without cavities.

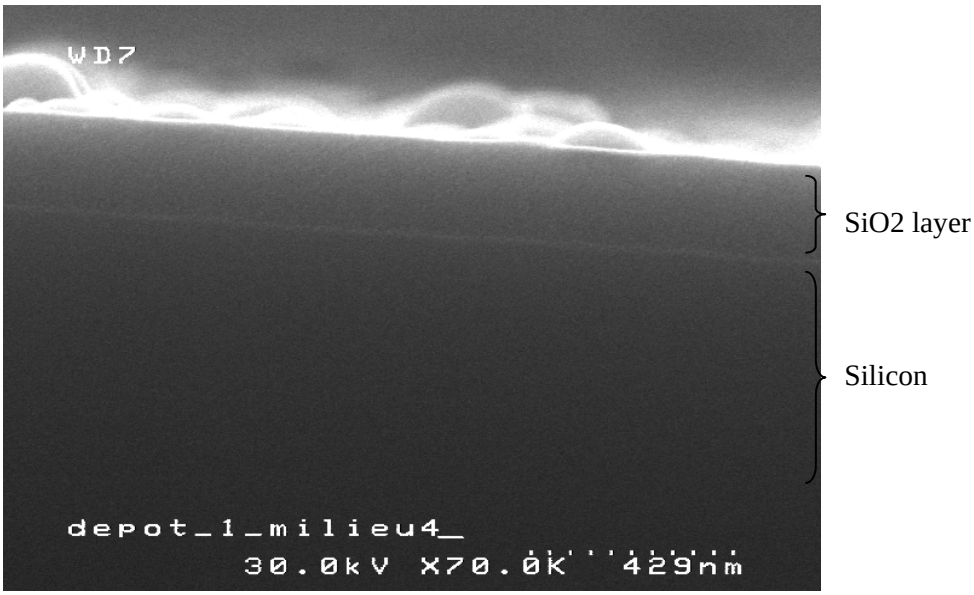

Figure 10 : SEM view of a SiO_2 film deposit

We compared FTIR spectra of four layers made with our technology with those of layers made with classical PECVD methods (Figure 11). They are very similar.

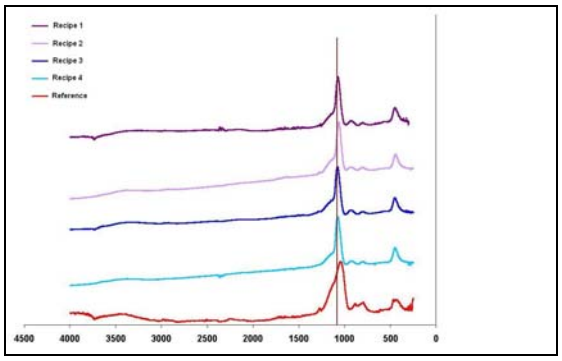

Figure 11 : Four FTIR spectra compared to those of a classical PECVD deposit (bottom)

VASE measurements show refractive index as a function of wavelength (Figure 12). Several materials made with different techniques have been compared in term of refractive index, and thus in term of density (Table 1). It appears that very dense layers can be deposited with atmospheric plasma. Indeed, the density is higher for our films than for sol-gel layers and nearly the same as PVD layers. Density has been evaluated at 1,7 g/cm^3.

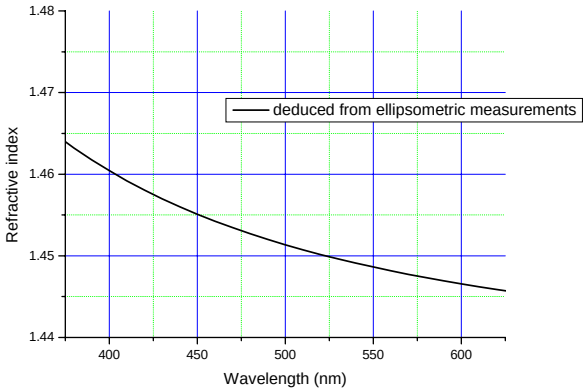

Figure 12 : Ellipsometry measurements of the silica-like film.

Technology	Ion Beam Sputtering	Evap. 250°C	AcXys plasma	Sol-Gel
n @ 600 nm	1.5	1.475	**1.446**	< 1.35

Table 1 : Comparaison of refractive indices (n) of the silica films deposited by different techniques.

Homogeneous deposits have been produced on 4” wafers (Figure 13). This is a very promising result, showing industrial viability of the process.

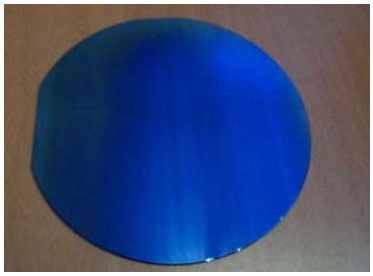

Figure 13 : Homogeneous silica film deposit on a 4" silicon wafer.

4. Towards lower temperatures

SiO_2 film deposition is produced from organosilicon precursors without preheating the substrate. This latter is naturally heated by the plasma and can reach 200°C, depending on the distance between the substrate and the plasma source, the plasma treatment time, and the nature of the substrate. The heat can be avoided by using several short time cycles so as to let the substrate cool.

A new way to decrease plasma temperature has been experimented with success. It is based on duty cycle control of the plasma power. Plasma is regularly switched on and off at 100 Hz with a duty cycle that can be set from 0 to 1. Thus, it is possible to monitor plasma temperature from ambient to approximately 200°C. With this method, deposition of a 150 nm SiO_2 layer has been completed at 50°C.

5. Deposition of TiO2 at low temperature

Similar experiments have been performed with TiO2 precursors. A TiO2 crystal thin film has been deposited at less than 300°C.

Acknowledgments

An important part of this work was realized by Rémy Maurau during his graduation internship at AcXys Technologies, with technical support from Patrick Lassagne and Laurent Lassagne. We would like to thank Dominique de Barros, Carmen Jiménez and François Weiss (Laboratoire des Matériaux et du Génie Physique) for their work on TiO2. FTIR measurements have been realized with the help of Michel Langlet. SEM measurements have been realized by Jérôme Thiault.

References

[1] BORVON G., BOUSQUET A., GOULLET A., GRANIER A., VAN DER LEE A., ROUESSAC V., Mechanisms involved in the transformation of ppHMDSO films into SiO_2-like by oxygen plasma treatment. *14th international colloquium on plasma processes*, Antibes 2003.

[2] LEADLEY S.R., O'NEIL L., O'HARE L.A., GOODWIN A.J., Atmospheric pressure plasma liquid deposition – a new route to high performance coatings. *14th international colloquium on plasma processes*, Antibes 2003.

[3] SAWADA Y., OGAWA S., KOGOMA M., Synthesis of plasma-polymerized tetraethoxysilane and hexamethyldisiloxane films prepared by atmospheric pressure glow discharge. *Phys. D : Appl. Phys.* 28 (1995) 1661-1669.

Thermal characterization of He-(x<5%)M (M=N_2,O_2,Ar or H_2) atmospheric microwave plasmas

C. Noël, R.P. Cardoso, G. Henrion and T. Belmonte

Laboratoire de Science et Génie des Surfaces-(CNRS-UMR 7570), INPL-Ecole des Mines
Parc de Saurupt - 54042 NANCY cedex, FRANCE

Abstract
In this work, the influence of different impurities (N_2, O_2, Ar and H_2) on the thermal behaviour of an atmospheric microwave plasma is studied. Substituting 500 ppm of N_2 by 500 ppm of H_2 makes the gas temperature vary by about 500 K. Infra-red thermal analyses of the fused silica tube confirm the sensitive influence of the additive gas on the thermal behaviour of the plasma.

Keywords. Atmospheric pressure glow discharge, Helium, TALIF, OES, Temperature measurements

1. Introduction

The development of applications of atmospheric pressure plasmas requires a better understanding of phenomena that control the discharges. Recent theoretical and experimental characterizations of atmospheric discharges in helium pointed out the importance of impurities in the description of the plasma [1-2]. For example, small amounts of additive gases (~1%) are known to play a role in the stability of Atmospheric Pressure Glow Discharges (APGD) [3].In the present work, the influence of different impurities is studied. The main criterion retained here to appreciate the influence of the impurities is the gas temperature which is determined either by simulating the rotational spectra of OH radicals [4] or from the Doppler broadened line shape the H_α and D_α lines measured by means of Two Photon Absorption Laser Induced Fluorescence (TALIF) [5]. Indeed, in the microwave cavity used as plasma source, huge thermal gradients are observed. In the flow conditions retained in these experiments, the Reynolds number is in the range from 2 to 15, whereas the Grashof number (Gr=$\frac{g\beta\rho_{ref}^2\Delta T_{ref}R^3}{\mu_{ref}^2}$ where g is the gravity, β the compressibility factor of helium, ρ the gas density, μ its viscosity and R, the radius of the tube) reaches 5340 at 3000 K. In this case, where the Gr/Re ratio is sufficiently high, instabilities are observed [6] since mixed flow conditions prevail. Recently, Castaños Martinez et al. [7] have shown the importance of thermal gradients on plasma contraction at sufficiently high pressure.

2. Experiment

The experimental device is presented in Figure 1. The gas mixture is introduced into a 28 mm inner diameter tube made of fused silica. The flow rate of Helium is 2000 sccm (standard cubic centimetre per minute). The microwave power is kept at a constant value of 300 W. All gases (He, N_2, H_2, O_2 and Ar) have the same level of purity (99.995%) and the flow rates are controlled by mass flow meters (typically between 1 sccm (~ten times higher than the amount of impurities initially contained in "pure" helium) and 100 sccm). The discharge is produced using a cavity connected to a microwave generator (2.45 GHz). Optical Emission Spectroscopy (OES) is carried out in the discharge using a HR640 Jobin Yvon spectrometer equipped with a 1200 gr/mm grating and a CCD detector. The spectral resolution is thus $\Delta\lambda \sim 0.33$ nm
For TALIF experiments in He-H_2 mixtures only, photo-excitation is provided by a YAG-pumped dye laser (Quantel TDL50). The Nd-Yag emission at 1064 nm is frequency doubled into a KDP crystal before pumping the dye cells. For our purpose, the dye laser operates with Rhodamine 640 to produce a 615 nm laser beam which is next frequency tripled (~205 nm). The two-photon absorption is then used to probe the Ly_β transition

at 102.57 nm. The detection set-up for TALIF measurement is made of the set: Photomultiplier, interference filter, amplifier and Boxcar presented in Fig. 1. Finally, deuterium is substituted to hydrogen to calibrate the full width at half maximum (FWHM) of the hydrogen adsorption peak [5].

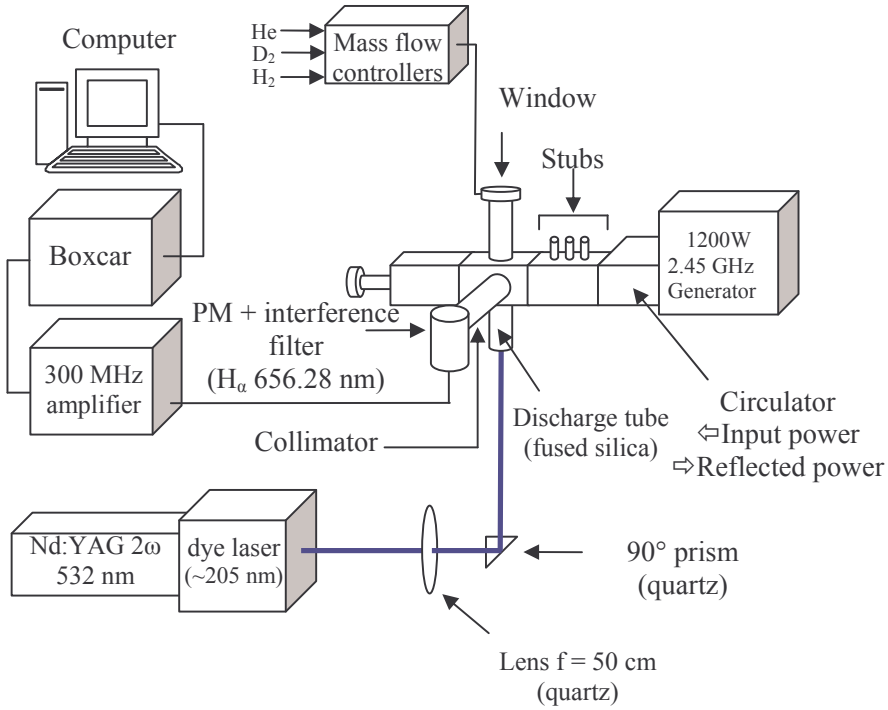

Figure 1: Experimental set-up.

3. Experimental results

Visible optical emission spectra of helium plasmas of different additive gases are depicted in figure 2. They are very similar to those presented in other kinds of discharges [8-9]. Dimmer emission is not detected at 300 W since the temperature of the gas is too high to keep these species at sufficiently high densities [7].
At 0.1% of additive gases, the emission spectra are very similar to those that would be obtained in discharges of the pure additive gases.

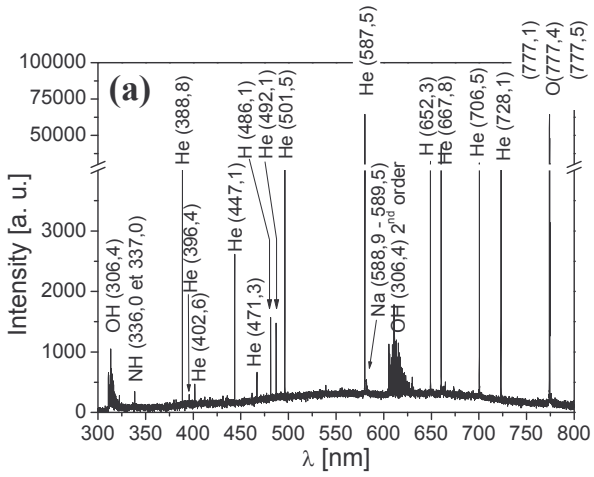

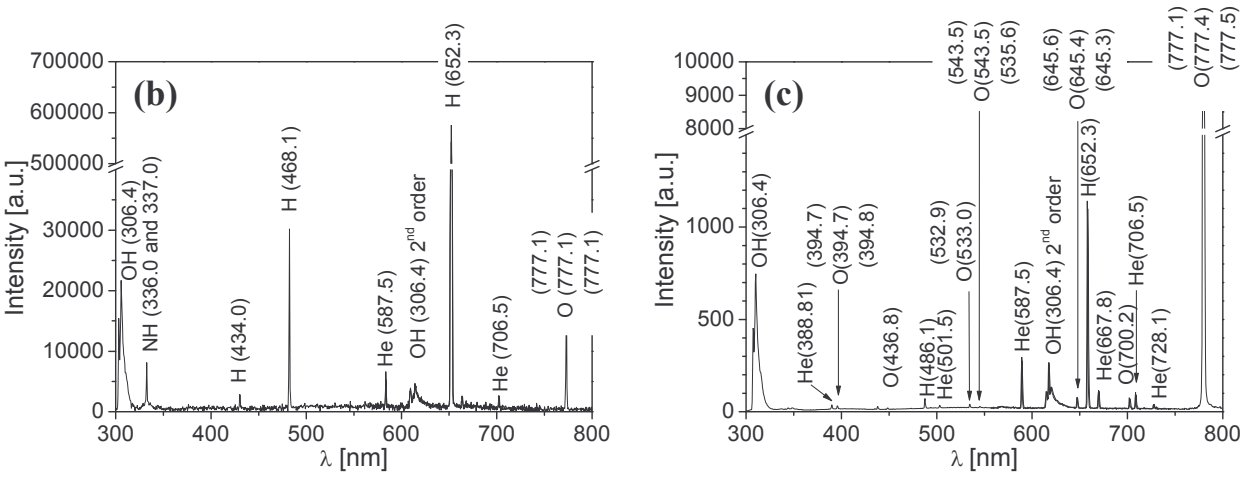

Figure 2: Optical emission spectra in the visible region of atmospheric helium plasmas (300 W) with (a) : 0 sccm of additive gases, (b) 0.1% H_2, (c) 0.1% O_2.

The presence of OH emission enables us to predict the temperature of the gas with a satisfying accuracy as already studied in detail by [10] in a very similar experimental arrangement to the present device.

3.1. Gas phase temperature

In a first step, a comparison is draw between the temperatures determined by OH rotational spectrum simulation and TALIF measurements (Figure 3). The mean temperature increases significantly from 0 to several hundreds of ppm of hydrogen (from 2700 K to about 3000 K). A discrepancy is noticed between OES and TALIF measurements between 0 and 2% of H_2 whereas at higher concentrations, both types of results merge.

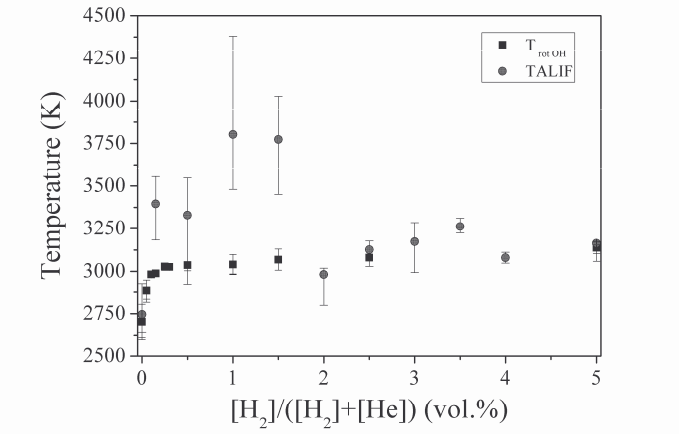

Figure 3: Comparison between temperatures determined by TALIF and synthetic spectra of OH from optical emission spectroscopy.

OH rotational temperature is determined from a spectrum of optical emission spectroscopy acquired from the whole volume of the plasma, whereas the TALIF measurement is spatially resolved. Furthermore, the reproducibility of TALIF results is much lower than that of OES as shown by error bars.

In a second step, the influence of different gases introduced as impurities in helium is studied. Results are reported in Figure 4. Clearly, it can be seen that nitrogen or argon cools the plasma whereas hydrogen or oxygen heats it. From 500 ppm N_2 to 500 ppm H_2, a difference of nearly 500 K is measured.

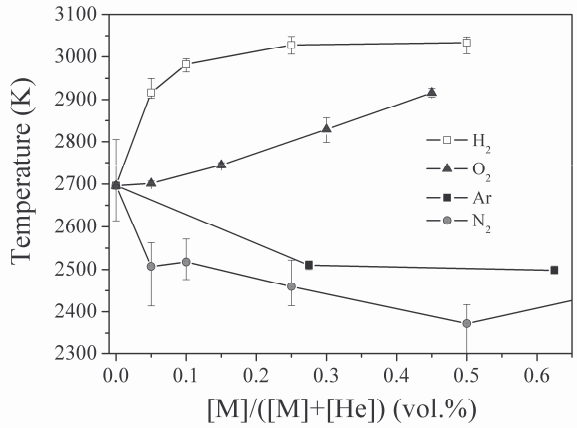

Figure 4: Influence of H_2, O_2, Ar and N_2 introduced as impurities in helium on the plasma mean temperature determined by OH rotational temperature.

This huge difference shows the importance of the additive gas on the thermal behaviour of the plasma, even at low concentrations.

3.2. Wall temperature

To evidence the role played by additive gases on the thermal behaviour of the plasma, even at low concentrations, infra-red thermal analyses of the tube enclosing the helium gas flow were performed. For these measurements, a square window is opened in the waveguide. Experimental results are depicted in Figure 5 in which the limits of the window are indicated by vertical arrows.

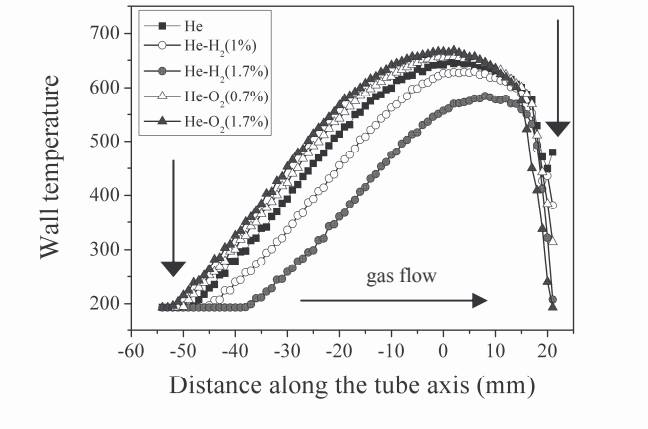

Figure 5: Wall temperature profiles measured by infra-red thermal camera for five different gas mixtures. The maximum temperature is close to the plasma location.

Clearly, the wall temperature of the fused silica tube increases when oxygen is introduced in helium whereas the opposite effect is noticed when hydrogen is introduced. With nearly one percent of each gas, the wall

temperature varies by 100 K. This effect should be enhanced with nitrogen. Experiments are in progress to confirm the effect of that gas on the wall temperature of the fused silica tube.
It is however striking to observe an opposite evolution to that already noticed for the gas temperature. We do not know yet the reason for such a behaviour even though it is likely related with the gas flow. Indeed, the gas temperature determined by OH spectrum simulation was measured along the tube axis. The resulting profile is provided in figure 6.

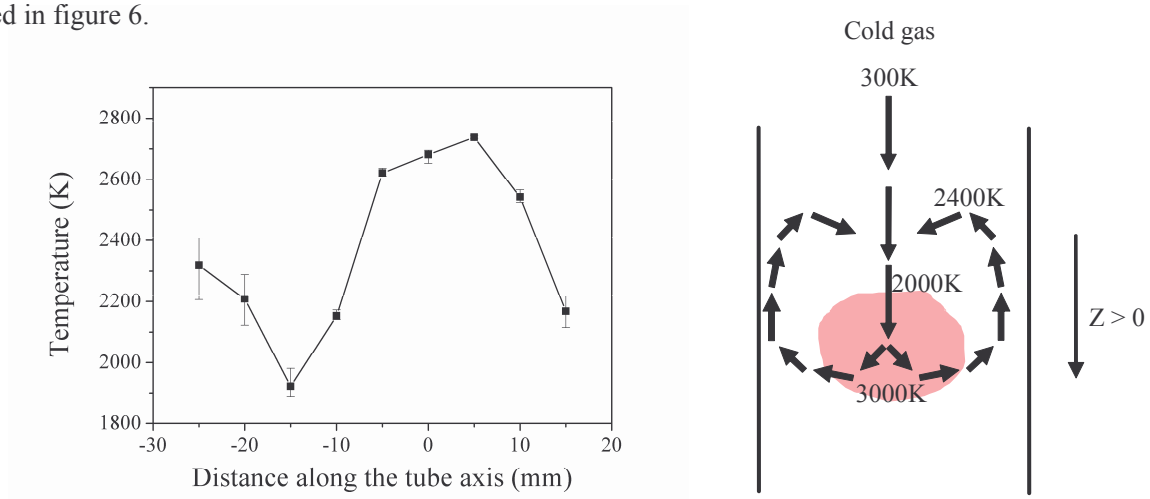

Figure 6: Gas temperature profiles along the axis of the discharge tube measured by simulation of OH emission spectrum. A He-3%H_2 mixture was used (300 W). Possible recirculation flows creating the drop of temperature observed just above the plasma.

It clearly appears that the gas mixture hydrodynamics is complex and recirculation flows probably occur. The minimum in temperature observed in figure 6 can only be due to a recirculation of the cold gas above the much warmer plasma.

4. Conclusion

The influence of small amounts of N_2, H_2, O_2 and Ar on the thermal behaviour of helium microwave discharges at atmospheric pressure was investigated. Even at low concentrations, additive gases strongly affect the thermal behaviour of the helium plasma.

5. References

[1] X. Yuan, L.L. Raja, Appl. Phys. Lett. 81 (2002) 814
[2] Y.B. Golubovskii, V.A. Maiorov, J. Behnke, J.F. Behnke, J. Phys. D: Appl. Phys. 36 (2003) 39
[3] F. Massines, A. Rahebi, P. Décomps, R. Ben Gadri, P. Segur, C. Mayoux, J. Appl. Phys., 83 (1998) 2950
[4] O. Motret, C. Hibert, S. Pellerin, J.M. Pouvesle, J. Phys. D: Appl. Phys. 33 (2000) 1493
[5] X.R. Duan and H. Lange, J. Phys. B: At. Mol. Opt. Phys. 37 (2004) 427
[6] H. van Santen, C.R. Kleijn, H.E.A. van den Akker, Int. J. Heat Mass Transfer. 44 3 (2001) 659
[7] E. Castaños Martinez, Y. Kabouzi, K. Makasheva, M. Moisan, Phys. Rev. E, 70 (2004) 066405
[8] A. Ricard, Ph. Décomps, F. Massines, Surf. Coat. Technol. 112 (1999) 1
[9] Y.-H. Lee, C.-H. Yi, M.-J. Chung, G.-Y.Yeom, Surf. Coat. Technol. 146-147 (2001) 474
[10] S. Youn Moon, W. Choe, Spectrochimica Acta, Part B, 58 (2003) 249

Influence of the process parameters on both the plasma and the silicon oxide film properties in an O_2/HMDSO PACVD process

M. Goujon[1], G. Henrion[1], T. Belmonte[1], P. Choquet[2], H. Michel[1]

1 Laboratoire de Science et Génie des Surfaces -(CNRS-UMR 7570), INPL-Ecole des Mines - Parc de Saurupt 54042 NANCY cedex, France
2 ARCELOR/RDCS - Domaine du Sart-Tilman - Boulevard de Colonster - BP 57 – B4000 LIEGE, Belgium

Abstract
An RF O_2/HMDSO plasma assisted chemical vapour deposition (PACVD) process, used for SiO_2 deposition, is analyzed by optical emission spectroscopy (OES) and Fourier transform infrared absorption spectroscopy (FTIRAS). OES investigation leads us to point out two different regimes according to whether the organic precursor is highly or slightly diluted in oxygen. Meanwhile, on the basis of FTIRAS measurements, the dissociation of the monomer is studied as a function of the dilution ratio of the monomer and the input RF power. Therefore, it is shown that the dilution rate to power ratio is the relevant parameter for the dissociation of the HMDSO molecule in the plasma. From these experimental results, a dissociation schema for the organosilicon precursor is proposed and results of a numerical modelling of the discharge are presented, which allow us to estimate the dissociation rate of HMDSO by electron impact.
From the comparison of FTIR analyses of the films with plasma characterization, direct correlations are drawn between the plasma composition and that of the deposited films.

Keywords
RF plasma ; Hexamethyldisiloxane ; Silicon oxide ; plasma modelling ; plasma diagnostics ; OES ; FTIR ; PACVD

1 - Introduction

RF capacitively coupled plasmas utilizing organosilicon precursors are widely used for SiO_x deposition for many applications such as improvement of wetability and adhesion, protective barrier coatings or anti-reflection films. Because the coating properties depend on the plasma and process parameters, the process plasmas have been widely investigated over the last decade, especially for what concern the use of organosilicon precursors such as hexamethyldisiloxane (HMDSO = $(CH_3)_3SiOSi(CH_3)_3$) [1-4]. These studies may be of useful interest in the development of numerical modelling aiming at the best description and understanding of the deposition process. However, the development of such a complete description suffers from the lack of basic data concerning the HMDSO molecule and the HMDSO–O_2 gas mixture. In particular, it is of prime importance to get knowledge in both the precursor fragmentation schema and the main chemical kinetic pathways (in the gas phase) involving the dissociation by-products. On the other hand, correlations have to be drawn between the plasma analysis and the film characterization in order to determine the growth mechanisms and the species that act as the coating precursors.
The goal of this paper is first to present and discuss experimental results dealing with the O_2/HMDSO RF plasma investigations in close connection with the film composition in order to improve the knowledge and the understanding of the deposition process. The obtained results will then serve as a basis to the establishment of a numerical modelling of the plasma kinetics, which is presented in the second part of this paper.

2 - Experimental arrangement

The complete experimental arrangement is describe in detail in ref [5]. Roughly speaking, experiments are carried out in a parallel-plate capacitively coupled radio frequency (13.56 MHz) plasma CVD reactor. The HMDSO gas line is temperature stabilized at 40°C to avoid condensation of the organic precursor inside the gas line. The total gas flow rate is adjusted with respect to the [HMDSO]/[O_2] ratio in order to keep the total pressure at a constant value of 80 Pa (0.6 Torr).
The gas phase is investigated by means of both optical emission spectroscopy (OES) and Fourier transform infrared absorption spectroscopy (FTIRAS). OES measurements are carried out over the spectral range 300-

900 nm with a spectral resolution of 0.039 nm. In the case of FTIR measurements, each spectrum is acquired over 40 scans with a resolution of 2 cm^{-1} to improve the signal to noise ratio. Owing to the CaF_2 windows that equip the plasma chamber, it was not possible to perform measurements below 1000 cm^{-1}.

3 – Plasma characterization

3.1 OES investigation

The variation of emission line intensity of the optical transitions of H (H_α 656 nm), O ($^5P–^5S_o$ 777 nm) and CO ($B^1\Sigma$-$A^1\Pi$ (0,2) 520 nm) are shown in figure 1. As reported in previous works [5, 6], the electron density and temperature do not change significantly with the monomer content and it is reasonable to consider the emission line intensity as representative of the atom (or radical) density.

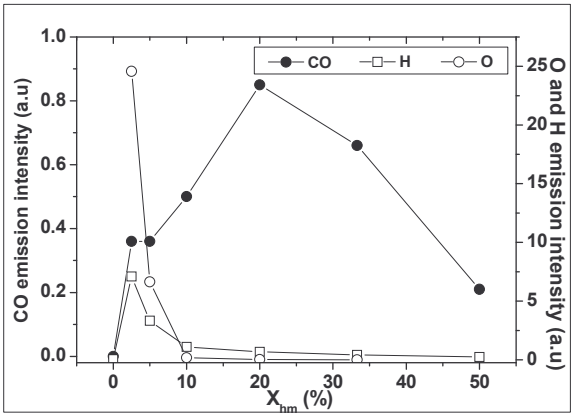

Figure 1 : O-777 nm (○), H-656 nm (□) and CO-520 nm (●) emission line intensity vs HMDSO content in O_2. P_{rf} = 100W

The variations of the line intensities with the monomer content in oxygen gas ($X_{hm} = \frac{[HMDSO]}{[HMDSO]+[O_2]}$) point out two different regimes.

- For X_{hm} < 20 %, the behaviour of the line intensity exhibits two different modes :
  - At first, when X_{hm} < 10%, the density of O-atoms decreases sharply while the one of carbon monoxide increases as X_{hm} increases. In fact, O-atoms are mainly issued from the dissociation of O_2 molecules by electron impact in the discharge and are lost through oxidation of carbon-containing species (especially CH_3) coming from the dissociation of the organic precursor to form CO. This loss process of atomic oxygen agrees the results reported by other authors in the case of RF [1] or microwave [7] plasmas. Thus, we can consider that O-atoms are consumed by oxidation reaction leading to the formation of CO radicals
  - As a consequence, for X_{hm} > 10%, O-atom density is close to zero and the production of CO comes from another process which consists mainly in carbon oxidation by molecular oxygen ($C + O_2 \rightarrow CO + O$). However, the reaction $HCO + O_2 \rightarrow CO + HO_2$ may also contribute to the formation of CO, especially when the concentration in CH_3 increases since the HCO radical is issued from the oxidation of the methyl radical ($CH_3 + O_2 \rightarrow HCO + H_2O$).
- For X_{hm} > 20 % the dilution of HMDSO in O_2 is low and only CO and H-atoms are the main observed species, the density of which decreases with increasing X_{hm}. Two effects can explain this behaviour. At first the consumption of atomic species to form large molecules, such as formic acid (CO_2H_2) or formaldehyde (COH_2). The second effect relates to the dissociation of the monomer by electron impact, the efficiency of which may decrease with increasing the quantity of the monomer. Both these effects are pointed out by the FTIR analysis of the gas phase, as discussed below.

3.1 FTIRAS analysis of the gas phase

As already reported by several authors [3-5, 8-10] the dilution rate of the organic precursor in oxygen plays a significant role in the fragmentation of the monomer. In fact, as depicted in figure 2, the IR absorption bands that are characteristic of the HMDSO molecule (CH_3 asym. stretch. 2966 cm^{-1} ; SiOSi asym. stretch. 1072

cm^{-1} and $SiCH_3$ sym. stretch. 1263 cm^{-1}) exhibit an increase as the amount of HMDSO in O_2 is increased. Nevertheless, the variation of the absorbance with X_{hm} is not linear -as one could expect- and is different according to whether the monomer is highly ($X_{hm} < 50\%$) or slightly ($X_{hm} > 50\%$) diluted in oxygen gas.
From these measurements, it is possible to define a dissociation ratio τ for each of the characteristic bond of HMDSO : $\tau = (A_o - A)/A_o$ where A_o and A stand for the area of the absorption band with the plasma off and on respectively. The τ-values deduced from figure 2 are reported in figure 3 that clearly show the influence of the dilution rate on the dissociation of the precursor.

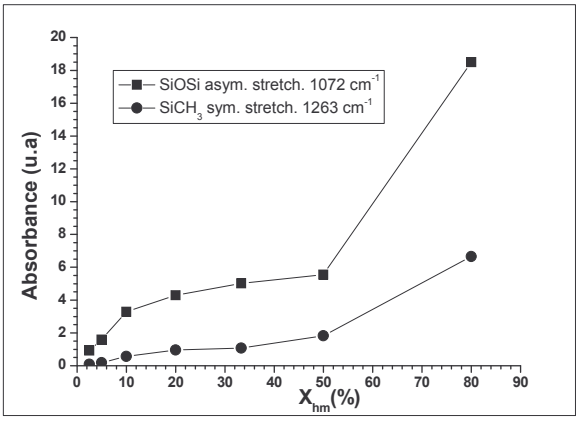

Figure 2 : Variation of the absorbance peak area of the characteristic bonds of the monomer vs the amount of HMDSO in O_2. $P_{rf} = 50W$

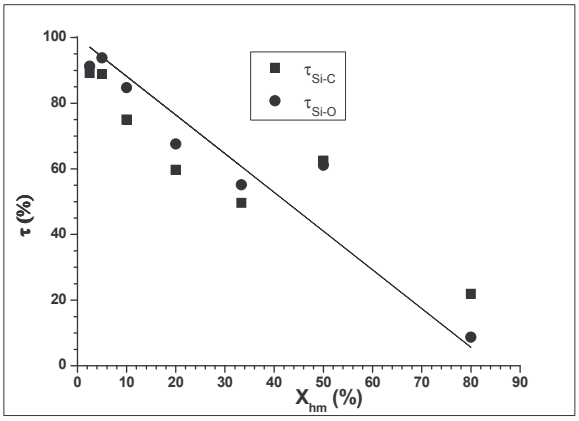

Figure 3 : Variation of the dissociation ratio of the characteristic bonds of the monomer vs the amount of HMDSO in O_2. $P_{rf} = 50W$

On the other hand, the breaking of the precursor bonds depends also on another major plasma parameter, namely the input RF power. Indeed, as soon as the RF power is switched on and increased, the characteristic absorption bands of the HMDSO molecule strongly decrease to reach a nearly constant level close to zero for an input power higher than 100 W (figure 4). That decrease in the absorption bands is significant of an increase in the dissociation of the organic precursor.
Therefore, it seems reasonable to assume that the dissociation of the monomer mainly occurs through electron collisions. Indeed, the electron density depends on the RF power (P_{rf}) and increases with increasing the input power [11]. Thus the above results may be summarized by looking at the behaviour of the dissociation rate as a function of the dilution rate to power ratio. As shown in figure 5, the variation of the dissociation rate seems to decrease linearly as X_{hm}/P_{rf} increases, which allows us to predict the τ-value from the knowledge of the two process parameters.

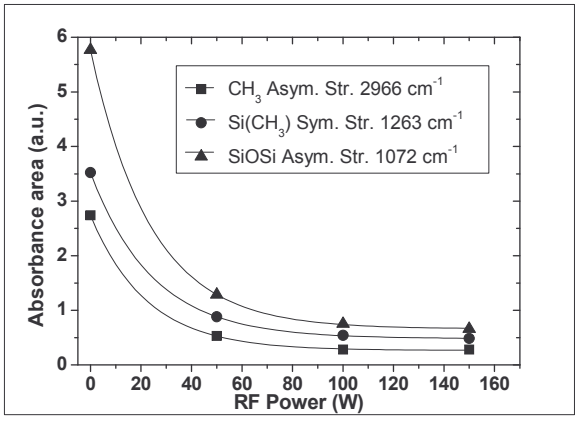

Figure 4 : Variation of the absorbance peak area of the characteristic bonds of the HMDSO molecule vs input power. Pure HMDSO plasma

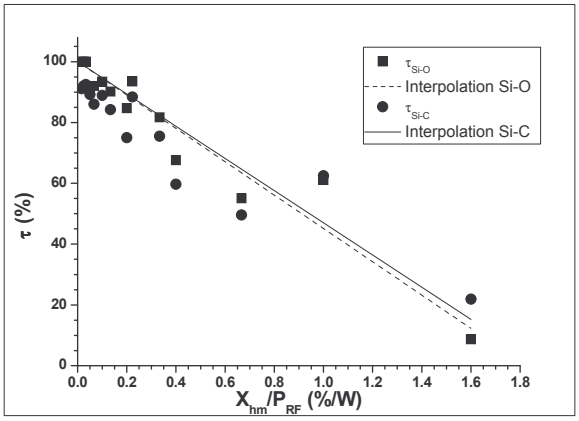

Figure 5 : Variation of the dissociation rate of the characteristic bonds of the monomer vs the dilution rate to power ratio.

4 – Correlation between the film and the plasma compositions

In order to establish some possible correlation between the film composition and the species present in the gas phase, we performed the analysis of the coatings using FTIR spectroscopy. Taking care to the deconvolution of the absorption bands of the films, we paid a particular attention to the following absorbing bonds in the films: Si-O-Si, 1072 cm^{-1} ; Si-OH, 921 cm^{-1} and Si-CH_3, 1260 cm^{-1}. From the comparative variation of these species in both the film and the plasma as a function of the amount of HMDSO in the gas mixture, it clearly appears that their behaviour in the gas phase and in the solid are strongly different ; such a comparison is given for the SiOSi bond in figure 7

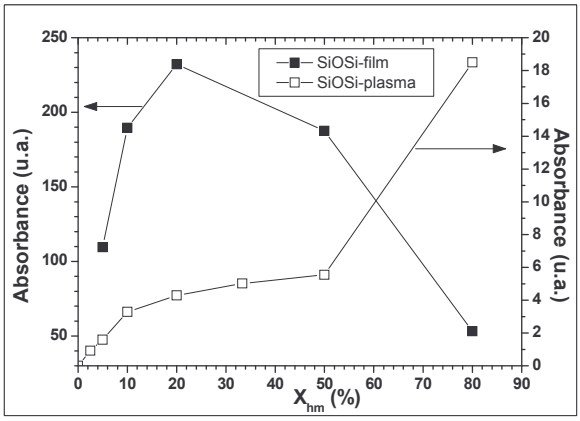

Figure 7 : Comparative absorbance of the SiOSi (1072 cm^{-1} bond measured in the gas phase and in the films vs HMDSO content in O_2.

However, the study of the relative variation of these species in both phases points out that a direct correlation exists between the composition of the gas phase and that of the deposited film (figure 8). The analytical interpolation of the experimental data points takes the form : $y = \frac{a}{(X_{hm} - b)^c}$; the value of the fitting coefficients are reported in the table below.

Table 1 : Fitting coefficients used in the interpolation of figure 7.

	a	b	c
SiOSi/$SiCH_3$ (plasma)	2.65	0	0.384
SiOSi/$SiCH_3$ (film)	1.85	5	0.384
SiOH/SiOSi (plasma)	3.76	2.5	0.658
SiOH/SiOSi (film)	2.83	4.17	0.658

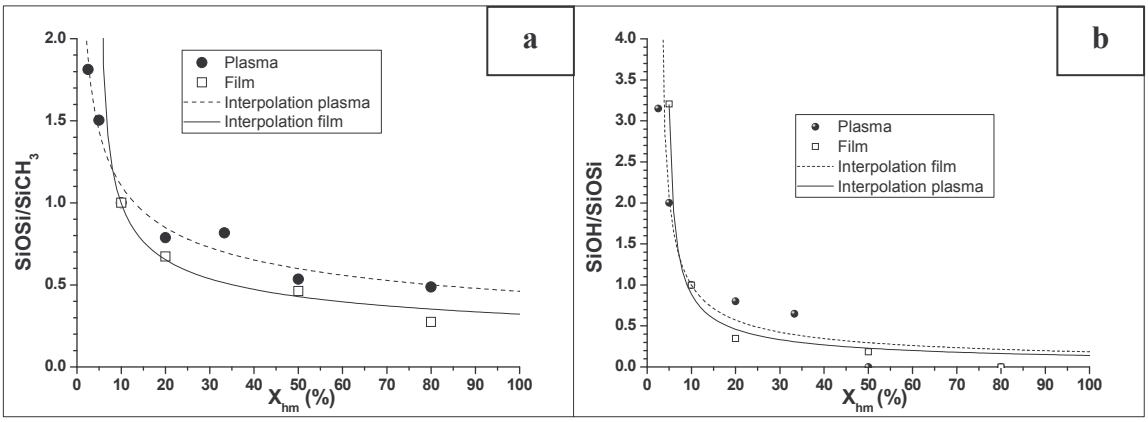

Figure 8 : Variation of the absorption band area relative to that of SiOSi. a) $SiCH_3$; b) SiOH

This interpolation allows us to describe the variation of the relative quantity of the different bonds in the films. Meanwhile, such an interpolation leads us to establish threshold values of the amount of the monomer (for X_{hm} = b) for which the films composition will be dominated by SiOH bonds with regard to SiOSi ones for X_{hm} slightly greater than 4.17% and by SiOSi bonds with regard to $SiCH_3$ ones for X_{hm} slightly greater than 5%

An important point to note concerns the silanol group whose relative concentration in the film is directly related to that in the plasma and is strongly reduced as the HMDSO amount is increased. In fact, the growth of SiO_2 films is achieved from two SiOH radical, as proposed by Selamoglu et al. [12]. Thus this direct correlation has great interest in offering the possibility of controlling the amount of silanol in the film through an in situ analysis of the plasma.

5 – Kinetic modelling

In order to complete the experimental investigation, we developed a simple numerical model aiming to describe the behaviour of the plasma gas. Owing to the lack of basic data concerning the HMDSO molecule and the HMDSO/O_2 gas mixture, we suppose that the monomer is broken by electron collisions according to:

$$(CH_3)_3\text{-Si-O-Si-}(CH_3)_3 + e \xrightarrow{K_{HMDSO}} 6CH_3 + SiO + Si$$

This implies that Si-O and Si-C bonds are supposed to be preferentially broken by electron impact whereas C-H is broken in a further step by oxidation through :

$$CH_3 + O \xrightarrow{K_{CH3}} CO + H_2 + H$$

where $K_{CH3} = 5.6.10^{-11}$ cm^3/s [13].

From the dissociation products of the previous reactions, the plasma chemistry develops to create more complex molecules such as CH_4, COH_2 or CO_2H_2. Thus the numerical model takes into account 62 chemical reactions describing the kinetics of 32 chemical species. The reaction rates are issued from the literature (a complete list of the reactions and reaction rates is given in [14]). The one-dimensional model consists in solving the balance equations for each species by considering the system has reached a steady state. According to the experimental reactor configuration, the neutral species are considered to run out across the electrode gap (4 cm). The electron number density involved in the dissociation equations of HMDSO and O_2 by electron impact, is issued from a fluid model developed previously to describe the behaviour of the charged particles [11] and is typically in the range $10^9 – 10^{10}$ cm^{-3}. The electron impact dissociation rate of the HMDSO molecule consists of an input parameter of the model and is adjusted by comparison with experimental results.

Some of the results obtained as a function of X_{hm} are presented in figure 6 for different K_{HMDSO} values.

Though some disagreements are observed between the experiments and simulations, the behaviour of the species issued from the numerical results for $K_{HMDSO} = 1.10^{-8}$ cm^3/s, seems consistent with that given by the experimental measurements, especially at high dilution rate of the organic precursor in oxygen.

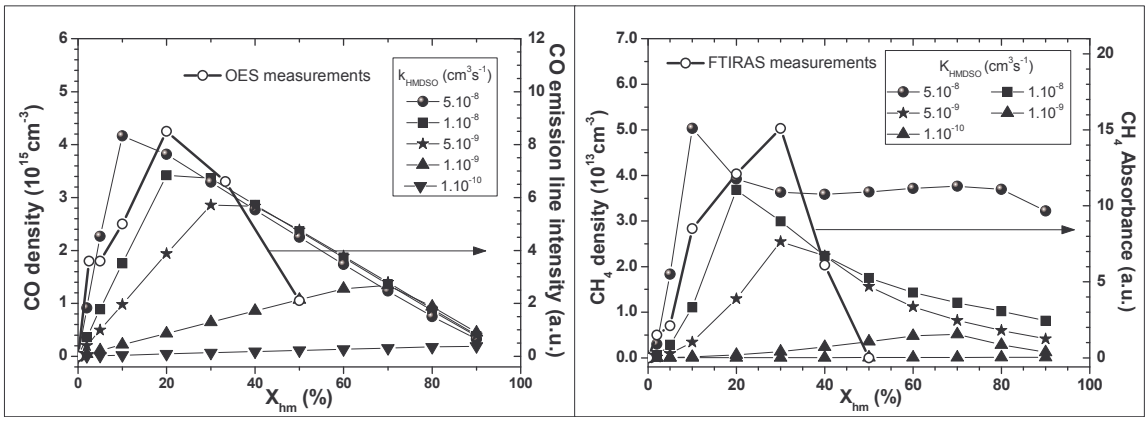

Figure 6 : Density of CH_4 (left) and CO (right) radicals issued from the kinetic modelling of the discharge for different K_{HMDSO}-values, and comparison with the corresponding experimental results.

However, some differences can be pointed out. For example the experimental maximum for CH_4 is around 30% whereas it is close to 20 % for the numerical results.
However, the comparison between experimental and numerical results points out the influence of the dissociation rate constant and justifies our assumption about the monomer dissociation by electron impact.

6 – Conclusion

Experimental investigation and numerical modelling of a RF capacitive O_2/HMDSO plasma used for SiO_2 deposition have been carried out. Experimental results have led us to highlight the dominating role of electron in the dissociation of the monomer while the simulation allowed us to estimate the electron impact dissociation rate of the monomer. In spite of some discrepancies between experimental results and numerical calculation, the simple model, which must be considered as a first step in the complete modelling of the O_2/HMDSO discharge, is able to roughly predict the behaviour of the main species in the discharge, especially at high dilution rate of the organosilicon precursor. From the comparison of the film analyses with the plasma results, it has been established that a strong correlation exists between the composition of the two phases (gas and solid) that may be useful for predicting the nature of the film, which may exhibit a mineral trend at high dilution rate or a more polymeric nature at low dilution of the monomer.

References

[1] R. Lamendola, R. d'Agostino, F. Fracassi, Plasmas and Polymer **2** (1997) 147-164
[2] M. T. Kim, Thin Solid Films **311** (1997) 157-163
[3] M. Creatore, F. Palumbo, R. d'Agostino, P. Fayet, Surf. Coat. Technol. **142-144** (2001) 163-168
[4] M. Creatore, F. Palumbo, R. d'Agostino, Plasmas Polym. **7** (2002) 291-310
[5] M. Goujon, T. Belmonte and G. Henrion, Surf. Coat. Technol. **188-189** (2004) 756
[6] M. Goujon, T. Belmonte and G. Henrion, International Conference on Metallurgical Coatings and Thin Films (ICMCTF 2004), San Diego (California), 19-23 Apr. 2004
[7] C. Vautrin, C. Boisse-Laporte, N. Benissad, A. Chausse, P. Leprince and R. Messina, Prog. Org. Coat. **38** (2000) 9-15
[8] A. Granier, M. Vervloet, K. Aumaille and C. Vallée, Plasma Sources Sci. Technol. **12** (2003) 89
[9] K. Aumaille, A. Granier, M. Schmidt, B. Grolleau, C. Vallée and G. Turban, Plasma Sources Sci. Technol. **9** (2000) 331
[10] K. Aumaille, C. Vallée, A. Granier, A. Goullet, F. Gaboriau and G. Turban, Thin Solid Films **359** (2000) 188
[11] M. Goujon, T. Belmonte and G. Henrion, Thin Solid Films **475** (2005) 118
[12] N. Selamoglu, J.A. Mucha, D.E. Ibbotson and D.L. Flamm, J. Vac. Sci. Technol. B **7** (1989) 1345
[13] R. Atkinson, D. L. Baulch, R. A. Cox, R. F. Hampson Jr., J.A. Kerr, M. J. Rossi and J. Troe, J. Phys. Chem. Ref. Data, **26** (1997) 521-1011
[14] M. Goujon, PhD Thesis, (2004) Institut National Polytechnique de Lorraine, Nancy, France. (*Available on demand at Gerard.Henrion@mines.inpl-nancy.fr*)

Application of Atmospheric Microwave Pure Steam Plasma to Treatment of Plastic Wastes

H.Sekiguchi, S.Nakanishi, M.Murakami and H.Arimatsu

Department of Chemical Engineering, Tokyo Institute of Technology, Tokyo, Japan

Abstract

Atmospheric steam plasma generated by microwave discharge was applied to the treatment of plastics. Three kinds of the plastics and their mixture were treated by the plasma. The results indicated that the gasification into H_2, CO, CO_2, CH_4 and C_2H_4 was successful, however, soot was also produced. The amounts of steam reacted per carbon content in the feed plastics were almost independent of the feed plastics and their mixtures. The results suggested that the steam plasma was a promising method to gasify plastic wastes.

Keywords

Steam plasma, microwave discharge, plastic wastes, and gasification

1. Introduction

The mass of plastic wastes has increased year by year and many studies have been carried out to treat them efficiently. Due to the development of plastic recycling systems, the percentage of plastic wastes treated for recycle has been raised greatly in this decade. However, it is not ideal level because plastic wastes are still increasing. Much effort is continuously put into the studies on plastic recycling systems to overcome this severe problem. In this study, atmospheric microwave pure steam plasma, which is one of advanced techniques in the plasma technology, is applied to treat various plastics. Atmospheric microwave discharge provides non-equilibrium plasma containing radicals, ions and electrons. These active particles efficiently decompose plastic wastes. Furthermore, it is advantage that water used as a plasma medium is cheap and safe for environment. Plasma is roughly classified to three kinds by their power frequency; direct current discharge, high frequency discharge, and microwave discharge. The microwave discharge does not require electrodes, which makes advantages that the system of the plasma torch is simple and the material component of electrodes do not contaminate the plasma. Recently, the atmospheric pure steam plasma using microwave discharge has been applied to the reforming of hydrocarbon, where the steam plasma is effective for generating hydrogen with CO [1, 2]. Microwave steam plasma supplies reactive radicals such as H, OH, and O in non-equilibrium state, resulting in high performance for the treatments of various materials. We have also carried out the preliminary study on the gasification of polyethylene using microwave plasma where the plasma gas was a mixture of argon and steam [3]. Plastics mostly consist of carbon and hydrogen, so that the treatment of plastics with the steam plasma likely produces synthesis gas containing CO and H_2 similarly to the reforming of hydrocarbon. Moreover in treating PVC by the steam plasma, Cl can be fixed with H into HCl, which will be easily absorbed with a scrubber. Hence, the proposed method is to produce synthesis gas and to treat halogen components simultaneously. The previous study has concluded that the microwave steam plasma has a potential to convert plastic into CO, CH_4 and H_2 effectively [3].

This study is placed as the second step for the treatment of plastic wastes with the steam plasma. Here we use three kinds of plastics; polyethylene (PE), polyethylene terephthalate (PET), polyvinylchloride (PVC) and mixtures of them since these plastics are utilized so much in the various fields. Powdered epoxy resin containing bromine (Br) is also treated with the steam plasma here. Usually printed circuit boards in electric instruments are made of this resin reinforced with glass fibers. To prevent burning, Br is added as a flame retardant into the resin. Due to the incombustibility, the wastes of the resin dust are generally disposed to landfill. Hence, we have preliminarily examined the possibility on the treatment of this fireproof plastic using the steam plasma.

2. Experimental

Figure 1 shows the experimental system which is almost the same as in the previous study [1,2] except for the power generator. The experiment was conducted with 2.45GHz microwave power supply giving a maximum power of 1.5kW. Steam was heated and introduced to the discharge zone in a quartz tube where microwave was irradiated through a wave-guide. Argon (Ar) was only employed for the ignition. These gases were supplied into the quartz tube through the brass block connected at the top of the tube. This brass block was designed to make a tangential flow in the quartz tube which was effective for the plasma stabilization. The size of the quartz tube was 700mm in length, 12mm and 10mm in outer and inner diameter, respectively. The tube had a branch from which the plastics were introduced into the steam plasma as illustrated in Fig.1. The plastics were attached to the tip of the quartz stick and the treatment was done to push the stick into the steam plasma. Commercial PE, PET, PVC and their mixtures were used as models of the plastic wastes. Product gas was gathered in a gas-sampling bag after cooling in the exhaust gas line to condense steam. Then the gas was quantitatively analyzed with gas chromatograph (GC). Ion chromatograph was also used for the analysis of halogen ion dissolved in water condensed in the exhaust gas line. The experimental conditions are summarized in Table 1.

Another experiment was carried out using a printed circuit board grinded. The board consisted of tetra bromine bisphenol A (TBBPA) type epoxy resin reinforced with glass fibers. The powdered samples having an average size of 10μm and 630μm were prepared by grinding the board. The powder was fed into the plasma from the top of the reaction tube shown in Fig.2 which was different from that used in the above experiment.

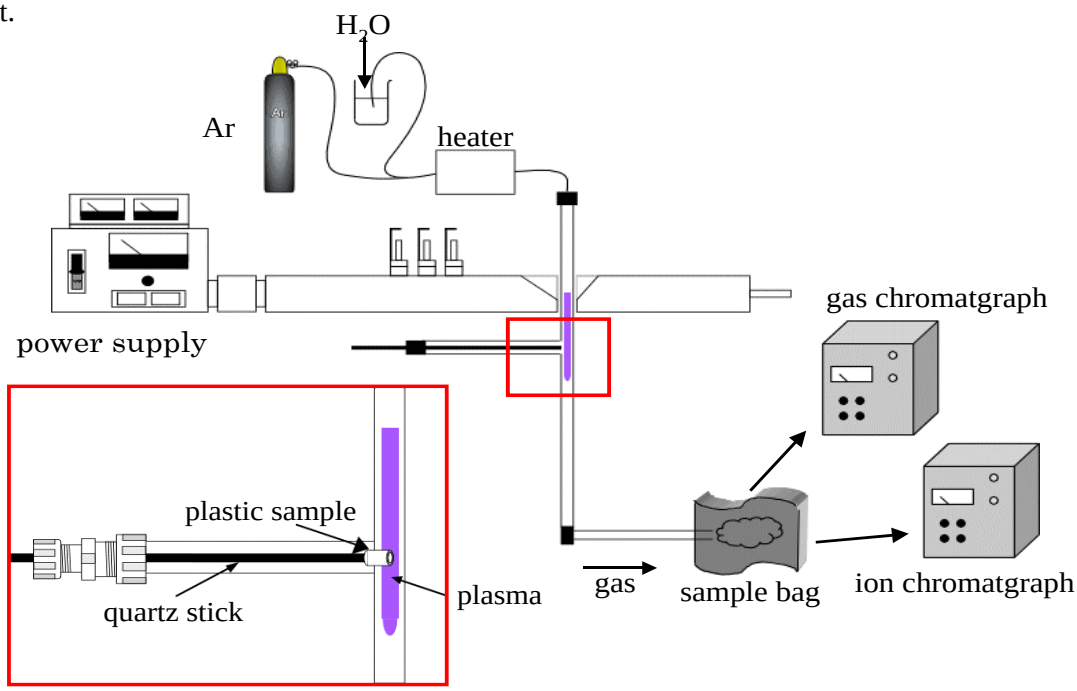

Fig.1 Experimental apparatus

Table 1 Experimental conditions

quartz tube	O.D. 12mm I.D. 10mm
H_2O flow rate	9.61L/min
input power	1.5kW 2.45GHz
plastic sample	0.01–0.30g

Fig.2 Reaction tube for treating TBBPA

3. Results and Discussion

The photo of the steam plasma is shown in Fig.3. The plasma was generated only near the wave-guide from which intensive emission of light was observed. The emission spectra could evaluate the temperatures of gas and electron in the plasma, hence, the measurements of the emission spectra were carried out using another steam plasma equipment with similar plasma conditions. The gas temperature and electron temperature were respectively estimated 2-3000K and 6-7000K from UV OH band [4] and the atomic emission spectra of hydrogen. Therefore, the steam plasma showed non-equilibrium similarly to microwave N_2 plasma [5].

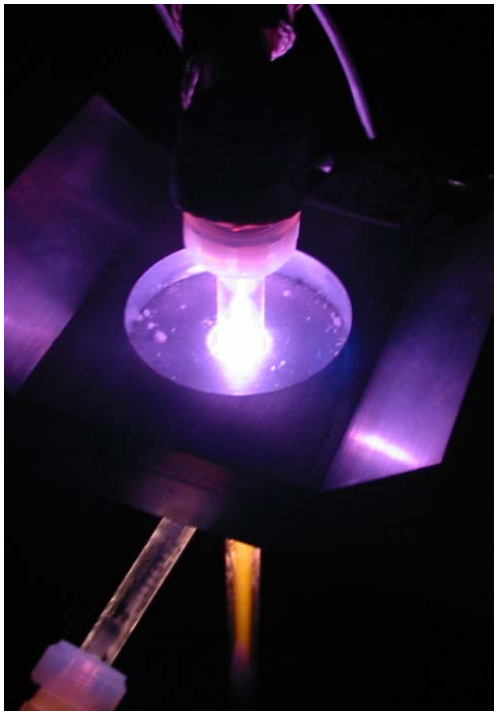

Fig.3 Steam Plasma

3.1 Treatment of PE, PET and PVC

The experimental results showed that the microwave steam plasma treated the plastics perfectly and the plastics were converted into gas and soot. The analysis with GC indicated that the product gas contained H_2, CO, CO_2, CH_4, and C_2H_4 in all the treatments of the plastics. Assuming only soot was produced except for the above gases, the amount of soot was estimated from the material balances of the feed and products. Figures 4 (a-c) show the results of the treatments of PE, PET and PVC respectively where the abscissa denotes carbon content in the feed plastics. The amounts of the gases increased with increasing the feed plastics and H_2 was most produced in all the treatments. The treatment of PVC indicated that soot was formed with highest selectivity. This might be because PVC was easily dechlorinated to form polyene structure in low temperature.

Figure 5 shows the carbon yield defined by the following equation:

$$Carbon\,Yield = \frac{\sum Carbon\ Amount\ Contained\ in\ Puroduct\ Gas}{Total\ Carbon\ Amont\ of\ \ Initial\ Feed\ Plastic} \quad (1)$$

The carbon yield for PE treatment was roughly independent of the feed amount. However, for the cases of PET and PVC, the yields decreased as the feed increased. As shown in Figs.4, soot was most produced in PVC treatment, hence, the carbon yield for PVC case appeared least among the three plastic cases.

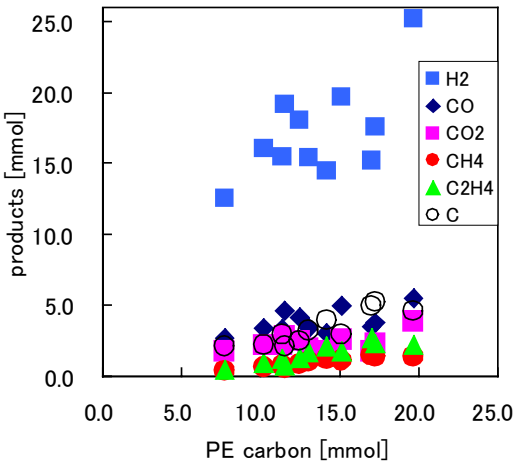

Fig.4(a) Amounts of products produced in the treatments of PE

Figure 6 shows the amount of steam reacted. The amount increased with increasing the feed plastic. As expected from Fig.5, H_2O was least reacted in PVC treatment.

To compare the results of the three plastics, the ratio of the reacted steam to carbon content in the feed plastic, that is, the amount of steam reacted per 1 mol carbon in feed, was indicated in Fig.7. Even when the data for three cases exhibited a scatter, a correlation between the ratio and the carbon content could be seen independently of the feed materials. This was because the reaction of carbon with steam to form H_2, CO and CO_2, which was endothermic with relatively large reaction energy, seemed to be a main mechanism of the gasification of the plastics. The ratio decreased with increasing the feed because more energy was required when more plastics were fed. This was clearly supported by Fig.6 where the amount of steam reacted increased with the feed plastic.

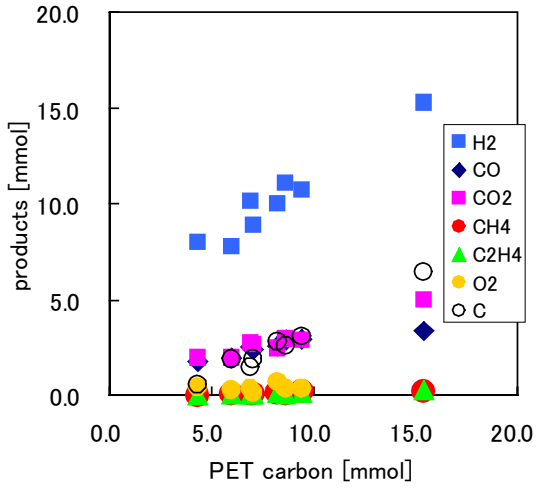

Fig.4(b) Amounts of products produced in the treatments of PET

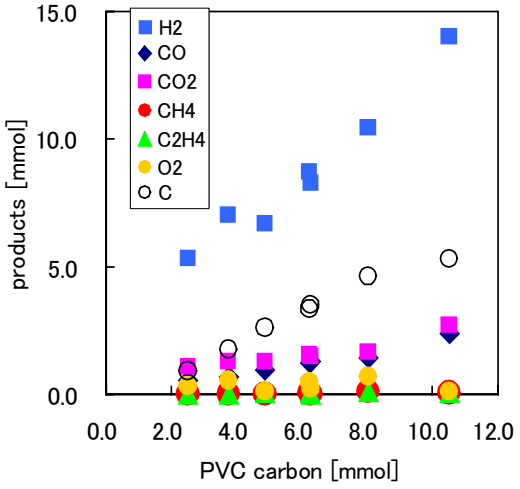

Fig.4(c) Amounts of products produced in the treatments of PVC

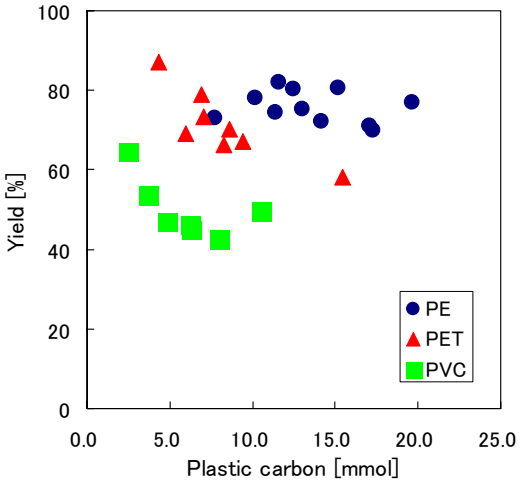

Fig.5 Carbon yield

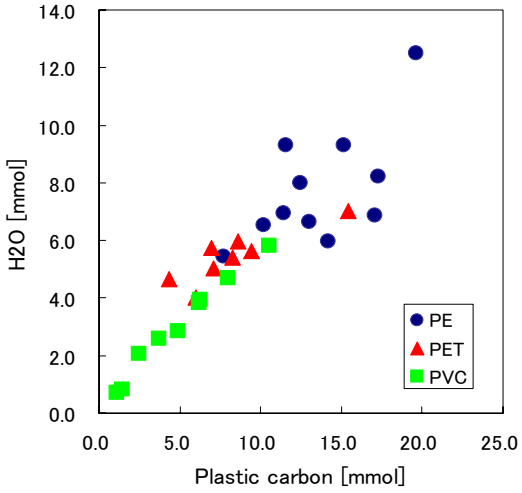

Fig.6 Amount of H_2O reacted

3.2 Treatment of a mixture of PE, PET and PVC

The results of the mixture treatment are shown in Fig.8 where PE and PVC were fed together. In the experiment, total carbon content in the feed plastic was adjusted to the same when samples of the mixture were prepared. The abscissa denotes the fraction of the plastics. The data for the mixed plastics were almost on the interpolations between the results for the pure plastic treatments, suggesting that the mixture did not affect the treatment. This could be also observed in Fig.10 where the amount of steam reacted was independent of the ratio of the plastics.

Similar behaviors were observed in the mixture treatments of PE-PVC and PET-PVC.

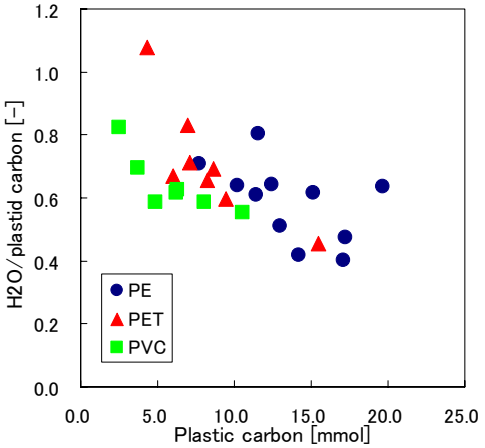

Fig.7 Reacted H_2O per 1mol carbon in feed plastic

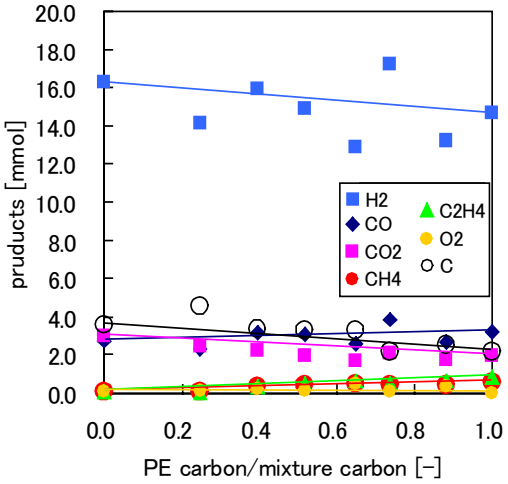

Fig.9 Amounts of products produced in the treatments of PE-PET mixture

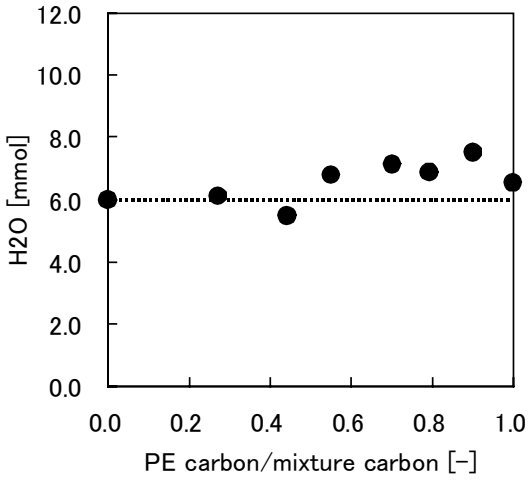

Fig.10 Amounts of H2O reacted in the treatments of PE-PET mixture

3.3 Energy efficiency

The recycling process for plastic wastes should be evaluated from the energy aspect. Therefore, the energy efficiency was defined by the following equation to evaluate the plasma treatment process:

$$\eta = \frac{\sum Combustion\ Heat\ of\ Puroduct\ Gas}{Total\ Combustion\ Heat\ of\ Initial\ Feed} \quad (2)$$

Fig.11 shows the efficiency of the treatments where all the data are plotted including the treatments of the pure and mixture plastics. The efficiency revealed almost higher than unity, indicating that the process could at least recover the initial energy in the feed plastics.

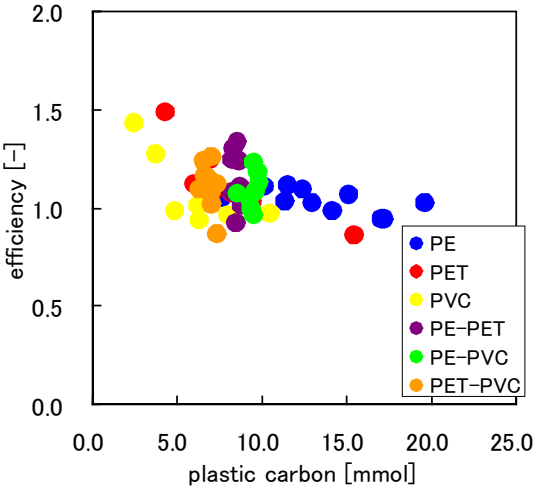

Fig.11 Energy efficiency

3.4 Treatment of powdered epoxy resin

Figure 12 shows the result of the epoxy resin treatment. Because the steam plasma was diminished when the powder was introduced, Ar was added at a flow rate of 12 l/min as a supporting gas. From the figure, the gasification into H_2, CO and CO_2 took place and larger sample showed better treatment. This might be because small particles were not well introduced into the plasma due to strong tangential flow regime in the reaction tube. The present results were regarded as preliminary data, therefore, further investigation using pure steam plasma should be carried out with substantial modification on the powder feed method.

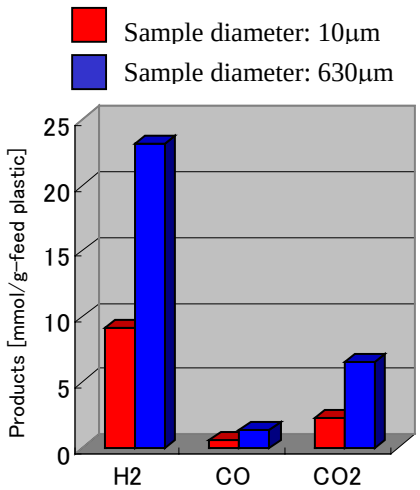

Fig.12 Results of epoxy resin treatment

3.5 Halogen detection in condensed water

The analyses of halogen ions existing in water condensed in the exhaust gas line were carried out using the ion chromatograph for the treatments of PVC and epoxy resin. Chloric ion was detected for the former case,

while, bromic ion was observed for the latter case. However, quantitative analyses could not be done for both the treatments.

4. Conclusion

The microwave pure steam plasma was used for the gasification of the plastics of PE, PET, PVC and their mixtures. The results indicated that all the samples were converted into H_2, CO, CO_2, CH_4 and C_2H_4. Soot was also produced. The amount of steam reacted per carbon content in the feed was almost independent of the feed plastics and their mixtures. Preliminary experiment for epoxy resin containing Br also indicated the possibility of the gasification of the resin. The results suggested that the steam plasma was a promising method to covert plastic wastes into valuable gases.

Acknowledgement

This research was partially supported by Plastic Waste Management Institute, Japan.

References

[1] H.Sekiguchi and Y.Mori, Thin Solid Films, **435** (2003) 44.
[2] S.Nakanishi and H.Sekiguchi, J. Jpn.Petro.Inst., **48**(2005), 22.
[3] H.Sekiguchi and T.Orimo, Thin Solid Films, **457** (2004) 44.
[4] C.Izarra, J.Phys.D., **33**(2000) 1697.
[5] M. D. Calzada, et al., J.Appl.Phys., **80** (1996) 46.

REFINING METALLURGICAL GRADE SILICON BY RF THERMAL PLASMA TREATMENT WITH MOLTEN BATH BIASING

A.Soric[1], M.Benmansour[1], N.Leone[2], P.Adam[2], D.Morvan[1], J.Amouroux[1]

[1]Laboratoire de Génie des Procédés Plasmas – Université Pierre et Marie Curie – ENSCP
11, rue Pierre et Marie Curie – 75231 Paris France
[2]Centre d'Etudes du Bouchet – DGA – Section Détection Physique
3, rue Lavoisier – 91710 Vert le Petit – France

Abstract

A RF thermal plasma process combined to a molten silicon bath polarization by a variable DC source was used to purify metallurgical grade silicon. The silicon sample was first molten by thermal argon plasma and then polarized via a direct voltage. Optical Emission Spectroscopy was used to follow the evaporation's kinetic of silicon and impurities during treatment. In addition to these on-line analyses, the sample chemical composition was given by Laser Induced Breakdown Spectroscopy. This work led to understand the role of sample biasing in the process of impurities elimination.
Keywords: thermal plasma, purification, silicon, polarization

1 Introduction

With an aim of meeting the needs for the fastly increasing photovoltaic market and reducing the manufacturing cost of solar cells, a certain number of processes were developed to produce photovoltaic grade silicon starting from metallurgical grade material [1,2,3]. The process developed in our laboratory leads to massive silicon purification by thermal plasma together with sample biasing. Molten silicon bath was polarized via a DC source to improve impurities elimination by influencing electrochemical mechanisms at plasma/silicon interface.

2 Experimental Setup

2.1 General Apparatus

The experimental apparatus is shown in figure 1. The part of the process concerning plasma purification consists of a stainless steel water-cooled reactor, a RF plasma torch (P = 20kW) equipped with an injector linked to the electrical ground and a copper water-cooled substrate holder in the axis of the plasma. The solid silicon sample is deposited on a graphite electrode used as substrate. This unit is sitting on the water-cooled copper substrate holder covered by a refractory material in order to prevent any contact between the plasma and electric ground. The last part of the apparatus is used for polarization of the sample. It consists in a DC generator connected to the graphite electrode by an alumina sheathed tungsten wire. In order to prevent HF current from the plasma generator to reach and disturb the DC generator, a HF filter is added to the electric circuit between the sample and the DC source.
Molten by the plasma, the silicon sample becomes conductor. At this time the sample is polarized to influence electrochemical mechanisms and, as a result, improve the plasma purification process.

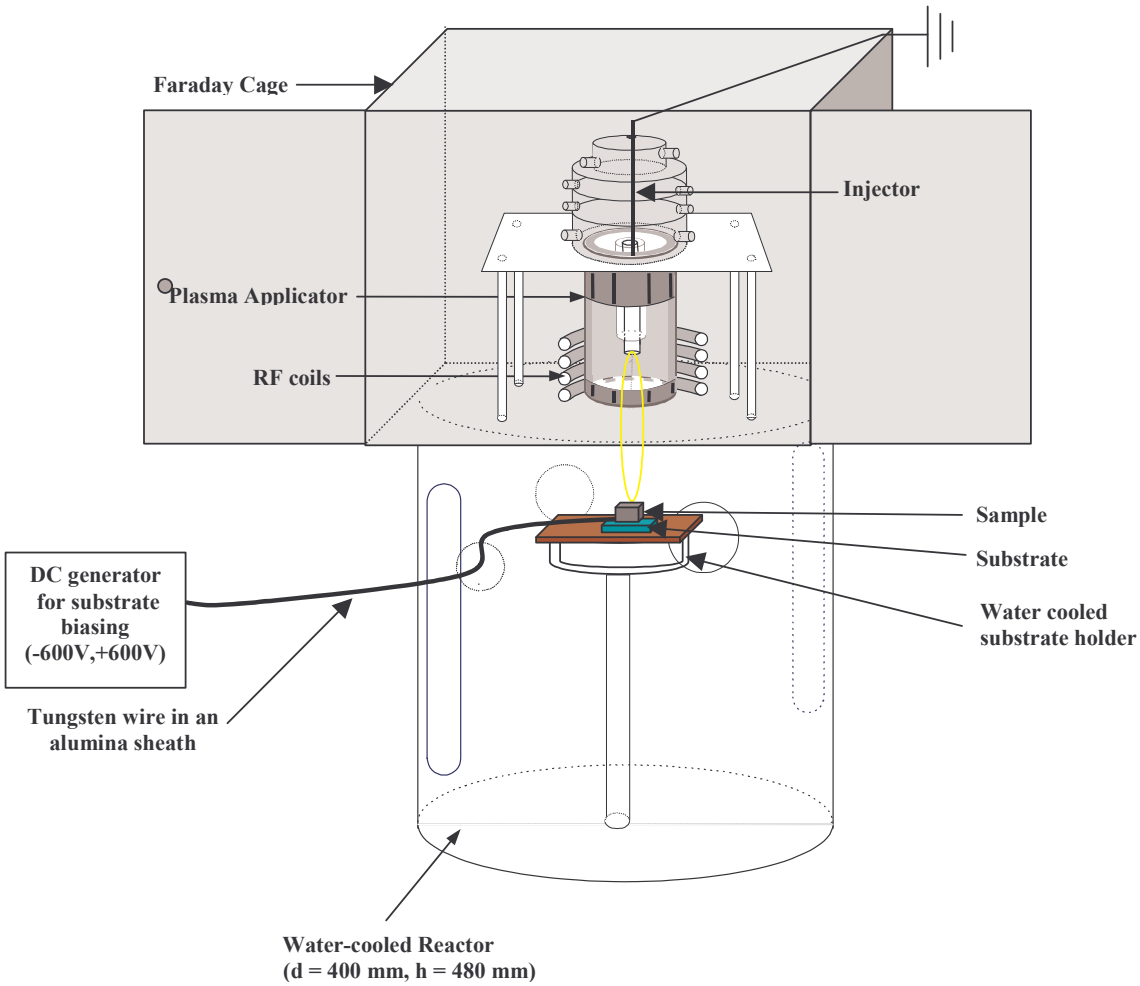

Figure 1: Experimental Apparatus

2.2 Polarization circuit

Before polarization we tried to determine the direction of the current in the circuit composed by the sample, the plasma and the injector. We deposited LiCl on our sample before plasma treatment without any bias. During treatment, we were able to see the direction of the current by following the direction of Li cations emitting in pink color. They were going upstream in the plasma as shown in figure 2.
Measurements with an amperemeter confirmed that there was already a closed electric circuit. Indeed we were able to measure a direct current of about 15 mA between the sample and the injector during the plasma treatment without any polarization from the DC source.

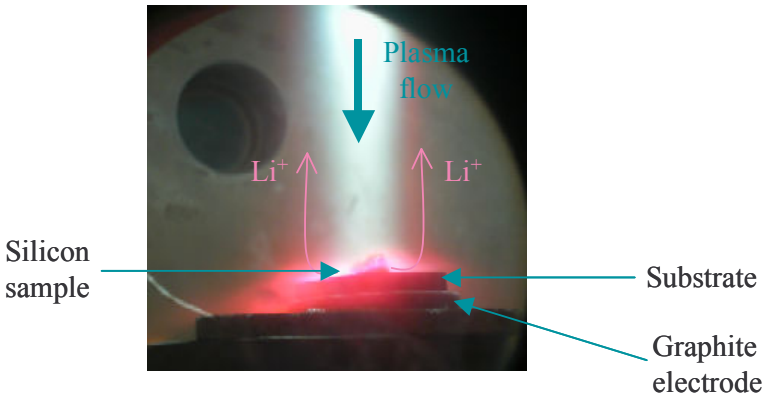

Figure 2: Photograph of a plasma treatment in the presence of LiCl

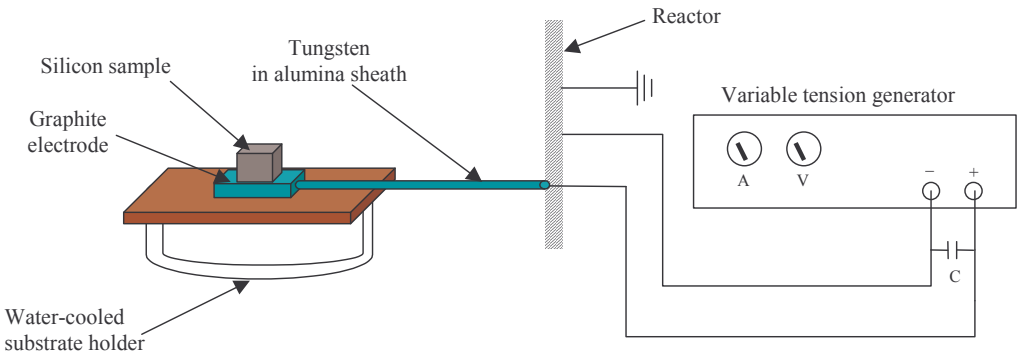

Figure 3: Scheme of polarization circuit

The potential was applied on the sample by the DC generator via a tungsten wire (figure 3). Indeed we have to simultaneously solve thermal and electrical problems to bring the current to the sample. Tungsten has both the characteristics because it's conductive and its melting point is above silicon's one (1410°C). Alumina sheath prevents any contact between plasma and polarization circuit.
The plasma generator (ν = 4,5 MHz) was responsible for a parasite RF signal disturbing DC generator's one. As a result, under these conditions, the electrochemical parameters of the polarization of the sample couldn't be controlled.
Measurements of RF and direct signals led to the elaboration of a specific RF filter permitting to prevent parasite signal from reaching the DC generator and consequently keep polarization process under control.
This filter was introduced in the polarization circuit between the sample and the DC generator.
It also revealed that this plasma had a floating potential of about +90 V.

3 On-line spectroscopic measurements of plasma emissions during treatment

3.1 Experimental conditions

During treatment, the plasma generator provides a 20 kW power. The plasmagene argon flow was set to 40L.min^{-1} and sheathing argon flow to 25 L.min^{-1}. The potential applied onto the sample was set to a define value between -25 V and +90 V. Treatment with on-line follow-up goes on 30 minutes.
The aim of these on-line spectroscopic analyses was to follow the purification's kinetics. This was done in order to know the evaporation processes taking place during the thermal plasma treatment.
On-line analyses were carried out by the means of an optical fiber pointing at the sample surface and connected to a CCD detector and a spectrometer. Spectra were recorded between 350 nm and 950 nm.
The first step consisted in recording the whole spectrum in the presence of argon plasma but without the sample to obtain argon reference.
Then, silicon sample was brought near to the plasma and melted. When the whole sample was molten a spectrum was recorded every 10 minutes for half an hour.

3.2 Results

Without sample, only argon lines were recorded. This spectrum was the mean of knowing which kind of species were evaporated from the sample by subtraction from the spectrum recorded during the sample purification.
In the presence of the molten sample, we recorded phenomena developing at the plasma-silicon interface. We observed evaporated silicon lines but also impurities lines like iron, aluminum or calcium. These elements are highly concentrated in metallurgical grade silicon and were eliminated by the evaporation phenomenon due to the thermal effect of the argon plasma and chemical effect of an added reactive gas like oxygen for boron elimination [4. Consequently, this technique permitted to follow the elimination's kinetic of impurities from the silicon sample as a function of time and experimental conditions like chemical composition of the plasma and sample biasing value.

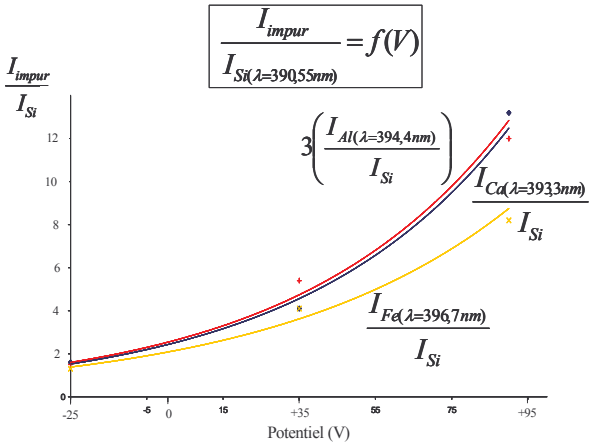

Figure 4: Ratio of impurities and silicon lines intensity versus sample potential

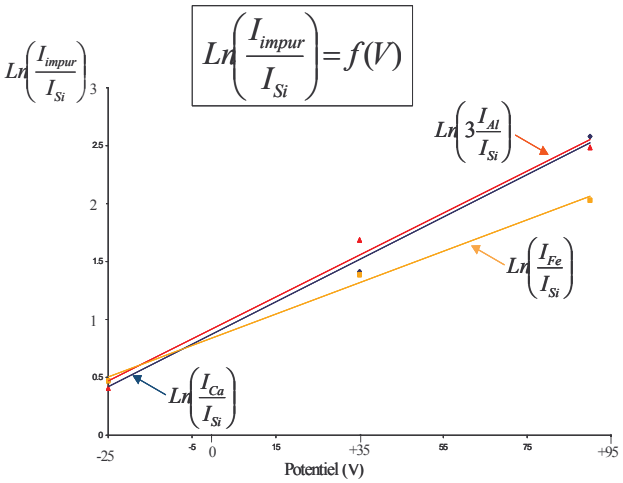

Figure 5: Ratio of impurities and silicon lines intensity versus sample potential

Analysis of figures 4 and 5 shows that the potential applied on the sample has a determining role in impurities evaporation phenomenon. Indeed, we can see that evaporation rate of cationic impurities increases with sample potential.
To confirm that these selective evaporations of impurities lead to the purification of the silicon sample, we compared the concentration of these elements in initial sample and in a plasma treated one by LIBS.

4 Laser Induced Breakdown Spectroscopy analyses

4.1 Principle of the technique

This method consists in focusing a laser pulse near the surface of the sample in order to create an intensive electric field on the focal point. A high quantity of energy is concentrated in a small volume so that the sample is locally vaporized producing a high thermal plasma (10,000 to 20,000 K). The molecules of the sample are completely dissociated during the plasma formation process and the plasma is mainly constituted of ionic and atomic species which characteristic de-excitation emission lines can be used for detection in less than 1 ms for one laser shot. Indeed photons resulting from plasma emission are collected by a spectrometer via an optical fiber. Spectroscopic analysis of atomic and ionic emissions of plasma relaxation gives complete information on chemical composition of the sample. These qualitative (atomic and maybe molecular composition) and quantitative spectrochemical analyses allow performing in-situ, fast and potential remote diagnosis.

4.2 Experimental procedure

For each sample we carried out 10 laser shots series. The 10 spectra obtained were superimposed to confirm the reproducibility of the analysis on the one hand and to know the general appearance of the spectrum by working out the average of all the spectra on the other hand. Therefore spectra obtained with the first and the second shots were systematically removed. This way, we avoided considering surface pollution of samples.
Then spectra were analyzed to know the exact elementary composition of each sample.
From parallelepiped of metallurgical grade silicon samples, thermal plasma leads to a specific geometry of the silicon due to the density differences between solid and liquid state during the fast crystallization at the end of the treatment.
The last area of crystallized silicon (area 1) formed on the sample surface seems to concentrate impurities as it can be seen on figure 6. We analyzed this portion of the sample, together with another area (area 2) at the other end of the sample.

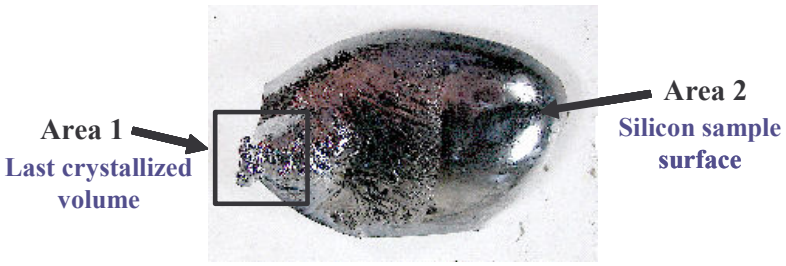

Figure 6: Photograph of a treated silicon sample

4.3 Results

LIBS spectra of metallurgical grade silicon and plasma treated silicon (area 1 and 2) are shown in figure 7.

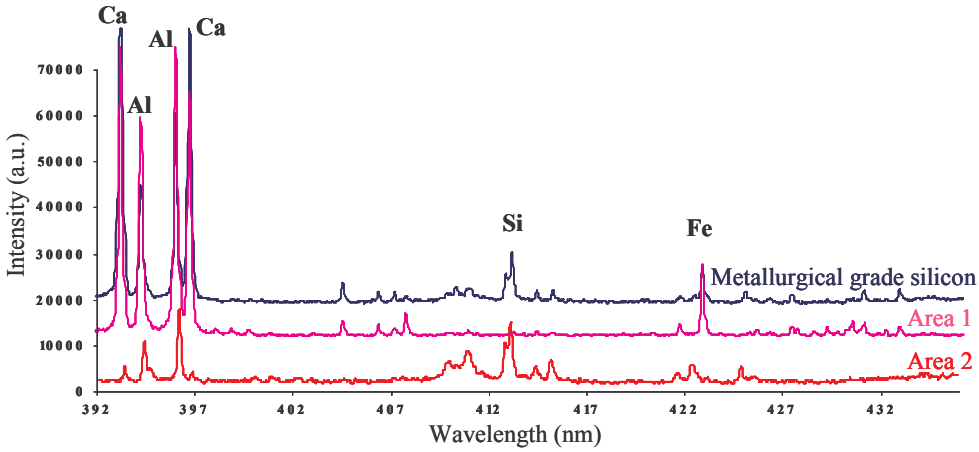

Figure 7: Comparison of LIBS spectra in the range of wavelength 392-432 nm

In order to be able to compare these spectra, we normalized relative intensities of emission lines in both areas of the plasma treated sample compared with intensity of the same lines in the metallurgical grade sample:

$$ratio = \frac{I_{\text{emission line of treated material}}}{I_{\text{emission line of metallurgical grade material}}}$$

Results are listed in the table below:

Impurities in metallurgical grade silicon (ratio = 1)	Plasma treated sample (Area 1)	Plasma treated sample (Area 2)
Fe	2,45	0,33
Al	1,26	0,53
Ca	1,50	0,29
C	0,75	0,52

Table 1: Comparison of impurities emission lines in metallurgical grade and treated samples

These results show that impurities are concentrated in area 1. During the melting process, impurities go up to the surface of the sample where they are partially evaporated. When the sample is crystallizing, impurities concentrate in the last liquid area of the purified sample. In the same way the concentration of impurities in area 2 shows that the sample was purified by the plasma treatment.

5 Conclusion

The use of *in situ* (Optical Emission Spectroscopy) and *ex situ* (LIBS) analyses demonstrated that plasma treatment leads to the purification of silicon samples.
With the same techniques, we were able to demonstrate that the potential applied onto the sample played a determinant role on the phenomenon of evaporation of impurities.
Indeed, emission spectra obtained during the treatment showed that evaporation of cationic impurities increased significantly with the applied potential.
These results let us to conclude that elimination of cationic impurities increases with the potential.
The reference potential value is the plasma potential one (+90 V). For potential values above this reference, transfers kinetic of cationic impurities from the liquid bath to the plasma would be improved. Investigations are currently performed for values bellow this reference. They should prove that the evaporation of anionic impurities is improved together with hydrogenation of the sample (carried out with Ar/H_2 plasma) for a potential value lower than the reference value.

Acknowledgement:
ADEME for financial support
J. Reboux, EFD engineer, for technical advice

References:

1 N.Yuge, M.Hanazawa, H.Baba, N.Nakamura, Y.Kato, Y.Sakaguchi, S.Hisawa, M.Obashi
PVSEC-11, Sapporo, Hokkaido, Japan, 1999, 115-118

2 M. Benmansour, E. Francke, D. Morvan, J. Amouroux, D.Ballutaud
Thin solid film – Vol. 403-404, pp. 112-115, 2001

3 C.Alemany, C.trassy, B.Pateyron, K.I.Li, Y.Delannoy
Solar Energy Materials and Solar Cells – Vol.72, pp.41-48, 2002

4 J. Amouroux, D. Morvan
Patent n° EP0045689, 1982

Multiplex Bioassay With ICP-MS

S.D. Tanner[1], O. Ornatsky[1], V.I. Baranov[1], D.R. Bandura[1], J. Dick[2]
1 Institute for Biomaterials and Biomedical Engineering, University of Toronto, Toronto, Canada.
2 University Health Network, Toronto, Canada.

Abstract
A novel ICP-MS based method of protein quantitation is discussed. Multiplexing capabilities of this technique are demonstrated for cell surface membrane receptors that are specific for a particular cell and are widely used in leukemia diagnosis. Experiments for the simultaneous identification of several surface and intracellular antigens in a human megakaryocytic leukemia-derived cell line were conducted. This new technique provides an innovative arena for ICP-MS in the analysis of biological samples.

1. Introduction

New technology that enables accurate protein quantitation is required in the booming area of proteomics and drug discovery as well as in areas of clinical and diagnostic testing. It is also important in biological research aimed at analyzing protein synthesis, function and disease at the molecular level. Currently, there are several existing techniques that are widely used for estimating protein concentration including: Bradford and Lowry assays, UV spectroscopy, organic mass spectrometry, HPLC, flow cytometry, ligand binding assays, ELISA (Enzyme Linked Immunosorbent Assay), and RIA (RadioImmunoAssay). Nevertheless, this extensive assortment of well-established analytical tools and research techniques remains insufficient for today's challenges. The failures of these methods relate to limitations in sensitivity, selectivity, dynamic range, and the ability to determine the concentration of several proteins simultaneously in an accurate and absolute manner (multiplexing). The realization that elemental analysis offers significant advantages to the field of protein quantitation has directed the development of several new methods of protein quantitation via Inductively Coupled Plasma Mass Spectrometry (ICP-MS) linked immunoassays [1-5]. This new technique provides an innovative arena for ICP-MS in the analysis of biological samples.

The ICP-MS technique maintains its well deserved place in the analysis of some biological samples and has been widely used for the quantitation of toxic elements, studying transport of metals, and monitoring the absorption and metabolism of metals and metallo-drugs, metallo-amino acids, metallo-proteins. In all of these cases, the bio-molecules being analyzed are already associated with a metal component. In contrast, the ICP-MS linked immunoassays provide a means to determine the concentrations of proteins that do not necessarily naturally contain a metal. To achieve this, ICP-MS immunoassays rely on the use of affinity products that include an elemental (mostly metal) containing tag. The most straightforward approach includes antibodies that have been raised specifically against the antigens (eg. proteins) of interest and tagged with metal.

ELISA with fluorescent tags and RIAs methods are under continuing development, with recent advances in microsphere immunoassays and flow cytometry reporting the ability to quantitate up to 15 targets almost simultaneously [6,7] with somewhat limited dynamic range. Although, it is feasible to have an optical emission detector capable of distinguishing more than 15 wavelengths (for example ICP-OE, Optical Emission) and an excitation system with significantly broad range, it is still physically impossible to create a set of non-interfering fluorophores for massively multiplexed assays. In the multiplex configuration, non-overlapping signal fluorescent dyes are required. This results in mismatched overlap of the excitation and absorption wavelengths, with a corresponding loss in sensitivity for some of the fluorophores. More significantly, the emission spectra are not well baseline-resolved. That is, some overlap of the fluorescent signals is obtained and this becomes important when the target antigen concentration differs substantially (a large signal in one channel overlaps strongly into the weaker signal channel).

2. Experiment and discussion.

The most important advantage of ICP-MS is its stability and matrix resistance. A large number of heavy metals and their isotopes will provide distinct signals that can be detected simultaneously. Thus many (>50) elemental tags could be created; the obtained intensity ratio vs. tag mass fingerprint could serve as a signature of the disease-state. Secondly, the abundance sensitivity of ICP-MS, a measure of the overlap of signals of neighboring isotopes, is large ($>10^6$ for the quadrupole analyzer), and this ensures independence of the detection channels over a wide dynamic range. The third key property is that MS is very sensitive.

Classes of reagents suitable for the ICP-MS application as well as specific tags for elemental analysis have not yet been developed. Commercially available immuno-reagents that contain elemental tags for unrelated purposes can be used. Fortunately, there is a variety of metal containing immuno-reagents such as gold-tagged antibodies that are routinely used in electron microscopy. It has been found that small gold clusters (1.4nm diameter) [8] and colloidal gold particles can be successfully analyzed by ICP-MS [1-5,9,10]. In addition, four lanthanide (Eu, Tb, Dy and Sm) tagged antibodies [11] produced for fluorescence-based ELISA methods (by PerkinElmer) were also found to be good candidates for ICP-MS based immunoassays [4]. Both the 1.4nm nanogold and lanthanide tags were determined to have several valuable characteristics for elemental analysis including, i) uniform size (number of atoms), ii) more than one tag atom per conjugate; iii) covalent attachment to antibodies, iv) biological inactivity with low steric hindrance, v) a reproducible ratio of tag to antibody, and vi) low natural background.

The protein targets already examined employing ICP-MS included Smad proteins (which play a role in cardiac muscle development) and various regulatory proteins found in human serum which are involved in the immune response, including: Immunoglobin (IgG), Interleukin-1beta(IL-1β), Interleukin-6 (IL-6), Interleukin-8 (IL-8), Interleukin-13 (IL-13), Interferon-gamma (IFN-γ) and Tumor Necrosis Factor-alpha (TNF-α) [1,3-5].

For example, Sandwich and competitive ELISA coupled to the ICP-MS detector yielded reproducible and linear responses to antigen concentration. They also enable 96 immunoassays to be run per plate. Primary antibody plates were found to be more sensitive than secondary antibody plates allowing lower levels of protein to be detected. This is probably due to the restricted well capacity of secondary antibody plates resulting from the steric hindrance of over-lying antibodies. A comparative study of three analytes in 81 patient samples (estriol, AFP and hCG), has been performed [3] where it was found that the ICP-MS detection reproduced results currently achieved on the same plates with fluorometers.

It should be evident that antigens having independent antibodies that are distinguishably tagged by elemental labels, can be determined simultaneously, or multiplexed using the ICP-MS. Five commercially available tags (Au, Sm, Eu, Dy, and Tb) enable a 5-plex assay assuming that the antibodies are not cross-reactive.

The cell surface membrane carries a host of receptors (antigens) that are specific for a particular cell. This is widely used in leukemia diagnosis since knowing the cell type, stage of maturation and receptor abundance determines the correct and personalized therapeutic intervention. Experiments for the simultaneous identification of several surface and intracellular antigens in a human megakaryocytic leukemia-derived cell line were conducted. Expression of intracellular oncogenic kinase Bcr/Abl, myeloid cell surface antigen CD33, human stem cell factor receptor c-Kit and integrin receptor VLA-4 were investigated using live and permeabilized leukemic cells. Current studies were performed with live and fixed cells using primary antibodies, which were detected by secondary antibodies linked to metals (Au, Eu, Tb, Sm). Depending on the abundance of antigens it was possible to use as little as 10,000 cells per 150 μl sample for several receptor identifications.

Comparative flow cytometric analysis was done on a four-color fluorescence capability FACScalibur™ flow cytometer (BD Biosciences, San Jose, CA) equipped with 488 nm argon-ion and

635 nm diode air-cooled lasers. Data acquisition and analysis was run through the BD CellQuest™ software. The following secondary fluorescent labeled antibodies were used: anti-mouse-phycoerythrine (PE) and anti-rabbit-fluoresceine-isothiocyanate (FITC); streptavidin-peridinin chlorophyll-a protein (StrAv-PerCP) and streptavidin-allophycocyanin (StrAv-APC) conjugates. Human monocyte cell lines MBA-1 and MBA-4, derived from Mo7e by stable transfection of p210 BCR/Abl expression plasmid were propagated in synthetic media supplemented with 10% fetal bovine serum.

Antibodies used to identify cell surface as well as intracellular antigens were obtained from commercial sources. Anti-CD33, mouse monoclonal, 2 mg/ml (Immunotech Inc. France); biotinylated anti-human SCFR/c-Kit antibody (CD117) (R&D Systems) and biotinylated anti-human Integrin alpha4 (CD49d or VLA-4) mouse monoclonal antibody (R&D Systems). Anti-BCR antibody raised in rabbit (Cell Signaling Tech) detects total levels of endogenous BCR and the p210 kDa Bcr/Abl fusion protein.

Cells in logarithmic growth phase were collected by centrifugation (1200 rpm, 10 min), washed once in PBS/10%FBS and counted in a hemocytometer. Cells were distributed into round bottom 5 ml flow cytometry tubes (BD Biosciences, USA) in triplicates for staining. Incubation of cells with primary antibodies was carried out on ice for 30 min. Permeabilization (BD Bioscience, Permeabilization solution #2); was done for 30 min at room temperature, after which the cells were washed and non-specific antigen sites were blocked with PBS/10%FBS; cells were then stained for intracellular antigens. After secondary antibody incubation (30 min, ice) cells for ICP-MS analysis were washed twice, centrifuged and pellets were dissolved in concentrated HCl (75 µl per tube) for 10 min at room temperature. As an internal standard for ICP-MS measurements, 75 µl of 1ppb Ir solution was added to each tube. Cells prepared for flow cytometry analysis were resuspended in PBS/10%FBS at $1x10^6$ cells/ml.

Three cell antigens, CD33, VLA-4 and c-Kit, were analyzed on the surface of live MBA-1 cells by ICP-MS. As secondary affinity reagents, NANOGOLD™ anti-mouse-Au (1:25) was chosen as the identifying agent for CD33 antigen; StAv-Tb (1:50) – for biotinylated anti-c-Kit, and StAv-Sm (1:50) – for biotinylated anti-VLA-4. MBA-1 cells were distributed into triplicate tubes at $1.5x10^5$, $3x10^5$, and $1x10^6$ cells per tube. There is a good correlation between the number of cells

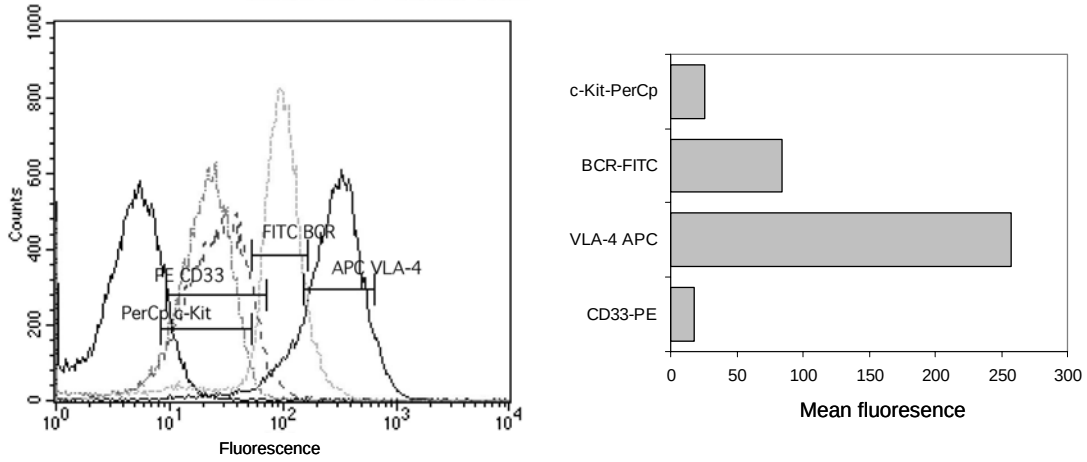

Figure 1.Simultaneous four-antigen staining of MBA-4 cells analysed by flow cytometry. Histogram representation of results with demarcations for geomean values (CellQuest software). Unmarked peak – autofluorescence of negative control cells; PerCp c-Kit – primary anti-c-Kit-biotinylated antibody and strepavidin-PerCp; PE CD33 – primary anti-CD33 and anti-mouse-PE secondary antibodies; FITC BCR – primary anti-BCR and anti-rabbit-FITC secondary antibodies; APC VLA-4 – primary anti-VLA-4-biotinylated antibody and streptavidin-APC. Bar graph representation of geomean fluorescence values.

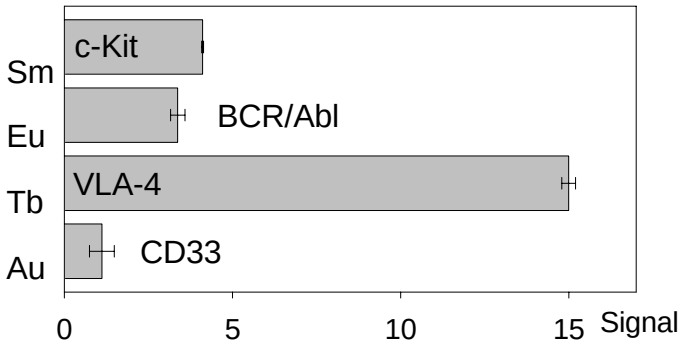

Figure 2. Simultaneous four-antigen staining of MBA-4 cells analyzed by ICP-MS. (background subtracted, corrected for the Ir internal standard, and differences in the size of the metal tags). Cells were stained with primary anti-c-Kit-biotinylated antibody and strepavidin-Sm; primary anti-CD33 and anti-mouse-Au secondary antibodies; primary anti-BCR and anti-rabbit-Eu secondary antibodies; primary anti-VLA-4-biotinylated antibody, and streptavidin-Tb.

used and signal obtained.

Live cells were also stained with anti-CD33 and anti-c-Kit, permeabilized, stained with a mix of anti-BCR, anti-mouse-Au, StrAv-Sm; finally stained with anti-VLA-4, followed with StrAv-Tb for ICP-MS (Figure 2). FACS was done simultaneously with the same cells and primary antibodies, followed by secondary antibodies labeled with fluorochromes. To obtain an accurate histogram of the sample stained with all four antibodies and fluorescent dyes, it was necessary to set compensation parameters using samples individually labeled with each fluorochrome-conjugated antibody. The resultant histogram is shown in Figure 1. To compare results of FACS with that of the ICP-MS data, mean fluorescent intensity values (GeoMean; CellQuest software) were obtained and are presented as a bar graph (Figure 1). Comparing Figure 1 and Figure 2 it is evident that both methods of antigen detection give similar results. Both methods indicate that the most abundant cell surface antigen is the integrin receptor VLA-4, with lesser amounts of intracellular kinase BCR/Abl, and cell surface antigens CD33 and c-Kit antigens.

Acknowledgements:

This work was funded in part by Genome Canada through the Ontario Genomics Institute.

References

[1] Baranov, V. I.; Bandura, D. R.; Tanner, S. D. - European Winter Conference on Plasma Spectrochemistry, Hafjell, Norway Book of Abstracts, p.85. (2001)

[2] Zhang, C.; Zhang, Z.; Yu, B.; Shi, J.; Zhang, X. - Anal.Chem. **74,** 96 (2002)

[3] Baranov, V. I.; Quinn, Z.; Bandura, D. R.; Tanner, S. D. - Anal.Chem. **74,** 1629 (2002)

[4] Baranov, V. I.; Quinn, Z. A.; Bandura, D. R.; Tanner, S. D. - J.Anal.Atom.Spectrom. **17,** 1148 (2002)

[5] Quinn, Z. A.; Baranov, V. I.; Tanner, S. D.; Wrana, J. L. - J.Anal.Atom.Spectrom. **17,** 892 (2002)

[6] Carson, R. T.; Vignali, D. A. - J.Immunol.Methods **227,** 41 (1999)

[7] De Jager, W.; te, V. H.; Prakken, B. J.; Kuis, W.; Rijkers, G. T. - Clin.Diagn.Lab Immunol. **10,** 133 (2003)

[8] http://www.nanoprobes.com

[9] Andreu, E. J.; Martin de Llano, J. J.; Moreno, I.; Knecht, E. - J.Histochem.Cytochem. **46,** 1199 (1998)

[10] Martin de Llano, J. J.; Andreu, E. J.; Knecht, E. - Anal.Biochem. **243,** 210 (1996)

[11] http://www.perkinelmer.com

Two-dimensional simulation of the interaction between plasma dynamics and bulk flow in direct current microdischarges

P.S. Kothnur[1] and L.L. Raja[1]
[1]*Department of Aerospace Engineering and Engineering mechanics, University of Texas at Austin, Austin, TX, USA*

Abstract

Direct current microdischarges permit the generation of plasmas over length scales of a few hundred microns. Here, a two-dimensional modeling study of the interaction between plasma dynamics and bulk flow in direct-current microdischarges is presented to support our proposed concept of a microdischarge-based small satellite electrothermal propulsion device. Results indicate that there is significant gas-heating with microchannel bulk flows, and that the gas temperature distribution depends strongly on the nature of the wall boundary condition. The possibility of intense gas-heating at micron length scales raises the prospect of new applications that exploit this concept.

Keywords High-pressure discharges, direct-current microdischarges, glow discharges, plasma-flow interactions, two-dimensional modeling

1. Introduction

Direct-current microdischarges (MDs) are discharges that allow the generation of plasmas at length scales of a few hundred microns. Microdischarges are operated at relatively high pressures (~10 Torr-1 atm) to overcome plasma quenching effects and achieve reasonable low breakdown and sustain voltages. Recently, these discharges have generated much interest due to possible applications such as sources of UV and visible radiation [1] and maskless etching of thin films [2]. Some attempts at diagnosing the microdischarge plasmas directly have been made [3]-[5]. These studies indicate that electron number densities are expected to range from 10^{17}-10^{20} m^{-3} depending on the geometric configuration, operating conditions and choice of gas. Further, these studies indicate the presence of high levels of excited states of ions with excitation energies of several tens of electron volts, suggesting that electron temperatures in microdischarges are much higher than in low-pressure glow discharges. Recently we have performed modeling studies in planar direct-current microdischarges using a one-dimensional model [6] and helium discharges in a microhollow electrode geometry using two-dimensional modeling [7]. Prominent features include presence of a sheath region comparable to the bulk plasma region, and high electron (several tens of eV) and gas (~1000 K) temperatures. Experimental observations of microhollow cathode discharges in the high-current high-pressure operating regime have also shown significant bulk gas heating, with gas temperatures of ~1000K being measured [8]. For some applications such as photonics [9], high gas temperatures are detrimental to performance, but in other applications such as microchemical reactors [10], high gas temperatures can be beneficial. Our motivation in studying this class of discharges arises from our proposed concept of electrothermal class of small spacecraft (1-10 kg) propulsion devices that utilize microdischarge based gas heating to provide highly controllable thrust levels. The focus of the present study is to explore the interactions between bulk flow and the plasma in a microchannel geometry using a two-dimensional self-consistent representation of the plasma and the flow. The objective of the study is to provide a fundamental understanding of underlying physical phenomena to aid the understanding and design of such devices.

2. Description of Model

The model is based on a two-dimensional multifluid description of the plasma, described in detail elsewhere [7], and the SIMPLE (semi-implicit pressure linked equations) approach [11] for the flow. A brief description of the model is presented below.

Assumptions (1) A continuum fluid approach is used to model the MD phenomena. This approach is reasonable for the relatively high pressure operation of the discharge. At a pressure of 300 Torr, the mean free path for electron-neutral collisions in helium is about 1 μm while gradient length scales are of order discharge dimension, or ~100 μm. (2) Fast secondary electrons emitted from the cathode are not treated explicitly. (3) A common gas

temperature is used for all the heavy species even though significant thermal nonequilibrium exists in microdischarges. Ion-neutral energy transfer length scales for a 300 Torr plasma is ~0.25 μm, which is much smaller than discharge dimensions. Ion energy is therefore locally redistributed among all heavy species, justifying the use of a common heavy species temperature. (4) Resonant excited species are neglected, and radiative energy transfer processes are ignored. This is a reasonable assumption for the high-pressure operation being considered. (5) Compressibility effects are ignored at the low flow velocities that are of concern here.

Governing Equations Multiple charged and neutral species are considered, as well as the effect of chemical reactions and surface interactions. The electric field is governed by the Poisson's equation, and the species number densities are governed by the species conservation equations incorporating generation and transport. The drift-diffusion formulation is used to compute the species number and energy fluxes, with the additional term to account for convection due to bulk fluid flow. The electron energy equation is used to determine electron temperature distribution and the gas energy equation is solved to capture the gas heating effects. Sources of thermal energy in the gas heating equation include elastic electron-neutral collisions and ion joule heating by the electric field. All equations are cast in full time-implicit form and solved using Newton-iterations. Six helium plasma species are considered—electrons, helium ions (He^+, He_2^+), helium metastable species (He^*, He_2^*) and background helium atoms are considered. High-pressure helium plasma chemistry taken from the literature (see Ref. [7] for values of rate constants and references) is used to compute source terms for the plasma species in the species continuity equation. Secondary electron coefficients of $\gamma^+ = 0.105$ for ions and $\gamma^* = 0.115$ for metastable species is chosen. These values have also been used in our previous work [7]. A circuit model comprising of a ballast resistor (~100 kΩ) is used to stabilize the solution.

A separate flow module based on the SIMPLE (semi-implicit pressure linked equations) methodology [11] is used to solve global conservation equations for the flow through the discharge. Solution of the flow proceeds via SIMPLE iterations for the continuity, momentum and energy equations. The gas density is updated after each iteration using the local gas temperature and the ideal gas law. Typically, about 20 iterations are needed to achieve convergence in the flow module. Since the flow time scales are typically much larger than plasma time scales, the flow solver module needs to be invoked only a few times during the plasma simulation to achieve converged results.

3. Results

Results are presented below for a microchannel configuration corresponding to a net flow rate of 192 sccm, and with an inlet Reynolds number based on the channel width and centerline velocity of about 25. A parabolic velocity profile with a centerline velocity of 20 m/s is imposed at the inlet. The net electrical power input to the system is about 0.1 W. Figure 1 shows the geometry of the microchannel discharge being considered. The configuration consists of anode and cathode surfaces of thickness 100 μm separated by a dielectric surface of thickness 100 μm. The channel width is 400 μm. A Cartesian grid with grid stretching near the walls provides adequate resolution of the relatively thick sheath regions.

Figures 2 and 3 show contours of different plasma and flow variables in the microchannel geometry. The contour lines for this figure and all other figures in this paper are at equally spaced intervals between the levels specified in the figures. The potential contours (shown in Fig. 2(a)) shows that electric fields in this discharge are localized, most of the electric potential gradients occurring in the cathode sheath region which is about 40 μm. Electron number density contours are shown in Figure 2(b). Peak electron and ion (not shown) number densities are about 10^{20} m^{-3}, and occurs along the centerline near the cathode surface. This value is consistent with available quantitative experimental data for microhollow cathode discharges in other noble gases [8] and molecular gases [12]. The electron number density distribution is relatively unaffected by the presence of the flow, as is the case with ions. Electron temperatures, shown in Figure 2(c), are of the order of 1 eV in the bulk of the discharge, and reach peak values of several tens of eV in the cathode sheath regions. Indirect evidence of high electron temperatures in microdischarges is provided by experimental studies of emission from high-lying

excited states of ionic species in noble gas microdischarges [13]. The electron temperature distribution is also relatively unaffected by the presence of bulk fluid flow.

Monomer and dimer metastable species number densities are shown in Figure 2(d) and 2(e). Both the metastable species are present in significant concentrations, with number densities of order 10^{20} m^{-3}. The predicted metastable species densities are of the same order as those measured experimentally in another type of microdischarge [8]. The monomer metastable species are also relatively unaffected by the presence of flow, and are primarily present in the region near the cathode surfaces. The presence of high-energy electrons in this region (as shown Fig. 2(c)) and the increased importance of quenching of metastable downstream of the electrodes are responsible for the observed localized nature of the monomer metastable species. In contrast to the monomer metastable species, the effect of flow on dimer species number densities is much more noticeable. Figure 2(e) shows the distribution of dimer metastable species number densities. The figure shows that significant dimer species concentrations can be found at locations several channel widths downstream of the discharge electrodes.

Figure 2(f) shows the bulk flow axial velocity contours in the discharge. The inflow velocity profile is modified due to density gradients caused by gas heating. The maximum velocity occurs along the centerline and reaches values as high as 60 m/sec for the case corresponding to adiabatic wall boundary conditions.

Figure 3 shows the gas temperature plots corresponding to a flow rate of 100 sccm. The figure shows results corresponding to different fixed wall temperatures of 500K (Fig. 3(a)) and 800K (Fig. 3(b)), and a third scenario corresponding to an adiabatic wall (Fig. 3(c)). Gas heating is significant, and gas temperatures near the cathode surface can reach values that are several hundreds of K higher than the ambient. The figure also shows that the gas temperature distribution is very sensitive to the wall boundary condition. Gas temperatures in the vicinity of the cathode are of order several 100's of K above the ambient, but it is quenched at the walls effectively owing to the low Reynolds numbers. In the limiting case of an adiabatic wall (no heat losses at the wall), the gas temperature is predicted to reach values as high as 1200K (Fig. 3(c)) downstream of the discharge. However, for realistic scenarios involving finite wall losses, the downstream gas temperature will be less than the value predicted by the adiabatic wall assumption. For example, Fig. 3(b) shows that when the wall temperature is fixed at 500 K, the gas temperature falls by about 200 K one channel width downstream of the cathode edge. A comparison of the source terms in the gas energy equation (not shown) indicates that ion joule heating is the primary source of energy in the gas energy equation as compared to electron-neutral elastic collisions.

4. Conclusions

Helium microdischarge phenomena in microchannel geometry in the presence of substantial bulk fluid flow are investigated using a two-dimensional self-consistent continuum model. Except for the dimer metastable species, all plasma parameters are relatively unaffected by the presence of bulk fluid flow. Charged species densities of the order of 10^{20} m^{-3} and metastable species densities of the order 10^{20} m^{-3} are observed, both values being consistent with experimental data available for other micron scale discharge geometries. Electron temperatures that are several tens of eV and gas temperatures of several hundreds of Kelvin higher than ambient are observed. The possibility of achieving intense gas heating in these micron-sized geometries raises the prospect of potential new applications such as our proposed microdischarge plasma thruster for small satellite propulsion. The gas temperature distribution is very sensitive to the nature of the wall boundary conditions, due to the low Reynolds numbers and quenching of gas energy at the wall. The results emphasize the localized nature of gas heating in hollow-electrode microdischarge geometries, as well as the need for the development of refractory materials to withstand such high temperatures, and insulating materials to limit wall losses.

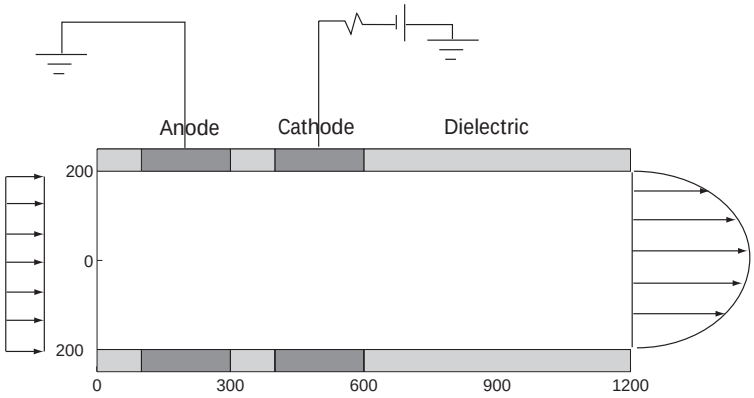

Figure 1. Schematic of microchannel discharge (all dimensions are in μm)

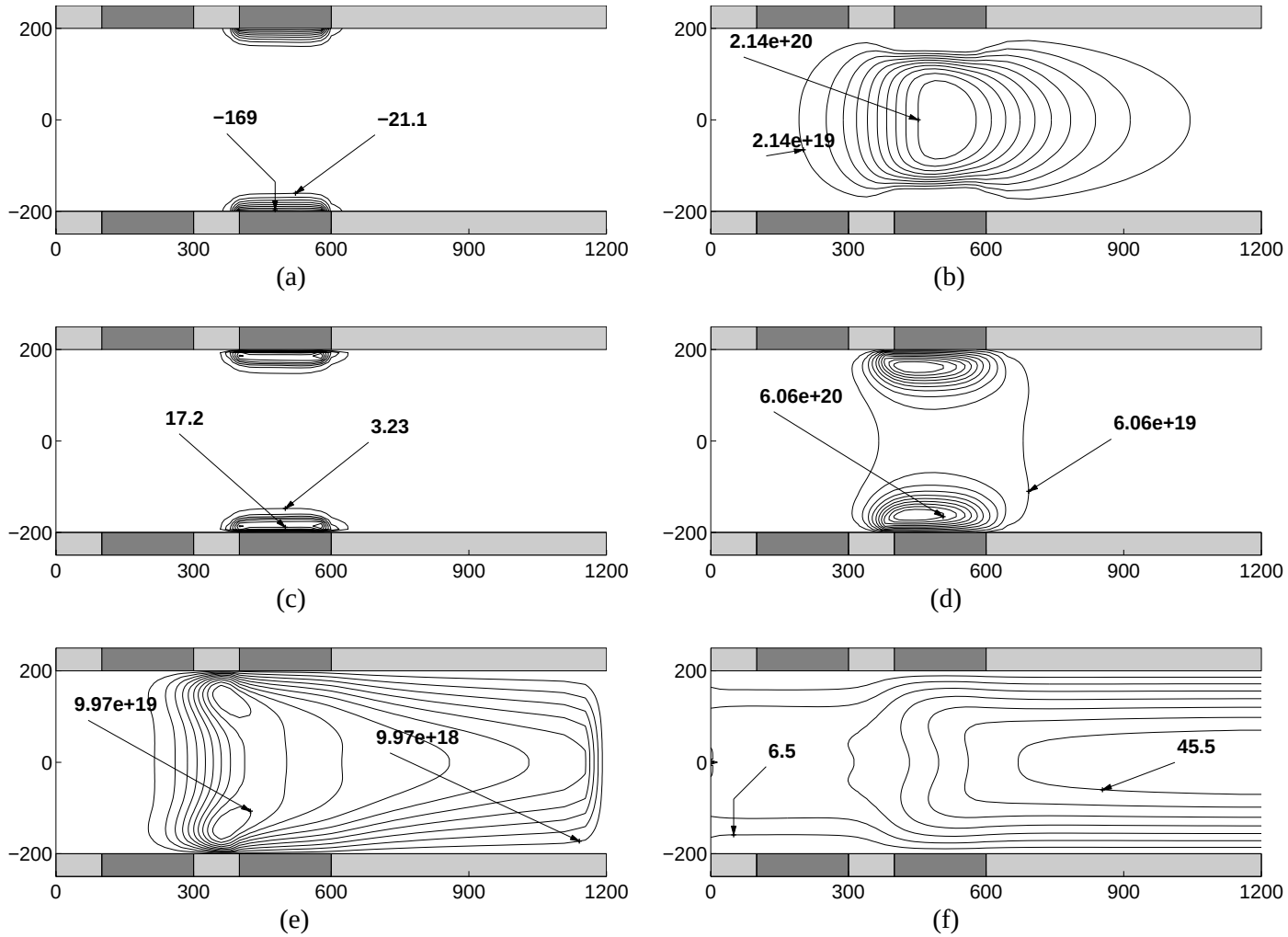

Figure 2. Contours of **(a)** Electric potential (V) **(b)** Electron number density (m^{-3})
(c) Electron temperature (eV) **(d)** Monomer metastable species number density (m^{-3})
(e) Dimer metastable species number density(m^{-3}) **(f)** axial velocity (m/s). All dimensions are in μm.

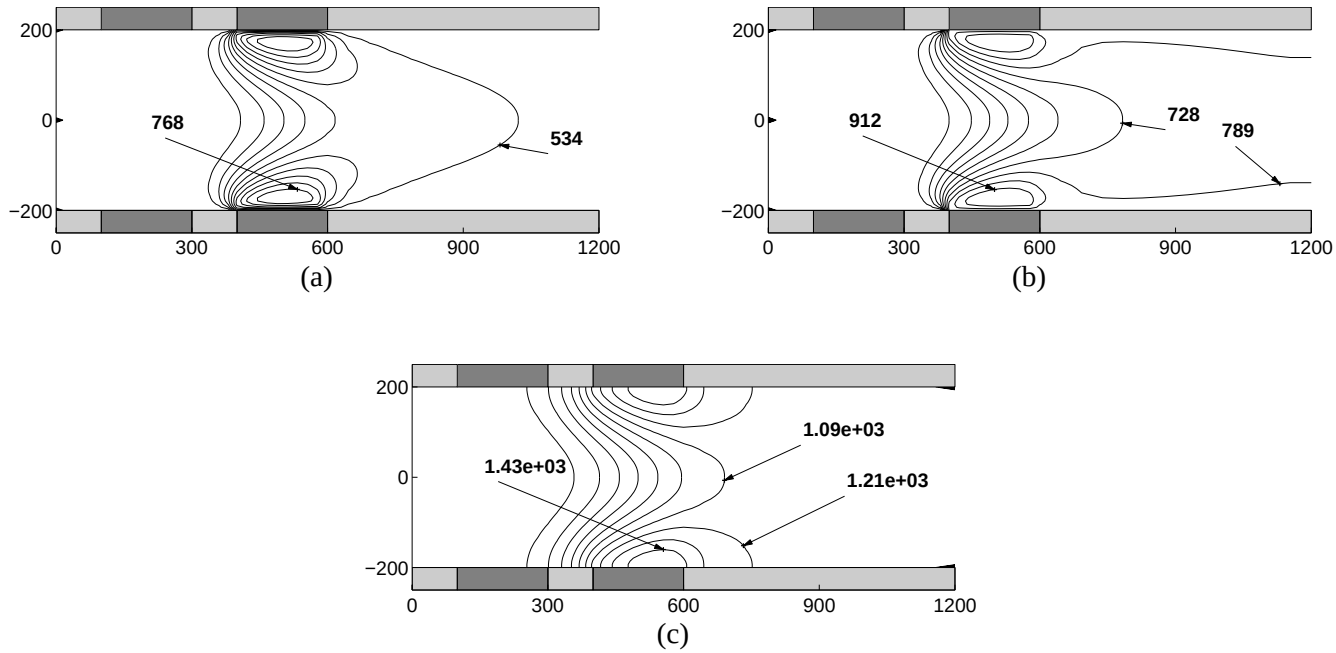

Figure 3. Gas temperature contours **(a)** T_{wall} = 500 K, **(b)** T_{wall} = 800 K, **(c)** adiabatic

References

[1] A. El-Habachi and K.H. Schoenbach. Applied Physics Letters, **72**, 22-24, (1999).
[2] R.M. Sankaran and K.P. Giapis. Applied Physics Letters, **79**, 593-595 (2001).
[3] R.H. Stark and K.H. Schoenbach. Journal of Applied Physics, **85**, 2075 (1999).
[4] K. Terashima, L. Howard, H. Haefka, and H.-J Guntherodt. Thin Solid Films, **634**, 281-282 (1996).
[5] F. Leipold, R.H. Stark, A. El-Habachi, and K.H. Schoenbach. Journal of Physics D, **33**, 2268 (2000).
[6] P.S. Kothnur, X. Yuan, and L.L. Raja. Applied Physics Letters, **82**, 529-531 (2003).
[7] P.S. Kothnur and L.L. Raja. Journal of Applied Physics, **97**, 043305-1-12 (2005).
[8] C. Penache, M. Miclea, A. Brauning-Demian, O. Hohn, S. Schossler, T. Jahnke, K. Niemax, and H. Schmidt-Bocking. Plasma Sources Sci. Technol. **11**, 476 (2002).
[9] S-J. Park, J. Chen, C.J. Wagner, N.P. Ostrom, C. Liu, and J.G. Eden. IEEE Journal of Selected Topics in Quantum Electronics, **8**, 139 (2002).
[10] D. Hsu and D.B. Graves. Journal of Physics D., **36**, 2898 (2003).
[11] S.V. Patankar, Numerical Heat Transfer and Fluid Flow, Taylor and Francis, (1980).
[12] F. Leipold, R.H. Stark, A. El-Habachi, and K.H. Schoenbach, J. Phys. D **33**, 2268 (2000).
[13] J.W. Frame, D.J. Wheeler, T.A. DeTemple, and J.G. Eden. Applied Physics Letters, **71**, 1165 (1997).

Microdischarge-assisted ignition characteristics of large-volume dielectric-barrier atmospheric pressure glow discharges

J. Shin and L. L. Raja

Department of Aerospace Engineering and Engineering Mechanics, University of Texas at Austin, Austin, Texas,USA

Abstract : Ignition characteristics of atmospheric pressure dielectric-barrier discharge (DBD) in the presence of dc microdischarges are studied in pure helium and pure nitrogen gas. The ignition voltages for various conditions are monitored with or without microdischarges being turned on. The substantial reduction of the ignition voltage for DBD is observed for both working gases when microdischarges are turned on. Somewhat localized glow forms within a discharge gap when high pressure DBD turns on in the presence of microdischarges. Intensified CCD image shows the structure and formation of localized glow discharge and I-V characteristics verifies a localized discharge mode is more like glow mode rather than a streamer mode.
Keywords : microdischarge, breakdown voltage, dielectric-barrier, atmospheric pressure

1. Introduction

Dielectric-barrier atmospheric pressure glow (APG) discharges are an excellent source of uniform, non-equilibrium glow plasmas at high pressures. These discharges can be used in large-volume, open-chamber processes such as sterilization [1], ozone generation [2], and aerodynamic flow control [3]. Due to the high *pd* (pressure-distance) value at high pressure, relatively high breakdown voltage (order of kilovolts) are required to successfully operate dielectric-barrier APG discharges. Helium gas has the lowest breakdown voltage of all APG working gases and several studies with helium gas have been reported [4-7]. In large-scale industrial processes, molecular gases such as nitrogen are desirable and in other applications such as aerodynamic flow control even attaching gases such as air are encountered. The breakdown voltage for dielectric-barrier APG can be exceedingly high in these cases resulting in difficulty in establishing a uniform glow mode [8]. This work explores an approach to reduce the breakdown and working voltage of dielectric-barrier APG discharge. We report the use of high-pressure microdischarges to seed the formation of large-volume dielectric-barrier APG discharges at lower voltages. Microdischarges such as the microhollow cathode discharge can be generated stably at low voltages in a number of working gases including attaching gases such as air [9, 10]. Microdischarges are a source of copious amounts of charged and radical species that can provide seed electrons for ignition of other discharges. Indeed, such microdischarges have been used to assist in the ignition of high-pressure arc lamps before [9], and have the potential for use in dielectric-barrier APG discharges, as is reported in this study.

2. Experiment setup and results

In this study, we employ a hybrid discharge configuration as shown in the schematic (Figure 1). A classical parallel-plate DBD configuration is modified to include an array of several microdischarges on one of the electrode surfaces. The upper electrode (aluminum) is powered while the microdischarge array is placed on the other side. The cathode layer of the microdischarges which also serves as the ground electrode for DBD faces the upper electrode. A mica layer (100 μm) is placed on the lower ground electrode which serves as the dielectric barrier, while the upper electrode has an alumina barrier (635 μm). The microdischarges have 342 μm

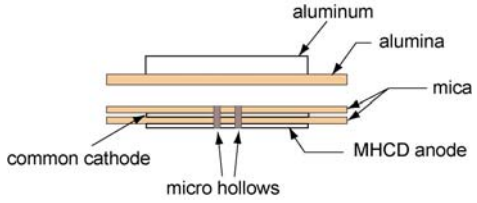

Figure 1. Discharge schematic for hybrid mode dielectric-barrier APG discharges.

hole with 150 kΩ individual ballast. Nickel or aluminum are used for microdischarge electrode and separated by 200 μm mica dielectric. Both helium and nitrogen working gases are studied. 5 mm and 6 mm gas gap are used for helium gas and 3 mm is used for nitrogen gas. The pressure is varied over a range of 300 Torr to 700 Torr. The main discharge (large-volume dielectric-barrier APG) is driven by an ac power supply with an oscillatory voltage of the order of 1-10's kHz. The microdischarge array is driven separately by a dc power supply.

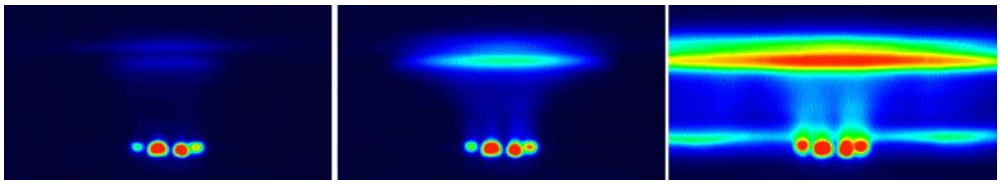

Figure 2. Images of DBD with 4 microdischarges being turned on at 15 kHz, 300Torr helium with 6 mm gas gap. DBD voltages are a) left : 427 V, b) center : 500 V, c) right : 700 V.

With a helium gas, a highly stable glow discharge can be obtained at high pressures. Figure 2 shows the time-averaged intensified CCD (ICCD) images of DBD in the presence of microdischarge array at 15 kHz, 300 Torr with 6 mm gas gap. For these conditions, the average ignition voltage is measured as 825 V with the microdischarges turned off. The microdischarges are switched on with a total power of 3.2 W for the four discharges array. With the microdischarges on, incipient localized glow is observed to form in the dielectric barrier gap at a DBD voltage as low as 427 V. The intensity of glow in the DBD gap increases as the external DBD voltage increases (center image). The discharge plume from microdischarges connects with localized glow. The I-V waveform in the Figure 3 tells that the localized glow discharge near the upper electrode is more like a classical DBD in that it has a single current pulse with tens of microsecond pulse width [4]. The asymmetric current pulse is caused by geometric asymmetry of discharge setup and this is consistent with time-resolved ICCD image where the localized glow discharge forms when the potential of powered electrode becomes negative. Further increase in voltage makes the glow discharge expands over the entire gap (right image in Figure 2) and generates positive current pulse even though it is still asymmetric in the magnitude. The glow in

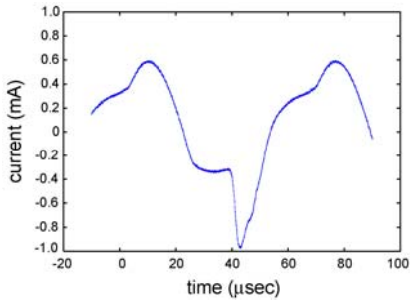

Figure 3. I-V waveform of hybrid mode DBD at 15 kHz, 300 Torr in helium with 6 mm gas gap. 4 mA microdischarges current and 500 V DBD voltage.

the bulk region is weaker than that of regular DBD and the positive glow is much weaker than negative glow. Changing the power input of the microdischarges can result in a change in the intensity of glow and the on-set voltage at which the dielectric-barrier APG is formed. The intensity of the glow becomes slightly stronger with an increase in the microdischarge current. This is different from the observation of Eden *et al.* [9], who report that the ignition voltage is insensitive to microdischarge current. The average ignition voltages of helium dielectric-barrier APG at different pressures are plotted in Figure 4. The discharge conditions are 5 mm gas gap at 15 kHz. A dotted line represents the breakdown voltage of DBD only, without microdischarge being turned on and is close to the theoretical estimate of the dc Paschen breakdown voltage for the gas in helium assuming a 0.01 secondary electron emission coefficient (γ_{se}) [11]. When the microdischarge is kept on, the ignition voltage of the glow (localized glow) is reduced by about 50 % (solid line) over the pressure range. At this point, the current pulse is weak and so is the emission intensity. Further increase in external voltage makes localized

dielectric-barrier APG abruptly expands over the entire electrode (overall glow) as indicated by the dot-dash line in the Figure 4. The voltage at which the glow extends over the entire dielectric-barrier volume is about 80-88 % of breakdown voltage without microdischarges on.

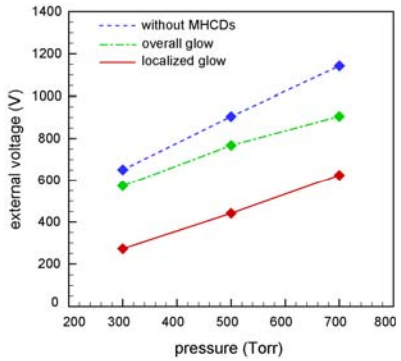

Figure 4. Ignition voltages of helium DBD with the presence of microdischarges at 15 kHz, 5 mm gas gap.

The same experiment is performed with nitrogen which requires much higher ignition voltage than helium. A DBD in nitrogen gas at high pressure has normally a mixed mode character where the streamers form within a uniform glow discharge and make current waveform appear noisy. Other studies have indicated that the streamer component can be reduced by using a Polyethylene Terephthalate (PET) dielectric with meshed electrode [8]. In contrast to helium case, the localized dielectric-barrier APG with the microdischarges on is much more confined to the centerline of microdischarge hole and appears to have peak intensity in the middle of discharge gap (Figure 5). The detail discharge structure inside localized glow in the figure looks similar to that of DBD and the current waveform shows the discharge is glow mode rather than streamer. A horizontal line in the discharge

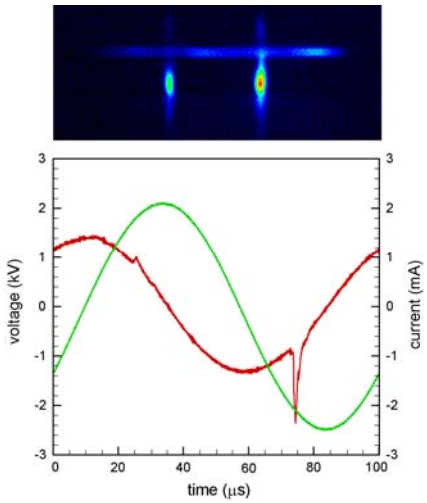

Figure 5. I-V waveform and corresponding discharge image when localized glow occurs in nitrogen gas at 300 Torr, 10 kHz with 4 microdischarges of 6mA on.

image is just a reflection from plexiglass frame. The ignition voltages for nitrogen gas at different pressures are plotted in Figure 6. The dot-dash line shows the breakdown voltage without microdischarges being turned on. The values are also close to the theoretical dc Paschen breakdown values with $\gamma_{se} = 0.1$. The solid line represents the ignition voltages when the localized glow (as in Figure 5) turns on within a discharge gap with the presence of microdischarges. A reduction in voltage for localized glow discharge is about 45% which is similar to helium experiment. For nitrogen case, the on-set of uniform glow discharge in the gap was hard to identify since the discharge mode continuously changes its intensity and current waveform along with gradually increasing streamer formation as the external voltage increases. The structure of overall glow is similar to that of helium

case in that the intense negative glow occurs at every half cycle and relatively weak glow is in the middle of a discharge gap with weak streamers formed within a glow.

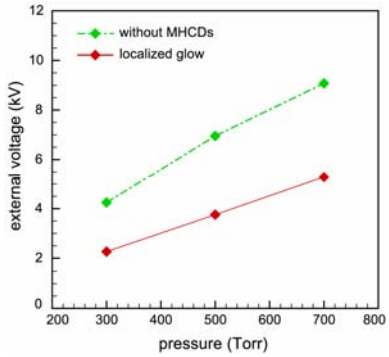

Figure 6. Ignition voltages of nitrogen DBD with the presence of microdischarges at 10 kHz, 3 mm gas gap.

Approximate electron number density (n_e) can be estimated by assuming a current is electron mobility (μ_e) limited. Electron number density $n_e = J / (e\mu_e E)$ where J is a current density, e is an electron charge ($=1.6\times10^{19}$) and E is an electric field. The values of μ_e with a valid range of a reduced electric field (E/p) are listed in the literature [11]. For the case in Figure 5, a reduced electric field (E/p) is 25.2 (V/cm·Torr) and it gives a value of $\mu_e p$ for nitrogen gas as 0.42×10^6 cm^{2}Torr/V·s. Stark *et al*. used a temperature dependent electron mobility approximation [10]. The gas temperature of air microdischarge is about 2000 K [12] but the extended plume can be expected to have a room temperature. Assuming gas temperature as 300 K in the localized glow region, $(\mu_e p)_T = (\mu_e p)_{To}$. The diameter of localized glow is approximately twice of microdischarge hole diameter. Assuming four localized glows have the same area, effective area $A = 4\times0.25\pi(2\times342\times10^{-4})^2 = 1.5\times10^{-2}$ cm^2. With a peak current of 2.4 mA, current density $J = I / A = 0.16$ A/cm^2 and hence $n_e \approx 9.4\times10^{16}$ m^{-3}. This verifies a localized glow is regarded as a dielectric-barrier glow discharge ($n_e \sim 10^{17}$ m^{-3}) rather than microdischarge ($n_e \sim 10^{20}$ m^{-3}).

3. Summary

In this study, we observe a significant reduction in the ignition voltage for glow discharge mode of dielectric-barrier high pressure discharge when the microdischarge is used. The reduction for localized glow discharge with microdischarges on in the dielectric-barrier gap is as low as 50% of ignition voltage of DBD without microdischarges. For uniform glow discharge in the dielectric-barrier gap, the reduction is about 80%. The current waveform for localized glow shows an asymmetric pulse with a low magnitude. The ICCD images show the localized glow discharge is formed only at the negative cycle of DBD power which is consistent with the asymmetry in the current waveform. The structure of the localized glow looks similar to that of a dielectric-barrier glow discharge except for its low intensity and asymmetric shape. The approximate calculation of electron number density as well as the current density waveform verifies that the localized glow is more like a dielectric-barrier glow discharge rather than a microdischarge. In our previous study, we showed that the breakdown and sustenance of dielectric-barrier APG discharge does not depend on the number density between current pulses. Instead, the ignition voltage is very dependent on pressure and gap distance with a given working gas. But this study shows that the breakdown of DBD at high pressure can be initiated at much lower voltage when there is an external source of high number density seed particles, such as the microhollow cathode discharges.

Reference

[1] M. Laroussi, G. S. Sayler, B. B. Glascock, B. McCurdy, M. E. Pearce, N. G. Bright, and C. M. Malott, IEEE Trans. Plasma Sci., **27**, 1 (1999).
[2] M. Kogoma and S. Okazaki, J. Phys. D, **27** (1994).
[3] C. L. Enloe, T. E. McLaughlin, R. D. VanDyken, K. D. Kachner, E. J. Jumper, and T. C. Corke, AIAA Journal, **42** (2004).

[4] J. Shin and L. L. Raja, J. of Appl. Phys., **94** (2003).
[5] F. Tochikubo, T. Chiba, and T. Watanabe, Jpn. J. Appl. Phys., **38** (1999).
[6] L. Mangolini, C. Anderson, J. Heberlein, and U. Kortshagen, J. Phys. D: Appl. Phys., **37** (2004).
[7] F. Massines, A. Rahebi, P. Decomps, R. Ben Gadri, P. Segur, and C. Mayoux, J. Appl. Phys., **83** (1998).
[8] Y. B. Golubovskii, V. A. Maiorov, J. F. Behnke, J. Tepper and M. Lindmayer, J. Phys. D: Appl. Phys., **37** (2004).
[9] J. G. Eden, C. J. Wagner, J. Gao, N. P. Ostrom, and S, J, Park, Appl. Phys. Letter, **79** (2001).
[10] R. H. Stark, K. H. Schoenbach, Appl. Phys. Letter, **74** (1999).
[11] Yu. P. Raizer, *Gas Discharge Physics*, (New York, Springer, 1991).
[12] R. Block, O. Toedter, and K. H. Schoenbach, Bull. Am. Phys. Soc., **43** (1998).

Effect of carbon precursor hybridization on plasma deposited films-structure and properties

D. Escaich[1], R. Clergereaux[1], S. Martin[2], P. Raynaud[1] and F. Gaillard[2]
[1] *Laboratoire de Génie Electrique de Toulouse*
Université Paul Sabatier - 118, Route de Narbonne 31062 TOULOUSE cedex 04 - France
[2] *Commissariat à l'Energie Atomique - Département des Technologies pour les Energies Nouvelles*
CEA Grenoble - 17, rue des Martyrs 38054 Grenoble cedex 9 - France

Abstract
Amorphous carbon layer are frequently deposited by PECVD because of its high control of film quality, high efficiency and reproducibility. Here, a study of carbon layers deposited at weak heat balance process is shown. The effect of the precursor type in a MMP-DECR reactor on the film properties is reproted. From FT-IR, spectroscopic ellipsometry and optical emission spectroscopy, links between plasma parameters and film structure and properties have been shown.
Keywords : amorphous carbon, PECVD, plasma, spectroscopic ellipsometry, FTIR

Introduction

Hydrogenated amorphous carbon (a-C :H) films received a great interest since their advent [1], owing to their wide range of properties, such optical transparency, mechanical hardness. It is well known that a-C:H have a complex structure essentially due to the different types of hybridisation of carbon atoms: tetrahedral sp^3, trigonal sp^2 or linear sp^1. More, hydrogen atoms come to complicate more the structure of these films. The properties of a-C:H films are mainly controlled the relative sp^2 to sp^3 bonding ratio, as the amount of sp^1 sites is usually negligible. It is commonly accepted that the graphitic sp^2 clusters is embedded in the sp^3 matrix [2]. The sp^2 sites are responsible for electrical and optical properties whereas the sp^3 sites govern mechanical properties.
Due to their easily optical tune properties [4], a-C:H films are very interesting. So, they have been extensively studied with a variety of optical characterization methods such as Fourier Transform Infra-Red spectroscopy (FTIR), and spectroscopic ellipsometry (SE).
The object of this article is to show the effect of precursor hybridizations on the plasma deposited films when the plasma power increases.

Experimental details

a-C:H films have been deposited on Si substrates from ethane (C_2H_6), ethylene (C_2H_4) and acetylene (C_2H_2) in a dual DECR plasma reactor. The substrate holder was at room temperature. This temperature was not maintained constant during the deposition. The plasma was produced using a working pressure of 1mT. The plasma power varies from 70 W to 800 W.
The gaz phase is observed with an optical emission spectrometer (OES) in the UV-visible range (200-900 nm).
The chemical structure of the C_xH_y films was characterized by Fourier Transform Infrared spectroscopy (FTIR) in the absorbance mode using a Bio-Rad (FTS60A) spectrometer. The thickness was estimated by profilometer (KLA-TENCOR Alpha-Step IQ). Optical characterisations are measured by spectroscopic ellipsometer (SOPRA GES-5). Refractive indexes, extinction coefficient, and gap of films are calculated using a Cauchy or Forouhi model.
Then, as it is described in the literature [5], it is able to calculate the sp^2 hybridized carbon proportion (Csp^2) from the SE measurements. This method use the comparison of the film n_{eff} or effective number of valence electrons per atom taking part in optical transitions at low energies (<9eV) with the one of a pure graphite layer at the same energy:

$$Csp^2{}_{a-CH} = \frac{n_{eff,a-CH}(E \le 9eV)}{n_{eff,graphite}(E \le 9eV)} \qquad (1)$$

with $n_{eff} = K \frac{A}{\rho} \int_0^{E_M} 2Enk.dE$ (2)

where A=12, ρ is the density and K a constant.

Finally, the hydrogen concentration can be evaluated from FTIR measurements [6] by using the equation:

$$\%\,H = B \cdot \int_{\nu_1}^{\nu_2} \frac{\alpha(\nu)}{\nu} \cdot d\nu \qquad (3)$$

where B is a constant which depends on the film thickness and a constant determined from a standard material containing C-H bonds. α represents the absorbance and ν_1 and ν_2 the wave numbers at the edges of the CH absorption peaks

Results and Discussion

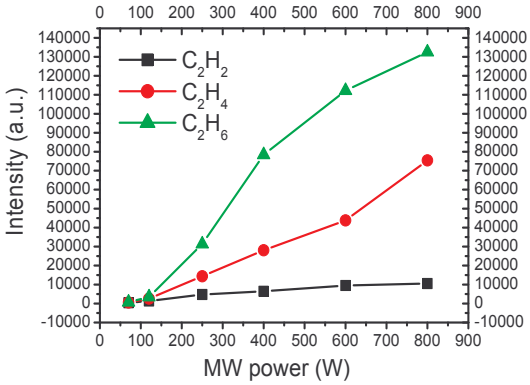

Figure 1 : H_α Optical emission vs. Micro wave power for C_2H_2, C_2H_4 and C_2H_6

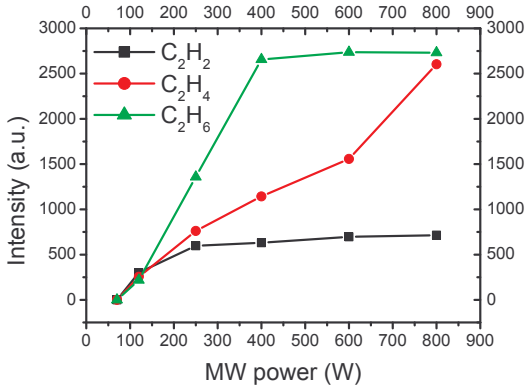

Figure 2: C_2 Optical emission vs. Micro wave power for C_2H_2, C_2H_4 and C_2H_6

The optical emission of these three type of discharge point to: first that C_2H_2 plasma are the less luminescent, different mechanism decomposition could explained this. Then, the C_2 emission at 516.5 nm intensity arises to a tableau at 400 W for C_2H_6 whereas the H_α intensity continues to growth. C_2H_2 gas has the same comportment but the tableau is obtained earlier, at 250 W. However, C_2H_4 plasma growths linearly when the power increases.

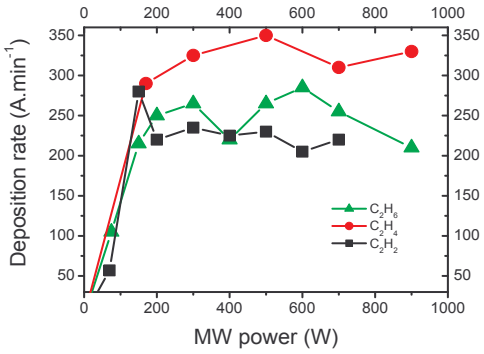

Figure 3 : Deposition rate vs. Micro wave power for C_2H_2, C_2H_4 and C_2H_6

Figure 3 shows the different deposition rate for each precursor. When the precursor should be completely dissociated, at high power, it appears that this deposition rate is equivalent for the three precursors, is equivalent. This phenomenon confirms the hypothesis we made that the number of carbon atoms is the parameter which control the deposition rate [7]. This rate is about 150 Å.min^{-1} with CH_4 precursor, 450 Å.min^{-1} with C_3H_8 precursor and here about 300 Å.min^{-1} with C_2H_4 precursor. Furthermore, it has been observed that C_2H_2 plasma, although they are generated at low pressure, produce powders. This behaviour can explain the weak difference of the deposition rate which is also observed with C_2H_6 precursor. For this last one, the plasma contains the large amount of H, an etching effect can be observed and limited the deposition rate.

The spectroscopic ellipsometry, in the range 0.25-1.6 µm, is a way to characterize film properties. Using a Cauchy model, the refractive index n and the extinction coefficient k can be calculated from ellipsometric measurements.
The variation of k (at 1.55 µm) and the amount of C-H bonds (% C-H) have the same shape for the three precursors (Figure 4). If we compare the three precursors, C_2H_6 films have the higher amount of CH bonds and C_2H_2 films the lowest ones. More films contain CH bonds, more k is high (Figure 6). Then, C-H bonds seem to play an important role on optical absorption. And, films which have the higher C_{sp2} rate present the higher value of k. Moreover, C_2H_2 films have the higher C_{sp2} rate and the C_2H_6 films the lowest (Figure 7). These last one are less absorbent than these first ones. So, it's obvious that CH bonds and the sp^2 hybridization of C atoms play a role in absorption property of the a-CH films, but C_{sp2} have a higher influence on this absorption.

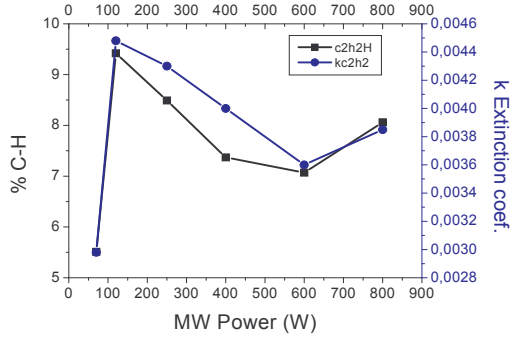

Figure 4: % CH bonds & k extinction coef. vs. Micro wave power for C_2H_2, C_2H_4 and C_2H_6

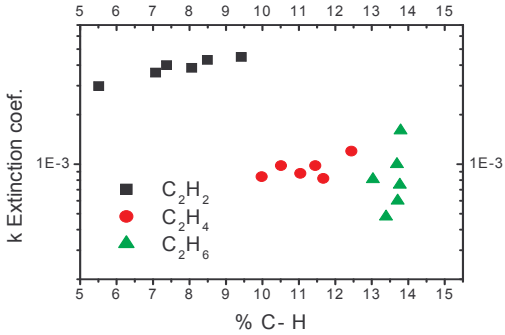

Figure 6 :k extinction coef. vs % CH bonds for C_2H_2, C_2H_4 and C_2H_6

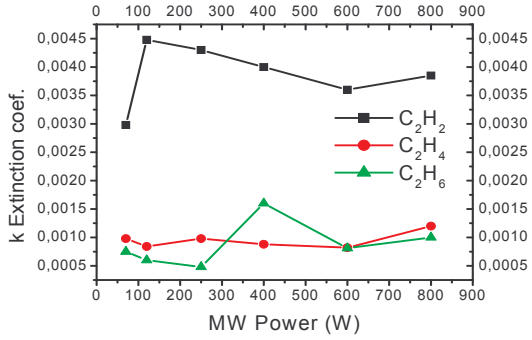

Figure 5 :k extinction coef. vs. Micro wave power for C_2H_2, C_2H_4 and C_2H_6

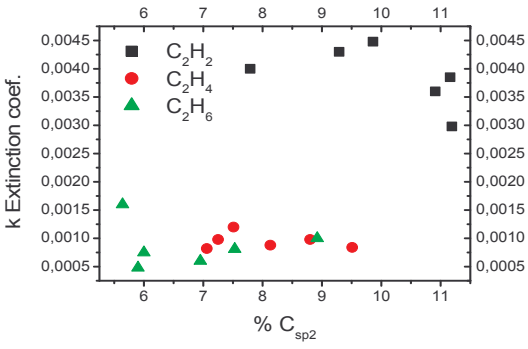

Figure 7 : k extinction coef. vs % C_{sp2} C_2H_2, C_2H_4 and C_2H_6

However, the evolution of the refractive index n is more complicate to understand (Figure 8) and to correlate. For C_2h_4 and C_2H_6 precursors, n evolutions are similar. Their evolutions comport three parts: first n growths, then reaches a plateau before falling. n values obtained with C_2H_4 is bigger than each

one obtained with C_2H_6 ; C_2H_4 films contain a higher rate of C_{sp2} (Figure 9). It is well know that in RF plasma, one way to improve n value is to increase the ionic bombardment during the deposition [8]. This bombardment result is to increase the C_{sp2} rate and decrease the amount of H in the film. So, the superior value of n for C_2H_4 films can be explained by a higher C_{sp2} rate. But, the C_{sp2} rate not control in totality the n value because some films obtain with C_2H_4 and C_2H_6 present a same concentration of C_{sp2} but have a different n as for example the sample at 600 W.

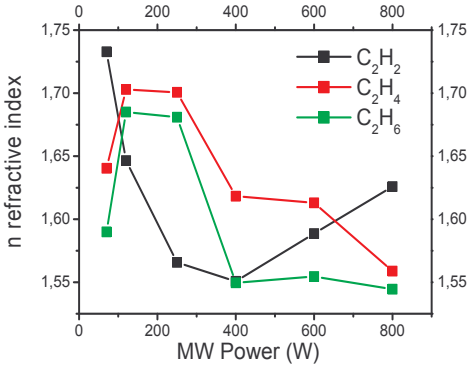

Figure 8: n refractive index. Vs MW power C_2H_2, C_2H_4 and C_2H_6

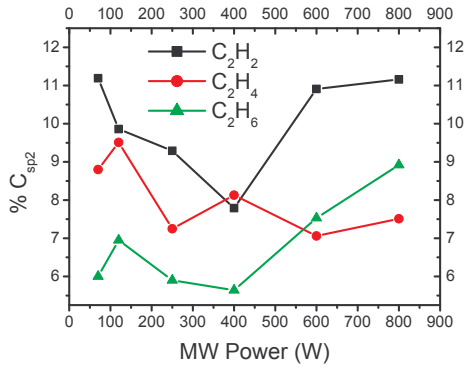

Figure 9 : % C_{sp2} vs. Micro wave power for C_2H_2, C_2H_4 and C_2H_6

Nevertheless, it is interesting to notice that for C_2H_6 precursor, from 400 W, all the curves show a particular comportment: n value stays constant, C_{sp2} rate increases linearly, and the intensity of C_2 optical emission arises a plateau too.
On the other hand, n evolution with plasma power for films realized with C_2H_2 precursor is less harebrained. The evolution of C_{sp2} and n according to the microwave power variation seem to have the same shape. The weak rate of hydrogen in this type of process could explain this behaviour. Due to this low amount of H, the ratio sp^2/sp^3 governs predominantly the properties of these films.

The FT-IR spectra set out the chemical structure of the different films realized. For each precursor, a particular signature is obtained (Figure 10). The absorption band of C_{sp2} carbon from, 1580 to 1680 cm^{-1}, present in the different film, is less and less intense when you consider C_2H_2, C_2H_4 and then C_2H_6.C_2H_6 has no double bond in its structure, this double bond forms during the process in or on the film. The deconvolution in 8 peaks at frequencies mentioned below in table 1 of the CH peaks around 2900 cm^{-1} of the Ft-IR spectra shows that sp^3 CH vibration at 2920 cm^{-1} is 4 to 5 times superior to the others contain in this remarkable peak. This behaviour is observed for the three precursors. So, as a general rule, these three types of films are essentially composed with C-C sp^3 bonds. This hypothesis is confirmed by the fact that the amount of C-H bonds and Csp2 bonds don't exceed about 10 %.

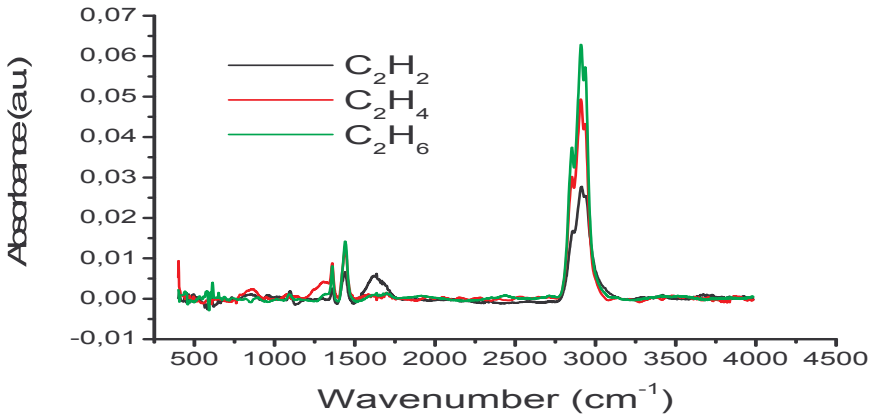

Figure 10 : FT-IR spectrum of a-CH films at 400 W

Bonding type	Stretching vibration (wavenumber (cm^{-1}))
sp^3 CH_2 symmetric	2850
sp^3 CH_3 symmetric	2865
sp^3 CH	2920
sp^2 CH_2 olifinic, symmetric	2950
sp^3 CH_3 asymmetric	2970
sp^2 CH olifinic	3000
sp^2 CH_2 olifinic asymmetric	3020
sp^2 CH aromatic	3045

Table 1 : Vvibrational frequencies [9]of CH_x peak

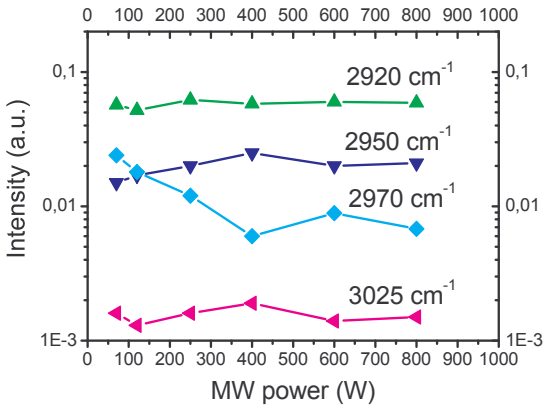

Figure 11: Peak intensity variation vs MW power for C2H4

For C_2H_6, the peaks intensities are near constant when the power increases, the totally decomposition of this gas from the lowest power could explain this. The constant value of H rate in the films reinforces this hypothesis. The evolution of the C_{sp2} rate is so explained by a bad estimation of the film density and then to an error on C_{sp2} estimation.
In the case of C_2H_4, the deconvoluated peaks intensities are also constant (Figure 11), except the peak at 2970 cm^{-1}, sp^3 CH_3, which decreases. This vibration represents the end of chains, so this decreasing can significated the chains' extension. And, the increasing of the peak at 2950 cm^{-1}, sp^2 CH_2 olifinic, shows a chain which became more sp^2 when the plasma power increases.
The same behaviour is observed with C_2H_2. Furthermore, the absorption peak at 2180 cm^{-1} (C_{sp1}) does not appear, even at lowest power: this triple bond is directly opened or broken and then, do not take part in the film's growth.
So, the hybridization or the H rate in the precursor leads to films with different chemical structure.

Conclusion

This study presents some results on three types of precursor. C_2H_2, C_2H_4 and C_2H_6 precursor have been studied and reveal that the structure and properties of the different films can be controlled with plasma parameters and precursor chemical structure. Material structures obtained are different with the precursor.
It is interesting to notice that C_2H_2 has different properties compared to the others ones. C_2h_4 and C_2H_6 are relatively close in terms of properties and chemical structure although the decomposition mechanisms seem to be different.
Furthermore, this kind of films, as they can be easily etched by oxygen plasma, could be used in microelectronic devices. Their tune properties offer a large range of applications.

References

[1] J. C. Angus, Y. Wang – Diamond and Diamond-like films and Coating 266, 173 (1991).
[2] J. Roberston – Adv. Phy. 35, 317 (1986).
[3] J. Roberston – Surface and Coating Technologies 50, 185 (1992).
[4] JC. Angus, P. Koidl, S. Domitz – Plasma Deposited Thin Films, CRC Press, Boca Raton, FL, 89 (1986).
[5] N. Savvides, J. Appl. Phys., **59**, 4133 (1986).
[6] N. Basu, J. Dutta, S. Chaudhuri, A.K. Pal, and M. Nakayama, Vacuum, **47**, 233 (1996).
[7] D. Escaich, R. Clergereaux, S. Martin, P. Raynaud, F. Gaillard, IVC 16 Conference, (2004).
[8] J.E. Bourée, C. Godet, R. Etemadi, B. Drévillon, Synthetic Metals, 76, 191-194 (1996).
[9] B. Dischler, A.Bubenzer, P. Koidl – Solid State Commun. 48, 105 (1983).

Amine rich coatings prepared by plasma polymerization of allylamine

A. Choukourov[1], H. Biederman[1], D. Slavinska[1], J. Hanus[1], J. Kousal[1], A. Grinevich[1], L. Hanley[2]
[1]Department of Macromolecular Physics, Charles University, 18000 Prague, Czech Republic
[2]Chemistry Department, University of Illinois at Chicago, Chicago, IL 60607-7061

Abstract
Plasma polymerization of allylamine is performed both in continuous wave (CW) and pulsed mode. The concentration of primary and secondary amines is evaluated by chemical derivatization technique. Secondary amines are found to be more abundant than primary amines. The maximum primary amine concentration of 7 NH_2 per 100 C atoms is obtained at low discharge power. Pulsed experiments with off-times in a range of 5-30 ms are remarkable for significantly higher deposition rate than that of continuous mode at the identical conditions.
Keywords: amines, pulsed plasma polymerization, chemical derivatization.

1. Introduction

Plasma polymerization is used to deposit polymer-like thin films by glow discharge of organic monomer vapors. Extensive research has examined the retention of amines by plasma polymerization of various amine-containing monomers [1-3]. However, allylamine is the most commonly utilized organic precursor. Amine containing plasma polymers can be utilized for modification of waste-water purification membranes [4, 5], as biocompatible surfaces in biomedical applications [6, 7] and in designing various sensors (for monitoring antigen-antibody interactions [8] or enzyme detection [9]).
In addition to CW mode, pulsing the plasma has been frequently applied to control surface chemical functionality by keeping the peak power constant while off-time (and average power) is varied [10-11]. The other way is to keep an average power constant with different peak powers [12-13]. These two approaches are compared here.

2. Experimental

Plasma polymerization of allylamine is performed in a reactor of a tubular type with capacitevely coupled 13.56 MHz excitation. The depositions are performed with a pressure of 25 Pa and a flow rate of 2.5 sccm. The average power ranges from 2 to 20 W and the duty cycle ranges from 1 (continuous wave or CW) to 0.1, with t_{on} of 2 ms (t_{off} 18 ms) utilized for pulsing experiments. A number of studies are also performed with t_{off} varying in 0.1-100 ms time domain with duty cycle and power being held constant.
Infrared measurements were performed using a Nicolet Impact 400 Fourier transform infrared (FTIR) spectrophotometer. The FTIR spectra of allylamine plasma polymer (pp-allylamine) deposited on intrinsic silicon wafers were acquired in transmittance mode with an uncoated silicon wafer used to record the reference spectrum.
XPS using a high-resolution monochromatic Al Kα x-ray source (15 keV, 25 mA emission current, VSW MX10 with 700 mm Rowland circle monochromator) and a 150 mm concentric hemispherical electron energy analyzer (VSW Class 150) is applied to determine the element composition of the films.
Chemical derivatization reactions with trifluoromethylbenzaldehyde (TFBA) and trifluoroacetic anhydride (TFAA) are performed to detect primary and secondary amines. The calculation procedure gives the amine concentration in number of groups per 100 carbon atoms and has been described in detail elsewhere [14]. The samples deposited on aluminum were cut into two pieces after plasma polymerization and stored in air. One piece was treated with TFBA for 8-10 and 60 days after deposition and the other with TFAA at the same intervals. Thus, all derivatization measurements of a given coating are performed on exactly the same film. XPS were acquired immediately before and after the derivatization reactions.
AFM (Quesant, Q-Scope™ 850) is applied in an intermittent contact mode (BBWavemode) to observe the surface and to measure the thickness of plasma polymers deposited on polished silicon. For the thickness measurements, a cellulose acetate mask was fixed on silicon substrate prior to deposition. After the deposition, the underlying cellulose acetate film was removed to produce a very sharp edge of plasma polymer, which was then scanned by AFM.

3. Results and discussion

The FTIR and the C 1s XP spectra of pp-allylamine are similar to those reported in literature [12] and not shown here. The presence of NH_x at 3200-3400 cm^{-1}, CH_x at 2850-2930 cm^{-1}, carbon double and triple bond structures at 2100-2200 cm^{-1} was confirmed. With increasing discharge power the intensity of carbon unsaturated bonds increases with respect to the other peaks, which is consistent with the results of the other authors [15] showing an increase in unsaturation of allylamine plasma polymer with power, mainly due to formation of nitrile groups.

The XPS analysis demonstrates that the chemical composition of pp-allylamine is very close to that of allylamine monomer. The film deposited at 2 W power in CW contains 64.5 at. % of C, 22.7 at. % of N and 12.8 at. % of O, whereas allylamine molecule has 75 at. % of C and 25 at. % of N. It should be also noted that there appears to be a slight decrease in nitrogen content with increasing average power both for CW and pulsed samples. Table 1 shows the elemental composition of plasma polymers deposited in the same experimental setup from diaminocyclohexane (DACH), ethylenediamine (EDA) and allylamine. The data for the precursors are also provided. The presence of several percent of oxygen in plasma polymers is due to ageing effects discussed in detail in [2]. Allylamine proves to be the best in terms of similarity of elemental composition to the parent monomer. The plasma polymer composition changes considerably in dependence of the monomer used. The nitrogen content increases in a pp-DACH/pp-Allylamine/pp-EDA sequence, being two times higher for pp-EDA than for pp-DACH. Similarly, the carbon component decreases in the same manner. The changes in film composition can be attributed mainly, but not exclusively, to the different composition of the precursor molecules. The least carbonaceous EDA produces the plasma polymer with the lowest carbon content. Nevertheless, DACH and allylamine monomers give different results. The molecular formula for DACH is $C_6N_2H_{14}$, and that of allylamine is C_3NH_7. Thus, the ratio between the elements in these two precursors is the same. However, allylamine deposits the films, which are very close to the precursor in elemental composition. The C/N ratio is 2.8 for pp-allylamine versus 3.0 for the monomer. In the case of DACH, the plasma polymer lacks nitrogen and C/N grows to 4.6. Among three monomers EDA molecule has the highest concentration of nitrogen, but it is the most vulnerable to the discharge. The nitrogen content drops from 50% in precursor to 33% in plasma polymer, and C/N increases almost two times from 1.0 to 1.9.

Table 1 The elemental composition of the plasma polymers and corresponding monomers

DACH				Experimental parameters
C, at. %	N, at. %	O, at. %	C/N	
75.9	16.4	7.7	4.6	2 W, 5 Pa, 0.85 sccm, 48 days aged plasma polymer
75	25	-	3.0	DACH monomer
EDA				
61.5	32.7	5.8	1.9	2 W, 5 Pa, 0.85 sccm, 49 days aged plasma polymer
50	50	-	1.0	EDA monomer
Allylamine				
64.5	22.7	12.8	2.8	2 W, 25 Pa, 2.5 sccm, 60 days aged plasma polymer
75	25	-	3.0	Allylamine monomer

XPS cannot by itself provide information about the amine concentration in plasma polymers and FTIR allows only qualitative estimation. Chemical functionalization prior to XPS analysis permits the unique identification of primary and secondary amine groups. Table 2 shows the amine concentration in pp-allylamine deposited in CW and the pulsed mode. Primary amines are efficiently formed, but secondary amines are more abundant. Stored in air, pp-allylamine films take up oxygen. Its concentration increases from ~8% after 8-10 days to ~13% after 60 days storage. However, both primary and secondary amines are found to be rather stable against oxidation in the air with NH_2 concentration slightly decreasing with time (Table 2). The same trend is observed for pulsed pp-allylamine.

When the peak power is held constant, pulsing does not have an effect on the concentration of primary amines. Primary amine content is the same for films deposited at 20 W in CW mode and at 2 W average power, D = 0.1 (with 20 W peak power) in a pulsed mode. However, the retention of the secondary amines is more effective in the case of pulsed pp-allylamine. In accordance with [3], the total amine concentration is higher for the pulsed polymerized samples. Thus, the observed increase in amine retention with longer off-times in our experiments is due to the secondary amines.

Table 2 Primary and secondary amine concentration in allylamine plasma polymers

Chemical group	Groups per 100 C atoms							
	CW				Pulsed			
	2 W		*20 W*		*2 W*		*20 W*	
	9 days	*60 days*	*9 days*	*60 days*	*9 days*	*60 days*	*9 days*	*60 days*
NH_2	7.2	5.5	4.4	3.7	4.1	4.3	1.8	1.6
NH	13.7	16.2	5.7	5.5	14.9	15.5	11.5	6.1
NH_2 + NH	20.9	21.7	10.1	9.2	19	19.8	13.3	7.7

Under constant average power conditions, the pulsing vs CW chemical changes are highly monomer dependent. Recent FTIR study of pulsed plasma polymerization of allylamine show noticeable increase of amine content with decreasing duty cycle [11, 12]. However, previous experiments with other monomers performed on a constant average power basis (i.e., with different peak powers) revealed no significant difference between samples prepared in CW and pulsed mode [13 and references therein]. However, the film composition was found to be strongly affected only by variation of average power. Our comparison of films deposited in CW vs. pulsed mode at constant average power (Table 2) confirms this finding, indicating that the total amine concentration does not depend strongly on the mode of operation (although the concentration of primary amines is slightly higher for the CW samples).

Overall, we have found that the power delivered into the discharge is the main parameter controlling the film composition. The films deposited at 2 W power in CW mode have twice as much total amine than those deposited at 20 W power. The difference between the pulsed polymerized samples is not large, but the trend is the same.

The chemical nature of this kind of plasma polymers is interesting not only in terms of elemental composition, but rather in terms of amine retention. The Fig. 1 provides the data on primary and secondary amine concentration for pp-DACH, pp-EDA and pp-allylamine obtained from the results of chemical derivatization. The most important point that should be addressed here is that the retention of primary amines is rather poor for all kinds of the monomers. The worst case is pp-EDA, which looses almost all of NH_2. Of all the monomers, EDA molecule is the richest with primary amines. However, pp-EDA contains only ~1 NH_2 per 100 C atoms. The best result is obtained using allylamine plasma polymerization. In this case, the concentration of primary amines is 5.5 per 100 C atoms, though it is still much lower than 33/100 C atoms of allylamine precursor.

The secondary amines are more abundant in all of the mentioned plasma polymers. The most remarkable is pp-EDA, in which the concentration of NH, in contrast to the lowest NH_2 content, is high, so that nearly all of the amines are of NH type. The pp-allylamine reveals approximately the same secondary amine concentration, but the fraction of primary amines is bigger. pp-Allylamine preserve more than half (~60%) of precursor's amines, though the most of them are transformed to secondary amine form. Compared to 18-20 NH_2 and NH groups per 100 C atoms for pp-EDA and pp-allylamine, the pp-DACH is much worse in terms of amine retention (only 10 groups per 100 C atoms).

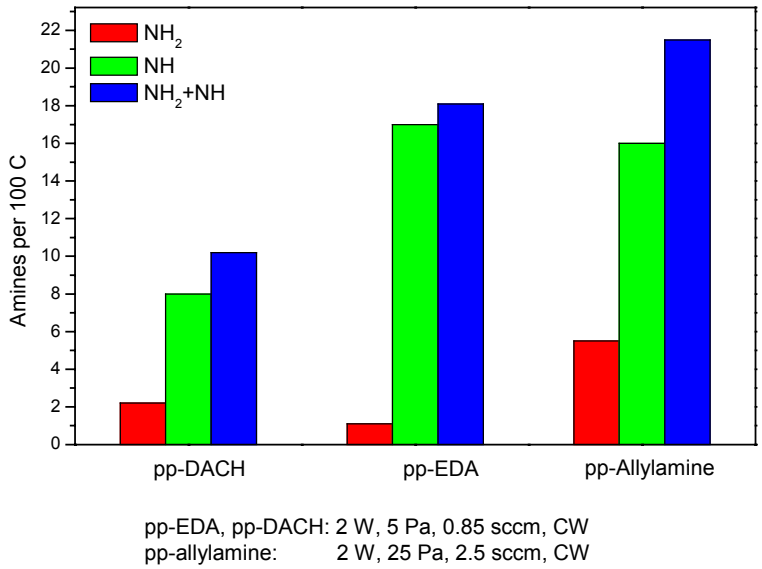

Fig. 1 The concentration of amines in plasma polymers. (Derivatization and XPS are performed in 48 days for pp-EDA, pp-DACH and in 60 days for pp-allylamine after deposition).

The chemical nature of the monomers is also seen in considerable difference in deposition rates (Table 3). The DACH molecule has the highest molecular mass (M=114 g/mol) and at given pressure this monomer supplies the biggest mass into the reactor volume, which makes the deposition rate of pp-DACH very high. EDA and allylamine have lower and almost equal molecular weights (60 and 57 g/mol, respectively), but the deposition rate of the latter is much higher. At given pressure the mass of allylamine and EDA precursor molecules contained in the reactor volume is almost the same given their similar molecular weights, so their difference in deposition rate can not be accounted for by different mass transfer on the surface. We believe that in the case of allylamine, plasma-induced reaction of carbon-carbon double bond of intact allylamine molecules with surface radicals plays a significant role in film formation.

Table 3 The deposition rates of amine containing plasma polymers, nm/min

Plasma polymer	flow 0.85 sccm	flow 2.5 sccm	Experimental parameters
pp-DACH	16		5 W, 5 Pa, CW, as-deposited
pp-EDA	4	2.5	
pp-allylamine		9	

The contribution of plasma-induced allylamine polymerization to the film growth is further supported by the pulsed experiments with varying off-time, other parameters (duty cycle 0.1, average power 2 W, pressure 25 Pa, flow rate 2.5 sccm) being held constant. Each deposition lasted for 10 minutes. The preliminary experiments found that the deposition rate is linear within at least half an hour of deposition. The thickness of plasma polymers was determined from the AFM images as shown in Fig. 2. It is worth noting that even ultra-thin pp-allylamine films (down to 5 nm) reveal the continuous character as deposited on silicon. For the films thinner than 5 nm, the roughness is of the same scale as the thickness. The term ‘film thickness’ is defined here as the distance between mean lines laid along the profiles of the film and the substrate. For comparison, pp-allylamine was deposited in CW mode (power 2 W, pressure 25 Pa, flow rate 2.5 sccm) with different deposition intervals.

The deposition rate of 0.4±0.1 nm/min was determined in CW mode. For the pulsed experiments, there is an interval of off-times between ~5 and ~30 ms where the deposition rate is much higher than that of CW at the identical conditions, reaching 1.80 nm/min. Out of the above range, the film growth is slower approaching the value of CW. Here we assume that the ion bombardment during on-time plays more or less destructive role in film formation. Taking into account that the characteristic time of bias decay during t_{off} is < 1 ms [16], there is still a certain ion flux on the surface at shorter off-times and the deposition resembles that in CW mode. At the t_{off} > 5 ms, the influence of charged particles on the polymerization processes when the plasma is off is minor. The film grows via the reaction of molecular fragments or intact monomer molecules with surface radicals. The deposition rate reaches maximum here. The decrease in deposition rate at the longer off-times is readily explained by completing recombination of the surface radicals with volume species. Apparently, at the t_{off} > 30 ms the majority of reactive species are already depleted.

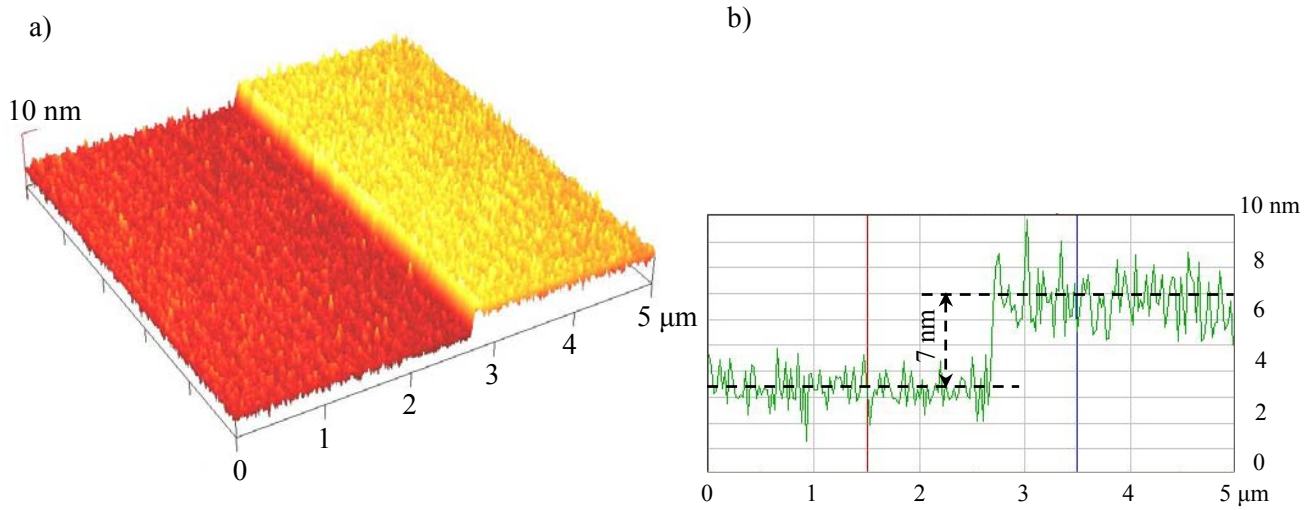

Fig. 2 pp-Allylamine deposited on Si (25 Pa, 2 W, CW): a) the AFM image; b) the film profile.

4. Conclusions

Allylamine is effective for deposition of amine rich coatings. The amine concentrations calculated here are close to those reported by others [3] and are significantly higher than amine concentration of plasma polymers deposited from other amine bearing precursors such as ethylenediamine and diaminocyclohexane. The highest values of amine content (7 NH_2 and 14 NH per 100 carbon atoms) were obtained for allylamine plasma polymers deposited at low (2 W) power. Both primary and secondary amines are found to be stable to oxidation on air with NH_2 concentration slightly decreasing with time.

CW and pulsed mode under equivalent average power input condition produce no noticeably different film compositions. However, pulsing at equivalent peak power results in increase of amine contents, which is due to secondary amines.

In the pulsing experiments with constant duty cycle and average power, a region of off-times between ~5 and ~30 ms exists where sharply increased values of film thickness are observed. This indicates a significant film formation during plasma off-time.

Acknowledgements

This work is a part of the research plan MSM 0021620834 that is financed by the Ministry of Education of the Czech Republic and partly was supported by the U.S. National Science Foundation through the grant 9986226.

References

[1] A. Choukourov, H. Biederman., D. Slavinska, M. Trchova, A. Hollander- Surf. Coat. Technol. **174-175**, 863 (2003).

[2] T. R. Gengenbach, H. J. Griesser- J. Polym. Sci. A **37**, 2191 (1999).

[3] J. G. Calderon, A. Harsch, G. W. Gross, R. B. Timmons- J. Biomed. Mater. Res. **42**, 597 (1998).

[4] R. C. Ruaan, T.-H. Wu, S.-H. Chen, J.-Y. Lai- J. Membr. Sci. **138**, 213 (1998).

[5] G. Pozniak, I. Gancarz, J. Bryjak, W. Tylus- Desalination **146**, 293 (1999).

[6] D. Y. Tseng, E. R. Edelman- J. Biomed. Mater. Res. **42**, 188 (1998).

[7] L. Dai, H. A. W. StJohn, J. Bi, P. Zientek, R. C. Chatelier, H. J. Griesser- Surf. Interface Anal. **29**, 46 (2000).

[8] E. Szili, H. Thissen, J. P. Hayes, N. Voelcker- Biosens. Bioelectron. **19**, 1395 (2004).

[9] D. Cokeliler, M. Mutlu- Anal. Chim. Acta **469**, 217 (2002).

[10] A. E. Lefohn, N. M. Mackie, E. R. Fisher- Plasmas and Polymers **3**, 197 (1998).

[11] A. K. Walker, H. Qui, Y. Wu, R. B. Timmons, G. Kinsel- Anal. Biochem. **271**, 123 (1999).

[12] Q. Chen, R. Foersch, W. Knoll- Chem. Mater. **16**, 614 (2004).

[13] R. B. Timmons, A. J. Griggs- Pulsed Plasma Polymerizations, In: Plasma Polymer Films, ed. H. Biederman, London, Imperial College Press (2004).

[14] A. Choukourov, J. Kousal, H. Biederman, E. R. Fuoco, S. Tepavcevic, J. Saucedo, L. Hanley- Vacuum **75**, 195 (2004).

[15] M. T. van Os, B. Menges, R. Foersch, G. J. Vancso, W. Knoll- Chem. Mater. **11**, 3252 (1999).

[16] C. L. Rinsch, X. Chen, V. Panchalingam, R. C. Eberhart, J.-H. Wang, R. B. Timmons- Langmuir **12**, 2995 (1996).

Thin film deposition on powder surfaces using atmospheric pressure discharge

V. Brüser, M. Hähnel, H. Kersten
Institute for Low Temperature Plasma Physics,Greifswald,Germany

Abstract
The deposition of SiO_x containing films on NaCl and KBr powder in dielectric barrier discharge under atmospheric pressure was investigated. As precursor hexamethyldisiloxane (HMDSO) and tetraethoxysilane (TEOS) in argon-oxygen gas mixtures were used. The deposited layers were studied by means of light microscopy, SEM, FTIR and XPS investigations. The particles were completely covered by SiO_x, with increasing oxygen concentration in the plasma the carbon content of the layer was decreased.
Keywords: Dielectric barrier discharge; Hexamethyldisiloxane; Tetraethoxysilane; Thin film deposition

1. Introduction

The dielectric barrier discharge (DBD) at atmospheric pressure has been used for many technical applications, for example ozone generation, gas cleaning, surface treatment of foils and fabrics [1]. Atmospheric pressure plasmas for surface treatment of materials become more and more important because in contrast to low pressure plasmas no vacuum devices are necessary. Therefore, batch processing can be avoided and treatment processes can be easily integrated into production lines.
For more than ten years the deposition of organosilicon layers on flat substrates has been studied by the use of various monomers [2, 3]. In this paper, the deposition of silicon containing thin films on powder particles is desribed. These coatings can be used as protection for luminescent particles or pigments against corrosion and humidity. Some pharmaceuticals need barriers for a slow release of the agent, too. The present contribution focuses on the deposition of SiO_x containing layers on powders. Hexamethyldisiloxane (HMDSO) and tetraethoxysilane (TEOS), respectively, were used as precursor.
For the modification of powder surfaces special techniques have to be applied to realize a homogeneous treatment. Therefore, the planar dielectric barrier discharge arrangement was combined with a vibrating conveyor device.

2. Experimental

In Fig. 1 the schematic diagram of the experimental apparatus is shown. The powder treatment system consists of three major parts: a mechanically agitating chamber for plasma treatment, a gas feeding system and a power source. On the bottom of the treatment chamber a planar surface dielectric barrier discharge arrangement is fixed. The discharge arrangement is made from a printed circuit board. One side of this circuit board is completely covered by a copper layer and represents the ground electrode. On the opposite side is the high voltage electrode consisting of an etched copper layer (Fig. 2). Between the stripes of the high voltage electrode a filamentary surface discharge is generated (Fig. 3). The bulk material of the circuit board consists of nonconducting material and represents the dielectric barrier. On the top of the treatment chamber a gas distributor for homogenous gas injection is arranged. The chamber is mechanically agitated by an electromagnet to move the powder through the plasma zone (Fig 1).
The atmospheric surface discharge is driven by a medium frequency pulse generator (Fourier Synthesis Pulse Generator, Ingenieurbüro Dr. Jürgen Klein) that has a frequency range between 1 Hz and 20 kHz and a maximum voltage of 20 KV. The pulse generator is controlled by a frequency generator (AFG 310 Sony/Tektronics).
Oxygen and argon are used as plasma gas. The liquid precursors hexamethyldisiloxane (HMDSO) and tetra-ethoxysilane (TEOS) are introduced by feeding argon through a bubbler. The gas composition in the plasma was investigated by mass spectrometry. Plasma treatments were carried out under following conditions:

Table 1 Treatment conditions

TEOS concentration [vol-ppm]	HMDSO concentration [vol-ppm]	Ar concentration [vol-%]	O_2 concentration [vol-%]	Gas flow [sccm]	Treatment time [min]
2000	/	95	4.8	210	30
/	1600	0..90	0..10	300	10

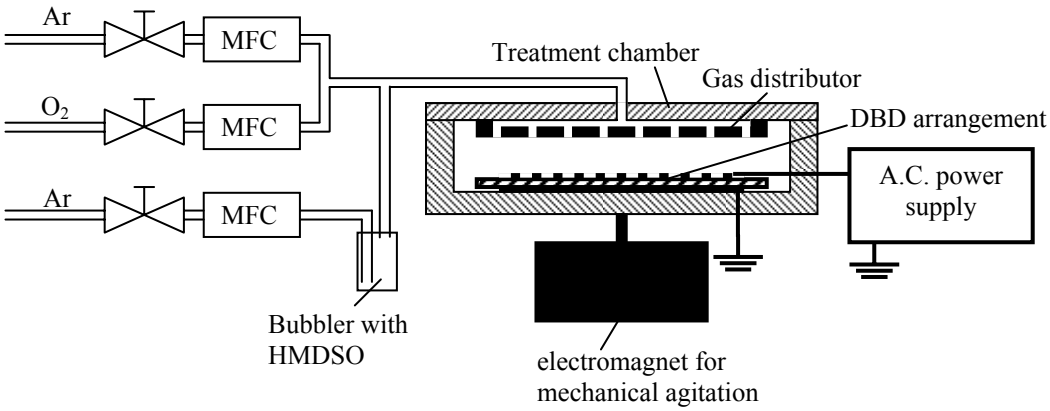

Fig. 1 Scheme of the experimental set-up

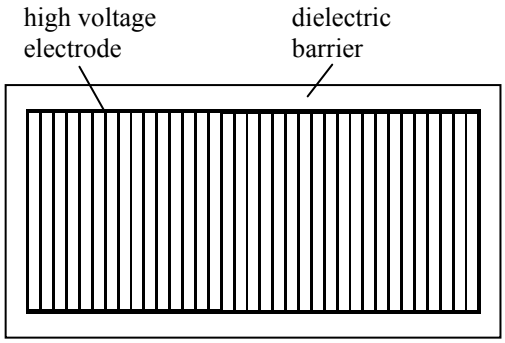

Fig. 2 Surface discharge arrangement (top view)

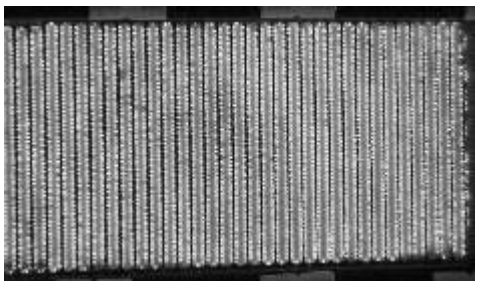

Fig. 3 Surface discharge

Silicon oxide containing layers have been deposited on NaCl and KBr powders used as model substances. The treated particles were characterized by light microscopy, scanning electron microscopy (SEM), infrared spectroscopy (FTIR), and photo electron spectroscopy (XPS).

3. Results and Discussion

Deposition in TEOS-Ar-O_2

NaCl powder was covered using TEOS precursor. The coated salt particles were examined with a light optical microscope and scanning electron microscope.

In Fig. 4 SiO_x coated crystals are shown. The NaCl crystals are completely covered by the layer. Later, the NaCl was removed by solving in water. Only a box consisting of the SiO_x containing material remains (Fig 5). Apparently, there are some holes in the layer which make a penetration of water into the box possible. A fraction of a solution residue of a coated NaCl was observed with SEM (Fig. 6). Also in this picture it is visible that the deposited coating consists of a compact layer. Hence, tiny (micro) glass boxes have been prepared.

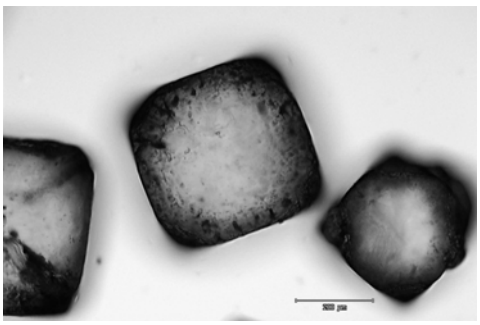

Fig. 4 NaCl particles coated in TEOS-Ar-O_2

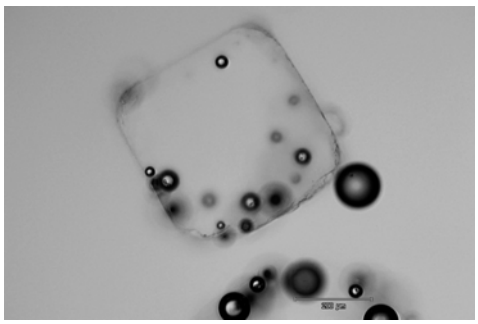

Fig. 5 Remaining coating after dissolution of NaCl crystal in water. The coating was deposited in TEOS-Ar-O_2.

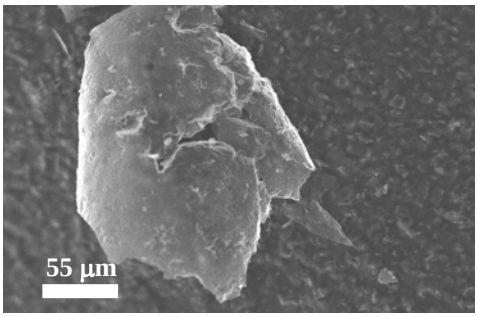

Fig. 6 Fraction of a SiO_x coating after dissolution of NaCl crystal in water. The coating was deposited in TEOS-Ar-O_2.

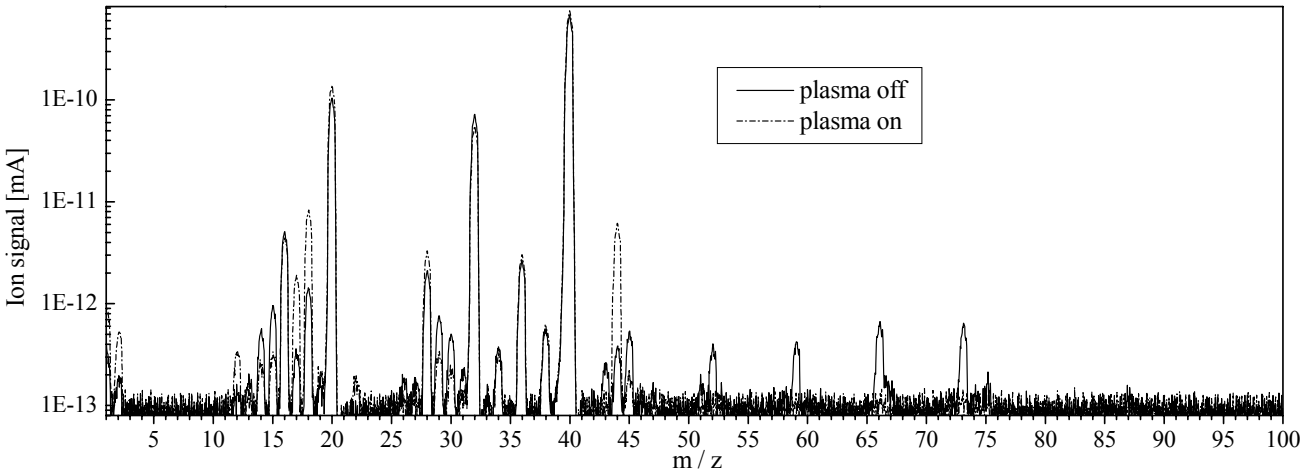

Fig. 7 Mass spectrum of HMDSO-Ar-O_2 mixture with and without discharge

Deposition in HMDSO-Ar-O_2

The gas phase of the treatment chamber containing Ar, O_2 and HMDSO was investigated by MS measurements (Fig. 7). With the used mass spectrometer only particle mass m/z ≤100 could be observed. In this range following signals can be related to HMDSO: CH_2^+ (m/z 14), CH_3^+ (m/z 15), $SiCH_3^+$ (m/z 43), $SiOH^+$ (m/z 45), $Si_2OC_2H_8^{++}$ (m/z 52), $SiC_2H_7^+$ (m/z 59), $Si_2OC_4H_{12}$ (m/z 66), $SiC_3H_9^+$ (m/z 73) and Si_2OH^+ (m/z 73) [4]. The signals disappear after ignition. However the content of CO_2 (CO_2^+, m/z = 44) and H_2O (H_2O^+ m/z = 18 and OH^+ m/z = 17) increases. This means, that HMDSO is mainly converted into the SiO_x layer, CO_2 and H_2O.

Fin ally, the composition of the deposited layer was investigated by XPS measurements. The plasma treatments were performed at four different oxygen concentrations in the range of 10-100 vol.-%. The content of oxygen in the layers of four treated samples remains almost constant (Fig. 8). The content of silicon and carbon slightly decrease with increasing oxygen concentration in the gas phase. At higher oxygen gas concentrations the content of Na and Cl of the coating increases. It is known, that at increasing oxygen concentration of Ar-O_2-HMDSO gas the thickness of deposited layers becomes smaller and the bulk of the particles can be detected [5].

In addition, the contents of SiC, SiO, SiO_2, SiO_3 and SiO_4 bonds in the coating were investigated [Fig. 9]. With increasing oxygen concentration in the plasma signals of SiO_3 and SiO_4 groups decrease and signals of SiC, SiO and SiO_2 groups increase. Apparently, in the films deposited at low oxygen concentrations not all carbon is bond on silicon. A part of carbon must be bond on oxygen or the content of C-C groups is higher. The plasma properties change with oxygen concentration due to the different ionization energies of oxygen and argon ($E_{ion,Ar}$ = 15,8 eV, $E_{ion,O2}$ = 12,5 eV). Hence, the decomposition of HMDSO depends essentially on the plasma properties.

The FTIR measurements of KBr coated in HMDSO-Ar-O_2 (10 vol-% O_2) show an absorption band of SiOSi at a wave number of 950 - 1250 cm^{-1} as shown in Fig. 10. However absorption bands between 1240 and 1300 cm^{-1} indicates $OSi(CH_3)_x$. These results are in accordance with the described XPS results.

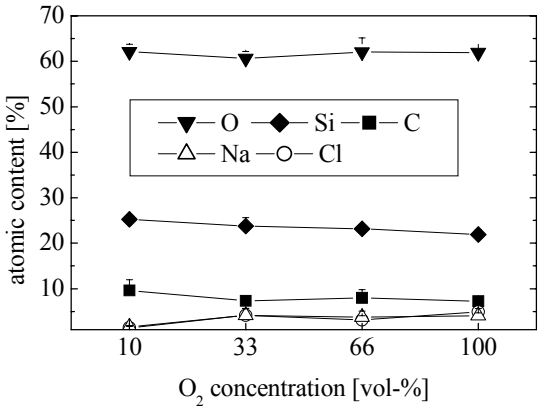

Fig. 8 Atomic content of O, Si, C, Na and Cl of coatings on NaCl deposited in HMDSO-Ar-O_2 with different oxygen concentrations

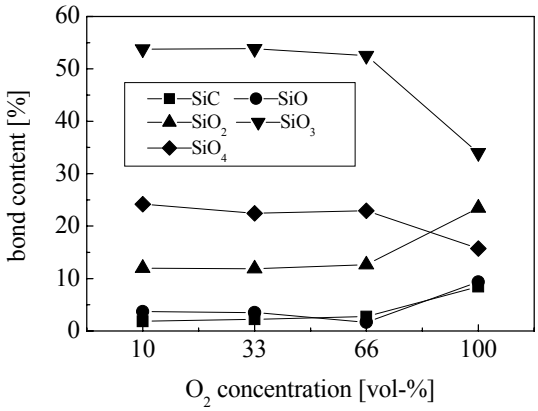

Fig. 9 Content of SiC, SiO, SiO_2, SiO_3 and SiO_4 bonds of coatings on NaCl deposited in HMDSO-Ar-O_2 with different oxygen concentrations

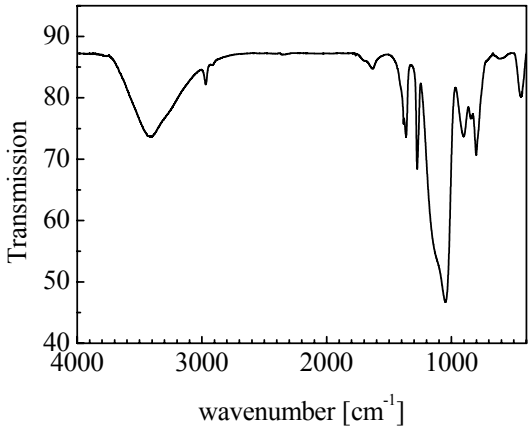

Fig. 10 FTIR spectrum of coated KBr particles

4. Summary

SiO_x containing layers have been deposited on powder particles by means of a mechanically agitated surface discharge arrangement. NaCl and KBr powders as model substances were treated using TEOS and HMDSO precursor. The coatings completely covered the crystals. In the plasma HMDSO is mainly converted to the film, CO_2 and H_2O. The deposited material contains Si, O and C. Contents of SiC and SiO_x bonds change with the oxygen concentration.

5. References

[1] R. Hippler, S. Pfau, M. Schmidt, K. H. Schoennach – Low Temperature Plasma Physics, WILEY-VCH Verlag Berlin GmbH, Berlin, 2001
[2] R. Foest, F.Adler, F. Sigeneger, M. Schmidt - Surf. Coating Technol. 163-164, 323 (2003)
[3] T. Opalinska, B. Ulejczyk, L. Karpinski, K. Schmidt-Szalowski - Polymery 49 (4), 257 (2004)
[4] R. Basner, R. Foest, M. Schmidt, K. Becker, H. Deutsch – Int. J. of Mass Spectrometry 176 3 (1998) 245
[5] A. Sonnenfeld, T. M. Tun, Zajickova, H.-E. Wagner, J. F. Behnke, R. Hippler – Proc. of the Int. Symp. on High Pressure, Low Temperature Plasma Chemistry, Hakone VII, Greifswald (2000) 445

The synthesis of carbon nano-particles in plasma-liquid system

V.Ya. Chernyak[1], V.V. Naumov[2], V.V.Yukhymenko[1],
V.A. Zrazhevskij[1], I.I. Prisyazhnevich[1]

[1]*Plasma Lab, Dept. of Physical Electronics, Faculty of Radiophysics, Taras Shevchenko Kyiv National University*
Prospect Acad. Glushkova 2/5, 03122 Kyiv, Ukraine; e-mail: chern@univ.kiev.ua
[2]*Photonics Lab, Institute of Fundamental Problems for High Technology, Ukrainian Academy of Science*
Prospect Nauki 45, 03028 Kyiv, Ukraine; e-mail: naumov@ifpht.kiev.ua

Abstract
A possibility of plasma-chemical synthesis of nanoparticles in heterophase gas-liquid plasma with use of the thermally nonequilibrium secondary discharge with a liquid electrode is investigated. Processing a toluene, a fine-dispersed soot powder containing micro- and nanosized carbon particles up to 10 nm is produced.
Keywords: plasma chemistry, synthesis, plasma-liquid system, secondary discharge, carbon nanoparticles.

1. Introduction

During the last years many research groups have investigated different methods of obtaining of carbon nano-particles by the use of the electric arc vaporization [1], catalytic pyrolysis and incomplete burning of hydrocarbons [2], laser ablation [3], microwave radiation [4], solar energy [5], and others. These methods are based mainly on the sublimation of a solid phase [6]. We propose an alternative approach – the plasma-chemical synthesis from a liquid phase using thermally nonequilibrium heterophase plasma [7]. This method is still poorly investigated but according to our experiments it can be a good method if it will be organized in due course. Among possible discharges of gas-liquid type, one type presents a special interest for us – it is the secondary discharge with a liquid electrode [8]. In this discharge, one electrode is connected with liquid while another electrode is maintained by the plasma flow from the auxiliary gas discharge [9]. Under the nonequilibrium plasma exposure including active electrons and temperature influence, the liquid hydrocarbon molecules can be decomposed through the partial oxidation/pyrolysis into the carbon source radical and atomic components, which then can form the carbon particles and structures.

In this work we present first results of our studies on the possibilities of the synthesis of carbon nanoparticles in plasma-liquid system using the toluene decomposition by the secondary discharge with a liquid electrode. Do not going into details of kinetics of plasma-chemical processes in this system we focus efforts on the experimental results first of all.

2. Experimental Methodology

The image and principal scheme of the experimental set-up used for studies of the process of plasma-chemical synthesis of carbon nanoparticles is shown in Fig. 1. It consists of a quartz glass & stainless steel reactor chamber and the electrical discharge system of gas-liquid type. We used a liquid toluene as a hydrocarbon-containing raw material and argon as a plasma-forming gas and transport gas flow. Argon was moved into the reactor top-down through the nozzle into the gap between two opposite rod copper electrodes, where the auxiliary arc discharge was burning and served as a source of plasma. Toluene was put into the reactor bottom-up through the hollow electrode and atomized through the nozzle as a spray of fine-dispersed droplets. The electric field of the secondary discharge was applied between the liquid electrode that served as cathode and the plasma flow of auxiliary arc discharge that served as anode for the secondary discharge at the same time. So the current of the secondary discharge passed through the blowing arc discharge plasma and through the dispersed gas-liquid medium. The discharge was powered by the HV DC source. In experiments we varied the current-voltage parameters, gas/liquid flow rates, and distance between the electrodes in order to optimize the process. The products of the plasma-chemical decomposition/pyrolysis and chemical vapor deposition/synthesis were collected and analyzed by available techniques of atom force microscopy (AFM), scanning electron microscopy (SEM) and optical microscopy (OEM).

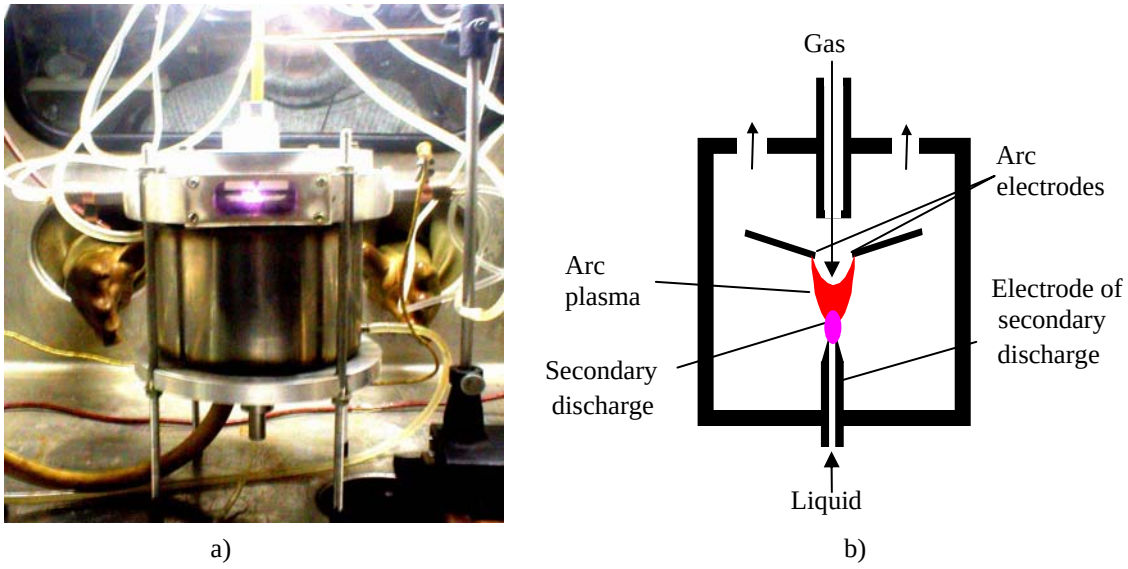

Fig. 1 Experimental set-up

3. Results and Discussions

In the result of the toluene treatment in the electro-discharge gas-liquid plasma-chemical reactor the output products were formed in three phases: (i) in a solid phase as a fine-disperse soot powder of black color; (ii) in a liquid phase as a fine-dispersed emulsion, and (iii) in a gas phase. The gaseous output products were taken out from the studied system and moved into another reactor, where they were burned in the auxiliary arc discharge. We were interested mainly by the liquid-phase and solid state output products collected in the primary reactor.

The obtained liquid-phase products after evaporating and cooling were deposited at the glass object plate in the form of a thin film with the incorporated carbon particles and were investigated with use of the optical electronic microscope. OEM analysis has shown the presence of microparticles with the sizes of 10 μm and less. Fig. 2 shows the typical OEM image of the carbonaceous deposits produced without any post-discharge purification. The obtained fine-dispersed carbon black powder was applied on the micaceous substrate and investigated with use of the atom force microscope. AFM analysis has shown the distribution of the large and small carbon particles with the sizes from 300 nm till 50 nm (Fig. 3). Since the heating of asphaltogenic mass led to polymerization of carbon-containing structures, in order to exclude the effects of the particles adhesion, the carbon black powder was crushed by the ultrasound method. For that purpose the powder was mixed with the distilled water, and the water solution was treated during several minutes by the ultrasound. After that water solution was evaporated, and the evaporation residue was investigated again by the AFM. In the result, the presence of carbon nanoparticles with the sizes of 5-10 nm were determined (Fig. 4).

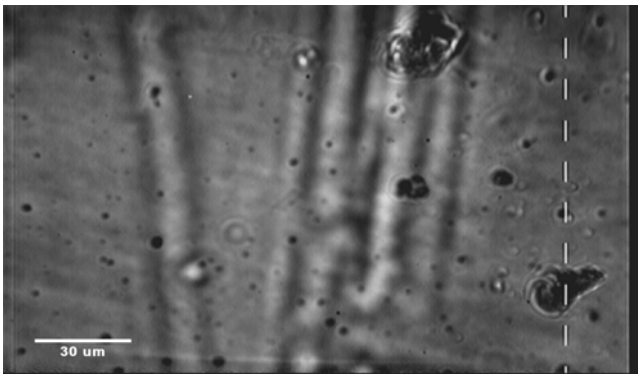

Fig. 2. Microphotograph image of the liquid film with carbon structures.

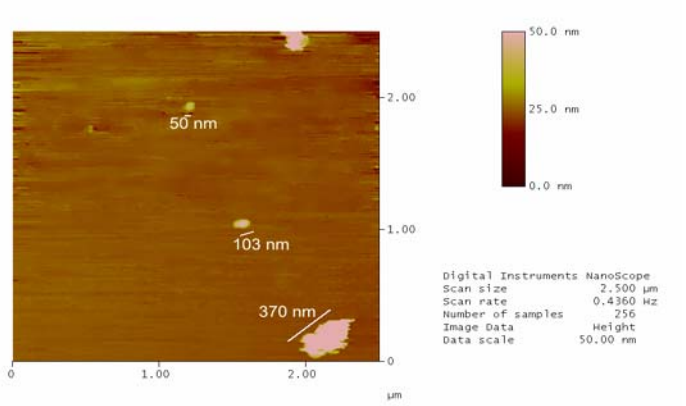

Fig.3. AFM image of dispersed carbon powder applied on the mica substrate.

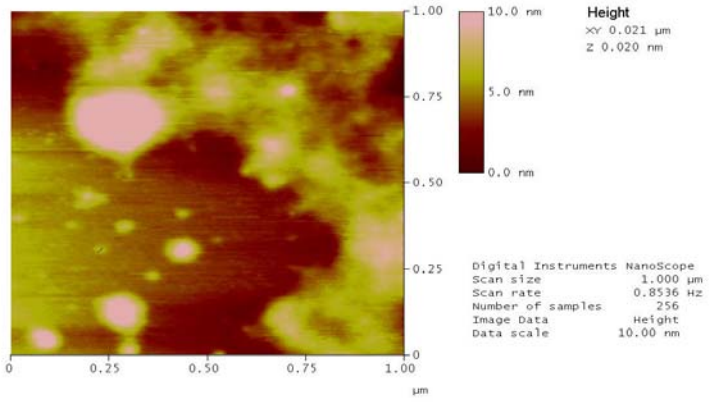

Fig.4. AFM image of dispersed carbon powder after the u.s. treatment.

Conclusions

We conclude that treatment of toluene in plasma-liquid system by means of the thermally nonequilibrium secondary discharge with a liquid electrode can be an effective method for producing of wide spectrum of carbon micro- and nanoparticles. The further research step will be a quantitative analysis of the yield/content and morphological characterization of the target nanostructures in the synthesized carbonaceous materials as well as the determination of efficiency and optimization of the process.

The work was partially supported by the Ministry of Education and Science of Ukraine.

References

[1] W. Kratshmer, *et al* - Nature, 347, 354 (1990); S Iijima – *Nature*. **354**, 56 (1991).
[2] J.B. Howard, A.L. Lafleur, Ya. Makarovsky, *et al* – *Carbon*. **30**(8) 1183 (1992).
[3] A. Thess, *et al* – Science. **273**, 483 (1996).
[4] Patent 568918 EP, Int.C1 CO1 B31/02 /W. Muller, U. Wirth, I. Semel: Hochst A.G. Publ. 10.11.1993.
[5] Patent 95-00440 WO, Int.C1. CO1 B31/02 /R.E. Smalley: William Marsh Rice Univ. Publ. 05.01.1995.
[6] A.V. Eletskii, B.M. Smirnov - *Physics-Uspekhi*. **163**(2) 33 (1993), **167**(9) 945 (1997), **172**(4) 401 (2002).
[7] V. Chernyak, S. Koval, V. Naumov - *Proc. 15th Intern. Symp. on Plasma Chemistry*, **IV**, 1447 (2001).
[8] V.Ya Chernyak, S.V. Olshevskii – *Ukr.J.Phys.* **50**(3) 243 (2005).

Plasma polymerization of evaporated conventional polymers

J. Hanus[1], J. Kousal[1], A Choukourov[1], H. Biederman[1], J. Zemek[2]

[1]*Faculty of Mathematics and Physics, Charles University, Prague, Czech Republic*
[2]*Institute of Physics, Academy of Sciences of the Czech Republic, Prague, Czech Republic*

Abstract

Thermal evaporation of polyethylene and polypropylene is performed with or without an activation of volatile fragments in a glow discharge. Without plasma assistance evaporated films are a mixture of aliphatic hydrocarbons. These films are not stable in contact with water. The activation in a glow discharge enhances cross-linking and the films become hydrocarbon plasma polymers. However, these plasma polymers resemble much more the original polymers.

Keywords

Evaporation of polymers, magnetron sputtering

1. Introduction

Evaporation of polymers has been attempted already in the 1960s [1,2]. The films were found composed of low molecular weight fragments and for better mechanical properties a post deposition UV light irradiation was recommended [2,3]. The evaporation of a large number of polymers has been treated by Hogarth and Iqbal [4]. We have decided to reinvestigate the above mentioned findings and compare a simple evaporation and "plasma assisted" evaporation [5] that may be seen as a specific plasma polymerization process.

2. Experimental

Evaporation of PP and PE was performed in cylindrical reactor pumped with rotary and diffusion pumps. The evaporation was performed in argon atmosphere at the presure 0.4 Pa and flow rate 2.5 sccm with or without simultaneous rf magnetron discharge (10 – 160 W). The magnetron equipped with a graphite target was aimed to initiate and sustain the glow discharge in Ar/hydrocarbon vapour mixture. Graphite known for its low sputtering yield was chosen to minimize the contribution of sputtering. The evaporation source was placed 5 cm above magnetron, and substrates were 10 cm and 15 cm above evaporation source for PP and PE, respectively. In the case of PP, a typical molybdenum evaporation boat was used. During the evaporation of PE, vigorous boiling led to bulk drops of polymer splashing out and reaching the substrates. A more sophisticated evaporation source was constructed, which consisted of a copper crucible with external heating delivered through the two molybdenum strips. The crucible was filled with a mixture of PE and copper granules to improve thermal transfer to the polymer. Evaporation temperature was controlled by a thermocouple and set to 350 °C for both polymers. The low-density polyethylene in granular form was purchased from Aldrich, and the polypropylene in sheet form was obtained from Goodfellow.

Silver coated glass for FTIR and water contact angle measurements and polished silicon for AFM analysis were used as substrates. Rf balanced planar magnetron 80 mm in diameter was driven by rf power supply ENI 600 W. Quartz crystal mirobalance was used for in-situ thickness monitoring. Quadrupole mass spectrometer (Hiden HAL 301 RC) was used for monitoring volatile fragments during the deposition proces. FTIR analyses were performed ex-situ on a Bruker Equinox 55 FTIR spectrometer, and XPS was performed on an angular-resolved x-ray induced photoelectron spectrometer ADES-400 (VG Scientific) equipped with Mg K^{α} radiation (1253.6 eV) and a rotable hemispherical energy analyser. AFM Quesant Q-scope 850 and Burleigh Metris 2000 were used for topography and thickness measurements.

3. Results and discussion

Films prepared by evaporation without magnetron discharge revealed similar roughness for both PP and PE (RMS 13.1 and 14.9 nm, respectively; measured at 20 micron scan size). When brought in contact with water they tend to swell and delaminate from the substrate surface. This might be an indication that evaporation of these polymers proceeds with significant thermal degradation of polymeric chains. As a result, the volatile fragments of lower molecular weight deposit a wax-like film, which is essentially a mixture of various hydrocarbon oligomers. To improve film stability a glow discharge was applied during evaporation. It was found that with increasing discharge power film roughness decreases down to 1.6 nm for PP at 80 W and 1.7 nm for PE at 120 W. AFM images show that in both cases at a certain power range the formation of branched sferulite-like structures occurs (10 W for PP and 40 – 120 W for PE at the evaporation temperature of 350 °C – Fig. 1). Deposition rate is very important for film formation and structure. It can be increased by higher evaporation temperature. However, in the case of PE, as the temperature of the source is raised above 400 °C vigorous boiling of the polyethylene happens. This causes an ejection of macroscopic particles of bulk polymer. These particles have sufficient energy to reach the substrate surface, and the surface is in this case very rough (Fig. 2).

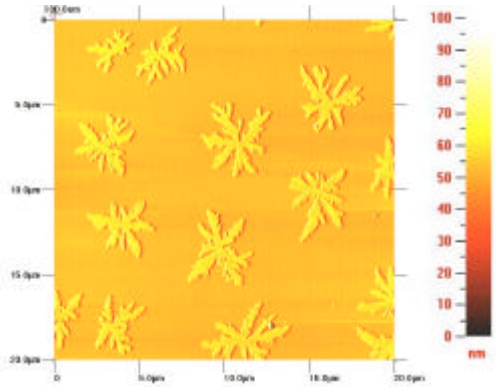

Fig. 1 . Sferulite-like structures on the PE film evaporated on Si at 350 °C with simultaneous 40 W discharge.

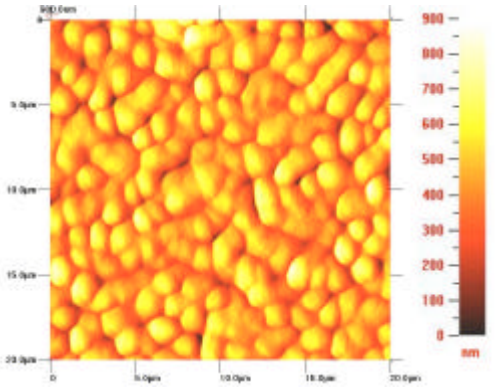

Fig. 2. PE film evaporated at 400 °C on Si with simultaneous 160 W discharge.

The application of a glow discharge during evaporation induced changes in a chemical composition as well. The FTIR spectra of the films deposited by evaporation of PP and PE with and without a glow discharge are presented in Fig. 3 and Fig. 4, respectively. The films evaporated without a glow discharge produce the spectra typical for aliphatic hydrocarbons with stretching and deformation vibrations of CH_x groups appearing slightly below 3000 and 1500 cm^{-1}, respectively. For both polymers, new peaks at 1650 and 1715 cm^{-1} develop with increasing discharge power. These can be assigned to C=C and C=O bonds, respectively. Furthermore, the spectra of the films prepared at low discharge powers are well resolved, whereas with increasing power the individual peaks widen and tend to merge. In the case of PP (Fig. 3), with increasing power the peaks related to absorption of CH_3 groups (2960 cm^{-1}) enhance with respect to CH_2 (2925 cm^{-1}). Comparison of the FTIR spectra of conventional polymers and of polymeric films prepared by magnetron sputtering [8, 9] to out present results shows that the films deposited without discharge are very similar to the classical bulk polymers. With increasing discharge power their chemical structure changes to that of plasma polymer films. The above findings indicate that glow discharge induces plasma polymerization processes, which in the case of hydrocarbon plasmas are generally recognized as based on radical addition, propagation and termination mechanism. This leads to the enhancement of cross-linking, oxidation and the enrichment of bonding environments of hydrocarbon groups. In the case of PE, the oxidation of the polymeric film is also indicated by an increase of a broad OH peak at 3500 cm^{-1}.

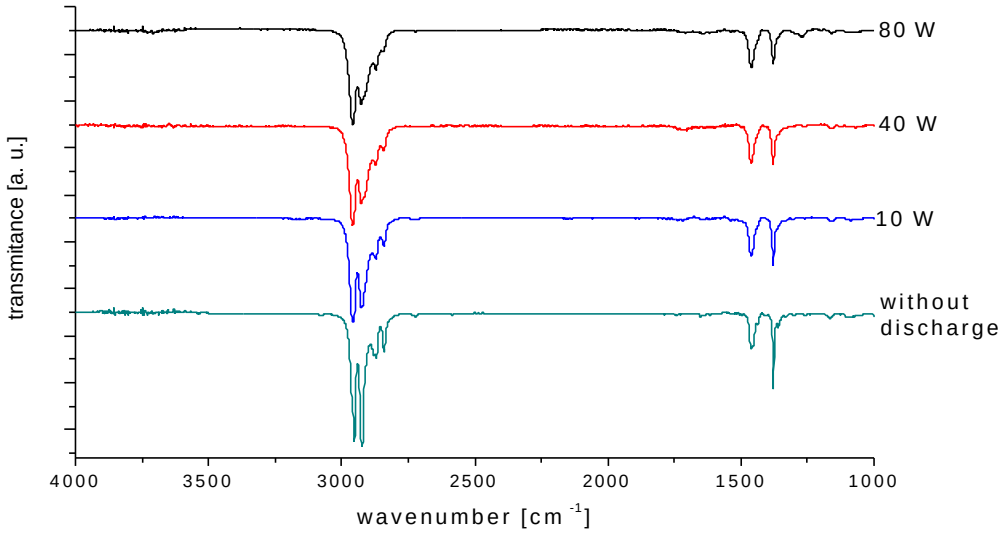

Fig. 3 The FTIR spectra of evaporated PP with or without glow discharge.

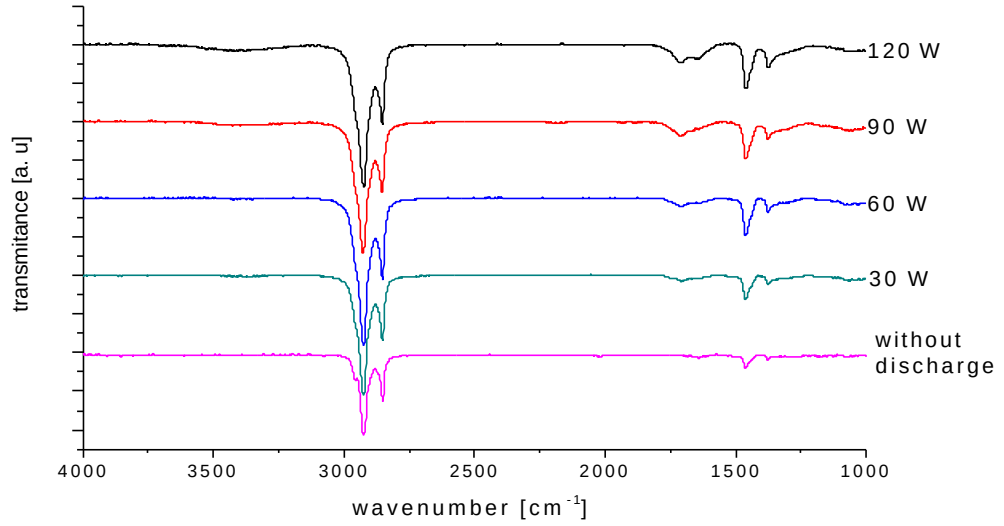

Fig. 4 The FTIR spectra of evaporated PE with or without glow discharge.

The high-resolution C 1s XPS spectra were measured on the PP evaporated films (not shown here). The spectra are featureless regardless the discharge power. However, the Full Width at Half Maximum increases from 1.5 eV for the sample deposited without glow discharge to 2.2 eV for the film prepared at 80 W. A slight asymmetry to the higher binding energy is also observed. We attribute the increase of the peak width and asymmetry to the contribution of carbon bound to oxygen functionalities. The elemental composition calculated from the XPS data is given in the Table 1. The atomic concentration of oxygen gradually increases from 2 % for the sample deposited without glow discharge to 16 % for the film prepared at 80 W. This supports the FTIR findings showing an enhancement of the film oxidation at higher discharge powers. The presence of a small amount of oxygen in the film deposited without discharge may be explained by the water absorbed in source materials. The mass spectral analysis of residual gases performed before and during the evaporation revealed

a considerable increase of intensity from the water species (17-19 amu) after the heating has been turned on. This is with good agreement with our previous work [8].

discharge power	C [at %]	O [at %]	O / C
no discharge	98	2	0.02
10 W	98	2	0.02
40 W	91	9	0.10
80 W	84	16	0.19

Table 1 Elemental composition of polymeric films prepared by evaporation of PP with simultaneous discharge obtained from XPS analysis.

Different chemical structure and surface morphology result in changes of water contact angle. With increasing power water contact angle decreases from 103° to 84° for PP and from 101° to 92° for PE (Fig. 5). The decrease of contact angle with increasing discharge power is in agreement with the chemical changes (increase of oxygen content). It may also be contributed by decrease of roughness, which is known to reduce contact angle on hydrophobic surfaces.

Mass spectrometry of neutral species was done during evaporation of PE, and the examples of the spectra are given in Fig. 6. In the case of evaporation without discharge, only Ar (ions Ar^+ 40 amu, Ar^{2+} 20 amu), water (ions H_2O^+ 18 amu, OH^+ 17 amu, H_3O^+ 19 amu), carbon (C^+ 12 amu) and low molecular weight hydrocarbon fragments (ions CH_x^+ 14 – 16 amu, $C_2H_x^+$ 27 – 29 amu and $C_3H_x^+$ 41, 43, 44 amu) are observed. Absence of higher hydrocarbon fragments has two possible explanations. First, the evaporated fragments may have mass beyond the ultimate limit of our mass spectrometer (300 amu). On the other hand, their partial pressure may be under the detection limit of the spectrometer. When the discharge is switched on (160 W discharge, evaporation temperature 400 °C), the higher hydrocarbon fragments up to $C_9H_x^+$ appear in the mass spectra. We attribute it to fragmentation of long hydrocarbon chain, which results in an increase of the partial pressure of the hydrocarbon components falling within the detection range of our spectrometer.

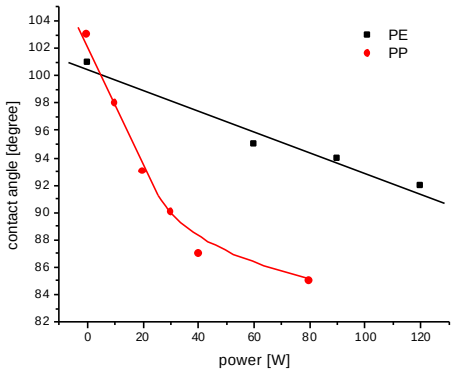

Fig. 5 Water contact angle on the films deposited by evaporation with or without glow discharge in dependence on discharge power.

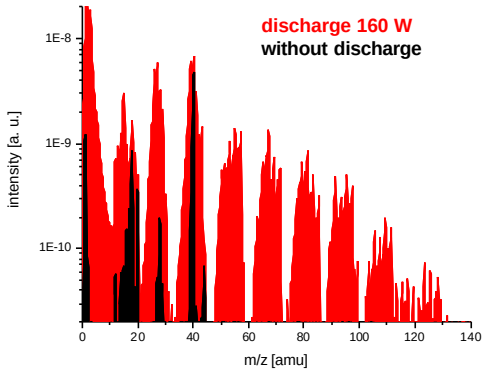

Fig. 6 The neutral species mass spectra during the evaporation of PE at 350 °C (black). Red peaks belong to the evaporation temperature 400 °C with 160 W discharge power.

3. Conclusions

It has been shown that films prepared by evaporation of PP and PE have similar chemical structure to that of conventional polymers. Dissolution in water implies that such films are composed of a mixture of the lower molecular weight hydrocarbon oligomers. The mechanical stability of these coatings can be improved if thermal evaporation is combined

with a glow discharge. Increasing the discharge power leads to the higher extent of cross-linking, and the films become hydrocarbon plasma polymers. However, at moderate discharge powers these hydrocarbon plasma polymers resemble the original polymers used for evaporation.

Acknowledgement
This work is a part of the research plan MSM 0021620834 that is financed by the Ministry of Education of the Czech Republic and partly was supported by OC 527.10(COST 527) also funded by the Ministry of Education of the Czech Republic. The authors thank Zdenek Strihal for part of AFM analysis and discussions.

References

[1] P. P. Luff, M. White, Vacuum, 18 (1968) 437 - 440
[2] P. P. Luff, M. White, Thin solid films, 6 (1970) 175 – 195
[3] N. Boonthanom, M. White, Thin Solid Films, 24 (1974) 295-306
[4] C.Hogarth and N.Iqbal, Phys. Stat. Sol., A65(1981) 12
[5] H. Biederman, I. Chudacek, D. Salvinska, P. Stulik, Proc. of ISPC 9, Italy, Bari 1989
[6] H. Usui, H. Koshikawa, K. Tanaka, J. Vac. Sci. Technol. A 13(5), Sep/Oct 1995, 2318 - 2324
[7] H. Usui, H. Koshikawa, K. Tanaka, S. Miyata, T. Watanabe, J. Vac. Sci. Technol. A 16(1), Jan/Feb 1998, 108 - 113
[8] V. Stelmashuk, H. Biederman, D. Slavinska, M. Trchova, P. Hlidek, Vacuum 75 (2004) 207–215
[9] I. Kholodkov, H. Biederman, D. Slavinska, A. Choukourov, M. Trchova, Vacuum 70 (2003) 505–509
[10] J. Kousal, J. Hanus, A. Choukourov, P. Hlidek, H. Biederman, D. Slavinska, J. Zemek, Surface & Coatings Technology, to be published
[11] N. Kasai, I. Sugimoto, Journal. of Applied Polymer Science, Vol. 73, 1869 - 1877 (1999)
[12] T. R. Gengenbach, H. J. Griesser, Polymer 40 (1999) 5079 - 5094

Formation And Electron-Ion Recombination Of N_4^+ Examined In Near-Atmospheric Pressure N_2

S. Adams[1], J. Williamson[2], C. DeJoseph, Jr.[1], and R. Lee[1]

1 Air Force Research Laboratory, Wright Patterson Air Force Base, USA
2 Innovative Scientific Solutions Inc., Dayton, OH, USA

Abstract

The time dependent behavior of molecular nitrogen ions, following pulsed photoionization of near atmospheric pressure N_2, has been investigated using multi-photon laser techniques and kinetic modeling. Measured time dependent fluorescence spectra, during and after pulsed laser resonance-enhanced multi-photon ionization of N_2, together with a coupled rate equation model, allowed for the determination of the absolute densities of N_2^+ and N_4^+ as these species evolved.

1. Introduction

As the primary component of our atmosphere, molecular nitrogen has been the subject of extensive spectroscopic analysis. Over the past century, the numerous electronic states of N_2 and N_2^+ have been well defined in terms of energy and transition probability[1]. Time resolved nitrogen spectra, generated under controlled excitation, can thus produce information on the kinetic behavior of selected nitrogen states, both neutral and ionized. In this study, ionization and recombination kinetics are investigated under conditions applicable to near atmospheric pressure nitrogen discharges. This kinetic information is of value in studies of combustion processes, atmospheric phenomena, and gas discharges for industrial or laboratory use. This work introduces a new technique for determining N_2^+ and N_4^+ kinetic behavior using pulsed laser spectroscopy together with kinetic modeling. The ion species of interest, N_2^+ and N_4^+, are produced by applying pulsed laser resonance-enhanced multi-photon ionization (REMPI) to a near-atmospheric pressure N_2 system and allowing ion-molecule reactions to proceed. Results of particular interest include the modeled N_4^+ formation and reaction phenomena in nitrogen and air.

2. Theory

It is well known that $N_2^+(X\ ^2\Sigma_g)$ ions can be produced by near-ultraviolet laser excitation of ground state $N_2(X\ ^1\Sigma_g)$ via several resonant absorption bands[2]. The strongest of these absorption bands can be attributed to transitions involving (2+2) or (3+1) REMPI combinations as shown in figure 1, with intermediate states $N_2(a\ ^1\Pi_g)$ and $N_2(b\ ^1\Pi_u)$ being resonant with the second or third photons, respectively. This REMPI technique has been used in previous studies at relatively low N_2 pressures, to preclude collisional processes, where information was sought on intermediate state energy levels or N_2^+ product energies[3]. The higher N_2 pressures in the work presented here allowed the study of a number of reactions of the time-dependent photoionization product $N_2^+(X)$. In particular, the formation of the molecular-ion cluster $(N_2)_2^+$, commonly known as N_4^+, proceeds rapidly for pressures near atmospheric by the three-body reaction[3]

$$N_2^+(X) + N_2 + N_2 \rightarrow N_4^+ + N_2 \qquad (1)$$

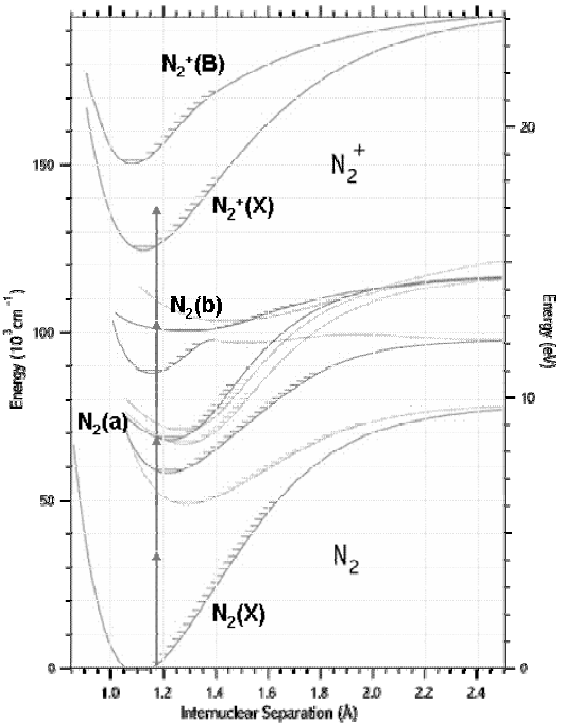

Figure 1. Energy level diagram of N_2 showing (2+2) and (3+1) multi-photon absorption processes through intermediate states $N_2(a)$ and $N_2(b)$

In the partially ionized environment following the REMPI pulse, the electron-ion recombination reaction becomes the primary loss mechanism for N_4^+ as[4]

$$N_4^+(X) + e^- \rightarrow N_2^* + N_2 \qquad (2)$$

Where N_2^* indicates an excited state of N_2. Specifically, this recombination channel leads to N_2 2nd positive system ($C\ ^3\Pi_u - B\ ^3\Pi_g$) fluorescence, which is observed and reported here for the first time using pulsed laser REMPI in N_2. The time dependence of this observed fluorescence, for times during and shortly after the laser pulse, provided information on the evolution of the electron-ion recombination, which was combined with known reaction rate constants to derive information on the time dependence of the N_4^+ density. Similar N_2(C-B) fluorescence has been previously observed in excitation of air by a short-pulse electron beam and attributed to N_4^+ recombination[5].

Also observed in this experiment is a relatively intense fluorescence corresponding to the 1st negative system, $N_2^+(B\ ^2\Sigma_u^+ - X\ ^2\Sigma_g)$, that occurs only during the laser pulse. To differentiate the two observed emission bands, the N_2^+(B-X) emission is henceforward referred to as "prompt fluorescence" while the N_2(C-B) emission discussed above is referred to as "delayed fluorescence". This prompt fluorescence has been mentioned in the literature[6], but its origin has not been thoroughly investigated. We have studied the possibility that the source of the prompt fluorescence is N_2^+(B) production resulting from a single photon photodissociation of N_4^+. With a sufficiently rapid build-up of N_4^+ by reaction (1), during the laser pulse, it is then energetically possible that N_4^+ laser photodissociation can occur and yield N_2^+(B) as a product from the reaction

$$N_4^+(X) + h\nu \rightarrow N_2^+(B) + N_2\ . \qquad (3)$$

Such excited state N_2^+(B) fragments have been experimentally observed from the photodissociation of N_4^+ with a laser in the range of 270-290 nm [7].

We have developed a coupled rate equation model, which describes the pressure and time dependence of both the delayed and prompt fluorescence signals originating from reactions (2) and (3). By using the appropriate known reactions rates along with the relative delayed fluorescence intensity data and the time dependent laser pulse intensity, the model determined the respective N_2^+ and N_4^+ densities that provide the best fit to the data. In general, the rate of temporal rise of the fluorescence signal was strongly dependent on the density of N_2^+ in reaction (1) while the post laser decay rate of the fluorescence was almost entirely dependent on the N_4^+ density (with $[N_4^+] \approx [e^-]$) in the recombination reaction (2). Fitting the delayed fluorescence rise and decay simultaneously allowed for this unique measurement technique of the absolute N_2^+ and N_4^+ densities.

3. Experiment

A pulsed ultraviolet laser, tunable within the 275-290 nm range, was used to photoionize N_2 gas via a resonance-enhanced multi-photon absorption process. The output of a 10 Hz Nd: YAG pumped dye laser operating with Rhodamine 6G dye over the wavelength range 550-580 nm was subsequently passed through a BBO frequency doubling crystal. This generated the working ultraviolet laser pulse with a linewidth of 0.02 cm^{-1} and a nominal energy of 4 mJ per pulse. The beam also passed through a variable uv attenuator to allow the power dependence of the laser absorption processes to be measured. The laser pulse energy was monitored with a beam back-reflection by a joulemeter which was then calibrated to calculate the working laser pulse energy. The uv pulse was then focused down with a 10 cm focal length lens to increase the optical power density and greatly enhance the multi-photon absorption process as the beam entered a quartz chamber with flowing N_2.

For this experiment, a fluorescence signal was collected from the laser focal region, in contrast to the normal REMPI procedures in which only an ion signal is collected. Observations of the fluorescence were restricted to the laser focal region of the chamber due to the relatively slow gas flow and the fact that most measurements

were taken within 100 ns of the laser pulse. The fluorescence induced by the laser absorption included two major bands at 337 nm, N_2(C-B), and 391 nm, N_2^+(B-X), respectively. The fluorescence was then collimated by a 5 cm diameter, 10 cm focal length lens and focused onto a fiber optic receiver with a second 10cm focal length lens. The optical signal was then coupled to a half-meter spectrometer equipped with a 1200 grooves/mm grating, blazed at 300 nm. The spectrally resolved fluorescence was recorded by an intensified charge-coupled device (ICCD) camera with a 512 x 512 pixel array. The camera was configured with a 2 ns optical gate that allowed for the reconstruction of a temporal profile of the fluorescence signal. Experimental control and data acquisition was accomplished with a PC using LabView software.

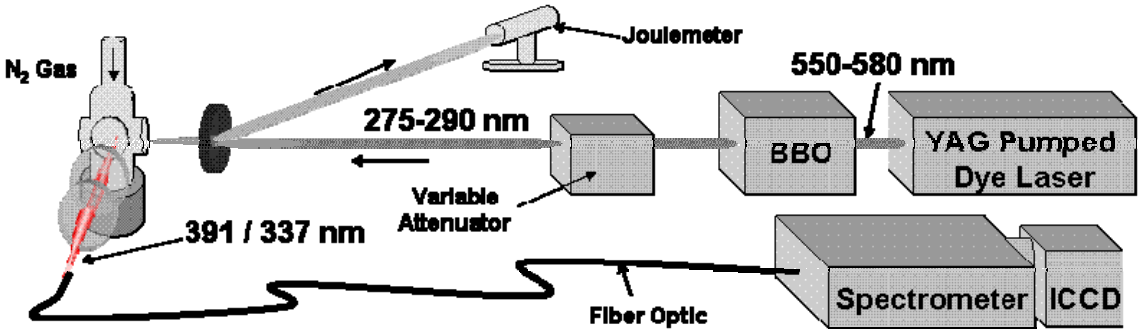

Figure 2: Sketch of experimental set up including laser source, quartz chamber, and optical detection apparatus.

4. Results and Discussion

• Laser Absorption Spectra

Measurements of the fluorescence intensity as a function of ultraviolet laser wavelength resulted in laser absorption spectra that were virtually identical when monitoring either the delayed fluorescence signal at 337 nm or the prompt fluorescence at 391 nm. Figure 3 shows an example of the fluorescence signal recorded at 391 nm as a function of laser wavelength. Several bandheads can be seen corresponding to resonant absorption from the $N_2(X\ ^1\Sigma_g)$ ground state to an intermediate state in the eventual formation of N_2^+. The bandheads of the intermediate N_2 states have been identified and are labeled on the plot with the vibrational sequence from $N_2(X,v''=0)$ in parenthesis. The bandheads corresponding to the $N_2(a\ ^1\Pi_g)$ and $N_2(b\ ^1\Pi_u)$ intermediate states are labeled in figure 3 by *a* and *b*, with less prominent features from $N_2(c_4'\ ^1\Sigma_u)$ and $N_2(b'\ ^1\Sigma_u)$ intermediate states being labeled by c_4' and b' respectively. The resonant absorption from ground state to $N_2(a\ ^1\Pi_g)$ is a 2 photon process where the absorption to the $N_2(b\ ^1\Pi_u)$, $N_2(c_4'\ ^1\Sigma_u)$ and $N_2(b'\ ^1\Sigma_u)$ states are all 3 photon processes.

Although the intensity distribution of absorption spectral features was independent of which fluorescence line was observed, it was dependent on other factors, such as laser power, as expected, but was also found to be dependent on pressure. For example, the rotational line intensity distribution within the N_2(a-X) bands was seen to change significantly as pressure varied from 100 Torr to 750 Torr. This pressure dependence was attributed to the rapid rotational quenching of the $N_2(a\ ^1\Pi_g)$ intermediate state during the laser pulse at higher pressure. The quenching altered the coupling scheme of the 2 photon ionization step since the probability of photoionization depends on a virtual intermediate state that is influenced by Rydberg states such as $N_2(o\ ^1\Pi_u)$ lying about 35,000 cm^{-1} above $N_2(a\ ^1\Pi_g)$[8]. The large fluctuations in the observed band intensities for the $N_2(b\ ^1\Pi_u)$ intermediate states was attributed to the rates of predissociation in the $N_2(b\ ^1\Pi_u)$ state which vary significantly with vibrational level. For the photoionization measurements discussed in the remainder of this paper, the laser wavelength was fixed at 283 nm, which corresponds with the bandhead of the a $^1\Pi_g$ – X $^1\Sigma_g$ (1, 0) resonant transition.

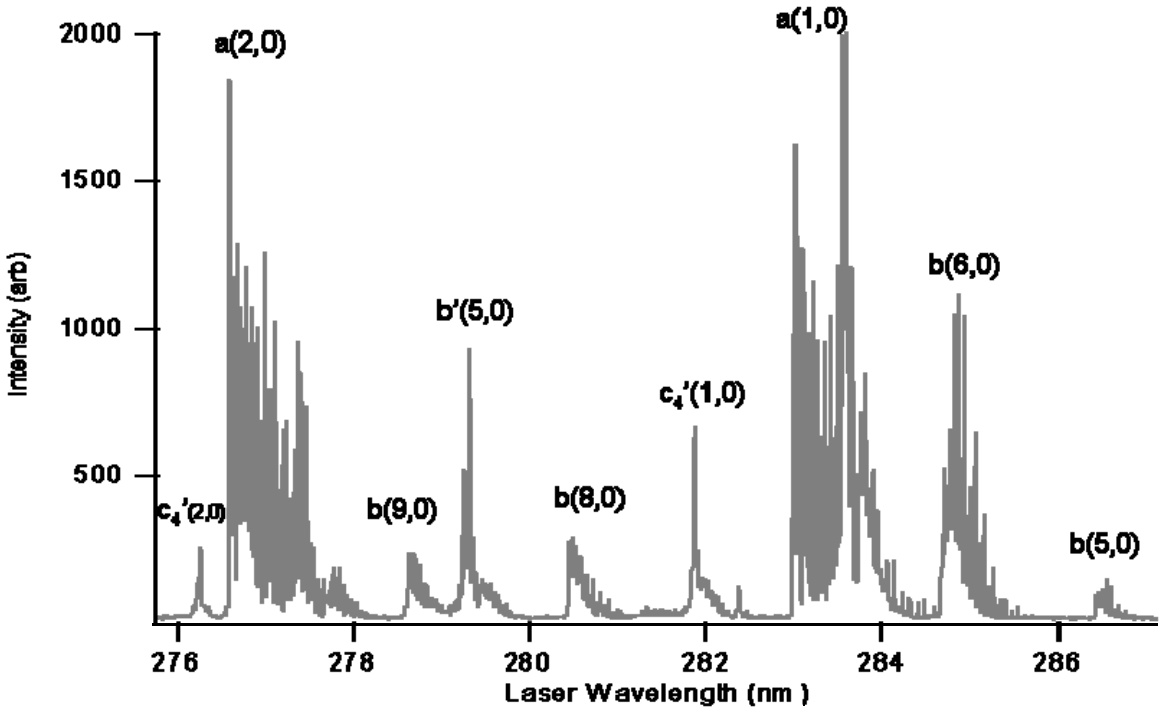

Figure 3: Example ultraviolet laser absorption spectrum taken in 750 Torr N_2 with bandheads labeled as a, b, c_4', and b' representing N_2^+ formation via resonant absorption through intermediate states $N_2(a^1\Pi_g)$, $N_2(b^1\Pi_u)$, $N_2(c_4'^1\Sigma_u)$ and $N_2(b'^1\Sigma_u)$ respectively.

• Fluorescence Data and Kinetic Model

Temporal profiles of the pulsed laser excitation, the prompt fluorescence and the delayed fluorescence are shown in figure 4 for an N_2 pressure of 250 Torr. Using known major reactions of the photolysis products and varying the laser absorption rates in the model, best fits were determined for both the prompt and delayed fluorescence (solid lines).

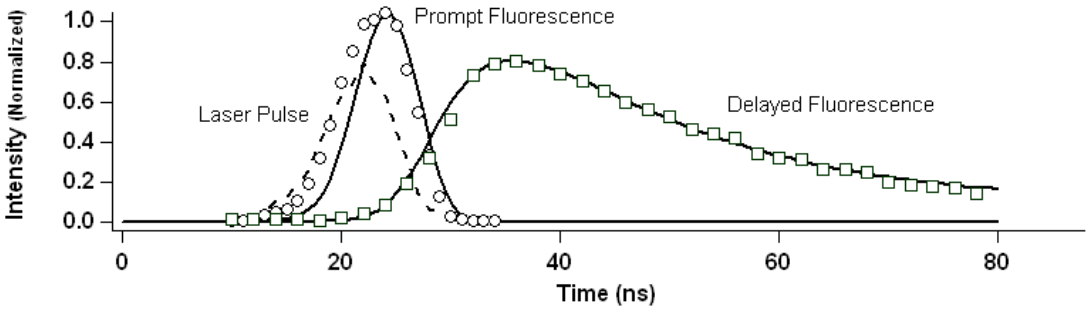

Figure 4: Experimental temporal profiles of laser pulse (dotted line), prompt fluorescence (circles) and delayed fluorescence (squares) with kinetic model fit of each fluorescence (solid lines)

The temporal rise of the prompt fluorescence was observed to slightly lag behind the exciting laser pulse rise and then sharply decay as the laser pulse diminished. This observation is consistent with our theory that the $N_2^+(B)$ upper state prompt fluorescence was produced only upon laser photodissociation of N_4^+. Since the N_4^+ formation was collisionally induced, the initial $[N_4^+]$ rise, and consequently the rise in $[N_2^+(B)]$ would be slightly slower than the laser rise time. The fluorescence, being a product of photodissociation, required the presence of the laser energy as well and thus decreased in intensity quickly as the laser decayed. At pressures below 100 Torr, formation of N_4^+ was calculated to be so slow that there would be minimal accumulation of N_4^+ before the laser

decayed. Our corresponding experiments found the prompt fluorescence signal did vary with pressure and was indeed very weak below 100 Torr.

As discussed earlier, the fitting procedure resulted as well in the determination of absolute densities of both N_2^+ and N_4^+ which are shown plotted as a function of time in figure 5. The plot clearly shows the importance of the N_4^+ ion species at our operating pressures, especially after the excitation source has been removed. The N_4^+ density continued to build until the laser pulse had terminated and the N_2^+ density became insignificant. The maximum ion density occurred shortly after the laser pulse at $[N_4^+] = 2x10^{13}$ cm^{-3}, which in 250 Torr of N_2 corresponds to a N_4^+/N_2 fraction of 2.5 ppm.

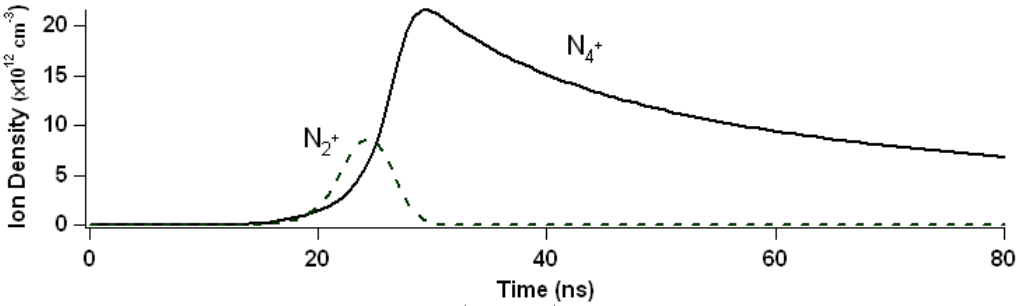

Figure 5: Temporal profile of absolute ion density of N_2^+ and N_4^+ in 250 Torr N_2 generated from kinetic model

5. Summary

Pulsed laser resonance-enhanced multi-photon ionization has been used in conjunction with temporally resolved fluorescence monitoring to study the kinetic behavior of N_4^+ and N_2^+ ions in near atmospheric pressure N_2. Mechanisms are proposed and modeled for the production of $N_2(C)$ and $N_2^+(B)$ during the photoionization and compared to fluorescence data. A least-squares fit of the measured, time resolved, fluorescence data to a coupled rate equation model allowed for the determinations of the absolute densities of both N_2^+ and N_4^+ during and after the laser pulse. This technique is adaptable to various system configurations or could be used in conjunction with other analytical techniques to more accurately determine N_4^+ or N_2^+ reaction rates at near-atmospheric pressure.

Acknowledgement

The authors gratefully acknowledged the technical assistance of Anthony DeCerbo. This work is partially supported by the Air Force Office of Scientific Research.

References

[1] A. Lofthus, P.H. Krupenie – J. Phys. Chem. Ref. Data 6, 113 (1977).
[2] P.M. Johnson, C.E. Otis – Annu. Rev. Phys. Chem. 32, 139 (1981).
[3] K.L. Carleton, K.H. Welge, S.R. Leone - Chem. Phys. Lett. 115, 492 (1985).
[4] M.C. Sauer, W.A. Mulac – J. Chem. Phys. 56, 4995 (1972).
[5] D.J. Eckstrom, J.S. Dickinson, R.M. Hill – J. Chem. Phys. 82, 1792 (1985).
[6] M. Alden, W. Wendt, – Optics Communications 69, 31 (1988).
[7] W. Ubachs, I. Velchev, and A. deLange – J. Chem. Phys. 112, 5711 (2000)
[8] B. Girard, G.O. Sitz, R.N. Zare, N. Billy, and J. Vigue – J. Chem. Phys. 97, 26 (1992)

SPECTROSCOPIC STUDY OF DC PLASMA-ENHANCED CVD FOR CARBON NANOTUBES SYNTHESIS

M.A. Bratescu[1), 2)], Y. Suda[1)], A. Okita[1)], Y. Sakai[1)], and O. Takai [2)]

[1)] Graduate School of Information Science and Technology,
Hokkaido University, North 14 West 9, Sapporo 060-0814, Japan
[2)] Graduate School of Engineering, Nagoya University
Furo-cho, Chikusa-ku, Nagoya 464-8603, Japan

Abstract
The formation of carbon nanotubes (CNT) in a dc plasma-enhanced chemical vapor deposition (PECVD) was investigated. It was found that an increase of the CH_4 gas pressure produces an increase of the relative density of the C_2, C_3 molecules and the clusters and a decrease of the excited carbon atom number density in plasma. It was observed that in 10 Torr pressure of CH_4 gas, the ratio between the intensity of the graphite peak (G peak) and the disorder peak (D peak) in the Raman spectrum and the length of the obtained CNT were maxims.

1. Introduction

CNTs are increasingly becoming one of the most important materials for various applications in electronics, optics and biophysics. Up to now, several synthesis methods for CNTs growth, such as arc-discharge [1], laser ablation [2], chemical vapor deposition (CVD) [3] and plasma-enhanced CVD (PECVD) [4] have been investigated. All of these techniques require high temperature for the growing process, which is obtained in an electric furnace or with a hot filament. In our experiment we used dc plasma, which provides the advantage that the metal catalyst was deposited by argon sputtering inside the same vacuum chamber where CNTs were produced on a silicon substrate heated by Joule effect. This PECVD set-up offered the possibility to study plasma composition in the vicinity of the silicon substrate by spectroscopic methods.

In the present work, the number density of the excited carbon atom was measured by laser absorption spectroscopy (LAS) method. Plasma composition and the relative number density of CH radical, C_2, C_3 molecules, H atom, and clusters were measured by optical emission spectroscopy (OES) method. The morphology of the synthesized CNTs in PECVD was probed with a scanning electron microscope (SEM). Raman spectroscopy and Fourier Transform Infrared Spectroscopy (FTIR) characterized the composition of CNTs.

It was found that an increase of the CH_4 gas pressure produces an increase of the relative density of the C_2, C_3 molecules and the clusters and a decrease of the excited carbon atom number density in plasma. It was observed that at 10 Torr pressure of CH_4 gas, the ratio between the intensity of the graphite peak (G peak) and the disorder peak (D peak) in the Raman spectrum and the length of the obtained CNT were maxims. The formation of CNT was explained by the neutral-neutral gas-phase chemical reactions in the high-pressure range of the CH_4 gas plasma.

2. Experimental results

2.1. Production of CNT

The experimental setup for CNT synthesis and plasma diagnostics is schematically shown in Fig. 1. CNT was produced in dc plasma in CH_4 gas.

The cathode was a cylindrical rod of Ni (99.99 %) with a diameter of 15 mm. The anode plate was made from stainless steel, with a diameter of 60 mm. The distance between the electrodes was 7 mm. The silicon substrate (Nilaco, 100, 10x10x0.625 mm, resistivity $\leq 0.02\ \Omega$ m) was set in the space between the cathode and the anode, at a distance of ~ 3 mm far from the cathode.

A nickel thin film was deposited on a silicon substrate by sputtering of the nickel atoms from the cathode, in dc argon plasma. The film thickness was controlled by the sputtering time. The nickel film thickness was evaluated knowing the sputtering yield (the mass of the sputtered metal from the cathode in one hour, at a

discharge current of one Ampere) for the energy of Ar^+ of 600 eV. The sputtering yield of nickel atoms for Ar^+ at 600 eV is 1.34 [5]. In the present experiment nickel film was deposited by Ar^+ at ~ 50 eV, at 20 mA discharge current, in 8 Torr argon pressure and during 10 minutes. From these experimental conditions we evaluate the nickel film thickness to be ~ 50 nm.

After depositing the nickel film, the silicon substrate was heated at 750ºC, using a Joule heater. The substrate temperature was measured with an optical pyrometer. Typical resistance of the substrate including the contact resistance, 500 Ω before heating, was decreased at ~ 3 Ω after heating, due to the increased temperature of the silicon substrate [6].

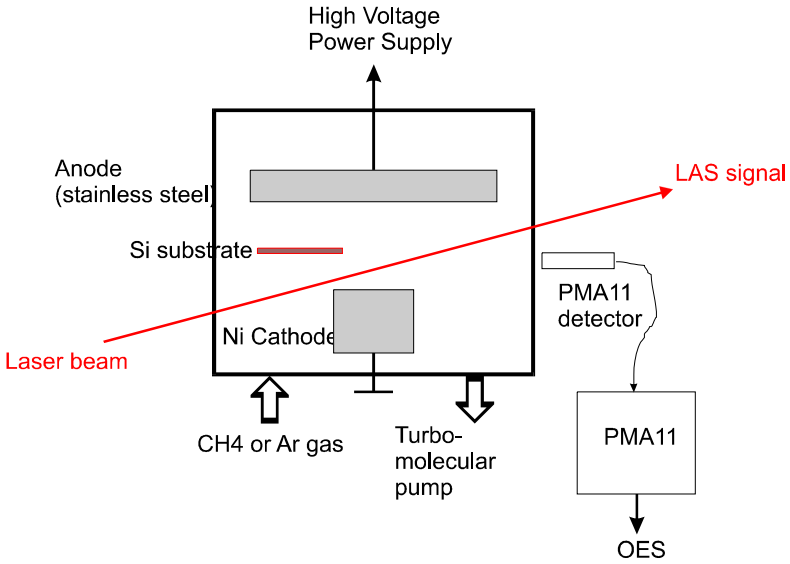

Fig. 1. Experimental setup.

A stable CH_4 discharge was obtained for gas pressures (p) from 2 Torr up to 20 Torr and for discharge currents (i) from 5 mA to 30 mA. The deposition time was one hour.

2.2. Plasma diagnostics

Plasma diagnostics consisted in: *(a)* measurements of the number density of the excited carbon atom by LAS, *(b)* measurements of the relative emission intensities of the excited CH radical, the excited C_2, C_3 molecules and clusters by OES and *(c)* calculation of the electron temperature from relative emission intensities of spectral lines of the hydrogen atom.

The number density of the excited carbon atom on $3^1P_1^0$ level (N_C) was measured with a commercial diode laser (DL: Hitachi 8325G, 40 mW maximum output with the central wavelength of 830 nm at 25°C). The DL wavelength ($\lambda = c/\nu$) was tuned to the resonance absorption of $C(3^1P_1^0 \rightarrow 3^1S_0)$ at λ_0^C = 833.744 nm. A photodiode (PD) and a lock-in amplifier (NF Electronic Instruments 5610B) were used to acquire the absorption signal [7]. The signal to noise ratio (S/N) of the $C(3^1P_1^o)$ atom absorption signal was ~ 10. The value of N_C was calculated by the following formula: $N_C = \left(8\pi g_i / g_j \lambda_0^2 A_{ji} L\right) \int_{\substack{absorption \\ line}} \left[1 - I(\nu)/I_0\right] d\nu$, where g_i (= 3) and g_j (= 1) are the statistical weights of the lower and the upper levels, respectively. A_{ji} (= 0.351×10^8 sec^{-1}) is Einstein coefficient for carbon transition at λ_0 = 833.744 nm. L is the absorption length, which is assumed equal to the diameter of the cathode (~ 15 mm). I_0 is the laser intensity before entering the plasma and $I(\nu)$ is the laser intensity after passing through the plasma. The dependence of N_C on p and i is shown in Fig. 2.

The emission spectrum of dc plasma CVD was analyzed in a range between 300 and 800 nm using a Hamamatsu PMA-11 (Photodiode Multichannel Analyzer) with 2 nm spectral resolution. The most intense OES

lines of the species produced by the decomposition of the CH_4 molecule were: CH radical at 431.4 nm ($A^2\Delta \rightarrow X^2\Pi$), 388.9 nm ($B^2\Sigma \rightarrow X^2\Pi$) and 314.3 nm ($C^2\Sigma \rightarrow X^2\Pi$), the C_2($A^3\Pi_g$) molecule (Swan System: $A^3\Pi_g \rightarrow X'^3\Pi_u$) and the C_3($^1\Pi_u$) molecule (Comet Head System: $^1\Pi_u \rightarrow {}^1\Sigma_g^+$), H atom at 656.3 nm (H_α), 486.1 nm (H_β) and 397.0 nm (H_ε). Many nickel lines were detected in OES from nickel atoms, which are sputtered from the cathode and excited in plasma (Fig. 3).

Table I lists some chemical reactions in gas-phase and the corresponding threshold energy, which can explain the appearance of C_2 molecule, C, H atoms and CH radical in plasma [8]. The gas-phase chemical reactions and the surface chemical reactions can explain the CNT formation in PECVD. In gas-phase the main chemical reactions are electron impact reactions (which conduct to dissociation, excitation, and ionization processes), neutral-neutral reactions and ion-neutral reactions. On the surface, the chemical interaction of neutrals and ions with the catalyst and the substrate are the most significant reactions.

Table I. Production of neutral radicals [8, 9]

No.	Reaction	Threshold (eV)
Electron impact reaction		
1.	$CH_4+e \rightarrow CH_3+H+e$	4.55
2.	$CH_4+e \rightarrow CH_2+H_2+e$	4.79
3.	$CH_4+e \rightarrow CH_2+2H+e$	9.31
4.	$CH_4+e \rightarrow CH+H+H_2+e$	9.19
5.	$CH_4+e \rightarrow CH_3+3H+e$	13.71
6.	$CH_4+e \rightarrow C+2H_2+e$	8.20
7.	$CH_4+e \rightarrow C+4H+e$	17.24
8.	$C_2H_2+e \rightarrow C_2+H_2+e$	6.33
9.	$C_2H_3+e \rightarrow C_2{+}{+}H+H_2+e$	7.98
10.	$C_2H_4+e \rightarrow C_2+2H_2+e$	8.14
11.	$C_2H_5+e \rightarrow C_2+2H_2+H+e$	9.72
12.	$C_2H_6+e \rightarrow C_2+3H_2+e$	8.30

No.	Reaction
Neutral-neutral reaction	
13.	$CH+CH \rightarrow C_2H_2$
14.	$CH+CH_2 \rightarrow C_2H_3$
15.	$CH+CH_3 \rightarrow C_2H_4$
16.	$CH+H \rightarrow C+H_2$
16.	$CH_2+CH_2 \rightarrow C_2H_4$
17.	$CH_2+CH_3 \rightarrow C_2H_5$
18.	$CH_2+H \rightarrow CH+H_2$
19.	$CH_3+CH_3 \rightarrow C_2H_6$
20.	$CH_3+H \rightarrow CH_4$

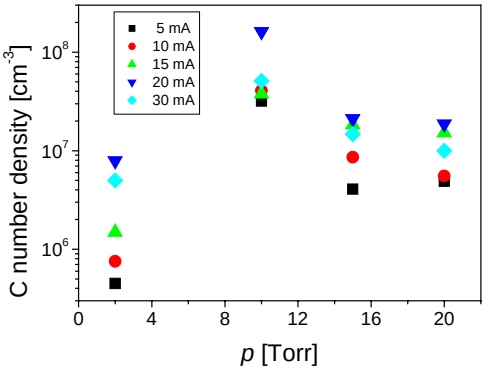

Fig. 2. Dependence of carbon number density on *p*.

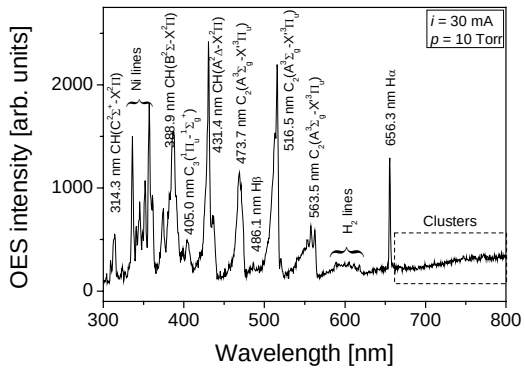

Fig. 3. OES spectra of dc CH_4 plasma (i = 30 mA and p = 10 Torr).

Assuming a quasi-thermal equilibrium in plasma, the electron temperature (T_e) was calculated using the ratio of the relative emission intensities of spectral lines of the hydrogen atom, using the relation: $kT_e = (E_\beta - E_\alpha)/(\ln(I_\alpha / I_\beta) + \ln(A_\beta g_\beta \lambda_\alpha / A_\alpha g_\alpha \lambda_\beta))$, where $E_{\alpha,\beta}$, $I_{\alpha,\beta}$, $A_{\alpha,\beta}$, $g_{\alpha,\beta}$, and $\lambda_{\alpha,\beta}$ are the upper level energy, the OES emission intensity, the Einstein emission coefficient and the wavelength of $H_{\alpha,\beta}$ lines, respectively [10]. Fig. 4 is shows the dependence of T_e on p, at i = 30 mA.

In OES, in the spectral region from 670 nm to 800 nm, a blackbody radiation was observed at different *p* and *i*. This continuum spectrum was attributed to the incandescence of hot carbon clusters or nanoparticles. The blackbody radiation is usually fit with the Planck function to determine particle temperature and to obtain a crude estimation of the particle size [11]. Similar results with the present OES results have been reported in Ref. [12], in a laser vaporization of a graphite/(Ni, Co) system for single-wall CNT synthesis.

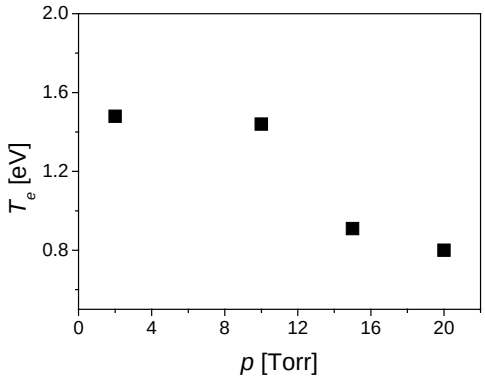

Fig. 4. Dependence of the electron temperature on *p* at *i* = 30 mA.

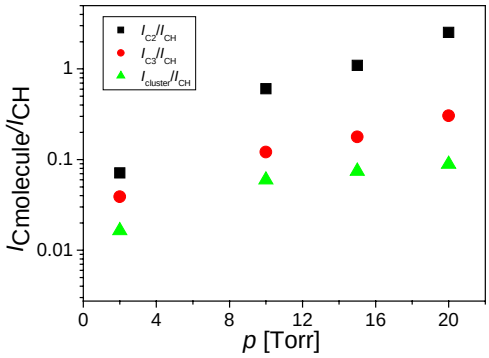

Fig. 5. Dependence of the relative densities of C_2, C_3 molecules and clusters on *p*, at *i* = 30 mA.

The relative intensity of the clusters in plasma is described by the OES intensity around 800 nm. The relative density of C_2, C_3 molecules and clusters are expressed as the ratios between the OES intensity of C_2, C_3 (I_{C2}, I_{C3}) and clusters ($I_{clusters}$), respectively and the OES intensity of the CH radical (I_{CH}), because the excitation energies of CH radical on $A^2\Delta$ level, C_2 molecule on $A^3\Pi_g$ level and C_3 molecule on $^1\Pi_u$ level are almost the same, ~ 3 eV. The dependences of the relative densities of C_2, C_3 molecules and clusters on *i* and *p* are shown in Fig. 5.

2.2 CNT analysis

CNTs were analyzed by Raman spectroscopy (JASCO NRS-1000HS), Fourier Transform Infrared Spectroscopy (FTIR, JASCO FT/IR 660 Plus) and scanning electron microscope (SEM, S4800, Hitachi).

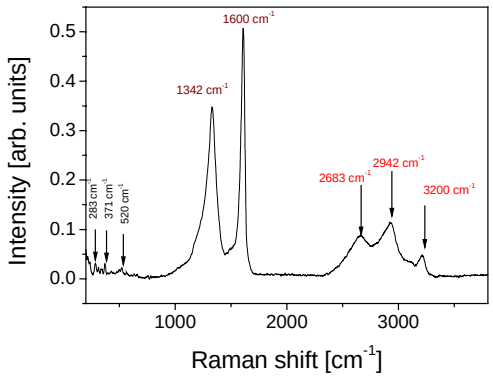

Fig. 6. Typical Raman spectrum of CNT produced in dc plasma, *p* = 10 Torr, *i* = 15 mA.

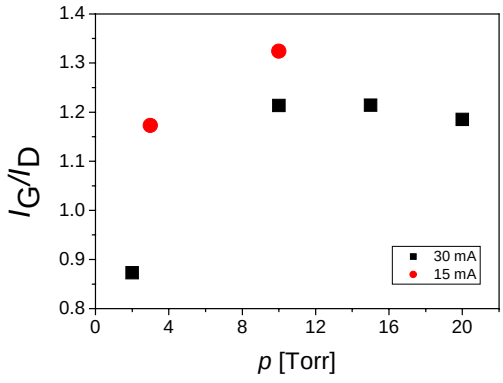

Fig. 7. Dependence of I_G/I_D on *p* and *i*.

Fig. 6 shows a typical Raman spectrum of CNT obtained in dc PECVD, in CH_4 gas. The Raman spectra of CNT have several peaks located between 200 and 3800 cm^{-1} [13, 14]. The most intense peaks occur at 1342 cm^{-1} (D peak), which indicates the presence of defects in graphite structure, and 1600 cm^{-1} (G peak), which represents E_{2g} Raman scattering mode of sp^2-hybridized carbon. Besides the D and G peaks, there are several smaller peaks at 283, 310, 337, 371 and 520 cm^{-1}. The peak at 520 cm^{-1} is due to the silicon substrate. The other four peaks are characteristic features arising from A_{1g} breathing mode of single-wall CNT [14]. These small peaks in Raman spectrum could suggest that a small quantity of single-wall CNT may be present in the deposition. The second-order Raman peaks of CNT occurs between 2000 and 3800 cm^{-1}. The peak observed at 2683 cm^{-1} and 3200 cm^{-1} is the second harmonics of D peak (2×1342 cm^{-1}) and G peak (2×1600 cm^{-1}), respectively. The peak at 2942 cm^{-1} is the sum of the D peak and G peak frequencies ($1342+1600$ cm^{-1}).

The degree of graphite in CNT can be characterized by the ratio between the intensities of G peak and D peak. Fig. 7 shows the dependence of I_G/I_D on p at two discharge currents.

From the transmission spectrum measured by a Fourier Transform Infrared (FTIR) spectrometer (JASCO FT/IR 660 Plus) (Fig. 8), IR absorption coefficient, $\alpha(\omega)$, was calculated. The thickness of the deposition was evaluated from SEM to be ~ 15 μm. The number of C-H bonds per unit volume was calculated as: $N_{CH} = A \int_{\substack{absorption \\ band}} \frac{\alpha(\omega)}{\omega} d\omega$, where A (= 1.35×10^{21} cm^{-2}) is a constant of the C-H_x stretching mode absorption around 3000 cm^{-1} and ω is the wavenumber [15]. N_{CH} was found to be ~ 2×10^{23} cm^{-3} for a deposition at i = 30 mA and p = 10 Torr.

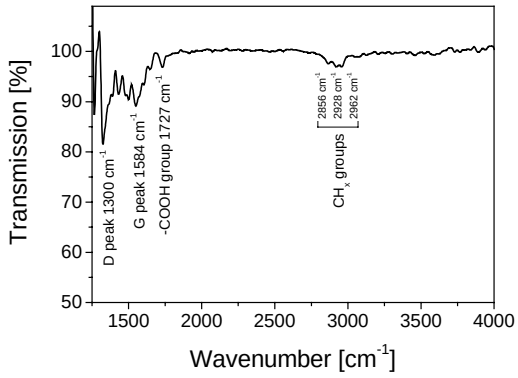

Fig. 8. A baseline corrected FTIR spectrum of CNT deposition in p = 10 Torr and i = 30 mA.

3. Discussion of the experimental results

The highest N_C was ~ 10^8 cm^{-3} in p ~ 10 Torr. N_C slightly depended on i. As p increased, N_C decreased and the relative densities of C_2, C_3 molecules and clusters increased (Fig. 2 and Fig. 5). As p increased T_e decreased (Fig. 4), and the number of dissociated molecules and clusters became smaller.

For the CNTs obtained in CH_4 plasma at p = 10 Torr and i ~ 15 – 30 mA, I_G/I_D was maxim, which corresponded to the same value of p where N_C was maxim. In this case, we can explain that in the formation process of CNT, the carbon atoms play a more important role than the bigger molecules of carbon. Hydrocarbon clusters and radicals contribute to amorphous carbon – hydrogen formation in the same time with CNT production. From SEM analysis presented (Fig. 9), we can observed that the obtained CNT are mixed with amorphous carbon. FTIR analyses proved that a large amount of amorphous carbon was also deposited (Fig. 8). The calculated value of N_{CH} was typical for a-C:H film, as reported in Ref. [15]. From SEM observation, CNT length was evaluated to be ~ 15 μm.

The presence of a high amount of sp^2 graphite in the composition of CNTs was also confirmed by the IR-active peak corresponding to G peak at 1584 cm^{-1} (Fig. 8). The peak at 1727 cm^{-1} corresponds to

nonconjugated carboxylic carbonyl group [16] and can be explained by oxidation of silicon substrate before deposition.

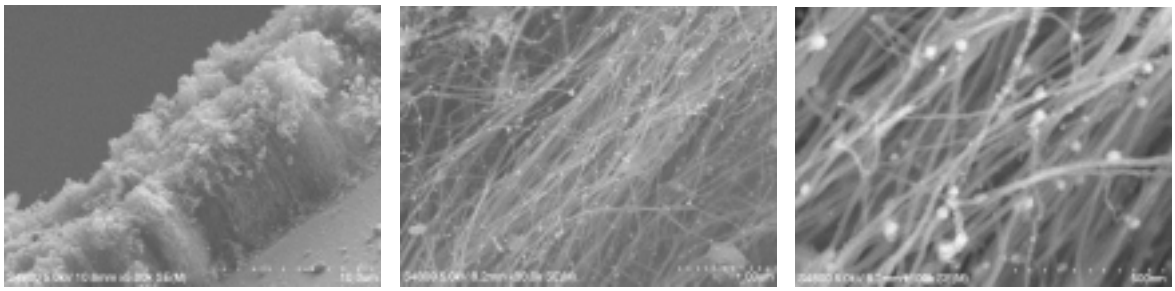

Fig. 9. SEM image of CNTs obtained in PECVD at i = 30 mA and p = 10 Torr.

These small peaks in Raman spectrum corresponding to the A_{1g} breathing mode of single-wall CNT (Fig. 6), could suggest that a small quantity of single-wall CNT may be present in the deposition [14].

4. Conclusions

The experimental results show that the maximum ratio of I_G/I_D was obtained when the number density of C atoms was maxim. The relative number density of the C_2, C_3 molecules and the clusters to the number density of CH radical increased with gas pressure. The increased number density of the C_2, C_3 and the clusters in plasma was determined by a low electron temperature and recombination processes. If the electron temperature was high, in low range pressure of CH_4 gas, the dissociation processes dominate in plasma. In this case, in low range pressure of CH_4 gas, the number density of C atoms was higher than in high range pressure.

The maximum length of CNT synthesized in PECVD in CH_4 gas, and the maximum ratio between G peak and D peak were obtained when the deposition was realized in 10 Torr pressure of CH_4 gas and 30 mA discharge current.

These experimental results cannot explain completely the mechanism of CNT formation.

References

[1] S. Iijima, Nature **354** (1991) 56 -
[2] A. Thess, et al., Science **273** (1996) 483 - 487
[3] W.Z. Li, et al., Science **274** (1996) 1701 - 1703
[4] L.C. Qin, D. Zhou, A.R. Krauss, D.M.Gruen, Appl. Phys. Lett., **72** (1998) 3437 - 3439
[5] M.A. Liberman, A.J. Lichtenberg, *Principles of plasma discharges and materials processing*, John Wiley&Sons, Inc., 1994, p. 289
[6] S. Chiashi, Y. Murakami, Y. Miyauchi, S. Maruyama, Chem. Phys. Lett., **386** (2004) 89 - 94
[7] M.A. Bratescu, Y. Sakai, D. Yamaoka, Y. Suda, H. Sugawara, Appl. Surface Science, **197** (2002) 257 - 262
[8] N.A. Morrison, C. William, W.I. Milne, J. Appl. Phys., **94** (2003) 7031 - 7043
[9] Y.H. Le Teuff, T.J. Millar, A.J. Marckwick, UMIST *Database for Astrochemistry*, http://www.rate99.co.uk
[10] W. Lochte-Holtgreven, *Plasma diagnostics*, AIP Press, 1995, p.181
[11] E.A. Rohlfing, J. Chem. Phys., **89** (1988) 6103 - 6112
[12] A.A. Puretzky, D.B. Geohegan, X. Fan, S.J. Pennycook, Appl. Phys. Lett., **76** (2000) 182 - 184
[13] S.M. Bachilo, et al., Science 298 (2002) 2361
[14] K. Kwok, W.K.S. Chiu, Carbon **43** (2004) 435 - 444
[15] S. Liu, S. Gangopadhyay, G. Sreenivas, S.S. Ang, H.A. Naseem, Phys.Rev.B, **55** (1997) 13020 - 13024
[16] N. Kouklin, M. Tzolov, D. Straus, A. Yin, J.M. Xu, Appl. Phys. Lett., **85** (2004) 4463 – 4465

Plasma deposited composite bioactive porous coatings for intrabone implants

V.I. Kalita[1], A.G. Gnedovets[1], A.I. Mamaev[2], V.A. Mamaeva[2], D.A. Malanin[3], V.B. Pisarev[3]

1 Laboratory of Physics, Chemistry and Technology of Coatings, A.A. Baikov Institute of Metallurgy and Materials Science, Russian Academy of Sciences, Moscow, Russia
2 Laboratory of Ceramic Coatings, Institute of Strength Physics and Materials Science, Siberian Branch of the Russian Academy of Sciences, Tomsk, Russia
3 Department of Traumatology and Orthopedy, Volgograd State Medical University, Volgograd, Russia

Abstract
Composite coating for intrabone implants as a combination of capillary-porous titanium coating with deposited bioactive ceramic top layer is proposed. Porous coating is formed on an implant surface by atmospheric plasma spraying and bioactive ceramic layer is deposited over it by microplasma process in electrolytic solutions. High values of porosity and bioactive nature of these composite coatings are favorable for bone tissue growing in and fastening its connection with an implant.
Keywords: biomaterials; porous coatings; implants; plasma spray

1. Introduction

Connection of a bone skeleton with the help of implants remains an important problem of clinical medicine and material science. Bone tissue should easily grow into the surface layer of an implant ensuring strong and reliable connection.

One of the impressive examples of porous coatings applications is their use in medicine as components of orthopedic or dental implants significantly enhancing their performance. Porous metal and ceramic coatings deposited on implants facilitate bone ingrowth and implant fixation. This application area for coatings is one of the fastest-growing areas in the field of biomaterials [1-3].

The most common surface coatings used for metal implants include sintered beads, diffusion bonded wire mesh, and metallic plasma sprayed porous coatings. In conventional plasma spraying process, the operating parameters are adjusted such that the metal powder particles (most often commercially pure titanium, typically ~200 μm in diameter) being injected into the plasma are only partially melted as they are being accelerated toward the substrate. Plasma sprayed coatings are commonly 500 to 1000 μm thick, but they do not form a regular three-dimensional interconnected array of pores. The porosity of these coatings reaches ~30%, and the maximum pore size is about 50–150 μm. Relatively low mechanical strength of the plasma sprayed coatings may be associated with low contact area between the deposited particles. The plasma sprayed coatings essentially form irregular surfaces with very little interconnected porosity throughout the thickness of the coating.

For bone to grow into the porous coating, certain minimum pore sizes must be achieved. If these minimums are not met, either soft tissue will form or ingrowth will not occur at all. Studies [1-3] have shown that the minimum pore size for load bearing implants, such as artificial hips and knees, should be approximately 100 to 150 μm. Most porous coatings intended for intrabone implants have pore sizes that range from 100 to 500 μm. Observations suggest that the performance of porous-coated implants depends on the pore structure as a function of both the degree of pore interconnectivity and the volume of porosity. In particular, performance of an implant is greatly enhanced by the use of osteoconductive materials (osteoconduction is defined as the ability of a material to encourage bone to grow toward and along its surface).

Surface engineering plays a particularly significant role in implants design since the bone grows onto the surface, thus affecting the quality of the bond between bone and implant. Bone ingrowth is dependent on the material and biological properties of the surface of the implant but at a great extent also on its surface parameters. The key factors in a porous structure design are the surface roughness, pore size and the amount of pore interconnectivity.

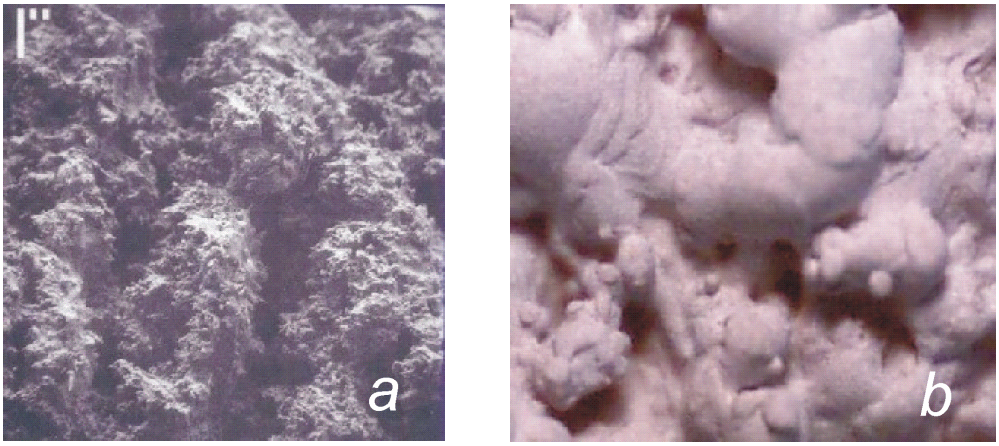

Fig. 1. SEM images of the surface of 3DCP Ti (a) and Ti+HA (b) coatings. Mark – 100 μm.

Bone fixation could be further maximized by means of deposition of hydroxyapatite (HA) layer over the porous coating on an implant. The osteoconductivity of HA facilitates bone contact by directing bone growth towards the implant and both to the coating. Osteoconductivity of HA coatings can guide bone growth into the pore space to enhance the mechanical bonding. With this aim microplasma electrolytic method could be used which allows receiving uniform bioceramic porous coatings on a complex geometrical relief.

A coating of HA, a major inorganic component of bone, on the metal surface has been suggested as the most effective way to give biocompatibility and osseoconductivity. Until today several coating techniques of HA on titanium alloys such as plasma spray coating, sputtering, chemical vapor deposition, electrophoresis, electrochemical deposition, and dip coating, have been explored and among these techniques plasma spray coating has mostly been highlighted for the applications. However, using plasma spray coating it is very difficult to obtain uniform HA coating and high bond strength between HA and Ti/Ti-alloy substrates.

A new concept of bone-implant volumetric boundary in the form of three-dimensional capillary-porous (3DCP) metallic (Ti) coating with deposited bioactive ceramic (BC) top layer (Fig. 1) is proposed in the present research. Porous titanic coating is formed on an implant surface by atmospheric plasma spraying (APS) and bioactive ceramic hydroxyapatite layer is deposited over it by microplasma process in electrolytic solutions.

2. Plasma spraying of porous coatings

The requirements to implants listed above, have stimulated a design of plasma sprayed porous coatings with regulable structure ensuring high osteoconductive properties and at the same time high strength characteristics of deposited surface layer. These conflicting objectives could be fulfilled by means of spatial separation of porous and condensed volumes of the coating. Such a new concept of bone-implant volumetric boundary in the form of three-dimensional capillary-porous titanium coatings was proposed in [4]. These coatings consist of cavities (open voids or valleys) and ridges (deposited material or peaks) growing from a surface of the substrate (Fig. 1a). The ridges may have micro-rough surface and include capillaries. The process of fabrication of 3DCP coatings is performed by atmospheric plasma spraying at off-normal spray angle of completely-molten particles to the substrate using Ti wire as a feedstock. The method of 3DCP coating buildup is based on the effect of shadow zones arising behind the particles already deposited to the substrate (e.g., [5]). The height of the ridges is of the same order as the mean height of the 3DCP coating. The surface area of the coating increases directly proportionally with the increase of the coating thickness, thus this type of coating is named three-dimensional.

Titanium used in 3DCP coatings is known as highly stable material which easily osseointegrates with bone [1-3]. Firstly, titanium is passive in aqueous solutions and the passive film that forms on titanium is stable even in a biological system. Secondly, oxide on titanium reacts with mineral ions, water and other constituents of biofluids that cause remodeling of the surface. It has been shown that calcium phosphate forms on the passive oxide film. The calcium phosphate formed on titanium is similar to apatite. Titanium therefore forms its own bioactive surface leading to osseointegration in a similar fashion to HA coated implants.

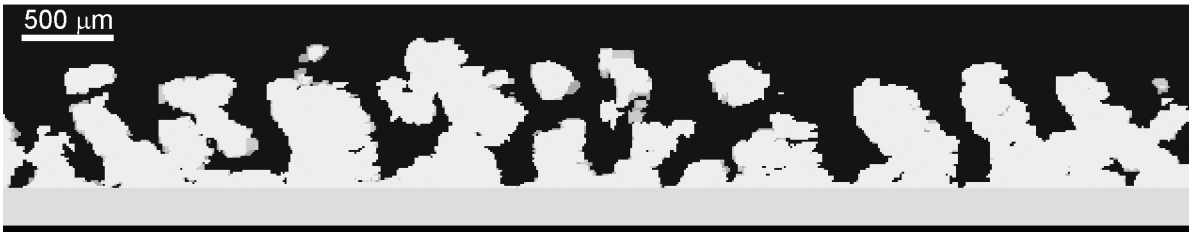

Fig. 2. Cross section of 3DCP coating. Spray angle θ = 30°. Computer simulations.

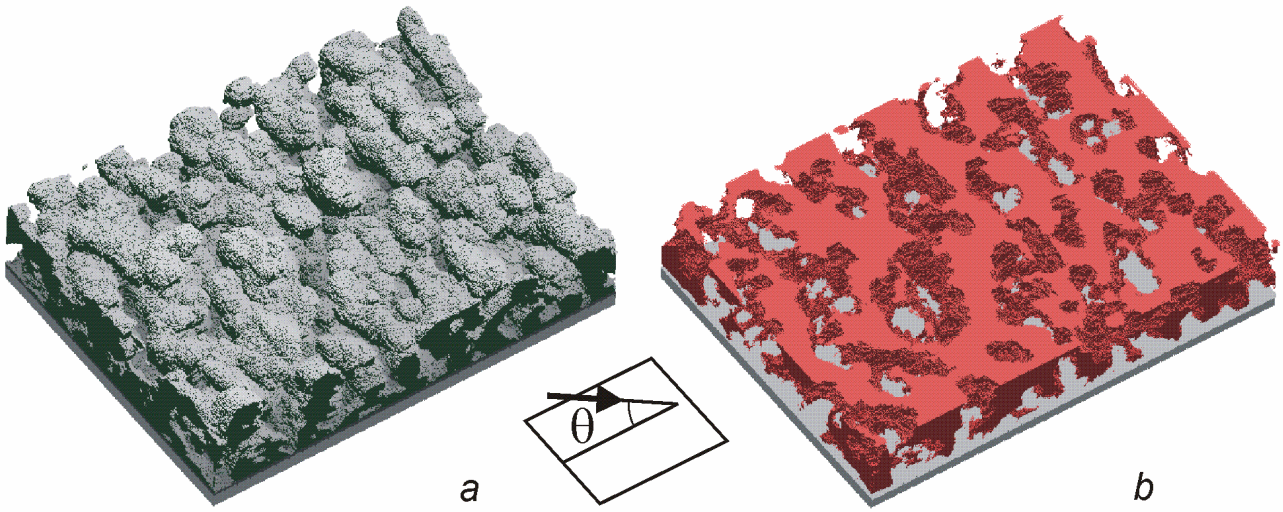

Fig. 3. 3D-images of 3DCP coating (*a*) and corresponding pore network (*b*). Spray angle θ = 30°. Substrate area 4×3 mm^2. Computer simulations.

The cavities represent the main porous fraction of the 3DCP coating; bone ingrowths into this volume. The structure of porous coating of this type itself promotes biological activity, since the size and shape of the cavities are favorable for bone ingrowth and healing.

Typical characteristics of plasma sprayed implant surface coatings are given in the Table 1. It is important to point out that experimental value of the volume available for bone ingrowth for 3DCP coatings is 6 times higher than the corresponding value determined for conventional plasma sprayed coatings [6].

Structural coating parameters were also predicted by numerical simulation of plasma spray coating build-up process using a three-dimensional discrete ballistic model. Depending on a sample geometry and angle of spray, typical numerical experiment describes layering of 20000−80000 individual particles. The model predicts coating porosity, thickness and roughness as functions of the spraying conditions. Depending on the deposited particles size and shapes of the resulting splats, different types of microstructures and porosities, and consequently different coating properties could be obtained. The simulation results for the spray angle θ=30° illustrating the coating structure and corresponding pore network which characterizes osteoconductivity are shown in Fig. 2 and 3.

Table 1. Characteristics of porous coatings deposited on intrabone implants

Parameter	Type of coating	
	Traditional plasma spray	3DCP coatings
Volume available for bone ingrowth, μm^3/ μm^2	71.0	413.9
Ra, μm	28.9	359
Rz, μm	144.9	824
Ra/Rz	0.155	0.436

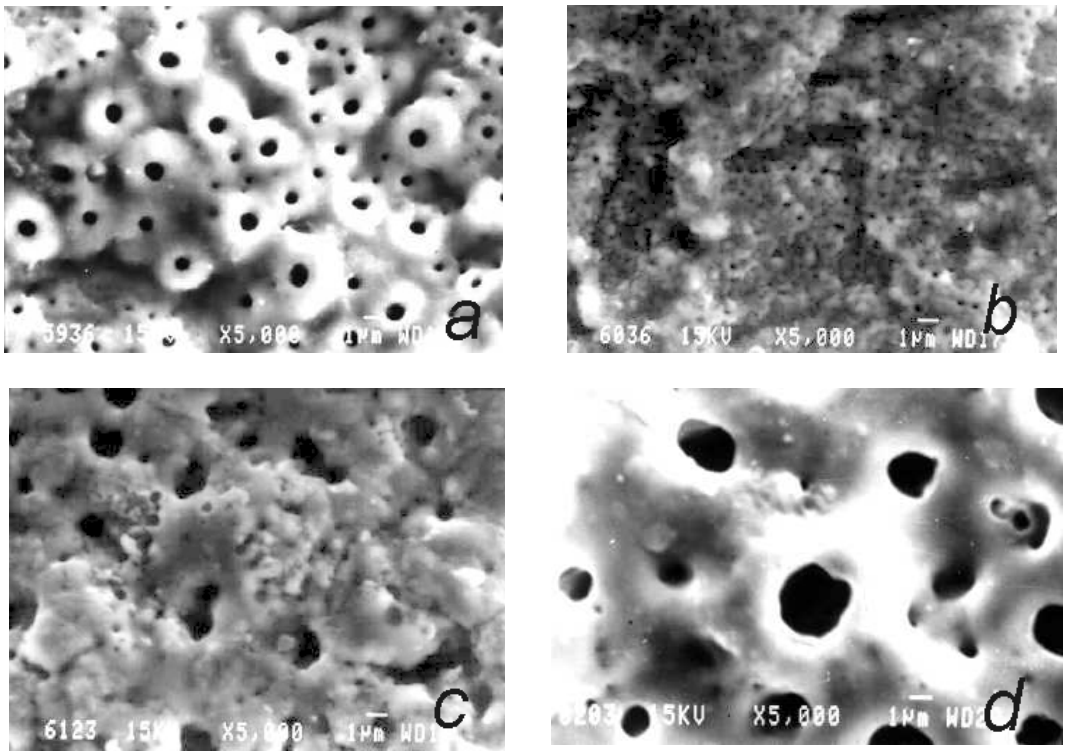

Fig. 4. Morphology of BC coatings deposited over 3DCP Ti coating in electrolytic solutions (Table 2). ×5000.

3. Microplasma deposition of bioactive ceramic coatings

Microplasma process is a room-temperature electrochemical method suitable for HA coating, and this technique may replace plasma spray coating. Microplasma electrolytic technique has the certain advantages on deposition of bioactive ceramic layers in comparison with conventional ways of deposition. Pulsed plasma deposition methods in solutions of electrolytes allow obtaining coatings with high adhesion due to high values of energy of local microplasma discharges on a surface of the processable sample, promoting creation of nanocrystal ceramic coatings. Microplasma process enables depositing BC films of uniform thickness on the coarce and rough surface of 3DCP Ti coatings over implants of complex shape [7,8]. This method can be applied for the formation of gradient coatings [9] with the internal layer consisting of thermodynamically stable TiO_2 formed by microplasma discharges generated at the surface and the outer nanostructured BC layer composed of Ca and P atoms.

During pulsed electrolytic microplasma process, BC coating is formed over titanium substrate consisting at least of two layers. The internal layer is composed of titanium oxides, and the external bioactive layer is sintered of calcium and phosphorus compounds and HA presenting in electrolyte as dispersed powder. The composition and structure of bioactive coating can be constructed: it depends on the composition of an alloy on which it is deposited, but in the greater degree on the composition of electrolyte. Also it is possible to design such properties of a coating as thickness, porosity, a roughness, and the pore sizes.

Table 2. Electrolyte composition and characteristics of BC coatings: element composition, thickness h, roughness R_a, pore surface concentration N, porosity P, pore diameter D

	Electrolyte composition	Ti	P	Ca	h, μm	R_a, μm	N, cm^{-2}	P, %	D, μm
(*a*)	Na_2HPO_4, HA	72.5	22.08	5.42	47	1.49	1×10^6	8	4.0
(*b*)	Na_2CO_3, HA	97.8	0.16	2.06	44	0.89	1×10^7	22	1.2
(*c*)	KOH, $Ca_3(PO4)_2$	96.6	3.19	0.23	33	0.86	9×10^6	14	2.5
(*d*)	Na_2HPO_4, $Na_2B_4O_7$, H_3BO_3	78.6	21.54	–	49	2.32	1×10^6	20	6.3

BC coatings on implants were obtained in electrolytic solutions containing calcium phosphates and HA at the applied voltage of 440 V and pulse duration 200 μs. BC coatings fabricated by microplasma process include crater shaped pores. BC coating composition, pore diameters and concentration depend strongly on electrolyte composition (Table 2, Fig. 4). All investigated coatings on titanium and its alloys have high chemical stability, they are not dissolved in acids and alkalis.

4. *In vivo* research

Research of fabricated implants *in vivo* was carried out with dogs (24 knee joints). The technique of experiment included formation of channels in distal epiphyses of femurs in which appropriate cylindrical implants (titanium rods 7 mm in length and 3.3 mm in diameter) were placed. Two types of surfaces were analyzed: implants without (control group) and with 3DCP Ti and BC coatings (experimental group). Results of biopsy have shown that implants with plasma sprayed porous Ti + HA coatings were strongly fixed in tissue of femoral condyle. A process of enchondral ossification was observed on the border between these implants and the bone tissue. Within the period of 16−24 weeks the bone beams have been formed directly integrating with coatings and repeating their surface relief (Fig. 5).

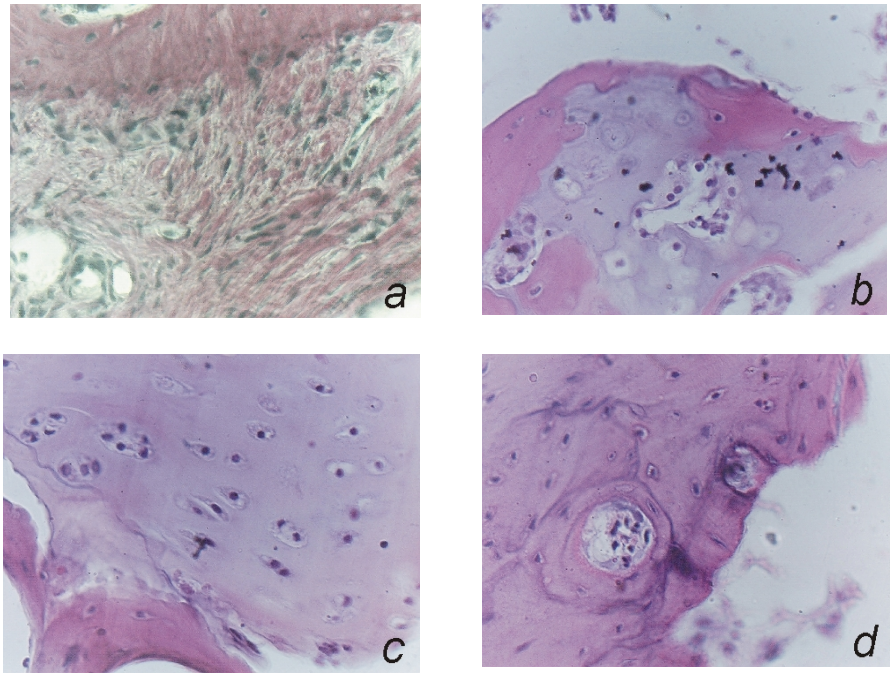

Fig. 5. Regenerative processes at the bone-implant boundary: (*a*) Ti implant without coating – increase in growth of the friable connective tissue around implant; (*b*) implant with 3DCP Ti coating – formation of clusters of chondrical tissue; (*c*) implant with 3DCP Ti + BC coating – processes of enchondrical ossification; (*d*) completing of the bone tissue formation. Dye: (*a*) Van Ghison; (*b*)–(*d*) heamatoxyline and eosin. ×400.

5. Intrabone implants with composite 3DCP Ti+BC coatings

The research of coating build-up process and porous structures obtained at off-normal spray angles have led to the development of the technology of fabrication of a new generation of effective composite porous coatings intended for intrabone implants.

The porosity of 3DCP coatings reaches 50%, and the widths of ridges and cavities may be regulated over a wide range from 5 up to 2700 μm. The small porosity (2–10 %) of the internal volume of the ridges allows achieving the values of adhesion and cohesion close to the values of feedstock (dense) sprayed materials. Special

conditions of plasma spraying process have allowed achieving the shear strength of 250 MPa at the coating porosity level of 45%. Favorable coating characteristics ensure reliable fastening a bone tissue in 3DCP coatings. One of the modifications of cementless hip prostheses with porous composite bioactive coating is shown in Fig. 6. About 80% of the surface of the prosthesis (Ti6Al4V) is covered by 3DCP Ti+HA coating with the thickness of 0.5–0.8 mm. This construction ensures reliable primary press-fit fixation and also secondary fixation due to osteointegration into the porous coating with bioactive top layer.

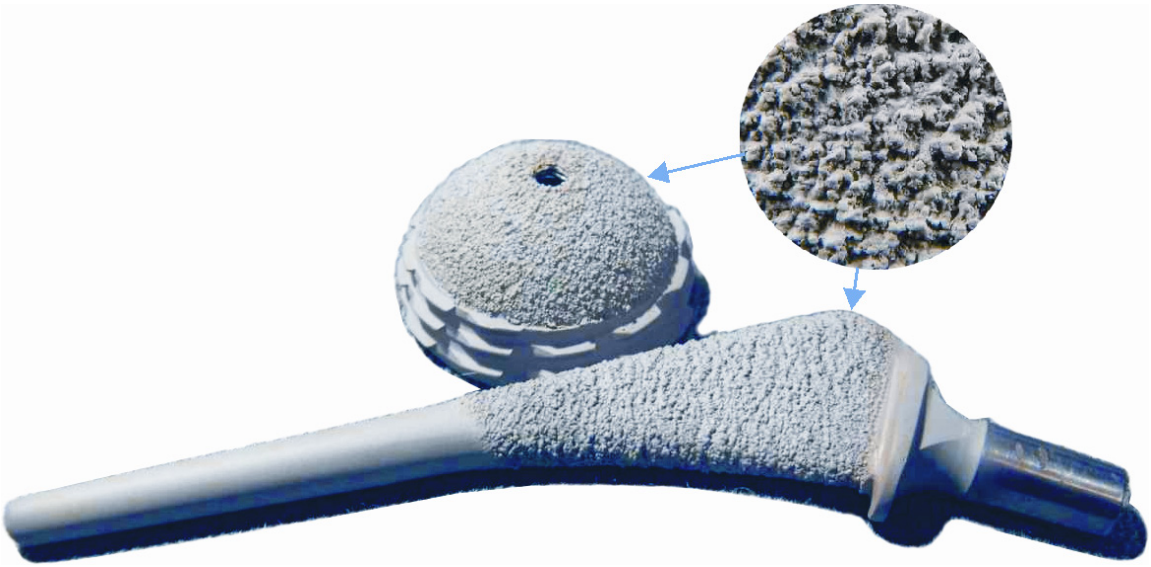

Fig. 6. Intrabone implants with 3DCP Ti+BC coatings.

6. Conclusion

Combined process of plasma spray-microplasma deposition of highly porous bioactive composite coatings with principally new structure and enhanced mechanical and operating characteristics has been developed. High values of porosity, surface area and excellent mechanical properties of 3DCP Ti + BC coatings proved to be favorable for bone tissue growing in and fastening of its connection with an implant. BC and 3DCP coatings successfully supplement each other by their surface structure: presence of micro and macroporosty is favorable for fastening of bone tissue on the implant surface. Bioactive properties of these coatings ensure high stability and strength of bone-implant bond.

References

[1] L. Sun, C.C. Berndt, K.A. Gross, A. Kucuk – J. Biomed. Mater. Res. **58**, 570 (2001).
[2] Handbook of Materials for Medical Devices – J.R. Davis, Ed., ASM Int., Materials Park, OH (2003).
[3] K.A. Hing, S.M. Best, K.E. Tanner, W. Bonfield, P.A. Revell – J. Biomed. Mater. Res. **68A**, 187 (2004).
[4] V.I. Kalita, V.A. Paramonov − Phys. Chem. Mater. Treatment. 6 (2002).
[5] M.P. Kanouff, R.A. Jr. Neiser, T.J. Roemer – J. Thermal Spray Technol. **7**, 219 (1998).
[6] D. D. Arola, M. K. McCain – J. Biomed. Mater. Res. **53**, 536 (2000).
[7] A.I. Mamaev, S.V. Vibornova, V.A. Mamaeva – J. Adv. Mater. **6** (1998).
[8] X. Nie, A. Leyland, A. Matthews – Surf. Coat. Technol. **125**, 407 (2000).
[9] Y.-M. Sung, Y.-K. Shin, Y.-W. Song, A.I. Mamaev, V. Mamaeva – Crystal Growth & Design. **5**, 29 (2005).

Engineering of plasma spray porous coatings

V.I. Kalita[1], A.G. Gnedovets[1]

[1] *Laboratory of Physics, Chemistry and Technology of Coatings, A.A. Baikov Institute of Metallurgy and Materials Science, Russian Academy of Sciences, Moscow, Russia*

Abstract
Novel technology of plasma spraying of three-dimensional capillary-porous coatings with principally new structure consisting of ridges and cavities has been developed. The process of fabrication of these coatings is performed under a sharp incidence angle of the plasma spray to the substrate. The method of spraying is based on the effect of shadow zones arising behind the particles already deposited to the substrate. Influence of the spray angle on coatings porosity, roughness and structure is investigated.
Keywords: porous coatings; computer modeling; plasma spray

1. Introduction

As a rule, porosity is considered to be a defect of plasma sprayed coatings. Nevertheless, highly porous coatings in some situations are desirable and they are widely used in various branches of technology, science, and medicine, serving like heat exchangers, catalytic surfaces, bioactive surface layers of intrabone implants, drug delivery elements, etc. The key factors in a porous structure design are the surface roughness, pore size and the amount of pore interconnectivity.

Structural, mechanical, and other properties of plasma sprayed coatings are controlled by the impingement, spreading and solidification of discrete molten particles which finally form splats on a substrate or previously deposited layers during plasma spraying process. The splat layering depends on the particle temperature and velocity at impact, the shape and topology of already deposited layers, the substrate temperature, the ability of the flattening particle to accommodate their pores, asperities, etc.

The advances in understanding of the process of plasma spraying have allowed controlling the coating properties, reliability and reproducibility. Recently, the important results of the intensive research in the field of plasma spraying both in experiments and modeling during the last five decades have been summarized in extended review publications [1,2].

The requirements of current technology have stimulated a design of plasma sprayed porous coatings with regulable structure ensuring high values of porosity, pore interconnectivity and at the same time high strength characteristics of deposited surface layer. These conflicting objectives could be fulfilled by means of spatial separation of porous and condensed volumes of the coating. Such a new concept of three-dimensional capillary-porous (3DCP) coatings was proposed in [3]. These coatings consist of cavities (open voids) and ridges (deposited material) growing from a surface of the substrate. The ridges may have micro-rough surface and include capillaries. The process of fabrication of 3DCP coatings is performed by atmospheric plasma spraying (APS) under a sharp incidence angle of completely-molten particles to the substrate. The method of 3DCP coating buildup is based on the effect of shadow zones arising behind the particles already deposited to the substrate (e.g., [4]). The height of the ridges is of the same order as the mean height of the 3DCP coating. The surface area of the coating increases directly proportionally with the increase of the coating thickness, thus this type of coating is named three-dimensional.

Various aspects of coating deposition at off-normal spray angles have been studied previously by different authors (e.g., [1,2] and literature cited therein) including peculiarities of coating buildup, splat formation, etc. However, as it was mentioned, in the majority of papers coating deposition at off-normal spray angles was considered as a process leading to the defective coating structure. At the same time, off-normal plasma spraying enables to create unique three-dimensional structures which could not be fabricated in any other technological process.

This paper describes the experimental and theoretical investigations of the coating growth at off-normal plasma spraying and the resulting structural and mechanical properties of 3DCP coatings.

2. Spraying conditions and coatings characterization techniques

In the experiments presented in this paper, the feedstock was commercially pure titanium powder with a particle size distribution ranging from 36 to 63 μm and mean particle size of 49.5 μm. The coatings with a thickness up to 1 mm were deposited onto flat and cylindrical (diameter 10 mm) titanium substrates at different spray angles (here and hereinafter, as is customary, the spray angle θ is defined as the angle between the substrate surface and the impacting particles trajectories).

For the coatings deposition, plasma torch (20 kW, atmospheric pressure $Ar+N_2$) with special nozzle ensuring plasma flow extraction from the coating deposition zone, local protection from atmospheric oxygen and eliminating the heat influence of the plasma flow on the coating and substrate was used. The design of the extracting nozzle led to an increase in the neutrality of a gas medium in a spraying spot, a decrease in the thermal effect of a plasma jet on a sprayed coating, and an increase in the efficiency of heating a powder in the plasma jet. Decreasing the temperature gradient across a plasma jet is another important factor. Moreover, the nozzle increases the maximum velocity of sprayed particles up to 200 $m \cdot s^{-1}$.

The structural coatings characteristics were measured using optical microscopy, SEM and image analysis. For the investigations of the surface of Ti 3DCP coatings, soft hardware complex based on high resolution SEM Hitachi-800 was used. Planimetric and stereometric morphological surface analyses were performed by means image processing program [3]. Porous structures of the plasma-sprayed coatings were also analyzed by mercury intrusion porosimetry (MIP). Mechanical tests of the deposited porous coatings were performed using Instron equipment and original methods including shear tests with a help of a matrix with orifices for sample streching.

3. Effect of spray angle on coating structure

In order to illustrate influence of the spray angle on the coating structure in a single experiment under the same operating conditions, the plasma torch was oriented perpendicularly to the axis of the titanium cylindrical rod substrate with a diameter of 10 mm. In this case, as it is clear from Figure 1, the spray angle θ varies continuously from 0 to 90° along the cylinder surface.

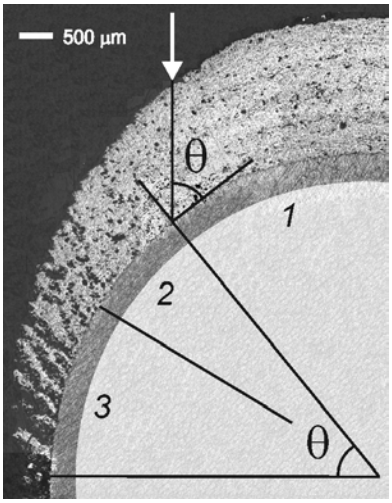

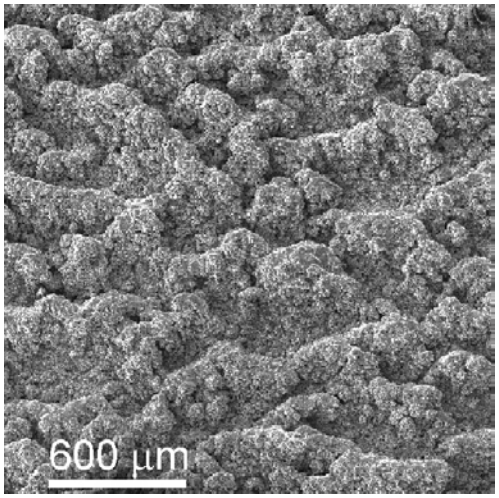

Figure 1. Cross section of cylindrical sample with plasma sprayed titanium coating (fragment). *1* – zone of low porosity, contains small-sized pores; *2* – transition zone, includes closed voids and large pores; *3* – zone of high porosity, consists of ridges. Arrow indicates the direction of spraying.

Figure 2. SEM image of the surface of titanium 3DCP coating deposited at the spray angle θ = 20°.

By its structure, the titanium coating sprayed onto the cylindrical substrate in some approximation could be divided into three zones (these zones are allocated on each side of the plane of symmetry which is normal to the cross section presented in Figure 1). In the central zone (*1*) the porosity is relatively low and the coating contains

pores which sizes do not exceed 20 μm. In the peripheral zone (*3*) the coating obtains a columnar structure and consists of ridges growing up from the substrate surface. The remaining zone (*2*) is transitional and includes closed voids and large pores with diameters of the order of ~60 μm. Depending on the spraying conditions (particles temperature, velocity, diameter, etc.), the dimensions of the transition zone are defined by the spray angles θ ranging from 40 to 50°.

The experiment with plasma spraying onto a cylinder is a visual demonstration of important morphological peculiarities of the coatings deposited at off-normal spray angles. While the mechanisms of pore formation in the central zone (*1*) are typical for traditional plasma spraying (incomplete filling of intersplat spaces by molten particles, splat curling, cracks, etc.), one more mechanism associated with the shadow effect described above appears in transitional (*2*) and especially in the peripheral (*3*) zones. Due to the relief shadowing, the absolute values of the local coating profile peaks heights and peak to peak distances increase with the decrease of the spray angle. Starting from some critical angle ($\theta < 40°$), isolated ridges appear on the substrate. It should be pointed out that the angle between a single ridge and the substrate surface does not coincide with the local spray angle; typical values of the slope angles of ridges are about 48–52° even at nearly zero spray angles. In the transition zone, during the process of growing up the neighboring ridges finally overlap each other, and as a result the closed pore network is formed within the coating. In the plane of the cross section (Figure 1) these large-sized pores are not connected with each other.

4. Coatings characterization

A series of titanium coating deposition experiments have been performed at a number of fixed values of the spray angle (Figure 2). Except traditional coatings characteristics such as roughness and porosity, various morphological parameters of porous coatings were considered: the equivalent pore diameter, defined as the diameter of a circle with the same area as the selected pore; the pore specific surface area, defined as the ratio of the surface of all the pores to the total volume; pore shape factor, defined as the ratio of lager to minor semiaxis of the ellipsoid inscribed into the real pore. These results are summarized in Table 1 and Figures 3 and 4.

Table 1. Morphological characteristics of Ti 3DCP coatings (SEM analysis).

Parameter	Spray angle	
	20°	30°
Total number of pores	$2.1 \cdot 10^5$	$2.9 \cdot 10^5$
Porosity, %	45.75	39.66
Minimum equivalent pore diameter, μm	0.54	0.61
Maximum equivalent pore diameter, μm	402.4	267.7
Mean pore diameter/dispersion, μm	1.86/13.5	1.77/10.3
Pores specific surface area, $\mu m^2/\mu m^3$	0.38	0.47
Pore shape factor	0.16–0.96	0.10–0.99

The experiments demonstrated that the amount of porosity and surface roughness increases slowly with decreasing the spray angle from 90° down to ~50°. After that a fast increase in these parameters occurs. These observations are in quite good qualitative agreement with the experimental results reported in [5] for alumina and titania composed particles deposited at off-normal spray angles.

Figure 4 compares the pore size distributions for the spray angles 90° and 30°. The allocation of pores in the coatings is of polymodal character. In the Ti 3DCP coating sprayed at 30° at least three groups of pores could be detected. The major part of porosity of the 3DCP coatings corresponds to large open voids – cavities between the ridges. The contribution of this type of pores with equivalent diameter of 100 μm and higher to the total coating porosity reaches 40–50%. The microstructure of the ridges is represented by the deformed solidified particles (splats) with the shapes typical to traditional thermal spraying process. In order to achieve the highest strength characteristics of porous coating, the ridges must be built-up of splats with maximum contact area between them. The sizes of the pores allocated in the ridges depend on the thickness of the formed splats which values according to experimental measurements may vary within 5–15 μm interval. Inclusion of semi-molten particles into the coating results in the appearance of pores with sizes close to the sprayed particle diameters.

Special conditions of plasma spraying process have allowed achieving the value of 250 MPa for the shear strength of 3DCP titanium coatings at the coating porosity level of 45% and surface roughness characteristics R_a = 359 μm, R_z = 824 μm, R_a/R_z = 0.436. The width of cavities of 3DCP coatings may be regulated over a wide range from 5 up to 2000 μm, and the width of ridges − from 200 to 2700 μm. Low porosity (2–10%) of internal volume of ridges allows to reach the values of adhesion and cohesion close to the values for initial (dense) spraying materials.

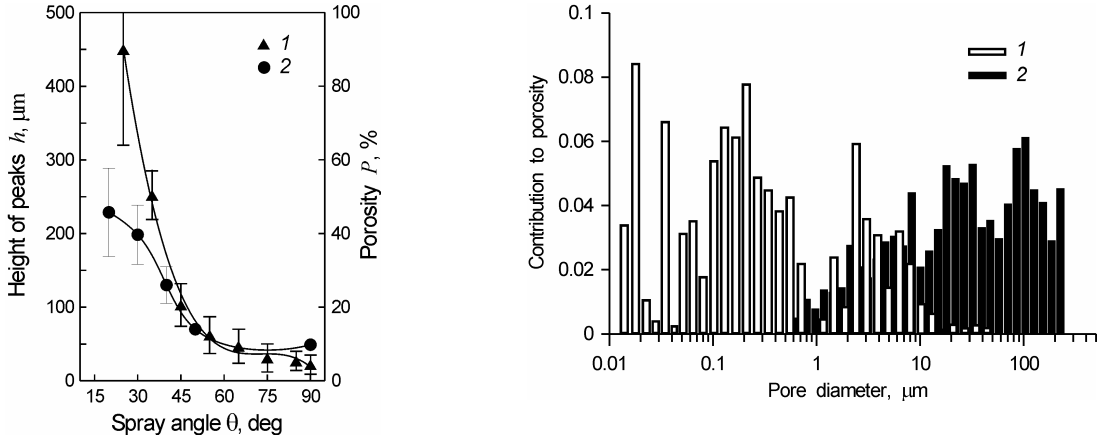

Figure 3. Dependencies on the spray angle θ of (*1*) profile peaks heights *h* and (*2*) coating porosity *P*.
Figure 4. Pore size distributions for the spray angles (*1*) 90° and (*2*) 30°.

5. Model description and simulation results

Structural coating parameters can be predicted by numerical simulation of plasma spray coating build-up process. In principle, a strict plasma spray coating growth model could be developed based on the detailed description of numerous (typically, about 10^4–10^5) individual collisions of deposited particles with a substrate, their deformation and solidification as a splats. However, this requires solving complex coupled problems of hydrodynamics and heat transfer for every particle-surface collision. Although tremendous progress has been made in this area [6,7], modern computers can simulate splat formation and interactions only of a few splats. Therefore, some simplified approach to obtain information concerning coating structure should be used, such as continuous [8], stochastic [9] or discrete ballistic [10] models.

A modified three-dimensional discrete ballistic model of coating build-up has been developed, which is based on simplified semi-analytical splat formation models proposed in [4,11]. The algorithm used in simulations can be described shortly as follows: (1) individual particle trajectory tracking; (2) calculation of the coordinates of the particle collision with the coating or substrate surface; (3) determination of the local angle of impact β which differs from the spray angle θ due to the complex coating surface topology; (4) deposition of the particle mass at a point of collision into a curved disk-shaped splat depending on the particle temperature, mass, velocity and local impact angle according to the rules similar to that of used in [4,11]; (5) coating update (Figure 5).

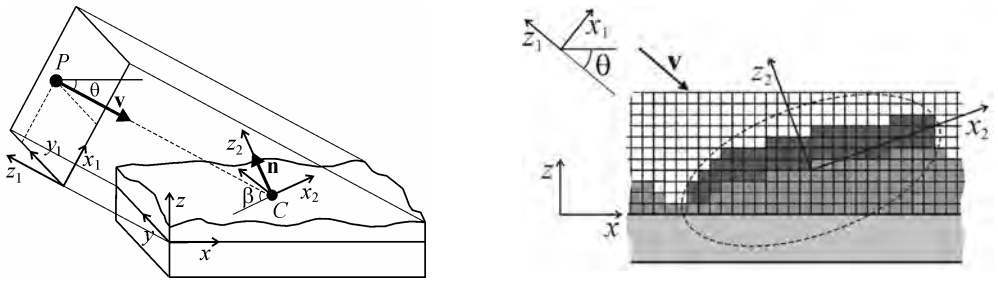

Figure 5. Coordinate system and schematic presentation of splat layering.

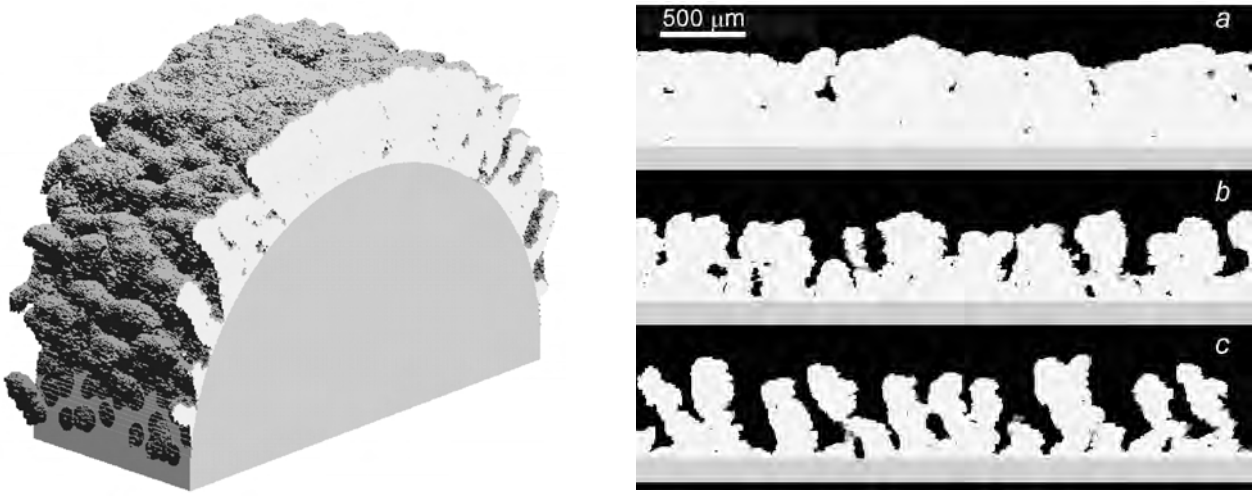

Figure 6. 3D image of cylindrical sample with plasma sprayed coating. Numerical simulation.
Figure 7. Coating cross sections for different spray angles θ: (*a*) 90°; (*b*) 45°; (*c*) 30°.

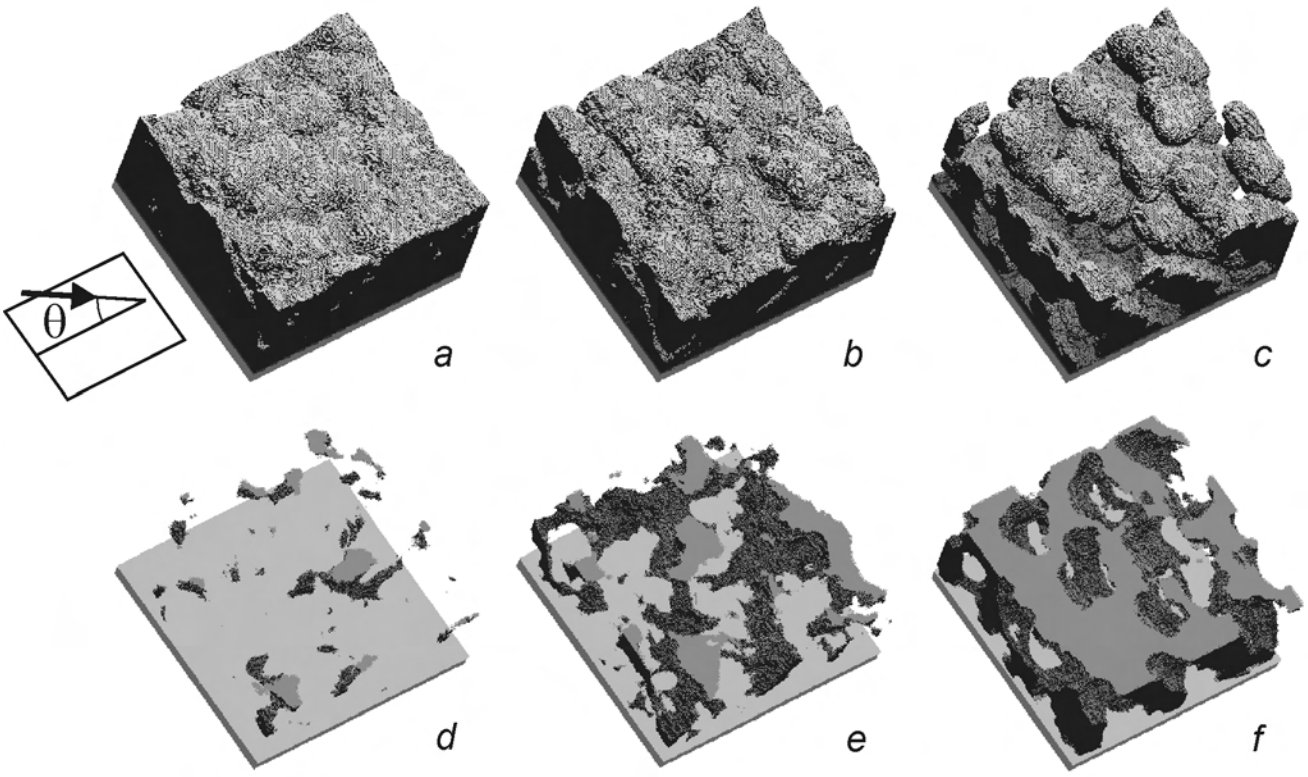

Figure 8. 3D images of coatings (*a*, *b*, *c*) and corresponding pore networks (*d*, *e*, *f*). Spray angles θ: (*a*, *d*) 90°; (*b*, *e*) 45°; (*c*, *f*) 30°. Substrate area 1000×1000 μm^2. Numerical simulation.

Depending on a sample geometry and angle of spray, typical numerical experiment describes layering of 20000−80000 individual particles. The simulation results illustrating influence of the spray angle on the coating structure for deposited Ti particles with diameter of 60 μm are shown in Figures 6−8. The model predicts coating porosity, thickness and roughness as functions of the spraying conditions. Depending on the deposited particles size and shapes of the resulting splats, different types of microstructures and porosities, and consequently different coating properties could be obtained.

Although several simplifying assumptions have been adopted in the model, in particular, semiempirical relations predicting the resulting shapes of the splats depending on the impinging molten particle impact parameters, the results of numerical simulations are in good qualitative agreement with experimental observations.

Conclusion

As a result of the studies of the process of coating formation at off-normal spray angles a novel technology of plasma spraying of highly porous coatings with principally new structure and enhanced mechanical characteristics was developed. These coatings consist of ridges growing from the surface of the substrate and separated one from another by cavities. The ridges may include micropores and capillaries. The total surface area increases directly proportionally with the increase of the thickness of the deposited coating. That is why this type of coatings was named as three-dimensional capillary-porous (3DCP). The process of fabrication of 3DCP coatings is performed under a sharp incidence angle of the plasma spray to the substrate and is based on the shadow effect.

Influence of the spray angle on morphological and mechanical characteristics of titanium coatings was investigated in experiments. It was found that in order to achieve the highest strength characteristics of porous coating, the ridges must be built-up of splats with maximum contact area between them. Low porosity of the internal volume of the ridges allows reaching the values of adhesion and cohesion close to the values of dense sprayed materials.

A three-dimensional discrete ballistic model based on the description of the consequence of individual molten spray particles impacts with the substrate was proposed for the interpretation of the experimental results and prediction of structural characteristics of deposited coatings depending on the spraying conditions.

The technology of plasma deposition of highly porous coatings is of great significance for biomedical applications, in particular, for enhancing bone ingrowth into the surface of implants [12]. High values of porosity, pore interconnectivity, large specific surface area and excellent mechanical properties of Ti 3DCP coatings proved to be favorable for bone tissue growing in and fastening of its connection with an intrabone implant.

References

[1] P. Fauchais – J. Phys. D: Appl. Phys. **37**, R86 (2004).

[2] P. Fauchais, M. Fukumoto, A. Vardelle, M. Vardelle – J. Thermal Spray Technol. **13**, 337 (2004).

[3] V.I. Kalita, V. N. Sokolov, V. A. Paramonov – Fiz. Khim. Obrab. Mater. **4**, 55 (2000).

[4] M. P. Kanouff, R. A. Jr. Neiser, T. J. Roemer – J. Thermal Spray Technol. **7**, 219 (1998).

[5] J. Ilavsky, A.J. Allen, G.G. Long, S. Krueger, C.C. Berndt, H. Herman – J. Am. Ceram. Soc. **80**, 733 (1997).

[6] J. Mostaghimi, M. Pasandideh-Fard, S. Chandra – Plasma Chem. Plasma Proc. **22**, 59 (2002).

[7] J. Mostaghimi, S. Chandra – Pure Appl. Chem. **74**, 441 (2002).

[8] Z. Djuric, P. Newbery P. Grant – Modelling Simul. Mater. Sci. Eng. **7**, 553 (1999).

[9] R. Ghafouri-Azar, J. Mostaghimi, S. Chandra, M. Charmchi – J. Therm. Spray Techn. **12**, 53 (2003).

[10] Y. Chen, G. Wang, H. Zhang – Thin Solid Films **390**, 13 (2001).

[11] J. Madejski – Int. J. Heat Mass Transfer **19**, 1009 (1976).

[12] A.G. Gnedovets, V.I. Kalita, D.I. Komlev, A.L. Yerokhin, A. Matthews – 16th International Vacuum Congress IVC-16, Venice, Italy, Conf. Proc. **1**, 398 (2004).

Characterization of laser ablation plasma ion source for thin film deposition in pulsed electric field

V.Yu. Fominski [1], A.G. Gnedovets [2], W. Scharff [3]

1 Department of Solid State Physics, Moscow State Engineering Physics Institute, Moscow, Russia
2 Laboratory of Laser Treatment of Materials, Baikov Institute of Metallurgy and Materials Science, Russian Academy of Sciences, Moscow, Russia
3 Diagnostic Systems, Institut fur Umweltanalysen, Ottendorf, Germany

Abstract
Experiments on pulsed laser deposition of Fe films on Si substrates were performed with the aim to analyze an energy spectrum and a dose of ions bombarding the film in strong pulsed electric fields. The goal of the study was to clarify the physical nature of the processes determining characteristics of the ion beam produced from the expanding plasma plume under different regimes of application of accelerating high-voltage pulses in order to establish the conditions in which it is possible to implant ions with a narrow energy spectrum.
Keywords: laser ablation; laser plasma; ion source; thin film deposition; ion implantation

1. Introduction

After irradiation of a target surface with nanosecond laser pulse, due to rapid material heating, evaporation and ionization, a plasma cloud is formed in front of the target and consequently expands away from the surface. Even at relatively low intensities near the threshold for ablation (0.2–1.0 $GWcm^{-2}$), measurements taken with nanosecond laser pulses, e.g. [1-3], show that the ablated material is significantly ionized, and the ions in the plasma plume obtain energies ranging up to several hundred of electron-volts. It was observed that both the mass flux and the average energy of the ions are strongly peaked about the target normal. The expansion of the plume is primarily driven by the plasma pressure gradients, but at the later stages there is an additional contribution from Coulomb interactions between the ions and the more mobile electrons and self-repulsion of the ions. The understanding of the temporal evolution of the ion energy distribution in the expanding cloud and the accompanying acceleration processes are of interest for many applications of laser-induced plasmas.

Vapor-plasma plumes initiated by high-intensity nanosecond laser pulses during irradiation of various materials may be employed in deposition of thin-film structures [4], as well as in generation of ion beams for the implantation processing of materials [5]. Depending on a processing parameters and applications, these laser-based technologies are known as pulsed laser deposition (PLD), pulsed laser ablation (PLA), ablation plasma ion implantation (APII), laser ion source (LIS), etc. In the past several years laser ablation techniques have received much attention, for example, in deposition of thin films and solid lubricants available for improving tribological functionality [6,7], semiconductor processing [3], etc.

The main advantage of the laser-based techniques is to generate ions of many elements by direct action on solid materials, instead of the conventional plasma immersed ion implantation (PIII), electron beam ion source (EBIS) and electron cyclotron resonance (ECR) sources which operate mainly on evaporated materials or gas mixtures. Ion source plasmas can be generated by laser beam from any solid material, even refractories and compounds, and requires no toxic precursor gases.

With pulsed laser deposition or implantation processes, the laser plume properties are known to depend critically on the laser fluence. But even at extremely high fluences of nanosecond laser pulse the ion energy does not exceed several keV. This energy is not high enough to initiate deep ion penetration, and hence the implanted layer is rather thin. The possibility exists of changing the conditions of film deposition by bombarding the surface with ions accelerated to sufficiently high energy by means of application of external electric field.

Since the first experiments on plasma immersion ion implantation [8], pulsed electric fields have been widely used in ion-implantation processing [9], as well as in adjusting the ion energy for plasma-enhanced deposition of thin films [10]. The possibility to increase the ion energy up to several tens of kilo-electron-volts using external electric fields in pulsed laser deposition of thin-film coatings was demonstrated in [3,6,7,11,12]. The method for accelerating ions from a laser ablation plume using pulsed fields is easy to implement; however, it is essential

that the ion dose and energy are precisely controlled to obtain the best properties of thin-film coatings. The ion beam may be controlled by varying the parameters of the high-voltage pulse, , the conditions of laser irradiation of the target, and the target-substrate geometry in the vacuum chamber.

The construction of a mathematical model that takes account of the mentioned above factors facilitates essentially the optimization of the conditions of thin-film formation. After the pioneering work [13] describing free plasma expansion into vacuum, tremendous progress has been achieved in the field of simulation of laser ablation plasmas (e.g., [14] and literature cited therein) but only a few theoretical investigations concern specific features of pulsed laser deposition or laser ion implantation in external electric fields.

In a number of studies [3,11], the dynamic sheath model of conventional PIII process [15] was adapted to the conditions of PLD (APII). A theory based on the Child–Langmuir law was applied to explain the long-time scale of the implanted ion current profile observed in laser ablation experiments with parallel target–substrate orientation [11]. This approach treats the case where the plasma plume is already in contact with the substrate and when the bias voltage is turned on.

This paper describes the results of the experimental and theoretical investigations of the factors that govern the dose and energy characteristics of ion bombardment during pulsed laser-induced deposition of thin films in strong pulsed electric fields. The goal of the study is to clarify the physical nature of the processes determining generation of the ion beam from the plasma plume under different regimes of application of accelerating electric pulse in order to establish the conditions in which it is possible to implant high-energy (>10 keV) ions with a relatively narrow energy spectrum. The investigations have been carried out with the Fe–Si system.

2. Experimental setup and diagnostic technique

A schematic diagram of the experimental setup is shown in Fig. 1. Q-switched Nd:yttrium-aluminum-garnet (YAG) laser with a wavelength of 1.06 μm and a laser pulse duration of 10 ns was used for the thin-film deposition. The laser beam guided by the scanning and focusing device was incident onto the target at an angle of 45°. The repetition rate of laser pulses was 10 Hz. The beam scanned the target area of 5×5 mm^2. The chamber was exhausted to a pressure of 10^{-4} Pa. A substrate was a Si(100) wafer located 8 cm away from the target, and the surfaces of the substrate and the target were oriented parallel to one another. The amplitude of the negative high-voltage pulse applied to the target reached 40 kV. The pulse generator activated from the laser-control unit triggered the high-voltage source with a given delay time relative to the laser pulse.

The processes proceeding in the laser-produced plasma upon applying high-voltage pulses were monitored by measuring the electric signals from the laser target. As it will be shown later, the signals measured at the target enable to receive important characteristics of the ion implantation process at the substrate. The energy and angular characteristics of the ion flow in the laser-generated plume were determined by measuring the time-of-flight (TOF) spectra with a detector.

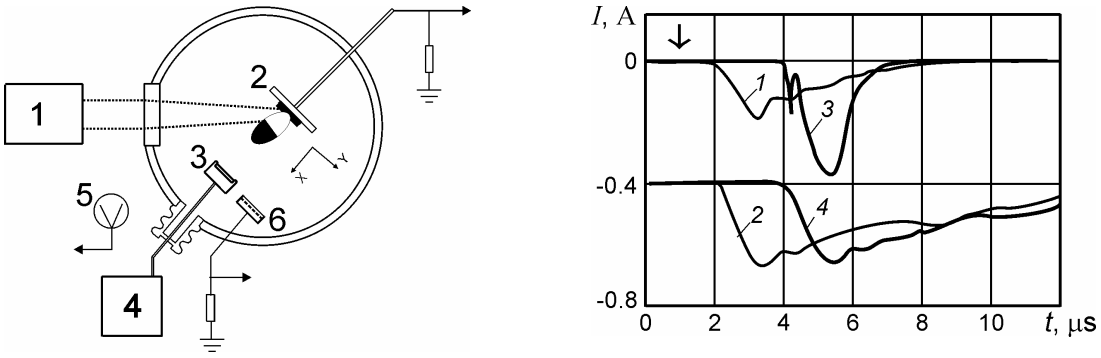

Figure 1. Schematic diagram of the main components of the experimental setup used for the pulsed laser deposition in pulsed electric fields and the detection of electric signals in the laser target: (*1*) Nd:YAG pulsed laser; (*2*) Fe target; (*3*) Si substrate; (*4*) pulsed high-voltage generator; (*5*) antenna; (*6*) ion detector.

Figure 2. Electric signals generated in the target (*1, 3*) and in the antenna (*2*, *4*) for different high-voltage pulse delay times of 1 and 3 μs. The moment of the laser pulse action is indicated by the arrow.

3. Characterization of laser ablation plasma ion sorce

In the experiments, the amplitude of the triangular high-voltage pulse (–40 kV) applied to the Si substrate and the laser fluence (7.5 J/cm^2) at the Fe target were fixed during the deposition. Owing to the high laser fluence at a relatively low power (20 mJ), the ionization of the laser plume was high, but the Fe vapor pressure near the substrate was low enough to avoid arcing.

The experiments on the detection of ion signals during free expansion (without external electric field) of the laser ablation plume in vacuum showed that the plume approached the substrate within ~2.5 μs after the beginning of the laser action. The ion density near the substrate increased for ~2 μs and, then, slowly decreased for ~10 μs. Measuring with a detector of the angular diagram of the laser-plume expansion in vacuum, it was found that the ion flux was peaked about the target normal in the angular range of ±30°. The ion energy did not exceed 400 eV, and the ion energy distribution obtained maximum within the interval of 150–200 eV.

The ion spectrum determined from the time-of-flight measurements was used to reconstruct the dynamics of the ion fraction of laser plume during its free expansion in vacuum. In particular, within 1 μs after the laser pulse the ion front propagates to a distance of ~2 cm from the target and the maximum plasma density decreases to ~6×10^{10} cm^{-3}. These data were used as the initial conditions for numerical simulations.

Parameters of the electric signals measured at the laser irradiated target depend significantly on the high-voltage delay time (Fig. 2). In the case when the accelerating voltage was turned on with the delay of 1 μs after the laser pulse, the electric signal at the target increased for ~1 μs and then decayed in a time interval of 6–7 μs.

Increase of the delay time resulted in the decrease of the signal length. If the high-voltage pulse was applied at the instant the ion front approached the substrate (delay time of 3 μs), the signal length reduced to ~2.5 μs, while the signal magnitude raised nearly twice. This signal initiated during the high-voltage rise time was formed at the peak of the accelerating voltage. In this case one may expect formation of the most narrow energy spectrum of the implanted ions. Further increase in the delay time leads to a smooth reduction of the signal amplitude.

4. Model description and simulation results

The particle-in-cell (PIC) algorithm was employed to solve the problem of ion source generation from the laser ablation plasma under conditions of varying density of the moving plasma plume in external electric field. The PIC code is a well-known tool for simulating plasma physics problems and it has been applied to a vast variety of problems, in particular, to description of both laser plasma expansion [16] and also conventional PIII processes [15].

Simulations were performed under several simplifying assumptions. A one-dimensional geometry was considered, since in vacuum the ablated plasma is sharply peaked and moves preferably in the forward direction along the normal to the target surface, especially after the high-voltage pulse is turned on. A representative time of laser plume formation is close to the laser pulse length (τ ~ 10 ns) and it is much less than duration of plasma expansion (several μs). By this reason, starting from an arbitrary time $t_0 >> \tau$, the plume propagation from the target to the substrate can be treated independently of the process of laser plasma ignition. To specify the initial plasma density and mass flow velocity, the experimental data were used. It was assumed that within 1 μs after the laser pulse, the plasma propagates to a distance x of 2 cm from the target and within this interval it obtains a bell-shaped density distribution $N_j(x)$ with the maximum value of 6×10^{10} cm^{-3}. The corresponding mass flow velocity is $u = 10^6$ cm s^{-1}. In the calculations typical values of the laser plasma temperature were employed: kT_j = 1 eV (here subscripts $j = i$ and e denote the plasma ions and electrons, respectively). The initial ion and electron velocity distribution functions $f_j(x,v,t=t_0)$ were presented by shifted Maxwellian distributions with the specified above parameters N_j, T_j and u corresponding to the plasma particles density, temperature and mass flow velocity, respectively.

As the boundary conditions for the Poisson equation, the known values of the potential at the grounded target $\varphi(x=0,t)=0$ and at the substrate $\varphi(x=x_s,t)=V_s(t)$ were used. The high-voltage pulse $V_s(t)$ applied to the substrate with the turn on delay τ_V was approximated by a triangular shape. The target – substrate distance was set equal to 8 cm. The total number of ions and also of electrons used in the simulations was up to 10^5.

Simulation of the laser plasma free expansion into vacuum shows that the first ions from the plume reach the substrate in ~2.3 μs and the maximum of the ion density arrives at the substrate within ~5 μs. Typical electric signals at the target and at the substrate are given in Fig. 3.

After accelerating voltage is turned on the electron flux to the target practically coincides with the ion flux to the substrate. This arises from the fundamental property of plasma to keep quasineutrality in the entire volume occupied by it. After application of the negative high voltage pulse, the ions from the plasma front are extracted by the accelerating field to the substrate. The electrons, on the contrary, are decelerated and they are not able to reach the substrate any more. Thus, in order to balance the ions outcome from the plasma, the surplus electrons are ejected from the plasma rear part and return back to the target. As a result, the electric signals at the substrate and at the target are close in shape within the whole period of the plasma expansion in the external electric field. In the experiments these signals are registered with unlike signs. Hence, the modeling results approve the validity of the monitoring of laser plasma ion implantation with a help of the signals from the target.

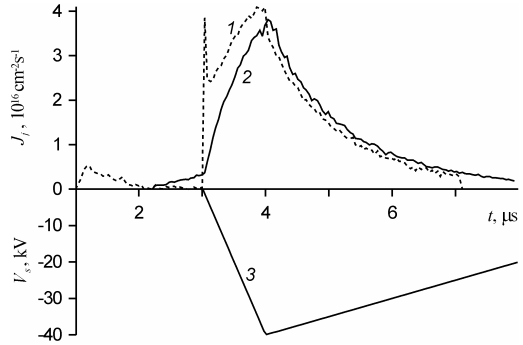

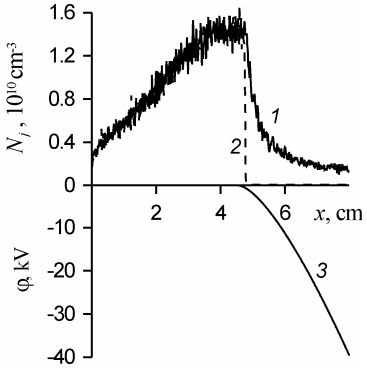

Figure 3. Variations with time t of the electron flux J_e at the target (*1*) and ion flux J_i at the substrate (*2*). Triangular high-voltage pulse V_s (*3*) is applied with the delay of $\tau_V = 3$ μs.

Figure 4. Spatial distributions of the number densities of ions N_i (*1*) and electrons N_e (*2*) and the plasma potential φ (*3*) during the plasma expansion from the target ($x = 0$) to the substrate ($x = 8$ cm) at the moment of time $t = 4$ μs. High-voltage pulse delay time $\tau_V = 3$ μs.

The representative structure of the expanding laser plasma at the stage of the action of the external electric field is shown in Fig. 4. During the whole process, in the major part of the expanding plume the quasineutrality condition is fulfilled, and the external electric field is almost completely screened by the plasma. At the plasma front, the charge separation takes place, and the ion sheath is formed between the plasma plume and the substrate. The ions are ejected to the substrate from the moving boundary of the plume where the electric field is very strong.

Computed dynamics of the ion density during the laser plume expansion in vacuum for the high-voltage pulse delay $\tau_V = 3$ μs is shown in Fig. 5. The ion current grows at the stage of the plume front movement toward the substrate (see also Fig. 3). Within this period of time the accelerating voltage after passing the absolute value maximum of 40 kV begins to decrease. Then the reverse motion of the plume front from the substrate to the target starts and thus the sheath extent increases. At the same time the expanding plasma as a whole continues its movement from the target to the substrate.

The simulations show that the ion energy spectrum and the ion bombardment time interval change to a great extent depending on the high-voltage pulse turn on delay time. Calculated ion fluxes to the substrate for different τ_V are presented in Fig. 6. Independently on the moment of the high-voltage switching on, the process of ion implantation is completed within the time of ~7–8 μs. An increase in the delay time τ_V leads to significant reducing of the high energy ion pulse at the substrate. For the delays $\tau_V \sim 3$–4 μs the calculated duration of the ion signal decreases to ~3 μs, and its amplitude grows nearly two times as compared to the case of $\tau_V \sim 1$ μs; this is in good agreement with the experimental data presented above. For larger turn on delays, a powerful signal of the accelerated ions is formed after relatively weak signal of the ions reaching the substrate before the high-voltage pulse is applied.

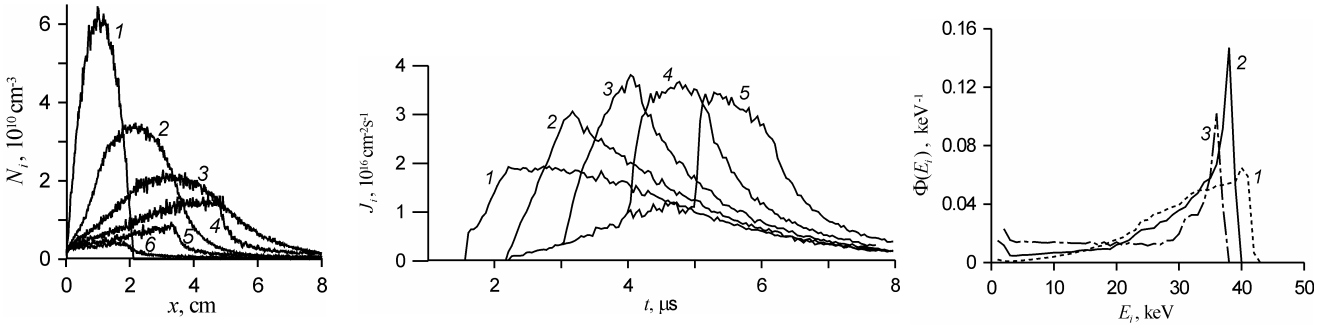

Figure 5. Dynamics of the ion density during the laser plume expansion for the regime with high-voltage delay τ_V = 3 μs. Digits near the curves (*1 – 6*) denote different moments of time t in μs.

Figure 6. Temporal variations of the ion flux density J_i at the substrate depending on the high-voltage pulse turn on delay time. Digits near the curves (*1 – 5*) denote delay times τ_V in μs.

Figure 7. Energy spectra of the ions bombarding the substrate for different high-voltage delays τ_V = 1 (*1*); 3 (*2*) and 5 μs (*3*).

The energy distributions of the ions bombarding the substrate for the regimes with different high-voltage pulse turn on delay times τ_V are given in Fig. 7. Simulation demonstrate that variations in time of a delay τ_V lead to noticeable changes in the resulting upper bound and width of the ion kinetic energy distribution. Calculations show that the upper bound of the ion energy distribution decreases from 43 to 40 keV as the delay time increases from 1 to 3 μs. At the same time, a fraction of high-energy ions increases.

5. Effect of high-voltage pulse parameters on laser ablation plasma ion source characteristics

For the conditions of the ion implantation to be optimized, it is necessary to select both proper conditions for the laser irradiation of the target and the time for the application of the high-voltage pulse. Both the results of numerical modeling and experiments with a triangular high-voltage pulse (with amplitude of up to 40 kV) demonstrated that the conditions proved to be optimal when laser pulses had medium power (20 mJ) and the delay of the high-voltage pulse was 3 μs.

Under these conditions, most of ions in the laser plume are concentrated in the space between the target and the substrate. Upon applying a high-voltage pulse, the plasma sheath quickly (in ~2–3 μs) spreads over the laser plasma; therefore, a major portion of the implanted-ion dose is acquired at the peak of the accelerating pulse. As large as 80% of implanted ions have a kinetic energy of approximately 30–40 keV.

Another implantation mode is implemented when the high-voltage pulse is applied with a short (~1μs) delay with respect to the laser pulse. In this case, the ions are accelerated from the front of the dense laser plasma; therefore, the ion-current pulse is governed by the dynamics of the laser plume, and its width is close to the target – substrate propagation time (~10 μs). Within this period of time, the accelerating voltage changed from −40 to 0 kV, which causes the energy spectrum of bombarding ions to broaden.

For long turn on delays (>5 μs), a broadening of the ion energy spectrum is due to the contribution of large amount of low-energy ions arriving to the substrate before the high-voltage pulse is applied. Only relatively small fraction of the ions can be accelerated to the required energies when the accelerating electric field is turned on. In addition, the ion energy broadening may occur because the implantation process involves all ions that are scattered throughout the vacuum chamber, in which the potential of the accelerating field varies from −40 kV (substrate) to 0 (chamber walls).

6. Conclusion

The potential of the laser ablation plasma as an effective ion source in the applied pulsed electric field was investigated. The experiments have demonstrated that pulsed laser deposition of thin films under applied high-voltage pulses provides means for the implantation of high-energy (several tens of keV) ions with a narrow

energy spectrum. In the experiments, it was established that the current characteristics of the plasma expanding from the target to the substrate depend significantly on the moment of application of the accelerating high-voltage pulses.

A physical model of laser-produced plasma expansion in vacuum in pulsed electric field based on the PIC algorithm was proposed for the interpretation of the experimental results and for the process optimization. Simulations demonstrated that variations in time of a delay τ_V lead to noticeable changes in the resulting upper bound and width of the kinetic energy distribution of implanted ions.

Both experiments with triangular high-voltage pulse and numerical simulations predicted that the ion energy spectrum occurred to be the optimal if the high-voltage pulse is applied at a moment of time (~3μs) when the ion component of the plume approached the substrate. In this case, the implanted ions have the highest energy close to the nominal value determined by the amplitude of the electric pulse. This regime is characteristic for the traditional plasma immersion ion implantation, when the ion current is governed by the dynamics of the plasma sheath in the substrate-to-target gap. An advance or delay in applying a high-voltage pulse causes the ion energy spectrum of bombarding ions to broaden.

By means of numerical simulation it was verified that the electron flux to the target practically coincides with the ion flux to the substrate after accelerating voltage is turned on, i.e. electric signals measured at the substrate and at the target are close in shape within the whole period of the plasma expansion in the external electric field. Thus, the modeling results approve the validity of the monitoring of laser plasma ion implantation with a help of the signals from the target.

In general, the investigations have demonstrated that the simple and cost-effective modified version of the traditional PLD technique provides the possibility of high-energy ion flux generation from laser ablation plasma for ion implantation and thin film deposition technologies.

Acknowledgment

This work was supported by the INTAS Grant No 03-51-4206 and the President of Russian Federation Grant for Leading Scientific Schools of Russia No NS-97.2003.2.

References

[1] B. Toftmann, J. Schou, T. N. Hansen, J. G. Lunney – Phys. Rev. Lett. **84**, 3998 (2000).
[2] F. Claeyssens, S.J. Henley, M.N.R. Ashfold – J. Appl. Phys. **94**, 2203 (2003).
[3] V.Yu. Fominski, V.N. Nevoiln, I. Smurov – J. Appl. Phys. **96**, 2374 (2004).
[4] Pulsed Laser Deposition of Thin Films. D.B. Chrisey, G.K. Hubler, Eds., Wiley, New York (1994).
[5] Yu.A. Bikovskii, V.N. Nevolin, V.Yu. Fominski. Ion and Laser Implantation of Metals, Energoatomizdat, Moscow (1991).
[6] V.Yu. Fominski, V.N. Nevoiln, R.I. Romanov, I. Smurov –J.Appl.Phys. **89**, 1449 (2001).
[7] V. Fominski, V. Nevoiln, R. Romanov, A. Smirnov, V. Titov, W. Scharff –Thin Solid Films **422**, 39 (2002).
[8] J. R. Conrad, J. L. Radtke, R. A. Dodd, J. Worzala, N. C. Tran, J. Appl. Phys. **62**, 4591 (1987).
[9] Handbook of Plasma Immersion Ion Implantation. A. Anders, Ed., Wiley, New York (2000).
[10] S. Qin, N. McGruer, C. Chan, K. Warner – IEEE Trans. Electron Devices **39**, 2354 (1992).
[11] B. Qi, R.M. Gilgenbah, Y.Y. Lau, M.D. Johnston, J. Lian, L.M. Wang, G.L. Doll, A. Lazarides, Appl. Phys. Lett. **78**, 3785 (2001).
[12] M.C. Jones, R.M. Gilgenbach, B. Qi, Y.Y. Lau, G.L. Doll, Appl. Phys. A **79**, 969 (2004).
[13] A.V. Gurevich, L.V. Pariskaya, L.P. Pitaievskii – Sov. Phys. JETP **22**, 449 (1966).
[14] A. Bogaerts, Z. Chen , R. Gijbels , A. Vertes – Spectrochim. Acta Part B **58**, 1867 (2003).
[15] P. K. Chu, S. Qin, C. Chan, N.W. Cheung, L.A. Larson – Mater. Sci. Eng. **R17**, 207 (1996).
[16] O. Ellegaard, T. Nedelea, J. Schoua, H.M. Urbassek. Appl. Surf. Sci. **197–198**, 229 (2002).

Global Model of Electronegative Discharges for Neutral Radical Control

S.J. Kim[1], J.T. Gudmundsson[2], M.A. Lieberman[1] and A.J. Lichtenberg[1]

[1]*Department of Electrical Engineering and Computer Science, University of California, Berkeley, USA*
[2]*Department of Electrical and Computer Engineering, University of Iceland, Reykjavik, Iceland*

Abstract
Electronegative plasmas driven by steady power and by time-modulated power, with oxygen as the feedstock gas, have been investigated utilizing volume-averaged (global) models of a cylindrical plasma discharge. The variations of the ratio of neutral radical to ion flux (Γ_O/Γ_+), depending on the chamber geometry and power modulation conditions, were examined using a simple model with uniform spatial profiles and a new model with non-uniform spatial profiles, and the results from the models were compared.
Keywords electronegative plasma, global model, neutral radical

1. Introduction

For the next generation plasma etching processes in the microelectronics industry, control and reduction of the ratio of neutral radical flux to ion flux (Γ_O/Γ_+) at the wafer surface is required to accomplish the patterning of the vertical etch profile in high aspect ratio features. To explore these processes, we investigated plasmas driven by steady power and by time-modulated power using various discharge models with oxygen as the feedstock.
The calculations of the plasma parameters have been made utilizing a volume-averaged (global) model of a cylindrical plasma discharge [1] [2] [3]. First, we used a simple model with uniform spatial profiles. In this model, all quantities are assumed to be uniform over a cylindrical discharge. This model can be applied to weakly electronegative discharges such as low pressure, high power, O_2 plasma [1]. However, there are significant errors in ignoring the effects of plasma profiles. Therefore, we have developed a new global model of cylindrical electronegative discharges with non-uniform spatial profiles and new expressions for the wall loss factors. This model is considered to be valid over a wider range of plasma parameters and pressures than the previous model.

2. Simple global model

This model assumes uniform spatial distribution of plasma parameters over the volume of bulk plasma, but includes a diffusive loss factor. However, the fluxes of both oxygen radicals and ions are approximated by assuming their densities are constant, $\Gamma_O = 1/4\, n_O v_O$ and $\Gamma_+ = n_+ u_B$, with v_O the oxygen thermal velocity and u_B the Bohm velocity. The global model consists of particle balance and power balance equations. In the particle balance equations, the reaction rates of O_2^+, O^- ions, electrons and the metastable oxygen molecules O_2 ($a\ ^1\Delta_g$) have been included. We consider pressures of 10 - 50 mTorr and plasma densities of 1×10^{10} - 1×10^{11} cm^{-3}. In this regime, the discharge is found to be weakly electronegative. A nearly sinusoidal waveform of the power pulse was used (rise and fall time = 50% of the pulse period). The power modulation period was varied to determine the optimum conditions for reduction of Γ_O/Γ_+. The effect of duty-ratio (on-time/period) on the reduction of Γ_O/Γ_+ was examined by comparing two different duty ratios (50% and 25%) together with a CW plasma case. Two chamber geometries with different aspect ratios (chamber height/diameter = 1/6 and unity) were examined to determine the influence of the surface-area/volume ratio. The diameter of the chamber was 30cm and the heights were 5cm and 30cm, respectively.
Figure 1 shows the plots of time-average flux ratio of oxygen neutrals to O_2^+ ions (Γ_O/Γ_+) with various pulse periods at 10 mTorr. The average power of smaller aspect ratio (b) is adjusted to yield similar values of steady state positive ion flux (Γ_+) on the wall as the aspect ratio of 1 in (a). At a fixed duty-ratio, the ratio Γ_O/Γ_+ is found to have a minimum value as the pulse period is varied, with the minimum value decreasing as the duty-ratio decreases. The pulse period that yields minimum Γ_O/Γ_+ decreases as the aspect ratio decreases. For steady-state discharges, reducing the aspect ratio by 6 leads to 43% reduction of Γ_O/Γ_+. For pulsed discharges, a 25% duty-ratio pulse with 50% rise and fall time can reduce the Γ_O/Γ_+ by an additional 27%.

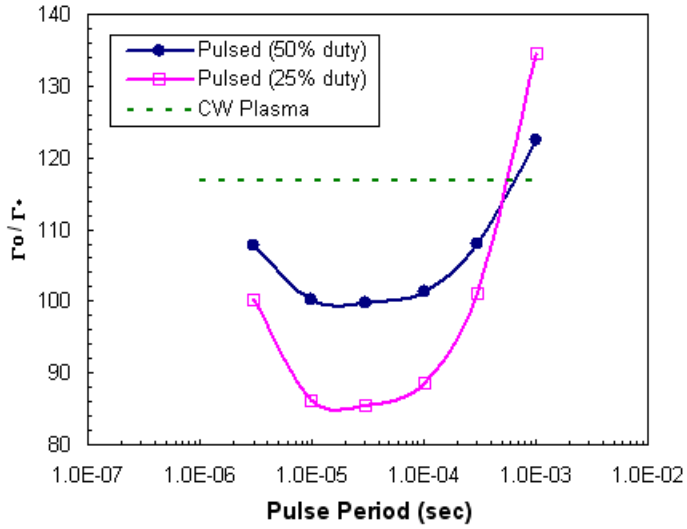

(a)

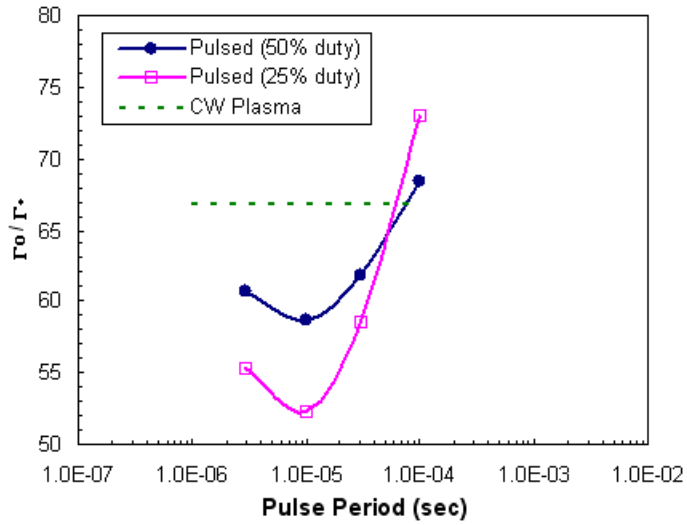

(b)

Figure 1. Time-average flux ratio of oxygen neutrals to O_2^+ ions (Γ_O/Γ_+) with various pulse periods based on simple global model. (a) height/diameter = 1, average power = 200 Watt, (b) height/diameter = 1/6, average power = 66 Watt. (The average power of (b) was adjusted to yield similar values of steady state positive ion flux (Γ_+) on the wall for (a) and (b).)

3. Improved model with non-uniform spatial profiles

To improve the accuracy of the simulation, we developed a new model which incorporates non-uniform spatial profiles of ions and neutrals rather than uniform profiles. In this new model, we combined three models of plane-parallel electronegative discharges which are accurate over different negative ion densities: (a) a low-pressure two-region parabolic model which has parabolic electronegative core with low-pressure electropositive edges [4] [5]; (b) a one region parabolic electronegative model applicable at low pressure and high electronegativity; and (c) a one-region flat-topped electronegative model applicable at higher pressure and higher electronegativity. Calculating the edge-to-center density ratio using these profiles, the new model has improved the overall

accuracy over a wider range of plasma parameters and pressures than the previous model. Denoting the edge-to-center positive ion density ratios for the three regimes as h_a, h_b and h_c, respectively, then the approximate results for the h_l factors are:

$$h_a \approx \frac{0.86}{\left(3+\eta\frac{l_p}{\lambda_+}\right)^{1/2}}\frac{1}{1+\alpha_0} \equiv h_{l0}\frac{1}{1+\alpha_0} \tag{1}$$

which approaches the constant electropositive result h_{l0} as electronegetivity α_0 becomes negligible,

$$h_b \approx \frac{1}{\gamma_-^{1/2}+\gamma_+^{1/2}\frac{\eta}{(2\pi)^{1/2}}\frac{l_p}{\lambda_+}}\frac{\alpha_0}{1+\alpha_0} \equiv h_{l\infty}\frac{\alpha_0}{1+\alpha_0} \tag{2}$$

which gives a result $h_{l\infty}$ that is independent of both α_0 and n_{e0} as α_0 becomes large, and

$$h_c \approx \frac{1}{\gamma_-^{1/2}+\gamma_+^{1/2}\frac{n_*^{1/2}}{n_{-0}^{1/2}}} \tag{3}$$

which depends on n_{-0} but is independent of α_0 and n_{e0}. In the above three expressions,

$$\eta=\frac{2\mathrm{T}_+}{\mathrm{T}_+ + \mathrm{T}_-};\qquad \gamma_-=\frac{\mathrm{T}_e}{\mathrm{T}_-};\qquad \gamma_+=\frac{\mathrm{T}_e}{\mathrm{T}_+};\qquad l_p=\mathrm{L}/2;\qquad n_*=\frac{15}{86}\left(\frac{8e\mathrm{T}_+}{\pi\mathrm{M}_+}\right)^{1/2}\frac{\eta^2}{K_{\mathrm{rec}}\lambda_+} \tag{4}$$

where l_p is the half-length of the system, the subscript + and – denote positive and negative ions, the subscript 0 denotes the center value, and K_{rec} is the positive-negative ion recombination coefficient. To obtain a single description of the fluxes covering the full parameter range, we use a linear ansatz that sums the h_l for three regimes to determine an overall h_l factor:

$$h_l = h_a + h_b + h_c\,;\qquad \Gamma = h_l\, n_{+0}\, u_{\mathrm{B}} \tag{5}$$

where the positive ion flux Γ is calculated as the product of the h_l, central positive ion density n_{+0} and the EP Bohm velocity, $u_B = (e\mathrm{T}_e/\mathrm{M})^{1/2}$.

We have also added particle balance equations for O_2 feedstock and O^+ ions, which were not implemented in the simple model. We introduced density-weighted averages for multiple positive and negative ion species, together with pressure-dependent effective volume and surface loss factors for the neutral species. To make the simulations more complete, we have also revised the chemical reaction coefficients used in the calculations based on recently reported results of cross section sets and measurements [6] [7].

After testing the new model with a steady-power discharge, we applied it to the time-modulation case. The same nearly sinusoidal waveform of the power pulse was used (rise and fall time = 50% of the pulse period) as in the simple model case. The power modulation period was varied and the effect of duty-ratio (on-time/period) was examined by comparing two different duty ratios (50% and 25%) together with the CW plasma case. Two aspect ratios that were same as the simple model case (height/diameter = 1/6 and unity) were examined to determine the influence of the surface-area/volume ratio.

Figure 2 shows the plots of time-average flux ratio of oxygen neutrals to O_2^+ ions (Γ_O/Γ_+) with various pulse periods at 10 mTorr, based on the new model. The average power of smaller aspect ratio (b) is adjusted to yield

similar values of steady state positive ion flux (Γ_+) on the wall as the aspect ratio of 1 in (a). At a fixed duty-ratio, the ratio Γ_O/Γ_+ is found to have a minimum value as the pulse period is varied, with the minimum value decreasing as the duty-ratio decreases. The pulse period that yields minimum Γ_O/Γ_+ also decreases as the aspect ratio decreases. For steady-state discharges, reducing the aspect ratio by 6 leads to 56% reduction of Γ_O/Γ_+. For pulsed discharges, a 25% duty-ratio pulse with 50% rise and fall time can reduce the Γ_O/Γ_+ by an additional 27%.

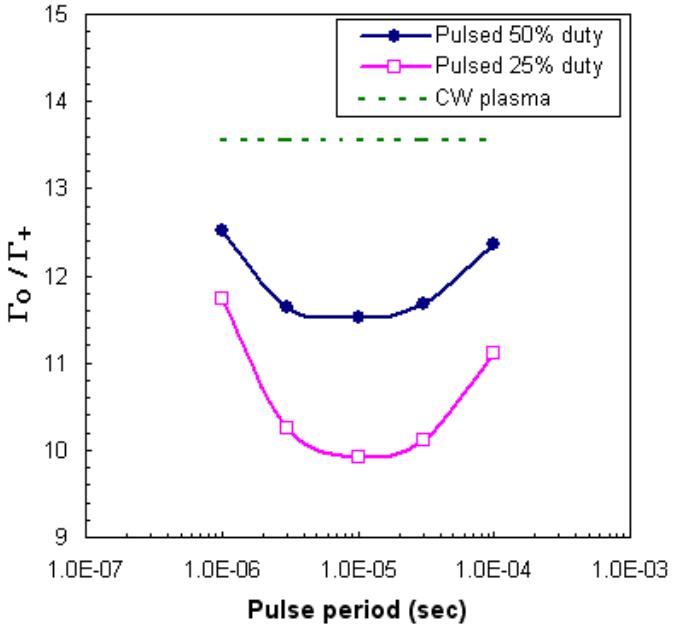

(a)

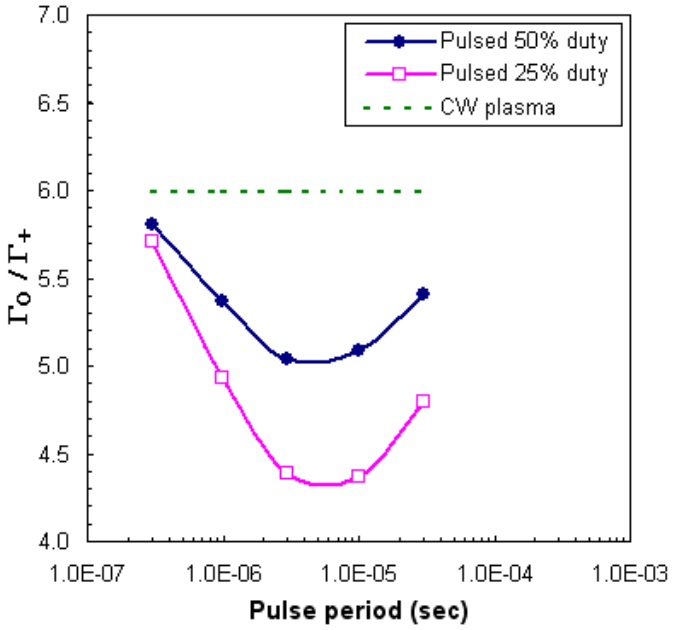

(b)

Figure 2. Time-average flux ratio of oxygen neutrals to O_2^+ ions (Γ_O/Γ_+) with various pulse periods based on the new model. (a) height/diameter = 1, average power = 400 Watt, (b) height/diameter = 1/6, average power = 102 Watt. (The average power of (b) was adjusted to yield similar values of steady state positive ion flux (Γ_+) on the wall for (a) and (b).)

In this new result, the range of the values of flux ratios (Γ_O/Γ_+) is almost 10 times lower than result of the simple model. This difference is the result of the various changes implemented in the new model, such as the introduction of wall loss factor for the neutrals, using a higher value of wall recombination coefficients for the neutral oxygen, different reaction coefficient sets together with the introduction of O^+ ions, and the difference in the calculation of positive ion loss factors. Nevertheless, the resulting trend of Γ_O/Γ_+ reductions at the smaller aspect ratio with the optimal pulse period and lower duty ratio is found to be similar to the simple model.

4. Conclusions

The electronegative plasmas driven by steady power and by time-modulated power, with oxygen as the feedstock gas, have been investigated utilizing volume-averaged (global) models of a cylindrical plasma discharge. The variations of the time-average flux ratio of oxygen neutrals to O_2^+ ions (Γ_O/Γ_+) depending on the chamber geometry and power modulation conditions were examined using a simple model with uniform spatial profiles and a new model with non-uniform spatial profiles, and the results from the models were compared. In both models, at a fixed duty-ratio, the ratio Γ_O/Γ_+ is found to have a minimum value as the pulse period is varied, with the minimum value decreasing as the duty-ratio decreases. The ratio Γ_O/Γ_+ is reduced in the chamber geometry with lower aspect ratio, and the pulse period that yields minimum Γ_O/Γ_+ also decreases.
In future work, we will compare the simulation results with measured experimental results.

References

[1] C. Lee, D.B. Graves, M.A. Lieberman and D.W. Hess: J. Electrochem. Soc. **141** (1994) 1546
[2] S. Ashida, C. Lee and M.A. Lieberman: J. Vac. Sci. Technol. A **13** (1995) 2498
[3] M.A. Lieberman and S. Ashida: Plasma Sources Sci. Technol. **5** (1996) 145
[4] I.G. Kouznetsouv, A.J. Lichtenberg and M.A. Lieberman: Plasma Sources Sci. Technol. **5** (1996) 662
[5] A.J. Lichtenberg, I.G. Kouznetsouv, Y.T. Lee, M.A. Lieberman, I.D. Kaganovich and L.D. Tsendin: Plasma Sources Sci. Technol. **6** (1997) 437
[6] J.T. Gudmundsson: J. Phys. D: Appl. Phys. **37** (2004) 2073
[7] J.T. Gudmundsson: A critical review of the reaction set for a low pressure oxygen processing discharge, report RH-17-2004, Science Institute, University of Iceland (2004)

Synthesis of carbon nanomaterials by thermal arc plasma

L. Fulcheri[1], T.M. Gruenberger[2], J. Gonzalez-Aguilar[1], H. Okuno[4], F. Fabry[2], E. Grivei[2], N. Probst[2], G. Flamant[3], J.C. Charlier[4]

[1] *Ecole des Mines de Paris, Centre for Energy and Processes, Sophia Antipolis, France*
[2] *Timcal Belgium S.A., Willebroek, Belgium*
[3] *PROMES-CNRS, Font Romeu, France*
[4] *University of Louvain, Unit of Physico-Chemistry and Physics of Materials, Belgium*

Abstract
Thermal plasmas open a new area for the bulk production of carbon nanostructures ranging from carbon black over fullerenes to carbon nanotubes with a high product selectivity.

Keywords : carbon black, fullerenes, nanotubes, 3-phase AC plasma system.

1. Introduction

Since the discovery of new forms of carbon such as Fullerenes and carbon nanotubes (CNT), in 1985, [1] and 1991, [2] respectively, carbon nanostructures remain at the forefront of the nanotechnology wave. However, carbon nanostructures have a long history : carbon black is indeed one of the oldest nanomaterials used by man since ancient civilizations in China and Egypt mixed soot into resins, vegetable oils or tar to create colors and inks. In addition, the first large scale industrial production of dispersed nanomaterials occurred with the production of carbon black early in the 20th century.

Continuous carbon black production techniques are usually based on combustion processes. These processes are characterized by a high level of CO_2 emissions since an important part of the carbon feedstock is burnt while the remaining part is converted into carbon black. In 2004, the carbon black industry was directly responsible for more than 25 million tons of CO_2 emissions (0.1 % of the total world CO_2 emissions). In addition, these processes hardly allow the independent control of some key processing parameters such as temperature profile, residence time or reactant concentration. On the other hand, present production techniques for fullerenes and carbon nanotubes production can only provide limited quantities and the availability of these new nanostructures in reasonable quantities, typically the order of several kilograms or tons, is a compelling necessity for the development of future applications.

In this context, new approaches using thermal plasma opens the way towards the mass production of carbon nanomaterials ranging from carbon black over fullerenes to nanotubes.

2. Apparatus

The overall process is presented in Figure 1. A 3-phase, 600 Hz, 260 kVA power supply is connected to a plasma torch, composed of three graphite electrodes, located at the top of the reactor. The plasma reactor is composed of a high temperature insulated chamber which upper part is equipped with a graphite nozzle where the hydrocarbon (HC) can be introduced. The external kiln of the reactor is water cooled. The system is equiped with a PTFE bag filter where carbon and gas are separated and collected. Gas network allows to provide different plasma gases or mixtures (N_2, Ar, He, CO, H_2) into the plasma system.

This technology, initially designed for the cracking of hydrocarbons [3-5], was adapted in order to treat solid carbon powders [6]. The overall process is illustrated in Figure 2. In this case, solid powder is transported together with the plasma gas to the arc zone. By opposition with the classical “arc process” generally used in fullerene and nanotube synthesis, the carbon rate is no more limited to the electrodes erosion but can be totally controlled. In addition, a system composed by a water cooled suction pipe combined with a recirculation loop was specially developed for the sampling of the species inside the reactor, their quenching and their transport up to a filter. This system has been designed to adjust the residence time and the quenching rate by changing the gas extraction point from the reactor and the gas flow rate in the recirculation loop. The reactant concentration being controlled by adjusting the plasma gas-precursor ratio.

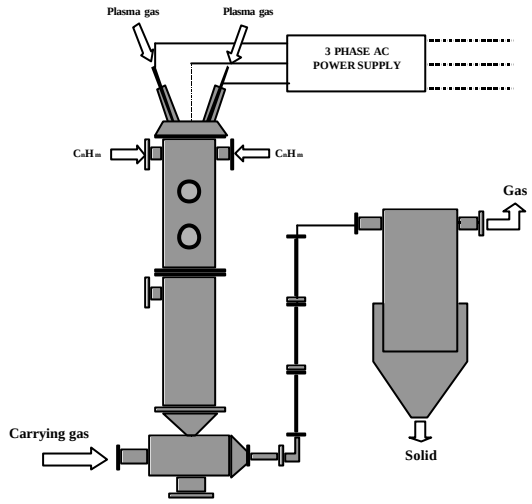

Figure 1 : Scheme of the plasma reactor for the production of carbon black (configuration 1)

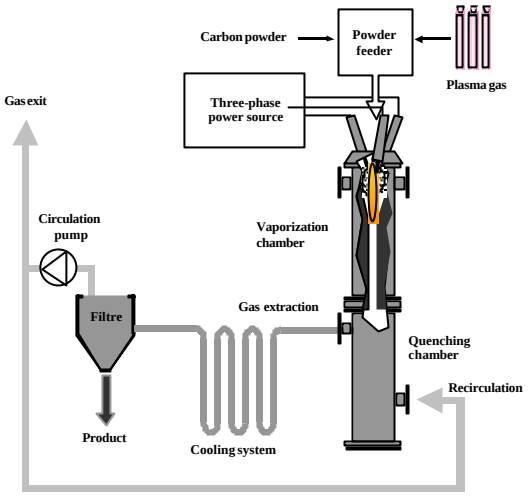

Figure 2 : Scheme of the plasma reactor for the synthesis of fullerenes and nanotubes (configuration 2)

Flow and wall temperatures were measured along the reactor. In the high temperature zones, the measurements were carried out by optical emission spectroscopy (OMS) and optical pyrometry, whereas R-type and K-type thermocouples were placed in the low temperature regions. The experimental set-up was in configuration 1 for carbon black production while configuration 2 was used for fullerenes and nanotubes synthesis.

3. Results

Carbon black

A large variety of carbon precursors (hydrocarbons), plasma gases, and operating conditions (flow rates, electrical power, injection points,…) have been investigated for the synthesis of carbon black. Depending on the operating conditions, different carbon black grades varying from typical low furnace blacks up to high temperature graphitised blacks could be obtained [7]. Figure 3 illustrates an example of typical structures obtained using colza oil as carbon feedstock. These structures are composed of branched-type aggregates, where central small spherical particles seem enrobed by a wrapping paper-like structure carbon layer. HRTEM shows that the elementary particles, which average diameter is around 30 nm, present a radial growth while the wrapping carbon layer shows a lateral growth, characteristic of high temperature carbon blacks, sometimes well crystallised.

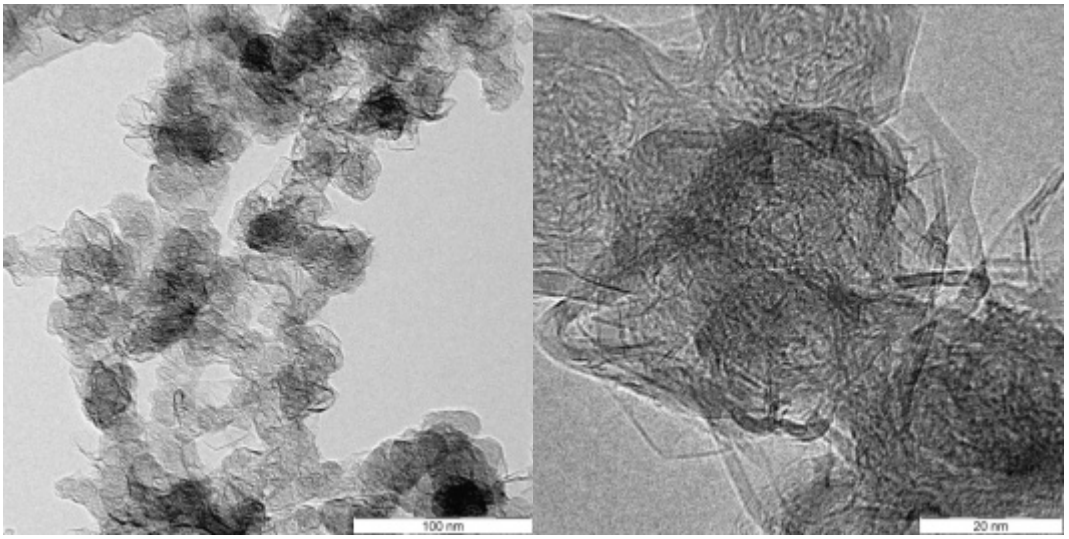

Figure 3 : TEM (left) and HRTEM (right) of a Plasma black aggregate obtained with colza oil

Fullerenes

For the production of fullerenes, pure dispersed carbon is introduced in the plasma reactor in the presence of an inert gas. Different parameters have been investigated: nature of the carbon precursor (acetylene black, graphite powder, carbon black,…) and plasma gases (He, Ar), arc current, gas and carbon flow rates, residence time and reactor geometries [8] . Contrary to the case of hydrocarbon cracking, where growth mechanisms are mainly governed by the hydrogen-carbon chemistry, the growth mechanisms are here based on the vaporisation-condensation of pure carbon into an inert atmosphere since neither hydrogen nor other carbon-combining gas is present in the system.

Figure 4 (left) represents the evolution of fullerene content in the soot (% C_{60} + C_{70}) versus carbon and gas flow rates (arbitrary unit) while Figure 4 (right) represents the fullerene yield evolution versus the two same parameters. These figures show the importance of the carbon dilution in the gas phase on these two parameters. So far the process for continuous fullerene synthesis is not fully optimised, however current yields typically of the order of 5 % (toluene extractable) have been obtained, the yield being however strongly dependent on throughput and noticeably higher yields have been achieved.

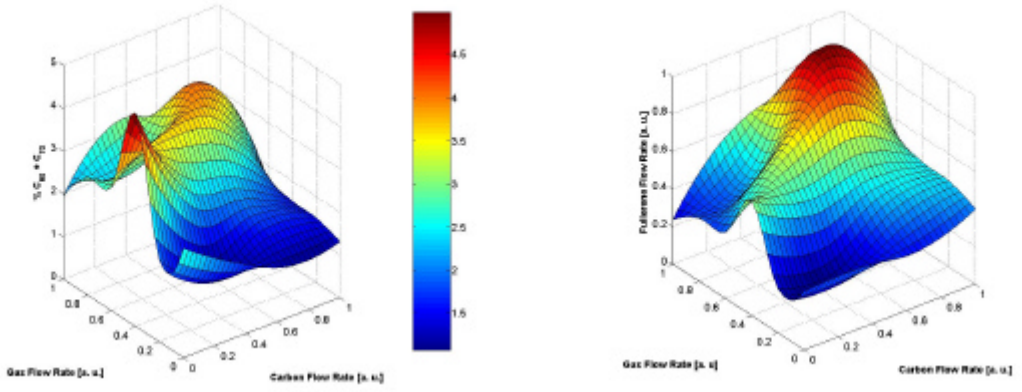

Figure 4 : Fullerene content and fullerene yield versus carbon and gas flow rates (arbitrary unit)

TEM analyses were performed on most fullerene soot. The obtained structures are radically different than the original precursors (acetylene black). Most structures show a typical “rounded” shape (left), very similar to those obtained by the arc or laser processes and described in literature, [9] while some other structures (right) present a very peculiar filamentous carbon organisation at the surface of the particle probably composed of nanocones.

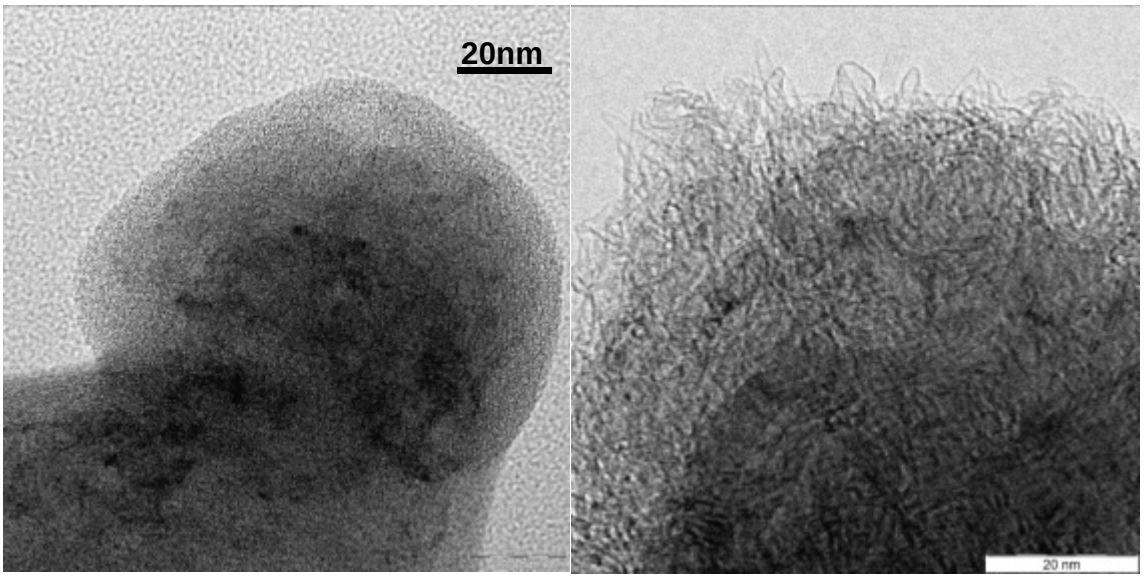

Figure 5 : TEM image of a typical “rounded shape” Fullerene soot (left). HRTEM detail of a filamentous surface of a fullerene soot (right).

Carbon Necklaces

Such structures represented in Figure 6 have been produced by injecting dispersed carbon together with a metal catalyst under a Nitrogen atmosphere (plasma gas), [10]. These nano-necklaces are up to several µm long with outer diameters in the range 50-100 nm. Carbon spheres are found to be regularly spaced along the filament. The necklace can include more than 50 units linked from the end of the bell to its head. In order to analyse their nano-structure, these carbon necklaces are also characterized by TEM, illustrating the repetition of an elementary unit looking like a nano-bell, sometimes filled. The joined segments in the carbon nano-necklaces are actually short variable-diameter compartments. Most unit are hollow however, some compartment are completely filled with the Ni-Co catalyst used during the synthesis. TEM and HRTEM pictures presented in Figure 7 show a high degree of graphitic organization of the carbon layers together with a detail showing intersection between two elementary successive cells.

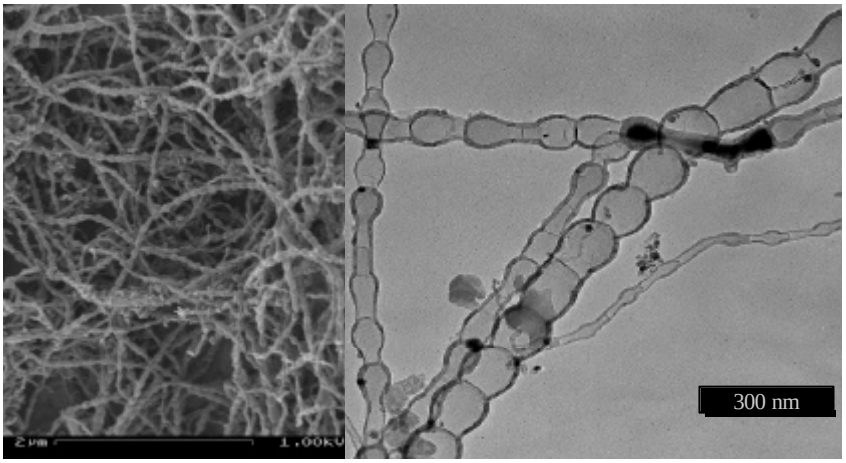

Figure 6 : SEM image (left) and TEM analysis (right) of the carbon "Necklaces" nanostructures

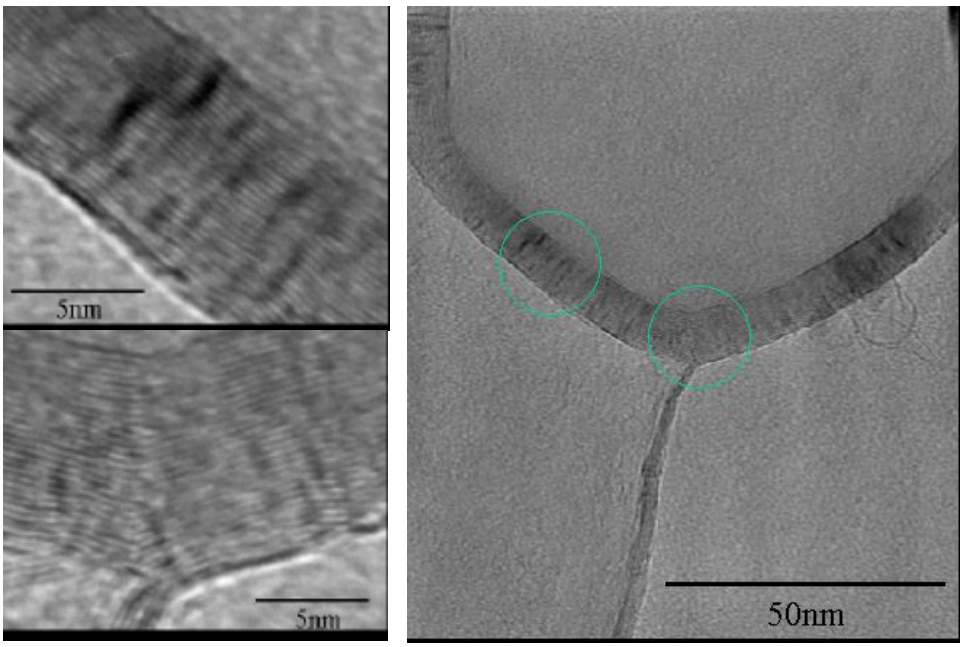

Figure 7 : HRTEM detail of the "Necklaces"carbon layers

These structures have some similarities with the "bamboo-like" ones but they differ from their typical rounded shape. This rounded shape suggests a similar growth mechanisms based on the absorption-segregation process of carbon into the metal catalyst, but differing by the temperature level: the metal catalyst being solid or liquid for "bamboo-like" and "necklaces" structures respectively.

Carbon Nanotubes

Single Wall Nanotubes (SWNT) have been obtained by injecting dispersed carbon together with a metal catalyst (generally cobalt or nickel) under an helium atmosphere and particular operating conditions, characterized by a high quenching velocity. SWNT, generally observed together with small metallic particles, often agglomerate to form bundles. Both bundles and particles can be covered by an amorphous carbon layer similar to fullerene soot. HRTEM images (right) indicate the presence of fullerenes molecules at the vicinity of a SWNT. At least one of the nanotube tips seems connected to metallic particles, what tend to be in agreement with the metal-carbon liquid droplet growth mechanism [11].

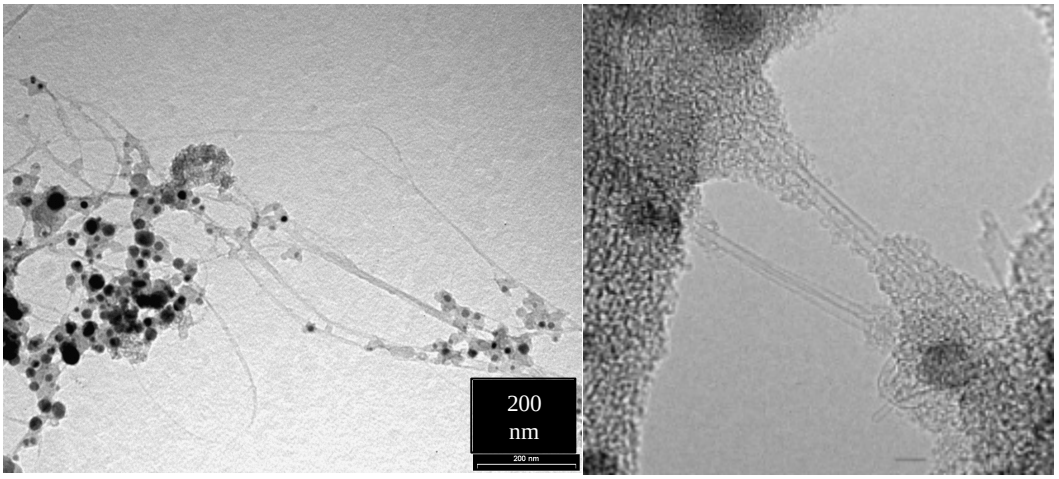

Figure 8 : TEM bundles of SWNT with metal particles (left) and detail by HRTEM (right)

Carbon Fibres

Another nanostructure family composed of long carbon chains has also been observed. Such structures represented on Figure 9 have been observed by injecting ethylene as carbon precursor together with a metal catalyst. The fibers diameter varies in the range of 20 – 50 nm with a length of few µm. Their structure seem composed of an axial stacking of carbon layers with a low graphitic organization. Similar structures have already been reported with the catalytic decomposition of hydrocarbons carried out at low temperature (< 1500 K), [12].

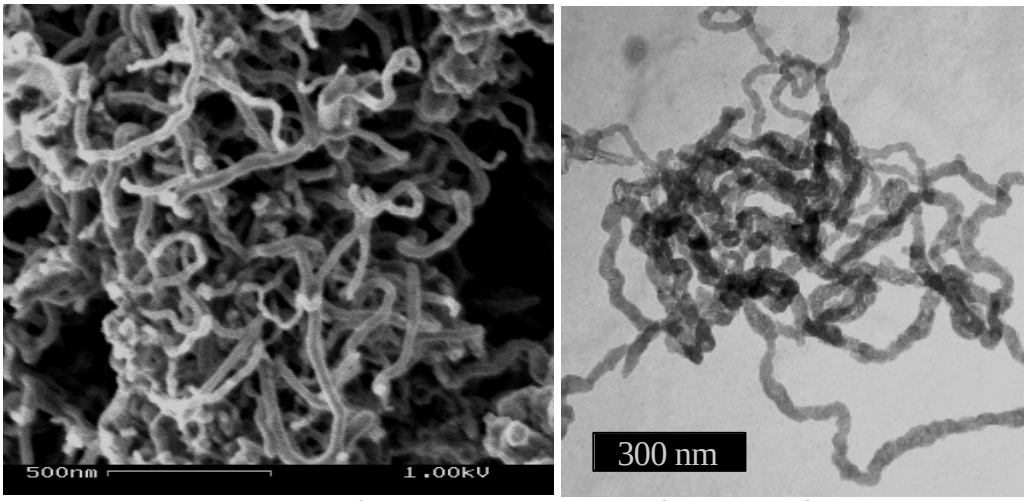

Figure 9 : SEM (left) and TEM (right) images of carbon nanofibres.

Conclusion

Plasma systems open a new area for the production of carbon nanostructures. These technologies are characterized by a very high versatility and flexibility. It has been demonstrated that the very same technology could be used for the production of a wide range of carbon nanostructures ranging from carbon black over fullerenes to carbon nanotubes with a high product selectivity. In the field of carbon black, the main difference with combustion methods is that the enthalpy applied to the system can be controlled totally

independently by means of an external electric power supply. As a consequence, any raw materials : liquid, solid or gaseous can be used, including waste oils, vegetable oils, plastics,…The process allows a more rational use of the raw material (100 % carbon yield), zero CO_2 emission on the site and the production of hydrogen as by-product. Finally, it is possible to control and de-correlate reaction temperature and aerosol concentration, two important parameters for the tailoring of final nanostructures. In addition, when using pure carbon under inert atmosphere, very high temperatures can be obtained (higher than 3,000 K up to 10,000 K) thus allowing in particular the vaporisation of carbon and the formation of chemical species such as C_1, C_2,.. whose species have been identified to play an important role as precursors for new carbon nanostructures such as fullerenes and nanotubes.

Acknowledgements
This work was supported by the European Commission under the TMR Programme, contract NANOCOMP, HPRN-CT-2000-00037 and the 'Competitive and Sustainable Growth' Programme, contract PLASMACARB, G5RD-CT-1999-00173.

References
[1] Kroto, H. W., Heath, J. R., O'Brien, S. C., Curl, R. F., and Smalley, R. E., *Nature* 318, 162 (1985).
[2] Iijima, S., Nature (London), 350, 320 (1991).
[3] L. Fulcheri, Y. Schwob, From Methane to Hydrogen, Carbon Black and,...Water, International Journal of Hydrogen Energy, vol 20, N° 3, pp. 197-202, 1995.
[4] L. Fulcheri, et. Al., A 3-Phase AC Plasma Process for Carbon Black Production from Methane, Thermal Plasma Processes, 19-21 Sept. 94, Aachem Germany, VDI BERICHTE NR 1166, pp 525-532, 1995.
[5] L. Fulcheri, et al., Characterization of a 3-phase AC plasma reactor for carbon black synthesis from natural gas, ISPC 12, August 21-25 1995, Minneapolis, MINNESOTA USA, vol III, pp 1159 - 1164.
[6] L. Fulcheri , Y. Schwob, F. Fabry, G. Flamant, L.F.P. Chibante, D. Laplaze, Fullerene Production in a 3 - Phase AC Plasma Process, *Carbon*, **38**, 5, 797-803 (2000).
[7] L. Fulcheri, N. Probst, G. Flamant, F. Fabry, E. Grivei, X. Bourrat, Plasma processing: a step towards the production of new grades of carbon black, Carbon 40 (2002) 169-176.
[8] T.M. Gruenberger, J. Gonzalez-Aguilar, L.Fulcheri, F. Fabry, E. Grivei, N. Probst, G. Flamant, J.C. Charlier, Continuous production of fullerenes and other carbon nanomaterials on a semi industrial scale using plasma technology, Electronic properties of molecular nanostructures, H. Kuzmani et al., Eds AIP, New york, 2001.
[9] S. Ijima et al., Structure of carbon soot prepared by laser ablaltion , J. Phys. Chem., Vol 100, pp 5839-5843, 1996.
[10] H. Okuno, E. Grivei, F. Fabry, T. M. Gruenberger, J. Gonzalez-Aguilar, A. Palnichenko, L. Fulcheri, N. Probst, J.-C. Charlier, Synthesis of carbon nanotubes and nano-necklaces by thermal plasma process, *Carbon*, **42**, 12-13, 2543-2549 (2004).
[11] Gavillet J, Loiseau A., Ducastelle F., Thair S., Bernier P., Stephan O., Thibault J., Charlier J.C., Microscopic mechanisms for the catalyst assisted growth of single-wall carbon nanotubes, Carbon 40 (2002), 1649-1653.
[12] R.T.K. Baker and P.S. Harris, the formation of filamentous carbon, Chemistry and Physics of Carbon, Vol. 14, 1978.

Electrical Characterisation of a low current-high voltage compact arc plasma torch

Jean-Damien Rollier, Laurent Fulcheri, José Gonzalez-Aguilar

Ecole des Mines de Paris, Centre for Energy and Processes, Sophia Antipolis, France

Abstract
A new compact plasma torch associated with a resonance power supply allows the generation of low power discharges (typically 100 W – 1 kW) under different regimes ranging from streamer over gliding arc to continuous discharges. The objective of this paper is a better understanding of the different observed behaviours through the determination of the main torch and power supply parameters, these two sub systems being highly coupled.

Keywords : high voltage, low current, compact arc plasma torch, electrical characterization, continuous, glidarc, streamer.

1. Introduction

Thermal plasmas have been widely used in industrial applications and more particularly in material related application requesting very high temperature. For lower temperature applications as those generally encountered in chemical gas processing, the use of non thermal plasmas (glidarc, glow discharge, DBD, corona, microwave…) is generally preferred for their lower energy consumption. In particular, non thermal plasmas have been emerging as an attractive alternative of standard (heterogeneous) catalytic systems. For example, the catalytic effect of non-thermal plasma for Synthesis gas production has already been demonstrated in several works [1-3]. This paper presents some advances obtained on a new low current high voltage compact arc plasma torch which is under development at CEP in the frame of gas phase chemical applications.

2. Experimental set up

The compact non thermal arc plasma torch is presented in Figure 2. The geometry is very similar to those encountered in classical high current DC plasma torches. An electric arc is established between a central (1) and an annular electrode (2). These two concentric electrodes being separated by a high voltage insulating ceramic material (3). A low current-high voltage arc discharge generated between the electrodes is blown down by a high velocity plasma gas injected radialy at the vicinity of the central electrode (4).
The generation of a low current high voltage arc discharge has been obtained using a power supply specially developed for this application. The power supply operates as a current source and it is based on a resonant converter technology. Here, a LC resonant circuit works as a selective filter: the current flowing to the load is controlled by the resonant tank impedance, which is controlled by the switching frequency in comparison with the tank resonant frequency (Figure 1). A 15,000 V maximum voltage can be obtained while maximum current is 660 mA. Contrary to high voltage transformers currently used for such applications, this power supply allows the continuous control of the arc current with a high accuracy in the range 200-600 mA. Tests have been performed using air as plasma gas with flow rates varying in the range 0.5 to 4 Nm^3/h using a mass flowmeter. Electrical signals have been analysed thanks to a 2 channels digital oscilloscope (HP 54615 B). Voltage measurements were performed using a 1:1000 probe (Elditest, GE3830) while discharge current was carried out using two methods (10 Ω shunt and a hall effect current probe : PR 30: LEM)

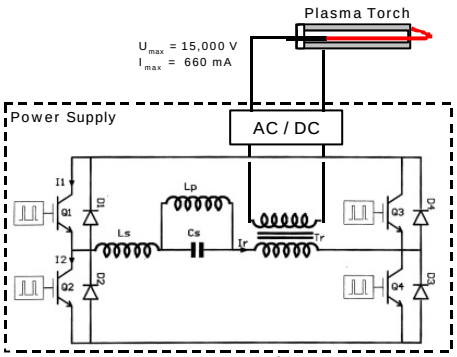

Figure 1: Electric scheme of the power supply

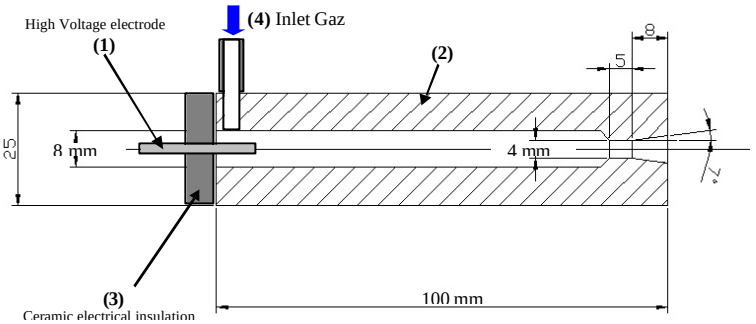

Figure 2: scheme of the compact plasma torch

3. Results

As shown in Figure 3, three different discharge regimes could be obtained by varying the arc current: a streamer regime at low current, a continuous regime at high current and a gliding arc regime at intermediate current. The boundaries between these different regimes is found to increase towards higher currents when increasing the air flow rate : at low flow rate (0.5 Nm^3/h), the limits between the streamer and gliding arc regimes and between the gliding arc and continuous regimes appear at 150 mA and 300 mA respectively. At high flow rate (4 Nm^3/h), the transitions take place at 300 mA and 430 mA respectively.

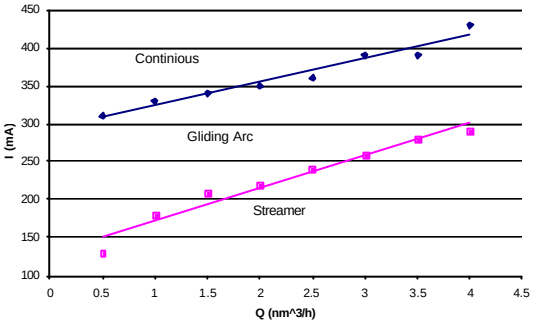

Figure 3: different discharge regimes versus current and flow rate

Figure 4 shows typical voltage and current time evolution for the three discharge regimes for streamer (a), gliding (b) and continuous (c) discharges obtained with a 2 Nm^3/h air flow rate and mean current 210 mA, 320 mA and 460 mA respectively.

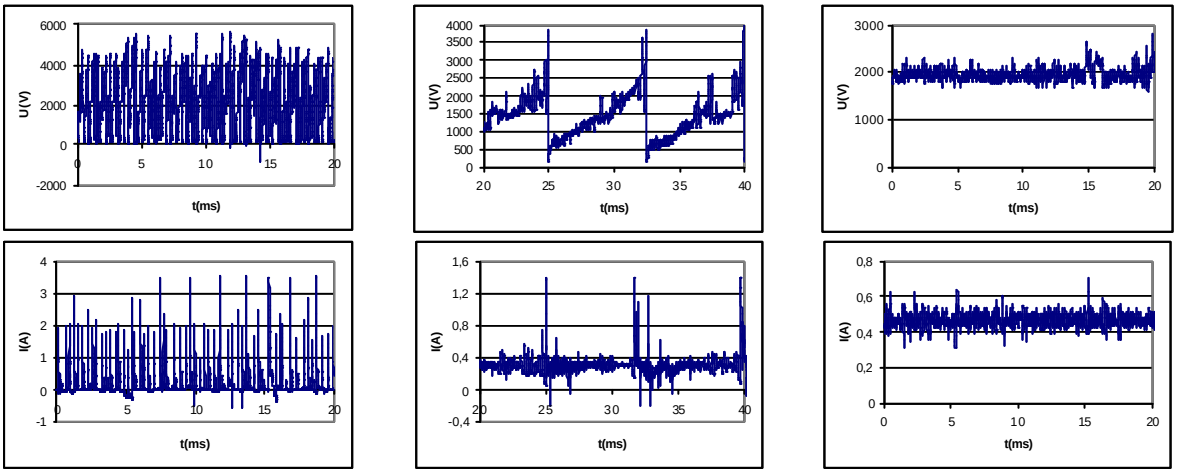

(a) streamer regime (b) gliding arc regime (c) continuous regime

Figure 4: Time evolution of voltage and current

Streamer regime

This regime, characterized by high frequency discharges (typically higher than 2 kHz), appears at low current and it is characterized by a typical noise resulting of the high discharge frequency. As shown in

Figure 7, the time evolution analysis of the current and voltage streamer discharge reveals two different zones : a first zone characterized by a current peak which corresponds to a breakdown at the inter electrode gap ; a second zone where the voltage increases linearly while the current decreases down to zero until a new breakdown occurs. Under these conditions, the discharge is very thin and remains short and located at the vicinity of the central electrode as shown in Figure 5 and Figure 6. Actually, this regime corresponds to the power supply limits which does not allow to maintain a dynamic control of the discharge under such low current high voltage conditions. This is in particular due to the power supply response time which is not adapted to the breakdown frequency.

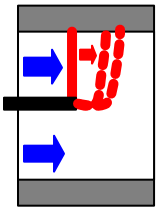

Figure 5 : Scheme of the streamer regime

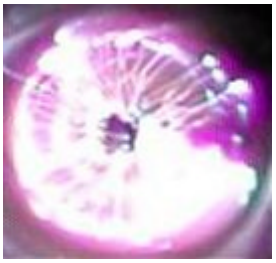

Figure 6 : Axial view of the streamer regime

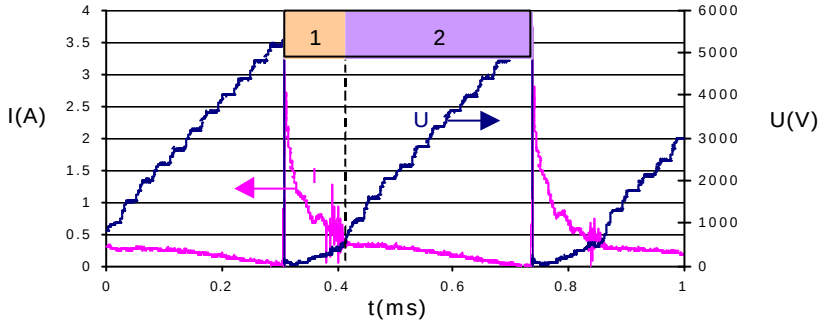

Figure 7 : Time evolution of of the current and voltage streamer discharge

Glidarc regime

This regime, characterized by a lower frequency (typically lower than 500 Hz) appears at higher current. As previously, the time evolution presented in Figure 8 shows a short current peak accompanying each breakdown. However, contrary to the previous case, the power supply allows an efficient control of the current which can be kept almost constant between two successive breakdowns since the response time of the power supply is lower than the breakdown periodicity.

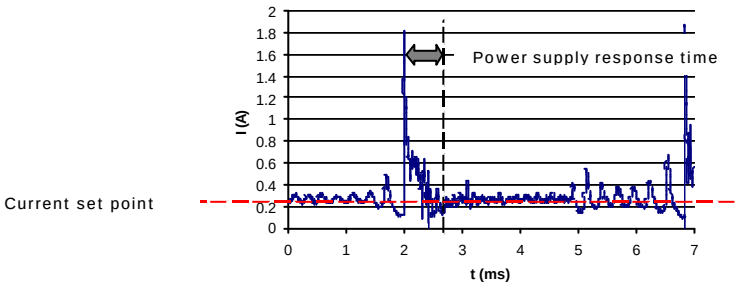

Figure 8 : Time evolution of current for the glidarc regime

The glidarc mechanism can be decomposed as follow [4-5]. After a breakdown occurring at the vicinity of the smallest inter-electrode gap, the arc is blown by the gas flow and its length increases. When increasing, the arc resistance increases together with the arc voltage up to reaching the breakdown voltage. Then, the arc stops, leaving the place to a new one. As a general rule, for given conditions (geometry, nature of the gas, gas flow rate), the higher the current the lower the glidarc frequency. This is the result of two opposite phenomena, the first one being the dominant one. One the one hand, the higher the current, the higher the arc temperature and the lower the arc resistance per unit of length so that the limit arc length can be increased

and the glidarc frequency decreased (the arc remaining "alive" more longer). On the other hand, the higher the current, the higher the arc cross section and the higher the drag force so that the relative arc shift (difference between gas and arc velocity) gets lower; the arc velocity increases and approaches the gas velocity (sweeping effect shrinks).
In addition, the arc current will also influence the dynamic behaviour of the arc through the "memory effect". Indeed the higher the current the higher the collision density and the concentration of ionised species.

This regime is strongly dependant on the hydrodynamic flow. The compact plasma torch developed at CEP has shown the existence of three different glidarc behaviours.

Regime "Glidarc 1"

This case is illustrated in Figure 9. The arc voltage varies between the breakdown voltage (approximately 3500 V) and the minimum voltage occurring once the arc is ignited at the smallest inter-electrode gap (A) (approximately 500 V). Depending on the gas flow rate, the arc length increases until the voltage reaches the breakdown voltage. The hydrodynamic conditions remaining almost constant between (A) and (B) as shown in Figure 10, the arc length and the arc voltage vary almost linearly versus time.

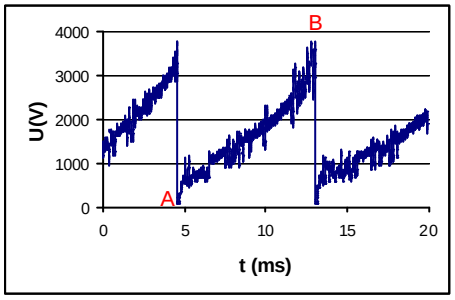

Figure 9 : Arc voltage time evolution "glidarc 1"

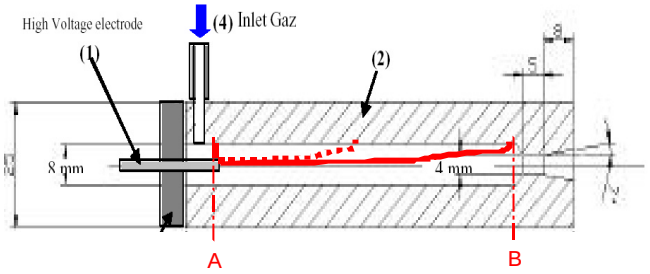

Figure 10 : Scheme "glidarc 1"

Regime "Glidarc 2"

When, for a given gas flow rate, the arc current is high enough, the arc is able to reach the output nozzle (B) before reaching the breakdown voltage as shown in Figure 11. In (B), the torch cross section decreases and the gas velocity is strongly increased. The arc is simultaneously accelerated and cooled down giving a stiff increase of the voltage slope (section [BC] in Figure 11). Both the breakdown and minimum voltages remain unchanged.

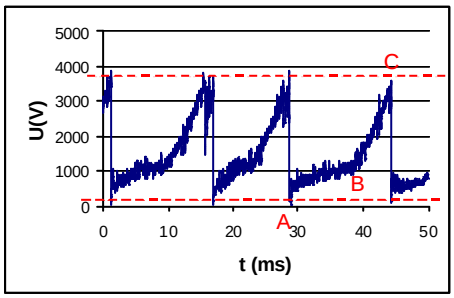

Figure 11 : Arc voltage time evolution "glidarc 2"

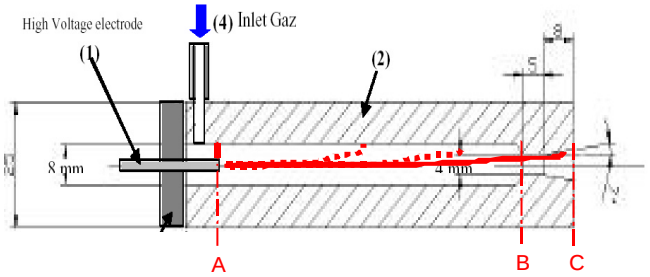

Figure 12 : Scheme "glidarc 2"

Under certain particular conditions, a third regime: "glidarc 3", intermediate between "regimes 2" and "continuous" may happen .

Regime "Glidarc 3"

Thanks to the "memory effect", it could happen that, after an arc extinction, a new breakdown will start directly from (B) as a result of a remaining ionised gas channel between A and B.

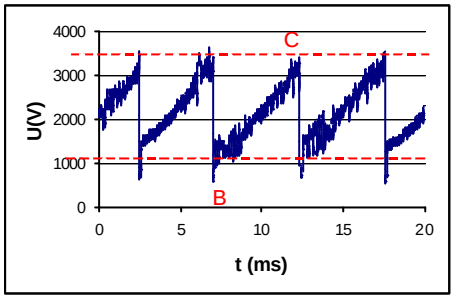

Figure 13 : Arc voltage time evolution "glidarc 3"

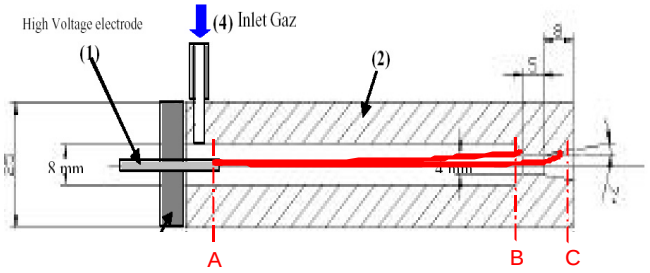

Figure 14 : Scheme "glidarc 3"

In this case, as shown in Figure 13, the minimum voltage, formally around 500 V for case 1 and 2, jumps very quickly to a higher level, typically 1000 V. This value corresponds approximately to the transition voltage observed in "regime 2" (point B in Figure 11).
In addition, the different "glidarc" regimes differ in term of frequency as shown in Figure 15. While frequencies vary continuously from "glidarc 1" to "glidarc 2", "glidarc 3" is characterised by higher frequencies what can easily be explained by different evolution zones of the arc, [A-B], [A-C] and [B-C] for regimes 1, 2 and 3 respectively .

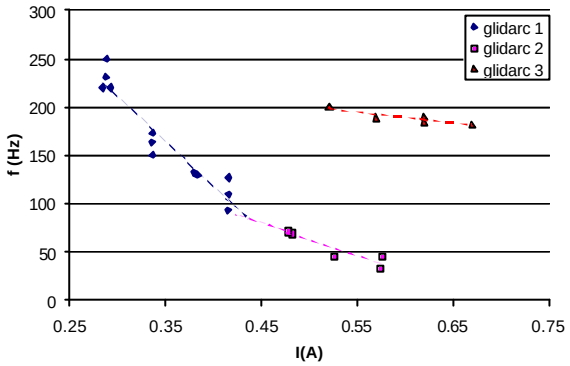

Figure 15 : Glidarc frequency versus arc current for the different arc regimes

To summarise this part, it has been demonstrated that the different glidarc regimes (1, 2 and 3) are mainly governed by the torch geometry, hydrodynamic conditions and arc current. The power supply allows a good control of the arc current for the different gliding arc regimes.

Continuous regime

Under certain conditions, it is possible to get a continuous stable discharge as shown in Figure 16. This is possible when the arc reaches the point C while the voltage remains lower than the breakdown value.

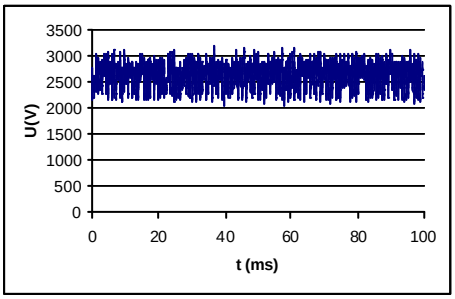

Figure 16 : Time evolution of the arc voltage for the continuous regime

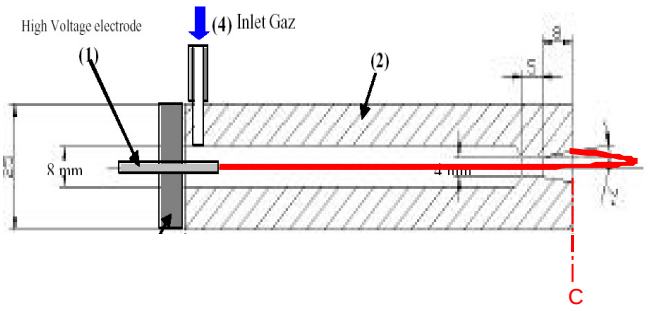

Figure 17 : Scheme of the arc for the continuous regime

As shown in Figure 18, for given conditions (gas flow rate and arc current), the arc voltage directly depends on the torch length. Consequently, it is possible to increase the torch length up to L_{max} by increasing the arc current. For $L = L_{max}$, the arc voltage equal the breakdown voltage corresponding to the smallest inter electrode gap. For higher lengths the continuous regime cannot be achieved.

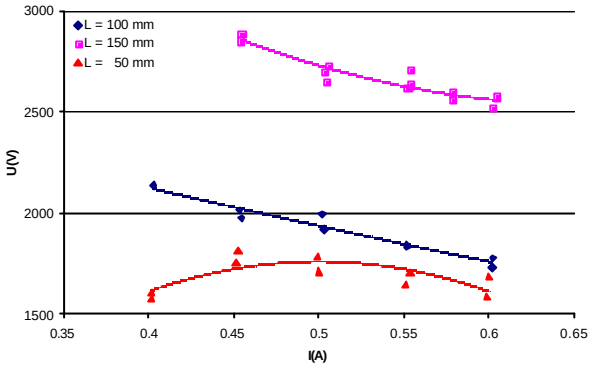

Figure 18 : Continuous regime mean characteristics versus torch length

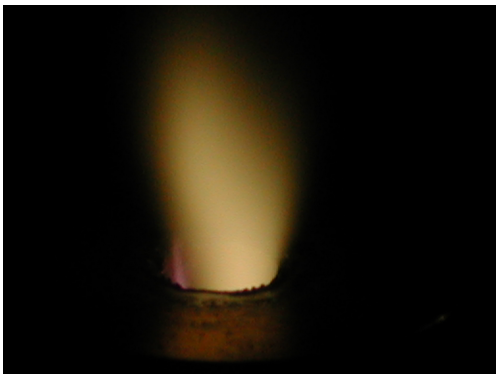

Figure 19: view of the plasma jet (continuous regime)

Conclusion

The new compact plasma torch associated to the resonance power supply allows obtaining low power discharges (typically 100 W – 1 kW) and different regimes ranging from streamer over gliding arc to continuous discharges under unusual current voltage characteristics (typically 100-500 mA, 2-10 kV). Contrary to conventional power supplies based on high voltage transformers currently used in gliding arc discharges systems, this power supply allows a continuous control of the mean discharge current with a high accuracy. This system is currently being tested in the frame of researches on plasma assisted hydrocarbon conversion.

Acknowledgements

This work was supported by RENAULT-SA.

References

[1] L. Bromberg, D. R. Cohn, A. Rabinovich, J. E. Surma and J. Virden, Compact plasmatron-boosted hydrogen generation technology for vehicular applications, Int. J. Hydrogen Energy, 24, 4 (1999), 341-350.

[2] M. G. Sobacchi, A. V. Saveliev, A. A. Fridman, L. A. Kennedy, S. Ahmed and T. Krause, Experimental assessment of a combined plasma/catalytic system for hydrogen production via partial oxidation of hydrocarbon fuels, Int. J. Hydrogen Energy, 27, 6 (2002), 635-642.

[3] T. Paulmier, L. Fulcheri, Use of non thermal plasma for hydrocarbon reforming *Chemical Engineering Journal*, 106, 59-71 (2005).

[4] Mutaf-Yardimci, A. V. Saveliev, A. A. Fridman, Thermal and non-thermal regimes of gliding arc discharge in air flow, J. Appl. Phys., 87, 4 (2000), 1632-1641.

[5] F. Richard, J.M. Cormier, S. Pellerin, J. Chapelle, Physical study of a gliding arc discharge, J. Appl. Phys., 79, 5 (1996), 2245-2250.

Investigation of the water gas shift reaction in a dielectric barrier discharge reactor

O. Aubry, A. Khacef and J.-M. Cormier

GREMI - Polytech'Orléans, 14 rue d'Issoudun, B.P. 6744, 45067 Orléans cedex 2, France
e-mail: olivier.aubry@univ-orleans.fr

Abstract

The aim of this study is to show that a Dielectric Barrier Discharge (DBD) at atmospheric pressure can be used to produce the water gas shift reaction. The inlet mixture composition and discharge electric parameters effects on the reactive species conversion rates and on the products concentration are studied. This preliminary investigation permitted to obtain a CO conversion rate close to 35%. A thermal modelling is compared to the DBD experimental data.

Keywords: Non thermal plasma, pulsed DBD, CO conversion

1. Introduction

The carbon monoxide is a pollutant stemming from the incomplete combustion of hydrocarbons but can be also produced during the steam reforming. CO is well known as dangerous for the health, the environment and for the fuel cell electrodes (CO level must be lower than 10 ppm to avoid electrodes poisoning). Recent works showed the possibility to produce hydrogen by a non thermal plasma technique from ethanol/water mixtures with results close to those obtained from catalytic reactors [1-4]. Nevertheless, the main disadvantage of the steam reforming is the high level of CO produced (up to 20% in catalytic and plasma processes). One possible way to reduce carbon monoxide is the water gas shift reaction (WGSR) which leads to H_2 and CO_2 following the reaction 1.

$$CO + H_2O \rightarrow CO_2 + H_2 \qquad \Delta H^0_{298} = -41 \text{ kJ.mol}^{-1} \qquad (1)$$

The steam reforming of bio-ethanol from the agriculture or agricultural residues associated with the WGSR can reduce the outlet CO leading to a nil global CO_2 balance. The amount of CO_2 produced is the same that consumed by the plants during their growth. The WGSR is widely studied in catalytic reactors [5-7].

In the present paper, an experimental investigation was conducted in order to demonstrate the feasibility of the WGS reaction by a pulsed Dielectric Barrier Discharges (DBD) reactor at atmospheric pressure. Until now, this reaction was described not possible by this technique. The influence of voltage and initial H_2O concentration on the CO and H_2O conversion rates and on the products mole fractions are presented.

2. Experimental

The inlet mixtures (CO/H_2O) were prepared in a gas handling system and their composition was controlled by calibrated mass flow controllers. Water vapour with controlled concentrations was added to the CO gas using controlled evaporator mixer CEM®. After mixing in the manifold, the gas reaches the reactor through a temperature-controlled line to avoid condensation. The reactor was placed inside a tubular furnace where the temperature is fixed at 120°C. The electrical discharge reactor used is a DBD reactor described previously [8]. The geometry was one of a wire to cylinder type with a tungsten wire (0.9 mm diameter) in a quartz tube with inner and outer diameter of 11 mm and 13 mm, respectively. An aluminium foil covered the dielectric tube and forms the outer electrode. The active volume of the DBD reactor can be adjusted by adjusting the length of the outer electrode. In this study, the reactor volume was fixed at 16 cm^3.

The DBD reactor is driven by a transformer powered by high-voltage ceramic capacitors (4 nF) disposed in Blumlein-like configuration. In this work, high voltages up to 40 kV output into pulses of 80 ns duration (FWHM) and short rise time (40 ns) are delivered. The pulse repetition rate could be varied from single shot to 220 Hz.

The time behaviour of voltage was measured using a Tektronix P6015A high voltage probe (1000x) and recorded on a Tektronix TDS 400A digital oscilloscope. Figure 1 shows an example of a typical recording of voltage across the electrodes as a function of time.

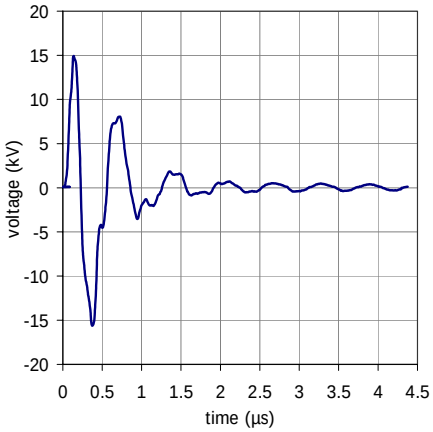

Figure 1. Typical recording of voltage pulse *vs.* time.

The outlet gas composition was analysed using micro gas chromatography (µGC, Varian CP2003-P) and Fourier Transform Infra Red spectroscopy (FTIR, Nicolet Magna-IR 550 series II). The µGC analyser was equipped with Molsieve 5Å and PoraPlot Q columns. The detection was assured by thermal conductivity detector (TCD) calibrated with standards of known composition.. The detected and analyzed species in that study are: H_2, CO, CO_2, and H_2O. The outlet H_2O concentration was estimated from C, H and O balances, since no other species were detected.

3. Results and discussion

Figures 2a and 2b show the influence of the inlet H_2O mole fraction and the applied voltage on the products mole fractions. Figure 2c presents H_2O and CO conversion rates as function of the inlet mixture composition and the applied voltage.

For the lowest applied voltage (20 kV), the H_2 and CO_2 mole fractions are constant in the range of inlet mixture composition studied (figure 2a). For higher applied voltage (30 kV), the H_2 and CO_2 concentrations depend strongly on the inlet mixture composition (figure 2b). When the inlet H_2O concentration rises from 0.40 to 0.80, H_2 and CO_2 mole fractions decrease from 0.11 and 0.105 to 0.08 and 0.067, respectively. H_2 and CO_2 mole fractions are in the same order of magnitude showing that CO and H_2O reacted mole by mole. Indeed, for a given mixture, the amounts of CO and H_2O consumed correspond to the CO_2 and H_2 produced.

We can observe (figure 2c) that the inlet H_2O mole fraction plays a major role on the conversion rate of the reactive species and on H_2 and CO_2 concentrations. An increase of the inlet H_2O leads to an increase of the consumption of the CO while H_2O conversion decreases. The CO conversion rate increases when the inlet CO concentration decreases.

The outlet concentrations and the conversion rates as a function of the voltage are shown in figure 3. One can note that, when the voltage increase, the H_2 and CO_2 mole fractions in the outlet gas increase from about 0.05 to 0.102. In the same time, H_2O and CO mole fractions decrease from 0.45 to 0.40 and, CO and H_2O conversion rate is multiplied by a factor 2 (figure 3b).

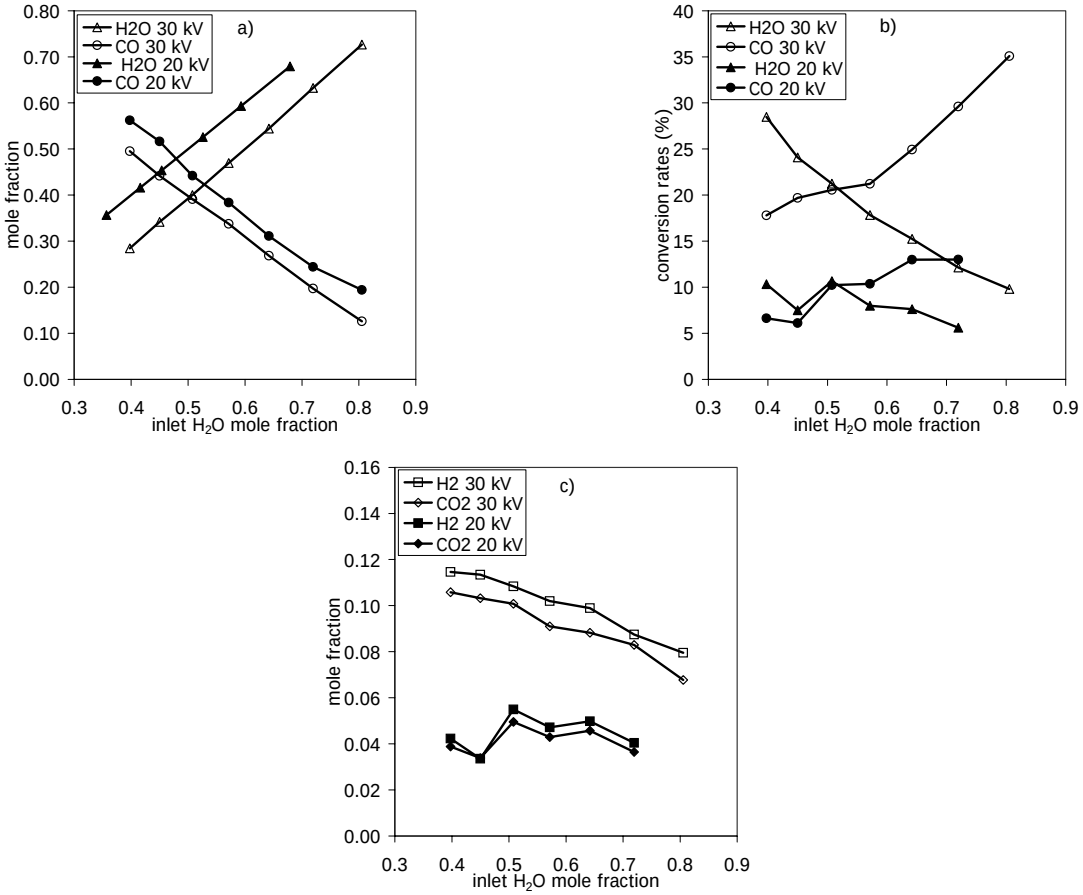

Figure 2. Influences of the inlet H_2O mole fraction and the peak voltage pulse on:
a) H_2O and CO mole fractions, b) CO and H_2O mole fractions and c) conversion rates of H_2O and CO.
Total flow gas = 147.5 sccm at 120°C.

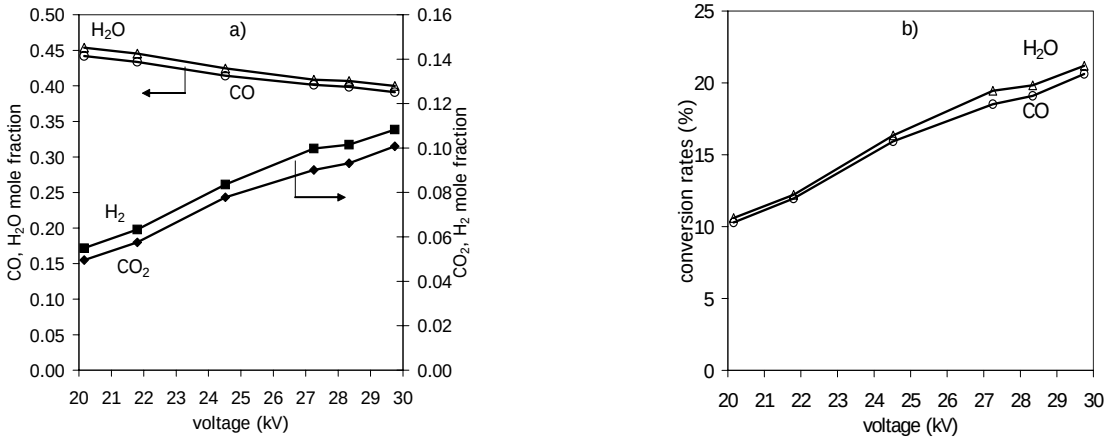

Figure 3. Effect of the applied voltage on: a) H_2O, CO, CO_2 and H_2 mole fractions
and b) CO and H_2O conversion rates.
Inlet mixture mole fractions: H_2O 0.508 - CO 0.492; total gas flow = 147.5 sccm; T = 120°C; f = 180 Hz.

Although the implied processes are typically non thermal one, it is interesting to compare the experimental results with classic kinetic models. Calculations obtained from Chemical Workbench 3.2 software [9] for a plug flow reactor are presented in figure 4. Two C-H-O mechanisms were used: GRImech 3.0 [10] (53 species and 325 reactions) and CH_4+O_2 combustion model from Chemical Workbench package (36 species and 134 reactions). We used these two models which led to similar results. The temperature of the plug flow reactor was adjusted to fit the experimental data.

Figures 4 show the mole fractions as a function of the inlet mixture composition. A fairly good agreement between the experimental and computational results is observed for the reactive species H_2O and CO (figure 4a). The profiles of the mole fraction and the trends *vs.* the inlet H_2O mole fraction are close to the experimental data. Gas temperatures used to simulate the non-thermal DBD reactor in GRImech and CH_4+O_2 combustion mechanisms are 1325 K and 1350 K, respectively.

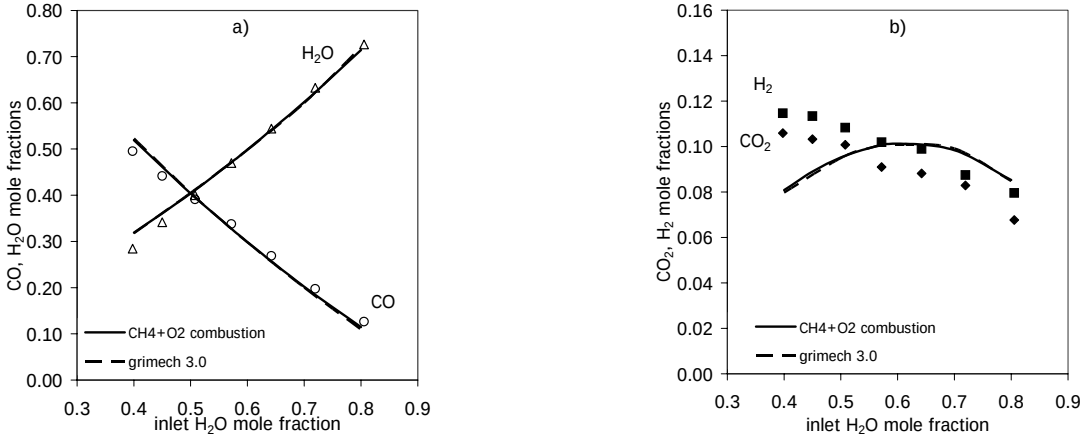

Figure 4. Effect of the inlet H_2O mole fraction on CO, H_2O, CO and H_2 mole fractions. Comparison between experimental data (symbols) and modelling (lines and dotted lines). Total gas flow = 147.5 sccm; T = 120°C; f = 180 Hz.

For a given gas mixture, the calculation using these two mechanisms gives close results concerning H_2 and CO_2 mole fractions. However, computed and experimental results are different in the range of low H_2O concentration. In that case, the mechanisms slightly underestimate the H_2 and CO_2 mole fractions values (about 0.11 for the experimental data and 0.065 for the modelling results). When H_2O concentration increases, modelling results shows an increasing of the products concentrations while the experimental data show a linear decrease.

From these comparisons between experimental and modelling results, we have simulated the effect of the voltage on the species concentration. The increase of the voltage is simulated by the increase of the gas temperature in the GRImech 3.0 plug flow reactor model. The increase of the applied voltage from 20 to 30 kV corresponds to an increasing of the gas temperature from 1288 to 1325 K, respectively (figure 5). A good agreement is obtained in the entire voltage domain studied for the species concentration.

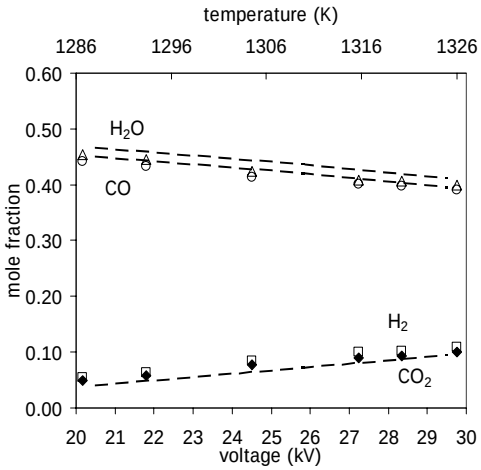

Figure 5. The effect of the inlet peak pulse on CO, H_2O, CO and H_2 mole fractions. Comparison between experimental data (symbols) and GRImech 3.0 modelling (dotted lines).
inlet H_2O mole fraction= 0.508; total gas flow = 147.5 sccm; T = 120°C; f = 180 Hz.

Conclusion

This work showed the potential of DBD reactor to realize the water gas shift reaction at atmospheric pressure. The conversion rates and the concentrations of the products were studied as functions of the inlet reactant mixture and the applied voltage. This preliminary investigation permitted to obtain conversion rates of CO close to 35% for the highest inlet H_2O mixtures studied. The applied voltage plays an important role in the CO conversion.

Results obtained from kinetic modelling show that the mechanisms used in the combustion chemistry are determining. The reactions implying electrons and ions, which are not taken into account in these models, can be then considered as initiators; they are followed by classic mechanisms which allow describing production of various species. We suggest representing a DBD reactor by an association of reactors models. The first reactor would represent a non thermal equivalent processing and the last one thermal reactor. To achieve real temperatures of the discharge reactor, vibrationnal and rotational temperatures measured by optical spectroscopy must be made and used in equivalent thermal models.

References

[1] O. Aubry, C. Met, A. Khacef, J.M. Cormier – Proc. Ninth International Symposium on High Pressure, Low Temperature Plasma Chemistry (Hakone 9), Padova (Italy), August 23-26 (2004)
[2] O. Aubry, C. Met, A. Khacef, J.M. Cormier - Chem. Eng. J. 106(3), 241 (2005).
[3] F. Auprêtre, C. Decorme, D. Duprez - Catal. Comm. 3, 263 (2002).
[4] J. Llorca, N. Homs, J. Sales, P. Ramirez de la Piscina - J. Catal. 209, 306 (2002).
[5] W. Ruettinger, O. Ilinich, R.J. Farrauto - J. Power Sources. 118, 61 (2003).
[6] Y. Choi, H.G. Stenger - J. Power Sources. 124, 423 (2003)
[7] O. Goerke, P. Pfeifer, K. Shubert - Appl. Catal. A: General. 263, 11 (2004)
[8] A. Khacef, J.M. Cormier, J.M. Pouvesle - J. Phys. D: Appl. Phys. 35 1491 (2002).
[9] Chemical Workbench 3.2 by Kintech Technologies, Moscow, Russia.
[10] G.P. Smith, D.M. Golden, M. Frenklach, N.W. Moriarty, B. Eiteneer, M. Goldenberg, C.T. Bowman, R.K. Hanson, S. Song, W.C.Gardiner Jr., V.V. Lissianski, and Z.Qin- www.me.berkeley.edu/gri.mech/

HYBRID PROCESSING OF TI6AL4V USING PLASMA IMMERSION ION IMPLANTATION COMBINED WITH PLASMA NITRIDING

M. M. Silva[1], M. Ueda[2], C. Otani[3], H. Reuther[4], C. M. Lepienski[5], P. C. Soares Jr.[5], J. Otubo[1]
[1]*Divisão de Engenharia Mecânica-Aeronáutica, Instituto Tecnológico de Aeronáutica, Praça Mal. Eduardo Gomes, 50, 12228-900 S.J.Campos, S.P, Brasil*
[2]*Laboratório Associado de Plasma, Instituto Nacional de Pesquisas, S. J. Campos, SP, Brasil*
[3]*Departamento de Física, Instituto Tecnológico de Aeronáutica, S. J. Campos, SP, Brasil – e-mail: otani@Ita.br*
[4]*Institute of Ion Beam Physics and Materials Research, Center Rossendorf, Dresden, Germany*
[5]*Departamento de Física Universidade Federal do Paraná, Curitiba, Brasil*

ABSTRACT

Because of its excellent combination of mechanical properties, corrosion resistance and chemical stability, the Ti-6Al-4V alloy is one of the most useful titanium alloys for aeronautical and biomedical applications. In case of wear absence, this material presents excellent corrosion resistance, including in the saline solutions media, similar to corporeal fluids, base of its bioengineering application. However, problems appear when localized wear starts causing intense corrosion. To improve corrosion wearing resistance, and fatigue strength as well, surface treatments by cold plasma plating and ionic implantation have been carried out. Present experimental work reports the surface characteristics improvements of Ti-6Al-4V alloy induced by a hybrid process performed by: Plasma Nitriding (PN) and Plasma Immersion Ion Implantation (PIII).

Key-words: Ti6Al4V, plasma, mechanical properties, biocompatibility

1. INTRODUCTION

The Ti-6Al-4V alloy is one of the most common titanium alloys intensively applied in aeronautical industries and also in biomedical areas [1]. This fact is attributed to its excellent combination of high mechanical and high chemical corrosion resistance [2,3], being the last characteristics originating from the passive oxide films formation on its surface [4,5] as a consequence of the surface oxidation process provided by contact with air [6]. This phenomenum almost avoid the penetration of oxidation process toward inner volume of this material which in turn minimize the metallic ion release into the biologic media [6]. The spontaneously formed oxide passivate the surface of this material leading to its biocompatible characteristics enhancement [4,7].

The major application for this material is in the area of aeronautic and space industries, allowing its use for some structural parts like for pressure vessels, aircraft turbines and compressor blades. Moreover, it has also been reported an important application of this material: for surgical implantations [1,7,8,9], due to its good characteristic of biocompatibility [1].

The Ti-6Al-4V alloy is classified as $\alpha+\beta$ alloy, presenting density of 4,43 g/cm^3, therefore 56% of the corresponding value of the steel and approximately double of the aluminum [10,11].

Despite of, above mentioned, very interesting characteristics of Ti-6Al-4V, this alloy presents a relatively poor tribological characteristics. Its friction coefficient is about 0,8 [12], and when a localized wear is started. This effect can cause through contacting surface an intense corrosion [11,13] producing ultimate damage of specimen produced by this material. To improve corrosion and wearing resistance, as well as fatigue strength, surface treatments such as cold plasma plating and ionic implantation have been investigated [11].

The present work aims to improve the tribological properties of the Ti6Al4V alloy treating it by a combination of two plasma assisted processes: Plasma Nitriding and Plasma Immersion Ion Implantation, in the sense to increase the nitride layer thickness as observed in another preliminary work [11].

2. EXPERIMENTAL PROCEDURE

The experiments were carried out on Ti-6Al-4V samples with 10 mm dia. x 1 mm thick disks. They were polished up to mirror like surface is achieved, mounted in a sample holder, and then they were adequately positioned in the reactor chamber, whose schematic diagram is presented in the figure 1. The plasma chamber was initially vacuum pumped up to residual pressure of 2,0 x 10^{-3} Pa and then argon gas is introduced for approximately 10 min. After this purging stage, the argon gas is replaced by nitrogen gas. Experimental conditions are resumed in Table I. Some samples were only treated by PIII process, while others were treated by combinations of PIII and PN processes. The ionic bombardment produced a heating condition of the samples to the temperatures up to 400 ºC.

All treated samples as well as the original Ti-6Al-4V sample (TAV), which has been taken as reference, were characterized by means of surface hardness using nanoindentation technique, chemical composition profile using Auger Electron Spectroscopy and surface topography uisng Atomic Force Microscopy. Two samples (TAV and #7) were analysed by means of its friction coefficient using the ball on disk method.

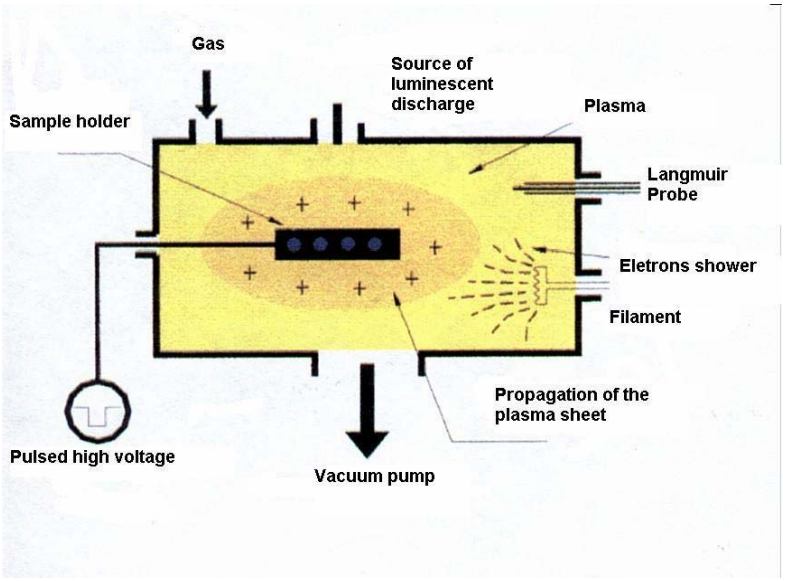

Figure 1 - Schematic diagram of experimental set up (plasma immersion ion implantation reactor)

Table I. Experimental conditions used.

Sample	1		2 and 4	3		5 and 6		7
Process	PIII	PN	PIII	PIII	PN	PIII	PN	PIII
Voltage (V)	10k	-700	17k	15k	-700	17k	-750	10
Pressure (Pa)	$8x10^{-2}$	$8x10^{-2}$	$7.2x10^{-2}$	$8x10^{-2}$	$8x10^{-2}$	$8x10^{-2}$	$8x10^{-2}$	$7,6x10^{-2}$
Time (min)	75	75	150	75	75	75	240	45
Frequency (Hz)	400		400	400		400		300
Pulse (μs)	20		20	20		20		50

3. RESULTS AND DISCUSSIONS

The results obtained from hardness measurement as a function of indentation penetration depth for representative samples are presented in Figure 2. A relatively small variation of hardness was observed for untreated sample (reference sample). This characteristic is a consequence of bulk homogeneity of the samples. All plasma treated samples showed larger variation of this parameter with penetration depth, which can easily inferred as due to the formation of a harder layer at surface of the sample. The comparative analysis of results originating from all treated samples showed that PIII + PN both for 75 min, presented most effective hardening of the material,

leading to the interpretation that this compound process can be a interesting alternative process if main objective of treatment is to improve the hardness of this material.

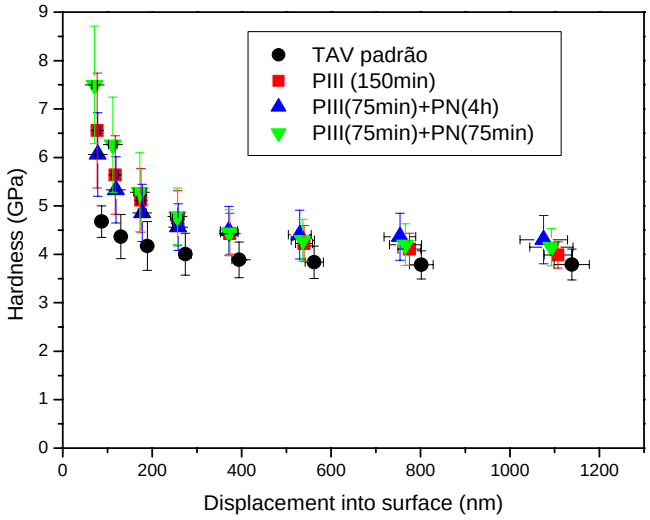

Figure 2 - Hardness of samples measured by nanoindentation technique (TAV is reference sample without any surface treatment)

The AES technique (Auger Electron Spectroscopy) can show the chemical composition at the surface of sample, and by its association of etching technique a depth dependent concentration profile for each element can be obtained. The figure 3-a shows the results obtained from reference sample (TAV) while figure 3-b corresponds to the results obtained from sample # 2. These results show that the carbon and oxygen are present in the original sample surface, probably forming TiC and TiO_2. The single PIII process can produce 65 nm thick nitride layer, while PIII + PN hybrid one performed for sample # 6 (not shown in figure 3) produced only 15 nm thick. This result can tentatively understand that is due to the concurrent sputtering process introduced by PN, which simultaneously with implantation of N by PIII removes the freshly forming nitride layer. This result is also confirmed by AFM analysis of surface. It was also verified that all treated samples presented a thin oxygen layer at its surface. It can be observed that the formation of complex compounds like oxide, carbide and nitride at the surface of the sample almost vanish the presence of vanadium and aluminum at the surface of samples. This effect is, for instance, suitable for many applications, specially for implantation [14].

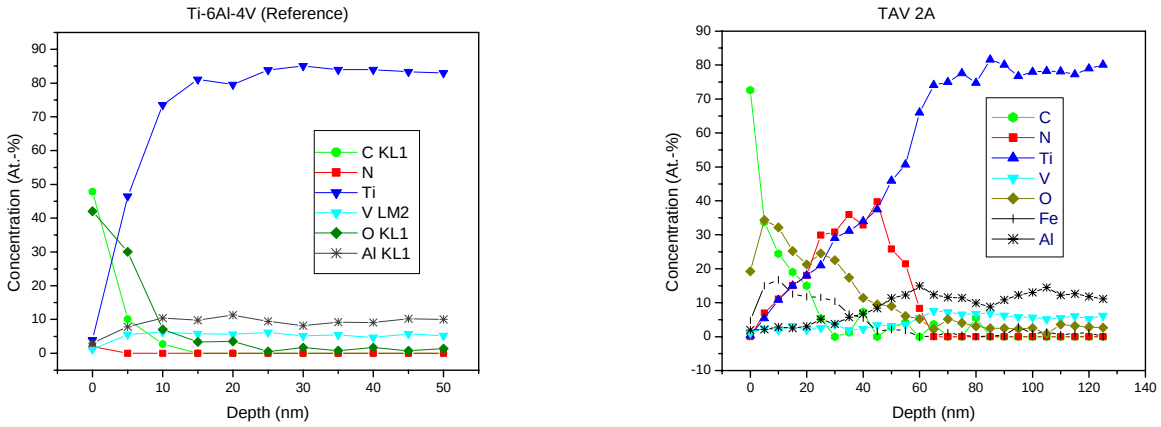

Figure 3 - Concentration of chemical elements as a function of surface depth obtained by AES technique.

Two representative 3-D micrographs obtained by AFM are presented in figure 4. The comparative analysis of these two micrographs leads to the confirmation of the AES results in the sense that the sample #4, treated only by PIII process presents larger RMS (Root Mean Square) roughness of 6,9nm, compared to the 1,8nm of sample #5. This means that PN process associated with PIII smoothen the sample surface probably sputtering process. All analyses shown evidence that both plasma based surface treatment processes can modify the mechanical properties of the Ti-6Al-4V alloy, probably, improving its tribological property.

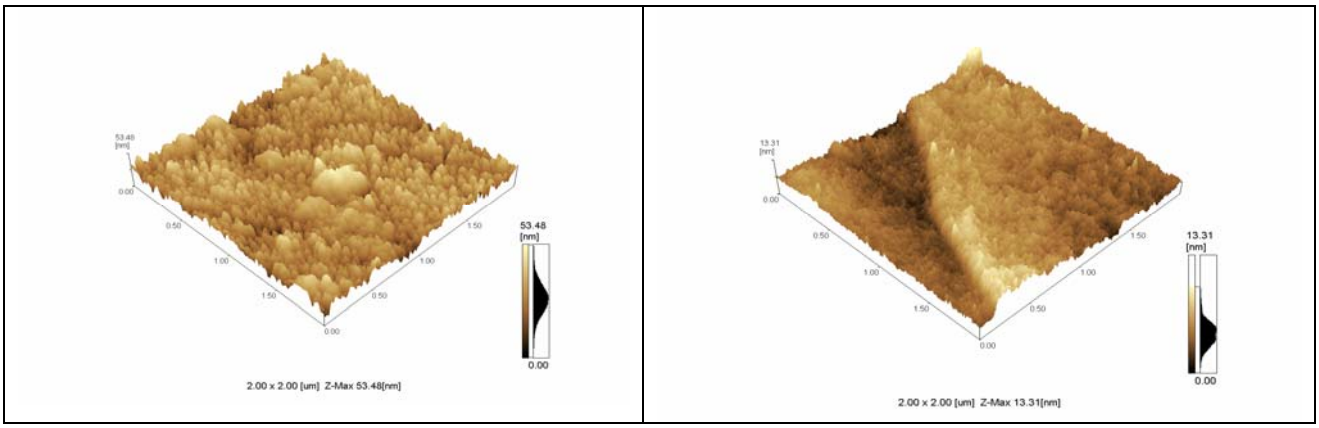

Figure 4 - AFM topography of: (a) sample 4 treated by PIII and (b) sample 5 treated by PIII + PN.

The figure 5 shows the ball on disk wear resistance tests results, for reference sample and for sample #7, treated by single PIII for 45 min. These tests allow us to confirm that the friction coefficient of original Ti-6Al-4V is about 0.8, which can be minimized to 0.3, as consequence of new material layer formed at its surface.

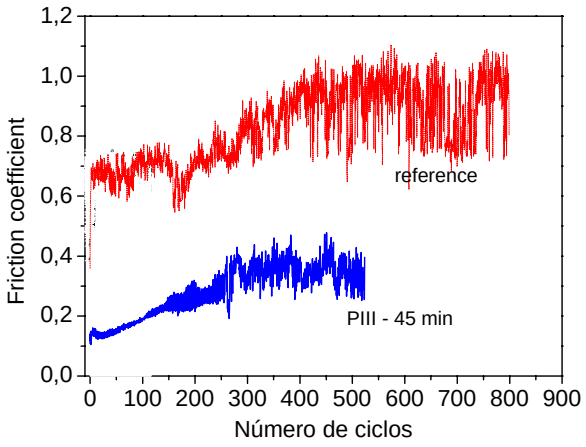

Figure 5 - Friction coefficient measurement results by ball on disk method

4. CONCLUSIONS

The set of results can lead us to the conclusions that the surface Ti-6Al-4V alloy properties can be modified by treatment processes performed in this work, being the single PIII the best process when deeply distributed nitrogen layer is requested for some specific application, but the combined PIII + PN process is more suitable to produce hardest and smooth surface.

The surface hardness increase induced in Ti-6Al-4V by processes studied can be attributed to nitrogen implantation effect, as confirmed by the nitrogen profile measurente by AES technique.

The deepest implantation of nitrogen was performed by PIII process for 150 min, producing 65 nm thick nitride layer. The thinnest nitride layer, with about 15nm, was observed in the material treated for PIII (75 min) + PN (240 min). These results are attributed to sputtering involved in the hybrid process.

New combinations of processing parameters are being carried out aiming thicker layer of implanted nitrogen with more hard and smooth surface sample production.

ACKNOWLEDGMENTS

This project is partially sponsored by the FAPESP.

REFERENCES

1) Nishiguchi, S. et al; The effect of heat treatment on bone-bonding ability of alkali-treated titanium. **Biomaterials** 20 P.491-500, 1999.
2) Cai, Z. et al; In vitro corrosion resistance of titanium made using different fabrication methods. **Biomaterials** 20 P.183-190, 1999.
3) Khan, M. A.; Williams, R. L.; Williams, D. F.; The corrosion behavior of Ti-6Al-7Nb and Ti-13Nb-13Zr in protein solutions. **Biomaterials** 20 P.631-637, 1999.
4) Mante, F. K.; Baran, G. R.; Lucas, B.; Nanoindentation studies of titanium single crystals. **Biomaterials** 20 P.1051-1055, 1999.
5) Baur, K.; Hornes, J.; The formation of intermetallic compounds in ion implanted aluminium and Ti-6Al-4V observed by X-ray absorption spectroscopy, **Surface Science** 436 P.141-148, 1999.
6) Apert, Ch.; **Metaux-Complements sur les metaux et alliages**, 1976. Class notes, École Nationale D´ingénieurs de Constructions Aeronautiques – Toulouse. P.279 a 317.

7) Brooks, R. Charlie; **Heat Treatment, Structure ans Properties of Nonferrous Alloys American Society for Metals**. Livro-American Society for Metals – University of Tennessee P.329-348 e 361-376, 1982.
8) Rinner, M.; Gerlach, J.; Ensinger, W.; Formation of titanium oxide films on titanium and Ti-6Al-4V by O_2 – plasma immersion ion implantation. **Surface Coatings Technology** 132 P.111-116, 2000.
9) Alonso, F. et al; Characterization of Ti-6Al-4V modified by nitrogen plasma immersion ion implantation. **Surface and Coatings Technology** 93 P.305-308, 1997.
10) **Bulletin Timet**. Properties and Processing Ti-6Al-4V. General Office, 1979.
11) Silva, M. M. **Modificação de Propriedades Superficiais da Liga Ti-6Al-4V pelo Processo Implantação Iônica por Imersão em Plasma**. 2001 These (Engenharia Aeronáutica e Mecânica) Instituto Tecnológico de Aeronáutica, São José dos Campos – SP.
12) Dong, H. et al; Surface engineering to improve tribological performance of Ti-6Al-4V. **Surface Engineering,** vol 13 n° 5 P.402-406, 1997.
13) Qiu, X. et al; Microestructural Study of Nitrogen-Implanted Ti-6Al-4V Alloy. **Nuclear Instrument and Methods in Physics Research** B59/60, P.951-956, 1991.
14) Zardiackas, L.D.; Mitchell, D.W.; Disegi, J.A.; Characterization of Ti-15Mo beta titanium alloy of orthopaedic implant applications. In: **Medical Application of Titanium and its Alloys.** American Society for Testing and Materials, 1996, p. 60-75.

Methane Steam reforming with oxygen in a sliding discharge reactor

F. Ouni, A. Khacef, and J. M. Cormier

GREMI-Polytech'Orléans, 14 rue d'Issoudun, BP 6744, 45067 Orléans Cedex 2, France
e-mail: fakhreddine.ouni@univ-orleans.fr

Abstract

Hydrogen-rich gas can be efficiently produced in compact plasma boosted reformers by the conversion of variety of hydrocarbon fuels including natural gas and diesel. Previous studies of methane steam reforming using a gliding arc reactor at atmospheric pressure, shows a promising results (H_2 concentration higher than 55%). In order to improve reactor efficiency, decreasing input electrical power and increasing methane conversion, small amount of oxygen was added to the CH_4-H_2O mixture.

Keywords: Steam reforming, methane, hydrogen, sliding discharge, non-thermal plasma

1. Introduction

Natural gas attracts considerable attention as an alternative energy source to petroleum. One of the reasons why it is possible for natural gas to become the first resource is its high H to C ratio compared to those of coal, and oil [1]. Accordingly, natural gas has a best future as a resource to product hydrogen. However, methane is one of the most stable molecules, and thus, it is difficult to induce a selective reaction using methane to produce special molecules.

There are several methods to produce synthesis gas (syngas) but most of them (40%) are obtained by steam reforming (SR) [2]. The conventional catalytic technology presents several shortcomings such as large size of the equipment, high investments and exploitation costs, limitations on rapid response, catalyst sensitivity to poisons, and extreme operating conditions that limit the lifetime of reactors [3]. Therefore, a process, which converts methane directly into syngas and other valuable products under sweet conditions, is expected to be a challenge from the viewpoint of industry as well as science. Plasma reformer seems to be one of the solutions. Plasma is known to be a very high energy density media and gives an attractive alternative for hydrogen and syngas production. In this approach, the plasma could replace catalysts and accelerates chemical reactions due to both temperature and active species effect. Plasma reactors represent an incisive approach by their simplicity, compactness and low price.

Produce hydrogen and syngas via methane steam reforming was experimentally investigated in various plasma reactor configurations [4]. Obtained results were promising (H_2 concentration higher than 55%).

Due to its high reactivity, oxygen was used in several processes working on hydrocarbons conversion into syngas in partial oxidation (POX) process.

$$CH_4 + \tfrac{1}{2} O_2 \Leftrightarrow 2H_2 + CO \qquad \Delta H = -36 \text{ kJ/mole} \qquad (1)$$

The reaction is exothermic and nor indirect heat exchanger neither catalyst are needed because of its high temperature. It was used in auto-thermal reformer to provide heat and to raise steam for the steam reforming endothermic reaction:

$$CH_4 + H_2O \Leftrightarrow 3H_2 + CO \qquad \Delta H = 206 \text{ kJ/mole} \qquad (2)$$

The present work is a continuation of our previous studies regarding the syngas production by steam reforming of methane [4]. We will present an experimental study of oxygen effect on the methane conversion and hydrogen production using glidarc discharge reactor at atmospheric pressure.

2. Experimental

The plasma reactor shown in Figure 1 consists of three anodes arranged around of a single cathode. Three channels electrical power supply is used to power up the three cascading discharges. Each channel consists of two transformers with rectifiers allowing two running phases: the ignition at high voltage and low current intensity, and a complementary energy supply with higher current.

Discharges are ignited between electrodes and then pushed by the gas flow. A magnet was used in order to produce a rotating effect in the discharge region. The discharge column is a plasma string with a visible diameter less than one millimeter that slides in the gas flow and the magnetic field region (figure 1). The plasma string performs a helix movement and looks like a wrapped wire around the cathode.

Using this type of reactors, plasma can sweep a large part of the inlet gas and maintains its non-equilibrium behavior. In the usual gliding discharges, the plasma thermalization was avoided by using external current limitation (resistors, reactors, etc).

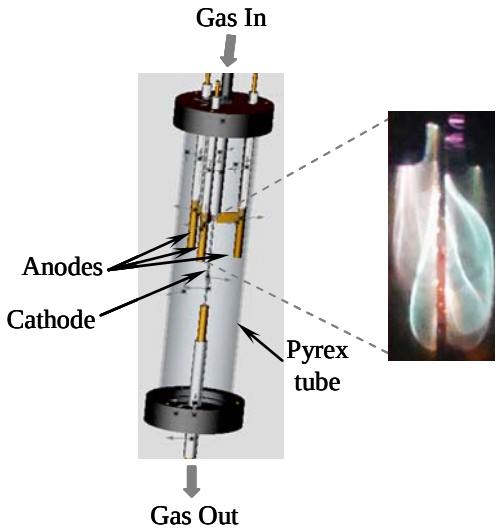

Figure 1: Schematic of the sliding discharge reactor

The discharge behaviour in a magnetic field is quite different than the usual gliding discharges. The first effect is the increase of the mixing properties of the reactor [4]. In the case of magnetic blow out, the force acting on the lengthening discharge column is proportional to the product between the current and the magnetic-field strength. This force produces a very rapid lengthening of the discharge column. The de-ionisation occurs much faster, leading to the mixing of the discharge gases with the cold gas through which the core is forced to pass in its rapid motion. Due to the magnetic field, a self-limitation of the current intensity is produced.

Figure 2 shows the typical voltage and current waveforms for one of the three discharges. For clarity of the diagram, the high voltage is plotted as a negative signal. As can be seen on this figure, the discharge behaviour is not definitely periodic due to the instabilities in the growing discharge. The electrical power is obtained by averaging results over a large number of periods.

All experiments were conducted at atmospheric pressure. The water and methane are mixed before injection in a heating line. The gas temperature was fixed at about 500 K for all the experiments. The exhaust gas from the reactor was passed through a condenser. The major gaseous components were analysed online and quantified using tow techniques: micro gas chromatography (µGC, Varian CP2003-P) and Fourier Transform Infra Red spectroscopy (FTIR, Nicolet Magna-IR 550 series II). The µGC analyser was equipped with Molsieve 5Å and PoraPlot Q columns and the detection was assured by thermal conductivity detector (TCD) calibrated with standards of known composition. The major gas components identified were H_2, CH_4, and CO. Also, a small amount of CO_2 and C_2 hydrocarbons have been detected (concentration lower than 1% in all cases studied).

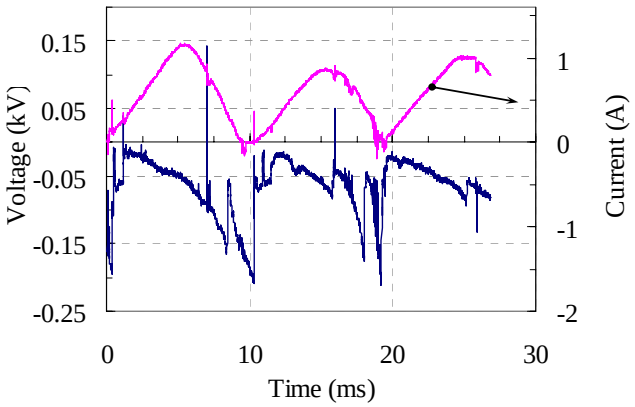

Figure 2: Typical voltage and current waveforms

3. Results and Discussion

Figure 3 shows an example of H_2, CO, CH_4 and CO_2 concentrations as a function of the inlet O_2 amount added in the CH_4-H_2O mixture. These results were compared with those obtained in the case of water-methane mixtures and showed in figure 4.

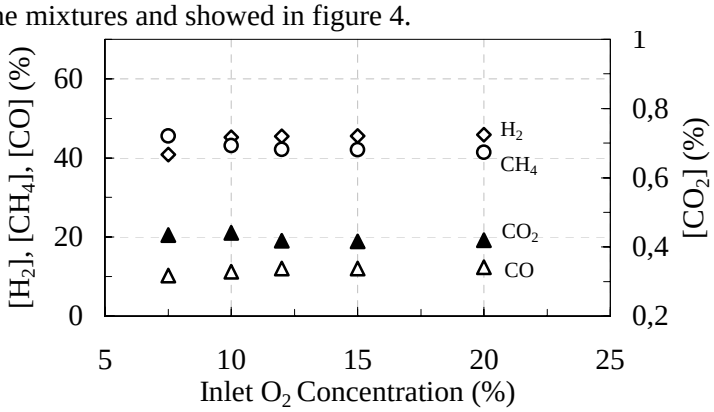

Figure 3: H_2, CH_4, CO and CO_2 concentrations as a function of O_2 concentration in H_2O-CH_4–O_2 mixtures. (Inlet gas temperature: 500 K, Electrical power: 830 W, flow rate: 15 L/min, Initial CH_4 molar fraction: 30 %)

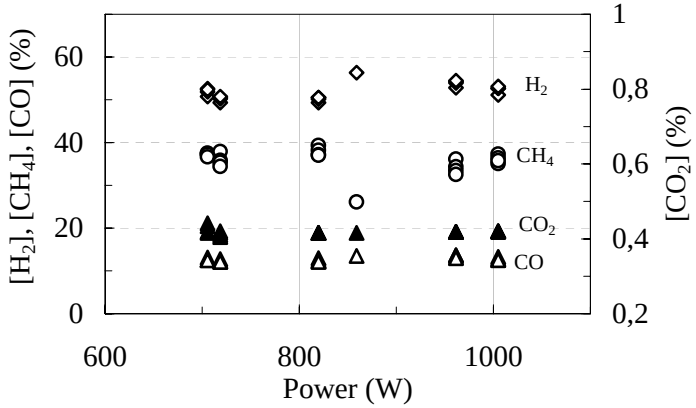

Figure 4: H_2, CH_4, CO and CO_2 concentrations as a function of electrical power in H_2O-CH_4 mixtures. (Inlet gas temperature: 500 K, Gas flow rate: 15 L/min, Initial CH_4 molar fraction: 30 %)

From figures 3 and 4, we note that, adding up to 20% of O_2 in methane-water mixtures do not affect significantly the CO, CH_4 and CO_2 concentrations obtained after plasma treatment. Nevertheless, the H_2 molar fraction slightly decreases in the case of presence of O_2. The addition of O_2 does not seem to be the solution to improve CH_4 conversion. It seems that oxygen reacts preferentially with H_2 to form H_2O.

Taking into account the main products identified at the reactor outlet and the decrease of the outlet H_2 molar fraction, we calculate the characteristic parameters (conversion, selectivity) of our process following the main possible reactions given below:

	CH_4 + H_2O ⇔ $3H_2$ + CO				**ΔH = 206 kJ/mole**	(1)
Initial (moles)	1	b				
Consumed (moles)	x					
Final (moles)	1-x	b-x	3x	x		

	CH_4 ⇔ $2H_2$+ C				**ΔH = 74.6 kJ/mole**	(2)
Initial (moles)	1-x					
Consumed (moles)	y					
Final MF	1-x-y	2y				

	$2H_2$ + O_2 ⇔ $2H_2O$				**H = -285.83 kJ/mole**	(3)
Initial (moles)	3x+2y	c	b-x			
Consumed (moles)	2y					
Final (moles)	3x+2y-z	c-z	b-x+2y			

The x, y, c, and z parameters represent the amount of methane consumed via the steam reforming reaction (equation 1), the amount of methane consumed via the cracking reaction (equation 2), the amount of inlet oxygen, and the amount of hydrogen converted in water, respectively. Accordingly, the total amount of methane converted will be equal to (x+y). The steam reforming and cracking reactions selectivity are calculated from the ratios (x/(x+y)) and (y/(x+y)), respectively. Figure 6 gives the results of these calculations as a function of the O_2 concentration added to the CH_4 - H_2O mixture. These results show that the addition of O_2 (up to 20%) promotes the cracking reaction (equation 2). In these experiments, one can note that a large quantity of soot was deposited on the plasma reactor wall in the case of high O_2 concentration and could be explained by the decrease of the H_2O/CH_4 molar ratio (<2) [5].

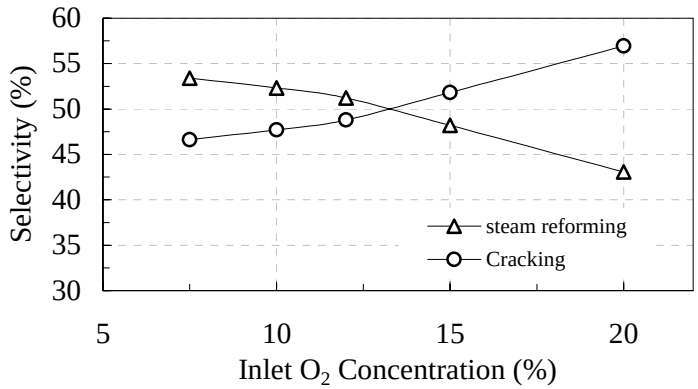

Figure 5: Selectivity variation us a function of the feeding parameters of the reactor

4. Conclusion

Compared with other processes, gliding arc reactor showed encouraging results and seems have a great future in the production of hydrogen from hydrocarbons. The addition of O_2 is not a solution to improve CH_4 conversion and to decrease input electrical power. Therefore, further investigations must be performed in order to increase both conversion and selectivity.

References

[1] S. Kado, K. Urasaki, Y. Sekine, K. Fujimoto - Fuel 82, 1377 (2003)
[2] C. Liu, R. Mallison and L. Lobbon - J. Catal. 179, 326, (1998).
[2] M.A. Pena, J.P. Gomez and J.L.G. Fierro - Appl. Catalysis A, 144, 7, (1996)
[4] I. Rusu, J.M. Cormier – Chem. Engin. J. 91, 23, (2003)
[5] A. Berman, R.K. Karn, M. Epstein, Appl. Catalysis A: General, 282, 73, (2005)

Removal of NOx and SO_2 from synthetic glass industry exhausts with pulsed dielectric barrier discharge

A. Khacef and J. M. Cormier

GREMI-Polytech'Orléans, 14 rue d'Issoudun, B.P. 6744, 45067 Orléans Cedex 2, France
E-mail: ahmed.khacef@univ-orleans.fr

Abstract

A gas phase oxidation process using a sub-µs pulsed DBD has been studied to simultaneously remove SO_2 and NOx from gas stream that simulated glass manufacturing industry exhausts. SO_2 and NOx ($NO+NO_2$) removal efficiencies are evaluated as a function of gas temperature, specific energy and inlet SO_2 concentrations. About 100% of the SO_2 are removed from the gas stream containing 163 ppm of SO_2 at an energy cost of about 45 eV/removed molecule. The SO_2 removal efficiency was not significantly affected by the temperature in the range 100-500°C. The fraction of NOx removed was limited to a value of 30% in all cases studied. These results indicate that DBD plasmas have the potential to remove SO_2 from gas streams without additives.

Keywords: Pulsed dielectric barrier discharge; SO_2 removal; NOx removal

1. Introduction

The reduction of harmful greenhouse gases, such as sulfur and nitrogen oxides - SO_2 and NOx (including NO and NO_2), from industrial processes and vehicle exhausts is one of the critical and urgent topics in environmental and pollution control researches. These molecules have adverse effects on human health and have a great contribution to acid rain which has had detrimental effects on ecosystems.

Removal of these pollutants from flue gases can be achieved by conventional methods combining wet scrubbers and catalytic converters. However, these methods require additives (ammonia, urea, or lime), catalyst, and additional waste water treatment processes.

Many recent investigations [1-2] have paid attention to new technologies and suggested that the non-thermal plasma (NTP) could be one of the most effective methods for simultaneously removal of SO_2 and NOx ($NO+NO_2$) from flue gas at relatively low energetic costs. NTP that has a low gas temperature and a high electron temperature can be produced by a variety of electrical discharge methods (pulsed corona discharge, barrier discharge, and dc discharge) [3-6] or electron beam irradiation [1,7]. Regarding their intrinsic properties well adapted to treat large gas quantities, pulsed corona and dielectric barrier discharge (DBD) techniques are two of the more commonly methods used for producing electrical discharge plasmas. In these plasmas, gas phase radicals such as hydroxyl (OH), hydroperoxyl (HO_2) and oxygen atoms (O) were generated that simultaneously oxidize SO_2 and NO to SO_3 and NO_2, respectively. These oxides react with water to form acids molecules consisting of H_2SO_4 and HNO_3, respectively. In an industrial application of this process, the acid molecules could be chemically neutralized with the added ammonia (NH_3) to form salts ($(NH_4)_2SO_4$ and NH_4NO_3) which can be recovered as a dry powder using conventional particle collector and can be sold as a useful product (agricultural fertilizer) [7].

In the present work, an experimental investigation was conducted to remove simultaneously SO_2 and NOx from simulated glass industry exhausts based on SO_2-NO-NO_2-O_2-H_2O-CO_2-N_2 mixtures using a sub-microsecond DBD at atmospheric pressure.

2. Experimental facility

The experimental system consists of a continuous flow gas generation system, laboratory-scale DBD reactor, and a gas detection system (Figure 1). The system was described in detail previously [8] but is briefly described for clarity.

Synthetic gas containing mixtures of O_2, N_2, NO, NO_2, CO_2, SO_2, and H_2O were prepared in a gas handling system. The gas composition was controlled with calibrated high-precision mass flow controllers. Water vapor with controlled concentrations was added to the gas mixture using controlled evaporator mixer CEM®. It consists of a liquid flow control, a carrier gas control and a mixing chamber for liquid and carrier gas with heat exchanger for total evaporation. This device can provide a high reproducibility and a very stable water vapor flow. After mixing in the manifold, the gas then passes through a temperature-controlled line which preheats the gas and prevents condensation. The compositions of the gas mixtures studied are shown in table 1. Experiments were conducted at two flow rates (3 and 10 L/min) corresponding to residence times of the flue gas in the DBD reactor of about 320 ms and 1.07 s, respectively.

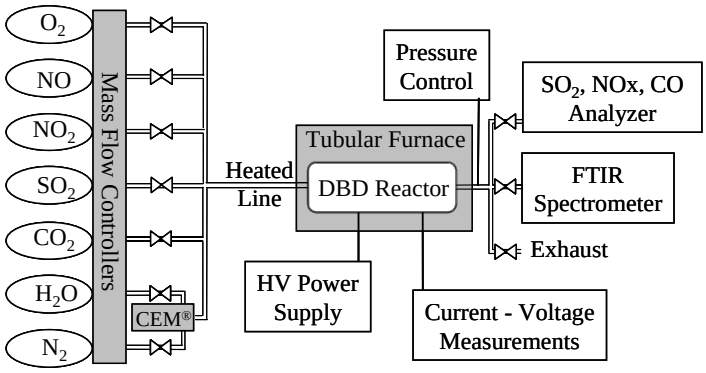

Figure 1: experimental arrangement

Table 1: Gas mixtures studied

	O_2	H_2O	CO_2	NO	NO_2	SO_2	N_2
Gas mixture #1	8%	16%	14%	523 ppm	49 ppm	163 ppm	62%
Gas mixture #2	8%	11.5%	16.5%	373 ppm	39 ppm	630 ppm	64%

The DBD reactor geometry was one of a wire to cylinder type. It consists of a 0.9 mm-diameter tungsten wire in a 16 mm-long quartz tube with inner and outer diameters of 11 mm and 13 mm, respectively. A brass mesh covers the dielectric tube and form the other electrode. The length of the outer electrode can be adjusted and then determine the active volume of the DBD reactor. Results presented in this paper were obtained with a plasma volume of about 16 cm^3. The DBD reactor was placed inside a tubular furnace and the gas mixture temperature can be adjusted from room temperature to 500°C.

The DBD reactor was powered by a home made high voltage pulses with amplitude up to 30 kV into 80 ns (FWHM) pulses and short rise times (40 ns) at variable pulse repetition rate (up to 200 Hz). The discharge pulse energy into the plasma was about 32 mJ. The fast voltage rise time allows achieving significant overshoot of breakdown voltages (kilovolts per nanosecond) and allowing working at larger reduced field values (E/n) than in AC-conventional DBD. The time-behavior of the voltage and the current, shown in figure 2, were measured with a Tektronix P6015A high voltage probe (1000x) and current transformer Europulse 9001. The signals from the probes were recorded on a Tektronix TDS 3034B digital oscilloscope.

The specific input energy which is the discharge energy to unit volume of the treated gas is given by:

$$E_s = \frac{E_p \cdot f}{Q} \qquad (1)$$

where E_p is the discharge pulse energy, f the pulse repetition frequency, and Q the gas flow rate at standard conditions (25°C and 1 atm). At a constant flow rate, changing the specific energy means changing either frequency and/or discharge pulse energy. In general, the experiments were performed with pulse energy of 32 mJ in the frequency range from 15 Hz to 160 Hz.

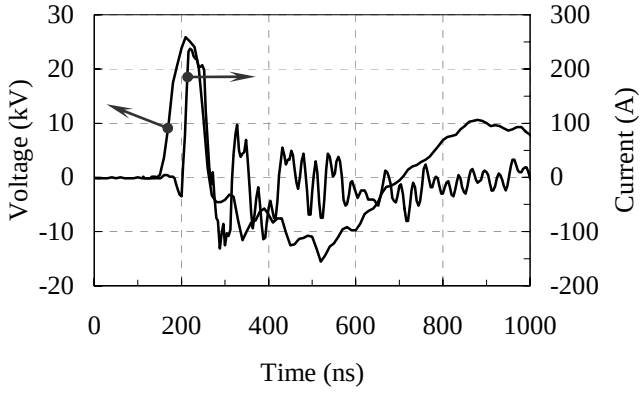

Figure 2: Typical voltage (a) and current (b) pulses

The product gases were analyzed online and quantified using Fourier transform infrared absorption spectrometer (FTIR, Nicolet Magna 550) equipped with a heated 10 m-multiple pass absorption cell. FTIR analysis collected 12 scans for each spectrum at a spectral resolution of about 0.5 cm^{-1}. Absorbencies were converted to concentrations using calibration plots. An electrochemical analyzer (QUINTOX KM 9006) was also used for monitoring continuously SO_2, NO, NO_2, NOx as well as CO levels in the gas stream.

3. Results

In the gas phase under oxygen and water rich conditions, DBD is a very effective means for oxidizing NO to NO_2 and SO_2 to SO_3 [9-12]. Analysis of gas composition at the outlet of the plasma reactor revealed the existence of compounds already reported in the literature. Beside the main products of the plasma such as NO_2, CO, and CO_2, we should highlight the presence of by-products such aldehydes (CH_2O, CH_3CHO), formic acid (CH_2O_2), ethyl and methyl nitrate ($C_2H_5ONO_2$, CH_3ONO_2). Figure 3 shows some species observed in the case of "dry mixture". Small amount of nitrous acid was measured indicating the presence of moisture in the system, possibly arising from the air supply or from moisture adsorbed onto the walls of the gas handling system.

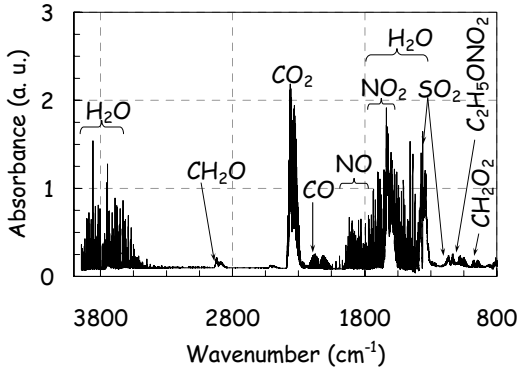

Figure 3: Typical FTIR spectrum: NTP processing of O_2 (8%)-CO_2 (14%)-NO (523 ppm)-NO_2 (49 ppm)-SO_2 (158 ppm)-N_2

The removal efficiency parameter is sometimes used instead of concentrations for the description of decomposition processes. For the molecule X (X could be SO_2, NO, or NOx) this parameter is defined by the following equation where the subscripts denote if the discharge was turned on or turned off.

$$\eta_X\ (\%) = \left(\frac{[X]_{Off} - [X]_{On}}{[X]_{Off}} \right) .100\% \qquad (2)$$

SO_2 removal efficiency η_{SO2} as a function of gas temperature is shown on figure 4 for selected SO_2 inlet concentrations $[SO_2]_{off}$ (158 ppm and 630 ppm) and specific energies E_s (10 J/L and 30 J/L). These measurements show that the highest SO_2 removal efficiency is obtained at temperature above the condensation of water and remain constant in the range 100-500°C. Even at relatively low specific energy (10 J/L), SO_2 removal efficiency higher than 80% was obtained at 163 ppm SO_2 inlet concentration. When SO_2 inlet concentration increase, the SO_2 removal efficiency decrease to a value of about 60% at $[SO_2]_{off}$=680 ppm. Although η_{SO2} is higher at a lower inlet SO_2 concentration, the amount of SO_2 molecules removed from the gas stream is larger for increasing inlet SO_2 concentration (figure 5). Note that the absolute SO_2 removal is a function of specific energy deposited to the gas. In our case, higher total removal can be achieved by operating at higher frequencies (see equation 1). These results could be compared with those using additives such as NH_3 and H_2O_2 in combination with corona discharge. The SO_2 removal efficiency is strongly correlated to energy cost per SO_2 removed molecule (W-value). As example, for the case of gas mixture#1, W-value for SO_2 is dramatically reduced to values scaling from ≈ 45 eV at 30 J/L down to ≈ 15 eV at 10 J/L.

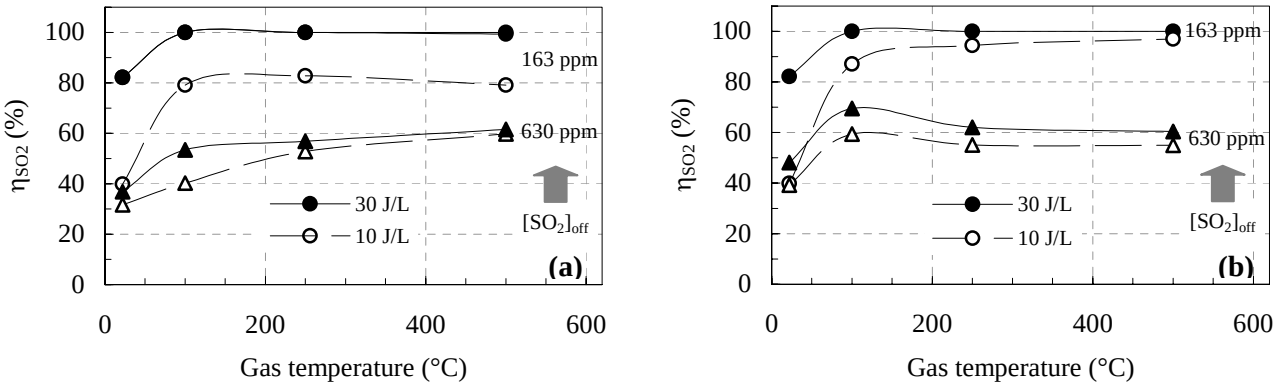

Figure 4: SO_2 removal efficiency as a function of gas temperature and specific energies for two different SO_2 initial concentrations (gas flue rate: a) 3 L.min^{-1}; b) 10 L.min^{-1}).

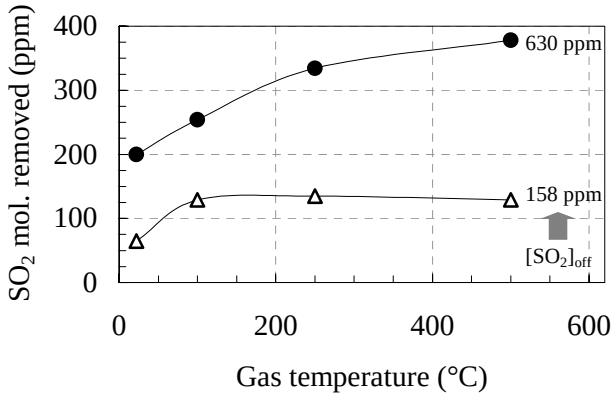

Figure 5: Amount of SO_2 molecules removed as a function of gas temperature for the two gas mixtures at flow rate of 3 L.min^{-1} and specific energy deposition of 10 J/L.

Output NO and NO_2 concentrations as a function of gas temperature for the gas mixture#2 is shown in figure 6. At a given temperature, the NO concentration decreases while that of NO_2 increases with increasing the specific energy deposition. The fraction of NOx (sum of NO and NO_2 concentrations) removed was limited to a

value of 30% in all cases studied in that work. These results could be explained by the NO_2 to NO reduction reactions that counterbalance the NO to NO_2 oxidation processes. One possible way to enhance NOx conversion is the introduction of a small amount of reducing agent (hydrocarbons or ammonia for example) as additives to increase the reactivity of the plasma [2,8,10,12].

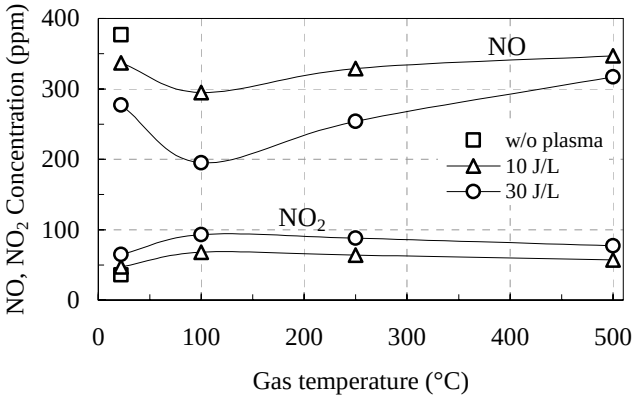

Figure 6: NO and NO_2 concentration as a function of gas temperature for two specific energies (10 and 30 J/L). Gas mixture#2, flow rate=10 $L.min^{-1}$.

4. Conclusion

The dielectric barrier discharge has been proved to be an effective tool to remove SO_2 and NOx pollution from simulated glass manufacturing industry exhaust at atmospheric pressure. Removal efficiencies of SO_2 and NOx are dependant on specific energy and inlet concentration of SO_2. For a specific energy of 30 J/L, simultaneous removal efficiencies for SO_2 and NOx at inlet concentrations of 163 and 570 ppm are as high as 100% and 30%, respectively.

Scaling these results to industrial flow rates (1000 $m^3.h^{-1}$) indicates that energy consumption three times lower than that of conventional technologies (SCR, SNCR, Reburning) can be obtained. In addition to environmental advantage, NTP process using pulsed DBD appears technically simple and economic compared with the other technologies.

References

[1] Non-thermal Plasma Techniques for Pollution Control, Part A and B, Eds B.M. Penetrante and S.E. Schultheis (New York: Springer-Verlag) (1993).
[2] J.Y. Park, I. Tomicic, G.F. Round, and J.S. Chang - J. Phys. D: Appl. Phys. 32, 1006 (1999).
[3] S. Masuda and H. Nakao - IEEE Trans. Ind. Appl. 26, 374 (1990)
[4] S.K. Dhali and I.J. Sardja - Appl. Phys. 69, 6319 (1991)
[5] B.M. Penetrante, M.C. Hsiao, J.N. Bardsley, B.T. Merrit, G.E. Vogtlin, P.H. Wallman, A. Kuthi, C.P. Burkhart, and J.R. Bayless - Pure & Appl. Chem. 68, 1083 (1996)
[6] D. Evans, L.A. Rosocha, G.K. Anderson, J.J. Coogan, and M.J. Kushner - J. Appl. Phys. 74, 5378 (1993)
[7] N.W. Frank - Radiat. Phys. Chem. 45, 989 (1995)
[8] A. Khacef, J.M. Cormier and J.M. Pouvesle - J. Phys. D: Appl. Phys. 35, 1491 (2002)
[9] J.J. Lowke and R. Morrow – IEEE Trans. Plasma. Sci. 23, 661 (1995)
[10] M.B. Chang, M.J. Kushner, and M.J. Rood - Plasma Chem. Plasma Process. 12, 568 (1992)
[11] W. Sun, B. Pashaie, S.K. Dhali, and F.I. Honea - J. Appl. Phys. 79, 3438, (1996)
[12] E.M. van Veldhuizen, L.M. Zhou, and W.R. Rutgers - Plasma Chem. Plasma Process. 18, 91 (1998)

On the use of a Non thermal Plasma for Hydrogen Fuel Enrichment

C. Met, E. El Ahmar, O. Aubry, J. M. Cormier, and A. Khacef

GREMI - Polytech'Orleans, 14 rue d'Issoudun, B.P. 6744, 45067 Orléans Cedex 2, France
e-mail: jean-marie.cormier@univ-orleans.fr

Abstract

A new promising technology based on plasma treatment of air-fuel mixtures in the thermal engines could provide new opportunities for obtaining substantial emissions reductions and improving the ignition of combustion. In this work, a first series of experiments using a plasma prototype reactor powered by a 10 kHz high voltage step-up transformer is presented. Results show an H_2 enrichment (4-10%) of inlet gas mixture after plasma treatment.

Keywords: Methane, hydrogen, non-thermal plasma

Introduction

Among the existing pollution sources, motor vehicles are seen as a major contributor to air pollution by nitrogen oxides (NOx), carbon monoxide and dioxide (CO and CO_2), unburned hydrocarbons (UHC), and fine particles matter (PM). Reducing the fuel consumption as well as the harmful exhaust emissions require an improvement of the engine combustion techniques and a better understanding of the physical-chemistry phenomena occurring during of the ignition and combustion phases in the engines.

Plasma reactor can generate electrical discharges in gas flow containing mixtures of air and hydrocarbons with controlled proportions. The plasma energy deposition is associated with the production of reactive species through electron-impact dissociation of gas molecules present in the gas flow. These radicals are the active species of the plasma that eventually lead to the acceleration of the hydrocarbon reformation reactions and, in the final step, a hydrogen rich gas mixture is obtained.

The plasma treatment could also improve the catalytic steam reforming process by decreasing the sensitivity to the type of hydrocarbon, lowering the poisoning risk of catalysts and extending their operating temperature window. The onboard hydrogen production could also improve the combustion starting in lean burn engines. The presence of hydrogen in the combustion chamber is supposed to greatly enhance the propagation velocity of the flame and avoids the ignition failures in lean burn engine. This effect is also beneficial on the NOx emission because dilution reduces the maximum temperature and leads to a low nitrogen oxides production. This approach is particularly attractive for the lean burn gasoline engines and engines running on natural gas because a small level of hydrogen can allow a correct operation.

In this work, first series of experiments using a "sliding discharge" with a prototype specially designed for motor bench tests were presented.

Experimental

The plasma reactor consists of two electrodes between which thread-like plasma develops. The operation mode of this type of reactor is very similar to the sliding discharge device described in previous publications [1-6]. Experimental reactor is shown in figure 1.

Air- CH_4 experiments were carried out with methane concentrations higher than the explosive limit (15%) [7-8] i.e. ranging between 16% and 35%. Mixtures with higher CH_4 concentration had been not studied because of carbon deposition phenomena.

The power supply operating conditions must be flexible in order to allow us a good synchronization between the discharge and the admission of gases in the engine combustion chamber. According to the

engine regime, the plasma treatment duration must be regulated. At a speed of 2000 round per minute, this duration is approximately 15 ms.

The energy deposition into the plasma could be varied by varying either the repetition frequency or the input voltage. In this work, adjustment of the input continuous voltage was selected in order to obtain a progressive variation of the injected energy into the plasma.

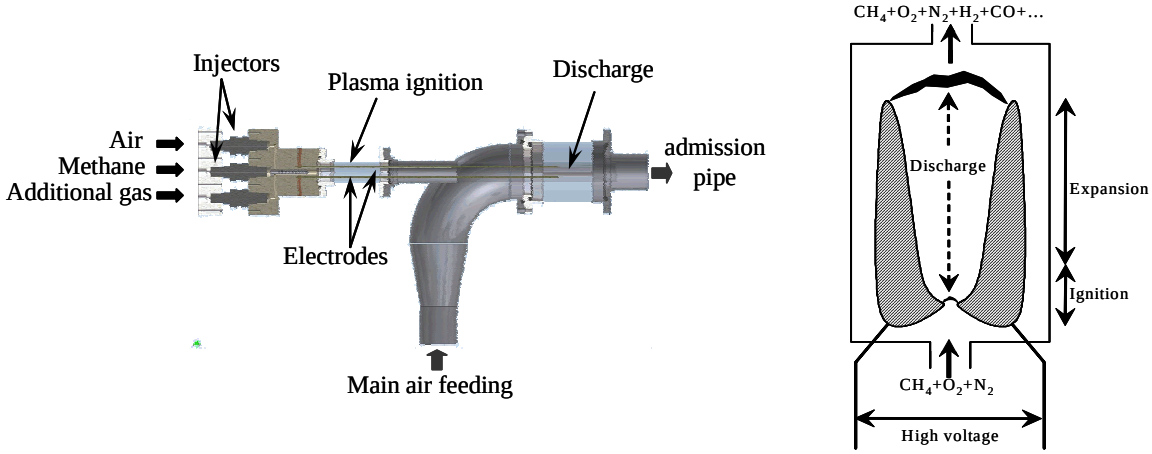

Figure 1: Experimental reactor
a) Motor bench reactor b) Schematic of sliding discharge

The current and voltage waveforms were measured using a Tektronix Hall effect probe TCP202 and a Tektronix high voltage differential probe ST500 connected to a voltage divider with a ratio of 0.01, respectively. The signals from the probes were recorded on a Tektronix digital oscilloscope TDS 460A and processed in a PC.

After plasma processing the exhaust gases were analyzed online and quantified using a Fourier Transform InfraRed absorption spectroscopy – FTIR - (Nicolet Magna 550) equipped with a heated 10 m-multiple pass absorption cell, and a micro Gas Chromatography - µGC - (VARIAN CP 2003P). In that exploring phase, the hydrogen, carbon monoxide, carbon dioxide and water production were mainly presented and discussed.

Results

a) Power variation

Total flow rate corresponding to these experimental conditions is constant (41 L/min, 19% of CH_4, 81% of air). Analysis gas results at the outlet reactor are given on figure 2.

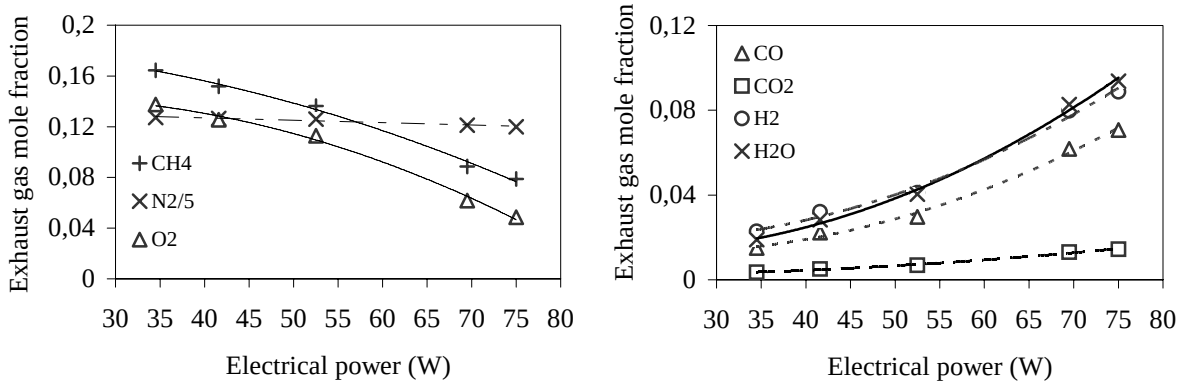

Figure 2: Exhaust gas composition as a function of electrical power (total flow rate=41 L/min)

As it can be seen in figure 2, non linear variation of CH_4 conversion and H_2 production are observed. As the power is increasing the CH_4 conversion and H_2 production are increasing. For the maximum power (75 W), the CH_4 conversion is about 58% and the H_2 production rate is about 9%.

b) Composition variation at constant air flow rate and constant electrical power

Air flow rate corresponding to these experimental conditions is constant (33 L/min). Average power determined from oscilloscope recording is 50 W. As shown on figure 3, the CH_4 consumption is corresponding to the H_2, H_2O, CO and CO_2 production. The CH_4 and O_2 concentrations decrease with the CH_4 inlet. The figure 3 shows that the enrichment of fuel in hydrogen is possible with the use of low electrical power.

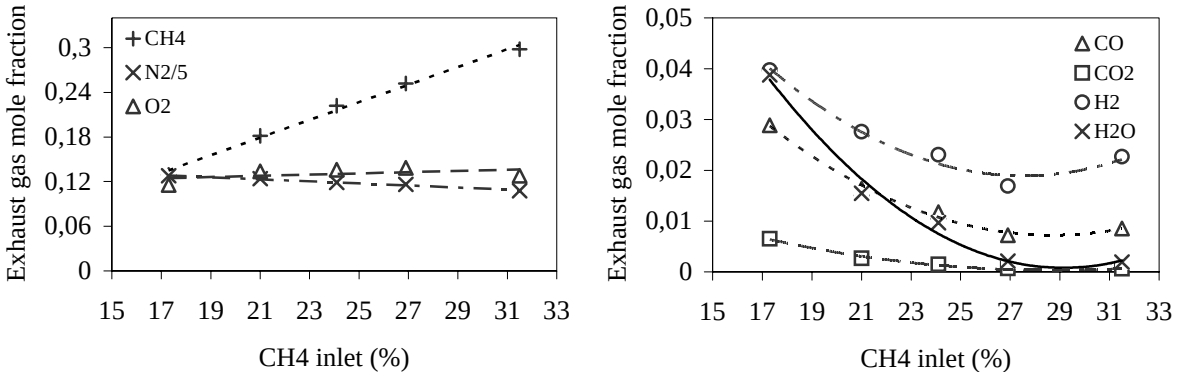

Figure 3: Exhaust gas composition as a function of CH_4 inlet(air flow rate=33 L/min, electrical power=50 W)

c) Outlet reactor temperature

Thermocouples were laid out at the outlet reactor in order to measure the gas temperature after the plasma treatment. The presence of the discharge produces a heating of the system. The energetic supply corresponds to two contributions: the first is the electrical power provided to plasma by Joule effect, the second is the energy provided by the exothermic reactions ignited by the plasma. Figure 4 shows the outlet gas temperature as function of CH_4 initial molar fraction. The outlet gas temperature decreases when the CH_4 initial molar fraction increases. The maximum gas temperature was observed for a CH_4 concentration of 17%, which corresponds to a strong reactivity of the system. This rise in temperature, which increases when one approaches the high explosive limit, is probably related to the starting of the combustion process.

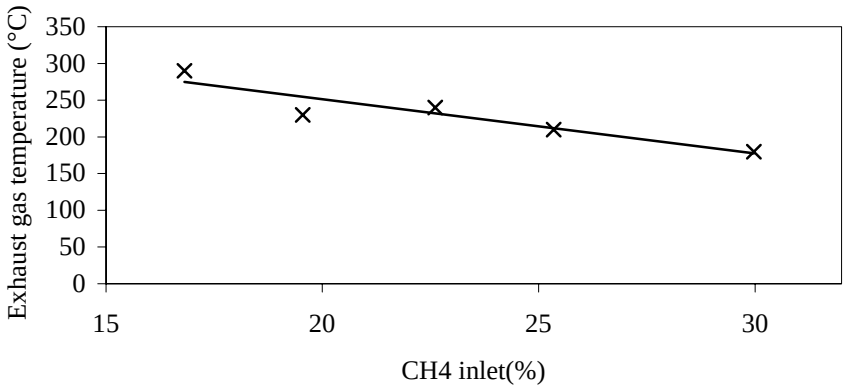

Figure 4: Outlet reactor gas temperature as a function of CH_4 inlet (air flow rate=33 L/min, electrical power=50 W)

d) Calorific value of the outlet mixture (CH_4-H_2)

The net calorific value of a mixture (C_m) is calculated from the relation $C_m = \Sigma(x_i.C)$, where x_i and C are the molar fraction and the net calorific value of each component, respectively.

The net calorific values of H_2 and CH_4 are 2.98 and 9.95 kWh/m^3, respectively. We calculated the net calorific value of the outlet CH_4 - H_2 mixture. Figure 5 shows that this calorific value is a decreasing function of the electrical power provided to plasma. Indeed, as previously announced, the effectiveness of

the conversion of methane into hydrogen is as high as the electrical power provided to plasma is high. For the maximum power (75 W), there is the weakest C_m (6.25 kWh/m^3). This result shows that the H_2 enrichment generates fuel mixtures releasing less energy (C_m value) than methane (C value). Then, it is obvious that the interest of such a treatment improve combustion processes as well as reduction of emitted pollutants.

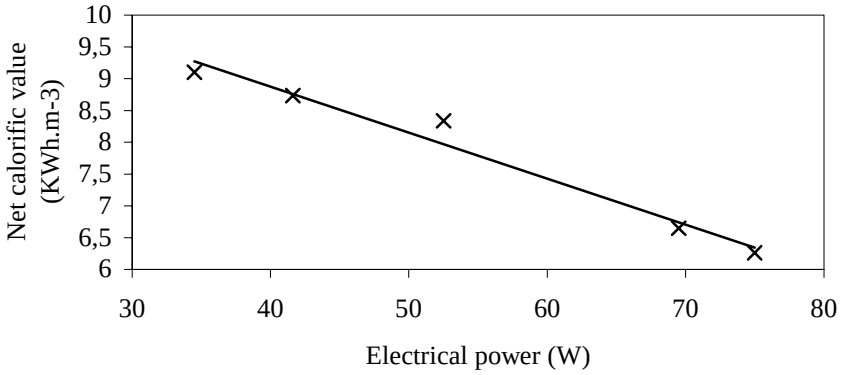

Figure 5: Net calorific value of CH_4-H_2 mixture as a function of electrical power (total flow rate=41 L/min)

The above results confirm the interest of the study for the corresponding application. Improvement of diagnostics for both plasma and chemical mechanisms is underway.

Conclusion

The treatment of methane - air mixture by plasma as well as the chemical analysis of the gas products was carried out. In the present work, only H_2, CO, CO_2 and H_2O were quantified. The molar fraction of hydrogen at exhaust gas is about 9% for an input electrical power of 75 W. We should now check that this quantity is suitable for inducing positive effects on the engine operation. Reduction of the net calorific value shows that the only interest would be to support the ignition of combustion and the emission reduction. Tests on the motor bench are envisaged soon.

Acknowledgment

This work was performed within the framework of the French energy program "improvement of the combustion techniques". The authors are grateful to CNRS and to the Ministère de la recherche for their financial support.

References

[1] S. Pellerin, F. Richard, J. Chapelle, J. M. Cormier, K Musiol - J. Phys. D: Appl. Phys., 33, 2407, (2000).
[2] A. Kaminska, J.M. Cormier, S. Pellerin, O. Martinie - J. High Temp. Mat. Proc., 5, (2001).
[3] J.M. Cormier and I. Rusu - Journal of Physics D: Applied Physics, 34, 2798, (2001).
[4] J.M. Cormier, I. Rusu, A. Kaminska - J. High Temp.Mat. Proc., 6, 421, (2002).
[5] I. Rusu, J.M. Cormier - Chemical Engineering Journal, 91, 23, (2003).
[6] I. Rusu, J.M. Cormier - International Journal of Hydrogen Energy, 28, 1039, (2003).
[7] C. Met, O. Aubry, F. Ouni, A. Khacef, J.M Cormier - Proc. IVth Non-Thermal Plasma Technology for Pollution Control and sustainable Energy Development, CD Rom ISNTPT 4, (2004).
[8] C. Met, J.M. Cormier, A. Khacef - Proc. IXth International Conference on Optimization of Electrical and Electronic Equipment, CD Rom OPTIM'04, (2004).

Plasma characterizations in a Hollow Cathode System for Thin Film Growth

H. S. Maciel, G. Petraconi, K. G. Grigorov, R. S. Pessoa and G. Murakami

Technological Institute of Aeronautics, Department of Physics – Plasma and Processes Laboratory (LPP), 12228-900, ITA – CTA, São José dos Campos, SP, Brazil.

Abstract

The application of the hollow cathode discharge (HCD) in plasma PVD processing is mainly based on two phenomena: the production of high-density plasma and the generation of hot electrons. In this work the plasma properties generated by a HCD system were studied by means of a Langmuir probe and mass spectrometry. Additionally AlN thin films were grown on silicon substrates at temperature in the range of (25 – 150) ºC and characterized with respect to the crystalline structure and morphology using XRD and AFM analyses respectively. The influences of the deposition parameters on the plasma properties were studied and the film properties were discussed.

1. Introduction

High-density plasma typical for the hollow cathodes discharges is based on efficient avalanche multiplication of electrons known as hollow cathode effect (HCE) [1]. The hollow cathode effect is a special situation for the glow discharge between two closely separated cathode surfaces. This effect occurs when the length of the cathode fall region becomes as large as the separation distance between the two cathodes. The loss of electrons is low because the negative walls of the cathode repel them and they oscillate between the cathodes. Thus, at the same power the hollow cathode exhibits a plasma density of one to two orders of magnitude higher than that of conventional planar electrodes. Hollow cathode discharges also have an important characteristic that combines two important processes, i.e. sputtering and excitation/ionization of the sputtered atoms [2, 3].

The optimization of the HCD system for application in plasma processing device extends the studies of ref. [3] and constitutes the main objective of this work. I order to implement the plasma-assisted deposition processes a thorough and detailed characterization of the plasma parameters was required. Besides the conventional Langmuir probe technique, plasma spectrometry is reliable and widely used technique.

2. Experimental set up

The deposition HCD system was allocated (shown in Fig. 1) in a cylindrical vacuum glass chamber of 130 mm internal diameter and 300 mm length. The chamber was preliminary evacuated using a combination of rotary and diffusion pumps to achieve a residual pressure of 10^{-2} Pa. The hollow cathode cavity consists of two parallel aluminum plates having as wording gas a mixture of argon and nitrogen within the pressure range of (10 – 50) Pa. The discharge was generated by a dc power supply of (0 – 1000) V and its electrical characteristics showed a dependence on the inter-cathode distance which was varied in range (3.5 – 1.5) cm. A Helmholtz coil was used to produce a low intensity and uniform B-field within the range of (0 – 30) × 10^{-3} T. The magnetic confinement increases the power density along the axis of the discharge.

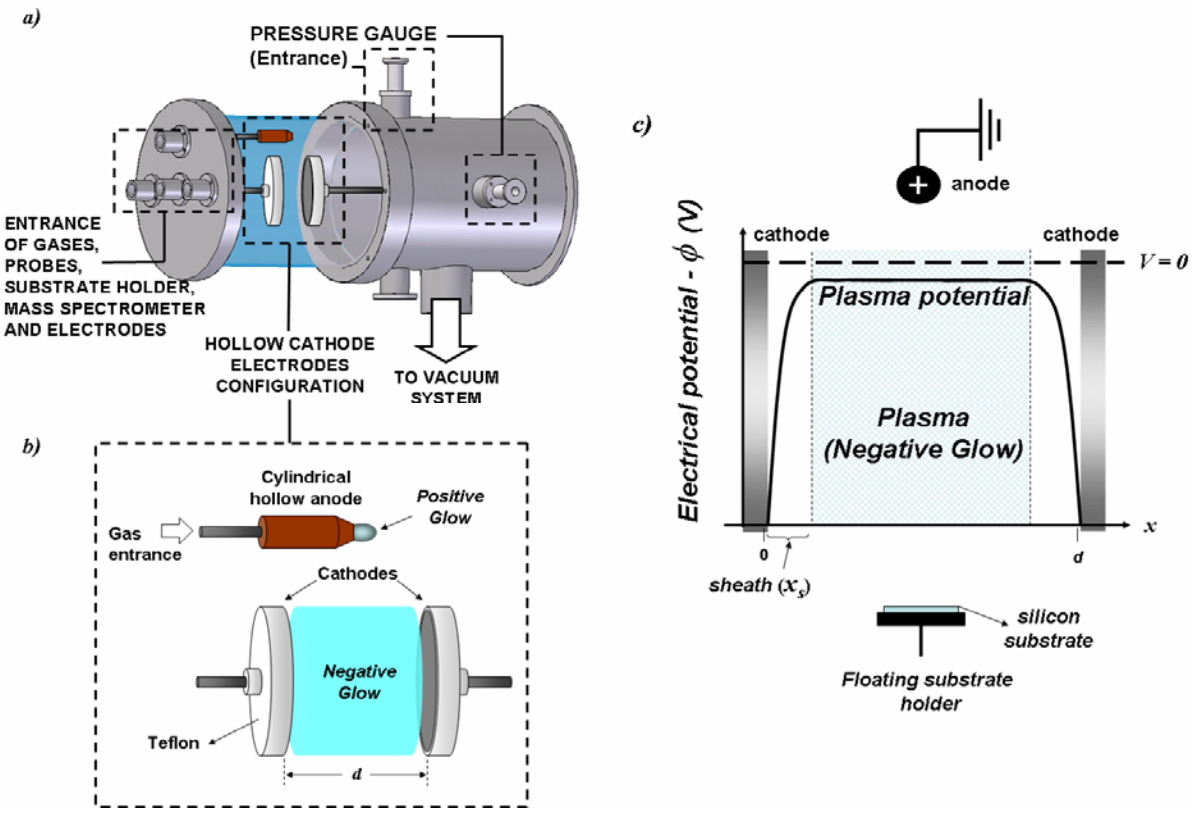

Figure 1. Schema of the HCD reactor - (a), HC source - (b) and deposition configuration - (c).

The Plasma diagnostic was carried out by Langmuir probes and mass spectrometry techniques. The Langmuir probe consists of a tungsten cylindrical electrode with area of 2-mm^2. The probe can be inserted into the vacuum chamber via accesses at frontal of the chamber. The hollow cathode electrodes can be moved axially along a traveling length of 150 mm. This layout enabled to place the probes at any distance from the HC source, so as to study different plasma regions. The measurements were performed at the same probe position and in different external discharge conditions.

A mass spectrometer AccuQuad^{TM} with a resolution of 1 amu was adapted to the vacuum chamber trough a drifting tube for monitoring the mass spectra for different discharge process parameters. The species were sampled through a micro orifice located at the mass spectrometer's entrance. The typical operation pressure within the mass spectrometer was 10^{-5} Pa. The collected spectra were recorded in the mass range from 1 to 100 amu.

The type of crystalline structure, orientation and grain size was investigated by Philips 1830 diffractometer in θ - 2θ scan mode. Moreover, the morphology of the surface and its roughness were studied using an Atom Force Microscope (AFM) SPM-9500 J3.

3. Results and discussion

3.1. Analysis of plasma parameters of the HC discharge

a) Langmuir Probe

Typical results of the HC plasma probe I-V measurements are given in Fig. 3-a showing a family of I-V plots designed for different products $P.d$, P and d being the pressure and inter-cathode distance respectively. As

one can see, the plots differ mostly in the electron saturation currents (I_{e0}), plasma potential (V_p) and floating potential (V_f).

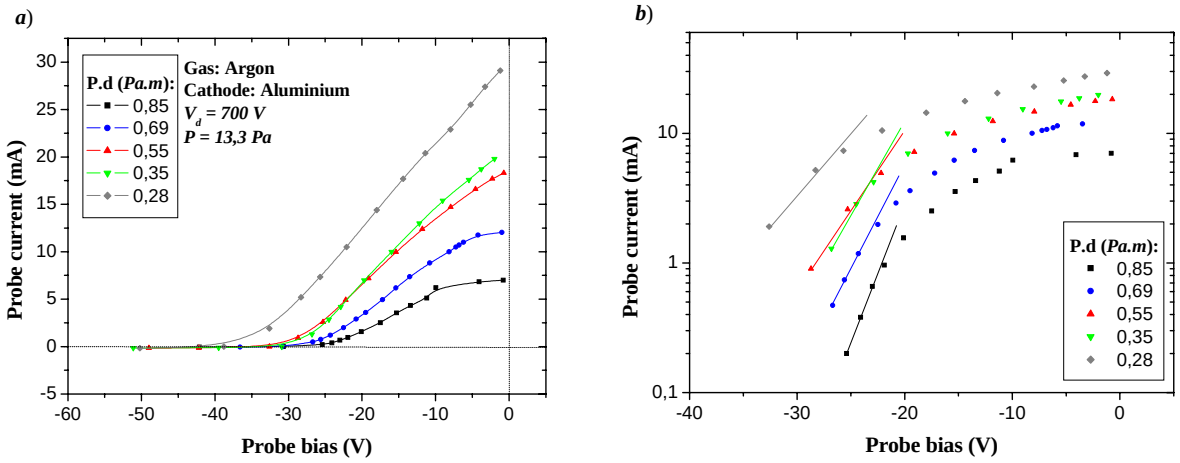

Figure 2. Probe current versus the probe bias for argon buffer gas (a); Probe Current (Ln) versus probe bias (b).

The plasma parameters (n_i, T_e, V_p, V_f, λ_D) are derived from the measured *I-V* characteristic assuming a Maxwellian distribution of electrons [7]. Special interest draws the region with probe voltages between the floating potential (the potential when $I_e = I_i$) and the plasma potential, $V_f < V < V_p$. The slope of the straight lines in this region (Figure 2-b) is related to the value of the electron temperature Te [3]. The values of the electron density n_e and the Debye length λ_D (1) has been calculated by using the conventional probe theory previously described in [4].

$$\lambda_D = 7400\left(\frac{T_e}{n_e}\right)^{1/2} mm \tag{1}$$

The plasma in this system is a type of "cold plasma" ($T_i << T_e$) and, therefore the differences between the plasma and the floating potentials are proportional to the electron temperature [4]. For a typical argon (M = 40) and nitrogen (M = 28) plasma, the proportionality factor is 5.40 and 5.19 respectively.

$$V_P - V_f = \frac{kT_e}{2e}\ln\left(\frac{2m_i}{\pi m_e}\right) = 5.4\frac{kT_e}{e} \text{ (Argon)} \tag{2}$$

These parameters are quite good in order to estimate the electric field E_s in the region of the plasma sheath around of an inserted sample in the volume of the plasma. Thus, through the values obtained by Eq. 1 and Eq. 2, we can evaluate the electric field in the plasma region assuming that no collisions occur within the probe sheath,

$$E_s = \frac{V_p - V_f}{n\lambda_D} \tag{4}$$

Hutchinson [4] got a relation between the thickness of the probe sheath (x_s) and the Debye length. For argon x_s = 4.97 λ_D and nitrogen x_s = 4.84 λ_D. All these parameters are calculated and listed in Table 1 for Ar and N_2 gases used in this work.

Table 1. The measured Ar and N_2 plasma parameters for operating conditions - V_d = 700V, P = 13.3 Pa, d = 2.5 cm.

Gas	n_p (10^{17} m^{-3})	T_e (eV)	V_p - V_f (V)	λ_D (μm)	x_s (mm)	E_s (kV/m)
Argon	1.4	4.5	25.9	34.0	0.17	152.3
Nitrogen	3.5	4.8	24.9	27.0	0.13	191.2

Figure 3 illustrates the electron density and the electron temperature as a function of the *P.d* parameter when different gases are used. To maintain plasma in reactive gas discharge higher currents are required than in cases of inert gases, as the argon. As observed, higher current densities (of the order of 10^{17} m^{-3}) and temperatures of electrons (between 1 and 4.5 eV) can be reached when reactive gases are used, i.e. the hollow cathode effect becomes more pronounced.

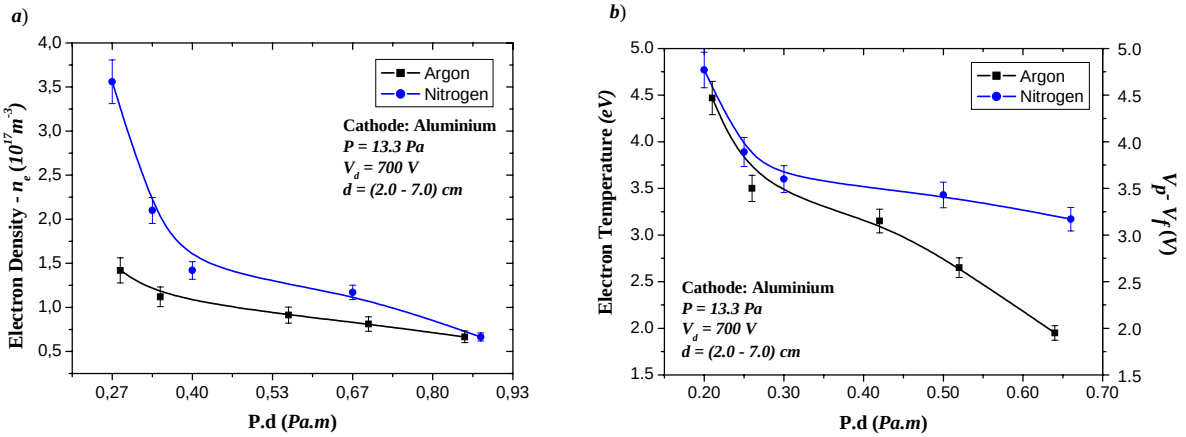

Figure 3. Electron density n_e versus the *P.d* product for Ar and N_2 gases (a); Electron temperature T_e and the probe potential sheath fall V_p - V_f versus the *P.d* product in the same experimental conditions (b). The discharge voltage is 700 V.

The application of perpendicular magnetic field to the cathode surface facilitates the ignition of the discharge and improves the HCE – increase the time of residence of electrons in the inter-cathode cavity and reduce the lateral diffusion. As a consequence the discharge current and the electron density are increased [3].

Interesting effect concerning the electron temperature when a magnetic field is applied was observed and displaced in Figure 4. In this figure, we also evaluate the variation of the potential fall in the sheath of the probe as function of *P.d*. It is known that the application of a magnetic field onto a glow discharge has equivalent effect to an increase of the pressure of the gas, leading to a reduction of the effective electron temperature. This effect is stronger at lower range of *P.d* as observed in Fig 4.

b) Mass Spectrometry

Due to the ion bombardment and the enhanced cathode temperature, the hollow cathode target can be sputtered and/or evaporated and it contributes to film growth when the source is used for film deposition. Through mass spectrometry technique some species in the plasma gas phase could be monitored for various operational conditions of the discharge. In Figure 5 the relative partial pressure (%) for AlN^+ and Al^+ peaks was plotted as function of the inter-cathode distance, for two pressure values. For discharges processes when the operation pressure is lower (left part of the curve) the curve indicates that the generation of molecules of aluminum nitrite reaches a maximum for *P.d* = 0,7 Pa.m. This tendency vanishes at higher-pressure values (right part of the curve).

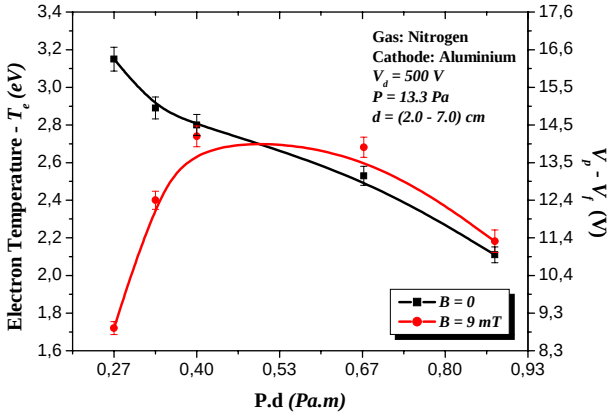

Figure 4. Electron temperature T_e and probe potential sheath fall V_p - V_f versus product $P.d$ for HCD in N_2 gas for two values of magnetic field.

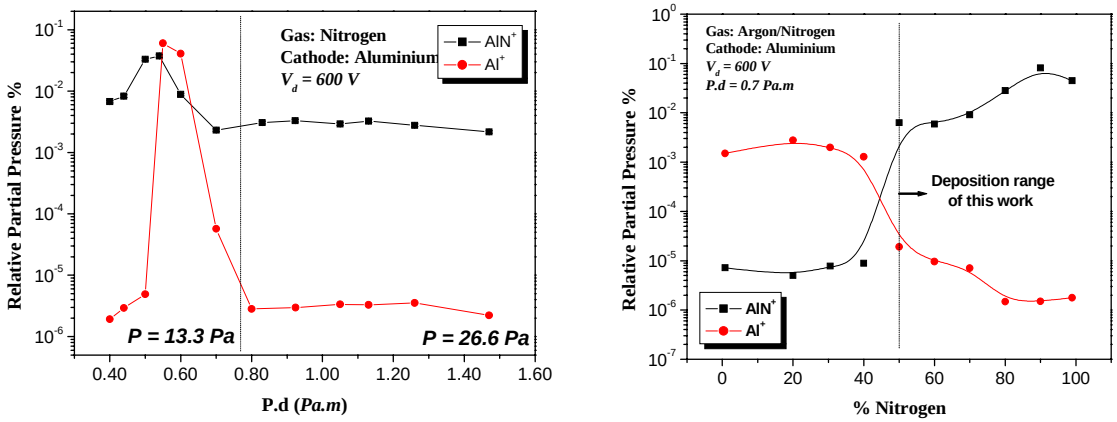

Figure 5. Variation of the aluminum (27 amu) and AlN^+ (41 amu) peaks for HCD in nitrogen gas for two pressure values - 13,3 and 26,6 Pa (a); Variation of the AlN and Al atom signals as a function of the percentage of nitrogen in the Ar gas mixture (b).

Fig 5-b shows one to one dependence describing the dynamic of the AlN formation as a function of the nitrogen gas content in the discharge. The growing rate depends on the nitrogen percentage. If nitrogen gas exceeds 40 % in the Ar-N_2 mixture the reactive film growth can reach and exceed the growth rate of pure metal (Al) film.

3.2. AlN-film analysis

Figure 6-a shows a typical AlN spectrum with very strong reflections at 32.88^o corresponding to AlN (100) crystalline orientations referring to the hexagonal type wurtzit. This sharp and intense peak is common for the highly textured phases similar to a single crystal. Besides the crystallographic orientation, another important parameter calculated is the coherent domain of reflection (CDR), which, in general, describes the dimensions of one crystal or grain containing micro crystals with identical spatial orientation of the axis a, b and c. The CDR was calculated using the Debye-Scherrer formula revealing a 100 nm sized domains grown in columnar way consisting of crystals oriented with his axe “c” parallel to the silicon surface. The topography of the crystals is

shown on Fig 6-b, which reveals smooth and densely packed surface. The mean grain radius is 20 nm with rms roughness of 2.5 nm.

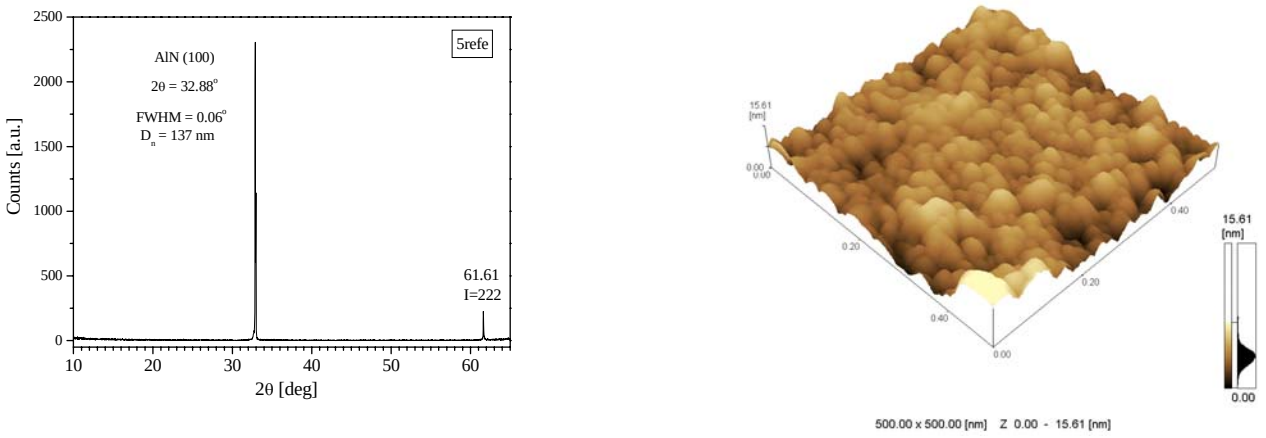

Fig. 6. X-ray diffraction pattern of sample deposited in 50% N_2 atmosphere at P = 13.3 Pa and V_d = 600 V (a); AFM scan in dynamic mode of AlN sample deposited for 15 minutes (b).

4. Conclusions

The plasma density and the electron temperature were measured in a HCD system by using a single Langmuir probe placed inside the plasma bulk and reaches the order of (10^{16} – 10^{17}) m^{-3} and (1 – 4) eV respectively at dc discharge voltage of 600 V. Detailed analysis of the plasma properties using probe techniques and mass spectrometry, at different nitrogen gas flows, could guide the establishment of favorable geometric and gas-pressure conditions for enhanced plasma parameters aimed at plasma material processing. The obtained optimal conditions allow growing of high quality AlN thin films with sufficient deposition rate assuring thus an alternative method for synthesis of this material.

Acknowledgement

The financial support of CAPES is strongly acknowledged.

References

[1] Little, P. F.; von Engel, A. Proceedings of the Royal Society of London. Series A, Mathematical and Physical Sciences, Volume 224, Issue 1157, pp. 209-227.
[2] D. Zhechev, V.I. Zhemenik, S. Tileva, G.V. Mishinsky, N. Pyrvanova, “A hollow cathode discharge modification as a source of sputtered atoms and their ions”, Nuclear Inst. and Methods in Physics Research, B 204, (2003) 387.
[3] Maciel H.S., Petraconi G., Pessoa R. S., "Studies of a hollow cathode discharge using mass spectrometry and electrostatic probe techniques", HAL – ICPP2004, http://hal.ccsd.cnrs.fr/ccsd-00001921/en, (2004).
[4] I.H. Hutchinson, “Principles of plasma diagnostics”, Cambridge University Press, New York, 1988.

Study of plasma-solid interaction in electronegative gases by the combination of particle simulation technique and evolutionary modelling

J. Šimek, R. Hrach, D. Sedlák, P. Jelínek

Charles University, Faculty of Mathematics and Physics, Department of Electronics and Vacuum Physics
Prague, Czech Republic

Abstract
Self-consistent particle models of plasma are precise, but the performance of standard algorithms is rather low. Another particle simulation technique of plasma-solid interaction is a non self-consistent one, where the distribution of electric potential near the substrate is given analytically. But the accuracy of these simulations is in general low as it depends on simplified assumptions about electric field used. The evolutionary modelling was used to combine good features of these two techniques.

1. Introduction

The understanding of processes in the boundary layer between plasma and immersed metal substrates is important both in probe diagnostics and in plasma-chemical technologies. However, the interpretation of experimental data is often difficult as the substrates or probes perturb their local surroundings. The application of Langmuir probe diagnostics of such plasma is limited, because the original theory was developed for the collisionless plasma only. The situation is more urgent in the case of electronegative plasma, as the presence of negative ions complicates not only the theoretical interpretation of experimental data but also the physical and chemical processes in plasma (see Fig. 1)

.

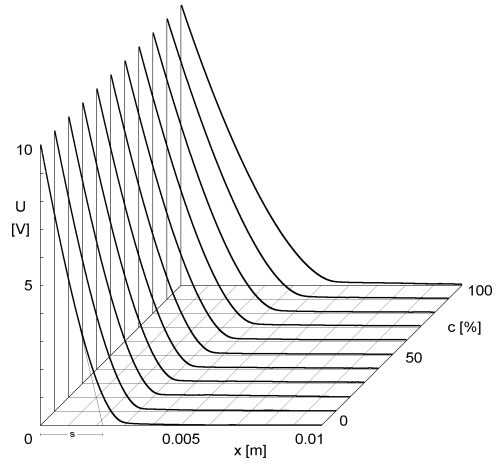

Fig. 1: Distribution of electric potential near the substrate for various concentrations of negative ions in plasma [1].

For the analysis of plasma-solid interaction besides standard experimental and theoretical methods of study, the technique of computer simulation proved to be very successful approach. The computer simulation technique seems to be very promising tool to analyse the cases where the theoretical description cannot be used – substrates of complicated forms, higher pressures, plasma consisting of more types of particles including negative ions, chemically active plasmas, plasma in magnetic field, etc. There are two basic techniques of the plasma sheath simulation – fluid modelling and particle simulation techniques. Fluid models are much more efficient, however their accuracy is very limited. The self-consistent particle models of collisional plasma can bring precise results but the performance of standard algorithms is rather low – in Fig. 2 there are shown time requirements of main parts of the self-consistent models of various spatial dimensions. Time demands of the

molecular dynamic part strongly increase with number of particles in the model. Also the solution of Poisson equation is very time consuming, being the crucial part for 3D model, where more sophisticated algorithms must be used. Sometimes an older particle simulation technique is used, when the distribution of electric potential near the substrate is given analytically by solving the diffusion equation for some simplified situations. In this case the number of charged particles in the model can be reduced and the performance of resulting code increased, however the accuracy of derived results is again low as it depends on the simplified assumptions about the local electric field used. In our contribution, we tried to combine good features of two particle simulation techniques, self-consistent and non self-consistent, in order to increase both the accuracy of simulation and the performance of resulting codes. For this purpose the evolutionary modelling technique was used, which is able among others to generalize various experimentally derived dependencies.

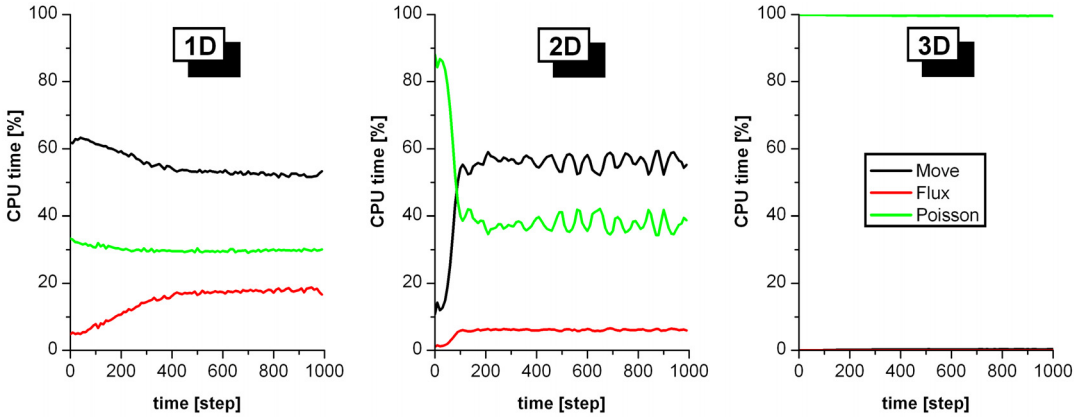

Fig. 2: Evolutions of time requirements for self-consistent models of different spatial dimensions. Main parts of the models are: source of particles (*Flux*), executing molecular dynamic part together with treatment of collisions (*Move*) and force calculations (*Poisson*). Real duration of 1 time step: 1D .. 0.2s, 2D .. 0.4s, 3D .. 250s (P4 3.2GHz).

2. Self-consistent models

The main task of our study is to analyse processes taking place during the interaction of plasma containing negative ions with immersed metal substrates. For this purpose the computer experiment analysing the multicomponent plasma containing electrons, positive ions, negative ions and neutral particles was prepared and the most precise technique of simulation was used – the self-consistent particle simulation approach.

The primary task is the study of sheath evolution and the determination of trajectories of charged particles both in the sheath and presheath. The typical particle model of plasma-solid interaction consists of following parts [2]:

- Source of particles – undisturbed plasma consisting of argon atoms, oxygen molecules, electrons, positive argon ions and negative molecular oxygen ions.
- Interactions – neutral particles are treated as neutral background with which the charged particles interact. For electrons elastic collisions, excitations and ionisations of neutral particles, possibly dissociative attachments with oxygen molecules are considered [3]. For ions elastic collisions, charge transfers and possibly detachments for negative oxygen ions are taken into account.
- Trajectories of charged particles – between scattering events the trajectories in both external and local electric fields are simulated using molecular dynamics method (leap-frog scheme).
- The scattering events are simulated using Monte Carlo method. Due to energy dependence of cross sections of interactions under consideration, the null-collision technique must be used.

- Force calculations – standard PIC technique is used in CIC modification, i.e. the forces are obtained from electric potential calculated from Poisson equation.

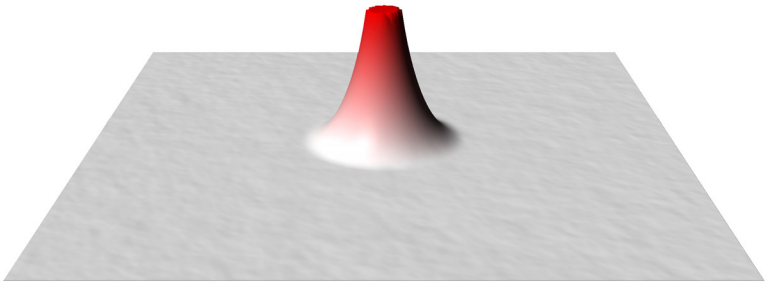

Fig. 3: Distribution of electric potential near the cylindrical probe

The cylindrical substrate was chosen, as it corresponds to the most common form of Langmuir probes. The dimensionality of prepared models was either 1D or 2D, i.e. one or two spatial coordinates and three velocity coordinates were used.

The results of self-consistent modelling of the sheath and presheath (see Figs. 1 and 3) can be used for the determination of the distribution of electric field U in the vicinity of substrates. For the determination of the distribution U various techniques can be used:

- Simple tabulating of results of self-consistent simulation.
- Approximation of derived data by simplified formulae by numerical methods.
- Preparation of analytical formulae by the evolutionary modelling technique,

the last method being the most sophisticated and increasing the performance of resulting codes. The self-consistent approach, especially in higher dimensions, is extremely time-consuming; therefore the reduction of demands on computer time is very desirable.

3. Evolutionary modelling

Evolutionary modelling is a computational method inspired by evolution. It is an optimisation technique that is able to generate functions on the basis of the principles of evolution genetic operators – selection, fitness evaluation, mutation and crossover. These functions are encoded in tables, which represent the compressed neighbourhood-matrix of the canonical acyclic graphs. An implementation of evolutionary modelling begins with a population of tables (typically randomly generated). Fitness value expressing quality of approximation is assigned to each table in the main loop of evolutionary modelling. Then selection operator is applied on evaluated population – tables that represent a better approximation (better fitness) have more chances to be "reproduced" than tables that have poorer quality. Crossover and mutation operators are applied on the new population. This is repeatedly performed until some stop-condition is fulfilled. The main problem in evolutionary modelling is finding efficient encoding and choosing sufficient crossover probability and mutation probability.

4. New generation of non self-consistent models

Standard non self-consistent models use very simplified formulae for the electric field distribution near the substrate so their results are not in most cases trustworthy enough. Our new approach consists of several steps. First, we developed self-consistent model corresponding to studied problem. Then we prepared large set of self-consistent results obtained for various combinations of discharge parameters and plasma compositions. This is the most time-consuming part, however, firstly, the calculation was performed for a limited number of

configurations only, secondly, the older results can be used and, thirdly, for some problems the self-consistent simulation can be performed in lower-dimensions. These data were then processed by program based on evolutionary modelling technique. With the help of genetic algorithms we are able to derive a set of formulae for the electric field distribution in the sheath region of plasma, i.e. generalization of potential distribution for various parameters.

After exact analytical formulae are derived, the much more effective non self-consistent approach can be used for similar conditions of simulation. As a result we can work with efficient computer technique, while the preciseness of results corresponds to original self-consistent calculations, i.e. is radically increased compared to old non self-consistent calculations. The numerical comparison of derived results shows that the increase in the computational speed is about 3 orders of magnitude for one- and two-dimensional simulations and at least 6 orders of magnitude for three-dimensional modelling, the exact values depend on the plasma parameters in the model.

5. Results

As an application of suggested approach one problem from the plasma physics is studied – the probe diagnostics in medium pressures. It is well known that the biased probe is surrounded by a local electric field attracting the charged plasma particles of one sign and repulsing the oppositely charged particles – see Fig. 4 for cylindrical configuration. However, the ability of probe to collect electric current depends not only on its geometry and bias, but also on the scattering of electrons and ions in the sheath and presheath. The theoretical interpretation of experimental results is based on the collisionless Langmuir theory and the collisions are included additionally by various approximations, the main question being if the scattering of charged particles in the sheath increases or decreases the probe current. With the help of these corrections the theory can be extended to slightly collisional plasma (Fig. 5), however it cannot be used in modern applications of high-pressure plasmas.

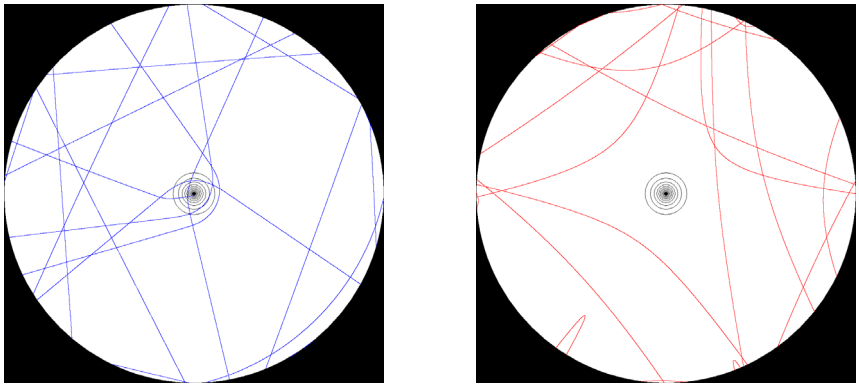

Fig. 4: Collisionless argon plasma, voltage bias +10 volts. Left – electrons, right – positive Ar ions.

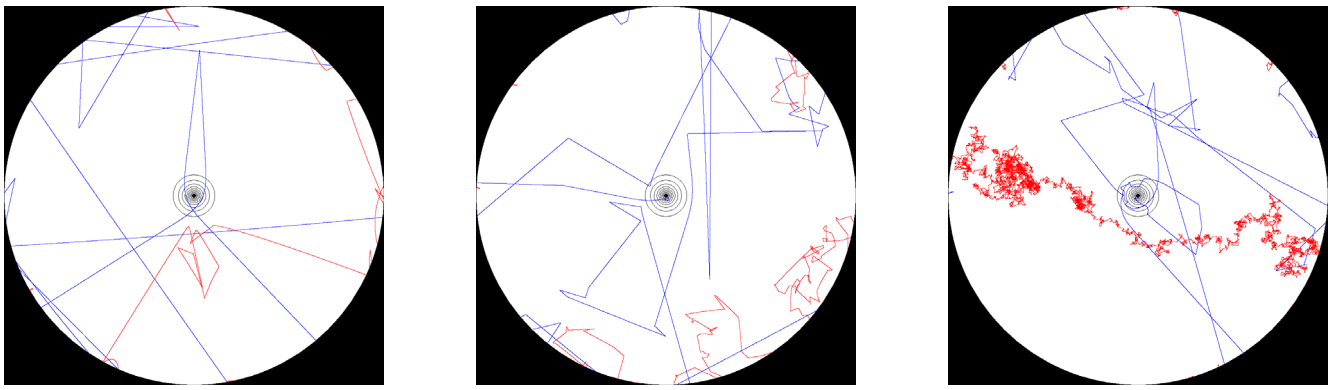

Fig. 5: Collisional argon plasma, voltage bias +10 volts, different pressures: left – 1.33 Pa, centre – 13.3 Pa, right – 133 Pa.

Examples of trajectories of individual charged particles in the vicinity of cylindrical biased probe are shown in Figs. 4 and 5. The changing character of the transport at higher pressures can be seen, especially for ions. Also the time demands are growing as the mean free paths decrease with increasing pressure and scattering events become more important.

6. Conclusions

If we summarise advantages and disadvantages of suggested approach, we can state that the standard non self-consistent models use very simplified formulae for the electric potential distribution, so their results are not precise enough. With the help of evolutionary modelling it is possible to obtain results with accuracy of self-consistent models but also with much less demands on computational time.

Acknowledgments

The work is a part of the research plan MSM0021620834 that is financed by the Ministry of Education of the Czech Republic and partly was supported of the Grant Agency of Charles University Prague, Grant No. 296/2004 and Grant Agency of Czech Republic, Grant. No. 202/03/H162.

References

[1] R. Hrach, V.Hrachová, M. Vicher - Computer Physics Comm. **147**, 505 (2002).
[2] R. Hrach - Czech J. Phys. **49**, 155 (1999).
[3] S.C. Brown - Basic Data of Plasma Physics: The Fundamental Data on Electrical Discharges in Gases. AIP Press, New York, 1994.

Morphological study of metal/dielectric composite films prepared by plasma chemical technologies

J. Šimek, R. Hrach

Charles University, Faculty of Mathematics and Physics, Department of Electronics and Vacuum Physics, Prague, Czech Republic

Abstract
Composite films of the structure metal/dielectric prepared by plasma chemical technologies far bellow the percolation threshold typically consist of metal objects with excellent uniformity. When characterising the structural properties of composite films the information about the forms of individual metal objects and about their distribution in dielectric matrix must be derived. The present contribution is devoted to the second task, both the well-known and new methods of mathematical morphology being used.

1. Introduction

The composite films represent class of promising materials [1]. Especially composite metal/dielectric films consisting of metal particles embedded into an oxide or polymer matrix have received more and more attention in last few years due to their interesting optical, mechanical and electrical properties.

Composite material can be obtained by embedding metal particles (Ag, Au, etc.) into a matrix of dielectric film (Al_2O_3, SiO_2, carbon, etc.). There exist several techniques for the preparation of composite films. One possibility is the thermal evaporation of the complete structure metal/oxide – the metal is evaporated from one source and the oxide film is deposited simultaneously from another one (e.g. [2]). Similar to that, in [3] composite films were obtained by the ion-beam sputter deposition technique. However, the most important technology is the plasma deposition technique. There are different ways to prepare metal containing plasma polymer films, such as simultaneous plasma etching and plasma polymerisation, plasma polymerisation of organometallic compounds, or simultaneous plasma polymerisation and metal evaporation. A great variety of these composite films can be achieved by using different polymers and metals [4]. The most popular are various fluoropolymers and films prepared by polymerisation of hydrocarbons. Even semiconductors have been embedded into a polymer matrix.

Depending on the concentration of metal atoms in the composite film there are three possible types of the metal containing dielectric structures: for small metal volume fraction the films consist of metal particles completely insulated from each other embedded in a polymer matrix, with increasing concentration of metal atoms the metal-dielectric transition is observed and metal objects form a percolation structure, and for high concentration of metal the composite films are created by metal layers with polymer inclusions. The main interest in the literature is given either to composite films with small amount of metal or to the films near the percolation transition, when the charge transport is studied. As there exists close connection between morphology of composite films and their physical properties (optical, electrical, etc.), the morphological analysis of composite thin films is very important.

2. Morphological analysis of composite structures

The goal of the morphological analysis of composite films is to characterise:

- the forms of individual metal objects in the film,
- the three-dimensional spatial distribution of objects.

TEM investigations reveal that bellow the percolation threshold the composite films prepared by plasma chemical methods consist of small nanometer-sized metal particles with excellent uniformity embedded in an amorphous dielectric matrix. In this case the analysis of size distribution of objects is based on the integral transform method [5] and the unfolding problem results in the determination of the distribution function of

objects' radii. With increasing metal concentration the forms of metal clusters become more complicated and the methods for their analysis are complicated too.

The second, more important task is to derive the spatial (three-dimensional) distribution of metal objects in the composite films on the basis of two-dimensional information. If the film is thin enough, it is possible to derive information about bulk composition and structure of composite films either from their planar sections or from their projections (see Fig. 1), while for the thicker layers the micrographs of the sections can be used only. There exist numerous methods designed for the study of metal films in two dimensions – i.e. for the morphological analysis of discontinuous or semicontinuous metal films created on dielectric substrates (e.g. [6] - [8]), however the methods well suited for the analysis of three-dimensional composite films must be yet created. Theoretical approach to the unfolding problem of composite films often leads to the nearly invincible difficulties; therefore a computer experiment would be more suited for that purpose.

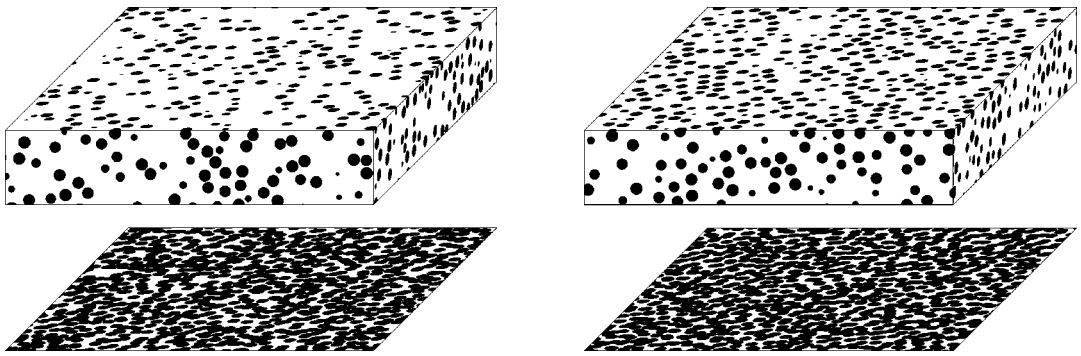

Fig. 1: Schematic view of two composite films with small volume metal fraction and various films parameters together with main sources of morphological information – planar sections and projections of the films.

In two dimensions the well-known methods based on the mathematical morphology [6] are commonly used. While direct application of these methods in three-dimensions is possible and leads often to interesting results (see e.g. [9] - [12]), the exact interpretation of derived results is not clear enough and detailed analysis is required. The main problem is that the available two-dimensional information is not sufficient for the complete reconstruction of three-dimensional distribution of objects and the results have probabilistic character only.

In our recent publication [13] we analysed several morphological algorithms intended for the spatial analysis of two-dimensional discontinuous metal films, tested their sensitivity for the determination of various physical parameters of island structures and suggested new one-number features. In the present contribution we extended this analysis upon morphological methods applicable to composite metal/dielectric films at low and medium volume metal fraction, when the composite layers consist of individual objects.

3. Model

For testing methods convenient for partial reconstruction of three-dimensional information from two-dimensional images a simple computer experiment was prepared. Our model of composite film with a small metal volume fraction, i.e. with so-called filling factor *ff*, is based on a hard-sphere technique. In a three-dimensional working region (typical dimensions are from 1000×1000×100 pixels to 5000×5000×500 pixels, pixel being the length unit in our model and the *z*-axis is oriented perpendicular to working region) metal objects are generated. The spherical form of objects is assumed in accordance with experiments. The object's diameters are either constant or have the Gaussian distribution of magnitudes.

The objects are generated randomly not touching each other. The minimum distance between edges of objects is a model parameter called diffusion zone ΔZ. For given number of objects and for given objects' radii there exists

a limit ΔZ_{max}. With the help of the model parameter $\Delta Z \in \langle 0, \Delta Z_{max} \rangle$ it is possible to influence the randomness of spatial distribution of objects in composite structure.

Simulated images used for the image analysis of composite films can be prepared either as a random sections parallel to the (x,y) plane or as projections of the whole working region. Examples of such images can be seen in Fig. 1 – left for $\Delta Z = 0$ and right for $\Delta Z = \Delta Z_{max}$.

There exist more sophisticated models based on various modifications of both hard-sphere and soft-sphere techniques, e.g. [12], however for our purpose of the algorithms testing the basic hard-sphere model is sufficient.

4. Results

For the purpose of analysis of various morphological methods a large set of simulated composite structures was prepared with different combinations of model parameters. Examples of parts of images derived from the simulated structures are demonstrated in detail in Figs. 2 and 3 (maximally random structures) and 4 (fully arranged structures).

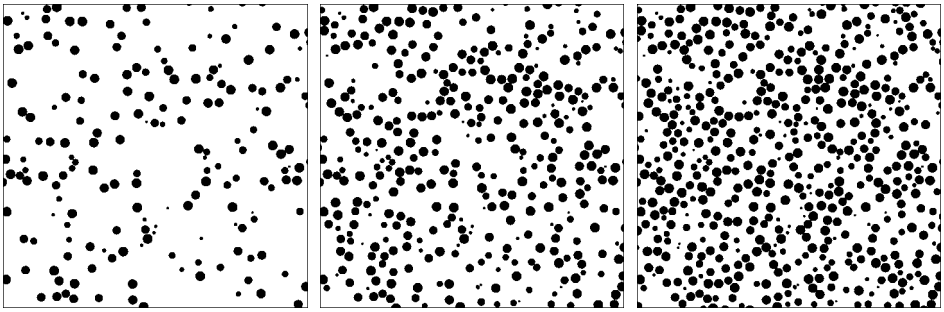

Fig. 2: Sections of composite structures generated with diffusion zone $\Delta Z = 0$ and filling factors *ff* equal to 0.1 (left), 0.2 (middle) and 0.3 (right).

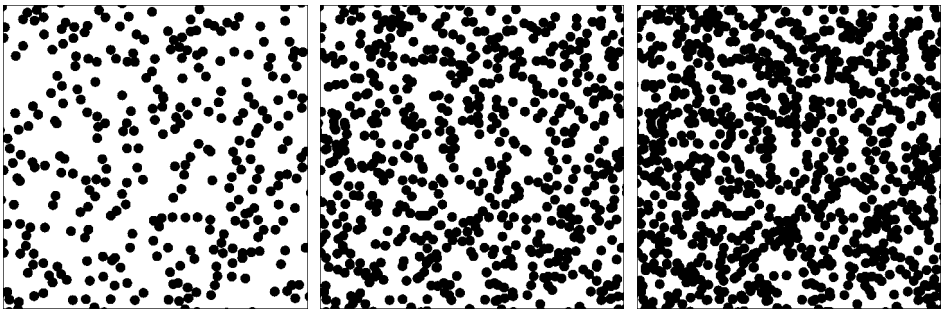

Fig. 3: Projections of composite structures generated with $\Delta Z = 0$ and *ff* = 0.1 for different film thicknesses – 100 (left), 200 (middle) and 300 (right).

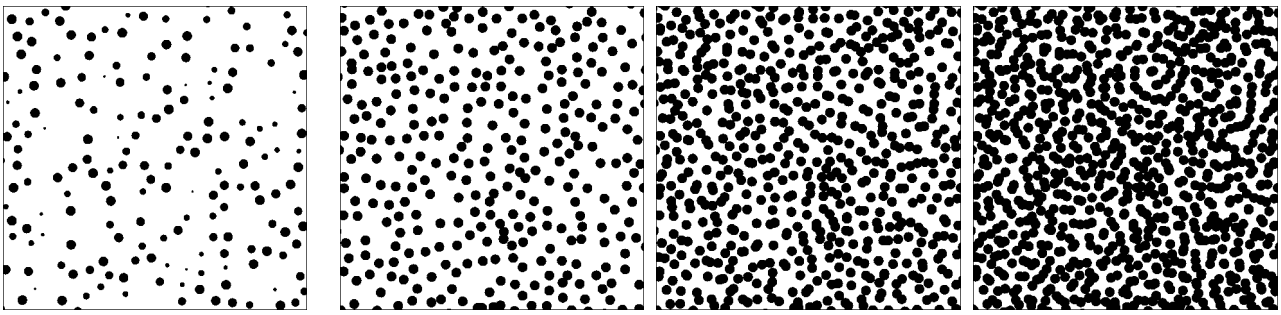

Fig. 4: Images of a composite structure generated with $\Delta Z = \Delta Z_{max}$ and $ff = 0.1$. Left: section, other images: projections for different film thicknesses – 100, 200 and 300 (right).

Morphological analysis of derived images was performed by a complete set of morphological algorithms: radial distribution function, distribution of nearest neighbours, contact distribution function, covariance, chord-length distribution, quadrat counts method and Voronoi tessellation. Some examples of obtained morphological characteristics can be seen in Figs. 5 and 6. These characteristics were obtained again for maximally random and maximally arranged structures.

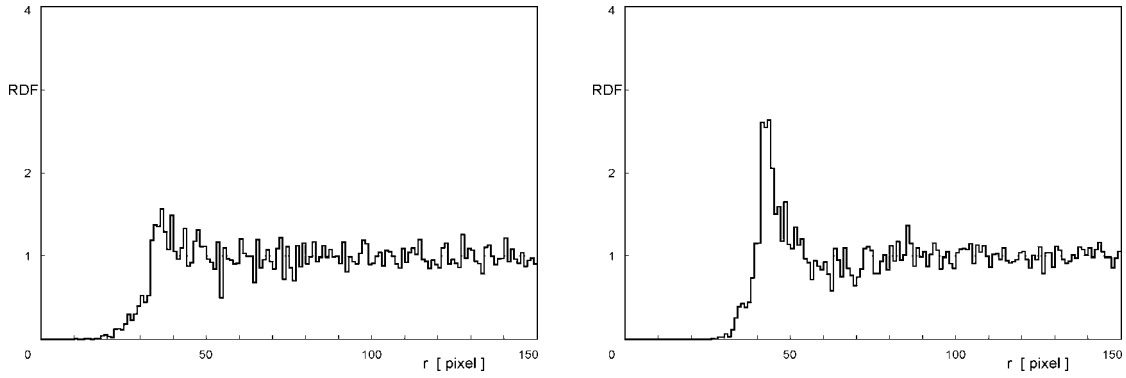

Fig. 5: Radial distribution function of images of sections of composite structures generated with diffusion zone $\Delta Z = 0$ (left) and ΔZ_{max} (right).

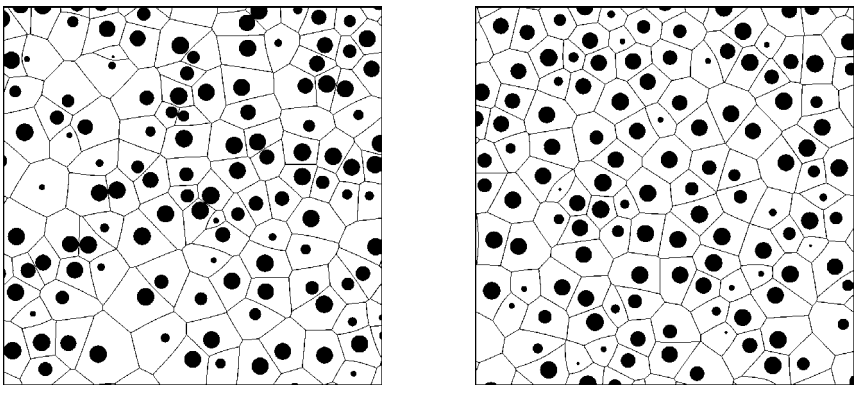

Fig. 6: Voronoi tessellation of images of sections of composite structures generated with diffusion zone $\Delta Z = 0$ (left) and ΔZ_{max} (right).

From these figures it can be seen, that some morphological methods are sensitive enough to the arrangement of objects in the composite structure, however that merely on the basis of morphological characteristics it is

difficult to describe the degree of arrangement quantitatively. For this purpose individual features of morphological methods [13] are much more convenient, because they can be created in accordance with the demands of individual studied systems.

5. Discussion

From the morphological analysis of images of both sections and projections of simulated composite structures it follows (e.g. [10]-[11]) that the Voronoi tessellation is one of the most sensitive morphological methods for the description of object arrangement in composite films. For this purpose we tried to suggest a set of features based on this method and to compare their efficiency for the quantitative characterisation of object arrangement in composites.

According to this method (sometimes known as Wigner-Seitz cells method) the whole image is divided into ´tiles´ or cells surrounding individual objects creating the image. The tiles consist of image pixels for which the distance to given object is minimal. The forms of these tiles depend on the degree of objects arrangement – see Fig. 6. However, as was shown in [13], the distribution of tiles depends not only on the distribution of objects in the image, but also on various technical parameters as the number of objects in image, on image resolution, etc. In order to remove the dependence of derived information on unimportant image parameters, it is necessary to introduce appropriate numerical feature, which will characterise the most important image properties.

In [13] for the description of two-dimensional discontinuous metal films three features based on the distribution of areas of Wigner-Seitz cells were suggested:

- the ratio of second and first moments of the distribution of areas of Wigner-Seitz cells,
- the mean value of the distribution of form factors of Wigner-Seitz cells, and
- the dispersion of the distribution of form factors of Wigner-Seitz cells.

It was found there that the first suggested feature for Wigner-Seitz cells is the best, however the more sensitive features can be derived from the radial distribution function criterion. For the analysis of images derived from three-dimensional composite films the situation differs from the case of discontinuous metal films. First, there exist two sources of information – sections and projections. It was found that the projections could be used for very thin composite layers only; therefore the analysis of images-sections of composite film is more universal. Second, as for composites the Voronoi tessellation (together with covariance function) is the most sensitive morphological method, we tested the features based on this method. Besides three numerical features suggested in [13] for two-dimensional discontinuous metal films, we applied and analysed several further features:

- angularity of individual cells (number of edges),
- length distribution of edges,
- distribution of angles between edges in the cell,
- distribution of perimeters of individual cells, etc.

This group of features we can denominate as differential and the first group as integral. Comparison of results obtained by both groups of numerical features indicates that while the second group brings more detailed information, the analysis of its results is much more difficult than analysis of the results obtained by integral features. Therefore the applicability of individual features depends on the purpose of morphological analysis of composite structures – if we need the global information about studied structure, the integral features are more convenient, if the details are important, some of differential features are used. The differences between individual differential features were found to be unimportant.

It was found that all features, both integral and differential, lose their accuracy for large filling factors because the objects become arranged. However, for large filling factors the composite films are changing their character as the dielectric-metal transition occurs and all physical mechanisms in films vary, therefore this decrease of sensitivity of suggested morphological features is unimportant.

6. Acknowledgements

The work is a part of the research plan MSM0021620834 that is financed by the Ministry of Education of the Czech Republic and partly was supported by the Grant Agency of Charles University Prague, Grant No. 237/2005 and Grant Agency of Czech Republic, Grant. No. 202/03/H162.

References

[1] H. Biederman, L. Martinu - Plasma Deposition, Treatments and Etching of Polymers. Academic Press, New York 1990.
[2] W. Yang, Z.N. Wang, Y.W. Du - Solid State Commun. **104**, 479 (1997).
[3] T. Ichinohe, S. Masaki, K. Kawasaki, H. Morisaki - Thin Solid Films **343-344**, 119 (1999).
[4] T. Noguchi, K. Gotoh, Y. Yamaguchi, S.J. Deki - J. Mater. Sci. Lett. **10**, 477 (1991).
[5] S. Novak, M. Sobotka, R. Hrach - Thin Solid Films Proc. **373**, 203 (2000).
[6] J. Serra - Image Analysis and Mathematical Morphology, Academic Press, London 1982.
[7] H. Ebeling, G. Wiedenmann - Phys. Rev. E **47**, 704 (1993).
[8] B. Bhattacharjee - Phys. Rev. E **67**, 041208 (2003).
[9] S. Novak, R. Hrach - Materials and Manufacturing Processes **17**, 97 (2002).
[10] S. Novak, R. Hrach, M. Vicher - Czech. J. Phys. **52**, 1329 (2002).
[11] S. Novak, R. Hrach - Le Vide **307** – Numero Speciaux, 258 (2003).
[12] R. Hrach, M. Svec, S. Novak, D. Sedlak - Thin Solid Films **459**, 174 (2004).
[13] J. Simek, R. Hrach - Thin Solid Films **466**, 16 (2004).

Modification of the acid/base surface adsorption properties of granular Carbon Black by means of O_2/NH_3 RF glow discharges

N. De Vietro[1], R. d'Agostino[1,2], P. Favia[1,2], F. Fracassi[1,2]

[1]*Department of Chemistry, University of Bari, Italy*
[2]*Istituto di Metodologie Inorganiche e Plasmi (IMIP) - CNR, Bari, Italy*

Abstract
CB granules and flat graphite slabs have been treated in O_2/NH_3-plasma in order to improve the adsorption of acid/basic chemical species from liquid and gas phase. Surface plasma modifications have been detected on flat graphite by means of XPS and WCA with water solutions at different pH [1-2]. Boehm titrations and tests with an home-made Pyrex glass system have been performed on CB to evaluate the adsorption properties for HCl and NH_3 in vapour/gas phase, respectively.
Keywords: CB, acid/base surface adsorption properties.

Introduction

Carbon Black (CB) is the commonly accepted generic name for a wide variety of finely divided carbonaceous powders or granules produced by the partial combustion or thermal decomposition of liquid or gaseous hydrocarbons under controlled conditions. The carbon content of CB materials usually ranges from 83 to 99 % [3], with oxygen and hydrogen being the other most common elements. The surface area, structure and composition of CB change widely, depending upon several factors in the manufacturing process and operating conditions.
Today, Carbon Black and related materials are widely utilized as reinforcing fillers in polymeric matrix, as adsorbents and filters for gases and liquids, as support for catalysts and for many other uses. For many years, for instance, CB has been the main inexpensive reinforcing filler in rubber goods [4]. It is used, also, as adsorbing material in cigarette filters with the aim of detaining toxic molecules (acids, bases, organics, etc.) produced during the combustion of tobacco.
Both surface chemistry and morphology of carbonaceous materials play a crucial role in adsorption, adhesion and other relevant properties. Surface chemical features of CB granules or powders are reported, in literature, to be successfully modified by low temperature plasma treatments in several kinds of electrical and geometrical systems. Most of them deal with O_2-based feeds, with the aim of increase the surface density of the O-functionalities and, consequently, the adsorption properties [5-6]. In fact, although handling fine particles materials in a low pressure environment and allowing an homogeneous plasma treatment is some what complicated and requires special reactor designs, many examples exist in literature about low pressure plasma processing of organic and inorganic powders substances [7-8]. Few studies are reported, however, on the knowledge of the authors on the possibility of tuning the surface acid/base character of carbon-based materials, while this approach is extensively utilized for flat polymers [9-10].
In this work granules of CB (0.1-2 mm; DC W60 16*25; *Filtrona*) and flat graphite slabs (1 mm thick, 3x3 cm, *Goodfellow*) have been plasma treated in a particular home-made rotating plasma reactor (**Figure 1**), able to keep stirred and homogeneously plasma-treated up 500 g of granular materials. RF (13,56 MHz) low pressure glow discharges fed with O_2, NH_3 and O_2/NH_3 mixtures have been utilized, at 20 and 100 W of input power in the conditions reported in **Table 1**.

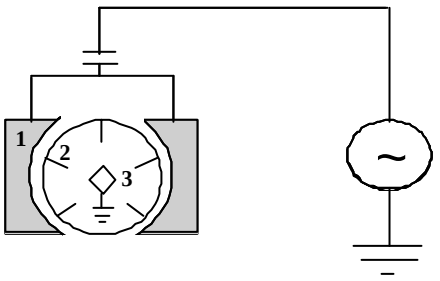

Fig.1: scheme section of the RF plasma reactor.
1) RF external electrodes; 2) internal glass wings solidal to the Pyrex chamber; 3) internal ground electrode.

	Flat graphite	*CB granules (10.00 g)*
Total flow rate	10 sccm	
O_2/NH_3 ratio	10/0; 8/2; 5/5; 2/8; 0/10	
rpm	/	50
RF power	20 W; 100 W	
Treatment time	2 min.	15 min.
Pressure	0.250 mbar	

Tab.1: Experimental conditions for plasma treatments of CB and flat graphite samples.

The chemical surface modifications, induced on plasma-treated CB, expressed in terms of C, O and N atomic percent, have been estimated by means of X-Ray Photoelectron Spectroscopy (XPS). Plasma parameters have been optimized (time, rpm), on CB and graphite, by means of XPS in order to have similar effects on the surface composition of the two different substrates. WCA measurements have been carried out, with water solutions at different pH, on flat graphite with the aim of studying the acid/base character imparted to the functionalized surface. Boehm's titrations [11] have been performed, with NaOH and HCl water solutions, on CB before and after plasma treatment, in order to tune the acid/base surface adsorption properties for basic and acid molecules in liquid phase, respectively. Finally, the surface adsorption properties modifications, for basic and acid compounds, have been tested in vapour/gas phase with an home-made Pyrex glass test system (**Figure 2**), with HCl vapours and NH_3 as probes. Particularly, the tunability of this kind of response has been taken into account by varying feed gas composition and input power of the discharge.

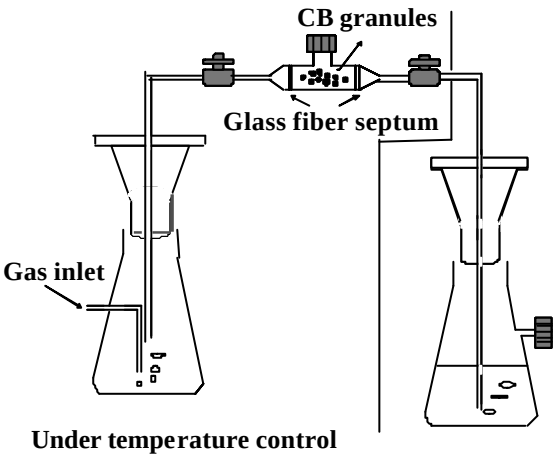

Fig. 2: Scheme of the home-made Pyrex glass system to test CB adsorption properties for acid or basic vapor/gas compounds.

Results and discussion

XPS and WCA measurements

From wide scan XPS of untreated flat graphite, only carbon and a small contamination of oxygen have been detected, whose relative approximate amounts are C1s 96.6 % and O1s 3.4 %, respectively. Small spot XPS survey spectra of CB untreated granules reveals traces of elements such as N, Na, Ca, K and Cl (< 1 %) besides C (89.9 %) and O (7.5 %) as the main surface elements. Graphite has been used as reference substrate for XPS analysis. The effect of O_2/NH_3-plasma treatments have been investigated, in terms of XPS atomic surface composition, on flat graphite plasma treated. Results on CB samples have been found similar.

Data are represented in **Figure 3**, where C, O, N atomic percent is reported as a function of the O_2 percent in O_2/NH_3 feed. C % and O % data for untreated samples are included.

As it can be easily observed, O and N surface content increases with the related gas source in the feed, O_2 and NH_3, respectively. This effect is stronger for oxygen, which also reaches a plateau (higher at higher power). At 100 W a larger introduction of N- and O-functionalities is observed. It is important to note that XPS data show that the treatment in a 100 % NH_3-plasma leads not only to the grafting of N-groups, but also to increase the surface oxygen density, probably due to the uptake of oxygen from air after the plasma treatment.

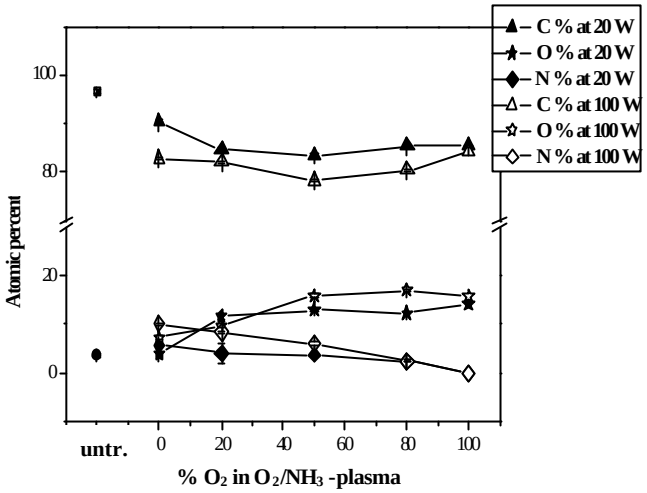

Fig. 3: XPS atomic percent for flat graphite treated in O_2/NH_3 RF plasma at 20 W and 100 W. All measurements were performed within 12 h from treatment.

WCA vs pH measurements have been performed on plasma treated graphite slabs. **Figure 4** reports only the results obtained at 100 W.

In all cases the contact angle is clearly lower than untreated graphite, due to the grafted polar groups. In pure O_2-plasma the treated surface becomes acid for the grafted O-groups, since WCA decreases with increasing pH. When NH_3 is added to the feed, a surface amphoteric behaviour develops, certainly due to the presence, at the same time, of both acid (O-containing) and basic (N-containing) groups. All WCA trends, in fact, besides 100 % O_2, show a drop at both ends, even though with different slope.

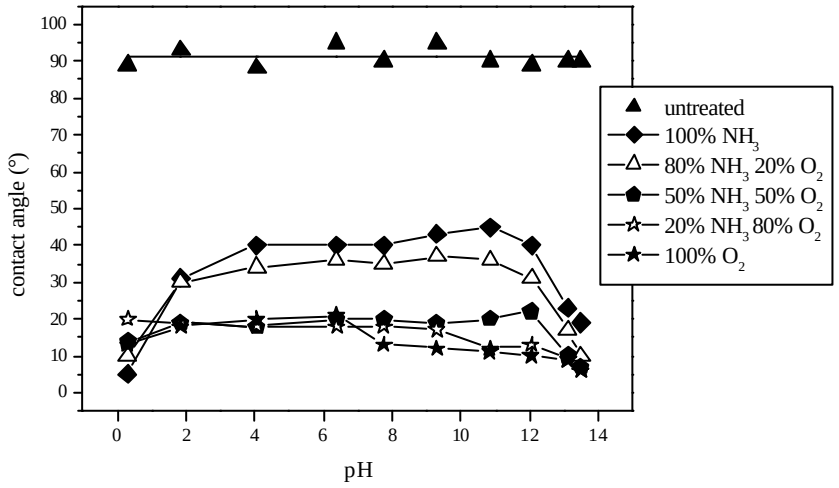

Figure 4: WCA vs pH data for flat graphite treated in O_2/NH_3 RF plasma at 100W.

Similar trends have been obtained at 20 W, with a less marked overall WCA decrease respect to untreated graphite, probably due to the *etching* effect of the plasma treatment, which is a function of the input power.

Boehm titrations

Surface adsorption properties of plasma treated CB granules in water have been tested with the titration method proposed by Boehm [11] for acid and basic compounds. A 20 ml volume of 0.02 N HCl or NaOH water solution was added to vials containing 1 g of untreated or treated CB granules. Samples have been shaken for 24 h at 180 rpm; after that, CB has been decanted from the solution. The unreacted excess of acid or base have been determined (five replicated per CB sample) by titration with NaOH or HCl 0.1 N.

The data, expressed as adsorbed equivalents of H^+ and OH^- per gram of CB, are shown in **Figure 5** as a function of the O_2/NH_3 composition of the plasma feed, at 20 and 100 W of RF power.

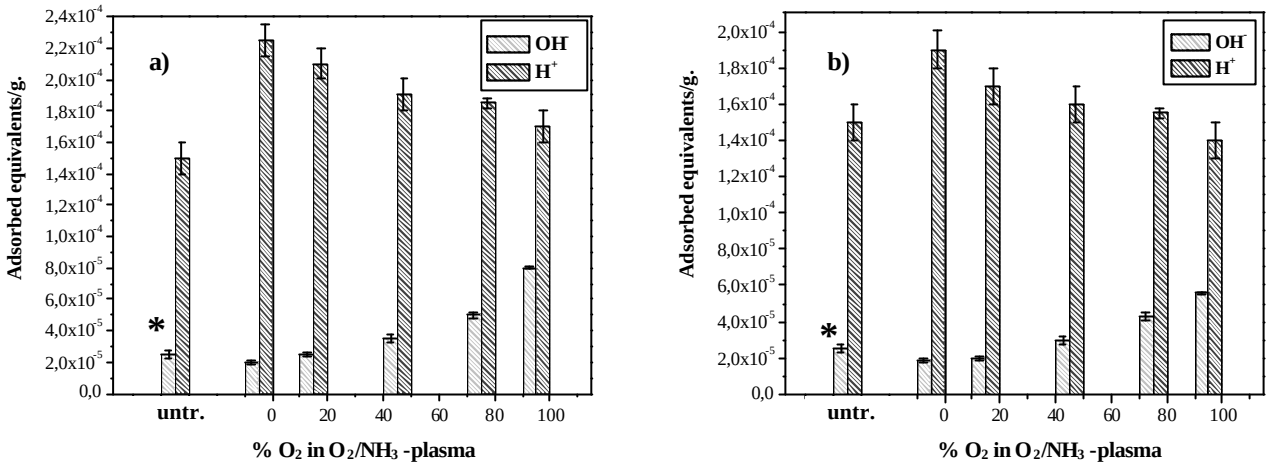

Fig. 5: Boehm's titration results for CB granules before and after plasma treatment at 20 W (a) and 100 W (b). All measurements have been repeated five time.
* OH^- is released from untreated CB.

It is possible to note that the untreated sample adsorbs a small amount of H^+ ions. From these data, moreover, we can conclude that the untreated CB samples give basic reaction with water. This is confirmed by the increase of pH (from 6.01 to 9.83) of 20 ml of bi-distilled water where 1g of untreated CB was kept under constant mechanical shake for 24 h. After any treatment in O_2/NH_3-plasma the CB surface increases the acid character and this effect becomes more clear increasing the O_2 content in the feed. On the contrary, CB becomes more and more basic increasing the NH_3 percent in the plasma. The treatment performed in a 100 % NH_3-plasma fed, imparts also a partial acid character to the surface. This amphoteric character can be probably justified taking in account the oxygen uptake from air after plasma treatment, as the XPS results, shown in Figure 3, have highlighted. Bohem results shown for CB agree with WCA vs pH data shown previously in Figure 4 for flat graphite. All data confirm that a NH_3-based plasma is more effective in imparting a basic character, than O_2-plasma in imparting an acid one. This is also evident by comparing the amount of H^+ equivalents adsorbed by the NH_3-treated surfaces respect to the corresponding OH^- amount retained by O_2-plasma modified CB surfaces.
This behaviour is more evident for samples treated at 20 W (Figure 5a); this is more clearly shown in **Figure 6**, where a comparison of the adsorbed equivalents percent of H^+ and OH^- are reported, respect to the initial ion concentration in HCl or NaOH solutions, for all CB samples.

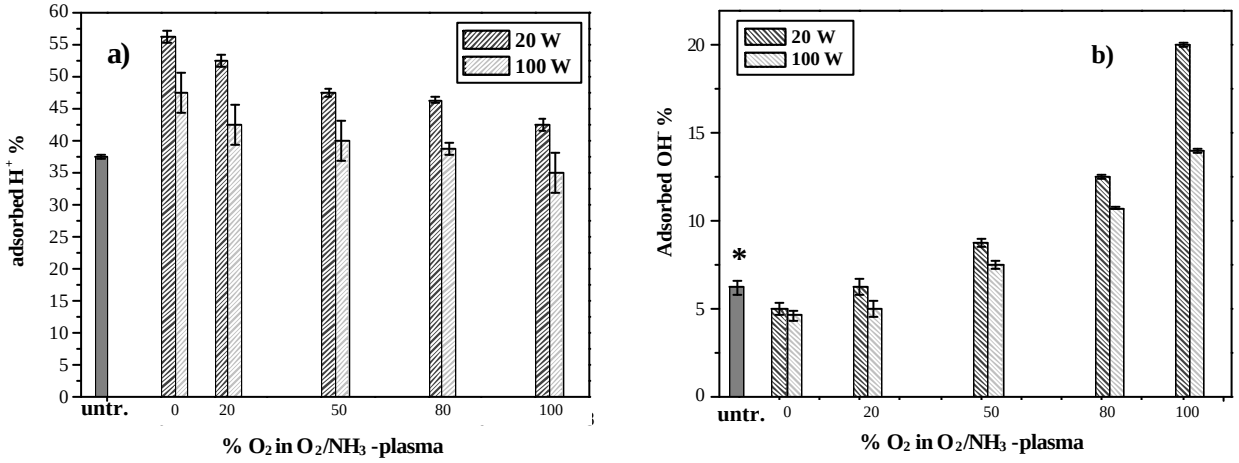

Fig. 6: H^+ (a) and OH^- (b) adsorbed equivalents percent (Boehm's titrations) for CB granules before and after plasma treatment at 20 W and 100 W. All measurements have been repeated five time.
* OH^- is released from untreated CB.

Acid/base vapour/gas adsorption tests

Acid/base surface adsorption properties for modified CB for vapour/gas compounds have been tested with an home-made test system schematized in Figure 2. Vacuum sealing is ensured by steel clamps. At the centre of the system there is a flask with 100 ml of HCl 12 N to test the basic adsorption properties of 0.1 g of CB granules, before and after plasma treatment. CB is positioned in a glass chamber in the system, between two glass fiber filters. All the system is under thermal control, maintained at 50 °C.

60 sccm of N_2 were used to strip HCl vapours from the flask. Vapours were collected in 100 ml of bi-distilled water contained in an external flask, at room temperature, after 20 min in contact with the CB granules. HCl collected was titrated with NaOH 0.2 N. From the difference between H^+ equivalents collected when the test chamber is empty and those titrated when 0.1 g of CB is in the chamber, we can estimate the amount of basic groups present at the surface of 1g of CB. To test the acid surface adsorption properties of treated and untreated CB, 15 sccm of NH_3 has been used. In this case, ammonia was collected in 100 ml of 0.15 N HCl, at room temperature, after 15 minutes in contact with 0.1 g of treated or untreated CB granules. NH_3 collected was determined by back-titration of the HCl solution utilizing NaOH 0.2 N. The amount of acid surface sites was estimated as seen above for basic sites. **Figure 7** displays the adsorbed equivalents percent of HCl and NH_3 as a function of the O_2 content in the O_2/NH_3 feed. Untreated samples adsorb only a small amount of acid or base, about 6 %, while plasma treatments induce a clear increment of the surface basic and acid adsorption properties. In particular, it is evident that the acid character rises with the O_2 percent in the gas feed while, on the contrary, the CB basic character increases with NH_3 amount. Also in this case, as for Boehm's titrations (Figures 5 and 6), NH_3 fed discharges result more effective than O_2 in modifying CB surfaces. In fact, the amount of HCl equivalents adsorbed by NH_3-treated surfaces is larger than the NH_3 retained by O_2-plasma modified ones.

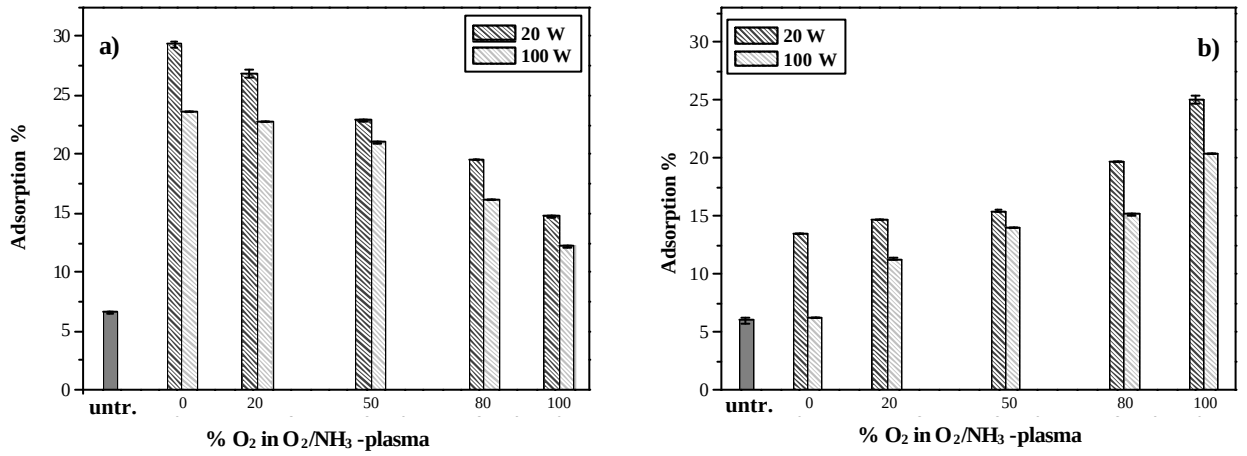

Fig. 7**:** Adsorption % data for CB granules before and after plasma treatment at 20 W and 100 W, for HCl (a) and NH_3 (b). All measurements have been repeated five time.

Also from this figure, the amphoteric behaviour of NH_3-plasma treated CB surfaces is evident, in agreement with Bohem's titrations results and WCA data. It is evident that plasma treatment at 20 W is more effective in modifying the acid/base surface character of carbonaceous substrates than the corresponding treatment at 100 W. Also this result agrees with Boehm's titrations conclusions.

Conclusions

In this work it has been shown that glow discharges, fed with O_2 and/or NH_3, can modify the surface chemical composition and improve the acid/base surface adsorption properties of CB granules, as a function of the input power and of the feed composition. O_2 RF-discharges, in detail, develop acid groups (O-containing), while NH_3 discharges develop basic ones (N-containing) and impart, after air exposure, an amphoteric behaviour to the carbonaceous substrates. Mixed O_2/NH_3-plasma treatments impart an intermediate acid/base surface character, which is a function of the O_2/NH_3 feed ratio. RF plasma modified

CB samples, furthermore, show an evident rise of their adsorption properties for acid and basic compounds in liquid and in vapour/gas phase.

References

[1] Fowkes, in Mittal and Anderson Jr., eds., Acid-Base Interactions, Relevance to Adhesion Science and technology, VSP, Utrecht, 1991.
[2] Fowkes, in Ind. Eng. Chem., 56, 40, 1964.
[3] Ihara, in Plasma-Processing of Polymers, d'Agostino, Favia, Fracassi, eds. Kluwer, Ac. Publ., NATO ASI series, E: Applied Sciences, Vol. 346, 1997.
[4] Tricas et al., in Compos Sci Technol, Vol. 63, No 8, 1155, 2003.
[5] Cascarini de Torre et al., in Carbon 3, 277, 1998.
[6] Ana B. Garcia et al., in Fuel 77, 613, 1995.
[7] Rajenndra Kumar et al., In Jour. of Materials Processing Technology, Vol. 113, 456, 2001.
[8] Takafumi Nakajima et al., in Thin Solid Films, Vol. 386, 208, 2001.
[9] Arefi Khonsari et al., in Plasma-Processing of Polymers, d'Agostino, Favia, Fracassi, eds. Kluwer Acad. Publ., NATO ASI series, E: Applied Sciences, 165, 1997.
[10] Creatore et al., in Plasmas and Polymers, Vol. 5, No. 3/4, 201, 2000.
[11] Boehm et al., in Angew. Chem. Internat., Edit. 3 (10), 669, 1964.

Experimental study of pattern formation in unipolar-pulsed dielectric barrier discharges

S.N. Abolmasov[1], T. Shirafuji[2] and K. Tachibana[3]

[1]Venture Business Laboratory, [2]International Innovation Center, [3]Department of Electronic Science and Engineering, Kyoto University, Kyoto, Japan

Abstract

Formation of complex patterns lateral to the current flow in a short planar dielectric barrier discharge system, excited by positive voltage pulses, is investigated experimentally. The current-voltage measurements and optical diagnostics provide evidence that patterned dielectric barrier discharges in helium, argon and krypton are driven by conditions of V_{gap}, j = const; similar to low pressure DC normal glow discharges. New mechanisms for pattern formation in gas discharge systems are proposed.

Keywords

Dielectric barrier discharge, unipolar-pulsed excitation, pattern formation, normal cathode spot

1. Introduction

Spatiotemporal pattern formation in systems driven away from equilibrium is a long-standing problem in many fields of science. Much work (mainly theoretical) has been done over the years to get a better understanding of the phenomenon [1]. It seems that pattern formation in DC discharges is related to the existence of a negative slope region in the voltage versus current characteristic curve of the discharge [2, 3]. The picture, however, becomes more complex in the case of dielectric barrier discharges (DBDs) due to their transient nature and, therefore, some authors believe that surface charge accumulated on the electrode dielectric may also come into play [4, 5]. Nevertheless, it is also believed that DBDs in short gaps are formed due to Townsend breakdown mechanism, similar to low-*pd* DC discharges (*pd*: pressure times discharge gap width) [4, 5]. It is reasonable, therefore, to assume that spatiotemporal patterns observed in DC discharges and those in DBDs are probably similar in nature. The aim of this study is to answer the question of whether it is true or not.

Since the problem is multiparametric it is important to simplify it as much as possible. Due to this reason, we have used: 1) pulsed excitation of DBDs (to control the voltage rise time independently of the frequency), 2) noble gases (to minimize elementary plasma processes) and 3) no gas flow (to simplify the gas dynamics).

2. Experimental

Fig. 1 illustrates a schematic of the electrode system used in the experiments. Two identical quartz plates with conducting, optically transparent [indium tin oxide (ITO)] coatings on their counter side were used as the electrodes, to permit the optical characterization of discharge uniformity using a digital camera. The transparency of the ITO coatings was about 80%. Four squares forming a cruciform structure on the periphery of the circular electrodes provided favorable wire-plane geometry for corona discharges. One of the electrodes was grounded while the other was powered by a unipolar-pulsed, high-voltage power supply

(positive pulses of amplitude up to 10 kV, 5 kHz repetition frequency, 50% duty factor). The electrode system with a 0.3 mm discharge gap was mounted inside a hermetic Pyrex cylinder pumped to a base pressure of about 1 mTorr. Discharges were generated in noble gases such as helium, argon and krypton. The voltage applied to the top electrode was measured with a 1:1000 high-voltage probe. The total current passing through the discharge was monitored by measuring the voltage drop across a 1 kΩ (low inductive) resistor that was placed in series with the grounded electrode. The displacement current (I) was determined by measuring the current (I_M) through a known capacitance (C_M = 22 pF) placed in parallel with the discharge cell [$I = C_g(dV/dt) = (C_g/C_M)I_M$, where C_g is the capacitance of the discharge gap]. The difference between the currents yielded the discharge current.

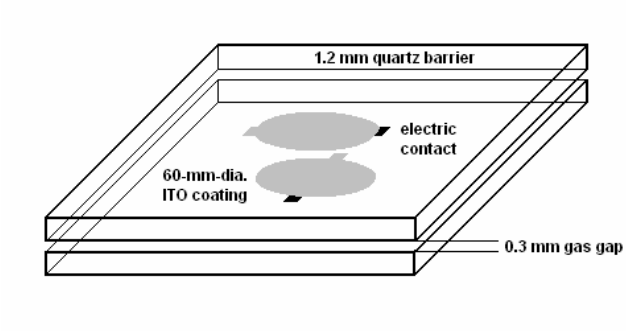

Fig. 1. Electrode geometry used in the experiments.

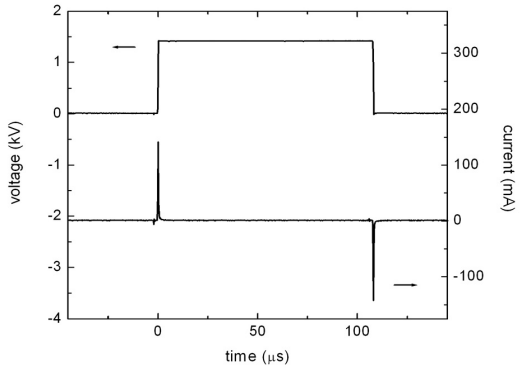

Fig. 2. Typical voltage/current oscillograms in the case of helium DBD at p = 260 Torr.

3. Results and discussion

Fig. 2 shows typical voltage and current oscillograms of a 5 kHz, unipolar-pulsed DBD. It can be seen that two current pulses corresponding to two consecutive discharges are generated per voltage pulse, similar to bipolar pulse excitation. The second discharge, which occurs at the falling edge of the voltage pulse, is induced by electric charges stored on the electrode dielectric during the initial discharge. The discharge duration is about 1 μs, as can be seen in Figs. 3 and 4. Here the images of helium and argon DBDs and their discharge current oscillograms show that the barrier discharges exhibit behavior similar to that found in DC glow discharges. Namely, as the discharge current is varied its density at the cathode remains unchanged, and the discharge area changes. Only when the discharge covers the entire electrode area, an increase in the applied voltage leads to a rise in the current density, and the discharge enters the abnormal glow regime (see two left images in Figs. 3 and 4). Note that the displacement (first) and discharge (second) current peaks in helium DBD usually appear separated from each other, which is not the case in argon and krypton DBDs. Fig. 4 shows the discharge current of argon DBD (after displacement current subtraction), indicating that the value of normal current density in argon is about two times higher than that in helium (Fig. 3). It should be emphasized that the breakdown voltage and normal current density values of krypton DBD were close to those of argon DBD within the pd-range under consideration [(3–23) Torr cm].

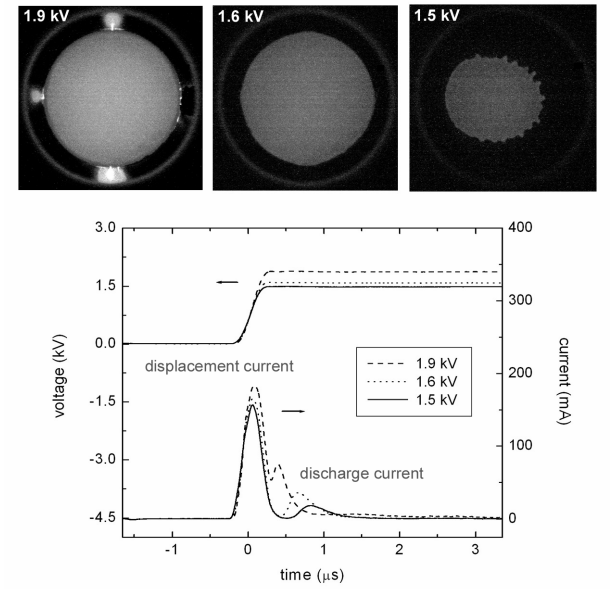

Fig. 3. Abnormal/normal discharge modes in helium at p = 600 Torr and their current/voltage oscillograms. (1 s exposure time)

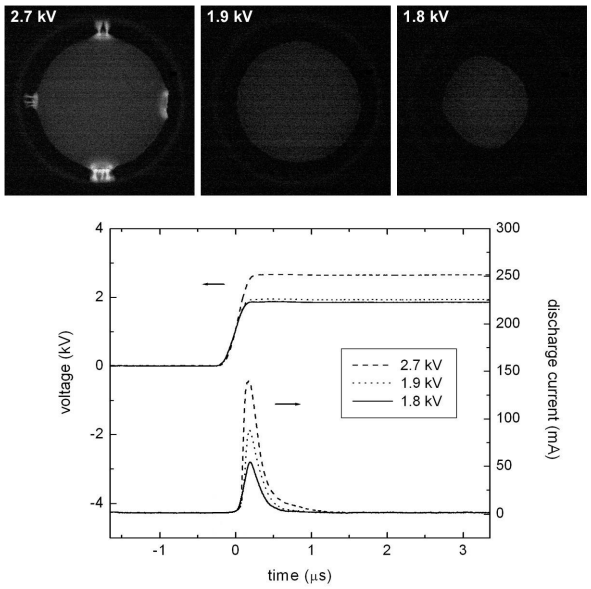

Fig. 4. Abnormal/normal discharge modes in argon at p = 200 Torr and their current/voltage oscillograms. (1/30 s exposure time)

Quasi-stationary discharge patterns were observed in helium with decreasing gas pressure (p < 600 Torr), while it was opposite in the case of argon and krypton (p > 200 Torr). The discharge current measurements combined with optical observations also confirmed that the patterned DBDs in the three noble gases operate in the normal glow regime.

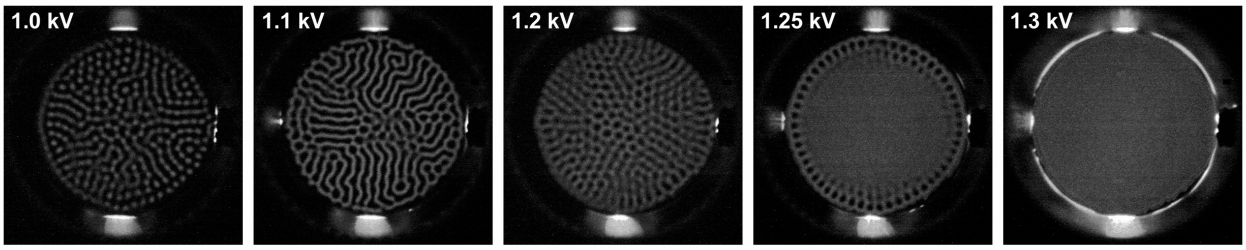

Fig. 5. Pattern formation in helium at p = 150 Torr: voltage amplitude dependence (voltage amplitude is shown in the upper left corner). (1 s exposure time)

Fig. 5 shows a typical pattern obtained in helium at p = 150 Torr which exhibits the well known transitions *dot pattern => stripes => hexagons => homogeneous state* and vice versa with increasing/decreasing voltage pulse amplitude. It can be seen that during the normal glow mode the luminosity of the pattern keeps constant (suggesting V_{gap}, j = const) and increases only when the discharge enters the abnormal glow mode at V = 1.3 kV. The pattern looks very similar to that reported in [6], where 40-125 kHz, 0.4 μs rise time, square wave excitation has been used to create DBDs in 0.05-0.06-mm-gaps between two plane-parallel, 0.076-mm-thick dielectric barriers (Corning 0211 Microsheet) in flowing helium at p = 760 Torr. It should be noted that despite a marked difference in the experimental devices, the voltage impulse rise time and

pd-factor (~ 4.5 Torr cm) are identical in both experiments. This fact speaks against dependence of the pattern upon impurities [7] and supports the importance of discharge current density value in the pattern formation. Note that at the moment of breakdown (or discharge termination by voltage decrease) the discharge appeared (disappeared) in the form of a large number of identical dots accompanied by diffuse corona discharge around the electric contact squares (1.0 kV case in Fig. 5).

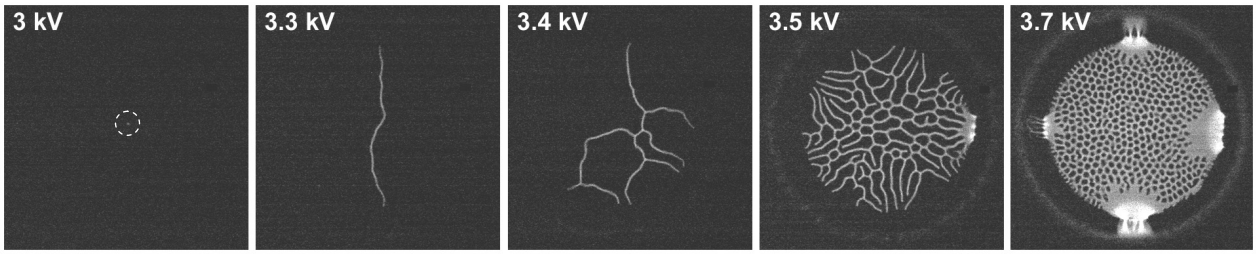

Fig. 6. Voltage amplitude effect on discharge pattern in argon at p = 600 Torr (voltage amplitude is shown in the upper left corner). (1/30 s exposure time)

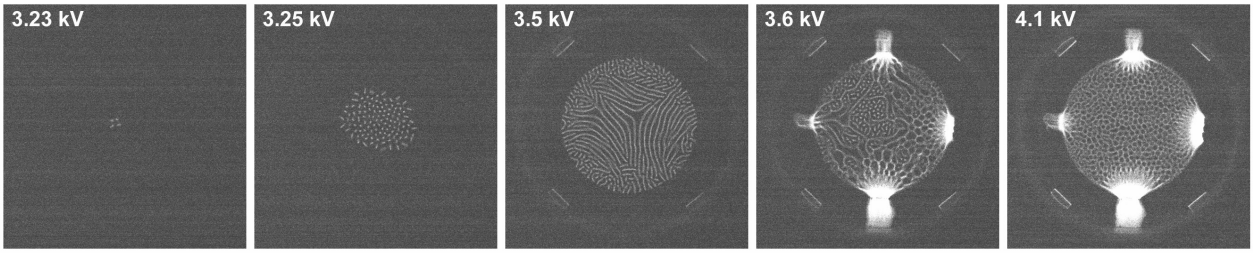

Fig. 7. Pattern formation in krypton at p = 600 Torr: voltage amplitude dependence (voltage amplitude is shown in the upper left corner). (1/8 s exposure time)

Unlike the patterned DBD in helium, the breakdown stage of patterned DBDs in argon and krypton is characterized by the presence of intense streamer-like corona and the appearance of stripe pattern, as can be seen in Figs. 6 and 7. Noteworthy, the low-voltage states here (with V < 3.6 kV) can only be obtained by lowering the discharge current and in both gases the discharge disappears in the form of one discharge dot (or normal cathode spot). One can also see that the hexagonal symmetry inherent to helium DBD is broken in argon and krypton DBDs and the discharge stripes here tend to split rather than merge. The later is probably a result of repulsive Coulomb force among the discharge stripes (or dots); the value of normal current density in argon (krypton) is somewhat higher than that in helium, as shown above. On the other hand, thermal effects also become more pronounced in argon and krypton. This is especially the case of krypton (because of its high atomic mass), in which such phenomena as quantization of discharge stripes (Fig.7: 3.5/3.6 kV) and replication of discharge dots (Fig. 7: 3.23/3.25 kV) were observed as the gas temperature (as well as the electrode temperature) reached a certain value. Thus, a pattern state in krypton DBD can depend on the discharge history– the phenomenon known in the DBD literature as a “memory effect” [5, 8]. According to the classification given in [7], the patterns shown in Figs. 5 and 6 can be classified as type I patterns, while that in Fig. 7 as type II pattern. It also seems that the radius of a discharge spot in these patterned DBDs is

inversely proportional to the atomic mass of the working gas (He > Ar > Kr). The same radius dependence upon gas type was also reported by Radu *et al.* [5] for AC driven DBDs in noble gases. Note that type II patterns behave qualitatively in the same way as (arc) cathode/anode spots (spots replicate from/into each other). Therefore, we assume that the physics involved in their formation is different from that of type I patterns.

Turning now to description of the pattern formation (type I patterns), it is interesting to raise the questions of why a Townsend discharge being homogeneous starts to constrict laterally as the discharge current is increased and what determines the radius of a constricted discharge channel (or normal cathode spot). Moreover, why in one case the discharge constriction leads to the formation of one normal cathode spot, while in the other it results in the appearance of a discharge pattern. To our knowledge, none of theoretical models existing today answer these questions; see, e.g., [2-4, 9].

Looking back over 35 years, by the early seventies Vlasov *et al*. [10] reported that the presence of negative glow plasma, whose thickness is several times larger than the length of cathode fall region l_c, is necessary for the existence of normal glow discharge mode. In other words, a subnormal discharge constricts laterally with an increase in discharge current only in the case of $pd > (pd)_{min}$ (on the right branch of the Paschen curve). For $pd < (pd)_{min}$ there is a direct transition from a subnormal to an abnormal discharge, which occurs without radial constriction; the subnormal and abnormal discharges cover the entire area of the cathode. For example, the normal cathode fall is established in neon when the distance between the electrodes equals to at least $4l_c$ [10].

A distinguishing feature of negative glow region is the existence of a reversal of the axial electric field which is related to the fact that the negative glow is analogous to externally sustained plasma [11]. Electrons emitted from the cathode and accelerated in the high, sheath electric field release their energy in the low-field region which defines the negative glow. Most textbooks on gas discharge physics [12-15] also indicate that the net space charge in this region is negative, composed of slow electrons. These electrons being located close to the cathode surface will feel the electrode surface charge concentrated on the electrode edge. The electrostatic repulsive force they exert because of their negative charges will constrict the discharge channel. During the constriction process the second repulsive force between slow electrons will grow and compensate finally the external repulsive force. Thus, the radius of normal cathode spot should be determined by the force balance. We believe that this is the scenario for how a normal cathode spot is established, in contrast to "multiplication maximum mechanism" described in [15].

On the other hand, our recent experiments [7, 16] as well as few observations reported by other authors [17 (see Fig. 7b), 18] show that the electrode boundary is likely to be responsible for the formation of type I patterns in short planar discharge systems (rather than "mysterious" negative differential conductivity [2, 3]). In this case, the electrostatic repulsive force among charged particles trapped on the electrode edge as well as edge corona discharge [7] might be possible triggering mechanisms for the pattern formation. Interestingly, the presence of corona discharge is most likely at the breakdown stage in patterned DBDs (Figs. 5, 6 and 7), while it is absent during the formation of one normal cathode spot and appears here only when the discharge becomes abnormal (Figs. 3 and 4).

4. Conclusion

The experimental results presented in this study show that DBDs in short gaps behave similar to low pressure (low-*pd*) DC glow discharges. The results also suggest (in addition to the results reported in [7]) that there are (at least) two mechanisms for pattern formation in gas discharge systems corresponding two types of discharge patterns. These mechanisms involve different physical processes and should, therefore, be treated in different manners. The first mechanism which is believed to be responsible for pattern formation in subnormal discharges involves processes at the electrode periphery. Consequently, the formation of type I patterns is an inherently three dimensional (3-D) problem which, in addition, requires a kinetic treatment of the electron dynamics due to the appearance of cathode layer [19]. Moreover, the pattern evolution can also take place in the normal glow regime, i.e., under conditions of V_{gap}, j = const, as experimentally shown above. On the other hand, thermal processes can cause the appearance of type II patterns, whose description would require taking into account thermodynamics. Thus it is clear that the negative differential conductivity alone (as a universal criterion) cannot explain a variety of experimentally observed patterns. In our view, Monte Carlo methods which are found to be useful in solving 3-D problems, albeit computer-time-intensive, might be helpful for the analysis of the phenomenon.

References

[1] M.C. Cross, P.C. Hohenberg - Rev. Mod. Phys. **63**, 857 (1993).

[2] K.G. Müller - Phys. Rev. A **37**, 4836 (1988).

[3] D.D. Šijačić, U. Ebert - Phys. Rev. E **66**, 066410 (2002).

[4] I. Müller, C. Punset, E. Ammelt, H.G. Purwins, J.P. Boeuf - IEEE Trans. Plasma Sci. **27**, 20 (1999).

[5] I. Radu, R. Bartnikas, G. Czeremuszkin, M.R. Wertheimer - IEEE Trans. Plasma Sci. **31**, 411 (2003).

[6] D.G. Boyers, W.A. Tiller - Appl. Phys. Lett. **41**, 28 (1982).

[7] S.N. Abolmasov, T. Shirafuji, K. Tachibana - IEEE Trans. Plasma Sci. **33**, to be published.

[8] U. Kogelschatz - IEEE Trans. Plasma Sci. **30**, 1400 (2002).

[9] E. Ammelt, Yu.A. Astrov, H.G. Purwins - Phys. Rev. E **58**, 7109 (1998).

[10] V.V. Vlasov, L.G. Guseva, B.N. Klarfeld - Proc. 10th ICPIG (Oxford, England, 1971) p. 98.

[11] J.P. Boeuf, L.C. Pitchford - J. Phys. D: Appl. Phys. **28**, 2083 (1995).

[12] B.N. Chapman - *Glow Discharge Processes* (New York: Wiley, 1980) Chap. 4.

[13] M.A. Lieberman, A.J. Lichtenberg - *Principles of Plasma Discharges and Materials Processing* (New York: Wiley, 1994) Chap. 14.

[14] J.R. Roth - *Industrial Plasma Engineering*: *Principles* (Bristol: IPP, 1995) Chap. 9.

[15] Yu.P. Raizer - *Gas Discharge Physics* 2nd ed. (Berlin: Springer-Verlag, 1997) Chap. 8.

[16] S.N. Abolmasov, T. Shirafuji, K. Tachibana - Proc. PSS/SPP-22 (Nagoya, Japan, 2005) p. 285.

[17] C. Radehaus, H. Willebrand, R. Dohmen, F.J. Niedernostheide, G. Bengel, H.G. Purwins - Phys. Rev. A **45**, 2546 (1992).

[18] I. Brauer, C. Punset, H.G. Purwins, J.P. Boeuf - J. Appl. Phys. **85**, 7569 (1999).

[19] I. Revel, Ph. Belenguer, J.P. Boeuf, L.C. Pitchford - Pure Appl. Chem. **71**, 1837 (1999).

Particle contribution to the radiative heat transfer in a plasma reactor: Continuum approach

J. Gonzalez-Aguilar[1], L. Fulcheri[1], G. Flamant[2]
[1]*Center for Energy Studies, Ecole des Mines de Paris, Sophia-Antipolis, France*
[2]*PROMES-CNRS, B.P. 5 Odeillo, F-66125 Font Romeu, France*

Abstract
Radiative heat transfer must include particles contribution in studies on thermal plasma gas-phase synthesis due to close relation between temperature and particle tailoring. This work explores an improved method for taking into account the particle presence. Expressions for the extinction and the scattering coefficients providing a dependence of the local temperature are given.

Key words : CFD modelling, radiation, absorption coefficient, scattering coefficient, soot.

1. Introduction

Particles contribute quite significantly to radiative heat transfer in plasmas processes. This contribution plays a crucial role when high requirements on temperature control are needed. This is usually the case in gas phase synthesis since the produced material tailoring depends on the particles thermal history [1, 2, 3].
In thermal plasma gas-phase synthesis of carbon nanostructures such as carbon blacks [4], fullerenes [5] or carbon nanotubes [6], plasma is used as a heat source for achieving the thermal decomposition or the vaporisation of a carbon feedstock. The requirements on the temperature control appear during all process stages from nucleation-aggregation to quenching, including annealing. In all of them, radiative heat exchanges are modified by the simultaneous actions of the synthesised nanoparticles and by the residual feedstock. Consequently, a good description of the particles effects on radiative transfer must be performed.
In a previous work [7], particles were considered to be non-diffusive Rayleigh emitters given that size parameter $x = \pi D/\lambda << 1$, with D, the particle diameter and λ, the wavelength. The complex refractive index was maintained constant at a certain value, which was related to the characteristic wall temperature inside the plasma reactor. However, internal temperature gradients could be high enough to invalidate the characteristic temperature concept that was used to define the soot refractive index. Therefore, this approach should be examined carefully in order to verify if a more sophisticated radiation model for improving the particulate effects on radiative heat transfer is required.
In this work, an improved version of the radiation model will be proposed and compared with the simple model. This new model, which includes the temperature dependence of the soot refractive index, is applied to the study of a geometry for soot formation from a hydrocarbon cracking by plasma using the commercial code Fluent.

2. General model

The radiation model was implemented in the framework of a general model devoted to study the thermal decomposition of methane by a nitrogen plasma jet. The general model assumes that the flow is highly turbulent and the gas is optically transparent and in local thermodynamic equilibrium.
A renormalization group (RNG) based k-epsilon model is employed for taking into account the turbulence. Within this model, the turbulent viscosity μ_t is calculated by $\rho C_\mu k^2/\varepsilon$, with ρ, the fluid density; k , the turbulent kinetic energy; ε , the dissipation of the turbulent kinetic energy and C_μ, a model constant equals to 0.0845.
The chemical composition is described by a non-premixed model. Two convection-diffusion equations are solved, which correspond to the mixture fraction $\bar{f}$ (or mass fraction originated from the hydrocarbon stream)

$$\frac{\partial}{\partial t}\left(\rho \bar{f}\right)+\nabla\cdot\left(\rho u \bar{f}\right)=\nabla\cdot\left(\frac{\mu_t}{\sigma_t}\nabla\bar{f}\right) \qquad (1)$$

and the mean mixture fraction variance $\overline{f''^2}$

$$\frac{\partial}{\partial t}\left(\rho\overline{f'^2}\right)+\nabla\cdot\left(\rho u\overline{f'^2}\right)=\nabla\cdot\left(\frac{\mu_t}{\sigma_t}\nabla\overline{f'^2}\right)+C_g\mu_t\Delta\bar{f}-C_d\rho\frac{\varepsilon}{k}\overline{f'^2} \tag{2}$$

where σ_t, C_g and C_d are model constants, whose values are 0.85, 2.86 and 2.0, respectively. The mixture fraction variance is used in the closure model describing turbulence-chemistry interactions. All instantaneous values of thermochemical scalars, such as density, temperature, and species mass fractions, are uniquely related to the mixture fraction and the enthalpy: $\varphi=\varphi(f,H)$. The time-averaged values are calculated as

$$\overline{\varphi}\approx\int_0^1\varphi\left(f,\overline{H}\right)p(f)df \tag{3}$$

where $p(f)$ is the probability density function (PDF), which describes the temporal fluctuations of f in the turbulent flow.

In this work, a β-function PDF has been chosen,

$$p(f)=\frac{f^{\alpha-1}(1-f)^{\beta-1}}{\int f^{\alpha-1}(1-f)^{\beta-1}df} \tag{4}$$

with

$$\alpha=\bar{f}\left[\frac{\bar{f}(1-\bar{f})}{\overline{f'^2}}-1\right]\ \text{and}\ \beta=(1-\bar{f})\left[\frac{\bar{f}(1-\bar{f})}{\overline{f'^2}}-1\right].$$

Reactive chemical species were limited to the following ensemble: C, C_2, C_2H, C_2H_2, C_2H_4, C_2N, C(s), CH_2, CH_3, CH_4, CN, H, H_2, HCN, N, N_2, NCN, NH, NH_2, NH_3.

Soot formation was incorporated by a two-step Tesner model [6], which involve two transport equations. They correspond to the soot mass fraction and the normalised radical nuclei concentration. It was assumed that CH_4 is the particle precursor.

3. Radiation model

The radiation model is based on the resolution of the radiative heat transfer equation:

$$\frac{dI(\mathbf{r},\mathbf{s})}{ds}+(a+\sigma_S)I(\mathbf{r},\mathbf{s})=a\,m^2\frac{\sigma T^4}{\pi}+\frac{\sigma_S}{4\pi}\int_0^{4\pi}I(\mathbf{r},\mathbf{s})\Phi(\mathbf{s}\cdot\mathbf{s}')d\Omega' \tag{5}$$

where $I(\mathbf{r},\mathbf{s})$ is the radiation intensity at position $\mathbf{r}$ and in the direction $\mathbf{s}$, a and σ_s are the absorption and the scattering coefficients, respectively, m is the complex refractive index, σ is the Stefan-Boltzmann constant, T is the local temperature and Φ is the phase function. For media with mono-dispersed particles, the absorption and the scattering coefficients are expressed as

$$a=\frac{3}{2}\frac{Q_{ext}f_v}{D},\ \sigma_S=\frac{3}{2}\frac{Q_{sca}f_v}{D} \tag{6}$$

with Q_{ext} and Q_{sca} the extinction and scattering efficiencies and, f_v, the volume fraction, which is defined as $\pi/6\cdot D^3\cdot n$, where n is the particles concentration. The extinction and scattering efficiencies are (to terms of order x^4) [8]

$$Q_{ext}=4x\,\mathrm{Im}\left\{\frac{m^2-1}{m^2+2}\left[1+\frac{x^2}{15}\left(\frac{m^2-1}{m^2+2}\right)\frac{m^4+27m^2+38}{2m^2+3}\right]\right\}+\frac{8}{3}x^4\,\mathrm{Re}\left\{\left(\frac{m^2-1}{m^2+2}\right)^2\right\}, \tag{7}$$

$$Q_{sca}=\frac{8}{3}x^4\left|\frac{m^2-1}{m^2+2}\right|^2. \tag{8}$$

The refractive index is calculated as a function of the temperature and the wavelength by using the theory proposed by Lee and Tien [9]. In order to estimate the local refractive index as a function of temperature, the characteristic wavelength is by applying the Wien's Law.

Discrete Ordinate Model is employed for solving eq. 5, as implemented in the CFD code FLUENT.

4. Test geometry and boundary conditions

A simple geometry was used to test the model described above. A cylinder of radius R and length L in which a plasma jet is injected axially and a hydrocarbon is introduced in the radial direction at a distance l from the top. Following table contains the boundary conditions.

	Momentum	Energy	Turbulence	Mixture Fraction	Soot	Radiation
Plasma Inlet	$\mathbf{u}(r)$	$T(r)$	$k(r)$, $\varepsilon(r)$	0	0	emissivity(T)
CH_4 Inlet	$\mathbf{u}(r)$	$T(r)$	$k(r)$, $\varepsilon(r)$	1	0	emissivity (T)
Outlet	Mass conservation	Extrapolated	Extrapolated	Extrapolated	Extrapolated	emissivity ($300K$)
Inner Wall	Non-slip Condition		Standard Wall Function [9]	$\partial f / \partial n = 0$	$\partial / \partial n = 0$	emissivity = 0.9
External Wall		300 K				

5. Results

Figure 1 shows the evolution of the complex refractive index as a function of temperature by using the radiation model described previously. Real and imaginary parts of the refractive index decrease monotonically with temperature. At temperatures higher than 1800 K, the real part of the refractive index is almost constant around 1.86, whereas the imaginary part changes smoothly between 0.68 and 0.52. Consequently, the previous approach, which assumed that the refractive index was constant, is roughly valid at high temperatures.

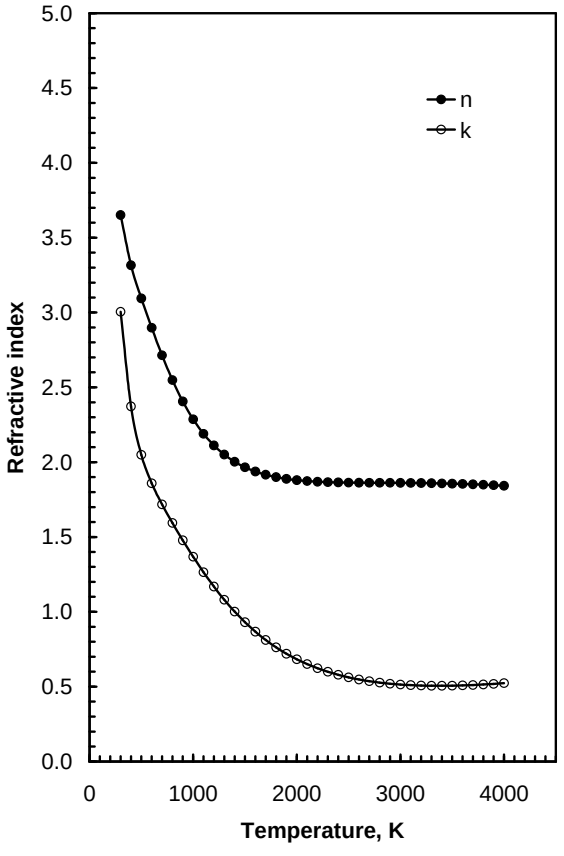

Figure 1. Refractive index versus temperature.

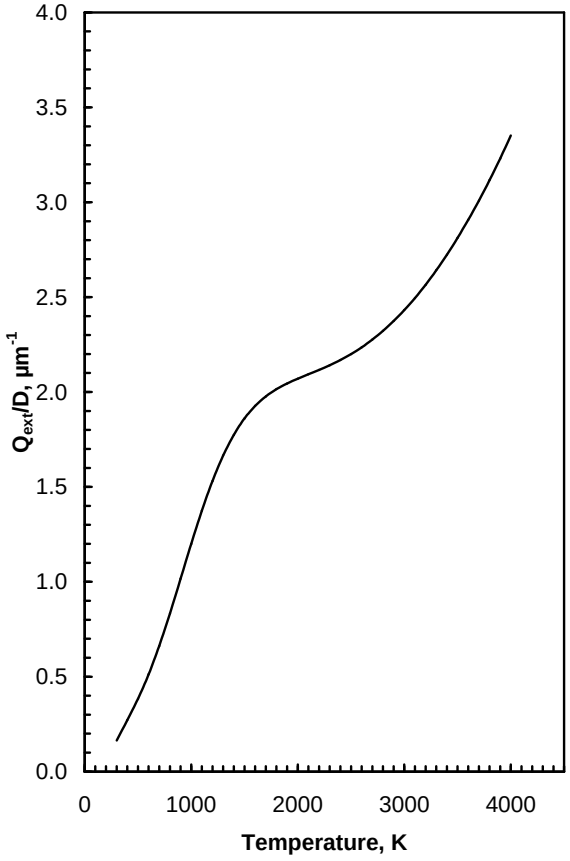

Figure 2. Absorption coefficient at Rayleigh limit.

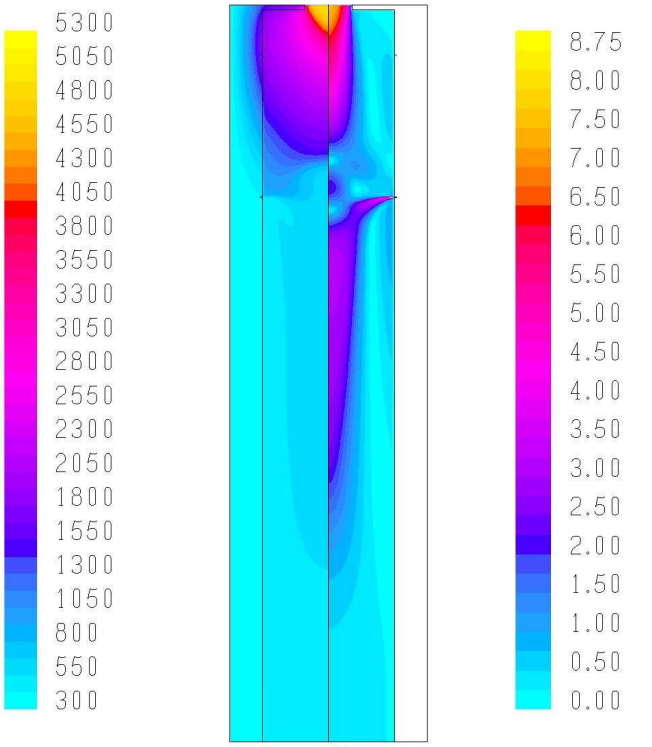

Figure3. (a) Temperature (K), (b) Velocity (m/s).

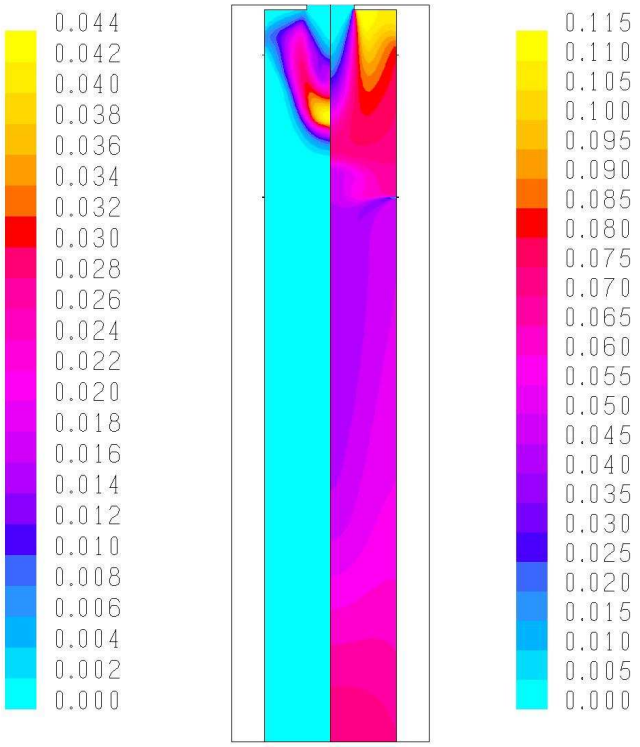

Figure 4. (a) Nuclei mass fraction (10^{15} particles/kg), (b) Soot mass fraction.

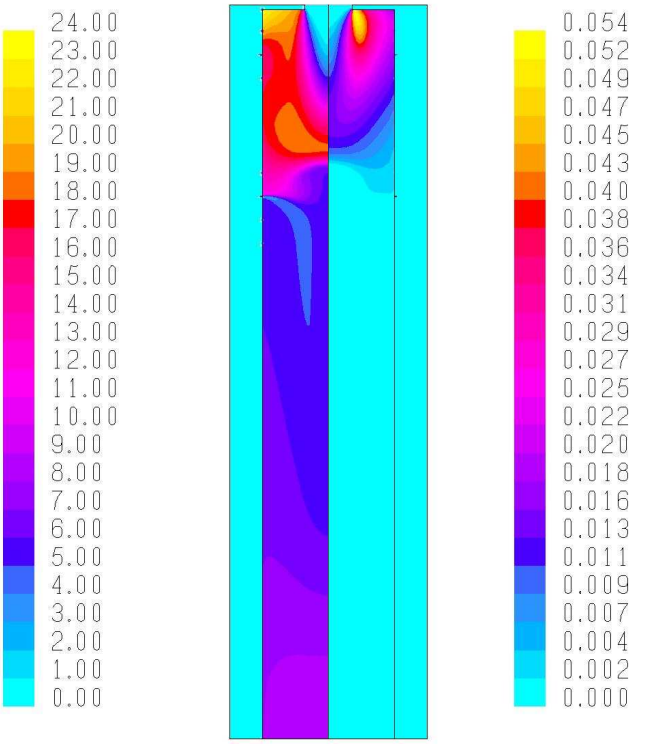

Figure 5. (a) Absorption and (b) scattering coefficients.

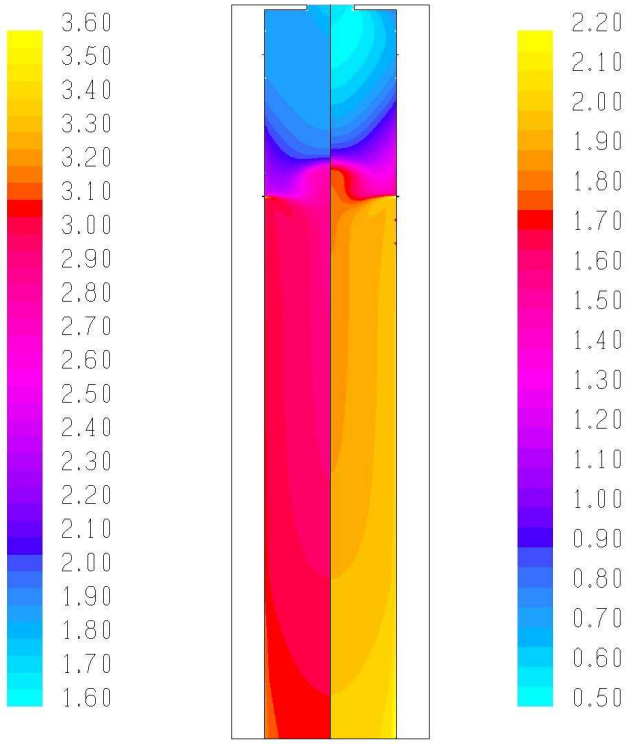

Figure 6. Complex Refractive index, $m = n - j\,k$. (Left) Real part, n and (Right) Complex part, k.

Figure 2 illustrates the absorption coefficient dependence on the temperature. In this picture, the absorption coefficient has been calculated in the Rayleigh limit (that neglects terms of order higher than one). Contrary to the refractive index, the absorption coefficient increases with the temperature, showing a small plateau around 2000 K. In the region comprised between 1000 K and 4000 K, the magnitude grows up by a factor three.
Series of figures from 3 to 6 shows typical field distributions obtained with the test geometry when methane is injected at $l = 0.25\ L$ and at 4.8 g/s flow rate. Two temperature zones become visible in figure 3.a. The first zone is characterised by temperatures higher than 1800 K, whereas the second has temperatures lower that 700 K. The limit between both regions, in which temperature quenches considerably, is located at methane injection level. Simulation shows that the gas cooling down is mainly caused by the mixing of the plasma and the methane jets, leading up to the thermal decomposition of methane. Thus, particle nucleation is placed in the contact region between the two jets, as seen in figure 4.a. Nevertheless, the soot is concentrated in the upper part of the reaction chamber just in the corner (fig. 4.b). This is due to the vortex generated by the plasma jet.
As result of the particle presence and the temperature, the absorption and scattering coefficients are higher in the upper temperature zone than in the lower. Both coefficients contribute to make more uniform the temperature field.
The refraction index is approximately constant within each temperature zone. In the hot zone, the refraction index change smoothly even if temperature varies between 4000 to 1800 K, as it is expected from its temperature dependence (fig.1). In the cold zone, the refraction index behaviour is caused by the uniformity of the temperature field.

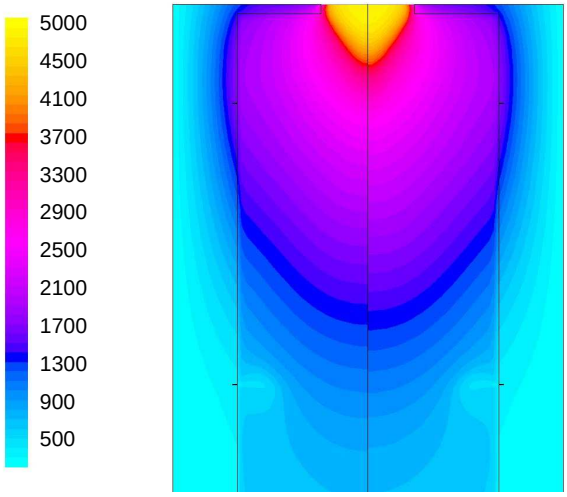

Figure 7. Temperature comparison $m = 1.86 - j\ 0.68$ (left) and $m(T)$ (right).

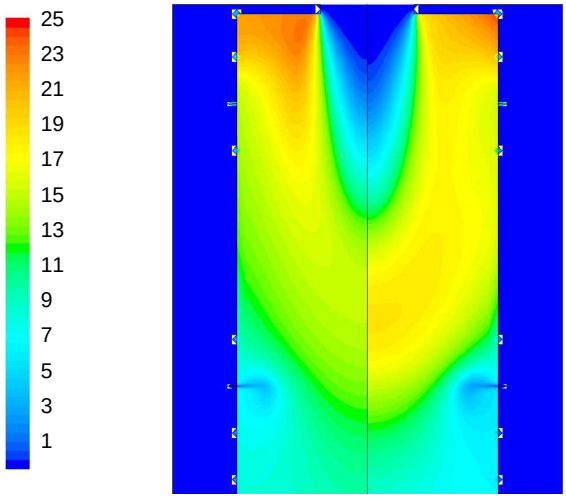

Figure8. Absorption coefficients comparison with $m = 1.86 - j\ 0.68$ (left) and $m(T)$ (right).

Therefore, absorption and scattering coefficients are mainly dependent on the volume fraction and the role of refractive index is secondary. Figure 7 and 8 shows the comparison of temperature and absorption coefficient distributions when the temperature dependence of the refractive index is taking into account or not. In this case, the refractive index is $1.86 - j\ 0.68$. Both approaches predict a mean free path of photons in the hot region between 4 cm and 10 cm. However, there is a deviation in the absorption coefficients as high as 20%.
Notice that if the chamber dimensions (radius or length) are larger than the photons mean free path, the medium will be optically thick, and the differences between the two approaches will decrease.

4. Conclusions

Radiative heat transfer must consider particles contribution in studies on thermal plasma gas-phase synthesis due to close relation between temperature and particle tailoring. This work explored an improved method for taking

into account the particle presence. Expressions for the extinction and the scattering coefficients are given providing a dependence of the local temperature.
The comparison of two models (constant and temperature-dependent refractive index) show that the assumption of constant refractive index is not valid at low volume fractions and gas temperatures lower than 1500 K. Then, it remains a good approach in the hot plasma zone.

References

[1] A. Gutsch, M. Kramer, G. Michael, H. Muhlenweg, M. Pridöhl, and G. Zimmermann, KONA **20**, 24 (2002).
[2] G. Kuhner, G. Dittrich, Chem. Ing. Technol. **44**, 717 (1972).
[3] R. E. Smalley, Acc. Chem. Res. **25**, 98 (1992).
[4] L. Fulcheri, N. Probst, G. Flamant, F. Fabry, E. Grivei and X. Bourrat, Carbon **40**, 169 (2002).
[5] L. Fulcheri, Y. Schwob, F. Fabry, G. Flamant, L. F. P. Chibante and D. Laplaze, Carbon **38**, 797 (2000).
[6] H. Okuno, E. Grivei, F. Fabry, T. M. Gruenberger, J. Gonzalez-Aguilar, A. Palnichenko, L. Fulcheri, N. Probst and J.-C. Charlier, Carbon **42**, 2543 (2004).
[7] J. Gonzalez-Aguilar, I. Dème, L. Fulcheri, T. M. Gruenberger, F. Fabry, G. Flamant , B. Ravary, High Temp. Material Processes **7**, 51 (2003).
[8] C. F. Bohren, D. R. Huffman, “Absorption and Scattering of Light by Small Particles”, John Wiley & Sons Inc., New York (1983).
[9] S. C. Lee, C. L. Tien, 18th Symposium International on Combustion, The Combustion Institute, 1159 (1981).

The role of negative ions in the sheath formation

P. Jelínek, R. Hrach, J. Šimek, V. Hrachová, P. Bartoš

Charles University, Faculty of Mathematics and Physics, Department of Electronics and Vacuum Physics
Prague, Czech Republic

Abstract
The transport of electrons and ions to metal substrates immersed into plasma is studied by computer experiment in the plasma of electronegative gases. As input data for modelling the results of both measurement and simulation of the dc glow discharge in oxygen/argon plasma were used. The formation of the sheath region and the spatial and temporal evolutions of distributions of individual charged species in the presence of negative ions are investigated.

1. Introduction

The interaction of both inert gas plasmas and chemically active plasmas with immersed substrates takes part in many technological applications as plasma processing of materials, plasma oxidation or plasma-assisted deposition processes. Special attention must be given to technologies using electronegative gases because of their importance in practice and in the same time the difficulties in theoretical description. The presence of three-component plasma containing besides electrons and positive ions also negative ions significantly alters the formation of the sheath and in such way modifies the fluxes of charged species to the substrate. As a consequence the detailed analysis of physical and chemical processes taking part during plasma-solid interaction in such plasmas is much more complicated and the theoretical description of both technological results and probe diagnostics is difficult, especially in dynamic regime. Therefore, in such plasmas the computational approach is a convenient alternative to the theory and computer experiments can help to analyse experimental data obtained in electronegative gases.

The theoretical/computational description of the complete process of electronegative plasma-solid interaction consists of several stages – characterisation of bulk properties of plasma, formation of sheath region and calculation of the transport of charged species from undisturbed plasma to metal substrate immersed into plasma, followed in some plasma chemical technologies by the description of physical or chemical processes on the surfaces of substrates.

In our contribution the sheath formation as a part of plasma-solid interaction in gas mixtures containing oxygen is studied by the combination of direct measurement and computer modelling. This study is a continuation of our contribution presented during the last 16th ISPC conference in Taormina [1]. Moreover, in the present 17th ISPC conference another contribution [2] is presented, devoted to the complementary problem, i.e. to the analysis of complete process of plasma oxidation of metals, where the plasma-solid interaction is one of the most important parts.

2. Volume processes

In the first part of our study the volume of the electronegative plasma is characterised. For this purpose two different techniques were used:

- experimental approach
- computational approach.

The measurements were performed in a positive column of dc glow discharge either in pure oxygen or in mixtures of oxygen with rare gases – argon, neon or helium. Our studies were made in a pressure range 67 to 800 Pa, the composition of mixtures and the discharge current being experimental parameters. For the study of plasma properties optical, microwave and probe diagnostics were used. Some experimental results can be found in [3], [4] as well as in [2]. Examples of obtained experimental results can be seen in Fig. 1. During the

measurements the axial electric field was determined together with the electron density, effective collision frequency and temperature of electrons for various combination of experimental parameters. Some of these experimental results were used as input data for following computer simulations.

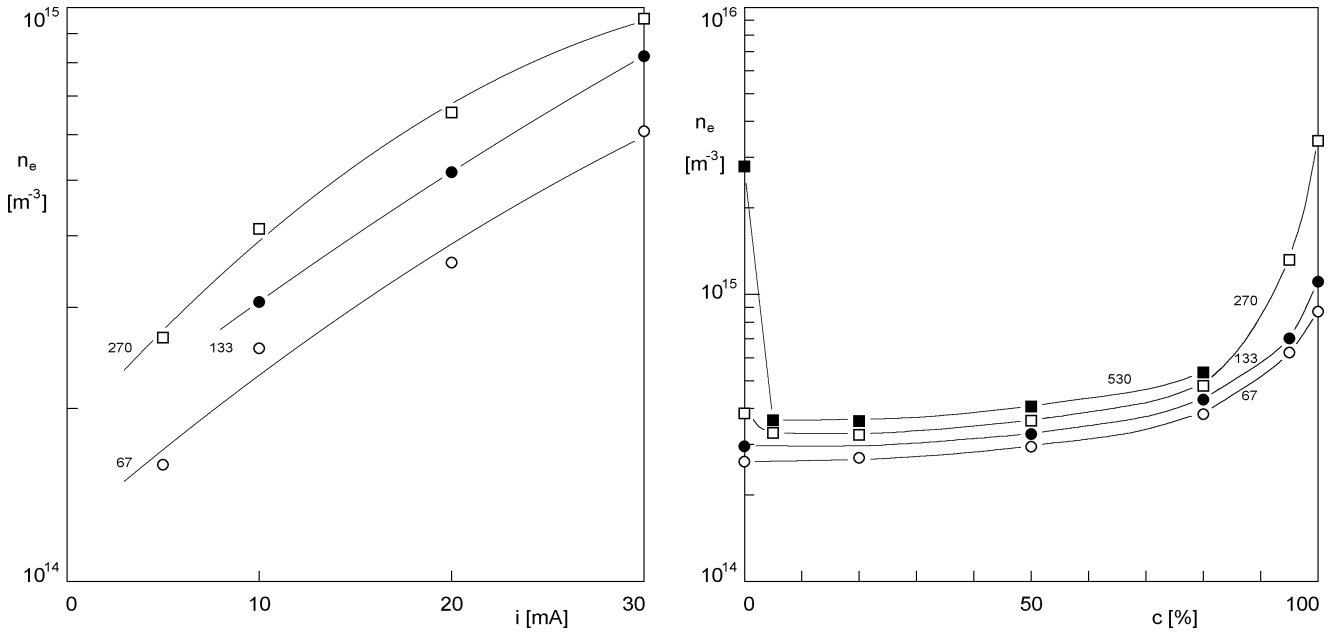

Fig. 1: Measured electron density n_e [1]. The parameter is a pressure of gas mixture in Pa.
Left – O_2 plasma, measurement in the dependence on discharge current i.
Right – O_2/Ne plasma, dependence on concentration of inert gas c.

Plasma composition in the undisturbed region was studied with the help of computer experiment, too. The model of bulk of oxygen plasma was based on a macroscopic kinetic approach, when the steady-state concentrations of various species can be found as a solution of a set of linear differential equations corresponding to conservation laws for individual species in the discharge – e.g. [5].

The model of O_2/Ar plasma consists in the present moment of 196 reactions between 21 types of neutral, charged and excited species. The reaction set includes the basic physical processes and consists of three parts – reactions between oxygen particles, reactions in argon and mixed reactions oxygen-argon. As a result the concentrations of the most important neutral and charged species in the plasma were derived for various discharge parameters – see Tab. 1.

neutral and excited species					
O_2: 1.0	O: 7.5×10^{-1}	$O_2(^1\Delta_g)$: 1.5×10^{-1}	$O_2(^1\Sigma_g^+)$: 4.3×10^{-3}	O_3: 7.7×10^{-5}	…
1.0	2.5×10^{0}	4.3×10^{-6}	2.0×10^{-3}	7.5×10^{-5}	…

positive charged species			
O_2^+: 1.6×10^{-6}	O^+: 5.2×10^{-10}	O_4^+: 3.0×10^{-10}	...
1.1×10^{-6}	2.0×10^{-9}	1.1×10^{-9}	...

negative charged species				
e: 1.3×10^{-6}	O^-: 2.6×10^{-7}	O_2^-: 8.6×10^{-9}	O_3^-: 4.6×10^{-10}	...
1.0×10^{-6}	8.8×10^{-8}	5.9×10^{-10}	1.1×10^{-10}	...

Tab. 1: Calculated concentrations of most important species in pure oxygen plasma. First line: 60 Td, second line: 100 Td.

The three most important negative species were found to be electrons and negative oxygen ions both atomic and molecular; the most important positive particle is the molecular oxygen ion. Results shown in Tab. 1 were obtained for the zero concentration of argon in the mixture. With increasing concentration of argon the number of positive argon ions increases and Ar^+ ions become the most important positive particle. In the same manner increases the influence of electrons among negatively charged particles.

3. Plasma-solid interaction

The steady-state results, both experimental and computational, mentioned in previous section were used as input data for the basic part of our study, which was devoted to the description of the transport of charged species through the region of disturbed plasma near the substrate.

It is known that the role of negative ions in the formation of sheath region in the vicinity of metal substrate immersed into plasma is very important. The reason of this behaviour is, that the creation of sheath and presheath is influenced not only by charges of interacting particles but also by their masses. While the masses of the main positive particles (Ar^+, O_2^+ and O^+) are comparable, the masses of the basic negative species – electrons and O^- ions – differ profoundly.

Therefore, our basic model was devoted to the analysis of the role of negative ions in the sheath formation. The technique of simulation used was a hybrid particle simulation approach, i.e. the combination of molecular dynamics and Monte Carlo methods (so-called method PIC-MC). In reality, we prepared several models, which differ in the dimensionality and geometry – models were either one-, two- or three-dimensional in space and described interactions of electronegative plasma with planar, cylindrical or spherical substrates. All models are self-consistent, i.e. charged particles generate during their transport to the substrates local electric fields that influence their further movement. This approach is rather precise, however extremely time-consuming. Therefore some sophisticated techniques of computer simulation must be applied, as the introduction of variable statistical weights of particles depending on their positions, switching between several time scales or changing the numbers of particles during the simulation.

All models are based on similar assumptions. Charged particles originate in undisturbed O_2/Ar plasma consisting of most important positive and negative species shown in Tab. 1. The number of species differs according to the purpose of modelling – for the study of sheath formation only the most important species, where the most of the charge is concentrated, are introduced (negative: electrons and O^- ions, positive: Ar^+ and O_2^+ ions). For the detailed analysis even the species with lower concentrations can be taken into account. Trajectories of charged particles were calculated by the combination of deterministic molecular dynamics method, when the equations of motion were solved by the Verlet algorithms. The scattering of charged particles by neutrals was treated by stochastic Monte Carlo method. The mean free paths for individual interactions were obtained from experiments [6] and their energy dependences were compensated by the null-collision technique. The types of interactions introduced into models were elastic scattering, charge transfer, excitation and ionisation. The input physical data for simulation were taken from the oxygen/argon dc glow discharge - pressure 133 Pa, ion and gas temperature 300 K, electron temperature between 20,000 and 30,000 K, time step for the Verlet algorithm given by the movement of electrons 10^{-11} to 10^{-12} s.

4. Results

Most of simulations were made for planar configuration, as this geometry corresponds to typical technological arrangement. In this case a simplified one-dimensional model can be used. The second analysed configuration was cylindrical, which can be studied either one- or two-dimensionally. As a result the distribution of electric potential in the sheath and presheath region was derived. The simulation enabled us to observe the changes in energy distribution functions of both electrons and ions during their transport through the sheath, to calculate the fluxes of charged particles and to derive energies of impinging particle on the surface of substrate. These results can be used in the study of plasma chemical technologies as plasma oxidation of metals.

The modelling was performed both in static and dynamic regimes. In static regime, when only steady state results are important, the simulation can be accelerated by introducing various time steps for electrons and ions. In order to study the influence of negative ions on the plasma properties near the substrates of immersed solids, the relative concentrations of these ions were changed as a parameter of modelling. While in real situation the concentrations of negative ions represent maximally several tenths of the total negative charge, our model parameter varied in the whole range from 0 to 100 %.

In Figs. 2 to 4 some results of simulations are presented – the distribution of electric potential in the sheath region (Fig. 2), concentrations of individual charges species in the distance *x* from the substrate (Fig. 3) and velocity and angular distributions of both electrons and ions near the substrate (Fig. 4, the solid lines denote theoretical Maxwell distributions).

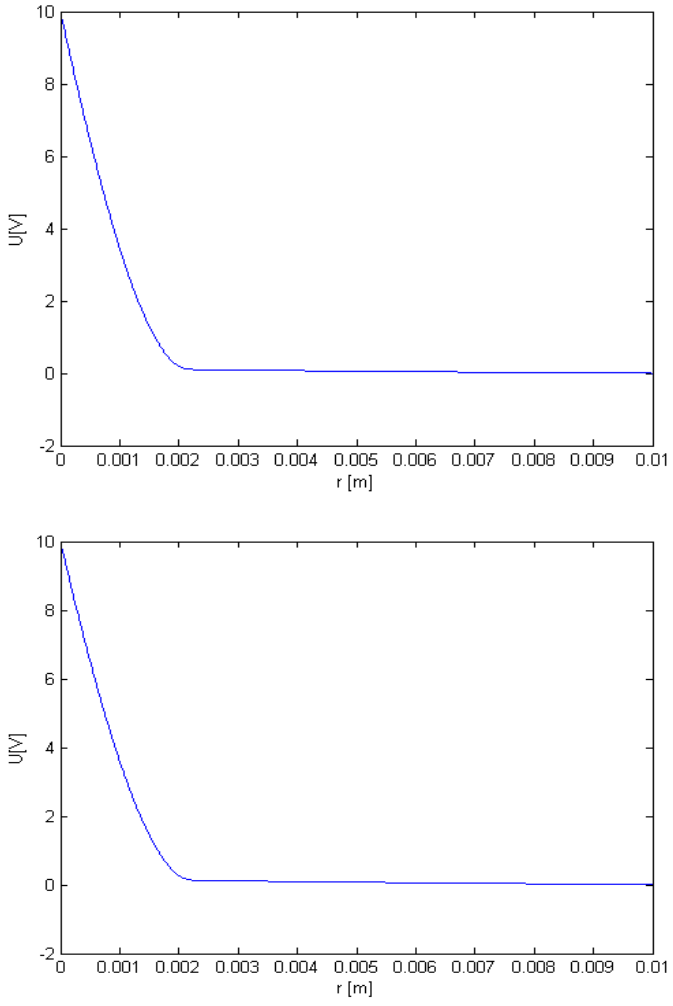

Fig. 2: Distribution of electric potential *U(x)* near the positively biased electrode for various relative concentrations of negative ions *c*. Relative concentration of negative ions 10 % - upper part, 20% - bottom part.

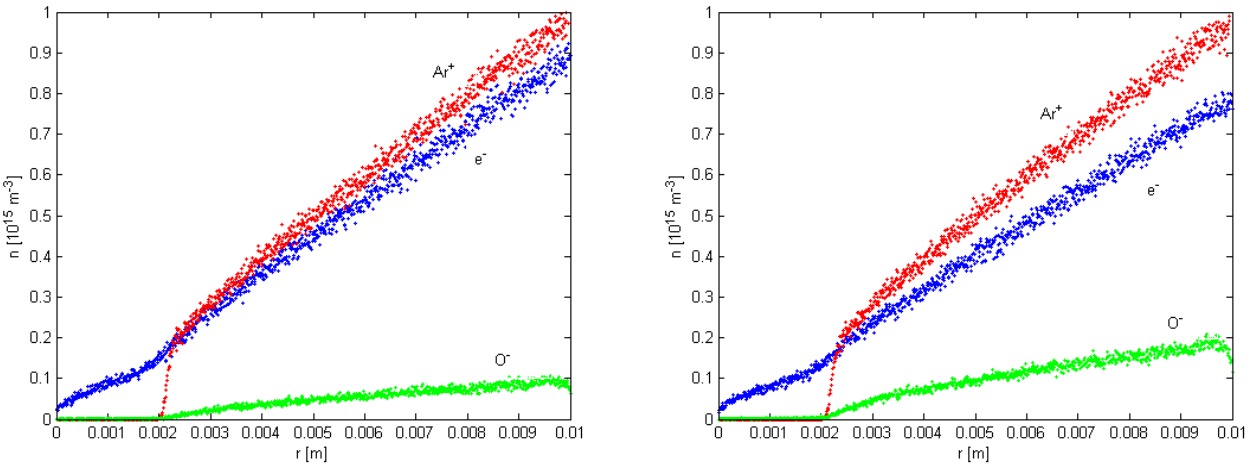

Fig. 3: Spatial distribution of concentrations of most important charged species *n(x)*.
Relative concentration of negative ions 10 % - left part, 20% - right part.

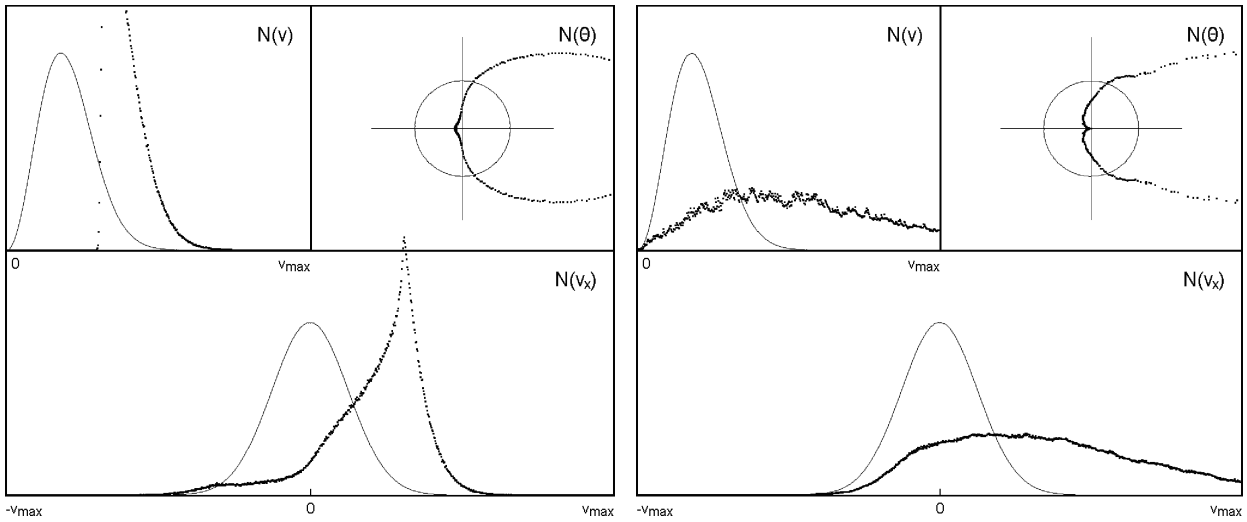

Fig. 4: Distributions of negatively charged particles impinging substrate – electrons (left) and ions (right).
Parameters: voltage bias +5 volts, relative concentration of negative ions 10 %.

5. Discussion

The presence of negative ions influences profoundly the properties of the sheath region, the transport of charged species from the plasma to immersed substrates and as a consequence all technological processes based on the application of electronegative plasmas. However, the different behaviour of electrons and negative ions can be demonstrated in the best way in dynamic regime, e.g. during application of step voltage bias or at higher frequencies. The most remarkable results can be obtained when the electric field in the vicinity of metal substrates reverses its sign and the space charge trapped in the sheath is suddenly released [7].

During the simulation there were observed some discrepancies in the role of negative ions during sheath formation derived by computer simulation compared to theoretical considerations. In order to clarify these differences another simulation of fundamental processes in plasma is now being performed and the first results will be published soon.

6. Acknowledgements
The work is a part of the research plan MSM0021620834 that is financed by the Ministry of Education of the Czech Republic and partly was supported by the Grant Agency of Charles University Prague, Grant No. 296/2004. The authors P. J. and J. Š. gratefully acknowledge the support of Grant GAČR 202/03/H162.

References

[1] R. Hrach, V. Hrachová, M. Vicher, J. Šimek - Proc. 16th Intern. Symp. on Plasma Chemistry ISPC-16, Taormina, Italy, p. 145 (2003).
[2] S. Novák, R. Hrach, J. Pavlík, V. Hrachová: Modelling of plasma-solid interaction during plasma oxidation process, Proc. 17th Intern. Symp. on Plasma Chemistry ISPC-17, Toronto, Canada (2005).
[3] V. Hrachová, A.-M. Diamy, O. Kylián, A. Kaňka, J.-C. Legrand - Behaviour of Glow and Microwave Discharges of Oxygen, in Advances in Plasma Physics Research, Volume II, NOVA, Science Publishers Inc., Hunhington, NY, USA 2003.
[4] A. Kaňka, V. Hrachová, O. Kylián - Proc. 15th Intern. Symp. on Plasma Chemistry ISPC-15, Orléans, France, Vol. IV, p. 1405 (2001).
[5] J.-C. Legrand, A.-M. Diamy, R. Hrach, V. Hrachová - Production of C2 Hydrocarbons from Methane Conversion in the Flowing Afterglow of a Dinitrogen Microwave Plasma: Experiments and Modeling, in Advances in Plasma Physics Research, Volume I, NOVA, Science Publishers Inc., Hunhington, NY, USA, Chapter 1, p. 1 (2001).
[6] S.C. Brown - Basic Data of Plasma Physics: The Fundamental Data on Electrical Discharges in Gases. AIP Press, New York (1994).
[7] R. Hrach, V. Hrachová, M. Vicher - Computer Physics Comm. **147**, 505 (2002).

Deposition of hydrocarbon films by means of helium-ethylene fed dielectric barrier discharges

F. Fanelli, R. d'Agostino, F. Fracassi

Department of Chemistry, University of Bari, Istituto di Metodologie Inorganiche e Plasmi - CNR, Bari, Italy

Abstract
The present work provides a detailed study of helium-ethylene glow dielectric barrier discharges. Particular attention has been given to different process parameters in order to clarify both discharge operational mode and coating properties. The effect of ethylene concentration, total gas flow rate, excitation frequency and applied voltage have been investigated. It has been observed that a polyethylene-like coating can be obtained with deposition rates ranging between 20 and 80 nm min^{-1}.
Keywords: glow dielectric barrier discharge, ethylene, deposition

Introduction

In recent years glow dielectric barrier discharges (GDBDs) have received an increased attention since they appear to be a promising alternative to low pressure plasmas for surface processing of materials even though, due to the quite restrictive conditions under which stable and homogeneous discharges can be obtained, an adequate process control is not available so far. Efforts are in progress to evaluate the utilization of this non-equilibrium plasma technique for surface modification of materials and for this purpose the generation of homogeneous dielectric barrier discharges in several gases is under study [1-5]. Particular attention should be given to the influence of process parameters on the operational mode of the discharge and to the fact that the addition of a reactive monomer to the feed gas, as it is required in deposition processes, can drastically affect discharge stability and behaviour.
Our study aims to contribute to this thematic by providing a detailed exploration of helium-ethylene fed glow DBDs in order to clarify both discharge behaviour and coating properties.
Plasma enhanced chemical vapour deposition (PECVD) of hydrogenated amorphous carbon (a-C:H) thin films at low pressure have been widely studied utilizing several monomers. A good process control, which allows to obtain deposits with defined characteristics, such as hydrogen concentration and Csp^3/Csp^2 ratio, has been achieved [6-9]. Interesting results have been reported since 70's; for instance in 1974 Kobayashi *et al.* [10] studied the plasma polymerization of ethylene and they obtained a polymer-like coating (high hydrogen content). The results were exploited to raise the hypothesis of a free-radical polymerisation mechanism that mainly occurs in the gas phase.
One of the first investigations of atmospheric pressure deposition in hydrocarbons containing discharges has been published in 1979 by Donohoe and Wydeven [11]. The polymerisation of ethylene diluted in He in an uniform atmospheric pressure pulsed discharge was described. In this pioneristic work a soft polymer with a low cross-linking degree was obtained. The polymerization of ethylene in He containing atmospheric pressure glow discharges (APGDs) has also been studied by Yokoyama *at al.* [12]. A polyethylene-like film similar to those deposited with low pressure PECVD was obtained. Many other studies concerning the hydrocarbon deposition in DBD have been reported in the scientific literature, and frequently also in a filamentary discharge regime [13-19].
In the present work the results of a-C:H thin film deposition in GDBD fed with helium-ethylene are reported. The effect of ethylene concentration, residence time inside the discharge and input power have been investigated. The discharge has been characterized by means of electrical measurements and optical emission spectroscopy. In order to obtain indications on the reactive fragments generated inside the discharge, the stable species contained in the gas effluent have been sampled and analysed using gas chromatography with mass spectrometry detection. The coatings has been characterized by means of XPS and FT-IR.

Experimental

The experimental apparatus consists of a parallel plate electrode system (5 mm of interelectrodic gap) contained in a Plexiglas box, each electrode (3 x 3 cm^2 area) is covered by a 0.6 mm thick Al_2O_3 plate (CoorsTek, 96% purity). The plasma is generated by means of an AC high voltage (HV) power supply, composed by a variable frequency generator (TTi TG215), a linear amplifier (Outline PA4006) and a high

voltage transformer (Montoux). The excitation frequency (f) can be changed in the range 0.5 kHz – 30 kHz and the applied voltage can be raised up to 10 kV_{rms}.
The discharge was fed with He-C_2H_4 mixtures (Airliquide, Helium C, Ethylene N35), the gas flow rates were controlled by MKS mass flow controllers. Feed gas was introduced in the interelectrodic zone through a slit and is pumped through a second slit positioned on the opposite side.
The electrical characterization of the discharge was performed with a digital oscilloscope (Tektronix TDS2014). The voltage applied to the electrodes was measured by means of a high voltage probe (Tektronix P6015). The discharge current (I_m) was evaluated by measuring the voltage drop across a 50 Ω resistor connected in series with the grounded electrode.
Optical emission spectroscopy was performed in the UV-Vis region using an Optical Multichannel Analyser (OMA) equipped with a monochromator (0.300 m focal length imaging monochromator SP-300i ACTON, 1200 g/mm grating) and a CCD intensified detector (SpectruMM^{TM} 100B, Princeton Instruments).
A stainless steel liquid nitrogen trap, located between the reactor and the rotary pump, allows to sample the stable species contained in the exhaust gas. The sampling was performed for three hours, then the trap was isolated and the condensate dissolved in nonane (Aldritch, 99+% purity) and analysed using gas chromatography with mass spectrometric detection. The GC apparatus (GC 8000^{Top} Thermoquest Corporation) is equipped with an J&B DB-1 capillary column (polydimethylsiloxane 0.25 μm thick stationary phase, length of 30 m, i.d. of 0.25 mm) and with a quadrupole mass spectrometer (Voyager, Finngan, Thermoquest Corporation). Mass spectra were recorded in the m/z range 15 – 500 u.m.a. at the standard ionizing electron energy of 70 eV. The products were identified by means of available libraries [20].
The chemical characterization of the coating was carried out by means of XPS analyses, performed with a PHI ESCA 5300 with non-monochromatic Mg K_α radiation (1253.6 eV), and by FTIR (Bruker Equinox 55 spectrometer) analyses of film deposited onto CaF_2 substrates. Film thickness was measured on substrate partially masked during deposition using an Alpha-Step® 500 KLA Tencor Surface profilometer at different positions inside the interelectrode gap (in the region 10 – 20 mm from the gas entrance inside the discharge area), i.e. as a function of gas residence time. In order to compare the results obtained under different experimental conditions, the average value of the deposition rate ($r_{d\ av}$) has been considered; at each experimental point an error bar corresponding to the minimum and maximum values of the measured deposition rate has been associated.
The experimental conditions utilized for the study are listed in table 1.

f (kHz)	V_a (kV_{pk-pk})	φ_{He} (slm)	$\varphi_{C_2H_4}$ (sccm)	[C_2H_4] (%)
20	2.8	2	2 –10	0.1 – 0.5
20	2.8	2 – 5	10 – 25	0.5
10 - 30	2.8	2	10	0.5
20	2.8 – 4.0	2	10	0.5

Table 1. Process parameters for GDBD in helium-ethylene mixtures

Results
The electrical characterization of the discharge has shown that microdischarges appears for excitation frequency lower than 9 kHz, whatever the concentration of ethylene in helium is. However, if the frequency is higher than 10 kHz a periodical discharge current signal can be observed up to 0.5 % of ethylene in the gas feed. Figure 1 shows that the current is periodical with the same period of the applied voltage and it is formed by only one peak per half cycle, as for a typical current signal of a GDBD in helium [4]. The higher the ethylene concentration, the higher the breakdown voltage and the discharge peak amplitude.
Moreover, the discharge current is formed by only one peak per half-cycle only if the applied voltage is lower than 3.4 kV_{pp}, while for higher values of the applied voltage, secondary current peaks appear in addition to the principal intense one (figure 2). The periodicity of the current signal and the individual current pulse duration suggest that the discharge is still homogeneous, even though it operates with successive breakdowns during a single half cycle. These multiple current pulses usually are produced when the applied voltage exceeds the breakdown voltage [21, 22].

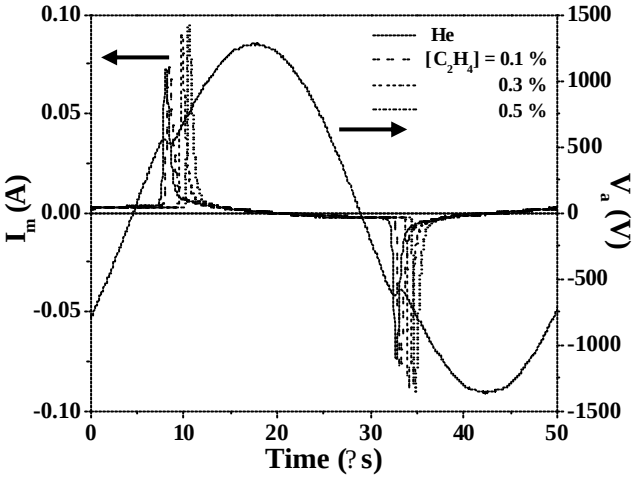

Figure 1. Applied voltage and measured current waveforms for pure helium and for three different ethylene concentrations (f = 20 kHz, V_a = 2.8 kV_{pp}, $[C_2H_4]$ = 0.1, 0.3, 0.5 %)

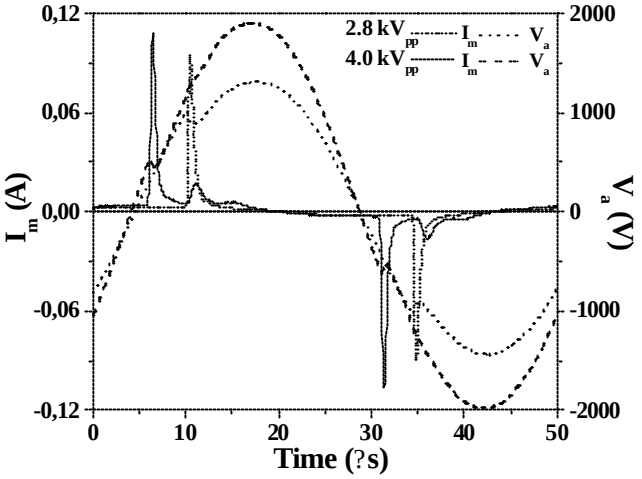

Figure 2. Applied voltage and measured current waveforms for two different values of the applied voltage (f = 20 kHz, V_a = 2.8 kV_{pp} and 4.0 kV_{pp}, $[C_2H_4]$ = 0.5 %).

As expected, as a consequence of the gas injection system the thickness of the deposit increases as a function of the distance from the gas admission (i.e. of residence time of the gas) inside the discharge area (figure 3). By increasing the frequency, i.e. the number of current pulses per unit of time, a linear growth of the discharge power can be observed together with a linear increase of the deposition rate from 20 nm min^{-1} up to 80 nm min^{-1} (figure 4). On the other hand by increasing the voltage at fixed excitation frequency, i.e. the energy per each half cycle, an approximately linear growth of the power density and a less pronounced increase of deposition rate is observed (figure 5).

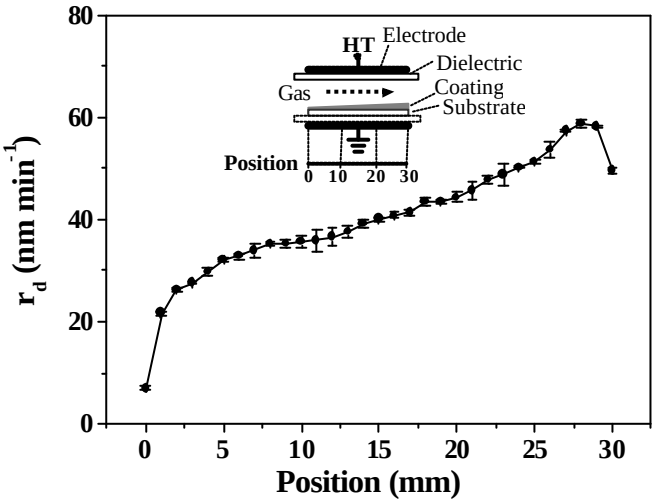

Figure 3. Schematic of the electrode system and typical deposition rate profile as a function of the position in the discharge area (f = 20 kHz, V_a = 2.8 kV_{pp}, φ_{He} = 2slpm, $\varphi_{C_2H_4}$ = 10 sccm, $[C_2H_4]$ = 0.5 %,)

Figure 6 shows the normalised FTIR absorption spectra of the deposits as a function of excitation frequency. The main spectral feature is the broad band between 3000 and 2800 cm^{-1}, due to CH stretching vibration modes and the two signals between 1480 and 1370 cm^{-1} due to CH_2 and CH_3 bending. Any olefinic CH signal can be observed. The intensity and the structure of the CH stretching band are consistent with an amorphous, weakly cross-linked and polymer-like structure with mainly hydrogen bonded to sp^3 carbon [6,

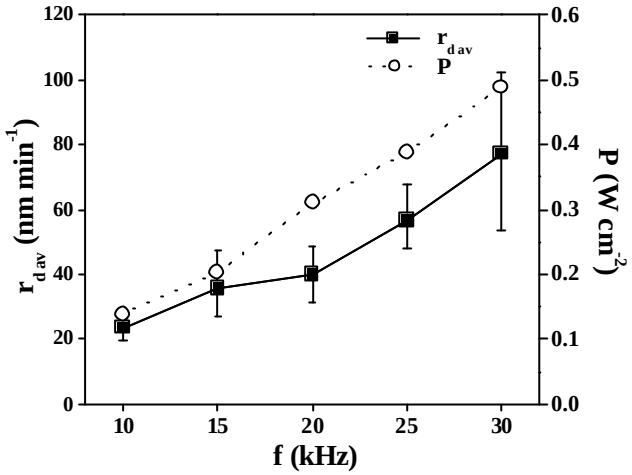

Figure 4. Deposition rate and discharge power as a function of frequency at a fixed applied voltage of 2.8 kV_{pp} ([C_2H_4] = 0.5 %).

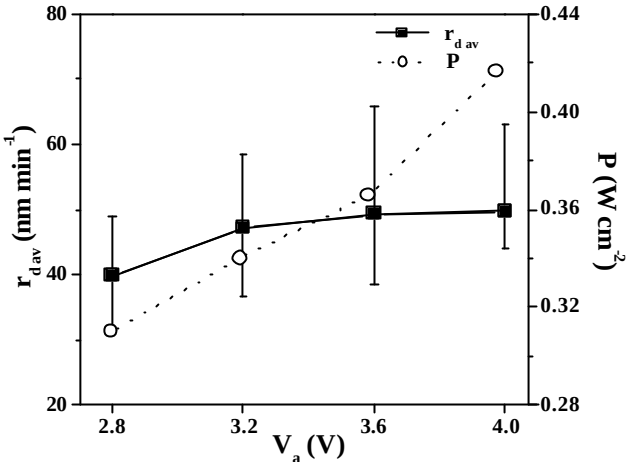

Figure 5. Deposition rate and discharge power as a function of applied voltage at a fixed frequency of 20 kHz ([C_2H_4] = 0.5 %).

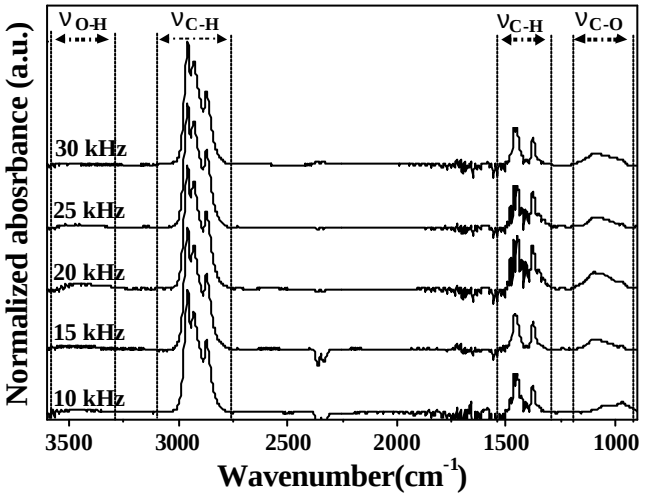

Figure 6. Normalized absorbance FTIR spectra of films deposited as a function of frequency (V_a = 2.8 kV_{pp}, [C_2H_4] = 0.5%).

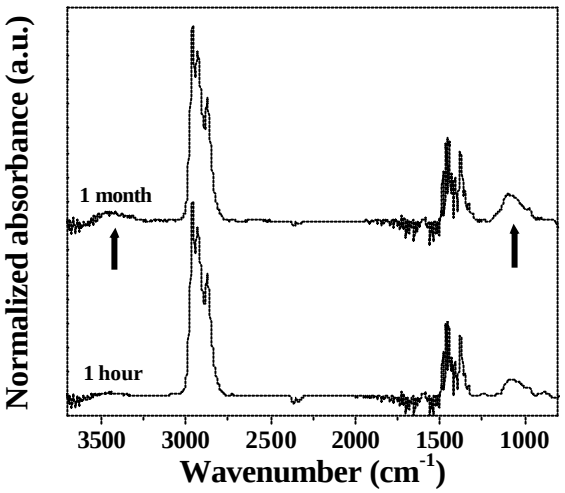

Figure 7. Normalized absorbance FTIR spectra of films deposited as a function of storage time (f = 20 kHz, V_a = 2.8 kV_{pp}, [C_2H_4] = 0.5%)

23-26]. Some oxygen is also contained in the coating in form of OH (3450 cm^{-1}) and C-O (1090 cm^{-1}) groups [24, 26]. These functionalities are due to O_2 and H_2O contaminations in the Plexiglas box, which generate oxygen containing groups during the deposition process, and/or to coating oxidation after atmosphere exposure. The FTIR spectra of figure 6 show that the chemical characteristics of the coatings is not appreciably affected by frequency variation; XPS analyses, on the other hand, show that oxygen concentration is lower than 3 % for all the experimental conditions explored.

In order to investigate the stability of the coating the FTIR analysis of a coating obtained at 0.5% C_2H_4, 20kHz and 2.8 kV_{pp} has been repeated after one month of storage in ambient air. Only a slight increase of the OH and C-O bands have been detected with respect of the as deposited film (figure 7). The oxygen uptake due to ageing is confirmed by comparing the XPS spectra performed after 1 hour and 1 month from deposition: the concentration of atomic oxygen increases from 0.8 % up to 2.5 %.

Optical emission spectroscopy investigation have been carried out in order to identify the main emitting species. For this purpose the emission of helium plasma has been compared with that of helium-ethylene plasma. He GDBD is characterized by intense emissions originated from helium and impurities i.e. nitrogen, oxygen and water; among contaminants, N_2^+ emission at 391 nm resulted the most intense. After ethylene addition to the feed gas, the total emission intensity of the spectrum decreases, the emissions of impurities

are drastically reduced (e.g. the emissions of oxygen containing species completely disappear for all ethylene concentrations) and the CH (4300Å system) and C_2 (Swan system) emissions appear.
Figure 8 shows a typical chromatogram of by-products sampled with the cold trap. The concentration of by-products is always very low and it is not affected by the experimental conditions. Several saturated and unsaturated hydrocarbons have been sampled, however butane is the most abundant specie.

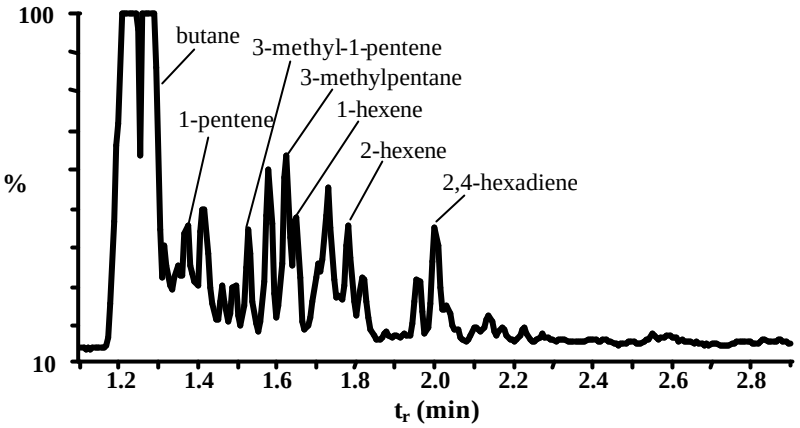

Figure 8. Typical gas-chromatogram of exhaust (f = 20 kHz, V_a = 2.8 kV_{pp}, $[C_2H_4]$ = 0.5 %, φ_{He} = 2slpm, $\varphi_{C_2H_4}$ = 10 sccm, sampling time = 3h).

Conclusion

The results shown in previous section allow to state that it is possible to deposit thin hydrocarbon films in a glow dielectric barrier discharge regime with good control of process parameters. In helium-ethylene GDBD the deposition of a soft polymer-like coating occurs and the high content of sp^3 carbon indicates the strong reactivity of the double bond present in the ethylene structure.
The oxygen uptake observed can be ascribed to contaminations in the discharge and/or to post-deposition reactions with atmospheric oxygen or water. It has been observed that by increasing the total gas flow rate, i.e. by reducing the gas residence time, the oxygen content of the coating can be reduced. The moderate ageing of the coating, evaluated with the oxygen uptake during storage indicate that the coatings are quite stables and do not contain high quantities of reactive species.
Since any evidence of powders formation has been obtained it is possible to suppose that the contribution of gas phase reaction to the polymerization process is quite low and that gas-surface reaction plays the major role. The results of GC-MS investigation and in particular the low concentration of by-products support this hypothesis, in fact only butane, derived from ethylene dimerisation, is formed in appreciable quantity.
Further investigations will be carried out for a better comprehension of the deposition mechanism.

Acknowledgements

Dr. Françoise Massines and Dr. Nicolas Gherardi (Laboratoire de Génie Electrique de Toulouse, Université Paul Sabatier, Toulouse, France) are gratefully acknowledged for the scientific support in the assembling of the experimental set-up.

References

[1] S. Kanazawa; M. Kogoma, T. Moriwaki, S. Okazaki - J. Phys. D: Appl. Phys. **21**, 5, 838-40 (1988).
[2] T. Yokoyama, M. Kogoma, T. Moriwaki, S. Okazaki - J. Phys. D: Appl. Phys. **23**, 1125-1128 (1990).
[3] S. Okazaki, M. Kogoma, M. Uehara, Y. Kimura - J. Phys. D: Appl. Phys. **26**, 889-892 (1993).
[4] F. Massines, A. Rabehi, P. Decomps, R. Ben Gadri, P. Segur, C. Mayoux - J. Appl. Phys. **83**, 2950-57 (1998).
[5] N. Gherardi, G. Gouda, E. Gat, A. Ricard, F. Massines - Plasma Sources Sci. Technol. **9**, 340-346 (2000).
[6] J. Robertson - Materials Science and Engineering **R 37**, 129-281(2002).
[7] N. V. Novikov, M. A. Voronkin, S. N. Dub, I. N. Lupich, V. G. Malogolovets, B. A. Maslyuk, G. A. Podzayarey - Diam. Relat. Mater. **6**, 574-578 (1997).

[8] N. Mutsukura, K. Miyatani - Diam. Relat. Mater. **4**, 342-345 (1995).
[9] P. Courdec and Y. Catherine - Thin Solid Films **146**, 93-107 (1987).
[10] H. Kobayashi, A. T. Bell and M. Shen - Macromolecules **7**, 3 (1974).
[11] K. G. Donohoe, T. Whydeven - J. Appl. Polym. Sci. **23**, 2591-2601 (1979).
[12] T. Yokoyama, M. Kogoma, S. Kanazawa, T. Moriwaki, S. Okazaki - J. Phys. D: Appl. Phys. **23**, 3, 374-7 (1990).
[13] O. Goossens, E. Dekempeneer, D. Vangeneugden, R. Van de Leest, C. Leys - Surf. Coat. Technol. **142-144**, 474-481 (2001).
[14] O. Goossens, S. Paulassens, D. Vangeneugden, H. Vrielinck, F. Callens, C. Leys and J. Meneve - New Diamond Frontier Carbon Technol. **13**, 4, 221-229 (2003).
[15] C.-P. Klages, M. Eichler and R. Thyen - New Diam. Front. Carb. Technol. **13**, 4 (2003).
[16] S. P. Bugaev, A. D. Korotaev, K. V. Oskomov and N. S. Sochugov - Surf. Coat. Technol. **96**, 123-128 (1997).
[17] D. Liu, G. Benstetter, Y. Liu, X. Yang, S. Yu and T. Ma - New Diam. Front. Carb. Technol. **13**, 4 (2003).
[18] R. Thyen, A. Weber, C.-P. Klages - Surf. Coat. Technol. **97**, 426-434 (1997).
[19] D. Liu, S. Yu, Y. Liu, C. Ren, J. Zhang, T. Ma - Thin Solid Films **414**, 163-169 (2002).
[20] NIST and Wiley libraries in MassLab Release 1.4 (GC/MS Data System Software Finngan).
[21] T. Nozaki, Y. Miyazaki, Y. Unno and K. Okazaki - J. Phys. D: Appl. Phys. **34**, 3383-3390 (2001).
[22] L. Mangolini, K. Orlov, U. Kortshagen, J. Heberlein, and U. Kogelschatz - Appl. Phys. Lett. **80**, 10 (2002).
[23] B. Dischler, A. Bubenzer and P. Koidl - Solid State Communications **48**, 2, 105-108 (1983).
[24] J. Rinstein, R. F. Stief, L. Ley and W. Beyer - J. Appl. Phys. **84**, 7 (1998).
[25] W. Jacob and M. Unger - Appl. Phys. Lett. **68**, 4, 475-477 (1996).
[26] I. Retzko, J. F. Friedrich, A. Lippitz, W. E. S. Unger - J. Elect. Spectro. Relat. Phenom. **121**, 111-129 (2001).

Effects of the spraying parameters on the evaporation of the sprays in radio frequency inductively coupled plasmas

Yanguang Shan, Javad Mostaghimi

Centre for Advanced Coating Technologies
Department of Mechanical & Industrial Engineering, University of Toronto, Canada

Abstract
A spray model was developed to study the effects of the spraying parameters on the evaporation and transportation of liquid spays in a 20.0 kW plasma torch. The heights that the spray can reach in the torch were predicted for a variety of spray parameters and hydrocarbon liquids. It was found the increase of the spray cone angle increases heat transfer between the spray and the plasma. The height of complete evaporation for liquid sprays increases with the increase of the liquid mass flow rate and droplet size.
Keywords: Spray model; liquid sprays; evaporation and transportation; inductively coupled plasma

1. Introduction

The trend in plasma synthesis and deposition processing has been that of the increasing use of the radio frequency inductively coupled plasma (RF-ICP) and the liquid or solution precursors. The radio frequency inductively coupled plasma has relatively large volume, lower plasma velocity, and more uniform temperature distribution. It allows better process control and axial material injection. In solution plasma spraying and thermal plasma chemical vapor deposition, liquid precursors are injected into the radio frequency inductively coupled plasma along the axial direction via a spray, where exposure to high temperatures makes them evaporate, decompose and react, and then form a hard coating/film onto a solid substrate. Wilden *et al.* [1] and Bouyer *et al.* [2] deposited silicon carbide (SiC) film by feeding different liquid precursors into a radio frequency inductively coupled plasma reactor. The properties of the sprayed or deposited coatings or films are extremely sensitive to process parameters. These include the torch operating conditions, droplet size distribution of the spray, the spray trajectory and evaporation within the discharge, species diffusion and reaction, substrate position and temperature. To get better quality coatings or films, it is necessary to understand the effect of these spraying parameters on the spraying process.

2. Models

A typical RF-ICP torch geometry is schematically shown in Fig.1.The model used here is an extension of the model developed by Mostaghimi [3]. The plasma was assumed to be in local thermodynamic equilibrium state, laminar and incompressible flow, 2-D axi-symmetric and optically thin. Both displacement currents and viscous dissipation effects were neglected. The time-dependent equations governing the conservation of mass, momentum, and energy along with the vector potential form of Maxwell's equations were solved simultaneously to get the temperature and flow fields of the plasma.

$$\frac{D\rho}{Dt} + \rho\nabla\cdot\vec{u} = S_c^s, \tag{1}$$

$$\rho\frac{D\vec{u}}{Dt} = -\nabla P + \nabla\cdot\mu\nabla\vec{u} + \vec{j}\times\vec{B} + \vec{S}_m^{\,s}, \tag{2}$$

$$\rho\frac{Dh}{Dt} = \nabla\cdot k\nabla T + \vec{j}\cdot\vec{E} - Q_R + S_E^{\,s}, \tag{3}$$

$$\rho\frac{DY}{Dt} = \nabla\cdot D_{AB}\nabla Y + S_c^{\,s}. \tag{4}$$

$$\mu_0\sigma\frac{\partial A_R}{\partial t} = \nabla^2 A_R - \frac{A_R}{r^2} + \mu_0\sigma\omega A_I, \quad (5)$$

$$\mu_0\sigma\frac{\partial A_I}{\partial t} = \nabla^2 A_I - \frac{A_I}{r^2} - \mu_0\sigma\omega A_R, \quad (6)$$

where ρ is the plasma density, t is time, P is pressure, μ is the viscosity, k is the thermal conductivity, D_{AB} is the diffusion coefficient , h is the enthalpy, T is the temperature, $\vec{u}$ is the velocity vector, Y is the vapor mass fraction, $\vec{j}$ is the current density vector and $\vec{j} = \sigma\vec{E}$, σ is the electrical conductivity, $\vec{B}$ is the magnetic induction, $\vec{E}$ is the electric field intensity, Q_R is the volumetric radiative loss, S_c^s, S_m^s, and S_E^s represent source terms due to plasma-spray interaction effects [4]. μ_0 is the permeability of free space. A_R and A_I are the real and imaginary parts of the vector potential, respectively. Details of the source terms and the initial and boundary conditions of this model can be found in Ref. [4].

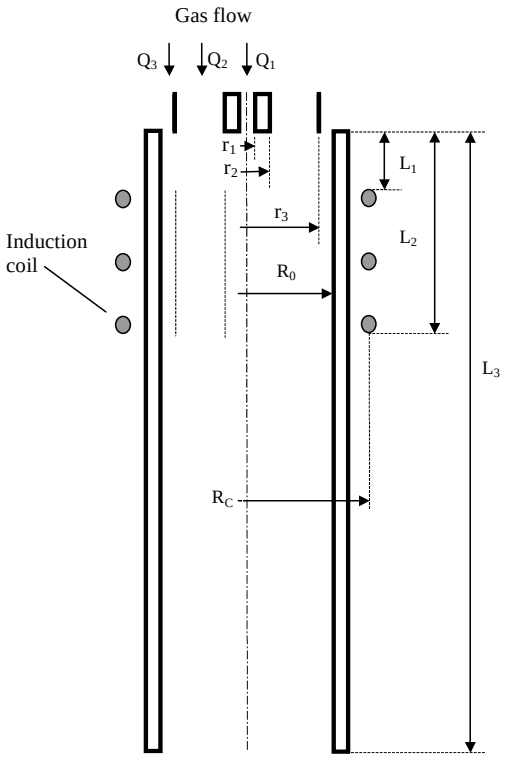

Figure 1 Torch geometry

The evolution of the spray was obtained by solving the spray equation [5]

$$\frac{\partial f}{\partial t} + \nabla_{x_i}\cdot(f\phi_i) = \dot{f}_{coll}, \quad (7)$$

where f is droplet probability distribution function, $\dot{f}_{coll}$ is the source term due to droplet collisions, x_i represents $\vec{x}, \vec{v}, r_d, T_d$, ϕ_i represents $\vec{v}$ $\vec{F}$, R, and $\dot{T}_d$, which are time change rates of velocity, radius and temperature for an individual droplet. $\vec{x}$ is the droplet position, $\vec{v}$ is the droplet velocity, r_d is the equilibrium radius of droplet, T_d is the droplet temperature which is assumed to be uniform within the droplet. The trajectory and evaporation model for an individual droplet is given in the Ref [4]

The droplet collisions calculation was performed for a pair of droplets if, and only if, they are in the same computational cell. Two types of collisions are accounted for. If the collision impact parameter b is less than a critical value b_{cr} the droplets coalesce, if b exceeds b_{cr} , the droplets maintain their sizes and temperatures but undergo velocity changes. The details for the calculation of droplet collisions were given in Ref. [5].

The spray model was implemented into the plasma model. The plasma phase was solved using SIMPLER method [6]. A stochastic Monte Carlo technique combined with the discrete particle method was used to determine the characteristics of the spray and the interactions between the spray and the plasma gas, as well as the droplet collisions within the spray [4, 5].

3. Results and discussion

The torch geometry and typical operating parameters of the ICP are listed in Table 1. All symbols in Table 1 correspond to those of Figure 1. First, the water spray was used in the calculations. A spray parametric study was followed. These parameters include: the liquid mass flow rate, the droplet size distribution, the spray cone angle,

and the injection velocity. The evaporation and the collisions of hydrocarbon spray droplets in plasma are also predicted. For the poly-disperse spray, the x-squared droplet size distribution with a 15.0 μm SMD (Sauter Mean Diameter) was used (Fig. 2). Droplets are introduced into the plasma from random positions behind the exit of the center tube of the torch. Droplet collisions model was turned off unless indicated.

Table 1 Torch geometry and typical operating parameters.

r_1: 0.5 mm	R_0: 25.0 mm	L_2: 74.0 mm	Inlet swirl:20.0 m/s	Q_1 (Ar): 3.0 L/min
r_2: 4.0 mm	R_c: 33.0 mm	L_3: 200.0 mm	Frequency: 0.5 MHz	Q_2 (Ar): 25.0 L/min
r_3: 20.0 mm	L_1: 10.0 mm	No. coils: 3	Forward Power: 20.0 kW	Q_3 (Ar): 72.0 L/min

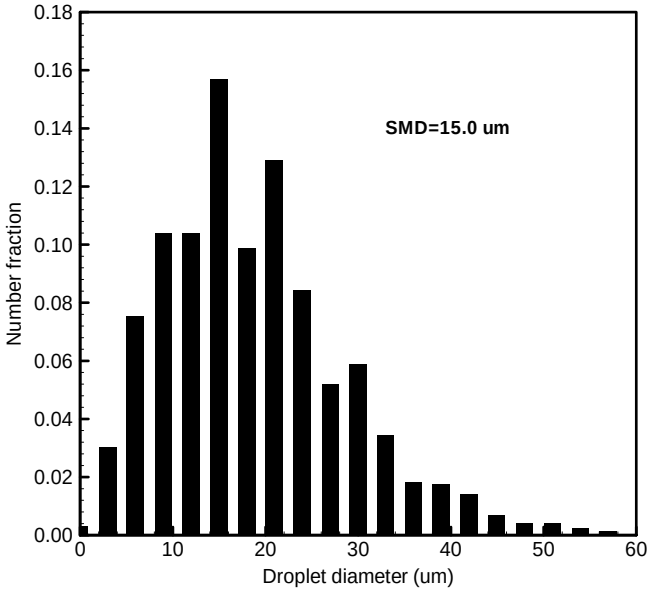

Figure 2 Droplet size distribution with SMD=15.0 μm.

3.1 Plasma fields and the spray evolution

Figure 3 shows the predicted quasi-steady state temperature, flow, and concentration fields of the plasma with the spray pattern. Very large gradients are evident. It can be seen that the plasma is cooled locally along the spray region. The droplets of the spray are delivered to downstream by the plasma gas. As the spray travels through the plasma, it evaporates and the vapor diffuses into the plasma gas.

3.2 The effect of the liquid mass flow rate on the spray evaporation

In this case, the liquid was injected into the plasma at mass flow rates of 1.0g/min, 3.0g/min, and 5.0g/min, respectively. The spray was poly-disperse with SMD=15.0 μm. The initial velocity of the injected droplets was 15.0 m/s. The spray cone angle was 15.0°. The maximum height where the spray completely evaporates in the plasma torch was recorded. The model predicts that a poly-disperse spray with a 7.5 μm SMD survives 108.5 mm, 117.1 mm, and 127.9 mm at liquid mass flow rates of 1.0 g/min, 3.0 g/min, and 5.0 g/min, respectively. As expected, since the increase of the mass flow rate leads to an increased cooling of the plasma, the height of complete evaporation of the spray in the plasma increases with the increase of the spray mass flow rate.

3.3 The effect of the spray cone angle on the spray evaporation

The liquid was injected into the plasma with different spray cone angles (0°, 15°, and 30°) at a 3.0 g/min mass flow rate. The other parameters were the same as those in section 3.2. The model predicts that a poly-disperse

spray with a 15 μm SMD survives 124.0 mm, 117.1 mm, and 114.9 mm at spray cone angles of 0°, 15°, and 30°, respectively. The height of complete evaporation decreases with the increase of the spray cone angle. It also shows that the effect decreases with the increase of the spray cone angle. This is because the increase of the spray cone angle leads to increased heat transfer between the spray and the plasma, but the droplets of the spray cannot penetrate into the high temperature region anymore when the spray cone angle reaches a certain value.

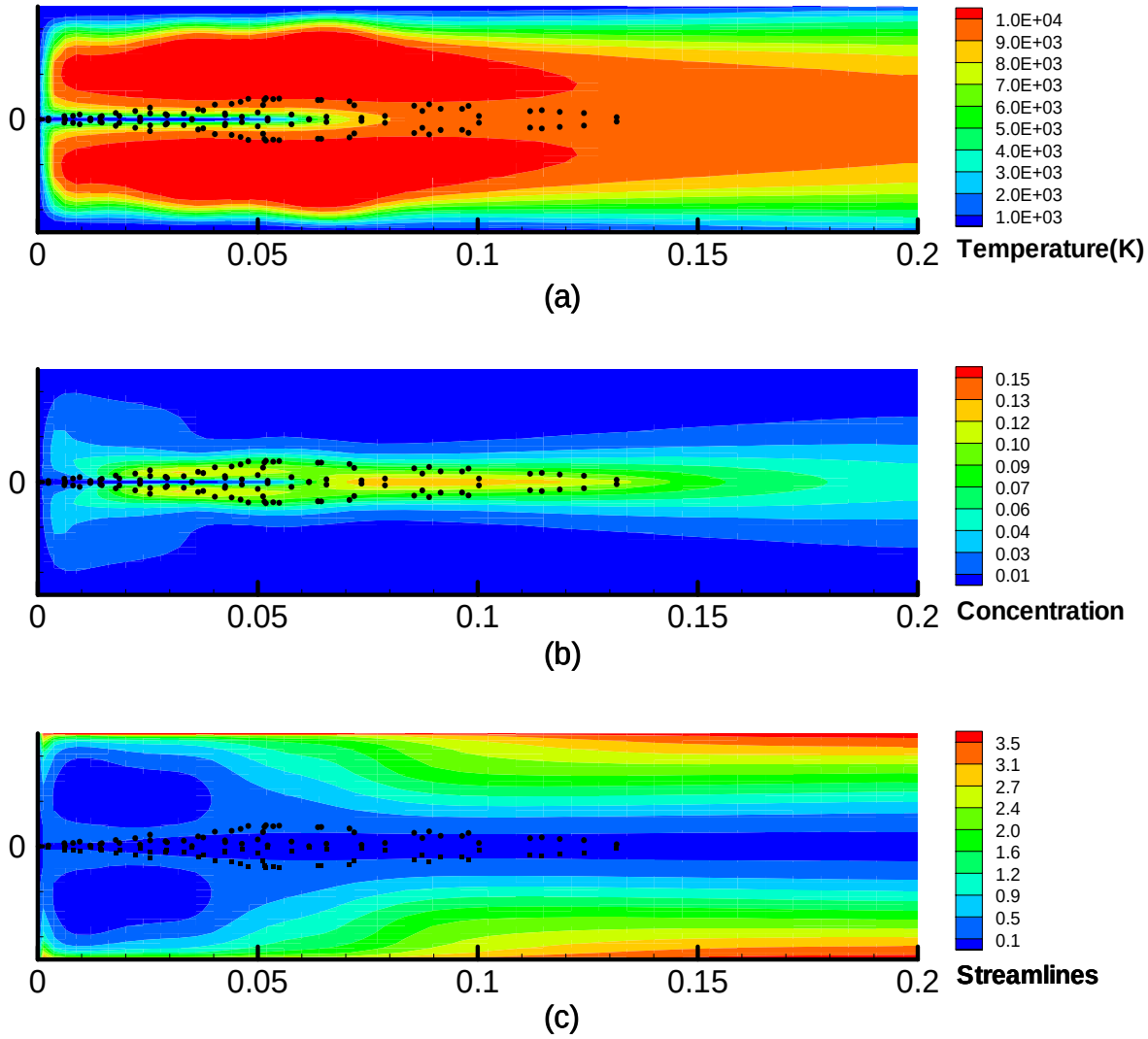

Figure 2: Plasma temperature, flow, and concentration fields with the spray pattern. (a) Temperature, (b) Vapor mass concentration, and (c) Normalized streamlines.

3.4 The effect of the injection velocity on the spray evaporation

The liquid was injected into the plasma with different initial velocities (5.0 m/s, 10.0 m/s, and 15.0 m/s) at a 3.0 g/min mass flow rate. The other parameters were the same as those in section 3.2. The model predicts that a poly-disperse spray with a 15 μm SMD survives 122.1 mm, 119.6 mm, and 117.1 mm at injection velocities of 5.0 m/s, 10.0 m/s, and15.0 m/s, respectively. Since the spray with a lower injection velocity leads to increased local cooling of the plasma than the spray with a higher injection velocity, the height of complete evaporation of the spray decreases with the increase of the injection velocity. However, if the injection velocity reaches such a value that the spray cannot obtain enough heat to evaporate, the height of complete evaporation of the spray will increase with the increase of the injection velocity.

3.5 The effect of the droplet size on the spray evaporation

The liquid was injected into the plasma with different Sauter mean diameters (10.0 μm, 15.0 μm, and 20.0 μm) at a 3.0 g/min mass flow rate. The other parameters were the same as those in section 3.2. The model predicts that the spray with a 10.0 μm SMD survives 103.4 mm, the spray with a 15.0 μm SMD survives 117.1 mm, and the spray with a 20.0 μm SMD survives 138.8 mm in the plasma, respectively. As expected, the height of complete evaporation of the spray increases with the increase of the Sauter mean diameter.

3.6 Modeling the evaporation of hydrocarbon sprays

The studies in previous sections were focused on the injection of water sprays into the radio frequency inductively coupled plasma. In thermal plasma chemical vapor deposition and hazardous liquid waste destruction technologies, hydrocarbon sprays are of great theoretical and practical importance. The injection and evaporation of several hydrocarbon sprays in the inductively coupled argon plasma was simulated in this section. Those hydrocarbon sprays are heptane (C_7H_{16}), dodecane ($C_{12}H_{26}$), and hexadecane ($C_{16}H_{34}$).

The hydrocarbon sprays were injected into the plasma at a mass flow rate of 3.0g/min. The spray was poly-disperse with SMD=15.0 μm. The initial velocity of injected droplets was 15.0 m/s. The spray cone angle was 15.0°. The droplet collision model was used to investigate the effect of droplet collisions on the evaporation of the spray. The results are shown in Table 2. The results in Table 2 show that droplet collisions in all cases lead to an increase in the height of complete evaporation for the liquid spray.

Table 2: The height of complete evaporation for hydrocarbon sprays in the plasma

Substances	The height of complete evaporation in the plasma	
	Without collisions	With collisions
Heptane (C_7H_{16})	57.5 mm	63.4 mm
Dodecane ($C_{12}H_{26}$)	64.3 mm	78.3 mm
Hexadecane ($C_{16}H_{34}$)	67.4 mm	77.2 mm
Water (H_2O)	117.1 mm	155.2 mm

4. Conclusions

A stochastic spray model was used to simulate the injection of liquid sprays into a 20 kW radio frequency inductively coupled plasma. The effects of spray parameters on the evaporation of liquid sprays were investigated. It was found that the liquid mass flow rate and the droplet size are the most important factors that influence the evaporation of the spray. The height of complete evaporation for liquid sprays increases with the increase of the liquid mass flow rate and droplet size. The increase of the spray cone angle leads to an increased heat transfer between the spray and the plasma. Droplet collisions may lead to an increase in the height of complete evaporation for the liquid spray. This model was also able to predict the evaporation and transportation of hydrocarbon sprays in the plasma under different operating conditions.

References

[1] J. Wilden, A. Wank, M. Asmann, J. Heberlein, *et. al*., Appl. Organometal. Chem., 15 (2001) 841.
[2] E. Bouyer, G. Schiller, M. Muller and R. Henne, Plasma Chem. and Plasma Process., 21 (2001) 523.
[3] J. Mostaghimi, K. C. Paul, and T. Sakuta, J Appl. Phys., 83 (1998) 1898.
[4] Y. Shan and J. Mostaghimi, Spectrochim. Acta Part B, 58 (2003) 1959.
[5] Y. Shan and J. Mostaghimi, Plasma Chem. and Plasma Process., 25 (2005) 193.
[6] S. V. Patankar, Numerical Fluid Flow and Heat Transfer, McGraw-Hill, New York, 1980.

Spectroscopic characterization of the non-isothermality in the atmospheric pressure air jet plasma in the blowing arc discharge

V.Ya. Chernyak[1], V.V. Naumov[2], I.I. Prisyazhnevich[1],
Yu.I. Slusarenko[1], V.V. Yukhymenko[1]

[1]*Plasma Lab, Dept. of Physical Electronics, Faculty of Radiophysics, Taras Shevchenko Kyiv National University*
Prospect Acad. Glushkova 2/5, 03122 Kyiv, Ukraine; e-mail: chern@univ.kiev.ua
[2]*Photonics Lab, Institute of Fundamental Problems for High Technology, Ukrainian Academy of Science*
Prospect Nauki 45, 03028 Kyiv, Ukraine; e-mail: naumov@ifpht.kiev.ua

Abstract
A specific case of the nonequilibrium atmospheric pressure air jet (APAJ) plasma in the blowing arc discharge is studied by optical emission spectroscopy (OES). From relative intensities of atomic lines and molecular bands, the temperatures of excitation of electronic states of free atoms, T_E, and vibrational and rotational states of molecules, T_V and T_R, were determined in different conditions. It is found there is no local LTE in APAJ plasma during its space/time evolution, and effects of the strong non-isothermally, $T_E > T_V > T_R$, have a place.
Keywords: plasma chemistry, blowing arc discharge, air jet plasma, non-equilibrium, non-isothermality

1. Introduction

Spectroscopic characterization of the air plasma in electric discharges is of permanent interest in many labs because of various important applications in plasma chemistry [1]. From the optical spectra emitted by plasma one can deduced all basic plasma parameters and its state: composition of chemical elements (according to emitted lines), populations of excited atoms and molecules upon energetic levels (from the intensity of spectral lines), densities of charged and neutral particles (from the broadening of spectral lines), temperatures of excitation of atomic and molecular states (from the relative or absolute spectral intensities). The main condition is a correct use of spectroscopic diagnostics in every specific case, e.g. application of the approximation of the optically thin plasma in conditions of high pressure, approximation of plasma quasi-neutrality and approximation of the local thermodynamic equilibrium (LTE) in conditions of high non-isothermality when characteristic temperatures of different plasma components may be differenced within the relation: electron temperature $T_e >$ vibrational temperature $T_V >$ rotational temperature $T_R \geq$ translation gas temperature T_g [2].

The factor of non-izothermality has a fundamental importance for efficiency of plasma-chemical processes in reactive plasma. While most of the discharge energy goes into the mean energy of electrons and not just to the gas heating, it gives the desirable reactivity and selectivity of plasma-chemical transformations [3]. Among possible types of nonequilibrium discharges: spark, corona, barrier, etc [4] which can produce non-thermal plasmas at high atmospheric pressures, one specific case is very interesting for us. This is a transverse arc in a blowing flow with a stationary current column or with a rotating one in a vortex flow. It is an intermediate case of the high-voltage low-current self-sustained discharge with a self-adjustable arc supported by the plasma flow [5]. It differs from the non-stationary gliding arc of Czernichowski type [6] by the fixed arc length. It also has a convective cooling of the plasma column by airflow but without conductive heat losses at the walls since this is a free arc jet. An intensive transverse ventilation of the arc plasma increases its ionization non-equilibrium and non-isothermality [7]. The blowing arc was tested successfully in different variants with the primary and secondary discharges in our current investigations in Kiev University for the plasma processing of various homo- and hetero-phase gaseous and liquid substances [8-9]. However, despite of achievements in practical applications, there are still enough issues for research. One of the main points is a mechanism of the transition from the quasi-equilibrium to non-equilibrium, i.e. from the thermal to non-thermal ionization.

In this work, we present results of our spectroscopic characterization of the air plasma in the transverse blowing arc discharge at atmospheric pressure conditions in order to determine the level of plasma non-isothermality and get more deep understanding in physics of non-equilibrium processes in such discharge.

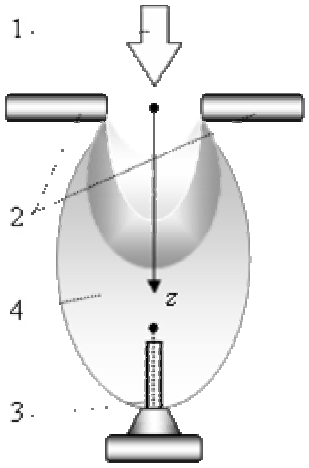

Fig.1. Scheme of the transverse blowing arc discharge: 1 is an air nozzle, 2 are the electrodes, 3 is the probe, 4 is the air plasma jet.

2. Experimental Methodology

Experiments were done for a scheme of the transverse blowing arc as shown in Fig.1. A free air jet ran from the nozzle top-down across two opposite electrodes where the discharge was burned and formed a bright crescent-shaped electric arc as well as a highly reactive plasma afterglow. We used the rod electrodes with diameter d = 6 mm. A nominal gap between electrodes from which we started was δ = 1 mm. Since electrodes were not cooled, the electric discharge energy was transferred totally to the air plasma. We applied electrodes made from the copper and graphite in order to see a spectroscopic difference. The air nozzle was axisymmetric, with the inner diameter $\varnothing$ = 1 mm, made from the stainless steel. It was installed vertically perpendicular to the electrode axis at the nominal length L= 20 mm and centered between electrodes. We used a standard technical air system supply with the flow controller. It was a high enough gasdynamic pressure in the airflow to blow out the electric arc downstream. In fact, we can regulate the arc discharge geometry as by the gap δ between electrodes and by the length L between the nozzle exit and electrodes. The last allows to control both the air blowing of the arc and the air cooling of electrodes. Then, we can regulate the airflow rate, G, and discharge current, I_d, in order to vary a process. The discharge was powered by the HV DC source with a dropping output characteristics at the ballast resistance in the circuit. Current-voltage parameters were measured by the standard digital electronics. For optical diagnostics, a classic method of optical emission spectroscopy was applied. The plasma radiation was detected by two means: 1) portable rapid PC-operated CCD-based multi-channel optical spectrometer MOSA (F/5, 1200 l/mm grating, 3648-pixel array TCD1304AP) that provides a wide wavelength survey within 200-1100 nm with a spectral resolution 0.3 nm; and 2) spectral machine KSVU23, including the scanning monochromator MDR23, photomultiplier FEU100, ADC controller and PC recorder, which provided a high spectral resolution up to 0.01 nm within 200-800 nm but slow scan speed. Measurements were conducted in different cross-sections along the arc jet. Images were normally focused by the quartz lens at the bench 5-focus distance from the arc directly on the spectral device entrance slit (0.025x0.2 mm). In case of MOSA, a fine long UV optical fiber with the microlens focusing was used. The spatial pointing accuracy was about 0.1 mm. For calibration, the etalon spectral sources: mercury, deuterium, and tungsten lamps were applied. Within the available spectrum of UV-VIS-NIR wavelengths, we monitored all remarkable emissions and identified all basic atomic lines of N, O, H as well as molecular bands of NO, N_2, O_2, OH and other excited species, which we were able to recognize [10]. For temperature diagnostics, we utilized relative intensities of the analytical CuI lines (a product of the electrode emission) and OI lines in order to determine the temperature of electronic states of free atoms, T_E, and we used the N_2 $2^{(+)}$ bands (a dominating component of the plasma-forming gas) in order to determine the temperature of vibrational states of excited molecules, T_V, by the Ornstein method as a commonly accepted approach in the thermal plasma [11]. This method does not require a calibration but for accuracy it needs well-resolved spectral lines covering the maximum difference in energies. It is assumed that plasma is optically thin and spectral lines are not self-absorbed. The gas kinetic temperature T_g was derived from the temperature of rotational molecular states, T_R, that is, because of a non-resolved rotational spectral structure, determined by the comparison of the measured spectral profile of individual N_2 $2^{(+)}$ bands and the theoretical spectra calculated on the known molecular constants for the N_2 *E-V-R* transitions, assuming the Boltzmann population distribution and using the Gauss-like instrumental line shape function $\Delta\lambda$. The necessary spectroscopic data were taken from the databases [12-13]. Errors in measurements of the emissivity did not exceed ±30%, temperatures were determined with the uncertainty ±15%. In order to increase the accuracy of measurements in conditions of spatial/temporal instabilities of the burning arc, the procedure of statistical averaging was performed. The min. exposure time was 7 ms, time between scans was 1 μs, max. signal accumulation time was 4 s. On this base, we draw the curves of changes of the specific emission intensities and characteristic temperatures along the plasma flow depending on the discharge current I_d and the airflow rate G. The overall studies were conducted within the range of variations I_d = 100-1000 mA and G = 20-220 cm^3/s at atmospheric pressure conditions.

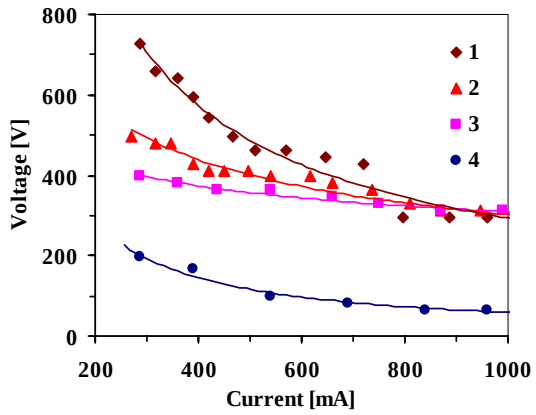

Fig.2. *I-V* curves of the blowing arc discharge in the air flow: G = 75 cm^3/s (curve 1), 40 cm^3/s (2), 20 cm^3/s (3), and 0 cm^3/s (4). P = 1 atm. Cu rod electrodes: d = 6 mm, δ = 1.5 mm, L = 20 mm.

3. Results and Discussions

A transverse arc discharge in the airflow was ignited with a high voltage at the shortest distance between the electrodes that corresponds to breakdown when the electric field reached ~3 kV/mm [4]. Under the action of the gasdynamic pressure of the incident air flow, the electric arc was forced to bow down and elongated along the stream, so that the current increased and the voltage dropped down a little bit. The air flow led not only to bending and to blowing of the arc current channel but also to stabilization of the plasma column due to the convective withdrawal of energy (radiative losses are neglected). Due to a high-speed flow, the air plasma jet had to be turbulized, and this additionally contributed to the suppression of the ionization-overheating instability in plasma. Thus, gas dynamics and convective heat mass transfer favored the steady arc burning.

Fig.2. shows the typical current-voltage characteristics of the transverse blowing arc discharge in comparison with the usual arc in air. As is seen, in the range of low currents the *I-V* curves have a dropping character as for the high-voltage discharges. It points out that the blowing arc has a self-adjusting length, and the current channel in the airflow is auto-stable despite of all visible non-uniformity and fluctuations in time and space. With the increasing airflow rate, the electric field strength increases. But in the range of high currents, the voltage becomes independent on the airflow rate. It is explained by the saturation of the carrying capacity of the electric arc in the discharge at the given geometry of electrodes.

Fig.3 shows a typical spectrum of the emission of the air plasma in the studied discharge as registered by MOSA (exposure time 20 ms). We see it is rich of spectroscopic information. We recognized here the nitride oxide NO γ-system ($A^2\Sigma^+$-$X^2\Pi$: (0-0) 226.3, (0-1) 236.3, (0-2) 247.1 nm, etc); nitrogen N_2^+ $1^{(-)}$ system ($B^2\Sigma^+_u$-$X^2\Sigma^+_g$: (0-0) 391.4, (1-0) 358.2, (1-1) 388.4, (0-1) 427.8 nm), N_2 $2^{(+)}$ system ($C^3\Pi_u$-$B^3\Pi_g$: (0-0) 337.1, (0-1) 357.7, (0-2) 380.5, (1-0) 315.9 nm, etc), and even weak N_2 $1^{(+)}$ system ($B^3\Pi_g$-$A^3\Sigma^-_u$: 570-750 nm). Among atomic lines, we identified hydrogen HI lines (Ballmer Hα 656.3, Hβ 486.1 nm), oxygen OI lines (777.3, 844.6, 926.0 nm), and nitrogen NI lines (746.8, 818.8, 868.3 nm). There are a lot of copper CuI lines due to the evaporation of electrodes (in case of graphite electrodes we saw nothing) but the strongest lines 324.7 and 327.4 nm are over-saturated, others are overlap with some N_2^+ $1^{(-)}$ and N_2 $2^{(+)}$ bands, so for diagnostics only CuI 510.5, 515.3, 521.8 and 578.2 nm were used. The choice of molecular bands for diagnostics was also optional because they were not always observed well. Thus, the interference of CuI lines and N_2 $2^{(+)}$ bands precluded the diagnostics of the OH $A^2\Sigma$-$X^2\Pi$ (0-0) bands at 306.4-308.9 nm. The appearance of the CN $B^2\Sigma^+$-$X^2\Sigma^+$ Violet bands at 388 nm and NH $A^3\Pi_i$-$X^3\Sigma^-$ UV band at 336 nm in the regime of high currents disturbed the diagnostics of nearby N_2^+ $1^{(-)}$ and N_2 $2^{(+)}$ bands. The NO γ-bands sometime were 3-5 times weaker. Therefore, the most results were obtained with the N_2 $2^{(+)}$ bands (0-0) 337.1, (2-4) 371.0, (1-3) 375.5, (0-2) 380.5, and (1-4) 399.8 nm. The band (1-4) was less intensive than the band (0-0) but it had a distortion-less spectral profile provided better *V-R* diagnostics.

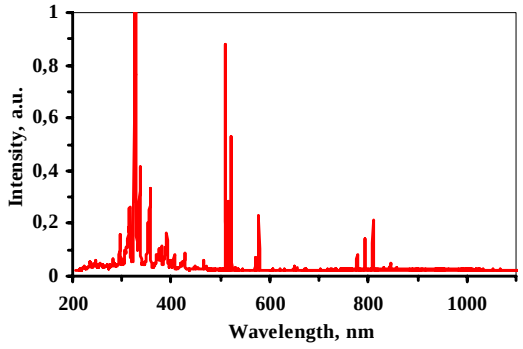

Fig.3. Emission spectrum of air plasma in the blowing arc discharge. P = 1 atm, G = 75 cm^3/s, U_d=0.6 kV, I_d = 400 mA, Cu electrode. z = 3 mm. $T_e \approx$ 0.7 eV; $T_V \approx$ 0.3 eV, $T_R \approx$ 0.1 eV.

A distinguishing feature of the plasma column in the transverse blowing arc discharge is their curvature along the flow, and so all dependencies of the emission intensities and spectral distributions in the plasma along the z-axe downstream are of non-linear character. Fig.4 shows typical dependencies of the emissivity I_λ(z) for the CuI line 510.5 nm in the discharge along the flow. Here, normalized curves 1-5 correspond to the airflow rates G = 40, 75, 110, 150, 190 cm^3/s and discharge current I_d = 200 mA. The absolute emissivity $I_{\lambda Cu}$ changes very much with

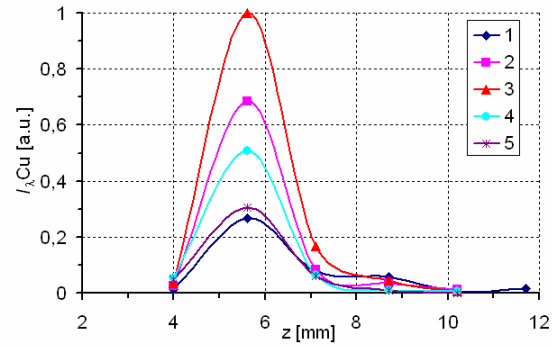

Fig.4. Emissivity of the CuI line 510.5 nm along the air plasma flow: G = 40 cm^3/s (curve 1), 75 cm^3/s (2), 110 cm^3/s (3), 150 cm^3/s (4), and 190 cm^3/s (5). I_d = 200 mA.

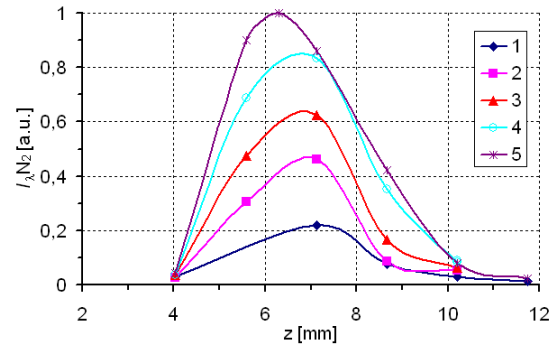

Fig.5. Emissivity of the N_2 $2^{(+)}$(0-0) band 337.1 nm along the air plasma flow: G = 40 cm^3/s (curve 1), 75 cm^3/s (2), 110 cm^3/s (3), 150 cm^3/s (4), and 190 cm^3/s (5). I_d = 200 mA.

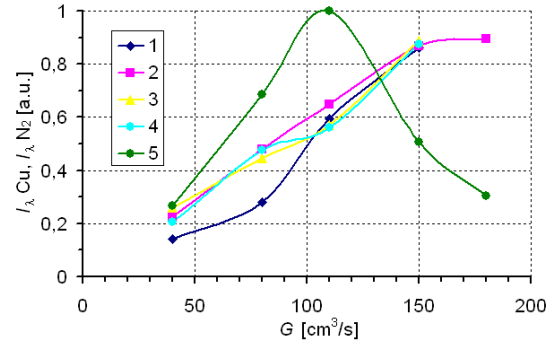

Fig.6. Emissivity of the N_2 $2^{(+)}$(0-0) band 337.1 nm (curves 1-4) and CuI line 510.5 nm (curve 5) vs. the airflow rate G. I_d = 100 mA (curve 1), 200 mA (2,5), 300 mA (3), and 400 mA (4). z = 5.5 mm.

the airflow rates G but the spatial position of its maximum I_λ^{max} at the distance z = 5.5 mm from the electrode axis and its longitudinal length $\Delta z \approx 2$ mm for all curves are almost constant. It tells about the quasi-stability of the arc current channel in the range of the used flow rates at the given arc discharge geometry. The observed effect of the "ignition" of the luminescence of electronically excited Cu atoms in the discharge plume tells about the overheating of electrons resulted from the kinetic non-equilibrium conditions in the gasdynamically moving and convectively cooling air plasma.

The distribution of the emission intensity of the N_2 $2^{(+)}$ head bands along the z-axe of the discharge also is non-monotonic character. Fig.5 shows typical dependencies of the emissivity $I_\lambda(z)$ for the N_2 $2^{(+)}$ (0-0) band 337.1 nm in the plasma along the flow. Here, normalized curves 1-5 also correspond to the airflow rates G = 40, 75, 110, 150, 190 cm^3/s and discharge current I_d= 200 mA. The comparison of longitudinal distributions $I_{\lambda Cu}$ and $I_{\lambda N2}$ in Fig.4 and Fig.5 tells that the $I_{\lambda N2}$ distributions are sufficiently larger and someway shifting downstream relatively to the $I_{\lambda Cu}$ curves. At the distance z = 10 mm the N_2 $2^{(+)}$ (0-0) emission is still visible, and taking into account the flow rate, we can estimate that the residence time of the excited species in the plasma flow is 0.5-2 ms. With above notes about the arc current channel and plasma dynamics, it evidences that the afterglow in this discharge is conditioned by the emission of electronically excited N_2 molecules.

With the discharge current I_d the absolute emissivity $I_{\lambda N2}$ 337.1 nm increased (by few tens percent) but it reacted more strongly (in direct proportion) to the increase in the airflow rate G. It is illustrated in Fig.6 by curves 1-4, taken at the distance z ≈ 5.5 mm for different values I_d = 100, 200, 300, 400 mA (see also Fig.5). In comparison with the almost linear dependence $I_{\lambda N2}(G)$, the dependence $I_{\lambda Cu}(G)$ is non-linear. This is clear shown in Fig.6 by the curve 5, given for the $I_{\lambda Cu}$ 510.5 nm at z ≈ 5.5 mm and I_d = 200 mA (see also Fig.4). The functional extreme of $I_{\lambda Cu}$ is obtained at G = 110 cm^3/s. Such behavior of the CuI emission can be explained by the fact that, on the one side, the increasing G at the fixed I_d should lead to the increase of the level of nonequilibrium of the air plasma due to the acceleration of the energy carry-over from the arc current channel, and therefore to the increase of the emissivity of Cu atoms. On the other side, with the increasing of the air flow and air-cooling, the erosion of electrodes and therefore the emission of Cu atoms decreased.

On the base of the measured relative intensities $I_{\lambda Cu}$ and $I_{\lambda N2}$, assuming the partial Boltzmann distribution and using the Boltzmann plot, the temperatures of electronic excitation of Cu atoms, T_E, and vibrational excitation of N_2 molecules, T_V, were determined. In this technique, the plot $\ln(I_{\lambda Cu}\lambda^3/gf) = \ln C - E_E/kT_E$ vs. E_E gives T_E (here E_E is the excitation energy, g is the statistical weight, f is the probability of atomic transition, C is a constant for all CuI lines); and the plot $\ln(I_{\lambda N2}\lambda^4/q) = \ln B - E_V/kT_V$ vs. E_V gives T_V (here E_V is the vibrational energy, q is the FCF probability of vibrational transition, B is the constant for

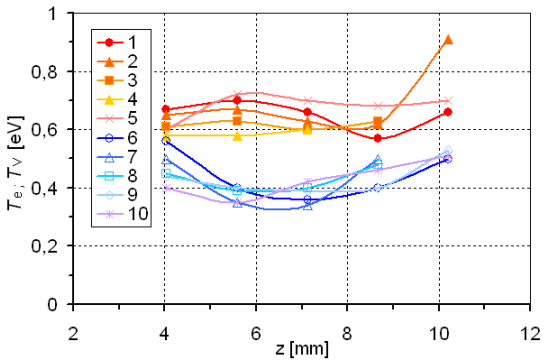

Fig.7. Electronic temperature of Cu atoms T_e (curves 1-5) and vibrational temperature of N_2 molecules T_V (curves 6-10) along the plasma flow: G = 40 cm^3/s (1,6), 75 cm^3/s (2,7), 110 cm^3/s (3,8), 150 cm^3/s (4,9), and 190 cm^3/s (5,10). I_d = 200 mA.

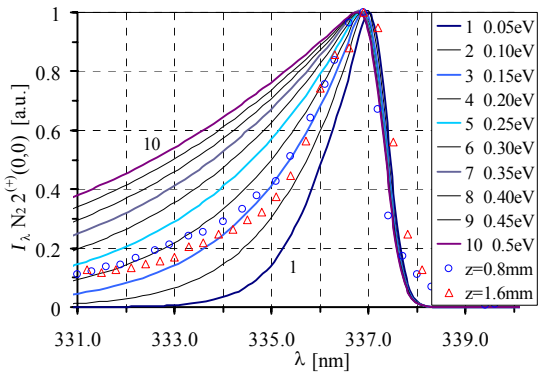

Fig.8. Emission spectra of the N_2 $2^{(+)}$(0-0) band 337.1 nm in the air plasma flow: experimental data (signs) vs. theoretical (curves) at different rotation temperatures T_R. G = 40 cm^3/s, I_d = 480 mA.

all considered N_2 bands). Due to a relatively high density of electrons that should be in the arc in air at atmospheric pressure, i.e. when inelastic electron collisions are high, we suggest $T_e \approx T_E$ as usual for such plasma [14].

As is expected, the electron temperature T_e and vibrational temperature T_V differenced very much, so that $T_e/T_V >> 1$ everywhere. At that, a level of non-isothermality is not permanent along the plasma flow. It depends not only on the discharge current I_d but also on the airflow rate G that is blowing the arc plasma column, providing convective heat mass transfer. Especially large temperature differences occur during the plasma relaxation in the afterglow zone. Fig.7 shows experimental dependencies T_e(z) and T_V(z) along the discharge at I_d = 200 mA for the different G: curves 1-5 are T_e, and curves 6-10 are T_V; curves 1, 6 are G = 40 cm^3/s; curves 2, 7 are G = 75 cm^3/s; curves 3, 8 are G = 110 cm^3/s; curves 4, 9 are G = 150 cm^3/s; and curves 5, 10 are G = 190 cm^3/s. As is seen, along the plasma flow the T_e is 0.7-0.6 eV while the T_V is 0.4-0.3 eV. The results obtained from the temporally and spatially integrated records are located in the core of the plasma column, and we suppose that the longitudinal distributions T(z) obtained from the spectra I_λ(z) are maximal due to averaging of the radial profile. The highest value $T_e \approx$ 1.4 eV was measured in the center of the arc at G = 0. In the blowing discharge, T_e decreases while T_V keeps longer. Then increasing the arc current I_d, the value T_e becomes larger. At the lager airflow rate G, the gradient T_e becomes smaller.

The non-equilibrium of the air plasma in the blowing arc discharge follows also from the estimation of the rotational temperature of electronically excited N_2 molecules, T_R. It was determined from the emission spectra of selected N_2 $2^{(+)}$ bands, assuming a Boltzmann population distribution and collisional termalization of rotational states. Here we suggested $T_g \approx T_R$ as usual in such plasma [14]. Fig.8 shows the results of numerical fitting of the V-R spectrum for the N_2 $2^{(+)}$ (0-0) band 337.1 nm, calculated at different T_R from 0.05 to 0.5 eV with the step 0.05 eV, from the curve 1 that is T_R = 0.05 eV to the curve 10 that is T_R = 0.5 eV, in comparison with the measured data (apparatus function Δλ=0.6 nm) at the distances z = 0.8 and 1.6 mm for G = 40 cm^3/s and I_d = 200 mA. The best contour fit of T_R is to be 0.15 eV. In fact, it differences from the T_V and T_e more than twice. Along the plasma flow, T_R keeps at the level 0.1-0.2 eV within experimental uncertainty, increasing slightly downstream due to the bulk gas heating. This evidences about kinetic non-equilibrium state in the discharge even without going into details of the kinetics of elementary plasma-chemical processes.

Thus, we found that during the evolution of the air plasma in the blowing arc discharge the characteristic temperatures varied very much depending on the power injected into the plasma. However, with the exception of the afterglow, within the arc zone the gas and electron temperatures are coupled at the level of T_g ~ 2000-3000 K and T_e ~ 8000-12000 K, respectively. This indicates, in the blowing arc we have the same transitional regime as in the gliding arc [15] when it is supported both by the thermal ionization (function of gas temperature) and by the direct electron impact (function of electric field). It is particularly remarkable that despite of atmospheric pressure, the air plasma in the blowing arc discharge remains ionizational non-equilibrium with the overheated electron component due to the effective convective heat carry-over. According to our estimation in comparison with the hypothetic case of LTE Saha's law, the degree of ionization nonequilibrium is as high as 10^2-10^3.

It is worth to note that besides the pure air, we tried out the blowing arc discharge for non-thermal ignition of air/spirit and petrol mixtures. This work is currently done at Kiev University, and results of pilot experiments are quit satisfied resulting in the fast ignition and expansion of the burning both across the flow and downstream. However, details are out of the scope of this paper and will be reported later.

Conclusion

1. We are convinced that a high-voltage transverse blowing arc discharge working in air of atmospheric pressure can be a source of non-thermal plasma with a relatively high level of ionization. We found that there is no local LTE in this arc discharge air plasma during its space/time evolution, and measured/estimated characteristic temperatures are within a relation: $T_e \sim T_E > T_V > T_R \sim T_g$, where the temperature of electronic excitation of free atoms differences from the temperatures of vibrational and rotational states of electronically excited molecules more then twice. Therefore, a conventional two-temperature approach with T_e for electrons and T_g for heavy particles is not valid in this case. Another character effect is an "ignition" of the plasma luminescence in the discharge plume resulted from the kinetic nonequilibrium conditions. The factors that effecting on the plasma non-equilibrium state, are not only electric parameters and discharge power injected into the plasma but also the gas dynamics and convective heat mass transfer in the plasma flow.
2. Taking into account the high plasma density, high electronic excitation temperature, easy control of the discharge potential and possibility of stimulation of selective chemical reactions at relatively low gas temperatures and high atmospheric pressures, we believe that this type of the nonequilibrium arc discharge in the atmospheric air flow can be very suitable for many technological applications including non-thermal plasma-assisted ignition/combustion of hydrocarbon fuels and plasma-enhanced modification of combustion products.
3. On the results of our investigations we conclude that even small variations in the air plasma conditions due to their spatial and temporal instability, decomposition, contamination, etc can produce large visual changes in the spectral emission which is functionally related with the temperatures and concentrations of plasma components, so the optical emission spectroscopy of electronically excited molecules and atoms in the air plasma could serve as a simple and reliable tool for the characterization and control of the non-equilibrium plasma state in the blowing arc discharge in different experimental conditions.

Acknowledgment

The work was partially supported by the Ukrainian Ministry of Education and Science and by the State Foundation for Basic Research.

References

[1] R. d'Agostino (Ed.) *et al - Proc.16th Intern. Symp. on Plasma Chemistry*, Taormina, Italy (2003).
[2] V.K. Zhivotov, V.D. Rusanov, A.A. Fridman - *Diagnostics of Non-Equilibrium Chemically Active Plasma*, Moscow: Atomizdat (1985).
[3] V.D. Rusanov, A.A. Fridman – *Physics of Chemically Active Plasma*, Moscow: Nauka (1984).
[4] Yu.P. Raiser - *Gas Discharge Physics*, Moscow: Nauka (1987); Berlin: Springer (1997).
[5] V.Ya. Chernyak - *Proc.3rd Intern. Seminar on Electrophysical and Thermophysical Processes in Low-Temperature Plasma*, Brno, Czech Republic (1999).
[6] A. Czernichowski - *Pure Appl. Chem.* **66** (6) 1301 (1994).
[7] V.V. Buchnev, S.D. Koval, V.Ya. Chernyak - *Bull. Kyiv Univ., Series: Physics&Math.* **1** 315 (2000).
[8] V. Chernyak, S. Koval, V. Naumov - *Proc.15th Intern. Symp. on Plasma Chemistry,* Orleans, France /Eds. A.Bouchoule *et al,* Orleans: GREMI, Vol. **IV** 1447 (2001).
[9] V.Ya Chernyak, S.V. Olshevskii – *Ukr.J.Phys.* **50**(3) 243 (2005).
[10] R.W.B. Pears, A.G. Gaydon - *The Identification of Molecular Spectra*, Chapman & Hall, London (1976).
[11] W. Lochte-Holtgreven - *Plasma Diagnostics*, Amsterdam: North-Holland (1968).
[12] K.P. Huber, G. Herzberg – *Constants of Diatomic Molecules*, N.Y.: Van Nostrand Reinhold Co. (1979).
[13] NIST Atomic Spectra Database. URL http://physics.nist.gov (2005)
[14] C.O. Laux, R.J. Gessman, C.H. Kruger *et al - J. Quant. Spectr. Radiat. Transfer* **68** 473 (2001).
[15] A. Fridman, A. Shirokov, A. Gutsol - *J.Phys.D:Appl.Phys.* **38** R1 (2005).

Surface Modification of Textiles by Pulsed Ammonia Plasma

X.J. Dai, L. Kviz, and R.J. Denning

CSIRO Textile & Fibre Technology, PO Box 21, Belmont, Geelong, Vic. 3216, AUSTRALIA

Abstract

The application of a pulsed ammonia plasma to produce high concentrations of $\cdot NH_2$ radicals for the introduction of amino functional groups on textile surfaces, particularly on wool, was investigated. It was found the pulsed ammonia plasma provides an effective plasma activation process and can be used to control chemical reactions on the substrate surface to effectively and selectively produce surface functionalities.

Keywords
Pulsed ammonia plasma, amino groups, polyethylene (PE), wool

1. Introduction

The attachment of amino groups to polymer surfaces is particularly attractive because amines are relatively reactive nucleophiles. Amino groups on the surface provide reactive sites for either covalent or interfacial adhesive bonding of chemical compounds that can be used to control interactions of the surface with its environment. Such functional groups on substrate surfaces have been widely applied to biomolecules and protein immobilization as well as in cell growth [1-4].

Amino groups are usually incorporated on the surface using either ammonia or amines in a plasma discharge. Ammonia is a non-polymer-forming gas, while amines deposit a plasma polymer layer. Continuous ammonia plasma has been used for the treatment of various materials and has been the subject of many papers [1, 5-8]. It has been reported that the primary amino radical ($\cdot NH_2$) is the species most likely to react with surface radicals produced by an ammonia plasma [6]. For a surface treatment it is essential that sufficient $\cdot NH_2$ radicals are produced that can effectively react with the substrate surface. Usually, in continuous ammonia plasmas, H_2 is added to the NH_3 feed to increase the production of $\cdot NH_2$ radicals [7]. In this work an alternate method of producing $\cdot NH_2$ radicals for the modification of textile surfaces, particularly wool fabrics, has been investigated using a pulsed ammonia plasma.

2. Experiment

A. Pulsed Ammonia Plasma

The experiments were performed in a 1.7 litre electrodeless plasma reaction chamber schematically shown in Figure 1. The chamber pressure was controlled using a rotary pump at a base pressure of less than 1×10^{-1} Pa. Electronic mass flow meters were used to monitor the inlet gas flow. Fabric samples were held on a horizontal support located at the chamber center.

Ammonia, provided by BOC Gases, with a purity of >99.99% was used without further purification. The pulsed plasma was produced by an RF generator, supplying RF power to the external antenna around the chamber through a matching network. RF power was pulsed at a range of frequencies and duty cycles (D), calculated as $D = \frac{T_{on}}{T_{on} + T_{off}}$, where T_{on} and T_{off}

are the time when the plasma is "On" and "Off" respectively. The average power, calculated as $P_{av} = P_{peak}$ x D, ranged from 10 to 20 W with duty cycles varying from 0.1 to 1 (Continuous Wave), where P_{peak} is the power applied during the "On" phase.

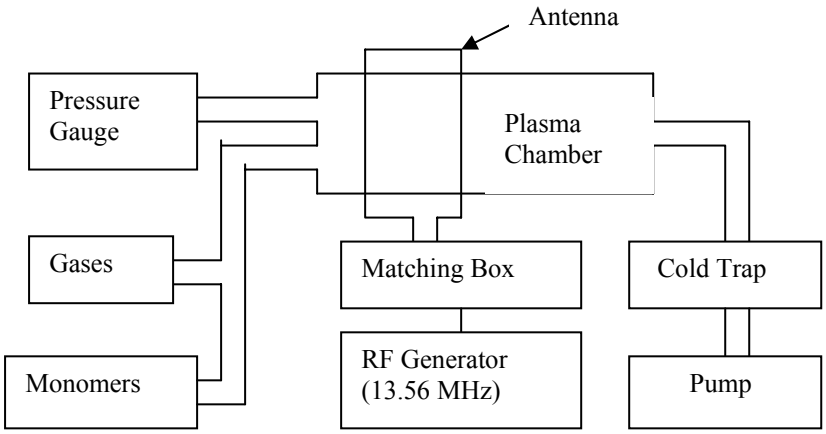

Figure1. Schematic diagram of the experimental apparatus

The RF pulse in gaseous ammonia produces $\cdot NH_2$ radicals as described in equations (1) and (2). The "Off" portion of the pulse provides sufficient time for grafting the $\cdot NH_2$ radicals to the textile surface with minimum interference by charged particles and UV photons. By selecting the plasma parameters, it is possible to optimize the surface reactions and minimize recombination reactions that form additional ammonia and ·NH radicals (3) or hydrazine (4) [9,10].

$$NH_3 + energy \rightarrow \cdot NH_2 + \cdot H \quad (1)$$

$$NH_3 + \cdot H \rightarrow \cdot NH_2 + H_2 \quad (2)$$

$$\cdot NH_2 + \cdot NH_2 \rightarrow NH_3 + \cdot \dot{N}H \quad (3)$$

$$\cdot NH_2 + \cdot NH_2 \rightarrow N_2H_4 \quad (4)$$

B. Materials and Surface Analysis

A lightweight plain woven wool fabric (155g/m^2), made from 20µm Australian merino wool, was used as the substrate in the experiments. Samples (15cm x 30cm) were cleaned using Soxhlet extraction in dichloromethane for 4 hours to remove residual processing lubricants and other possible contaminants. Polyethylene (PE) was used as a reference substrate because of the similarity of its surface energy to that of normal wool. The PE samples were ultrasonically cleaned in a hexane/isopropyl alcohol (1:1) mixture for 30s and then air dried.

Changes to the surface chemistry of the samples were observed using X-ray photoelectron spectroscopy (XPS) in a Kratos analytical AXIS-HSi equipped with a monochromatised Al Kα X-ray source at a power of 200 W (10kV and 20mA). The samples were mounted on a multi-sample holder using double-sided adhesive tape. A jet of dry nitrogen was used to remove any loose contamination (dust) from the sample surface. Typical pressures during analysis were between 2 and 5 x 10^{-6} Pa. Survey spectra for identification of all elements and their atomic concentrations were obtained over the range 0 - 1200 eV. High resolution spectra (40eV pass energy) were then recorded for selected elements (e.g. O, C, N, S) in order to obtain more specific data regarding chemical structure.

A Digital Instruments Dimension 3000 scanning probe microscope was used to examine the adhesion force and topographical nature of the sample surfaces before and after the plasma treatment. The instrument was operated in contact mode using a silicon nitride probe, consisting of a V-shaped cantilever (nominal spring constant κ = 0.12 N/m) with a square pyramidal tip, to acquire images and force curves in air. Scanning Electron Microscope was conducted using a Hitachi S4100 Field-Emission Scanning Electron Microscope (FeSEM), operating at 1KV with a 5mm working distance using carbon-coated film and fabric samples.

Surface energy changes of wool were measured using the Wilhelmy balance principle as described previously [11]. This method was further developed [12] for measuring the changes in the surface energy of plastic films and synthetic fabrics through a calibration curve established from the net water absorption values measured using the Wilhelmy method and the absolute values from Softal test inks [13] (range 34 mJ/m^2 - 72 mJ/m^2 non-continuous).

3. Results and Discussion

As many plasma parameters may affect the properties of the modified surface, we focused on a number of key plasma parameters in our experiments to determine the most suitable experimental conditions for grafting amino groups to the surface. The variables investigated included pulse frequency, duty cycle, RF power, pressure, and treatment time. From simple water drop tests, we found that the most hydrophilic surfaces were produced at a duty cycle, D of 0.2 and a pulse frequency, f of 200Hz. These two parameters were maintained constant for the remainder of the work.

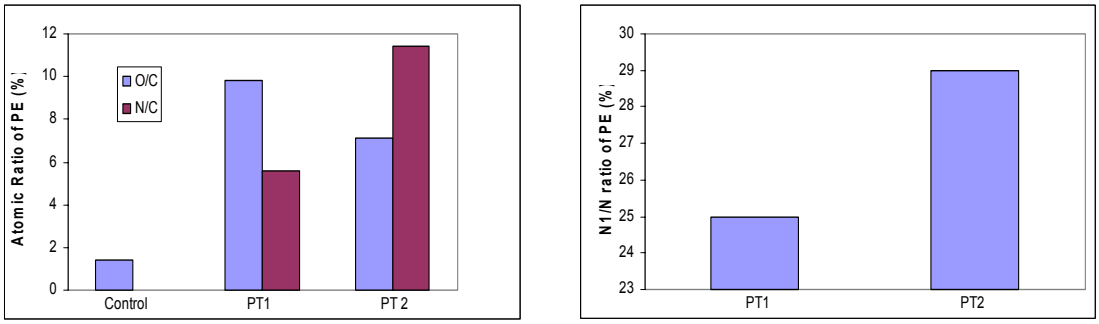

(a) (b)

Figure 2 XPS elemental ratio of PE before and after the pulsed NH_3 plasma treatments
(PT1: P_{av}=15W, p=7 Pa, t=20sec; PT2: P_{av}=15W, p=30 Pa, t=40sec)
(a) Atomic ratio N/C and O/C; (b) Atomic ratio of N1/N

Figure 2 shows the XPS results for PE before and after treatment with the pulsed ammonia plasma. The atomic ratios of nitrogen to carbon (N/C) and oxygen to carbon (O/C) (Figure 2(a)) are significantly different for the different plasma treatment conditions (PT1 and PT2). The higher O/C ratio at a pressure 7 Pa (PT1) is consistent with previous work that found that the highest concentration of atomic oxygen (n[O] peak) was produced at an oxygen pressure of 5 Pa [14] using a similar plasma source to that used here. The N/C ratio increased in going from PT1 to PT2, as well as the ratio of primary amine groups (N1) to total nitrogen (N) (N1/N) shown in Figure 2(b). It is believed that the increase of N/C and N1/N ratios at the plasma condition PT2 was due to the pressure change (30Pa) as the surface energy reached the saturation level at a treatment time of approximately 20 seconds (see Figure 6). Therefore, the adjustment of some plasma parameters allows the selective production of reactive species and modification of the surface.

Although PE has a similar surface energy to the bound lipid layer on the wool fiber surface, wool has a much more complex surface [15]. It is characterized by a highly cross-linked protein matrix acylated with fatty acids, predominantly 18-methyleicosanoic acid [16]. The fatty acids are believed to be attached to the surface protein via a thioester linkage to cysteine residues with the hydrocarbon tail oriented directly away from the surface [17]. Figures 3 (a) and (b) shows the XPS elemental ratios, O/C, N/C, S/C (sulfur to carbon) and N1/N for untreated and treated wool fabrics. Compared to untreated wool, the total nitrogen content of the plasma treated wool surface increased by 66% and the primary amine content increased by 200%.

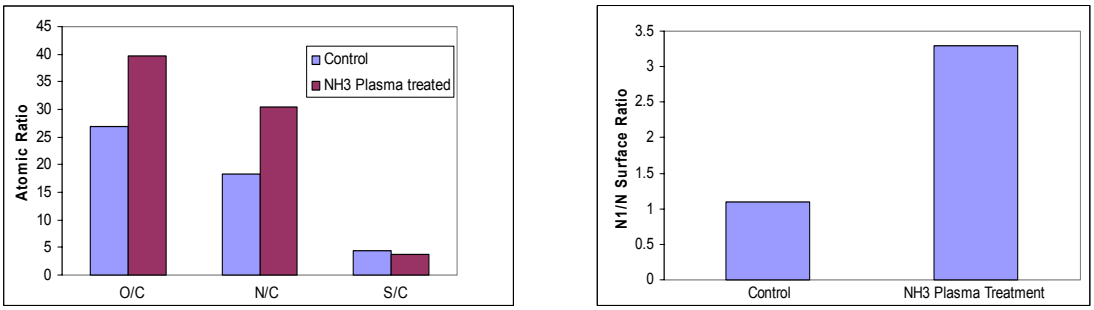

(a) (b)

Fig. 3 XPS elemental ratios of wool before and after the pulsed NH_3 plasma treatment (P_{av}=15W, p=9pa, t=20sec)
(a) Atomic ratios O/C, N/C, S/C; (b) Atomic ratio of N1/N

An important indicator for ammonia plasma surface modification is an improvement in the adhesion of polymers to the surface. The improvement can be achieved by increasing the surface energy following introduction of reactive groups. The ammonia plasma modifies the surface by grafting nitrogen and oxygen polar groups, which are detected by XPS analysis. The modified surface was further characterized using an AFM to measure force distance curves and by wettability measurements to assess surface energy changes.

Figures 4 and 5 show the force distance curves measured by AFM for untreated and the pulsed ammonia plasma treated PE and wool respectively.

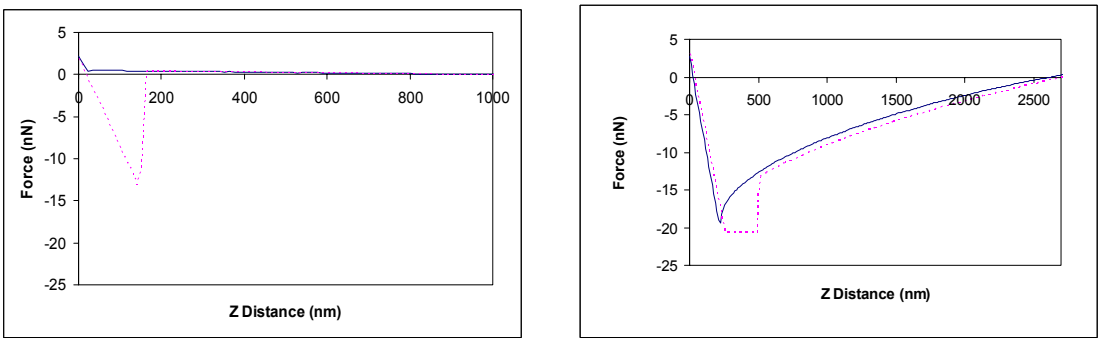

(a) (b)

Figure 4 The force-distance curves of PE measured by AFM
(a) untreated; (b) the pulsed NH_3 plasma treated, P_{av}= 20W, p=30Pa, t=60sec

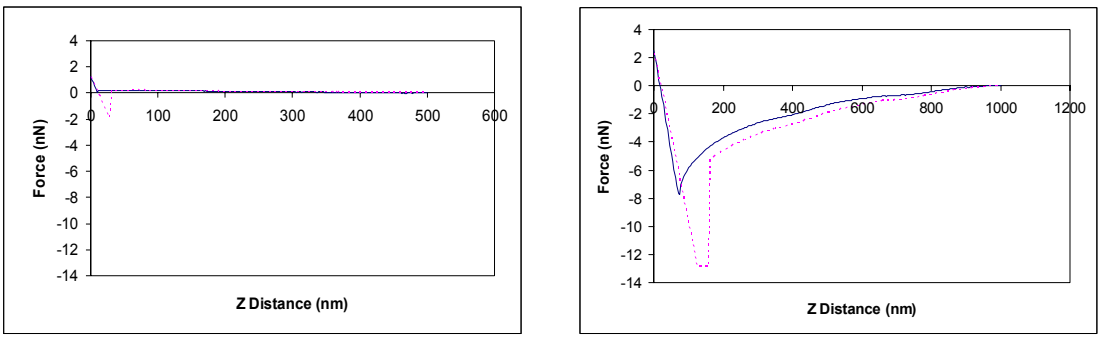

(a) (b)

Figure 5 The force-distance curves of wool measured by AFM
(a) untreated; (b) the pulsed NH_3 plasma treated, P_{av}= 20W, p=20Pa, t=40sec

The X-axis is the distance (in Z direction) from the base of the AFM cantilever to the sample surface. The solid lines are approach curves and dotted lines are retract curves. In Figure 4(a), in the region of Z distance from 20nm to 1000nm the tip is above the sample surface and no force is experienced by the tip. At 20 nm it touched the surface and further movement in the Z distance resulted in a positive force (deflection) on the cantilever. At about 2 nN the tip is retracted but adheres to the surface until about –14 nN before pulling loose. This value (14nN) represents the adhesion between the tip and the sample surface. For the treated PE (Figure 4(b)), there is a strong attraction between the tip and the sample surface in air out to about 2500 nm, as well as adhesion during retraction. (Note: the adhesion spike has been truncated due to the signal going off the detector). Similar results can be seen for the wool, shown in Figures 5(a) and (b). The results show that there are much greater adhesion forces and attraction forces between the surface and the AFM tip for the pulsed NH_3 plasma treated PE and wool than the controls.

These results are in agreement with the wettability measurements, shown in Figure 6. As the plasma treatment time increased, the surface energy change increased, before reaching saturation (72 mJ/m^2 for PE and 62 mJ/m^2 for wool) at a treatment time of approximately 20 seconds.

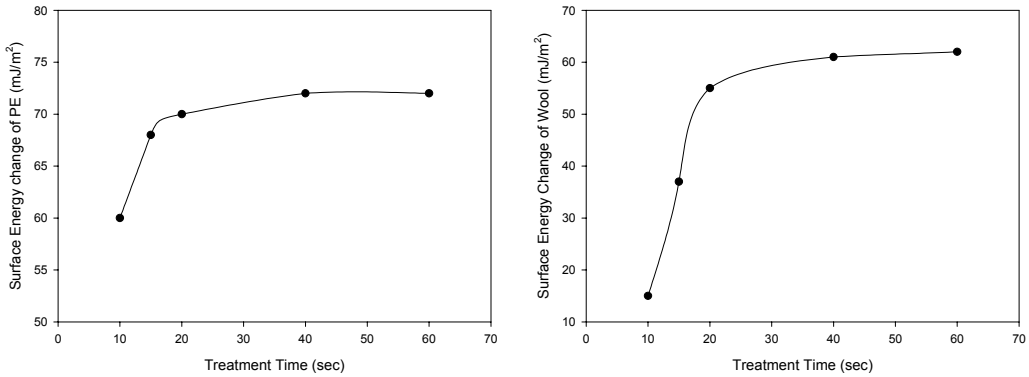

(a) (b)

Figure 6 Surface energy changes of PE (a) and wool (b) via the pulsed NH_3 plasma treatment time
P_{av}=15W, p=30Pa

SEM images of the treated and untreated wool fibres show no significant change on surface physical structure, indicating the pulsed ammonia plasma is a mild form of surface modification.

4. Conclusion

It has been demonstrated that a pulsed ammonia plasma is an effective method for grafting amino functional groups onto the surfaces of PE and wool. It has also been shown that surface functionality can be selectively modified and the relative concentration of primary amine groups grafted onto the surface varies with the plasma treatment conditions. Wettability measurements show that the surface energy is significantly increased after the pulsed ammonia plasma treatment while AFM measurements show that surface adhesion can also be greatly improved.

Acknowledgments

The authors would like to thank Dr. T. R. Gengenbach for the XPS measurements and his valuable discussions, Dr. J. Maxwell for the AFM measurements and Dr. M. Huson for the data analysis and his valuable discussions, Mrs. C. Coombs for the SEM images, and Drs. D.J. Evans and R. Cranston for their valuable discussions.

References

1. M. Tatoulian, F. Arefi-Khonsari, J. Amouroux, S. Ben Rejeb, A. Martel, N. Fischer Durand, J.F. Lawrence, and F. Le Goffic, *Plasma and Polymers,* ***3****(4), 211(1998)*
2. I. Gancarz, J. Bryjak, G. Pozniak, W. Tylus, *European Polymer Journal,* ***39****, 2217(2003)*
3. D.A. Puleo, R.A. Kissling, M.-S. Sheu, *Biomaterials,* ***23****, 2079 (2002)*
4. Y. Wan, J. Yang, J.L.Yang, J. Bei, S. Wang, *Biomaterials,* ***24****, 3757 (2003)*
5. J. Kurdi, H. Ardelean, P. Marcus, P. Jonnard, F. Arefi-Khonsari, *Applied Surface Science,* ***189****, 119(2002)*
6. R. d'Agostino, F. Cramarossa, S. DeBenedictis & G. Ferraro, *Plasma Chemistry and Plasma Processing,* ***1****, 19 (1981)*
7. P. Favia, M.V. Stendardo, and R. d'Agostino, *Plasma and Polymers,* ***1****, 91(1996)*
8. T.R. Gengenbach, X.M. Xie, R.C. Chatelier, and H.J. Griesser, *J. Adhesion Sci. Technol.* ***8****(4), 305 (1994)*
9. M.H. Hanes and E.J. Bair, *The Journal of Chemical Physics,* ***38****(3), 672(1963)*
10. S. Holmes & P. Schwartz, *Composites Science and Technology* ***38****, 1 (1990)*
11. X.J. Dai, S.M. Hamberger, and R.A.Bean, *Australian Journal of Physics,* ***48****, 939 (1995)*
12. X.J. Dai, L. Kviz, P. S. Turner, and N. Finn, *Atmospheric Pressure Glow Discharge (APGD) and Applications in Technical Textiles*, *CSIRO Internal Report, 2003.*
13. SOFTAL Electronic, Measuring surface tension of plastics
14. X.J. Dai, *Australian Journal of Physics,* ***49****, 1169 (1996)*
15. X.J. Dai, F.M. Elms, G.A. George, *Journal of Applied Polymer Science,* ***80****, 1461 (2001)*
16. A.P. Negri, H.J. Cornell, D.E. Rivett, *Text. Res. J,* ***63****, 109 (1993)*
17. D.J. Evans, R.D. Denning, and J.S. Church, *Interface of Keratin Fibres with their Environment, in "Encyclopedia of Surface and Colloid Science," Marcel Dekker, Inc., 2628(2002)*

Effects of Microstructure on Reflectance of Thermal Barrier Coatings

T. Ma, M. Kambara, K. Eguchi, T. Yoshida

Department of Materials Engineering, the University of Tokyo, Tokyo 113-8656, Japan

Abstract

Reflectance of YSZ and Al_2O_3-YSZ coatings with different microstructures was compared at room temperature. It is clearly observed that the specially engineered microstructure, produced by the twin hybrid thermal plasma spraying system, affect substantially the coating's reflecting capability. Plasma spray PVD coating with cross-bracing structure has higher reflectance compared to the plasma powder sprayed coatings with splats construction, and the typical EB-PVD coatings. This indicates the coating prepared by thermal plasma PVD possesses added advantage as TBC in suppressing the radiative heating particularly at high temperature use.

Keywords TBCs, microstructure, reflectance

1. Introduction

Thermal radiation in infrared region plays an important role in the heat transfer process especially at the temperature higher than 1700K, due to its intensity proportional to the fourth power of temperature. Thermal barrier coatings (TBCs), used in aircraft and gas turbines for thermal insulation, are expected to have higher light reflectance, together with lower thermal conductivity, which are important issues for the next generation TBC system. In general, at a given material, the reflectance varies significantly with its microstructure and the surface conditions. This in turn suggests that effective thermal insulation of TBC can be achieved by controlling its microstructure. A special ZrO_2-8%Y_2O_3 coating with multiple sharp interfaces within its columnar microstructure produced by EB-PVD was reported in Ref.[1], in which the continuous flux of the vapor cloud was periodically input by using a shutter mechanism. It revealed that the picturesque multiple layer structure is beneficial to increase the reflectance. Y. Kagawa[2,3] reported another ZrO_2/Al_2O_3 multilayer coating produced by spin coating process and its light reflectance showed a repeated increase/decrease behavior. The constant value of the difference between neighboring peak-to-peak wavelength suggested that the origin of the increase/decrease was interference of reflected light at the ZrO_2/Al_2O_3 interfaces. These reports indicate that microstructure is one of the factors affecting reflectance. In this paper, the effect of novel microstructure on reflectance is presented for YSZ and Al_2O_3-YSZ composite TBCs prepared by plasma spraying technology.

2. Experimental

YSZ and Al_2O_3-YSZ coatings with different microstructures were prepared by the twin hybrid thermal plasma spraying system, in which two hybrid plasma torches are equipped. This system allows production of a variety of TBCs with PVD and/or splats structure, by tuning input power, powder size, powder feeding rate, distance from torch to substrate, and so on.[4,5] In order to maintain low substrate temperature during deposition, water-cooled substrate holder was used. The

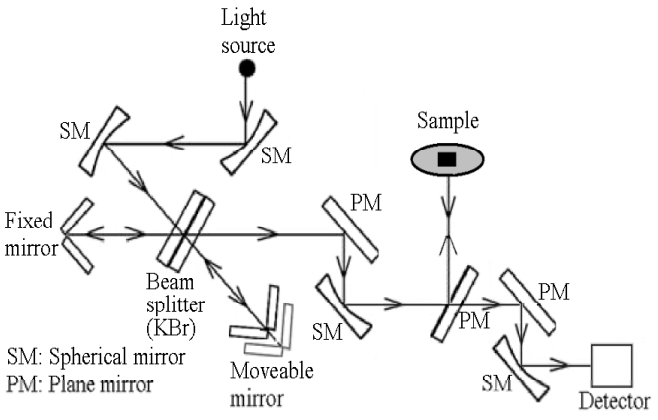

Fig.1 Schematic of an optical system for the measurement of IR reflectance

substrate temperature was measured by a thermal couple. In the interest of evaluating the reflective characteristics only from the freestanding coatings, the TBCs were deposited on graphite plates so that they can be removed easily from the substrates. All specimens were carefully polished under the same condition (1200 surface finish and slurry polished) and the cross sections were observed by FE-SEM (JEOL-6340, Japan). The reflectance perpendicular to the specimen surface was measured by Fourier-transform infrared spectrometer (FT/IR-670 Plus, JASCO Corp, Japan). The optical system for the measurement of IR reflectance is shown in Fig.1. Although the reflective property at high temperatures should be measured, the measurement was carried out at room temperature due to less significant dependence of reflectance of zirconia on temperature.[3,6]

3. Results and discussion

Figure 2 shows the cross sections of the typical specimens produced by twin hybrid thermal plasma spraying system. Specimens (a) and (b) represent the columnar YSZ PVD structure, which were prepared by spraying smaller powder less than 15μm in diameter on the stationary water-cooled substrate. The distance from torch to substrate was different in the processing. There are some additional layers formed within the PVD columnar grains (hereafter called cross-bracing structure) in the specimen (a), whereas no such special structure is present in the specimen (b). On the other hand, (c) and (d) are the typical powder sprayed structure consisted of YSZ and Al_2O_3-YSZ composite splats. These were prepared with one torch (c) and twin torches (d) by injecting 63~88μm powders on a rotating substrate during deposition.

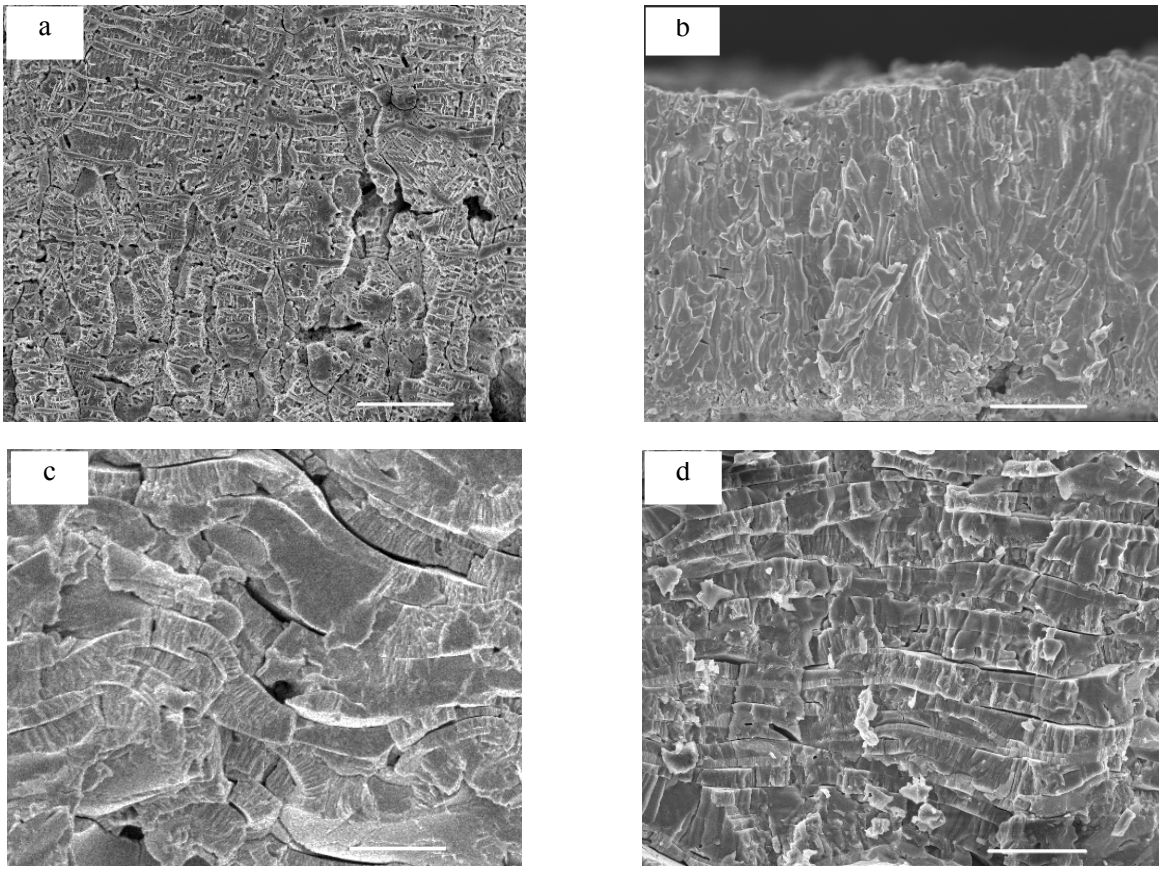

Fig.2 Cross sectional micrographs of TBCs with different microstructures; the white bar represents 20μm. (a) 8YSZ PVD structure with aligned layers within columnar grains, torch-substrate distance: 50 mm; (b) 8YSZ PVD structure, prepared under similar conditions as the case (a) except the torch-substrate distance: 30 mm; (c) 8YSZ powder sprayed structure; (d) Al_2O_3-8YSZ powder sprayed composite structure.

The reflectance of these specimens was measured as a function of wavelength of IR light as shown in Fig.3. The theoretical reflectance R for ZrO_2 and Al_2O_3 by an estimation with Fresnel's Law[7] ($R=\left[(\bar{n}-1)/(\bar{n}+1)\right]^2$, where $\bar{n}$ is refractive index) is also included in Fig.3. The refractive index of ZrO_2 is 2.0-2.1 at wavelength range 1.0-5.0μm[8], the index for Al_2O_3 is 1.68, 1.65, 1.62, 1.60 at wavelength of 2μm, 3μm, 4μm, 5μm, respectively[3]. It shows that the specimens with splats structure have lower reflectance than the theoretical values. No big difference is found between (c) and (d) despite their different compositions. The wavy surfaces and micro pores inside the splats of (c) and (d) as observed in Fig.2 may scatter the incident light randomly and therefore reduce the reflectance measured at right angle. This implies that microstructure is an additional factor to affect the reflecting capability besides material property and surface condition. On the other hand, the reflectance of the PVD specimens is found to be higher than the theoretical values. This may be caused by the fact that the vertically aligned dense PVD columnar grains effectively reflect the incident light to the right angle. In addition, the cross-bracing grains within PVD columnar crystals as shown in Fig.4, which are t′ phase formed due to rapid cooling rate during deposition, make possibly additional contribution to enhance the reflectance. In fact, the light with a wavelength, λ, reflected at an object with a certain thickness, can be enhanced when the quarter wavelength criteria ($-1/4\,\lambda < \delta < 1/4\,\lambda$, where δ is optical path length) is applied[10]. In the case of the Infra-red (λ =1-10μm) incident perpendicular to a platelet grain, the light reflection will be enhanced when the thickness is smaller than 1.25μm. From Fig.4, in comparison, the average thickness of the grains aligned transversely is roughly estimated to be around 0.5-1.2μm, which is in good agreement with the size of the object calculated from the criteria above.

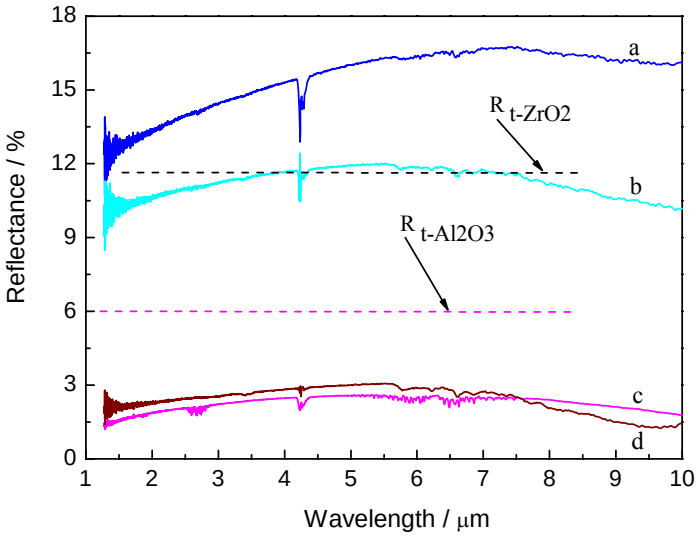

Fig.3 Reflective curves of TBCs with different microstructures of (a)~(d) shown in Fig.2. $R_{t\text{-}ZrO2}$ and $R_{t\text{-}Al2O3}$ are theoretical reflectance for ZrO_2 and Al_2O_3, respectively. The depressions at wavelength of 4.2μm are thanks to absorbance of carbon dioxide in the air.[9]

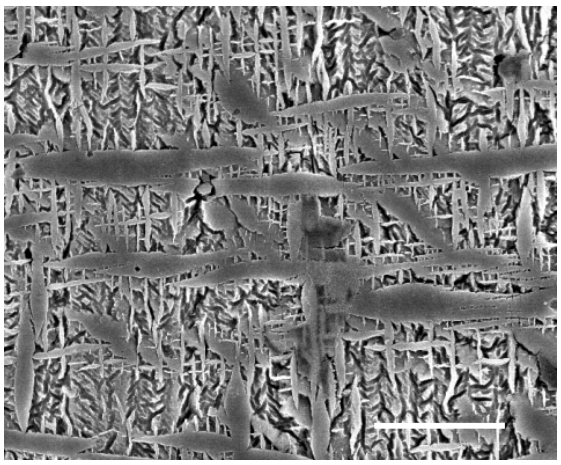

Fig.4 Cross sectional micrograph of the coating with cross-bracing grains, the white bar represents 5μm.

Electron beam physical vapor deposition (EB-PVD) and atmospheric plasma spraying (APS) are the other two kind of typical processes for TBC preparation. In order to compare the coatings' reflective property produced by different processing, several specimens prepared by Plasma Spraying PVD, EB-PVD and APS were carefully polished at the same

conditions to obtain the uniform surface roughness. Fig.2 (a) and Fig.5 show cross section micrographs of this three kind of coatings, of which reflectance was measured as a function of wavelength of light as shown in Fig.6. It can be seen that APS coating has the lowest reflectance in this comparison. This is because the cracks, pores and wavy surfaces within the specimen greatly decreased the measuring reflectance at right angle. As for EB-PVD, though it seems no significant porosities in the coating, the vertical gaps between the columnar crystals decrease the density and may enhance the absorption of incident radiation at normal direction. The coating produced by plasma spraying PVD has the highest reflectance because of its high density, low porosity and special cross-bracing structure, which has been analyzed in the above paragraph.

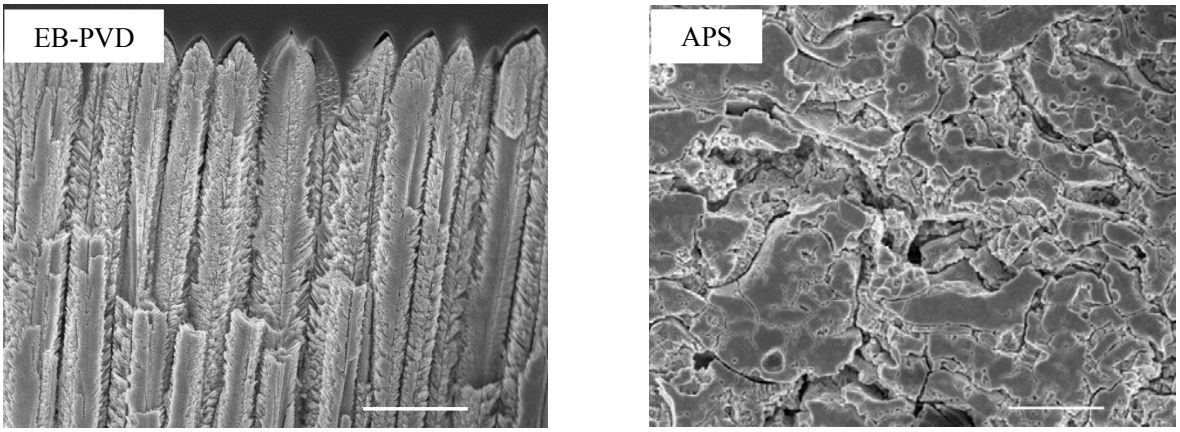

Fig.5 Cross section micrograph of TBCs prepared by EB-PVD and APS processing, the white bar represents 20μm.

Additional experiments are needed to confirm the detailed effects of microstructure on reflectance of TBCs. Nevertheless, the present results clearly indicate that the coatings with cross-bracing PVD structure, produced by twin hybrid thermal plasma spraying system, have high potential as TBC used at higher temperatures.

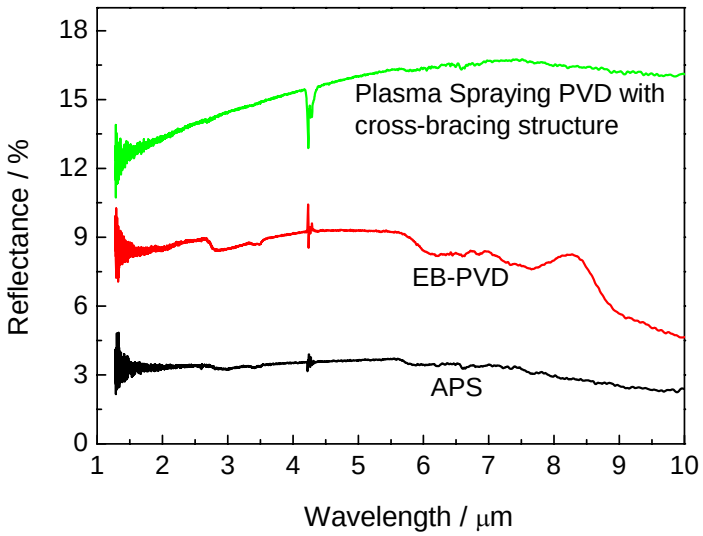

Fig.6 Reflective curves of thermal barrier coatings prepared by different process.

Acknowledgement

This work was supported by NEDO. The authors are also grateful to Professor Kagawa and Dr. Matsumura for their kind help in reflectance measurements.

References

[1] J. Singh, D.E. Wolfe. Journal of Materials Science, Vol.39, (2004) 1975-1985
[2] K.Matsumura, T.Naganuma, Y. Kagawa. Advanced Engineering Materials, No.4, (2003.5) 226-228
[3] T.Naganuma, Y. Kagawa. Acta Materialia, Vol.52, (19), (2004.11) 5645-5653
[4] H. Huang, K. Eguchi, T. Yoshida. Science and Technology of Materials, Vol.4, (2003) 617-622
[5] H. Huang, K. Eguchi, M. Kambara, T. Yoshida. Materials Science Forum, Vol.475-479, (2005) 2883-2886
[6] J.I. Eldridge, C.M. Spuckler, K.W. Street. Proceedings of the 26th Annual International Conference on Advanced Ceramics & Composites, Jan. 13-18, (2002) 417-430
[7] W.D. Kingery, H.K. Bowen, D.R. Uhlmann. Introduction to ceramics, John Wiley & Sons, Inc, 1976

[8] D.L.Wood, K. Nassau. Applied optics, Vol.21, (16), (1982.8) 2978-2981
[9] J. Manara, R. Brandt, J. Kuhn, J. Fricke. High temperature-high pressure, Vol.32, (2000) 361-368
[10] I. Yamaguchi. Applied Optics, Published by OHM, 1998.6

Experimental investigation of the magneticlly enhanced RF discharge in methane.

S.V. Avtaeva, T. M. Lapochkina and D.K. Otorbaev*

Kyrgyz-Russian Slavic University, *Kyrgyz National Academy of Sciences, Bishkek, Kyrgyz Republic.

1. Abstract

Under conditions of the coronal equilibrium in the magnetically enhanced capacitive RF discharge in methane inverse populations of the excited hydrogen states were observed. These populations of excited states of hydrogen atoms can form in the dissociative recombination of H_2^+ ions: $H_2^+ + e \to H + H^*$. Also the molecular hydrogen parameters and ratio of atomic hydrogen to molecular hydrogen were investigated using spectroscopy methods.

2. Introduction

At present time low-temperature plasma in mixtures of hydrocarbon containing gases with noble gases and hydrogen is an object of greeting interest. This is cased with applications of the plasma for plasma deposition of amorphous hydrogenated carbon films. In the plasma deposition methods, the structure and properties of deposited carbon films can be varied widely by changing the deposition parameters.

In this paper the populations of hydrogen atom excited states, hydrogen molecule distributions on vibrational and rotational energy levels, and ratio of atomic hydrogen to molecular hydrogen in the magnetically enhanced RF discharge in methane were investigated using emission spectroscopy methods.

3. Experimental details

A magnetically enhanced asymmetric capacitive coupling RF reactor was used in the experiments. The reactor chamber consisted of the stainless steel cylindrical vessel of diameter 30 cm and height 25 cm with ports to allow optical diagnostics. The chamber walls were grounded. RF power (frequency 13.56 MHz) from a RF generator was applied to the stainless steel plane square electrode ($10\times10\times1.6$ cm^3) arranged in the middle of the chamber. The power supply was connected to the electrode through a special matching device. Two magnetic coils induced a homogeneous magnetic field with respect to the vertical symmetry axis in the chamber. The discharge operating parameters were adjusted in the range: power 90÷110W, methane pressure 1 ÷ 5 Pa, magnetic field 50÷200 G. An optical system based on a high-resolution monochromator and photomultiplier was used to measure the spectral line intensities.

4. Hydrogen atom distributions on energy levels

The emission spectrum of the magnetically enhanced RF discharge in methane was studied in the wavelength range of 420-660 nm. In the spectrum hydrogen spectral lines of Bulmer's series and molecular bands of CH-radicals and molecular hydrogen were observed. The effect of the magnetic field on intensities of hydrogen spectral lines and the molecular bands was studied. Relative intensities of Bulmer lines H_α, H_β, and H_γ were used for investigation of the hydrogen atom distributions on the excited states with quantum numbers n=3, 4 and 5. In a case of the coronal equilibrium populations N_k of excited atomic states can be presented as

$$N_k = N_0 N_e \cdot \sigma_{\max} \langle \sigma(\varepsilon) v_e \rangle \cdot \tau_k . \qquad (1)$$

Here $\sigma(\varepsilon)$ is a form –function identical for all excited states, as the excitation cross sections of Bulmer lines H_α, H_β, H_γ have close dependencies on electron energy [1], $\sigma_{\max}$ is the excitation cross section in maximum and τ_k is lifetime of the excited state. Under invariable conditions in the discharge the equation (1) can be written as

$$N_k \propto const \cdot \sigma_{\max} \tau_k , \qquad (2)$$

where *const* has the same value for all three excited states . As one can see, relative populations of the hydrogen excited states weakly depend on discharge parameters in the case of coronal equilibrium. On the other hand, population of the excited state N_k is related with spectral line intensity I_{ki} : $N_k = const \cdot \frac{I_{ki} \cdot \lambda_{ki}}{A_{ki}}$ (3).

Relations (1) and (3) were used for reconstruction of the hydrogen atom distributions on excited states theoretically and experimentally, accordingly. Dependencies of $\ln(N_k) \sim \ln\left(\frac{I_{ki}\lambda_{ki}}{A_{ki}}\right)$ and $ln(N_k) \sim \ln(\sigma_{\max} \cdot \tau_k)$ on the excited level energy of hydrogen atoms are shown in figure 1. Discharge operating parameters for each of five experimental derived distributions are presented in table 1. When doing the theoretical calculations we neglected the differences in the excitation energy of the excited states (n=3, 4 and 5). Taking this difference into account would result in increase in population of low energy levels relative to upper levels.

Table 1. Operating parameters of the RF discharge in methane, which correspond to atomic hydrogen distributions on excited states presented at figure 1.

1	2	3	4	5
W=90 W *P=1 Pa* *B=50 G*	*W=90 W* *P=1 Pa* *B=100 G*	*W=90W* *P=1 Pa* *B=200 G*	*W=90 W* *P=5 Pa* *B=200 G*	*W=110 W* *P=5 Pa* *B=200 G*

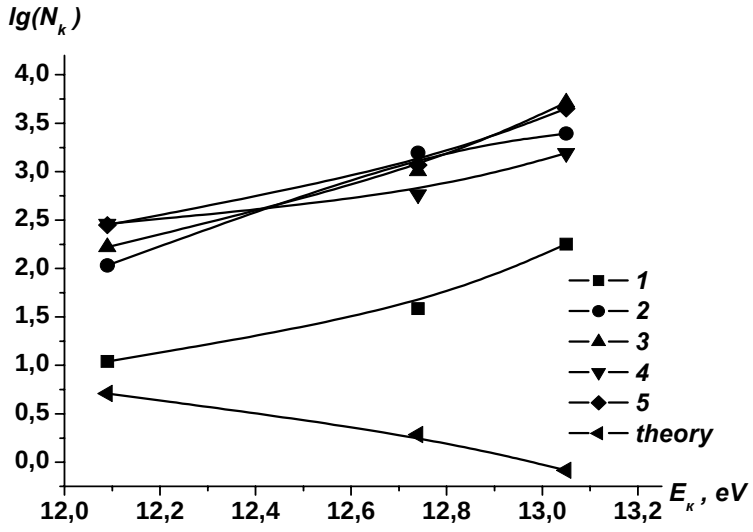

Figure 1. Dependencies of $\ln(N_k) \sim \ln\left(\frac{I_{ki}\lambda_{ki}}{A_{ki}}\right)$ (1÷5) and $ln(N_k) \sim \ln(\sigma_{\max} \cdot \tau_k)$ (theory) on energy of the excited states for Balmer H_α, H_β, H_γ lines.

As one can see (figure 1), in the RF discharge in methane the inverse populations of the excited hydrogen states are realized. These hydrogen atom distributions on excited states cannot be explained in terms of processes of the direct excitation of hydrogen atoms by electron impact or directly in the dissociative excitation by interactions of electrons with methane molecules.

As it was shown in simulations [2], in the capacitive RF discharge in methane rather high concentration of hydrogen molecular ions is realized. H_2^+ ions can be effectively destroyed in the dissociative recombination $H_2^+ + e \to H + H^*$. The ionization energy of H_2 molecule equal to *15.42 eV*, the dissociation energy of H_2^+ ion equal to *2.65 eV* [3]. So the energy defect equal to *12.77 eV*, this energy is close to excitation energy of the excited state of hydrogen atom H^* (n=4) E_β*=12.74 eV* (H_β) and, hence, process of $H_2^+ + e \to H + H(k=4)$ will be resonant, practically. The dissociative recombination of H_2^+ ions can also lead to creation hydrogen excited states H^* with n=3 or 5, however, the creation rates for H^*(n=3) will be the lowest. Most effectively dissociative recombination run by collisions of molecular ions with slow electrons, for H_2^+ the process cross section increases from ~10^{-16} cm^2 to ~ 10^{-14} cm^2 under decrease in electron energy from 1 eV to 0.01 eV [4]. Thus, the dissociative recombination cross section exceeds the cross sections of the direct excitation of H^*(n = 3, 4, 5) by electron

impact from the ground state of hydrogen atom [1] in $\sim 10^2 \div 10^4$ times. It is necessary to notice, that under average electron energy of 2÷3 eV typical for capacitive RF discharges the electron energy distribution function (EEDF) at energies of 12÷13 eV is essentially lower than in energy range of 0.01÷1 eV, (at T_e=2 eV ratio F (13 eV)/*F* (1eV) $\sim 10^{-2}$). In that way, rate constant of the H_2^+ dissociative recombination with creation of the excited hydrogen atoms H^* ~ in 10^5 times will exceed rate constant of direct excitation of H^*(n = 3, 4, 5) by electron impact from the ground state of H. Hence, the dissociative recombination of H_2^+ can form inverse population of the excited states of hydrogen atoms in the RF discharge in methane.

5. Molecular hydrogen

In the emission spectrum of the magnetically enhanced capacitive RF discharge in methane a plenty of molecular hydrogen lines in the wave length ranges of 4400 – 4800 Å and 4900 – 6400 Å, including Fulcher system of H_2 ($d^3\Pi_u\nu' - a^3\Sigma_g\nu''$; $\nu'= \nu''= 0,1,2,3$) are observed. The typical view of vibrational bands of Fulcher system H_2 ($d^3\Pi_u\nu' - a^3\Sigma_g\nu''$; $\nu'= \nu''= 0,1,2,3$) liying in the wave length range from 6000 Å to 6400 Å is shown in figure 2. At equilibrium hydrogen molecule distribution on the vibrational levels the vibrational temperature of the molecular hydrogen can be appreciated on best coincidence of an experimentally measured distribution of intensities in vibrational bands of the Fulcher system with theoretically calculated distributions [5]. In this case vibrational distribution function is defined by expression:

$$f_v = \frac{1}{Q_v} e^{-G(v)hc/kT_{vib}}, \qquad (4)$$

here v is the vibrational quantum number, $G(v)$ is the vibrational energy term, T_{vib} is the vibrational temperature in the ground state , Q_v is the vibrational partition function, and c, h, k are known constants.

The vibrational distribution of hydrogen molecules in an exited state is connected with the vibrational distribution in the ground state by expression [5]:

$$f_v'(v') \propto \sum_{v^0} q_{v^0 v'} f_v(v^0) e^{-\Delta E_{vib}/kT_e}, \qquad (5)$$

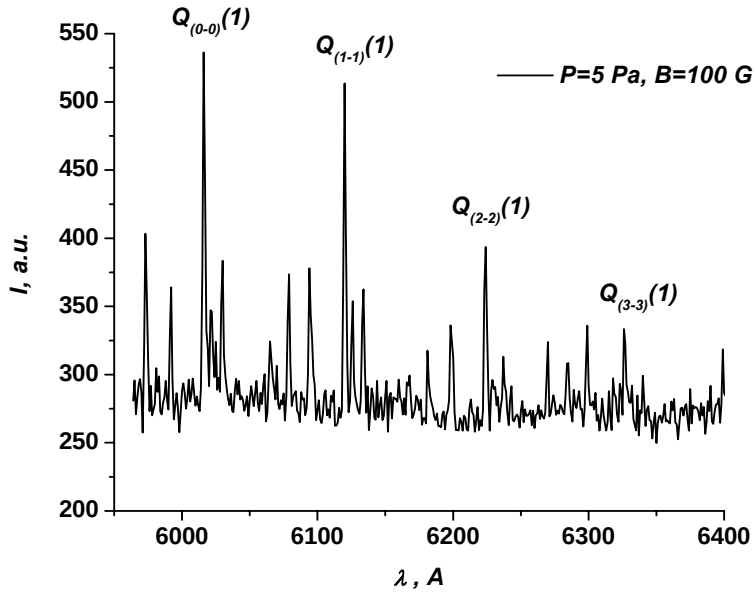

Figure.2. The typical view of a part of the Fulcher system spectrum in emission of the RF discharge in methane.

where ΔE_{vib} is difference in energies of vibrational levels with quantum numbers v' and v^0 in exited and ground electronic states, T_e is the electron temperature, and $q_{v^0 v'}$ - the Franck-Condon factors.

The vibrational band intensity distributions is determined by Franck-Condon factors $q_{v'v''}$ for the radiative decay: $I_{v'v''} \propto f'(v') q_{v'v''}$. (6)

The typical intensity distribution in the vibrational bands of the Fulcher system $H_2(d^3\Pi_u\nu' - a^3\Sigma_g\nu''; \nu'= \nu''= 0,1,2,3)$ observed in the emission spectrum of the RF discharge is presented in figure 3. The theoretically distributions calculated for equilibrium distribution of hydrogen molecules on vibrational levels is also presented in figure 2. Intensity values are normalized to intensity value of the (1-1) vibrational band.

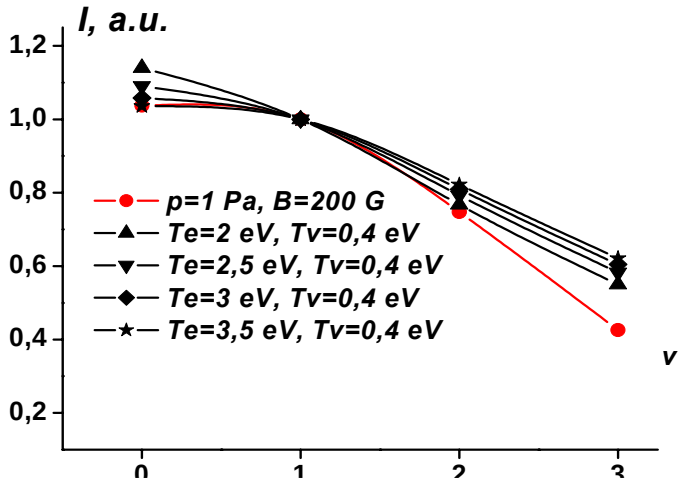

Figure. 3. Intensity distributions of vibrational bands of the Fulcher system in emission spectrum of the RF discharge (P=1Pa, B=200G) and theoretically calculated distributions at the given values of Te and Tv.

vibrational quantum number. It results in reduction

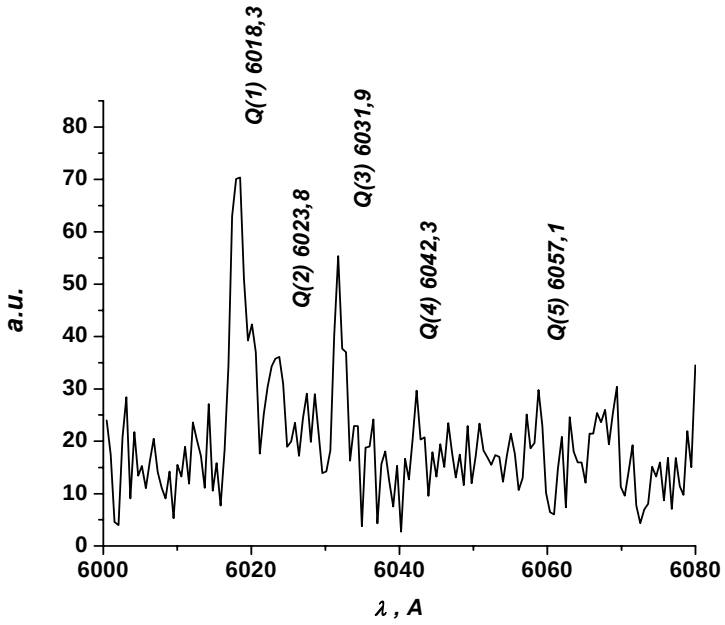

Figure 4. The typical view of spectrum of (0-0) vibrational band of the α-Fulcher system.

As at pressure 1 Pa, so at 5 Pa the experimentally observed intensity distributions in the vibrational bands of the Fulcher system essentially differ from equilibrium distributions, the vibrational levels with quantum numbers v'=2 and v'=3 are noticeably impoverished in comparison with equilibrium distributions. The return situation is observed at magnetic field 50 Гс and methane pressure 1 Pa.

Taking into account that the most part of molecules are on two lower vibrational levels it is possible to define vibrational temperature for two-level system. Vibrational temperature of molecular hydrogen determined by this way lays in limits of 0,2-0,5 eV.

Apparently, observed distributions of hydrogen molecules on vibrational levels testify about increase in rate constants of elementary processes with participation of vibrationally - exited hydrogen molecules with growth of populations of the vibrational levels with higher quantum numbers in comparison with equilibrium populations.

Intensity distributions of rotational lines in the (0-0) vibrational band of the Fulcher system were used for measuring the rotational temperature of hydrogen molecules. Also ratio of atomic hydrogen to molecular hydrogen were determined using optical actinometry method on ratio of relative intensities of the H_α*(6563 Å, n'=3→n=2)* and the Q1 rotational line of the (0-0) vibrational band of the Fulcher system.

The typical view of the (0-0) vibrational band of the α-Fulcher system is shown in figure 4. Rotational temperature of hydrogen molecules in the RF discharge in methane was determined on distribution of relative intensities of Q rotational lines in the (0-0) vibrational band of the Fulcher system. The rotational temperature T'_{rot} of hydrogen molecules in the exited state $d^3\Pi_u$ was determined on inclination of rectilinear dependence of $\ln\left[\frac{I_{K'K''}}{g_I(2K'+1)}\right]$ on

F(K'). Here $I_{K'K''}$ is rotational line intensity, K is rotational quantum number, g_I is degeneracy due to the nuclear spin, g_I =1 for even rotational levels and g_I =3 for odd rotational levels, $F(K')$ is the rotational energy term. Molecule rotational energy distribution function in excited state is connected with the distribution function in the ground state by expression:

$$f'_{rot}(K') = \sum_{K^0} R_{K^0K'} f^0_{rot}(K^0), \qquad (7)$$

where K^0 and K' are quantum numbers, $R_{K^0K'}$ are the Hönl-London factors. This relationship was used to get dependence of T^*_{rot} on (T_{rot}). The received values of the rotational temperature of hydrogen molecules in the ground state were in the temperature range of 480-570 K. The rotational temperature grows with increase in magnetic field and methane pressure.

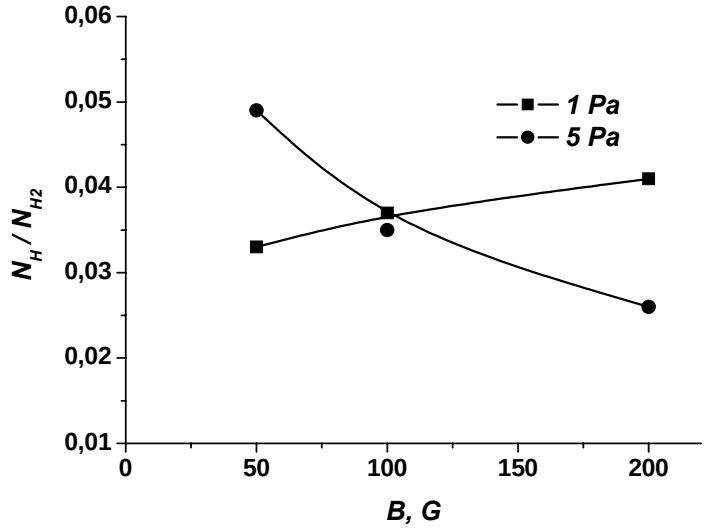

Figure 5. Ratios of atomic and molecular densities as a function of magnetic field and methane pressure in the RF discharge in methane.

In conditions of coronary equilibrium the intensity ratio of atomic and molecular lines of hydrogen can be used for determining density ratio of atomic and molecular hydrogen. Density ratio of atomic to molecular hydrogen is connected with ratio of relative intensities of the atomic line H_α*(6563 Å, n'=3→n=2)* and the rotational Q (*k=1*)-line of the*(0-0)* vibrational band of H_2 α-Fulcher system by relationship:

$$\frac{N_H}{N_{H_2}} = \frac{I_{H_\alpha}}{I_{H_{F(0-0,1)}}} \cdot \frac{\lambda_{H_\alpha}}{\lambda_{H_F}} \frac{\frac{f'_{rot}(k=1)}{Q_r}\sigma^{(0-0)}_{em}}{A_{H_\alpha}\tau^H_{n=3}\sigma^{H(n=3)}_{\max}} \cdot \frac{1}{(1+C_{thr}(\varepsilon))}, \qquad (8)$$

here N_H, N_{H2} are atomic and molecular hydrogen densities; $I_{H\alpha}$, $I_{HF(0-0,1)}$, $\lambda_{H\alpha}$ λ_{HF} are relative intensities and wave lengths of the atomic line H_α*(6563 Å, n'=3→n=2)* and the rotational Q (*k=1*)-line of the*(0-0)* vibrational band of H_2 α-Fulcher system, $f'_{rot}(k=1)$ is the population probability of the rotational level with *k=1*, Q_r is the rotational partition function, $A_{H\alpha}$ is the transition probability for H_α, $\tau^H_{n=3}$ is radiative lifetime for H_α, $\sigma^{H(n=3)}_{\max}$, $\sigma^{(0-0)}_{em}$ are excitation cross sections, $C_{thr}(\varepsilon)$ is the correction factor, which is taking into account a difference in dependencies of the cross sections on electron energy [5].

At figure 5 ratios of N_H / N_{H_2} as dependencies on methane pressure and magnetic field are shown. One can see, the opposite dependencies of N_H / N_{H_2} on magnetic field were observed at pressure 1 and 5 Pa. Growth of N_H / N_{H_2} ratio with increase in magnetic field at pressure 1 Pa is caused by increase in electron density and, as a result, by growth of dissociation rates both methane and its radicals, and hydrogen molecules by collisions with electrons. Change in dependence of N_H / N_{H_2} on magnetic field with increase in pressure is apparently caused by reduction of free path length of atoms and radicals with increase in pressure and corresponding growth of return processes rates, resulting in formation together with other products and molecular hydrogen. As it was shown in [6], atomic hydrogen density in the magnetically enhanced capacitive RF discharge in methane under similar conditions changes in a range $7*10^{10} \div 6*10^{11}$ см$^{-3}$. Taking into account the

calculated values of N_H / N_{H_2}, values in a ranges of (1.9÷2.5)*10^{12}см$^{-3}$ at pressure 1 Pa and 8.1*10^{12} см$^{-3}$ ÷2.3*10^{13}см$^{-3}$ at pressure 5 Pa have been received for molecular hydrogen densities.

References.

[1] Jr. J.D. Walker and R.M.S. John. J. of Chem. Phys. **61,** 2394 (1974)**.**
[2] D. Herrebout, A. Bogaerts, M. Yan, R. Gijbels, W. Goedheer, and E. Dekempeneer. J of Appl. Phys. **90,** 570 (2001).
[3] B.M. Smirnov. Physics of low-ionized gas. Moscow: Nauka.(1978).
[4] A.V. Eletskiy and B.M. Smirnov. Elementary processes in low-temperature plasma. In book: Encyclopedia of low-temperature plasma. Moscow: Nauka. **1**, 229 (2000).
[5] M.J. de Graaf. A new hydrogen particle source. Ph. Thesis. Netherlands. Eindhoven Technical University. (1994).
[6] S.V. Avtaeva, M.Z. Mamytbekov, and D.K. Otorbaev. J. Phys. D: Appl. Phys. **30**, 3000 (1997).

A New Type of Arc Plasma Reactor with Twelve-Phase Alternating Current Discharge for Synthesis of Carbon Nanotubes

Tsugio Matsuura, Keiji Taniguchi and Takayuki Watanabe
Industrial Technology Center of Fukui Prefecture, 61Kawai-Washizuka, Fukui, 910-0102, Japan
Professor Emeritus, Fukui University, 2-1302 Nakano, Fukui, 918-8186, Japan
Tokyo Institute of Technology, 4259 Nagatsuta, Midori-ku, Yokohama, 226-8602, Japan

Abstract
A new type of arc plasma reactor with twelve-phase alternating current (AC) discharge for synthesis of carbon nanotubes (CNTs) is proposed. A couple of six discharge electrodes by which have mutually electrical connection between them to enlarge the high temperature regions in the reactor are arranged to three dimensional locations. A new method of CNTs fabrication by this reactor which accomplishes to enlarge the suitable growth region in high-purity and at high yield was developed.

Keywords Arc plasma, Twelve-phase AC discharge, Carbon nanotubes

1. Introduction

A large number of applications for arc plasma have been used for the welding and cutting of metals up to this time. Arc plasma as the energy source with effective heat efficiency has been also tried to open new technological field for better global environment with related new industrial markets, including plasma chemical reaction.

In general, the power source for generating arc plasma is accomplished by using a direct current (DC) power supply. This is the larger the capacity the higher the cost of apparatus for inverting from AC to DC. On the other hand, the single-phase and the three-phase AC power supply have already been proposed for the same application fields. Since these systems have a characteristic of intermittent discharge, the high power arc plasma systems generated by AC power supply have not been fully developed. In order to improve this defect, a multiple-phase AC power supply has been developed. To obtain a more effective arc plasma generator by expanding this concept, we have developed a twelve-phase AC power supply [1]. The most important advantage of this system is that there are large number of discharging paths among electrodes in comparison with the case of the single-phase and the three-phase systems. Therefore, some of the plasmas always exist for continuing smoothly the discharging action. It seems as if this system was driven by the DC power supply instead of actual commercial AC power supply (60 Hz) [2].

Since CNTs discovered in 1991 at first time [3], many researchers have been provided its unique physical and chemical properties, and applications to nano-scale devices. Several methods for synthesis of CNTs such as DC arc-discharge [3, 4], laser ablation and thermal chemical vapor deposition (CVD) have been presented. The DC arc-discharge method can synthesize CNTs in highest quality than the other methods mentioned above. However its yields are much lower. Up to date, CVD method is the mainstream of mass fabrication of CNTs. In order to avoid the disadvantage of the DC arc-discharge method, the twelve-phase AC arc-discharge method is proposed here. The purpose of this paper is to describe the techniques for obtaining its method and to show the experimental results for synthesizing CNTs by using this new type of arc plasma reactor.

2. Twelve-phase AC power supply for arc plasma reactor

2.1 Three-phase to twelve-phase conversion

Figure 1 shows the electrical circuit diagram of the transformers for converting from the three-phase AC to the twelve-phase AC and the schematic connection diagram of the plasma reactor. The input of the three-phase power supply is connected to 200V commercial power lines. The primary coils of transformers are divided into two parts: one is the Δ connection and the other is the Y connection. The twelve-phase power supply can be realized by the combination of these circuits. From the Y connection, the voltage components V_x, V_y, V_z, V_x', V_y', and V_z' of the six-phase AC are defined by the following equations:

$$V_i = V_m \sin(\omega t - \frac{n}{3}\pi), (i = x, y, z), (n = 0,2,4) \quad (1)$$

$$V_i' = V_m \sin(\omega t - \frac{n}{3}\pi), (i = x, y, z), (n = 1,3,5) \tag{2}$$

where V_m and f are the maximum value of the sinusoidal wave and the frequency of the AC (60 Hz), respectively.

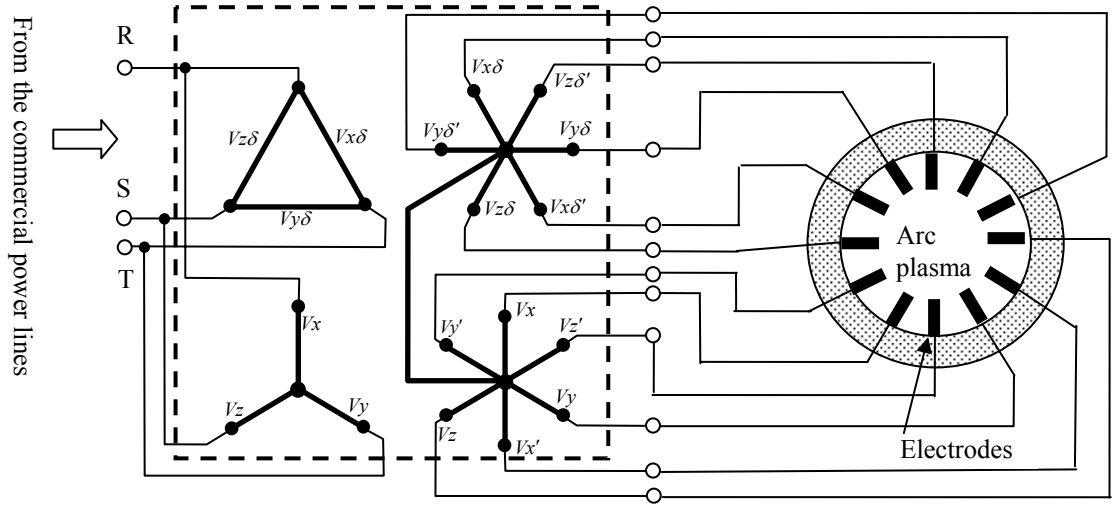

Fig. 1 Electrical circuit diagram and schematic temporary connection diagram of the plasma reactor

From the Δ connection, the voltage component $V_x\delta$, $V_y\delta$, $V_z\delta$, $V_x\delta'$, $V_y\delta'$, and $V_z\delta'$ are defined by the following equations:

$$V_i\delta = V_m \sin(\omega t - \frac{n}{6}\pi), (i = x, y, z), (n = 1,5,9) \tag{3}$$

$$V_i\delta' = V_m \sin(\omega t - \frac{n}{6}\pi), (i = x, y, z), (n = 7,11,15) \tag{4}$$

2.2 Advantages of the twelve-phase AC discharger

The configuration of twelve electrodes are symmetrically arranged to bring out the advantages of the twelve-phase discharge. The geometrical arrangement of the tips of electrodes is indicated in Fig. 2. In the case of the distance between electrodes No.5 and No.7 is unity, the ratio of the distance among other electrodes have the values as shown in the same figure.

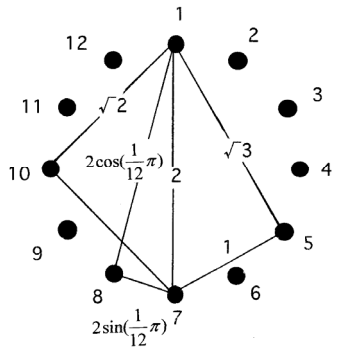

Fig. 2 The geometrical arrangement of the tip of electrodes

In general, the voltage applied between each electrodes and neutral point of the secondary coil of the transformer for the twelve-phase AC power supply can be described by following equation.

$$V_i = V_m \sin(\omega t - \frac{(i-1)}{6}\pi), (i = 1.....12) \tag{5}$$

From this equation, we can obtain the difference of the voltage between the electrode No.1 and the others. These are explained as follows:

$$V_2 - V_1 = 2\sin(\frac{1}{12}\pi)V_m \cos(\omega t + \frac{1}{12}\pi) \tag{6}$$

$$V_3 - V_1 = V_m \cos(\omega t + \frac{1}{6}\pi) \tag{7}$$

$$V_4 - V_1 = \sqrt{2}V_m \cos(\omega t + \frac{1}{4}\pi) \tag{8}$$

$$V_5 - V_1 = \sqrt{3}V_m \cos(\omega t + \frac{1}{3}\pi) \tag{9}$$

$$V_6 - V_1 = 2\cos(\frac{1}{12}\pi)V_m \cos(\omega t + \frac{5}{12}\pi) \tag{10}$$

$$V_7 - V_1 = 2V_m \cos(\omega t + \frac{1}{2}\pi) \tag{11}$$

Here we should notice that the ratio of the voltage amplitudes in equations (6)-(11) is equal to the ratio of the geometrical distances shown in Fig. 2. As the phase shift is kept constant every moment by the combination of transformers, the values of voltage/distance among each electrode are also constant every moment.

2.3 Power supply for the twelve-phase AC discharge

To realize the power supply for the generation of twelve-phase AC discharge, twelve pieces of single-phase AC arc welding transformer (DAIHEN B-250) were used. These welders are the conventional ones and have a dropping characteristic. The input voltage, the maximum non-loading output voltage, the typical loading voltage, the wattage and the range of output currents are 200 V, 80 V, 32.5 V, 12.4 kW and from 75 A to 250 A, respectively. Two pairs of six transformers are connected to the commercial AC line (three-phase 200 V, 60 Hz) with the figures of Δ and Y connections. Twelve output lines from the transformers are directly connected to the corresponding electrodes of the reactor.

Fig. 3 Setup of the twelve-phase AC power supply

Fig. 4 Photograph of the twelve-phase AC arc discharge

Fig. 3 shows the setup of the twelve-phase AC power supply. The picture of the twelve-phase AC arc discharge is shown in Fig. 4. Typical voltage and current waveforms of the single-phase AC arc discharge and the twelve-phase ones are shown in Fig. 5 and Fig. 6, respectively.

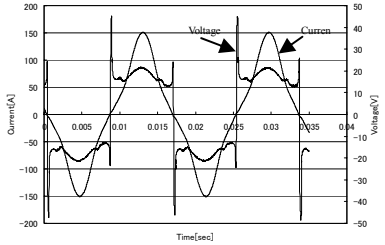

Fig. 5 Voltage and current waveforms in case of single -phase AC

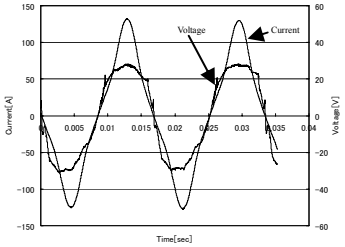

Fig. 6 Voltage and current waveforms in case of twelve-phase AC

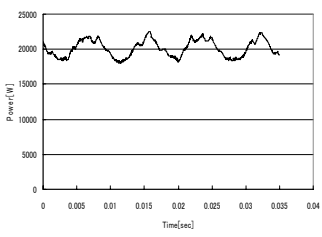

Fig. 7 Total power waveform in case of twelve-phase AC

Fig. 6 indicates the twelve-phase AC arc discharges which do not have an intermittent discharge. The waveform of the total power in the case of twelve-phase is also shown in Fig. 7. The ripple of the total power was 6.3%.

3. Synthesis of carbon nanotubes

3.1 A new type of arc plasma reactor

A new type of arc plasma reactor with twelve-phase AC discharge for mass fabrication of CNTs is shown in Fig. 8. The CNTs were produced by a twelve-phase AC arc discharge among carbon electrodes in helium gas. The electrodes of graphite rod 12mm in diameter, 500mm in length having the purity of 99.995% are configured horizontally in the reactor as shown in Fig.4. Since the electrodes are consumed by evaporation, the arc gaps among electrodes are kept constant by the motor-drive systems of which are adjusted by the voltage among them.

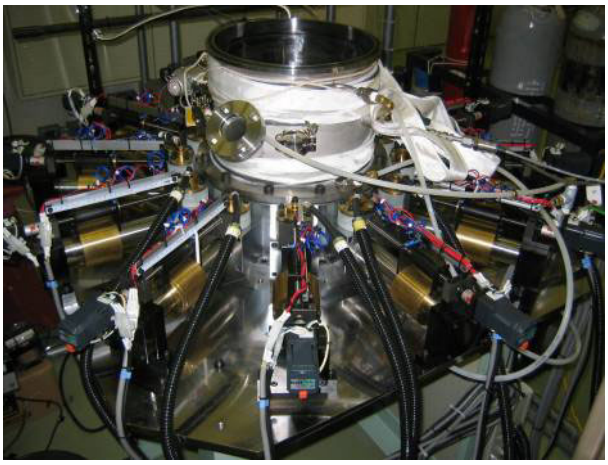

Fig. 8 A new type of arc plasma reactor for mass fabrication of CNTs

3.2 Experimental setup

Figure 9 shows the schematic diagram of the experimental setup inside of the reactor. The substrate made of the stainless steel plate (sus304, 50 mm in width, 320 mm in length and 1 mm in thickness) suspended from the ceiling of the reactor. The tip of the substrate was apart 10 mm above from the center of twelve electrodes configuration. The diameter of the plasma surrounded by the tips of twelve electrodes is approximately 60 mm.

After purging in the chamber, helium gas (purity 99.99%) is introduced and sets at 600 torr. The discharging voltage and its current are 20-45 V and 70-100 A, respectively. The carbon electrodes contain nickels as the catalyst for CNTs synthesis at 10wt. %.

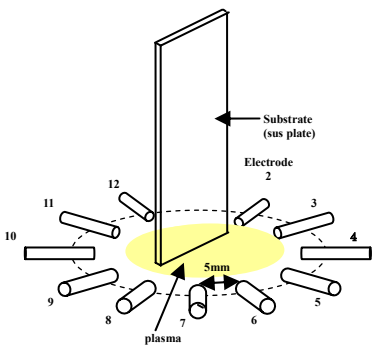

Fig. 9 Schematic diagram of the experimental setup inside the reactor

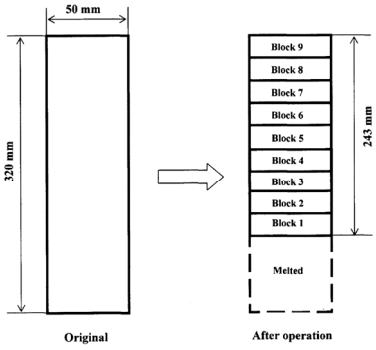

Fig. 10 Substrate for CNT deposition (original and after operation)

3.3 Experimental results and discussion

The CNTs synthesis is strongly related to the temperature of condensation and growth of carbon

molecules in plasma [5, 6], therefore the deposition was carefully analyzed to investigate the effect of deposition temperature. During the discharge for one hour, CNTs were prepared from the evaporation of the electrodes. A lot of soot-like deposit was obtained on the surface of the substrate as well as on the inner surface of the reactor. Figure 10 shows the original substrate and after operation one. The surface of remained substrate was divided equally into nine blocks. The deposit on the substrate is carefully gathered from nine sampling blocks. The products were examined using scanning electron microscopy (SEM), transmission electron microscopy (TEM) and Raman spectroscopy with a 514.5nm Ar^+ laser and were also characterized by using an energy dispersive X-ray analysis (EDX)

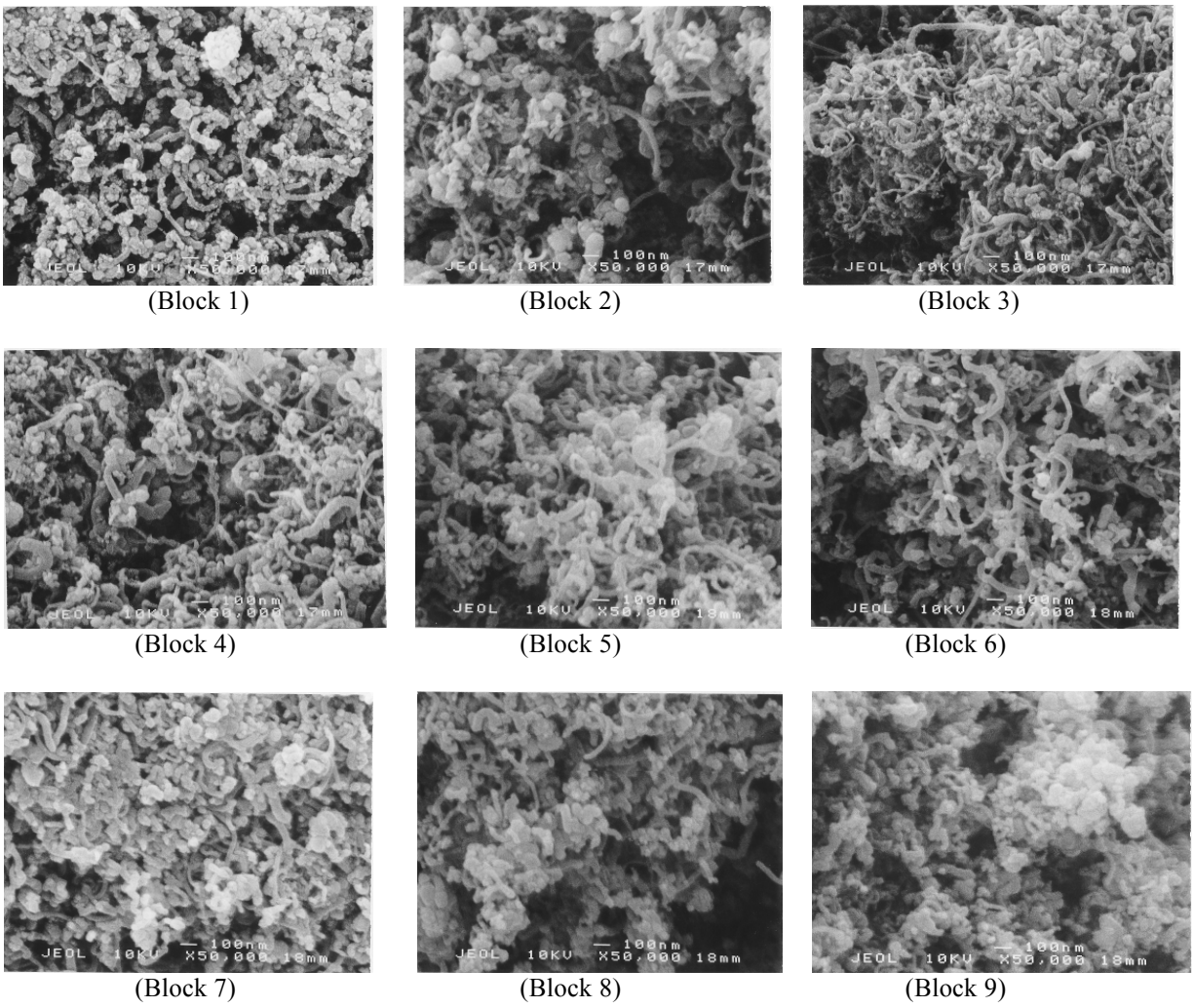

Fig. 11 SEM images of the CNTs from gathering nine blocks on the substrate

The SEM images of crude samples at each block of the substrate are shown in Fig.11. The clusters of carbon particles which are considered to be amorphous carbons are much more observed at the images of blocks 1, 2, 7, 8, and 9 in comparison with the images of blocks 3-6. On the contrary, CNTs with much less amorphous carbons are observed at the images of blocks 3-6. The surface temperature at the tip of block 1 of the substrate is estimated at 1400 degree Celsius of its melting point. The surface temperature of the bottom of block 9 was measured at 800 degree Celsius by using the thermocouples. From these evaluations, the temperature distribution on the substrate can be roughly estimated with the linear assumption of the temperature distribution. The optimum temperature for CNTs synthesis is approximately in the range from 1000 to 1250 degree Celsius. This result was congruous well with previous report [7]. From the morphological observation of blocks 2 and 8, even though their locations are not suitable for fabrication of CNTs, the length of it in block 8 is shorter than that of block 2. The multi-walled CNTs of 20 nm-40 nm in diameter shown in Fig. 12 were produced not only on the substrate but also on the wall of reactor. Nickel particle filled with the CNTs shown in Fig. 13 was identified by the energy dispersive X-ray spectrometry.

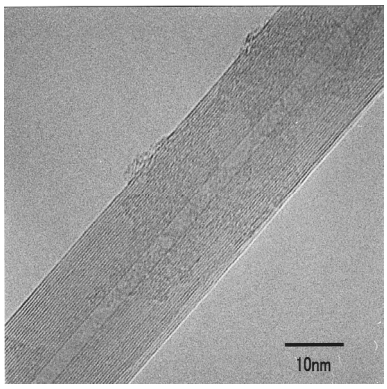

Fig. 12 TEM image of the multi wall CNTs

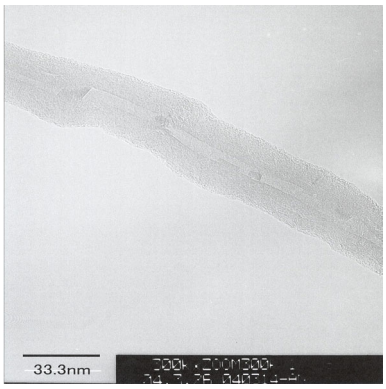

Fig. 13 CNTs filled with nickel particles

Raman spectrum shown in Fig. 14 contains the G-band (1580 cm^{-1}) and the D-band (1360 cm^{-1}). In general, the G-band shows the CNT oriented peak and the D-band shows the amorphous carbon or the structure defects of CNTs oriented peak. The synthesis of CNTs is not clearly found out on the block 1 shown in Fig.14 (a). Fig.14 (c) shows CNTs and the amorphous carbon are both synthesized on the block 8. On the contrary, the strong peak of G-band caused by synthesis of CNTs was appeared on the block 6 shown in Fig.14 (b). These results were congruous very much with the morphological observation of SEM images mentioned above.

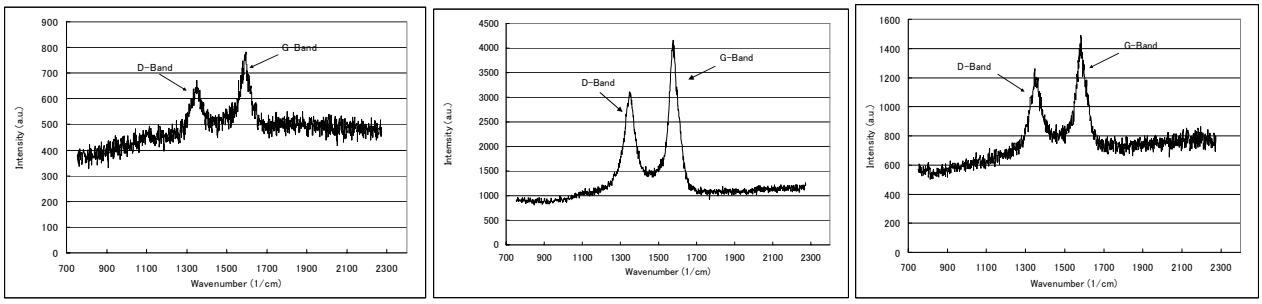

(a) block 1 (b) block 6 (c) block 8

Fig. 14 Raman spectrum of the CNTs on the substrate

4. Conclusions

We have described the techniques for obtaining the new type of arc plasma reactor with twelve-phase AC discharger. This configuration can provide the attractive advantages of the arc plasma in superior stability and long continuity. A new method of CNTs fabrication by using this reactor which accomplishes to enlarge the suitable growth region in high-purity and at high yield was developed. The optimum temperature for CNTs synthesis is approximately in the range from 1000 to 1250 degree Celsius. The multi-walled CNTs of 20 nm-40 nm in diameter were produced

5. References

[1] T.Matsuura, O.Tago, H.Tshujino, K.Taniguchi, Proceedings of International Conference MODELLING, SIMULATION & IDENTIFICATION, C-212, 81 (1994).
[2] T.Matsuura, K.Taniguchi, H.Makida, The Japan Society of Waste Management Experts, 8, 1 (1997).
[3] S.Iijima, Nature, 354, 56 (1991).
[4] T.W.Ebbesen and P.M. Ajayan, Nature, 358, 220 (1992).
[5] M.Yudasaka, T.Ichihashi, S.Iijima, J. Phys. Chem., B102, 10201 (1998).
[6] Y.Saito, New Diamond and Frontier Carbon Technology, 9, 1 (1999).
[7] T.Sugai, H.Omote, S.Bandow, N.Tanaka, and H.Shinohara, J. Chem. Phys., 112, 13 (2000).

MAGNETIZED PLASMA IN CYLINDRICAL COORDINATES – EXPERIMENT AND MODEL

A. Marek[1], M. Holík[1], O. Bilyk[1], I. Picková[1], R. Apetrei[2], R. Schrittwieser[2], Codrina Ionita-Schrittwieser[2], P. Kudrna[1], M. Tichý[1]

1 Faculty of Mathematics and Physics, Charles University in Prague, Czech Republic
2 Department for Ion Physics, University of Innsbruck, Austria

Abstract
We report on experimental and theoretical study of dc magnetized discharge in cylindrical magnetron device. The experimental study encompasses Langmuir probe and emissive probe diagnostics the theoretical one 2D Particle-In-Cell (PIC) model of the dc discharge in the mentioned system.
Cylindrical magnetron, Langmuir probe, emissive probe, Particle-In-Cell

1. Introduction

Magnetically confined plasma is used in a wide range of plasma applications. DC magnetized discharges are commonly used in plasma processing e.g. for thin film layer coating and etching. In our work we concern on dc magnetized discharge in cylindrical magnetron device. The theoretical description of plasma as well as understanding of processes and mechanism of discharge formation is easier due to symmetrical configuration of magnetron device.

2. Experimental device

Our cylindrical magnetron device has been in detail described e.g. in [1] so that only a brief description will be given here. Cylindrical magnetron consists of two coaxial electrodes – grounded stainless steel tube (anode) and water cooled cathode at its axis. Discharge area is constrained by two metallic limiters connected to cathode potential. Plasma in cylindrical magnetron is confined by homogenous magnetic field parallel to the anode axis. This is created by couple of magnetic coils and can vary up to 40 mT. The cylindrical magnetron is schematically depicted in figure 1. Magnetron usually operates in noble gases at pressures 1 – 10 Pa. Cylindrical magnetron device is evacuated by turbomolecular pump backed by dry compressing piston pump. The ultimate pressure is below 10^{-2} Pa. Plasma parameters in magnetron can be determined by means of electrical probes located in radially movable feedthrough in the central plane of magnetron. Some experimental data presented here were obtained in another cylindrical magnetron that differs from above-mentioned only in length of discharge area (30 cm instead of 12 cm) and electrodes diameter. Let us to denote these two magnetrons like "longer"

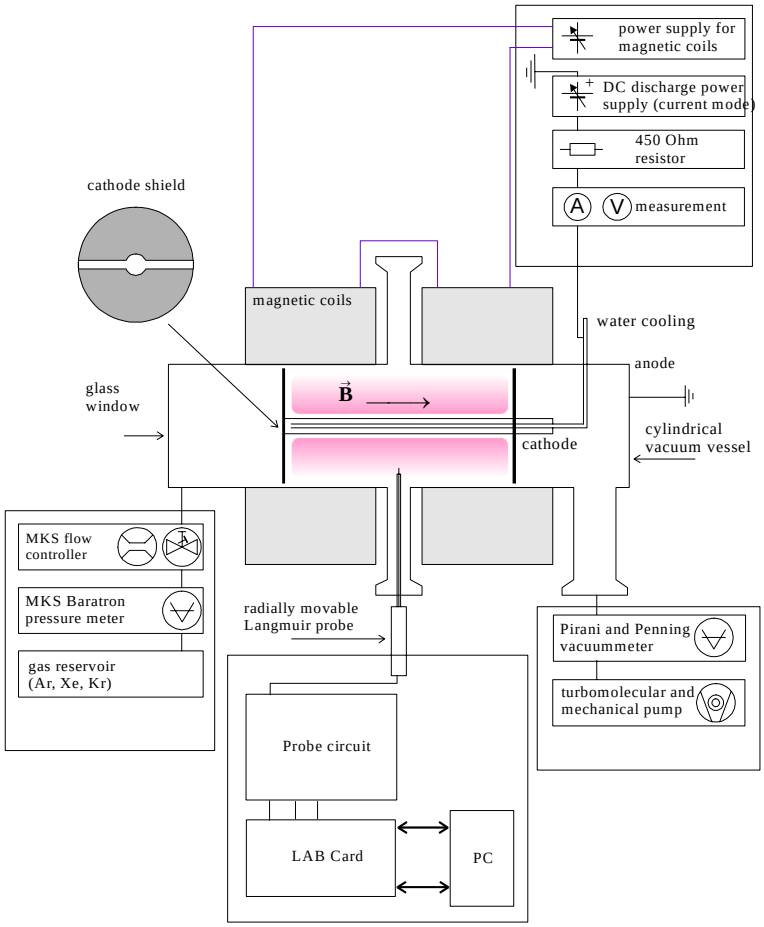

Figure 1: Cylindrical magnetron scheme. Faculty of Mathematics and Physics, Charles University in Prague.

and “shorter” for easier handling in this text. Cathode radius of the “longer” magnetron is 9 mm, anode radius is 28 mm. Dimensions of the “shorter” magnetron are given in figure 2.

3. Particle-In-Cell model of the magnetron

For theoretical description of the discharge in magnetron we used two dimensional Particle-In-Cell code OOPIC [2] developed at the University of California, Berkeley. 2D model of discharge is needed because discharge is not homogenously distributed along the whole discharge region [3]. The scheme of the region for the 2D PIC simulation of a discharge in the cylindrical magnetron is depicted in figure 2. In order to reduce computational effort we placed reflecting boundary to the middle of the magnetron and we simulated only half of the discharge area length (from the center of the discharge region to the left limiter). Though only one half of the discharge area in magnetron was modeled, simulations still needed relatively huge computational power because Debye length in magnetron is typically tens of micrometers and needs to be resolved by grid.

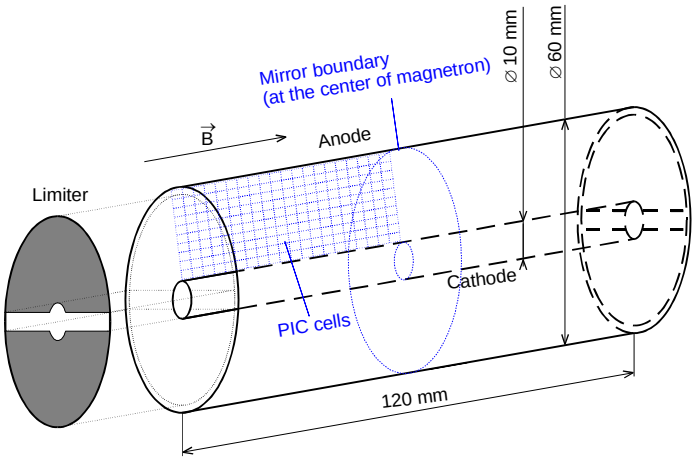

Figure 2: Scheme of region for 2D PIC simulation of discharge in the “shorter” magnetron.

4. Comparison of PIC results with experiment

An example of computational results of OOPIC model is presented in figure 3. Comparison of computational density profile with Langmiur probe data is given in figure 4 for two different experimental conditions. Considering that maximum of the electron density is proportional to the applied power we can see satisfactory agreement of model results with experimental data. Electron density maximum is approx. at the

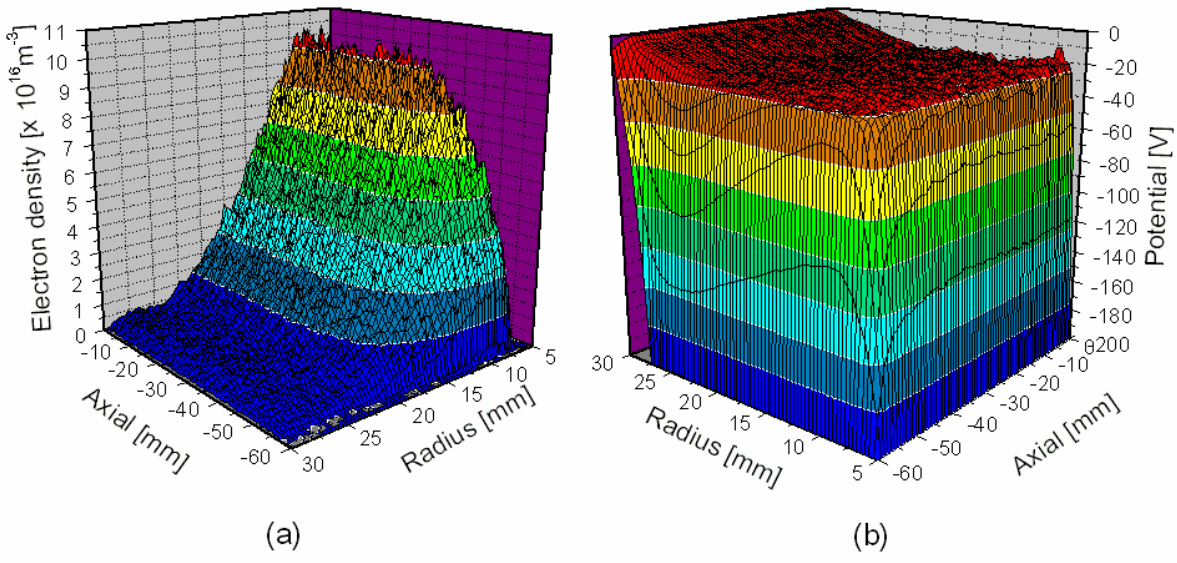

Figure 3: OOPIC simulation results of Argon discharge in magnetron at p = 4 Pa, B = 20 mT, $U_{Cathode}$ = -200 V. Data are from snapshot taken at discharge time t = 6,4.10^{-7}s. Density profile used for initial condition was obtained from former simulation with rougher computational grid. Zero of axial coordinate denotes center of magnetron; r_{Anode} = 30 mm; $r_{Cathode}$= 5 mm. Cell dimension is comparable with Debye length (i.e. 500×1250 cells).
(a) electron density profile, (b) potential profile (for better view 90° clockwise rotated).

same position in experiment as well as in PIC simulation. Electron density fall profile corresponds better with data obtained at higher magnetic field (25 mT, 5 Pa – note ratio of the magnetic induction and pressure B/p= 5 mT/Pa is the same in both experimental cases) in region of positive column. Potential profile obtained in the simulation is depicted in figure 3b. We can see relatively broad region, where the plasma potential remains practically constant – positive column. It is good result in comparison with our former 1D PIC simulations [4] and also former 2D simulations using grid with larger cells [5] (and also presented in printed abstract of this symposium), where we observed relatively big potential fall in this region. Recent results depicted in figure 3 were obtained in simulation with more precise grid. Length of cells was already comparable with Debye length. Although the broad region of the almost constant potential was observed in this simulation (i.e. well developed region of the positive column), anode fall is relatively big (approx. 20 V) and reach relatively far into the discharge volume. In contrast to that, experimental data obtained via Langmuir probe diagnostics showed that the potential fall in the anode region as well as in the positive column is only a few volts at these experimental conditions. More detailed view of the potential obtained in the simulation (figure 3b) is depicted for three different axial positions in figure 5.

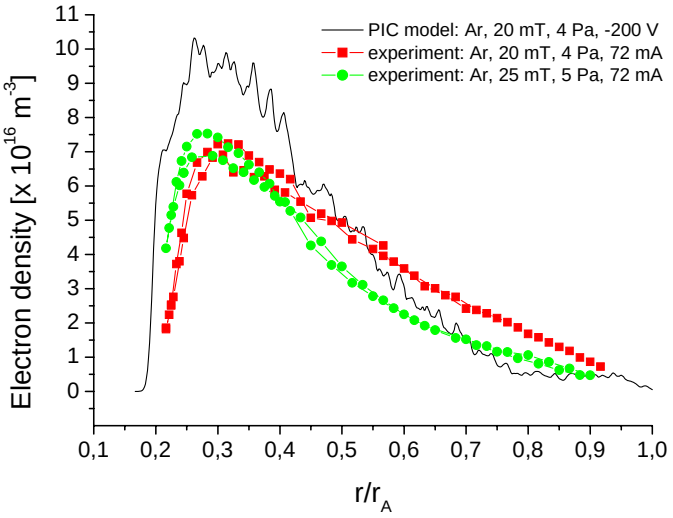

Figure 4: Comparison of computational density profile with data obtained in magnetron via Langmuir probe. r_A is anode diameter

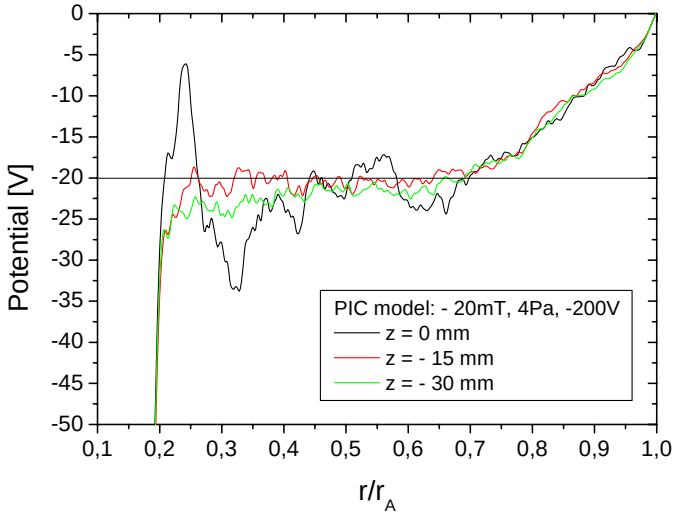

Figure 5: Detail of computational potential profile at three different axial positions. r_A is anode diameter, z = 0 denotes the center of the magnetron.

In order to validate experimental plasma potential profile by another independent method we measured plasma potential profile in cylindrical magnetron by emissive probe too (in fact with kT_e/e difference [6]). These measurements have been realized in the "longer" magnetron. Emissive probe data are depicted in figures 6 and 7. According to dependence of the floating potential on the probe heating that is depicted in figure 6 we set operating point for our next measurements. We chose heating current I_{HEAT} = 1.3 A that was already good approximation of plasma potential at given experimental conditions. Emissive probe data (see figure 7) confirmed results obtained by Langmuir probe: potential fall in the region of the positive column was only a few volts as well as the potential fall in the anode region.

Large potential fall in anode region can be caused by some of these factors: a) grid is not still precise enough, b) discrepancy is observed because of the noise in potential caused by small number of superparticles per one cell, c) model doesn't involve all processes participating in burning discharge (especially proper description

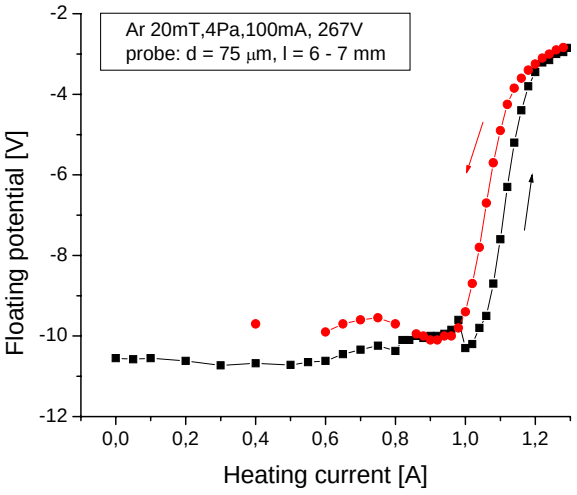

Figure 6: Heating characteristics of emissive probe. Operating point determined at 1.3 A.

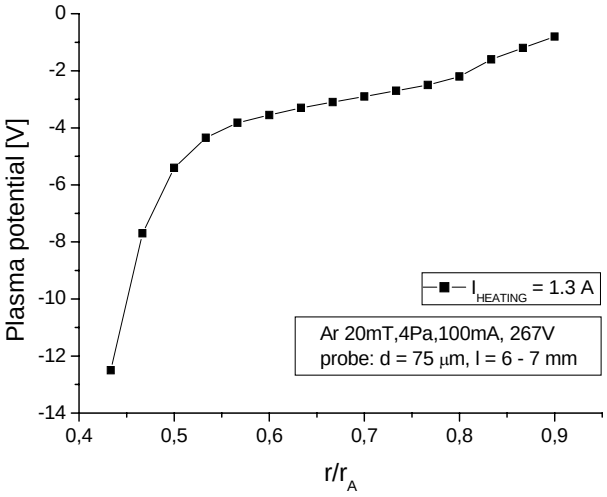

Figure 7: Radial profile of plasma potential obtained by strongly emitting probe in "longer" magnetron.

of plasma interaction with anode surface). Solution of this discrepancy of the model with experiment will be object of our future work.

Conclusion

Experimental and theoretical study of dc magnetized discharge in cylindrical magnetron device was presented at this place. Results of 2D PIC simulation were compared with data obtained by means of Langmuir probe and emissive probe diagnostics. Despite that qualitative agreement of simulation with experiment was found in electron density profiles, further improvement of model is needed because of discrepancy in potential profile. Simulation resulted to potential profile with well developed region of positive column but with relatively big anode fall, that protrudes relatively far into the discharge volume. This phenomenon doesn't correspond with experiment.

Acknowledgments

The work was financially supported by Czech Science Foundation, grants 202/03/H162, 202/03/0827 and 202/04/0360, by project COST action 527.70, by the Ministry of Education, Youth and Sports, Research plan MSM 1132000002 and by EURATOM. Thanks are also due to University of Greifswald, Germany, which provided us with the cylindrical magnetron system.

References

[1] E. Passoth, P. Kudrna, C. Csambal, J.F. Behnke, M. Tichý and V. Helbig, J. Phys. D: Appl. Phys. 30 (1997) 1763-1777.

[2] J.P. Verboncoeur, A.B. Langdon and N.T. Gladd, Comp. Phys. Comm. 87 (1995) 199-211.

[3] M. Holík, O. Bilyk, A. Marek, P. Kudrna, J.F. Behnke, M. Tich´y: Contrib. Plasma Phys. **44** (2004) 613-618.

[4] J.F. Behnke, C. Csambal, J. Rusz, P. Kudrna, M. Tichý, Czech. J. Phys. 50, Suppl. S3 (2000) 427-432.

[5] M. Holík, I. Pickova, O. Bilyk, A. Marek, P. Kudrna, J.F. Behnke and M. Tichy, Plasma Polymers and Related Materials (in print)

[6] M. Y. Ye and S. Takamura, Phys. Plasmas 7 (2000) 3457-3463.

ON THE ELECTRIC CHARACTERISTICS OF A PLASMA REACTOR WITH MAGNETIC ANNULAR ARC

L. Charakhovski[1], A. Gorbunov[1], S. Zhdanok[1], V. Ermachenko[1], A. Essiptchouk[2], A. Marotta[2], H. Maciel[3]

[1]*Heat- and Mass Transfer Institute (HMTI), National Academy of Sciences, Minsk, Belarus*
[2]*Institute of Physics, State University of Campinas (UNICAMP), Campinas, Brazil*
[3]*Technological Institute of Aeronautics (ITA), Sao Jose dos Campos, Brazil*

Abstract
It is known that nanotubes can be synthesized from carbon monoxide in a plasma reactor with Atmospheric Pressure High-Voltage Discharge (APHVD) at electric field about 1 kV/cm. This field is sufficient for formation of excited molecules of CO in plasma, owing to collisions with the high-energy electrons. Excited CO molecules are capable of activating the synthesis of nanomaterial. At the same time, the gas translational temperature can be remained on optimal level, appropriate for synthesis (about 700-800 K). However, APHVD is operated at low power only, not more than 0.2-0.3 kW. In this work we propose that similar conditions can be attained with much higher power in a plasma reactor with magnetic annular arc. The results of the study of electrical characteristics of such reactor are represented.

1. Introduction

Carbon nanotubes (CNT), considered as a new form of pure carbon, attract attention due to its unique mechanical and electrical properties. The growing number of applications for CNT has resulted in their increasing demand. Major obstacle in wide application of CNT consists in exclusively high cost and absence of large-scale manufacturing techniques. Nowadays, several methods of CNT production are being actively studied in laboratories. Most of them involve the variation of three principal techniques such as arc discharge, laser vaporization of graphite targets and chemical vapor deposition. All above-mentioned methods are exclusively labor-intensive and inefficient, which restrains scaling up their production for application in various industries. Thus, the development of new technique and technology for continuous production of CNT is very important now.

As it was shown in [1,2], a relatively high yield of carbon nanomaterial can be obtained in plasma reactor with Atmospheric Pressure High-Voltage Discharge (APHVD). This discharge is characterized by substantial non-equilibrium effects and is attractive for many potential applications. The authors [1,2] attained nanomaterial productivity at a rate of 1.5 g/hr with plasma reactor of 0.25 kW electric power. A methane-air mixture was used as plasma-forming gas. X-ray analysis showed that produced carbon material includes single wall carbon nanotubes (25-30%), fullerenes (12-20%) and diamond fraction (nearly 2-5%). By hypothesis of the authors [1,2], the proposed technique of CNT manufacturing consists in performing the Boudouard CO disproportionation reaction with participation of vibrationally excited molecules of carbon oxide [3]

$$\begin{gathered} \mathrm{CO}(v)+\mathrm{CO}(w) \rightleftarrows \mathrm{CO_2}+\mathrm{C} \\ E_v + E_w \geq 5.5\ \mathrm{eV} \end{gathered} \qquad (1)$$

where carbon monoxide molecules CO(v) and CO(w) are in vibrational quantum states v and w. Exceeding the reaction activation barrier of 5.5 eV can be achieved by the excitation of upper vibrational levels of CO molecules by electrons accelerated in high electric field. Since the activation energy for this reaction is provided by vibrational energy mode, the gas kinetic temperature can be kept at a value in the range 700-800 K, suitable for carbon nanomaterials formation.

By its electric characteristics, APHVD occupies intermediate position between glow and arc discharges and is realized in a relatively wide range of discharge voltage (~1–10 kV) and direct current (~0.02–0.2 A). In the experiments [1,2] the discharge electric field was near to 1 kV/cm at currents of 100-120 mA. As it is well known, the more effective formation of carbon nanomaterials occurs over the catalysts containing atoms of Fe,

Ni, Zr, Mo, Co. In APHVD the cathodes, made from these metals, serves as the source of catalytic particles regulated by erosion.
The serious drawback of APHVD is the transition into low-voltage electric arc discharge at current exceeding 0.2-0.3 A, which limits the net power of the installation. In order to avoid this limitation we investigated plasma chemical reactor, based on Magnetic Annular Arc (MAA), as possible apparatus for effective realization of Boudouard CO disproportionation reaction at continuous regime for large scale CNT production. Basically, MAA constitute an electric arc rotating between two coaxial electrodes in the presence of high intensity axial magnetic field at atmospheric pressure. At this kind of installation it is possible to attain a high electric field at substantially higher discharge current.

2. Experimental setup

The schematic drawing of the experimental setup is shown in Figure 1. The installation was equipped with copper ring electrodes. The outer electrode was the cathode, inner diameter of 50 mm, and anode (inner electrode) with outer diameters of 36, 48 or 48.8 mm for different experiments. Thus, a radial inter-electrode arc gap was 7, 1 or 0.6 mm, respectively. The electrodes in the form of narrow rings were isolated from the adjacent part of the setup by thermal- and electro-insulating spacers. The insulation permits to limit axial displacement of the arc and hold the arc length nearly the inter-electrode gap.
The whole system was equipped with a coaxial magnetic-arc-deflection system composed of a pair of solenoids. The solenoids create magnetic field up to 3.7 Tesla. Under the action of Lorentz force the electric arc rotates at high frequency, which was measured by photo-sensor mounted opposite the inter-electrode gap. For more stable axial location of the arc, we applied local decrease in the magnetic field obtained by location of solenoids at proper distance one from another.
The experiments were carried out at atmospheric pressure in air.

3. Results and Discussion

In Figure 2 we present one of the most important characteristics of MAA, i.e. the arc voltage *U* versus magnetic field *B* for three different inter-electrode gaps. We see that the arc voltage increases linearly with magnetic field, while it was practically independent on the arc current (in the range up to 600 A) for our experiments. This phenomenon was observed elsewhere [4,5].

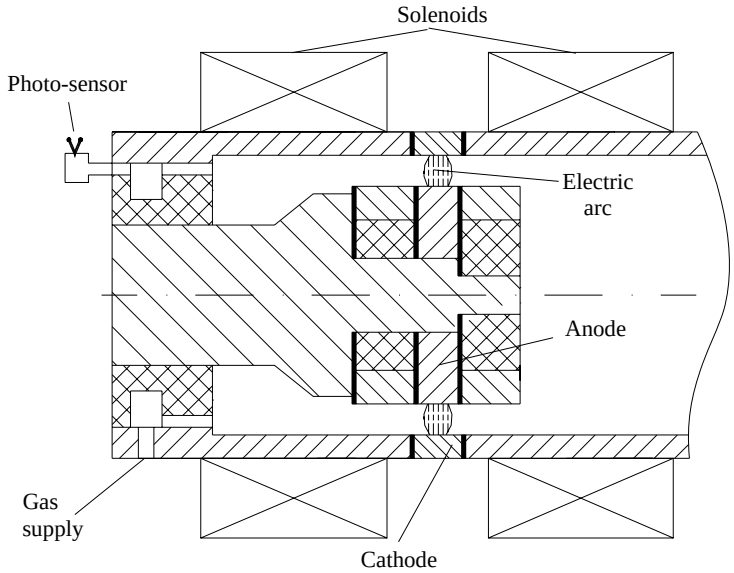

Figure 1. Experimental setup.

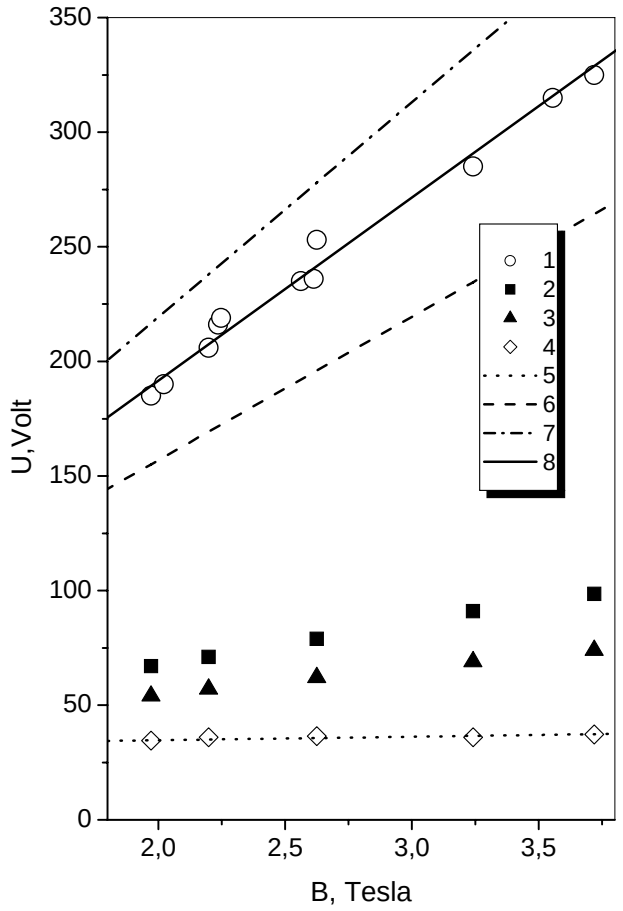

Figure 2. The arc voltage versus magnetic field for arc current of 350 A in air. Experimental data: 1 - points with inter-electrode gap of 7 mm; 2 – 1mm; 3 – 0.6 mm. 4 – U_0 from linear extrapolation of points 2 and 3 to *L=0* mm; 5 – linear fitting of U_0; 6 - radial gap between electrodes 7 mm. Calculations in accordance with eq. (4): 6 – $V_{ion}=V_{Ar}$, $m=m_{Ar}$; 7 – $V_{ion}=V_{N2}$, $m=m_{N2}$; 6 – $V_{ion}=V_{N2}$, $m=m_{Ar}$.

Besides of large inter-electrode gap, L=7 mm, we have measured discharge voltage drop U at ultra short gaps: L = 1 and 0.6 mm. Then, assuming linear dependence $U(L)$, the sum of near- electrode (cathode and anode) voltage drops $U_0=U(L=0)$ was obtained as a result of linear extrapolation of arc voltages obtained on short gaps. Points 4 in Figure 2 (closed symbols) represent the result of linear extrapolation U to inter-electrode gap of L=0. This points can be approximated by a linear function of magnetic field $U_0(B)$. Thus we can conclude that for high magnetic fields arc column voltage (without U_0) and, respectively, effective electric field $E=U/L$ in arc column are linear functions of magnetic field.

Theoretical explanation of the linear nature of *U-B* dependence for the first time has been proposed for the diffuse vacuum electrical discharges in the homopolar devices, and based on the hypothesis of critical ionization velocity v_c of plasma [6,7]. According to this hypothesis, starting with a certain small degree of ionization, the plasma velocity increases with magnetic field but no increase in ionization takes place, until the critical velocity v_c is reached. A further increase in the magnetic field leads to no increase in velocity but an increase in the degree of ionization. In other words, the drift velocity of plasma component in the magnetic field has a constant value for given gas, until total ionization was achieved. In the works [6,7] it was considered a situation where a plasma and a neutral gas are in relative motion across magnetic field. Rapid ionization occurs when a free relative kinetic energy source corresponding to motion perpendicular to the magnetic field in the system exceeds the ionization potential of the neutrals. A critical velocity for anomalous ionization was therefore hypothesized by Alfvén [6] to exist at

$$\frac{1}{2}mv_c^2 = eV_{ion}. \qquad (2)$$

Here e is the magnitude of the electronic charge, V_{ion} is the ionization potential, and m is the mass of a neutral particle. Above v_c the energy in the relative motion should be rapidly used to ionize the neutral gas.

This process, called the critical ionization velocity (CIV), is essentially an instability-driven ionization mechanism where neutral gas is ionized in a more abrupt and efficient manner than can be accounted for by classical means (binary collisions, thermal electron impact, photoionization, charge stripping, charge exchange, etc...).

Subsequently a similar explanation of *U-B* linear dependence was extended to the magnetic annular arcs. There were attempts to explain the phenomenon by a sort of collective interactions, microturbulence, etc., but a rigorous theory of ionization mechanism was not elaborated, until now [6-10]. In the absence of the azimuthal

uniformity of the discharge, i.e., in the spoke-similar arc discharges *U-B* dependence keeps linear nature and could be calculated, using the same formulas as diffuse discharge [11-14].

Theoretical studies and observations of staged CIV interactions in the laboratory have characterized the phenomenon as one in which the free energy source associated with the directed kinetic energy of the relative motion between two plasma components excites plasma micro-instabilities. These instabilities would then channel a substantial part of the relative kinetic energy to heat electrons preferentially creating a substantial population of electrons with energies above V_{ion}, which would then contribute to a substantially enhanced ionization process. The energy going into ionization ultimately comes from the relative motion (i.e. the arc column kinetic energy) and consequently the CIV interaction results in slowing down the relative velocity to near v_c during the interaction.

The instability, typically of the lower hybrid mode, is originally ignited by the cross-streaming of "seed" charged particles (arc column) in the neutral gas with respect to plasma particles and maintained through the cross-streaming between newly created and old charged particle populations. The lower hybrid wave can easily be destabilized by an ion beam perpendicular to magnetic field when the beam velocity is above the ion thermal speed. It must be emphasized that in all CIV scenarios a "seed" of charged particle must initially exist in the neutral gas.

In strong magnetic fields the ion drift $\vec{v}_E$ perpendicular both electric $\vec{\mathbf{E}}$ and magnetic $\vec{\mathbf{B}}$ fields

$$\vec{v}_E = \frac{\vec{\mathbf{E}} \times \vec{\mathbf{B}}}{B_0^2}. \qquad (3)$$

Integrating (3) in the inter-electrode gap and assuming $v_E=v_c$ we obtain the arc voltage in the form

$$U = U_0 + v_c BL, \qquad (4)$$

where U_0 – the sum of near-electrode voltage drops.

The calculated value of arc voltage *U* is shown in the Figure 2 (see lines (6)-(8)). The calculation on the base of nitrogen data (as the main component of plasma) showed the values of arc voltage below obtained experimental points (line 6). For this case the sum of energy of dissociation (9.756 eV) and ionization (15.5 eV, see [15]) of nitrogen was used as $V_{ion}=V_{N2}=25.256$ eV and $m=m_{N2}=4.65\times10^{-26}$ kg.

Following Alfven's hypothesis, one expects a burning voltage must be corresponding to the critical velocity of the specimen with lowest relation V_{ion}/m. The argon is well-known as easiest-to-ionization and heaviest component of air and posses the lowest value of V_{ion}/m. The arc voltage corresponding to critical velocity on the base of argon data (V_{ion} = 15.76 eV, $m=m_{Ar}=6.62\times10^{-26}$ kg) is shown as line 7 in the Figure 2 and exceeds the experimentally obtained one.

Assuming that, first of all, the argon atoms are ionized and owing to posses the greatest mass they can easy dissociate and ionize other specimen of air. Thus for this process we calculated the arc voltage using ionization potential of nitrogen $V_{ion}=V_{N2}$ and argon mass $m=m_{Ar}$. In this case, calculated values of arc voltage *U* agrees well with the experimental points 1 (see line 8 in Figure 2).

In accordance with (4) the electric field in MAA can be estimated as $E=Bv_c$. Thus for the CO-H_2-N_2 mixture, utilized in APHVD experiments, even for a pair C-H_2 with lowest ionization potential we obtain an electric field that exceeds 1 kV/cm at 5 Tesla. This value is approximately the same as for the APHVD. In practical situations the electric field in multi-component plasma depends on main phenomenon of interaction (exchange channel) between plasma components. Hence, it is possible to find experimentally appropriate regimes and local of reaction zone within reactor with relatively low mean temperature and substantial contribution in vibration energy of carbon monoxide in order to perform the mentioned Boudouard CO disproportionation reaction. Moreover, MAA permits to scale-up the power and utilize catalyst of different kind and phase: solid, liquid, gas.

4. Conclusion

Electric characteristic of plasma chemical reactor based on Magnetic Annular Arc were studied. It was shown that there is a possibility to obtain the conditions when discharge plasma exists in non-equilibrium state at atmospheric pressure. Specific characteristic of installation is high electric field, which linearly depends on applied magnetic field. An instability-driven ionization mechanism, where neutral gas is ionized in a more

abrupt and efficient manner, is assumed to explain observed phenomenon. By hypothesis, a substantial part of the relative kinetic energy is channeled to heat electrons, preferentially creating a substantial population of electrons with energies above ionization energy. This permit attains the highest values of electric field, similar to APHVD. The plasma chemical reactor is dedicated to perform Boudouard CO disproportionation reaction in order to obtain the carbon nanoparticles in large scale.

References

[1] S.A. Zhdanok, I.F. Buyakov, A.V. Krauklis, A.P. Solntsev, A.E. Shashkov, G.P. Okatova – Synthesis of Carbon Nanotubes under Thermal and Kinetic Non-Equilibrium Conditions. Contr. Papers of School-Seminar "Non-Equilibrium Processes and their Applications", Minsk, HMTI (2002).

[2] S.A. Zhdanok, I.F. Buyakov, A.P. Chernukho, A.V. Krauklis, A.E. Shashkov, A.P. Solntsev – Carbon Nanotubes Synthesis under Non-equilibrium Conditions. "Nanotechnology in Physics, Chemistry and Biotechnology", St-Petersburg (2002).

[3] E. Plonjes, P. Palm, G.B. Vismanathan, V.V. Subramaniam, I.V. Adamovich, W.R. Lempert, H.L. Fraser, J. W. Rich – Synthesis of single-walled carbon nanotubes in vibrationally non-equilibrium carbon monoxide. Chem. Phys. Lett., **352,** (2002).

[4] W.E. Powers, R.M. Patrick – Magnetic Annular Arc. The Physics of Fluids, 10, **5** (1962).

[5] R.M. Patrick, A.M. Schneiderman – Performance Characteristics of a Magnetic Annular Arc. AIAA Journ. **4 (**1966).

[6] H. Alfven – Collision between a Nonionized Gas and a Magnetized Plasma. Rev. of Mod. Phys.,4, **32 (**1960).

[7] U.V. Fahleson – Experiments with Plasma Moving through Neutral Gas. Phys. of Fluids, 1, **4 (**1961).

[8] E.Y. Choueiri, A.J. Kelly, R.G. Jahn – The Manifestation of Alfven's hypothesis of critical ionization velocity in the performance of MPD thrusters. In 18th Int. Electric Propulsion Conf., Alexandria, Virginia, USA, AIAA-85-2037, (1985).

[9] E.Y. Choueiri, A.J. Kelly, R.G. Jahn – Current-driven instabilities of an electromagnetically accelerated plasma. In 20th Int. Electric Propulsion Conf., Garmisch-Partenkirchen, W. Germany, AIAA-88-042, (1988).

[10] E.J. Sheppard, M. Martinez-Sanchez – Nonequilibrium Ionization in MPD thrusters. In 21th Int. Electric Propulsion Conf., Orlando, Florida, USA, AIAA-90-2608, (1990).

[11] J.A. Fay, R.A. Cochran – An Actuator-Disk Model for Azimuthally Nonuniform MPD Arcs. AIAA Journ., 9, **7 (**1969).

[12] G.W. Garrison, R.T. Smith – Characteristics of Magnetic Annular Arc Operating Continuously at Atmospheric Pressure. AIAA Journ., 9, **8 (**1970).

[13] R.A. Cochran, J.A. Fay – Occurrence and Behavior of Current Spokes in MPD Arcs. AIAA Journ., 5, **9 (**1971).

[14] R. Kribel, C. Eckdal, R. Lovberg – Properties of the Rotating Spoke in an Unstable Pulsed MPD Arc. 5, **9 (**1971).

[15] E.W. McDaniel. Collision Phenomena in Ionized Gases. J. Wiley & Sons, New-York, 1964.

Characterization via image analysis of the arc spray using two different wires

M.P. Planche, H. Liao, C. Coddet

LERMPS, UTBM, Site de Sévenans, 90010 Belfort Cedex – France

Abstract
The aim of this study was to investigate the droplets formation in the wire arc spraying process using simultaneously two different materials, namely copper and steel, in order to better understand the role of each electrode on in-flight particle properties when changes are performed in the process. Particles were collected at the spray distance in different points in the spray jet and average content and particle sizes were determined from image analysis. The evolution of particle characteristics showed important modifications in function of the radial position or the electrode nature. Finally, the role of each electrode was related to the droplets formation and coating characteristics in view of optimizing the arc spray process.

1. Introduction

Wire arc spraying is a technique that uses two conductive, consumable wires. A continuous d.c. arc sustained by an electrical source melts the crawling wire tips. A wire arc spray gun consists of a nozzle that directs a high velocity air jet to the wire tips and a wire feed mechanism that moves the wires forward. A gas flow atomizes the tips of the melting wires and accelerates the resulting small droplets toward the substrate being coated. The gas stream is responsible for forming the initial droplets after the removal of the molten material from the wire tips (primary break up), for atomizing the larger droplets (secondary break up) and for accelerating them towards the substrate. Then, higher gas velocities will result in the generation of finer particles which are accelerated to higher velocities [1, 2]. Dynamic forces of the atomizing gas stream are acting on the arc as well as on the droplets lead to different particle sizes, which, in turn, determine the coating properties [3]. In the d.c. two wires arc spray process, one of the wires is connected to the positive electrode, the other to the negative one. According to the results presented in the literature [4, 5], an important difference between those two electrodes exists leading to an asymmetric melting behaviour of two wires. Indeed, the anode melts slowly, resulting in elongated relatively large droplets while the cathode melting is rather localized which gives rise to relatively small droplets. As a consequence, this uneven melting affects the spray pattern and the coating structure [6]. Moreover, depending on the working parameters, deposit microstructures and properties can be strongly affected by the noticeable differences in the thermal and the kinetic backgrounds of the formed particles [7]. Therefore, in this study, the role of the electrodes, either anode or cathode, was considered with the objective of pointing out the differences between them in terms of particle characteristics and coating properties. A set of measurements was performed to quantify the characteristics of particles at several locations in the jet. For each location, particles were also collected in water and image analysis allowed to determine the percentage and size of each material. Some coatings were also sprayed and their thickness and microstructures analysed. Some correlations were then searched in order to demonstrate the role of each electrode in the particles formation.

2 Experimental procedures

2.1 Wire arc spray process and parameters

A TAFA 9000 arc spray gun (Tafa Inc. Concord, NH) was used for this work. A current of 150A, a voltage of 30V and 100 m^3/h atomizing air flow rate were set up for all the experiments. 1.6 mm diameters steel and copper wires were produced by Tafa®, respectively referenced 38T and 05T. The composition of these wires is given respectively in table 1 and table 2.

Table 1. Composition of TAFA 38T wire.

Element	Fe	C	P	S	Mn	Si
% in weight	97.7	0.8	0.4	0.3	0.7	0.1

Table 2. Composition of TAFA 05T wire.

Element	Cu	Zn	Pb	Sn	Si	Mn
% in weight	97.7	0.04	0.01	0.8	0.3	0.8

The main properties of these materials are summarized in table 3.

Table 3. Properties of Fe and Cu.

	Copper	Steel
Melting temperature (K)	1358	1808
Vaporisation temperature (K)	2840	3023
Density (kg/m^3)	8920	7874
Thermal conductivity (W/m.K)	401	80.2

2.2 Particles collection

Particles were first collected by directing the spray jet onto water at the location corresponding to the coating built up. The scheme of this procedure was already described in [2]. A receptacle of water was used to collect the particles passing through a 2.5 mm diameter capillator. The time of spray for this static position was about 60 seconds in order to collect enough particles. Then, depending on the nature of the electrodes, experiments were systematically performed with the two arrangements; i.e. copper anode / steel cathode and steel anode / copper cathode. Particles collection was performed at the constant axial distance of 150 mm from the nozzle exit and for three different radial locations: -2 cm, 0 and 2 cm relatively to the spray jet centre. After proper drying, photographs of the particles were taken. A photograph of these particles collected in the jet axis is given in Fig. 1 as an example.

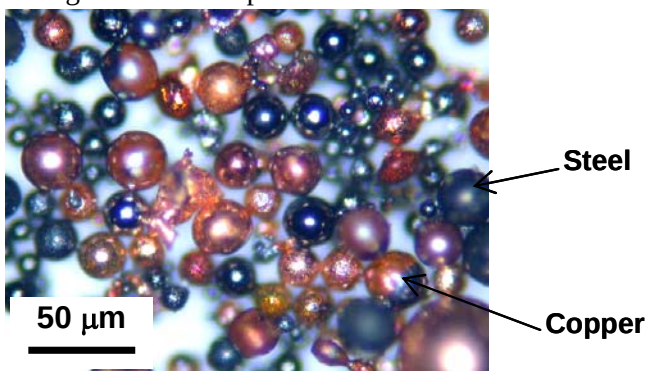

Figure 1. Photograph of collected particles.

It can be first observed that all the particles are spherical and solidified during impact on water and second, that steel particles can be easily distinguished from that of copper. It can be noted too that droplets from the two wires are not in contact during their flight because only individual droplet composed either of steel or of copper is observed. Thus, a clear identification of steel and copper particles was possible, leading to the determination of their respective number fraction and average diameter and allowing a statistical treatment of the data.

2.3 Coating built up

The substrates were prepared with grit blasting and placed 150 mm from the gun on a stationary mound. Polished cross sections of the sprayed coatings were digitalized using a Nikon EPIPHOT optical microscope coupled with a Nikon COOLPIX E955 digital camera. Pictures were taken at different radial locations in the coating corresponding to those of the particle collection, as shown in Fig. 2.

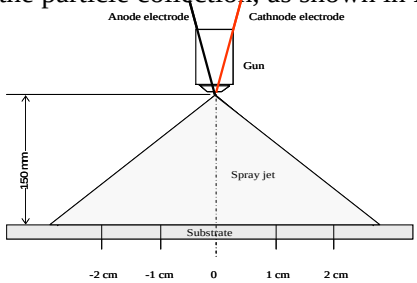

Figure 2. Locations of coating cross sections.

About 20 pictures were taken in order to cover an area important enough around the defined locations. The analyzed area of one picture is 50x40 µm² and the total area corresponds to 80000 m² for one location.

Magnification, field of vision and illumination conditions were kept unchanged to ensure consistency of these pictures and then to obtain a significant comparison between them. Because some colour differences are well marked between each specimen, an image analysis program using the RGB value as a colour criterion was used to clearly recognize the different features in the coating. This way, the area fraction of each element could be estimated with accuracy.

3 Experimental results

3.1 Analysis of the collected particles

The obtained pictures were digitalized using the «Graftek» software®. An example of images is given in Fig. 3 corresponding to particles collected in the central location in the spray jet with a steel anode and a copper cathode (Fig. 3.a) and a copper anode and a steel cathode (Fig. 3.b). Comparing these images, it can be clearly observed that important modifications in particle characteristics in terms of size and number exist when electrodes material are changed. Steel particles are bigger when steel is used as anode and only a few copper particles are present in this case; an anode copper leads to a better homogeneity of the type of particles not only in size but also in number. Statistical measurements were made on about 600 to 800 particles for each experiment in order to estimate the average diameter of each type of particles as well as their respective number fraction.

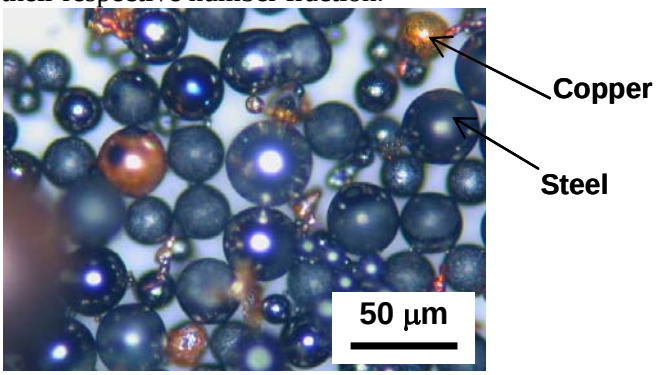

Figure 3.a. Particles in the centre of the jet sprayed with a steel anode and a copper cathode.

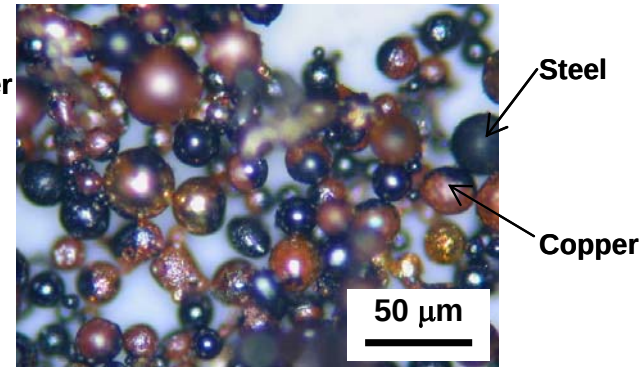

Fig. 3.b. Particles in the centre of the jet sprayed with a copper anode and a steel cathode.

3.1.1 Evolution of the average number fraction of individual wires

Fig. 4 (a) and 4 (b) present the results obtained at three different locations in the spray jet at 150 mm from the gun exit.

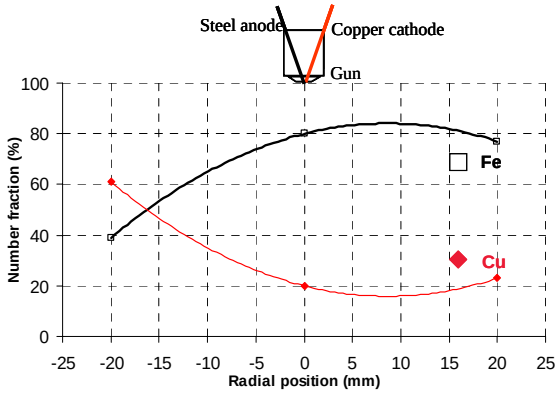

Figure 4.a. Evolution of the number fraction of particles sprayed with a steel anode and a copper cathode.

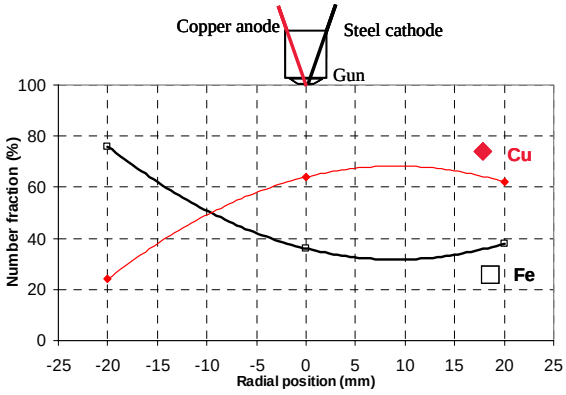

Figure 4.b. Evolution of the number fraction of particles sprayed with a copper anode and a steel cathode.

It can be observed that these particles ratii are largely dependant on the electrodes nature and on the location in the spray jet. Indeed, when the analysis location changes radially from – 2 to + 2 cm, inversed evolutions are observed demonstrating the cross – over behaviour of the particles during their flight. That leads to a percentage for one type of material the highest in location the furthest from the original position of the wire. Moreover, using steel anode conduces to obtain a number fraction almost majoritary (33% to 78%) in

comparison to that obtained with copper anode that does not exceed 64%. The same observation can be made for cathode electrodes with a number of steel particles always bigger than that of copper particles. One parameter allowing to explain this phenomenon is the difference of the melting temperature of these two materials. With a melting temperature the lowest for copper, it can be supposed that some copper droplets can instantaneously disappear due to vaporization restricting finally drastically the number of copper droplets in the image analysis.

3.1.2. Evolution of the average particle diameter of individual wires

The respective evolutions of steel and copper diameters are given in figure 5 corresponding to a process working either with steel anode / copper cathode (Fig 5 a) or with copper anode / steel cathode (Fig 5 b). These evolutions are function of the radial positions at 150 mm from the gun exit.

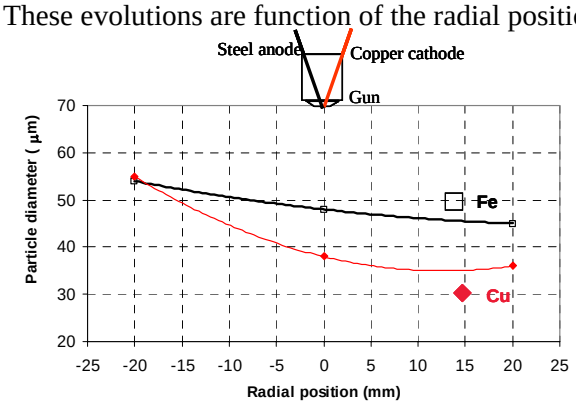

Fig. 5.a. Evolution of the diameter of particles sprayed with a steel anode and a copper cathode.

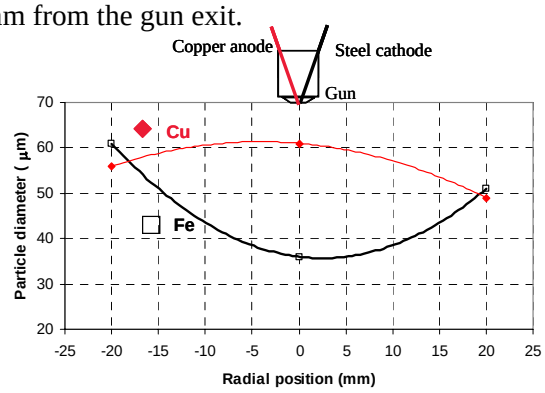

Figure 5.b. Evolution of the diameter of particles sprayed with a copper anode and a steel cathode.

Looking at the evolutions of particle diameter obtained for the same locations (Fig. 5), anode electrode allows to obtain the bigger diameters in comparison to those produced by the cathode. As already observed through high speed camera imaging [4], this is due to the diffuse attachment of the arc at the anode tip which heats a large part of the wire surface creating consequently droplets with big diameter. Respectively, the smaller diameters corresponding to the cathode electrode are attributed to the constricted attachment of the arc which is responsible of the very small detachments of molten metal. Moreover, for the location in the jet centre, the particles generated by copper anode have a bigger diameter (60 µm) than that given by steel anode (48 µm). That can be explained by their melting temperature difference which makes the melting of copper wires easier and leads to the formation of bigger particles.

3.1.3 Evolution of the average volumetric percentage

From the results obtained by both evolutions (numerical fraction and droplet diameter), the average volumetric percentage of each material can be deduced using the following relations:

$$V(steel) = N(steel)\frac{\pi}{6}d^3(steel) \quad (1)$$

$$V(copper) = N(copper)\frac{\pi}{6}d^3(copper) \quad (2)$$

where N is the number and d the mean diameter of each material.

$$\%\ of\ copper = \frac{V(copper)}{V(Total)} \quad (3)$$

where $$V(Total) = V(copper) + V(steel) \quad (4)$$

Fig. 6 presents the evolution of these percentages for the two different process combinations. The role of the anode is clearly demonstrated because the volumetric percentages obtained either for steel anode or for copper anode are superior to 85% in the jet axis which are the result of the higher diameters found in this location. It appears also that a minor percentage of copper exists in the eccentric positions (-2 and +2 cm) relatively to steel percentages. Consequently, these results suggest that the contribution of the anode electrode in the coating built up will be largely preponderant. Moreover, with the low melting temperature of

copper, it can be assumed that the smallest copper particles can instantaneously disappear due to vaporization phenomena decreasing finally their contribution in the volumetric percentages.
This conclusion if confirmed by the determination of the mean volumetric fractions for the three locations. Indeed, it is interesting to note that a globally minor volumetric fraction (50 %) of copper exists in comparison to steel one (65 %). To conclude, that proves the copper disappearance because the velocity imposed on the wires advance is the same. This remark will be confirmed in the future by the coating microstructure analysis.

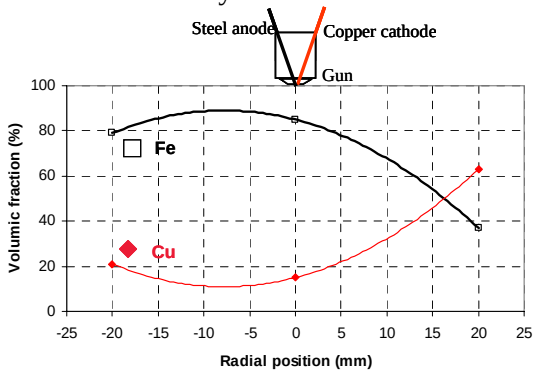

Figure 6.a. Evolution of the volumic fraction of particles sprayed with a steel anode and a copper cathode.

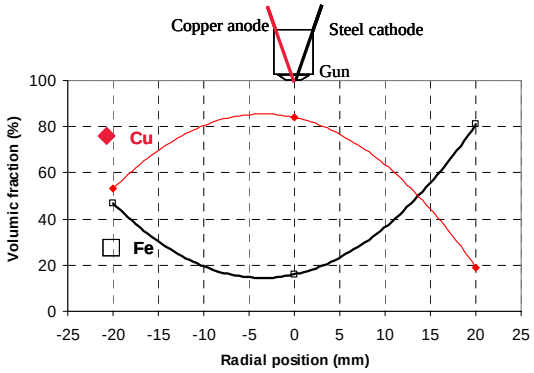

Figure 6.b. Evolution of volumic fraction of particles sprayed with a copper anode and a steel cathode.

4 Coating microstructure

From image analysis of a cross section of sprayed deposit, typical microstructure of these deposits is given in figure 7. This figure corresponds to the microstructure obtained at 150 mm from the gun exit for respectively steel anode / copper. This image reveals predominant regions including dark and light colours which correspond respectively to copper and steel materials. Using the image analysis program to distinguish the different colours present in the coating, the area fraction of steel and copper can be quantitatively defined and compared to previous results.

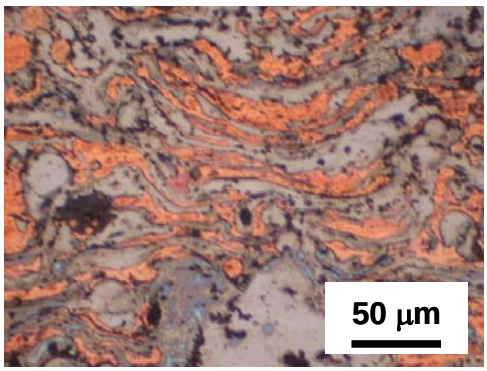

Figure 7. Typical microstructure of coating sprayed with steel anode and copper cathode in the jet centre at 150 mm from the gun exit.

Figures 8 gives the microstructures of deposits obtained at the two eccentric positions (+ 2 and – 2 cm relatively from the jet axis) and for the two different electrodes arrangements corresponding respectively to steel anode / copper cathode (Fig 8 a) and to copper anode / steel cathode (Fig 8 b).
The variations of steel and copper contents along the cross section of the deposit follow the same tendency than that presented by particle analysis i.e. the cross behaviour of the particles during their flight is clearly observed. It can be observed that the highest quantity of one or the other material regardless to the fact of where the measurements are performed. In order to give a quantitative description of material distribution in the different coatings, its cross section are digitalized by using an optical microscope and the images analyzed via the computer image analysis. Due to random phenomenon which takes place in the spray process, it can be assumed that the area fraction determined from the images analysis is directly proportional to the volumetric fraction previously examined. In conclusion, after comparing these results, a good correlation can be found between the two giving no more than 5% difference between them.

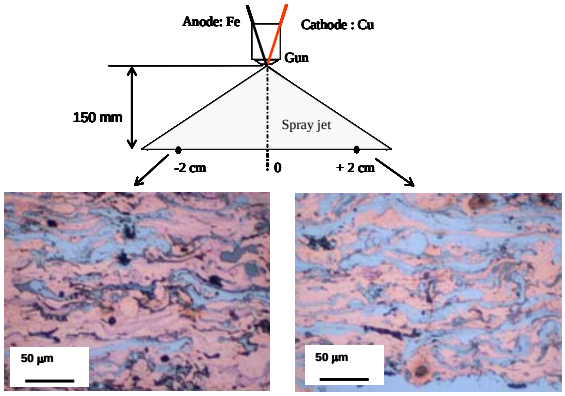

Figure 8.a. Microstructures of coating sprayed with a steel anode and a copper cathode at +2 and -2 cm from the jet axis.

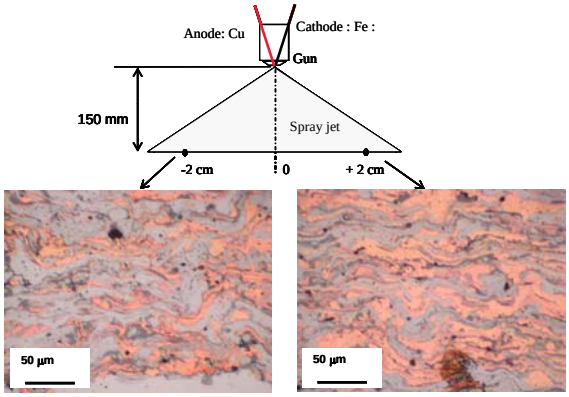

Figure 8.b. Microstructures of coating sprayed with a copper anode and a steel cathode at +2 and -2 cm from the jet axis.

5 Conclusion

Commercially available 1.6 mm in diameter TAFA steel (30T) and copper (05T) wires are sprayed together with the TAFA 9000 spray process at a voltage of 30V with a current intensity of 150 A with a total 100 m^3/h air as atomizing gas. With the help of a specific set up dedicated to collect the particles at different radial locations, + / -2 cm relatively from the jet axis and at 150 mm from the gun exit, the analysis of these collected particles allows to quantitatively define the electrode function in terms of particles production.It is interesting to observe that while steel particles increase from the left to the right, copper particles decrease in the similar way accordingly, regardless to the fact that copper and steel wires are positioned on the right and left hand side of the axes of symmetry respectively. That demonstres the cross over behaviour of the particle trajectories. Finally, it is proved that the asymmetric melting, droplet forming and detaching behaviour of the two wire tips affect the spray pattern, especially the coating microstructure. Appreciable differences are pointed out in coatings containing a majority of steel or copper relatively to the material anode used for spraying. Then, it is clearly shown that the use of steel anode leads to greater percentage of this material than that corresponding to copper anode. In conclusion, the microstructure analysis presents the same material content distribution as that already estimated by image analysis, with a maximum deviation between them not higher than 5 %. It has been proved that the smallest copper particles produced by the hottest electrode (the anode) vaporize immediately leading to losses of this material in the coating.

References

[1] H. Steffens, "*Metallurgical changes in the arc spraying of steel*" , Br. Weld, Vol 134, n°4, p.597-605

[2] M.P. Planche, A. Lakat, H. Liao, C. Coddet "*Investigations of in-flight particles characteristics through DPV measurements and correlation with impact analysis and coating properties*", In Proc. Thermal Spray 2003 : Advancing the Science & Applying the Technology, (ed) C Moreau and B. Marple, published by ASM Int., Materials Park , OH , Orlando (2003), p.1175-1182

[3] X. Wang, D. Zhuang, E. Pfender, J. Heberlein, W. Gerberich, 1994, "*Effect of Atomizing Gas Pressure on Coating Properties in Wire Arc Spraying*", Proceedings of the 7th International Thermal Spray Conference, Boston, Massachusetts, Proceedings edited by C.C. Berndt and S. Sampath, Pub. ASM International, (1994), p. 587-592

[4] N. Hussary, J. Heberlein, "*Investigations of arc behaviour and particle formation in the wire arc spray process using a high speed camera*", in Thermal Spray Surface Engineering via Applied Research, (ed) C.C. Berndt, published by ASM Int., Materials Park , OH, Montreal, (2000), p. 737-742.

[5] T. Watanabe, X. Wang, S. Heberlein, E. Pfender, W. Herwig, "*Voltage and current fluctuations in wire arc spraying as indications for coating properties*", in Thermal Spray : 'practical solutions for engineering problems', Ed. C.C. Berndt, published by ASM Int., Materials Park, Ohio-USA, (1996), p. 577-583.

[6] M. Kelkar, N. Hussary, J. Schein, J. Heberlein "*Optical diagnostics and modelling of gas and droplet flow in wire arc spray*", In Proc. Thermal Spray 1998 : Meeting the challenges of the 21 st century, (ed) C Coddet, published by ASM Int., Materials Park , OH , Nice (1998), p.329 – 334

[7] M.P. Planche, H. Liao, C.Coddet "*Relationships between in-flight particle characteristics and coating microstructure with a twin wire arc spray process and different working conditions*", in Journal of Surface Coating T, 182, (2004), p.215-226

Acknowledgments

The authors would like to express their thanks to the financial support of this research from ANVAR.

Abrasion Resistant Coatings for Glazing Applications Technology Scale up

T. Miebach, C. D. Iacovangelo, M. Mercedes, T. W. Kim, W. A. Morrison

GE Global Research Center, General Electric Company, Niskayuna, NY, USA

Abstract
We have investigated the different aspects of arc design with regard to industrialization criteria in an effort to optimize the arc design. Examples will be given of how arc design can be modified to improve arc efficiency and performance. Principles to compare and characterize different arc designs in the coating process were developed. Finally, during this work an understanding of the deposition process was sought and some insights were gained on the relationship between arc and/or plasma parameters and the performance of the deposited coating.

Keywords
Expanding thermal plasma, abrasion resistant coating, plasma arc design

Introduction

GE Global Research has been actively pursuing the coating of polymer surfaces with a variety of coatings that allow plastics, such as polycarbonate, to be used to replace glass in transportation and architectural window applications [1]. Plasma based deposition processes have been used in the past to generate various relevant functional coatings, e.g. abrasion resistant or UV absorbing coatings, at substrate temperatures low enough to be compatible with most plastics. However, most plasma deposition processes are not able to coat polymer surfaces at high rates and uniformly over large areas and thus have not been proven to be cost effective.

Schram and Kroesen, at the Eindhoven University of Technology (EUT), developed a deposition process using an individual expanding thermal plasma source (ETP) [2]. It was shown previously that the ETP technology could be used to apply a large variety of coatings at a high rate (typically in the order of 2-30 micron/min) over areas with a diameter in the range of 10-15 cm. Schaepkens et al. reported on the scalability of this process and the development of a unique, high-rate, large area plasma deposition process at General Electric to generate various functional coatings on polymeric substrates [3,4]. The process relies on the integration of a multiple individual ETP sources into an array to form a multi-source plasma deposition setup. Large areas can be coated by translating large area substrates past the array. It has been shown that the versatile control of parameters in the ETP setup (i.e. arc current, gas flow rates and working pressures) enables specific tuning of the film properties (i.e. chemical composition, optical and mechanical properties) [5].

EXATEC LLC was founded as a joint venture of Bayer Material Science and GE Advanced Materials specifically with the automotive market in mind. EXATEC is developing technologies to enable the use of polycarbonate in automotive glazing systems and its R&D covers all processes and manufacturing steps. As part of this portfolio of technologies, plasma enhanced chemical vapor deposition (PECVD) using an ETP arc as the plasma source is used for the vacuum deposition of an abrasion resistant layer on polycarbonate substrates. This technology was successfully scaled to a production scale unit at EXATEC's facility in Wixom, MI, USA. In the process of scale up a variety of issues were addressed, the reactor design, the accommodation of larger substrates, the industrialization of the arc design, process development and coating performance, to name a few.

This work will focus on the subject of plasma arc design, its implications on arc performance and the industrialization process. Maecker first introduced the ETP arc in 1956 [6]. Modifications to the original design were made to study non-ideal plasma effects [7] and the physics of strongly flowing cascaded arcs plasma [8]. Changes were made by Kroesen for the development of the plasma deposition process [2,9], but since then little or no changes were reported.

For the use of an ETP arc in an industrialized application a variety of aspects need to be considered. Functional aspects related to process development have been described in numerous references cited above.

With the process scale up the question of variability (arc to arc for multiple arc systems) and stability (in extended operation) becomes of interest. Also to be considered are aspects of cost. Both, initial cost and operations cost, the latter related to reliability and serviceability, come to the forefront. We have investigated the different aspects of arc design with regard to the criteria above in an effort to optimize the arc design. Reducing the number and complexity of the components involved is one strategy to address the requirements above. Examples will be given of how arc design can be modified to improve arc efficiency and performance. Criteria to compare and characterize different arc designs in the coating process were developed. Finally, during this work an understanding of the deposition process was sought and some insights were gained on the relationship between arc and/or plasma parameters and the performance of the deposited coating.

Experimental

The experimental approach was to investigate the effect of arc design changes on the plasma properties and ultimately coating performance. The different arc designs were characterized by total ion flux measured in amps (A). The amount of argon that is ionized was measured by a Langmuir probe [10]. A commercial probe, SmartProbe™ from Scientific Systems, Ltd., was used. This is an automated Langmuir probe system including an auto linear drive, which provided spatially or time resolved measurements of a wide range of plasma parameters. The probe was positioned perpendicular to the arc on a linear drive capable of scanning across the plasma jet. The ion flux was measured at about 25cm from the plasma source, i.e. at the same position as a typical working distance (WD). From the measured current-voltage (I-V) curve different plasma parameters can be derived. The key measurement parameter gained from the I-V curve that is used for the subsequent calculations in this work is the uncorrected ion flux P_i measured in mA/cm^2. To characterize an arc, the uncorrected ion flux is measured as a function of radial distance across the expanding plasma at the given WD. The data obtained is fitted to a Gaussian distribution and from the area under the curve (A_r) and width (w_r, Gaussian width) obtained from this fit the total ion flux was calculated as

$$Total\ Ion\ Flux = A_r w_r \sqrt{\pi/2} \qquad (1)$$

This total ion flux together with the width of this Gaussian distribution will be used to describe and compare the expanding thermal plasma process conditions.

Coating depositions were done at 45 mTorr process pressure. In the examples given below, the substrate were 4”x 4” pieces of commercially available silicon hard coated polycarbonate sheets from GE Structured Products. The substrate was coated with 2 layers of abrasion resistant coatings. Each layer was deposited by passing the sample by the arc using 0.19 standard liters per minute (slm) of D4 under the arc conditions described below. A first coating was applied at an oxygen flow rate of 0.3 slm and the second layer at an oxygen flow rate of 0.8 slm. The coating performance was evaluated with regard to coating thickness, adhesion and abrasion resistance. The coating thickness was measured by incorporating pieces of silicon chips on top of the substrate to be coated and the thickness measured *ex situ* using spectroscopic ellipsometry. The coating adhesion was determined according to the ASTM D3359 cross hatch test before and after a 3-day immersion in 65 ºC water and is expressed as a ranking from 0B to 5B. Taber abrasion resistance was determined in accordance with ASTM D1044, i.e. the increase in haze measured after 1000 cycles of Taber abrasion using CF-10 wheels with a 500 g load was measured.

Results and discussion

The expanding thermal plasma arc is an example of a wall stabilized plasma source. The original EUT arc, as described by Kroesen [2] and shown in Figure 1, consists of three cathodes and an anode separated by a stack of four or more electrically isolated copper plates. The copper plates define the plasma channel in which the arc column is stabilized. In addition, this plasma channel provides the flow restriction, which leads to an increased pressure in the arc housing where the arc originates at the cathode.

One approach to meet the requirements for an industrialized arc outlined above is to simplify and reduce the number of components. A single, adjustable cathode has been described in the patent literature [11]. Using Langmuir probe measurements, no difference was observed utilizing three vs. one cathode for an EUT style arc. The advantage of an adjustable arc is in the potential to adjust for arc-to-arc variability and long term arc drift during operation.

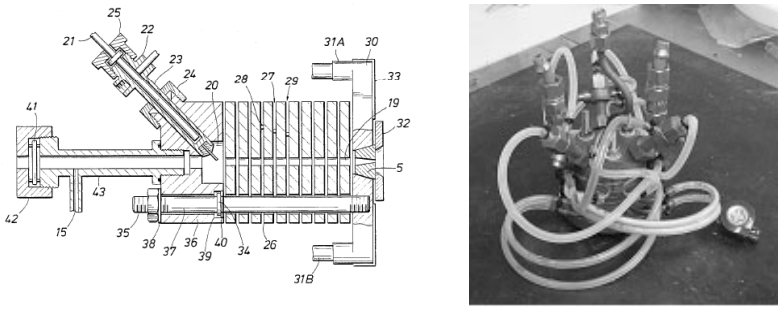

Figure 1: Schematic design and picture of the original EUT design

To investigate the possibility of changing the cascade plate (CP) design, various styles and numbers of cascade plates were investigated. Selected data is summarized in Table 1. Different comparisons can be made from this data table. Comparing data sets A, B and C one can see the effect on total ion flux with changing number of cascade plates at constant diameter. An initial drop in ion flux is observed going from 4 to 2 cascade plates. This is accompanied by a loss in power corresponding to the reduced plasma resistance because of the shorter channel length. Reducing the number of CP from 2 to 1, however, the total ion flux remains the same, while the arc power drops further. Examples C through F illustrate that the ion flux can be recovered and indeed exceeded by reducing the channel diameter of the single CP. With decreasing channel diameter the power requirements to run at constant currents increases. In addition, the amount of total ion flux generated with the input power indicates varying efficiencies of the different designs.

Data set	***CP Design***	***Orifice Diameter*** [mm]	***Number of CP***	***Total Ion Flux*** [A]	***Gaussian Width*** [mm]	***Power*** [kW]	***Efficiency (flux/power)*** [A/kW]
A	Straight	4	4	47.8	219	2.87	16.7
B	Straight	4	2	39.7	201	2.00	19.9
C	Straight	4	1	39.8	206	1.55	25.7
D	Straight	2.54	1	52.8	220	2.09	25.3
E	Straight	2	1	72.2	241	2.85	25.3
F	Straight	1.8	1	77.9	248	3.62	21.5
G	Cone	1.3 / 3.4	1	47.5	227	2.36	20.1
H	Invt. cone	3.4 / 1.3	1	58.0	242	2.70	21.5

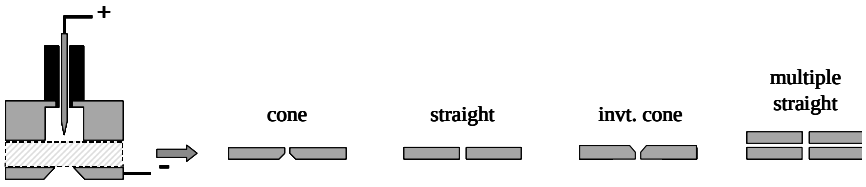

Table 1: Summary of cascade plate design changes investigated. All arcs were measured under identical current controlled conditions (2.0 slm Ar flow, 70 A arc current and 45 mTorr chamber pressure)

Examples G and H illustrate that this interaction between the plasma and the cascade plate is even more complex. A cascade plate with a cone shaped orifice was investigated in two different configurations. While, from a flow dynamics perspective, both configurations represent similar conductance, the interaction with the plasma leads to different ion flux and arc power.
The data presented in Table 1 illustrates the effect changes in cascade plate geometry can have on the flux and Gaussian width. This geometry dependence adds to the typical arc control parameters, argon flow and arc current. Combining results from all straight channel arc designs, Figure 2 shows the dependence of total ion flux, Gaussian width and arc power on CP diameter, argon flow and current.

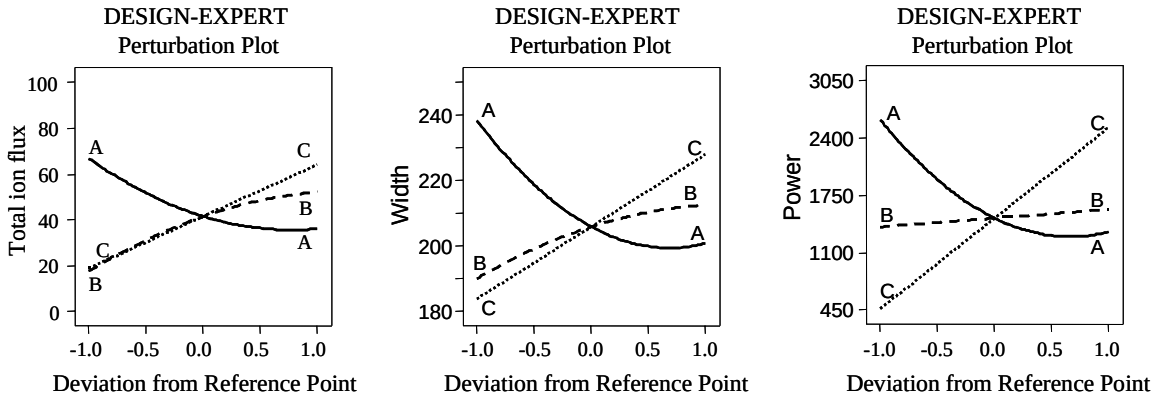

Figure 2: Pertubation plot showing observed trends for total ion flux, Gaussian width and power as a function of CP orifice diameter (A, solid line), argon flow (B, dashed line) and arc current (C, dotted line).

Trends for the three arc parameters are very similar. With decreasing CP orifice diameter, the ion flux, Gaussian width and power increase exponentially. The same parameters increase linearly with current. The argon flow reaches a limiting plateau. The interaction between argon flow and current can shift this plateau indicating a current and an argon limited operating region. Little effect of argon flow on power is observed. While the trends shown here are for a single straight CP, they hold true for any of the investigated CP designs or numbers. What does change is the magnitude of the trends with respective geometries.

The data so far shows that a multitude of parameters can be applied to change the output of the arc. One of the very practical questions is how to compare the different arc designs and operating parameters with respect to coating performance. For this purpose, coating depositions were made with two different arc designs. The first arc designs that were used are the original EUT arc design as shown in Figure 1 using four CP and a triple cathode. The comparison was made to a single cathode, single CP design with a 1.8 mm orifice diameter shown in Figure 3.

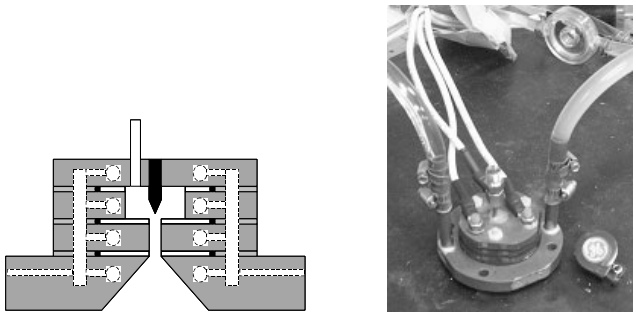

Figure 3: Schematic design and picture of a single CP arc design (patent pending)

Depositions were made at a range of ion flux. This range was achieved by employing various combinations of argon flows and currents. Figure 1 shows the obtained coating thickness for a two pass coating as a function of total ion flux. The data includes depositions by both arcs and a good correlation was observed.

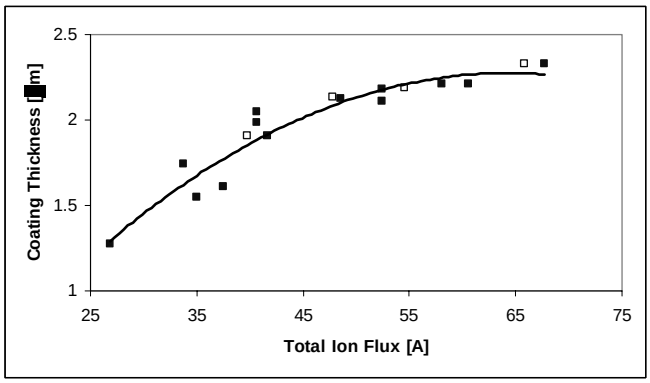

Figure 4: Coating thickness as a function of ion flux for both arc designs investigated.

In addition to this correlation on coating thickness a comparison of the coating Taber abrasion performance is made in Table 2. The Taber abrasion performance at identical arc conditions (i.e. argon flow and current, data set I + J) shows a significant difference between the two arcs (1.7 % and 6.6 % Δhaze for the two arcs, respectively). Data sets K + L shows the same two arcs adjusted to bracket a much narrower ion flux range, which gave virtually identical performance.

Data set	***Orifice Diameter*** [mm]	***Number of CP***	***Argon flow*** [slm]	***Current*** [A]	***Total Ion Flux*** [A]	***Thickness*** [µm]	***Taber abrasion Δhaze*** [%]
I	4	4	2	60	39.8	1.91	1.7
J	1.8	1	2	60	65.8	2.33	6.6
K	4	4	2	70	47.8	2.13 (0.04)	1.3 (0.3)
L	1.8	1	1.65	55	54.6	2.19 (0.08)	1.4 (0.2)

Table 2: Comparison of two arc designs

Summary

We have investigated the different aspects of arc process and design with regard to industrialization criteria in an effort to optimize the arc design. It was shown that the combination of argon flow, arc current and CP geometry can change the output of the arc over a wide range with respect to total ion flux, Gaussian width and arc power. Depositions of abrasion resistant layers using different arc designs showed that total ion flux was the central parameter to achieve parity between different arc designs.

Acknowledgements

The authors would like to acknowledge Exatec, LLC in general for funding this work and in particular Steve Gasworth, Global Plasma Technology Manager, for continuous support and discussions. Also acknowledged for continuous discussions is Prof. Richard van de Sanden at Eindhoven University of Technology.

[1] a) D. Katzamberis, K. W. Browall, C. D. Iacovangelo, M. Neumann, H. Morgner *Progress in Organic Coatings* **34**, 130 (1998) b) K. W. Browall, C. W. Reed, D. Katsamberis *NATO ASI Series, Series 3: High Technology **21**(Protective Coatings and Thin Films)*, 565 (1997).
[2] a) D. C. Schram, G. M. W. Kroesen *US Patent No. 4,871,580*, (October 3, 1989) b) W. G. J. H. M. van Sark *Handbook of Thin Film Materials*, H. S. Nalwa, Ed., Academic Press, **Vol. 1**, 79 (2002).
[3] M. Schaepkens, S. Selezneva, P. Moleker, C. D. Iacovangelo *J. Vac. Sci. Technol. A*, **21**(4), 1266 (2003).
[4] M. C. M. van de Sanden, P. J. van den Oever, M. Creatore, M. Schaepkens, T. Miebach, C. D. Iacovangelo, R. C. M. Bosch, M. Bijker, M. Evers, D. C. Schram, W. M. M. Kessels *Ann. Techn. Conf. Proc.-Soc. Vac. Coat.* **47th**, 43 (2004).
[5] Y. Barrell, M. Creatore, M. Schaepkens, C. D. Iacovangelo, T. Miebach *Surf. Coat. Technol.* **180-1**, 367 (2004).
[6] H. Z. Maecker *Naturforsch.* **11a**, 457 (1956).
[7] a) R. J. Rosado *An investigation into non-equilibrium effects in thermal argon plasmas*, PhD thesis, Eindhoven University of Technology (Oct. 1981) b) C. J. Timmermans *An investigation of pulsed high density plasmas*, PhD thesis, Eindhoven University of Technology (May 1984).
[8] J. C. M. de Haas *Non-equilibrium in flowing atmospheric plasmas*, PhD thesis, Eindhoven University of Technology (Sept. 1986).
[9] G. M. W. Kroesen *Plasma depositions investigations on a new approach*, PhD thesis, Eindhoven University of Technology (Mar. 1988).
[10] a) M. A. Lieberman, A. J. Lightenberg *Principles of plasma discharges and materials process*, Wiley Interscience (1994) b) J. D. Swift, M. J. R. Schwar *Electrical Probes for Plasma Diagnostics*, American Elsevier (1969)
[11] a) M. Schaepkens, C. D. Iacovangelo, T. Miebach, *US Patent application, US 2004/0040833* (Mar. 4, 2004) b) M. D. Bijker, L. P. M. Clijsen, F. C. Dings, R. L. J. R. Pennings *PCT patent application WO2004/105450* (December, 2, 2004).

Theoretical and experimental validation of an arc discharge model based on the balance of the energy equation

J. L. Tapia[1], J. Pacheco-Sotelo[1, 2], M. Pacheco[2], J. S. Benitez-Read[1, 2], R. López-Callejas[1, 2] G. Zissis[3], S. Bhosle[3].

[1] *Instituto Tecnológico de Toluca, México*

[2] *Instituto Nacional de Investigaciones Nucleares, México*

[3] *Centre de physique des Plasmas et de leurs Applications de Toulouse, France*

Abstract

This paper presents an improved physical model for a high intensity discharge, derived from the balance of energy equation. The effects of energy dissipation caused by conduction and radiation are also considered. The resultant model is presented in Matlab as a two terminal device. The model's validity has been confirmed with experimental measurements. Analytical results reveal that the efficiency and the modulation depth of the plasma temperature at low frequency, can be improved using a square current power supply.

Keywords- HID lamp modeling, Electronic ballast design, plasma temperature modulation depth, square current power supply.

1. Introduction

Discharge lamp modeling is essential in the investigation and design of high frequency converters for high intensity discharge (HID) lamps and plasma torches.

A very extensive research, concerning arc lamp models can be found in the literature [1-2]. One of the most successful models is the balance of energy model [3], which considers the conservation of energy equation in the discharge column. The electric field applied in the discharge column, gives the power transmitted to the electrons and then transferred to the gas atoms via elastic and inelastic collisions among electrons, atoms and other species participating in the discharge. Consequently the gas is heated up and then removed by thermal conduction, radiation, convection and diffusion. The two latter forms can be ignored because the lamps are normally operated in vertical position and the conduction effect predominates over the diffusion effect [4].

The increment of temperature inside the lamp can be deduced from the Elenbaas-Heller equation, [5], including the radiation losses and using the concept of "effective temperature" (T_{eff}) (Channel Model). The HID is supposed to have a constant temperature T_{eff} for the cylinder radius $r \langle R_{el}$, (where R_{el} is the radius of the electrode), for $r \rangle R_{el}$ the current density and radiation intensity are negligible, since the temperature is very low in this zone. The model incorporates significant aspects of physical mechanisms occurring in the HID. A mathematical description of this instantaneous conductance $\left(g = {}^{i_a}\!/\!_{V_a} \right)$ was first proposed by O. Mayr [3], who assumes that the conductance increases exponentially with the thermal energy stored in the arc.

Among existing models, two approaches are of particular importance in terms of their ability to simulate the electrical characteristic of a lamp over a wide frequency range an easy implementation on electrical simulation software [6], [7]. In [6] a Matlab HID lamp model was proposed; however does not take into account the lamp physical process, which is critical and essential to the lamp performance. In [7] a Pspice HID lamp model that can be used for high and low frequency operation has been proposed, but its interface is complicated for the user.

The model described in this paper, was implemented in MATLAB as a two terminals device. The aim of this model is its user-friendly interface and is able to predict the HID behavior at different frequencies and power requirements. Using the results obtained with the proposed model we can investigate and establish the compromise between supply current frequency and waveform shape to improve the luminous efficacy. Also we can obtain some measures related with the efficiency discharge for example the modulation depth of the plasma temperature.

2. HID Modeling

The fundamental idea of the developed MATLAB model (Figure 1) consists in the representation of the HID lamp as a voltage dependent source. It is well know that:

$$I_{lamp} = \frac{V_{lamp}}{R_{lamp}} \tag{1}$$

where I_{lamp} is the instantaneous current trough the lamp, V_{lamp} is the instant voltage, R_{lamp} is the instantaneous lamp's electrical resistance, which can be obtained by solving $R_{Lamp} = \int_V L/(\sigma_\Sigma S) dV$. In this last equation σ_Σ is the global conductance of the plasma being equal to the sum of the specific conductance of gases that compose the plasma, V is the volume, L and S are the discharge length and cross-section respectively.

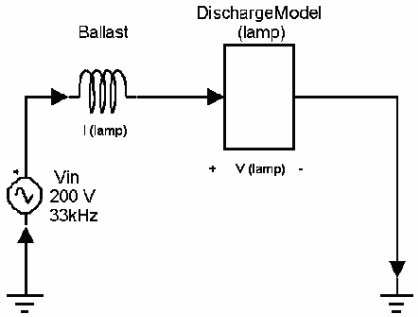

Figure 1. Model proposed for a HID discharge.

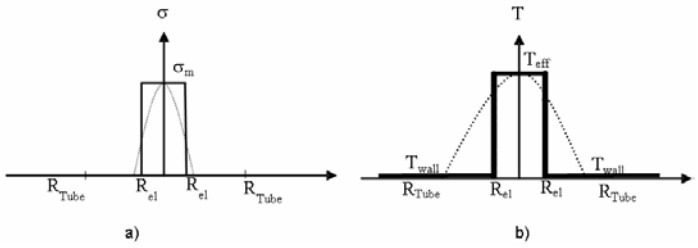

Figure 2. Channel model assumptions a) distribution of conductivity σ along the arc column radius b) distribution of temperature along the arc column radius.

For weakly ionized plasma the conductance is it giving by: [8]

$$\sigma_i = \sigma_{oi} \frac{T^{0.75}}{\sqrt{p}} e^{\frac{-E_i}{2kT}} \tag{2}$$

where σ_{oi} is a constant of each gas component i, T is the arc's core temperature, p is the pressure of the gas, E_i is the ionization energy for each element and k is the Boltzmann's constant. As can we see the conductance depends strongly on the temperature; therefore to describe the electrical process of the HID lamp, the thermodynamic state should be explained. Based on the equation of the power balance we can determine the heat increment in the arc using the following equation.

$$dQ = (P_{in} - P_{out})dt = mC_p dT \tag{3}$$

where the input power to the lamp is P_{in}, P_{out} is the power losses (radiation P_{rad} plus conduction P_{cond}), dt is the increment of time. m is the discharge cylinder mass, C_p is the heat capacity, and dT is the temperature increment. In addition, if we consider that $m = \varphi V$ where: φ is the density and V is the volume, then by using Eq. (3) we can find the discharge temperature, which is necessary to know the electrical characteristics of the lamp.

$$\frac{dT}{dt} = \frac{(P_{in} - P_{rad} - P_{cond})}{\varphi V C_p} \tag{4}$$

The present study was conducted under some simplified considerations of the channel model shown in Figure 2.

1. The arc in the high pressure lamp is confined to a plasma cylinder.
2. The plasma is in a Local Thermal Equilibrium (LTE) state.
3. The arc is composed of a two-layer cylinder:
    - The radius of the internal layer is equal to the electrode radius, R_{el}
    - The external radius of the external layer is equal to the arc tube internal radius.

- The arc´s length is equal to the gap between electrodes.

4. All physical properties in each layer are constant.
5. Electrical current only appears in the internal layer core.
6. The energy (P_{out}) losses are due to radiation and heat conduction.
7. The influence of the arc´s tube, electrodes and bulb is neglected.

Under these assumptions, the increase in heat per a unit length can be expressed by:

$$dQ = \left[c_{arc}\varphi_{arc}\pi R_{el}^2 + K_{Tred}c_{per}\varphi_{per}\pi\left(R_{tube}^2 - R_{el}^2\right)\right] \tag{5}$$

where c_{arc}, c_{per} are the heat capacity of the internal and external layers respectively; $\varphi_{arc}, \varphi_{per}$ represent the density of the internal and external layer's medium, consequently; R_{tube}, R_{el} - arc cavity and electrodes radius, respectively, K_{Tred} -factor keeping the temperature reduction in the arc's periphery

The input power to the lamp per unit length P_{in} is:

$$P_{in} = \frac{V_{lamp}I_{lamp}}{L_g} \tag{6}$$

where: L_g is the distance between electrodes.

The formula for the radiated energy P_{rad} :

$$P_{rad} = 2\pi R_{el}\varepsilon(T) \tag{7}$$

where: $\varepsilon(T)$ arc's surface emissivity. The heat conduction losses P_{con} are described by the law:

$$P_{con} = k(T - T_{amb}) * 2\pi R_{el} \tag{8}$$

where $k = k(T)$ coefficient of heat transfer.

By taking into account the lamp geometry and all the energy losses (P_{out}), a differential equation that describes the state of the arc, can be deduced:

$$\frac{dT}{dt} = \frac{\frac{v_{lamp}\ i_{lamp}}{L_g} - 2\pi R_{el}\left[\varepsilon(T) + \kappa(T - T_{amb})\right]}{\pi\left[c_{arc}\ \varphi_{arc}\ R_{el}^{\ 2} + k_{Tred}\ c_{per}\ \varphi_{per}\ (R_{tube}^{\ 2} - R_{el}^{\ 2})\right]} \tag{9}$$

To solve this equation, we use the numerical values of the parameters: $c_{arc}, c_{per}, \varphi_{per}, \varphi_{arc}$ in [7]. The procedure of solution adopted in this study is summarized in Figure 3. We use this algorithm to know the discharge's temperature, and from this we can obtain the arc's surface emissivity $(\varepsilon(T))$, the coefficient of heat transfer $(k(T))$ and the discharge electrical characteristics.

Figure 4 shows the block diagram of the developed Matlab HID model, which considers two input variables (discharge's current and voltage) needed to solve the energy balance equation.

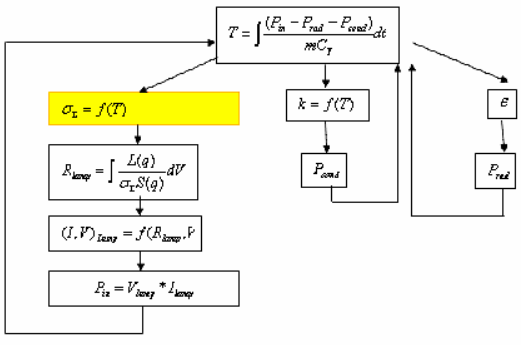

Figure 3. Structured solution for the described equation.

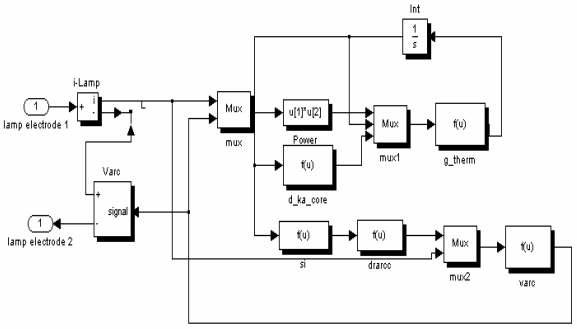

Figure 4. Block diagram of HID lamp model.

3. Simulation and experiments

The HID model implemented in MATLAB was verified using some experimental measurements. In order to compare the model response and lamp's experimental characteristics, it was necessary to power the lamp and then acquire the values of current and voltage. As we can see (Figure 5) the model response shows a good correspondence with the experimental results at low frequency (60 Hz).

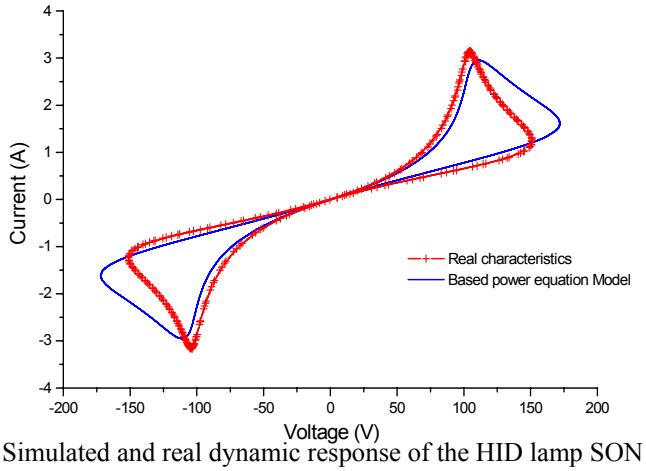

Figure 5. Simulated and real dynamic response of the HID lamp SON T- 400, 60 Hz.

Figure 6 shows the model's high frequency performance. We can observe that the simulated dynamic response for the HID at high frequency shows also a good correspondence with the experimental results; so the model emulates the lamp operation at high and low frequency, according the experimental behavior of the lamp.

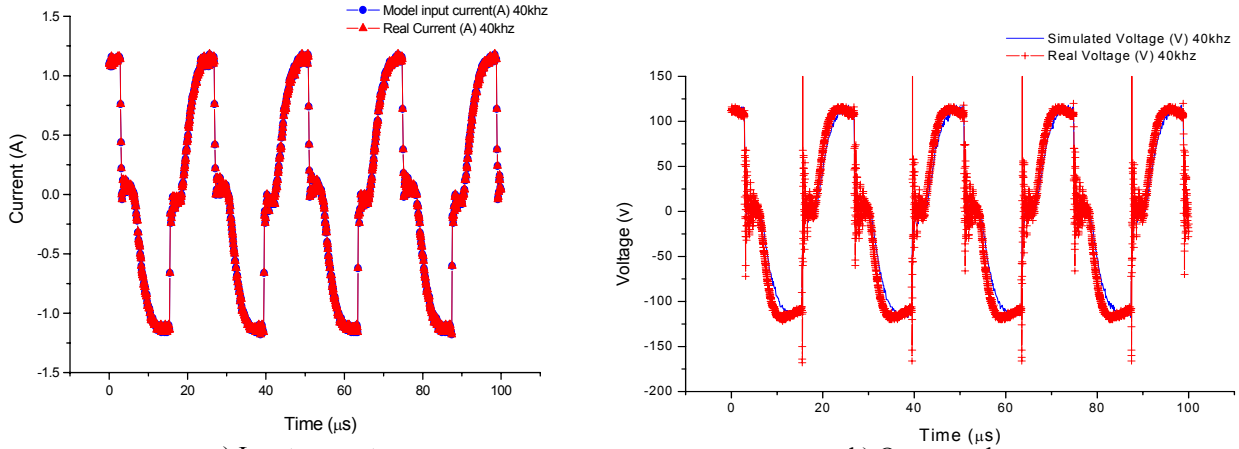

a) Input current b) Output voltage

Figure 6. Simulating and real dynamic response of the HID current and voltage 40 kHz.

4. Influence of current waveform on HID lamp operation.

New electronic components and converters structures, make possible operate HID lamps at different frequencies and waveforms. A problem presented in high frequency operation is the occurrence of discharge distortions caused by acoustics waves.

Efficient light production in ac-supplied HID lamp is strongly dependent on plasma conditions during the complete half-cycle. A significant luminous efficacy gain is obtained by using sinusoidal current waveform with frequencies of tens of kilohertz or with rectangular current waveforms at lower frequencies (1-4 kHz.).

Simulations of the lamp conductance at several operating conditions can be useful to select a supply frequency and current waveform for electronic ballast design.
When the HID works with a sinusoidal current supply at low frequency, the electrons and ionized atoms have enough time to recombine, but when this discharge is operated at higher frequencies electrons and ions do not recombine, and the charge carrier density is high enough at each current reversal, and not extra power is needed to reignite the discharge [9]. The change of discharge conductance occurring by these effects can be observed in Figure 7; a strong variation in the conductance can be obtained working with sinusoidal waveforms at low frequencies while working with rectangular waveforms these variations are hardly minimized.

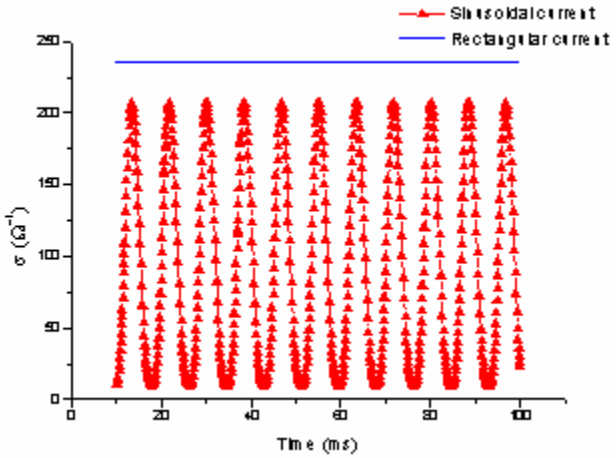

Figure 7. Conductance variations of HID lamp supplied with sinusoidal current and with rectangular waveform at 60 Hz.

The variation in the conductance is associated with efficiency. In this case the luminous efficacy of HID lamp supplied with sinusoidal current depends on frequency waveform and on the phenomenon of saturation related with the time constant of electron temperature [10]. At least two sustancial advantages can be obtained using rectangular current:

- The absence of the cataphoresis effects (normally they occur under dc operation).
- The absence of discharge distortion by acoustic resonance, because it is possible to work at low frequencies, where acoustic resonance does not longer exist.

5. Modulation Depth of the Plasma Temperature

A very useful parameter for lamps designers is the Modulation Depth of the Plasma Temperature MDPT $\left(\Delta T/T\right)_f$, which relates the temperature variations with respect the average temperature occurring in the HID as a function of the operation frequency f .

The model described here Figure 4 was supplied with both waveforms: rectangular and sinusoidal, at different frequencies.The average temperature and the temperature variations can be deduced in function of the operation frequencies, the data obteined are depicted in Figure 8. We can see that the MDPT of the plasma discharge is reduced from 25% at 60Hz to 1% at 12 KHz, if a sinusoidal current is used. When a square wave pulse is applied, the MDPT is notably reduced (lower than 2%) even at low frequencies.
Therefore, by using a converter square wave pulses the thermal strengths in the electrode material is considerably reduced and the lamp life time is generally extended.
Operating at low MDPT results in remarkable improvement of the power factor. Thus, the operation characteristics of the HID lamp under square wave pulses would appear to approach those found under DC operation, but avoiding the cataphoresis effect in the electrodes.

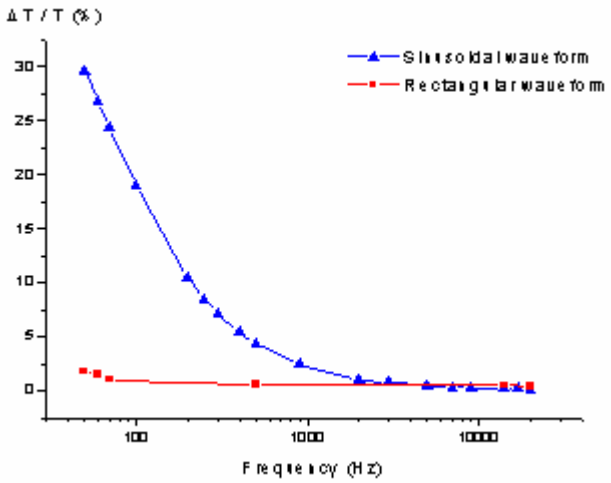

Figure 8. Modulation depth of the plasma temperature in a 400W HID lamp as a function of supply current's waveform and frequency

6. Conclusion

By using the balance of energy equation occurring in an electrical discharge, a simple and effective model has been developed. This model, emulates the behavior of HID working at low and high frequencies. The solution was implemented in MATLAB and presented as a two terminal element compatible with electronic circuit simulators.

Using this model we showed that the current waveform has a strong influence on the luminous efficiency in HID lamps. Rectangular current waveform operation at 60 Hz offers higher efficiency than that obtained when sinusoidal waveforms are used. This efficiency increase is caused by the faster current polarity reversal at each half cycle and, therefore, the plasma retains a higher degree of ionization. The gain obtained with rectangular current supply remains constant in a wide range of frequencies. However the rise time must be small (some μs), otherwise the gain in efficiency will be smaller and frequency dependent.

7. References

1. J.J. de Groot, J. A: J. M. van Vliet. "The high pressure sodium lamp", Philips Technical Library, MacMillan Education, (1986).
2. Shan Lu, Zhongyuan Cheng, Bin WU. "Modeling of Neon Tube Powered by High Frequency Converters". IECON 02 Industrial Electronics Society, Vol.1, pp. 288-293, (2002).
3. Mayr, O. "Beitrage zur Theorie des Statischen und des Dynamischen Lichtbogens", Archiv für Elektrotechnik, Band 37, Heft 12, pp. 588-608, (1943).
4. Wei Yan, S.Y. Ron Hui. "An Improved High-Intensity Discharge Lamp Model Including Acoustic Resonant Effect on the Lamp Arc Resistence". IEEE Trans. On Power Electronics., Vol. 19, N°6, (2004).
5. Raizer P. Yuri."Gas Discharge Physics", Germany: Springer, Ch 10, pp 271-284,(1997).
6. J.C Antón, G. Zissis. "An Equivalent Conductance Model for High Intensity Discharge Lamps", p. 1494-1498, IEEE Transactions of Plasma Science, Vol. 23, (1995).
7. M. Shvartsas and S. Ben-Yaakov, "A Pspice compatible model of high intensity discharge lamps", in Proc. IEEE power Electronics Specialists Conf., pp 1037-1042, (1999).
8. V. G. Levitch, Kurs teoretitcheskoj physiki, Phismatgiz, Moska, USSR, T.1, (1962).
9. Seebaches, P. J., Perturbation of an Energy-Balance. Model: Time Constants of Low-Current Cascade Arcs in Argon, p. 171-176, IEEE Transactions of Plasma Science, Vol. 23, (1995).
10. Walter Kaiser. "Influence of Frequency and Current Waveform on Low-Pressure Sodium Lamp Operation". IEEE Trans. On Ind. Appl., Vol. 37, N°2, (2001).
11. Ali Bulent Cambel, "Plasma Physics and Magnetofluid-Mechanics", pp. 169-174, McGraw-Hill, (1963).

An Improved ZCT Buck Converter for Plasma Torches

C. E. Torres[1], J. O. Pacheco[1, 2], M.Pacheco[1], F. Ramos[1], J.S. Benitez-Read[1,2]
[1] *Instituto Tecnológico de Toluca, México.*
[2] *Instituto Nacional de Investigaciones Nucleares, México.*

Abstract
The Buck Converter here proposed successfully sustains a plasma discharge with high power transfer efficiency. To avoid the excessive semiconductor power dissipation during commutations, a resonant snubber cell is introduced to achieve zero-current transitions. The operation principle under steady-state is presented.
Keywords: Buck Converter, state-variables analysis, Zero Current Switching, Plasma Torch

1. Introduction

In order to obtain a good performance of the plasma torch operation, it is necessary to use a current supply instead of a voltage supply. In this work a Buck Converter (BC) is proposed as a current source for the excitation of a plasma torch. The BC is one of the most studied systems [1, 2] with a wide variety of applications. The structure of this type of converter is very simple (just a few elements are needed to control high current intensities); it is of low cost and easy to control. Nevertheless, the available commercial semiconductors still do not have neglectable internal resistance R_{DS}, when the semiconductor is in its ON state. Normally, the R_{DS} value is around 16mΩ. Although it seems to be a quite low resistance, when high intensity currents of about 100A flow, the power dissipation becomes an important drawback. To avoid this effect, several transistors (Q_1, Q_2, Q_3) are connected in parallel, as shown in figure 1, representing a good option to decrease the equivalent serial resistance R_{DS}. In consequence, the power dissipation is reduced in the converter. All these transistors are controlled with just one single pulse width modulation (PWM) signal.

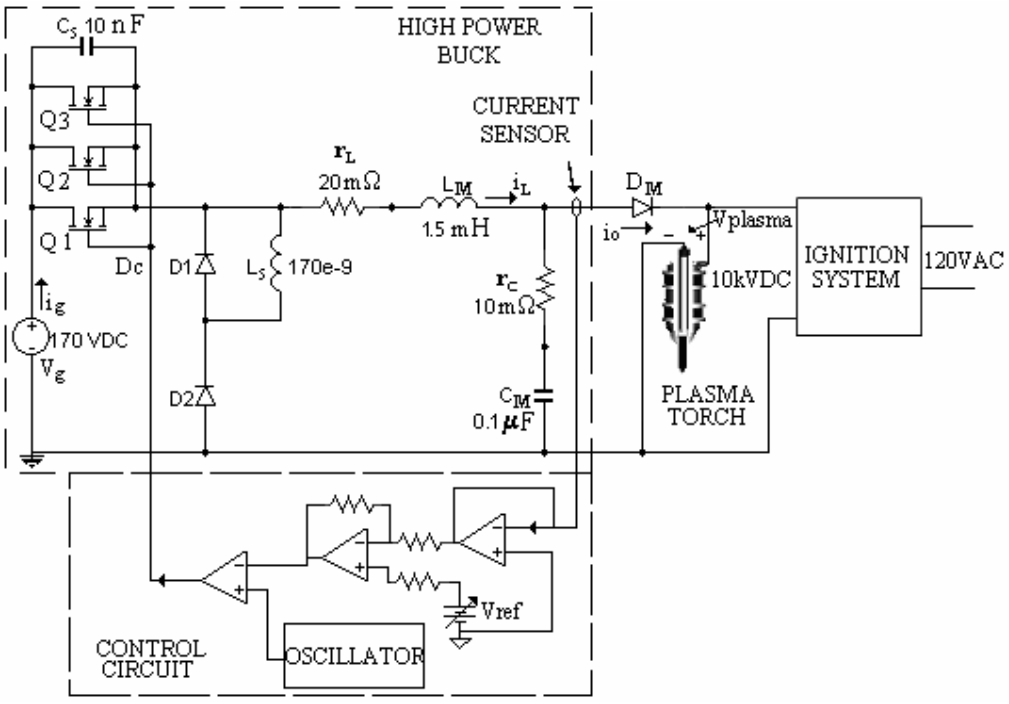

Figure 1. Complete power supply system with Buck Converter.

The system proposed is depicted in figure 1, the BC is connected to the plasma torch. The ignition system is also included in this figure, but it is only used during the plasma ignition. The BC is used to sustain the normal operation of the plasma torch. The diode D_M is used to protect the BC against high voltage impulsions, during the ignition phase. A very simple active snubber cell provides Zero Current Switching

(ZCS) [3]. This snubber cell is implemented by using a quasi resonant circuit with no significant cost and neither complexity. The elements composing this snubber cell are D_1, D_2, L_s and C_s. L_S is of 170nH approximately which this is obtained from di/dt of D1, C_S is of 10nF. The incorporation of a snubber circuit improves the efficiency during the commutation of this converter because it can operate with soft switching successfully at very wide load ranges at considerably high frequencies [3-5]. The main transistors (Q_1, Q_2, Q_3) do not have any additional voltage and current stress.

2. State-variable analysis.

A powerful analysis habitually used to deduce the behavior of power electronic systems is based on state variable analysis [6-8]. It allows the formulation of a transfer function relating the plasma voltage (P_{lasma}) respect to the duty cycle (δT), which is necessary, to propose a closed loop control for the plasma current flowing trough the plasma torch. The state variable analysis includes the parasitic elements such as the equivalent resistance r_C of the filter capacitor C_M and those of the inductance r_L. The elements conformed the snubber cell are only considered in the simulation, appearing in the numerical results section.

The BC behavior can be linearized by using state-variable analysis. The Bode plots obtained in the next section, can be used to determine the appropriate compensation in the feedback loop for the desired steady state and transient responses.

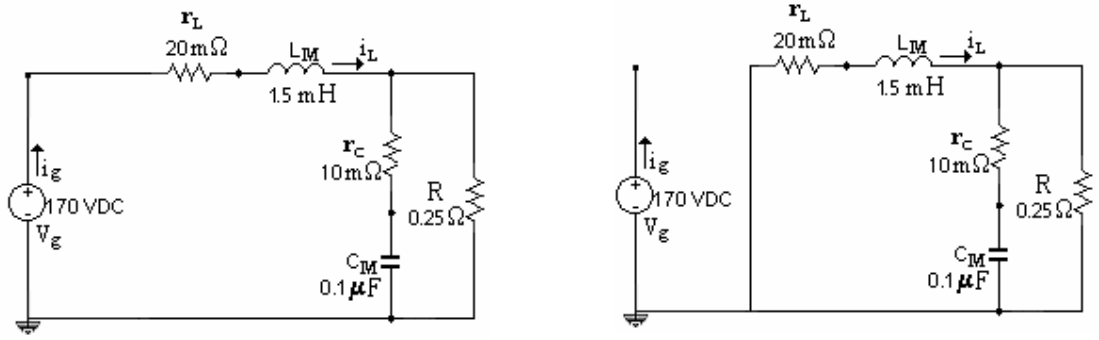

a) b)

Figure 2. Circuits state of BC, a) ON state and b) OFF state.

The canonical form of the state-variables is:

$$\overset{*}{\mathbf{x}} = \overline{\mathbf{A}}\,\mathbf{x} + \overline{\mathbf{B}}\,\mathbf{u} \qquad , \qquad \mathbf{y} = \overline{\mathbf{C}}\mathbf{x}$$

During each circuit state a linear approaching is obtained by means of the state-variable vector **x** consisting of the inductor current $\dot{x}_1$ and the capacitor voltage $\dot{x}_2$. In this power converter operation, two circuit states exists (figure 2): one state corresponds to when the switch (Q1...Q3) is ON and the other, when this switch is OFF as is shown in figure 2 a) and b) respectively. Therefore, during each circuit state we can write the following state equations:

$$\left[\dot{\mathbf{x}}\right] = \mathbf{A_1}\left[\mathbf{x}\right] + \mathbf{B_1}\,V_g \qquad 0 \le t \le \delta T$$
$$\left[\mathbf{V}_C\right] = \mathbf{C_1}\left[\mathbf{x}\right]$$

$$\left[\dot{\mathbf{x}}\right] = \mathbf{A_2}\left[\mathbf{x}\right] + \mathbf{B_2}\,V_g \qquad \delta T \le t \le T$$
$$\left[\mathbf{V}_C\right] = \mathbf{C_2}\left[\mathbf{x}\right]$$

Where $\mathbf{A}_1$, $\mathbf{A}_2$, $\mathbf{B}_1$, $\mathbf{B}_2$, $\mathbf{C}_1$ and $\mathbf{C}_2$ are matrices; ***x*** and $\boldsymbol{V}_C$ are state variables. Using Laplace transformation and some others algebraic operations, a generalized expression, considering all matrices element is obtained [8]:

$$G(s)\frac{\tilde{v}_o(s)}{\tilde{d}(s)} = C\left[sI - A\right]^{-1} \bullet \left[(A_1 - A_2)X_{dc} + (B_1 - B_2)V_d\right] + \left[(C_1 - C_2)X_{dc}\right] \qquad (1)$$

When transistors are in ON state, the equations obtained are (2) and (4), while for the OFF state, the equations are (3) and (4).

$$\dot{x}_{1ON} = -\frac{(Rr_c + Rr_L + r_c r_L)}{L_M (r_c + R)} x_1 - \frac{R}{L_M (r_c + R)} x_2 + \frac{V_g}{L_M} \tag{2}$$

$$\dot{x}_{1OFF} = -\frac{(Rr_c + Rr_L + r_c r_L)}{L_M (r_c + R)} x_1 - \frac{R}{L_M (r_c + R)} x_2 \tag{3}$$

$$\dot{x}_{2ON-OFF} = \frac{Rx_1 - x_2}{C_M (r_c + R)} \tag{4}$$

The state variables of interest are equations (5).

$$\text{With} \quad \dot{x}_2 = \frac{dv_C(t)}{d(t)}, \dot{x}_1 = \frac{di(t)}{d(t)} \tag{5}$$

Matrices $\mathbf{A}_1$ and $\mathbf{A}_2$ have the same values; therefore buck matrices are evaluated as:

$$A_1 = A_2 = \begin{bmatrix} -\frac{(r_c + r_L)}{L_M} & -\frac{1}{L_M} \\ \frac{1}{C_M} & -\frac{1}{RC_M} \end{bmatrix} \quad B_1 = \begin{bmatrix} \frac{1}{L_M} \\ 0 \end{bmatrix} \quad B_2 = \begin{bmatrix} 0 \\ 0 \end{bmatrix} \tag{6}$$

Finally, the transfer function describing the Buck circuit is obtained:

$$G(s)\frac{\tilde{v}_o(s)}{\tilde{d}(s)} = v_g \left(\frac{r_C C_M}{L_M C_M}\right) \left(\frac{s + \frac{1}{r_C C_M}}{s^2 + \left[\frac{1}{RC_M} + \frac{r_C + r_L}{L_M}\right] s + \frac{1}{L_M C_M}} \right) \tag{7}$$

By including the variables representing the radial resonant frequency (ω_o) and the switching radial frequency (ω_c) in (4), a new equation is deduced:

$$G(s) = \frac{\tilde{v}_o(s)}{\tilde{d}(s)} = v \left(\frac{\omega_o^2}{\omega_c} \right) \left(\frac{s + \omega_c}{s^2 + 2\zeta\omega_o s + \omega_o^2} \right) \tag{8}$$

Where it can be found by comparison of (7) and (8):

$$\omega_o = \frac{1}{\sqrt{L_M C_M}}, \omega_c = \frac{1}{r_C C_M}, \zeta = \frac{1}{2R}\sqrt{\frac{L_M}{C_M}} + \frac{(r_C + r_L)}{2}\sqrt{\frac{C_M}{L_M}} \tag{9}$$

3. Numerical results

According with the real components used in the BC prototype the parameters given in equations (5), (6), can be established: r_C=10mΩ; r_L=20 mΩ; C_M=0.1μF; L_M=1.5mH; V_g=170VDC. During plasma torch stable operation, at equilibrium point, the plasma discharge can be represented by a 0.25Ω resistance. By substitution of all these parameters and by using some Matlab commands, a Bode diagram can be obtained describing the BC behavior for a frequency range (10 to 10^{10} rad/seg) as it is appreciated in figure 3. By

analyzing the Bode diagram a compensator circuit can be proposed in the feedback loop to improve the converter stability [9, 10, 11].

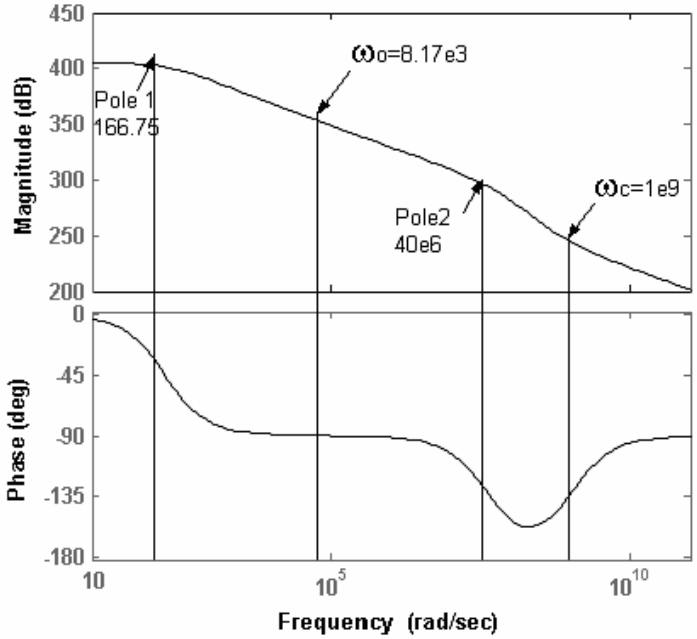

Figure 3. Bode Diagram of Buck Converter

To show a comparison between hard and soft switching, 3 circuits were simulated by using ORCAD software:

- the first circuit was conform without snubber and with one transistor or single hard switch (SHS),
- the second without snubber and with three transistors or three MOS in hard switch (TMHS),
- the third is analyzed with three MOS and with snubber cell or three MOS in soft switch (TMSS).

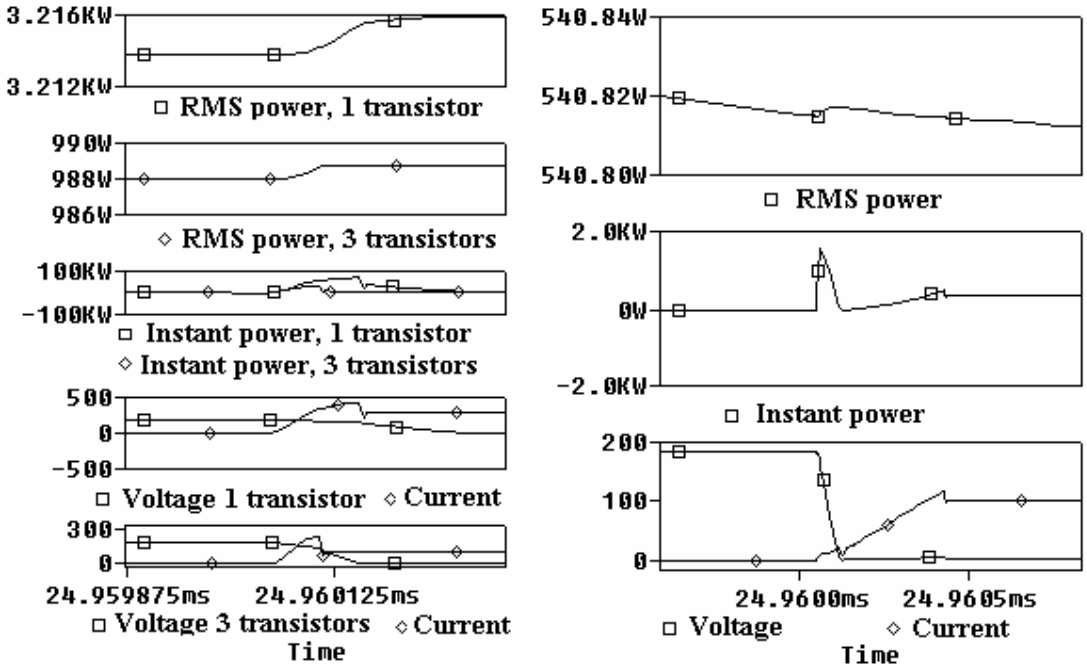

a) b)

Figure 4. Simulation with a) hard commutations and b) soft commutations.

Results are presented in figure 4. A comparison between SHS and TMHS is illustrated in figure 4a. In the power graph, it can be appreciated that the power in the TMHS is 989W, while in the SHS is about 3.21kW. The instantaneous power peak in the TMHS is at about 20kW and in the SHS is at about 80kW. The low power occurring in the TMHS is certainly due to its low resistance obtained in the parallel arrangement of the three transistors, instead of just one transistor.
In figure 4b, results of the TMSS simulation are shown; as we can see, the RMS power is 540W and the instant power peak is 1.8kW. A significant dissipation reduction is obtained because the MOS are switched under zero current conditions thanks to the snubber cell operation.

4. Conclusions

All semiconductor devices operate under soft switching. The MOS transistors are subjected to no additional voltage and current stresses. This converter operates successfully under variable load conditions appearing during plasma torch operation. Consequently, the dissipation losses are minimized and the energy transfer to the plasma torch is achieved with very high efficiency of nearly 92% at full power capacity.
By using the transfer function, a simple closed loop control can be proposed to improve the stability of the current source.
A generalized state-plane analysis method for soft-switching Buck Converter was presented in this paper. By applying this, a simple computer-aided analysis and mathematical modeling could be realized.

The operational behavior and stability of the Buck Converter is analyzed during duty cycle variations. However, some other specific effects appearing during finite switching times during experimental tests are not treated in this work.

5. References

[1] R. Orugati "Inductor voltage control of buck-tipe single phase ac-dc converter", IEEE Trans. Power Electron., Vol**.15**, pp 411-417, (2000).
[2] H. Bodur, A.F. Bakan, "An Improved ZCT-PWM DC–DC Converter for High-Power and Frequency Applications" IEEE Trans. Power Electron., Vol. **51**, No. 1, pp 89-95, (2004).
[3] B. P. Divakar and D. Sutanto, "Optimum Buck Converter with a Single Switch", IEEE Trans. Power Electron., Vol. **4**, pp636-642, (1999).
[4] H. Bodur and A. F. Bakan, "A new ZVT-ZCT-PWM dc-dc converter", IEEE Trans. Power Electron., Vol. **19**, No 3, pp 677-684, (2004).
[5] H. Bodur, A.F. Bakan and M. Bayasal, "A detailed analytical analysis of a passive resonant snubber cell perfectly constructed for a pulse with modulated d.c.-d.c. buck converter", Electrical Engineering, Springer-Verlag, Berlin, Germany, Vol **85**, Num.1, pp. 45-52, (2003).
[6] C. T. Rim, G. B. Joung and G. H. Cho, "A state-space modeling of non-ideal dc-dc converters", PESC, pp. 943-950, (1988).
[7] A. Barrado, A. Lázaro, J. Pleite, R. Vázquez, J. Vázquez, and E. Olias, "Linear-non-linear control (LnLc) for dc-dc buck converters: stability and transient response analysis", IEEE, pp 1329-1335, (2004).
[8] N. Mohan, "Power Electronics: Converter, Applications and design", Second Edition. John Wiley, pp.229-261, (1989).
[9] B. J. Patella, A. Prodié, A. Zirger and D. Maksimovié, "High-frecuency digital PWM controller IC for dc-dc converters", IEEE Trans. Power Electron., Vol **18**, No. 1, pp 438-446, (2003).
[10] C. Gatlan, "Ac to Dc PWM Voltage Source Converter Under Hysteresis Current Control" in Proc. Int. Symp. on Industrial Electronics '97, Vol. **2**, pp. 469-473, (1997).
[11] G. Kopasaki, "Fuzzy Current-Mode Control and Stability Analysis", NASA, Glenn Research Center, Cleveland Ohio, pp. 24-28, (2000).

Functionalization of Polyethylene by Ammonia Dielectric Barrier Discharge Microplasma

Yuri Noma[a,*], Haruki Kataoka[a], Kaoru Higashi[b], Katsuro Oda[b], Daisuke Ishihara[a], and Kazuo Terashima[a]

[a]*Department of Advanced Materials Science, Graduate School of Frontier Sciences, The University of Tokyo, 5-1-5, Kashiwanoha, Kashiwa, Chiba 277-8561, Japan*

[b]*Institute of Industrial Science, The University of Tokyo, 4-6-1 Komaba, Meguro-ku, Tokyo 153-8505, Japan*

ABSTRACT: Dielectric barrier discharge NH_3/He microplasma (NH_3/He-DBDMP) under a high-pressure environment close to atmospheric pressure (720-730 Torr) has been employed for the local surface functionalization of amino groups on the surface of bulk polyethylene. Optical emission spectra were taken by varying the applying voltage and gas flow rate to study the characteristics of the microplasma and to find a suitable condition for functionalization. The incorporation of amino groups on the local surface (500 μm in diameter) by the microplasma treatment has been identified by X-ray photoelectron spectroscopy (XPS).

KEYWORDS : dielectric barrier discharge (DBD), ammonia, polyethylene, localized treatment, optical emission spectroscopy (OES), Lissajou method, x-ray photoemission spectroscopy (XPS)

Ⅰ. INTRODUCTION

Functionalizing polymer substrates by plasmas has wide range of applications [1]. By adding functions to the surface of the polymer, surface properties can be altered. However, achieving functionalization by conventional low-pressure plasmas requires expensive high-vacuum systems and overall long time from preparing to the treatment. In order to solve these problems, dielectric barrier discharge microplasma (DBDMP) under a high-pressure environment close to atmospheric pressure (720-730 Torr) is a suitable tool. DBDMP can be generated in high-pressure environment with low power, which leads to both high-density ($\sim 10^{12}$ cm^{-3}) and low-temperature plasma (several hundred K for gas temperature) [2]; hence saving both power and time for functionalization without employing expensive high-vacuum systems. Additionally, DBDMP can easily control the functionalization point in limited space both two dimensionally and three dimensionally. This localization can be applied to micro electro mechanical system (MEMS) and polymerization technique used for developing immunosensor [3]. Not only limited space but also large area can be functionalized by arrayed DBDMPs.

In this study, NH_3/He -DBDMP has been employed for the local surface functionalization of amino groups on the surface of bulk polyethylene. We focus on both characterization of NH_3/He-DBDMP and also the incorporation of local surface by the microplasma treatment.

Ⅱ. EXPERIMENTAL SETUP

Figure 1 shows a schematic of our system to generate the DBDMP. The system consists of a function generator, an amplifier, a main chamber, a microplasma torch, and a rotary pump. To keep the gas isolated from the air outside, the pressure of the main chamber is maintained at 720-730 Torr. The holder is set in

front of the torch so that the gap between the torch and the substrate will be 500 μm when treating the center of the polymer substrates. NH_3/He-DBDMP is generated at the end of the microplasma torch, in a quartz tube with an inner diameter of 500 μm. The stainless steel wire (300 μm in diameter), which penetrates through the hole of the quartz tube, is the driving electrode, and the conductive paste around the quartz tube is the grounding electrode. Together, it serves as a capacitively coupled electrode with dielectric barrier in between. Gases (NH_3 and He) are introduced through the flow meter and the pressure was monitored with a vacuum gauge. Irrespective of the NH_3 gas flow rate, the He gas flow rate is always kept constant at 200 sccm during the experiment. The NH_3/He-DBDMP (500 μm in diameter) actually generated in this system is shown in Figure 2.

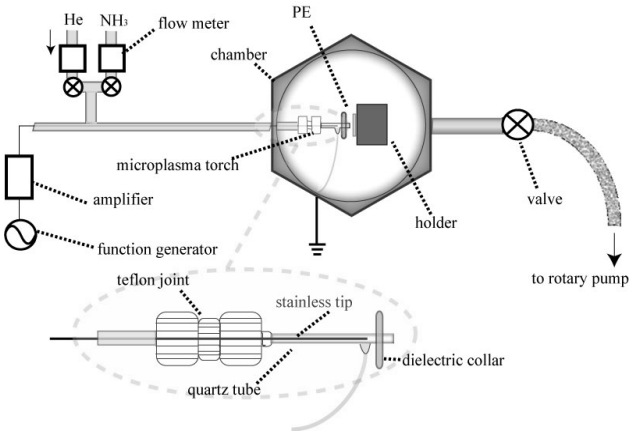

Fig. 1 Schematic diagram of the experimental setup.

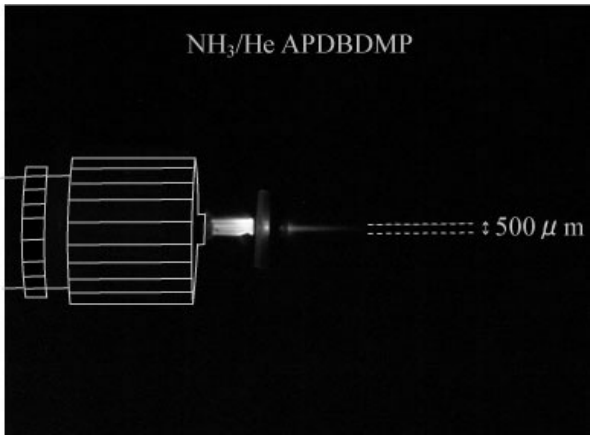

Fig. 2 NH_3/He-DBDMP (V = 1.9 kV, f = 7 kHz, Q_{NH3} = 5 sccm, Q_{He} = 200 sccm).

The polymer substrate used in this study is a low-density polyethylene (SANPLATEC). Samples were prepared in the form of 0.5 mm thick square-shaped coupons (10×10 mm). They are purified by extraction with hexane/isopropyl alcohol mixture for 1 hour and stored in a desiccator prior to each plasma treatment.

To study the characteristics of the NH_3/He-DBDMP, optical emission spectroscopy was performed with Acton Research Corporation SpectraPro-300i monochromator with a focal length of 300 mm equipped with 1200 grooves/mm grating, and photons were detected with Acton Research Corporation CCD detection system for analysis of the 310-360 nm domain.

The power consumption of the NH_3/He-DBDMP is measured with Lissajou method, which is illustrated in Figure 3. The voltages across the discharge electrodes from the oscilloscope (TDS 5104 digital phosphor oscilloscope) are plotted as a function of the voltage across the test capacitor C_{test}. The power consumption is obtained by measuring the area of the Lissajou curve and multiplying it to capacitance C_{test} and the frequency of the applying voltage V (Figure 6) [4].

The local incorporation of the NH_3/He-DBDMP treated polyethylene surface is identified by XPS measurements. The XPS apparatus we employed in this experiment is a PHI

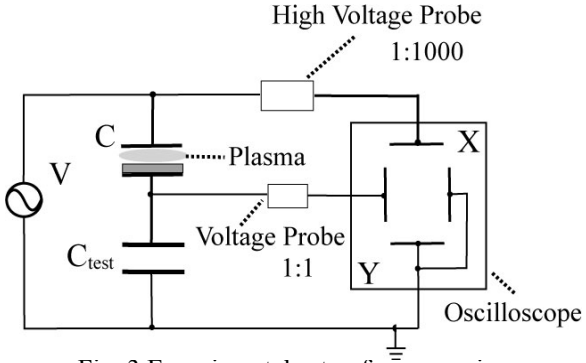

Fig. 3 Experimental setup for measuring NH_3/He-APDBDMP power consumption.

Quantum2000, using monochromated AlK_{α}(1486.7eV) radiation, the analysis area being 200 μm in diameter. The electron take-off angle used is 45°. To avoid differential charging effects of nonconducting polyethylene samples, an electron flood gun is used for neutralizing. The binding energy analysis was referenced to the C1s signal of the aliphatic hydrocarbon at 285 eV. The peak fitting was done by using Multipak V6.1A software and for the peak shape, a mixture of Gaussian and Lorentzian was chosen. Furthermore, by measuring the atomic concentrations of N1s on 361 points over NH_3/He-DBDMP treated area, we have succeeded to map and visualize the locality of NH_3/He-DBDMP treatment. The distance between the nearest measurement points is 300 μm.

Ⅲ. RESULTS AND DISCUSSION

A. Characterization of the microplasma by optical emission spectroscopy (OES)

In this study, we focused on NH radicals, which play an important role in functionalization of amino groups to find a suitable condition for functionalizing amino groups on polyethylene surface with our system. Figure 4 is the optical emission spectra of NH radicals as a function of applying voltage. It shows that as the applying voltage increases, the intensity of the radicals increases. However, 1.9 kV is the maximum limit of applying voltage in our system because the discharge mode transit to arc and ends up destructing the electrode part.

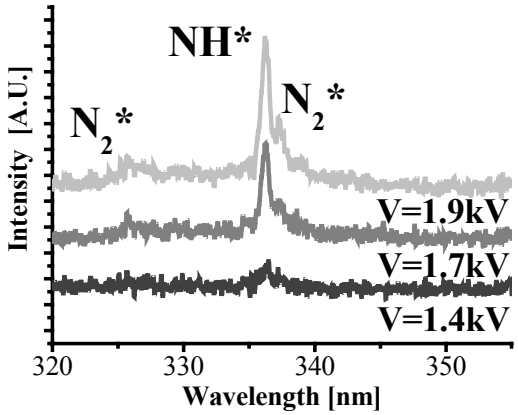

Fig. 4 OES spectra of NH radical as a function of applying voltage V (f = 7 kHz, Q_{NH3} = 5 sccm, Q_{He} = 200 sccm).

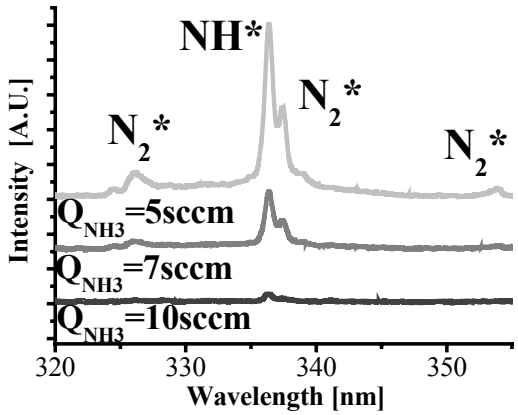

Fig. 5 OES spectra of NH radical as a function of NH_3 gas flow rate Q_{NH3} (V =1.9 kV, f = 7 kHz, Q_{He}= 200 sccm).

On the other hand, Figure 5 is the optical emission spectra of NH radicals as a function of NH_3 gas flow rate. Note that the He gas flow rate is constant at 200 sccm. It shows that as the NH_3 gas flow rate increases, the intensity of the radicals decreases. This is explained by the Penning effects of helium metastables. He metastable particles consume their energy by dissociating and ionizing ammonia. When NH_3 gas flow rate increases, NH_3 particles receiving energy from He metastables increase although the He gas flow rate does not change. Hence the mean energy that NH_3 particles get from He metastables decreases, and dissociated and ionized NH_3 particles before flowing outside of the electrodes decrease. Taking into account that formation of NH radicals involves dissociation and ionization, the explanation agrees well with the result. We must also note that in our system, 5sccm was the minimum limit of the stable NH_3 gas flow.

B. Power measurement of the microplasma by Lissajou method

The power consumption of the NH_3/He-DBDMP is obtained by multiplying the capacitance C_{test} and the frequency of the applying voltage to the area of the Lissajou curve (Figure 6), and under the suitable condition for amino groups functionalization in this study (V = 1.9 kV, f = 7 kHz, Q_{NH3} = 5 sccm, Q_{He} = 200 sccm), it was 6.2 mW. Comparing the result to the power consumed by the other conventional plasmas employed in surface treatment system, it is about 1/10,000~1/1,000.

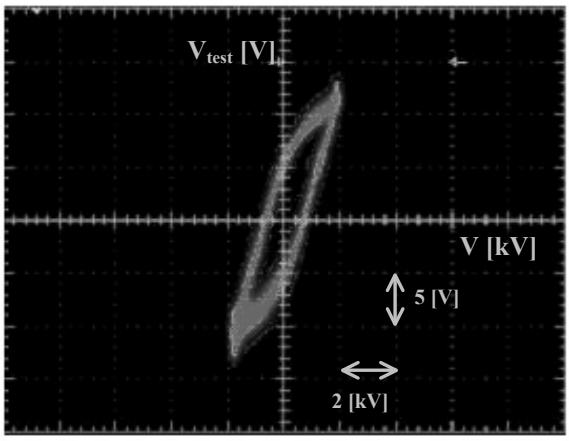

Fig. 6 Lissajou curve (V = 1.9 kV, f = 7 kHz, Q_{NH3} = 5 sccm, Q_{He} = 200 sccm).

C. Characterization of microplasma treated polyethylene surface by X-ray photoelectron spectroscopy

Three kinds of surface treated polyethylene samples by NH_3/He-DBDMP under the suitable condition for amino groups functionalization in this study (V = 1.9 kV, f = 7 kHz, Q_{NH3} = 5 sccm, Q_{He} = 200 sccm) were measured by XPS. They differ in the treatment time (1, 10 and 100 s). The results show that the longer microplasma treatment time, the more N and O components get incorporated on the surface of the polyethylene (Figure 7).

The C1s peak of the nontreated polyethylene is composed of a single peak centered at 285 eV corresponding to the methylene groups. The NH_3/He-DBDMP treatment broadens this C1s peak, which indicates the incorporation of new functional groups on the surface of a polyethylene. However, it is difficult to determine and quantify the C-NH_2 from the C1s spectra since there are too many kinds of combining possibilities of functional groups. Figure 8 is the deconvoluted high-resolution spectra of N1s. It shows that two different peaks can fit the N1s peak, and quantities of the nitrogen-containing groups incorporated on the surface were evaluated from them. The lower binding energy peak at 399 eV corresponds to the amino

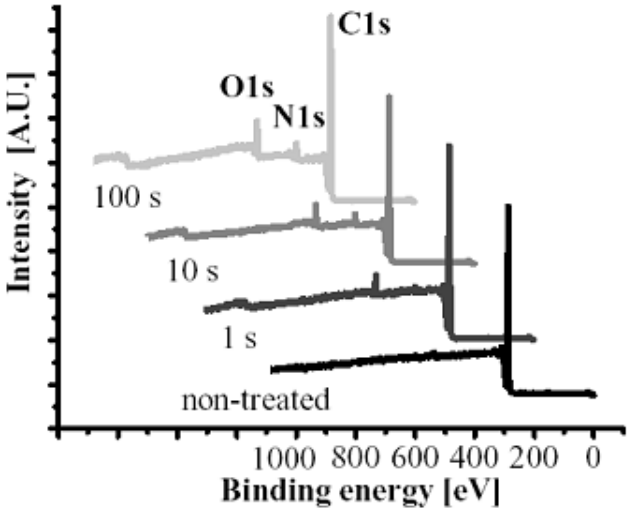

Fig. 7 XPS spectra of nontreated (a) and NH3/He 1s (b), 10s (c), 100s (d) microplasma-treated polyethylene.

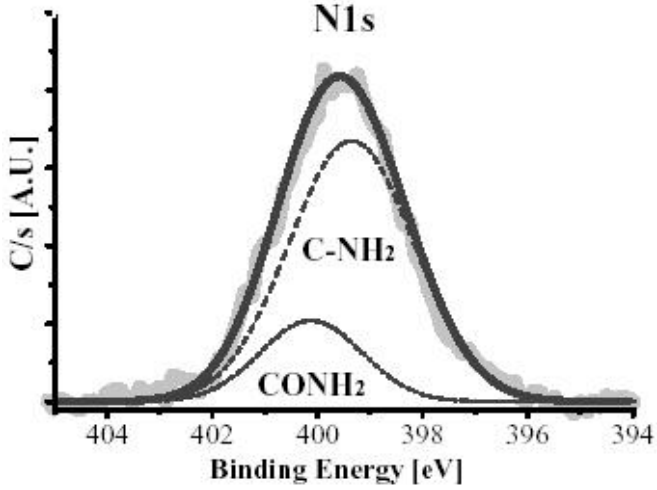

Fig. 8 Deconvoluted high-resolution XPS spectra of N1s.

groups (C-NH_2) and the higher binding energy peak at 400 eV corresponds to amide groups ($CONH_2$). Table Ⅰ shows that although the power dissipated into the plasma is small(1/10,000~1/1,000), almost the same or more quantity of amino groups are functionalized on the surface of polyethylene compared to other plasma surface treatment. Moreover, selectivity of amino groups functionalization (NH_2/N) in this work is relatively high compared to other works. The O1s peak can be also deconvoluted into two different peaks. The lower binding energy peak corresponds to carbonyl groups and the higher binding energy peak corresponds to ether or alcohol.

Figure 9(a) and (b) are the results of localization mapping of N1s XPS signal counts for 1 s and 100 s treatment respectively. We have achieved localized N1s area which is about 500 μm in diameter at 1s treatment. The size corresponds to the inner diameter of quartz tube. Although, it apparently shows that as the treatment time increases, the N1s incorporated area spreads. This fact indicates the possibility of the even smaller N1s functionalized area below 1 s treatment time.

Table Ⅰ. Comparison of Polymer Functionalization Results Reported in Other Literatures and Our Result.

Polymer	Treatment time (s)	Power (W)	Gas	Pressure (Torr)	O/C	N/C atomic	NH_2/C ratio%	NH_2/N	Ref.
PE	3	9.6	NO in N_2 atmosphere		23.8	5.38	2.05	38	[5]
PE	300～	?	NH_3	?	-	-	-	44.6	[6]
PE	10	0.0062	NH_3/He	720-730	5.78	4.06	2.74	74.16	this work
PE	216	5	NH_3	0.38	13.6	12.8	-	-	[7]
PP	1	50	NH_3	1.5	6～7	9	-	-	[8]
PS	10	40	N_2/H_2	0.12	16.3	8.75	4.48	67.4	[9]
PET	120	50	N_2	0.1	58	10	-	-	[10]
PET	120	50	NH_3	0.1	35	3	-	-	[10]

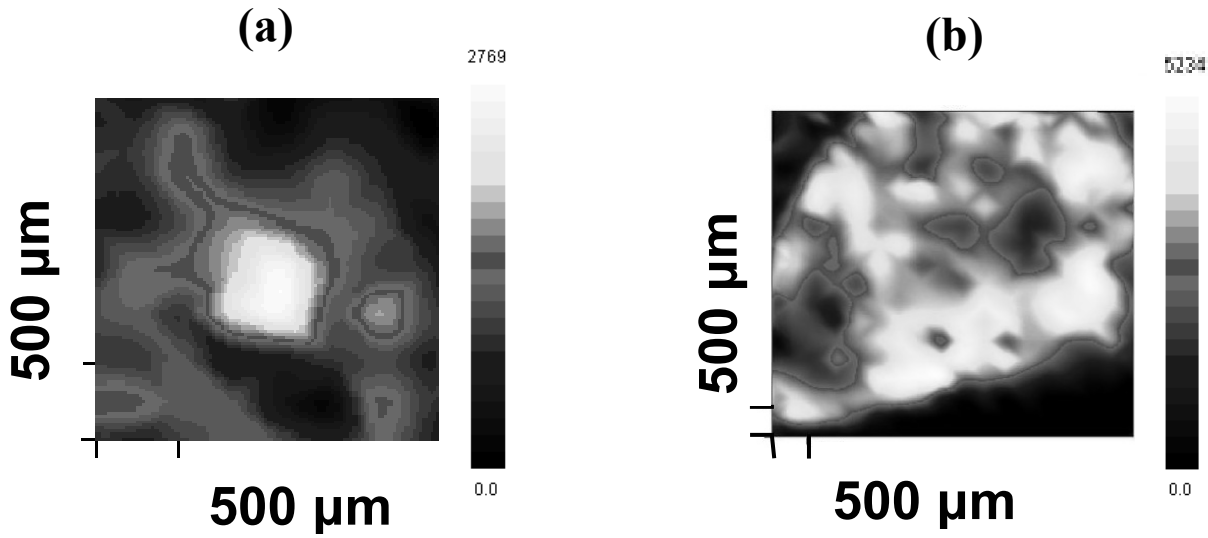

Fig. 9 Localization mappings of XPS N1s signal counts for (a) 1 s and (b) 100 s microplasma treatment, respectively.

Ⅳ. CONCLUSIONS

The amino groups were functionalized on a local surface of the low-density polyethylene by NH_3/He-DBDMP. Optical emission spectroscopy (OES) has been used for the characterization of the NH_3/He-DBDMP. Intensity of the NH radicals which play an important role on functionalizing amino groups, increases as applying higher voltage and as lowering the NH_3 flowing rate. The latter result can be explained by the mean energy that NH_3 particles recieve from He metastables. Lissajou method has been used to obtain the total power consumption of the NH_3/He-DBDMP in our system and it was 6.2 mW under the condition of V = 1.9 kV, f = 7 kHz, Q_{NH3} = 5 sccm, and Q_{He} = 200 sccm. The value is about 1/10,000~1/1,000 of those of other conventional plasma surface treatment system. X-ray photoelectron spectroscopy has been used for the characterization of NH_3/He-DBDMP treated polyethylene surface. The data from XPS shows that the increase of treatment time results in the increase of N and O components incorporation on the surface of the polyethylene. Although the power dissipated into the plasma is small, almost the same or more quantity of amino groups are functionalized on the surface of polyethylene compared to other plasma surface treatment. This is the advantage of the high-density plasma generated at atmospheric pressure in a small space. The results of localization mapping to visualize the locality of NH_3/He-DBDMP treatment show that as the treatment time increases, the N1s incorporated area spreads. This fact indicates the possibility of the even smaller amino groups functionalized area for shorter treatment time.

ACKNOWLEDGEMENT

This work was supported financially in part by Specific Research of Priority Areas (Microplasma) (Grant No. 15075202) from The Ministry of Education, Culture, Sports, Science and Technology.

REFERENCES

[1] N. Inagaki , *Plasma Surface Modification and Plasma Polymerization*, Technomic Publishing Company, (1996)

[2] D. Ishihara, Y. Kasaki, Y. Shimizu, T. Sasaki, N. Koshizaki, and K. Terashima, Thin Solid Films, unpublished

[3] S. Kurosawa, H. Aizawa, Z. A. Talib, B. Atthoff, and J. Hilborn, Thin Solid Films, **374** (2000), 262-267

[4] H.-E. Wagner, R. Brandenburg, K. V. Kozlov, A. Sonnenfeld, P.Michel, and J.F. Behnke, Vacuum **71** (2003), 417-436

[5] John B. Lynch, Paul D. Spence, David E. Baker, and Timothy A. Postlethwaite, J Appl Polym Sci, **71** (1999), 319-331

[6] Hana Drnovska, Lubomir Lapcik Jr., Vilma Bursikova, Josef Zemek, and Ana M. Barros-Timmons, Colloid Polym Sci, **281** (2003), 1025-1033

[7] F. Bretagnol, M. Tatoulian, F. Arefi-Khonsari, G. Lorang, and J. Amouroux, Reactive & Functional Polymers, **61** (2004), 221-232

[8] M. Tatoulian, F. Arefi-Khonsari, N. Shahidzadeh-Ahmadi, and J. Amouroux, Int. J. Adhesion and Adhesives **15** (1995), 177-184

[9] Meng-Jiy Wang, You-Im Chang, and F. Poncin-Epaillard, Langmuir, **19** (2003), 8325-8330

[10] Norihiro Inagaki, Kazuo Narushima, Norio Tuchida, and Kohji Miyazaki, J. Polym Sci: Part B: Polym Phys, **42** (2004), 3727-3740

Etching of high-*k* and metal gate materials using electron cyclotron resonance chlorine-containing plasmas

Kazushi Osari, Tomohiro Kitagawa, Keisuke Nakamura, Kazuo Takahashi, Kouichi Ono

Department of Aeronautics and Astronautics, Graduate School of Engineering, Kyoto University, Kyoto, Japan

Abstract

Etching characteristics of high-*k* dielectric materials (HfO_2) and metal electrode materials (Pt, TaN) have been studied in high-density chlorine-containing plasmas. The etching of HfO_2 was performed in BCl_3 without rf biasing, giving a high etch selectivity of >10 over Si and SiO_2. The etching of Pt and TaN was performed with high and low rf biasing, respectively, giving a high etch selectivity of >8 over HfO_2 and SiO_2 in Ar/O_2 for Pt and in Ar/Cl_2 for TaN.

Keywords: high-*k*, plasma etching, ECR, gate oxides, gate electrodes, HfO_2, Pt, TaN

1. Introduction

As integrated circuit device dimensions continue to be scaled down, increasingly strict requirements are being imposed on plasma etching technology. The requirements include the etch anisotropy, profile control, feature size or critical dimension control relative to the mask layer, selectivity to the mask and underlying layers, and also microscopic uniformity of these etch parameters. For gate etch processes, a precise control of the profile and critical dimension of gate electrodes and a high selectivity to gate oxides have historically been the two most important issues to be addressed. In practice, the gate width of advanced microelectronic devices is projected to be scaled down to much less than 100 nm, and the thickness of gate oxides is also reduced down to 2 nm or less for conventional SiO_2.

Regarding gate dielectrics, the technological challenge continues for growing ultrathin SiO_2 films of high quality, to maintain the gate capacitance without increasing the gate leakage current and reducing the oxide reliability; however, the ultimate solution would rely on high dielectric constant (*k*) materials. Recent efforts have been made to replace SiO_2 with silicon-oxynitrides of slightly higher dielectric constant, and nowadays, new high-*k* (>20) dielectrics or metal oxides such as Al_2O_3, HfO_2, ZrO_2, and their silicates and aluminates are being developed to replace SiO_2 [1,2]. In practice, the metal oxides give the required specific gate capacitance at a considerably larger thickness as compared to SiO_2. In integrating these materials into device fabrication, an understanding of the etching characteristics of high-*k* materials is strongly required for their removal prior to forming the source and drain contacts. It should be noted that high-k dielectrics are generally difficult materials for etching, owing to their non-volatile etch products or halogen compounds.

Moreover, for gate stacks with high-*k* dielectrics, gate electrodes of conventional poly-crystalline silicon (poly-Si) tends to cause some problem of the depletion layer present in doped poly-Si gate materials. Thus, for lower equivalent oxide thicknesses, recent efforts have also been made to replace poly-Si gate electrodes with metal gates of WN, TiN, TaN, Ru/RuO_2, Pt, and/or Ir [1,2]. It should be noted that some of these metals (Pt, Ir) are also difficult materials for etching, owing to their non-volatile halogen compounds.

Plasma etching of high-*k* oxides and metal electrodes has been studied in the application of ferroelectric materials, buffer layers, and capacitor dielectrics to memory devices. However, only a few studies have recently been concerned with the plasma etching of high-*k* dielectrics [3-13] and metal electrodes [11,13] for the application of high-*k* gate stacks. Pelhos *et al*. studied the etching of high-*k* gate dielectric $Zr_{1-x}Al_xO_y$ thin films in helical resonator plasmas with Cl_2/BCl_3 [3]. Sha *et al*. investigated the etching of ZrO_2 in electron cyclotron resonance (ECR) plasmas with Cl_2/Ar [4] and BCl_3/Cl_2 [6], and also the etching of HfO_2 in ECR BCl_3/Cl_2 plasmas [7,8]. Norasetthekul *et al*. reported on the etching of HfO_2 in inductively coupled plasmas (ICP) with Cl_2/Ar, SF_6/Ar, and $CH_4/H_2/Ar$ [5]. Moreover, Maeda *et al*. reported on the HfO_2 etching in ICP CF_4 and $Cl_2/HBr/O_2$ plasmas [9]. Chen *et al*. investigated the etching of HfO based high-*k* films in ICP plasmas with Cl_2/HBr and CF_4/CHF_3 [10]. Emphasis of most of these studies has been placed on etch chemistries giving an etch selectivity of >1 over the underlying Si [3-8] and SiO_2 [9], and further on a better understanding of the physics and chemistry underlying the processing. More recently, Kota *et al*. have reported on the etching of metal/high-*k* stacks ($TiN/TaN/HfO_2$) in ICP plasmas with BCl_3- based chemistries [11]. It is further noted that the etching of high-*k* dielectrics is also indispensable with low ion energies and/or less ions, for chamber cleaning of the chemical vapor deposition (CVD) and atomic layer deposition (ALD) apparatuses to prepare high-*k* thin films.

We have investigated the high-density plasma etching of HfO_2 with attention being focused on etch chemistries and plasma conditions to achieve a much higher selectivity of >>1 over Si and SiO_2. We found the highly selective

etching of HfO_2 over Si in ICP fluorocarbon plasmas [12]; in some detail, the selectivity was >5 in C_4F_8/Ar plasmas, where carbon and/or carbonaceous species would work as surface inhibitors on Si, contributing to the high selectivity. Moreover, we demonstrated that the HfO_2/Si selectivity is further increased to >>10 in C_4F_8/Ar/H_2 plasmas, where the fluorocarbon polymer deposition on Si would be enhanced significantly by adding H_2, as in the situation of high selective etching of SiO_2 over Si with fluorocarbon plasmas.

This paper presents a highly selective etching of HfO_2 over the underlying Si and SiO_2 in ECR chlorine-containing plasmas without rf biasing [13]. The idea is that the lowered energy of incident ions would reduce the etch rates of Si and SiO_2 significantly as compared to HfO_2, thus contributing to the high selectivity. The paper also presents the etching of Pt and TaN in ECR chlorine-containing plasmas [13], with emphasis on the etch anisotropy and selectivity of metal electrodes over HfO_2 and SiO_2 (over the underlying high-*k* and the mask materials).

2. Experimental

The experimental setup is shown in Fig. 1 for ECR plasma etching. The plasma reactor consisted of a plasma and a specimen chamber grounded. A set of solenoid coils were placed around the former, providing divergent magnetic fields to produce and transport ECR plasmas to a sample for etching in the specimen chamber. The discharge was established by 2.45-GHz right-hand circularly polarized microwaves of TE_{11} mode injected trough an entrance quartz window at the top of the plasma chamber, and the 875-G ECR resonance was located near the end of the plasma chamber. The specimen chamber, 36 cm in diameter and 40 cm long, had an end port for pumping and several side ports for diagnostics, containing a 16-cm-diam floating electrode or substrate holder ~20 cm downstream (B≈200 G) from the ECR resonance region. The electrode was water cooled, and capacitively coupled to a 13.56-MHz rf power supply through an impedance matching network for additional rf biasing. Feedstock gases employed were Cl_2 BCl_3. O_2, and their mixtures with Ar, being introduced into the reactor, evacuated to a base pressure $<10^{-6}$ Torr, through a set of small holes at side walls of the reactor. The experiments were performed at incident microwave powers of nominally P_{MW}= 400-600 W, rf bias powers of nominally P_{rf}=0-150 W, and a gas flow rate of 40 sccm in total; the reactor gas pressure was varied from P_0=5 to 20 mTorr (0.665 to 2.66 Pa).

The etched depth was measured by stylus profilometry; in some cases, the film thickness of dielectrics was measured by optical interferometry, and the film thickness of metals was obtained from the sheet resistance measured by the four probe method. The etch rates were calculated by dividing the etched depth or thickness by the etching time. Moreover, the chemical composition on wafer surfaces was examined with x-ray photoelectron spectroscopy (XPS), and the etched profile was with scanning electron microscopy (SEM). In addition, several diagnostics were employed to characterize the plasma around the wafer position during processing: optical emission spectroscopy (OES), microwave interferometry, and Langmuir probe measurement.

Samples for etching were 50-nm-thick HfO_2 films prepared by CVD on Si substrates, and 200-nm-thick Pt and TaN films prepared by reactive sputtering on thermally oxidized Si substrates. Separate Si and thermal SiO_2 substrates were employed for reference of etching. To examine the etched profiles, patterned samples were also employed with a 200-nm-thick hard mask (SiO_2 mask) pattern feature of lines and spaces, where the nominal pattern width was in the range 0.4–10 μm. It is noted here that the Pt samples had 10-nm-thick Ti films deposited as an adhesion layer between Pt and SiO_2. The samples were cleaved into 2 cm^2 pieces, and attached on a 6-in.-diam Si wafers, which were then mechanically clamped into place on the wafer stage; backside helium was injected for increased wafer thermal contact.

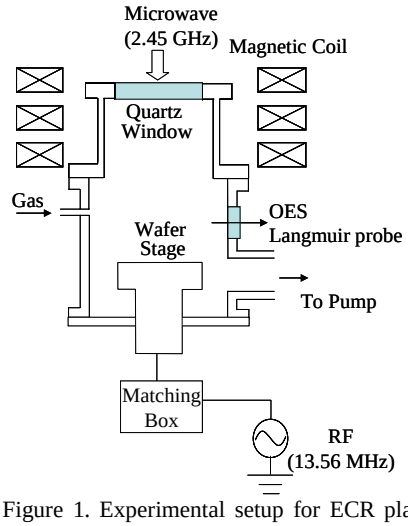

Figure 1. Experimental setup for ECR plasma etching.

3. Results and Discussion

3.1 Etching of high-k dielectrics

Figures 2(a) and 2(b) shows the etch rates of HfO_2, Si and SiO_2 in BCl_3 without rf biasing, as a function of pressure P_0 at P_{MW}=600 W and as a function of microwave power P_{MW} at P_0=10 mTorr, respectively. The gas flow rate was 40 sccm in total. The etching of HfO_2 films occurred at pressures between P_0=8 and 12 mTorr. The etch rate of HfO_2 was about 5 nm/min in maximum at P_0=10 mTorr, where the etch selectivity was >10 over Si and SiO_2. It should be noted that at lower P_0≤6 mTorr, the deposition occurred on all surfaces of HfO_2, Si, and SiO_2, and that at

higher $P_0 \geq 15$ mTorr, the etching of HfO_2 did not occur; moreover, the etching of Si and SiO_2 was found to occur only at around P_0=8 mTorr. The Langmuir probe measurements indicated that at P_0=10 mTorr with P_{MW}=600 W, the difference between the plasma and floating potentials was V_p-$V_f \approx 15$ V, increasing and decreasing with increasing and decreasing the P_0, respectively. In addition, as the microwave power was increased from P_{MW}=400 to 600 W at P_0= 10 mTorr, the etch rates of all the films increased, where the HfO_2 etch rate was in the range 3-5 nm/min and the selectivity of HfO_2 over Si and SiO_2 exceeded 10.

Figure 2(c) shows the etch rates of HfO_2, Si and SiO_2 in BCl_3 without rf biasing, as a function of pressure P_0 at P_{MW} =600 W, derived from the data of Figure 2(b) after removal of the deposited films on surfaces by using the solvent of alcohol. It should be noted that at low pressures $P_0 \leq 6$ mTorr, the etching was found to occur on HfO_2 surfaces, while the etching was insignificant on Si and SiO_2 surfaces. Figure 2(d) shows the etched depth or thickness of HfO_2, Si and SiO_2, measured as a function of time in BCl_3 without rf biasing, at P_0=5 mTorr and P_{MW}=600W. It should be noted that the etching of HfO_2 was found to occur during approximately <0.5 min, and then the deposition occurred on HfO_2; in contrast, on Si and SiO_2 surfaces, only the deposition occurred after the induction period.

Figure 3 shows SEM micrographs of the HfO_2, Si and SiO_2 surfaces exposed to ECR BCl_3 plasmas without rf biasing during 5 min at P_{MW}=600 W and P_0=5 and 10 mTorr. At P_0=5 mTorr, all surfaces of HfO_2, Si, and SiO_2 were found to be rough, or the surface morphologies were poor, probably owing to the films or materials deposited. In contrast, all the surfaces were smooth at P_0=10 mTorr, on which the etching occurred.

Figure 4(a) shows the XPS spectrum of Hf $4f_{7/2}$ and Hf $4f_{5/2}$, obtained from HfO_2 sample surfaces for three different conditions: (i) HfO_2 surfaces before plasma exposure; and HfO_2 sample surfaces exposed to BCl_3 plasmas without rf biasing during 5 min at P_{MW}=600 W and P_0= (ii) 5 mTorr (deposit- ed) and (iii) 10 mTorr (etched). Note that the conditions (ii) and (iii) correspond to those of Figure 3.

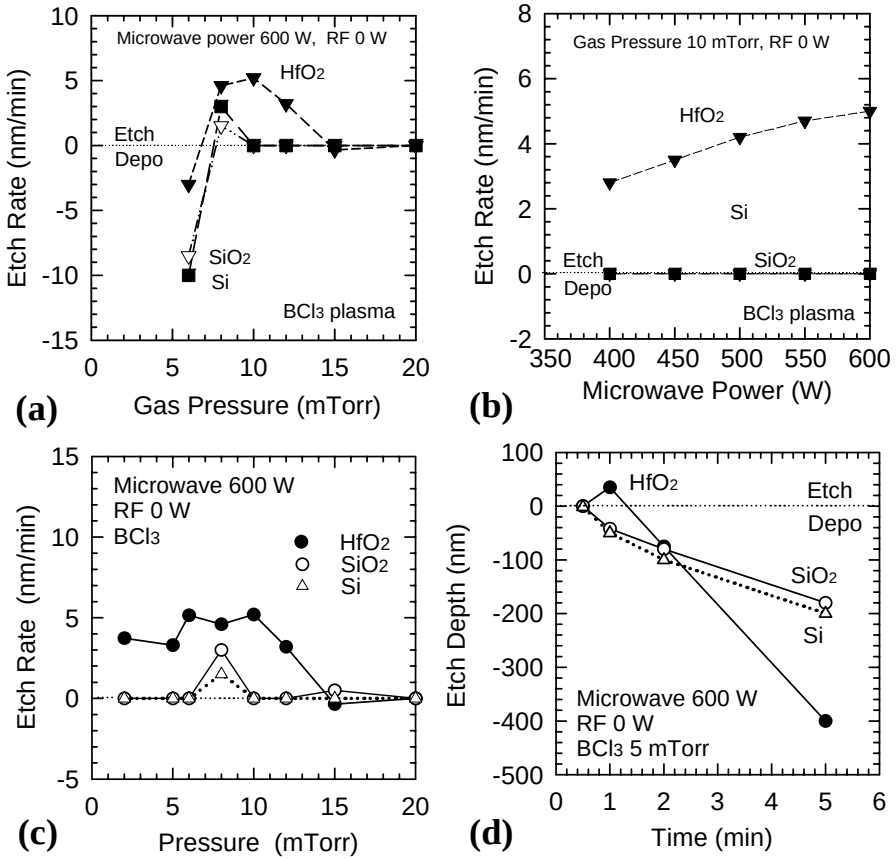

Figure 2. Etch rates of HfO_2, Si and SiO_2 in ECR BCl_3 plasmas without rf biasing, (a) as a function of pressure P_0 at P_{MW}=600 W and (b) as a function of microwave power P_{MW} at P_0=10 mTorr. The gas flow rate was 40 sccm. Also shown were (c) the etch rates derived from the data of (a) after removal of the deposited films on surfaces, and (d) the etched depth or thickness measured as a function of time at P_0=5 mTorr and P_{MW}=600 W.

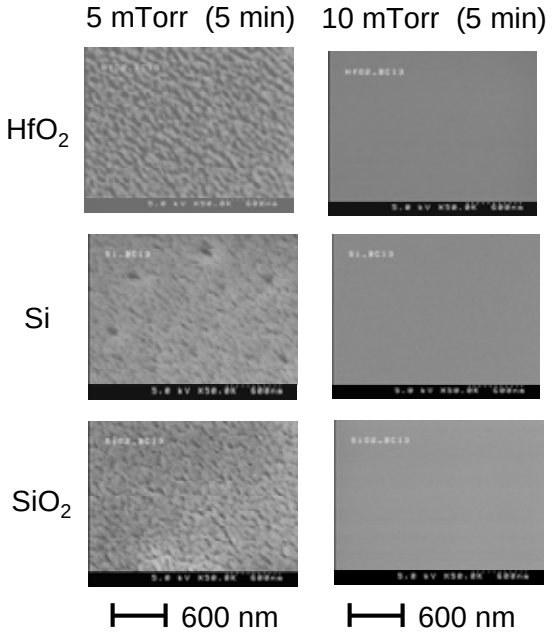

Figure 3. SEM micrographs of the HfO_2, Si and SiO_2 surfaces etched in (or exposed to) ECR BCl_3 plasmas without rf biasing during 5 min at P_{MW}=600 W and P_0=5 and 10 mTorr.

Also shown is the spectrum obtained from (iv) Si surfaces exposed to BCl_3 plasmas under the same operating conditions of (ii). The similar spectrum of Hf 4*f* was observed from (i) virgin and (iii) etched HfO_2 surfaces, while the spectrum intensity was relatively small from (ii) HfO_2 sample surfaces obtained under deposition conditions, implying that the deposited surfaces were covered with thin films or material layers containing no Hf species.

Figure 4(b) shows the XPS spectrum of Cl 2*p* and B 1*s*, obtained from HfO_2 and Si surfaces for the same conditions of Figure 4(a). No significant spectrum was observed from (i) virgin and (iii) etched HfO_2 surfaces. Note that no peaks on the etched surfaces may be attributed to the exposure of samples to atmosphere after the experiment. In contrast, the similar spectrum of Cl 2*p* and B 1*s* was observed from (ii) HfO_2 and (iv) Si sample surfaces obtained under deposition conditions, implying that some BCl_x species or films were deposited on all the surfaces of interest. Moreover, Figure 4(c) shows the XPS spectrum of O 1*s* from HfO_2 and Si surfaces for the same conditions of Figures 4(a) and 4(c). The similar O 1*s* spectrum was observed from (i) virgin and (iii) etched HfO_2 surfaces, being attributable probably to Hf-O bonding of HfO_2. In contrast, the O 1*s* spectrum on (ii) HfO_2 and (iv) Si sample surfaces under deposition conditions exhibited a chemical shift attributable possibly to B-O bonding, which may be caused by the exposure of samples to atmosphere containing O_2 after the experiment.

It should be concluded that HfO_2 thin films can be etched with a high selectivity over Si and SiO_2 in high-density BCl_3 plasmas without rf biasing. At lower pressures, the deposition of BCl_x occurs on all the surfaces of interest; however, on HfO_2 surfaces, the deposition follows the etching that occurs during a few tens of seconds after some induction period. If the deposition can be suppressed under some

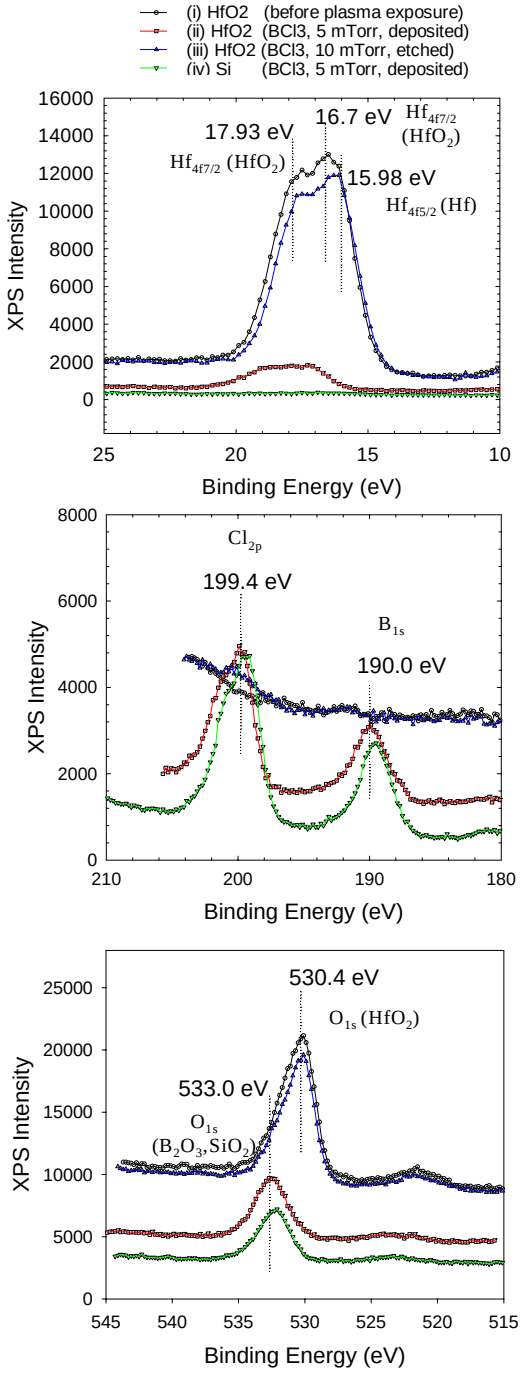

Figure 4. (a) XPS spectrum of Hf $4f_{7/2}$ and Hf $4f_{5/2}$, obtained from HfO_2 surfaces (i) before plasma exposure and (ii)(iii) exposed to BCl_3 plasmas without rf biasing during 5 min at P_{MW}=600 W and P_0=5 and 10 mTorr. Also shown is (iv) the spectrum obtained from Si surfaces exposed to BCl_3 plasmas under the same conditions of (ii). Moreover, XPS spectrum of (b) Cl 2*p* and B 1*s* and (c) O 1*s* were obtained from HfO_2 and Si surfaces for the same conditions of (a).

operating conditions, the HfO_2 etch rate would be significantly enhanced.

3.2 Etching of metals

Figures 5(a) and 5(b) show the etch rates of Pt, TaN, HfO_2, SiO_2 and Si as a function of Cl_2 concentration ratio in Ar/Cl_2 and as a function of O_2 concentration ratio in Ar/O_2, respectively, under the condition at a microwave power of P_{MW}=600W, an rf bias power of P_{rf}=150 W, and a pressure of P_0=10 mTorr. The gas flow rate was 40 sccm in total. Under these conditions, the peak-to-peak amplitude of the rf bias voltage was measured to be in the range V_{pp}=440-530 V. The etch rate of Pt in Ar/Cl_2 was about several tens of nm/min, being almost independent of Cl_2 concentration. The selectivity of Pt was in the range 0.4-1.5 over HfO_2, and in the range 0.9-1.6 over SiO_2, indicating that highly selective Pt etching over HfO_2 and SiO_2 is difficult in Ar/Cl_2. Note that under these conditions, the TaN etch rate exceeded > 300 nm/min when adding a small amount of Cl_2, probably owing to the formation of highly volatile products $TaCl_x$.

In contrast, by adding a small amount of O_2 to Ar, the etch rates of TaN, HfO_2, SiO_2, and Si significantly decreased, while the etch rate of Pt decreased slightly, resulting in a high etch selectivity of > 8 over HfO_2 and SiO_2 with >20% O_2 added. These results of the etching behavior of Pt is similar to previous studies for the application of high-*k* metal oxides to capacitor dielectrics in memory devices [14-16]; in practice, the etching of Pt relies primarily on physical sputtering through energetic ion bombardment on surfaces.

Figures 6(a) shows the etch rates of Pt, TaN, HfO_2, SiO_2 and Si as a function of Cl_2 concentration ratio in Ar/Cl_2, under the condition at a microwave power of P_{MW}=600W, an rf bias power of P_{rf}=30 W, and a pressure of P_0=10 mTorr. Under these conditions, the peak-to-peak amplitude of the rf bias voltage was measured to be in the range V_{pp}=100-160 V. Note that under these low rf bias power conditions, the etching of Pt did not occur, owing to lowered energy of ion bombardment; moreover, without rf biasing, the etching did not occur for all the metal films of interest. The etch rate of TaN increased significantly with increasing Cl_2 concentration, being about 200 nm/min in pure Cl_2, where a high etch selectivity of > 8 was achieved over HfO_2 and SiO_2. Figure 6(b) shows the etch rates of TaN and Pt as a function of rf bias power P_{rf} at 50% Cl_2 added in Ar/Cl_2, otherwise under the same condition of Figure 6(a). The threshold of P_{rf} or incident ion energy was found to be significantly lower for TaN than for Pt;

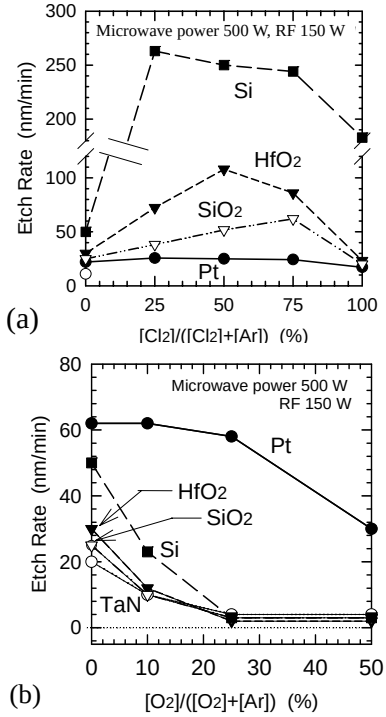

Figure 5. Etch rates of Pt, TaN, HfO_2, SiO_2, and Si (a) as a function of Cl_2 concentration ratio in Ar/Cl_2 and (b) as a function of O_2 concentration ratio in Ar/O_2, under the condition at a microwave power P_{MW}=500W, an rf bias power P_{rf}=150 W, and a pressure P_0=10 mTorr. The gas flow rate was of 40 sccm in total.

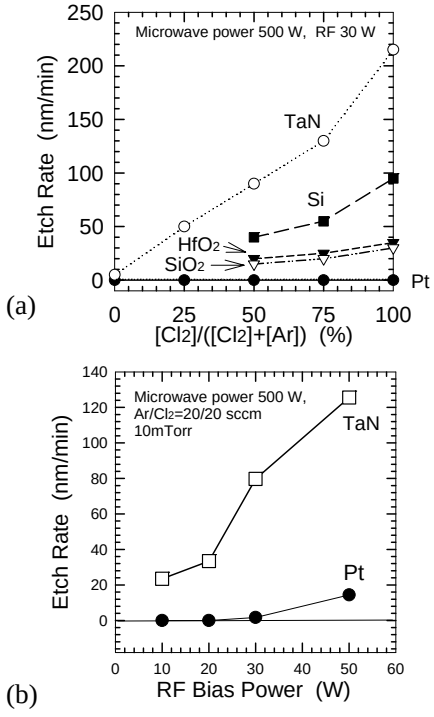

Figure 6. (a) Etch rates of Pt, TaN, HfO_2, SiO_2 and Si as a function of Cl_2 concentration ratio in Ar/Cl_2, under the condition at P_{MW}=500W, P_{rf}=30 W, and P_0=10 mTorr. Also shown are (b) the etch rates of TaN and Pt as a function of P_{rf} at 50% Cl_2 added in Ar/Cl_2, otherwise under the same condition of Figure 6(a).

in practice, the etching of TaN may occur at P_{rf}=0 or without rf biasing after some breakthrough at the beginning of etching. These results imply that the etching of TaN relies primarily on ion-assisted etching, with the chemical nature being high as compared to Si.

Figure 7 shows SEM micrographs of a nominally 0.4 μm line feature of Pt and 0.6 μm line feature of TaN, approximately just etched at 20% O_2 in Ar/Cl_2 with P_{rf}=150 W for Pt and at 75% Cl_2 in Ar/Cl_2 with P_{rf}=30 W for TaN; otherwise, the operating conditions were the same for Pt and TaN with P_{MW}=500 W and P_0=10 mTorr. A hard (SiO_2) mask was employed for the patterned samples. The etched profile of Pt was outwardly tapered, owing to the redeposition of etch or sputter products on feature sidewalls [14-16]. In contrast, the etched profile of TaN was found to be almost anisotropic, probably owing to the ion-enhanced etching that occurred.

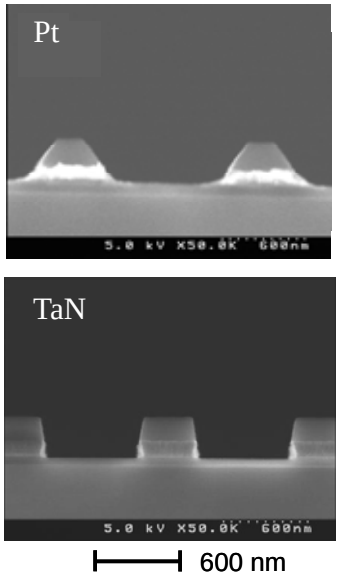

Figure 7. SEM micrographs of a 0.4 μm line feature of Pt and TaN, etched at 20% O_2 in Ar/Cl_2 with P_{rf}=150 W for Pt and at 75% Cl_2 in Ar/Cl_2 with P_{rf}=30 W for TaN. Other -wise, the operating conditions were the same for both with P_{MW}=500 W and P_0=10 mTorr,

4. Conclusion

Etching characteristics of high-*k* dielectric materials (HfO_2) and metal electrode materials (Pt, TaN) have been studied using high-density ECR chlorine-containing plasmas. Attention was focused on etch chemistries and plasma conditions to achieve a high etch selectivity of >>1 for HfO_2 over the underlying Si and SiO_2; regarding Pt and TaN, the emphasis was placed on the etch anisotropy and selectivity of metal electrodes over HfO_2 and SiO_2 (over the underlying high-*k* and the mask materials). The etching of HfO_2 was performed in BCl_3 without rf biasing, giving a high etch selectivity of >10 over Si and SiO_2. The etching of Pt and TaN was performed with high and low rf biasing, respectively, giving a high etch selectivity of >8 over HfO_2 and SiO_2 in Ar/O_2 for Pt and in Ar/Cl_2 for TaN. Further investigations are now in progress for the etched profiles and for the etching of stacks of metals/high-*k*, along with the numerical simulation of the feature profile evolution concerned and with a better understanding of the physics and chemistry underlying the phenomena observed.

This work was supported by NEDO/MIRAI project and by Taiyo Nippon Sanso Corp.

References

[1] M. Hirose: Oyo Buturi **71** (2002) 1091 [in Japanese]
[2] A. Toriumi, T. Horikawa and T. Nabatame: Nikkei Microelectronics Dec. (2002) 163 [in Japanese].
[3] K. Pelhos, V.M. Donnelly, A. Kornbilt, M.L. Green, R.B. Van Dover, L. Manchanda, Y. Hu, M. Morris and E. Bower: J. Vac. Sci. Technol. A **19** (2001) 1361.
[4] L. Sha, B.-O. Cho and J.P. Chang: J. Vac. Sci. Technol. A **20** (2002) 1525.
[5] S. Norasetthekul, P.Y. Park, K.H. Baik, K.P. Lee, J.H. Shin, B.S. Jeong, V. Shishodia, D.P. Norton and.J. Pearton: Appl. Surf. Sci. **187** (2002) 75.
[6] L. Sha and J.P. Chang: J. Vac. Sci. Technol. A **21** (2003) 1951.
[7] L. Sha, R. Puthenkovilakan, Y.-S. Lin and J.P. Chang: J. Vac. Sci. Technol. B **21** (2003) 2420.
[8] L. Sha and J.P. Chang: J. Vac. Sci. Technol. A **22** (2004) 88.
[9] T. Maeda, H. Ito, R. Mitsuhashi, A. Horiuchi, T. Kawahara, A. Muto, T. Sasaki, K. Torii and H. Kitajima: Jpn. J. Appl. Phys. **43** (2004) 1864.
[10] J. Chen, W.J. Yoo, Z.Y. Tan, Y. Wang and D.S.H. Chan: J. Vac. Sci. Technol. A **22**, (2004) 1552.
[11] G.P. Kota, S. Ramalingam, S. Lee, B. Coene- grachts and C. Lee : Proc. 4th Int. Symp. Dry Process, Tokyo, 2004 (IEEJ, Tokyo, 2004) p. 133.
[12] K. Takahashi and K. Ono: Proc. 4th Int. Symp. Dry Process, Tokyo, 2004 (IEEJ, Tokyo, 2004) p. 369; submitted to J. Vac. Sci. Technol..
[13] K. Nakamura, T. Kitagawa, K. Osari, K. Takahashi and K. Ono, presented at the 2005 JSAP Spring Meeting, Tokyo, 2005, 30a-G-5 (unpublished).
[14] T. Shibano, K. Nakamura and T. Oomori: J. Vac. Sci. Technol. A **16** (1998) 502.
[15] K. Ono, T. Horikawa, T. Shibano, N. Mikami, T. Kuroiwa, T. Kawahara, S. Matsuno, F. Uchikawa, S. Satoh, and H. Abe: Tech. Dig. 1998 Int. Electron Devices Meet. (IEDM), San Francisco, 1998 (IEEE, Piscataway, N.J., 1998) p. 803.
[16] K. Shibano, K. Nakamura, T. Takenaga and K. Ono: J. Vac. Sci. Technol. A **17** (1999) 799.

X-ray scattering for in situ observation of nano sized silicon clusters during Meso Plasma fast rate epitaxy

M. Kambara, Y. Hamai and T. Yoshida

Department of Materials Engineering, The University of Tokyo, Tokyo 113-8656, JAPAN

Abstract

X-ray scattering measurement was attempted to observe in situ the possible formation of nano size clusters during medium pressure plasma CVD, in which high rate epitaxial growth has been achieved. X-ray beam was focused in the plasma/substrate boundary and the scattered signals were collected at an angle of 30˚. A distinguishable difference in intensities was observed before and during deposition, and was also varied with the silane gas flow rate, RF power input and the working pressure. These variations are potentially explained by altered size and number density of scatters, plausibly silicon clusters formed in the plasma / substrate boundary, which might be responsible for the morphological change of the film observed.

I. Introduction

In the course of film growth from vapor, atom and/or molecular precursors in an environment ahead of the solid growth interface determine critically the development of microstructure and the resultant properties of the solid. This is due mainly to its degree of spatial freedom in controlling the chemical and physical characteristics of the precursors. As a result, high pressure processing in general achieves enhanced deposition rates owing to its increased number density but tends to form agglomerated structures due to excessive particle coagulation. However, it would be still possible to attain effective precursor arrival, migration and accommodation on film surface if the precursors are to be controlled appropriately. Physical modeling on particle formation from high temperature plasma environment has predicted the nucleation of up to 1nm size clusters in the plasma/substrate boundary region and its significant contribution to an enhanced deposition rate [1]. Indeed, homoepitaxial silicon films have been produced at a rate as fast as 100nm/sec, as well as polycrystalline silicon thick films at 1μm/sec by medium pressure plasma (Meso Plasma) [2,3]. In addition, the possible presence of nano sized precursors in these experiments was supported by the ex-situ techniques such as microtrench and TEM observation [4]. These in turn imply that the processing is tuned or controlled to realize high rate deposition of a variety of films if the characteristic information of such nano clusters through direct observation is made possible.

Characterization of these in-flight (nucleating and growing) nano sized particles is typically carried out by Time-Of-Flight [5], Differential Mobility Analyze [6] and Laser scattering. Although the first two techniques allow analysis of particles as small as several nano meter sizes, these require collection of the particles from the reaction environment. This implies that, as an in-situ technique, these techniques are not applicable to the cases where nano particles are in reaction, nucleating and growing, during collection. Light scattering, on the other hand, can be a choice to observe particles in reaction based on Rayleigh or Mie scattering criteria [7]. However, the size of the particle to be observed is critically limited by the wavelength of the light used, which is several hundreds of nano meters at the smallest if laser is used as a light source. Therefore, to observe several nano sized particle, light with much smaller wavelength, such as X-ray, have to be employed. So far, only one group has attempted Soft X-ray scattering to observe soot inception in combustion flame at atmospheric pressure condition [8]. However, no attempt of this measurement has been reported for thin film processing where the nano sized clusters play critically essential roles upon controlling the structure.

In this work, we have thus adopted x-ray scattering to Meso Plasma CVD for observation of nano clusters in rather high dense and in-reaction environment, and evaluated its feasibility of being an in-situ technique to control nano particle formation during processing.

II. EXPERIMENTAL

Meso plasma CVD and X-ray scattering experiment has been carried out in the inductively coupled plasma with argon carrier gas (12slm) as shown in a schematic experimental set up of Fig.1.

The reaction chamber was initially evacuated up to 10^{-4}Pa. Silicon thin films were deposited under various pressures (6~50Torr), silane gas flow rates (5~20sccm) and RF power inputs (10~20kW) conditions. The temperature of the substrate was monitored at the bottom by the thermocouple inserted from the water-cooled copper substrate holder.

The X-ray beam generated with a copper target at 40kV and 2mA was focused with a focal diameter of 700μm at the plasma/substrate boundary, and the scattered light was collected by a solid-state detector (SSD) placed at scattering angles of 5˚ and 30˚. The slits were positioned in the X-ray path appropriately to eliminate the possible noise (multiple-scattered X-ray at chamber wall) and to collect the signal from only the plasma flame. In addition, to avoid the emission of Ar and Si, Ni filters were also placed in front of SSD counter to collect the X-ray at Cu Kα energy, which is the sum of the scattered X-ray from plasma / natural gases and from possible clusters within the plasma / substrate boundary region.

Measurement at a certain deposition condition was carried out under high vacuum before deposition (V_0), in the Ar plasma (P), during deposition with silane gas injection (D) and after deposition under high vacuum (V). This set of measurements allows an evaluation of the effects of residual gases, plasma and substrate (or the thin film deposited) on the intensities measured. The net intensity from the particles was then obtained by subtracting intensities during deposition from that in Ar plasma, and was compared with the morphology of the film so produced.

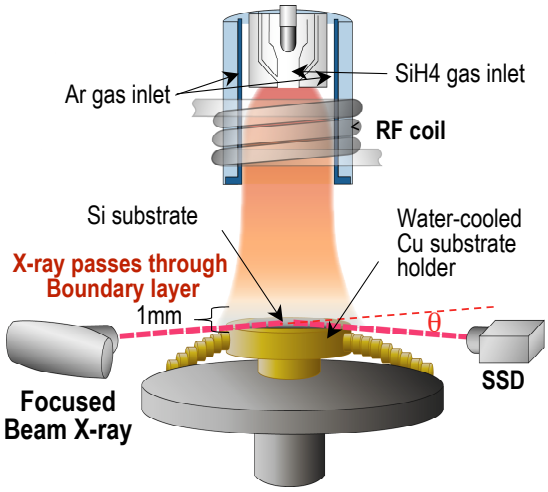

Fig.1 Schematic illustration of the experimental set up. Plasma carrier gas and silane gas were injected from top of the coil. The X-ray tube and SSD counters are positioned in the same horizontal plane which is tuned to the substrate position with sub-mm precision.

III. Results and discussions

Prior to the measurement during deposition, the effect of the environment gas species on X-ray intensity was measured. Figure 2 show the pressure dependences of scattered (transmitted) intensity by He, N_2 and Ar gases, measured at 0˚ and 30˚, respectively, and compares with those calculated with absorption coefficients and atomic scattering factors. In the case of 0˚, for all the gases, a monotonic decrease in intensity was observed with increasing the total pressure, although the intensity through Ar gas decreases rather rapidly in contrast to less significant influence of pressure of He and N_2. On the other hand, for the case of the scattering at 30˚, the scattering intensity increases monotonically with pressure for He and N_2, while that by Ar gas decreases, having the maximum at around 50Torr. These variations show a good agreement with the calculated pressure dependence. This is explained qualitatively by the combined contribution of the increased number densities of both the absorbing medium and of scattering objects with an increase in the pressure. In addition, it should be noted that no remarkable difference in intensity was observed between in the Ar plasma compared to that for natural Ar due probably to less ionization in the meso

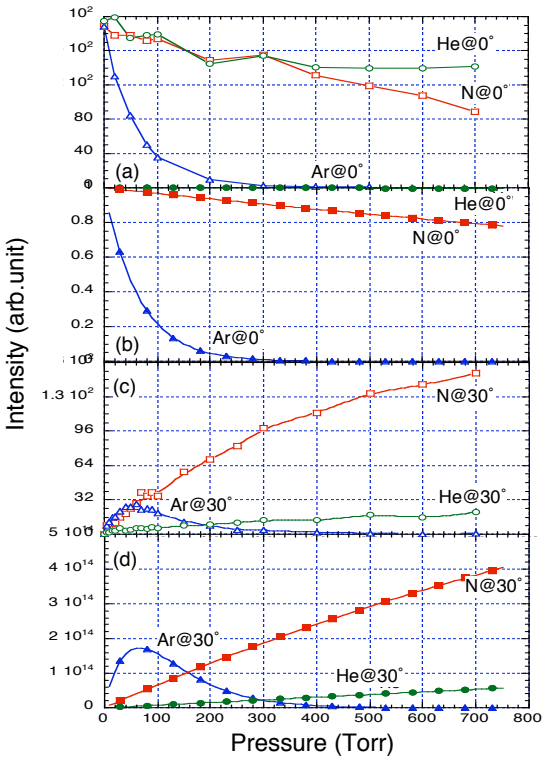

Fig.2 Pressure dependences of X-ray intensity through various gas atmospheres:
(a) experiment measured at 0˚, (b) calculation at 0˚, (c) experimental at a scattering angle of 30˚ and (d) calculation at a scattering angle of 30˚.

plasma condition.

The effect of the X-ray beam position on the x-ray intensities was then measured. Figure 3 shows the time evolution of the scattered intensity, measured at 30˚ before and after plasma deposition, at different X-ray - substrate positions. By fixing the X-ray beam position constant, the substrate height was changed so that the beam passes (a) within the plasma core flame, (b) through the possible plasma/substrate boundary layer and (c) at the bottom of the boundary and possibly interacts with substrate. In the case of (a), no detectable signal was collected under vacuum (10^{-4} Pa) after deposition (V), indicating no effect of interaction of X-ray with substrate, while the intensity during deposition (D) is nearly the same with or slightly smaller than that at plasma (P). On the other hand, the arrangement of (b) attains higher and distinguishable intensity of (D) than that of (P) although the intensity (V) is also increased after deposition. This tendency is found further enhanced in the case of (c).

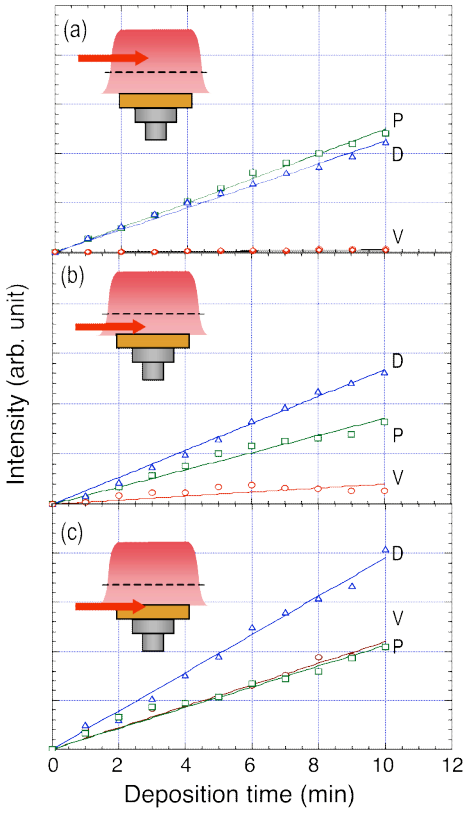

Fig.3 Time evolution of X-ray intensities, measured in Ar plasma before deposition (P), during deposition (D) and under vacuum after deposition (V), for the different substrate to X-ray beam positions; (a) X-ray in the plasma flame, (b) in the boundary and (c) at substrate. The height of substrate for (a) and (c) is lower and higher by1mm than that for (b), respectively. (all the intensities are already subtracted by the intensity measured at the initial high vacuum (V_0)).

As a general tendency, an addition of hydrogen gas to Ar plasma leads to an increase in transmitted X-ray and to a decrease in the scattering intensity. Similar tendency could be expected for silicon vapor, as the scattering cross section (atom scattering factor) and absorption coefficient for Si and H are smaller than those for Ar. As a result, when the silane gas was injected in the Ar plasma and dissociated into silicon and hydrogen atoms, the scattering intensity could be reduced from that only of Ar gas. This effect is substantially dependent on the amount of silane gas injected, but reasonably accounts for the slight decrease in the intensity (D) than (P) as observed in the case of (a).

On the other hand, the possible sources for an increase of (D) than (P) would be either the substrate (films grown) interaction or some other scattering objects or both. The effect of the former is clearly identified by the intensity (V) measured after deposition in vacuum, as is observed in the cases of (b) and (c). Recalling that the intensity (D) is the sum of the X-ray scattered by all the possible scattering objects in the boundary region, the subtraction of (V) from (D)-(P) gives a contribution only from the additional scatters within the boundary excluding the effect from the film or substrate. In the case of (c), this amount was estimated to be nearly negligible, which clearly indicates that the intensity (D) is fully due to the interaction with the film. In contrast, the amount of (D)-(P)-(V) for the case of (b) remains finite and suggests the presence of the additional scattering objects upon injection of silane gas despite the small number density of the silicon atoms in this experiment of the order of $10^{14}/cm^3$. Considering less significant scattering by silicon atoms evident from the case of (a), therefore the possible scattering object would be the silicon clusters formed by the gas phase condensation in the boundary between plasma / substrate.

Another important result involved in this set of measurements is that the appropriate height of the x-ray from the substrate is identified for observation of the clusters. Also, it should be noted that the intensity for each measurement varies with time rather linearly, suggesting the deposition process environment was carried out at steady state.

At a fixed X-ray beam and substrate arrangement, measurement was carried out at various plasma deposition conditions. Figure 4 summarizes the changes in the scattering intensity from scatters with (a) total pressure at a constant silane gas flow rate of 20 sccm and power of 15 kW, (b) silane gas flow rate at a constant total pressure of 6 Torr at 15kW and (c) RF power input at silane gas flow rate of 20

sccm and 6 Torr (all other deposition conditions are maintained constant). Note that these intensities are the net scattering intensities from scatters (possibly clusters) after subtracting that at plasma from that at deposition. It is clear that the intensity increases with increasing the total pressure and silane gas flow rate. These results would be largely affected by an increased number density of the scatters. On the other hand, the similar increase in the intensity was observed when the RF power input was increased, although the pressure and the silane gas flow rate were both maintained constant. This is partly because the scattering intensity increases with decreasing the size of scatterers as is calculated from the Mie scattering theory (forward scattering becomes pronounced if the size of scatters increases in contrast to the wavelength of light, leading to a decrease in the intensity at larger scattering angles). This tendency is further enhanced by the increased number density of smaller scatterers at a fixed number of atoms (at a constant reaction gas concentration). Simultaneous and multiple measurements at several scattering angles should be needed for quantitative characterization of the scatterers. Nevertheless, as shown in Fig.5, the structure of the films deposited at different RF powers was found to vary from aggregation of nano grains to epitaxially planar growth interface, as has been observed in Meso Plasma CVD [3]. It is therefore plausible that there is an obvious correlation between the intensity and the film morphology, and also that the possible clustering of silicon atoms is responsible for the structural variations of the films.

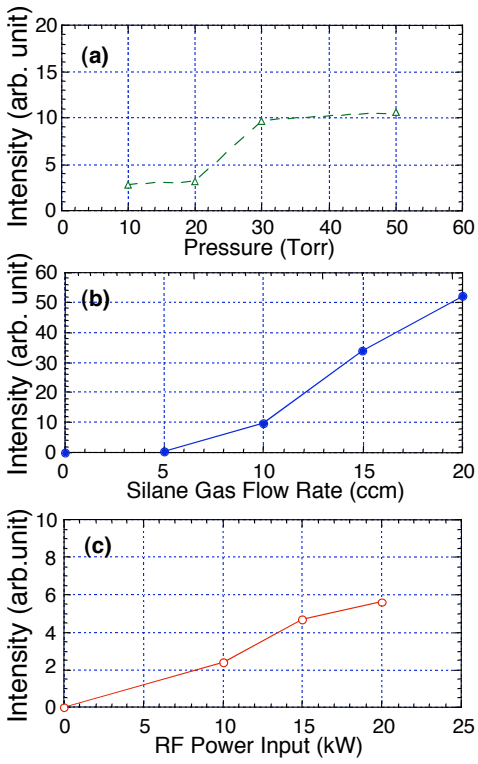

Fig.4 Variation of the scattered X-ray intensities with (a) pressure, (b) Silane gas flow rate and (c) RF power input.

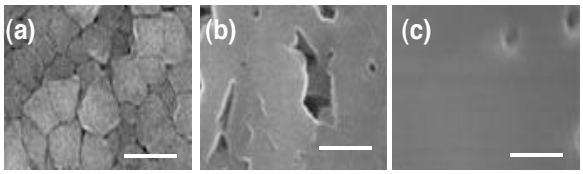

Fig.5 SEM surface images of the films deposited at different plasma RF power input; (a) 10kW, (b) 15kW and (c) 20kW.

IV. Conclusions

In situ X-ray scattering measurement was attempted to observe the possible cluster formation during meso plasma CVD. When the X-ray passes through the plasma /substrate boundary, the scattering intensity during deposition was distinguishably increased compared to that at only Ar plasma. Furthermore, this difference in the intensity was altered with the plasma conditions, while various microstructures were also observed in the films so deposited. These results potentially suggest that the additional scatters, plausibly Si clusters, were formed in the plasma / substrate boundary and could influence substantially on the evolution of the film structures. Although detailed analysis and establishment of this technique are necessary, as such the x-ray scattering was found effective to observe the condensation process in situ.

References

[1] P. Han and T. Yoshida; J. Appl. Phys., 92[8] (2002) 4772.
[2] Y. K. Chae, H. Ohno, K. Eguchi and T. Yoshida, J. Appl. Phys. 89 (2001) 8311.
[3] M. Kambara, H. Yagi, M. Sawayanagi, and T. Yoshida: J. Appl. Phys. submitted.
[4] Y. Takamura, K. Hayasaki, K. Terashima and T. Yoshida: J. Vac. Sci. Technol., B15 (1997) 558.
[5] T. Hihara and K. Sumiyama, J. Vac. Sci. Technol. B17 (1999)1923.
[6] T. Seto, T. Nakamoto, K. Okuyama, M. Adachi, Y. Kuga and K. Takeuchi; J. Aerosol. Sci. 28 (1997) 193.
[7] Y. Hayashi and K. Tachibana; Jpn. J. Appl. Phys., 33 (1994) L476.
[8] J. P. Hessler, S. Seifert, R. E. Winans and T. H. Fletcher, Faraday Discuss., 119 (2001) 395.

Infrared spectroscopic study of the deposition process using methane plasma

H.Shibata[1], T.Katagiri[1], K. Iwatsuji[1], M.Shinohara[2], Y.Matsuda[2], and H. Fujiyama[1]

[1]Graduate School of Science and Technology, Nagasaki University, Japan

[2]Department of Electrical Electronic Engineering, Nagasaki University, Japan

Abstract

We investigate the film-deposition process by CH_4/Ar plasma, using infrared spectroscopy in multiple internal reflection geometry (MIR-IRAS). The IRAS data show that sp^2- and/or sp- C_XH_Y species predominantly stick on Si substrates, when ratio of partial pressure of CH_4 to total pressure is low, and that sp^3-CH_X species predominantly stick on it when the ratio is high. We think that chemical states of the deposited films can be controlled by changing the fraction of CH_4.

1. Introduction

Methane (CH_4) plasma has been widely employed to deposit many kinds of carbon related materials, such as diamond, diamond like carbon (DLC), carbon nanotube and so on. In order to synthesize these materials precisely we must control chemical states of films from the initial stage of film deposition. Of course, many efforts have contributed to the fundamental understanding of their growth process. However, the growth process has not been fully understood yet. This is because there are many parameters to synthesize the carbon related materials. One of them is dilution gas. Argon (Ar) and hydrogen (H_2) are usually used as dilution gas in the CH_4 plasma process. It is well known that hydrogen content is high in the films deposited using the H_2/CH_4 plasma, compared with that deposited using Ar/CH_4 plasma.

We investigate the film-deposition processes by Ar/CH_4 plasma, using in-situ and real time infrared absorption spectroscopy in multiple internal reflection geometry (MIR-IRAS).

2. Experiments

An MIR-IRAS monitoring system was installed in a plasma enhanced chemical vapor deposition (PECVD) reaction chamber equipped with a plasma source and a gas delivery system in this study,

as shown in Fig. 1. The base pressure of the chamber was maintained below 1×10^{-6} Torr. Plasma excitation was accomplished by a 13.56 MHz rf power of 10 W through a π-type matching network to a coil wrapped around a 30 mm diameter Pyrex tube. The total pressure is set at 0.1 Torr. The Ar and CH_4 gas mixture was introduced into the Pyrex tube. The ratio of the partial pressure of CH_4 to the total pressure (CH_4+Ar) was changed. Radicals and other species generated in the rf field region were transported to the downstream region and reacted on a Si sample mounted 20 cm apart from one end of the helical antenna.

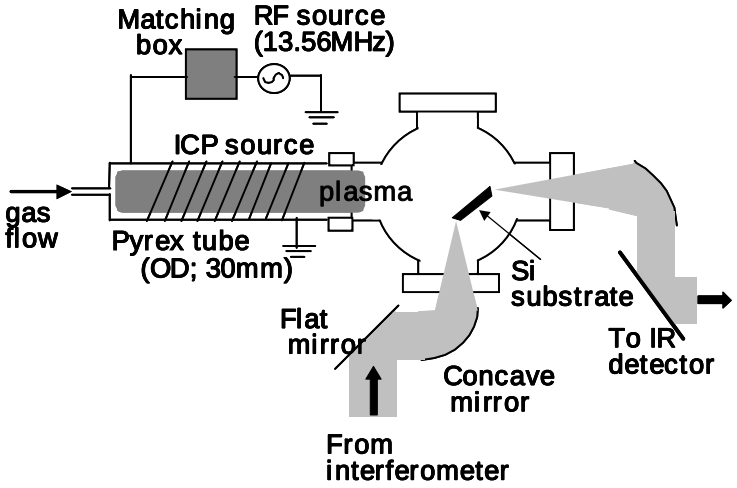

Fig.1 Experimental setup

The Si(100) sample surfaces used here were treated with the traditional RCA cleaning before the sample was set in the chamber. The chemical state of the surface was monitored using the MIR-IRAS technique. The samples were 0.5 × 10 × 40 mm^3 with 45^o bevels on each of the short edges. Infrared radiation that exited an interferometer (BOMEM MB-100) was focused at normal incidence onto one of the two bevels of the sample, and traveled through the wafer with internally reflecting about 80 times. The radiation that exited the sample at the other bevel was focused onto a liquid-N_2-cooled HgCdTe (MCT) detector.

3. Results and discussion

Fig.2 shows IRAS spectra of Si(100) surface that was exposed to CH_4/Ar plasma when the ratio of partial pressure of CH_4 to the total pressure was 50 %. The broad peaks are observed at frequencies more than 3000 cm^{-1} from the initial stage. The peak increases its intensity as plasma

exposure time passes. These peaks are attributed to sp^2- and/or sp- CH_X species [1]. Another peak is also observed around 2165 cm^{-1}. It is due to the C≡C species. The sp^2- and/or sp-CH_X species play an important role in film deposition from the initial stage in this condition.

Fig. 3 shows the IRAS spectra of Si(100) surface that was exposed to CH_4/Ar plasma when the ratio of partial pressure of CH_4 to the total pressure was 80 %. Three peaks are observed at frequencies less than 3000 cm^{-1}. The shapes of the spectra are essentially the same as that obtained from the exposure of Si surface to H_2/CH_4 plasma generated at 0.1 Torr [2]. These peaks are attributed to sp^3-CH_X species. No clear peaks are observed at frequencies more than 3000 cm^{-1} and at around 2165 cm^{-1} in Fig.3. It indicates that there are little sp^2- and/or sp-CH_X species in the film. Then, we consider they little contribute to the film deposition in this condition.

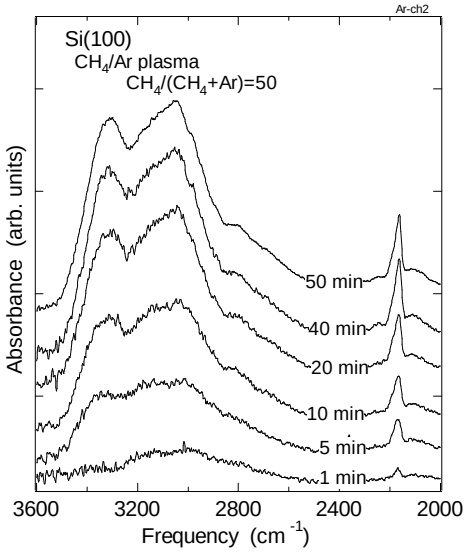

Fig. 2 IRAS spectra of Si surface that was exposed to CH_4/Ar plasma generated by a 13.56 MHz rf power of 10 W at 0.1 Torr. The partial pressure of CH_4 is 50% of the total pressure.

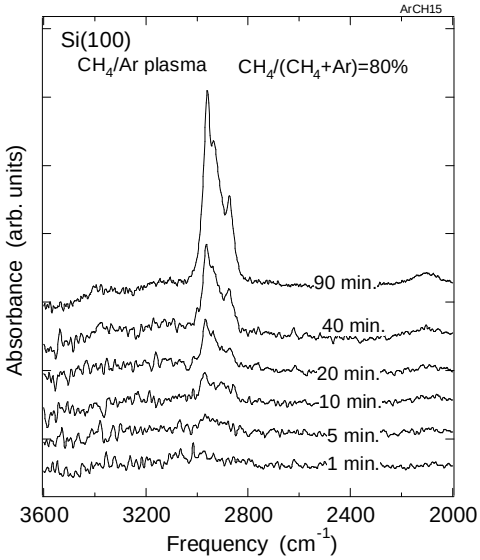

Fig. 3 IRAS spectra of Si surface that was exposed to CH_4/Ar plasma generated by a 13.56 MHz rf power of 10 W at 0.1 Torr. The partial pressure of CH_4 is 80% of the total pressure.

The CH_4/Ar plasma predominantly generated sp^2- and/or sp- C_XH_Y species, which stick on Si substrates, when the ratio of partial pressure of CH_4 to the total pressure is low. On the other hand, the plasma predominantly generates sp^3-CH_X species such as -CH_3 radicals when the ratio is high. These results indicate that the chemical states of the deposited film can be controlled by changing the ratio of partial pressure of CH_4 to the total pressure. We also suggest that the difference can be attributed to plasma-generated species. We think that the plasma-generated CH_X species is

dehydrogenated by the generation of ArH species in the CH_4/Ar plasma, and that as a result, the sp^2- and/or sp- CH_X species are easily formed when the ratio of partial pressure of CH_4 is low. Further studies are needed in order to clarify this consideration.

4. Conclusion

We have investigated the film-deposition process by CH_4/Ar plasma, using infrared spectroscopy in multiple internal reflection geometry (MIR-IRAS). The IRAS data showed that sp^2- and/or sp- C_XH_Y species stick on Si substrates, when ratio of partial pressure of CH_4 to total pressure is low, and that sp^3-CH_X species stick on it when the ratio is high. We think that the chemical states of the deposited films can be controlled by changing the ratio of the partial pressure of CH_4 to the total pressure.

Acknowledgments

This research was partially supported by a Grant-in-Aid for Young Scientists (B), No. 15760023, from the Ministry of Education, Culture, Sports, Science and Technology (MEXT) of Japan.

Reference

[1] G. Socrates: “Infrared and Raman Characteristic Group Frequencies” (Wiley, Chichester, 2001).

[2] M. Shinohara, T. Kuwano, Y. Kimura and M. Niwano, Thin Solid films **435**, 13 (2003).

Synthesis of AlN spherical nano-structured composite particles using transferred type DC arc plasma

Mikimasa Iwata*, Shizue Furukawa, Tadashi Amakawa and Kazuo Adachi

Central Research Institute of Electric Power Industry (CRIEPI), Yokosuka, JAPAN
(*m-iwata@criepi.denken.or.jp)

Abstract
Aluminum nitride (AlN) composite particles consisting of nano-particles dispersed on the surface of spherical micro-particles are one of the materials necessary for developing solid insulating materials with high thermal conductivity. This paper describes the synthesis of AlN composite particles using transferred type DC arc plasma. The diameters of micro-particle and nano-particle were controlled by varying the travelling time of the raw particles in the arc plasma and the flow rate of reacting/quenching gas.

1. Introduction

Downsizing of electrical equipment has meant that such equipment now requires a high thermal conductivity. To develop polymer insulating materials with high thermal conductivity, it is necessary to add large quantities of ceramic particles with high thermal conductivity, e.g. aluminum nitride (AlN), to organic insulating materials. Using composite particles consisting of nano-particles dispersed on the surface of spherical micro-particles is considered a good way of achieving a high ceramic particle content [1]. However, the conventional method for synthesizing composite particles requires the plural processes of synthesizing the spherical micro-particle, and the nano-particle, and mixing the two kinds of particles [2]. Another method using a spray fluidized bed granulator requires only one process for synthesizing the composite particles. However the method requires long process-time because the composite particles are synthesized by gradual agglomeration of small particles [3]. Therefore, another simple method for synthesizing the composite particles needs to be developed. On the other hand, in order to synthesize the insulating materials, it is necessary to clarify the optimal composite particle conditions, that is, the shape of synthesized particles, the volume fraction of micro-particles in the synthesized particles [4] and diameters of micro-particle and nano-particle. Therefore it is important to develop a simple method of controlling the particle conditions of synthesized composite particles.

The method utilizing transferred type arc plasma is considered a good choice for synthesizing nano-particles with a high production rate and lower costs, because the transferred type arc plasma has a long high temperature zone and the advantage of making it easy to upgrade plasma power [5]. We may expect to synthesize composite particles simply by controlling the evaporation conditions of the raw material in the transferred type arc plasma and the reacting/quenching conditions of the raw material vapour. This paper describes the synthesis of AlN composite particles using transferred type DC arc plasma. The influences of operating parameters on the shape of the synthesized particle, the volume fraction of micro-particles in the synthesized particles and the diameters of micro-particle and nano-particle were clarified.

2. Experimental conditions and analyzing method

2.1 Experimental setup and conditions

Figure 1 shows the experimental setup. A transferred type arc plasma was generated between a tungsten cathode of a plasma torch and a graphite anode in a chamber. The distance between the two electrodes (plasma length) was 25-75 mm. The cathode consisted of a tube-shaped electrode, and the anode a rod-shaped electrode, and the two electrodes were water-cooled. The raw material (crushed AlN particle) was injected into the arc plasma through the cathode using a plasma gas (nitrogen [N_2]). The flow rate of the plasma gas was 5-20 litres/min. By varying the flow rate of the plasma gas and the plasma length, the travelling time of raw particles in the arc plasma was changed. Diameter of the raw AlN particle was below 25 μm with a feed rate of 2.1 g/min and a feed time of 1-2 minutes. DC arc current was 140 A and arc voltage 100-150 V. A suction pipe was positioned downstream from the anode. The distance between the anode and the tip of the suction pipe was 100 mm. A reacting/quenching gas was blown into the suction pipe. Ammonia (NH_3) was used as the reacting/quenching gas. The flow rate of the reacting/quenching gas was 5-20 litres/min. The surface of the raw AlN particle would evaporate in the arc plasma and the aluminum

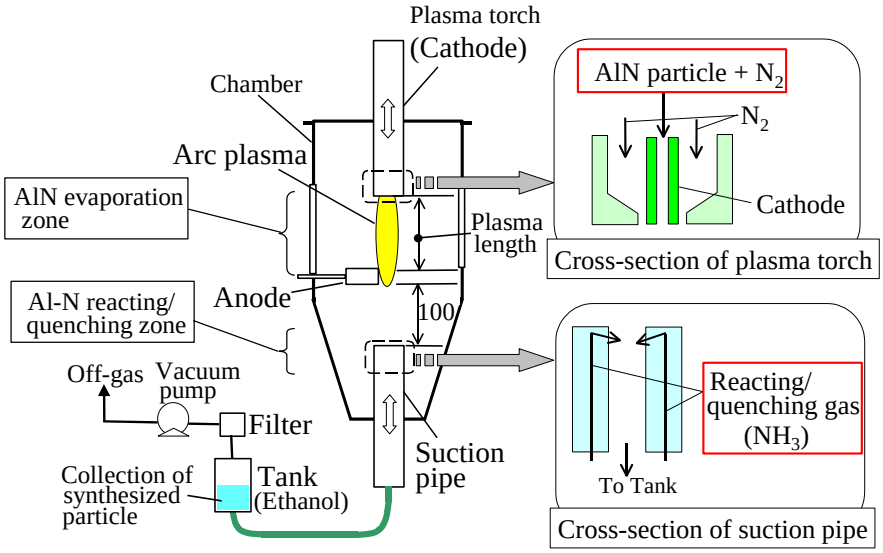

Figure 1. Experimental setup.

(Al) gas would surround the AlN particle, then the Al gas would react with and be quenched by the reacting/quenching gas. Therefore, composite particles consisting of nano-particles dispersed on the surface of spherical micro-particles would be synthesized. The synthesized particles were collected in a tank. The off-gas was exhausted through the suction pipe, the tank and a filter using a vacuum pump. The tank contained ethanol in order to prevent the oxidation of the synthesized particles. The pressure in the chamber was 20-50 kPa.

2.2 Method of measuring velocity of particles in arc plasma and temperature of arc plasma

The flight velocity of the AlN particles in arc plasma was estimated by video observation. Some bright lines were observed in the arc plasma owing to high emission from AlN particles in the arc plasma. The exposure time of the video observation was 1 ms. The flight velocity of the particle was estimated using the length of the observed bright lines and the exposure time. The spectroscopic observation of the arc plasma was carried out. The temperature of the arc plasma was determined by comparing the observed intensities of two spectral lines, i.e. 694.5 nm and 742.3 nm of nitrogen atom, assuming that the arc plasma was in local thermodynamic equilibrium (LTE). The upper energy levels of these spectral lines are 13.6 eV and 12.0 eV respectively.

2.3 Method of analyzing the synthesized particles

The AlN content in the synthesized particle was analyzed by x-ray diffraction (XRD) using the same method as in reference [5]. The shape and diameter of the synthesized particle were analyzed by scanning electron microscopy (SEM) and transmission electron microscopy (TEM). By image processing of the SEM photograph, the degree of circularity and projected area equivalent diameter of the synthesized particle were measured using the same method as in reference [6].

The average diameter of the synthesized particles was measured by the Brunauer-Emmett-Teller (BET) method. Using the projected area equivalent diameter and the average diameter of the synthesized particles containing micro-particle and nano-particle, the diameters of micro-particle and nano-particle were estimated.

3. Experiment results and discussions

3.1 Velocity of particles in arc plasma and temperature of arc plasma

The velocity of particles injected into the arc plasma was determined approximately 10 m/s, 20 m/s and 40 m/s, when the flow rate of plasma gas was 5 litres/min, 10 litres/min and 20 litres/min, respectively. The travelling time of raw particles in the arc plasma was estimated using the measured velocity and the plasma length.

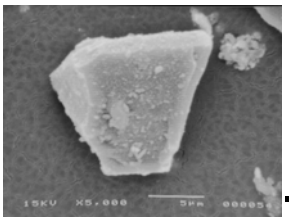

(Degree of circularity : 0.70)

(a) Raw particle

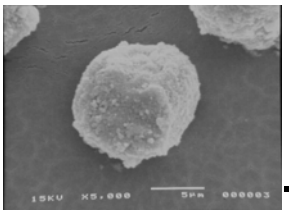

(Degree of circularity : 0.82)

(b) Synthesized particle

Figure 2. SEM photographs of particles.

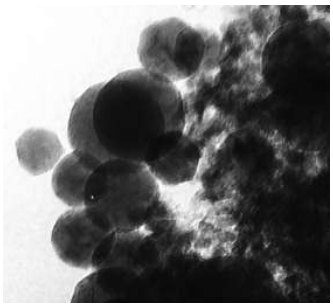

Figure 3. TEM photograph of synthesized particle surface

The temperature of the arc plasma in the central-axis was determined approximately 7,000 K. The radial temperature distribution was estimated by fitting in with the numerical result [7] of the radial temperature distribution of nitrogen arc plasma. The radially average temperature of the arc plasma was determined approximately 3,500 K, assuming that the diameter of arc plasma was 20 mm by video observation and the temperature of the plasma edge was 3,000 K because the radiation intensities of nitrogen arc plasma increases abruptly when the temperature was more than 3,000 K [8].

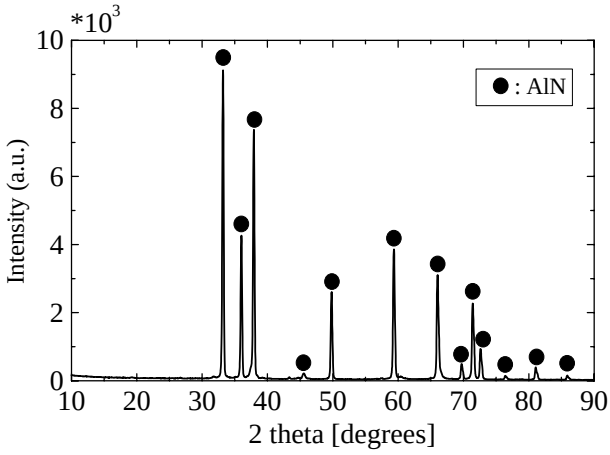

Figure 4. XRD profile of synthesized particles.

3.2 Shape and surface state of synthesized particles

Figures 2(a) and (b) show SEM photographs of the raw and synthesized particles, respectively. The shape of the raw particle was angular and that of the synthesized particle became relatively spherical. As described in the previous paper [6], the average degree of circularity of raw particles was 0.75 and that of synthesized particles increased to approximately 0.9 when the travelling time of raw particles in the arc plasma increased more than 2 ms. Figure 3 shows a TEM photograph of the synthesized particle surface. The TEM observation clarified that many small particles less than 100 nm adhered uniformly to the surface of the synthesized particle.

3.3 AlN content in synthesized particles

Figure 4 shows an example of an XRD profile of the synthesized particles. Only AlN peaks were observed in the XRD profile. The AlN content in the synthesized particles was estimated at more than 99 %. However, a weak Al peak was observed in an XRD profile when the travelling time of raw particles in the arc plasma was relatively long (5 ms) and the flow of the reacting/quenching gas was relatively little (5 litres/min). It was considered that the result was due to the condensation of non-reacted Al gas that was generated from the evaporation of the raw AlN particle in the arc plasma. Figure 5 shows the calculation result of the condensation temperature of non-reacted Al gas for the NH_3/AlN system. The calculation method was described in reference [5]. Calculation conditions (molar rate, pressure) were similar to the experimental conditions described in section 2.1. As the non-reacted rate of Al gas increased and the ratio of NH_3/AlN decreased, the condensation temperature of the Al gas increased. When the travelling time of raw

particles in the arc plasma was relatively long (5 ms) and the flow of the reacting/quenching gas was relatively little (5 litres/min), the quantity of the Al gas was so much that non-reacted rate of Al gas would be high and the ratio of NH_3/AlN would be low, therefore, the condensation temperature of the Al gas would be 1,600-1,800 K. On the other hand, the temperature of the space where the reacting/quenching gas was blown in the suction pipe was measured in reference [5]. The measured temperature of the space was 1,600-1,700 K. Hence, the non-reacted Al gas would condense and the some Al nano-particles would be synthesized, when the travelling time of raw particles in the arc plasma was 5 ms and the flow of the reacting/quenching gas was 5 litres/min.

Both these results and the result mentioned in section 3.2 suggest that the surface of the raw AlN particle evaporated in the arc plasma and the consequential generated Al gas reacted with and was quenched by the NH_3 gas, and finally AlN nano-particles were synthesized and adhered to the surface of the spherical micro-particles.

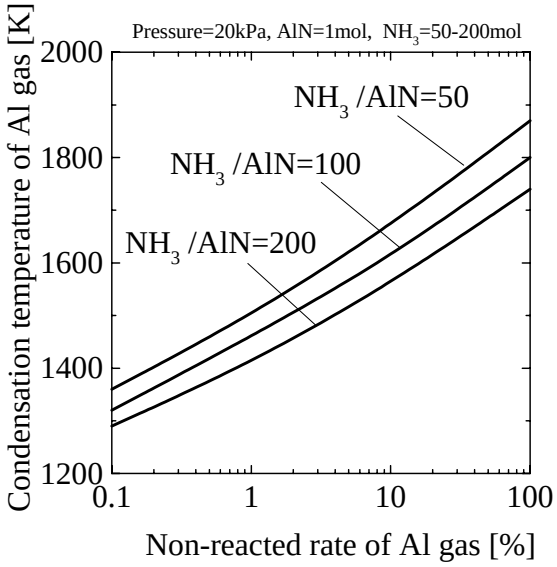

Figure 5. Condensation temperature of non-reacted Al gas for NH_3/AlN system.

3.4 Diameter of micro-particles

The circular plots in figure 6 show the diameter of micro-particles obtained from experiments. The diameter of the micro-particles in the synthesized particles decreased as the travelling time of raw particles in the arc plasma increased.

The broken curves in figure 6 show the calculated results of change in diameter of particles. The calculations took into account the decrease in particle diameter with the particle progress in the arc plasma using the same method as in reference [6]. The temperature of the arc plasma was set around the 3,500 K measured as an average temperature of the arc plasma in section 3.1. Calculations for figure 6 showed good agreement with the experimental results except the case that t_P was 5 ms. The video observation clarified that the arc plasma had a tendency to bend when t_P was 5 ms because the flow rate of plasma gas was relatively little (5 litres/min) and the plasma length was relatively long (50 mm). Therefore, it is considered that the raw particles passed through the relatively low temperature zone (e.g. 3,200 K) of the arc plasma and the calculation for figure 6 did not show good agreement with the experimental results when t_P was 5 ms.

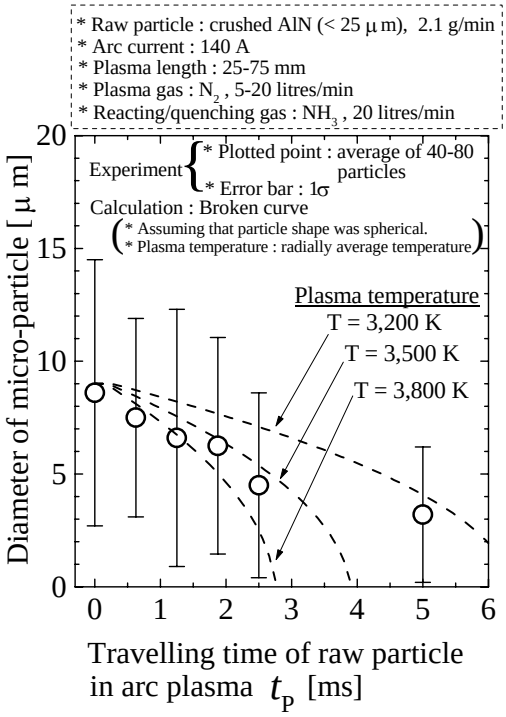

Figure 6. Dependence of diameter of micro-particles on its travelling time in arc plasma.

3.5 Volume fraction of micro-particles in the synthesized particles

The volume of vapour that was origin of the nano-particles was calculated using the diameter difference between the raw particles and the micro-particles. It was considered that the all nano-particles synthesized from the vapour were not collected in the suction pipe of the chamber because the vapour has a tendency to

spread in all directions. The collection rate of the nano-particles in the suction pipe was approximately 10 % in the previous report [9]. Therefore, the adherence rate of nano-particles on the micro-particle to all synthesized nano-particles was set at 10 %. The volume fraction of micro-particle in the synthesized particles was determined using these values mentioned above.

The circular plots in figure 7 show the volume fraction of micro-particles in the synthesized particles obtained from experiments. The volume fraction of micro-particles decreased as the travelling time of raw particles in the arc plasma increased. The volume fraction of micro-particles changed from 80 % to 50 % by varying the travelling time of raw particles in the arc plasma from 2 ms to 5 ms. The broken curves in figure 7 show the calculated results of change in the volume fraction of micro-particles. The calculation result was obtained using the calculated results of figure 6. The temperature of arc plasma was set around the 3,500 K measured as an average temperature of the arc plasma in section 3.1. Calculations for figure 7 showed good agreement with the experimental results except the case that t_P was 5 ms. The result was due to the same reason as mentioned in section 3.4.

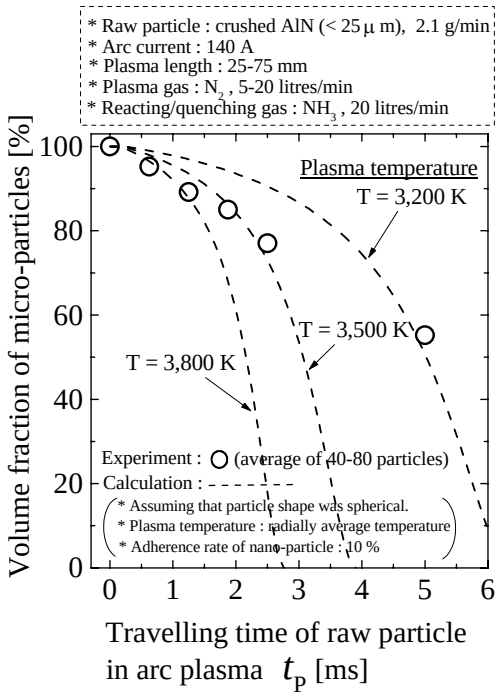

Figure 7. Volume fraction of micro-particles in synthesized particles.

3.6 Diameter of nano-particles

As shown in figure 8, the diameter of the nano-particles in the synthesized particles (circular plots) increased from 20 nm to 40 nm, when the travelling time of raw particles in the arc plasma increased from 1 ms to 5 ms. The diameter d of the nano-particles was investigated numerically using a Brownian collision-coalescence model as follows [10],

$$d = k * T^{0.2} * V^{0.4} \text{ ------ } (1)$$

where T is the temperature of the nano-particle synthesized space, V is the vapour density in the nano-particle synthesized space and k is constant.

The broken curve in figure 8 show the calculated results of change in diameter of nano-particles using the equation (1) when the diameter in case of t_P = 0.6 ms was basis. The temperature T was measured in the previous paper [5]. The vapour density V was calculated using the diameter difference between the raw particle and the micro-particle of the synthesized particle as shown in figure 6. The calculation result showed a similar tendency to the circular plots.

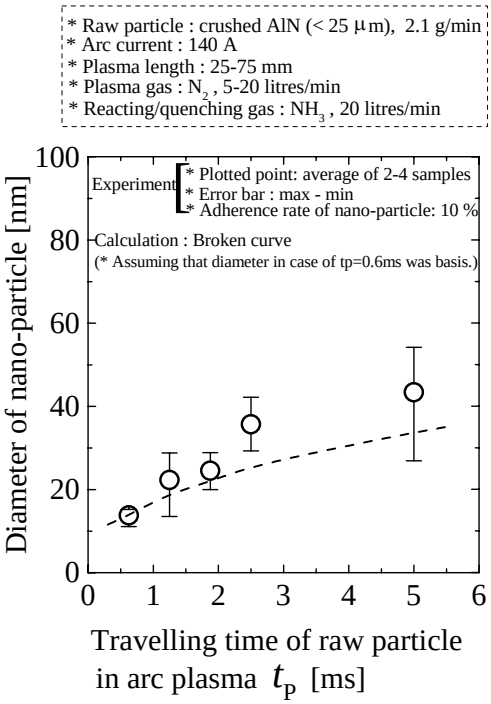

Figure 8. Dependence of diameter of nano-particles on its travelling time in arc plasma.

As shown in figure 9, the diameter of the nano-particles (circular plots) decreased from 80 nm to 40 nm when the flow rate of reacting /quenching gas increased from 5 litres/min to 20 litres/min. The broken curve in figure 9 show the calculated results of change in diameter of nano-particles using the equation (1) when the diameter in case of F_{RQ} = 5 litres/min was basis. The vapour density V was calculated assuming that V decreased inverse proportionally as F_{RQ} increased. The calculation result showed a similar tendency to the circular plots.

4. Conclusions

AlN composite particles consisting of nano-particles dispersed on the surface of spherical micro-particles were synthesized by simple method of using transferred type DC arc plasma. When the travelling time of the raw AlN particle (< 25 μm) in the nitrogen arc plasma was more than 2 ms, the degree of circularity of raw particles increased from 0.75 (raw particle) to approximately 0.9 and the shape of the synthesized particle was nearly spherical. The TEM observation clarified that many small particles less than 100nm adhered uniformly to the surface of the synthesized particle.

The volume fraction of micro-particles in the synthesized particles and the diameters of micro-particle and nano-particle were controlled by varying the travelling time of the raw particles in the arc plasma from 2 ms to 5 ms and the flow rate of reacting/quenching NH_3 gas from 5 litres/min to 20 litres/min. The experimental results of the diameters showed a similar tendency to the calculation results. From these results, the way to control the AlN composite particle conditions was clarified.

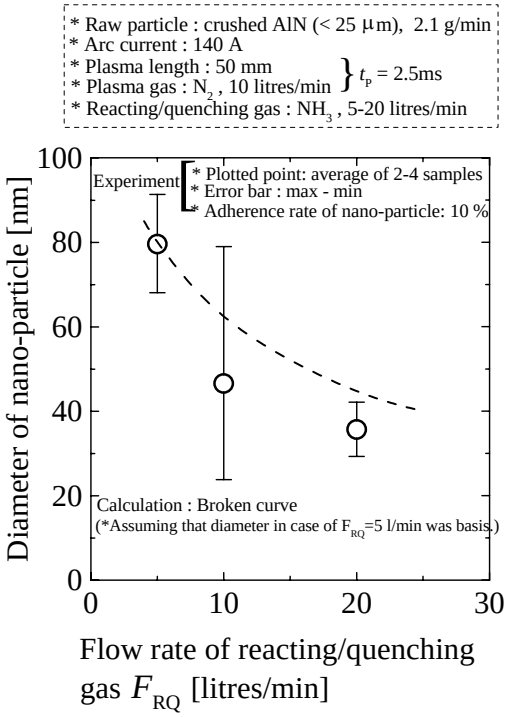

Figure 9. Dependence of diameter of nano-particles on flow rate of reacting/quenching gas.

Acknowledgements

The authors wish to thank Dr. S. Ito of CRIEPI for his helpful discussions.

References

[1] H. Hosoda and T. Yamada: *J. J. Dental Materials and Devices*, **11**, 331 (1992)
[2] N. Ashizawa and K. Masters: *Proc. 4th Int. Drying Symp.*, 364 (1984)
[3] H. Tsujimoto, K. Nagata, T. Yokoyama, T. Kamata, K. Terashita and K. Miyanami: *J. Soc. Powder Technology Japan*, **37**, 107 (2000)
[4] K. Sawai: *SEMI Technology Symp.*, 473 (1989)
[5] M. Iwata, K. Adachi, S. Furukawa and T. Amakawa: *J. Phys. D: Appl. Phys.*, **37**, 1041 (2004)
[6] M. Iwata, S. Furukawa, K. Adachi and T. Amakawa: *Proc. of 15th Int. Conf. on Gas Discharges and their Applications*, **2**, 985 (2004)
[7] S. Furukawa, M. Iwata, K. Adachi and T. Amakawa: *CRIEPI Report*, W02022 (2003)
[8] Y. Naghizadeh-Kashni, Y. Cressault and A. Gleizes: *J. Phys. D: Appl. Phys.*, **35**, 2925 (2002)
[9] M. Iwata, S. Furukawa, K. Adachi and T. Amakawa: *CRIEPI Report*, W02012 (2003)
[10] G. D. Ulrich: *Combus. Sci. Technol.*, **4**, 47 (1971)

Reduction of Oxygen Content in Atmospheric Plasma Jet: Shrouding by Reactive and Nonreactive Gas

T. Kavka, M. Hrabovsky, O. Chumak, A. Maslani

Institute of Plasma Physics, ASCR, Za Slovankou 3, Prague, Czech Republic

Abstract
The ambient air is entrained intensively into atmospheric pressure thermal plasma jets. A system for shielding plasma jet has been used to improve jet characteristics and reduce oxygen content. Two gases have been applied as a shroud gas – argon and acetylene. Argon shrouding resulted in slight changes of the plasma jet properties. The plasma jet became wider with small reduction of the oxygen content. Acetylene caused strong decrease of the oxygen content due to chemical reactions. Temperature of the plasma jet as well as velocity increased.

Keywords: entrainment shroud

1. Introduction

Plasma spraying of metals is usually accompanied by oxidation of sprayed material, which affects resulting coating. The plasma spraying is a two stage process. In the first stage particles are introduced into the plasma jet, where they are heated, melted and accelerated toward the substrate, where the second stage, i.e. deposition, cooling down and solidification takes place. Processes occurring in both stages have an influence on resulting coating properties and one of the serious problems is oxidation mentioned above. Although the second stage, during which the deposited solidified material interact with ambient atmosphere consisted mostly of the air, is much longer than the first stage, the in-flight oxidation in the high temperature environment plays critical role in the resulting oxide content in the sprayed coatings. In-flight oxidation begins due to gas-solid interaction during heating of particles in the plasma jet containing oxygen from air entrained into the jet. Hence, reduction of the oxygen content in the plasma jet is a question of great importance.

There are several methods how to avoid or at least reduce oxygen content in plasma jets. The simplest and the most economical method is shroud nozzle attached to the exit of the plasma torch. The shroud nozzle can provide both a solid shield and a gas shroud. The solid shield acts as a barrier preventing the air entrainment into the jet. In a gas shroud the solid shield is replaced by gas formed around the jet preventing mixing of the plasma with air [1]. Usually gases contained in plasma forming medium (e.g. Ar, N_2) are used as a shroud gas and they are supplied close to the exit nozzle parallel to the main flow. In the present paper the effect of the reactive gases as acetylene, methane and a mixture of oxygen with hydrogen is studied together with the effect of nonreactive argon shroud gas. Reactive gases combust intensively when react with oxygen in the plasma jet and are significantly more effective for decreasing the oxide content in plasma sprayed powders. Previous study of metallic coatings sprayed with different shrouding gases has shown that inert shrouding is ineffective in decreasing the oxide content and the oxide layers are thicker in comparison with the shrouding by reactive gases [4].

The aim of the present paper is a study of the shroud effect on the properties and composition of the plasma jet. Both the shroud gas and the solid shield were used in experiments. The effect of shroud gas nature and flow rate on properties of the plasma jet is discussed.

2. Experimental setup

Plasma jet was generated by hybrid argon-water plasma torch [5]. The schematic diagram of the torch with the shielding system is shown in Figure 1. The plasma jet generated by this torch is formed a mixture of argon, supplied along the cathode in the upstream part of the torch, with water vapor, which entrances and mixes up with argon plasma in the downstream water stabilized part. A long arc column results in high arc voltage and thus, high power given rise to high temperatures of the plasma. The important feature of the torch is the external rotating anode, which provides reduction of the strong erosion of the anode surface in the atmosphere containing

oxygen. The anode makes it difficult to provide good protection of the arc column close to the exit nozzle in the air atmosphere. That is why in the present experiments the shielding system was positioned at the distance 25 mm from the exit nozzle downstream the anode.

The system for shielding consisted of a ring for shroud gas distribution and supply, and a solid wall. The ring was 78 mm in diameter and 10 mm in width of the front part (Fig. 2). It was made of stainless steel and was not cooled. Several holes with diameter of 1 mm were made in the ring to distribute shroud gas around the plasma jet. The shroud gas flow was directed parallel to the jet axis. The solid wall was made from a ceramic tube 100 mm in length, which was placed downstream the ring. The tube was removable and was not water cooled. The ceramic wall protected surrounding of the plasma jet from air entrance altering surrounding atmosphere. The shielding system was centered with the respect to the exit nozzle. First, the feeding of the shroud gas was made through one tube entering to the distributing ring at its top (Fig. 2 a)). But this arrangement turned out to be unsatisfactory as it could not provide proper distribution of the shroud gas around the jet. As a result the flow rate of the shroud gas at the bottom part of the ring was higher than at the top part. To avoid improper distribution the ring was divided inside into three sections by partitions and shroud gas was supplied from three different sides (Fig. 2 b)).

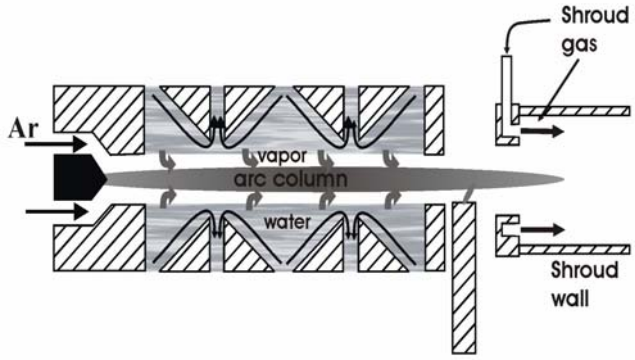

Figure 1 Hybrid argon-water torch with the system for shielding

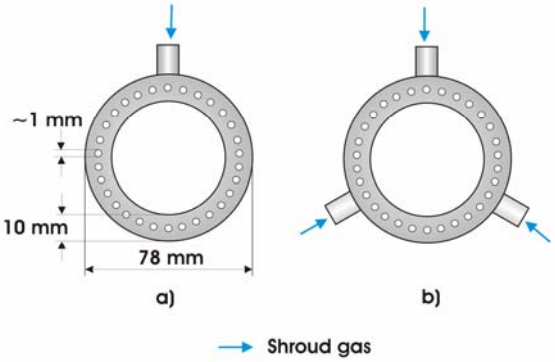

Figure 2 The ring for gas shroud distribution: a) one gas entrance; b) three gas entrances

The choice of the shroud gases was dictated not only by necessity to reduce oxygen content entrained from the surrounding, but also by plasma gas contained oxygen from the products of dissociation and ionization of water. Several gases were applied. First, effect of nonreactive argon was studied. Further, argon was replaced with reactive acetylene, methane, and safety mixture of hydrogen with nitrogen (5% of H_2). The problem with gas distribution appeared when pure acetylene was used as shroud gas. At the temperatures about 400 °C the pyrolysis of acetylene starts. As the ring was not cooled its temperature rose fast during acetylene combustion. The carbon precipitated inside the ring blocking the holes. To avoid this effect acetylene was mixed with nitrogen.

Measurements of the plasma jet characteristics were done with the help of the enthalpy probe system connected to the mass spectrometer. Enthalpy probe allowed to measure plasma jet temperature and velocity while mass spectrometer was used to determine plasma composition. The plasma torch was moved in horizontal and vertical direction allowing a scanning of free jet in axial and radial directions with the step of 5 mm.

All present measurements were done under atmospheric pressure conditions. In all experiments argon flow rate was 17.5 slm and arc current was 300 A. Arc voltage under these conditions was about 250 V, which corresponded to arc power of 75 kW. Such a high arc power resulted in high heat fluxes in the plasma jet in spite of strong air entrainment and it was impossible to make measurements in the regions close to the nozzle because of the permissible level of heat flux, which could be sustained by enthalpy probe tip. The enthalpy probe scanned

the jet at the distance of 200 mm from the exit nozzle, which corresponded to the 65 mm from the end of the ceramic wall.

The freezer was inserted into the gas sample line of the enthalpy probe system to avoid entrance of water vapor into the system, which could damage it. As enthalpy probe evaluate gas characteristics based on the measured gas composition, the recalculation of all measured characteristics should be done due to the fault determination of the gas composition. But present measurements were done at the distance of 200 mm from the exit nozzle. At such a distance plasma jet represents mostly heated ambient gas rather than plasma forming gas because of the strong entrainment. The amount of plasma forming medium drops here to about 5%. Under these condition the error caused by water vapor, which was not taken into account, was negligible and measured values supposed to be equal to real values of the jet characteristics.

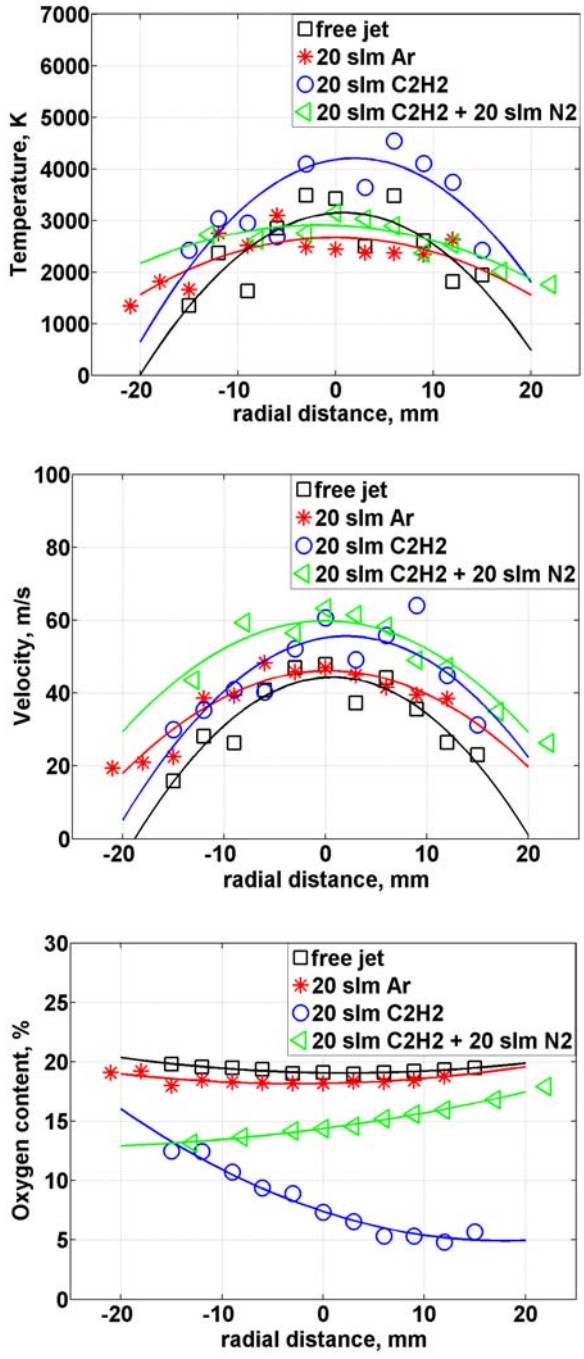

Figure 3 Properties of the plasma jet at the distance 200 mm without shroud gas and with argon and acetylene shrouding (shrouding with the ceramic tube)

3. Results and discussion

The plasma jet generated by hybrid argon-water torch is characterized by an intensive interaction with surrounding atmosphere and air entrainment [6]. The effect of the shroud gas was studied for two cases – with and without ceramic wall. Figure 3 represents properties of the plasma jet then solid wall was applied, while in the Figures 4 and 5 there are results then ceramic tube was removed.

Temperature, velocity and oxygen content in the jet are shown for free jet, when no shroud gas was applied, and for the cases of shrouding by argon and acetylene and its mixture with nitrogen. The oxygen percentage in the free jet shows that the jet consisted mostly of the heated air. The zero point on the x axis corresponds to centerline of the jet, which is usually shifted with respect to plasma torch axis because of interaction of the main plasma flow with an anode jet [7].

The results showed just small effect of the argon shrouding on the properties of the plasma jet. The profiles of the plasma jet characteristics shows that the shroud gas improved free stream region as plasma jet became wider without strong gradients at the jet fringes. Temperature of the jet went down slightly because of the influence of cold argon consuming a part of energy from the jet for its heating. The velocity of the jet remained unchanged. Concentration of oxygen decreased just a little. Further increasing of the argon flow rate up to 120 slm resulted just in minor changes of oxygen content in the jet center accompanied by minor

temperature reduction. These results indicate that air entrainment is most intensive in the part of the jet close to the nozzle exit, which was not protected by the gas shielding while in the region, where shroud gas acted, entrainment rates already slowed down.

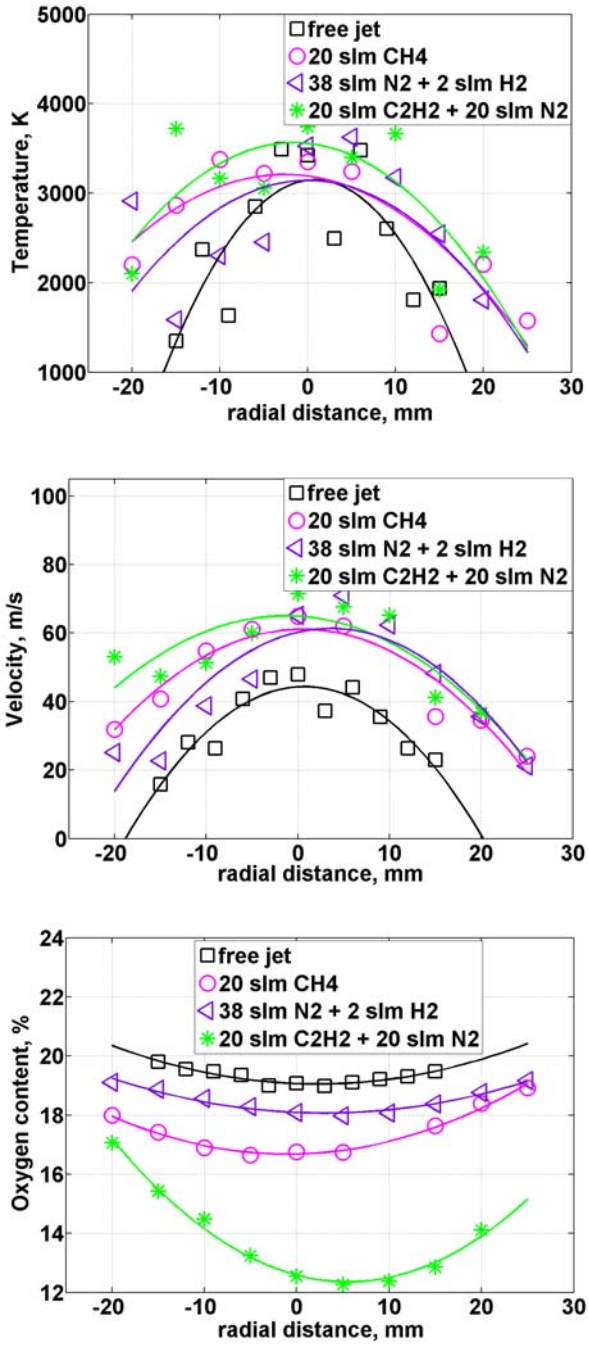

Figure 4 Properties of the plasma jet at the distance z = 200 mm without shroud gas and with CH_4, N_2/H_2 and C_2H_2/N_2 shrouding (shrouding without the ceramic tube)

Argon shroud gas was replaced by reactive acetylene. The acetylene reacts very intensively with the oxygen already at the temperatures near 300 °C. A reaction of acetylene with oxygen results in the formation of carbon oxides. Moreover, the injection of acetylene introduces a further energy source as the combustion heat of 58.6 MJ/m3 will be released. The results showed strong changes of the plasma jet characteristics when acetylene was applied. Oxygen content was reduced when acetylene flow rate was increased and already 20 slm of acetylene allowed reducing oxygen content to values about 5 % at the jet centerline. Temperature and velocity of the jet increased. This effect was caused by a reaction of oxygen with acetylene accompanied by heat evolution. Consequently, the high-temperature high-velocity region was extended significantly. This is expected to provide better particle heating and acceleration with less particles oxidation, and thus improving spraying process efficiency and deposition quality. The shifted profile of the oxygen content was caused by nonuniform distribution of the shroud gas due to the holes, which became cluttered because of acetylene pyrolysis.

Mixing of acetylene with the same amount of nitrogen resulted in better distribution of the shroud gas around the jet. As nitrogen is diatomic gas it consumed energy from the plasma flow for the dissociation. Thus, adding of nitrogen caused reduction of temperature. Moreover, higher total shroud gas flow rate resulted in a higher discharge velocity of the shroud gas through the holes. This could affect process of acetylene combustion. On the other hand, higher shroud gas flow rate led to smaller velocity gradients at the jet fringes, which in turn reduced process of the plasma jet deceleration caused by entrainment. Thus, plasma jet velocity was increased.

In the Figure 4 there are results of the experiments when ceramic tube was removed and only the effect of the shroud gas was studied. In addition to mixture of acetylene with nitrogen, methane and the mixture of nitrogen with hydrogen were examined. Methane is also combustible, but is more stable and its pyrolysis starts at much higher temperatures, which allowed us to use it without addition of other gases. Like acetylene, methane is also a source of heat as its combustion is accompanied by release of 37 MJ/m^3

of heat. In the reaction of combustion one molecule of methane binds 2 molecules of O2, whereas molecule of acetylene 2.5. In spite of this, methane is preferable as a shroud gas since it is better to store and to handle. Beside these, a safety mixture of hydrogen with nitrogen was examined in the experiments – 5 % of H_2.

Similarly as in case of the ceramic tube, shroud gas apply resulted in the flattening of the plasma jet characteristics for all shroud gases. Using of the H_2/N_2 mixture led to increasing of the temperature at the plasma jet fringes, while centerline temperature was unchanged. Temperature of the jet was a little higher when acetylene and methane were used because of the released heat of combustion. Velocity increased for all shroud gases, the centerline velocity increased by almost 30 % from 45 m/s to near 60 m/s. The results show that H_2/N_2 shrouding only replaces air from the ambient atmosphere and thus reduces available oxygen to be entrained from the surrounding. Hydrogen binds oxygen atoms but its amount is too small to provide proper oxygen elimination. Acetylene and methane not only replace air but also consume significant amount of oxygen in

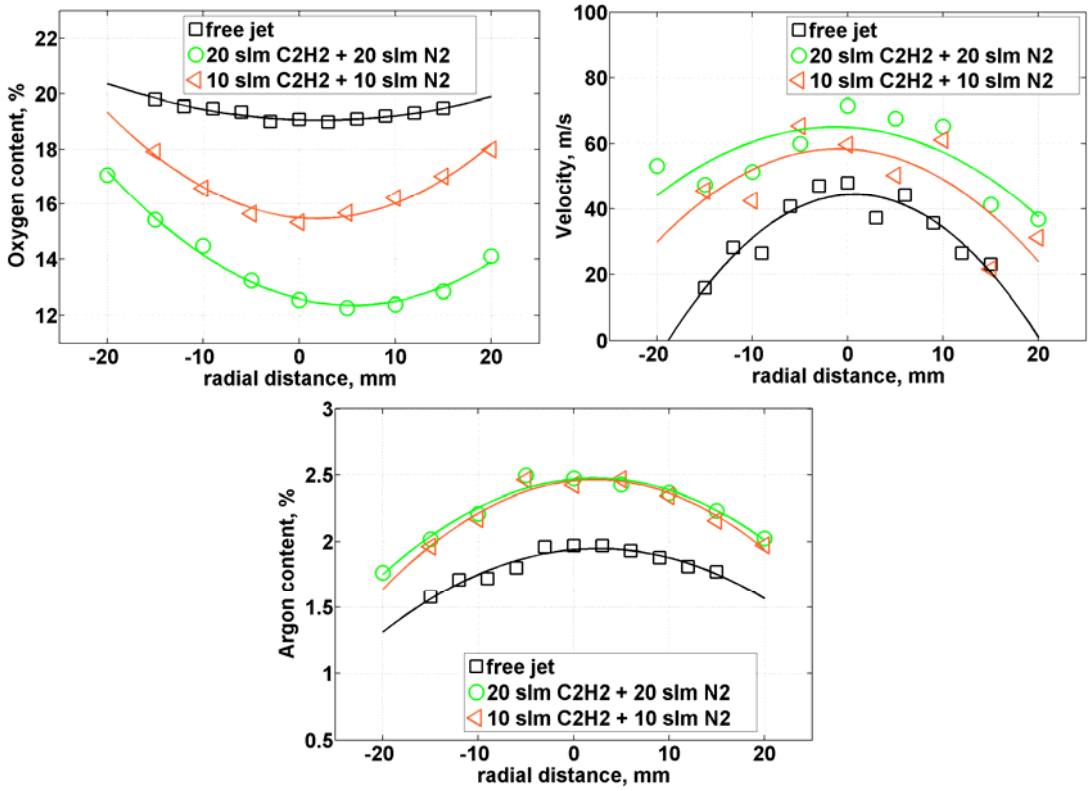

Figure 5 Effect of the shroud gas flow rate on the properties of the plasma jet at the distance z = 200 mm without the ceramic tube

process of combustion. Acetylene shrouding provided the best results of oxygen reduction together with improvement of the plasma jet characteristics.

The effect of acetylene flow rate is illustrated in Figure 5. Acetylene flow rate was set to the values of 10 and 20 slm. Acetylene was mixed with the same amount of nitrogen to get 50 % mixture. Oxygen content decreased for higher flow rates of the shroud gas, while velocity increased. The argon content reflects amount of plasma in the plasma jet. The plasma content increased when C_2H_2/N_2 shrouding was used, but it was almost independent on shroud gas flow rate. Increasing of the shroud gas flow rate had no effect on the center of the jet and had only negligible effect on the plasma jet fringes. The results confirmed that the entrainment process was slowed down when C_2H_2/N_2 mixture was supplied what would be the consequence of two factors. As the shroud gas discharges from the holes its starts to react intensively with air. Reaction of the acetylene with oxygen is

accompanied by heat release, which results in heating of the plasma jet surrounding. Thus, air bubbles getting into the plasma jet in the process of the entrainment [8] and cooling and slowing down the jet have lower density and could travel quicker in the plasma jet in comparison with cold air bubbles. The process of the plasma jet velocity reduction slows down. Moreover, in contrast to stagnant air surrounding, shroud gas moves concurrently with the plasma jet reducing velocity gradients at the jet fringes and slowing down the process of the bubble formation.

4. Conclusions

The effect of the shroud gas was studied on the plasma jets generated by hybrid DC torch with water-argon stabilization of arc. The shroud gas was distributed around the jet with the help of the ring with holes. Different reactive and nonreactive gases were used for shrouding – pure argon, acetylene, and methane and mixtures of nitrogen with acetylene and hydrogen. The ceramic tube was also tested to improve shielding of the jet as it protected plasma jet surrounded from the air entrance.

The study showed that entrainment of the surrounding air into the jet is significant even with shrouding. The highest entertainment rates are at the regions close to the exit nozzle, where high velocity plasma flow enters to the stagnant ambient air. That is why protection of this part of the jet is a question of great.

All shroud gases used in experiments affected plasma jet making the profiles of the jet characteristics flattened with higher temperatures and velocities and reduced amount of oxygen. Ar and H_2/N_2 shrouding only replace air from the jet surrounding, while CH_4 and C_2H_2 shrouding remove oxygen in the process of combustion as well. Moreover, both acetylene and methane are a source of extra heating as a large amount of heat release during combustion, which would provide better particle heating. Acetylene improved plasma jet characteristics most of all used shroud gases but difficulties connected with handle this unstable gas force to replace it with more stable methane which would be the best shielding gas from the tested in present experiments.

Acknowledgement

The authors gratefully acknowledge the support of this work by the Grant Agency of the Czech Republic under the project No. 202/05/0669.

References

[1] D.T. Gawne, T. Zhang, B. Liu – Surface and coating technology 153 (2002).
[2] I. Thomson, V. Pershin, J. Mostaghimi, S. Chandra - Plasma Chem. Plasma Process. **21**, 1 (2001).
[3] K. D. Kang, S. H. Hong - J. Appl. Phys. **85**, 9 (1999).
[4] K. Volenik, F. Hanousek, P. Chraska, J. Ilavsky, K. Neufuss – Materials Science and Engineering A272 (1999).
[5] V.B. Brezina, M. Hrabovsky, M.Konrad, V.Kopecky and V.Sember - Proc. Of 15th Int.Symp. on Plasma Chemistry (ed. A.Bouchoule et al.), Vol.III, 9-13 July 2001, Orleans (2001).
[6] T. Kavka, M. Hrabovsky - Czechoslovak Jour. of Physics **52** (2002).
[7] M. Hrabovský, O. Chumak, T. Kavka, V. Kopecký - Proc. of 12th Workshop on Plasma Technology, September 2004. TU Ilmenau
[8] E. Pfender, J. Fincke, R. Spores - Plasma Chem. Plasma Process. **11** (4) (1991).

Experimental investigation of industrial ashing equipment

C. Hayden

Plasma Research Laboratory, School of Physics, Dublin City University, Ireland
Email: Chanel.Hayden@dcu.ie

Abstract
An experimental investigation was carried out on industrial ashing equipment by means of mass spectrometry and optical emission spectrometry (OES) diagnostic techniques. The tool under analysis comprises of an upstream Microwave-RF downstream configuration at an operating pressure of 850mT. The neutral species present in the discharge (N, O, NO, N_2O, NO_2) were analysed for a variety of physical conditions and compared with a simple kinetic model.
Keywords Radio-frequency (rf), ashing, photoresist, UV-VIS (ultraviolet-visible)

1. Introduction

O_2-N_2 plasmas are widely used in a number of industrial processes such as surface treatment [1], cleaning and polymer etching [2]. Microelectronic devices are manufactured by a sequence of processes in which layers of materials are grown or deposited then etched in a particular pattern, plasma ashing is one such process. Etching involves a chemical solution, which can sometimes leave a residue on the substrate affecting the performance of a device. Ashing is the process of removing photoresist residue from an etched wafer. This is accomplished by using a plasma source to create single atom reactive species that combine with photoresist to form 'ash', which is removed by the vacuum system. This procedure may also change the chemical character of the polymer in desirable ways such as improved adhesion properties. The reactor configuration can greatly affect the etch rate, for instance plasmas generated by microwave achieve faster polymer etching than rf sources [3]. A number of gas mixtures can be employed in this process, for example O_2 and N_2 or SF_6 and O_2, in this case O_2 and N_2 are used. The ashing tool consists of a downstream plasma configuration (see figure 1) in which plasma is formed remotely by a microwave plasma source and channelled to the wafer through a diffuser plate or showerhead. The wafer is placed on a heated radio-frequency (rf) chuck in the downstream region, which enhances ion bombardment on the surface. This type of arrangement allows electrically charged particles time to recombine before they reach the wafer surface and prevents damage to the substrate. The process gases are used in a specific proportion from which the microwave plasma source generates the monatomic reactive species. The reactive species recombine at different rates, leaving some active species available for processing the wafer. In this paper we will present a spectrometric analysis of an ashing discharge. We will also discuss a global model representation of this equipment.

2. Experimental

Figure 1 shows the experimental arrangement with one of the diagnostic connections in place. It consists of two plasma regions separated by a diffuser plate or showerhead. In the upper region, the working gas enters a plasma cavity where it is excited by a 1 kW microwave source operating at 2.45 GHz. This reaction area is separated from the main discharge by gas transport piping and a diffuser plate. The plasma is sustained by a continuous flow of 810 sccm O_2, 90 sccm N_2 at 850mT. The efflux from the microwave discharge flows though a showerhead into the downstream chamber containing the work-piece, which rests on a rf powered electrode. This rf chuck is heated to about 65˚C and operates at 13.56 MHz with a power of approximately 200 W. The work-piece is therefore exposed to energetic ions produced by the downstream capacitive discharge and a flux of radicals produced predominantly in the upstream source. The diagnostics are applied on the downstream chamber as access to the microwave region is very limited. In this experiment, a Pfeiffer QMS200 quadrupole mass-spectrometer was used to analyse relative concentrations of chemical species. As the mass-spectrometer is pressure sensitive with a maximum limit of 1e-4 mBar while the operating pressure of the tool under investigation is of the order of 1e-3 mBar, the set-up required the inclusion of a diaphragm. A number of apertures of varying diameters were tested to obtain an optimum signal. In this case, a 0.25 mm aperture yielded the strongest signal. It was placed between the outer chamber wall and a gate-valve

connecting the mass-spectrometer with the appropriate adaptors. The neutral species present in the discharge (N, O, NO, N_2O, NO_2) were analysed for a variety of physical conditions.

Optical Emission Spectrometry measurements were performed using a custom built optical fiber probe and feed-through with Ocean Optics HR2000 and USB2000 spectrometers. These spectrometers have ranges of 200-650 nm and 200-875 nm respectively, see Table 1. The optical fiber was a 400 μm solarisation-resistant material designed for measurements in the UV-VIS range of the spectrum. The probe was first enclosed in ceramic tubing so that only the tip was exposed before inserting into the plasma. A number of measurements were taken for a range of microwave and rf power settings as well as varying gas fractions.

Table 1. Optical Spectrometer Configuration

Spectrometer		**HR2000**	**USB2000**
ICCD Camera No. of pixels Size of pixel		200-1100 nm 1 x 2048 14μm x 200μm	200-1100 nm 1 x 2048 14μm x 200μm
Grating Grating tuned		600 lines/mm 195-645 nm	600 lines/mm 180-875 nm
Focal length		101 mm	42 mm
Reciprocal Dispersion	(min λ) (max λ)	16.47 nm/mm 16.19 nm/mm	39.61 nm/mm 38.29 nm/mm
Resolution	(min λ) (max λ)	0.231 nm/pixel 0.227 nm/pixel	0.554 nm/pixel 0.536 nm/pixel
Slit width		5 μm	defined by fiber
Mean Instrumental Width		(0.3±0.1) nm	(1.6±0.3) nm

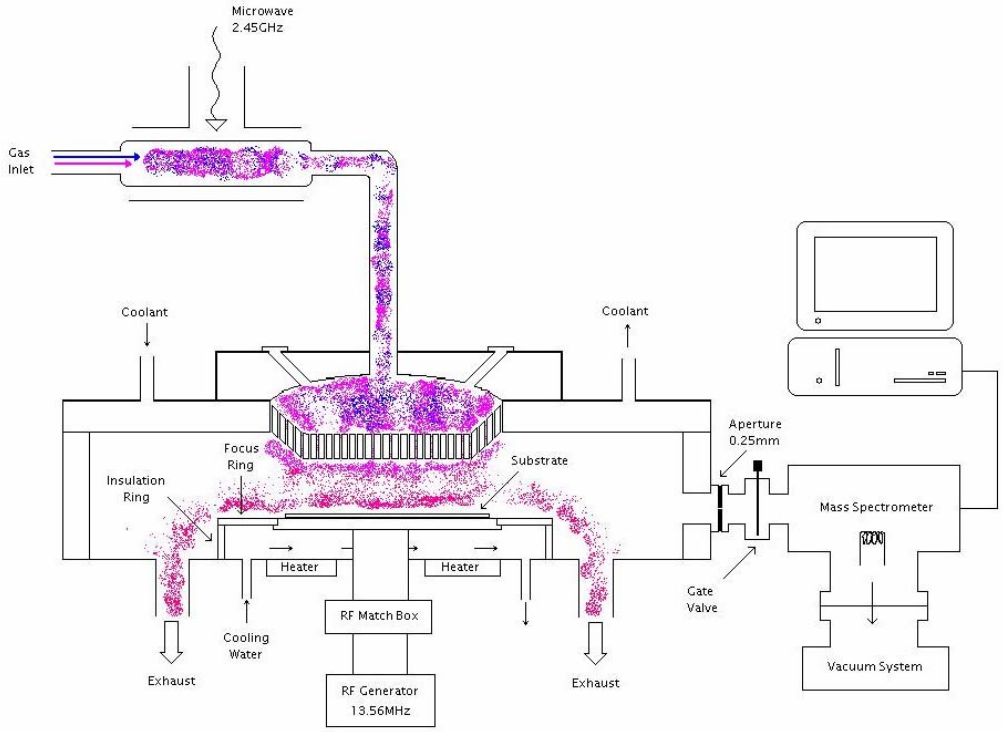

Figure 1. Experimental set-up.

3. Results

Experiments were performed to investigate the effects of gas pressure, microwave power, rf power, gas flow rate and gas composition on the plasma. Signals for a number of neutral species resulting from the O_2-N_2 discharge were analysed from mass-spectrometric data taken. Firstly, the gas fraction of O_2-N_2 was fixed at 810sccm O_2 and 90sccm N_2 for varying microwave power values from 750 to 2000W with rf power on (at 195W) and off. Figure 2 (a) and (b) show the variation in signal for O_2 and N_2 respectively at 850mT.

In figure 2(a), there is an almost linear decrease in ion current with increasing power for both rf on and off. When the rf power is extinguished the signal is greater, indicating a higher neutral density. Figure 2(b) shows very little change in signal with rf power off except at higher microwave powers.

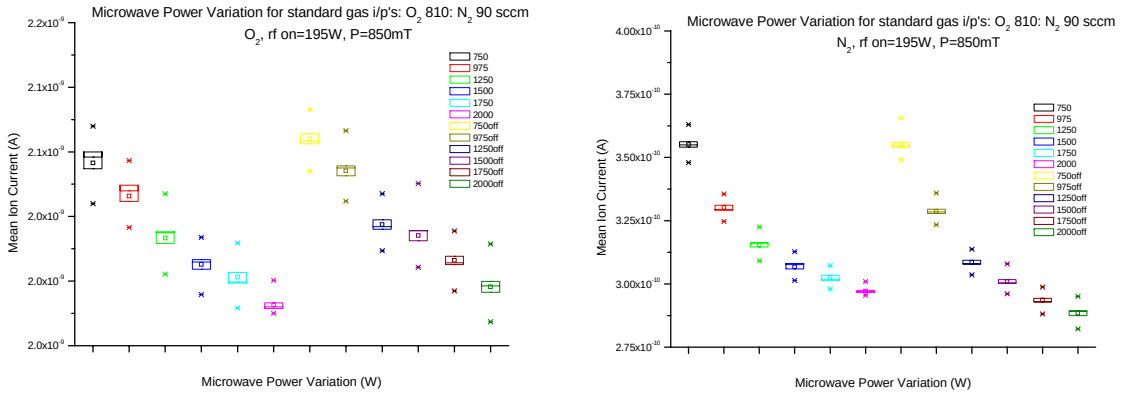

Figure 2. Mean variation in signal current with microwave power from 750-2000W, with rf on=195W, rf off=0W, pressure=850mT for (a) O_2 (b) N_2

Decreasing the pressure from 850mT to 700mT gave rise to reduced errors as shown figure 3(a) and an overall increase in signal current. Figure 3(b) displays the signal obtained for NO increasing with microwave power. The signal is greater when rf power is extinguished.

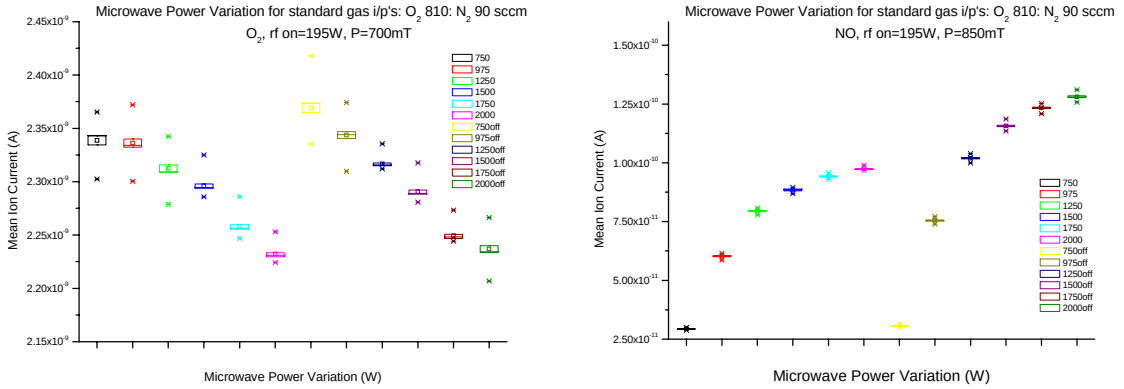

Figure 3(a) O_2 signal variation with microwave power for rf on and off at 750mT (b) NO at 850mT

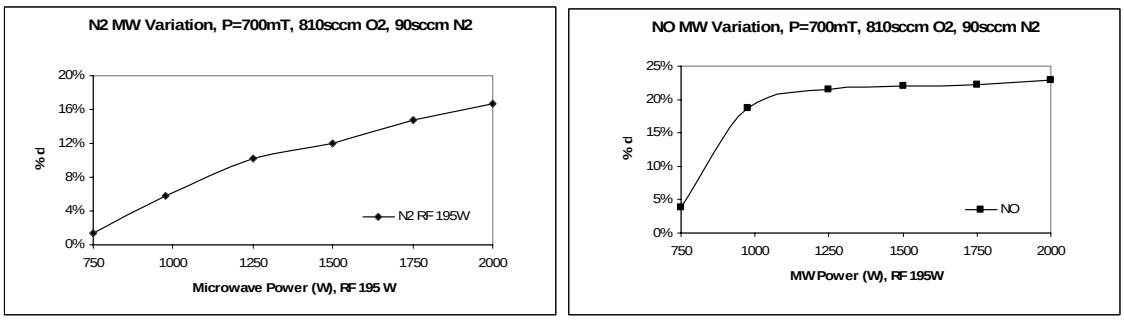

Figure 4. These graphs show the normalized percentage dissociation (%d) of (a) N2 and (b) NO for microwave power variation at 700mT with rf power fixed at 195W.

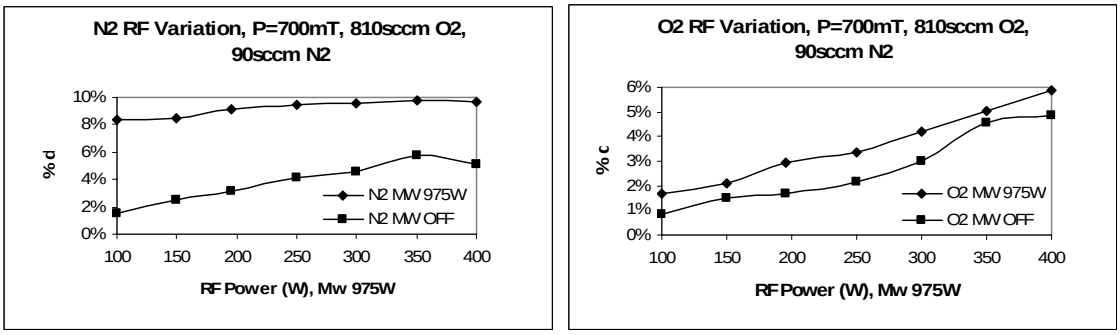

Figure 5. The plots above show the dissociation (%d) of (a) N2 and (b) O2 for changes in rf power values with microwave power off and at 975W.

With a fixed gas fraction of O_2-N_2 for varying microwave and rf power values, the corresponding dissociation degree was calculated. Low ion current signals for N_2O and NO_2 were observed for microwave power changes with a decrease in signal for both species when the rf source is extinguished.

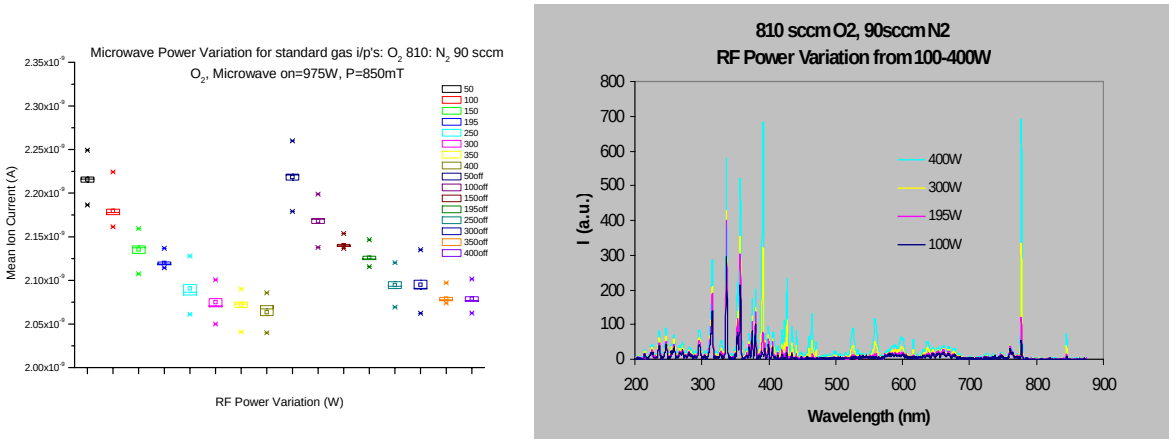

Figure 6. (a) RF power variation of O_2 current signal at 850mT from 50-400W and (b) Optical emission spectra of O_2 for variations in rf power from 100-400W.

Varying external parameters such as power, pressure and gas ratio, result in different excited states thus shifts in intensity and wavelength can be observed. Monatomic radicals increase in intensity as can be seen @777nm and 845nm, Molecular radical @761nm doesn't show changes in intensity for increasing power

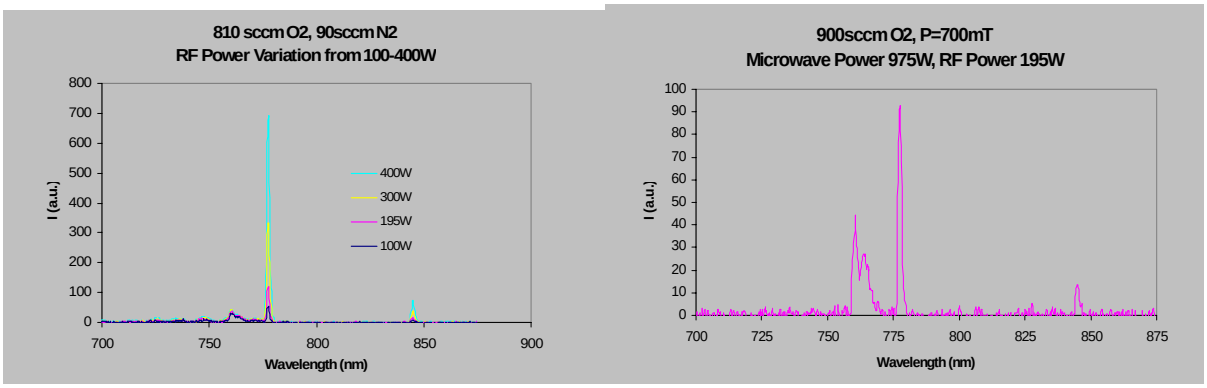

Figure 7. Optical emission spectra of (a) rf power variation from 100-400W for 810sccm O_2, 90sccm N_2 and (b) 900sccm O_2 at microwave 975W, rf 195W.

Global Model Solver - Predict spatially averaged quantities. Good: low computational cost, can have complex chemistry. Bad: limited accuracy, no spatial information. Electron power, gas flow-rates, chamber geometry, gas temperature and numerous chemistry sets are used to simulate the experiment.

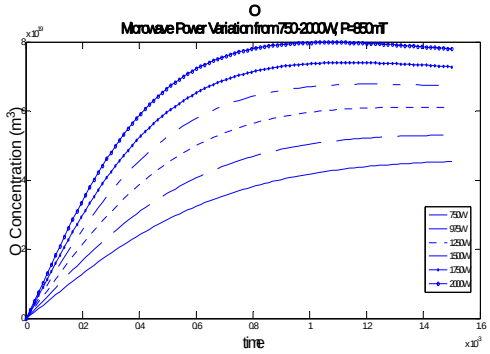

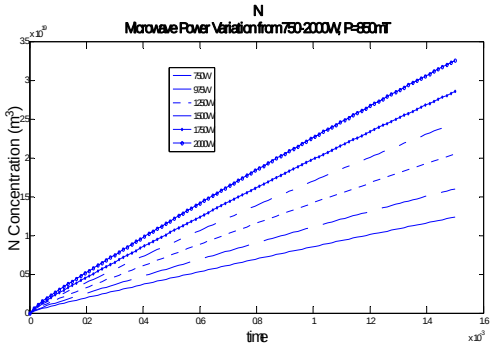

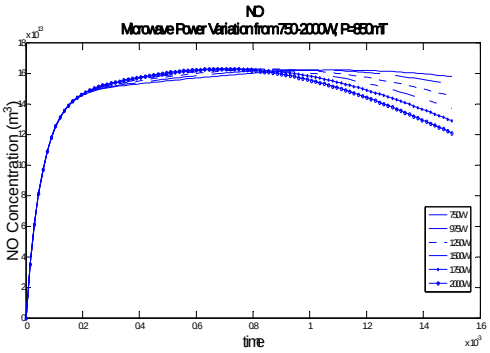

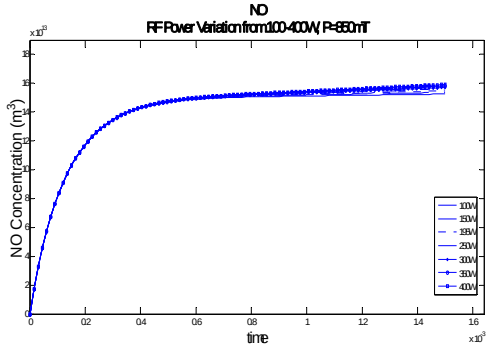

Changes in rf power have less affect on concentration of NO

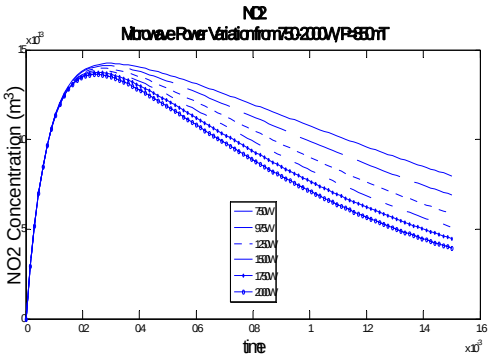

NO2 reacts with O to form NO and O2

4. Conclusion

There is very limited space for applying diagnostics to a tool and so customisation is often required.
Ensure stability of mass-spec. The percentage dissociation for O_2 and N_2 increased with rising rf power however this percentage dropped when the microwave power was extinguished as shown in Figure 2 above. Ion current signals were higher for microwave off due to a greater volume of the neutral gas reaching the downstream region before being excited and dissociated into radicals. The concentration of NO and NO_2 was found to grow with increasing microwave power with N_2O decreasing. The results were compared with a simple kinetic model and some agreement was found.

References

[1] V. Premachandran, Appl. Phys. Lett. **55**, 2488 (1989).
[2] T.H. Lin, M. Belser, Y. Tzeng, IEEE Trans. Plasma Sci. **16**, 631 (1988).
[3] J.E. Heidenreich, J. Paraszczak, M. Moisan, G. Suave, J. Vac. Sci. Technol. B **6**, 288 (1988).

Modification of the Polyester Fabric Hydrophobicity with Atmospheric Dielectric Barrier Discharge

J. Píchal[1], T. Vatuňa[2], J. Koller[1], L. Aubrecht[1], P. Špatenka[2]

[1]Department of Physics, Czech Technical University, Faculty of Electrical Engineering, Technická 2, 166 27 Praha 6, Czech Republic

[2]Department of Material Science, Technical University of Liberec, Faculty of Mechanical Engineering, Hálkova 6, 461 17 Liberec, Czech Republic

e-mail: pichal@fel.cvut.cz

Abstract

Paper presents results of experiments investigating possibility of synthetic fibres´ hydrophobicity improvement with the atmospheric dielectric barrier discharge. For experiments polyester (PES) fibres (fabric) were used. Experiments were performed in air under atmospheric pressure. There were studied relation between modification time, discharge power and hydrophobicity expressed by area of feathering and also modification effect aging .

Keywords: atmospheric dielectric barrier discharge, plasma modification, PES fabric, hydrofobicity

1. Introduction

At present synthetics and among them polyester are widely used in industry, but applied finishing methods are often confronted with strict environmental protection laws. These problems and pursuit of low cost production result in permanent search for alternative finishing and treatment methods. This single-minded effort is also continually paid to the polyester fibres characteristics improvement (because of the polyester low wettability, high hydrophobicity, low adhesion, high oil impurities cohesion and undesirable electric discharge generation) since begin of the polyester production.

The most reliable way to improve them seems to be the change of surface characteristics, adhesion and corresponding surface energy being those often used.

At present there is a large number of methods for fibers´ surface formation during manufacturing. Surface formation resulting in fibres higher wettability, higher adhesion and dyeability etc. can be performed e.g. by enzymatic hydrolysis, chemical grafting, laser application or low pressure and atmospheric pressure plasma application.

Plasma consists of many excited particles modifying the fibre surface. The effect of the surface plasma modification depends on properties of used gas, because of methane, ethylene, ethanol participation in the graftage, oxide, tetrafloromethane (CF4) and ammonia can be used for sloughing, or noble gases as helium, neon, argon etc. effectivity as admixtures for better chemical processes initialisation. Modification characteristics also depend on properties of the used working gas and the way of plasma generation. Atmospheric plasma seems to be the most suitable both from the economical perspective (low running cost in contrary with the low plasma processes) and from ecological point of view (it is a solvent free and dry process and it is characterized with extreme low chemicals consumption in contrary with chemical processes). One of ways to get the atmospheric plasma is the dielectric barrier discharge.

Manufacturing the composite of tyre cord PES fibres and styrene-butadiene rubber (SBR) matrix in car industry [1] was accompanied with problems connected with adhesion. Beside them fibres were also polluted with lubricants from preceding technological operations. Desired modification could be performed e.g. with classical chemicals application, but this method was unsuitable from ecological point of view. Further possibility was the plasma treatment. Combination of the clean up with acetone and atmospheric nitrogen plasma treatment led to improvement of adhesion of about 100%. The modification effect was sufficiently permanent in time.

Another example of nitrogen dielectric barrier discharge application was creation of hydrophilous surface for palladium catalyzer absorption simplification [2] in case of electroless nickel deposition, necessary treatment time in nitrogen plasma had been very short (1s).

To improve the deep coloring effect of polyethylene terephtalate fabric, anti reflective coating layers had been deposited on the surface of the fabric with two different organo-silicon compounds as HMDS, TTMSVS using atmospheric pressure plasma [3]. The best results of the deep coloring effect on PET fabric had been obtained from the HMDS polymerized film treated for 15 minutes and TTMSVS polymerized film

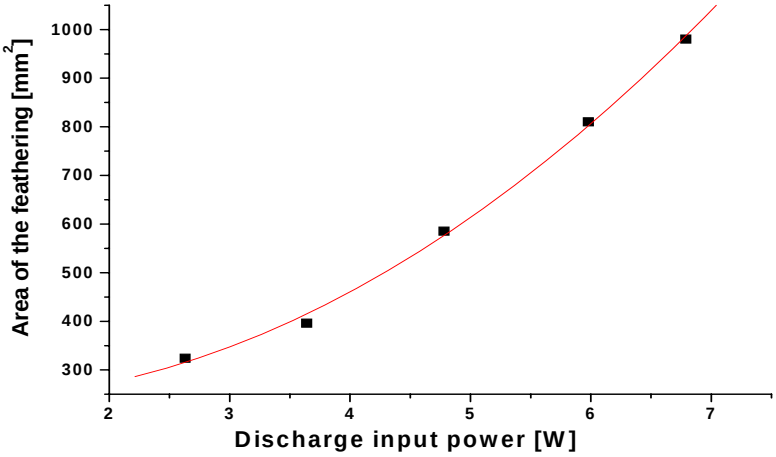

Fig. 1. Feathering area dependence on dielectric barrier discharge input power.

treated for 5 minutes. Sputter-etched PET fabric had also shown good coloring effect at atmospheric pressure of He/O_2 mixed gas.

Dielectric barrier discharge was also used on industrial scale for textile modification. New equipment for a two-meter-wide textile plasma activation is mentioned in [4]. Its efficient inlet system gave the opportunity to reduce the oxygen concentration in the plasma treatment chamber in continuous operation mode significantly, so that treatment could be performed in a defined process gas composition independent on the environment. Hydrophilic as well as hydrophobic and oleophobic modification on textiles could be performed on the same equipment by change of its parameters.

Technical textiles can be also effectively protected against water and oil penetration in a cost-effective dry dielectric barrier discharge-based continuous plasma process using Ar/FC_4 mixtures [5].

Plasma Ireland produces industrial equipments substantially improving bonding of PET textiles with polyurethane resin as measured by peel strength via grafting of polar groups [6].

In industrial praxis it is sufficient if modification effect time duration is limited to a shorter time period, when special procedures, e.g. dying, would be performed. Therefore there is no need for search of methods leading to permanent modification effect so that we consider the modification effect reduction after some days as unimportant in praxis.

This contribution supplements preceding works reporting results of polyester fabric modification by atmospheric corona discharge [7] and by low-pressure radio-frequency and microwave discharges [8]. Our research focused on a systematic study of possibilities of the polyester fabric hydrophobicity control and modification efficiency in atmospheric dielectric barrier discharge. Experiments were performed in air, because of its attractive low cost, and there was studied connection between dielectric barrier discharge input power and polyester fabric's hydrophobicity and modification effectivity.

2. Experimental

For all experiments there were used specimens made from the polyester cloth with the trade name Tesil 12. Their cleaning consisted of following steps: specimen double washing in water solution of a proper washing agent, rinsing in running water, double washing in distilled water, chemical cleaning and drying before discharge application.

Dielectric barrier discharge was generated between two large plane iron electrodes, both with diameter 45 mm and 10 mm thick. One of them was grounded. The glass barrier was created with a (83×83) mm, 2 mm thick glass table stuck to the other electrode. The interelectrode distance was fixed at 10 mm. The electrodes were put into open cylindrical vessel (diameter 153 mm, height 146 mm). Textile specimens were placed right on the grounded large plane electrode during modification. All experiments were performed in stationary air under atmospheric pressure $(743 \div 754)$ torr and room temperature $(20 \div 22)°C$. A.C. voltage $(6{,}8 \div 10{,}4)$ kV was applied to the electrodes, typical discharge current values were hundreds of μA. Modification time was $(30 \div 600)$ seconds.

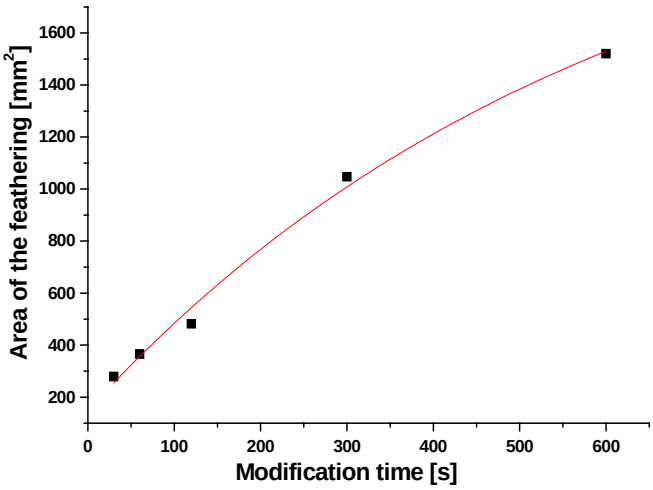

Fig. 2. Feathering area dependence on modification time.

Modification efficiency was compared by means of hydrophobicity, which was evaluated by the drop test [9], 20 µl of distilled water being the test liquid. Relevant feathering spot size was recorded with a ccd camera, the area of the spot in the 60th second after start of the test was used as the standard for the evaluation. The experiment was stopped if the drop did not soak into the fabric after 10 minutes from the start.

Results and discussion

Feathering area grew in proportion both to the atmospheric dielectric barrier discharge input power and modification time. More effective modification expressed by the treated fabric area changes could be achieved by the discharge input power rise (Fig. 1). For in experiment used input power values the feathering area-time dependence seemed to be sharply rising, hence small change of input power resulted in greater change of the hydrophobicity. Reached modification efficiency maximum corresponded to the input power of 6,8 W. Unfortunately, we did not probably reach potential modification efficiency maximum, when treated fabric surface would be fully saturated with active particles. This reality caused by disposable power supply properties seemed to be confirmed with feathering area–modification time characteristic (Fig. 2), too.

Experiments showed that the fabric modified with dielectric barrier discharge had an increased sorption. The modification effectivity (i.e. effect permanency) had changed in time, during first 24 hours the feathering spot size and hence also modification effectivity had sharply diminished (Figs. 3, 4). The curve shape changes might be connected with the modification degree of the fabric, i.e. the efficiency drop might be connected with the transformation of created hydrophilous function groups on the surface of fabric. Transformation might be caused by chemical reactions of created hydrophilous function surface groups with air components. Dipoles orientation might also changed backwards in time coming into the primary orientation. Five days after modification there was measured no important difference in hydrophobicity of modified and unmodified specimens. Modified fibres were stocked in air at atmospheric pressure.

Comparison with results of similar experiments performed with an atmospheric corona discharge [7] indicate that modification by atmospheric dielectric barrier discharge might be more appropriate tool for the polyester fabric modification than the atmospheric corona discharge.

Conclusions

1) Atmospheric dielectric barrier discharge modification effect grew with both the discharge input power and modification time duration rise. It seems, that its potential modification efficiency maximum, when treated fabric surface would be fully saturated with active particles, was not reached during our experiments.
2) The modification effect had sharply diminished in time. Study of the polyester fabric RF

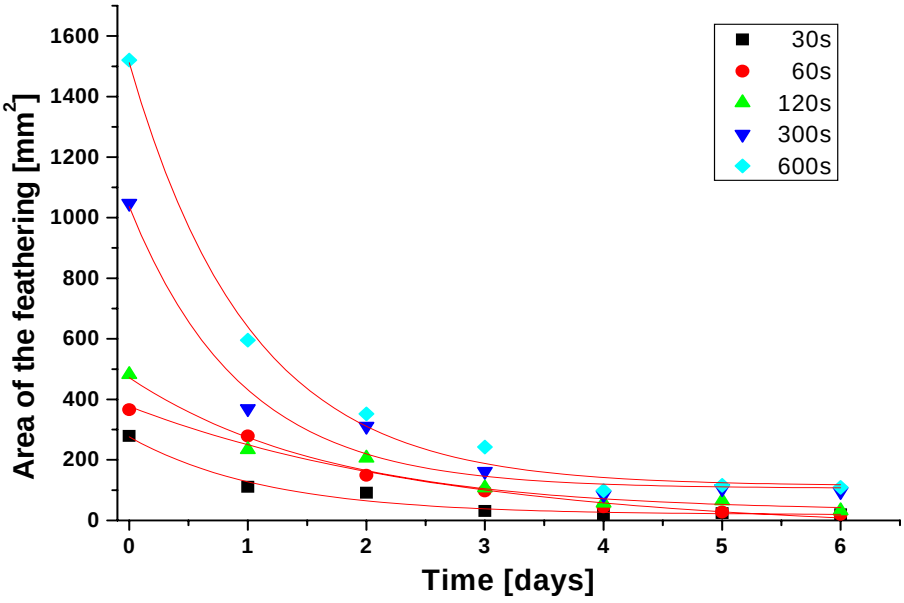

Fig. 3. Air barrier discharge plasma polyester fabric modification effect aging expressed in the feathering spot size time changes for different modification times.

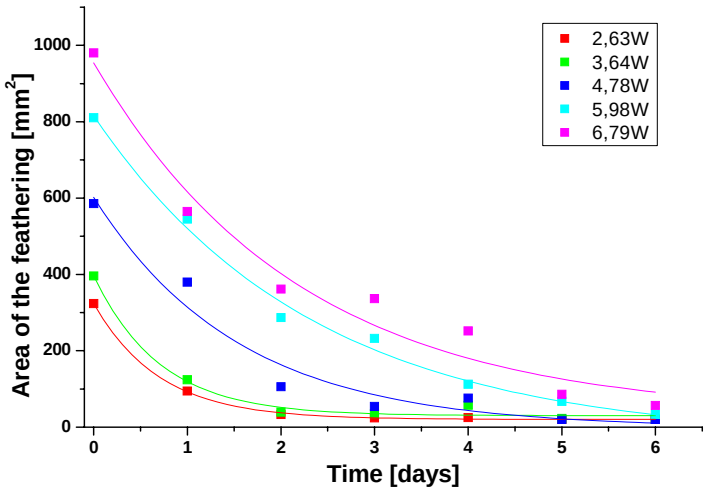

Fig. 4. Air barrier discharge plasma polyester fabric modification effect aging expressed in the feathering spot size time changes for different discharge input power

3) atmospheric dielectric barrier discharge modification effect aging expressed in the feathering spot size time changes indicated that the modification effect evidently lasted for about 48 hours, and then became extinct. 5 days after modification there was measured no important difference in hydrophobicity of modified and unmodified specimens.
4) Modification with atmospheric dielectric barrier discharge might be more appropriate tool for the PES fabric modification than the atmospheric corona discharge [7].

Acknowledgement

This work was supported by the projects MSM OC 527.60, OC 527.120, MSMT 1M4531477201 and LB 00B090.

References

[1] H. Krumpa, M. Šimor, I. Hudec, M. Jaššo, A.S. Luyt; Adhesion strength study between plasma treated polyester fibers and a rubber matrix, Applied Surface Science, **240** (2005), 268–274.

[2] M.Šimor, J.Ráhel, M.Čermák, Y.Imahori, M.Štefečka, M.Kando; Atmospheric-pressure plasma treatment of polyester nonwoven fabric for electroless plating, Surface and Coating Technology, **172** (2003), 1-6.

[3] H.Lee, H.Kim, K.Lee; Anti-reflective coating for the deep coloring of PET fabric using an atmospheric pressure plasma technique, Surface and Coating Technology, **142-147** (2001), 468-473

[4] T.Bahners, T.J.Heimbach, J.Erdmann, A.Lunk, T.Stegmaier, N.Weber; Flexible characteristics, TM, **6** (2001), 12-13.

[5] A.Dinkelmann, V.Arnim, A.Lunk, T.Stegmaier, M.Shakhatre, I.P.Vinogradov, T.Bahners; Deposition of water-oil repellent coating on technical textiles in a DBD at Atmospheric pressure, Proc. of 9th International Conference on Plasma Surface Engineering; Garmisch-Partenkirchen; Germany; 13-17th September, 2004.

[6] www.plasma-ireland.com

[7] J. Pichal, J Koller, L. Aubrecht, T. Vatuna, P. Špatenka, J. Wiener; Application of atmospheric corona discharge for PES fabric modification. Czech. J. of Phys. **54** (2004), C828-C834.

[8] T. Vatuna, P. Spatenka, , J. Pichal, J. Koller, L. Aubrecht, J. Wiener; PES fabric plasma modification. Czech. J. of Physics, **54** (2004), C475-C482.

[9] A.M. Wrobel et. al. ; Polymer, **1** (1978), 908–912.

[10] Pastore CH.M., Kiekens P.: Surface Characteristic of fibers and textiles; Marcel Dekker, Inc.(2001); 49-57; ISBN 0-8247-0002-3

Theoretical Analysis of In-Flight and After-Impact Particle Chemistry in Plasma Spraying

D. Kolman[1], K. Volenik[2]

[1] *Dept. Mechanical Engineering, Czech Technical University, Prague, Czech Republic*

[2] *Institute of Plasma Physics, Czech Academy of Sciences, Prague, Czech Republic*

This paper describes a comprehensive model for the simulation of the interaction of a multi-species particle with its surrounding gas phase. The interactions modeled include heat and mass transport from/to the particle and the corresponding transports inside the particle. Furthermore, chemically limited processes at the particle surface, and phase changes and stoichiometric constrains inside the particle are considered. The model is applied to iron and steel in-flight and after-impact oxidation, and the results are compared to experiments.

Keywords: Modeling, Plasma Spraying, Oxidation, Iron, Chromium

1. Introduction

Chemical changes accompanying inevitably heating, melting, impingement and solidification of particles during plasma spraying are a serious although frequently unsolicited phenomenon. In case of metals, oxidation and reduction changes are of greatest importance. In any case, an understanding and a subsequent control of these changes are of vital interest to both academia and industry.

The rate of any reaction between the particle and the gas phase species is determined by an interplay of several processes - reactant and/or product diffusion through the particle gas phase boundary layer; surface reactions; reactant and/or product diffusion through the altered subsurface layer; and reaction at the interface between the already altered layer and the bulk. Each of these processes may be rate limiting and all have to be considered simultaneously. Individual process rates are quite temperature sensitive, thus the extent of the transformation has to be traced from particle introduction into the plasma up to its impact at the substrate. Furthermore, spatial and temporal oscillation of the plasma background pose a question whether we study of "typical" particle or particle ensemble. This contribution studies changes of a *typical* particle, both *in-flight* and *after-impact* at a substrate. Some of the mathematical details of the model may be found in [1].

2. Components of the analysis

The system that is being modeled consists of a spherically symmetric particle together with its adjacent gas-phase boundary layer. For the description of the species transport across the boundary layer species continuity equation in terms of mole fractions is utilized. It has be shown numerically that the pressure equilibration time is much smaller that other time scales, thus convection trough the boundary layer has not to be considered. The energy transport is described by an analogous equation of conservation of energy written in terms of temperature. All equations include a temporal change of the respective quantities, a diffusion term and a source term due to homogeneous chemical reactions in the gas phase.

The passage from the gas-phase to the condensed phase and vice versa is described by surface chemical reactions and their kinetic rates. In general, additivity of the reactions with respect to both gas-phase and condensed species is assumed. Apart from the purely chemical processes, vaporization of the condensed species is also considered.

There exists always a layer under the surface of the particle that has already undergone some chemical modification – an altered zone. In the situation under consideration it is usually strictly distinguishable from the bulk material and thus these two zones are conveniently treated separately. Transport of chemical species in any of these two zones is given by a diffusion equation, energy transport by a heat conduction equation. Due to the fact that the relationship between temperature and enthalpy in the region of phase changes is not unique, the heat

transfer equation can not be expressed directly in terms of temperature and temperature is therefore computed from enthalpy separately using a more complicated relation.

At the interface between the altered zone and the bulk zone, infinite reaction rates are assumed and the composition of the altered zone is limited by stoichiometric considerations only.

Finally, the growth of the altered zone and particle size change are given by the sum of the appropriate surface reaction rates and vaporization rates, respectively.

3. Implementation details

1D unsteady species and energy conservation equations in all media are discretized both in space and time and a set of finite difference equations is formed. On a single time level, composition and gas-phase energy equations are solved implicitly with a tri-diagonal Gauss elimination, condensed phase energy equation is solved explicitly with a time sub-stepping. The extend of the altered zone is being traced, and, when appropriate, a new computation point is added. Thermodynamic and transport properties as well as chemical reaction rates are evaluated locally in each computational point and in each time step. A Unified Approximation for Mixture Transport Properties for Multicomponent Boundary Layer Applications is applied in the gas-phase [2].

It has been shown previously [1] that in case of metal oxidation there is no strong melt circulation on the surface of the particle that would keep removing the oxide from from the surface into the interior of the particle. On the other hand, impermeable oxide layer has lead to insufficient metal vaporization. Thus, the particle is assumed to be covered with the oxide, most of the time molten, but the metal vapor forming under the oxide layer is allowed to escape from the particle.

Finally, during the after-impact analysis, particle spreading is modeled by a particle macroscopic mechanical energy balance following [3].

4. In-flight and after-impact oxidation and vaporization of alloy particles

The model introduced above is applied to oxidation, vaporization, impact and spreading of metallic alloy particles, in particular to Fe-Cr particles in a water-stabilized plasma torch of the Institute of Plasma Physics in Prague [4]. In this case, both Fe and Cr form a range of oxides: FeO to Fe_3O_4 and Cr_2O_3 to Cr_3O_4. Data on surface reaction rates and diffusion rates for the temperature range under consideration are almost nonexistent and are mostly extrapolated and/or estimated from analogous problems. Metal vaporization rates are given by Langmuir equation, oxide vaporization is negligible. In general, Cr oxidation is at least an order of magnitude faster than Fe but diffusion in chromium oxide is more than an order of magnitude slower than in iron oxide. It should be noted that oxidation reactions are considered irreversible but metal vaporization is limited by the corresponding equilibrium vapor pressure.

After some minor optimization with respect to the in-flight experimental data, the following oxidation and vaporization rates were obtained:

Fe oxidation rates (mol/m²s)

2Fe(c)+O2=>2FeO(c)	$R = 3\cdot 10^4 \exp(-16000/T) C_i S_i$	[extracted from 5,6]
Fe(c)+O=>FeO(c)	$R = 4\cdot 10^3 \exp(-10170/T) C_i S_i$	[est. by analogy with other metals 7,8]
Fe(c)+OH=>FeO(c)+H	$R = 4\cdot 10^3 \exp(-10170/T) C_i S_i$	[same activity as O]

where C_i is the concentration of the participating gas phase species, S_i is the fraction of the corresponding unbounded metal atoms at the oxide surface.

Cr oxidation rates (mol/m²s): order of magnitude faster that Fe

4/3Cr(c)+O2=>4/3$CrO_{3/2}$(c)	$R = 6\cdot 10^5 \exp(-16000/T) C_i S_i$
2/3Cr(c)+O=>2/3$CrO_{3/2}$(c)	$R = 8\cdot 10^4 \exp(-10170/T) C_i S_i$
2/3Cr(c)+OH=>2/3$CrO_{3/2}$(c)+H	$R = 8\cdot 10^4 \exp(-10170/T) C_i S_i$

Metal vaporization (mol/m²s): $V = \frac{p_i^{eq} X_i - p_i}{\sqrt{2\pi W_i RT}} = \frac{A_i \exp\left(-B_i/T\right) X_i - p_i}{\sqrt{2\pi W_i RT}}$

Fe(c) <=> Fe(g) $A_i = 1.30 \cdot 10^{11}$, $B_i = 43980$ [after 9]

Cr(c) <=> Cr(g) $A_i = 1.16 \cdot 10^{11}$, $B_i = 41190$ [after 9]

where p_i is the actual vapor pressure of the corresponding gas-phase species, X_i is the fraction of the corresponding metal atoms at the metal-oxide interface.

The second decisive factor in the oxidation process are the diffusion rates of the ions inside the condensed material:

First, the allowed ranges of oxides formed have been determined to be:

FeO to Fe_3O_4 i.e. $Fe_{1+a}O_{4/3}$, $a \leq 1/3$

Cr_2O_3 to Cr_3O_4 i.e. $Cr_{1+b}O_{3/2}$, $b \leq 1/8$

Next, the diffusion coefficients have been determined (m²/s):

Fe↔O in solid FeO $D = 1.18 \cdot 10^{-6} \exp(-14954/T)$ [10]

Fe↔O in molten FeO $D = 1.50 \cdot 10^{-3} \exp(-14954/T)$ [11]

Cr↔O in solid Cr_2O_3 $D = 1.37 \cdot 10^{-5} \exp(-30500/T)$ [10]

Cr↔O in molten Cr_2O_3 $D = 5.30 \cdot 10^{-6} \exp(-15400/T)$ [est.]

Finally, adjustable multipliers have been introduce to make diffusion in “foreign” oxide more difficult,

Fe in $CrO_{3/2}$ d = 0.05

Cr in FeO d = 1.00

The particles under consideration are either pure iron or steel AISI 410 with 13 wt% chromium. The particle SMD is 120 μm. Typical in-flight residency time is about 10 ms, and the gas composition is assumed for simplicity to be composed of 50% air + 50% water vapor. The particle experiences gas-phase temperatures between 500 K and 3500 K depending on its particular trajectory (determined within the computation).

After impact, in the time range considered, the particle cools slightly bellow its solidification temperature. Typical time for which the splat surface is exposed to the ambient atmosphere before it is covered by another impacting particle is estimated from the mass load, the target size and the spraying deposition efficiency, and is found to be about 20 ms.

5. Results and discussion

This section presents results concerning the influence of alloy composition, and both time development and integrated results are shown. First, simulation results for in-flight oxidation are given.

Figure 1. depicts the temporal development of the boundary layer temperature that the particle feels, particle surface (oxide) temperature, volume of iron oxide and volume of chromium oxide as they are recorded during the flight in case of steel particles. Similarly, Figure 2. shows the same quantities for pure iron particles.

When we compare the two above cases it is seen that the temperature situation does not differ much: The increasing temperature of the surrounding leads to a corresponding increase in the oxide temperature - the little kink around 3 ms is the release of the latent heat of melting. At after about 2/3 of the flight time, the particle accumulates enough heat and starts to be cooled by the relatively cold gas in the tail of the jet.

The oxidation situation, on the other hand, is quite different: The take-off of the oxidation is slightly delayed to about ½ of the flight time in case of the chromium steel, then a strong chromium oxidation takes place with iron oxidation volume lagging significantly behind, and, eventually, chromium oxidation and iron oxidation rates become smaller and almost identical. In case of pure iron, oxidation starts little earlier and more gradually already in the solid phase but after the zenith in the temperature, the oxidation rate decreases too.

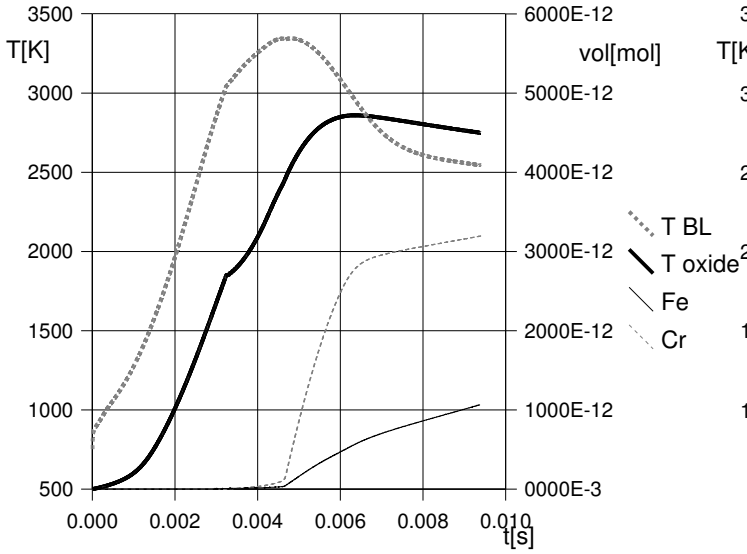

Figure 1. In-flight development of boundary layer temperature, oxide temperature, and FeO and $CrO_{3/2,}$ molar volumes, steel 13 wt% Cr.

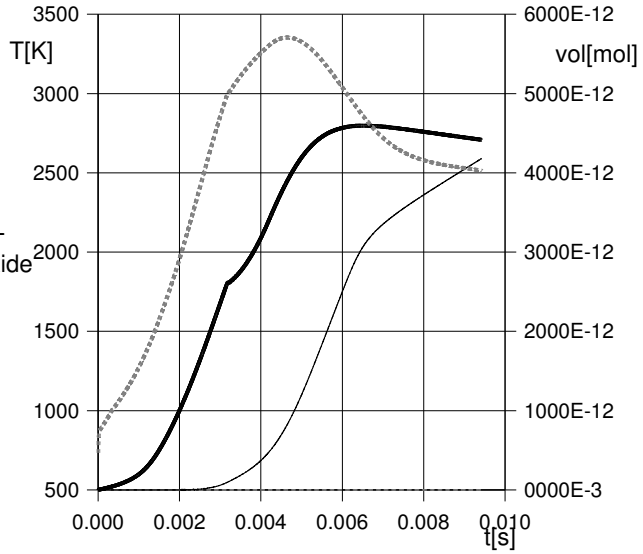

Figure 2. In-flight development of boundary layer temperature, oxide temperature and FeO molar volume, pure iron.

The corresponding results for the situation after impact are shown in Figure 3. Here, only oxide volumes are shown, one curve corresponds to the temporal development of the iron oxide in case of oxidation of pure iron, and the other two curves represent the iron and chromium oxide volumes in case of 13 wt% steel. Here, the oxidation in case of pure iron is much higher than in case of the chromium steel, and in both cases is almost linear in time as the particle surface and its temperature do not change (after first few milliseconds) in time. In both cases, this is oxidation bellow the particle melting temperatures for most of the exposure time.

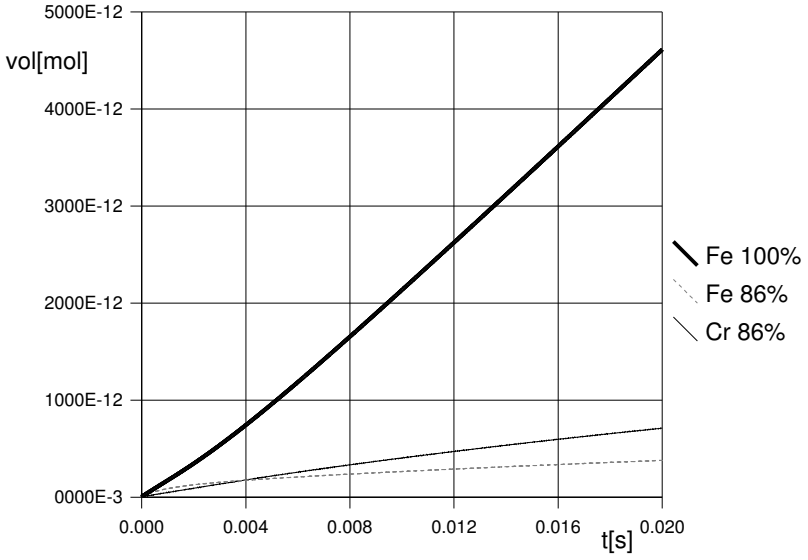

Figure 3. After-impact development of FeO and $CrO_{3/2}$ molar volumes, pure iron and steel 13 wt% Cr (14 vol%).

6. Comparison with experimental data

After some tuning of the kinetic parameters, the trends agree well with experimental data, namely the chromium content, trends in the overall oxidation extent and the dependence on whether it is in-flight or after-impact oxidation. The results are summarized and compared with experimental data in Figures 4 and 5. (The minor difference in the initial chromium content is accidental).

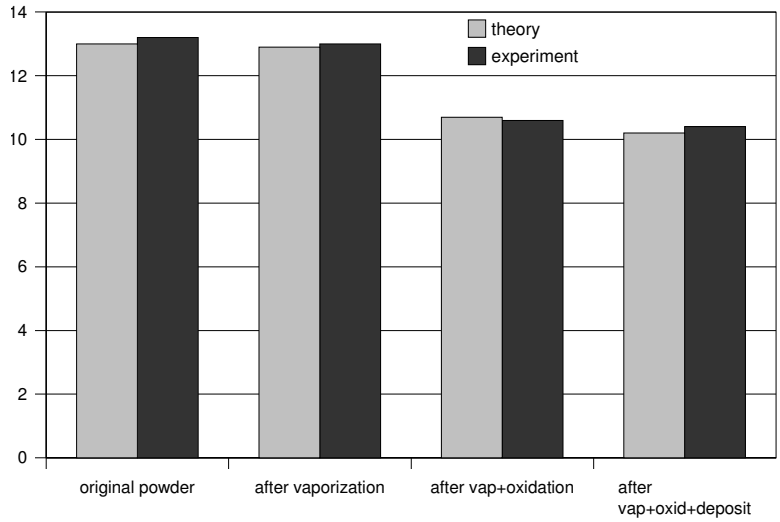

Figure 4. Chromium content [wt %] in steel 13 wt% Cr at various stages of processing - comparison of theory with experiments. Note that „after vaporization“ represents the in-flight content of the whole particle, „after vap+oxidation“ represents the in-flight content of the metal alloy only.

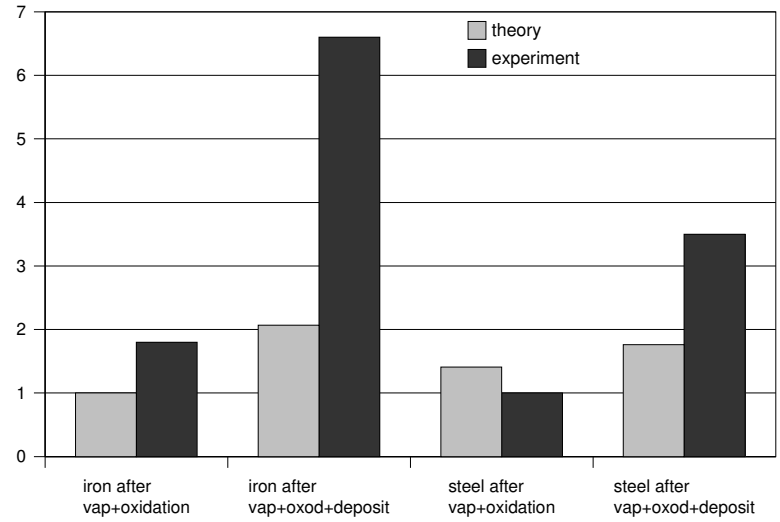

Figure 5. Oxygen content [wt %] in iron and steel 13 wt% Cr at various stages of processing - comparison of theory with experiments.

Figure 4 gives the experimental and simulated values of chromium weight content in the material at various stages of its processing. Thus, this figure tells us whether the composition results obtained are correct. Figure 5, on the other hand, provides similar data for oxygen content found in the material and serves thus as an indicator of the correctness of the overall oxidation extent.

In case of after-impact oxidation, the oxidation extent is visibly underestimated. The only plausible explanation to it is an underestimate of the splat surface area (experiments show mostly splashing whereas simulation considered an orderly splat). The lower oxidation rate after impact in case of steel reflects well with the

overall character of chromium steels, i.e. the chromium is added into it exactly for the purpose of reducing oxidation under standard conditions.

7. Summary and conclusions

In this work, the latest development on a comprehensive model for theoretical analysis of in-flight and after-impact chemistry is reported. The model includes a finite difference simulation of the heat and mass transport through different phases involved in the process, and is particularly suitable for the studies of oxidation/reduction of alloy particles. This is demonstrated on an analysis of the oxidation of pure iron and of the commercial steel AISI 410 under the water-stabilized plasma spraying conditions.

As the model is rather complex, its use requires an estimate of a range of kinetic parameters. A set of such parameters for the system Fe-Cr-O and the appropriate plasma gas environment (oxidation, vaporization and diffusion rates) has been developed and to a certain degree optimized, and has been presented above.

It may be said that the model and its kinetic parameters succeeded in reproducing the experimental observations, namely it gives the right proportion between iron and chromium oxidation. Also, as judged from the indirect evidence of the chromium content, the vaporization assumptions and rates seem to be correct (it is experimentally impossible to obtain direct vaporization data). The predicted values differ in the total oxidation extent after impact when being lower than the data obtained with the water-stabilized plasma system of the Institute of Plasma Physics in Prague. This discrepancy may be rectified by a better representation of the splat surface area considering splashing of the deposited material.

Acknowledgment

This work was possible thanks to the Fellowship of the Humboldt Foundation and the Support of the Czech Science Foundation under #106/03/0710.

References

[1] Kolman, D., Theoretical Analysis of Particle Chemistry in Plasma Spraying, 12th Workshop Plasma Technology, Sept. 2004, TU Ilmenau, Germany

[2] Barlett, E.P., Kendall, R.M., Rindal, R.A., An Analysis of the Coupled Chemically Reacting Boundary Layer and Charring Ablator, Part IV, A Unified Approximation for Mixture Transport Properties for Multicomponent Boundary Layer Approximation, NASA Aerotherm Report No. 66-7, Part IV

[3] Zhang, H., Theoretical Analysis of Spreading and Solidification of Molten Droplet During Thermal Spray Deposition, Int. J. Heat Mass Trans. 42 (1999) 2499-2508

[4] Hrabovsky, M., Konrad, M., Kopecky, V., Measurement of Velocity of Individual Particles Injected into Oxygen – Hydrogen Plasma Jet, *Progress in Plasma Processing of Materials 1999, Proc. of 5th International Thermal Plasma Processing Conf.*, P. Fauchais, J. Amouroux, eds., St. Petersburg, 1998

[5] Robertson, D.G.C., Jenkins, A.E., The Reaction of Liquid Iron and its Alloys in Pure Oxygen, *Heterogeneous Kinetics at Elevated Temperatures*, G.R. Belton, W.L. Worrel, eds., Plenum Press, New York, 1970

[6] Distin, P.A., Whiteway, S.G., Kinetics of Vaporization and Oxidation of Liquid Iron Levitated in Flowing Helium-Oxygen, Canad. Metal. Quart. 9(2), 1970

[7] Gusakov, A.G., Raspopov, S.A., Vecher, E.E., Voropayev, A.G., Interaction of Tantalum with Diatomic and Atomic Oxygen at Low Pressures, J. Alloys Comp. 201, 1993

[8] Raspopov, S.A., Gusakov, A.G. *et al.*, Kinetics of Zirconium Oxidation by Atomic and Molecular Oxygen at Low Pressures, J. Chem. Soc., Faraday Trans. 93(11), 1997

[9] Leitner, J., unpublished results, June 2003

[10] Goto, K.S., *Solid State Electrochemistry and its Applications to Sensor and Electronic Devices*, Material Science Monographs 45, Elsevier, 1988

[11] Li, Y., Lucas, J.A., Fruehan, R.J., Belton, G.R., The Chemical Diffusivity of Oxygen in Liquid Iron Oxide and Calcium Ferrite, Metal. Mater. Trans. B, 31B, Oct. 2000

Elaboration and Grafting of Cold Plasma Organo-phosphorus polymer on Polyamide 6 : New approach to flame retardancy

A. Mazzah[1], I. Errifai[2], C.Jama[2], R. Delobel[3] and R. De jaeger[1]

[1]*LASIR, CNRS UMR 8516, USTL, 59650 Villeneuve d'Ascq*
[2]*Laboratoire PERF UPRES EA n° 1040, ENSCL, 59650 Villeneuve d'Ascq*
[3]*CREPIM, Parc d'Activités de la Porte Nord, 62700 Bruay-La-Buissière*

Abstract

In order to improve the fire retardancy properties of the polyamide-6 (PA6), vinylphosphonic acid monomer (VPA) was graft-polymerized onto the PA6 using a low-pressure microwave plasma process. The property was achieved by creating covalent bonding between PA6 and the phosphorus polymer. The grafting and the polymerization processes were characterized by IR (ATR), the thermal stability by TGA and the fire retardancy performances by LOI and UL94 tests.

Keywords: Cold plasma; Vinylphosphonic acid; Fire retardancy; Polyamide.

1. Introduction

In the course of our studies aimed at making polyamide-6 fire retardant, several studies have been performed using cold remote plasma enhanced vapor deposition [1-4], or using cold plasma polymerization of a fluorinated acrylate [5,6].

This work is a part of an ongoing project to study the effectiveness of the plasma-induced graft polymerization (PIGP) procedure as a novel method to confer new and durable properties to synthetic polymers, without altering their bulk properties. With the PIGP procedure, an argon microwave (MW) plasma is used to induce, in one step, the grafting and the polymerization of acrylic, or vinylic monomers containing the functional groups needed to impart the desired properties. One advantage of PIGP procedure is that the polymerization occurs with structure retention of the monomer. Furthermore, the desired properties are obtained by creating covalent bonds between the substrate and the growing polymer on the surface leading to a durable effect.

In this study, the PIGP procedure is used to impart durable flame retardant properties to polyamide-6 (PA6) using functional monomers containing phosphorus, such as vinylphosphonic acid (VPA) (Fig.1). The argon microwave (MW) plasma is used to induce the polymerization of VPA according to the reaction presented in figure 2. The treated (PA6) were characterized by IR (ATR) spectroscopy and thermal analysis. The fire retardancy performances of the coated PA6 were evaluated using Underwriters Laboratories (UL 94) and limiting oxygen index (LOI) tests.

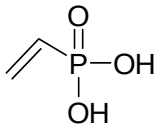

Fig. 1 : Vinylphosphonic acid

Monomer (VPA)

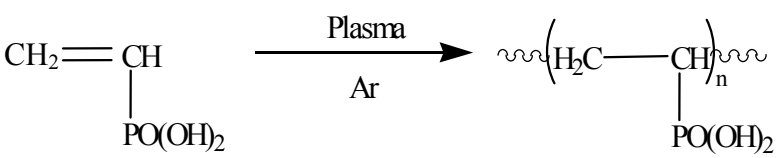

Fig. 2 : Reaction of plasma induced polymerization of VPA

2. Experimental

2.1. Materials

Polyamide 6 plates ($10\times10\times0.3$ cm^3) were prepared from pellets supplied by Radilon company using a darragon press at 260 °C under a pressure of 10^6 Pa. The monomer (VPA), the photo-initiator 2-hydroxy-2-methylpropiophenone (Darocur1173) and the solvents butanol-1 and ethanol were purchased from Aldrich Company and were used as received. Argon and Oxygen gases were obtained from Air Liquide Company.

2.2. Cold plasma process

The experimental set-up is described elsewhere [7,8]. An argon glow discharge was generated in an aluminum reactor chamber (27 l) at 2.45 GHz with a continuous out power ranging from 0 to 600 W. The chamber was pumped down to 10.7 Pa using a pump (E2M28 PEPE, Edwards), and the argon gas was introduced into the chamber at a certain flow rate. When the pressure becomes constant, the generator was switched on and adjusted to a certain power value, which gives rise to a continuous glow discharge.

2.3. Graft polymerization process

In the first step the polyamide plates were rinsed using ethanol and dried for 5h at 70 °C. Then after, they were pre-treated by an oxygen plasma (flow rate: 0.5 l/min; P = 100 W, t = 10 min) and subsequently a 6 µm film of VPA in Ethanol solution (200 g/l) in the presence of 3.5% by weight of the Darocur 1173 was applied onto the PA6 surface. In the next step, the samples were treated by Ar plasma (flow rate: 0.5 l/min; P = 250 W; t = 30 min). Finally, the treated plates were washed at room temperature with Ethanol for 24 h, in order to remove the residual monomer and dried at 70 °C.

2.4. Poly(vinylphosphonic acid) deposit characterization

The kinetic of the reaction of polymerization was followed by using ^{31}P NMR. The spectra were recorded using Brucker WP 300. The chemical shifts were expressed in ppm using H_3PO_4 (85%) as external reference. The deposits were characterized using FT-IR technique. The Infrared spectra were recorded using a Perkin-Elmer Spectrometer one, continuously variable-angle ATR accessory equipped with a diamond crystal.

Thermogravimetric (TG) analyses were performed using a Setaram apparatus from 20 to 800 °C at a heating rate of 10 °C/min under air flow (Air Liquide grade, 5×10^{-7} m^3/s measured in standard conditions). Samples in the powder form were placed in an open vitreous silica pans. Precision of temperature measurements was ±1.5 °C.

2.5 Fire retardancy performances of coated PA-6

The limiting oxygen index (LOI) test was measured according to the standard oxygen index test (ASTM D2863/77) [9] with a Stanton Redcroft instrument. This test provides a comparative numerical value for research and quality control. It is based on the determination of the limiting percentage of oxygen in a nitrogen oxygen mixture which will just sustain the candle-like burning of a sample. The UL 94 vertical burning test was measured according to ASTM D635-77 [10]. A burner flame is applied to the free end of the specimen for two 10 second intervals separated by the time it takes for flaming combustion to cease after the first application. Two sets of 5 specimens are tested. Different criteria are recorded for each specimen as indicated in table 1. The best flame retardancy rating of V-0 is achieved when the after-ignition burn time is less than 10s in each ignition and no drips are allowed.

3. Results and discussion

3.1. Kinetic study

The kinetic of the polymerization of VPA induced by an Ar plasma have been investigated by studying the influence of the power of the plasma as a function of time. The experiments were monitored by ^{31}P NMR spectroscopy.

For various treatment times, the ratio p = I_p (polymer) /(I_p(monomer)+I_p(polymer))

Where: I_p(polymer) is the intensity of NMR signal from phosphorus in polymer structure and I_p(monomer) is the intensity of NMR signal from phosphorus in the monomer form.

This ratio allows the conversion rate monomer to polymer p and the amount $1-p$ of remaining VPA monomer to be evaluated. Figure 3 shows the evolution of the remaining amount of VPA monomer versus time of treatment for different microwave powers. Four phases can be observed. In the first one (0 – 4 min) the rate of conversion of the monomer increases with MW power. This increase can be correlated to the increase of the concentration of radicals emanating from the Darocur decomposition. In the second phase, the monomer concentration remains quite stable. It is characterized by an increase of the deposit viscosity and by the formation of a superficial film. The third phase corresponds to a decrease in the kinetic of polymerization due to the fact that the diffusion of the active species through the film becomes the limiting factor. The last phase corresponds to the termination reactions.

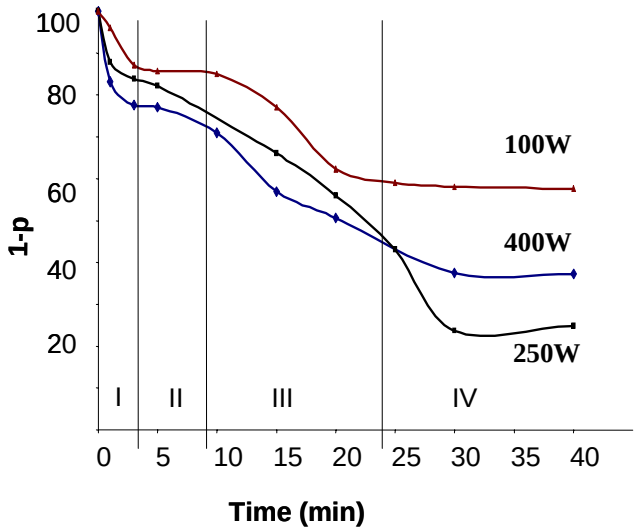

Figure 3: Kinetics of polymerization in an Ar MW plasma of VPA with 3.5% (w/w) Darocure (Ar flow rate=500 sccm; thickness film=6 µm).

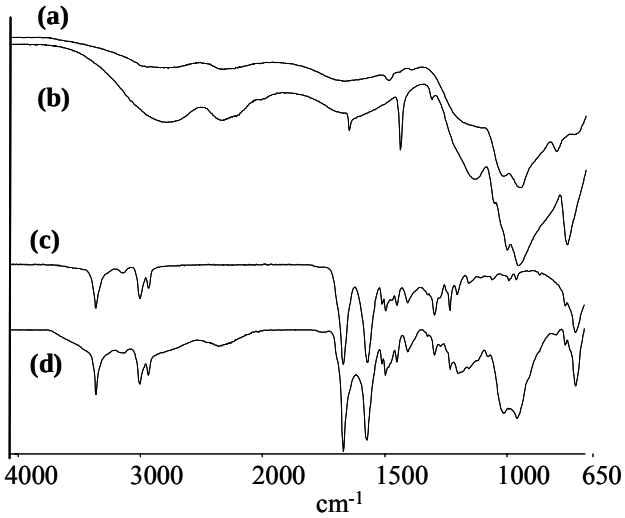

Figure 4: IR (ATR) spectra of VPA monomer (a), polyVPA (b); virgin PA(6) (c) and PA6-g-polyVPA (d).

3.2. Surface characterization

3.2.a. ATR-IR spectroscopy

Figure 4 shows the ATR-IR spectra of VPA monomer (a), polyVPA (b); virgin PA(6) (c) and the PA6-g-poly(VPA) (d), after washing with Ethanol for 24 hours. AVP spectrum shows the main characteristic bands at 727, 924 and 1103 cm^{-1} corresponding respectively to ν(P-C), ν(P-OH) and

ν(P=O). The two bands at 1405 and 1614 cm^{-1} are characteristic of the vinyl group (δCH_2= and νC=C). The polymerization induces logically the disappearance of these last bands as evidenced from the polyVPA spectrum. The PA6-g-polyVPA spectrum (d) compared to the virgin PA6 (c) shows the characteristic absorption bands at ν = 2286 cm^{-1}, ν = 1165 cm^{-1} and ν = 979 cm^{-1} corresponding to the νOH, ν(P=O) and ν_{as} P-O(H) respectively. However, the absorption bands characteristic for ν N-H (3296 cm^{-1}), ν_s and ν_{as}(C-H) (2864 and 2934 cm^{-1}), Amide (I) (νC=O) and Amide (II) (νC-N + δN-H) (1635 and 1540 cm^{-1}) of PA-6 are still visible which indicates that the depth of the deposited layer is lower than the analyzed depth (≈1µm).

3.2.b. Thermogravimetric analysis

Figure 5 shows TGA curves for virgin PA6 (a), PolyVPA (b) (polymerized under Ar Plasma, VPA in 1-Butanol solution (200 g/l) in the presence of 3.5% by weight of the Darocur 1173 (flow rate: 0.5 l/min; P = 250 W; t = 30 min)) and PA6-g-PolyVPA (c). Evidently, the orgnophosphorus layer reduces the thermal stability as indicated by a decrease in the onset temperature of degradation. The temperature for 10% mass loss $T_{10\%}$ decreased from 315 °C for virgin PA6 to 240 °C for PA6-g-PolyVPA. It can also be seen from Fig.5 that the orgonophosphorus coating has a strong effect on the char forming tendency. Whereas the virgin PA6 degrades completely upon heating to 600 °C, a thermally stable residue is formed at 600 °C of 20wt% for the PA6-g-PolyVPA. This residual weight increases up to 40 wt%, when the PA6-g-PolyVPA is treated with 0.5M aqueous solution of sodium hydroxide (NaOH), as presented in Fig.6. It is possible that this increase in the char yield arise as a result of surface cross-linking, assisting in retaining material in the condensed phase during combustion and encouraging the formation of char as previously reported by Wilkie and al [11-12]. Moreover, an increase of temperature of the major step of degradation is observed. Indeed, it passes from 240°C to 317°C when the PA-g-PolyVPA is treated with 0.5M NaOH. This increase could be explained by the loss of the acidic character of the polyVPA layer leading to the formation of a more thermally stable residue at a higher temperature.

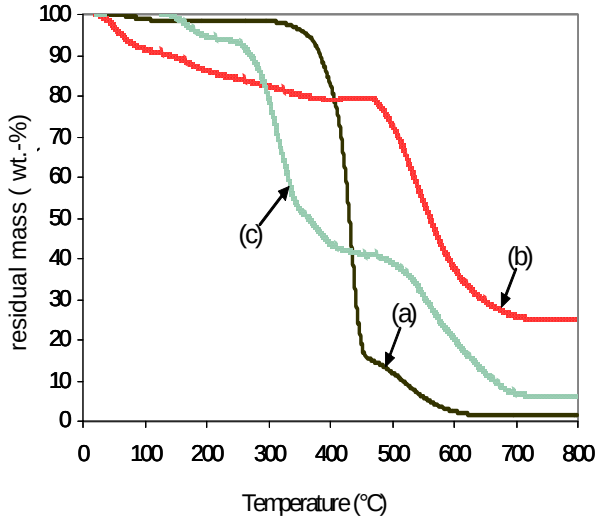

Figure 5: TG curves for virgin PA6(a), polyVPA(b) and PA6-g-polyVPA (c)

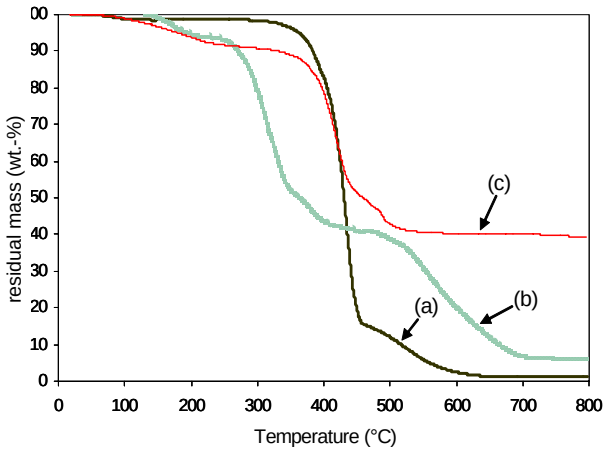

Figure 6: TG curves for virgin PA6(a), PA6-g-polyVPA (b) and PA6-g-polyVPA treated by 0.5M NaOH (c)

3. 3. Fire retardancy performances of PA6-g-PolyVPA

The LOI values for virgin and treated PA6 are given in table 2. It shows that the fire performances of PA6-g-PolyVPA are increased. Indeed, the LOI of the grafted PA6 is higher than that of unmodified PA6. The performance depends on the concentration of VPA solution. The highest LOI, obtained by treating the PA6 with a pure VPA, reaches a value of 45% and the UL 94 rating correspond to V0.

Criteria Conditions	**V-0**	**V-1**	**V-2**
Total flaming combustion for each specimen	≤10 sec	≤30 sec	≤30 sec
Total flaming combustion for all 5 specimens of any set	≤50 sec	≤250 sec	≤250 sec
Flaming and glowing combustion for each specimen after second burner flame application	≤30 sec	≤60 sec	≤60 sec
Cotton ignited by flaming drips from any specimen	NO	NO	YES
Glowing or flaming combustion of any specimen to holding clamp	NO	NO	NO

Table 1. Material Classification

Samples	**LOI (vol. %)**	**UL 94 rating**
Virgin PA6	25	NC
PA6-g-polyVPA (600g/l)	29	V1
PA6-g-polyVPA (800g/l)	35	V0
PA6-g-polyVPA (pure VPA)	45	V0

Table 2: UL rating and LOI values for virgin PA6 and the PA6-g-VPA

4. Conclusion

In the present work we have investigated a new approach to the flame retardancy of polyamide 6 using a cold plasma process by grafting and polymerizing the vinylphosphonic acid VPA onto the PA6 surface. This modification leads to significant reductions in flammability as evidenced by increased LOI values and increased yields of char formation during oxidative degradation. These performances are explained by the fact that the phosphorus acid -containing groups are active in the condensed phase by assisting intermolecular cross-linking promoting the formation of a protective char layer.

References

[1] S. Bourbigot, C. Jama, M. Le Bras, R. Delobel, O. Dessaux, P. Goudmand - Poly. Deg. Stab. **66**, 153(1999).

[2] C. Jama, A. Quédé, P. Goudmand, O. Dessaux, M. Le Bras, R. Delobel, S. Bourbigot, J. W Gilman, T. Kashiwagi - « Fire retardancy and Thermal stability of Materials Coated by Organosilicon Thin Film using a Cold Remote Plasma Process », in : Fire and Polymers Materials and Solution for Hazard Prevention, G. L. Nelson, C. A. Wilkie, Eds., American Chemical Society Publication, Washington 2001, chapter 16, ACS Symp. Ser. **797**, 200(2001).

[3] C. Jama, A. Quédé, H. Sadiki, O. Dessaux, P. Goudmand, R. Delobel, M. Le Bras, - « Studies of Plasma Applied Polymer Fire Retardant Coatings », in : Recent Advances in Flame Retardancy of Polymeric Materials, Vol.12, M. Lewin, Ed., Business Communications Co Inc., Norwalk pp. 127-136(2001).

[4] C. Jama, A. Quedé, M. Le Bras, R. Delobel, P. Goudmand, O. Dessaux, S. Bourbigot, J.W. Gilman, T. Kashiwagi - Abstr . Pap. Am. Chem. Soc. PMSE **83**, 75(2000).

[5] I. Errifai, C.Jama, M. Le Bras, R. Delobel, R. De Jaeger, A. Mazzah, L.Gengembre - Journal of surface and coating technology **180- 181**, 297(2004).

[6] I. Errifai, C.Jama, M. Le Bras, R. Delobel, R. De Jaeger, A. Mazzah - Polymeric Materials : Science and Engineering **91**, 392 (2004).

[7] F. Hochart, J. Levalois-Mitjaville, R. De Jaeger - Polymer **41**, 3159(2000).

[8] F. Hochart, R. De Jaeger, J. Levalois-Grützmacher - Surface and Coatings Technology **165**, 201(2003).

[9] ASTM, Standard D2863/77, American Society for Testing and Materials, Philadelphia, PA, 1977.

[10] Underwriters laboratories, Northbrook, AINSI/ASTM D635-77, 1977.

[11] D. D. Jiang, Q. Yao, M. A. McKinney, C. A. Wilkie - Polym. Deg. Stab. **63**, 423(1999).

[12] N. M. Langer, C. A. Wilkie - Poly. Adv. Technol. **9**, 290(1998).

Exploring Radical-Surface Interactions During Plasma Etching and Deposition

Ellen R. Fisher, Department of Chemistry Colorado State University, Fort Collins, CO 80523-1872

Abstract:

Plasma-enhanced chemical vapor deposition (PECVD) and plasma etching are an integral to the microelectronics industry as well as to development of biomaterials, hard coatings and other widespread applications. Many mechanistic details for plasma processing of materials remain unknown. Understanding surface interactions of plasma species provides critical molecular level information about plasma processing. In addition, power dissipation and energetics are also important for elucidation of mechanistic details in plasmas. The imaging of radicals interacting with surfaces (IRIS) technique examines interactions of radicals during plasma processing of a variety of materials. This technique combines molecular beam and plasma technologies with laser-induced fluorescence (LIF) to provide spatially-resolved 2D images of radical species involved in film formation or etching. IRIS allows for direct determination of radical-surface interactions *during* plasma processing. Furthermore, IRIS provides direct information on the energetics of plasma-generated radicals as well as for species scattering off of surfaces. Specifically, IRIS provides data on the kinetic translational temperature and the rotational temperature of radicals in plasma systems. IRIS data for species in PECVD and etching environments will be presented. This work concentrates on the energetics of radicals such as SiH, CH, OH, and SO_2 during deposition or etching of silicon-based or carbon-based materials. Comparisons will be made between the surface interactions of individual species (i.e. comparison of the main group hydrides indicates not all open shell molecules are highly reactive) to elucidate the chemistry of both the molecules and the plasma processes.

Plasma Chemical Behavior of Inductively Coupled Fluorocarbon Plasmas

H. Fukumoto, K. Ono and K. Takahashi

Department of Aeronautics and Astronautics, Graduate School of Engineering, Kyoto University, Kyoto, Japan

Abstract

Chemical behavior has been simulated of inductively coupled plasmas. The fluorocarbon gases, CF_4 and C_4F_8, were employed in the simulation, and the results were compared with each other. There was little difference in the spatial distribution of electron density and temperature between CF_4 and C_4F_8 plasmas; on the other hand, there was large difference in some chemical species between in the two.

1. Introduction

Radio-frequency discharges in low-pressure fluorocarbon gases have been widely used for the etching of thin SiO_2 layers on Si in the microelectronics fabrication [1]. During plasma etching, several different kinds of reactive ions and neutrals occur in the plasma, being incident on substrate surfaces being etched: feedstock gas species and their fragments (or reactants), reaction products (or etch products) from the substrate, impurities from chamber walls, and mask materials. An etching process is much complicated because it contains many chemical reactions and many chemical products. The composition of neutrals and ions depends on many kinds of conditions: ICP input power, pressure, mass flow rate, material and temperature of electrodes and chamber walls, material of wafer, and so on.

In the near future, the process of ultra large scale integrated circuit (ULSI) devices will need a precisely controlled process technology for processing micro structures with sub 0.1-μm patterns and aspect ratios of over 10 on 30-cm-diameter wafers. To achieve the technology, it is necessary to produce uniform ion fluxes by using low-pressure and high-density plasmas. Many kinds of plasmas sources are being researched and developed. However, there are many problems to be solved, arising from the existence of magnetic fields, complicated dissociation of reactive gases, interaction with chamber walls, and so on [2]. Thus, a better understanding of the chemical behavior of reactive plasmas for etching is strongly required, to develop an advanced plasma etching technology for microelectronics and MEMS devices. In this work, the chemical behavior is simulated of inductively coupled fluorocarbon plasmas, to understand the spatial structure of plasmas.

2. Modeling

A schematic of the ICP source studied is shown in Fig. 1. The reactor has a radius R=15 cm and a length H=9 cm, with a dielectric window at the top of the chamber. The plasma is generated by a five-turn RF coil driven at radio frequencies of 13.56 MHz. The coil current induces time-varying magnetic fields which in turn induce the electric fields that couple the rf power to the plasma electrons within a skin depth layer near the plasma-dielectric interfaces. A wafer stage 10 cm in radius is located at the bottom of the chamber. Feedstock gas is supplied through a gas inlet ring located just under the dielectric window, being pumped away through an annular ring vacuum pump port.

Maxwell's equations are solved to obtain the power deposition into the plasma. The power deposition profiles are then used in the electron energy equation to calculate electron temperatures. The rate coefficients for chemical reactions, which are a function of electron temperature, are transferred as

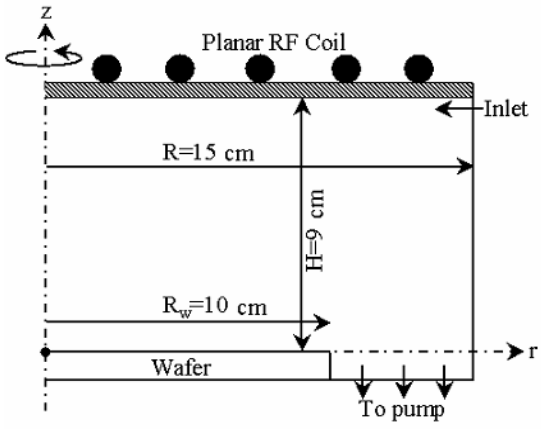

Fig. 1. A schematic of the ICP reactor studied in the present simulation.

source and sink terms to the charged and neutral species rate equations. At plasma-surface boundaries, the surface site balance model acquires fluxes of reactants from the plasma fluid model, implements surface reaction mechanisms, assigns surface coverages, and then places back fluxes of products to the plasma fluid model as boundary conditions. Electron density gives the plasma conductivity used in Maxwell's equations. By iterating these procedures until the solution converges, a self-consistent steady-state solution can be obtained.

The electromagnetic fields are obtained by solving Maxwell's equations. In this study, the rf spiral coil is approximated by concentric coils. With the axisymmetric assumption, we only consider the azimuthal component of the inductive electric field E_θ.

$$\nabla^2 E_\theta = j\omega\mu_0\sigma E_\theta, \tag{1}$$

where σ is the plasma conductivity, ω is the driven frequency, and μ_0 is the permeability of vacuum.

The diffusion and chemical reactions are taken into account for neutral species. We employed Fick's law instead of solving full momentum equations. This reduces computational time tremendously as compared to solving Navier-Stokes equations. The flux of the kth neutral species is given by

$$\boldsymbol{\Gamma}_k = -D\nabla n_k, \tag{2}$$

where D is the diffusion coefficient, and n_k is the kth neutral density. Then, the continuity equation of the kth neutral species is expressed as

$$\frac{\partial n_k}{\partial t} = -\nabla\cdot\boldsymbol{\Gamma}_k + \sum_j R_{kj}, \tag{3}$$

where R_{kj} is the production/destruction rate of the kth neutral species due to the reaction event j. Neutral species also flow into and out of the discharge as a result of pumping. For the feedstock gas, only the particles entering the chamber have to be considered. The gas temperature is assumed to be uniform at room temperatures (T_n = 300 K = 0.026 eV).

The fluid approach is adopted to model the behavior of charged species as well. A Maxwellian electron energy distribution function (EEDF) is assumed. Kimura *et al*. measured the EEDF in an inductively coupled CF_4 plasma source with Langmuir probes, and they showed that the EEDF is Maxwellian even at pressure of 2 mTorr [3]. Then, the electron energy balance is expressed as

$$\frac{\partial}{\partial t}\left(\frac{3}{2}n_\mathrm{e}k_\mathrm{B}T_\mathrm{e}\right) = W - \nabla\cdot\boldsymbol{q}_\mathrm{e} - \upsilon_\mathrm{m}\frac{3m_\mathrm{e}}{M}n_\mathrm{e}k_\mathrm{B}\left(T_\mathrm{e}-T_\mathrm{n}\right) - \sum_j R_{\mathrm{e}j}\Delta H_{\mathrm{e}j}, \tag{4}$$

where T_e is the electron temperature, ν_m is the electron momentum transfer collision frequency, M_n is the mass of neutral species, $R_{\mathrm{e}j}$ is the rate of the inelastic electron impact collision j, $\Delta H_{\mathrm{e}j}$ is the inelastic electron-impact collision energy loss/gain in the jth collision, and k_B is the Boltzmann constant. The electron energy flux $\boldsymbol{q}_\mathrm{e}$ is composed of heat conduction and convection as

$$\boldsymbol{q}_\mathrm{e} = -\kappa_\mathrm{e}\nabla T_\mathrm{e} + \frac{5}{2}k_\mathrm{B}T_\mathrm{e}\boldsymbol{\Gamma}_\mathrm{e}, \tag{5}$$

where $\boldsymbol{\Gamma}_\mathrm{e}$ is the electron flux, and κ_e is the electron thermal conductivity given by

$$\kappa_\mathrm{e} = \frac{3}{2}k_\mathrm{B}D_\mathrm{e}n_\mathrm{e}. \tag{6}$$

The drift diffusion approximation is employed to model the electron and ion fluxed in the chamber. To avoid solving the plasma sheath structure, we assume the continuity equation covers all of the chamber area except for the sheath region. Based on the assumption of the quasi-neutrality

$$\sum\nolimits_+ n_+ = \sum\nolimits_- n_-, \tag{7}$$

and congruence of flux

$$\sum\nolimits_+ \boldsymbol{\Gamma}_+ = \sum\nolimits_- \boldsymbol{\Gamma}_-, \tag{8}$$

which means that the total positive ion flux out of any region is equal to the total negative ion and electron flux, and that the plasma is treated with the ambipolar diffusion model. Here, subscripts '+' and '-' indicate positive ions and negative ions/electrons, respectively. The continuity equation for the ith charged species is then

described as

$$\frac{\partial n_i}{\partial t} = -\nabla \cdot \left(\mu_i n_i \boldsymbol{E} - D_i \nabla n_i\right) + \sum_j R_j, \tag{9}$$

where the sum of R_j is over the collisions that produce or destroy the ith ion. With the drift-diffusion approximation, the ith ion flux is given by

$$\boldsymbol{\Gamma}_i = \mu_i n_i \boldsymbol{E} - D_i \nabla n_i. \tag{10}$$

Here, the diffusion coefficient D_i and the mobility μ_i of the ith ion are given by

$$D_i = \frac{k_B T_i}{M_i \nu_{\text{in}}}, \quad \mu_i = \frac{q}{M_i \nu_{\text{in}}}, \tag{11}$$

where q, M_i, T_i are the charge, mass and temperature of the ith ion, and ν_{in} is the ion-neutral collision frequency. $\boldsymbol{E}$ is the plasma electrostatic field derived from the flux balance of charged species. Substituting eq. (10) into eq. (8), we have

$$\boldsymbol{E} = \frac{\sum_+ D_+ \nabla n_+ - \sum_- D_- \nabla n_-}{\sum_+ \mu_+ n_+ + \sum_- \mu_- n_-}. \tag{12}$$

Chemical species in C_4F_8 plasma are assumed to be more than in CF_4 plasma. In CF_4 plasma, we assume CF_4, CF_3, CF_2, CF, F, CF_3^+, CF_2^+, CF^+, F^- and electron. In C_4F_8 plasma, we assume C_4F_8, C_2F_3, C_2F_4, C_3F_5, C_3F_7, $C_2F_3^+$, $C_2F_4^+$, $C_3F_5^+$ and $C_3F_7^+$ in addition to species already assumed in CF_4 plasmas. The reactions assumed in the gas phase are 21 in CF_4 plasma and 51 in C_4F_8 plasma [4-9]. They contain ionizations, dissociations and recombinations of the species.

3. Results and Discussion

The nonlinear partial differential equations were discretized in space with finite-volume approximations. Then, we integrated the set of ordinary equations with the fully implicit scheme, assuming an initial two-dimensional profile for all of the species densities and electron temperature. When the time variations in these quantities disappear, the calculated values correspond to the solutions for the steady state. The ICP power at 13.56 MHz is applied, and CF_4 or C_4F_8 pure gas is supplied into the chamber. The nominal operating conditions are: a gas pressure of 20 mTorr, an ICP power of 250 W, and a mass flow rate of 200 sccm.

The volume-averaged densities of ions and electrons are compared in Fig. 2. The density of CF_3^+ is the largest among the positive ions in CF_4 and C_4F_8 plasmas. That is as large as the electron density. The density of CF_2^+ in CF_4 plasma is much larger than that in C_4F_8 plasma. The spatial distribution of CF_2^+ is shown in Fig. 4. In the following figures, the CF_4 plasma is indicated by (a) and the C_4F_8 plasma is indicated by (b). The density peak in Fig. 4 (a) is around z-axis; on the other hand, the density peak in Fig. 4 (b) is under the forth coil from the most inner coil. The peaks positions are different from each other in Figs. 4 (a) and (b). In addition, the densities of $C_2F_4^+$ and $C_3F_5^+$ in Fig. 2 are major among the positive ions in C_4F_8 plasma. It is supposed that the reactions (13) and (14) play an important role.

$$C_4F_8 + CF_2^+ \rightarrow C_3F_5^+ + C_2F_4 + F, \tag{13}$$

$$C_2F_4 + CF_2^+ \rightarrow C_2F_4^+ + CF_2. \tag{14}$$

The volume-averaged compositions of neutral radicals are compared in Fig. 3. The densities of F are the largest in CF_4 and C_4F_8 plasmas. It is supposed that the F is derived from many kinds of the dissociations. The densities of CF_2 are not large different between CF_4 and C_4F_8 plasmas, nor those of CF_3. However, the density of C_2F_5 in CF_4 plasma is much larger than in C_4F_8 plasma though the C_2F_5 is generated from CF_2 and CF_3. To help to comprehend the large difference in the density of C_2F_5, the spatial distributions of CF_2 and CF_3 give a good direction. The spatial distribution of CF_2 is shown in Fig. 5 and that of CF_3 is shown in Fig. 6. In Fig. 5 and Fig. 6, the distributions of CF_2 and CF_3 in C_4F_8 plasma are mostly flat over the whole computed area; on the other hand, those in CF_4 plasma are steeper than those in C_4F_8 plasma, and so the density peaks in CF_4 plasma are clear. The peaks positions in CF_4 plasma are under the coils and correspond to each other. Thus, the C_2F_5 in CF_4 plasma may be generated much more efficiently than in C_4F_8 plasma.

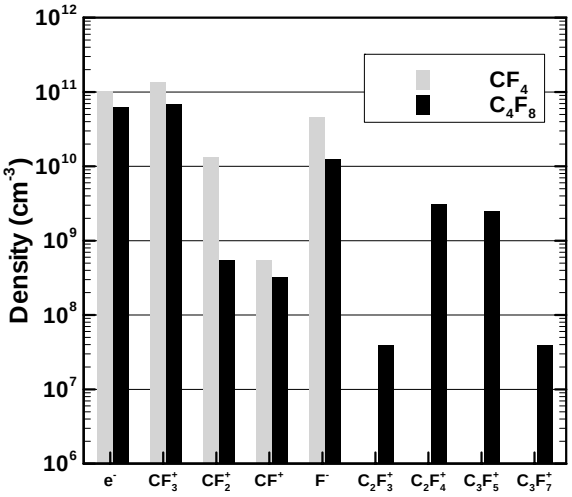

Fig. 2. Volume-averaged concentration of ions in CF_4 plasma and C_4F_8 plasma.

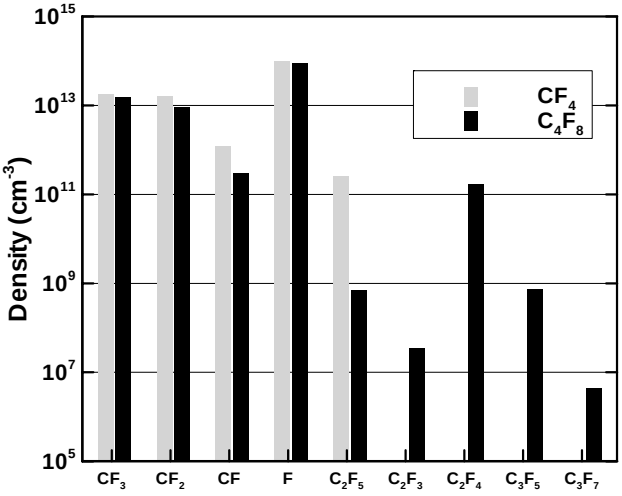

Fig. 3. Volume-averaged concentration of neutral radicals in CF_4 plasma and C_4F_8 plasma.

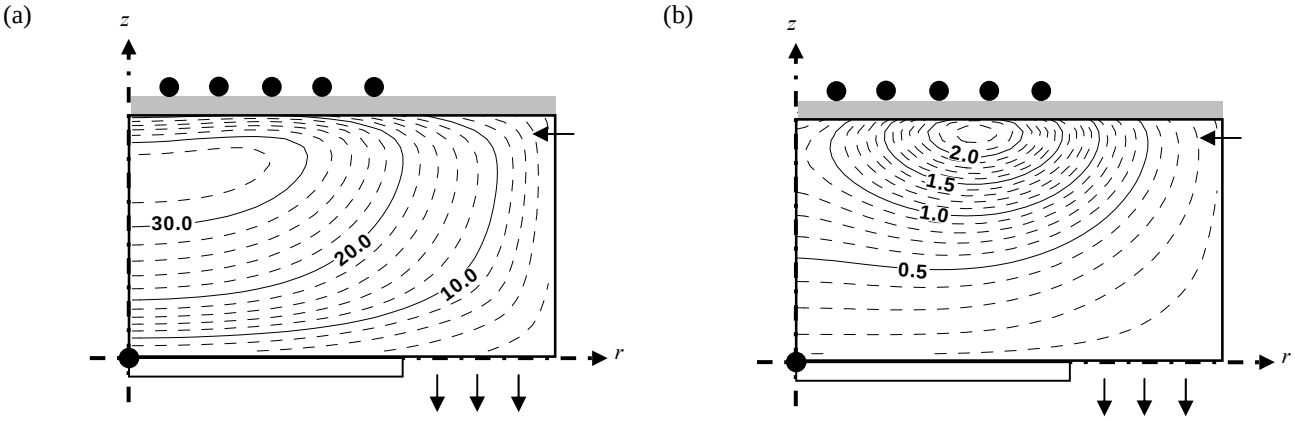

Fig. 4. Spatial distribution of the CF_2^+ density ($\times 10^9$ cm^{-3}) (a) in CF_4 plasma and (b) in C_4F_8 plasma.

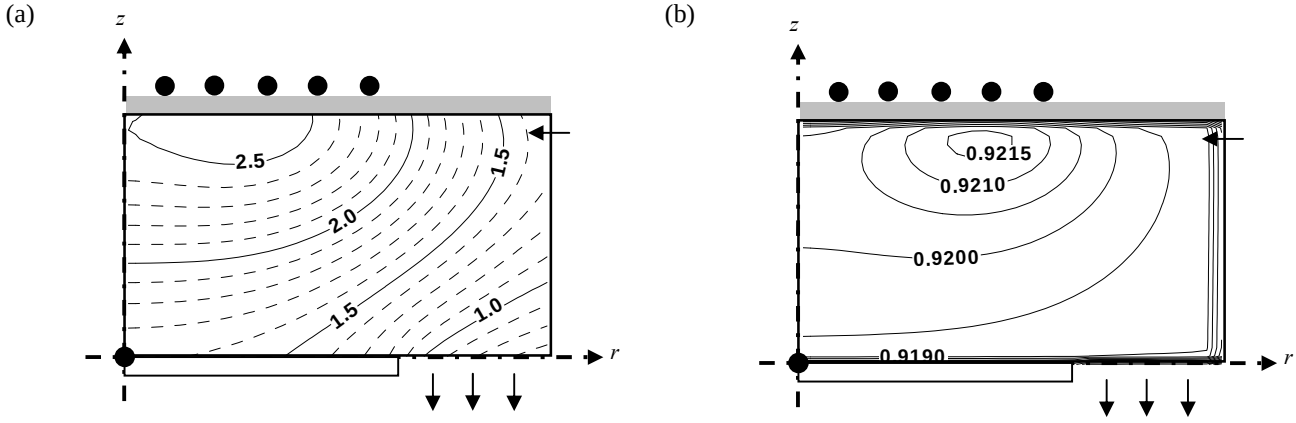

Fig. 5. Spatial distribution of the CF_2 density ($\times 10^{13}$ cm^{-3}) (a) in CF_4 plasma and (b) in C_4F_8 plasma.

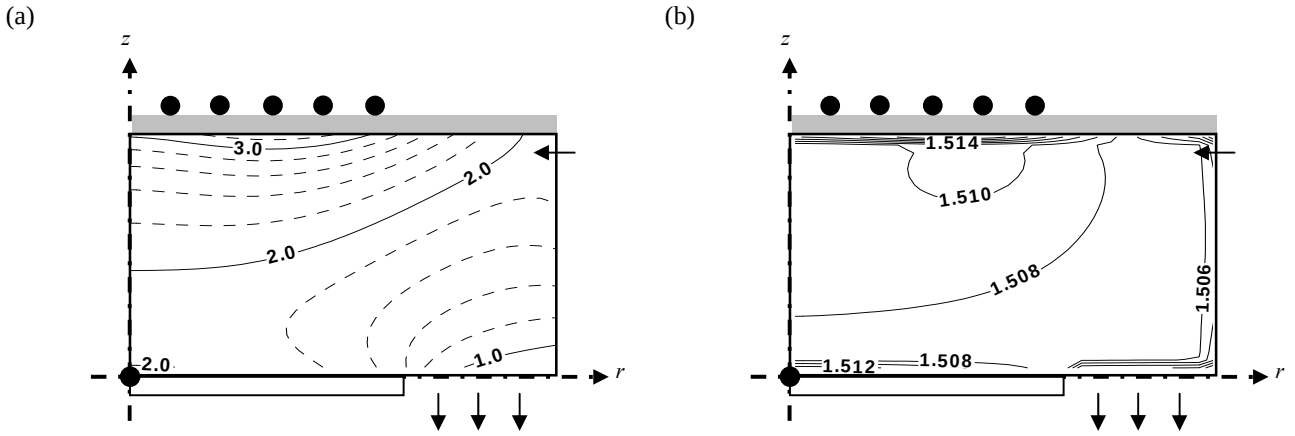

Fig. 6. Spatial distribution of the CF_3 density ($\times 10^{13}$ cm^{-3}) (a) in CF_4 plasma and (b) in C_4F_8 plasma.

The spatial distribution of electron density is shown in Fig. 7 and that of electron temperature is shown in Fig. 8. In Figs. 7 (a) and (b), the electron density peaks are observed in under the coils. The temperature peaks are just under the forth coil from the most inner coil in Figs. 8 (a) and (b). The temperature in Fig. 8 (b) is lower than in Fig. 8 (a) over the whole computed area. The electron energy may be absorbed more in C_4F_8 plasma than in CF_4 plasma because there are more reactions of ionization and dissociation in C_4F_8 plasma. The distributions shapes are quite similar over the whole computed area between (a) and (b) in Fig. 7 and Fig. 8.

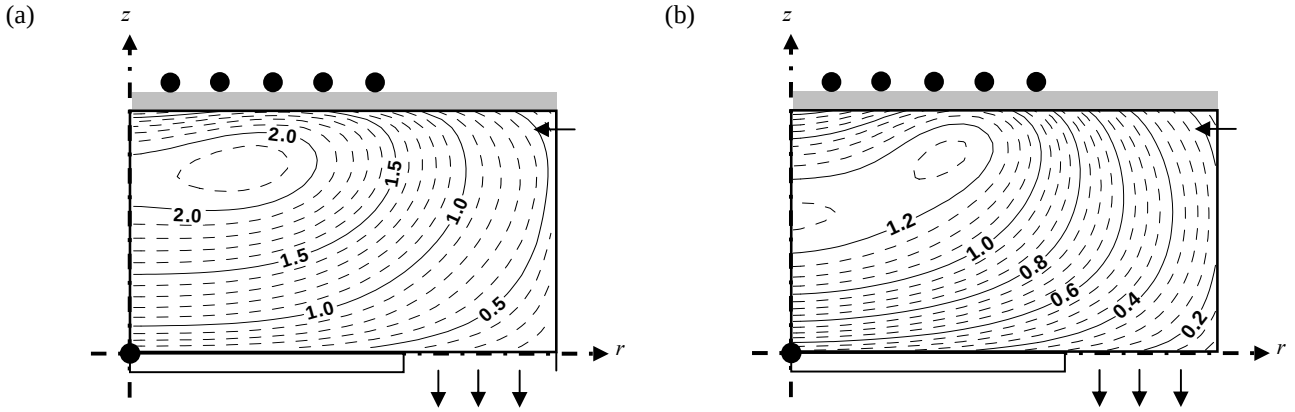

Fig. 7. Spatial distribution of the electron density ($\times 10^{11}$ cm^{-3}) (a) in CF_4 plasma and (b) in C_4F_8 plasma.

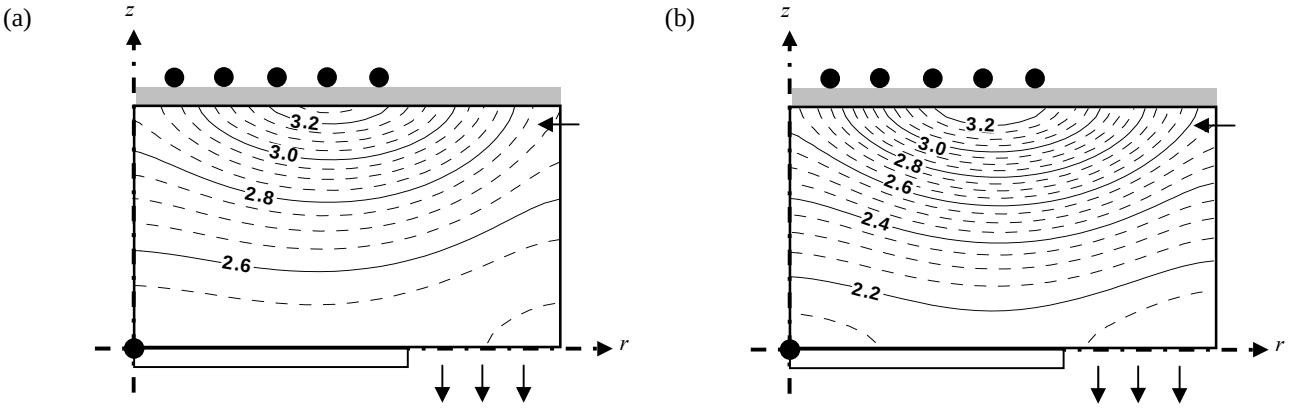

Fig. 8. Spatial distribution of the electron temperature (eV) (a) in CF_4 plasma and (b) in C_4F_8 plasma.

For further discussion, we investigated the inductively coupled CF_4 and C_4F_8 plasmas with a quadrupole mass spectrometer. Figure 9 shows the mass spectra without electron beams for ionization. The both of plasmas was at a gas pressure of 20 mTorr, an input power of 280 W, and a gas flow rate of 2.5 sccm. The ion energy, which corresponded to the plasma potential concerned, was measure to be 16 V in Fig. 9 (a) and 14 V in Fig. 9 (b). Many chemical species are observed which could not be assumed in the simulation. Some common properties are found in the simulation and the measurement. In Fig. 2 and Fig. 9 (a), regarding the CF_x^+ ions (x=1-3) in CF_4 plasma, the concentration is lager for species with lager x. In Fig. 2 and Fig. 9 (b), the $C_2F_4^+$ and $C_3F_5^+$ in C_4F_8 plasma are major species in positive fluorocarbon ions.

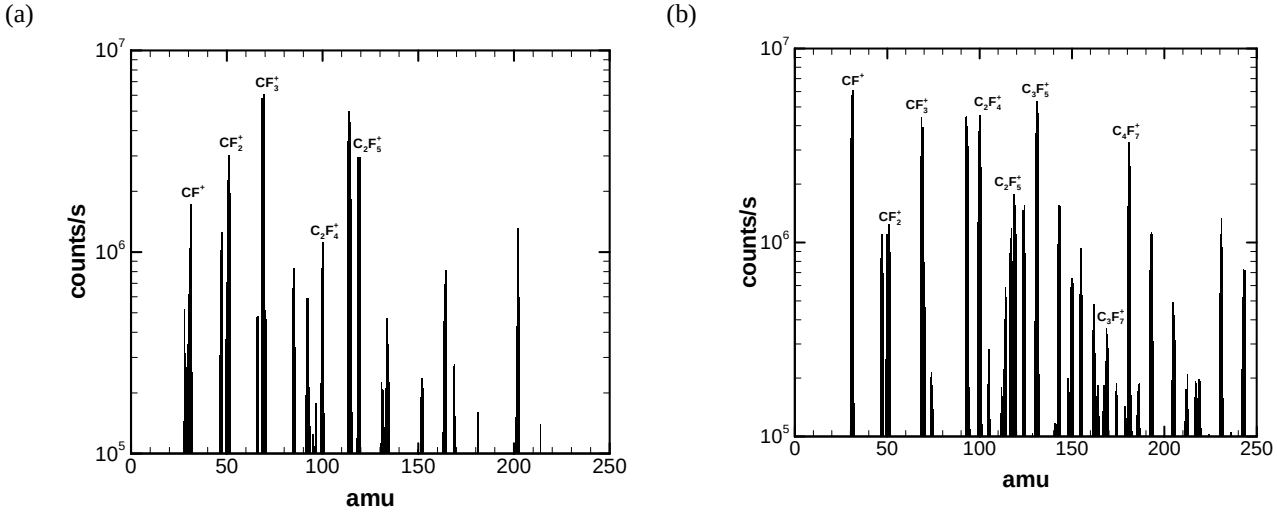

Fig. 9. Mass spectrum for inductively coupled (a) CF_4 plasma and (b) C_4F_8 plasma, without electron beams for ionization.

4. Conclusions

A two-dimensional fluid simulation of inductively coupled CF_4 and C_4F_8 plasmas source has been performed. The fluid model consisted of Maxwell's equations, rate equations for neutrals and ions, and energy balance equation for electrons. The surface reaction model employed a concept of surface coverage. By coupling these models, steady state solutions were obtained in a self-consistent fashion. The numerical results clarified the internal structure of inductively fluorocarbon plasmas. There was little difference in the spatial distributions of electron densities and temperatures between CF_4 and C_4F_8 plasmas; on the other hand, there was large difference in the spatial distributions of some chemical species between in the two. Some results from the simulation and the measurement corresponded to each other.

References

[1] C. Lee, D. B. Graves and M. A. Lieberman: Plasma Chemistry and Plasma Processing **16** 99 (1996).
[2] T. Tokuyama *et al.*: Cho-bisaikako gijutsu [in Japanese].
[3] T. Kimura and K. Ohe: Plasma Source Sci. Technol. **8** 553 (1999)
[4] H. H. Hwang, K. James, R. Hui and M. J. Kushner: J. Appl. Phys. **69** 7419 (1991).
[5] N. V. Mantzaris: J. Appl. Phys. **77** 6169 (1995).
[6] S. Rauf and M. J. Kushner: J. Appl. Phys. **82** 2805 (1997).
[7] H. Hayashi, S. Morishita, T. Tatsumi, Y. Hikosaka: J. Vac. Sci. Technol. A **17** 2557 (1999).
[8] G. I. Font, W. L. Morgan and G. Mennenga: J. Appl. Phys. **91** 3530 (2002).
[9] A. V. Vasenkov, X. Li, G. S. Oehrlein and M. J. Kushner: J. Vac. Sci. Technol. A **22** 511 (2004).

Modification of graphite powders in a thermal RF induction plasma

R. Mach[1], H.-E. Maneck[1], B. Röhl-Kuhn[1], B. Peplinski[1], S. Benemann[1], B. Strauss[1], W. Schütz[2], G. Kühn[1], J. Friedrich[1]

[1]*Federal Institute for Materials Research and Testing, Unter den Eichen 87, D-12205 Berlin, Germany*
[2]*FutureCarbon GmbH, Gottlieb-Keim-Strasse 60, D-95448 Bayreuth, Germany*

Abstract

A thermal RF induction plasma of standard design have been used to modify graphite particles. The materials were treated in an argon/oxygen-plasma to modify the morphology and the surface of the particles. During plasma treatment the former platelet graphite particles were converted into spheroidized, rounded or potato-shaped particles. Additionally the particle surfaces were modified by introducing oxygen functionalities and the specific surface area of the graphite was reduced.

1. Introduction

Graphitic or graphitized carbonaceous materials are widely used as anode materials for Lithium-ion rechargeable batteries. To increase the performance, cycle life, stability and safety of this type of energy storage device, the development of high performance carbon materials is urgently required. In this connection, the surface characteristics, the pore structure and the morphology of the carbon material have a quite special relevance.
A thermal RF induction plasma of standard design, normally used for the synthesis of nanopowders, for spheroidization of meltable substances or for the deposition of coatings, have been used to modify graphite particles.

The graphite particles were treated in an argon-oxygen-plasma to modify the morphology and the surface of the particles with respect to the using as anode materials in Lithium-ion rechargeable batteries.

The plasma treated graphite particles were analyzed by scanning electron microscopy (SEM), X-ray photoelectron spectroscopy (XPS), and specific surface area (BET).

2. Experimental

In this study, two different artificial graphite powders, which consist mainly of nonspheric, irregular, and flat particles, have been treated under various reactive thermal plasma conditions. The graphite powders were modified in a thermal RF induction plasma at atmospheric pressure. The RF induction plasma has proven to be a very attractive tool both for the thermal treatment of powders and for materials synthesis. The use of inert atmospheres and the absence of electrodes produces the very clean plasmas, which are essential for some processing applications. Additionally, RF induction plasma can be made much larger and more uniform than other thermal plasma systems. Moreover, thermal plasma techniques offers the advantage of a continuous one-step process with the potential for a versatile, cost-effective technology for the industrial-scale production of many advanced materials for demanding applications in high tech industries.

The laboratory-manufactured moderate-scale RF induction plasma synthesis facility mainly consisted of four components: the plasma torch with radio frequency generator, the graphite powder and gas supply systems, the water-cooled reactor together with the heat exchanger, and the filter system for powder collection. The principle of the reactor has been described previously in detail [1]. The plasma torch consists of an air-cooled quartz confinement tube of 50 mm diameter surrounded by a three-turned induction coil of 30 mm length and 60 mm diameter. The plasma torch was powered by a radio frequency power supply (Steremat, Berlin, model GI5/5D-047, maximum plate power 5 kW, nominal frequency 2.5 – 5 MHz) operating at a frequency of 4 MHz and a plate power of 3 kW. The discharge parameters were kept constant in the experiments. The upstream part of the

set-up was the distribution head made of stainless steel. This distribution head combines the probe for powder injection and the inlet of the plasma gases into the discharge chamber, the sheath gas to protect the walls and the central plasma-forming gas. The sifted graphite powders (smaller than 50 µm and 50-80 µm diameter), carried by an argon gas, is injected into the hot plasma core through a graphite probe. The graphite probe was installed in the axis of the distribution head, and it was adjusted so that the tip position was located at the first turn of the induction coil.

The torch is discharged into the downstream part that consists of a water-cooled steel reactor. The reaction zone is followed by a quench zone, in which the gases and the particles are rapidly cooled. The high temperature reacting system was quenched by adding cold argon gases at the reaction zone exit. In addition a water-cooled quenching chamber was located after the reactor allowing cooling by gas expansion.

The plasma treated graphite powders were collected by solid-gas separation on a cloth filter.

The plasma was operated with argon and various argon-oxygen-mixtures as central and sheath gas, respectively. The powder feed rate was 35 - 100 g/h.

3. Results

For the plasmachemical modification of graphite two different graphite powders of the sieve fractions 50 – 80 µm (graphite powders A) and < 50 µm (graphite powders B) have been used. Both starting materials consist mainly of relatively flat irregular polyhedral surfaces and are characterized by a relatively high content of very small particles. This two types of particles were plasma treated using an Ar/O_2 plasma of different oxygen content. Fig. 1 shows the SEM images of the starting and the plasma treated graphite powders A of the 50-80 µm sieve fraction. It is clearly shown in the SEM images, that during the plasma treatment the structure of the particles was modified by oxidation forming rounded particles. The shape of the former irregular platelet particles were converted into spheroid and potato-like particles. At the same times the content of the small particles was drastic diminished. This effect is attributed to the evaporation of carbon as well as to the formation of carbon oxides during passing the plasma zone.

Fig. 2 shows the SEM images of the graphite powders B (sieve fraction < 50 µm) before and after plasma treatment. The plasma treated material at low oxygen

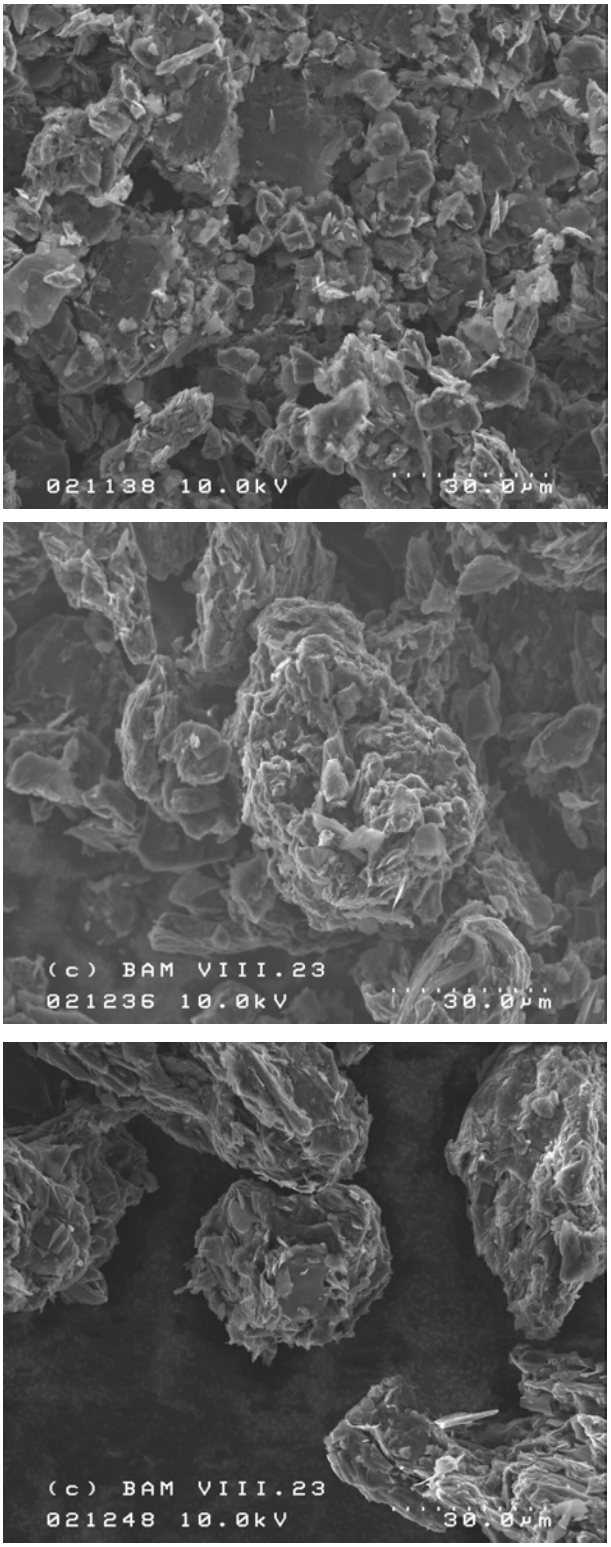

Fig. 1: Evolution of morphology of the graphite powders A (50-80 µm) by plasma treatment. SEM images of the starting powder (top) and the plasma treated graphite powders at lower (middle) and higher (bottom) oxygen concentration in the plasma gas.

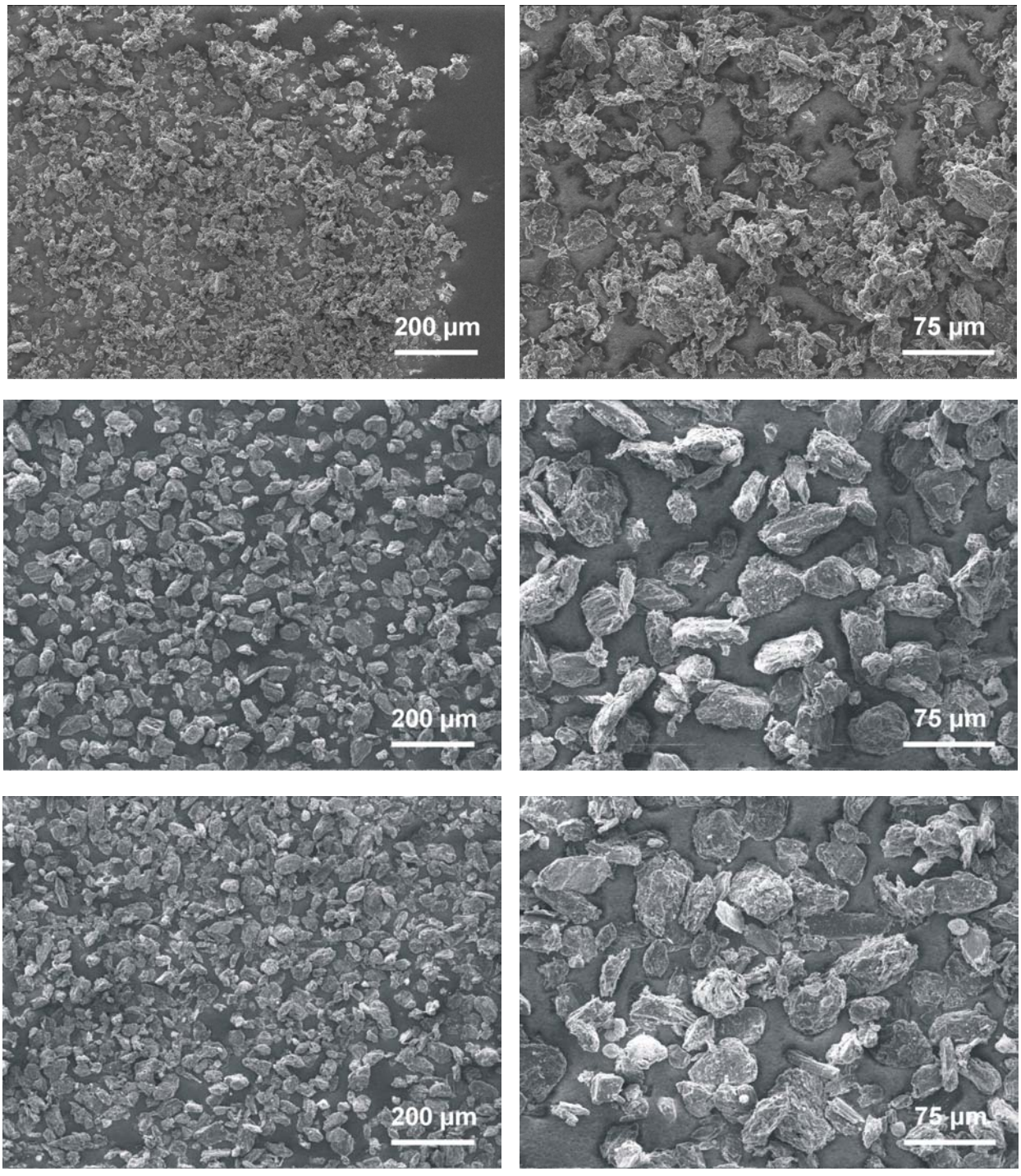

Fig. 2: Evolution of morphology of the graphite powders B (<50 µm) by plasma treatment. SEM images of the starting powder (top) and the plasma treated graphite powders at lower (middle) and higher (bottom) oxygen concentration in the plasma gas.

and high oxygen partial pressure shows clearly the spheroidized, rounded and potato-like graphite particles. The effect of the spheroidization is observed independently of the particle size used in the experiments (Figs. 1 and 2). Both the formation of the spheroidized particles and the diminishing content of the small particles are favored by increasing content of oxygen in the plasma gas.

XPS investigations shows that the surface of the graphite particles were modified by introducing oxygen functionalities in the range of up to 4.5 at % depending of the oxygen content of the plasma gas (Fig. 3 and 4). The O1s XPS spectra of the starting powder A and the plasma-treated powders at low and higher oxygen content in the plasma gas shows 1.8, 2.9, and 4.5 at % oxygen, respectively. This oxygen on the surface belongs to different functional oxygen groups. Peak fitting shows that the surface groups consists mainly of -C-OH, >C=O and -COOH groups.

The starting graphite powders A shows a BET surface area of 3.7 m^2/g. After the plasma treatment with lower and higher oxygen content in the plasma gas the BET surface area was reduced to 2.8 and 2.4 m^2/g, respectively (Fig. 5). This demonstrates clearly that the specific surface area of graphite particles can be drastic reduced by treatment in an Ar/O_2 plasma.

The spheroidization of the particles together with the formation of oxygen functionalities at the particle surface and the reduction of the BET surface area are good assumptions to improof the electrochemical properties of graphite powders for use as anode material in Lithium-ion rechargeable batteries. Therefore the plasma modified graphite powders were used to prepare anodes for Li-ion rechargeable batteries and the electrochemical properties were tested. The discharge capacity of cells with anodes made of the plasma-treated graphite powders was clearly improved in comparison to the cells with anodes made of the original graphite powders [2].

Summary

The thermal RF induction plasma has been used to modify the morphology and the surface of graphite particles. It has been found, that during argon-oxygen plasma treatment the former platelet graphite particles were converted into spheroidized, rounded or potato-like particles. At the same times the content of the small particles was drastic reduced.

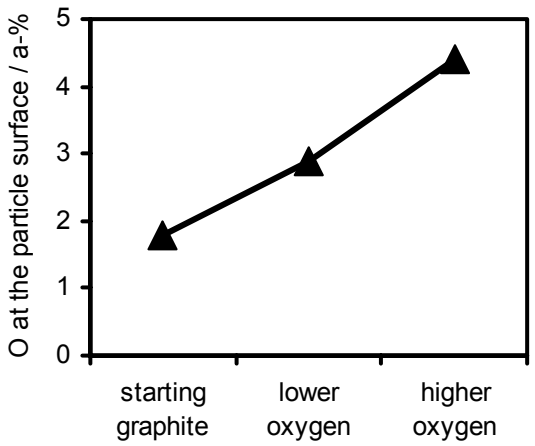

Fig. 3: Oxygen content by XPS of the starting graphite powders A (50-80 µm) and the plasma-treated powders at different oxygen concentration in the plasma gas.

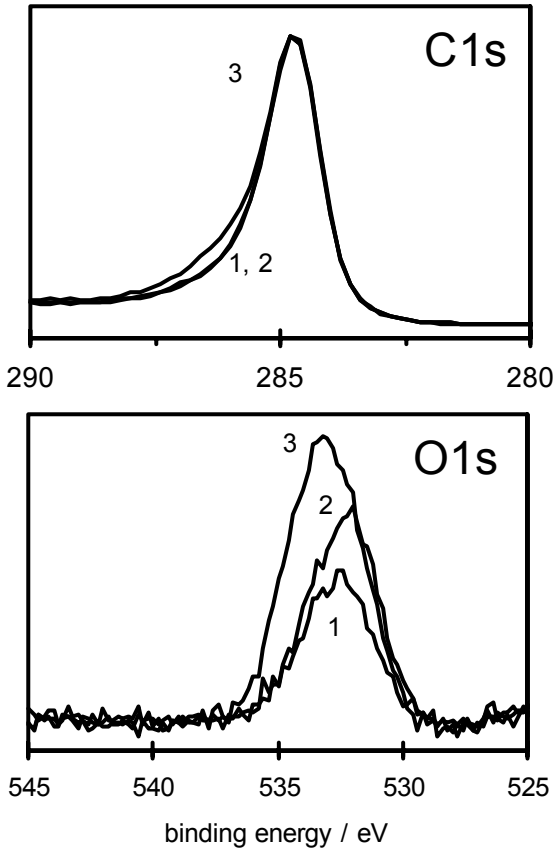

Fig. 4: XPS spectra of graphite powders A (50-80 µm)
(starting powder (1) and the plasma treated powders at lower (2) and higher (3) oxygen content in the plasma gas).

The graphite particles found to be modified in the surface by introducing oxygen functionalities mainly consisting of -C-OH, >C=O and -COOH groups. Additionally, during plasma treatment the specific surface area of the graphite was reduced.

The plasma treated graphite powders were used to prepare anodes for Li-ion-batteries which shows excellent charge/discharge efficiency during cycling.

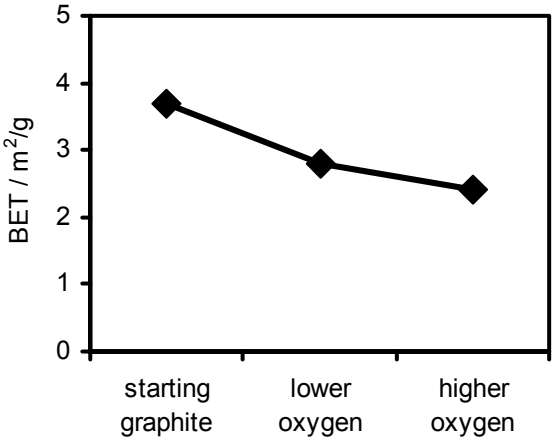

Fig. 5: BET surface area of the starting graphite powders A (50-80 µm) and the plasma-treated powders at different oxygen concentration in the plasma gas.

Acknowledgement

This work has been carried out with the financial support of the German Ministry for Research and Education in the project INES under contract number FKZ: 0327304H

References

[1] R. Mach, H.-D. Klotz, K.-D. Suhrke, H. Drost, F. Oleszak, C. Olschewski and I. Kosche, VDI-Berichte 1166, VDI-Verlag Düsseldorf, (1995) 301

[2] H.-E. Maneck, R. Mach, B. Röhl-Kuhn, B. Strauss, B. Peplinski, G. Kühn, J. Friedrich, U. Storr, M. Wohlfahrt-Mehrens and L. Jörissen, Extended Abstracts of the Battery and Fuel Cell Materials Symposium, Graz (Austria) 18.-22.4.2004, 155

Synthesis of Nanostructured Carbonaceous Materials by Thermal Decomposition of Methane Using DC Thermal Plasmas

Keun Su Kim[1], Kwang-Sik Lee[2], Won Tae Ju[2], and Sang Hee Hong[1]

[1] *Department of Nuclear Engineering, Seoul National University, Seoul 151-742, Korea*
[2] *Plasnix Co., Ltd., Seoul 151-742, Korea*

keywords: Carbon nanosheet, DC plasma torch of hollow electrodes type, thermal plasma processing, methane decomposition

Abstract

Crumpled carbon nanosheets (CNSs) of a quasi-two-dimensional graphite structure are synthesized by thermal decomposition of methane using a DC plasma torch of hollow electrodes type operated in a reversed polarity mode. FE-SEM images show that the synthesized products solely consist of a large number of individual CNSs, which are stacked with random orientation and interlaced each other. The material analyses of BET and XRD indicate that the CNSs synthesized by this new method have excellent physico-chemical properties such as large surface area and highly graphitized structure with good crystallization.

1. Introduction

A sheet-like carbon structure named as carbon nanosheet or nanowall, has been reported as a common by-product during fullerenes and carbon nanotubes (CNTs) preparations by using arc discharge or laser ablation method [1]. This material has a high aspect ratio with good chemical stability due to its sheet-like graphitic structure, and such unique properties are very attractive for storage of hydrogen gases and fuel cell applications [2]. Moreover, the CNSs with sharp and ultra thin edges of less than 20 nm can be utilized as effective electron emission sites in the fabrications of high-performance vacuum electronic devices [2-3]. Compared to other self-assembled carbon nanostructures such as CNT and fullerene, only limited knowledge has been so far established on the property and production of CNSs, and more intensive studies on CNSs are now needed to explore their further potential applications.

Recently, physical properties of CNSs have been investigated by examining field emission characteristics of them [3], and the samples used in these lab-scale experiments have been grown mostly by plasma enhanced chemical vapor deposition (PECVD) techniques, in which well-aligned and ultra thin CNSs were successfully synthesized from decomposition of methane. For an expansion of their commercial usage, mass and continuous productions of high purity CNSs are essential. However, conventional arc discharge methods are inevitably accompanied by other carbon allotropes like CNT and fullerene [1], and CVD methods are usually subject to low product yields [2]. Above all, both the existing processes are basically operated in a batch mode and are not easy to be scaled up.

For the above reasons, a new method for the preparation of high quality CNSs in a continuous mode is proposed in this experimental work utilizing a DC thermal plasma torch. Thermal plasmas have been broadly used in material industries for synthesis of new materials by taking advantages of their high enthalpy contents and temperatures around 2,000 ~ 20,000 K [4]. Therefore, a high growth rate of CNSs is achievable with thermal plasmas due to a bountiful supply of carbon atoms generated from a thorough decomposition of feedstock, i.e., methane (CH_4). The physico-chemical properties of the synthesized CNSs are also investigated by some microscope images, X-ray diffraction and static gas adsorption techniques. Finally, in order to find effects of torch input conditions on the formation of CNSs, a series of processing experiments are conducted with three different levels of input power.

2. Experimental setup

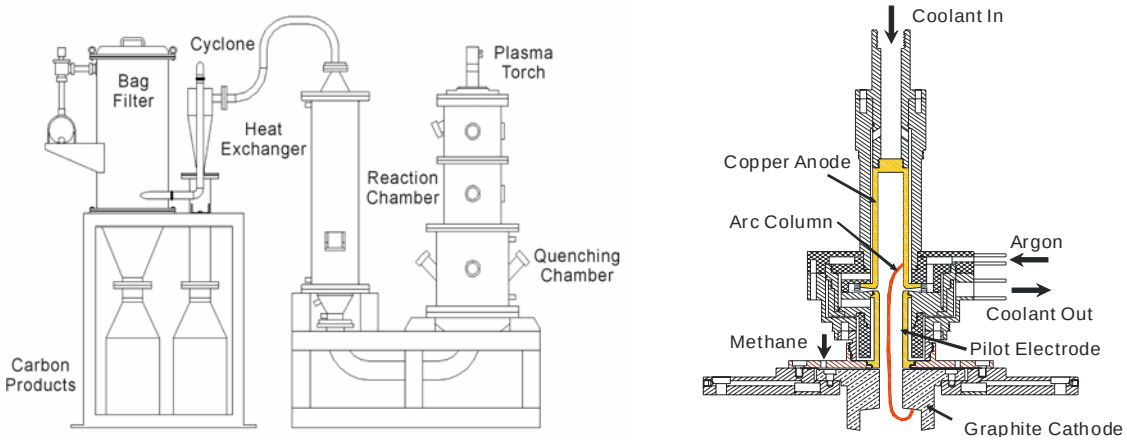

(a) (b)

Fig. 1. Schematic layout of a DC thermal plasma processing system (a) and cross-sectional view of a DC plasma torch of hollow electrodes type (b) used for synthesis of carbon nanosheets (CNSs).

For a continuous synthesis of high quality CNSs, a prototype reactor system mounted with a DC plasma torch are built as shown in Fig. 1. The reactor system consists of four major parts: a reaction chamber, a quenching chamber, a heat exchanger and a particle collection system (i.e., bag filter and cyclone). The stainless steel reaction chamber (0.32 m in outer diameter, 0.65 m in length) contains a graphite liner (0.1 m in inner diameter) surrounded by thermal insulator in order to extend high temperature reaction regions by minimizing thermal losses to the reactor wall.

Among a variety of DC thermal plasma torches, a plasma torch of hollow electrodes type has been chosen as a heat source because it is appropriate for high power operations up to several hundreds kW and can use any kind of gas as a plasma forming gas [4]. Instead of adopting a conventional electrode polarity of inner-cathode and outer-anode configuration, a reverse polarity operation mode with a graphite cathode extruded is employed to reduce erosion rates of both the electrodes and to avoid formation of unwanted impurities from electrode wear. Moreover, a feedstock gas of CH_4 is directly injected into the graphite cathode region for its complete decomposition. The overall processing system for thermal plasma aided material synthesis has the following additional advantages:

1) in a reverse polarity, plasma flows become more turbulent because of the chaotic motion of cathodic arc root at the torch exit, and mixing of reactants with hot plasma gases are significantly enhanced.
2) the hot graphite cathode wall provides a high-temperature environment in the injection region of feedstock in contrast with a water-cooled cold copper cathode.
3) the direct injection of feedstock inside the graphite electrode region usually results in an increment of arc resistance and the corresponding arc power subsequently rises by about 20 ~ 40 %.
4) a strong electric field (~ 10^5 V/cm) near the cathode region is formed and it is considered as an important factor influencing the growth mechanism of self-assembled carbon nanostructures.

The material properties of the produced carbonaceous materials are analyzed by field emission scanning electron microscope (FE-SEM, JEOL, JSM-6330F), transmission electron microscope (TEM, JEOL, JEM-1010), X-ray diffraction (XRD, Bruker, D-5005) and static gas adsorption techniques of Brunauer-Emmett-Teller (BET).

3. Experimental results and discussion

3.1. Methane decomposition experiments

The synthesis experiments for CNSs are performed with a DC power of about 48 kW and argon is used as a plasma forming gas. For the stable generation of plasma jets, the Ar flow rate of 140 slpm is kept constant and the CH_4 gas of 20 slpm is introduced into the plasma in the cathode region without addition of any catalyst. All experiments are conducted under an atmospheric pressure environment with the reactor pre-heated for 8 minutes.

Figure 2 shows the temporal evolutions of reactor temperature and arc voltage measured during the methane decomposition experiments. Just after injection of methane at 8 min, the reactor temperature drops a little, but recovers its original value in several minutes. Since the temperature is measured at the entrance of the quenching chamber (z = 500 mm from the torch exit), the maximum temperature measured here is somewhat low (800 K) compared with that at the torch exit. As expected in the torch design, the arc voltage increases rapidly from 140 V to 220 V after methane injection, and eventually has a saturated value of 180 V. Therefore, the relevant arc power rises by about 40 % without increasing arc current. For a 12-minute operation, a few tens of grams of carbonaceous materials are collected from the cyclone and the bag filter.

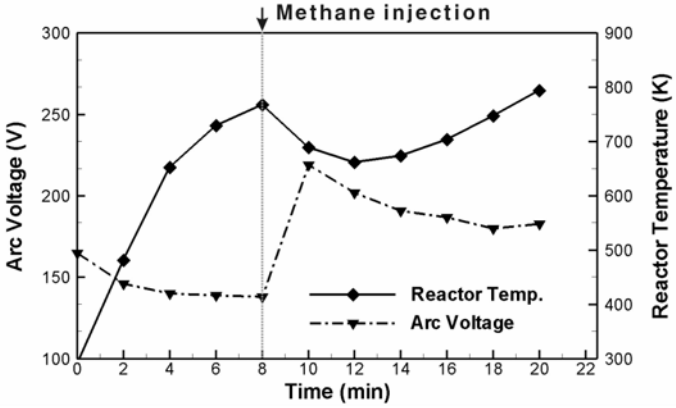

Fig. 2. Changes of reactor temperature and arc voltage measured with time during the methane decomposition experiments when methane injection of 20 slpm starts at 8 min after the torch ignition (arc current = 250 A).

3.2. Material property analyses on the produced carbonaceous materials

The morphological properties of the produced carbonaceous materials are investigated by FE-SEM images. As clearly seen in Fig. 3, the main products solely consist of a large number of individual CNSs, which are randomly oriented and interlaced each other. The width and height of the produced CNSs ranges from 100 nm to 150 nm. The thin edges of the CNSs are also clearly identified from their FE-SEM images and the average thickness of the CNSs is estimated to be less than about 10 nm from Fig. 3(b). Since most of the CNSs prepared from CVD methods are usually grown on the substrates for a long processing time, they resemble vertically standing walls [2]. But in the present thermal plasma process, the CNSs grow primarily in the free space and then they are stacked in the collection chamber. Therefore, the overall features of the final products look like a coral as appeared in Fig 3(a).

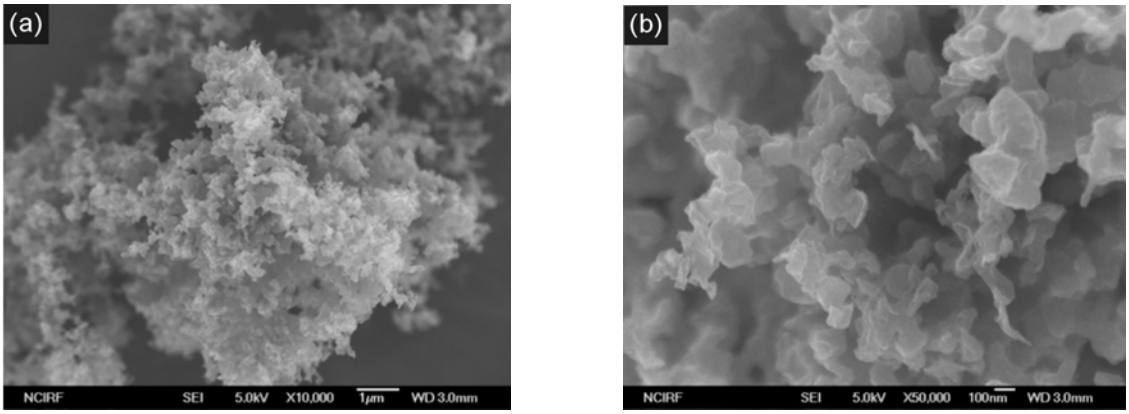

Fig. 3. FE-SEM images of the carbon nanosheets (CNSs) produced by the DC thermal plasma process.

Figure 4 is the TEM images showing micro-structures of the individual CNSs synthesized in this work. The dark fringes observed in the TEM images indicate the graphene layers of the CNSs and represent the cross sections of the planar surfaces of the CNSs. The observed graphene layers are parallel to the adjacent ones and stacked orderly along the c-axis (crystallographic axis) with a uniform interval. Thus it is certain that the CNSs possess well-aligned graphitic structures. The thickness of the stacked graphene layers ranges from 5 nm to 15 nm and its average value is estimated as about 10 nm from a partially enlarged image in Fig. 4(b). The other surfaces perpendicular to the c-axis are transparent in the TEM images, which reveal indirectly that the thickness of the produced CNSs are very thin.

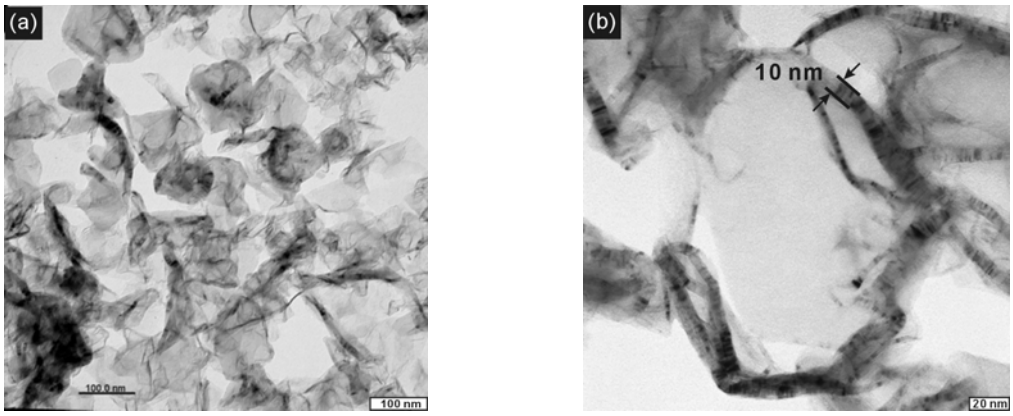

Fig. 4. TEM images of the carbon nanosheets (CNSs) produced by the DC thermal plasma process.

The micro-structural properties of the CNSs are further investigated using an XRD method and Fig. 5 shows the typical X-ray diffraction patterns of the produced CNSs. From the reflection peak of a (002) plane, the interplanar distance (d_{002}) of the (002) plane is calculated as 3.44 Å, which is very close to that of bulk graphite (3.35 Å). As a first-order approximation, the crystallite size (L_c) of the individual CNSs is also calculated as 10.6 nm by the Debye-Scherrer formula. These results are well consistent with the previous SEM and TEM observations, in which the average thickness of the CNSs is found as 10 nm. It is concluded from the XRD analysis that the produced CNSs are strongly graphitized with a high degree of crystallization. Since a good crystallinity usually provides higher electrical conductivity, the synthesized CNSs are expected to have a great potential for conductive applications such as electrical cell. Moreover, the internal structures of the CNSs consist of the well-ordered graphene layers, which are known as one of the toughest two-dimensional structure. Thus the products would be more robust and versatile in practical applications compared with other one-dimensional structures like CNTs and nanofibers.

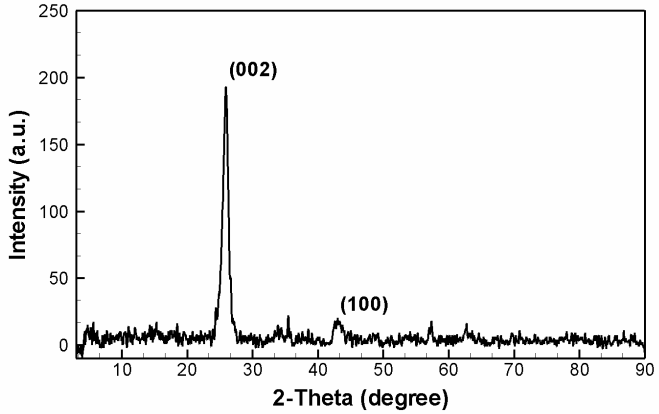

Fig. 5. X-ray diffraction (XRD) patterns of the produced carbon nanosheets (CNSs).

From the morphological structures of the CNSs observed in the previous FE-SEM images, it is expected that the produced CNSs have a larger specific surface area because of their corrugated sheet-like features. A standard BET with nitrogen adsorption test is carried out for determining the specific surface area of produced CNSs, which turns out to range from 41.5 to 48.4 m^2/g much higher than those of natural graphite (1.7 ~ 6.0 m^2/g) and exfoliated graphite sheets (24.1 m^2/g). Therefore, this synthesized material can also serve as a good conductive catalyst in various practical applications for improving performance of other functional materials.

In order to find effects of torch input power conditions on the formation of CNSs, a series of experiments have been conducted with three different levels of input power as listed in the Table 1.

Table. 1. Various torch operation conditions for methane decomposition experiments.

Input Power (kW)	Current (A)	Avg. voltage(V)	Argon (slpm)	Methane (slpm)
16 kW	100	161	120	20
32 kW	180	179	130	20
48 kW	250	193	140	20

Figure 6 compares the morphologies of the various carbonaceous materials synthesized under the different power conditions. As clearly seen in the images, the sizes of the products are reduced as the input power decreases. In the low power condition, the plasma temperature is considerably cooled down by injection of cold methane gas. Under such a low temperature condition, the growth or graphitization process of the carbon materials is not significant and most of the products remain as tiny carbon particles having a turbostratic structure. As the input power increases, however, the sizes of the products become larger due to a long residence time of the reactant in the high temperature region, and the morphologies of the products also change from a spherical shape to a two-dimensional sheet-like one. The differences among the reaction products are apparently appeared in the following TEM image in Fig. 7.

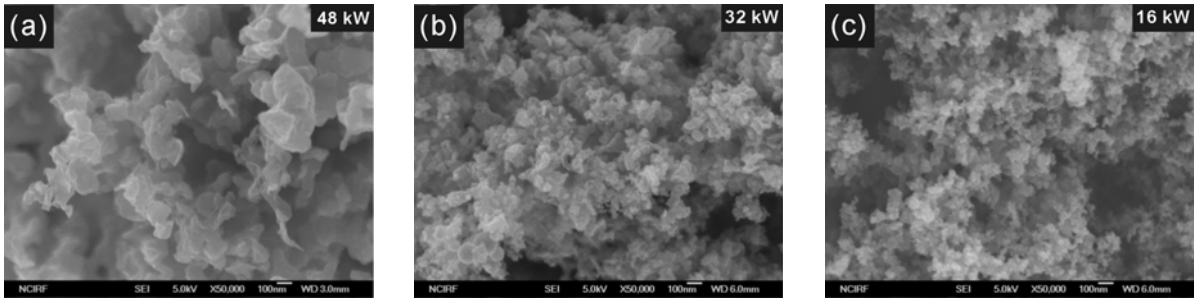

Fig. 6. FE-SEM images of the carbonaceous materials synthesized under three input power conditions.

Two kinds of carbonaceous materials, A and B, are found in the TEM image of Fig. 7, and they seem to be synthesized under different torch conditions of low and high powers, respectively. The fine spheroidally shaped particles (marked as ‘A’, 20 ~ 30 nm in size), which used to be typically observed in the TEM images of the conventional carbon blacks (CBs) [5], are fused together to form a chain of particles. The foregoing images of the CNSs, shown in Fig. 4, are also observed in Fig. 7 marked as ‘B’. It is believed from the above results that carbon atoms are likely to be synthesized into spherical CBs (i.e., isotropic and quasi-amorphous structure) under a low temperature condition. On the other hand, in a high temperature condition, carbon atoms grow into highly crystallized CNSs, which exhibit strong anisotropies in their structural dimension and physical property.

The anisotropic growth mechanism of CNSs under thermal plasma environments is a very interesting and curious aspect to be closely examined. In the present thermal plasma processing system, there is no asymmetric source affecting the direction of carbon atoms growth, while in the conventional CVD method, biased electric fields and catalysts are usually provided in order to guide an anisotropic growth of carbonaceous materials [2]. Wire-shaped CNTs are also observed in the carbon deposits collected from the inner surface of the graphite cathode as shown in Fig. 8.

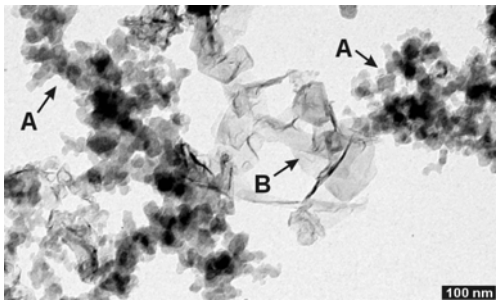

Fig. 7. TEM image of coexisting carbon blacks (A) and carbon nanosheets (B), which seem to be synthesized under different power conditions of the plasma torch.

The CNTs are well-aligned in one direction and considerable carbon flakes (i.e., sheet-like carbon) are observed nearby the roots of the CNTs as well. During the thermal plasma process, the cathodic arc root is attached to the cathode inner surface, which is then exposed to high temperature and high velocity of thermal plasma flows. Thus it can be conjectured that the high temperature and directional plasma flows inside the graphite cathode may contribute to the anisotropic growth of the carbonaceous materials. From such a physical reasoning, an external injection of hydrocarbons near the torch exit into the turbulent and relatively low-temperature plasma jets normally results in a synthesis of CB-like carbonaceous materials [5].

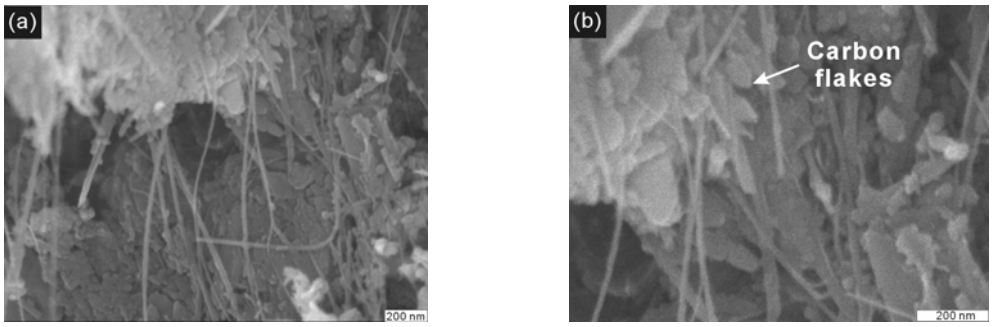

Fig. 8. FE-SEM images of the carbon nanotubes (CNTs) and carbon flakes synthesized inside the cathode.

4. Conclusion

A new DC thermal plasma processing system has been developed to make an attempt to produce high quality CNSs in a continuous manner. In the experiments, randomly distributed CNSs with thin edges are successfully synthesized from methane decomposition using the new processing system. The synthesized CNSs exhibit high degree of crystallization and possess high specific surface areas as well because of their corrugated sheet-like features. Thus the CNSs are expected to have better electric conductivity and adsorption capacity, which are very attractive features for various industrial applications such as energy storages and fuel cells. Though the detailed growth mechanism of CNSs in the thermal plasma environment is not ascertained, high temperature atmosphere and strong directional flows inside the electrodes may play an important role in the formation of CNSs. Finally, the results of various material analyses indicate that the DC thermal plasma process developed in this work will be very effective for the mass production of CNSs with the advanced properties.

References

[1] Y. Ando, X. Zhao, and M. Ohkohchi, *Carbon* **35**, 153-158 (1997)
[2] Y. Wu, P. Qiao, T. Chong, and Z. Shen, *Adv. Mater.* **14**, 64-67 (2002)
[3] N.G. Shang, F.C.K. Au, X.M. Meng, C.S. Lee, I. Bello, and S.T. Lee, *Chem. Phys. Lett.* **358**, 187-191 (2002)
[4] S.L. Camacho, *Pure Appl. Chem.* **60**, 619-632 (1988)
[5] L. Fulcheri, N. Probst, G. Flamant, F. Fabry, E. Grivei, and X. Bourrat, *Carbon* **40**, 169-176 (2002)

Characterization of microhollow cathode discharges

B. N. Sismanoglu and J. Amorim

Departamento de Física, Instituto Tecnológico de Aeronáutica, Centro Técnico Aeroespacial, 12228-900, São José dos Campos, SP, Brazil.

Abstract

This work is devoted to the study of the electrical characteristics of microhollow cathode discharges (MHCD) at moderate to high-pressure in argon for different geometries. Experiments have been performed to determine the so-called Paschen's curves, that is, the dependence of the breakdown voltage on the product between the electrodes gap and gas pressure (p*d*). Using MHCD, stable discharges could be ignited for pressures ranging from 12 to 800 Torr, in a very wide range of current densities and electrodes materials.

Keywords: microhollow cathode discharges, breakdown, moderate pressure non-thermal plasma

1. Introduction

A microhollow cathode discharge device (MHCD) consists of a metallic cathode with a hole in the center and an arbitrarily shaped metallic anode, separated by an insulator (mica in our case). When a discharge is ignited in such a configuration, the negative glow is spatially confined in the cathode cavity. The electric field in this region creates a trough, which is responsible for the strong acceleration of the electrons. It may cause an oscillatory motion of the electrons in the cavity (pendulum electrons), between the two opposite cathode fall regions. These pendulum electrons can undergo many ionizing collisions with the background gas thus creating a high-density plasma which emits intense radiation [1,2]. Secondary electrons emitted from the cathode area come to enhance this phenomenon. The range of discharge operating pressure varies inversely with the hole diameter *D* of an MHCD. For atmospheric-pressure operation the hole diameter must be in order of $100\mu m$ [3].

Such micro discharges are in the category of non-thermal plasma, $T_e >> T_i$, and its low operation cost, allied to small size and low power consumption, is an attractive to the plasma applications possibilities in industry, like surface treatment, generation of UV and VUV radiation, reduction of pollutants, gas lasers, biological decontamination, thin film deposition, mainly in a high pressure operation. Microplasmas can be generated in a high-pressure operation, in accordance with the White-Allis similarity-law, in rare and molecular gases or in air. In argon gas operation, for example, an MHCD with hole size of about $200\mu m$ lead the operation of discharges at pressures of about *1000 Torr* [3].

2. Experimental set-up

The electrodes of our open MHCD are made of 100μm thick molybdenum or cuprum foils separated by a $250\mu m$ spacer of mica with holes from *200* to $700\mu m$ (diameter) through cathode, dielectric, and anode. A closed MHCD in a cathode plane geometry (for anode hole diameters smaller than 700μm) were also used in these experiments. Supply voltages were typically between *250 V to 700 V* and sustaining glow (discharge) voltages were in the range of *200 V - 400 V* for Ar. Discharge currents I_{DIS} varied between *0.1mA* and *8.0 mA*. The experiments were performed for an (*pD*) interval between 0.24 and 56 Torr cm. The operating gas was moderate to high-pressure Ar, between *12* to *800 Torr*. The electrode system is placed in a cylindrical quartz chamber with *10 cm* diameter and *16cm* length. Before each experiment the chamber was cleaned, dried and evacuated to about *1mTorr*. After that, was filled with pure argon gas (*99.995%*) and placed at the desired pressure. A series of $47K\Omega$ resistors were used to limit the discharge current. Experiments with

atmospheric air were also developed. A digital camera was used to record the appearance of the glow discharge.

3. Experimental results

In Fig. 1 is shown the evolution of the current with voltage applied to an open MHCD in Ar, DC operated when current and pressure were varied. In these curves the normal and subnormal mode of glow discharge is observed.

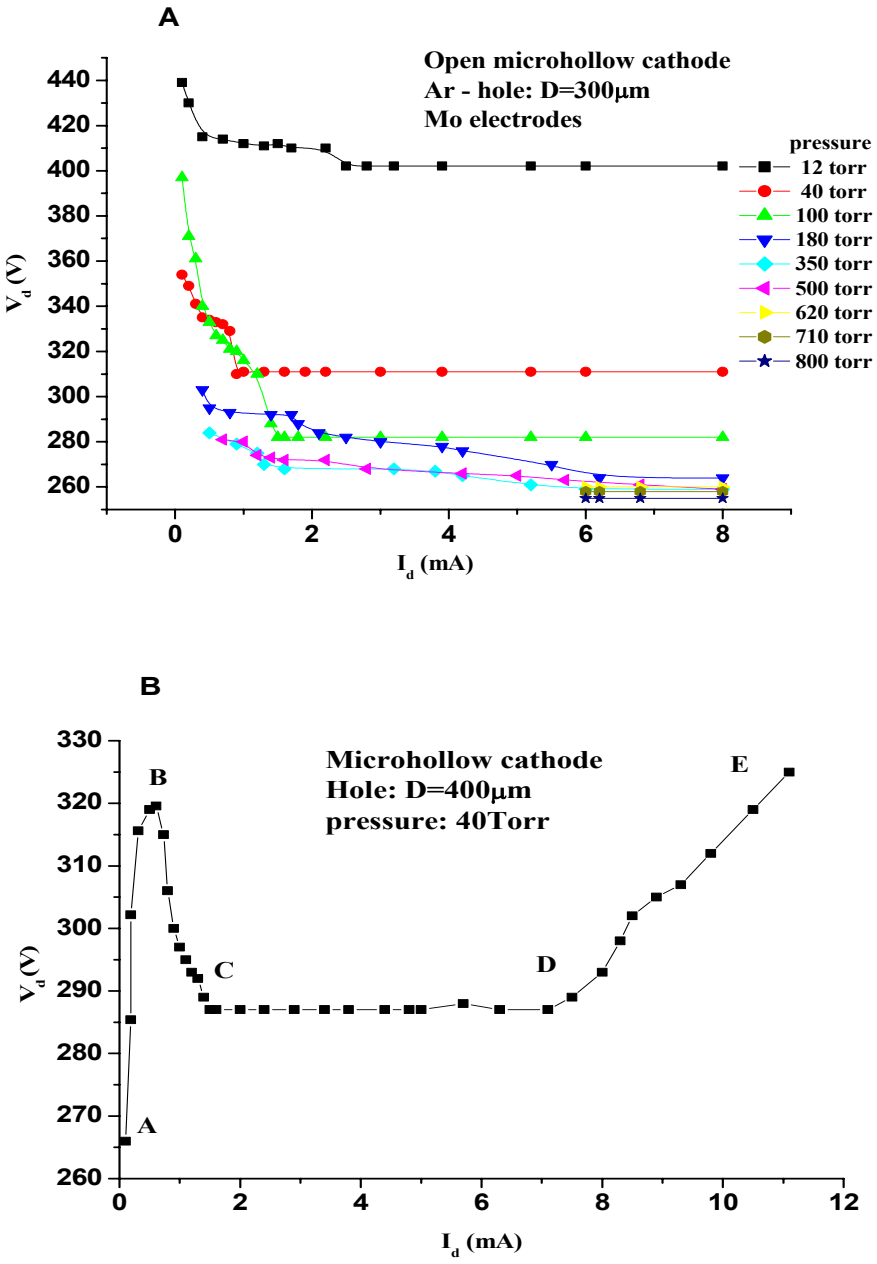

Fig. 1. (A) V-I characteristics for open MHCD operated in Ar with hole diameter of *300μm* at various operating pressures. (B) V-I curve for a hole diameter of *400μm* at *40Torr*.

Fig. 1A shows V-I characteristics of an open MHCD in Ar in the pressure range of *12 – 800 Torr*. As pressure increases, the sustaining voltage decreases due to more favorable conditions for ionization.
Fig. 1B graphs, the Townsend discharge mode (AB region) in low current and a positive differential resistance followed by a hollow cathode mode (BC region), were a drop of the voltage follows from the amplification of DC discharge current. In this region is established the hollow cathode effect in the cathode cavity. The confinement of the discharge inside the hole can be seem by the optical appearance of the glow. With the increasing of the discharge current, one can observe the gradually expansion beyond the cavity covering the cathode surface. The normal glow discharge mode, with constant voltage and increasing current (CD region) precede the anomalous glow discharge (DE region), where a positive slope in the current-voltage characteristics is observed. We, generally, avoid the abnormal mode of operation, beyond *10mA* due to overheating of the sample. On the other hand, limiting the cathode surface, the positive slope in I-V curve is always present. A closed microhollow cathode consists of a metal-insulator-metal device with a blind hole in the cathode surface.

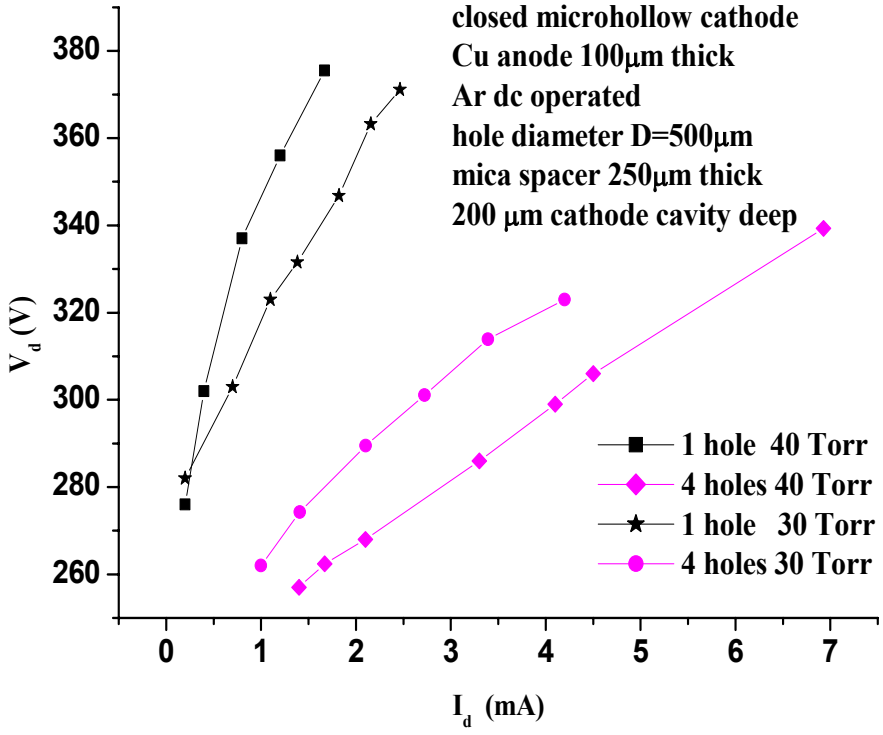

Fig.2. V-I characteristics for closed microhollow cathode DC operated in Ar, with hole diameter of *500μm* at a pressure of *30* and *40Torr*, for *1* and *4* holes (parallel operated).

In this configuration a positive slope is observed in V-I characteristics and a parallel operation is possible (Fig.2). Here, the plasma serves like a resistor of approximately *15KΩ* at a pressure of *30 Torr*. In this case the plasma was ignited in a four holes plate in Ar dc operation. With an increasing of the pressure, keeping V_d constant, a higher current is needed to maintain the glow lightening in all holes. We can limit the cathode area covering it with an insulator [4]. This way, in open microhollow cathode configuration, a jumping to abnormal mode is observed after gas ignition occurs. Here again, a parallel stable operation is possible without ballasting the individual discharges. Fig. 2 shows the I-V curve for MHCD operated with one and

four holes. As can be seen, the positive slope of I-V curve is present in both cases. In four holes operation the sustaining voltage is reduced for a given discharge current.

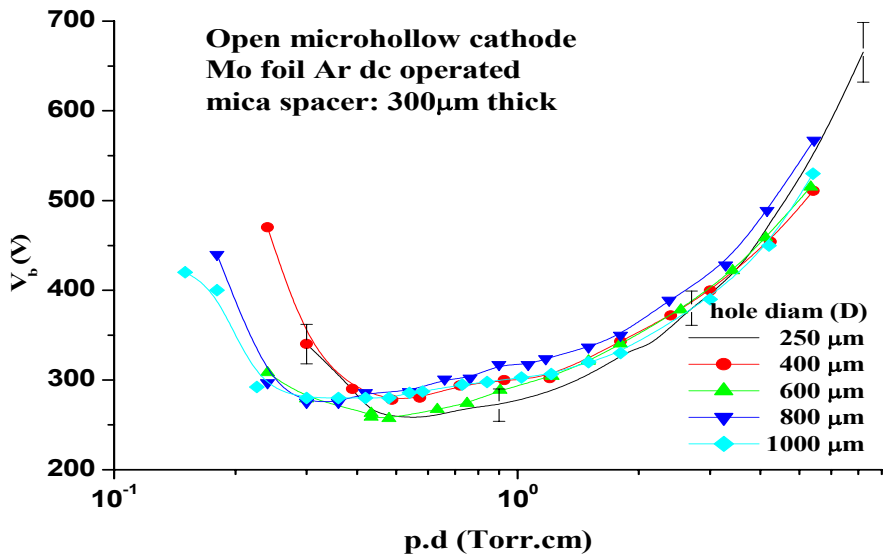

Fig. 3. Paschen curve for microhollow cathode discharge for various hole diameter.

To obtain the Paschen curve of the MHCD, large load resistors were used to limit the discharge current, and hence assuming a Townsend mechanism of breakdown. In Fig.3 shows Pashen's curves for various hole diameters, for MHCD with mica spacer d = *500μm*, in Ar DC operation. According to the Allis-White similarity law, the *pD* product is in the rage of 1 to 10 Torr cm, for hollow cathode operations. The different size holes MHCD does not change very much the breakdown voltage for pd greater than 0.3 Torr cm.
Figure 4 presents Paschen´s curves for MHCD´s constructed with different materials. Aluminum is the material that favors the operation at lower voltages while nickel and molybdenum needs high voltages for breakdown.

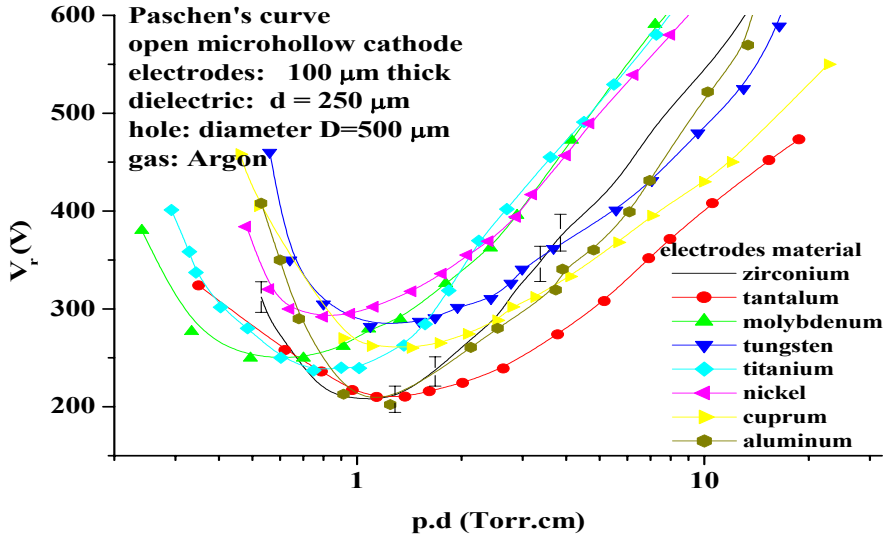

Fig. 4. Paschen´s curve for microhollow cathode discharges for different cathode materials.

Mechanically drilled holes has non-uniform opening surface, with incorporated micro-protrusions in it. This, allied with the cathode surface roughness, and for a small gap spacing (of several microns) between electrodes (mica thickness), induces phenomena of electron field emission and tunneling. For this gap, the macroscopic electric field becomes very large and the field emission may be responsible for the breakdown in low pressure operations, instead of Townsend electron avalanche mechanisms.

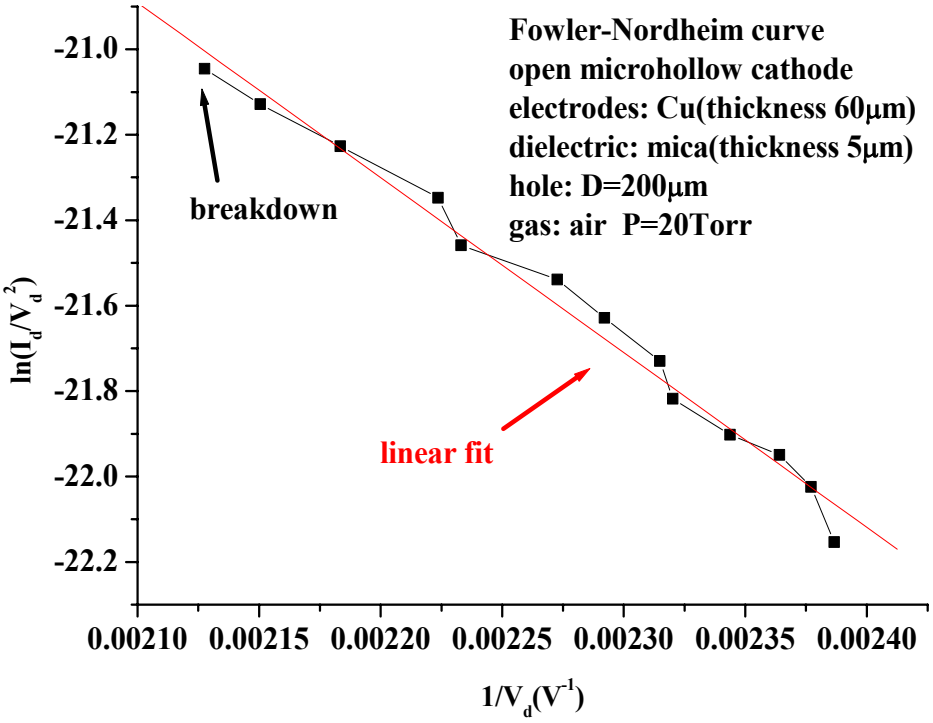

Fig. 5. Fowler-Nordheim plot for $5\mu m$ gap device, near breakdown.

One can use the Fowler-Nordheim equation and obtain a microscopic electric field just above the cathode surface to observe this quantum phenomenon. The total current I_d is given by $I_d = (\lambda a S F^2/\Phi) \exp(-\mu b \Phi^{3/2}/F)$, were a and b are universal constants given by $a = 1.5414.10^{-6} A\ eV\ V^{-2}$ and $b = 6.8309\ eV^{-3/2}\ V\ nm^{-1}$[5], λ and μ are generalized correction factors, Φ is the work function for the relevant point of the emitting surface, $F = \beta E$ is the microscopic electron field, for a field amplification factor β. The I-V curve was plotted for microhollow cathode, in air discharge operated at *20 Torr*, Cu cathode with a single $200\mu m$ diameter hole and a very thin mica spacing (about $5\mu m$) the electrodes. In figure 5 a straight line, with negative slope, was obtained when $ln(I_d/V_d^2)$ is plotted versus V_d^{-1}, a so-called FN plot, for this device configuration. It was employed $\Phi = 4.6\ eV$ for Cu electrodes, which lead us to obtain $\beta = 80$ and $F = 10V/nm$, which is a good value for a local microscopic field needed to start the field emission.

4. Conclusions

The V-I characteristic of the open MHCD (Fig. 1) was measured and found to be similar to the well-known characteristic of a low-pressure glow discharge, showing different modes of operation. At low current it

presents a Townsend mode followed by a transition to a normal glow discharge. The Townsend discharge is characterized by small current (typically less than *0.5 mA*). The charge density in the hole is low and does not disturb the electric field between the electrodes, which is in this case mainly axial oriented. Increasing the current, the axial electric field begins to be distorted by the space charge accumulated inside the cathode and a strong radial electric field develops. The potential distribution in the gap becomes strongly non-uniform and the cathode fall is generated. The enhanced electric field at the cathode facilitates ionization processes and correspondingly a fall in the sustaining voltage and a rise in the current is observed [3]. The discharge concentrates inside the hole.

The breakdown voltage depends on the nature of the gas at the same pd product. A Paschen's curves are given in Fig. 4 for open MHCD´s. All of that have the well-known Paschen curve "U" shape. It can be seen that in the region of the minimum, for Cu and Mo electrodes in Ar gas operation, the breakdown voltage and the $(pd)_{min}$ product are in reasonable agreement to the ones found in literature [1]. However, in microhollow cathode operations, as in low pressure hollow cathode operations, the left-hand Paschen's curve is shifted to a lower breakdown voltage, compared to a plane-plate glow discharge. This is in accordance with the hollow cathode effect, due mainly to the "pendulum electrons", which ionizes more efficiently, in low pressures, compared to a glow discharge. Due to micro protrusions existing around the opening hole there is an enhancement of the local electric field, lowering the breakdown voltage. This high local electric field can emit electrons by tunneling or field emission process, and for small gaps, be the responsible for the breakdown process.

4. References

[1] Yu P Raizer 1997 *Gas Discharge Physic* (New York, Springer).
[2] D J Sturges and H J Oskam, Journal of Applied Physics **35**, 2887(1964).
[3] R H Stark and K H Schoenbach, Applied Physics Letters **74**, 25 (1999).
[4] K H Schoenbach, A El-Habachi, M M Moselhy, W Shi and R H stark, Physics of Plasmas **7**, 2186 (2000).
[5] R G Forbes, Solid-State Electronics **45**, 779(2001).

Sol-gel Coatings on Ambient Plasma on Polymers

Srikantha Sahu[1], Shirshak Dhali[1], Bakul Dave[2]

[1]*Department of Electrical & Computer Engr., Southern Illinois University, Carbondale, IL62901*
[2]*Department of Chemistry and Biochemistry. Southern Illinois University, Carbondale, IL62901*

Abstract

Here we discuss the properties of sol-gel coatings on addition polymers treated with ambient plasma. The plasma is generated by a coaxial dielectric barrier discharge operating at atmospheric pressure in Argon or Helium carrier gas. The afterglow interacts with the surface and the ambient air. Contact angle measurements and peel strength measurements were done to study the effectiveness of plasma treatment.

1. Introduction

Radio frequency (RF) plasma treatments at low pressures have been employed to improve the surface properties of commodity polymers, increasing the range of potential applications for these materials. In applications were adhesion is important, the required treatment need not be specific. However, in applications involving biomaterials, the treatment would be very specific. The reactive species in plasma, resulting from ionization, dissociation, and excitation processes, include positive and negative ions, neutral species, atoms, metastables, and free radicals. Inductively coupled inert gas plasmas, that are commonly used in these applications have species with a broad range of energies: Plasma components include ions (10-30 eV), electrons (0-10 eV), and UV and vacuum UV radiation. In reactive gas plasmas such as oxygen, ablation or etching occur, resulting in the formation of small volatile degradation products. In inert gas plasmas, the dominant process is hydrogen abstraction [1].

Plastics constitute the majority of engineering materials due to their versatility and applications. While the plastics offer major advantages in terms of cost-effectiveness, ease of forming different shapes and architecture and their compatibility with traditional materials, the plastics suffer a serious drawback in comparison to ceramics when it comes to optical and mechanical properties as well as long term degradation due to thermal and UV radiation. Especially vulnerable in this context are the addition polymers, which mostly comprise of stand-alone architectures without any protective coatings. Design of suitable coatings that can seamlessly integrate with the polymer structures during post-processing steps can not only confer stability against environmental factors but also provide value-added benefits to vast applications field of plastics in general.

At low pressures, the ions will play an important role in the interaction causing polymer degradation and crosslinking [2]. In atmospheric pressure discharges, the role of ions is not important, whereas metastables and radical chemistry becomes important. Choi et al have shown that the metastable He^* in a helium discharge is capable of scission of polymers in a polypropylene surface [3].

From a manufacturing point, ambient plasmas operating at atmospheric pressure is desirable compared to low pressure confined processing. We have used ambient atmospheric pressure plasma to treat polymer surfaces prior to sol-gel coatings. The contact angle measurements and peel test indicate improved adhesion. However, these plasmas are very different from

low pressure plasma commonly used for polymer treatment. The energetic ions are absent and most plasma chemical reactions are based on neutral chemistry.

At atmospheric pressures, essentially there are two methods for producing non-thermal plasmas; (1) a corona discharge and (2) a barrier-type ac discharge. The dielectric-barrier discharge, also known as a silent discharge or a partial discharge, is widely used in industry for ozone synthesis. This discharge is intermittent and the current exhibits a large number of spikes when the discharge is burning. Experimental investigations in atmospheric air have

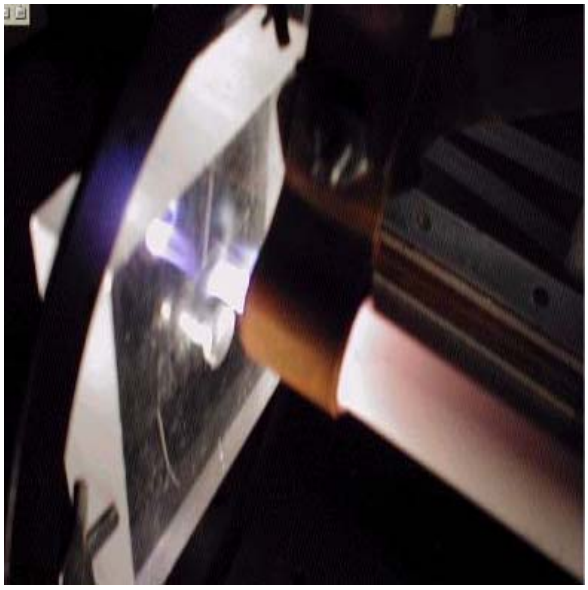

Figure 1: Picture of an RF ambient plasma treating a sample of plastic

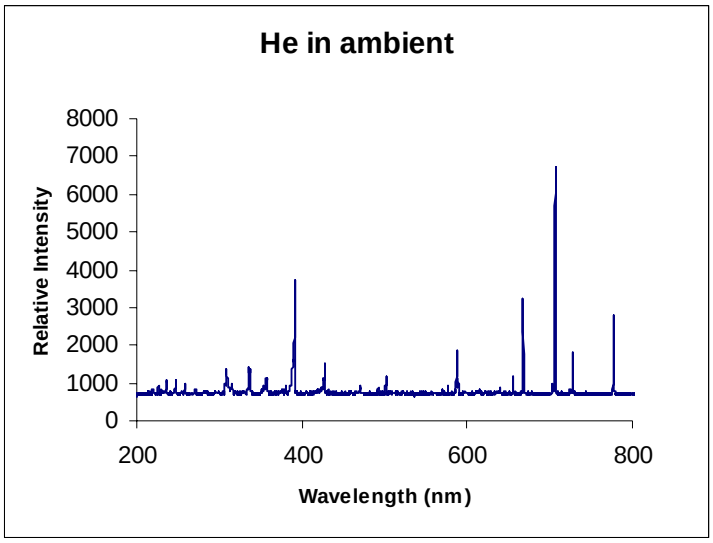

Figure 2: Optical emission spectra of He afterglow in ambient air.

demonstrated that current flows on a large number of partial discharges. These partial discharges are best characterized by streamers, which are a result of space charge dominated transport at high electric fields [4].

2. Results and Discussions

Shown in Fig. 1 is the picture of atmospheric pressure plasma treatment of a sample of plastic. In the configuration shown, the discharge is "struck" in a noble gas (Argon) and the reactive gas is added in the afterglow. The centered electrode is bored to allow the reactive gases to flow into afterglow. This is critical for the stability of the discharge: Gases like H_2 and O_2 are attaching and change the physical characteristics of the discharge. Due to increase in breakdown voltage, even for concentration of reactive gases in few percentages, it is difficult to strike a discharge using radio frequency (RF). From our experience, RF is the most suitable power source because it can be tuned to the load easily compared to low frequencies. The plasma is an afterglow and is not confined between electrodes like conventional plasma. This has the advantage of treating blind holes and difficult to reach areas of molded parts. This type of a source can also be mounted on a robotic arm with proximity sensors. The plasma has both convective and diffusive flow. The force of the gas flow produces a directional flow and density gradient produces diffusive flow. In plasma chemical devices, the aim is to produce desired radicals to carry out a particular reaction. The main thrust for atmospheric pressure plasma for our application is the production of high-energy metastables, H and O radicals. The ambient afterglow discharge is a cold discharge with most of its energy being utilized for the production of excited species. The afterglow interacts with the ambient gas and a typical optical emission

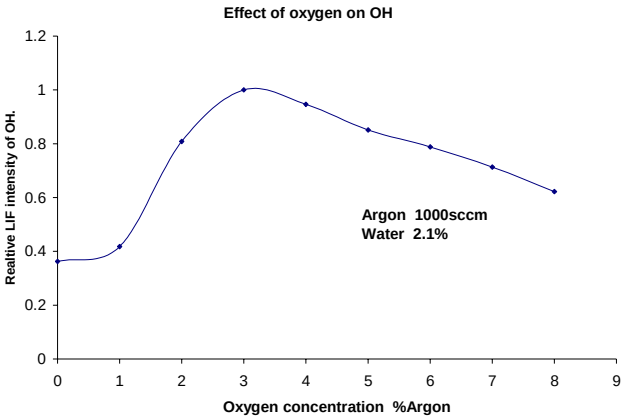

Figure 3: The relative concentration of OH for different gas composition.

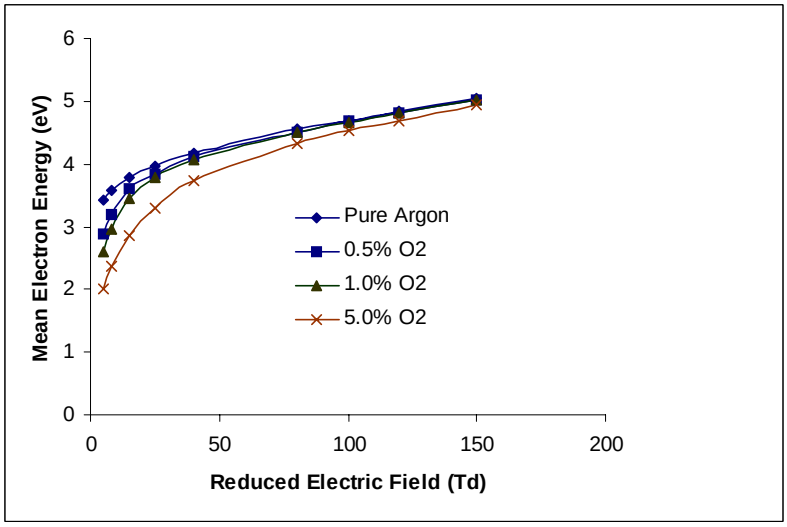

Figure 4: Calculated mean energy of different composition of Oxygen in

spectrum of the helium afterglow is shown in Figure 2. The highest peak in the spectrum is $O^*(3p \rightarrow 3s)$ at 777.2. Clearly the He metastables excite the oxygen molecules to produce excited oxygen atoms. Experimental investigation of OH radicals can be done with Laser Induced Fluorescence. Figure 3 shows the Laser Induced Fluorescence (LIF) intensity in an Argon/H_2O/O_2 discharge. The OH increases with O_2 concentration up to a certain point and then decreases due to the adverse effect of increasing O_2 concentration on the discharge.

In order to understand the influence of discharge parameters such as gas composition and discharge power on the radical concentration, a model has to be developed for the afterglow plasma. The model starts with Monte-Carlo calculations of the electron energy distribution function. The cross section data required for these calculations was obtained from the Joint Institute for Laboratory Astrophysics website (http://jilawww.colorado.edu/research/colldata.html). The electron energy distribution function is then used to calculate all electron related rates and mean electron energy, a plot of which is shown in Fig. 4. From the power and voltage applied to the discharge, the electron density and the rates can be estimated.

The use of silica-based coatings has been used to alter the properties of polymers and metals. For polymeric substrates, the silica-based coatings have been largely through the use of chemical and/or physical vapor deposition processes. The films of silica and other oxides modify the properties of plastics such as optical properties including anti-glare, anti-reflection, permeability of gases, and to protect food products from oxygen. The coatings in these applications have focused on nonporous silica or oxides layers deposited using high energy curing process. On the other hand, liquid phase deposition of silica layers on plastics has also been accomplished using hexafluorosilicic acid as means to enhance their optical properties. The use of sol-gel methods using alkoxysilane precursors requires polymeric substrate that can exhibit covalent or hydrogen bonding with silicate species. With hydrophilic polymers such polyester sol-gel coatings can be deposited directly due to interactions of silicate species with the polymer. However, with addition polymers such as polyethylene, polypropylene, and polystyrene, which only contain hydrocarbon chains, the deposition of sol-gel coatings usually requires pretreatment of the polymer surface for

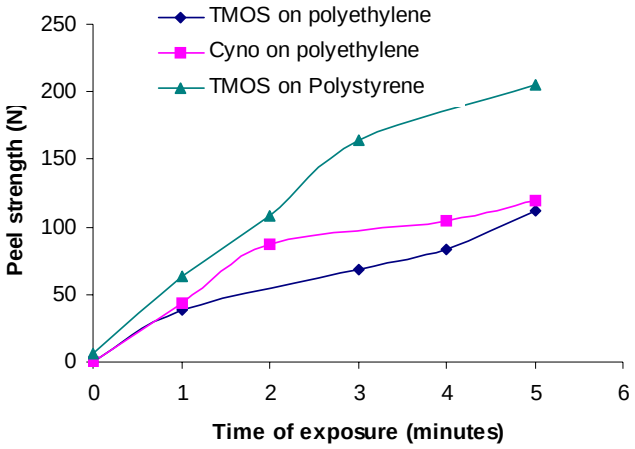

Figure 6: Peel strength of sol-gel coatings on polyethylene and polystyrene.

adhesion. The use of plasma to activate the surfaces of such polymers has been shown to facilitate the deposition of sol-gel overlayers [5].

The sol-gel process is a low temperature solution-based method for making ceramic oxide glasses such as SiO_2, SnO_2, TiO_2, V_2O_5 etc. In the sol-gel process, a suitable precursor (usually an alkoxo or chloro complex) is hydrolyzed to generate a solid-state polymeric oxide network. Initial hydrolysis of the precursor generates a liquid sol, which ultimately turns to a solid porous gel. The procedure involves formation of glass from a solution phase, and considerable flexibility in inorganic, organic, or biological modification of the resulting material is possible [6].

The afterglow interacts with the surface and the ambient air. In such plasmas, optical emission spectroscopy shows the presence of excited oxygen molecules and oxygen atoms [7]. The surface modification can occur by oxidation of plastic surface with the oxygen radicals available in plasma of atmospheric pressure. Hydroxyl-(-OH-) AND KETO-(=O) groups formed in the surface act as anchor points for chemical reactions with the ink and adhesive. The oxidation of the surface leads to an elevated surface energy level and in most cases increased adhesion. The increased surface energy due to plasma treatment is indicated by the lowering of contact angle with treatment time as shown in Figure 5.

The treated samples were coated with various types of sol-gels. Figure 6 shows the 180 degree peel strength of coatings with exposure time. The peel strength increases with increasing treatment time. However different sol-gel coatings show different behavior depending on the substrate. The cyno- precursors did not form coating on polystyrene even with plasma treatment.

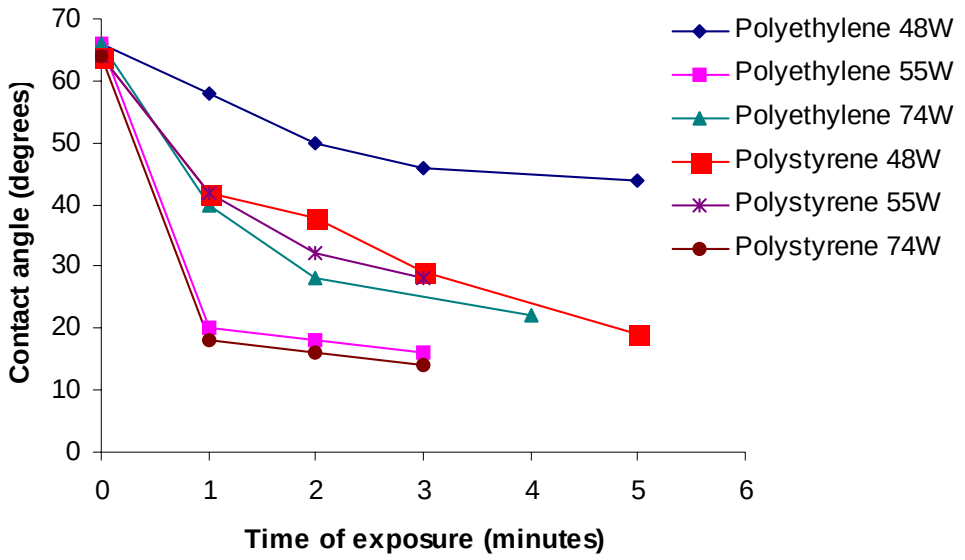

Figure 5: Contact angle of Polyethylene and polystyrene for different exposure time as a function of input power.

3. Conclusions

The experimental results indicate that surface treatment of addition polymers improve the hydrophilic properties of polymer surfaces and produce improved adhesion of sol-gel coatings.

This work was partially supported by a grand from the National Science Foundation.

References

[1] France, R., and Short, R. D. Plasma Treatment of Polymers J. Chem. Soc., Faraday Trans. Vol 93, pp 3173-3178 (1997).

[2] Friedrich F., A. Meyer_plath, I. Retzko, G. Kuhn, and R. Mix, Comparision of different plasmachemical processes for the formation of monotype functionalized polymer surfaces , CD ROM proceedings of the 16^{t} International Symposium on Plasma Chemistry, Edited by R. d'Agostino, P. Favia, F. Fracassi, F. Palumbo, University of Bari. (2003).

[3] Choi, Y. H. Y. H. Kim, H. J. Kim, K. H. Paek, W. T. Ju, and Y. S. Hwang, Characterization of polypropylene surface treted by atmospheric pressure ejected plasma for adhesion improvement, CD ROM proceedings of the 16th International Symposium on Plasma Chemistry, Edited by R. d'Agostino, P. Favia, F. Fracassi, F. Palumbo, University of Bari (20030.

[4] Dhali, S. K., and A. K. Pal. 1988. Numerical simulation of streamers in SF_6. Journal of Applied Physics. Vol. 63, 1355(1988).

[5] M. C. Coen, R.Lehmann, P. Groening, and L. Schlapbach, Modification of the micro- and nanotopgraphy of several polymers by plasma treatments Appl. Surf. Sci. Vol. 207, 276-286 (2003)

[6] Dave, B. C.; Dunn, B.; Valentine, J. S.; Zink, J. I. 1998 Sol-Gel Matrices for Protein Entrapment, Immobilized Biomolecules in Analysis: A Practical Approach F. S. Ligler, and A. E. G. Cass (eds) Oxford University Press, pp 113-134(1998).

[7] J. Y. Jeong, J. Park, I. Henins,S. Babayan, V. J. Tu, G. S. Selwyn, G. Ding, R. F. Hicks, Reaction Chemistry in theAfterglow of an Oxygen-Helium,Atmospheric-Pressure Plasma,, Journal of Physical Chemistry A Vol 34, 8027–8032 (2000).

Destruction of dichloromethane by thermal plasma

B. Bournonville, D. Guenadou and E. Meillot

CEA Le Ripault, BP 16, 37 260 Monts, France

Abstract
A new-patented process employing thermal plasma for the destruction of organic halogen liquid wastes is proposed. Using plasma torch as high temperature source, this safe system can destroy a great variability of wastes, even mixed together. At the exit of the process, only no-toxic compounds are produced as atmospheric gases, liquid water and halogen sodium salt. As test molecule, dichloromethane has been treated: the results show a complete destruction with reject of clean gases in the atmosphere.
Keyword: inductive thermal plasma, waste destruction, organic halogen liquid, dichloromethane.

1. Introduction

The manufacturing of numerous products from human activity generates a lot of wastes. The quantity and the variety of wastes increase with the global industry development. At the same time, environmental laws evolve and create severe stresses leading to more and more important stocks of wastes without elimination way. Then, most of gas, liquid or solid wastes must be treated, recycled or destroyed.
Destroying wastes, which cannot be easily and safety recycled, can be really feasible by combustion if these wastes do not present high temperature stability and do not imply toxic off-products after burning. Destroying toxic high-stability wastes requires high-energy processes. For this reason, thermal plasma processes, which present a high energy power and a great adaptability, have been first applied for vitrifying fly ashes from domestic waste incinerators, for example, with the EUROPLASMA process. Another application concerns also asbestos vitrifying by the same process. State of the art shows many thermal plasma processes destroying gases or vitrifying solid wastes. After solids, the second application has been to destroy gases such as ozone depleting gases. For example, the PLASCON process has been developed to remove CFC but also liquids such as dichlorophenoxyacedic (2-4 D) or oils contaminated by PCB [2]. Other plant is the one built by NIPPON STEEL CORP. in Japan to remove chlorofluorocarbons [5]. Other research papers have been proposed using different kinds of plasma [3-6].
In nuclear industry, the problem is more significant due to the adding of radioactivity. The 1991's French law, called BATAILLE law, stipulated that different ways of elimination must be explored to stock or to diminish and to store the wastes emanated from nuclear activities. That is why, the French atomic energy agency, CEA, has high interests for all new industrial treatments of diversified wastes.
To response to the directives, CEA has decided to study, in first step, chemical destruction of no-radioactive halogen organic mixed wastes in a new process based on thermal inductive plasma torch. In a first step, this process has destroyed pure organic molecules without halogen. All introduced products show a rapid and total destruction and induce the formation of no-toxic gases. These experiments validate the feasibility of the process with no halogen molecules. Then, the process has been validated with dichloromethane as an example of halogen organic molecules. This process, in progress to be patented, has been studied as an answer to elimination or reduction of nuclear waste stocks; so, its economical evaluation has not yet been performed.
The aim of this process is to destroy completely a wide range of halogen liquid wastes, pure or mixed, and to exhaust only no-toxic gases with trapping the halogen molecules as mineral salts. Its final aim is to develop a clean process for treatment of radioactive organic halogen compounds.

2. Description of the process

Thermodynamic and kinetic simulations permit the operating condition definition before experiment. To avoid formation of toxic $COCl_2$ and solid carbon (soot), hydrogen and oxygen are required in the recombination zone. They are introduced as liquid water form. Simulation predictions have shown a very fast destruction of dichloromethane and formation of simple molecules with 2 or 3 atoms (CO, CO_2, HCl, H_2, Cl) by atom recombination. To achieve oxidation of explosive H_2 and toxic CO, oxygen, as air injection, is added. This leads to no CO and H_2 left, without NOx formation.
Short description of the pilot is presented here without details due to the in-progress-patent study. Inductive plasma torch, PL 50 gun from TEKNA Inc., working with argon/hydrogen mixing, transforms the electric

energy into mainly thermal energy at the head of the reactor (figure 1). It is a double-flux gun, one in the central network of the torch (only argon), the second along the wall as sheath gas (mixture of argon and hydrogen). Air as plasma gas is not an appropriate opportunity because of NOx formation. This kind of technology presents the interest of using a wide range of gases and the introduction of compounds-to-destroy directly inside the torch, in the highest temperature zone and that, without any gun material degradation. The gases are ionized at high temperature (more than 12 000 K) as thermal plasma and flow inside the reacting chamber. This one presents a studied design to avoid cold areas, with a refractory wall. Wastes and water adding are introduced in the plasma plume at the head of the reaction chamber.
The high temperatures, allied with a long time life (less than 1 s) of the products in the hot zone, lead to vaporize and to break up completely the molecules, even the most stabilized one, in elementary atoms. The molecular flow rates of the two fluids (wastes and water) are in correlation such as the carbon and halogen atom numbers from wastes and the oxygen and hydrogen atom numbers can react following the reactions:

$$C + 2O \leftrightarrow CO_2 \qquad (1)$$

$$Cl + H \leftrightarrow HCl \qquad (2)$$

An excess of water can saturate the previous reactions. At the end of the first destruction zone, an air introduction accelerates and achieves the oxidation of carbon and hydrogen. After complete reactions, the off-gases are cleaned in a wet treatment unit with soda to trap halogen atoms, and then are cooled by a heat exchanger. Pump unit has two goals: firstly evacuating the off gases and secondly regulating the inside pressure in the process.

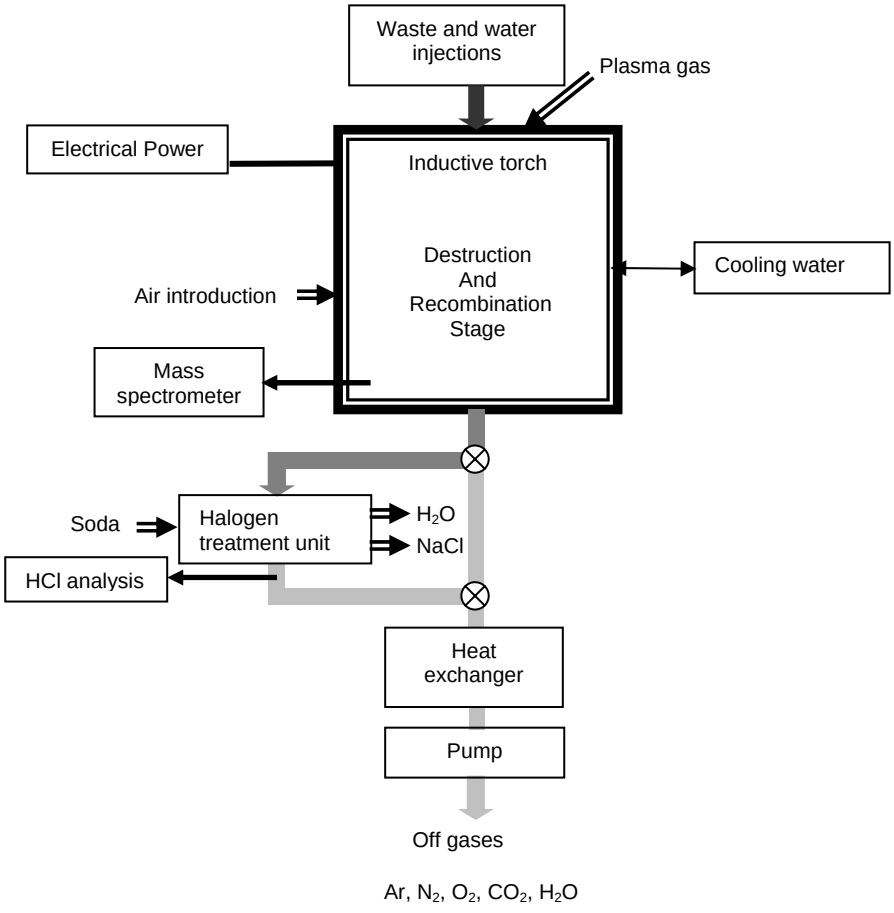

Figure 1: Simplified set-up of the process.

3. Operating conditions and analysis setup

3.1 Operating parameters

The main operating parameters are collected in Table 1. Argon and hydrogen are introduced in the torch to generate the thermal plasma. Hydrogen increases the enthalpy of the gases. The plate power is around 41 kW. Due to the rather bad thermal efficiency of inductive gun, less than 50% of the electric power is

transferred to the gases at the torch exit. The products to destroy, here dichloromethane, are injected in the plume. For dichloromethane destruction, the water flow rate ratio is depending on the equation (3). An excess of water is introduced to saturate the basic reaction in the first step.

$$CH_2Cl_2 + 5H_2O \leftrightarrow CO_2 + 2HCl + 3H_2O + 2H_2 \qquad (3)$$

Table 1: operating parameters of the process.

Parameters	Values and units
Argon central flow rate	30 slpm
Argon sheath flow rate	105 slpm
Hydrogen sheath flow rate	7 slpm
Plate power	41 kW
Additional air flow rate	200 slpm
Dichloromethane flow rate	15.8 g/mn
Additional water flow rate	17.0 g/mn
Soda initial concentration in treatment unit	7% mass
Pressure	$0.9\ 10^5$ Pa

3.2 Analysis materials

Gases are analysed at the end of reaction zone, after air introduction, by mass spectrometer (PFEIFFER VACCUM type MONISTAR GSD 300 C2). Several thermocouples measure the gas temperature, before and after air injection for example, to control the well-done oxidation reactions. Before exhaust into the atmosphere, HCl concentration measurements are realized with an OLDHAM analyser (LASERGAS 2000).

4. Results

The results are presented versus experimental time. All experimental parameters have been recorded each two minutes. Several injections have been carried out in the same test and so experiments can show the rather good stability of the process because of test duration. Dichloromethane and water feedings are represented by darkest grey zone while, before and after the injection, only water introduction is coloured in brightest grey to clean the injection system and reactor.

4.1 Gas temperature

In the destruction and recombination stage, just before air adding and without liquid injection, the gas temperature has risen up to around 1200 °C (first curve of Figure 2) when the thermal equilibrium was steady. This temperature, measured quite far from the plasma torch, is in good agreement with simulation results [1]. These results imply that the high upstream temperatures are efficient to destroy completely the wastes.

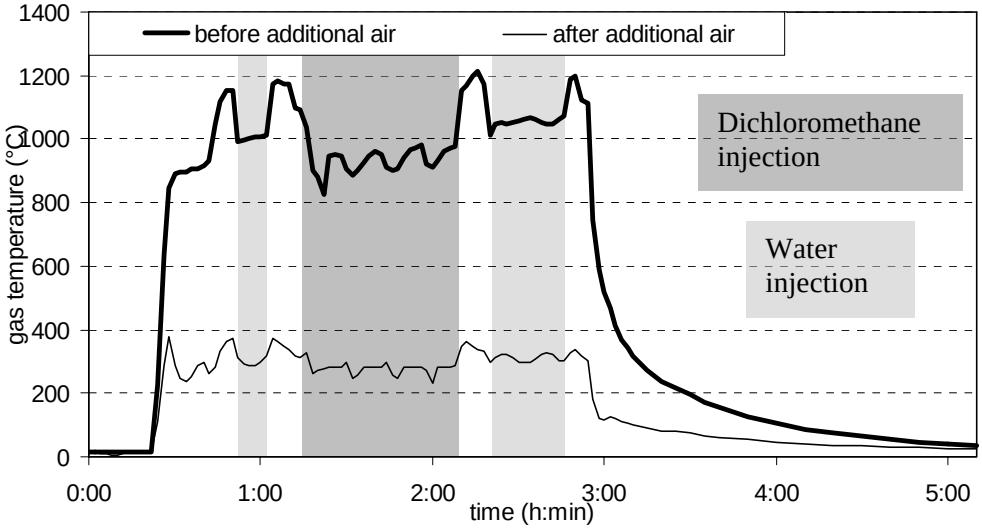

Figure 2: Gas temperature during dichloromethane injection experiment.

The only water introduction (at the flow rate of 28 g/mn) into the plasma induces a temperature drop of about 150°C (Figure 2), due to molecular decomposition, at the first step of the temperature measurement. Introducing the dichloromethane/water mixture in the process has leaded to the severe temperature drop: the temperature was less than 1000 °C during around fifty minutes after one hour and a quarter time. Although the volume flow rate of dichloromethane and water was similar than single water injection, the temperature drop during the dichloromethane injection is more important due to the endothermic reaction of the hydrochloric acid formation. After three hours experiment, the process has been stopped. The gas temperature has decreased rapidly first and more slowly in a second time: this effect is due to the energy stored in the refractory wall.
After air adding and still without liquid injection, the gas temperature has risen up to nearly 375°C (second curve on Figure 2). The curve has the same trend than the previous one with less amplitude.

4.2 Gas composition

After molecular combinations, the mass spectrometer analyses show the presence of only simple molecules: Ar, N_2, O_2, CO_2, H_2O, and HCl. No dichloromethane has been detected. Then, the destruction and removal efficiency must be very high (close to 100%).
With these analyses, following the evolution of the gas composition versus time is possible (Figures 3, 4 and 5). Some analyses have been rejected because there were incoherent, certainly due to electromagnetic interference.

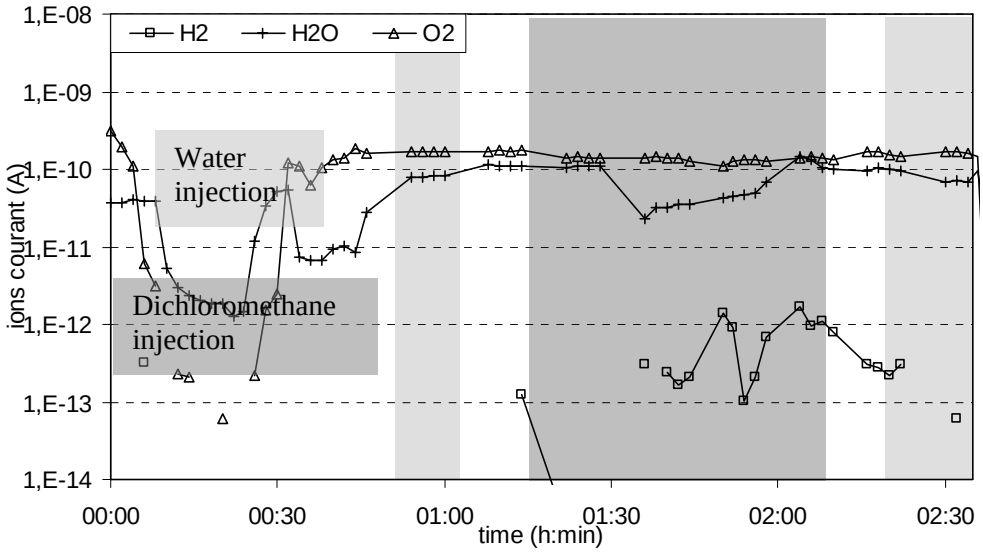

Figure 3: H_2, H_2O and O_2 composition signal during dichloromethane injection experiment.

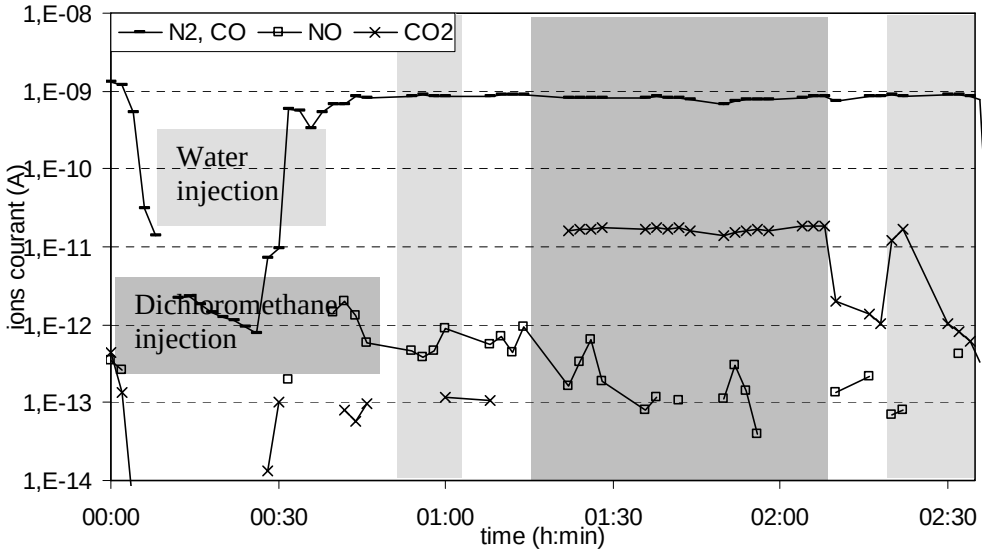

Figure 4: N_2, NO, CO and CO_2 composition signal during dichloromethane injection experiment.

In Figure 3, only H_2, H_2O and O_2 compositions are first plotted, process working. O_2 appears in excess while H_2 seems completely transformed in vapour. The water evolution is particular. The quantity of steam has increased with the beginning of the Ar/H_2 plasma. Then, in the first half of the dichloromethane injection, a notable decrease has appeared. After that, the water quantity has increased regularly until the end of the dichloromethane injection. Assumptions about water deposition by condensation on cold walls and deposit saturation could be proposed.
In Figure 4, results concerning carbon and nitrogen oxidation are presented. Firstly, if CO and N_2 are plotted together, due to similar molecular mass, this curve remains stable during plasma presence although the CO_2 line shows important increases when dichloromethane is injected. So, if the carbon oxidation has not been completely achieved, that has stayed at low level. At the beginning of the second water injection, there is a short peak of CO_2 due to the injection tube cleaning. Secondly, nitrogen oxides have left under low concentrations, process working, and so no nitrogen oxide treatment unit is needful.

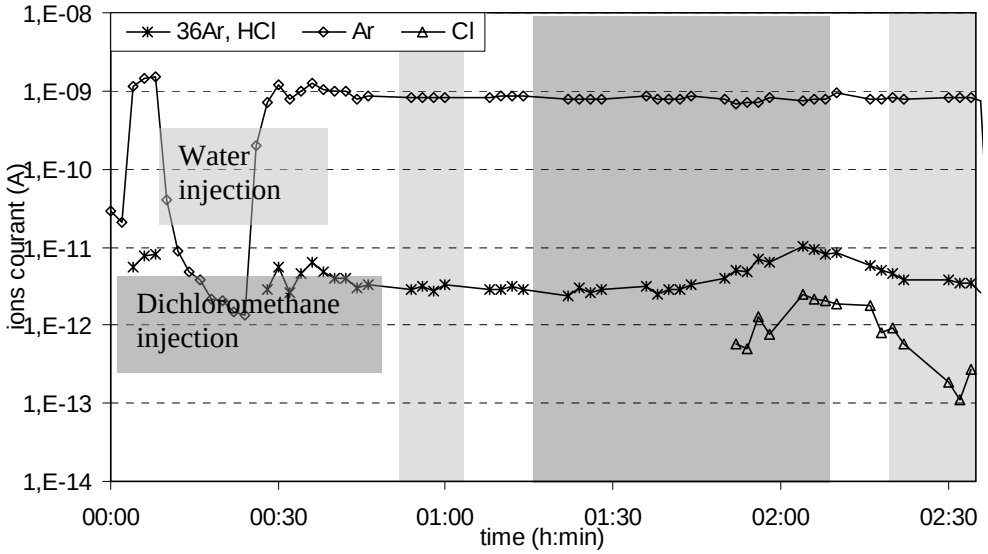

Figure 5: Ar, HCl and Cl composition signal during dichloromethane injection experiment.

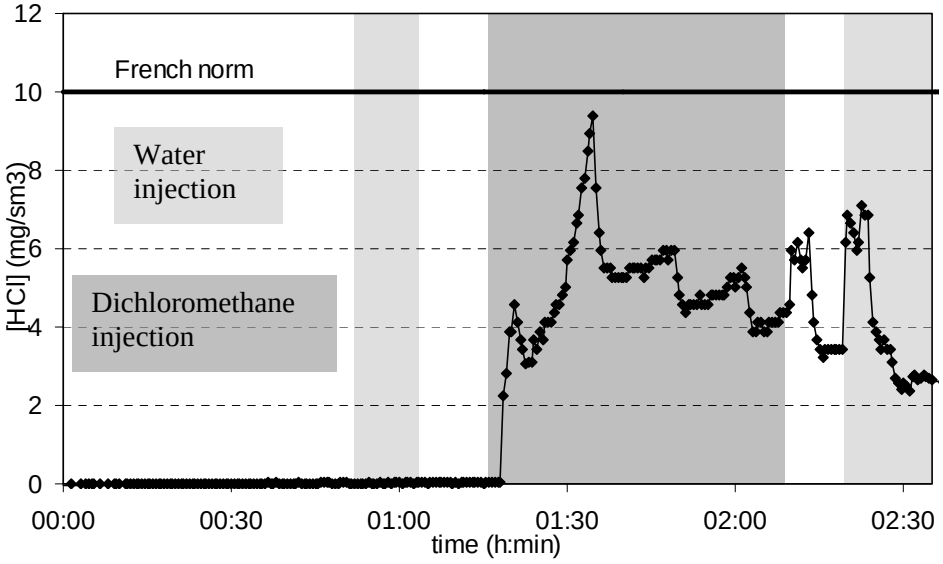

Figure 6: Hydrochloric acid ejection into atmosphere during dichloromethane injection experiment.

Figure 5 shows signals of chloride species and also argon for the main line. This one does not evolve while dichloromethane injection or no. So, the evolution of the second line, which indicates the presence of both argon (^{36}Ar) and hydrochloric acid, proves only appearing of hydrochloric acid when injection working. Unlike the CO_2 evolution, which has increased and decreased drastically when the dichloromethane injection

started and stopped, the hydrochloric acid evolution has been smoother. The delay before seeing the hydrochloric acid is higher than for CO_2 and the increase of HCl concentration, as its decrease, has been progressive. The increases in H_2O and HCl seem to follow the same slope. Their evolution could be linked by a saturation phenomenon.
After air addition, the gas cools down on cold wall. Consequently, there is an important condensation of steam on the reactor wall. When dichloromethane is introduced into the plasma, a great HCl formation appears and the hydrochloric acid has a great affinity with liquid water. Then, a part of HCl dissolves into the condensed water. So, when the liquid is saturated by hydrochloric acid, equilibrium is obtained and the HCl concentration in the gas increases enough to be detected by the mass spectrometer. A great quantity of liquid highly concentrated in HCl (40% of the introduced chlorine) has been founded at the bottom of the reactor, before halogen trap unit. That's confirmed this hypothesis.
After that, the gas treatment unit has trapped efficiently hydrochloric acid gas and has limited its concentration in off gases (Figure 6). The HCl concentration is always lower than 10 mg/sm^3 (the French HCl off-gas concentration norm used for dangerous waste incineration [7]): when the treatment unit parameters have been correctly fixed, equilibrium has started and the concentration was less than 6 mg/sm^3. This light concentration of gaseous hydrochloric acid during the dichloromethane injection indicates also the well-operating treatment of the process, which trap 60% of introduced chlorine.

5. Conclusion

Due to necessity of destroying high stability liquid halogen wastes, a new process has been proposed and is in progress to patent. Based on thermal inductive plasma torch and working with water adding in the hot destruction area, it is safe and robust.
The measured temperatures, before additional air injection, far from the plasma zone, are high and in correlation with previous simulation results. They represent the first evidence of the good destruction rate.
After additional air, the gas composition, caught by mass spectrometer analyses, is exempt of initial products to destroy, here dichloromethane. The process presents a very high destruction rate: only no toxic but simple gas molecules have been rejected into the atmosphere after a gas treatment for hydrochloric acid. In this case, chloride has been trapped as minerals salts.
New developments are carried on: after simple products such as dichloromethane or chloroform [8], destructions of several halogen liquid waste mixtures are in progress. Optimisation study of operating parameters will also be proceeded.

References

[1] Guenadou D., Meillot E., May 2004, Modelling of Inductively Coupled Plasma Flows in a Reactor: Comparison with Experimental Results, Proceedings of International Thermal Spraying Plasma 2004, Thermal Spray Solution Advances in Technology and Applications, ED. German Welding Society, OSAKA, JAPAN.
[2] Murphy A.B., December 1999, Plasma Destruction of Gaseous and Liquid Wastes, Annals of the New York Academy of Sciences, Vol. 891.
[3] Snyder H., Fleddermann C., October 1997, Decomposition of Dichloroethane in a plasma Arc jet Reactor: Experiment and Modelling, IEEE Transactions on Plasma Science, Vol. 25, N° 5.
[4] Suzuki M., Komatsubara M., Umebayashi M., Akatsuka H., December 1997, Conversion of Chloride Waste into Oxide by Microwave Heated Oxygen Plasma, Journal of Nuclear Science and Technology, Vol. 34, N° 12.
[5] Takeuchi S., Takeda K., Uematsu N., Komaki H., Mizuno K., YoshidaT., 1995, Proceedings of the 12th International Symposium on Plasma Chemistry, Vol. II, Ed. J. Heberlin, D. Ernie, J. Roberts, Minneapolis, USA.
[6] Yargeau V., Soucy G., Boulos M., 1999, The Treatment of a Water-Based Toxic Waste using Induction Plasma Technology, J. Plasma Chemistry and Plasma Processing, Vol. 19, N° 2
[7] French decree "Arrêté du 20 septembre 2002 relatif aux installations d'incinération et de co-incinération de déchets dangereux", Journal Officiel de la république française 1er décembre 2002, pp. 19789-19801.
[8] Bournonville B., Thellier C., Guenadou D., Meillot E., 2005, Destruction of Organic Halogen Liquid Waste in Thermal Plasma, Proceeding of WasteEng05 the 1st International Conference on Engineering for Waste Treatment, Albi, France.

Characterization of plasma properties in an oxygen cutting arc

John Peters[1], Joachim Heberlein[1] and Jon Lindsay[2]

[1]*University of Minnesota Mechanical Engineering Minneapolis, MN 55455*
[2]*Hypertherm Inc. Hanover, NH 03755*

Abstract:

Temperatures in a plasma arc cutting system were measured using optical emission spectroscopy. Several methods were used to calculate the temperature and absolute ion emission intensity was found to be the best technique for temperature determination. Using this temperature measurement method the effects of arc current, plasma flow rate and torch geometry were determined. The arc current had a large effect on the plasma temperature, while the flow rate and geometry affect the expansion of the plasma jet leaving the torch nozzle.

Introduction:

Plasma arc cutting is a widely used industrial process in the metal fabrication industry. It uses a transferred arc to melt a conductive work-piece while a high speed gas jet removes the molten material. The plasma properties, as well as the cutting performance, are strongly influenced by several cutting process parameters. Some of these process design parameters include: geometry of the torch nozzle, shield gas flow configuration, plasma and shield gas flow rates and plasma cutting current. The goal of this investigation is to understand the effect of many of these parameters on the characteristics of the cutting plasma. This research will improve understanding of the plasma cutting arc, which can lead to improvements in plasma cutting torch design, as well as develop tools that can be useful in the torch design process.

Experimental setup:

The plasma source for this investigation is a Hypertherm HT2000 plasma cutting system. Major components of this system include a power supply, high frequency starter, gas supply and controls and a cutting torch. During cutting, a conductive work-piece is connected as the anode in the cutting system. In this experiment the work-piece has been replaced by a water-cooled rotating copper ring, which allows operation of the torch without the cost or by-products associated with cutting material. Measurements of the plasma arc are obtained using a CCD camera and spectrometer. Figure 1 shows a schematic of the experimental setup including components of the cutting system, optics and measurement equipment. The experimental torch setup is the same used for previous cutting torch studies [1].

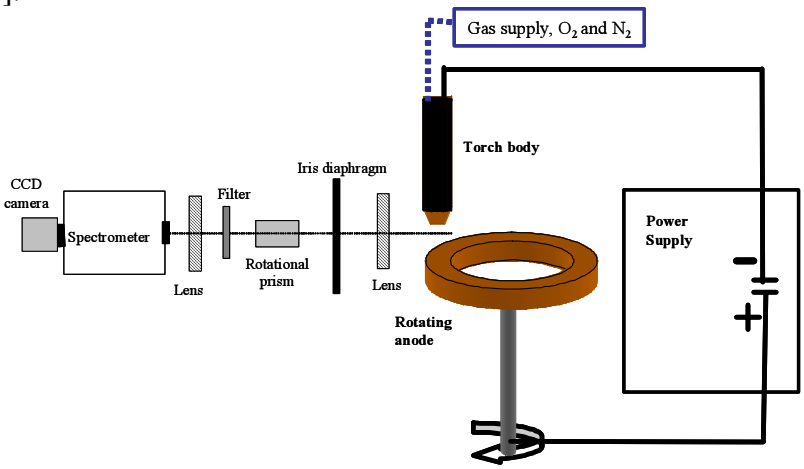

Figure 1. Schematic of experimental setup.

The optical components shown in fig. 1 magnify and rotate the arc image before it enters the spectrometer. The CCD detector used has a spectral resolution of 0.01 nm and a spatial resolution of 0.018 mm. Rotation of the image allows application of the high spatial resolution to the arc radius. Axial measurements are obtained by traversing the optical system up and down along the arc axis. Spatial resolution in the axial direction is 0.5 mm. In order to provide sufficient access to the plasma for measurement, the torch is mounted 15 mm above the surface of the anode. This standoff distance is much larger than the common cutting standoff of 3 to 4 mm.

The internal torch components greatly influence cutting performance and are therefore an important topic in this study. Figure 2a shows the components of the cutting torch, often referred to as torch consumables because they need to be replaced periodically. Each consumable set has a hafnium cathode set in water-cooled copper. The plasma gas flows through a copper nozzle with a shroud or shield gas flowing on the outside of the nozzle. Two consumable geometry designs are commercially available for the HT2000. The standard consumable set is shown in fig. 2a while fig. 2b shows a consumable set geometry with the trade name of HySpeed consumables. The major difference between the two consumable sets is in the length and shape of the nozzle bore and the introduction of the shield gas to the plasma jet.

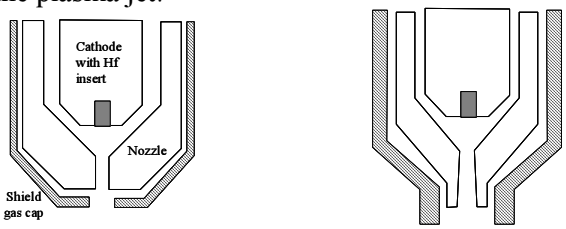

Figure 2. Torch consumables for standard geometry (a) and HySpeed geometry (b)

Typical operating conditions are a current of 200 A with a plasma gas flow of 39 slm of oxygen and a shield gas flow of air at 130 slm. In the case of the experimental investigation the shield gas flow is changed to pure oxygen to aid in the interpretation of the spectroscopic data. The nozzle exit diameter of standard consumables is 2.08 mm and 2.48 mm for HySpeed consumables.

The plasma temperature can be determined from the spectroscopic data. With certain assumptions about the plasma, i.e. it is in LTE and at 1 atm pressure, the plasma emission of a specific line of a given species can be related to the temperature. This relationship is shown in fig. 3 for an oxygen atom line and an oxygen ion line.

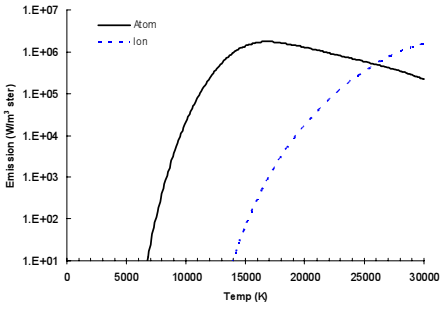

Figure 3. Plasma emission vs. temperature for oxygen atom and oxygen ion emission lines

Several possibilities for temperature calculation are available in this arc because both atomic and ionic oxygen exist. From the atomic emission lines the temperature may be derived from an absolute intensity measurement of the plasma together with a tungsten calibration source. The temperature is then obtained from data similar to that in fig 3. The ratio of different lines of the same species can be used to construct a Boltzmann plot to determine the temperature. If the temperature in the center of the arc is higher than the temperature of

maximum emission for atomic lines, the norm temperature or off-axis peaking method can be used. Oxygen ions can be used with the absolute intensity method and the Boltzmann plot method. Also, if both atomic and ionic emission lines are visible at the same location in the arc, their ratio can be used for the temperature calculation. A total of 6 distinct possible methods for determining the temperature from spectroscopic measurements exist for this plasma source.

Results:

Radial temperature profiles were obtained using all of the available calculation methods. Figure 4 shows the temperature values obtained from methods based on atomic lines (fig. 4a) and ion emission lines (fig. 4b) All measurements were taken at a distance of 7 mm from the exit of the shield cap using the standard consumable geometry. The dashed line at 1 mm indicates the location of the edge of the nozzle.

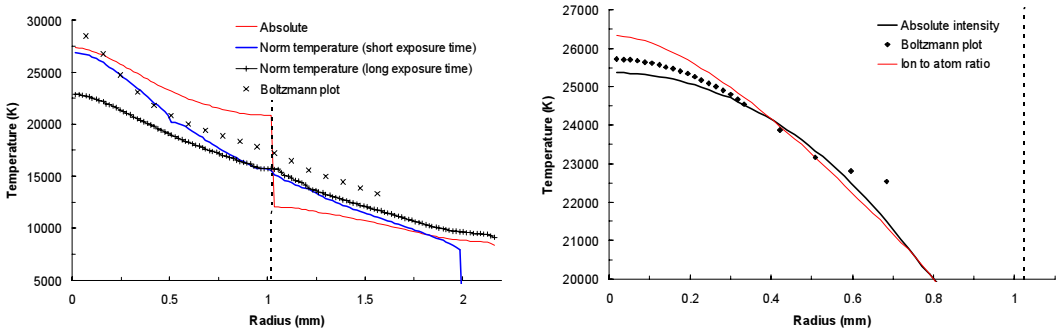

(a) **(b)**

Figure 4. Radial temperature profiles for different temperature calculation methods based on atoms (a) and ions (b)

Emission from the atom lines shows an off-axis maximum that allows for the use of the norm temperature method. Figure 4a contains 2 profiles derived using the norm temperature method. The difference between the two profiles is the exposure time. A short exposure time (~10μs) and a long exposure time (~10ms) were used. The long exposure integrates the emission over the exposure time. Temperatures from long exposure time measurements show very little variation between measurement repetitions. The short exposure time results in a large difference between repetitions, but also in consistently higher temperatures at the arc center. The same off-axis peak that is used for calibration in the norm temperature method leads to the discontinuity in the temperature profile when using the absolute method. The calibrated emission profile does not reach a maximum value that is as large as the maximum possible emission value. Because the use of the norm temperature method uses this peak for calibration, there is no discontinuity in the results from this method, only a lower temperature value in the center and a higher value below the norm temperature. The Boltzmann plot data support the existence of a higher temperature in the arc center. Three lines were available for the Boltzmann plot.

Temperature measurement methods that rely on the emission from oxygen ions are shown in fig 4b. These measurements show a temperature near 26000 K in the center and the agreement between these methods is much better. Because 7 lines were used for constructing the Boltzmann plot, the results from this method should be fairly accurate. Good agreement between the Boltzmann method and the absolute line intensity method is also a sign that the assumption of atmospheric pressure, needed for the absolute intensity method, is valid at the measurement location. The ion to atom line ratio is also very similar to the other ion based measurements at the arc center. The effects of exposure time are much smaller for the ion lines.

Radial temperature profiles at several locations along the axis of the arc are obtained from the absolute intensity method using ion emission lines. Measurements without the shield cap were made to characterize the plasma in the region immediately after the nozzle exit, while measurements with the shield gas flow were made to simulate actual operating conditions.

Figure 5 shows radial temperature profiles at several axial distances from the nozzle exit plane using the standard consumable geometry. This figure clearly shows the under-expanded nature of the plasma jet leaving the torch nozzle. The arc quickly expands outward and the temperature decreases significantly in the first 1.5 mm after the nozzle exit. This is followed by a rapid increase in the temperature 2.5 mm from the exit plane then a much slower axial temperature drop. At all axial locations, the intensity of the ion emission is not large enough to provide a measurement beyond the edge of the nozzle radius of 1 mm.

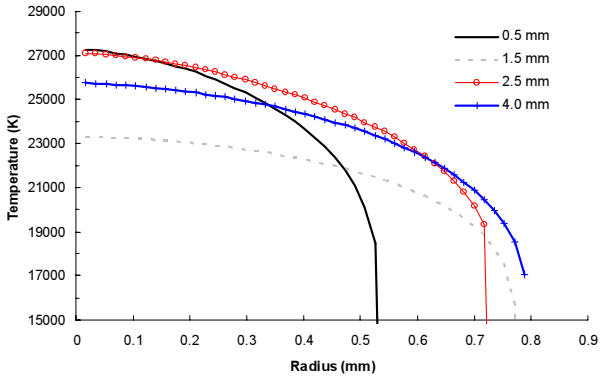

Figure 5. Radial temperature profiles at several axial locations from the nozzle exit plane. Temperature was calculated using absolute ion emission and standard consumables

Figure 6 shows the centerline arc temperature calculated using the absolute ion line intensity method along the axis of the arc for 3 different plasma gas flow rates at currents of 200 A and 160 A using standard consumables without shield flow. Increasing the flow rate increases changes in temperature in the expansion region of the jet. The locations of the maximum and minimum temperatures are also shifted downstream with increasing flow rate. There is no measurable change in the arc temperature due to changes in the plasma gas flow rate beyond the expansion region.

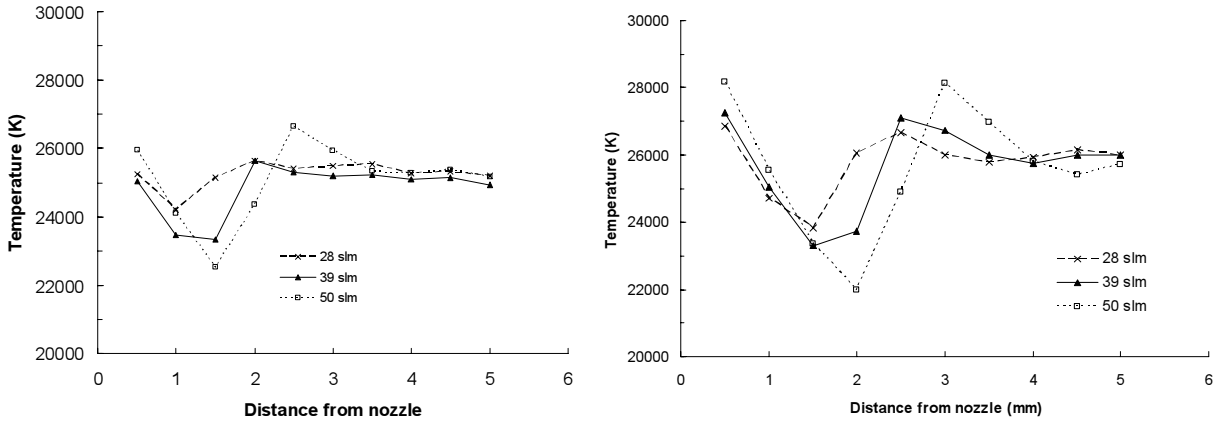

(a) **(b)**

Figure 6. Centerline temperatures for different plasma gas flow rates at 160 A (a) and 200 A (b)

Reducing the current from 200 A to 160 A reduces the fully developed temperature after the expansion region by 900 K. For the same flow rate the expansion region is shifted downstream and the temperature extremes are increased for increasing current. The radius of the high temperature region measured with the ion lines was also smaller for 160 A.

The plasma temperatures produced by the two consumable geometry designs were also compared. This comparison was performed with and without the shield cap in place. The shield cap covers most of the large temperature fluctuations in the expansion region. The shield gas flow itself has the small effect of lowering the arc temperature for the first 1.5 mm downstream of the shield cap for the standard consumables and has no measurable effect on temperature for the HySpeed consumables. In fig. 7 the centerline temperatures for both consumable types are shown. Solid lines indicate measurements made when operating with a shield gas flow of 130 slm of oxygen and dashed lines indicated that the shield cap was removed for measurement near the nozzle exit.

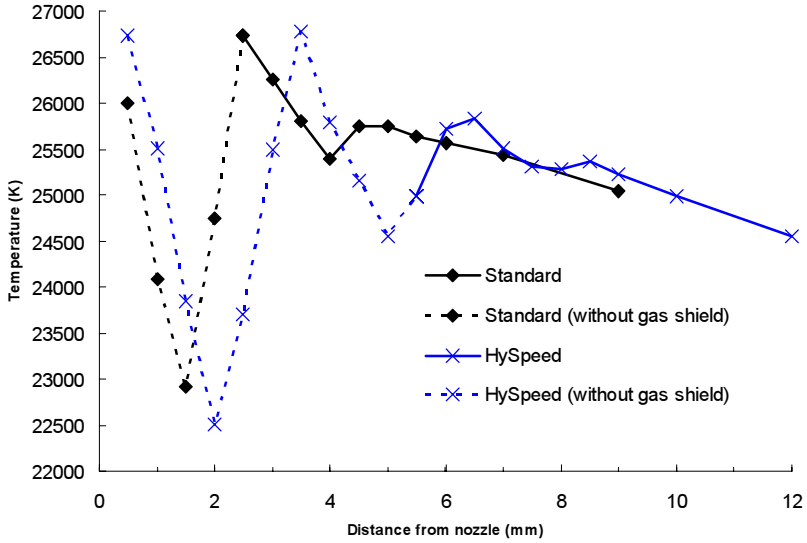

Figure 7. Centerline temperature for standard and HySpeed consumables with shield gas flow (solid lines) and with the shield cap removed (dashed lines)

The major difference between the consumable geometries is seen in the jet structure in the arc expansion region. HySpeed consumables show 3 well defined temperature peaks at 3.5 mm, 6.5 mm and 8.5 mm from the nozzle exit while the standard consumable peaks are seen at 2.5 mm and 4.5 mm from the nozzle exit. Once the jet expansion is complete the temperatures of the two consumable geometries are very similar.

Discussion:

For temperature measurement in this 200 A cutting arc, ion emission gives the most accurate values. Good agreement between the ion line methods is an indicator that there are no errors in system calibration, application of the measurement method or major violations of the underlying assumptions in the central region of the arc. Atom emission lines also give temperature values that are within 15% of the values calculated using the ion lines, another indicator of the accuracy of the temperature values obtained. The ion lines are most useful because they are most sensitive to temperature changes in the temperature range near the center of the arc. This high sensitivity allows the detection of small changes that result from design changes in the cutting system. This advantage of sensitivity can be seen from fig. 3, above 15000 K the change in emission with temperature is very small for the available atomic lines but is quite large for ion lines up to a temperature of 30000 K.

The steepest temperature gradient in the arc is near the edge of the nozzle radius. In this region the ion emission drops off quickly limiting the application of this method to the central region of the arc. Unfortunately, the atom line emission is not very sensitive in this region and these lines still have a large uncertainty in temperature measurement. Besides errors introduced due to a lower sensitivity of the emission coefficient with respect to temperature, short term intensity fluctuations (~100 μs) have been observed in the arc fringes indicating fluid dynamic instabilities. Time resolved measurements in the arc fringes will yield different temperature values

than time averaged measurements. In addition, the temperature values may not be valid in this arc fringe region due to deviation from LTE, which is assumed for all the calculation methods.

Because the jet exiting the nozzle is under-expanded, there are axial fluctuations in temperature as the jet adjusts to match atmospheric pressure. The pressure is also changing in this region [2]. When using the absolute line intensity method to calculate plasma temperature, a pressure of 1 atm is assumed. A violation of this assumption will lead to errors in the temperature calculation. The Boltzmann plot method is independent of the pressure because it is the relative emission from several lines. However, the Boltzmann plot is not as sensitive as the absolute line intensity method and is more affected by sources of uncertainty in the measurement. Large changes in temperature are visible using this method but smaller differences are not detectable. The absolute intensity method was still used in the expansion region because the error due to the pressure assumption in the absolute method is acceptably small [3]. It has been estimated that a pressure deviation 20% at 20000K leads to a temperature error of 200 K. The emission is also much more sensitive to changes in temperature. A 20% change in pressure will produce the same change in emission as a 2% change in temperature.

Arc current had the strongest influence on the temperature of the arc. Changes in the nozzle geometry or plasma gas flow rate only changed the expansion region of the arc. The observed changes are consistent with a change in the pressure inside the nozzle. For a given flow rate, decreasing the current leads to a smaller arc which gives more area for cold gas flow through the nozzle. This reduces the pressure drop in the nozzle and makes the jet expansion region shorter with smaller temperature changes.

Conclusions:

A spectroscopic method for measuring the temperature has been used to characterize a plasma cutting arc. The accuracy of this system has been established by using several different methods of temperature measurement which all give similar results. With this system ion line emission is the best method for temperature measurement, and this method is capable of detecting the effects of several cutting torch design parameters on the plasma temperature. The arc current has the most influence on arc temperature, while the nozzle geometry and gas flow rate influence the jet expansion at the torch exit.

Acknowledgement:

Funding of this study by Hypertherm Inc. is gratefully acknowledged.

References:

[1] J. Peters, J. Heberlein, C. Hackett. ISPC 16 2003.

[2] P. Freton, J. J. Gonzalez, F. Camey Peyret, A. Gleizes. J. Phys. D: Appl. Phys. **36** (2003) 1269-1283.

[3] C. Pardo, J. Gonzalez-Aguilar, A. Rodriguez-Yunta, M. A. G. Calderon. J. Phys. D: Appl. Phys. **32** (1999) 2181-2189.

Axial distributions of the potential in plasma of secondary discharges with a liquid electrode

V.Ya. Chernyak[1], V.V. Naumov[2], I.L. Babich[1], Yu.V. Voevoda[1]

[1]*Plasma Lab, Dept. of Physical Electronics, Faculty of Radiophysics, Taras Shevchenko Kyiv National University*
Prospect Acad. Glushkova 2/5, 03122 Kyiv, Ukraine; e-mail: chern@univ.kiev.ua
[2]*Photonics Lab, Institute of Fundamental Problems for High Technology, Ukrainian Academy of Science*
Prospect Nauki 45, 03028 Kyiv, Ukraine; e-mail: naumov@ifpht.kiev.ua

Abstract
The probe and spectroscopy studies of a two-phase gas-liquid plasma system with a secondary electric discharge with a liquid electrode are presented. The existence of the jump of the electric field potential at the plasma-liquid interface and its dependence on the current and polarity of the discharge is demonstrated. Its shape, amplitude and pulsations depend on the distance from the liquid surface. It is found that during the cw burning of the secondary discharge in water vapors of low pressure, plasma is effectively enriched by free hydrogen.
Keywords plasma chemistry, gas-liquid plasma, secondary discharge, potential jump, hydrogen

1. Introduction

Plasma chemistry long time has been developing commonly considering plasma as a chemical active medium, which activity is instituted by high temperatures and high concentrations of reactive components: ions, electrons, radicals, excited particles, and photons [1]. Today it became clear the charge for such high activity of plasma is a low selectivity of plasma-chemical transformations, i.e. chain multi-channeling and weak control of processes. It is generally supposed the main way of increasing a plasma-chemical selectivity lies in moving from the thermal to non-thermal plasma. However, existing gas-discharge sources of non-equilibrium plasma can provide at best only the non-isothermality. It means the situation when the temperature of electrons differs from characteristic temperatures of heavy particles at the average energy of electrons lower than energies where the cross-sections of excitation for inelastic processes, such as dissociation of molecules, are maximal [2]. It is hard to advance the cause in the bulk plasma even in the transitional mode of non-thermal plasma, but it is possible to extend opportunities by organizing the heterophase plasma, providing branched contact between gas-discharge plasma and solid- or/and liquid substances. In this direction, two-phase gas-liquid plasma systems are of great interest [3]. They are based on self-maintained discharges having one or two immersed electrodes. Among them, electrolytic glow, corona, spark, barrier, gliding arc, and others are well-known [4]. But, despite of wide usage of these discharges, their physics and chemistry in gas-liquid systems are not studied well. Many discharges still have no theoretical description for explanation of electric-physical phenomena occurring in the positive column, near-electrode zones, and especially at the plasma-liquid interface. The main peculiarity of such plasma systems is the presence of the free liquid surface which represents an intense emitter of liquid molecules brought into the discharge volume at the atomization of liquid solution and formation of gaseous plasma-chemical products. The second peculiarity is conditions of gas-liquid plasma generation, corresponding to the saturated vapor pressures at given temperatures. For aqueous solutions, the lower pressure limit can be reached only under the continuous exhaust pumping. Under such conditions, the electric discharge burning represents the ascending branch of the Paschen curve, which determines the development of thermal plasma instabilities. Other factor contributing to the development of ionization instabilities in gas-liquid plasma is related with a presence of negative ions. Despite all problems, it is clear that gas-liquid plasma systems can be very effective because of (i) transition to non-thermal plasma with a high level of ionization nonequilibrium; (ii) realization of uniform parameters at the plasma-liquid interface, and (iii) efficient control during discharge operation. On the ground of the above consideration, a special interest for us presents the secondary gas-liquid discharge with a liquid electrode, supported by means of the auxiliary plasma flow [5]. In this discharge, one electrode is immersed in liquid while another belongs to the auxiliary self-maintained discharge in gas-vapor medium. In the present work, we study physical properties of such plasma-liquid system at low-pressure (~ 1 Torr) conditions.

2. Experimental Methodology

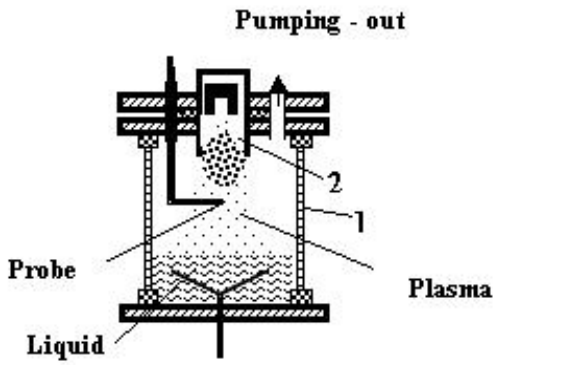

Fig. 1. Plasma chemical reactors for investigation of plasma-liquid systems of low pressure.

The scheme of the experimental setup used for studies of the low-pressure plasma-liquid system is depicted in Fig. 1. It consisted of the quartz vacuum chamber 1 and the electrical discharge system of gas-liquid type including the coaxial-end discharger 2. The electric field of the secondary discharge was applied between the metallic electrode immersed into liquid volume and the auxiliary discharge plasma source that anode served as an electrode for the secondary discharge at the same time. The distance between the source of the plasma flow and the liquid surface did not exceed 7 cm, while the height of the liquid column above the immersed electrode was 2-3 cm. This electrode had a conic form with diameter 6 cm, providing a stable state of the liquid surface under the discharge operation. The working liquid solution was distilled water. The discharge is powered by the DC source at the ballast resistance $R = 4$ kΩ in the circuit. Current-voltage parameters were measured by standard digital electronics. In order to measure the spatial distributions of the potential of the electric field in plasma-liquid system, we used a plasma probe technique. The probe of diameter 300 μm and 1 mm long was connected via the divider with a division factor 2,000 directly to the inverting entrance of the oscilloscope. The ionometric technique was also available for plasma diagnostics. For optical diagnostics, besides imaging photography, a method of optical emission spectroscopy was applied. The plasma radiation was monitored by the portable rapid PC-operated CCD-based multi-channel UV-VIS-NIR optical spectra analyzer in the range of wavelengths 200-1100 nm (spectral resolution 0.3 nm). For spatial point-to-point monitoring, a fine long optical fiber with a micro-lens focusing was used (pointing accuracy ~0.1 mm). For calibrations, the etalon spectral lamps were applied. From the measured spectra the population and temperatures of electronically excited atoms of hydrogen and oxygen were determined by the method of relative intensities [6] (diagnostic uncertainty ±10%). Measurements were conducted in different cross-sections along the secondary discharge at different polarities the electrodes.

3. Results and Discussions

Fig. 2 presents photo images of the low-pressure secondary discharge system operation in the absence of water: (a) is the burning of the auxiliary coaxial-end discharge; (b) is the secondary discharge at a positive polarity of the conic electrode, and (c) is the secondary discharge at a negative polarity of the conic electrode.

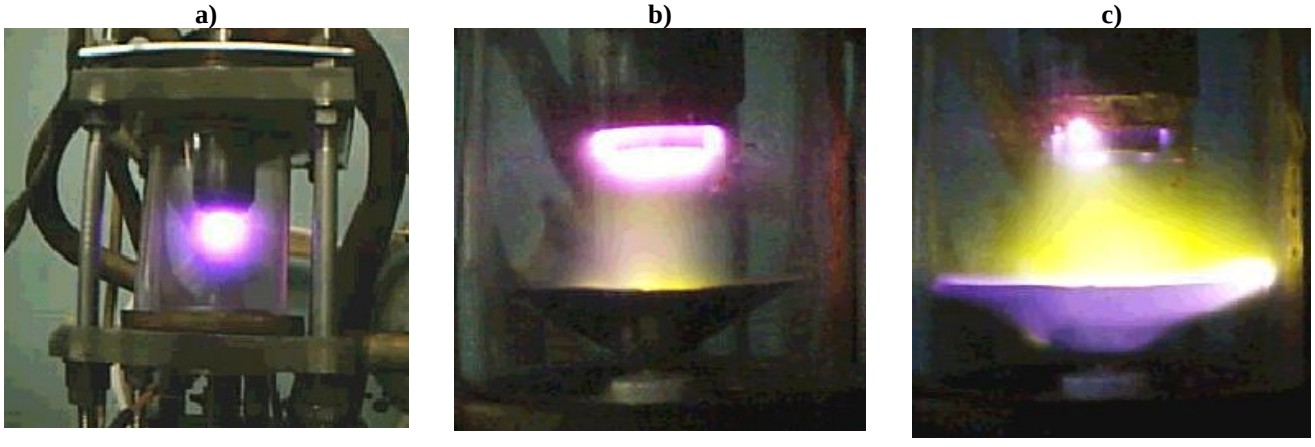

Fig.2. Photos of the low-pressure secondary discharge system without liquid electrode.

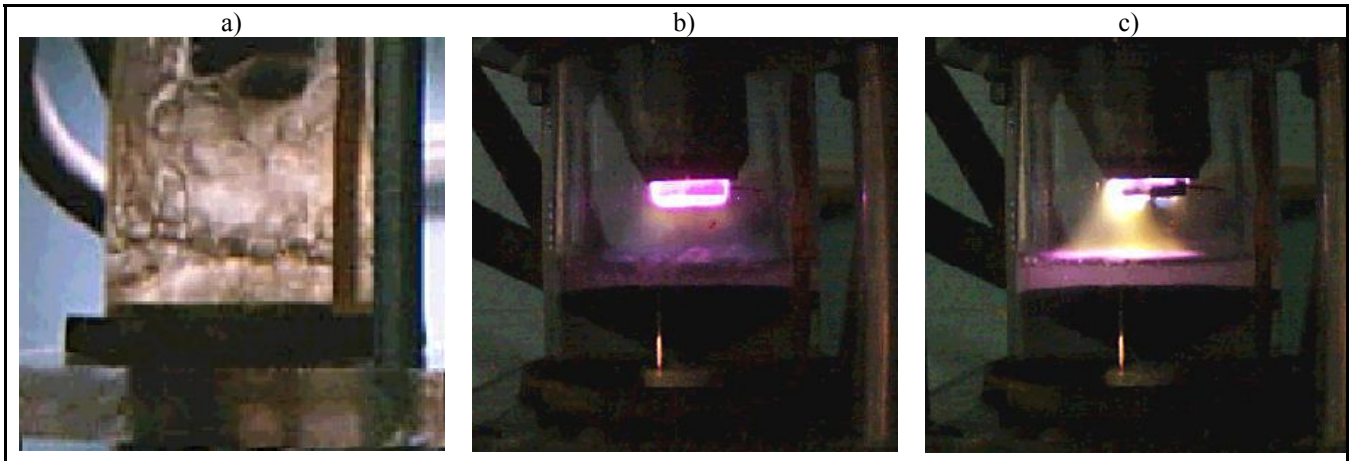

Fig. 3. Photos of the low-pressure plasma-liquid system with liquid electrode.

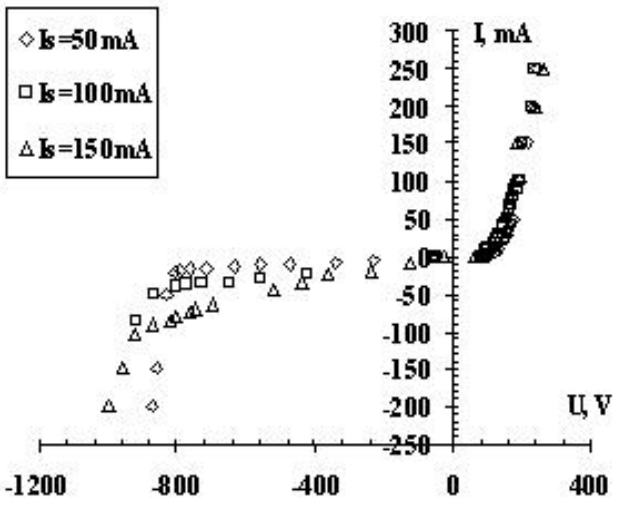

Fig. 4. Volt-ampere charecteristics of the secondary discharge.

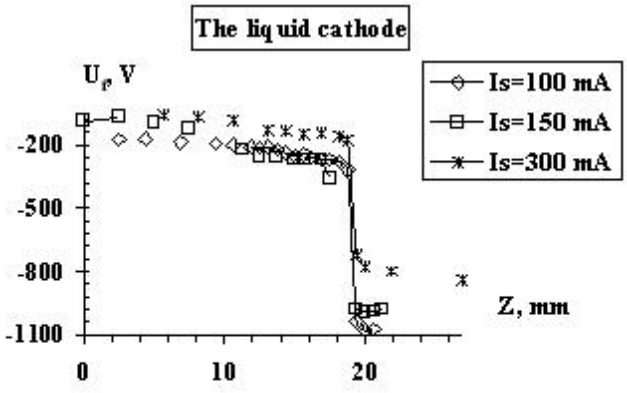

Fig. 5. Axial distribution of the floating potential of the electric field in plasma-liquid system with liquid cathode.

The feature of the secondary discharge operation in the presence of water was its vigorous boil on reaching the pressures below the saturated vapor pressure at given temperature (see photo in Fig. 3a). After complete evaporation of dissolved gases (vacuum outgassing took several minutes) the water boiling was ended and the secondary discharge was switched on. Fig.3b and Fig.3c present images of the plasma-liquid system operation with a live discharge for two different modes: (b) is the secondary discharge with a positive polarity of the immersed electrode ("liquid cathode"), and (c) is the secondary discharge with a negative polarity of the immersed electrode ("liquid anode"). In both modes the plasma column has a truncated cone-shape with extension at the liquid surface. Its size varies as the discharge current. The state of the liquid surface also depends on the discharge conditions. In case of the negative polarity of the liquid electrode its surface was quite normal (without visual bifurcations).

The measurements of current-voltage characteristics of the secondary discharge in plasma-liquid system have shown that in the range of low currents its behavior is similar to usual *I-V* curves of the probe, while in the range of high currents it has a sharp growth character as for the secondary gas discharge in strong electric fields [2]. Typical dependences of the secondary discharge current I_d at different potentials of the liquid electrode U_d and various values of the auxiliary discharge source current I_s are given in Fig. 4. The measurements of the axial distribution of the floating potential of the electric field in plasma-liquid system with a liquid cathode at the typical value of the secondary discharge current I_d = 150 mA and different currents of the auxiliary discharge I_s = 50-300 mA are presented in Fig. 5. Here, a distance from the auxiliary discharge downstream is 2 cm. These

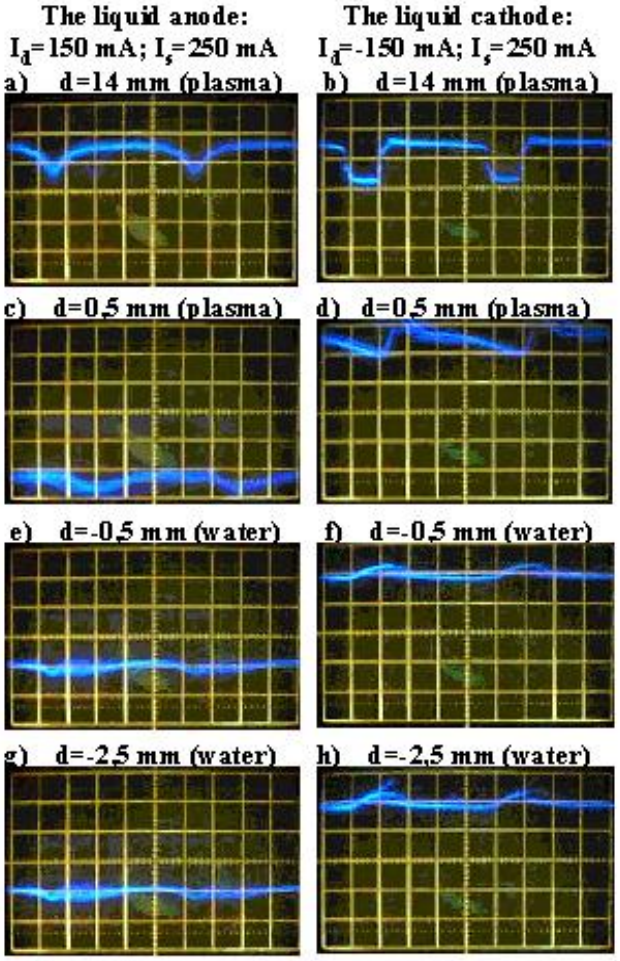

Fig. 6. The probe signals on an inverted unclosed entry oa oscillograph at different distances of a probe from plasma - liquid border.

measurements indicate the existence of a region near the liquid surface where the axial gradient of the plasma potential rises sharply. Such an increase of the voltage where plasma contacts liquid, can be interpreted as a decrease of the electroconductivity due to the process of dissociative attachment of electrons to H_2O molecules: $e+H_2O=OH^-+H$. It is assumed that mobility of negative ions OH^- near the liquid surface is lower than mobility of positive ions H^+ [5]. At the same time, a potential jump at the plasma-liquid interface can be associated with the basic peculiarity of the secondary discharge maintained due to the plasma flow from the auxiliary discharge. There is always a jump of the potential between the electrode and surrounding plasma due to a shielding effect of space charges. It gives possibility to control the secondary discharge voltage jump near its electrode by variation of the auxiliary discharge voltage, if the jump width is less than the free electron path length. The probe measurements revealed also a fact of pulsations of the potential caused by the ripple voltage of the power supply. Their amplitude and shape vary along the discharge and depend on the distance from the liquid surface and polarity of electrodes (Fig. 6). The peak amplitude is situated near the output electrode of the auxiliary discharge.

The results of optical emission spectroscopy of plasma-liquid system in the secondary discharge with a liquid electrode after the vacuum outgassing have shown the presence of wide spectrum of excited species in output products including components of dissolved gases but most intensive emissions belong to hydrogen-containing species: H (atomic lines of Ballmer series Hα 656.3 nm, Hβ 486.1 nm, Hγ 434.0 nm), OH ($A^2\Sigma$-$X^2\Pi$ 0,0-band at 306-309 nm) and oxygen (atomic lines OI 777.3, 844.6, and 926.0 nm). Fast response of the CCD spectrograph (min exposure time ~7 ms) allowed to explore the temporary changes in intensities of the emission of separate atomic lines H and molecular bands OH during the secondary discharge burning within the time t = 1-30 min. This monitoring has shown that in the modes with a liquid anode the intensity of H lightly increases with the magnification of time of treatment. The monitoring of the modes with a liquid cathode has revealed a strong decrease of intensity of H and a gradual decrease of intensity of OH. The representative dependence of intensity I_λ for the Hα line 656.3 nm is given in Fig. 7. The corresponding dependences for the temperature of electronic excitation of H atoms T^* determined from the relative intensities I_λ are presented in Fig. 8. The values T^* vary in the range from 0.4 to 0.5 eV depending on the discharge conditions. They have somewhat different character of dependency: in the modes with a liquid cathode the T^* decreases, while in the modes with a liquid anode the T^* grows. The obtained dependences $I_\lambda(t)$ and $T^*(t)$ allowed to make the estimation of concentration of released hydrogen. It turned out that the number of H atoms has tendency to increasing, and its greater accumulation is in plasma-liquid system with a liquid cathode. Apparently, basic mechanism of formation of hydrogen in the low-pressure plasma-liquid system is connected with electrochemical processes near the metallic electrode immersed in water. This deduction correlates with the above note about the stability of the liquid surface in plasma-liquid system with a liquid cathode.

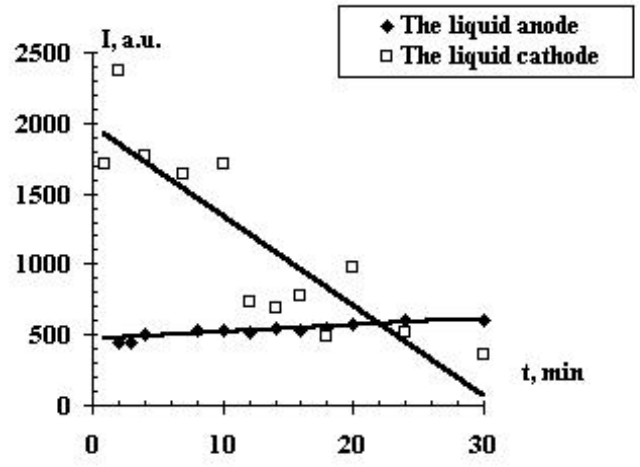

Fig. 7. Dependence of intensity of a hydrogenous line H_α of a burning time of the discharge.

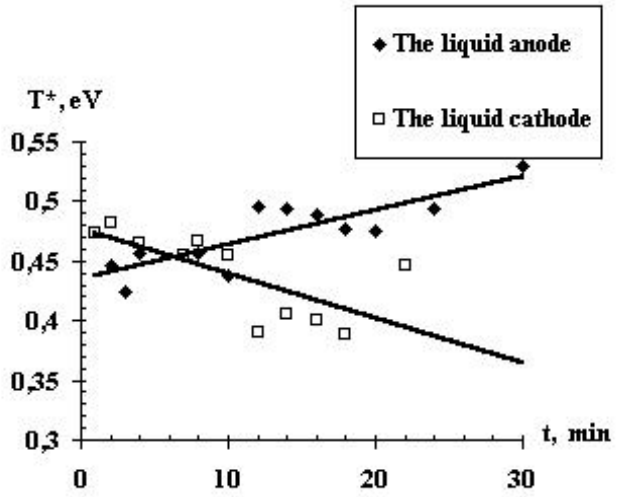

Fig. 8. Dependence of the population temperatures for electronic levels of a hydrogen atoms from a burning time of the discharge.

Conclusions

On the results of our investigation of the secondary discharge with a liquid electrode, supported by the auxiliary plasma flow based on the discharge in water vapors of low pressure, we can conclude the following:

- In the two-phase plasma-liquid system under conditions of the low-pressure secondary discharge with a liquid electrode, a jump of the electric field potential on the gas-liquid interface exists. It depends on the current and polarity of the discharge. The pulsations of the potential are caused by the ripple voltage of the power supply. Their amplitude and shape vary along the discharge and depend on the distance from the liquid surface and polarity of electrodes. The peak amplitude lies near the anode of the auxiliary discharge.
- The current-voltage characteristics of the secondary discharge with a liquid electrode are similar to those for typical secondary gas discharges. In case when the potential of the liquid against plasma is positive, the current is by two orders higher than that in case of the negative potential.
- The emission spectroscopy of the plasma-liquid system in the low-pressure secondary discharge has shown the presence of wide spectrum of excited species in output products including components of dissolved gases but most intensive emissions belong to hydrogen-containing species H and OH. The population temperature of H atoms determined from the relative intensities varies in the range 0.4-0.5 eV depending on the discharge conditions. At that time the concentration of H atoms has tendency to increasing. It means that during the cw burning of the secondary discharge in water vapors at low pressure, plasma is effectively enriched by free hydrogen.

The work was partially supported by the Ministry of Education and Science of Ukraine.

References

[1] V. Rusanov, A. Fridman – *Physics of Chemically Active Plasma*, Nauka: Moscow (1984); V. Zhivotov, V. Rusanov, A. Fridman - *Diagnostics of Chemically Active Plasma*, Atomizdat, Moscow (1985).
[2] Yu.P. Raiser - *Gas Discharge Physics*, Nauka, Moscow (1987); Springer, Berlin (1997).
[3] E.M. van Veldhuizen (Ed.) - *Electrical discharges for environmental purposes: fundamentals and applications*, New York: Nova Science Publishers Inc. (2000).
[4] V. Chernyak, S. Koval, V. Naumov - *Proc. 15th Intern. Symp. on Plasma Chemistry*, IV, 1447 (2001).
[5] V.Ya Chernyak, S.V. Olshevskii – *Ukr.J.Phys.* **50**(3), 243 (2005).
[6] V.Ya. Chernyak, V.V. Naumov, I.L. Babich *et al* - *Bull.Univ. of Kiev, Series: Physics,* 4, 379 (2004).

Microwave heating of a ceramic sample

Yu.V. Bykov [1], V.E. Semenov[1], O.N. Kanygina[2], E.B. Kulumbaev[2], V.M. Lelevkin[2]

[1] *Institute of Applied Physics of the Russian Academy of Sciences, Nizhny Novgorod, Russia*
[2] *Kyrgyz-Russian Slavic University, Bishkek, Kyrgyz Republic*

Abstract
A two-dimensional magnet-gas-dynamic model is considered for the ceramic material microwave heating in a channel of the rectangular waveguide. The alumina and surrounding air characteristics are calculated at atmospheric pressure in microwave radiation field at frequency of 2.45 HHz.

Introduction

In our days modern technologies are intensively applied to manufacture ceramic products, using microwave radiation, which allows realization of porous materials and gas phase [1-2] volumetric heating. The Institute of Applied Physics RASc has created special equipment of 20 kWt for ceramic materials treatment in continuous (electromagnetic fields frequencies 30-85 HHz) and pulse (several hundreds kilowatts; electromagnetic fields frequencies 110-170 HHz) modes. The materials obtained at microwave heating have better mechanical characteristics and resistance to fissuring, because in multi-mode cameras fed by the microwave radiation a high uniformity of the power volumetric distribution is realized.

In this work a self-consistent two-dimensional model of the ceramic cylinder stationary microwave heating in the rectangular waveguide is developed due to electromagnetic wave H_{10} power dissipation in Earth's gravitational field.

Model

We consider a microwave heating of the ceramic pattern of cylindrical shape, oriented perpendicular to wide walls of the rectangular waveguide of section $a \times b$ (fig.1) at the expense of electromagnetic power dissipation supplied by the TE-wave with components $\vec{E}(0;\, E_y = E;\, 0)\exp(i\omega t - ikz)$, $\vec{B}(B_x;\, 0;\, B_z)\exp(i\omega t - ikz)$. Stationary heating is ensured by heat removing from the cylinder surface due to heat conductivity and laminar convective cooling in gas environment (air at atmospheric pressure). In two-dimensional approximation we neglect the characteristics changes along the electric-field intensity vector (along the cylinder axis in parallel with narrow walls of the waveguide).

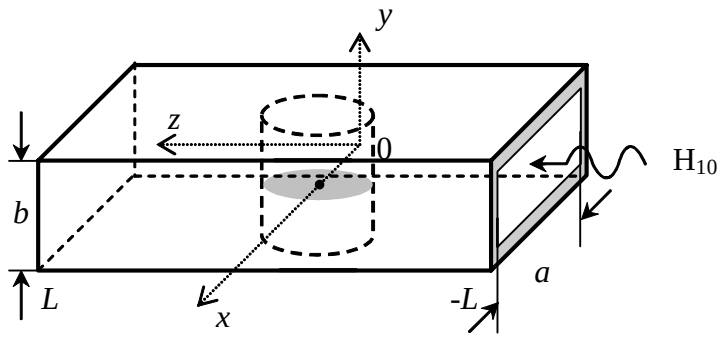

Figure 1. Scheme of the ceramic cylinder microwave heating in the rectangular waveguide.

Equations. We describe a process of microwave heating in Cartesian rectangular coordinates (fig.1) on the basis of stationary continuity equations, Navier-Stokes equations, power balance and wave equations:

$$\frac{\partial}{\partial x}(\rho u) + \frac{\partial}{\partial z}(\rho w) = 0$$

$$\rho u\frac{\partial u}{\partial x} + \rho w\frac{\partial u}{\partial z} = -\frac{\partial p}{\partial x} + 2\frac{\partial}{\partial x}\left(\eta\frac{\partial u}{\partial x}\right) + \frac{\partial}{\partial z}\left[\eta\left(\frac{\partial u}{\partial z} + \frac{\partial w}{\partial x}\right)\right] - \frac{2}{3}\frac{\partial}{\partial x}\left[\eta\left(\frac{\partial u}{\partial x} + \frac{\partial w}{\partial z}\right)\right] - (\rho_\infty - \rho)g_x$$

$$\rho u\frac{\partial w}{\partial x}+\rho w\frac{\partial w}{\partial z}=-\frac{\partial p}{\partial z}+\frac{\partial}{\partial x}\left[\eta\left(\frac{\partial u}{\partial z}+\frac{\partial w}{\partial x}\right)\right]+2\frac{\partial}{\partial z}\left(\eta\frac{\partial w}{\partial z}\right)-\frac{2}{3}\frac{\partial}{\partial z}\left[\eta\left(\frac{\partial u}{\partial x}+\frac{\partial w}{\partial z}\right)\right]-(\rho_\infty-\rho)g_z$$

$$\rho uC_p\frac{\partial T}{\partial x}+\rho wC_p\frac{\partial T}{\partial z}=\frac{\partial}{\partial x}\left(\lambda\frac{\partial T}{\partial x}\right)+\frac{\partial}{\partial z}\left(\lambda\frac{\partial T}{\partial z}\right)+\frac{1}{2}\omega\varepsilon_0\varepsilon_I E^2;\frac{\partial^2 E}{\partial x^2}+\frac{\partial^2 E}{\partial z^2}+\frac{\omega^2}{c^2}(\varepsilon_R-i\varepsilon_T)E=0.$$

Here: $\vec{V}=(V_x=u,\ V_z=w)$- is velocity; p - pressure; T - temperature; $\vec{g}=(g_x,g_z)$ - gravitational acceleration vector; ρ, C_p, η, λ - density, thermal capacity, viscosity, thermal conductivity; ε_R, ε_I - real and imaginary parts of complex dielectric permeability; $\omega=2\pi f$ - cyclic frequency; $k=\sqrt{(\omega/c)^2-(\pi/a)^2}$ - longitudinal propagation number; c – velocity of light; ε_0 - electric constant; i - imaginary unit.

Boundary conditions are set on a rectangular contour of the accounted region $0\le x\le a, -L\le z\le L$ (fig.1):

on inflow boundary – the conditions of normal gas inflow at given pressure and superposition of incident and reflected electromagnetic waves in the rectangular one-mode waveguide are:

$$z=-L\ :\ p=p_0,\ u=0,\ \partial(\rho w)/\partial z=0,\ T=T_\infty,\ E=\left[E_I\exp(-ikz)+E_R\exp(ikz)\right]\sin(\pi x/a);$$

on outflow boundary – the conditions of normal outflow or inflow of gas and passed electromagnetic wave are:

$$z=L\ :\ p=p_0,\ u=0,\ \partial(\rho w)/\partial z=0,\ \partial T/\partial z=0,\ E=E_T\exp(-ikz)\sin(\pi x/a);$$

on side boundaries – the conditions of "adhesion" on cold ideally conducting waveguide walls are:

$$x=0;a\ :\ u=0,\ w=0,\ T=T_\infty,\ E=0,$$

where E_I, E_R, E_T are amplitudes of incident, reflected and passed H_{10} waves.

Solution technique is based on the end-to-end account at which a self-adjointness of tasks in solids and gases on boundaries of their separation is reached by introduction of transport factors, determined as average harmonic ones [3]. We make the discretation of the equation by the method of control volume. The pressure field is calculated with help of the SIMPLER-procedure [3]. Temperature in the center of pattern's profile $(a/2, 0)$ is T_0, input microwave power P_I is determined interactively. Boundary conditions for E will be reduced to radiation conditions:

$$z=-L\ :\ \frac{\partial E}{\partial z}-ikE=-2ikE_I\exp(-ikz)\sin(\pi x/a),\quad z=L\ :\ \frac{\partial E}{\partial z}+ikE=0.$$

As the wave equation determines the amplitude of the electric field intensity to a free constant multiplier, the first condition is substituted by the correlation $z=-L:\tilde{E}=\sin(\pi x/a)$. An interactive character of the condition on the right boundary is saved. The obtained numerical solution $\tilde{E}(x,z)$ is scaled $E(x,z)=K_E\tilde{E}(x,z)$ with coefficient $K_E=|E_0|/|\tilde{E}|$ at $x=a/2,\ z=0$. The module $|E_0(a/2,0)|$ ensures the power balance for current (on given iteration) values of required variables in control volume with temperature T_0. By the obtained field $E(x,z)$ we calculate amplitudes E_I, E_R, E_T and respective microwave powers $P_{I,R,T}=kE_{I,R,T}^2 ab/4\mu_0\omega$.

Results

For an example one made calculation of pattern of the ceramic (baked alumina, density 97%) microwave heating in air at atmospheric pressure in the rectangular waveguide 72×32 mm with the electric field intensity f = 2.45 HHz. Thermo-physical characteristics of Al_2O_3 and air are given by temperature functions. Spatial orientation of the waveguide in Earth's gravitational field is g = 9.8 m/s^2, $\vec{g}(0, g_z=-g)$, $\vec{g}(g_x=-g, 0)$.

As a result of accounts it was found (fig.2) that the ceramic cylinder profile is drain for vector of Umov-Pointing. The electric field propagation around axis is "saddle" (in the cylinder center minimum field is realized toward the wave propagation and maximum – in transverse location). "Focusing" field's effect is observed on backside of the cylinder profile directed toward waveguide H_{10}-wave propagation, where maximum temperature value is realized.

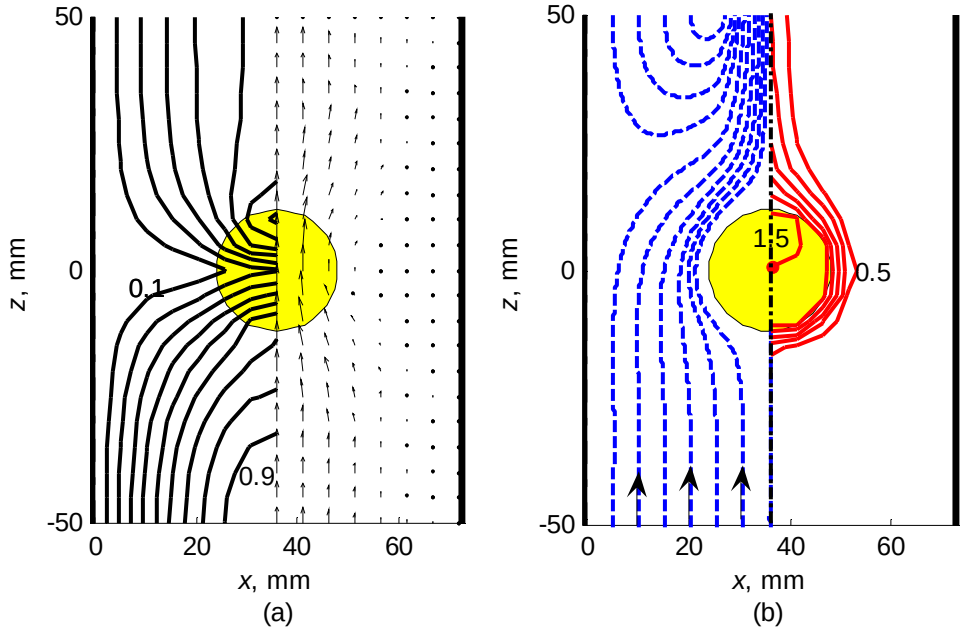

Figure 2. (a) Isolines of the electric field intensity module E/E_*, from 0.1, pitch 0.1 (E_*=0.59 kV/cm); a field of Umov-Pointing vector; (b) isotherms from 0.1, pitch 0.2 kK and 1.5 kK (firm lines) and gas flow lines (dotted line) at natural convection: $g_z = -g$; $V_{ext} = 0$ (P_I = 1.18 kW; P_R = 0.35 kW;P_d = 0.05 kW; P_T = 0.78 kW).

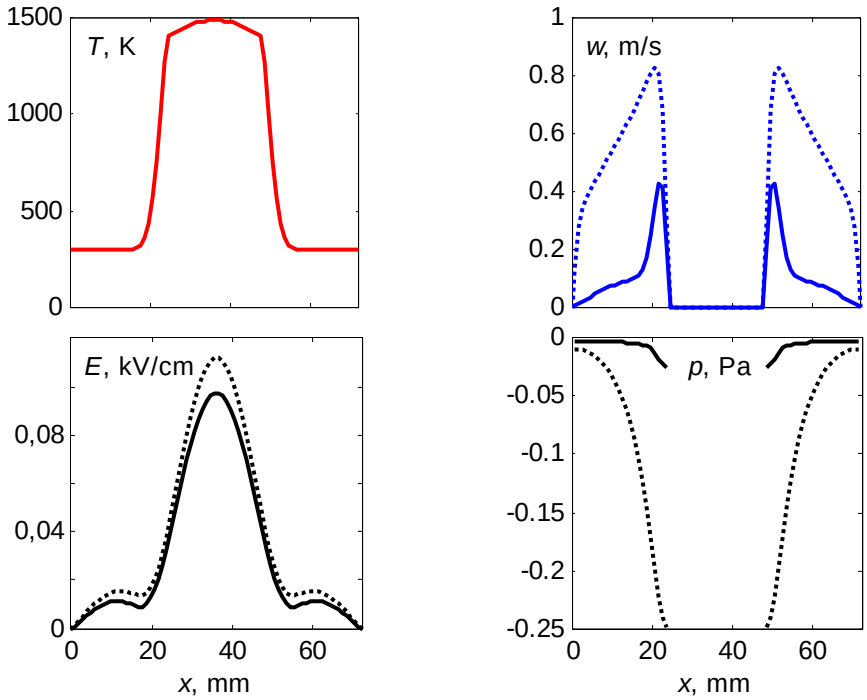

Figure 3. Temperature distribution T, velocity components w, module of the electric field intensity $|E|$ and pressure p at $z = 0$; $g_z = -g$; $V_{ext} = 0$ (firm lines); 0.5 m/s (dotted line).

At natural convection ($V_{ext} = 0$) a picture of gas flow lines and heat flows on the waveguide walls rather depend on the ceramic cylinder spatial orientation in Earth's gravitational field (fig.2, 5a). But this influences little the product heating.

A degree of temperature field heterogeneity in the cylinder profile, a temperature and gas-dynamic structure of the exterior cooling gas flow essentially depend on a type of convective cooling. At gas pumping in the waveguide (forced convection) a cold gas flow intensively cools the cylinder front, increasing a temperature gradient in the product (fig.3-4) and, accordingly, expands the isotherm on the cylinder back (fig.5b). When the velocities of a cold gas, blowing around a ceramic cylinder are $V_{ext} > 1$ m/s, a role of natural convection similar the waveguide orientation in gravitational Earth's field is inessential.

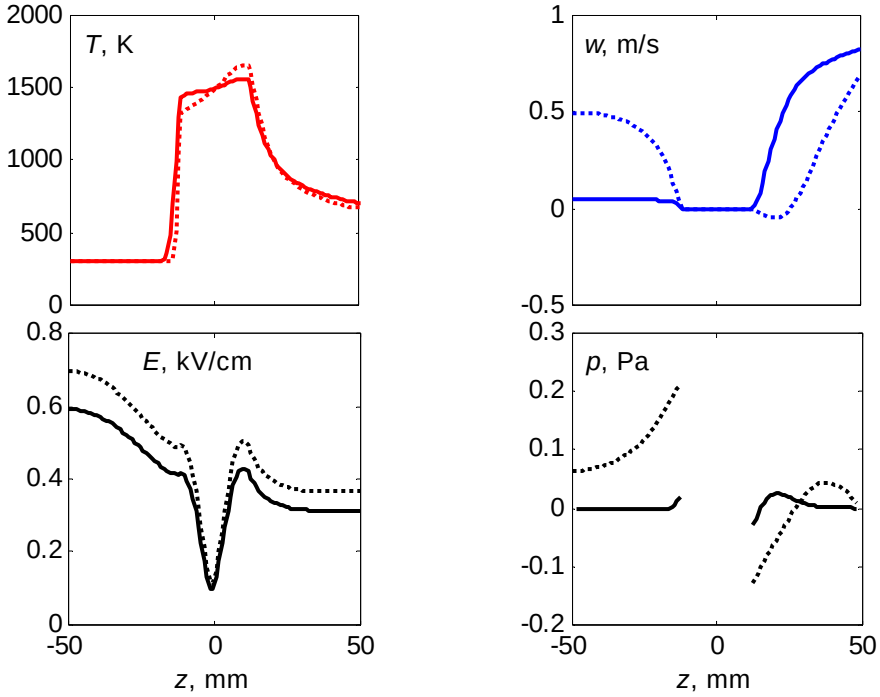

Figure 4. Distributions of temperature T, velocity w, the electric field intensity module $|E|$ and pressure p at x = 36 mm; $g_z = -g$; $V_{ext} = 0$ (firm lines); 0.5 m/s (dotted lines).

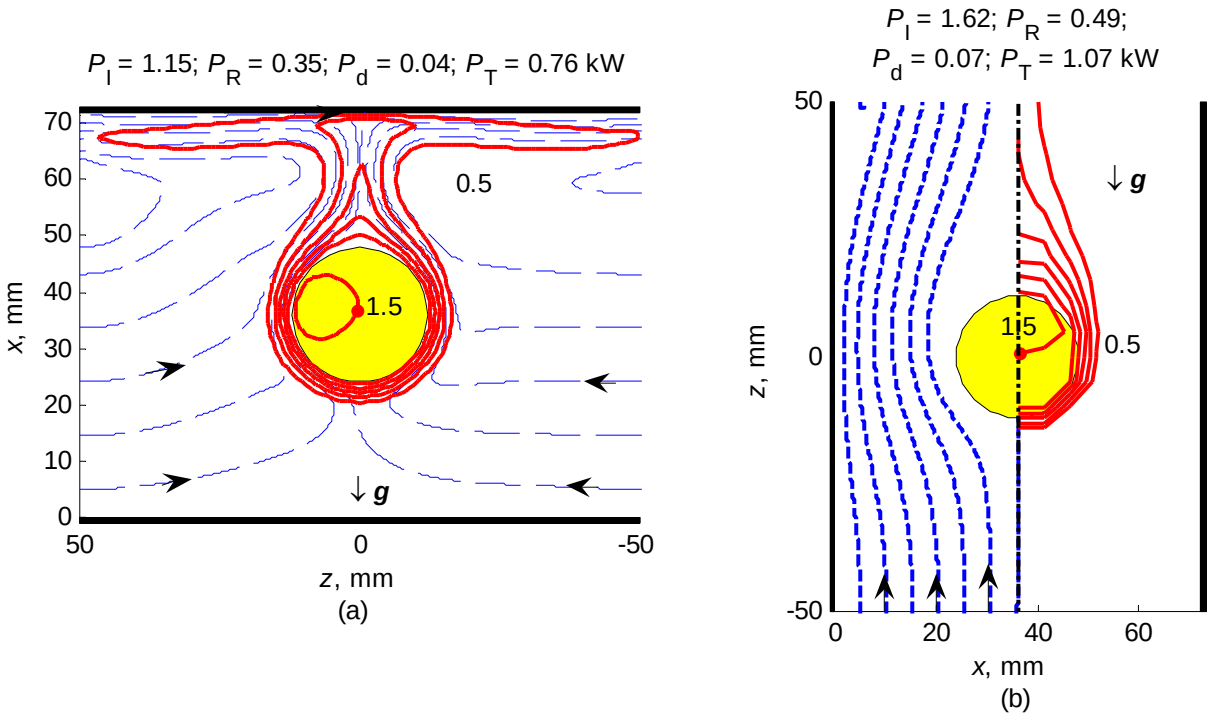

Figure 5. Isotherms in kK (firm lines) and gas flow lines (dotted lines) at natural convection (a) $g_x = -g$; $V_e = 0$; (b) $g_z = -g$; $V_{ext} = 0.5$ m/s.

Literature

1. Yu. Bykov, A. Eremeev, V. Flyagin, et. al., Ceramic Transactions **53**, 133 (1995).
2. Yu. Bykov, S. Gusev, V. Holopsev, et. al., Nanostructured Materials **6**, 855 (1995).
3. S. Patankar, *Numeral Heat Transfer and Fluid Flow* (McGraw-Hill, New York, 1980).
4. V.S. Éngel'sht, V.Ts. Gurovich, G.A. Desyatkov, *et al.*, *The Theory of Electric Arc Column* (Nauka, Novosibirsk, 1990), Vol. 1.

PETROCOKE PLASMA-STEAM GASIFICATION

M. Khan[1], L. Khan[2], V.G. Lukiaschenko[3], V.E. Messerle[3] and A.B. Ustimenko[3]*

[1] *National Interest Corporation, USA;*
[2] *Illinois State Geological Survey, USA;*
[3] *The Combustion Problems Institute, Kazakhstan*

* *ust@ntsc.kz*

Abstract

This paper presents a numerical analysis and experimental investigation of air and steam plasma gasification of petrocoke. Numerical analysis was carried out using the software package TERRA. From the data produced from the analysis, the optimal medium and operating parameters for the gasification process were discovered. Using these results, preliminary experiments on plasma steam gasification of petrocoke were carried out, producing high quality Syngas. The numerical calculations and experimental results corresponded with one another.

Introduction

The world's petroleum reserves are limited. Based on current global consumption, it has been estimated that this reserve will be depleted in approximately 40 to 60 years. Due to the dwindling petroleum supplies, the development and usage of secondary oil sources such as: lake oil, oil sands, and soils near oil fields and pipelines, is crucial. During the production of hydrocarbons, the thermal processing of oil sands also produces petrocoke. Petrocoke is solid fuel consisting of fixed carbon, tar and ash. Direct utilization of petrocoke is difficult because of its hardness and high tar content. A potential use of petrocoke is plasma gasification in air or steam medium that converts the organic mass of coke into high-calorific synthesis gas ($CO + H_2$) prevents nitrogen and sulphur oxides production in the plasma reactor.

Numerical analysis showed that from both energy and ecological standpoint steam gasification using an internal heat source is the process of choice. Using a plasma gasifier source in the steam gasification process allows for the production of high quality syngas without the dilution with incineration gases. Steam gasification using a plasma gasifier was chosen for experimental investigation. High quality syngas was produced from the petrocoke. Its yield reached 93.6% which correlated with predicted syngas concentration ($CO + H_2 = 97\%$).

1. Numerical analysis

Petrocoke produced from Canadian oil sands was used in the study. The petrocoke is composed of (mass %): C = 69.65; $C_{3.28}H_{60.67}$ = 25.428; H_2O = 0.99; S = 5.64; SiO_2 = 1.305; Al_2O_3 = 0.778; Fe_2O_3 = 0.6; CaO = 0.099; K_2O = 0.068; MgO = 0.052; Na_2O = 0.037; Hg = 0.003. The organic mass was approximately 97% and the mineral mass was only 3%. Note in nature there is no such substance as $C_{3.28}H_{60.67}$. It is conventional molecular formula characterizing the hydrocarbon component of the coke.

To select a more rational way of gasification, thermodynamic analysis of the processes of air and steam petrocoke gasification was performed. Software package TERRA [1] was used for thermodynamic modelling of the pertocoke plasma gasification. This software was created for high-temperature process computations and is based on the principle of maximizing entropy for isolated thermodynamic systems in equilibrium. TERRA has its own database of thermochemical properties for more than 3,500 chemical agents over a temperature range of 300 to 6,000K. Calculations were performed using the following initial data: temperature was varied from 400 to 4,000 K at pressure 0.1 МПа. The first set of calculations the feed was assumed to consist of 100 kg of coke plus 460 kg of air. In the second set of calculations the feed was assumed to consist of 100 kg of coke plus 120 kg of water steam. The gas phase species (Fig. 1), degree of coke gasification (Fig. 2) and specific power consumptions for the processes (Fig. 3) were calculated for the both variants.

Using air gasification (Fig. 1) in a temperature interval of 1,000 to 2,600 K the gas phase mainly consists of molecular nitrogen (N_2) and synthesis gas (CO + H_2). When the concentration of hydrogen is about 26.9% (T=1,400K), the concentration of carbon monoxide is about 22.9% and the concentration of nitrogen is about 47.4%. Under these conditions the sulfur is presented as hydrogen sulfide (H_2S) with a concentration of less than 0.7%. Oxidant concentration (H_2O and CO_2) in this temperature interval does not exceed 2.1%. At the temperature over 2,000 K in gas phase atomic hydrogen (H) is present. Its concentration reaches 35.9% by the temperature 4,000 K. At the temperature exceeding 2,200 K hydrogen sulfide dissociates onto atomic sulfur (S) and sulfur hydride (SH). Total maximal concentration of them is about 0.5%. At temperature above 3,000 K in gas phase hydroxyl (OH) and atomic oxygen (O) appears. Their total concentration is about 1.5%. At temperature exceeding 3,200 K in gas phase nitrogen oxide (NO) is noticed. Its concentration reached 1,500 ppm.

Using steam gasification in a temperature interval of 1,200 to 2,800 K, the gas phase (Fig. 1 on the right) mainly consists of synthesis gas. When the concentration of hydrogen was about 67% (T=1,400K), the concentration of carbon monoxide was about 29.8% and sulfur was present as sulfur hydrogen (about 0.8%). The oxidants concentration (H_2O and CO_2) is not exceed 2.5% in that temperature range. At temperatures greater than 2,000 K atomic hydrogen is appeared in gas phase. Its concentration reaches 62.2% at the temperature 4,000 K. At temperatures greater than 2,200 K hydrogen sulfide dissociates into atomic sulfur and sulfur hydride with total maximal concentration of them reaching 0.5%. At temperatures greater 3,000 K in gas phase hydroxyl and atomic oxygen is appeared. Their total concentration was less than 1.5%. In contrast to the air gasification, in the process of steam gasification nitrogen oxides are not formed.

Note that concentration of syngas obtained in the process of steam gasification is significantly greater one got in the process of air gasification.

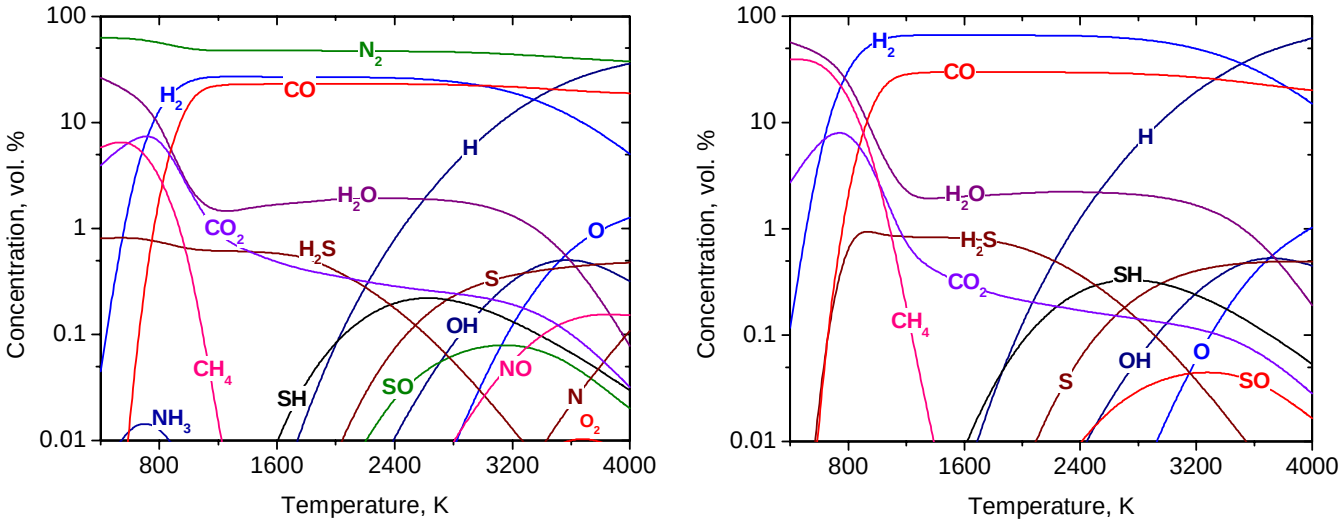

the petrocoke air gasification

the petrocoke steam gasification

Figure 1. Concentrations of gas phase species (organic mass) variation with temperature

One of the main features of the petrocoke gasification process is the dependence of degree of carbon gasification on temperature (Fig. 2). It was calculated in accordance with the following formula.

$X_c = \frac{C_{init} - C_{fin}}{C_{init}} \cdot 100\%$, where C_{init} and C_{fin} is initial carbon concentration in the petrocoke and final carbon concentration in the solid residue at current temperature of the process correspondingly.

Gasification degree increases with the temperature in the both variants and reaches 100 % at close and relatively low values of temperature, which are 1,000 K for air gasification and 1,050 K for steam gasification of the petrocoke. Thus for the both variants carbon from the petrocoke completely transforms into the gas phase mainly in the form of CO (Fig. 1).

Specific power consumptions for the gasification processes were calculated by the difference of working medium (petrocoke and oxidant) enthalpy in initial (T=298 K) and final (current temperature of the process) conditions. The calculations results for the both processes are presented in Fig. 3. At that specific power consumptions were related to one kilogram of initial petrocoke (curves 1 and 3) and to one kilogram of the target product syngas (curves 2 and 4). At the temperatures above 1,000 K specific power consumptions increase smoothly with the gasification processes temperature. Note that in the temperature interval from 1,400 to 2,600 K, where syngas concentration is maximal (Fig. 1) and practically permanent, specific power consumptions for the both processes smoothly increase. It is significant that absolute values of specific power consumptions related to one kilogram of petrocoke (curves 1 and 3) both for steam and for air gasification are almost equal, at that specific power consumption for the process of air gasification in temperatures above 1,900 K is even slightly greater one for steam gasification. But values of specific power consumptions related to one kilogram of syngas are different noticeably for the both variants (curves 2 and 4). For example at temperature 1,400 K, when syngas concentration has its maximal value, specific power consumption for the process of steam gasification of petrocoke is quite less than one for the process of air gasification and amount to 3.24 and 4.46 kW·h/ kg of syngas correspondingly.

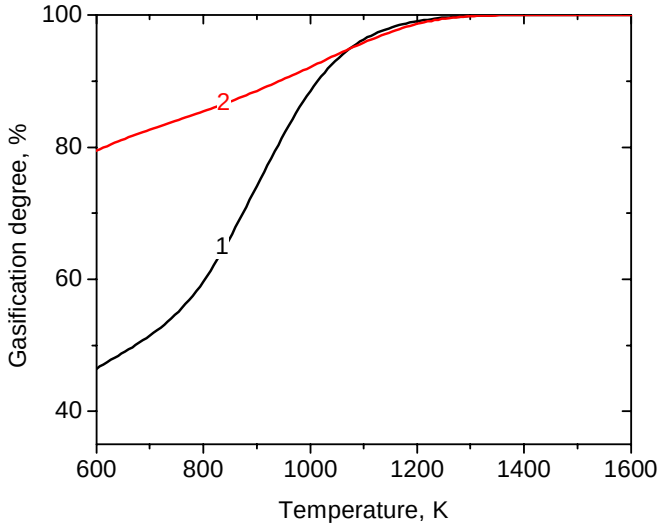

Figure 2. Petrocoke gasification degree variation with temperature

1 – air gasification; 2 – steam gasification

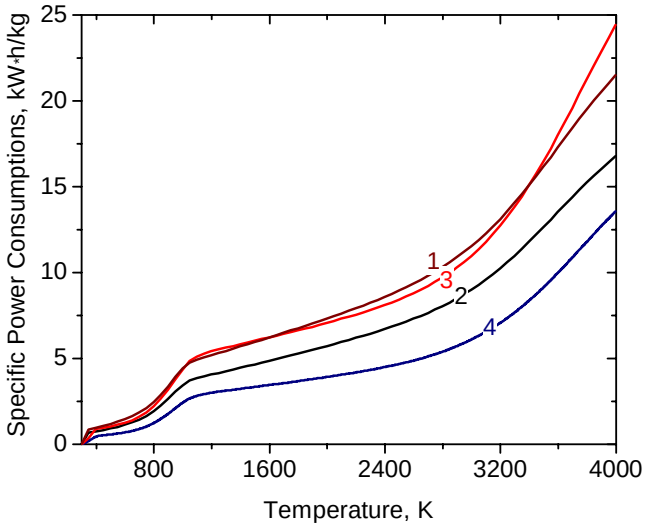

Figure 3. Specific power consumptions for the process of petrocoke gasification variation with temperature

1, 2 – air gasification; 3, 4 – steam gasification; 1, 3 – values related to 1 kg of coke; 2, 4 – values related to 1 kg of syngas

Thus numerical investigation showed that both from energy and ecology point of view for petrocoke gasification more perspective process is its steam gasification with use of internal heat sourse. And for example this sourse could be plasma one. It will allow getting the temperature required for the process of gasification without additional fuel incineration and the target product syngas dilution with inert products of combustion.

Plasma-steam gasification of petrocoke allows converting the organic mass of the coke into high-calorific synthesis gas ($CO + H_2$) that is free from nitrogen and sulphur oxides in a plasma reactor. This conversion can be written as following gross-reaction: $C + H_2O = CO + H_2 - Q = 131500$ kJ/mol. The plasma sourse energy compensates the heat absorbing or endothermic effect Q of this reaction. This process is widely known for power coal gasification [3-9].

2. Experiment

Petrocoke plasma steam gasification experiments were conducted on the laboratory gasifier with 100 kW of nominal electric power (Fig. 4) [2]. The gasification process was carried out according to the following procedure: an arc was fired between the rod and ring electrodes in the combined plasma reactor 1. Then, coke-dust from coke feeder 7 was fed through two ejectors mounted on the reactor cover. Fed through the ejectors steam pulverized the coke-dust over the cross-section of the gasifier. The steam-pulverised coke mixture entering to the arc zone, heated to high temperatures by the arc rotating in magnetic field, thus producing a two-phase plasma flow where the coke gasification occurred. The solid residue produced in the process was withdrawn through the orifice plate 2 into the slag catcher 3. The gaseous products were withdrawn into a ventilation system through gas and slag separation chamber 2 than through chambers for synthesis gas removal 4 and hydration 6. As a result of experiments on the basis of material and heat balances making up, the major indexes of coke plasma gasification were found.

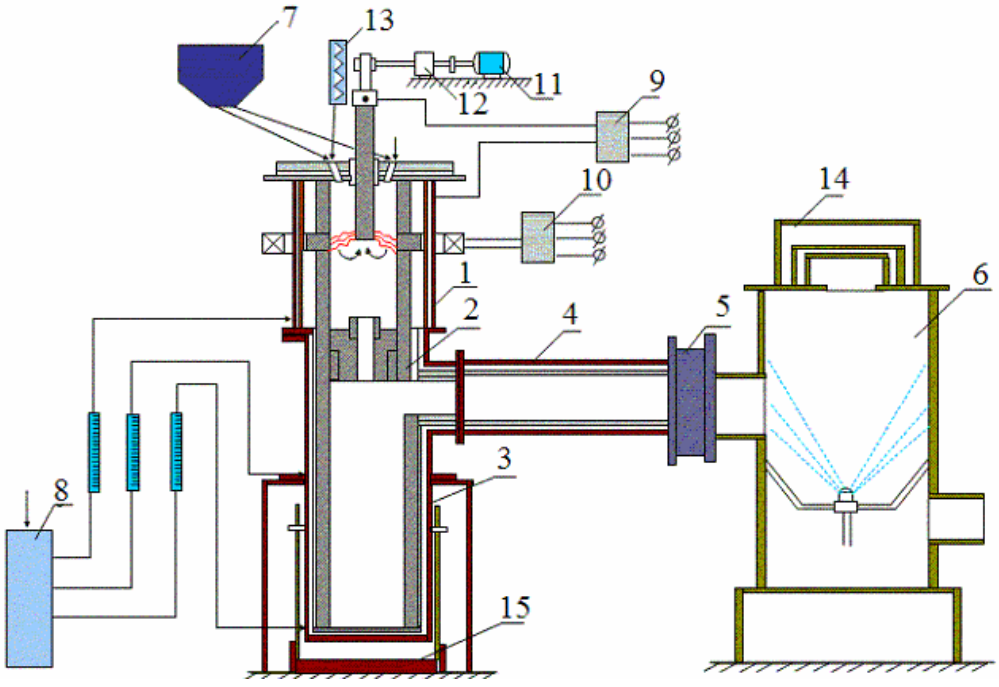

Figure 4. Scheme of Plasma Unit for Coke Steam Gasification.

1 – plasma gasifier; 2 – gas and slag separation chamber and orifice; 3 – slag catcher; 4 – chamber of synthesis gas removal; 5 –the system of gas flow measure; 6 – chamber of hydration; 7 – pulverized coke feeder; 8 – the cooling system; 9, 10 – electric power supply system; 11, 12 – gear for rod electrode supply; 13 – water steam generator; 14 – safety valve; 15 – stand for slag catcher.

To control the installation efficiency and to define the process integral indexes like mass averaged temperature, specific power consumption, syngas concentration, coke gasification degree components of the mass and heat balance of the experimental plant were measured.

The equations of material and heat balance of the experimental set-up take the following form:

$$G_2 + G_3 + G_4 + G_5 = G_6 + G_1 + G_7 \text{ , kg/h} \quad \text{and} \quad W_0 + W_1 = W_2 + W_3 + W_4 + W_5 + W_6 \text{ , kW,}$$

where G_2, G_3, G_4, and G_5 are the flow rates of coke, steam, carrier gas for coke pulverisation, and electrode graphite, respectively; G_6, G_1, G_7 are the mass rates of slag (solid residue), effluent gases, and pulverised coke (fume and fine particles) being removed, respectively; W_0 is the heat output of the arc, W_1 is the heat supplied with steam at T = 405 K; the heat losses to the cooling water in the unit assemblies are: W_2 from the reactor; W_3 from the gas and slag separation chamber; W_4 from the synthesis-gas cooling chamber; W_5 from the slag catcher; W_6 from the heat carry-over in the effluent gas stream.

The arc electric power is determined from wattmeter. The heat input in steam is calculated as: $W_1 = G_3 \cdot H_1$, kW, where $H_1 = H°_{405K} + \Delta H°_{steam} = 0.05 + 0.63 = 0.68$ kW·h/kg of steam. $\Delta H°_{steam}$ is the heat of vaporization.

The heat loss in the effluent gases is determined from the effluent gas temperature (T_g), flow rate (G_1), and composition obtained through the gas analysis. The measured temperature, pressure, and composition of gases are fed into the TERRA code [1] and the specific enthalpy of the effluent gases is computed for specified values of the parameters mentioned above. The gas mixture heat output is calculated as follows:

$$W_6 = H_6 \cdot G_1 \text{ , kW, where } H_6 = \int_{300}^{T_g} C_p \cdot dT \text{ is the specific enthalpy of the gas mixture.}$$

Thus, except for W_6, all the components of the heat balance equation are measured during the experiment. At that metering error of water flow for heat losses of the experimental plant determination is less that 1% of meter scale. Metering error of the cooling water temperature is ±0.1 K. Chromel-alumel and platinum-platinum-rhodium thermocouples provide measuring of outgoing gas temperature. The gas temperature metering error is ±0.01 K. For high temperature measurements infrared thermometers allowing to measure temperature to 4000 K were used. Metering errors depends on temperature interval of measurements and can reach ±2% from measured temperature. Measurement system Prowirl 77F used for measuring steam flow through reactor allows measuring flow range of 10^{-3} to 10 m^3/s. It provides measurements of the flow values within 0.1% accuracy. For the outgoing gases flow measurement differential manometer is used. The accuracy for its values is also within 0.1%. One of the major components of the experimental plant is the system of coke-dust supply to the gasifier. Metering error of the dust consumption is not less than ±0.5 g/s.

The gas is subject to chromatographic analysis. Carrier gas is helium or argon, detectors are thermal conductivity sensors. Analysis of the light gas like H_2, CO, O_2, N_2 and CH_4 is provided in the columns filled with molecular sieve CaX and analysis of CO_2 in the columns filled with silica gel. Absolute calibration method was used for the chromatograph data handling. A sampling is implemented in several point of the installation including plasma reactor. The composition of the solid residue is examined by chemical and X-ray phase analyses. To determine carbon gasification degree absorption-weight method is used. According to absorption-weight method carbon is determined through the carbon dioxide that is formed as a result of the solid residue sample combustion and following absorption of it by ascarit (KOH or NaOH covering asbestos).

Conditions of the experiments and their results are shown in Table 1. The plasma reactor power was 60kW in the both experiments. At that measured thermal efficiency of the plasma gasifier was about 80%.

It is seen from the table that the ratio of steam flow to the petrocoke consumption was varied in interval 1.2-1.4. The steam flow initial temperature was 140^{O}C. The petrocoke gasification degree (Xc) varied from 76.3 to 78.6%. The increased concentration N_2 and O_2 in comparison with calculated ones can be explained by uncontrolled air inflow through sealing disks of the unit as it works under discharge 10-15 mm of water lift. The

synthesis gas maximal yield was 93.6%. That is in good agreement with the predicted syngas concentration ($CO + H_2 = 97\%$).

Table 1. Experimental results

G_{COKE}, kg/h	G_{STEAM}, kg/h	Concentration, vol.%				T, K	Xc, %
		H_2	CO	N_2	O_2		
2.5	3.5	53.5	33.9	11.8	0.8	2,500	76.3
2.5	3.0	57.4	36.2	6.0	0.4	2,960	78.6

The received from the petrocoke syngas is a high-quality power gas, and it can be used for synthetic liquid fuel (methanol) synthesis: $CO + 2H_2 = CH_3OH$ [4]. Syngas [3] of this quality is high-potential reducing agent instead of metallurgical coke for iron ore direct reducing. Also plasma steam gasification is perspective method for hydrogen production through water steam decomposition by petrocoke carbon.

Acknowledgments

The authors gratefully acknowledge the European Commission for this work funding through the ISTC (Project K-746) and personally Professor F. Lockwood for his support and coordination of the research project.

References

[1]. E.I.Karpenko, V.E.Messerle, B.G.Trusov, S.S.Tutebaev, A.B.Ustimenko. Modelling of Plasmochemical Processing of Solid Fuels // Combustion and Plasmochemistry, V.1, N4, P. 291-310, (2003).

[2]. E.I.Karpenko, V.E.Messerle, A.B.Ustimenko. Plasma-Fuel Systems for Enhancement Coal Gasification and Combustion // Presentations Abstracts of 30th International Symposium on Combustion //University of Illinois at Chicago, July 25-30, 1I5-19; P. 110, (2004).

[3]. V.E.Messerle, Sh.Sh.Ibraev, V.A.Frolov, A.V.Pukhov. Syngas Production by Plasma Coal Gasification Process // Journal of High Temperature Chemical Processes. V. 1, P. 51-55, (1992)

[4]. G.N.Kruzhilin. Plasma Gasification of Coal // Vestnik (Bulletin) of Academy of Science of the USSR, N12, P. 69-79, (1980)

[5]. G.N.Kruzhilin, G.N.Khudiakov, P.A.Tselischev. Plasma Gasification of Coal // Chemistry of Solid Fuel, N1, P. 34-38, (1981)

[6]. I.Georgiev, B.I.Mikhailov. Temperature and Medium Compound Influence to Power Consumptions at Plasma Gasification of Various Quality Brown Coals // Proceedings of the Academy of Sciences of the USSR, Series of Technical Sciences, Fascicle 4, N15, P.83-89, (1987)

[7]. M.F. Zhukov, B.I.Mikhailov, A.S.Anshakov. Steam-Water Plasmatrons for Pyrolysis and Conversion of Hydrocarbons // Plasma Gasification and Pyrolysis of Coals. Moscow: G.M.Krzhizhanovski ENIN, P.111-123, (1987)

[8]. R.A. Kalinenko, A.P. Kuznetsov, A.A. Levitsky, V.E. Messerle, V.E. Mirokhin, L.S. Polak, Z.B. Sakipov, A.B. Ustimenko. Pulverized Coal Plasma Gasification // Plasma Chemistry and Plasma Processing V. 13, N1, P.141-167, (1993)

[9]. Jieshan Qiu, Xiaojun He, Tianjun Sun, Zongbin Zhao, Ying Zhou, Shuhong Guo, Jialiang Zhang, Tengcai Ma. Coal gasification in steam and air medium under plasma conditions: a preliminary study // Fuel Processing Technology V. 85 P. 969– 982, (2004)

Plasma-deposited thin films, useful for medical and biotechnological applications

This contribution will focus on several applications of polymers in contact with a biological environment. Thus, the requirements for appropriate interaction (often summarized as biocompatibility) of the respective materials surfaces with living cells (mammalian as well as prokaryotic cells) and bio-molecules will be discussed in the frame of usually mentioned surface properties like wettability etc.
Following some short remarks on polymers in general and on those used for biomedical application will be given.

In a following step several plasma-chemical approaches for the generation of well defined surfaces with uniform functionalities are described. A short discourse on the historical development and the state of the art of these approaches will be presented. The needed densities and availability of the functionalities, so far possible, will be given in functions per surface area or per film volume. The surface analytical methods useful for the qualitative and quantitative estimation of the chemical functions on surfaces and in thin films will also be shortly presented. The different plasma-chemical strategies for the deposition of a chemically uniform film on surfaces are evaluated with respect to their technical and economical appropriateness. From this viewpoint stability aspects will be discussed. Therefore a short overview on stability aspects of plasma modified surfaces will be given

Beside surface properties like surface energy, surface charges and roughness the aspects of structuring (2D) and penetration into trenches, fissures and pores (3D) will be discussed. Examples of plasma-carboxylated two- and three-dimensional structures will be shown and discussed with respect to the penetration depth.

Some special applications as for example the production of regio-selective finished surfaces of separation membranes, a field where an unique potential of plasma-technology is obvious, will be presented in more detail.

For surface preparation of polymers by glow discharges and related techniques, some implications on reactors have to be taken into account and will be discussed as well as some analytical tools, which are appropriate for the development of surfaces useful for biotechnological application.

Finally an outlook on future needs (from a biotechnological viewpoint) and trends in plasma technology (with respect to polymer modification) will be given.

TOWARDS A NEW ERA OF PLASMA SPRAY PROCESSING

T. Yoshida
Department of Materials Engineering, The University of Tokyo, Tokyo 113-8656, Japan
e-mail : yoshida@plasma.t.u-tokyo.ac.jp

For the last 30 years, I have been engaged in studying plasma processing based on materials science, namely, plasma materials engineering. I started with the study of thermal plasma processing, especially plasma-particle interaction and co-condensation process of high temperature vapors, and then expanded to the ultrafine particle synthesis and to thermal plasma PVD, CVD and powder spraying for coating applications. 10 years ago, I also started to utilize medium pressure plasma with an aim at super-high rate deposition of pure silicon, and found that the peculiar characteristic of this plasma is suitably called “Meso-plasma” as a new category of plasmas. Looking back my research carrier, the research field would be characterized mainly by the words: plasma and vapor condensation, and is fortunately fit to the recent global trend of materials R&D which is shifting from “monolithic” to “materials system” and from “bulk” to “thin film & coating”, although this was not the case 30 years ago.

It is, on the other hand, a clear consensus that the primary factor in materials development is “affordability” and it must be considered at every step in processing; unless otherwise, all the efforts are only for the sake of research. It is thus a natural consequence that the plasma processing, as an affordable and effective thin film & coating technology, is attracting global attentions in materials engineering. Unfortunately, however, the current plasma spray thin film & coating technology seems not yet to reach the sufficient level to meet the requirements from the fields where this technique was not applicable in the past. In fact, considering the present status of all the thin film & coating related markets on the basis of this technology developed over the last thirty years and its future possible evolution, the rapidly growing desires, such as the next-generation thin film devices and nano-coatings, would not be fully gratified if the currently available technologies are only used. I suppose that I am not the only one who believes that new standpoints and principles with the fundamental research concept should be introduced from both plasma processing science and materials science & engineering perspectives.

In this context, this lecture will point out the disregarded but important issues involved in the conventional plasma spray processing and infer the future potential of novel plasma spray processing with an use of extended feedstock like gases, liquids and various sized powders. In particular, special attention will be given to our recent challenges aiming at a development of novel deposition processes for silicon films by maso-plasma CVD, and of thermal barrier coatings by novel comprehensive plasma spraying.

Nanoparticles and Plasmas

Steven L. Girshick
University of Minnesota, Minneapolis, USA

Long before the term “nanoparticle” was coined it was known that plasmas are one of the most effective ways to synthesize ultrafine particles, with nanoscale dimensions, of many different substances. Since the 1960s both DC and RF thermal plasmas have been used to generate ultrafine powders for various applications, particularly for production of advanced ceramics. On the other hand, starting around 1990 interest began to grow in the problem of unwanted nucleation of contaminant particles in low-pressure semiconductor processing plasmas. Over the last several years there has been an enormous increase in the level of research activity, in contexts ranging from the deliberate synthesis of nanoparticles in low-pressure plasmas, for applications such as advanced solar cells, optical displays and electronic devices, to use of thermal plasmas for high-rate production of nanoparticle films as superhard coatings. At the same time, the continued shrinking of microelectronics feature sizes is making the nanoparticle contamination problem ever more challenging.

This lecture will give an overview of nanoparticles in both thermal and nonthermal plasmas, and will review the current state of understanding of nanoparticle nucleation, growth, coagulation, charging and transport in plasmas. Current research in our laboratory at the University of Minnesota is focused on three broad themes. The first involves the use of thermal plasmas to synthesize nanoparticles at high rates, but then seeks to develop approaches either to deposit these nanoparticles in controlled fashion (*e.g.* by hypersonic impaction or aerodynamic focusing) so as to form useful nanostructured materials, or to process the particles in flight (*e.g.* by growing films on particle surfaces), or both. The second theme involves studies of particle nucleation in chemically reacting low-pressure plasmas, including both deposition and etching systems. Particle nucleation in nonequilibrium plasmas exhibits a rich range of phenomena, many of which are not found in thermally-driven systems. The final theme concerns the development of computational models that simulate nanoparticle formation and dynamics in plasmas. This work ranges from the development of more efficient numerical methods for solving the aerosol general dynamics equation, two-way coupled to detailed plasma/chemical kinetic models, to Monte Carlo simulations of particle transport.

PLASMA AIDED COMBUSTION

S.M.Starikovskaia, I.N.Kosarev, E.I.Mintoussov, A.Yu.Starikovskii
Moscow Institute of Physics and Technology, Dolgoprudny, 141700, Russia

Abstract

The efficiency of nanosecond discharges as active particles generator for plasma assisted combustion and ignition has been investigated. The study of nanosecond barrier discharge influence on a flame propagation and flame blow-off velocity was carried out. With energy input negligible in comparison with burner's chemical power, a double flame blow-off velocity increase was obtained. The present paper shows that, besides proper form of energy input, proper organization of discharge is of great importance. It was found that active particles (O and OH primarily), which are produced in the streamer head under its action, play the most significant role in the effect of combustion acceleration. The model of flame acceleration, suggested in the previous work, was confirmed by the new experimental data. Ignition of homological series of hydrocarbons from CH_4 to C_4H_{10} under the action of nanosecond discharge was investigated. Significant shift of ignition delay time in comparison with autoignition was obtained for all mixtures. Experiments with ignition by excimer laser flash-photolysis were carried out to study the role of excited atomic species in the ignition of combustible mixtures.

Introduction

The problem of the uniform ignition and efficient combustion of a gas mixture is of crucial importance from both scientific and technological standpoints. The oxidization of a fuel proceeds via a chain mechanism, which is very fast. The delay time of ignition is limited by the rate at which active centers are produced, usually by thermal dissociation. For this reason, the total rate of reaction is, in fact, higher with artificial initiation of a chain. The easiest way to produce free radicals is to decompose the weakest bond of a molecule.[1] The two mechanisms by which a discharge can affect a gas should be taken into account when using a discharge to initiate combustion. For discharges resulting in the formation of an equilibrium (or nearly equilibrium) plasma (e.g., sparks and arcs), the main factor that reduces the delay time of ignition is local heating of gas and, accordingly, the increase in rate of thermal dissociation.[2–4] In the case of a nonequilibrium plasma, the main mechanism initiating chain reactions is dissociation and excitation of molecules by electron-impact. The question of the efficiency of using nonequilibrium plasmas still remains open despite of the fact that theoretically even relatively small amount of atoms and radicals ($\sim 10^{-5}$–10^{-3} of the total number of the gas particles) can shift equilibria in the system and initiate a chain reaction.

In the present paper we analyze three radical – influenced chemically reacting systems: plasma assisted combustion of premixed fuel – air mixtures at atmospheric conditions; plasma assisted ignition of homological series of hydrocarbons in preliminary heated mixtures and ignition of mixture containing N_2O and hydrogen by laser flash-photolysis and the discharge.

Combustion Experiment

The main part of the experimental setup is a quartz nozzle with rectangular section. Three different nozzles, with 2.2, 2.5 and 4.3 mm in width and the same length of 30 mm were investigated. Stainless steel 0,8 mm thick high-voltage electrode was placed inside the nozzle, and the grounded electrodes were situated near the nozzle edges, parallel to them. In order to prevent a transition of the discharge into a spark form, they were set tightly into quartz tubes. On applying a voltage to the gap, a barrier discharge occurred, so the maximum possible current was limited by the dielectric. You can find more detailed description of the setup in.[5]

To fix the point of streamer start and the number of streamers as well, the high-voltage electrode has a number of pins on its upper edge. Two electrodes were used - with 8 and 15 pins, so the number of streamers could be 16 or 30 respectively. The nozzle and images of discharge and flame are presented in fig.1.

Earlier it was shown by the authors in[5] by picosecond ICCD camera images that the energy inputs in the mixture only during the first 10-20 ns of pulse duration, and then the region of energy release moves beyond the zone of mixture flow and is situated near the grounded electrodes. To increase the effectiveness

of energy input, the principal scheme of high-voltage generator has been changed entirely. Instead of rotation interruptor scheme with pulses of 77 ns FWHM, we used the idea of magnetic compression to reduce the pulse length. In the present work we used three different types of pulses: with FWHM 7, 19 and 24 ns. The voltage on the discharge gap could be 14 kV or 22 kV, the nanosecond pulse polarity was positive. Pulse repetition rate could be varied within the range of 400-1000Hz.

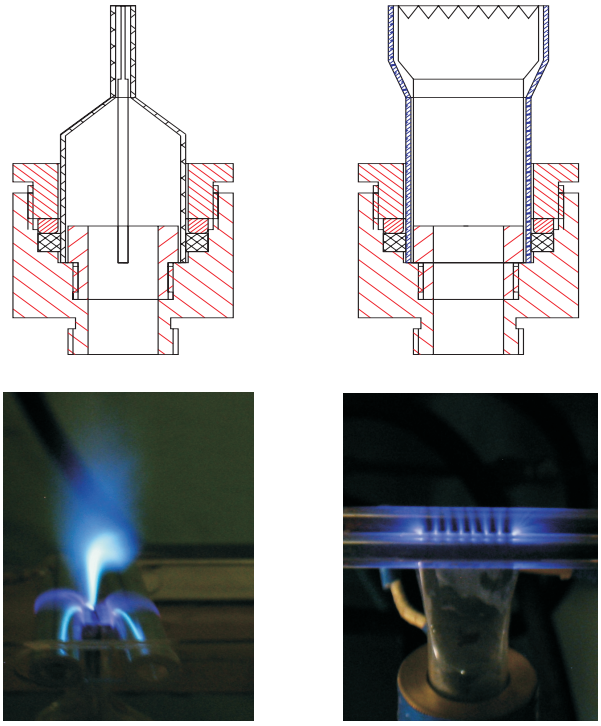

Figure 1: Quartz nozzle and discharge view

The investigations of active particles production were performed by emission spectroscopy methods. The recording facility consisted of CCD-line (spectral range of $\lambda = 200$–800 nm) and MDR-41 monochromator (with an operating range of $\lambda = 190$–600 nm and a linear dispersion of 0,96 nm/mm). The optical system was calibrated using a standard emission source (a calibrated DDS-30 deuterium arc lamp emitting in the range 190–500 nm).

Combustion. Results and Discussion

It was shown in,[1] that in processes of combustion acceleration and flame velocity increase the main role is played by active particles (such as O, H, OH and so on), which are responsible for chain branching. The production of additional centers results in acceleration of chemical kinetic processes. Another important feature is the proper organization of energy input. The energy should be put inside the gap and lead to radical production (instead of gas ionization or thermal heating). Streamer type of discharge totally corresponds to these condition. The main area, where active particles are produced, is the streamer head, which is quite small (~ 0.05 cm for typical voltages of 10–20 kV[6]), but has high values of reduced electric fields (up to 800 Td).

We used two different high-voltage electrodes - with 8 and 15 pins. In fig 2 and fig 3 the comparison of the discharge influence on propane-air flame blow-off velocity is shown. It's seen quite well that both types of electrodes lead to flame acceleration for the cases of 14 kV and 22 kV. But the effectiveness of such influence is different - the effect is greater for 15-pin electrode (Fig.4), because of the larger quantity of streamer. So, the flame stabilization occurs due to the plasma action and hardly depends on the local overheating near the steel plate pins, because estimations shows that overheating is greater in case of 8-pin electrode.

The energy input in both cases was the same and was equal approximately to 2-5 mJ per pulse (2-5 W of total power). This value corresponds to 0,5% of the chemical power of the burner. The equivalent value of gas heating by this energy is 10-20 K. This fact confirms the thesis about the importance of the way we put energy in the mixture.

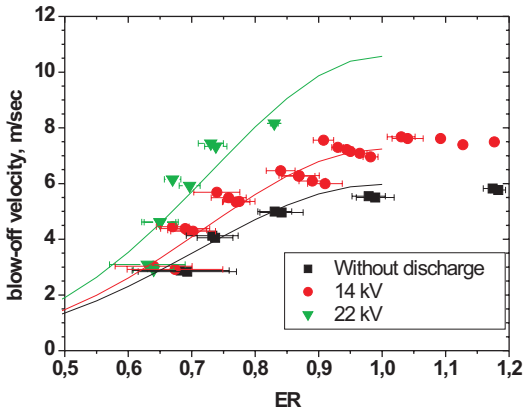

Figure 2: Flame blow-off velocity increase with 8-pin HV electrode

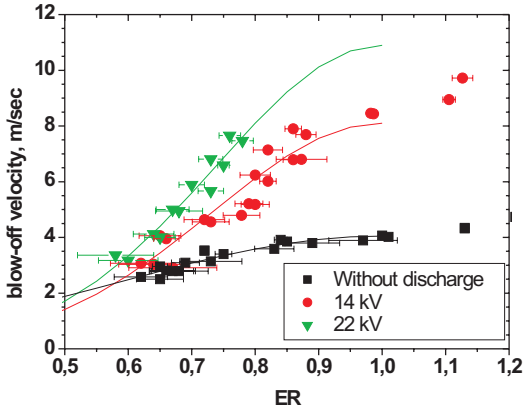

Figure 3: Flame blow-off velocity increase with 15-pin HV electrode

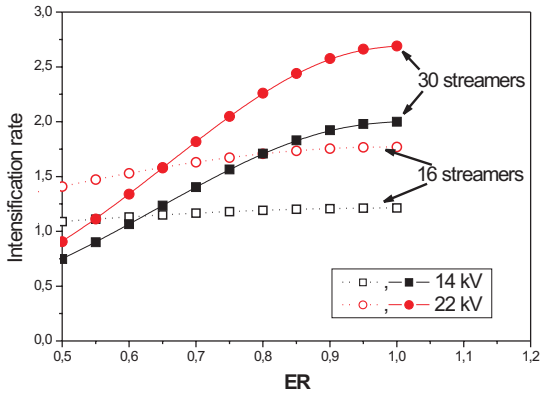

Figure 4: The comparison of the effectiveness of influence. 8-pin versus 15-pin HV electrode

We just have showed that if we are making pulse shorter (24 ns vs 77 ns in the previous work[5]), we can increase the efficiency of energy input (we've reduced energy input more than 2 times, and still have the same increase in flame blow-off velocity). But the duration of pulse should be greater than the time

of streamer propagation through the gap where mixture flows, to provide full overlapping of the nozzle by the streamer. The streamer velocity was calculated in,[6] and is equal to 0.6 mm/ns under the voltage of 22 kV, so in the case of 14 kV, as in our experiment, the velocity value is even lower. On the images (Fig.5) it is shown that in the regimes near blow-off point streamer prefers go through the weakly ionized zone just below the flame instead of the shorter way. Calculations were made for the time of the gap overlapping, and the result is approx. 8 ns in the case of 2 mm nozzle (track length is 5 mm), and even greater in the case of 4.3 mm nozzle.

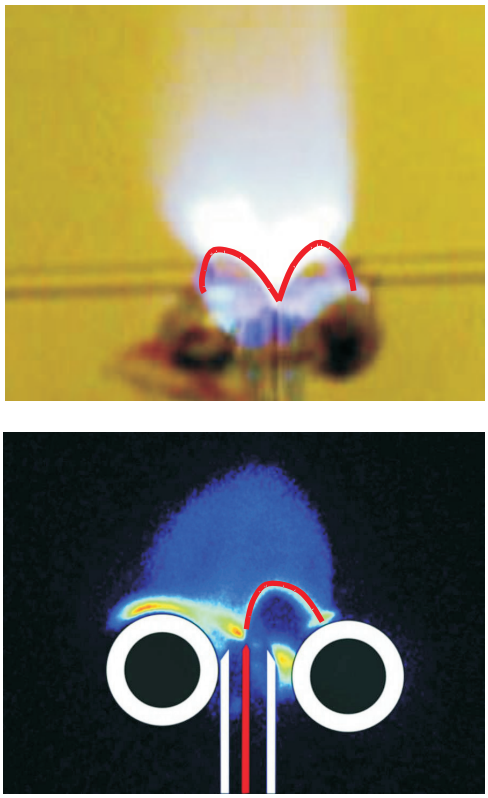

Figure 5: The streamer track in the gap. Top image was obtained by common camera, bottom one - by ICCD picosecond camera, the gate is 1 ns

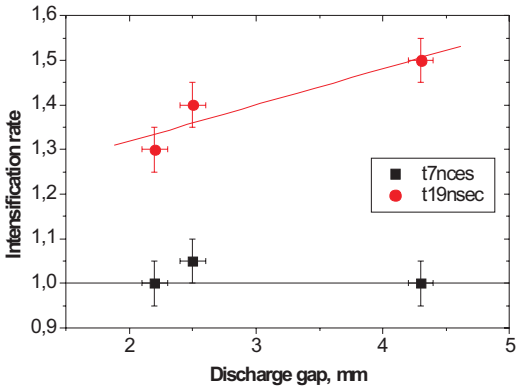

Figure 6: The discharge influence on flame blow-off velocity for different pulse durations

To confirm these arguments, a number of experiments has been performed. Two types of additional line pieces were used to provide different pulse duration (FWHM 7 ns and 19 ns). It was found that at frequency 500 Hz and ER=0.8 19 ns pulse is much more efficient than 7 ns one for all three nozzles, and

the advantage of using 19 ns grows with nozzle widening (Fig.6), as it was predicted earlier.

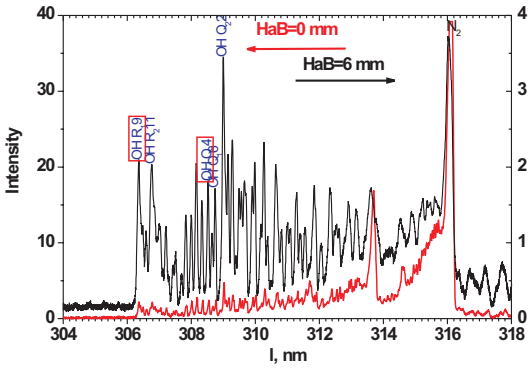

Figure 7: OH* spectra in methane-air flame under discharge action at HaB=0 mm and HaB=6 mm

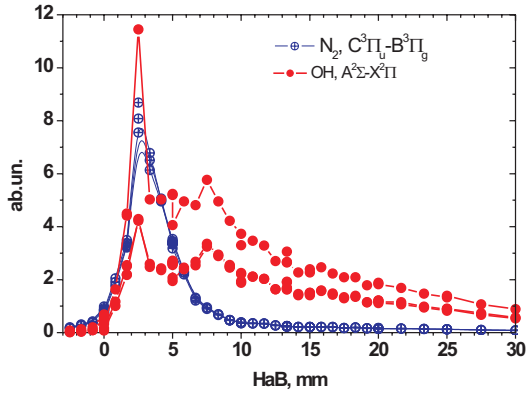

Figure 8: OH* profile along the HaB in methane-air flame

A series of experiments were made to prove the correctness of the model of flame acceleration and kinetic scheme, suggested in the previous work.[5] It's worth to remind that, according to,[5] the main role is played by radicals, which appears under the non-equilibrium nanosecond discharge action. That's why it's very important to make spectroscopic investigation of the flame itself and the flame under discharge action. In,[5] the profile of OH radical along the height above burner in propane-air flame was presented. That result was based on the non-resolved spectrum ($OH(A^2\Sigma, v' = 0 \rightarrow X^2\Pi, v'' = 0)$) at 306.4 nm with quite a large apparatus function of monochromator (2.4 nm). This caused a question, is the first peak of the typical "two-humped" spectrum connected with N_2 production in the discharge (second positive system of nitrogen $C^3\Pi_u \rightarrow B^3\Pi_g$ has intense lines on the wavelengths of 315.9 nm (1→0), 313.6 nm (2→1) and 311.6 (3→2))? In the present work, using CCD-line with signal accumulation mode, it became possible to obtain rotationally resolved spectrum of OH radical in methane-air flame. The spectra of OH* for two different heights (0 mm and 6 mm) above the burner are presented in fig.7. It's distinctly seen that in the region below 310-312 nm we can use any rotational line of OH* spectrum to build the dependence between OH* emission and height above burner (HaB). The result is presented in fig.8, and this figure confirms the previously obtained one for propane-air mixture as well as the importance of OH radical in flame and the similarity of kinetic processes, which lead to flame blow-off velocity increase, for the vast majority of premixed hydrocarbon-air flames. The results for methane-air flame blow-off velocity increase (fig.9) are in agreement with this theory.

Using OH rotationally resolved spectra, the rotational temperature was calculated. The technique of temperature determination is described in.[7] We used the ratio of $R_1(9)$ (λ=306.3565 nm) line and $Q_1(4)$ (λ=308.3278 nm) line. In the case of equilibrium flame, the rotational temperature, obtained in a such

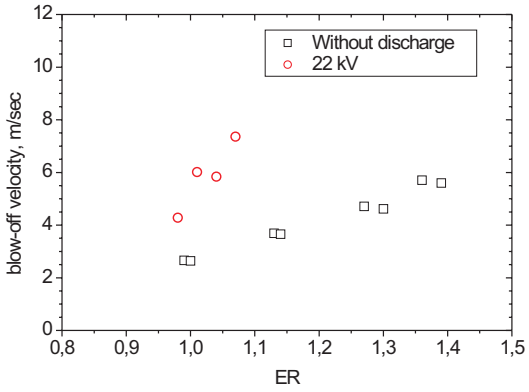

Figure 9: Methane-air flame blow-off velocity increase

way, is close to the translational temperature (the radiative time of living of $A^2\Sigma$ level is 690 ns,[8] and the typical time between particles collisions is about 30 ns, so the Boltzmann distribution of particles at rotational levels occurs before radiation). Experimental OH rotational temperature profiles along the height above burner in methane-air flame are presented in fig.10

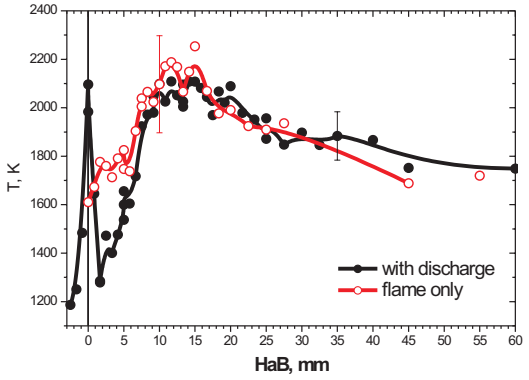

Figure 10: Experimental OH rotational temperature profile along the HaB in methane-air flame

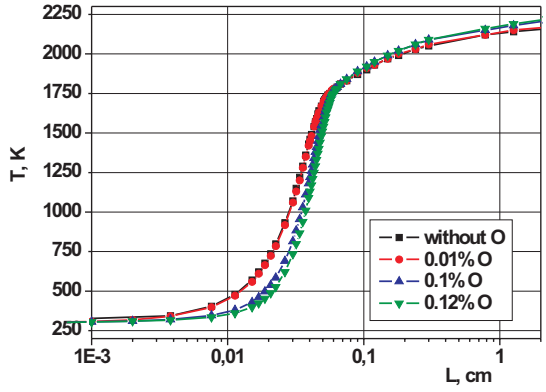

Figure 11: Calculated temperature profile along the HaB in methane-air flame

The comparison of experimental profile with calculated one shows a good data agreement. The theoretical model is based on changing in initial mixture composition under the discharge action.

An additional proof to the suggested theory and the model of radical influence lies in the results of experiments with $Ar/O_2/C_3H_8$ mixture. We have changed the nitrogen in the mixture to argon in order to prevent active particles formation. According to the model, the main channel of O and OH production is the quenching of electronically-exited triplet states of N_2 on the oxygen molecules in processes:

$$N_2(A^3\Sigma_u^+) + O_2 \rightarrow N_2(X^1\Sigma_g^+) + O + O; \quad (1)$$
$$N_2(B^3\Pi_g) + O_2 \rightarrow N_2(X^1\Sigma_g^+) + O + O; \quad (2)$$
$$N_2(C^3\Pi_u) + O_2 \rightarrow N_2(X^1\Sigma_u^+) + O + O; \quad (3)$$
$$N_2(a'^1\Pi_g) + O_2 \rightarrow N_2(X^1\Sigma_u^+) + O + O. \quad (4)$$

or dissociation of oxygen molecule, which can proceed via its electronically excited states:

$$O_2(\text{el.exc.}) \rightarrow O(^3P) + O(^3P); \quad (5)$$
$$O_2(\text{el.exc.}) \rightarrow O(^3P) + O(^1D). \quad (6)$$

So, the substitute of nitrogen to argon should reduce the amount of atomic oxygen and decelerate flame in comparison with $N_2/O_2/C_3H_8$ mixture. Indeed, the results (fig.12) showed that the phenomenon in argon mixture is much more weaker. This is an evidence for our flame acceleration model.

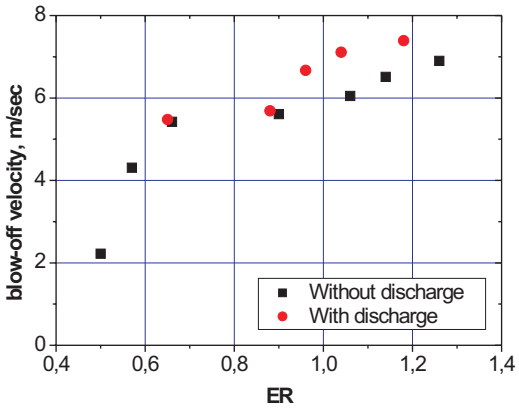

Figure 12: Flame blow-off velocity increase for $Ar/O_2/C_3H_8$ mixture

Ignition Experiment

The influence of nonequilibrium plasma pulsed discharge as an ignitor of combustible mixtures at various pressures and temperatures were investigated via shock tube technique. Experiments were carried out behind a reflected shock wave, as in classic experiments on the autoignition of combustible mixtures.[9,10] The experimental setup (see Fig. 13) consisted of a shock tube (ShT) with a discharge cell (DC), a gas evacuation and supply system, a system for ignition with discharge, and a diagnostic system. The shock tube (25×25-mm square cross section) had a 1.6 m long working channel. The length of the high-pressure cell (HPC) was 60 cm. There were two pairs of windows for optical diagnostics along the stainless-steel working channel. The last section of the shock tube with a 25×25-mm square cross section was made from 40 mm thick plexiglas and had eight optical windows (quartz and MgF_2). The metal end plate (EP) of the tube served as a high-voltage electrode. Another electrode was the grounded steel section of the shock tube.

The nanosecond discharge was initiated at the instant at which the reflected shock wave arrived to the observation point (point A in Fig. 13). High-voltage pulses were produced with a Marx type high-voltage generator (HVG). At the output of the forming line, the voltage growth rate was about 8 kV/ns, which

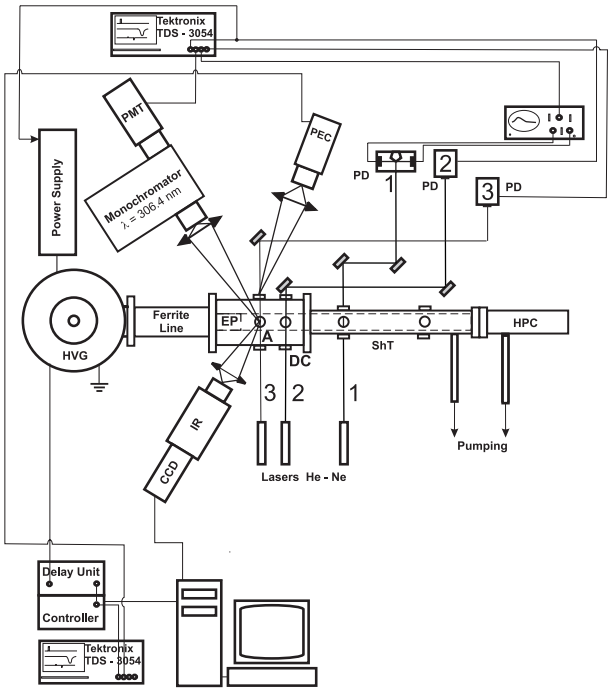

Figure 13: Scheme of the experimental setup. CCD — A — cross-section of measurement, CCD-camera, DC — discharge cell, EP — end plate, HPC — high pressure cell, HVG — high voltage generator, ShT — shock tube, PD — photodiode, PEC — photoelectric cell, PMT — photomultiplier.

enabled the operation of the gas discharge in the form of a fast ionization wave (FIW) in the dielectric section of the shock tube. The velocity of the ionization wave front was 10^9–10^{10} cm/s, depending on the experimental parameters.

The diagnostic system consisted of a system for monitoring the shock wave parameters, a system for detecting ignition, a system for studying the spatial structure of the discharge and combustion, and a system for monitoring the electric parameters of the nanosecond discharge. Velocity of a shock wave was measured by Schlieren system consisted of three HeNe lasers and a set of photodiodes (PD). The gas density (ρ_5), pressure (P_5), and temperature (T_5) behind the reflected shock wave were determined from the known initial gas mixture composition, the initial pressure, and the velocity of the incident shock wave. Ignition delay time was controlled using OH emission ($\lambda = 306.4$ nm, $A^2\Sigma(v' = 0) \rightarrow X^2\Pi(v'' = 0)$ transition) in microsecond time scale. Simultaneously we controlled emission from the discharge with nanosecond time resolution, current through the discharge cell and voltage drop between high-voltage electrode and cross-section of measurement.

Ignition. Results and Discussion

As a reference result, we considered data obtained for the methane – synthetic air stoichiometric mixture, diluted by argon.[11] What is important that we came back to this mixture during 1.5 years with a gap of a half of a year, and a summary of all these data, published, for example, in,[12] confirms an excellent reproducibility of the results.

The question about efficiency of ignition of different hydrocarbons in homological series by the nanosecond discharge is still remains open. This part of the paper is devoted to results of experimental investigation of ignition delay under the action of a nanosecond discharge. The experiments were carried out with a set of stoichiometric mixtures $C_xH_{2x+2} : O_2$ (20%) diluted by Ar (80%) for hydrocarbons from CH_4 to C_4H_{10}. The temperature behind the reflected shock wave (T_5) varied from 980 to 1630 K, and the pressure (P_5) was 0.17 to 1.0 atm. Composition of investigated mixtures is represented in Table 1.

The strongest change in OH emission intensity had been observed for methane – oxygen mixture, diluted by argon. This is shown in Fig. 14. For the conditions of this pair of experiments, Schlieren signals are practically the same, but discharge (it is indicated by a vertical line in the Figure) shifts the ignition delay by hundreds of microseconds. The same effect, but less pronounced, is observed for all series of hydrocarbons. As an example, difference in emission with and without discharge is represented

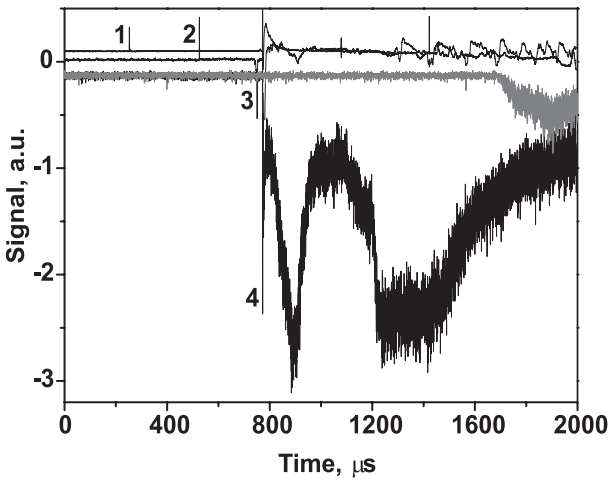

Figure 14: Typical oscillograms from Schlieren detectors (upper curves) and from photomultiplier (two lower curves). Methane–containing mixture. 1, 2 – direct shock wave, 3 – reflected shock wave, 4 - discharge. Gray curve from photomultiplier corresponds to autoignition, black one – to ignition by FIW.

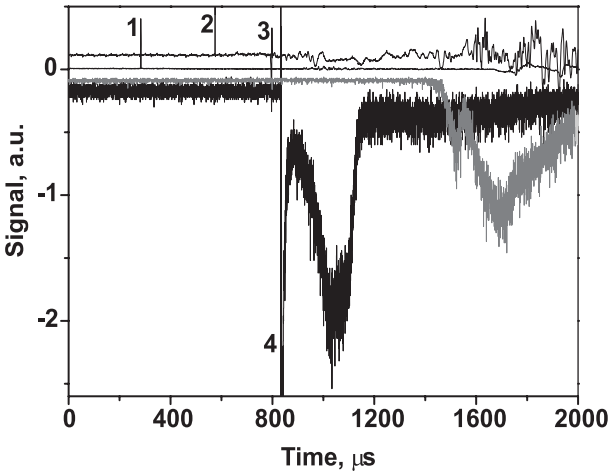

Figure 15: Typical oscillograms from Schlieren detectors (upper curves) and from photomultiplier (two lower curves). Butane–containing mixture. 1, 2 – direct shock wave, 3 – reflected shock wave, 4 - discharge. Gray curve from photomultiplier corresponds to autoignition, black one – to ignition by FIW.

Table 1: Investigated mixtures

Alkane	CH_4	C_2H_6	C_3H_8	C_4H_{10}
	6.7%	4.4%	3.3%	2.7%
O_2	13.3%	15.6%	16.7%	17.3%
Ar	80%	80%	80%	80%

for butane – oxygen mixture, too (see Fig. 15).

Figures 16–19 demonstrate dependence of ignition delay time for autoignition and ignition by nanosecond discharge for all investigated mixtures. It is clearly seen that ignition delay is well-pronounced in all the cases. Difference for C_4H_{10} is the strongest in a region of 1100–1200 K, while for C_3H_8 the difference is practically constant within a range of 1400–1600 K and comprises about 200 K.

Energy measurement have been performed for different mixtures. The results are demonstrated in the Fig. 20. It is obvious that the energy values are of the same order of magnitude as in methane-containing mixture. This is quite clear, because for mixture with 80% of Ar dilution and $13 - 17\%$ of O_2, energy input into discharge will be determined preferably by Ar–O_2 mixture. It is seen from the Figure, that

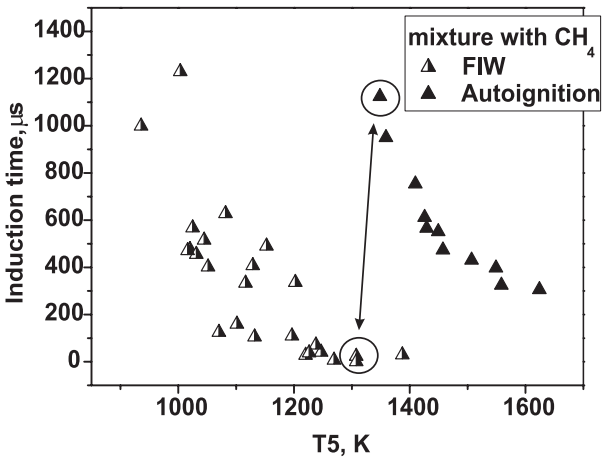

Figure 16: Ignition delay time *vs* temperature for methane – containing mixture.

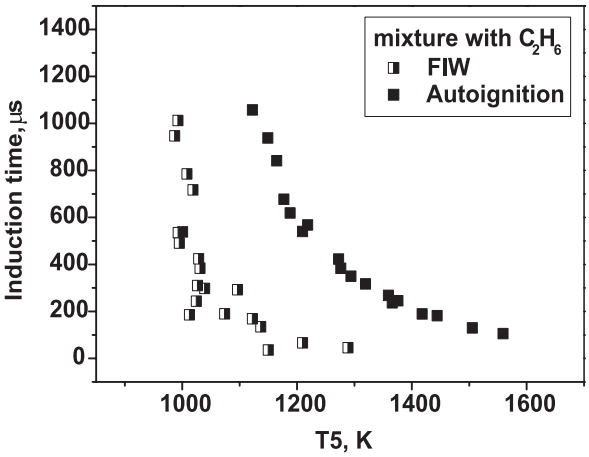

Figure 17: Ignition delay time *vs* temperature for ethane – containing mixture.

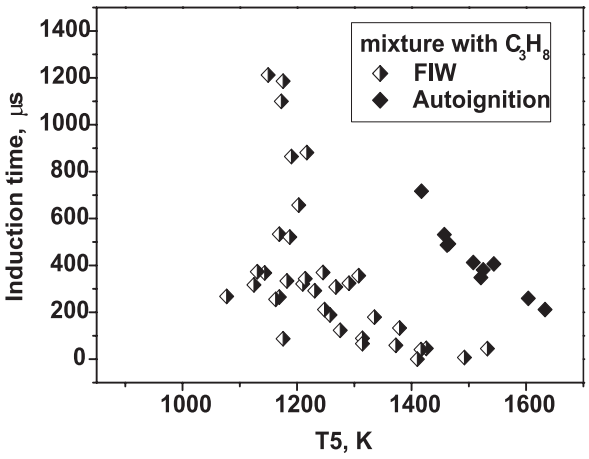

Figure 18: Ignition delay time *vs* temperature for propane – containing mixture.

the main part of experimental point is within interval 7-13 mJ/cm^3 (this region is separated with two horizontal lines).

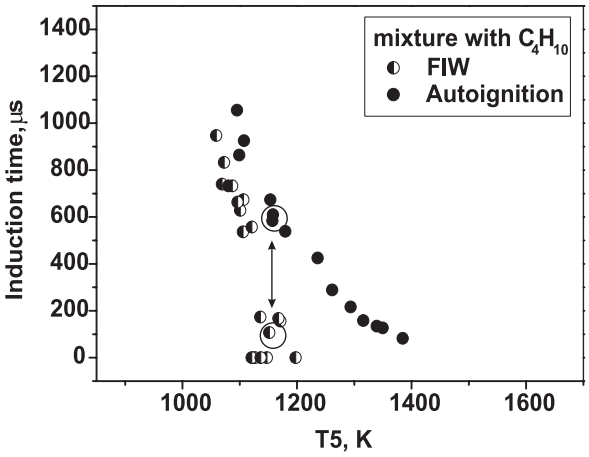

Figure 19: Ignition delay time *vs* temperature for butane – containing mixture.

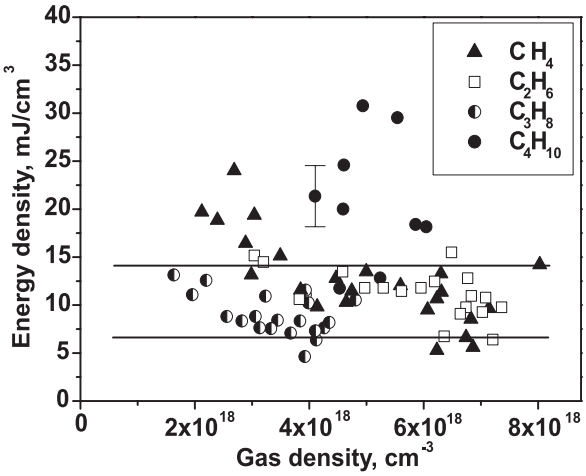

Figure 20: Energy input into a gas for different gases.

Laser Ignition. Experiment

The diagnostic system used for ignition by the discharge was modified to control ignition by laser flash-photolysis. A flash of UV-radiation of ArF excimer laser ("Center of Physical Devices" production, Troitsk, $\lambda = 193$ nm) was organized behind the reflected shock wave instead of the nanosecond discharge. Laser output reached 0.2 J. The laser radiation was supplied to the dielectric section of the shock tube through the optical window perpendicularly to the shock tube axis in the same cross-section were we performed measurements in a case of the ignition by nanosecond discharge. Laser spot had approximately rectangular shape with 5×21 mm dimensions and was controlled by special sensible paper.

A piroelectric detector (PEM21) with 21 mm diameter of receiving site was used to determine energy input from laser radiation into the gas. Signal from PEM21 was controlled every time before the experiment, when the system was pumped up to 10^{-2} Torr and then during the experiment. Knowing spectral transmission of MgF_2 windows in this spectral range (were controlled by Varian Cary50 Spectrophotometer) we calculated energy input into a gas. We organized experiment so, that energy input in the discharge and energy input from a laser were within one order of magnitude. We controlled initial gas pressure and shock wave velocity, and parameters behind the reflected shock wave were calculated as in the previous case. Ignition delay time was calculated from the OH emission at 306 nm.

The experiments were repeated with the same mixture for autoignition, discharge initiation of ignition and ArF flash-photolysis. Ignition delay times were compared for all cases. To make these experiments, we chosen N_2O as a main absorbing component. Really, N_2O is known to be very efficient as an oxidant. On the other hand, it absorbs radiation at 193 nm better than molecular oxygen. To demonstrate this, cross-sections of molecular oxygen and N_2O molecule are represented in the Fig. 21. So, experiments

were performed in gas mixture N_2O:H_2:Ar = 1:1:8. In our earlier experiments 1% of CO_2 was added to a gas mixture for control of a gas temperature using emission in IR range of spectrum.

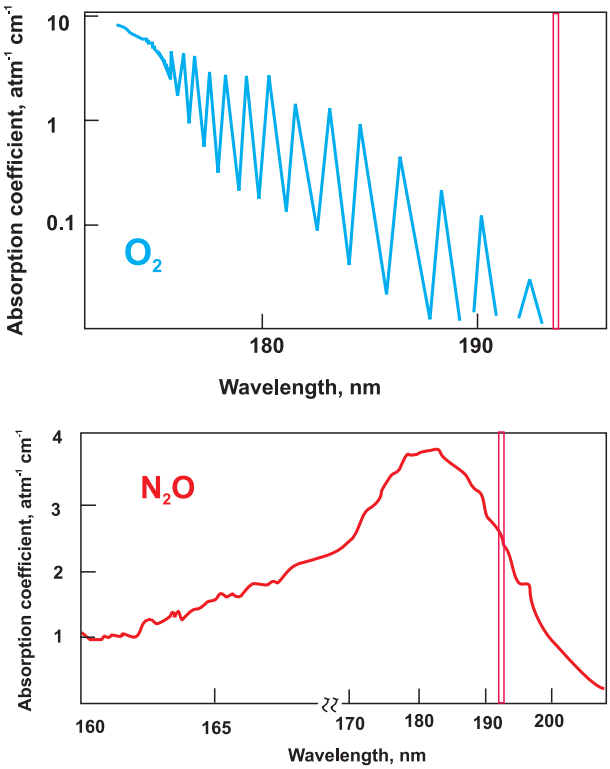

Figure 21: Cross-section of absorption: **a** — for molecular oxygen, **b** — for nitrous oxide. Region of ArF laser generation is marked with vertical lines.

Laser Ignition. Results and Discussion

Typical energy input in a gas in experiments with flash-photolysis is demonstrated by Fig. 22. The shape of a laser beam is quite uniform It is represented in a right hand side of the figure. Energy value obtained by piroelectric gauge was divided by volume 5x20x25 mm, where 25 mm is a transverse size of a shock tube channel.

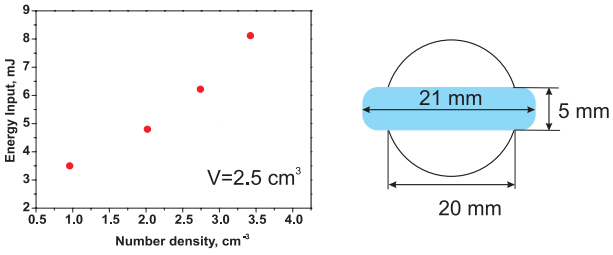

Figure 22: Typical energy input in experiments with laser flash–photolysis. A shape of a laser beam is on the right part of a figure.

It is known that N_2O photolysis takes place via the reactions:

$$N_2O + h\nu = N_2 + O(^1D), \tag{7}$$

$$N_2O + h\nu = N_2 + O(^4S), \tag{8}$$

at this weight of reaction (7) is 99%. $O(^1D)$ is a metastable atom, its life time is 150 s, and usually it looses excitation in collisions with other species. It may destruct N_2O via the reactions

$$N_2O + O(^1D) = N_2 + O_2, \tag{9}$$

$$N_2O + O(^1D) = NO + NO. \tag{10}$$

On the other hand, $O(^1D)$ has to be active in ignition. The results of our preliminary experiments (with 1% CO_2 in gas mixture) demonstrated no effect on ignition delay, in spite of a fact that nanosecond discharge shifts the threshold by hundreds of K, which is typical for this discharge in different gas mixtures. Behavior of mixture with 1% CO_2 additive is illustrated by Fig. 23.

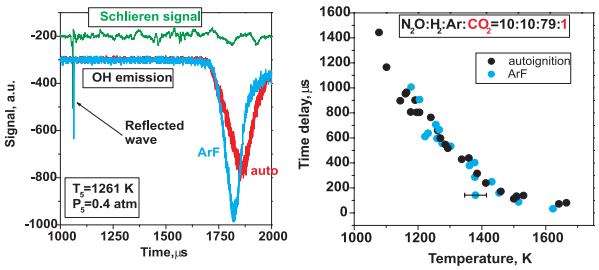

Figure 23: Typical oscillograms and time delay dependence upon gas temperature for gas mixture with additive of carbon dioxide.

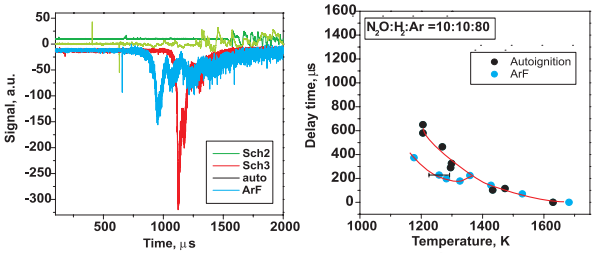

Figure 24: Typical oscillograms and time delay dependence upon gas temperature for gas mixture without additive of carbon dioxide.

We tried to use mixture N_2O:H_2:Ar = 1:4:5 (also with 1% CO_2) and to focus laser radiation, but we were not able to shift the ignition delay. At the same time, in gas mixture N_2O:H_2:Ar = 1:1:8 without CO_2 additives we have obtained some systematic result, which is represented in the Fig. 24. We obtained at least four points, where ignition by laser differed significantly from autoignition.

Previous analysis demonstrate the following: on one hand, CO_2 is rather strong quencher[13] of $O(^1D)$ radicals:

$$O(^1D) + CO_2 = O(^3P) + CO_2^*. \tag{11}$$

Constant rate for the reaction (11) is $2 \cdot 10^{-11}$ cm^3/s, and typical estimated time of $O(^1D)$ destruction in our system due to the presence of CO_2 may be as short as 2 μs. On the other hand, there is a lot of species, even in our system, which are much more active as excited oxygen atoms quenchers. They are, first of all, water and molecular hydrogen. In principle, water is a final product of combustion process and its amount may not be enough on the initial stage to prevent CO_2 to quench atomic oxygen. As for hydrogen, it do quenches $O(^1D)$, but this is one of main helpful reaction in our system. We believe, that this point need to be investigated more carefully. It is necessary to obtain results for the shift of ignition delay by flash–photolysis again, just to be sure that they are reproducible and to analyze them.

Conclusion

The study of efficiency of nanosecond discharge plasma on combustion and ignition process has been carried out. The following conclusions could be made:

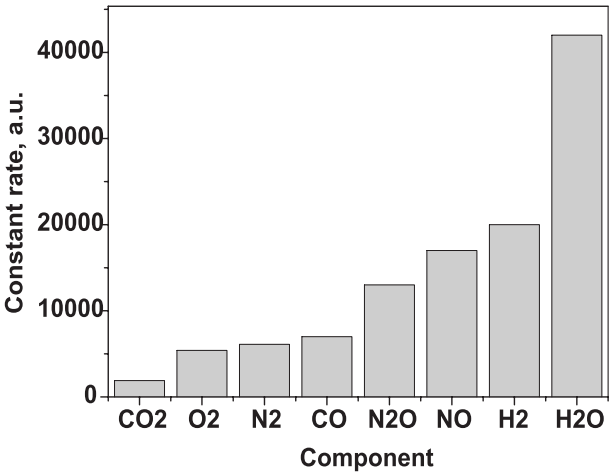

Figure 25: Comparison of constant rates for quenching of excited oxygen atom.

For nanosecond plasma assisted combustion, with energy input negligible in comparison with burner's chemical power, a double propane-air flame blow-off velocity increase was obtained. It was shown experimentally that the results for methane-air flame are similar with propane-air one. Besides proper form of energy input, proper organization of discharge is of great importance. It was found that the effectiveness of plasma-assisted combustion depends on type of discharge, pulse duration, pulse repetition rate and other parameters, which are responsible for active particles production. It was found that active particles (O and OH primarily), which are produced in the streamer head under its action, play the most significant role in the effect of combustion acceleration. The model of flame acceleration, based on nitrogen quenching on oxygen molecules, with production of O and OH radicals, was confirmed by the new spectroscopic investigations and experiments with $Ar/O_2/C_3H_8$ mixture, where discharge influence is small because of the absence of mechanism of active particles production.

The investigation of efficiency of the nanosecond discharge to ignite homological family of hydrocarbons has been started. Gas mixtures of methane, propane and butane has been investigated under the same experimental conditions. It is demonstrated that high-voltage nanosecond discharge is an efficient tool of ignition of different hydrocarbons. Results for the ignition delay and shift of a temperature threshold under the action of nanosecond discharge have been obtained experimentally.

Experiments to investigate ignition delay shift under the action of excimer laser flash-photolysis have been organized. It was found that small additives of CO_2 may influence significantly on the results. Preliminary analysis of possible mechanisms of $O(^1D)$ de-excitation has been performed. Ignition delay shift under the action of flash-photolysis has been obtained systematically in four points. Additional experiments are planned to prove or refute these preliminary results. In a case we will obtain the ignition delay shift it will be possible to estimate efficiency of excited atoms in the process of ignition. In a case the experiments will not demonstrate the difference between autoignition and ignition by flash-photolysis, we will have a ponderable reason to organize investigation of influence of charged particles (ions) on the ignition delay.

Acknowledgments

This work was partially supported under Grants by PR0-1349-MO-02 EOARD/CRDF, 02-03-33376, 02-15-99305, 01-02-17785 of Russian Foundation for Basic Research; Project 1440 by ISTC; Award MO-011-0 of the CRDF and Grant 02-3.2-97 by Ministry for Higher Education of Russian Federation, Project No. MD-334.2003.02 of the Grants of President RF for young scientists. The authors are grateful for Mr.E.Kukaev and Dr.S.Pancheshnyi for their help in adjustment of the equipment and organization of preliminary experiments and for fruitful discussions.

References

[1] N.N. Semenov, Nobel Lecture, December 11, 1956
http://www.nobel.se/chemistry/laureates/.

[2] L.S. Polak, A.A. Ovsiannikov, D.I. Slovetskii and F.B.M. Vurzel', Theoretical and Applied Plasmochemistry. M.: Nauka, 1975, p. 222.

[3] D.A. Eichenberger and W.L. Roberts, Combust. Flame, **118**, 1999, 469.

[4] E. C. Samano, W. E. Carr, M. Seidl, and Brian S. Lee, Review of Scientific Instruments, **64**(10), 1993, 2746–2752.

[5] E.I. Mintoussov, S.V. Pancheshnyi, A.Yu. Starikovskii. AIAA paper **2004–1013**.

[6] M.M.Nudnova, S.V. Pancheshnyi, A.Yu.Starikovskii Pressure Dependence of the Development of Cathode-Directed Streamer, XV International Conference on Gas Discharges and their Applications, Toulouse, 2004.

[7] S. Pellerin, J.M. Cormier, F.Richard, K.Musiol, and J. Chapelle. J.Phys.D.: Appl.Phys., **29**, 1996, 726–739.

[8] K.P.Huber and G. Herzberg. Molecular Spectra and Molecular Structure. IV. Constants of Diatomic Molecules. Litton Educational Publishing, Inc., 1979.

[9] GL Schott and JL Kinsey, J. Chem. Phys. 29 (1958) 1177–1182.

[10] K.A. Bhaskaran and P. Roth, Progress in Energy ang Combust. Science 28 (2002) 151–192.

[11] S.A. Bozhenkov, S.M. Starikovskaia and A.Yu. Starikovskii, Combust. Flame, **133**, 2003, 133–146.

[12] 5. S.M. Starikovskaia, E.N. Kukaev, A.Yu. Kuksin, M.M. Nudnova and A.Yu. Starikovskii. Combust. Flame, **139**, 2004, 177–187.

[13] Cvetanovic R.J., J.Chem.Phys., **43**, 1965, 1450.

Production of B-doped multi-walled carbon nanotubes by arc discharge in water

M. Bystrzejewski[1], H. Lange[1], A. Huczko[1], M. Ruemmeli[2] and T. Gemming[2]

[1] *Department of Chemistry, Warsaw University, Pasteur 1, 02-093 Warsaw, Poland*

[2] *IFW Dresden, Helmholtzstr. 20, 01069 Dresden, Germany*

Abstract

Boron-doped multi-walled carbon nanotubes (MWCNTs) were generated by arc discharge in water by using B-doped graphite electrodes. The product morphology was studied by SEM and HRTEM microscopy. The structure features were determinated by Raman and EELS spectroscopy. Optical emission spectroscopy (OES) was performed to evalute the temperature and C_2 content distributions in arc plasma.

1. Introduction

Since the discovery of multi-walled carbon nanotubes (MWCNTs) in 1991 [1], they have been extensively studied for various applications. Their small dimension, high strenght and the remarkable physical properties make them very promising emmiters for field emission devices. Due to the size-effect and structure diversivity of nanotubes, the physical properties strongly depend on their stucture, size and chemical composition. Different diameter, length and chirality of MWCNTs give a rise to diverse physical and mechanical properties. It is believed that the atom inclusions into hexagonal network such as nitrogen, phosphorus or boron can enhance e.g., MWCNTs' eletronic properties by creating electrons or holes.
Boron-doped MWCNTs were synthesized by using many various techniques including dc arc discharge [2], microwave plasma chemical vapor deposition [3], laser vaporization method [4], and substitution reaction [5]. Recently [6], we reported that arc discharge in water generates various carbon nanostructures (nanotubes, onions, and encapsulates). In this study we report boron-doped MWCNTs synthesis by arc discharge in water by using B-doped homogeneous graphite electrodes.

2. Experimental

The equipment, based on a gas phase arc-discharge system previously used for fullerenes and CNTs formation [6], was modified to facilitate a continous d.c. arc discharge in water. The anode and cathode (6 mm diameter) were immersed to a depth of ca. 3 cm in deionized water (1 dm^3) contained in a transparent glass trough. The electrodes were aligned horizontally. The brass electrode holders were free to mowe, forward and backward, which enabled proper electrode gap adjustment to be made during arc discharge (Fig. 1).

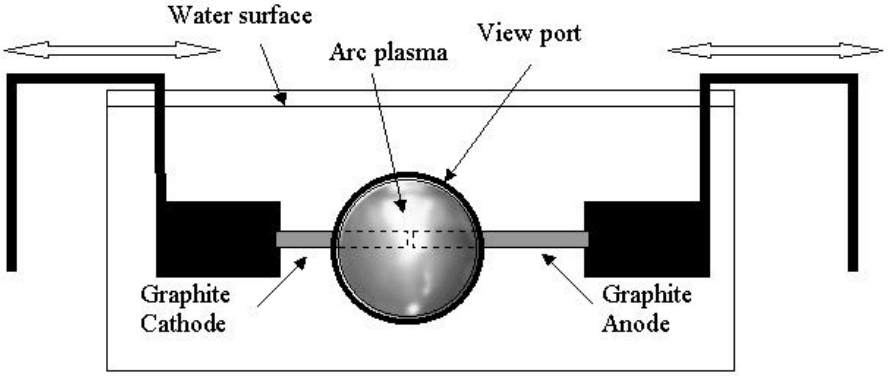

Fig. 1. Electrodes arrangment for arc discharge in water.

Upon ignition the electrode gap was maitained at ca. <0.7 mm, to avoid arc disruption We used a digitally controllable power suplly with constant voltage output up to 90 V. Four tests were performed, where boron content in the anode was varied between 0 and 11 at. % (Table 1).

Table 1. Experimental detail.

Test No.	Current [A]	Voltage [V]	Anode erosion rate [mg s^{-1}]	Boron concentration in anode [at. %]
1	40	28	2.5	0
2			2.4	1
3			3.1	3
4			3.2	11

During discharge, the spectroscopic features of the plasma emission were monitored optically by using a ST8 CCD camera coupled with a high resolution spectrograph, in order to identify the atomic lines and molecular bands. Considering quantitative diagnostics, such a task in the case of the arc discharge in water is a very difficult one because of high arc fluctuation, small arc gap, and progressing decrease of water transparency caused by carbon particles dispersed in water. Therefore, the information characterizing the plasma was inferred only from C_2 radical radiation which is mainly associated with the Swan band system d ^3Đ_g a $3Đ_u$. The emission band 0-0 (516.5 nm) was used for temperature assesment and contribution of carbon in the plasma phase evaluation. The C_2 content was determined applying the method based on the phenomenom of self-absorption which highly influences the intensity of the band with respect to the intensity of the non-overlapped rotational component [7].

The collected products from the bottom of the reactor were analyzed by using scanning electron microscopy (ultra high-resolution field emission SEM, Leo 1530). The samples were also subjected to ultrasound treatment in ethanol for 15 min, and then transferred to a Cu grid coated with a holey carbon film for high-resolution transmission electron microscopic investigations (HRTEM, Jeol 3010). Raman spectroscopy (Jobin YvonSpex T64000) was applied to evaluate the structure features of the products.

3. Results and discussion

Fig. 2 shows the SEM pictures obtained in test 1-4. The product consisted of mainly carbon nanotubes, but other carbon nanoparticles are also present. The amount of CNTs increase with increasing the boron content in the anode. These nanotubes are ca. several nm in diameter, and a few micrometers in length. In the case of 11% B-doped anode thicker bundles of MWCNTs were found (Fig. 2D). The abudance of CNTs increased also with increasing the B concentration in anode. The highest yield of CNTs was obtained in test 4 (Fig 2D). These result could suggest, that boron favours the formation of CNTs.

The morphological details were investigated by HRTEM (Fig. 3). Based on the images, the diameter of MWCNTs was found to be between 10 and 25 nm. There were no correlation beetwen boron content in the anode and the diameter of obtained carbon nanotubes. The graphitization degree of MWCNTs decrease with boron concentration, what is clearly seen in Figs. 2C and D. The graphene sheets are not planar, due to the substitution carbon by boron atoms. This phenomena was also shown earlier [8]. The thin amorphous coating (ca. 1-2 nm) was observed in samples from tests 3 and 4.

The produced MWCNTs were also studied by Raman spectroscopy. First-order Raman measurements were performed using a 647.1 nm laser. There were two peaks located at ca. 1330 and 1590 cm^{-1}, corresponding to D and G lines of graphite, respectively. The D band is normally explained by relaxation of the wave vector selection rule due to the effect of the finite size of the crystal in the material [9]. The D/G ratio increases also with the decreasing of the graphite crystal size and its crystallization degree. The latter is also related with the presence of boron in the hexagonal lattice of graphite. Fig. 4 indicates that the I_D/I_G ratio increses with increasing the boron concentration. This implies that boron decreases the graphitiziation. Thus, the boron-doping effect strongly influences the crystallinity of CNTs. This results was also discussed with HRTEM ivestigation. In the case of the sample obtained in test 3 we measured the B content in the individual CNTs by EELS technique. It was found to be 1.0 +/- 0.4 at. %. It means, that ca. 30% of the starting amount of boron was incorporated in CNTs fomation. The measurements of B content in other samples are under way.

The carbon arc discharge in water is similar to that of a standard carbon arc discharge in helium [6]. The strongest bands and lines are still asosciated with C_2 radicals (d ^3Đ_g a ^3Đ_u, e.g., 516.5 nm), carbon atoms and ions. The average plasma temperature in water was found to be ca. 4000-6000 K. The obtained

temperatures for all electrodes were within the same range. The C_2 column density was between $1*10^{15}$ and $6*10^{15}$ cm^{-2}. It follows from thermodynamics that at such temperatures and C_2 content the total carbon vapor pressure is between 3 and 54 kPa. These results are similar to those obtained in helium, during arcing B-doped anodes [10].

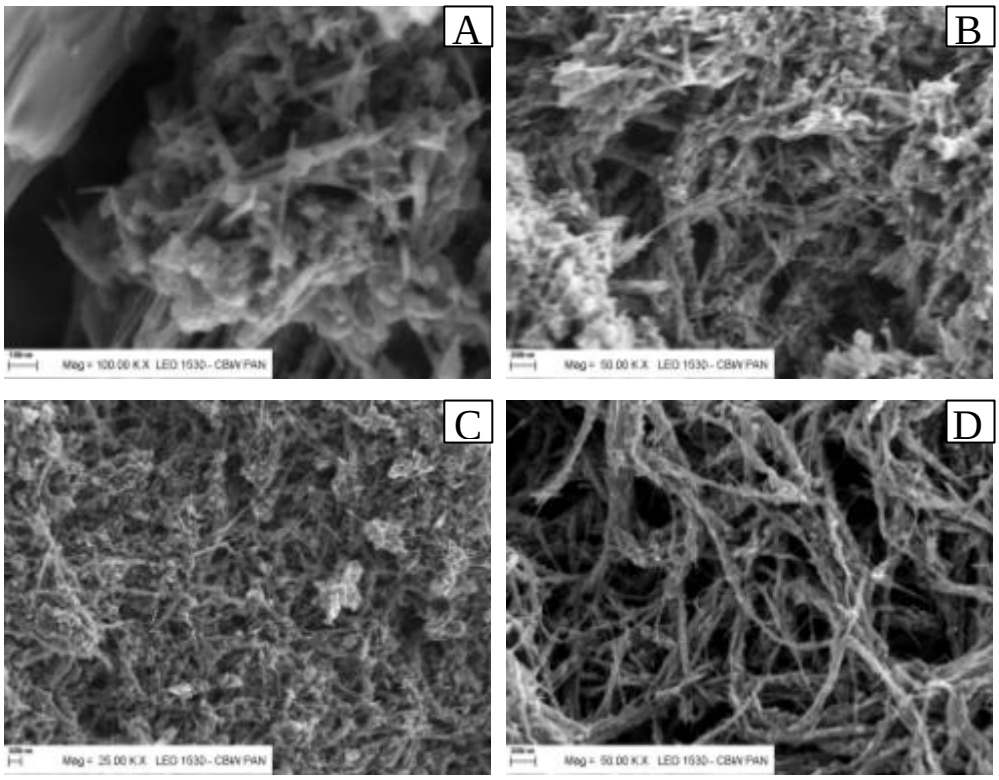

Fig. 2. SEM images of product obtained in test 1 (A), 2 (B), 3 (C), and 4 (D).

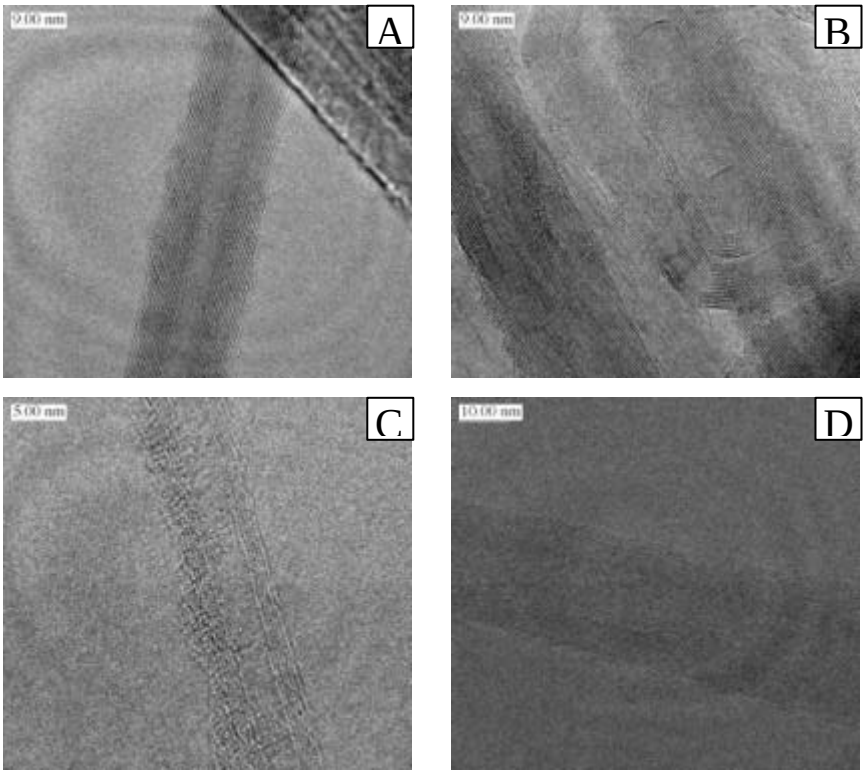

Fig. 3. HRTEM images of product obtained in test 1 (A), 2 (B), 3 (C), and 4 (D).

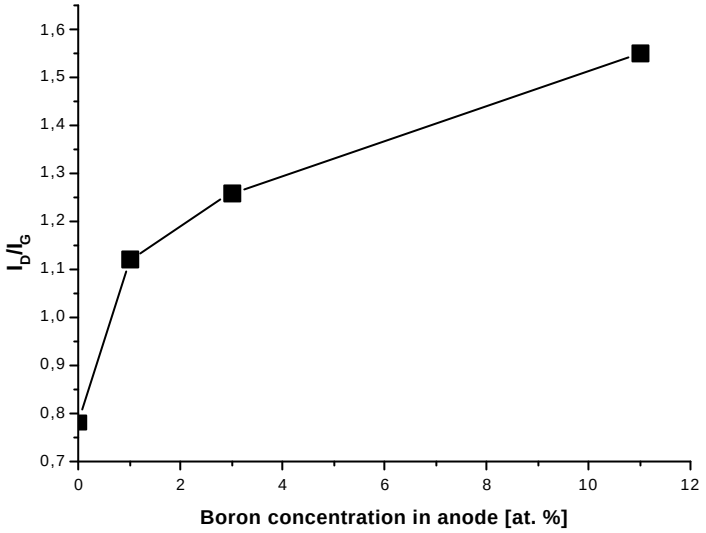

Fig. 4. I_D/I_G ratio of undoped and various concentrations of boron-doped CNTs.

4. Conclusion

We have demonstrated the production of B-doped MWCNTs in the arc discharge in water. The boron concentration in anode strogly influenced the yield and the structure of obtained MWCNTs. The temperatures and C_2 contents were similar to those observed in carbon arc in helium gas. This study has also shown that water arc-discharge technology simplifies the traditional He discharge for nanostructured carbons production: no special equipment, vacuum or gas are needed.

Acknowledgment. This work was supported by the Committee for Scientific Research (KBN) through the Department of Chemistry, Warsaw University, under Grant No. 3 T08D 012 28.

References

[1] S. Iijima, Nature (London), 56, 354 (1991).
[2] Ph. Redlich, J. Loeffler, P.M. Ajayan, J. Bill, F. Aldinger, M. Ruhle, Chem. Phys. Lett., 465, 260 (1996).
[3] C.F. Chen, C.L. Tsai, C.L. Lin, Diamond and Related Materials, 1500, 12 (2003).
[4] K. McGuire, N. Gothard, P.L. Gai, M.S. Dresselhaus, G. Sumanasekera, A. M. Rao, Carbon, 219, 43 (2005).
[5] W. Han, Y. Badno, K. Kurashima, T. Sato, Chem. Phys. Lett., 368, 299 (1999).
[6] H. Lange, M. Sioda, A. Huczko, Y.Q. Zhu, H.W. Kroto, D.R.M. Walton, Carbon, 1617, 41 (2003).
[7] H. Lange, K. Saidane, M. Razafinimanana, A. Gleizes, J. Phys. D: Appl. Phys., 1024, 32 (1999).
[8] T. Shirasaki, A. Derre, M. Menetrier, A. Tressaud, S. Flandrois, Carbon, 1461, 38 (2000).
[9] R.J. Nemanich, S.A. Solin, Phys. Rev. B, 392, 20 (1979).
[10] H. Lange, A. Huczko, P. Byszewski, E. Mizera, H. Shinohara, Chem. Phys. Lett., 174, 289 (1998).

Effect of substrate geometry on deposition of thermally sprayed coating particles

V. R. Srivatsan, Q. Zhu, A. Dolatabadi
Department of Mechanical and Industrial Engineering, Concordia University, Montreal, Canada.

Abstract
Simulations of solid particles in a highly compressible gas flow in a high velocity thermal spray process are presented. The Lagrangian method is used for tracking the particles in the gas phase. Effects of geometric configuration of the substrate and particle landing position for different particle sizes are analyzed. It is found that the geometry of the substrate and size of particles have a significant effect on the normal velocity of the particle upon impact on a substrate. Deviation of particle trajectory for various particle sizes is presented.

Key words: Deposition efficiency; Substrate geometry; Lagrangian particle tracking.

1. Introduction:

Thermal spray coatings are formed by the impingement of a stream of particles in high temperature on a substrate. Extensive use of thermal spray process is found in the aerospace, power generation and more recently in automotive industries to provide protective coatings on components that are exposed to heat, corrosion, and wear. For example, in HVOF process, a mixture of fuel and oxygen fed in to a specially designed nozzle; ignites at a high pressure and this combustion accelerates the particle fed along with the carrier gas inside a converging–diverging nozzle. By the interaction with the gas phase, the injected particles attain high velocity (above 400 m/s) at relatively low temperature (less than 2400ºC), thereby gaining high kinetic and thermal energy. High particle kinetic energy coupled with high thermal energy, upon impact leads to the formation of a dense, well adhered coating.

The goal of any thermal spray process is to attain high deposition efficiency. In practice, from 20% up to 55 % of the particles fed to a spray gun escape from the field and are not deposited on the substrate, which leads to low deposition efficiency [1]. This is the result of having many particles with low normal velocity upon impact on the substrate [2]. For industrial applications, improving the deposition efficiency is a critical task to be taken in to consideration. A close inspection of the gas-particle flow near the substrate shows that the curvature of the substrate is an important factor which determines the gas flow field in the region near the substrate [3].

In this work we have attempted to study the effect of geometry of the substrate and size of the particles on deposition efficiency by analyzing the gas flow and the particle trajectory and impact velocity near the substrate. We have compared the flow pattern near the substrate of three different shapes i.e., Flat, Concave, and Convex. Consequently, the trajectory of the particles of different sizes and their deposition characteristic on the above mentioned substrates were examined.

2. Methodology:

A thermal spray process usually involves supersonic viscous turbulent flow with solid particles. In order to capture the characteristics of the gas-solid particles flow, a compressible two-phase flow analysis is required. The governing equations are solved for the gas phase in an Eulerian frame, and equation of motion for a solid particle in the Lagrangian framework. Inert solid spherical particles are modeled, and a uniform temperature distribution inside each particle is considered (lumped capacitance system). A four-step chemical reaction [3] is used to model the combustion.

2.1 Governing Equations:

2.1.1. Gas phase

The governing equations for the gas phase are the continuity, momentum, energy, and ideal gas state equations for viscous, compressible, and turbulent flow. The equations are expressed in Cartesian tensor form with the Einstein summation convention:

Continuity Equation:

$$\frac{\partial \rho}{\partial t} + \frac{\partial (\rho u_j)}{\partial x_j} = 0 \tag{1}$$

Momentum Equation:

$$\frac{\partial}{\partial t}(\rho u_i) + \frac{\partial}{\partial x_j}(\rho u_j u_i) = -\frac{\partial p}{\partial x_i} + S_{u_i} + \frac{\partial}{\partial x_j}\left\{\mu_{eff}\left(\frac{\partial u_i}{\partial x_j} + \frac{\partial u_j}{\partial x_i}\right) - \frac{2}{3}\mu_{eff}\frac{\partial u_l}{\partial x_l}\delta_{ij}\right\} \tag{2}$$

Energy Equation:

$$\frac{\partial}{\partial t}(\rho H) + \frac{\partial}{\partial x_j}(\rho u_j H) - \frac{\partial p}{\partial t} = \frac{\partial}{\partial x_j}\left(\lambda \frac{\partial T}{\partial x_j} + \frac{\mu_t}{\mathrm{Pr}_t}\frac{\partial h}{\partial x_j}\right) + S_E + \frac{\partial}{\partial x_j}\left\{u_j\left[\mu_{eff}\left(\frac{\partial u_i}{\partial x_j} + \frac{\partial u_j}{\partial x_i}\right) - \frac{2}{3}\mu_{eff}\frac{\partial u_l}{\partial x_l}\delta_{ij}\right] + \mu\frac{\partial k}{\partial x_j}\right\} \tag{3}$$

where $\mu_{eff} = \mu + \mu_t$, $H = h + \frac{1}{2}(u_i u_i) + k$, λ, k, and S are effective viscosity, total enthalpy, thermal conductivity, turbulent kinetic energy, and source terms, respectively. The standard k-ε turbulence model of Launder and Spalding [4] is considered, where k is the turbulent kinetic energy and ε is the rate of its dissipation.

2.1.2 Particle Phase

The motion of each particle in the gas-particle flow is modeled by the Lagrangian particle tracking method. Two-way coupling between the gas and particulate phases is provided by source terms in the momentum and energy equations which include the effect of particulate phase on the gas phase. The equation of motion for a particle in the gas flow is as follows [5]

$$m_p \frac{d\vec{U}_p}{dt} = \frac{1}{2}\rho_g A_p C_D \left(\vec{U}_g - \vec{U}_p\right)\left|\vec{U}_g - \vec{U}_p\right| + \vec{F} \tag{4}$$

where m_p is the mass of particle, U_p and U_g are instantaneous particle and gas velocities, respectively. ρ_g is the gas density, A_p is the particle cross-sectional area and F denotes external forces such as gravitational force. Integrating the above equation of motion for a particle, results in the particle velocity. Second integration over the time step will result in the particle position.

2.2 Numerical Technique

This work uses Fluent™ version 6.1.22 computer code, which is commercially available from Fluent.Inc technology. A finite volume method for predicting flows at supersonic speeds is employed for an axi-symmetric geometry. The primary variables are the velocity components, pressure and temperature in Cartesian coordinates. Density is linked to pressure via an equation of state. The computational domain is subdivided into a number of quadrilateral control volumes.

All the dependent variables and fluid properties are stored in the control volume center i.e., cell-centered. Integrating the conservation laws over each control volume, results in systems of non-linear algebraic equations which are solved simultaneously.

3. Results and Discussion:

We have presented the results obtained for the three substrate configurations with two different particle sizes. The behavior of the gas phase is first analyzed and then the trajectory of particle in the gas phase is observed and the results are discussed below.

3.1 Gas Phase

General characteristics of the flow for three different substrates (Flat, Convex and Concave) are shown in Figure 1-a, b, and c, respectively. At the throat section of the nozzle, the Mach number is around 1 and as the sonic flow expands in the diverging section of the nozzle, a supersonic flow develops in this region. Finally, the high speed gas leaves the nozzle with an average Mach number of 2.3. Four or possibly five shock diamonds can be identified before the flow stabilizes to atmospheric pressure due to the fact that shocks are attenuated by turbulent shear layers. Furthermore, the gas flow is decelerated and diverted near the substrate. A bow shock can be observed near the substrate as a result of the jet impingement on the wall. It is evident from these results that the flow regime is changed significantly near the substrate due to the gas flow impingement on the wall. More importantly, variation of the flow regime is strongly dependent on the shape of the substrate. Resolving the supersonic flow and its interaction with the coating particles in this critical region (i.e. near the substrate) is eminent to predict particle conditions such as particle trajectory, velocity, and temperature upon impact.

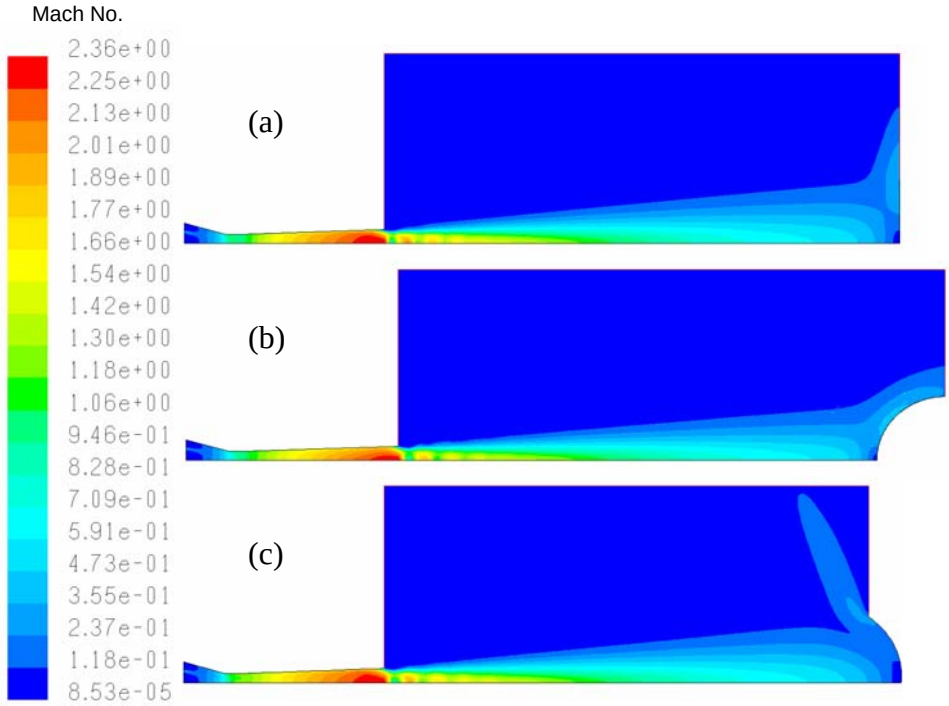

Figure 1: Mach number Contour of gas impinging on (a) Flat (b) Convex and (c) Concave Substrates

3.2 Particle Phase:

Figure 2 illustrates velocity of Nickel particles with a diameter of 10 μm impacting on substrates with three different shapes. The trajectory of particles near the substrate is significantly altered for the three different geometries. This is mainly due to the variation of the strength and shape of bow shocks formed over the three different geometries (Figure 1). A close inspection of the results of particle trajectories near the substrates shows that the particle landing position on the substrate also differs from each other for the three different shapes. Here, as the particle size is too small (in the order of 10 micron), some of the particles are flushed away by the gas before impinging on the substrate. Moreover, as it is shown in Figure 2-b due to the convex nature of the substrate, the particle streams which are injected slightly away from the centerline are deviated and their deposition on the substrate is questionable. However, for the concave substrate case (Figure 2-c) the inward curvature traps even those particle streams which are away from the centerline.

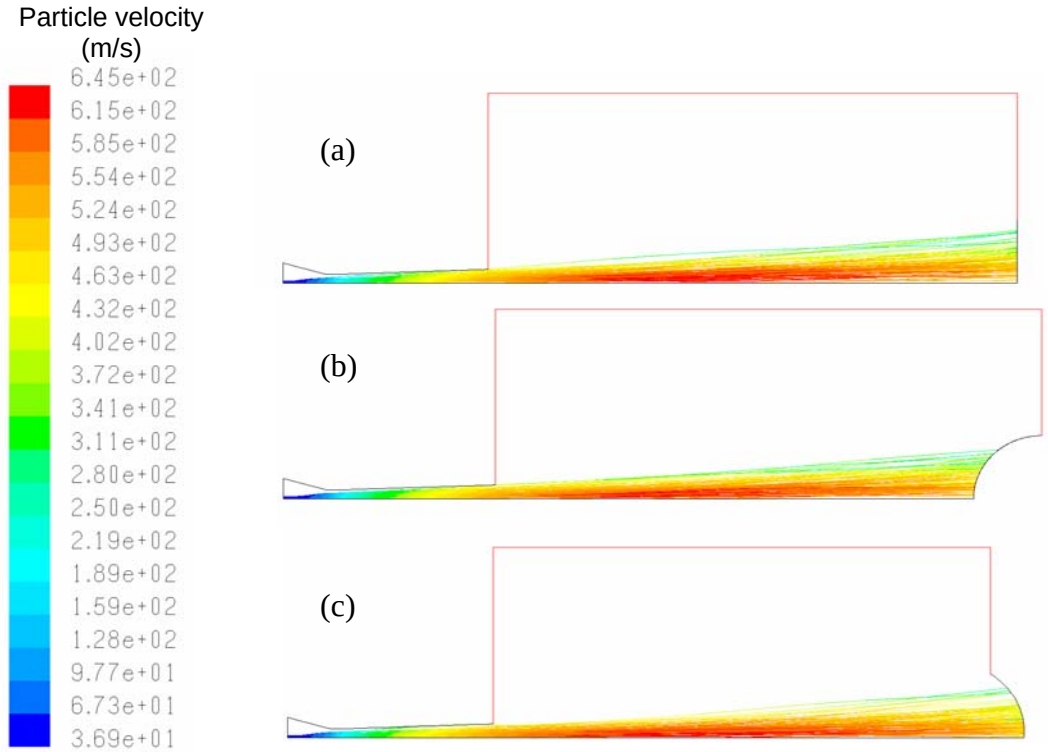

Figure 2 Particle trajectory and velocity with a size of 10 μm for (a) Flat, (b) Convex, and (c) Concave Substrates

Study of heavier particles with a size of 30 μm is shown in Figure 3. In this case, the deviation of particle trajectory from the centerline is smaller compared to that of 10 micron particles. This can be described by evaluating the particle Stokes number, which is the ratio of particle response time to a time characteristic of the fluid motion. Stokes number would be in the order of 10^2-10^3. With such high Stokes numbers, particles do not respond quickly to the variation of the gas velocity field. Because of this, the heavier particles are less sensitive to the bow shocks consequently to the shape or curvature of the substrate. This effect can be observed by comparing the results shown in Figure 3 for flat, convex, and concave substrate configurations.

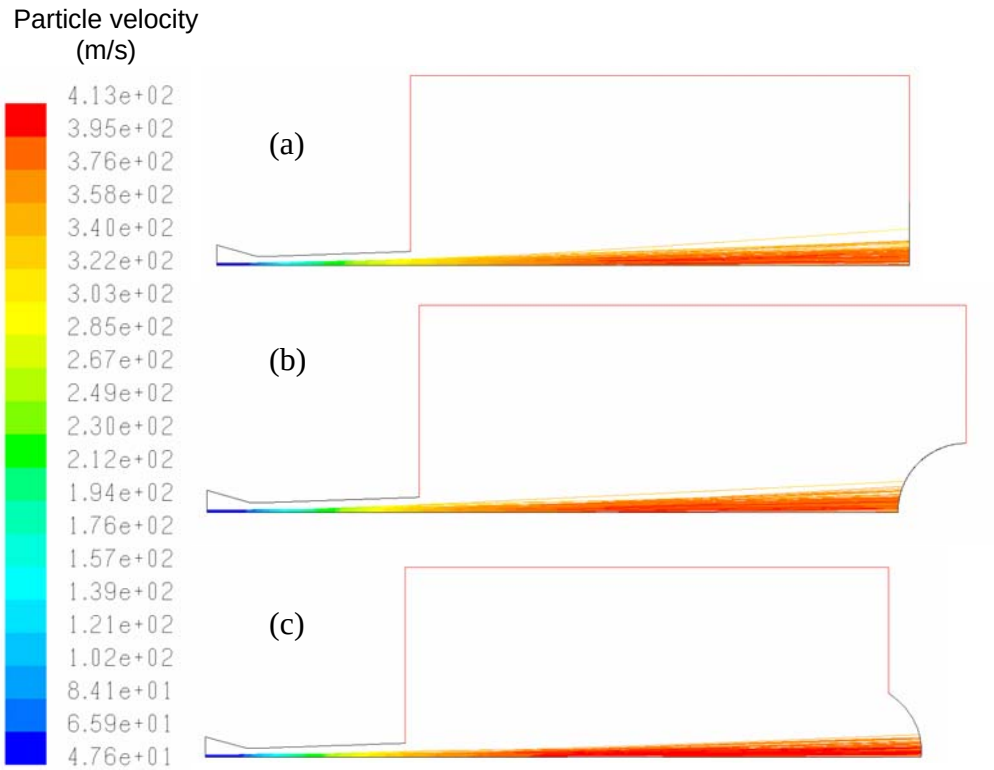

Figure 3: Particle trajectory and velocity with a size of 30 µm for (a) Flat, (b) Convex, and (c) Concave Substrates

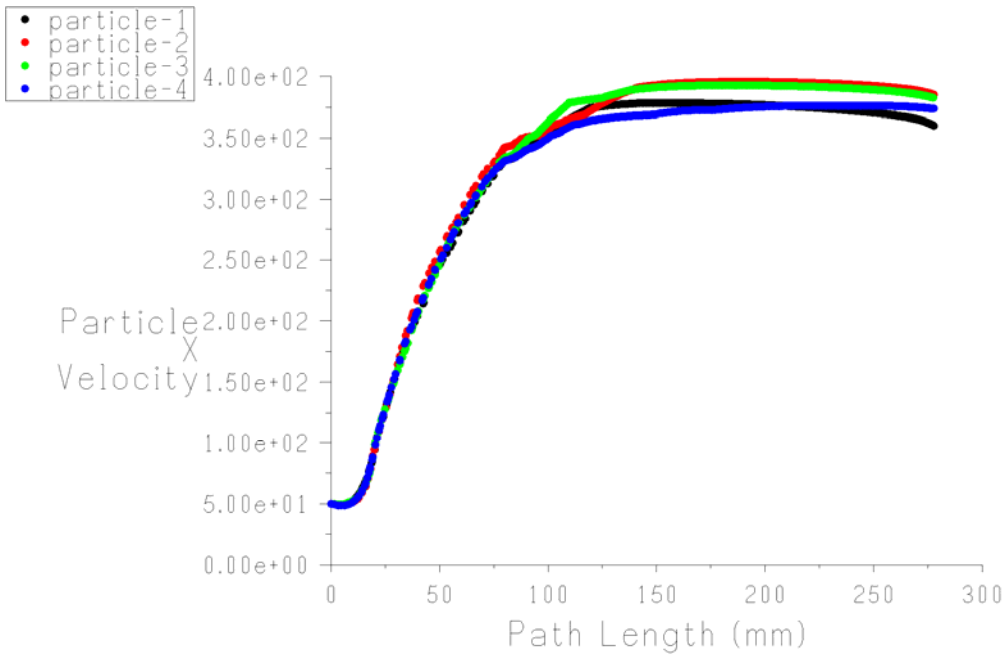

Figure 4: Plot of Axial Velocity Vs Path Length

These observations lead to a conclusion that heavy particles have better chances of sticking to the substrate. However, the particle landing velocity is an important factor for deposition of particles on the substrate. Figure 4 shows the plot between particle velocity and path length of 4 particle streams with a size of 30 μm. It is clear that the velocity of 30 micron particles is least affected by the presence of shocks near the nozzle exit and near the wall. It is also observed that the average particle velocity near the wall is 400 m/s. This gives particle sufficient kinetic energy, which when added to the thermal energy, makes the particle stick well on the substrate.

4. Conclusion and Future Work:

The effects of substrate geometry and particle size on deposition of coating particles are studied in this work and results were presented for different substrate geometries with various particle sizes. It is found that, smaller particles deposit easier on a concave substrate than on the other two. Interestingly, it is observed that particles with higher sizes have better chance to stick on the substrate, irrespective of the shape of the substrate on which they impact.

The future work will be dedicated in finding out an optimum size of the particle which attains maximum normal velocity upon impact on a substrate. Focus will also be made to extend the supersonic zone of the gas phase and smooth transition of flow from supersonic to subsonic velocities, which would minimize the loss of impact velocity of particles, providing sufficient kinetic energy, which in turn, increases the deposition efficiency.

5. Reference:

[1] N. Sinha, B.J. York, A. Hosangadi, S.M. Dash, First-principles-based computational fluid dynamic (CFD) model of thermal spray deposition process, in: Proceedings of the Eighth National Thermal Spray Conference, Houston, TX, 1995, pp. 199–206

[2] X. Yang, S. Eidelman, Numerical analysis of a high-velocity oxygen fuel thermal spray system, Journal of Thermal Spray Technology 5 (2) (1996)175–184.

[3] A. Dolatabadi, J. Mostaghimi, M. Ivanovic, Numerical modeling of particle laden flow in HVOF torch with gas shroud, in: Proceedings of the International Thermal Spray Conference, Montreal, Quebec,Canada, 2000, pp. 105–113.

[4] B.E. Launder, D.B. Spalding, The numerical calculation of turbulent flows, Comput. Meth. Appl. Mech. Eng. 3 (1974) 269–289.

[5] C. Crowe, D. Stock, A computer solution for two-dimensional fluid–particle flows, International Journal of Numerical Methods. Eng. 19 (1976) 185–196.

The plasmacatalytical removal of an azo dye : Orange G

F. Abdelmalek[1]; F. Belabbes[1]; A. Addou[1]; J.L. Brisset[2]

[1]*Laboratoire des Sciences et Techniques de l'Environnement et de la Valorisation. Faculté des Sciences de l'Ingénieur, Université de Mostaganem. Algérie*
[2]*Laboratoire d'Electrochimie Interfaciale et de Chimie Analytique. Faculté des Sciences Université de Rouen. France.*

Abstract :
Exposure of TiO_2 aqueous suspension of Orange G to activated species of humid air non thermal plasma of gliding arc leads to oxidative degradation. We demonstrate that there is an optimum TiO_2 concentration (2g/L) at the which the rates of decolorization and degradation are maximum.
The decolorization efficiency and COD reduction were 100% and 91.7% respectively, while they were only 98.4% and 63.5%without catalyst.This results were obtained after 180 min of treatment.

Keywords:
Non thermal plasma; gliding arc; Orange G; plasmacatalysis; UV-VIS spectra; TiO_2

1. Introduction

Various textiles industries use different types of organics dyes. Fifteen percent of the world production of dyes is lost during the dyeing process and it released in textile effluent. The release of those colored wastewaters has serious consequences for the environment. It is well know that some azo-dyes are highly carcinogenic [1]. Classical waste removal processes such as biodegradation, flocculation, ozonation, adsorption are currently used, but they become inadequate [2,3] nowadays with respect to the more drastic imposed environmental regulations.
Advanced oxidation processes have been used to treat various organic pollutants [4-7]. Among these processes, heterogeneous photocatalysis was found as an emerging destructive technology leading to the total mineralization of organics dyes [8-18].
In this study, we propose the use of an advanced oxidation process: the gliding arc technique which generates reactive species OH°. We considered the gliding arc as a new degradation technique which is able to degrade pollutant molecules [19, 20]. We report in this work on the results relevant to the treatment of TiO_2 aqueous suspension of azo dye (Orange G) of this particular non-thermal plasma.

2. Experimental section

Orange G was purchased from Accros Organic (Fig. 1) and used as received without further purification. Titanium dioxide Merck (surface area 11 m^2/g) was used as catalyst. Other chemicals used in the study were of analytical reagent grade quality. The colored suspensions were magnetically stirred in the dark for 60 min to reach the adsorption equilibrium. Aliquots were taken at regulars intervals, centrifuged and filtered through 0.45 μm filter.
The gliding arc system was described previously [21]. An electric is created between two metallic electrodes raised a convenient voltage difference (10 kV). The arc is blown away by a gas flow air the axis of the system and glides towards the end of the electrode before it breaks and a new arc forms. A plasma is generated by the arc in a volume located at the tips of the electrodes.
A UV-VIS spectrophotometer "Biomat 3 (Thermospectronic)"was used to the determination of the decolorization at the maximum of absorbance $\lambda = 478$ nm.
The mineralization of the dye was monitored by measuring the chemical oxygen demand (COD) using the French AFNOR norm. The organic matter was oxidized by potassium dichromate $K_2Cr_2O_7$. The excess of potassium dichromate was measured out by Mohr salt titration.
COD was calculated from the expression

$$COD\ (mg\ O_2/L) = 8000\ X\ (V_{MB} - V_{MS})\ X\ N_M\ /V_0$$

Where V_{MB} and V_{MS} are the volumes of standard Mohr salt solution used for the blank and the sample respectively. N_M is the normality of Mohr salt solution, and V_0 is the volume of the sample.

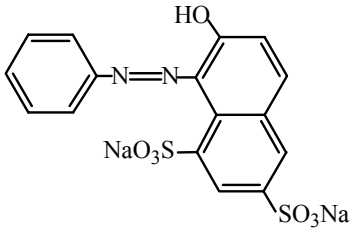

Fig.1. Structure of Orange G

3. Results

3.1 Treatment in absence of TiO_2

-The spectrum of Orange g in the visible region exhibits a main band with a maximum at 478 nm and a shoulder at 440 nm. The band at 478 nm reveals the presence of the azo form, whereas the shoulder at 440 nm indicates the presence of the azo form.

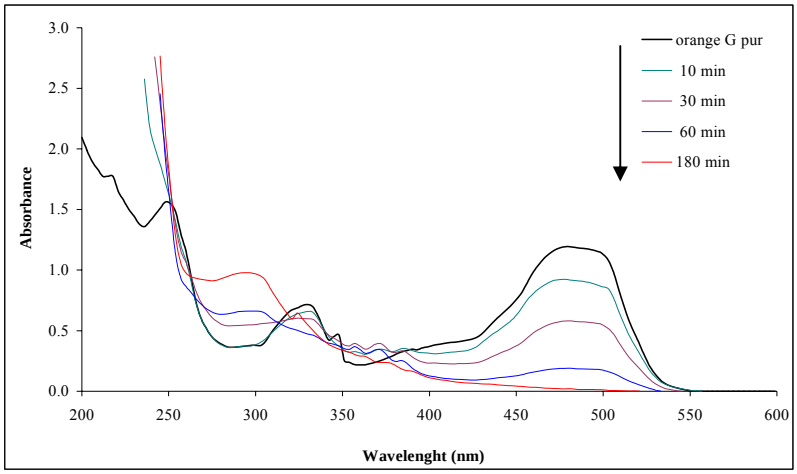

Fig. 2. UV-VIS spectra of the aqueous solution of Orange G at t=0 and after 10, 30, 60, 180 minutes of plasma treatment. C_{OG} = 80 µM, pH = 5.4

It is well known that azo group (–N=N–) of the Orange G is the basic reason for its visible color. We observed (fig.2) the visible absorbance of the dye solution becomes lower. These is explained by considering the breaking down of the azo bond and the formation of smaller products [22, 23]. The absorbance peaks in the visible region disappeared during plasma treatment (Fig. 3). In the meantime, new peaks between 200 and 260 nm appeared, which indicates new structure units formed. The 260 nm absorbance peak is attributed to the multi-substituted benzene (e.g., benzendicarboxylic acid [24] produced from degradation of the naphtalene ring (330 nm) [25].

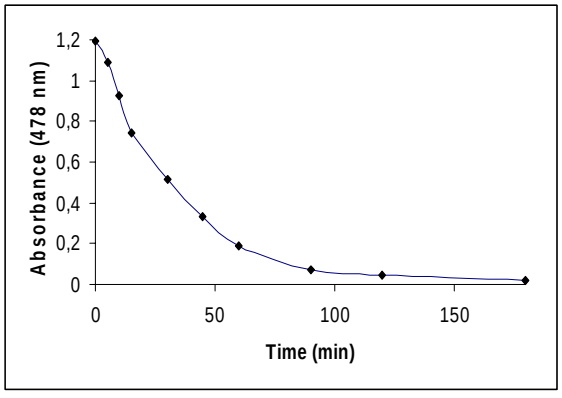

Fig. 3. Plasma decolorization of Orange G (80 µM)

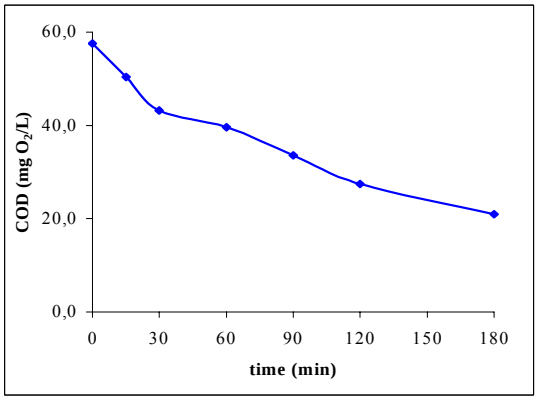

Fig. 4. Plasma degradation of Orange G (80 µM)

The degradation of Orange G has been followed using the COD. The disappearance of the COD expresses the mineralization of the dye by oxidation reaction by hydroxyl radicals, which follows the equation (1):

$$C_{16}H_{10}N_2O_7S_2^{2-} + 21O_2 \longrightarrow 16CO_2 + 2NO_3^- + 4H^+ + 2SO_4^{2-} + 3H_2O \quad (1)$$

The COD values decreased as the treatment time increased as we can see on figure (4). The COD removal of Orange G was 63% after 3 hours of treatment, while the color removal was 98.41%. We noticed that the decolorization is easier than COD removal (Table. 1).

Table.1. Effect of plasma treatment on decolorization and degradation of Orange G

time (min)	% Decolorization	% Degradation
0	0	0
5	8.81	
10	22.57	
15	37.42	12.5
30	56.62	25
45	72.32	
60	84.23	31.25
90	94.04	41.67
120	96.39	52.26
7180	98.41	63.54

3.2 Treatment in presence of TiO_2

a. Effect of catalytic dose

The dye solution (80 µM) was exposed to system plasma/TiO_2 during 180 minutes with different catalytic doses (0.5 g/L, 1 g/L, 1.5 g/L, 2 g/L, 2.5 g/L, 3 g/L). Table. 2 shows percent decolorization and degradation of dye as function of catalytic dose. The decolorization and increases with increase in catalytic dose

At 2 g/L the dye was found to be almost completely decolourized (100%) after 180 minutes of treatment, while the degradation rate reaches the maximum (91.67%). Hence, an optimum catalytic dose 2 g/L was selected.

Table. 2. Effect of Catalytic dose on decolorization and degradation of Orange G treated by plasma/TiO_2

Catalytic dose (g/L)	% Decolorization	% Degradation
0	98.41	63
0.5	99.16	70.83
1	99.33	72.50
1.5	99.75	83.33
2	100	91.67
2.5	99.92	83.33
3	99.83	78.33

The decrease in the percentage of degradation at higher catalyst loading may be due to deactivation of activated molecules by collision with ground state molecules. Agglomeration and sedimentation of TiO2 particles were observed elsewhere when 2.5 g/l of catalyst was added to the dye solution [26].

b. Effect of pH

At the start of the treatment the pH was 5.4, but during the process of degradation the pH decreased and at the end it was measured to be < 2.

The non-thermal plasma generates OH° radicals which are responsible for strong oxidising properties; while the NO° radicals are know as parent molecules for acid derivatives HNO_2, HNO_3 which induce a steep pH lowering of the solution.

For the Orange G, the decrease of pH favors it degradation. During the treatment, there is a combination effects of OH° radicals created from plasma and OH° radicals produced on the surface of TiO_2 (eq. 2). If the dye is adsorbed on the TiO_2 surface, it can be both oxidized by OH° and/or by photogenerated holes (eq. 3).

$$TiO_2 + h\upsilon \longrightarrow e^-_{Cb} + h^+_{vb} \quad (2)$$

$$H_2O + h^+_{Vb} \longrightarrow OH^\circ + H^+ \quad (3)$$

Also the adsorbed dye molecules may be directly oxidized by the valence band holes to form dye radical cations which ultimately cause dye degradation [25-29].

c. Effect of the optimum catalytic dose

The decolorization was studied in the presence and absence of 2 g/l of TiO_2, which is the optimum catalytic dose. Figure 5 shows a plot of percent decolorization of Orange G versus treatment time. The reaction was found to be less in the absence of catalyst. Figure 6 shows the degradation in the presence and absence of catalyst, the rate of mineralization is higher with TiO_2, the dye was found to have mineralized to the extent of 91.67%, while it was 63% without catalyst, after 180 minutes of treatment. The results are indicating that TiO_2 is a prerequisite for the plasma degradation process.

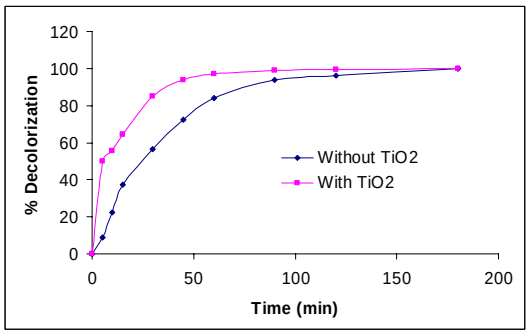

Fig. 5. Decolorization with and without TiO2

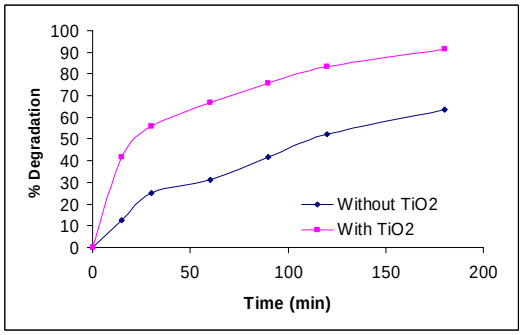

Fig.. 6. Degradation with and without TiO_2

d. Kinetic analysis

Ours results show that the plasma/TiO_2 process is efficient to degrade azo dyes in aqueous solution and to remove solution color. The kinetic study show a first order kinetic for the decolorization and the degradation as confirmed by the linear transform $\ln(C_0/C) = - kt$. The rate constants were as follows:

- Decolorization in absence of TiO_2: $k = 0.0316\ min^{-1}$, $R^2 = 0.995$
- Decolorization with 2 g/l of TiO_2: $k = 0.0509\ min^{-1}$, $R^2 = 0.983$
- Degradation in absence of TiO_2: $k = 0.0054\ min^{-1}$, $R^2 = 0.987$
- Degradation with 2 g/l of TiO_2: $k = 0.0127\ min^{-1}$, $R^2 = 0.971$

Conclusion

The degradation of the azo dye Orange G by non-thermal plasma has been studied in aqueous medium. We have shown that the gliding arc technique is efficient for azo dye degradation. It is explicitly exhibited by the absorbance decrease, color disappearance and COD decrease in azo dye solution under study.

Exposure of Orange G solution to the non-thermal plasma in the presence of TiO_2 gives the best efficiency for lower treatment time. The influence of the concentration of TiO_2 has been evaluated: the plasmacatalytic reaction was favoured by an optimum catalytic dose.

The results indicate that the decolorization is faster with TiO_2 and the mineralization could be achieved up to 90%

References

[1] M.V. Correia, T. Stephenson, S.J. Judd, «Characterization of textiles wastewaters: a review», Environ. Tech.s. **15**, 917-919 (1994).

[2] S. Dai, W. Song, T. Li, Y. Zhuang, « Study on azo dyes structure-biodegradability relationships », Advances in Tech. Seminar. **4**, 1-9 (1996).

[3] S. Dai, Y. Zhuang, Y.Chen, L. Chen, « Study on the relationships between structure of the synthetic organic chemicals and their biodegradability », Environ. Chem. **14**, 354-367 (1995).

[4] A.T. Sugiarto, S. Ito, T. Ohshima, M. Sato, J. Skalny, « Oxidative decoloration of dyes by pulsed discharge plasma in water », J. of Electrostatics. **58**, 135-145 (2003).
[5] I. Arslan, I.A. Balciogul, D. W. Bahnemann, «Advanced chemical oxidation of reactive dyes in simulated dyehouse effluent by ferrioxalate-Fenton / UV-A and TiO_2 / UV-A processes», Dyes and Pigments. **47**, 207-218 (2000).
[6] S. Nam, V. Renganathan, P.G. Tratnyek, «Substituant effects on azo dye oxidation by the Fe^{III} – EDTA-H_2O_2 system», Chemosphere. **45**, 59-65 (2001).
[7] T.C. An, X.H. Zhu, Y.Xiong, «Feasibility study of photoelectrochemical degradation of methylene blue with three-dimensional electrode-photocatalytic reactor», Chemosphere. **46**, 897-903 (2002).
[8] B. Neppolian, H.C. Choi, S. Sakthivel, B. Arabindoo, V. Murugesan, «Solar/UV induced photocatalytic degradation of three commercial textile dyes», J. Hazard. Mat. B. **89**, 303-317 (2002).
[9] C. Zhu, L. Wang, L. Kong, «Photocatalytic degradation of azo dyes by supported TiO_2 + UV in aqueous solution», Chemosphere. **41**,303-309 (2000).
[10] C. Hachem, F. Bocquillon, O. Zahraa, M. Bouchy, «Decolourization of textile industry wastewater by the photocatalytic degradation process», Dyes and pigments. **49**, 117-125 (2001).
[11] Galindo, P.Jacques, A. Kalte. «Photochemical and photocatalytic degradation of an indigoid dye : a case study of acid blue 74 (AB74) ». Journal of Photochemistry and photobiology A: Chemistry. **141**, 47-56 (2001).
[12] C. Guillard, H. Lachheb, , A. Houas and all. «Influence of chemical structure of dyes, of pH and of inorganic salts on their photocatalytic degradation by TiO_2 comparison of the efficiency of powder and supported TiO_2 ». Journal of photochemistry and photobiology. **158**, 27-36. (2003).
[13] H. Lachheb, E. Puzenat, A. Houas, M. Ksibi, « Photocatalytic degradation of various types of dyes in water by UV/Irradiation titana», Appl. Catal. B: Evironnmental. **1025**, 1-16 (2002).
[14] M. Mrowetz, C. Pirola, E. Selli, « Degradation of organic water pollutants through sonophotocatalysis in the presence of TiO_2», Ultrasonics Sonochemistry.**10**, 247-254 (2003).
[15] I.K. Konstantinou, A.A. Triantafyllos, « TiO_2-assisted photocatalytic degradation of azo dyes in aqueous solution: kinetic and mechanistic investigations a review», Appl. Catal. B: Environnmental. **49**, 1-14 (2004).
[16] S. Sakthivel, B. Neppolian, M.V. Shankar, B. Arabindoo, M. Palachamy, V. Murugesan, « Solar photocatalytic degradation of azo dye: compari son of photocatalytic efficiency of ZnO and TiO_2», Solar Energy Materials & Solar Cells. **77**, 65-82 (2003).
[17] W. kan, Z. Jianying, L. Liping, Y. Shiying, C. Yingxu, « UV or visible light photodegradation of AO7 on TiO_2 particles: the influence of inorganic anions», J. Photochem. and Photobio. A: Chemistry, (2004). In press. [18] Guangming Liu, Xiangzhong Li, Jincai Zhao, Satoshi Horikoshi, Hisao Hidaka, « Photooxidation mechanism of dye alizarin red in TiO_2 dispersions under visible illumination : an experimental and theorical examination», J. of Molecular Catalysis A : Chemical.**153**, 221-222 (2000).
[19] A. Doubla ; F. Abdelmalek; K. Khelifa; A. Addou; J.L Brisset "Post-discharge plamachemical oxidation of iron (II) complexes" J. Applied. Electrochim. **33**, 73-77 (2003).
[20]- F. Abdelmalek; S. Gharbi; B. Benstaali; A. Addou; J.L Brisset, . "Plasmachemical Degradation of Azo Dyes by humid air plasma: Yellow Supranol 4 GL, Scarlet Red Nylosan F3 GL and industrial waste", Water. Research. **38**, 2338-2346 (2004).
[21]- D, Moussa, F. Abdelmalek, B. Benstaali, A. Addou,E. Hnatiuc, J.L. Brisset. "Acidity control of the gliding arc treatment of aqueous application to polluant abatement and biodecontamination". Eur. Phys. J. Appl. Phys. **29**, 189-199 (2005).
[22] J. Bandara, C. Morrison, J. Kiwi, «Degradation/decoloration of concentrated solutions of Orange II. Kinetics and quantum yield for sunlight induced reactions via Fenton type reagents», J. Photochem. Photobio A: Chemistry. **99**, 57-66 (1999).
[23] M. Zhu, X. Huang, H. Shen, «Aromatic azo compounds as spectrphotometric kinetic assay substrate for HRP», Talanta. **53**, 927-935 (2001).
[24] J. Cao, L. Wei, Q. Huang, S. Han, « Reducing degradation of azo dye by zero-valent iron in aqueous solution», Chemosphere, **38 (3),** 565-571 (1999).
[25] E. Guivarch, S. Trevin, C. lahitte, «Degradation of azo dyes in water by Electro-Fenton process», Environ, Chem, Lett. **1**, 38-44 (2003).
[26] J. Lea, A.A. Adesina, « The photo-oxidative degradation of sodium dodecyl sulfate in aqueous TiO_2 suspensions», J. Photochemistry and Photobiology A : Chemistry. **118**, 111-122 (1998).

[27] C.M. So, M.Y. Cheng, J.C. Yu, P.K. Wong, « Degradation of azo dye Procion Red MX-5B by photocatalytic oxidation», Chemosphere. **46**, 905-912 (2002).
[28] J.M. Herrmann, F. Jansen, R.A. Van Santen, « Water treatment by Heterogeneous photocatalysis in environmental catalyst», Imperial College Press, Catalytic Science Series, London. **1**, 171-194 (1999).
[29] R.J. Davis, J.L. Gainer, G. O'Neal, I. Wu, « Photocatalytic decoloration of wastewater dyes», Water Evironnment Research. **66**,50-53 (1994).

Methane Conversion to Valuable Products Using Catalytic Enhanced Dielectric-Barrier Discharge

N. Seyed Matin*; A. H. Jalili; H. Savadkoohi; R. Ahmadi; M. Khodagholi; and S. Vasheghani Farahani;

National Iranian Oil Company(NIOC), Research Institute of Petroleum Industry (RIPI), Qom Road, P. O. Box 18745-4391, Tehran, Iran

*Corresponding author, Email: matinn@ripi.ir

Abstract- Methane conversion to higher hydrocarbons and valuable products using a plasma activated and the hybrid dielectric-barrier discharge (DBD)-catalyst reactor was investigated under ac high voltage conditions. Perovskite type and ZSM-5 employed as the catalyst in this study. The experiments were carried out in a quartz tube with external diameter of 9 mm and the reaction zone with length of 15cm, at atmospheric pressure. Methane and oxygen as reactants and helium as a dilution gas were used in the experiments. The effect of system variables including CH_4/O_2 ratio in the feed, applied voltage and feed flow rates and also catalyst have been studied. The results show the selective production of syngas and C_2 hydrocarbons. In the blank DBD reactor without catalyst the feed composition ratio CH_4/O_2 =4 and feed flow rate 40ml/min gives the maximum methane conversion about 8% at 8kV for applied voltage. The main product in the DBD reactor filled with zeolite was syngas at optimum temperature 200^{o}C. The experiments show that at the studied temperature range in this work, both blank and filled DBD reactors with zeolite produce syngas as the main product. The optimum voltage for C_2 and C_2H_4 production in the hybrid catalyst-plasma reactor in this study was between 8- 10 kV. The maximum 40% yield for syngas production at temperature 200^{o}C in the presence of zeolite catalyst in the DBD reactor was achieved. At the catalyst free DBD reactor the production of syngas at the studied temperature reveals the temperature independency and is about 30%. The hybrid perovskite type catalyst-DBD reactor shows no enhancement in the results at studied temperature range.

Keywords: dielectric barrier discharge, zeolite, methane conversion, plasma, syngas

Introduction- Methane contributes to the building up green house effect. Any success in the research of a utilization of methane will help to slowing down a green house gases production. On the other hand the relatively abundant resource of natural gas and its low cast makes it as a good choice for carbon-based fuel, and other chemicals. Presently natural gas uses mostly as an fuel in industry and household heating devices, with no economic value and negative environmental impacts.

Methane can be indirectly converted to liquid chemicals, traditionally known as GTL(Gas to Liquid). Methane is converted to syngas (i. e. H_2 and CO) through steam reforming, partial oxidation and/or steam-CO2 reforming processes. Syngas under high pressure and relatively high temperature conditions in the presence of catalyst (e.g. Cobalt or Fe catalysts) produces wide rang of hydrocarbons, from C_1 to wax. In the other process methane under high temperature condition and the presence of catalyst, is directly converted to higher hydrocarbons mainly ethylene, that is known as OCM (Oxidative Coupling of Methane) [1, 2]. The tough thermodynamic conditions, product selectivity problem, catalyst deactivation, make researchers to investigate the other applicable ways mainly plasma technology[3-9]. In this study the conversion of methane to higher hydrocarbons and syngas via gas discharge is investigated.

Experimental Setup –The details of experimental system used in this study has been given in ref. [8]. Nevertheless we give the brief description here. The set up consist of home made power supply, reactant feeding system, quartz reactor and gas

chromatograph for product analyzing, Figure (1). Methane and oxygen are introduced as the feeds and helium employed as diluent gas.

Results and Discussion- In this study the effects of feed ratio, applied voltage, feed flow rate and the presence of catalyst on the methane conversion and product selectivity are investigated.

Figure (2) shows the methane conversion as a function of applied voltage. The methane conversion increases with enhancement of the applied voltage. Increasing of methane conversion with applied voltage is the same trend for catalyst-DBD and blank DBD reactors. In the same way methane conversion is raised with reactant residence time in the reactor. Figures (3)-(5) show that the methane conversion and ethane and ethylene yield how impact by CH4/O2 ratio in the feed. Figure (6) shows the product selectivity in the DBD reactor with the presence of perovskite type catalyst as a function of applied voltage. As it can be seen the maximum methane conversion in the presence of perovskite catalyst and room temperature is less than 6%. The perovskite catalyst is in favor of the reaction selectivity to C2 production. The low conversion of methane affects the C2 yield in the presence of perovskite catalyst and generally the product yields in DBD reactor. Figure (7) shows the variation of product selectivity in the blank DBD reactor with applied voltage. As it can be seen the maximum yield of C2 production is about 4%, which is comparable with results of perovskite -DBD reactor at room temperature. Of course it should be mentioned that the activation temperature for this type of catalyst is high (more than 550^{o}C) in the traditional methods (i. e. without plasma) for methane conversion such as OCM. Anyway this study conducted for investigation of the likely synergic effects of catalyst and plasma in the DBD reactor at room temperature. Since plasma can provides enough electron for catalyst surface for electron transfer reactions between catalyst surface and gas phase reactants, even at room temperature. Figure (8) shows the product yield as a function of system temperature in the case of zeolite-DBD reactor hybrid. As it can be seen the main products is syngas with about 40% yield.

Conclusion – In this work the catalyst-DBD hybrid reactor and blank DBD reactor were studied for their ability in methane conversion to higher hydrocarbons and valuable products. Results of this study show the low methane conversion and also good product selectivity in catalyst-DBD hybrid reactor. The ZSM-5-DBD hybrid reactor shows good selectivity for syngas production.

Refrences

[1] L. H. Lunsford, Catal. Today**, 63,** 165 (2000).

[2] Gerard P. Laan Van Der, and A. A. C. M. Beenackers, Catal. Rev. Sci. Eng., **41**, 255 (1999).

[3] Y. P. Raizer, "Gas Discharge Physics", Springer-Verlag, 1991.

[4] S. L. Yao, T. Takemoto, F. Ouyang, A. Nakayama, E. Suzuki, A. Mizuno, and M. Okumoto, Energy & Fuels, **14**, 459 (2000).

[5] B. Eliasson, C.-J. Liu, and U. Kogelschatz, I&EC, Res., **39**,1221 (2000).

[6] D. W. Larkin, L. L. Lobban, and R. G. mallinson, Catal. Today, **71**, 199 (2001).

[7] T. Jiang, Y. Li, C.-J. Liu, G.-H. Xu, B. eliasson, and B. Xue, Catal. Today, **72**, 229 (2002).

[8] F. M. Aghamir, N. Seyed Matin, A. H. Jalili, M. H. Esfarayeni, M. A. Khodagholi and R Ahmadi, Plasma Sources Sci. Technol. **13**, 707 (2004).

[9] M. Heintze, and B. Pietruszka, Catal. Today, **89**, 21 (2004).

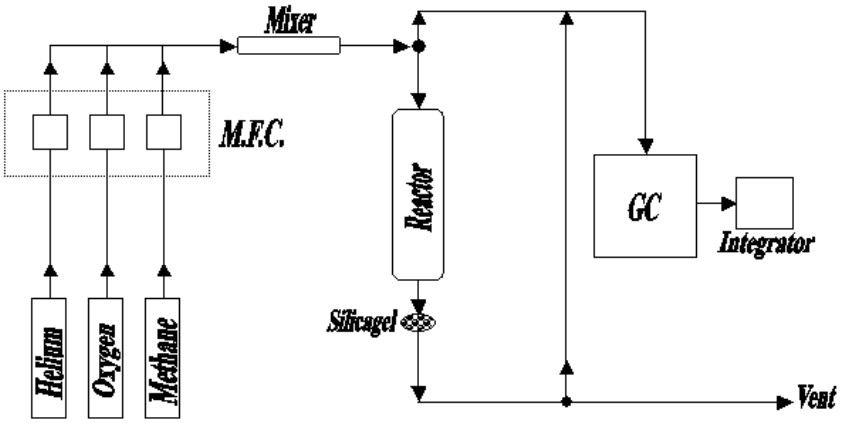

Figure (1)

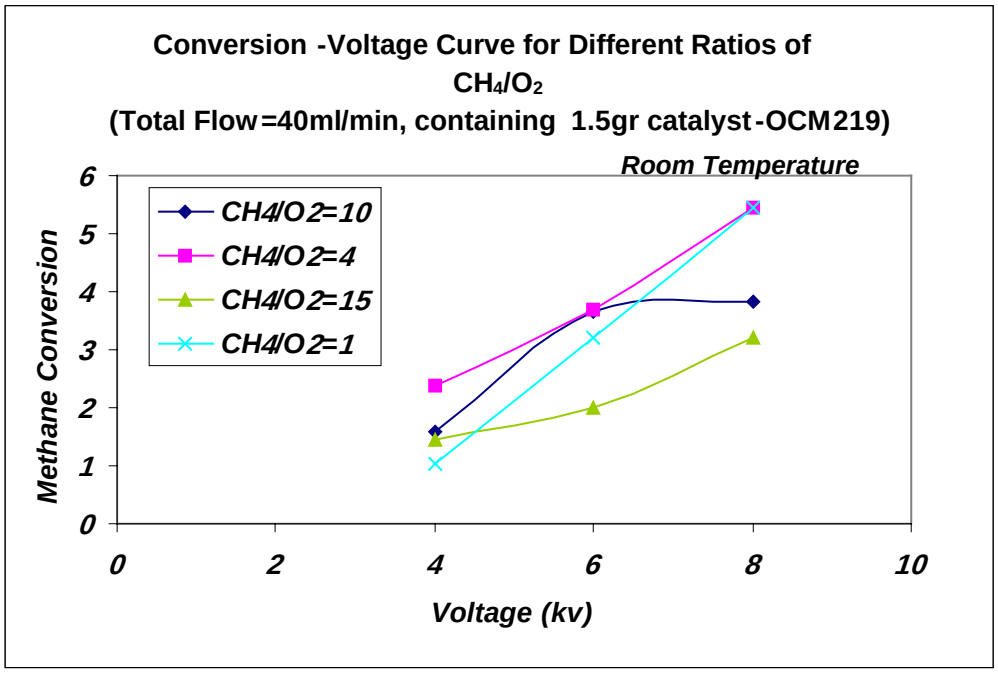

Figure (2)

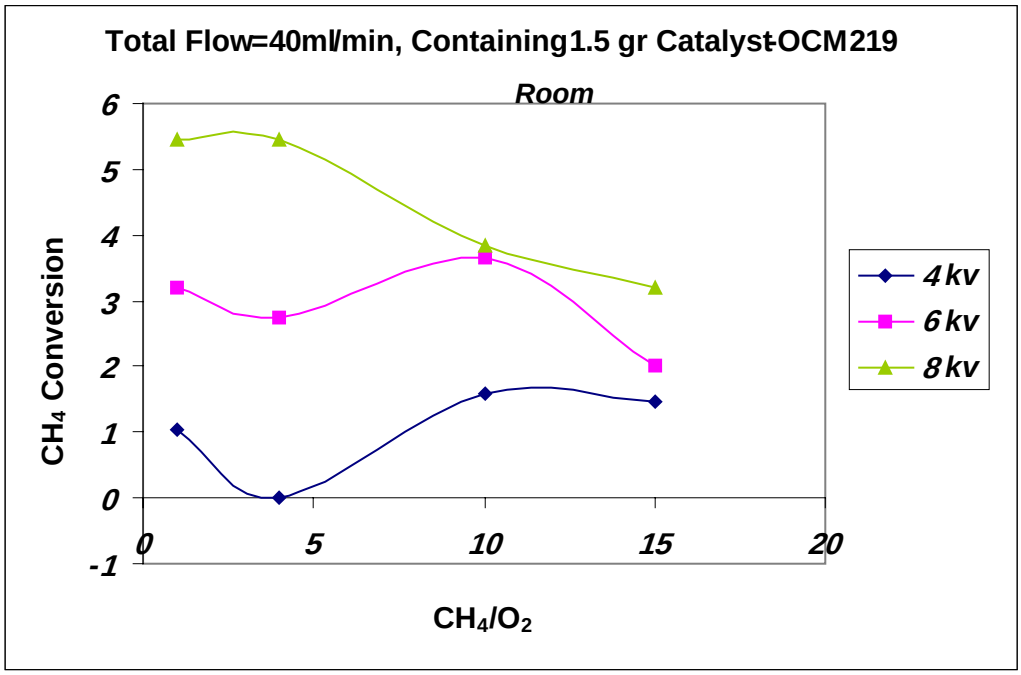
Total Flow=40ml/min, Containing1.5 gr Catalyst-OCM219
Room
6
5
4
3
2
1
0
-1
0
5
10
15
20
CH4 Conversion
CH4/O2
4 kv
6 kv
8 kv

Figure (3)

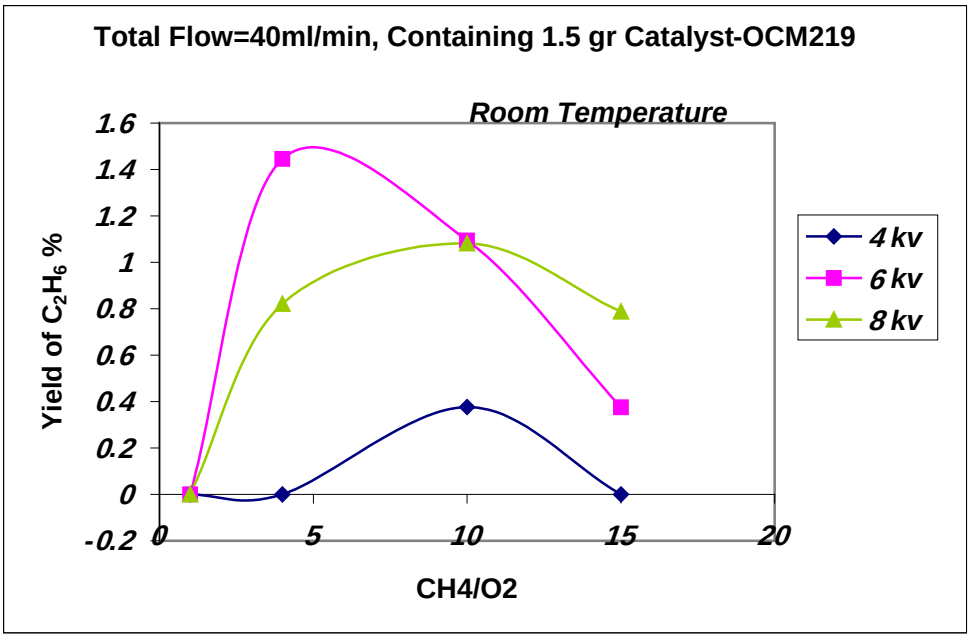

Figure (4)

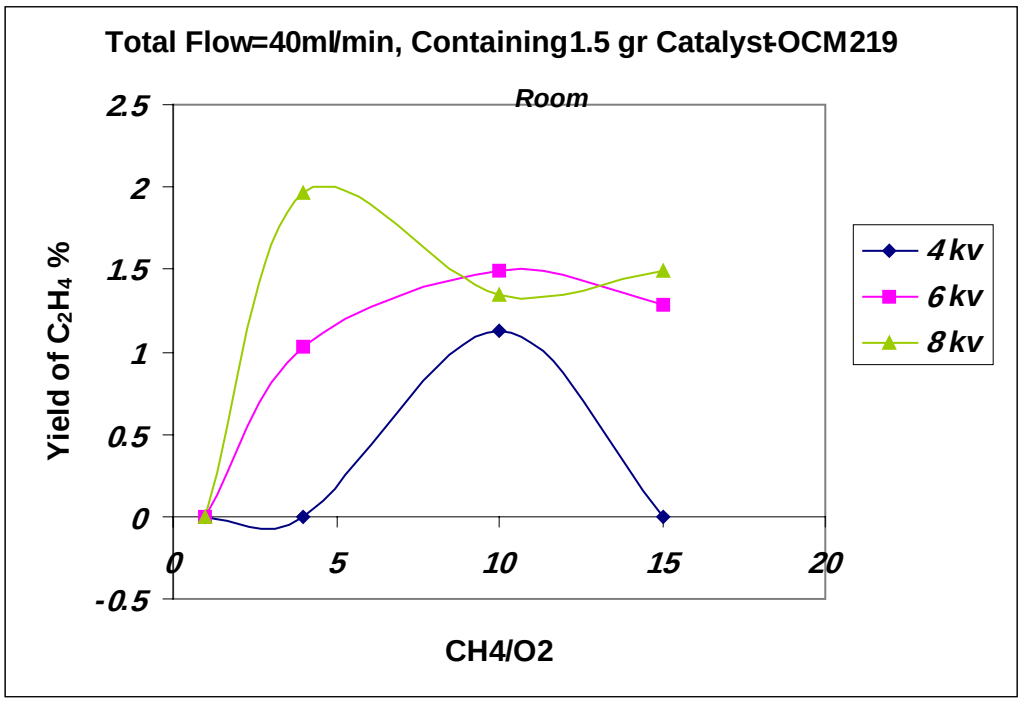

Figure (5)

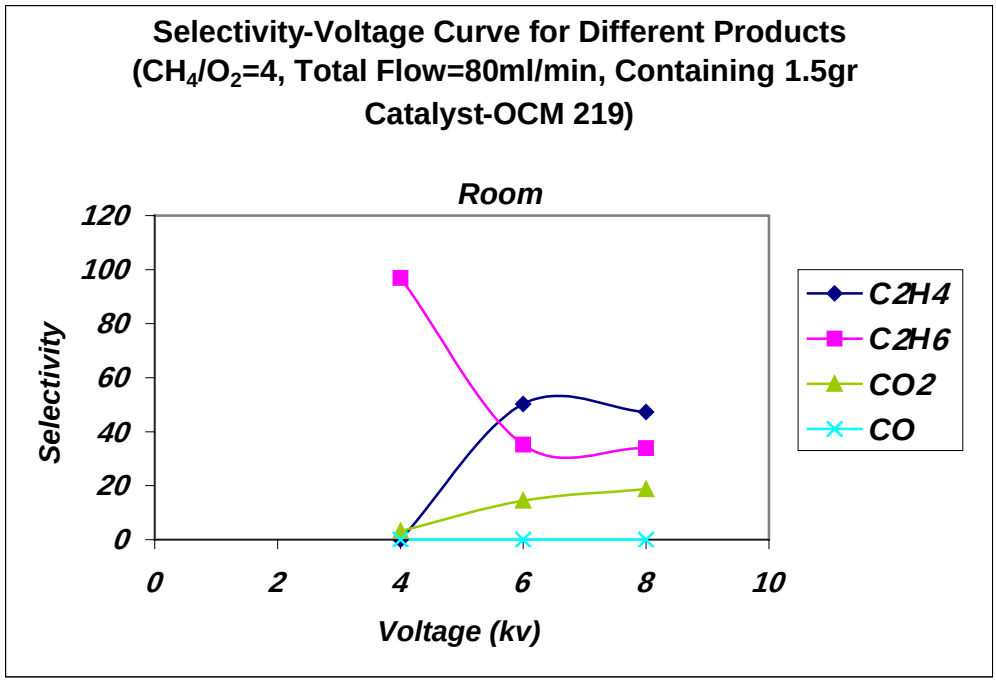

Figure (6)

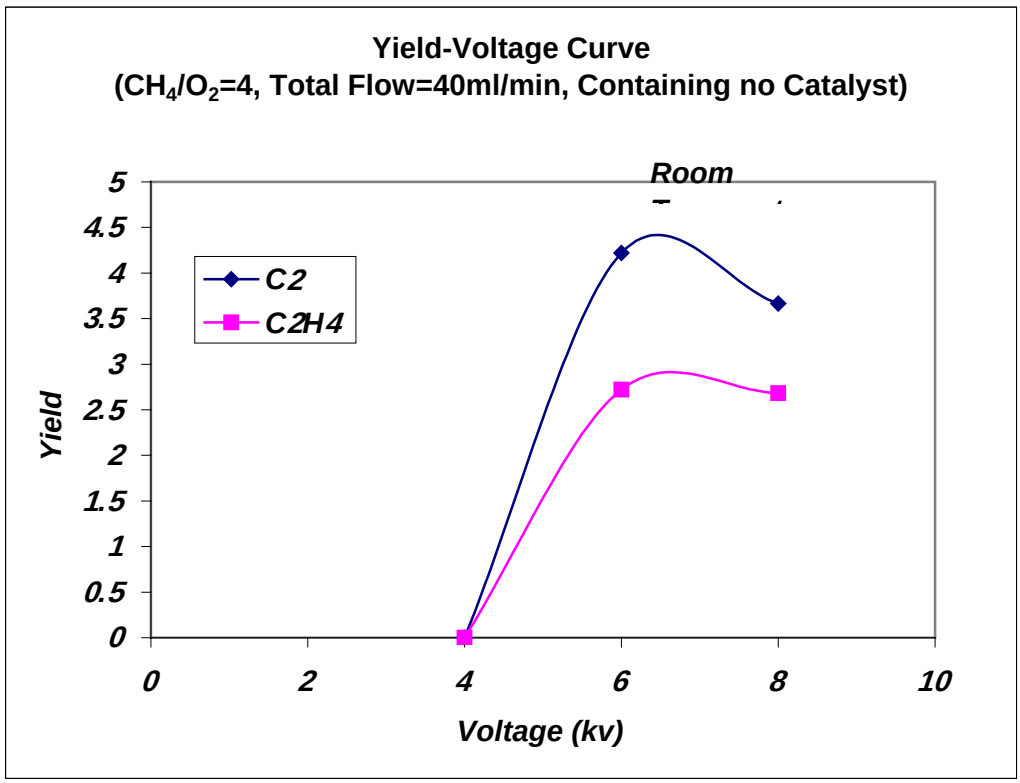

Figure (7)

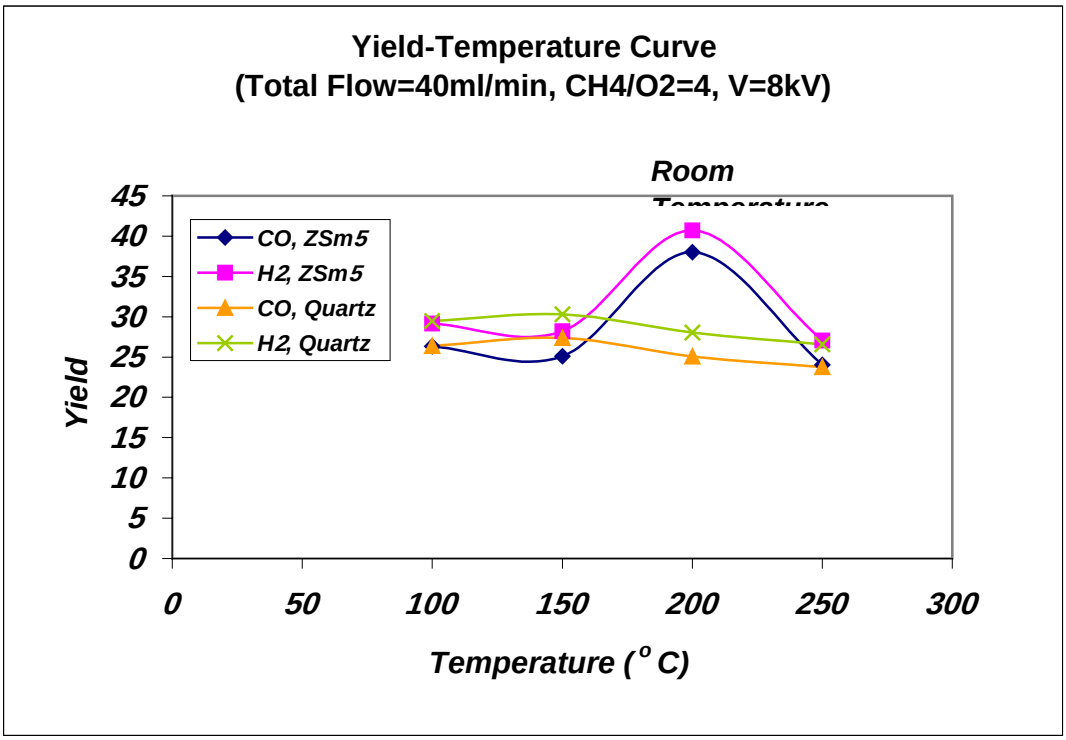
Yield-Temperature Curve
(Total Flow=40ml/min, CH4/O2=4, V=8kV)
Room
Temperature
CO, ZSm5
H2, ZSm5
CO, Quartz
H2, Quartz
Yield
45
40
35
30
25
20
15
10
5
0
0
50
100
150
200
250
300
Temperature (°C)

Figure (8)

Time-dependent two-dimensional two-temperature chemical non-equilibrium model of Ar-N_2 pulse modulated induction thermal plasmas: Influence of coil-current modulation on thermal non-equilibrium

Yasunori Tanaka

Division of Electrical and Computer Engineering, Kanazawa University, Kakuma, Kanazawa 920-1192, JAPAN

Abstract

The author developed a time-dependent two-dimensional two-temperature chemically non-equilibrium (TD-2D-2T-NCE) model for an unique high-power Ar-N_2 pulse-modulated induction thermal plasma (PMITP) to obtain variations in electron and heavy particle temperatures, particle composition as well as the gas flow field considering the diffusion, convection and reaction rate effects. Influence of modulation conditions of the coil current were numerically studied on the temperature and gas flow fields in such an Ar-N_2 PMITP.

1. Introduction

The pulse-modulated induction thermal plasma (PMITP) or the high-power pulse-modulated inductively coupled plasma (high-power PMICP) is one of the advanced breakthrough techniques in thermal plasma fields. This PMITP technique has been developed by Ishigaki *et al.*, and Sakuta [1, 2] to encounter difficulty of the control of thermal plasma temperature and also to introduce a new function of thermal plasma system. Modulation of the coil current sustaining induction thermal plasmas enables one to control the time-averaged temperature of thermal plasmas, and also gas flow velocity periodically. In addition, introduction of thermal and chemical non-equilibria even in thermal plasmas by a sudden application of the electromagnetic field in pulse-modulated operation is expected to enhance controllability of reactions and temperature in thermal plasmas.

In order to investigate such unique PMITP behaviors, experimental and numerical approaches have been made. For example, Ohashi *et al.*have applied the PMITP to the improvement of luminescence of ZnO emission[4]. The author and co-workers have been experimentally studying the stable operation region, transient response, and temperature control of the PMITP [3]. We also developed a thermofluid PMITP model on the assumption of local thermal equilibrium (LTE) [5]. This LTE model supported to understand the transport of mass, momentum, energy, gas flow and temperature fields in the PMITP. However, further understanding of reactions and particle density distributions in the PMITP has greatly been required for the advanced material processings in non-LTE states. For this purpose, we have so far developed a one-temperature chemically non-equilibrium model of Ar-N_2 PMITP in transient state [6], and also a two-temperature chemical non-equilibrium model of Ar-N_2 induction thermal plasmas but in steady state [7]. The Ar-N_2 induction thermal plasmas can be used for high-speed nitriding processes of materials. This two-temperature chemical non-equilibrium model considers diffusion and convection, reaction rate effects on particle composition, transport and thermodynamic properties. In this paper, the author newly develops and reports a time-dependent two-dimensional two-temperature and chemically non-equilibrium (TD-2D-2T-NCE) model for Ar-N_2 PMITP considering reaction rates and difference between electron and heavy particle temperatures. The use of this model makes it possible to investigate pulse-modulation conditions on electron and heavy particle temperature fields, as well as the evolution in particle density distributions considering reaction rates, convection and diffusion effects. From this model, it was found that lower SCL and longer off-time enhances deviation between electron and heavy particle temperatures just after a sudden increase in coil-current amplitude.

2. Modelling of Ar-N_2 PMITP

2.1. Hypothesis

The following are assumed in Ar-N_2 PMITPs in the present calculation: (a) In Ar-N_2 PMITPs, there are only the electron and seven heavy particles: Ar, Ar^+, N_2, N_2^+, N and N^+. (b) All heavy particles have the same temperature with a Maxwellian energy distribution function. On the other hand, the electron energy distribution function also follows the Maxwellian law although its mean energy is not always equal to that of heavy particles. This means that electron temperature T_e can be different from heavy particle temperature T_h. (c) Electrons lose their kinetic energies through elastic collisions with heavy particles and also through inelastic collisions involving related ionization and dissociation reactions. However, the present calculation ignores inelastic collision involving electronic, rotational and vibrational excitations for simplicity. (d) The energy required for a reaction is supplied from the electron kinetic energy if one of the reactants is the electron. The released energy from a reaction is transferred to the electron kinetic energy if one of the products is the electron. Otherwise, the energy is exchanged from or to the kinetic energy of heavy particles. (e) The plasma has an axissymetric structure. (f) The gas flow is laminar. (g) The optically thin assumption is made. (h) Pressure in the PMITP

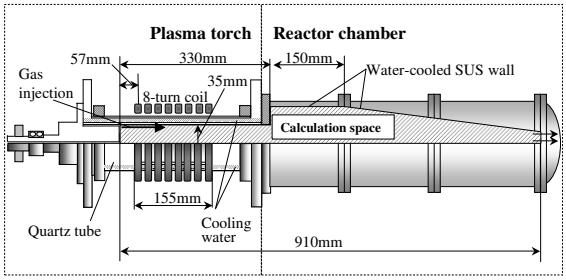

Fig. 1. Plasma torch configuration and calculation space.

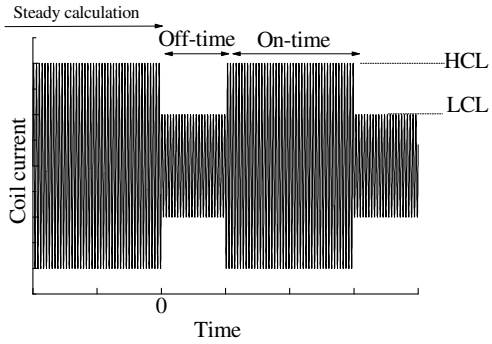

Fig. 2. Coil current for sustaining the pulse-modulated induction thermal plasmas

is approximately the atmospheric pressure. (i) Quasi-neutrality of electrical charges is established. (j) The displacement current by alternative electric field is neglected.

2.2. Governing equations, reactions, thermodynamic and transport properties

On the basis of the hypothesis mentioned in the previous section, Ar-N_2 PMITP behavior can be expressed in Table.1 In this table, Eq.(1) is the mass conservation equation, Eqs.(2) and (3) are the momentum conservation equations for axial or radial direction, respectively, Eq.(4) the energy conservation equation of heavy particles, Eq.(5) the energy conservation equation of the electron, Eq.(6) the mass conservation equation of species j, Eq.(7) is the Maxwell equation for vector potential. In addition, Eqs.(8) and (9) indicate the phasors of electromagnetic fields using the derived phasor of the vector potential, Eq.(10) is the reaction heat per unit volume and time, Eq.(11) the enthalpy concerning the translational motion of heavy particles, Eq.(12) the energy transfer from elastic collisions between electrons and heavy particles, Eq.(13) the relative thermal velocity between the electron and heavy particles, Eq.(14) the relation between number density n_j and molar fraction Y_j of species j, Eq.(15) the equation of state, Eq.(16) the quasi charge neutrality. It should be noted that a time-dependent two-temperature model was adopted for considering thermal non-equilibrium effect in this work. At the same time, chemical non-equilibrium effects were also taken into account here. These governing equations were simultaneously solved by the SIMPLE method.

Table 2 indicates the reactions taken into account in this calculation. Thirty reactions including 15 forward and their backward reactions were considered. These are the same reactions taken into account in the previous paper [7]. The reaction rates of these forward reactions α_ℓ^{f} were assumed to follow the Arrhenius' law.

Thermodynamic and transport properties such as the electrical conductivity σ, the viscosity η, the translational thermal conductivity of heavy particles $\lambda_{\mathrm{h}}^{\mathrm{tr}}$, the thermal conductivity of electrons $\lambda_{\mathrm{e}}^{\mathrm{tr}}$, and the effective diffusion coefficients for species j, D'_j, were calculated using the first order approximation of Chapman-Enskog method. These formula are described in Eqs.(21)–(28) [7].

2.3. Plasma torch, calculation space and conditions

Figure 1 shows a schematic diagram of the plasma torch used in the experiment and treated in the present calculation. The plasma torch is composed of two coaxial quartz tubes cooled by water. This torch has an eight-turn induction coil, which is connected with a MOSFET inverter power source through an L-C series matching circuit. A reaction chamber is installed at the downstream of the plasma torch. The wall of this chamber is cooled by flowing water.

In this calculation, the cross section of the plasma torch and the reaction chamber as hatched in Fig.1 was set for the calculation space. The gas flow rates of Ar and N_2 were set to 100 and 2.5 slpm, respectively. Pressure at center of the torch head was fixed at 101 325 Pa. The boundary conditions were the same to those in the previous literature [7] except the coil-current modulation. Figure 2 illustrates the coil-current waveform involving the definition of modulation parameters. The pulse modulation produces four controllable parameters: the higher current level (HCL), the lower current level (LCL), the on-time and off-time as described in this figure. The shimmer current level (SCL), which is a ratio of lower to higher current levels (LCL/HCL), is also defined. The on-time is fixed at 10 ms.

First, calculation was made for steady state of Ar-N_2 induction thermal plasma without coil-current modulation at a fixed input power of 27 kW. Using this steady state calculation result as an initial value, transient state calculations were performed for gas flow, temperature and particle density fields for eight modulation cycles of the coil current.

Tab. 1. Governing equations.

Mass conservation:

$$\frac{\partial \rho}{\partial t} + \frac{\partial (\rho u)}{\partial z} + \frac{1}{r}\frac{\partial (r\rho v)}{\partial r} = 0 \tag{1}$$

Momentum conservation:

$$\begin{aligned}\frac{\partial (\rho u)}{\partial t} &+ \frac{\partial (u\rho u)}{\partial z} + \frac{1}{r}\frac{\partial (rv\rho u)}{\partial r} \\ &= -\frac{\partial p}{\partial z} + 2\frac{\partial}{\partial z}\left(\eta \frac{\partial u}{\partial z}\right) \\ &+ \frac{1}{r}\frac{\partial}{\partial r}\left[\eta r\left(\frac{\partial u}{\partial r} + \frac{\partial v}{\partial z}\right)\right] + \mu_0 \sigma \Re[\dot{E}_\theta \dot{H}_r^*]\end{aligned} \tag{2}$$

$$\begin{aligned}\frac{\partial (\rho v)}{\partial t} &+ \frac{\partial (u\rho v)}{\partial z} + \frac{1}{r}\frac{\partial (rv\rho v)}{\partial r} \\ &= -\frac{\partial p}{\partial r} + \frac{\partial}{\partial z}\left[\eta\left(\frac{\partial v}{\partial z} + \frac{\partial u}{\partial r}\right)\right] \\ &+ \frac{2}{r}\frac{\partial}{\partial r}\left(\eta r \frac{\partial v}{\partial r}\right) - 2\eta\frac{v}{r^2} + \mu_0 \sigma \Re[\dot{E}_\theta \dot{H}_z^*]\end{aligned} \tag{3}$$

Translational energy conservation of heavy particle:

$$\begin{aligned}\frac{\partial (\rho h')}{\partial t} &+ \frac{\partial (u\rho h')}{\partial z} + \frac{1}{r}\frac{\partial (rv\rho h')}{\partial r} \\ &= \frac{\partial}{\partial z}\left(\lambda_{\mathrm{h}}^{\mathrm{tr}} \frac{\partial T_{\mathrm{h}}}{\partial z}\right) + \frac{1}{r}\frac{\partial}{\partial r}\left(r\lambda_{\mathrm{h}}^{\mathrm{tr}} \frac{\partial T_{\mathrm{h}}}{\partial r}\right) \\ &+ \sum_{j\ (j\neq \mathrm{e})}^{N}\left[\frac{\partial}{\partial z}\left(\rho D_j' h_j' \frac{\partial Y_j}{\partial z}\right) + \frac{1}{r}\frac{\partial}{\partial r}\left(r\rho D_j' h_j' \frac{\partial Y_j}{\partial r}\right)\right] \\ &- \sum_{\ell\ (\beta_{\mathrm{e}\ell}^{\mathrm{f}} \cdot \beta_{\mathrm{e}\ell}^{\mathrm{r}} = 0)}^{L} \Delta Q_\ell + E_{\mathrm{eh}}\end{aligned} \tag{4}$$

Energy conservation of electron:

$$\begin{aligned}\frac{\partial}{\partial t}\left(n_{\mathrm{e}}\frac{5}{2}\kappa T_{\mathrm{e}}\right) &+ \frac{\partial}{\partial z}\left(u n_{\mathrm{e}}\frac{5}{2}\kappa T_{\mathrm{e}}\right) + \frac{1}{r}\frac{\partial}{\partial r}\left(rv n_{\mathrm{e}}\frac{5}{2}\kappa T_{\mathrm{e}}\right) \\ &= \frac{\partial}{\partial z}\left(\lambda_{\mathrm{e}}^{\mathrm{tr}}\frac{\partial T_{\mathrm{e}}}{\partial z}\right) + \frac{1}{r}\frac{\partial}{\partial r}\left(r\lambda_{\mathrm{e}}^{\mathrm{tr}}\frac{\partial T_{\mathrm{e}}}{\partial r}\right) \\ &- \frac{\partial}{\partial z}\left(\frac{1}{m_{\mathrm{e}}}\frac{5}{2}\kappa T_{\mathrm{e}}\Gamma_{\mathrm{e}z}\right) - \frac{1}{r}\frac{\partial}{\partial r}\left(r\frac{1}{m_{\mathrm{e}}}\frac{5}{2}\kappa T_{\mathrm{e}}\Gamma_{\mathrm{e}r}\right) \\ &- \sum_{\ell\ (\beta_{\mathrm{e}\ell}^{\mathrm{f}} \cdot \beta_{\mathrm{e}\ell}^{\mathrm{r}} \neq 0)}^{L} \Delta Q_\ell + \sigma \dot{E}_\theta \dot{E}_\theta^* - P_{\mathrm{rad}} - E_{\mathrm{eh}}\end{aligned} \tag{5}$$

Mass conservation of species j (for N, N^+, N_2^+, Ar^+):

$$\begin{aligned}\frac{\partial (\rho Y_j)}{\partial t} &+ \frac{\partial (u\rho Y_j)}{\partial z} + \frac{1}{r}\frac{\partial (rv\rho Y_j)}{\partial r} \\ &= \frac{\partial}{\partial z}\left(\rho D_j' \frac{\partial Y_j}{\partial z}\right) + \frac{1}{r}\frac{\partial}{\partial r}\left(r\rho D_j' \frac{\partial Y_j}{\partial r}\right) \\ &+ m_j \sum_{\ell=1}^{L}(\beta_{j\ell}^{\mathrm{r}} - \beta_{j\ell}^{\mathrm{f}})\left(\alpha_\ell^{\mathrm{f}} \prod_{i=1}^{N} n_i^{\beta_{i\ell}^{\mathrm{f}}} - \alpha_\ell^{\mathrm{r}} \prod_{i=1}^{N} n_i^{\beta_{i\ell}^{\mathrm{r}}}\right)\end{aligned} \tag{6}$$

Maxwell equation by vector potential:

$$\frac{\partial^2 \dot{A}_\theta}{\partial z^2} + \frac{1}{r}\frac{\partial}{\partial r}\left(r\frac{\partial \dot{A}_\theta}{\partial r}\right) - \frac{\dot{A}_\theta}{r^2} = \bar{i}\mu_0 \sigma \omega \dot{A}_\theta \tag{7}$$

$$\dot{H}_z = \frac{1}{\mu_0}\frac{1}{r}\frac{\partial}{\partial r}(r\dot{A}_\theta), \quad \dot{H}_r = -\frac{1}{\mu_0}\frac{\partial \dot{A}_\theta}{\partial z} \tag{8}$$

$$\dot{E}_\theta = -\bar{i}\omega \dot{A}_\theta \tag{9}$$

Reaction heat per unit volume and time:

$$\Delta Q_\ell = \psi_{\mathrm{reac}\ell}\left(\alpha_\ell^{\mathrm{f}} \prod_{i=1}^{N} n_i^{\beta_{i\ell}^{\mathrm{f}}} - \alpha_\ell^{\mathrm{r}} \prod_{i=1}^{N} n_i^{\beta_{i\ell}^{\mathrm{r}}}\right) \tag{10}$$

Translational enthalpy of heavy particles:

$$h' = \sum_{j\neq \mathrm{e}} Y_j h_j', \qquad h_j' = \frac{1}{m_j}\left(\frac{5}{2}kT_{\mathrm{h}}\right) \tag{11}$$

Energy transfer from electron to heavy particles:

$$E_{\mathrm{eh}} = \sum_{j\neq \mathrm{e}} \frac{3}{2}\kappa(T_{\mathrm{e}} - T_{\mathrm{h}})\frac{2m_j m_{\mathrm{e}}}{(m_j + m_{\mathrm{e}})^2} n_j n_{\mathrm{e}} \pi \bar{\Omega}_{\mathrm{e}j} \bar{v}_{\mathrm{e}j} \tag{12}$$

$$\bar{v}_{\mathrm{e}j} = \sqrt{\frac{8\kappa T_{\mathrm{e}}(m_{\mathrm{e}} + m_j)}{\pi m_{\mathrm{e}} m_j}} \tag{13}$$

Relation between mass density and mass fraction:

$$n_j = \frac{\rho Y_j}{m_j} \tag{14}$$

Equation of state:

$$\rho = \frac{p}{\dfrac{Y_{\mathrm{e}}}{m_{\mathrm{e}}}\kappa T_{\mathrm{e}} + \displaystyle\sum_{j\neq \mathrm{e}} \frac{Y_j}{m_j}\kappa T_{\mathrm{h}}} \tag{15}$$

Quasi-neutrality:

$$\frac{Y_{\mathrm{e}}}{m_{\mathrm{e}}} = \frac{Y_{\mathrm{Ar}^+}}{m_{\mathrm{Ar}^+}} + \frac{Y_{\mathrm{N}_2^+}}{m_{\mathrm{N}_2^+}} + \frac{Y_{\mathrm{N}^+}}{m_{\mathrm{N}^+}} \tag{16}$$

Balance of mass fraction:

$$Y_{\mathrm{Ar}} = Y_{\mathrm{Ar}}^{\mathrm{TOT}} - Y_{\mathrm{Ar}^+} \tag{17}$$

$$Y_{\mathrm{N}_2} = Y_{\mathrm{N}_2}^{\mathrm{TOT}} - Y_{\mathrm{N}} - Y_{\mathrm{N}^+} - Y_{\mathrm{N}_2^+} \tag{18}$$

Admixture ratio N_2 to Ar:

$$Y_{\mathrm{N}_2}^{\mathrm{TOT}} = \frac{m_{\mathrm{N}_2} Q_{\mathrm{N}_2}}{m_{\mathrm{Ar}} Q_{\mathrm{Ar}} + m_{\mathrm{N}_2} Q_{\mathrm{N}_2}} \tag{19}$$

$$Y_{\mathrm{Ar}}^{\mathrm{TOT}} = 1.0 - Y_{\mathrm{N}_2}^{\mathrm{TOT}} \tag{20}$$

Effective diffusion coefficient of heavy particle:

$$D_j' = \frac{1 - Y_j}{\displaystyle\sum_{k\neq j} \frac{x_i p \Delta_{ij}^{(1)}}{\kappa T_{\mathrm{h}}}} \tag{21}$$

Electrical conductivity:

$$\sigma = \frac{e^2}{\kappa T_{\mathrm{e}}} \frac{n_{\mathrm{e}}}{\displaystyle\sum_{j\neq \mathrm{e}} n_j \Delta_{\mathrm{e}j}^{(1)}} \tag{22}$$

Viscosity:

$$\eta = \sum_{j=1}^{N} \frac{m_j n_j}{\displaystyle\sum_{i=1}^{N} n_i \Delta_{ij}^{(2)}} \tag{23}$$

Translational thermal conductivity of heavy particle:

$$\lambda_{\mathrm{h}}^{\mathrm{tr}} = \frac{15}{4}\kappa \sum_{i\neq \mathrm{e}} \frac{n_i}{\displaystyle\sum_j \xi_{ij} n_j \Delta_{ij}^{(2)}} \tag{24}$$

Translational thermal conductivity of electron:

$$\lambda_{\mathrm{e}}^{\mathrm{tr}} = \frac{15}{4}\kappa \frac{n_{\mathrm{e}}}{\displaystyle\sum_j \xi_{\mathrm{e}j} n_j \Delta_{\mathrm{e}j}^{(2)}} \tag{25}$$

$$\frac{1}{\Delta_{ij}^{(1)}} = \frac{3}{8}\sqrt{\frac{\pi\kappa T_{\mathrm{h,e}}(m_i + m_j)}{2m_i m_j}} \frac{1}{\pi \bar{\Omega}_{ij}^{(1,1)}} \tag{26}$$

$$\frac{1}{\Delta_{ij}^{(2)}} = \frac{5}{16}\sqrt{\frac{\pi\kappa T_{\mathrm{h,e}}(m_i + m_j)}{2m_i m_j}} \frac{1}{\pi \bar{\Omega}_{ij}^{(2,2)}} \tag{27}$$

$$\xi_{ij} = 1 + \frac{(1 - m_i/m_j)(0.45 - 2.54 m_i/m_j)}{(1 + m_i/m_j)^2} \tag{28}$$

where t: time (s), r: radial position (m), z: axial position (m), u: axial flow velocity (m/s), v: radial flow velocity (m/s), ρ: mass density (kg/m^3), p: pressure (Pa), T_{h}: heavy particle temperature (K), T_{e}: electron temperature (K), P_{rad}: radiation loss (W/m^3), n_j: number density of species j (m^{-3}), Y_j: mass fraction of species j, x_j: mole fraction of species j, m_j: mass of species j (kg), $\Gamma_{\mathrm{e}r}$, $\Gamma_{\mathrm{e}z}$: radial and axial electron flux due to ambipoler diffusion (1/m^2/s), α_ℓ^{f}, α_ℓ^{r}: rate coefficients of forward and backward reaction ℓ, respectively, $\beta_{j\ell}^{\mathrm{f}}$, $\beta_{j\ell}^{\mathrm{r}}$: stoichiometric number of species j in forward and backward reaction ℓ, μ_0: permeability of vacuum (H/m), κ: Boltzmann constant (J/K), $\dot{A}_\theta$: vector potential (V·s/m), ω: angular frequency of coil current (rad/s), $\dot{E}_\theta$: electric field strength (V/m), $\dot{H}_z$: axial magnetic field strength (A/m), $\dot{H}_r$: radial magnetic field strength (A/m), $\bar{i}$: complex index ($\bar{i}^2$=−1), $\psi_{\mathrm{reac}\ell}$: reaction heat for reaction ℓ (J), $\pi\bar{\Omega}_{ij}^{(1,1)}$: momentum transfer collision integrals (m^2), $\pi\bar{\Omega}_{ij}^{(2,2)}$: viscosity collision integrals (m^2), Q_{Ar}: Ar gas flow rate (m^3/s), Q_{N_2}: N_2 gas flow rate (m^3/s), N: total number of species, L: total number of reactions.

Tab. 2. Reactions taken into account in the present calculation.

N^o	Reaction			a_ℓ	b_ℓ	c_ℓ	Reaction heat $\psi_{\mathrm{reac}\ell}$ (eV)	Dep.Temp. for forward	Dep.Temp. for backward
1	$N_2 + N_2$	$\rightarrow$	$N + N + N_2$	4.98×10^{-9}	−1.5	113260	9.759	T_h	T_h
2	$N_2 + N$	$\rightarrow$	$N + N + N$	2.49×10^{-8}	−1.5	113260	9.759	T_h	T_h
3	$N_2^+ + N$	$\rightarrow$	$N_2 + N^+$	1.30×10^{-19}	0.5	0	−1.047	T_h	T_h
4	$N_2^+ + e$	$\rightarrow$	$N + N$	2.49×10^{-8}	−1.5	0	−5.821	T_e	T_h
5	$N^+ + e + e$	$\rightarrow$	$N + e$	2.29×10^{-20}	−4.5	0	−14.534	T_e	T_e
6	$N_2^+ + N_2 + e$	$\rightarrow$	$N_2 + N_2$	6.07×10^{-34}	−2.5	0	−15.580	T_e	T_h
7	$N_2^+ + N + e$	$\rightarrow$	$N_2 + N$	1.66×10^{-35}	−2.5	0	−15.580	T_e	T_h
8	$N^+ + N_2 + e$	$\rightarrow$	$N + N_2$	6.07×10^{-34}	−2.5	0	−14.534	T_e	T_h
9	$N^+ + N + e$	$\rightarrow$	$N + N$	1.66×10^{-35}	−2.5	0	−14.534	T_e	T_h
10	$Ar + e$	$\rightarrow$	$Ar^+ + e + e$	-	-	-	15.760	T_e	T_e
11	$Ar + Ar$	$\rightarrow$	$Ar^+ + e + Ar$	-	-	-	15.760	T_h	T_e
12	$N_2 + Ar$	$\rightarrow$	$N + N + Ar$	2.49×10^{-8}	−1.5	113260	9.759	T_h	T_h
13	$N_2 + Ar^+$	$\rightarrow$	$N + N + Ar^+$	2.49×10^{-8}	−1.5	113260	9.759	T_h	T_h
14	$N_2^+ + Ar + e$	$\rightarrow$	$N_2 + Ar$	1.66×10^{-35}	−2.5	0	−15.580	T_e	T_h
15	$N^+ + Ar + e$	$\rightarrow$	$N + Ar$	1.66×10^{-35}	−2.5	0	−14.534	T_e	T_h

3. Results and discussions

3.1. Temperature variation

Figure 3 shows the time evolution in T_e and T_h at (z, r)=(165 mm, 16 mm) for SCL=60 % at an on-time/off-time of 10/5 ms, respectively. This position corresponds to the one at which T_h is the highest in steady state. Both the temperatures T_h and T_e have periodical changes according to the coil-current modulation. After five cycles from pulse-modulated operation, a periodical steady state can be seen in the temperature evolutions. Another important fact in this figure is that T_e rapidly increases just after a sudden increase in coil-current amplitude. This rapid increase in T_e leads to 500 K higher T_e than T_h, which means an introduction of thermal non-equilibrium condition even in high-power atmospheric-pressure plasmas.

Figures 4 and 5 show two-dimensional time variations in electron temperature (T_e) and heavy particle temperature (T_h) fields in an Ar-N_2 PMITP during off-time and on-time durations, respectively. Unique and large changes in T_e and T_h can be found especially around the plasma torch region. An decrease in coil-current amplitude from t=104 to 110 ms decays both T_e and T_h, and then the high-temperature area with T_e and T_h >9000 K is shrunk as represented in Fig.4. This decrease in coil-current amplitude, however, extends an area around 8000 K to the downstream portion of the plasma torch. This is due to an fluid inertia effect in the atmospheric-pressure plasmas in this case. On the other hand, an increase in the coil-current amplitude increases both T_e and T_h in the plasma torch region, and then these reaches beyond 9000 K as indicated in Fig.5. It can be also seen that T_e and T_h below 6000 K do not change so much around the downstream of the reaction chamber.

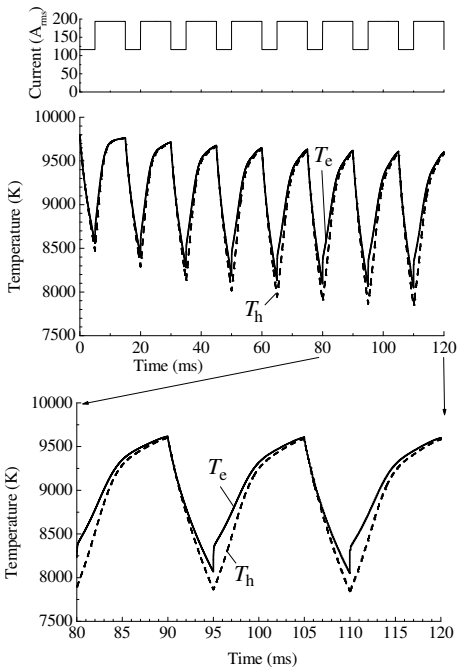

Fig. 3. Time evolution in T_e and T_h at high-temperature point in an Ar-N_2 PMITP for SCL=60 %.

3.2. Enhancement of deviation from thermal equilibrium by coil-current modulation

In order to verify deviation from thermal equilibrium in the PMITP, the dynamic behaviors of the radial distributions of T_e and T_h are depicted for an on-time duration from t=110 to 114 ms in Fig.6. The sudden increase in coil-current amplitude at t =110 ms rapidly increases T_e with time at radial position r > 15 mm, i.e. around the tube wall. After that, T_h around r < 25 mm gradually increases with time. Thus, thermal non-equilibrium condition that means $T_\mathrm{e} > T_\mathrm{h}$ can be found near the tube wall. In this way, pulse-modulation of the coil-current amplitude yields a thermal non-equilibrium condition in transient state even in high-power high-pressure plasmas. Around the plasma center axis, we can confirm T_e close to T_h, which indicates that thermal equilibrium condition is almost established there.

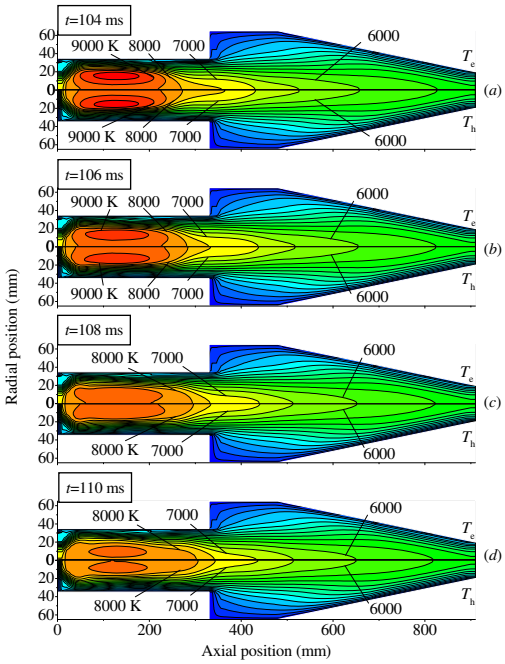

Fig. 4. Transient distributions of T_e and T_h during 'off-operation' in an Ar-N_2 PMITP.

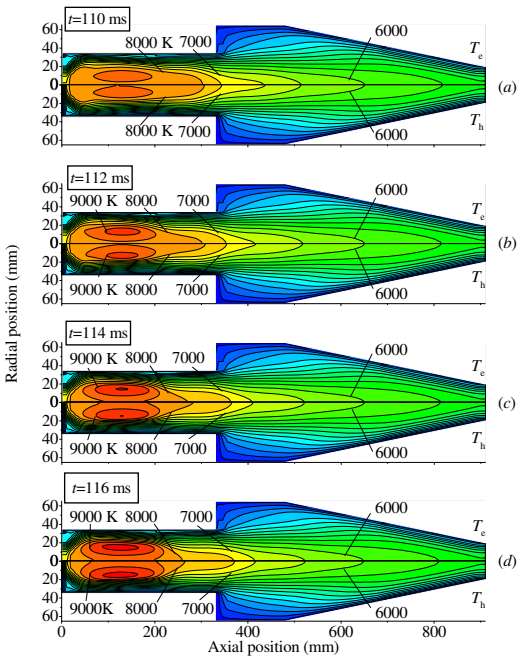

Fig. 5. Transient distributions of T_e and T_h during 'on-operation' in an Ar-N_2 PMITP.

3.3. Dynamic behavior of N atom density distribution

It is very important to investigate transient distributions of nitrogen atomic density in the plasma torch and the reaction chamber for nitriding processings [8]. Figures 7 and 8 depicts dynamic behavior of N atomic density in Ar-N_2 PMITP for SCL=60 % at on-time/off-time=10/5 ms. Remember that the effects of reaction rates, convection and diffusion were considered in this calculation. Nitrogen atoms have higher density around axial positions $320 < z < 370$ mm, i.e. around the inlet of the reaction chamber. This means that the above axial positions may be preferable for nitriding processings of materials. The N atoms are also found to be modulated and controlled with coil-current amplitude modulation. Such N atoms are produced mainly by dissociation of N_2 around $20 < r < 25$ mm in high-temperature region in the plasma torch, and then they are transported to the downstream portion around radial center of the plasma torch by gas flow convection. On the other hand, N atom density at further downstream portion $z > 500$ mm in the reaction chamber hardly changes with the coil-current modulation.

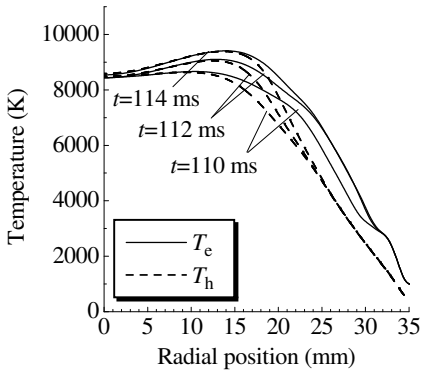

Fig. 6. Transient radial distributions of T_e and T_h during 'on-operation' at an axial position of 155 mm in an Ar-N_2 PMITP for SCL=60 %.

3.4. Effect of modulation condition on temperature variation

Next, effect of the coil-current amplitude modulation conditions such as SCL and off-time were also studied on temperature variation and deviation from thermal equilibrium. Figure 9 presents time evolutions in T_e and T_h at (z, r)=(165 mm, 16 mm) for various SCL at a fixed on-time/off-time of 10/5 ms. It can be noticed that lower SCL causes lower T_e and T_h just before on-operation, which indicates that setting SCL can control minimum values of T_e and T_h in modulation cycle. Just after on-operation, for example at t =50 or 65 ms, only T_e increases much more rapidly than T_h. This is because the higher electric field strength is applied suddenly to the plasmas with on-operation, and accelerates the electrons there. This rapid increase in T_e means that large deviation from thermal equilibrium can be realized by decreasing SCL even in this atmospheric pressure high-power plasmas.
Figure 10 shows the effect of off-time on T_e and T_h variations and deviation from thermal equilibrium. It is seen that longer off-time can causes larger modulation in T_e and T_h and larger deviation from thermal equilibrium.

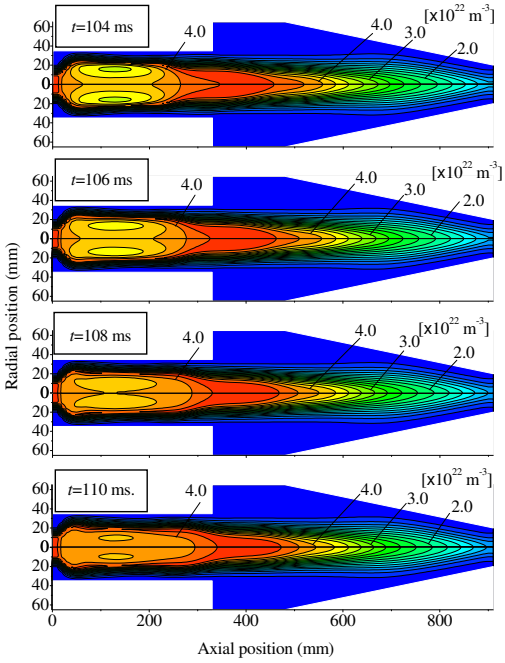

Fig. 7. Transient distributions of N atomic density during 'off-operation' in an Ar-N_2 PMITP.

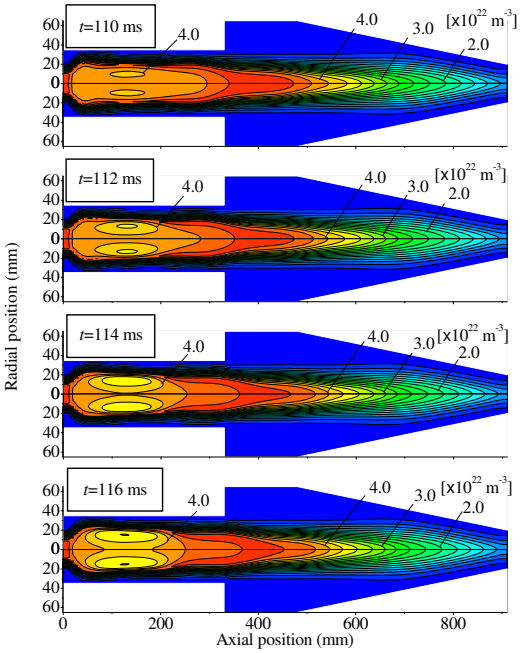

Fig. 8. Transient distributions of N atomic density during 'on-operation' in an Ar-N_2 PMITP.

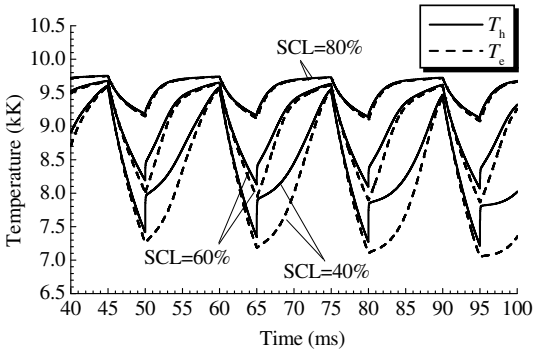

Fig. 9. Time evolutions in T_e and T_h at high-temperature point in an Ar-N_2 PMITP for various shimmer current levels.

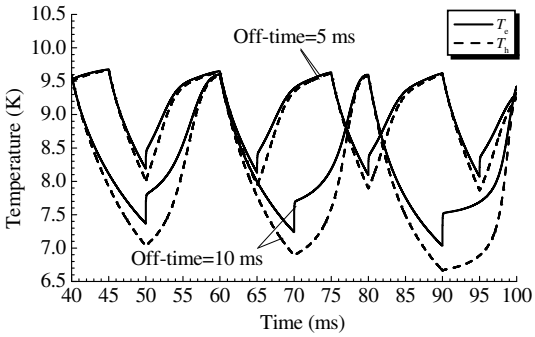

Fig. 10. Time evolutions in T_e and T_h at high-temperature point in an Ar-N_2 PMITP for off-times.

4. Conclusions

The author developed a time-dependent two-dimensional two-temperature chemically non-equilibrium model for high-power Ar-N_2 PMITP. Using this model, the controllability of electron and heavy particle temperatures, thermal non-equilibrium and N atomic density in the PMITP were investigated. The results revealed that lower shimmer current level and longer off-time was found to cause larger temperature variation and larger deviation from thermal equilibrium.

References

[1] T.Ishigaki et al.- Appl. Phys. Lett., **71**, 3787 (1997)

[2] T.Sakuta, T.Ishigaki - Pure Appl. Chem., **71**, 1845 (1999)

[3] Y.Tanaka, T.Sakuta - Plasma Sources Sci. & Tech., **12**, 69 (2003)

[4] N. Ohashi et al. - J. Appl. Phys., **93**, 6386 (2003)

[5] M.M.Hossain et al.- Thin Solid Film, **435**, 19 (2003)

[6] Y.Tanaka, T.Sakuta - Trans. MRS-J., **29**, 3403 (2004)

[7] Y.Tanaka - J. Phys. D: Appl. Phys., **37**, 1190 (2004)

[8] Y.Tanaka et al. "High-speed surface nitridation of titanium using Ar-N_2 pulse-modulated induction thermal plasmas", ISPC-17 (2005)

High-speed surface nitridation of titanium using Ar-N_2 pulse-modulated induction thermal plasmas

Yasunori Tanaka,T.Muroya and Y.Uesugi

Division of Electrical and Computer Engineering, Kanazawa University, Kakuma, Kanazawa 920-1192, JAPAN

Abstract

This paper addresses high-speed surface nitridation of a titanium metal using novel high-pressure high-power pulse-modulated induction thermal plasmas (PMITP or high-power PMICP). The PMITP method is one of unique techniques for controlling electron and heavy particle temperatures and radical densities in time domain in high-power thermal plasmas. Pulse-modulation of the coil current sustaining Ar-N_2 PMITPs was found to enhance N atom flux flowing into the downstream chamber. The irradiation of Ar-N_2 PMITPs made nitridation of the titanium metal surface within five minutes with little thermal damages.

1. Introduction

High-power induction thermal plasmas around atmospheric pressure have great advantages such as remarkably high enthalpy and high radical density compared with cold plasmas, and little contamination because of no electrodes. From these advantages, induction thermal plasmas have been widely used for many material processing fields such as syntheses of nanopowders, superconducting and diamond films. However, their too high enthalpy is difficult to be controlled only by the conventional setting of gas flow and electrical input powers to thermal plasmas under steady states. This uncontrollable high enthalpy may cause thermal damages on the substrates and grown films. In order to control this high enthalpy and temperature, we have developed a pulse-modulated induction thermal plasma (PMITP) system. This system can modulate the amplitude of coil current sustaining thermal plasmas [1]–[3]. Such the coil-current modulation leads to thermal plasmas under transient states, and enables us to control thermal plasma temperature and radical density in time domain. Furthermore, it can promote chemical and thermal non-equilibrium states even in high-power atmospheric pressure plasmas. We have investigated unique dynamic behaviors of such a PMITP by experimental and numerical approaches [4]–[6]. Recently, Ohashi *et al.* have applied the PMITP to the hydrogen doping on ZnO [7]. They successfully found that irradiation of the Ar-H_2 PMITP can dope hydrogen atoms into ZnO and then improve its photoluminescence. However, there have been still a few reports on application of the PMITP to the material processings.

In the present work, we report experimental results about the first trial application of Ar-N_2 PMITPs to the high-speed surface nitridation of titanium metal. It is known that nitridation generally requires a long processing time about several hours using conventional methods such the gas nitriding method and the ion nitriding method. In the present experiment, spectroscopic observation was carried out to find the radiation intensity of nitrogen atomic spectral line around the installed position of titanium metal targets. Titanium target surface was found to be modified to TiN by irradiation of Ar-N_2 PMITP within five minutes with little thermal damages.

2. Pulse modulation of coil current for PMITP

Figure 1 shows essential elements of pulse amplitude-modulation of the coil current for sustaining a PMITP. The PMITP is established by the amplitude-modulated coil current with a fundamental frequency of 450 kHz in our case. The pulse modulation of the coil current induces four controllable parameters. They are 'HCL' which is the higher current level, 'LCL' the lower current level, 'on-time' the time period with the higher current level and 'off-time' the time period with the lower current level. Setting these four parameters can change dynamic behaviors of the PMITP. However, it is noted that these parameters have a relationship for stable operation of the PMITP [3]. We also define 'SCL; shimmer current level' as a ratio LCL/HCL. The control of these parameters can bring the following expected features and effects: (i) control of time-averaged power and temperature/enthalpy of the thermal plasmas in time domain, (ii) extremely high or low electromagnetic field operation can be made during on/off-operation of the coil-current, (iii) thermally and/or chemically non-equilibrium effects in thermal plasma could be introduced by sudden application of the electric field.

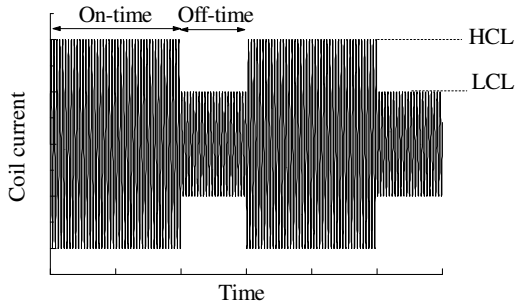

Fig. 1. Pulse-modulated coil current.

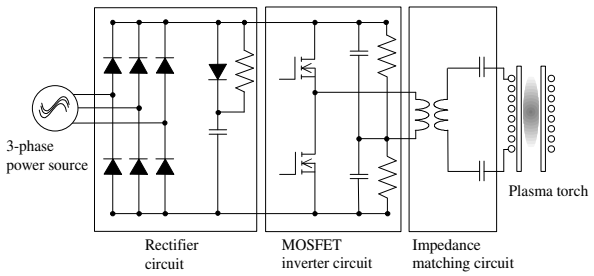

Fig. 2. Electric circuit system for pulse-modulated induction thermal plasmas.

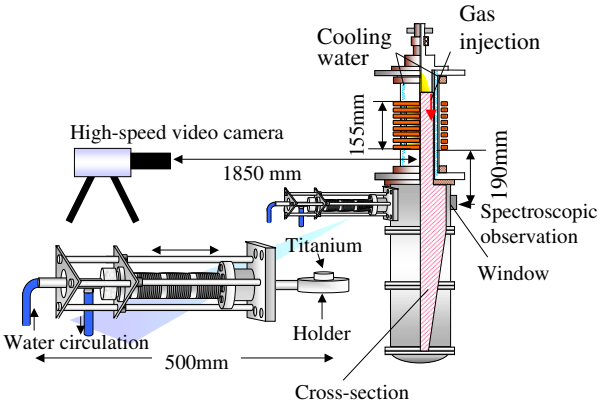

Fig. 3. Plasma torch and target holder.

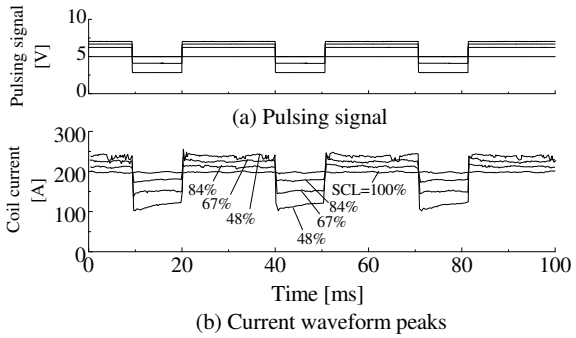

Fig. 4. Coil current controlled for a fixed time-averaged power of 15 kW.

3. Experimental setup and experimental conditions

For sustaining a PMITP with a high-power conversion efficiency, we adopted a MOSFET inverter power supply for a power source. Figure 2 shows the electric circuit system for PMITP used in the experiment [3]. The system includes four parts: a rectifier circuit, an inverter circuit, an impedance-matching circuit and an induction plasma torch. The rectifier circuit has six diodes with a smoothing capacitor to produce dc power. The dc power is converted into ac one with the inverter circuit including two MOSFET (Metal Oxide Semiconductor Field Effect Transistor, rated 150V/460A) units. These units are operated at a fundamental frequency of 450 kHz. The MOSFET inverter part has a much higher power-conversion efficiency over 85 % than a conventional vacuum tube during dc/ac inverter performance. A MOSFET inverter power supply was connected to the induction coil through a series LC matching circuit. This system can modulate the 450 kHz current with a hundred several amperes by controlling fire angle of the MOSFETs.

Figure 3 illustrates a schematic diagram of the plasma torch for PMITPs. The plasma torch is composed of two coaxial quartz tubes with a 330 mm length. The inner tube has an inside diameter of 70 mm. Between these two tubes, cooling water flows to keep the temperature of the tube wall to be 300 K. This plasma torch has an eight-turn induction coil around the quartz tube. At downstream portion of the plasma torch, a water-cooled reaction chamber is installed. This chamber has a tapered shape to make rapid cooling of the hot gas in this chamber. Argon and nitrogen gas mixture was supplied as a sheath gas along the inside wall of the inside quartz tube. Total gas flow rate was fixed at 100.0 slpm. Nitrogen gas flow rate Q_{N_2} was set to a value from 0.0 to 9.0 slpm. Pressure inside the chamber was fixed at 31 kPa (=230 torr) with an automatic feed-back pressure controller. The “on-time” and “off-time” was set to 10 and 5 ms, respectively.

A two-piled titanium metal target with a diameter of 15 mm and a thickness of 5.0 mm was located on a water-cooled target holder in irradiation experiments. The target holder was fixed at 190 mm below the coil-end to make nitridation of the target surface by Ar-N_2 PMITP irradiation. The irradiation time was set to 3–10 minutes.

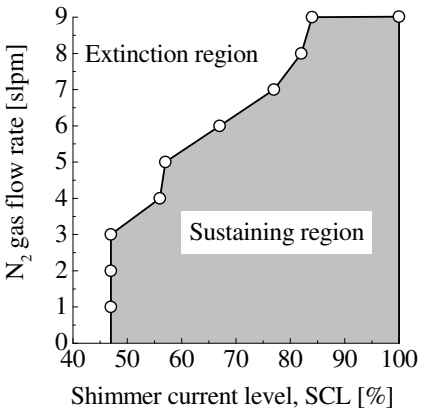

Fig. 5. Stable operation region of Ar-N_2 PMITP at a time-averaged input power of 15 kW at a pressure of 31 kPa. The total gas flow rate is 100 slpm.

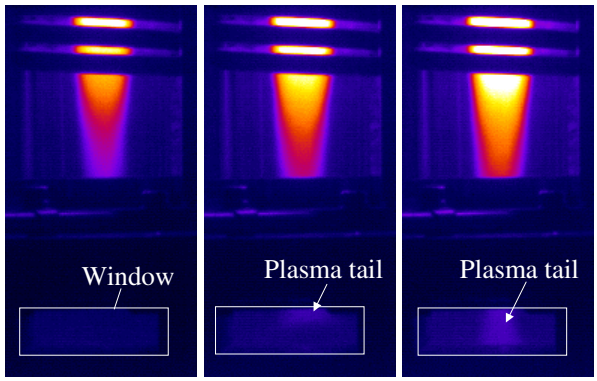

(a) SCL=100% (b) SCL=70% (c) SCL=40%

Fig. 6. High-speed video pictures of visible light emission from 98%Ar-2%N_2 PMITP at a time of its maximum volume in a modulation cycle. Pressure is 31 kPa. The time-averaged input power is fixed at 15 kW.

Optical emission spectroscopic (OES) observation was also carried out at 190 mm below the coil through the observation window installed at downstream portion of the plasma torch. In this OES method, we measured time evolution in radiation intensities of a nitrogen atomic line at a wavelength of 746 nm. A high-speed video with a complementary metal-oxide semiconductor (C-MOS) optical array sensor was also set up at 1850 mm far from the plasma torch. This C-MOS sensor has a sensitivity for visible light between 400–800 nm. The exposure time of this high-speed video camera was set to 10 μs, whereas a frame rate was independently set to 3200 frame/s.

4. Control of fixed time-averaged input power into thermal plasma

In the present experiments, a time-averaged electric input power to the inverter power supply in a modulation cycle was fixed for any modulation condition. This is to find modulation effects of the coil current on the internal state of thermal plasmas under the almost same electric power cost condition. Figure 4 depicts the pulsing signal and the controlled coil-current amplitude in this fixed time-averaged power condition. For SCL=100%, the coil-current amplitude was fixed at constant value. For the modulation cases, on the other hand, the HCL was controlled to be higher while the LCL was lower than those in SCL=100% case.

5. Experimental results

5.1. Stably sustaining region of the Ar-N_2 PMITP

Stable sustain of the Ar-N_2 PMITP is necessary for any applications. This stable sustain of the PMITP is limited by modulation and gas flow conditions. Figure 5 presents the experimentally obtained stably-sustaining region of Ar-N_2 PMITP at a fixed power of 15 kW. At SCL=100 %, i.e. in continuous operation mode, Ar-N_2 induction thermal plasma can be established in Q_{N_2} range of 0–9 slpm. However, in the coil-current amplitude modulation mode, Ar-N_2 PMITPs cannot be sustained for a higher Q_{N_2}, which leads to extinction of the plasmas. Figure 5 shows that increasing ratio of Q_{N_2} to the total gas flow makes it difficult to sustain Ar-N_2 PMITP. This difficulty arises mainly from energy consumption necessary for dissociation, vibrational and rotational excitations of N_2 molecules. Furthermore, decreasing SCL reduces the sustaining region of Ar-N_2 PMITP as indicated in this figure. This is ascribed to larger disturbances of the coil current by the lower SCL modulation. The Ar-N_2 PMITP should be operated in this stably sustaining region.

5.2. Dynamic behavior of Ar-N_2 PMITP observed with a high-speed video camera

First of all, we investigated the unique dynamic behavior of Ar-N_2 PMITPs. A high-speed video capture is useful for understanding the dynamic behavior of two-dimensional visible light emission region from Ar-N_2 PMITP. The region with high visible-light emission generally corresponds to the high-temperature region for thermal plasmas. Figure 6 represents high-speed video pictures around the downstream portion of the plasma

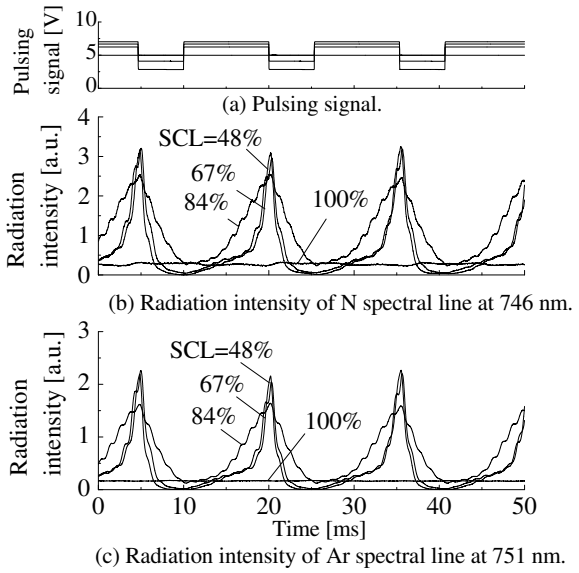

Fig. 7. Time evolutions in radiation intensities of N atomic line at 746 nm and Ar atomic line at 751 nm in 98%Ar-2%N_2 PMITP. The pressure is fixed at 31 kPa, the time-averaged input power is 15 kW.

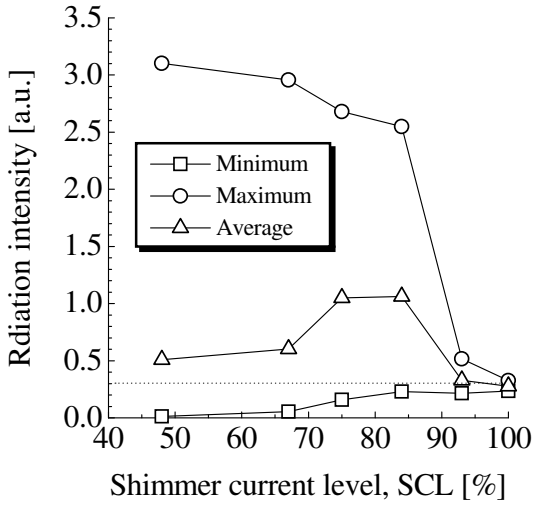

Fig. 8. Dependence of radiation intensity of N atomic line at 746 nm on shimmer current level in 98%Ar-2%N_2 PMITP.

torch and the observation window in the reaction chamber. The observation window position corresponds to the target position in irradiation experiments described later. These pictures were taken at just before off-operation at SCL=70 and 40 %. At just before off-operation, the volume of plasmas becomes its maximum in the coil-current modulation cycle in the modulation modes. As seen in these figures, at SCL=100 %, i.e. in continuous operation mode, the high light emission area from plasmas is smaller than those in the modulation case, and the light from the "plasma tail" around the observation window cannot be seen. However, the plasma tail can be found from the observation window in the modulation mode. This indicates that decreasing SCL causes a large variation in PMITP and then the plasma tail reaches much more to the downstream portion.

5.3. Enhancement of N excited atom flux by current-modulation

We made spectroscopic observation of the plasma tail from the observation window at 190 mm below the coil end to find dynamic behaviors of Ar-N_2 PMITP in detail. Figure 7 (a) indicates the pulsing signal, and Figs.(b) and (c) indicate time evolutions in radiation intensities of a N atom spectral line at a wavelength of 746 nm and that of an Ar atomic line at 751 nm, respectively. The radiation intensities of the N atomic line and the Ar atomic line can be found to change periodically with the modulation of the coil current.

For modification of metal surfaces, radicals and excited particles flux of N atom onto the metal surface is of importance. The radiation intensity I_{N746} of the N atomic line measured here is expressed by

$$I_{\mathrm{N746}} = \int_{\Omega} N_m A_{mn} h\nu_{mn} dV = A_{mn} h\nu_{mn} \int_{\Omega} N_m dV = A_{mn} h\nu_{mn} \bar{N}_m \tag{1}$$

where N_m is the number of the excited N atoms with an upper level m, A_{mn} the transition probability from levels m to n, h the Planck constant, ν_{mn} the frequency of photon, Ω the observation region, $\bar{N}_m$ the number of excited N atoms with an upper level m in Ω region. This equation means that variation in the measured radiation intensity I_{N746} is proportion to variation in the number of excited N atoms $\bar{N}_m$ in the observation region. It is thus considered that the number of excited N atoms $\bar{N}_m$ itself is modulated and changed as indicated in Fig.7(b). We can also see that changing SCL cause differences in waveform of I_{N746}, and thus difference in dynamic behavior of $\bar{N}_m$. Smaller SCL produces a sharp or spike-like change in waveform of I_{N746} around coil-current transition from HCL to LCL. It also enhances peak values of I_{N746} just before off-operation. This means that decreasing SCL enhances the number of N atoms flowing into the reaction chamber just before off-operation.

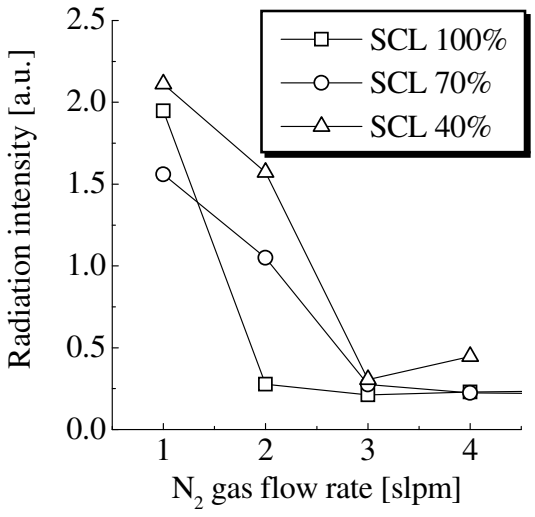

Fig. 9. Dependence of radiation intensity of N atomic line at 746 nm on N_2 gas flow rate.

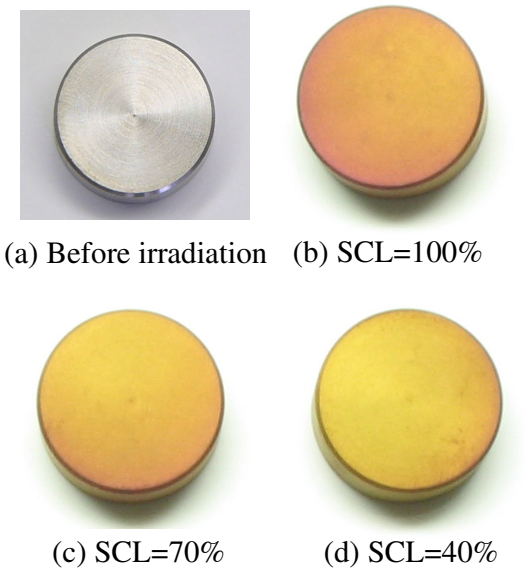

Fig. 10. Photograph of Ti surface irradiated by 98%Ar-2%N_2 PMITP at a time-averaged power of 15 kW at a pressure of 31 kPa. Irradiation time is 5 min.

Fig.8 plots these peak and minimum values of I_{N746} versus SCL. The time-averaged I_{N746} were also evaluated from the measured I_{N746} as follows:

$$I_{N746}^{Tave} = \frac{1}{2T_{cyc}} \int_{t}^{t+2T_{cyc}} I_{N746} dt \tag{2}$$

where T_{cyc} is the modulation cycle time which was set to 15 ms in this case. This quantity I_{N746}^{Tave} is proportion to the time-averaged $\overline{N}_m$ flowing into the reaction chamber. As seen in this figure, the maximum radiation intensity markedly increases with reducing SCL, while the minimum decreases with reducing SCL. This represents that controlling SCL can enhance peak value of $\overline{N}_m$ flowing into the chamber just after off-operation. Another important fact is that the time-averaged I_{N746}, i.e. I_{N746}^{Tave} increases with reducing SCL. This result means that the modulation of the coil current enhances the total excited N atomic flux produced in the plasma torch into the reaction chamber. This may also enhance nitridation reactions in the chamber in irradiation experiments.
Figure 9 shows dependence of the time-averaged radiation intensity of the N atomic line I_{N746}^{Tave} on N_2 gas flow rate Q_{N_2}. Increasing Q_{N_2} decreases I_{N746}^{Tave} for any SCL in spite of an increase in N atom as an injected gas. This is due to temperature decay by increasing Q_{N_2}. The molecule N_2 have a large vibrational and rotational cross sections around 2.0–3.0 eV, and requires dissociations by impact of electrons. These consumes the electron energy and then the temperature. The essential point in this figure is that decaying rate of I_{N746}^{Tave} on Q_{N_2} is smaller in the modulation mode than in the continuous mode at SCL=100 %. As a result, I_{N746}^{Tave} at SCL=70 % is higher than that at SCL=100 %, especially at Q_{N_2}=2.0 slpm. This means that total N atomic flux can flow more effectively into the reaction chamber in modulation mode than in continuous mode.

5.4. Irradiation experiments of Ar-N_2 PMITP to the Ti target

To investigate enhancement effect of N atom flux by Ar-N_2 PMITPs around the reaction chamber, a titanium metal target was installed at downstream portion of the plasma torch as indicated in Fig.3 for its nitridation. The titanium can be an indicator for N atomic flux in the reaction chamber. Figure 10 indicates photographs of Ti surface irradiated by 98%Ar+2%N_2 PMITP at 15 kW at a pressure of 31 kPa. Irradiation time is 5 minutes. Gold-like color, which is TiN color, can be seen from these surface in any SCL case. However, some violet color is also seen around the target for SCL=100 %. Figure 11 represents SEM observation results of the target surface irradiated by Ar-N_2 PMITP. The surface originally has a circle Little thermal damage can be found for the surfaces of the targets.

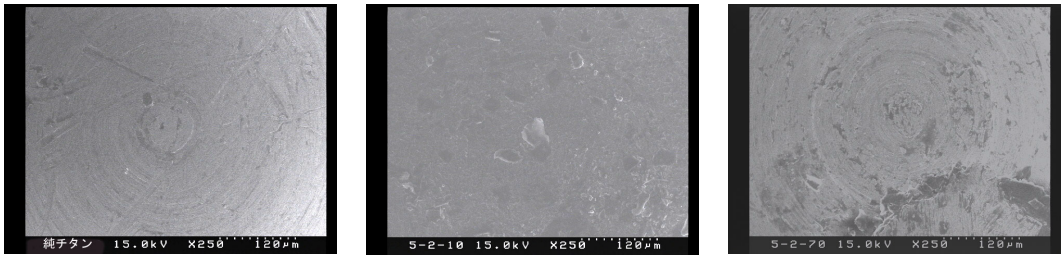

(a) Before irradiation. (b) SCL=100%. (c) SCL=70%

Fig. 11. SEM Photograph of Ti surface irradiated by 98%Ar+2%N_2 PMITP at 15 kW at a pressure of 31 kPa. Irradiation time is 5 min.

5.5. XRD analysis of surface by Ar-N_2 PMITP irradiation

In order to find the surface crystal composition, XRD analysis were made for the targets irradiated by the Ar-N_2 PMITP. Figure 12 shows the XRD spectra of Ti surface before and after irradiation by Ar-N_2 PMITP. For a Ti target before irradiation, only Ti spectra can be found. After irradiation of Ar-N_2 PMITP, TiN spectra can be seen for any SCL cases. These spectra is seen to be influenced by SCL. At SCL=70 %, Ti_2N spectra at 34 and 52^o are seen. This might be due to insufficiency of N atom flux and temperature. These results indicate that controlling SCL can change surface crystal state of the target.

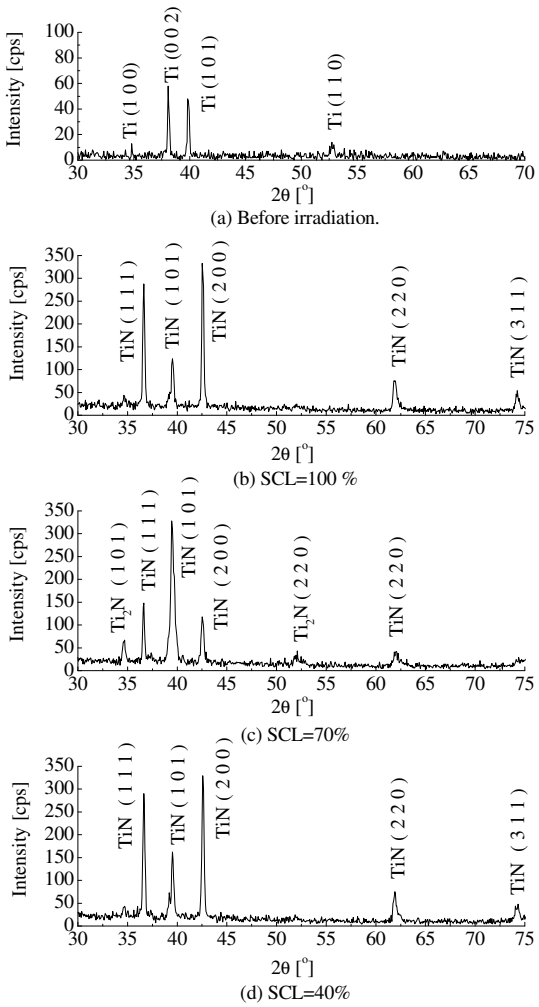

Fig. 12. XRD spectra of Ti surface irradiated by 98%Ar-2%N_2 PMITP at 31 kPa. The irradiation time is 5 min.

6. Conclusions

The Ar-N_2 pulse-modulated induction thermal plasma was applied to the surface nitridation of titanium. The modulation of the coil current causes a much more transport of excited nitrogen atoms to the downstream portion of the plasma torch, which may promote surface nitridation of the target. The target surface irradiated by Ar-N_2 PMITP was analyzed by a XRD analyzer. The result indicates TiN spectra was influenced by shimmer current level of the coil current modulation.

References

[1] T.Ishigaki et al.- Appl. Phys. Lett., **71**, 3787 (1997)

[2] T.Sakuta and T.Ishigaki - Pure Appl. Chem., **71**, 1845 (1999)

[3] Y.Tanaka and T.Sakuta - Plasma Sources Sci. & Tech., **35**, 2149 (2002)

[4] Y.Tanaka - J. Phys. D: Appl. Phys., **37**, 1190 (2004)

[5] M.M.Hossain, Y.Tanaka, T.Sakuta - Thin Solid Film, **435**, 19 (2003)

[6] Y.Tanaka, T.Sakuta - Trans. IEE of Japan, **123-A**, 469 (2002)

[7] N. Ohashi et al.- J. Appl. Phys., **93**, 6386 (2003)

RF Thermal Plasma Processing of Visible-Light Responsive Iron- and Nitrogen-Doped TiO_2 Photocatalytic Nanocrystals

J.-G. Li,[1] X.H. Wang,[1] H. Kamiyama,[1,2] N. Ohashi,[1] Y. Moriyoshi,[2] T. Ishigaki[1]

1Advanced Materials Laboratory, National Institute for Materials Science, Tsukuba, Japan

2 Department of Materials Science, Hosei University, Tokyo, Japan

Abstract

Visible-light responsive Fe- and N-doped TiO_2 nanocrystalline powders have been synthesized via Ar/O_2 RF thermal plasma oxidizing mists of liquid precursors containing Ti^{4+} and the dopant elements. Structure and optical properties of the powders are characterized by XRD, TEM, SEM, Raman spectroscopy, and UV-Vis spectroscopy. Both Fe- and N-doping narrow the bandgap of TiO_2, allowing visible light responses of the powders and hence their potential applications as photocatalysts under visible light illumination.

Keywords RF thermal plasma, TiO_2 nanocrystals, N-doping, Fe-doping, phase structure, bandgap, photocatalysis

1. Introduction

TiO_2 remains the most promising photocatalyst up to date but is only activated by irradiating with ultraviolet (UV) light due to its relatively wide bandgap (~3.2 eV). As UV light accounts for only ~5% of the solar energy compared to visible light (~45%), any shift in its optical response from UV to the visible spectral range will have a remarkable positive effect on the practical application of the material. There seem two general approaches to achieve visible light responses of TiO_2: substituting the Ti sites of TiO_2 lattice with metal cations, mainly transition metals like Fe^{3+} [1], and doping TiO_2 with nonmetallic elements, typically nitrogen [2]. The synthesis of Fe-doped TiO_2 has been achieved by wet chemical routes, but either post annealing that exclusively results in phase segregation is necessary or the Fe/Ti ratio in the resultant powders significantly deviates from that of the starting solution. N-doping is generally made by annealing pure TiO_2 powders under N-containing atmospheres (usually NH_3), but has drawbacks of non-uniform dopant distribution, as the nitriding reaction starts at particle surfaces. RF thermal plasma is characterized by its extremely high temperature (up to ~10^4 K) and rapid heating and cooling rates (~10^{5-6} K/s), which are particularly suitable for the synthesis of both lightly and heavily doped oxides with homogeneous dopant distribution and good crystallinity in a very short time. We report here the synthesis of Fe- and N-doped TiO_2 nanocrystals via Ar/O_2 thermal plasma oxidation of liquid precursor mists. The use of mists ensures atomic level mixing of the elements and high supersaturation of the evaporated species upon plasma oxidation, which favors nanocrystal formation upon condensation. The effects of dopant on phase structure and photo-response of the resultant TiO_2 powders are investigated in detail.

2. Experimental

The experimental conditions for the synthesis of Fe-doped TiO_2 nanopowders are as follows: plate power, 25kW;

central gas, 30L/min of Ar; sheath gas, 70L/min of Ar plus 20L/min of O_2; atomization gas, 5L/min of Ar; chamber pressure, 66.7kPa; precursor feeding rate, 3.5-4.0g/min. Fe-doped TiO_2 nanoparticles are synthesized by injecting organic solutions containing titanium tetra-*n*-butoxide (TTBO) and ferrocene (Fe/Ti=0-20at%, stabilized with diethanolamine (DEA, DEA/TTBO=1:1 in molar ratio) into the center of the thermal plasma plum through an atomization probe.

The fundamental conditions for synthesizing N-doped TiO_2 powders are the same as described above, except that the O_2 flow rate in the plasma sheath ($Ar+O_2$=90 L/min) was varied in the range 10-90L/min to investigate its effects on the phase constituent and nitrogen content of the resultant powders. DEA is employed here not only as a stabilizer for TTBO but also as the nitrogen source. To achieve effective doping, a higher DEA/TTBO molar ratio of 4 was used.

Characterizations of the nanopowders were achieved by elemental analysis, XRD, TEM, SEM, Raman spectroscopy, and UV-Vis spectroscopy. Photocatalytic activities of the powders were evaluated via bleaching methyl orange solutions under visible light (>400 nm) irradiations.

3. Results and discussion

Chemical analysis confirmed that the prescribed Fe/Ti molar ratios (*R*) in the precursor solutions have been kept to the final powders. XRD analysis (Fig. 1) revealed that the resultant nanopowders exclusively contain anatase and rutile. At dopant concentrations up to *R*=5at%, the XRD patterns show normal peaks with symmetric shapes (Fig. 1). Fe-doping dramatically promotes rutile formation, due to the oxygen vacancies created for charge compensation upon substituting Fe^{3+} for Ti^{4+} sites. Metastable anatase instead of thermodynamically stable rutile is formed as the major phase in the undoped sample, which is consistent with our predictions obtained through theoretical calculations based upon classical nucleation theory, that is, anatase preferentially nucleates from deeply undercooled TiO_2 melts while rutile from less deeply undercooled ones [3].

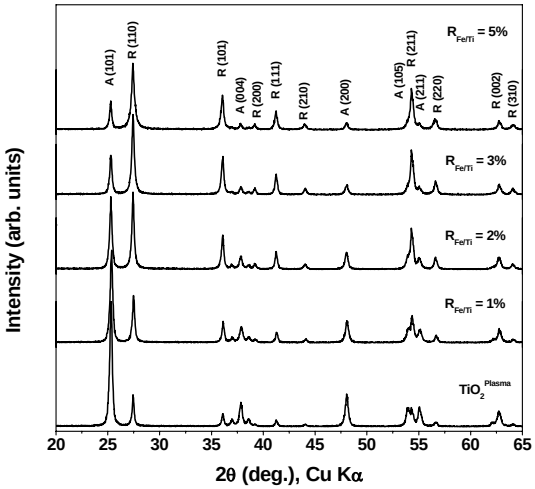

Fig. 1. XRD patterns of the powders with *R* up to 5at%.

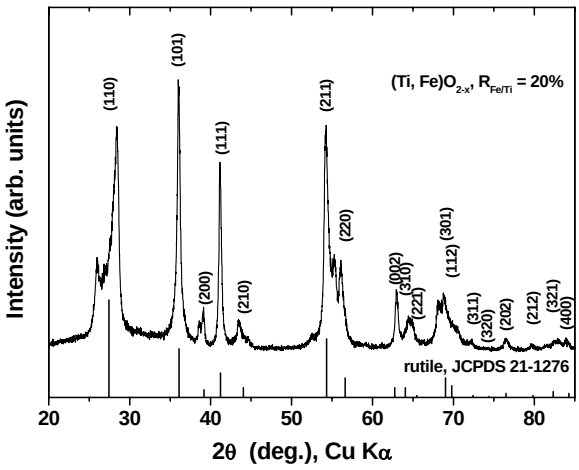

Fig. 2. XRD pattern of the powder with *R*=20at%.

In the heavily doped samples (R=10 and 20at%), The diffraction peaks expect for (101), (111), and (002) exhibit asymmetry, which was enhanced with increasing R (Fig. 2). The asymmetric peaks, with (110) in particular, are significantly broadened and weakened, which reflects misalignment of the slabs in such a way that the d-spacing was not well defined in the [110] direction. Figure 3 shows Raman spectra of the powders with R up to 20at%. Special attentions were paid to the anatase E_g mode at 146.2 cm^{-1} and the rutile E_g mode at 448.1 cm^{-1}, as increasing the oxygen vacancies in the crystal structure of TiO_2 causes right-hand shift of the former while left-hand shift of the latter [4], which was clearly observed at R up to 2at%. At higher R values, the E_g mode of rutile keeps constant at ~402.5 cm^{-1}, suggesting that the oxygen vacancy level in the rutile structure has reached its maximum. Besides, significantly decreased intensities were observed for the Raman bands with increasing Fe^{3+}addition, mainly owing to the increased absorption of the excitation light by the sample. TEM observations indicate that the surplus oxygen vacancies in the samples with R above 2at% cluster to form extended defect structure like crystallographic shear plane (Fig. 4). Iron doping lowers the energies for both indirect and direct transitions TiO_2 (Fig. 5), suggesting their potential use as photocatalysts under visible light illuminations.

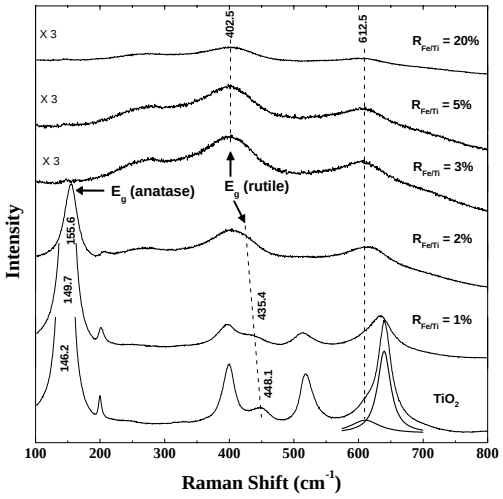

Fig. 3. Raman spectra of the Fe-doped TiO_2 samples

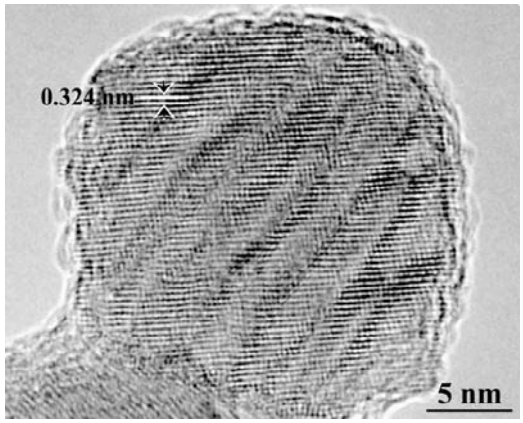

Fig. 4. TEM image showing the clustering of oxygen vacancies

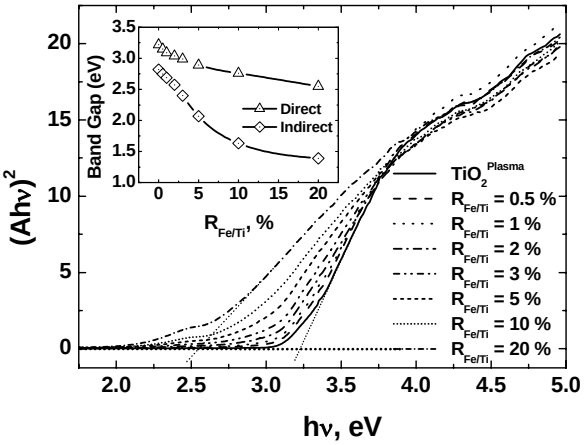

Fig. 5. Bandgap narrowing of TiO_2 by Fe^{3+} doping

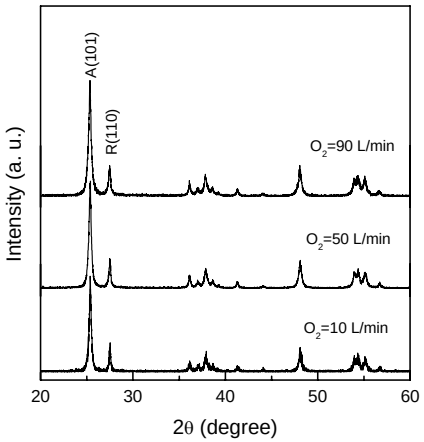

Fig. 6. XRD patterns of the N-containing TiO_2 powders

For N-doped TiO_2 samples, XRD analysis (Fig. 6) shows that they contain only anatase and rutile, and again, metastable anatase was formed as the major phase (>70 wt%), irrespective of the oxygen input rates in the plasma sheath. The anatase content tends to increase at a higher O_2 flow rate (Fig. 7), which might be understood from the facts that (1) the increased addition of diatomic oxygen gas improves thermal conductivity of the thermal plasma, which causes deeper undercooling of the TiO_2 melt at the plasma tail and therefore favors anatase nucleation [3], and (2) a higher O_2 input reduces oxygen deficiencies in the TiO_2 gas clusters, beneficial to anatase formation upon gas phase condensation. A similar phenomenon was observed during our previous work on TiO_2 synthesis via RF thermal plasma oxidation of TiC and TiN particles [5,6]. The nitrogen concentration tends to increase along with the anatase content (Fig. 7), implying that nitrogen is readily doped into the anatase lattice. The powders show weak dependence on the O_2 input in the plasma sheath, and have average crystallite sizes of ~40 nm and specific surface areas of ~30-50 m^2/g. Figure 8 shows typical morphologies (SEM) of the plasma generated N-doped TiO_2 powders. Though particles having diameters bigger than 100 nm are present, most of the crystallites have sizes around 35 nm and are largely dispersed. These two distinctly different types of particle morphologies were considered to be due to the different trajectories of the precursor mists in the hot zone of the thermal plasma.

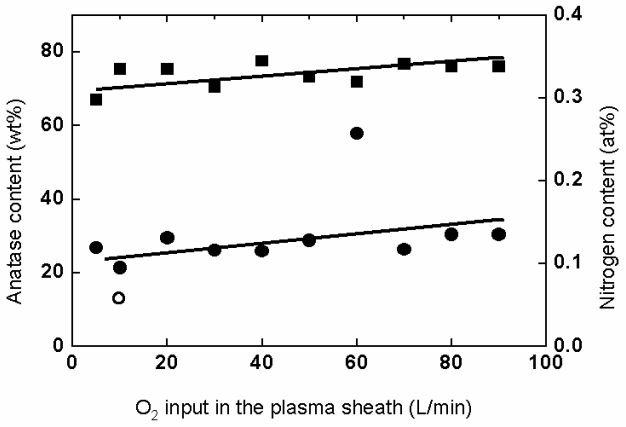

Fig.7. Anatase and N contents of the powders, as a function of the O_2 input in the plasma sheath.

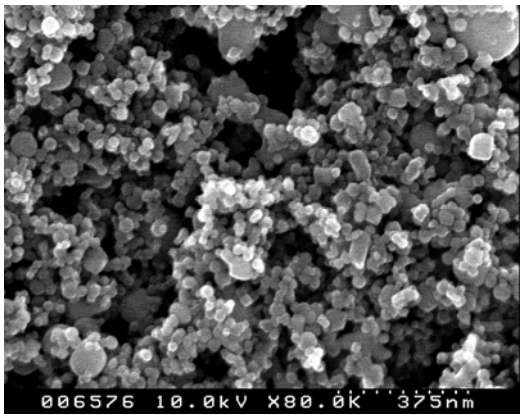

Fig. 8. SEM micrograph showing morphology of the N-doped TiO_2 powder synthesized with 10L/min of O_2 input

Figure 9 shows UV-Vis spectra of the TiO_2 powder synthesized with 10 L/min of O_2 input in the plasma sheath, compared with that of the Degussa P25 powder. The P25 powder has a bandgap of ~3.04 eV, while the N-doped powder exhibits a narrowed one of ~3.00 eV, showing bandgap narrowing of the N-doped TiO_2. the N-doped TiO_2 powders exhibit higher efficiencies than Degussa P25, a model photocatalyst, in the bleaching of methyl orange solution (100 μ mol/L) under visible light (>400 nm) irradiation (Fig. 10).

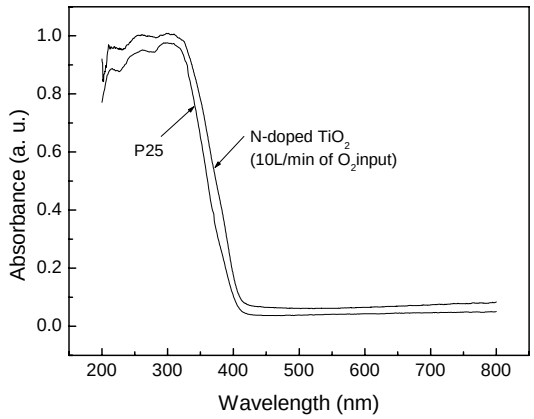

Fig. 9. UV-Vis spectra of P25 and N-doped TiO_2

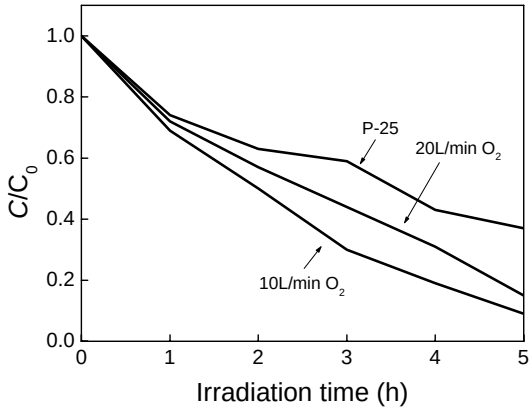

Fig. 10. Bleaching of 20μM methyl orange solution

References

[1] M.R. Hoffmann, S.T. Martin, W. Choi, D.W. Bahnemann - Chem. Rev. 95, 69 (1995).

[2] R. Asahi, T. Morikawa, T. Ohwaki, K. Aoki, Y. Taga – Science 293, 269 (2001).

[3] Y.-L. Li, T. Ishigaki - J. Cryst. Growth 242, 511 (2002).

[4] J.C.Parker, R.W. Siegel-Appl. Phys. Lett. 57, 943 (1990).

[5] S.-M. Oh, J.-G. Li, T. Ishigaki – J. Mater. Res. 20, 529 (2005).

[6] Y.-L. Li and T. Ishigaki – J. Phys. Chem. B 108, 15536 (2004).

Influence of Sulfur and Fluorine Containing Thermal Plasma Treatment of Graphite Powders on the Anode Performance of Lithium-Ion Rechargeable Battery

T. Ishigaki[1], H. Tanaka[1], M. Kurihara[2], N. Ohashi[1], J.-G. Li[1], S. Maruyama[2], Y. Moriyoshi[3]

[1] *Advanced Materials Laboratory, National Institute for Materials Science, 1-1 Namiki, Tsukuba, Ibaraki 305-0044, Japan*
[2] *TDK Corp., Device Development Center, Saku, Japa*
[3] *Hosei University, Department of Materials Science, Koganei, Japan*

Abstract
Spherical artificial graphite powders, so-called as mesocarbon microbead powders, were treated in Ar-H_2-SF_6 radio-frequency inductively coupled thermal plasma. Sulfur and fluorine incorporated into particles. An anode of lithium-ion rechargeable battery made from plasma-treated powder had a discharge capacity as much as 13% greater than that made from untreated powder, while its irreversible capacity loss (ICL) was as much as 9% less. More interestingly, the specific ICL calculated by dividing the ICL by surface area decreased as the surface area increased.
Keywords: Lithium ion rechargeable battery; Anode material; Graphite powder; Surface modification; Electrochemical property.

1. Introduction

Carbonaceous materials have been proven to be an inexhaustible source for scientific research and technological development, such as electrode of lithium ion rechargeable battery [1,2]. Surface and chemical modifications are usually the first step for the application of carbon materials [3,4]. The modifications can change surface composition and structure, active surface area (ASA) and total surface area (TSA), which all play important roles in carbon chemical reactions and applications. The concept of ASA was firstly introduced by Laine and his co-workers in 1963 [5]. The way used to characterize the ASA was to remove surface defects by heat treatment and then measuring the amount of oxygen subsequently chemisorbed. The extent of ASA was thought to be a function of such properties of the carbon as crystallite size, crystallite orientation, vacancy concentration in the basal plane, and impurity concentration, type, and location.

For battery applications, the electrochemical lithium intercalation and de-intercalation capacities are important characteristic of carbon materials, which strongly influence the energy density. While, during the first charge and discharge cycle, an irreversible capacity loss (ICL) always exists, and the ICL has been attributed to the solid electrolyte interphase (SEI) formation and other side reactions. Carbon surface structure has a great influence on the ICL of electrodes [6].

Radio frequency inductively coupled thermal plasma (RF-ICP) treatment has been proved to be a successful way to modify carbon surface for its high temperature, high energy density, high chemical reactivity properties and high heating and cooling rate (~10^6K/min) [7]. The aim of this work is to study the effect of Ar-H_2-SF_6 plasma treatment induced active surface of MCMB powder on the electrochemical properties of the anodes made from these materials [8].

2. Experimental set-up

The carbon used in this investigation was mesocarbon microbeads (MCMB), which is a kind of artificial graphite. The RF induction plasma generating and powder feeding apparatus have been shown elsewhere [9]. The plasma conditions were set as follows: Power, 40kW; plasma gas, Ar 15 L/min; sheath gas, Ar (60 L/min) and H_2 (3 L/min). The powder carrier gas was a mixture of Ar and SF_6, and its total flow rate was set as 10 L/min, in which the SF_6 flow rate was changed from 0.4 to 1.0 L/min. The plasma was generated at the reactor pressure of 27 and 53 kPa. Surface morphology of MCMB powders was observed using scanning electron

microscopy (SEM, HITACHI S-5000). Surface area was measured by N_2 adsorption using the Brunauer-Emmett-Teller (BET) method (BEL JAPAN, BELSORP18). Oxygen content measurement was performed on an oxygen/nitrogen analyzer (HORIBA, EMGA-650). Sulfur content measurement was carried out on a carbon/sulfur analyzer (LECO CS-444). Fluorine content was measured by ion chromatography. Fourier transform infrared (FTIR) experiments were carried out on a BIO-RAD FTS-65 FTIR spectrometer. Electrochemical properties were measured in non-aqueous solvents containing 1 M $LiClO_4$. Sample electrodes were prepared by following way: Poly vinylidene fluoride was used as the binder and slurry was spread on copper foil and dried at 150℃ under vacuum for one hour; a 1mol/cm^2 solution of $LiClO_4$ in a 50:50 mixture of ethylene carbonate (EC) and diethyl carbonate (DEC) was used as the electrolyte; the electrochemical cell was set up in a dry box under argon atmosphere and the charge/discharge behavior of the cell was measured galvanostatically at the current density of 0.25 mA/cm^2 between 0 and 3 V vs. Li/Li$^+$ at 25℃.

3. Results and discussion

Figure 1 shows typical surface morphologies of the original MCMB and the plasma treated MCMB powders. The original MCMB in Fig.1(a) has polyhedral shape, while Fig. 1 (b) reveals that some particles have a lot of holes after plasma treatment. Figure 2 gives the FTIR results on the original and the plasma treated powders. The peak at 1716cm^{-1} in plasma treated sample represents the C=O double bond stretching vibration in the form of C–C=O, and peaks at 1222cm^{-1}, 1364cm^{-1} and 984cm^{-1} represent the C=S bonds, which are attributed to the chemical reactions of carbon and sulfur. Figures 1 and 2 prove that the surface structure and chemical composition of MCMB have changed greatly after plasma treatment, which should be responsible for the change of the electrochemical properties

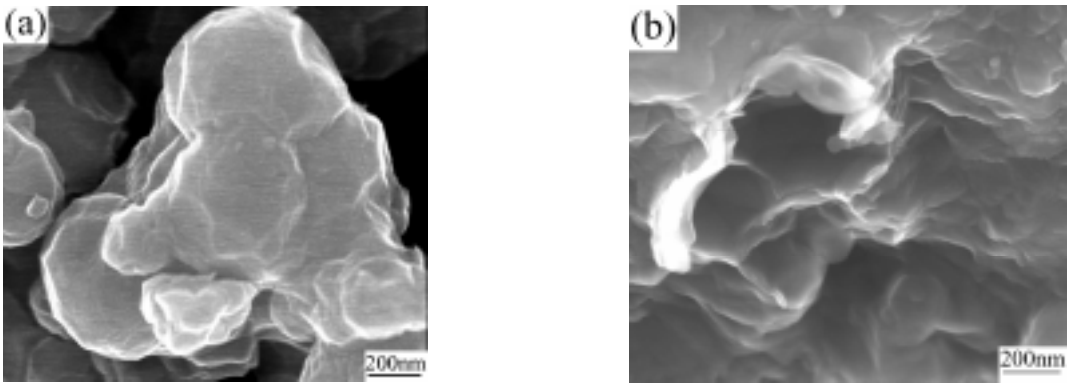

Fig. 1 Surface morphologies of original and plasma treated MCMB; (a) original MCMB. (b) plasma treated MCMB.

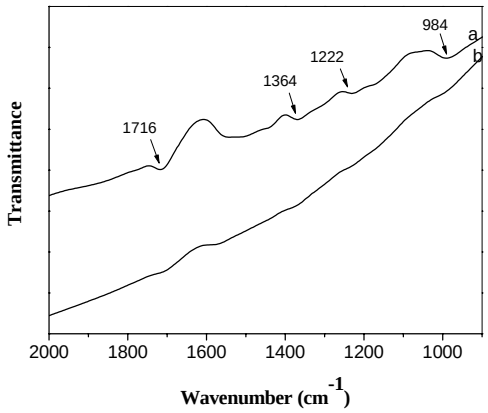

Fig. 2 FTIR results of original and plasma treated MCMB; (a) original MCMB. (b) plasma treated MCMB.

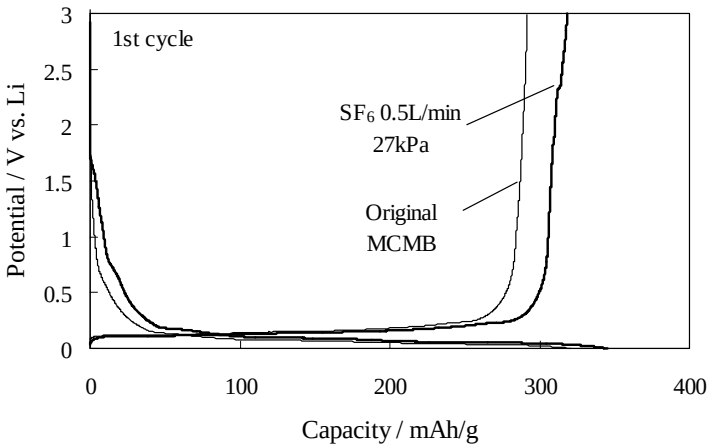

Fig. 3 First charge/discharge curve of original MCMB and plasma treated MCMB (SF_6 flow rate: 0.5L/min; reactor pressure: 27kPa).

Figure 3 shows the first charge/discharge curves of the original and the plasma treated MCMB powders (SF_6 flow rate: 0.5L/min; reactor pressure: 27kPa). It can be seen that the plasma treatment gave the great increase of discharge capacity at the first charge/discharge cycle. Figure 4 shows the relationship between the specific ICL and the BET surface area. This figure demonstrates that the specific ICL (the calculation method is dividing ICL by TSA) decreases with the increase in BET surface area, and the relationship is approximately exponential. The curve also suggests that the carbon surface is not uniformly active for irreversible capacity loss. Figure 5 shows the relationship between the specific ICL (the calculation method is dividing ICL by the content of O+S+F) and the content of O+S+F. Since the content of active site of O+S+F can be an indicator of the ASA, this figure demonstrates that that the ASA is not the only reason to be responsible for the ICL. Figure 5 also shows that within certain extent of ASA, the specific ICL decreases with the increase in ASA.

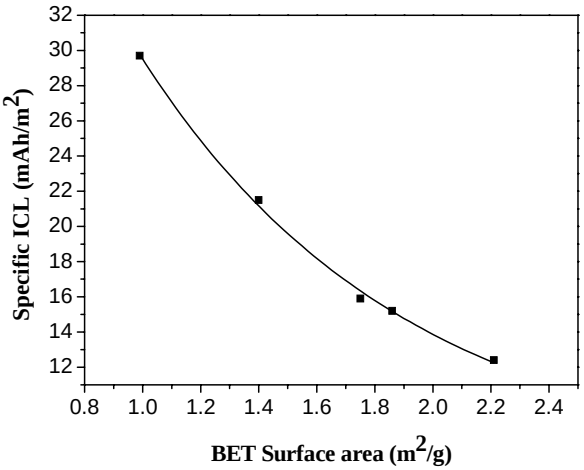

Fig. 4 Relationship between the specific irreversible capacity loss (in respect to the BET surface area) and BET surface.area

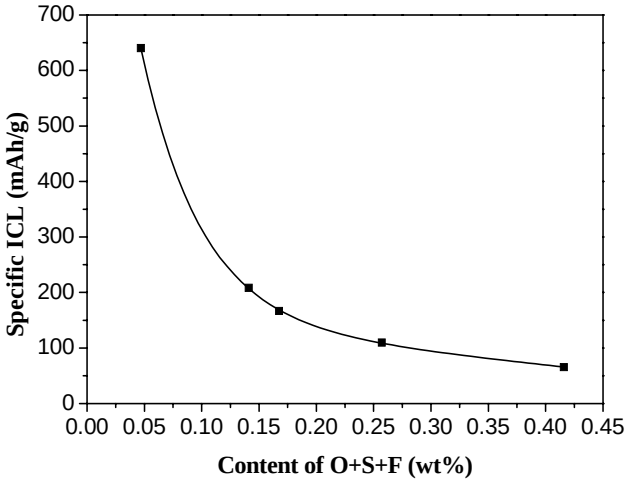

Fig. 5 Relationship between the specific irreversible capacity loss (in respect to the content of O+S+F) and the content of O+S+F.

5. Conclusion

In summary, we have demonstrated that the electrochemical properties of MCMB as an anode of lithium-ion rechargeable battery have a great relationship with the surface area and active surface area. Within certain extent, the specific irreversible capacity loss decays nonlinearly with the increase of surface area and active surface area.

References

[1] M. Inaba, Z. Ogumi, *IEEE Electrical Insulation Magazine*, **17**, 6(2001).
[2] Z. Ogumi, A. Sano, M. Inaba, T. Abe, *J. Power Sources*, **97**, 156(2001).
[3] J.Y. Xu, Y. Hu, L. Song, Q.A. Wang, W.C. Fan, Z.Y. Chen, *Carbon*, **40**, 450(2002).
[4] J.Y. Xu, Y. Hu, L. Song, Q.A. Wang, W.C. Fan, G.X. Liao, Z.Y. Chen, *Carbon*, **40**, 2964(2002).
[5] N. R. Laine, F. J. Vastola, P. L. Walker, Jr., J. Phys. Chem., **67**, 2030(1963).
[6] G. C. Chung, S. H. Jun, K. Y. Lee, M. H. Kim, *J. Electrochem. Soc.*, **146**, 1664(1999).
[7] M. Kurihara, S. Maruyama, K. Oh'e and T. Ishigaki, *Chem. Lett.*, **27**, 715(1998).
[8] H. Tanaka, J. Y. Xu, M. Kurihara, S. Maruyama, N. Ohashi, Y. Moriyoshi, T. Ishigaki, *Carbon*, **42**, 3229(2004).
[9] H. Tanaka, T. Osawa, Y. Moriyoshi, M. Kurihara, S. Maruyama, T. Ishigaki and H. Kanda, *Thin Solid Films*, **435**, 205(2003).

CARBON/PHENOLIC COMPOSITE ABLATION UNDER DROPLET IMPINGING : DIAGNOSTICS OF A BENCH TEST

S. Bansard[1], M. Vardelle[1], J.M. Déoclézian[2], P. Fauchais[1]

[1] *SPCTS, University of Limoges, Limoges, France.*
[2] *Snecma Solid Propulsion, Le Haillan, France.*
E mail : mvardelle@unilim.fr

Abstract :

The design of solid fuel engine nozzle requires a good knowledge of the recession behaviour of the ablative thermal barrier (heat transfer and ablation processes). The use of aluminium-enriched propergol results in the formation of alumina droplets that impinge and form a liquid film at the nozzle surface modifying the ablation processes. To validate an aerothermochemical model developed by Snecma Solid Propulsion, an experimental simulation has been developed to characterize and measure the surface recession of a carbon/phenolic composite under the impact of alumina droplets.
This paper presents the experimental setup which combines two direct current (d.c.) plasma torches in a controlled atmosphere chamber that are used both to fuse and accelerate alumina particles. The behavior of the alumina droplets before impact (velocity and temperature) and the plasma fields close to the target are examined.
The recession measurements are obtained through a feedback control of the position of the sample top. Recession rate evolution has been studied according to experimental parameters

Introduction :

The development of spatial engines is based on the regularity, reliability of the engine and the improvement of the ratio carried weight to that of the engine. That is why for many years, engines with solid propergols have been developed [1, 2]. Using composite materials appeared very rapidly to be the solution to palliate the weight of the refractory materials used at the beginning while keeping their mechanical resistance [3, 4]. However these materials are submitted to very severe stresses: temperatures over 3000K, high and low pressure (0.1 to 4 MPa), very aggressive chemical environnement (OH, CO, Cl…). Besides to increase the thrust during the take off, the solid propergol is enriched with aluminium particles. During combustion they react with oxygen increasing the combustion temperature and thus the thrust by 6 to 8%. However this combustion produces alumina particles resulting in a multi phase flow, adding to the stresses of the composite wall impact and chemical erosion. For example Fabignon [5] shows that these alumina particles result in the formation of an alumina liquid film on the nozzle wall. However, models of the nozzle wall surface recession such as that developed by SNECMA Solid Propulsion, do not predict very well the phenomena, even after backing the model to experiments. The wall recession is underestimated. Thus it is mandatory to understand the history of the alumina film from its right beginning (interaction drop-solid) to its elimination (reaction film-wall, liquid feeding and ejection) through its evolution (study of the interfaces liquid-wall and drop-liquid). This work presents the experiment developed to simulate the hot multi-phase flow with two spray d.c. plasma torches in a controlled atmosphere chamber and the results of the carbon/phenolic composite ablation for different conditions.

Experiment:

- **Description of the experimental set up developed at SPCTS Laboratory (Limoges, France):**

The aim of this set-up is to reproduce the impacts of liquid alumina particles onto a composite flat substrate as well as the formation of a liquid alumina film keeping the substrate temperature over 2300K. Unfortunately, the real conditions (chemical composition and pressure) cannot be reproduced. To achieve a rather flat particle flux, two d.c plasma torches have been chosen to limit the gas velocity. These torches have an anode-nozzles with internal diameter of 8 mm, and an angle between both, which can be varied between 40 and 120 (see fig 1). For each torch the power dissipated in the gas can reach 20kW and the mean gas temperature close to the chamber wall can be over 900K. Thus the chamber walls are water cooled

under a pressure of 1.2 MPa. The chamber comprises two parts: a cylinder where the two torches are positioned with windows allowing optical diagnostics and a cone to evacuate the hot gases and particles. The pressure in the chamber is controlled by a primary vacuum pump and a monitored vane. The argon atmosphere (to avoid a too fast substrate oxidation) is kept at 50 kPa.

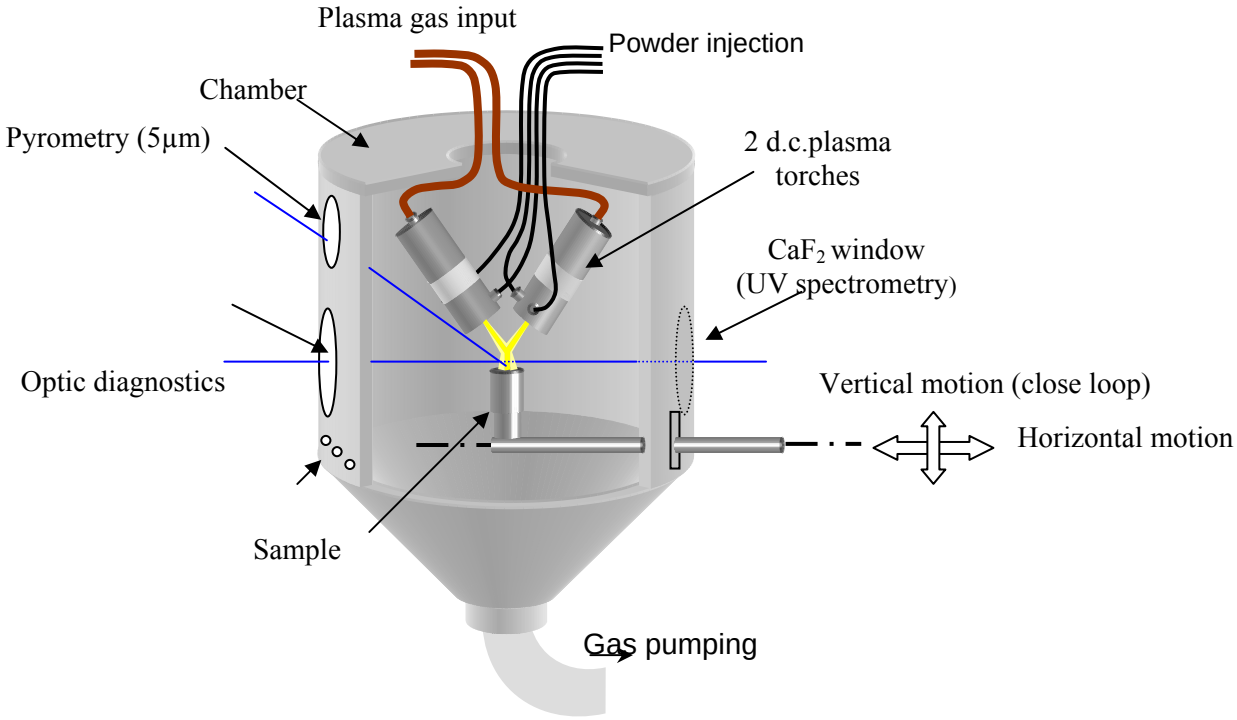

Fig1: Scheme of the experimental set-up

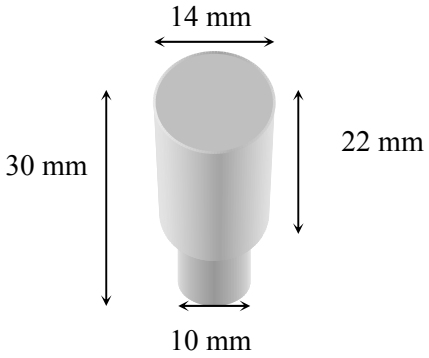

Fig 2: Geometrical aspect and dimensions of the carbon/phenolic

The substrate made of carbon/phenolic has the size shown in fig2. The useful height (upper part) is 22mm. In order to achieve a regular heating and wear of the substrate it rotates at 200 r.p.m. The substrate holder is water cooled but the rotating axis which can reach temperatures as high as 3000K is made of tungsten. The substrate holder can be moved up and down at a variable velocity controlled by the position of the substrate top measured with the help of a laser (λ=632.8nm) and a photodiode. This system allows keeping the substrate position constant and thus following its erosion by the relative displacement of the substrate holder.

Particles are injected orthogonally to both torches axis, the injector 1.8 mm in internal diameter being disposed internally in the plane of the two torch axis. Thus with the rotation of the substrate, the powder distribution is almost flat onto a disk 12mm in diameter centred on the substrate axis. Powder feed rates can be varied between 1 and 3 kg for each torch for alumina particles in the size range 10 – 40 µm.

- **Diagnostic techniques**

The species present in the plasma jets have been determined by emission spectroscopy. The plasma jet temperature is measured by using the OH band at 306 nm according to a method developed by De Izzara [6]. Of course the spectrum intensity is much lower in argon atmosphere because of the low oxygen pressure. An imaging technique with a CCD camera has also been used allowing comparing very rapidly different torch working conditions. Of course the camera was calibrated with spectroscopic measurements. As the temperature below 2500K is difficult to measure with OH bands in the jet fringes the position where the

extremity of a rod of alumina (1mm in diameter) melts, allows determining the position were temperatures reach 2326K.

The heat flux received by the composite substrate has been measured with the help of a water cooled calorimeter: typical values are between 1 and 10 MW/m2.

The velocity of the in-flight alumina particles was measured with the Spray Watch.

The surface temperatures of the substrate and alumina film were measured with an IR pyrometer (4.87 – 5.3 µm), wavelength range where the plasma emission is very low [7]. Using a grey filter and calibrating the pyrometer has allowed extending the temperature range up to 3500K. The windows are made of CaF_2, and corrections are made to account of its absorption. The alumina emissivity is that proposed by Rosenbaun et al [8]. Thermocouples (W-W.Rh) disposed at different distances along the substrate axis allow measuring the temperature gradient within it.

Results and discussion

All results will be presented for the working conditions summarized in fig 3 caption.

- **Characterization of the plasma jet**

Fig 3 shows a typical temperature distribution of the two plasma jets. The informations given by the different techniques are complementary.

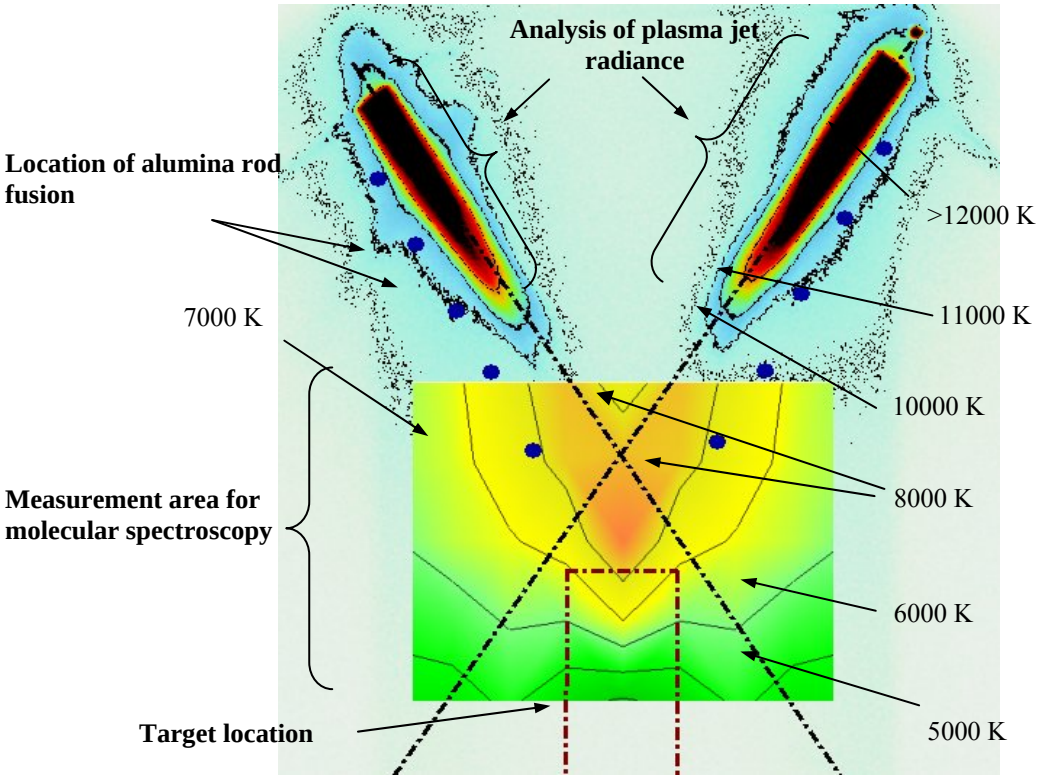

Fig 3: Temperatures distributions obtained with different diagnostics working conditions: anode-nozzle i.d. 8mm, I=600A, Ar-H2 plasma (45-15 slm) flowing in air at $p=10^5$ Pa, angle of both torches=60°

The importance of the hydrogen percentage on the heat flux imposed to the substrate for the 60° torch angle is shown in fig 4.

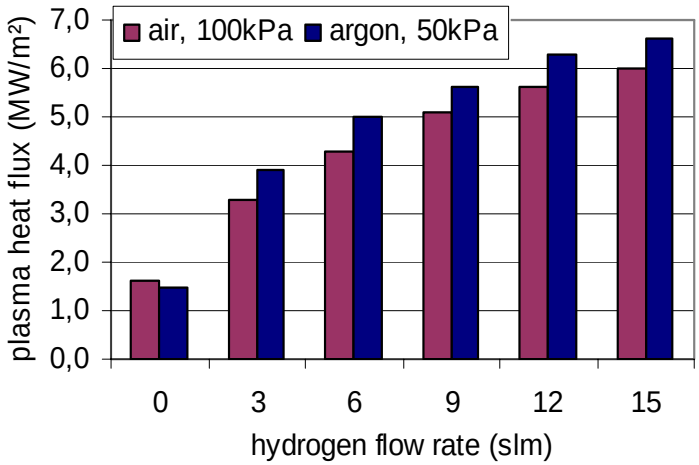

Fig4: Heat flux received by the calorimeter (working conditions of fig 3)

- **Study of the sample erosion**

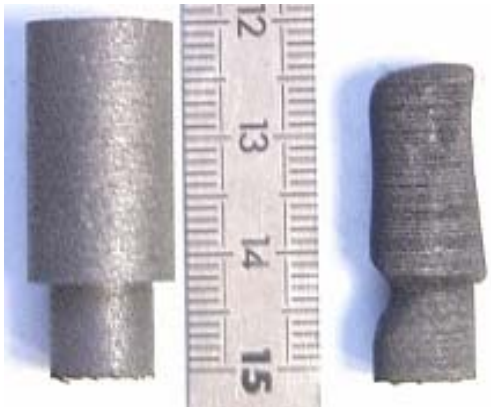

Fig 5 : Initial sample (left) submitted to the plasma as shown in fig 6.

Fig 5 shows the evolution of the aspect of the initial sample (left) submitted to the plasma without powder in argon atmosphere during 90 sec.

Almost no surface recession can be observed (less than 1mm). It seems that the sample has been a little expanded in spite of a mass loss of 25%. In air atmosphere, the mass loss is over 42% with a surface recession of 4mm in height and 3 mm in diameter. As soon as the powder is injected the wear of the sample is drastically increased. First when increasing the powder flow rate, the relative velocity of recession increases linearly with the powder mass flow rate, and then reaches a plateau for a powder flow rate of about 3kg/h

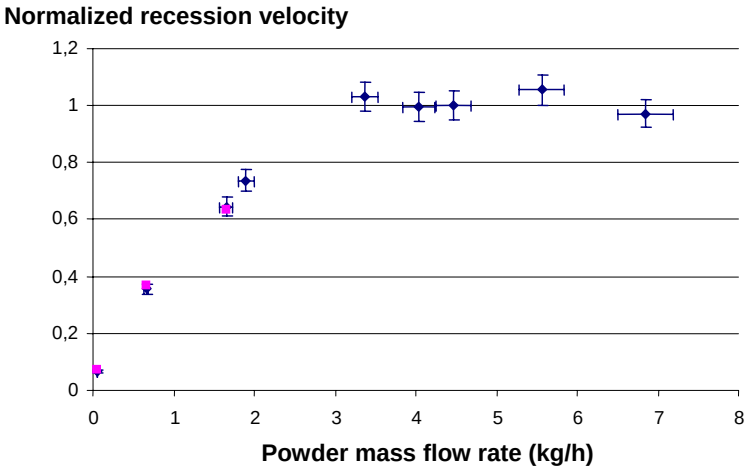

Fig 6: Normalized recession velocity evolution with alumina mass flow rate (in each torch).

This result is confirmed by the results presented in fig 7, representing the time-evolution of the normalized displacement of the sample for different powder flow rates.

Normalized recession velocity

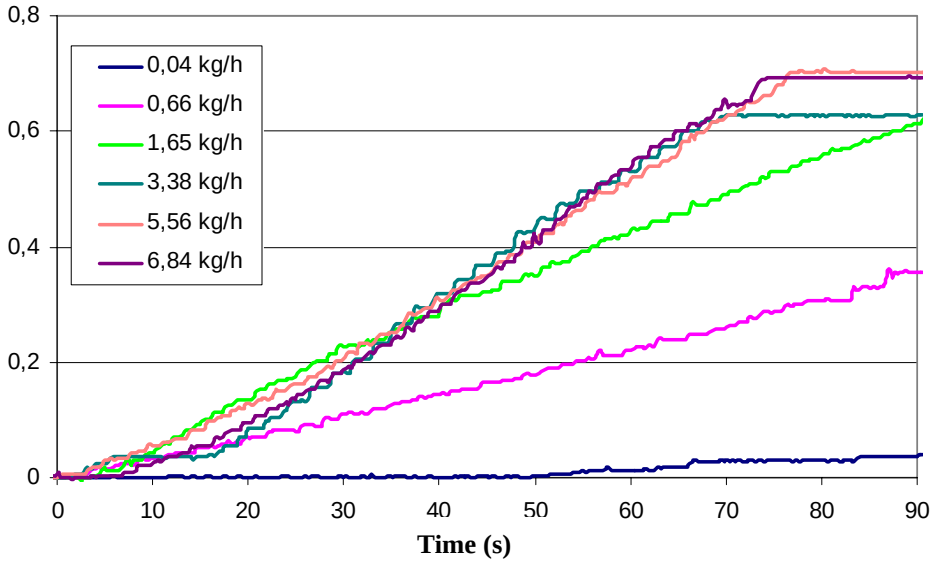

Discussion: Without the powder the wear of the sample is mainly due to the reaction of the hot carbon with oxygen to form CO. Of course in air atmosphere this wear is drastic. However it is relatively limited in argon controlled atmosphere due to the relatively low pressures of oxygen. When looking at the surfaces with SEM it can be observed that the fibres are no more imbedded in the phenolic resin and they exhibit a sharp-pointed tip. This phenomenon is probably due to the evaporation of the fibres by the very important heat flux (see fig 4). With alumina particle a typical observation is shown in fig 8.

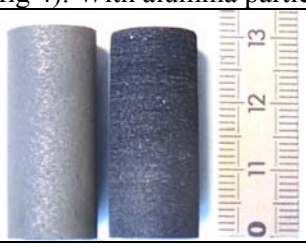	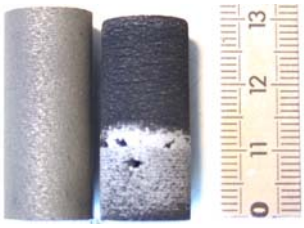
Without powder	Powder flow rate : 0,04 kg/h
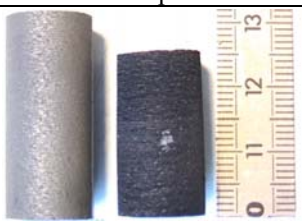	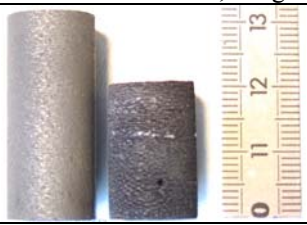
Powder flow rate : 0,66 kg/h	Powder flow rate : 1,65 kg/h
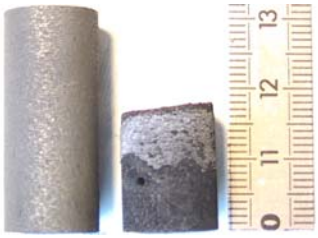	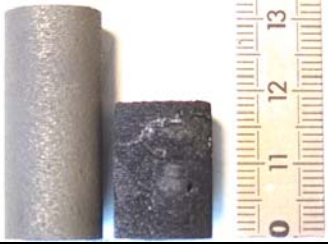
Powder flow rate : 3,38 kg/h	Powder flow rate : 5,56 kg/h

Fig 8: Surface of the composite material after the alumina particle impacts. Magnification 800

The aspect is similar to that observed in air for samples submitted to oxyacetylenic flame or a laser. Fibres exhibit well marked brushes already observed under the impact of solid particles [9]. It is also possible observing holes in certain areas which means that chemical reactions between alumina and fibres

could have occurred. Moreover, in the chamber spherical particles of alumina in which pieces of fibres are imbedded can be collected. Alumina buttons in a graphite crucible were submitted to the plasma jet. When plasma heating a closed graphite crucible containing the composite and an alumina button, the composite fibres look the same as those observed after alumina impact and fibres seem to have reacted with liquid alumina. Works are in progress to reproduce these experiments in a furnace where temperatures of 2500K can be achieved.

Conclusion

An experimental set-up with two d.c. spray torches in a controlled atmosphere chamber has been realized to follow the wear of carbon/phenolic composites. The sample movement is continuously controlled to keep the distance plasma-sample constant during the sample wear. First the sample has been submitted to the plasma jet alone and then to molten alumina particles which flow rate was varied between 0.2 and 6 kg/h. The erosion rate increases linearly with the powder mass flow rate, but over a critical value of the later, the erosion rate reaches a plateau. The erosion phenomena are first a pyrolysis of the phenolic resin, followed by the weakening of the fibre resistance by chemical reaction liquid alumina – carbon fibre.

References

[1]. Ellis R.A. "*Solid rocket motor nozzles.*" NASA, SP-8115.(1975)
[2]. Ryan R.S. "*A History of Aerospace Problems, Their Solutions, Their Lessons.*" NASA Technical Paper 3653.(1996)
[3]. Nettles A.T. "*Basic mechamics of laminated composite plates.*" NASA, 1351.(1994)

[4]. Barret C. "*Launch vehicle flight control augmentation : using smart material and advanced composite.*" NASA, TP 9305.(1995)

[5]. Fabignon Y. "*Synthèse des travaux sur la modélisation et la simulation numérique du dépôt d'alumine dans le MPS P230.*" Rapport technique ONERA, RT 109/6133 DEFA/Y.(1999)

[6]. Izarra[2] C. De. "*Computer simulationof the UV OH band spectrum.*" International Journal of Modern Physics C(2000) 11(5): 1-12.

[7]. Renault T, Vardelle M., and Fauchais P., *Choice of an IR- pyrometer to measure the surface temperature of a coating during its formation in air plasma spraying*, High temp. Material Processes, 6, (4), (2002), 469-490
[8]. Rozenbaum O., Meneses D. De Sousa, Auger Y., Chermanne S.,Echegut P. "*A spectroscopic method to measure the spectral emissivity of semi-transparent materials up to high temperature.*" Review of Scientific Instruments(1999) 70(10): 4020-4025.

[9]. Tewari U.S., Harsha A.P., Häger A.M.,Friedrich K. "*Solid particle erosion of carbon fibre- and glass fibre-epoxy composites.*" Composites Sciences and Technology(2003) 63: 549-557.

Selective oxygen plasma etching of amorphous phases in composite organic thin films

R. Murillo[1] Y. Segui[1] , C.Petcu[2], G. Dinescu[2]

[1] *Laboratoire de Genie Electrique , University of Toulouse, CNRS, France*
[2] *National Institute for Lasers, Plasma and Radiation Physics, Magurele MG-16, 07712, Bucharest, Romania*

1 Abstract

Organic materials consisting of mixed amorphous and crystalline phases were obtained by using a sublimable di-para-xylylene crystalline monomer .The process combines recondensation with plasma polymerization techniques in the same reactor. The materials were submitted to oxygen plasma etching experiments. It is shown that the etching process of the amorphous plasma polymerized film is significantly more effective than the etching of the crystalline phases embedded in the material.

2 Introduction

The aim of the present work is to investigate the oxygen plasma interaction mechanisms with organic materials surfaces in amorphous or crystalline phases. There are many situations where organic materials, polymers are in contact with oxygen containing plasmas. Such as, in plasma sterilization, the microbes and bacteria have to be removed. Infection free surfaces are created. Organic contaminants have to be removed from metallic or polymeric surfaces before further process like painting, soldering or gluing. To avoid wet cleaning which lead up products detrimental for the environment, considerable efforts have been made to promote plasma cleaning [1-3]. In other applications, like polymer surface treatment, a surface roughening, surface structuring (or nanostructuring) can be necessary, accompanied by modification of surface topography and change of its physical and chemical properties.

In many of the above mentioned situations, the surface cleaning or modification are apparently due to the plasma selective attack of the crystalline and amorphous phases of the material. Consequently, it would be of interest to examine the phenomena associated to the plasma etching of amorphous and crystalline phases of materials. Aiming to that, materials consisting of organic microcrystals embedded in amorphous matrix have been specially prepared, starting from the crystalline dimer di-para-xylylene (DPX) and using condensation and plasma polymerization, and where submitted to oxygen plasma. The materials were characterised by using XRD, AFM, SEM and profilometer measurements.

3 Experimental

The experimental set-up used for film deposition presented in figure 1 was also described previously in detail [4]. A tubular glass reactor of 8 cm external diameter, 50 cm long was used, provided with flanges at both ends, appropriate for substrate and precursor cell holding and with ports for vacuum measurement and gas admission. The plasma was generated in argon atmosphere by applying a radiofrequency (13.56 MHz) voltage between two external annular electrodes placed on the glass tub. The DPX vapors were produced by heating a sublimation cell (glass ampoule). The vapours are transported toward a water cooled substrate

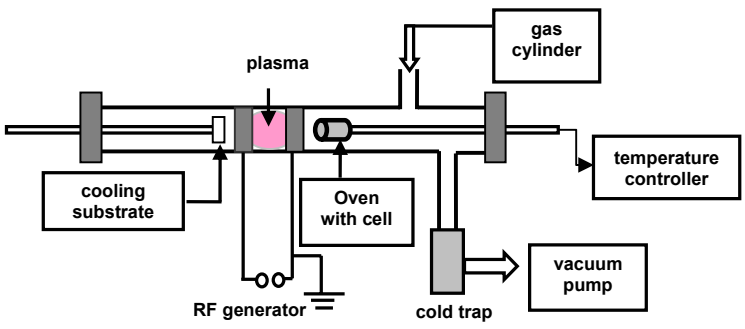

Figure 1. Experimental set-up – schematic view

by a gas flow (argon) at low pressure (10^{-1} mbar). Along their way from the cell to substrate the vapours pass across the RF discharge zone where plasma is present when the RF voltage is applied to the electrodes.

The heating of the sublimation cell was performed by a home made low caloric capacity electrical oven. The sublimation temperature was measured with a thermocouple placed in the wall of the sublimation cell and maintained at values appropriate for the process via a temperature controller, with errors in the range of 1-2 Celsius degrees.

Plasma etching was performed in a bell jar reactor represented in figure 2. This reactor was made up with a Pyrex glass cylinder closed by two stainless steel plates. The cylinder was 32 cm in diameter and 31 cm high. A Trivac D 25B was used as a primary pump. Gas was introduced by the upside of the reactor, controlled by a MKS mass flow controller. A MKS Baratron capacitance manometer was used to check the pressure.

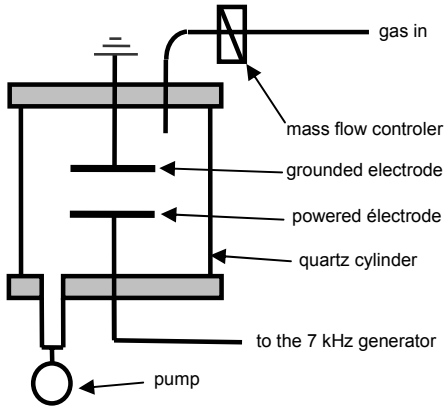

Figure 2. Low frequency plasma reactor used for etching

The two stainless steel parallel plates electrodes, 10 cm in diameter, were powered by a low frequency amplifier at 7 KHz. The sample was placed on the powered electrode. Plasma power was calculated from the measurements of the discharge current and voltage across the electrodes. The reactor was first pumped down to 0.1 Pa , and then pure molecular oxygen was introduced. The flow rate has been controlled to achieve a pressure of 53 Pa (400 mTorr). The injected power was about 0.35W during two run of 2 minutes each.

The process was controlled by OES. Atomic oxygen emission at 844 nm was recorded. The argon (5%) was introduced to attempt actinometric measurements. Unfortunately due to a very low electronic density of the etching oxygen plasma, the density of atomic oxygen was very low and the main path to produce excited atomic oxygen was found to be a dissociation /excitation process of molecular oxygen. These phenomena make unreliable the actinometric measurements, and further studies are necessary in order to describe the processes.

The monomer decomposition was monitored by OES measurements, the carbon containing radicals (CO, CH) appearing in the spectra during the plasma process. As substrate silicon, quartz, glass may be used. The deposited films were studied by X-Ray Diffraction (XRD), Atomic Force Microscopy (AFM), Scanning Electron Microscopy (SEM), revealing the amorphous/crystalline nature of the material. The modification of the amorphous/crystalline mixed material due to oxygen plasma etching was done by SEM measurements.

4 Results and discussion

4.1 Deposition of the mixed phase organic material

The method for precursor injection used in this work was the DPX sublimation. In the usual plasma polymerization methods, the sustaining species necessary for film growth are obtained by feeding plasma with vapors of organic or metalo-organic volatile substances, in liquid state at process temperature. This work differs strongly in comparison to the usual methods, the vapors being obtained by sublimation of a solid state precursor. As it is known [5], the properties of the material are dependent on the W/F (W power, F mass flow) composite parameter known as Yasuda parameter. It was previously shown for parylene-like thin film deposition by DPX plasma polymerization that the quality of material is strongly dependent of this parameter as well. Consequently, the control of power and mass flow has a great importance for the process.

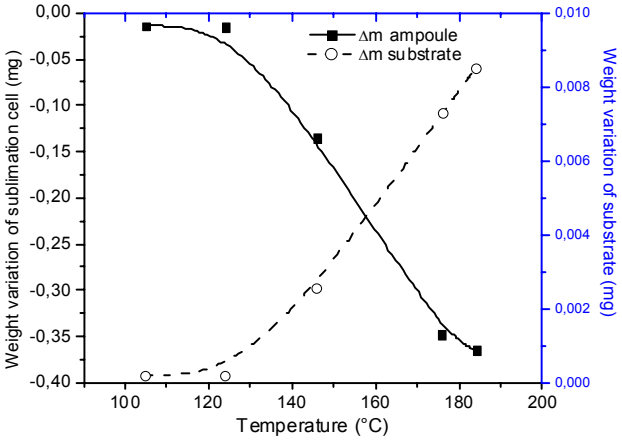

Figure 3. Temperature dependence of DPX amount sublimated from the cell, and recondensed on the substrate.

Whereas the power control is quite easy with normal radiofrequency generators provided with auto matching, the control of mass flow can be very difficult due to the particularities of sublimation process. Indeed, around the sublimation temperature the sublimation rate is strongly dependent on the temperature.

An experiment was performed in which the mass loss of the sublimation cell was measured for different sublimation temperature. The dependence of the mass loss on temperature is shown in figure 3. It is seen that the mass loss changes rapidly with the temperature, in such a manner that a small variation in temperature produces a large variation of the mass flow. One concludes that a precise and rapid temperature control is necessary in order to insure a good reproducibility. This was realized with a small resistive tubular oven having a small caloric capacity and inserted directly into the plasma reactor. The sublimation cell, consisting of a glass ampoule was placed inside this oven.

A condensation experiment was performed simultaneously with the sublimation experiment. The mass of a cooled silicon substrate was measured before and after the sublimation step, for various sublimation temperatures. The results are presented in the Figure 3 as well.

In figure 4, the XRD pattern of a sample obtained from a condensation experiment is shown. It proves that the mass increase is due to the deposition of material having a crystalline structure which was identified as being that of DPX.

The crystallites growth during the condensation process was studied by AFM. The images presented in figure 5 are recorded at 10x10 μm^2. For short recondensation times, 30 seconds and 1 minute respectively, we can see small particles on the substrate (figure 5 a, b). When increasing the recondensation time, the dimension of the particles starts to increase (figure 5 c, d). The crystallites size varies from about 300 nm up to a few microns, depending on the recondensation time.

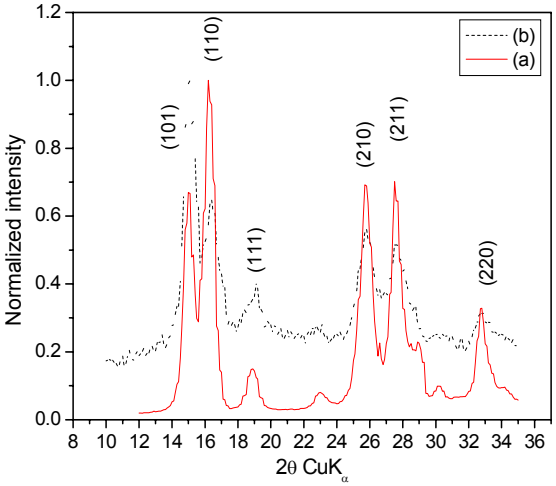

Figure 4. The XRD pattern of the material collected at substrate a) without RF discharge b) with RF discharge (20 W)

In the presence of the RF discharge the vapours created by sublimation are fragmented by collisions with plasma particles and transported to the substrate. A material containing both crystalline and amorphous phases can be realized at low power values, when only partial decomposition of DPX is realized. An example of XRD pattern of a sample obtained for such a mixed phase material is presented in figure 5b. For power values that are high enough to produce the complete decomposition of DPX vapours amorphous films are formed [1].

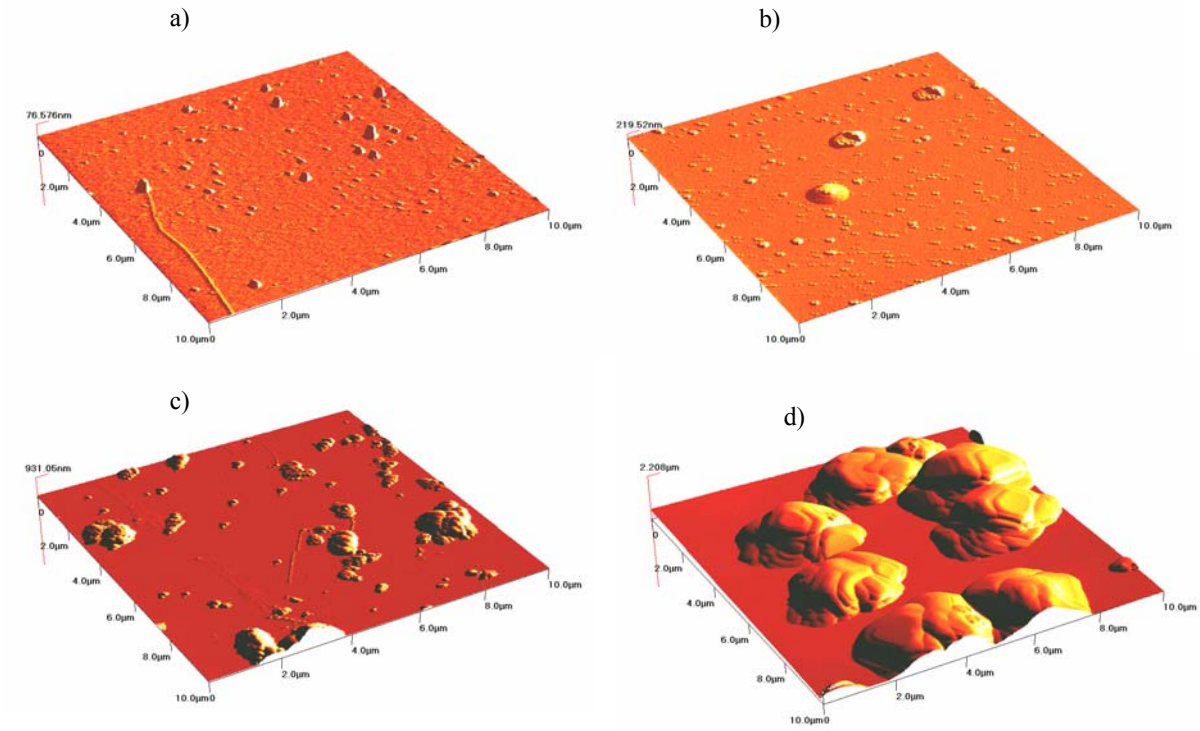

Figure 5. AFM images of the material deposited at different recondensation times:
a) 30 seconds; b) 1 minute; c) 5 minutes; d) 15 minutes

4.2 Etching experiments

The film was deposited at 40 W, for 10 min, at 3.8 mbar argon pressure. Figure 6(a) and 6(b) are pictures of the deposit before etching. We can see two strips on the left side and on the bottom of the picture 6(a),. They have been made with a blade on the samples by removing out the deposited material in order to increase the visibility of the film on the substrate and to create a position reference for the SEM observation after etching. The fine lines along the strips can be associated to the micro-trenches made on the sample due to the softness of the removed material.

White spots are images of the microcrystals of di-para-xylylene, deposited together with the parylene-like amorphous phase (in grey) during the course of the fabrication of the layer. These spots are more visible on the picture 6(b), done with a higher magnification (x8000).

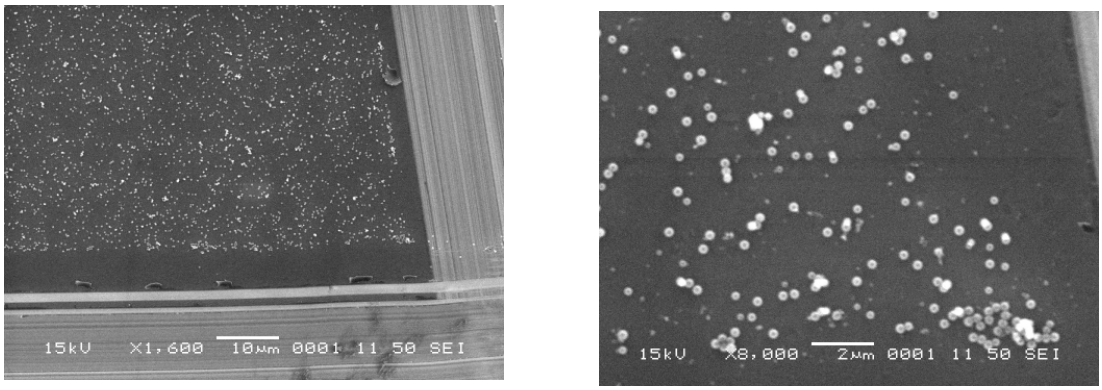

Figure 6. SEM images of a composite thin film before etching at a x1600(a) and a x8000(b) magnification

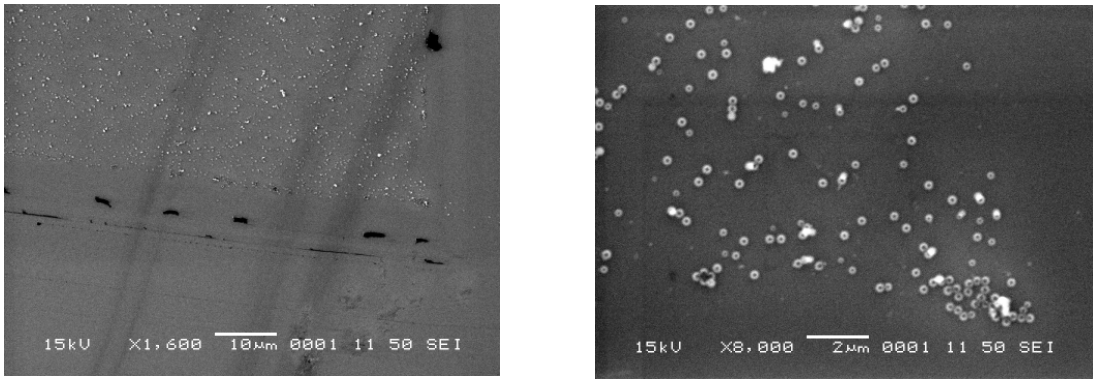

Figure 7. SEM images after 2 min of O_2 plasma etching at a x1600(a) and a x8000(b) magnification

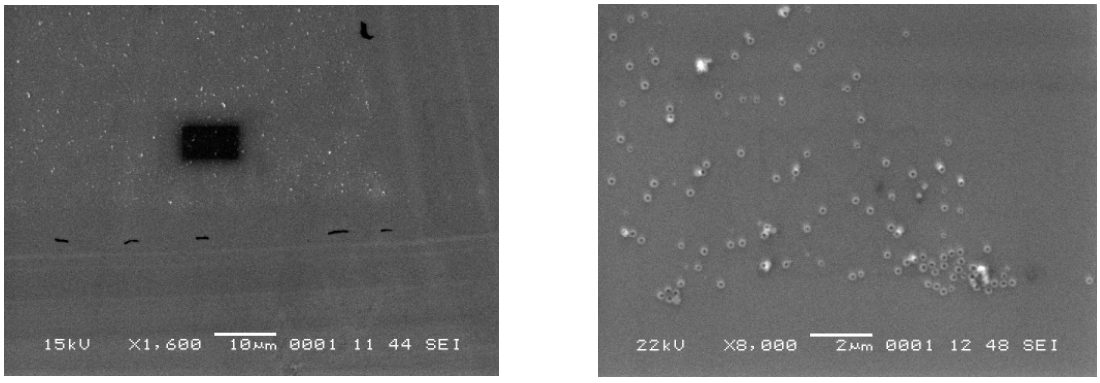

Figure 8. SEM images after 4 min of O_2 plasma etching at a x1600(a) and a x8000(b) magnification

Figure 7 (a) and (b) represent the same area than figure 6(a) and (b). Those pictures have been taken after a two minutes O_2 plasma treatment in the reactor represented in figure 2. The amorphous smooth phase is no longer visible whereas the white crystallites are still visible.

Pictures on figure 8(a) and (b) show the same area after a second treatment of two minutes of O_2 plasma. The smaller crystals have disappeared but the majority of them are still here.

We can consider spherical the shape of the microcrystals. Low frequency O_2 plasma etching is mainly anisotropic. If less than half of the volume of each microcrystal has been etched, it cannot be revealed with a top view of the surface. That's why we can't rigourously conclude that microcrystal etching is more efficient than amorphous phase etching. The amorphous phase thickness knowledge and the microcrystals diameter knowledge would permit us to conclude about O_2 plasma etching selectivity between amorphous and crystalline phase. Due to the amorphous phase softness, it was nearly impossible to measure the layer thickness with a profilometer. However, it appears clearly from figures 7 and 8 that only the crystalline part of the sample remains visible after 2 to 4 minutes under O_2 plasma. If we consider that microcrystals and amorphous layer thicknesses are close,, we can conclude that the amorphous phase etching process is significantly more effective than the crystalline phases etching.

Conclusion

A technique of mixed phase (amorphous and crystalline) organic materials growth was described. The materials consist of microcystals embedded in an amorphous matrix. The technique is based on the use of sublimable crystalline monomers. The vapours obtained by sublimation are used as precursors in the growth process. The material is obtained by combining in the same experimental set-up the condensation and plasma polymerization.

Materials deposited by this technique from di-para-xylylene monomer were submitted to oxygen plasma etching experiments. It is shown that amorphous parylene-like layer disappear from the surface faster than the crystalline phases embedded in the material. On the assumption that amorphous phase thickness and microcrystals diameter are close, we can conclude that the etching process of amorphous parylene-like film is significantly more effective than the etching of the crystalline phases embedded in the material.

References

[1] T. Belmonte, J.M. Thiebault, H. Michel, R.P. Cardoso, A. Maliska J. Vac. Sci and TechnolA .Part 1 20(2002) 1347-1352 and Part 2 20(2002) 1353-1357

[2] D. Mezerette, T. Belmonte, R. Hugon, T. Czerwiec, G. Henrion, H. Michel Surface and Coating Technol. 169-170 (2003) 181-185

[3] M. Gaillard, P. Raynaud, A. Ricard Plasma and Polymers 4 (1999) 241-246

[4] B. Mitu, S. Bauer-Gogonea, H. Leonhartsberger, M. Lindner, S. Bauer, G. Dinescu, Surface and Coating Technologies, 174-175 (2003) 124-130

[5] H. Yasuda, Glow discharge polymerisation, in: J.L. Vossen, W. Kern (Eds.), Thin Film Processes, Academic Press, New York, San Francisco, London, 1978, pp. 361-400.

Gas absorption properties of plasma deposited organosilicon thin films

Y. Segui[1], S. Sahli[2], A. Bellel[2], S. Mouissat[2]

[1] *Laboratoire de Génie Electrique, University of Toulouse/ CNRS, France*
[2] *Laboratoire de Microsystemes et Instrumentation, University Mentouri of Constantine, Algeria*

Introduction

It is well known that plasma polymer films are not perfectly stable after deposition. This change is due to chemical reactions of radicals with themselves and with the surrounding molecules.
In most cases these undesirable evolutions is considered as a drawback to use these films in microelectronics devices. However it was proposed to gain benefits from gas absorption on plasma films by developping gas sensors. (1–3). On the other hand during the deposition process adsorption of species at the surface is one of the key phenomena controlling the growing process. It is then important to analyse the adsorption of gases especially the monomer molecule introduced in the plasma reactor. In this paper adsorption of various gases : organosilicon monomer, H_2O, alcool, ketones at the surface of plasma films was observed and analysed as a function of the nature of the gas and the plasma parameters used for the deposition . Hexamethyldisiloxane (HMDSO) was used as a monomer and a quartz crystal microbalance (QCM) measures the thickness and the deposition rates and the mass adsorbed on the film after the introduction of different gases in the reactor.

Experiments:

A bell jar reactor with two parallel plate electrodes was used for deposition of plasma films from HMDSO. A silicon substrate is located on the lower electrode to measure the thickness of the film. The plasma is powered by a low frequency power supply (7 kHz) and the power was actually calculated from the measurements of the discharge current voltage across the electrodes and phase between current and voltage signals.. The reactor is first pumped down to 10^{-3} mbars then the monomer is introduced and the working pressure adjusted with a needle valve.
The quartz crystal was mounted at the edge of the plasma. Of course the deposition rate on the quartz was much smaller than on the substrate.
The resonance frequency of the quartz before any deposition was 6 MHz. The sensitivity of the oscillation frequency shift was 1 Hz and is directly related to the mass deposited on the quartz crystal. The well known Sauerbrey equation (4)

$$T_f = (N_q d_q / d_f f_q^2)\,(f_q - f_c) \qquad (1)$$

where T_f is the film thickness (deduced from the mass, density and deposition area)

d_q and d_f are the quartz and film densities

N_q a constant depending on the quartz

f_q and f_c are the resonant frequencies for the uncoated and coated quartz

gives a relationship between the frequency shift and the deposited mass. Note that in our case, the frequency shift was always negligible compared to the oscillation frequency (Hundred Hz against MHz), the deposited mass is then proportional to the frequency shift.
In our experiment we first start by depositing a film. The deposited thickness was recorded by the measurement of the frequency shift assuming density of 2 g/cm^3. Then the reactor was pumped down and various gas introduced. Then the frequency shift due to the absorption of molecules from the gas phase was recorded as a function of time.

Results and discussion:

Figure 1 shows the frequency shift during several successive depositions. It can be pointed out that the deposition rate is different during the two first runs then reaches a stable value. We believe this result show the role of the nature of the substrate. The surface was initially made of a gold layer deposited on the quartz; this surface was step by step covered by the plasma film As soon as the initial quartz surface was completely coated, the growth rate remains constant.

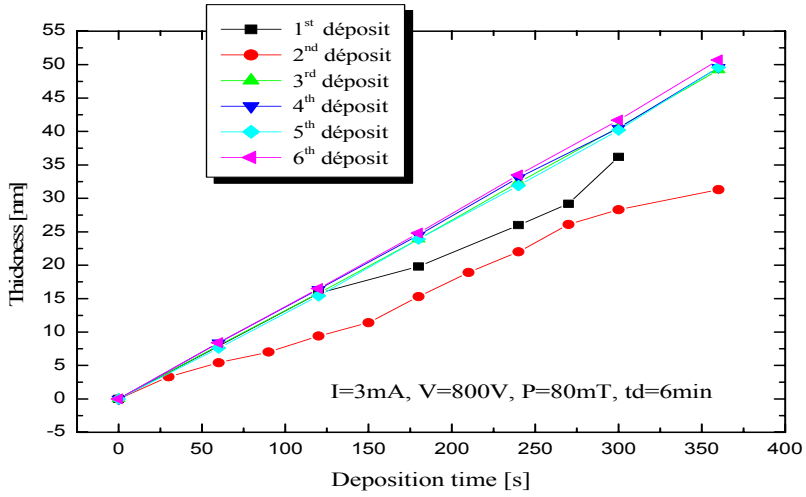

Figure 1 : Deposition kinetics for successive layers on the same quartz substrate

Monomer and water adsorption on the deposited film:

During the deposition process monomer molecules as well as its fragments adsorb on the surface of the growing film and contribute to its formation . It is then interesting to get a quantitative evaluation of this effect at least for monomer molecules.

Figure 2 shows the frequency shift due to the adsorption of HMDSO molecules on plasma deposited film from HMDSO. In this experiment, the pumping units were stopped after deposition. The valve introducing HMDSO was wide open ; then we assumed that adsorption occurs at the vapour pressure of HMDSO at 20°C which is about 40mBars. For comparison, adsorption on uncoated quartz was shown on the same figure. Obviously the plasma deposited layer enhanced the mass adsorbed on the surface. Also, the adsorption kinetic is slow since a steady state wasn't reached after 60mn.

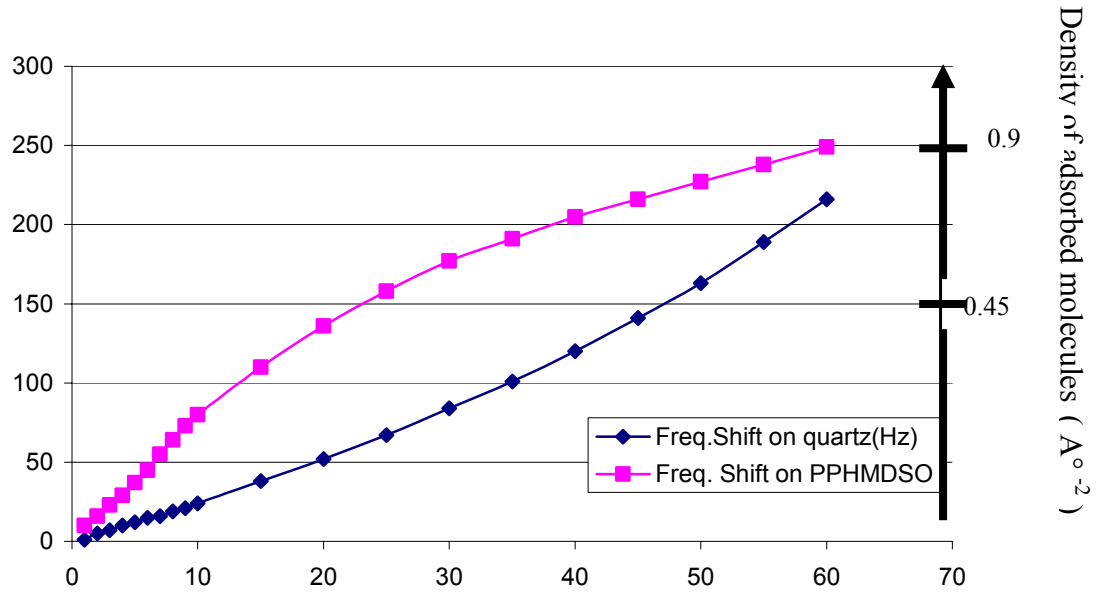

Figure 2: Adsorption of HMDSO molecules on Plasma polymerized HMDSO films and on the uncoated quartz.

Firstly, we checked that the frequency shift was not induced by some change in the working pressure in the reactor; in fact no change was recorded if argon is used to fill the reactor from the base pressure to 100 mBars. Hence the frequency shifts observed later are due to the absorption of molecules on the plasma film.
A larger adsorption might be due to an increase of the roughness (under certain conditions, plasma films deposited from HMDSO exhibited a "cauliflower" shape which increases the real surface interacting with the gas phase) [5]. Roughness measurements gave the same values for coated and uncoated quartz. Then only the nature of the surface can explain the differences in the amount of HMDSO adsorbed.
It is well known that QCM is only sensitive to the mass. It is useful to calculate the number of adsorbed molecules per unit area. This calculation is made using Eq (1), the mass of HMDSO (162 uma)and the Avogadro number. The practical equation becomes :

$$n\ (cm^{-2}) = 4.56 \cdot 10^{13}\ \Delta f\ (Hz)$$

where n is the number of adsorbed molecules per square centimetre.
The result of this calculation is given on the vertical axis on the right side of the figure.
The experimental values show that some of the adsorbed molecules diffuse into the film or we might have several adsorbed layers. For example, a frequency shift of 300 Hz would mean 1.4 molecules per $A°^2$ which is obviously impossible if a single monolayer without diffusion into the film is considered.
Another interesting molecule is water. Same procedure than before was followed: after deposition, pumping system was stopped then water vapour was introduced and it is assumed that the adsorption process took place under the water vapour pressure at 20°C which is
Figure 3 shows the adsorption kinetic of water molecules on coated and uncoated quartz. Also the mass was translated in terms of molecules per unit area (vertical axis on the right side).
A larger adsorption was also observed on the plasma film compared to the uncoated quartz.

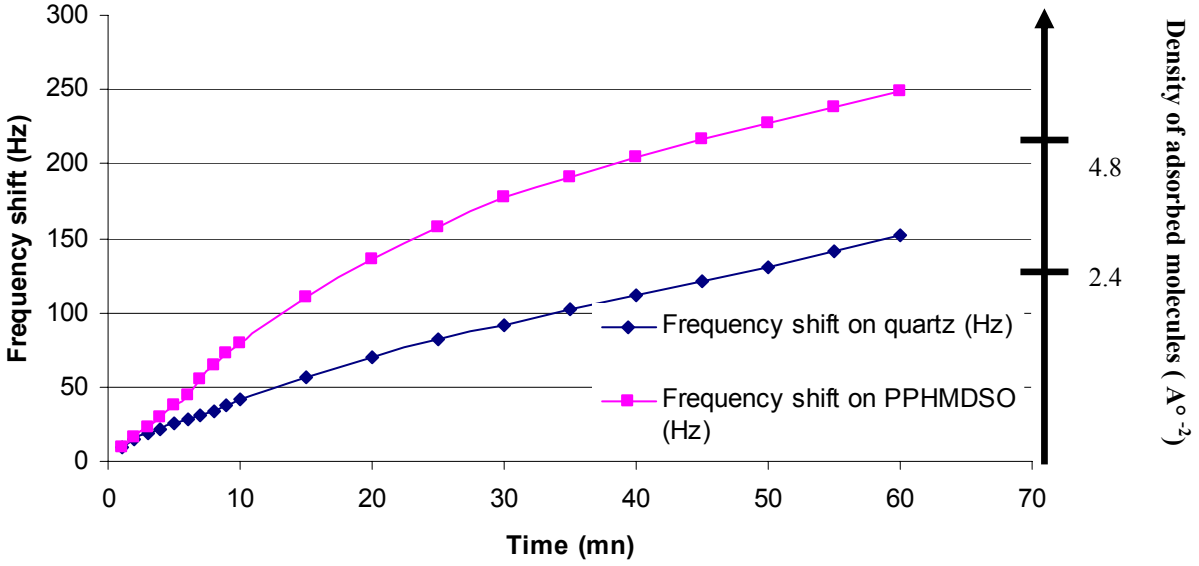

Figure 3 : Frequency shift (left axis) and density of water molecules adsorbed (right axis) on a quartz surface and on a plasma deposited film from HMDSO

Calculations of the number of water molecules adsorbed per unit area on the surface gave the practical equation:

$$n\ (cm^{-2}) = 24.18\ \ 10^{13}\ \Delta f\ (Hz)$$

A frequency shift of 200 Hz gives 48.36 10^{15} molecules /cm^2 which corresponds to 4.8 molecules / $A°^2$.
The size of o water molecule is about 9 $A°^2$. Then water molecules are probably diffusing inside the film or form clusters at the surface or both.

Same experiments using different thicknesses have been made. The idea is that if there is no diffusion inside, adsorption would be independent of the thickness since the surface will be supposed the same for each sample.
Results are shown on figure 4. Obviously there is an effect of the thickness. Surprisingly, it seems that the adsorption is reduced whereas the thickness of the film increases. We expected an opposite variation. The reason could be due to our experimental procedure. In fact a plasma film is deposited then, absorption measurements are carried out. In a second step a second layer was deposited on the first one and new absorption measurements are made and the thickness in supposed to be the addition of the two layers. So, some errors could be introduced due to the fact that several successive absorption measurements are made on the same quartz and there is no evidence that all the adsorbed molecules during the first step desorbed before the second step. Nevertheless, if the surface was the only parameter controlling absorption no differences would be expected because the plasma parameters for deposition were kept constant. Then, surface and subsurface properties are involved in the adsorption process.

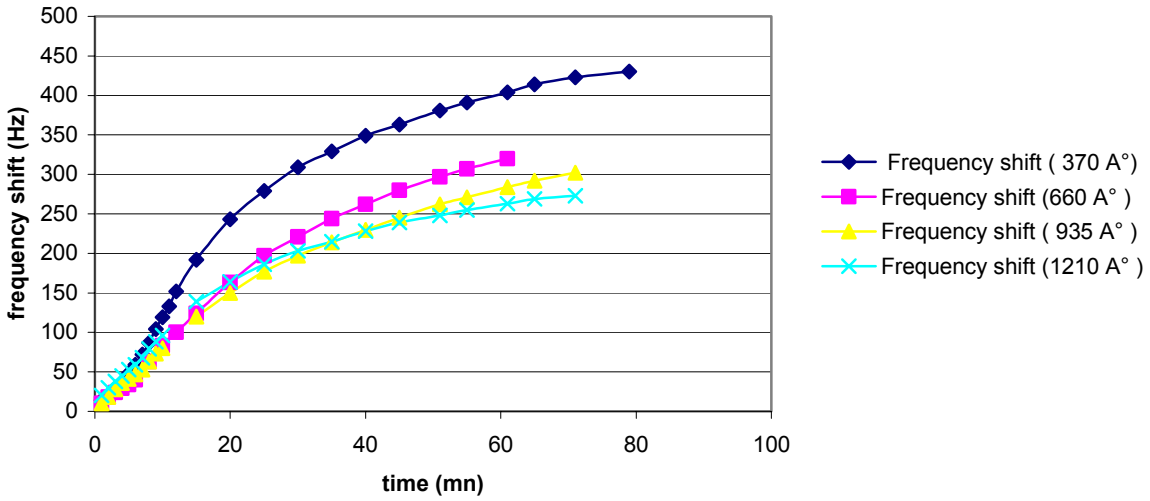

Figure 4: Frequency shift due to adsorbed water on plasma deposited HMDSO films of different thicknesses.

Adsorption of HMDSO, water , ethanol and propanol:
A comparison of HMDSO, water and two alcohols was made to control the role of the polarity and size of the adsorbed molecules. A plasma film 100nm thick was deposited from HMDSO. Then the tested molecules were introduced. For each experiment the pressure of the gas phase is the vapour pressure at 20°C.
Figure 5 shows the results in terms of frequency shift . These results could lead to a wrong estimation of the adsorption process. In fact they have to be translated in terms of number of adsorbed molecules per unit area, as shown on figure 6. A° square has been choosen for a better representation of the phenomena at a molecular scale.

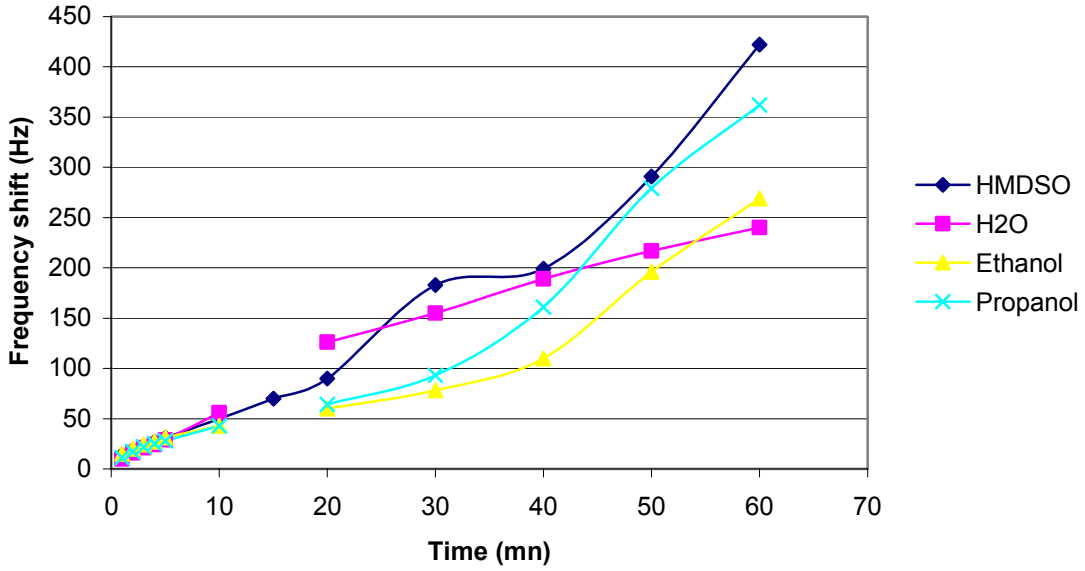

Figure 5 : Frequency shift due to the mass adsorbed on the plasma film for four different molecules.

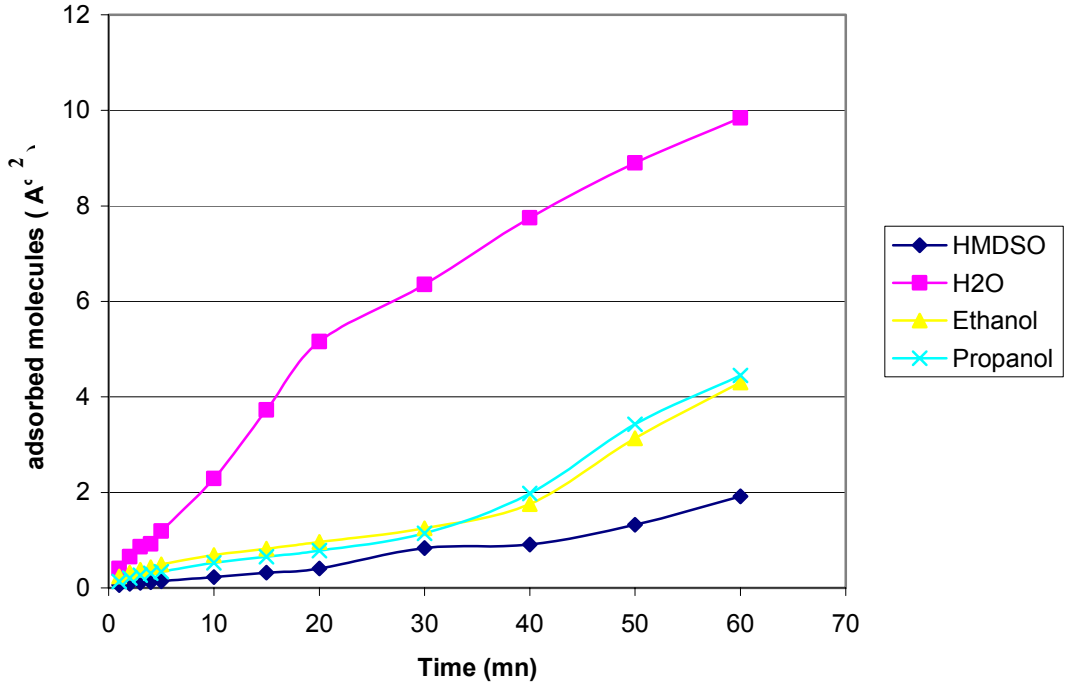

Figure 6 : Results of figure5 re- plotted in terms of number of adsorbed molecules per $A°^{2}$

Now it can clearly be seen that the large and weakly polar HMDSO molecules are much less adsorbed than the smaller and polar water and alcohol molecules. Size effect between ethanol and propanol doesn't play an important role. Water is the most easily adsorbed molecule and their densities clearly involve either a diffusion process inside the film or clusters of molecules at the surface.

Effect of the structure of the surface on the absorption:

Up to now, all the experiments where made on plasma deposited films from pure HMDSO. Previous papers report and discuss the structure and composition of these films [6 – 8]. As expected from the structure of the monomer, - Si – O – Si – is the backbone of the plasma polymer film. The presence of C – H and Si – $(CH_3)_x$ IR absorption bands (with x = 1, 2 or 3) give evidence of the organic part of the deposit.

Before adsorption experiments, these films are submitted to an oxygen plasma. The result of this post treatment is to crosslink the first monolayers due to the etching of the organic part of the plasma film.
A typical example of the effect of the post treatment on HMDSO and water adsorption is given on figure 7.

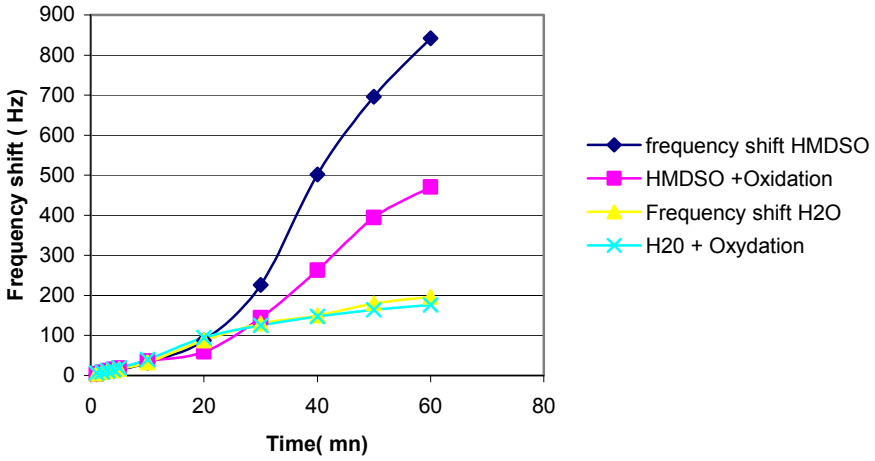

Figure 7: Adsorption of HMDSO and H2O molecules before and after a post treatment of plasma films by an oxygen plasma.

The post treatment reduces by a factor of 2 the mass of HMDSO adsorbed . This is probably due to the crosslinking of the first monolayers of the plasma film making much more difficult the diffusion into the bulk. Moreover a closer examination of our results shows that the treatment has almost no effect during the first 15 mn . Up to this time the surface is mainly involved ; diffusion process become important at longer times whereas all the adsorption sites on the surface are occupied.
Water molecules due to their much smaller size are not very sensitive to the crosslink as shown on figure 7.

Conclusions:

Adsorption of non polar, polar, large and small molecules on plasma deposited HMDSO films have been carried out. A quantitative evaluation of the mass and number of molecules adsorbed was made using a QCM which gives a very good sensitivity. Adsorption is in all cases much larger on plasma films than on a uncoated quartz crystal. We demonstrate that this difference is not due to a change in the roughness. Among all the molecules tested so far, largest adsorption occurs for water molecules probably due to their ability to diffuse inside the film. The lowest adsorption was observed for the molecules use to produce the plasma film. They are weakly polar and their size is very large. Crosslinking the surface of the film using an oxygen plasma reduces drastically the adsorption of large molecules and doesn't change the adsorption of water.

References

[1] V. Georgieva, E. Radeva, L. Spassov – Vacuum 58(2000)
[2] F. Kraus, S. Cruz, J. Müller – Sensors and Actuactors B88 (2003)
[3] M.L.P. da Silva, I.H. Tan, A.P. Nascimnto Filho, E. Galeazzo, D.P. Jesus – Sensors and actuactors B91(2003)
[4] G.Z. Sauerbrey Physik 155, (1959)206
[5]D. Hegemann, U. Vohrer, C. Oehr and R. Riedel- Surface and Coatings Technologies 116-119(1999)1033
[6] Y. Ségui, Plasma déposition from organosilicon monomers in Plasma Processing of Polymers, NATO ASI Series Applied Sciences, Vol 346, 1997 ; R. d' Agostino, P. Favia and F. Fracassi Editors
[7] P. Raynaud, B. Despax, Y. Ségui and H. Caquineau – Plasma Processes and Polymers, 2(2005) 45
[8] K. Aumaille, C. Vallée,A. Granier, A. Goullet, F. Gaboriau, G. Turban Thin Solid Films, 359(2000)188

Surface Sterilization Using a Low-Temperature Atmospheric Plasma Brush

Q.S. Yu,[1] C. Huang,[1] F.-H. Hsieh[2], H. Huff,[2] Y.X. Duan[3]

[1]*Department of Chemical Engineering, Center for Surface Science and Plasma Technology, University of Missouri-Columbia, Columbia, MO 65211, USA*
[2]*Department of Biological Engineering, University of Missouri-Columbia, MO 65211, USA*
[3] *Los Alamos National Laboratory, Los Alamos, NM 87545, USA*

Abstract

This study investigated the sterilization effects of a new atmospheric plasma source, which is a brush-shaped direct current (DC) glow discharge of argon created under one atmospheric pressure. With nutrient broth and standard methods agar as supporting media, a cell reduction in a level of 6 orders of magnitude was observed for both *Escherichia coli* and *Micrococcus luteus* with a few minutes of plasma treatment. The plasma treatment effects on the bacteria cell structures were examined using scanning electron microscopy (SEM).

Keywords: DC glow discharge; atmospheric plasma; sterilization; *Escherichia coli*; *Micrococcus luteus*

Introduction

Rapid, safe, and effective sterilization process is of utmost importance in protecting not only the hospital patients, but the public in general by supplying safe foods, clean water and air. Although the traditional heat based sterilization methods are being extensively used, there is urgency in developing new and improved technologies for sterilization, pasteurization, disinfection. Such urgency is because of the more and more extensive use of heat-sensitive tools nowadays as well as the appearance of heat-resistance microorganisms, such as prion, the protein which causes Creutzfeldt-Jacob disease, more commonly known as "mad cow disease" [1]. In these cases, the traditional heat-based sterilization techniques such as autoclaving (moist heat) and ovens (dry heat) are not suitable.

Sterilization by low-temperature plasmas, which are partially ionized gases, is an alternative to conventional and/or traditional sterilization methods. Low-temperature plasmas, which can be easily created at low-pressure (e.g., less than 10 torr) by applying an electrical field, contains a huge amount of reactive species including various atoms, ions, energetic electrons, UV irradiation. Because of the existence of these reactive plasma species, low-temperature plasma technique has proven to be an effective alternative to many existing sterilization methods. Since early 1990s, several types of plasma sterilizers are now commercially available in the market and are being used in biomedical areas [2]. In spite of their excellent sterilization efficiency, the currently available plasma sterilization processes with regard to medical uses have several major limitations, such as the restricted volume of the plasma reactor and one or more vacuum and chemical cycles required during the process.

Low-temperature atmospheric plasma is a new emerging plasma technology. Because it is operated in open-air, the use of such an atmospheric plasma torch can easily overcome the limitations imposed by the currently available vacuum-based plasma sterilizers. Since it is operated at one atmospheric pressure, atmospheric plasma eliminates the use of vacuum equipment and thus significantly reduces the cost as well as the operation complexity. Such atmospheric plasma techniques can be used not only for surface sterilization and/or decontamination in biomedical, food areas, but also with potential applications in biological warfare defense such as in killing anthrax or other biological warfare agents [3-5].

Results and discussions

In this study, a novel atmospheric cold plasma technology, an atmospheric cold plasma brush (ACPB) [6] with a proprietary design, was investigated for a rapid and effective destruction of various bacteria. The pictorially views of this plasma source operated with argon gas is shown in Fig. 1.

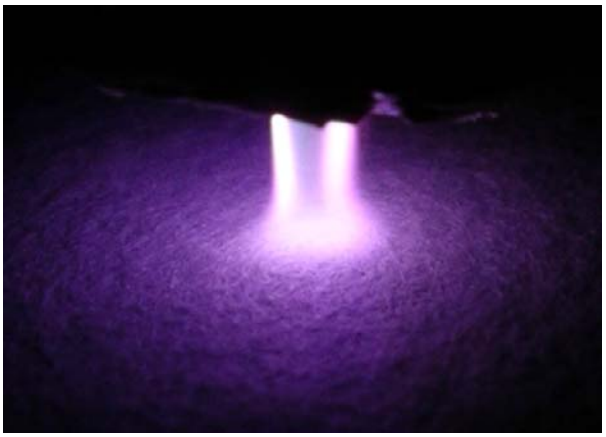

FIGURE 1. Pictorial view of APB plasma source.

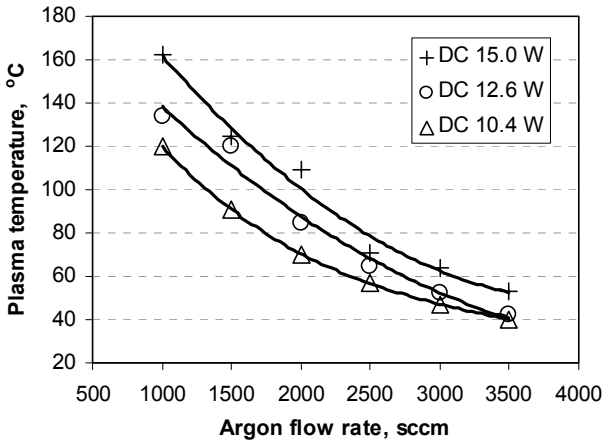

FIGURE 2. Gas phase temperature of APB with argon flow rate.

Such an atmospheric argon plasma source can be operated under very low electric power level (several watts), and as a result very low plasma temperature can be achieved [6]. Fig. 2 shows the gas temperature of this argon atmospheric plasma measured using thermocouple method at various plasma conditions. It can be seen the gaseous temperature of the plasma could reach 40 ^{o}C under the plasma conditions shown in Fig. 2.

1. *Plasma sterilization effects on Escherichia coli and Micrococcus luteus*

With filter papers as supporting media, bacteria of *Escherichia coli* and *Micrococcus luteus* were subjected to the low-temperature atmospheric plasmas of argon. The plasma conditions was controlled at 1500 sccm of argon flow and 15 W of DC power input, which give the gas phase temperature of 125 ^{o}C. Fig 3 shows the survival curves of the two bacteria as a function of plasma exposure time. As can be seen in Fig. 3, 90% of *Escherichia coli* were killed within 2 minutes of plasma exposure; and only 1% *Escherichia coli* colony was detected after 5 minute plasma exposure. In the case of *Micrococcus luteus*, 90% of the cells were killed after a 15 second exposure, while no colonies grew on the agar plate after a 3 minute plasma exposure.

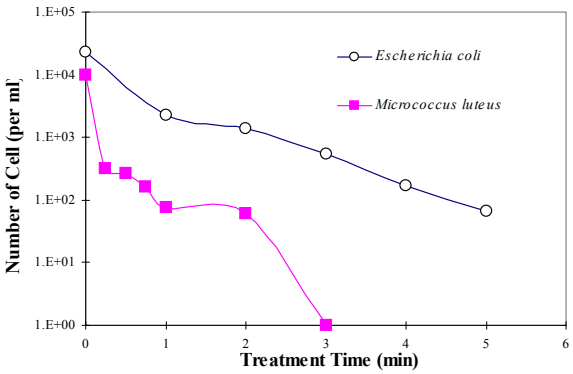

FIGURE 3. Survival curves of *Escherichia coli* and *Micrococcus luteus* on filter paper medium after argon atmospheric plasma treatment with argon flow rate of 1500 sccm and DC power input of 15 W.

2. *Effects of supporting medium*

The plasma sterilization effects on *Escherichia coli* and *Micrococcus luteus* were investigated with different supporting media, including nutrient broth, standard methods agar, and the filter paper. Fig. 4 shows the survival curves of two bacteria on these supporting media upon argon plasma exposure. As shown in Fig. 4, among the three media, plasma treatment enables the fastest cell reduction of 6 orders of magnitude on nutrient broth. When seeded in nutrient broth, a 6 orders of magnitude *Escherichia coli* cell reduction requires 3 minute plasma treatment; and *Micrococcus luteus* needs 2 minute plasma exposure. With standard methods agar, one

more minute plasma treatment is required for *Escherichia coli* when compared with nutrient broth media. While seeded in filter paper, both two bacteria needs the longer exposure times in order to achieve the similar level of cell reduction.

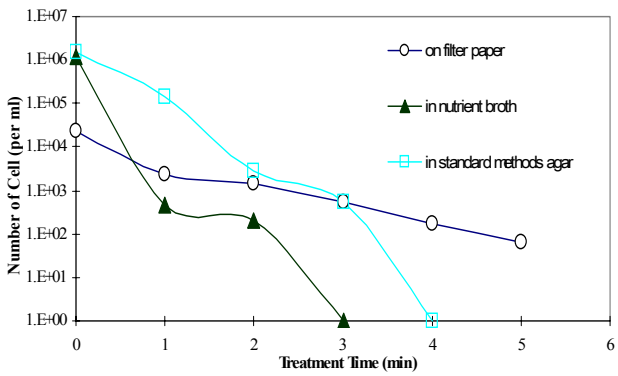

(a) *Escherichia coli*

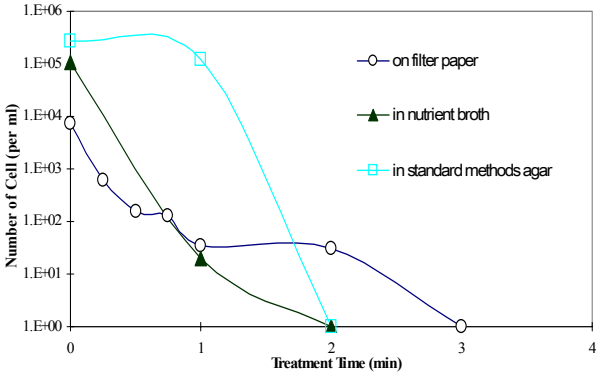

(b) *Micrococcus luteus*

FIGURE 4. Survival curves of (a) *Escherichia coli* and (b) *Micrococcus luteus* in various supporting media after argon atmospheric plasma treatment with argon flow rate of 1500 sccm and DC power input of 15 W.

The fast plasma killing of the two bacteria on nutrient broth is mainly because of the direct attack of plasma species on the bacteria cells. It was observed that the droplets of the nutrient broth dried out within one minute plasma exposure. This enables direct contact of the plasmas to the bacteria cells. With nutrient broth as supporting medium, no stain of *Escherichia coli* and *Micrococcus luteus* was observed after 4 minute plasma treatment. A possible reason for the very different plasma sterilization time is the plasma penetrating efficiency with different culture mediums. The filter paper used in this study is a porous solid and requires plasma penetration to kill the bacteria cells resided inside the pores. The colloid state of agar could slow down the plasma penetration but was eventually destroyed through evaporation of water with longer plasma treatment time.

3. *Effects of heat and gas blowing on cell reduction*

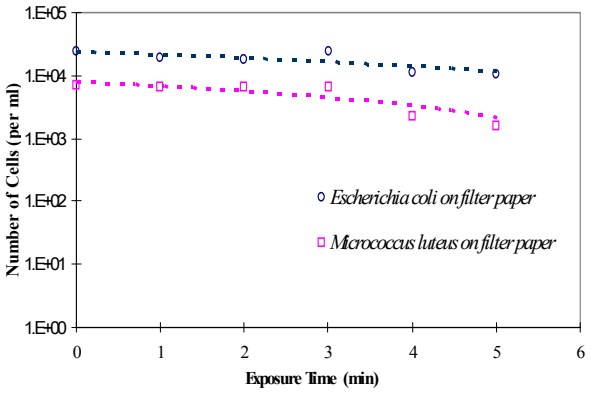

(a) dry heat effect

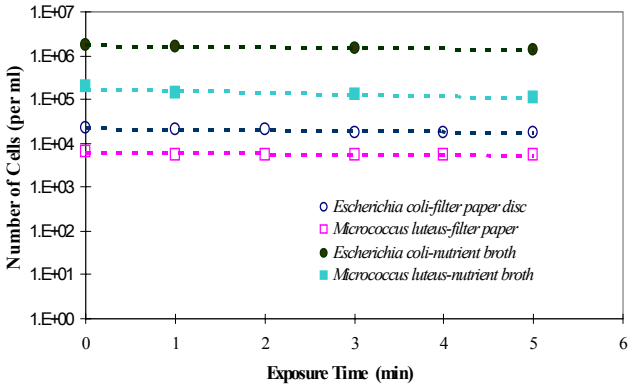

(b) gas blowing effect

FIGURE 5. Sterilization effects of at 125°C and at a 1500 sccm on Escherichia coli and Micrococcus luteus seeded on filter paper and nutrient broth.

In order to distinguish the plasma sterilization effects from the possible heat effect of the plasmas, a sterilization test to elucidate the dry heat effect was performed using a temperature controllable oven (Fisher Scientific Isotemp Vacuum Oven Model 282 A). Under the operating condition studied, the gas phase temperature of the

argon plasmas was 125 ^{o}C. Therefore, *Escherichia coli* and *Micrococcus luteus* on filter papers was kept inside the oven with temperature set at 125 ^{o}C. The cell survival curves of the two bacteria subjected to the dry heat was shown in Fig 5(a). It was confirmed that the 125 ^{o}C dry-heat treatment did not show any killing effect on both bacteria within 5 minute exposure. These data indicated the heat carried by the argon atmospheric plasmas did not contribute to the sterilization effects shown in Figs. 3 and 4.

A high follow rate of argon higher than 500 sccm is necessary in order to blow the argon glow discharge out of the discharge chamber and form a free brush-shaped plama jet. To determine if the high flowing plasma gas could blow the bacteria cell off the supporting media, the blowing effect of argon gas on the two bacteria was examined by flowing the argon gas at the same flow rate (1500sccm) without igniting electrical discharge. Fig. 5 (b) shows the cell survival curves of *Escherichia coli* and *Micrococcus luteus* on different supporting media with argon gas blowing on the surface. From Fig. 5 (b), it can be seen that the high flow argon gas did not reduce the cell number of both bacteria on all three supporting media. The results shown in Fig. 5 indicate that the sterilization effects of argon plasmas are due to the presence of reactive plasma species, but not the heat or the high flowing gas it carries.

4. *Effects of plasma conditions*

In creation of atmospheric plasmas, the power input and gas flow not only affect the plasma density, but also the plasma temperature s shown in Fig. 2. Consequently, it is expected that these plasma operating parameters should have a certain degree of influence on the plasma sterilization results. Therefore, the effects of power input and argon flow rate of the plasma on the sterilization of the two bacteria were also examined.

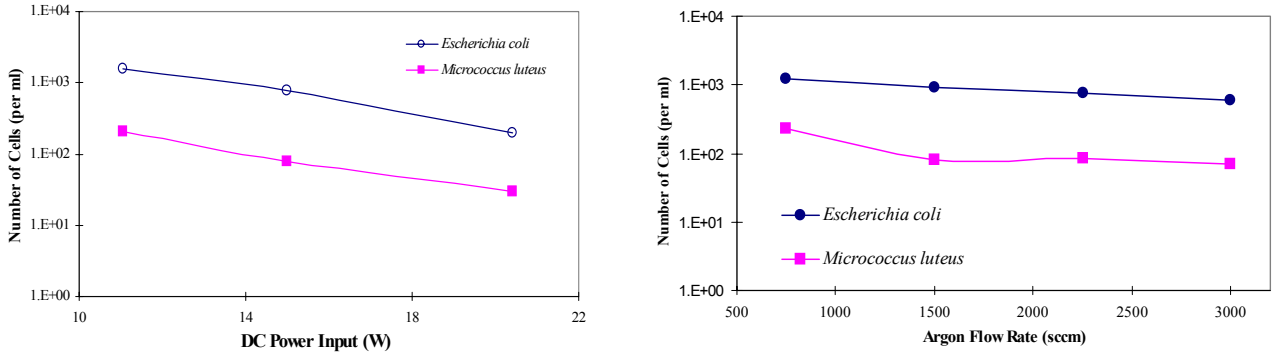

FIGURE 6. The surviving cell numbers of *Escherichia coli* and *Micrococcus luteus* on filter papers as a function of plasma parameters: (a) plasma power and (b) argon flow rate after 1 minute plasma treatment under condition, if not specified in the plots, of 1500 sccm argon and 15 W DC power input.

Fig. 6(a) shows the cell survival number changes of both *Escherichia coli* and *Micrococcus luteus* on filter paper medium with DC power input of the plasma under a fixed argon flow at 1500 sccm and plasma treatment time of 1minute. It can be seen that higher DC power input did result in fast killing of both bacteria. Fig. 6(b) shows cell survival number changes of the two bacteria with argon flow rate of the plasmas under a fixed DC power of 15 W and plasma treatment time of 1 minute. Since it doesn't affect plasma density, the change of argon flow rate in the plasmas did not affect the bacteria killing rate.

5. *Effects of remote plasma* exposure

In atmospheric plasmas, the plasma species could lose its energy or reactivity in a very short time due to the much higher collision frequency among the plasma particles. The life time of the reactive plasma species is much shorter when compared to that in low-pressure plasmas. As a result, the plasmas could lose their reactivity dramatically in a remote position (away from the glow). To examine the sterilization effects of a remote plasma, the bacteria seeded in filter papers were subjected to plasma exposure in the down stream at a position 2 mm away from the glow. The long-life plasma species from the plasmas were allowed to diffuse and get in contact with the bacteria cells resided on the supporting media. Fig. 7 shows a comparison of the cell survival curves of

the two bacteria upon a remote plasma exposure and direct plasma exposure. It was observed that the remote plasma exposure causes much slower cell reduction on *Micrococcus luteus* than the direct plasma exposure.

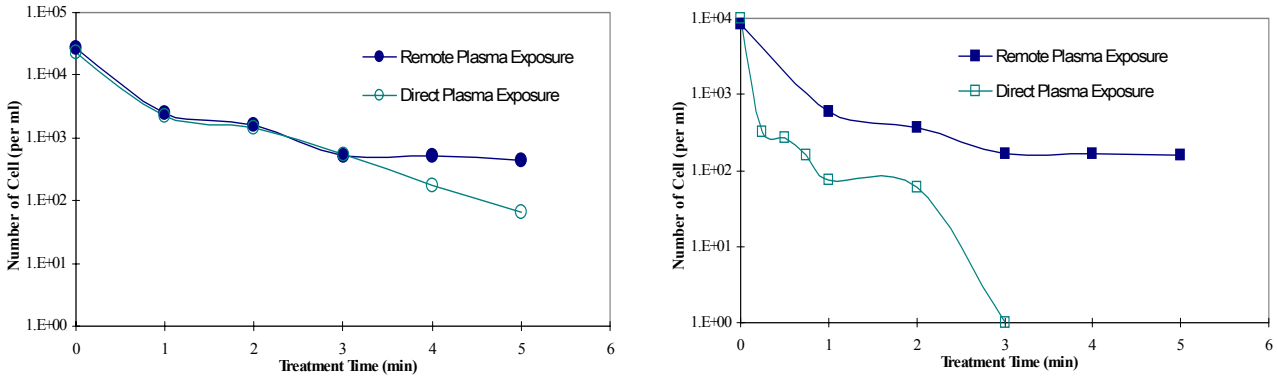

(a) *Escherichia coli* (b) *Micrococcus luteus*

FIGURE 7. Comparison of the survival curves of *Escherichia coli* and *Micrococcus luteus* on filter papers under direct plasma exposure and remote plasma exposure (2 mm away from the plasma glow). Argon atmospheric plasma conditions are 1500 sccm argon and 15 W DC power input.

6. *SEM images of plasma treated Escherichia coli and Micrococcus luteus*

SEM measurements were used to examine the cell structure changes of the two bacteria upon plasma treatments. Figs. 8 and 9 show the SEM images of untreated and plasma treated *Escherichia coli* and *Micrococcus luteus* respectively. From Fig. 8, it was observed that the *Escherichia coli* cells were severely damaged and only some cell debris was detected by SEM with the argon plasma sterilized samples. The SEM measurements on *Micrococcus luteus* shown in Fig. 9 provided the similar information, i.e. the bacteria cells were damaged by argon plasma treatment. After the plasma treatment, the size of *Micrococcus luteus* cells was significantly reduced and the shape of the dead cells was distorted. The distorted cell shape shown in Fig. 9 indicated that the lipid moieties have been lost after the plasma treatment.

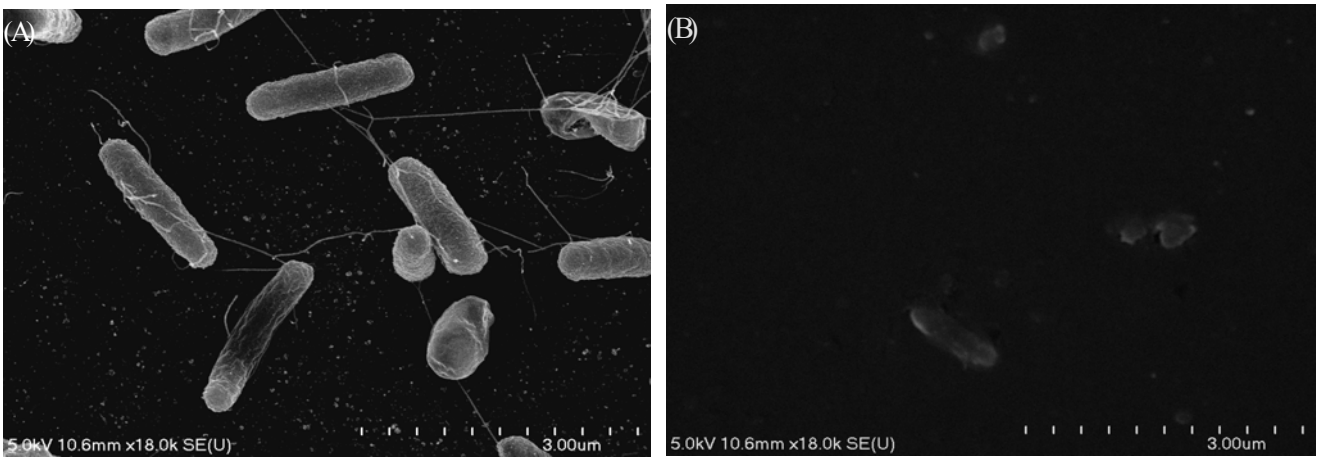

FIGURE 8. Scanning electron micrographs of (A) untreated *Escherichia coli* control and (B) 5 min plasma treated *Escherichia coli* seeded on filter paper under plasma condition of 1500 sccm and 15 W DC power input.

A possible sterilization mechanism of argon atmospheric plasma is the continuous impact on the bacterial cells by energetic plasma species such as argon ions, electronically excited neutrals. The characteristic energies of the argon ions and neutrals is in the level of ~ 15 eV and >11 eV, which are much higher than the bonding energy of the organic molecules constituting microorganisms. Thus, even simple argon plasmas should have sterilization ability to destroy various microorganisms. D.A. Mendis et al. suggested charged particles might cause the

rupture of the outer membrane of the bacterial cell [7,8]]. Therefore, the plasma exposure could eventually damage the cell structure or the cell membrane, and consequently destroys the viability of the cells.

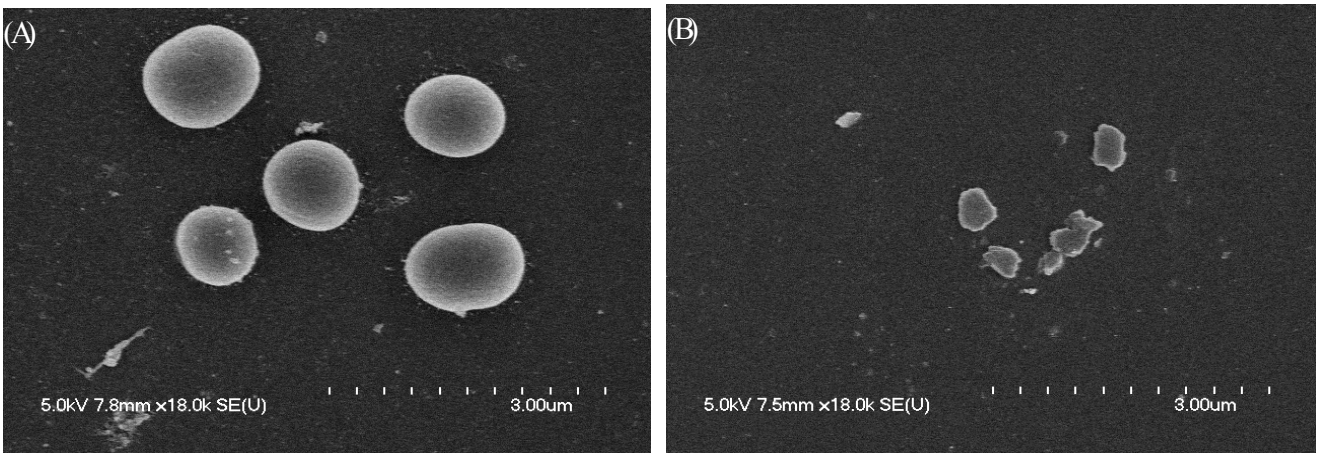

FIGURE 9. Scanning electron micrographs of (A) untreated *Micrococcus luteus* control and (B) 5 min plasma treated *Micrococcus luteus* seeded on filter paper under plasma condition of 1500 sccm and 15 W DC power input.

Conclusions

The plasma sterilization capability demonstrated through this study indicated the tremendous potential of this low-power driven atmospheric plasmas as a promising alternative sterilization technique. Such a low-power atmospheric plasma source is cost effective in both fabrication and operation, simple and safe to use, requires much less treatment time as compared with traditional sterilization methods. The low-power feature of such an atmospheric plasma source makes it not only applicable to various heat-sensitive materials or device, but is also practical to assemble an array of individual plasma brushes for sterilizing large surface or object. This study is our first step to demonstrate the applicability of low-power atmospheric plasma source in sterilization application. Further investigation focusing on elucidation of plasma chemistry effects on sterilization efficiency are being performed in our laboratories and the results will be reported and published in due course.

Acknowledgement

This study was supported by the Faculty Startup Funds of College of Engineering and the Bioprocessing and Biosensing Center of University of Missouri-Columbia (MU). The authors would thank the personnel of MU Electron Microscopy Core Facility for performing the SEM measurements.

References

[1] M. Laroussi, "Plasma-based sterilization", International Conference on Phenomena in Ionized Gases, Proceedings, 26th, Greifswald, Germany, July 15-20, 2003, **4,** 11-12, (2003)

[2] P. T. Jacobs and S. M. Lin, "Sterilization Processes Utilizing Low-Temperature Plasma", in "Disinfection, Sterilization and Preservation", 5th, edition, SS. Block Ed., Philadelphia, Lippincortt Willams & Wilkins, p.747-763 (2001).

[3]M. Laroussi, IEEE Trans. Plasma Sci., **vol. 24**, no. 3, p. 1188-1191 (1996).

[4] K. Kelly-Wintenberg, A. Hodge, T. C. Monite, L. Deleanu, D. Sherman, J. R. Roth, P. T. Tsai, and L. C. Wadsworth, J. Vac. Sci. Technol. A, **vol.17**, no. 4 , p. 1539-1544 (1999).

[5]K. Kelly-Wintenberg, T. C. Monite, C. Brickman, J. R. Roth, A. K. Carr, K. Sorge, L. C. Wadsworth, and P. T. Tsai , J. Industrial Microbiol. Biotechnol., Vol. **20**, no. 1, p. 69-74 (1998).

[6] Y.X. Duan, C. Huang, and Q.S. Yu, "Low-temperature direct current glow discharges at atmospheric pressure", IEEE Trans. Plasma Sci., in press (2005)

[7] D.A. Mendis, M. Rosenberg, and F. Azam, IEEE Trans. Plasma Sci., **vol. 28,** no. 4, p. 1304 (2000).

[8] M. Laroussi, D.A. Mendis, and M. Rosenberg, New Journal of Physics, **vol. 5**, p. 41.1-41.10 (2003).

Absolute Cross Sections of C_{60}^-, C_{60}^+ Formation, Electron and Photon Thermoemission Induced by Electron Impact

A. A. Vostrikov[1, 2], D. Yu. Dubov[1, 2], A. A. Agarkov[1], S.V. Drozdov[1], V. A. Galichin[1]

[1] *Institute of Thermophysics SB RAS, Acad. Lavrentyev ave., 1, Novosibirsk 630090, Russia*

[2] *Novosibirsk State University, Pirogova, 2, Novosibirsk 630090, Russia*

Abstract

The method of intersecting beams of C_{60} fullerene clusters and of electrons was used to investigate the formation of C_{60}^+ and C_{60}^- ions and the radiation. The ionization σ^+ and electron-attachment σ^- cross sections were measured for electron energy E_e = 0.1 ÷ 100 eV. For E_e < 0.5 eV, the formation of C_{60}^- was found to be defined by the polarization capture of an *s*-electron. The "delayed" ionization under collision of C_{60}^* with the surface was observed. The rate of radiative cooling of C_{60}^{+*} ion was found to be $5.5 \cdot 10^5$ eV/s at $T(C_{60}^{+*})$ = 3150 K.

1. Introduction

Fullerenes are distinguished by their exceptional stability towards fragmentation. The dominant dissociation channel – the evaporation of C_2 unit – begins within typical mass spectrometric time scale only after pumping into C_{60} cluster several tens of eV (see review [1] and references therein). This fact gives rise to different decay modes of these metastable highly energized nanoparticles, i.e. actively studied "delayed" autoionization of energy-rich C_{60} cluster [2]. Radiative cooling of C_{60} [3, 4] is competitive to decay channels.

Large number of inner degrees of freedom results in quasicontinuous function of C_{60}^- formation in reaction $C_{60} + e^-$ [5]. In this process the largest attachment cross section is achieved at $E_e \to 0$, and at E_e > 7.5 eV the C_{60}^- states which are unstable against electron auto-detachment are formed.

2. Experimental

Figure 1 shows the scheme of experimental setup. An electron beam 2.5 mm in diameter was formed with an oxide-coated cathode 1 and electron-optical diaphragms 2 and 3. Collector assemblies 5-7 ensured a complete accumulation and recording of the ions, $I^{+,-}$, and electron, i_e, currents. The electron energy E_e was set by the voltage between electrodes 1 and 4. The scale of energy E_e was calibrated by the retarding potential method. The retarding potential between electrodes 6 and 4 at which the current i_e was reduced by a factor of two was taken to be equal to E_e. The magnetic field between magnets 8 prevented the electron beam from broadening.

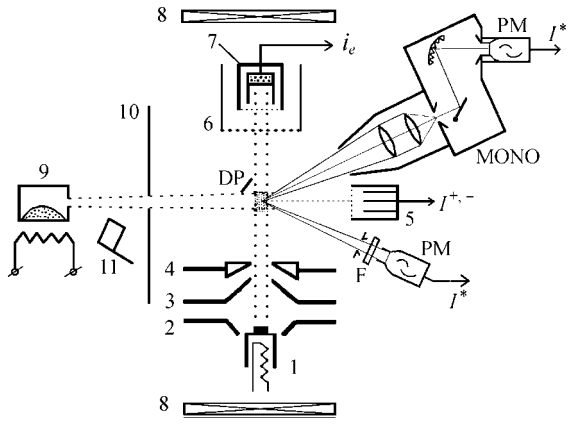

Fig. 1. Experimental setup.

The beam of fullerene clusters was formed by using C_{60} vapor flowing from an effusion source 9 through an opening 2.4 mm in diameter and was collimated by a diaphragm 10 with a 3-mm aperture. In order to take into account the contribution made to the ion current and to radiation by the background gas of the vacuum chamber (the pressure of this gas was about $4 \cdot 10^{-5}$ Pa), the C_{60} beam was cut off by an electromagnetic gate 11, whereby the ion current and the photon flux from the background gas could be measured.

In the energy region E_e greater than the width of the energy distribution function f_e(E) of electrons (0.3 eV

in this study), the absolute values of the cross section $\sigma^+(E_e)$ and $\sigma^-(E_e)$ are determined by the formula [6] $\sigma^{+,-} = I^{+,-} / (i_e \cdot n \cdot l)$, where n is the density of C_{60} clusters in the region of beam intersection, and l is the length of this region. The density n was determined on the basis of the weight of the C_{60} clusters condensed over a fixed time in a trap mounted on the beam path. For $E_e < 0.3$ eV, the cross section $\sigma^-(E_e)$ was determined by comparing the E_e dependences of the currents $I^-(C_{60}^-)$ and $I^-(SF_6^-)$. It is well known that the formation of SF_6^- ions is caused by *s*-electron capture and is characterized by a narrow resonance at $E_e \to 0$ [7].

Radiation from the region of beams intersection was recorded by a system of short-focus lenses, a monochromator (MONO) with the spectral range of 200-800 nm, inverse dispersion of 3.2 nm/mm, 0.3-mm slits, and a photomultiplier (PM). The spectral sensitivity of the optical system was determined with the aid of a reference tungsten lamp. In order to increase the signal, a wideband filter F with the transmission band at half-height of $\Delta\lambda$ = 150 nm and a center at λ = 500 nm could be placed instead of the monochromator. The spatial sensitivity of the optical system was determined by scanning with a point source.

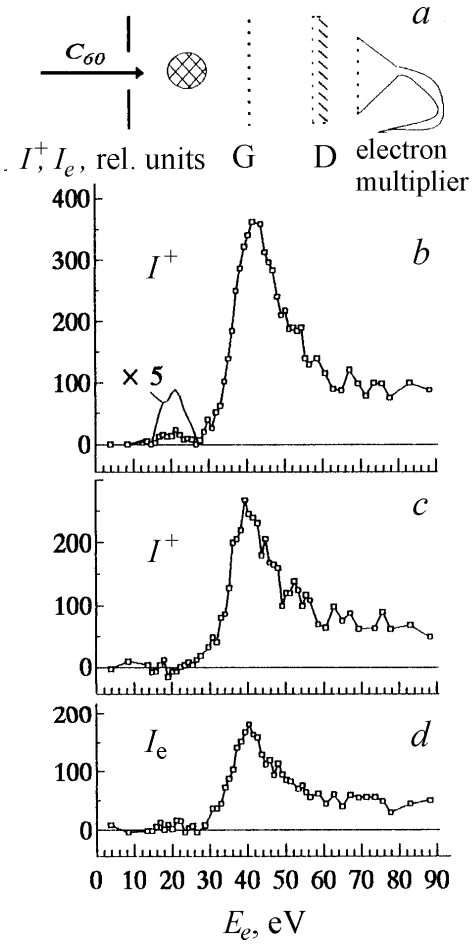

Fig. 2. Scheme of the surface-induced delayed ionization experiment (a); the behavior of ion (b, c) current and electron (d) current resulted from surface impact as a function of the energy E_e. The values of electrode voltages for grid G, dynode D and multiplier, respectively, are: (b) –30, +3200, –2100; (c) +30, –600, –2100; and (d) +30, –3200, –2100 V.

In order to identify the contribution of C_{60}^{+*} ions to the total radiation, an electric field between deflecting plates (DP) was applied to the beam intersection region. The fact that the field of the plates did not distort the geometry and the parameters of the electron beam was checked by measuring the intensity of radiation from the short-lived states of N_2^{+*} ($B^2\Sigma_u^+$) ion. The modulation of the electron beam (with a frequency of 80 Hz) and synchronous detection of signals improved the signal-to-noise ratio.

The effect of surface-induced ionization of C_{60}^{**} formed by electron impact was observed in an experiment with the scheme shown in Fig. 2a. The following elements were placed on the fullerene-beam axis downstream the region of intersection with the electron beam: at a distance of 26 mm – a grid G, then 3 mm from the grid – a louvered dynode D with the second grid in front of it, and 7 mm from dynode – a channel electron multiplier. The aluminum plates of the dynode D arranged at an angle of 45° with respect to the C_{60} beam were used as the target. The second grid in front of dynode ensures a uniform electric field between G and D. The total transparency of the grids was as large as 90%, therefore we disregard the collisions with their surface and take into consideration only collisional ionization of C_{60}^{**} with the louvered dynode. The primary C_{60}^+ and C_{60}^- ions that were formed upstream of the grid G were retarded by the field of the grid G and of the electrode D. This was tested at E_e = 0.2 and 52 eV, which correspond to the maximal cross sections for the formation of negative and positive C_{60} ions (see below). The time of C_{60} travel in the beam from the region of interaction with electrons to the grid G (estimated from the average velocity of C_{60} clusters in effusive beam at 744 K, 174 m/s) was about 150 μs.

3. Results and Discussions

Surface-induced C_{60} ionization. The formation of C_{60}^+ over a time scale of the order of the time it takes a molecule to traverse the

electron beam may be referred to as fast ionization. The term delayed ionization (DI) is used to denote the formation of C_{60}^{+} ions after the escape of an excited C_{60}^{*} cluster from the beam intersection region. An electron may be emitted from the cluster either because of the statistical distribution of energy over the internal degrees of freedom (thermionic emission) or upon decay of primary quantum excitation.

We know of only one study where DI was observed after the excitation of C_{60} by electron impact [8]. The electron-energy dependence of the DI current, $I^{+}(E_e)$, in [8] peaked at E_e = 43 eV and was attributed to the excitation of C_{60} to long-lived Rydberg states (longer than 130 μs) which decayed in an electric field.

In this study we have found the electron-induced formation of C_{60}^{**} metastable states, which decayed at surface collision with C_{60}^{+} formation. The Fig. 2b, c, d gives the E_e dependences of currents $I^{+}(C_{60}^{+})$ of ions and I_e of electrons formed at C_{60}^{**} impact to aluminum target in 150 μs after C_{60}^{**} formation. In contrast to the results of [8], we did not find any effect of electric fields up to 3.5 kV/cm. For this reason, we believe that the DI current was associated, first of all, with the existence of long-lived (metastable) electron-excited states C_{60}^{**}, which decayed into a C_{60} ion and an electron upon hitting the metal surface. The dependence $I^{+}(E_e)$ characterizes the cross section of C_{60}^{**} metastable states formation σ^{**}. The maximum of σ^{**} is shown to be at E_e = 41.5 eV. It is remarkable that this value is essentially equal to the threshold energy of fragmentation $C_{60} \rightarrow C_{58} + C_2$ by electron impact [9]. Possibly, the fragmentation limits the life-time of C_{60}^{**}. Note that, in Fig. 2, a small maximum is observed of the DI current at an energy E_e = 21 eV, which coincides with the plasmon excitation energy in C_{60} [12, 13]. This remarkable fact indicates directly that quantum excitations contribute to DI.

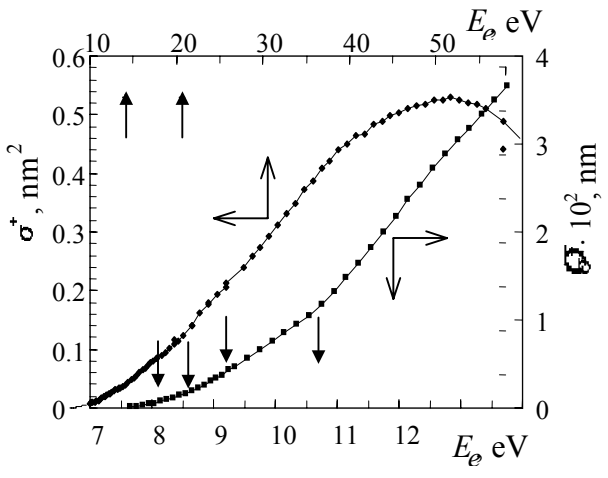

Fig. 3. Cross section of C_{60}^{+} formation.

Electron-induced ionization of C_{60}. The fast ionization of C_{60} by electron impact was investigated, for example, in [10, 11], with the cross sections $\sigma^{+}(E_e)$ measured there being markedly different. In this study, we measure the cross section $\sigma^{+}(E_e)$ up to E_e = 60 eV. The measured values of $\sigma^{+}(E_e)$ are given in Fig. 3, where the initial segment is shown on an enlarged scale. One can see that a maximum of $\sigma^{+}(E_e)$ = 0.53 nm^2 is attained at E_e = 52 eV. At the initial segment of the $\sigma^{+}(E_e)$ plot, we can clearly see breaks at E_e = 8.1, 8.6, 9.2, 10.7, 14.1, and 20.5 eV (indicated by arrows). These breaks correspond to autoionization states of C_{60}. The first two values coincide with the positions of breaks on the curves of $\sigma^{+}(E)$ for the photoionization of C_{60} [12]. The values of energy E_e = 10.7 and 20.5 eV are close to the plasmon excitation energy [13], and C_{60}^{2+} ions show up at $E_e \approx$ 20 eV [14].

Because the dependence $\sigma^{+}(E_e)$ proved to be linear between the breaks, we determined the ionization potential of C_{60}, U_i = 7.6 eV, by extrapolating the linear segment to the region E_e < 8.1 eV. For the ionization of C_{60} by synchrotron radiation, the value of U_i = 7.58 eV was obtained [12].

Electron attachment to C_{60}. The electron attachment to C_{60} cluster was investigated, for example, in [15, 16, 17], but the absolute values of $\sigma^{-}(E_e)$ did not measured.

Figure 4 gives the E_e dependences of the cross section σ^{-}: points 1 – experiment, curve 2 – calculation. The nonmonotonicity of the dependence 1 for E_e < 0.2 eV is due to the increase in error of I^{-}/i_e ratio with decreasing E_e. It was found that the measured at E_e < 0.3 eV $I^{-}(SF_6^{-})$ and $I^{-}(C_{60}^{-})$ currents are fitted well with the

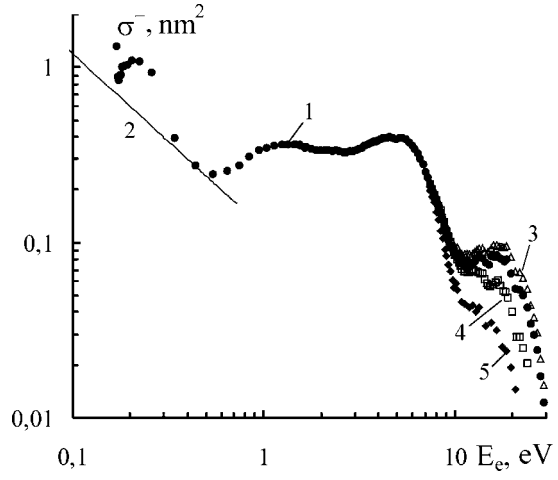

Fig. 4. Cross section of C_{60}^- formation.

dependences $I^- = \int_0^\infty \sigma^-(E_e) f_e(E_e) dE_e$, where $\sigma^-(C_{60}^-)$ are given by expression for polarizative caption [18]: $\sigma^- = (\pi a_0^2/2E_e)\cdot\{1 - \exp[-4(2\alpha E_e)^{1/2}]\}$. Here a_0 – Bohr radius, other values are taken in atomic units, α is the polarizability of C_{60}. We used the mean of the values obtained in [19]: $\alpha(C_{60})$=756. At E_e > 7.5 eV, C_{60}^- ions are unstable against electron autodetachment, and the observed cross section $\sigma^-(E_e)$ depends on the time t it takes an ion to travel the distance from the formation point to the ion collector. Figure 4 shows the effective cross sections $\sigma^-(E_e)$ for five values of time t : (3) 40, (1) 60, (4) 80, and (5) 100 μs.

Thermoemission of electrons and photons. Earlier we observed, that the spectrum of radiation in the wavelength range λ = 300 up to 800 nm from the region where the beam of C_{60} clusters and the electron beam intersect is similar to the Planck radiation spectrum [4, 20]. An analogous spectrum was observed in [3] in the case of evaporation of C_{60} by laser irradiation. Here we have found that the main contribution to radiation comes from C_{60}^{+*} ions which are produced as a result of thermionic emission and determined the main radiative characteristics of these ions.

Figure 5 gives the radiation intensity as a function of the electric-field strength, ξ, between the deflecting plates DP (see Fig. 1) at E_e = 40 (curve 1) and 65 eV (curve 2). The radiation was detected with an optical filter. The same figure also shows the calculated electric-field-strength dependence of the residence time of a C_{60}^+ ion in the observation region, t(ξ) (curve 3). One can see that the main contribution to radiation comes from C_{60}^+ ions. For high values of ξ, the time t and, hence, the intensity of ion radiation are proportional to $\xi^{-1/2}$. By expressing the dependences $I^*(\xi)$ in terms of coordinates $I^*(\xi)$ and $\xi^{-1/2}$ and extrapolating them to the

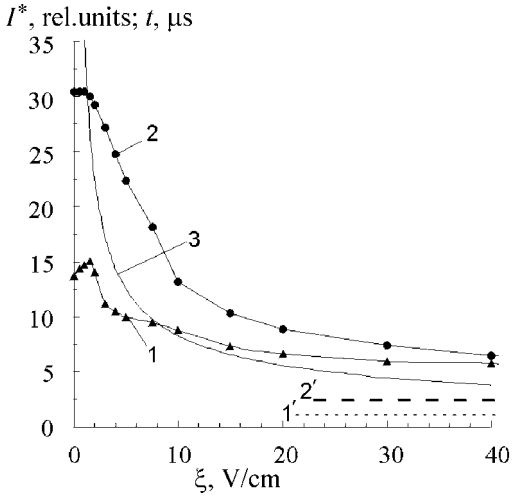

Fig. 5. The intensity of radiation from C_{60}^* and C_{60}^{+*} (1, 2) and the residence time of C_{60}^{+*} ion in the observation region as functions of the electric-field strength. Contributions from C_{60}^* neutrals (1', 2') (see text).

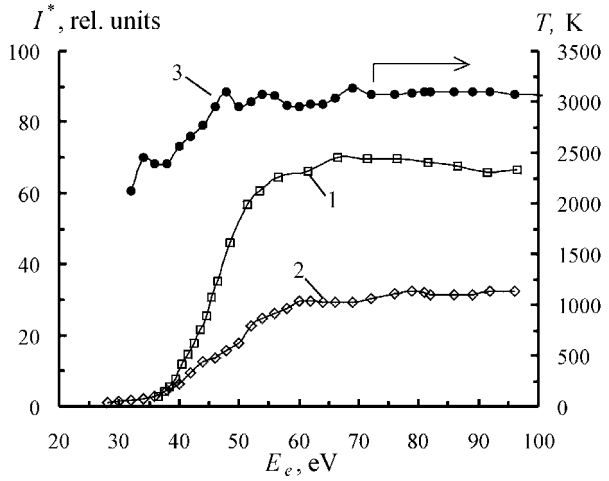

Fig. 6. The intensity of radiation (1, 2) and the temperature of radiating particles (3) as functions of the electron energy E_e.

origin, we have found that the contribution of neutral particles to radiation does not exceed 16 and 4% at E_e = 40 and 65 eV, respectively. In Fig. 5 these values are indicated by lines 1' and 2'.

Figure 6 gives the E_e dependences of I^* during measurements of radiation in the scheme with a filter (points 1) and with a monochromator (λ = 540 nm, $\Delta\lambda$ = 3 nm) (points 2). Also given in Fig. 6 is the brightness temperature as a function of $T(E_e)$ (points 3) obtained by approximation of radiation spectra at different values of E_e by the modified Planck formula from [4, 21]. In the wavelength range of $[\lambda, \lambda + \Delta\lambda]$, such a particle emits a photon flux

$$j(\lambda, T) = 2\pi c S \Delta\lambda \varepsilon_0 \left\{ \lambda^4 \left[\exp\left(\frac{hc}{\lambda k_B T} \right) - 1 \right] \right\}^{-1}, \qquad (1)$$

where $S = 4\pi d^2$ is the area of the radiating sphere of diameter d, and $\varepsilon_0(\lambda, T)$ is the emissivity (blackness factor) of particle.

The behavior of $I^*(E_e)$ suggests that the contribution of C_{60}^+ to radiation becomes dominant for E_e > 33 eV. The temperature $T(E_e)$ = 3150 K is established at $E_e \geq$ 47 eV. This is possibly due to the E_e dependence of the energy ΔE_v transferred from the electron to the cluster. According to the calculation results of [22], the internal energy of C_{60} at T = 3150 K is approximately equal to 37 eV. Adding U_i = 7.6 eV and substracting the energy of C_{60} in the effusive beam we obtain ΔE = 40 eV.

The cross section σ^* of the production of a radiating C_{60}^{+*} ion by electron impact is determined by comparing the intensities of radiation from C_{60}^{+*} and $N_2^{+*}(B^2\Sigma_u^+)$ at a wavelength λ = 391 nm as measured on the basis of the same experimental scheme. We have $I(N_2^{+*})/I(C_{60}^{+*}) = n_N \sigma_N^* / (n \sigma^* t j)$, where n_N and n denote the density of N_2 and C_{60} in the region of beams intersection, $\sigma_N^* \approx 1.7 \cdot 10^{-3}$ nm^2 is the cross section of excitation of observable radiation from N_2^{+*} [23], and $t = 3.5 \cdot 10^{-5}$ s is the time during which the C_{60}^{+*} ion traverse the optical-observation region. The lifetime of $N_2^{+*}(B^2\Sigma_u^+)$ is $\tau^* = 6 \cdot 10^{-8}$ s >> t, that is, the current of N_2^{+*} ions is equal to the photon flux. From the ratio $I(N_2^{+*})/I(C_{60}^{+*})$ at E_e = 60 eV, we obtained $\sigma^* \approx 2 \cdot 10^{-2}$ nm^2. This value appeared to be approximately 20 times smaller than the maximum cross section for C_{60} ionization by electron impact, but it is much larger than σ_N^* for $N_2^{+*}(B^2\Sigma_u^+)$ radiation.

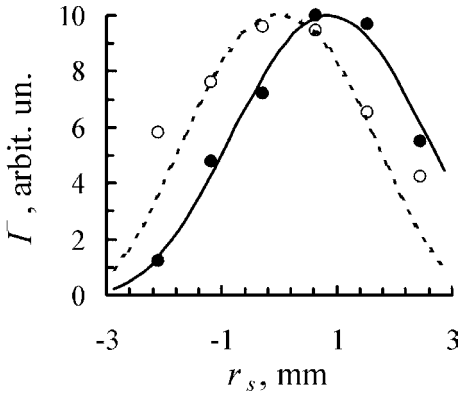

Fig. 7. The transverse profiles of electron-induced radiation (E_e = 70 eV) of the C_{60}^{+*} (•) and $N_2^{+*}(B^2\Sigma_u^+)$ (o) ions.

The kinetics of thermionic emission and of radiation was determined from a comparison of the experimental and calculated dependences (per C_{60}^{+*} ion) of the radiation intensity I^* on the electric field strength of the DP plates, assuming the first-order approximation for the kinetics of formation of C_{60}^{+*} ions by thermionic emission. The radiative cooling constant was taken from integration of Eq.(1) over the wave length. The calculation parameters were d = 1 nm, and T = 3150 K 6 ms, l = 540 nm,.The best agreement between calculations ond experimental data was obtained at ε_0 = 6 and thermionic emission time τ_e = 6 μs. This results in the rate of radiative loss of energy by a C_{60}^{+*} ion of $5.5 \cdot 10^5$ eV/s.

The delay of radiation due to the finite time of thermionic emission is clear manifested in measurements of transverse

profile of the C_{60}^{+*} emission region. This profile together with the profile of $N_2^{+*}(B^2\Sigma_u^+)$ radiation at a wavelength λ = 391 nm are shown in Fig. 7 with black circles and open circles correspondingly. Both profile were measured without electric field. Due to small lifetime the profile of $N_2^{+*}(B^2\Sigma_u^+)$ emission coincides with the profile of the exciting electron beam (corrected for the spatial sensitivity of our optical system) and corresponds well to calculations on the assumption that electron beam is cylindrical (see dash line in Fig 7). The maximum of the C_{60}^{+*} ion profile appears to be shifted downwards the beam moving to 0.9 mm, which at average cluster velocity 174 m/s corresponds to delay time 6.1 μs. The scatter of the data on the rate constant for C_{60}^{*} delayed autoionization is rather large. For example, with data taken from [24], we obtained the rate constant $1.2\cdot10^5$ s^{-1} at the C_{60}^{*} cluster temperature 3100 K, i.e. the ionization characteristic time 8.6 μs, cluster temperature 3200 K results in values $2.9\cdot10^5$ s^{-1} и 3.4 μs, correspondingly. Thus in our experiments it is the delayed ionization that is responsible for radiating ions formation.

Acknowledgements

This study was supported by the Russian Foundation for Basic Research (projects 03-03-32055 and 03-03-32241).

References

[1] E. E. B. Campbell, R. D. Levine - Annu. Rev. Phys. Chem. **51**, 65 (2000).
[2] J. U. Andersen, E. Bonderup, K. Hansen - J. Phys. B: At. Mol. Opt. Phys. **35**, R1 (2002).
[3] R. Mitzner, E. E. B. Campbell - J. Chem. Phys. **103**, 2445 (1995).
[4] A. A. Vostrikov, D. Yu. Dubov, A. A. Agarkov - JETP Letters **63**, 963 (1996).
[5] M. Lezius, P. Scheier, T.D. Märk - Chem. Phys. Lett. **203**, 232 (1993).
[6] D. Rapp, P. Englander-Golden - Chem. Phys. **43**, 1464 (1965).
[7] D. Klar, M.-W. Ruf, H. Hotop - Chem. Phys. Lett. **189**, 448 (1992).
[8] H. Lin, K. Han, Y. Bao, *et al.* - J. Phys. Chem. **48**, 12495 (1994).
[9] S. Matt, B. Dunser, M. Lezius, *et al.* - J. Chem. Phys. **105**, 1880 (1996).
[10] M.S. Baba, T.S.L. Narasimhan, R. Balasubramanian, C.K. Mathews - Int. J. Mass Spectrom. Ion Proc. **114**, R1 (1992).
[11] V. Tarnovsky, P. Kurunczi, S. Matt - J.Phys. B **31**, 3043 (1998).
[12] J. De Vries, H. Steger, B. Kamke *et al.* - Chem. Phys. Lett. **188**, 159 (1992).
[13] D. Ostling, P. Apell, A. Rosen - Z. Phys. D **26**, 282 (1993).
[14] R. Worgotter, B. Dunser, P. Scheier, T.D. Märk - J. Chem. Phys. **101**, 8674 (1994).
[15] J. Huang, H.S. Carman, R.N. Compton - J. Phys. Chem. **99**, 1719 (1995).
[16] O. Elhamidi, J. Pommier, R. Abouaf – J. Phys. B **30**, 4633 (1997).
[17] V. Kasperovich, G. Tikhonov, V.V. Kresin – Chem. Phys. Lett. **337**, 55 (2001).
[18] C.E. Klots - Chem. Phys. Lett. **38**, 61 (1976).
[19] P. W. Fowler, P. Lazzeretti, R. Zanasi - Chem. Phys. Lett. **165**, 79 (1990).
[20] A.A. Vostrikov, A.A. Agarkov, D.Yu. Dubov - Russ. Chem. Bull. **49**, 276 (2000).
[21] C. E. Bohren, D. R. Huffman - Absorption and Scattering of Light by Small Particles, Wiley, New York, 1983.
[22] E. Kolodney, B. Tsipinyuk, A. Budrevich - J. Chem. Phys. **102** (1995) 9263.
[23] W. L. Borst, E. C. Zipf - Phys. Rev. A **1** (1970) 834.
[24] A. Bekkerman, B. Tsipinyuk, A. Budrevich, E. Kolodney - J. Chem. Phys. **108** (1998) 5165.

Dose Dependence of Surface Hardness

by Low Energy Ion Irradiation on PMMA

(JAPAN)

M. Arai, E. Hatsugai, N. Hamamura, T. Iwao, and M. Yumoto

(*Musashi Institute of Technology in Japan*)

Abstract

It will know that a low energy ion irradiation is a powerful method for nm order modification of polymer surface properties of polymers. If sp^3 coupling are formed at the surface of PMMA(polymethylmethacrylate) by ion irradiation, an improvement of wear resistance and hardness will be expected. In the report, change of the hardness and the chemistry bonding by the low energy N_2 ion irradiation on to PMMA is reported. It is also reported that the result of HOPG(Highly Oriented Pyrolytic Graphite) for the clarification of the structure of PMMA.

1. Introduction

In light guide, optical fiber, optical disk, and liquid crystal display (LCD), etc. that support the information technology the importance of the transparent polymer material has risen. Especially PMMA is called the alias organic glass, and excels in the transparency, possesses a low birefringent rate, and is used widely. However, when this is used as an optical material such as displays and lenses, it is necessary to improve wear resistance. Generally, the coating method is used for the improvement of wear resistance. But, because the thickness of the coating layer by the method is a micrometer order, the coating material influences an optical characteristic of the material. Then, it is necessary to form the structure of the nanometer order like a hard film such as DLC(Diamond Like Carbon) and CN_x(Carbon Nitride) on the surface.

The ion irradiation method of the energy of several 100 eV is one of the surface modification method. This method can control the properties in the thin modified layer depending on the kind of the irradiated molecules and atoms, and a kinetic energy of the irradiated ions. Especially, it is reported that the ion irradiation with its penetration kinetic energy of 100eV is effective to the formation of the covalent binding (sp^3 bond). Moreover, the depth the ion in to the material is a nanometer order. Therefore, it can be expected that it is an effective technique for forming the modified layer along the demand of the mentioned above.

By the way, the development of the surface layer with some functions polar component surface energy and a by the nitride processing is paid to attention because nitrogen compounds is a material with high stability. For instance, it is reported that the surface of the sample an improvement of abrasion resistance[(1)] and a large magnitude of smooth surface was obtained[(2)].

In this report, the aim with PMMA by the acceleration energy 100 eV, is to clarify the structure of the modified layer on PMMA which the hardness is improved by the nitrogen ion irradiation with its energy of 100 eV. But, it is very difficult to identify the structure of the polymer. Then, the change of the structure by the nitrogen ion irradiation is investigated by using HOPG as the analysis of the structure is easier. The relation between the change of the hardness of PMMA after low energy ion irradiation processing and the change of elation between chemical structures obtained of HOPG is shown and is discussed.

2. Experimental

<2•1> Surface Treatment

Figure 1 shows the schematic diagram of treatment apparatus. Before the irradiation, the chamber was evacuated to less than 1.3×10^{-4} Pa. The gas used was commercial grade nitrogen (purity 99.999%). Under the pressure at 1.3×10^{-2} Pa, ions were accelerated by 100 V constant, and the amount of the irradiation has been changed as a parameter within the range from 1.5×10^{15} to 6.0×10^{16} ions/cm^2. Sample were a commercial PMMA plate(8 mm × 8 mm × 0.5 mm) and the HOPG plate(ZYB grade, 6 mm × 12 mm × 1.7 mm). The PMMA sample was washed by using an ultrasonic washing with ethanol for ten minutes, and was dried in a desiccator to remove impurities on the surface. After the surface treatment, the sample was taken out in the atmosphere, for the surface analysis.

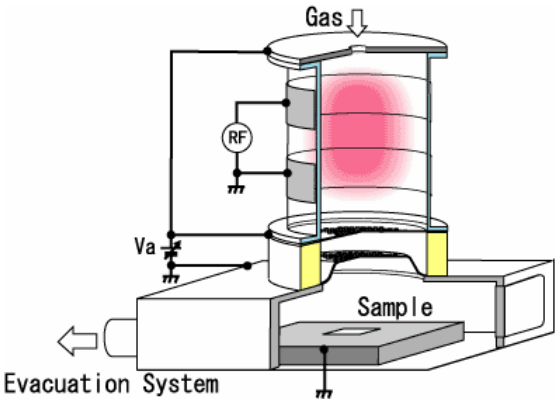

Fig.1 Processing system

<2•2> Analysis Method of Sample Surface

The sample were analyzed by using AR-XPS(X-ray Photoelectron Spectroscopy) (Surface Science Instruments SSX-100, X-ray source (Al Kα) : 1487 eV) and Raman spectroscopy(HORIBA Jobin Yvon T-64000, excitation light source : 514.5 nm). Because the sample during the measurement was exactly electrified, the electron of 10eV was irradiated on the sample by the neutralizing gun.

Figure 2 shows the principle of the depth profile analysis. In fact, the analyzer is anchored in position, and the sample stand is rotated. X rays are incidence from the direction of the rotation axis of the sample stand.

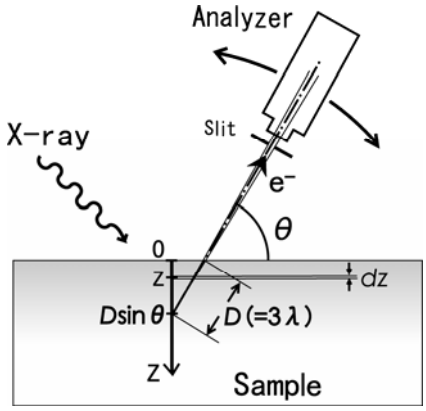

Fig.2 Angle-resolved XPS[2]

The depth profile of each atom was calculated by using equation (1).

$$I = \int dI = \int_0^{D\sin\theta} \frac{1}{\sin\theta} k(z) S \sigma E n(z) \exp\left(-\frac{z}{\lambda \sin\theta}\right) dz \quad \cdots (1)$$

Where, I is the spectrum intensity, $n(z)$ is the depth profile of the composition which corresponds to the number of photoelectrons generated at the depth z, θ is the photoelectron take off angle, λ is the electron inelastic mean free path, S is the X-ray irradiation area, and k(z) is a compensation function in the measurement device.

<2•3> Surface Harness Measurement

The Nanoindentation test machine(Hysitron, Triboscope) was used for the measurement of hardness. The diagrammatic illustration of the metrology is shown in Figure 3 [(3)]. The needle made of the diamond is operated in the vertical direction, and the pushing load is continuously changed. The method is a method of dynamically measuring the sinking crowding to it, and can evaluate a very thin reforming layer. The hardness of the sample is requested by the except load curve of load-displacement curve. When the pushing depth at permissible capacity at rated load center distance P_{max} assumes that the project area in the area where h_{max} and the pushed needle have come in contact with the sample is A, hardness H of the sample is defined by the equation (2). To adjust the needle invasion depth to several nm, the load added to the needle was assumed to be 4μN for PMMA and 10μN for HOPG.

$$H = \frac{P\max}{A} \quad \cdot \cdot \cdot (2)$$

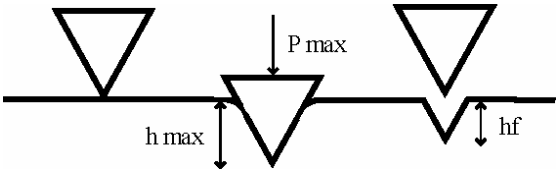

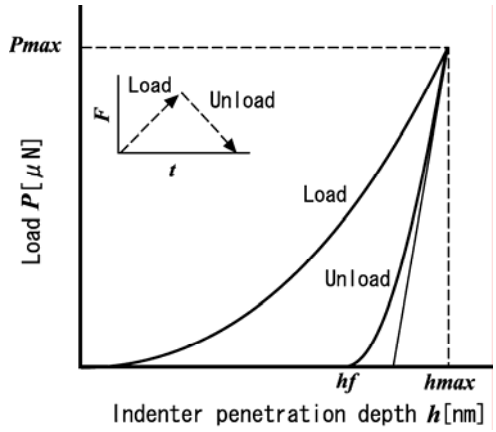

Fig.3 Hardness measurement of nanoindentation test[(3)]

3. Experimental Results and Discussion

<3•1> Hardness Measurement

Figure 4 shows the results of the hardness measurement by the nanoindentation test. The test was repealed ten times, and the bar in the figure shows the maximum and the minimum values.

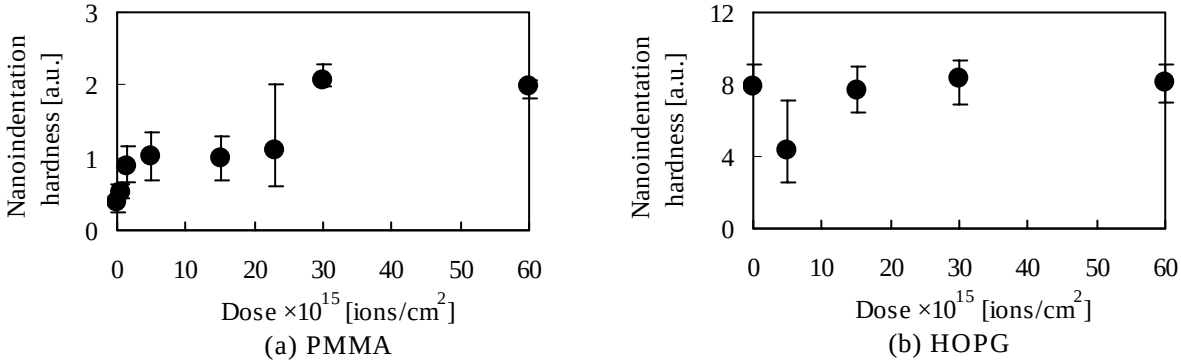

Fig. 4 N_2 dose dependent of surface hardness

Hardness of PMMA which ion was irradiated increased depending on the amount of ion irradiation. Hardness increases suddenly around the most at amount 3.0×10^{16} ions/cm^2. Its magnitude increased about three times compared with the untreatment PMMA, and showed saturation with the value. Hardness decreased in HOPG in case of a small amount of the irradiation, often that hardness increased, too, depending of the amount of the irradiations. Hardness increased up to the amount 3.0×10^{16} ions/cm^2 of the

irradiation as well as PMMA, and hardness was saturated. The untreated HOPG is a high density material. Therefore, it hardness is high. However, the hardness decreased under the small amount of irradiation. It is said that HOPG to which the ion is irradiated will become an amorphous structure. Afterwards, the change of the structure was introduced and change of the might hardness increase by the ion irradiation. That is, it is expected that the structure of PMMA and HOPG in amount of 3.0×10^{16} ions/cm^2 irradiation may be similar.

<3•2> Change of composition

Figure 5 shows the N_2 dose dependence of composition.

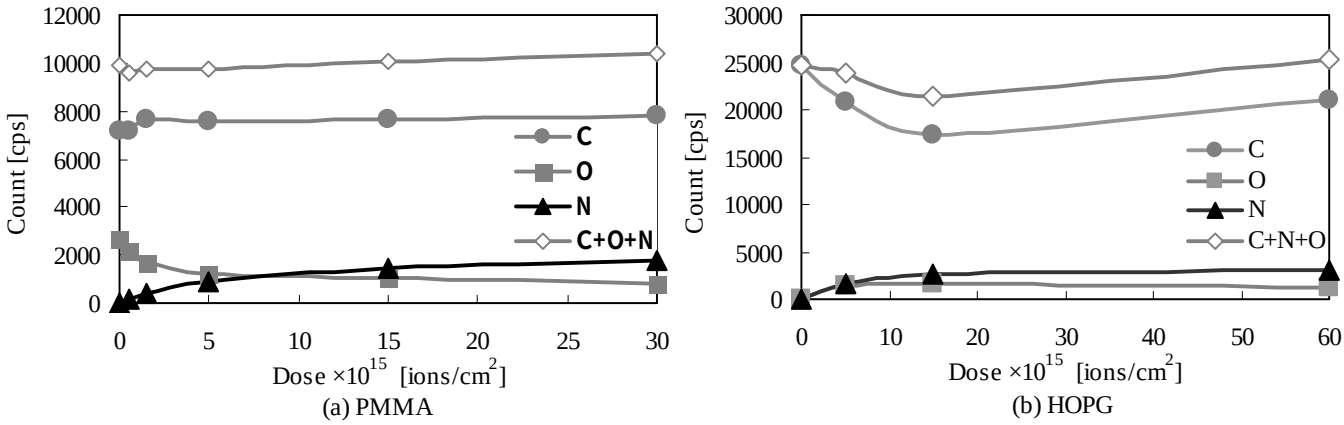

Fig.5 N_2 dose dependence of composition

In PMMA, oxygen decreaseds as the amount of the irradiation increase, and nitrogen increased. The binding energy of hydrogen is lower than that of the carbon and oxygen though hydrogen cannot be measured by XPS. It is thought that combination of hydrogen and oxygen such as C-H and C=O is resolved by the ion irradiation, and the nitrogen is introduced. Because sum of the each composition increased a little by increasing the amount of the irradiation, it is thought that the density on the surface of the sample increases by the ion irradiation. It is thought that binding of nitrogen and the carbon is chiefly effective in the improvement of hardness because an increase of nitrogen irradiation into the sample and of the hardness.

In HOPG, the carbon decreased by the ion irradiation with a little amount of the irradiation. And nitrogen and oxygen were introduced. Afterwards, the composition of the carbon and nitrogen increased, and oxygen didn't increase. The composition of oxygen didn't depend on the change in the amount of the irradiation. It is thought that the oxygen that adhered to the surface was introduced by the ion irradiation as. Sum of each composition increased depending on the amount of the irradiation.

It is thought that the reason why the hardness shown in Figure 4 decreases under a small amount of iradiation is that itsthe density falls, and it changes into an amorphous structure. Based on the above results, it is thought that bindings of nitrogen and the carbon is chiefly effective in the improvement of hardness.

<3•3> Density Distribution

Figure 6 shows the calculated results of the density profile against distribution to the amount of the irradiation.

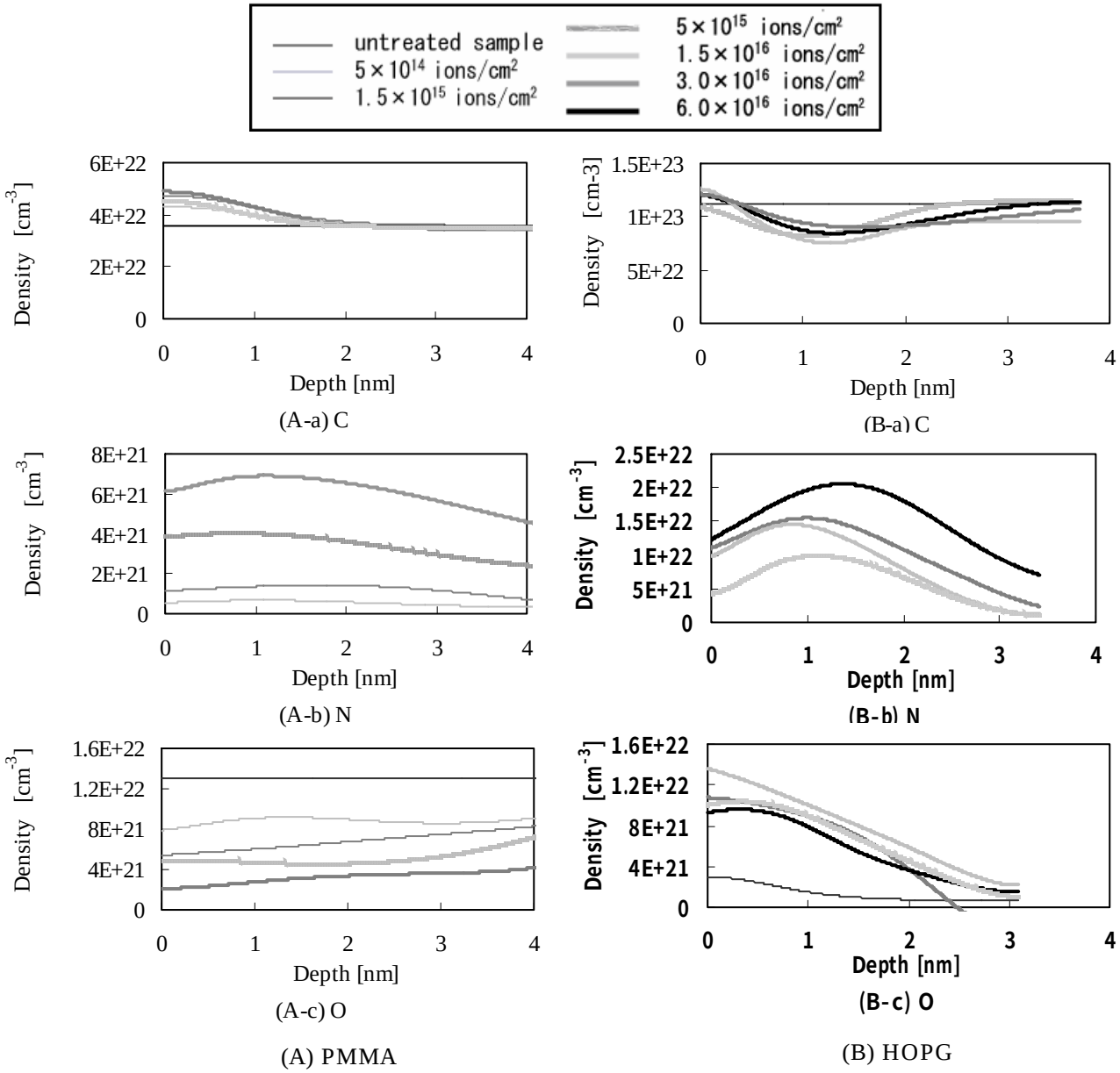

Fig.6 Depth profile of Carbon, Oxygen and Nitrogen

In PMMA, nitrogen was introduced into the sample amount of 1-2nm the depth of. Oxygen was resolved on the surface, and the density of the carbon increased on the surface of the sample. The amount of the introduction of nitrogen increased, and oxygen decreased for an increase in the amount of the irradiation. The improvement in the hardness was anticipated with basing on the increase of the combination of charcoal element and nitrogen, because there are small changes of the density of the charcoal element for the increase in the amount of radiation. In HOPG, nitrogen, around depth was introduced into the sample of 1-2nm. Oxigen was introduced at the surface, and the carbon decreased up to 1 to 2 nm depth, and the density was increases mean the surface. The change according to an increase in the amount of the irradiation appears only to nitrogen. It is expected that the improvement of hardness is brought about by uniting nitrogen and the carbon having increased as well as PMMA from the above-mentioned result.

<3･4> chemical structure

From the hardness improvement are brought about the introduction of the combination including charcoal element and nitrogen. However, it is very difficult to analyze the PMMA surface of the nm order. Bond state of PMMA can be forecast from the connection state of HOPG because it is expected that connection state of PMMA and HOPG after the ion irradiation is similar. Then, the result of analyzing combined state of HOPG by the Raman spectrum analysis method is shown in Figure 7.

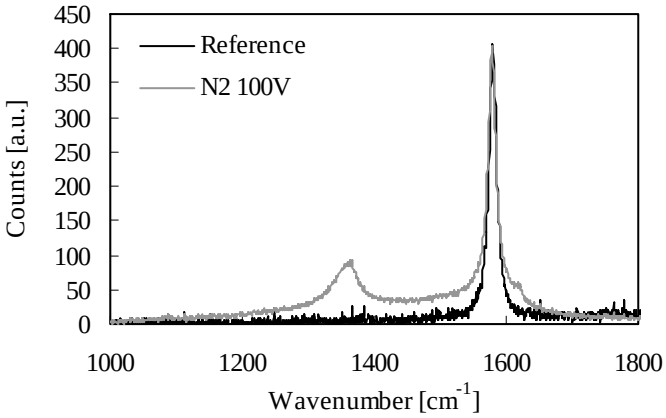

Fig.7 Raman Spectra (HOPG)

D band in the vicinity of 1360cm^{-1} and G band in the vicinity of 1580cm^{-} show the sp2 bonding and the sp^3 bonding the carbons respectively. The resalts showed that the sp^3 bonding of C-N was detected.

It is clear that the sp3 bonding of C-C and C-N is generated to HOPG by the nitrogen ion irradiation. Based on the above result, It is expected that there is a possibility that the sp3 bonding of C-C and C-N is generated also in PMMA, and hardness increases from this.

4. Conclusions

The hardness of, PMMA by nitrogen ion irradiation increased about three times hardness compared with untreated PMMA. Chemical bonding of C and N is chiefly related to the improvement of hardness. It is expected that the improvement of the hardness of PMMA by which nitrogen ion irradiation is due to the formation of the sp^3 structure of C-C and C-N, because the sp^3 structure of C-C and C-N was formed on the HOPG surface by nitrogen ion irradiation.

References

(1) J. Robertson : “Diamond-like-carbon ”, Pure&Appl.Chem., 66, .9, 1789-1796 (1994)

(2) Hamamura, Yumoto and Sakai : “Depth Profile of Modified Layer on Polymer Surface by Exposure to High E/n Discharge(Ⅱ) ”, T. IEE Japan. A. 121, 5, 453-458 (2001) in Japanese

(3) Miyake : “Deposition and Microtribology of Super Hard Films”, J. Surf. Fin. Soc. Japan., 51, 4, 390-397 (2000)

Effect of crosslinking structure on Modified PMMA by using Low Energy Ion Irradiation

E. Hatsugai, M. Arai, T. Iwao, N. Hamamura, M. Yumoto
(Musashi Institute of Technology, Japan)

Abstract

The surface modification of PMMA was done by using low energy ion irradiation. It is known that an irradiation of low energy ions for surface modification forms a thin modified layer of several nm with a crosslink formation. In this paper, the effect of the crosslinking structure on diffusion prevention of the dyeing molecule in modified layer is analyzed. The dyeing agent of PMMA was used to evaluate an amount of the penetration in by the diffusion in the modified layer. If the crosslinking structure is formed by the surface modification, the diffusion of a dyeing agent should be prevented. Ion dose or ion accelerating voltage is changed, and correlation of crosslinking layer and experimental condition is analyzed quantitatively by measuring transmittance or absorbance as a difference of amount of diffusion of dyeing agent. In this paper, the relation between crosslinking structure and diffusion control of molecule is clarified from these results.

1. Introduction

Polymer materials have many excellent properties in the field of the optoelectronics such as a high mass production, a lightweight, a low price and a high transparency. Especially, PMMA (poly-methyl-methacrylate) which has a high transmittance is used in various fields such as an optical fiber and an optical lens. However, it has a low wear-resistance, and its surface gets small cracks easily and the transparency decreases. Therefore, an improvement of a low wear-resistant is required.

It is well-known that formation of the crosslinking structure at the surface is effective for an improvement of a wear-resistance [1]. On the other hand, to give a wide range refractive-index distribution in an optical waveguide, some dopants are dispersed in the waveguide. In this case formation of crosslinking structure is useful for preventing the diffusion of dopant. Thus, the various functions can be obtained by formation of crosslinking structure at the surface.

An irradiation of low energy ions for surface modification is expected to obtain a thin modified layer of several nm with a crosslink formation [2][3]. If the crosslinking structure is formed in the sample surface by carrying out ion the irradiation, the surface becomes stable chemically and it is possible to be hard to melt to a solvent. Actually, when the solvent was dropped, it was shown that there were few amounts of the dissolution [4].

In this paper, the effect of the crosslinking structure on diffusion prevention of the molecule in modified layer is analyzed. The dyeing agent of PMMA was used in order to evaluate the quantitatively. If the crosslinking structure is formed by the surface modification, invasion of a dyeing agent should be prevented. Then, the correlation of a crosslinking layer and processing conditions was quantitatively analyzed by measuring the difference in the transmissivity of light when changing the ion energy. In this paper, the relation between crosslinking structure and diffusion control of molecule is clarified from these results.

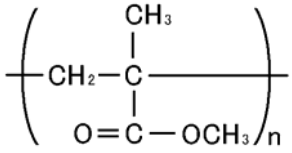

Fig. 1: Molecular structure of PMMA

2. Experiment

2.1 Experimental setup

Processing system is shown in figure 2. Before the irradiation, the chamber was evacuated to less than 1.3×10^{-4}Pa.The gas was commercial nitrogen. Under the pressure at 1.3×10^{-2}Pa, the irradiation was carried out. The ion dose was 1.0×10^{-16}ions/cm^{-2} in which nitrogen concentration of the sample shows saturation. Ion accelerating voltage was 100 and 1000V. The sample was a commercial PMMA film of 0.2mm in thickness.

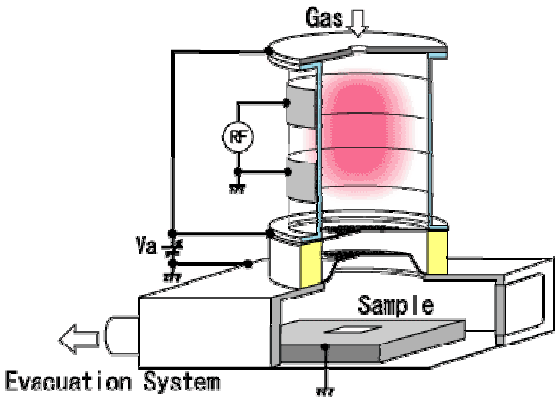

Fig. 2: Processing system

2.2 Transmittance measurement procedure of untreated sample when dyeing time is changed

Dye was diluted to 5% with the aqua pura, and was warmed up to 70 degrees C. Untreated sample was dipped 15min, 30min, and 60min in the dyeing agent. After dyes, the sample was cleaned by an ultrasonic way in an aqua pure bath for ten minutes and was dried up. After that, transmittance and the absorbance were measured.

2.3 Transmittance measurement procedure of treated sample when ion accelerating voltage is changed

The surface processed both sides respectively by ion acceleration voltage 100V and 1kV. Dye is diluted to 5% with the aqua pura, and it warms it to 70 degrees C. Treated sample dyed green leaving 60min in the dyeing agent. After dyes, the sample was cleaned by an ultrasonic way in an aqua pure bath for ten minutes and was dried up. After that, transmittance was measured.

3. Result and discussion

3.1 Transmittance measurement result of untreated sample when dyeing time is changed

Measurement result of transmittance is shown in figure 3, measurement result of absorbance is shown in figure 4, and absorbance area at each processing time is shown in figure 5. The relation between absorbance:A and transmittance:T is $A=\log_{10}1/T$. Transmittance is large in green wavelength area for 460nm to 570nm as shown Fig.3. There is absorption in the wavelength areas other than green (Fig.4). The absorbance area grows depending on the dye time (Fig.5). The results show that the dyeing agent diffuses in to the sample as time passes.

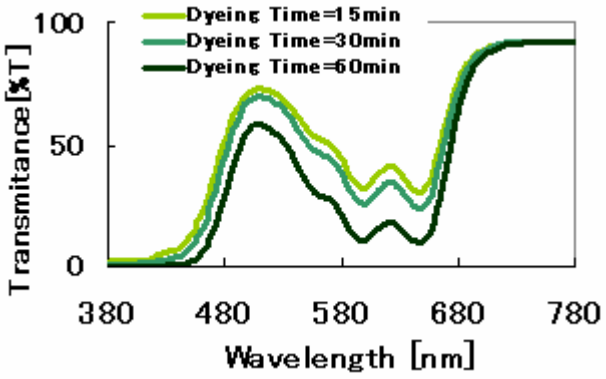

Fig. 3: Transmittance (Sample: Uuntreated, Dyeing time [min] = 15, 30, 60)

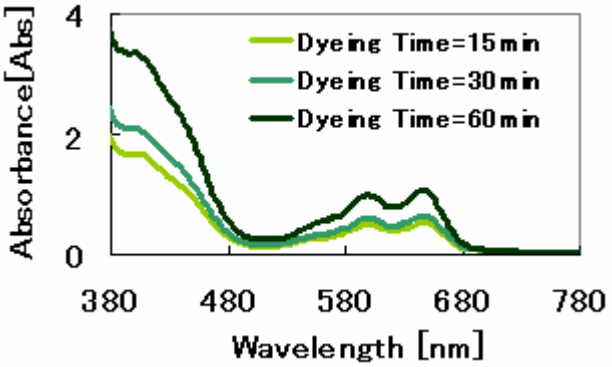

Fig. 4: Absorbance (Sample: Uuntreated, Dyeing time [min] = 15, 30, 60)

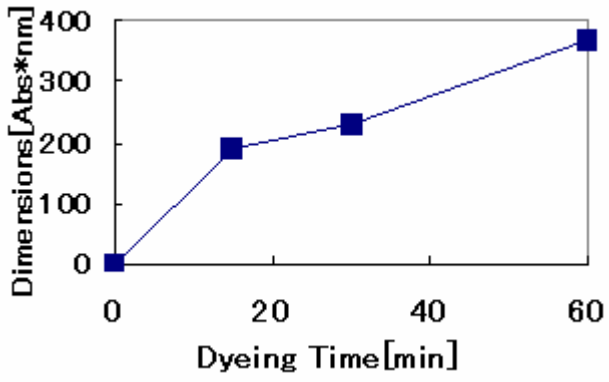

Fig. 5: Integral of Absorbance

Here, the result is dominated by a diffusion phenomenon assuming one-dimensional. Thus the diffusion of the dyeing agent follows diffusion equation shown by equation (1).

$$\frac{\partial u}{\partial t} = D\frac{\partial^2 u}{\partial x^2} \qquad (1)$$

u: Concentration of dyeing agent, *D*: diffusion coefficient, *t*: time, *x*: distance

The one-dimensional solution of the diffusion equation is an equation (2).

$$u(x,t) = \frac{1}{\sqrt{4\pi Dt}}\exp\left(\frac{-x^2}{4Dt}\right) \qquad (2)$$

Then, equation (1) was assumed D=1, t=15, 30, and 60, and calculated. Figure 6 shows the result. Moreover, the calculation result of equation (3) is shown in figure 7.

$$U = \int_0^{\infty} \frac{1}{\sqrt{4\pi Dt}}\exp\left(\frac{-x^2}{4Dt}\right)dx \quad (3)$$

It is understood that the concentration area increases depending on the dye time (Fig. 7).

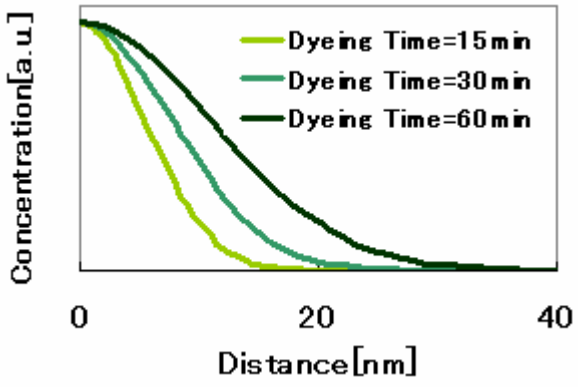

Fig. 6: Solution of Diffusion Equation (T = 15, 30, and 60, D = 1)

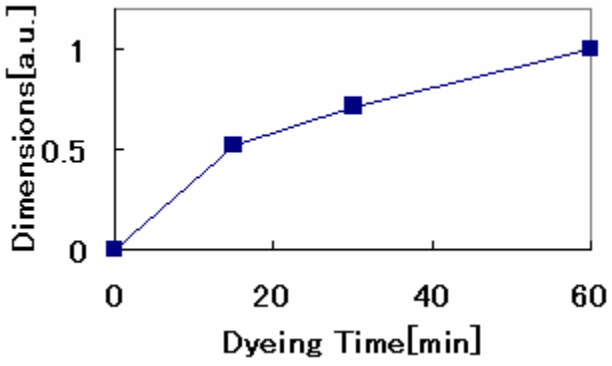

Fig. 7: Concentration area

3.3 Transmittance measurement result of treated sample when ion accelerating voltage is changed

If the crosslinking structure is formed by the surface modification, diffusion of a dyeing agent should be prevented. Then, the difference of the transmittance when the ion accelerating voltage was changed was measured. Figure 8 shows the ratio of the transmittance of dyed sample and sample not dyed by processing it under the same condition. Moreover, the absorbance is shown in Figure 9. Figure 10 shows the result of the change in the absorbance area when the accelerating voltage is changed. Transmittance increased when the ion acceleration energy raised (Fig.8). In a word, when the ion accelerating voltage rises, it is shown that the amount of the invasion of the dyeing agent is a little (Fig.9). Absorbance of treated sample with the ion accelerating voltage 1000V as compared with 100V is about 1/10 decreased (Fig.10).

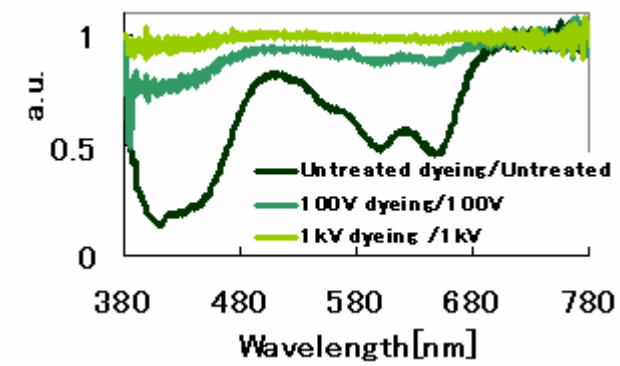

Fig. 8: Transmittance (Sample: Treated Ion energy [V] = 0, 100, 1000)

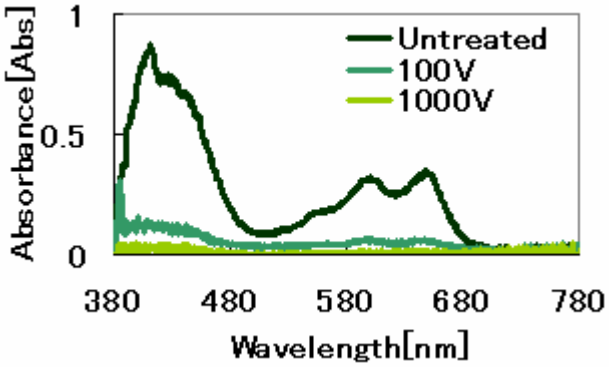

Fig. 9: Absorbance (Sample: Treated, Ion energy [V] = 0, 100, 1000)

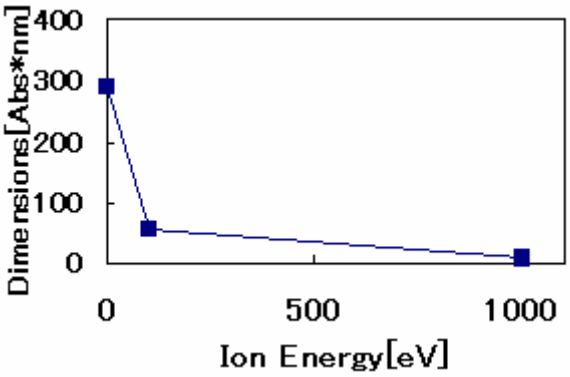

Fig. 10: Dimensions of Absorbance

This phenomenon follows the diffusion equation as mentioned above. Here, it is thought that modified layer and bulk have changed because of formation of crosslinking layer on the surface. From the result of projected range, the invasion depth of nitrogen is 1.2nm in 100V, 5.6nm in 1000kV respectively. It is assumed that the diffusion coefficient of surface 1.2nm and 5.6nm is approximately 1/10, 1/30, and 1/100 of the bulk, and calculated the diffusion equation (1). Figure 11 shows the result. Figure 12 shows each concentration area. When the diffusion coefficient of surface 1.2nm is 1/10, 1/30, and 1/100 of the bulk, the concentration area decreases about 17%, 47%, 87% respectively (Fig. 12). When the diffusion coefficient of surface 5.6nm is 1/10, 1/30, and 1/100 of the bulk, the concentration area decreases about 68%, 81%, 89% respectively (Fig. 12). Difference of amount of invasion was able to be detected as a difference, when there was one digit difference of the diffusion coefficient, if the thickness of the modified layer is only 0-6nm (Fig. 11).

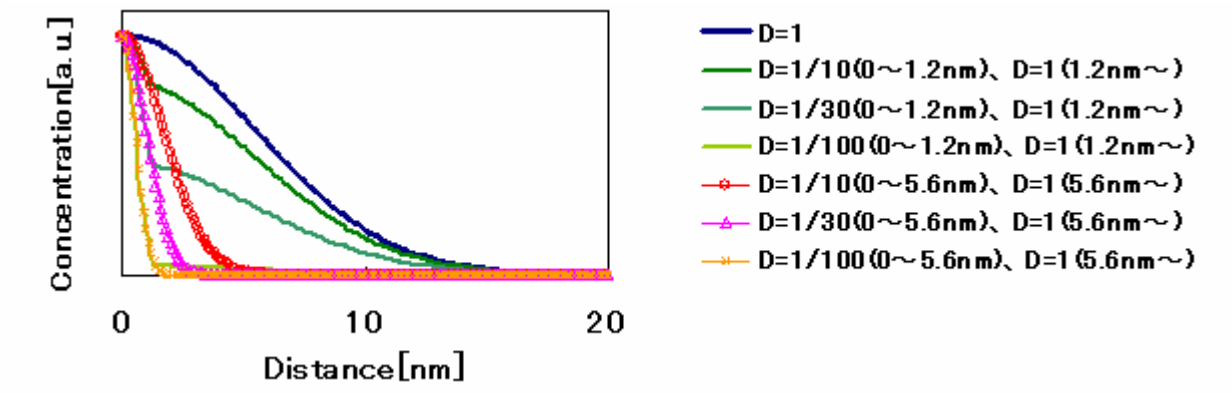

Fig.11: Solution of Diffusion Equation (T = 1, D= 1, 1/10, 1/30, 1/100)

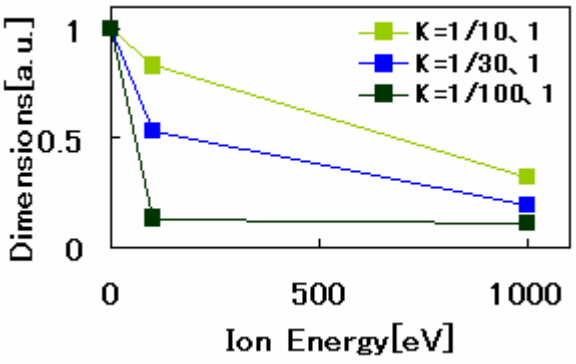

Fig.12: Concentration area

Here, the cross section of surface by ion irradiation was modeled as shown in figure 13. The crosslinking structure was formed thickly since the ion with high energy penetrated deep in to the sample. According, it is thought that the dyeing agent was prevented from diffusing. The crosslinking structure was formed thinly since the ion with low energy penetrated shallow, it is thought that the dyeing agent come through the crosslonking structure and diffuses to the bulk.

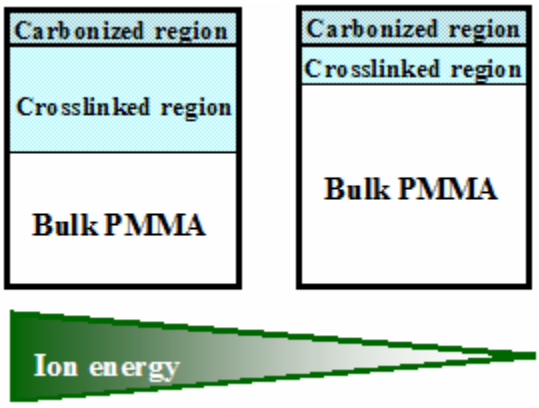

Fig. 13: Cross-sectional model

Conclusion

The surface modification of PMMA was done by using low energy ion irradiation. An irradiation of low energy ions for surface modification is expected to obtain a thin modified layer of several nm with a crosslink formation. In this paper, the effect of the crosslinking structure on diffusion prevention of the molecule in modified layer was analyzed. The dyeing agent of PMMA was used to evaluate an amount of diffusion in the modified layer. As a result, the absorbance decreases by 80%, 97% with irradiating the nitrogen ion of 100eV, 1000eV compared with the untreated. Difference of amount of invasion was able to be detected as a difference, when there was one digit difference of the diffusion coefficient, if the thickness of the modified layer is only 0-6nm.

References

[1]Hayashi, Fukushima, Kikuchi, Kusano, Nanto and Kinbara: “Surface Processing of PTFE using Discharge under High E/n condition-Comical Stability of Processed Surface-”,J.Surf.Fin.Soc.Japan.,53,7,471-474(2002)

[2]H.Schonhorn and R.H.Hsnsen: “Surface Treatment of Plymars for Adhesive Bomding”,J.Appl.Sci., 11,1461-1474(1967)

[3]Y.Koval: “Mechanism of etching and surface relief development of PMMA under low-energy ion bombardment”,J.Vac.Sci.Technol. B22,.2, 843-851 (2004)

[4]Hatsugai, Hamamura, Iwao and Yumoto: “Introduction of crosslinking structure on Modified PMMA by using Low Energy Eon Irradiation -Effect of crosslinking structure on diffusion prevention of molecule-”,T.IEEJ.P-18-466(2004) in Japanese

Refractive index control of polymer thin film by using plasma enhanced polymerization

Tetsuji Sato, Kazunori Moriki, Motoshige Yumoto

Musashi Institute of Technology, Tokyo, Japan

Abstract

The polymer waveguide was fabricated by using plasma enhanced polymerization for refractive index control. Because the single-mode optical waveguide of specific refractive index difference becomes pretty large such as about 4.6 percent currently, there is a problem with bad optical coupling efficiency when light is coupled from the optical fiber to the waveguide. It is necessary to reduce the specific refractive index difference to improve the optical coupling efficiency. It aimed to examine whether the refractive index control of one small digit was possible in this research to improve the optical coupling efficiency with the optical fiber now. From the result, it has been understood to be able to reduce the specific refractive index difference by one digit.

1. Introduction

A silica (SiO_2-GeO_2) thin film that deposited on the silicone substrate by using the flame hydrolyzing method is used for an optical coupler and an optical splitter, etc. that are the optical devices for wavelength division multiplexing communications, currently. It is necessary to heat-treat it by a thousand and several hundreds K in order to make this deposited thin film transparent. This fabrication of the optical functionality device mixed with other materials difficultly. On the other hand, the low-cost polymer waveguide can be fabricated by the solvent evaporating easily after spreading the dissolved polymer by using the spin court method. Moreover, because it is also possible to disperse a nonlinear optical low molecule etc., it is used to make an optical switch and wavelength conversion of the optical functionality device etc. However, the form of the film thickness control with high accuracy and a steep boundary with the different kind material thin film is difficult in the spin court method. Therefore, the development of the polymer thin film form technology by a dry process is hoped.

The benzene of monomer for the core layer and the cyclohexene for the clad layer are confirmed to be able to fabricate the single-mode waveguide of 0.6 micrometers in core diameter by previous researches. Because the core diameter of waveguide becomes very small at 0.6 micrometers, in the case of coupling the light between the optical fiber and the optical functionality element, it is necessary to improve the coupling efficiency. As for the fiber-optic communication, the single-mode fiber of about 9 micrometers in core diameter is used generally. It is necessary to fabricate the waveguide with the core of the film thickness at the same level in order to improve the coupling efficiency. Therefore, it is necessary to adjust the specific refractive index difference between the core and clad to about 0.35 percent. The single-mode optical waveguide of specific refractive index difference becomes pretty large such as about 4.6 percent currently.

In this paper, the refractive index is controlled such as one small digit in order to improve the optical coupling efficiency with the optical fiber. Then, the ratio of double bond in the formed film was changed by controlling the ratio of benzene and cyclohexene of the monomer material, and it was tried to control the

refractive index. Moreover, the ratio of fluorine in the film formed was changed by controlling the ratio of Ar and CF_4 of atmospheric gas, and it was tried to control the refractive index.

2. Experiment

Figure 1 shows pattern diagrams of plasma CVD experiment. The pyrex glass of 200 mm in the diameter was used for a reactive room. After the oxide film on the surface of the silicon substrate of 10 mm × 10 mm had been removed, it is put on the earth electrode of a parallel plate electrode of the electrode distance 100 mm in the diameter 35 mm. It was made to evaporate at the room temperature by using benzene and cyclohexene of the material, and they were introduced into the reactive jurisdiction throughtheflow meter. Moreover, Ar and CF_4 of the atmosphericgas were introduced in a reactive tube different from the material monomer.

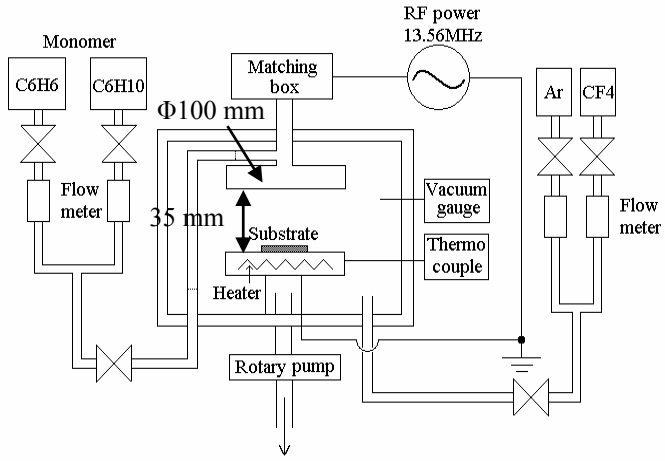

Fig.1 Schematic view of plasma enhanced polymerization equipment

The substrate was heated and to temperature was set at 373 K, because it is prevented from remain unreacted monomer in the polymer film. However, when the a-C:H thin film is heated to 573 K or more, it is reported to do CH_4 and H desorption [1]. Moreover, it is reported that it is necessary to reduce impressed electric powers up to about 0.01 W/cm^2, in order to suppress the generation of dangling-bond caused by desorption of hydrogen, and to obtain the polymer state thin film [2]. Therefore, an applied electric power was to be 1W. In addition, the pressure in the chamber was to be 0.3 and 0.4 in the case of Ar and CF_4, respectively, because it is reported that in there is no change the ratio of $C_4H_2^+/C_4H_3^+$ and $C_6H_6^+/C_6H_5CH{=}CH_2^+$ within the range of pressure from 0.3 to 0.65 Torr in the case of making the styrene into a monomer material, changing pressure, the RF electric power and analyzing mass spectrometry in the chamber [3].

As valuation method, the refractive index of formed thin film is measured by using spectrum ellipsometer and the structure of the thin film was evaluated by using FT-IR and XPS.

3. Results and discussion

3. 1 Refractive index control by changing the benzene and cyclohexene of material mixture gas

The refractive index of deposited thin film was measured from 600-1600 nm by using the spectroscopic ellipsometer. The refractive index in the case of 800 and 1300 nm is shown in Figure 2. The refractive

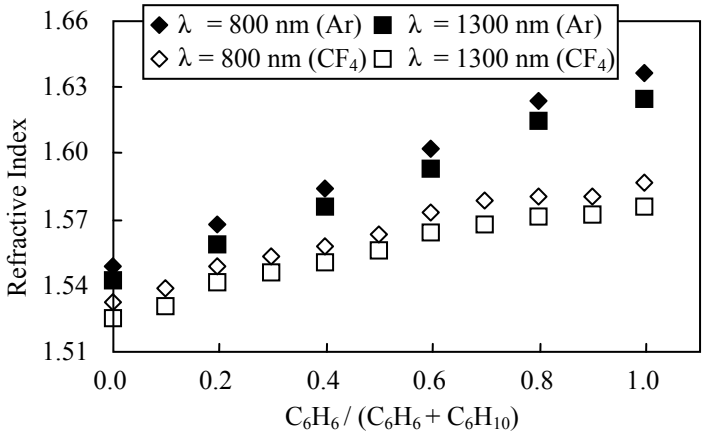

Fig.2 Refractive index change in each wavelength

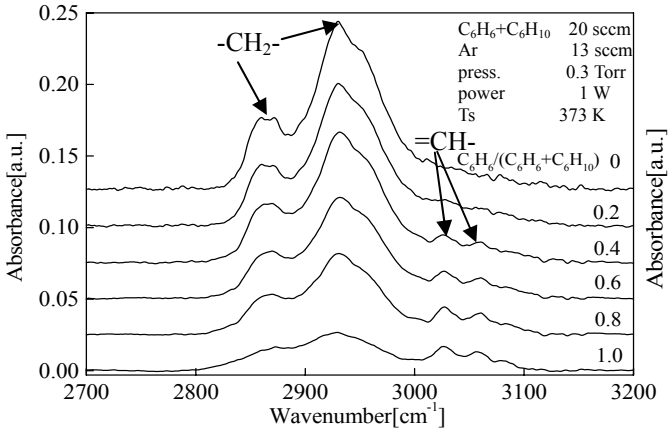

Fig.3 FT-IR spectrum of polymerization film on Si at Ar

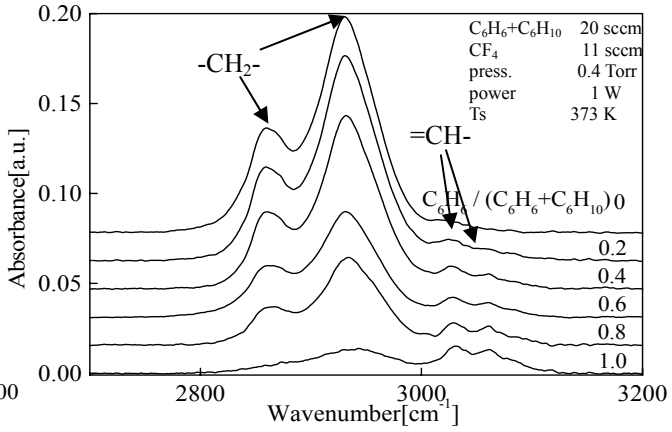

Fig.4 FT-IR spectrum of polymerization film on Si at CF_4

index increases in proportion to the mixture ratio of benzene. This slope of Ar and CF_4 becomes 0.09 and 0.05, respectively. Therefore, it is possible to make the specific refractive index difference between the core and clad below 0.5 percent, because the difference of mixture ratio between them becomes 0.07 (Ar) or 0.14 (CF_4).

Figure 3 shows the FT-IR spectrum of the thin film formed in the Ar atmospheric gas. Figure 4 shows the FT-IR spectrum of the thin film formed in the CF_4 atmospheric gas. The 2860 and 2924 cm^{-1} of wavenumbers indicate an infrared absorption spectrum of the CH stretching vibration that originates in the sp^3 (CH_2) bond. The 3030 and 3060 cm^{-1} of it indicate an infrared absorption spectrum of the CH stretching vibration that originates in the sp^2 (CH) bond [4]. The infrared absorption with CH stretching vibration of the sp^3 (CH_2) bond was compared with it of the sp^2 (CH) bond. When the mixture ratio of benzene increases, the sp^2 bond increases. The refractive index depends on the ratio of sp^2 and sp^3 in a thin film. In fact, the amount of the double bond can be controlled.

3. 2 Refractive index control by changing Ar and CF_4 of atmospheric mixture gas

Figure 5 shows the refractive index change in the formed thin film. The refractive index decreases by increasing the mixture ratio of CF_4. A decrease in the refractive index examined whether it was the one by what influence by using the XPS measurement.

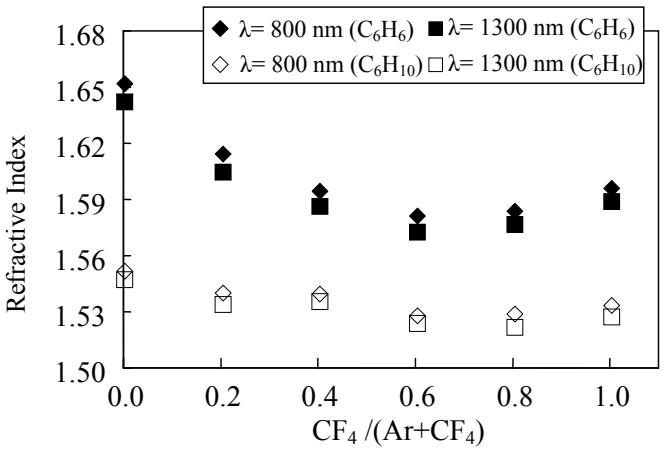

Fig.5 Refractive index change in each wavelength

The amount of the introduction of the fluorine when benzene and cyclohexene of the material gas are used is shown in Figure 6 and the C1s spectrum is shown in Figure 7. The amount of the introduction of fluorine increases rapidly between from 0 to 0.2 of mixtures ratio of CF_4. The amount of the introduction of fluorine becomes constancy at 0.2 or more. The mixture ratio of CF4 becomes 0.2, a small amount of fluorine entering from Figure 7 for benzene and it is thought that the

structure has CF (aromatic), CF, and CF_2 [5][6]. Moreover, the film from which the shake up peak was seen was made. These structures might be not change with fluorine at 0.2 or more. The mixture ratio of CF_4 is 0.2 for cyclohexene and it is thought that the structure has CHF, CF, and CF_2. Moreover, the shake up peak was not seen. These structures might be not change with fluorine at 0.2 or more. It is thought that the mixture ratio of Ar and CF_4 is changed as a result, and the structure doesn't change with fluorine. It is thought that the refractive index decreased by the difference of the amount of the introduction of fluorine.

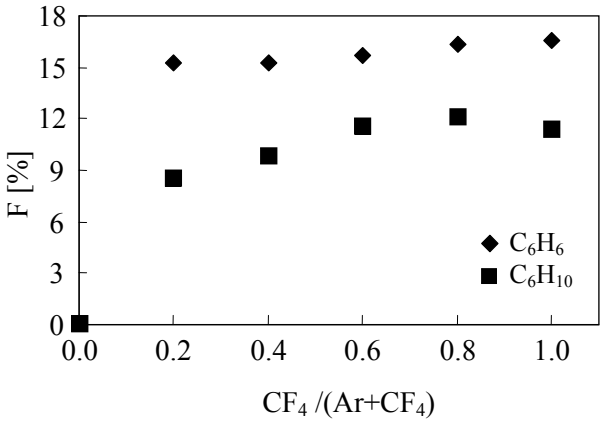

Fig.6 Introduction amount change in fluorine

Therefore, it is possible to make the specific refractive index difference between the core and clad below 0.35 percent, because the difference of mixture ratio between them becomes 0.05 (benzene) or 0.15 (cyclohexene).

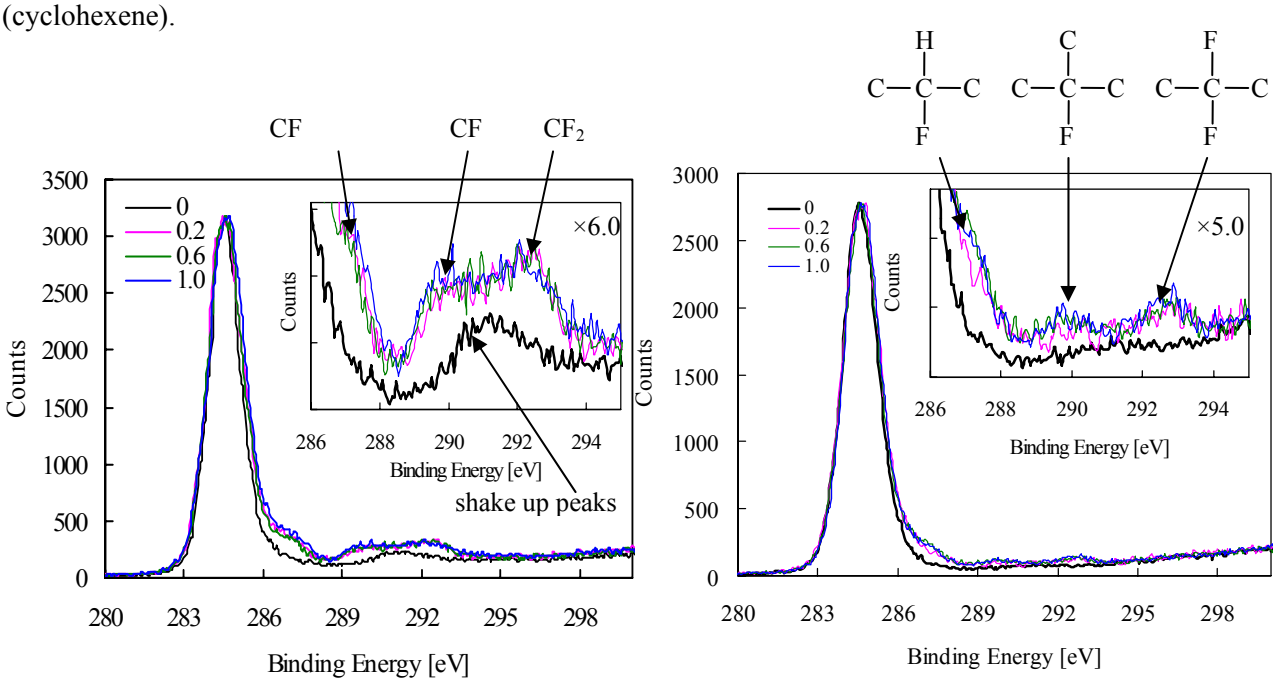

Fig.7 C1s spectrum

4. Conclusion

The refractive index clarified the straight change into the mixture ratio by changing the ratio of the sp^2 bond and the sp^3 bond by changing the mixture ratio of material benzene and cyclohexene. It is possible to make the specific refractive index difference between the core and clad below 0.5 percent, because the difference of mixture ratio between them becomes 0.07 (Ar) or 0.14 (CF_4). The single-mode waveguide of the core diameter 5 micrometer core can be formed with the specific refractive index difference below 0.5 percent.

Acknowledgement

The authors wish to thank to assistant professor T. Iwao of the Musashi Institute of Technology for his fruitful suggestions, and Prof. F. Koyama and assistant professor T. Sakaguchi of Tokyo Institute of Technology microsystem research center to using the spectroscopic ellipsometer.

References

[1]Y. Bounouh, M. L. Theye, A. Dehbi-Alaoui, A. Matthews, J.P.Stoquert, Phys. Rev. B, Vol. 51, pp.9597-9605, 1995.

[2]Kaplan, F. Jansen, M. Machonkin, Appl. Phys. Lett., Vol. 47, pp. 750-753, 1985.

[3]Meng Chen, Tsin-Chi Yang and Xiao Zhou, J. Poly. Sci. Part. B, Vol. 34, pp.113-120, 1996.

[4]J.Ristein, R. T. Stief, L. Ley and W. Beyer, J. Appl. Phys, Vol. 84, pp.3836-3847, 1998.

[5]Licheng M. Han et.all, JOURNAL OF APPLIED PHYSICS, Vol. 84, pp.439-444, 1998.

[6]T. Martin, Galiya Sh. Maikov, Carmen I. Butoi, Ellen R. Fisher, J. Vac. Sci. Tecynical. A, Vol. 22, pp.227-235, 2004.

Enhanced magnetron sputtering deposition of NiO by gas flow modulation

I. Hotovy[1], J. Huran[2], D. McPhail[3], V. Rehacek[1]

[1] *Faculty of Electrical Engineering and Information Technology, Slovak University of Technology, Ilkovicova 3, 812 19 Bratislava, Slovakia*
[2] *Institute of Electrical Engineering, Slovak Academy of Sciences, Dubravska cesta 9, 841 04 Bratislava, Slovakia*
[3] *Department of Materials, Imperial College, Prince Consort Road, London SW7 2BP, U.K*

Abstract
We present the pulsed dc magnetron sputtering method in which a nickel target is sputtered in a mixture of argon and reactive gas oxygen. The flow rate of oxygen is modulated periodically in time and during deposition when oxygen flows is cut off to remove the oxide formed on the target. Modulated deposition process was monitored directly by optical emission spectroscopy, the deposition rate and partial pressure measurement. The variations of atomic ratio in NiO films were revealed by SIMS method.
Keywords: reactive magnetron sputtering, gas flow modulation, nickel oxide, SIMS

1. Introduction

Magnetron discharges in reactive gases are currently used for deposition of compound films. Reactive magnetron deposition can be used for oxides deposition, but it is a complex process, the kinetics of which occur in several stages: transport of gas into the reaction zone [1], conversion of molecules into active states (ionization, dissociation, excitation, etc. [2]), transport of active particles towards the surfaces (target, substrate and chamber walls), their interaction with surfaces [3] and the removal by pumping from the chamber of the resultant products. Behavior of process and thin film properties will be affected then by extension of each stage. Moreover, the overall process is reactive (reactive gas is nitrogen, inert gas is argon), and thus to a great extent non-linear and show hysteresis in the process parameters. Thus the gas flow conditions and final composition of the gas mixture can play a significant role in these processes. Reactive magnetron discharge regime can be unstable due to the relation between the sputtering and the consumption of oxygen either by the target or by the deposited film. Generally reactive sputtering with metal target is often faced with the following difficulties. One is reduction of deposition rate due to the presence of reactive gases. The other is formation of a compound at the target surface caused by a reaction with induced gas. The second phenomena are called poisoning of the target and sometimes cause poor reproducibility of film formation. In reactive sputtering it may be possible to obtain the desired compound composition with several different combination of processing parameters [4]. It is therefore very important to be able to individually control these parameters [5]. Modulation of the flow modulation of oxygen was investigated as a possible method of enhancing the deposition process when preparation oxide and nitride films [6-8]. The flow rate of oxygen is modulated periodically in time and during deposition when oxygen flows is cut off to remove the oxide formed on the target [9-11].

Here we present the pulsed dc magnetron sputtering method in which a nickel target is sputtered in a mixture of argon and reactive oxygen gas. The mass flow rate of oxygen is modulated in the fashion of a rectangular wave function. The influence of the oxygen flow rate on the deposition rate, the target potential and the Ni/O ratios in NiO thin films are investigated.

2. Experimental

The experiments were carried out in the experimental apparatus which contained of a dc custom-built magnetron sputtering source with a Ni target. Measurements of flow conditions were realized at constant total pressure of the working mixture and its value was 0.5 Pa. The flow rate of oxygen was modulated periodically in time (Fig.

2). During the first period, the oxygen flow was on for 45 s and in the second period, O_2 flow was cut off (5 s). A constant pulse period of T=50 s was used. The oxygen mass flow rates were 10, 30 and 50 sccm, respectively, during t_{on}=45 s, whereas the injection of oxygen was completely stopped during t_{off}=5 s. In this study, the rectangular wave function has been used because it appears as the simplest of the possible flow modulations. The discharge power was maintained at 600 W.

The light emitted from discharge was collected from a certain point near the target by two UV lenses and 1 mm aperture (mounted in between) onto the entrance slit 0.3 m monochromator Bentham M300E. A photomultiplier Hamatsu R955 was mounted just behind the exit slit of the monochromator. The photomultiplier signal was sent to current supply, then to analogue-digital converter and the spectra stored on a microcomputer. This optical system was mounted upon a vertically moving table, which enables us to observe the emitted light from plasma along the target. The spectral range between 300 and 900 nm was investigated. In order to study the influence of oxygen flow 10, 30 and 50 sccm, respectively, on the OES spectra we selected Ni (352.4 nm), Ar (751.4 nm) and O (777.0 mm) lines on which to focus. Partial pressure measurements were realized at the constant values of pumping speed and of chamber volume by a capacitance manometer (MKS Baratron). The changes of deposition rates ware monitored by a thin film thickness and deposition rate monitor (Inficon) with a quartz crystal sensor head. A quadrupole SIMS instrument Physical Electronics PHI ADEPT 1010 with primary ion beam Cs^+ was used to depth compositional analysis of NiO films prepared by this process.

3. Results and discussion

In our previous study we defined the sputtering modes for the continuous addition of oxygen at NiO deposition [11]. The oxygen flow rates we used here were based on these results. The conditions of the oxygen flow rates and period were respectively 10 sccm and 50 s, 30 sccm and 50 s, 50 sccm and 50 s. The first condition corresponds to the experimentally observed condition for the metal-sputtering mode while the two other conditions are valid for the oxide-sputtering mode for the continuous addition of oxygen.

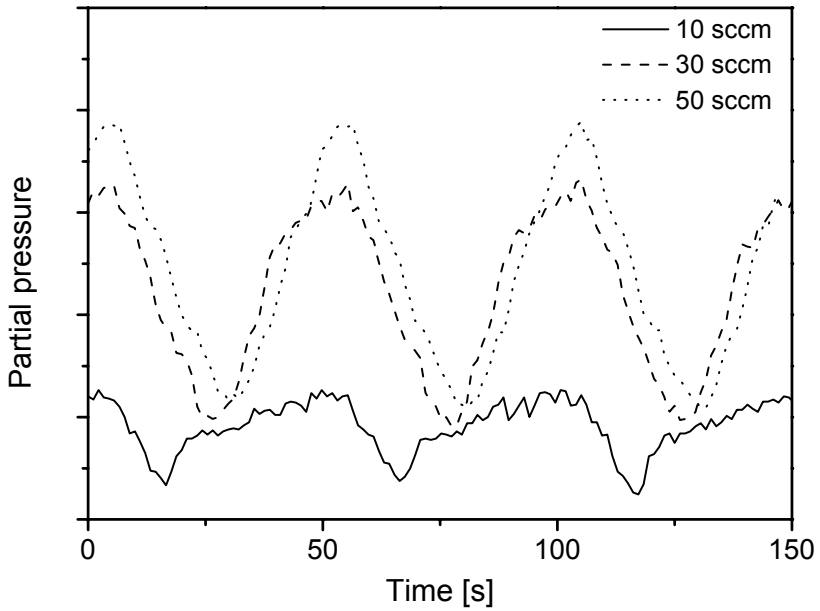

Fig. 1: Oxygen partial pressure in the deposition chamber during an oxygen-on and oxygen-off period.

The partial pressure measurements were realized at constant values of pumping speed and of chamber volume without the plasma. Fig. 1 shows the change of the partial pressure of oxygen during an oxygen-on and oxygen-off period for various oxygen flows. The time for the increase and decrease of the partial pressure is determined

by pumping speed, chamber volume and oxygen flow. Using the modulation unit we controlled the oxygen flow and this lead to an oscillating oxygen concentration during the sputtering process. When the oxygen flow is cut off, the partial pressure will be decreased and the decrease in the partial pressure will enhance the deposition rate. This can be explained by an increased pumping speed resulting from gettering of oxygen by continuously deposited nickel.

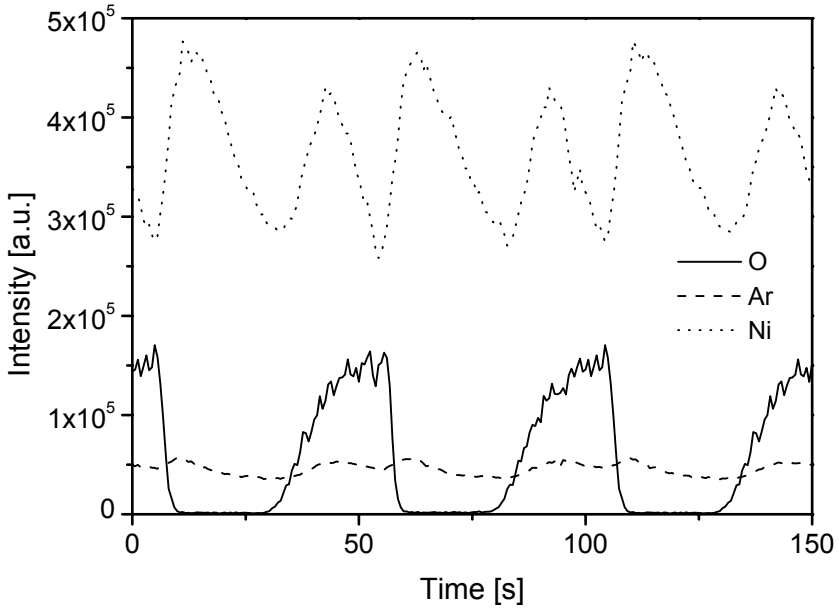

Fig. 2: Time dependencies of OES signals of nickel, oxygen and argon for periodic oxygen addition 50 sccm.

OES yields interesting information on excited species, atoms, molecules and radicals present in the plasma as well as qualitative variations of these species with respect to the discharge conditions. The corresponding variations of the intensities of Ni (352.4 nm), O (777.0 nm) and Ar (751.4 nm) lines against the oxygen flow rate are given in Fig. 2. We note that the changes are due to the oxygen modulation and they reflect the coverage of the target. During the oxygen-off period the peak intensity from Ni line rapidly increases while the oxygen OES signal indicating the concentration of excited oxygen molecules in the plasma decreases.

The variations of the deposition rate and real time measurements of the nickel target potential for the periodic oxygen addition were recorded (Fig. 3). The maximum NiO deposition rate was observed for 10 sccm oxygen flow and its value is almost constant. We suppose that this deposition process remains predominantly in the metal-sputtering mode, because the Ni target potential exhibits weak changes from 430 to 445 V. The poisoning compound layer on the surface of the target is thin enough and partially formed to rapidly restore the process in metal-sputtering mode. For 30 and 50 sccm oxygen flow rate, respectively, the poisoning compound layer is thicker and the oxidized surface expands. Sputtering yield is reduced as well as the deposition rate. The metal-sputtering mode cannot achieve and is vanished under the oxide-sputtering mode. In the oxide-sputtering mode the poisoning of the target becomes serious because of the higher secondary electron emission coefficient of the oxide compared to that of pure metal, the total number of electrons near the target increases and hence a higher target current can be achieved at lower voltage. Therefore, it can be seen that the target potential changes in the range from 318 to 385 V but the characteristic values for the metal-sputtering mode were not reached. This conclusion is in agreement with the partial pressure measurements when we observe the higher values that are characteristic for metal-sputtering mode.

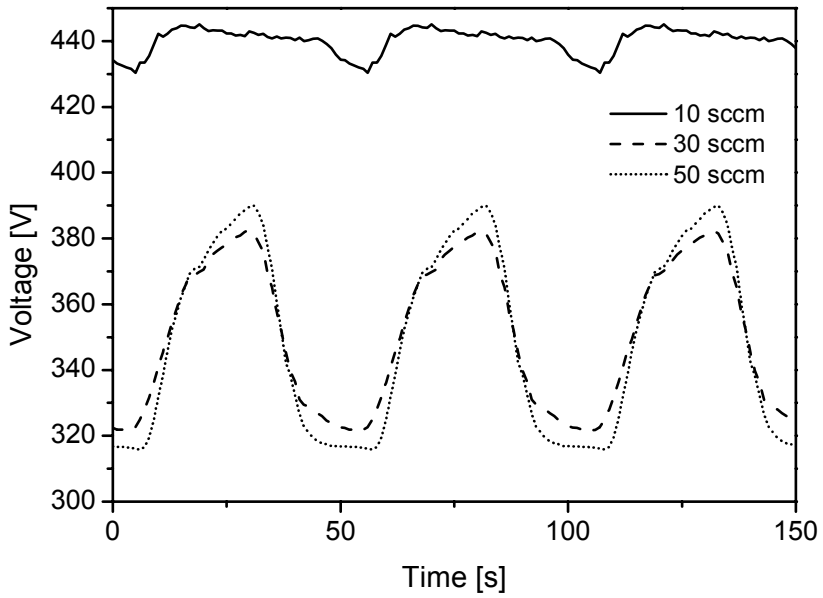

Fig. 3: Real time measurements of nickel target potential for periodic oxygen addition.

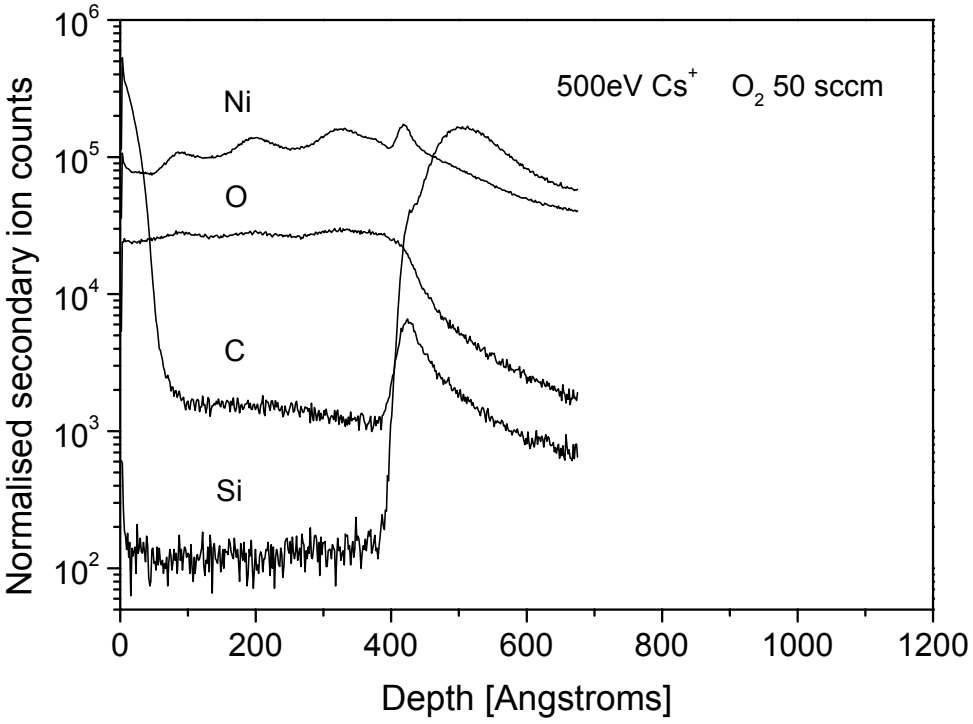

Fig. 4: SIMS depth profile taken from NiO film prepared at 50 sccm oxygen flow.

Some samples on silicon substrates have been deposited by repeated oxygen-on and oxygen-off cycles during three periods. In the case of the sample prepared at 10 sccm oxygen flow rate the SIMS depth profiling shows that the composition of the layer is essentially invariant with depth and the level of Ni and O are not practically affected by periodic oxygen addition. On the other hand, SIMS measurements from samples prepared at 30 and 50 sccm oxygen flow rate clearly record the oscillation of Ni and O in the depth profile (Fig. 4). Then, the

behavior of the Ni target potential changes not only the deposition rate but also the composition and variations of Ni/O atomic ratios in NiO films. We conclude that in order to get a higher NiO deposition rate in the oxide-sputtering mode, pulsing of the oxygen flow rate is a suitable method. The enhancement of the deposition rate is caused by processes on the target during removal of oxide compounds from its surface. It was found that the oxygen concentration strongly increases immediately when the O_2 flow is cut off. Then, pulsing of oxygen affects the NiO growth process and chemical composition of the films.

4. Conclusion

A controlled pulsing of the oxygen flow rate has been investigated for reactive magnetron deposition of nickel oxide thin films. A sputtering process to enhance and change the deposition rate and the target potential of NiO in the reactive magnetron system was proposed using flow modulation of oxygen. This pulsing method can modify and control the properties of the films and suppress the instabilities in the reactive sputtering. By this process thin NiO films with the different Ni/O ratios can be deposited alternatively and the multilayered film results.

Acknowledgements
The work was supported by the Scientific Grant Agency of the Ministry of Education of the Slovak Republic and Slovak Academy of Sciences, No. 1/0170/03 and by Science and Technology Assistance Agency under the contract, No. APVT-20-021004.

References

[1] T. Larson, H.O. Blom, C. Nender and S. Berg, J. Vac. Sci. Technol, **A6,** 1832 (1988).
[2] D.K. Hohnke, D.J. Schmatz and M.D. Hurley, Thin Solid Films, **118,** 301 (1984).
[3] S. Kadlec, J. Musil and J. Vyskocil, J. Vac. Sci. Technol, **A8,** 1560 (1990).
[4] S. Zhu, F. Wang and W. Wu, J. Vac. Sci. Technol, **A17,** 70 (1999).
[5] S. Berg, T. Larson and H.O. Blom, J. Vac. Sci. Technol, **A4,** 594 (1986).
[6] S. Hofmann, Thin Solid Films, **191,** 335 (1990).
[7] N. Martin, A.R. Bally, P. Hones, R. Sanjines, F. Levy, Thin Solid Films **377-378,** 550 (2000).
[8] H. Sekigichi, T. Murakami, A. Kanzawa, T. Imai, T. Honda, J. Vac. Sci. Technol. **A14,** 2231 (1996).
[9] R.P. Howson, N. Danson, I. Safi, Thin Solid Films **351,** 32 (1999).
[10] N. Martin, R. Sanjines, J. Takadoum, F. Levy, Surface and Coating Technol. **142-144,** 615 (2001).
[11] S. Kimura, T. Honda, D. Fukushi, J. Vac. Sci. Technol. **A17,** 3312 (1999).
[12] I. Hotovy, J. Huran, J. Janik, A.P. Kobzev, Vacuum **51**, 157 (1998).

Deposition of SnO_2 nanostructured thin films by PECVD : role of the excited O_2 species on the film properties

J. Pulpytel, M. Jubault, W. Morscheidt, J. Amouroux, F.Arefi-Khonsari

Laboratoire de Génie des procédés Plasmas, ENSCP-Université Pierre et Marie Curie Paris VI, Paris, France

Abstract

Nanostructured tin oxide thin films were fabricated by a PECVD process. The threshold ionization technique (TIMS) was used to measure O_2 ($^1\Delta_g$) and O_2 ($^1\Sigma_g^+$) densities during the deposition of tin oxide. The densities of these species have been correlated with the effective electron temperature and electron density determined by integration of the electron-energy-distribution-function (EEDF). Furthermore, these results have been shown to be correlated to the trend of the electronic conductivity of SnO_2 thin films.

1. Introduction

SnO_2-based materials are widely used in many fields. Among all tranparent conductive oxides (TCO), SnO_2:F is the most often used to make energy-conserving windows, due to its low emissivity ("low-e") [1]. In addition, due to the excellent properties for sensors, SnO_2 has become the most investigated material for metal oxide sensors since the first Tagushi sensors in 1970 [2]. The optical and electrical performance of a TCO depends not only on its chemical composition, but also on the method used for its preparation.

Argon/oxygen/tetramethyltin ($Sn(CH_3)_4$ or TMT) were used to deposit tin oxide films using a capacitively coupled RF 13.56 MHz reactor. The latter was composed of nanosized particles (6-10 nm) in particularly interesting for gas sensing applications [3] but also for transparent conductive coating on polymers [4].

The present paper describes mass spectrometric measurements of O_2 ($^1\Delta_g$) and O_2 ($^1\Sigma_g^+$) densities using the threshold ionization technique (TIMS) and EEDF measurements via a Langmuir probe technique. The correlation between these two diagnostic methods is investigated. The electronic conductivities of tin oxide thin films determined from four-point probe measurements was monitored as a function of certains deposition parameters and related to the relevant plasma characteristics. Morphological and structural analyses from transmission electron microscopy (TEM) are also reported.

2. Experimental

The geometry of the experimental setup for TIMS and EEDF measurements is shown in Fig. 1. A capacitively coupled discharge (CCD) was produced in a 16 cm diameter cylindrical stainless steel vessel, between two parallel plates separated by a distance of 3 cm. The shower-head powered aluminum electrode was 10 cm in diameter and the grounded stainless steel one was 3 cm in diameter. The voltage of the RF signal at the powered electrode is recorded using a Tektronix P6015 high-voltage probe and a Lecroy waverunner LT 342 oscilloscope. The system can be evacuated to a base pressure of $8x10^{-4}$ Pa ($6x10^{-6}$ Torr). Mixtures of argon/oxygen, controlled by MKS mass flow controllers (1259 B), were studied first, before introducing small quantities of TMT (0.5-2%) with a MKS vapor source mass flow controller (1150C). The total flow and the operating pressure were kept constant at 10 sccm and 15 Pa (110 mTorr) respectively.

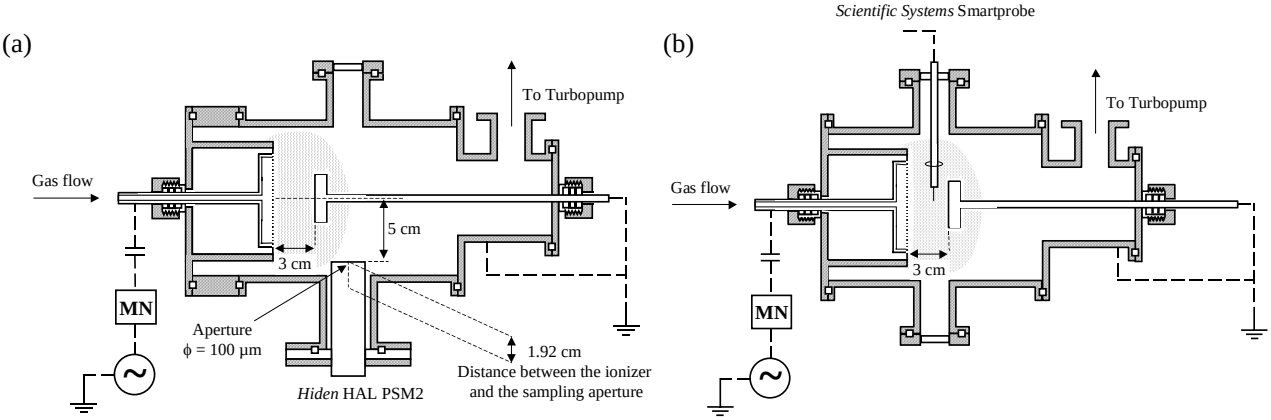

Fig. 1. (a) Schematic of the capacitively coupled plasma reactor with the singly differentially pumped mass spectrometer. (b) Schematic of the capacitively coupled plasma reactor and the Langmuir probe.

A Hiden PSM2 quadrupole mass spectrometer was mounted to detect neutral species from the plasma. The 100 µm diameter aperture was located 8 cm from the center of the plasma. The distance between the ionizer and the sampling aperture was 1.92 cm. A base pressure of 1.3×10^{-6} Pa (10^{-8} Torr) was achieved in the mass spectrometer chamber, and the operating pressure in the mass spectrometer increased up to 1.1×10^{-4} Pa (8×10^{-7} Torr) for 15 Pa (110 mTorr) in the plasma chamber. The electron energy scale was standardized by argon, the ionization energy of which is $I(Ar\ ^1S_0 \rightarrow Ar^+\ ^2P_{3/2}) = 15.8$ eV. The width in the energy distribution of the electron beam is about 0.5 eV at half-maximum.

The Langmuir probe system was a RF compensated Smartprobe from Scientific Systems. The tungsten wire (10 mm, 190 µm ϕ) was introduced in the center of the discharge, where the electron density was measured to be above 5.10^9 cm^{-3} enabling an effective auto-cleaning of the tip. Probe cleanliness was verified by the similiraty of the EEDF recorded sequentially at the same conditions.

For electrical measurements, the room temperature sheet resistance of the films was determined using the four-point probe method (Keithley 224 and 195A). A JEOL 100 CXII (100 KeV) microscope was used for TEM observations on ultrathin tin oxide thin films prepared under the conventional preparation method ; the films were mechanically polished and thinned with ionic bombardment. The TEM images were analysed with the software Visilog 5.4.

3. Measurements of O_2 ($^1\Delta_g$) and O_2 ($^1\Sigma_g^+$) densities by TIMS

Considering the mass spectrum of the figure 2, the signal on mass 32 attributed to O_2^+ is shown as a function of the energy of the electrons emitted by the filament. The ionization potential of O_2 molecules is at $E_I = 12.2$ eV. However, when the discharges were initiated, O_2^+ ions have been detected before the ground-state ionization threshold indicating a population of electronically and vibrationally excited species. The 10 % decrease in the O_2^+ intensity at high energies with "Discharge On" is probably due to the dissociation of molecular oxygen to atomic one. According to the equation (1), the density of singlet O_2 (O_2 ($^1\Delta_g$) and O_2 ($^1\Sigma_g^+$) denoted as O_2*) is obtained by [5] :

$$\frac{n_{O_2^*}^{On}}{n_{Ar}^{Off}} = \left(\frac{A^{O_2^* \rightarrow O_2^{*+}}}{A^{Ar \rightarrow Ar^+}} \right) \left(\frac{\lambda^{Ar \rightarrow Ar^+}}{\lambda^{O_2 \rightarrow O_2^{*+}}} \right) \left[\frac{\alpha(Ar^+)}{\alpha(O_2^+)} \right] \qquad (1)$$

where n_{Ar}^{Off} is the number density of Ar in the ionization chamber (plasma off), $A^{O2 \rightarrow O2^{*+}}$ and $A^{Ar \rightarrow Ar^+}$ are the slopes of the linear fits to O_2^{+*} signal and Ar^+ signal respectively. $\lambda^{O2^* \rightarrow O2^{*+}}$ and $\lambda^{Ar \rightarrow Ar^+}$ are the slopes of the linear fits of the cross sections of ionization of O_2* and Ar ionization respectively, assuming that the ionization cross sections for the molecules at corresponding excess energies were almost equal, i.e. $\lambda^{O2^* \rightarrow O2^+} \cong \lambda^{O2 \rightarrow O2^+}$. The parameter $\alpha(Y)$ is estimated to be $(m/e)^{-0.85}$ and is the Y specie m/e dependent transmission efficiency of the quadrupole mass filter and the m/e dependent detection coefficient of the detector.

This yields a density of singlet oxygen molecules between 3×10^{13} - 4×10^{14} cm^{-3} and a density ratio up to 18% of the total O_2 molecules as shown in Fig. 3.

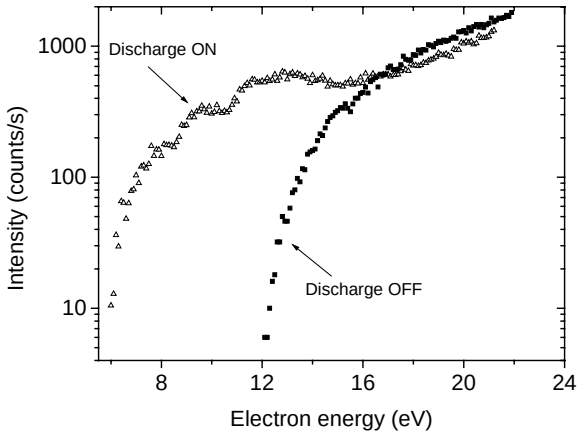

Fig. 2. TIMS with m/e = 32 for 34% Ar – 66% O_2 mixture, P = 15 Pa(110 mTorr), RF voltage = 550 V.

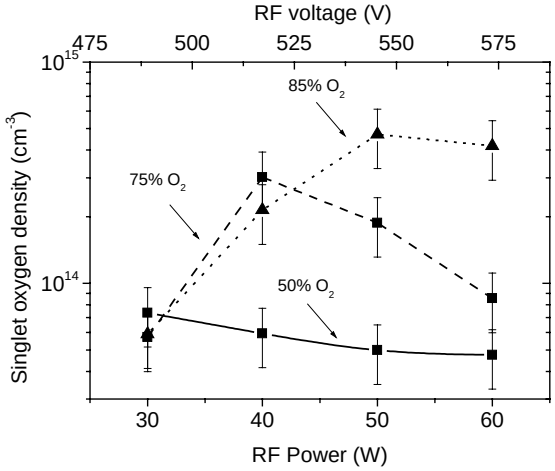

Fig. 3. Density of singlet oxygen molecules as a function of O_2 mole percentage in the feed gas.

4. Langmuir probe EEDF measurements

In our previous work [6], the EEDF or F(ε) was not reported. The electron-energy-probability-function (EEPF) or f(ε) can be determined with the Druyvesteyn formula (2) [7] :

$$f(\varepsilon) = \frac{2 \cdot I_e^{''}}{e^3 \cdot A} \cdot (2 \cdot m)^{1/2} = \frac{F(\varepsilon)}{\sqrt{\varepsilon}} \qquad (2)$$

where I_e" is the second derivative of the current, m and e are the electron mass and charge respectively, A is the probe area and ε is the probe potential with respect to the plasma potential. In our discharges, the EEPF at 15 Pa (110 mTorr) can be represented as a bi-Maxwellian with a cold-electron group having temperature T_{ec} and density n_{ec}, and a hot-electron group characterized by T_{eh} and n_{eh}. These parameters can be obtained by integration of the EEDF (3), (4) :

$$n = \int F(\varepsilon) \cdot d\varepsilon \qquad (3) \qquad T_e = \frac{2}{3} \cdot \int \varepsilon \cdot F(\varepsilon) \cdot d\varepsilon = \frac{2}{3} \cdot \langle \varepsilon \rangle \qquad (4)$$

An EEPF obtained by the probe is shown in Fig. 4. The evolution of the electron temperatures are also shown in Fig. 5.

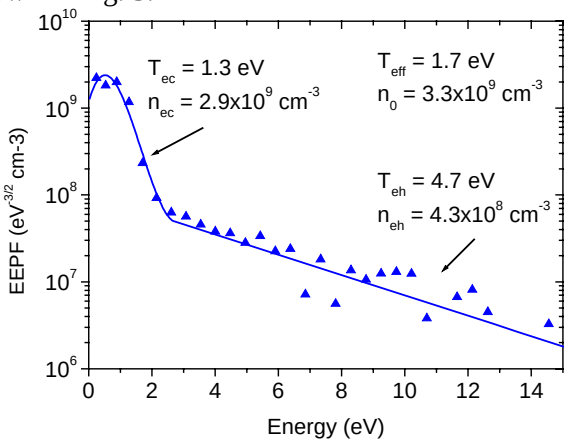

Fig. 4. The EEPF measured in an Ar(25%)/O_2(75%) discharge at 390 V and 15 Pa.

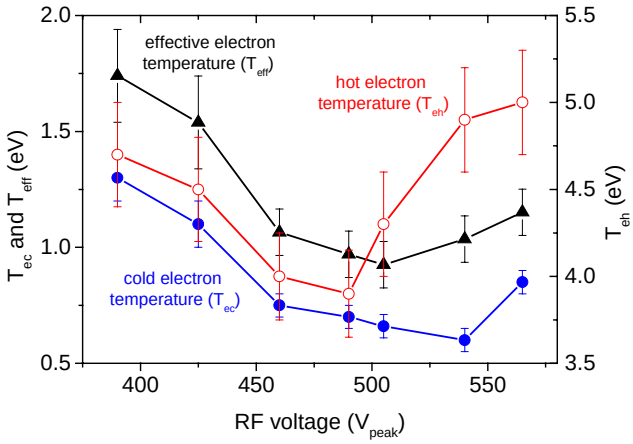

Fig. 5. Electron temperatures and effective electron temperature in an Ar(25%)/O_2(75%) discharge at 15 Pa.

5. Electrical properties of SnO_2 thin films

The sheet resistance R_s of our tin oxide films have been determined by 4-point probe measurements.
The figure 6 shows the evolution of the sheet resistance for undoped tin oxide thin films.

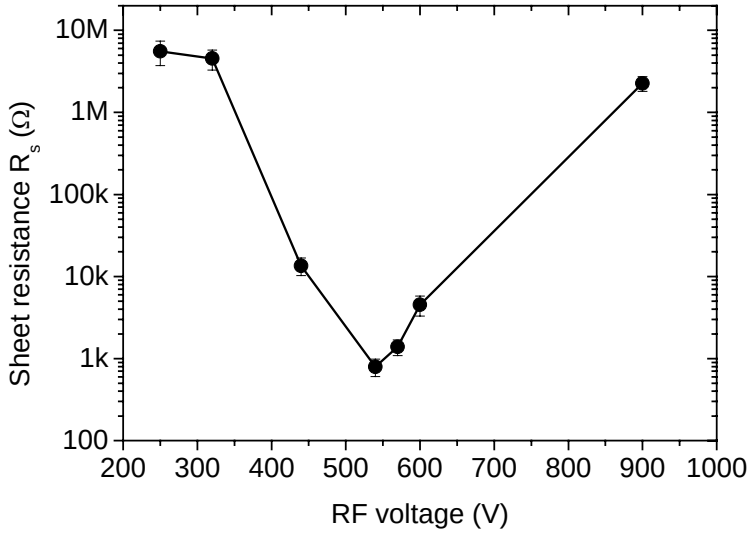

Fig. 6. Tin oxide sheet resistance as a function of the RF voltage for 1% TMT–24% Ar–75% O_2 at 15 Pa

6. Nanostructure of SnO_2 thin films

Figure 7 shows the TEM image of a SnO_2 sample with a 100,000 magnification. The micrograph exhibits a uniform and continuous distribution of spherical nano-sized grains (6-10 nm) agglomerated . A statistical analysis of the size distribution obtained by image analysis is shown in Fig. 8.

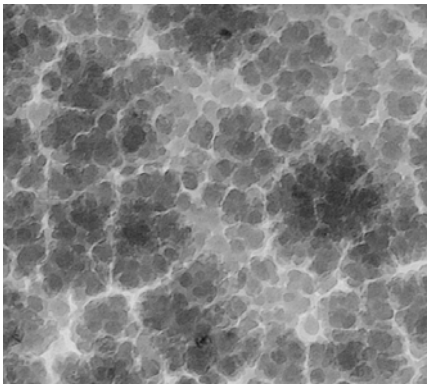

Fig. 7. Transmission electron microscopy of tin oxide nanoparticles thin films (x 100,000).

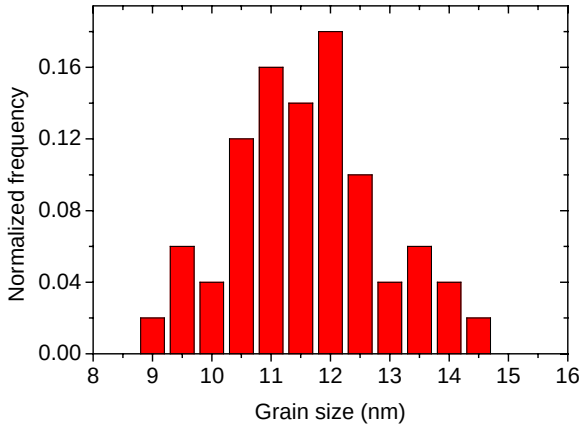

Fig. 8. Histogram of particle diameters obtained from image analysis.

7. Correlations between TIMS and Langmuir probe measurements

In what follows the results are presented in Fig. 9. On one hand, the effective electron temperature measured at low voltage is a few electron-volts (1.5-1.7 eV) with an electron density of the order of 10^9 cm^{-3}. By increasing the RF voltage, the electron temperature drops dramatically to about 0.9 eV, while the electron density rises to $2x10^{10}$ cm^{-3}. Then, the electron temperature rises again after a critical voltage denoted by V_{probe}* at 505 V. This phenomenon has been also observed in other discharges too [8]. On the other hand, the densities of singlet oxygen molecules increases up to $3x10^{14}$ cm^{-3} for a critical voltage denoted by V_{TIMS}* at 515 V, then decreases. By coupling Langmuir probe measurements with TIMS ones, one can conclude that the trend of the singlet molecular oxygen formed in the discharge is what could be expected, i.e. at 0.9 eV, where the effective electron temperature is minimum, the concentration of singlet oxygen is maximum. This may be explained by the effective electron temperature which is close to the energy levels of O_2 ($^1\Delta_g$) and O_2 ($^1\Sigma_g^+$), respectively at 0.97 eV and 1.63 eV, so a large population of electrons can populate these energy levels and this is why a maximum of the concentration of these species has been observed.

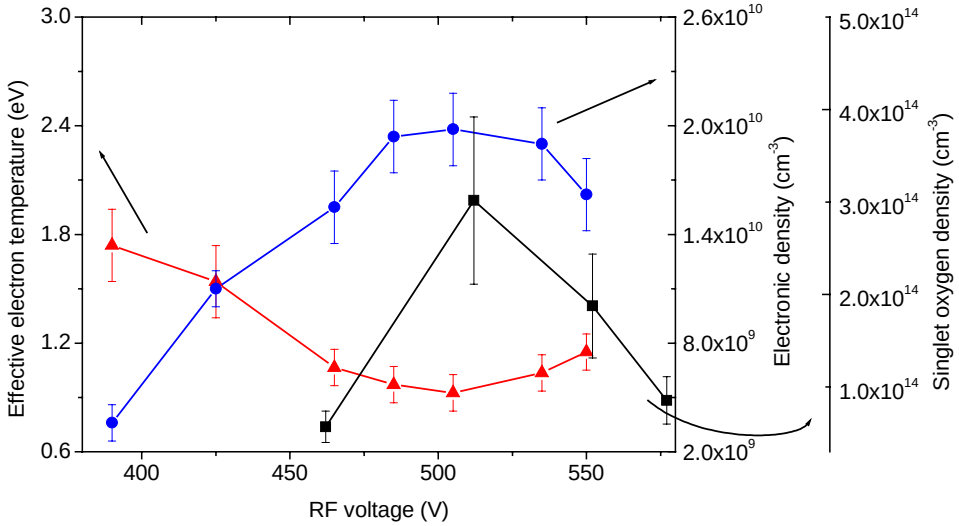

Fig. 10. The correlation between TIMS and Langmuir probe measurements for 25% Ar – 75% O_2 at 15 Pa

8. Influence of the singlet oxygen density on tin oxide thin films resistance

Figure 10 shows the decrease of the SnO_2 sheet resistance as a function of the increase of density of singlet molecular oxygen. These results show that excited molecular oxygen is one of the species which plays an important role in the carbon stripping of the deposited films leading to conductive ones.

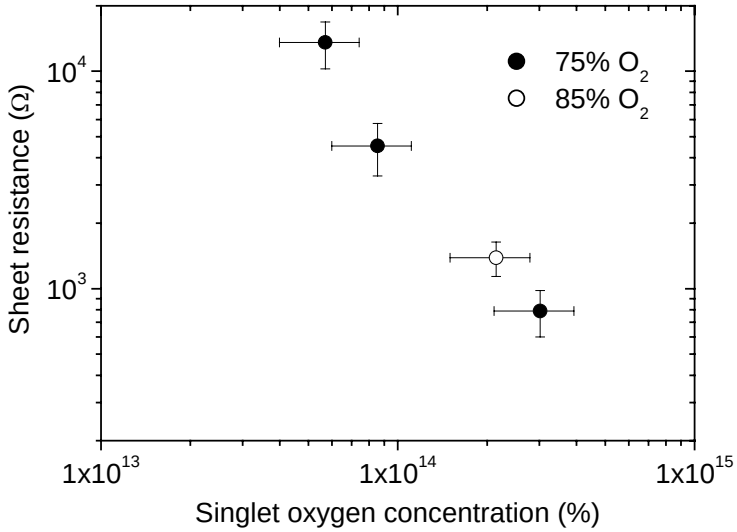

Fig. 10. SnO_2 sheet resistance as a function of the singlet oxygen density for 75% O_2 and 85% O_2 mixtures at 15 Pa

9. Conclusion

By combining mass spectrometric study and Langmuir probe measurements, it has been possible to explain the evolution of the singlet oxygen molecules, and the change in the sheet resistance of the thin films deposited. The trend of the variation of the O_2 ($^1\Delta_g$) and O_2 ($^1\Sigma_g^+$) is ruled by the energetic characteristics of the discharge. Indeed, the maximum density of such species has been observed at the highest electron density and the lowest temperature. The deposition of carbon free tin oxide films may be explained by the high chemical reactivity of singlet molecular oxygen amongst other species with organic compounds.

References

[1] D.S. Ginley, C. Bright, MRS Bulltetin/August 2000, 15 (2000)
[2] N. Bârsan, U. Weimar, J. Phys.: Condens. Matter **15**, 813 (2003)
[3] F. Hellegouarc'h, F. Arefi-Khonsari, R. Planade, J. Amouroux, Sens. actuators. B, Chem. **73-1**, 27 (2001)
[4] J. Pulpytel, M. Ghasemi, H. Cachet, D. Festy, F. Arefi-Khonsari, ISPC 16, Taormina, Italy (2003)
[5] H. Singh, J. W. Coburn, D. B. Graves, J. Vac. Sci. Technol. **A18(2)**, 299 (2000)
[6] J. Pulpytel, F. Arefi-Khonsari, W. Morscheidt, J. Phys. D: Appl. Phys. **38**, 1, (2005) (in press)
[7] V.A. Godyak, A.S. Khanneh, J. Appl. Phys. **73(8),** 3657 (1992)
[8] A. Melzer, R. Flohr, A. Piel, Plasma Sources Sci. Technol., **4**, 424 (1995)

The Mechanism for Forming the Hot rotational distribution of CH Molecules

A.V. Filippov[1], Yu.A. Mankelevich[2], A.F. Pal[1], T.V. Rakhimova[2], A.N. Ryabinkin[2], A.O. Serov[2], A.Yu. Yuriev[2]

[1]Troitsk Institute for Innovation and Fusion Research, Troitsk, Moscow reg., Russia

[2]Nuclear Physics Institute of Moscow State University, Moscow, Russia

Abstract

The paper is devoted to the study of the RF discharge utilized for carbon film deposition. The emission spectroscopy method is applied for plasma diagnostics. The formation of CH molecule non-equilibrium rotational distribution is found. The chemical mechanism of production of the hot rotational distribution of CH molecules is considered.

Keywords

Emission spectroscopy, RF discharge, Chemical Vapour Deposition, Rotational temperature, Honl-London factors.

1. Introduction

Nowadays the Chemical Vapour Deposition (CVD) of thin films having different composition and morphology is widely used in scientific research and technology. An RF discharge is very often used for that purpose due to the possibility of decreasing the rate of electrode erosion in such a discharge and, therefore, eliminating the electrode material impact on the quality of the obtained films. In the present work an RF discharge in pure methane is used to deposit carbon films of various morphology. The emission spectroscopy method was used for plasma diagnostics. The CH $A^2\Delta \rightarrow X^2\Pi_r$ (431.4 nm) emission band was investigated in detail. It is shown that rotational temperature $A^2\Delta$ does not correspond to the gas translational temperature. The analysis of the formation of CH molecule non-equilibrium rotational distribution was carried out.

2. Experimental setup

The experiments were carried out on the setup whose scheme is in fig.1. The volume of the working chamber is about 40 dm^3. The plasma-forming gas was methane, it was activated by the RF discharge with frequency f = 5.28 MHz. The deposition was carried out on silicon substrates situated on the bottom powered electrode. Both one-electrode and two-electrode schemes were used for the deposition. In the latter case the gas gets into the discharge gap of 2.5 cm in length through 170 holes in the top ground electrode. The electrode diameter is 10.0 cm. Typical conditions of the deposition film experiment are as follows: the RF voltage amplitude is 400 V, the gas flow is 1 sccm, and the gas pressure is varied within 4÷40 Pa. Significant self-bias in the potential of the powered electrode was observed in the both installation schemes (up to 95% of the amplitude).

For pressures higher than 10 Pa there usually occurs the growth of fine dispersed hydrogen-carbon structures rather than diamond-like films. This can be explained by the change in the mechanism of electron growth in the discharge at the increase in the pressure (transformation from the low current α-regime of the RF discharge to the high-current γ- regime [1]). It should be noted that α- and γ- regimes differ, in particular, in the temperature of electrons in the middle area of the discharge gap [2].

Optical spectra of the discharge glow were investigated in the two-electrode scheme. There are two glow regions of the discharge in methane in the visible range: one is above the electrode layer of the power electrode, the other is close to the electrode surface (fig.2).

As the pressure grows, the top glow region goes down and its volume decreases. Hydrogen lines H_β (486.1 nm) and H_γ (434.0 nm), and CH $A^2\Delta \rightarrow X^2\Pi_r$ (431.4 nm) emission band system are most intensive. The glow near the top electrode was not observed within the investigated pressure range in the experiments. The radiation from different glow regions was in turns focused upon the monochromator input slit, the spectral resolution being higher than 0.4 nm. A CCD-array with a linear characteristic was used as a emission-measuring device. The discharge glow spectra were obtained for various methane pressures: 40, 21, and also for 6.6 and 4.4 Pa, all these pressures are typical for a CVD-process.

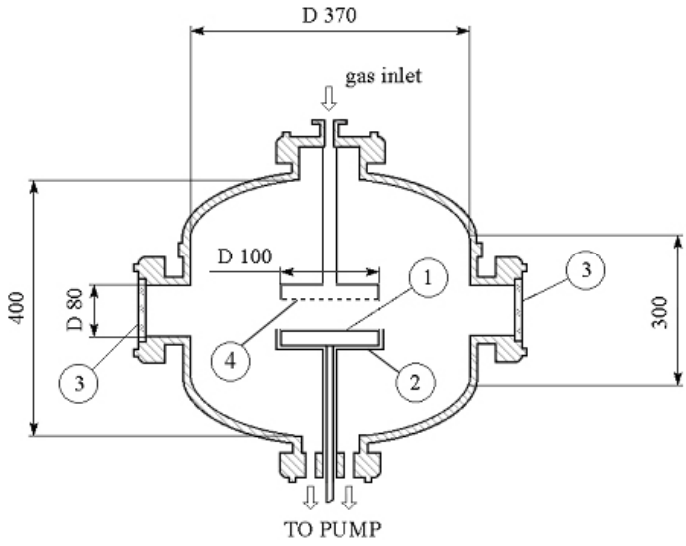

Fig. 1. The scheme of the working chamber of the RF discharge for depositing diamond-like films by the CVD method. 1 – the substrate; 2 – the movable low electrode; 3 – the optical window; 4 – the grid grounded electrode.

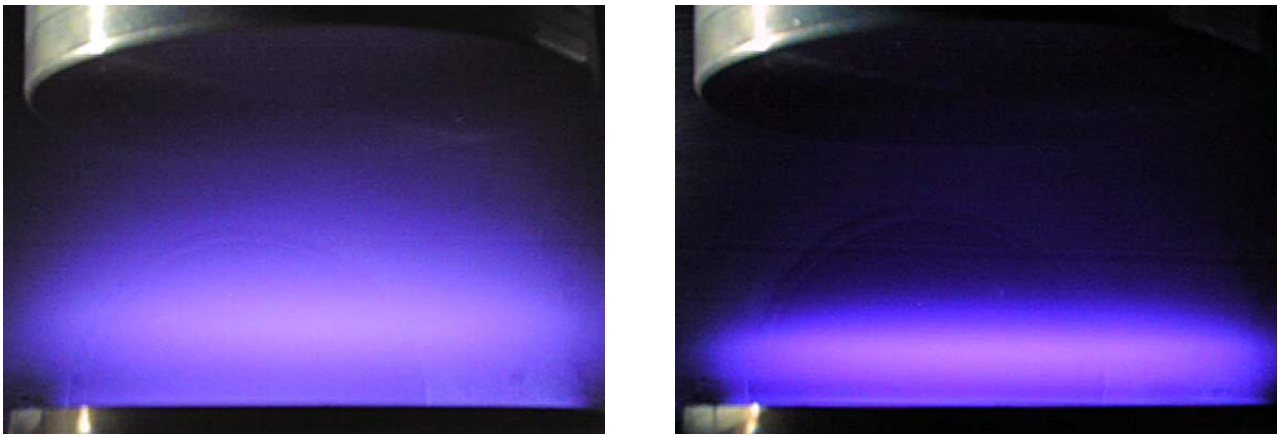

P = 6 Pa P = 19 Pa

Fig. 2. Typical images of the RF discharge glow in methane under different pressures

3. Discussion

One of the most important parameters of the weakly ionized plasma is the temperature of the neutral gas that directly or indirectly influences practically all the processes occurring in plasma. The temperature determines the rate of physical and chemical processes, the direction and the intensity of thermal flows, the reduced electric field strength and the average energy of electrons, the width of spectral lines etc. To determine the gas temperature the method of relative intensities for electronic-vibrational-rotational (EVR) lines of two-atom molecules is used [3].

In this paper the CH $A^2\Delta \rightarrow X^2\Pi_r$ band system was investigated. The spectroscopic data of these states were taken from [4-7]. For the Boltzmann distribution of rotation levels with the temperature T'_{rot} the intensities of the spontaneous radiation of the individual EVR line are determined by the following expression [7-9]:

$$I_{n'v'J' \rightarrow n''v''J''} \propto \cdot \left(\nu_{n'v'J' \rightarrow n''v''J''}\right)^4 S_e q_{v'v''} S_{J'J''} g_{s,a} \exp\left(-\frac{hcF'(J')}{kT'_{rot}}\right) \quad (1)$$

where $\nu_{n'v'J' \rightarrow n''v''J''}$ is the wave number of the $n'v'J' \rightarrow n''v''J''$ transition, n indicates the electron state, v is the number of the vibrational level, J is the total momentum of the rotational level, the values with one prime refer

to the top state, those with two primes to the low one; S_e is the electron momentum of the transition, $q_{v'v''}$ is the Frank-Condon factor, $S_{J'J''}$ is the Honl – London factor, $F'(J')$ – is the rotational term of the top level, $g_{s,a}$ is the value that takes into consideration the difference between statistic weighs of symmetric and anti-symmetric states of homo-nuclear molecules, h is the Plank constant, c is the light velocity, k is the Boltzmann's constant.
The rotational terms of doublet states were determined from relationships [8]:

$$F_1(J) = \nu_0 + B_v\left[\left(J+\tfrac{1}{2}\right)^2 - \Lambda^2 - \tfrac{1}{2}\sqrt{\Lambda^2 Y(Y-4) + 4\left(J+\tfrac{1}{2}\right)^2}\right] - D_v\left[\left(J-\tfrac{1}{2}\right)\left(J+\tfrac{1}{2}\right) - \Lambda^2\right]; \quad (2)$$

$$F_2(J) = \nu_0 + B_v\left[\left(J+\tfrac{1}{2}\right)^2 - \Lambda^2 + \tfrac{1}{2}\sqrt{\Lambda^2 Y(Y-4) + 4\left(J+\tfrac{1}{2}\right)^2}\right] - D_v\left[\left(J+\tfrac{1}{2}\right)\left(J+\tfrac{3}{2}\right) - \Lambda^2\right]; \quad (3)$$

where $\nu_0 = T_e' - T_e'' + G_{v'}' - G_{v''}''$, $G_v = \omega_e\left(v+\tfrac{1}{2}\right) - \omega_e x_e\left(v+\tfrac{1}{2}\right)^2 + \omega_e y_e\left(v+\tfrac{1}{2}\right)^3 + \omega_e z_e\left(v+\tfrac{1}{2}\right)^4 + \ldots$,
$B_v = B_e - \alpha_e\left(v+\tfrac{1}{2}\right) + \gamma_e\left(v+\tfrac{1}{2}\right)^2 + \ldots$, $D_v = D_e + \beta_e\left(v+\tfrac{1}{2}\right) + \ldots$, v is the number of the vibrational level, $Y = A/B$.

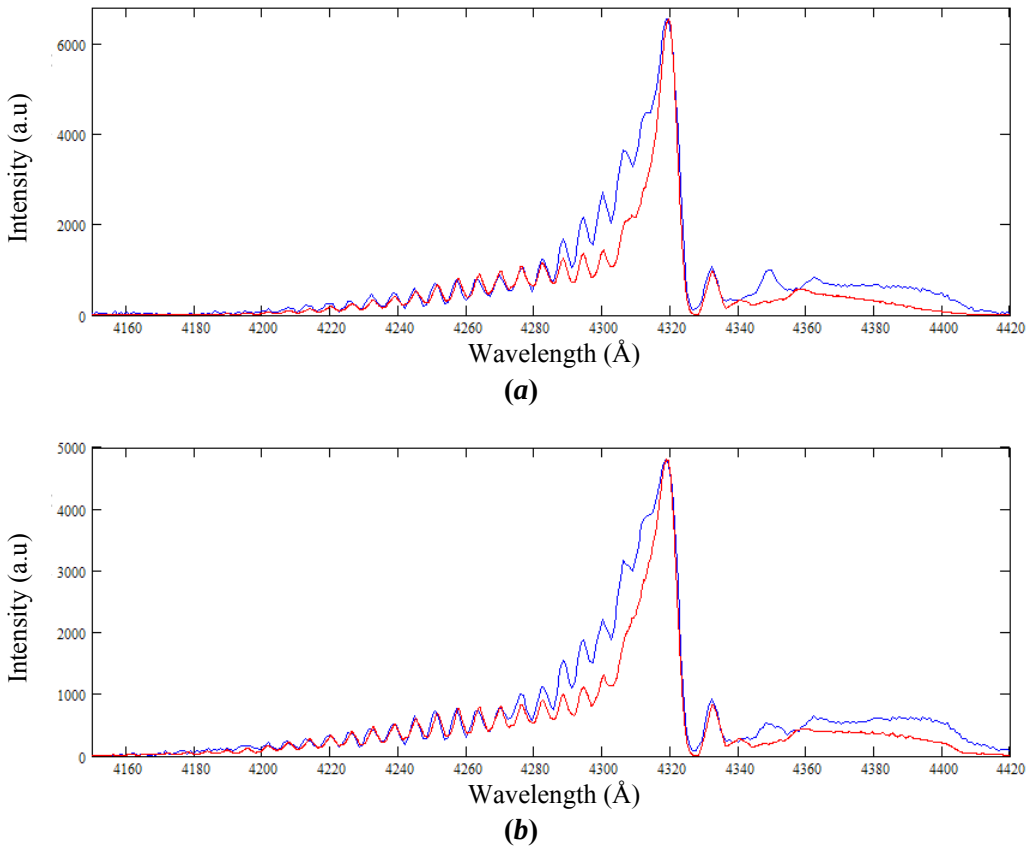

Fig. 3. Experimental and calculation spectra of CH molecules in $A^2\Delta \rightarrow X^2\Pi_r$ system bands at the pressure of 40 Pa, U_{RF} = 400 V, the self-biase of U_{bias} = 340 V, f = 7 MHz.
(*a*) the top glow area, the rotation temperature of T_{rot}=1900 K, the vibration temperature of T_{vib}=2900 K, the maximal glow intensity of I_{max}= 6557 a.u.
(*b*) the low glow area, T_{rot}=2900 K, T_{vib}=2900 K, I_{max}= 4814 a.u.

The Honl - London factors were calculated according to [8]. It should be noted that the levels with the vibration number $N' > 27$ for the zero vibrational level pre-dissociate, therefore, they were not taken into consideration in the calculation. In figures 3-4 there is a comparison of experimental and calculation spectra of CH molecule glow in the Δv=0 sequence in the RF discharge under different pressures of methane. In calculations, separate

peaks were summed with the apparatus function having a triangle shape with the half width at half height of 0.19 nm. Rotational and vibrational temperatures were adjusted to the best coincidence for the line intensities. The temperatures calculated in such a way are shown in Table 1.

Table 1. Rotational and vibrational temperatures of CH molecule glow in two regions at various pressures.

Pressure, Pa		40	21.8	6.6	4.6
Top glow	T_{rot}, K	1900	2300	4300	4500
	T_{vib}, K	2900	2700	2700	2800
Low glow	T_{rot}, K	2900	3500	4400	4400
	T_{vib}, K	2900	2900	2700	2600

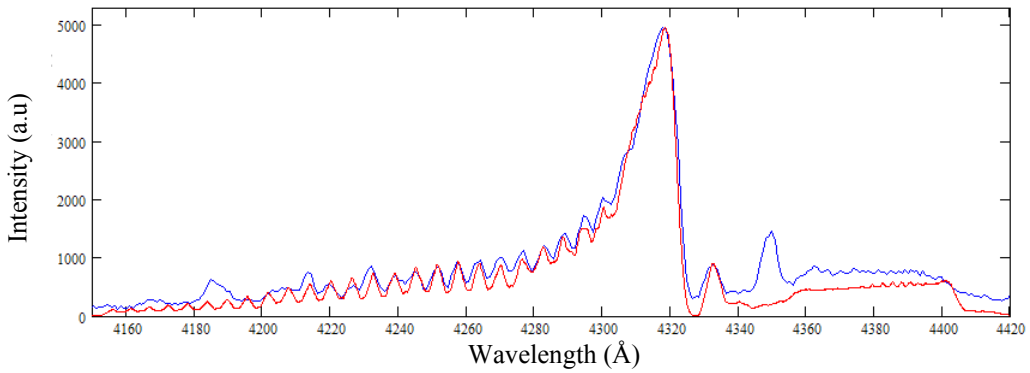

(a)

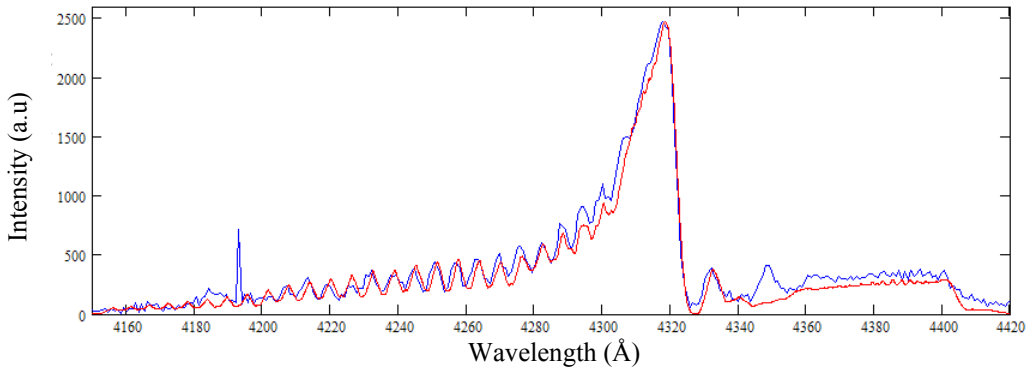

(b)

Fig. 4. Experimental and calculation spectra at the pressure of 4.6 Pa, U_{RF}= 400 V, U_{bias} = 397 V, f = 7 MHz.
(*a*) the top glow area, T_{rot}=4500 K, T_{vib}=2800 K, I_{max}= 4964 a.u.
(*b*) the low glow area, T_{rot}=4400 K, T_{vib}=2600 K, I_{max}= 2476 a.u.

According to figures 3 and 4, the rotational distribution of CH molecules in the excited $A^2\Delta$ states has a high rotational temperature, up to 4400 K, that very much exceeds the gas temperature estimated by other methods and not exceeding 1200 K. That makes it possible to conclude that the emission in the given band system for the studied regions of RF discharge parameters cannot be used for determining the gas temperature. Comparison of the calculation spectrum with the experimental one results in two features in the behavior of spectra at the gas pressure variation. The first feature is as follows: the growth of the pressure is accompanied by the decrease in the rotational temperature, down to the gas one, that indicates a rising role of the rotational relaxation with the growth of the pressure. The other feature is as follows: there is increase in the divergence between the calculation and experimental results within low rotation levels $J = 1.5 \div 6.5$ of the main branches R_1 and R_2. It

should be noted that according to the calculation of spectra the closely spaced $A^1\Pi \rightarrow X^1\Sigma^+$ Duglas-Hersberg band system of CH^+ ions, $B^2\Sigma^- \rightarrow X^2\Pi_r$ band system of CH molecules for the sequence $\Delta v=-1$, $d^3\Pi_g \rightarrow a^3\Pi_u$ Swan band system of C_2 molecules for the sequence $\Delta v=2$ as well as emission of C_3 molecules (which are within 4050 Å) do not make any contribution into this spectrum region. The calculation with two rotational temperatures did not bring to the better agreement either. Therefore, it is necessary to find the reason for the divergence between the calculation and experimental spectra within 4280 – 4320 Å wavelengths.

It is known that at electron excitation of molecules the rotational distribution function for the ground state is repeated in the exciting state due to the rotation number selection rules. Therefore the high rotational temperature of CH molecules in the $A^2\Delta$ state indicates that either the main exciting mechanism is the indirect electron impact and it is required to search for other mechanisms of exciting CH molecules to the $A^2\Delta$ state, or the thermodynamic equilibrium between rotational and translational degrees of freedom fail to be established. The analysis of chemical processes of CH formation showed that there was no real chemical mechanism of creating CH molecules in the exited state due to the small binding energy between C and H. And the processes of dissociative excitation of methane molecules by an electron impact with the formation of $CH(A^2\Delta)$, which should actively take place within the near cathode region at the input of the gas into the discharge area, are not important under our conditions. That is indicated by the above mentioned absence of the methane glow in the top area of the discharge gap (fig.2).

The calculation of the gas composition for our conditions was carried out according to the model including 98 chemical processes. Table 2 contains the gas composition, which was established in 4 ms from the initial mixture of 20%H + 20%H_2 + 60%CH_4. The starting pressure was set to be equal to 40 Pa, the gaseous temperature was 800 K. Table 3 shows the basic processes of the chemical model in which CH molecules and singlet $CH_2(S)$ molecules with excitation energy of 0.357 eV participate and these processes play an important role in forming a strong non-equilibrium excitation of rotational degrees of freedom of CH molecules. In our opinion the mechanism of the non-equilibrium formation is as follows.

In exothermal reactions (5) and (28) which are the primary channels of CH molecule formation, the energy defect is used for making the rotational non-equilibrium of CH molecules in the ground state. According to Table 2, the main components of gaseous mixture in the working chamber are hydrogen and methane molecules, whose rotational constants (60.8 cm^{-1} for H_2, 5.24 cm^{-1} for CH_4) considerably differ from the rotational constant of CH molecules (14.9 cm^{-1} in the ground state). Therefore the rotational relaxation of CH molecules is highly complicated in such a system.

Table 2. Established composition of gaseous mixture (T_g=1019 K, $N = 2.845\times10^{15}$ cm^{-3}) in the discharge from the original mixture 20%H + 20%H_2 + 60%CH_4, under the pressure of 40 Pa and the temperature of 800 K.

Radical	N, cm^{-3}	Radical	N, cm^{-3}	Radical	N, cm^{-3}	Radical	N, cm^{-3}
H	1.55×10^{14}	C	4.35×10^{10}	**CH_3**	2.46×10^{14}	C_2H_3	5.98×10^{10}
H_2	9.86×10^{14}	CH	1.98×10^{10}	**CH_4**	1.41×10^{15}	C_2H_4	8.49×10^{12}
C_2	7.14×10^{6}	CH_2	1.03×10^{11}	C_2H	8.36×10^{7}	C_2H_5	2.96×10^{11}
$C_2(X)$	1.02×10^{5}	$CH_2(S)$	5.16×10^{10}	C_2H_2	4.17×10^{12}	C_2H_6	3.47×10^{13}

Let's estimate the acceptable for the considered mechanism rate coefficient of the rotational relaxation rate from the condition of the typical rotational relaxation time being greater than the lifetime of CH molecules. With taking into account the fact that the basic loss channels are processes (3), (27), (31) and (33), the lifetime of CH molecules is determined according to the following relationship:

$$\tau_{CH} \approx \left(k_3[H]+k_{27}[H_2]+k_{31}[CH_3]+k_{33}[CH]\right)^{-1} \approx 4.3\ \mu s.$$

This time interval is an order of the magnitude longer than the radiation lifetime of the $A^2\Delta$ state, equal to 500 ns [6], therefore, the basic loss channel for the excited state is the radiation decay. Finally we have the following estimation for the rotation relaxation coefficient:

$$k_{rot} < \left(N\tau_{CH}\right)^{-1} \approx 1.6\times10^{-10}\ cm^3/s.$$

where N is the methane density. The obtained constant is quite reasonable, therefore we can conclude that the presented mechanism for forming the hot rotational distribution of CH molecules is physically consistent and quite possible. To establish final details of the mechanism for the non-equilibrium formation it is necessary to carry out the calculation of the rotation kinetics of CH molecules for each level, that is rather a complicated problem at present due to no valid coefficients.

Table 3. The basic processes with participation of CH and $CH_2(S)$ radicals

No. of the process in the model	Process	Process rate ($cm^{-3}s^{-1}$)	Rate constant k (cm^3/s)	Energy defect ΔE (eV)
3	$H + CH \rightarrow C + H_2$	8.42×10^{14}	2.74×10^{-10}	1.01
5	$H + CH_2(S) \rightarrow CH + H_2$	4.00×10^{14}	4.98×10^{-11}	0.473
6	$CH + H_2 \rightarrow H + CH_2(S)$	1.18×10^{12}	6.06×10^{-14}	-0.473
27	$CH + H_2 \rightarrow H + CH_2$	7.52×10^{14}	3.86×10^{-11}	-0.116
28	$H + CH_2 \rightarrow CH + H_2$	4.21×10^{15}	2.63×10^{-10}	0.116
31	$CH + CH_3 \rightarrow H + C_2H_3$	2.42×10^{14}	4.98×10^{-11}	2.32
33	$CH + CH_4 \rightarrow H + C_2H_4$	2.78×10^{15}	9.96×10^{-11}	2.56
41	$CH_2(S) + H_2 \rightarrow CH_3 + H$	5.92×10^{15}	1.16×10^{-10}	0.610
42	$CH_3 + H \rightarrow CH_2(S) + H_2$	1.35×10^{16}	3.53×10^{-13}	-0.610
43	$CH_2(S) + CH_3 \rightarrow H + C_2H_4$	3.35×10^{14}	2.64×10^{-11}	3.06
45	$CH_2(S) + CH_4 \rightarrow CH_3 + CH_3$	2.56×10^{15}	3.52×10^{-11}	0.586
46	$CH_3 + CH_3 \rightarrow CH_2(S) + CH_4$	3.61×10^{14}	5.98×10^{-15}	-0.586
67	$CH_2(S) + C_2H_6 \rightarrow CH_3 + C_2H_5$	1.56×10^{14}	8.72×10^{-11}	0.809
73	$CH_2(S) \rightarrow CH_2$	4.85×10^{15}	9.40×10^{4}	0.357
74	$CH_2 \rightarrow CH_2(S)$	8.03×10^{13}	7.80×10^{2}	-0.357
97	$CH_4 \rightarrow CH_3 + H$	2.82×10^{14}	2.00×10^{-1}	-4.50
98	$CH_4 \rightarrow CH_2(S) + H_2$	2.82×10^{14}	2.00×10^{-1}	-5.11
Processes 97 and 98 are the dissociation by an electron impact with $n_e k_{total} = 0.4\ s^{-1}$.				

The work was supported by Russian Foundation for Basic Research, project projects 05-02-17258*a* and SS-1257.2003.2.

References

[1]. B. Smeets, V. Van den Bergh, R. Jacobs, L. Eersels, J. Meneve and E. Decempeneer - J. Phys. III France, **2**, 1461 (1992).
[2]. Yu.P. Raizer, M.N. Shneider, N.Ya. Yatzinko - High frequency capacitor discharge. Moscow, Nauka (1995).
[3]. G. Herzberg - Molecular spectra and molecular structure. 1. Spectra of diatomic molecules. N. Y.: D. van Nostrand (1951).
[4]. K.F. Huber, G. Herzberg - Molecular spectra and molecular structure. IV. Constants of diatomic molecules. N. Y.: D. van Nostrand (1979).
[5]. B.M. Krupp - The Astrophysical Journal **189,** 389 (1974).
[6]. S.W. Reeve, W.A. Weimer - J. Vac. Sci. Tech. **13**(2), 359 (1995).
[7]. L.A. Kuznetzova, N.E. Kuz'menko, Yu.Ya. Kuzyakov - Probabilities of optical transitions of diatomic molecules, Moscow, Nauka (1980).
[8]. I. Kovacs - Rotational structure in the spectra of diatomic molecules. Budapest, Akademiai Kiada (1969).
[9]. N.E. Kuz'menko, L.A. Kuznetzova, Yu.Ya. Kuzyakov - Frank-Condon factors of diatomic molecules, Moscow State University (1984).

Atmospheric Pressure Deposition of Micropatterned N-rich Plasma-Polymer Films for Tissue Engineering

P.-L. Girard-Lauriault[1], F. Mwale[2], M. Iordanova[2], C. Demers[2], P. Desjardins[1], S. Lerouge[3], and M.R. Wertheimer[1*]

[1.] *Department of Engineering Physics, Ecole Polytechnique, Montreal, Canada*
[2] *Lady Davis Institute for Medical Research and Department of Surgery, McGill University, Montreal, Canada*
[3] *Department of Radiology, Université de Montréal, Montreal, Canada.*
* *Corresponding author: michel.wertheimer@polymtl.ca*

Abstract. A novel atmospheric-pressure plasma-polymerised, nitrogen (N)-rich ("PPE:N") thin film material has been deposited using a pilot-scale dielectric barrier discharge (DBD) reactor. Characteristics of PPE:N deposits are described in detail. Adhesion, proliferation and micropatterning of different cell types, for example, the usually non-adherent U-937 human macrophages, is demonstrated. The critical role of N concentration, [N], is discussed.
Keywords: dielectric barrier discharges (DBD), deposition, biomaterials, cell adhesion, cell patterning.

1. Introduction

Biotechnological applications show an ever-increasing need for surfaces permitting control over cell functions. These so-called "smart" surfaces are specifically engineered to provide solutions to particular challenges. For example, chondrocytes which are rounded *in vivo* become flattened and fibroblastic when cultured on conventional culture plates. One possible solution involves the use of nano-/micro-patterned surfaces that permit greater control of the cell environment. By creating an array of cell-adhesive islands in a non-adherent matrix, the spreading of cells may be limited [1], and ultimately control over phenotype conservation and gene expression may be achieved. It is known that most cell types do not adhere to hydrophobic polymer surfaces like polyethylene, polypropylene, polystyrene or PTFE. However, hydrophilic surfaces, for example those functionalized by plasma or VUV treatments [2], are known to promote cell adhesion. A good example is the commercial product "Primaria"^{TM}, plasma nitrided polystyrene [3]. We report a promising novel material, nitrogen-rich plasma-polymerised ethylene (PPE:N), which is deposited on various substrates of interest, using an atmospheric pressure dielectric barrier discharge (DBD) apparatus in this laboratory. Its characteristics, high nitrogen content and high surface energy, render it a promising candidate for providing tailored solutions to the challenges described above. In this study we present the characteristics of this novel thin film material and of its cell-adhesive properties. We demonstrate reproducible, selective adhesion of U-937 human macrophages, epiphyseal and growth plate chondrocytes, mesenchymal stem cells, aortic vascular smooth muscle cells (VSMC) and dermal fibroblasts on PPE:N surfaces. Finally, we show the critical importance of nitrogen concentration, [N], by correlating the adhesion of different cell types on surfaces with varying [N], as we also reported elsewhere [4].

2. Experimental Methodology

2.1 Deposition of PPE:N and Micropatterning

The topics of plasma chemistry and plasma polymerisation are well covered in some excellent monographs [5, 6], and will not be addressed in detail here. While much of that literature relates to low-pressure, non thermal ("cold") plasmas, "cold" plasmas generated at atmospheric pressure via the use of so-called dielectric barrier discharges (DBD) have gained increasing importance in recent years [7]. The plasma-polymerised PPE:N films discussed here are exclusively of this latter variety, although they may in principle also be produced via traditional low-pressure plasma techniques [6]. PPE:N films were deposited on several types of polymer substrates identified below; these were placed on a 2 mm thick float glass plate (see below). Biaxially oriented polypropylene (BOPP) was the main substrate material for cell-culture experiments; this 50 μm thick isotactic polymer film, graciously provided by 3M Company, has been described elsewhere [2]. However, to suit the

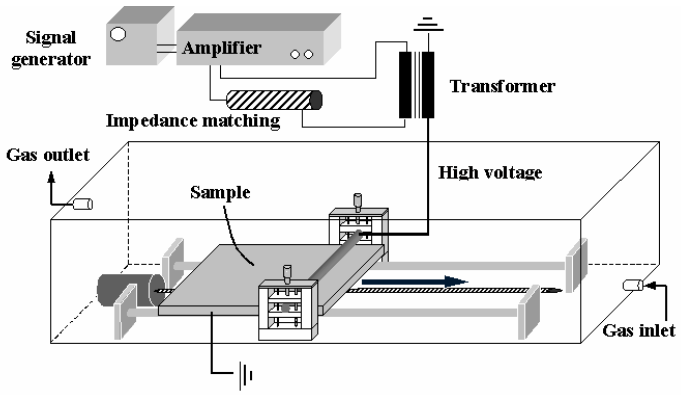

Figure 1: Schematic diagram of the DBD plasma deposition apparatus.

needs of other applications, PPE:N was also deposited on a variety of other substrates, for example, 125 μm thick PTFE used in endovascular implants, 25 μm thick PET, and 50 μm thick Teflon® FEP film.

Figure 1 depicts the atmospheric pressure DBD apparatus used for depositing the PPE:N films [8]; it comprises a grounded, planar Al electrode and a cylindrical, dielectric-coated stainless steel high voltage (HV) electrode. The 2 mm thick glass plate mentioned earlier is placed on the planar Al electrode and it serves as a second dielectric layer, as described in detail elsewhere [8]. The precursor gas mixture is introduced into the discharge zone, an adjustable 1 mm wide gap between the HV electrode and the glass plate, using a gas diffuser (not shown on Fig. 1) to ensure the requisite high gas purity. Gas flow rates (N_2 – 10 standard liters/minute, slm; C_2H_4 – 5 to 60 standard cm^3/minute, sccm) are controlled by electronic mass flow controllers. The roughly 1 cm wide plasma zone is generated with a commercial power source and transformer (Enercon Industries, model LM2727-03, 450 kVA maximum output) at a typical frequency of 10 kHz and peak voltage of 18 kV. After the carefully precleaned substrate was introduced into the DBD system, the latter was purged with the precursor gas flow for approximately 10 min. The discharge was then initiated and monitored with a digital oscilloscope, the voltage and current being measured with the help of a resistive probe (Tektronix, model P6015A) and a 50 Ohm resistor, respectively. The substrate was made to move back and forth under the HV electrode at precisely controlled speed, 10 mm/s, for up to two dozen cycles, depending on the desired PPE:N film thickness. For the micropatterning experiments, special 25 μm thick Kapton® polyimide masks were placed over the substrate. These masks were fabricated with an excimer laser coupled to a precise positioning system, to create the following square arrays of circular holes (hole diameter -pitch): 30 μm – 60 μm; 30 μm – 200 μm; 100 μm – 200 μm, with array areas ranging from 1 to 4 cm^2. Care was taken to assure intimate contact between the mask and substrate surface during deposition runs.

2.2 Materials Characterisation and Cell Culture

A detailed description of characterisation and cell culture methodologies is available elsewere [4], so that only a rapid overview is presented here. PPE:N films were characterised by X-ray photoelectron spectroscopy (XPS) and by attenuated total internal reflectance FTIR (ATR-FTIR) to gather information about surface composition and functional groups, including quantification of the functionality of greatest interest, primary amines, which was obtained by chemical derivatisation with trifluoromethylbenzaldehyde [9]. Contact angle goniometry (CAG) measurements were carried out according to the method of Owens and Kaelble [10], from which the surface free energy, γ_s, can readily be determined. Individual PPE:N dots were imaged with an atomic force microscope (AFM) in contact mode. Film thickness, d, and refractive index, n, of PPE:N films were measured using a variable-angle spectroscopic ellipsometry (VASE), and values of d were also confirmed by profilometry (Dektak) measurements of steps created with the Kapton® masks.

Prior to each of the cell culture experiments, individual cell lines were suspended and counted in medium that generally consisted of Dulbecco's modified eagle medium (DMEM) with 5 to 10 % fetal bovine serum (FBS). For each experiment a 100 μl volume of cell suspension, containing typically $2X10^5$ cells, was carefully pipetted onto a 1 cm^2 PPE:N surface that was previously placed face-up on the flat bottom of a 24-well plate for cell

culture. All cell types were left to adhere to the substrate surfaces in a humidified incubator at 37°C, 5% CO_2 in air, for 1h before careful removal of the remaining medium with a pipette. Fresh cell-free medium was then pipetted into the wells (1 ml in each well) and photomicrographs of the surfaces were taken.

3. Results and Discussion

3.1 Material Characteristics

As mentioned in section 2.2, elemental compositions of the PPE:N films obtained by XPS, combined with ATR-FTIR data, permitted us to semi-quantitatively determine the concentrations of functional groups at the sample surfaces. Typical elemental concentrations ranged from 17 to 36 at.% nitrogen, [N], about 4 at.% oxygen, [O], the balance being carbon. Hydrogen is, of course, also present in the films but cannot be detected by XPS; high [N] values, as determined from eq. (1),

$$[N] = \frac{N}{N+O+C} \times 100\% \qquad (1)$$

are the main attribute of these PPE:N films, in comparison to other work in the literature; to the best of our knowledge, no earlier work has reported [N] as high as the value of 36.3% we observe here. Regarding [O], even though oxygen is excluded from the precursor gas, long-lived free radicals and other active species at the sample surface can react with oxygen and/or water vapour when the sample is exposed to the ambient atmosphere [6, 8]. The [O] value was minimised by lengthy storage of samples in feed gas mixture after the discharge had been terminated. Also, since the material described is a highly cross-linked plasma-polymer, it does not undergo the well-known "hydrophobic recovery", or aging effect observed in plasma surface modification techniques [8], so that surface elemental concentrations are stable over time. In fact, such stability was demonstrated by comparing 6 month-old PPE:N coatings on BOPP with samples freshly deposited under the same conditions: none of the characterisation methods detected any significant differences between the two sample groups. The value of [N] in PPE:N can be readily and reproducibly controlled by varying C_2H_4 concentration, $[C_2H_4]$, in the feed gas, higher $[C_2H_4]$ resulting in lower [N] in the deposited films. This control over PPE:N composition is an important attribute of our methodology, in that it enables controlled adhesion of different cell types simply by changing [N], as will be shown below.

ATR-FTIR spectra show the main functional groups in the PPE:N to be amines (their order cannot be determined by this method), nitriles and some amides. High resolution XPS of the N 1s peak can indicate relative concentrations of different N-species, but cannot provide quantitative information. Given the random structure of plasma polymers [6], any particular functional group can possess a broad distribution of binding energies. This assertion has been confirmed by high resolution XPS spectra taken also with a narrow monochromatic X-ray source (0.3 eV width, compared with 0.7 eV for the ESCALAB instrument); all spectra were similar in shape and width, which confirms that the broad convoluted peaks result from a distribution of energies rather than from polychromatic X radiation. Primary amine concentrations, $[NH_2]$, were found to vary from 5 to 10 % NH_2/N, the most abundant being at 3.5% NH_2/C, similar to literature data for plasma-modified polymer surfaces [11]. Interestingly, $[NH_2]$ does not appear to depend strongly on $[C_2H_4]$ in the precursor gas.

The films' surface energy, γ_s, indicative of their wettability by aqueous media, was found to increase with rising [N] from 27.0 mN/m (or dynes/cm) for virgin BOPP to about 58 mN/m for [N]=30%, similar to Guimond's findings for BOPP surfaces modified by DBD treatments with pure N_2 gas [8]. Here, too, the ~ 30 mN/m increase is entirely due to that in the polar component, γ_s^p, in turn related to the content of highly polar groups (amines, amides, etc.). In view of the above, it is not surprising that cell adhesion should manifest strong correlation with γ_s and wettability, as evidenced in section 3.2 below. The deposition rate, R, (from profilometry and ellipsometry measurements) of PPE:N films was found to vary with $[C_2H_4]$ in the precursor gas. Values of R ranged from about 2 nm/s (for $[C_2H_4]$ = 5 sccm) to 9 nm/s (for $[C_2H_4] \approx 30$ sccm), comparable to values found in the plasma-polymerisation literature [6]. In all conditions, R is sufficiently high and not a limiting factor in this study; all cell culture experiments were carried out using 150-200 nm thick films.

Figure 2 A shows a photomicrograph of a "30-200" Kapton® mask; well-defined dots of deposit are visible on the substrate at the same magnification (not shown here). For the case of a 200 nm deposit on an unmasked

glass surface, each dot had a height of about 150 nm, measured by Dektak and by AFM, on account of some masking by the 25 μm thick Kapton® film. An AFM image of a single dot (Fig. 2 B) shows the well-defined 30 μm diameter "mound"; note that for visual purposes the Z scale has been amplified 100-fold compared with the X and Y scales. The deposition was well confined by the mask, which was in good contact with the surface, since no film was deposited outside the 30 μm boundary.

3.2 Cell Culture

In order to demonstrate the great potential of PPE:N for cell culture and tissue engineering, a wide variety of experiments have been conducted, many using nominally 200 nm of PPE:N with 29.5 % [N], deposited on the substrate of particular interest. This choice constituted a compromise between adequate surface energy and deposition rate values. All of the cell types under study were first cultured on large-area coated surfaces that were partially masked during deposition, in order to compare adhesion on the bare substrate and on PPE:N. Figures 3 A to D are representative examples of these experiments. Substrates for each cell type were deliberately chosen to induce adhesion contrasts, so that the cells adhered to the coating but not to the substrate (U-937 human macrophages, epiphyseal and growth plate chondrocytes on BOPP, and mesenchymal stem cells on Teflon^{TM} FEP), or to simulate a specific application (VSMC and fibroblasts on PTFE). In all cases, cells were seen to selectively adhere to PPE:N after one hour of contact with cell suspensions. The adhesion contrast is particularly strong and noteworthy in the case of the U-937 macrophages, since these cells are non-adherent to almost all previously known cell culture surfaces [12]. Of equal interest was the finding that the cells maintained a rounded morphology after adhesion. To investigate the viability of cells on PPE:N for extended periods of time, the following proliferation studies were undertaken: U-937 macrophage cell suspension was left in contact with the surface for 1h before removing medium and excess cells, in the presence only of culture medium; cell counts were then performed and cells were found to survive and proliferate on the PPE:N surface, an important finding for future applications [12]. Following these experiments, a macrophage suspension was left in contact with a micropatterned (30 μm holes, 200 μm pitch) BOPP surface for 1h (see Fig. 3 E). Evidently, small groups of up to ten cells adhered readily and selectively only to the PPE:N islands, as anticipated from the results presented above. A suspension of growth plate chondrocytes was also left in contact for 1h with a different (100 μm holes, 200 μm pitch) micropatterned surface, since 30 μm holes were found to be inadequate. To test the longevity of these chondrocytes on the patterned surface, they were kept in culture for 9 days before a micrograph was taken (Fig. 3 F). This experiment, too, clearly shows that chondrocytes adhered selectively to micropatterns, even after many days in culture [2].

In the preceding paragraph and in Fig. 3 A to D we have noted that an [N]-rich PPE:N deposit, with [N] = 29.5%, evidently constitutes a surface on which all cell types examined readily adhered and proliferated. In view of this fact and of our ability to vary [N] at will, the following additional sets of experiments were conducted in order to examine cell adhesion behaviour at lower [N] values: U-937 macrophages and growth plate chondrocytes were cultured on PPE:N-coated BOPP substrates, but now the [N] values were systematically decreased by enriching the N_2/C_2H_4 gas mixture with ethylene during plasma deposition of the PPE:N coatings. Coated substrates with [N] values ranging from 36.3% downward to 17.5% were then exposed to concentrated cell suspensions for 1 hr durations, following which photomicrographs of the cell cultures were taken. Figure 3 G and H show such micrographs of macrophages for the cases [N] = 25% and 23%, respectively. Clearly, a

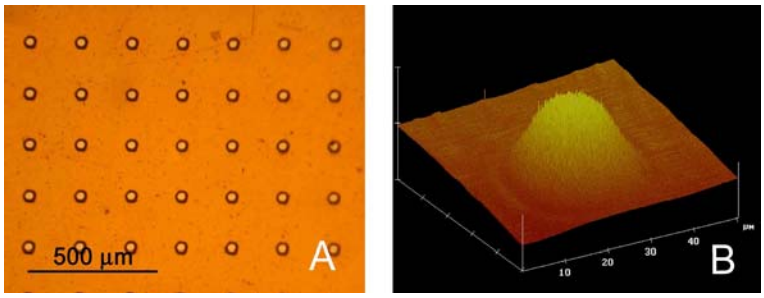

Figure 2: PPE:N film micropatterning : Kapton ® mask – (A) 30 μm holes every 200 μm; (B) AFM image of a single 30 μm PPE:N dot, shaped like a "mound".

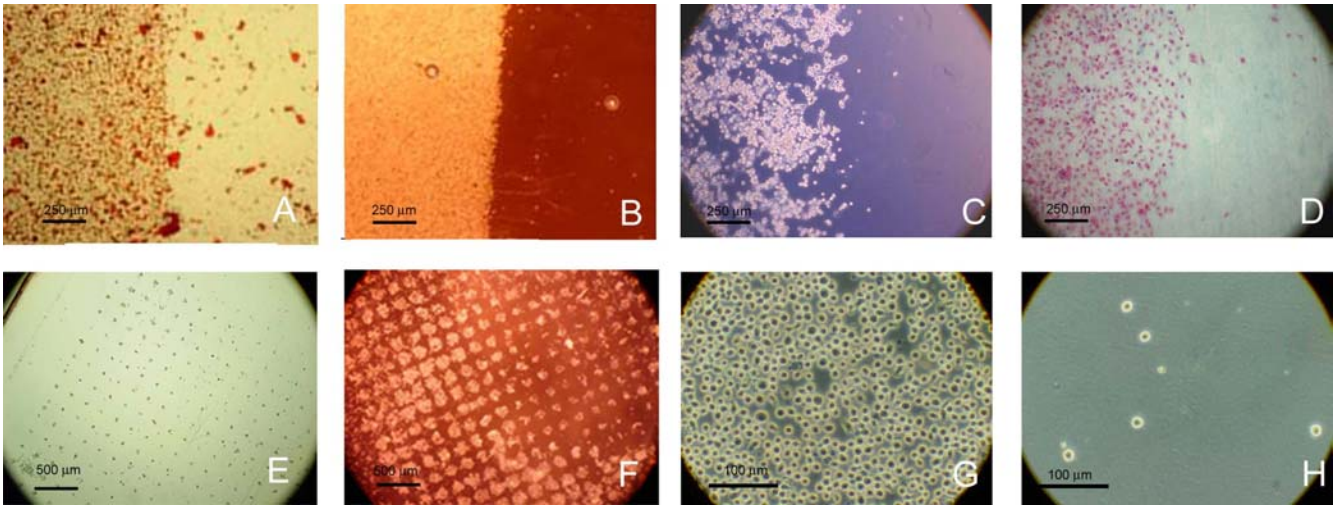

Figure 3: Cell culture and micropatterning on various substrates: Cell adherence to PPE:N coatings with [N] = 29.5% on partially-masked surfaces, with coatings and cells on the left sides of the images: (A) growth plate chondrocytes on BOPP, (B) human U-937 macrophages on BOPP, (C) fibroblasts on Teflon FEP, and (D) VSMC on PTFE. Cell adhesion on PPE:N-micropatterned BOPP substrates: (E) U-937 macrophages, and (F) growth plate chondrocytes. Adhesion of U-937 macrophages to PPE:N films (on BOPP) of varying [N], after 1hr of culture: (G) 25%, (H) 23%.

"critical" value of nitrogen concentration, $[N]_{crit}$, exists between 25% and 23%, a value below which this cell-type does not adhere to PPE:N. The micrographs shown here are typical and fully representative for many repeated experiments: for [N] ≥ 25%, adhering cells formed a single continuous monolayer after 1 hr, even if the cell suspension was highly concentrated. On the contrary, for [N] < 25%, the observed number of cells adhering to the PPE:N surfaces was no different from the case of uncoated, pristine BOPP (or polystyrene, PS, or other commercial polymers), namely virtually nil. A similar series of experiments was also conducted with growth plate chondrocytes, where the value of $[N]_{crit}$ was found to lie between 19% and 17.5%.

As proposed by Ohl, Schröder and their collaborators [1, 11, 14], these observations are probably related to the concentration of surface-near primary amine ($-NH_2$) groups: the higher the [N] value, the greater is the likelihood that the concentration of such groups, $[NH_2]$, is also high. The protonated amine group possesses a localised positive charge which may, in aqueous solution at physiological pH values, attract negatively charged biomolecules. In view of their known high reactivity, amine groups are therefore believed to covalently couple proteins, thereby giving rise to immobilisation of biomolecules and cell adhesion.

4. Conclusions

Novel, nitrogen-rich PPE:N thin films have been deposited using an atmospheric pressure plasma polymerisation technique that is both economical and efficient. An important attribute are their high, stable and adjustable nitrogen content, relatively high primary amine concentration, and their high surface energy (wettability). Also, since we are dealing with deposition (as opposed to surface modification), PPE:N films can be applied on many different substrates, including inorganic ones. Based on these characteristics, PPE:N is an excellent candidate for cell culture and tissue engineering experiments, including those on micropatterned surfaces created with the help of Kapton® masks used here. The present cell culture experiments have shown that PPE:N promoted selective adhesion of many cell types, including the usually non-adherent human U-937 macrophages. Micropatterned adhesion of cells on PPE:N islands was rapid and effective; in the case of growth plate chondrocytes the pattern was conserved, even after 9 days in culture. Finally, we have demonstrated the existence of a "critical" nitrogen concentration, $[N]_{crit}$, of these PPE:N coatings below which specific cell lines did not adhere to the surfaces.

Acknowledgements

The authors gratefully acknowledge financial support from NanoQuebec, the Natural Sciences and Engineering Research Council of Canada (NSERC, to P.-L.G.-L., P.D., and M.R.W.), AO Foundation Switzerland (to F.M.), and the Canadian Institutes for Health Research (CIHR) (to F.M. and S.L.).

References

[1] A. Ohl, K. Schröder, Surf. and Coatings Technol. **116-119**, 820 (1999)
[2] N. A. Bullett, D. P. Bullett, F.-E. Truica-Marasescu, S. Lerouge, F. Mwale, M. R. Wertheimer, Appl. Surf. Sci. **235**, 395 (2004)
[3] P. LaRocca, S. Baker, Cell Line **6**, 1 (1996)
[4] P.-L. Girard-Lauriault, F. Mwale, M. Iordanova, C. Demers, P. Desjardins, M. R. Wertheimer**,** Plasma Proc. Polym.. **2**, 263 (2005)
[5] R. Hippler, S. Pfau, M. Schmidt, K. H. Schoenbach, Eds., "Low Temperature Plasma Physics", Wiley-VCH, Berlin (2001)
[6] H. K. Yasuda, "Plasma Polymerisation", Academic Press, London (1984)
[7] U. Kogelschatz, Plasma Chem. Plasma Process. **23**, 1 (2003)
[8] S. Guimond, I. Radu, G. Czeremuszkin, D. J. Carlsson, M. R. Wertheimer, Plasmas and Polymers **7**, 71 (2002)
[9] P. Favia, M. V. Stendardo, R. d'Agostino, Plasmas and Polymers **1**, 91 (1996)
[10] D. H. Kaelble, "Physical Chemistry of Adhesion", John Wiley and Sons, New York (1971)
[11] A. A. Meyer-Plath, B. Finke, K. Schröder, A. Ohl, Surf. and Coatings Technol. **174-175**, 877 (2003)
[12] Y.K. Gong, M. R. Wertheimer, F. Mwale, F. M. Winnik, J. Biomat. Sci. Polym. Ed. **15**, 1423 (2004)
[13] F. Truica- Marasescu, M. R. Wertheimer, J. Appl. Polym. Sci. **91**, 3886 (2004)
[14] A. A. Mayer-Plath, K. Schröder, B. Finke, A. Ohl, Vacuum **71**, 391 (2003)

Effect of electrical excitation type on the removal of isopropyl alcohol from dry air using a dielectric barrier discharge

J. Jarrige, N. Blin-Simiand, F. Jorand, L. Magne, S. Pasquiers, C. Postel

Laboratoire de Physique des Gaz et des Plasmas, Bât. 210, Université Paris XI , 91405 Orsay cedex, France

Abstract
The conversion of isopropyl alcohol (IPA) in a transient filamentary plasma (DBD discharge) has been studied in dry air. It has been shown that the removal efficiency of IPA is greatly improved when the electrical excitation of the DBD is changed from an AC to a pulsed one. Carbonated oxidation by-products are mainly acetone, CO and CO_2. Preliminary experiments have been also performed using a photo-triggered discharge which allows to obtain an homogeneous plasma. Same products have been detected.
Keywords - Dielectric barrier discharge - Phototriggered discharge - VOC abatement - Isopropanol

1. Introduction

The removal of molecular atmospheric pollutants by non-thermal plasmas is under investigation since the beginning of the eighties, and it has been shown that transient electrical discharges, such as dielectric barrier (DBD) or corona discharges, are powerful means to eliminate Volatile Organic Compounds (VOCs) at low concentration (less than 1 %) in the ambient air [1-4]. Isopropyl alcohol (IPA), $CH_3CH(OH)CH_3$, is one of the VOC molecule for which few studies have been performed up to now [5-7]. This molecule is widely used in chemical industries for extraction or purification of products such as oils, gum, perfume, ... It is also used as a solvent in paints and varnishes. In this paper, we examine the effect of the electrical excitation type of a DBD working at 1 bar and ambient temperature on the removal of IPA from dry air. However, because of the strong non-homogeneity of such a plasma, a detailed understanding of the chemistry involved in the pollutant removal and formation of by-products is quite hard to achieve. Therefore, in order to get a more precise knowledge of this chemistry, we have also undertaken experiments using a photo-triggered discharge [8]. Owing to the medium homogeneity, this type of pulsed high pressure pre-ionised discharge allows useful comparison between experimental results and predictions of self-consistent 0D-discharge and kinetic models. Formerly designed for the development of high-power lasers [9, 10], the photo-triggering technique has been more recently applied to gas mixtures ($N_2/O_2/H_2O$) relevant for atmospheric pollutant removal, such as NO [11] or light olefins [12]. In the present work, type of by-products which followed oxidation of IPA in the non-homogeneous reactive medium of DBD discharges are compared to those detected at the exit of a photo-triggered discharge reactor.

2. Experimental set-up

The first experimental set-up was composed of three parts : (i) a continuous gas flow generating system, (ii) a DBD reactor, and (iii), a gas sampling analysis and detection system. The dry air-like (20 % O_2) flow was kept constant at 0.7 sl/mn. The liquid IPA was continuously injected with a syringe through a vaporizer producing gaseous IPA. The alcohol streamed along a glass rod located at the center of a heated tube through which air flowed. The DBD reactor was made of a pyrex tube (inner diameter 11 mm, wall thickness 1.6 mm) [13]. The high voltage central electrode was made of stainless steel screw (diameter 3 mm). The grounded outer electrode (10.7 cm long) was made of stainless steel wire mesh and covered up the outside of the dielectric. Two types of power supply have been used to energize the DBD, firstly, an AC type working at a frequency of 50 Hz with an adjustable peak-to-peak voltage between 1 and 60 kV, and, secondly, a pulsed type with a positive polarity at a fixed peak voltage of 40 kV and with a repetition frequency which can be chosen between 1 Hz and 1 kHz. The electrical energy deposited in the discharge has been determined either using the Lissajous figure method (for AC excitation), or following measurements of the voltage and current time evolutions (for pulsed excitation) using adapted probes. The treated gas mixture was flowing from the DBD reactor to the gas analysis apparatus (Micro Gas Chromatography CP-4900) equipped with a thermal conductivity detector.
On the other hand, the photo-triggered discharge cell has been described in detail in reference [12]. An homogeneous plasma is obtained between two flat electrodes, 24 cm in length and 2 cm in width, separated

by a gap d=1.2 cm. These electrodes are inserted in an acrylic cell which acts as insulator, and are connected to the output of a symmetrical one-stage Fitch generator. The lower electrode is electrically grounded while the upper one, the cathode, is perforated with many 1 mm in diameter holes over a surface 24x2 cm^2. An auxiliary corona discharge device is located under the cathode in order to uniformly pre-ionise the discharge volume (57.6 cm^3) through the holes, by UV-photons. In the present experiment, the electrical energy deposited in the discharge is 300 mJ per pulse. The current pulse duration of the main discharge is 30 ns with a peak value of about 1.5 kA. The total pressure of the N_2/O_2/IPA mixture has been fixed to 400 mbar in order to achieve a well reproducible homogeneous discharge from shot to shot at a repetition frequency up to a few Hz, with a gas flux fixed to 1 sl/mn. Infrared Fourier transform spectroscopy has been used to detect molecules at the exit of the photo-triggered reactor. The spectrometer is a MIR8000 from Oriel, with a maximum spectral resolution of 0.5 cm^{-1}, equipped with a long path absorption cell (Infrared Analysis model V-16).

3. Removal of IPA by dielectric barrier discharges

In figure 1 and 2 are shown the IPA concentration measured at the exit of the DBD, $[IPA]_{exit}$, as function of the specific deposited energy, E_{dep} (in Joule/litre), in the case of the AC (fig.1) and pulsed (fig.2) electrical excitation, and for five values of the initial pollutant concentration, $[IPA]_0$, ranging from 50 ppm up to 640 ppm.

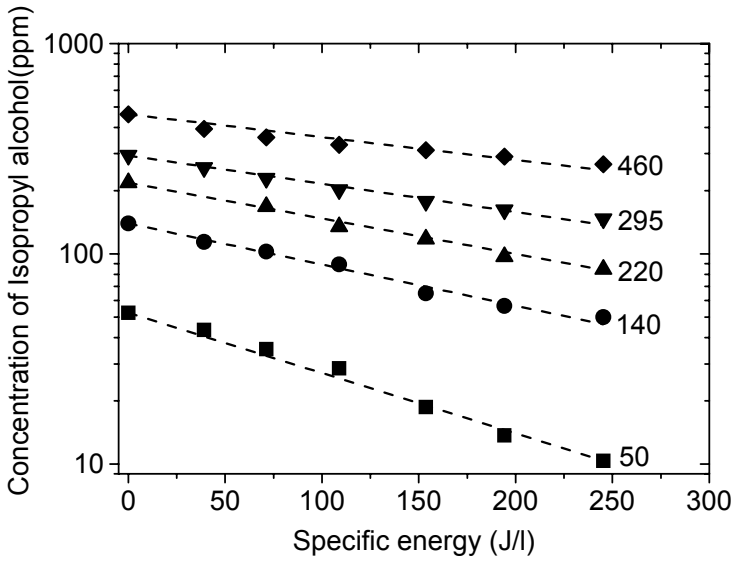

Figure 1 - Concentration of isopropyl alcohol at the exit of the DBD reactor as function of the specific deposited electrical energy, for AC excitation. Values of the initial concentration are given on the figure, in ppm.

$[IPA]_{exit}$ exhibits an exponential decrease when E_{dep} increases up to 250 J/l, i.e.

$$[IPA]_{exit} = [IPA]_0 \exp(-E_{dep}/\beta) \quad (1)$$

where the β parameter increases linearly when $[IPA]_0$ increases,

$$\beta_{AC} = 130 + 0.604\ [IPA]_0 \quad (2)$$

This law is identical to the one already observed in many studies on VOC removal by filamentary discharges [3, 4]. It has been also obtained when the DBD is energized using the pulsed electrical excitation, for an initial IPA concentration between 140 ppm and 640 ppm. In this case we have determined the following β parameter function,

$$\beta_P = 77 + 0.157\ [IPA]_0 \quad (3)$$

for $[IPA]_0$ higher than 200ppm; at low concentration, 140 ppm, β_P is lower than the value given by (3).

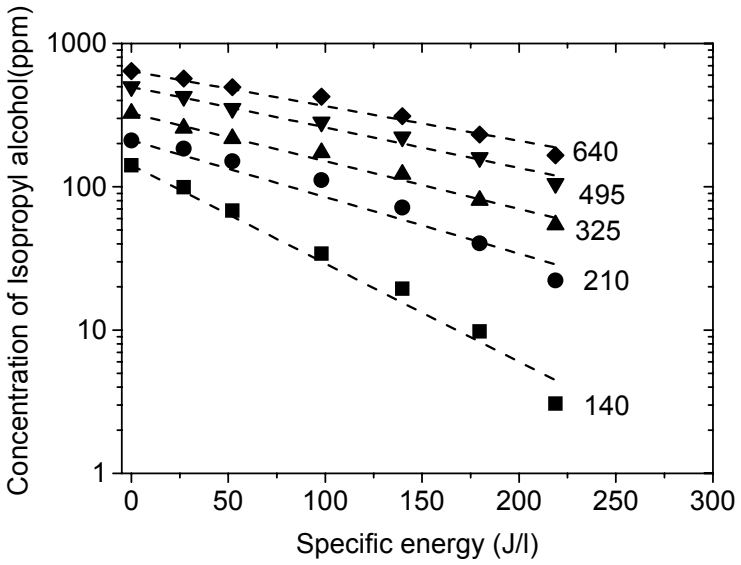

Figure 2 - Concentration of isopropyl alcohol at the exit of the DBD reactor as function of the specific deposited electrical energy, for pulsed excitation. Values of the initial concentration are given on the figure, in ppm.

In figure 3 are plotted evolutions of β_{AC} and β_P versus $[IPA]_0$. It can be seen that β_P is much lower than β_{AC}, which means that the removal of isopropyl alcohol is much easier to achieve in the case of a pulsed electrical excitation of the DBD than in the case of the AC excitation. Such an effect has been previously observed for the removal of NO from diesel engine exhaust gases [14], and we have also obtained very recently similar results on acetaldehyde in dry air [13].

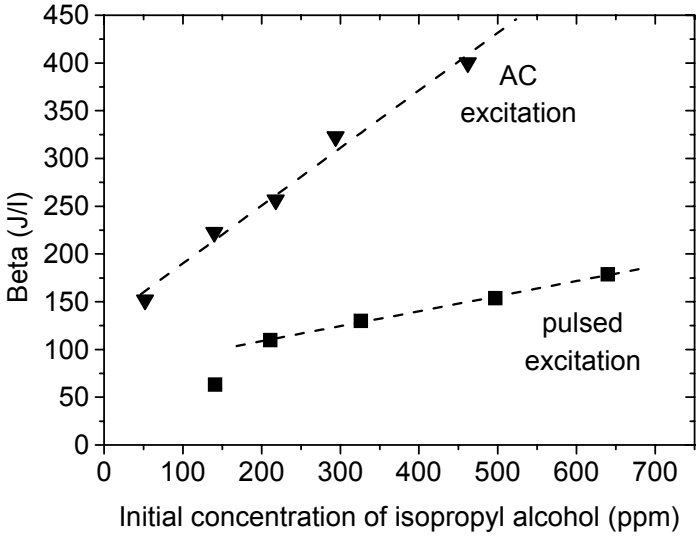

Figure 3 - The β parameter for AC and pulsed electrical excitation of the DBD.

4. By-products

The detected molecules at the exit of the DBD reactor have been the following (beside H_2O, which concentration has not been quantified) : $CH_3C(O)CH_3$ (acetone), CO, CO_2, H_2 and C_2H_4. No other compounds have been detected using Micro Gas Chromatography, and no solid or liquid deposit has been seen on the discharge tube walls. Acetone and carbon oxides are the most important products. In figure 4 are plotted concentration values of all molecules, as a function of the specific energy, in the case of the pulsed electrical excitation and for an initial IPA concentration value equal to 640 ppm. The total carbon

concentration is given in figure 5, taking into account the carbon contained in the remaining IPA for each value of the deposited energy.

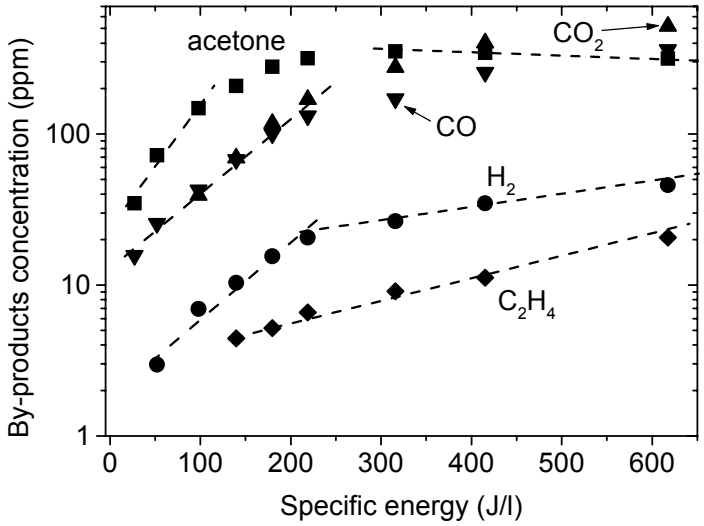

Figure 5 - Concentration of by-products at the exit of the DBD reactor as function of the specific deposited electrical energy, for the pulsed excitation and an initial concentration of IPA equal to 640 ppm.

It can be seen in figure 5 that the acetone concentration rapidly increases when the deposited energy increases up to 300 J/l. However it decreases slowly for higher energy values. In this experiment, the energy is increased through the increase of the discharge repetition frequency (the applied voltage is constant). As the gas flow is kept constant, the increase of the frequency induces the increase of the number of discharges performed in the mixture. As a result acetone molecules are also removed. On the other hand, CO and CO_2 concentrations exponentially increase when the energy increases up to 250 J/l. The ratio between this two concentration values is close to unity, except for the highest energy values for which the CO_2 concentration is slightly above the CO one. In this range of energy, the increase of the carbon oxides concentrations is less pronounced than in the low energy range.

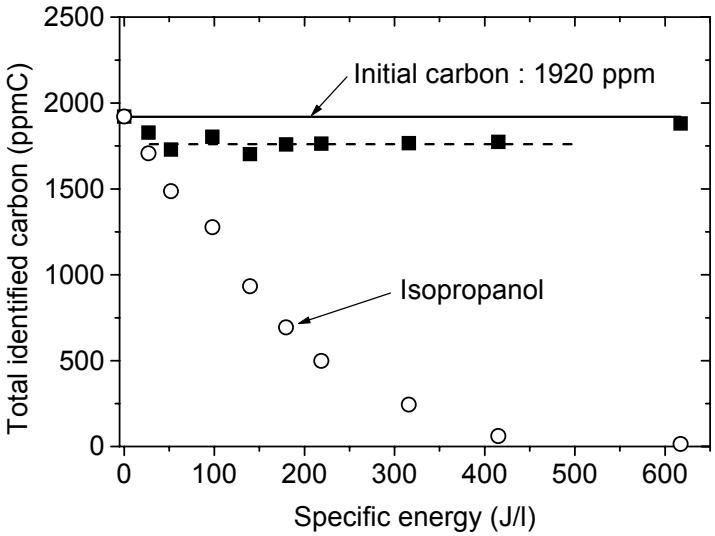

Figure 6 - Total identified carbon concentration at the exit of the DBD reactor as function of the specific deposited electrical energy, for the pulsed excitation and an initial concentration of IPA equal to 640 ppm.

The carbon balance shown in figure 6 emphasizes that the concentration of unidentified products is only 160 ppmC for the chosen experimental conditions, in the whole energy range studied. IPA molecules are in great part converted to acetone and carbon oxides.

The same by-products have been detected at the exit of the photo-triggered reactor, except C_2H_4. Moreover the FTIR spectra show the presence of formaldehyde (CH_2O) and formic acid (HCOOH) molecules, as it can be seen in figures 7a and 7b on which are displayed the absorbance measured in the long path cell after subtraction of the acetone and isopropanol contribution. Some products remain unidentified. Works are in progress to quantify IPA removal and concentration of by-products, for the photo-triggered discharge, using both FTIR spectroscopy and gas chromatography coupled with mass spectrometry.

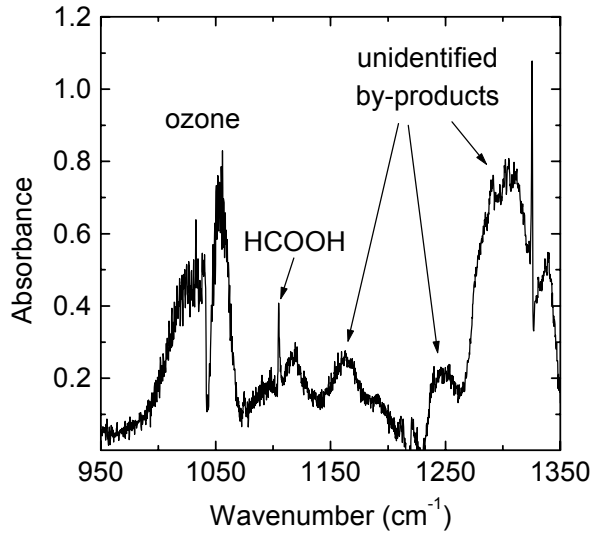

Figure 7a - Example of FTIR spectrum measured at the exit of the photo-triggered reactor. Identification of ozone and formic acid.

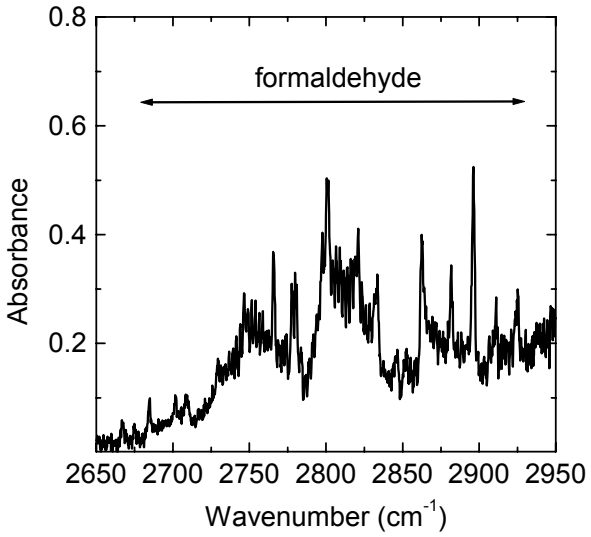

Figure 7b - Example of FTIR spectrum measured at the exit of the photo-triggered reactor. Identification of formaldehyde.

5. Simplified kinetic analysis

One can suggest well-known kinetic mechanisms to explain the removal of IPA and the production of acetone. Indeed the IPA molecule can be oxidized to give the 2-hydroxypropyl radical, $CH_3C(OH)CH_3$, according to the two following reactions [15],

$$O + CH_3CH(OH)CH_3 \rightarrow CH_3C(OH)CH_3 + OH \quad (R1)$$

$$OH + CH_3CH(OH)CH_3 \rightarrow CH_3C(OH)CH_3 + H_2O \quad (R2)$$

Thus acetone is produced by reaction of 2-hydroxypropyl with oxygen atoms,

$$O + CH_3C(OH)CH_3 \rightarrow CH_3C(O)CH_3 + OH \quad (R3)$$

or by reaction with oxygen molecules,

$$O_2 + CH_3C(OH)CH_3 \rightarrow CH_3C(O)CH_3 + HO_2 \quad (R4)$$

Acetone can be also oxidized as follows,

$$O + CH_3C(O)CH_3 \rightarrow CH_3C(O)CH_2 + OH \quad (R5)$$

$$O + CH_3C(O)CH_3 \rightarrow CH_3C(O)CH_2 + H_2O \quad (R6)$$

but rate constants for reactions (R5) and (R6) are respectively two order and one order of magnitude lower than those of reactions (R1) and (R2). This can explain, almost qualitatively, experimental results plotted in figure 5. However such a simple scheme has not yet been clearly demonstrated, as far as IPA removal and acetone production are concerned in absolute values. Moreover, analysis of the gas mixture reactivity reveals that by-products such as CH_2O, HCOOH, CO and CO_2 should not be formed directly after the first steps described above. A complete kinetic modeling of the N_2/O_2/IPA mixture is under development in order to achieve a comprehensive understanding of experimental results obtained with the photo-triggered discharge, and to see how this kinetic can help in the interpretation of the effect of electrical excitation type on IPA removal and by-products formation in filamentary discharges.

6. Conclusions

Type of the electrical excitation of the dielectric barrier discharge has a great influence on the removal of isopropyl alcohol in dry air. A pulsed excitation is much more efficient than an AC excitation. Explanations

are probably to be found in a higher production rate of oxygen atoms. Other molecules have to be studied also, for example hydrocarbons or aldehydes. Future works will be devoted to a detailed kinetic analysis of the N_2/O_2/IPA mixture homogeneously energized by the photo-triggered discharge.

References

[1] *Non-Thermal Plasma Techniques for Pollution Control*. Penetrante B and Schultheis S (eds) 1993 NATO ASI Series Vol.G34, parts A and B, (Berlin : Springer-Verlag).
[2] *Electrical discharges for environmental purposes. Fundamentals and applications.* Van Veldhuizen E-M (ed) 2000 NOVA Science Publishers.
[3] K. Yan, E. van Heesch, A. Pemen, P. Huijbrechts - Plasma Chem. Plasma Proc. **21**, 107 (2001).
[4] Y. Mok, C. Nam, M. Cho - IEEE Trans. Plasma Sci. **30**, 408 (2202).
[5] S. Masuda, S. Hosokawa, X. Tu, Z. Wang - J. Electrost. **34**, 415 (1995).
[6] Z. Falkenstein - J. Adv. Oxid. Technol. **2**, 223 (1997).
[7] T. Oda, R. Yamashita, I. Haga, T. Takahashi, S. Masuda - IEEE Trans. Ind. Applicat. **32**, 118 (1998).
[8] B. Lacour, V. Puech, S. Pasquiers - Recent. Res. Devel. Applied. Phys. **6**, 149 (2003).
[9] R. Riva, M. Legentil, S. Pasquiers, V. Puech - J. Phys. D **28**, 856 (1995), and references therein.
[10] B. Lacour, S. Pasquiers, C. Postel, V. Puech - Appl. Phys. B **72**, 289 (2001), and references therein.
[11] M. Rozoy, C. Postel, V. Puech - Plasma Sources Sci. Technol. **8**, 337 (1999).
[12] S. Pasquiers, C. Postel, L. Magne, V. Puech, G. Lombardi - J. Adv. Oxid. Technlol. **7**, 108 (2004).
[13] A. Chiper, N. Blin-Simiand, F. Jorand, S. Pasquiers, G. Popa, C. Postel - This conference.
[14] A. Khacef, J-M. Cormier, J-M. Pouvesle - XVIth International Symposium on Plasma Chemistry, Taormina, Italy (22-27/06/2003).
[15] W. Mallard, F. Westley, J. Herron, R. Hampson, D. Frizzell - NIST chemical kinetics database (version 2Q98) (1998).

Cavity ringdown measurements of NH and NH_2 in an Ar-NH_3-SiH_4 expanding thermal plasma for silicon nitride deposition

P.J. van den Oever, J.H. van Helden, J.L. van Hemmen, R. Engeln,
D.C. Schram, W.M.M. Kessels, and M.C.M. van de Sanden

Dept. of Applied Physics, Eindhoven Univ. of Technology, P.O. Box 513,5600 MB Eindhoven, The Netherlands

Abstract

The densities of NH and NH_2 radicals in an expanding Ar-NH_3 and Ar-NH_3-SiH_4 plasma were determined as a function of the NH_3 and SiH_4 flow. The NH and NH_2 radicals were measured using cavity ringdown absorption spectroscopy and the typical densities are in the order of 2×10^{12} cm^{-3} for NH and 6×10^{12} cm^{-3} for NH_2. A simple reaction scheme that explains the observed trends is presented. Finally, the detection of N radicals in the plasma by threshold ionization mass spectrometry is demonstrated.

Silicon nitride, expanding thermal plasma, cavity ringdown spectroscopy, NH and NH_2 radicals

1. Introduction

Ammonia plasmas have numerous applications in industry. They are, for example, used for surface treatment of polymers to improve the wettability and biocompatibility, for surface passivation of electronic devices and for nitridation of dielectric and metallic materials. However, one of the most important applications of NH_3-based plasmas is the deposition of silicon nitride films, that are used for encapsulation purposes of organic LEDs, as dielectric materials in the microelectronics industry and as antireflection coating on (multi-)crystalline silicon solar cells. These films are generally deposited from N_2-SiH_4 reactant mixtures [1,2] or from NH_3-SiH_4 reactant mixtures [3]. Despite the widespread use of amorphous silicon nitride (a-SiN_x:H) in industry, the exact growth mechanism of these films from NH_3-SiH_4 plasmas is not known. For example, the role of silane radicals, ammonia radicals, and possibly aminosilane radicals [4] in the growth process is still not resolved. To obtain insight into the role of the various radicals in the plasma we have carried out absolute density measurements of NH and NH_2 radicals in a remote Ar-NH_3 and Ar-NH_3-SiH_4 plasma by means of cavity ringdown spectroscopy (CRDS). Furthermore, we have used threshold ionization mass spectrometry (TIMS) to detect nitrogen radicals in the Ar-NH_3 plasma.

2. Experimental setup

Figure 1 gives an overview of the experimental setup that consists of the expanding thermal plasma setup, the laser system and optics used for cavity ringdown spectroscopy and the Hiden threshold ionization mass spectrometer. The expanding thermal plasma has been described extensively in the literature [5,6]. Briefly, a cascaded arc plasma source creates a plasma at high pressure (~ 400 kPa) that subsequently expands from a conical shaped nozzle into a low pressure reactor (~ 20 Pa). The plasma is created in a channel filled with Ar gas between three cathode tips and one common anode, that are separated by 4 cascaded plates at floating potential. For a pure Ar plasma, the ionization degree of the plasma depends on the source current and can be as high as 15 %. In downstream region, the electron temperature and heavy particle temperature are low (~ 0.3 eV) and the ion and electron density are in the order of 10^{13} cm^{-3}. Due to the low electron temperature, the highly reactive ions initiate the dissociation reactions with the precursor gases that are injected in the downstream region. This is different from radiofrequency plasma sources, that rely on electron induced chemistry. Processing steps, such as etching or deposition, take place in the downstream region where other precursor gases, such as NH_3 and SiH_4 are injected. In this particular experiment, NH_3 is injected in the nozzle and SiH_4 is injected in a ring situated 10 cm downstream from the nozzle.

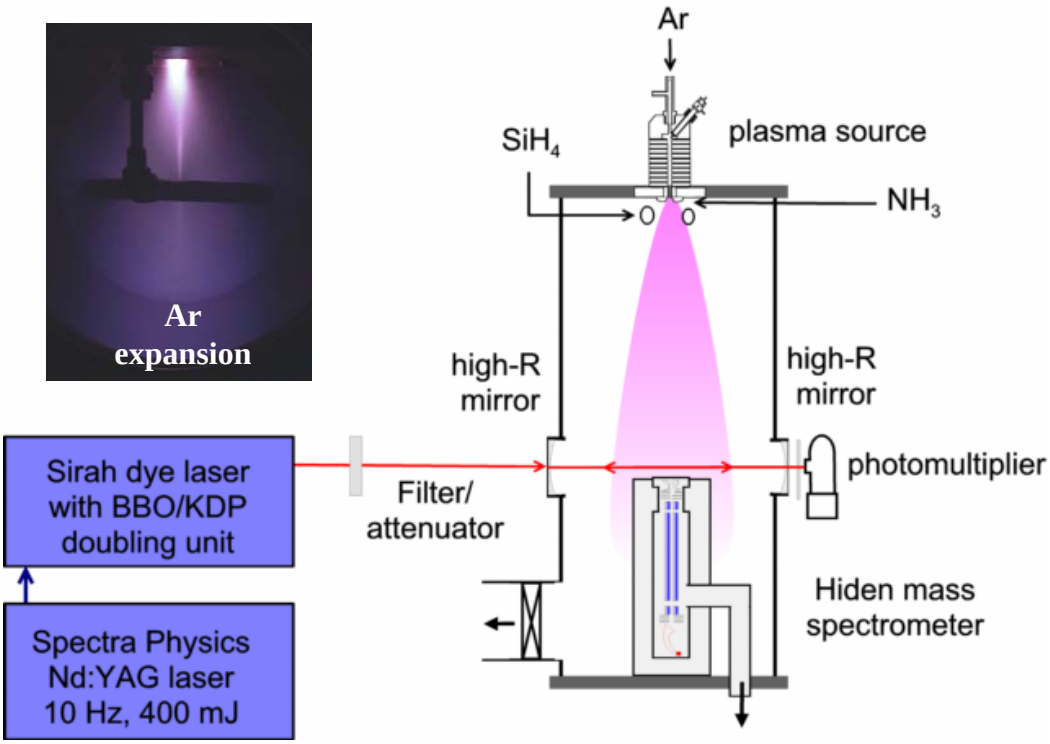

Figure 1: A schematic overview of the experimental setup with the cascaded arc plasma source, the laser system used for cavity ringdown spectroscopy and the Hiden mass spectrometer. The inset shows a typical Ar plasma expansion.

The NH and NH_2 densities were measured by cavity ringdown spectroscopy. This sensitive absorption measurement technique is very suitable for gas phase measurements of radicals in a plasma. It is based on the detection of the lifetime of an optical pulse inside a high finesse cavity that consists of two plano-concave, high reflectivity mirrors. The decay rate of the light intensity in the cavity is measured through one of the mirrors. If an absorbing medium is present in the cavity, the lifetime of the light pulse in the cavity will be shortened. The difference in lifetime (ringdown times) between an empty cavity and a cavity with absorbing species can be related to the density of the absorbing species in the cavity, when information on the cross section and absorption path length is known. In our experiment, the density of the NH radical was determined using the "isolated" $P_{3,3}(9)$ absorption line of (0,0) band of the $A^3\Pi \leftarrow X^3\Sigma^-$ transition at 339.52 nm (29543.25 cm^{-1}), while the NH_2 radical was detected at the "isolated" $\Sigma^P Q_{1,7}$ absorption line of the (0,9,0) – (0,0,0) band of the $\tilde{A}^2A_1 \leftarrow \tilde{X}^2B_1$ transition at 597.21 nm (16744.53 cm^{-1}). The peak absorption cross sections of both lines are similar (3.4 10^{20} m^2 for NH and 5.5 10^{20} m^2 for NH_2 at a gas temperature of 1750K), but the partition functions (state sums) used for the calculation of the total densities are different due to more rotational and vibrational freedom of the triatomic NH_2 [7].

In all experiments described in this paper, the plasma source was operated on a argon flow of 55 standard cubic centimeter per second (sccs) and the current through the channel was 45 A. NH_3 is injected in the nozzle with flows varying between 0 and 17 sccs, while the pressure in the reactor was kept constant at 20 Pa by changing the position of the gate valve to the pumps. Silane (SiH_4) was injected in a ring at approximately 10 cm from the nozzle. Usually, at a position of 39 cm from the source a substrate holder is placed that can be used for the deposition of silicon nitride films. All cavity ringdown measurements have been done at 36 cm from the plasma source (3 cm in front of the substrate holder). However, the substrate holder can be replaced by a threshold ionization mass spectrometer to measure radicals and stable species in the plasma beam. The sampling orifice of the mass spectrometer is situated 56 cm from the plasma source.

3. NH and NH_2 densities in an Ar-NH_3 expanding plasma jet

Figure 2 shows the absolute densities of NH and NH_2 radicals measured at 36 cm from the plasma source as a function of the injected NH_3 flow. The arc current used is 45 A and the downstream pressure was kept constant at 20 Pa. The NH density increases rapidly and saturates at a value of 2.0×10^{12} cm^{-3} for NH_3 flows greater than ~3 sccs. The NH_2 density shows a different behavior than the NH density. It increases more gradually and reaches a level of 6.0×10^{12} cm^{-3} at an injected flow of 17 sccs, but does not saturate. Langmuir probe measurements in the Ar-NH_3 plasma have shown that the ion density decreases by 3 orders of magnitude when 3 sccs NH_3 is injected in the plasma. Therefore, the saturation of the NH density at 3 sccs suggests a production mechanism for NH that is ion dominated. We propose the following basic reactions to explain the observed trends for the NH and NH_2 radical densities. First, the argon ion reacts with the ammonia molecule, creating molecular ions:

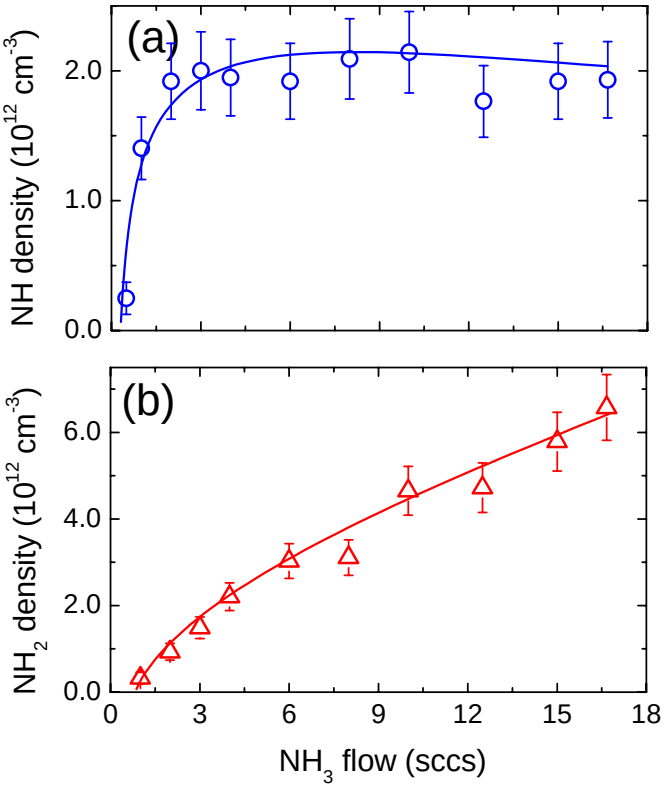

Figure 2: The NH (a), NH_2 (b) and NH_3 (c) density in an expanding Ar-NH_3 plasma. The lines are a guide to the eye.

$$Ar + NH_3^+ \rightarrow \begin{matrix} Ar + NH_3^+ \\ Ar + NH_2^+ + H \\ ArH^+ + NH_2 \end{matrix} \qquad (1)$$

This reaction has a rate constant of $1.85\text{x}10^{-9}$ cm^3s^{-1} and the channel that results in NH_3^+ is dominant [8]. Subsequently, the NH_3^+ recombines dissociatively at a very fast rate (rate constant ~$1\text{x}10^{-7}$ cm^3s^{-1}):

$$NH_3^+ + e \rightarrow \begin{matrix} NH + 2\,H \\ NH + H_2 \\ NH_2 + H \end{matrix} \qquad (2)$$

The dissociative recombination reaction results in NH and explains the saturation of the NH density when the ion density has diminished drastically (for NH_3 flows greater than 4 sccs). Reaction (2) also produces NH_2, but the NH_2 density does not saturate for higher NH_3 flows. Therefore, additional NH_2 is most likely produced by another reaction that is especially important for high NH_3 flows. One of the possibilities for this reaction is the following ion-molecule reaction:

$$NH_3^+ + NH_3 \rightarrow NH_4^+ + NH_2 \qquad (3)$$

This reaction produces NH_2 radicals, particularly at high NH_3 flows and has a rate of $1.7\text{x}10^{-9}$ cm^3s^{-1} [9], which is comparable to the rate of reaction (1). Also the dissociative recombination of NH_4^+ that is produced by reaction (3) leads to NH_2. Another reaction that can possibly explain the observed NH_2 trend is the atomic H induced dissociation of NH_3 molecules.

To check the proposed reaction scheme, we measured the NH density and the NH_3 consumption as a function of the argon ion flow from the plasma source. For both cases, we found a linear dependence on the Ar^+ flow, which is consistent with the expectations based on the proposed reaction scheme [7]. The NH_2

density, however, does not show a pronounced increase as function of the Ar^+ flow, which also indicates a different production mechanism for NH and NH_2 radicals [7].

4. NH and NH_2 densities in an Ar-NH_3-SiH_4 expanding plasma jet

Figure 3 shows the NH and NH_2 density in an Ar-NH_3-SiH_4 plasma as a function of the silane flow for a NH_3 flow of 17 sccs. The plasma source current is 45 A and the downstream pressure is 20 Pa. After a small initial increase, the NH density decreases gradually reaching a value of ~ 1.5×10^{12} cm^{-3} for an injected SiH_4 flow of 5 sccs. The NH_2 density decreases faster when SiH_4 is injected. For 5 sccs SiH_4 in the plasma, the NH_2 density is comparable to the NH density and approximately 1.5×10^{12} cm^{-3}. The decrease of the NH density might be explained by a competition between the charge transfer reaction of Ar^+ with SiH_4 and of Ar^+ with NH_3 [reaction (1)]. For NH_2, the decrease is much more pronounced and therefore, another loss mechanism is probably dominant. One possibility for this mechanism is a reaction of NH_2 radicals with silane radicals creating aminosilanes radicals. The initial increase in NH density for low SiH_4 flows might be caused by a change in the surface reaction probability for a depositing and non-depositing environment.

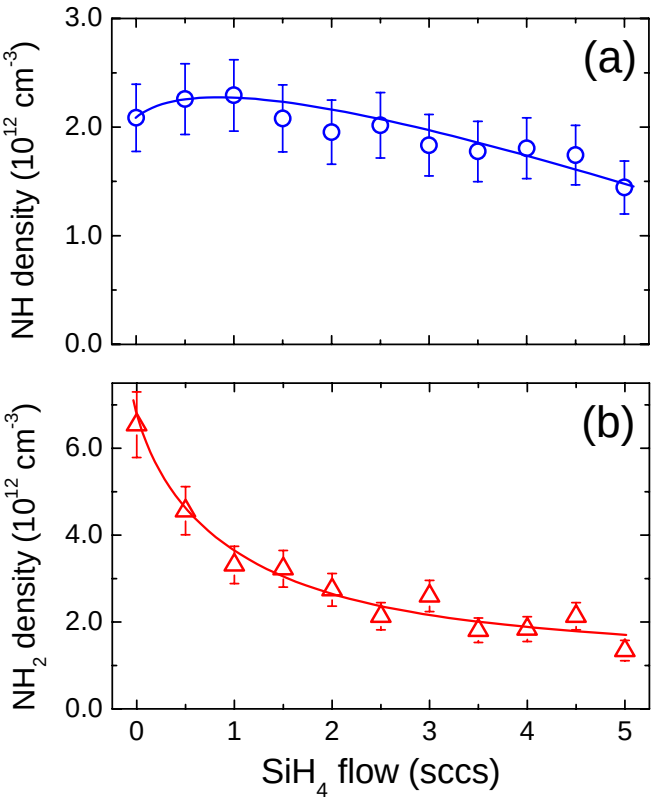

Figure 3: The NH (a) and NH_2 (b) density versus the injected SiH_4 flow. The lines are a guide to the eye.

5. Detection of N radicals

N radicals are much easier detected my mass spectrometry than by cavity ringdown spectroscopy, because the optical transitions of the N radical are in the vacuum ultra violet. Therefore, we used threshold ionization mass spectrometry (TIMS) [1] to detect N radicals in an Ar-NH_3-SiH_4 plasma. TIMS is based on the fact that direct ionization of a radical by an electron ($N + e \rightarrow N^+ + 2e$) requires less energy than dissociative ionization of a parent molecule ($NH_3 + e \rightarrow N^+ + H_2 + H + 2e$). For example, direct ionization of a N radical requires ~ 15 eV, while dissociative ionization of NH_3 resulting in N^+ requires ~ 23 eV. Here we present the first measurements of N radicals in an Ar-NH_3 plasma. Figure 4 shows the number of counts at mass 14 versus the electron energy for an Ar-NH_3 plasma ("plasma on") and for an Ar-NH_3 gas mixture

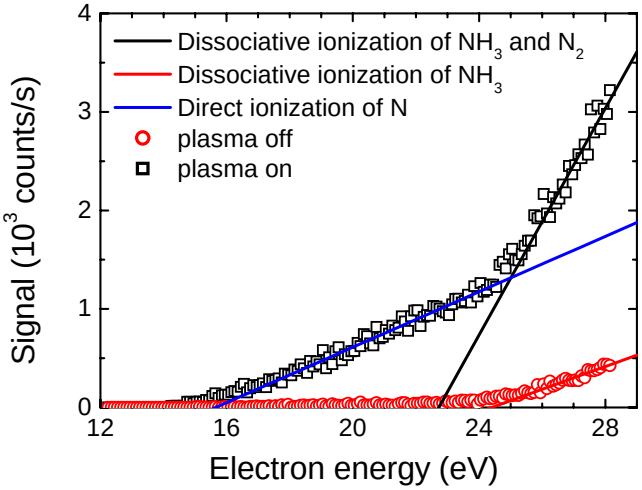

Figure 4: The signal of the mass spectrometer at mass 14 as a function of the electron impact ionization energy for plasma on and plasma off situation (Ar-NH_3 plasma).

("plasma off"). Clearly the signal for plasma on shows two distinct regions that are related to direct ionization of N radicals and to the dissociative ionization of NH_3 molecules. However, for the plasma on case, the slope of the dissociative ionization is steeper than for the plasma off case, which is not expected as NH_3 is consumed by the plasma. This indicates that also the dissociative ionization of N_2 molecules (~24 eV) that are created in the plasma contributes to the plasma on signal. This contribution can not be distinguished from the contribution of dissociative ionization of NH_3 (~23 eV) due to the small energy difference between both cases. By looking at the slope of the signal at low electron energy, the contribution of N radicals can be distinguished from the contribution of dissociative ionization of NH_3 molecules and N_2 molecules. For the plasma off signal, only the contribution of dissociative ionization of NH_3 molecules is present.

6. Conclusions

In this contribution, we have presented the NH and NH_2 density in an expanding Ar-NH_3 plasma jet measured by means of cavity ringdown spectroscopy. The maximum NH density is in the order of 2×10^{12} cm^{-3}, while the maximum NH_2 density is approximately 6×10^{12} cm^{-3}. The trends as a function of NH_3 flow, however, are different, suggesting a different production mechanism for both radicals. When SiH_4 is injected in the Ar-NH_3 plasma, the densities of both NH and NH_2 radicals decrease to approximately 1.5×10^{12} cm^{-3}. The different trends of both radicals as a function of the SiH_4 flow suggest again different loss mechanisms. In the future, threshold ionization mass spectrometry will be extended by N radical measurements as a function of NH_3 and SiH_4 flow and by measurements of SiH_x (x=0-3) radicals in the Ar-NH_3-SiH_4 plasma. The densities of these radicals as a function of several plasma parameters (flow ratio, current, pressure) will be valuable information to identify the main growth precursor for silicon nitride films.

Acknowledgements

The authors thank M.J.F. van de Sande, J.F.C. Jansen, A.B.M. Hüsken, and H.M.M. de Jong for their technical assistance. This study has been supported by the Netherlands Foundation for Fundamental Research on Matter (FOM) and by the Netherlands Ministry of Economic Affairs, the Ministry of Education, Culture and Science and the Ministry of Public Housing, Physical Planning and Environment (E.E.T.-project "HR-CEL"). Carolien Lamers is acknowledged for her contribution to the measurements. The research of W.K. has been made possible by a fellowship of the Royal Netherlands Academy of Arts and Sciences (KNAW).

References

[1] W.M.M. Kessels, F.J.H. van Assche, J. Hong, D.C. Schram, and M.C.M. van de Sanden - J. Vac. Sci. Technol. A **22**, 96 (2004)

[2] W.M.M. Kessels, F.J.H. van Assche, P.J. van den Oever, and M.C.M. van de Sanden - J. Non-Cryst. Solids **338-340**, 37 (2004)

[3] J. Hong, W.M.M. Kessels, W.J. Soppe, A.W. Weeber, W.M. Arnoldbik, and M.C.M. van de Sanden - J. Vac. Sci. Technol. B **21**, 2123 (2003).

[4] D.L. Smith, A.S. Alimonda, C-C. Chen, S.E. Ready, and B. Wacker - J. Electrochem. Soc. **137**, 614 (1990).

[5] W.M.M. Kessels, C.M. Leewis, M.C.M. van de Sanden, and D.C. Schram - J. Appl. Phys. **86**, 4029 (1999).

[6] M.C.M. van de Sanden, R.J. Severens, W.M.M. Kessels, R.F.G. Meulenbroeks, and D.C. Schram - J. Appl. Phys. **84**, 2426 (1998); J. Appl. Phys. **85**, 1243 (1999).

[7] P.J. van den Oever, J.H. van Helden, C.C.H. Lamers, R. Engeln, D.C. Schram, M.C.M. van de Sanden, and W.M.M. Kessels - submitted for publication

[8] R. Derai, G. Mauclaire, and R. Marx - Chem. Phys. Lett. **86**, 275 (1982)

[9] M.P. Skrzypkowski, and R. Johnsen - Chem. Phys. Lett. **274**, 473 (1997)

Novel plasma reactor with bottom rotary electrode for plasma-enhanced chemical vapor deposition of nanostructured films

R. Prikryl[1], V. Cech[1], P. Hedbavny[2], N. Inagaki[3]

[1]*Institute of Materials Chemistry, Brno University of Technology, Brno, Czech Republic*
[2]*Vakuum Praha, Prague, Czech Republic*
[3]*Laboratory of Polymer Chemistry, Shizuoka University, Hamamatsu, Japan*

Abstract
A novel plasma reactor has been developed in scope of the joint Czech-Japan project. The plasma system is aimed at preparation of functionally nanostructured thin films of high reproducibility. Controlled deposition of the nanostructured films is a new technological step for creative design and application of complex film systems in smart materials. Functionally gradient and/or multilayered nanostructured thin films of continuously or quasi-continuously varying physicochemical properties are worthwhile as compatible interlayers among distinct materials.

Keywords: PE CVD; thin film; multilayer; gradient film

1. Introduction

Technological applications of new materials often require them to be in the form of thin films. Many thin-film processing techniques have been developed for the fabrication of monolayers and single layers. Some of the techniques are able to prepare high quality thin films with high reproducibility. This level of technology has enabled us to deal with more complicated film systems. Over the last ten years, scientists from varying backgrounds have rallied around a versatile new method for the synthesis of multilayer thin films [1]. Because the layer-by-layer assembly method provides opportunities for creative design and application of function-specific films, the field has experienced an initial period of exponential growth. In complex systems, new properties appear that are not observed for each individual component. Plasma-enhanced chemical vapor deposition (PE CVD) is one of the perspective techniques [2] suitable for deposition of complex film structures.

In PE CVD, chemical activation is achieved by supplying electrical power to a gas at reduced pressure (10^{-1}–10^{3} Pa). At that pressure, the application of a sufficiently high voltage creates a visible glow, called glow discharge plasma. The low temperature plasma consists of about equal concentration of ions and electrons. Charge recombination processes and relaxation of electronically excited atoms and molecules cause the visible glow. The electrical power is coupled into the gas through the mediation of plasma electrons. The energetic electrons in the plasma ionize the gas, if only to a minor extent – about one part per million. The electrons chemically activate a much larger fraction of the gas, about 1 percent. The increased chemical activity of the gas (monomer vapor) results primarily from dissociation of the molecules into smaller species, called radicals. Radicals are chemically unsaturated and therefore capable of chemical reactions at high rates; they are the species that react at a surface (substrate) and contribute to film formation. Plasma polymerization is a film-forming process, in which growth of low-molecular-weight molecules (monomers) into high-molecular-weight molecules (polymers) occurs with the assistance of the plasma energy [3]. It should be emphasized, that the adjective "plasma" does not mean a kind of activated species propagating polymeric chains in plasma polymerization in contrast to radical or ionic polymerizations. The term "plasma" means an energy source to initiate polymerization reactions. In many cases, polymers formed by plasma polymerization show distinguished chemical composition, and chemical and physical properties from those formed by conventional polymerizations, if the same monomer is used for the two polymerizations. This uniqueness of plasma polymers results from the reaction mechanism of the polymer-forming process.

2. Nanostructured films

Plasma-polymerized organosilicones constitute a class of materials with a rich and varied scientific background. This class of materials possesses a special characteristic, which distinguishes it from other

plasma polymers. It is the ability to vary and control the degree of organic/inorganic character (that is, the carbon content) by appropriate choice of fabrication variables. This allows one to control many physico-chemical properties over wide ranges resulting in an extraordinary potential for useful applications, which are now only beginning to be tapped. The organosilicon plasma polymers are widely observed with respect to the potential for optical, mechanical and electronics applications. These materials were reviewed in Ref. 4,5.

The mechanical properties (hardness, Young's modulus, adhesion, internal stress) of thin films are of great importance with respect to applications such as protective coatings to improve wear resistance or possibly as lubrication. Therefore thin films of quite different mechanical properties are required. Multicomponent materials such as composites require functional films (interlayers) that are embedded among components (reinforcing fiber, polymer matrix) to improve their compatibility and it is expected that ductile and flexible films of the elastic modulus value about 10^0 GPa are expected to fulfill the demands [6]. The Young's modulus and thickness of the interlayer are among the main parameters influencing composite performance [7]. Model calculations even suggest controlling the composite strength and toughness by varying the interlayer modulus [8]. Experimental data drawn from the literature indicate that thin films of variable moduli can be deposited even by the same monomer using plasma techniques. However, most of the materials, such as a-Si:H [9], a-SiN:H [10], a-SiO_2:H [10], a-C:H [9,11] or a-SiCO:H [12], are too stiff materials of the modulus higher than 40 GPa (Fig. 1).

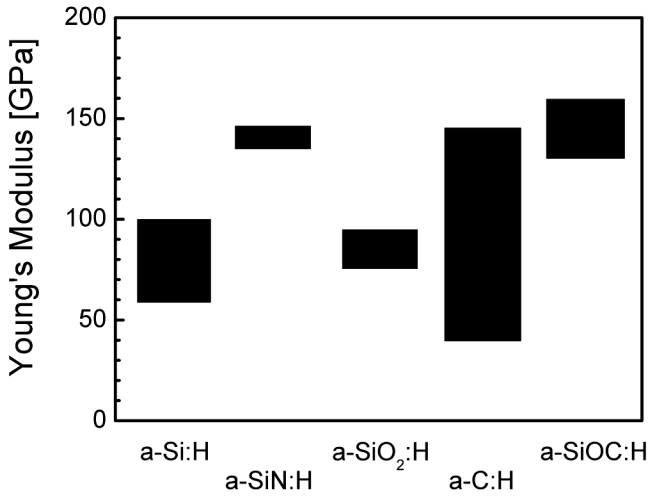

Fig. 1. Range of elastic modulus corresponding to thin films prepared by plasma techniques.

Our team in cooperation with research workers in UK was successful in deposition of hydrogenated amorphous silicon oxycarbide (a-SiCO:H) single layers of RF-power controlled Young's modulus (4 – 40 GPa) [13,14]. The soft and highly elastic films of a thickness ranging from 15 nm to 4 μm were deposited on planar glass and silicon substrates using an inductive coupling plasma system [15]. Our films were prepared at a relatively low power density, and the lower plasma energy therefore seems to be the reason for the reduced elastic modulus. Monomer molecules are more activated and fragmented forming a higher density of free radicals, if the plasma energy increases, and the reactive species results in a highly cross-linked polymer.

In general, a utilization of interlayer with the modulus about that of the polymer matrix (3-4 GPa) or even lower results in problems with a very sharp fiber/interlayer interface (Fig. 2(b)). A simple gradient interlayer could suit better; see Fig. 2(c). In that case, both the interfaces are not so sharp and the interlayer material is not so stiff. More sophisticated modulus profile can be suggested to ensure a strong but tough composite using a functionally gradient nanostructured interlayer; see Fig. 3 (solid line) [16]. Preparation of an interlayer with chemical and physical properties continuously varying from those of the fiber to those of the matrix without any interface could be an ambitious aim.

Multilayer thin films (sandwiches) can be prepared using the fabrication "bottom-up". Thus, a nanostructured interlayer can be prepared as layer-by-layer (Fig. 3, dashed line), where the film thickness of a single layer could be only several tens of nanometers and single layers have to be bonded each other using strong chemical bonds. We could construct a functionally gradient nanostructured interlayer "without" interfaces if any coating technology would be able to prepare film of continuously varying properties in one deposition. Such a nanotechnology could be worth for formation of the controlled interphase in

multicomponent materials. With respect to our experience we expect that the plasma-enhanced chemical vapor deposition has the potential to be successful in preparation of functionally nanostructured thin films.

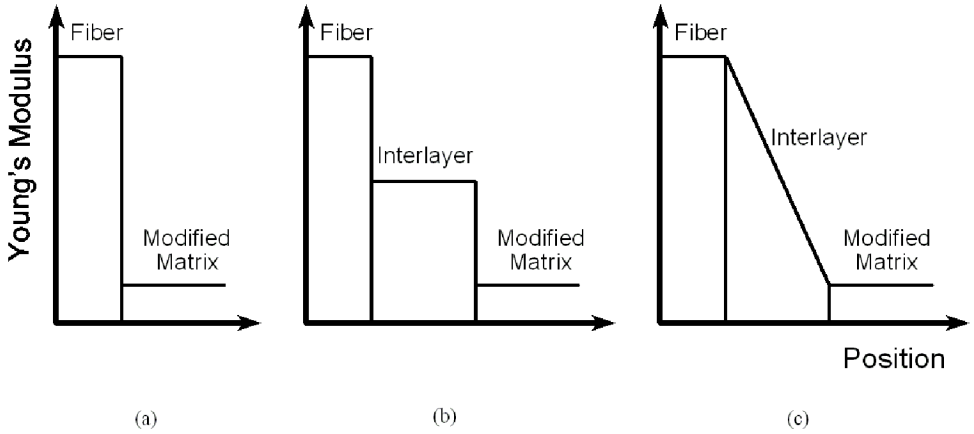

Fig. 2. Schematic illustration of the elastic modulus profile across the fiber/interlayer/matrix composite system (multicomponent material): (a) without interlayer, (b) homogeneous interlayer, (c) gradient interlayer.

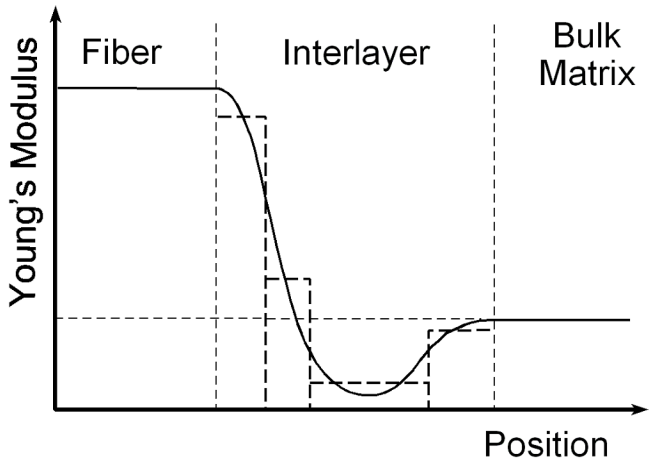

Fig. 3. Schematic illustration of elastic modulus profile across the fiber/interlayer/matrix composite system (multicomponent material) with a functionally gradient nanostructured interlayer prepared as layer-by-layer (dashed line) or in one deposition (solid line).

3. Technological apparatus

A novel plasma reactor has been developed in scope of the joint Czech-Japan project (2002-2004) supported by the Czech and Japan Ministry of Education. The plasma system (Fig. 4) is aimed at preparation of functionally nanostructured thin films of high reproducibility. The internal setup of our deposition chamber, using plan-parallel electrodes, was derived from a typical capacitive coupling system, but our apparatus of new creative design was equipped with many non-standard components. A special construction of bottom rotary electrode (ø 114 mm) (Fig.5) enabled us to stick in/out samples (Fig.6) into/from the chamber under vacuum, and so without reactor contamination, using a magnetic drive (linear and rotary, BOC Edwards) and a special load lock mounted inside of differentially pumped side chamber. Next, the rotary electrode can be heated/cooled ranging from –100 to 300 °C and biased ranging from –500 V to +500 V. An upper electrode (ø 135 mm) of shower-type can be positioned in a distance of 20 – 60 mm from the bottom one. A movable substrate shutter can be used to deposit film at steady-state plasma conditions. An RF-generator (Cesar 1310, 13.56 MHz, 1000 W, Dressler) was connected to the system using an automatic matching network (VM 1000A, Dressler). It was possible to achieve a range of effective power density from 1×10^{-4} to 4×10^{0} W cm^{-3} (1×10^{-3} to 4×10^{0} W cm^{-3}) using pulsed (continuous) plasma regime with respect to the movable top electrode.

A turbomolecular pump (TMU 261 P, Pfeiffer Vacuum) with a dry scroll pump (TriScroll 300, Varian) as the first stage and an LN2-cooled trap were selected to evacuate the system in order to eliminate oil vapor, minimize a rest of water in all vacuum chambers and thus acquire the basic pressure ~ 10^{-6} Pa. Cleaning of the system, substrate pretreatment, and deposition process were automatized via control unit.

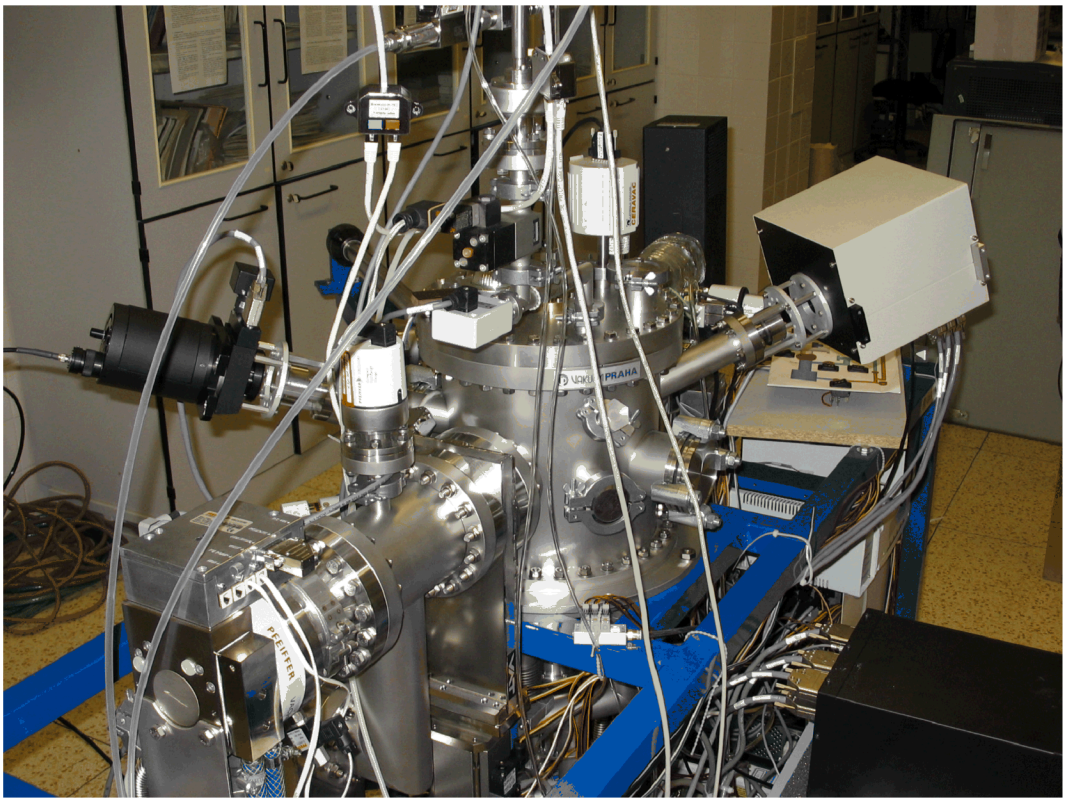

Fig. 4. A real view of new technological apparatus.

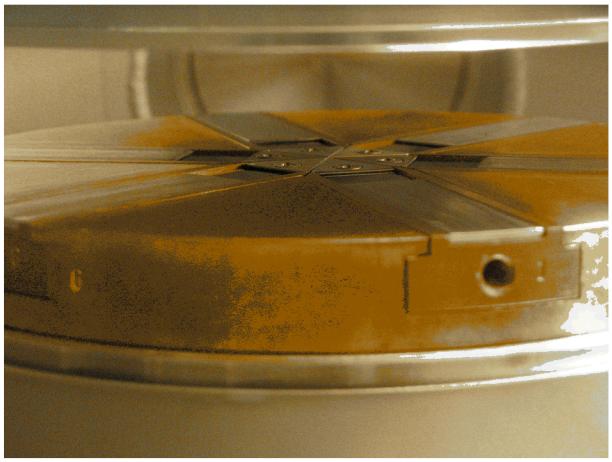

Fig. 5. Bottom rotary electrode with substrate holders inside.

Fig. 6 Substrate holders.

The reactor was equipped by mass spectrometer (Process Gas Analyser HPR-30, Hiden Analytical), in-situ spectroscopic ellipsometer (UVISEL, Jobin Yvon), and optical emission spectrometer (Triax 550, Jobin Yvon) to monitor the plasma process and film growth (Fig. 7). The in-situ ellipsometry enables analyses not only single layers but also multilayers [17-19] with respect to their thicknesses and optical constants. New numerical simulations enabled fast analyses of measured ellipsometric data corresponding to complex

multilayer and gradient nanostructures. The optical constants of a newly grown ultrathin layer should be used as a feedback for the control of deposition conditions during a nanostructure growth. This is a new conception of a controlled plasma process (PE CVD).

Controlled deposition of the functionally nanostructured thin films is a new technological step for creative design and application of complex film systems in smart materials. Functionally gradient and/or multilayered nanostructured thin films of continuously or quasi-continuously varying physicochemical properties are worthwhile as compatible interlayers among distinct materials.

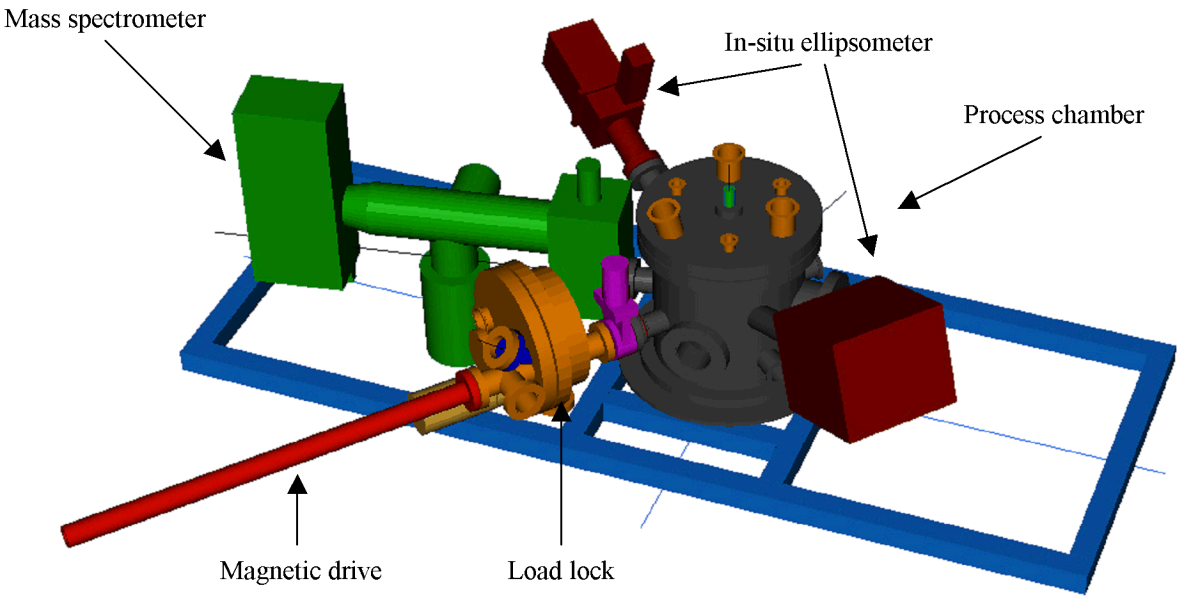

Fig. 7. Schema of process chamber with load lock, magnetic linear drive, mass spectrometer, and in situ ellipsometer.

4. Conclusion

We are going to promote our experience with a deposition of single layers of controlled properties. The controlled construction of nanostructured multilayers and gradient thin films of a given elastic modulus (hardness) and/or refractive index profiles, using the plasma-enhanced chemical vapor deposition (PE CVD), is the main objective of new activities. Thin and ultrathin single layers and functionally nanostructured thin films will be deposited using a high-tech RF capacitive coupling system equipped by in-situ spectroscopic ellipsometer, optical spectrometer and process gas analyzer. The deposition system will be automatized to enable precise and fast varying of deposition conditions via control unit (PC) and all the deposition process (pretreatment of substrate, deposition steps, post-treatment of layered structure) will be programmed. Analyses of measured ellipsometric data provide optical parameters during the growth of complex multilayer or gradient nanostructures. The optical constants of a newly grown ultrathin layer will be used as a feedback for the tuning of deposition conditions during a nanostructure growth. This is quite a new conception of the controlled plasma process (PE CVD). Selected organosilane monomers and their mixtures with a gas together with other suitable silane and non-silane monomers have to be utilized for the preparation of functionally nanostructured thin films with controlled organic/inorganic character. The deposited films and their layered nanostructures will be extensively characterized by microscopic and spectroscopic techniques in order to determine surface morphology, microstructure, and chemical structure. Selected mechanical and optical parameters across the nanostructured thin film will be determined as a function of deposition conditions and the structure-property relations will be discussed as well. We expect that new properties and phenomena could appear in such complex systems that are not observed for each individual component.

Acknowledgements: This work was supported in part by the Czech Ministry of Education (contracts COST 527.110 and P12.001) and the Czech Science Foundation (contracts 104/03/0236 and 104/04/P138).

References

1. G. Decher, J. B. Schlenoff (Eds.), *Multilayer Thin Films*, Wiley-VCH, Weinheim 2003.
2. F. Jansen, Plasma-enhanced chemical vapor deposition. In *Handbook of Vacuum Science and Technology* (D.M. Hoffman, B. Singh, and J.H. Thomas, Eds.), London, Academic Press, 1997.
3. N. Inagaki, *Plasma Surface Modification and Plasma Polymerization*, Lancaster, Technomic Publ., 1996.
4. A. M. Wrobel and M. R. Wertheimer, in *Plasma Deposition, Treatment, and Etching of Polymers*, R. D'Agostino, Ed., Academic Press: New York, 1990, Chapter 3.
5. Y. Segui, in *Plasma Processing of Polymers*, R. D'Agostino, P. Favia, and F. Fracassi, Eds., Kluwer Academic Publishers, Dordrecht, 1997, p. 305.
6. A. P. Kettle, F. R. Jones, M. R. Alexander, R. D. Short, M. Stollenwerk, J. Zabold, W. Michaeli, W. Wu, E. Jacobs, and I. Verpoest, Composites Part A 29, 201 (1998).
7. M. Labronici and H. Ishida, Comp. Interfaces 2, 199 (1994).
8. L. J. Broutman and B. D. Agarwal, Polym. Eng. Sci. 14, 581 (1974).
9. X. Jiang, K. Reichelt, B. Stritzker, J. Appl. Phys. 66, 5805 (1989).
10. D. Rats, V. Hajek, and L. Martinu, Thin Solid Films 340, 33 (1999).
11. J. C. Sanchez-Lopez, C. Donnet, J.L. Loubet, M. Belin, A. Grill, V. Patel, and C. Jahnes, Diam. Rel. Mater. 10, 1063 (2001).
12. J. F. Zhao, P. Lemoine, Z.H. Liu, J.P. Quinn, P. Maguire, and J.A. McLaughlin, Diam.Rel.Mater.10, 1070 (2001).
13. V. Cech, A.A. Goruppa, J. Vanek, and F.R. Jones, Proc.16thInt.Symp. Plasma Chemistry, Taormina 2003, 6pages.
14. V. Cech, F.R. Jones, R. Prikryl, and J. Vanek, Proc. NANO 03, Brno, 2003, pp.129.
15. V. Cech, R. Prikryl, R. Balkova, J. Vanek, and A. Grycova, J. Adhesion Sci. Technol. 17 1299 (2003).
16. V. Cech, F.R. Jones, R. Balkova, A.A. Goruppa, J. Vanek, and R. Prikryl, Int. Conf. Interfaces and Interphases in Multicomponent Materials, Balatonfured 2003.
17. C. Valee, A. Goullet, F. Nicolazo, A. Granier, G. Turban, J. Non-Cryst. Solids 216, 48 (1997).
18. K. Aumaille, C. Vallee, A. Granier, A. Goullet, F. Gaboriau, G. Turban, Thin Solid Films 359, 188 (2000).
19. Spectroscopic Elipsometry (brochure), Jobin Yvon, Horiba Group (www.jyhoriba.com).

Chemical properties of plasma-polymerized vinyltriethoxysilane

V. Cech[1], J. Vanek[1], V. Perina[2], J. Zemek[3]

[1]*Institute of Materials Chemistry, Brno University of Technology, Brno, Czech Republic*
[2] *Nuclear Physics Institute, Academy of Sciences, Rez near Prague, Czech Republic*
[3] *Institute of Physics, Academy of Sciences, Prague, Czech Republic*

Abstract
Plasma-polymerized thin films of vinyltriethoxysilane were deposited on IR-transparent silicon wafers using plasma-enhanced chemical vapor deposition. Deposited films were characterized by spectroscopic techniques (RBS, ERDA, XPS, FTIR) in order to compare their elemental composition and chemical structure. We were able to influence/control the elemental composition and chemical structure of the plasma polymer films in relatively wide ranges by increasing the effective power.

Keywords: PE CVD; thin film; organosilicon; FTIR; RBS; ERDA; XPS

1. Introduction

The vinyltriethoxysilane (VTES) monomer is one of silane coupling agents [1] recommended for surface modification of glass fibers employed as reinforcements for polyester-matrix composites. The VTES molecule is a multifunctional one, which reacts at one end with the glass surface and at the other end with the polymer matrix. In principle, a polysiloxane interlayer prepared by wet chemical process from VTES should provide a strong but tough bond [2] between the reinforcement and the polymer matrix. However, the real polycondensed film is heterogeneous [3] with respect to the uniformity and film thickness. The molecules of silane coupling agent have a tendency towards self-condensation, forming siloxane oligomers rather than complete bonding with the glass surface [4,5], which results in deterioration of composite performance. We would like to introduce a plasma-polymerized vinyltriethoxysilane (pp-VTES) as homogeneous film (interlayer) and demonstrate a variety of the films with respect to their chemical properties that could be controlled by deposition conditions.

2. Experimental

Pp-VTES films were deposited on IR-transparent silicon wafers using a helical coupling pulsed-plasma system (13.56 MHz); details on the apparatus have been described in Ref. 6. The vacuum system was evacuated to a pressure of 5×10^{-3} Pa and then flushed with argon gas (10 sccm) for 10 min. A basic pressure of 2×10^{-3} Pa was established in the deposition chamber after flushing. Monomer vapor at a mass flow rate of 0.45 sccm (process pressure was 0.02 mbar) was introduced into the deposition chamber using a dose valve. The plasma was ignited at a selected effective power ranging from 0.05 to 25 W, using pulsed plasma with t_{on} = 1 ms and a total power of 50 W. When the deposition process was ended, all the apparatus was flushed by argon gas and after 30 min the chamber was flooded by air to atmospheric pressure and the prepared specimen conveyed from the chamber into a desiccator to avoid contamination before measurements.

Films of the thickness ranging from 0.2 to 1.4 μm were subjected to chemical analysis. The elemental composition, atomic surface density, and density of thin films were studied by conventional and resonant Rutherford Backscattering Spectrometry (RBS) and Elastic Recoil Detection Analysis (ERDA) methods using Van de Graaf generator with a linear electrostatic accelerator. The depth profiles of heavy elements were measured by RBS using 2.73 MeV alpha particles impinging perpendicularly on sample surface and detected scattered under the laboratory scattering angle of 170 deg. The Si and C, O content were measured by using 2.4 MeV protons as projectiles. The reason for this is the enhanced selectivity for some lights elements as admixtures. The ERDA and RBS with incident beam of 2.75 MeV alpha particles at 75 deg to sample surface normal was simultaneously measured. The hydrogen atoms recoiled under the angle of 30 deg were detected with a surface barrier detector covered with 12 μm thick Mylar stopping foil. Similar uncovered surface barrier detector was used for simultaneous detection of alpha particles scattered under the laboratory scattering angle of 170 deg. Small aluminium propeller covered by thin gold layer and checked by simultaneously measured RBS monitored the amount of impinging alpha particles needed for ERDA

normalization. The RBS was evaluated by computer code GISA 3 [7] and the ERDA by SIMNRA code [8] both using cross-section values from SigmaBase. The charge of impinging alpha particle was not measured directly and thus the evaluation of RBS with alpha particle was used to estimate amount of impinging alpha particles needed for ERDA normalization. The estimated accuracy of composition measurements was about 5 at%.

The Si, C and O bulk contents were correlated with the surface one determined from analyses of the photoelectron spectra using X-ray Photoelectron Spectroscopy (XPS). The composition of elements in the surface region (top 6–8 nm) of the deposited layers was studied by XPS on an ADES 400 VG Scientific photoelectron spectrometer using Mg K_α (1253.6 eV) photon beam at the normal emission angle. Atomic concentrations were determined semi quantitatively assuming the model concerns a solid that is homogeneous in composition [9]. Peak areas were corrected for inelastic background [10], photoelectron cross-sections, asymmetry parameters [11], inelastic mean free paths [12], and the measured transmission function of the electron energy analyzer [13]. The estimated accuracy of composition data was about 2 at%.

Infrared measurements in the wavenumber range from 400 to 4000 cm^{-1} were carried out using a Nicolet Impact 400 Fourier transform infrared (FTIR) spectrophotometer in an H_2O-purged environment. Transmission spectra were obtained on films deposited on one-side polished crystalline silicon wafers. An absorption subtraction technique was applied to remove the spectral features of Si wafers. The spectral resolution was 2 cm^{-1}. Approximately 128 scans were recorded to achieve the signal-to-noise ratio.

3. Results and discussion

It was possible to prepare continuous and homogeneous coatings on planar substrates with a film thickness ranging from 15 nm to 2 μm. The film thickness and optical constants were determined from ellipsometric data (UVISEL Jobin Yvon). Optical data were processed using a model of single homogeneous film on the semi-infinite silicon substrate. The deposition rate varies as a function of the effective power in a range of 1–120 nm min^{-1} and the film thickness could be controlled by deposition time. The surface roughness (RMS) of pp-VTES films measured only several nanometers as obtained using AFM (Accurex IIL, Topometrix).

The bulk elemental compositions corresponding to the pp-VTES film deposited at different power and were evaluated from RBS/ERDA measurements are given in Fig. 1. There was no evidence about a depth profile in measured spectra of films with the film thickness up to 2 μm and thus we could state that the films were homogeneous. We can notice form the Fig. 1 that the hydrogen concentration was almost the same (40 – 45 at%) for all the films. However, the carbon concentration increased and oxygen and silicon concentrations decreased significantly when the effective power was enhanced.

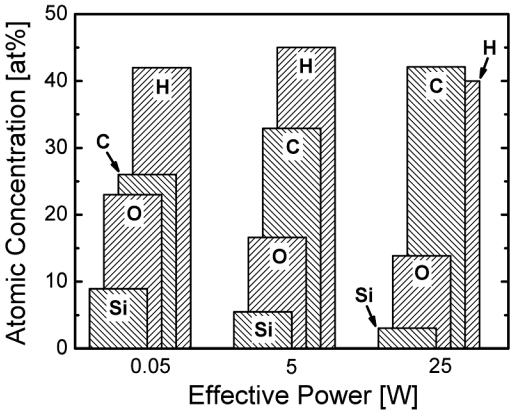

Fig. 1. Elemental composition of pp-VTES films deposited at different power determined form RBS/ERDA.

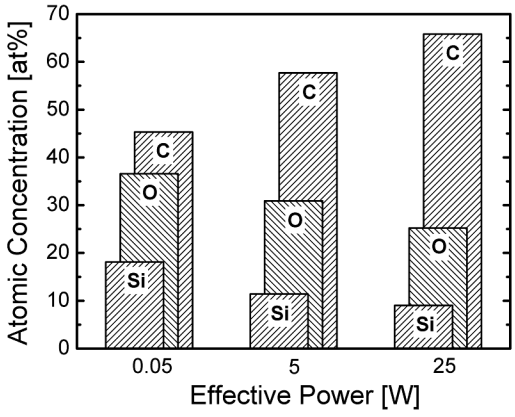

Fig. 2. Elemental composition of pp-VTES films deposited at different power determined form XPS.

Using the same samples, the elemental compositions at the surface layer (6-8 nm) of pp-VTES films were determined from the integral intensities of the C 1s, O 1s, and Si 2p signal of the XPS spectra recorded. The determined atomic concentrations (Fig. 2) exhibited the same trends with respect to the power as the

previous data (Fig. 1). Carbon, oxygen and silicon concentrations evaluated from RBS/ERDA measurements were recalculated eliminating the hydrogen concentration in order to enable comparison between the bulk and surface data (XPS), see Fig. 3. We could find a perfect agreement among the concentration values corresponding to bulk and surface data. The difference is only up to 5 at%, which is within an accuracy of the RBS method.

Element ratios in the monomer molecule compared with those for pp-VTES films prepared at different power gave a picture about great changes in plasma polymer (Fig. 4). The ratios were calculated using the bulk concentrations (RBS/ERDA). One can see that the organic/inorganic character of the film, represented by the element ratio of C/Si, varied in a wide extent from 2.9 to 13.9, when the power was enhanced. In a similar way, the O/Si ratio increased from 2.6 to 4.6 and, the C/O ratio increased from 1.1 to 3.0, when the effective power was enhanced form 0.05 to 25 W. The determined results revealed that the plasma polymer deposited at low power (0.05 W) was deficient of carbon atoms and that one deposited at higher power (25 W) was deficient of silicon atoms. The molecular formula of the monomer, $SiO_3C_8H_{18}$, and the plasma polymer one, $SiO_3C_6H_{8.2}$, corresponding to the pp-VTES film deposited at a power of 5 W, seemed to be similar but the chemical structure of plasma polymer was quite different.

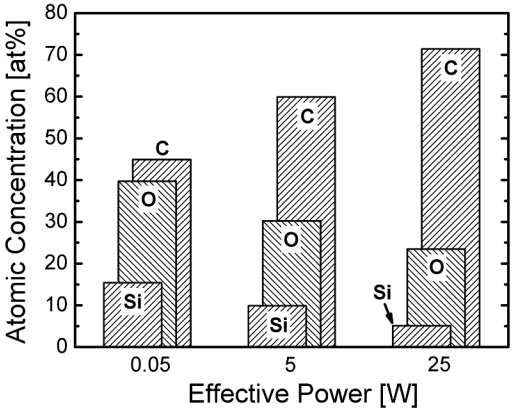

Fig. 3. Carbon, oxygen and silicon concentrations evaluated from RBS/ERDA measurements and recalculated eliminating the hydrogen concentration.

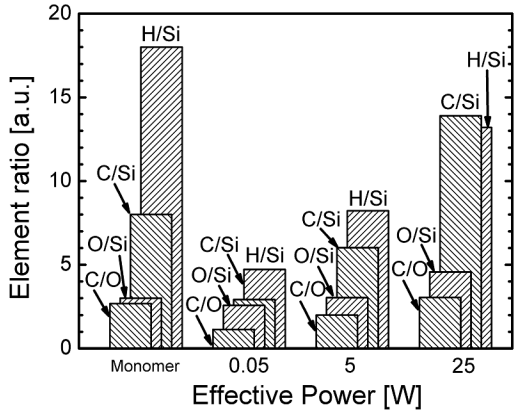

Fig. 4. Comparison among element ratios corresponding to monomer molecule and pp-VTES films deposited at different power.

Figure 5 shows typical FTIR spectra of the pp-VTES films prepared at different effective power (0.05, 5, 25 W). The absorption bands at 2970–3000 cm^{-1} were assigned to CH_3, CH_2 stretching vibrations [14] and a decreased intensity corresponding to the methyl groups evidenced a decrement of this species in plasma polymer films deposited at high power (25 W). Two bands (965 cm^{-1} and 1163 cm^{-1} [14]) assigned to the Si–O–C stretching vibration in ethoxy groups were not evident in spectra of high-power deposited pp-VTES film and this phenomenon corresponded well to a descent of methyl groups. The CH_2 asymmetric stretching vibrations at 3058 cm^{-1} [15], C=C stretching vibrations at 1600 cm^{-1} [15], CH_2 deformation vibrations at 1410 cm^{-1} [15], and =CH waging vibrations at 1010 cm^{-1} [15] corresponding to the vinyl groups were not apparent in all IR spectra of pp-VTES films. The pp-VTES films seemed to be free of vinyl groups or plasma polymer could content a low density of the groups as the absorption bands were of low intensity even at the monomer spectrum. Increasing the power, a new absorption band could be found at 3200–3700 cm^{-1} assigned to the OH stretching vibrations [14,15] and one at 1710 cm^{-1} corresponding to the carbonyl stretching vibrations [16]. The dominant absorption band in all the spectra could be found at a range of 1000–1200 cm^{-1}. The absorption band at 1072 cm^{-1} [16] corresponds to the Si–O–Si/Si–O–C stretching vibrations in continuous random network, which forms the basic chemical structure of the material prepared at lower power (0.05 and 5 W). The band decreased when the effective power was enhanced (25 W).

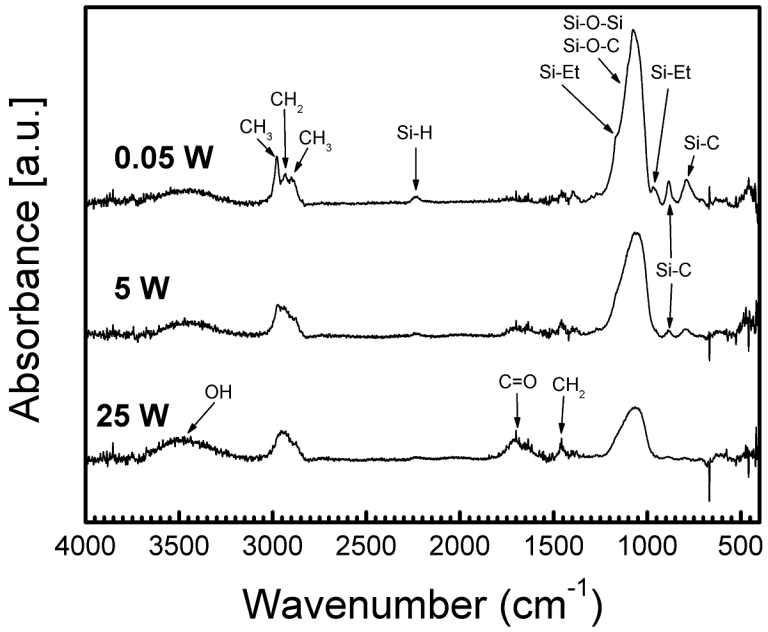

Fig. 5. Infrared spectra of pp-VTES films deposited at different power.

4. Conclusion

Plasma-polymerized vinyltriethoxysilane (pp-VTES) films were deposited on planar silicon substrates using pulsed plasma (PE CVD). The deposition rate could be controlled by power and the thickness of plasma polymer film could be easily varied in a range of 15 nm – 2 μm with the film surface relatively flat. Ellipsometric and RBS/ERDA data gave evidence about the single homogeneous film. The bulk (RBS/ERDA) and surface (XPS) elemental composition of films agreed within an error up to 5 at%. The hydrogen concentration was almost the same (40 – 45 at%) for all the pp-VTES films. The organic/inorganic character of the pp-VTES film was varied extensively and can be expressed by bulk element ratio of C/Si, which increased from 2.9 to 13.9, when the effective power enhanced from 0.05 W to 25 W. Molecular formulas of the monomer and plasma polymers deposited at different power varied as follows:

Monomer	$SiO_3C_8H_{18}$
0.05 W	$SiO_{2.6}C_{2.9}H_{4.7}$
5 W	$SiO_{3.0}C_{6.0}H_{8.2}$
25 W	$SiO_{4.6}C_{13.9}H_{13.2}$

The pp-films were constituted by Si–O–Si/Si–O–C network with side ethoxy groups that decreased when increasing the power. The absorption bands corresponding to the C=O and OH stretching vibrations were apparent for plasma polymer films deposited at higher power. However, the vinyl groups in the pp-VTES were not confirmed by FTIR spectroscopy even if a very low power was used.

Acknowledgements: This work was supported in part by the Czech Ministry of Education (contracts COST 527.110 and P12.001) and the Czech Science Foundation (contract 104/03/0236).

References

1. J.G. Marsden, in I. Skeist, (Ed.), Handbook of Adhesives, Chapman & Hall, New York, 1990, p. 536.
2. J-K. Kim and Y-W. Mai, Engineered Interfaces in Fibre Reinforced Composites, Elsevier, Amsterdam, 1998.
3. D.W. Dwight, in A. Kelly, C. Zweben (Eds), Comprehensive Composite Materials, Elsevier, Amsterdam, 2000, Volume 1.
4. G.M. Nishioka, J. Non-Cryst Solids, 120, 102 (1990).
5. W. Wang, A.T. Dibenedetto, J. Adhesion, 68, 183 (1998).
6. V. Cech, R. Prikryl, R. Balkova, J. Vanek, and A. Grycova, J. Adhesion Sci. Technol. 17, 1299 (2003).

7. J. Saarilahti and E. Rauhala: Interactive personal-computer data analysis of ion backscattering spectra, Nucl. Instrum. and Methods in Physics Research B64, 734 (1992).
8. M. Mayer, SIMNRA User`s Guide, Forschungscentrum Julich, Inst. fuer Plasmaphysik, 1998.
9. J.F. Moulder, W.F. Stickle, P.E. Sobol, and K.D. Bomben, Handbook of X-ray Photoelectron Spectroscopy, Perkin Elmer Co., 1992.
10. D.A. Shirley, Phys. Rev. *B*, 5, 4709 (1972).
11. I.M. Band, Y.I. Kharitonov, and M.B. Trzhaskovskaya, At. Data Nucl. Data Tables, 23, 443 (1979).
12. S. Tanuma, C. J. Powell, and D. R. Penn, Surf. Interface Anal., 17, 911 (1991).
13. P. Jiricek, Czech J. Phys., 44, 261 (1994).
14. V.P. Tolstoy, I.V. Chernyshova, V.A. Skryshevsky, Handbook of Infrared Spectroscopy of Ultrathin Films, John Wiley & Sons, New Jersey, 2003.
15. D. Lin-Vein, N.B. Colthup, W.G. Fateley, J.G. Grasselli, The Handbook of Infrared and Raman Characteristic Frequencies of Organic Molecules, Academic Press, San Diego, 1991.
16. C. Vallee, A. Goullet, A. Granier, A. van der Lee, J. Durand, J. Non-Cryst. Solids 272 (2000) 163.

Relationship between plasma phase composition and deposit chemical structure in DECR HMDSO plasmas under various microwave powers

Patrice Raynaud, Bernard Despax, Yvan segui, Isabelle Savin and Richard Clergereaux
Laboratoire de Génie électrique (UMR 5003), 118 Route de Narbonne, F-31062 Toulouse Cedex, France
raynaud@lget.ups-tlse.fr and despax@lget.ups-tlse.fr

Abstract:
The composition of HMDSO microwave plasma phase at 4.10^{-3} mbar and of the corresponding films were studied by FTIR spectroscopy, under different power conditions. We have shown that the thin film composition is related to the plasma phase composition The interpretation of these observations led to a proposal involving a chemical mechanism: the increasing decomposition of HMDSO into by-products, which themselves decompose all the more as power increases, plays a determining role.
Keywords: hexamethyldisiloxane, plasma, gas phase infrared spectroscopy, SiOxCHy

1. Introduction

Under plasma conditions, thin film deposition often results from the surface reactions of neutral active species. Therefore, the properties and the quality of deposited film depend on the relative contribution of these species to the film growth. Understanding how the dissociation conditions affect these contributions provides important guidance in finding the mechanism leading from the initial precursors to the film formation. This paper focuses on the hexamethyldisiloxane (HMDSO) dissociation mechanism and the resulting species as well as the relationship between these species and the nature of the deposit. Although ions can also be important for deposition and film properties, in our case the deposition is mainly due to neutral active species. No direct analyses of HMDSO dissociation products can be found in the literature. It has only been indirectly studied. The works carried out by Magni [1] and Alexander [2] in radiofrequency discharges using mass spectrometry suggest a breaking of both Si-O and C-Si bonds after electron impact. Besides, studies in microwave discharge using Direct Electron Cyclotronic Resonance (DECR) [3-5] have shown that a large production of hydrocarbon molecules is an evidence of C-Si bond breaking in HMDSO plasma. Besides the HMDSO thermal dissociation may also lead to other organosilicon species [6].A determination of HMDSO by-products under different radiofrequency plasma conditions (100 mTorr) was undertaken by F.Fracassi et al [7]. They essentially detect many linear and cyclic oligomers containing -$(CH_3)_2$SiO-chemical group.The aim of this work is to contribute to the understanding of HMDSO plasma deposition mechanism at very low pressures (few mbar) through the Fourier transform infrared analysis of the gas phase and the the chemical analysis of the deposits.

2. Experimental

The experimental reactor coupled to the gas infrared measurement setup, schematically represented in figure 1, has been described elsewhere [3,4]. The optical length of the infrared beam can be adjusted by multi-reflection to a maximum of 44 m. The spectra were recorded by means of Biorad FTS 60A FTIR spectrometer. The data reported were obtained with a resolution of 0.5 cm^{-1}. The detection threshold of our IR setup was around 5 10^{10} molecules.cm^{-3}. The plasma was a MMP-DECR at 2.45 GHz. The analyses were carried out at a total pressure of 4.10^{-3} mbar with power ranging from 60 to 600 watts. As during a run the mirrors and KBr windows could be covered with a deposit, a particular attention was paid to estimate the mirror coverage by a deposit. Before each experiment, a base line was recorded as the background for the new experiment. Moreover, spectra of the empty reactor were recorded after each run. After a run, no significant signal was obtained on the mirrors with respect to infrared measurement in the plasma gas phase. Fourier Transform Infrared spectroscopy (FTIR) gives information on the neutral species present in the plasma.

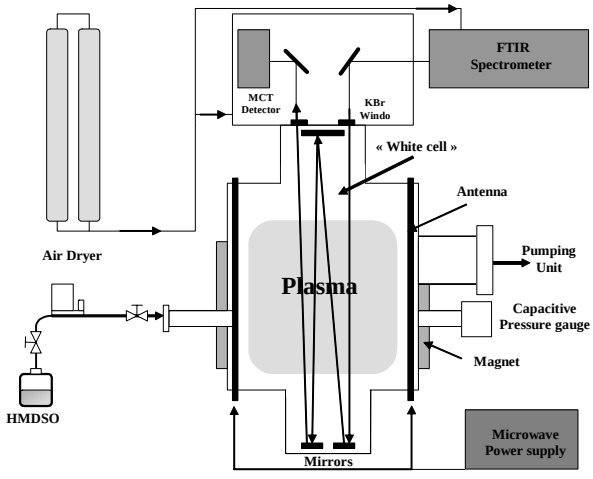

Figure 1: Microwave reactor coupled to the gas infrared measurement setup

3. Results and discussion

A. Pure hexamethyldisiloxane FTIR spectra.

The Beer Lambert law was checked at different pressures with a 40 m path length within the pressure range used in our experiments. Figure 2 shows a typical HMDSO spectrum. An identification of HMDSO bands has been already done in previous works [1,3][4][8]. Table 1 lists the bands observed in the present study. In the νCH regions, the asymmetric stretching CH_3 mode, the symmetric bending CH_3 mode (ν_s δ CH_3 in Si $(CH_3)_x$ $1 \leq x \leq 3$) and two rocking modes (ρCH_3 in $Si(CH_3)_x$) respectively appear at 2964 cm^{-1}, 1260 cm^{-1} and 850, 834 cm^{-1}(weak shoulder). Besides, in the νSiO regions, the stretching mode of Si-O-Si bridge band appears at 1072 cm^{-1}.

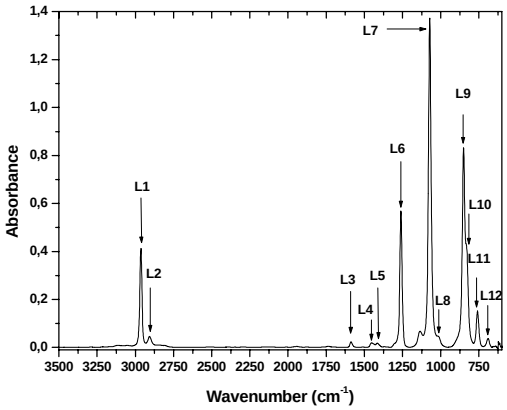

Figure 2: Pure HMDSO FTIR spectrum at 4.10^{-3}

B. Analysis of the plasma phase

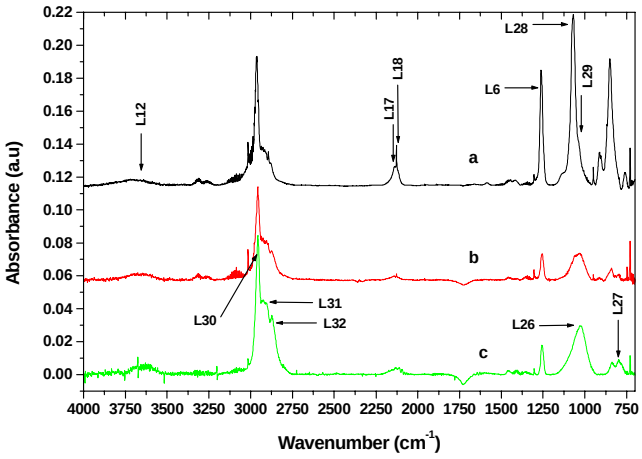

Figure 3: Plasma FTIR spectra at different microwave powers: a (60 W), b (170 W), c (600 W),

In order to accurately examine the HMDSO by-products in the plasma phase we have to get rid of the residual HMDSO spectrum bands (Figure 3). At low microwave powers, figure 3a clearly shows IR bands at 3660 cm^{-1}, 2138 cm^{-1}, 2128.5 cm^{-1}, 1260 cm^{-1}, 850 and 834 cm^{-1}. The presence of hydrocarbons is also observed. The bands at 2128.5 cm^{-1}, 2138 cm^{-1}, 914 cm^{-1}, 903 $cm^{-1}$are in the range of SiH bands. The main difference with respect to the initial plasma spectrum is the appearance of an important band at 1068 cm^{-1} which could be the signature of Si-O-Si bridge which normally appears at 1072 cm^{-1} for the monomer HMDSO. This slight wavenumber shift is probably due to a small Si-neighbourhood modification. A very small shoulder also appearsg at 1025 cm^{-1}. A study of HMDSO radiofrequency discharges [7] at about 100 mbar showed the production of tetramethylsilane (TMS) , trimethylsilanol, ethyltrimethylsilane, pentamethyldisiloxane(PMDSO), ethylpentamethyldisiloxane. At low plasma power in DECR (60W), our spectra do not show any TMS bands such as the 868.7 cm^{-1}(vs) and 1254 cm^{-1} absorbtion bands [4]. A theoretical work from McKean [9] for $(CH_3)_3SiH$ (TriMS) predicted a very strong absorption at 2128.5 cm^{-1}. Except the very strong band appearing around 2128.5 cm^{-1}, the TriMS bands are more difficult to identify in the plasma because of their low amplitudes with respect to the other bands. Nevertheless, one of the bands either at 903 or at 914 cm^{-1} can be assigned to the SiH bending mode of TriMS. According to McKean[9] this mode is at 908 cm^{-1}. The presence of this species at low power can partly explain the m/z peaks at 73 $(Si(CH_3)_3^+$, M^+_{TriMS} -1) and 59 $(SiH(CH_3)_2^+$, M^+_{TriMS} -15) observed in mass spectrometry [2]. Besides, the band at 1068 cm^{-1} together with the remaining bands at 1262 cm^{-1} and 850 cm^{-1} indicate the presence of some products with the same structure as HMDSO. PMDSO should be the molecule involved considering the SiH stretching band at 2139 cm^{-1} and one of the SiH bending bands at around 910 cm^{-1}. The m/z peak at 133 $(H(CH_3)_2SiOSi(CH_3)_2^+$, M^+_{PMDSO}- 15) in mass spectrometry also detected by Alexander [2] argues for the presence of PMDSO. Finally the very weak band at 3660 cm^{-1} could indicate the presence of trimethylsilanol traces. Thus, PMDSO, TriMS and hydrocarbons seem to be the main HMDSO by-products present in the gas phase under low power conditions. The situation seems more complex under high power conditions (600 W) with the presence of bands at 2956 cm^{-1}, 2924 cm^{-1} 2878 cm^{-1} and 1025 cm^{-1}(Fig.3c). However, with respect to the gas phase spectrum under low-power conditions (60 W), the strong increase of the CH stretching bands in the 2900 cm^{-1} range, the disappearance of the bands at 2128.5 cm^{-1}, 850 $cm^{-1}$and 759 cm^{-1}, and the

band shift from 1068 to 1022 cm^{-1} are worth mentioning and can draw comments. The first interesting observation concerns the TriMS absence which is unambiguously characterized by the 2128.5 cm^{-1} band disappearance. The band disappearance at 1068 cm^{-1} clearly indicates no significant PMDSO presence. As a confirmation of the HMDSO, PMDSO and TriMS disappearance, the band at 850 cm^{-1}, which is a signature of $-Si(CH_3)_3$ in these monomers, shifted to 837 cm^{-1}. This behaviour implies a modification of chemical environment of the $-Si(CH_3)_3$ group. Moreover, the $-Si(CH_3)_3$ amount is low at this power as revealed by the weakness of the 837 cm^{-1} band and the disappearance of the weak band at 760 cm^{-1} corresponding to Si-C in $-Si(CH_3)_3$.

HMDSO gas phase	Plasma HMDSO - 60 W	Plasma HMDSO - 600 W
	(L12) 3660 (vw)	3660 (w)
	Acetylene and methane band (L13) 3290 (L14) 3016	3290 3016
(L_1) 2964 (s) C-H a-stretching	2963 (L1)	2958 (vs)
(L_2) 2907 (w) C-H s-stretching	(L15) 2916 (L16) 2894	(L23) 2924 (L24) 2873
	(L17) 2137, (L18) 2128	(L25) 2132
(L3) 1587(vw)		
(L4) 1452(vw)	1443 ethylene	1404
(L5) 1414(vw)		
	1305 CH_4	1303 CH_4
(L6) 1260 (s) CH_3 s-bending in $Si(CH_3)$	(L 6) 1262 (vs)	1256 (vs)
1135 (w)		
(L7) 1072 (vs) Si-O-Si a stretching	(L28) 1068 (vs) (L29)1025 vw)	
(L8) 1017 (vw)		(L26)1022 (vs) $Si-CH_2-Si$ or Si-O-Si
	(L19) 949 ethylene	
	(L20) 914 (w), (L21) 903 (w)	
(L9) 850(vs) CH rocking in $Si(CH_3)_3$	850 (vs)	
(L10) 834(vw) CH rocking		837 (s)
		(L27) 796 (s)
(L11) 759(qs) Si-C s..stretching in $Si(CH_3)_3$	(L11)759	$Si-C_3$ in $Si(CH_3)_3$
	(L22) 729 acetylene	729 acetylene
689(w)	694	

Table 1: Comparison between the infrared bands of HMDSO gas phase and the bands present under low power conditions (60 watt) and high power conditions (600Watt).
(vs):very strong, (s) (strong), (qs) quite strong, (w) weak, (vw) very weak

The modification of the main band at 1072 cm^{-1} attributed to Si-O-Si bridges in pure HMDSO also draws comments on the evolution of the gas phase species. Under low power conditions, the appearance of species such as PMDSO leads to a band at 1068 cm^{-1}. This 4 cm^{-1} shift is consistent with the slight chemical modification between HMDSO and PMDSO. Under high power conditions, only a broad band at 1022 cm^{-1} comes as a signature of Si-O-Si. This 50 cm^{-1} shift from the reference position in pure HMDSO and the broadening of the band result from a larger structural change in the Si-O-Si bridge-containing molecules. Based on Li et al. [10], this wavenumber shift to lower energy can be attributed to the molecules containing small siloxane chains with a gradually increasing molecular weight. The appearance of a band at 796 cm^{-1} indicates either the presence of Si-O-Si bending mode or that of Si-C with an environment different from $Si(CH_3)_3$. Under high power conditions, the slight increase of the OH band at around 3660 cm^{-1} is also noteworthy and reveals the reaction between ≡Si-O° and the hydrogen at the deposit surface to form SiOH-containing products in the gas phase Notice that in the gas phase of HMDSO/oxygen plasma, Creatore et.al [11] detected a large amount of such products.

C. Relationship between the gas phase composition and the deposit composition

The band between 1040 and 1020 cm^{-1} pertaining to the infrared spectrum of HMDSO plasma deposits (Fig.4a - 60 W) has been ascribed to Si-O-Si stretching mode in a disturbed environment $-((CH_3)_2SiO)_n-$. Recall that the Si-O-Si stretching mode in the HMDSO gas phase peaked at 1072 cm^{-1} and that the difference between monomer and deposit is mainly due to carbon substitutions by oxygen atoms to form the (Si-O)n backbone with some CH_3 or CH_2 branching on silicon site [10]. Actually, the spectra recorded at low and high power were different to each other (Fig. 4 spectra normalized to the same thickness, Table 2). At low power

(60 W), the spectrum exhibits a main band at 1032 cm^{-1} (Table 2, Fig.4a) whereas the deposit spectrum under a high power shows a broad band at around 1022 cm^{-1} (Table 2, Fig.4c). Another feature in the deposit spectrum under a low power condition (60 W) is a very small Si-H content whereas for deposits obtained at higher powers (>150 Watt, Fig 4b and c, Table 2), this content is large.Taking into account the preceeding gas phase analysis, the following global comment can be drawn. Under low powers, the gas phase mainly contains hydrocarbon molecules, trimethylsilane, pentamethyldisiloxane and a large amount of HMDSO whereas the deposit is characterized by Si-O-Si bridges (1034 cm^{-1}), a low SiC (or Si-O) content (796 cm^{-1}), a large $Si(CH_3)_3$ content (840 and 760cm^{-1}) and a very low content of SiH bonds (2129 cm^{-1}). On the other hand at a high power (600 W), molecules possibly containing $(Si-O)_x$ coupled with a large amount of hydrocarbon branching seems to be dominant in the gas phase. Then the deposit contained with Si-O-Si bridges (1023 cm^{-1}) as well as a significant ≡Si-H amont (2139 cm^{-1}), a large Si-C (or Si-O) amount (796 cm^{-1}) and very few $Si(CH_3)_3$ groups(834 cm^{-1}). Note that no significant Si-OH bonds were detected in the deposit although infrared spectra show the presence of few silanol groups in the gas phase. The low concentration in the gas phase can explain the absence of Si-OH in the deposit. The following interpretation can be given to the preceding observations. Although the presence of a $-(Si-O)_n-$ backbone is on the whole unquestionable, the occurrence of a few $Si-CH_2-Si$ bridges or $Si-CH_2-CH_x$ – is possible. Indeed, recent papers on thin film deposition from hexamethyldisilane [12] have shown that the infrared spectrum of deposits exhibits a broad band at 1020 cm^{-1} which has been ascribed to the $Si-(CH_2)n-Si$ bridge (wagging mode $1 \leq n \leq 2$). Obviously, this deposit does not contain Si-O bonds. The presence of the CH_2 groups at 2873 cm^{-1} in the gas phase and 2876 cm^{-1}(Fig. 4c, Table 2) in the deposit could indicate the presence of some $Si-CH_2-Si$ or $Si-CH_2-CH_x$ bridges -.Taking into account the presence of molecular species in the gas phase such as CH_4, TriMS and PMDSO as assumed by mass spectrometry [2][5][7] and confirmed by our work, it is clear that the radicals associated with these species, i.e., °CH_3, °$Si(CH_3)_3$ and $(Me)_3SiOSi$ °$(Me)_2$ radicals could be involved in the deposition process. These radicals also partly react with the surface to form volatile stable molecules in addition to the deposit. We underline the fact that the dissociation products after gas-phase recombination or/and species desorption by surface recombination lead to the stable molecules detected in the gas phase. It can be seen from our results that surface effects cannot be ignored to correctly understand the origin of some neutral species in the gas phase. This remark is even more important under our plasma conditions since the pressure in the reactor was lower than 5 10^{-3} mbar keeping the probability of chemical reactions in the gas phase very low. Besides, let also remark that under high power, the large HMDSO consumption can favour the electron interaction with HMDSO by-products leading to a partial modification

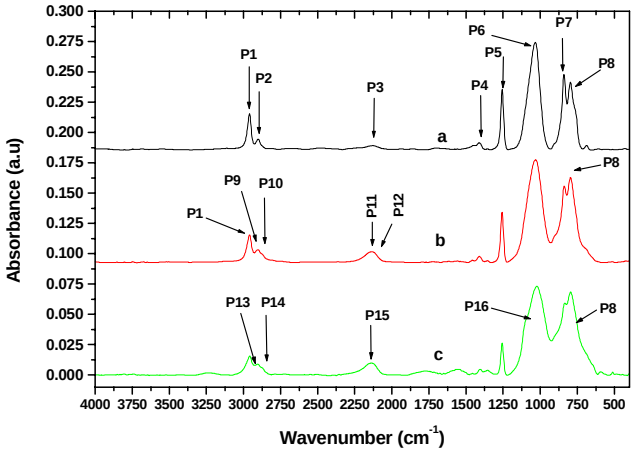

Figure 4: Deposit FTIR spectra at different microwave powers: a (60 W), b (170 W), c (600 W). The spectra are normalized to the thickness

Plasma HMDSO 60 W	**Plasma HMDSO 170 W**	**Plasma HMDSO 600 W**
(P_1) 2960 (s) C-H a-stretching	(P_1)2960	2958 (vs)
(P_2) 2902 (w) C-H s-stretching	(P_9) 2905 (P_{10}) 2894	(P_{13}) 2905 (P_{14}) 2876
(P3) 2129 (vw)	(P_{11}) 2136 (P_{12}) 2128	(P_{15}) 2140
		1570
		1457
(P_4) 1412(vw)	1411	1406
(P_5) 1257 (s) CH_3 s-bending in $Si(CH_3)$	1258	1257
(P_6) 1034 (vs) Si-O-Si a stretching	1032	(P_{16}) 1022
(P_7) 834(vw) CH rocking		837
(P_8) 796	(P_8) 796	(P_8) 796
687(w)	694	

Table 2: Comparison between the infrared bands (in cm^{-1}) of HMDSO plasma deposits obtained under different power conditions.

of the deposition process chemistry. In this respect, the large production of hydrocarbon in the gas phase explains the carbon deficit in the deposit as measured by XPS. Indeed, the C/Si ratio decreases below 2 in the deposit instead of 3 in HMDSO. Moreover, taking into account, the global oxygen deficit concerning the HMDSO by-products, it is consistent to find an increase of [O]/[Si] ratio in the deposit with respect to HMDSO ([O]/[Si] =0.5). That was found in reference [2] at a low power ([O]/[Si] =0.7) and in reference [13] at a high power ([O]/[Si])= 1) . These last observations lead to the conclusion that both carbon and silicon atoms are missing in the deposit as compared to the HMDSO atomic composition. This is consistent with the large amount of stable species such as hydrocarbons, $H\text{-}Si(CH_3)_3$ or $(CH_3)_3\text{-}(CH_3)_2Si\text{-}O)x\text{-}Si\ H(CH_3)_2$ and so on, which are present in the gas phase and pumped out. This view is confirmed by the work of Fracassi et al. [7] who detected these kinds of products in HMDSO radiofrequency discharges. Alexander et al. [2] have shown, by means of TOF SIMS analysis of deposits that a lot of heavy ionized fragments involved few $-(Si{=}CH_2)$ units which were attributed to $Si\text{-}CH_2\text{-}Si$ breaking. Nevertheless as already shown, the deficit of both carbon and silicon compared to oxygen in the deposit is compensated by their excess in the gas phase.

D. Mechanism proposal

At a low power, the mechanism assumed by Magni [1] appears to be quite consistent with our results. They proposed the following dissociation reactions :

$$(CH_3)_3SiOSi(CH_3)_3 + e^- \rightarrow (CH_3)_3SiO°Si(CH_3)_2 + CH_3° + e^-$$
$$(CH_3)_3SiOSi(CH_3)_3 + e^- \rightarrow °Si(CH_3)_3 + (CH_3)_3SiO° + e^-$$
$$\text{or } (CH_3)_3SiOSi(CH_3)_3 + e^- \rightarrow °Si(CH_3)_3 + (CH_3)_2SiO + °CH_3 + e^-$$

Three out of the obtained radicals, $(CH_3)_3SiO°Si(CH_3)_2$, $CH_3°$ and $°Si(CH_3)_3$ can explain the presence of TriMS, PMDSO and methane in the gas phase as described above. Of course, these radicals may also contribute to the deposit and to polymer chain ends. The large content of $Si(CH_3)_3$ (840 cm^{-1}) in the deposit could also be related to the $Si(CH_3)_3$ radicals.

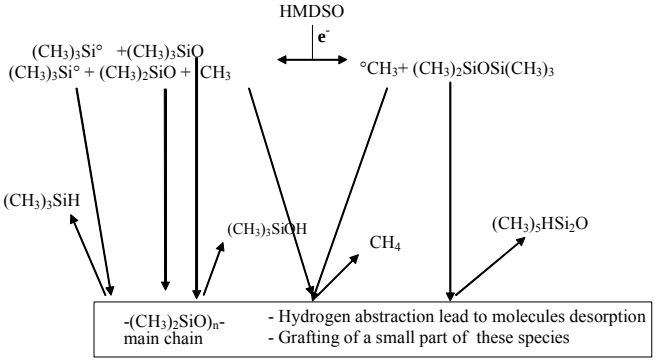

Figure 5: Simplified reaction pathway for deposition at low powers.

The main structure of the deposit based on a -(SiO)- backbone probably arises from the other two radicals whose generic formula is $(CH_3)_xSiO$. Two arguments are in favour of this proposal. Firstly, the atomic composition of these radicals is quite close to the O/Si ratio observed in the film. Secondly, the very weak band at 3660 cm^{-1} (O-H bonds) could confirm the presence of $(CH_3)_3SiO°$ radical which can induce the silanol production by hydrogen abstraction from the deposit surface. Moreover, the FTIR spectrum of the gas phase at intermediate power (170 Watt, Fig.3b) shows a broad band with a maximum between 1055 cm^{-1} and 1030 cm^{-1}. This indicates the presence of molecules containing $-((CH_3)_2SiO)_x-$ ($2 \leq x \leq 3$) as shown by Fracassi in radiofrequency discharge [7] and confirmed by mass spectrometry [2]. Based on the proposed mechanism, the only means to obtain these small oligomers is the reaction of $(CH_3)_xSiO$ species with each other in order to increase the $-(SiO)_y-$ chain length (Fig. 5). In any situation, the deposit composition (O/Si ≈1) leads to the conclusion that the most reactive and probably the main mechanism for deposition is:

$$\text{either } n\,(CH_3)_3\,SiO° \rightarrow (CH_3)_3Si\text{-}(OSi(CH_3)_2)_{n-2}\text{-}Si(CH_3)_3 + (n\text{-}2)\,CH_3$$
$$\text{or dangling bond} + n(CH_3)_2SiO \rightarrow \text{site-}[(CH_3)_2SiO]_{n-1}\text{-}(CH_3)_2Si\text{-}O°$$

At higher powers (≥ 400 Watt) in the gas phase, the large CH bands at around 2957, 2924 and 2873 cm^{-1} with respect to $Si\text{-}(CH_3)_x$ and Si-O-Si bands let us think that the heavy stable hydrocarbon molecules or/and hydrocarbon groups are grafted onto siloxane-like species containing chains such as : $((CH_3)_2Si\text{-}O)_x\text{-}Si\text{-}(CH_2)_y\text{-}Si$ or $((C_xH_y)_2Si\text{-}O)_z$. If we consider the corresponding deposits, the hydrocarbon group content (between 2959 cm^{-1} and 2876 cm^{-1}) is very low with respect to that of the SiH, $SiCH_3$ and Si-O-Si groups. In the layer, the importance of the bands at 796 cm^{-1} (SiC or Si-O) with respect to the very weak band at 834 cm^{-1} ($Si(CH_3)_3$) indicates the disappearance of the $Si(CH_3)_3$ group in the deposit. These last observations on the deposition process could be explained based on a modification of the discharge composition. At a high power, HMDSO is almost totally consumed and the gas phase is dominated by its by-products. Then,

electrons can also interact with these by-products to form new radical species which can contribute to the deposition process (Fig.6). For instance, reactions such as the following might be possible :

$$CH_4 + e^- \rightarrow CH_3^{\bullet} \text{ and } CH_2^{\bullet\bullet} \text{ and } CH^{\bullet\bullet\bullet} + x\, H^{\bullet} + e^-$$

$$HSi(CH_3)_3 + e^- \rightarrow H^{\bullet}Si(CH_3)_2 + CH_3 + e^-$$

$$PMDSO + e^- \rightarrow H(CH_3)_4{}^{\bullet}Si_2O + CH_3 \text{ and } H(CH_3)_2{}^{\bullet}SiO \text{ (or } H(CH_3)SiO + {}^{\bullet}CH_3) + {}^{\bullet}Si(CH_3) + e^-$$

It can be noticed that the obtained radicals contain Si-H bonds which can explain the presence of such bonds in the deposit.

As observed in the infrared spectra of both the gas phase and the deposit, the gradual change in composition from low power to high power is due to a combination of HMDSO depletion and HMDSO by-product formation. This obviously leads to variable chemical composition of the deposits even though the main chain is controlled by SiO oligomerization.

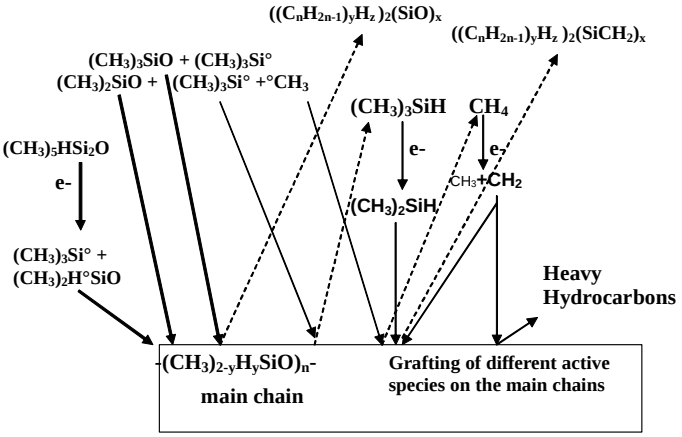

Figure 6: Simplified reaction pathway for deposition at high powers (>100 Watt)

5. Conclusion

Plasma deposition processes from siloxane monomers have only been described so far in the literature as the formation of a $(Si\text{-}O)_n$- backbone resulting from the siloxane break-up of organic groups in the gas phase or at the surface.It is commonly assumed that the dominant reactive gas phase species are the main deposit precursors. The present work reveals a more complex situation. It is especially interesting to note that the deposit structure is more or less a kind of reverse of what is in the gas phase. Broadly speaking, given the chemical structure of the initial monomer and its fragmentation, just a few basic chemical species are involved in the deposition process whereas the other active radicals partly react with the surface to form volatile molecules. At low powers, the species issued from the primary HMDSO dissociation stages dominate the process. The radical surface reaction produces stable species such as TriMS, PMDSO and CH_4 obtained after a radical recombination. On the other hand, $(CH_3)_xSiO$ seems to be the main deposit precursors. At a higher power the HMDSO byproducts in the gas phase are also dissociated by electronic impact producing new radicals which contribute to the deposit. This leads to an increase of the grafting rate of the (Si-O) chains in the films. Meanwhile the length of the siloxane chains in the gas phase increases. This is also the case in the deposit as shown by the shift of the Si-O-Si stretching towards energy as low as 1020 cm^{-1} and a large decrease in the $Si(CH_3)_3$ group amount. This shift could also be favoured by the formation of -Si-CH_2-Si - bridges.

References

[1] D. Magni, Ch Deschenaux, Ch Hollenstein, A. Creatore and P.Fayet, J.Phys. D; Appl. Phys.**34**, 87 (2001)

[2] M.R. Alexander, F.R. Jones and R.D.Short, Plasma and Polymers, **2**, 277 (1997)

[3] P. Raynaud, Y. Segui, G. Balmer, A. Boulanger and R. Burke, J. Phys. D: Appl. Phys.**, 30** , L23 (1997)

[4] P. Raynaud, C. Marlière, D. Bertomieux, Y. Segui, J. Durand, R. Burke, J. Phys. IV France **8**, Pr7-265 (1998)

[5] N. Benissad, K. Aumaille, A. Granier and A. Goulet, Thin Solid films **384**, 230 (2001)

[6] J. Kupčik, Z. Bastl, J. Šubrt, J. Pola, V. Papadimitriou, A. Prosmitis and P. Papagiannnakopoulos, J. Anal. and Appl. Pyrolysis **57**, 109 (2001)

[7] F. Fracassi, R. d'Agostino, F. Fanelli, A. Fornelli and F. Palumbo, Plasma and Polymers **2**, 277 (1997)

[8] G. F. Leu, A. Brockhaus, and J. Engemann, Surface and Coatings Technology **174-175**, 928 (2002)

[9] D. C. McKean, Spectrochimica Acta Part A **55**, 1485 (1999)

[10] K. Li, O. Gabriel and J. Meichsner, J. Phys. D: Appl.Phys. **37**, 588 (2004)

[11] M. Creatore, F. Palumbo and R. d'Agostino, Plasma and Polymers **7,** 291 (2002)

[12] A. M.. Wrobel, A. Walkiewicz-Pietrzykowska, Y. Hatanaka, S. Wickramanayaka and Y. Nakanishi, Chem. Mater.**13**, 1884 (2001)

[13] A. Zenasni, PHD thesis, Université Paul Sabatier (Toulouse) September (2003)

Complete Oxidation of Volatile Organic Compounds Using Plasma-Driven Catalysis and Oxygen Plasma

H.H. Kim, A. Ogata, S. Futamura

Advanced Industrial Science and Technology (AIST), Tsukuba, Japan

Abstract

In this paper we will present a complete oxidation technology of volatile organic compounds (VOCs) using a cycled operation of adsorption and decomposition of adsorbed VOCs using oxygen plasma. This cycled operation system was developed based on the extraordinary oxygen-dependent characteristics of the plasma-driven catalyst system. Complete decomposition of VOC to CO_2 was achieved with this cycled system using oxygen plasma without forming CO and any nitrogen oxides. The influence of VOC concentration and the temperature condition of oxygen plasma will be discussed.

Keywords; Nonthermal Plasma, Corona discharge, Plasma-Driven Catalysis, Oxygen plasma, Volatile organic compound (VOC), Catalyst

1. Introduction

Volatile organic compounds (VOCs) released into the atmosphere as a consequence of man-maid emission undergo a complex physical-chemical transformations before they are decomposed or deposited to the earth's surface. Many of these VOCs are considered to be carcinogenic, teratogenic and mutagenic. There is, therefore, an urgent need to develop more effective and inexpensive techniques for the treatment of VOCs. Application of nonthermal plasma (NTP) technology has been investigated for the removal of SO_2, NOx, odors, and VOCs from many industrial fields [1-3]. Substantial progress has been achieved during the last two decades [4]. In the practical application of NTPs for the abatement of VOCs, suppression of harmful byproducts is required as well as the high energy efficiency.

One of the remarkable recent trends in the NTP application for air pollution control is the combination of NTP with catalyst in either of single-stage or two-stage [5-7]. The single-stage and the two-stage process are referred to as plasma-driven catalysis (PDC) and plasma-enhanced catalysis (PEC), respectively. It has been reported by the authors that the PDC system is much more efficient than that of the ordinary gas-phase homogeneous plasma reactors (dielectric-barrier discharge, pulsed corona, surface discharge) in terms of energy efficiency, carbon balance, byproduct etc [8]. Decomposition of various aromatic compounds showed CO_2 selectivity of around 75%, which was 30-40% higher than those with the conventional plasma reactors [9]. Continuous operation of the PDC system showed stable performance without any catalyst deactivation over 150h. Table 1 summarizes the differences between the conventional NTP alone processes and the PDC system. Both the plasma alone and the PDC system are not influenced by gas hourly space velocity

Table 1. Comparison of NTP alone and plasma-driven catalysis

Parameter	Plasma alone	PDC
Kinetics	First-order $\eta(\%) = \{1 - \exp(-k_E \cdot \mathrm{SIE})\} \times 100$	Zero-order $\eta(\%) = \frac{k_E \cdot \mathrm{SIE}}{C_0} \times 100$
GHSV (residence time)	No influence	No influence
Oxygen content	No influence	Large influence
Carbon balance	Poor	Good
Aerosol formation	Yes	No
IP *vs* decomposition efficiency	Highly related	Unrelated

* The rate constant k_E is referred to as energy constant. The unit for first-order and zero-order are LJ^{-1} and $ppm \cdot J^{-1}L$, respectively.

(i.e. residence time) because the characteristic time of plasma chemical reactions is usually short enough relative to the gas residence time. Kinetics of VOC decomposition in the PDC system shows a zero-order, which indicates the important role of surface reaction in the decomposition of VOCs. Maximum applicable energy to the PDC reactor should be less than about 120 J/L because formation of nitrogen oxides sharply increases at SIE above this value. In this sense, the flow-type PDC reactor only can be applied for the decomposition of VOCs with concentrations below about 100 ppm. One important characteristics of the PDC system that we focused on in this work is the influence of oxygen content on the decomposition efficiency. In contrast to the plasma alone processes, which show constant performance at given specific input energy regardless of oxygen content, the decomposition efficiency of VOC in the PDC system shows almost linear increase with oxygen content. In addition to the decomposition efficiency, the selectivity of CO_2 also remarkably increased with oxygen content. Based on the highly oxygen content-dependent property of the PDC system a cycled system of adsorption and the decomposition of adsorbed VOCs using oxygen plasma has been proposed by the authors. The expected advantages of this cycled process include high energy efficiency, high CO_2 selectivity and no formation of nitrogen oxides.

2. Experimental

Figure 1 shows the concept of the cycled process for the complete destruction of VOCs. This system is operated in two separated modes of adsorption and the decomposition of adsorbed VOCs using oxygen plasma. This cycled process is based on the highly oxygen content-dependent behavior of the PDC system. The experiment system consisted of two PDC reactors, valves, AC power supply, gas cylinders, mass flow controllers, and Fourier transform infra red (FITR) spectrometer (Perkin Elmer, Spectrum One). The catalysts used in the PDC reactor were 2.0 wt% Ag/TiO_2 catalysts. Two PDC reactors were connected in

parallel. In the adsorption mode VOC is removed by adsorption on the catalyst surface without plasma application. When the catalyst bed reached a saturated adsorption, then the gas flow was switched to the other line for continuous adsorption. The catalyst bed reached saturated adsorption was then purged with oxygen and the decomposition of adsorbed VOC was started with oxygen plasma. Benzene was used as model compound of VOC in this work. The additional cost for the use of oxygen can be minimized by operating the decomposition cycle at closed system after purging the catalyst bed with oxygen.

Adsorption mode was operated at room temperature to maximize the benzene adsorption on the catalyst. Regeneration mode using oxygen plasma was operated at room temperature and 100 ^{o}C to know the effect of temperature on the decomposition of adsorbed benzene.

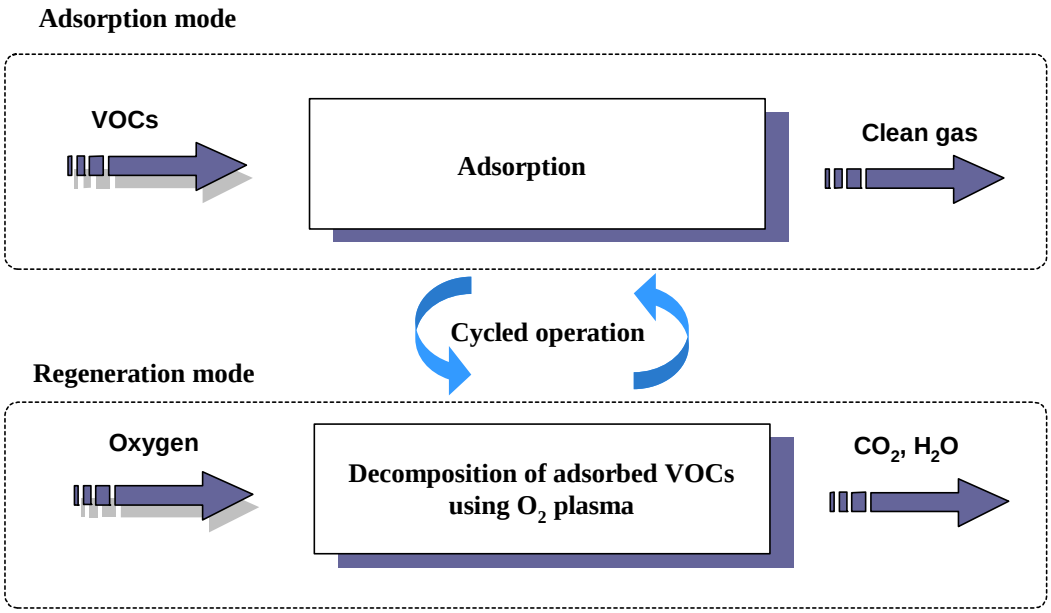

Figure 1. Schematic diagram of the cycled process for the complete destruction of VOCs.

Discharge power of the oxygen plasma was measured using V-Q Lissajous figure method. A condenser of 100nF capacitance connected in series to the ground line of the plasma reactor. The charge Q (i.e. time-integrated current) was measured with a 10:1 probe. Specific input energy (P/Q_f) is the ratio of discharge power (P_{dis} in watt) in the plasma reactor to gas flow rate (L/min).

$$\text{SIE (J/L)} = \frac{P_{dis}}{Q_f} \times 60 \qquad (1)$$

In the case of the cycled operation equivalent specific input energy (SIE_{eq}) was introduced to evaluation the energy consumption.

$$\text{SIE}_{eq}\text{ (J/L)} = \frac{(P_{dis})_{Ave}}{(Q_{Ads})_f} \times \frac{T_{Oxy}}{T_{Ads}} \times 60 \qquad (2)$$

Here, $(P_{dis})_{Ave}$ and $(Q_{Ads})_f$ indicate the average discharge power of oxygen plasma for the decomposition of adsorbed VOC and gas flow rate during the adsorption, respectively. T_{Oxy} and T_{Ads} indicate the period of oxygen plasma and the time of adsorption, respectively.

3. Results and Discussion

Figure 2 shows the required energy for the complete decomposition of benzene using the cycled process using oxygen plasma. Time to reach breakthrough in the adsorption was varied from 30 to 95min depending on the inlet benzene concentrations. Oxygen plasma completely oxidized the adsorbed benzene to CO_2., which is impossible with the conventional plasma alone processes or the flow-type PDC system. The SIE_{eq} for the decomposition of adsorbed benzene largely depended on the benzene concentration. The higher the benzene concentration, the larger the SIE_{eq} for the complete decomposition of adsorbed benzene. These results can be explained by the zero-order kinetics of the PDC system. In the zero-order kinetics the amount of VOC decomposition is only determined by SIE but not by the concentration of benzene. Our preliminary data indicated that the specific input energies to achieve complete decomposition of 60 ppm and 205 ppm benzene were about 150 J/L and 310 J/L, respectively. It should be noted that the values shown in the Figure 2 indicate the required energy to decompose the adsorbed benzene with more than 99% CO_2 selectivity. Temperature actually had no influence on the SIE_{eq} within the tested conditions. The data obtained at room temperature and 100 ^oC fell on single line. Further enhancement can be possible by optimizing the plasma parameters for the regeneration mode and the use of proper adsorbent/catalyst.

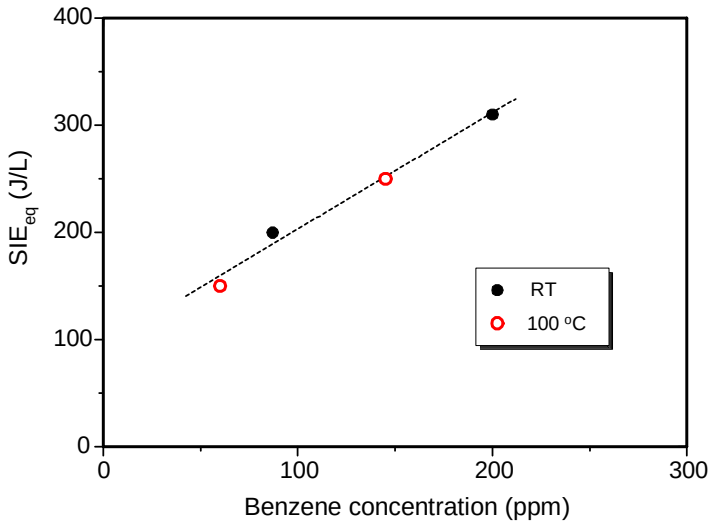

Figure 2. Required energy for the complete decomposition of benzene using the cycled operation system. PDC reactor packed with 2.0wt% Ag/TiO_2 catalysts was used. Adsorption was operated at room temperature in both cases.

When nitrogen is present in gas mixture plasma can produce nitrogen oxides. Figure 3 shows the formation of nitrogen oxides (NO_2 and N_2O) in the flow-type PDC system as a function of the oxygen content in the gas stream. In the gas-phase plasma processes nitrogen oxides exist in different oxidation level; NO, N_2O, NO_2, N_2O_5, HNO_2, HNO_3. On the other hand, nitrogen oxides exist mostly as NO_2 and N_2O in the outlet of the PDC reactor. Therefore only NO_2 and N_2O were measured in this study. The formation of NO_2 changed drastically with the oxygen content. The maximum formation was found at 10% oxygen and then decreased with further increase of oxygen. On the other hand, formation of N_2O was quite sensitive to the oxygen content below 10%, and was slow down at higher oxygen content. From the data shown in Figure 3, it can be

concluded that the increase of oxygen partial pressure can reduce the formation of nitrogen oxide. However, it is difficult to suppress the formation of nitrogen oxides completely. In order to complete the decomposition of adsorbed VOC in a short time, it will be necessary to maintain the specific input energy much higher than those of the flow-type PDC reactor. These results indicated that the operation of the regeneration mode must be done at 100% oxygen to minimize the formation undesirable byproducts.

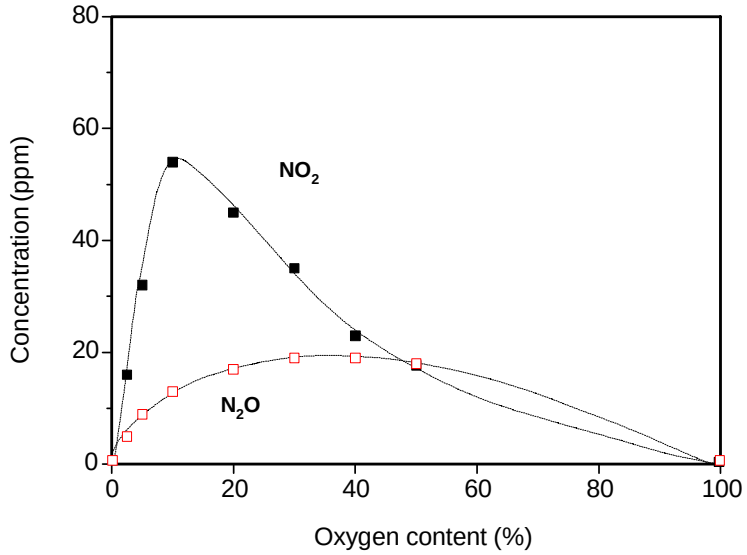

Figure 3. The effect of oxygen content on the formation of NO_2 and N_2O in the flow-type PDC system. Specific input energy was 130 J/L.

References

[1] A. Mizuno, J.S. Clements, R.H. Davis, *IEEE Trans. Ind. Applicat*. **22**, 516-522 (1986)

[2] B. M. Penetrante, S. E. Schultheis, Non-Thermal Plasma Techniques for Pollution Control; Part A: Overview, Fundamentals and Supporting Technologies & Part B: Electron Beam and Electrical Discharge Processing, Springer-Verlag (1993)

[3] S. Masuda, *Pure & Appl. Chem*. **66**, 727-731 (1988)

[4] H.H. Kim, *Plasma Processes & Polym*. **1**, 91-110 (2004)

[5] A. Ogata, H. Einaga, H. Kabashima, S. Futamura, S. Kushiyama, H.H. Kim, *Appl. Catal. B: Environ*. **46**, 87-95 (2003)

[6] S. Futamura, H. Einaga, H. Kabashima, L. Y. Lee, *Catal. Today* **89**, 89-95 (2004)

[7] A. Ogata, D. Ito, K.Mizuno, S. Kushiyama, T. Yamamoto, *IEEE Trans. Ind. Applicat*. **37**, 959-964 (2001)

[8] H.H. Kim, H. Kobara, A. Ogata, S. Futamura, *IEEE Trans. Ind. Applicat*. **41**, 206-214 (2005)

[9] H.H. Kim, A. Ogata, S. Futamura, *J. Phys. D: Appl. Phys*. **38**, 1292-1300 (2005)

Gas-phased Pulsed Corona for wastewater treatment- comparative study.

L.R. Grabowski [1], E.M. van Veldhuizen[1], A.J.M. Pemen[2], A. Pokryvailo[3], Y.Yankelevich[3], W.R. Rutgers[1]

[1] *Department of Physics ,Technische Universiteit Eindhoven (TU/e),The Netherlands*
[2] *Department of Electrical Engeneering ,Technische Universiteit Eindhoven (TU/e),The Netherlands*
[3]*Propulsion Physics Laboratory, Soreq NRC, Israel*

e-mail: e.m.v.veldhuizen@tue.nl

Abstract
In the framework of European project "ytriD" two reactors for water treatment with corona pulsed discharges have been studied. In one reactor there is a water film on the bottom, in the other there is aerosol spray. The ozone generation and phenol removal have been investigated for the two available reactors. Both reactors proved their high efficiency in ozone production (~80 g/kWh in ambient air) and phenol removal (up to 48 g/kWh). The phenol conversion yield increased up to ~90 g/kWh with addition of $FeSO_4$ or NaOH.

Keywords: pulsed corona discharge, ozone creation, phenol removal, water cleaning

1. Introduction

Low-temperature plasma applications for environmental purposes are intensively studied and implemented. Many recent studies have been focused on the industrial gas cleaning only. Pulsed corona discharge, one of the Advanced Oxidation Techniques (AOT's), is widely used in that field [1,2]. Recently, attempts to use pulsed corona technique for wastewater treatment have been successfully undertaken [3,4,5]. In those tests corona was created in the liquid phase. Relatively new approach [6] is the creation of the electrical discharges in the air phase. In such configuration, pulsed corona becomes a powerful source for the ozone and other radicals, with high oxidation potentials. Active species created in the air phase are diffused easily into the thin layer of liquid, where they can react with impurities.

Within the framework of European project "ytriD" [7] two reactors to study the effects of corona on wastewater are available. Those reactors utilize two different approaches to the problem of transport of the reactive species in to the liquid phase. In the first one -aerosol reactor- the liquid is sprayed in form of aerosol between electrodes. The reaction takes place in the droplets and at their surface. In the second one, called Corona Above Water (CAW) reactor, discharge takes place in air phase, above thin layer of liquid. As a model molecule to study the reactors' cleaning efficiency, the phenol was chosen because of its well-known chemistry and use by other authors [6,8].

Both reactors proved their very good efficiency in the ozone production and phenol removal [10], there is still need for optimizing process and reactors for obtaining even better efficiency. The improvements can be done: i) to the electrical setup (changing the electrical properties of the system), ii) to the chemical process (additives), iii) to the physical conditions (gap distance, wire length). Previous studies show that the conversion efficiency of corona discharges can likely be improved by the application of additives. Addition of NaOH [8] (leading to increase of pH level) and Fe(II,III) salts [9] can significantly improve the decomposition of phenol in pulsed corona discharges reactors.

2. Experimental set-ups

Reactors and electrical systems.

The reactors and electrical circuits have been described in [10]. The CAW reactor is a hermetic construction, to prevent the corona products from escape. The reactor envelope is made of Perspex; its inside dimensions are 8x5.5x38cm. The sidewall thickness is 10mm and bottom wall 4mm. The 4 electrodes, 0.2 mm in diameter, are placed in cover of the reactor. The horizontal distance between the electrodes is 2cm. The cathode is placed outside the reactor, at the bottom side. The gap between cathode and anodes is 4,5cm. The bottom section of the CAW reactor is made from one piece of Perspex, to prevent sparking and

leakages. Compared to [10], the system operates at lowered voltage and current for better stability.. The setup can operate with frequencies from 5-25 Hz with the pulse duration of ~100ns, with the ~40kV voltage peak and 80A of current. The energy value for performed experiments is in the range of 50-60mJ per pulse, i.e. the average power is only 0.25-0.5W. The reactor can operate in a batch type configuration or the water flow system can be incorporated.

The aerosol reactor build in Soreq [11] is a metal cylinder with 120 L of volume. Inside a system of cathodes and anodes is placed. The distance between the electrodes is 3cm. The liquid and the air supply system are connected at the bottom of the reactor. A compressor is installed in the system. Its function is to recycle the air, containing large amount of ozone, back to the reactor. The residence time of the liquid in the reactor is ~1min. The liquid flow is 15L/h. The reactor is driven by a compact all solid-state power supply. Energy per pulse is up to 0.5J with a repetition rate up to 1kHz, i.e. power up to 500W.More detail on the power supply can be found in [11].

Measurements setup

The ozone concentration is measured by the absorption technique using an Ocean Optics HR2000 spectrometer. As a light source the deuterium lamp is used. The ozone concentration values are taken at 266nm wavelength. In CAW reactor optical fibers with lenses are placed in the discharge area. In the aerosol reactor probes are positioned at the duct connecting output of the reactor with compressor.

For concentration measurements of the phenol solution a LIF setup is constructed using a Quantel Brilliant Ultra YAG laser with 4 mJ/pulse output at 266 nm and an Ocean Optics HR2000 spectrometer. The system is calibrated for the range between 1 and 0,1 mMol/L of phenol solution. The calibration curve gives a very good fit (R^2=0,98). Comparative tests with HPLC technique show very small differences (<2%) between those two measuring techniques.

3. Results and discussion

Effect of atmosphere medium on ozone production process

In the first test the ozone concentration was measured in CAW reactor. The electrical system operated with 45kV voltage measured at the reactor with 80A of current. Calculated energy per pulse was 50mJ.

Fig.1 indicates the effect of gas composition on ozone concentration. The reactor was filled with ambient air or with oxygen. For those two cases the ozone concentration above the liquid was observed as well as the removal of phenol from a 150ml of 1mMol/L solution was determined.

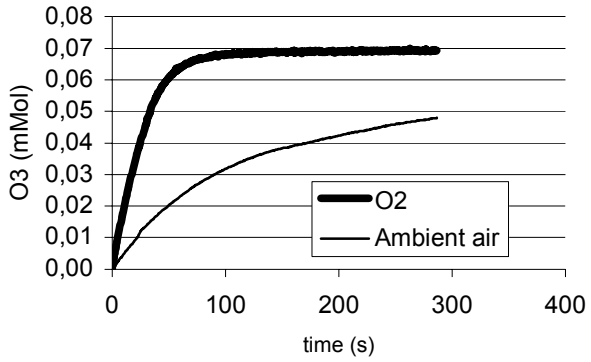

Fig.1. Ozone creation in ambient air and oxygen atmosphere

As is shown in the graph in Fig.1 the oxygen atmosphere significantly influences the ozone production rate. The yield of ozone calculated from the initial slopes rise from 80g/kWh in case of ambient air, up to 190g/kWh for oxygen atmosphere.

Effect of reactor fillings on ozone creation process

Fig.2 presents the effect of different reactor fillings on ozone concentration. The reactor was filled with ambient air (total air volume of 780ml), with 150mL deionized water and 150 ml of 1mMol/L phenol solution (total air volume 650ml both). The ozone yield has been calculated from the starting slope, it leads to 85 g/kWh.

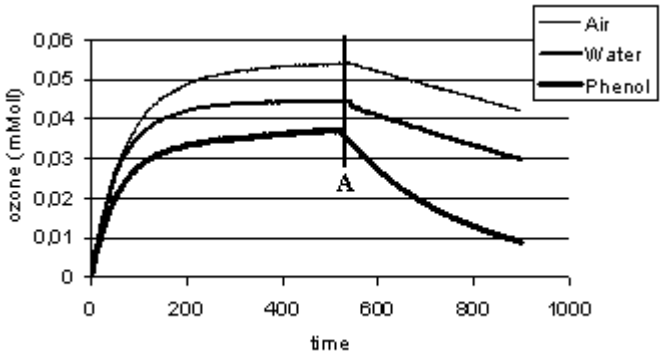

Fig.2. Ozone creation and dissipation for different fillings of the reactor.

As can be seen in the graph, the shapes of the initial lines of ozone concentration are also similar. After around 60s the linear growth changes due to saturation. It is clearly seen that type of filling highly influences the ozone concentration in the reactor. This is expected because in presence of water and phenol solution the mass transfer process starts. Ozone molecules diffuse in to the liquid where they are scavenged by the water molecules as well as transited in to OH* radical [12]. In case of phenol solution additional reaction with phenol molecules takes place [13].

The total ozone concentration after 500s has been calculated. In the reactor filled with air 27mMol of ozone were produced. The presence of deionized water 4mMol of total ozone created had been diffused in to the water. The presence of phenol solution decreased it again with same amount, leading to 19mMol of ozone in the air after 500s.

In the next part of the experiment the corona was turned off after 500s (line A on the graph) and the decay of ozone has been observed. As is shown in Fig.2 the curves for ozone concentrations in reactor filled with air and water have similar slopes. From simulations it was obtained that, for the reactor filled with air the main mechanism for ozone degradation is its degradation in the volume. Layer of liquid has no significant influence on the ozone decomposition. When the maximum level of ozone saturation in water is reached no more ozone molecules are transferred into the liquid phase, thus the decomposition in volume become predominant. This is consistent with the result of fig.2.

In presence of phenol solution the ozone molecules in boundary phase reacts with phenol and its by-products allowing more ozone to transfer from the air phase. The faster decay of ozone concentration in air confirms this idea. This result is also useful to improve the simulation model. The initial part of the decomposition curve has an exponential shape. After 300s 45% of phenol was removed leading to the yield of 48g/kWh.

Effect of pH value on phenol removal

Fig.3 shows the dependence of the pH solution on phenol removal. The different amounts of NaOH and HCl have been added to 150 ml of 1mMol/L phenol solution to obtain desired levels of pH. In the next step the solutions had been treated with the corona for 5 min. With the pH level of 2 29% of the phenol had been removed. With increasing the pH value the removal rate increase.

At pH=5, which corresponds 1mMol phenol solution without addition, 45% of phenol had been removed. Increasing pH value above 6 causes the removal rate to increase with even higher rate. At pH=10 the phenol removal reached 90%. The yields of phenol removal are shown in Tab.1. The experimental results are in

agreement with reaction mechanism reported by other authors. With acidic condition the direct reaction between ozone and phenol molecules becomes predominant. At high pH values OH* radicals decompose less likely allowing the phenol molecules to react with them. Thus the phenol decomposition increases.
During treatment of phenol solution the drop of pH has been observed (Hoeben 1999). It is explained by the creation of organic acids, like acetic acetic and muconic acid from the phenol decomposition. Thus that effect negatively influences the efficiency of the process with time. On the other hand slight increase of pH above 6 can significantly improve the phenol removal. Results of performed experiments will help to create more effective system.

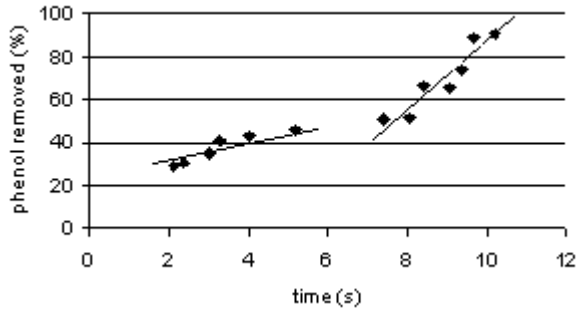

Fig.3 Phenol removal as a function of pH value

Effect of additives on phenol removal

Addition of several metals, which have special oxygen transfer properties, can affect the efficiency of the treatment process. The Fenton's reactions involving iron-catalyzed hydrogen peroxide are well known [9]. In this catalytic reaction hydrogen peroxide can react with iron(II) and iron (III) ions creating, among other species, the hydroxyl radical. OH* radical is used later in the cleaning process.

The phenol removal rate was significantly improved when the addition of 100mMol/L FeSO4 was added to 1 mMol/L of phenol solution. As can be seen in Tab.1 The addition the 3ml addition of Fe2+ solution increased the phenol removal rate up to 94%, with phenol yields up to 98 g/kWh. The obtained result indicates that Fenton's catalytic reaction took place. It also reveals that the amount of H_2O_2 created by the decomposition of ozone in water [12] is sufficient for Fenton's reaction to start.

Table.1 Phenol removal and yield with different additions

	Phenol removed (%)	Phenol yield (g/kWh)
1 mM/L phenol	45	48
pH=2	29	30
pH=10	91	95
Fe2SO4 1ml	69	72
Fe2SO4 2ml	86	90
Fe2SO4 3ml	94	98

Ozone creation and phenol removal in aerosol reactor

The ozone concentration profiles were measured in the aerosol reactor operating with different electrical settings. Lines 1 and 4 in fig.4 indicate the corona power dependence on the ozone creation process. The increase in input power from 20W with ozone yield of 55 g/kWh (line 1) to 50W with yield of 104 g/kWh (line 3) significantly influences the ozone concentration. However, for given input power the use of higher energy pulses with lower frequencies leading to faster ozone build-up and higher yield up to 140 g/kWh (line 2).

To check the cleaning efficiency of the aerosol reactor initial tests with treatment of 1 mMol/L phenol solution were performed. The samples of solution for different electrical settings of the power source were collected. Results showed the 60% removal for repetition rate of 200Hz and 200mJ per pulse. The yield of phenol reaches the value of 21 g/kWh. For 500Hz repetition rate and 280 mJ per pulse 92% of phenol

been removed, while phenol yield drops to 9 g/kWh. Results indicate that the residence time of the liquid in the reactor may be not sufficient to fully penetrate the liquid droplets by the ozone molecules. These results show that there is a trade-off between high removal yield and high cleaning efficiency.

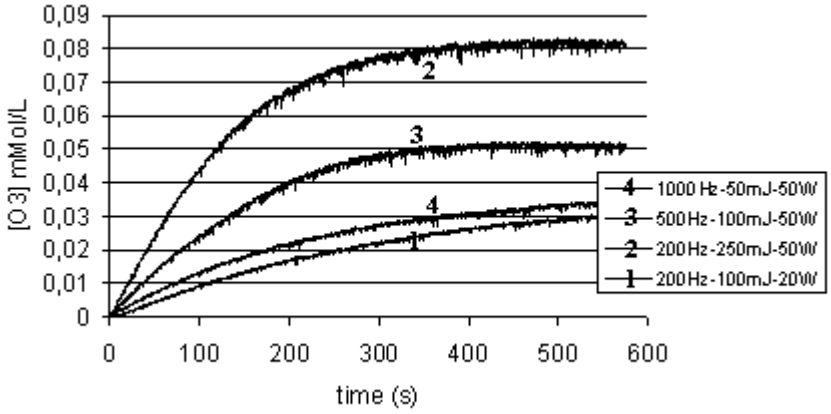

Fig.4. Ozone concentration profiles depend on the pulse energy and frequencies

4. Conclusions

The effect of several chemical and electrical properties on ozone creation and phenol removal was investigated. The CAW technique has proven its high efficiency in ozone production and phenol removal. The ozone concentration in the reactor reaches level of 0.08mMol/L (4g/m^3), and yields of up to 90 g/kWh in ambient air and 190 g/kWh in oxygen atmosphere. The reactor is capable of removing up to 45% of phenol with yield of 48 g/kWh in 5 min. The increase of pH due to NaOH addition can increase the removal up to 91% and phenol yield up to 95 g/kWh in 5 min. The additional creation of the hydroxyl radicals in presence of iron salts (Fenton's reactions) increased the phenol conversion up to 94% and yields to 98 g/kWh. The air phase discharge is capable of creating the sufficient amount of H_2O_2 molecules for Fenton's catalytic reaction to start. Ozone concentration profiles obtained with aerosol reactor indicates the need of use less frequent, high energy pulses. The aerosol reactor is very efficient source of ozone. The aerosol reactor is capable of removing up to 92% of phenol with very short residence time (<1 min).

Obtained results will help to create a chemical model of the conversion process and implement it to industrial application, which is the final stage of the ytriD project.

Acknowledgement

This work is financially supported by the European Commission under contract no. GRD1-2001-40374.

References

[1] E. M. van Veldhuizen, *Electrical Discharges for Environmental Purposes, Fundamentals and Applications,* Huntington, Nova Science Publishers, Inc., New York (2000).
[2] Y.L.M. Creyghton, *Pulsed Positive Corona Discharges*, PhD thesis, TU Eindhoven, September 1994.
[3] A.A. Joshi, B.R. Locke, P. Arce, W.C. Finney, J. Hazard. Mat. **41**(1995)3.
[4] P. Sunka, V. Babicky, M. Clupek, P. Lukes, M. Simek, J. Schmidt, Plasma Sources Sci. Technol. 8(1999)258.
[5] B. Sun, M. Sato, J.S. Clements, J. Phys. D: Appl. Phys. 32(1999)1908.
[6]W.F.L.M. Hoeben, E.M. van Veldhuizen, W.R. Rutgers, G.M.W. Kroesen, J. Phys. D: Appl. Phys. **32**(1999)L133.
[7] www.phys.tue.nl/EPG/YTRID.
[8] N. Sano, T. Fujimoto, T. Kawashima, D. Yamamoto, T. Kanki, A. Toyoda *S aP Tech., Volume 37, Issue 2, 2004*
[9] D. Grymonpré, A. Sharma, W. Finney and B. Locke Chemical Engineering Journal, Volume 82, 2001
[10] L.R.Grabowski , E.M. van Veldhuizen, A.J.M. Peemen, W.R. Rutgers, ISNTPT16, JAOT, in press
[11] A. Pokryvailo, Y. Yankelevich, M. Wolf, E. Abramzon, E. Shviro, S. Wald, A. Welleman, IEEE Pulsed Power Conf. 2003.
[12] N.C.Baird, J. of Chemical Education, vol.7, 1997

Diagnostics of Surface Wave Plasmas for Giant Materials Processing

H. Sugai, Y. Nojiri, T. Ishijima, E. Stamate and H. Toyoda

Department of Electrical Engineering and Computer Science, Nagoya University
Furo-cho, Chikusa-ku, Nagoya 464-8603, Japan

Abstract

A meter-scale high-density *surface wave plasma* (SWP) for manufacturing giant microelectronics devices such as liquid crystal display and solar cell is diagnosed with several techniques. Standing modes of surface waves at 2.45 GHz are detected by a movable antenna, and the measured wave distributions are in good agreement with FDTD simulation of surface waves. Three dimensional measurements of electron density and temperature are made by a Langmuir probe array movable in meter-scale. In order to obtain information of radical distribution in large-area plasma, *wide-view* OES (optical emission spectroscopy) technique is developed. Applications of SWP to silicon thin films deposition and silicon oxidation processes are presented along with electron density monitoring by a *surface wave probe*.

1. Introduction

There has been a great need for meter-scale plasma sources for giant materials processing. The typical examples of giant plasma processing are thin film transistor manufacturing for meter-size LCD (liquid crystal display) panel, deposition of silicon thin films for photovoltaic power generation, surface coating of housing glass plate for UV and IR light cut, hardening plastic materials, surface modification of paper and plastic films to give either hydrophobic or hydrophilic properties, and abatement of toxic gases.

To date, linearly-long magnetron plasma sources have been used for sputter deposition of electrically conductive thin films on the materials which are conventionally moved normal to the plasma axis. On the other hand, large-area capacitively coupled plasmas (CCPs) have widely been used for large-scale CVD and etching processes. However, the 13.56 MHz CCPs have drawbacks of low plasma densities ($<10^{10}$ cm^{-3}). Recent studies of CCPs produced at the discharge frequency in a range of VHF (30 – 100 MHz) revealed considerable increase in plasma density, however standing wave effect and edge effect significantly degrade the plasma uniformity. Thus, the VHF CCPs are classified to be medium-density and medium-size plasmas.

Recently, we have developed a new technology for production of large-area uniform high-density plasmas based on surface wave excitation at 2.45 GHz [1]. The key technologies employed here are a dielectric-filled waveguide and a careful design of slot antenna array. In the preliminary experiments, using a large discharge vessel of 1 m in length and 0.3 m in width, we obtained a plasma density of ~$5x10^{11}$ cm^{-3} with ~10 % uniformity in 2.5 kW argon discharge at 50 mTorr.

Here, we describe the giant microwave discharge technology and present the plasma characterization by several diagnostic tools, together with some examples of applications of the large plasmas to materials processing.

2. Production of Meter-scale Microwave Plasma

The critical challenges for production of meter-scale microwave plasmas are (1) how to avoid huge atmospheric pressure (eight tons/m^2) acting on a dielectric window for microwave injection, and (2) how to design an antenna-plasma coupling so as to attain the plasma uniformity over meter-size. The first issue was dodged by employment of a dielectric-filled waveguide and antenna system, which is contained in a low-pressure plasma chamber. Figure 1(a) shows a conventional method of microwave plasma excitation where a thick dielectric

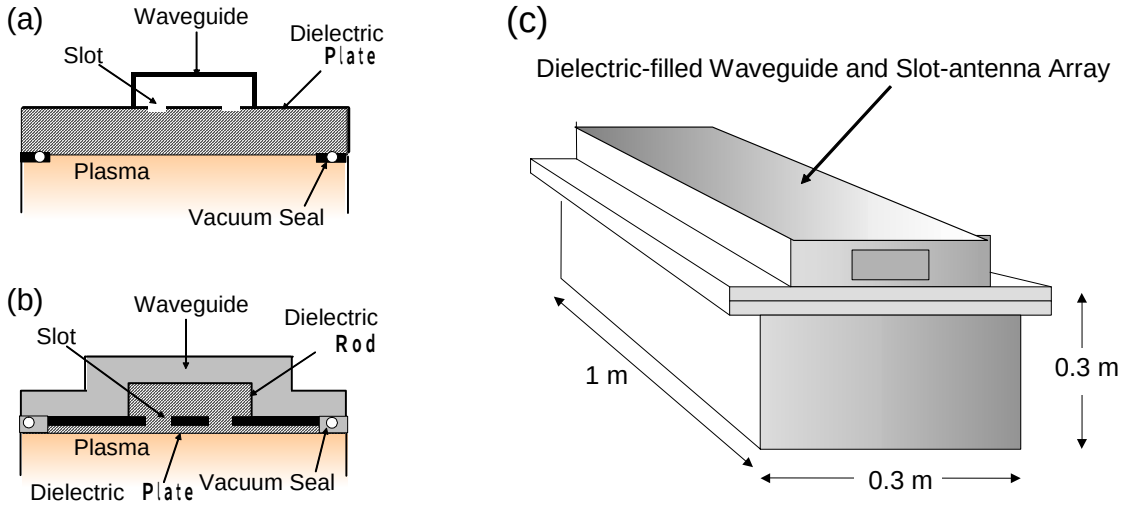

Fig. 1. (a) Conventional microwave injection through thick dielectric plate, (b) a new type of microwave injection through thin dielectric plate under dielectric-filled waveguide, and (c) schematic view of a meter-size microwave plasma apparatus.

plate (> 7 cm thick for a 1 m^2 quartz plate) is required to make vacuum seal between a plasma chamber and a waveguide with slot-antenna array. Such thick dielectric plate is extremely expensive and inconvenient for maintenance, and it also leads to a difficulty in control of surface wave excitation.

Thus, we developed a new scheme of microwave injection illustrated in Fig. 1(b). Here the waveguide is inserted into a plasma chamber with a vacuum seal using a dielectric partition inside the waveguide. As shown in Fig. 1(b), the slot antenna array and the large-area dielectric window are installed underneath the waveguide at the same ambient pressure as the plasma region. Since there exists no pressure difference in both sides of the large dielectric plate, no mechanical stress acts on the plate, and hence the plate thickness can be made as small as possible, say 1 cm or less, in spite of meter size.

In this scheme, the waveguide pressure is same as the plasma chamber pressure, so that unfavorable anomalous discharges might occur inside the waveguide and near the slot antennas due to the much stronger

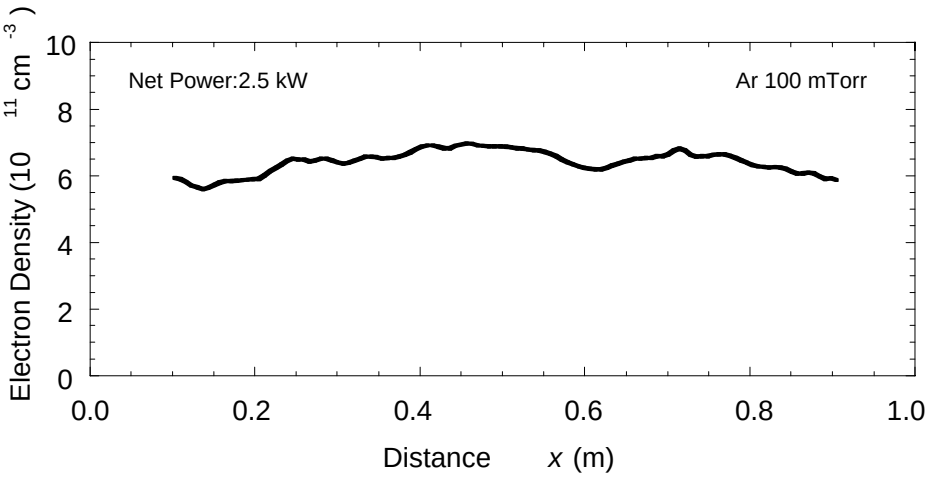

Fig. 2. The axial distribution of electron density produced by 2.45 GHz 2.5 kW microwave at 100 mTorr in argon.

microwave field intensity than in the plasma chamber. In order to prevent a stable plasma from such accidental discharges, the spaces inside the waveguide and the slots were fully plugged with dielectric material (quartz).

The second issue mentioned above was solved by a careful design of slot antenna array. Firstly, the design should meet a requirement of impedance matching at the waveguide entrance port between the microwave source and the load including the quartz-filled waveguide, slots, and open space. Secondly, in order to generate a meter-size uniform plasma, the slot antenna array is required to radiate the same microwave power from each slot which is distributed at the same interval along the waveguide axis in parallel to the *x*-axis.

These requirements were fulfilled in the present antenna array according to analytical approach and numerical simulations of electromagnetic fields; 25 slots aligned in two parallel lines along the x-axis, the slot size and spacing properly adjusted for obtaining a good impedance matching.

As a result, the new microwave injection scheme carefully designed in this way turned out to successfully work in producing a high-density large flat plasma in a chamber (1 m x 0.3 m x 0.3 m) shown in Fig. 1(c). For example, Fig. 2 shows the axial profile of electron density measured by a motor-driven Langmuir probe system in the discharge conditions of 2.5 kW, 100 mTorr argon. The electron density as high as $6x10^{11}$ cm^{-3} was obtained with a sufficient uniformity over one meter in length. A plasma of one-meter-square in area will easily be produced by installing three identical waveguide systems similar to the present waveguide system.

3. Microwave Field Measurement

In the SWP produced by microwave discharge at 2.45 GHz, surface waves propagating underneath a quartz plate parallel to the x-y plane were detected by a movable antenna. The standing modes of surface waves were successfully identified to be *m*=26 in the *x*-direction and *n*=11in the *y*-direction. Figure 3 compares the wave intensity profile in the *y*-direction measured in the experiment (solid line) and simulated in the relevant FDTD (*finite difference time domain*) method (dashed line). Here the wave electric field in the *z*-direction was measured at the distance *z*=1.5 cm from the quartz plate at the electron density of $6.4x10^{11}$ cm^{-3} produced by the microwave power of 2.5 kW in argon at 100 mTorr. As seen in Fig. 3, a very good agreement was obtained between the experiment and the simulation, suggesting the excitation of mode *n*=11 in the in the y-direction.

The similar comparison of the x-direction revealed the excitation of longitudinal mode *m*=26.

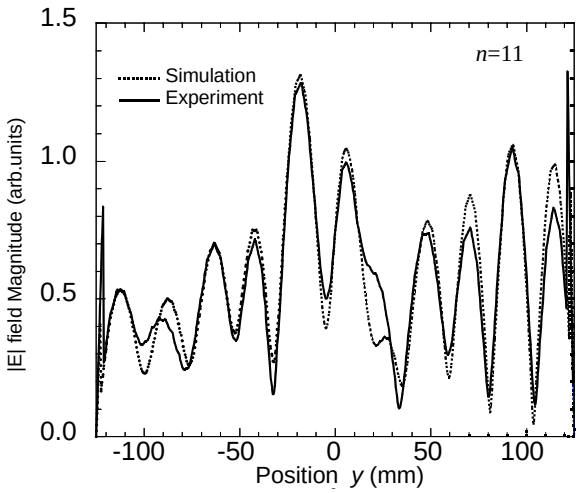

Fig. 3. Comparison of microwave field distributions along the y-direction between the experiment and the simulation.

4. Three-D Langmuir Probe Measurement

Three dimensional measurements of electron density and temperature were made by a Langmuir probe array movable in meter-scale. The linear probe array along the *y*-axis, which can be shifted along the *z*-axis, is driven along the *x*-axis by a stepping motor system. Computer-controlled data acquisition of probe *V-I* curves enables the three-dimensional measurement of electron density, temperature, and potential in the meter-scale plasma. Figure 4 shows the electron density as a function of the position *y* for the different discharge powers at 100 mTorr in argon. At low powers, the plasma is localized at the slot region ($y < 4$ cm). However, at the power higher than 2 kW, a fairly uniform high-density ($6x10^{11}$ cm^{-3}) plasma of 30 cm in width and 100 cm in length

was generated.

The observed plasma expansion with microwave power is well explained taking account of a wave propagation characteristics and the power balance. Namely, the surface wave launched from each slot propagates along the quartz plate in the *y*-direction, depositing the wave energy to electrons. The waves are reflected at the position giving the surface wave (SW) resonance at the density 3.6×10^{11} cm^{-3}, below which the waves are evanescent. As the discharge power is increased, the electron density increases and the SW resonance points shift outward, which in turn gives rise to successive expansion of the plasma width.

Such behavior is quantitatively examined based on the equation of power balance in a global model: the absorbed power is consumed for creation of electron-ion pairs in gas phase and the Bohm loss to walls. Comparison between the estimated plasma width and the measured width showed a good agreement not only for a pure argon discharge, but also an oxygen-mixure discharge.

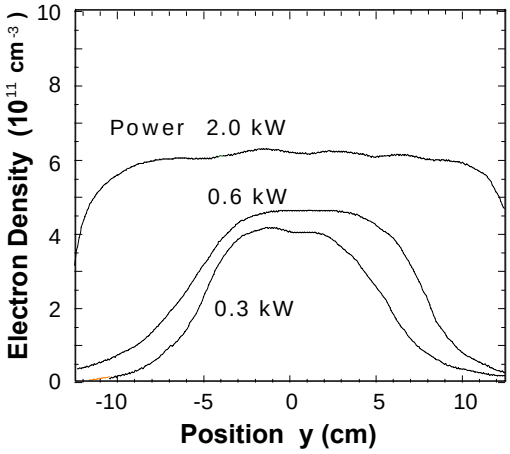

Fig. 4. Electron density profile along y-direction.

5. Wide-view OES Measurement

Optical emission spectroscopy (OES) is a simple and convenient tool to obtain information of radical species, plasma density, and electron energy distribution function. The OES measurement is conventionally done picking up the optical emission from plasma through a line-of-sight along a narrow beam. In order to obtain the information over a large area at a glance, a *wide-view OES* is developed where the optical emission is taken in a wide angle from a narrow viewing port. Combining optical filterswith this system enables *actinometry* measurement of radical species distribution in a large volume plasma.

6. Applications of SWP and Surface Wave Probe

Applications of SWP to meter-scale thin films formation are promising in manufacturing giant electronic devices. With liquid crystal display process in mind, plasma oxidation of silicon surface at low wafer temperatures is reported with oxygen radical detection. Furthermore, in order to apply the SWP to solar cell processing, we present high-speed deposition (>10 nm/s) of micro-crystalline silicon films at 500 K obtained in 20 % SiH_4/H_2 discharge, while poly-crystalline silicon films of large grain size (>200 nm) at 700 K are formed in 2 % SiH_4/H_2 discharge [2].

In such reactive plasmas, a conventional Langmuir probe is useless due to contamination of the probe surface. A novel tool, *surface wave probe* [3, 4] enables us to measure the local absolute electron density even when the probe surface is soiled with processing plasmas. The tool relies on absorption of surface waves resonantly excited around the probe head at critical frequencies, which mainly depend on the electron density. Recent improvement of this technique expands an applicable range of electron density from 10^8 to 10^{12} cm^{-3}, and of discharge pressure from 10^{-4} to 10 Torr.

References

[1] H. Sugai, Y. Nojiri, K. Takasu, T. Ishijima, E. Stamate, 57th Gaseous Electronics Conf. (Bunratty, Ireland, 2004), in Bulletin Amer. Phys. Soc. **49**, No. 5, p.10 (2004).

[2] H. Toyoda, Y. Hotta, H. Sugai, Abstracts 15th Sympo. Material Soc. Japan (Tokyo, 2004), p. 138.

[3] H. Kokura, K. Nakamura, I. Ghanashev and H. Sugai: Jpn. J. Appl. Phys. **38**, 5262 (1999).

[4] K. Nakamura, M. Ohata and H. Sugai: J. Vac. Sci. Technol. **A21**, 325 (2003).

NUMERICAL INVESTIGATION OF NO EFFECT ON THE IGNITION OF HYDROGEN AND HYDROCARBONS IN NON-PREMIXED LAYERS OF COLD FUEL AND HOT AIR

V.A. Bityurin, A.N. Bocharov and E.A. Filimonova
Institute for High Temperatures of RAS, Izhorskaya , 13/19, 125412, Moscow, Russia

Abstract
To determine a range of temperatures and corresponding to them NO concentrations for purposes of plasma-assisted combustion the axi-symmetric problem of the radial development of electrical arc channel was carried out. The one-dimensional combustion simulation of cold H_2 (T_0=300 K) and air (T_0=790-200 K) and chemical kinetics combustion modeling in H_2-air and CH_4-air mixtures holding the different NO percentage (10^{-3}-3%) was performed. The comparison with experiment in the counter-flow jets was done.
Keywords: ignition, induction time, chemical kinetics mechanism, electrical discharge, simulation.

1. Introduction

On study of plasma-assisted combustion it is widely used several kind of electrical discharges. One of them is arc discharge. The arc discharge was employed under investigation of the ignition and combustion in the counter-flow jets of oxidant (air) and cold fuel (gaseous propane) in the work [1]. The products of reactions initiated by arc discharge differently influence ignition of non-premixed layers of fuel and oxidant. One-dimensional simulation of mixing and combustion showed that the ignition time in each point of combustion zone is determined by the multi-component diffusion [2]. Radicals (O atoms) in hot air zone resulting from discharge play a part of source of high-enthalpy component and bring to the growth of temperature due to recombination and other chemical reactions, and O atom weakly affects the induction time [2]. This is the principle distinction from the preliminary premixed fuel and oxidant where the presence of radicals reduces the induction time appreciably. Other important component produced in discharge zone is nitrogen oxide. Its concentration may amount to some percents. Experiments carried out in H_2-air mixture [3] and in the counter-flow jets [4] showed nitrogen oxide may promote hydrogen and hydrocarbons combustion under rather low temperatures of 770-1300 K in some range of pressure, temperatures and NO concentrations.

In given paper to determine the nitrogen oxide influence area on ignition time and temperature the axi-symmetric problem of the radial development of electrical arc channel in air was carried out. The radial dependences of temperature and NO concentration in several time instants were obtained. The goal of modeling was to find the main processes, which affect the ignition rate and temperature ignition limit. The one-dimensional simulation of NO effect on induction time in the system of cold hydrogen (T_0=300 K) and sufficiently hot air (T_0=790-1100 K) holding the different NO percentage (10^{-3}-3%) was performed. The comparison with results in preliminary mixed fuel and air, and with experiment in the counter-flow jets was done. The chemical kinetics mechanism of hydrocarbons (CH_4, C_2H_2, C_3H_8) oxidation and combustion was assembled to describe the influence of NO on theses processes. The dominated reactions for every stage, induction time in dependence on temperature, CH_4 and NO content in CH_4-air mixture are presented.

2. Simulation of electrical arc discharge

The computational model used in simulating the evolution of electric discharge is basically described in [5]. In the current paper options related to the non-equilibrium plasma are omitted and it is assumed that both heavy particles and electrons have the same temperature at any location of the plasma bulk. The discharge is supposed to occur in the gap between two flat electrodes. The length of the gap is taken to be 1 cm. External electric circuit is assumed to provide 1 Ampere DC current in the gap. It is also guessed that electric field strength has only one component aligned with the electrode-to-electrode direction. Neglecting near-electrode phenomena one can consider all plasma properties unchangeable in the electric current flow direction. Finally, axi-symmetric discharge is considered. All these assumptions allow formulating the one-dimensional axi-symmetric problem to calculation of plasma properties in the gap.

The numerical model is based on a solution to Navier-Stokes equations coupled with the mass conservation equations for every species. The source terms in the species conservation equations are evaluated from 7 species chemical kinetics model. Transport properties of multi-component fluid are estimated on the base of temperature approximations to collision integrals of viscous and diffusion type. Details are referred to [6, 7]. Thermodynamic properties of species are determined by specifying the formation enthalpies and polynomial dependencies of constant-pressure heat capacities on temperature. Ideal gas equation-of-state is assumed to hold for every species, and Dalton's law is used to determine the gas pressure. Relationship between electric field strength and total current is resulted from Ohm's law. To complete total plasma resistance is to be calculated.

Initial and boundary conditions are specified as follows. As initial state the plasma column is specified, in which Gaussian distribution of temperature and electrons along radius is given. Typically, 0.5 mm was used as the half-width of Gaussian; at-axis temperature was taken between 5500-7000K; at-axis electron mole fraction was tried between $10^{-6} – 10^{-5}$. The electrons were balanced with NO^+. Initial radial distribution of density is calculated at pressure $P_0 = 10^5$ Pa, and temperature distribution described above. Symmetry conditions are set at the symmetry axis, i.e. zero radial derivatives for all variables except radial velocity are specified at the axis, and zero radial velocity is set at R = 0. At the outer boundary distant from the symmetry axis on 4 cm, zero derivatives are specified along with fixed static pressure value, $P_0 = 10^5$ Pa.

In Fig.1 the temperature and NO radial distributions in the vicinity of arc channel is presented. The thin horizontal and vertical lines mark the range of low temperature T=770-1100 K where nitrogen oxide may accelerate the oxidation process of hydrogen. According to Fig.1 these temperatures are corresponded [NO]=0.05-1%. The NO concentration is "frozen" when airflow drifts NO from discharge zone and may achieve the amount more then 1 percent. In general the formation near discharge of some NO distribution is determined by velocity of airflow, pressure and fuel flow rate. Non-uniform NO distribution in airflow may bring to cellular structure of ignition and non-uniform character of initial stage of combustion.

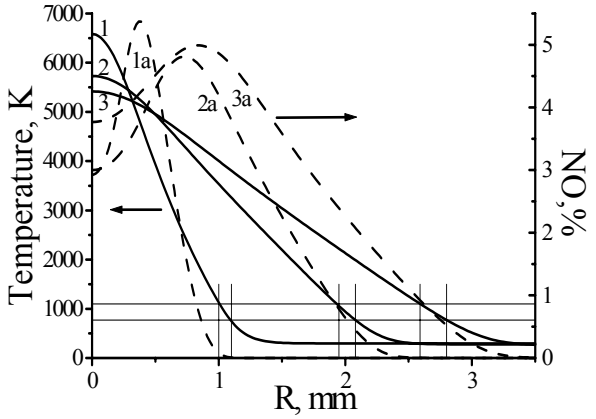

Fig.1. Radial evolution of arc channel in air. Dependences are given for different instants of time: 1,1a - 40 μs, 2,2a - 500 μs, 3,3a – 800 μs . Thin lines mark the ranges where sensitization of ignition is possible: T=770-1200 K, [NO]=0.05-1%.

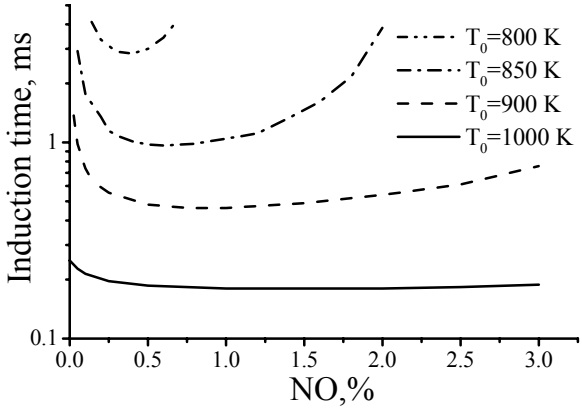

Fig.2. Induction time in dependence on initial NO content in hot air at the boundary of fuel and oxidant layers for several temperatures of hot zone. (H_2 layer is at T_0=300K).

3. Discussion of results

3.1. Ignition of hydrogen in non-premixed mixture

The calculations showed non-monotone ignition character at the boundary of two layers in dependence on NO concentration as well as in stochiometric H_2-air mixture. The NO influence already begins with a small concentration, for example, 10 ppm for mixture. The induction time was defined in the maximum of H atom concentration; this moment corresponds to the temperature of 1600 K at the boundary of layers. Fig.2 illustrates

the dependence of induction time on NO percentage for H_2 and air layers at initial air temperature of 800-1000 K. The minimum induction time τ_{in} at $P=10^5$ Pa and $T_0=900$ K of air is observed at 0.5-1% NO and equal to ≈460μs, whereas in the stochiometric mixture $\tau_{in}=225$ μs. Nitrogen oxide virtually does not influence ignition of hydrogen at $T_0 \geq 1100$ K for non-premixed gases and stochiometric mixture. These results are in agreement with experimental dependences [3,4]. In the absence of NO at $T_0<930$ K and in the presence of 2.1% NO at $T_0=850$ K the ignition at the boundary of two layers did not occur at the time less 4.2 ms (residence time of ignition kernel in the reaction volume). It is noted τ_{in} rapidly increases near $T_0=900$ K without NO, and for stochiometric mixture τ_{in}~6 ms at $T_0=910$ K as in experiment [8] as in our calculations.

In Fig.3 the dependence of temperature ignition limit as a function of NO concentration in air is shown. Corresponding to these temperature values the ignition time at the boundary is found in the range of 3-4.2 mc. The results of experiments in counter-flow jets [14] at strain rate $k_{exp}=300$ $s^{-1}$are indicated by symbols. The distance between two nozzles was equal to 2 cm. These values are limited the residence time of ignition kernel in the reaction zone. In given work the calculation domain was limited by 2 cm and the boundary between cold and hot layers was located in the middle of domain. The direct comparison is possible only taking into consideration a tangential component of flow velocity, for example, in two-dimensional simulation, because of counterflow improves the mixing, and as a consequence, accelerates the ignition. However, in experiment [9] the ignition temperature at $P_0=10^5$ Pa virtually was insensitive to strain rate in the fairly wide range. In Fig.3 one can see if a conterflow is available the temperature ignition limit decreases from 910 K without NO to 770 K with 0.14% NO, but in calculations it decreases from 930 K to 790 K at 0.3% NO.

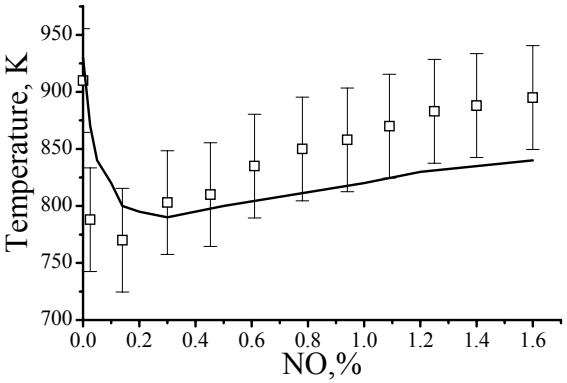

Fig.3. Ignition temperature in dependence on NO concentration in air at the boundary of two layers (H_2 layer is at $T_0=300$ K). The lines are modeling, symbols are experiment [4].

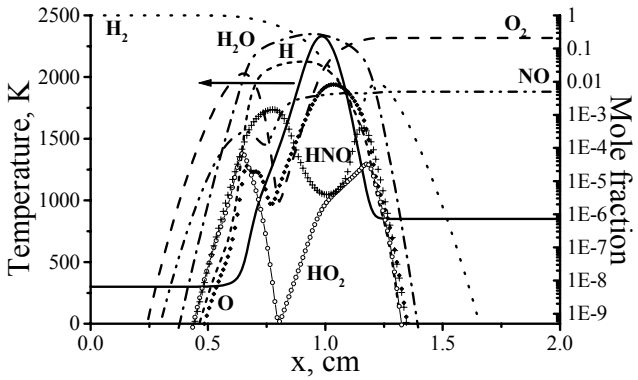

Fig.4. Temperature and concentrations of components within 1.2 ms in ignition kernel. H_2 layer is at $T_0=300$ K, air layer is at $T_0=850$ K, $[NO]_0=0.5\%$.

During induction time a mixing zone of fuel and oxidant amounts to some millimeters, its width is determined by diffusion and thermal conductivity. The distribution of most components at ignition instant and combustion has a non-monotone behavior with some extremums (see Fig.4). The size of combustion zone may define with respect to H_2O profile line; it is about 1 cm. The behavior of NO_2 is close to HO_2 profile line.

In the combustion process with NO the chemical kinetics scheme and role of individual components are changed, for example, HO_2. This radical facilitates branching instead of termination of chain (reactions (5), (6)). The main reactions, which result in sensitization of ignition or prohibit the branching of chain under certain conditions of temperature and concentrations, are following:

$$H_2+O_2 \leftrightarrow OH+OH \quad (1)$$
$$H+O_2+H_2 \leftrightarrow HO_2+H_2 \quad (2)$$
$$H+O_2+O_2 \leftrightarrow HO_2+O_2 \quad (3)$$
$$H+O_2+N_2 \leftrightarrow HO_2+N_2 \quad (4)$$
$$HO_2+NO \leftrightarrow OH+NO_2 \quad (5)$$

$H+NO_2 \leftrightarrow OH+NO$ (6)
$O+NO_2 \rightarrow NO+O_2$ (7)
$NO_2+M \leftrightarrow O+NO+M$ (8)
$H+NO+M \leftrightarrow HNO+M$ (9)
$OH+NO+M \leftrightarrow HNO_2+M$ (10)

Reactions (1)-(5) essentially influence the initial combustion process and induction time. At high initial NO concentration the disappearance of O and H atoms in interacting with nitrogen oxide becomes appreciable and the combustion process does not develop (reactions (8)-(10)). The kinetic scheme included 15 components and 77 elementary reactions. The constants rates have been taken mainly from [10]. This kinetic scheme has been tested (without NO) on experiments [3,8,11] and results of comparison was very good.

The modeling showed the maximum temperature shift was observed at $[NO]_0$=0.3% and equal to 140 K (without NO T_0=930 K) for non-premixed layers of H_2 and air, and 175 K (without NO T_0=915 K) for stoichiometric H_2-air mixture. The ignition occurred at time ~4 ms.

3.2. Ignition of hydrocarbons in preliminary mixed gases

Chemical kinetics mechanism included about 1000 elementary reactions for 160 components, which may be reduced according to conditions of modeling. Rate constants of reactions were taken from many sources. Some of them are pointed out in the work [12] devoted to $DeNO_x$ in the presence of hydrocarbons from exhaust gas on the base of non-thermal plasma processes. The kinetic scheme has been applied a test to experiments of CH_4 conversion in the presence of NO at T=800-1000 K with low concentrations of these species of 100-200 ppm [13], and ignition delay measurements in the shock tube in methane-ethane mixture [14]. The simulated results agree well with the experimental data.

Fig.5a shows the typical concentration profiles at temperatures of lower 1600 K for mixture of 9.5%.CH_4+19%O_2+71.5% N_2. The first stage (t < 1 ms) is characterized by CH_3, OH, H and O radical production mainly in the reactions

$CH_4 \rightarrow H + CH_3$ (11)
$CH_4 + O_2 \rightarrow HO_2 + CH_3$ (12)
$HO_2 + NO \rightarrow OH + NO_2$ (5)
$O_2 + CH_3 \rightarrow O + CH_3O$ (13)
$O_2 + CH_3 + M \leftrightarrow CH_3O_2 + M$ (14)
$O_2 + CH_3 \rightarrow O + O + CH_3$ (15)
$O_2 + CH_3 \rightarrow OH + CH_2O$ (16)
$NO + CH_3O_2 \rightarrow CH_3O + NO_2$ (17)
$CH_3O + M \rightarrow H + CH_2O + M$ (18)
$H + O_2 \rightarrow O + OH$ (19)
$O + CH_4 \rightarrow OH + CH_3$ (20)
$H + CH_4 \rightarrow H_2 + CH_3$ (21)
$OH + CH_4 \rightarrow H_2O + CH_3$ (22)

Profiles of O and H radicals are close to the OH concentration behavior. The duration of this stage depends only initial temperature and matrix gas.

The second stage named of conversion stage is beginning when OH and H concentrations achieve the first maximum (t ~ 1 ms in Fig.5a). The hydrocarbon (CH_4, C_2H_6, C_3H_8 and other) and oxygen concentrations are slowly decreasing at almost constant temperature in contrast of rapid production of main conversion products (H_2 and CO) due to reactions (3)-(5), (10), (14)-(22) and

$H + O_2 + CH_4 \rightarrow HO_2 + CH_4$ (23)
$CH_3 + NO_2 \rightarrow CH_3O + NO$ (24)
$H + NO_2 \rightarrow OH + NO$ (6)
$O_2 + HNO \rightarrow OH + NO_2$ (25)
$CH_3O + NO \rightarrow CH_2O + HNO$ (26)
$OH + CH_2O \rightarrow H_2O + CHO$ (27)
$O_2 + CH_2O \rightarrow HO_2 + CHO$ (28)

$$H + CH_2O \rightarrow H_2 + CHO \quad (29)$$
$$CHO + M \rightarrow H + CO + M \quad (30)$$
$$O_2 + CHO \rightarrow HO_2 + CO \quad (31)$$
$$CH_2O + M \rightarrow H_2 + CO + M \quad (32)$$

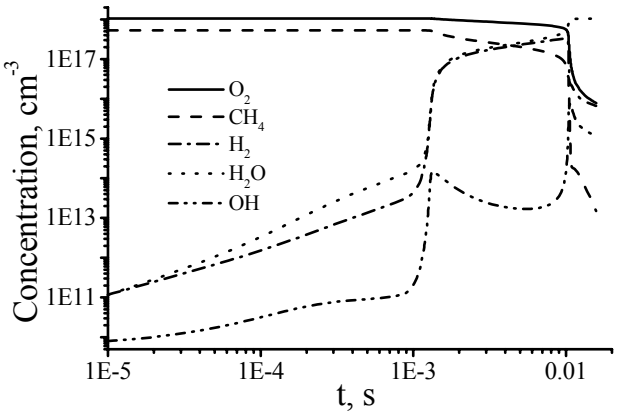

Fig. 5a. Concentrations of some components as a function of time in combustion of 9.5%.CH_4+19%O_2+71.5% N_2 mixture. T_0=1300 K, $P_0 = 10^5$ Pa.

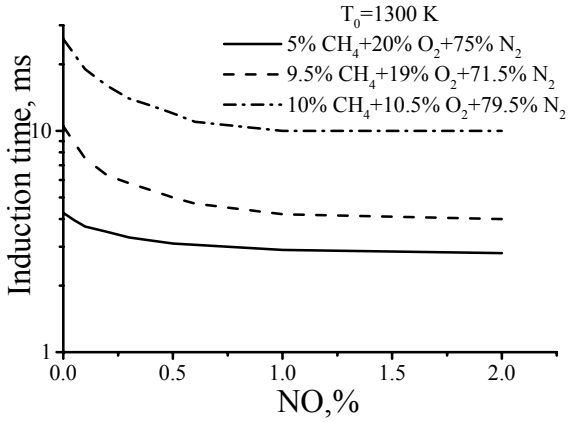

Fig. 6. Induction time in dependence on initial NO content for several methane mixtures. $P_0 = 10^5$ Pa.

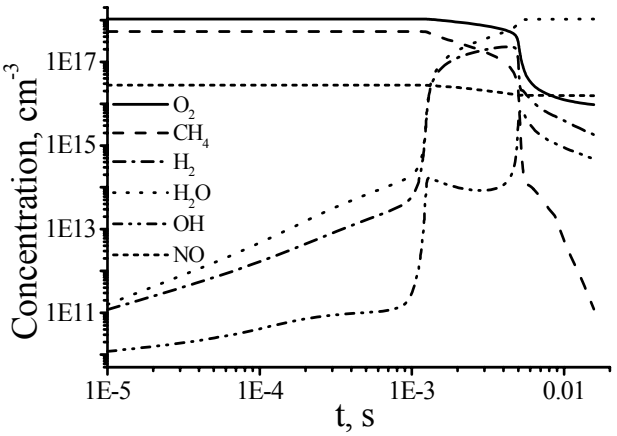

Fig. 5b. Concentrations of some components as a function of time in combustion of 9.5%.CH_4+19%O_2+71.5% N_2 mixture with 0.5% NO. T_0=1300 K.

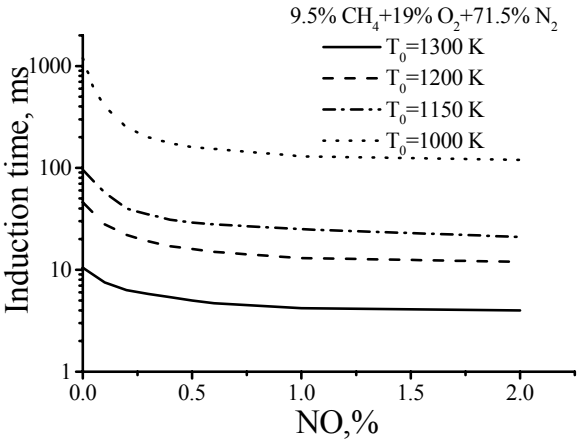

Fig. 7. Induction time in dependence on initial NO content for several temperatures for stochiometric methane mixture.

At the ignition moment (t=10.5 ms in Fig.5a) in the case of poor and stochiometric mixtures the H_2, CO, CH_4 concentrations are sharply decreasing and OH concentration achieves the second maximum. Third stage is combustion stage with CO_2 and H_2O formation and temperature growth. Following leading reactions of final step together with reactions (6), (18), (22), (27), (29)-(31) are dominating:

$$H_2 + OH \rightarrow H + H_2O \quad (33)$$
$$OH + CH_3OH \rightarrow H_2O + CH_3O \quad (34)$$
$$OH + CH_3OH \rightarrow H_2O + CH_2OH \quad (35)$$
$$OH + OH \rightarrow O + H_2O \quad (36)$$

$OH + HO_2 \rightarrow O_2 + H_2O$ (37)
$OH + CO \rightarrow H + CO_2$ (38)
$CO + HNO \rightarrow CO_2 + NH$ (39)
$CHO + NO_2 \rightarrow H + CO_2 + NO$ (40)
$HO_2 + CHO \rightarrow OH + H + CO_2$ (41)

NO addition doesn't influence the duration of first stage but shortens the conversion stage. Fig. 5b demonstrates this effect in the presence of 0.5% NO for the same mixture as noted above in Fig.5a. Duration of conversion stage is reduced by a factor of two basically owing to reactions (5), (6), (17), (24), (25) and depends on NO content in mixture. HO_2 radical also facilitates branching of chain as in combustion of hydrogen however influence of terminating reactions (8)-(10) is less evaluated then in H_2 combustion. For this reason 2% NO and 1% NO result in similar diminution of conversion stage (See Fig.2 and Fig.7).

In Fig.6 one can see the summary result of NO effect on induction time for poor, stoichiometric and rich methane mixtures at T_0=1300 K. Induction time is decreased from 4.25 ms to 3.2 ms and from 26 ms to 12 ms for poor and rich mixtures correspondingly. At NO content more than 0.5% induction time almost doesn't change.

The most pronounced NO effect on reduction of induction time exhibits at low initial temperature. It is obvious from Fig. 7. Results are presented for stoichiometric methane mixture at four initial temperatures. At T_0=1000 K the induction time is reduced by the order of magnitude from 1.2 s to 120 ms..

4. Conclusions

Thus, NO effect on ignition and combustion takes place in comparatively narrow range of temperatures and sufficiently wide range of NO concentrations. Induction time at the boundary of fuel and oxidant with different temperatures (H_2 and air) is greater than induction time for stochiometric H_2-air mixture by a factor of two and more under considered conditions. The ignition temperature is shifted to lower values, at more than 100 K. In hydrocarbon–air mixtures NO affects only the conversion stage of combustion process shortening it up to the order of magnitude.

This work was supported by Program No 20 of Russian Academy of Sciences.

References

[1] A.I. Klimov, V.A. Bityurin et al. - In Proc. of The 4nd Workshop on Magneto-plasma-aerodynamics in Aerospace Applications, 9-11 April, Moscow, Russia. 192 (2002).
[2] V.A. Bityurin, A.N. Bocharov, E.A. Filimonova and A.I. Klimov - In Proc. of The 15 Inter. Conf. on Gas Discharges and their Applications, 5-10 Sept., Toulouse, France. 973 (2004).
[3] M. Slack and A. Grillo - Investigation of Hydrogen-Air Ignition Sensitized by Nitric Oxide and by Nitrogen Dioxide, NASA Report CR-2896. 38 P. (1977).
[4] Y. Tan, C.G. Fotache and C.K. Law - Combustion and Flame. **119**, 346 (1999).
[5] A. Bocharov, S. Leonov, I. Klement'eva, V. Bityurin - In Proc. of 41st Aerospace Sciences Meeting and Exhibit, Reno, NV, AIAA Paper 2003-5878 (2003).
[6] A.I. Zubkov, G.A. Tirskiy, V.A. Levin, V.I. Sakharov - Motion of bodies in Earth's and Planet's Atmospheres with Supersonic and Hypersonic Velocities under Conditions of Chemical Conversions, Heat Transfer and Radiation. Rep. No.4507, Institute of Mechanics of Moscow State University (1998).
[7] A.V. Andriatis, S.A. Zhluktov, I.A. Sokolova - J. Mathematical Modeling. **4**, No 1(1992).
[8] A.D. Snader, J.Z. Robertson et al.- Shock tube studies of flue-air ignition characteristics. Tech. Report AFAPL-TR-65-9, 1965.
[9] C.G. Fotache, T.G. Kreutz, D.L. Zhu and C.K. Law - Combust. Sci. and Tech. **109**, 373 (1995).
[10] D.L. Baulch et al J. Phys. Chem. Ref. Data . **21**,411 (1992)
[11] G.I. Schott, J.L. Kinsey - J. Chem. Phys. **29**, 1177 (1958)
[12] E.A. Filimonova**,** Y. Kim, S.H. Hong, and Y.H. Song - J. Phys. D: Appl. Phys. **35**, 2795 (2002)
[13] J.H. Bromly and F.J. Barnes et al. – Combust Sci. Tech. **115**, 259 (1996)
[14] L.J. Spadaccini and M.B. Colket - Prog. Energy Combust. Sci. **20**, 431 (1994).

Full Paper

Aerosol Assisted Plasma Deposition of Barrier Coatings using Organic-Inorganic Sol-gel Precursor Systems**

By Dirk *Vangeneugden,* Sabine Paulussen, Olivier Goossens, Robby Rego* and *Klaus Rose*

Hybrid organic-inorganic monomers and sol-gel systems thereof, obtained via wet-chemical hydrolysis, were atomised and introduced in an atmospheric pressure dielectric barrier discharge (DBD). The obtained coatings were analysed by means of Fourier transform infrared spectroscopy (FTIR), Raman spectroscopy and field emission scanning electron microscopy (FESEM). Films deposited on PET foil were tested for their oxygen barrier properties. Plasma assisted coating deposition of the sol-gel systems proved to be superior to wet-chemical application and conventional thermal or UV curing. However, the best barrier performance was obtained with a coating from a new high molecular weight non-hydrolysed siloxane precursor.

Keywords: DBD plasma, barrier coating, aerosol deposition, sol-gel, hybrid materials

[*] Dr. D. Vangeneugden, Dr. S. Paulussen, Dr. O. Goossens, Dr. R. Rego
Plasma Technology Group
Materials Department
VITO - Flemish Institute for Technological Research
Boeretang 200, B-2400 Mol (Belgium)
E-mail: Dirk.Vangeneugden@vito.be

Dr. K. Rose
Fraunhofer-Institut fuer Silicatforschung
Neurerplatz 2, D-97082 Wuerzburg (Germany)

[**] The presented work is carried out in the framework of SOLPLAS, a project funded by the European Commission under the Fifth Framework Growth Program (GRD1-2001-41847). We thank the EC for funding and all partners for the excellent cooperation.

1. Introduction

The use of polymer films has increased drastically over the last decades. The range of applications is very divers and still expanding: from food packaging over medical components to substrates for electronic displays.[1] However, the demanded specifications for polymer films are also increasing systematically as well as the pressure on their environmental impact and production costs. Today, one of the key challenges is to develop alternative environmental save and improved barrier coating technologies against water and gas permeation.
Barrier coating technologies for polymer films can be subdivided roughly in two categories: atmospheric and vacuum based technologies. The atmospheric techniques consist of applying a lacquer followed by a post-curing treatment (thermal, UV or e-beam irradiation). Vacuum coatings mainly concern aluminium metallization or, when transparency is a requisite, metal oxide (MeOx) deposition. The limitations of these state-of-the-art technologies are related to barrier performance and/or cost and functionality. The values for oxygen transmission rates (OTR) and water vapour transmission rates (WVTR) realized industrially today are 1-3 orders of magnitude higher than targeted for future demanding applications (OTR ≈ WVTR ≈ 10^{-2}).[2] Today, only some very specific multilayer combinations of lacquers and MeOx coatings have

demonstrated acceptable overall performance.[2-4] The complexity of the processes to obtain such a multilayer significantly increases the process costs. Moreover, some films are incompatible with vacuum deposition technology due to out-gassing. The presented work aims at the development of a novel atmospheric plasma deposition technology which offers better performance and increased functionality at reduced cost.

Low temperature atmospheric pressure plasma treatment by means of dielectric barrier discharges (DBD) constitutes an emerging technology for foil treatment.[5] The technology is closely related to current industrial corona treatment which is widely used in foil production and finishing processes.[6,7] DBD systems have been developed and optimised for the sterilization and activation of surfaces before printing, gluing or top-coating.[5,8-12] However, in recent years laboratory and semi industrial scale experiments have demonstrated the interesting capabilities of this technology for in-situ coating deposition.[13-18] This can be done by injection of gaseous or vaporized chemical precursors in the plasma discharge. Unlike low pressure plasma deposition which generally targets metal oxide or nitride coatings, atmospheric pressure DBD is most suited for deposition of organic and hybrid organic-inorganic coatings. Moreover, atmospheric plasma technology allows to circumvent one of the major drawbacks of current low pressure plasma technologies: the need for expensive and limited volume vacuum equipment.

Until recently, the variety of coating precursors used in DBD deposition was limited to gaseous chemicals and liquid precursors with a high vapour pressure and/or high thermal stability which considerably limited the coating capabilities. Furthermore, deposition rates are in most cases to low (e.g. 1 µ/h for siloxanes) to meet the requirements for in-line production.[2] The use of nano-sized aerosols enables to overcome the latter limitations. It allows to make use of the full variety of chemical compounds available today and to increase the deposition rates drastically. The presented work describes the deposition of hybrid organic-inorganic nano-composite coatings by injection of hybrid precursors and sol-gel systems thereof (ORMOCER®) to the plasma as aerosol particles formed by atomisation.[19,20]

2. Results and Discussion

Sol-gel coatings of silicon oxide are known to give good barrier properties.[19,20] Common sol-gel precursor systems for these coatings are made by controlled hydrolysis of e.g. tetraethoxysilane (TEOS). (Figure 1) These transparent coatings have a dense and highly cross-linked silicate structure but are also quite brittle.

In order to reduce the brittleness of sol-gel coatings organic building blocks can be incorporated. This can be done by preparing sol-gel systems using organically modified precursor compounds like glycidoxypropyltrimethoxysilane (GLYMO), methacryloxypropyltrimethoxysilane (MEMO) or propyltrimethoxysilane (PTMO). (Figure 1) The resulting hybrid organic-inorganic coatings are more flexible due to a lower oxidic cross-link density.[19] Aerosols of these (partially) hydrolyzed sol-gel precursors have been introduced into a nitrogen DBD plasma.

The criterion for the selection of these monomers is the expected difference in behavior under plasma conditions due to the presence of different functional groups. During sol-gel processing, hydrolysis and condensation of organically functionalized alkoxysilanes result in the formation of an inorganic pre-polymer bearing some functional groups. The latter can act as an anchor point for the formation of an additional organic network which may be formed under plasma conditions.

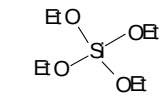

Tetraethoxysilane
TEOS

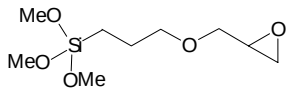

Glycidoxypropyltrimethoxysilane
GLYMO

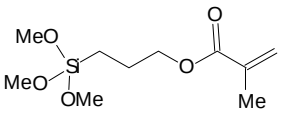

Methacryloxypropyltrimethoxysilane
MEMO

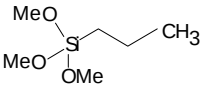

Propyltrimethoxysilane
PTMO

Figure 1: Silane sol-gel precursors

TEOS will form an inorganic network on hydrolysis bearing no organic groups. An inorganic network is also formed by hydrolysis of GLYMO and MEMO. However, the functional groups present in these compounds allow additional organic cross-linking via epoxide and acrylate polymerization, respectively. PTMO forms an inorganic backbone bearing non-reactive saturated hydrocarbon (propyl) group. As a consequence, pre-polymers of the latter have not much possibilities to react further via conventional chemical polymerization routes.

From all previously mentioned hydrolyzed solutions a plasma coating could be obtained, except from the TEOS-solution. The latter gave rise to a powder like deposition, which can be explained by the absence of organic groups on the inorganic prepolymer. Depending on the type of precursor, the plasma conditions and the set-up used, deposition rates varied between 40 and 175 nm/min. (Table 1)

Table 1: Plasma deposition rates of pure and hydrolized sol-gel precursor

Precursor	Coating thickness (nm)	Deposition time (min)	Deposition rate (nm/min)	Physical appearance
TEOS	500	10	50	smooth coating
GLYMO	300	10	30	smooth coating
MEMO	400	10	40	smooth coating
PTMO	1000	10	100	smooth coating
TEOS sol-gel	---	2	---	powder
GLYMO sol-gel	250	2	125	smooth coating
MEMO sol-gel	400	10	40	smooth coating
PTMO sol-gel	350	2	175	smooth coating

Coating thickness was measured close to the gas inlet. In stationary plasma deposition experiments coating thickness generally decreases substantially in relation to the distance from the gas inlet. Results of plasma deposition experiments with non-hydrolized silane precursors are also included in Table 1. Although the hydrolized precursor systems are diluted in alcohol, deposition rates of the sol-gel systems seem to be higher than those obtained via direct plasma deposition of the precursors.

Under equal conditions, the growing rates obtained with the PTMO and GLYMO sol-gel systems were significantly higher than the one obtained with the MEMO sol-gel system. The reason for this is still unclear. The fact that the PTMO sol-gel system polymerizes easily and gives rise to a smooth coating proves that polymerization does not occur exclusively in the classical chemical way. Figure 2 shows FESEM pictures of cross sections of plasma coatings obtained from the hydrolyzed precursor solutions.

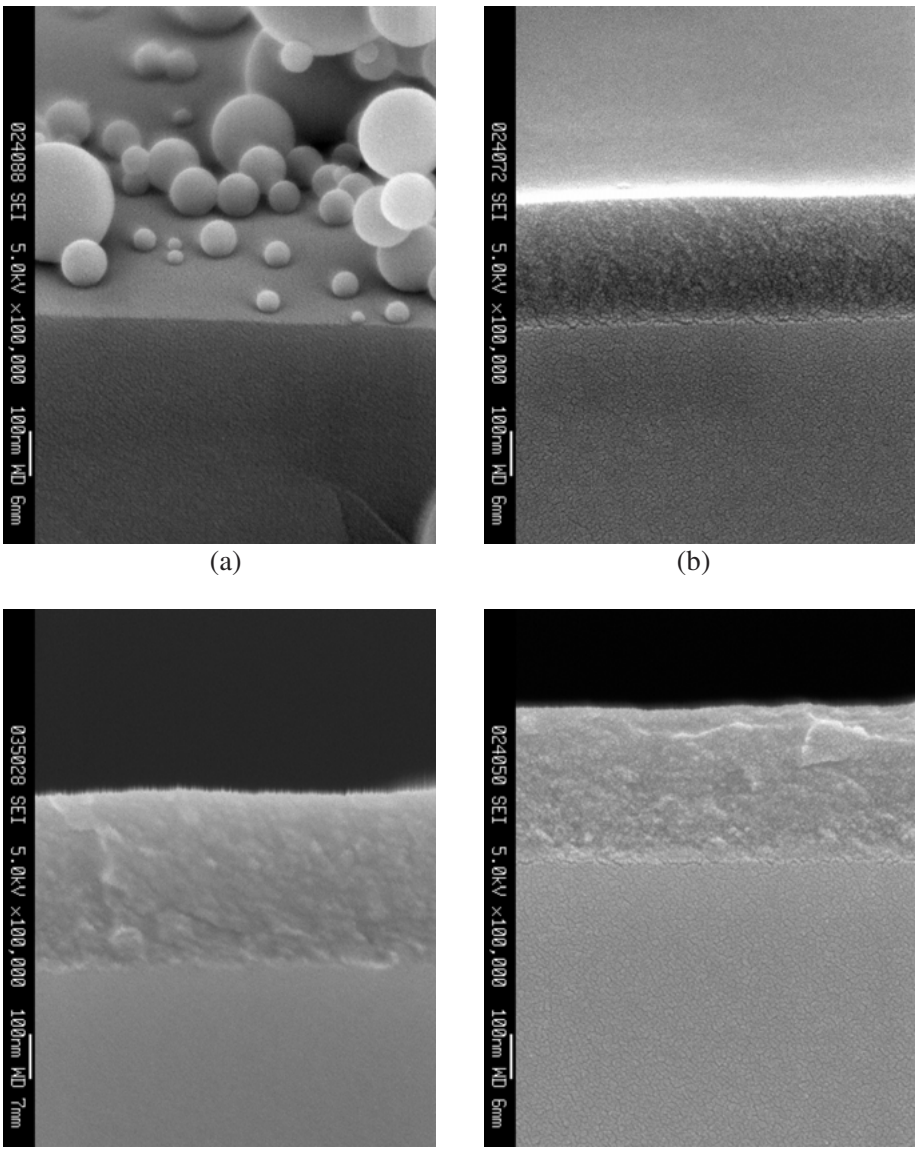

(a) (b)

(c) (d)

Figure 2: FESEM pictures of cross sections of plasma depositions obtained from hydrolyzed solutions of TEOS (a), MEMO (b), PTMO (c) and GLYMO (d). Pictures (a) and (b) were taken under a tilting angle of 25°. Deposition times were 2 minutes except for the MEMO-solution (10 minutes).

Transparent and homogeneous coatings from GLYMO and MEMO sols were obtained both after conventional curing (GLYMO: 1 h/130 °C; MEMO: 20 sec UV curing at 5,93 J/cm^2) and by plasma deposition/curing. In both cases organic cross-linking (GLYMO: ring opening polymerization; MEMO: radical initiated –C=C-polymerization) and inorganic Si-O-Si cross-linking/condensation occurred.
The organic cross-linking/polymerization was observed via IR-spectroscopy (Figure 3a + 3b). The GLYMO spectra exhibit the formation of a carbonyl signal (plasma: 1690 cm^{-1}, thermal: 1725 cm^{-1}) indicating the ring opening reaction. The MEMO spectra show a significant decrease of the –C=C-double bond (1640 cm^{-1}) indicating organic polymerization.

A completely different behavior was found for plasma and thermally cured PTMO. In PTMO no reactive organic polymerizable group is present. Hence, only SiOH condensation reactions are possible under classical conditions. Films obtained by plasma deposition were non-sticking, whereas films obtained after thermal curing (1-5 h/130°C) were still sticky. During thermal treatment only SiOH condensation can take place, which is not as effective as in TEOS. During plasma deposition/curing additional organic cross-linking is expected to takes place. The IR spectrum of thermally cured PTMO is identical to the non-cured film, whereas the spectrum of plasma cured PTMO exhibits a carbonyl signal at 1695 cm^{-1} indicating also oxidation reaction in the organic chain (Figure 3c).

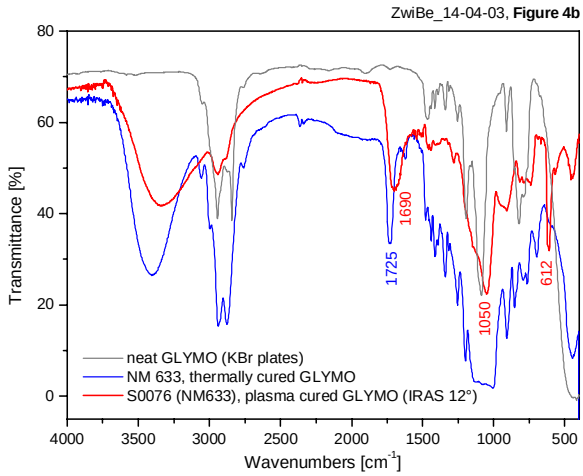

a)

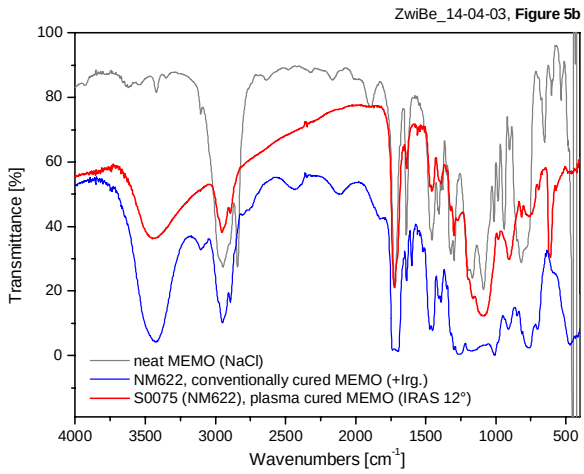

b)

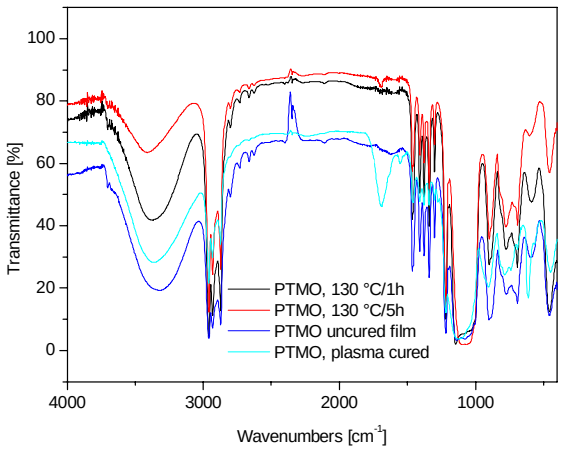

c)

Figure 3: FTIR spectra of a) GLYMO, b) MEMO and c) PTMO precursors and sol-gel based coatings thereof after both conventional (thermal or UV) and plasma curing/deposition

Raman spectra of conventional (thermal) and plasma cured PTMO sol-gel coating shows that the aliphatic groups are not strongly affected or decomposed by the plasma treatment. (Figure 4) The fingerprint regions in the Raman spectra of plasma cured and thermally cured PTMO layers show identical signals. However, the fact that the thermally cured PTMO layer is still sticky while the plasma cured layer is not, indicates that an additional cross-linking process is taking place under plasma conditions. Since there are no significant differences in the Raman signals of $-CH_2-$ and $-CH_3$ groups, it could be assumed that plasma improves the cross-linking and curing of the inorganic siloxane network for PTMO sol-gel systems. More thorough analysis with FTIR and Si-NMR should be able to clarify the differences in chemical structure of both types of coating.

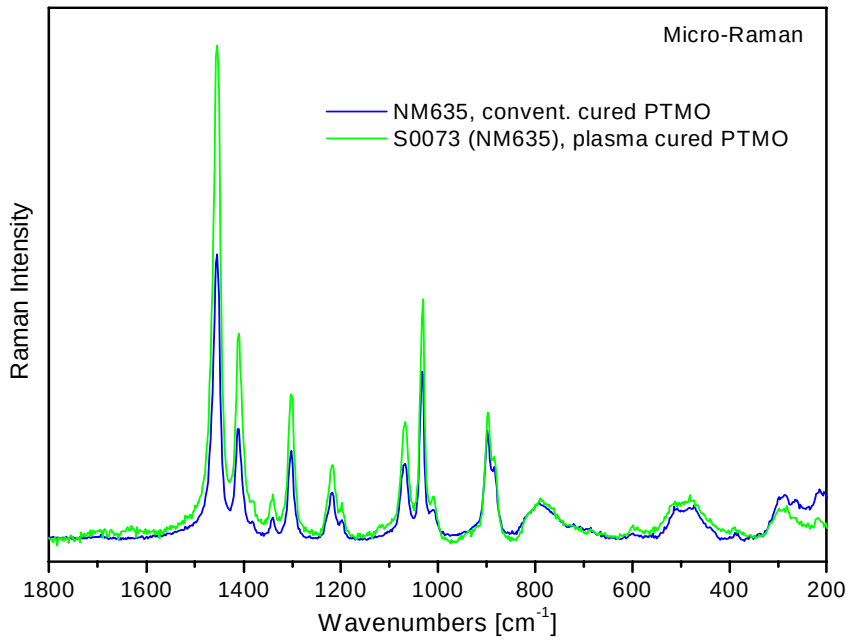

Figure 4: Raman spectra of the plasma cured and thermally cured coatings obtained from a hydrolyzed PTMO solution.

In order to evaluate the influence of plasma induced cross-linking on the physical coating properties, the oxygen permeability of coated PET films was determined. Both thermally and plasma cured coatings were three micron thick. As can be seen in Figure 5, the oxygen permeability decreases significantly from thermally cured PTMO to plasma cured PTMO coatings on PET films. The reason is the more densely cross-linked structure obtained after plasma curing.

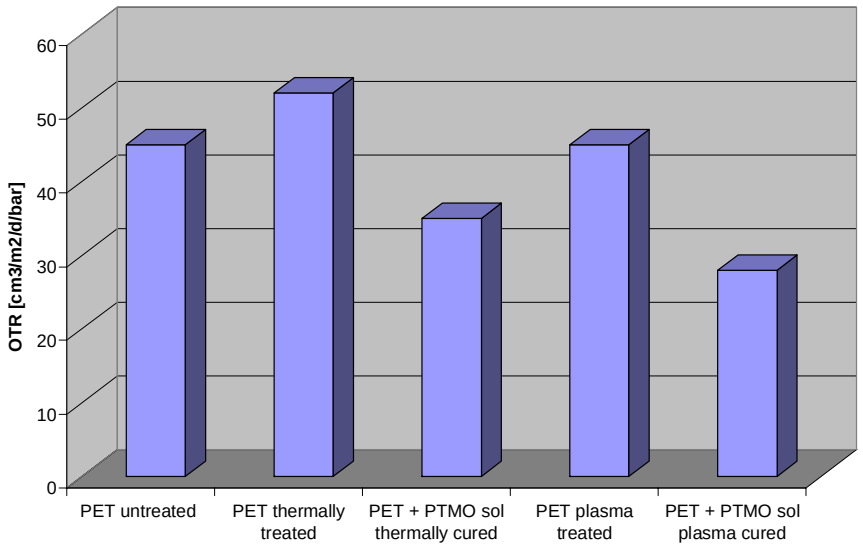

Figure 5: Oxygen permeability of PTMO sol-gel coated PET after conventional curing and plasma deposition/curing

In order to obtain even better barrier coating properties and higher deposition rates for DBD plasma coatings the addition of a high molecular weight inorganic cross-linker (Bayresit) to the sol-gel systems was investigated. (Figure 6)

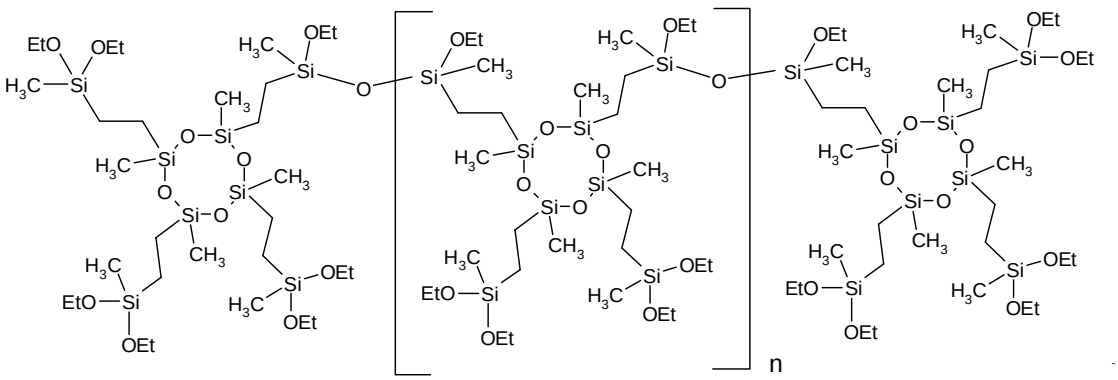

Figure 6: Chemical structure of Bayresit

Under standard curing conditions (MEMO: UV-curing; PTMO, GLYMO: thermal curing) coatings were still sticky and very soft indicating non-sufficient curing. This effect cannot be explained up to now. However, a first preliminary plasma deposition of a Bayresit/PTMO sol-gel system (50:50 molar ratio) resulted in a well cured film. Furthermore and rather surprisingly, plasma coatings obtained from the latter

compound in its pure form gave rise to very low oxygen transmission rates (< 10 cm³/m²/d/bar on PET). (Figure 7)

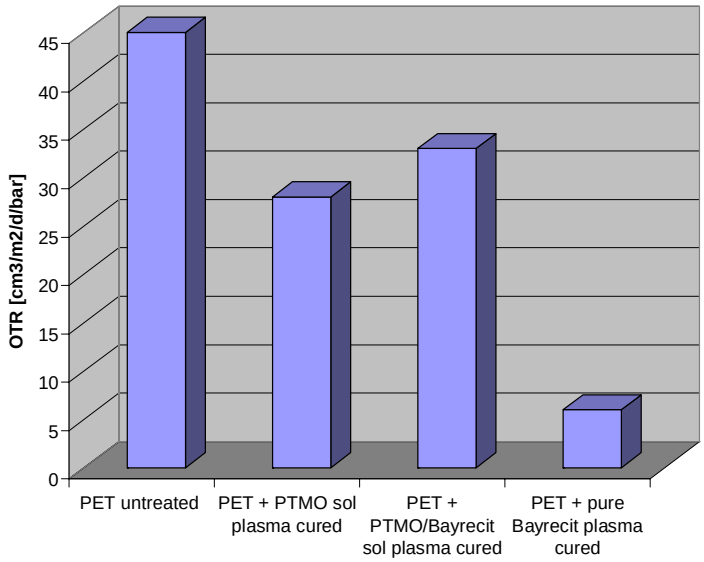

Figure 7: O_2-permeation of plasma coated PET films

3. Conclusions

Sol-gel technology opens-up a wide range of chemical possibilities in coating deposition, especially with respect to nanoscopic variations of inorganic and organic groups or structural elements. Coatings prepared from these materials can be tailored towards many different applications including barriers, scratch resistance and many others. However, the classical curing processes (thermal and UV) do not always exploit the full potential of these materials.

The presented work shows that plasma curing of aerosol droplets of hybrid sol-gel precursor solutions prior and during deposition on a substrate surface is advantageous to conventional wet-chemical coating and subsequent thermal or UV curing. Due to the high surface area of the atomized sol and the extremely reactive plasma environment, increased cross-linking takes place. This results in faster curing and better barrier properties of the obtained coatings.

However, the best barrier performance was obtained with a coating from a new high molecular weight non-hydrolysed siloxane precursor. Further experiments should allow to improve the barrier performance even more and to gain more insight in the exact physico-chemical structure of these coatings.

4. Experimental

The experimental configuration of the DBD system consists of two parallel electrodes (160 x 180 mm), both covered with an insulating borosilicate glass plate of 3 mm thickness. (Figure 8) In order to perform tests in a controlled atmosphere, the electrode configuration is mounted in a closed vessel which is evacuated and subsequently filled with the carrier gases before deposition is started. To ensure stable plasma operation, the gap between the electrodes is limited to 2 millimetres. Plasma discharges were generated by a 20 kV/200 mA AC power supply (Melec) with variable frequency connected to a high voltage transformer. The maximum output power is 3 kW and the frequency can be varied in the range of

50 Hz- 100 kHz. The discharge voltage is measured by means of a high voltage probe (Tektronix P6015A) while the discharge current is measured by means of a current probe (Tekronix A6312). The discharge current and discharge voltage are monitored on a digital oscilloscope (Tektronix TDS 3052). The carrier gas is introduced between the parallel plates by a gas distribution unit. The gas flow rate is controlled by mass flow controllers (MKS Instruments, Multi Gas Controller 647B).
The reported deposition experiments were performed in nitrogen (15 l/min) at a frequency of 9 kHz and power densities between 0.5 to 1.5 W/cm^{2}. Polydisperse submicron aerosols of the liquid precursors and sol-gel systems were added to the gas flow by means of an atomizer (TSI, model 3076 or model 9306A). Deposition times were set at 2 to 10 minutes.

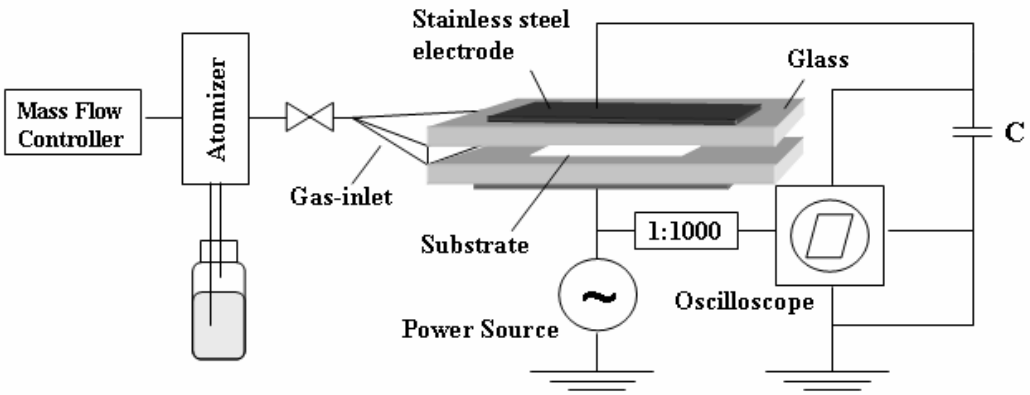

Figure 8: Experimental setup of DBD equipment

The hydrolysis conditions of the monomers and the stability of the sols were investigated. The use of ethanol in a ratio of silane precursor:ethanol = 2:1 and the use of hydrochloric acid as a catalyst have been found advantageous for the synthesis of stable sols. In the case of GLYMO and MEMO very stable sols were obtained exhibiting only a slight increase of viscosity and a low increase of molecular weight after 3-4 weeks of storage at 25 °C. The PTMO and the TEOS sols gelled after 12 days and 17 days respectively. Storage under freezing conditions increases the stability significantly. (Figure 9)

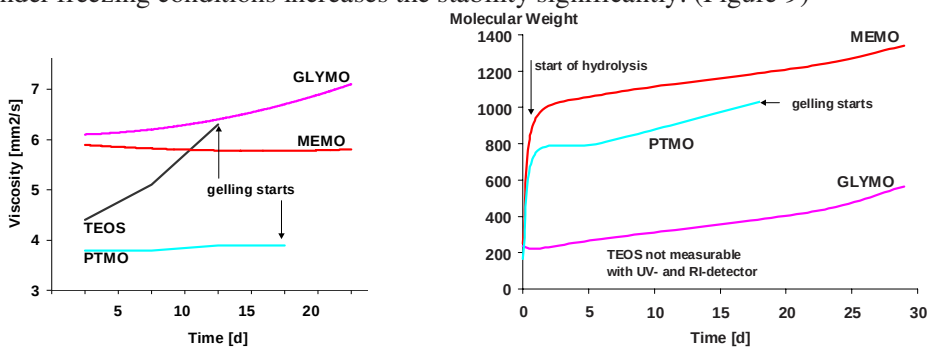

Figure 9: Stability of precursor sols at 25 °C (left); Molecular weights given relative to polystyrene standards (right)

Combinations of Bayresit as inorganic cross-linker with the coating forming and plasma active silanes MEMO, GLYMO and PTMO resulted in stable sols after hydrolysis (sol-gel processing). In general a lower amount of water had to be used for the hydrolysis reaction in order to obtain stable sols. In case of

stoichiometric amount of water gelling occurred very rapidly. This effect indicates clearly the high degree of cross-linking which is achieved after sol-gel processing.

To obtain suitable samples for the different analytical techniques, various substrates are placed between the electrodes such as glass slides, pieces of single and double polished silicon wafers, pieces of plastic foil (PET) and polished stainless steel platelets.
The deposits were characterized by various surface analysis techniques. The coating thickness was determined by a UBM-Microfocus profilometer. Cross-sections of the plasma polymer coatings were studied by field emission scanning electron microscopy (FESEM, JSM-6340F, Jeol). Oxygen transmission rates (OTR) were measured according to DIN 53380 at 23 °C and 50 % relative humidity. A Nicolet Nexus FT-IR spectrometer equipped with a Spectra Tech ATR module (Thermo, USA) was used for the deduction of functional groups present in the coating.

References

1 C.A. Harper, E. M. Petrie, *Plastics Materials and Processes: A Concise Encyclopedia*, Wiley-VCH, Verlag Berlin **2003**.
2 Y. Leterrier, *Progress in Materials Science* **2003**, 48, 1.
3 J. D. Affinito, *Surf. Coat. Tech.* **2000**, 133-134, 528.
4 M. Schaepkens, T. Won Kim, A. Gün Erlat et al., *J. Vac. Sci. Technol. A* **2004**, 22(4), 1716.
5 J.R. Roth, *Industrial Plasma Engineering Volume 2 Applications to Nonthermal Plasma Processing*, IOP Publishing, Philadelphia **2001**.
6 A. Villermet, P. Cocolios, G. Rames-Langlade et al., *Surf. Coat. Tech.* **2003**, 174-175, 899.
7 U. Kogelschatz, G. Eliasson, W. Egli, *Pure Appl. Chem.* **1999**, 71, 1819.
8 R.B. Gadri, J.R. Roth, T.C. Montie et al., *Surf. Coat. Tech.* **2000**, 131, 528.
9 M. Moisan, J. Barbeau, M.-C. Crevier et al., *Pure Appl. Chem.* **2002**, 74, 349.
10 O. Goossens, E. Dekempeneer, D. Vangeneugden et al., *Surf. Coat. Tech.* **1999**, 119, 812.
11 M. Aouinti, P. Bertrand, F. Poncin-Epaillard, *Plasmas Polym.* **2003**, 8, 225.
12 C. Sun, D. Zhang, L.C. Wadsworth, *Adv. Polym. Tech.* **1999**, 18, 171.
13 L.J. Ward, W.C.E. Schofield, J.P.S. Badyal et al., *Chem. Mater.* **2003**, 15, 1466.
14 S. Martin, F. Massines, N. Gherardi et al., *Surf. Coat. Tech.* **2004**, 177-178, 693.
15 C. Klages, M. Eichler, R. Thyen, *New Diamond Front. C Tech.* **2003**, 13, 175.
16 R. Foest, F. Adler, F. Sigegener, M. Schmidt, *Surf. Coat. Tech.* **2003**, 163-164, 323.
17 A. Sonnenfeld, T.M. Tun, L. Zajíčková et al., *Plasmas Polym.* **2001**, 6(4), 237.
18 O. Goossens, S. Paulussen, D. Vangeneugden et al., *New Diamond Front. C Tech.* **2003**, 13(4), 221.
19 K.-H. Haas, S. Amberg-Schwab, K. Rose et al., *Surf. Coat. Tech.* **1999**, 111, 72.
20 K.-H. Haas, S. Amberg-Schwab, K. Rose, *Thin Solid Films* **1999**, 351, 198.

Effect of synthesis conditions on the morphology of ZnO powder produced in RF thermal plasma

Z. Károly, L. Gál, J. Szépvölgyi

Institute of Materials and Environmental Chemistry, Chemical Research Center, HAS
H-1525 Budapest, POB 17, Hungary

Abstract
We have investigated the synthesis of nanophase ZnO particles in inductively coupled RF thermal plasma reactor. Precursor materials were the solutions of zinc-nitrate-hexahydrate that was sprayed into the plasma flame. Particles nucleated from aqueous solutions were usually bigger than those nucleated from ethanol solutions if other conditions were unchanged. We found good correlation between the mean particle size of the product particles and the total gas flow rate in the plasma reactor.

Keywords
Zinc-oxide, nanophase particles, RF plasma

1. Introduction

The electronic and optical properties of ceramic materials are greatly influenced by the size, morphology, purity and chemical composition of the particles they comprised. Nanophase ZnO with different morphologies has potential applications in varistors, gas sensors, catalysts, pigments, ceramics, electrical and optical devices [1]. Besides, ZnO is one of the few oxides that show quantum confinement effects in an experimentally accessible size range [1]. Consequently, synthesis and morphology control of ZnO nanoparticles has received great attention recently. Several routes have been developed for the synthesis of ZnO powder such as hydrothermal synthesis [2], precipitation [3], sol-gel technique [4], spray pyrolysis [5], thermal decomposition etc. This work is aimed at preparing nano-sized ZnO particles in inductively coupled, RF thermal plasma reactor.
Intrinsic features of RF thermal plasmas provide favorable conditions for the synthesis of nanophase particles. The extremely high temperature prevailing in the center of the plasma is capable of evaporating most of the precursor materials. Rapid cooling of vapors taking place in the tail flame results in very fine particles as a result of high supersaturation. By-products, if there is any, are usually removed as gas. One of the main advantages of thermal plasmas that chemically less complicated, low cost materials could do as precursors.
Precursor materials injected into the hot region of the plasma are vaporized, the vapors are quenched rapidly outside the plasma flame, and nano-sized particles are formed due to high supersaturation. In contrast to model calculations, our experiences revealed that solid powders fed into the plasma do not evaporate totally. This results from the fact that even feeding is difficult to realize, and precursor particles are either oversized (having mean particle size of several ten microns) or heavily agglomerated with high porosity. For the aforementioned reasons, in this work precursors of ZnO synthesis have been sprayed into the plasma as solutions. We have investigated the mechanism of particle formation and the effect of the synthesis conditions on the morphology of formed particles.

2. Experimental

The experimental apparatus consisted of an RF generator attached to a four-turn RF inductively coupled plasma torch (TEKNA PL35), a reactor chamber, a cyclone and a filter. Scheme of the experimental setup was presented in other papers [6]. Air and argon were used as sheath and plasma gas, respectively. Gas flow rates and plate power were varied in the different tests. Precursors were aqueous and ethanol solution of $Zn(NO_3)_2 \cdot 6H_2O$ of various concentration.. A peristaltic pump was used to deliver the liquid feedstock at a constant a rate of 8 $ml \cdot min^{-1}$ to the atomizer nozzle, where it was dispersed by 3 $l \cdot min^{-1}$ of argon gas into fine droplets. The obtained powder was collected from the reactor wall and from the cyclone, respectively. Crystal phases of the product

were determined by XRD. Mean crystallite size was calculated from the peak broadening of particular XDR peaks. SEM and TEM apparatus was used to reveal the particle morphology of the as-prepared powders.

3. Results and discussion

Operating conditions and main characteristics of product powders are summarized in Table 1. Product particles show great differences in terms of morphology, size and crystalline nature, as well. Comparison of typical XRD patterns of the products made from aqueous and ethanol solutions, respectively, are shown in Fig.1.

Table 1 Operating conditions and results of nanosized ZnO production

Test	Precursor		Flow rates	Plate power	Size	Fraction of
	solution	Molarity	$l \cdot min^{-1}$	kW	nm	ZnO, %
1	aqueous	2,0	60	19	165	95
2	aqueous	1,5	71	21	-	68
3	aqueous	2,0	70	20	141	26
4	aqueous	1,0	73	23	123	100
5	ethanol	1,0	90	15	123	100
6	ethanol	1,1	91	15	123	100
7	ethanol	1,1	120	15	52	100
8	ethanol	1,3	73	23	247	100
9	ethanol	1,0	76	23	197	100
10	ethanol	1,6	65	16	329	100
11	ethanol	1,0	65	16	329	100

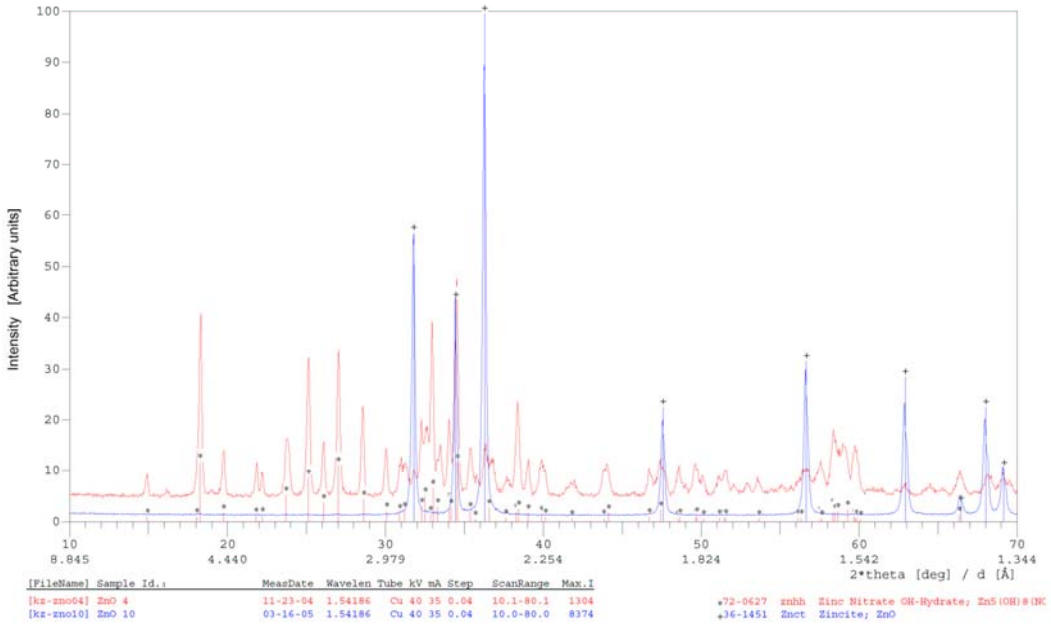

Fig. 1 XRD patterns of products

When starting from ethanol solution feedstock, product material invariably consisted of well-crystallized ZnO phases (blue line in Fig. 1). Peaks refer to a hexagonal wurtzite structure with lattice constants of a=0.325 nm and c= 0.521 nm. In contrast, using aqueous solution precursors, the abundance of peaks besides the characteristic peaks of ZnO crystals (red line in Fig. 1) indicates the presence of other nitrate hydroxide hydrate phases. Although, complete decomposition of zinc nitrate hexahydrate finishes up to 350°C, several factors such as low residence time, dense loading that retard the thermodynamic equilibrium to be attained, result in a partial decomposition only. It is confirmed by the correlation established between the proportion of the hydroxide phases remained after treatment in the product and the applied specific power (Fig. 2). It appears from the correlation that higher specific power is required in order to obtain pure ZnO powders. In this point of view particular route entails much higher power consumption due to the rather high proportion of water to be evaporated.

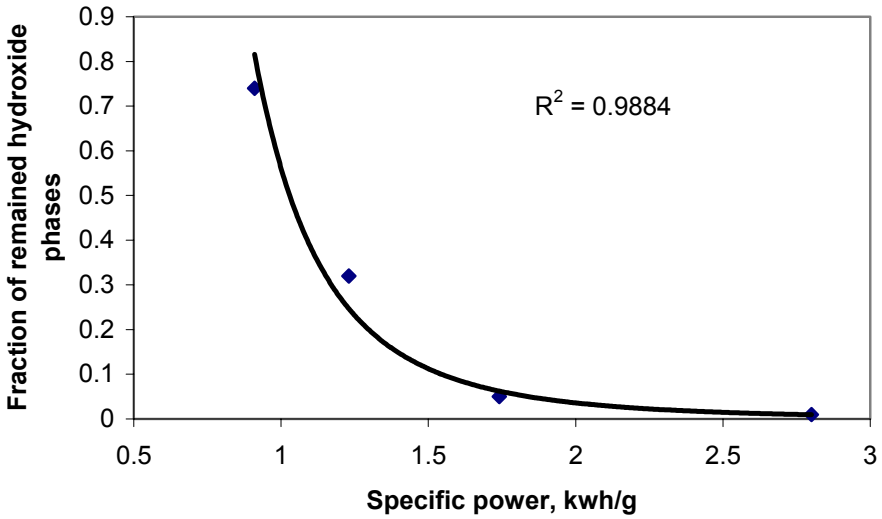

Fig. 2 Effect of the specific power on transformation of precursors

In terms of mean particle size, particles produced from ethanol solution were generally smaller in comparison with aqueous solution counterparts. The mean size was affected in the greatest extent by the total gas flow rates of plasma gases. Quite a good correlation could be established between them despite the fact that size determination from XRD peak broadening inherently entails about 10% uncertainty above calculated values of 100 nm. According to the correlation (Fig. 3), mean particle size can be decreased by increasing gas flow rates. Increased flow rate has twofold effects: it reduces the residence time of the nucleated particles in the hot region and also reduces the volume concentration of Zn-containing species in the vapor. Gas flow rate is, however, limited by the suction capacity of the vacuum pump. Effects of other process parameters on the mean size were negligible.

Morphology of product particles exhibit great diversity; dots, rods, tetrapods and spheres could also be observed among them. Even the particular test resulted in particles of various morphologies simultaneously, however, their ratio varied in each test. Different morphologies suggest different crystallization mechanisms.

According to the general procedure for synthesis of nanophase materials by plasma treatment, the nanophase particles nucleate from the vapor phase by homogeneous condensation as a result of high super-saturation due to rapid cooling. Depending on the residence time a nucleated particle spend in the hot zone, particles may grow further by condensation or coagulation. The simultaneous presence of dots, nanorods (Fig. 4a) or particles of other shapes is presumably the consequence of the different thermal history of the species. In some tests, most of the powders are made up tetrapod-shaped ZnO crystals of different size (Fig. 4b). The arms of these tetrapods are single crystal hexagonal ZnO with a [0001] growth direction. It is under debate whether the nuclei of

tetrapod ZnO structure are metallic zinc [7] or zinc-suboxides (ZnO_x) [8] The lack of atomic zinc lines in the range of 200-600 nm on the optical spectrographs confirms the latter mechanism. Nevertheless, it seems to be evident that tetrapods can be developed in an atmosphere being locally deficient in oxygen.

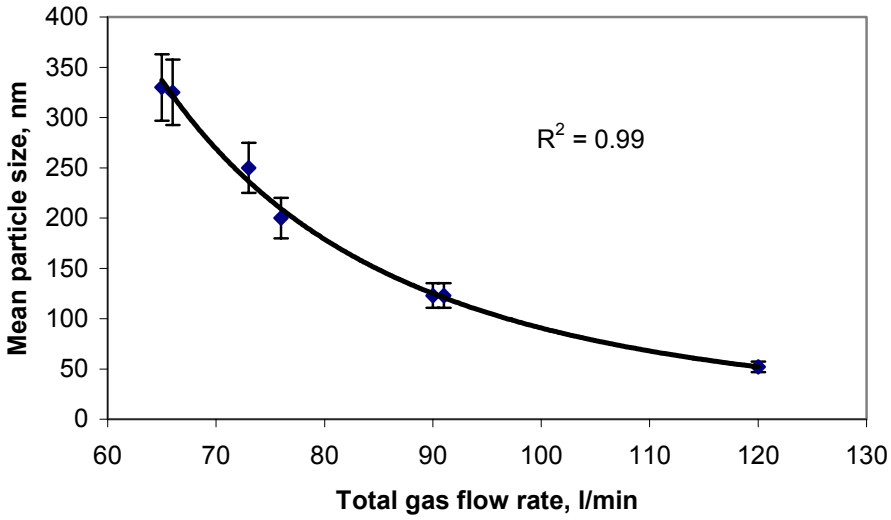

Fig. 3 Effect of gas flow rate on the mean particle size

Nucleation in aqueous solution tests did not follow the above mechanism, but rather resembles flame spray processes. The solvent, water molecules evaporate from the fine droplets, while nucleation takes place within the supersaturated droplets. As a result, relatively large, submicron or micron sized, tabular or spherical grains are formed that consisted of primary particles of 100-200 nm size (Fig. 5). Using sufficiently high power, this particle-to-particle conversion mechanism could be altered and nano-sized or tetrapod particles can also be prepared.

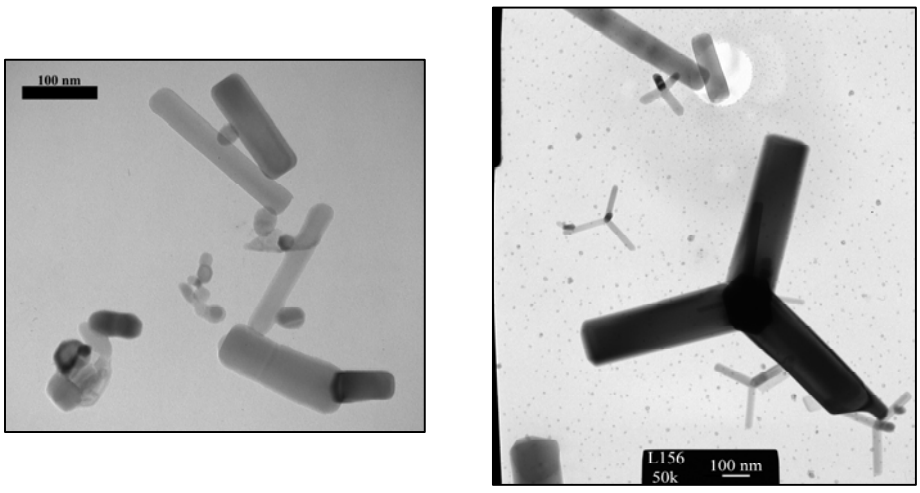

a b

Fig. 4 TEM images of nanophase ZnO particles

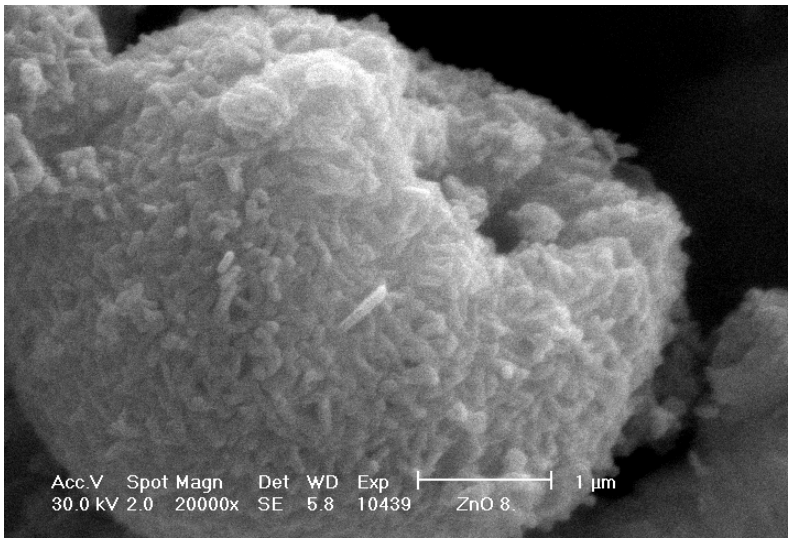

Fig. 5 SEM image of a ZnO grain synthesized from aqueous solution

4. Conclusions

We have investigated the preparation of nanophase ZnO particles in RF thermal plasma reactor from different precursors. We found that the flow rate of the working gases has the greatest effect on mean particle size that was generally higher starting from aqueous solution. Particles differed in size and morphology even in the same test. It can ultimately be attributed to the strongly different trajectories and thermal histories of nucleated particles.

Acknowledgement

The authors acknowledge the financial support of the Hungarian Scientific Research Fund (OTKA) under grant No. T047360.

References

[1] J. Wang, L. Gao - Inorganic Chemistry Comunications 6 877 (2003).
[2] C.H. Lu, C. H. Yeh - Ceramics International 26 351 (2000).
[3] T. Trindade, J.D. Pedrosa, P. O'Brian - J. Eur. Ceram. Soc. 11 275 (1993).
[4] M. Bender et al. - Thin Solid Films 418 45 (2002).
[5] I. Stambolova et al. - Mater. Chem. Phys. 63 104 (2000)
[6] L. Gál, I. Mohai, Z. Károly, J. Szépvölgyi, J. Gubicza – ISPC 17 (2005)
[7] R. Wu, J. Wu, C. Xie, J. Zhang, A. Wang – Mater. Sci. & Eng. A 328 (2002)
[8] F.Z. Wang, Z.Z. Ye, D.W. Ma, L.P. Zhu, F. Zhuge – Materials Letters 59 (2005)

How Can the Carbon Black Yield From Freons Be Raised in Thermal Plasma Decomposition?

K.A. Főglein, J. Szépvölgyi

Institute of Materials and Environmental Chemistry, Chemical Research Center, Hungarian Academy of Sciences
H-1525 Budapest, POB 117, Hungary

Abstract
Freon decomposition in RF thermal plasma conditions was investigated in this work. The main reaction product was solid soot. Correlations were established among conditions of processing and soot yield.

Introduction
Carbon nanomaterials exhibit a rich polymorphism including nanosized particles, single- and multi-wall carbon nanotubes (CNTs), fullerenes [1], necklaces, graphitic onions, toroids, boxes etc. Each discovery of a new morphology in carbon materials opens to new field of application. It is expected that these structures have potential impact in applicative domains such as molecular electronics or high strength composite materials.
Carbon materials are mainly produced by conventional techniques such as arc discharge, laser ablation, chemical vapor deposition (CVD), AC-plasma, MW-plasma or RF plasma technologies. Structure and amount of synthesized carbon nanostructures strongly depend on the applied technique.
In this work decomposition of freons was studied in RF thermal plasma, in a systematic way. Our goal was to establish the effect of reaction conditions leading to maximum yield of carbon black as main product of decomposition.

Experimental
The RF induction plasma torch used in this work had a standard design with a quartz glass confinement tube of 27 mm I.D. The plasma reactor was connected to air-cooled quenching and powder collection sections. The plasma power was provided by a 3-turn induction coil from an RF generator operating at an oscillator frequency of 27.17 MHz.
High-purity argon was used as plasma (8 $l \cdot min^{-1}$ (STP)) and sheath (21 $l \cdot min^{-1}$ (STP)) gases, and also as the carrier gas of reactants. Oxygen or hydrogen gases, if any, were added to the carrier gas with a flow rate of 0.6 $l \cdot min^{-1}$ (STP).
Analytical grade model compounds, such as CCl_4, $CHCl_3$, CH_2Cl_2 and $CFCl_3$ were injected in a swirl direction through a transverse slot into the plasma tail flame region. The solid main product was mainly condensed on the wall of the reactor, and also in the collector and the filter. The soot was extracted by toluene using the Soxhlet method to separate its carbon black content.

Experimental design
The experiments were designed by computer code STATISTICA. Four factors at three levels each were considered in the experimental planning (Table 1).

Table 1. The factors and their levels

Factors		***Levels***		
		1	***2***	***3***
Power [kW]		1.6	2.1	2.6
Plasma gases		Ar	Ar + O_2	Ar + H_2
Model compounds	*F-Cl-H*	C-F-Cl_3	C-Cl-Cl_3	C-H-Cl_3
	0, 1, 2 H	C- Cl_2-Cl_2	C-HCl-Cl_2	C-H_2-Cl_2
Sampling place		Reactor	Collector	Filter

Results and Discussions

To find relationship between parameters of processing and carbon black yield, the plasma conditions should be characterized in a complex way. For this reason we defined the specific energy of processing (E_{SP}, $kWh \cdot g^{-1}$) as follows:

$$E_{SP} = \frac{P}{G} \tag{1}$$

where P is the plate power (kW) and G is the feed rate of precursor ($g \cdot h^{-1}$).

The soot contained adsorbed organic compounds on its surface, which were removed by toluene extraction. The carbon black yield from decomposition ($Y_{C(s)}$, %) was calculated by the following equation:

$$Y_{C(s)} = \frac{M \cdot G_{C(s)}}{144 \cdot G} \tag{2}$$

where $G_{C(s)}$ is the formation rate of extracted carbon black ($g \cdot h^{-1}$), G is the feed rate of precursor ($g \cdot h^{-1}$) and M is the molas mass of precursor (g/mol).

Dependence of $Y_{C(s)}$ on the composition of precursor

Previous investigations [2] revealed that in neutral conditions the carbon black yield ($Y_{C(s)}$) changes as a function of specific energy along a Gaussian curves. The carbon black yield is plotted against the specific energy in Fig 1. In experiments presented in this work not the total energy range that could be considered in particular system was studied only some characteristic sections have been investigated in order to determine the E_{SP}, where the E_{SP}-$Y_{C(s)}$ function reaches its maximum..

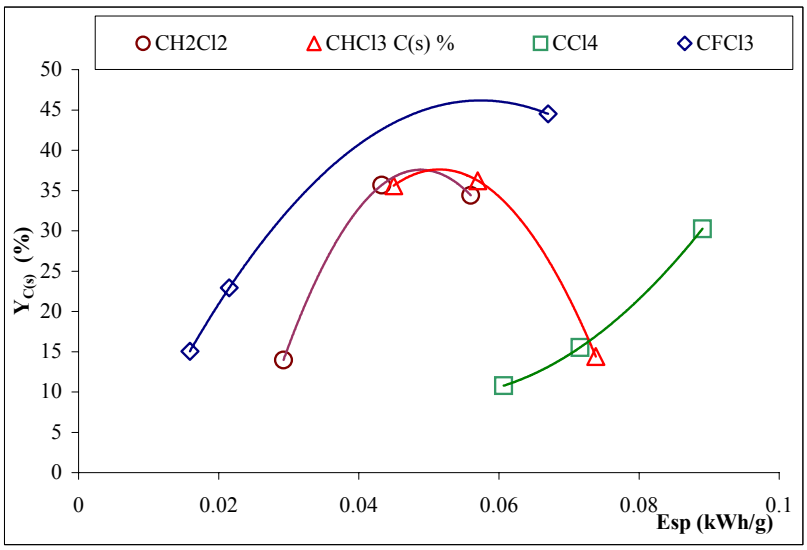

Figure 1. Carbon black yield as a function of specific energy of processing

Run of the E_{SP}-$Y_{C(s)}$ curves in Fig. 1 is explained as follows:

- At low E_{SP} values the plate power is not enough for the complete decomposition to atoms and remains radicals in the system. Carbon black yield rises with increasing E_{SP}, caused by the higher effectiveness of precursor decomposition.
- At high E_{SP} values complete decomposition is possible, caused by the higher temperature of plasma flame. The products make a stay in the hot zone for a longer period. This fact facilitates the formation of

high order hydrocarbons on the soot surface, accompanying by the drop of C(s) concentration in the system.

- The maximum E_{SP} values occur where the first mechanism turns into the second one.

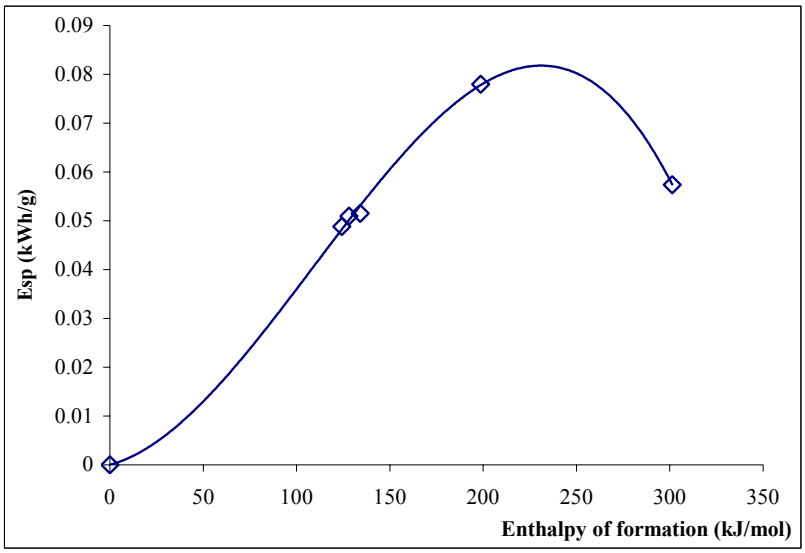

Figure 2. Specific energies belonging to maximum carbon black yield as plotted against formation enthalpy of precursors

Specific energy values belonging to maximum carbon black yield depends on the formation enthalpy of precursors (Fig. 2). After having determined this curve for a given plasma system, it can be used to predict for other precursors the probable E_{SP} where $Y_{C(s)}$ reaches its maximum.

Dependence of $Y_{C(s)}$ on sampling spot in the $CFCl_3$ case

Carbon black yield of $CFCl_3$ was the highest among precursors studied in this work. Thus, it was investigated in more detailed later on. We observed that for $CFCl_3$ the maximum yield of carbon black depended on the spot of sampling, as well (Fig. 3).

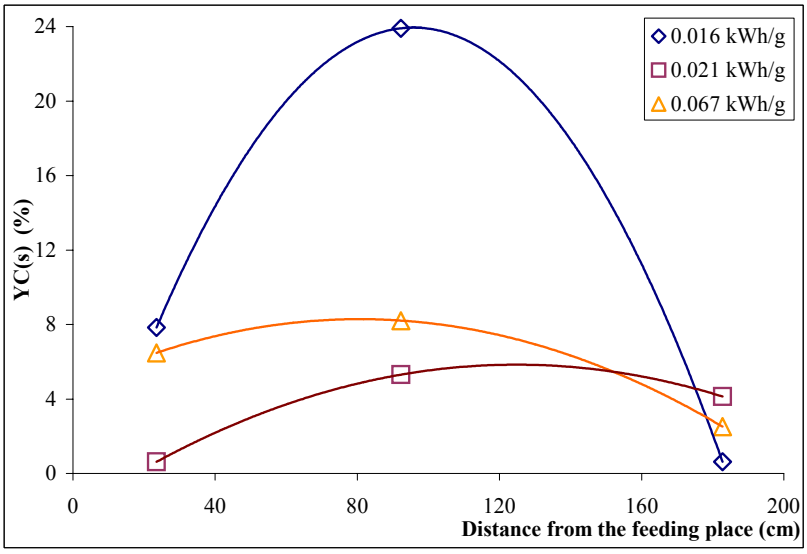

Figure 3. Dependence of $Y_{C(s)}$ on the spot of sampling at different specific energies for $CFCl_3$

Close to the spot of feeding the C(s) concentration was low due to formation of small organic compounds which condensed on the reactor wall. At greater distances from the feeding spot the solid product, in addition to carbon black, contained different organic molecules crystallized on the surface of the carbon black as it had been proved by GC-MS investigations [3].

Dependence of $Y_{C(s)}$ on the quality of carrier gas in the $CFCl_3$ case

The carbon black yield depended on the composition of the gas phase, too. The gas composition was changed by adding hydrogen or oxygen to the carrier gas. Changes of $Y_{C(s)}$ as a function of distance from feeding spot for different gas compositions (pure Ar, 0.5% O_2 + 99.5% Ar, 0.5% H_2 + 99.5% Ar) are plotted in Fig. 4. Run of curves in pure argon and hydrogen-argon mixture is rather similar which refers to similar reaction mechanisms in both cases. In the presence of oxygen, the carbon black yield is very low, and it is actually independent of the spot of sampling.

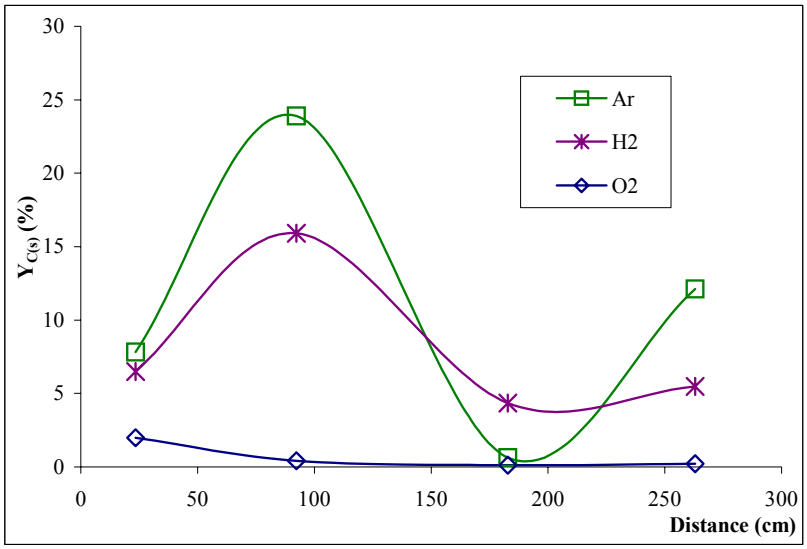

Figure 4. $Y_{C(s)}$ as a function of distance from the feeding spot for $CFCl_3$ in different atmospheres

Evaluation of experimental data by computer code STATISTICA

Experimental results were evaluated by computer code STATISTICA in order to establish the effect of process parameters on $Y_{C(s)}$. Several Greco Latin Squares (GLSs) were drawn and analyzed. Results of calculations are plotted in 3 by 3 GLSs where we distinguished three of four factors only (Fig. 5) or in the 4 by 4 ones, where we applied all factors (Fig. 6). We established that:

- At a given sampling spot, the lowest carbon yield was achieved for CCl_4, while the highest for CH_2Cl_2.
- The carbon yield depended directly on the plate power.
- Both in oxidative and reducing conditions, the carbon black content of the soot decreased as compared to decomposition in argon atmosphere.
- Soot of highest carbon black content was collected from the reactor and from the gas filter, respectively.

Another goal of our work was to test the significance of different factors as above. For this reason the Square Sum (SS) was calculated for all GLSs. Their average is plotted in Fig. 7. The higher the Square Sum, the greater is its effect on carbon black production. The results can be summarized as follows:

- Composition of carrier gas has the greater effect on $Y_{C(s)}$.
- Plate power and composition of precursors actually have similar effect on $Y_{C(s)}$.
- Spot of sampling actually does not influence the carbon black yield.

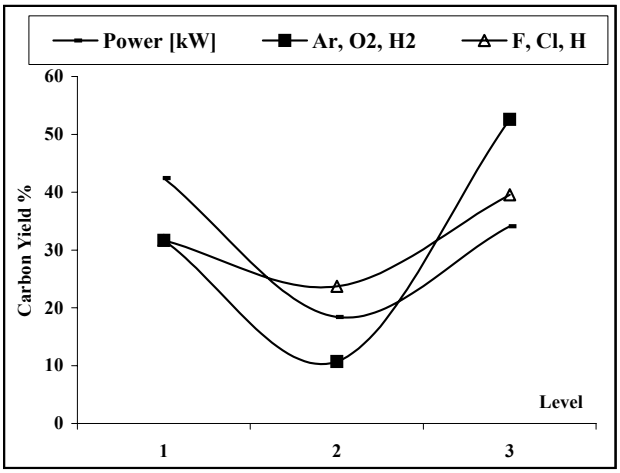

Figure 5. F-Cl-H systems - Sampling from the same place

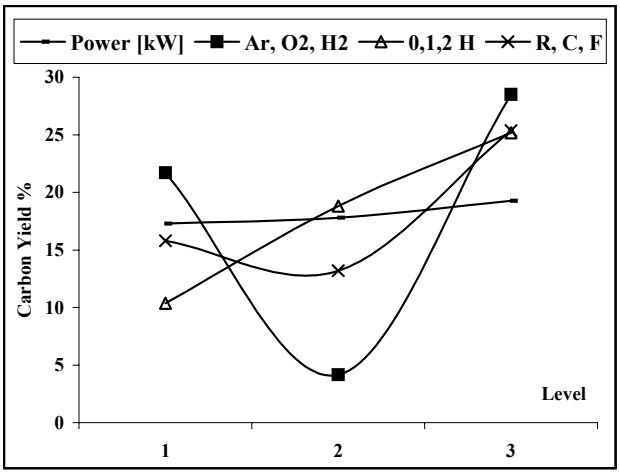

Figure 6. All four factors for the 0, 1, 2 H systems

Conclusions

The carbon black yield from decomposition of different freons can be increased by changing the conditions of thermal plasma processing as follows:

- **Plasma gas**: using pure Ar plasma instead of Ar-H_2 or Ar-O_2 ones;
  - H_2 decreases the carbon black content of the soot, because hydrogen facilitates formation of hydrocarbons.
  - O_2 depresses the soot yield, but it increases the carbon black content of the soot.
- **Specific energy:** the task is to determine the maximum of E_{SP}-$Y_{C(s)}$ function for each model compound.
- **Flow rate of carrier gas:** the lower, the better, because the degree of decomposition depends on the feed rate of precursors.
- **Distance of sampling spot from the feeding point**: for each model the maximum of E_{SP}-sampling distance correlation should be determined by experiments

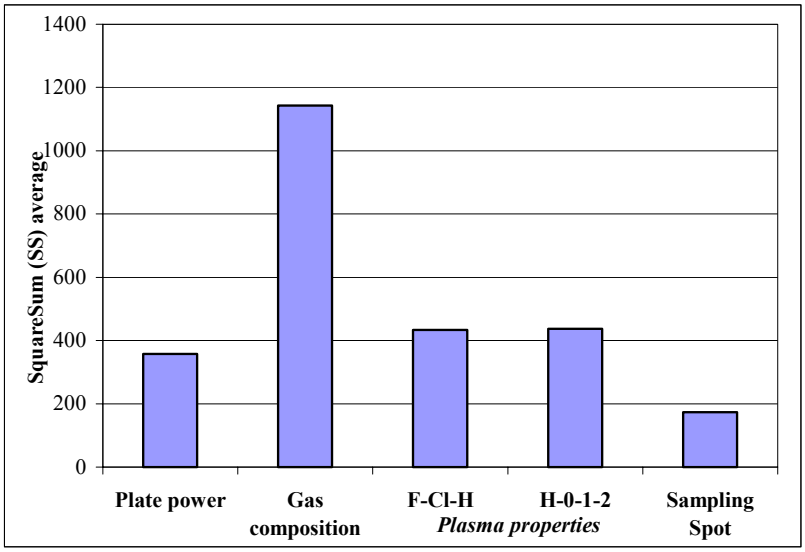

Figure 9. The effect of different factors on the carbon production

Acknowledgement

This work has been supported by Hungarian Scientific Research Fund (Project No. T047360).

References

[1] B. Todorovic-Markovic, Z. Markovic, I. Mohai, Z. Károly, L. Gál, K. Főglein**,** P.T. Szabó, J. Szépvölgyi - Chem. Phys. Lett. 378, 3 (2003).

[2] J. Szépvölgyi, M.T. Beck, S. Kéki, I. Mohai – Proc. ISPC-12, Minnesota, Vol. VIII. pp. 1165 (1995).

PRODUCTS OF CCl_2XY DECOMPOSITION IN THERMAL PLASMA

K.A. Főglein, P.T. Szabó, J. Szépvölgyi

Institute of Materials and Environmental Chemistry, Chemical Research Center, Hungarian Academy of Sciences
H-1525 Budapest, POB 17, Hungary

Abstract
Decomposition of different CFCs (of CCl_2XY stoichiometry) has been studied in RF thermal plasma reactor in order to find correlations among conditions of processing, degree of decomposition and composition of products. Mechanism of decomposition depended on the composition of model compounds. In addition to gaseous products, solid soot and different halogenated hydrocarbons were identified as main products of decomposition.

Keywords: Freons, RF thermal plasma, decomposition

Introduction

Conversion of freons into more useful species is a great challenge even nowadays. Solid, liquid and gaseous products can form during their decomposition. In addition to decomposition of freons and thus, to decrease their harmful environmental impacts, much attention is being paid to transform particular materials to useful products such as carbon spheres and carbon nanostructures. These products have great potential of application p as emitters for field emission arrays, nano-composite fillers, manifold energy storage devices and secondary battery electrodes [1,2]. Equally great theoretical and practical importance was given to the production of C_2 hydrocarbons, synthesis gas and methanol as useful chemicals [3]. Formation of harmful gaseous products could be avoided by setting the plasma conditions properly. To initiate conversion of freons, the strong C-F and C-Cl bonds should be broken and halogens should be taken off the system. It can be realized by different methods, including pyrolysis, direct oxidation, catalytic reactions and decomposition in electrical discharges or thermal plasmas. This work is aimed at revealing the differences in product distribution during the decomposition of model compounds of various compositions in thermal plasma conditions.

Experimental

The RF induction plasma torch has a standard design with a quartz glass plasma confinement tube of 27 mm I.D. The plasma reactor was connected to air-cooled quenching and powder collection sections. The plasma power was provided by a 3-turn induction coil from an RF generator operating at an oscillator frequency of 27.17 MHz. High-purity argon was used as plasma (8 $l \cdot min^{-1}$ (STP)), sheath (21 $l \cdot min^{-1}$ (STP)) gases and also as the carrier gas of the reactants. Oxygen, if any, was added to the carrier gas with a flow rate of 0.6 $l \cdot min^{-1}$ (STP).
Analytical grade model compounds, such as CCl_4, $CHCl_3$ and $CFCl_3$, were injected in a swirl direction through a transverse slot into the plasma tail flame region. After having reached the steady-state operation samples were taken from the exhaust gas. These samples were immediately analyzed by GC-MS. The solid soot was mainly condensed on the reactor wall. The soot was extracted by toluene using the Soxhlet method and the extracts were subjected to GC-MS analysis.
The GC-MS measurements were carried out on a VG-ZAB2-SEQ mass spectrometer connected to a HP 5890 gas chromatograph. A 50m long HP-5MS fused silica capillary column was used for separation. Helium was applied as carrier gas with a flow rate of 2 ml min^{-1}. The temperature was programmed as follows: 80°C for 4 min then increased by 5°C min^{-1} up to 250°C and kept there for 10 min. The mass range of mass spectrometer was 30-800 m/z.
In order to identify the gaseous decomposition products, a 100 µl sample was collected from the exhaust gas by a gas-tight Hamilton syringe. The sample was subjected to GC-MS analysis. Another 100 ml sample was collected by an IR gas-cell for FT-IR monitoring. FT-IR measurements were carried out on a PE FT-IR spectrometer equipped by a DTGS detector.
The processing conditions where characterized by the specific energy defined as follows:

$$E_{sp} = P/G \quad (1)$$

where E_{SP} is the specific energy of processing ($kWh \cdot g^{-1}$), P is the plate power (kW) and G is the feed rate of precursors ($g \cdot h^{-1}$). The unreacted fraction of model compounds during plasma treatment was calculated from the results of FT-IR analysis by the following equation:

$$UF = 100 \cdot (1-F_{in}/F_{out}) \quad (2)$$

where UF % is the unreacted fraction, F_{in} is the amount of model compound in the feed material (mol) and F_{out} in the exhaust gas.

Results and Discussions

Decomposition of model compounds in Ar plasma

It was found that decomposition of different models started and completed at different specific energies. $CFCl_3$ decomposed more easily as compared to CCl_4 and $CHCl_3$ (Fig. 1). Its decomposition is taking place through formation of different intermediates, such as CCl_4, CF_3Cl, CF_4, and CF_2Cl_2 [4]. The plasma temperature and the mean residence time of intermediates in the hot zone determined the composition and the amount of intermediates. The higher the specific energy, the longer the residence time of models in the plasma flame region. Thus, beyond a minimum value of UF, concentration of $CFCl_3$ slightly increased with increased E_{SP} in the exhaust. It can be explained by the cross-reactions of intermediates leading to the re-formation of CF_3Cl.

$$2\ CF_2Cl_2 \rightarrow CF_3Cl + \mathit{CFCl_3} \quad (3)$$
$$CCl_4 + CF_3Cl \rightarrow CF_2Cl_2 + \mathit{CFCl_3} \quad (4)$$

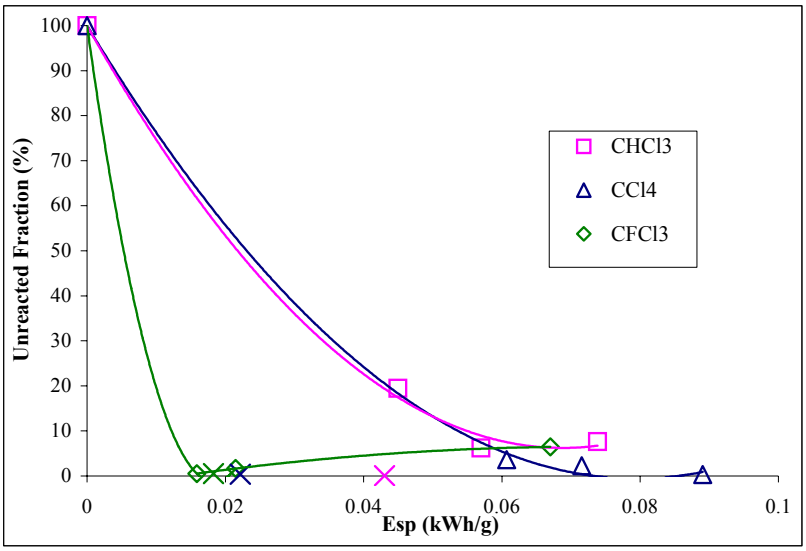

Figure 1. The unreacted fraction of $CHCl_3$ as a function of specific energy

No complex intermediates are formed during decomposition of CCl_4 and $CHCl_3$, respectively [5]. CCl_4 and $CHCl_3$ can be re-formed directly from the primary products of their decomposition. Thus, CCl_4 and $CHCl_3$ could re-form more easily at lower E_{SP} values than $CFCl_3$. However, at higher specific energies this difference disappears.

Formation of soot in CCl_4 decomposition in Ar plasma

In all cases, oot was formed as main solid product of decomposition. It consisted of carbon black, and on its surface it contained halogenated organic compounds which were extracted by toluene. The solid residue of the extraction was carbon black. The soot and carbon black yields in the CCl_4 case are plotted in Fig. 2. The soot yield was defined as the rate of soot mass related to the mass of precursor. The carbon black yield was calculated as the ratio of the carbon black mass related to the mass of carbon in CCl_4 to be treated. Fig. 2 reveals that both soot and carbon black increase with specific energy It is explained by the higher gas temperature and the longer residence time of intermediates in the hot zone leading to more soot formation and also to the formation of more complex organic molecules adsorbed on the surface of soot particles.

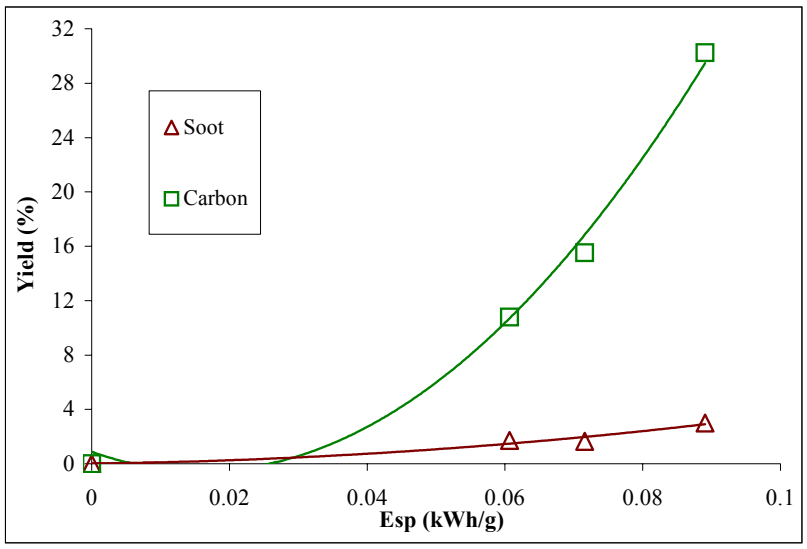

Figure 2. Soot yield and carbon yield as a function of plasma energy

The effect of the carrier gas flow rate in $CHCl_3$ decomposition

It was found that decomposition of $CHCl_3$ depended on the flow rate of carrier gas and hence, on the feed rate of $CHCl_3$ (Fig. 3). At lower flow rates, concentration of precursor was lower, while its mean residence time was longer in the hot plasma zone. It resulted in a more complete decomposition i.e. less unreacted $CHCl_3$. Increase of the flow rate led to higher precursor concentration and shorter residence time in the hot zone. Thus, the unreacted part of $CHCl_3$ increased with the flow rate of carrier gas.

Effect of the plasma gas composition on the $CFCl_3$ decomposition

In addition the pure argon plasma, decomposition of model compounds was investigated in argon-oxygen plasma, as well. In order to compare efficiency of decomposition in the presence and in absence of oxygen, respectively, the experimental data were extrapolated to unreacted fraction of 10%. Specific energies relating to particular decomposition were plotted against specific energy in Fig. 4. Decomposition of CCl_4 and $CHCl_3$ was more effective in oxygen. However, decomposition of $CFCl_3$ was actually not affected by changing the composition of plasma gas in given limits.

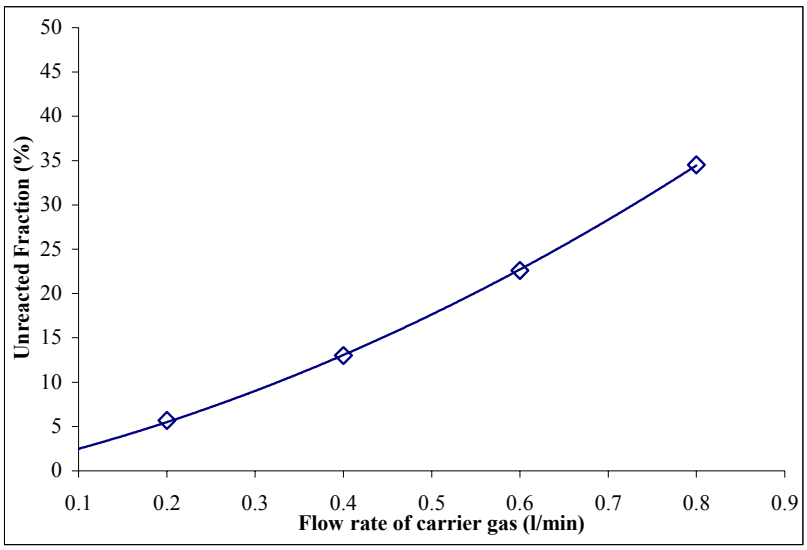

Figure 3. Decomposition rate as a function of carrier gas flow rate

Analysis of the extract from the soot and the exhaust of processing

Results of the GC-MS analyses of extracted fractions and that of FT-IR analyses of exhaust of processing are summarized in Table 1. It can be established that:

- Per-chlorinated products are very stable and they formed even in the presence of hydrogen.
- Chlorine is removed from the system in the presence of oxygen only.
- Replacement of one chlorine atom with one hydrogen atom led to formation of chloro-hydrogenated benzene derivatives, in addition to per-chlorinated benzene.
- Replacement of two chlorine atoms with hydrogen atoms resulted in formation of per-chlorinated and per-hydrogenated products, as well as HCl.
- Increase of hydrogen atoms in the model compounds decreased the number of products.
- Dimethyl-benzene was a very stable product that could form even from the hydrogen contamination of plasma gas.
- Replacement of one chlorine atom with fluorine atom led to formation of fluoro-chloro-benzene derivatives.
- Presence of oxygen in the plasma gases depressed soot formation; however, it increased the carbon black content of the soot.
- Addition of hydrogen to the plasma gas resulted in more soot formation.

Conclusions

On the basis of experiments as above, the following conclusions can be drawn:

- The model compounds decomposed with different rates according to different reaction mechanisms.
- The main product of decomposition was; its carbon black content increased with specific energy of processing.
- Poly-halogenated hydrocarbons were formed in different compositions and different amounts from different freons.

Table 1. Compounds determined in the extract and the exhaust, respectively

Model compound	**$CHCl_3$**				**CCl_4**				**$CFCl_3$**					
Products	**Gas**		**Extract**		**Gas**		**Extract**		**Gas**			**Extract**		
	Ar	**O_2**	**Ar**	**O_2**	**Ar**	**O_2**	**Ar**	**O_2**	**Ar**	**O_2**	**H_2**	**Ar**	**O_2**	**H_2**
HCl														
Cl_2		+				+				+				
CCl_4					+	+			+	+				
Ethene, -fluoro, -trichloro									+	+	+			
1,2,2,trichloro-ethene	+	+	+	+	+	+			+	+	+			
Benzene-dimethyl												+	+	+
Benzene, -methyl, -chloro			+	+										
Benzene, -difluoro, -tetrachloro									+	+	+	+	+	+
Benzene, 1,3 dichloro, 2-fluoro									+					
Benzene, -fluoro, -pentachloro									+	+	+	+	+	+
Benzene, hexachloro	+	+	+	+	+	+	+	+			+	+		
1,3 Cyclopentadiene, 1,2,3,4-tetrachloro-5-(dichloromethylene)			+	+			+	+				+	+	+
Cyclobutane, -dichloro, 3,4-bis dichloromethyl-ene			+	+			+	+						
Styrene, -octachloro			+	+			+	+						
Naphtalene, -octachloro			+	+										
Butadiene, -hexachloro	+	+	+	+	+	+	+	+	+	+	+			
Benzofurane, -4,5,7-trichloro, 2 methyl									+	+	+			

References

[1] J. Hahn, J.H. Han, J.E. Yoo, H. Y. Jung, J.S. Suh - Carbon 42 877 (2004).
[2] R. Hatakeyama, T. Hirata, H. Ishida, T. Hayashi, N.Sato - Thin Solid Films 316 51 (1998).
[3] A.M. Diamy, R. Hrach, V. Hrachova, J.C. Legrand - Vacuum 61 403 (2001).
[4] K.A. Főglein, J. Szépvölgyi, P.T. Szabó, E. Mészáros, E. Pekker-Jakab, I.Z. Babievskaya, I. Mohai, Z. Károly - Plasma Chem. Plasma Proc. 25 3 (2005).
[5] K.A. Főglein, P.T. Szabó, I.Z. Babievskaya, J. Szépvölgyi - Plasma Chem. Plasma Proc. 25 3 (2005).

Influence of the Characteristics of Precursors on Fullerene Formation in RF Thermal Plasma Reactor

Z. Marković[1], B. Todorović-Marković[1], Z. Nikolić[4], I. Mohai[2], Z. Farkas[3], Z. Károly[2], J. Szépvölgyi[2]

[1] *"Vinča" Institute of Nuclear Sciences, POB 522, 11001 Belgrade, Serbia and Montenegro*

[2] *Institute of Materials and Environmental Chemistry, Chemical Research Center, Hungarian Academy of Sciences, H-1525 Budapest, POB 17, Hungary*

[3] *Department of Silicate Chemistry and Materials Engineering, Veszprém University H-8200 Veszprém, Egyetem u. 2, Hungary*

[4] *Faculty of Physics, University of Belgrade, POB 316, 11001 Belgrade, Serbia and Montenegro*

Abstract

Five synthetic graphite powders (4827-Asbury Mills, KS4 and KS6-Timcal, graphite-Aldrich and flake - Alfa) having different mean particle size in the range of 3 to 12 μm were processed in the thermal plasma reactor at atmospheric pressure. In the experiments, effects of feed rate of graphite powder and the helium content of plasma flame on the fullerene yield were studied.

Keywords: RF plasma, fullerenes, graphite

1. Introduction

Since fullerenes may become important building blocks of future technologies such as optoelectronics and photovoltaics, and products such as batteries and fuel cells, development of a technology for large scale production of fullerene at low cost seems to be a topic of outstanding importance [1-3].

Thermal plasma methods for fullerene synthesis have not been investigated in details up to now, in spite of the intensive research on fullerenes, which dates back several years. Many questions are still not answered, especially those regarding the synthesis of higher fullerenes. No feasible technology was developed and implemented for the industrial production fullerenes [2].

A previously developed theoretical model of fullerene formation established that the fullerene yield depended on the following parameters: *(i)* concentration of evaporated carbon in the reactor, *(ii)* mean velocity of the plasma gases in the plasma region and *(iii)* the maximum plasma temperature [4,5]. Inductively coupled, radiofrequency (RF) thermal plasmas offer good possibilities to meet these requirements: more voluminous plasma flames are formed with lower gas velocities compared to arc plasmas. Thus, the mean residence time of reactive species in the hot plasma region is longer in RF thermal plasmas. Powder-like fullerene precursors can be easily introduced into RF plasmas and the feed rate of powders can be changed independently of the RF plasma parameters.

In the present work, five graphite powders from different producers were tested as potential precursors of fullerene synthesis in RF plasma reactor. Our first goal was to establish the optimum particle size for the effective evaporation of graphite particles. It is obvious that the lower is the particle size the evaporation is more effective. However, fine carbon particles are susceptible to agglomeration and agglomerated particles evaporate with lower efficiency than separate ones. The highly efficient evaporation is a key factor in terms of C_2 concentration in the plasma reactor because high value of C_2 concentration facilitates fullerene formation.

2. Experimental procedure

Different graphite powders (4827 from Asbury Mills, KS4 and KS6 from Timcal, flake from Alfa Aesar and graphite from Aldrich) were treated in a thermal plasma reactor at atmospheric pressure. The mean particle size of particular powders varied in the range of 3 to 12 μm. The RF power was produced by a generator operating at 3-5 MHz. A plate power of 30 kW was coupled inductively to a TEKNA PL-35 torch connected to the water-cooled plasma reactor, cyclone and dust filter [5]. Typical gas compositions

of RF plasma are presented in Table 1. The graphite powder was injected axially to the top of the plasma flame with feed rates from 30 to 180 $g \cdot h^{-1}$.

Table 1. Typical gas compositions in the RF plasma reactor.

No.	Sheath		Central	Carrier	Helium
	(Ar, slpm)	(He, slpm)	(He, slpm)	(He, slpm)	(%v/v)
1	50	0	18	3	30%
2	34	22	18	12	60%

Morphology of precursors was characterized by scanning electron microscopy (SEM, Philips XL30 ESEM). The mean crystallite size (L_{002}) was determined from the Fourier (Voight method) analysis of single XRD-line profile. The mean particle size of precursors was measured by laser diffraction technique using Malvern Master Particle Sizer M6.10. The specific surface area of precursors was determined by BET method.

In our experiments, the main product was solid soot collected mainly from the reactor wall. To separate fullerenes, the soot was extracted by toluene at a 100 mg solid/10ml liquid ratio for one minute at 20°C. Amount of fullerenes in the filtered extract (defined as fullerene yield) was measured by UV-VIS spectrophotometer against reference solutions.

3. Results and discussion

Morphological properties of graphite powders used as precursors are presented in Table 2. The highest fullerene yield was obtained with KS4 graphite as precursor (Fig. 1). The other precursors exhibited significantly lower fullerene yields. No direct correlation was found between the mean particle size of precursors (D_{50}) and the fullerene yield. In spite of their similar D_{50} and D_{90} values, processing of Timcal KS4 and Asbury 4827 powders led to quite different fullerene yields. Thermal conductivity of the powders may have a strong effect on the evaporation rate as well.

Table 2. Morphological properties of graphite powders used as precursors.

Precursor	D_{50} (µm)	D_{90} (µm)	S* ($m^2 \cdot g^{-1}$)	$L_{002}{}^{b}$ (Å)	D_{50}/L_{002}
Asbury 4827	3.2	6.3	118	87	370
Timcal KS4	3.7	6.4	26	118	310
Timcal KS6	4.4	7.3	20	109	400
Alfa flake	7.6	14.1	10	144	530
Aldrich powder	11.8	27.5	13	140	840

* Specific surface area

The thermal conductivity of graphite particles cannot be measured in a direct way. For this reason, we defined the ratio of mean particle size and crystallite size (D_{50}/L_{002}), as a parameter characterizing thermal conductivity of precursor. It is reasoned by the fact that particular ratio is proportional to the number of crystallite boundaries, and thus, to the thermal conductivity of graphite powder. The lower this ratio, the higher the thermal conductivity is (Table 2).

Plotting of fullerene yield against D_{50}/L_{002} ratio (Fig. 2) revealed that the highest fullerene yield was obtained in processing of KS4 graphite, which had the lowest D_{50}/L_{002} ratio. The Asbury 4827 graphite is also characterized by a low D_{50}/L_{002} ratio. However, much lower fullerene yield was obtained from this precursor than it could be expected from the D_{50}/L_{002} ratio. It is explained by the extremely high specific surface area of Asbury 4827 graphite (Table 2). The high specific surface area refers to porous microstructure that reduces thermal conductivity.

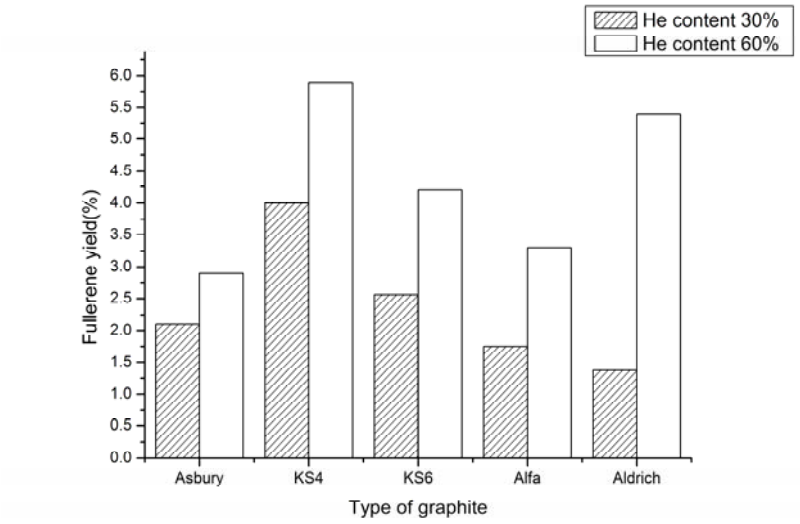

Fig. 1**.** Fullerene yield from different precursors at plate power of 30 kW and different helium content of plasma gas

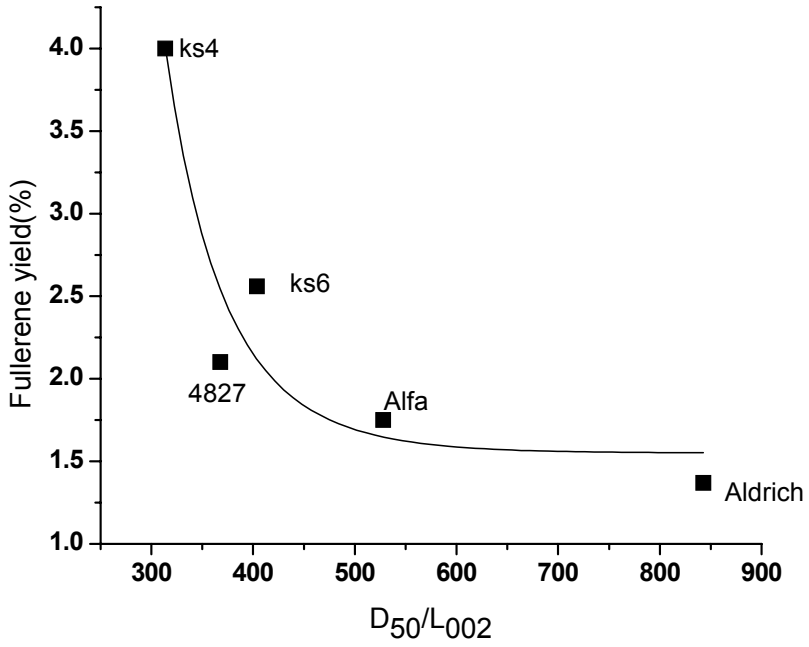

Fig. 2**.** Fullerene yield as plotted against precursor parameter of D_{50}/L_{002} at 30% helium content in the plasma gas

The fullerene yield (i.e. the fullerene content of soot) and the production rate (i.e. mass of fullerene produced in unit time) are plotted against feed rate of KS4 powder in Fig. 3. The fullerene yield decreased, while production rate increased with feed rate. Similar tendencies were observed during processing of other precursors, as well. For KS4 graphite, the highest fullerene yield was 5.9%. Lower fullerene yields and production rates were obtained from other precursors as compared to KS4 graphite.

The fullerene yield was plotted against feed rate of precursors at different gas compositions in Fig. 3. It was observed that increase of the helium concentration from 30% to 60% resulted in 50% increase in fullerene yield. It refers to the importance of heat transfer phenomena in fullerene formation in particular conditions.

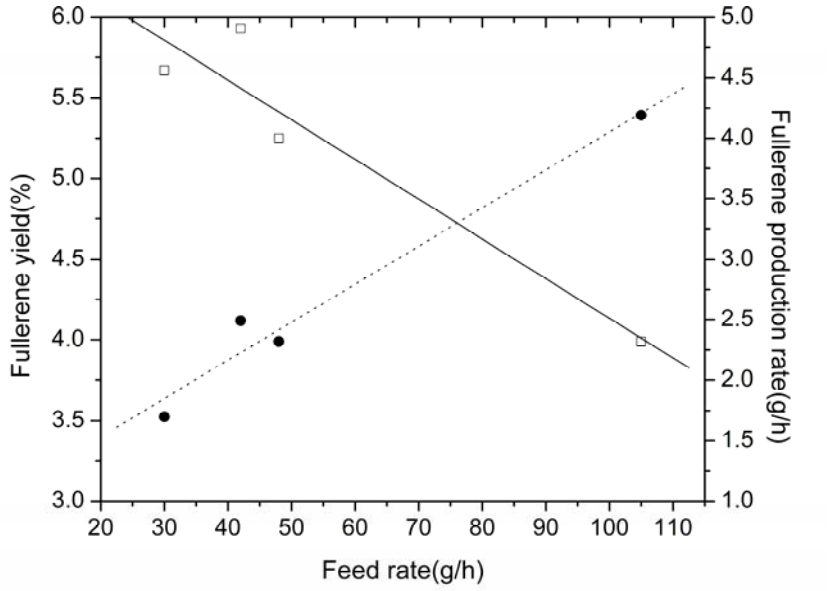

Fig. 2**.** Fullerene yield (full line) and production rate (dashed line) as plotted against feed rate of precursor KS4.

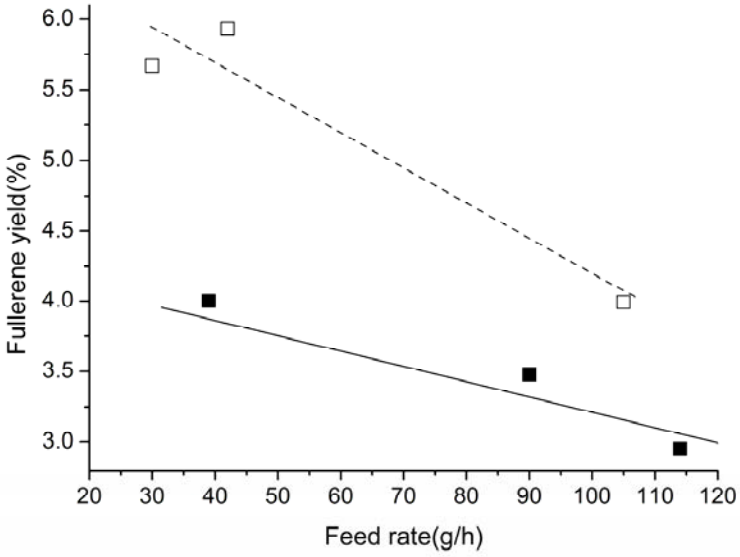

Fig. 3. Fullerene yield as plotted against feed rate of precursor KS4 at different gas compositions (helium concentration of 30% and 60% are represented by full and dashed lines, respectively).

The main factors having effect on the synthesis of fullerenes from graphite powders in RF thermal plasma reactor are as follows: *(i)* the properties of precursors and *(ii)* the plasma parameters. Both factors have significant effect on the concentration of C_2 radicals in the high temperature zone. It is well known that C_2 radicals are the basic blocks of fullerenes.

On the basis of information from the relevant literature and results presented in this work, fullerene formation in RF thermal plasma conditions takes place in the following steps:

- Heating of particles injected into the plasma flame to their sublimation temperature (~4000K). Particles of different size reach this temperature at different sites of the plasma flame, and hence, in different times. The heating time for the smallest (1-5 μm) particles is in the microsecond range. The largest particles (15-20 μm) are heated to 4000K in about 100 μs [6].
- Evaporation of graphite particles at about 4000K. Particles are evaporated roughly in the same period of time as required for their heating.
- Formation of chains, rings, polycyclic structures and defective cages [7].
- Transformation of defective cages to perfect structure upon annealing. A cluster of C_{60} is formed in 2 ns at 3000 K. Transformation into a perfect fullerene structure needs annealing for about 52 ns [8, 9].

The main physical properties of precursor that determine heating and evaporation rate are the mean particle size and the heat conductivity. Our calculations and experiments demonstrated that particle size is an important factor of processing. Particles of characteristic size above 20 μm cannot evaporate in given plasma conditions. On the other hand, a decrease in the particle size did not result in a monotonous increase of fullerene yield. It is well known that the heat conductivity of disordered carbon structures, such as carbon black, can be lower of 2-3 orders of magnitude than that of ordered carbon structures, like graphite. Differences in structural orderliness of precursors may lead to differences in their heat conductivity, as well. Although Asbury graphite has the lowest particle size, its particles can be heated to the sublimation temperature for a relatively long period of time, due to its rather disordered structure and porous nature. The Aldrich graphite and Alfa flake have the most ordered structure and hence, the highest thermal conductivity. However, they contain bigger particles, as well, that hardly evaporate.

In Figs. 4. and 5. SEM micrographs of KS4 and Aldrich graphite powders before and after RF plasma processing are presented. Cumulative volume distribution vs. particle diameter was calculated for all graphite powders by the Diameter Distribution Analyzer software [10]. Extent of evaporation, defined as the volume of particles having diameters lower than 1μm related to the total volume of particles, were found as 13% for KS4 and 3% for Aldrich graphite. These graphite powders resulted in the highest (KS4) and lowest (Aldrich) fullerene yield, respectively, at 30kW plate power and 30 % helium content of the plasma gas (Fig.1).

On the SEM micrographs of products (Figs. 4b. and 5b.), both non-evaporated and evaporated particles can be observed. Condensed carbon formed spherical, nano-sized particles, while the non-evaporated graphite preserved its disk-like shape. Presence of non-evaporated particles in the condensation zone of the plasma reactor results in fast deposition of gaseous carbon species onto surface of particles. To verify the catalytic effect of the solid surface or the impurities of graphite on fullerene formation needs further investigations. Even the detrimental effect of the fast deposition cannot be excluded.

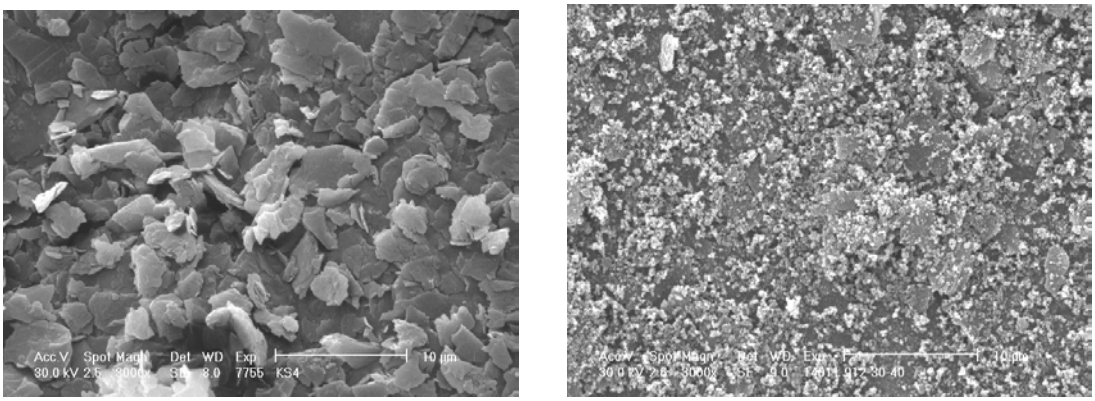

a b

Fig. 4. SEM micrographs of the KS4 graphite precursor (a) and the soot produced there from at 30 kW and 30% of He in the plasma gas (b).

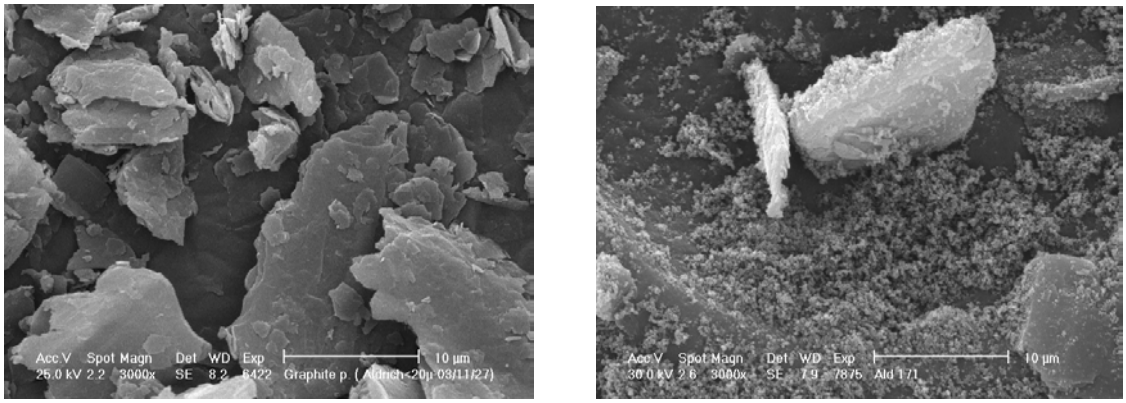

a b

Fig. 5. SEM micrographs of the Aldrich graphite precursor (a) and the soot produced there from at 30 kW and 30% of He in the plasma gas (b).

4. Conclusion

Five graphite powders (4827 from Asbury Mills, KS4 and KS6 from Timcal, flake from Alfa Aesar and graphite from Aldrich) having different mean particle size were processed in an RF thermal plasma reactor at atmospheric pressure. It was found that the mean particle size of precursors has an important, but not exclusive effect on the evaporation efficiency. Micro-structural orderliness of precursors, which determines their thermal conductivity, is another significant property that should be considered in the interpretation of observed phenomena. In this work, KS4 graphite from Timcal proved to be the best precursor of fullerene synthesis.

From plasma parameters affecting fullerene yield, effects of the feed rate of precursors and composition of plasma gas were studied in details. The fullerene yield decreased, while the production rate increased with the feed rate. High helium content of the plasma gas favoured evaporation of graphite particles, and thereby, promoted fullerene formation. It was reasoned by the good thermal conductivity and high ionisation potential of helium.

Acknowledgment

The authors thank the support of the Hungarian Scientific Research Fund (Project No. T047360) and the Ministry of Science and Environmental Protection of Republic of Serbia (Project No. 2018). Special thanks for Asbury Mills and Timcal Co. for supporting their graphite powders.

References

[1] D. Guldi, J. Mater. Chem., **12**, 1978 (2002).

[2] H. Maruyama, S. Tomonoh, J.M. Alford, M.E. Karpuk, Full. Nanotubes & Carb. Nanostr., **12**, 1 (2004).

[3] H. Takehara, M. Fujiwara, M. Arikawa, M.D. Diener and J.M. Alford, Carbon, **43**, 311 (2005).

[4] Z. Marković, B. Todorović-Marković, T. Jokić, P. Pavlović, P. Stefanović, J. Blanuša and T. Nenadović, Full. Sci. & Technol., **6**, 1057 (1998).

[5] B. Todorović-Marković, Z. Marković, I. Mohai, Z. Károly, L. Gál, K. Főglein, P.T. Szabó and J. Szépvölgyi, Chem. Phys. Lett., **378**, 434 (2003).

[6] E. Bourdin, P. Fauchais and M. Boulos, Int. J. Heat Mass Transfer, **26,** 567 (1983).

[7] Yu.E. Lozovik and A.M. Popov, Uspehi fizicheskih nauk, **167**, 751 (2002).

[8] Y. Yamaguchi and S. Maruyama, Chem.Phys. Lett., **286/3-4**, 336 (1998).

[9] S. Maruyama and Y. Yamaguchi, Chem. Phys. Lett., **286/3-4**, 343 (1998).

[10] Z. Nikolić, DDA software, version 2.0, (2003).

3-D Turbulent Modelling of an ICPT with Detailed Gas Injection Section

V. Colombo, E. Ghedini, A. Mentrelli

Department of Mechanical Engineering (D.I.E.M.) and Research Centre of Applied Mathematics (C.I.R.A.M.)
University of Bologna, Via Saragozza 8, 40123 Bologna, Italy
Phone: +39 (0)51 2093978, Fax: +39 (0)51 582528 e-mail: colombo@ciram.unibo.it

Abstract
The aim of this work is to investigate in a realistic manner the behaviour of inductively coupled plasma torches operating at atmospheric pressure, by means of an improved turbulent version of the 3-D model based on customized CFD commercial code FLUENT© previously used to describe configurations with simplified gas inlet section [1-4].

1. Introduction

Standard numerical models of Inductively Coupled Plasma Torches (ICPTs) in literature usually make the assumption of laminar and uniform velocity field for the inlet boundary conditions [5]. Moreover the modelled inlet section is positioned near the bottom of the induction coil in order to reduce the computational domain. The details of the inlet gas section of the ICPTs are thus neglected, overcoming also the necessity of a turbulence model which should be necessary in this high velocity and low viscosity region.
In this work the gas injection section of an industrial Tekna Plasma Systems Inc PL-35 plasma torch is included in the model without geometry simplifications, refining the mesh at the injection points, in order to perform a more realistic simulation of the inlet region of the discharge and to investigate the effects of the inlet turbulent region on the simulation results. In particular, special attention is devoted to the modelling of the actual inlet gas section, which is characterized by two different sets of 8 and 18 circumferentially distributed injection points with a diameter of 0.8 mm for the tangential plasma gas and the axial sheath gas, respectively. A carrier gas introduced axially by means of an injection probe is also considered.
The standard Reynolds Stress Model is used to describe turbulence phenomena in the discharge. Unlike in the previously studied configurations with simplified gas inlet section, the use of a turbulent model is here necessary due to the high Reynolds numbers occurring near the gas injection regions as a consequence of the low argon viscosity value at ambient temperature and of the high gas injection velocity related to the small dimensions of the inlet points.

2. Modeling assumption

The mathematical model is based on the hypothesis of optically thin *Ar* plasma under local thermodynamic equilibrium (LTE) condition and includes the coupled set of continuity, momentum, energy and turbulence transport equations for the plasma flow along with the vector potential equations for the electromagnetic field, taking into account the actual shape of the helicoidal induction coil. The operating conditions are: discharge power of 15 kW, RF induction frequency of 3 MHz and inlet mass flow rates of 60, 15 and 2.5 slpm for the sheath, plasma and carrier argon gases, respectively. Details on the model and the geometry can be found in [1-5].
Simulations are performed over a network cluster of double processor calculators in order to use the full capabilities of the 3-D modelling in a time-dependent framework.

3. Results

In Fig. 1(a) the temperature field is shown in a 3-D view in order to underline the effects on the discharge of the actual coil shape. The views for two planes passing through the axis of the torch are presented in Fig. 1(b) for a more detailed rapresentation of the temperature field. The direct comparison of the temperature fields resulting from the two different models done in Fig. 2, shows that in terms of shape and 3-D displacement the main behavior of the discharge is the same for the two models. The differences are located mainly in the upstream region near the probe side and near the exit section. Another comparison between tangential velocity fields done

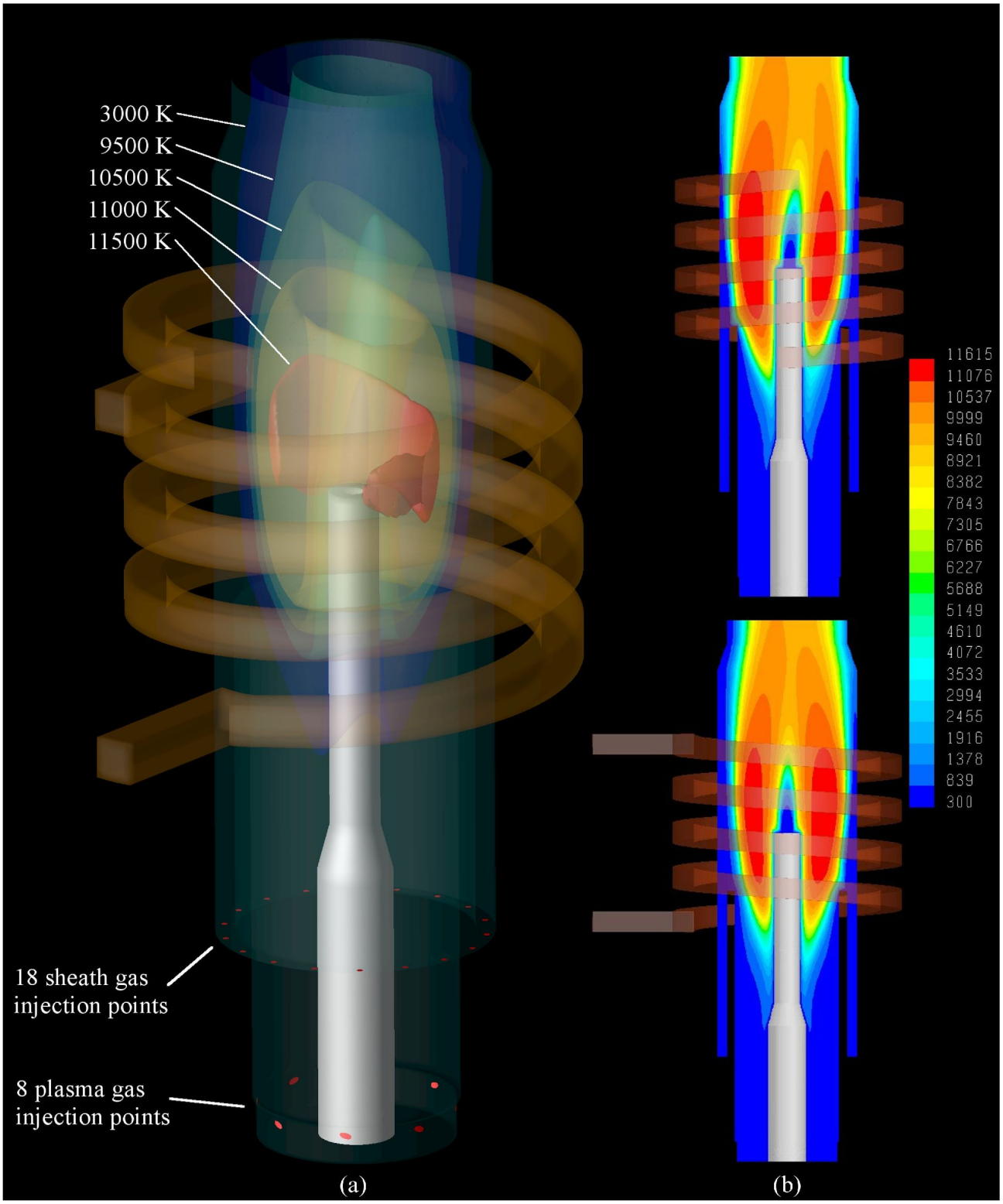

Fig. 1 Temperature fields [K] in a fully 3-D view and on two orthogonal planes passing through the axis of the torch. Operating conditions for the ICPT Tekna PL-35 are: discharge power of 15 kW, RF induction frequency of 3 MHz and inlet mass flow rates of 60, 15 and 2.5 slpm for the sheath, plasma and carrier Argon gases, respectively

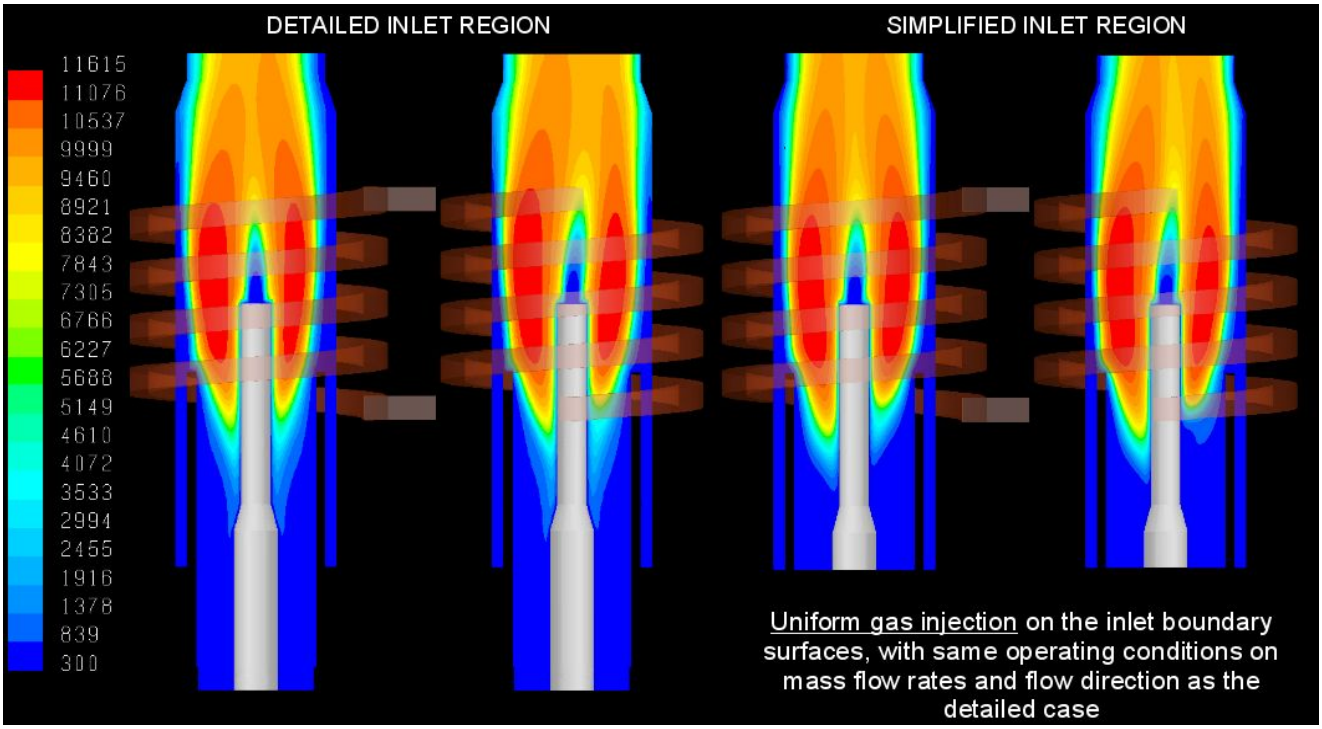

Fig. 2 Comparison between temperature fields [K] for the detailed and the simplified inlet region model.

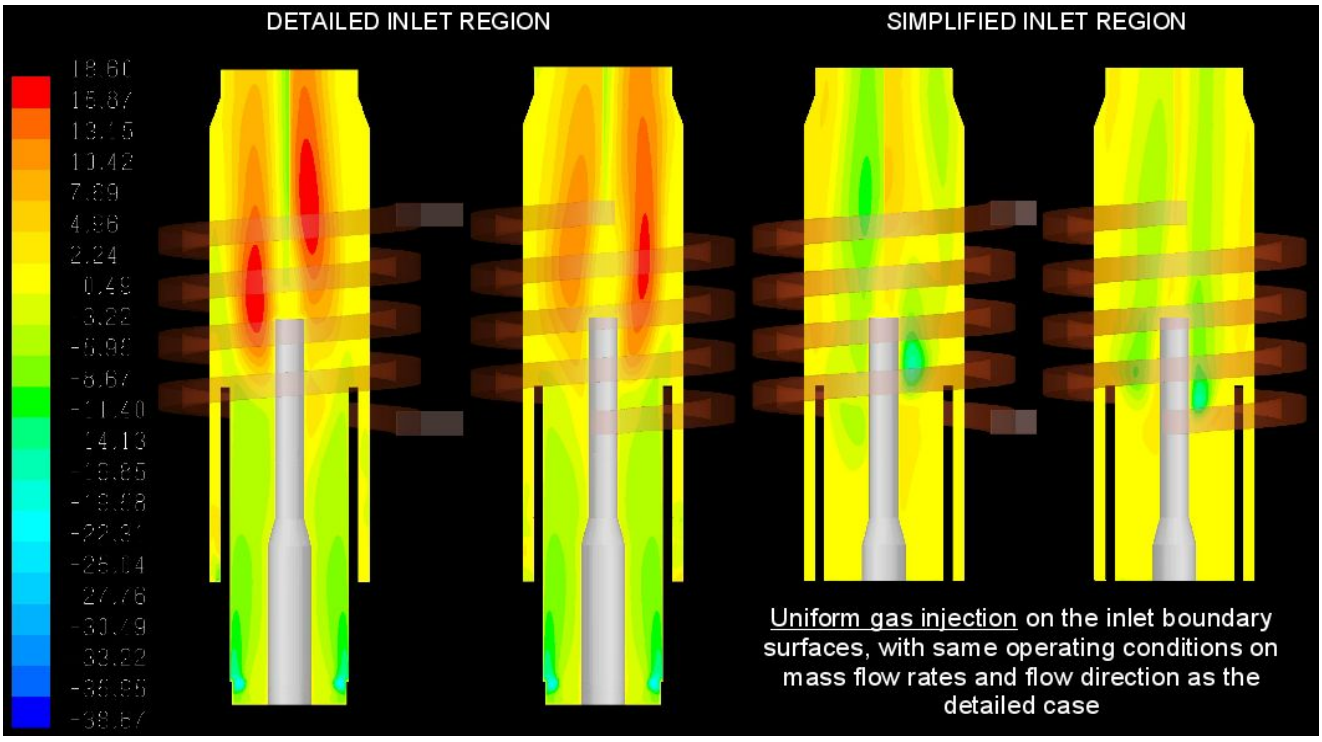

Fig. 3 Comparison between tangential velocity fields [m/s] for the detailed and the simplified inlet region model.

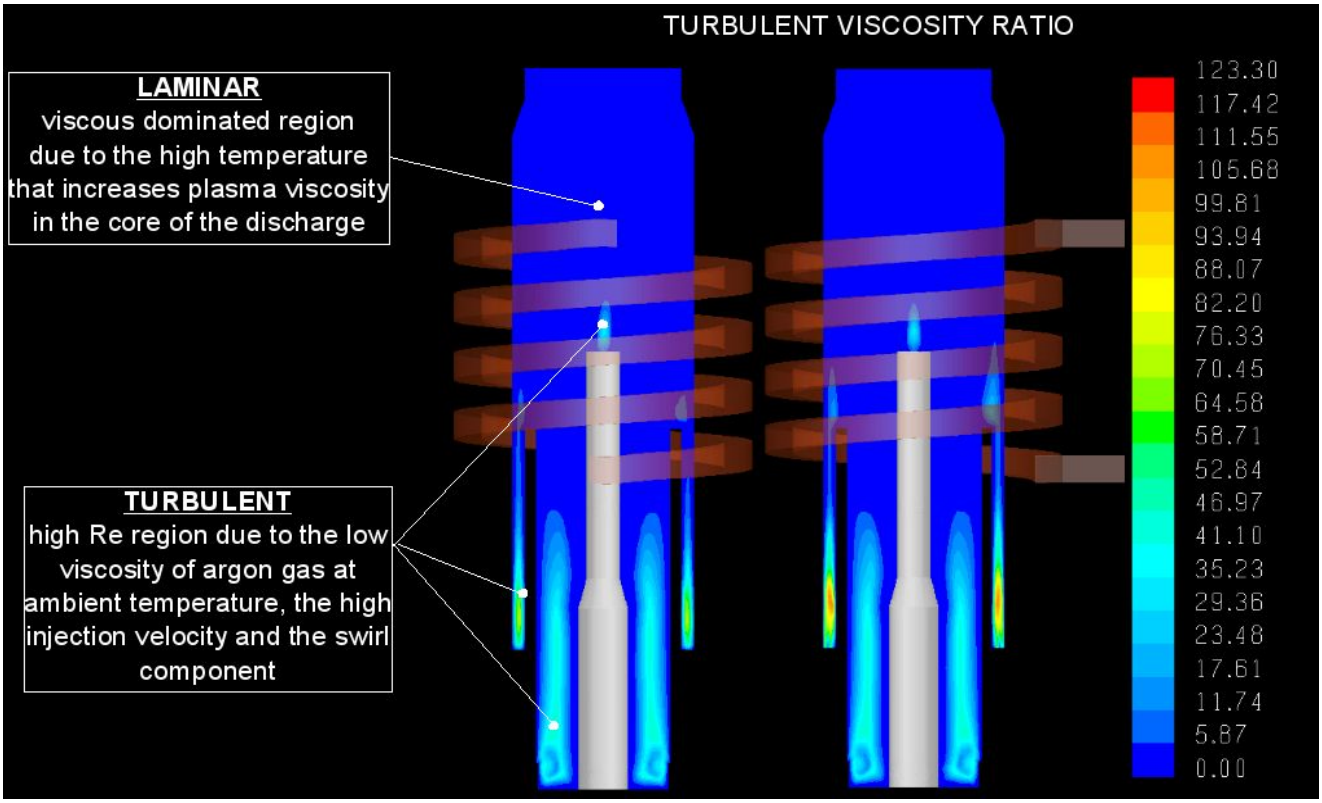

Fig. 4 Turbulent viscosity ratio for the detailed inlet region model.

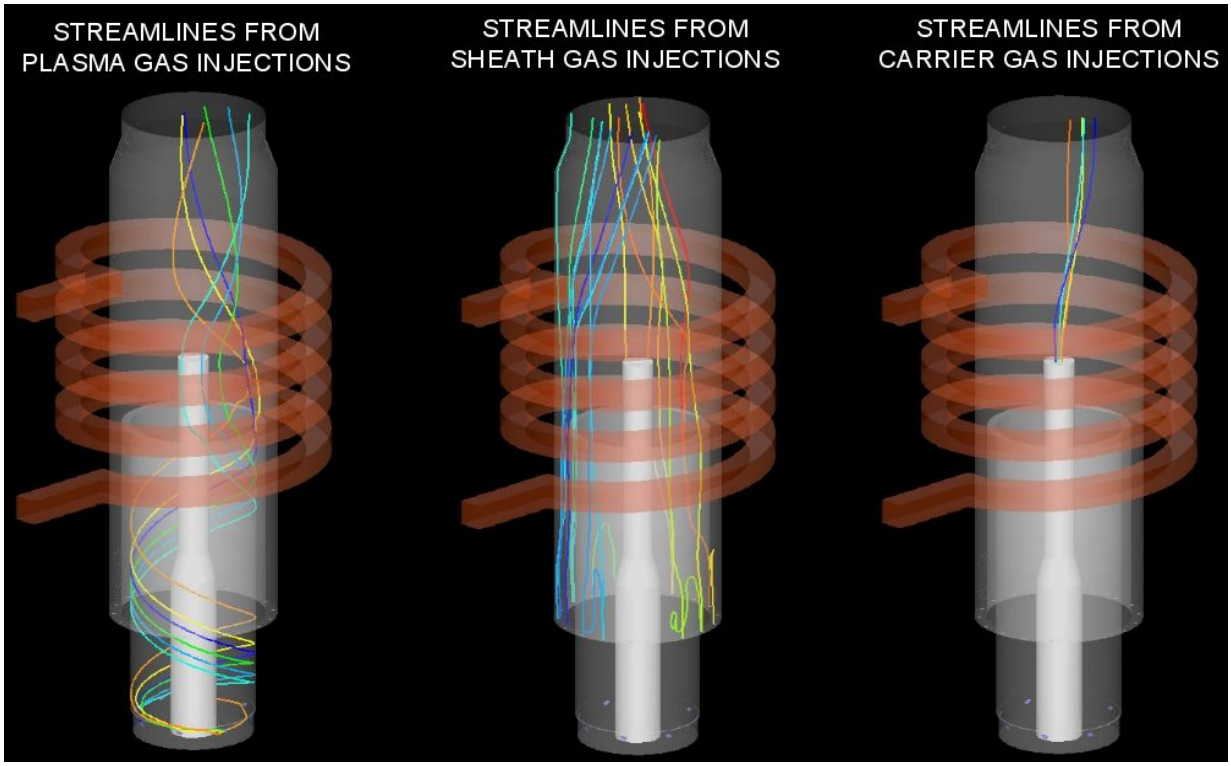

Fig. 5 Streamlines starting from carrier, sheath and plasma gas injection points.

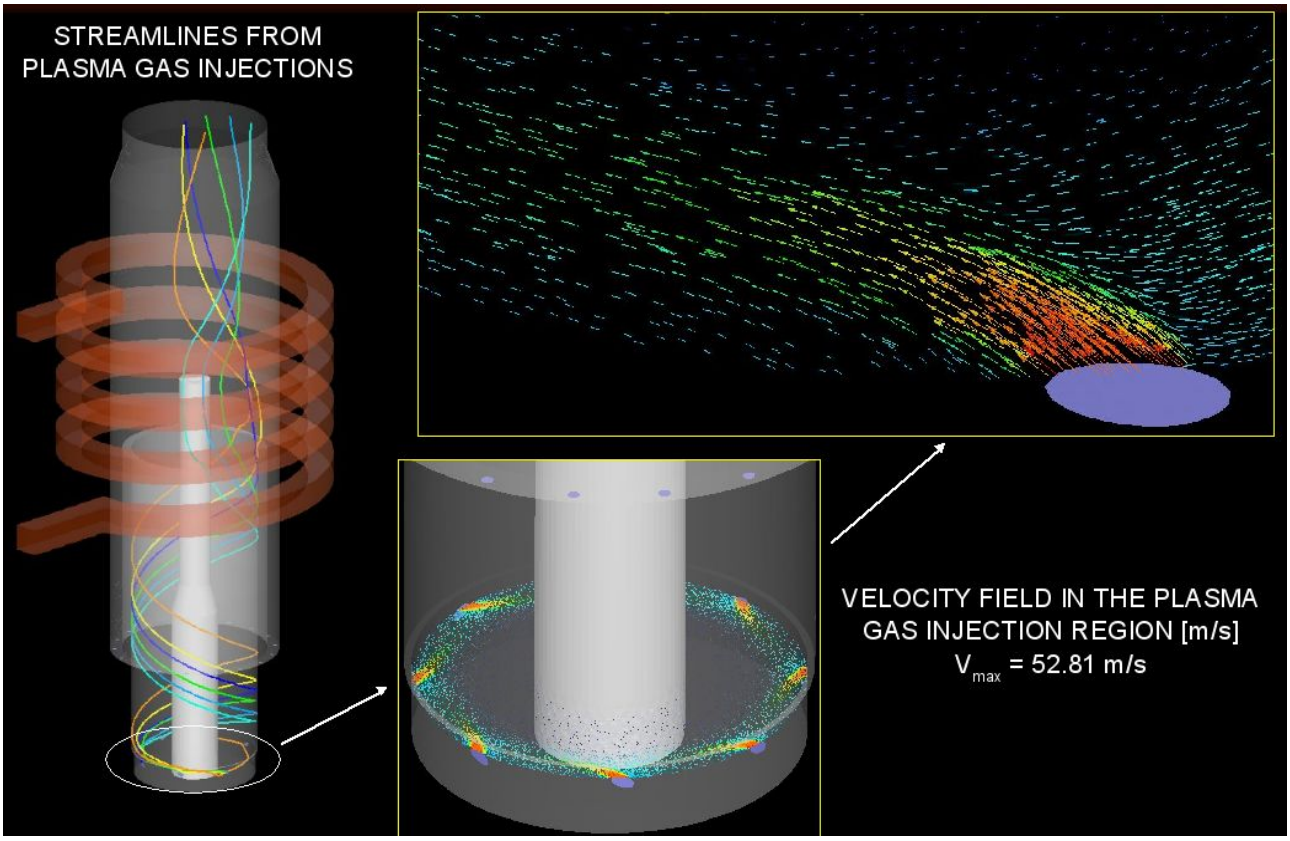

Fig. 6 Details of the velocity field in the plasma gas inlet section.

in Fig. 3, shows a very different characterization in terms of direction and magnitude for the two different models. The turbulence affected region is shown in Fig. 4 where the turbulence viscosity ratio shows that the inlet region of the plasma and the sheath gas inlet section is characterized by non negligible turbulence effects, while the discharge is quite laminar due to the high viscosity of the plasma [6]. In Fig. 5 the streamlines generated from the different inlet gas region are presented. The plasma gas shows a strong swirl direction in the upstream region and the streamlines cross the core of the discharge in the coil region while the sheath gas streamlines tents to remain near the wall in order to avoid the excessive heating of the confinment tube. Fig. 6 shows the details of the velocity vector in the plasma gas inlet region.

4.Conclusions

Comparisons between simplified and detailed modelling of the inlet regions of an industrial ICPT show that differences on the simulation results are mainly on the velocity field and in a less order of magnitude on the temperature field. The computational cost of this more complex fluid dynamic modelling (domain size and model complexity due to the RSM) is thus justified for the fields of application in which the knowledge of the velocity of the plasma plays an important rule, like the simulation of particle thermal history and trajectory inside an ICPT discharge.

References

[1] D. Bernardi, V. Colombo, E. Ghedini, A. Mentrelli, *Three-Dimensional Modelling of Inductively Coupled Plasma Torches*, Eur. Phys. J. D, **22**, 119-125, 2003

[2] D. Bernardi, V. Colombo, E. Ghedini, A. Mentrelli, *Three-Dimensional Effects in the Modelling of ICPTs. I - Fluid Dynamics and Electromagnetics,* Eur. Phys. J. D, **25**, 271-277, 2003

[3] D. Bernardi, V. Colombo, E. Ghedini, A. Mentrelli, *Three-Dimensional Effects in the Modelling of ICPTs. II - Induction Coil and Torch Geometry,* Eur. Phys. J. D, **25**, 279-285, 2003

[4] D. Bernardi, V. Colombo, E. Ghedini, A. Mentrelli, *Comparison of different techniques for the FLUENT-based treatment of the electromagnetic field in inductively coupled plasma torches*, Eur. Phys. J. D, **27**, 55-72, 2003
[5] J. Mostaghimi, M.I. Boulos, Plasma Chem. Plasma Process. **9**, 1 (1988)
[6] K. Chen, M.I. Boulos, J. Phys. D.: Appl. Phys. **27** ,946-952 (1994)

Acknowledgments
This work was performed with partial financial support from the Italian Ministry of Education, University and Scientific Research (M.I.U.R.) national project COFIN-2002 and from the National Group for Mathematical Physics (G.N.F.M.) of the Italian Institute of High Mathematics.

3-D Simulation of Powder Injection in Various ICPT Configurations

V. Colombo[1], E. Ghedini[1], A. Mentrelli[1], T. Trombetti[2]

[1]*Department of Mechanical Engineering (D.I.E.M.) and Research Center for Applied Mathematics (C.I.R.A.M.)*
Università di Bologna, Via Saragozza 8, 40123 Bologna, Italy
Phone: +39 (0)51 2093978, Fax: +39 (0)51 582528 e-mail: colombo@ciram.ing.unibo.it

[2]*Department of Mechanical Engineering (D.I.E.M.), Università di Bologna, Bologna, Italy*

Abstract

In this paper, numerical simulations of the trajectory and heating history of powders injected through a carrier gas in inductively coupled plasma torches working at atmospheric pressure have been performed within a fully 3-D FLUENT©-based model [1-3], taking into account the effects of plasma-particle interaction and the turbulent dispersion of the particles, in the frame of a stochastic approach.

1. Introduction

Inductively coupled plasma torches (ICPTs) are successfully used as high-temperature sources in a wide range of applications, such as spheroidization and purification of both metallic and ceramic powders. However, the effectiveness of these processes strongly depends on a large number of parameters, including the torch operating conditions and the type and characteristics of the injected powders. This causes the try and fail approach to be expensive and difficult to carry out. In this frame, numerical modeling represents a useful tool that may help in the design and optimization of these processes. Several numerical models have been developed in a recent past: 2-D axisymmetric models [4,5] for the analysis of the motion and heating history of the particle inside the torch region, as well as 3-D models to simulate thermal plasma jets with particle and carrier gas injected downstream of the torch exit [6]. Recently, a new 3-D FLUENT-based model for the evaluation of the trajectory and thermal history of particles injected, by means of an injection probe, together with a carrier-gas, into ICPTs working at atmospheric pressure has been presented by the authors [7]. In this paper we present a selection of new results obtained for different types and characteristics of the injected particles.

2. Modeling assumptions

The fully 3-D FLUENT-based model previously developed by the authors [1,2], suitably modified to keep into account the appropriate source-sink terms in the continuity, momentum and energy equations, is employed to calculate plasma temperature and velocity fields in the torch region. Continuity, momentum and energy equations are solved for optically thin plasmas under the assumptions of LTE, while an extended grid model is adopted for the treatment of the electromagnetic field. Simulations are performed over a network cluster of double processor calculators in order to use the full capabilities of the 3-D modelling. A Reynolds Stress Turbulence Model is used in order to predict turbulence inside the discharge and in the reaction chamber. Particles are fed both axially, with injection velocity equal to that of the carrier gas, at the exit section of the torch; they are assumed to be spherical with no internal temperature gradients. Particles trajectory and thermal history are obtained by solving the motion and energy balance equations, respectively, also accounting for particle evaporation effects and turbulence dispersion, as done in [6,7] with the final aim of putting into evidence the importance of a 3-D treatment of the problem for particular working conditions of the torch within various injection procedures. Computational domain for the particle tracking is here extended also downstream the torch region in order to simulate powders behaviour at the exit of the system, so allowing one to suitably design the reaction chamber typically used in this kind of induction plasma processing of materials. Numerical results are presented for different particle diameters. The effects of the particle injection on the plasma is suitably taken into account by adding proper exchange terms in the fluid dynamics equations, as explained in [3]. The particles trajectory is obtained by solving the following equation of motion:

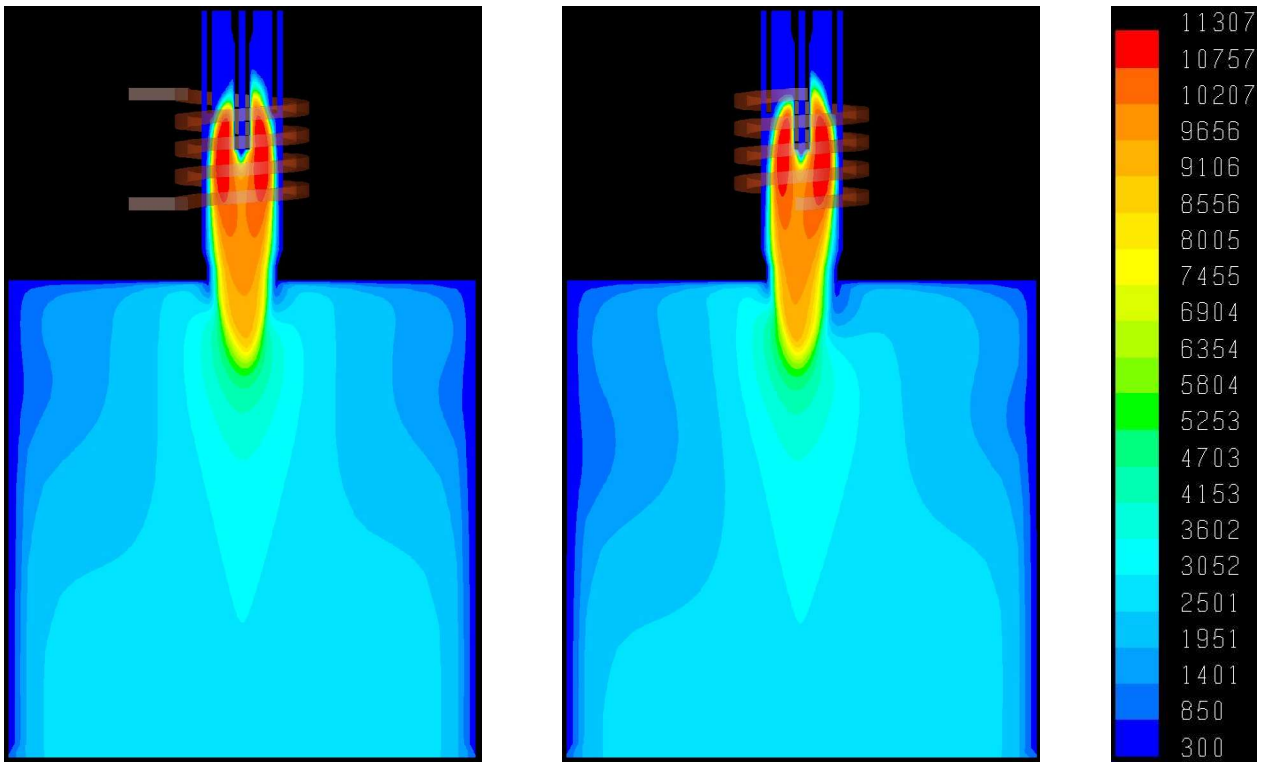

Fig. 1 Plasma temperature [K] in two perpendicular planes passing through the axis of the torch; operating conditions for the Tekna PL-35 torch are: Q_1 (Ar carrier gas)=0.5 slpm; Q_2 (Ar plasma gas)= 15 slpm; Q_3 (Ar sheath gas)= 60 slpm; f = 3 MHz; P= 10kW, <u>without</u> partcles injection.

$$\rho_p \frac{d\mathbf{v_p}}{dt} = \left(\frac{3\rho_\infty C_D}{4d_p}\right) |\mathbf{v}_\infty - \mathbf{v_p}| (\mathbf{v}_\infty - \mathbf{v_p}) + \mathbf{g}(\rho_p - \rho_\infty)$$

where $\mathbf{v}_\infty$ and ρ_∞ are the velocity and density of the plasma. In order to take into account turbulence dispersion $\mathbf{v}_\infty$ is the sum of the mean velocity (obtained by the RANS approach) and a stochastic contribution due to the turbulence intensity in every point of the domain. $\mathbf{v}_p$, d_p, ρ_p are the velocity, diameter and density of the particle, respectively; $\boldsymbol{g}$ is the gravitational acceleration; C_D is the drag coefficient which is calculated as in [6] but neglecting the Knudsen (rarefaction) effect. The heating history of the particle in the solid-phase is obtained by solving the energy balance equation:

$$m_p c_p \frac{dT_p}{dt} = A_p h_c (T_\infty - T_p) - A_p \epsilon\sigma \left(T_p^4 - T_a^4\right)$$

where mp and A_p are the mass and the surface area of the particle; c_p and ρ are the specific heat and the emissivity of the particle material; σ is the Stefan--Boltzmann constant; T_a is the room temperature and h_c is the convective coefficient. As soon as the particle temperature reaches the melting point, it is assumed to remain constant and the liquid-phase fraction x, is calculated by integrating the equation:

$$\frac{dx}{dt} = \frac{6q}{\rho_p d_p \lambda_m}$$

where q is the net specific heat flux transferred to the particle, and λ_m is the melting latent heat of the particle material. As soon as the evaporation

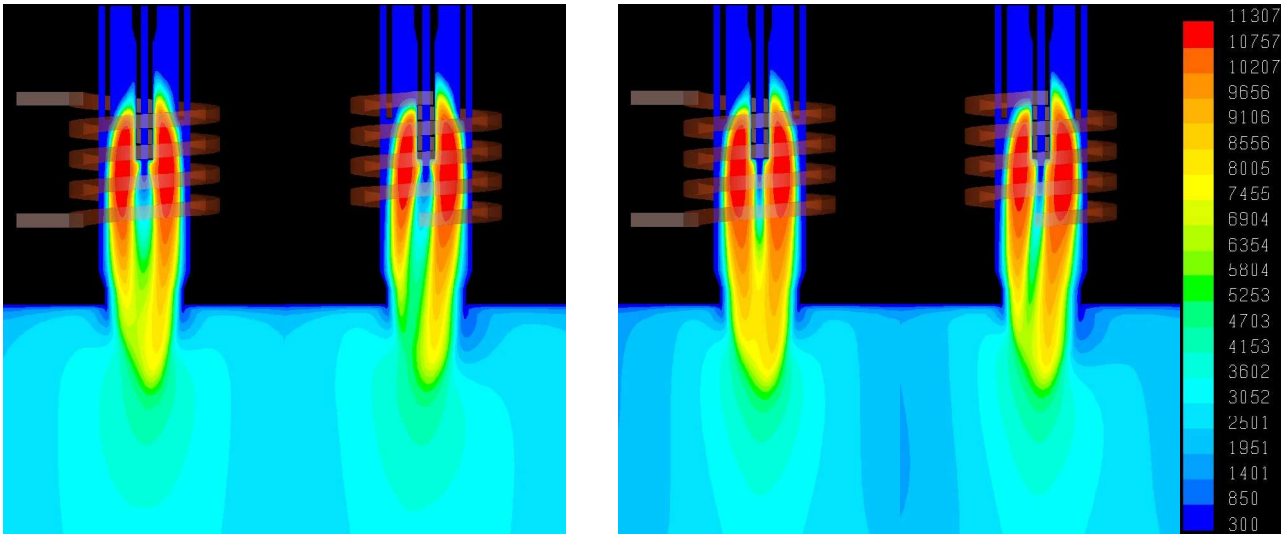

(a) (b)

(c)

Fig. 2 Plasma temperature [K] in two perpendicular planes passing through the axis of the torch; operating conditions for the Tekna PL-35 torch are: Q_1 (Ar carrier gas)=0.5 slpm; Q_2 (Ar plasma gas)= 15 slpm; Q_3 (Ar sheath gas)= 60 slpm; f = 3 MHz; P= 10kW, with 20 g/min of Al_2O_3 particles with diameter (a) d = 25 μm, (b) d = 50 μm and (c) d = 100 μm.

point is achieved, the temperature of the particle is kept constant while its diameter reduces itself according to the following law:

$$\frac{dd_p}{dt} = -\frac{2q}{\rho_p \lambda_v}$$

Details on the model used in this work can be found in [3]. It is worth noting that, in the present model, no mass transfer between particles and plasma is accounted for; i.e. the eventual evaporated fraction of the particles does not alter the composition of the surrounding plasma gas, which is considered to be always pure argon.

3. Simulation results

In Fig.1 the plasma temperature fields on two planes perpendicular one to each other for the case with no particle injection are shown for a Tekna PL-35 plasma torch working under operating conditions characterized by Q_1 =0.5 slpm; Q_2 = 15 slpm; Q_3 = 60 slpm, with respect to to the schematic of the torch given in [7]. The

frequency *f* of the current flowing in the torch coil is equal to 3 Mhz and the discharge power, P, is set to 10kW.

In Fig. 2, Fig.3 and Fig.4, we present simulation results concerning the injection of Al_2O_3 particles with diameters in the range 25 - 100 μm in a Tekna PL-35 plasma torch working under the same operating conditions as the case reported in Fig. 1, but for the presence of particle injection. In Fig. 2(a) the plasma temperature on two perpendicular planes passing through the axis of the torch is shown for the case with injection of particles with diameter equal to 25 μm; In Fig. 2(b) and in Fig. 2(c) the same visualization as reported in Fig. 2(a) are given for the case with injection of particles with diameter equal to 50 μm and 100 μm, respectively. In Fig. 3(a), Fig. 3(b) and Fig. 3(c), the plasma axial velocity magnitude for the same operating conditions and particle injection corresponding to the cases shown in Fig. 2(a), Fig. 2(b) and Fig. 2(c), respectively, are shown. In Fig. 4(a), Fig. 4(b) and Fig. 4(c), we present the particle concentration fields corresponding to the cases shown in Fig. 3(a), Fig. 3(b) and Fig. 3(c), respectively.

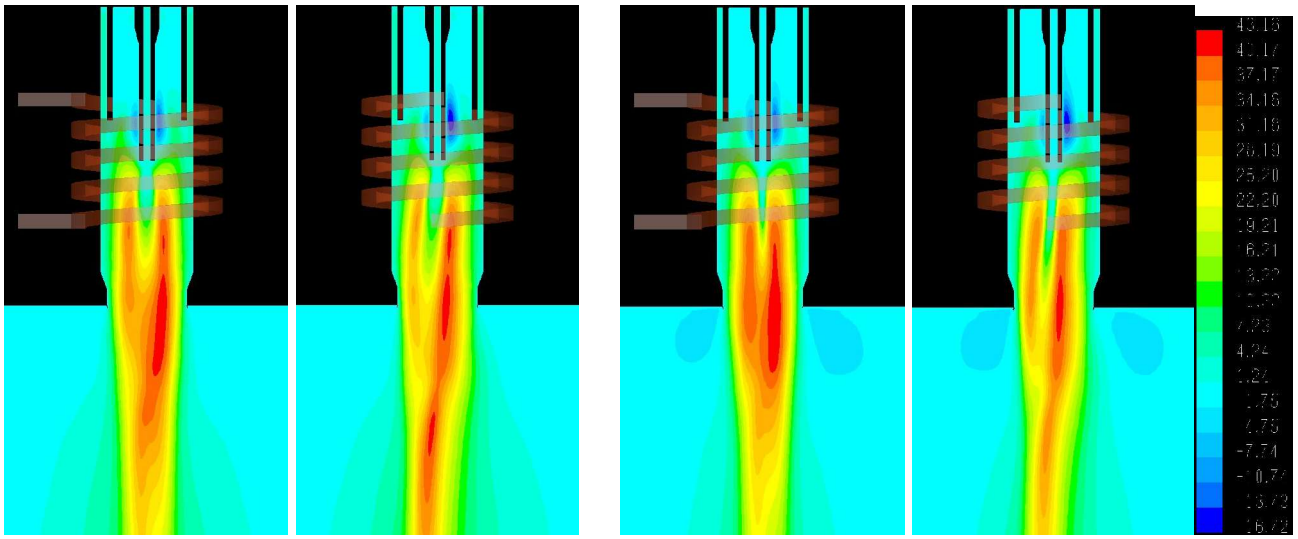

(a) (b)

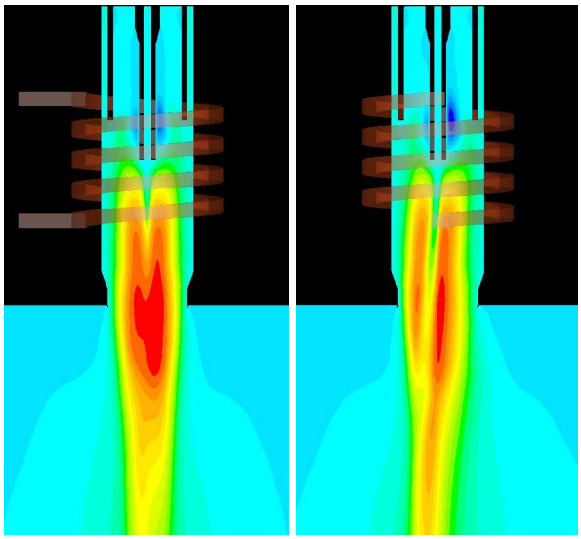

(c)

Fig. 3 Plasma axial velocity magnitude [m/s] in two perpendicular planes passing through the axis of the torch; operating conditions for the Tekna PL-35 torch are: Q_1 (Ar carrier gas)=0.5 slpm; Q_2 (Ar plasma gas)= 15 slpm; Q_3 (Ar sheath gas)= 60 slpm; *f* = 3 MHz; P= 10kW, with 20 g/min of Al_2O_3 particles with diameter (a) d = 25 μm, (b) d = 50 μm and (c) d = 100 μm.

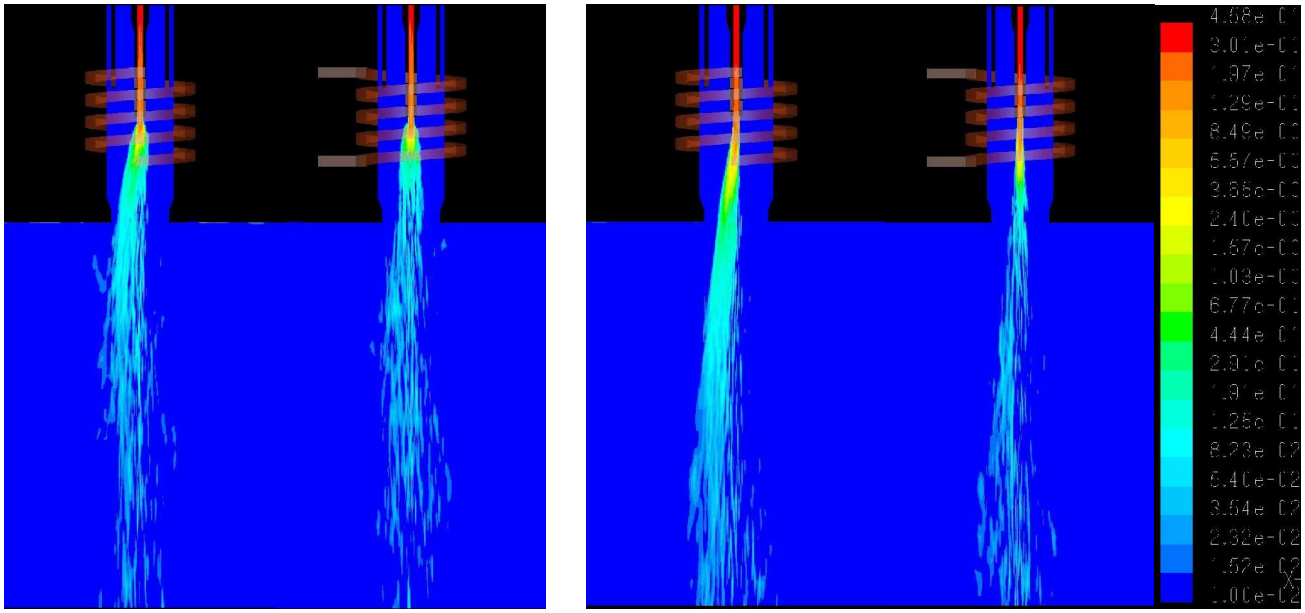

(a)

(b)

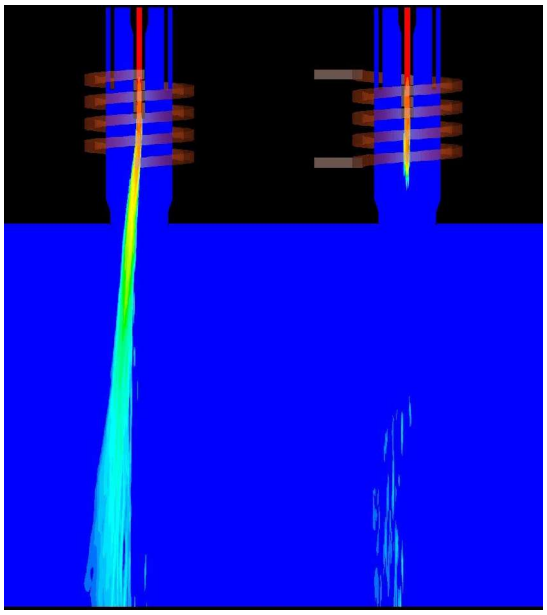

(c)

Fig. 4 Particle concentration [Kg/m^3] in two perpendicular planes passing through the axis of the torch; operating conditions for the Tekna PL-35 torch are: Q_1 (Ar carrier gas)=0.5 slpm; Q_2 (Ar plasma gas)= 15 slpm; Q_3 (Ar sheath gas)= 60 slpm; f = 3 MHz; P= 10kW, with 20 g/min of Al_2O_3 particles with diameter (a) d = 25 μm, (b) d = 50 μm and (c) d = 100 μm.

Finally, in Fig. 5 the thermal history of three particles injected through the same injection point are given as a function of the curvilinear coordinate of the particles along their path, in order to show the effect of the paricle stochastic traking in the three cases previously analyzed.

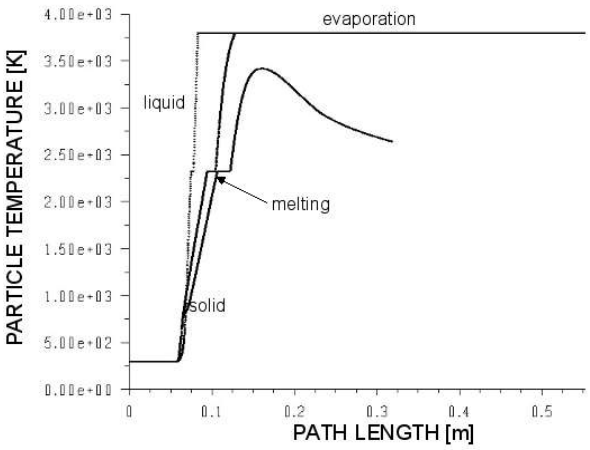

(a)

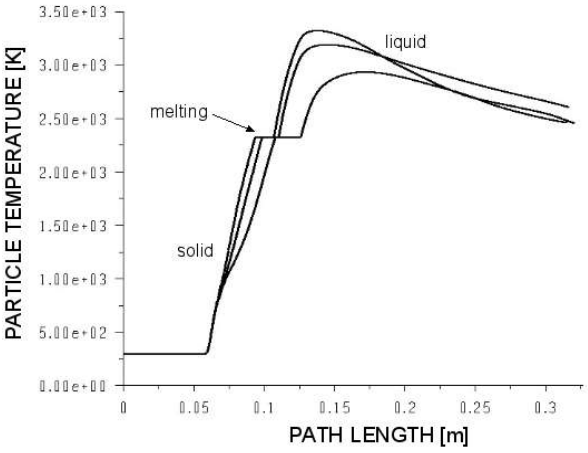

(b)

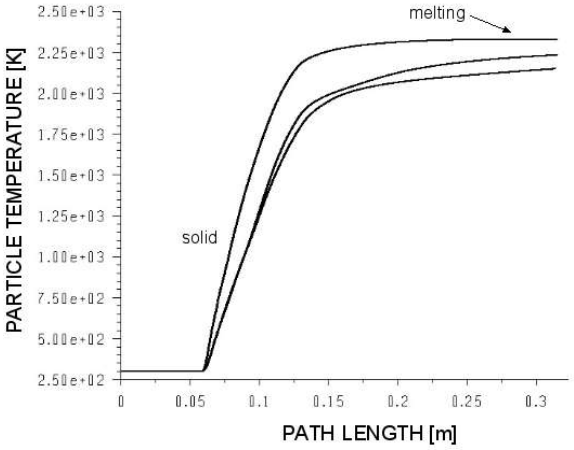

(c)

Fig. 5 Plasma axial velocity magnitude [m/s] in two perpendicular planes passing through the axis of the torch; operating conditions for the Tekna PL-35 torch are: Q_1 (Ar carrier gas)=0.5 slpm; Q_2 (Ar plasma gas)= 15 slpm; Q_3 (Ar sheath gas)= 60 slpm; f = 3 MHz; P= 10kW, with 20 g/min of Al_2O_3 particles with diameter (a) d = 25 μm, (b) d = 50 μm and (c) d = 100 μm.

References

[1] D. Bernardi, V. Colombo, E. Ghedini, A. Mentrelli, *Three-Dimensional Effects in the Modelling of ICPTs. I - Fluid Dynamics and Electromagnetics,* Eur. Phys. J. D, **25**, 271-277, 2003

[2] D. Bernardi, V. Colombo, E. Ghedini, A. Mentrelli, *Three-Dimensional Effects in the Modelling of ICPTs. II - Induction Coil and Torch Geometry*, Eur. Phys. J. D, **25**, 279-285, 2003[3] D. Bernardi, V. Colombo, E. Ghedini, A. Mentrelli, T. Trombetti, *3-D numerical simulation of fully-coupled particle heating in ICPTs*, Eur. Phys. J. D, **28**, 423–433, 2004

[4] P. Proulx, J. Mostaghimi, M.I. Boulos, Plasma-particle interaction effects in induction plasma modeling under dense loading conditions, Int. J. Heat Mass Transfer 28 7, 1327-1336 (1985)

[5] R. Ye, P. Proulx, M.I. Boulos, Particle turbulent dispersion and loading effects in an inductively coupled radio frequency plasma, J. Phys. D: Appl. Phys. 33, 2154-2162 (2000)

[6] H.-P. Li, X. Chen, Three-Dimensional Modeling of the Turbulent Plasma Jet Impinging upon a Flat Plate and with Transfers Particle and Carrier-Gas Injection, Plasma Chem. Plasma Process., 22 1, 27-58 (2003)

[7] D. Bernardi, V. Colombo, E. Ghedini, A. Mentrelli, *3-D Numerical Analysis of Powder Injection in Inductively Coupled Plasma Torches,* in press on IEEE Trans. on Plasma Science-Images in Plasma Science, Feb. 2005

Acknowledgments

This work was performed with partial financial support from the Italian Ministry of Education, University and Scientific Research (M.I.U.R.) national project COFIN-2002 and from the National Group for Mathematical Physics (G.N.F.M.) of the Italian Institute of High Mathematics.

Time Dependent 3-D Numerical Simulation of Transferred Arc Plasma Treatment

V. Colombo, E. Ghedini, A. Mentrelli

Department of Mechanical Engineering (DIEM) and
Research Centre of Applied Mathematics (CIRAM)
Università di Bologna, Via Saragozza 8, 40123 Bologna, Italy
Phone: +39 (0)51 2093978, Fax: +39 (0)51 582528
e-mail: andrea.mentrelli@mail.ing.unibo.it

Abstract

A 3-D time-dependent numerical model useful for the analysis of a dc transferred argon arc has been developed. The model allows to investigate the influence on the behaviour of the arc and on the evolution of the temperature distribution inside the anode of an external magnetic field induced by a current flowing in a moving leading wire parallel to the axis of the cathode. If the current of the arc and the current of the external conductor have opposite directions, the magnetic fields mutually repel and the arc is deflected losing its natural axisymmetric configuration. This practice to obtain a deflected arc may find applications in the industrial processing of materials as, for example, in surface treatment of metallic substrates.

Keywords: transferred arc plasma torches, magnetic deflection, numerical simulations, thermal treatment.

1. Introduction

The aim of this work is to investigate by means of a 3-D time-dependent numerical model the behavior of a transferred arc plasma operating at atmospheric pressure, for the treatment of a metallic substrate material [1], using a customized version of the CFD commercial code FLUENT® [2,3]. Unsteady flow and heat transfer equations are solved together with the two equations of the RNG k-ε turbulence model and with the equations of the scalar potential and of the vector potential, for an argon plasma in local thermodynamic equilibrium, over a computational domain that includes the region between the two electrodes, where the discharge takes place, as well as the anodic region. The developed model allows also the evaluation of the effects of the presence of an external magnetic field generated by a electric direct current flowing in a moving leading wire whose axis is parallel to the axis of symmetry of the cathode on the shape and characteristics of the arc and on the evolution of the temperature distribution inside the metallic substrate on which the arc is attached.
It is well known that, if the current of the arc and the current flowing in the leading wire have opposite directions, the magnetic fields repel reciprocally. As a consequence, the electric arc is deflected and its natural axisymmetric configuration is lost. Such a practice to obtain a deflection of the electric arc has found in recent years useful application in the industrial processing of materials as, for example, in surface treatment of metallic substrates.
With this regard, even though several excellent papers have been published in the recent past on the 2-D and 3-D modelling of transferred arc in both undeflected and deflected arc configurations (for example, [4-8] just to name but a few), a time-dependent 3-D numerical study of the transferred arc plasma torch including the anodic region in the computational domain has not been developed so far, to the authors' knowledge. So, we propose to evaluate the transient effects of an imposed external magnetic field on the three-dimensional shape of the arc and on the evolution of the temperature distribution inside the anode on which the arc is attached, with the final aim of optimizing the treatment process of the metallic substrate. The effects on the substrate temperature evolution of different patterning for the arc treatment and of different current intensities and positions of the leading wire with respect to the torch have been investigated.

2. Modelling approach

The 3-D time-dependent model developed at the University of Bologna [3] for the simulation of atmospheric pressure transferred arc plasma torches both in undeflected and magnetically deflected configurations relies on the following main assumptions:

- the plasma is supposed to be optically thin;
- the plasma is supposed to be in local thermodynamic equilibrium (LTE);
- the viscous dissipation is neglected;
- the plasma flow is assumed to be turbulent and it is modelled by the FLUENT®-implemented RNG k-ε model;
- electrode sheaths are not taken into account;

Under these assumptions, the governing equations of mass, momentum and energy may be written as follows:

$$\frac{\partial \rho}{\partial t} + \nabla \cdot (\rho \mathbf{u}) = 0$$

$$\frac{\partial (\rho \mathbf{u})}{\partial t} + \nabla \cdot (\rho \mathbf{u}\mathbf{u}) = -\nabla p + \nabla \cdot \left[\mu \left(\nabla \mathbf{u} + \nabla \mathbf{u}^T\right)\right] + \mathbf{J} \times \mathbf{B} + \mathbf{F}$$

$$\frac{\partial (\rho h)}{\partial t} + \nabla \cdot (\rho \mathbf{u} h) = \nabla \cdot \left(\frac{k}{c_p} \nabla h\right) + \mathbf{J} \times \mathbf{E} - Q_R$$

and the scalar and vector potential equations are the following:

$$\nabla \cdot (\sigma \nabla V) = 0$$

$$\nabla^2 \mathbf{A} = -\mu_0 \mathbf{J}$$

In the previous equations **u** is the plasma velocity, h is its enthalpy, T is the temperature, p is the pressure, ρ is the plasma density, k is the plasma thermal conductivity, c_p is the plasma specific heat, μ is the plasma viscosity, **E** is the electric field, **B** is the magnetic induction, **J** is the arc current density, Q_R is the volumetric radiative losses, σ is the plasma electrical conductivity, μ_o is the magnetic permeability of the free space, V is the scalar potential, **A** is the vector potential. The magnetic induction, **B**, is obtained from the vector potential, **A**, by means of the relation: $\mathbf{B} = \nabla \times \mathbf{A}$. Finally, the term **F** appearing in the Navier Stokes equation is the deflecting force acting on the arc due to the current in the leading wire. This force may be readily obtained by means of the relation $\mathbf{F} = \mathbf{J} \times \mathbf{B_C}$ once the external magnetic induction $\mathbf{B_C}$ has been calculated with the following formulae:

$$B_{C,x} = \mu_o I_C \frac{\cos(\arctan(y/x))}{2\pi\sqrt{x^2+y^2}}$$

$$B_{C,y} = \mu_o I_C \frac{\sin(\arctan(y/x))}{2\pi\sqrt{x^2+y^2}}$$

$$B_{C,z} = 0$$

where B_{Cx}, B_{Cy} and B_{Cz} are the Cartesian components of the external magnetic induction generated by the current (whose intensity is I_C) flowing in the leading wire, parallel to the z-axis (the axis of symmetry of the cathode) [6].

The selected turbulence model is the FLUENT®-implemented RNG-based k-ε one, which is a two-equations model with a form similar to the standard k-ε model derived from the instantaneous Navier-Stokes equations using a mathematical technique called "renormalization group" (RNG) methods. The two equation of the model are the following:
Ù

$$\frac{\partial}{\partial t}(\rho k) + \frac{\partial}{\partial x_i}(\rho k u_i) = \frac{\partial}{\partial x_j}\left(\alpha_k \mu_{\text{eff}} \frac{\partial k}{\partial x_j}\right) + G_k + G_b - \rho\epsilon - Y_M$$

$$\frac{\partial}{\partial t}(\rho\epsilon) + \frac{\partial}{\partial x_i}(\rho\epsilon u_i) = \frac{\partial}{\partial x_j}\left(\alpha_\epsilon \mu_{\text{eff}} \frac{\partial \epsilon}{\partial x_j}\right) + C_{1\epsilon}\frac{\epsilon}{k}(G_k + C_{3\epsilon}G_b) - C_{2\epsilon}\rho\frac{\epsilon^2}{k} - R_\epsilon$$

where G_k is the generation of turbulence kinetic energy due to the mean velocity gradients; G_b is the generation of turbulence kinetic energy due to buoyancy and Y_M represents the contribution of the fluctuating dilatation in compressible turbulence to the overall dissipation rate. Finally, α_k and α_ε are the inverse effective Prandtl numbers for k and ε, respectively [9].

The governing equations described so far are solved by the FLUENT® solver on a structured computational grid made up of hexahedrons and prisms. The *User-Defined Scalar* (UDS) approach, described in [10] has been adopted for the treatment of the electromagnetic field, while the extra source terms appearing in the transport equations have been implemented by means of *User-Defined Functions* [9] suitably implemented.
The number of cells making up the grid varies between 1.0×10^6 and 1.8×10^6, while the time-step adopted throughout the calculations is kept constant throughout the simulations ($\Delta t = 10\times10^{-5}$ s).
The thermodynamic and transport coefficients of the argon plasma used for the numerical simulations are those given in [11].
The calculations have been performed by PlasMac, a cluster of workstations available at CIRAM & DIEM of the University of Bologna. Such a resource allows for a large reduction in computational time as well as for the treatment of complex computational domain otherwise not manageable with traditional personal computers.

The arc configuration and the implemented boundary conditions are the same as those presented in [6]. In all the simulation presented in this paper the argon flow rate is equal to 0.0003 Kg/s.

3. Selected results

In Fig. 1(a) and in Fig. 1(b), the plasma temperature fields on two planes perpendicular one to each other and passing through the axis of the cathode are shown for the case of undeflected arc configuration (the current flowing in the external conductor is $I_C = 0$). In Fig. 1(c) and in Fig. 1(d) the temperature fields inside the metallic substrate are shown, for the same two planes of Fig. 1(a) and Fig. 1(b), respectively, and under the same operating conditions, while in Fig. 1(e), the temperature field on the upper surface of the anode (interface plasma-anode) is shown. It may be noticed that the temperature field is both the discharge region and the anodic region is axisymmetric because of full axisymmetric configuration of the torch.

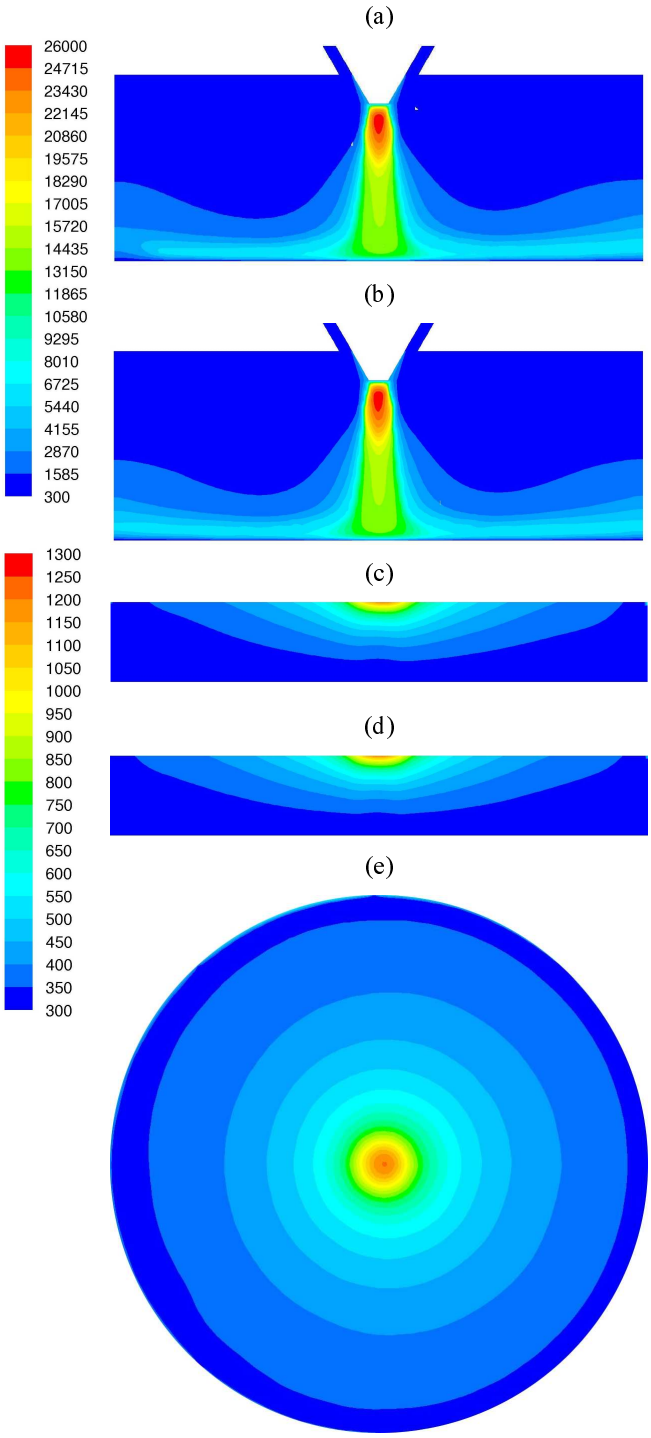

Fig. 1. Temperature distribution [K] in the discharge region (a,b) and inside the anode (c,d) on two planes perpendicular to each other and passing through the axis of the cathode, and on the upper surface of the anode (e) in absence of deflecting current.

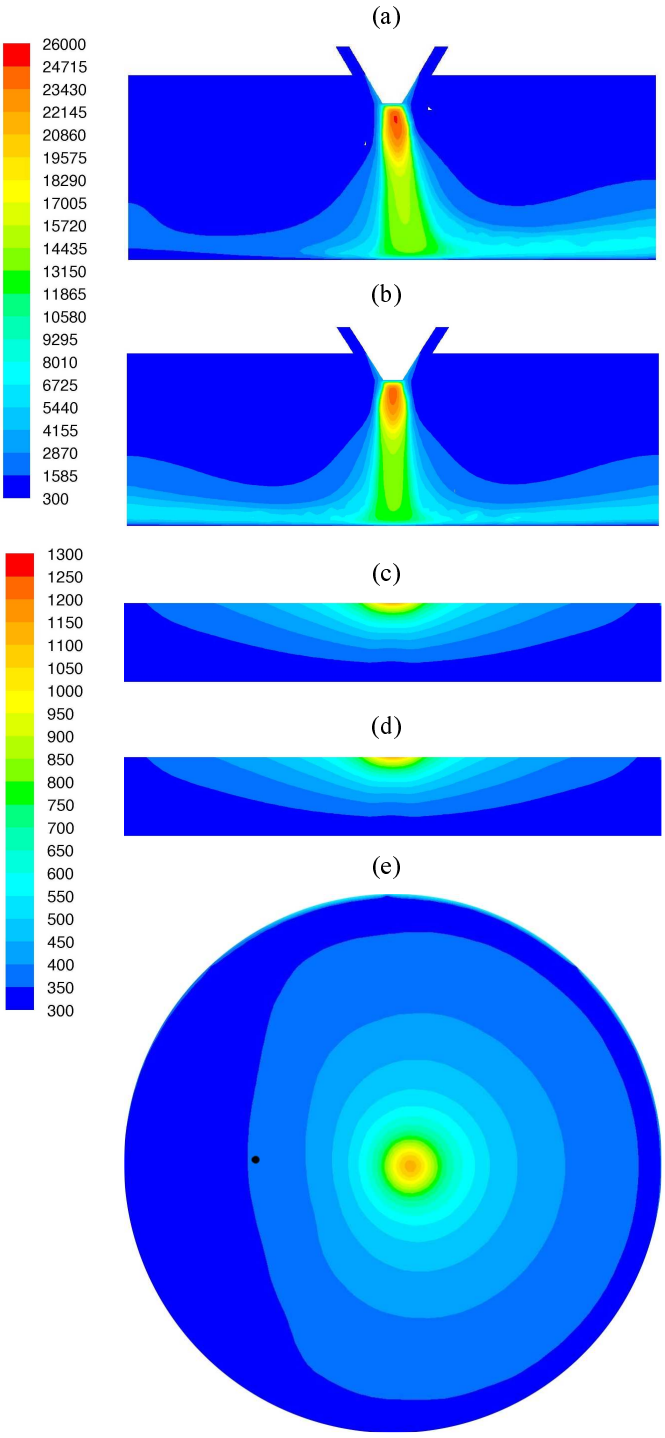

Fig. 2. Temperature distribution [K] in the discharge region (a,b) and inside the anode (c,d) on two planes perpendicular to each other and passing through the axis of the cathode, and on the upper surface of the anode (e). The position of the wire is evidenced by the black dot if Fig. 2(e).

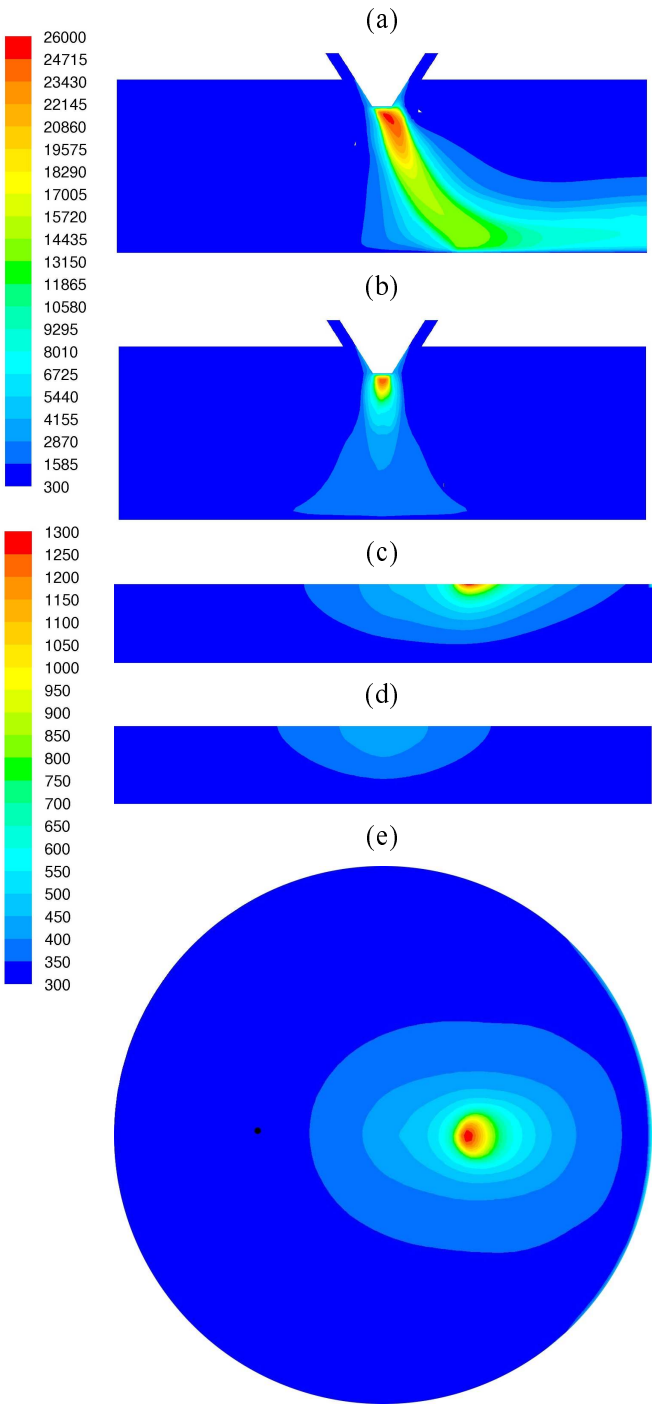

Fig. 3. Temperature distribution [K] in the discharge region (a,b) and inside the anode (c,d) on two planes perpendicular to each other and passing through the axis of the cathode, and on the upper surface of the anode (e) at *t=0* with a deflecting current flowing in a moving wire whose instantaneous position is evidenced by the black dot in Fig. 3(e).

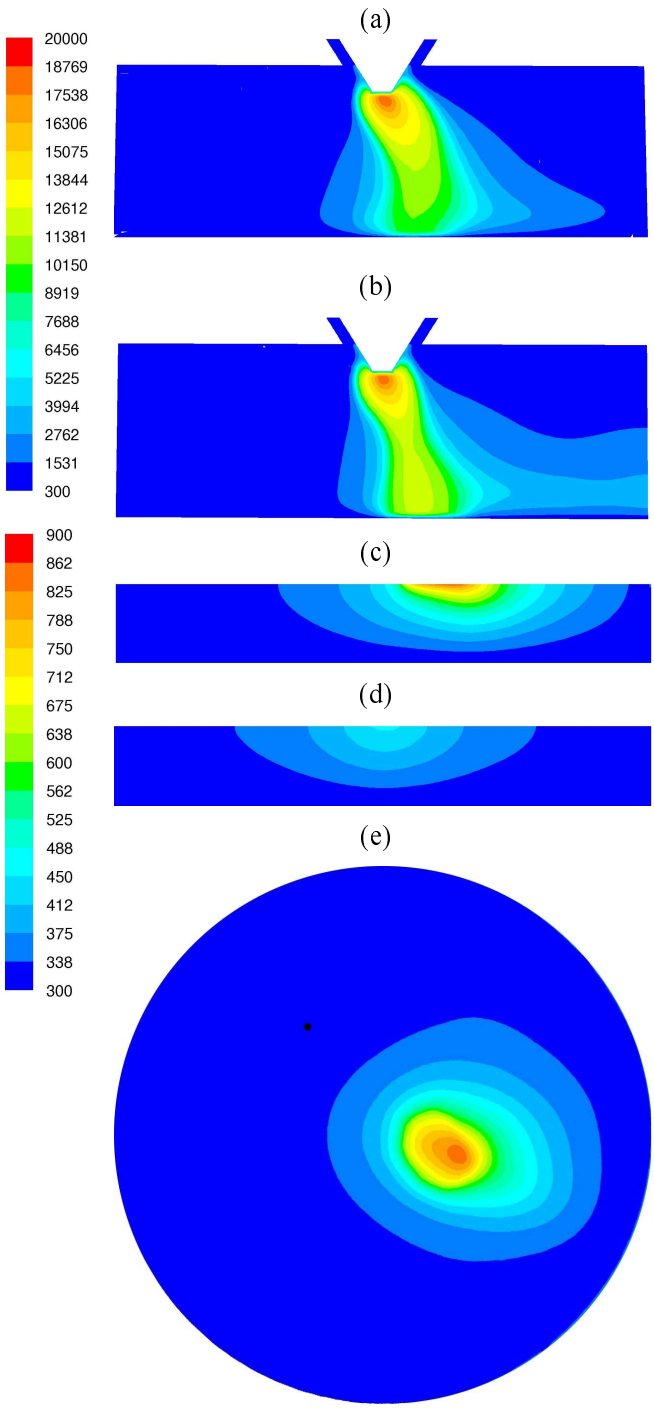

Fig. 4. Temperature distribution [K] in the discharge region (a,b) and inside the anode (c,d) on two planes perpendicular to each other and passing through the axis of the cathode, and on the upper surface of the anode (e) at *t = 0.16 s* with a deflecting current flowing in a moving wire whose instantaneous position is evidenced by the black dot in Fig. 4(e).

If Fig. 2(a) and in Fig. 2(b) the plasma temperature fields on the same planes as those of Fig. 1(a) and Fig. 1(b) are given for the case in which the electric arc is deflected by the presence of a magnetic field induced by a current flowing in a wire parallel to the axis of the cathode and with intensity I_C = 50 A. In Fig. 2(c) and Fig. 2(d) the corresponding temperature fields inside the substrate are shown, for the same two planes of Fig. 2(a) and Fig. 2(b) and under the same operating conditions. Finally, in Fig. 1(e), the temperature field on the upper surface of the anode is given. In this case, the symmetry of the discharge and of the temperature distribution in the substrate is lost because of the presence of the deflecting external magnetic field. In Fig. 2(e) the position of the leading wire in which the current flows is evidenced by the black dot.
In Fig. 3 and in Fig. 4, the results of a time-dependent simulation are presented. In this case, the leading wire in which the deflecting current flows is fixed for $t < 0$ and it starts moving around the axis of the cathode with an angular velocity $\omega = 2\pi$ at $t = 0$, keeping its axis parallel to the axis of the cathode. In Fig. 3(a-d) and Fig. 4(a-d) the temperature fields in the discharge and in metallic substrate are shown for the times $t = 0$ and $t = 0.166$ s. Fig. 3(a,b) and Fig. 4(a,b) give, for these two different instant times, the plasma temperature fields on two planes orthogonal one to the other and both passing through the axis of the cathode, one of these two planes containing the wire. In Fig. 3(c,d) and in Fig. 4(c,d) the temperature distribution inside the metallic anode and on the same planes of the corresponding Fig. 3(a,b) and 4(a,b) are shown.
The position of the wire at $t=0$ is evidenced in Fig. 3(e), while its position after $t=0.166$ s is evidenced in Fig. 4(e).

References

[1] V. Colombo, A. Mentrelli, T. Trombetti, *Time Dependent 3-D Modelling of Laser Surface Heating for the Hardening of Metallic Materials*, Eur. Phys. J. D **27**, 239-246, 2003
[2] D. Bernardi, V. Colombo, E. Ghedini, A. Mentrelli, *Three-Dimensional Time-Dependent Modelling of Magnetically Deflected Transferred Arc,* IEEE Trans. on Plasma Science - Images in Plasma Science **33**, 2, Part I, 2005
[3] S. Melini, *Analisi fisica e modellazione tridimensionale per la caratterizzazione stazionaria e dipendente dal tempo finalizzata al progetto di torce al plasma a corrente continua ad arco trasferito*, Thesis (in Italian), University of Bologna, Italy, 2004
[4] G. Speckhofer, H.-P. Schmidt, *Experimental and Theoretical Investigation of High-Pressure Arcs-Part II: The Magnetically Deflected Arc (Three-Dimensional Modeling)*, IEEE Trans. Plasma Sci. **24** 4, 1239-1248, 1996
[5] P. Freton, J.J. Gonzales, A. Gleizes, Comparison between a two- and a three-dimensional arc plasma configuration, J. Phys. D.: Appl. Phys. **33**, 2442-2452, 2000.
[6] A. Blais, P. Proulx, M.I. Boulos, *Three-dimensional numerical modelling of a magnetically deflected dc transferred arc in argon,* J. Phys. D: Appl. Phys. **36**, 488-496, 2003
[7] F. Lago, J.J. Gonzales, P. Freton, A. Gleizes, *A numerical modelling of an electric arc and its interaction with the anode: Part I. Two-dimensional model*, J. Phys. D: Appl. Phys. **37**, 883-897, 2004
[8] J.J. Gonzales, F. Lago, P. Freton, M. Masquère, X. Franceries, *A umerical modelling of an electric arc and its interaction with the anode: Part II. The three-dimensional model – influence of external forces on the arc column*, J. Phys. D: Appl. Phys. **38**, 306-318, 2005
[9] FLUENT 6.1 User's Guide (January 28, 2003), FLUENT Inc., Lebanon, NH, 2003
[10] D. Bernardi, V. Colombo, E. Ghedini, A. Mentrelli, *Comparison of Different Techniques for the FLUENT-Based Treatment of the Electromagnetic Field in Inductively-Coupled Plasma Torches*, Eur. Phys. J. D **27**, 1, 55-72, 2003
[11] A.B. Murphy, *Transport coefficients of hydrogen and argon-hydrogen plasmas*, Plasma Chem. Plasma Process., **20**, 279–297, 2000

Acknowledgments

This work was performed with partial financial support from the Italian Ministry of Education, University and Scientific Research (M.I.U.R.) national project COFIN-2002 and from the National Group for Mathematical Physics (G.N.F.M.) of the Italian Institute of High Mathematics.

3-D Modelling of DC Transferred Arc *Twin Torch* for Asbestos Inertization

V. Colombo, E. Ghedini, E. Malfa(*), A. Mentrelli

Department of Mechanical Engineering (DIEM) and
Research Centre of Applied Mathematics (CIRAM)
Università di Bologna, Via Saragozza 8, 40123 Bologna, Italy
Phone: +39 (0)51 2093978, Fax: +39 (0)51 582528
e-mail: colombo@ciram.unibo.it

(*) *Centro Sviluppo Materiali (CSM S.p.A.)*
Piazza Caduti 6 Luglio 1944, 1 - 24044 Dalmine (BG), Italy
Phone: +39 (0)35 697939 , Fax: +39 (0)35 697945
e-mail: e.malfa@c-s-m.it

Abstract

The aim of this work is to investigate by means of a 3-D numerical model the fluid flow and temperature distribution of a plasma transferred electric arc discharge generated between two suspended metallic electrodes. This *twin torch* device is used inside a plasma furnace for hazardous waste incineration and asbestos inertization. Flow and energy equations are solved for an optically thin plasma under conditions of LTE, while the electromagnetic field equations are solved in their scalar and vector potential form.

Keywords: transferred arc plasma torches, numerical simulation, hazardous waste incineration.

1. Introduction

In the past, research on the subject of DC transferred arc *twin torch* systems has been done [1] concerning 3D simulation of flows inside a plasma furnace devoted to combustion/vitrification of radioactive wastes, based on a molten glass bath under an electric arc transferred between two metallic parallel electrodes (cathode and anode) under the hypothesis that the arc shape closes itself through the molten bath. The arc domain was modelled on a 3D structured mesh representative of the SHIVA melter geometry integrating two parallel torches, providing results on the plasma side for electrical potential, arc shape, and temperature of the plasma and comparing them with some experimental results such as emission spectroscopy or arc observation with an high speed camera. Also results for glass domain are given for an example through velocity, temperature and volumetric power distributions and shape of the obtained glass ingot.
Centro Sviluppo Materiali (CSM) S.p.A. is one of the most important European industrial research centres in the field of materials (steel, special alloys and ceramics), related manufacturing processes, coating technologies dedicated to wear and tear, corrosion and thermal insulation problems and innovative forming technologies (rapid prototyping, hydroforming, superplastic forming, laser welding). CSM started to use plasma torches in 1987 carrying out, with commercial torches, a 1 MW plant installed in an Italian steel-works for liquid steel temperature control (about 1550 °C) in a continuous casting plant [2]. For application over waste, characterized by problems of corrosion and high turbulence, CSM developed its own dedicated plasma torches that assure high reliability and high efficiency. Particular attention was also paid to enhance the most important torch components (electrodes and nozzles) using specific CSM competence: special materials, coating technologies, advanced mechanical design, thermal fluid-dynamic simulation. In this direction the development of a 3-D plasma arc model used on FLUENT® code has been carried out recently in cooperation with the University of Bologna.

2. Modelling approach

2.1 Governing equations

A three-dimensional computational model useful for the simulation of a transferred arc plasma torch involves the

simultaneous solution of the coupled set of non-linear fluid-dynamic, electromagnetic and energy transfer equations.

The main simplifying assumptions on which the developed model relies are the following:
- the discharge is stationary;
- the plasma is described as a simple mono-component fluid;
- the plasma is optically thin and in local thermodynamic equilibrium (LTE);
- the turbulent plasma flow is described by the renormalization group (RNG) turbulence model;

Taking into account the previous assumptions, the equations of the conservation of mass and momentum take the following form:

$$\nabla \cdot (\rho \mathbf{v}) = 0$$

$$\nabla \cdot \rho \mathbf{v}\mathbf{v} = -\nabla p + \nabla \cdot \tau + F_L$$

being ρ the density of the fluid, $\mathbf{v}$ the velocity of the fluid, p the pressure, τ the stress tensor and F_L the Lorentz force due to the interaction of the conductive fluid and the electromagnetic field. The energy equation is solved without taking into account the viscous dissipation:

$$\nabla \cdot \rho \mathbf{v} h - \nabla \cdot k \nabla T - \frac{5}{2}\frac{k_B}{e}\left(\mathbf{j} \cdot \frac{1}{C_p}\nabla h\right) = Q_J - Q_R$$

where h is the enthalpy of the fluid, k is the thermal conductivity of the fluid, k_B is the Boltzmann constant, e is the electron charge, $\mathbf{j}$ is the current density and C_P is the specific heat at constant pressure of the fluid.
The last term on the left hand side of the equation represents the enthalpy transport due to stream of the conductive electrons. Finally, Q_J is the energy dissipated in the discharge by Joule effect and Q_R represents the radiative losses.
The equations for the calculation of the electrostatic potential V, and of the vector potential $\mathbf{A}$, are the following:

$$\nabla \cdot \sigma \nabla V = 0$$

$$\nabla^2 \mathbf{A} + \mu_0 \mathbf{j} = 0$$

where σ is the electrical conducibility of the plasma, $\mathbf{j} = \sigma\mathbf{E} = -\sigma \nabla V$ represents the current density and μ_o is the magnetic permeability of the vacuum. The electromagnetic equations are solved, by the FLUENT® solver, by means of a *user-defined scalar* (UDS) approach, in a way similar to that described in [3].
In all the performed calculations, the required database of thermodynamic and transport properties has been worked out starting from the raw data calculated at CSIRO (Sydney, Australia) [4,5].
The calculations have been performed by PlasMac, a cluster of workstations available at CIRAM & DIEM of the University of Bologna. Such a resource allows for a large reduction in computational time as well as for the treatment of complex computational domain otherwise not manageable with traditional personal computers.

2.2 The twin torch configuration

The *twin torch* configuration is schematically represented in Fig. 1.

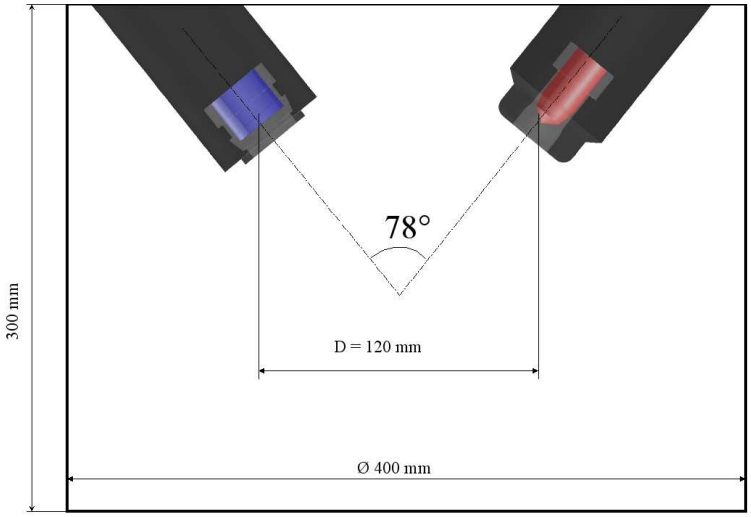

Fig.1 The twin torch configuration.

The computational domain does not extend to the whole reactor, since the simulation of the complete three-dimensional configuration would be too computationally expensive. The domain is thus limited to the region between the cathode and anode where the discharge takes place, as shown in Fig. 1.
The profile of the current density on the cathodic surface is given as a boundary condition. In the simulations performed, this profile is parabolic:

$$\mathbf{j}(r) = -\sigma \nabla V = -j_{max}\left[1 - \left(\frac{r}{R_0}\right)^2\right]$$

where $j_{max} = 0.8\times10^7$ A/m^2 is the maximum value of the current density on the cathode, r is the distance from the axis of the cathode, R_0 is a reference value calculated imposing a given value of the total current, I, on the cathodic surface. On the anodic surface the electrical potential is assumed to be zero, while on all the other surfaces of the model the current flux is assumed to be zero. The temperature value given as a boundary condition on the anodic and cathodic surfaces comes from previous calculations developed by CSM S.p.A.; on all the other surfaces the temperature is fixed at 500 K. The FLUENT®-implemented pressure-outlet condition is selected as a boundary condition for the momentum equation on the external boundaries of the computational domain, while the traditional *no-slip* condition is imposed on all the solid walls. In the performed *twin torch* simulations the working gas is either pure Ar or a mixture of Ar-H_2 with an H_2 content equal to 5% by volume, treating the plasma as a one-component fluid and so neglecting the demixing effects [6] .

3. Simulation results

The results presented in this section come from numerical simulations of the *twin torch* under operating conditions typical of the industrial applications developed at CSM S.p.A. The electrical current of the arc I imposed on the surface of the cathode as a boundary condition, is equal to 1500 A and to 1000 A, while the anodic and cathodic gas flow rates are, respectively, 5.34 m^3/h and 4.74 m^3/h.
A three-dimensional visualization of the isotemperature surfaces in the pure Ar discharge for both the cases of 1500 A and 1000 A are reported, respectively, in Fig. 2(a) and in Fig. 3(a), in which the deflection of the anodic and cathodic plasma jets due to the repulsive effects induced by the Lorentz force are appreciable. A more detailed visualization of the plasma temperature fields in the regions close to the two electrodes is reported in Fig. 2(b) and in Fig. 3(b) for the cases with I = 1500 A and with I = 1000 A, respectively.
An analysis of Fig.2(a) and Fig.3(a) highlights that, as the total electric current I of the arc decreases, the extension of the high temperature region of the discharge decreases too, although the shape of the discharge remains qualitatively almost unchanged. The decrease in the volume of the high temperature region of the

discharge is strictly related to the decrease in the total amount of the energy dissipated in the discharge by Joule heating.

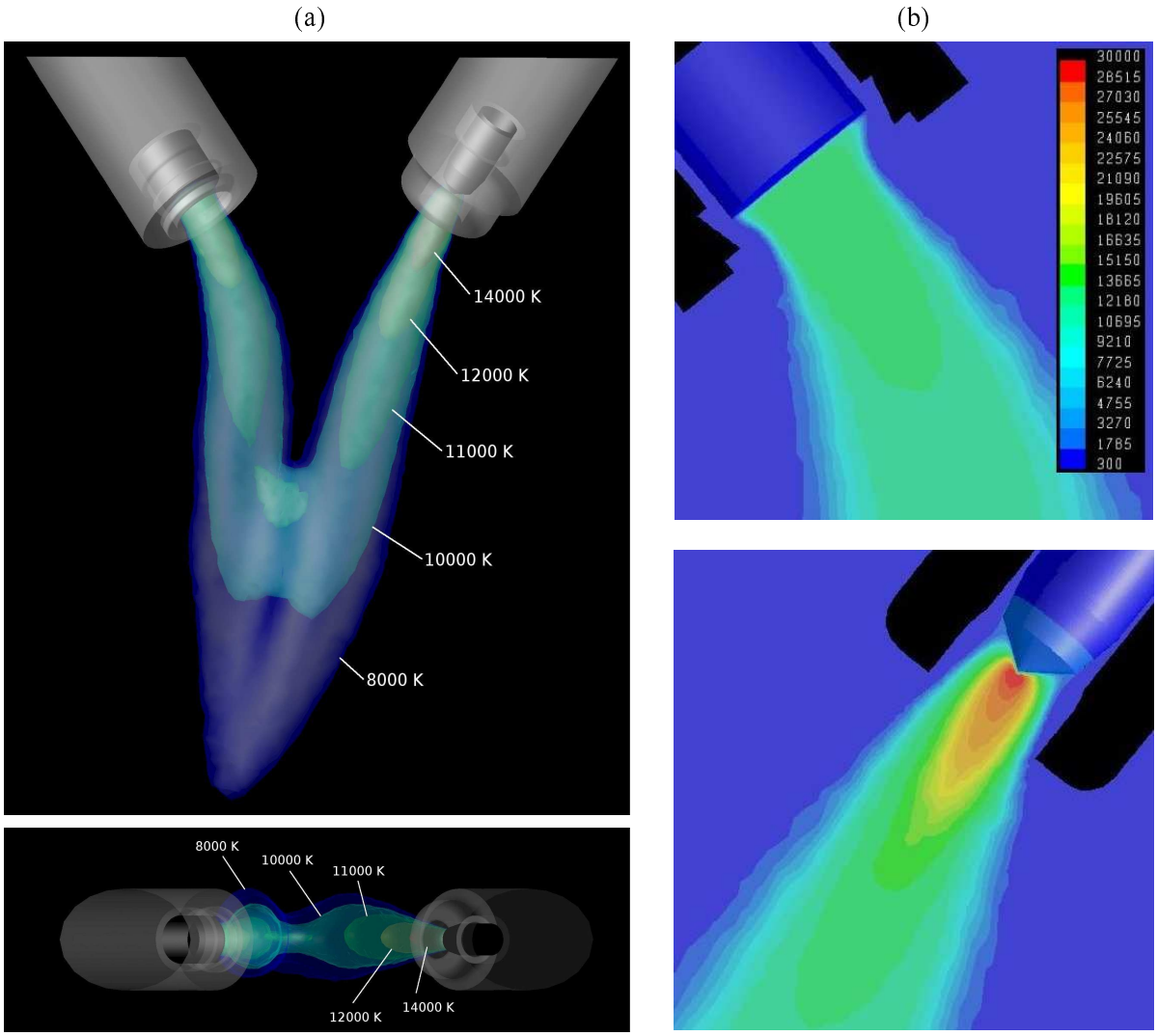

Fig. 2. Isotemperature surfaces in the discharge (a) and details of the plasma temperature [K] in the region close to the anodic (top) and cathodic (bottom) surfaces (b). Operating conditions: I=1500 A; pure Ar as working gas.

The maximum plasma temperature, located close to the cathodic surface, is close to 30000 K for both the cases presented in Fig. 2(a) and in Fig. 3(a), while in the proximity of the anodic surface the plasma temperature reaches a value close to 12000 K. It is interesting to note that these values of the plasma temperature close to the electrodes are mainly influenced by the maximum value of the current density on the surfaces of the electrodes, and are not noticeably influenced by the total electric current of the arc.

The *twin torch* configuration has also been simulated under operating conditions in which an homogeneous mixture of Ar and H_2 is injected as working gas. In this case, the diffusion of the two species has been neglected due to the low content of H_2 considered in the present case (equal to 5% by volume).
In Fig. 4(a) a three-dimensional visualization of the plasma temperature isosurfaces for the *twin torch* operating with the considered Ar-H_2 mixture under the operating conditions characterized by total electric current I = 1500 A is shown. The main difference between the plasma temperature presented in Fig. 4(a) and the one

presented in Fig. 2(a) (referring to a *twin torch* operating under the same conditions but for the composition of the gas, which is pure Ar), consists in higher values of the plasma temperature close to the anodic region. In fact, in the simulation with Ar-H_2 mixture a value close 14000 K is found, while for pure Ar case, in the same region a temperature close to 12000 K was found. From the comparison of these two figures, it may also be noticed that the macroscopic behavior of the discharge is not considerably affected by the injection of such a quantity of H_2. A detailed visualization of the plasma temperature fields in the anodic and cathodic regions is shown in Fig. 4(b).

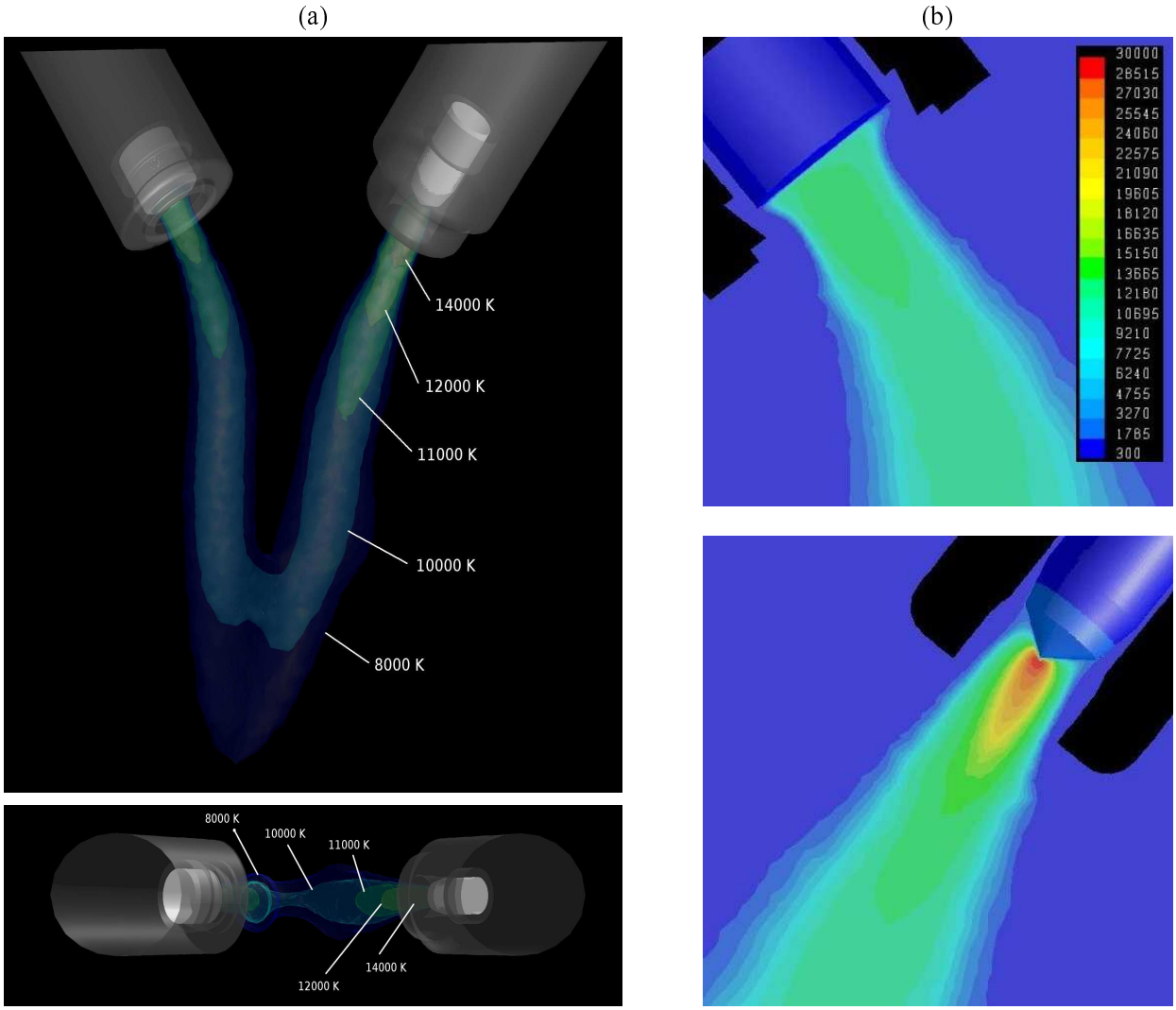

Fig. 3. Isotemperature surfaces in the discharge (a) and details of the plasma temperature [K] in the region close to the anodic (top) and cathodic (bottom) surfaces (b). Operating conditions: I=1000 A; pure Ar as working gas.

Acknowledgements

This work has been performed in the frame a research contract between University of Bologna (DIEM) and Centro Sviluppo Materiali (CSM S.p.A.).

Partial financial support for the University of Bologna group from the Italian Ministry of Education, University and Scientific Research (M.I.U.R.) national project PRIN 2002.

The authors would like to thank Dr. A.B. Murphy (CSIRO, Sydney, Australia) for having provided the raw database of thermodynamic and transport properties of the Ar and Ar-H_2 plasmas that the authors have suitably elaborated and adapted to their needs.

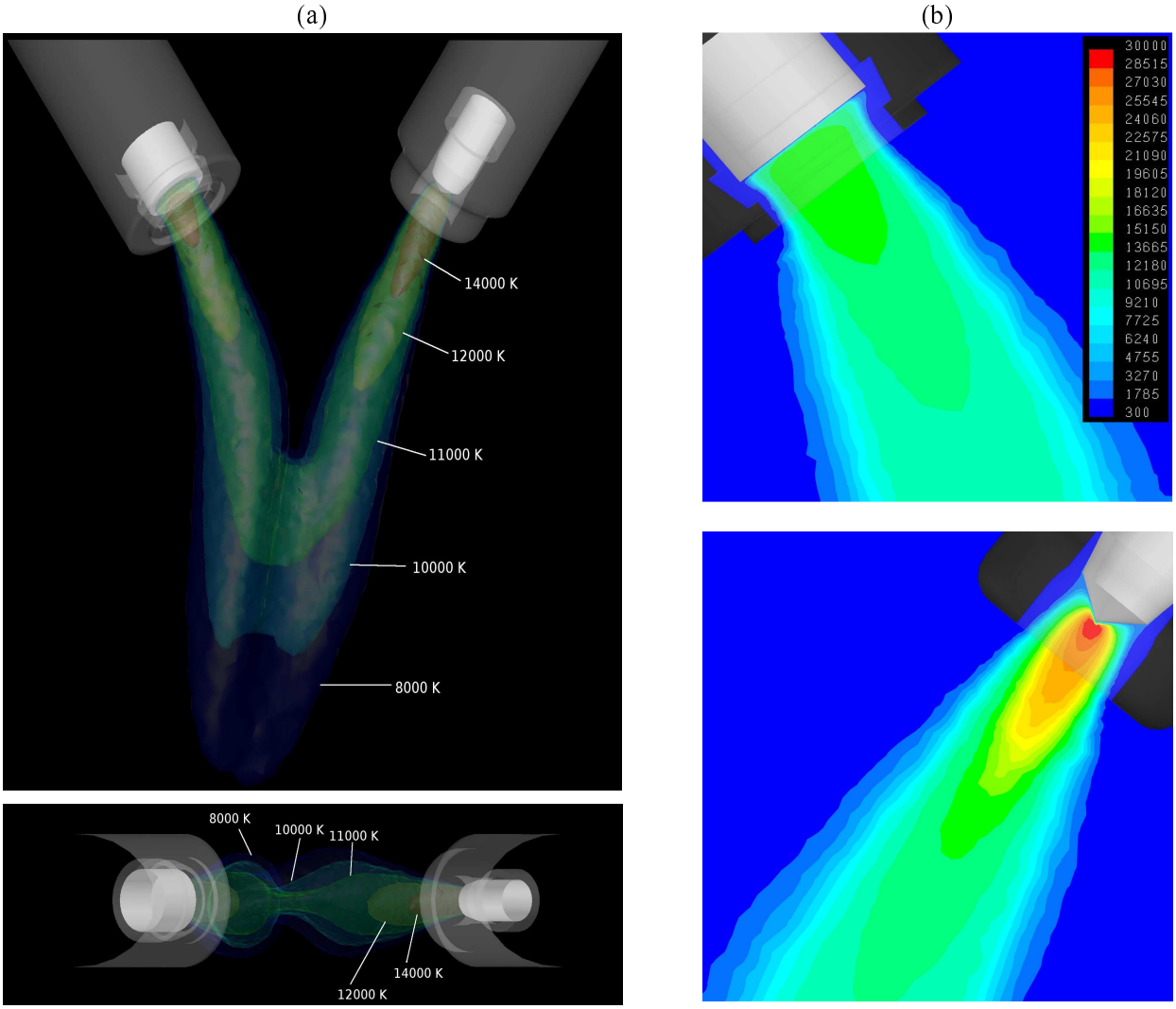

Fig. 4. Isotemperature surfaces in the discharge (a) and details of the plasma temperature [K] in the region close to the anodic (top) and cathodic (bottom) surfaces (b). Operating conditions: I = 1500 A; mixture Ar-H_2 (5% H_2 content) as working gas.

References

[1] B. Barthelemy, C. Girold C. Delalondre, B. Paya, J.M. Baronnet, *Modeling a pilot-scale combustion-vitrification furnace under oxygen plasma arc transferred between twin torches*, Proceedings of the 16th International Symposium on Plasma Chemistry (ISPC-16), Taormina, Italy, 22-27 June 2003.

[2] F. Salvati, *Application of Plasma System for Tundish Heating*, Proceedings of the 1st European Conference on Continuous Casting, Firenze, Italy, 1991

[3] D. Bernardi , V. Colombo, E. Ghedini, A. Mentrelli, *Comparison of Different Techniques for the FLUENT®-Based Treatment of the Electromagnetic Field in Inductively-Coupled Plasma Torches*, Eur. Phys. J. D., **27**, 55-72, 2003

[4] A.B. Murphy, C.J. Arundell, *Transport Coefficients of Argon, Nitrogen, Oxygen, Argon-Nitrogen, and Argon-Oxygen Plasmas*, Plasma

[5] A.B. Murphy, *Transport Coefficients of Hydrogen and Argon-Hydrogen Plasmas*, Plasma Chem. Plasma Process., **20**, 279-297, 2000

[6] A.B. Murphy, *Demixing in free-burning arcs*, Physical Review E, **55**, 7473-7494, 1997

Time Dependent 3-D Simulation of a DC Non-Transferred Arc Plasma Torch: Anode Attachment and Downstream Region Effects

V. Colombo, E. Ghedini

Department of Mechanical Engineering (D.I.E.M.) and Research Center for Applied Mathematics (C.I.R.A.M.)
Università di Bologna, Via Saragozza 8, 40123 Bologna, Italy
Phone: +39 (0)51 2093978, Fax: +39 (0)51 582528 e-mail: emanuele.ghedini@unibo.it

Abstract
The aim of this work is to investigate by means of a 3-D time-dependent numerical model the plasma flow and heat transfer inside a DC non-transferred arc plasma torch operating at atmospheric pressure [1-6], using a customized version of the CFD commercial code FLUENT©.

1. Introduction

Modeling of a DC non transferred arc is a very difficult task since the discharge is often characterized by instabilities due to the anode-arc attachment motion that leads to strong fluctuations of the temperature and velocity fields in times of the order of the 10^{-5} s [1,2]. In the recent literature the modeling of this kind of devices [3-5] is performed by means of 3-D codes but restricted to steady state configurations. Recently a 3-D time dependent model has been presented [6] enforcing the restriking of the anode in the region of the torch where the electric is sufficiently high, by means of a modification of the anode boundary conditions, following some experimental observations.
In this work a 3-D time dependent model is developed to simulate the behavior of a DC non-transferred plasma torch without any external assumption on the anode restriking and attachment in order to achieve a self consistent model. Moreover the downstream expasion of the plasma jet after the torch nozze is included in the domain, using a LES turbulence model.

2. Modeling assumption

Unsteady flow and heat transfer equations are solved together with the scalar and vector electromagnetic potential equations, for an Ar optically thin plasma under conditions of LTE. We refer to [3,6] for the details on the equations and on the boundary conditions since they are basically the same. Geometry is taken as in [3] in order to have a literature basis for comparison. Cathode and anode regions are taken into account in a simplified way, neglecting the non equilibrium effects of the sheath region. The current is I = 150A and is imposed on the cathode tip, while the gas mass flow rate inlet is of $4x10^{-4}$ Kg/s with a swirl angle of 30°. The motion and the restrikes of the discharge on the anode wall, resulting from the drag of the flow particles acting on the anode spot, are obtained without any external enforcement on the placement of the new attachment (as done in [6]). Instead, an uniform zero electric potential condition on the anode wall is imposed as boundary condition. Due to the low time step size (10^{-6} s) needed for the description of the transient phenomena inside the torch, an advanced LES turbulence model with a Smagorinsky-Lilly subgrid-scale model [7] is used in order to describe the turbulence effects on the flow field, solving the dynamic behavior of the larger scale turbulence eddies.
Simulations are performed over a network cluster of double processor calculators due to the large computational requirements of the unsteady model and the grid refinement needed for the turbulence model in a full 3-D environment.

3. Results

In order to capture the unsteady movements of the anode attachment and the details of the turbulence eddies the time step used in this simulation is $2.5x10^{-6}$s. In Fig. 1 the electric potential contours are shown on the isosurface at 8000 K at different times. A first restrike is shown from t = 0ms to 0.15ms, while for t = 0.3ms to 0.6ms the arc anode attachment is moving downstream under the effects of the fluid dynamic drag force, with a slowly increasing of the maximum voltage. It is possible to see also that the point of attachment slightly rotates due to the presence of the swirl component on the velocity. The other restrikes occour for t = 0.75ms and t =

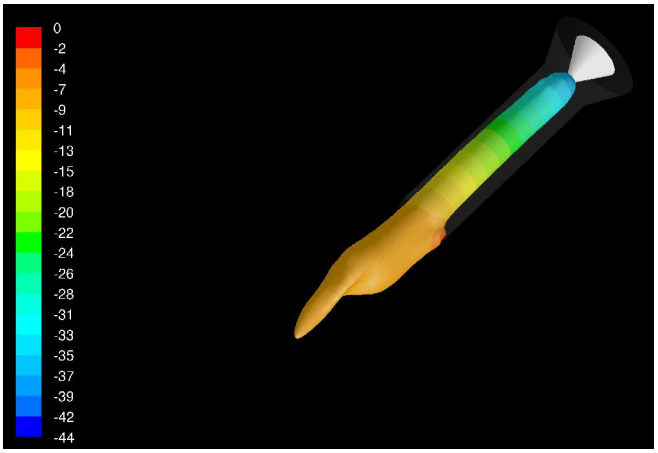

0 ms

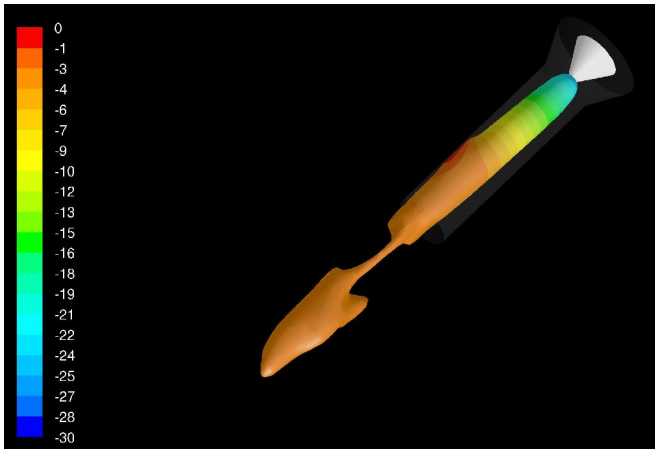

0.15 ms

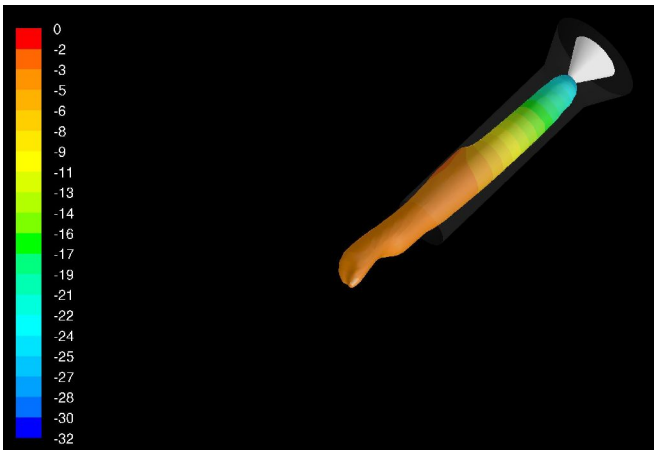

0.3 ms

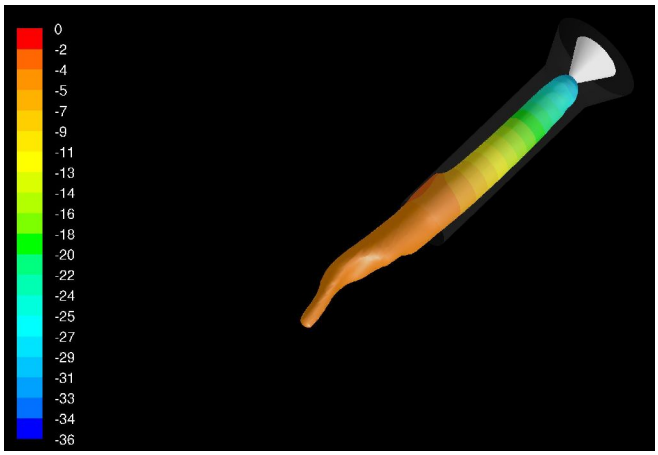

0.45 ms

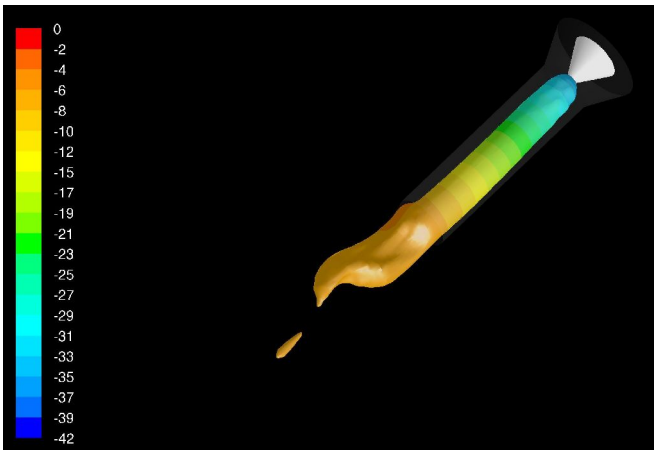

0.60 ms

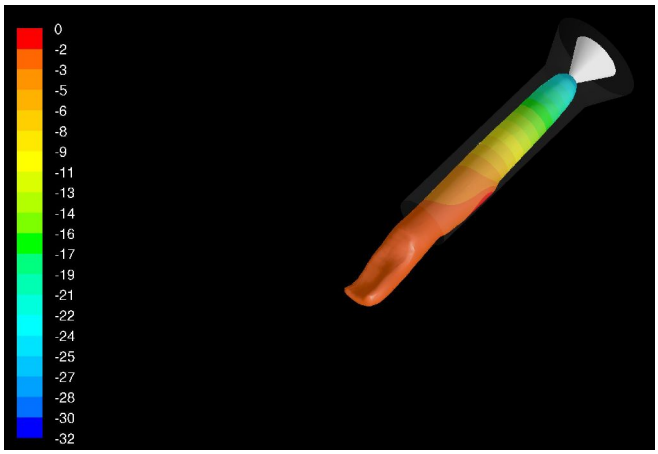

0.75 ms

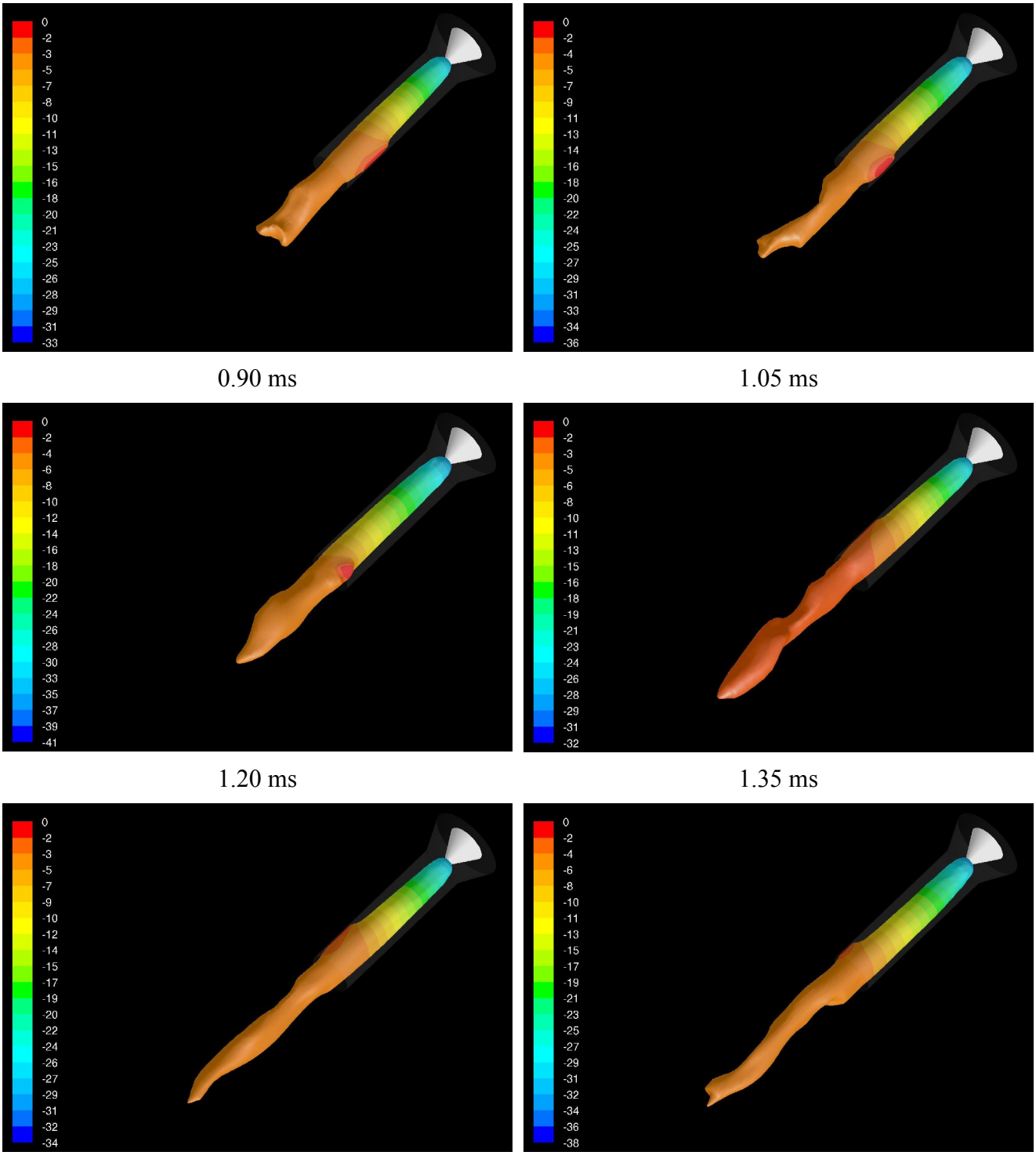

Fig. 1 Instantaneous electric potential [V] on the isosurface at 8000 K in different times.

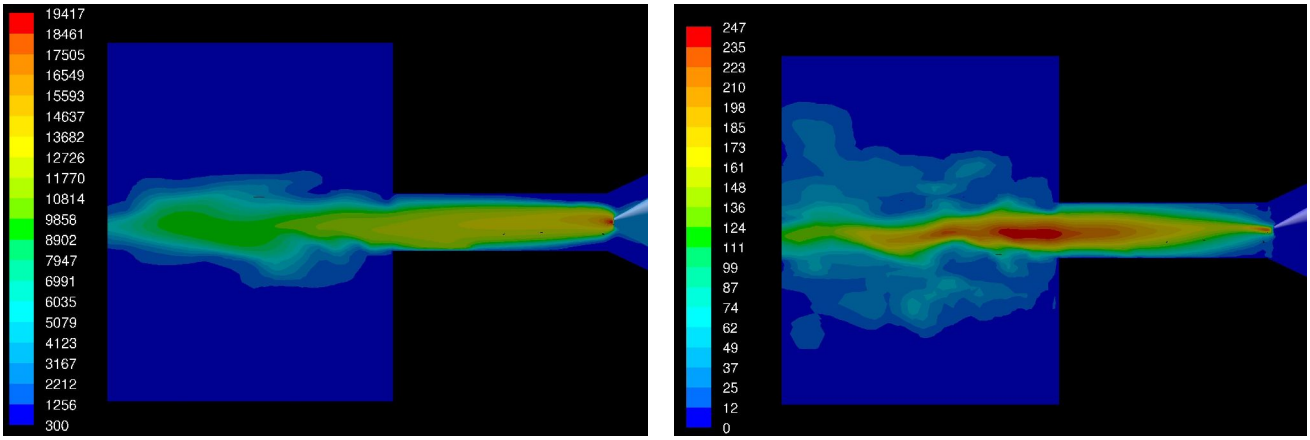

(a) (b)

Fig. 3 Instantaneous (a) temperature field [K] and (b) velocity field [m/s] on a plane for t = 1.50ms.

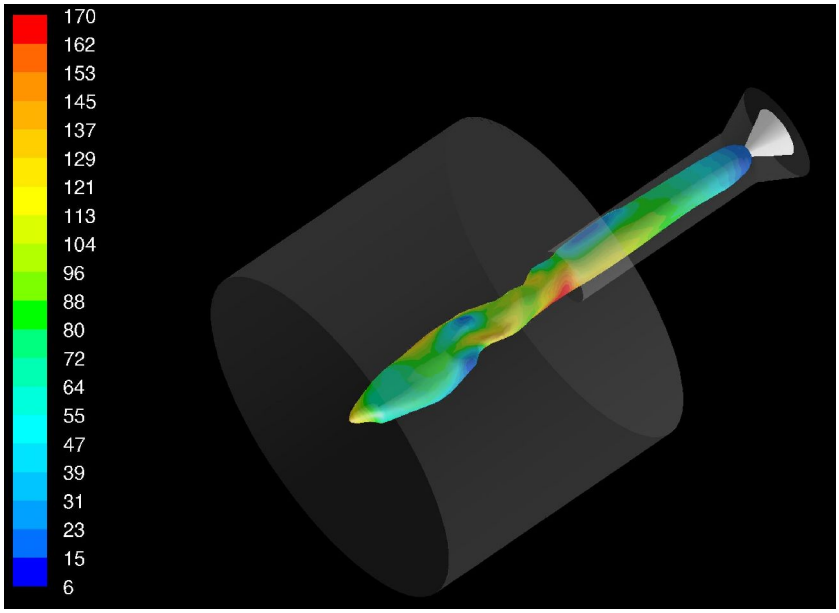

Fig. 4 Instantaneous velocity magnitude [m/s] on the isosurface of 7000K for t = 1.50ms.

1.35ms. The shape of the 8000 K isosurface after the exit nozzle of the torch is quite irregular due to the LES turbulence model, that describes the instantaneous flow field at every time step without any time filtering as done in the RANS models (for example k-ε or RSM). These figures can be interpreted as images taken from an high speed camera with a low shutter speed. In Fig. 2 the instantaneous temperature and velocity fields are shown on a plane passing through the axis of the torch. Again is possible to see the strong irregular shape of these fields in the region downstream the nozzle, expecially for the velocity. Inside the torch cylinder the flow field is quite laminar, due to the high viscosity of the plasma and the smaller length scale. In Fig. 4 the velocity magnitude is plotted on the 7000K isosurface in order to put in evidence the low speed of the plasma gas in the point of the anode attachment. This point is seen by the fluid particles as an obstacle on their motion, due to the high viscosity of the plasma forming the arc spot. The low temperature gas flows around it and the maximum on the velocity magnitude is located on the opposite wall side. In Fig. 5 the instantaneous electric potential on the isosurface of $3x10^6$ A/m^2 for t = 1.50ms is shown, underlining the point of attachment and the path of the current inside the discharge.

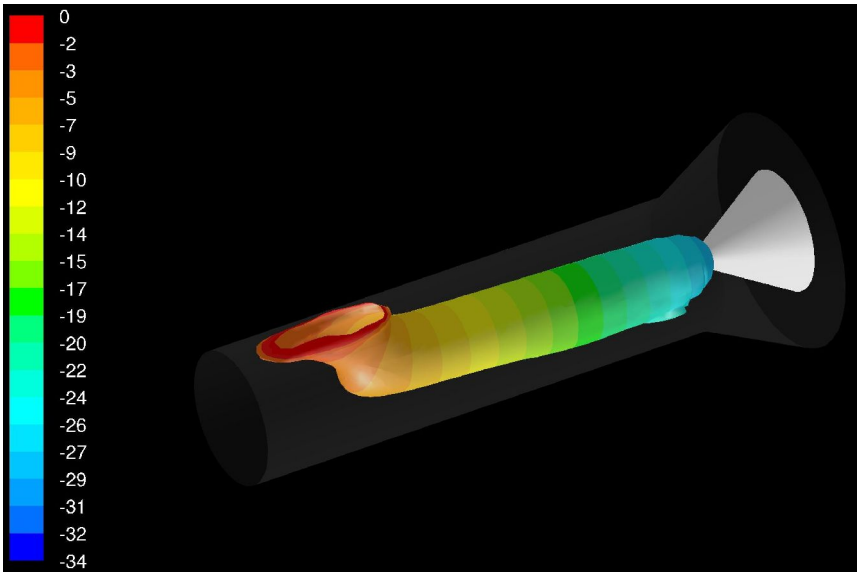

Fig. 5 Instantaneous electric potential [V] on the isosurface of $3x10^6$ A/m^2 for t = 1.50ms.

Conclusions

Simulation results of a 3-D time dependent LES model of DC non-transferred arc have been presented. The anode attachment motion and restrike is described without any external assumption. Results seems to be quite in agreement with experimental observations done in [1,2]. This model is far from being perfect, especially in the anode boundary layer treatment where the non equilibrium effects have been neglected and seems to be very important in the evaluation of the location of the restrikes. Another important step will be the comparison of the results with experimental measurements in order to tune the model, since the LES approach is still in a stage of verification in the different fields of application in which it could be used. The next step will be a two temperature model in order to take into account the anode attachment in a more accurate way.

References

[1] J.F. Coudert, P. Fauchais, *High Temp. Mat. Proc.* **1**, 2 (1997)
[2] P. Fauchais, *J. Phys. D: Appl. Phys.* **37** (2004) R86R108
[3] He-Ping Li, Xi Chen, *J. Phys. D: Appl. Phys.* **34** (2001) L99L102
[4] J.J. Gonzalez, P. Freton, A. Gleizes, *J. Phys. D: Appl. Phys.* **35** (2002) 31813191
[5] He-Ping Li, E. Pfender, Xi Chen, *J. Phys. D: Appl. Phys.* **36** (2003) 1084-1096
[6] C. Baudry, G. Mariaux, A. Vardelle, C. Delalondre, E. Meillot, *Proceedings of ISPC-16*, n. 558, Taormina, Italy (2003)
[7] M. Germano, U. Piomelli, P. Moin and W.H. Cabot, *Phys. Fluids A* **3** (1991) 1760–1765

Acknowledgments

This work was performed with partial financial support from the Italian Ministry of Education, University and Scientific Research (M.I.U.R.) national project COFIN-2002 and from the National Group for Mathematical Physics (G.N.F.M.) of the Italian Institute of High Mathematics.

3-D Fluidynamic and Plasma Characterization of DC Transferred Arc Plasma Torches for Metal Cutting

V. Colombo, E. Ghedini, A. Mentrelli

Department of Mechanical Engineering (D.I.E.M.) and Research Centre of Applied Mathematics (C.I.R.A.M.)
University of Bologna, Via Saragozza 8, 40123 Bologna, Italy
Phone: +39 (0)51 2093978, Fax: +39 (0)51 582528 e-mail: colombo@ciram.unibo.it

S. Dallavalle, M. Vancini
Cebora S.p.A., Via Andrea Costa 24, 40057 Cadriano di Granarolo, Italy
Phone: +39 (0)51 765000, Fax: +39 (0)51 765222 e-mail: mauro.vancini@cebora.it

Abstract
The aim of this work is to investigate by means of a 3-D numerical model the behaviour of a transferred arc plasma torch operating at atmospheric pressure, for the cutting of a metallic substrate material, using a customized version of the CFD commercial code FLUENT©. The metallic substrate and the keyhole are included in the computational domain in order to take into account their effects on the flow field of the discharge at the nozzle exit. The detailed gas injection section and the cathode chamber are included in the computational domain as well.

keywords: plasma cutting torches, transferred arc plasma torches, metal cutting.

1. Introduction

Transferred arc plasma torches are widely used in industrial cutting process of metallic materials because of their ability to cut a wide range of metals and because of the very high productivity that can be achieved with this technology [1]. The plasma arc cutting process is characterized by a transferred electric arc that is established between an electrode that is part of the cutting torch (the cathode) and another electrode that is the metallic workpiece to be cut (the anode). In order to obtain a high quality cut and a high productivity (low cutting time) the plasma jet must be, among the other things, as collimated as possible and must have the higher achievable power density. With this regard, modelling and numerical simulation may be very useful tools for the investigation of the characteristics of the plasma discharge generated in these kind of devices, as well as for optimization of industrial cutting torches. In recent years, numerical simulation has gained popularity as a tool for torch design and a lot of excellent papers have been published on this topic (se, for example, [1-4], just to name but a few).
In this paper we present a three-dimensional numerical model recently developed by some of the authors within a customized version of the CFD commercial code FLUENT© in the framework of a research contract between the University of Bologna and Cebora S.p.A.
Fluid flow and heat transfer equations are solved together with the coupled electromagnetic ones for an air optically thin plasma assumed to be in local thermodynamic equilibrium. The details of the gas injection section and of the cathode chamber are included in the computational domain in order to determine the effects of the geometry on the flow field characteristics of the discharge and to optimize it in the design phase.
The metallic substrate with the keyhole is included in the computational domain only for electrical and fluid-dynamics purposes, in order to take into account its effect on the flow field of the discharge at the nozzle exit. Experimental measurements are performed in order to evaluate the keyhole shape and diameter for different cutting conditions. In order to investigate the behavior of the device during pre-cutting phase 2-D simulation of the non-transferred nozzle-attached arc are also considered.

2. Modelling approach

Two-dimensional and three-dimensional computational models for the simulation of a transferred arc plasma torch require the simultaneous solution of the coupled set of non-linear fluid-dynamic, electromagnetic and

energy transfer equations. Such computational models have been developed starting from previously developed numerical models implemented by some of the authors for the simulation of atmospheric pressure inductively coupled plasma torches [5] and of transferred arc plasma torches both in free-burning arc configuration and in configuration with gas injection [6].
In the model developed for plasma cutting torch presented here, turbulence phenomena are taken into account by means of a k-ε RNG model in order to better describe the flow field inside the device.

The main simplifying assumptions on which the developed models rely are the following:
- the discharge is stationary;
- the plasma is described as a simple mono-component fluid (air);
- the plasma is optically thin and in local thermodynamic equilibrium (LTE);
- the turbulent plasma flow is described by the renormalization group (RNG) turbulence model;

Taking into account the previous assumptions, the equations of the conservation of mass and momentum take the following form for the three dimensional case:

$$\nabla \cdot (\rho \mathbf{v}) = 0$$

$$\nabla \cdot \rho \mathbf{v}\mathbf{v} = -\nabla p + \nabla \cdot \tau + F_L$$

being ρ the density of the fluid, **v** the velocity of the fluid, p the pressure, τ the stress tensor and F_L the Lorentz force due to the interaction of the conductive fluid and the electromagnetic field. The energy equation is solved without taking into account the viscous dissipation:

$$\nabla \cdot \rho \mathbf{v} h - \nabla \cdot k \nabla T - \frac{5}{2}\frac{k_B}{e}\left(\mathbf{j} \cdot \frac{1}{C_p}\nabla h\right) = Q_J - Q_R$$

where h is the enthalpy of the fluid, k is the thermal conductivity of the fluid, k_B is the Boltzmann constant, e is the electron charge, **j** is the current density and C_P is the specific heat at constant pressure of the fluid.
The last term on the left hand side of the equation represents the enthalpy transport due to stream of the conductive electrons. Finally, Q_J is the energy dissipated in the discharge by Joule effect and Q_R represents the radiative losses.
The equations for the calculation of the electrostatic potential V, and of the vector potential **A**, are the following:

$$\nabla \cdot \sigma \nabla V = 0$$

$$\nabla^2 \mathbf{A} + \mu_0 \mathbf{j} = 0$$

where σ is the electrical conducibility of the plasma, $\mathbf{j} = \sigma\mathbf{E} = -\sigma \nabla V$ represents the current density and μ_o is the magnetic permeability of the vacuum.
The electromagnetic equations are solved, by the FLUENT® solver, by means of a *user-defined scalar* (UDS) approach, in a way similar to that described in [7].
The equation for the two-dimensional case are a subset of the presented equations and will not be presented here.
The thermodynamic and transport coefficients of the air plasma used for the numerical simulations are those given in [8].

All calculations have been performed by PlasMac, a cluster of workstations available at CIRAM & DIEM of the University of Bologna. Such a resource allows for a large reduction in computational time as well as for the treatment of complex computational domain otherwise not manageable with traditional personal computers.

3. Results

As a first step in the analysis of this kind of device, a two-dimensional axi-symmetric non-transferred configuration of a CP-160 CEBORA plasma cutting torch has been simulated. This configuration is typical of the first ignition phase of the cutting torch, where the pilot arc is approached to the workpiece in order to establish the transferred configuration in which the cutting phase will be initiated. In the first non-transferred phase the anode is the nozzle of the torch, while in the second transferred phase the anode is the workpiece to cut. The effect of the inlet pressure on the non-transferred discharge shape is shown in Fig. 1. A first effect is the increase on the inlet pressure that leads to an increase on the plasma maximum temperature reached inside the nozzle. A second effect is on the attachment point of the discharge to the anode which is dragged downstream by the increased velocity of the fluid that tents to create a low temperature gas shield on the internal cylindrical surface of the nozzle, preventing the attachment of the arc point in this position. For a sufficiently high pressure the arc is closed on the nozzle exit surface. The two-dimensional code predicts a cylindrical uniform attach due to its intrinsic limitations, while the actual attachment will be a single spot due to the magnetic constriction forces.

The three-dimensional model has been applied to a CP-200 CEBORA plasma cutting torch, including the details of the inlet gas section as shown in Fig. 2. A detail of the temperature field resulting from simulation is shown in Fig. 3 while the electric potential on the 13000 K isosurface is shown in Fig .4. The inclusion of the inlet region allows a better understand the characteristics of the flow in the upstream region of the plasma chamber and to perform a better design of the torch component. An example is in Fig. 5, where the turbulence viscosity ratio in the inlet region is shown.

References

[1] V.A. Nemchinsky, *Plasma flow in a nozzle during plasma arc cutting*, J. Phys. D: Appl. Phys. 31, 3102-3107, 1998.

[2] J. Gonzalez-Aguilar, C. Pardo Sanjurjo, A. Rodriguez-Yunta, M. Angel Garcia Calderon, *A theoretical study of a cutting air plasma torch*, IEEE Transactions on Plasma Science, **27,** 1, 1999.

[3] P. Freton, *Etude d'un arc de découpe par plasma d'oxygène. Modélisation – expérience*, PhD Thesis (in French), Universite Paul Sabatier, Toulouse III, France, 2002.

[4] P. Freton, J.J. Gonzalez, A. Gleizes, F. Camy Peyret, G. Caillibotte, M. Delzenne, *Numerical and experimental study of a plasma cutting torch*, J. Phys. D: Appl. Phys. **35,** 115131, 2002.

[5] D. Bernardi, V. Colombo, E. Ghedini, A. Mentrelli, *Three-dimensional modelling of inductively coupled plasma torches*, Eur. Phys. J. D, **22,** 1, 119-125, 2003.

[6] D. Bernardi, V. Colombo, E. Ghedini, S. Melini, A. Mentrelli, *Three-dimensional time-dependent modelling of magnetically deflected transferred arc*, IEEE Transaction On Plasma Science, **33**, 2, 428-429, 2005.

[7] D. Bernardi, V. Colombo, E. Ghedini, A. Mentrelli, *Comparison of different techniques for the FLUENT-based treatment of the electromagnetic field in inductively-coupled plasma torches*, Eur. Phys. J. D **27**, 1, 55-72, 2003.

[8] M. Capitelli, G. Colonna, C. Gorse, A. D'Angola, *Transport properties of high temperature air in local thermodynamic equilibrium,* Eur. Phys. J. D., **11**, 279–289, 2000.

Acknowledgments

Work performed in the frame a research contract between University of Bologna (D.I.E.M.) and Cebora S.p.A.

Partial financial support for the University of Bologna group from the Italian Ministry of Education, University and Scientific Research (M.I.U.R.) national project COFIN-2002 and from the National Group for Mathematical Physics (G.N.F.M.) of the Italian Institute of High Mathematics. The Authors wish to thank Christian Diego Di Sanzo, Olaf Marzocchi and Giovanni Masini for their contribution in 2D modelling and experimental activities in the frame of this work.

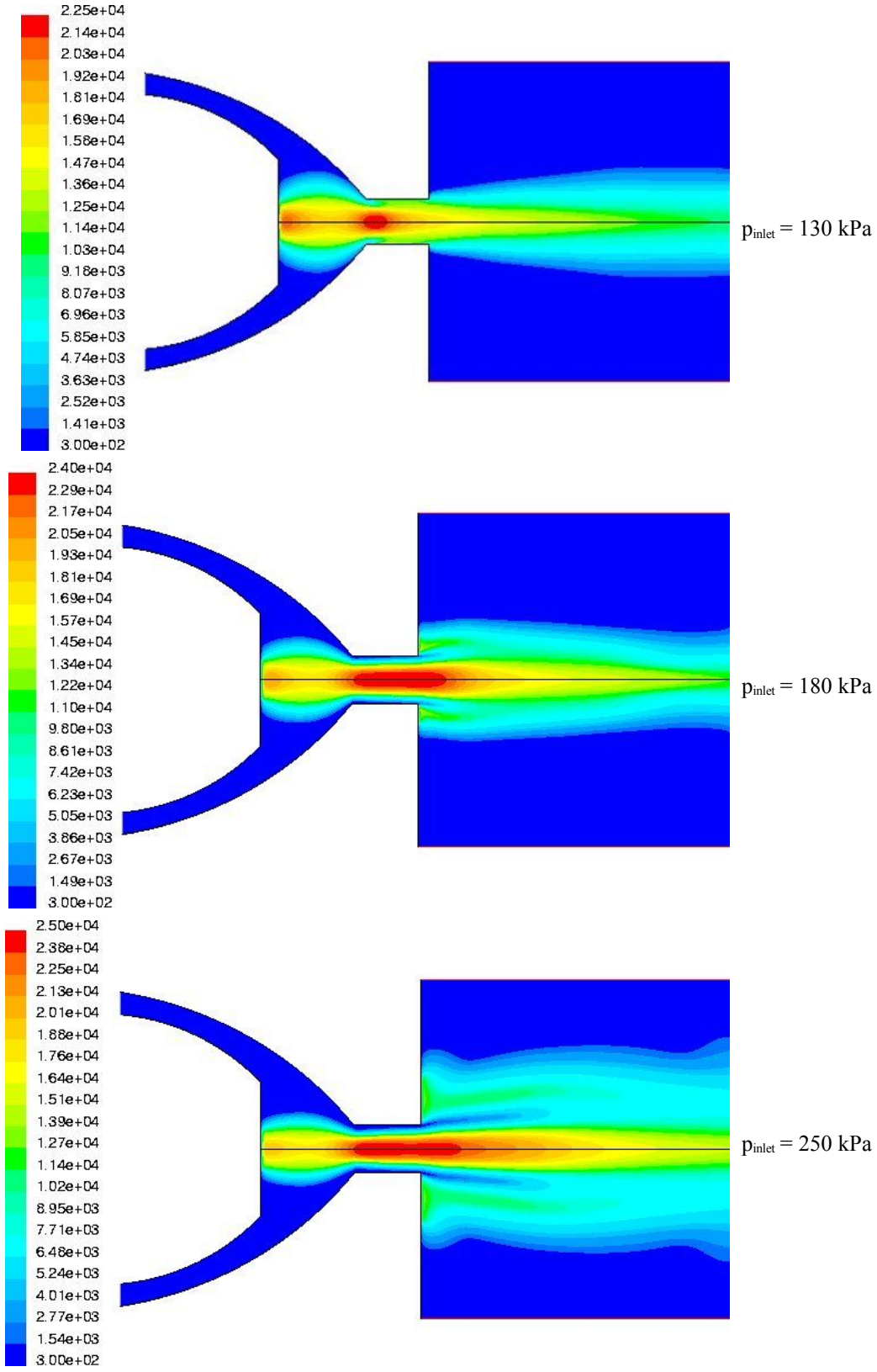

Fig. 1 Temperature fields [K] for a CP160 plasma torch with 1.8 mm nozzle diameter, operating at different inlet absolute pressure with a current I = 180 A.

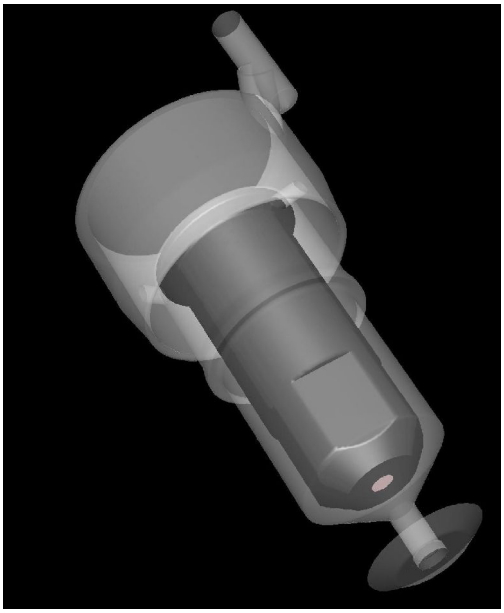

Fig. 2 3-D visualization of the geometry of the plasma cutting device CP200. Details of the inlet gas region are included in the computational domain.

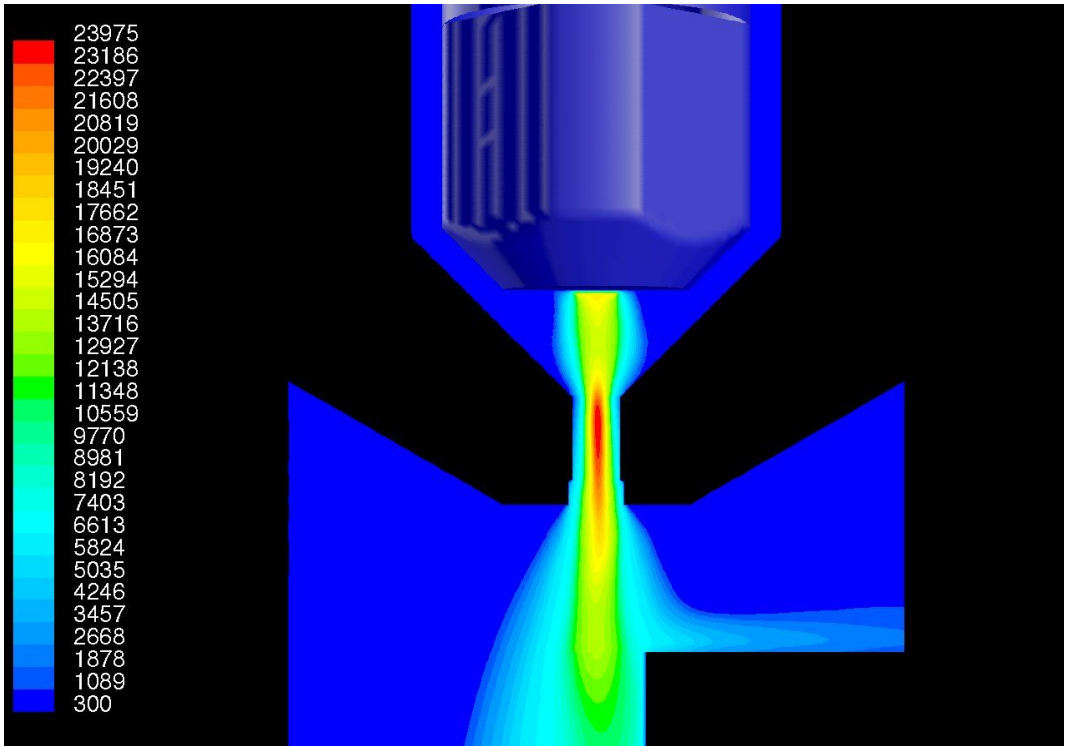

Fig. 3 Detail of the temperature field [K] in the nozzle region of the plasma cutting device CP200 for a 1.8 mm nozzle diameter, 160 A of cathode current and 400kPa (absolute) at the inlet.

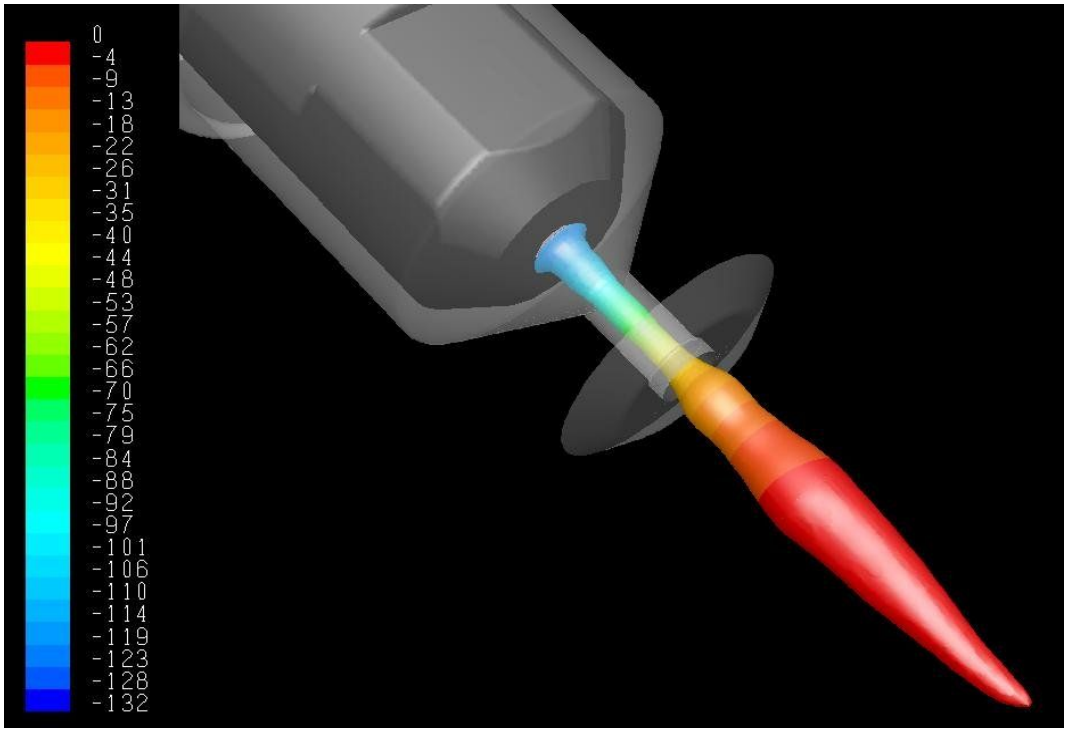

Fig. 4 Electric potential [V] on the 10000 K isosurface for a plasma cutting device CP200 with a 1.8 mm nozzle diameter , 160 A of cathode current and 400kPa (absolute) at the inlet.

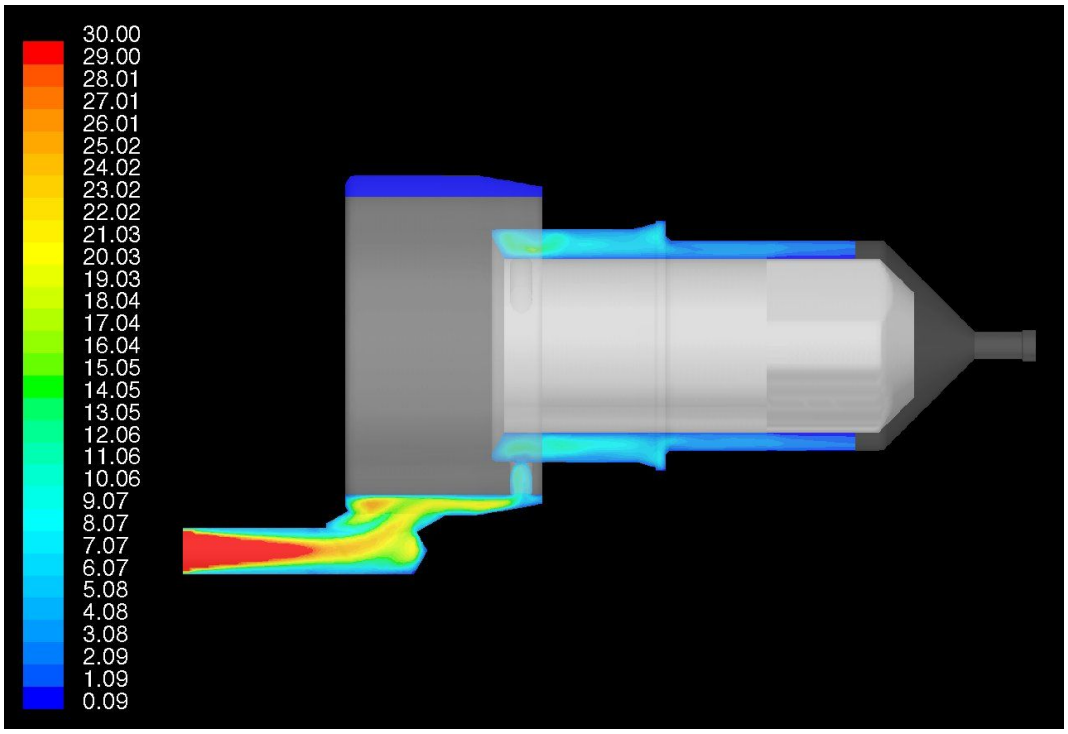

Fig. 5 Turbulence viscosity ratio in the inlet section of a plasma cutting device CP200 with a 1.8 mm nozzle diameter, 160 A of cathode current and 400kPa (absolute) at the inlet.

Two hollow needles-to-mesh electrical discharge with TiO_2 catalyst for VOC decomposition

S. Pekárek[1], D. Neirynck[2], C. Leys[2], M. Pospíšil[3] and J. Krýsa[3]

[1]*Czech Technical University, FEE, Technická 2, 166 27 Prague 6, Czech Republic*
[2]*Ghent University, Department of Applied Physics, Faculty of Engineering, Rozier 44, B-9000 Ghent, Belgium*
[3]*Institute of Chemical Technology, Technická 5, 166 28 Prague 6, Czech Republic*

Abstract
The results of studies of operational regimes of the two hollow needles-to-mesh electrical discharge enhanced by the mixture of air or mixture of air with n-heptane are given. The n-heptane decomposition efficiencies for the discharge with stainless steel mesh, with the mesh coated by the layer of TiO_2 or with the mesh covered by TiO_2 globules are presented.
Keywords: DC electrical discharge, catalyst, VOC decomposition.

1. Introduction

The non-thermal plasma based technologies are becoming more and more important for a wide range of applications such as destruction of volatile organic compounds (VOC) in air streams, because of their energy selectivity and their capability for the simultaneous removal of various pollutants [1-4]. Corona discharge (DC, AC or pulsed), dielectric barrier discharge in a confined space and others have been tested for these purposes [4]. Recently, it has been shown that a combination of non-thermal plasma with catalysis leads to very promising results for the destruction of atmospheric pollutants at relatively low energy cost [5-8].
The corona discharge reactors involve different electrode configurations, a wire-to-cylinder most frequently, a corona torch, a point-to-plate and a multi-point-to-plate.
The corona discharge is a relatively low power electrical discharge. Both discharge stabilization and discharge power enhancement can be achieved by applying a gas flow with respect to the active electrode. Contrary to the electrode system and gas flow regime proposed in [1, 6, 9], in this paper we proposed a hollow-needle-to-mesh electrode configuration in which an atmospheric pressure discharge is enhanced by a mixed VOC/air flow through the needle electrode [2]. The advantage of this arrangement of the airflow with respect to the active electrode is that all the mixture passes through the discharge and therefore is affected by the plasma chemical processes.
Titanium dioxide (TiO_2) is an n-type semi-conductor, biologically and chemically inert, and existing in rutile and anatase phase. A series of its energy levels is associated with covalent bonding between atoms composing the crystallite (valence band) and a second series of spatially diffuse higher energy levels is associated with conduction in the macromolecular crystallite (conduction band) [10]. Both series are strictly separated by a fixed energy gap of 3.2 eV [12]. Incidence of UV light of a higher energy than this band gap, e.g. originating from de-excitation processes in the plasma-reactor, can promote electrons from the valance band to the largely vacant conductance band. Simultaneously, a positive hole with strong oxidizing capability is formed [10, 11]. In order for photo-catalysis to be productive chemically, electron-hole pair recombination followed by energy dissipation as heat, must be suppressed by fast trapping either of the electrons, or the holes or both, not exceeding the time constant of recombination which is a fraction of nanoseconds [10, 12]. The anatase TiO_2 is predominantly used, because it has a higher O_2 adsorbing capacity than rutile TiO_2 [10]. The contaminating organic substrates themselves can react as adsorbed traps for the photo-generated holes.
In this paper the operational regimes of the reactor and the results of an n-heptane decomposition study are presented. This study was performed using a stainless steel mesh electrode, either uncoated or coated by a TiO_2 layer or as base structure for a layer of Aerolyst TiO_2 catalyst globules, produced by the Degussa AG. We used two needles to increase the energy density and to test possible scaling for future application.
For our experiments we chose n-heptane $CH_3(CH_2)_5CH_3$ because it is a common part of organic solvents and automotive fuels (petrol) and because it represents a wide group of saturated hydrocarbons.

2. Experimental arrangement

The experimental set up is shown in Figure 1. In a cylindrical plasma-chemical reactor, an electrical discharge is created between two hollow stainless steel needles and a mesh electrode. The needles with inner and outer diameter of 0.7 mm and 1.2 mm respectively and a 15° sharp tip, are placed in a diametrical plane of the reactor, one at each side of the reactor axis, in fact the mirror axis for the needle positions. The tip's inner faces are pointing towards each other and the inter-needle distance w is set to 9 mm. A metallic mesh R 0.60, made by M-Metall Italy, situated perpendicularly to those needles, is used as a second electrode. The rhombus mesh cells have dimensions 0.60×0.50 mm^2 and thickness 0.15 mm. In this study, two types of mesh are used, namely a mesh with a TiO_2 coating and an uncoated mesh used as underlying base structure for a 3 mm thick catalyst bed of TiO_2 globules. The inter-electrode distance d is varied from 4 mm to 10 mm by a 2 mm step.

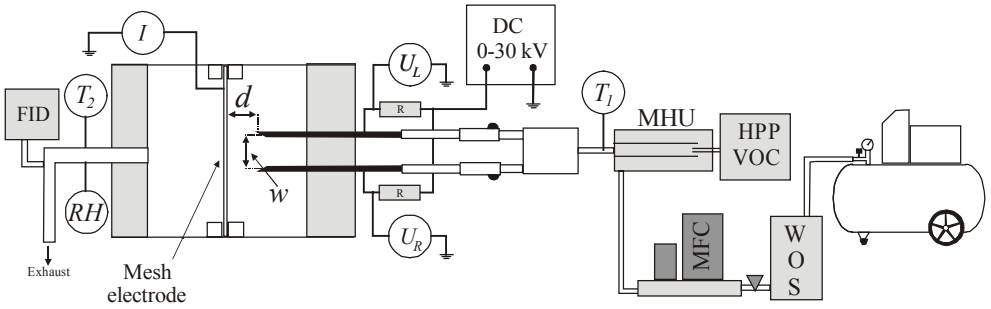

Figure 1. Experimental arrangement

A gas flow, either clean environmental air or a mixture of air and n-heptane, passes through the needles. A compressor supplies the required pressure. Before entering the needles, the air is dried and cleaned by the water and oil separator WOS. A Bronkhorst mass flow controller sets the flow rate. The air enters the mixing and heating unit MHU that is preheated to the temperature of 90°C. In this unit, a precise dosage of n-heptane is added to the preheated air using a high-pressure pump HPP followed by the evaporation of the n-heptane at temperature 150ºC. The mixture temperature is measured by a thermocouple T_1.

A DC power supply provides voltage up to 30 kV. The polarity of the needles can be changed. Both needles have a ballast resistor R = 5.30 MΩ. At the output of the reactor, two sensors are placed to detect both the outlet temperature T_2 and the relative humidity RH. For the purposes of an n-heptane decomposition study, there is also a FID total hydrocarbon analyser HC 51 (measuring range 0 -1300 ppm) present at the outlet.

3. Experimental results

3.1. Electrical discharge in air

The first set of experiment was devoted to the study of stable operational regimes of the discharge in air. The V-A characteristics were obtained for different inter-electrode distances and for different polarities of the needles. For d = 10 mm, the inter-electrode distance exceeded the inter-needle distance and the existence of a potential difference between both needles, originating from a possible asymmetry in the mutual needle positioning and a slightly different tip curvature, caused an unstable discharge. In order to obtain the highest possible energy density, with regard to future decomposition studies, we chose d = 8 mm. Therefore only for this distance the V-A characteristic is shown in figure 2. Negatively and positively biased needles reveal a V-A characteristic different in shape and voltage levels, which is obviously due to different discharge mechanisms for both polarities. To be self-sustaining a positive corona requires a lower voltage, i.e. lower fields (13.8 kV/cm versus 15.6 kV/cm), because of lower losses.

3.2. Electrical discharge in the mixture of air with n-heptane

For discharges in the mixture of air with n-heptane, again differently biased needles result in different V-A characteristics. Figure 3 shows that for needles biased negatively, the voltage increases for low currents and then

reaches a plateau, rather than it reaches a maximum, as was the case for discharges in air. For positive biased needles, again a maximum is obtained. However, the voltages are significantly higher than for discharges in air. This is not seen for negatively biased needles. This could be explained by photon absorption in n-heptane, limiting the creation of secondary electrons in a discharge with needles biased positively. Still the voltage level for positively biased needles remains for all current levels significantly lower than for negatively biased needles. Therefore, the latter configuration is chosen for further decomposition studies.

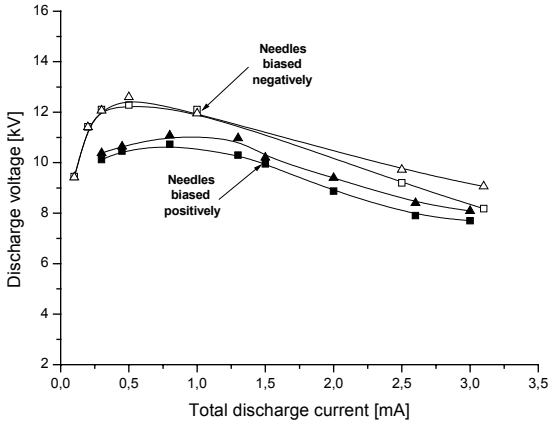

Figure 2. V-A characteristics for two-needles-to-mesh discharge in a air; Q_{AIR} = 20.3 slm; d = 8 mm. (left needle: squares, right needle: triangles)

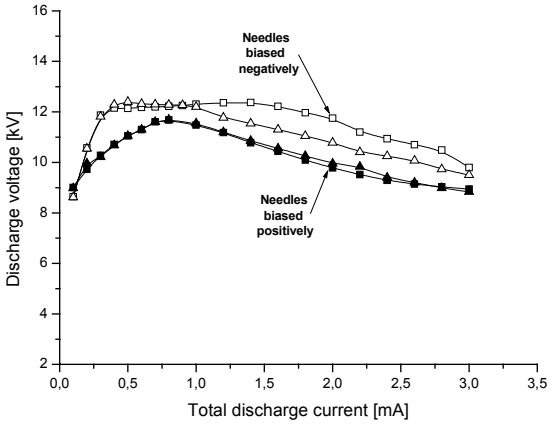

Figure 3. V-A characteristics for two-needles-to-mesh discharge in a mixture of air with n-hepatane; n-heptane concentration = 33 ppm; Q = 20.3 slm; d=8 mm. (left needle: squares, right needle: triangles)

3.3. Decomposition studies

All results described in this section were performed with the discharge with the needles biased negatively, as explained in previous section. The experiments were performed for three different secondary electrode configurations, namely with an uncoated stainless steel mesh, a stainless steel mesh coated with a layer of TiO_2 and a stainless steel mesh as a base structure for a layer of TiO_2 catalyst globules.

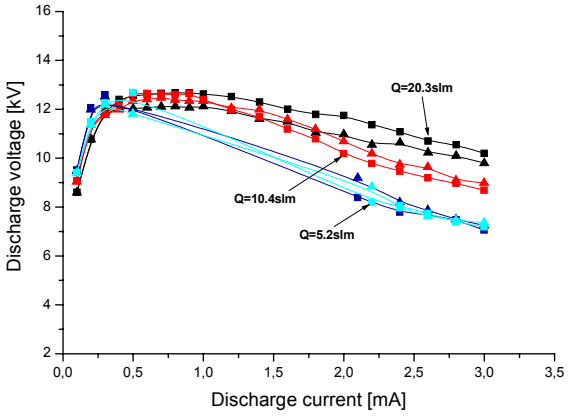

Figure 4. V-A characteristics for two needles to uncoated mesh discharge in a mixture of air and n-heptane. Needles biased negatively; d=8 mm; n-heptane concentration = 33 ppm. (left needle: squares, right needle: triangles)

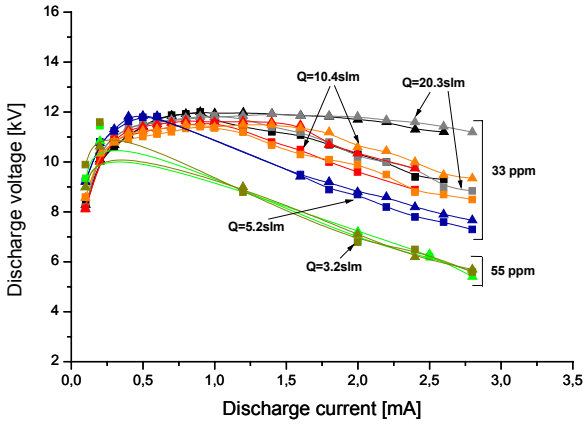

Figure 5. V-A characteristics for two needles to coated mesh discharge in a mixture of air and n-heptane. Needles biased negatively; n-heptane concentration = 33 ppm, d = 8 mm. (left needle: squares, right needle: triangles)

The V-A characteristics for these experiments are shown in figures 4, 5 and 6 respectively. The values of decomposition efficiencies for the first two sets of experiments were obtained for the discharge current of 2.8 mA at different flow rates. They are presented in Table 1. The experimental results for the TiO_2 globules are not included in this table because the removal efficiencies for different power densities were obtained at constant flow rate through a variation of the input electrical power.
Figure 6 also includes the V-A characteristic of the discharge in air. The airflow rate in both cases was 5.2 slm.

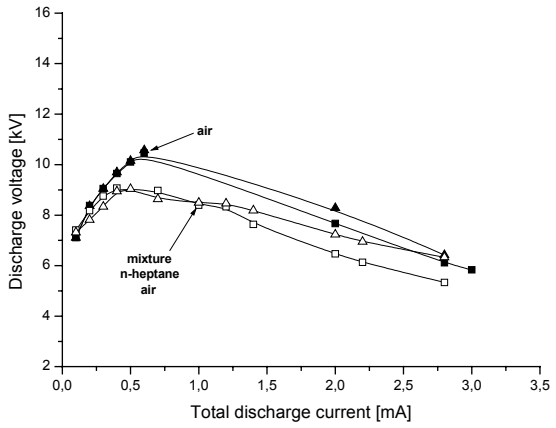

Figure 6. V-A characteristics for two needles to mesh with a layer of TiO_2 granules discharge in air and in the mixture of air with n-heptane; Q=5.2 slm; needles biased negatively; d = 8 mm; n-heptane concentration = 33 ppm. (left needle: squares, right needle: triangles)

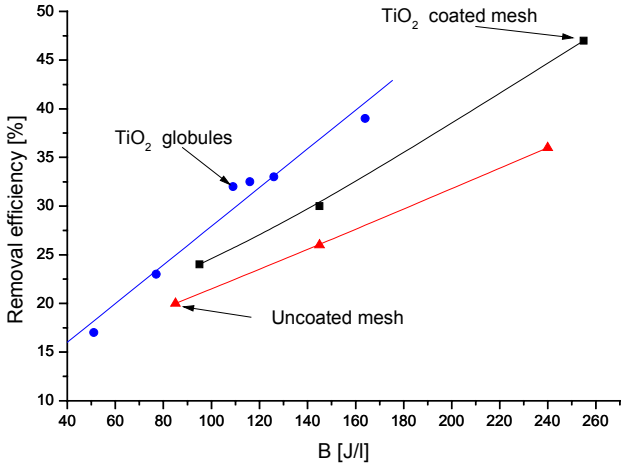

Figure 7. Decomposition efficiency versus energy density for discharge in a mixture of air and n-heptane. Needles biased negatively, d = 8 mm; n-heptane concentration = 33 ppm.

Table 1. Removal efficiency vs. flow rate and mesh type;
Needles biased negatively; d = 8 mm; n-heptane concentration = 33 (55*) ppm.

Flow Rate [slm]	20.3	10.4	5.2	3.2
Uncoated mesh	20	26	36	--
Coated mesh	24	30	47	37.5*

3.4. Decomposition studies – Summary

The decomposition efficiencies versus energy density for the discharge in the mixture of air with n-heptane for the discharge with an uncoated mesh, mesh coated with TiO_2 layer and finally for the discharge with the layer of TiO_2 globules on the mesh are shown in Fig. 7. In order to obtain high energy density the inter-electrode distance d was chosen to be 8 mm.

4. Conclusions

The layer effect of the TiO_2-coated mesh on V-A characteristics of the discharge in the mixture of air with n-heptane can be seen from the comparison of Fig. 4 and Fig. 5. As far as the decomposition experiments were performed with the inter-electrode distance d = 8 mm, the comparison was made for this distance only. From these two figures it is seen, that for all three flow rates coating of the mesh in the region of low currents

decreases discharge voltage. For higher currents the difference between V-A characteristics for coated and uncoated mesh is smaller.

Significant difference however exits among V-A characteristics for the discharge with the layer of TiO_2 globules on the mesh and the discharge with an uncoated mesh and the mesh coated with the layer of TiO_2. The results obtained from the comparison of Figs. 4, 5 and Fig.6 for the flow rate 5.2 slm reveal that for particular current the discharge with TiO_2 globules requires smaller voltage.

From Fig. 7 it is seen that n-heptane decomposition efficiency increases with increased energy density. It is also seen that for particular energy density the decomposition efficiency is the highest for the discharge with the layer of the TiO_2 globules, smaller for the mesh coated with the layer of TiO_2 and the smallest for the discharge with an uncoated mesh. These results can be explained by the effect of photo catalyst TiO_2 on decomposition efficiency. In case of TiO_2 globules the photo catalysts area exposed to the UV emitted from the discharge is higher than for the case of TiO_2 coated mesh, therefore the decomposition efficiency must be higher.

Acknowledgement

This work was supported by the Grant Agency of the Czech Republic under contract 202/04/0728 and by and the Czech-Flemish scientific cooperation research program under contract No. 2004-2005-03. The authors would also like to thank the Degussa AG, Germany, for providing the Aerolyst TiO_2.

References

[1] R.Vertriest, R.Morent, J.Dewulf, C.Leys, H.Van Langenhove - Plasma Sources Sci. Technol. **12**, 412 (2003).
[2] S.Pekárek, V.Kříha, M.Pospišil, I.Viden - J. Phys. D: Appl. Physics **34**, L117 (2001).
[3] M.Pospišil, I.Viden, M.Šimek, S.Pekárek - Int. J. Vehicle Design **27**, 306 (2001).
[4] K.Urashima, J.S.Chang - IEEE Trans. Dielectrics and Electr. Insul. **7**, 602 (2000).
[5] T.Ohkubo, D.Li, D.Yakushiji - J. Adv. Oxid. Technol. **6**, 75 (2003).
[6] R.Morent, J.Dewulf, N.Steenhaut, C.Leys, H.Van Langenhove - Proc. XV Intern. Conf. on Gas Discharges and their Applications, Toulouse, **2**, 749 (2004).
[7] T.Oda, T.Takahashi, K.Yamaji - IEEE Trans. Ind. Applications **38**, 873 (2002).
[8] D.Li, D.Yakushiji, S.Kanazawa, T.Ohkubo, Y. Nomoto - J. Electrostat. **55**, 311 (2002).
[9] Yu.Akishev, O.Goossens, T.Callebaut, C.Leys, N.Napartovich, N.Trushkin - J. Phys. D: Appl. Physics **34**, 2875 (2001).
[10] M.A.Fox and M.T.Dulay - Chem. Rev. **93**, 341 (1993).
[11] E.Pelizzetti and C.Minero - Electrochim. Acta **38**, 47 (1993).
[12] M.R.Hoffmann, S.T.Martin, W.Choi and D.W.Bahnemann - Chem. Rev. **95**, 69 (1995).

Formation of Modified Layer on HOPG by Low-energy Ion Bombardment

N.Hamamura and A.Yoshida
Musashi Institute of Technology
1-28-1 Tamazutsumi Setagaya-kuTokyo 158-8557, Japan

Abstract

An ion irradiation at low-energy of < 1 keV is expected to introduce a thin modified-layer about several nm onto polymers or carbon materials. Using the irradiation with nitrogen ion, a formation of a nitrogen containing diamond like carbon is expected to introduce on the surface. In the report, to clarify the structure of modified-layer, nitrogen ion irradiation to HOPG (highly oriented pyrolytic graphite) was carried out. As the result, it was suggested that the irradiated nitrogen is introduced preferentially at the edge or at the defect of basal plane.

Keywords: HOPG, Nitrogen ion irradiation, Modified-layer, Depth profile, Chemical bonding state

1. Introduction

Surface modification of polymers using gaseous plasmas is one of a method for improvement its properties such as a wettability and an adhesivity. The authors have studied on surface modification of polymers by using nitrogen plasma under high $\boldsymbol{E}/\boldsymbol{n}$ ($\boldsymbol{E}$: electric field, $\boldsymbol{n}$: gas density) condition [1] and low-energy nitrogen ion irradiation. From the result, a wettability and an adhesivity were improved with nitrogen introduction. And, the properties such as an increase of a chemical stability and of hardness were improved. It is considered that not chemical functional groups but also a bridged structure exist in the modified-layer. And, it was deduced that the improvement was accelerated by the irradiation of nitrogen ions about 100 eV. By the way, during the processing, many kind of active species such as electron, radical, and UV or VUV are also irradiated. Many researchers have studied on the contribution of active species to improvement of the property [2][3]. And, a structure of the modified-layer was suggested which consists of polar groups on the surface and bridged structure below the surface to several mm [3]. However, it is not fully characterized for thin surface layer about several nm.

To characterize the structure of the modified-layer, the authors have used AR-XPS (angle resolved X-ray photoelectron spectroscopy) to obtain the depth profile, which is able to analyze the sample surface with nondestruction. As the result, irradiated with the ion energy of 100eV on the sample, nitrogen introduction was occurred preferentially about 3nm below the surface. It was deduced a formation of thin modified-layer of several nm and an existence of a bridged structure including carbon-nitrogen bond [4]. And, the existence of the structure brought about the increase of surface hardness was suggested. However, the characterization requires thin analysis depth about several nm on the surface, a reaction process during the irradiation and characterization of the modified-layer was not clarified. In case of carbon materials as the sample, it is expected that a kind of nitrogen containing amorphous DLC (diamond like carbon) may form on the surface. And, the structure is able to characterize by using Raman spectroscopy which depth is several 10 nm. Using a commercial graphitic plate as the sample [5], the structural change by the irradiation was detected a little because of poor reproducibility. Therefore, the sample is required to use materials which composition and the structure have been clarified.

In the report, using HOPG as the samples, the analyses on the chemical bonding state were carried out to clarify the ion energy and dose dependence on the formation.

2. Experiments

2.1 Ion irradiation

Samples were commercial ZYB grade HOPG which size was 6 x 12 x 1.7 mm^3. Nitrogen ion was irradiated onto the samples which surface was peeled off using adhesive tape. Figure 1 shows a schema of

experimental setup. Before the irradiation, the chamber was evacuated to less than 1.0×10^{-4} Pa. The gas was commercial nitrogen. Under the pressure at 1.3×10^{-2} Pa, the irradiation was carried out using an iongun of VARIAN #981-2043. The distance between the substrate and the iongun was 100 mm. Irradiation area on the sample was 10 mm in diameter. The ion dose was 1.0×10^{17} cm^{-2} in which nitrogen concentration of the sample shows saturation [5].

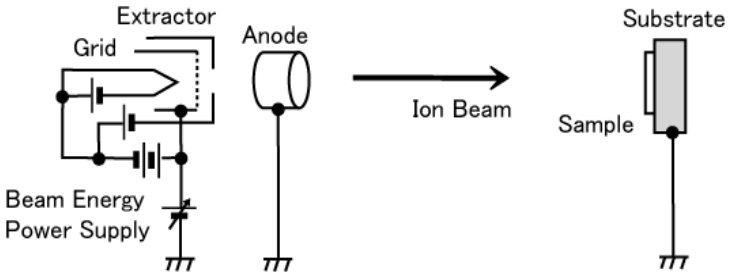

Fig.1 Experimental setup

2.2 Characterization

The samples were analyzed by using AR-XPS, Raman spectroscopy, and FT-IR.

AR-XPS was carried out using Surface Science Instruments SSX-100 which X-ray source was Al Kα 1486 eV. Figure 2 shows a schema of AR-XPS and the profiles were calculated using equation 1.

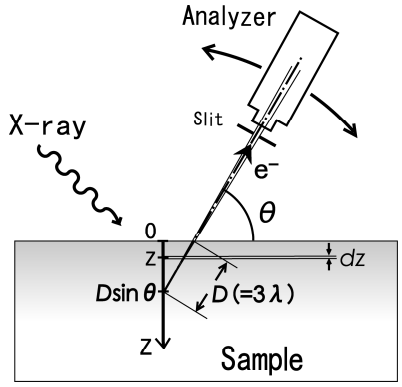

Fig.2 Angle-resolved XPS

$$I = \int dI = \int_0^{D\sin\theta} k(z) S \sigma E n(z) \exp\left(-\frac{z}{\lambda \sin\theta}\right) dz \qquad (1)$$

Where, I is the spectrum intensity in depth at z, $n(z)$ is the depth profile of the composition which corresponds to the number of photoelectrons generated in the depth at z., θ is the photoelectron take off angle, λ is the electron inelastic mean free path, S is the X-ray irradiation area, and $k(z)$ is a compensation function in the measurement device.

Varying θ and detecting I, $n(z)$ is obtained.

Chemical bonding state of carbon was analyzed by using micro Raman spectroscopy of HORIBA Jobin Yvon T-64000 of which spot size was 1 mm and the wavelength for the excitation is 514 nm.

3. Results and discussion

3.1. Structure of modified-layer

Table 1 shows composition of the sample analyzed by XPS. Nitrogen was detected on the irradiated surface. Increasing the energy, nitrogen concentration on the surface was increased. The oxygen contamination was detected several % and was depended little on the ion energy. It is deduced that the oxygen contamination is occurred preferentially after the irradiation.

Figure 3(a) shows Raman spectra. Irradiated the samples, G-band at 1560 cm^{-1} decreased and D-band about 1360 cm^{-1} appeared and increased. The result suggests a degradation of C-(sp^2)C and a generation other bonding on the surface by the irradiation. A broad peak around 1450 cm^{-1} appeared. The peak corresponds C-N bonds. Increased with the introduction of nitrogen, an introduction of C-N bonds is expected. On the other hand, the peak is also corresponds to a fluorescence of C-(sp^3)C bonds which often detected using longer excitation wavelength of Raman spectroscopy. Using the excitation light with short wavelength is required to distinguish these bonding states.

Table 1 composition of irradiated sample

Energy [eV]	C [%] ([cps])	N [%] ([cps])	O [%] ([cps])
Reference	95.6 (4739)	0 (0)	4.4 (217)
50	77.8 (3461)	14.2 (634)	8.0 (357)
100	76.5 (3198)	15.5 (648)	8.0 (336)
200	76.9 (3188)	15.3 (633)	7.8 (325)
500	78.9 (3244)	14.5 (595)	6.6 (271)
1000	79.1 (3260)	13.1 (540)	7.8 (321)

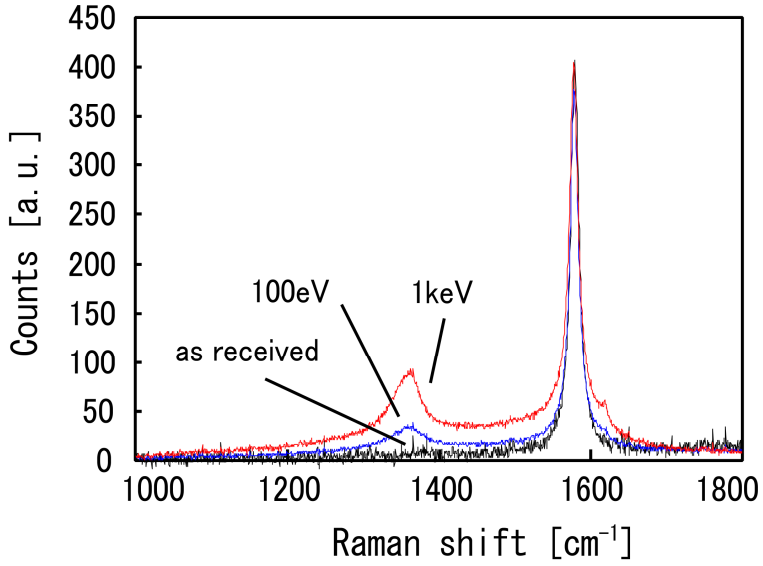

(a) Raman spectra

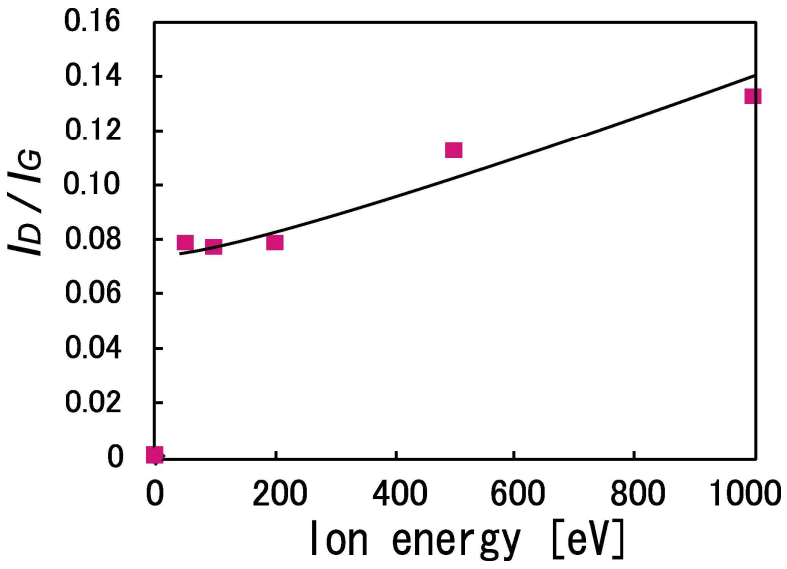

(b) I_D/I_G

Fig.3 Raman spectra and I_D/I_G

I_D/I_G peak ratio of D-band to G-band is shown in figure 3(b). Increased the ion energy, the ratio increased. The increase corresponds a destruction of C-(sp^2)C and a generation of other bonding state. Thus, it is considered that the destruction depends on the increase of the ion energy. On the other hand, increasing the ion energy, an increase of the implantation depth is considered. The analysis depth of Raman spectroscopy is about several 10 nm. Thus, increasing the modified-layer, it is considered that D-band is easily detected. It is also suggested that the increase of D-band is due to an increase of the thickness of the modified-layer.

Figure 4 shows depth profiles of nitrogen in the sample. Nitrogen concentration increased about 2 nm at 100 eV and about 3 nm at 1 keV from the surface. Increasing the ion energy, nitrogen was introduced inner region. Using SRIM2003 calculation in case, the ion range was estimated 0.8 nm at 100eV and 3.5 nm at 1 keV respectively. The implantation depth obtained by the depth profile showed agreement with that of SRIM calculation. The result suggests that the thickness of the modified-layer depended on the ion energy without the structural change. Increasing the energy, the thickness is due to increase.

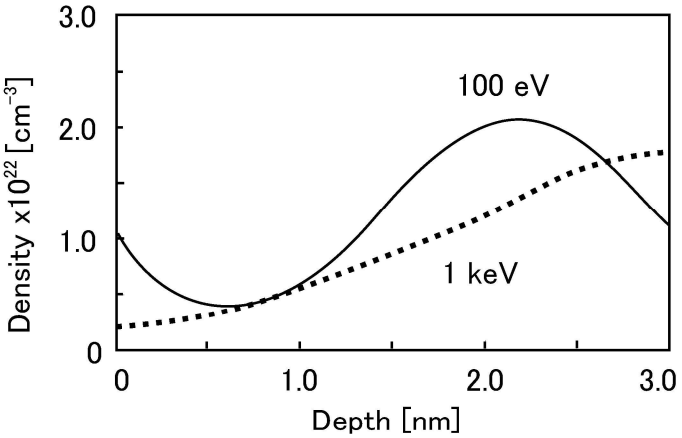

Fig.4. Depth profiles of nitrogen

Figure 5 shows C1*s* and normalized N1*s* XP core level spectra. Irradiated the samples, C1*s* spectra were broadened to higher binding energy which contain C-(sp^3)C or C-N bonds. A decrease of the peak about 285eV corresponded to C-(sp2)C suggests a degradation of C-(sp^2)C of HOPG and a formation of the modified-layer on the surface, which shows agreement the spectral change of Raman spectra shown in Fig. 3. N1*s* spectra after the irradiation showed same shape and were depended little on the ion energy. Thus, the chemical bonding state of nitrogen in the modified-layer is depended little on the ion energy. Increasing the ion energy with the same ion dose, increase of the thickness without change of chemical bonding is considered.

The spectrum is able to separate into three peaks A, B, and C which corresponded to C-NH_2 or pyridine like (A), pyrrole like or quarternary nitrogen (B), and N-O (C). However, it is also agreed generally that the peak A and the peak B attributed to CN(sp^3) and CN(sp^2) [6]. Thus, other analysis is required to clarify the chemical bonding state.

3.2. Introduction process of modified-layer

From the above discuss, it is considered that the structure of the modified-layer does not depend on the ion energy and the introduction is depended on the ion dose. Increasing the ion energy, the thickness of the modified-layer is increased and it is expected that chemical bonding states will be detected using FT-IR.

Figure 6 shows infrared spectra of the samples irradiated with the energy of 1 keV, which obtained by subtraction the spectrum before the irradiation. A peak at 1750 cm^{-1} was detected, which corresponds to oxygen containing groups such as –COOH or >C=O. The peak changed a little by the ion dose.

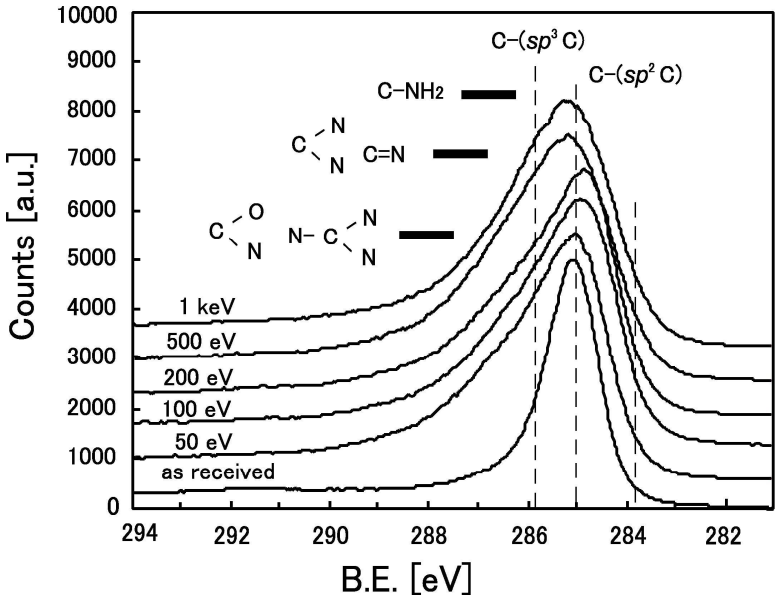

(a) C1*s*

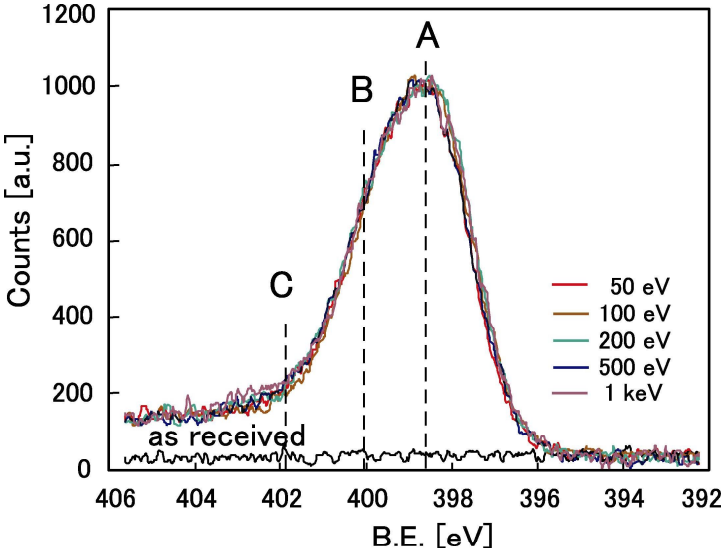

(b) N1*s*

Fig.5 XP core level spectra

Two peaks at 870 cm^{-1} and at 660 cm^{-1} were detected on the irradiated sample, which correspond to a defect of basal plane. A broad peak around 3200 cm^{-1} corresponds to primary or secondary amines. And, a peak at 1350 cm^{-1} corresponds to anilines. A pyridine like nitrogen was detected as a weak peak around 800 cm^{-1}. A quarternary nitrogen was detected little. Thus, it is considered that irradiated nitrogen is introduced preferentially at the defect or at the edge of basal plane. Increased the ion dose, these peak decreased. It is considered that the defect of the basal plane was increased and the modified-layer was decomposed by increase of the ion dose.

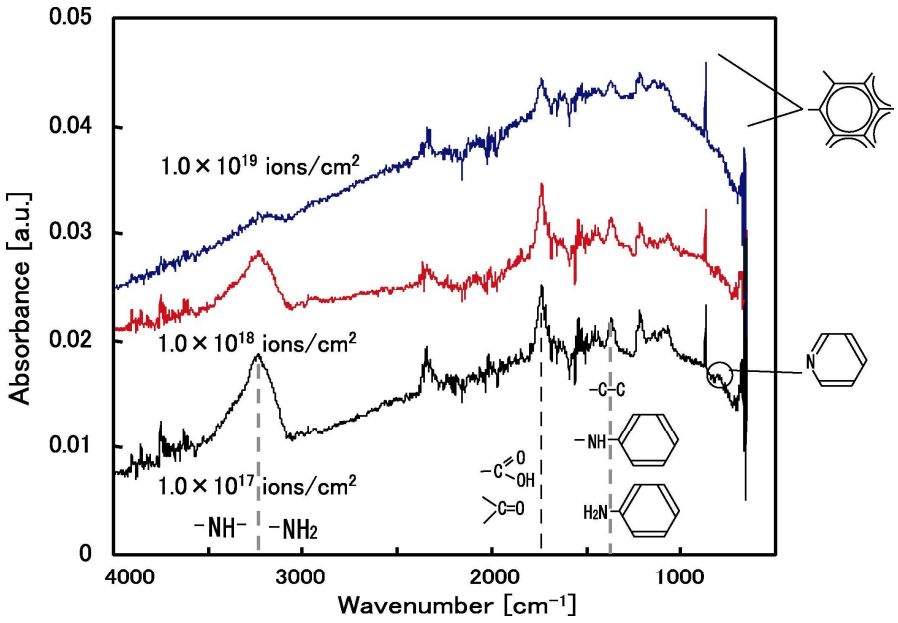

Fig.6 Infrared absorption spectra

4. Summary

The reaction mechanism during low energy nitrogen ion irradiation of HOPG was studied. And, the structure of the modified-layer was characterized. From the result, it was summarized as follows.

(1) Increasing the ion energy, the thickness of the modified-layer increased without structural change.

(2) Increasing the ion dose, the defect of basal plane was increased.

(3) Nitrogen introduction occurred preferentially at edge plane or at the defect of basal plane. And, the formation of pyridine or amine group is suggested.

References

[1] N.Hamamura, M.Yumoto, and T.Sakai: International Conference of Gas Discharges and Their Applications, pp.56-59 (2002)

[2] L.J.Gerenser: J. Vac. Sci. Technol. A, 6, 5, pp.2897-2903 (1988)

[3] E.M.Liston, L.Martinu, and M.R.Wertheimer : J. Adhesion. Sci. Technol., 7, 10, pp.1091-1127 (1993)

[4] H.Kanai, N.Hamamura, and M.Yumoto : T. IEE Japan. A, 121, 5, pp.453-458 (2001), *in Japanese*

[5] N.Hamamura, T.Onodera, M.Yumoto, and T.Sakai: ISPC-15, pp.1925-1930 (2001)

[6] J.E. Klemberg-Sepieta, O. M. Kuttel. L. Martinu and M. R. Wetheimer: J. Vac. Sci. Technol. A, 9, pp.2975-2981 (1991)

SYNTHESIS OF ALUMINUM NANOPARTICLES USING DC THERMAL PLASMA

B. Zhang[1], B. Liu[1], T. Renault[1], S. L. Girshick[1], and M. R. Zachariah[2]

1 Department of Mechanical Engineering, University of Minnesota, Minneapolis, MN, USA
2 Department of Mechanical Engineering, University of Maryland, College Park, MD, USA

Abstract
A process involving a subsonic thermal plasma expansion is reported for the synthesis of aluminum nanoparticles. Parametric studies of particle formation were performed. Particles were characterized by scanning mobility particle sizing, scanning and transmission electron microscopy, and electron dispersive X-ray spectroscopy. The produced aluminum particles had number-mean diameters below 20 nm. Particles were found to consist of a crystalline aluminum core encapsulated in a thin oxide surface layer.

Keywords: aluminum nanoparticles, thermal plasma synthesis

Introduction

Energetic materials are chemical compounds or mixtures that store significant quantities of energy. They typically include propellants, explosives, and materials for pyrotechnics. Metals that have been used or considered for these purposes include aluminum, titanium, magnesium, boron, zirconium and beryllium. Among these metals, aluminum has been used extensively [1]. For conventional size solid propellants, the reaction kinetics are largely controlled by mass transport rates between reactants, which establishes the limit of the energy release rate. However, when the particle size is reduced, especially into the nanometer range, the rate of diffusion-controlled processes becomes comparable to that of chemical reactions, resulting in a sharp increase in the rate of energy release [2]. Consequently there has been an increased research effort regarding the use of nano-aluminum in high-energy explosives, and aluminum nanoparticles are claimed to produce more rapid and efficient burning of solid propellants than other existing powders, thus gaining interest for applications such as rocket fuels [3-4].

Compared to other available methods of producing nanoparticles, such as thermal evaporation [5], electrochemical methods [6], and laser methods [7], thermal plasma methods can achieve high-rate synthesis of nanoparticles. Because of the high temperatures in the reaction zone, thermal plasmas can be used for complete dissociation of reactants into their elements. This leads to considerable chemical flexibility with regards to reactants.

Experimental procedures and results

A schematic of the particle synthesis apparatus and associated diagnostics is shown in Figure 1. An argon-hydrogen plasma is generated by a DC arc at near-atmospheric pressure, and is expanded in subsonic flow through a ceramic nozzle to ~53 kPa pressure. The main plasma gases, argon at a flow rate of 30 slm and hydrogen at 0.5 slm, are controlled by mass flow controllers. $AlCl_3$ was used as the aluminum precursor. $AlCl_3$ is a powder at room temperature, with a normal sublimation temperature of 183°C. $AlCl_3$ vapor was generated by subliming $AlCl_3$ powder (anhydrous, reagent grade, Alfa Aesar) in a packed bed similar to the one used by Powell et al [8]. The packed bed is composed of a stainless steel tube filled with 5-mm-diameter glass beads (Chemglass Inc.). Heating wire follows a serpentine path inside the bed to facilitate uniform heating in the range of 165-180°C. Preheated argon, with flow rate ranging from 100-200 sccm, was used to mix and carry the $AlCl_3$ vapor from the packed bed to the reactor. The amount of $AlCl_3$ vapor introduced into the reactor was determined from calibration runs in which the packed bed was weighed before and after a period of reactant injection. The $AlCl_3$ feed rate is affected by the flow rate of argon carrier gas. The mixture of heated argon and $AlCl_3$ vapor is delivered to the reac-

tion chamber through well insulated lines, and through an injection ring and nozzle ports into the plasma. The injection ring and nozzle ports are water cooled, which potentially causes the problem of $AlCl_3$ condensation and clogging of the feed path. To avoid this both the injection ring and the nozzle ports are internally wrapped with mica insulation.

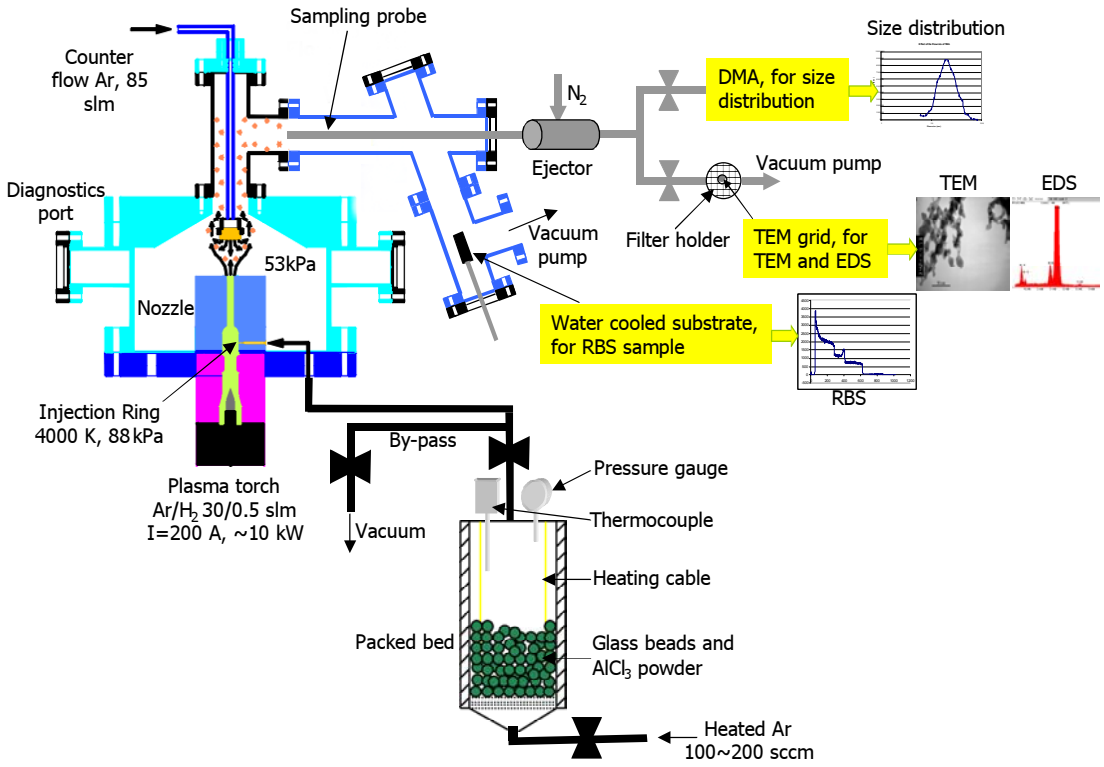

Figure 1. Schematic of system for synthesizing and characterizing aluminum nanoparticles.

Based on modeling of temperature profiles, aluminum particles are expected to nucleate near or shortly downstream of the nozzle exit. A cold argon counterflow opposes the plasma jet exiting the nozzle. The purpose of the counterflow is to provide dilution and cooling, so as to reduce both particle coagulation and particle-particle coalescence, thereby maintaining small primary particle size. Balancing of the momenta of the plasma jet and the counterflow produces a stagnation layer, as seen in Figure 2.

For on-line size distribution measurements a capillary sampling probe is inserted into the reactor downstream of the counterflow tube. The sample passes to a two-stage nitrogen ejector, which dilutes it typically by a factor of approximately 6000, thereby suppressing further coagulation and particle growth. The diluted sample then passes to a scanning mobility particle sizer (SMPS), which consists of a differential mobility analyzer (DMA, TSI model 3085) in series with a condensation particle counter (CPC, TSI model 3007). Measurements of particle size distributions were obtained for various sets of operating conditions. Conditions that varied included the hydrogen flow rate, the flow rate of the argon carrier gas containing the $AlCl_3$ vapor, and whether the argon counterflow was on or off. The hydrogen flow rate was found to have little effect on particle size distributions for the range of flow rates tested (0.5-2.5 slm), and thus only the 0.5-slm case is reported here.

Figure 3 shows measured size distributions for various reactant carrier gas flow rates. By weighing the packed bed before and after the experiment, it was determined that the 200-sccm carrier gas case corre-

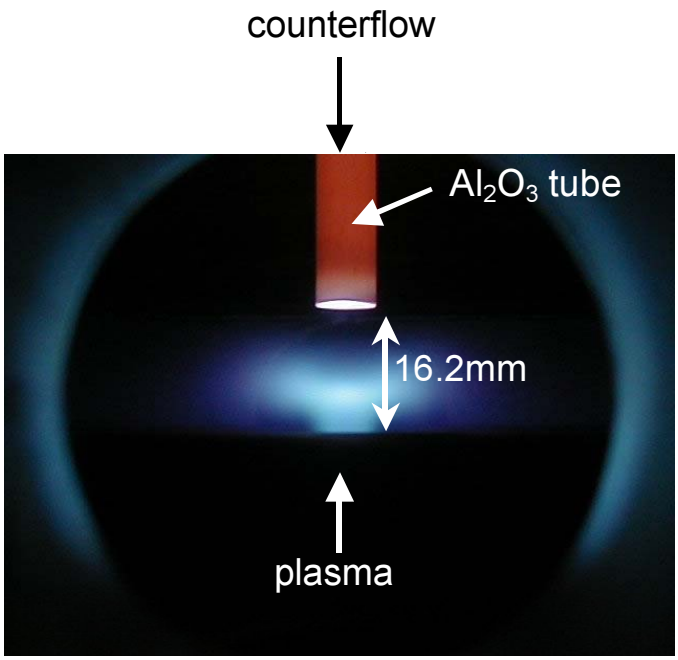

Figure 2: Photograph of stagnation layer obtained with a counterflow of 85 slm argon. A small amount of methane has been added to the counterflow to enhance the stagnation layer luminosity.

sponded to a $AlCl_3$ vapor flow rate of ~20 sccm. For given packed bed temperature the $AlCl_3$ vapor flow rate scales on the carrier gas flow rate. Higher precursor flow rates are seen to produce higher particle concentrations, which in turn favors particle coagulation, resulting in larger values of number-mean particle diameter. For the above running conditions (200 sccm carrier gas, counterflow on), SMPS measurements show a peak in the particle number distribution around 17 nm.

A counterflow configuration has previously been used to control particle size and size distribution [9]. Figure 4 shows measured particle size distributions with and without use of counterflow. The decrease in particle concentration with counterflow corresponds with the dilution due to the counterflow. This decreased particle concentration causes coagulation to be reduced, and therefore the mean particle size is smaller in the case with counterflow on.

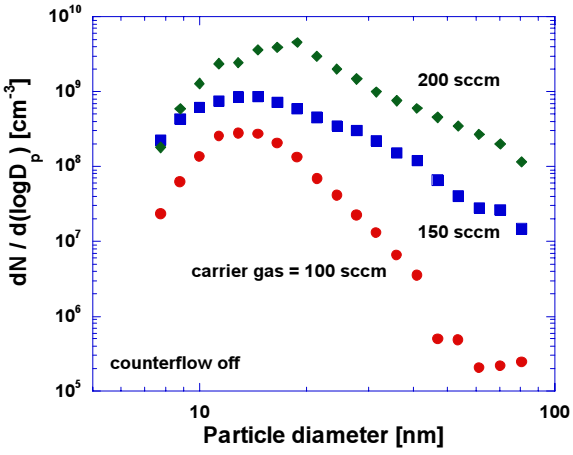

Figure 3. Measured particle size distributions for various flow rates of the reactant carrier gas.

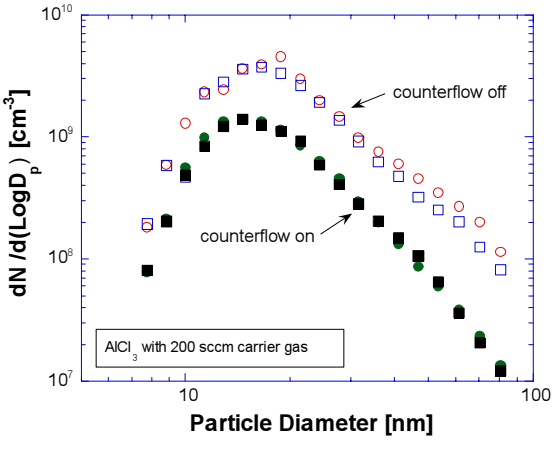

Figure 4. Measured particle size distributions, with and without use of counterflow.

Samples for scanning electron microscopy (SEM) were obtained from the orifice plate inside the dilution ejector. SEM analysis was obtained with a JEOL-6500 FEG SEM at 15kV operating voltage and a working distance of 9.5 mm. Transmission electron microscope (TEM) grids were placed on a filter holder downstream of the ejector. TEM images were obtained with a JEOL 1200 (accelerating voltage ~120kV) and, for high-resolution TEM (HRTEM), a FEI Tecnai G2 30 FEG (accelerating voltage ~300kV).

An SEM image of particles produced in the base case experiment is shown in Figure 5. Particles appear to be spherical and unagglomerated. An example of a TEM micrograph of aluminum particles produced in the base case and deposited onto a filter holder located downstream of the ejector is shown in Figure 6. The TEM image indicates that these particles are mostly smaller than 20 nm, consistent with the SMPS measurements. Energy dispersive X-ray spectroscopy (EDS) analysis of these particles is shown in Figure 7. The EDS spectrum shows a clear aluminum peak, and also indicates the presence of oxygen.

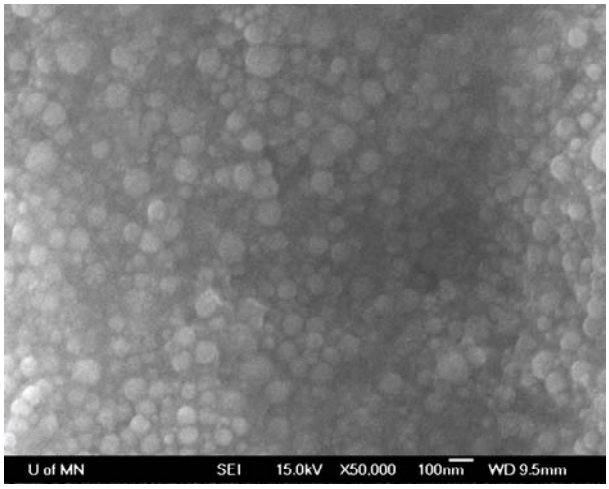

Figure 5. SEM image of particles deposited on ejector orifice plate.

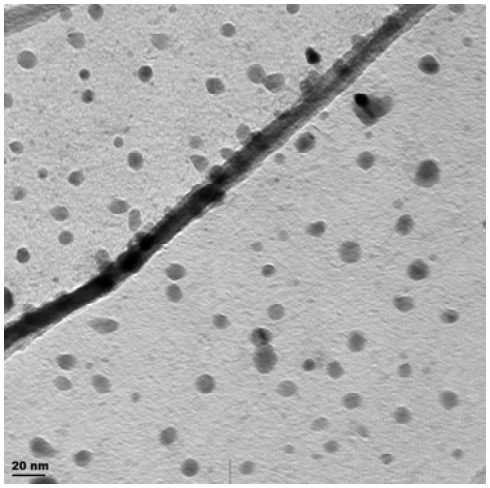

Figure 6. TEM image of particles deposited onto filter holder located downstream of ejector. Long wire in image is from TEM grid.

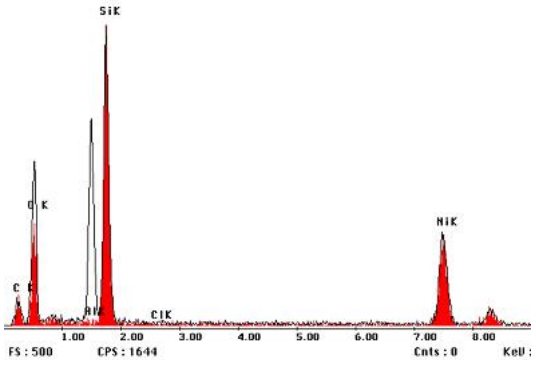

Figure 7. EDS analysis of particle elemental composition. Shaded peaks are from the background signal due to the C-coated Si_3N_4 TEM grid.

Aluminum nanoparticles readily oxidize when they are removed from the reactor, as a result of which it is difficult to obtain TEM analysis of bare Al particles. A previous surface characterization study [10] showed that when Al nanoparticles are exposed to air for a short time they became covered with a < 5-nm-thick amorphous and compact surface oxide layer. Figure 8 shows HRTEM images of a relatively large (~125-nm diameter) particle. The image shows that this particle has an amorphous layer with a thickness of 2-5 nm. The (111) lattice fringe shown in the circled area of the image on the right has a measured lattice spacing of 2.344 ±0.013 Å, in good agreement with the lattice spacing for (111) aluminum of 2.338 Å [11]. Combining these observations with the EDS measurements, one can conclude that the particles have a crystalline aluminum core with an amorphous oxide coating, consistent with results from the literature [10]. Due to the highly pyrophoric property of aluminum particles, especially when the particles are in the nanoscale size range, the particles need to be isolated from contact with air. Partially oxidizing the particles to form a thin alumina layer at the surface is one easy and common way to accomplish this, as the oxide layer can inhibit further diffusion of oxygen, thereby maintaining the aluminum core. However, from the viewpoint of potential applications for the aluminum nanoparticles, for example as solid propellants, a drawback of this approach is that the oxide layer is a barrier to reaction, as the oxide layer must crack open before combustion can occur. An alternative approach is to coat the particles with a non-oxide passivating layer of some other substance, possibly a polymer, that can serve as a diffusion barrier to oxygen until the shell is burned off. A study of such an approach is currently in progress.

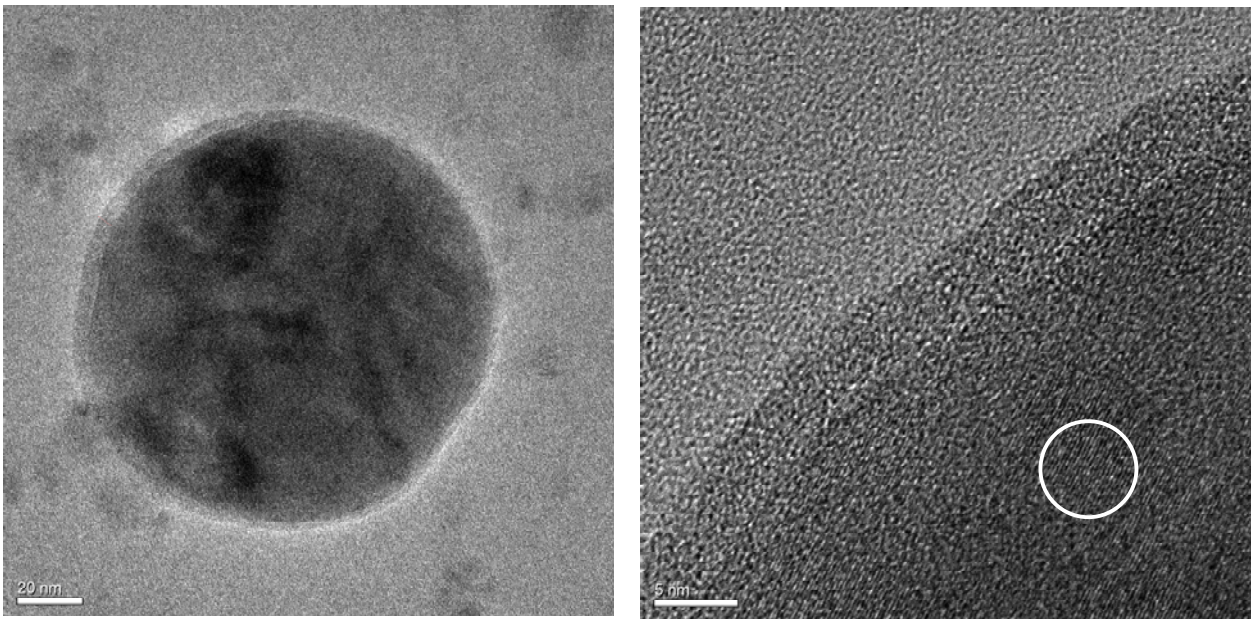

Figure 8. High-resolution TEM images of an aluminum particle with an amorphous surface layer. Circle on image on right highlights lattice fringes associated with (111) aluminum.

Conclusions

A DC thermal plasma process has been used to produce aluminum nanoparticles with the use of $AlCl_3$ vapor as precursor. Number-mean particle sizes were below 20 nm. Spherical, nonagglomerated aluminum particles were obtained, coated with a thin oxide layer. Particle concentrations and size are affected by the $AlCl_3$ vapor flow rate and by the use of a cold counterflow. Studies are in progress to further control the particle size and to passivate these pyrophoric particles by forming suitable coatings.

Acknowledgments
This work was partially supported by the Defense-University Research Initiative in NanoTechnology (DURINT) of the U.S. Army Research Laboratory and the U.S. Army Research Office under agreement number DAAD-190110503, and by the Minnesota Supercomputing Institute.

References
[1] K. K. Kuo and M. Summerfield, Fundamentals of Solid-Propellant Combustion, vol. 90, AIAA, New York, 479 (1984).
[2] T.M. Tillotson, A.E. Gash, R.L. Simpson, L.W. Hrubesh, J. Satcher and J.F. Poco – J. Non-Cryst. Solids **285**, 338 (2001).
[3] J.T. DeSena and K.K. Kuo – J. Propulsion Power **15**, 794 (1999).
[4] P. Brousseau and C. J. Anderson – Propell. Explos. Pyrotech. **27**, 300 (2002).
[5] R. W. Armstrong, B. Baschung, D. W. Booth and M. Samirant – Nano Lett. **3**, 253 (2003).
[6] S. Banerjee, S. Roy, J. W. Chen and D. Chakravorty – J. Magnetism Magnetic Mater. **219**, 45 (2000).
[7] S. Elizer, N. Eliaz, E. Grossman, D. Fisher, et al., Phys. Rev. B **69**, 144119 (2004).
[8] Q. H. Powell, G. P. Fotou and T. T. Kodas – Chem. Mater. **9**, 685 (1997).
[9] K. L. Steffens, M. R. Zachariah, D. P. Dufaux and R. L. Axelbaum – Chem. Mater. **8**, 1871 (1996).
[10] X. Phung, J. Groza, E. A. Stach, L. N. Williams and S. B. Ritchey – Mater. Engg. **A359**, 261 (2003).
[11] H.E.Swanson and E. Tatge, Standard X-Ray Diffraction Powder Patterns, National Bureau of Standards Circular 539, Vol. 1, 12 (1953).

Nitrogen Absorption by Fe-Cr Alloys in Low Pressure Glow Discharge: An Thermodynamic Approach

S.A. Sarmiento[1] and J.L.R. Muzart[2]

[1]Universidad de Pamplona-FCB-GIOP-Departamento de Física y Matemáticas-A.A.1046-Pamplona-NS-Colombia-asarmientos@unipamplona.edu.co
[2]UFSC-CTC-LabMat-Bloco "B"-EMC-Campus Universitário-Trindade-Caixa Postal 476-CEP.888040-900-Florianópolis-SC-Brasil-muzart@materiais.ufsc.br

Abstract
Nitrogen solubility in Fe-Cr alloys treated in H_2+N_2 abnormal glow discharge (AGD) is investigated at different temperatures for a better understanding of the thermodynamic process. The glow was sustained by a DC pulsed source with 700 V of amplitude and variable pulse width to adjust the AGD power and thus, the sample temperature. Sample temperatures were between 860 and 1100°C a discharge pressure of 10 Torr. For times between 15 and 60 minutes mass yielding of the samples was measured after treatment and its structure analyzed by X-ray diffraction. With a increase in chromium content a mass increase is observed after AGD treatment. Samples with chromium content higher than 13%, partially transform its initial ferritic structure to austenitic and CrN structures at 950°C. At a temperature of 1100°C only samples with 28% chromium content showed any structural transformation after 60 minutes. In iron samples the role of the sputtering processes evidently predominates over the thermodynamic ones due to the loss of mass and its unchangeable structure, after abnormal glow discharge treatment.
Keywords: Nitrogen absorption, Low pressure Abnormal Glow Discharge, Thermodynamic process.

1. Introduction

The equilibrium content of nitrogen [N] in steel depends on three variables of state: temperature T, nitrogen partial pressure P_N and the alloy concentration of the steel. Equation (1) allows quantifying the different possibilities of enhancing the poor solubility of pure iron [1]

$$\ln[N]_{Fe-X} = \ln[P_N] - e_N^X[X] - \frac{\Delta H_o}{RT} - \frac{\Delta S_o}{R} \qquad (1)$$

An increase in the partial pressure of the nitrogen and the addition of an alloying element *X* with negative interaction parameter e_N^X (see Table 1[2,3]) will support the nitrogen solubility. Because ΔH_o is proportional to e_N^X a ternary high chromium alloy (e_N^X <0) will show a decrease of nitrogen solubility in all three phases upon heating as shown in Figure 1 [4,5].

Nitrogen solubility in steel can be achieved in the cathode of an abnormal glow discharge (AGD) with nitrogen atmosphere [6]. The N_2+H_2 gaseous mixture is a good atmosphere for the AGD nitrogen absorption process because it provides a better energetic distribution of nitrogen ionic species [7] and improves the interaction of nitrogen species with the cathode surface [8]. Recent works also shows that N_2+H_2 atmosphere with very low partial pressure of H_2 decreases the AGD power and enhance the nitrogen transference of plasma to alloy sited on the discharge cathode [9].
In this work nitrogen solubility in Fe and Fe-Cr alloys, treated in N_2+H_2 AGD, is investigated at different temperatures to better understand the thermodynamic process.

Table 1-First and second order interaction parameters e_N^X and $r_N{}^X$ of different alloying elements [2,3].

X	$e_N{}^X$	$r_N{}^X$
Ti	-0,930	-
V	-0,098	(6,2/T)-0,00005
Nb	-0,050	(5,14/T)-0,0018
Cr	-0,048	(3,3/T)-0,001
Mn	-0,021	(0,80/T)-0,00038
Mo	-0,013	0,000079
W	-0,002	-
Cu	0,006	-
Co	0,010	-
Ni	0,011	0,000035
Al	0,040	-
Si	0,043	-
B	0,083	-
C	0,118	(-28/T)+0,035
N	0,13	-

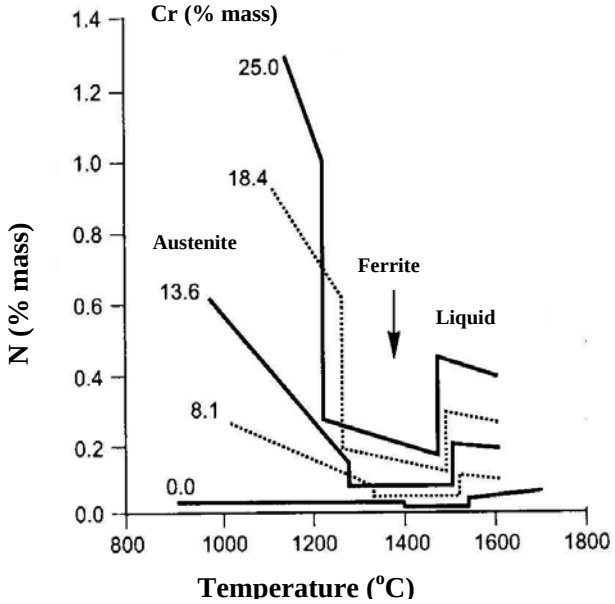

Figure 1-Nitrogen solubility of Fe-Cr alloys in equilibrium with atmosphere of 1 bar [4,5].

2. Experiment

The samples used were cylinders with 8,70 mm in diameter and height of between 3,50 and 4,50 mm prepared by powder metallurgy standard procedures [10,11], utilizing iron carbonyl powder and master alloy powder of 74% chromium content. Pure iron samples were also submitted to this process. Table 1 shows chromium content of Fe-Cr alloys submitted to nitrogen absorption on the cathode of 80% $N_2$and 20% H_2 AGD. Pressure was 10 Torr and flux 4 cm^3/s. The glow was sustained by a DC pulsed source of a rectangular

Table 1-Chromium contents of Fe-Cr alloys measured by EDX.

Alloy	1	2	3	4
Cr (% in mass)	13,9	18,7	23,6	28,4

signal with a 700 V amplitude and pulse variable width (8-180μs) to adjust the AGD power and thus, the sample temperature. Before nitrogen treatment the samples were cleaned during 15 minutes in 80%Ar+20%H_2 AGD [9,10] at a pressure of 10 torr a flux of 4 cm^3/s and temperature 900°C. Treatment temperatures were between 860 and 1100°C during 15 minutes. Nitrogen absorption times up to 60 minutes at 1100°C were also used.

After treatment, sample mass variation was measured with a four figure electronic balance. Structural analysis of the treated samples was carried out by X ray diffraction (XRD) with Cu K_α radiation.

3. Results and discussion

3.1. Power versus Temperature

Figure 2(a) shows the relationship between temperature and power (Pulse width: T_{ON}) in 80% N_2+20% H_2 AGD used in the nitrogen absorption process. Temperature increases from 40 to over 78 μs as a result of greater number of ions and neutrals impinging on the cathode surface and then transferring their kinetic energy [12,13] when pulse width is increased at the same pressure, gaseous mixture and flux conditions.

3.2. Nitrogen absorption

Figure 2b presents mass yielding (Δm) obtained by the samples after nitrogen absorption in AGD. The decrease in Δm with the temperature observed in Figure 2b could be related to the thermodynamic behavior of Fe-Cr alloys (Equation 1) which predicts a nitrogen loss when the temperature is increased [4,5]. Besides thermodynamic considerations, the sputtering process, inherent to AGD, could also influence the mass yielding by causing it decrease when the temperature is increased. This is because temperature increase is associated to an increase of T_{ON}, as shown in Figure 2b, and also the quantity of ions and neutrals that impact the sample surface per pulse. Thus, when temperature is increased, the sputtering process decreases Δm. It is

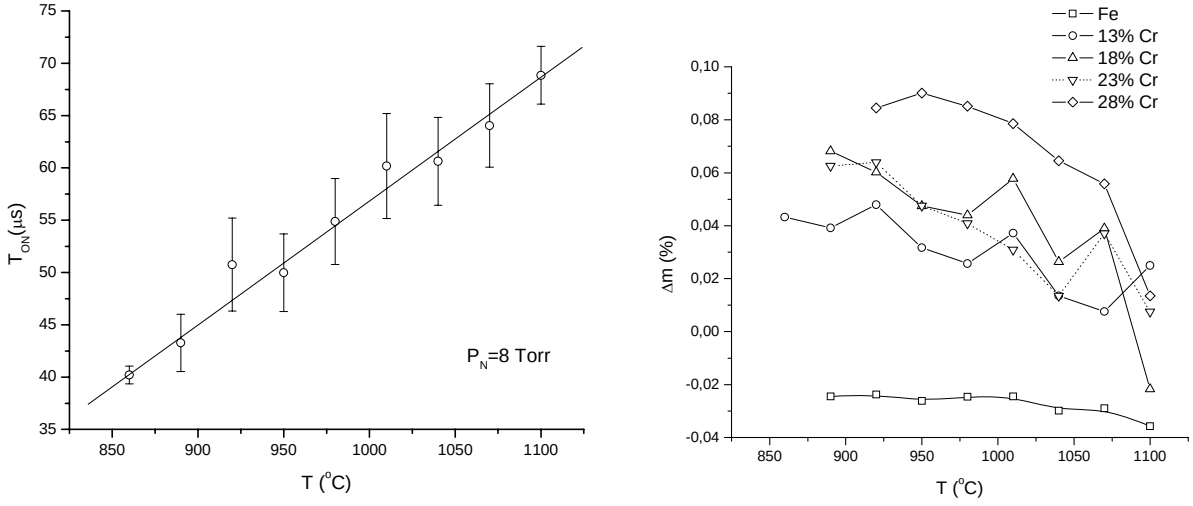

(a) **(b)**

Figure 2-a) Cathode temperature of AGD versus discharge power (T_{ON}) and b) sample mass variation versus temperature during 15 minutes of treatment.

difficult to determine the contribution of each competitive process (thermodynamic of Fe-Cr system and sputtering) on Δm increase and in some cases, it is only possible to observe the dominant process. That is, when Δm is positive, it is the thermodynamics of the nitrogen absorption in Fe-Cr system, which predominate. On the other hand, when Δm is negative, the sputtering is the predominant process.
The increases in Δm with a chromium content, shown in Figure 2b, also agrees with equation 1 when Δm is considered as a function of the chromium content, in Fe-Cr alloy, and the interaction parameter (e_N^X see Table 1) of it alloy is included.
Iron samples showed a Δm negative at all temperatures in N_2+H_2 AGD which reveals that sputtering prevails over the thermodynamic process of nitrogen absorption by the iron network in these experimental conditions. Nitrogen absorption in iron at the temperatures used would need much higher nitrogen partial pressure similar to gaseous metallurgical process [1]. Indeed, energetic nitrogen species yielded in AGD can be sufficient to satisfy the nitrogen absorption requirements in Fe-Cr stainless steel alloys, at these temperatures, but this in not sufficient for pure iron where nitrogen solubility is very poor [14,15].

3.3-XRD

XRD spectres of Fe-Cr alloys submitted to AGD at 950°C during 15 minutes are shown in Figure 3a for all chromium content utilized. Besides the characteristic peaks of Fe-Cr alloy ferritic structure (α), diffractograms of Figure 3a also shows an austenitic phase (γ) and chromium cubic nitride (CrN) peaks in samples with chromium content higher than 13%. Thus, nitrogen absorption partially transform the existing ferritic phase, in these alloys, and promotes the appearance of austenite and chromium nitride with chromium content of 21% which was studied by Quiu [16].
Because of the absence of any additional structure in samples with 13% of chromium, the nitrogen must be in solid solution in its original crystalline network.
Chromium nitride observed by XRD presents a formation free energy $\Delta G_T°$ as a function of the temperature as shown in Figure 3b for 1 atm of nitrogen pressure [17]. As shown in Figure 3b, at a nitrogen partial pressure of 10 Torr and a temperature of 950°C, CrN formation is not possible from a thermodynamic point of view. However, in the presence of plasma, as studied by Vepřek [18], the equilibrium temperature of thermodynamic systems can be changed and reaction rates can also be increased. Here, favorable conditions are generated by the presence of energetic species rich in nitrogen, coming from the cathodic region, so, thermodynamic equilibrium is dislocated to regions of higher temperatures and CrN kinetic formation is favoured. These chromium nitride precipitates were produced at yet higher temperatures (950°C) than those predicted in Figure 3b (~800K).
Nitrogen absorption at 1100°C only reports structural changes for samples with 28% of chromium content, after 60 minutes (as shown in diffractogram of Figure 4). Under these conditions the nitrogen quantity absorbed is sufficient to promote α→γ structural transformation in Fe-Cr alloy but is not sufficient for CrN formation. Nitrogen absorbed in samples with lower chromium content must be insufficient to saturate the ferritic network and thus transform their structures.
Iron samples didn't show any structural transformation after AGD treatment under the conditions used in this work. This confirms the previous results shown in Figure 2b where the sample presents loss of its mass. In pure iron, sputtering is the process that prevails over a possible thermodynamic process in the Fe-N system. In fact, at higher temperatures than 950°C and lower pressures utilized in AGD, all iron nitrides are not stables [19]. This also explains why iron nitrides do not appear in the structures of Fe-Cr stainless steel studies.

4. Conclusions

After Fe-Cr alloys were treated in AGD under the above mentioned conditions the following conclusions may be drawn:
Temperature decreases mass yielding of Fe-Cr alloys in AGD, as does the gaseous metallurgical process.

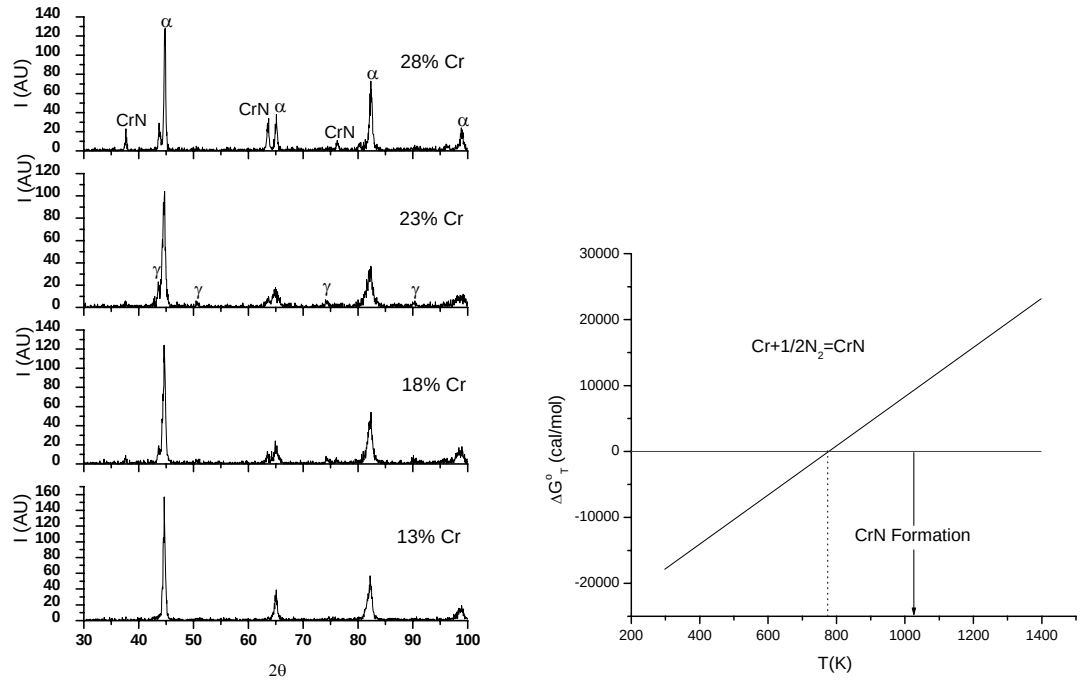

(a) **(b)**

Figure 3-a) XRD of Fe-Cr alloys after 15 minutes in N_2+H_2 AGD at 950°C and b) Formation free energy against temperature for CrN at 1 atm nitrogen pressure.

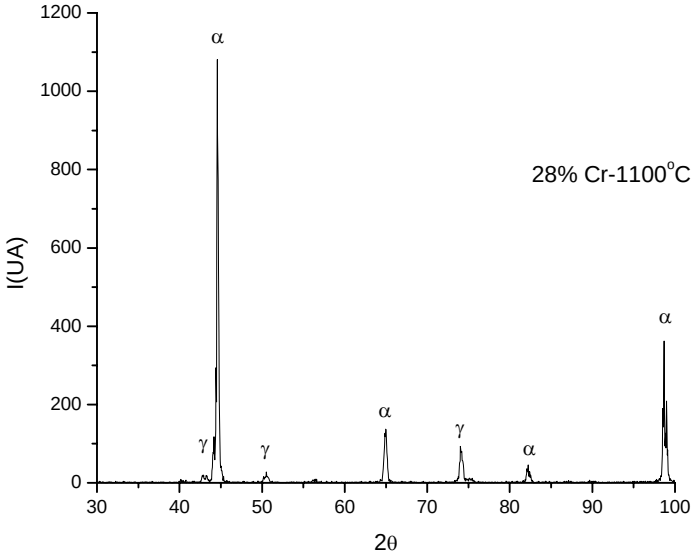

Figure 4-XRD for 28% Cr sample after 60 minutes in AGD at 1100°C.

Mass increase in Fe-Cr stainless steel alloys made evident the role of chromium in attracting nitrogen to wards the inside of the iron alloys, which agree with the thermodynamic behavior of the gaseous metallurgical process.

Nitrogen absorbed by samples with chromium content higher than 13% changed its ferritic structure to nitrogen austenite and NCr precipitates.
Nitrogen absorbed by 13% chromium alloy may be in solid solution in its crystalline network.
At 1100°C the nitrogen supply by the AGD is not sufficient to satisfy the thermodynamic requirements of nitrogen absorption in Fe-Cr alloys. To increase the quantity of nitrogen absorbed it may be necessary to increase the treatment time or the chromium content of the alloy.
In iron samples the sputtering is the predominant process and the thermodynamic processes inherent in the Fe-N system are absent.

5-Acknoledges

We wish to acknowledge the financial support given by Colciencias enabling the participation in the present symposium.

6-References

[1] Gavriljuk, V. J., Berns, H., High Nitrogen Steels, Springer-Verlag Berlin Heilderberg, 1999.
[2] Satir-Kolorz, A., Feichtinger, H. K., Speidel, M. O., Literaturstudie und Theoretische Betrachtungen zum Lösungsverhalten von Stickstoff in Elsen-, und Stahlguβ-Schmelzen, Gieβereiforschung, V. 42, n. 1, p. 36-49, 1990.
[3] Schürmann, E.,Kunze, H. D., Gieβereiforschung, V. 19, p. 101-108, 1967.
[4] Zeng, XH, Satir-Kolorz, A., Feichtinger, H. K., HNS'88-High Nitrogen Steels, p. 75, Ins. Met., London, 1989.
[5] Feichtinger, H. K., Zeng, XH., Thermodinamik und Verfahrenstechnik der Herstellung von Stickstoff-Stählen, 1991.
[6] Venugopalan, M., Basic Processes in Glow Discharge Plasmas, Nuclear Instruments and Methods in Physics Research, V. B23, p. 405-417, 1987.
[7] Berg, M., Budtz-Jorgensen, C. B., Reitz, H., Schweitz, K. O., Chevalier, J., Kringhoj, P., Bottiger, J., On Plasma Nitriding of Steels, Surface and Coatings Technology, V. 124, p. 25-31, 2000.
[8] Ricard, A., Czerwiec, T., Belmonte, T., Bockel, S., Michel, H., Detection by Emission Spectroscopy of Active Species in Plasma-Surface Processes, Thin Solid Films, V. 341, p. 1-8, 1999.
[9] S.A. Sarmiento, J.L.R Muzart, P.A.P Wendhausen, Nitrogen Introduction in Stainless Fe-Cr Alloys Sinterized and Submitted to Abnormal Glow Discharge, Proceedings of GD2004, Toulouse, 5-10 September, 2004
[10] S.A. Sarmiento, J.L.R. Muzart, Introdução deNitrogenio em Ligas Inoxidáveis de FeCr, Sinterizadas e Submetidas a uma Descarga Luminescente Anormal, Tese, UFSC, Brasil, 2003.
[11] Thümmler, F., Oberacker, R., Introduction to Powder Metallurgy, The Institute of Materials, London,1993.
[12] Chapman, B., Glow Discharge Processes, John Wiley and Sons, New York, 1980.
[13] Engel, A. Von, Ionized Gases, AIP Press, 2ª ed.,New York, 1994.
[14] Zeng, XH, Satir-Kolorz, A., Feichtinger, H. K., HNS'88-High Nitrogen Steels, p. 75, Ins. Met., London, 1989.
[15] Feichtinger, H. K., Zeng, XH., Thermodinamik und Verfahrenstechnik der Herstellung von Stickstoff-Stählen, 1991.
[16] Qiu, C., Thermodynamic Analysis and Evaluation of the Fe-Cr-Mn-N System, Metallurgical Transactions A, V. 24A, p. 2393-2409, 1993.
[17] Kubaschewski, O., Alcock, C. B., Metallurgical Thermochemistry, Pergamon Press, 5ª edição, 1979.
[18] Vepřek, S., Plasma-Induced Plasma –Assisted Chemical Vapour Deposition, Thin Solid Films, V. 130, p. 135-154, 1985.
[19] Wriedt, H. A., Gokcen, N. A., Nafziger, R. H., The Fe-N (Iron-Nitrogen) System, Bulletin of Alloy Phase Diagrams, V. 45, n. 4, p. 355, 1987.

Experimental Studies on a Sub-microsecond Pulsed Dielectric Barrier Discharge at Atmospheric Pressure

XinPei Lu and Mounir Laroussi
Electrical and Computer Engineering Department &Center for Bioelectrics
Old Dominion University, Norfolk, VA 23529

ABSTRACT:

In this paper, non-thermal atmospheric pressure plasma is generated by a pulsed dielectric barrier discharge with different mixtures of helium and nitrogen. The gas temperature is found to be about 350K. The UV emission power density, P_{UV}, reaches its highest level when 5 to 10 percent N_2 is mixed to a balance of helium. Further, the emission spectra show that the UV is emitted by NO. In addition to NO, excited N_2, N_2^+, OH and He are also present in the plasma. The concentrations of NO and NO_2 are also measured.

Keywords: Pulsed Discharge, UV, Radicals, Atmospheric Pressure, Cold Plasma.

I. INTRODUCTION:

Because of their enhanced chemistry at low operating temperatures, atmospheric pressure non-thermal plasmas have recently become the enabling technology in several emerging novel applications such as surface modification of polymers, biological and chemical decontamination of media, and aerodynamic drag reduction and shock wave mitigation [1-3].

To enhance the ionization and excitation processes, fast rising voltage pulses (pulse widths from tens to hundreds nanoseconds range) were suggested by several researchers. Liu and Neiger [4,5] and Laroussi et al. [6] applied sub-microsecond unipolar pulses to dielectric barrier discharges (DBD) at low pressure and high pressure, respectively. Liu and Neiger [4] found that the energy efficiency for ozone synthesis is 30% higher with pulsed DBD than that driven with sine wave voltages. Mildren and Carman [7,8] found that the UV power output from a xenon excimer lamp driven by ~150ns short pulses had an energy efficiency three times higher than the same lamp excited by sine wave voltages.

An attractive feature of pulsed discharges is that two consecutive plasma ignitions occur per each applied voltage pulse. The first ignition occurs at the voltage pulse rising edge, and the second at the falling edge of the voltage pulse [4-6]. The second discharge ignites without energy input from the external circuit, the required voltage being provided by the accumulated surface charges left from the first discharge. This process ultimately leads to a much improved power transfer to the plasma.

In this paper, a study of the UV emission and active species generation efficiency from an atmospheric pressure pulsed DBD for various gas mixtures containing different percentages of He and N_2 is presented. First, a brief discussion on the current-voltage characteristics of the discharge is presented. Then, the gas temperature is measured by comparing the experimental N_2(C-B) 0-0 transition spectrum with simulation results. This is followed by a detailed study of the UV emission power density from the discharge for different percentages of He and N_2 and different pulse frequencies. To identify the excited species responsible for the UV emission and other chemically important species, emission spectroscopy was used. Because of the presence of oxygen (from residual traces of air), molecules such as NO and NO_2 were formed. Therefore, a calibrated multi-gas detector was used to measure the absolute concentrations of NO and NO_2 for different pulse frequencies.

II. EXPERIMENTAL SETUP

The discharge device comprises two parallel electrodes separated by a gap. One of the electrodes is made of a 2" x 2" aluminum plate covered by an alumina (Al_2O_3) sheet (See Figure 1). The dimensions of the Alumina sheet are: 75mm × 75mm × 1mm. The second electrode is made of a copper disc (diameter of 5.7 cm) with several holes through which the operating gas is injected. The diameter of the holes is about 1mm. The distance between nearby holes is 5mm. This copper electrode is not covered by a dielectric. The distance of the gap between the electrodes is adjustable from 1mm to few centimeters. The gas flows out of the holes and into the discharge gap. A multi-gas manifold with flow meters was used to adjust the percentage of He and N_2. The

plasma was driven by a pulse generator capable of producing narrow high voltage pulses (pulse width few hundreds ns) at adjustable repetition rates. Detailed description of the pulsed power supply can be found in [6].

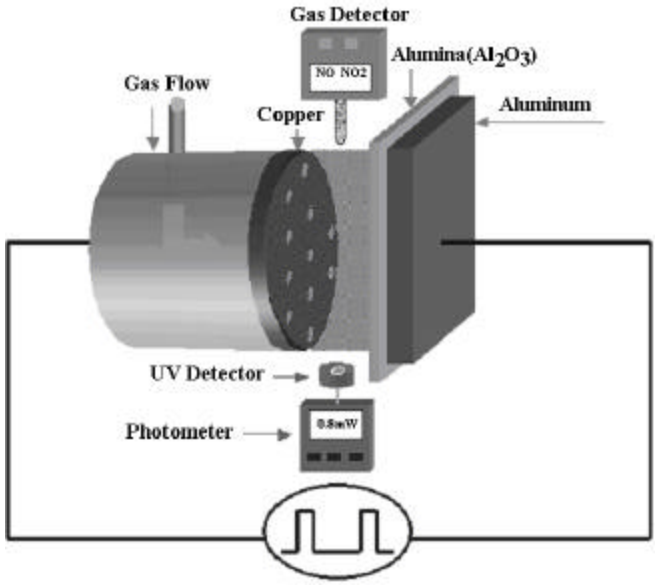

Fig. 1 Experimental setup of the discharge system with diagnostics.

For the identification of excited species and the determination of gas temperature, optical emission spectroscopy (OES) was conducted with a half-meter spectrometer (Acton Research SpectraPro 500i). To carry out absolute measurements of the emitted UV power, a radiometer/photometer (International Light. Inc. Model: IL1400A)(165-310nm) was used. The distance from the UV detector to the axis of the copper disk was 6cm. To identify the excited species responsible for the UV emission, and the other chemically important species present in the plasma, emission spectra in the 200-800nm range were recorded. The absolute concentrations of NO and NO_2 were measured by a multi-gas detector (RAE System: Model PGM-7840). The gas detector was located 1cm from the plasma surface.

III. EXPERIMENTAL RESULTS

Except when indicated otherwise, the following experimental results were obtained when the applied voltage, pulse width, and the gap distance were set to V_a=9kV, t_{PW}=500ns, and d_{gap}=2mm, respectively.

3.1 Current-Voltage Characteristics

Figure 2 shows the applied voltage pulse, V_a, the voltage across the dielectric, V_d, the voltage across the gas gap, V_g, and the corresponding discharge current, I_{dis}. Helium with traces of air was the operating gas. The voltage pulse repetition rate is 1 kHz. Two distinct current pulses indicating two consecutive discharges are clearly visible. The first pulse occurs at the rising front of the voltage pulse and the second current pulse occurs at the falling front of the voltage. These two current pulses are about 100 ns wide. The current curve shown in Figure 2 represents the actual discharge current, which was obtained by subtracting the displacement current (due to cable capacitance, the dielectric equivalent capacitance, and the gas gap equivalent capacitance) from the total measured current [6].

The voltage across the dielectric is calculated by the ratio of the time integral of the current through the DBD and the dielectric capacitance, C_d (C_d = 145 pF) [6]. The voltage across the gas gap is simply given by: $V_g = V_a - V_d$. Note that V_g exhibits a negative pulse when the applied voltage, V_a, decays. This negative pulse is induced by the charges previously collected on the surface of the dielectric plate. It is this voltage pulse that is responsible for the re-ignition of the discharge and the occurrence of a second current pulse at the falling edge of the applied voltage pulse.

Figure 3 shows the total power supplied or received by the power supply, P_{supp}, and the power dissipated in the plasma, P_{gas}. P_{supp} is the product of the total current supplied by the power source and the applied voltage

V_a. P_{gas} is the product of I_{dis} and V_g. During the first rising front of the applied voltage P_{supp} includes both the power dissipated in the plasma and the reactive power stored in the various capacitors (cable, dielectric, and gas). At the falling front of the applied voltage the sign of P_{supp} is negative which represents a power returned to the power source. The curve representing P_{gas} shows the power dissipated in the plasma during the first and the second discharge.

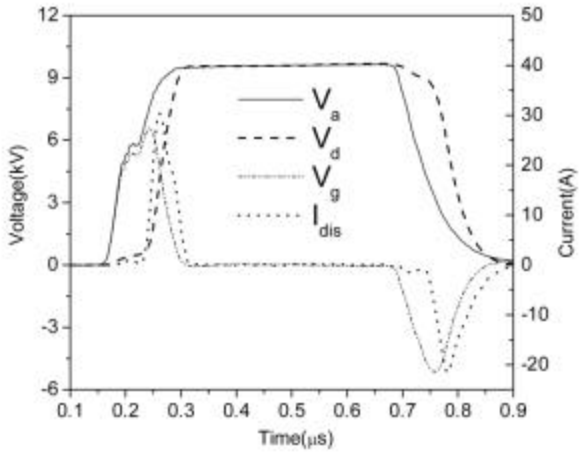

Fig. 2 Applied voltage, V_a, voltage across the dielectric, V_d, voltage across the gas gap, V_g, and the discharge current, I_{dis}, versus time. Operating gas: Helium with traces of air . Gap distance is 2.5 mm and pulse rep-rate is 1 kHz. [6]

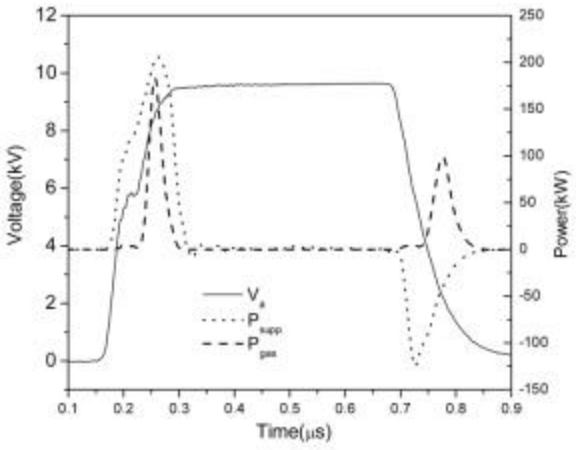

Fig. 3 Applied voltage, supply power, P_{supp}, and gas dissipated power, P_g, versus time. When P_{supp} is positive the power is supplied from source to load, and when P_{supp} is negative the power is restored from load to source [6]

3.2 Gas Temperature Measurement

One of the attractive features of non-equilibrium plasmas is that the gas temperature remains close to room temperature. Here, the gas temperature was determined by analyzing the rotational structure of the N_2 second positive system emission. This rotational structure contains information on the rotational temperature. Because of the low energies needed for rotational excitation and the short transition times, molecules in the rotational states and the neutral gas molecules are in equilibrium. Therefore, the gas temperature can be directly inferred from the rotational temperature [9]. To determine the gas temperature, we compared the experimentally measured spectra with simulated spectra of the 0-0 band of the second positive system of nitrogen at different temperatures. It was estimated that the gas temperature was about 350K for helium plasma. When different percentages of N_2 were added to helium, it was found that the gas temperature did not change appreciably. In addition, when the pulse frequency was increased from 1kHz to 10kHz, the gas temperature only increased slightly (less than 50K).

3.3 UV Power Measurement

The integrated UV power emitted by the discharge was measured for various mixtures containing different percentages of He and N_2. When only helium is used as operating gas, the emitted UV power density, P_{UV}, increased linearly with the pulse frequency, reaching about 0.18mW/cm^2 at 10kHz. When only nitrogen is used P_{UV} initially increased with the pulse frequency, but around 6 kHz, it reached a saturation value of about 90 μW/cm^2.

To optimize the UV emission power density, helium mixed with different percentages of N_2 was used. Figure 4(a) shows that, for three different percentages of N_2 in a He balance, P_{UV} increases linearly with pulse frequency, and is much higher than that when only He or N_2 is used. According to Figure 4(a), P_{UV} is highest when 10 % of nitrogen (He(90%) + N_2(10%)) was used. In this case, P_{UV} is more than 4 times higher than that of the helium only case. To further investigate how the percentage of N_2, R_{N2}, affects P_{UV}, we measured P_{UV} with

He((100- R_{N_2})%)+ N_2(R_{N_2} %) as operating gas mixtures at a fixed pulse frequency of 2kHz. Figure 4(b) shows that, when the percentage of N_2 was increased from 0 to 5 percent, P_{UV} increased from about 0.07mW/cm^2 to 0.23mW/cm^2. Increasing the percentage of N_2 up to about 10 percent did not greatly affect the value of P_{UV}. However, further increase of N_2 beyond 10% led to a decline in P_{UV}.

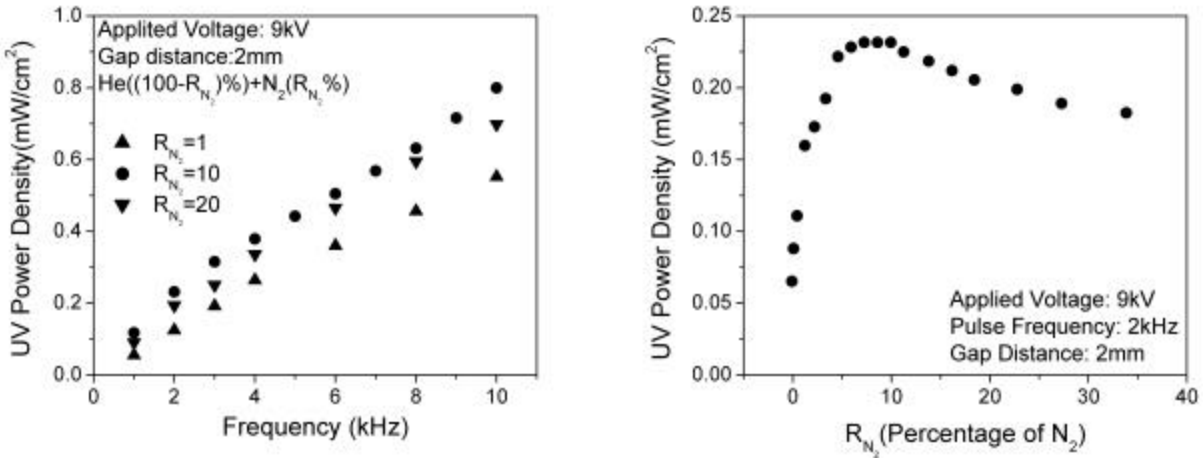

(a) (b)

Fig. 4 UV emission power density versus pulse frequencies for (a) UV emission power density for three different percentages (1%, 10% and 20%) of N_2 in a N_2/He mixture, versus pulse frequency and (b) UV emission power density versus the percentage of N_2 at a fixed pulse frequency of 2kHz. (R_{N2}: percentage of N_2)

3.4 Emission Spectra

To better understand the UV emission characteristics, and to identify the presence of chemically reactive excited species in the plasma, emission spectroscopy was used to measure the emission spectra in the 200-800 nm wavelength range, under different gas operating conditions. For all of the recorded emission spectra, the pulse repetition rate f was 1kHz, and the operational parameters of the spectrometer were unchanged (grating: 1200g/mm, slit width: 100μm).

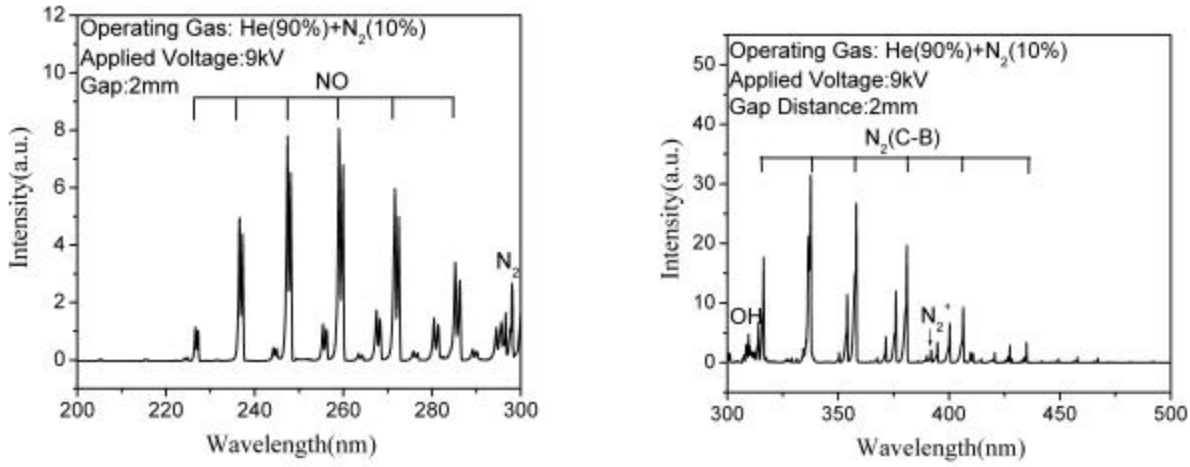

(a) (b)

Fig. 5 Emission Spectra from (a) 200nm to 300nm and (b) 300nm to 500nm for the He(90%) +N_2(10%) plasma. Trace amounts of oxygen are present from residual air.

Figure 5(a), which shows the emission spectra from 200 to 300 nm for a He(90%) + N_2(10%) mixture, clearly indicates that excited NO are the main source of the UV emission with contribution from the N_2(C-B) emission. Varying the percentages of He and N_2 we observed similar emission spectra but with weaker

intensities. Spectra in the wavelength range 300-500nm (Figs. 5(b)) reveal the presence of excited OH, N_2 and N_2^+ in the plasma. Helium emission was observed in the 500nm – 800nm wavelength range.

3.5 Measurement of NO and NO_2 Concentrations

Since most of the emission in the UV range was found to originate from NO and since NO is easily oxidized to NO_2 by reaction with O_2, O_3, etc [10,11], we measured the absolute concentrations of NO and NO_2. A multi-gas detector was used for this task. The maximum measured NO and NO_2 concentrations for a He(90%) + N_2(10%) mixture were about 8ppm and 4ppm, respectively.

IV. DISCUSSION

The results presented above clearly show that the optimal UV emission comes from the He(90%) + N_2(10%) plasma, where nitrogen oxide, NO, dominated this emission (the residual traces of air provided the oxygen to form NO). This optimized UV emission can be explained as follows. In order to enhance UV emission, NO had to be excited to the NO($A^2\Sigma^+$) state (Excitation energy E_{NO*}=5.5 eV). This can occur via collisions with helium metastables, He*, or with $N_2(C^3\Pi_u)$ (Excitation energy E_{N2*C}=11.1 ev). According to the spectra that we measured, the N_2(C-B) emission intensity from the plasma with a He(90%) + N_2(10%) mixture was several times higher than that of a helium only or nitrogen only plasmas. Because the mass of N_2 is 7 times higher than that of He, the NO excitation cross section by $N_2(C^3\Pi_u)$ is likely to be higher than that by He^*. Therefore, the plasma with the higher $N_2(C^3\Pi_u)$ concentration will excite more NO, and as a result emits more UV. To confirm this assumption, we also measured the N_2(C-B)(0-0) transition bandhead intensity (337nm) for different percentages of N_2 and He mixtures. The experimental results show that the emission intensity of this bandhead has a very similar behavior as that of the emitted UV power density shown in Fig. 4(c).

Since most of the UV emission came for the excited NO molecule, the presence of trace amounts of oxygen is therefore required. However, if too much oxygen is added to the gas mixture, the UV emission drops drastically. When just 1% of oxygen was added to a He (89%) + N_2 (10%) mixture, the intensity of the NO emission lines between 200 nm and 300 nm became very weak. Two reasons contribute to this result: 1. In the presence of oxygen NO is quickly oxidized to NO_2. Measurements of the absolute concentration of NO_2 showed a two order of magnitude increase (up to 500 ppm of NO_2) when 1% of oxygen was added; 2. Since oxygen has a large electron attachment cross-section, it affects the electron energy distribution function in a way that results in less excited species and consequently less UV emission.

Another important observation was that the UV emission power density from a nitrogen plasma was weaker than that from a helium plasma (both in the presence of trace amounts of air). This is because without the presence of He metastables, the only pathway to excite the ground state of N_2 to N_2(C) state is via electron impact. This process cross-section is smaller than that via He*. So the concentration of N_2(C) state is lower and as a result less NO is excited and less UV is emitted from the nitrogen plasma.

V. CONCLUSION

The electrical and emission characteristics of a diffuse pulsed dielectric barrier discharge were investigated in this paper. The gas temperature of the plasma was measured to be close to 350K. The UV emission power density, P_{UV}, measurements show that proper mixture of He and N_2 improves the UV emission dramatically. With 5 to 10 percent of N_2 mixed with He, P_{UV} reached about 0.8mW/cm^2 (for f = 10kHz), and was more than 4 to 9 times higher than that for He or N_2 plasmas, respectively. The emission spectra show that most of the UV was emitted by excited NO and N_2. The emission spectra from a He(90%) + N_2(10%) plasma show relatively high concentrations of excited NO and N_2. In addition to NO, NO_2 and excited OH, N_2^+, O were detected.

VI. ACKNOWLEDGEMENT

This work was supported by the US Air Force Office of Scientific Research (AFOSR).

VII. REFERENCES

[1] R Dorai and M J Kushner, J. Phys. D: Appl. Phys. **36**, 666(2003).

[2] M Laroussi, IEEE Trans. Plasma Sci. **24**, 1188(1996).

[3] S. Kuo and D. Bivolaru, Phys. Plasmas **8**, 3258 (2001).
[4] S. Liu and M. Neiger, J. Phys. D: Appl. Phys. **34**, 1632(2001).
[5] S. Liu and M. Neiger, J. Phys. D: Appl. Phys. **36**, 3144(2003).
[6] M. Laroussi, X. Lu, V. Kolobov, and R. Arslanbekov, J. Appl. Phys. **96**, 3028(2004).
[7] R.P. Mildren and R.J. Carman, J. Phys. D: Appl. Phys. **34**, L1(2001).
[8] R.J. Carman and R.P. Mildren, J. Phys. D: Appl. Phys. **36**, 19(2003).
[9] G. Faure and S. M. Shkol 'nik, J.Phys.D:Appl.Phys. **31,** 1212(1998).
[10] I.A Kossyi, A. Yu. Kostinsky, A.A. Matveyev and V.P. Silakov, Plasma Sources Sci. Technol. **1**, 207(1992).
[11] J. T. Herron, J. Phys. Chem. Ref. Data. **28**, 1453(1999).

SPECTROSCOPIC DETERMINATION OF THE TEMPERATURE IN AN EXPANDING H_2O-AR DC ARCJET

V. Sember. A. Mašláni
Institute of Plasma Physics, ASCR, Za Slovankou 3, 182 21 Prague, Czech Republic

Abstract
Optical emission spectroscopy is used to determine the temperature in a supersonic plasma jet expanding from a H_2O-Ar dc arc torch into a chamber maintained at a pressure of 4 kPa. The excitation and ionization temperatures are derived from argon, oxygen and hydrogen atomic lines, and argon ionic lines. The rotational and vibrational temperatures are obtained from UV OH $A^2\Sigma \rightarrow X^2\Pi$ bands. Various stages of departure from thermodynamic equilibrium are found for populations of both atomic and molecular excited states.

Keywords
Optical emission spectroscopy; Supersonic plasma jet; Argon; OH radical, Nonequilibrium

1. Introduction

The contribution addresses the problem of temperature measurement in a supersonic plasma jet of thermal plasma source by means of optical emission spectroscopy (OES). Jets of this kind are generated by expanding plasma from a remote source into a low-pressure chamber, the pressure being typically in the range of 10^0-10^1 kPa, and can be utilized, among others, for fast deposition of dense coatings [1]. Depending on the nozzle design and ratio of the inlet to chamber pressure, a variety of plasma flow structures is obtained: from subsonic to under- or overexpanded supersonic with a normal shock wave and/or oblique shock wave boundary [2].

Because of its simplicity and non-intrusive nature, the latter being the main advantage in supersonic conditions, OES is widely used powerful diagnostic technique, which can readily provide a wealth of information about excited species. Although the low-pressure supersonic jet is usually far from thermodynamic equilibrium, the kinetic temperature of free particles can be still well established. The question what is the relation between the temperatures obtained by OES, which in fact characterize a partial equilibrium among a particular manifold of excited states, and the electron or heavy particle temperatures is still open. Usually it is believed that the electronic excitation or vibrational temperatures are close to the electron temperature and the rotational temperature is close to the heavy particle temperature. Expanding plasma jets, however, are characterized by strong recombination resulting in an overpopulation of higher excited states with respect to the ground state and even if an apparent Boltzmann equilibrium is established among these states, the temperature derived from a Boltzmann diagram could be different from the electron temperature, e.g. [3],[4]. Molecular spectra, on the other hand, can be dominated by the radiation from nascent molecules, the ro-vibrational distribution of which is controlled by a particular chemical reaction in question rather than by elastic collisions of particles, e.g. [5][6].

2. Experimental arrangement

The measurements were performed on the plasma jet generated by the hybrid water-argon dc arc torch in a low-pressure chamber. In the hybrid torch the arc chamber is divided into short cathode part, where the arc is stabilized by tangential argon flow, and the rest is stabilized by a water vortex [7]. The operating parameters were: current 200 A, voltage 140 V, argon flow rate 13 slm, and chamber pressure 4 kPa. The spectra were recorded with a Jobin-Yvon imaging spectrograph Triax 550 fitted with a CCD detector. The spectral resolution with a grating 1200 grooves/mm was about 0.08 nm in the spectral region of 300 nm. The jet was strongly under-expanded with a well-pronounced expansion region without a noticeable oblique shock structure followed by a relatively faint normal shock front, after which the expansion continued subsonically. The electron number density decreased from $4\text{x}10^{22}$ m^{-3} at the exit nozzle down to $1.5\text{x}10^{21}$ m^{-3} in the expansion region before the shock front.

3. Spectroscopic methods

The electronic excitation temperature T_{ex} was derived from Boltzmann diagrams of all sufficiently resolved argon, oxygen and hydrogen (Balmer H_β-H7) atomic lines detected in VIS and near IR region. We also calculated the ionization temperature T_S from the ratio of emission coefficients of argon ionic and atomic lines using Saha equation and the electron number density obtained from Stark broadening of H_β line. Note that by the term 'temperature' we understand the parameter characterizing a particular distribution of the excited states population assumed to be in thermodynamic equilibrium.

Figure 1 shows typical Boltzmann diagrams obtained from argon atomic lines at three different positions in the plasma jet. The first one is taken at the nozzle exit on the jet centerline and reveals almost perfect Bolzmann distribution of the excited level populations with a well defined excitation temperature. The next two ones are taken respectively at the boundary and at the core of the jet in the expansion region near the shock front. These two diagrams demonstrate that the lowest measured 4p states with the upper level energy around 1.07×10^5 cm^{-1} (~13 eV) are underpopulated with respect to the higher states and that this underpopulation increases towards the core of the expansion region. The Boltzmann temperature obtained from higher excited states T_{ex}^{H} (Ar I) is then taken as the excitation temperature T_{ex} (Ar I). In the case of Boltzmann diagrams obtained from oxygen and hydrogen atomic lines shown in Figure 2 this effect is negligible.

The rotational T_{rot} and vibrational temperatures T_{vib} were obtained by fitting UV OH $A^2\Sigma \rightarrow X^2\Pi$ bands measured in the region of 280-319 nm to the simulated spectra using LIFBASE software [8]. The ro-vibrational

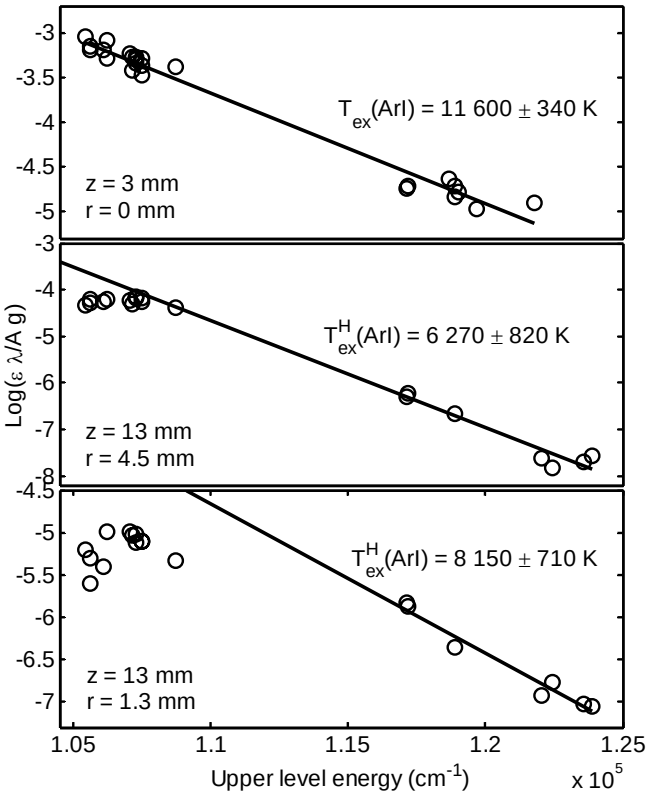

Figure 1. Boltzmann diagrams of Ar I lines at three positions in the plasma jet; *z* and *r* are respectively the distance from the nozzle exit and radial distance from the jet centerline.

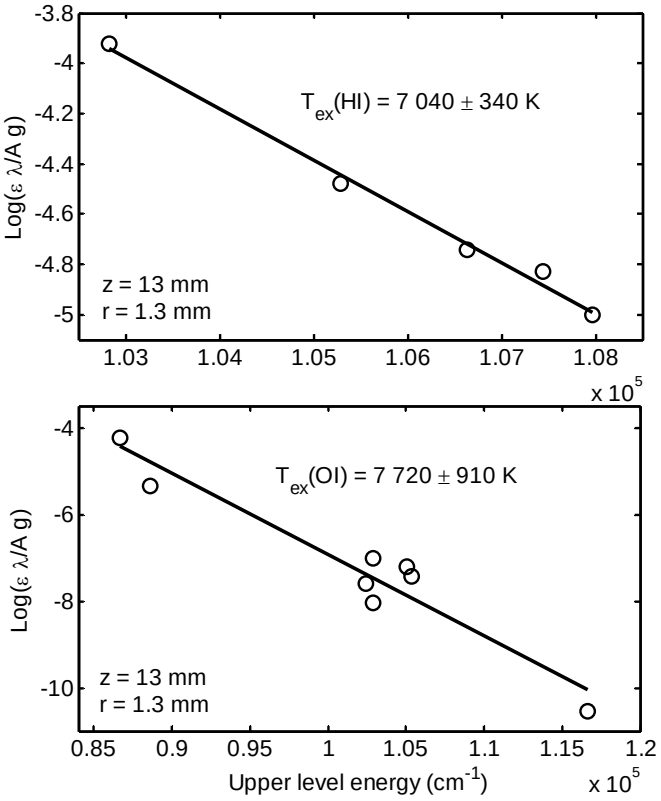

Figure 2. Boltzmann diagrams of H I and O I lines in the expansion region close to the jet centerline.

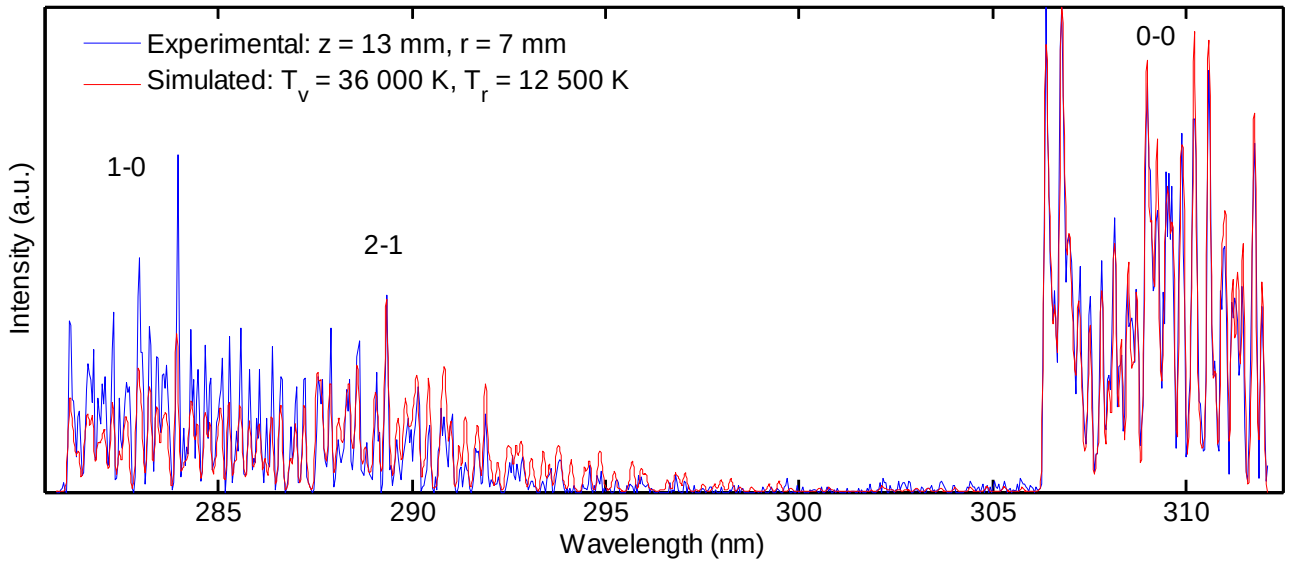

Figure 3. Experimental and fitted simulated OH spectrum at the periphery of the jet in the expansion region.

structure in our spectra was not sufficiently resolved to examine Boltzmann diagrams of rotational and vibrational level populations. To characterize the ro-vibrational distribution at least qualitatively, we fitted the different parts of the measured spectra separately. Thus, the rotational temperature T_{rot}(0-0) was derived by fitting the part of the vibrational transition 0-0 that is unaffected by other significant transitions, the vibrational temperature T_{vib} (1-0, 2-1) by fitting the part of the spectrum dominated by vibrational bands 1-0 and 2-1, and the same approach was used to obtain T_{rot} (1-0) and T_{vib} (0-0, 1-0).

Figure 3 demonstrates one of the most extreme result of the fitting procedure corresponding to the experimental spectrum taken at the far periphery of the jet in the expansion region. The spectrum comprises a vibrational sequence $\Delta v = 1$ and the vibrational band (0-0). The best fit gives a very high vibrational temperature resulting mainly from a relatively high intensity of the sequence $\Delta v = 1$ with respect to that of the sequence $\Delta v = 0$. On the other hand, the intensity ratio of the bands (2-1) and (1-0) corresponds apparently to a quite lower temperature. Note that OH spectra, in contrast to the atomic spectra, are evaluated only at the jet periphery and without applying Abel inversion, and they are just as they were measured and calibrated for spectral response.

4. Results

We performed two series of measurements. The first one was focused on the measurement of OH spectra and H_β line within the whole supersonic domain. The second series included atomic spectra of argon, hydrogen and oxygen, and since it was much more time consuming, it was restricted only to two distinctive positions in the plasma jet, i.e. at the nozzle exit and in the expansion region near the shock front. Since our experiment was not quite reproducible, the results for both series are slightly different.

Results of the first series are summarized in Figure 4. The figure represents radial profiles of all the calculated temperatures together with the profiles of electron number density. The latter can serve as an indication of the shape of the jet core. There are noticeable differences between each calculated temperature that increase towards and even beyond the jet boundary. On the other hand, both rotational and vibrational pairs of the temperature seem to converge to the same value near the jet core. This value is, however, different for both rotational and vibrational temperature, especially in the expansion region as the rotational temperature increases with increasing distance from the nozzle. Notice that we can distinguish between ‘hot’ and ‘cold’ both rotational and vibrational distributions. There is also sharp increase of the temperature T_{vib} (0-0, 1-0) close to the jet boundary.

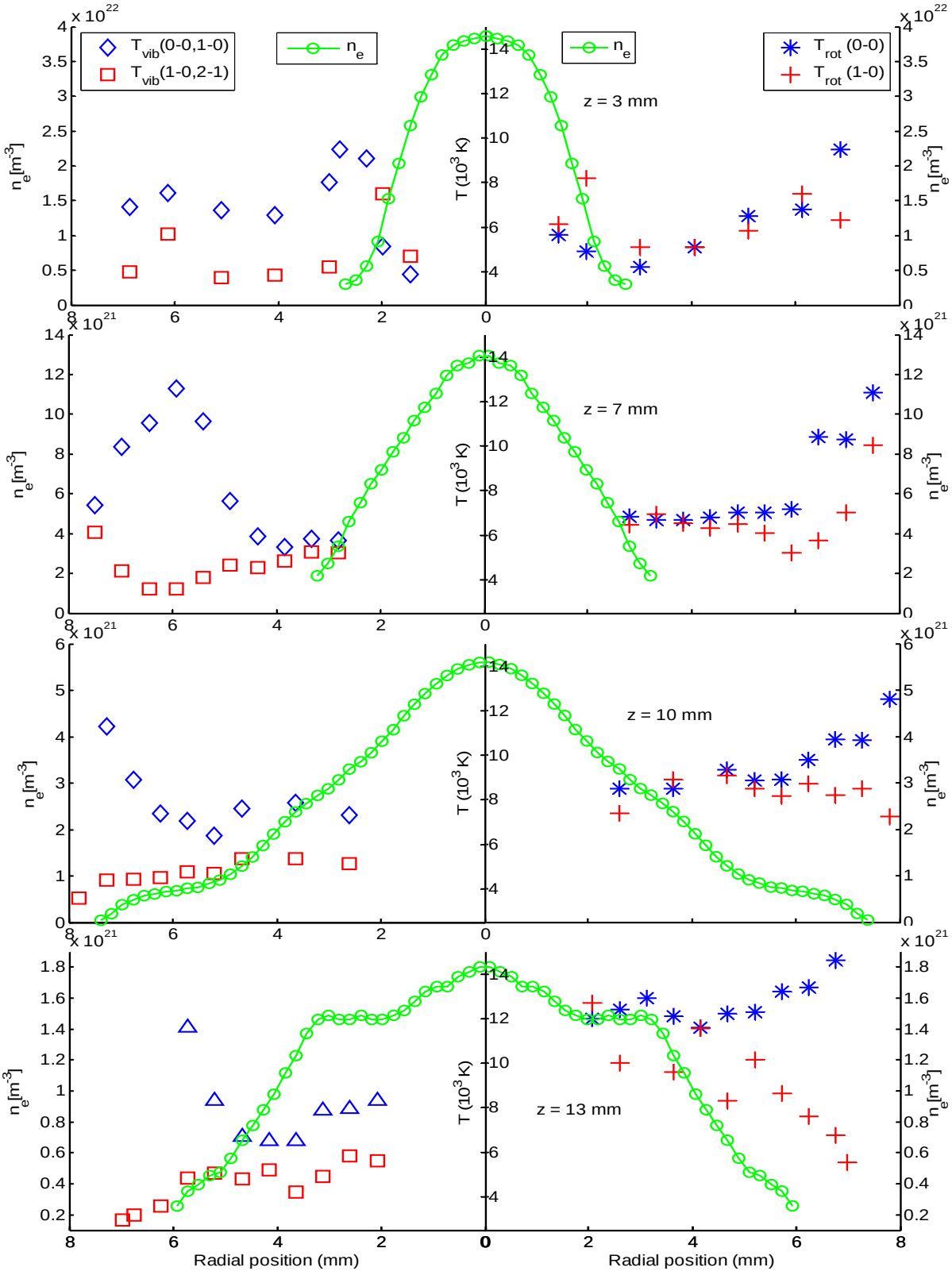

Figure 4. Radial profiles of rotational and vibrational temperatures, and electron number density at four distances z from the exit nozzle.

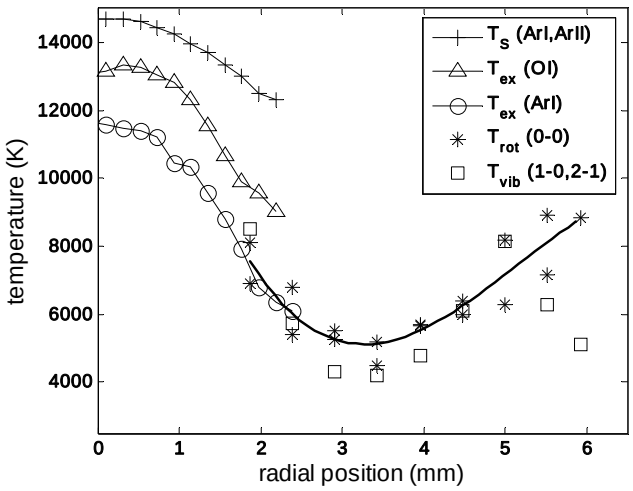

Figure 5. Radial profiles of the temperature at the nozzle exit.

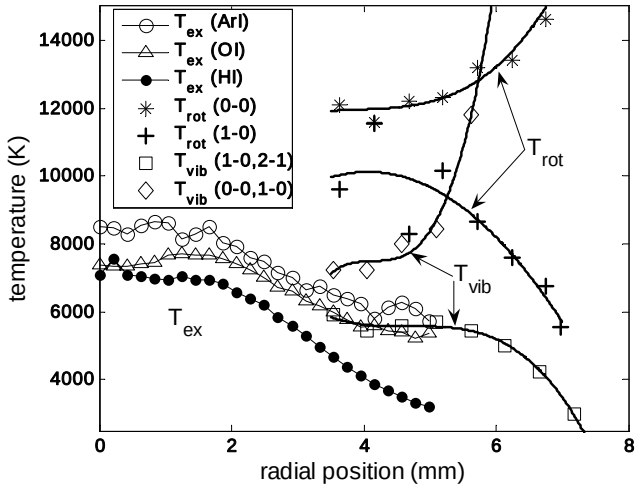

Figure 6. Radial profiles of the temperature in the expansion region.

Figures 5 and 6 show results of the second series of measurements at the nozzle exit and in the expansion region respectively. At the nozzle exit, the atomic excitation temperature T_{ex} (Ar I) is obtained from the complete Boltzmann diagram as no sign of overpopulation of higher excited states was noticed. Boltzmann diagram of O I lines gives a little bit higher excitation temperature than that of Ar I lines but still within the estimated error. T_{ex} (H I) was not determined as the hydrogen lines were too broad. The 'Saha' temperature T_S is of about 3000 K higher than T_{ex} (Ar I) on the jet axis and this difference increases to 5000 K close to the jet periphery. Both rotational and vibrational temperatures agree well with T_{ex} (Ar I) at the jet periphery and increase outside the jet boundary ($r > 3$ mm). The results suggest that the jet at the nozzle exit is relatively close to LTE and the elevated T_S at the jet periphery can be explained by diffusion of free electrons.

In the expansion region, the excitation temperatures derived from atomic spectra are similar with the maximum in the jet core around 8 000 K. The figure reveals once again the 'hot' and 'cold' character of both rotational and vibrational distributions and this effect increases with increasing radius. The idea of superposition of two independent distributions is supported by the fact that for some 0-0 bands the fitting procedure gives not only the temperature much higher than that of 1-0 band but also the temperature that is close to the latter one. There is, however, a noticeable difference between rotational and vibrational temperatures. While the vibrational temperature approaches the atomic excitation temperature at the jet periphery, the rotational temperature significantly exceeds the excitation temperature and is much higher than at the nozzle exit.

4. Conclusions

The results can be summarized as follows:

- Populations of higher atomic states remain close to the Boltzmann distribution for the whole supersonic region. The lower excited states, as indicated in the case of argon 4p states, are underpopulated, which is typical for recombining plasmas. It is, however, not quite evident to what extent the atomic excitation temperature represents the electron temperature. Nevertheless, the comparison of temperatures obtained from both atomic and molecular spectra suggests that at the nozzle exit the plasma can be close to the local thermal equilibrium.
- The rotational temperature is much higher in the expansion region than the vibrational temperature, which seems to be in contrast to the assumption that the former should represent the heavy particle temperature and the latter the electron temperature.
- The intensity distribution in the OH spectra can be interpreted as a result of both the departure from the thermal equilibrium and superposition of 'hot' and 'cold' OH radicals, which can be interpreted as a result of

competition between various chemical reactions leading to the creation of OH radical and collisional relaxation.

- We assume that reactions with argon metastable states may be responsible for the high vibrational excitation at the jet boundary [9], and an extremely 'hot' rotational distribution outside the jet can be explained by photodissociation of H_2O that is supposed to be abundant in the chamber atmosphere [10].

Acknowledgement
This work was supported by the Grant Agency of the Czech Republic under the project No. GA202/05/0669.

References

[1] R. Engeln, S. Mazouffre, P. Vankan, I. Bakker and D.C. Schram – Plasma Sources Sci. Technol. **11**, A104 (2002).
[2] S.E. Selezneva, M. Rajabian, D.V. Gravelle and M.I. Boulos – J. Phys. D: Appl. Phys. **34**, 2862 (2001).
[3] B. van der Sijde, J.A.M. van der Mullen – J. Quant. Spectrosc. Radiat. Transfer **44**, 39 (1990).
[4] V. Sember, D.V. Gravelle and M.I. Boulos – J. Phys. D: Appl. Phys. **35**, 1350 (2002).
[5] V. Linss, H. Kupfer, S. Peter and F. Richter – J. Phys. D: Appl. Phys. **37**, 1935 (2004).
[6] D.A. Levin, C.O. Laux, C.H. Kruger – J. Quant. Spectrosc. Radiat. Transfer **61**, 377 (1999).
[7] V. Březina, M. Hrabovský, M. Konrád, V. Kopecký, V. Sember – Proc. of 15th ISPC **III**, 1021 (2001).
[8] J. Luque and D.R. Crosley, "LIFBASE: Database and spectral simulation (version 1.5)" – SRI International Report MP 99-009 (1999).
[9] J.B. Leblond, F. Collier, F. Hoffbeck and P. Cottin – J. Chem. Phys. **74**, 6242 (1981).
[10] K. Tabayashi, K. Shobatake – J. Chem. Phys. 88, 6242 (1988).

Deformation and Solidification Process of Single Sprayed Zirconia Droplets Impinging on Substrate – In-situ Measurement and Numerical Simulation –

K. Shinoda, A. Yamada, T. Koseki, T. Yoshida

Department of Materials Engineering, Graduate School of Engineering, The University of Tokyo, Tokyo, Japan

Abstract

We developed an in-situ measurement system that enables us to correlate the splat morphology of each droplet with its thermal history during its impinging on substrate. In this study, we have measured the impacting process of yttria-stabilized zirconia droplets by the developed in-situ measurement system. The viscosity of zirconia was estimated via in-situ measurement and was compared with that of alumina. The kinematic viscosity of zirconia at melting point is approximately three times smaller than that of alumina. The most interesting finding is that the plateau-like area was observed in the thermal history. It indicated that the solidification process can occur near the end of the flattening process.

Keywords In-situ measurement, yttria-stabilized zirconia, rapid deformation and solidification, splat morphology, SOLA-VOF, supercooling

1. Introduction

With the increase of the operation temperature of gas turbines, which is now reaching the application limit of Ni-base superalloys, the microstructure of yttria-stabilized zirconia (YSZ) coatings as the main component of thermal barrier is demanded to be controlled at nano level[1]. Therefore, the number of basic researches is increasing to elucidate elementary processes in plasma spraying such as deformation and solidification of droplets impinging on the substrate. However, those processes have not been yet fully understood because the sprayed droplets are too small (10 – 100 μm) and their deformation and solidification are too fast (1 – 10 μs) to measure precisely. Moreover, the lack of high temperature physical properties of YSZ prevents us from numerically simulating these processes precisely.

Moreau *et al*. firstly measured the temperature of TiC particles impacting on a stainless steel substrate under dc plasma spraying via a double-wavelength fiber optic and showed the feasibility of infrared monitoring of the temperature of a plasma sprayed particle at the moment of and immediately after the impact[2]. Moreau *et al.* also monitored cooling rates of molybdenum particles impinging on substrates, and investigated the influence of coating thickness on the cooling rates of plasma-sprayed particles impinging on those substrates[3, 4]. Vardelle *et al*. developed a measurement system consisting of two high-speed two-color pyrometers and measured the temperature, the velocity, and the size of a zirconia particle prior to its impact on a steel substrate and its flattening and cooling during impinging under dc plasma spraying[5, 6]. Gougeon and Moreau developed simultaneous independent measurement of splat diameter and cooling time during impact on a substrate of plasma-sprayed molybdenum particles, in which they measured the shading area of laser beam during spreading[7]. However, the correlations between the splat morphology and the measurement results are not always sufficient in their system. More recently, direct observation of droplet impact by a high-speed CCD camera coupled to a microscope was reported and the impact behaviors such as rebound, deposition, splashing, spattering, were systematically studied[8]. The system was effective in evaluating splashing mode; however, the thermal history during impact could not be measured.

In this context, we have developed an in-situ measurement system that enables us to correlate splat morphology of each droplet with its thermal history[9-11]. We have measured and investigated the deformation and solidification process of sprayed YSZ droplets by the developed in-situ measurement system with the help of numerical simulation.

2. Experimental

The in-situ measurement system used is shown schematically in Fig. 1. The system consists mainly of a hybrid plasma spraying system, a single particle collection apparatus, two sets of emission detectors, and a data storage apparatus. The hybrid plasma spraying system consists of an rf power supply of 4 MHz-60 kW, a dc power supply of 10 kW, a dc-rf hybrid plasma torch, and an airtight chamber. This system made it

possible to measure the deformation and solidification process under a wide variety of conditions such as: 1) wide range of powder size up to 100 μm, 2) particle velocities ranging from 20 to 70 m/s, and 3) various atmospheres as well as a wide pressure range.

The way how to collect single sprayed particles is described in detail in the Ref[9]. Two optical systems were used to detect the thermal emission from a particle. One was used to measure the surface temperature and velocity of an in-flight particle immediately before the particle impinged, and was connected to the collimator, which is utilizing the method developed by Sakuta and Boulos[12]. We selected 500/ 800 nm and 700/ 1000 nm wavelengths for the measurement of particle temperature before and during impact, respectively. The detected signal of in-flight particle itself works as a trigger for the record of sequential measurement for the event of particle flattening. The other system was connected to the emission condenser that consisted of two optical lenses with the focal lengths of 40 mm and 70 mm. This condenser focused at an angle of 20 degrees on the substrate and its viewing field on the substrate was an ellipse of 1.7 mm – 5 mm. The sets of photomultipliers used were Hamamatsu-made R1104/R1104 and R943-02/R3310-02 for 500/800 nm of the in-flight particle measurement and for 700/1000 nm of the impact, respectively. The data were collected by a digital oscilloscope and sent to a PC via GP-IB. The droplet diameter was calculated from the volume of the deposited splat. The volume was measured precisely with a three-dimensional laser microscope, KEYENCE VK-8500, that could measure the three-dimensional morphology, which was also used to examine the backside of splats. In addition, the substrate holder was designed to be movable horizontally with a speed up to 1 mm/s in order to avoid overlapping of the substrate. The substrate temperature was controlled by an electric heater made of molybdenum spiral wire and measured by thermocouple set below the substrate.

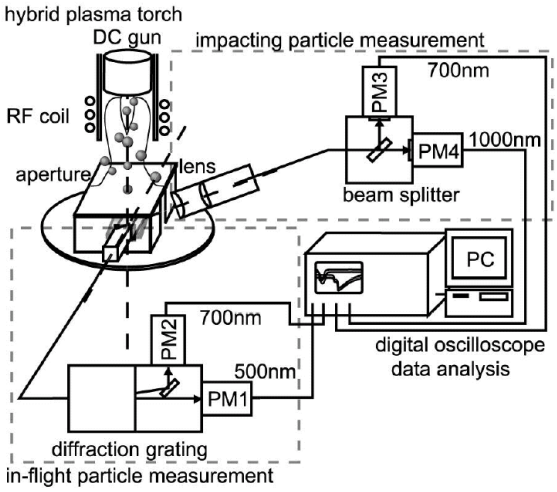

Fig. 1. Schematic diagram of the in-situ measurement system.

Table 1 shows the spraying conditions. Powders are injected into the dc plasma jet at an angle of 30 degree from the torch axis through a tube of 2 mm in internal diameter passed through inside the anode. Fused and crushed 8YSZ powder with size distribution ranging from 63 to 88 μm was used. 8%H_2-Ar atmospheric hybrid plasma was adopted to spray powders onto a quartz substrate. The substrate measured 25 mm long by 10 mm wide by 0.6 mm thick, and its surface roughness was 0.04 μm. The stand-off distance was set to 80 mm. The powder feeding rate was adjusted below 0.6 g/min to limit the number of particles impinging on the substrate. The substrate temperature was set at approximately 700 K to obtain disk-shaped splat[13]. The sampling rate was set to a 0.1 μs interval and the sampling point was 5000 pts for each channel, for each splat. When emission signals are detected, a shutter set above the BN plate was closed; the signals are recorded; the substrate is moved about 1 mm; then the shutter is opened again and next trial run is started. In this manner, 15 to 20 splats were collected in each experiment.

Table 1. Typical Experimental conditions

Parameters	Settings
Internal diameter of dc torch (mm)	6
Dc Ar gas flow rate (slm)	10
Dc current (A)	300
Internal diameter of rf torch (mm)	40
Rf tangential Ar gas flow rate (slm)	10
Rf radial Ar gas flow rate (slm)	30
Rf radial H_2 gas flow rate (slm)	5
Rf input power (kW)	50
Powder carrier gas flow rate (slm)	2
Powder feeding rate (g/min)	0.6
Stand-off distance (mm)	80
Substrate temperature (K)	700

3. Results & Discussion

Figure 1 shows laser microscope images of a single sprayed splat from both top and bottom side and the 1:1 corresponding waveforms to the splat. This particle impinged the substrate at 48 μm in diameter, 65 m/s in velocity, and 3550 K in temperature. The diameter of splat was 163 μm; hence, the degree of flattening was 3.4. Cooling rate was estimated from the initial gradient of temperature during impact to 8.1 $\times 10^7$ K/s and the thermal contact resistance was, therefore, estimated to be 5.3×10^{-6} m^2K/W.

On the other hand, the lack of knowledge of the high-temperature properties of zirconia has clearly prevented the development of realistic simulation. In reality, there are only few papers referring the

viscosity. For example, Fantassi *et al.* assumed constant value of 0.04 Pa·s[14] and Vardelle *et al.* used the equation: μ[Pa·s] = 0.1exp(-2.95+5993/T)[6] based on an analogy with the temperature dependence of alumina viscosity. Hence, we have estimated the viscosity of zirconia, μ, by substituting the results into the model: $D/d = 0.83Re^{0.2}$[15]. Each value could be fitted by the Arrhenius-type equation: μ[Pa·s] = 0.0037 exp (6100/T) revealing 0.028 Pa·s at 3000 K as shown in Fig. 3. The viscosities of alumina reported in literatures[16-21] are also shown for the purpose of comparison. The viscosity of zirconia does not increase rapidly with the increase of supercooling, which was different from what was expected. This low viscosity in the supercooled region will be the main reason why supercooled droplets can show similar flattening degree with superheated droplets[11]. The kinematic viscosities at melting points of zirconia (3000 K) and alumina (2328 K) are 4.9×10^{-6} m^2/s and 1.5×10^{-5} m^2/s[21], respectively. The value of zirconia is approximately three times smaller than that of alumina, which suggests that zirconia particles may flatten better than alumina particles once they are fully melted. Note that the activation energy for zirconia viscosity was derived as 51 kJ/mol, which is much lower than the value of 247 kJ/mol proposed by Sudreau *et al.* and rather close to the values 87 kJ/mol and 68 kJ/mol estimated by Grosse and Hirai relationships for metallic alloys, respectively[22]. The derived value of μ is only a rough estimation; nevertheless, the fact that we can deduce even the unknown viscosity of zirconia clearly reveals the powerfulness of our approach.

A Numerical simulation of the droplet impact processes about the splat shown in Fig. 2 has been conducted by basically solving the full Navier-Stokes and energy equations coupled with the Volume of Fluid (VOF) approach to track the surface of a deforming droplet. We adopted the 2-dimensional impact model utilizing SOLA-VOF algorithm, which was firstly developed by Pasandideh-Fard *et al.*[23, 24] and extended to include supercooling effects by Chae *et al.*[25]. The thermo physico-chemical properties of zirconia and quartz glass substrate used here were shown in Table 2. The simulation result shows flattening degree is 4.5, which is 20 % higher value than the experimental value.

Figure 3 shows the 700 and 1000 nm emission waveforms from the particle during the impact. Surface temperature calculated from the waveforms and the dimensionless diameter derived from numerical simulation are also shown in the figure. Calibration of the temperature during impact was performed by equalizing impact temperature with in-flight temperature of the particle. Noise reduction or smoothing was conducted by using Savitzky-Golay method[26]. The spreading time estimated from the measurement is 2.1 μs, and is in a good agreement with the 90 % spreading time, 2.2 μs, derived from the numerical calculation. The difference in flattening degree between the experiment

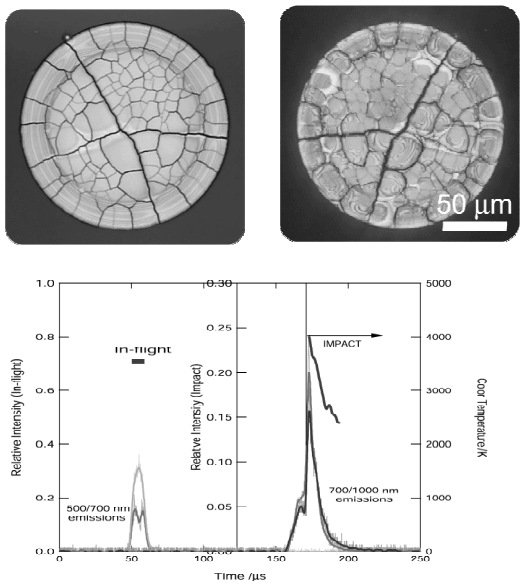

Fig. 2. 1:1 correspondence between emission signals and the splat

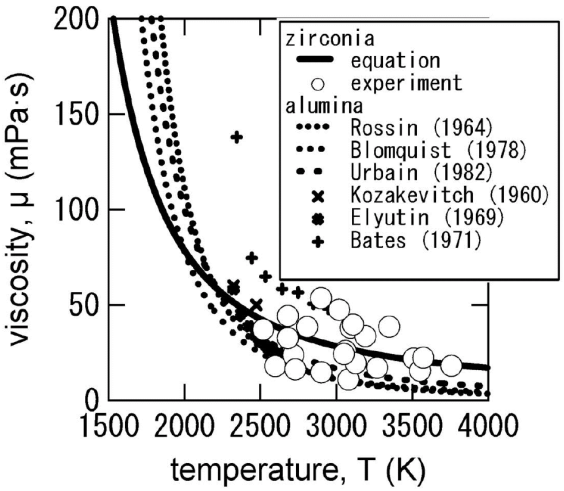

Fig. 3. Estimated viscosity of zirconia. Viscosities of alumina are quoted from Kozakevitch (1960), Rossin (1964), Elyutin (1969), Bates (1971), Blomquist (1978), and Urbain (1982).

Table 2. Physico-chemical properties of droplet and substrate materials used in numerical simulations.

materials	ρ (kg/m^3)	C_p (J/kgK)	k (W/mK)	σ (N/m)
zirconia (l)	5700	713	2.32	0.43
zirconia (s)	5700	604	2.32	
quartz	2000	900	1.17	

Properties were quoted from Vardelle (1995) and Chase (1998).

and the simulation may be explained by the effect of shrinkage, because we observe the rim of collected splat is much larger than that of calculated splat. This is consistent with the previous suggestion[7] that actual splat should show large shrinkage. The most interesting finding is that the plateau-like area is observed around 4.6 μs after the impact. This plateau indicates that in this droplet the solidification started near the end of the deformation process. Further investigation is needed to confirm this, but the obtained results suggest that the solidification can start near the end of the flattening and may affect the flattening process.

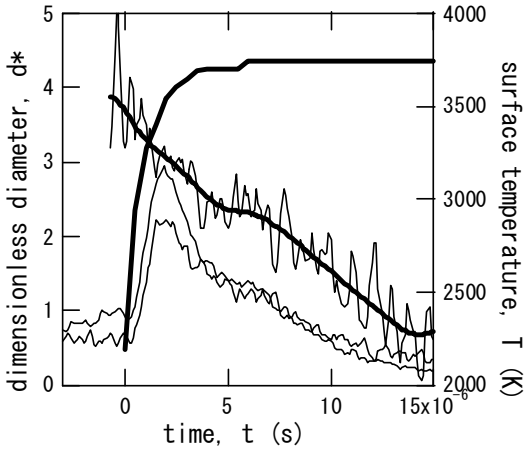

Fig. 4. Measured thermal history and calculated dimension less diameter during particle impact.

4. Conclusion

In-situ measurement of deformation and solidification process was conducted via highly developed in-situ measurement system. It enabled us to collaborate with numerical simulation in addressing solidification problems. The most interesting findings is that solidification may occur around the end of flattening process.

Acknowledgements

The present research was supported in part by a Grant for 21st Century COE Program 'Human-Friendly Materials based on Chemistry' from the Ministry of Education, Culture, Sports, Science, and Technology of Japan.

References

[1] H. Huang, K. Eguchi, T. Yoshida - Sci. Technol. Adv. Mater., 4, 6 (2003).
[2] C. Moreau, P. Cielo, M. Lamontagne, S. Dallaire, M. Vardelle - Meas. Sci. Technol., 1, 8 (1990).
[3] C. Moreau, M. Lamontagne, P. Cielo - Surf. Coat. Technol., 53 (1992).
[4] C. Moreau, P. Cielo, M. Lamontagne - J. Therm. Spray Technol., 1, 4 (1992).
[5] M. Vardelle, A. Vardelle, P. Fauchais, C. Moreau - Meas. Sci. Technol., 5, 3 (1994).
[6] M. Vardelle, A. Vardelle, A.C. Leger, P. Fauchais, D. Gobin - J. Therm. Spray Technol., 4, 1 (1995).
[7] P. Gougeon, C. Moreau - J. Therm. Spray Technol., 10, 1 (2001).
[8] C. Escure, M. Vardelle, P. Fauchais - Plasma Chem. Plasma Process., 23, 2 (2003).
[9] K. Shinoda, R. Takenoshita, Y. Kojima, T. Yoshida - *in the Proc. of* 16th ISPC, Taormina, Italy (2003).
[10] K. Shinoda, A. Yamada, T. Koseki, T. Yoshida - *in the Proc. of* ITSC, Osaka, Japan (2004).
[11] K. Shinoda, Y. Kojima, T. Yoshida - J. Therm. Spray Technol., (in press).
[12] T. Sakuta, M.I. Boulos - Rev. Sci. Instrum., 59, 2 (1988).
[13] K. Shinoda, P. Han, T. Yoshida - *in the Proc. of* 15th ISPC, Orleans, France (2001).
[14] S. Fantassi, M. Vardelle, A. Vardelle, P. Fauchais - J. Therm. Spray Technol., 2, 4 (1993).
[15] T. Yoshida, T. Okada, H. Hamatani, H. Kumaoka - Plasma Sources Sci. Technol., 1, 3 (1992).
[16] P. Kozakevitch - Rev. Met., 57 (1960).
[17] R. Rossin, J. Bersan, G. Urbain - Rev. Hautes Temper. et Refract., 1 (1964).
[18] V.P. Elyutin, V.I. Kostikov, B.S. Mitin, Y.A. Nagibin - Zhur. Fiz. Khimii, 43 (1969).
[19] J.L. Bates, C.E. McNeilly, J.J. Rasmussen - *in the Proc. of* Mater. Sci. Res. (1971).
[20] R.A. Blomquist, J.K. Fink, L. Leibowitz - Am. Ceram. Soc. Bull., 57, 5 (1978).
[21] G. Urbain - Rev. Int. hautes Temper. Refract., 19, 1 (1982).
[22] F. Sudreau, G. Cognet - Nucl. Eng. Des., 178 (1997).
[23] M. Pasandideh-Fard, Y.M. Qiao, S. Chandra, J. Mostaghimi - Phys. Fluids, 8, 3 (1996).
[24] M. Pasandideh-Fard, J. Mostaghimi - Plasma Chem. Plasma Process., 16, 1 (1996).
[25] Y.K. Chae, J. Mostaghimi, T. Yoshida - Sci. Technol. Adv. Mater., 1, 3 (2000).
[26] A. Savitzky, M.J.E. Golay - Anal. Chem., 36, 8 (1964).

Gasification of Biomass in Water-Stabilized DC Arc Plasma

M. Hrabovsky[1], V. Kopecky[1], M. Konrad[1], M. Hlina[1], T. Kavka[1],
G. van Oost[2], E. Beeckman[3], J. Verstraeten[3], J. Ledecky[4], E. Balabanova[5]

[1]*Institute of Plasma Physics, ASCR, Za Slovankou 3, Prague 8, Czech Republic*
[2]*Department of Applied Physics, Ghent University, Rozier 44, B-9000 Gent, Belgium*
[3]*EnviTech S.A., Belgium,*
[4]*Ateko a.s., Hradec Kralove, Czech Republic*
[5]*Institute of Electronics, Bulgarien Academy of Science, Sofia, Bulgary*

Abstract
Pyrolysis of biomass in thermal plasma was experimentally studied in reactor with dc arc plasma torch stabilized by combination of gas flow with water vortex. Crushed wood was used as a model substance for treatment of organic waste materials. Temperature distribution within the reactor, power balances of the process and composition of produced gas were measured. Synthetic gas with high content of hydrogen and CO was produced.

Key words: plasma pyrolysis, biomass, dc arc gas/water plasma

1. Introduction

The gasification of biomass to produce synthesis gas (syngas) offers an alternative to fossil fuels. Since syngas contains hydrogen and carbon monoxide, it has the potential to be used as a re-burning fuel to reduce NO_x emissions. Common biomass gasification technologies are based on the reaction between a heated carbon source with limited amounts of oxygen and steam. Thermal plasma offers possibility of decomposition of biomass by pure pyrolysis in the absence of oxygen. In the process all energy needed for gasification comes from plasma, no energy for decomposition is produced by combustion. The process acts also as energy storage – electrical energy is transferred to plasma energy and then stored in produced syngas. The main advantage is better control of composition of produced gas, higher heat capacity of the gas and reduction of unwanted contaminants like tar, CO_2 and higher hydrocarbons.

Most of the experiments with plasma pyrolysis have been performed with arc plasma torches with relatively high flow rates of plasma gas. Production of syngas from wood in plasma generated in ac air plasma torches is discussed in [1]. Coal gasification in hydrogen, air and steam plasma was studied in [2, 3]. In [4] wood was gasified in steam plasma. The mean enthalpy of plasma, given by ratio of net arc power to gas flow rate, was usually not higher then 10 MJ/kg [1 - 4]. The high flow rate of plasma ensures good mixing of plasma with treated material. However, produced synthetic gas contains components of plasma gas, usually nitrogen and oxygen if air or nitrogen are used as plasma gases [1, 3]. The usage of mixtures of inert gas with hydrogen [5, 6] eliminates this disadvantage but it increases cost of the technology. Therefore steam was used as plasma gas in [2, 4].

In this paper a dc plasma torch with gas/water stabilized arc, usually applied for plasma spraying, is used [7]. Plasma gas is mixture of steam with small amount of argon. Due to principle of arc stabilization by water vortex the flow rate of plasma gas is very low and plasma enthalpy is more than 200 MJ/kg and mean plasma temperature more than 15 000 K [7, 8]. This is the main difference from gas plasma torches with steam used as plasma gas [2, 4] where temperatures are lower then 4 000 K. The utilization of high enthalpy, high temperature plasma offers advantages in possibility of adjusting high reaction temperature. As low amount of plasma carries high energy, the power needed for heating of plasma to reaction temperature is very low and the efficiency of utilization of plasma power for waste destruction is extremely high. The paper describes first series of experiments in the plasma reactor with high enthalpy gas/water plasma torch designed for destruction of solid waste materials and gasification of biomass.

2. Experimental system

The experimental plasma-chemical reactor (Fig. 1) with water-cooling system has been designed to operate at a wall temperature up to 1700 C. The inner lining of the reactor was made from special

refractory ceramics. Ceramic insulation wall with the thickness of 400 mm reduces power loss to the walls. All parts of reactor chamber were water-cooled and calorimetric measurements on cooling circuits were made. The material container was equipped with a continuous material supply system with controlled flow rate. The pressure in the supply conveyer was automatically kept higher then the

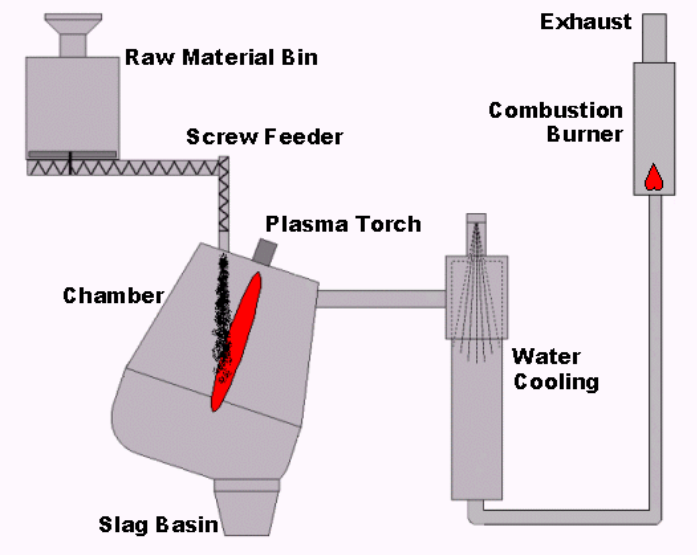

Fig. 1. Schematics of experimental reactor for plasma pyrolysis

pressure inside the reactor by controlled nitrogen flow to prevent reactor gases flow into the material supply system. Crushed wood was supplied to the reactor and was injected into plasma jet in the position about 30 cm downstream of the input plasma entrance nozzle at the reactor top. It was partially gasified during its flight within the jet, the non-gasified part of the wood falls onto the bottom of the reactor where it was gasified in the hot gas flow. The exit tube for exhaust gas was in the upper part of the reactor, so as the produced gases passed through the zone of high temperature within plasma jet or close to it. Inputs for additional gases for control of reactor atmosphere are at three positions in the upper part of the reactor.

Table 1. Experimental parameters

	Run 1	Run 2
Arc current [A]	350	450
Arc power [kW]	95	138
Steam plasma flow rate [g/s]	0.2	0.25
Argon plasma flow rate [slm]	12	12
Torch efficiency [%]	58	59
Argon flow rate in anode chamber [slm]	20	33
Nitrogen flow rate [slm]	4	4
CO_2 flow rate [slm]	23	0
Power loss to the reactor [kW]	16	18
Power available for material treatment [kW]	39	63
Material (wood) mass flow rate [kg/hour]	20	20
Humidity of treated wood [%]	7	7

The gas produced in the reactor flowed through the connecting tube to the quenching chamber, which was created by a cylinder with the length of 2 m. At the upper entrance of the cylinder the gas was quenched by a spray of water from the nozzle, positioned at the top of the cylinder. The water flow

rate was automatically controlled to keep the temperature of gas at the end of quenching chamber at 300 ^{o}C. The gas then flows into the combustion chamber where it is combusted in the flow of the air. Plasma was produced in the torch with dc arc stabilized by combination of gas flow and water vortex [7]. The torch generates an oxygen-hydrogen-argon plasma jet with extremely high plasma enthalpy and temperature. The torch is attached to the reactor at the reactor top. The anode of the torch is created by a rotating water-cooled disc, which is positioned outside the arc chamber downstream of the torch exit nozzle [7]. The anode of the torch was thus inside the reactor and it was separated from the reactor volume by a water-cooled wall. Additional argon was supplied into the anode chamber to protect anode from flow of reaction gases. Plasma enters the reactor volume through the nozzle with diameter of 40 mm in this wall.

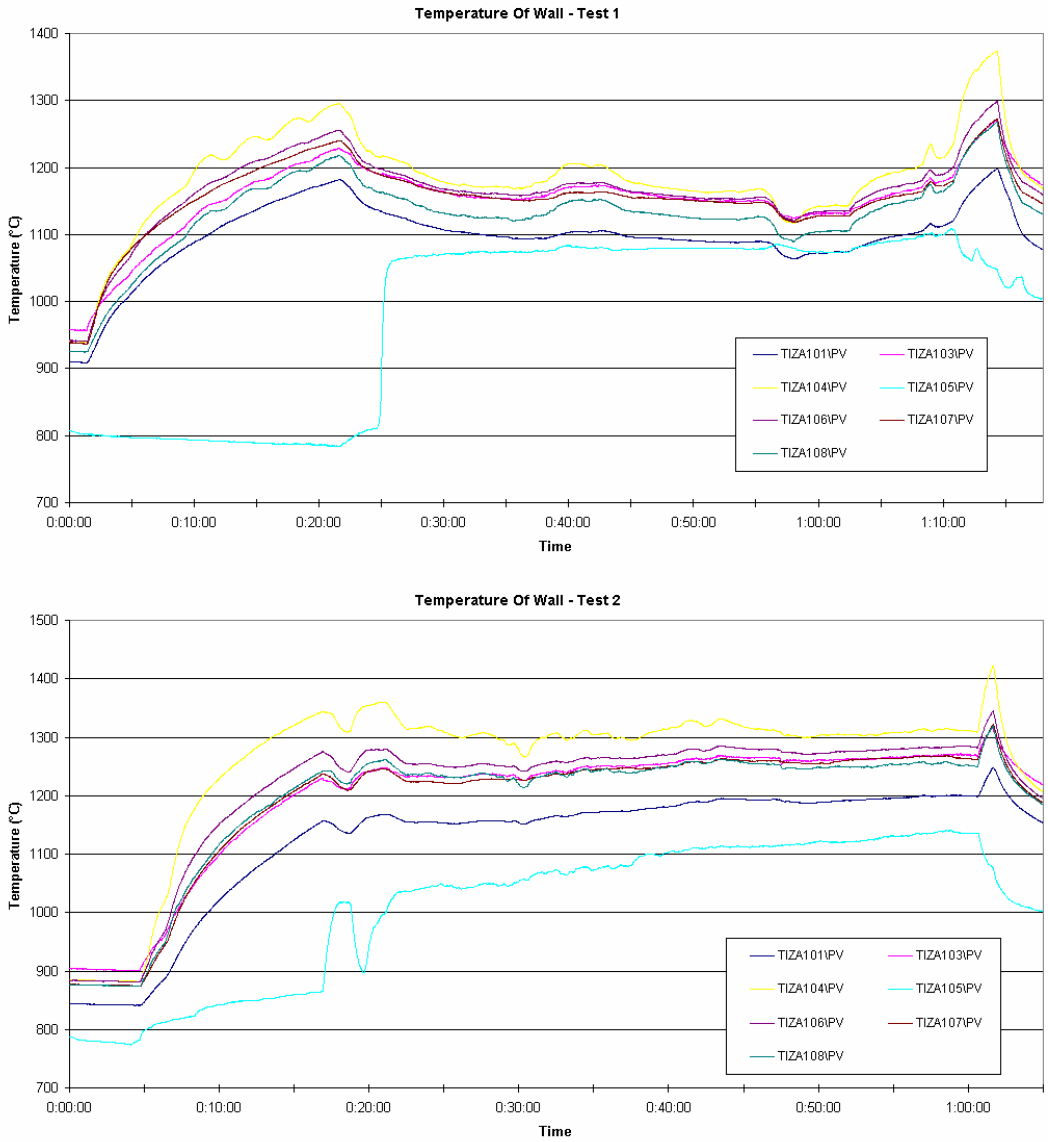

Fig. 2. Temperatures of reactor wall in several positions (TIZA 101, 103, 104, 106, 107, 108) and temperature of produced syngas at position of gas sample collection (TIZA 105).

Measuring system included monitoring of plasma torch operation parameters, temperatures in several positions inside the reactor and calorimetric measurements on cooling water loops. The temperature of inner wall of the reactor was measured in six positions by thermocouples. The flow rate of reaction gas was measured using a Pitot-static tube flow meter, gas temperature was measured at the input and output of quenching chamber. The composition of produced gas was measured at the output of reactor

before the gas enters the quenching chamber. The tube for collection of samples was cooled by the water spray at the input of the quenching chamber. The gas analysisys was made by a quadruple mass spectrometer Balzers QMS 200. As the gas can contain some amount of steam which could after condensation block or damage the inputs of the spectrometer, the freezing unit was connected into the gas sample circuit.

3. Results.

Before the experiments the reactor was pre-heated by the gas burner to temperature about 900°C. The results of two runs are presented in this paper. At each run the torch was operated for about one hour. The basic experimental parameters are in Table 1. The flow rate of crushed wood was the same in the both runs, the water content in the wood was 7% of weight. CO_2 was added into the reactor in the first run to increase the oxygen content and to reduce production of solid carbon deposits within the system.

The temperatures of inner wall of the reactor in several positions during the both runs are shown in Fig. 2. The time of arc ignition corresponds to the sudden steep increase of temperatures at the time t = 1.5 min in the first run and the time t = 5 min in the second run. The time of start of supply of the wood was t = 20 min in the first run and t = 16 min in the second run. The temperature of gas measured at the output of the reactor, where samples for gas analysis were taken, is shown in Fig. 2 as well. The sudden changes of the temperature at the beginning of wood supply were caused by adjusting the thermometers into their measuring position in the center of the exhaust tube. The temperature of gas is somewhat lower then the reactor temperature as the gas was cooled down in the exhaust tube.

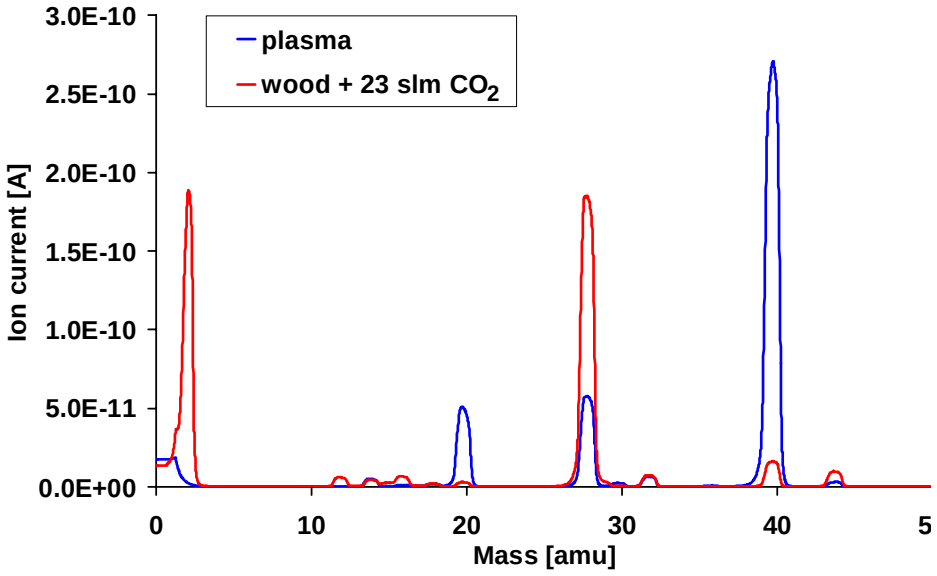

Figure 3. Mass spectra of exhaust pyrolysis gas (red) compared with the gas spectrum without material feeding (blue).

It can be seen that the differences of temperatures at different positions does not exceed 150°C despite of the fact that the reactor is heated by concentrated plasma jet with high velocity and temperature and low mass flow rate. Natural turbulence of generated plasma jet as well as disturbances of plasma flow caused by the interaction with solid evaporating material ensure strongly turbulent conditions within the reactor and thus sufficiently homogeneous heating of all parts of the reactor volume. After material is injected the temperatures fell down but were stable for the whole time of material feeding. Small differences in temperatures measured in different positions prove good mixing process in the reactor. The temperature increase at the end of the records correspond to reduction of flow rate of material.

Table 2. Composition of gases at the output from the reactor (in volume %)

	H_2	CO	CO_2	O_2	Ar	N_2
No material fed	0.5	-	0.5	1.3	89.1	8.6
Run 1 – sample 1	46.3	45.2	1.9	1.6	5.1	-
Run 2 – sample 1	40.6	43.4	5.3	2.4	8.4	-
Run 2 – sample 2	42.0	44.3	3.4	2.5	7.8	-
Run 1 – theory	44.0	47.8	0	2.0	5.5	0.7
Run 2 – theory	45.9	45.1	0	0.4	7.9	0.7

The example of mass spectrum of exhaust gas compared with the mass spectrum of gas flowing from the reactor without material feeding is shown in Fig. 3. Results of analysis of gas samples are shown in Table 2. The first line gives the composition of exhaust gases in case when only plasma torch was operated. Equilibrium concentrations of reaction products, calculated for experimental flow rates of input substances under the assumption of complete decomposition of cellulose, water and CO_2 into hydrogen and carbon monoxide, are shown for the both runs in the last two lines of Table 1. It can be seen that in the both cases almost complete decomposition of wood into mixture of hydrogen and carbon monoxide occurred, the concentration of CO_2 was only several percent. Argon concentrations correspond to the flow rate of argon into the torch and the anode chamber, flow rate of nitrogen corresponds to amount of nitrogen in pressure control input of the material feed conveyer. The results show that all material was decomposed in the reactor and thus sufficient heat transfer takes place in the reactor between flowing plasma, solid injected material and produced gases.

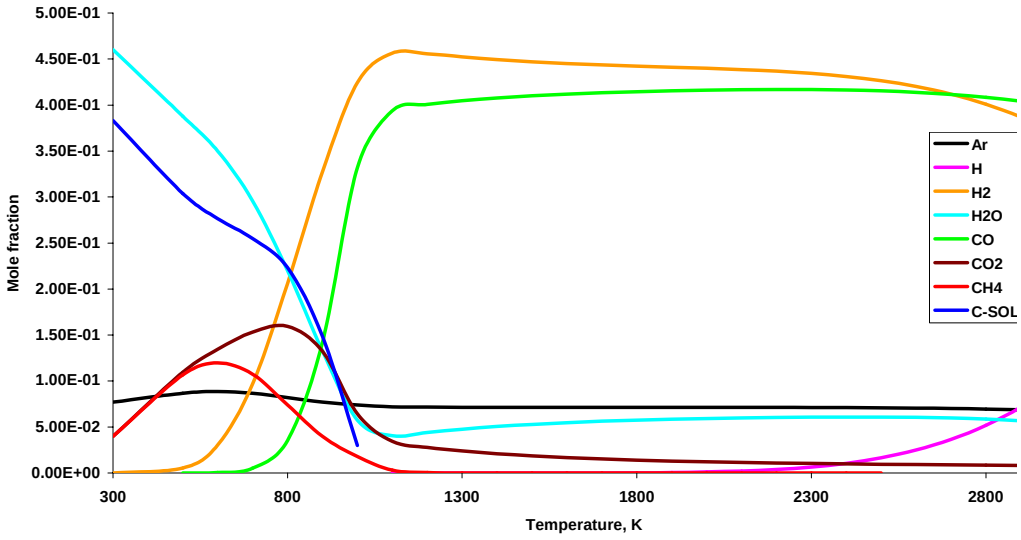

Fig. 4. Equilibrium composition of mixture of cellulose (1 mol) and water (1 mol) in dependence on temperature calculated using code ASTRA.

For comparison, the temperature dependence of composition of mixture of 1 mol of cellulose with 1 mol of water, which approximately corresponds to the test conditions, calculated under the assumption of existence of thermodynamic equilibrium using the computer code ASTRA, is shown in Fig. 4. It can be seen that for temperatures above approximately 1000°C the reaction gas is composed mostly from mixture of hydrogen with CO with small percentage of CO_2, steam and argon.

4. Conclusions.

The plasma reactor for pyrolysis of waste was operated with wood used as a model substance. High enthalpy, low plasma flow rate plasma jet generated in hybrid gas/water torch was used as a source of plasma. The experiments prove that homogeneous heating of volume of plasma reactor and proper mixing of plasma with treated material were ensured despite of very low plasma mass flow rate. The conditions within the reactor ensure complete destruction of tested substance. Synthetic gas with high content of hydrogen and carbon monoxide and low concentration of carbon dioxide with high caloric value was produced. The concentration of hydrogen is higher than the maximum values reported for classical treatment of biomass. The main advantage of use of plasma torch with water-stabilized arc is in composition and low flow rate of plasma. The content of other gases commonly present in gas stabilized systems is very low. In further experiments the effect of experimental conditions on mass and energy balances of the process will be studied.

Acknowledgement

The authors gratefully acknowledge the support of this work by the Grant Agency of the Czech Republic under the project No. 202/05/0669.

References

[1] Rutberg P.G., Bratsev AN, Ufimtsev AA, Plasmochemical technologies for processing of hydrocarbonic raw material with syngas production, J. of High Temp. Mat. Process. 8 (2004), 3, 433-446.

[2] Mikhailov B., Plasma gasification of coal, Thermal Plasma and new Materials Technology, ed. O.P. Solonenko, M.F. Zhukov, Vol. 2, Cambridge Interscience Publish., 1995, 345-369.

[3] Zasypkin I.M., Nozdrenko G.V., Production of acetylene and synthesis gas from coal by plasma chemical methods, Thermal Plasma Torches and Technologies, Vol II., ed. O.P. Solonenko, Cambridge Interscience Publish., 2001, 234-243.

[4] Kezelis R., Mecius V., Valinciute V., Valincius V., Waste and biomass treatment employing plasma technology, J. of High Temp. Mat. Process. 8 (2004), 2, 273-282.

[5] Zhao ZL, Huang HT, Wu CZ, Li HB, Chen Y., Biomass pyrolysis in an argon/hydrogen plasma reactor, Chem. Engineering & Technology 24 (2001), 11, 197-199.

[6] Zhao ZL, Plasma gasification of biomass in a downflow reactor, Abstract of Papers of the American Chemical Society 226: U536-U536 048-FUEL Part 1, SEP 2003.

[7] V.Brezina, M.Hrabovsky, M.Konrad, V.Kopecky, V.Sember, Proc. 15th Int.Symp.on Plasma Chemistry, Orleans, 9-13 July 2001, Vol.III, p. 1021-1026.

Influence of the applied frequencies on plasma characteristics in dual frequency reactors: a numerical study

V. Georgieva and A. Bogaerts
Department of Chemistry, University of Antwerp (CDE), B-2610 Antwerp, Belgium

Abstract
A one-dimensional particle-in-cell/Monte Carlo (PIC/MC) model is used to investigate the influence of the applied frequencies on the plasma characteristics in $Ar/CF_4/N_2$ discharges sustained in dual frequency reactors. The simulations were carried out for a high frequency (HF) of 27, 60 or 100 MHz and a low frequency (LF) of 1 or 2 MHz. It is observed that the decoupling of the two sources is possible with increasing the applied HF to very high values (above 60 MHz) and it is not defined by the frequency ratio.
Keywords PIC/MC method, dual frequency reactor, CF_4 plasma.

1. Introduction

Dual frequency reactors were introduced in the early 90s but recently there has been an increasing interest and study of these systems [1-6]. The two-frequency scheme allows independent control of the ion flux and ion bombardment energy, which is important for surface etching applications, and this cannot be achieved by the conventional single frequency capacitively coupled (cc) reactor.
The purpose of the present work is to study the influence of the applied frequencies on the plasma characteristics in $Ar/CF_4/N_2$ discharges by means of a PIC/MC method. In Sec. 2 the input parameters and the outline of the model are given. In Sec. 3 the results of the simulation, such as the plasma density, ion current, electron and ion average energies and energy distributions, average sheath potential and width, and ionization rates, are presented and discussed. Finally, in Sec. 4 a summary is given.

2. Description of the model

A schematic diagram of the cc rf reactor considered in this study is shown in Fig.1. The plasma is sustained between two parallel plates, each 20 cm in diameter and separated from each other by 2 cm. One of the electrodes is driven by a dual frequency voltage source, i.e. the applied voltage is

$$V = V_{HF}\sin(\omega_{HF}t) + V_{LF}\sin(\omega_{LF}t), \quad (1)$$

where V_{HF} and V_{LF} are the HF and LF voltage amplitudes, and ω_{HF} and ω_{HF} are the applied HF and LF. The other electrode is grounded. The computation is based on a one-dimensional coordinate space and three-dimensional velocity space PIC/MC algorithm. The motion of the charged particles is simulated by the PIC method using the standard explicit 'leap frog' finite difference scheme [7].
The collisions between the charged particles are added by combining the PIC model with a MC procedure [8, 9]. The charged species, which are followed in the model, are: electrons, Ar^+, CF_3^+, N_2^+, F^-, and CF_3^- ions.

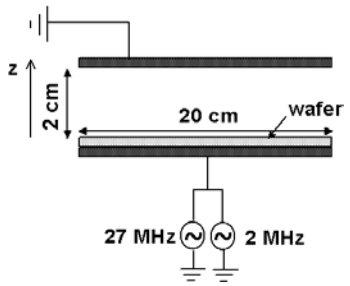

FIG. 1. Schematic diagram of the reactor

The interactions between the particles are treated by a MC method. To calculate collision probabilities, it is necessary to have the corresponding collision cross-section data, which are not always available. Hence, the present model uses several techniques to define the collision probabilities even when the collision cross-sections are unknown. The outlines of all techniques and the data for electron-neutral and ion-neutral collisions, electron-ion and ion-ion recombination considered in the model are given elsewhere [3,4]. We recall here only the expression for the energy width ΔE of the ion energy distribution function (IEDF) in dual frequency reactors, which was obtained in Ref. 4 and will be used to discuss the results

$$\Delta E = \frac{8\lambda_2 e\overline{V_s}}{3\bar{s}\omega_{LF}}\left(\frac{2e\overline{V_s}}{M}\right)^{1/2}, \quad (2)$$

where $\overline{V_s}$ and $\bar{s}$ are the average sheath potential and width, respectively, λ_2 is a parameter determined from the sheath potential plot as a function of the phase in the LF cycle and $\lambda_2 \le 1$, ω_{LF} is the applied LF, M is the mass of the ion, and e is the electron charge.

3. Results and discussion

The calculations are performed for an $Ar/CF_4/N_2$ mixture at a ratio of 0.8/0.1/0.1 at a pressure of 30 mTorr. The gas temperature is set to 300 K. The choice of the grid spacing and the time steps is defined by the accuracy criteria for PIC/MC codes with explicit mover [10].

Figure 2 presents the simulation results, averaged over one or two LF cycles, for the plasma density in the discharge center (a), the ion current density at the powered electrode (b), and the electron energy in the discharge center (c) as a function of the LF voltage amplitude. The calculated characteristics for the (27+2) MHz case are averaged over 2 LF cycles since one LF cycle does not contain an integer number of HF cycles. The HF voltage amplitude is kept at 200V, while the HF is 27, 60, or 100 MHz. The LF voltage amplitude is 0, 100, 200, 300 or 400 V and the LF is 1 or 2 MHz. The simulations for (27+1) MHz, when the LF voltage is higher than 200 V, could not be performed because the two sheaths expand and become comparable with the electrode gap, so that the plasma cannot be sustained.

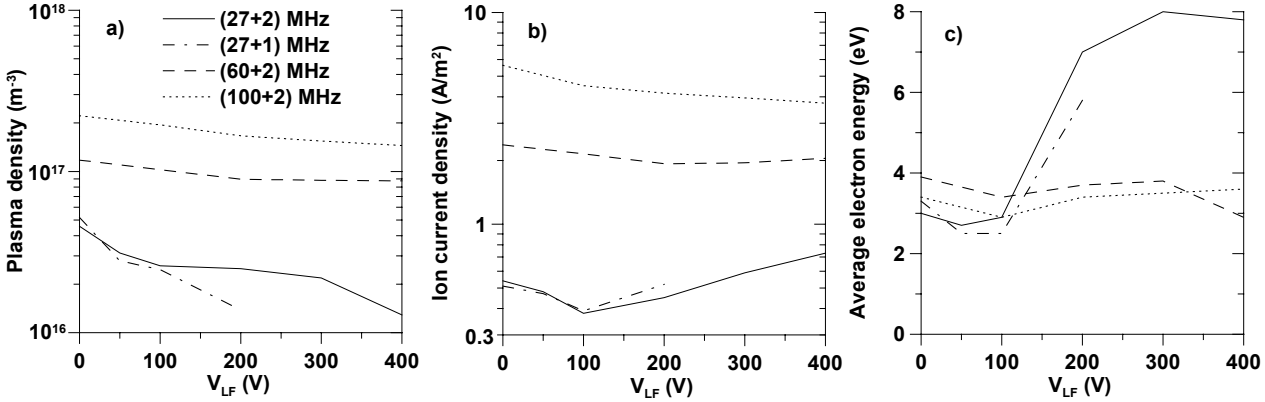

FIG. 2. Calculated plasma density (a), ion current density (b), and electron energy (c), averaged over the LF cycle as a function of the applied LF voltage amplitude at different frequency regimes; V_{HF} = 200 V.

It can be seen that for all investigated frequency schemes the introduction of the second LF voltage source decreases the plasma density in the discharge center [Fig. 2(a)]. Further, the drop is not very pronounced for the (60+2) and (100+2) MHz cases, while it decreases more clearly with increasing LF voltage for the other two frequency schemes. The ion current density exhibits a similar behavior as the plasma density for the (60+2) and (100+2) MHz regimes [Fig. 2(b)]. For the (27+2) and (27+1) MHz cases the ion current density shows a minimum at a LF voltage of 100 V and because of that, we made an additional simulation at 50 V. It is observed that the ion current decreases with varying the LF voltage from 0 till 100 V and it increases with further increase of the LF voltage, i.e. the ion loss increases. On the other hand, the electron energy also increases abruptly after 100 V [Fig. 2(c)] and consequently, the ionization rate, i.e. the ion production increases. The net effect of these processes is, however, a drop in the plasma density. The average electron energy shows little dependence on the LF voltage for the (60+2) and (100+2) MHz cases. Although the (27+1) and (60+2) regimes have a similar HF/LF ratio, it is observed that the LF voltage source has substantial influence on plasma density and ion current density at a HF of 27 MHz and the decoupling is possible only at higher primary frequencies. Therefore, independent control of plasma density and ion current is determined by the primary frequency and not by the frequency ratio, which was also experimentally observed [2].

Figure 3 shows the simulation results, averaged over one or two LF cycles, for the sheath potential (a) and width (b), and ion bombardment energy of Ar^+ and CF_3^+ ions (c). The calculated N_2^+ energy has values close to that of the Ar^+ and therefore we do not present it. A rise in the LF voltage leads to an increase of the sheath potential

and to an expansion of the sheath [Fig. 3(a) and (b)]. A similar behavior of the sheath width was observed experimentally [2] and numerically [6].

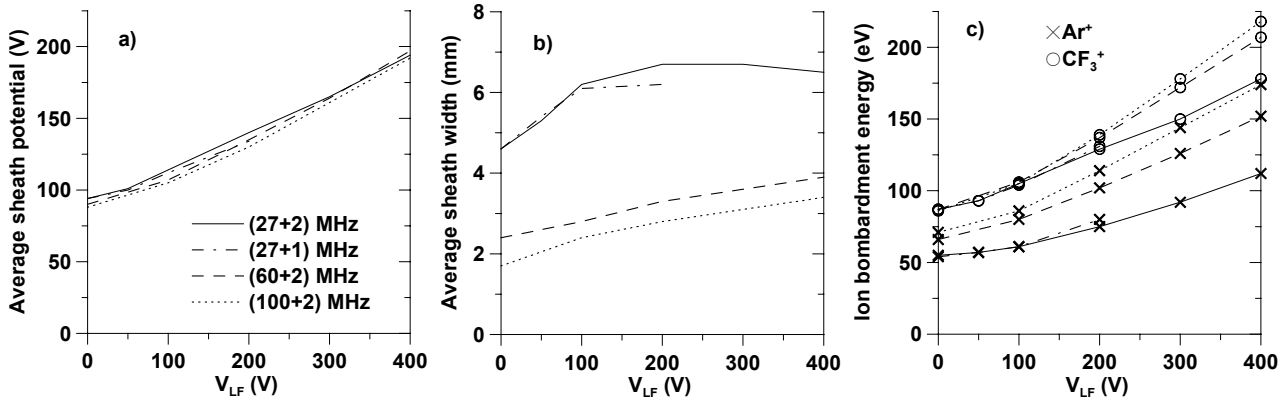

FIG. 3. Calculated sheath potential (a) and width (b), and Ar^+ and CF_3^+ bombardment energy (c), averaged over the LF cycle as a function of the applied LF voltage amplitude at different frequency regimes; V_{HF} = 200 V.

The ion energy [Fig. 3(c)] increases with the LF voltage because the sheath potential increases. Since the CF_3^+ ion does not experience charge exchange (see Ref. 4 for details about ion-neutral collisions), and therefore retains its energy, its average energy at the electrodes is higher, in comparison with the other two ions for the same operating conditions.

It is impossible to present the IEDF for all simulated operating conditions due to limited space, so that we have chosen to present them at a LF voltage of 200 V for the four frequency schemes (Fig. 4). The bimodal structure of the IEDF in the dual frequency reactors was discussed in detail elsewhere [4]. Figure 4 shows that the energy width, ΔE, increases with the HF when the LF is the same (cf. solid, dashed and dotted lines). According to Eq. (2) the energy width does not depend on the HF explicitly. However, it is inversely proportional to the average sheath width, which decreases with increase of the primary frequency [Fig. 3(b)]. The average sheath potential and the parameter λ_2 are calculated to be almost the same for the (27+2), (60+2) and (100+2) MHz cases. Furthermore, it is observed that the IEDF is broader when the LF is lower (cf. the solid and dash-dotted lines). Indeed, the energy width is inversely proportional to the LF in Eq. 2. The average sheath potential and width [Fig 3(a) and (b)], as well as the parameter λ_2 are calculated to have close values for the (27+2) and (27+1) MHz schemes. Consequently, the energy width increases with increasing the HF or decreasing the LF. The same behavior was observed for the other applied LF voltage amplitudes.

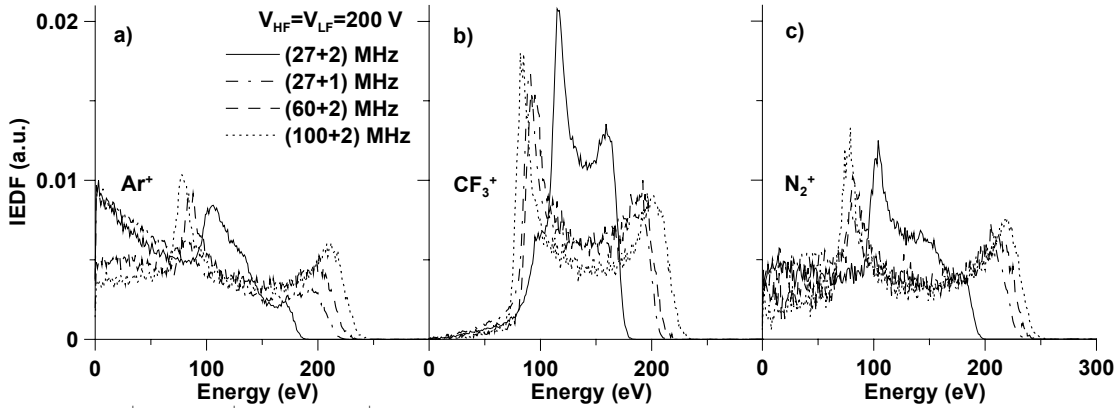

FIG. 4. Calculated Ar^+ (a), CF_3^+ (b), and N_2^+ (c) IEDF, averaged over the LF cycle, at HF and LF voltage amplitudes of 200 V at different frequency regimes.

Concerning the influence of the HF, it appears from Fig. 2 and 3 that the plasma density and ion current increase, and the sheath width decreases with HF, for the same LF voltage. The electron energy is between 3 and 4 eV for

the (60+2) and (100+2) MHz cases, and it increases with the LF voltage for the other two frequency schemes. The average ion energy [Fig. 3(c)] increases with HF because the sheath width decreases, and consequently the ions experience fewer charge exchange and elastic collisions with neutrals on their way to the electrodes, and therefore they retain their energy. A similar dependence of the plasma characteristics on the driving frequency was found in single frequency reactors [11].

A more detailed investigation of the simulations for a HF of 60 MHz and a LF of 1 or 2 MHz, keeping the LF voltage constant at 200 V or 0 V, i.e. single frequency scheme, and varying the HF voltage, shows that the plasma density and ion current density are only weakly affected by the second LF voltage source. Figure 5 presents the simulation results, averaged over the LF cycle, for the plasma density in the discharge center (a), the ion current density at the powered electrode (b), and the electron energy in the discharge center (c). The solid lines denote the results as a function of the LF voltage when the HF voltage is kept constant at 200 V for the (60+2) and (60+1) MHz cases. The dashed lines represent the calculations as a function of the HF voltage keeping the LF voltage constant at 200 V for the (60+2) and (60+1) MHz cases. Finally the dash-dotted lines illustrate the results for a single frequency reactor of 60 MHz, as a function of the driving voltage.

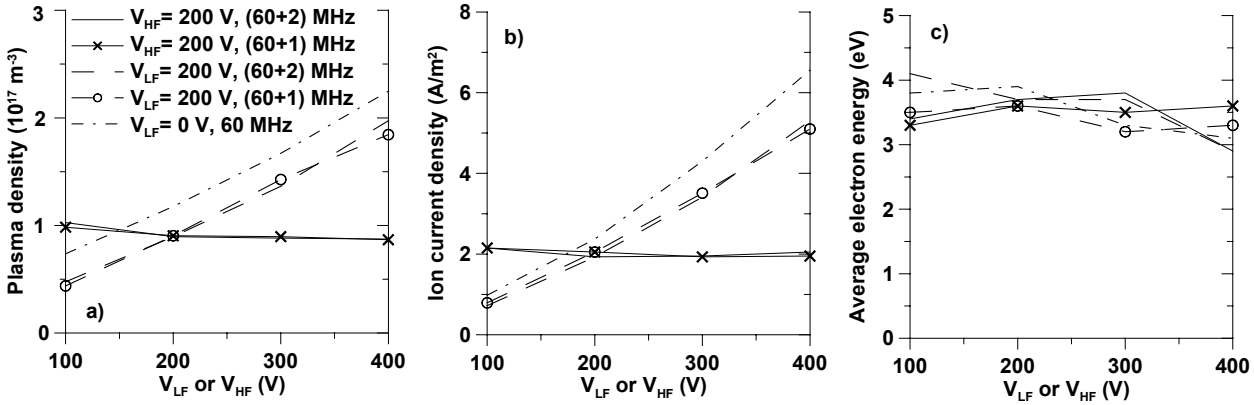

FIG. 5. Calculated plasma density (a), ion current density (b), and electron energy (c), averaged over the LF cycle as a function of the applied LF or HF voltage amplitude at different frequency regimes.

The plasma density slightly decreases from 10^{17} to $9\text{x}10^{16}$ m^{-3} when the LF voltage increases from 100 to 400 V and the HF voltage is kept at 200 V (solid lines) for both the (60+2) and (60+1) MHz cases. The ion current density is also nearly independent from the LF voltage and its value is about 2 A/m^2. The average electron energy in the bulk varies between 3 and 4 eV. It can be seen that for the (60+1) MHz case the LF voltage does not affect the EEPF and ionization rate [Fig. 6 (a) and (b), respectively]. The same is observed for the (60+2) MHz case and therefore, we do not present these results.

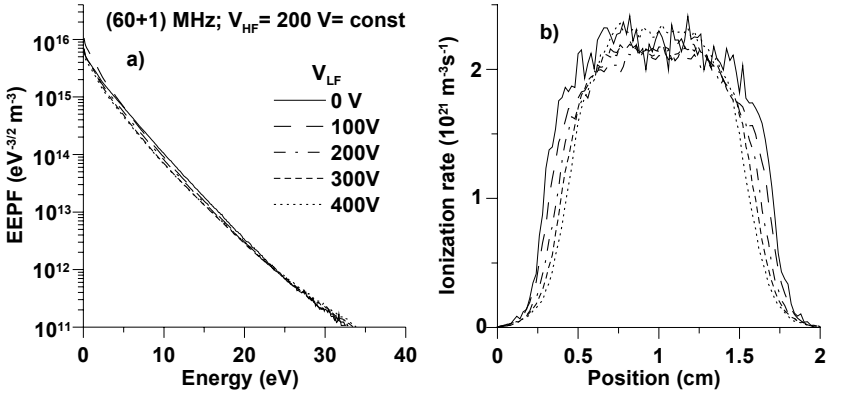

FIG. 6. Calculated EEPF (a) and ionisation rate (b) at a HF voltage of 200 V and LF voltages of 0, 100, 200, 300 and 400 V for the (60+1) MHz regime.

For the opposite operating condition, i.e. when the HF voltage is varying and the LF voltage is kept constant at 200 V, it is found that the plasma density scales linearly with the HF voltage [Fig. 5(a), dashed lines]. It increases from $5\text{x}10^{16}$ to $2\text{x}10^{17}$ m^{-3}. The same scaling law was observed in single frequency reactors [12]. Consequently, the plasma density shows the same dependence on the driving frequency, as if the second voltage source was not connected. However, the values of the plasma density are somewhat lower in comparison with the single frequency regime at the same driving voltage amplitudes [compare the dashed and dash-dotted

line in Fig. 5(a)]. It was already observed that introducing the second voltage source decreases the plasma density for any of the investigated frequency schemes [Fig. 2 (a)].

The ion current density increases with HF voltage from 0.7 to 5.3 A/m^2 [Fig. 5(b), dashed line] for both (60+2) and (60+1) MHz cases. It is found to scale as $j \sim V_{HF}^{3/2}$, which is similar to the scaling law in single frequency regime [Fig. 5(b), dash-dotted line]. Therefore, like the plasma density, the ion current density shows the same dependence on the driving frequency as if the second voltage source was not connected, but its values are somewhat lower than that in the single frequency reactor for the same HF voltage amplitude.

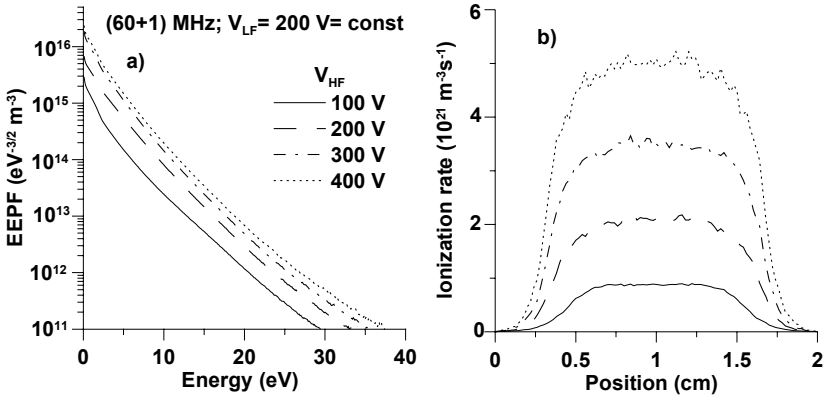

FIG. 7. Calculated EEPF (a) and ionisation rate (b) at a LF voltage of 200 V and HF voltages of 100, 200, 300 and 400 V for the (60+1) MHz regime.

The electron energy in the bulk varies between 3 and 4 eV [Fig. 5 (c)]. It can be seen that the slope of the EEPF is almost the same for all investigated HF voltage amplitudes [Fig. 7(a)] for (60+1) MHz, and the distribution is more or less Maxwellian so that the average electron energy does not change considerably. The number of high energy electrons increases with HF voltage and consequently the ionization rate also increases [Fig. 7(b)]. Similar behavior of the averaged energy, EEPF, and ionization rate is observed for the (60+2) MHz and single frequency reactor.

The sheath potential increases linearly with the applied voltage and consequently with the LF or HF voltage amplitude [Fig. 8(a) and see Eq. (1)]. The sheath expands with increasing the LF voltage [Fig. 8(b), solid lines], and it contracts with increasing the HF voltage [Fig. 8(b), dashed line] in the dual frequency regime, but it is wider in comparison with the single frequency case for the same HF voltage (compare with dash-dotted line). The sheath width is only weakly dependant on the applied voltage in the single frequency case [Fig. 8(b), dash-dotted line]. Other authors also observed that the applied voltage did not influence the sheath width in a single frequency reactor [12]. The average ion bombardment energy [Fig. 8(c)] increases with the LF or HF voltage amplitude, because the sheath potential increases with the applied voltage. The average ion energy increases with decrease of the LF because the IEDF is broader [see Fig. 9(a) and Eq. 2].

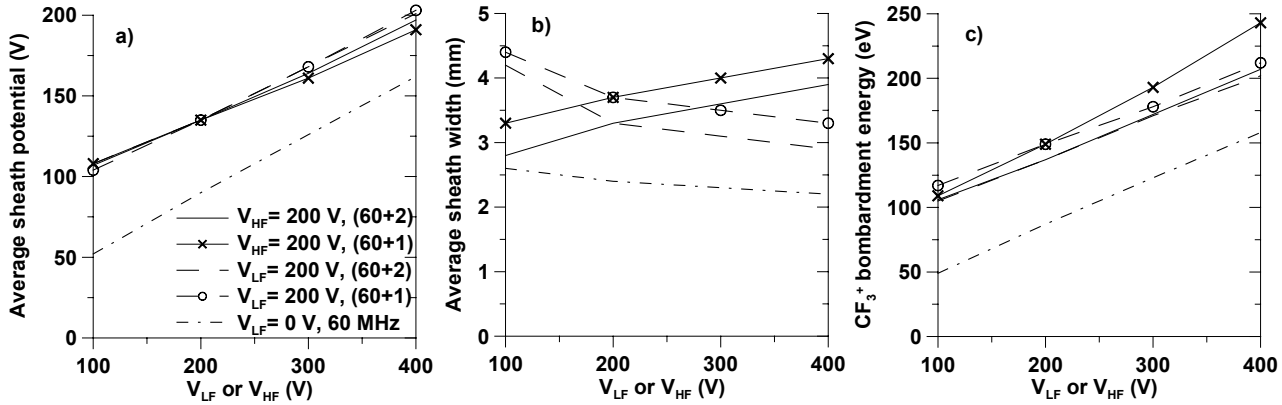

FIG. 8. Calculated sheath potential (a) and width (b), and CF_3^+ bombardment energy (c), averaged over the LF cycle as a function of the applied LF or HF voltage amplitude at different frequency regimes.

Figure 9 presents the CF_3^+ IEDF for the (60+1) and (60+2) MHz cases at HF and LF voltages of 200 and 100 V,respectively, (a), and dependence of the IEDF on the LF voltage (b) or HF voltage (c) for the (60+1) MHz

regime. The CF_3^+ ions reach higher energy with decrease of the LF or increase of the applied voltages. This behavior is observed for the other considered positive ions and for all the investigated frequency schemes. It was shown above that the IEDF is broader with increase of the HF (see Fig. 4). Consequently, the ion energy depends on both voltage sources and cannot be controlled only by the LF source.

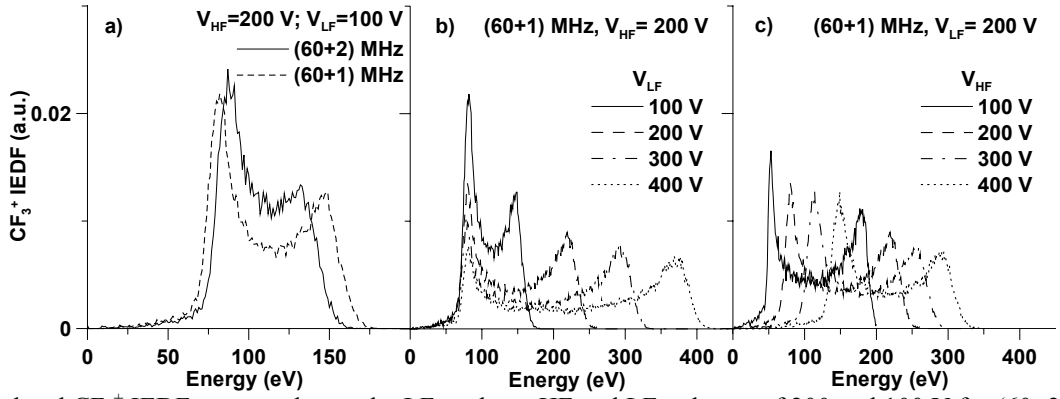

FIG. 9. Calculated CF_3^+ IEDF, averaged over the LF cycle, at HF and LF voltages of 200 and 100 V for (60+2) and (60+1) MHz cases (a), at different HF voltage amplitudes (b) and LF voltage amplitudes (c) for the (60+1) MHz case.

4. Summary

A detailed numerical investigation by means of the PIC/MC method was made to study the influence of the applied frequency sources on the plasma characteristics in $Ar/CF_4/N_2$ plasmas in a dual frequency reactor.

It is observed that the decoupling of the two sources is possible with increase of the applied HF to values of 60 MHz and higher, and it is not defined by the frequency ratio. The plasma density and ion current density show the same dependence on the driving voltage as if the second voltage source was not connected, but their values are somewhat lower than that in the single frequency reactor for the same HF voltage amplitude. The electron energy, EEPF and ionization rates are almost unaffected by the LF source. The plasma density and ion current increase, and the sheath width decreases with HF when the other operating conditions are the same. The average ion bombardment energy increases with HF or LF voltage amplitude when the other voltage amplitude is kept constant, because the sheath potential increases with the sum of the applied HF and LF voltages. Finally, the IEDF is broader with increasing the HF or decreasing the LF.

Acknowledgments

We would like to thank R. Gijbels for helpful discussions. This research is sponsored by the Federal Services for Scientific, Cultural and Technical Affairs of the Prime Minister's Office through IUAP – V.

References

[1] H. H. Goto, H.-D. Löwe, and T. Ohmi, J. Vac. Sci. Technol. A **10**, 3048 (1992).

[2] T. Kitajima, Y. Takeo, and T. Makabe, J. Vac. Sci. Technol. A 17, 2510 (1999); T. Kitajima, Y. Takeo, Z. Lj. Petrović, and T. Makabe, Appl. Phys. Lett. 77, 489 (2000).

[3] V. Georgieva, A. Bogaerts and R. Gijbels, J. Appl. Phys. **94**, 3748 (2003); J. Appl. Phys. **93**, 2369 (2003).

[4] V. Georgieva, A. Bogaerts and R. Gijbels, Phys. Rev. E **69**, 026406 (2004).

[5] J. K. Lee, N. Yu. Babaeva, H. C. Kim, O. V. Manuilenko, and J. W. Shon, IEEE Trans. Plasma Sci. **32**, 47 (2004).

[6] P.C. Boyle, A. R. Ellingboe, and M. M. Turner, Plasma Sources Sci. Technol. **13**, 493 (2004); J. Phys. D **37**, 697 (2004).

[7] C. K. Birdsall and A. B. Langdon, *Plasma Physics via Computer Simulation* (McGraw- Hill, New York, 1985).

[8] V. Vahedi and M. Surendra, Comput. Phys. Commun. **87**, 179 (1995).

[9] A. Okhrimovskyy, A. Bogaerts, R. Gijbels, Phys. Rev. E **65**, 037402 (2002).

[10] E. Kawamura, C. K. Birdsall and V. Vahedi, Plasma Sources Sci. Technol. **9**, 413 (2000).

[11] M. Surendra and D. B. Graves, Appl. Phys. Lett. 59, 2091 (1991).

[12] M. Surendra and D. Graves, IEEE Trans. Plasma Sci. **19**, 144 (1991).

Removal of Methanol and Dimethyl Sulfide by Pulsed Corona Discharge: Energy Efficiency and Byproducts Formation

E.H. Lock, A.V. Saveliev, L.A. Kennedy

Department of Mechanical and Industrial Engineering, University of Illinois at Chicago, Chicago, USA

Abstract
The removal of methanol and dimethyl sulfide in a pulsed corona discharge is studied experimentally varying process parameters such as applied voltage, pulse repetition rate, initial concentration of pollutant, temperature and humidity of the process stream. Specific consideration is given to the formation of unwanted byproducts. Total removal costs are evaluated using emission credit method and required electric energy inputs.
Keywords: pulsed corona, pollution control, methanol, dimethyl sulfide

1. Introduction

Non-thermal plasma techniques have shown very promising results to address the current increasing pollution problems caused by a variety of sources such as hydrocarbon burning electric power generating plants, diesel engines exhausts, paper mills, steel and chemical production plants. Among other pollutants successfully treated with plasmas are volatile organic compounds such as toluene, trichloro-ethylene, acetone, methanol, dimethyl sulfide, carbon tetrachloride, etc. [1, 2].

For complete characterization of pollutant removal process, not only the removal efficiency but also the generation of byproducts and cost of their secondary treatment must be considered. However, there are a limited number of studies analyzing formation of byproducts during plasma assisted removal of VOCs [3]. In the present work, the influence of the process parameters such as temperature, humidity, and pulse repetition rate on the destruction efficiency of methanol and dimethyl sulfide is studied experimentally using a pulsed corona discharge reactor. Another objective of this work is to evaluate the costs of the removal process and find the optimal condition for application of the industrial scale plasma removal systems. Considerable attention is directed towards the effect of humidity since there are conflicting reports describing humidity effect on the efficiency of the removal process and byproduct formation. The byproducts generated during the destruction of methanol and dimethyl sulfide are identified and the influence of process parameters on their concentrations is studied.

2. Experimental Approach

A schematic diagram of pulsed corona reactor is shown in Fig. 1. The corona discharge is generated in a wire-in-cylinder coaxial electrode system by a thyratron-based variable-voltage, variable-frequency power supply. The delivered power was varied from 0.2 to 12 W by controlling the high voltage pulse amplitude and the pulse repetition rate that ranged from 15 to 1000 Hz. Pulses of approximately 100 ns duration and 10 ns rise time were transmitted to the corona electrode by means of a 50 Ω coaxial cable. The inner high voltage electrode was 0.5 mm diameter Inconel wire. The outer electrode was 1 m long cylindrical stainless steel tube with a 22.2 mm internal diameter. An external aluminum jacket surrounded the outer electrode in order to achieve uniform heating of the reactor. The reactor was placed in tubular furnace (model 3200, Lindberg, Inc) that was operated over the temperature range 50 to 180 °C. A series of J-type thermocouples were used to ensure the uniformity of temperature at various reactor points.

To evaporate the liquid compounds and to properly mix the different chemicals, a stainless steel mixing chamber, heated to 160 °C and filled with glass beads, was placed before the reactor. Because of the different chemical nature of dimethyl sulfide (DMS) and methanol, two different approaches were used to generate industrial-like streams. Methanol was dissolved in water and pumped with a syringe pump (Model 200, KD Scientific) and sprayed into the gas stream. DMS was supplied as a gas mixture using nitrogen as a balance gas. A mass flow controller measured the inlet gas flow rate that was maintained at 2 slm during all experiments.

This resulted in residence times of 7 seconds. The air was provided by a dry zero air supply that insures no influence of residual humidity or organic compounds from the room air.

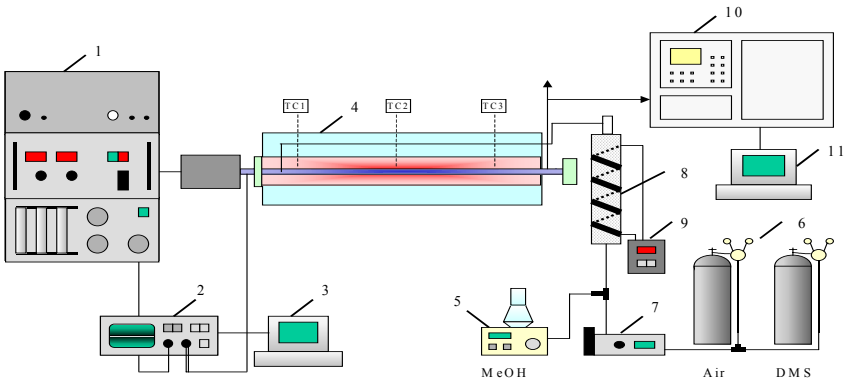

Fig. 1. Schematic of the experimental setup: 1 - pulsed power supply, 2 - oscilloscope, 3,11 -computers, 4 - pulsed corona reactor, 5 - syringe pump, 6 - air and DMS supply cylinders, 7 - mass flow controller, 8 - mixing chamber, 9 - temperature controller, 10 - gas chromatograph.

Voltage was measured using a high voltage probe (Model D 6015 A, Tektronix Inc.), current measurements were performed using a current monitor (Model 411, Pearson Inc.). Electrical characteristics were acquired with a digital oscilloscope (HP 546126 B) and the digitized wave forms were transmitted to a computer and analyzed with HP 34801A Bench Scope software. Concentrations of VOCs were determined using a gas chromatograph (Varian Inc, Model 3800), analyzing input and output samples. CO, NO_x and SO_2 were measured with a CO Analyzer (Thermo Environmental Instruments), a NO_x Analyzer (Thermo Environmental Instruments) and a SO_2 Analyzer (Horiba), respectively.

The figures of merit used in this work are the destruction and removal efficiency (DRE), and the specific energy input (SEI). The destruction and removal efficiency is defined as a ratio of the difference between the initial concentration C_0 and final concentration C to the initial concentration C_0. DRE is dimensionless and it is usually presented as a percentage. In the economic evaluation of the removal process the price of electricity and fines associated with pollutant emissions are taken into account.

3. Results and Discussion

The initial pollutant concentration for these experiments was 1000 ppm. The pulse repetition rate of 1000 Hz for methanol and 250 Hz for dimethyl sulfide and voltage of 12 kV were held constant. Figure 2 presents the influence of temperature and humidity variation on the removal efficiency of methanol and dimethyl sulfide. An increase of temperature results in increase of the electron mean energy leading to higher removal efficiencies. The effect of humidity on the experimental results is more intriguing. For both pollutants the best results were observed at absolute humidity of 0.5 %. This suggests the important role of water and, in particular, OH radicals in oxidation and removal of organic species. Small amounts of added water vapor effectively contribute to the removal process, while high water contents reduce removal efficiencies. Studies by Ono and Oda [4] on OH concentration at different humidity levels show that the maximum concentrations of OH radicals are produced at humidity of 0.5 %, which is in agreement with our findings. However, increase in

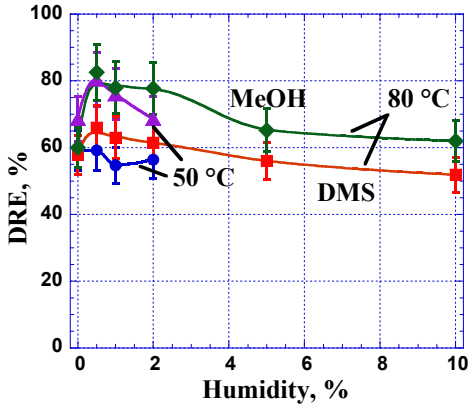

Fig. 2. DRE dependence on humidity. The initial concentrations of methanol and DMS are 1000 ppm.

humidity beyond 0.5% reduces the efficiency of the process affecting the electron distribution function and mean electron energies attainable at given peak voltages. As a result the pollutant removal for 5% and 10 % humidity are much lower compared to the 0-2% humidity levels.

Due to the small pulse duration (~100 ns) and large interpulse intervals, the pulses at repetition rates below o.1 MHz are practically independent from each other. For a constant flow rate, SEI is proportional to the pulse repetition rate and power input to the single corona pulse. The energy of the pulse, in turn, can depend on chemical composition of the gas, e.g. humidity level and pollutant concentration. As shown in Fig. 3, the removal of dimethyl sulfide with initial concentration of 1000 ppm requires much less energy compared to removal of the same methanol concentration. The power of the pulse for DMS was varied only slightly for 50 and 80 °C resulting in almost constant SEIs. In the case of methanol the increase of temperature produced slightly higher SEI values. At a constant temperature, increasing the humidity levels decreases SEI due to the lower electron temperatures, lower ionization rates and, hence, lower discharge currents.

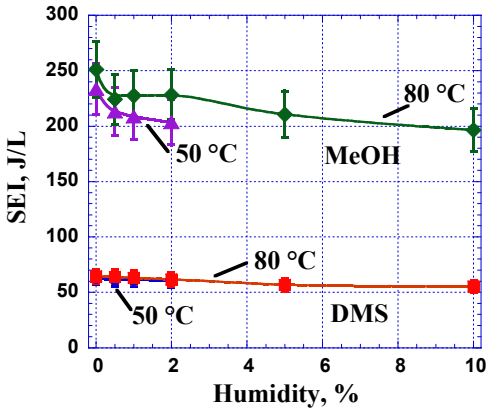

Fig. 3. SEI dependence on humidity for 1000 ppm methanol and dimethyl sulfide streams.

In summary, temperature increases the mean electron energy that has twofold effect: it increases the removal efficiency and the specific energy input. Humidity increases the efficiency until the threshold of 0.5%. Further increase of humidity causes decrease in efficiency and in power levels due to the reduction of electron temperatures.

The above observation raises the question how the energy of the generated electrons affects the removal efficiency and byproducts generation. Two ways to control discharge power were implemented in our experimental studies. The power input can be control independently by a variation of peak pulse voltage and by a variation of pulse repetition rate. The experimental results obtained using these approaches are shown in Fig. 4. In one set of experiments (case 1) the voltage was increased from 8 kV to 14 kV keeping the pulse repetition rate constant at 250 Hz. In another set (case 2) the peak pulse voltage of 8 kV was kept constant and the repetition rate was increased from 250 Hz to 1316 Hz. Other experimental conditions included temperature of 80 °C, initial pollutant concentrations of methanol and DMS equal to 1000 ppm and 800 ppm respectively and 0% humidity. As shown in Fig. 4, increasing the energy of the pulse causes much stronger increase in both efficiency and byproducts levels. For example, for DMS at power of 3W the differences in the efficiencies and NO_2 levels between cases 1 and 2 are respectively 15 % and 15 ppm. There are also different trends for two cases: raising the energy of the pulse causes exponential increase, while raising the frequency causes linear increase of NO_2 concentration and the removal efficiency. High energy electrons (e.g., from electron beam sources) are usually considered to be favorable for achieving the high removal efficiencies at low SEIs. However, as suggested by our results, these energetic electrons could be more effective in generation of unwanted byproducts as well. To find the most favorable conditions for pollution control always means to find the best compromise between the attainable removal efficiency and byproducts levels. In particular, the acceptable byproduct levels can be defined using the permissible exposure limits (PEL) set by the Occupational

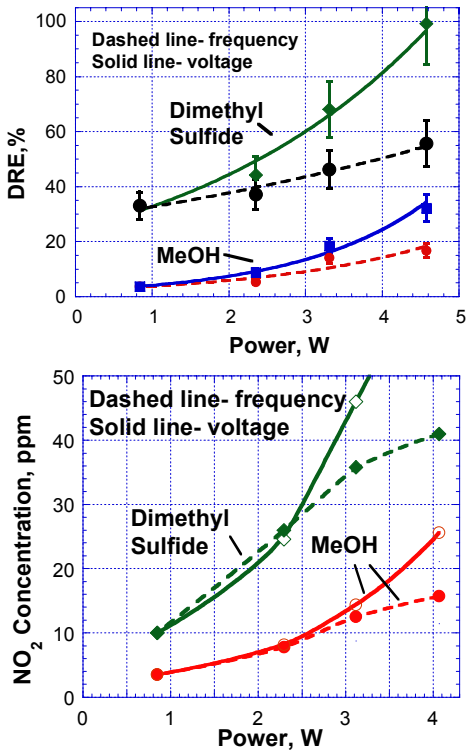

Fig. 4. DRE and NO_2 dependence on power.

Safety and Health Administration [5] and by the permissible amounts of pollutants that can be discarded in the atmosphere. For example, in the case of methanol PEL value is 200 ppm. This suggests that for a stream initially containing 1000 ppm of methanol a removal efficiency of 80 % and above will be required.

Byproducts formed during methanol destruction include CO and NO_x. CO is very dangerous and unwanted byproduct in any waste treatment process. It is generated by oxidation of HCO, HC_2O, CH_2, CH_2OH, CH_2CO and other intermediate products in the removal process of methanol and dimethyl sulfide. CO is also produced from reactions of CO_2 with N and O radicals. DMS oxidation processes have been studied extensively in atmospheric chemistry. These studies suggest that the major oxidation products are SO_2, NO_x and CO. Unfortunately studies on the plasma destruction of DMS are scarce. In our experiments we detected small amounts of methanol formed at intermediate powers. These trace amounts can completely destroyed applying higher SEIs. Simultaneous formation of NO_2 and SO_2 as byproducts occurs in the case of dimethyl sulfide removal. This suggests a possible interaction between their formation pathways. Indeed, as shown in Fig. 4, the generated concentrations of NO_2 for DMS are larger by almost a factor of two compared to methanol. Possible explanation for this can be attributed to reactions of sulfur containing radicals such as CH_3S, CH_3SOO, CH_3SO and CH_3SO_2 with NO and NO_2. SO_2 is very dangerous byproduct because of its oxidation in the troposphere to H_2SO_4 and is considered as a potential cause for the acid rain. No intermediate species like HNO_2, HNO_3, HSO_3, H_2SO_4 were detected in the output.

Figure 5 shows the processing of the stream with initial methanol concentration of 1000 ppm. Almost complete destruction of methanol is achieved at energy input of 300 J/l. However, the corresponding values of formed CO and NO_2 at this point are 1200 ppm and 80 ppm, respectively. At further power increase, the level of CO ppm starts to drop decreasing to about one third of the maximum value at 800 J/l. At the same time NO_2 level increases linearly with power reaching 250 ppm; this is 3 times higher than the previous value of 80 ppm. These results show that another important issue related to the selection of the optimal operating conditions is to know the price of discarding into the atmosphere a certain type of pollutants. Although the penalties for higher byproduct amounts in the exhaust streams are determined on case-by-case basis, the new policy of emission trading allowed us to conduct approximate cost analysis.

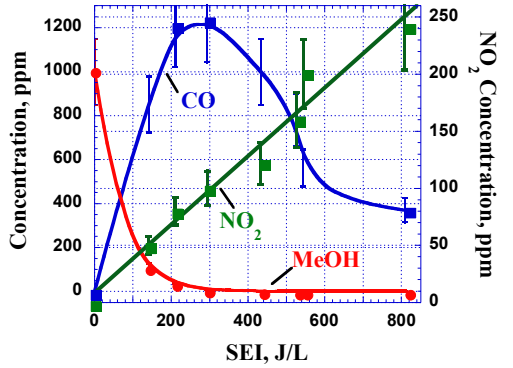

Fig. 5. Byproduct generation by removal of methanol.

The prices (per ton) for NO_x, SO_x and VOC emissions [6] are evaluate as \$1000, \$175, and \$3500, respectively. The price for CO is assumed to be \$150 based on reports from other sources. The cost of electricity is taken as 5.8 cents per kWh [7]. The cost analysis was performed for a gas flow rate of 100,000 m^3/h. For initial concentration of 1000 ppm, the estimated cost of untreated methanol emissions is 385 \$/h. The post treatment cost includes the cost of emitted CO, NO_2, and residual methanol. It initially drops with applied power and then slightly increases (Fig. 6). The total cost is the sum of the post treatment emission cost and the cost electricity. As shown in Fig. 6, the total cost has a minimum of approximately \$350 and then increases due to increase of electrical cost. However, by working at the conditions corresponding to this minimum savings can been realized by using pulsed corona discharge reactor.

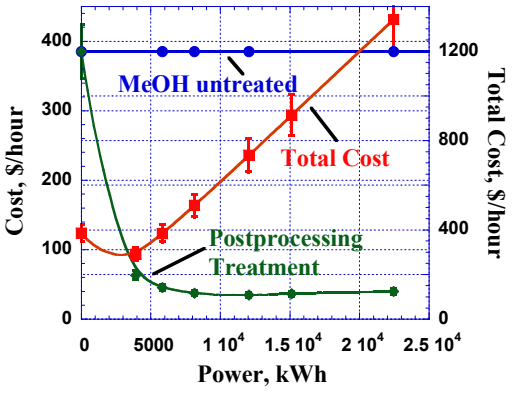

Fig. 6. Cost analysis of treatment of 1000 ppm methanol stream with flow rate of 100,000 m^3/h.

In addition to NO_2 and CO, SO_2 and methanol are formed as byproducts during the removal of dimethyl sulfide. The experiments were performed at the same operating conditions as described for Fig. 4. As shown in Fig.7, with increase of the power the SO_2 concentration raises to almost 700 ppm for the initial concentration of dimethyl sulfide of 800 ppm. This means that almost all of the latter is converted to SO_2. The increase of the power first leads to increase of methanol concentration to 50 ppm and than to its decrease. This implies that methanol would be completely destroyed by higher powers. The generated NO_2 and CO levels are less than 100 ppm and 600 ppm, respectively. The cost analysis for this system at the higher flow rate is presented in Fig. 8. As was shown above dimethyl sulfide was easier to remove than methanol. The lower electrical power is needed for this pollutant removal, which mean that savings as high as 600 $/h are realized. So based on our cost analysis for methanol and dimethyl sulfide it can be concluded that depending on the pollutant type and initial pollutant concentration pulsed corona discharge can be a successful pollution control technique.

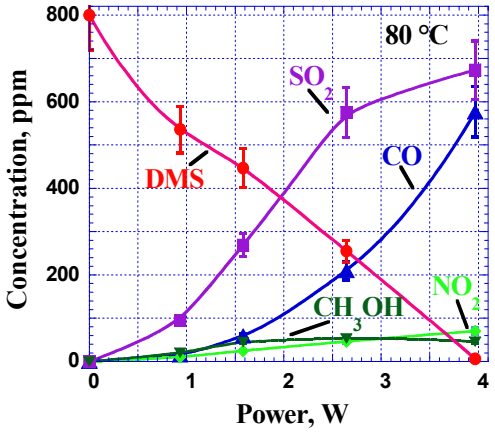

Fig. 7. Byproduct generation by removal of dimethyl sulfide.

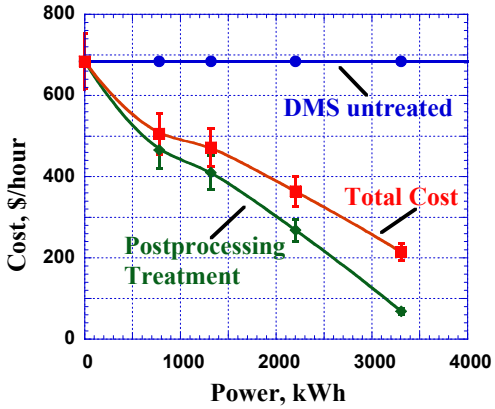

Fig. 8. Cost analysis of treatment of 800 ppm dimethyl sulfide.

4. Conclusions

In this paper the removal of the volatile organic compounds (methanol and dimethyl sulfide) and the influence of the process parameters such as temperature, humidity, pulse energy and pulse repetition rate are studied experimentally. Byproducts that are generated for these two pollutants are measured and the total cost of their treatment for industrial scale system is evaluated. It is shown that the mean electron energy is increased with temperature resulting in higher removal efficiencies and specific energy inputs. Small amounts of water vapor increase the effectiveness of the pollutant oxidation process until the threshold observed at absolute humidity of 0.5 %. Further increase of water content in the air stream causes decrease in the efficiency at given peak discharge voltages. At higher the mean electron energies the amounts of generated byproducts are large. This raises the question of finding the optimal process conditions as a compromise between required removal efficiency and acceptable byproduct levels.

References

[1] Y.S. Mok, C.M. Nam, M.H. Cho, I. Nam - IEEE Trans. Plasma Sci. **30**, 408 (2002).

[2] K. Yan, E.J.M. van Heesch, A.J. M. Pemen, P.A.H.J. Huijbrechts - Plasma Chem. Plasma Proc. **21**, 107 (2001).

[3] S. Futamura, T. Yamamoto - IEEE Trans. Ind. Appl. **33**, 447 (1997).

[4] R. Ono, T. Oda, - J. Electrostatics **55**, 333 (2002).

[5] www.osha.gov

[6] www.pert.org

[7] www.oeb.gov.on.ca

A STUDY OF NANOCRYSTALLINITY IN nc-Si, nc-Si, C and nc-Si, Ge FILMS DEPOSITED BY PECVD

M. M. Giangregorio, M. Losurdo, P. Capezzuto, G. Bruno
Institute of Inorganic Methodologies and of Plasmas IMIP-CNR via Orabona, 4 – 70126 Bari, Italy

Abstract

Si-based thin films, including nc-Si, $Si_{1-x}Ge_x$ and $Si_{1-x}C_x$ alloys, have been deposited by plasma enhanced chemical vapor deposition (PECVD) using SiF_4:H_2, SiF_4:GeH_4:H_2 and SiF_4:CH_4:H_2 plasmas, respectively. The SiF_4-based plasmas are characterized by the fact that low flux of CH_4 and GeH_4 are used for incorporation of C and Ge in the alloys. The correlation between alloys nanostructure and optical properties is investigated using Raman and ellipsometry spectroscopies. The role of fluorine atoms in the growth chemistry and material nanostructure is discussed.

1. Introduction

Basic capabilities of silicon technologies, including photovoltaics, electronics and optoelectronics [1-3], can be improved by "bandgap engineering" using Si-based alloys, such as silicon germanium ($Si_{1-x}Ge_x$) and silicon carbon ($Si_{1-x}C_x$), which provide a tunable band gap from values lower than 1eV using $Si_{1-x}Ge_x$ to values higher than 2.5eV using $Si_{1-x}C_x$ [4]. Apart from alloy composition of amorphous thin films, nanostructure is an additional factor for tuning properties and functionality. For instance, nanocrystalline silicon (nc-Si) is widely investigated for optoelectronics, due to its photoluminescence, which can be tuned by the crystallite size. Nano/microcrystalline silicon is attractive for thin film transistors (TFTs) and $Si_{1-x}Ge_x$ and $Si_{1-x}C_x$ alloys are used for solar cells.

In this paper, we present a study of the nanotructure and optical properties of hydrogenated $Si_{1-x}Ge_x$:H and $Si_{1-x}C_x$:H alloys deposited by plasma enhanced chemical vapor deposition (PECVD) using SiF_4:GeH_4:H_2 and SiF_4:CH_4:H_2 plasmas, respectively. These non-conventional plasmas proposed as alternative to generally used hydrogenated systems such as SiH_4-CH_4-H_2 [5] and SiH_4-GeH_4-H_2 [6] presents the advantage of small addition of CH_4 or GeH_4 to the SiF_4 plasma for incorporation in the film of C% and Ge% higher than 40%.The role of fluorine atoms, compared to hydrogen atoms, on the material structure and composition is discussed. The impact of alloys films heterogeneity on the optical gap is focused. Spectroscopic ellipsometry (SE) is used to establish a correlation between the film structure and optical response.

2. Experimental

Deposition of (a) silicon, (b) $Si_{1-x}C_x$ and (c) $Si_{1-x}Ge_x$ films with different structure going from amorphous to nanocrystalline were deposited by parallel-plate r.f. 13.56 MHz PECVD on Corning glass, at a pressure of 0.3 Torr, a r.f. power in the range 10-30W and at a temperature of 250°C, using fluorinated (a) SiF_4-H_2 plasmas with a SiF_4/H_2 ratio in the range 0.1-10 to have film with different structure, (b) SiF_4-CH_4-H_2 plasmas, with a SiF_4 flux of 20 sccm, while the CH_4 flux was varied in the range 0.1-0.3 sccm to have films with different carbon content while the H_2 flux was changed in the range 0.1-30 sccm to have film with different structure and (c) SiF_4-GeH_4-H_2 plasmas, with SiF_4 and H_2 fluxes of 10 and 1 sccm, respectively, while the $GeH_4/(SiF_4+GeH_4)$ ratio was varied in the range 0-5 to have films with different germanium content and different structure.
The film anatomy has been analyzed by spectroscopic ellipsometry (SE).

Spectroscopic ellipsometry measures the change in the polarization state of light when it interacts with an optical system. SE spectra of the real, $\langle\varepsilon_1\rangle$, and imaginary, $\langle\varepsilon_2\rangle$, parts of the pseudodielectric function, $\langle\varepsilon\rangle = \langle\varepsilon_1\rangle + i\langle\varepsilon_2\rangle$, were acquired with a phase modulated spectroscopic ellipsometer (UVISEL-Jobin Yvon) in the range 0.75-6.5eV. SE spectra were analyzed using the Bruggeman effective medium approximation (BEMA) [7]. The dielectric functions of nc-Si with grain size of ≈3nm [8] and of a-Si from ref. [9] were used.

Optical functions of $Si_{1-x}C_x$:H films were analyzed using the tetrahedron model [10] for representation of the Si-C bond configuration. Using this approach, we discerned films with the same overall carbon content but with different nanostructure and Si-C bond configurations

The approach used to analyze optically the $Si_{1-x}Ge_x$:H thin films consists in parameterization of the dielectric function $\varepsilon(E) = \varepsilon_1(E)+i\varepsilon_2(E)$ as a function of the photon energy, E, using the Tauc-Lorentz equation [11-12] that fits amorphous semiconductor dielectric functions over a wide energy region. The energy gap, obtained by the parameterization procedure, gives information on the incorporated Ge content and on the film structure.

SE results are corroborated by Raman measurements. The composition of alloys was determined from energy dispersive spectroscopy (EDS) and X-ray photoelectron spectroscopy (XPS).

3. Results

Figure 1a shows the dependence of the film crystalline and amorphous volume fraction and of microporosity as a function of the SiF_4/H_2 ratio. With the decrease of the SiF_4/H_2, the crystalline fraction, fc, increases while the amorphous fraction, fa, decreses. Indeed the nanostructure changes also depending on other experimental parameters such as the He dilution. Figure 1b shows the imaginary, $<\varepsilon_2>$, part of the pseudodielectric function of silicon films deposited at a SiF_4/H_2 ratio of 2 (low ratio) and 6 (high ratio). The presence of the E_1 and E_2 peaks at 3.4eV and 4.2eV gives evidence of the crystallinity of the silicon films which is enhanced in films deposited at low SiF_4/H_2 ratio (sharper E_1 and E_2). The crystallinity of the silicon films, determined by the SE analysis, has also been confirmed by Raman measurements (see inset in figure 2b) which shows the predominant peak at ~510cm^{-1} due to the TO vibration of Si crystallites.

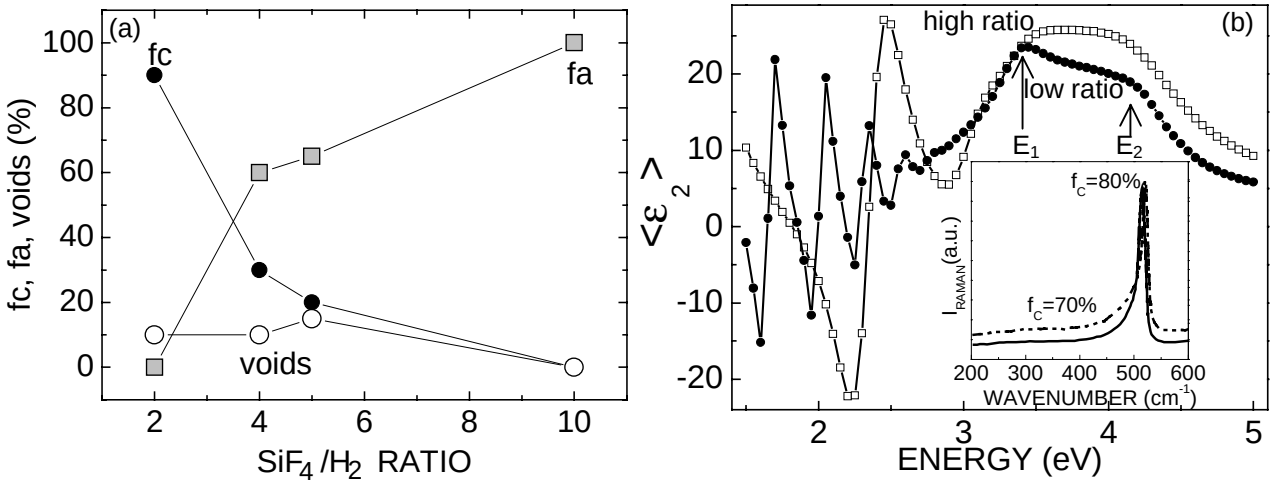

Fig. 1: (a) Dependence of μc-Si the film crystallinity and microporosity on the SiF_4/H2 ratio; (b) Imaginary, $<\varepsilon_2>$, part of the pseudodielectric function of silicon films deposited at a SiF_4/H_2 ratio of 2 (low ratio) and 6 (high ratio). Raman spectra of silicon films with different crystalline fraction, fc, is also reported in the inset.

The SiF_4/H_2 ratio acts on the relative concentration of the fluorine atoms and of the film building-blocks, which have been identified in the SiFx radicals and atomic hydrogen [13-14]. These results indicate an important role of the fluorine atoms in the improvement of film nanocrystallinity and in controlling the film nanotructure. In particular, fully nanocrystalline films with large grains are obtained at the border-line between the Si deposition and etching processes, the latter being operated by fluorine atoms, as discussed in the below.

The SiF_4/H_2 ratio is an important parameter also for deposition of $Si_{1-x}C_x$ alloys. Figure 2a shows the SE spectra of the imaginary part, $<\varepsilon_2>$, of the pseudodielectric function of films deposited at different

SiF_4/H_2 ratio and the same CH_4 flux of 0.2sccm. The films resulted to have the same carbon content, C%=14, but different structure. In particular, the broad peak at approximately 3.6 eV is indicative of the amorphous character of the sample deposited at SiF_4/H_2=4 and a r.f. power of 20W. Conversely, the presence of the E_1 and E_2 CPs at about 3.4 eV and 4.2 eV, characteristic of crystalline silicon, gives evidence of the nanocrystallinity of the sample, which has been deposited at SiF_4/H_2=40 and a r.f. power lower than 15W. These spectra provide evidence that the optical properties of $Si_{1-x}C_x$ alloys depend, not only on C content, but also on nanocrystallinity. In particular, the blue-shift of the interference system for the nanocrystalline sample indicates a higher optical gap for materials with a crystalline phase present. The presence of Si-crystallites with a grain size of ≈10nm can be also seen in the Raman spectrum shown in the inset of figure 2a.

The effect of the alloy composition and silicon nanocrystalline volume fraction on the optical band gap is summarized in Fig. 2b. Here, the E_{04} gap, which is defined as the energy at which the absorption coefficient, α, is 10^4 cm^{-1}, is shown. The E_{04} gap increases with the carbon content, in agreement with theoretical and experimental analyses [15] but for the same C% the segregation of silicon nanocrystallites in a SiC matrix further increases the E_{04} gap value. Therefore, the advantage of nc-$Si_{1-x}C_x$:H alloys is that a lower C% (7%) results in E_{04} gap values as high as that of amorphous a-$Si_{1-x}C_x$:H film with very high (>27%) C-content.

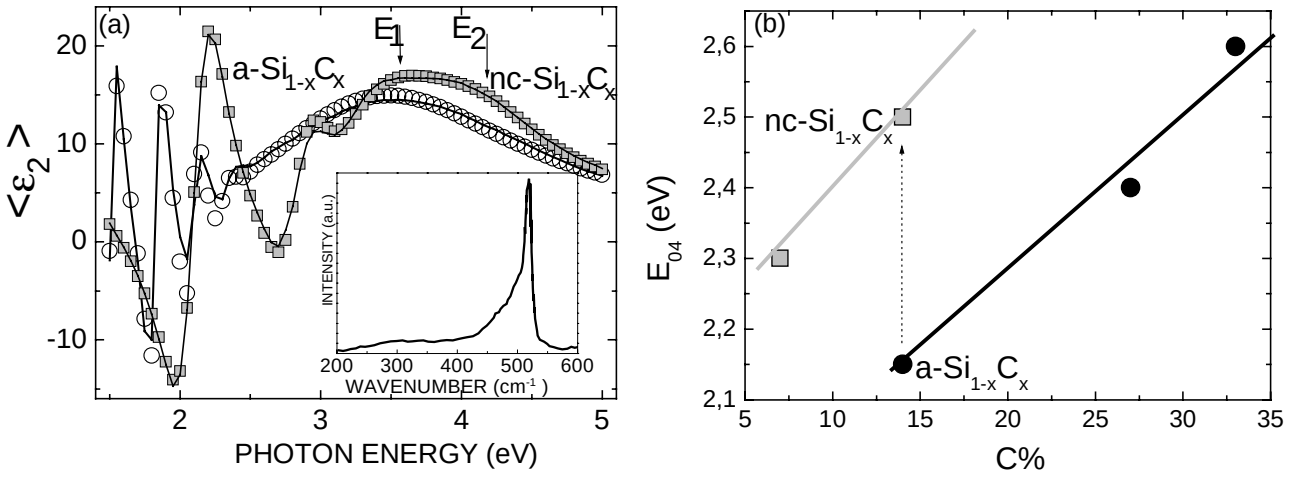

Fig.2: (a) Experimental (symbols) and calculated (line) SE spectrum of the imaginary part, $<\varepsilon_i>$, of the dielectric function of a-$Si_{1-x}C_x$ and nc-$Si_{1-x}C_x$ films with different structure. Raman spectrum of nanocrystalline nc-$Si_{86}C_{14}$ film is shown as inset; (b) Plot of the E_{04} optical gap of a-$Si_{1-x}C_x$ (full symbols) and nc-$Si_{1-x}C_x$ (empty symbols) as a function of carbon content and nanostructure.

Figure 3a shows the SE spectra of the real, $<\varepsilon_1>$, and the imaginary, $<\varepsilon_2>$, parts of the pseudodielectric function of hydrogenated silicon-germanium ($Si_{1-x}Ge_x$:H) films deposited on silicon substrate at a different $GeH_4/(SiF_4+GeH_4)$ % ratio, resulting in a Ge content ranging from 25% to 60%.

The optical properties of the $Si_{1-x}Ge_x$:H films were parameterized by a "five-parameters" Tauc-Lorentz dispersion equation [11-12]. The Tauc-Lorentz parameterization gives the values of the band-gap as a function of Ge-content, which are summarized in Fig. 3b. Here, various values reported in literature are indicated as gray region. A bandgap value of 1.42 eV is found for the $Si_{0.4}Ge_{0.6}$ alloy, which cannot be explained by the Ge content, but is related to quantum effect due to the presence of Ge nanocrystals. The presence of Ge nanocrystals has also been found by Raman measurements. Raman spectra for the films with the extreme compositions of $Si_{0.75}Ge_{0.25}$ and of $Si_{0.4}Ge_{0.6}$ are shown in Fig. 4. The spectrum of the $Si_{0.75}Ge_{0.25}$ film is typical of an amorphous alloy with broad lines centered at ~290, 400 and 470cm^{-1} corresponding, respectively, to Ge-Ge, Ge-Si and Si-Si vibrations. No evidence of segregation of micro- or nanocrystalline

silicon and or of the alloys phase is found. Conversely, the narrower mode of Ge-Ge bonds at ~270 cm^{-1} indicates that Ge nanocrystals segregate in the Ge-rich $Si_{40}Ge_{60}$ alloy, impacting on the optical gap.

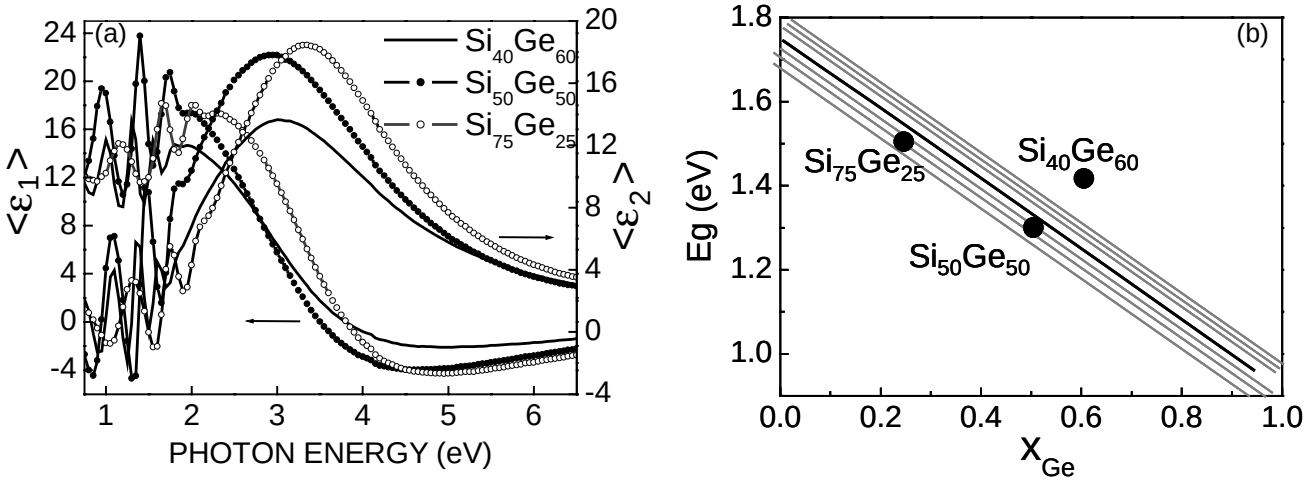

Fig.3: (a) Experimental (symbols) and calculated (line) SE spectrum of the real, $<\varepsilon_r>$, and the imaginary part, $<\varepsilon_i>$, of the dielectric function of $Si_{1-x}Ge_x$:H films with different Ge content; (b) Dependence of the optical gap of $Si_{1-x}Ge_x$:H on Ge composition. Circles are for experimental value for our samples. Shadow area is for data from various samples in literature.

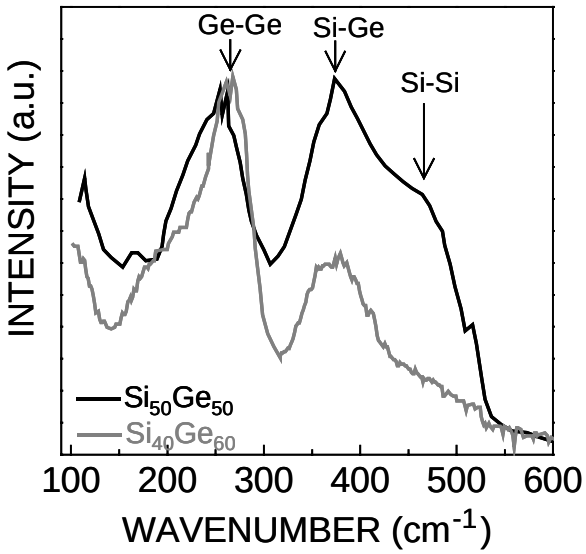

Fig. 4: Raman spectra of $Si_{1-x}Ge_x$ alloys with different composition

4. Discussion

Hydrogenated SiH_4-based and fluorinated SiF_4-based plasma systems are characterized by different chemical behaviors. This difference is enhanced in deposition of nano-crystalline materials, where the deposition/etching competition determines the overall growth. In particular, it is known that in SiH_4-H_2 plasmas, the silicon nanostructure depends on H_2 dilution and, hence, on the concentration of atomic hydrogen, which is the etchant enhancing the degree of crystallinity [16]. In the hydrogenated system the

etching rate follows the order C>Si>Ge. This means that in the Si:Ge binary system, atomic hydrogen will preferentially etch Si than Ge, whereas C is preferentially etched than Si in Si:C
In the fluorinated SiF_4 system, the etchant specie is atomic fluorine. In this case, the etching rate follows the order Ge>Si>C. Therefore in the binary Si:Ge, Si is preferentially etched than Ge, while Si is preferentially etched with respect to C in Si:C.
The growth of nc-Si films from SiF_4-H_2 plasmas, according to the deposition/etching chemical model, [17-18], is determined by a balance between deposition promoted by H atoms ($r_G=k_G[SiF_x]$ [H]) and etching processes operated by fluorine atoms ($r_E=k_E[F]$), giving reason of the crucial importance of the SiF_4/H_2 ratio in deposition of microcrystalline thin films.
In SiF_4-CH_4-H_2, the SiF_4/H_2 ratio is important since it controls the relative concentration of the atomic fluorine and hydrogen, the former etching the amorphous Si-phase (while they do not etch the carbon because of the low desorption rate of CFx radicals that are well known to be precursors for the deposition of fluoro-polymers[19]), the latter etching preferentially the amorphous C-phase. Being the fluorine atoms stronger etchant, the amorphous-to-microcrystalline Si transition occurs, resulting in segregation of Si crystallites in the a-$Si_{1-x}C_x$ matrix.
In the case of SiF_4-GeH_4-H_2 plasma mixtures for deposition of $Si_{1-x}Ge_x$ alloys, atomic fluorine preferentially etches the amorphous Ge-phase, promoting segregation of Ge nanocrystallites in the Ge-rich alloys.

5. Conclusions

Silicon, $Si_{1-x}C_x$ and $Si_{1-x}Ge_x$ thin films with different microstructure have been deposited by PECVD using SiF_4:H_2, SiF_4:GeH_4:H_2 and SiF_4:CH_4:H_2 plasmas. It is found that the flux ratio of the fluorinated- to-hydrogenated precursors is an important parameters for the control of the film nanostructure. The description of the complex anatomy of the films has evidenced the key role of the F-atoms density, and, hence, of the etching-to-deposition competition in determining the nanocrystallinity of the film. It is found that Si nanocrystallites preferentially segregate in a-$Si_{1-x}C_x$ matrices, whereas Ge nanocrystallites preferentially segregate in a-$Si_{1-x}Ge_x$ matrices. The impact of the film nanostructure on optical gap is also discussed, and it is found that segregation of a nanocrystalline phase yields an increase of the optical gap.

References

[1] D.A.Anderson, W.E.Spear, Philos.Mag. **35**, 1 (1977).
[2] Y.Catherine, G.Turban Thin Solid Films **60**, 193 (1979).
[3] S.Tsuda, H.Tarui, H.Dohjo, K.Watanabe, Y.Hishikawa, T.Takahama, H.Nishiwaki, T.Fukatsu, S.Nakayama, M.Nakano, Y.Kuwano, Jpn. J.Appl. Phys. **25**, 1795 (1986).
[4] M. Losurdo, M.M. Giangregorio, P. Capezzuto, G. Bruno, F. Giorgis, J.Appl. Phys. **25**, 1795 (1986).
[5] A. Desalvo, R. Galloni, R. Rizzoli, C. Summonte, F. Giorgis, C. F. Pirri, E. Tresso, P. Rava, J. Appl. Phys. **81**, 7973 (1997).
[6] W.Paul, D.K.Paul, B.Von Roedern, J.Blake, S.Oguz, Phys. Rev. Lett. **46**, 1016 (1981).
[7] M.Losurdo, R.Rizzoli, C.Summonte, P.Capezzuto, G.Bruno, J. Appl. Phys **88**, 2408 (2000).
[8] M.Losurdo, M.M.Giangregorio, P.Capezzuto, G.Bruno, M.F.Cerqueira, E.Alves, M.Stepikova App. Phys. Lett. **82**, 2993 (2003).
[9] D.E.Aspnes, A.A.Studna, E.Kimnsbron Phys. Rev. B **29**, 768 (1984).
[10] K.Mui, F.W.Smith, Phys. Rev. B **35**, 8080 (1987).
[11] G.E.Jellison Jr., F.A.Modine Appl. Phys. Lett. **69**, 371 (1996).
[12] G.E.Jellison Jr., F.A.Modine Appl. Phys. Lett. **69**, 2137 (1996).
[13] G. Bruno, P. Capezzuto, G. Cicala, J. Appl. Phys. **69**, 7256 (1991).
[14] M.Losurdo, M.M.Giangregorio, P.Capezzuto, G.Bruno, Proceedings of the 19th European Photovoltaic solar energy Conference (2004) 3DV.1.27.
[15] J.Robertson, Phil. Mag. B **66**, 615 (1992).
[16] Y.Hamakawa, Y.Matsumoto, G.Hirata, Mater. Res. Symp. Proc. **164**, 291 (1990).
[17] A.Matsuda, Thin Solid Films **337**, 2310 (1999).
[18] M.Losurdo, M.M.Giangregorio, A.Grimaldi, P.Capezzuto, G.Bruno Eur. Phys. J. Appl. Phys. **2**6, 187 (2004).
[19] B.E.E.Kastenmeier, P.J.Matsuo, J.J.Beulens, G.S.Oehrlein, J.Vac. Sci. Technol. A **14**, 2802 (1996).

Computational Simulation of Arc Melting Process with Complex Interactions

H.Nishiyama[1], T.Sawada[1], H.Takana[1], M.Tanaka[2] and M.Ushio[2]

[1]*Institute of Fluid Science, Tohoku University, Sendai, Japan*

[2]*Welding and Bonding Research Institute, Osaka University, Suita, Osaka, Japan*

Abstract

The real-time computational simulation of arc melting performance with considering complex interactions and solid-liquid mushy zone in molten anode has been successfully conducted for providing the fundamental data for highly economical performance arc melting process. The configuration of molten anode predicted by realistic numerical model shows the quantitative agreement with the experimental data. The effect of sulfur content concentration in molten metal on the welding structure is discussed in detail. Finally, the heat exchange efficiency and molten cross-sectional area are evaluated under different cathode vertex angles for optimum welding process with high efficiency.

Keywords: Arc melting system, complex interactions, mushy zone, real-time computational simulation

1. Introduction

Arc flow can be regarded as one of the multi-functional fluids, since it has high-energy flux, various gases selectivity and electromagnetic controllability[1]. Since the stable and controlled heating can be performed easily by an arc, it has been extensively utilized as arc melting systems[2] such as arc welding for material processing and arc ash melting for environmental processing. However, the arc processing needs relatively higher cost compared with the conventional treatment by combustion, since the arc can be produced only by large electric power and also the expensive electrodes and reactor are easily consumed for short running time[3]. For this reason, the optimization of operating conditions for the improvement of melting performance and high process efficiency has been expected eagerly in the industrial world. Nevertheless, it is experimentally difficult to clarify the physical phenomenon in detail and to optimize the operating conditions of an arc-electrodes system, since the thermofluid field of an arc and the interaction between an arc flow and molten anode are very complex in the extreme conditions. Therefore, the numerical modeling is expected to be one of the effective approaches to solve this problem. In the most of the previous numerical modelings, an arc flow and electrodes are treated separately and boundary conditions are partly given by using experimental data. Furthermore, the influence of solid-liquid mushy zone[4] in molten anode on the molten pool structure has not made clear yet so far.

In the present study, computational simulation of arc melting system with complex interactions are carried out with the purpose of providing the fundamental data for high performance arc melting process. In the electromagnetic thermofluid analysis, the integrated system modeling is proposed considering the complex interactions between arc flow and molten anode interface with temperature dependent surface tension and also considering solid-liquid mushy zone in molten anode[4]. The computational domain covers the entire region

including arc flow, electrodes, molten anode pool, mushy zone. Based on this integrated system modeling, the effects of sulfur content concentration in molten anode and cathode vertex angle on the molten pool structure and heat exchange efficiency are clarified numerically.

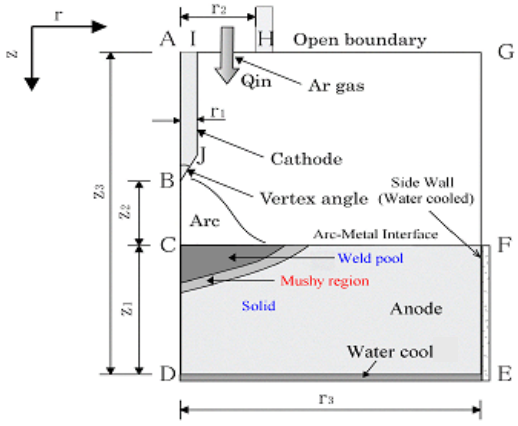

Fig.1 Computational domain for arc melting system.

2. Arc Flow Analysis

2.1. Governing Equations

Figure 1 shows a schematic illustration of a free burning arc-electrodes system and the coordinate system. In order to derive the governing equations, the following assumptions are introduced here[5].

1) The argon arc is regarded as an ideal gas and a continuous fluid. It is optically thin in Local Thermodynamics Equilibrium (LTE) state.
2) The thermofluid field is laminar, steady and axisymmetrical two-dimensional (2D).
3) The induction magnetic field has an axisymmetrical and azimuthal component.
4) There are temperature dependent thermodynamic and transport properties.
5) The surface tension on molten pool interface is given as a function of temperature.
6) The viscosity in the solid-liquid mushy zone is given as a function of liquid fraction.
7) The viscous dissipation and compressed work are neglected.
8) Only radiation loss from argon is considered.
9) Radiation, evaporation and deformation on the both cathode and anode surfaces are neglected for simplicity.

Under these assumptions, the governing equations for arc and electrodes region are presented as follows.

Conservation of Mass

$$\frac{\partial \rho_{Ar,a}}{\partial t} + \frac{\partial}{\partial z}\left(\rho_{Ar,a} u\right) + \frac{1}{r}\frac{\partial}{\partial r}\left(r\rho_{Ar,a} v\right) = 0 \tag{1}$$

Conservation of Momentum

$$\begin{aligned}\frac{\partial}{\partial t}\left(\rho_{Ar,a} u\right) + \frac{\partial}{\partial z}\left(\rho_{Ar,a} u^2\right) + \frac{1}{r}\frac{\partial}{\partial r}\left(r\rho_{Ar,a} uv\right) &= -\frac{\partial p}{\partial z} + 2\frac{\partial}{\partial z}\left(\eta_{Ar,a}\frac{\partial u}{\partial z}\right) \\ + \frac{1}{r}\frac{\partial}{\partial r}\left(r\eta_{Ar,a}\left(\frac{\partial u}{\partial r} + \frac{\partial v}{\partial z}\right)\right) - \frac{2}{3}\frac{\partial}{\partial z}\left(\eta_{Ar,a}\left(\frac{\partial u}{\partial z} + \frac{1}{r}\frac{\partial (rv)}{\partial r}\right)\right) &+ j_r B_\theta + \rho_{Ar,a} g\end{aligned} \tag{2}$$

$$\begin{aligned}\frac{\partial}{\partial t}\left(\rho_{Ar,a} v\right) + \frac{\partial}{\partial z}\left(\rho_{Ar,a} uv\right) + \frac{1}{r}\frac{\partial}{\partial r}\left(r\rho_{Ar,a} v^2\right) &= -\frac{\partial p}{\partial r} + \frac{\partial}{\partial z}\left(\eta_{Ar,a}\left(\frac{\partial v}{\partial z} + \frac{\partial u}{\partial r}\right)\right) \\ + \frac{2}{r}\frac{\partial}{\partial r}\left(r\eta_{Ar,a}\frac{\partial v}{\partial r}\right) - \frac{2}{3}\frac{\partial}{\partial r}\left(\eta_{Ar,a}\left(\frac{\partial u}{\partial z} + \frac{1}{r}\frac{\partial (rv)}{\partial r}\right)\right) &- \eta_{Ar,a}\frac{2v}{r^2} - j_z B_\theta\end{aligned} \tag{3}$$

Conservation of Energy

in the arc region:

$$\frac{\partial}{\partial t}(\rho_{Ar} h)+\frac{\partial}{\partial z}(\rho_{Ar} hu)+\frac{1}{r}\frac{\partial}{\partial r}(r\rho_{Ar} hv)=\frac{\partial}{\partial z}\left(\frac{\lambda_{Ar}}{C_{p_{Ar}}}\frac{\partial h}{\partial z}\right)+\frac{1}{r}\frac{\partial}{\partial r}\left(\frac{r\lambda_{Ar}}{C_{p_{Ar}}}\frac{\partial h}{\partial r}\right)$$
$$+\frac{j_z^2+j_r^2}{\sigma_{Ar}}+\frac{5}{2}\frac{k_b}{e}\left(\frac{j_z}{C_{p_{Ar}}}\frac{\partial h}{\partial z}+\frac{j_r}{C_{p_{Ar}}}\frac{\partial h}{\partial r}\right)-Ra-\frac{(\dot{q}_{c\leftrightarrow Ar}+\dot{q}_{a\leftrightarrow Ar})dS}{dV} \quad (4)$$

inside the electrode for solid phase:

$$\frac{\partial}{\partial t}(\rho_{c,a}h)=\frac{\partial}{\partial z}\left(\frac{\lambda_{c,a}}{C_{p_{c,a}}}\frac{\partial h}{\partial z}\right)+\frac{1}{r}\frac{\partial}{\partial r}\left(\frac{r\lambda_{c,a}}{C_{p_{c,a}}}\frac{\partial h}{\partial r}\right)+\frac{j_z^2+j_r^2}{\sigma_{c,a}}+\frac{(\dot{q}_{c\leftrightarrow Ar}+\dot{q}_{a\leftrightarrow Ar})dS}{dV} \quad (5)$$

inside the anode molten pool and the solid-liquid mushy zone :

$$\frac{\partial}{\partial t}(\rho_a h)+\frac{\partial}{\partial z}(\rho_a hu)+\frac{1}{r}\frac{\partial}{\partial r}(r\rho_a hv)=\frac{\partial}{\partial z}\left(\frac{\lambda_a}{C_{p_a}}\frac{\partial h}{\partial z}\right)+\frac{1}{r}\frac{\partial}{\partial r}\left(\frac{r\lambda_a}{C_{p_a}}\frac{\partial h}{\partial r}\right)+\frac{j_z^2+j_r^2}{\sigma_a}+\frac{\dot{q}_{a\leftrightarrow Ar}dS}{dV} \quad (6)$$

Heat flux between the cathode and the arc :

$$\dot{q}_{c\leftrightarrow Ar}=-\lambda_{c\leftrightarrow Ar}\left(\frac{\partial T}{\partial z}+\frac{\partial T}{\partial r}\right)-\frac{|\mathbf{j}_e|}{e}\left(\frac{5}{2}k_b T_{Ar}+e\phi_c\right)+\frac{|\mathbf{j}_i|}{e}\cdot eV_{Ar}-\varepsilon_c\alpha T_c^4 \quad (7)$$

Heat flux between the anode and the arc :

$$\dot{q}_{a\leftrightarrow Ar}=-\lambda_{a\leftrightarrow Ar}\frac{\partial T}{\partial z}+\frac{j_z}{e}\left(\frac{5}{2}k_b T_{Ar}+e\phi_a\right)-\varepsilon_a\alpha T_a^4 \quad (8)$$

Enthalpy :

$$h=\int_0^T C_{p_{Ar,a,c}}dT+f_L L \quad (9)$$

Conservation of electric current

$$\frac{\partial}{\partial z}\left(\sigma_{Ar,a,c}\frac{\partial}{\partial z}\phi\right)+\frac{1}{r}\frac{\partial}{\partial r}\left(r\sigma_{Ar,a,c}\frac{\partial}{\partial r}\phi\right)=0 \quad (10)$$

Ohm's law

$$j_z=-\sigma_{Ar,a,c}\frac{\partial\phi}{\partial z},\quad j_r=-\sigma_{Ar,a,c}\frac{\partial\phi}{\partial r} \quad (11)$$

Ampere's rule

$$\frac{1}{r}\frac{\partial}{\partial r}(rB_\theta)=\mu_0 j_z \quad (12)$$

2.2. Boundary Conditions

Figure 1 shows computational domain. Arc melting system consists of a cylindrical thoriated tungsten cathode (W+2wt%Th) and a stainless anode (SUS304). The roots of both electrodes are cooled at 300K. The boundary conditions for thermofield and electrical potential are summarized below.

in the arc region and cathode region

symmetric axis AB : $\frac{\partial T}{\partial r}=0,\quad \frac{\partial\phi}{\partial r}=0$

symmetric axis BC : $\frac{\partial T}{\partial r}=0,\quad \frac{\partial\phi}{\partial r}=0,\quad \frac{\partial(\rho u)}{\partial r}=v=0$

outflow boundary FG : $\frac{\partial^2 T}{\partial r^2}=0,\quad \frac{\partial\phi}{\partial r}=0,\quad \frac{\partial(\rho u)}{\partial r}=\frac{\partial(r\rho v)}{\partial r}=0$

outflow boundary GH : $\frac{\partial^2 T}{\partial r^2}=0,\quad \frac{\partial \phi}{\partial z}=0,\quad \frac{\partial(\rho u)}{\partial z}=\frac{\partial(\rho v)}{\partial z}=0$

inflow boundary HI : $T=300\mathrm{K},\quad \frac{\partial \phi}{\partial z}=0,\quad u=u_{in},\quad v=0$

cooled cathode surface IA : $T=300\mathrm{K},\quad -\sigma_{\mathrm{W}}\frac{\partial \phi}{\partial z}=j_{in}$

cathode surface IJB : $u=v=0$

in anode and molten pool region

symmetric axis CD : $\frac{\partial T}{\partial r}=0,\quad \frac{\partial \phi}{\partial r}=0,\quad \frac{\partial(\rho u)}{\partial r}=v=0$

cooled anode surface DE : $T=300\mathrm{K},\quad \phi=0,\quad u=\mathrm{v}=0$

anode side EF : $T=300\mathrm{K},\quad \phi=0,\quad u=\mathrm{v}=0$

arc-anode interface CF :

On the anode surface (CF), solid, liquid phase and solid-liquid mushy zone appear depending on liquid fraction f_L defined as a function of temperature. Phase is decided by the solidus line (1740K) and liquidus line (1750K) of stainless steel.

$$\begin{cases} \text{solid phase } (T_a < T_{solidus}): & f_L=0,\quad u=\mathrm{v}=0 \\ \text{solid-liquid mushy zone } (T_{solidus} < T_a < T_{liquidus}): & f_L=\dfrac{T_a-T_{solidus}}{T_{liquidus}-T_{solidus}},\ u=0,\ -\eta_{\mathrm{a}}\dfrac{\partial v_a}{\partial z}=-\eta_{\mathrm{Ar}}\dfrac{\partial v_{Ar}}{\partial z}+\dfrac{\partial \gamma}{\partial T}\dfrac{\partial T}{\partial r} \\ \text{liquid phase } (T_{liquidus} < T_a): & f_L=1,\ u=0,\ -\eta_{\mathrm{a}}\dfrac{\partial v_a}{\partial z}=-\eta_{\mathrm{Ar}}\dfrac{\partial v_{Ar}}{\partial z}+\dfrac{\partial \gamma}{\partial T}\dfrac{\partial T}{\partial r} \end{cases}$$

2.3. Numerical Conditions and Procedures

Table 1 shows the system configuration and operating conditions. The thermofluid field is solved by Semi-Implicit-Method for Pressure Linked Equation (SIMPLE) method[6] using Tri Diagonal-Matrix Algorithm (TDMA). The electromagnetic field is solved by SOR method. In this study, 90 of grid points are applied in both axial and radial directions. The thermo-dynamic and transport properties of argon, tungsten and stainless steel are given as a function of temperature.

Table 1. System configuration and operating conditions.

Operating pressure	$p_0=1.013\times10^5$ Pa
Arc current	$I=150$ A
Gas flow rate	$Q_{in}=15$ l/min
Cathode radius	$r_1=1.6$ mm
Nozzle radius	$r_2=10.8$ mm
Anode radius	$r_3=25$ mm
Cathode vertex angle	$\theta=30^\circ, 60^\circ, 90^\circ, 120^\circ$
Anode thickness (SUS304)	$z_1=10$ mm
Sulfur content	$n_s=40,\ 220$ ppm
Electrode gap	$z_2=5$ mm
Computational axial length	$z_3=25$ mm

3. Numerical Results and Discussion

Figure 2 shows the shape of molten pool approximately 20 seconds after arc generation under the condition of cathode vertex angle of 60° and high sulfur content. The available experimental result[7] is also shown for comparison. Although comparing with experiment, melting width in radial direction on the surface of anode is a little narrower due to thermal nonequilibrium effect near anode surface, relatively a good agreement with the experimental data is observed. This confirms that the proposed numerical model with solid-liquid mushy zone is valid when dealing with the arc melting process.

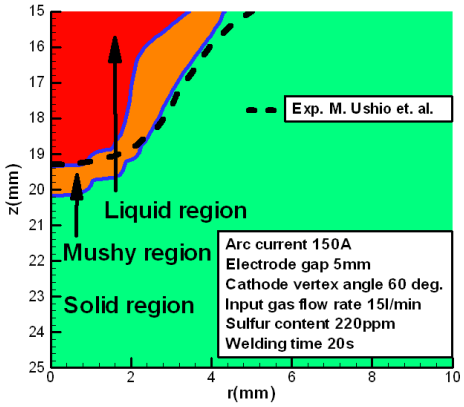

Fig.2 Comparison of numerical molten pool and experimental one.

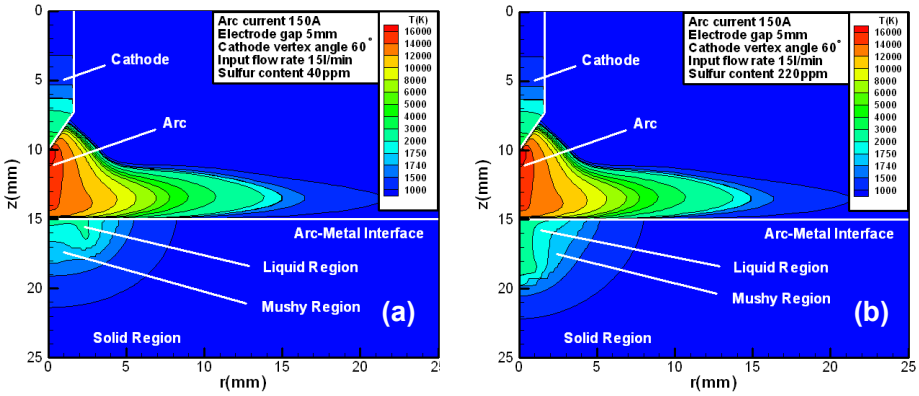

Fig.3 Effect of sulfur content on the arc melting process and molten pool penetration ((a) in case of sulfur content 40ppm, (b) 220ppm).

Figures 3(a) and 3(b) show the effect of sulfur content on the molten pool penetration. It is found that sulfur content does not affect the arc flow so much, however, the welding structure changes drastically by sulfur content. In the case of low sulfur containing in SUS304 as shown in Fig.3(a), the molten metal spreads outward due to the dominant shear force from cathode jet and outward surface driven flow at the arc-molten anode interface. On the other hand, in the case of high sulfur containing in SUS304, the molten pool penetrates downward in the core region due to the inward surface driven flow resulting from surface tension and heat concentration in the core region.

Figure 4(a) shows the input electrical power, heat input to anode material and heat exchange efficiency as a function of cathode vertex angle. Figure 4(b) shows the effect of cathode vertex angle on the cross-sectional area of weld penetration. Here, heat exchange efficiency η is defined as the ratio between heat input to the anode and input electrical power to the arc melting system. It is found from Fig.4(a) that almost the constant heat exchange efficiency of ~80% is maintained regardless of cathode vertex angle, although the input electrical power decreases with the increase of cathode vertex angle due to less electrical current concentration near the cathode tip. As shown in Fig.4(b), the largest cross-sectional area of weld penetration can be obtained for the cathode vertex angle

of 60° due to effective heat transfer.

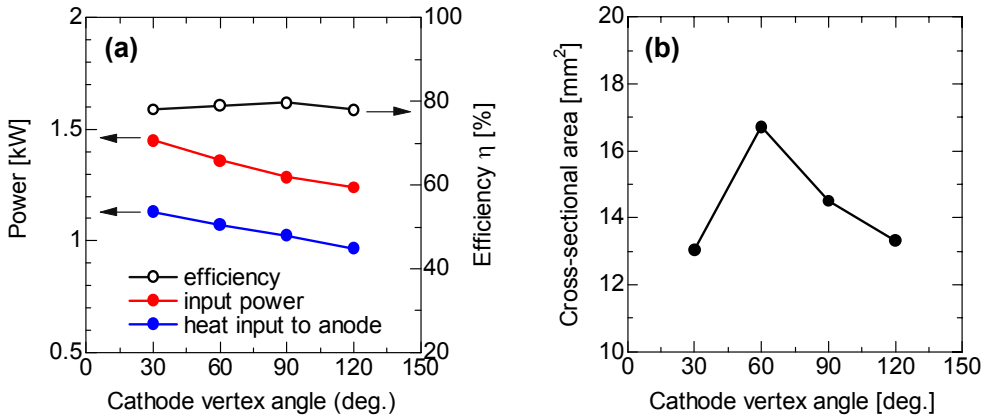

Fig.4 Effect of cathode vertex angle on (a) input power, heat input to anode and heat exchange efficiency, (b) cross-sectional area of weld penetration for sulfur content of 220ppm.

4. Concluding Remarks

For the optimization of arc melting system, the present study proposed the new numerical model considering the complex interactions between arc flow and molten anode interface with temperature dependent surface tension and also considering solid-liquid mushy zone in molten pool. Based on this numerical model, real-time computational simulation of arc melting system is conducted with the purpose of providing the fundamental data for high quality arc melting process. The results obtained from this study can be summarized as follows:

(1) The shape of molten pool predicted from this numerical model considering solid-liquid mushy zone shows a good agreement with the experimental data. Therefore, the numerical model proposed in this study is valid when dealing with the arc melting process.

(2) The welding structure changes drastically by sulfur content. In the case of low sulfur content, the molten metal spreads outward due to the shear force from cathode jet and outward surface driven flow at the arc-molten anode interface. On the other hand, in the case of high sulfur content, the molten pool penetrates downward in the core region due to the inward surface driven flow and heat concentration in the core region.

(3) Almost the constant heat exchange efficiency of ~80% is maintained regardless of cathode vertex angle. The largest cross-sectional area of weld penetration can be obtained for the cathode vertex angle of 60°.

Reference

[1] "Functional Fluids and Intelligent Fluids", ed. by Japan Society of Mechanical Engineers, Corona Pub. Corp. Ltd., Tokyo, (2000), 48. (in Japanese)

[2] H.Nishiyama, T.Shimizu and T.Sato, *ISIJ. Int*., **44** (2004), pp.268-274.

[3] E.Pfender, *Plasma Chem. Plasma Process*., **19** (1996), 21.

[4] M.Goodarzi, R.Choo, T.Takasu and J.M.Toguri, *J. Phys. D: Appl. Phys.*, **31** (1998), pp.569-583.

[5] R.C. Bianchini, R.C.Favalli, M.M.Pimenta and R.N. Szente. *J. Phys. D: Appl. Phys*., **33** (2000), p.134.

[6] S.V.Patankar, *Hemisphere Pub. Corp*., New York, (1980).

[7] M.Tanaka, H.Terasaki, M.Ushio and J.J.Lowke, *Plasma Chem. And Plasma Processing*, **23** (2003), pp.585-606.

Plasma enhanced chemical vapour deposited amorphous silicon carbide films

J. Huran[1], I. Hotový[2], N.I. Balalykin[3], A.P. Kobzev[3], J. Pezoltd[4]

[1] *Institute of Electrical Engineering, Slovak Academy of Sciences, Dúbravská cesta 9, 841 04 Bratislava, Slovakia*
[2] *Faculty of Electrical Engineering and Information Technology, Slovak University of Technology, Ilkovičova 3, 812 19 Bratislava, Slovakia*
[3] *Joint Institute for Nuclear Research, 141980 Dubna, Moscow Region, Russia*
[4] *Institut fuer Werkstofftechnik, Technische Universitaet Ilmenau, PF 100565, D-98684 Ilmenau, Germany*

Abstract
Amorphous silicon carbide (a-SiC_x:H) films have been deposited by plasma enhanced chemical vapour deposition from $CH_4/SiH_4/NH_3$ plasma on n-type (0.015 Ωcm) crystalline silicon (c-Si) in a small volume parallel plate plasma reactor. The elemental composition of the films has been studied using RBS and ERD analysis. Chemical bonding in the films has been studied using the IR technique. The surface morphology and topography of the deposited films have also been characterized by atomic force microscopy.
Keywords: silicon carbide, plasma deposition, RBS, AFM, IR.

1. Introduction

In recent years, nanotechnology has become widely applied in the life sciences, electronics and optoelectronics where it has come to play an increasingly important role. Silicon carbide is a material with remarkable potential for applications in nanotechnology. It shows superior characteristics as a semiconductor and excellent resistance to high temperature, abrasion and radiation [1]. In addition to high-temperature applications, SiC has potential for use in high-power and high-frequency [2]. However, SiC has several advantages over other wide-band gap semiconductors at the present time including commercial availability of substrates [3], known device processing techniques, and the ability to grow a thermal oxide for use as masks in processing, device passivation layers, and gate dielectrics. Furthermore, SiC can also be used as a thin buffer layer for the growth of diamond films on silicon substrates [4]. For example, a-$Si_{1-x}C_x$:H was used as a wide window material to enhance the conversion efficiency of amorphous solar cell. The significance of this material follows from the fact that its electrical and optical properties can be controlled by varying the carbon, silicon and hydrogen composition of the film.

N-doped SiC films have been prepared by various techniques, which include: pyrolysis of polymer precursors [5], chemical vapour deposition (CVD) at elevated temperatures [6], bias-assisted hot filament (CVD) [7], radio frequency plasma-enhanced CVD (PECVD) [8], microwave PECVD [9], electron cyclotron resonance PECVD [10], pulsed laser deposition [11], ion beam sputtering [12] and reactive magnetron sputtering [13]. PECVD technique offers an attractive opportunity to fabricate amorphous hydrogenated N-doped amorphous hydrogenated SiC films at intermediate substrate temperatures and it provides high quality films with good adhesion, good coverage of complicated substrate shapes and high deposition rate.

In this contribution the attention has been focused on the structural properties of a-$Si_{1-x}C_x$:H films prepared by the plasma enhanced chemical vapour deposition (PECVD) of silan SiH_4 and methane CH_4 as a function of the flow rate. Samples with different amounts of N were achieved by a small addition of ammonia NH_3 into the gas mixture of silane SiH_4 and methane CH_4. The properties were investigated by RBS, ERD, IR and AFM measurement techniques.

2. Experimental

PECVD silicon carbide films were deposited in a high frequency parallel-plate plasma reactor, in which the frequency, the RF power and the substrate temperature were maintained at 13.56 MHz, 0.06 Wcm^{-2}, and 350°C respectively. The diameter of electrodes was 12 cm, and they were 6 cm apart. The RF power was fed to the

upper electrode, while the lower electrode, which held the substrates, was grounded. A n-type silicon wafer with resistivity 0.015 Ω cm and (111) orientation was used as the substrate for the a SiC:H films. Prior to deposition, standard cleaning was used to remove impurities from the silicon surface, and the 5% hydrofluoric acid was used to remove the native oxide on the wafer surface. The wafer was then rinsed in deionized water and dried in nitrogen ambient. A gas mixture of SiH_4, CH_4 and NH_3 was directly introduced into the reaction chamber, and the flow rates of these gases were 10 sccm, 20-40 sccm and 2-5sccm respectively. The concentration of silicon carbon and nitrogen was determined by RBS method. The hydrogen concentration was determined by the ERD method. For this purpose the $^4He^+$ ion beam from a Van de Graff accelerator at JINR Dubna was applied. The energy 2.4 MeV was chosen. The target was tilted at an angle of 15^o with respect to the beam direction and the recoiled protons were measured in forward at an angle of 30^o. Chemical compositions were analyzed by infrared spectroscopy. The IR spectra were measured from 2000 to 400 cm^{-1}. Film morphology was assessed by Atomic Force Microscopy.

3. Results and discussion

The thickness and refractive index of the SiC films were measured by a Gaertner Ellipsometer. For technological conditions which represented by samples T1 and T2 with the flow SiH_4 10 sccm, the CH_4 40 sccm and the NH_3 5 and 2 sccm, respectively, the deposition rate was 5 nm per minute and refractive index was in the range 2.2-2.3. For samples T3 and T4, SiH_4 flow 10 sccm, CH_4 flow 25 sccm and NH_3 flow 2 and 5 sccm, respectively, the deposition rate was 4 nm/min and the refractive index was in the range 2.3-2.4. Our results show that the deposition rate increases if the flow of CH_4 is increased, however the value of refractive index is decreases. Figure 1 show RBS spectra of four samples T1, T2, T3 and T4 with different deposition conditions of the deposited amorphous silicon carbide films.

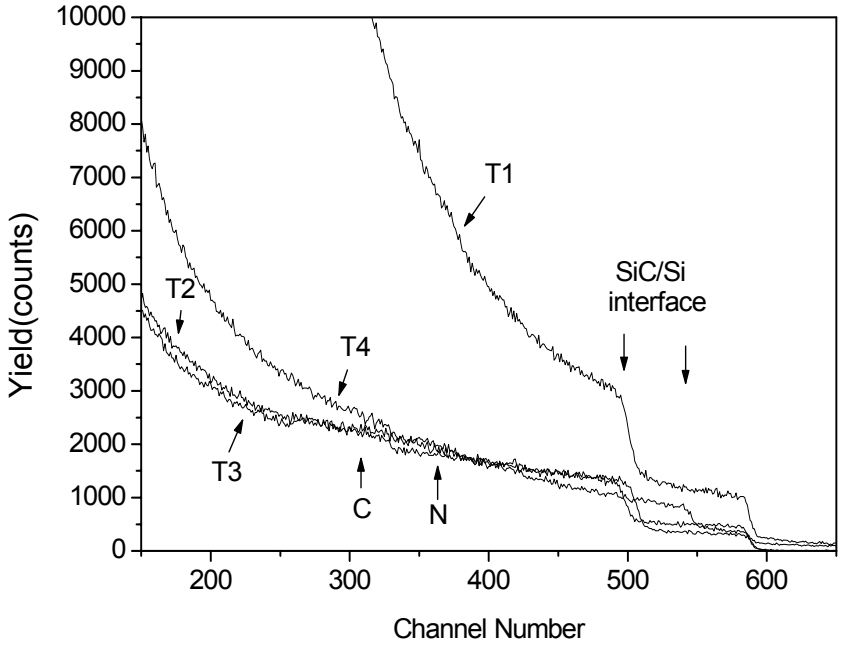

Fig. 1: RBS spectra of SiC films deposited onto a silicon substrate for 2 MeV alfa particles detected at scattering angle of 170^o. The spectra are for samples T1 (thickness of film 220 nm), T2 (190 nm), T3 (210 nm) and T4 (170 nm).

After modelling, we can show from calculated results the presence of small amounts of oxygen but the concentrations of hydrogen in the SiC films are approximately 20 at. %. In the case of samples T1and T2 the concentration of silicon, carbon and nitrogen are 25, 40 and 10-12 at.% respectively. The concentration of Si and C in samples T3 and T4 are 30, 35 and 10-12 at % respectively. There was no evidence of the substrate mixing into the films. Hydrogen was detected by means of elastic recoil detection. The ERD analyses show that the amount of incorporated H for samples T1, T2, T3 and T4 were 22 at %, 20 at % 19 at % and 18 at % respectively. The concentration of H increases with increasing CH_4 flow. The IR spectra in Figure 2 revealed the main absorption region between 500 and 1500 cm^{-1} due to the presence of Si-C, Si-H, Si-N and N-H bonds.

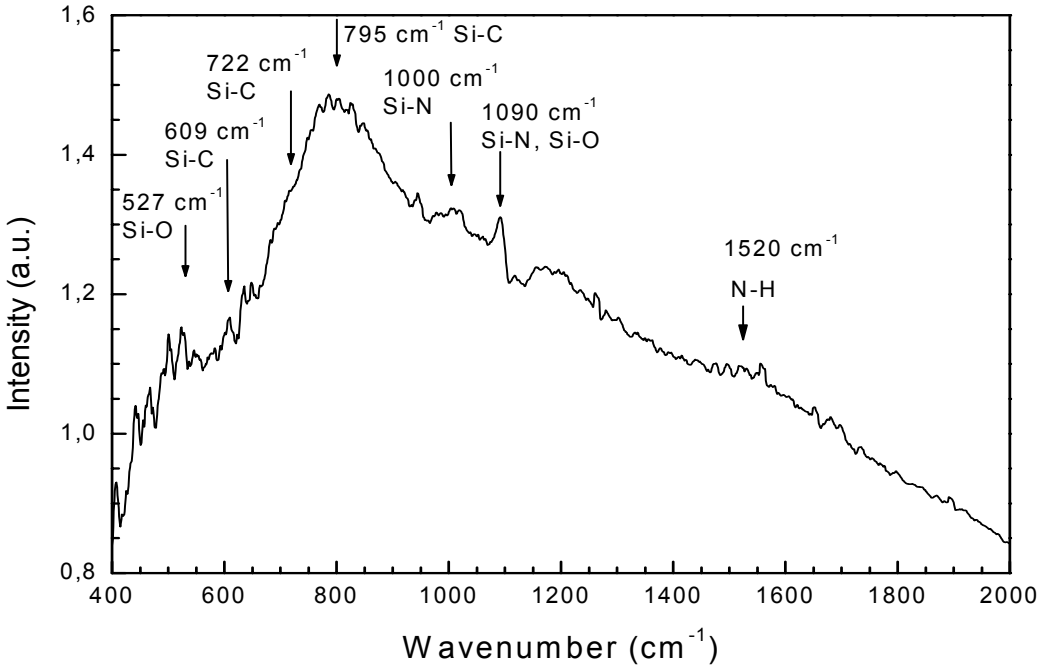

Fig. 2: Typical infrared spectra for all samples T1, T2, T3 and T4. Differences of IR spectra between samples are very small.

The AFM micrographs (Figure 3.) of the SiC films prepared by PECVD reveal that the film surface is rather smooth and compact. The mean roughness R and the root mean square RMS of the samples, as deduced from the AFM analysis, are similar.

4. Conclusion

We have investigated the structural properties of amorphous silicon carbide films prepared by plasma enhanced chemical vapour deposition The experimental results obtained from this work can be summarized as follows. The RBS results showed that the concentrations of Si, C and N in the films are practically the same. The concentration of hydrogen was determined by the ERD method and the value is approximately 20 at %. The films contain a small amount of oxygen. IR results showed the presence of Si-C, Si-N, N-H, and Si-O bonds.

Acknowledgements

The work was supported by the Scientific Grant Agency of the Ministry of Education of the Slovak Republic and Slovak Academy of Sciences, No. 1/4151/24, 1/0170/03 and by Science and Technology Assistance Agency under the contract No. APVT-20-021004.

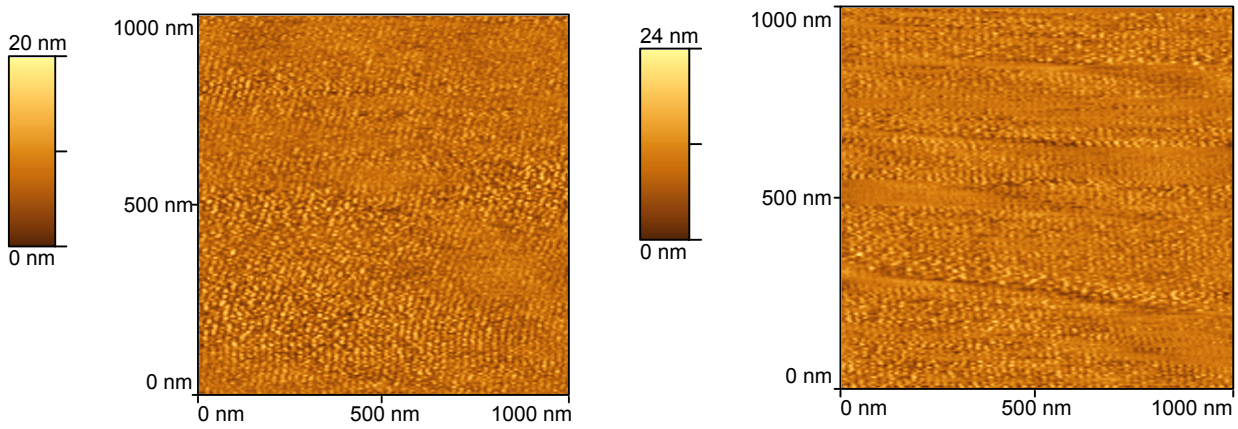

Sample T1 Sample T3

Fig. 3: AFM micrographs showing the surface (1000 x 1000 nm^2) of samples T1 and T3.

References

[1] S. Matsui, T. Kaito, J. Fujita, M. Komuro, K. Kanda, Y. Haruyama, J. Vac. Sci. Technol. **B18,** 3181(2005).
[2] R.J. Trew, J.B. Yan, P.M. Mock - Proc. IEEE **79,** 598 (1991).
[3] Advanced Technology Materials, Inc., 7 Commerce Drive, Danbury, CT 06810-4169.
[4] E.G. Wang - Physica **B185,** 85 (1993).
[5] R. Riedel, H.-J. Kleebe, H. Schönfelder, F. Aldinger – Nature **374,** 526 (1995).
[6] A. Bendeddouche, R. Berjoan, E. Beche, R. Hillel – Surf. Coat. Technol. **111,** 184 (1999).
[7] Z. Gong, E.G. Wang, G.C. Xu, Y. Chen – Thin Solid Films **348,** 114 (1999).
[8] H. Sachdev, P. Sheid – Diamond Relat. Materials **10,** 1160 (2001).
[9] J.-Y. Wu, C.-T. Kuo, P.-J. Yang – Mater. Chem. Phys. **72,** 245 (2001).
[10] F.J. Gomez, P. Prieto, E. Elizalde, J. Piquerasa – Appl. Phys. Lett. **69,** 773 (1996).
[11] G. Soto, E.C. Samano, R. Machorro, L. Cota - J.Vac. Sci. Technol. **A16,** 1311 (1998).
[12] Z. He, G. Carter, J.S. Colligon – Thin Solid Films **283,** 90 (1996).
[13] T. Berlind, N. Hellgren, M.P. Johansson, L. Hultman – Surf. Coat. Technol. **141,** 145 (2001).

Controllable Thermofluid Field of Reactive Plasma Jet Impinging onto the Substrate

H. Nishiyama[1], T. Sato[1], G. Chiba[1] and H. Takana[1]

[1] *Institute of Fluid Science, Tohoku University, Sendai, Japan*

Abstract

When the nonequilibrium Ar/N_2 plasma jet is impinging onto the substrate, the effects of operating pressure, applied magnetic field on radiation intensity from nitrogen radicals, plasma jet configuration near substrate and heat flux into the substrate are experimentally clarified. Finally, constant value control of radiation intensity, substrate heat flux, jet axis deviation and jet width fluctuation are achieved by using PI control method with suppressed fluctuation to stabilize an unstable plasma jet.

Keywords: Control, Plasma jet, Unstable behavior, Substrate, Nitriding

1. Introduction

Plasma jet has been extensively utilized for material processes and waste treatments so far [1-3]. Since there are rotating arc root behaviors in the torch, pulsating particle carrier gas flow, turbulent behavior in the downstream and strong interaction with the substrate, plasma jet is easily apt to experience the unstable behaviors [4, 5]. Especially it is very important to suppress the unstable plasma-substrate interaction and make the impinging jet more stable for high quality processes of surface modification and coating on the substrate. However, there are few papers concerning control of plasma jet for material processing [6-10].

The main objective of the present paper is to clarify experimentally the correlations between operating conditions and plasma jet characteristics in order to determine the important controlled and manipulated variables, when the nonequilibrium Ar/N_2 plasma jet is impinging onto the substrate for nitriding. The effects of operating pressure, applied magnetic field on radiation intensity from nitrogen atomic radicals, heat flux into the substrate, fluctuating jet axis and jet width are clarified. Finally, feedback control system is successfully constructed to achieve constant value control of nitrogen atom radiation from plasma near substrate and heat flux into the substrate by operating back pressure. The jet axis deviation and jet width fluctuation are effectively suppressed for stabilization by applied magnetic field using PI control method.

2. Experimental setup and procedures

The details of the experimental facilities are omitted here [8]. Table 1 shows the experimental conditions in the present study. The SUS303 substrate (W 34 mm × H 160 mm × T 22 mm) is set vertically in the middle of the test section held by two solenoidal coils. *Z* axis shows the flow direction and *r* axis shows perpendicular to *z* axis, respectively. The origin is the center of the substrate. Heat

Table 1 Experimental conditions

1st gas	Ar
1st gas flow rate	30 (Sl/min)
1st discharge current	30 (A)
1st discharge power	0.9 (kW)
2nd gas	N_2
2nd gas flow rate	30 (Sl/min)
2nd discharge current	80 (A)
2nd discharge power	5.6 (kW)
Background pressure	650~1100 (Pa)
Axial magnetic flux density	0~0.44 (T)

and r axis shows perpendicular to z axis, respectively. The origin is the center of the substrate. Heat flux into the substrate is measured by water cooled heat flux sensor (CAPTEC) embedded in the substrate. The substrate can be moved transversely to obtain the continuous data. The radiation intensity emitted from Ar/N_2 plasma is measured by optical analyzer (330-1100 nm) and by Si photodiodes (400-1000 nm) especially for control. The radiative plasma jet behavior is visualized by CCD camera at the sampling rate of 1/60 s to evaluate the jet axis and width of oscillating plasma jet. The jet width is defined as the radial distance between two radial locations showing half maximum radiation intensity. The fluctuating intensity is the ratio of standard deviation to averaged jet width. Furthermore, jet axis location is defined as the centerline between defined jet widths.

Figure 1 shows a schematic illustration of feedback control systems for an unstable plasma jet impinging onto a substrate. The control systems consist of a detecting element for the controlled values such as heat flux, radiation intensity, monitored jet axis and jet width, a control element for outputting the PI control signal and a final control element for a manipulated variables such as applied magnetic flux density and background pressure. The transfer function for PI control method is given by Eq.(1) as follows [11]:

$$G(s) = K_p\left(1 + \frac{1}{T_I s}\right) \tag{1}$$

where K_p, T_I are gain constant and integral time, respectively.

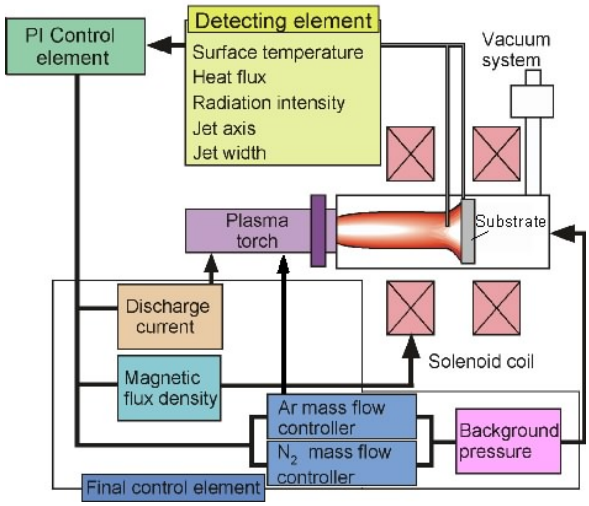

Figure 1 Schematic illustration of feedback control systems

3. Experimental results and discussion

3.1 Thermolfluid characteristics

Figure 2 shows the iso-contour of substrate heat flux as functions of background pressure and applied magnetic field intensity. The substrate heat flux at stagnant point r = 0 mm can be increased nearly two times by operating background pressure, although there is a little effect of applied magnetic flux density. This means that the background pressure is dominant operating valuable for controlling substrate heat flux.

Figure 3 shows the iso-contour of relative radiation intensity of 821.6 nm near substrate as functions of background pressure and applied magnetic field intensity. This radiation intensity is the strongest and comes from nitrogen atom. The radiation intensity increases considerably for lower background pressure and higher magnetic flux due to the plasma jet elongation toward downstream.

3.2 Control characteristics

Figure 4 shows the PI control characteristics substrate heat flux by operating background pressure based on their correlations as shown in Fig.2. When the discharge current I_p changes like step from 80 A to 90 A as a disturbance, the substrate heat flux can be kept nearly constant value of 55 kW/m^2 at stagnation point for K_p = 25 and T_I = 2.4 seconds.

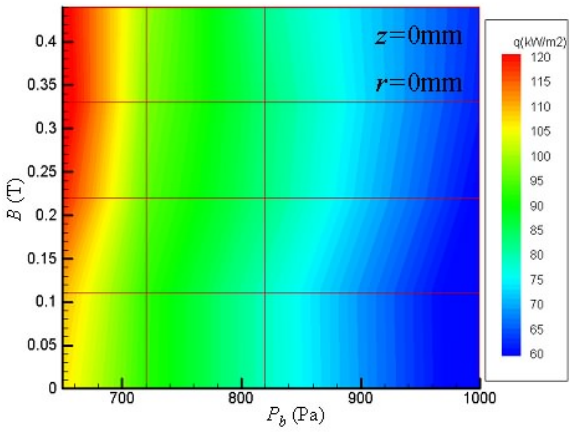

Figure 2 Iso-contour of substrate heat flux

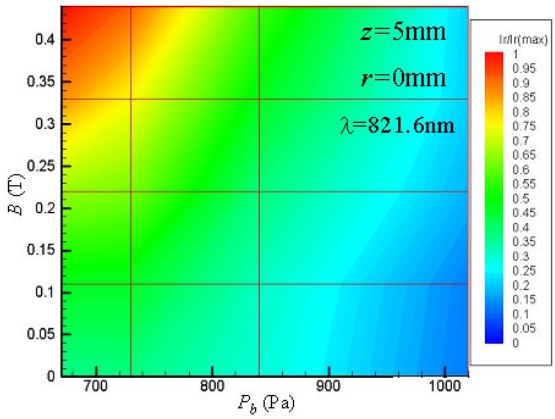

Figure 3 Iso-contour of radiation intensity from nitrogen atom

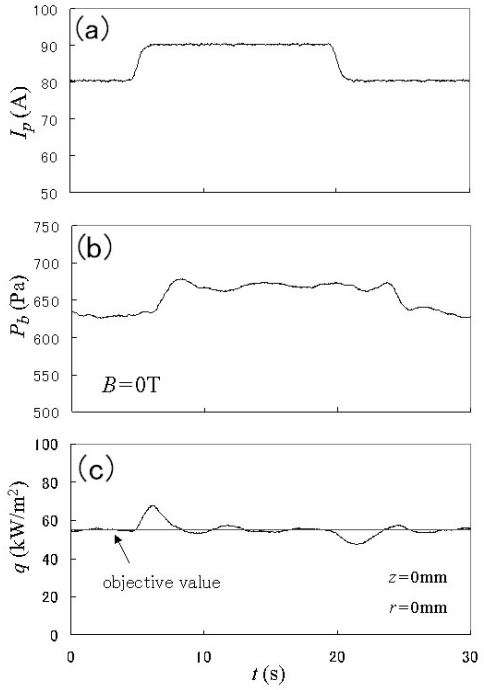

Figure 4 PI control characteristics of substrate heat flux

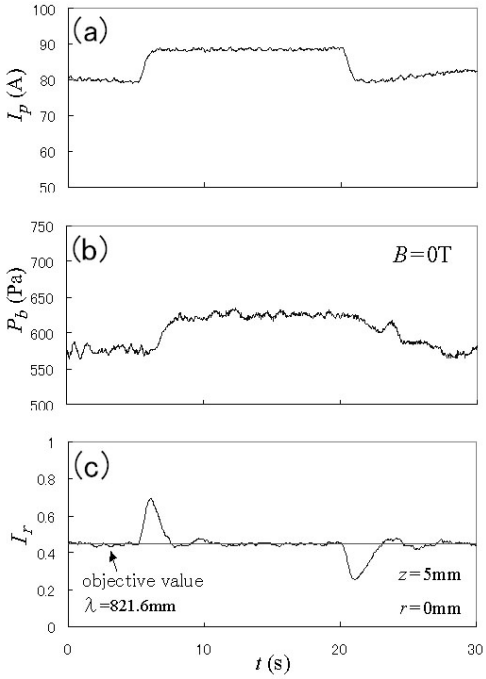

Figure 5 PI control characteristics of radiation intensity from nitrogen atom

Figure 5 shows the PI control characteristics of radiation intensity of nitrogen atom at 821.6 nm by operating background pressure based on their correlations as shown in Fig.3. When the discharge current I_p changes as the same behavior as in Fig.4, the radiation intensity can be kept constant value of 0.45 adjacent to substrate for K_p = 1300 and T_I = 2.4 seconds. This means that number density of nitrogen atom can be kept constant against a disturbed discharge current prior to impinging for high quality substrate nitriding.

Figure 6 shows the step response of jet axis position to the applied magnetic flux density. a' means the standard deviation of jet axis position in the radial direction. When the magnetic field is applied like step from 0.05 T to 0.44 T, the standard deviation and fluctuation intensity of jet axis position are decreased effectively.

Figure 7 shows the PI control characteristics of jet axis position for constant value of 1.5 adjacent to substrate by applying magnetic field for K_p = 0.04 and T_I = 0.6 seconds. It takes about 6 seconds to approach to the desired constant value. This shows that the plasma jet behavior can be stabilized and become axisymmetry by applying magnetic field.

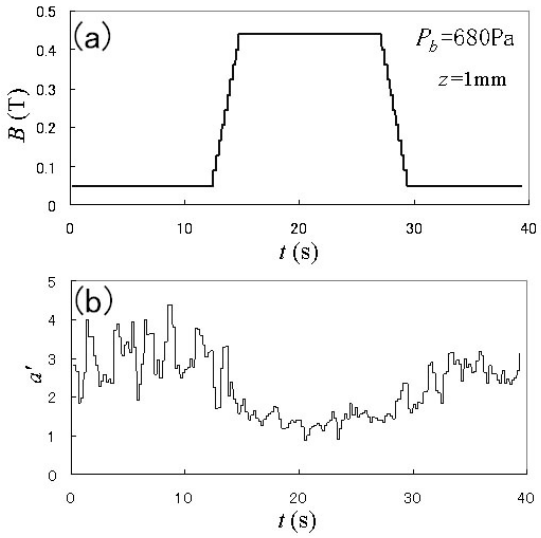

Figure 6 Step response of jet axis position to applied magnetic field

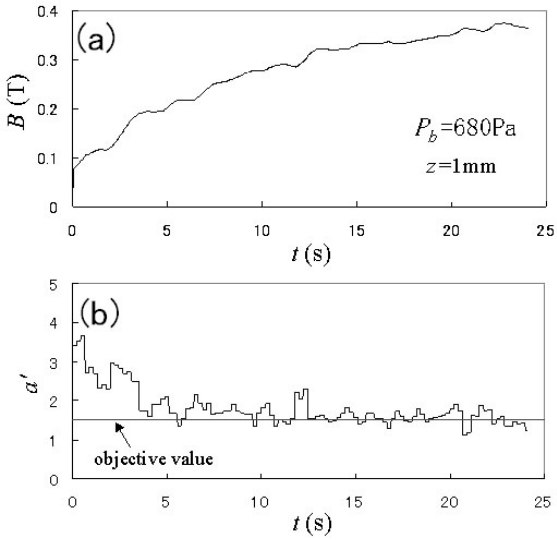

Figure 7 PI control characteristics of jet axis position

4. Conclusion

The correlation between operating conditions and controlled variables for argon/nitrogen plasma jet impinging onto the substrate is clarified experimentally. The control characteristics of impinging reactive plasma jet are obtained for high quality nitriding. The results obtained in the present study are as follows.

(1) The substrate heat flux and radiation intensity from nitrogen radical atom adjacent to substrate can be kept constant by operating background pressure using PI control method against a disturbed discharge current.
(2) The unstable behavior of impinging plasma jet onto the substrate can be stabilized by applying magnetic field effectively.

Acknowledgements

The present study was partially supported by a grant-in-aid for Scientific Research from the Japan Society for Promotion of Science and a 21st Century COE Program Grant of the International COE of Flow Dynamics from the Ministry of Education, Culture, Sports, Science and Technology. The authors would like to thank senior technician Mr. Kazunari Katagiri, student Mr. Shota Niikura with Institute of Fluid Science, Tohoku University and Mr. Hirotake Watashima with Quattro Systems & Co. for their eager helps in the experiments.

References

[1] E. Pfender, Pure Appl. Chem., **60**, 591 (1988).
[2] H. Nishiyama, Pure Appl. Chem., **71**, 1899 (1999).
[3] O. P. Solonenko and M. F. Zhukov, Thermal Plasma and New Materials Technology, **2** (Cambridge Interscience Press, Cambridge), (1995).
[4] S. Nityalendra, et al., J. Phys. D: Appl. Phys., **33**, 270 (2000).
[5] M. Hrabovsky, et al., High Temp. Materials Process., **1**, 167 (1997).
[6] J. F. Bisson, et al, Proc. of the Int. Thermal Spray, 715 (2001).
[7] L. Beall, et al., Proc. of the 15th Int. Thermal Spray Conf., Nice, 815 (1998).
[8] H. Nishiyama, et al., J. Phys. D: Appl. Phys., **30**, 2804 (1997).
[9] H. Nishiyama, et al., Plasma Devices and Operations, **10**, 157 (2002).
[10] H. Nishiyama, et al., Vacuum, **73**, 691 (2004).
[11] Handbook of Automatic Control: Fundamental, (Ohmsha, Ltd., Tokyo), (1983).

In-flight Treatment of Titanium Dioxide Nano Particles Using a DC-RF Hybrid Plasma Flow System

K. Kawajiri[1], J. H. Seo[2], N. Sato[3], S. H. Hong[4], H. Nishiyama[1]

[1]*Institute of Fluid Science, Tohoku University, Sendai, Japan*
[2]*Plasmix Co., Ltd., Seoul National University, Seoul, Korea*
[3]*Institute of Multidisciplinary Research for Advanced Materials, Tohoku University, Sendai, Japan*
[4]*Department of NuclearEngineering, Seoul National University, Seoul, Korea*

Keywords: Nano particle, In-flight particle treatment,DC-RF hybrid plasma,Optimization, Statistical analysis

Abstract

A DC-RF hybrid plasma flow is used for in-flight particle processing, where particle size of rutile TiO_2 particles is converted from 2 micrometer to submicron. Four typical particle size distributions of obtained products are confirmed after the treatment. The size of ultra fine particles (UFPs) is nearly 100 nm. The mean particle diameter of UFPs becomes small with decreasing operating pressure. The conversion ratio from the initial precursors to UFPs increases with decreasing operating pressure, decreasing swirl gas flow ratio and injecting a large amount of quench gas flow rate. Operating conditions are optimized to decrease mean particle diameter of UFPs, increase its conversion ratio and stabilize a plasma flow simultaneously by multi-input and multi-objective optimization method. Finally, conversion ratio from initial precursors to UFPs, whose mean particle diameter is 140 nm, is nearly 90 % by stable plasma flow by the optimized operating conditions.

1. Introduction

A thermal radio frequency inductively coupled plasma (RF-ICP) flow has been investigated intensively for material processing so far, because it has prominent advantages for in-flight treatment because of plasma purity, large volume, steep temperature gradient, long residence time and easy controllability by flow condition. Injected precursors are evaporated momentary and complex metallurgical reactions are taken place in an RF-ICP flow. On the other hand, it has also some disadvantages due to the large effect of flow condition on the plasma characteristics, such as plasma instability and strong back flow by a recirculation due to Lorentz force at an RF coil region. Then, a DC-RF hybrid plasma flow is expected to overcome such disadvantages of an RF-ICP flow for material processing [1]. A DC-RF hybrid plasma flow is produced by combining a supplemental direct current (DC) plasma jet with an RF-ICP flow, and it has been investigated by some researchers [2-6]. Compared with a conventional RF-ICP flow, there is prominent advantages in a DC-RF hybrid plasma flow because it is possible to inject reactants axially to the centerline region from the torch head and then, the reactants can obtain high enthalpy during passing though the plasma core region with much acceleration by a DC plasma jet. This unique feature could be utilized for in-flight particle treatment because evaporation of solid particles needs much more enthalpy than some other reactants such as gas or gel. The application of a DC-RF hybrid plasma flow system has been investigated by Yoshida intensively.

In the present study, the in-flight treatment of rutile TiO_2 particle is investigated. Rutile TiO2 is very attractive material in these days because its reactivity such as absorption and dissociation can be enhanced by producing a stable oxygen vacancy on its surface by annealing or sputtering [7]. In addition, a DC-RF hybrid plasma flow has good advantages in dealing with such stable materials at high temperature, which cannot be dealt by chemical process. The fundamental correlation between operating conditions and

properties of produced TiO_2 fine particles is clarified comprehensively for in-flight particle treatment using a DC-RF hybrid plasma flow system. Finally, the operating conditions are optimized by multi-input and multi-objective optimization [8] to achieve the most efficient processing by a DC-RF hybrid plasma flow system in viewpoints of particle size, conversion rate and plasma stability.

2. Experimental Setup

A DC-RF hybrid plasma system consists of RF plasma torch, DC plasma torch, reaction chamber, powder feeder, gas supply control systems for an RF plasma torch and a DC plasma torch, monitoring system and vacuum system.

Figure 1 (a) shows the schematic illustration of a DC-RF hybrid plasma flow system with gas injections. This system consists of a 3-turn RF induction coil, DC electrodes, which are installed at the top of an RF torch. There are mainly four kinds of gas injection modes to control a plasma flow. The sheath gas, which is the main gas to produce an RF plasma flow, is injected from the narrow space between the inner wall of the quartz tube whose diameter is 44 mm and the DC torch outside, respectively. The central gas is injected from the central gas nozzle at the center of the DC torch. The central gas is discharged to produce a DC plasma jet. The swirl gas is mixed in the sheath gas before injection into the RF torch, and circumferential velocity of the sheath gas swirl is controlled by the swirl gas ratio in the sheath gas. The carrier gas is injected diagonally from the two carrier gas nozzles on both sides of the central gas nozzle. Operating pressure is controlled by the flow valve in front of the rotary pump.

Figure 1 (b) shows the schematic illustration of the inside of a DC-RF hybrid plasma torch and the particle collector. The quench gas is injected from the copper tube ring with the 12 inside inlets of 2 mm diameter into the centerline region radially at 130 mm downstream.

In this study, RF power, DC power, carrier gas flow rate are fixed at 7 kW (4MHz, 7 kV, 1A), 1 kW (40 V, 25A) and 4 l/min, respectively, to clarify the fundamental effects of inlet flow condition on the characteristics of the obtained products such as particle size and structure. Commercial rutile TiO_2 particles with diameter of 2 micrometer (Wako Chemical, Japan) are employed as initial precursors. Its are provided at 250 mg/min for one minute by the carrier gas. Experiments are conducted for one minute. The products attached on the inside surface of the quartz tube and that accumulated on the collector bottom, both which are shown in Fig. 1 (b), are independently collected for comparison. The particle size distribution is measured by particle size analyzer (MT3000, Microtrac Inc. , USA) after 9 minutes ultra sonic treatment. On the other hand, the obtained samples are characterized by X-ray diffractometry (XRD) analysis (RINT2000, Rigaku, Japan) using CuKα radiation. Particle size and morphologies are characterized by scanning electron microscope (SEM) (S4100, Hitachi, Japan).

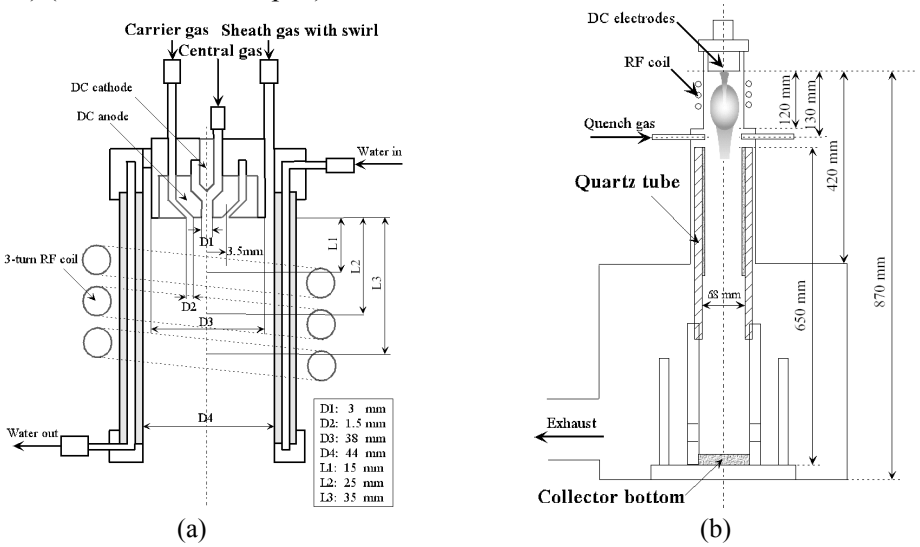

Figure 1. Schematic illustrations of (a) a DC-RF hybrid plasma system and (b) the detailed design of torch region

3. Experimental Results

Figure 2 shows particle size distributions of obtained products at various operating pressures; where sheath gas flow rate Q_{Sh}, swirl gas ratio R_{Sw}, central gas flow rate Q_C, carrier gas flow rate $Q_{Carrier}$ and quench gas flow rate Q_Q are 20 l/min, 1, 3 l/min, 4 l/min and 0 l/min, respectively. Typical four peaks are confirmed in the figure. The smallest particles, which have polygonal shape as shown in Fig. 3, are produced by homogeneous nucleation [9-10] and called as ultra fine particles (UFPs) in this study. These UFPs are accumulated on the collector bottom as agglomerates because these have large specific surface and easily agglomerates each other. The second smallest peak is from fine particles (FPs), which is produced by heterogeneous nucleation on the submicrom size particles of the initial precursors. These submicron size particles can pass through the plasma core region without evaporation because of small heat transfer due to large Knudsen effect. Then such particles act as seeds in a nucleation region at the plasma tail. The third smallest peak is from no treated particles (NTPs), which pass through the plasma core region without evaporation. The largest peak is from large agglomerated particles (LAPs), which are produced from the agglomerates by sintering due to long residence time and large heating in the plasma tail region.

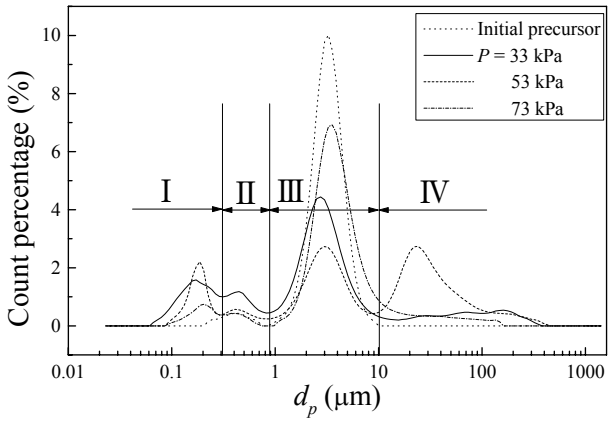

Figure 2 Particle size distribution at various operating pressures

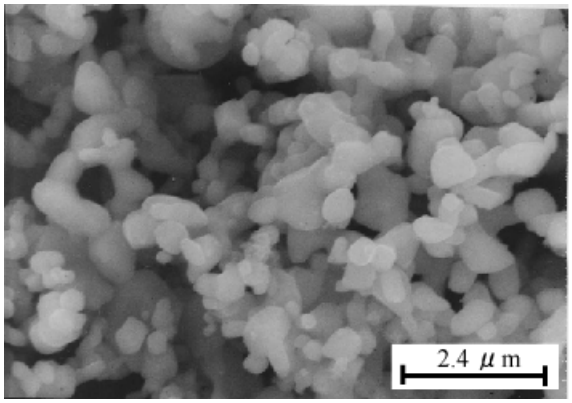

Figure 3 SEM image of UFPs

Figure 4 shows mean particle diameter and cumulative percentage of UFPs in Fig. 2. Mean particle diameter of UFPs increases with increasing operating pressure. Several conditions are required to suppress particle growth, such as rapid removal of nuclei from the nucleation region, decrease in density of nuclei and supersaturation [11-12]. Particle residence time in the nucleation region at the plasma tail increases with increasing operating pressure because particle velocity at the plasma core region is decelerated by a recirculation due to Lorentz force [13]. In addition, particle heating also becomes prominent with increasing operating pressure because of long particle residence time and decrease in Knudsen effect [14-16] and then, evaporation increases with increasing operating pressure. Therefore, particles grow large during the long residence time and large nuber density of nuclei in the nucleation region at large operating pressure. On contrary to it, the cumulative percentage of UFPs decreases with increasing operating pressure.

Figure 5 shows particle size distribution with the various quench gas flow rates. When the quench gas flow rate is 20 l/min, the effect of the quench gas is small because the quench gas is entrained by a strong recirculation at the coil downstream region and diffused into the plasma flow without reaching the nucleation region [17]. However, the effect of the quench gas flow becomes prominent with a large amount of the quench gas flow rate of 50 l/min. Supersaturation [18] is produced at the plasma tail region, where nucleation takes place, by a large amount of quench gas because the quench gas penetrates the coil downstream recirculation without being entrained.

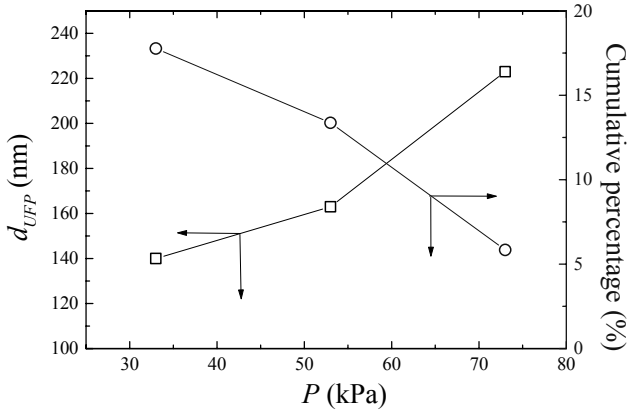

Figure 4 Mean particle diameter and cumulative percentage of UFPs

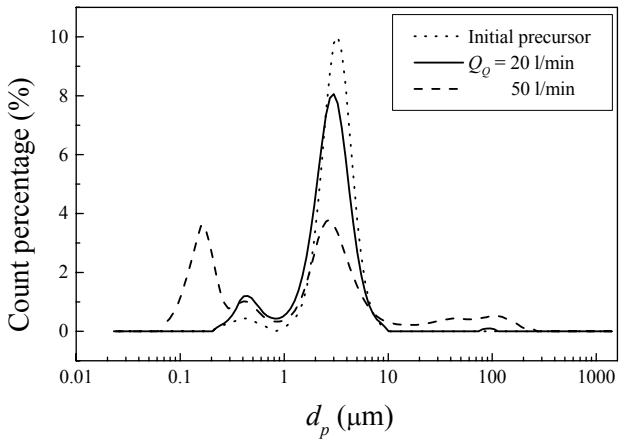

Figure 5 Particle size distribution at quench gas flow rates at 33 kPa

4. Optimization

Multi-input and multi-objective optimization, in which factorial design approach and genetic algorism are combined [8], is conducted. Fixed operating conditions are carrier gas flow rate of 4 l/min and RF power frequency of 4 MHz in this study. Working gas is argon. Initial precursor is rutile TiO_2 of 2 μm and supplied at 76.2 mg/min The following seven parameters, such as operating pressure (P kPa), sheath gas flow rate (Q_{Sh} l/min), central gas flow rate (Q_C l/min), swirl gas ratio (R_{Sw}), quench gas flow rate (Q_Q l/min), RF power (P_{RF} kW) and DC power (P_{DC} kW) are employed as input parameters in the present study. These input parameters are assigned to Taguchi type full factorial design of OA (L_8) in Table 1 as linear model; where RF powers of 9 kW and 10 kW are obtained from RF plate voltages of 6 kV and 6.5 kV, and anode currents of 1.5 A and 1.6 A, respectively. DC powers of 1 kW and 2 kW are obtained from DC voltages of 40 V and 80 V, and constant DC current of 25 A, respectively. The following output parameters are evaluated for the products obtained from the collector bottom. Mean particle diameter (d_{UFP} nm) of UFPs and conversion ratio ($R_{Conversion}$ %) from the initial precursors of 2 μm to UFPs distributions are chosen as output parameters. Additionally, disappearance RF power (P_d kW), which is measured when RF-ICP flow is distinguished with decreasing RF power, is also employed as important output parameter. This parameter shows the plasma stability. Injection rate of the initial precursors strongly depends on the plasma stability. The obtained results for the operating conditions in Table 1 are shown in Table 2. Conversion ratios from the starting material to UFPs are more than 70 % for these operating conditions because of large powers of an RF-ICP and a DC plasma jet.

Table 1 Taguchi type full factorial design of OA_8

Cond. No.	P (kPa)	Q_{Sh} (l/min)	Q_C (l/min)	R_{Sw}	Q_Q (l/min)	P_{RF} (kW)	P_{DC} (kW)
1	30	20	3	0	20	9	1
2	30	20	3	1	40	10	2
3	30	40	4	0	20	10	2
4	30	40	4	1	40	9	1
5	50	20	4	0	40	9	2
6	50	20	4	1	20	10	1
7	50	40	3	0	40	10	1
8	50	40	3	1	20	9	2

Table 2 Experimental results

Cond. No.	d_{UFP} (nm)	$R_{Conversion}$ (%)	P_d (kW)
1	131	82.75	5.50
2	127	84.70	6.24
3	138	80.41	6.36
4	133	88.47	5.28
5	133	78.35	8.28
6	136	75.32	6.49
7	127	78.12	7.13
8	127	81.03	4.41

Table 3 shows the contribution ratios (%) of input parameters on the each output; where the negligible input parameters, whose neglects are determined by F-test described, are shown by underlined,

and the contribution ratio of RF power on the disappearance RF power does not exist.

The following three equations showing the correlation between the input parameters and the each output parameter are obtained from the Tables 2 and 3 in a DC-RF hybrid plasma flow system.

$$d_{UFP} = 131.5 + 7(Q_C - 3.5) - 0.15(Q_Q - 30) \quad \text{.....(1)}$$

$$R_{Conversion} = 81.14 - 0.294(P - 40) + 0.086(Q_{Sh} - 30) + 2.473(R_{Sw} - 0.5) + 0.127(Q_Q - 30) - 3.013(P_{RF} - 9.5) \quad \text{.....(2)}$$

$$P_d = 6.21 + 0.037(P - 40) - 0.042(Q_{Sh} - 30) + 0.784(Q_C - 3.5) - 1.211(R_{Sw} - 0.5) + 0.052(Q_Q - 30) \quad \text{.....(3)}$$

Figure 6 shows the Pareto-optimal resolutions to minimize mean particle diameter of UFPs, maximize conversion ratio to UFPs and minimizing disappearance power simultaneously. UFPs less than 130 nm are obtained at large conversion ratio of nearly 90 % under a stabilized plasma flow by multi-input and multi-objective optimization.

Table 3 Contribution ratios of the input parameters on the output parameters

	d_{UFP} (nm)	$R_{Conversion}$ (%)	P_d (kW)
P (kPa)	3.52	57.42	10.88
Q_{Sh} (l/min)	0.39	4.96	14.14
Q_C (l/min)	76.56	1.70	12.50
R_{Sw}	3.52	10.16	29.85
Q_Q (l/min)	14.06	10.66	22.06
P_{RF} (kW)	1.56	15.09	
P_{DC} (kW)	0.39	0.00	1.02
e	9.38	6.67	10.60
T	100.00	100.00	100.00

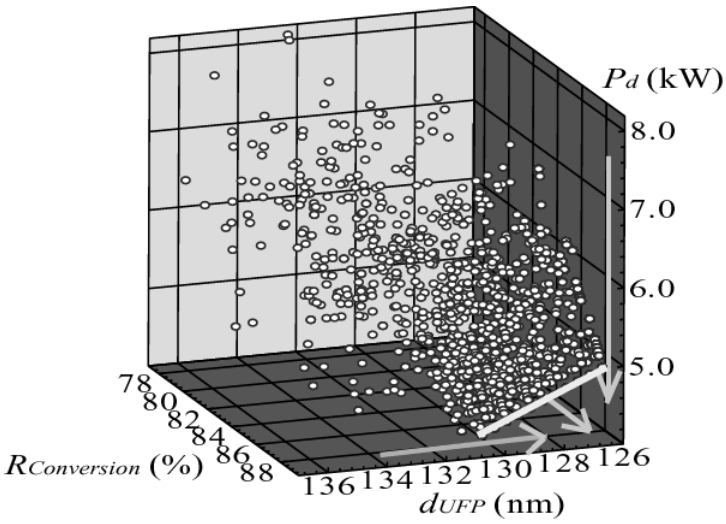

Figure 6 Pareto-optimal resolutions obtained by multi-input and multi-objective optimization

5. Conclusions

1. Several typical distributions of obtained products are confirmed in this study. The mean size of ultra fine particles due to homogeneous nucleation is nearly 100 nm and it increases with increasing operating pressure because particle residence time in the condensation region becomes small.
2. Quench gas effect of producing ultra fine particles becomes prominent at a large amount because a small amount of quench gas is diffused into the plasma core region by a strong recirculation due to Rorentz force.
3. The operating condition is optimized by multi-input and multi-objective optimization to decrease the mean size of ultra fine particles, increase the conversion ratio to ultra fine particles and stabilize the plasma flow during the processing. Under the optimized operating condition, the mean size of ultra fine particles is less than 130 nm, the conversion ratio is nearly 90 % and the plasma flow is very stable during the processing.

Acknowledgements

We would like to give our sincere thanks to senior technician Mr. Kazunari Katagiri in our laboratory, and also to Mr. Tsutomu Watanabe and Mr. Norio Ito in the institute workshop. This research was partially supported by a grant-in-aid for Scientific Research (B) from the Japan Society for Promotion of

Science (2003-2005) and a 21st Century COE Program Grant of the International COE of Flow Dynamics from the Ministry of Education, Culture, Sports, Science and Technology.

References

[1] T. Yoshida, T. Tani, H. Nishimura and K. Akashi, *J. Appl. Phys*. **54-2**, 640 (1983).
[2] J. H. Seo, Ph. D. Thesis, Seoul National University, Seoul, Korea, 2004.
[3] K. Kawajiri, T. Sato and H. Nishiyama, *Surf. Coat. Technol.* **171**, 134(2003).
[4] J. W. Mckelliget and N. El-kaddah, *Metallurgical Tras. B* **21B**, 589 (1990).
[5] S. W. Nam, H. Nishiyama and S. Kamiyama, *JSME Int. J. B* **39-1**, 134 (1996).
[6] M. Shigeta, Ph. D. Thesis, Tohoku University, Sendai, Japan, 2004.
[7] A. L. Linsebigler, G. Lu and J. T. Yates Jr. , *Chem. Rev.* **95**, 735 (1995).
[8] K. Kawajiri and H. Nishiyama, *Thin Solid Films* (2005), in press.
[9] P. Kong, T. T. Huang and E. Phender, *IEEE Trans. Plasma Sci.* **14-4**, 357 (1986).
[10] S. L. Girshick, *Plasma Source Sci. Technol.* **3** , 388 (1994).
[11] R. W. Siegel, *Mater. Sci. Eng.* **A168**, 189 (1993).
[12] C. G. Granqvist and R. A. Buhman, *J. Appl. Phys*. **47-5**, 2200 (1976).
[13] M. I. Boulos, *IEEE Trans. Plasma Sci.* **4-1**, 28 (1976).
[14] X. Chen and E. Pfender, *Plasma Chem. Plasma Process.* **3-3**, 351 (1983).
[15] X. Chen and E. Pfender, *Plasma Chem. Plasma Process.* **3-1**, 97 (1983).
[16] X. Chen and E. Pfender, *J. Eng. Gas Turbines and Power* **107**, 147 (1985).
[17] Z. Njah, J. Mostghimi and M. Boulos, *Int. J. Heat Mass Transfer* **36-16**, 3909 (1993).
[18] S. V. Joshi, Q. Liang, J. Y. Park and J. A. Batdorf, *Plasma Chem. Plasma Process.* **10-2**, 339 (1990).

Glow Characterization in Plasma Deposition Systems

Qingsong Yu, Chun Huang, YenFong Chan, Mary Gilliam, H.K. Yasuda

Department of Chemical Engineering, Center for Surface Science and Plasma Technology, University of Missouri-Columbia, Columbia, MO 65211, USA

Abstract

The nature of the glow formed in plasma polymerization systems is significant different from simple gas plasmas, in which the well-known *negative glow* is the dominant glow. Investigation to direct current (dc) glow discharges of a series of typical organosilicon and hydrocarbon monomers indicated that *cathode glow* constitutes the characteristic glow in plasma polymerization systems. Plasma diagnostic results obtained from these plasma deposition systems indicated that polymerizable species are mainly created in *cathode glow* region.

Keywords: plasma polymerization, DC glow discharge, trimethylsilane, hydrocarbons, cathode glow, dissociation glow, negative glow, optical emission spectroscopy

Introduction

Plasma deposition of organic gases or vapors in an electrically ignited glow discharge has found wide applications in both high-tech and traditional industries. However, the reaction mechanism in plasma deposition, e.g., how chemically reactive species are created and how these species influence the deposition characteristics and properties, has not been well-understood to date. Due to the difficulty in characterizing deposition plasmas, the ionization concept gained by the analysis of an inert gas discharge is generally applied to plasma polymerization processes. Our recent studies on plasma deposition in direct current (dc) glow discharges indicates that, however, the glow formation and glow characteristics in a glow discharge of organic gas, which deposits materials, are significantly different from that in an inert gas discharge [1-3]. In a dc discharge of an inert gas, the dominant glow, i.e., the well-known negative glow where ionization mainly occurs developed at a distinctive distance away from the cathode, whereas the cathode remained in the dark space [4-5]. In a strong contrast to this situation, in dc plasma deposition systems, the dominant or primary glow was the cathode glow, which formed on the cathode surface. In a dc glow discharge, the location of the plasma glow represents the electron energy level therein. Therefore, the discovery of the dominant cathode glow in dc deposition processes has extremely important implications in the understanding of electric breakdown and creation mechanisms of chemically reactive species in depositing plasmas, i.e. through electron-impact dissociation and/or ionization of organic molecules. In this study, the glow formation in DC glow discharges of a series of organic monomers was investigated using optical photography and optical emission spectroscopy (OES) and the results thus obtained are presented and discussed.

Experimental

A bell-jar type reactor was used in capturing the luminous gas phases. The bell-jar has the dimension of 46 cm in height and 44.5 cm in diameter. A cold rolled steel plate (10.2 cm by 15.2 cm by 0.08 cm) was used as the center electrode, which is the cathode in DC discharge. The two counter-electrodes consisting of a pair of cooled titanium electrodes (18.1 cm by 18.1 cm by 0.16 cm) equipped with magnetic field assembly (magnetron) were placed 10 cm apart. Eight pieces of permanent magnet bars were attached equidistantly on the backside of each anode with the south-pole pointing to the center of the iron plate. The magnetic field strength of each magnet ranged from 700 gauss to 800 gauss. The use of magnetron counter electrodes is not essential to this study. However, it is much easy to identify the negative glow by the use of magnetron anode, because the anode magnetron creates a funnel shaped negative glow and makes the boundary of the negative glow easier to be identified.

Results and discussions

1. Glow discharge of an organosilicon

Fig. 1 depicts the luminous gas phase in DC glow discharge of Ar and trimethysilane (TMS) with one cathode positioned in the middle of two magnet-enhanced anodes (i.e., anode magnetrons). It was noted that, in Ar discharge (Fig.1a), the center cathode was always surrounded by a dark space. At the same time, a well recognizable funnel-shaped negative glow exists in some distance away from the cathode on both sides, because two magnet-enhanced anodes are used against one center cathode plate. The funnel-shaped negative glow appears with anode magnetrons.

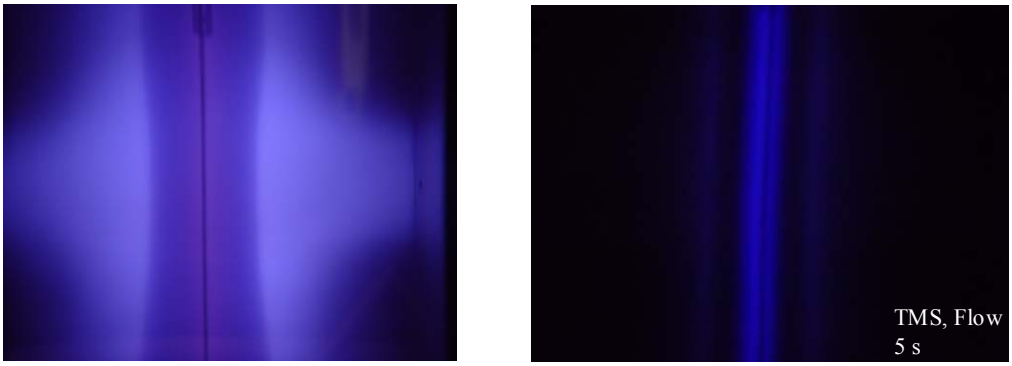

(a) Ar discharge (b) TMS discharge

Figure 1. Pictorial view of dc glow discharges of (a) argon and (b) trimethysilane (TMS): 1 sccm gas flow, 50 mtorr, 5 W dc power input.

In a strong contrast to Ar glow discharge, as shown in Fig. 1b, a *cathode glow* appeared on the cathode surface constitutes the primary glow in TMS glow discharge system. Under similar discharge conditions, the primary cathode glow in TMS discharge is weaker than the negative glow observed in Ar discharge. In TMS discharge, the cathode glow which literally adhered to the cathode surface evidently indicated that cathode glow is a low-energy glow because of its intimate position from the cathode. In other words, it is reasonable to consider that the primary cathode glow in TMS glow discharge is due to the dissociation of TMS molecules caused by slow or low-energy electron-impacts. It is also important to recognize that, in TMS DC glow discharge, a very feeble or secondary glow exists away from the cathode (approximately the same location where the negative glow was observed with Ar discharge).

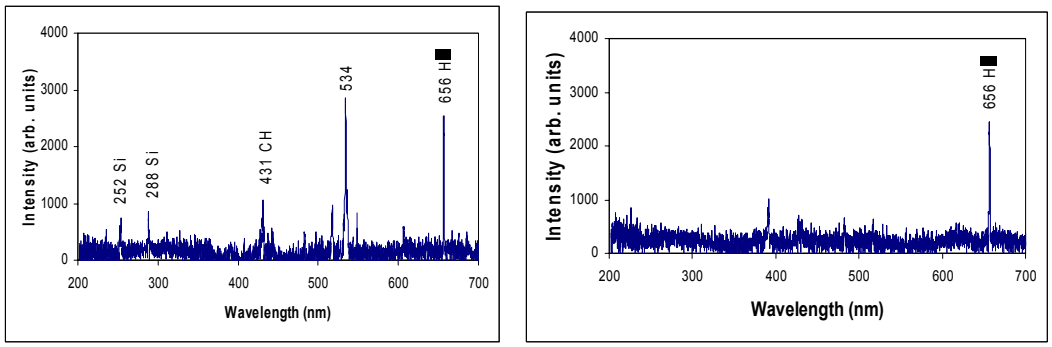

(a) OES of cathode glow (b) OES of negative glow

Figure 2. Optical emission spectra (OES) measured from (a) *cathode glow* and (b) *negative glow* in a DC glow discharge of trimethylsilane (TMS): flowing system, 1 sccm TMS, 50 mtorr, DC power 5W

The OES spectra measured from *cathode glow* and *negative glow* in TMS dc plasmas were shown in Fig. 2. From Fig. 2, it can be seen that the feature of optical emission in *cathode glow* is significantly different from that in negative glow. In the *cathode glow*, the reactive species such as CH free radicals and Si atoms that can contribute to plasma polymerization govern the photo-emission spectrum as shown in Fig. 2a. Although not identified at this time, the strong emission at ~ 534 nm appeared in OES spectrum of *cathode glow* has been

verified to be from a polymerizable species by monitoring its emission intensity change with discharge time in a closed TMS DC discharge system. In contrast, as seen from Fig. 2b, the Hα emission line from hydrogen atoms dominates the optical emission from negative glow in a TMS DC glow discharge.

2. Glow discharges of hydrocarbons

Consistent results were also obtained from plasma systems of a series of hydrocarbon monomers, including methane, ethane, n-butane, ethylene, and acetylene. The pictorial views of these hydrocarbon plasma polymerization systems are shown in Figure 3.

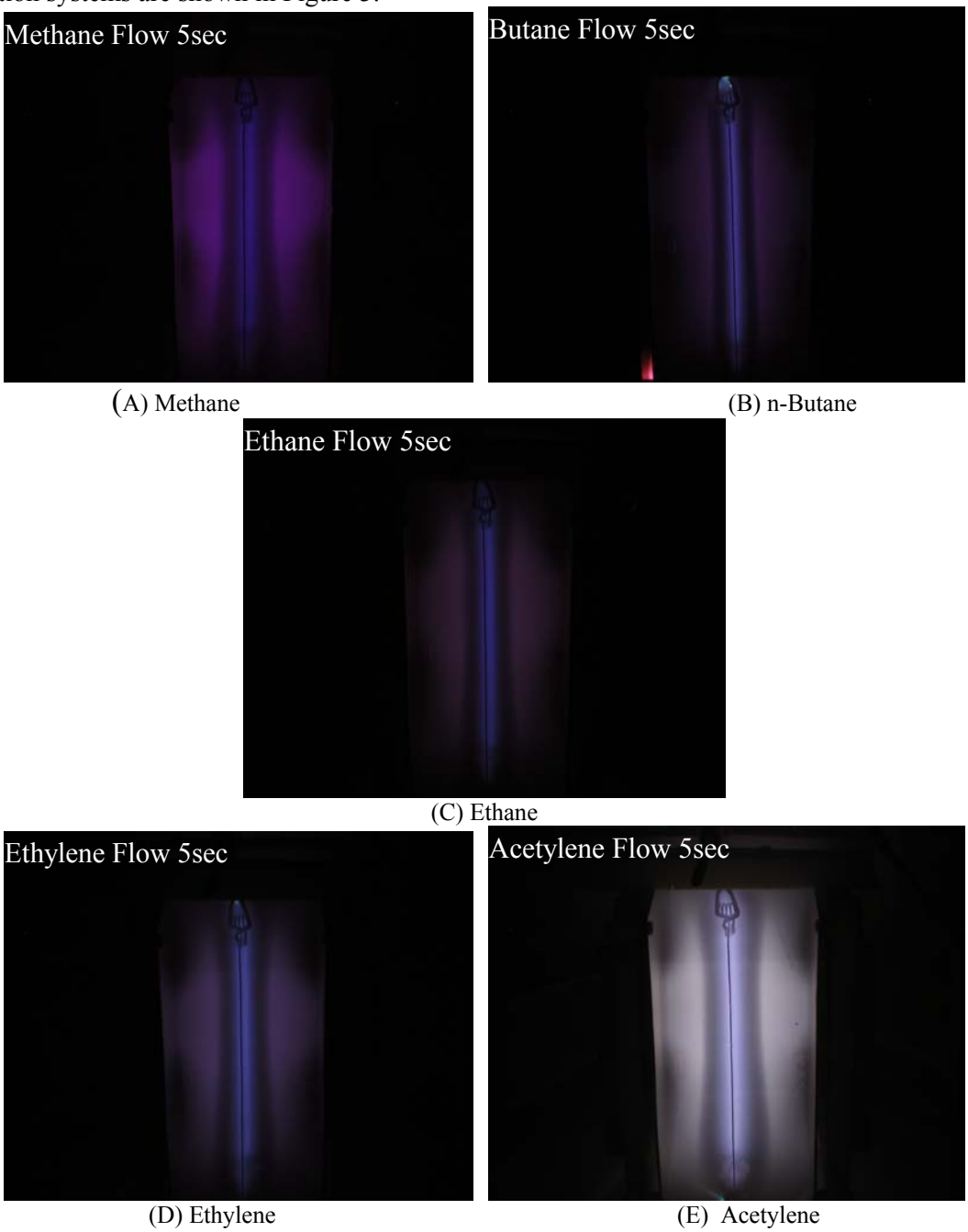

(A) Methane (B) n-Butane

(C) Ethane

(D) Ethylene (E) Acetylene

Figure 3. Pictorial view of DC glow discharges of (A) methane, (B) n-Butane, (C) Ethane, (D) Ethylene, and (E) Acetylene in a flow reactor system. Conditions are 1sccm hydrocarbon, 50 mtorr system pressure, 5 watt direct current power input.

It can be seen in Fig. 3, as a characteristic glow in plasma polymerization systems, the strong *cathode glow* was observed in DC glow discharges of the all the hydrocarbon monomers examined. The relative intensity of the both cathode glow and negative glow varies with the hydrocarbon monomer structures. While the *cathode glows* showed similar glow intensity, the secondary negative glow intensified with the increase in the H/C ratio of the monomers, CH_4 (A: H/C = 4) > C_2H_6 (C: H/C = 3) > C_4H_{10} (B: H/C = 2.5). In contrast, the glow intensity of both *cathode glow* and *negative glow* intensified while the chemical structure changes from saturated Ethane (C) to unsaturated Ethylene (D: double bond) and Acetylene (E: triple bond). Fig. 4 shows the OES spectra from both the *cathode glow* and *negative glow* regions of methane, ethane, and acetylene DC polymerization systems.

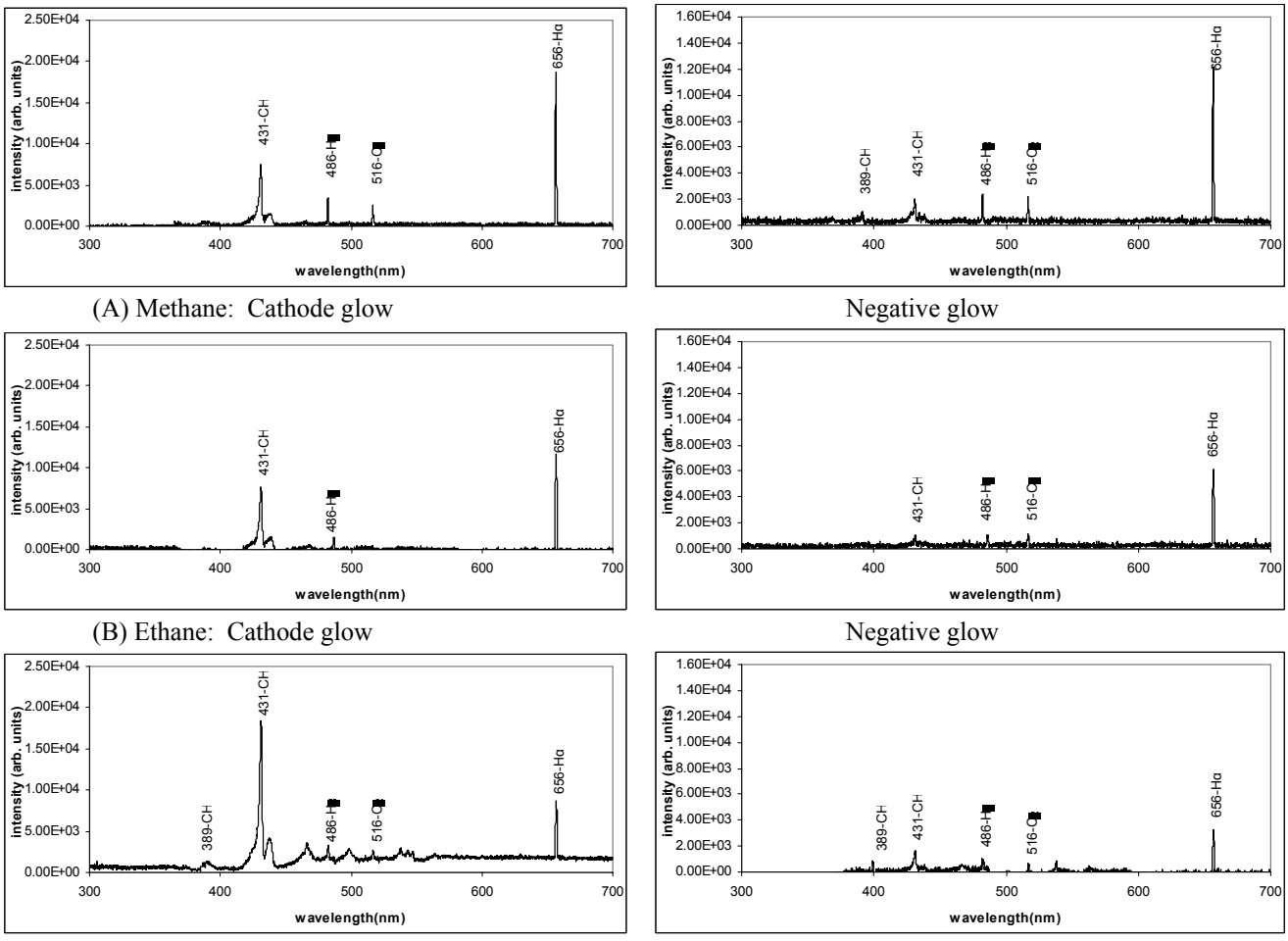

Figure 4. Optical emission spectra (OES) measured from *cathode glow* and *negative glow* regions in a DC glow discharge of (A) methane, (B) ethane, and (C) acetylene in a flowing reactor system with 1 sccm monomer, 50 mtorr, DC power 5W.

From the OES spectra shown in Fig. 4, the photo-emission of CH free radicals that can contribute to plasma polymerization as intermediate precursors mainly appeared in the *cathode glow* region of the plasma systems. In contrast, the main photo-emission from the *negative glow* region of the plasma systems is Hα species, which are non-polymerizable. It was also noticed that the bright *cathode glow* observed in acetylene glow discharge as shown in Fig. 3 gave rise to the strongest photo-emission of CH free radicals. These OES data is well consistent with the rapid deposition of acetylene monomer in a glow discharge under similar plasma conditions. Since the cathode glow is attached to cathode surface, the electron energy level in cathode *glow region* is much less that in the *negative glow* region. The low-energy electrons in the *cathode glow* are considered are mainly responsible for the dissociation of the monomer molecules and especially these unsaturated hydrocarbons such as ethylene

and acetylene. Therefore, a brighter *cathode glow* was observed in Fig. 3 and stronger photo-emission from CH species, an intermediate product of the dissociation reaction of the hydrocarbon molecules upon electron-impact, was detected by OES measurements from acetylene glow discharge shown in Fig. 4.

3. Glow discharges in a closed reactor system

Plasma polymerization was performed in a closed reactor system with an aim to investigate the glow dependence with chemical species in the system. Fig. 5 shows the glow characteristic change of Ethane DC glow discharge with discharge time. It was found that, in the initial plasma polymerization stage, the *cathode glow* constituted the dominant glow of the system. However, the cathode glow became weaker with the increase of the discharge time, i.e. plasma polymerization time. Eventually, the secondary *negative glow* became the primary glow of the system.

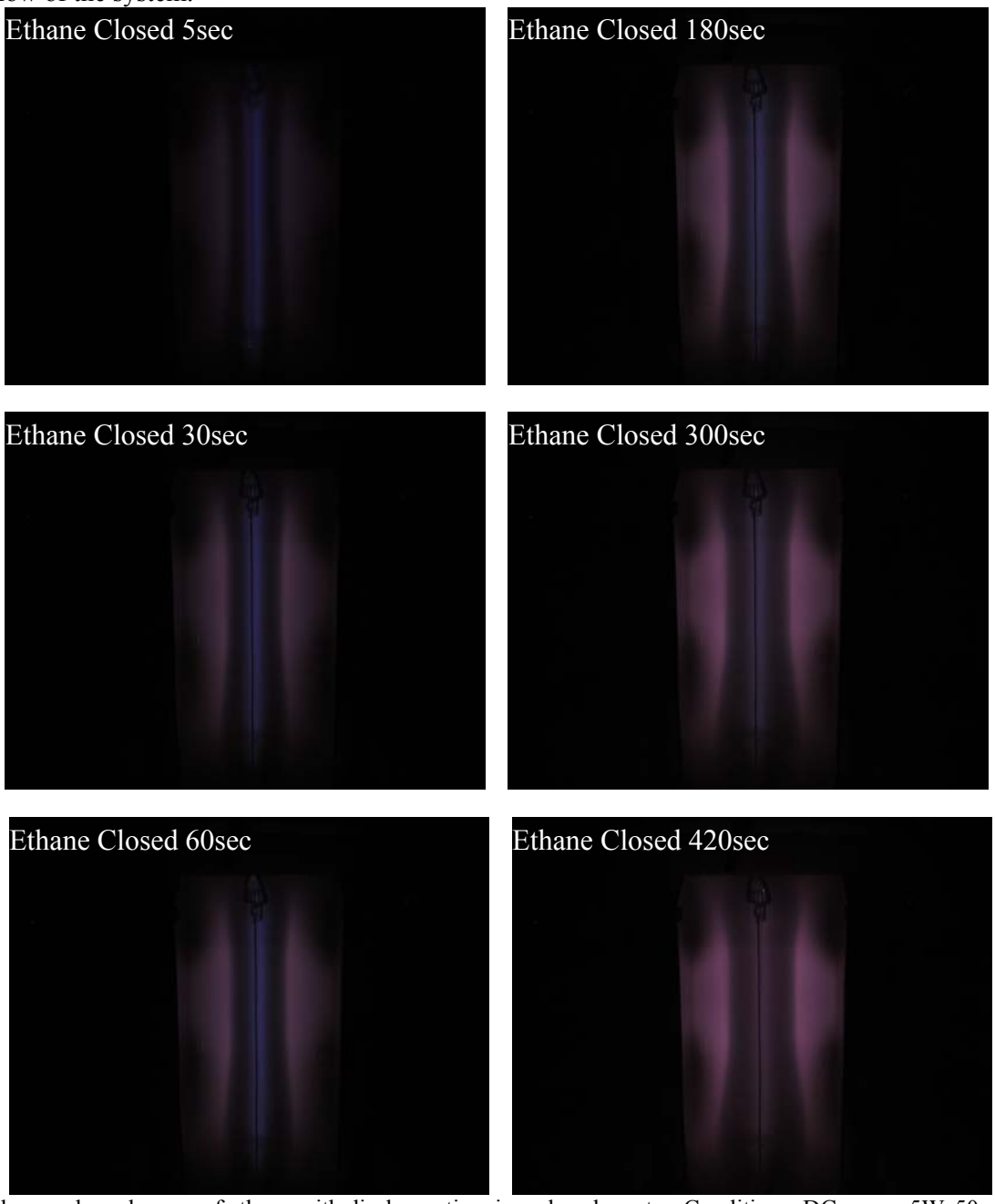

Figure 5. Plasma glow changes of ethane with discharge time in a closed reactor. Conditions: DC power 5W, 50 mtorr.

OES was used to monitor the emission intensity change of the major photo-emitting species in both glow regions of Ethane glow discharges in a closed reactor. Fig.6 shows the time dependence of emission intensity of CH and H species from both *cathode glow* and *negative glow*. It can be seen the CH species disappeared after a certain period of plasma polymerization due to material deposition to solid phase. In contrast, after the disappearance of CH species, the Hα emission reached a saturated level that is corresponding to the stronger *negative glow* as observed in Fig. 5. These results obtained in a closed plasma polymerization system further confirmed that the cathode glow is mainly responsible for the creation of polymerizable species, while the *negative glow* is related to non-polymerizable species.

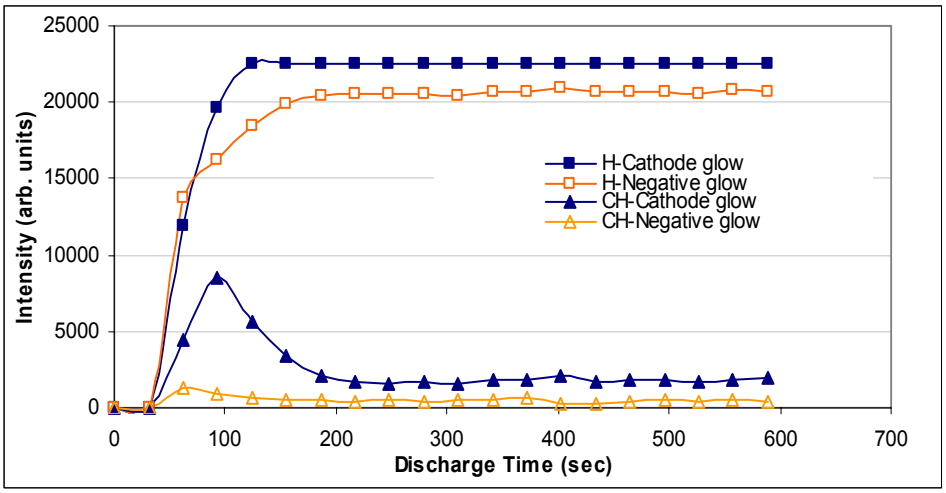

Figure 6. Time dependence of emission intensity of CH (431nm) & H_α species from *cathode glow* and *negative glow* regions in DC glow discharges of ethane in a closed reactor with 50mtorr system pressure and 5 watt DC power input.

Conclusions

The results obtained in this study clearly indicated that the glow formation in a plasma polymerization system is very different from that in a simple gas plasma system such as argon. The *cathode glow* in which low-energy electron impact dissociation occurs is the characteristic glow of a plasma polymerization or deposition system. In contrast, the negative glow formed in a position away from the cathode that contains high-energy electrons dominates in simple gas glow discharge systems. OES investigation on plasma polymerization systems of both organosilicon and hydrocarbon monomers indicated that the *cathode glow* is the plasma region where the main polymerizable species are formed. On the other hand, the negative glow is where the non-polymerizable species such as H atoms were observed. It can be concluded that, in a DC plasma polymerization system, the low-energy electron impact dissociation in the cathode glow mainly contributes to the creation of plasma polymerizable species and therefore control the plasma polymerization process.

Acknowledgement

This study was supported in part by the University of Missouri Research Board and the Faculty Startup Fund of College of Engineering, University of Missouri-Columbia.

References

[1] H.K. Yasuda and Q.S. Yu, J. Vac. Sci. Technol.; **A 22(3),** 472-476 (2004)
[2] H.K. Yasuda and Q.S. Yu, Plasma Chemistry and Plasma Processing; **24**, 325-351 (2004)
[3] Q.S. Yu, C. Huang, H.K. Yasuda, J. Polym. Sci.: Part A: Polym. Chem.; **42**, 1042-1052 (2004)
[4] B. Chapman, Glow Discharge Processes; Wiley: New York, pp. 77-133 (1980)
[5] G. Francis, "The Glow Discharge at Low Pressure" in Handbuch der Physik; Flügge, S., Ed.: Springer-Verlag: Berlin; **Vol. 22(2),** pp. 53-208 (1956)

Novel Plasma Sterilization Technique Using Volume Wave Plasma Excited by 2.45 GHz Microwaves

M. Nagatsu[1], F. Terashita[1], L Xu[1], H. Nonaka[1], K. Ninomiya[1], T. Nagata[2], Y. Koide[2], S. Nanko[3], and I. Kurawaki[4]

[1]*Faculty of Engineering, Shizuoka University, 3-5-1 Johoku, Hamamatsu 432-8561 Japan*
[2] *Hamamatsu University School of Medicine,1-20-1 Handayama, Hamamatsu 431-3192 Japan*
[3] *Nissin Inc., 10-7 Kamei-cho, Takarazuka 665-0047 Japan*
[4]*GMA, Co. Ltd., 3898-1, Asaba-cho, Iwata-D.C., 437-1101 Japan*

Abstract

In this study, we investigated the internal sterilization technique using microwave-excited volume-wave plasma. To produce the volume-wave plasma, we employed the planar cylindrical microwave launcher installed inside the vacuum chamber. The spores of population of 10^6 were irradiated with volume-wave plasma discharges in He and O_2 mixture gas. It is noted that when the spores were set inside of the plasma discharges, they were completely killed within 1 min discharge. It is also found from the SEM analysis that spores after oxygen plasma irradiation had changed significantly in length and width, due to the chemical etching process by the oxygen radicals. The present results demonstrated a successful internal sterilization with volume-wave plasma at a relatively low temperature less than 70 °C.

1. Introduction

Sterilization of medical instruments has been conventionally performed using a dry-heat or hot-steam technique for heat-resistant materials, or the ethylene-oxide gas for heat-sensitive materials. However, there are various issues in the present sterilization methods; for example, the former method is limited to use the sterilized materials, such as the metal or glass implements. As for the ethylene-oxide gas sterilization, the environmental problems due to its toxicity are recently concerned. Therefore, it is desired to develop a new type of sterilization technique, which makes it possible to sterilize the medical instruments safely and rapidly at low temperature.

Up to now, various low-temperature plasma sterilization techniques have been developed using low-pressure glow discharges[1], glow discharges at atmospheric pressure[2-4], downstream plasma produced by microwave excitation[5], moving atmospheric microwave plasma[6] and surface- wave plasma.[7-9]

The problem of the plasma sterilization is essentially on the treatment of the surface only. In order to sterilize inside the medical instruments wrapped with perforated plastic packing, it is required to produce the plasma inside

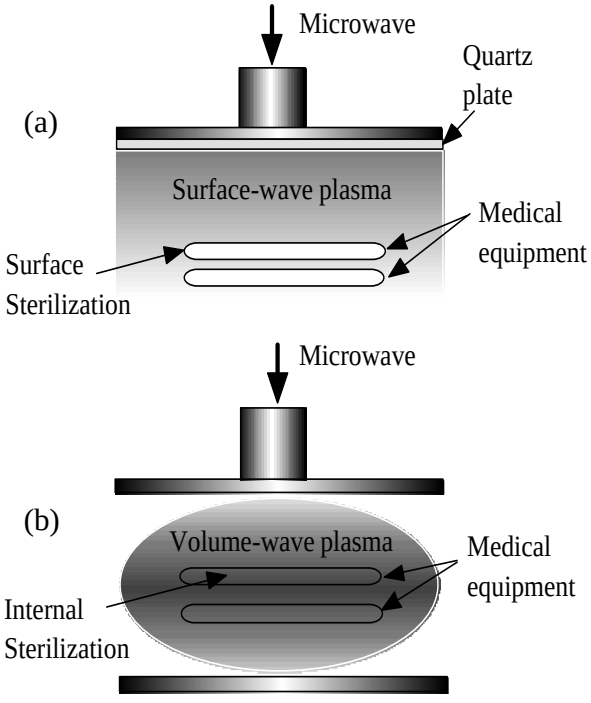

Fig. 1 Schematic drawings of (a)surface-wave plasma and (b)volume-wave plasma sterilization techniques.

the packing material. To overcome this problem, we propose here to use the volume wave plasma for plasma sterilization, as shown in Fig. 1.

2. Experimental setup

Schematic drawing of the experimental setup to produce the volume-wave plasma is shown in Fig. 2[10]. The inner diameter and the height of cylindrical vacuum chamber are 250 mm and 500 mm, respectively. The chamber is pumped down to order of mTorr by a rotary pump. Microwave launcher consisted of a coaxial waveguide and a cylindrical planar cavity, inside of which a thin dielectric plate was used. In this launcher system, the vacuum was sealed by an O-ring in a small area, so that the thickness of quartz plate was reduced significantly. A circular quartz plate having a diameter of 220 mm and a thickness of 8 mm was used inside the planar microwave launcher. A stainless steel punched plate with a hole-diameter from 8 mm was attached on the quartz plate as shown in Fig. 2. The narrow gap between the cylindrical side of quartz plate and the metal wall of microwave launcher was set to be 4 mm. The 2.45 GHz microwave guided by a rectangular waveguide was transferred to the microwave launcher via a coaxial waveguide.

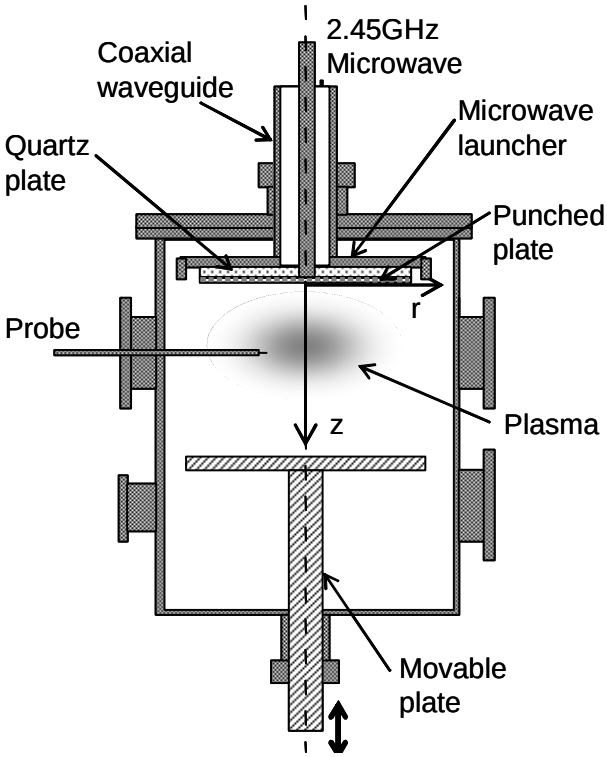

Fig. 2 Schematic drawing of the experimental setup of volume-wave plasma with a planar microwave launcher.

Output power of 2.45 GHz magnetron was variable from zero to 1.5 kW. Microwave through a number of apertures of punched plate penetrate into the chamber as evanescent wave. By adjusting the position of facing metal plate, VWP discharge can be produced between the launcher and metal plate, as shown in Fig. 3. As the biological indicators (B.I), we used *Bacillus subtilis* of a population of 10^4 to 10^8 and *Bacillus stearothermophilus* of a population of 1.5×10^6.[11]

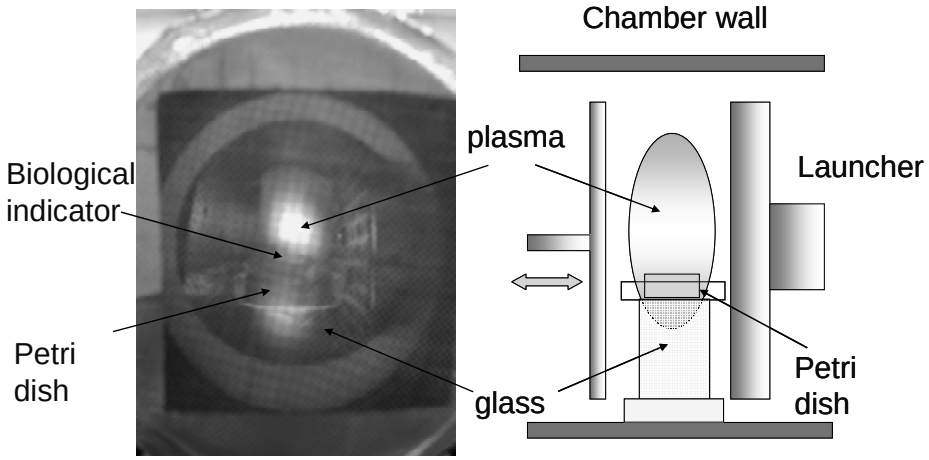

Fig. 3 Photograph of the He/O_2 plasma discharge taken from the side port window(left) and a schematic drawing of its cross-sectional view(right).

The spores were put on the Petri dish located just below the plasma ball, as shown in Fig. 3.

3. Results and discussion

First, we measured the electron density and temperature profiles of volume-wave plasma (VWP) using a double probe technique. Figure 4 shows the photograph of VWP and the geometrical relation between the plasma and the probe. Scanning the probe radially, we measured the density and temperature distributions, as shown in Fig. 5. Peak electron density was roughly 5~7x10^{10} cm^{-3} which is comparable to the cutoff density of 7.4x10^{10} cm^{-3} for 2.45 GHz microwave. The electron temperature in the center region was of 5~6 eV.

In the VWP sterilization measurements, we used two types of biological indicators. One type of B.I. is *B. Subtilis*, where the spores are painted inside the glassine strip having a size of 5 mm x 37 mm. A set of steri-chart having spore populations from 10^4 to 10^8 [11] was used in the volume wave plasma sterilization without taking them off wrapped glassine envelopes.

We varied the plasma irradiation period up to 10 min and simultaneously measured the stage temperature using thermo label sheets attached on the surface of Petri dish. After the plasma irradiation, the spores are incubated in culture tubes during several days at the incubation temperature of 35-40 °C for *B. subtilis*. It was found that B.I. having spores of 10^5 and 10^6 were sterilized for 10 min He/O_2 plasma discharge. The temperature of the Petri dish was roughly 70 °C or less from the measurement using a thermal label. Thermal damage of wrapping paper or strip was not seen at all.

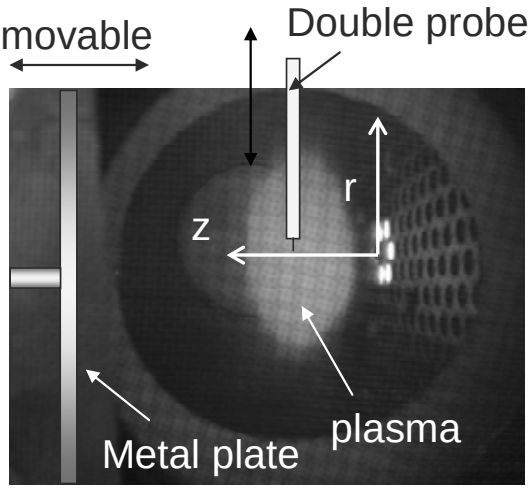

Fig. 4 Photograph of volume-wave plasma and schematic drawing of the double probe measurement.

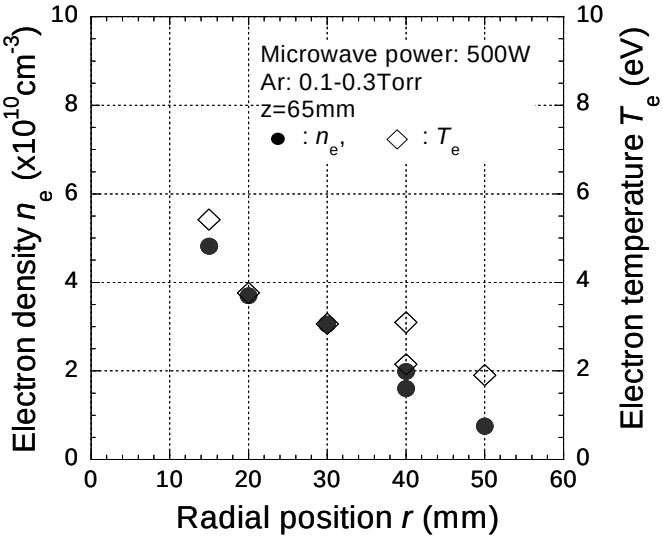

Fig. 5 Radial profiles of electron density and temperature in the volume-wave plasma.

To study the survival curves of the VWP sterilization, we used another B.Is, where the spores of population of 1.5~3x10^6 were painted on the small stainless steel disc. [11] Spores were directly irradiated by the plasma ball for different plasma discharge durations at different positions with respect to the plasma ball. Figure 6 shows the results of colony-counting measurements for different spore positions; that is, inside of the plasma, edge of the plasma and outside of the plasma, respectively. It is noted that the spores were killed within one minute in case of inside the plasma ball. The D value was evaluated from the slope of survival curve to be 20 sec or less. The temperature of the glass dish was heated to roughly 90°C or less, possibly due to the strong interaction with the CW plasma discharge. But it is believed that the spores are not killed by the heat effect under the present experimental conditions. At the edge region of the plasma ball, spores were reduced rapidly

in early plasma irradiation period, but the surviving spores decreased with a slightly slow rate. To confirm the sterilization, it will need about 20 min assuming a linear decay. Here temperature was roughly 70 °C or less. Away from the plasma ball, the sterilizing effect was weakened significantly. In the case of outside the plasma region, it will take longer plasma treatment. The D-value was estimated as roughly 4 min.

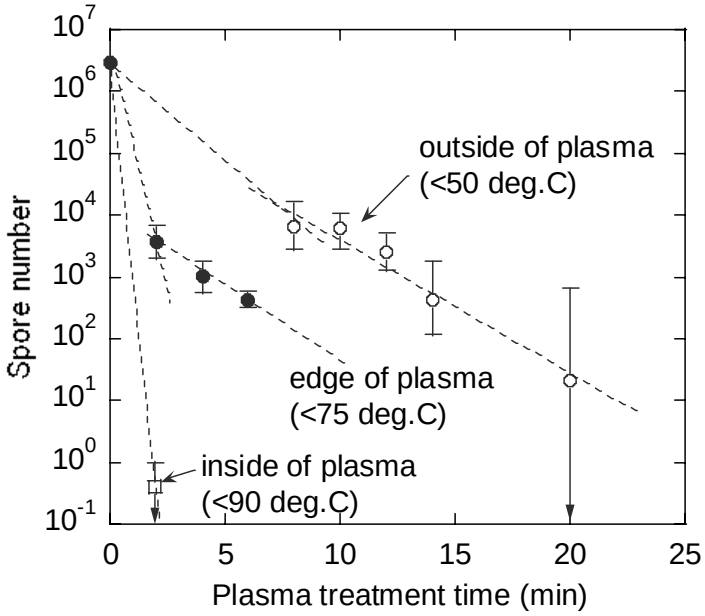

Fig. 6 Survival curves of spores irradiated with the VWP at different position; inside, edge and outside of the plasma ball.

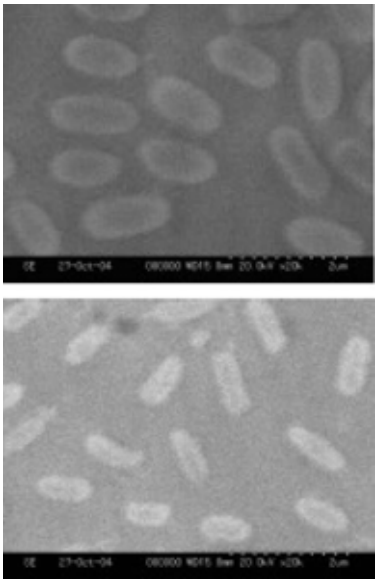

Fig. 7 SEM images of the spores irradiated by the oxygen plasmas for 2 min (top, not sterilized) and ones for 8min.(bottom, sterilized).

The spores irradiated by the volume wave plasma were studied using the Scanning electron microscope(SEM). Figure 7 shows the SEM images of spores treated for 2 min and 8 min plasma discharges. In the former case, the spores were not killed, so that the spores had almost the same shapes as those of original ones. In the latter case, however, the spores were sterilized and their sizes were significantly reduced. These results were very similar to the previous experimental results of surface wave plasma sterilization with pure oxygen plasma discharge.[8, 9]

4. Conclusion

In this study, we investigated the internal sterilization technique using microwave-excited volume wave plasma for application to the sterilization of the wrapped medical instruments. The volume-wave plasma was produced using the internally installed microwave launcher. The density of the plasma ball was measured with the double probe and we found that the electron density was comparable or lower than cutoff density. The spores of population of 10^4 to 10^8 were irradiated for different durations by the volume-wave plasma discharges in He and O_2 mixture gas. We confirmed that the spores of a population of 10^6 were sterilized with 10 min VWP treatment even though the BI strip was packed with the glassine envelope. Especially, it is noted that when the spores were irradiated directly with plasma discharge, they were killed within 1 min of plasma discharge. It is also found from the SEM analysis that spores after oxygen plasma irradiation had changed significantly in length and width, due to the chemical etching process by the oxygen radicals. The present results showed the successful sterilization with volume-wave plasma at a relatively low temperature less than 70 °C.

Acknowledgments

This work has been partly supported by Grant-in-Aid for Scientific Research from Japan Society for the Promotion of Science(JSPS), regional new consortium projects from Ministry of Economy, Trade and Industry(METI) and Grant from the Regional Science Promotion(RSP) program of the Shizuoka Organization for the Creation of Industries. The authors would like to acknowledge Nissin Inc. for supporting the microwave oscillator systems.

References

[1] I. A. Soloshenko, V.V. Tsiolko, V. A. Khomich, et al: Plasma Phys. Report, **26** 792 (2000).
[2] T. C. Montie, K. Kelly-Wintenberg, J. R. Roth: IEEE Trans. Plasma Sci., **28** 41 (2000).
[3] M. Laroussi, I. Alexeff, W. L. Kang, IEEE Trans. Plasma Sci., **28** 184(2000).
[4] V.Yu. Bazhenov, et al,: *Proc. 15th Int. Symp. Plasma Chemistry*, Orleans, France Vol. II, 3005 (2001).
[5] M. Moisan, J. Barbeau, S. Moreau, J. Pelletier, et al, Int. J. Pharmaceutics **226** 1 (2001).
[6] J. Ehlbeck, A. Ohl, M. Maas, U. Krohmann, et al, Surface Coatings Technol., **174-175** 493(2003).
[7] S. Lerouge, M. R. Wertheimer, R. Marchand, et al. J. Biomed. Mater. Res., **51** 128 (2000).
[8] M. Nagatsu, F. Terashita, Y. Koide, Jpn. J. Appl. Phys., **42** L856 (2003).
[9] M. Nagatsu, F. Terashita, L. Xu, et al, to be published in Appl. Phys. Lett. (2005).
[10]A. Ogino, K. Naito, F. Terashita, S. Nanko and M. Nagatsu, Jpn. J. Appl. Phys. **44** L352 (2005).
[11] Instruction manual of Raven Biological Laboratories,Inc. ATCC #12980.

Production of Large-Area Processing Plasma Using Novel Microwave Launchers

M. Nagatsu[1], K. Naito[1], A. Ogino[1] and S. Nanko[2]

[1]*Faculty of Engineering, Shizuoka University, 3-5-1 Johoku, Hamamatsu 432-8561, Japan*
[2]*Nissin Inc. 10-7 Kamei-cho, Takarazuka 665-0047, Japan*

Abstract

We developed a novel type of planar cylindrical microwave launcher installed inside the vacuum chamber for the production of large-area processing plasma. Microwave launcher consisted of a coaxial waveguide and a cylindrical planar cavity, inside of which a large-area thin quartz plate was inserted. We tested two types of microwave launchers, one was a closed cylindrical cavity structure and the other was a leaky open cavity structure. With a 1.5 kW microwave source, we have demonstrated the production of large-area, surface-wave plasma (SWP) using Ar gas. With the microwave launcher of a leaky open cavity structure, SWP with a spatial uniformity of ±3.5 % over 160 mm in radius was achieved at pressure of 20~30 Pa. Numerical analyses using the electromagnetic wave simulator, MAFIA, have been also carried out to study the electric field distribution radiated from the microwave launcher and to explain the experimental results.

1. Introduction

For large-size ULSI manufacturing or meter-size liquid crystal display panel, it has been required to develop the large-area uniform plasma sources. In plasma CVD, such as deposition of amorphous silicon, carbon nanotube or crystalline diamond films, the large-area plasma source has been also needed. However, it is not easy to achieve the plasma uniformity over the large cross section. Among the various plasma devices, surface wave plasma (SWP) is one of promising plasma sources satisfying the requirements for a compact, large-area plasma processing tool[1-6]. So far, we have been developing the large-area SWP excited by 2.45 GHz microwaves[7-9] or 915 MHz UHF waves[10] using a slot antenna excitation. In the SWP, a density jump has been observed when the incident power or operating gas pressure changed. This originated from the surface-wave mode, determined from the boundary conditions between the dielectric window and plasma, in addition to the chamber geometry and incident wave frequency [11]. Thus, by increasing the incident power or gas pressure, the plasma density satisfying a certain surface-wave mode was selectively allowed. From the practical aspects, such a discontinuous behavior of the plasma density is undesirable for the actual material processing. Another problem in enlarging the plasma device is the dielectric window for vacuum sealing. For enlargement of the chamber cross section, it is needed to use a thick, large dielectric plate to withstand a huge pressure force. Therefore, reduction of thickness of dielectric window is also another remaining issue.

In order to overcome these problems, we have developed a new type of microwave launcher installed inside the vacuum chamber [12]. Microwave launcher consisted of a coaxial waveguide and a cylindrical planar cavity, inside of which a thin dielectric plate with 500 mm diameter and 10 mm thickness was inserted. Huge pressure force can be held by a thin quartz plate in the proposed internally mounted launcher. In the proposed launcher, furthermore, resonant cavity mode was determined by the cavity geometry independently of plasma density. Therefore, it is expected that mode jump was avoidable in the present system. Preliminary experiments have been carried out to demonstrate the plasma production using a large-area

plasma chamber with a diameter of 600mm and a height of 350mm. To understand the experimental results, we also performed numerical analysis of electromagnetic wave fields using the MAFIA field simulator.

2. Experimental Set-up

Schematic drawing of the experimental setup with a microwave launcher is shown in Fig. 1[12]. The 2.45 GHz microwave guided by a rectangular waveguide was transferred to the microwave launcher via a coaxial waveguide. Microwave power of 2.45 GHz magnetron is variable from zero to 1.5 kW. The vacuum chamber was pumped down to order of mTorr by a rotary pump. For the measurements of plasma parameters, we used a Langmuir probe with a 0.7 mm-diameter platinum wire tip. In Fig. 2, we show a schematic drawing of the assembled microwave launchers. A circular quartz disc having a diameter of 500 mm and a thickness of 10 mm was used inside the planar microwave launcher. Two types of cavity structures were used. In TYPE I launcher, stainless steel punched plate with a hole-diameter from 4 mm to 10 mm was attached over the quartz plate. Microwave can penetrate through small holes as evanescent waves to produce the plasma. In TYPE II launcher, a half-size metal plate was attached in the center of the quartz surface to form a leaky open cavity.

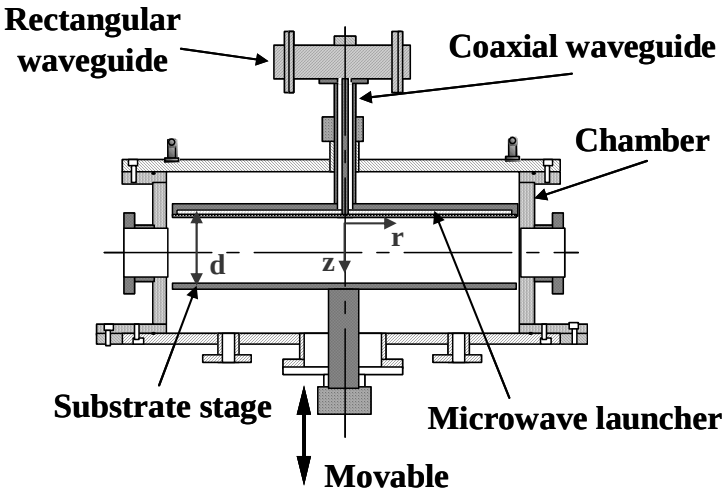

Fig.1 Schematic drawing of the experimental setup with a planar microwave launcher.

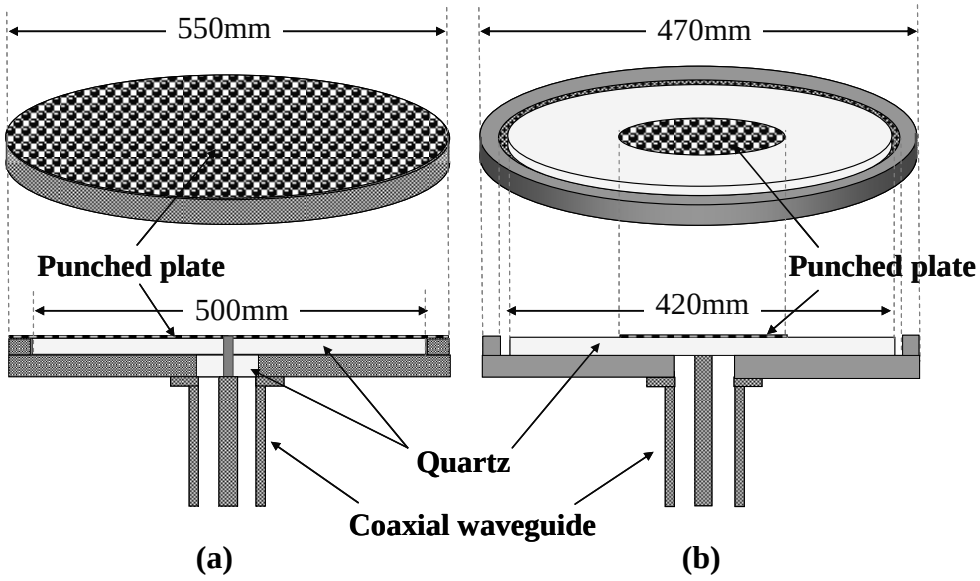

Fig. 2 Structures of microwave launchers of (a) TYPE I and (b) TYPEII, where in TYPE I, a punched plate having a hole size of 4-10mm was attached to the front surface and inTYPE II, a metal plate was partly attached in the center of the quartz surface.

3. Experimental results and discussion

We tested the plasma production using two types of internally mounted microwave launchers, shown in Fig. 2. Figure 3 shows pictures of Ar plasma discharges in case of TYPE I launcher, where microwave power was 500 W and 1.5 kW at pressure of 74 mTorr. These pictures were taken from the small side-port, so that they showed only a part of plasma discharge. As shown in Fig. 3, plasma discharge spreads radially as the incident power increases. When the input power was increased to 1.5kW, plasma discharge was gradually spread over the whole area of the launcher without any density jump. Spatial distributions of ion saturation currents were measured by scanning the

Langmuir probe horizontally at the axial position of z=4 cm far from the launcher surface. Here, microwave power was 1 kW at pressure of 74 mTorr. It is shown that density profile is peaked at the central region. Electron density at the center corresponds to roughly $1\sim2\times10^{11}\,cm^{-3}$. Plasma density rapidly decreased with the radial position. As it will be described later, density profile is closely related with the spatial distribution of electric field penetrating through the small holes of punched metal plate. Hence, we also tested another structure of microwave launcher, TYPE II launcher, in which the circular stainless steel plate with a diameter of 200 mm was used to hold the quartz plate in place of punched plate, as shown in Fig. 2(b). Picture taken from the side-port was shown in Fig. 5. With this type of launcher, we observed more uniform density profile over a diameter of 400 mm, as shown in Fig. 6, which was measured at z=11cm from the launcher. Electron density corresponds to roughly $5\times10^{9}\sim10^{10}\,cm^{-3}$, which is fairly low compared with the results in TYPE I launcher, because a strongly hollow type of profile near the launcher was diffused out and smeared out in the down stream region. When

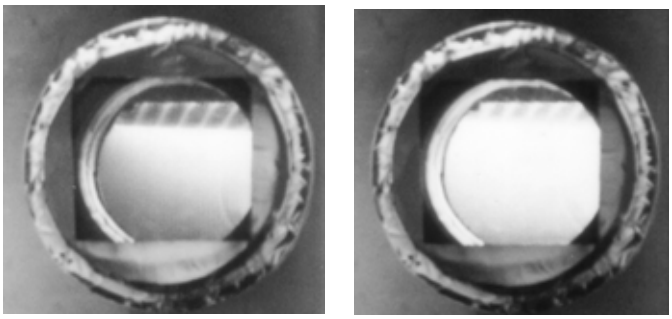

Fig. 3 Pictures of Ar plasma discharges in case of TYPE I launcher where microwave power was (a)500 W and (b)1.5 kW at pressure of 74 mTorr.

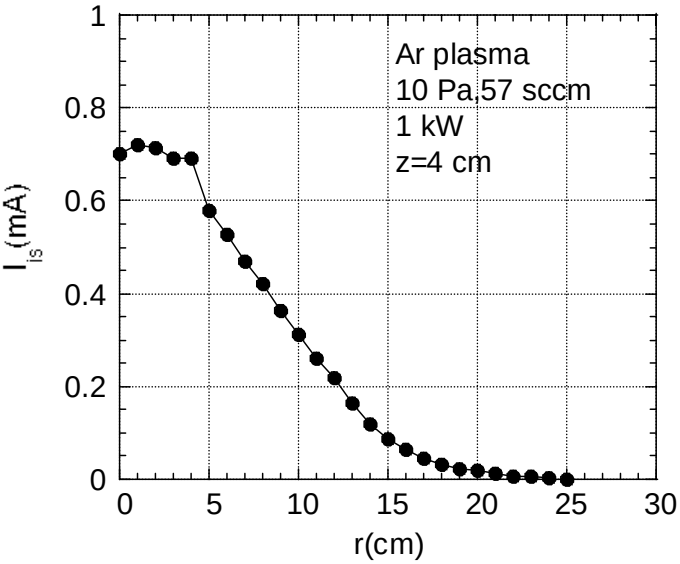

Fig. 4 Spatial distribution of Ion saturation currents in case of TYPE I launcher where microwave power was 1 kW at Ar gas pressure of 74 mTorr.

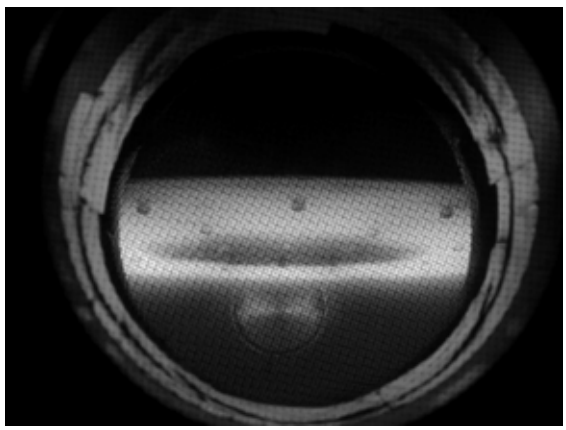

Fig. 5 Pictures of Ar plasma discharges in case of TYPE-II launcher where microwave power was 1kW at pressure of 190 mTorr.

increasing the input power up to 1.5 kW, density smoothly changed without any density jump.

Figure 6 shows the spatial distributions of ion saturation currents measured by the Langmuir probe at axial position of z=11 cm far from the launcher surface. Here, microwave power was varied from 100 W to 1.3 kW at Ar gas pressure of 140 mTorr. As shown in Fig. 6(a), uniform density profiles over a diameter of 300 mm were obtained for the input power rage from 500W to 1 kW. Here, the electron density was estimated to be roughly ~10^{10} cm^{-3}. When the incident power was less than 500 W, the ring shape plasma was produced surrounding the metal punched plate. With increasing the power, the plasma was broadened over the microwave launcher. Figure 6(b) show the ion saturation current versus the incident power at different radial positions. It is seen that the density linearly increased without any density jump as the incident power.

To investigate the field distribution launched from the microwave launcher, we performed the numerical simulation using the MAFIA. Figure 7 shows results of field analysis of the spatial distribution of electric filed intensity in the cases of TYPE I and TYPE II launchers. In case of TYPE I, the microwave field is fully spread toward the edge of the launcher and forms a concentric resonant field pattern of TM_{08} mode. Microwave can penetrate into the vacuum chamber through a number of small holes of the punched plate, as evanescent waves. Figure 7(a) shows one example of spatial distribution of field intensity radiated from the TYPE I launcher. It is seen that the field strength is strong in the central region of the launcher. This is consistent with the plasma density distribution shown in Fig. 4, where the plasma density will be peaked at the center. On the contrary, Fig. 7(b) shows that the electric field propagates through the quartz plate in the central part and uniformly radiate toward the vacuum chamber. It suggests that plasma will be produced just below bare quartz

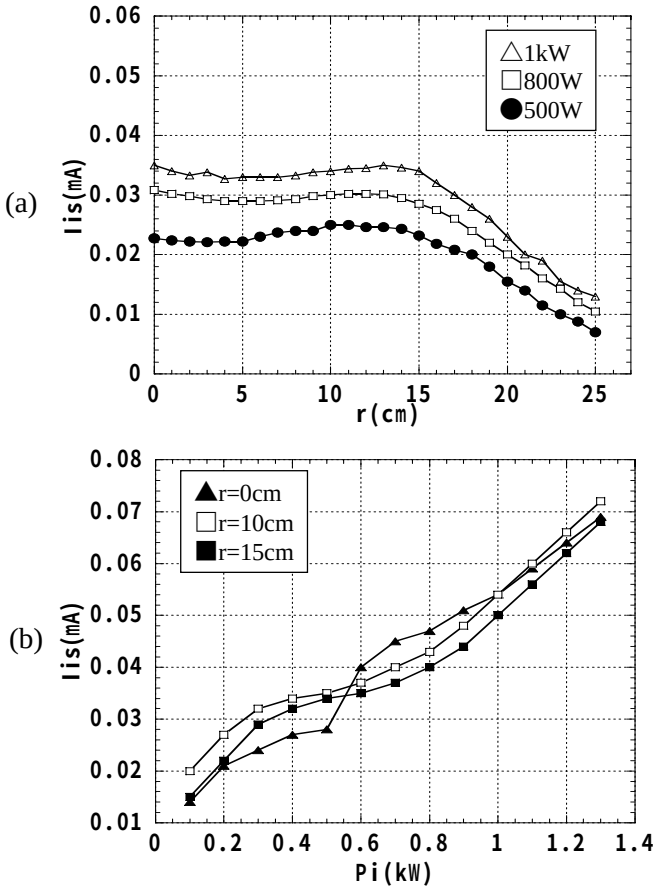

Fig. 6 (a) Radial profiles of ion saturation currents and (b) relation between the ion saturation currents and incident power in Ar plasmas.

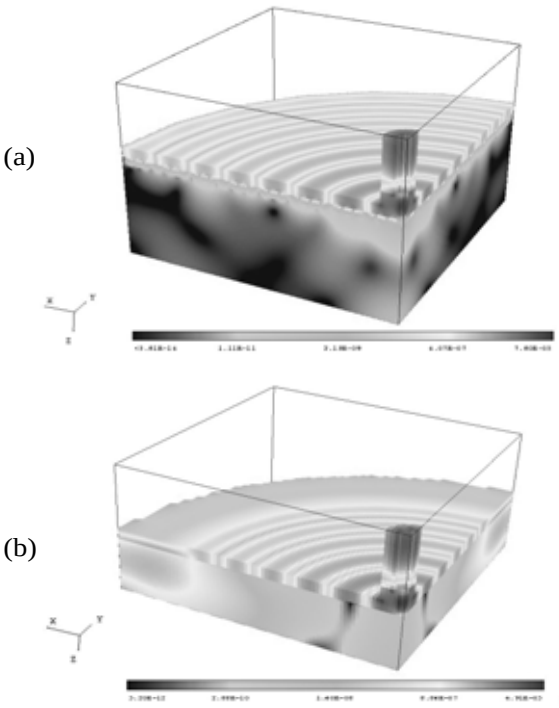

Fig. 7 Field intensity distributions of electric filed intensity in cases of (a) TYPE-I and (b) TYPE-II launchers.

surface. Actually, the ring shape plasma can be produced along the quartz surface, as shown in Fig. 5. Near the launcher surface, plasma had a strongly hollow type distribution. However, due to the particle diffusion, plasma became more uniform in the downward region, as shown in Fig. 6.

Lastly, it is noted that wave field penetrating through a number of small holes is of evanescent wave. From the MAFIA simulation, we found that the decay length of evanescent wave is typically 8-10mm in the free space. Plasma will be produced by the evanescent waves penetrating through the small holes, depending on the wave field strength. Thus, to obtain more uniform density profile, it will be necessary to design the punched plate with spatially controlled hole distributions.

4. Conclusion

In this study, we demonstrated novel type of planar cylindrical microwave launchers installed inside the vacuum chamber for production of large-area processing plasma. Two types microwave launchers with a diameter of 550 mm, closed and open cavity structures were tested to compare plasma production. A large-area thin quartz plate having a thickness of 10~15 mm was used for vacuum sealing in the planar cylindrical launcher. Field analysis using the electromagnetic field simulator has been carried out to study the electric field distribution radiated from the launcher and to explain the experimental results. We demonstrated that the microwave plasma having a diameter of roughly 300 mm was successfully produced using TYPE II launcher at Ar gas pressure of 0.5~1 Torr and an input power of 500-1500W.

Acknowledgements

This work has been supported by Grants-in-Aid for Scientific Research of Japan Society for the Promotion of Science(JSPS) and partly by the regional new consortium projects of Ministry of Economy, Trade and Industry (METI). It has been performed under the 21st Century COE Program “Research and Education Center of Nanovision Science” by JSPS. The authors would like to acknowledge Nissin Inc. for supporting the microwave oscillator system in the present work.

References

[1] K. Komachi and S. Kobayashi, J. Microwave Power Electromagn. Energy, 25 (1990) 236.
[2] G. Sauve, M. Moisan and Z. Zakrzewski, J. Microwave Power Electromagn. Energy, 28 (1993) 123.
[3] F. Werner, D. Korzec and J. Engemann, Plasma Sources Sci, Technol. 3 (1994) 473.
[4] E. Bluem, S. Bechu, C. Boisse-Laporte, P. Leprince, et al., J. Phys. D: Appl. Phys. 28 (1995) 1529.
[5] M. Nagatsu, G. Xu, M. Yamage, M. Kanoh and H. Sugai, Jpn. J. Appl. Phys., 35, (1996) L341.
[6] I. Odrobina, J. Kudela and M Kando, Plasma Sources Sci, Technol. 7 (1998)238.
[7] M. Nagatsu, G. Xu, I. Ghanashev, M. Kanoh and H. Sugai, Plasma Sources Sci. Technol. 6 (1997) 427.
[8] M. Nagatsu, I. Ghanashev and H. Sugai, Plasma Sources Sci. Technol. 7 (1998) 230.
[9] H. Sugai, I. Ghanashev and M. Nagatsu, Plasma Sources Sci. Technol. 7 (1998) 192.
[10] M. Nagatsu, A. Ito, N. Toyoda and H. Sugai, Jpn. J. Appl. Phys., 38, (1999) L679.
[11] I. Ghanashev, M. Nagatsu and H. Sugai, Jpn. J. Appl. Phys., 36, (1997) 337.
[12] M. Nagatsu, Proc. of 5th Int. Workshop on Microwave Discharge and Application, edited by A. Ohl, Greifswald Germany (2003) pp.222-230.
[13] J. D. Jackson, Classical Electrodynamics (New York; Wiley) Chap.8, p235.

Low Temperature Sterilization Using CW and Pulsed Surface-wave Plasmas

L. Xu[1], F. Terashita[1], H. Nonaka[1], K. Kondo[1], T. Nagata[2], Y. Koide[2], S. Nanko[3], I. Kurawaki[4] and M. Nagatsu[1]

[1]*Shizuoka University, 3-5-1 Johoku, Hamamatsu 432-8561, Japan*
[2]*Hamamatsu Univ. School of Medicine, 1-20-1 Handa-yama, Hamamatsu 431-3192, Japan*
[3]*Nissin Inc., 10-7 Kamei-cho, 665-0047 Takarazuka, Japan*
[4]*GMA, Co. Ltd., 3898-1, Asaba-cho, Iwata-D.C., 437-1101, Japan*

Abstract

Low-temperature plasma sterilization has been experimentally demonstrated using surface-wave plasma excited by a 2.45 GHz microwave. We used *Geobacillus stearothermophilus* spores with a population of 10^6 as biological indicators(BIs), and irradiated them with oxygen plasma discharges generated with CW microwave power of 750 W or pulse-modulated microwave instantaneous power of 1.5 kW. All the BI samples were sterilized by irradiating them for 150 sec total microwave on time or longer.

Keywords: surface-wave plasma, oxygen plasma, plasma sterilization, pulse-modulated SWP

1. Introduction

Conventional methods used in the sterilization of medical instruments have been mainly performed using dry heat or hot steam autoclave for heat resistant instruments, and ethylene oxide (EtO) gas for heat sensitive instruments. The disadvantage of the dry heat or hot steam sterilization is that they can only be applied to instruments that can withstand the high temperatures. The disadvantages of EtO gas sterilization are that EtO is toxic, carcinogenic, inflammable and the threat to the environment of chlorofluorocarbons (CFCs). As well, it takes one or more weeks for the EtO levels to return to safe levels, which is much longer than the time required to sterilize the equipment. Another type of sterilization method, which combines hydrogen peroxide gas with an RF discharge plasma, is commercially available.[1] Currently, this equipment is assumed to effectively sterilize due to the high concentration of hydrogen peroxide rather than to the plasma component.

At present, various low-temperature plasma sterilization techniques have been developed, such as low-pressure glow discharge [2], glow discharges at atmospheric pressure [3,4], downstream plasma produced by microwave excitation [5,6], moving atmospheric microwave plasmas [7], and surface-wave plasmas [8-10]. The plasma sterilization method has certain advantages over conventional methods, including a low sterilization temperature (often less than 70°C) and a short sterilization period of several minutes to 1 hour.

Previously, we reported that a 6-order reduction in spores could be achieved after only a 3-minute irradiation with low-pressure oxygen surface-wave plasma.[9] In this paper, we investigated the effect of low-temperature sterilization using continuous microwave (CW) and pulse-modulated surface-wave plasmas (SWPs). The effect of nitrogen gas addition on the sterilization was studied in the oxygen plasma.

2. Experimental Setup

A schematic drawing of the SWP device is shown in Fig. 1. The 2.45 GHz microwave guided by a rectangular waveguide was fed into the stainless steel chamber (diameter of 40 cm and height of 40 cm) filled with discharge gas, through slot antennas cut in the broad face of each waveguide.[11] The launched

microwave power can be variable from zero up to 3 kW. We can operate pulse-modulated plasma discharges using the pulsed microwave system with a modulation frequency from DC to 80 kHz. The vacuum chamber was pumped down to the order of 10^{-5} Torr with a turbo-molecular pump. For the experiments on plasma sterilization, we utilized the O_2 discharges at pressure of about 30~70 mTorr and 120~130 mTorr with O_2 gas flow rate of 200 sccm; we also utilized N_2 and N_2-O_2 discharges at pressure of about 60~90 mTorr with total gas flow rate of 100 sccm. As for the biological indicators (BIs), we used a population of $1.5x10^6$ and $3.0x10^6$ *Geobacillus stearothermophilus* spores (ATCC No.12980) painted on a small stainless steel disc.[12] These BI samples were placed in Petri dishes set onto substrate stage with a diameter of 20 cm about 15~23 cm below the quartz vacuum window. During plasma irradiation, the stage temperature was measured using thermo-label sheets attached to the Petri dish under a piece of thin glass. The piece of thin glass was used to avoid any direct interaction between plasma and thermo-label sheet.

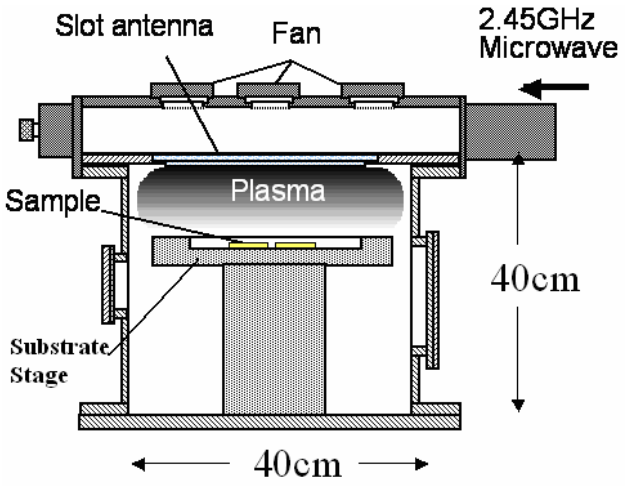

Fig. 1 Cross-sectional view of the surface-wave plasma device with a diameter of 40 cm.

After plasma irradiation, the spores were incubated in culture tubes with culture solution for 7 days at an incubation temperature of 55~60 °C as is standard for *Geobacillus stearothermophilus*. After the incubation process in the culture tubes, we determined whether the spores were perfectly sterilized or not. The color of the culture solution changed from purple to yellow, if the spores were still viable. Since we use the *Geobacillus stearothermophilus* with a population of $1.5x10^6$ and $3.0x10^6$, we assume that successful sterilization is at least a 6-order reduction in viable spore population from its original value.[12]

3. Experimental Results and discussion

First, we showed the experimental results of the oxygen plasma sterilization of $1.5x10^6$ *Geobacillus stearothermophilus* spores while substrate stage was about 15 cm below the quartz window, discharge pressure was at about 30~70 mTorr, O_2 gas flow rate was 200 sccm.

We utilized oxygen plasma excited by 500 W, 750 W, 1000 W, 1500 W and 2000 W CW power. Two BI samples for each plasma irradiation period were simultaneously put on the Petri dish on the stage. One sample was used for the incubation test and the other was used for the colony counting method. The plasma irradiation period was varied from 30 sec by 10-second steps, while CW power was kept at 1000 W and 1500 W. The Petri dish temperature increased from 20°C at room temperature to 60°C after 130 s plasma discharge excited by 1 kW CW power or 50 s plasma discharge excited by 1.5 kW CW power.

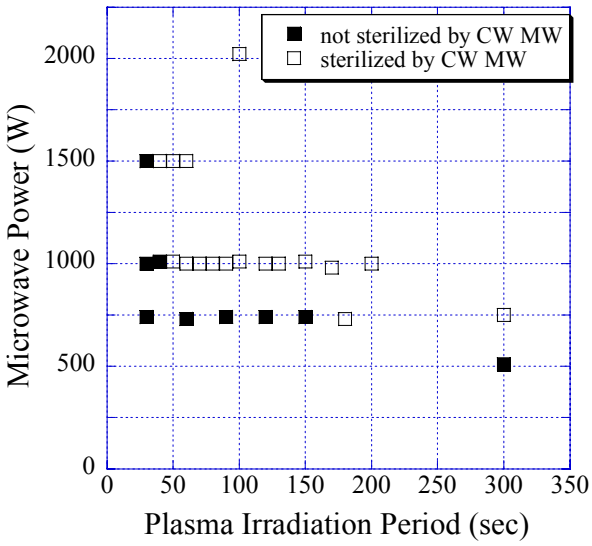

Fig. 2 Experimental results of sterilization between CW microwave power and plasma irradiation period.

The sterilization effect could be confirmed for

samples irradiated for 50 s or longer while CW power was 1 kW and samples irradiated for 40 s or longer while CW power was 1.5 kW. We also tested other parameter conditions using CW plasma as shown in Fig. 2. We draw the conclusions that BI can be sterilized by CW oxygen plasma under conditions: a) CW power should not be less than 700 W; b) plasma irradiation period should not be less than 40 sec; and c) at least total microwave energy of 50 kJ is needed.

In our previous paper, we reported BI could not be sterilized by argon plasma excited by 700 W CW power.[10] We also tested the sterilization effects of the oxygen radicals and UV radiation emitted from the oxygen plasma. We deduced from the experiment that the spores were mainly killed by some chemical reactions with oxygen radicals, rather than the UV radiation in the oxygen plasma experiment.[8] To study the detail of oxygen radicals, we have been investigating pulse-modulated microwave plasma sterilization.

In order to investigate temperature increase caused by irradiation of oxygen plasma excited by pulse-modulated microwave power, we used 1 kHz pulse-modulated microwave power with on-duration of 500 μs and instantaneous power of 1.3 kW. The plasma irradiation period was varied from zero to 5 min by 30-second steps. The stage temperature increased from 23°C at room temperature to 35°C after 5 min plasma irradiation. We tested several different parameter conditions by using the pulsed microwave system. We varied the pulsed modulation frequency of the pulsed operation, the microwave on-duration, the instantaneous microwave power and the total microwave on time. After the incubation process, the sterilization effects could be confirmed as shown in Fig. 3. From these results, we draw the conclusion that the least instantaneous microwave power and the total microwave on time needed for pulse-modulated microwave plasma sterilization are roughly determined from the total microwave energy of 200 kJ.

Figure 4 shows the results of colony count measurements for CW and pulsed microwave sterilization. We noted here that microwave pulses having instantaneous power of 2.0-2.2 kW with on-duration of 10 μs could sterilize the spores with almost the same sterilization characteristic as in the CW

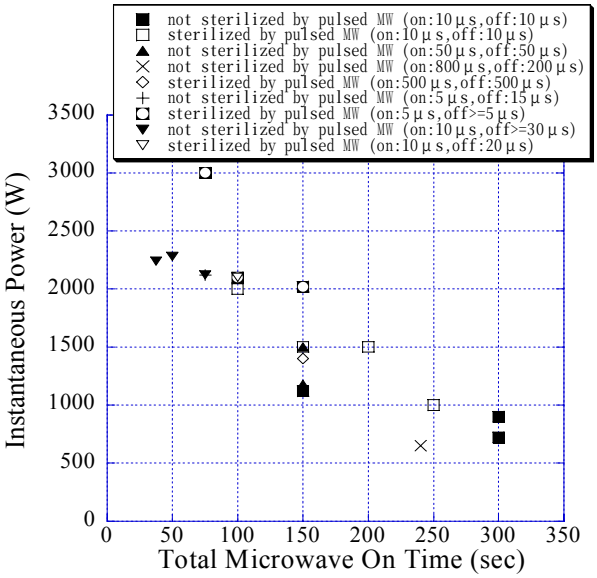

Fig. 3 Experimental results of sterilization between instantaneous microwave power and total microwave on-time.

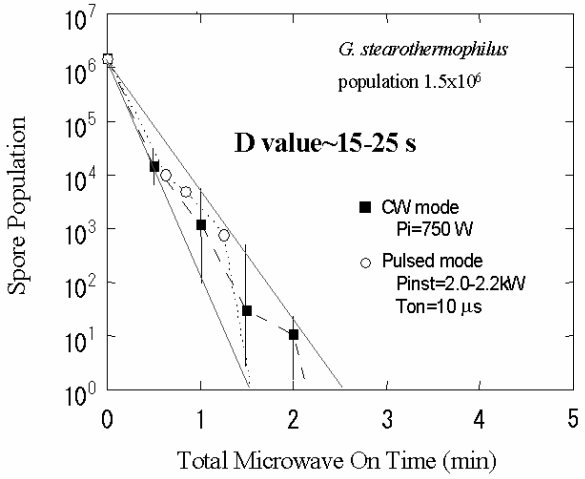

Fig. 4 Comparison of survival curves of CW and pulsed microwave plasma sterilization.

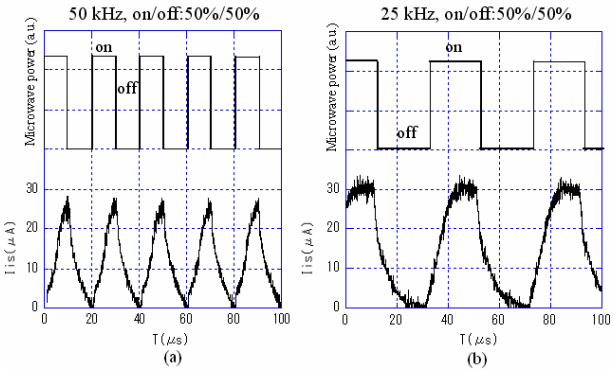

Fig. 5 Probe signals of pulse-modulated oxygen plasmas: (a)modulation frequency =50 kHz, (b)modulation frequency =25 kHz

operation, with the D-values of 15~25 s.

To study lifetime of oxygen plasmas, we applied diagnostic method by a Langmuir single-probe. The probe was inserted into chamber 55 mm below the quartz window. Negative bias voltage was 30 V, and the resistance in the probe circuit was 1 kΩ.

Under the conditions that gas pressure was 60 mTorr and duty ratio was 50%, we obtained two waveforms of ion saturation current produced when pulsed modulation frequency was 50 kHz and 25 kHz, respectively as shown in Fig. 5. From the waveforms of ion saturation currents, we found that plasma density saturated about 10 μs after the microwave onset. After the turn-off of the microwave pulses, ion saturation currents decayed with different time constants, that is, they initially decayed with a time constant of about 10 μs and then decayed with a longer time constant of about 30 μs. Thus, there existed plasma particles during 30 μs at least. It is expected that the oxygen with metastable states, such as $O^*(^1D)$ or $O_2^*(^1\Delta_g)$, can play an important role in the sterilization process.

Next, we showed the experimental results of the oxygen plasma sterilization of 3.0×10^6 *Geobacillus stearothermophilus* spores while substrate stage was about 23 cm below the quartz window, discharge pressure was at about 120~130 mTorr, O_2 gas flow rate was 200 sccm.

In Fig. 3, we noted a special case of two different on-duration periods with instantaneous microwave power of 1.5 kW and total microwave on time of 150 s had different sterilization results. These results might be explained by considering the effect of oxygen radicals. To study the characteristics of oxygen plasma sterilization using pulse-modulated microwave, we fixed instantaneous power at 1.5 kW and on/off duty ratio as 50%, then changed on-duration per modulation signal when total microwave on time kept same. Figure 6 showed the latest sterilization results by using pulse-modulated microwave oxygen plasma. From the figure, we found all the BI samples were sterilized by pulse-modulated oxygen plasma when the total microwave on time was longer than 150 s. Based on the thermo-label measurements, it was shown that the surface temperature of Petri dish during the 300 s processing period (150-s total microwave on time plus 150-s total microwave off time) was always less than 70°C. While the total microwave on time was shorter than 150 s, we found the longer on-duration per pulse was required,for the shorter total microwave on-time. Related with Fig. 5, the reason might be when total microwave on time is fixed, total saturation period of ion saturation current increases with on-duration per pulse. During longer saturation period of ion saturation current, more efficient oxygen radicals, which are considered as key factor in oxygen plasma sterilization, can be generated.

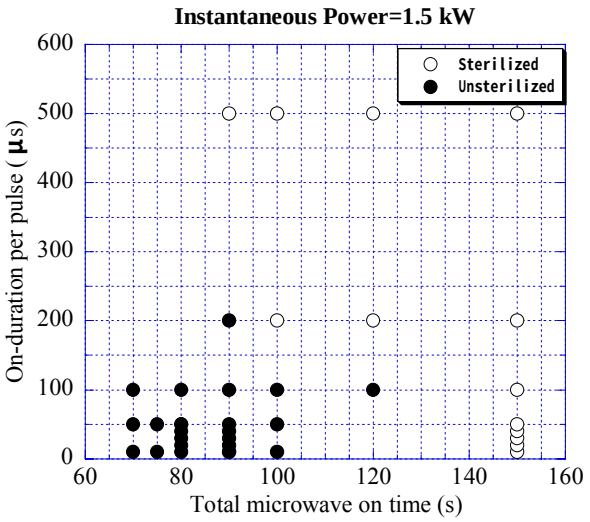

Fig. 6 Experimental results of sterilization between on-duration per pulse and total microwave on time.

Since discharge pressure and position of placed BI samples were changed, we tested O_2 discharge CW SWPs using *Geobacillus stearothermophilus* spores again. The sterilization effect could be confirmed for samples irradiated by oxygen plasma for 150 s or longer while CW power was 750 W.

At last, we showed effects of nitrogen gas addition in sterilization experiments using CW SWP. We utilized 3.0×10^6 *Geobacillus stearothermophilus* spores while substrate stage was about 23 cm below the quartz window, discharge pressure was at about 60~90 mTorr, total gas flow rate was 100 sccm. We fixed microwave power at 750 W.

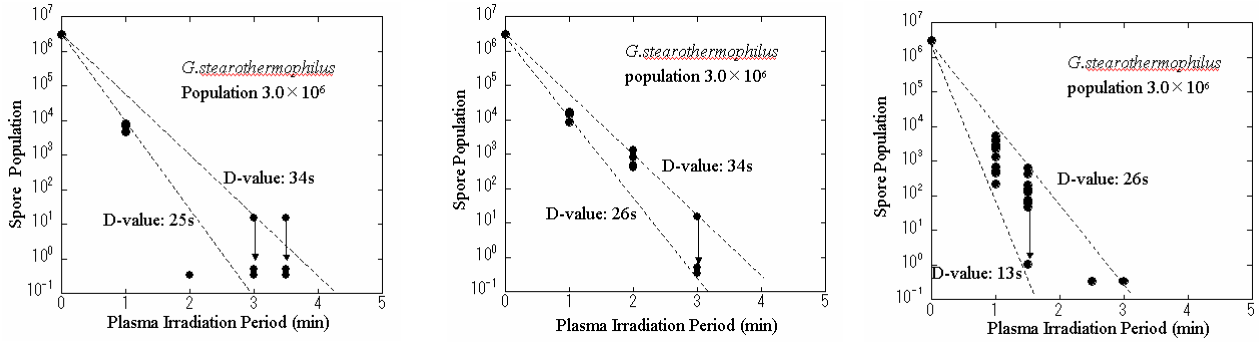

(a) pure O_2 plasma (b) pure N_2 plasma (c) N_2-O_2 plasma

Fig. 7 Survival curves for *G.. stearothermophilus* spores irradiated by 2.45 GHz surface-wave plasma.

The survival curves measured with the colony count method were shown in Fig. 7. Here, we defined the D-value as the time taken to decrease the number of spores by one order. From Fig. 7(a), we found that D-value was roughly 25~34 s and the shortest sterilization period were 3.5 min (210 s) for 100 sccm O_2 plasma. From Fig. 7(b), D-value was roughly 26~34 s and the shortest sterilization period was 3 min (180 s) for 100 sccm N_2 plasma. From Fig. 7(c), D-value was roughly 13~26 s and the shortest sterilization period was 3 min (180 s) for 20 sccm O_2 and 80 sccm N_2 gas mixture discharge plasma. The gas mixture consisting of 20% O_2 and 80% N_2 was similar to the compositions of air. Therefore, sterilization using air discharge SWPs is expected.

To study the shape and size of the spores before and after irradiation by different gas species discharge plasmas, we carried out measurements using a scanning electron microscope (SEM). It was shown that the length and width of the spores dramatically decreased after only a 4 min oxygen plasma irradiation. The ellipsoidal spores shrank to jellybean-like slender shapes.[9] This could be attributed to chemical etching by the oxygen radicals generated in the oxygen plasma. However, in the case of the nitrogen plasma, the spore shapes were almost identical to the original ones, which differed from the findings with oxygen plasma or oxygen radical irradiation. This result could possibly be caused by UV photons emitted by the nitrogen plasma. In the case of 20 sccm O_2 and 80 sccm N_2 gas mixture discharge plasma, the width of the spores seemed a little broader than the one in the case of pure oxygen plasma. We deduced the higher percent of O_2 in discharge gas was set, the slimmer shape of spores could be obtained.

4. Conclusion

In the present paper, we reported the effects of low-temperature plasma sterilization using CW and pulse-modulated surface-wave excited oxygen plasmas. When discharge pressure was at about 30~70 mTorr, O_2 gas flow rate was 200 sccm, BI samples with $1.5\text{x}10^6$ *Geobacillus stearothermophilus* spores were completely killed by being irradiated for 50 s or longer while CW power was 1 kW and being irradiated for 40 s while CW power was 1.5 kW. When discharge pressure was at about 120~130 mTorr, O_2 gas flow rate was 200 sccm, all the BI samples with $3.0\text{x}10^6$ *Geobacillus stearothermophilus* spores were sterilized by pulse-modulated oxygen plasma when the total microwave on time was longer than 150 s and instantaneous power was kept at 1.5 kW.

We also reported the effects of low-temperature plasma sterilization using CW nitrogen plasma. When discharge pressure was at about 60~90 mTorr, total gas flow rate was 100 sccm, microwave power was kept at 750 W, BI samples with $3.0\text{x}10^6$ *Geobacillus stearothermophilus* spores were sterilized after 3 min N_2 or N_2-O_2 plasma irradiation.

Acknowledgments

This work has been partly supported by Grant-in-Aid for Scientific Research from Japan Society for the Promotion of Science(JSPS), regional new consortium projects from Ministry of Economy, Trade and Industry(METI) and Grant from the Regional Science Promotion(RSP) program of the Shizuoka Organization for the Creation of Industries. The authors would like to acknowledge Nissin Inc. for supporting the microwave oscillator systems.

References

[1] P. T. Jacobs and S. M. Lin: *Disinfection, Sterilization and Preservation*, Ed. S. S. Block, 5th ed. Lippincortt Williams & Wilkins, Chap. 38, pp 747 (2000).

[2] I. A. Soloshenko, V. V. Tsiolko, V. A. Khomich, et al.: Plasma Phys. Report **26** 792 (2000).

[3] T. C. Montie, K. Kelly-Wintenberg, J. R. Roth: IEEE Trans. Plasma Sci. **28** 41 (2000).

[4] M. Laroussi, I. Alexeff, W. L. Kang: IEEE Trans. Plasma Sci. **28** 184 (2000).

[5] M. Moisan, J. Barbeau, S. Moreau, J. Pelletier, M. Tabrizian, et al.: Int. J. Pharmaceutics **226** 1 (2001).

[6] N. Philip, B. Saoudi, M. C. Crevier, M. Moisan, J. Barbeau, and J. Pelletier: IEEE Trans. Plasma Sci. **30** 1429 (2002).

[7] J. Ehlbeck, A. Ohl, M. Maas, U. Krohmann, T. Neumann: Sur. Coatings Technol. **174-175** 493 (2003).

[8] S. Lerouge, M. R. Wertheimer, R. Marchand, M. Tabrizian, L'H. Yahia: J. Biomed. Mater. Res. **51** 128 (2000).

[9] M. Nagatsu, F. Terashita and Y. Koide: Jpn. J. Appl. Phys. **42** L856 (2003).

[10] M. Nagatsu, F. Terashita, L. Xu, et al, to be published in Appl. Phys. Lett. (2005).

[11] M. Nagatsu, T. Sano, N. Takada, T. Hirao and H. Sugai: Jpn. J. Appl. Phys. **39** L929 (2000).

[12] Instruction manual of Raven Biological Laboratories,Inc. ATCC #12980.

Synthesis of Carbon Nanotubes with Ni-C Composite Clusters Using Microwave Plasma CVD

M. Nagatsu[1], A. Ogino[1], T. Yoshida[1], T. Matsuda[1], T. Tanaka[1], H. Tatsuoka[1], K. Murakami[2] and M. Fujimoto[3]

[1] *Faculty of Engineering, Shizuoka University, 3-5-1 Johoku, Hamamatsu 432-8561 Japan*

[2] *Research Institute of Electronics, Shizuoka University, 3-5-1 Johoku, Hamamatsu 432-8011 Japan*

[3] *Innovative Joint Research Center, Shizuoka University3-5-1 Johoku, Hamamatsu 432-8561 Japan*

Abstract

Synthesis of carbon nanotubes(CNTs) using microwave plasma CVD with catalytic nanoclusters has been studied. Nickel-carbon composite nanoclusters were fabricated using the dc arc discharge using a pair of graphite-Ni composite electrodes in a vacuum chamber filled with He and methane mixture gas at 50~100 Torr. Large-area surface-wave plasma (SWP) device with a diameter of 400 mm was used for growth of CNTs on the Ni-C clusters evaporated-Si substrate. Surface morphology has been studied using the field emission type scanning electron microscope (FE-SEM) and transmission electron microscope (TEM). It was found that the diameters of multi-walled CNTs were reduced from 50~100 nm in the case of Ni-evaporated Si to roughly 20 nm or less by using the present technique.

1. Introduction

Recently, field emission performances of carbon nanotubes(CNTs) have been extensively studied aiming at developing the cold electron emitter materials for the next generation flat panel display. Compared with other materials, such as the diamond film or diamond-like carbon films, CNTs have great advantages of lower emission electric fields and larger emission currents[1]. In general, the closely grown CNTs have a poor emission performance because of the field screening effect [2,3]. In order to achieve good emission performance, it is necessary to grow CNTs having a high aspect ratio, i.e., a ratio of CNT length to its diameter. Moreover, CNTs should be grown at a spatially regulated position.

So far, CNTs have been fabricated using various types of production techniques. For instance, DC arc discharge has been originally studied for production of single-walled CNTs[4,5]. In this technique, the CNTs have grown on the top of cathode electrode directly. For the practical use of CNTs, they have been purified as separated CNT wires and used by painting and holding on the substrate. Thus it might be awkward to use them as spatially regulated field emitters, as described above. On the other hand, the thermal CVD or plasma CVD techniques have been widely studied to grow CNTs on the catalyst deposited on the substrate beforehand. In the thermal CVD, it is often reported that single-walled CNTs could be produced. However, when the deposition area is too small, CNTs lay down due to Van der Waar's force. Thus, it is important develop the technique to grow single-walled CNTs vertically on the small catalyst surface in thermal CVD method. In the plasma CVD technique, it is reported that multi-walled CNTs were often produced. Nevertheless, advantages of plasma CVD are to be capable of growing vertically aligned CNTs by applying bias voltage between the substrate and plasma and of growing them uniformly over the large-area substrate.

In this study, we propose to grow CNTs with narrower diameter using the catalytic Ni-C nanoclusters prepared with the DC arc discharge in He and methane mixture gas.

2. Experimental Set-up

A schematic drawing of the experimental setup is shown in Fig. 1.[6] Surface-wave plasma (SWP) was produced in a 400 mm-diameter, cylindrical vacuum chamber by introducing a 2.45 GHz microwave through a quartz window via slot antennas[7,8]. A heater stage was installed about 15 cm below the quartz window of the microwave launcher inside the vacuum chamber. Growth of CNTs was carried out on the <100> n-type silicon wafer substrates placed on the substrate stage installed inside the chamber. Effective area of the substrate stage was 200 mm in diameter, where the substrate temperature could be controlled up to 850 °C by external heater and water-cooling system. Silicon substrates were cleaned beforehand by acetone in an ultrasonic bath and then Ni-C clusters were deposited on them using vacuum evaporation technique.

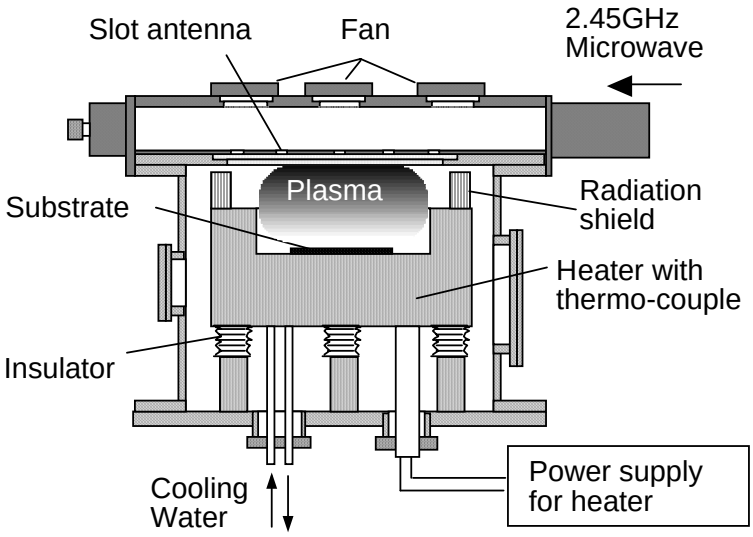

Fig. 1 Schematic drawing of the experimental setup for surface-wave plasma CVD.[6]

The SWP was sustained by the microwave power of 700W at gas pressure of 10 Torr for discharge duration of 10 min. The Ni-C nanoclusters were prepared using dc arc discharge method, as shown in Fig. 2. Stainless-steel vacuum chamber with 200 mm in diameter[9] was evacuated down to mTorr by rotary pump and then filled with He gas only or He and methane mixture gas at about 50~200 Torr. One of two graphite electrodes was made by molding Ni powders with graphite cements. By flowing a high current of 100 ~200 A between two electrodes, various Ni-C clusters were produced. Soot produced in arc discharge was collected with a cover and they were mixed with ethyl alcohol in the ultrasonic bath to select small size of clusters out from the clear supernatant liquid. Filtered soot including small size Ni-C clusters was painted and annealed on silicon substrate before CNT growth procedure. The CNT growth was carried out with two different plasma discharges; that is, a mixture gas of H_2, Ar and CH_4 at the gas flow rates of 100sccm, 50sccm and 20sccm, and a mixture gas of N_2 and CH_4 gas at 150sccm and 20sccm. During plasma discharge, substrate stage was kept at temperature of 700~750°C. For comparison, we also carried out the CNT growth on Ni evaporated silicon substrate under the same plasma discharge conditions.

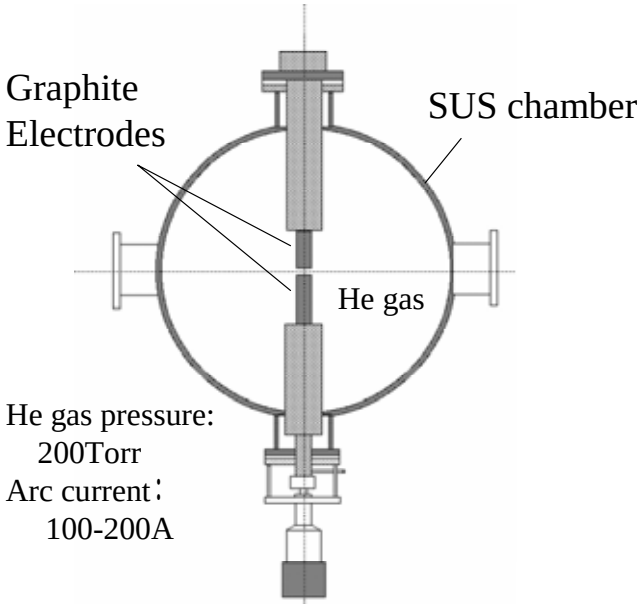

Fig. 2 Schematic drawing of experimental setup for production of Ni-C nanoclusters.

3. Results and discussion

The structures of Ni-C clusters were analyzed with transmission electron microscope (TEM). Figure 3 shows typical TEM images of Ni-C composite clusters. It is seen that the clusters consisted of nano-sized Ni spherical grains and carbon layers surrounding each Ni grain, as shown in Fig. 3(a) and 3(b). Figure 3(a) shows TEM image of grape-like structures of Ni-C clusters, where sizes of Ni grains are typically 5 nm or less. Figure 3(b) shows the image of an isolated cluster with a slightly larger diameter of 10 nm. It shows the lamellar crystal structure of Ni atoms with an interlayer distance Δ of 0.17 nm are surrounded by several carbon layers with an interlayer distance Δ of 0.34 nm.

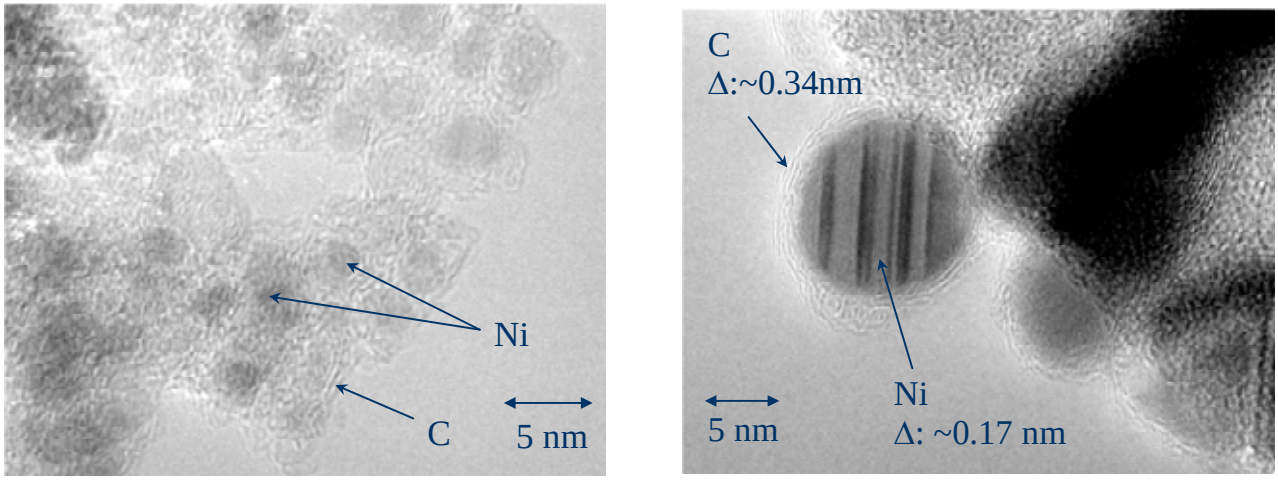

(a) (b)

Fig. 3 TEM images of Ni-C composite clusters; (a) grape-like structure of clusters and (b) isolated structure of N-C cluster.

To discuss the difference between the CNTs in the cases of conventional Ni evaporated method and the present technique, we analyzed them using the field-emission type of scanning electron microscope(FE-SEM) Figure 4 shows multi-walled CNTs with diameter of typically 50~100 nm randomly grown on Ni evaporated Si substrate. We tested two discharge conditions, that is, one is the case of H_2, Ar and CH_4 mixture gas, and the other is that of N_2 and CH_4 mixture gas. In the former case, Ar was added to obtain the more stable discharge in surface-wave plasma. Here, total gas flow rates were kept to be 170 sccm for both the cases.

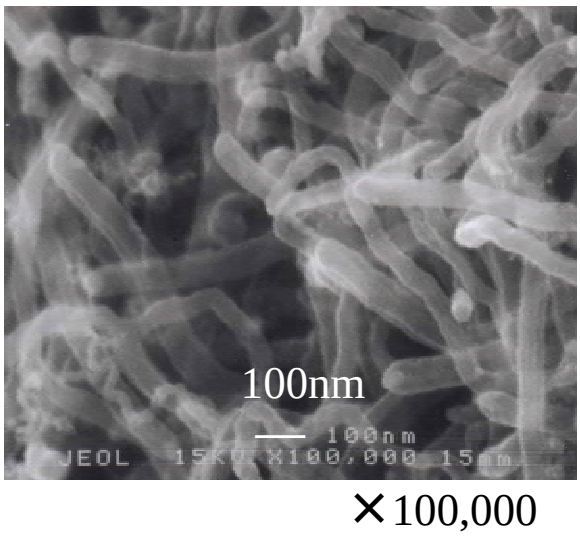

Fig. 4 FE-SEM image of CNTs grown on the Si substrate, where Ni film was used as catalyst and deposited beforehand.[6]

Figure 5(a) shows the FE-SEM of the CNT samples deposited on the Ni-C clusters deposited Si substrate with a mixture gas of H_2, Ar and CH_4 at the gas flow rates of 100sccm, 50sccm and 20sccm.

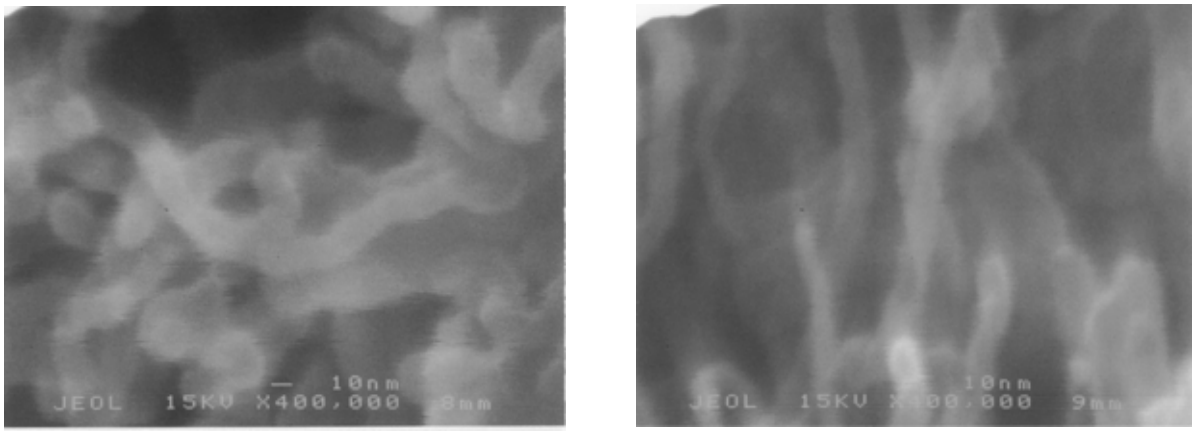

(a) x 400,000 (b) x 400,000

Fig. 5 FE-SEM images of CNTs deposited by SWP with (a)H_2, Ar and CH_4 mixture gas and (b) N_2 and CH_4 mixture gas, when Ni-C clusters were used as catalyst.

Although a various sizes of CNTs were observed, narrower ones had diameter of 10~20 nm. Figure 5(b) shows the FE-SEM of the CNT samples when a mixture gas of N_2 and CH_4 were used at the gas flow rates of 150sccm, and 20sccm. Typical sizes of CNTs were almost the same as those in Fig. 5(a).

To investigate fine structure of CNTs, we have carried out the TEM analysis of CNTs. Figure 6 shows one of typical images of TEM analysis of multi-walled CNTs in the case of N_2 and CH_4 mixture gas. It clearly shows the multi-walled CNT structure having 26 carbon layers surrounding a catalytic Ni cluster.

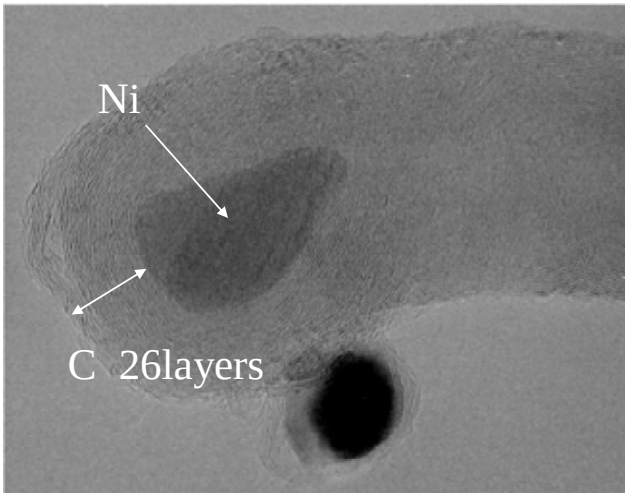

Fig. 6 TEM image of CNT deposited by SWP with N_2 and CH_4 mixture gas.

4. Conclusion

Synthesis of CNTs using microwave plasma CVD with catalytic nanoclusters has been studied. Catalytic nanoclusters were fabricated using the dc arc discharge using a pair of graphite-Ni composite electrodes in a vacuum chamber filled with He gas at 50~100 Torr. Nanoclusters with a number of Ni-C composites deposited on the cover in the vacuum chamber were used as the catalyst for the carbon nanotube growth. Large-area surface-wave plasma (SWP) device with a diameter of 400 mm was used for growth of CNTs on Ni-C cluster evaporated Si substrate. The surface morphology has been studied using the field emission type scanning electron microscopy (FE-SEM) and transmission electron microscope (TEM). It was found that the diameters of CNTs was reduced from 50~100 nm to roughly 20 nm or less by using the present technique.

Acknowledgments

This work has been supported in part by the Grants-in-Aid for Scientific Research and performed under the 21st Century COE Program “Research and Education Center of Nanovision Science” by the Japan Society for the Promotion of Science.

References

[1] W. I. Milne, K. B. K. Teo, M. Chhowalla, G. A. J. Amaratunga, S. B. Lee, et al, Diam. Relat. Mater. **12** (2003) 422-428.

[2] L. Nilsson, O. Groening, C. Emmenegger, O. Kuettel, E. Schaller, et al, Appl. Phys. Lett. **76** (2000) 2071-2072.

[3] J. S. Suh, K. S. Jeong, J. S. Lee, I. Han, Appl. Phys. Lett. **80** (2002) 2392-2394.

[4] S. Iijima, Nature **354** (1991) 56.

[5] S. Iijima, T. Ichihashi, Nature **363** (1993) 603.

[6] M. Nagatsu, T. Yoshida, S. Kurita and K. Murakami, Appl. Surf. Sci. **244**/1-4 (2005) 111-114.

[7] M. Nagatsu, T. Sano, N. Takada, W. X. Guang, T. Hirao and H. Sugai, Jpn. J. Appl. Phys. **39** (2000) L929-L932.

[8] M. Nagatsu, T. Sano, N. Takada, N. Toyoda, M. Tanga and H. Sugai, Diam. Relat. Mater. **11/3-6** (2002) 976-979.

[9] S. Sasaki, N. Kitagawa, N. Takada and M. Nagatsu, Jpn. J. Appl. Phys. **36** (1997) 7399.

Characteristics of Plasma CVD on Inner Surface of Micro Channel

M.Kadowaki[1], A.Yamamoto[2], S.Mori[1], and M.Suzuki[1]

[1]*Department of Chemical Engineering, Tokyo Institute of Technology, Tokyo, Japan*

[2]*The Research Association of Micro Chemical Process Technology (MCPT), Japan*

Abstract

We have developed plasma CVD method using low pressure dielectric barrier discharge in a micro channel, such as a narrow capillary or a channel graved in a Pyrex chip. And we have investigated the possibility of uniform deposition on the inner surface by using our plasma technique and obtained successful results. In this work, we would like to describe the generation of a packed bed plasma as another type of microplasma, which is discharged in a narrow capillary filled with small particles, and to report the qualitative characteristics of the plasma CVD on the inner surface of the packed bed capillary.

Keywords

microplasma, dielectric barrier discharge, chemical vapor deposition, particle, packed bed

1. Introduction

Various microplasmas have been developed and many basic and application studies have been done since the concept of microplasma was proposed. In particular, application studies of microplasmas in the fields of micro total analysis system (μ-TAS) and microelectromechanical system (MEMS) have been developed extensively. Although various studies relate to the inner wall modification of a micro channel utilizing a microplasma [1,2], there have been relatively few studies that tried to investigate plasma chemical vapor deposition (P-CVD) on the inner surface of a sealed micro channel without using a lithography technique.

We have developed P-CVD method using low pressure dielectric barrier discharges in a micro channel, such as a narrow capillary or a channel graved in a Pyrex chip with electrodes attached to the outer surface. And we have investigated the possibility of uniform deposition of platinum thin film on the inner surface by using our plasma technique and obtained successful results [3]. Our electrode arrangement has the important advantages that the length of the gap is not limited to the order of a micron, and that it can be adjusted. Since the electrode arrangement makes it capable to adjust the gap to a few centimeters, it is possible to attain a low spark voltage even at low pressure of the order of a few torrs, according to Paschen's law. Low pressure CVD processes have the advantages of making the adhesion of films to a wall surface possible, and of enabling precursors to be introduced effectively into a CVD reactor even if, such as is the case of organometallic compounds, which they have a low vapor pressure. In addition, it is expected that the microplasma with the electrode arrangement can be applied to P-CVD on the inner surface of channels that have complex shapes, because the plasma can be generated without inserting an electrode.

In this paper, after summary of our previous study we would like to describe the generation of a packed bed plasma as another type of microplasma, which is generated in a narrow capillary filled with small particles, and to report the qualitative characteristics of the P-CVD on the inner surface of the packed bed capillary.

2. Experimental

In our previous work, the micro capillary plasma was generated by dielectric barrier discharge between

cylindrical graphite electrodes (ϕ4mm) pierced by a capillary as shown in Fig. 1. A fused silica capillary of 450μm o.d., 320μm i.d., and 150mm length was used. The precursor, platinum bisacetylacetonate $Pt(C_5H_7O_2)_2$ (Aldrich, 97%), was used. The capillary temperature and precursor temperature were fixed to 200 °C and 170 °C, respectively. For details of the previous work the reader should refer to [3].

Fig 2 shows the schematic diagram of the P-CVD apparatus in this work. The packed bed plasma was generated with a similar electrodes arrangement pierced by a capillary to the previous work. The glass capillary of 1.5mm o.d., 1.0mm i.d., and 140mm length was packed with glass beads (300μm ~ 500μm) or silica gel particles (200 μm ~ 500 μm). The flow rate of carrier gas was controlled with a mass flow controller (Model 3200SR, KOFLOC). Helium and oxygen mixture was used as the carrier gas. The pressure in a capillary was measured at the upstream and downstream point of the capillary by pressure gauges and the average value was defined as the system pressure. The precursor of palladium hexafluoroacetylacetonate ($Pd(C_5HF_6O_2)_2$) was set in the heated tube located at the upstream of the capillary, vaporized, and introduced into the capillary. Carrier gas and the precursor vapor flowed through the capillary in the direction of the grounded upstream electrode towards the downstream electrode where high voltage was applied. The temperature of the heated tube filled with the precursor was fixed to room temperature (22~27 °C), and the atmosphere temperature around the capillary was measured by a thermocouple. A high voltage power amplifier (Model 20/20C, Trek) was used as the power supply. Plasma current and input power were measured by a Lissajous figure on a digital oscilloscope.

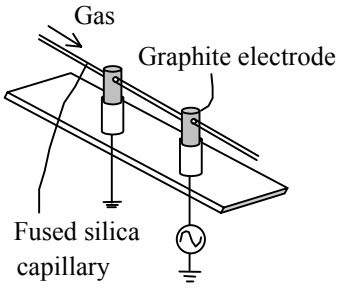

Fig. 1 Schematic diagram of the electrode arrangement of the micro capillary plasma.

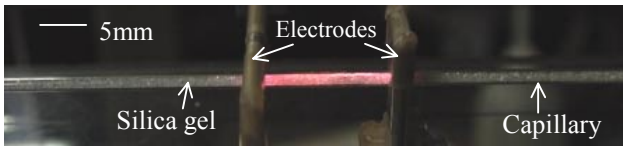

Fig. 3 The photograph of the packed bed plasma.
V_{peak}=7 kV, Pressure=45 Torr, (helium)
f=4 kHz, Power=13mW

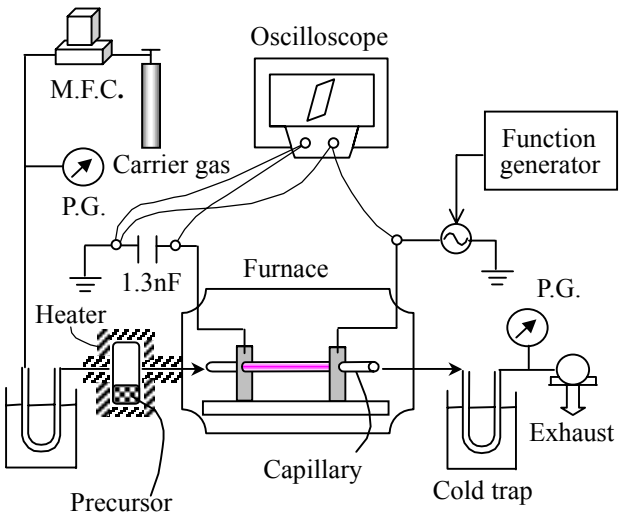

Fig. 2 Schematic diagram of the P-CVD apparatus.

3. Results and Discussion

3.1 Plasma CVD in a micro capillary

This section discribes the outline of our previous study.

Fig. 4(a) shows the profiles of the platinum amount deposited on inner surface of a fused silica capillary by the P-CVD method. These results were obtained by varying the frequency. An increase in frequency

corresponds to an increase in input power. The times required for film deposition completion are 30sec (2kHz), 150 sec (5kHz), and 375 sec (10kHz), respectively. The upstream and downstream electrode positions are located between –12~–8 mm and 8~12 mm, respectively. Note that the scale of the longitudinal axis is logarithmic. The results indicate that as input power is increased, the time required for film deposition completion is longer, and the deposited amount is larger.

Fig. 4(b) shows the profiles, which indicate the progression in time for similar experimental conditions. The figure shows that little platinum is deposited around the point of the downstream electrode at 50 sec and 120sec. In these conditions, the decomposition of the precursor and film deposition mostly takes place at the upstream range in the plasma and the precursor is no longer transported to the range around the downstream electrode. In addition, judging from little deposition in the range of –20~–4 mm after 50 sec, it is clear that the plasma discharge region is shortened as film deposition proceeds. Therefore, it seems reasonable to conclude that film deposition starts locally at the inner surface attached with an upstream electrode, and is completed at a downstream electrode.

Hence, we can suggest the model as shown in Fig. 5. When the plasma discharge in a capillary is maintained between a downstream electrode and the end of a deposited film, it is reduced in length automatically as film deposition proceeds, as shown in Fig. 5(a). This phenomenon works effectively to create uniform films in the P-CVD process even if the concentration gradient of the precursor in the microchannel is steep. After completion of film deposition, surface discharge at the outer surface around electrodes is generated as shown in Fig. 5(b).

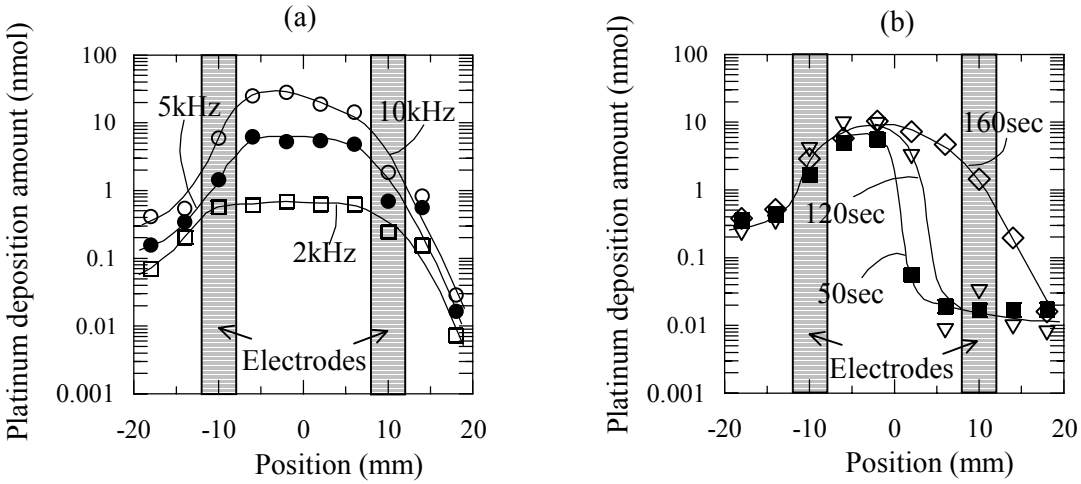

Fig. 4 Profiles of the platinum amount deposited on inner surface of a fused silica capillary varying plasma frequency (a) and deposition time (b).

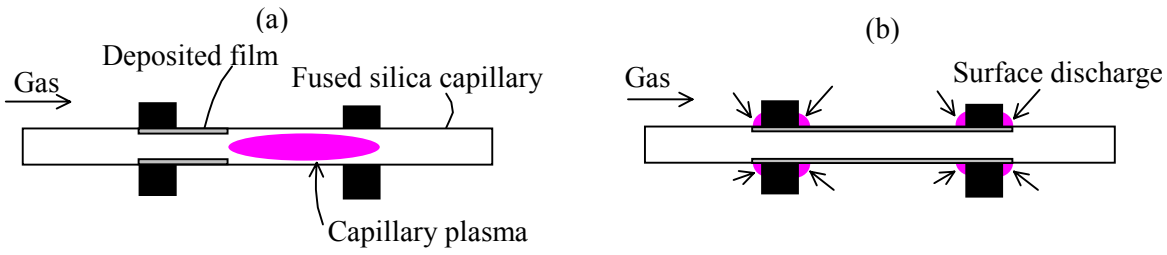

Fig. 5 Schematic illustrations of the discharges during deposition (a) and after deposition (b).

3.2 Plasma generation in a packed bed capillary

Microplasma in a capillary packed with glass beads or silica gel particles can be generated successfully between electrodes as shown in Fig. 3. The discharge space size is limitted to the order of a micron by the particles and the capillary wall. Igniting the plasma in a capillary packed with particles requires higher spark voltage than in a capillary without them. Also the pressure, which provides the Paschen's minimum spark voltage, is higher. For example, the helium plasma in a capillary packed with silica gel particles can be generated above $4kV_p$ and $7kV_p$ with the electrode gap of 8mm and 12mm, respectively under the optimum pressure of about 40 torr, while in a capillary without them about $2kV_p$ with the approximate gap under a few torrs. Considering that the product of pressure (torr) and gap (cm) which provides the minimum spark voltage is 2.5 torr·cm in helium atmosphere according to Paschen's law, the gap length would be about 600 μm. We can recognize from these facts that in a packed bed plasma reactor, the practical gap length for Paschen's law should be the space size surounded by particles, while the electrodes gap decides the electric field strength. So, for a longer capillary P-CVD, plural electrodes are effective since it is possible to adjust the electrode gap to a shorter one, igniting plasma at a lower voltage.

3.3 Plasma CVD in a packed bed capillary

Fig.6 shows photographs of the plural electrodes arrangement and of the capillary with the deposited thin film including palladium without packing paticles. This film was deposited by P-CVD for 150 minutes under the condition of 3 torr and low freaquency (800 Hz) after 90 minutes P-CVD under the condition of 6 torr and high frequency (5kHz). Gas composition, applied peak voltage and capillary temperature were fixed to $He/O_2=1/1$, $V_p=1.5kV_p$, and room temperature, respectively. It is observed that the positions attached electrodes have deep brown color because of precuesor decomposition promoted in the cathod sheath region near the electrodes. Also it is found that the film color under the high freaquency condition is deeper than under the low frequency one and the color shades into transparent brown gradually downstream as shown in Fig. 6. Therefore, it is clear that the film deposited under the low freaquency condition is thinner than under the high freaquency one and that the film thickness has gradient downstream. We can conclude that plasma frequency under fixed voltage condition is an important parameter, which decides the film thickeness and gradient.

The plasma is not extinguished even when the film is deposited all over between the electrodes. Why this result is different from our previous work, which shows that the end of the deposited film can work as an

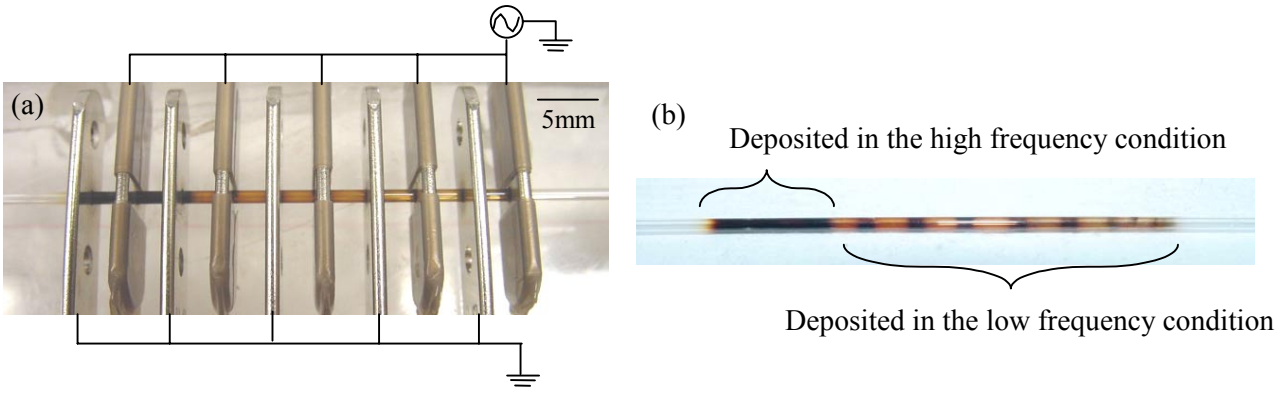

Fig. 6 Photographs of the plural electrodes arrangement (a) and of the capillary with a deposited thin film including palladium without packing paticles (b).

electrode to shorten the plasma region automatically, is that the electrical conductivity of deposited film in this work is different from previous one since low substrate temperature decreases film conductivity in P-CVD [4].

Fig. 7 shows the photograph of the capillary packed with glass beads and the deposited thin film including palladium at the substrate temperature of 130 °C. The film is black metallic and must have high electric conductivity because of the high substrate temperature. In fact the plasma is shortened as deposition proceeds. However, the deposited film is not uniform contrary to our previous results. The cause of the difference has not yet been found. The film is deposited also on the surfaces of glass beads in the capillary.

In the case of the capillary packed with silica gel particles, the precursor is not transported to the plasma region, being adsorbed to the silica gel particle surface in the range of the capillary entrance as shown in Fig. 8. In the case that the precursor is adsorbed on silica gel particles before packing in the capillary subsequence plasma treatment decomposes the adsorbed precursor to change the silica gel color from yellow to black. However, generating the plasma in a capillary packed with silica gel adsorbed by the precursor requires higher applied voltage than with not adsorbed.

Fig. 7 The photograph of the capillary packed with glass beads and the deposited thin film including palladium at the substrate temperature of 130 °C.

Fig. 8 Silica gel particles adsorbed by $Pd(hfac)_2$.

Conclusion

In this work, we described the generation of a packed bed plasma as another type of microplasma, which was generated in a narrow capillary filled with small particles and reported the qualitative characteristics of the P-CVD in the packed bed capillary. We conclude the following:

(1) Microplasma in a capillary packed with glass beads or silica gel particles can be generated successfully. And the generating condition is much different from the one without packing particles.
(2) For a longer capillary P-CVD, plural electrodes are effective.
(3) In the case of packed glass beads, P-CVD is done successfully although the film uniformity has a problem. The P-CVD process behavior is dependence on some parameters such as plasma frequency and substrate temperature. Quantitative research of the dependency is a further issue.
(4) In silica gel particles, the precursor transport is blocked by adsorption to the surface of them.

References

[1] H. Yoshiki, A. Oki, H. Ogawa, Y. Horiike, Thin Solid Films 407 (2002) 156.
[2] J. K. Evju, P. B. Howell, L. E. Locascio, M. J. Tarlov, J. J. Hickman, Appl. Phys. Lett. 84 (2004) 1668.
[3] M. Kadowaki, H. Yoshizawa, S. Mori, M. Suzuki, to be published in Thin Solid Films.
[4] E. Feurer, H. Suhr, Thin Solid Films 157 (1988) 81.

Surface analysis of plasma induced reactions on organic model substrates

M. Giza, J. Raacke, G. Grundmeier

Max-Planck-Institute for Iron Research, Duesseldorf, Germany
E-mail: grundmeier@mpie.de

Abstract

The influence of reactive species from an oxygen plasma on an organic model surface has been investigated by the use of a plasma cell which was developed for in-situ FTIR spectroscopy as well as in-situ Kelvin probe measurements of plasma modified surfaces. The presented application of this new in-situ analytical device shows that the monolayer sensitive infrared absorption spectroscopy in combination with the measurement of work function is suitable to provide new insights in plasma induced surface modifications.

Keywords: Fourier transform infrared spectroscopy, Kelvin probe, oxygen plasma, self-assembly monolayer, in-situ diagnostic.

1. Introduction

Self-assembly films of organic molecules have been employed as model systems for the investigation of surface functionalization of polymers by cold plasmas. In this case the chemical composition, degradation and disorientation of molecular chains, orientation of polar groups which are introduced in non-polar monolayer are of interest [1].
Ex-situ investigations of plasma modified organic surfaces are not able to eliminate the undefined influence of the environment, which contains species such as organic molecules, carbon dioxide, water and oxygen. These species lead to a change in the surface chemistry and ex-situ analytical methods are not really showing the surface properties directly after the plasma modification. This has led to some in-situ investigations of plasma processes [2, 3]
The content of the here presented work is the application of a plasma cell which is combined with in-situ infrared reflection absorption spectroscopy (IRRAS) and in-situ Kelvin probe (KP). The sample under investigation is a self-assembled monolayer (SAM) of octadecylmercaptane which was functionalized in an oxygen plasma. The influence of the oxidation to the surface chemistry and work function is reported.

2. Experimental details

The experimental setup as already described in [3] is shown in Fig. 1. The sample holder can be moved by a stepper motor with defined velocities through the plasma zone to the diagnostic position. A set of electrodes allows the generation of low pressure remote plasmas by applying an alternating, pulsable, and adjustable voltage (typically 30.7 kHz). The plasma treated surface can be analyzed by Fourier transform infrared spectroscopy (Biorad Excalibur 3000) and a Kelvin probe.
Flame annealed gold surfaces were used for the here presented fundamental studies, which consist of monoatomically flat terraces with Au(111) orientation. These surfaces can then be covered with self-assembled organo thiol monolayers (octadecylmercaptane) which were adsorbed from a $2x10^{-3}$ M ethanol solution.

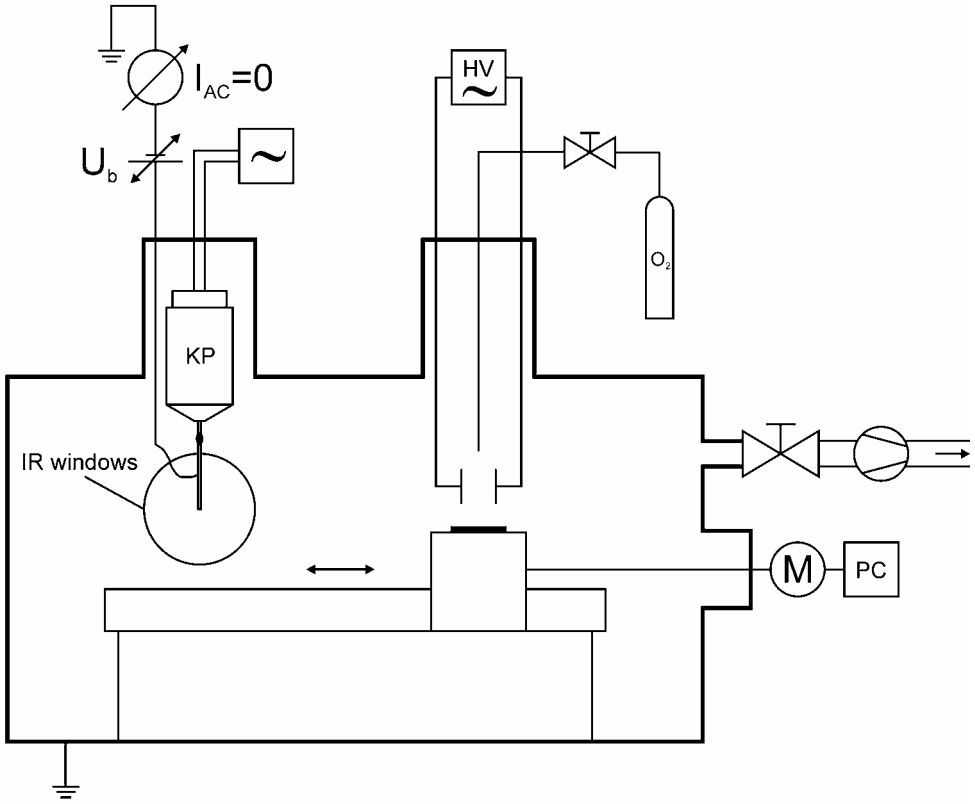

Fig. 1: Experimental set-up of the combination of in-situ FT-IRRAS and KP with a plasma cell [3]

3. Results and discussion

A self-assembled monolayer of octadecylmercaptane was treated in an oxygen plasma and the changes of the surface chemistry and potential were measured in-situ by FT-IRRAS and the Kelvin Probe.
Fig. 2 shows infrared absorption spectra after the modification in each case relative to the untreated state. Subsequently, the surface was exposed to an oxygen plasma (at a pressure of 0.3 mbar) four times for 1 s and for 4 s in a final step. The oxygen plasma treatment leads to an etching of the hydrocarbon chains (2850-2980 cm^{-1}) and to a build up of carbonyl functions (1720 cm^{-1}). The CH_2/CH_3 peak ratio increases after each plasma treatment. This behavior suggests that the etching process starts from the outer surface of the monolayer with the oxidative removal of the CH_3 functions. This assumption could be confirmed by ToF-SIMS measurements of the monolayer before and after exposure to the oxygen plasma. These ex-situ measurements show a significant increase of oxygen amount in the layer after the plasma treatment with nearly constant concentration of sulfur-oxygen compounds.

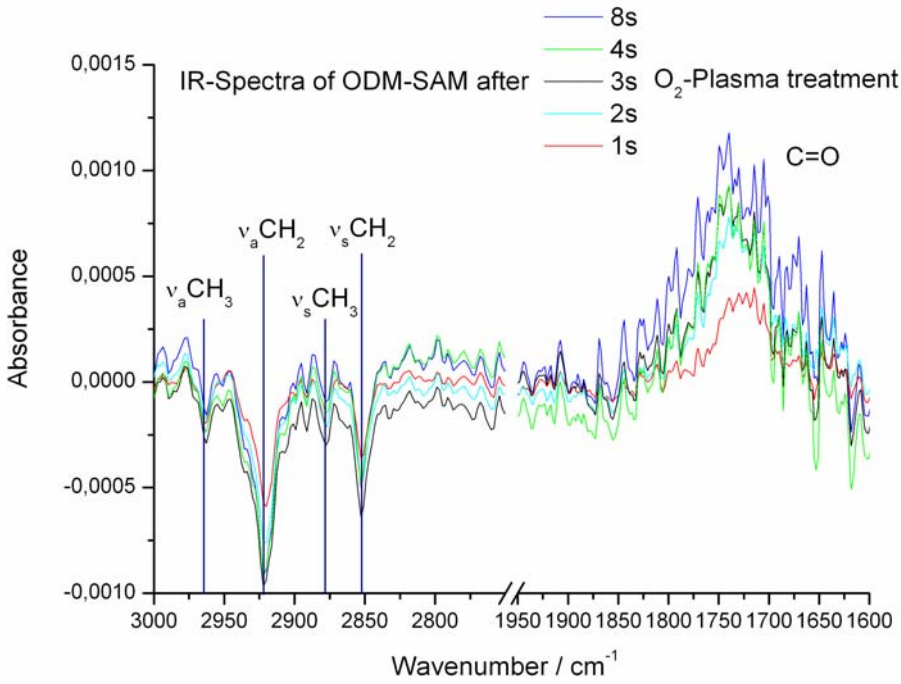

Fig. 2: FT-IRRAS measurements of an oxygen plasma treated octadecylmercaptane self-assembly monolayer

This indicates that no significant oxygen diffusion through the monolayer occurs. The proper description of the mechanism of such plasma-surface interaction requires further in-situ investigations.
Parallel to the etching of the hydrocarbon chains carbonyl functions are generated on top of the surface. The intensity of this carbonyl peak increases with etching time up to a maximum level.

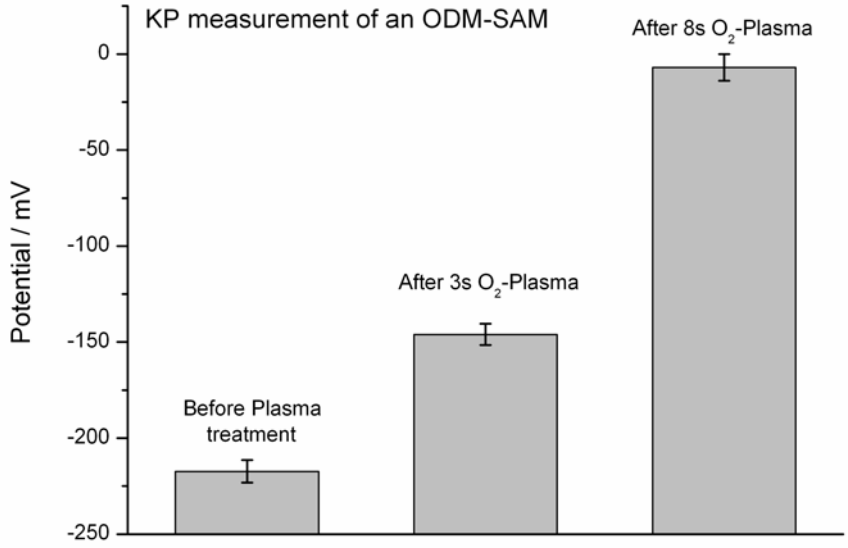

Fig. 3: Influence of oxygen plasma treatment on the surface potential of an octadecylmercaptane self-assembly monolayer

Parallel to the record of infrared spectra, in-situ surface potential measurements have been done. The signals of the Kelvin probe before and after selected plasma treatments are shown in Fig.3. The surface potential increases by about 85 mV after 3 s oxygen plasma and by further 125 mV after additional 5 s of plasma treatment. The reason for the increasing surface potential is a floating dipole layer composed of the carbonyl groups at the ends of the hydrocarbon chains. This can be modeled theoretically by the Helmholtz equation [4]:

$$\Delta V = \frac{\mu \cos\theta}{A\varepsilon\varepsilon_0} \qquad (1)$$

which represents the change of potential in a parallel plate capacitor due to the introduction of a dipole layer. The numerator describes the dipole moment component perpendicular to the surface and the denominator the effective area of each dipole and the dielectric constant of the layer.

4. Conclusions

The experiment described above shows that with in-situ measurements on well defined model surfaces an extremely high sensitivity for changes in the surface chemistry on the subnanometer scale can be achieved. This approach eliminates any undefined influence of the environment. With the described experimental setup a very powerful tool was realized for future in-situ investigations of plasma-surface interactions and for tailoring of well defined surface layers.

Acknowledgement

Financial support from Bundesministerium für Bildung und Forschung (BMBF) is gratefully acknowledged.

References

1. Friedrich, J., et al., Surface & Coatings Technology, 1998. **98**(1-3): p. 1132-1141.
2. Meichsner, J. and Li, K., Applied Physics a-Materials Science & Processing, 2001. **72**(5): p. 565-571.
3. Raacke, J., Giza, M., and Grundmeier, G., Surface and Coating Technology in press, 2005.
4. Taylor, D.M., Advances in Colloid and Interface Science, 2000. **87**(2-3): p. 183-203.

Two dimensional time-dependent self-consistent modeling of non-transferred plasma torches

N. Sakthivel and S. Chaturvedi
Institute for Plasma Research, Bhat, Gandhinagar-382 428, INDIA

Abstract
We have performed axisymmetric, 2-D, time-dependent, self-consistent fluid modeling of non-transferred plasma torches. The current density distribution is calculated accounting for the complex geometry and the spatio-temporal variation of resistivity of the partially-ionized plasma. The code can handle a variety of plasmagen gases, including mixtures. Radiation loss is calculated ignoring reabsorption. The plasma parameters obtained at the torch exit have been compared with published experimental and theoretical results.
Keywords: torch, non-transferred, radiation, current density, MHD, plasma

1. Introduction

Plasma torches have been employed as sources of thermal plasmas for a number of applications. Early modeling of plasma torches covered only the plume region, assuming a temperature and velocity profile at the torch exit. During the past decade, a variety of work has been reported including the arc as well as plume regions [1-4]. These studies, by and large, are subject to two major limitations. Firstly, all these studies have assumed some spatial variation of the current density through the plasma, based on experimental studies of free-burning arcs [5]. The current density distribution in the arc region and the anode-cathode potential difference have been calculated numerically based upon the assumed current density profile. This needs prior knowledge of the current density profile for specifying the boundary conditions. In reality, the current density should be determined self-consistently by the spatial distribution of electrical resistivity, the system geometry and the applied voltage. Secondly, most of these studies solve only the steady-state equations. This means that they cannot provide information related to temporal variation in torch parameters, such as fluctuations in electrode voltage, which occur even during normal operation. Furthermore, several applications, such as plasma pyrolysis, require determination of transients due to injection of extra material into a pre-existing torch.

There is, therefore, a pressing need for a time-dependent analysis which determines the current density distribution self-consistently with fluid parameters. We are attempting to satisfy this need, and the present work is the first step in that direction.

In this paper, we report on a two-dimensional (2-D), axisymmetric, time-dependent, self-consistent model of non-transferred plasma torches. The current density distribution has been calculated self-consistently with fluid flow for a given potential at the electrodes. The model can be applied to fairly complex geometries, limited only by the need for axisymmetry. In this paper, we describe the mathematical models used and compare our results with published data.

2. Mathematical model and Assumptions

Fluid flow in this model is determined by a solution of the Navier-Stokes equations for conservation of mass, momentum and energy. This is accomplished using a locally-modified version of the Conchas-Spray code [6]. Conchas-Spray is a time-marching finite-difference code that uses a partially -implicit numerical scheme, which can handle Lagrangian, Eulerian or mixed meshes. The detailed equations can be found in [6].

The spatial variation of the current density inside the torch is calculated by solving the current continuity equation for the given torch geometry and the applied potential, using a modified form of a Finite Element code listed in Ref.[7]. This equation is given by

$$\nabla.(\sigma \nabla\phi) = 0$$

where σ is the space- and time-dependent electrical conductivity, ϕ is the electric potential and the current density $\underline{\mathbf{J}} = -\sigma \nabla\phi$.

The density- and temperature–dependent plasma electrical conductivity has been calculated using the SIGDCS code [8], which takes into account both electron-neutral and Coulomb collisions. Inclusion of both contributions is necessary when dealing with plasmas having a degree of ionization less than unity, when neither type of collisional process may be neglected [8]. The applied potential difference V(t) between the electrodes has been allowed to vary in time according to a proportional feedback algorithm for an assumed current waveform I(t). This is an approximation to the constant-current power supply commonly used in such systems.

The temperature- and density-dependent average charge state and enthalpy of the plasma have been calculated using the IONMIX code [9]. IONMIX calculates the steady state distribution of different charge states for a mixture of elemental species. This calculation is done by assuming detailed balancing, taking into account processes like collisional ionization and recombination, radiative recombination, dielectronic recombination, collisional excitations and deexcitation,and radiative dacay. The rate coefficients are based upon the hydrogenic approximation. The required ionization potentials for different charge states are experimental values taken from the literature [10]. For this work, we have used IONMIX to generate charge state and enthalpy tables for an argon plasma, over the required range of densities and temperatures.

As a first step, the plasma is assumed to be optically thin; hence radiation loss is accounted for by using a volumetric loss rate that neglects re-absorption. The temperature-dependent volumetric radiation loss data for argon have been taken from [1].

Electromagnetic forces have not been taken into account in the present version of the model, but will be added soon. The code can handle a variety of plasmagen gases, including mixtures. To our knowledge, this is the first time-dependent, fully self-consistent MHD model of plasma torches. This will allow us to self-consistently predict the spatio-temporal evolution of plasma and arc parameters for different torch configurations (geometry, dimensions, flow rates, applied potential).

The following major assumptions have been made in the present version of the study:

1. The arc and the fluid flow are assumed to be axisymmetric.
2. The arc is assumed to be in local thermodynamic equilibrium (LTE), so a single temperature prevails for all plasma components.
3. The plasma is assumed to be optically thin – however, we plan to add a radiation transport model.
4. The cathode tip is assumed to be flat.
5. There is no swirl at the inlet and the flow is laminar – the fluid solver is, however, capable of handling swirl as well as turbulent flow.
6. Electromagnetic forces have been ignored – however, this feature is now being added.

3. Computational Domain and Boundary Conditions

The computational domain used in this study is given in Fig.1, which is very similar to the one used in [1] except for slight deviations in the cathode dimensions and the inflow area. The gas is injected at the inlet (line BC). The inflow density is arbitrarily taken to be 1.784×10^{-3} g/cm^3, while the inflow temperature is taken as 1,000 K [2]. The axial velocity (v_r) at the inlet is assumed to have a parabolic profile, given by

$$v_r = v_{max} \ [1.0 - (r/R_{max})^2] \qquad 0 \le r \le R_{max}$$

where r=0 at the rightmost edge of the cathode, v_{max} is the maximum velocity at the inlet and R_{max} is the radial distance between the cathode and anode. The peak inflow velocity has been adjusted to get the required mass inflow rate. The radial velocity (u) is set to zero at the inlet. A no-slip boundary condition has been assumed at

the electrode boundaries. Along EF, we have assumed a free-slip boundary condition. A continuative outflow boundary condition (zero gradients in all quantities) has been assumed along GF. AG is the axis of symmetry.

For the solution of $\phi(r,z)$ and the current density profile J(r,z), appropriate potentials are applied to the cathode and anode surfaces, the difference between these being the inter-electrode voltage V(t).

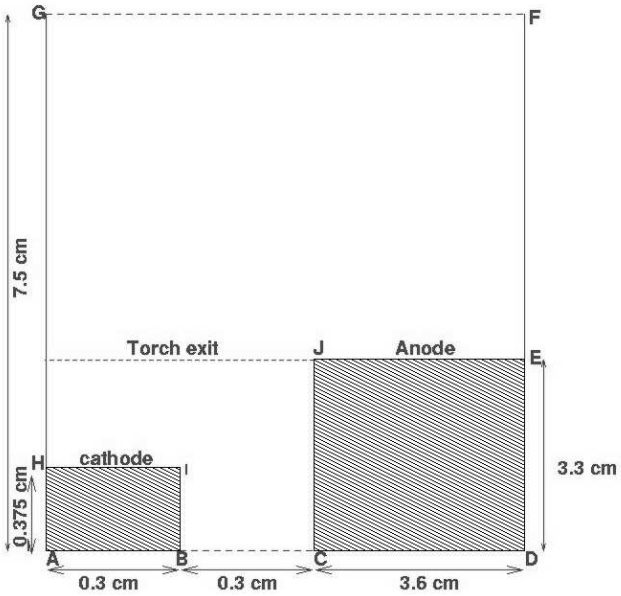

Figure 1. Schematic of computational domain of the plasma torch used in this study (not to scale).

4. Validation and Comparison

a) Preliminary Validation

The validation of the 2-D code has been carried out at each stage of its implementation and development. In the first stage, the code implementation has been checked with a sample problem as given in [6]. This involves an internal combustion engine with a chamfered bowl geometry, with octane spray injection into a cylinder containing air. The mixture is ignited and the progress of the flame front is followed. The results were compared with the results of [6] and a good match obtained. In the second stage, for fluid flow problems, we considered fluid flow in a cylindrical pipe with a constant cross section. Nitrogen gas enters at one end of the cylinder and exits at the other end. The study was carried out for both subsonic and supersonic flow. The inflow velocity profile was taken as parabolic, similar to that obtained in laminar flow through a pipe. This yields maximum velocity near the axis of symmetry and zero velocity at the outer walls, corresponding to a no-slip boundary condition. The maximum velocities chosen for supersonic and subsonic flow were 600 m/sec and 15 m/sec, respectively. In both cases, the inflow gas mass density was taken as 1.09×10^{-3} g/cc and the temperature as 300 K. At the exit, axial gradients of all fluid quantities were assumed to be zero and the radial velocity was also set to zero. In both cases, we obtained good conservation of energy and mass and "reasonable" spatial profiles of fluid quantities.

In the third stage, a typical non-transferred arc torch geometry was examined. This consists of a small flat cathode near the axis of symmetry and a ring anode near the outer wall, very similar to Figure 1. The gas enters in the annular space between the electrodes. In this case too, the inlet velocity profile has been taken as

parabolic, with a maximum velocity of 15 m/sec. In this stage, calculations were performed for two different problems. The first was gas flow without any joule heating. In the second case, we assumed a constant joule heating rate in some cells lying in the arc region. In both cases, mass and energy conservation were found to be acceptable.

The finite element code [7] that has been used for calculating the current density distribution has been validated in both rectangular and cylindrical geometry with electrodes by assuming a constant resistivity and voltage throughout the domain. Conservation of the total current across different axial locations has been checked and found to be correct.

b) Comparison with published results

Since the present work yields the temporal variation of spatial profiles, it is necessary to run the simulation long enough for fluid parameters to reach a quasi-steady-state. It is only at that point that a meaningful comparison can be made with published steady-state results.

In this section, we present our predictions of time-dependent operating conditions in the torch and compare plasma parameters with Westhoff's experimental data and predictions for the B23 case [1]. This involves a system where a hot argon plasma, created within the arc region, flows out of the torch exit into an argon environment. The operating current is 250 A, the mass inflow rate is 0.29 g/sec, and there is no swirl at the inlet. The computational domain used in this study is given in Figure 1. The specified density and temperature at the torch inlet for argon are 1.784×10^{-3} g/cc and 1000 K respectively.

Figure 2 shows the temporal variation of mass outflow rate. The mass outflow rate oscillates between 0.1 – 0.5 g/sec, more-or-less symmetrically around the constant inflow rate. The calculated voltage for this case in [1] is 20.1 volts for an experimentally-measured current of 250 Amps. In our study, we have allowed the voltage to vary according to a feedback control algorithm using only proportional control. The control parameter has been adjusted so as to produce a mean current of 250 Amps. The current and voltage variation are shown in Figures 3 and 4 respectively. The mean current stays around 250 Amps and the mean voltage stays around 14.5 V. However, this voltage does not include the electrode fall. Allowing for a cathode drop of around 4.5 volts, this shows reasonable agreement with the reported value of 20.1 volts [1].

Figure 5 compares our estimates of the radial temperature profile near the torch exit with numerical and experimental data from Westhoff [2]. Westhoff's data were reported at a distance of 1 mm from the torch exit, while we are reporting our results at 0.75 mm from the exit. Over the radial extent of the cathode, and of the anode, our temperatures are consistently lower than those from Westhoff. However, in the intervening gap, our temperatures are higher. Figure 6 shows a comparison of the radial profiles of axial velocity near the torch exit. Since experimental measurements are not available, only simulations results are compared. We find that our predictions are higher by a factor of up to 4.7. We are presently unable to account for this discrepancy.

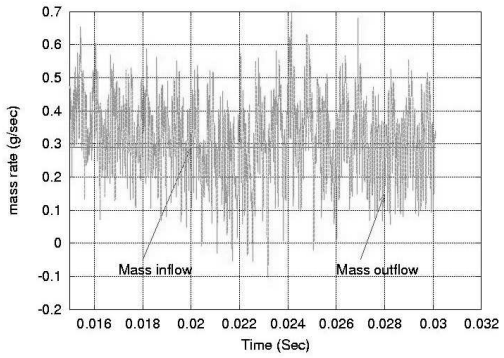

Figure 2: Time dependent mass outflow rate along line GF. The mass inflow rate is also shown for comparison.

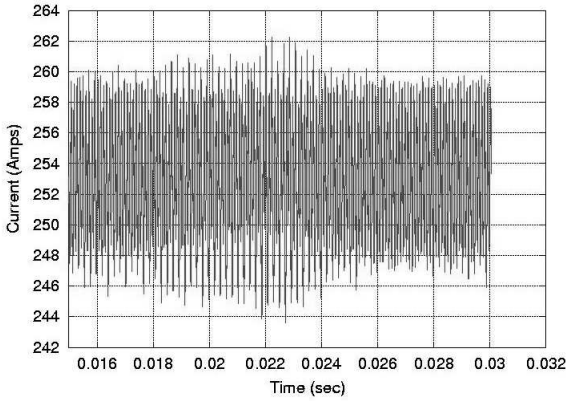

Figure 3: Time dependent variation of torch current

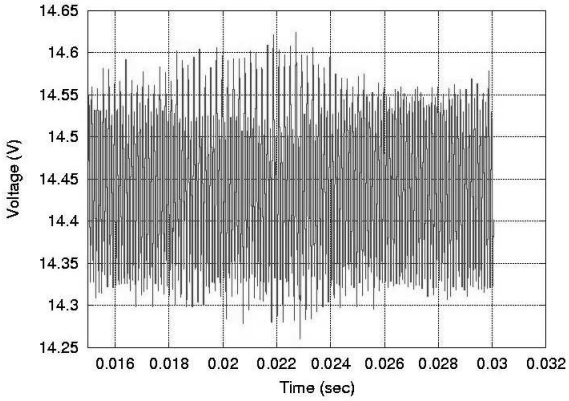

Figure 4: Time dependent variation of torch voltage, due to proportional control algorithm

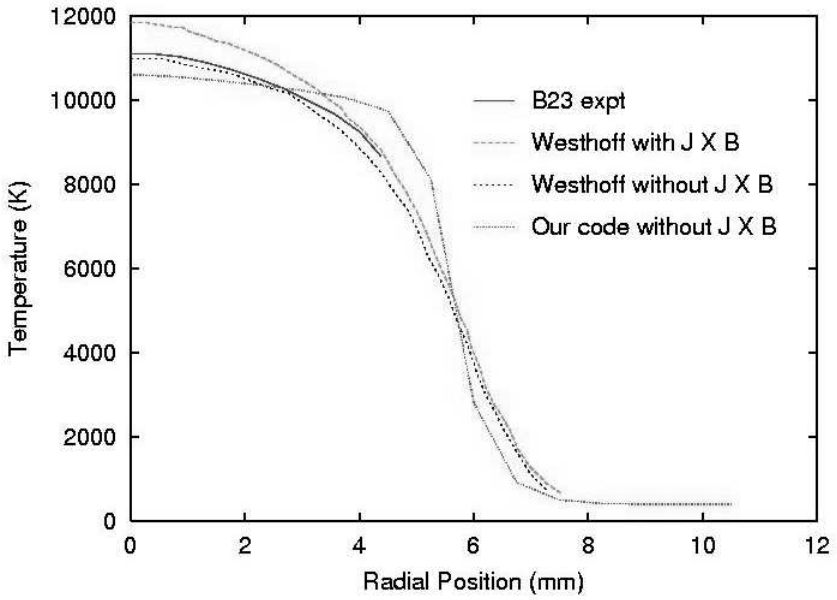

Figure 5: Comparison of temperature profiles in the radial direction near torch exit

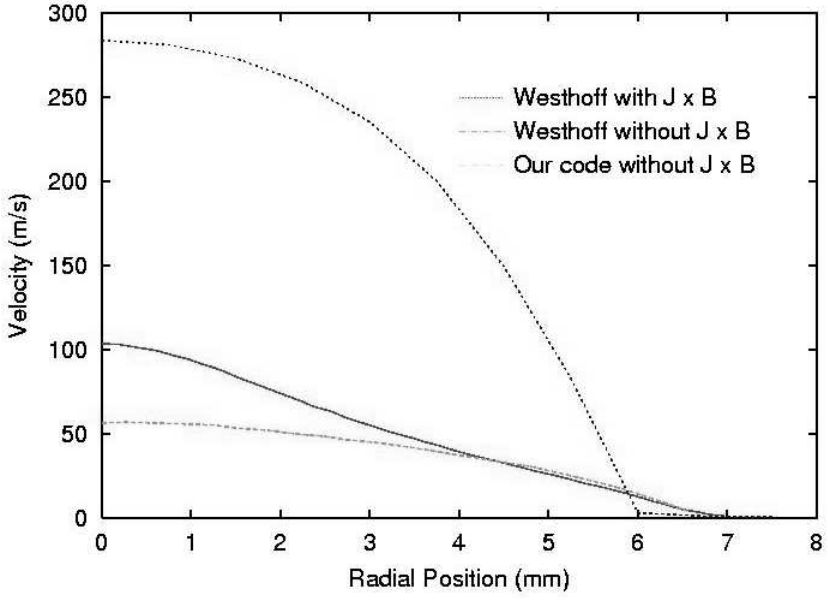

Figure 6: Comparison of axial velocity profile along radial direction near torch exit

5. Conclusions and future work

We have performed axisymmetric, 2-D, time-dependent, self-consistent fluid modeling of non-transferred plasma torches. The model includes a self-consistent calculation of the current density profile throughout the plasma. To our knowledge, this is the first time-dependent, fully self-consistent MHD model of plasma torches. This will allow us to self-consistently predict the spatio-temporal evolution of plasma and arc parameters for different torch configurations.

A comparison of our code results with published work shows that the predicted voltage variation, as well as the radial temperature profile at the torch exit, are in fairly good agreement. However, substantial differences exist in the axial velocity level, which needs further analysis.

In the future, apart from attempting to understand this discrepancy, we also plan to include electromagnetic forces as well as a more sophisticated model for radiation transport.

References

[1] Richard Westhoff, "Modeling the Non-Transferred Arc Plasma Torch and Plume for Plasma Processing", PhD Thesis, Massachusetts Institute of Technology, May 1992.

[2] R. Westhoff and J. Szekely, "A Model of Fluid, Heat Flow, and Electromagnetic Phenomena in a Nontransferred Arc Plasma Torch", J. Appl. Phys. 70(7), 1 Oct. 1991.

[3] A. B. Murphy and P. Kovita, "Mathematical Model and Laser-Scattering Temperature Measurements of a Direct-Current Plasma Torch Discharging into Air", J. Appl. Phys. 73 (10), (15 May 1993).

[4] R.C. Favalli and R. N. Szente, "Physical and Mathematical Modeling of Non Transferred Plasma Torches", Brazilian Journal of Physics, Vol. 28, no.1 (March 1998)

[5] K.C. Hsu, K. Etemadi, and E. Pfender, "Study of the Free-Burning High-Intensity Argon Arc", J. Appl. Phys. 54, 3 (March 1983).

[6] L.D Cloutman, J.K. Dukowicz, J.D. Ramshaw, A.A. Amsden, "CONCHAS-SPRAY: A Computer Code for Reactive Flows with Fuel Sprays", LA-9294-MS, May 1982.

[7] J. N. Reddy, "An Introduction to the Finite Element Method", Tata McGraw-Hill, 2003.

[8] D.A. Erwin and J.A. Kunc, "Scalar DC Electrical Conductivity of Partially Ionized Gases", Comp. Phys. Communications, 42 (1986) 119-125.

[9] J.J. MacFarlane, "IONMIX: A Code for Computing the Equations of State and Radiative Properties of LTE and Non-LTE plasmas", Computer Physics Communications, 56, (1989) 259.

[10] R.L. Kelly and D.E. Harrison, Atomic Data 3 (1971).

Plasma polymerization of C_6F_6 at high substrate temperature of low-*k* applications and its *in situ* FTIR gas phase diagnostics

T. Shirafuji[1] and K. Tachibana[2]
[1]*International Innovation Center, Kyoto Univ., Sakyo-ku, Kyoto 606-8501 Japan*
[2]*Dept. Electronic Sci. & Eng., Kyoto Univ., Kyoto-daigaku-katsura, Nishikyo-ku, Kyoto 615-8510 Japan*

Abstract

Amorphous fluorinated carbon films have been prepared by plasma enhanced chemical vapor deposition method using C_6F_6 at substrate temperature of 400°C. Thermal stability up to 400°C is automatically achieved. Dielectric constant of the films is 2. Infrared absorption spectra of the films have indicated that the films contain benzene rings, and F/C ratio is unity as seen in monomer molecules. No film deposition has been observed if C_4F_8 or C_5F_8 is used as a source monomer at this substrate temperature.

Keywords plasma polymerization, C_6F_6, low-k, thermal stability, in situ FT-IR

1. Introduction

In ultra-large-scale integrated circuits (ULSI), it is necessary that the dielectric constant k of inter-metal dielectric (IMD) should be low for decreasing resistance-capacitance time delay. A few years ago, it had been said that k<2 would be required in 2005. However, due to difficulties in the low-k integration, practical application of new low-k materials has been always achieved a few years later of scheduled ITRS roadmap. Recently, we have reported possibility of k<2 with a-C:F (porous) films using two monomers of C_5F_8 and C_6F_6 as shown in **Fig.1** [1]. However, its thermal stability was poor. Therefore, we have changed our target to k=2 with high thermal stability (>400°C). In this work, we have performed film deposition at 400°C.

In the case of a-C:H and/or SiOC, high temperature deposition is relatively easy, because its deposition rate is reasonably high. However, in the case of a-C:F, its deposition rate fairly decreases with increasing substrate temperature, which has been demonstrated by using C_4F_8 [2]. In order to achieve high deposition rate, we have used C_5F_8 instead of C_4F_8. However, its deposition rate was not enough, and crack has been observed after cooling the samples [3].

Therefore, we examined C_6F_6, because it has benzene structure with pi-bonded carbons, which enhanced polymerization and high deposition rate will be expected. If this is possible, needless to say, thermal stability up to deposition temperature is certified automatically. In addition to this, benzene structure is thermally stable. Therefore, its structure and F/C ratio will be kept even after landing on the high temperature substrate. This may work to increase k-value because relatively low F/C ratio of unity of C_6F_6 is not favorable in comparison to conventional Teflon (F/C=2). However, its structural symmetry may work to reduce polarization and k-value.

In this paper, we report that low-k (k=2) a-C:F with carbon ring structure is available by plasma polymerization of C_6F_6 at 400°C, and its reaction mechanisms are discussed on the basis of *in situ* FTIR diagnostics of gas phase of the C_6F_6 plasma.

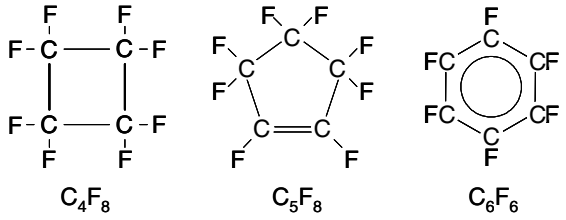

Fig.1 Molecular structure of fluorocarbon monomers, which can be used for preparation of fluorinated carbon films.

2. Experimental

Films were deposited with PE-CVD (or plasma polymerization as described later) method using C_6F_6 as a monomer and ICP as a plasma source. Substrate temperature T_{sub} was varied from room temperature (RT) to 400°C. Flow rate and pressure the monomer was 5 sccm and 50 mTorr, respectively. Typical deposition time was 30 min. RF power was 100 W. Chemical composition of the films was characterized by FTIR and XPS. Thermal stability of the films was characterized by measuring residual thickness after thermal treatment at 400°C for 30 min in N_2 ambient. Dielectric constant of the films was determined by capacitance measurements of MIS structure of Al/Film/p^+-Si.

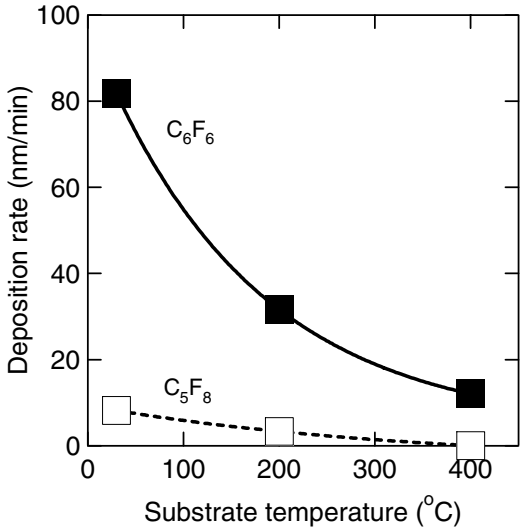

Fig.1 Deposition rate of the films deposited with C_5F_8 and C_6F_6.

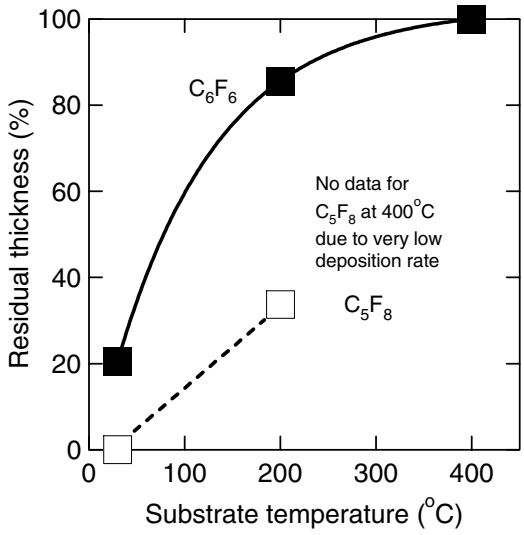

Fig.2 Residual thickness of the films, deposited with C_5F_8 and C_6F_6, after thermal treatment at 400oC for 30 min in N2 ambient.

3. Results and discussion

3.1 Deposition rate (at 400°C)

Figure 1 shows film deposition rate as a function of T_{sub}. For comparison, data for C_5F_8 and C_6F_6 are shown in the figure. Deposition rate of C_6F_6 at room temperature is as high as 80 nm /min, while that of C_5F_8 is 10 nm/min under the same condition. Deposition rate for both monomers decreases with increasing T_{sub} as known generally even in the case of C_6F_6. However, the most important fact is that C_6F_6 plasma can deposit films even at high T_{sub} at which C_5F_8 plasma cannot deposit films as can be understood from the data for T_{sub}=400°C. This is due to highly polymerizing nature of π bonds in benzene ring in C_6F_6.

3.2 Thermal stability (residual thickness)

Figure 2 shows residual thickness of the films after thermal treatment at 400°C for 30 min in N_2 ambient. As can be seen in the figure, the films deposited with C_6F_6 have higher thermal stability in comparison to C_5F_8. Especially for the films deposited at room temperature, the film from C_5F_8 is not left on the substrate after the thermal treatment, while the film from C_6F_6 remains 20% of initial thickness. Regarding the films deposited at 400°C, the films from C_5F_8 may have thermal stability up to 400°C. However, due to impossibility of film deposition from C_5F_8 at 400°C, no data for T_{sub}=400°C can be presented for C_5F_8 in the figure. On the other hand, needless to say, the film deposited with C_6F_6 at 400°C shows thermal stability up to 400°C automatically, because it has been deposited at 400°C.

3.3 Dielectric constant

Figure 3 shows relative dielectric constant of the films deposited with C_6F_6 at RT, 200 and 400°C. Regarding the films deposited at room temperature, their dielectric constant is as high as 2.8 for as deposited films and

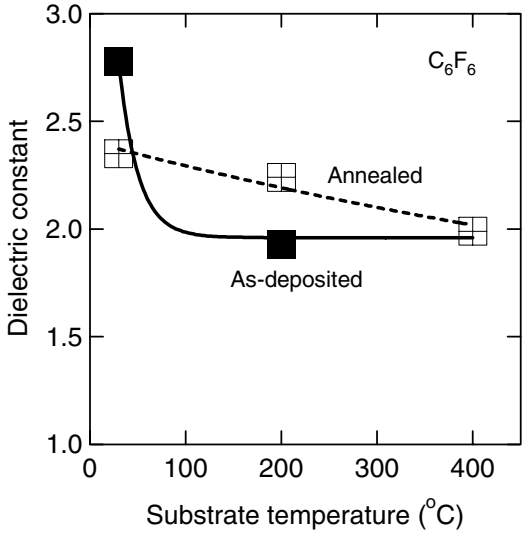

Fig.3 Dielectric constant of the films deposited with C_6F_6 at RT, 200 and 400°C. Dielectric constant after the thermal treatment is also shown for comparison.

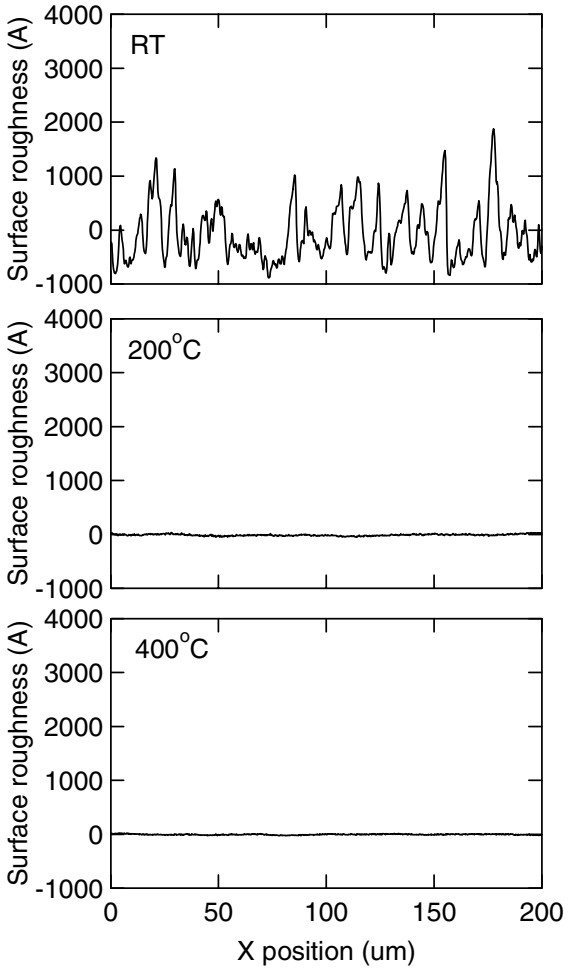

Fig. 4 Surface roughness observed on the films deposited at room temperature, and smooth surface on the films deposited at 200 and 400°C.

decreases to 2.4 after thermal treatment. Causes of this are not clear at present, surface roughness may cause this phenomenon, because only the samples deposited at room temperature have quite rough surface as shown in **Fig.4**. This roughness can be explained by high sticking probability of precursors. Because of highly polymerizing nature of C_6F_6, its product through electron impacts must have the similar nature, and surface migration to smoothen surface should be suppressed, which leads to rough surface. The films deposited under such condition, must be less cross-linked and poor thermal stability as indicated in **Fig.2** and **3**.

For the films with smooth surface, k-value increases or is stable after thermal treatment. Slight increase of k-value for the films deposited

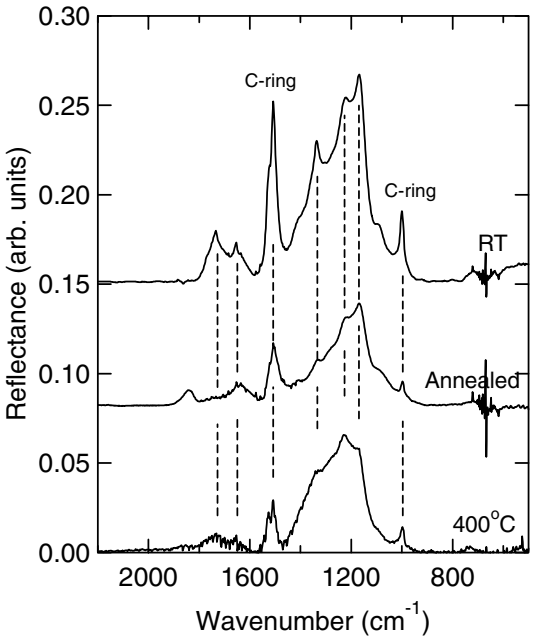

Fig.5 FTIR spectra of the films deposited with C_6F_6 at room temperature and 400°C. Spectrum after thermal treatment of RT deposited films are shown for comparison,

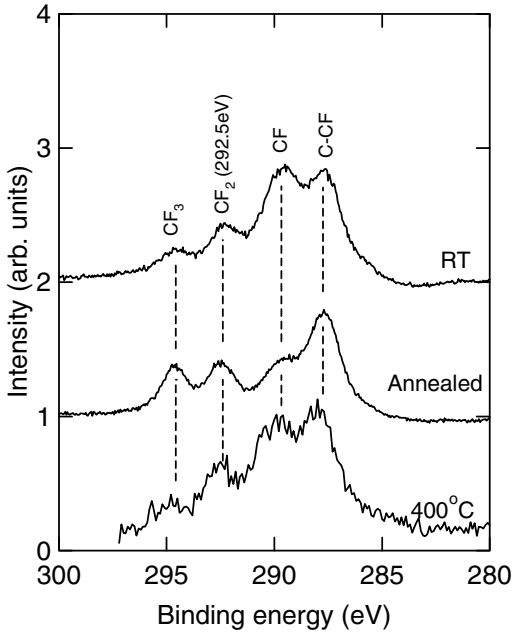

Fig.6 C(1S) region of XPS spectra of the films deposited with C_6F_6 at room temperature and 400°C. Spectrum after thermal treatment of RT deposited films are shown for comparison,

at 200°C can be explained by shrinking of the films because its thickness reduction is only 20%, while that of C_5F_8 film is as high as 60% or more which cannot be explained by only shrinking but also vaporization of the film.

The films deposited at 400°C, as expected, do not show marked variation in k-value after thermal treatment at 400°C, namely, they are stable at 400°C.

3.4 Structure of the films

As long as characterizing k-value and thermal stability, they are perfect as a low-k material with k=2. In order to see how they are realized, structural properties of the films were investigated by FTIR and XPS.

Figure 5 shows FTIR spectra of the films deposited with C_6F_6 at room temperature and 400°C (Spectrum after thermal treatment of RT deposited films are shown for comparison). These spectra are not resemble to conventional broad IR absorption peak corresponding to random amorphous a-C:F structure. As indicated in the figure, clear carbon ring IR peaks are observed, which means that benzene ring structures are incorporated in the films, and suggesting electron impact in the plasma does not lead full fragmentation of the monomers (with keeping monomer's original molecular shape). This scheme should not be termed as CVD but polymerization which incorporates functional structure of the monomers in the deposited films.

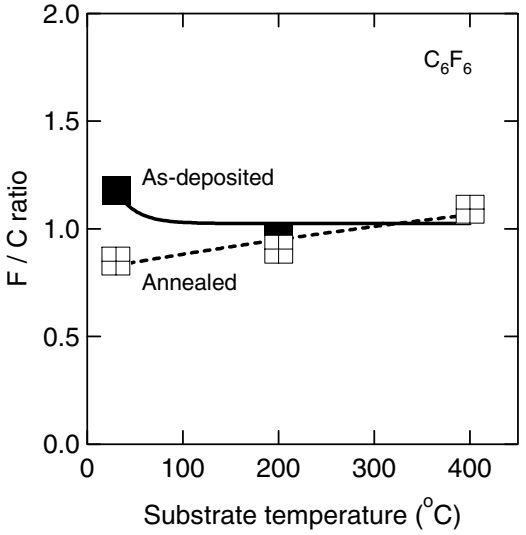

Fig. 7 F/C ratio of the films as a function of substrate temperature.

XPS spectra of the films also support above model. **Figure 6** shows XPS spectra of the film deposited at 400°C together with that at RT and after thermal treatment. The films deposited at room temperature and 400°C show similar XPS spectra. However, the spectra after thermal treatment of the RT deposited films show reduction of C-F bond peak intensity. As the thickness reduction of RT deposited films is as large as 80% after the thermal treatment (this is considered to be due to vaporization), weakly bonded C-F containing structure exists in the films. This structure is also suggested by quite large surface roughness of the films deposited at room temperature as described above subsection. On the other hand, the film deposited at 400°C did not show marked difference in XPS spectra after the thermal treatment.

By using relative sensitivity and instrument function, F/C ratio can be calculated from area intensity of C(1S) and F(1S) region of XPS spectra. **Figure 7** shows F/C ratio of the films, in which F/C ratio is close to unity as in the case of C_6F_6 monomer. Although this data also support incorporation of ring structure with C-F bonds, F/C=1 is smaller than F/C=2 for Teflon, which has k=2. Therefore, k=2 for F/C=1 cannot be explained by conventional model of F/C ratio vs. k-value for amorphous a-C:F films which contains only random network of C-C and C-F_x. At this moment, we do not have quantitative theory to explain k=2 for F/C=1.

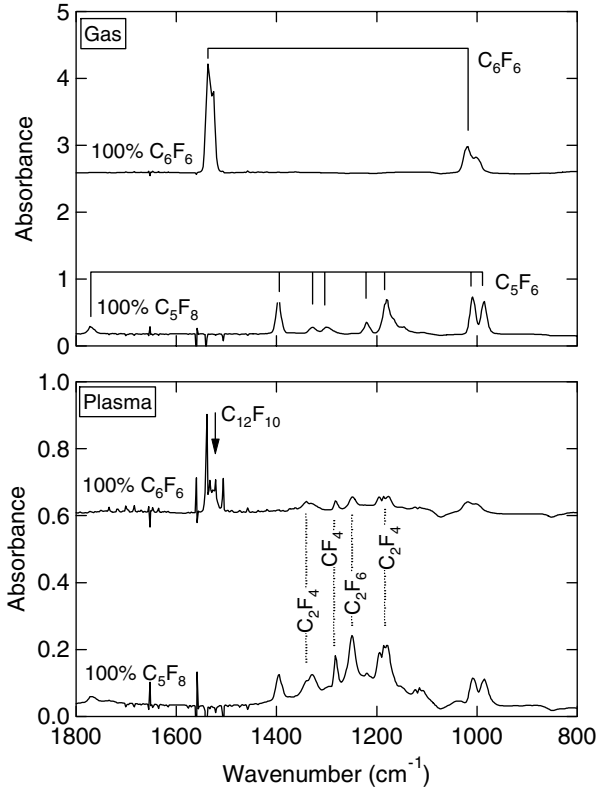

Fig.8 *In situ* FTIR spectra of the gas phase of C_6F_6 and C_5F_8 gas / plasma.

However, this must have relationship to symmetric structure of C-F ring structure brought by nature of C_6F_6 monomers.

3.5 *In situ* FTIR

As described above, C_6F_6 plasma can prepare unique a-C:F (or a-C:F:C_6F_x amorphous/polymer blend). In order to investigate deposition mechanisms, *in situ* FTIR of the gas phase has been performed. **Figure 8** shows spectra of the gas and plasma of C_6F_6 (together with those of C_5F_8 for comparison). As can be seen in the figure, the plasma of C_6F_6 does not show small molecules such as CF_4, C_2F_4 and C_2F_6 which are pronounced in the case of C_5F_8. This means that C_6F_6 molecule is not fully fragmented in the gas phase (while C_5F_8 is mostly fragmented to less carbon containing species). In the plasma of C_6F_6, the interesting peak appears in the spectrum, which is not observed in C_5F_8 plasma, namely, $C_{12}F_{10}$. Production of $C_{12}F_{10}$ suggests that $C_6F_6+e \rightarrow C_6F_5+F+e$ and $2C_6F5 \rightarrow C_{12}F_{10}$ are occurring in the gas phase. As the large pressure reduction has been observed just after ignition of plasma, this must be occurring in the gas phase. However, quite high deposition rate on the room temperature substrate, this reaction must be occurring also on the surface (surface polymerization). As this model can explain C-rin g incorporation in the films deduced from IR spectra of the films, F/C=1 and majority of C-F and C-CF deduced from XPS investigation, this model is considered to be the most probable one for our C_6F_6 plasma polymerization process.

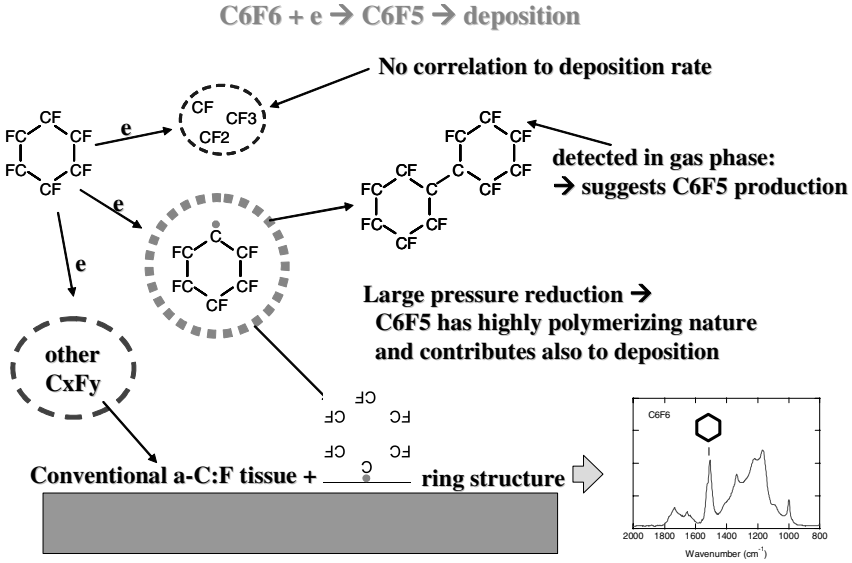

Fig.9 Proposed deposition model for C_6F_6 plasma.

4. Summary

Amorphous fluorinated carbon films with C-ring structures have been prepared by plasma enhanced chemical vapor deposition method using C_6F_6 at substrate temperature of 400°C. Deposition rate reduction due to higher substrate temperature can be suppressed by highly polymerizing nature of C_6F_6. Film availability at 400°C, which is not achieved by the other monomers such as C_4F_8 and C_5F_8, has realized thermal stability up to 400°C. Dielectric constant of the films is 2 even for F/C ratio of almost unity, which may be due to symmetric structure of C-F ring structure. Infrared absorption spectra of the films have indicated that the films contain the benzene rings in their amorphous tissue. In situ FTIR observation has suggested that C_6F_5 and C_xF_y (not fragmented CF_x) are contributing to the film deposition for preparing C-ring structure and amorphous a-C:F structure, respectively.

Acknowledgments

This work has been partly supported by Kyoto Nano-Technology Cluster, Grand-in-Aid of MEXT, Japan, and NEDO/MIRAI Project.

References

[1] T. Shirafuji, A. Tsuchino, T. Nakamura and K. Tachibana: Jpn. J. Appl. Phys. 43 (2004) 2697.

[2] T. Shirafuji, Y. Hayashi and S. Nishino: Advanced Metallization Conference 1999, Mater. Res. Soc. Symp. Proc., ULSI XV (2000) 425.

[3] T. Shirafuji, A. Kamisawa, T. Shimasaki, Y. Hayashi and S. Nishino: Thin Solid Films, 374 (2000) 256.

In situ FTIR diagnostics of DVS-BCB plasma used for plasma polymerization of low-*k* films

T. Shirafuji[1], T. Wakai[2], Y. Nishimura[2] and K. Tachibana[2]
[1]*International Innovation Center, Kyoto University, Sakyo-ku, Kyoto 606-8501 Japan*
[2]*Dept. Electronic Sci. & Eng., Kyoto Univ.., Kyoto-daigaku-katsura, Nishikyo-ku, Kyoto 615-8510 Japan*

Abstract
Plasma polymerization of DVS-BCB has been performed for preparation of low-*k* SiOC films. Films have shown dielectric constant of ~2.3, but it increased to 3.3 for higher RF power. The causes of the increase in dielectric constant are discussed on the basis of the data of *in situ* gas phase FT-IR diagnostics of the plasma and characterization of the films.
Keywords plasma polymerization, low-k, in situ FTIR

1. Introduction

In ultra-large-scale integrated circuits, it is necessary that the dielectric constant k of inter-metal dielectric should be low for decreasing resistance-capacitance time delay. Many materials and process techniques have been proposed for the low-*k* applications. Due to this frequent change of materials and processing methods, low-*k* engineering is always under construction. In order to fulfill up-coming requirements smoothly, "scaling rule" should be applied also to low-*k* materials, where processing method is fixed, and only minor changes in monomers are required [1]. This kind of approach can be realized only for polymerization and/or co-polymerization methods using monomers with suitable functional groups, and a plasma polymerization method has been proposed by Kikkawa *et al* [2], in which divinyl siloxane-bis-benzocyclobutene (DVS-BCB) shown in **Fig.1** has been used as the first attempt.

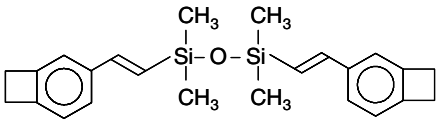

Fig.1 Structure of DVS-BCB monomer.

However, this monomer was not used for plasma polymerization before, and nobody knew its reaction mechanisms in the gas phase and/or surface. Therefore, in order to clarify decomposition scheme and deposition mechanisms, and also its correlation to film properties, we must perform *in situ* diagnostics of plasma polymerization of DVS-BCB.

In our previous work, we have investigated effects of plasma exposure on DVS-BCB monomer coated on substrate surface using *in situ* FTIR reflection spectroscopy, in which UV irradiation has been revealed to work for bond breaking [2]. In this work, we have performed gas-phase diagnostics of DVS-BCB plasma together with structural and electrical characterization of the deposited films.

2. Experimental

Experimental setup is shown in **Fig.2**. As the DVS-BCB was liquid source and had quite low vapor pressure, liquid mass flow controller and vaporizer were used, and all the reactor walls (except windows) were heated up to 200°C. Although configuration of plasma source was ICP (13.56MHz), it seemed to be operated under CCP mode due to quite high operation pressure. Vaporizer temperature was 180°C, where Ar gas was used as a carrier gas with 500 sccm, and flow rate of DVS-BCB was 0.102 g/min. Under this condition, DVS-BCB/Ar was fed into reactor until total pressure reached 3 Torr. Film deposition experiments were performed under this condition as a function of RF

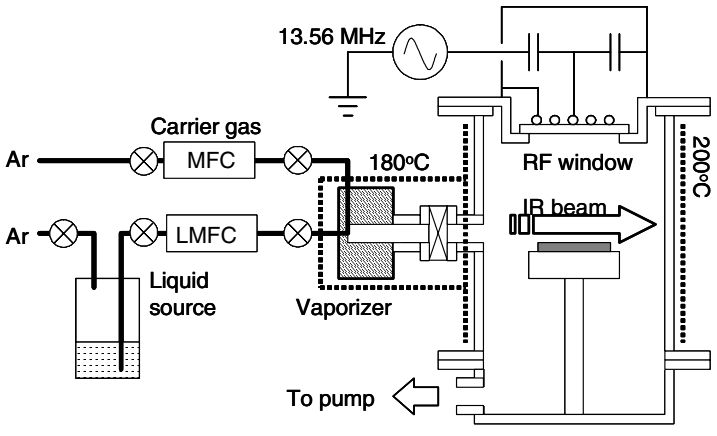

Fig.2 Schematic illustration of experimental apparatus.

power. In order to investigate decomposition scheme of the monomer as a function of discharge time, gas-phase diagnostics were performed on closed reactor without gas flow and pumping. Chemical structure of the deposited films was investigated with FT-IR and XPS. Relative dielectric constant was obtained from capacitance of the films by constructing MIS structure with Al, film and p^+ c-Si substrate. Measurement frequency was 1 MHz.

3. Results and Discussion

3.1 Deposition rate

Figure 3 shows deposition rate of the films as a function of RF power. With increasing RF power from 50 to 100 W, deposition rate increases from 5 to 23 nm/min, and saturates for higher RF power. This means that rate determining step is decomposition of the monomers for 50-100 W. For higher RF power, on the other hand, it turns out to be supply of the monomers, and excess decomposition of the monomers may occur in this condition. Therefore, by characterizing properties of the films deposited under these conditions, it is expected that effects of excess decomposition of the monomers on the structure and dielectric properties of the films.

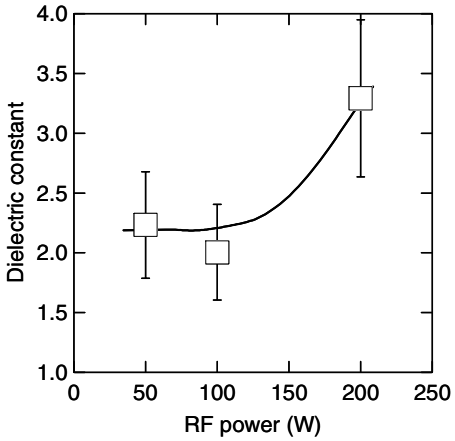

Fig.4 Relative dielectric constant of the films as a function of RF power.

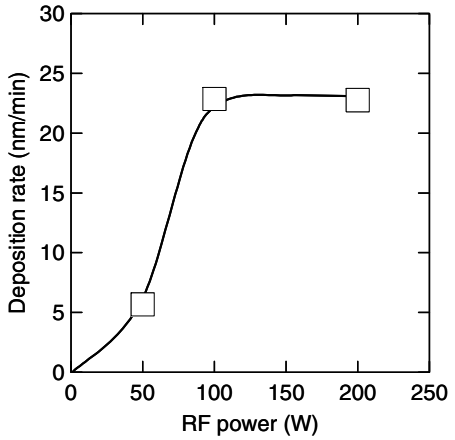

Fig.3 Deposition rate of the films as a function of RF power.

3.2 Relative dielectric constant

Figure 4 shows relative dielectric constant of the films as a function of RF power. As expected from variation of deposition rate as a function of RF power, dielectric constant of the films deposited at lower RF power shows lower value. As the spatial uniformity of the film thickness was quite poor for our present experimental setup (namely, source monomer was fed from a side of the reactor), thickness of the film where the MIS structure is prepared is not obtained. Therefore, the film thickness was obtained by averaging the thickness around the area of MIS structure. The error bar in **Fig.4** is due to this thickness uncertainty. Although there remain several technical issues, the data in Fig.4 show that relative dielectric constant of 2~2.5 can be obtained. For practical use of these films as a low-k film, mechanical strength and thermal stability must be examined. This will be carried out in future. Before going to practical issues, we have investigated deposition mechanisms of the films by characterizing film structure and gas phase of the plasma.

3.3 Chemical structure of the films

Figure 5 shows infrared absorption spectra of the films deposited at 50, 100 and 200 W. The vertical axis in the figure is absorption coefficient calculated from absorbance and thickness of the films, and peak intensity (or area) is proportional to density of these chemical bonds in the films. As shown in the figure, chemical bonds detected by IR spectroscopy are Si-O-Si, Si-CH_3, CH_x, C-ring and Si-H_x, in which most of the components comes from structure of the monomer except Si-H_x bonds. Cyclobutene and vinyl group are not detected in the spectra, which means these bonds are used for polymerization, and mainly affected (or attacked) by electron impact in the plasma.

The film deposited at low RF power of 50 W, highly amount of carbon-containing groups are detected in the spectrum, which suggests that deposition condition is not closer to CVD condition characterized by high fragmentation of monomers, but polymerization in which only limited parts of a monomer is decomposed by electron impact. In this condition, lower dielectric constant is expected. With increasing RF power, density of carbon-containing group decreases, and film structure becomes closer to amorphous SiO_x, which may lead

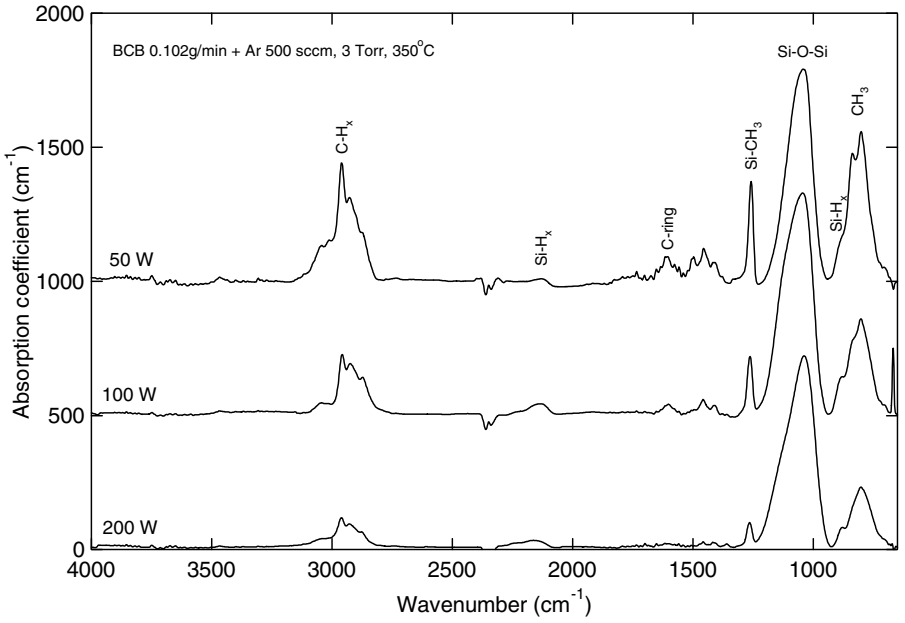

Fig.5 IR absorption coefficient of the films deposited with BCB/Ar plasma as a function of RF power.

increase of dielectric constant. At the same time, density of Si-H_x bonds increases. In order to generate Si-H bonds in the films, H atoms must be removed from C-H_x groups attached on the monomers in the gas phase, which also means that this condition is highly fragmenting condition for the monomers.

Figure 6 shows relative composition of Si, O and C in the films. Density of hydrogen is not represented in the figure because the H atoms cannot be detected by XPS. However, most of H atoms are regarded to be attached as C-H_x group as can be understood from IR absorption spectra of the films. Regarding density of C atoms relative to Si or O atoms, it is 4 or 8 even for the condition with the highest C density. These value is quite smaller than the ratio of C/Si or C/O in a monomer structure (12 or 24). This result suggests that some parts in monomer structure are detached by electron impact, and becomes stable species to be exhausted out of deposition zone. As the vinyl groups are weak bridge in the monomer and benzene ring is stable structure, vinyl groups in the monomer are considered not to be simply opened, but also decomposed. The ratio of Si/O is always 2 even for higher RF power of 200 W, this means that Si-O-Si in the monomer is tough structure in comparison to the other groups in the monomer.

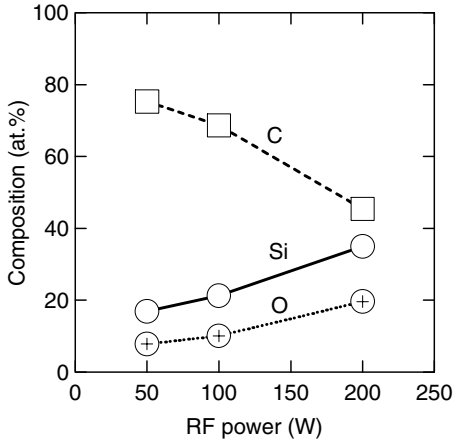

Fig.6 Composition of the films as a function of RF power, which was calculated from relative intensity of XPS spectra of the films (instrument function is also considered).

3.4 Gas-phase diagnostics

Figure 7 shows *in situ* IR absorbance of the gas phase of reactor after discharge for 0, 2, 6 and 10 seconds. As seen in the figure, intensity of the IR absorption peak decreases with increasing discharge duration except for the peak at ~2000 and 900 cm^{-1}. The structure of a BCB molecule consists of Si-CH_3, Si-O-Si and benzene ring with cyclo-butene group, and vinyl group as shown in **Fig.1**. IR absorption peaks for these structures are indicated on the **Fig.7**. As can be understood from the figure, decrease rate of the peak intensity is not the same for each other. For better understanding of this behavior, variation of intensity for these peaks has been plotted as a function of discharge duration, which is shown in **Fig.8**.

Vinyl and cyclo-butene show the fastest decomposition rate. In

the

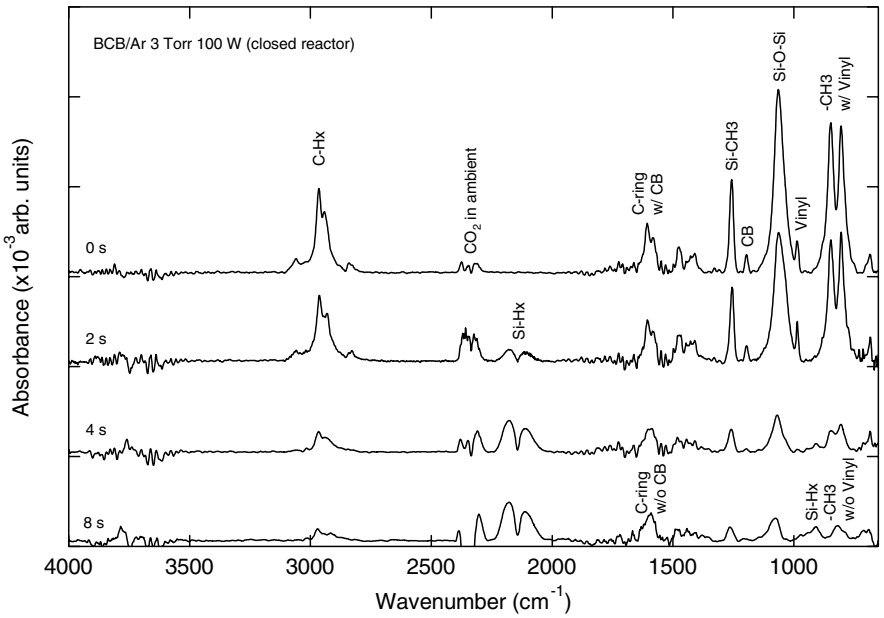

Fig.7 In situ gas-phase IR spectra of BCB/Ar plasma in closed reactor as a function of discharge time.

spectrum after 10-second discharge, these peaks disappear completely. This can be explained by chemical instability of these chemical bonds, because they contain double bonds which easily open by electron impact with smaller energy, which supports speculation deduced from film structure analysis.

On the other hand, the peaks for benzene ring, Si-O-Si and Si-CH_3 still exist even after 10-second discharge. Therefore, these chemical structures can be incorporated in the films. This is consistent to the results of chemical structure analysis of the films.

With increasing discharge duration, several peaks change their peak shape. For example, the benzene ring at 1600 cm^{-1} has two peaks before discharge, and its peak shape turns into one peak after 8-second discharge. This must be due to that cyclo-butene ring associated with benzene ring has been opened by electron impact, and a vibration mode due to association of cyclo-butene has disappeared. Similar trend is seen at around 800 cm^{-1}, where C-H_x mode exists. In this region, all the C-H_x bonds are contained. Before discharge, BCB contains CH_3, CH_2 in vinyl. As the vinyl structure rapidly disappear within the first 8 seconds, the peak profile with two peaks

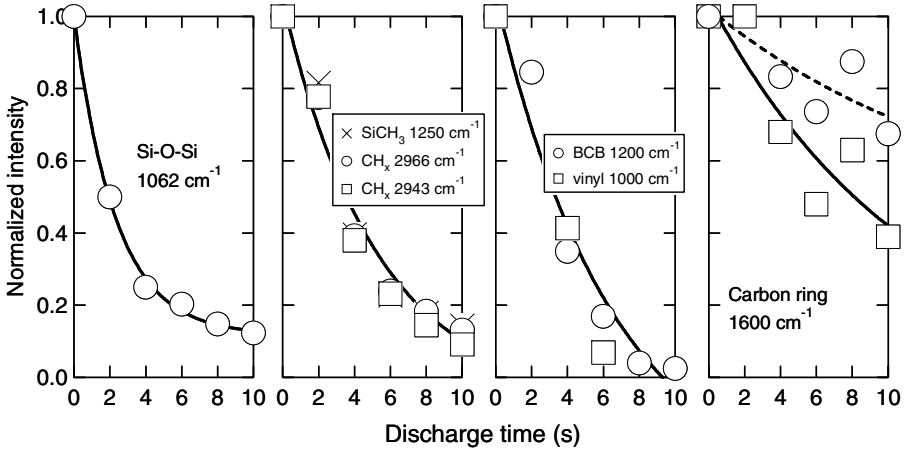

Fig.8 IR peak intensity of several chemical bonds detected in the gas phase as a function of discharge time.

disappear and becomes one peak after 10-second discharge. Except for the fact that benzene ring at 1600 cm^{-1} still exists and a new peak appears at 900 cm^{-1}, entire peak profile in the range of 1800-650 cm^{-1} is quite similar to that for HMDSO molecule, because chemical structures contained in the HMDSO are only Si-O-Si and $Si-CH_3$.

As shown in **Fig.7**, two peaks at 2100 cm^{-1} are generated with increasing discharge duration. Although these peaks are similar to R and P branch of SiH_4, Q branch was not observed. Although CO has absorption peak at the similar region, variation of CO_2 is not consistent to this peak. Therefore, this result suggests that Si-H containing species are created in the gas phase. As the films contain Si-H bonds, especially for higher RF power, bond breaking of Si-C-H is considered to occur at higher RF power, and H atoms attach to Si.

4. Summary

Plasma polymerization of DVS-BCB has been performed for preparation of low-k SiOC films. Films showed dielectric constant of ~2.3 for lower RF power of 50 W, but increased to 3.3 with increasing RF power to 200 W. Structural analysis of the films suggested that C-containing parts were reduced in the case of higher RF power. Gas phase diagnostics results suggested that, as a possible reason for the reduction of C-containing species, higher RF power brings about higher decomposition of C-containing bonds and/or detachment of C-containing groups from the monomer, which was faster than those for Si-O-Si and benzene rings. Furthermore, much higher RF power leaded also Si-C-H bond breaking and production of Si-H containing species, which were incorporated in the films.

Acknowledgments

This work has been supported by NEDO/MIRAI Project.

References

[1] T. Kikkawa, Ext. Abst. ADMETA 2003: Asian session, 1-2, p.4 (2003).

[2] T. Wakai, T. Shirafuji and K. Tachiban a, Proc. 21st Symp. Plasma Processing, Jan. 28-30, 2004, Hokkaido Univ., A1-10, p.34 (2004).

Experimental Investigations of Spatial and Temporal Distributions of Oscillations in a Thermal Plasma Jet

J. Hlina, J. Gruber and J. Sonsky

Institute of Electrical Engineering, Academy of Sciences of the Czech Republic, Prague, Czech Republic

Abstract
Series of images from a high-speed CCD camera were used for evaluations of spatial distributions of hydrodynamic fluctuations and their temporal evolution in a thermal plasma jet. The evaluation procedure was based on the fast Fourier transform and wavelet analysis of time series reflecting the evolution of the plasma jet optical radiation in each pixel of the camera record. The results have shown the existence of various types of oscillations differing in both the locations of maximal amplitudes and their temporal stability.

Keywords
Thermal plasma jet, hydrodynamic fluctuations, CCD camera, fast Fourier transform, wavelet analysis.

1. Introduction

Thermal plasma jets are being used in a growing number of applications where the thermal transport in the jet or between the jet and an inserted body is important for the efficiency of technological processes. The energy transfer is influenced significantly by turbulent phenomena [1,2] which manifest themselves also as a modulation of the plasma jet optical radiation and can be thus recorded and analysed [3]. The effects of vortex structures on the characteristics of a plasma jet are stressed by the resulting entrainment of external air [4]. Experimental investigations of these processes are important because the theoretical models of thermal plasma jets still do not include realistic involvement of turbulence [5] and more experimental results concerning plasma instabilities are needed [6]. In this work we describe the results of investigations of oscillations detected in a thermal plasma jet based on analysis of their spatio-temporal characteristics mainly by means of wavelet analysis of CCD camera records. These investigations build on a previous work dealing with mapping of spatial distribution of the oscillations [7] by means of the fast Fourier transform (FFT).

2. Experimental arrangement and results

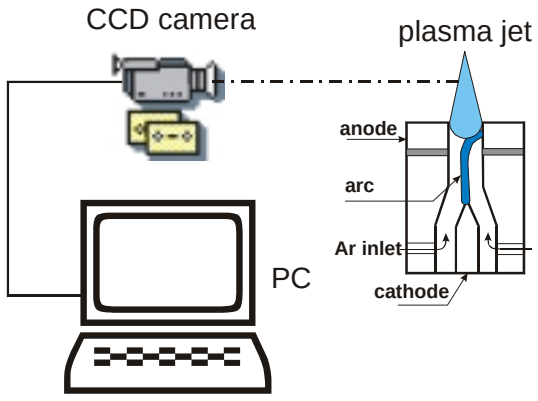

Fig.1. Experimental arrangement.

The experiments were carried out (Fig.1) using a vertically oriented cascaded d.c. fed arc torch working with argon with a typical arc length about 30 mm. The torch design was of a common type with a conical cathode and cylindrical anode working also as an output nozzle. The arc current was 100 A and the arc voltage 30-60 V depending on the gas flow rate which was varied in the range 10-80 slm. The gas heated by the arc discharge exited the plasma torch through the orifice with the diameter 8 mm. Records of the plasma jet radiation (examples are in Fig.2, colours represent the total optical radiation intensity) contained 4096 shots of the plasma jet acquired by a high-speed, black/white, 8 bit CCD camera with the frame frequency 33 kHz and resolution 72 x 96 pixels.

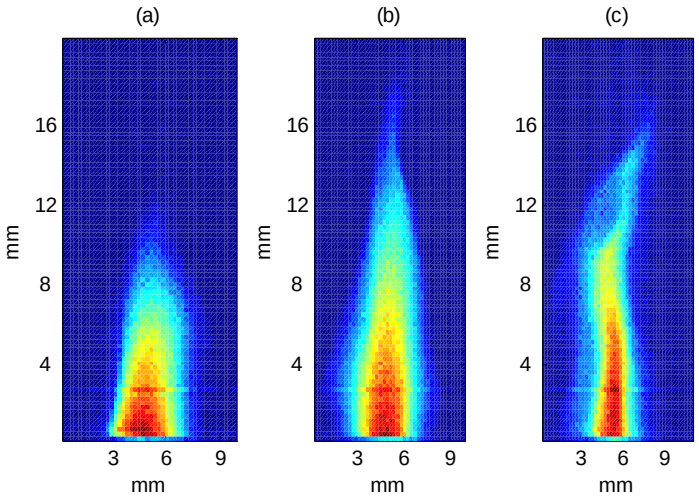

Fig.2. Examples of plasma jet images taken at 10 (a), 20 (b) and 60 slm (c).

The evaluation of the acquired data is possible using the FFT of data series reflecting time evolution of the signal recorded in each pixel of the CCD camera chip. The FFT yields frequency spectra with peaks showing significant oscillations in the plasma jet. The examples of frequency spectra in Fig.3 for the gas flow rates 10, 20 and 60 slm are the summations of FFT amplitudes in the whole plasma jet and show except the distinct peak at 300 Hz (which is caused by the modulation of the arc current) several peaks reflecting oscillations of a hydrodynamic origin. The spatial distribution of FFT

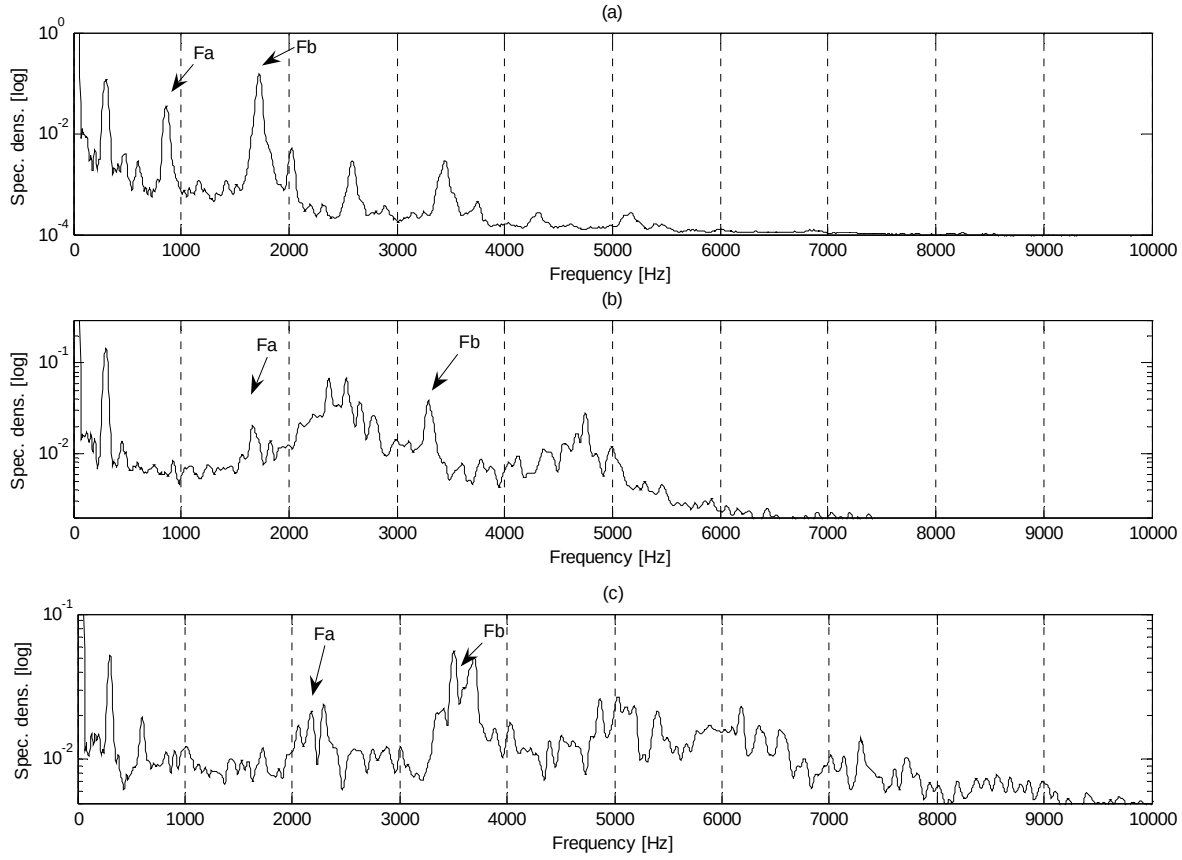

Fig.3. Frequency spectra at 10 (a), 20 (b) and 60 slm (c) with labels showing frequencies used for wavelet analysis.

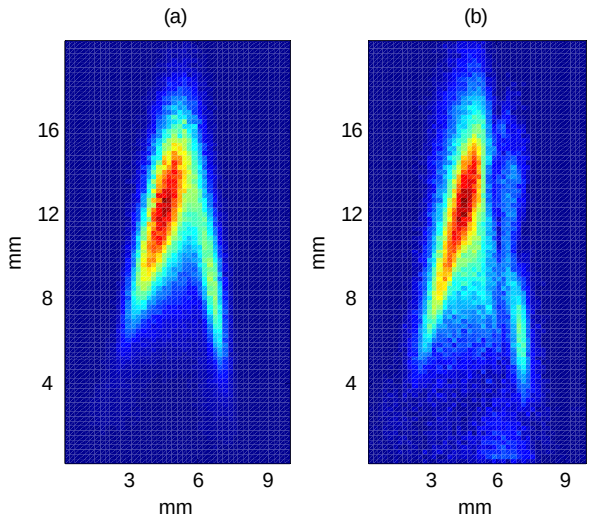

Fig.4. Comparison of spatial distribution of oscillations acquired by means of FFT in range 2300-2600 Hz (a) and wavelet analysis, scale 13 (b), at 20 slm.

amplitudes may be used to see the spatial distribution of oscillations on an arbitrary frequency in the spectrum.

The same data series have been used in this work mainly for the wavelet analysis on some chosen frequencies indicated in Fig. 3. The wavelet analysis was carried out using the complex Morlet wavelet. In the case of this wavelet type the relation between the wavelet pseudofrequency f and wavelet scale is $f=f_s/a$, where f_s is the sampling frequency (Hz) and a the wavelet scale given in number of samples. Using the complex wavelets, it is possible to study separately the behaviour of the real and imaginary components which reflect the coincidence of amplitudes or phases of the wavelet with the analysed signal. In our case we can so reveal the regions of significant occurrence of the studied oscillations and shifts of their location in time. The evolution of correlations on wavelet scales corresponding to

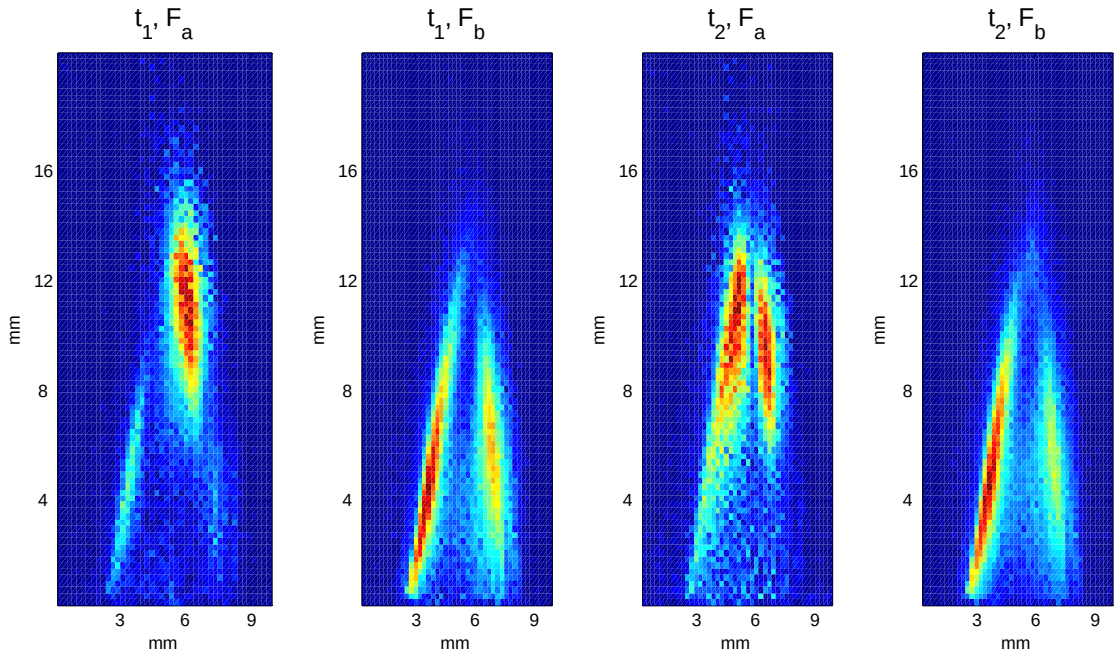

Fig.5. Distributions of oscillations for wavelet scales 38 and 19, corresponding to frequencies F_a, F_b, respectively, indicated in frequency spectra on Fig. 3a and at instants of time t_1, t_2. Gas flow rate 10 slm.

the chosen frequencies show then the temporal evolution of oscillation amplitudes on these frequencies. The summation of the wavelet correlation coefficients in the time series should result in the same spatial distribution of oscillation amplitudes as that acquired by the FFT and may be thus used e.g for checking

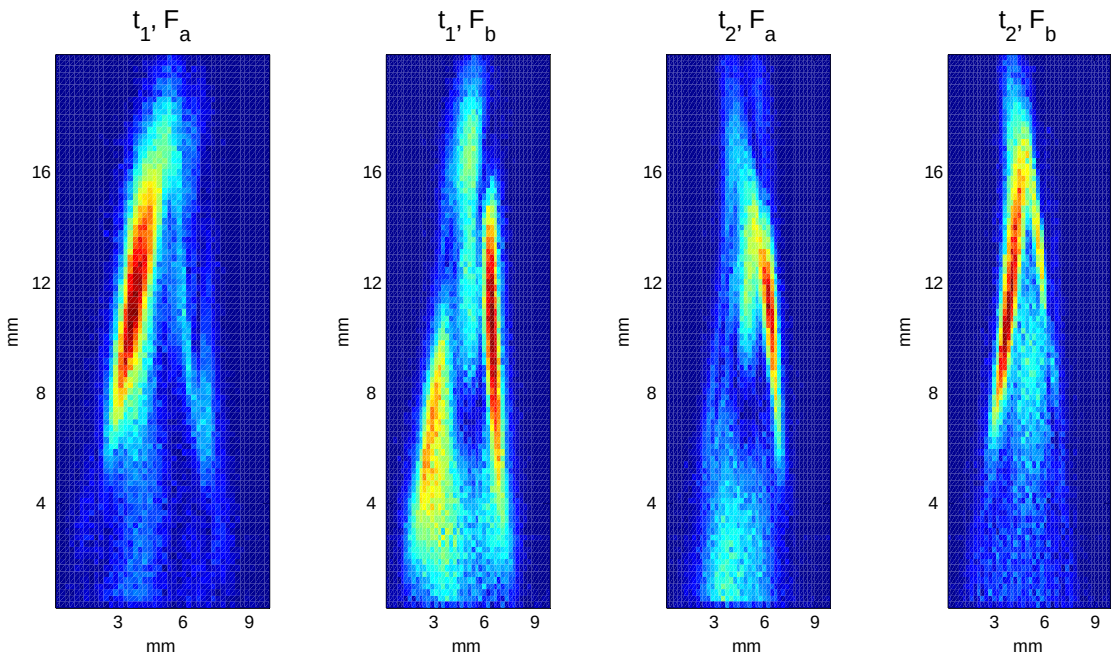

Fig.6. Distributions of oscillations for wavelet scales 20 and 10, corresponding to frequencies F_a, F_b, respectively, indicated in frequency spectra on Fig. 3b at two instants of time t_1, t_2. Gas flow rate 20 slm.

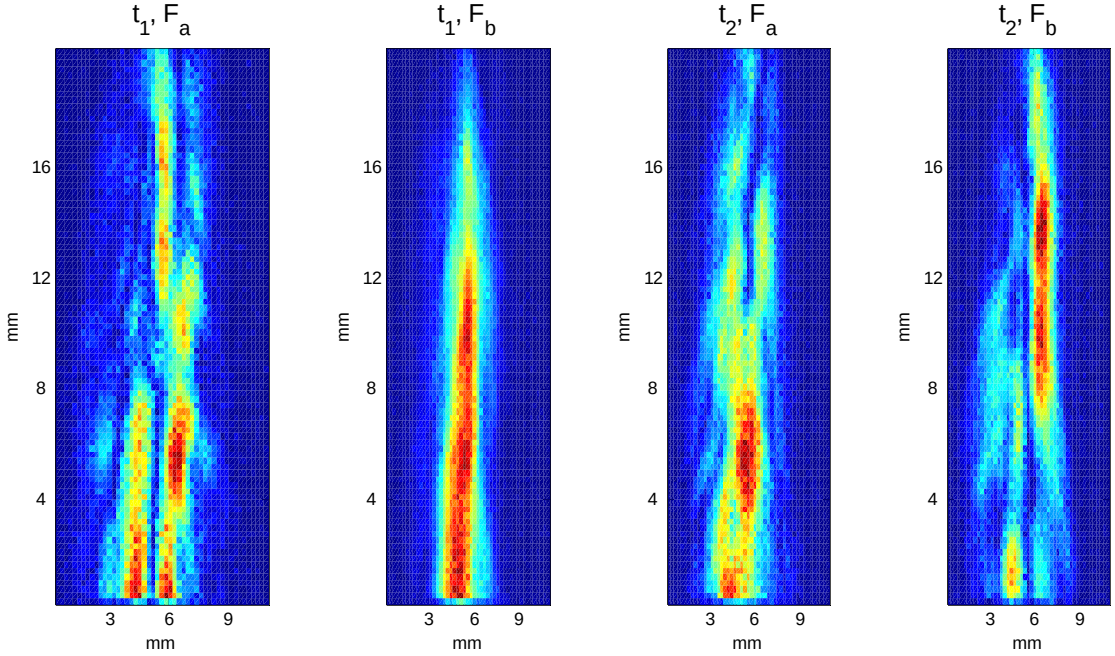

Fig.7. Distributions of oscillations for wavelet scales 15 and 9, corresponding to frequencies F_a, F_b, respectively, indicated in frequency spectra on Fig. 3c at two instants of time t_1, t_2. Gas flow rate 60 slm.

the correctness of the wavelet scale selection (an example of this comparison for the gas flow rate 20 slm and frequency Fb=2540 Hz in Fig.4 - corresponding to the wavelet scale 13).

Some examples of spatial distributions and their temporal changes for significant oscillations are in Figs.5–7. Each of the figures shows distributions of oscillations for two frequencies (F_a, F_b) indicated in frequency spectra on Fig. 3 and two instants of time for the gas flow rates 10, 20 and 60 slm.

3. Conclusion

Previous results [7] achieved by the FFT analysis of the images taken with a CCD camera have shown that most of oscillations occurring in thermal plasma jets are generated mainly on the jet boundaries or tail and their relative intensities may be sometimes distributed strongly asymmetrically, while the amplitudes corresponding to the plasma jet modulation introduced by the ripple of the arc current at 300 Hz show distributions with several maxima at distinct plasma jet regions or a distribution similar to the plasma jet total radiation intensities. The wavelet analysis is able to complete these findings with the information concerning the temporal stability or instability of the spatial distributions. The investigations of wavelet amplitudes derived by the application of the Morlet complex wavelets have shown that while the spatial distribution of some hydrodynamic oscillations at low gas flow rates may be relatively stable (scale 38 - frequency 870 Hz at 10 slm), the spatial location of all oscillations at higher gas flow rates (exceeding 20 slm) changes irregularly in time. Further increase of the flow rate (60 slm) leads to frequent localization of oscillations in the plasma jet core alternatively with splitting into many regions throughout the whole jet area characterising the transition to global plasma jet oscillations and strong turbulence. This work does not contain results dealing with investigations of the imaginary component of the complex wavelet analysis that yield phases of the oscillations and enable to study the velocity of their propagation in the jet which will be dealt with in another paper. The results have shown that the application of the wavelet analysis to records of a plasma jet optical radiation using high-speed CCD cameras may present a powerful tool in investigations of turbulent phenomena in plasma jets especially in studies of temporal instabilities of oscillations and relating heat transport phenomena.

Acknowledgement

The work was supported by the Czech Science Foundation under the grant contract 202/05/0728. The experimental data were acquired in the laboratory of the Institute of Thermomechanics AS CR. This opportunity is greatly acknowledged.

References

[1] Krejcí L., Dolinek V., Sopuch P., Nenicka V., Hlina J.: *Nonlinear convective heat transfer in a transitional plasma plume,* Annals of the New York Academy of Sciences **891**, 333-339 (1999).

[2] Fox M. D., Kurosaka M., Hedges L., and Hirano K.: *The influence of vortical structures on the thermal fields of jets,* J. Fluid Mech. **255**, 447-472 (1993).

[3] N. Singh, M. Razafinimanana, J. Hlina: *Characterization of a dc plasma torch through its light and voltage fluctuations,* J. Phys.D: Appl. Phys. **33**, 270-274 (2000).

[4] Russ S., Strykowski, Pfender E.: *Mixing in plasma nad low density jets*, Experimnets in Fluids **16**, 297-307 (1994).

[5] Fauchais P., Vardelle A.: *Pending problems in thermal plasmas and actual development*, Plasma Phys. Control. Fusion **42**, B365-B383 (2000).

[6] Heberlein J.: *New approaches in thermal plasma technology*, Pure Appl. Chem. **74**, 327-335 (2002).

[7] Hlina J., Sonsky J., Nenicka V.: *Mapping of spatial distribution of oscillations in a thermal plasma jet*, Symposium TPP 8 Thermal Plasma Processes, Strasbourg, June 24-28, publ. in High Temperature Material Processes **8**, 215-220 (2004).

ELECTRON DRIFT AND IONISATION IN Ne-Xe GAS MIXTURES

J. de Urquijo[1], J.L. Hernández-Ávila[2] and E. Basurto[2]

[1]*Centro de Ciencias Físicas, Universidad Nacional Autónoma de México, P.O. Box 48-3, 62251, Cuernavaca, Mor., México*
[2] *División de Ciencias Básicas e Ingeniería, Universidad Autónoma Metropolitana, Av. San Pablo 180, 02220 México, D.F., México*

Abstract

We have measured the electron drift velocity v_e, the density-normalised longitudinal diffusion coefficient ND_L and the density-normalised ionisation coefficients α/N in the Xe-Ne mixtures over a wide range of the density-reduced electric field strength E/N from 1.4 to 200 Td. The values of v_e and α/N are in general in good agreement with the calculated values with the Bolsig code. In contrast, the experimental ND_L values disagree strongly with the calculated ones.

1. Introduction

The mixtures of noble gases with Xe are nowadays used in the Plasma Display Panel industry as a means to generate UV light from microdischarges in which the Xe atoms play an important role. Also, this kind of mixtures with Xe are used for building detectors like wire chambers and proportional counters in the high energy physics experiments, where data such as the drift velocity are essential. There is at present a great deal of activity related to the simulation and modelling of such discharges in order to improve their efficiency [1]. Among the many swarm data and cross sections needed for a meaningful and comprehensive model, a thorough knowledge of the electron drift velocity v_e and diffusion coefficients, as well as the density-normalised ionisation coefficients α/N in these mixtures is essential. We report on the measurement of these swarm coefficients over a wide range of the density-normalised electric field intensity E/N from 2 to 200 Td (1 Townsend = 10^{-17} V cm^2).

2. Apparatus and measurement technique

The electron drift velocities and the density-normalised ionisation coefficients were derived from the analysis of pre-breakdown electron avalanches observed from a Pulsed Townsend Experiment (PTE) [1-3]. The apparatus and the analytical techniques have been described previously in detail [1,2]. Briefly, the PTE is based on the measurement of the displacement current due to electrons and ions drifting in a parallel-plate discharge gap. The initial current is initiated by the release of photoelectrons from the cathode by a UV light pulse from a nitrogen laser (1 ns, λ=337 nm, 1.4 mJ). These photoelectrons and their progeny brought about by ionising collisions drift to their corresponding electrodes. Provided that the electrons are much more mobile than the ions, and that no electron detachment takes place (as in the present case, since no negative ions are formed) then the measured current can be separated into two components, namely fast and slow, corresponding to electrons and ions, respectively. Thus, we have used the electron component to derive the electron drift velocity from the measurement of the transit time of the electrons, and the ionisation coefficient from the exponential growth of the avalanche. The longitudinal diffusion coefficient was obtained from a curve fitting procedure to the electronic transients to the formula [5]

$$i_e(t) = \frac{n_0 q_o}{2T_e} \exp(\alpha v_e t)\left\{\left[1-\phi\left(\frac{(v_e+\alpha D_L)t-d}{\sqrt{4D_L t}}\right)\right]+\exp\left(\frac{v_e+\alpha\ D_L}{D_L}d\right)\left[\phi\left(\frac{(v_e+\alpha\ D_L)t+d}{\sqrt{4D_L t}}\right)-1\right]\right\} \qquad (1)$$

where n_o is the initial photoelectron number, q_o is the electron charge, d is gap spacing, T_e=d/v_e is the electron transit time, and

$$\phi(x) = \frac{2}{\sqrt{\pi}} \int_0^x exp(-u^2)\, du \qquad (2)$$

is the error function

The purity of Ne Xe was 99.999%. The total gas mixture pressure range used was 0.5-40 torr. The measurements were performed at room temperatures over the range 293-300 K. The gap distance was kept fixed at 3 cm to within an accuracy of 0.001 cm.

3. Results

To our knowledge, no previous data of the drift velocity, the density normalized longitudinal diffusion coefficient or the density normalized ionisation coefficient have been published in the literature. It appears that, whenever the knowledge of these coefficients is needed, resort is made of the simulation codes to derive them. The overall precision of our measurements is $\approx$1.5% for v_e, $\approx$ 6-10% for ND_L and $\approx$6% for α/N.

3.1 Electron drift velocities

The drift velocity of electrons in the Ne-Xe mixtures is shown in Fig. 1 for Xe concentrations of 2%, 5%, 20%, 30%, 50% and 100% covering a wide range of E/N from 1.4 to 200 Td. It seems that there exists a well defined dependence of the drift velocity with the Xe concentration, since v_e increases with an increase of the Ne content for fixed E/N.

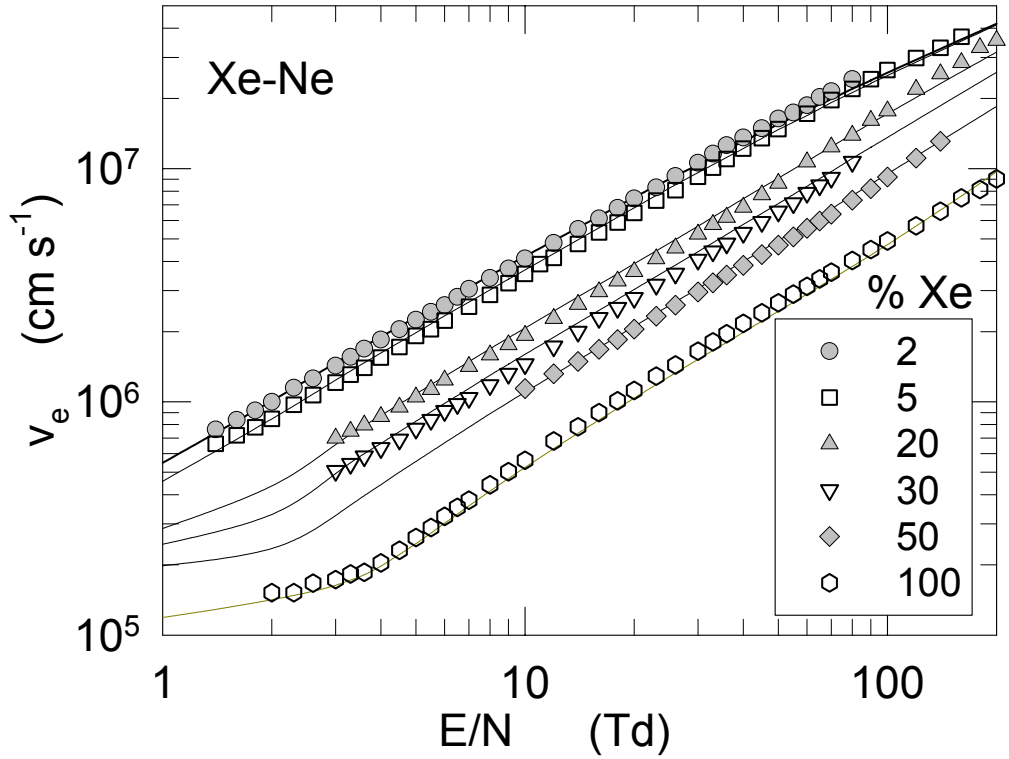

Figure 1. The electron drift velocity in the Xe-Ne mixtures as a function of E/N. Symbols, experimental data; lines, Bolsig calculations, with the exception of that for 100% Xe, which belongs to a Monte Carlo calculation [4]. For the sake of clarity, the Bolsig calculations for the mixtures with 2% and 10% Xe are not shown.

In the absence of previous data for comparison, we have resorted to use the Bolsig Code [6] to calculate these coefficients for the mixtures and to a recent Monte Carlo calculation for pure Xe [7]. The results are also plotted in the same figure, and are indicated by the solid lines. In general, the agreement between our data for the drift

velocity in the mixtures and the Bolsig calculations is very good over most of the ranges, within quoted uncertainties. On the other hand, even though the agreement with the Bolsig calculations for pure Xe was good, this code is only able to provide v_e data for Xe for E>9 Td. Thus we have compared our data with the Monte Carlo calculations [7], as shown in Fig. 1, in which the agreement seems to be excellent over the whole E/N range.

3.2 Longitudinal diffusion coefficients

The density-normalized longitudinal diffusion coefficients ND_L are shown in Fig. 2 for only two mixtures, since we have noticed a great discrepancy between our measurements and the Bolsig calculations, as it becomes apparent in this figure. Firstly, it appears that over the region of E/N being investigated, the ND_L values increase slightly with E/N, for E/N>10 Td. As with the electron drift velocities, for fixed E/N, ND_L increases steadily as the amount of Xe in the mixture is decreased. The Bolsig calculations depart strongly from our data in magnitude by factors between two and three, and the trend of the curves at low E/N contradicts that of the experimental values.

We are of the opinion that new calculations, with more powerful and accurate codes than Bolsig, which is a two-term code, could help resolve this discrepancy. It is also worth stressing the fact that the agreement between our data and the Bolsig calculations was very good, since it is known that the two-term codes are accurate for the calculation of this transport coefficient.

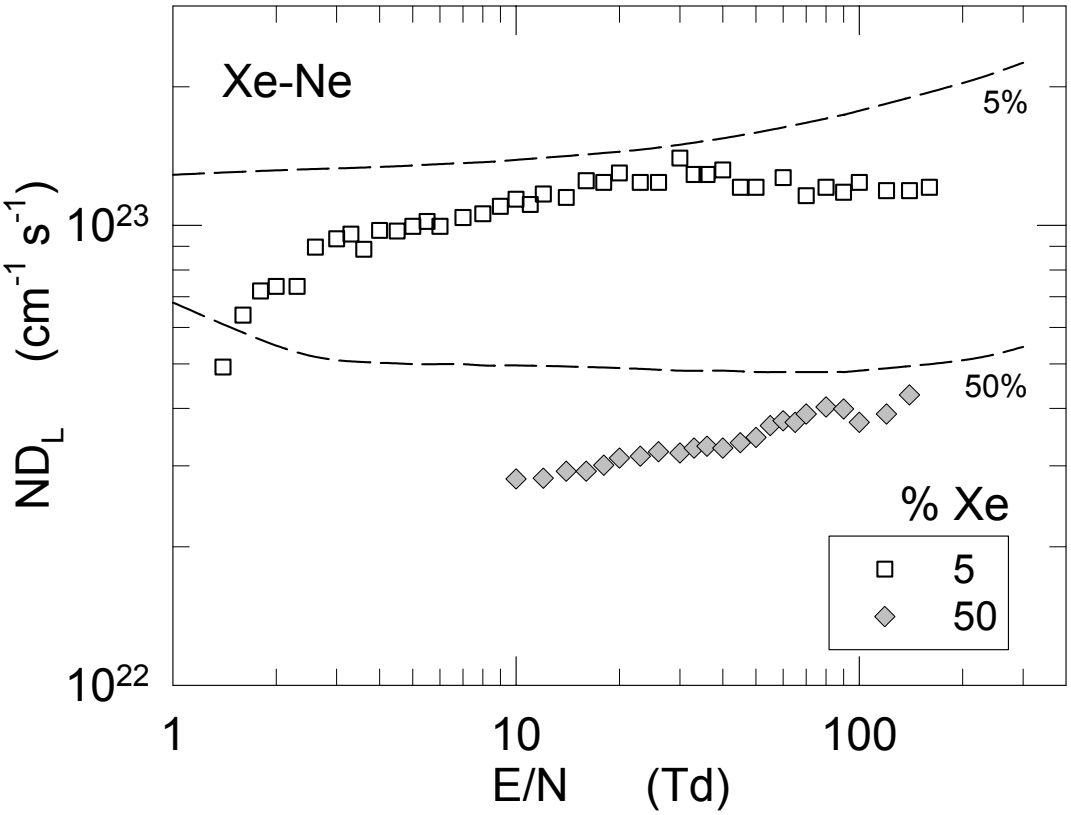

Figure 2. The present density-normalized longitudinal diffusion coefficient ND_L of electrons in the Xe-Ne mixtures (5% and 50% Xe only) (symbols). The solid lines represent the Bolsig calculations for this coefficient.

3.3 Ionisation coefficients

The density-normalised ionisation coefficients are shown in Fig. 3 as a function of E/N. Again, a well defined dependence with the Xe content is observed. For fixed E/N, the α/N values increase as the Xe content in the mixture decreases. The solid lines through the points correspond to the Bolsig calculation. Thus, with the

exception of the data for 2% Xe for E/N<40 Td and 30% Xe for E/N>20 Td, the agreement between measurements and calculations is very good. As regards comparison with other data, to the best of our knowledge there are no α/N values for the Xe-Ne mixture with which to compare.

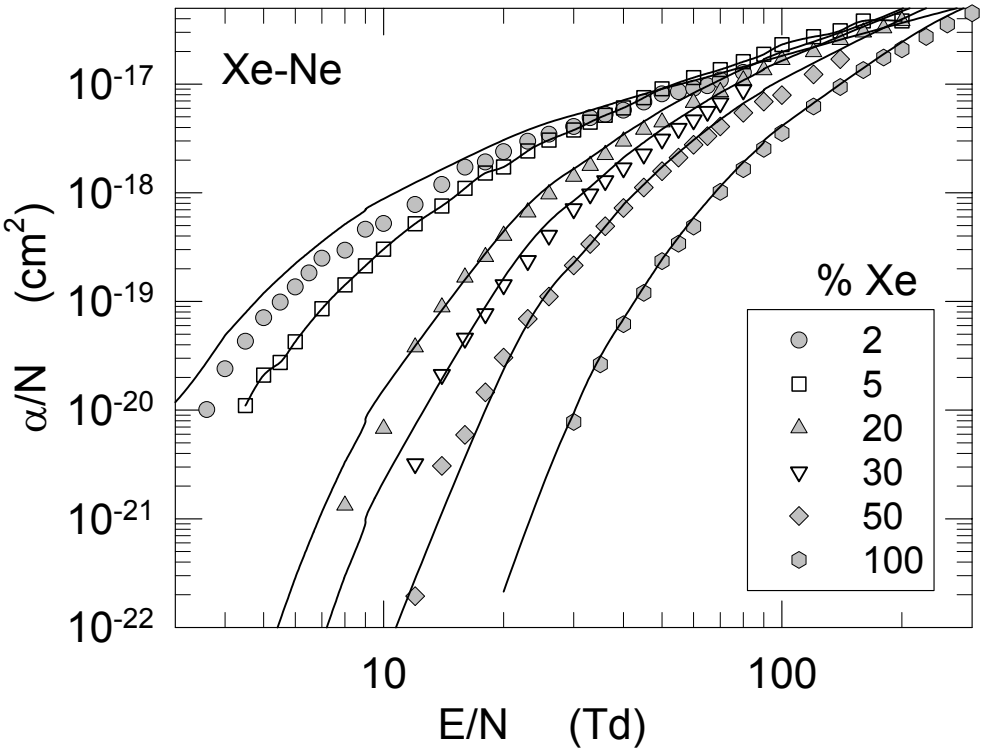

Figure 3. The density-normalised ionisation coefficient in the Xe-Ne mixtures as a function of E/N. The solid lines correspond to the Bolsig calculations.

4. Conclusion

We have measured the electron drift velocity, ionisation coefficients and longitudinal diffusion coefficients for the Xe-Ne mixture over a wide range of E/N. In general, we have found good agreement with the Bolsig calculations for v_e and α/N, but strong disagreement with the longitudinal diffusion coefficients. More comprehensive and accurate calculations are needed to resolve this matter.

Acknowledgements

This work was supported by Project DGAPA UNAM IN104501, IN102305 and UAM 2250216. The authors are grateful to A. Bustos and E. Ortíz for their technical assistance.

References

[1] J-P Bouef, *J. Phys. D* **36**, R53 (2003)

[2] J. de Urquijo, C. Arriaga, I. Alvarez, C. Cisneros, *J. Phys. D* **32**, 41 (1999).

[3] J. de Urquijo, I. Alvarez, C. Cisneros, *Phys. Rev. E* **60**, 4990 (1999).

[4] H. Raether, *Electron Avalanches and Breakdown in Gases*, Butterworths, London, 1964

[5] J. Brambring, *Z. Physik* **179,** 532–8 (1964)

[6] Bolsig Code. Free software from Kinema Software, Monument, CO.

[7] O. Šašić, J.Jovanović, Z.Lj. Petrović, J. de Urquijo, R. Castrejón, J.L. Hernández-Ávila and E. Basurto, *To be published in Phys. Rev. E*

Experimental study of a flowing nitrogen glow and pink afterglow

J. Henriques[1,2] and A. Ricard[1]

1 CPAT, Université Paul Sabatier, 118 rte de Narbonne, 31062 Toulouse, France
2 Center for Plasma Physics, Instituto Superior Técnico, 1049-001 Lisboa, Portugal

Abstract

High frequency discharges and respective post-discharges are investigated by means of emission spectroscopy and NO - titration. In the present conditions a strong pink afterglow is formed in the post-discharge region, this extended field free region is rich in active species such has nitrogen atoms, vibrationally and electronically excited nitrogen molecules and ions. The experimental results are interpreted using a kinetic model [1].

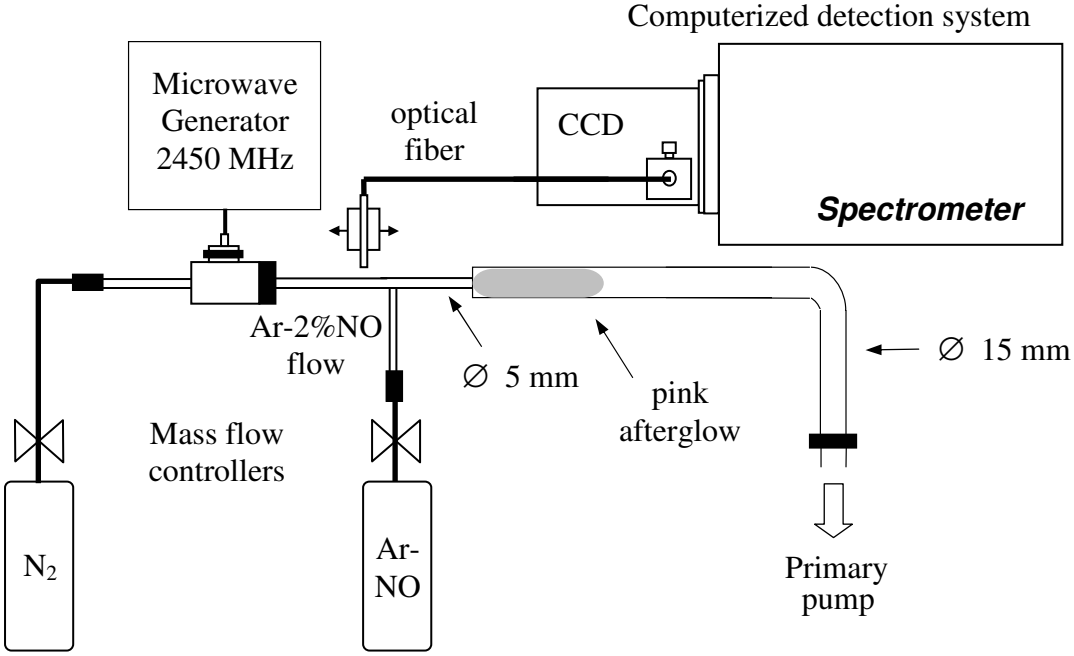

Figure 1. Experimental setup showing the discharge and post-discharge reactor.

Experimental setup

The experimental arrangement is reproduced in Fig. 1. High frequency discharges are produced using a Surfatron (at $\omega/2\pi$ = 2.45 GHz) in a quartz tube with 5 mm of internal diameter (i.d.) sealed to a bent quartz tube of i.d. 15 mm. The high frequency power transmitted to the plasma can vary between 30 to 150 watts, with a negligible reflected power. The total gas flow can be adjusted from 0.1 to 10 $L_n\,min^{-1}$ and the gas pressure in the chamber can be adjusted from 0.1 to 50 Torr. An Ar-2%NO gas mixture can be injected in the 5 mm i.d. quartz tube after the end of the discharge. The plasma and afterglow lights are collected by a quartz optical fiber connected to a Jobin-Yvon 270M spectrometer (1200 grooves mm^{-1} grating), equipped with a CCD detector.

Experimental Measurements

Emissions from the N_2 1st positive system (1st pos.) at 775.3 nm (see Fig. 2), 2nd positive system with the 367 – 380 nm sequence and 1st negative system at 391.4 nm (see Fig. 3) and vibrational spectra of the 1st pos.

N_2(B,v'=7 – 12) in the range between 570 – 610 nm (see Fig. 4), are studied as a function of the axial position in the discharge and post-discharge regions.

The rotational spectra of the N_2, 1st pos. at 775.3 nm allows us to determine the rotational temperature of N_2 as indicated in reference [2], measuring the intensity ratio of the P1/P2 rotational branches. In these measurements we have assumed that the N_2, 1st pos. rotational temperature is near the plasma gas temperature. The atomic nitrogen density at the end of the plasma column is measured by using the N_2 580nm band intensity which is calibrated by NO titration.

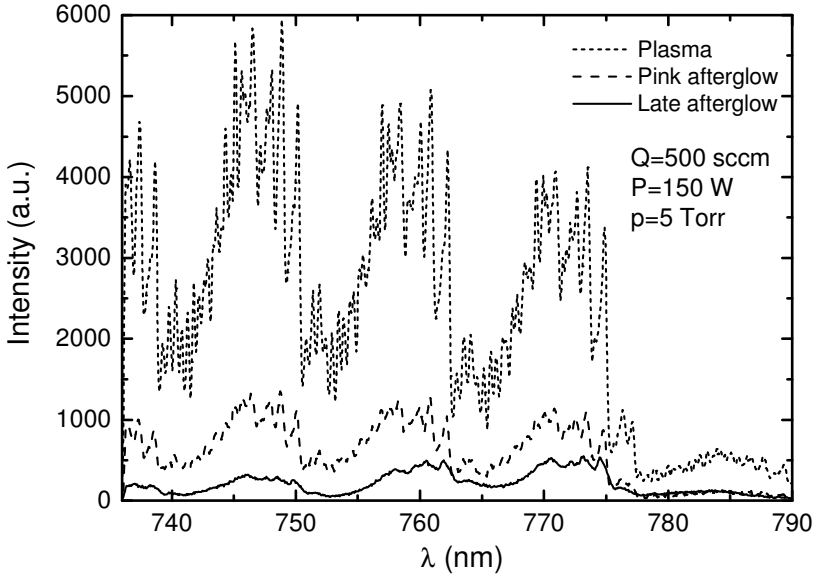

Figure 2. Emission spectra between 730 and 790 nm measured in the plasma at the gap (short dash line), in the beginning of the pink afterglow (dash line) and in the late afterglow (solid line).

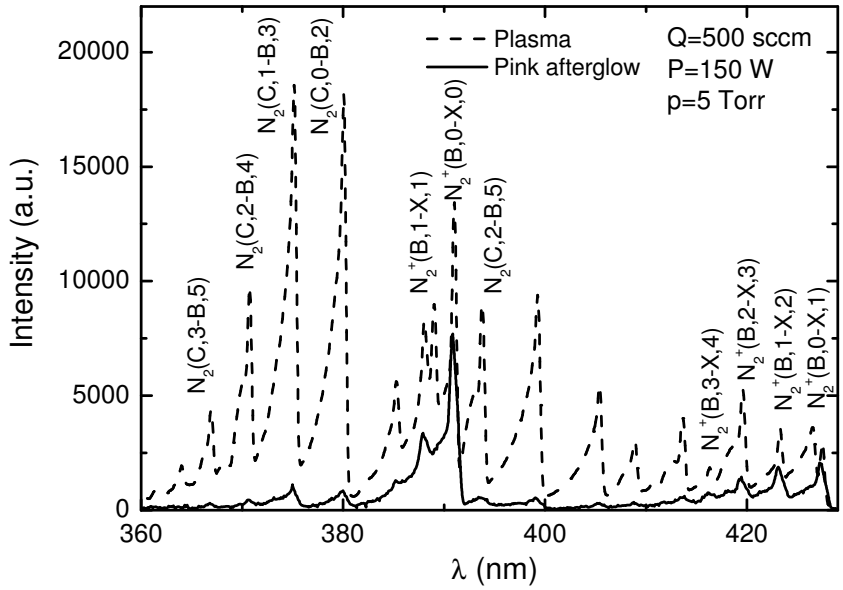

Figure 3. Emission spectra between 360 and 430 nm measured in the plasma at the gap (dash line) and in the beginning of the pink afterglow (solid line).

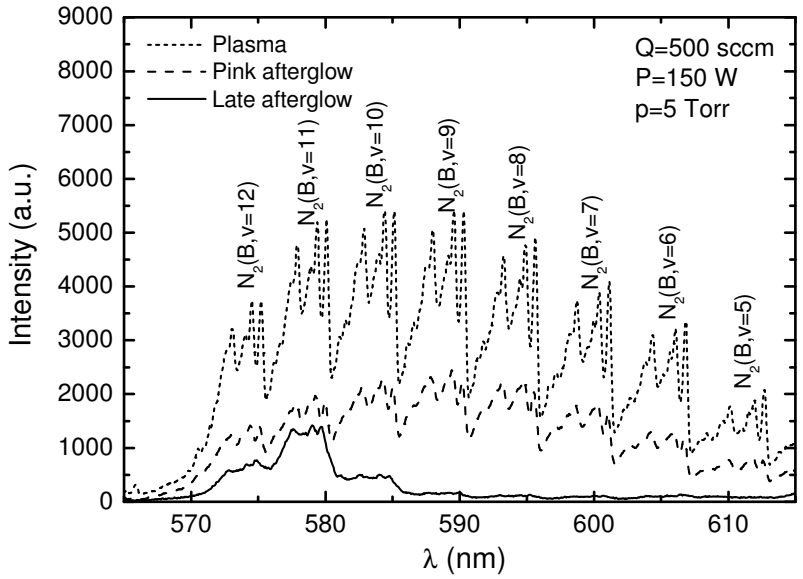

Figure 4. Emission spectra between 560 and 620 nm measured in the plasma at the gap (short dash line), in the beginning of the pink afterglow (dash line) and in the late afterglow (solid line).

Results

The ratio between the emission intensity lines of the transitions N_2^+(B,0–X,0) and N_2(C,0–B,2) increases 15 times from the gap to the beginning of the afterglow (see Fig. 3 and 5). The strong emission of the transition N_2^+(B,0–X,0) after the discharge end is the signature of the pink afterglow.

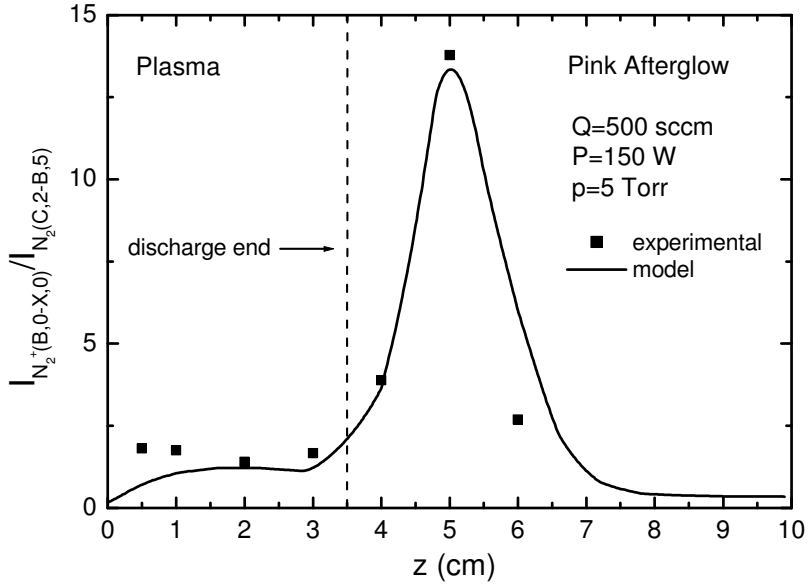

Figure 5. Axial distribution of the measured (black square) and theoretical (solid line, see ref. [1]) intensity ratios of N_2^+(B,0-X,0) over N_2(C,2-B,5) in the plasma and in the pink afterglow.

The gas temperature as determined from the rotational structure of the N_2 (1st pos.) increases from 500 K close to the gap to 950 K in the middle of the discharge column, remaining almost constant until his end. After the discharge end the temperature decreases slightly, attaining 650 K at 6 cm from the gap (see Fig. 6).

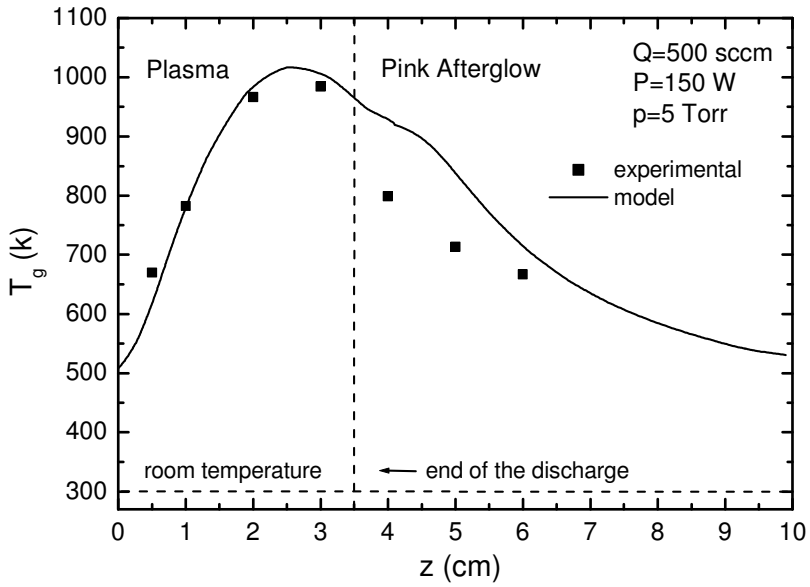

Figure 6. Axial distribution of the measured (black square) and theoretical (solid line, see ref. [1]) gas temperatures in the plasma and in the pink afterglow.

The vibrational distributions of $N_2(B,v'=7–12)$ in the discharge and in the pink afterglow remain almost unchanged. In the late afterglow an overpopulation of the $N_2(B,v'=11)$ is observed (see Fig. 7). The N – atom density measured by NO titration at the end of the pink afterglow is of 8.3×10^{14} cm^{-3} (uncertainty of 20 %).

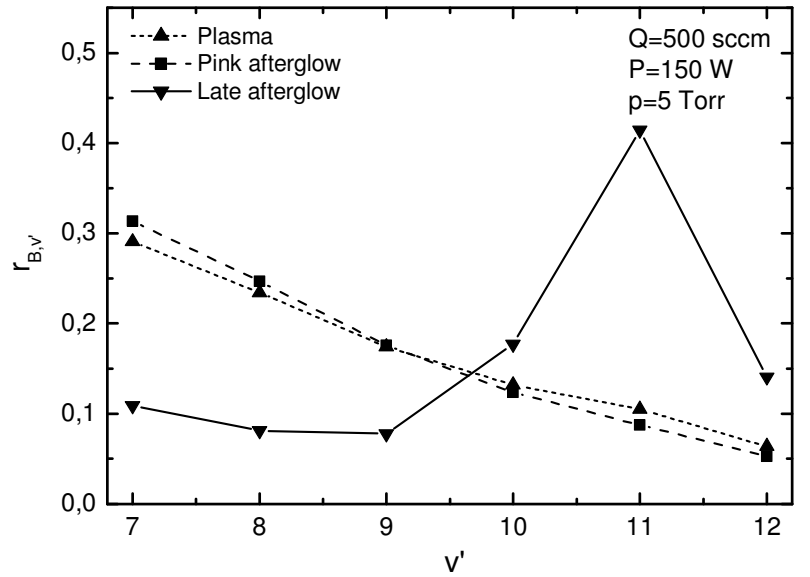

Figure 7. Normalized vibrational distributions $r_{B,v'}$ of $N_2(B,v')$ for v' = 7 – 12 in the plasma and afterglows.

Interpretation of the results

The sharp increase between the intensity ratio of the transitions $N_2^+(B,0\text{-}X,0)$ and $N_2(C,2\text{-}B,5)$ is directly related to the relaxation after the discharge end (field free region) of the vibrational distribution function (VDF) and of the electronic energy distribution function (EEDF). $N_2(C)$ is produced mainly by electronic impact in the plasma (more than 60%) with a small contribution of the pooling reaction $N_2(A) + N_2(A) \rightarrow N_2 + N_2(C)$ [3] (more than

30%). Due to the decrease of the electric field towards the end of the plasma, the electronic energy decreases and the productivity of these two reactions is equalized. After the plasma end the productivity of the pooling reaction between the flowing $N_2(A)$ metastable molecules grows in importance (see Fig. 8) together with the collisions between $N_2(B)$ and the growing vibrationally excited $N_2(X,v>12)$ states : $N_2(B) + N_2(X,v>12) \rightarrow N_2(C) + N_2(X,v=0)$ [4].

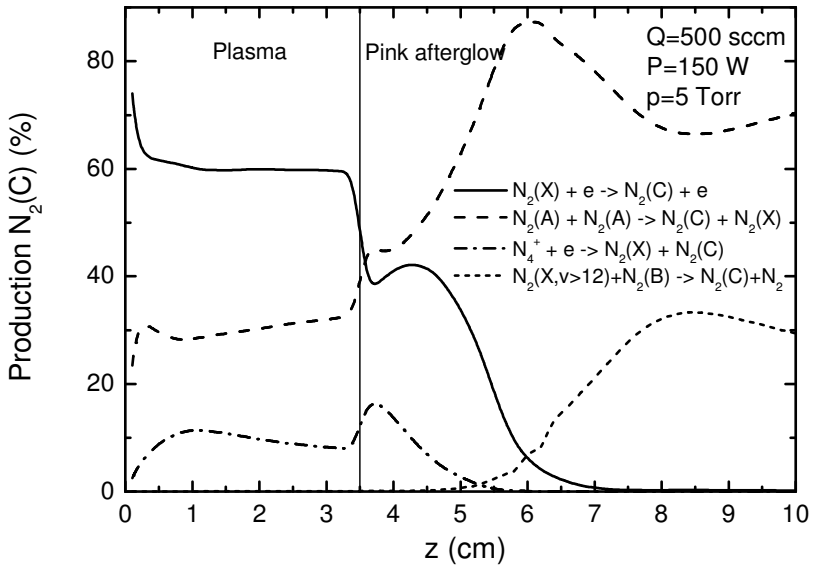

Figure 8. Calculated axial distribution of the $N_2(C)$ production channels in the plasma and in the pink afterglow.

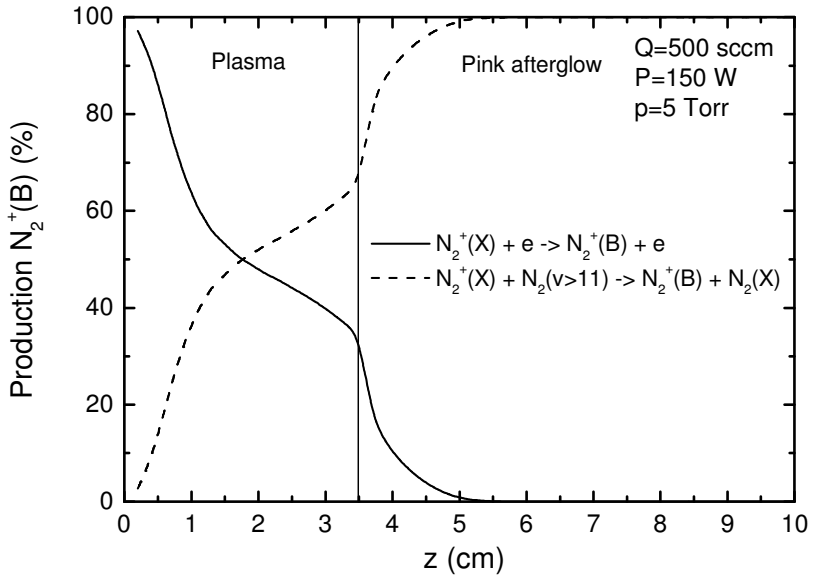

Figure 9. Axial distribution of the $N_2^+(B)$ production channels in the plasma and in the pink afterglow.

$N_2^+(B)$ is produced mainly by electronic impact in the discharge close to the gap, by the reaction $N_2^+(X) + e \rightarrow N_2^+(B) + e$. With the approach of the end of the discharge this reaction becomes less important and his productivity is equalized in the middle of the discharge (z = 2 cm) to the one of the reaction $N_2^+(X) + N_2(X,v>11) \rightarrow N_2^+(B) + N_2(X,v=0)$ [5]. After the end of the discharge the production of $N_2^+(B)$ is made almost entirely by collisions between $N_2^+(X)$ and the growing vibrationally excited $N_2(X,v>11)$ states (see Fig. 9). The

production of $N_2^+(B)$ is made mostly via $N_2^+(X)$. In the discharge $N_2^+(X)$ is produced mainly by the Penning ionization reaction $N_2(a') + N_2(a') \rightarrow e + N_2^+(X) + N_2(X)$ [6] (> 60%), by electronic impact reactions $N_2(X,A,B,a') + e \rightarrow N_2^+(X) + e$ and also by the penning ionization reaction $N_2(A) + N_2(a') \rightarrow e + N_2^+(X) + N_2(X)$ [6]. In the strong pink afterglow region (between 3.5 and 7 cm), $N_2^+(X)$ is produced mainly by penning ionization involving the flowing molecular nitrogen metastables $N_2(A,a')$. After that $N_2^+(X)$ is produced by the charge transfer reaction $N_4^+ + N_2 \rightarrow N_2^+(X) + N_2 + N_2$ [1,5] and N_4^+ is produced by the $N_2(a')$ flowing metastable and the growing vibrationally excited $N_2(X,v>12)$ states (see Fig. 9): reaction $N_2(X,v>24) + N_2(a') \rightarrow N_4^+ + e$ [7].

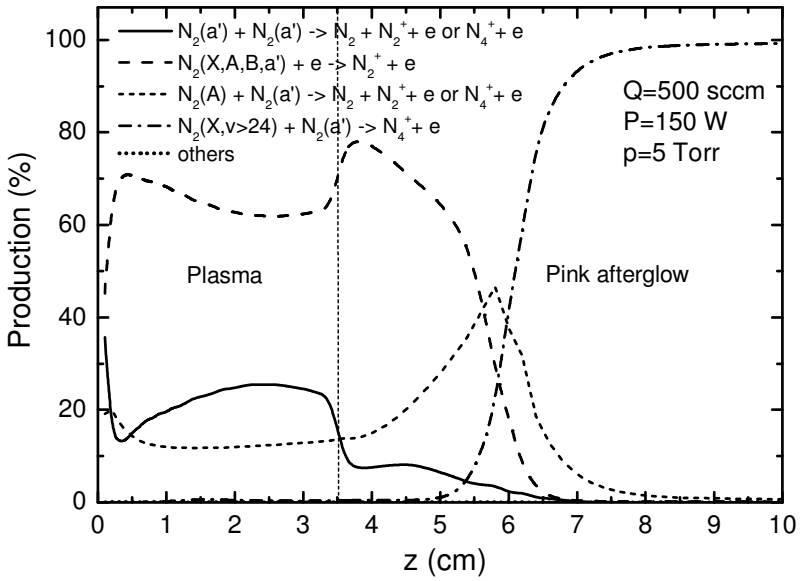

Figure 9. Axial distribution of the charge (N_2^+ and N_4^+) production channels in the plasma and in the pink afterglow.

Conclusion

A nitrogen glow and pink afterglow were produced and experimentally investigated by means of optical spectroscopy and NO - titration. The experimental results were interpreted using a kinetic model. An increase of 15 times in the emission intensity ratio of $N_2^+(B,0–X,0)$ over $N_2(C,0–B,2)$ were observed from the gap to the beginning of the afterglow. This effect is the consequence of the strong production of $N_2^+(X)$ in the pink afterglow by the Penning ionization reactions $N_2(A,a') + N_2(a') \rightarrow e + N_2^+(X) + N_2(X)$ followed by the reaction $N_2^+(X) + N_2(X,v>11) \rightarrow N_2^+(B) + N_2(X,v)$. A good agreement was obtained between the experimental and theoretical results.

Acknowledgements

This work was performed under the auspices of the Portuguese Ministry of Science and Technology through the research grant POCTI SFRH/BPD/11587/2002.

References

[1] J. Henriques, E. Tatarova, V. Guerra and C.M. Ferreira, J. Appl. Phys. (2002) **91** 5622
[2] L. Hochard, Escampig 18^E (1994) 336
[3] L.G. Piper, J. Chem. Phys. (1988) **88** 231
[4] D.I Slovetskii, Mechanisms of Chemical Reactions in Nonequilibrium Plasmas (Nauka, 1980)
[5] V. Guerra, P.A. Sá and J. Loureiro, Eur. Phys. J. Appl. Phys. (2004) **28** 125 – 152
[6] V. Guerra, J. Loureiro, Plasma Sources Sci. Technol. (1997) **6** 361
[7] A.A. Matveyev and V.P. Silakov, Plasma Sources Sci. Technol. (1999) **8** 162

Two-dimensional Modeling on Filamentary Mode of Dielectric Barrier Discharge in Nitrogen at Atmospheric Pressure

J. I. Kim, J. M. Park, D. Lee, S. I. Choi, and S. H. Hong

Department of Nuclear Engineering, Seoul National University, Seoul, 151-742 Korea

Abstract

Filamentary mode characteristics of dielectric barrier discharge (DBD) in atmospheric-pressure nitrogen are studied numerically by a fully two-dimensional simulation, in which the dynamics of a single streamer in the parallel-disk DBD are analyzed by the spatio-temporal plasma characteristics with an axi-symmetry. Simulation results describe not only the formation and propagation process of a streamer in the filamentary mode of the DBD but also the distinctive discharge phases of avalanche, streamer, and decay. It is revealed that the filamentary discharge is extinguished due to the surface charges accumulated on the dielectric barriers.

Keywords

Dielectric barrier discharges, Filamentary discharges, Streamer, Numerical modeling

1. Introduction

Dielectric barrier discharges (DBDs) as typical sources of atmospheric non-equilibrium plasmas are generated by applying high voltage to the electrodes, one or both of which are covered with the dielectric barriers. Since DBDs are simply operated without expensive vacuum equipment and make abundant chemically active species, they are widely used in numerous industrial applications such as ozone production, decomposition of gaseous pollutants, surface treatment of polymers, excimer lamps, and plasma display panels [1]. For their more effective applications, however, it is essential to fully understand the inherent discharge characteristics of DBDs. The filamentary and homogeneous (or diffusive) modes of the discharges are known to exist in DBDs according to their operating conditions. Each discharge mode of the DBD has its own formation mechanism and discharge characteristics, and especially the filamentary discharges, which are caused by the evolution of a streamer, play an important role in the plasma chemistry.

Extensive numerical studies on a streamer as a kind of an ionizing wave have been conducted because the streamer has such properties of a fast velocity and highly localized dynamics that the experimental research has been limited to some extent. To overcome the weakness of 1.5-dimensional modeling assuming a constant radius of the streamer channel [2], two-dimensional modeling on a single streamer was attempted for a discharge without dielectric barriers [3]. Especially in the DBD, it is of importance to take effects of surface charges due to their essential role in preventing the filamentary discharge from transferring to an arc discharge. In the present numerical work, the filamentary mode of DBD in nitrogen at atmospheric condition is studied by a fully two-dimensional modeling for a single streamer channel with different radii, in which an azimuthally symmetry about its propagation axis is assumed in cylindrical coordinates.

2. Theoretical model

2.1. Governing equations

A hydrodynamic drift model is employed for the numerical simulation on the filamentary mode of DBD. The fluid approach used broadly in a streamer modeling is not only simple to deal with but also productive with sufficiently reasonable results. Since the response time which takes electrons to reach an equilibrium state at atmospheric pressure is shorter than the time constant for electric field **E** to change due to the effects of space charges, it is assumed that the average velocity and momentum of electrons are instantly in equilibrium with

electric field [4]. In other words, the relaxation time and distance of the electron momentum and energy are so short that it is possible to take advantage of the 0th-order moment equations to describe electron and ion motions macroscopically. The governing equations are then given for electrons (e) and ions (i) as follows:

$$\frac{\partial n_e}{\partial t} + \nabla \cdot (n_e \mathbf{v_e}) = S_e \tag{1}$$

$$\frac{\partial n_i}{\partial t} + \nabla \cdot (n_i \mathbf{v_i}) = S_i \tag{2}$$

$$\mathbf{v_e} = \mu_e \mathbf{E}, \quad \mathbf{v_i} = \mu_i \mathbf{E} \tag{3}$$

where n is the number density, $\mathbf{v}$ is the drift velocity, S is the particle source term, and μ is the mobility.

Diffusion of charged particles is neglected and only electron impact ionization is considered in the source term for the sake of simplicity. Townsend's ionization coefficient α is dependent on a reduced electric field E/P due to a local field approximation. Then, α = 5.7 P exp(-260P/E) (cm^{-1}), $\mu_e = 2.9\times10^5$/P (cm^2/V·s), and $\mu_i = 2.6\times10^3$/P (cm^2/V·s) for nitrogen gas where P is the pressure in Torr [3] and set to be 760 here. The electric field is found from the following Poisson equation,

$$\nabla \cdot (\varepsilon \nabla \phi) = -e(n_i - n_e), \quad \mathbf{E} = -\nabla \phi \tag{4}$$

The governing equations are discretized based on a finite difference method (FDM). The continuity equations are solved by an upwind method and a fine grid is used to minimize numerical diffusions. A fast direct method is applied to the Poisson equation by using a sparse matrix solver, UMFPACK library, [5].

2.2. Initial and boundary conditions

A computational domain for describing the single streamer characteristics in a filamentary mode is a discharge gap of 0.2 cm between two parallel dielectric barrier disks, each of which covering a cathode or anode surface has a thickness of 0.1 cm. The origin of the axi-symmetric cylindrical coordinates (r, z) is placed at the center of the cathode barrier disk. A quasi-neutral plasma of a Gaussian profile is assumed to be initially exist in front of the cathode barrier surface as an initial condition for electron and ion densities: $n_e(r,z) = n_i(r,z) = n_0\ exp[-\{r^2+(z-d)^2\}/\delta^2]$ where $n_0 = 10^3$ cm^{-3}, d = 0.03 cm, and δ = 0.02 cm. The electron density at the cathode barrier surface is determined from the flux of secondary electrons emitted by ion bombardments.

Assuming that all of the charges moving toward the dielectric barriers are accumulated on the dielectric surfaces without dissipation, the equation for the surface charges on the dielectric barriers are given as

$$\frac{\partial \sigma_e}{\partial t} = n_e \mathbf{v_e} \cdot \hat{\mathbf{n}}_z, \quad \frac{\partial \sigma_i}{\partial t} = n_i \mathbf{v}_i \cdot \hat{\mathbf{n}}_z \tag{5}$$

where σ is the surface charge density and $\hat{\mathbf{n}}_z$ is the unit vector from plasma toward the dielectric barrier.

The electrostatic potential at the anode is set to 11 kV, the cathode potential to zero, and the derivatives of the potential vanish at the radial boundary of the cylindrical discharge chamber. The boundary condition for the potential at the interface between plasma and dielectric barrier is expressed as

$$\frac{\partial \phi}{\partial z} - \varepsilon_r \frac{\partial \phi_D}{\partial z} = \frac{e}{\varepsilon_0}(\sigma_i - \sigma_e) \tag{6}$$

where ε_r is the relative permittivity of dielectric material, and ϕ and ϕ_D are the electric potentials on the plasma and dielectric barrier sides, respectively.

3. Results and discussion

Temporal evolution of electron density at an early phase of discharge is shown in Fig. 1. The electron density grows exponentially with time as electrons move toward the anode barrier until 7.0 ns. It represents a Townsend discharge phase, in which electron multiplication dominates by electron impact ionizations due to frequent collisions between electrons and neutral atoms. There is little distortion of electric field during this avalanche stage since the effect of space charges is negligible. This stage could be omitted when the initial plasma density is high enough to affect the applied electric field. In that case, positive and negative streamers immediately propagate toward both of the dielectric barriers.

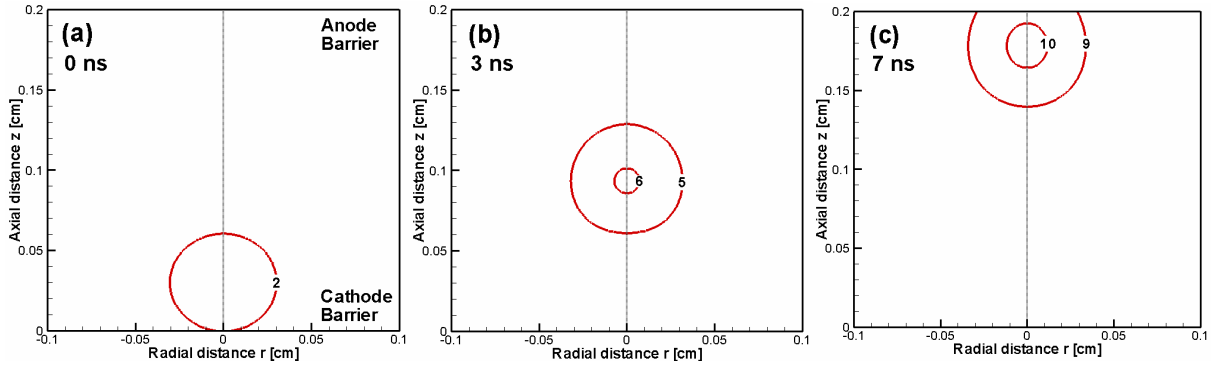

Fig. 1. Contour plots of electron density in a logarithmic scale at (a) 0 ns, (b) 3 ns, and (c) 7 ns during an avalanche phase in a parallel-disk DBD. The cathode and anode barrier disks are placed at z = 0 and at z = 0.2, respectively. Numbers typed on the contour lines are the power of 10, i.e., 2 stands for 10^2 cm^{-3} of electron density.

After the avalanche phase, the electric field near the anode dielectric barrier begins to decrease. Figure 2 shows the time change of highly distorted electric field during the propagation of a cathode-directed streamer. It takes several tens of *ns* for the streamer to be formed before the electron density is built up above about 10^{11} cm^{-3}.

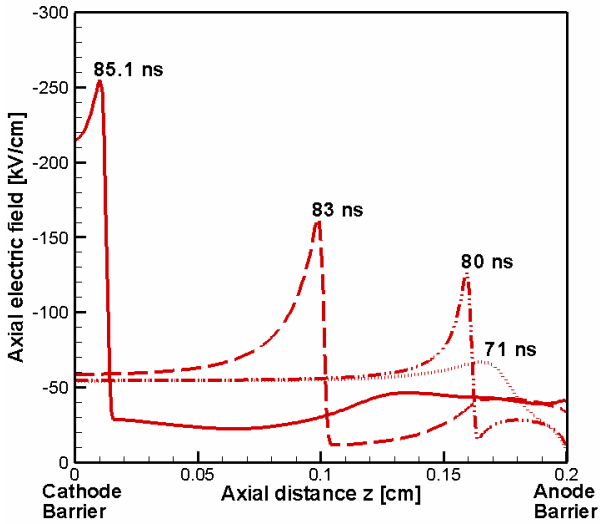

Fig. 2. Time variation of axial electric field along the axis (r = 0) during the streamer propagation from the anode barrier (z = 0.2) to the anode barrier (z = 0).

From the spatio-temporal profiles of electron density in Fig. 3(a), the velocity of the streamer propagation approximates to 10^7 cm/s and the radius of the streamer is about 400 μm. Since these results are similar to those obtained from the discharge case with no dielectric barriers [6], the dielectric barriers appear not to have much influence on the streamer propagation stage. As seen in Fig. 3(b), horseshoe-like distributions of space charges

are built up near the streamer head, but the net space charge density is low inside the streamer channel. This results in strong electric fields near the streamer head of net positive charges, while near-zero fields inside the streamer channel of a quasineutral plasma region. However, shielding of the electric field inside the streamer is not perfect because of a finite dielectric relaxation time of plasma [3]. The time evolution of detailed electric field distributions is plotted in Fig. 3(c). The steep gradients of electric fields appear at the streamer head due to large displacements between electrons and ions. The energetic electrons, which will generate abundant chemically active species in the filamentary mode of DBDs, are produced in this region.

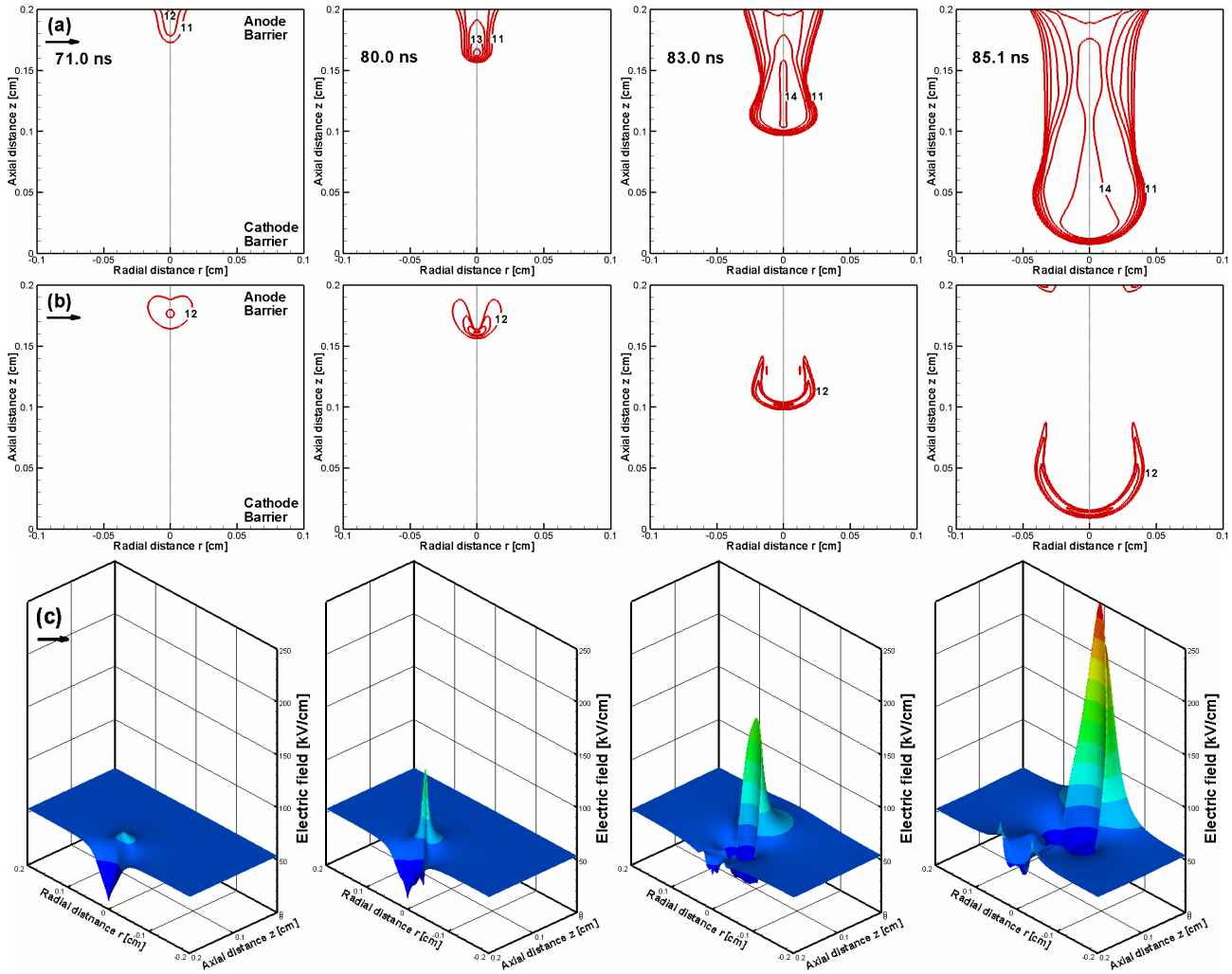

Fig. 3. Contour plots of (a) electron density, (b) net space charge density, and (c) electric field strength during the streamer propagation from the anode (z = 0.2) to cathode (z = 0) barriers in a parallel-disk DBD at 71.0 ns, 80.0 ns, 83.0 ns, and 85.1 ns from left to right column, respectively. Numbers typed near the contour lines in (a) and (b) are the power of 10, i.e., 11 stands for 10^{11} cm^{-3} of particle density.

Figure 4 shows a decay phase of the streamer discharge, in which the electric field vanishes with time and the electron density practically sustains a stationary state. The electrons on the cathode barrier are radially extended with time as seen in Fig. 4(a), and the electric fields at the streamer head decay with time reaching the cathode dielectric barrier in Fig. 4(b). A high electric field strength of over 900 kV/cm decreases rapidly within only a few 10 μm in front of the cathode barrier surface. This locally intensive cathode fall moves outward radial direction and disappears quickly. After the streamer arrives at the dielectric barrier surface at t = 85.2 ns, a single

filament channel is formed between two dielectric barriers and the discharge current records its maximum value of 1.8 A. Figure 5 shows an evolution of the discharge current density which demonstrates the filamentary mode of DBD – formation of the streamer channel and quenching of the discharge. As discussed above, one cycle of the filamentary discharge consists of the distinct discharge phases: avalanche, streamer propagation, cathode fall formation, and decay. After formation of a single filament channel, the discharge current a bit slowly decreases owing to the weakened motion of free charges, and then the filamentary discharge is finally extinguished.

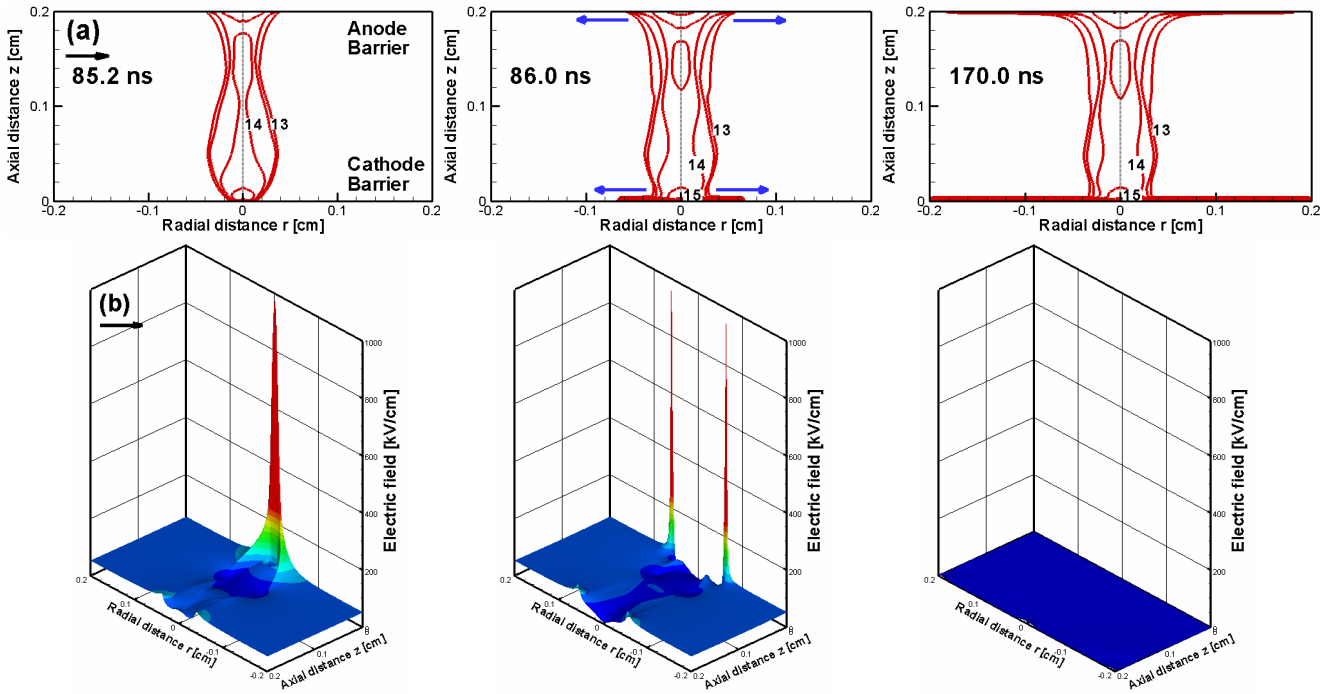

Fig. 4. Contour plots of (a) electron density and (b) electric field strength during a decay phase between the cathode (z = 0) and anode (z = 0.2) barriers in a parallel-disk DBD at 85.2 ns, 86.0 ns, and 170.0 ns from left to right column, respectively. Numbers typed near the contour lines in (a) are the power of 10, i.e., 13 stands for 10^{13} cm^{-3} of electron density.

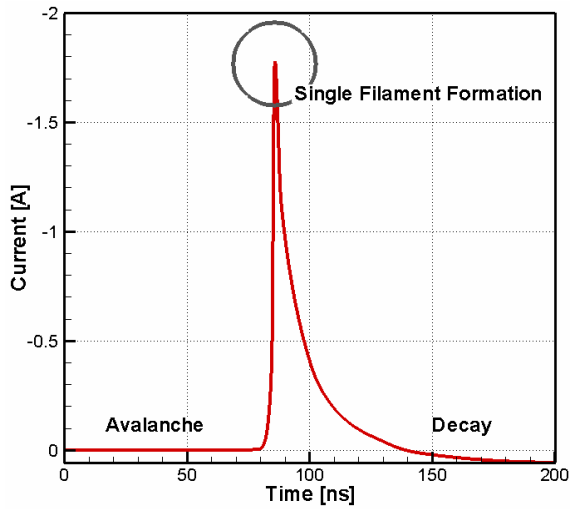

Fig. 5. Time evolution of discharge current during a filamentary discharge in a parallel-disk DBD with an initial uniform electric field of 54 kV/cm.

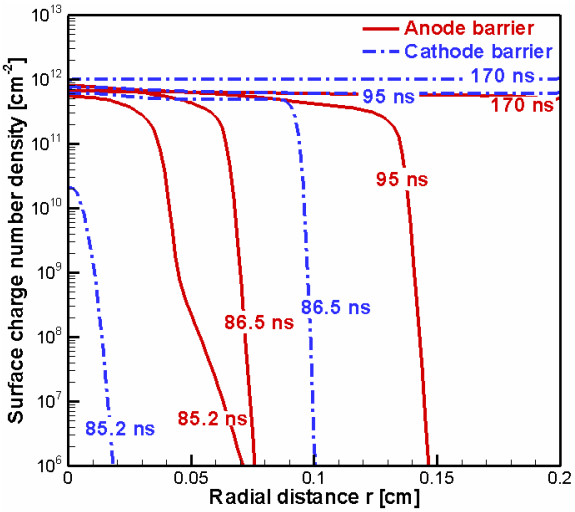

Fig. 6. Time variations of radial distributions of surface charges on both the dielectric barrier surfaces in a parallel-disk DBD.

The surface charges deposited on the dielectric barriers play an important role in shielding the applied electric field and in preventing the filamentary discharge from changing to an arc discharge. Time-varying surface charges accumulated on the dielectric barrier disks are drawn in Fig. 6. The surface charges deposited on the barrier surfaces rapidly increase after the streamer arrives at the cathode barrier, and then they become to spread radially outward direction on the surfaces. As the surface charges are distributed uniformly on the barrier surfaces, they make the applied electric field shielded in the discharge gap. The single filamentary discharge is thus quenched because of the net surface charges of opposite polarities accumulated on the surfaces of a pair of the dielectric barriers.

4. Conclusion

A two-dimensional modeling on parallel-plate type DBD in atmospheric-pressure nitrogen is carried out in order to study the filamentary discharge characteristics and the streamer dynamics. The simulation results show that the space charges in the DBD manly affect the formation and propagation of the streamer, and that a very steep electric field appears in front of the cathode barrier surface as the streamer head approaches to it. As a thin filament channel connects the dielectric barriers to each other, the discharge current reaches its maximum value, and subsequently, the discharge is quenched due to the accumulation of the surface charges. For a more realistic modeling of the filamentary mode of DBD, it is suggested that the detailed loss mechanism and radial behavior of the surface charges accumulated on the dielectric barrier should be taken into account in the future work.

References

[1] U. Kogelschatz, B. Eliasson, and W. Egli, Pure Appl. Chem. **71**, 1819 (1999).
[2] A. J. Davies, C. J. Evans, and P. M. Woodison, Proc. IEE **122**, 765 (1975).
[3] S. K. Dhali and P. F. Williams, J. Appl. Phys. **62**, 4696 (1987).
[4] B. Eliasson and U. Kogelschatz, IEEE Trans Plasma Sci. **19**, 309 (1991).
[5] T. A. Davies. Available: http://www.cise.ufl.edu/research/sparse/umfpack
[6] A. A. Kulikovsky, J. Phys. D: Appl. Phys. **28**, 2483 (1995).

Theoretical Analysis of Factors Affecting NOx Removal Performance by Barrier Discharge

T. Shoyama[1], S. Senda[1], Y. Yoshioka[1]

[1] *Department of Electrical Engineering, Kanazawa Institute of Technology, Ishikawa, Japan*

Abstract

NOx removal process was analyzed using a simplified micro-discharge model and by solving the rate equations and diffusion equation simultaneously. As the results, it became evident that (1) the temperature rise in the discharge channel had a negative effect on NO removal performance, (2) the existence of N_2 metastable state influences the NO removal performance if the quenching reaction of the metastable state N_2 is small and (3) wave form of the applied voltage has smaller effect on NO removal performance except the case that pulse discharges concentrate in a short period.

1. Introduction

NOx removal from diesel exhaust gas is difficult by conventional technologies. Thus, NOx removal techniques using non-thermal plasmas like silent discharge and corona discharge have been investigated actively so far. The principal mechanism of NOx removal by non-thermal plasmas is the oxidization of NO to NO_2 by O radical and O_3. However, it became apparent that the energy efficiency of this process is not enough for industrialization. In order to find ways to improve the energy efficiency, it is necessary to investigate the NO removal paths more in detail [1]. We developed a simulation model, which calculates the various chemical reactions induced by discharge, and also reactions induced by the diffused radicals to the outside of the discharge channel [2]. In this paper, we investigated the effects of three factors affecting NO removal performance, such as temperature rise of the inside of a discharge channel, the existence of N_2 metastable state $N_2(A^3\Sigma_u^+)$ and voltage waveform.

12. Analytical Method

2.1 Model of a micro discharge and calculating conditions

Here, we describe a model of a micro discharge and calculation conditions which were used in the analysis. In the silent discharge device, many micro discharges occur in the air gap between electrodes covered with a dielectric plate by applying AC high voltage. Fig.1 shows the electric equivalent circuit of silent discharge. We focused to a one micro discharge, and the micro discharge in the gap is assumed as a discharge of a small capacitor C_1. Fig. 2 is a model of one micro discharge structure.

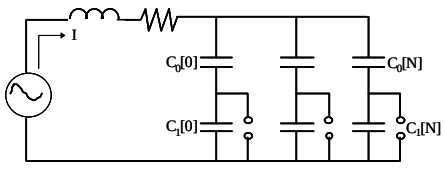

Fig.1 Equivalent circuit of silent discharge

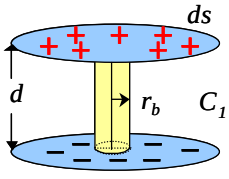

Fig.2 Model of one micro discharge

Table.1 shows various physical parameters, and Table.2 shows the parameters values, which were calculated by the equations written in Table 1. As the micro discharge area is *ds*, the number of parallel

Table.1 Description of various physical parameters

$$ds = \frac{d \cdot C_1}{\varepsilon} = \frac{d}{\varepsilon} \cdot \frac{q}{V_g} = \frac{d \cdot I \cdot \tau}{\varepsilon \cdot V_g} \quad \cdots\cdots\cdots\cdots\cdots\cdots \quad (1)$$

$$m = \frac{S}{ds} = \frac{\varepsilon \cdot V_g \cdot S}{d \cdot q} \quad \cdots\cdots\cdots\cdots\cdots\cdots \quad (2)$$

$$C_1 = \varepsilon \cdot \frac{ds}{d} \quad \cdots\cdots\cdots\cdots\cdots\cdots\cdots \quad (3)$$

$$Q = \frac{1}{2} \cdot C_1 \cdot \left(V_g{}^2 - V_b{}^2 \right) \cdots\cdots\cdots\cdots\cdots \quad (4)$$

$$I = \pi \cdot r_b{}^2 \cdot J \quad \cdots\cdots\cdots\cdots\cdots\cdots\cdots \quad (5)$$

$$h = \frac{P}{m \cdot Q} \quad \cdots\cdots\cdots\cdots\cdots\cdots\cdots \quad (6)$$

$$t_{\text{int}} = \frac{1}{h} \cdot \frac{Rd}{100} \quad \cdots\cdots\cdots\cdots\cdots\cdots\cdots \quad (7)$$

$$Rd = \frac{t_1}{t_h} = \frac{t_1}{2f} \quad \cdots\cdots\cdots\cdots\cdots\cdots\cdots \quad (8)$$

$$n_e = \kappa \cdot \frac{1}{q_e \cdot v_{de} \cdot (E/n)} \cdot \frac{P_s}{d \cdot n} \quad \cdots\cdots\cdots\cdots\cdots \quad (9)$$

Where, q : electric charge per a single micro-discharge(C), κ: dissipation factor of electrons(=0.55), q: electron charge(C), v_d: drift velocity of electron in electric field, n: Gas density(cm^{-3}), P_S :power density in micro discharge channel(W/cm^2).

Table.2 Parameter values

No.	Parameters	Value and Unit
P(1)	Current density *J*	1000 A/cm^2
P(2)	Micro discharge channel radius r_b	0.01 cm
P(3)	Discharge duration τ	3 ns
P(4)	Discharge power *P*	100 W
P(5)	Electrode area *S*	750 cm^2
P(6)	Gap distance *d*	0.3 cm
P(7)	Gas temperature *T*	323 K
P(8)	Breakdown voltage V_g	9000 V
P(9)	Discharge stop voltage V_b	3000 V
P(10)	Area of micro capacitor *ds*	0.532 cm^2
P(11)	Discharge current *I*	0.314 A
P(12)	Capacitance of micro-discharge *C*	0.157 pF
P(13)	Parallel micro-discharge *m*	1408
P(14)	Discharge energy *Q*	5.65 μJ
P(15)	Frequency of discharge times *h*	12554 s^{-1}
P(16)	Discharge interval t_{int}	39.8 μs
P(17)	Electron density n_e	2.79×10^{14} cm^{-3}
Gas composition N_2:O_2:NO=78%: 15%: 200ppm		

micro-discharges in the electrode area *S* becomes *m*, which is calculated by Eq. (2).

Followings are the calculation conditions. When AC voltage is applied to the discharge device, pulse micro discharges occur only when the gap voltage exceeds the breakdown voltage of the gap. Many radicals are generated by collision of molecules with the energetic electrons, and at the same time they react with the gas molecules during the discharge period. However, there are no radical generations during the non-discharge period. Thus, the non-discharge period is the period, when the residual radicals diffuse from the discharge channel and react with pollutants. The ratio *Rd* defined as Eq.(8) is the ratio of discharge period in a half cycle, and it varies with the wave form of the applied voltage. Usually, *Rd*=50%. So in the case that the frequency *h*=250Hz, the micro discharges occur for 1ms, and they don't occur for another 1ms, namely the discharge period comes at 1ms intervals. The discharge period continues for 40ms, and after 40ms, the chemical reactions are induced by residual reactive species and finally all the reaction products reach the equilibrium state. Location of pulse micro discharge was assumed to be at the same place all time.

The electron density in the micro discharge channel n_e was calculated by Eq.(9). A reduced electric field *E*/*n* in the gap was assumed as constant value of 100Td. An electron consumption rate κ of 0.55 was used from the literature [3]. *P*(1)~(3) in Table.2 are very important physical parameters, and the typical physical values that reported by Dr. Kogelschatz were used as shown in Table 1 [4], *P*(4) is a calculation condition, and *P*(5)～(6) are the dimension of our discharge device, and *P*(11)~(18) are values of the physical

parameters, and they are calculated from the typical physical values of $P(1)$~$P(3)$ by Eq.(1)~(8).

2.2 Calculating method of chemical reactions and diffusion

Diffusions of various species from a micro-discharge channel are governed by Eq.(10) in a micro-discharge model which is illustrated in Fig.3.

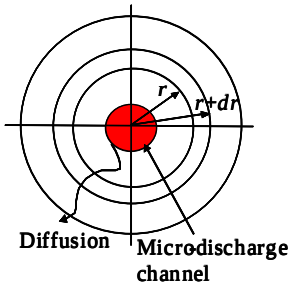

Fig.3 micro-discharge model

$$\frac{\partial c}{\partial t} = D \cdot \left(\frac{\partial^2 c}{\partial r^2} \right) + \frac{D}{r} \cdot \frac{\partial c}{\partial r} + \Gamma \quad \text{.....(10)}$$

$$\Gamma = k_1 \cdot [A] \cdot [B] + k_2 \cdot [A] \cdot [E] + \cdots \quad \text{.....(11)}$$

Where, $[X]$: density of substance X(cm^{-3})

Boundary condition at an edge of analyzing area is $dc/dr=0$. D (cm^2/s) means a diffusion coefficient, and as a D value, $0.41 cm^2/s$ was used. Γ in Eq.(11) is an amount of chemical reaction, which is calculated by the multiplication of the reaction rate k(cm^3/s-2body reaction, cm^6/s-3body reaction) and the density of gas molecules(cm^{-3}). The calculation took 161 reactions and 24 species into consideration, and the reaction rates were taken from NIST database [5] and Ikebe's report [6].

3. Results and discussion

3.1 Influence of local elevation of temperature on NO removal performance

When the many successive micro-discharges occur in the same channel, a portion of discharge energy is deposited in the volume of the micro-discharge channel. Gas temperature in the volume will increase by the deposited energy. On the other hand, since the reaction rates depend on the gas temperature, we investigated the effect of local elevation of gas temperature on NO removal performance. The elevation of gas temperature was calculated by solving the heat conduction equation and the NO removal performance was calculated by solving Eq. (10), considering the change of the reaction rate at high temperature.

At first, we estimated the temperature rise per single micro-discharge. In Eq. (9) of Table 1, the electron consumption rate κ was used, and κ means the rate of discharge energy used for radical reactions. According to the literature [3], κ was estimated as 0.55. If we think it from the other side, it is understood that the rest of the energy, namely (1-κ), is used for vibrational / rotational excitation and for ionization. So we assumed a half of the residual energy, namely R_T=0.225, was used for the temperature rise. On this assumption, the temperature increase $d\theta$ per single micro-discharge was calculated as 10.4K by using Eq.(12). Here, gas in the discharge device is air. Eq.(13) shows the heat conduction equation applied to our micro-discharge model.

$$d\theta = \frac{Q \cdot R_T}{c \cdot w} = \frac{C \left(V_g^{\,2} - V_b^{\,2} \right) \cdot R_T}{2 \cdot c \cdot w} \quad \text{.....(12)}$$

$$\rho \cdot c \cdot \frac{\partial T}{\partial t} = \frac{\lambda}{r} \left\{ \frac{\partial}{\partial r} \left(r \cdot \frac{\partial T}{\partial r} \right) \right\} \quad \text{.....(13)}$$

Where, c: specific heat (J/kg K), w: weight of micro discharge channel volume, ρ: mass density (kg/m^3), λ: thermal conductivity (W/m K).

Fig.4 shows gas temperature distribution of radial direction in the micro-discharge model. When t=39ms, gas temperature T at the center of micro-discharge reached the maximum value of 510K. After this time,

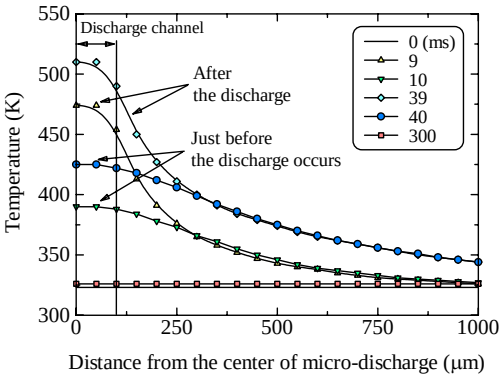

Fig.4 Temperature distribution

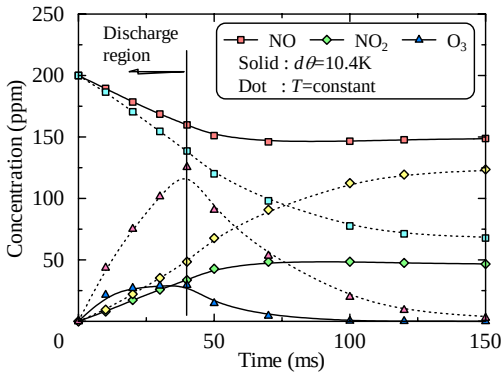

Fig.5 Time variation of NO, NO_2 and O_3 concentration

Table.3 NO removal/formation reactions and each reaction rate [5]

No.	Reaction	Reaction Rate $k(T)$
$k(1)$	$NO+O_3 \rightarrow NO_2+O_3$	$1.5*10^{-12}\exp(-1300/T)$
$k(2)$	$O+NO+O_2 \rightarrow NO_2+O_2$	$8.6*10^{-32}(T/300)^{-1.8}$
$k(3)$	$O+NO+N_2 \rightarrow NO_2+N_2$	$1.0*10^{-31}(T/300)^{-1.8}$
$k(4)$	$NO_2+O \rightarrow NO+O_2$	$1.7*10^{-11}\exp(-300/T)$
$k(5)$	$N+O_2 \rightarrow NO+O$	$1.5*10^{-11}\exp(-3601/T)$
$k(6)$	$N+O+N_2 \rightarrow NO+N_2$	$2.6*10^{-31}T^{-0.5}$

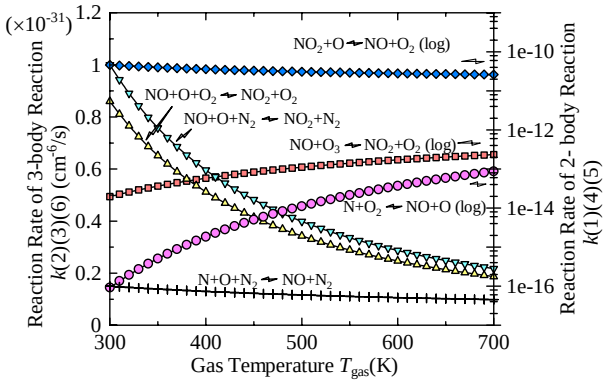

Fig.6 Dependence of reaction rate on temperature

decrease of the gradient of temperature distribution continued and finally, the gas temperature reached the equilibrium state of 326K.

Fig.5 shows the time variation of the concentrations of NO, NO_2 and O_3. At first, let's consider the case of NO. When the elevation of gas temperature was taken into consideration, NO concentration (solid line) was 150ppm at 150ms. On the other hand, when T is constant, NO concentration was 70ppm at same time. It was calculated that the NO removal efficiency was 40.9g/kWh at constant T and 15.9g/kWh at elevated temperature respectively. It is evident that NO removal rate decreases when the temperature rise is considered. The reason why is explained as follows.

The first reason is in the difference of O_3 concentration. O_3 is an important substance for the oxidation of NO to NO_2. But, it is well known that O_3 dissociates at high temperature. In fact, as it is seen in Fig. 5, in the case that temperature rise is considered, O_3 concentration (solid line) is smaller than the one in the case that T is constant (dot line). Therefore, the amount of oxidization of NO by O_3 decreased.

The second reason is the activation of NO formation reaction by N and O radicals. Table.3 shows typical NO removal and formation reactions and also their reaction rates. Fig.6 shows the dependence of reaction rate on temperature. Reaction rates which increase with temperature rise are $k(1)$: $NO+O_3 \rightarrow NO_2+O_2$ and $k(5)$: $N+O_2 \rightarrow NO+O$, and the other reaction rates are all declined. If the reaction rate $k(1)$ became large at higher temperature, the oxidization of NO by O_3 did not increase. Because, the O_3 concentration decreases with the temperature. But, NO formation reaction rate $k(5)$ at 500 K increases about 10^2 times as high as the rate at 323K. And the amount of generated N radical is not varied by the temperature elevation. Thus, NO formation reaction by N radical becomes very effective. In summary, the reasons that NO removal

Table.4 Typical reactions and reaction rates relating $N_2(A)$

No.	Reaction	Reaction Rate	Ref.
$k(7)$	$N_2+e \rightarrow N_2(A)+e$	$3.37*10^{-10}$	[7]
$k(8)$	$N_2(A)+O_2 \rightarrow N_2+2O$	$2.0*10^{-12}$	[8]
$k(9)$	$N_2(A)+N_2 \rightarrow N_2+N_2$	$2.7*10^{-11}$	[8]
		$1.9*10^{-13}$	[9]
		$<3.0*10^{-18}$	[10]

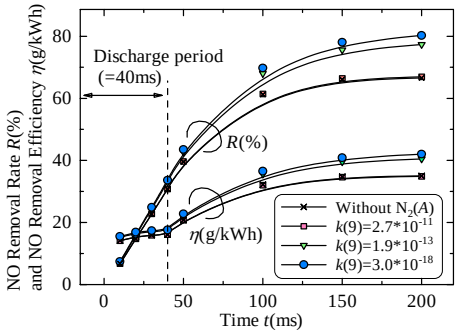

Fig.7 Influence of $N_2(A)$ on NO removal

performance becomes worse are concluded as the degradation of NO oxidization by O_3 and the activation of NO formation reaction by N radical.

3.2 Influence of the N_2 metastable state $N_2(A^3\Sigma_u^+)$

It is known that when electron energy is low, O_2 is dissociated into O radicals by N_2 excited in a metastable state in addition to the direct collision with electron. Previous model did not consider the metastable state of the N_2. Since the exhaust gases include high concentration of N_2, this reaction is very important. Here, we considered 15 reactions associated with $N_2(A^3\Sigma_u^+)$ (hereinafter $N_2(A)$). Table.4 shows a $N_2(A)$ generation reaction and typical $N_2(A)$ quenching reactions. Reaction rate $k(7)$ is the value when E/n=150Td[7]. Regarding the reaction rate $k(9)$ of $N_2(A)$ quenching reaction, there are a couple of data, but they are extended in a wide range (10^{-11}~10^{-18}). As the result of calculations, it was found that the reaction rate $k(9)$ ($N_2(A)+N_2 \rightarrow N_2+N_2$) is a very important value, because it almost determines the influence of $N_2(A)$. In this study, various values of $k(9)$ were used and investigated their effect on NO removal.

Fig.7 shows the influence of $N_2(A)$ on NO removal rate R(%) and also on NO removal efficiency η(g/kWh). When $k(9)$ is 10^{-11}, R and η have no difference with the previous result (without $N_2(A)$). Because, if $k(9)$ reaction is active, almost all of $N_2(A)$ which generated by electron collision, is quenched by N_2. However, when $k(9)$ of 10^{-13} and 10^{-18} were used, R and η became large. Especially, the difference of NO removal performance is quite apparent at the time after discharge has stopped. Namely, NO removal rate R at t=200ms is 78% for $k(9)=1.9*10^{-13}$ and 67% for case of the previous work, respectively. This comes from difference of O_3 concentration in the time after-discharge period. Because the lifetime of O and N radicals are very short, NO removal reaction in the after-discharge period is done by the residual substance, especially by O_3. Thus, O radicals generated by $N_2(A)$ are mainly used for O_3 generation reaction, and not for the direct oxidation of NO to NO_2. When $k(9)$ is 10^{-18}, O_3 concentration increases as much as 30% in comparison with the case without $N_2(A)$.

The effects of $N_2(A)$ on NO removal performance are summarized as follows. (1) If $N_2(A)$ quenching reaction rate $k(9)$ is low, the oxidization of NO by O_3 will increase. (2) If the reaction rate $k(9)$ is high, since almost all of $N_2(A)$ are consumed by N_2, the effect of $N_2(A)$ on NO removal performance is not so large. (3)Although $N_2(A)$ is able to produce O radicals, NO oxidation is mainly done by O_3, because O radicals soon changes to O_3.

3.3 Influence of voltage waveform

The barrier discharge usually occurs intermittently in a half cycle and the time period that discharge occurs is a period that dV/dt of the applied voltage is large. So the discharge period can be controlled by the voltage

waveform of applied voltage. Here, we introduce a parameter *Rd* which is defined as the ratio of discharge period to total period, and investigated the effect *Rd* on NO removal performance. If *Rd* is small, it means that the discharge concentrates in a short period and there are relatively long period of time without discharge. As for the wave form of applied voltage, trapezoid wave form corresponds to small *Rd*, and sinusoidal wave form gives larger *Rd*. In this study, *Rd* was changed in keeping with the constant input energy. In the practical calculation, the interval between the successive pulse discharges was changed in accordance with Eq.(7) without changing the number of micro-discharges.

Fig.8 shows relation between the discharge ratio *Rd* and NO removal performance (*R* and η). It is evident that both *R* and η deteriorate at smaller *Rd* than about 30%. It comes from a difference of the amount of O_3 destruction. When the time interval t_{int} between successive pulse discharges is large, namely when *Rd* is large, O_3 generated around discharge channel can diffuse to the surroundings without destruction by discharge, which leads to the improvement of NO removal performance. But the improvement is not so large.

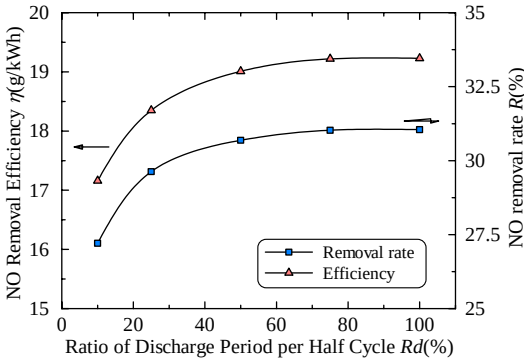

Fig.8 *Rd* vs. NO removal performance

4. Conclusion

Three factors affecting NO removal performance were investigated using a micro-discharge model, which takes the chemical reactions and diffusion of species into consideration. Principal results obtained in this work are summarized as follows.

(1) Temperature elevation in micro discharge volume makes the NO removal performance worse. It is because that NO formation reaction by N radical is activated at higher temperature. (2) Influence of N_2 metastable state depends on the reaction rate of $N_2(A)$ quenching reaction, namely the reaction $N_2(A)+N_2 \rightarrow N_2+N_2$. (3) When the ratio of the discharge period *Rd* is large, namely when *dV*/*dt* of applied voltage is small, η and *R* improve a little better. But, this factor is not so effective for the improvement of NO removal performance.

References

[1] A. C. Gentile, M. J. Kushner: J. Appl. Phys. **79**, 3877 (1996)

[2] Y. Yoshioka, T. Shoyama: HAKONE9, CD-ROM (2004)

[3] J. Kitayama, M. Kuzumoto: J. Phys. D: Appl. Phys, **30**, 2453-2461 (1997)

[4] U. Kogelschatz, B. Eliasson: Marcel Dekker, INC, 581-605 (1995)

[5] NIST Kinetics Database: http://kinetics.nist.gov/index.php

[6] K. Ikebe, K. Nakanishi, and S. Arai: T. IEE Japan, Vol.109-A, No.11 (1989) (in Japanese)

[7] H. Kusunoki, K. Ito, K. Onda: IEEJ Trans. PE, Vol.123-B, No.12 (2003) (in Japanese)

[8] H. Matzing: Adv. Chem. Phys. Vol. 80, 6315-402 (1991)

[9] R. Dorai: Doctor's thesis, Department of Chemical and Biomolecular Engineering, University of Illinois

[10] J. T. Herron:J. Phys. Chem. Ref. Data, Vol. 28, No. 5 (1999)

Characterization of the organic coating onto nanoparticles treated in acetylene plasma

G. Le Dû[1], N. Célini [1,2], F. Bergaya[2], D. Debarnot[1], F. Poncin-Epaillard[1]

[1] *Laboratoire Polymères Colloïdes et Interfaces (UMR CNRS 6120), Université du Maine, Avenue O. Messiaen, 72085 Le Mans, France*

[2] *Centre de Recherche sur la Matière Divisée (UMR CNRS 6619), Université d'Orléans, 1B, Rue de la Férollerie 45071 Orléans Cedex 02, France*

Abstract

The good properties of polymer nanocomposites are due to the good dispersion of the filler in the polymeric blend. The dispersion of clay particles is achieved with the use of plasma technique as an alternative route to alter the hydrophilic character of the clay. The plasma-polymer coated onto silicon wafer was characterized as composed of aliphatic groups and its growth was correlated to the fragmentation of acetylene in the electrical discharge and the issued reactive species detected by optical emission spectroscopy.

Keywords : acetylene, plasma, OES, hydrophobic coating

1. Introduction

In the field of polymer composites, a new class of materials with better mechanical, electrical or permeability properties has emerged in the past decade: the nanocomposites. They are composed of a polymer matrix and filler whose dispersion in the polymeric blend will grant the better final properties. Their dispersion is controlled by the interaction energy between the filler particle and the polymer chains [1]. The dispersion of clay particles can not be achieved without a pre-treatment of each individual layer of the clay since both products are incompatible. Therefore, the cohesion of the blend is obtained when an organic molecule, i.e. tensio-active molecule [2,3] is absorbed onto the clay surface. To alter the hydrophilic behavior of the clay, the dry plasma technique can be proposed as an alternative route to the synthesis of the organo-clay usually run in wet organic or aqueous medium with all the difficulties for the environmental protection with such synthesis route [3].Clays such as Wyoming montmorillonite and Laponite RD are treated in acetylene plasma to modify their surface properties and to improve their compatibility towards the polyethylene. The acetylene fragments will precipitate as hydrocarbonated coating onto the clay layer and will give an apolar – organophilic character to the clay surface.

Acetylene plasmas are nowadays mostly used in the deposition of the diamond –CH like film. Stoykov and al [4] proposed a model that analyses the clusterisation kinetics in a low pressure acetylene rf discharge in order to predict the temporal evolution of all different reactive gaseoues species and the mechanism of clusterisation. This model takes into account the neutrals species, hydrocarbonates cycles, positif and negative ions and electrons. Gordillo-Vasquez and Albella [5-6] studied the effect of different plasma parameters, the pressure and the rf power influence, on the $C_2H_2(1\%)/H_2/Ar$ rf discharge chemistry in the diamond nanofilm synthesis. The argon proportion was also varied. Benedikt [7-8] used the Cavity Ring Down Spectroscopy (CRDS) to characterize the species in an Ar/ C_2H_2 arc plasma. The detected C_2, C_2H, CH radicals seem to play an important role in the deposited layer growth mechanism.

The aim of this study is to analyse the acetylene plasma chemistry in order to optimize the plasma parameters to obtain a deposited layer with the lowest polar energy. The plasma-polymer layer is also fully characterized by different surface analyses such contact angle measurements, X-ray photospectroscopoy and FTIR spectroscopy.

2. Dependence of the plasma- polymer properties versus the plasma parameters

In the attempt to determine the optimum conditions for obtaining the most hydrophobic layer, different plasma parameters were tested: the duration (t, 1-7 mn), the discharge power (P, 10-40 W), and the gas flow (Q, 10-30 sccm). Depending on these parameters, the plasma polymer shows a hydrophobic character with a surface energy around 45 $mJ.m^{-2}$ and its FTIR spectrum is mostly composed of the C-H stretching and bending respectively at 2925, 2856 and 1387, 657 cm^{-1} suggesting the presence of CH_2 and CH_3, the C=C stretching vibration band at 1645 cm^{-1} and the C-C stretching vibration band at 1008 cm^{-1}. No bands at 2200 cm^{-1} and 2100 cm^{-1} corresponded to C≡C stretching bands, are found suggested that the acetylene molecule is fragmented into C=C, C-C and C-H. Some stretching bands of carbonyl, ketone and hydroxyl functions respectively at 1855, 1695 and 3446 cm^{-1} are noticed. Similar attribution reported by other authors [9-12] and assigned to a post-oxidation of the plasma-polymer with air rather than the plasma phase contamination, since no oxygen was

detected by OES. By XPS spectroscopy, the plasma-polymer was also prooved to be essentially composed of hydrocarbon functions (around 90 %). The examination of the C1s high-resolution peak shows the existence of three components corresponding to different nature of carbon bonds. The main component fixed at 285 eV is related the polymer hydrocarbon structure and represents the C-C and C-H bonds. The second component located at 286.5 eV indicates the presence of species containing C-O bonds such as alcohol, ether. The component at 287.6 eV reveals the presence of C=O bonds assigned to aldehyde and ketone. The percentage of chemical bonds determined by the ratio (total C1s peak area/bond C peak area), corresponds to 78.9 % C-C and C-H bonds, 18.1 % of C-O bonds and 3 % of C=O bonds, with these plasma parameters.

The effect of the gas flow (Fig. 1a) was determined with constant power of 20 W and duration of 1 mn. With a small addition of acetylene in the reactor (10 sccm), the surface energy of the substrate and its polar component decrease rapidly respectively of 27 % and of 80 %. Its apolar componant increases of 78 %. Then, with higher flow, the surface energy slowly decreases and reaches a plateau equal to 48 $mJ.m^{-2}$, while the apolar energy tends to 42 $mJ.m^{-2}$. With a fixed 30 sccm flow and power of 10 W and duration equal to 1 mn (Fig 1b), the total surface energy diminishes of 35 % and reach a plateau value of 47 $mJ.m^{-2}$. The apolar surface energy increases of 81 % and remains constant (43 $mJ.m^{-2}$) for longer duration. The polar surface energy is minimal, i.e. 6.8 $mJ.m^{-2}$, at 1 mn. Varying the power input with duration equal to 1 mn and flow of 30 sccm shows that the decrease of total surface energy and the increase of its polar componant reach at 20 W a plateau value, respectectively of 47 $mJ.m^{-2}$ and around 40 $mJ.m^{-2}$ (Fig 1c). Therefore, the optimum conditions to the obtention of the hydrophobic layer whose polar surface energy is equal to 3.9 $mJ.m^{-2}$ correspond to 20W of power input, 30 sccm of gas flow and 1 minute of duration.

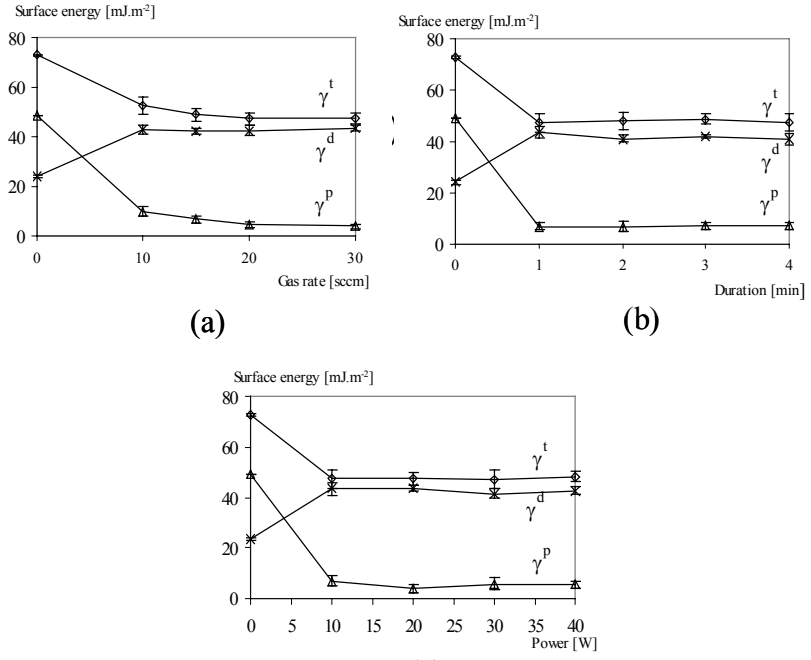

Fig. 1. Surface energy of plasma-polyacetylene versus (a) the gas flow (P=20 W, t=1 minute), (b) the duration (P=10 W, $F(C_2H_2)$=30 sccm), (c) the power input ($F(C_2H_2)$=30 sccm, t=1 mn).

3. Chemical composition of the acetylene plasma phase analysed by optical emission spectrocopy

This study deals with the detection of emissive species in the 300-800 nm range. The global spectrum (Fig. 2) consists of the different lines of the species in the plasma such as CH, C_2, CH^+, H_β et H_2. The highest line is the signature of CH at 431.4 nm. This radiation is the Q–branch of the (0,0) transition in the $A^2\Delta$ -$X^2\Pi$ system. CH is also representated at 388.9 nm due to the Q-branch radiative transition (0,0) of $B^2\Sigma$ -$X^2\Pi$ system. However this line can also be the C^+ signature : according to the spectrocopic tables, C^+ emits in this wavelenght area at 386.8 and 387.1 nm. C_2 is also shown at 453.6 nm for the transition (2,3) of the Swan system and at 404.6 nm for the transition (2,3) of Deslandres system. The lines at 546.1 and 506.8 nm are assigned to the emissive radiation at 545.9 and 505.5 nm of H_2. Unfortunately, both signatures of C_2 and H_2 overlap and it is difficult to assign some lines to C_2 or H_2 precisely, or a C_2/H_2 contribution. The dual lines are : the 468.1 nm line which can be either C_2 at 468.4 nm from Swan system (transition 4,3) or H_2 at 468.3 nm. The 471.1 nm line may be assign to C_2 at 471.5 nm from Swan system (transition 2,1) or H_2 at 486.1 nm; and the

542.1 nm line can correspond to C_2 transition (6,7) at 541.3 nm from Swan system or to H_2 at 545.9 nm. H is detected by its H_β signature at 486.1 nm. CH^+ appears in the emission spectrum at 374.8 nm and 379.8 nm assigned to (2,0) and (4,1) radiative transitions from the $A^1\Pi$ system of CH^+. Moreover, a continuum between 420 and 600 nm is shown : ones could be tend to attribute it to the hot carbonate particule incandescence produced in the discharge [11]. Indeed, such continua were observed on carbonated particles producted in graphite laser assisted evaporation. In our case, this assumption would suppose particule temperature of 5000 K which is impossible at this rf power and this gas pressure.Benedikt and al [8] assumed that it is known that excited C_2H emits a continuum band light in the visible region and similar continuum band emission was also observed using optical emission spectroscopy (OES).

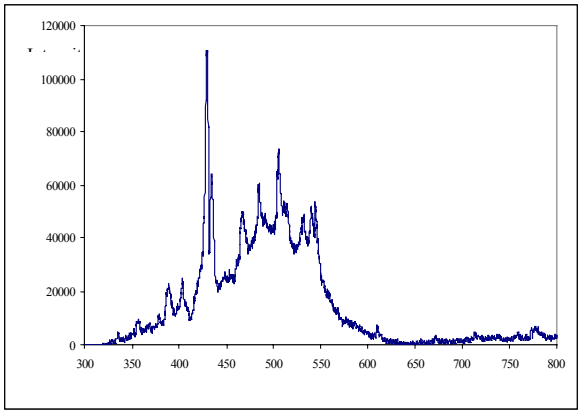

Fig. 2: Optical emission spectrum of the rf acetylene plasma in the 300-800nm range (Q_{C2H2}=10 sccm, P=10W)

By actinometry, a quantitave analysis of the discharge parameters (rf power and pressure) was carried out over the principal plasma species by following the CH^+ line at 374.8 nm, CH at 431.4 nm, C_2 at 435.3 nm, H_β at 486.1 nm, and H_2 at 545.5 nm. Argon was chosen as actinometer in so far as it does not interfere with acetylene.

The study of the gas flow influence (Fig. 3a) on the plasma composition was carried out at constant rf power (20W) and the acetylene flow was varied from 10 to 35 sccm. At a constant acetylene flow of 10 sccm, the concentration of H is the highest in the plasma phase. Then it continuously falls down by nearly 50%: the H consummation is then higher than its production. Indeed, the H production is due to the dissociation of acetylene and CH who both increase, to the deshydrogenation reactions to form C_xH_y compounds. The reactions between CH, CH_2, and C_XH_Y then consume it [5-8,13]. Between 10 and 35 sccm, H_2 decreases. It can be due to the dissociation of H_2 to form H whose rate is more important or to the association with CH to form CH_3 or CH_2. CH always rises as the acetylene flow rises. From 10 to 20 sccm, the raise is important whereas from 20 sccm this raise slows down. At 20 sccm, CH becomes majoritar behind H and H_2. CH is producted by the C_2H_2 dissociation and the $C_2H_2^+$ electronic recombinaison and consumed during the collisions between two CH molecules, with other molecules CH_x or with H_2 [5-8,13]. When the acetylene flow goes up, the CH line also rises up : the CH production is due to the likely acetylene dissociation. C_2, CH^+ appear in less quantity than H, H_2 and CH. Their concentrations smoothly vary with the acetylene flow. CH^+ slightly falls down. When the inlet gas rate increases, the amount of C_2H_2 increases. In our reactor, gas flow and pressure are linked : When the pressure increases, the mean path free decreases and the collision probability increases.The $C_2H_2^+$ electronic dissociation and and the CH ionisation product CH^+. It is then used in the collisional reactions with C_2H_2 [5-8,13]. As the collisions increase, $CH^+$is more used by collision reactions, and the CH^+ line intensity decreases in spite of the augmentation of C_2H_2 and CH. C_2 rate smoothly varies with C_2H_2 inlet gas. To conclude, the influence of the inlet flow is not negligable on the plasma phase composition. The C_2H_2 dissociation increases to produce CH which will recombine with other molecules when acetylene flow and the pressure increase in the reactor. Those results agree with Stoykov and al [4], Gordillo-Vazquez and al [5-6] : the pressure has a drastic effect on the amount of neutrals and more especially on CH whose production is more important when the inlet gas flow and the pressure increase. Morover, whatever the acetylene gas flow is, CH and H are more important than CH^+, C_2 and H_2. This leads to think that the most reactive species are CH and H, one or both of them are the plasma precursor of the hydrophobic caracteristic of the deposit.

The line intensities were measured for the different rf power and then plotted in Fig. 3b. This figure shows that in the plasma phase CH is the main specie. When the rf power increases, the chemical composition

of the plasma phase smoothly varies : CH decreases as the power increases up to 30W. For upper power values, CH reaches a plateau. CH^+ stays still :CH^+ and CH are mainly producted by the C_2H_2 dissociation . The CH^+ spectra line intensity is slightly affected by the augmentation of the rf power. H_2,C_2 and H slightly decrease. To conclude, the rf power has a weak influence on the chemical composition of the plasma phase. These results agree with Gordillo and al [5-6] who assumed that the rf power influence is weak.

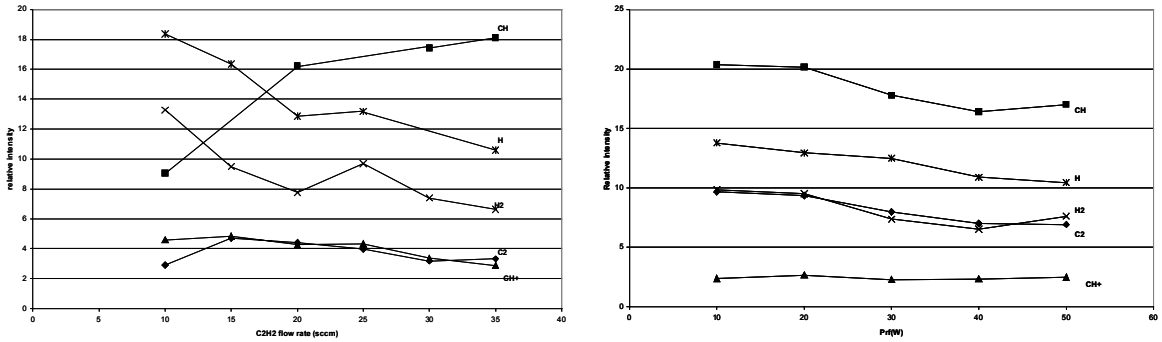

(a) (b)

Fig. 3: Evolution of the major spectra line (a) versus C_2H_2 inlet flow rate (P= 20 W) and power (Q_{C2H2} = p = 4,2.10^{-2} mbar)

4. Plasma species responsible of the growth of the plasma-polymer

From the optical emission spectroscopy technique, we know that CH and H are the main species in the plasma phase. The correlation between the CH and H densities in the plasma phase and the polar energy on the surface of the deposited layer is linear (Fig. 4). The polar energy of the deposit surface decreases when the CH density increases whereas it increases when the H density in the plasma phase increases. To obtain a hydrophobic deposit, the formation of CH must be enhanced, the plasma parameters (pressure, inlet gas rate and RF power) must improve the acetylene dissociation. The experiments shows that for a flow rate of 20 sccm and a rf power of 20 W the maximum rate of CH is detected in the plasma phase.

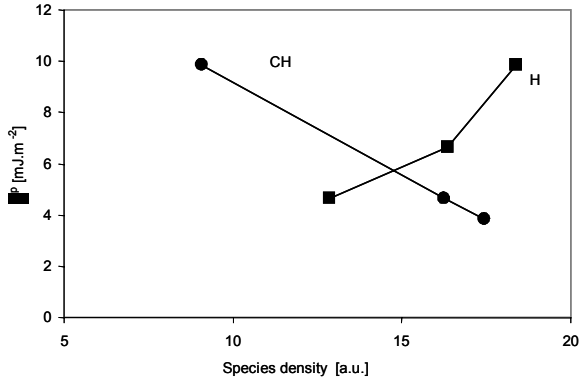

Fig. 4: correlation between the CH and H densities in the plasma phase versus the polar energy of the coated surface

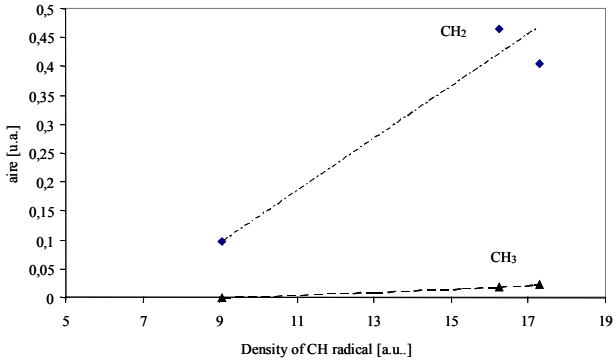

Fig. 5 : Correlation between the CH density in the plasma phase and CH_2 ,CH_3 concentrations in th eplasma polymer (P=20W)

Fig. 5 represents the evolutions of the CH_2 and the CH_3 groups analysed by FTIR spectroscopy versus the variation of CH density. When the CH density increases in the plasma phase, both amounts of methylene and methyle groups on the surface analysed by IR spectroscopy increase. The amount of CH_3 is less influenced by the CH density in the plasma phase

4. Conclusion

The most reactive species are CH and H detected by optical emission spectroscopy, one or both of them are the plasma precursor of the hydrophobic caracteristic of the deposit. The plasma-polymer, coated onto silicon wafer was characterized with different surface analyses. Its structure is composed of CH, CH_2, CH_3 groups, double carbon-carbon bonds and few oxygen-carbon bonds. The different plasma parameters were chosen to lead to the most hydrophobic coating with surface energy lower than 3.9 $mJ.m^{-2}$. The correlation between the CH and H densities in the plasma phase and the polar energy on the surface of the deposite is linear. The polar energy of the deposit surface decreases when the CH density increases whereas it increases when the H density in the plasma phase increases. To obtain a hydrophobic deposit, the formation of CH must be enhanced , and therefore the acetylene dissociation too. CH seems to be the plasma precursor for the surface functionalisation. The CH density increases in the plasma phase, both amounts of methylene and methyle groups in the plasma polymer increases. The rf power does not influence a lot the chemical composition of the plasma phase.

References

[1] R. A. Vaia, H. Ishii, E. P. Giannelis, Chem. Mater. **5**, 1694 (1993).
[2] P.Bala,; B. K.Samantaray,; Srivastava, S. K. Mat. Research Bul. **35**, 1717(2000).
[3] G. Lagaly, Solid State Ionics, **22**, 43 (1986).
[4] S Stoykov, C. Eggs, U. Kortshagen, J. Phys. D: Appl. Phys. **34**, 2160 (2001).
[5] F. Godillo-Vazquez, J. Albella, Plasma Sources Sci. Technol. **11**, 498 (2002).
[6] F.Gordillo-Vasquez, Plasma Sources Sci. Technol., **13**, 50 (2004).
[7] J. Benedikt , K.G.Y. Letourneur, M. Wisse, D.C. Schram, M.C.M. van de Sanden, Diamond and Related Materials **11,** 989 (2002).
[8] J. Benedikt , R.V. Woen , S.L.M. van Mensfoort , V. Perina , J. Hong , M.C.M. van de Sanden, Diamond and Related Materials **12** (2003) 90–97
[9] C. Nah, M.-Y. Huh, J. M. Rhee, T.-H Yoon,. Polym. Int. **51**, 510 (2002).
[10] I. Retzko, J. F. Friedrich, A. Lippitz, W. E. S. Unger, J. Elec.Spec.related Phenom. **121**, 111 (2001).
[11] S. I. Ivanov, S. H. Fakirov, D. M. Svirachev, Eur. Polym. J. **14**, 611 (1978).
[12] H. Yasuda, M. O. Bumgarner, H. C. Marsh,; N. Morosoff, J. Polym. Sci., **14**, 195 (1976).
[13] A. Golanski, J. P. Stoquert, F. Piazza, P. Kern, E. Laemmer, A. Deruyver, F. S. Schulze, L. McDonnell, Journal of Applied Physics, **93,** 10,5911 (2003)

Plasma polymerized polyaniline used as sensitive layer for gas sensors

Dominique Nicolas-Debarnot, Fabienne Poncin-Epaillard

Laboratoire Polymères-Colloïdes-Interfaces (UMR CNRS 6120), Université du Maine, Avenue Olivier Messiaen, 72085 Le Mans, France

Abstract
Polyaniline has been synthesized using plasma technique. Different plasma conditions have been studied in order to minimize the surface degradation and to obtain the polyaniline layer which can be used for gas detection.

Keywords: Plasma, deposition, polyaniline.

1. Introduction

Most of gas sensors available on the market are semiconducting ones, measuring a conductivity alteration under gas adsorption. These sensors, based on tin dioxide, operate at high temperature to ensure sensor sensitivity and selectivity. However, their performances, specially selectivity, have to be improved. To improve gas sensors characteristics, novel sensitive organic layers, electronic conducting polymers, were developed. The interest of these materials has been recognized by the awarding of the Nobel prize in Chemistry in 2000 to A.J. Heeger, A.G. MacDiarmid and H. Shirakawa [1,2], who synthesized the first conducting polymers and proved their potentialities in a large number of applications. Besides, some commercial electronic noses are based on electronic conducting polymers organized in an array [3]. The advantages of conducting polymers compared to inorganic materials used until now are their diversity, their easy synthesis and particularly, their sensitivity at room temperature. Polypyrrole has been one of the first polymers used in gas sensors. However, it shows a low sensitivity, a high response time and an incomplete desorption of gas molecules, *i.e.* an incomplete reversibility of the sensor response. So, the research were extended to polyaniline (PANi) [4].

Common routes to synthesis polyaniline are chemical and electrochemical routes. In this study, PANi is elaborated using an original, clean method: the plasma technique. As the sensitive sites for gas molecules are NH^+ groups, the aim is to obtain the highest concentration of N-containing groups, i.e. the highest electrical conductivity of the PANi layer by varying the parameters of the plasma. The plasma parameters studied are the discharge power, the polymerisation time and the use of a dilution gas (argon or nitrogen).

2. Materials and methods

Polyaniline thin films were deposited onto silicon substrates oxidized in order to obtain a 100 nm silica layer. The cleaned substrate was placed into the plasma reactor where the plasma is induced thanks to a radio-frequency generator. The pressure into the reactor during the polymerization was maintained at 0.02 torr for all the experiments whereas the discharge power, the polymerization time and the reactive gases (aniline, aniline + 1 sccm argon or aniline + 1 sccm nitrogen) varied.

The obtained polyaniline films were then characterized by thickness and wettability measurements, FTIR and XPS analyses.

3. Characterization of plasma polymerised polyaniline

3.1. Thickness measurements

The polyaniline layer grows linearly with time as shown in figure 1(a). Figure 1(b) presents the influence of the discharge power and the use of a dilution gas such as nitrogen or argon in the gas phase, on the thickness of the layer. Whatever the discharge power is, the thickness is more important without the presence of a dilution gas. Nitrogen or argon seems to act more like dilution agent than etching one. Moreover, after 20 W and whatever the reactive gases used, the thickness decreases proving that after this discharge power, the plasma phase may contain in majority ions which degrade the surface. Then, after a discharge power of 20 W, degradation becomes predominant compared to deposition.

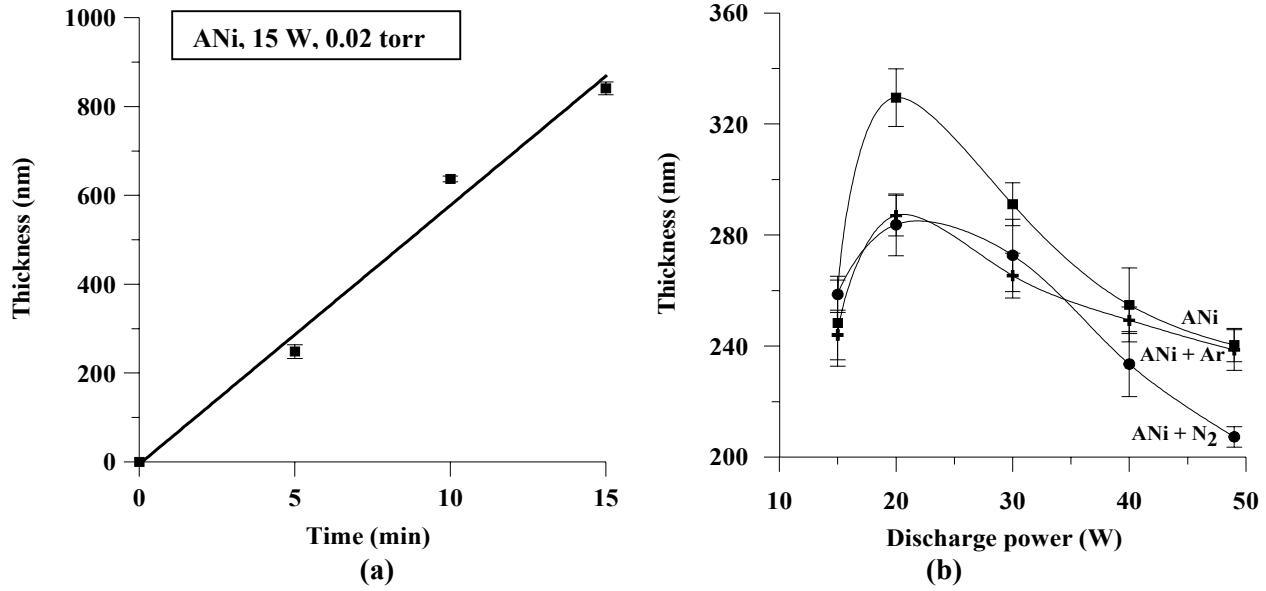

Fig. 1. Evolution of the thickness of plasma polymerized polyaniline versus (a) time and (b) discharge power.

In conclusion, it is better to use a discharge power lower than 20 W to avoid degradation and to favour deposition. Moreover, a longer polymerization time is preferable to obtain a thicker layer and then a more conductive one.

3.2. Surface energy determination

The polar component of the surface energy increases with discharge power and more when the reactive gas is just composed of aniline without a dilution gas. When the discharge power increases, the number of polar groups, i.e. N-containing functionalities (amine, imine, nitrile) increases. The increase of the polar component occurs almost totally between 15 and 20 W. Note that the total surface energy of the plasma polyaniline is comprised between 50 to 55 $mJ.m^{-2}$.

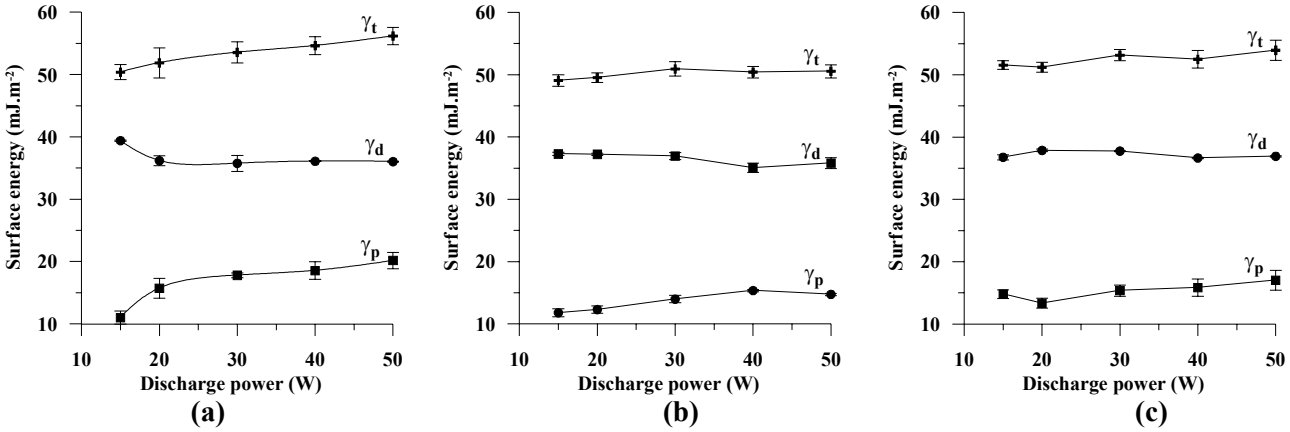

Fig. 2. Surface energy of plasma-polymerized polyaniline according to the precursor gas: (a) aniline or (b) aniline + 1 sccm N_2 or (c) aniline + 1 sccm Ar. (pressure=0.02 torr, polymerization time=5 min)

However, after deposition of a drop (water or diiodomethane) to measure the contact angle and then determine surface energy, we observe the formation of cracks accross the polyaniline films, only when the precursor gas is just composed of aniline and the discharge power is 20 W (pressure=0.02 torr). We attribute this phenomenon to excessive tensile stresses. Stress in thin films results in a thermal component and an intrinsic one [5]. The thermal stress is due to the difference in thermal expansion coefficients between the

substrate and the film. Then, after film deposition, differential contractions occur on cooling. The intrinsic stress is a function of the microstructure and stoechiometry of the film which strongly depend on the deposition method and then, process parameters [6]. The intrinsic stress is also function of the thickness of the film [5]. It has been found that the intrinsic stress is influenced by incorporated impurities [7] and ambient humidity after deposition [8]. In our experiments, intrinsic stress due to a too high deposition rate seems to be responsible for the formation of these cracks.

In conclusion, with aniline as precursor, the discharge power must be 15 W to avoid cracks across the film.

3.3. FTIR spectra

The FTIR spectrum of aniline is shown in figure 3. The two bands at around 3350 and 3450 cm^{-1} are attributed to primary aromatic amine N-H stretch. The bands between 3000 and 3100 cm^{-1} are due to aromatic C-H stretch. The two dominant peaks at 1500 and 1600 cm^{-1} are due to benzene ring C=C stretch; at around 1600 cm^{-1}, there is also the deformation of primary aromatic N-H. At 1300 cm^{-1}, the absorption of C-N bond stretch occurs. Finally, the peaks at 700 and 750 cm^{-1} correspond to C-H out-of-plane deformation of a mono-substituted benzene ring.

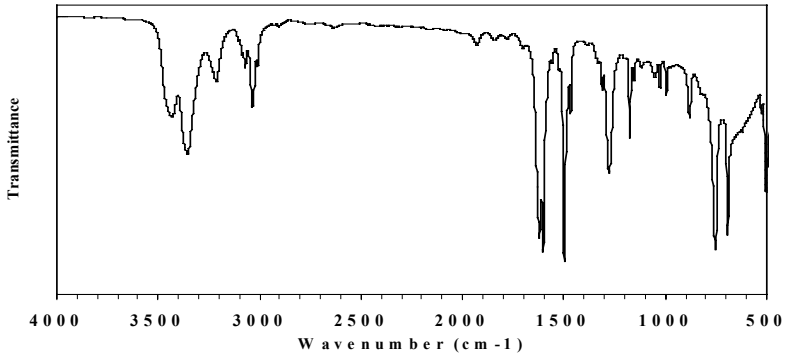

Fig. 3. FTIR spectrum of the aniline monomer

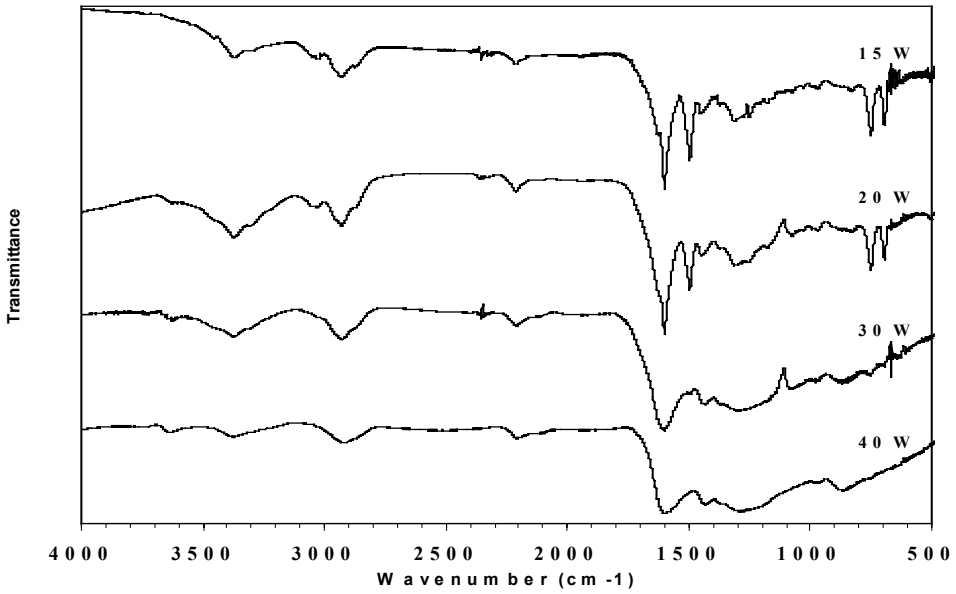

Fig. 4. FTIR spectra of plasma-polymerized polyaniline obtained at different discharge powers. (Aniline, pressure=0.02 torr, polymerization time=15 min)

Figure 4 presents FTIR spectra of plasma polymerized polyaniline at different discharge powers. At 30 and 40 W, the bands become broader which is typical of a highly disordered polymer. This result is in agreement with the evolution of the thickness with the discharge power (Figure 1(b)), showing the degradation of the film at 30 and 40 W. Compared to the monomer, the plasma-polyaniline elaborated at 15 and 20 W shows absorption at around 2900 cm^{-1} due to saturated C-H stretch, proving then the breakage of the benzene ring during plasma deposition. Moreover, we observe a peak at 2200 cm^{-1}, which can be assigned to aromatic nitrile stretch. We can attribute the peaks at 700 and 760 cm^{-1} to the C-H out-of-plane deformation of meta and ortho di-substituted benzene ring, respectively. The weak peak at 830 cm^{-1} may correspond to para di-substituted benzene ring. According to Wang et al., the weak intensity of this last peak compared to the meta and ortho substitution is the sign of a branched structure in the polymer [9].
The polymerization time does not influence the structure of the polymer as proved by figure 5. The same bands are observed on all the spectra. Therefore, a higher polymerization time is preferable to increase the electrical conductivity of the layer.

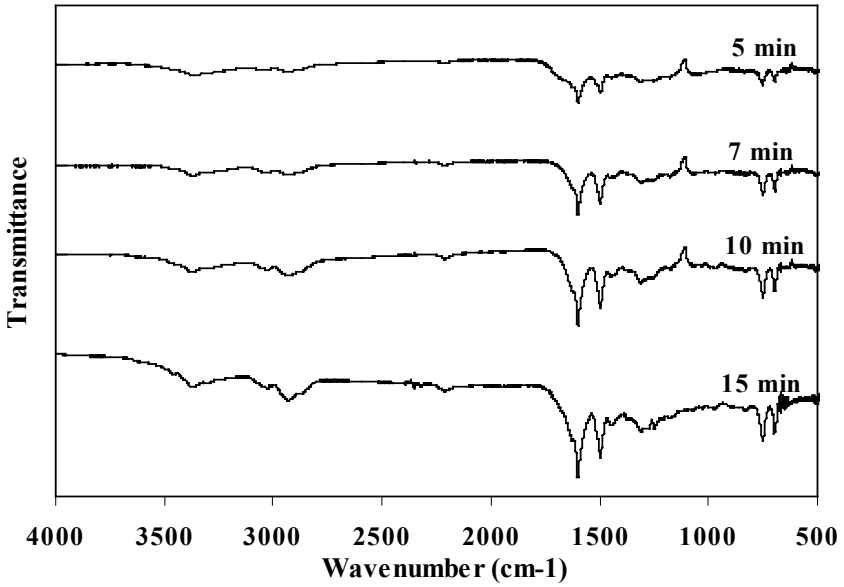

Fig. 5. FTIR spectra of plasma-polymerized polyaniline obtained at different polymerization times. (Aniline, discharge power=15 W, pressure=0.02 torr)

3.4. XPS analysis

The C 1s and N 1s XPS core-level spectra of plasma polymerized polyaniline are presented in figure 6. The C 1s spectrum can be decomposed into three components at 284.9, 286.2 and 287.3 eV, attributed to aliphatic and aromatic C-H and C-C, C-N and C-O groups, respectively. The N 1s spectrum is composed of a single peak at 399.5 eV corresponding to -NH- groups. According to literature, the N 1s XPS spectrum of polyaniline synthesized by chemical way shows two components of almost similar intensities, attributed to -NH- and -N= groups [10]. This result could be the sign of the formation, by plasma, of oligomers which contain a higher quantity of -NH- groups. Whatever the discharge power and the precursor gas are, the same decomposition of C 1s and N 1s XPS spectra can be made.

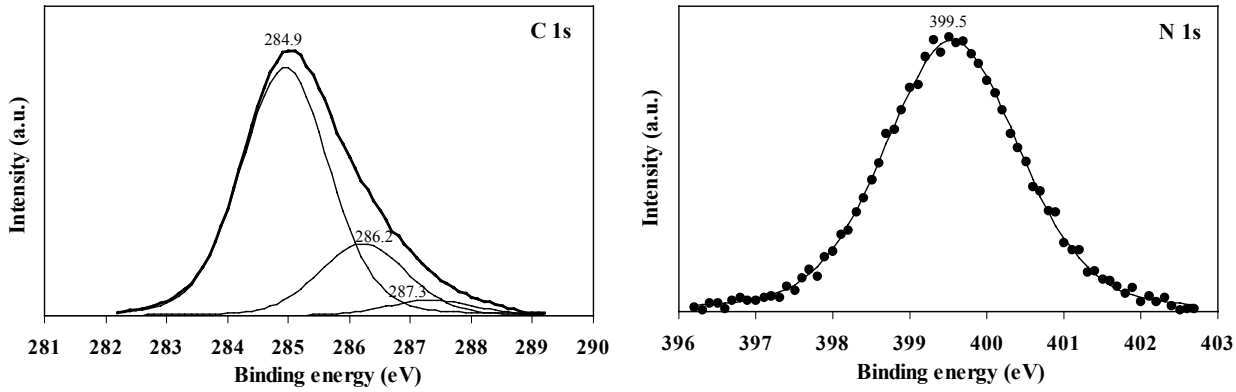

Fig. 6. Typical C 1s and N 1s XPS core-level spectra of plasma-polymerized polyaniline. (Aniline, discharge power =15 W, pressure=0.02 torr, polymerization time=5 min)

The C/N ratios (Table 1) remain almost the same whatever the discharge power is, when the used precursor gas is aniline. If the precursor gas is aniline with 1 sccm N_2, the C/N ratio decreases when the discharge power increases, showing then a higher incorporation of N-containing groups. If the precursor gas is aniline with 1 sccm Ar, the C/N ratio increases with the discharge power. So, a high power favours the breakage of the C-N bonds, this hypothesis is confirmed by the C-C/C-N ratio (table 2) which increases with the discharge power. So, we can conclude that the addition of argon in aniline gas phase is not interesting for gas sensor application since argon leads to a decrease in N-containing groups which are the gas absorption sites.
At 30 and 40 W, the C/N ratio is lower when the reactive gases are aniline with 1 sccm N_2 than when it is only aniline. It would the sign of a higher incorporation of N-containing functions if N_2 is added to aniline gas phase but as the C-C/C-N ratio is almost the same for the two kind of reactive gases, the additional N-containing functions would not link to carbon.
At 15 and 20 W, C/N and C-C/C-N ratios are almost the same for aniline or aniline + 1 sccm N_2 reactive gases. To increase N-containing groups, the nitrogen flow have certainly to be increased.

Table 1- C/N ratio of plasma polymerized polyaniline according to the discharge power and precursor gas

	ANi	**ANi + 1 sccm N_2**	**ANi + 1 sccm Ar**
15 W	10	10.4	10.4
20W	10.5	10.2	11.2
30 W	10.2	9.2	11.5
40 W	10.6	9.5	12.2

(pressure=0.02 torr, polymerization time=5 min)

Table 2- C-C/C-N ratio of plasma polymerized polyaniline according to the discharge power and precursor gas

	ANi	**ANi + 1 sccm N_2**	**ANi + 1 sccm Ar**
15 W	3.45	3.4	3.6
20W	3.8	3.9	3.8
30 W	3.9	3.5	3.9
40 W	3.3	3.3	4.1

(pressure=0.02 torr, polymerization time=5 min)

Conclusion

This work shows that to be used for gas detection, the polyaniline layer must be prepared at low discharge power for the deposition rate to be low and for the layer to be not degraded. Moreover, the polymerization time must be important to increase the film thickness and then the electrical conductivity since time doesn't influence the polymer structure. Finally, the addition of nitrogen to aniline in the gas phase seems to be promising as the N-containing groups increase.

References

[1] A.J. Heeger, *Synth. Met.* 125 (2002) 23-42.
[2] A.G. MacDiarmid, *Synth. Met.* 125 (2002) 11-22.
[3] A. Guadarrama, M.L. Rodriguez-Mendez, J.A. de Saja, J.L. Rios, J.M. Olias, *Sens. Act. B* 69-3 (2000) 276-282.
[4] D. Nicolas-Debarnot, F. Poncin-Epaillard, *Analytica Chimica Acta* 475 (2003) 1-15.
[5] K. Ramkumar, A.N. Saxena, *J. Electrochem. Soc*., 139/5 (1992) 1437.
[6] M.S. Haque, H.A. Naseem, W.D. Brown, *J. Appl. Phys*., 81/7 (1997) 3129.
[7] B. Bhushan, S.P. Murarka, J. Gerlach, *J. Vac. Sci. Technol. B*, 8 (1990) 1068.
[8] H. Sankur, W. Gunning, *J. Appl. Phys.*, 66/2 (1989) 809.
[9] J. Wang, K.G. Neoh, L. Zhao, E. T. Kang, *J. Colloid and Interface Science* 251 (2002) 214-224.
[10] J.G. Master, Y. Sun, A.G. MacDiarmid, *Synth. Met.* 41 (1991) 715.

Surface Modification of self assembled monolayers by the CO_2 plasma

N. Delorme[1], D. Debarnot[1], J.F. Bardeau[2], A. Bulou[2], F. Poncin-Epaillard[1]

[1] *Laboratoire Polymères Colloïdes et Interfaces (UMR CNRS 6120), Université du Maine, Avenue O. Messiaen, 72085 Le Mans, France*

[2] *Laboratoire de Physique de l'Etat condensé (UMR CNRS 6087), Université du Maine, Avenue O. Messiaen 72085 Le Mans, France*

Abstract

The elaboration of multilayers onto oxidized silicon wafer using a self-assembled octadecyltrichlorosilane (OTS) monolayer treated by CO_2-plasma is presented. The plasma effect onto the surface of the SAM was characterized by wettability measurements and X-ray spectroscopy. The structural properties of modified monolayers were investigated by X-ray reflectivity and AFM microscopy. The formation of multilayers was then demonstrated by grafting a second layer of OTS.

Keywords

SAMs, multilayers, plasma functionalization, X-ray reflectivity, atomic force microscopy

1. Introduction

Self-assembled monolayers (SAMs) have attracted increasing interests over the past 20 years due to their ability to form spontaneously highly organized organic structures on different substrates. A long linear hydrocarbon chain favoring upright monolayer ordering on the surface and a terminal functional group defining the surface functionality [1-6]. Alkylsiloxane SAMs have emerged as one of the most widely studied SAMs [7] due to its convenient attachment to hydroxyled and/or oxided surfaces and to its applications in microfluidic [8,9] protein adsorption [10] chromatography [11] and molecular electronic [12].

The surface modification of SAMs was little studied [13-17]. In most of the cases such an exposure results in either partial or total damage. One of the perspectives of modification of alkylsiloxane SAMs is the plasma processing. Whereas this method is widely applied in microelectronics or chemical modification of polymeric surfaces, there are only few examples for plasma treatment on SAMs [13-14]. In this study, we used silicon wafers that were functionalized with octadecyltrichlorosilane (OTS) to demonstrate the ability to prepare a layer-to layer self assembly system after surface modification by a CO_2 plasma treatment. OTS was selected as a model of higly-packed organic monolayer. The thickness and the density of the monolayer were controlled by X-ray reflectivity measurements whereas the surface homogeneity was studied by atomic force microscopy (AFM).

2. Formation of the OTS precursor monolayer

Quality of the OTS monolayer was preliminary demonstrated by the high water contact angle (110°±2), and by the analysis of X-ray reflectivity curves. In Fig. 1, we show the Fresnel normalized XR curve of silicon wafer functionalized by OTS-SAM and the best reflectivity fit as the solid line which describes the two well-defined Kiessig fringes. The fringes spacing of 0.240 $Å^{-1}$ which is inversely proportional to the total film thickness and the Q_z value of the first minimum at 0.125 $Å^{-1}$ (denoted Q_{zmin}) are good indicators of the quality of the SAM yielding to an approximate total film thickness of 25 (±1) Å. The full analysis of the XR curve gives a fully description of both orientation and density packing of the OTS monolayer. All the parameters found in this analysis were obtained from a four-layer model: a silicon substrate, a silicon oxide layer, a transition layer and the OTS monolayer. Structure of OTS monolayers have been studied by such various means as FTIR-ATR spectroscopy, X-ray diffraction and X-ray reflectivity, evidencing that OTS monolayers were composed of close packed, generally vertical chains *all trans* extended. As the total film thickness calculated from the Q_{zmin} is in agreement with a highly dense OTS monolayer with alkyl chains in *all-trans* conformation , we have performed constrained fits in which the length and the electron density of the hydrocarbon chain was fixed to it expected nominal values i.e. 0,316 $e^-.Å^{-1}$. The parameters which are allowed to vary during the fit are therefore the thickness of the OTS layer, the thickness of the silicon oxide layer, the roughness of each interface and the transition oxide parameters.

The fit yields roughness lower to 4 Å indicating the presence of atomic-level smooth interfaces. The thickness of the silicon oxide layer was found to be 12.9 Å which was in good agreement with the value proposed by Brzoska et al. for the typical thickness of the native silicon oxide layer on silicon substrate (10-15 Å). The parameters obtained for the transition layer (i.e. electron density and thickness) can be attributed to a

complex interface between the silicon oxide layer and the alkyl chains of the OTS monolayer. Therefore, the fitting analysis of the X-ray reflectivity curve provides a reliable measure of the thickness of the layers, the electron density and interface roughness consistent with a highly ordered OTS-SAM with fully extended hydrocarbon in all-trans conformation.

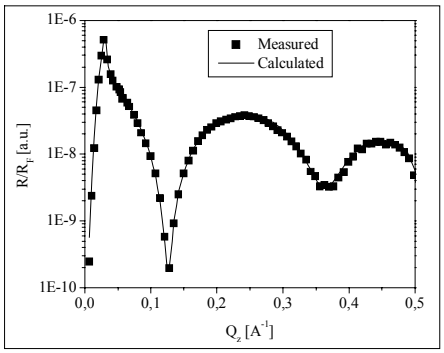

	ρ [$e^-.Å^{-3}$]	roughness [Å]	thickness [Å]
Substrate	0.710(*)	0.7	-
Oxide layer	0.682(*)	0.2	12.9
Transition layer	0.601	3.1	3.5
OTS layer	0.316(*)	2.8	23.0

Fig. 1. Calculated, measured X-ray reflectivity curves and data of OTS film grafted on silicon substrate.

The coverage of the monolayer surface was studied by AFM (Fig. 2). RMS roughness determined from the AFM image (180nm×180nm) is found to be 0.15 nm indicating that, at this scale, surface is smooth. The lack of default in a wider scale (1μm×1μm) confirms the high degree of homogeneity of the OTS-SAM. Thus, this observation is consistent with the structural studies which clearly indicated the formation of a dense and oriented perpendicularly OTS monolayer.

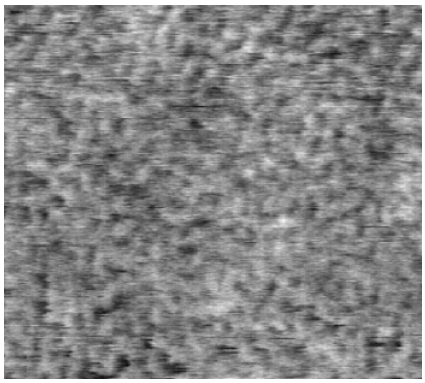

Fig. 2. AFM image of the OTS monolayer (tapping mode – Image size = 180 nm × 180 nm).

Methyl-terminated monolayers such as OTS, are known to be chemically resistant because of their poor reactivity. Thus, in order to elaborate a multilayer system on such monolayer, modification of the surface chemistry is needed.

3. CO_2-plasma surface modification of the OTS monolayer

In order to modify chemically the surface of the OTS monolayer, CO_2-plasma was preferred to O_2 plasma because the degradation processes are less efficient. Four parameters can be monitored with the plasma reactor used in this study : *P* the power, *F* the gas flow, *t* the treatment duration and *d* the distance between the bottom of the excitator and the sample. Parameters *P* and *F* were chosen to be the most effective to introduce hydroxyl (C-OH) and carboxyl groups (-COOH) onto organic surface. The distance *d* was kept to be maximal (~70 cm). We expected that this positioning will enable to expose OTS monolayer predominantly to only radicals which are responsible of the functionalization since electrons and ions responsible of the degradation do not exist in the post-discharge.

The effect of the plasma treatment onto the OTS monolayer was evaluated by following the evolution of the water contact angle as function of the plasma treatment duration (Fig. 3). A decrease of the water contact angle is observed since the first seconds of the plasma treatment until treatment

duration of 150 s, and then a plateau is observed. Such variation could be assigned to the progressive introduction of polar functions onto the monolayer surface leading, for the plasma duration of 150 s, to a surface saturation with polar functions.

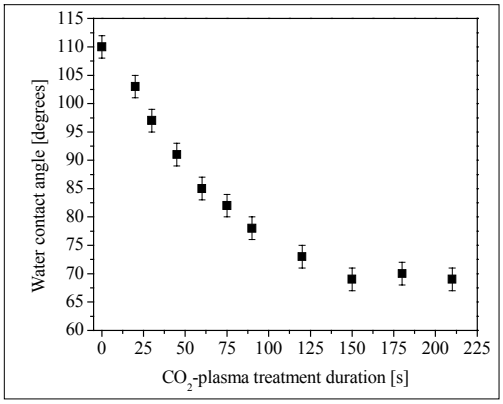

Fig. 3. Evolution of the water contact angle as function of the CO_2-plasma treatment duration.

To confirm these results, surface chemical composition was determined by X-ray photoelectron spectroscopy (XPS). After decomposition of the XPS signal of the plasma treated monolayer, it can be seen the appearance of three components at 286.1, 287.4, and 288.7 eV corresponding to C-O, C=O, and COO groups, respectively. Thus, XPS analysis confirms that CO_2-plasma introduces reactive polar groups onto the surface of the OTS film. Table 1 shows a progressive increase of the polar groups proportions (C-O, C=O, and COO) with the treatment duration until 210 s. As the immersing time was further prolonged, the decrease of the proportions of polar functions can be associated to the degradation of the monolayer surface caused by fragmentation of chains containing polar groups.

time [s]	C/O	% C-C	% C-O	% C=O	% COO
0	-	100	0	0	0
20	2.7	85	10	3	2
45	2.2	81	12	5	2
60	1.9	70	19	7	4
120	2.0	68	20	8	4
210	1.8	71	18	8	3

Table 1. Effect of CO_2-plasma treatment time on the surface chemical composition of the OTS film determined by XPS

In order to evaluate the effect of the degradation processes onto the structure of the monolayer, we performed X-ray reflectivity measurements as a function of the plasma treatment duration. In Fig. 4, we observed that above a treatment time of 120 s, the position and the height of the first minimum don't change. Such a result indicates that under these treatment conditions, electron density and thickness of the plasma treated monolayer remain the same that the non treated one. This result clearly indicates that until the treatment duration of 120 s, the degradation of the monolayer may be negligible.

On the contrary, for the duration of 210 s alterations of both height and position of the first minimum of the reflectivity curve are observed indicating the decrease of the plasma treated monolayer density. The shift of the first minimum towards low Qz wave vector transfers and the decrease of the contrast are likely due to the decrease of the initial OTS monolayer density and the polymerization of removed molecular chains on the top-most surface. Consistently, the decrease of the densities of polar groups observed by XPS measurements was interpreted as the result of the degradation of the monolayer

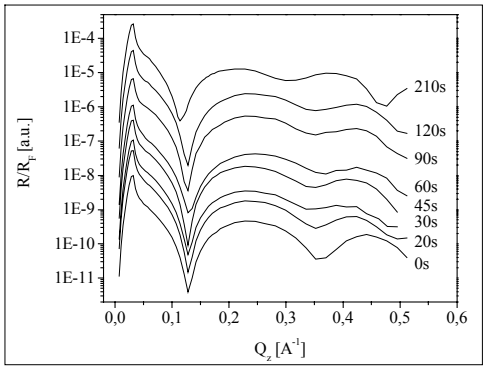

Fig. 4. Evolution of the reflectivity curves as function of the CO_2-plasma treatment duration.

Surface structure of the plasma treated monolayer was monitored using AFM. topography images (Fig. 5) indicate that the plasma treatment of 120 s doesn't modify the surface structure of the monolayer. Furthermore RMS rugosities were comparable between plasma treated monolayer (RMS = 0.28 nm) and the initial OTS monolayer (RMS = 0.23 nm); under these conditions, the monolayer is not degraded by the plasma treatment. On the contrary, AFM image of the 210 s plasma treated monolayer shows the structural modification of the surface with the appearance of hills and holes. The observed increase of the RMS roughness to 0.49 nm indicates a modification of the surface morphology associated to the degradation of the monolayer.

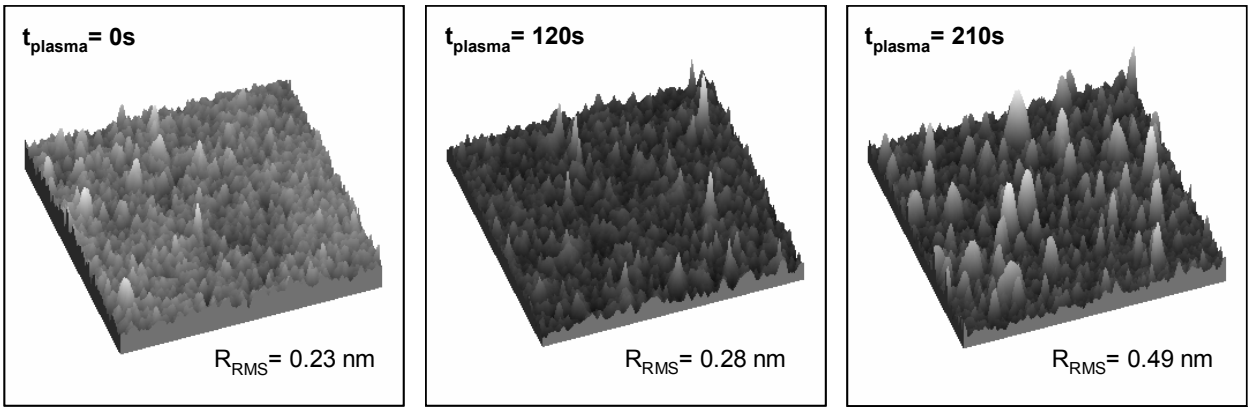

Fig. 5. AFM topography and RMS rugosity of monolayers treated by CO_2-plasma (Image size = 400×400 nm).

In order to optimize the grafting of a second layer onto the modified SAM surface one first needs to choose plasma conditions for which the functionalization is maximum and the degradation minimum. The chemical composition and structural studies of the treated OTS monolayer allow us to conclude that the plasma treatment duration of 120 s was very efficient. Indeed, for these conditions the surface modification of the OTS monolayer is maximum and proceeds without degradation.

4. Formation of the bilayer

In order to demonstrate the ability of grafting a second layer onto the plasma functionalized OTS monolayer, we have chosen to use similar OTS molecules. Indeed, the presence of C-OH and COOH groups introduced by the plasma treatment onto the surface should allow the grafting of a second layer of alkyltrichlorosilane molecules.

The efficiency of the grafting reaction was followed by measuring the water contact angle (Table 2). As shown before, the water contact angle decreases from 110°(±2) for the OTS monolayer to 72°(±2) for the 120 s plasma treated monolayer because of the introduction of polar groups by plasma onto the surface. After the deposition of a second layer of OTS molecules, the water contact angle increases to a value of 103°(±2) indicating the formation of a new hydrophobic layer without reaching the value obtained with the first OTS

monolayer. Such a result can be explained by le lack of presence of homogeneous second OTS layer due to the presence of non reactive groups such as –C=O and residual $–CH_3$ of the first layer which don't allow the grafting of OTS molecules leading to a second OTS layer less organized than the OTS monolayer (Fig. 6).

Sample	Water contact angle
OTS monolayer	110° (±2)
CO_2-plasma treatment (t = 120s)	72° (±2)
Grafting of a second OTS layer	103° (±2)

Table 2. Evolution of the water contact angle during the formation of a second OTS layer.

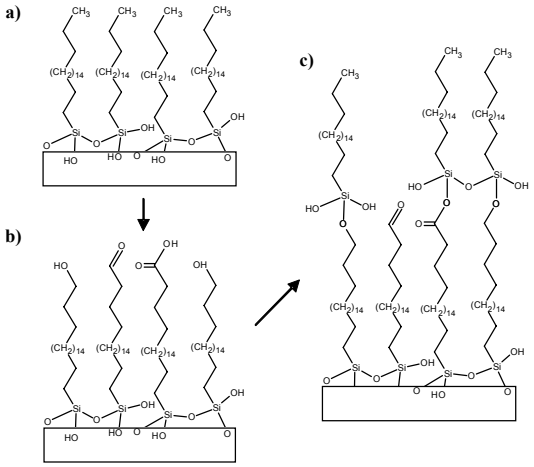

Fig. 6. Representation of the structure of a) OTS monolayer, b) CO_2-plasma treated monolayer, and c) after the grafting of the second OTS layer.

X-ray reflectivity measurements were performed in order to characterize the structure of the new OTS layer. Figure 8 indicates that the position of the first minimum was shifted from 0.128 $Å^{-1}$ for the plasma treated monolayer to 0.065 $Å^{-1}$ after the deposition of the second OTS layer. This shift corresponds to an increase of the total thickness from 24.5 to 48.3 Å indicating that the formation of a second layer of OTS molecules was achieved. However, although the position of the first minimum is consistent with the calculated data in a model taking into account two similar layers, we were not able to find a realistic model explaining the XR curve. The explanation is probably the complexity of the different interfaces and layers composing our system.

References

[1] A. Ulman, Chem. Rev., **96**, 1533 (1996).
[2] P. Silberzan, L. Léger, D. Ausserré, J. J. Benattar, Langmuir, **7**, 1647 (1991).
[3] J. B. Brzoska, I. Ben Azouz, F. Rondelez, Langmuir, **10**, 4367 (1994).
[4] A. Parikh, A. N. Allara, I. Ben Azouz, F. Rondelez, J. Phys. Chem., **98**, 7577 (1994).
[5] D. H. Flinn, D. A.Guzonas, R.-H.Yoon, Coll. Surf. A: Physicochem.Eng. Asp., **87**, 163 (1994).
[6] M. E. McGovern, K. M. R. Kallury, M. Thompson, Langmuir, **10**, 3607 (1994).
[7] R. Maoz, J. Sagiv, J. Coll. Interf. Sci., **100**, 465 (1983).
[8] B. Zhao, J. S.Moore, D. J.Beebe, Science, **291**, 1023 (2001).
[9] Y. Feng, Z.Zhou, X. Ye, J. Xiong, Sensors and Actuators A, 108, 138 (2003).
[10] P.Ying, G. Jin, Z.Tao, Coll. Surf. B, **33**, 259-263(2004).
[11] M. J. Wirth, R.W. P. Fairbank, H. O. Fatunmbi, Science, **275**, 44-47 (1997).
[12] I. Willner, V. Pardo-Yissar, E. Katz, K. T. Ranjit, J. Electroanalyt. Chem., **497**, 172-177(2001).

[13]W. E. S. Unger, A. Lippitz, T. Gross, J. F. Friedrich, C. Wöll, L. Nick, Langmuir, **15**, 1161-1166(1999).
[14] F. Rondelez, F. Moriere, O. Bouloussa, M. Tatoulian, F. Arefi-Konsari, P. D'otaviantonio, J. Amouroux, A. Jupin, proceed.15th ISPC, I, 257-262(2001).
[15] S. V. Roberson, A. J.Fahey, A.Sehgal, A.Karim, Appl. Surf. Sci., **200**, 150-164(2002).
[16] S. Hoeppener, R. Maoz, J. Sagiv, Nano Lett., *3*, 761-767(2003).
[17] E. A.McArthur, T. Ye, J. P. Cross, S. Petoud, E. Borguet, J. Am. Chem. Soc. Comm., 126, 2260-2261(2004).

Time-frequency analysis of sound signal in the partial electrical discharges

Toshiyuki Nakamiya[1], Daiki Sasahara[2], Kenji Ebihara[2], Tomoaki Ikegami[2] and Ryoichi Tsuda[1]

[1]*Department of Information Science, Kyushu Tokai University, Toroku9-1-1, Kumamoto 862-8652,Japan*
[2]*Graduate School of Science and Technology, Kumamoto University, Kurokami 2-39-1, Kumamoto 860-0082, Japan*

Abstract

The fundamental experiments were carried to examine the tracking phenomenon that was one of the main causes of fire breaking. AC high voltage was applied to one of the electrode. As the electrode, the following samples were prepared: the mesh plate, the flat ribbon cable and the ignition plug. The current, voltage waveforms of partial discharge and the sound signal detected by the condenser microphone were stored in the memory Hi-coder. In this scheme, Short Time Fourier Transformation (STFT) and Continuous Wavelet Transform (CWT) were applied to discriminate the acoustic sound of the partial discharge and the dominant frequency components were studied. It was found that the estimates provided by CWT have better accuracy and precision than those obtained with STFT on the data sets of sound signal.

Keywords STFT, Continuous Wavelet Transform, micro discharge, mesh type electrode, dielectric barrier discharge

1. Introduction

The fires caused by arc tracking phenomenon are about 700/year in Japan. The dust accumulated in the plug for the power supply of household utensils is main reason for the arc tracking phenomena. Electrical current will flow through dusts only when the dusts contain water. If the moisture is continuously replenished, the currents will be sustained. It is thought that small leakage currents through such contamination cause degradation of the plug material leading to the partial discharge, charring or igniting combustible materials around the discharge. The combined effects of surface moisture and pollutants cause leakage currents across the surface of the insulator, which can lead to formation of carbonized tracks [1]. A more energetic arc through the carbonized dusts might cause a fire under the right conditions. The similar phenomenon occurs on the electronic circuit board of computer and household electric appliance. The deposited dust carbonizes with a long time, and it becomes a cause of the arc tracking phenomenon [2]. We proposed the procedure to detect the tracking phenomenon using the acoustic signal due to the partial discharge. The fundamental experiments to examine the characteristics of the discharge were performed. AC high voltage was applied to one of the electrode. The partial discharge was generated by the applying high voltage and initiated the acoustic sound. In this scheme, the STFT and the CWT were applied to discriminate the acoustic sound of the partial discharge and the dominant frequency components were studied.

2. Experimental procedures

The fundamental experiments were carried to examine the tracking phenomenon that was one of the main causes of fire breaking. The schematic diagram of experimental equipment is shown in Fig.1.

The following three type of electrode were used to simulate the arc tracking phenomenon: the mesh type electrode, the flat ribbon cable and the ignition plug. The structure of the mesh type electrode is shown in Fig.2. In the mesh type electrode, the microscopic hole of 200μm diameters has been opened in great numbers. The cover glass(22mm x 24mm,Thickness: 0.12～0.17mm) is held between mesh electrode (30mm x 50mm) of the 2 sheets, and the gap length of mesh type electrode is 0.5～1.0mm. The flat ribbon cable (ϕ:1.1mm, length:100mm) is used in order to connect the mother boards of personal computer. The ignition plug (gap: 1.5mm) is used for automobile engine.

We generated the partial discharges using the electrode in order to understand the fundamental relationship between the partial discharge and the acoustic sound properties. One of the electrode was connected to the high voltage terminal through the resistance 200kΩ. Other terminal was grounded. The sound signal was generated by the partial discharge of the electrode. The high voltage (2∼15kV, 60Hz) produced by the neon transformer was applied to the electric wire. The current, voltage waveforms of partial discharge and the sound signal detected by the condenser microphone were stored in the memory Hi-coder 8855(Hioki). The sampling frequency was 1 MHz and the measurement time was 1 second. Data analysis was performed using MATLAB with the Signal Processing toolbox and Wavelet toolbox. (The Mathworks, Inc.)

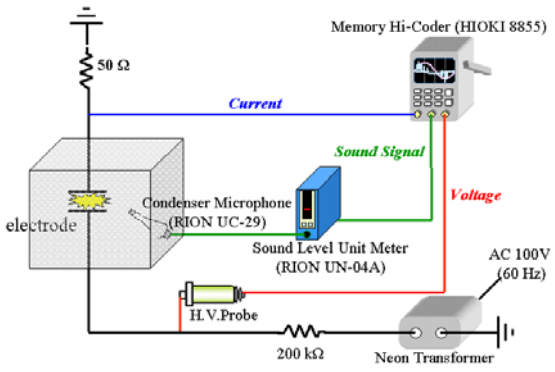

Fig.1. Measurement circuit of waveforms.

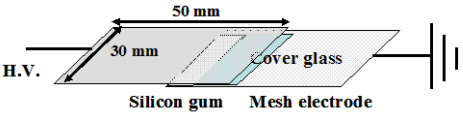

Fig.2. Mesh type electrode

3. Time-frequency analysis of sound signals

3.1 Short Time Fourier Transform (STFT)

The Fourier transformation mainly used in frequency analysis is not suitable for the analysis of the unsteady signal. The basis of Fourier transformation infinitely spreads in the time domain. Gabor extended the applicability of Fourier transform method dividing the input signal into segments. The signal in each window can be assumed to be stationary. The STFT for a given signal $f(t)dt$ can be expressed as

$$\hat{f}(\omega,b)=\int_{-\infty}^{\infty}\frac{1}{2\sqrt{\pi}\sigma}e^{-\frac{(t-b)^2}{\sigma^2}}e^{-i\omega t}f(t)dt \qquad (1)$$

σ is the window width of the window function, b is the time shift parameter[3]. Equation (1) shows that $\hat{f}(\omega,b)$ is the function of ω, b. Therefore, the time-frequency analysis became possible by Eq. (1). The squared magnitude of the STFT, $\left|\hat{f}(\omega,b)\right|^2$ is called spectrogram. It can be used to obtain the energy distribution of the signal along the frequency direction at a given time.

3.2 Continuous Wavelet Transform (CWT)

The wavelet transform converts a signal from time domain to the time-scale domain. Wavelet analysis involves the breaking up of a single prototype function called the mother wavelet. $\psi^{(a,b)}(t)$ is obtained by scaling the mother wavelet $\psi(t)$ at time b and scale a

$$\psi^{(a,b)}(t)=\frac{1}{\sqrt{a}}\psi\left(\frac{t-b}{a}\right) . \qquad (2)$$

When a becomes large, the basis function $\psi^{(a,b)}$ becomes a stretched version of the prototype, which can be useful for analysis of the low-frequency components of the signal. On the other hand, when the scale parameter is small, the basis function $\psi^{(a,b)}$ will be contracted, which is useful for the analysis of the high-frequency components of the signal [3].

As a mother wavelet, the gabor wavelet is used.

$$\psi(t) = \frac{1}{2\sqrt{\pi}\sigma} e^{-\frac{t^2}{\sigma^2}} e^{-it} \qquad (3)$$

Equation (3) is similar to the STFT which is used the Gaussian function in window function. So it is easy to compare with the analytical results of the STFT and the CWT. In this paper, real part of gabor function is used as a mother wavelet (σ =8).

$$\psi(t) = \frac{1}{2\sqrt{\pi}\sigma} e^{-\frac{t^2}{\sigma^2}} \cos(t) \qquad (4)$$

Therefore the wavelet transform of a continuous signal is defined as:

$$\hat{f}(a,b) = \frac{1}{\sqrt{a}} \int_{-\infty}^{\infty} \frac{1}{2\sqrt{\pi}\sigma} e^{-\frac{(t-b)^2}{\sigma^2 a^2}} \cos\left(\frac{t-b}{a}\right) f(t)dt \qquad (5)$$

where the signal $f(t)$ is transformed by the mother wavelet (Eq. (3)). Similar to the spectrogram, the squared magnitude of the CWT, $\left|\hat{f}(a,b)\right|^2$ is called scalogram and can be used to obtained the energy distribution of the signal over the entire time-scale plane.

4. Results and Discussion

4.1 Mesh type electrode

There was no partial discharge at the applied voltage of 2kV in the mesh type electrode. The partial discharge appeared at the applied voltage of 2.5kV. Figure 3 shows the voltage and the current waveforms with applied voltage of 2.5kV. The discharge current appears within 1/4 half-cycles which increase or decrease from 0V at the voltage value. The discharge current flows during 1.7ms～2.8ms, 9.9ms～11.3ms and 18.7～19ms. The current value is 2.7mA even in the maximum. The current waveform is pulse-like, and it seems to generate the dielectric barrier discharge, because the cover glass has been inserted between the electrodes.

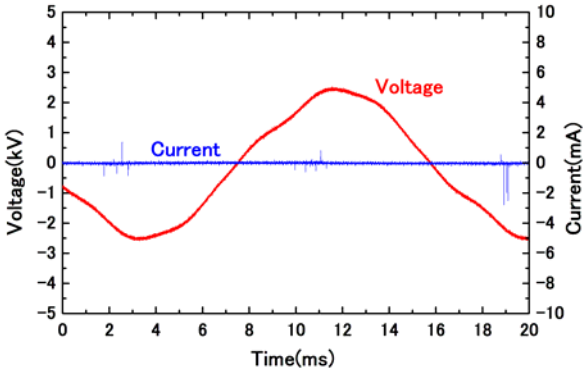

Fig.3. Voltage and current waveforms with applied voltage of 2.5kV.

When AC 2.5kV voltage is applied in the electrode, the measurement result of sound and current waveforms are shown in Fig.4. The acoustic signal is observed in the form superimposed on the drift signal, and the maximum value of the amplitude is 2.6mV.

When AC 2.5kV is applied to the mesh type electrode, the time-frequency spectrum of sound signal with dielectric barrier discharge is shown in Fig.5. The frequency characteristics of the sound signal are studied by STFT. The sound signal steadily contains the high frequency components. The frequency components of 20kHz or less are almost contained over all time. The spectrum at the

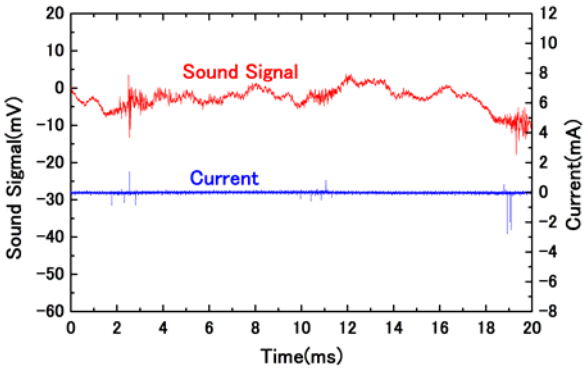

Fig.4. Sound signal and Current waveforms with applied voltage of 2.5kV.

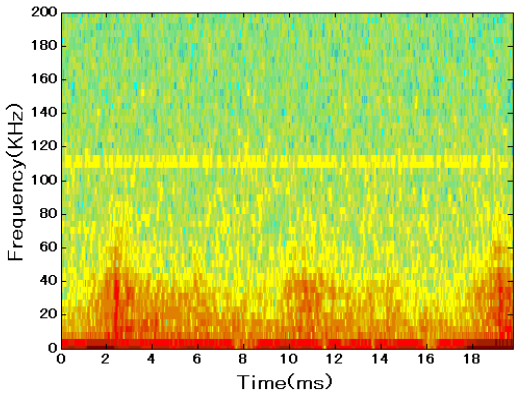

Fig.5. STFT spectrogram of sound signal with applied voltage of 2.5kV.

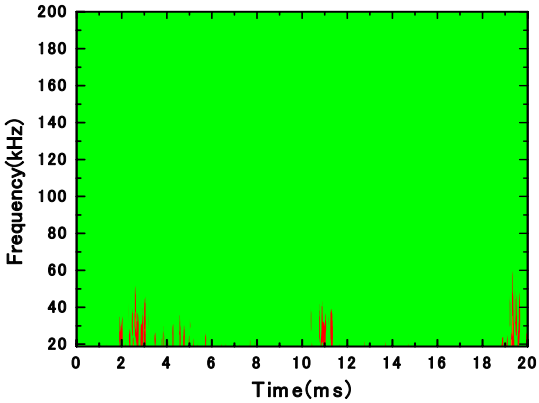

Fig.6. CWT scalogram of sound signal with applied voltage of 2.5kV.

applied voltage of 2.5kV with partial discharge has the dominant frequency components. The frequency components over 40kHz appear during 2ms～3ms, 10ms～12ms and 18～20ms. These results show that the partial discharge can be detected by observing the sound signal. They are almost same with the time in which the pulse-like current is generated.

When AC 2.5kV is applied to the mesh type electrode, CWT scalogram of sound signal with dielectric barrier discharge is shown in Fig.6. The frequency components over 40kHz appear during 2.1ms～3.3ms, 10.9～11.3ms and 19.2～19.7ms. These results of the CWT are good agreement with the time period of acoustic signal with the dielectric barrier discharge.

4.2 Flat ribbon cable

The flat ribbon cable is used as an electrode. Figure 7 shows the voltage and the current waveforms with applied voltage of 15kV. The pulse-like discharge current flows during 0.3ms～4ms, 8.6ms～12.6ms and 16.6～19.7ms. The current value is 32.9mA even in the maximum. The discharge current appears within 1/4 half-cycles which increase or decrease from 0V at the voltage value. The flat ribbon cable is covered with vinyl chloride and the pulse-like waveforms of the discharge current indicate dielectric barrier discharge.

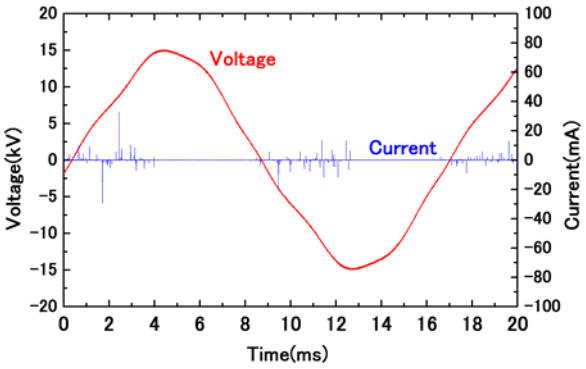

Fig.7. Voltage and current waveforms with applied voltage of 15kV.

Figure 8 shows the sound signal and the current waveforms with applied voltage of 15kV. The acoustic signal is observed in the form superimposed on the 8ms period (125Hz) signal, and the maximum value of the amplitude is 8.3mV.

When AC 15kV is applied to the flat ribbon cable, the time-frequency spectrum of sound signal with dielectric barrier discharge is shown in Fig.9. The sound signal steadily contains the high frequency components. The frequency characteristics of the sound signal are studied by STFT and wavelet. The spectrum at the applied voltage of 15kV with partial discharge has the dominant frequency components. The frequency components over 80kHz appear during 0.5ms～4.5ms, 9ms～13ms and 18～20ms. This results show that the

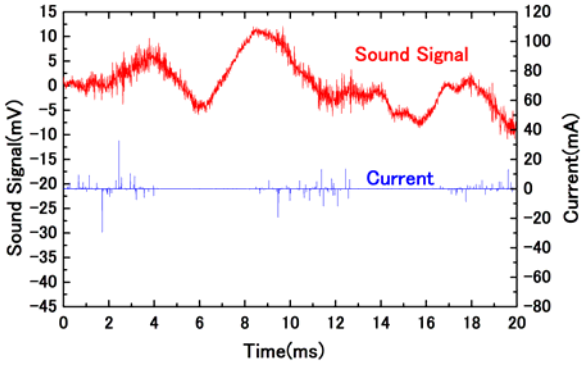

Fig.8. Sound signal and Current waveforms with applied voltage of 15kV.

partial discharge can be detected by observing the sound signal. It is almost same with the time in which the pulse-like current is generated.

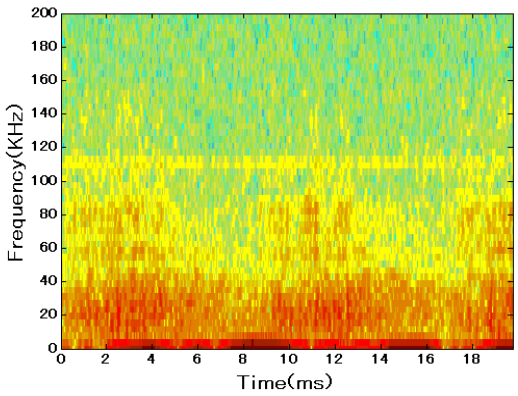

Fig.9. STFT spectrogram of sound signal with applied voltage of 15kV.

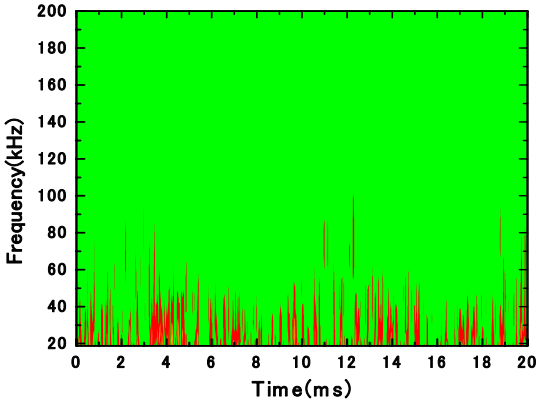

Fig.10. CWT scalogram of sound signal with applied voltage of 15kV.

When AC 15kV is applied to the flat ribbon cable, the CWT scalogram of sound signal with dielectric barrier discharge is shown in Fig.10. The frequency components over 80kHz appear during 1.1ms～3.5ms, 11.0ms～12.3ms and 18.7～20.0ms. These values by CWT are comparatively well agreement with the time of acoustic signal by the dielectric barrier discharge.

4.3 Ignition plug

When AC 7kV voltage is applied in the ignition plug, the measurement result of sound and current waveforms are shown in Fig. 11. As well as electrode using the mesh type electrode or the flat ribbon cable, the pulse-like current with the electric discharge is generated. The electric discharge has been generated at 11.6ms, 12.7ms and 18.8ms. The current maximum value is 270mA. This value is large compared with the electrode using meshed electrode or the flat ribbon cable. In addition, the acoustic signal also shows 1.8V in the maximum. This result shows that the arc discharge has been generated.

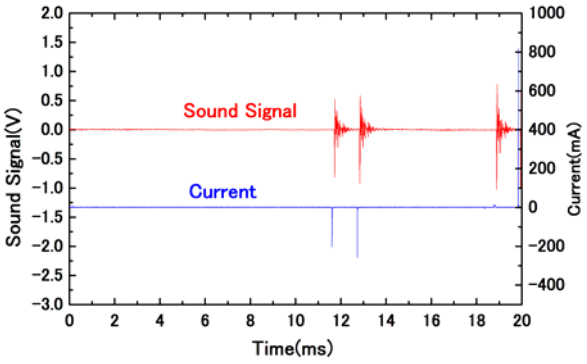

Fig.11. Sound signal and Current waveforms with applied voltage of 7kV.

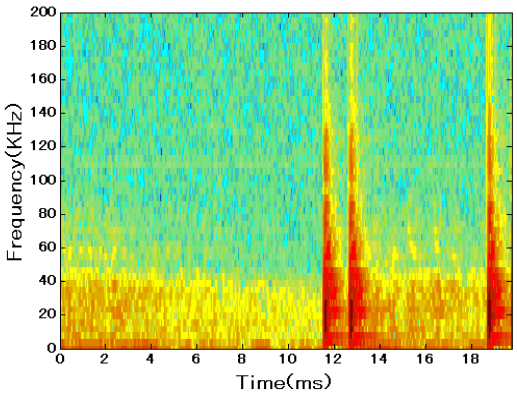

Fig.12. STFT spectrogram of sound signal with applied voltage of 7kV.

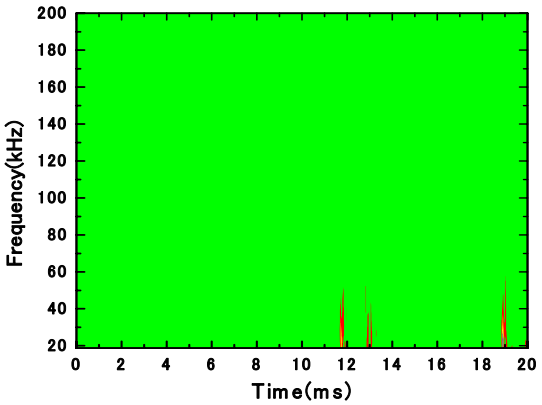

Fig.13. CWT scalogram of sound signal with applied voltage of 7kV.

The acoustic signal has been retarded from arc discharge at 0.1ms. It propagates at 3cm in 0.1ms, as the temperature in the laboratory is made to be 30℃, and The propagation distance is almost same with the distance of the microphone and the ignition plug.

Figure 12 shows the analyzing result of the acoustic signal by STFT with applied voltage of 7kV. The sound signal steadily contains the frequency components of 40kHz or less over all time. The signals with the frequency components over 100kHz are detected at 11.7ms, 12.8ms and 18.8ms. This value is almost same with the time of acoustic signal by the arc discharge.

When AC 7kV is applied to the ignition plug, the CWT scalogram of sound signal is shown in Fig.13. The frequency components over 45kHz appear at 11.7ms, 12.8ms and 18.9ms. These values by CWT are fairly good agreement with the time of acoustic signal by the arc discharge.

4. Conclusions

The fundamental experiments to examine the tracking phenomenon were carried. The high voltage of alternating current was applied to the electrode such as the mesh type electrode, the flat ribbon cable and the ignition plug. STFT and CWT were applied to discriminate the acoustic sound of the partial discharge and the dominant frequency components were studied. The following results are obtained:

1. When AC 2.5kV is applied to the mesh type electrode, the discharge current flows during 1.7ms～2.8ms, 9.9ms～11.3ms and 18.7～19ms. The current waveform is pulse-like, and it seemed to generate the dielectric barrier discharge. CWT scalogram of sound signal shows that the frequency components over 40kHz appear during 2.1ms～3.3ms, 10.9～11.3ms and 19.2～19.7ms.
2. The pulse-like discharge current flows during 0.3ms～4ms, 8.6ms～12.6ms and 16.6～19.7ms, when AC 15kV is applied to the electrode of flat ribbon cable. The CWT scalogram of sound signal with dielectric barrier discharge shows that the frequency components over 80kHz appear during 1.1ms～3.5ms, 11.0ms～12.3ms and 18.7～20.0ms.
3. When AC 7kV voltage is applied in the ignition plug, the electric discharge has been generated at 11.6ms, 12.7ms and 18.8ms. The CWT scalogram of sound signal shows that the frequency components over 45kHz appear at 11.7ms, 12.8ms and 18.9ms.
4. The calculation results by the CWT are more accurate compared with the STFT results.

References

[1]M.J.Billings, A.Smith and R.Wilkins, IEEE Trans. Elec.Insul. IE-2, p.131(1967).
[2]T.Nakamiya,T.Tanaka,K.Ebihara,T.Ikegami,Chung-Seog.Choi and R.Tsuda, SPP-21, p.282(2004).
[3]Charles K. Chui, 'An Introduction to Wavelets', ACADEMIC PRESS,INC.

CONTROLLING THE ATMOSPHERIC GLOW STABILITY

E.Aldea[1,2], P. Peeters[1], H.de Vries[2], M.C.M van de Sanden[1]

[1]*Department of Applied Physics, Eindhoven University of Technology, POB 513, 5600 MB Eindhoven The Netherlands*
e-mail e.aldea@tue.nl, m.c.m.v.d.sanden@tue.nl; www.etp.phys.tue.nl
[2] *TRL Laboratory , Fuji-Photo Film B.V , Tilburg The Netherlands ; Oudenstaart 1,Postbus 90156 5000 LJ Tilburg The Netherlands, www.fuji-research.com*

1. Abstract

Commonly atmospheric glow plasma can be straightforwardly generated only in He or very pure nitrogen and at relatively low power density. In this paper it is shown that through electronic suppression of the unstable plasma modes the atmospheric glow can be generated at high power density and in a variety of gases. It is argued that not the pre-ionization but the plasma stabilization is the key factor in atmospheric glow generation.

2. Introduction

Due their huge potential for cost efficient industrial applications uniform atmospheric plasmas (atmospheric glow) attracted a lot of interest in the recent years. Most of the atmospheric plasmas are generated in filamentary unstable form and the existence of atmospheric glow is a quite intriguing exception. It is widely believed that atmospheric glow generation is related to a large pre-breakdown pre-ionization [1-5]. This theory is based on the reasoning that pre-ionization would suppress the avalanches space charge and will eliminate the possibility of a filamentary streamer breakdown [1]. Nevertheless the link between pre-ionization and atmospheric glow generation it is still under debate. They are several experimental evidences that atmospheric glow can be generated with a negligible pre-ionization [6,7]. Moreover at the relatively low electric fields and gaps conditions under which atmospheric glow is commonly generated, the space charge of the avalanches is negligible. Thus the streamer breakdown is impossible and the pre-ionization is not necessary [6]. To our opinion not pre-ionization is the key factor in atmospheric glow generation but plasma stability. There is no plasma physics law forbidding the generation of an atmospheric glow *if the streamer breakdown does not occur.* There are however several reasons for which the generation of a *stable and uniform glow* at atmospheric pressure is rather improbable. Due to the large pressure a fast growth of instabilities due to large collision rates will occur. These instabilities will be slow damped (due to the slow diffusion) so a local perturbation will growth very fast and will remain localized generating a tendency of plasma to filamentate .As it will be argued in this paper the straightforward generation of atmospheric glow in He is the result of ionization cross-section peculiarities that makes plasma in He very stable to perturbations. Atmospheric plasma generation in other gases requires the suppression of the unstable plasma modes. Only in this atmospheric glow can be generated at high power density and for a variety of gases.

3. Experimental

The plasma was generated in He, Ar, N2 , Ar/O_2 , N_2/O_2 and air (gas flow speed 0.5-1 m/s), between two parallel electrodes (electrode gap 1 mm, plasma surface 60 cm^2). The discharge was operated in air surroundings or in a controlled environment. In the case of discharge in air surroundings it was estimated that at the standard flow conditions of 1 m/s there are hundreds of ppm of air due to the leaks in the reactor from the surroundings. In another set-up the purity of environment was strictly controlled by vacuuming the system up to $8*10^{-2}$ mbar and

filling it afterwards with gas up to atmospheric pressure. In this case the impurities are estimated to be of few ppm. No significant differences were noted in the plasma I-V characteristics or plasma uniformity and stability between the two set-ups. Glow generation was investigated using as surfaces in contact with plasma polyethylene naphthalene (PEN) , polyethylene teraphtalate (PET) , polyethtlene (PE) of 100-200 μm thickness , and alumina coated on metal (~500μm thick) .The high voltage (0.2-8 kV, 5-450 kHz) was applied to the electrodes using a system consisting of a computer controlled pulse generator and a power amplifier. The current and voltage waveforms were recorded through a computer controlled TDS 3034 B TEKTRONIX oscilloscope (sampling resolution 1 ns, bandwidth 350 MHz). The current flowing through the APG reactor was measured using (Tektronix CT-1 and TCP 202) current probes. In order to monitor the plasma uniformity the spatial distribution of the light emitted by the plasma was recorded using a DALSA Eclipse fast CCD camera (integration time 13μs).

4. Plasma instability

Plasmas at atmospheric pressure tend to be extremely unstable due to a critical combination of fast growth of perturbations and slow perturbation damping. As it will be argued below the fast growth of perturbation is due to the plasma generation at pd values (pressure *gap) much larger than the optimum pd value where the plasma stability to perturbations is optimal. The relatively large value of the **pd** product of order of 100 mbar*cm is determined by the high pressure and the practical need of having a gap of the order of at least one millimeter.
The slow damping of perturbation is mainly due to the small diffusion coefficient at atmospheric pressure and thus of a slow diffusion of ions, vibrationally excited molecules and metastables. The diffusion is so slow that a perturbation in the charge or excited species density will need milliseconds to diffuse over a millimeter. The tendency of a fast growth of instabilities can be demonstrated by evaluating plasma stability to the common thermal/ionization instability [8,9]. This instability is common because all local perturbations of ionization are also changing the temperature and are likely to trigger a thermal instability. For example if the temperature increase locally due to some perturbation the particle density **n** will decrease because the pressure remains constant in the neighborhood of the perturbed area. Then **E/n** (E is the electric field) will increase. Consequently the ionization rate will increase which in turn will increase again the temperature. At the atmospheric pressure due to high collision rate the temperature will follow in very short time (10-100 ps) the changes in the current density . Note that this instability occurs after the breakdown and it can not be suppressed by a pre-breakdown pre-ionization. The ionization is already large enough when the thermal/ionization instability occurs.
If one neglects the perturbation damping the speed of variation of the current density will be given by :

$$\frac{d\ln j_{plasma}}{dt} = S_0 + \frac{d\ln j_{plasma}}{d\ln(E/n)}\frac{d\ln(E/n)}{d\ln T}\frac{d\ln T}{dt} = \frac{1}{1-\beta\left(\frac{d\ln j_{plasma}}{d\ln(E/n)}\right)}\Phi_0 \qquad (1)$$

where : j_{plasma} is the plasma current density, $\Phi o = \delta j_{plasma}/dt j_{plasma}$ is the initial perturbation in current density ,T is the absolute temperature and β is the feedback coefficient of the plasma temperature to the perturbation reflecting the increase of absolute temperature in percents when the plasma current increase with one percent. To have a stable plasma β must be as small as possible and the plasma current density must not change to much with the electric field i.e :

$$\beta\left(\frac{d\ln j_{plasma}}{d\ln(E/n)}\right) << 1 \qquad (2)$$

If the condition given by eq.2 is not fulfilled than the denominator of eq.1 will tend to zero and the amplification of perturbation can occur explosively.

The feedback coefficient β will be larger if the plasma power is larger or if the gas is molecular one (due to the storing of energy in the vibrational levels). This may be the why reason atmospheric glow generation at large power densities or in molecular gases is very difficult. Using the general formula for the current density of glow plasma given in [8] one can see that at low current density (below the normal glow current density) the derivative of the current density on the electric field has a sharp minimum at the Stoletov point where the breakdown voltage is minimum as function of **pd**. The pd value of this minimum is determined by the ionization cross section and mean free path of electrons. For most of the gases the pd value is much larger than optimum pd. Incidentally for He plasma the pd of minimum breakdown voltage is large (~100 mbar*cm) which makes this plasma more stable to ionizations perturbations at atmospheric pressure. The low breakdown voltage of He is also a reflection of the fact that at millimetric gaps He is very close to the minimum value of the breakdown voltage. A numerical simulation of Boeuf et al. [10] indicated also that at breakdown He plasma is extremely stable to voltage perturbations.

The equation (2) may be rewritten as :

$$\beta\left(\frac{d\ln j_{plasma}}{d\ln(E/n)}\right)=\beta\frac{\frac{dI}{I}}{\frac{dV_{plasma}}{V_{plasma}}}=\frac{\frac{dI}{dV_{plasma}}}{\frac{I}{V_{plasma}}}=\beta\frac{R}{r}<<1 \qquad (3)$$

where I is the plasma current, V_{plasma} is the voltage drop on plasma , r is the dynamic resistance of the plasma (dI/dV_{plasma}) and R is the plasma resistance (I/V_{plasma}). The ionization instability will growth very fast if :

$$\beta\frac{R}{r}<=1\Rightarrow\frac{r}{R}>=\beta \qquad (4)$$

The ratio of dynamic to static resistance *must be of order of unity or larger in order to have a stable plasma*. Thus if the thermal/ionization instability is indeed a risk at atmospheric pressure one will expect that the IV characteristics of plasma will have a low ratio of the dynamic to static resistance. This is indeed the case. In all our experiments we observed that the filamentary plasmas or the unstable plasmas have a low ratio of dynamic to static resistance *r/R*. For example in Fig. of filamentary plasma in Ar1 it is presented the IV characteristic. In Fig. 2a one can note that even the He plasma has at the end of the discharge a low dynamic resistance. Due to this instability the plasma will switch in another mode of lower dynamic resistance, which is giving the current peak observed in Figs.2. Note that it is clear that the instability observed in Figs.2 cannot be linked with a deficit of pre-ionization. It is developing at a moment when the current and the pre-ionization are large enough. Also it is not an instability developed due to a over-voltage at the breakdown as assumed in [10]. The probable source of perturbation is the surface of material in contact with the plasma.

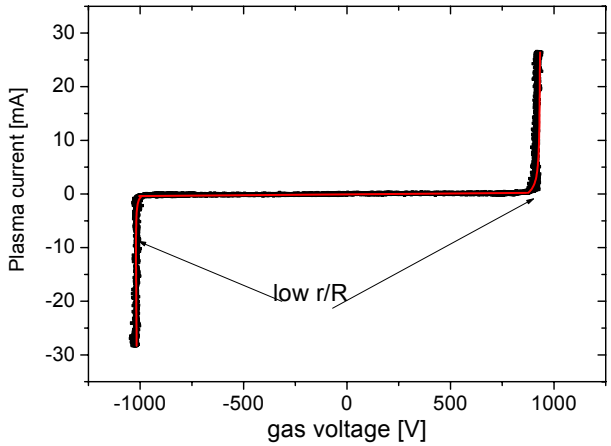

Fig.1 Filamentary plasma
Ar d=1 mm, f=12 kHz, PEN dielectric

Impurities or a local pin-like shape of the surface topography can trigger changes in secondary ionization and field electron emission. In [4-6] it was demonstrated that the nature of cathode material affects significantly the plasma stability.

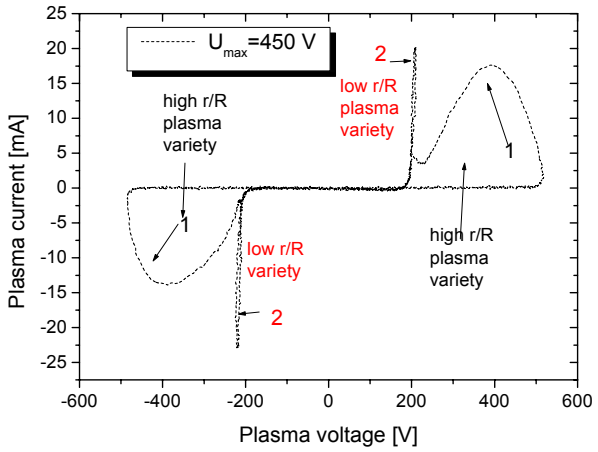

Fig.2a Plasma I-V characteristics for f=10.8 kHz, d=1 mm, U_{max}=450 V

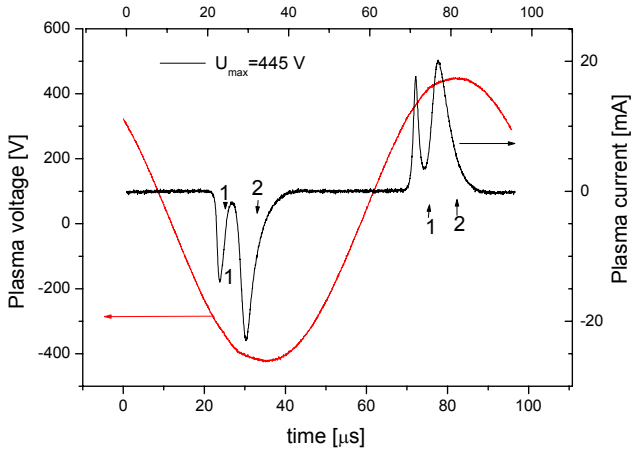

Fig.2b Multiple discharge pulses in He triggered by the plasma instability
f=10.8 kHz, d=1 mm, U_{max}=420-450 V

5. Plasma stabilization

The development of instabilities and of filamentation must be prevented in order to generate the stable glow variety. The peculiar low *r/R* ratio of the unstable plasmas can be exploited in order to suppress electronically this plasma variety. In Fig.3 the IV characteristics of a electronically stabilized Ar plasma are presented and in Fig.4 a those of a Ar+10% O_2 plasma. One can note that to the contrary of the case presented in Fig.1 for most of the current pulse duration the electronically stabilized plasmas have a *r/R* ratio of a stable plasma of order of unity. Moreover the spatial distribution of the light emitted by the plasma is not anymore filamentary but uniform (see Fig.5).

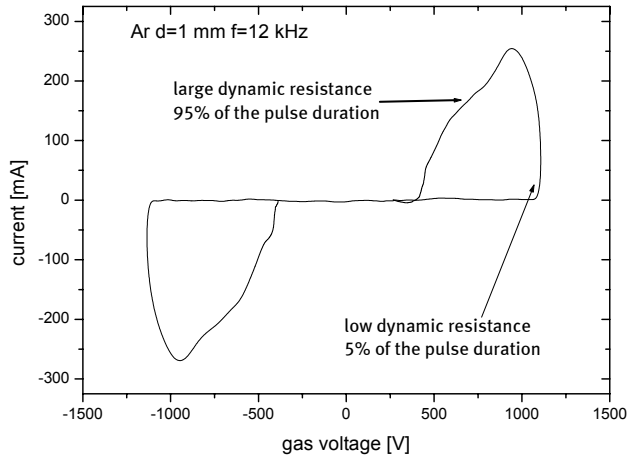

Fig.3 I-V characteristic of a stabilized Ar plasma d=1 mm, f=12 khZ, PEN dielectric

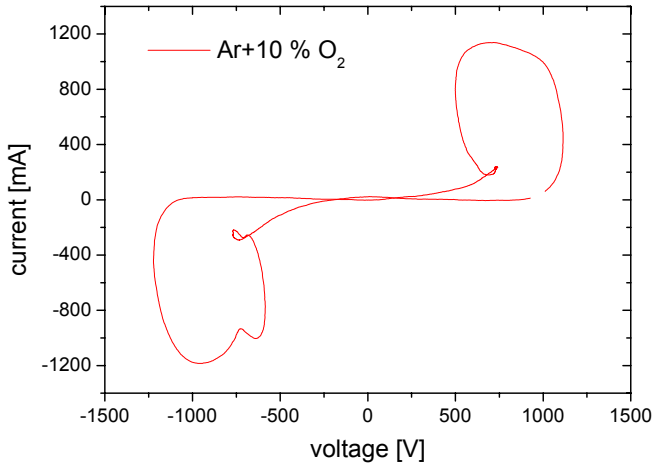

Fig.4 I-V characteristic of a stabilized Ar/O_2 plasma d=1 mm, PEN dielectric

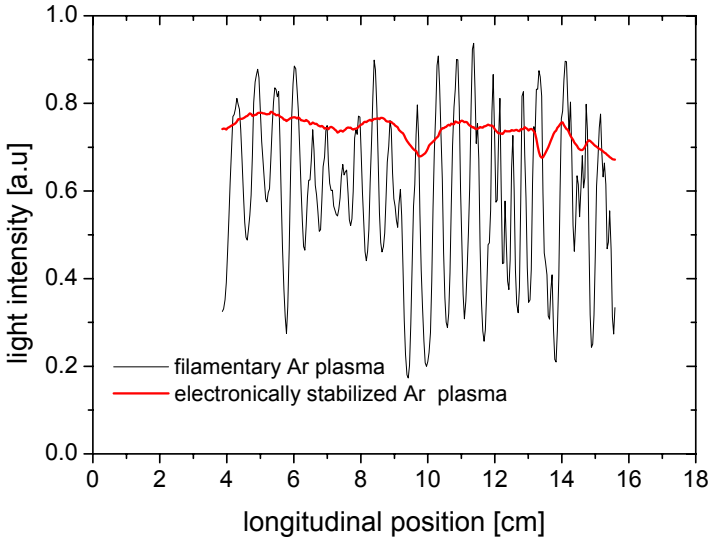

Fig.5 Spatial distribution of a filamentary and electronically stabilized Ar plasma

In Figs 6 are presented the IV characteristic of nitrogen plasma before and after electronic stabilization. The common form of atmospheric glow in nitrogen can be generated only at low power density below (1 W/cm^3) and is extremely unstable switching in a filamentary form when the voltage is increasing with 10-20% above the breakdown voltage or more than 0.01 % of oxygen is added to the discharge.

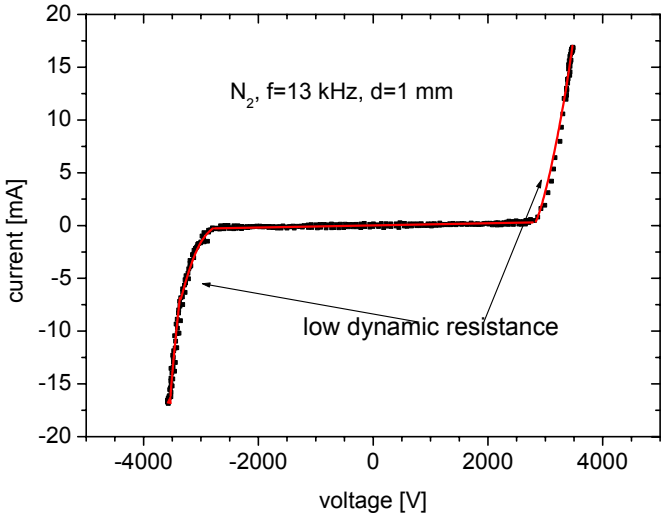

Fig.4a I-V characteristic of N_2 Townsend discharge d=1mm f=12 kHz, PEN dielectric

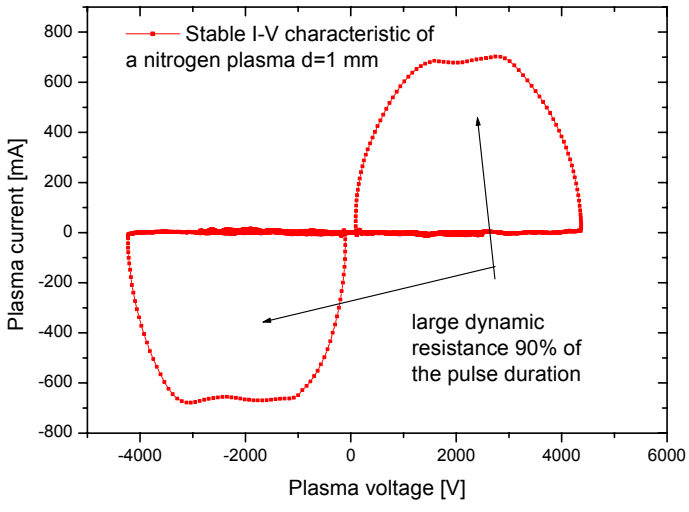

Fig.4b I-V characteristic of a stabilized N2 discharge

Again as one can see in Fig.6a the reason of this instability is the low *r/R* ratio of the IV characteristics. In this case the low *r/R* ratio is due to the fact that the common form of atmospheric glow in nitrogen is a Townsend discharge. For such discharges the current is extremely sensitive to any change in voltage [8]. After the electronic stabilization a discharge variety of larger dynamic resistance is generated (see Fig.5b). This electronic stabilized discharge is stable up to several percents of oxygen added to the discharge. Also it can be generated at large power density. In this way the surface energy of PP a notorious hydrophobic polymer can be increased to 66 mJ/m after a exposure of only 0.5 s in a nitrogen atmospheric glow [12].

A method of plasma stabilization is the limitation of the speed of the current growth *dI/dt* during the plasma breakdown. During the breakdown plasma has a negative dynamic resistance in order to limit the *dI/dt* the voltage applied to the plasma should not decrease during this phase of plasma generation. This is done by inserting in series with the AGP reactor a choke coil that operates in the saturation regime during the plasma generation [11].

6. Conclusions

Thermal/ionization instability is the key factor, which is preventing the atmospheric glow generation. Excepting He atmospheric plasma generation requires the suppression of the unstable plasma modes. Several dedicated electronic circuits were developed for this purpose. Only in this way we succeeded to generate the atmospheric glow at high power density and for a large variety of gases.

References

[1] F. Massines, P. Ségur, N. Gherardi, C. Khamphan and A. Ricard Surf. and Coatings Technology, Volumes 174-175, (2003)
[2] Yu. Golubovskii , V.Maiorov, J.Behnke, J.F.Behnke *J. Phys. D: Appl. Phys*. **36** (2003) 39–49
[3] I. Radu , R. Bartnikas, G. Czeremuszki, M.R Wertheimer *IEEE Trans. Plasma Sci.* 31,411 (2003)
[4] H.de Vries, E.Aldea, F.Mori, M.C.M van de Sanden, US Patent 20040007985
[5] H. de Vries, F. Mori, E. Aldea, M.C.M. van de Sanden**,** EP # 1403902, 2004.
[6] E.Aldea, P.Peeters, H. de Vries, M.C.M van de Sanden *in print in Surf. and Coat. Technol*.
[7] S.Jichul , R. Laxminarayan, J.Appl.Phys. **94**,12, 7408 (2003)
[8] Y.P.Raizier, *Gas discharge physics*, Springer Verlag, 1991
[9] Yu Akishev, O Goossens, T Callebaut, C Leys, A Napartovich, N Trushkin J. Phys. D: Appl. Phys. **34 ,** 2875 (2001)
[10] J.P.Boeuf and C.Pitchford Invieted lecture 17-th Escampig to be published in Plasma Sources. Sci and Tech.
[11]] H.de Vries, F.Mori, E.Aldea, M.C.M van de Sanden US Patent 6774569,(EP 1381257) 2004
[12] P.Peeters, E.Aldea, H de Vries, M.C.M van de Sanden Proceedings of SVC 2005

Manufacturing Nanostructured Coatings and Micropatterns Using a Thermal Plasma Process

J. Hafiz, R. Mukherjee, X. Wang, P. H. McMurry, J. V. R. Heberlein, and S. L. Girshick

Department of Mechanical Engineering, University of Minnesota, Minneapolis, USA

Abstract

In this paper we present results from the synthesis and deposition of Si-Ti-N nanostructured coatings using hypersonic plasma particle deposition. Focused particle beam deposition of micropatterns using aerodynamic lenses demonstrates promise in the synthesis of structures constructed from SiC nanoparticles. This study analyzes individual nanoparticles, nanostructured coatings and micropatterns, with particular emphasis on phase composition, morphology and particle/grain size distributions.

1. Introduction

Nanostructured materials are attractive candidates for advanced friction and wear-resistant coatings due to their potentially enhanced mechanical properties. Furthermore, generation of patterned ceramic microstructures made of nanoparticles has potential applications in microelectromechanical systems (MEMS). We have developed a one-step method called hypersonic plasma particle deposition (HPPD) to produce and deposit nanoparticles using a thermal plasma reactor [1]. In the HPPD process, particles are deposited on a substrate by hypersonic impaction to form a coating, or are deposited as micropatterns using focused particle beam deposition [2]. This paper analyses Si-Ti-N nanostructured coatings synthesized and deposited with the HPPD process. Micropatterns consisting of Si and SiC nanoparticles deposited at room temperature using the focused particle beam are also examined. Patterns were also deposited into gear molds using the coating deposition stage at elevated temperatures. Additionally, in-situ particle size distribution measurements were performed using a sampling probe interfaced to an extraction/dilution system in series with a scanning mobility particle sizer (SMPS) [3]. These data were compared to measurements obtained from X-ray diffraction peak broadening using the Warren-Averbach method [4].

2. Experimental Setup

HPPD involves a one-step process in which nanoparticles are both synthesized and deposited. The details of the experimental apparatus and operating conditions have been described previously [1] and are briefly explained here. In the HPPD process, vapor phase reactants are injected into a thermal plasma where high temperatures at the injection location dissociate the reactants into their elemental constituents. The gaseous mixture is expanded through a cooled ceramic nozzle driving the nucleation of nanoparticles, which are then accelerated in a hypersonic jet. The particles are deposited on a substrate by hypersonic impaction to form a coating, or are deposited as micropatterns after passing through an aerodynamic lens assembly. The experimental setup is shown schematically in Figure 1.

In the film deposition stage a molybdenum substrate (Module A in Fig. 1) is positioned normal to the flow, and particles as small as a few nanometers in diameter impact the substrate at high velocity to form a dense, nanostructured coating. The position of the substrate is 2 cm away from the exit of the ceramic nozzle.

In the focused particle beam deposition process, nanoparticles from the nozzle are collimated into a tight beam using an aerodynamic lens assembly consisting of a set of thin-plate orifices mounted inside a cylinder (Module B in Fig. 1) [5,6]. The entire unit is made of stainless steel, with the lenses spaced 47 mm apart. The gas inside the lens assembly contracts and expands as it passes through each of the lenses. Sufficiently small particles follow the gas, whereas large particles are lost to the walls. Particles of intermediate sizes are pushed closer to the centerline. Our lens assembly focuses 10-100 nm particles into a collimated beam with a diameter of a few tens of microns. An accelerating nozzle is placed at the end of the barrel, beyond which the flow undergoes another expansion to pressures around 1 Pa. The focused nanoparticles are then deposited onto a motion-controlled substrate to form micropatterns or onto TEM grids for off-line analysis.

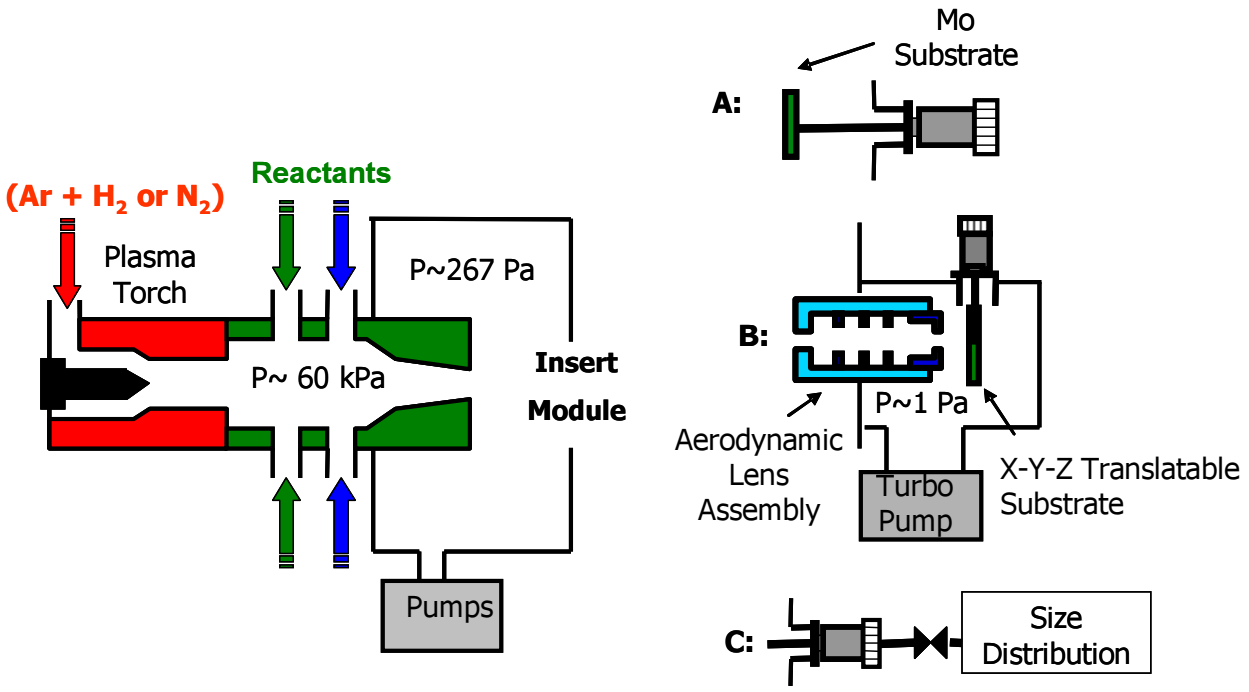

Figure 1: Schematic of the HPPD system

The HPPD process has been used to deposit nanostructured films composed of elements from among the following: silicon, titanium, carbon and nitrogen. The reactants include silicon tetrachloride and/or titanium tetrachloride, with methane additionally injected to produce the carbides, and nitrogen or ammonia to produce the nitrides.

Several techniques have been employed to investigate properties of nanoparticles prior to deposition, and structures constructed from these nanoparticles. A sampling probe interfaced with a scanning mobility particle sizing (SMPS) system allows in-situ access to particles in the hot gas jet for measurement of size and charge distributions (Module C in Fig. 1). During measurements, the sampling probe was placed 2 cm away from the nozzle, corresponding to the substrate standoff distance for film deposition. X-ray diffraction (XRD) spectra were obtained with a Bruker AXS microdiffractometer (CuKα) as well as a Siemens 5005 diffractometer. Scanning electron microscopy (SEM) was performed with a JEOL 6500 field emission gun (FEG) microscope equipped with an energy dispersive spectrometer. Transmission electron microscopy (TEM) was performed using a JEOL 2010 FEG TEM.

3. Results and Discussion

3.1. Si-Ti-N Coating Deposition

Si-Ti-N nanostructured films have shown good promise as potential candidates for high hardness and friction resistance applications [7]. We have synthesized Si-Ti-N coatings of 10-50 μm thickness on molybdenum substrates at deposition rates of 2-30 μm/min, depending on reactant flow rates, at substrate temperatures ranging from 400-1000°C. (All substrate temperatures quoted refer to the deposition surface.) Our previous study has shown the coatings to consist of TiN nanocrystals surrounded by an amorphous Si_3N_4 matrix [8].

To determine the effect of plasma gases on coating properties, we synthesized coatings with a plasma gas mixture of either Ar + N_2 (30 slm + 2.5 slm) or Ar + H_2 (30 slm + 2.5 slm) at substrate temperatures of 940 °C. For both cases the reactant flow rates were identical. X-ray diffraction spectra of films synthesized with a plasma gas mixture of Ar + H_2 show the presence of crystalline TiN, $TiSi_2$, and Ti_5Si_3, while films synthesized

with an Ar + N_2 mixture show only crystalline TiN (Fig. 2). The difference in crystalline phases present in the coatings can be attributed to the effect of extra nitrogen available during the synthesis process. Studies on the phase stability of Si-Ti-N have indicated that nitrogen activity plays a key role in changing phase components [9]. When the partial pressure of N is sufficiently high, Si does not form a stable titanium silicide phase. In our system, the partial pressure of nitrogen is increased significantly by adding extra N_2 as one of the plasma gases, resulting in the formation of only TiN with Si existing in an amorphous phase. These results indicate that we can switch crystalline phases in our coatings by changing the plasma gases.

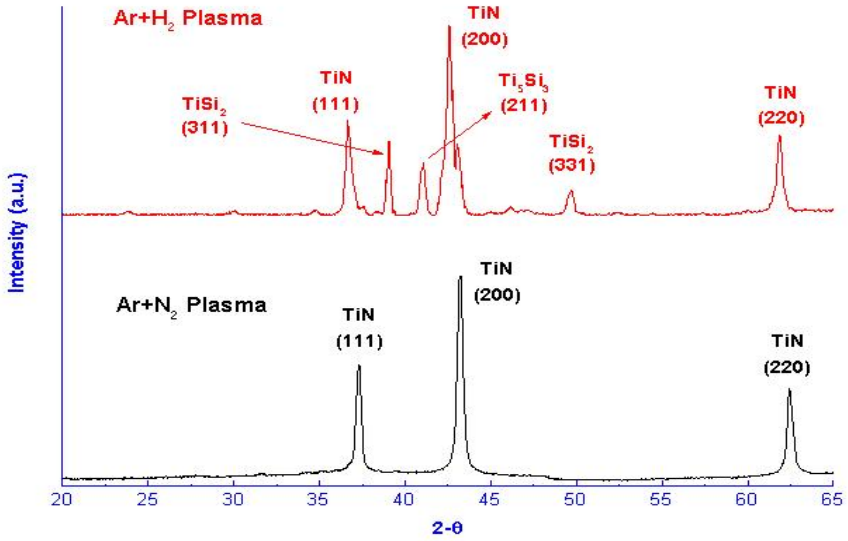

Figure 2: X-ray diffraction spectra of Si-Ti-N coatings deposited with an Ar + H_2 plasma gas mixture (top) and an Ar + N_2 mixture (bottom). The flow rates are: $SiCl_4$ 20 sccm, $TiCl_4$ 120 sccm and NH_3 500 sccm.

However, particle size distribution measurements performed for the same flow rates using either an Ar + H_2 or a Ar + N_2 gas mixture showed only a small difference (Fig. 3). The modes of the distributions for both cases are approximately 14 nm. It may be concluded that even though changing the plasma gas mixture results in different

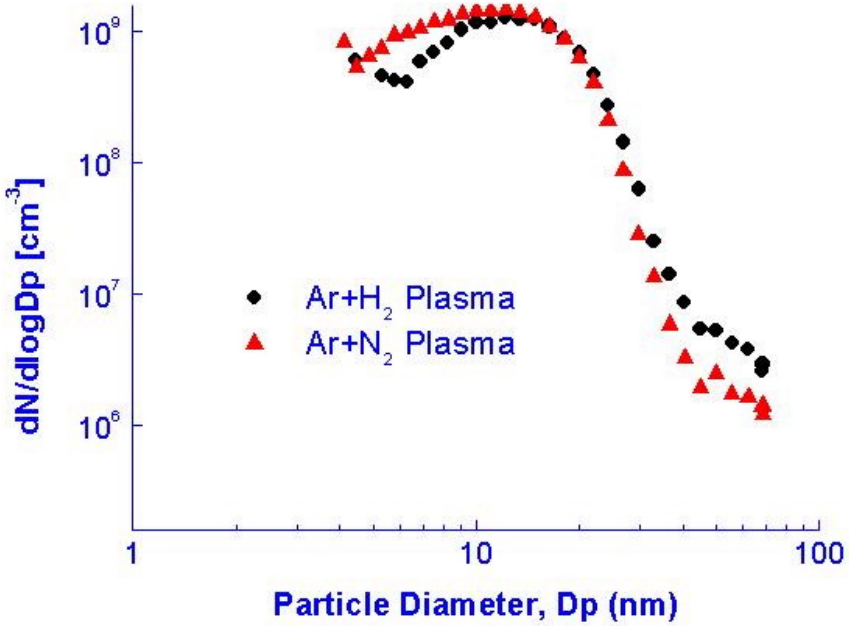

Figure 3: In-situ size distributions of particles synthesized with different plasma gas mixtures

crystalline phases, it does not significantly affect the size of the impacting particles forming the coatings.

In addition to the near real-time SMPS measurements, crystallite size was also determined from broadening of the Bragg reflections obtained from XRD measurements of the coatings. The Warren-Averbach (WA) method was utilized for this analysis, as researchers have found it to be more accurate than other methods when dealing with grain sizes in the nanometer range [10]. However, size determination could only be performed for coatings synthesized using the Ar + N_2 gas mixture. A disadvantage of WA analysis is that it requires multiple non-overlapping peaks of a phase for accurate size determination. As coatings synthesized using an Ar + H_2 mixture did not contain more than one distinct peak for any phase, accurate size analysis could not be performed. Crystallite size determined from the broadening of TiN reflections for the Ar + N_2 case showed the mean size to be 14.9 nm, corresponding well with the SMPS measurements. It is interesting to note that the mode of the distribution from the SMPS data and the mean size from XRD peak broadening were similar, even though the SMPS measures all synthesized particles, whereas the WA analysis provided information only concerning crystalline TiN. The results indicate that for the deposition conditions examined, the size of the TiN crystallites may be representative of the overall grain size distribution in the film.

3.2. Focused Beam Deposition

In concert with standard microfabrication techniques, focused nanoparticle beams can be used to deposit lines or patterns, or to build three-dimensional objects, made out of nanoparticles. We are currently pursuing micromolding of MEMS devices by filling micromachined silicon molds with focused nanoparticles. Molds were fabricated by standard photolithography tools and dry etched using deep reactive ion etching (DRIE). Figure 4a shows a microgear-shaped mold fabricated using DRIE. This mold was filled using SiC nanoparticles collimated by the aerodynamic lens system. The gear mold was rastered across the nanoparticle beam at a velocity of 50 μm/s. The time required for the deposit to cover three microgear molds (250 μm diameter separated by 100 μm) was on the order of 15 min. Cross-sectional SEM of a completely filled gear mold with a depth of ~8 μm is shown in Figure 4b. It should be noted that micropattern deposition on the Si substrate is carried out at room temperature, although the possibility of substrate heating exists for additional control of deposit properties.

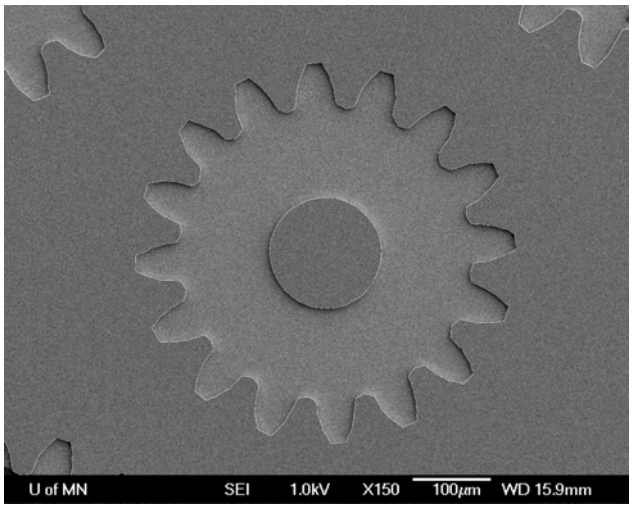

Figure 4a: Micromachined silicon gear mold.

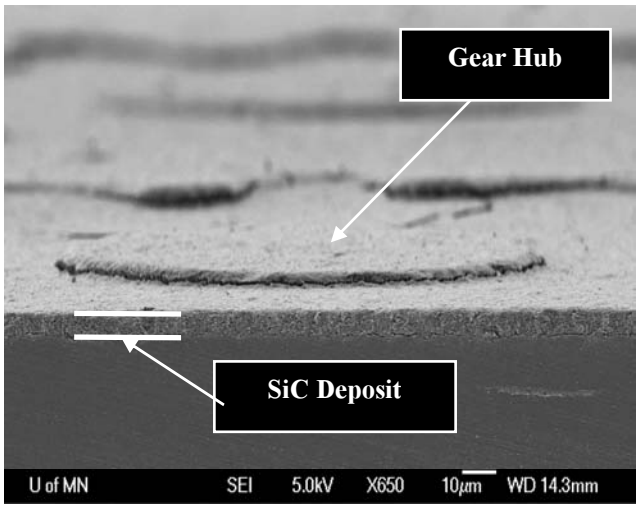

Figure 4b: Cross-section of mold filled by a layer of SiC nanoparticles from the focused beam.

We have conducted a number of experiments to characterize nanoparticles passing through the lens assembly. Studies of individual particles allow us to relate properties of the micropatterns to their nanostructure. These experiments were performed by removing the Si substrate and replacing it with a substrate containing TEM girds for off-line analysis of individual particle properties. Figure 5 shows a high-resolution TEM image highlighting

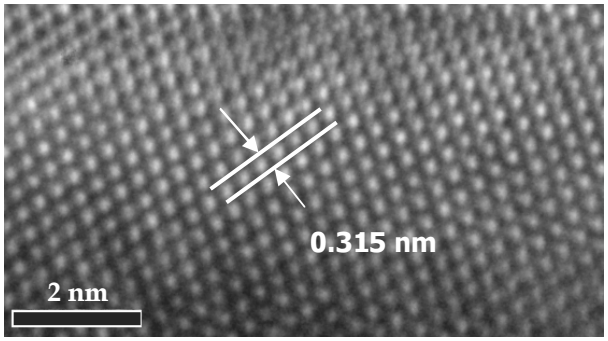

Figure 5: High-resolution TEM image of a crystalline Si nanoparticle collected using aerodynamic focusing.

the crystalline nature of a 100-nm-diameter Si particle collected on a copper grid. The calculated fringe spacing of the particles is 0.315 nm, corresponding to the Si (111) phase, which has a lattice spacing of 0.314 nm. The highly crystalline nature of the Si particle is typical of particles collected after the lens assembly.

In additional experiments, we also filled gear molds by replacing the molybdenum substrate used in the film deposition setup. This was done to utilize the high rate deposition capabilities and higher substrate temperatures attainable in the hypersonic impaction stage. Preliminary results (Fig. 6) illustrate a cross section image of a gear partially filled with a film of Si-Ti-N nanoparticles.

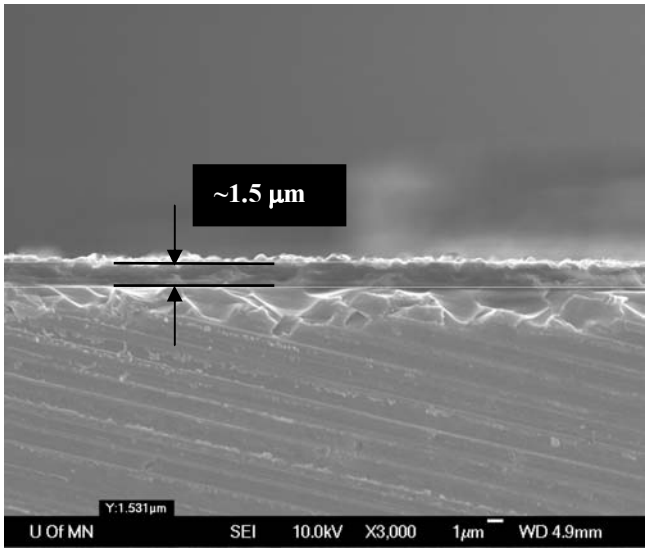

Figure 6: Cross-section of Si-Ti-N nanoparticle film deposited in "valley" of a gear mold using the film deposition stage. Substrate temperature ~650-800°C, 1-minute deposition.

4. Conclusions

The work reported here presents results using the HPPD process to deposit nanocomposite coatings and nanostructured micropatterns. The phase distribution in the Si-Ti-N coatings was studied as a function of plasma gases. When the plasma gases contained Ar + H_2, crystalline phases in the coatings consisted of TiN, $TiSi_2$, and Ti_5Si_3. When the system was switched to a plasma gas mixture of Ar + N_2, the only crystalline phase was TiN. However, there were only small differences in particle size distributions between the two cases. Size distribution measurements indicate the mode of the impacting particles to be ~14 nm in diameter. This corresponded well with the average size of the TiN crystallites in the films obtained from Warren-Averbach analysis.

Focused beam deposition presents a new and promising approach for fabricating hard microparts for MEMS systems. Results show that particles being focused through the lens system are primarily crystalline in nature. Preliminary experiments illustrate the capability of the deposition process to completely fill 8-μm-deep microgear molds with SiC nanoparticles. This approach has the potential for high-rate coating applications as well as for micromolding and free-form fabrication of nanostructured materials.

Acknowledgments
This work was partially supported by NSF grant DMI-0103169 and NSF IGERT grant DGE-0114372. Transmission electron microscopy was carried out at the Center for Microanalysis of Materials, University of Illinois, which is partially supported by the U.S. Department of Energy under grant DEFG02-91-ER45439. Assistance of J.-G. Wen during TEM operation is gratefully acknowledged.

References
[1] S. L. Girshick, J. V. R. Heberlein, P. H. McMurry, W. W. Gerberich, D. I. Iordanoglou, N. Rao, A. Gidwani, N. Tymiak, F. Di Fonzo, M. H. Fan and D. Neumann, "Innovative Processing of Films and Nanocrystalline Powders: Hypersonic Plasma Particle Deposition of Nanocrystalline Coatings", 2002, Editor K. L. Choy, Imperial College Press, London.

[2] F. Di Fonzo, A. Gidwani, M. H. Fan, D. Neumann, D. I. Iordanoglou, J. V. R. Heberlein, P. H. McMurry, S. L. Girshick, N. Tymiak, W. W. Gerberich and N. P. Rao, "Focused Nanoparticle-Beam Deposition of Patterned Microstructures," Applied Physics Letters **77**, 910–912 (2000).

[3] X. Wang, J. Hafiz, R. Mukherjee, S. L. Girshick, J. V. R. Heberlein, and P. H. McMurry, "System for in situ Characterization of Nanoparticles Synthesized in a Thermal Plasma", Plasma Chemistry Plasma Processing, accepted for publication.

[4] B. E. Warren, "X-ray Diffraction", Addison-Wesley, Reading, 1969.

[5] P. Liu, P. J. Ziemann, D. B. Kittelson, P. H. McMurry, "Generating Particle Beams of Controlled Dimensions and Divergence I. Theory of particle motion in Aerodynamic Lenses and Nozzle Expansions", Aerosol Science Technology, **22**, 293-313 (1995).

[6] P. Liu, P. J. Ziemann, D. B. Kittelson, P. H. McMurry, "Generating Particle Beams of controlled Dimensions and Divergence II. Experimental Evaluation of Particle Motion in Aerodynamic Lenses and Nozzle Expansions", Aerosol Science Technology, **22**, 314-324 (1995).

[7] S. Veprek, A. Niederhofer, K. Moto, T. Bolom, H.-D. Männling, P. Nesladek, G. Dollinger, A Bergmaier, "Composition, nanostructured and origin of the ultrahardness in nc-TiN/a-Si_3N_4/a- and nc-$TiSi_2$ nanocomposites with Hv=80 to ≥ 105 Gpa", Surface & Coatings Technology, **133-134**, 152-159 (2002).

[8] J. Hafiz, X. Wang, R. Mukherjee, W. Mook, C.R. Perrey, J. Deneen, J.V.R. Heberlein, P.H. McMurry, W.W. Gerberich, C.B. Carter and S.L. Girshick, "Hypersonic plasma particle deposition of Si–Ti–N nanostructured coatings", Surface & Coatings Technology, **188-189**, 364-370 (2004).

[9] S. Sambasivan and W. T. Petuskey, "Phase chemistry in the Ti-Si-N system: thermochemical review with phase stability diagrams", Journal of Materials Research, **9**, 2362-2366 (1994).

[10] A. Niederhofer, P. Nesládek, H. -D. Männling, K. Moto, S. Veprek, and M. Jílek, "Structural properties, internal stress and thermal stability of nc-TiN/a-Si_3N_4, nc-TiN/$TiSi_x$ and nc-$(Ti_{1-y}Al_ySi_x)N$ superhard nanocomposite coatings reaching the hardness of diamond", Surface & Coatings Technology, **120-121**, 173-179 (1999).

Modelling of plasma-surface interactions during plasma oxidation process

S. Novák[1], R. Hrach[1,2], J. Pavlík[1], V. Hrachová[2]

[1] *J. E. Purkyně University, Institute of Science, Department of Physics, Ústí nad Labem, Czech Republic*
[2] *Charles University, Faculty of Mathematics and Physics, Department of Electronics and Vacuum Physics, Prague, Czech Republic*

Abstract
The complete process of plasma oxidation of metals in oxygen plasma consists of several stages: activation of oxygen in discharge, transport of charged species from undisturbed plasma to metal substrate immersed into the plasma, processes on the surface and the growth of oxide layers including the ion transport through growing oxide film. In the contribution the plasma oxidation of aluminium and tin in pure oxygen and in oxygen/argon mixtures is analysed, the methods of study being both the direct measurement and computer simulation.
Keywords: plasma oxidation, plasma volume processes, sheath, computer simulation, AFM.

1. Introduction

Thin dielectric films are very important in many material engineering disciplines. There exist various techniques for preparation of dielectric films, the oxidation being one of the most important of them. The high-temperature processes as thermal oxidation or chemical vapour deposition often give rise to defect formation; therefore the low-temperature processes are popular. The plasma oxidation, utilizing highly activated oxygen plasma, is one of the low temperature techniques used to grow dielectric films on metal surfaces [1]. Substrates immersed into plasma are held on various biases relative to plasma. Typical procedure is the plasma anodisation, when the positive external bias is applied in order to enhance the diffusion of oxygen ions through the growing oxide layer, however the oxidation without external bias or even with negative biases is sometimes used too.

For the study of plasma oxidation there exist several reasons: to understand the mechanisms of plasma oxidation of metal thin films, to find basic factors playing the dominant role in studied process, and to find factors determining the properties of created oxide films. During our previous studies [2]- [3] it was found that the combination of two approaches – experimental and computational – is very efficient method for the analysis of physical and chemical processes taking place in the plasma oxidation of metals.

2. Bulk processes – Experimental study

The first part of our computer experiment, i.e. activation of oxygen in the discharge and transport of obtained charged species to the substrate, is based on experimental data obtained by measurements performed in our two laboratories. In the laboratory of J. E. Purkyně University the experiments were carried out in the system for the plasma chemical surface modifications of thin films [4]. Two types of discharges were applied: DC glow discharge and 13.56 MHz RF discharge in pure oxygen and in oxygen/argon mixtures. The DC flowing discharge was produced in the Pyrex tube at typical parameters: total gas pressure 50 Pa, flow rate 2.5×10^{-4} $l \cdot s^{-1}$, discharge current 25 mA. In the same ranges of gas pressures and flow rates an RF discharge was produced, too. For the diagnostics of the discharge process, a movable cylindrical Langmuir probe and optical emission spectroscopy system consisting of quartz fiber, spectrometer and CCD camera were used. Beside these measurements the visualization of the field of intensities emitted by plasma was performed by CCD camera with combination of various filters. The main experimental results were electron temperatures and densities and their radial profiles in the discharge tube, the spatial distribution of discharge and above all the plasma emission spectra enabling to analyse various atomic transitions in argon and oxygen.

In the laboratories of Charles University the measurements were made mostly in the positive column of DC glow discharge in the mixtures of rare gases containing oxygen (combinations: pure oxygen, oxygen/argon, oxygen/neon and oxygen/helium) in the pressure range 67 to 800 Pa and for discharge currents in limits 5 to 30 mA [5]. For the study of plasma properties various diagnostics were used – optical, microwave and probe

diagnostic method. The main studied plasma parameters were the axial electric field in the discharge, the electron density and electron temperature for the basic experimental parameters: composition of gas mixture, its pressure and discharge parameters.

As examples of obtained results some characteristics are presented in Figs. 1 and 2. These results can be used both as input data for the following modelling and for testing of results derived by our computer experiments.

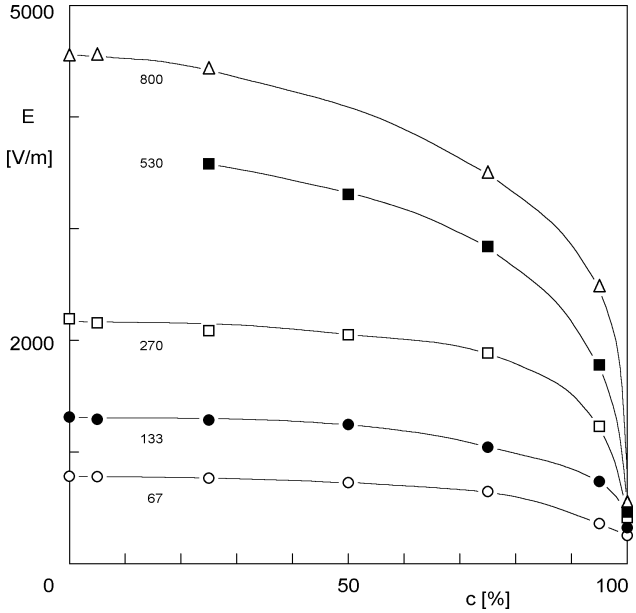

Fig. 1: Measured intensity of axial electric field *E* in the oxygen/argon plasma in the dependence on the concentration *c* of argon in the mixture. Discharge current 20 mA. Parameter: pressure of the mixture in limits 67-800 Pa [5].

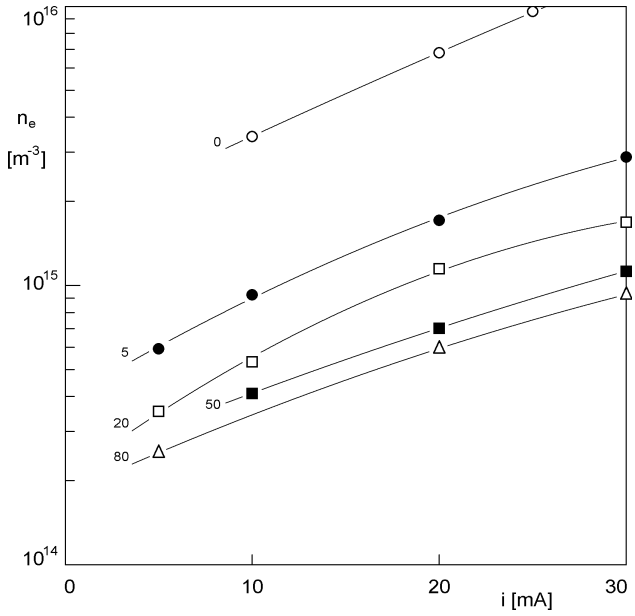

Fig. 2: Measured electron density n_e in the oxygen/neon plasma in the dependence on the discharge current *i*. Pressure 800 Pa. Parameter: concentration of neon in the mixture (0-80 %) [5].

3. Bulk processes – Computational study

As a second method for the study volume processes in plasma, a computer experiment was prepared. The numerical simulation of the plasma composition is based on a macroscopic kinetic approach (e.g. [6]). In reality there exist several similar models – for pure oxygen discharge and for mixtures of oxygen with various rare gases. The model of the oxygen/argon plasma consists of nearly two hundred reactions between 15 kinds of neutral, charged and excited particles (electrons; O, O_2, O_3, O^-, O^+, O_2^-, O_2^+, O_3^-, $O(^1D)$, $O_2(^1\Delta_g)$, $O_2(^1\Sigma_g^+)$; Ar, Ar^+, Ar^*). This set of reactions includes the basic physical processes in O_2/Ar plasma – ionisation, recombination, dissociative attachment, dissociative recombination, radiative attachment, direct dissociation, three-body collisions and excitation. The reaction set consists of three parts – reactions between oxygen particles, reactions in argon and mixed reactions oxygen-argon. The attention is paid to evaluation of the influence of individual chemical reactions on the resulting products, especially on those important from the point of view of plasma oxidation of metals (i.e. electrons and negative oxygen ions).

In the macroscopic kinetic approach, it is necessary to analyse the reactions in the model and to prepare the large set of partial differential equations describing the concentrations of individual species in plasma. The complete model is too complicated and very difficult to solve. However, if both the drift and diffusion terms can be neglected, the set of ordinary differential equations is obtained in the form

$$dn_i / dt = A_i(n_1,\ldots,n_m) - B_i(n_1,\ldots,n_m), \quad i = 1, 2,\ldots, m,$$

where n_i is the concentration of the i-th specie and m is the total number of species in the suggested mechanism – e.g. 15 in our oxygen/argon model. The creation and loss processes A_i and B_i consist of the terms $\pm k_p \cdot n_a$; $\pm k_p \cdot n_a \cdot n_b$ or $\pm k_p \cdot n_a \cdot n_b \cdot n_c$, where rate constants k_p may depend on gas temperature T_g or electron temperature T_e. The correspondence with experimental conditions can be obtained through these rate constants as well as through the input concentrations of basic species in the discharge. The resulting set of stiff equations was integrated with the help of a semi-implicit extrapolation Bader-Deuflhard method [7].

As a result, the time dependencies of neutral, excited and ionised products were obtained for various discharge parameters. For our experimental conditions, the concentrations found for O_2 glow discharge at E/N = 60 Td [2] were used for further simulation (all concentrations are given in relative scale – compared to concentration of molecular oxygen):

- neutral and excited species:
  O_2: 1.00 O: 7.53×10^{-1} $O_2(^1\Delta_g)$: 1.48×10^{-1} $O_2(^1\Sigma_g^+)$: 4.34×10^{-3} O_3: 7.70×10^{-5}
- positive charged species:
  O_2^+: 1.60×10^{-6} O^+: 5.17×10^{-10} O_4^+: 3.00×10^{-10} ...
- negative charged species:
  electrons: 1.33×10^{-6} O^-: 2.62×10^{-7} O_2^-: 8.60×10^{-9} O_3^-: 4.64×10^{-10} ...

The corresponding concentrations of particles for oxygen/argon plasma are modified by the presence of argon atoms, the most important positive charged specie being the Ar^+ ion. The relations between oxygen and argon particles depend on the concentration of oxygen in the mixture.

The model of physical and chemical processes in the bulk of oxygen plasma results in the steady-state concentrations of most important stable products. For further simulation as well as for the whole process of plasma oxidation of metals the relative concentrations of two basic negatively charged species – electrons and atomic oxygen ions – is very important. This ratio depends on discharge parameters alike on the concentration of oxygen in the mixture. The sheath properties depend in large extent on the masses of main charged species and

while for positive ions (Ar^+, O_2^+ and O^+) these masses are comparable, for negative species the situation is quite different.

3. Transport through the sheath

The following part of our computer experiment analyses the transport of charged particles through the region of disturbed plasma near the substrate. The model of charge transport through both the sheath and presheath is based on a hybrid particle simulation technique, i.e. on the combination of molecular dynamics and Monte Carlo methods (e.g. [8]). In our contribution the self-consistent approach of modelling was used; it is extremely time-consuming. Taking into account the planar form of the most of oxidized substrates and in order to simplify the simulations, the planar geometry of the model was used, too. This assumption enables to use the spatially one-dimensional approximation for the simulation. It increases the performance of the simulation, however slightly decreases the accuracy of obtained results [9].

The model consists of the following standard parts:

- Source of particles:
  Undisturbed plasma consisting of electrons, positive ions and negative ions with the total concentration of particles of one sign of the order of 10^{15} m^{-3} with Maxwell velocity distributions. The numbers of species and their relative concentrations are taken from the study of volume processes, either experimental or computational. If only qualitative estimations of processes in the sheath are sufficient, only the main species containing the majority of the charge (positive: Ar^+ and either O_2^+ or O^+, negative: electrons and O^-) are included. For detailed calculation it is possible to include much larger number of charged species.
- Equations of motion:
  Newton´s equations of motion were solved by the second order Verlet algorithm.
- Force calculation:
  The movement of particles is influenced by self-consistent electric field created by other particles and by substrate bias. For its determination the standard PIC technique was used [8]. By this technique the interactions between charged species are handled.
- Interactions:
  A minimal set of basic interactions between charged and neutral species in the sheath was used. This set consists of elastic collisions, excitation, ionisation and charge transfer interactions with mean free paths given by experimental data [10]. The interactions are treated by the Monte Carlo method, so the resulting code is of the type PIC-MC.

In this part of our computer experiment, we calculated the changes of concentrations and energy distributions of both electrons and ions originating in the bulk plasma during their transfer through self-consistent electric field in the transient region between plasma and metal electrode. As a result of this simulation the sheath properties (its thickness and potential distribution) were obtained together with basic characteristics of charged particles and their changes during the transport from undisturbed plasma to the surface of immersed substrates (the fluxes of different types of charged species, their energy and angular distributions both in the sheath and in the close vicinity of the substrate). Some examples of obtained results can be found in our second contribution [11].

4. Processes on the surfaces of immersed substrates

The last part of the computer experiment is the simulation of basic processes on the substrate – impingement of charged particles, their reflection, secondary emission, etc. This simulation is supported again by experimental data obtained by various techniques – the composition and depth profiles of oxide films were studied by Secondary Ion Mass Spectrometry, the morphology of oxide surfaces and surface roughness were performed by Atomic Force Microscopy. The experiments were carried out in the system for the plasma chemical surface modification of thin films. In these experiments two types of discharges were applied. Besides the DC discharge, the experimental characteristics of which were used as inputs for our modelling, the RF discharge at 13.56 MHz in both pure oxygen and oxygen/argon mixture was used, too. In order to compare our computer experiment even with these data, the dynamical processes were included into the model of the transport of charged particles

through the sheath region. The combination of all above-mentioned diagnostics and computational techniques enables us to analyse the plasma oxidation process in detail and to discuss the role of most important plasma parameters in this process. It has been proven that the method of plasma oxidation is a possible applicable alternative method for preparing thin oxide films.

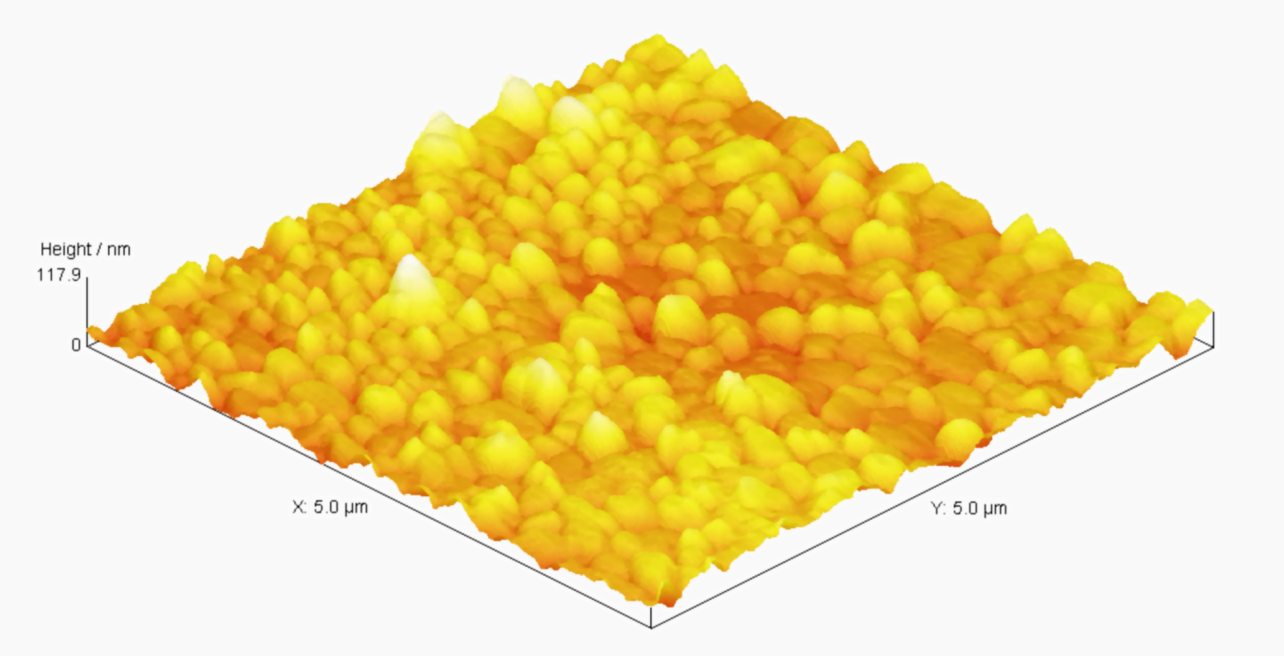

Fig. 3: AFM three-dimensional image of surface of thin SnO_2 film prepared by plasma oxidation of thin tin film.

5. Discussion

The main experimental results in bulk processes were electron temperatures and densities and their radial profiles in the discharge tube, the spatial distribution of discharge and above all the plasma emission spectra enabling to analyse various atomic transitions in argon and oxygen. These results can be used both as input data for the following modelling and for testing of results derived by our computer experiments. Computational studies showed that the relative concentration of electrons and atomic oxygen ions is very important. This ratio depends on discharge parameters alike on the concentration of oxygen in the mixture. The sheath properties depend in large extent on the masses of main charged species and while for positive ions these masses are comparable, for negative species the situation is quite different. As a result of simulations the sheath properties were obtained together with basic characteristics of charged particles and their changes during the transport from undisturbed plasma to the surface of immersed substrates. We can say it has been proven that the method of plasma oxidation is a possible applicable alternative method for preparing thin oxide films.

6. Acknowledgements

The work is a part of the research plan MSM0021620834 that is financed by the Ministry of Education of the Czech Republic. The authors S.N. and J.P. acknowledge the support of the projects COST OC 527.50 and 1P05OC013. The authors R.H. and V.H. acknowledge the support of Grant Agency of Charles University Prague, Grant No. 296/2004.

References

[1] J. Siejka, J. Perriere - Plasma Oxidation, in Physics of Thin Films, Vol 14, p. 81, Academic Press Inc., Boston (1989).

[2] J. Pavlík, Z. Strýhal, S. Novák, A. Macková, V. Peřina, M. Vicher, R. Hrach - Vide **56**, No 300 – Suppl., 85 (2001).

[3] J. Pavlík, Z. Strýhal, M. Vicher, R. Hrach, A. Macková, V. Peřina - Proc. 16th European Conf. on Atomic and Molecular Physics of Ionized Gases ESCAMPIG 16 / ICRP-5, Grenoble, France, Vol. I, p. 351 (2002).

[4] J. Pavlík, S. Novák - Proc. 13th Intern. Symp. on Plasma Chemistry ISPC-13, Beijing, China, Vol. III, p. 1183 (1997).

[5] R. Hrach, V. Hrachová, M. Vicher, J. Šimek - Proc. 16th Intern. Symp. on Plasma Chemistry ISPC-16, Taormina, Italy, p. 145 (2003).

[6] J.-C. Legrand, A.-M. Diamy, R. Hrach, V. Hrachová - in Advances in Plasma Physics Research, Vol. I, Chapter 1, NOVA Science Publ. Inc., New York (2001).

[7] W.H. Press, S.A. Teukolsky, W.T. Vetterling, B.P. Flannery - Numerical Recipes in Fortran 77/90, Second Edition, Cambridge Univ. Press, p. 735, (2002).

[8] R. Hrach - Czech. J. Phys. **49**, 155 (1999).

[9] R. Hrach, P. Jelinek, J. Simek, O. Barina, M. Vicher - Czech. J. Phys. **54**, C671 (2004).

[10] S.C. Brown - Basic Data of Plasma Physics: The Fundamental Data on Electrical Discharges in Gases, AIP Press, New York (1994).

[11] P. Jelínek, R. Hrach, J. Šimek, V. Hrachová: The role of negative ions in the sheath formation, Proc. 17th Intern. Symp. on Plasma Chemistry, Toronto, Canada (2005).

Line strengths of the methyl radical ν_2 band for plasma chemistry and astrophysical applications

G.D. Stancu[1], P.B. Davies[2], J. Röpcke[1]

[1] *INP-Greifswald, F.-L.-Jahnstr. 19, D-17489 Greifswald, Germany*
[2] *Department of Chemistry, University of Cambridge, Lensfield Rd, CB2 1EW, Cambridge, U.K.*

Abstract
Concentration measurements of the methyl radical rely on the data availability of spectroscopic properties such as the line strength. New measurements of line strengths of several transitions of the ν_2 fundamental band have been carried out. In the present work the temperature dependencies of the line strength from cryogenic temperatures up to moderate plasma temperature has been calculated.

Keywords:
methyl radical, infrared spectroscopy, line strength, transition dipole moment,

1. Introduction

The key role of the methyl radical in plasma kinetics, combustion, diamond deposition and semiconductor technologies has been demonstrated in numerous studies. The presence of the methyl radical in space has also been confirmed. Concentration measurements of the methyl radical (CH_3) in laboratory plasmas and in interstellar space are commonly made by IR spectroscopy of the ν_2 band. It has been demonstrated that detection of CH_3 in plasma processing reactors [1] and in the atmospheres of planets in our solar system [2] is most appropriately carried out by detection of the ν_2 band. The accuracy of concentration measurements depends on spectroscopic data such as the transition dipole moment or the line strength. New experimental values of the transition dipole moment and the line strengths have been published [3]. Here the temperature dependencies of the line strengths in the range of diamond plasma processing down to cryogenic temperatures will be presented.

2. Theoretical aspects

One of the physical quantities that can be measured by absorption spectroscopy is the integral value of the absorption coefficient (K_ν). The relationship between the total concentration (N) of the particles and K_ν is given by the following equation:

$$K_\nu = S(T)N \qquad (1)$$

where *S(T)* is the line strength of the specific absorption line at the equilibrium temperature *(T)* of the medium. The relationship between the line strength and the transition dipole moment is given by (2):

$$S(T) = \frac{8\pi^3}{3hc}\nu_{mn}\frac{g_m \exp\left(-\frac{E_m}{kT}\right)}{Q(T)}|\mu|^2 H_{KJ}\left[1-\exp\left(-\frac{hc\nu_{mn}}{kT}\right)\right] \qquad (2)$$

where ν_{mn} is the transition frequency, μ is the transition dipole moment, H_{KJ} is the Hönl-London factor, Q(T) is the total partition function, g_m is the degeneracy and E_m the energy of the lower level. Some comments can be made about equations (1) and (2). First if the concentration of CH_3 can be independently measured by another method or technique then the line strength can be obtained. In order to calculate μ we have to calculate the temperature dependent factors namely: the Boltzmann energy factor, the partition function and the stimulated emission factor. In this work the determination of the CH_3 concentration was made using decay measurements of the absorption coefficient during the off phase of the discharge. The principle of the method is described in detail in reference [3]. The transition dipole moment was found to be 0.215(0.025) D. Using the new value of μ the line strengths can be calculated for a wide temperature range and for several transitions.

Equation (2) relating the line strength and the transition dipole moment contains the total partition function $Q(T)$ and the total statistical weight, g_m, where $Q(T) = Q_E Q_V Q_R Q_{NS}$ and $g_m = g_e g_v g_J g_K g_{ns}$

(*E, e* – electronic; *V, v* – vibrational; *R, J,K* – rotational; *NS, ns* – nuclear spin; components). Special attention was given to the calculations of the total partition function, particularly the vibrational partition function at higher temperature and the rotational partition function at very low temperatures. Under the experimental conditions used here it can be safely assumed that only the ground electronic state is populated. The first excited state lies at 46305 cm^{-1}. Hence Q_E = 1 and, provided the spin-rotation splitting is not resolved, g_e = 1 also. The vibrational partition function is a product of the partition functions of all four normal modes,

$$Q_v = \prod_1^i \left[1 - \exp\left(-hc\nu_i / kT\right)\right]^{-g_V} \qquad (3)$$

where g_v is the vibrational mode degeneracy. The wavenumbers and degeneracies of the fundamental modes of CH_3 used to calculate Q_V are: ν_1=3004.8 cm^{-1} (g_v=1), ν_2=606.453 cm^{-1} (g_v=1), ν_3=3160.821 cm^{-1} (g_v=2) and ν_4=1396 cm^{-1} (g_v=2). In earlier works the vibrational partition function has been calculated using only the ν_2 and ν_4 modes. Figure 1 shows that above 1000 K this assumption begins to seriously underestimate the vibrational partition function.

The ν_2 band is a parallel band ($\Delta K = 0$) and non-degenerated, hence g_v = 1. Each rotational level for a symmetric top molecule also has a rotational degeneracy g_J and g_K: $g_J = 2J+1$, g_K = 1, for levels with K = 0 and g_K = 2 for levels with K = 1,2,3…. Because CH_3 is a planar molecule of the D_{3h} symmetric group, the reflection of the nuclei in the centre of mass produces a configuration that can be obtained by simple rotations of the molecule. The inversion doubling of the levels does not occur with the result that g_k = 1 for all K.

The rotational partition function, Q_R, for a planar symmetric top (D_{3h} symmetry) in which nuclear spin effects are ignored is given by,

$$Q_R = \sum_{J=0}^{\infty}\sum_{K=0}^{J}(2J+1)\exp(-\left[BJ(J+1)+(C-B)K^2\right]\frac{hc}{kT}). \qquad (4)$$

At sufficiently high rotational temperatures this expression approximates to

$$Q_R = \sqrt{\frac{\pi}{B^2C}\left(\frac{kT}{hc}\right)^3}, \qquad (5)$$

where B and C are the rotational constants. At high temperature the nuclear spin effects can be included through the nuclear spin partition function Q_{NS}:

$$Q_{SUM} = Q_{NS}Q_R = (2I+1)^3\frac{1}{\sigma}\sqrt{\frac{\pi}{B^2C}\left(\frac{kT}{hc}\right)^3} \qquad (6)$$

where we have assumed three equivalent nuclei with non-zero spin (I = 1/2) i.e. CH_3. σ is the symmetry number which is 6 for D_{3h} symmetry. Q_{NS} represents the number of the arrangements of the H nuclear spins of the CH_3 molecule. Specifically then for CH_3,

$$Q_{sum} = \frac{8}{6}\sqrt{\frac{\pi}{B^2C}\left(\frac{kT}{hc}\right)^3}. \qquad (7)$$

The nuclear spin degeneracy, g_{ns}, associated with each rotational level is included implicitly in the approximate equation (7). At low temperatures this equation is no longer valid and must be replaced by the exact sum, equation (4), modified to include the specific g_{ns} for each level. For a symmetric top molecule (D_{3h}) the value of g_{ns} depends on the quantum number K of the rotational level.

The statistical weights due to nuclear spin for K > 0 are:

$$g_{ns} = \frac{1}{3}(2I+1)(4I^2+4I+3) \text{ for } K = 3n\,;\ I = 1/2 \qquad 8(a)$$

$$g_{ns} = \frac{1}{3}(2I+1)(4I^2+4I) \text{ for } K \neq 3n\,;\ I = 1/2 \qquad 8(b)$$

Since CH_3 is a planar molecule, it consequently belongs to the D_{3h} point group. In this case, with three identical nuclei of spin *I*, the weight factors due to the nuclear spin for the levels with K = 0 are:

$$g_{ns} = \frac{1}{3}(2I+1)(2I+3)(I+1) \quad \text{for J even} \qquad 9(a)$$

$$g_{ns} = \frac{1}{3}(2I+1)(2I-1)I \quad \text{for J odd} \qquad 9(b)$$

Thus, the K = 0 and J odd lines are missing.

We have g_{ns}=4 for K=3n, g_{ns}=2 for K≠3n, n=1,2,3,… and g_{ns}=4 for K=0 and J even. The transitions which take place from the levels with K = 3, 6, 12… have double weight in comparison with the others. As a result, largerer absorption coefficients will be obtained. Since A_2 rotational levels are not allowed then K=0 and J odd levels are missing [4] (the H nuclei follow Fermi statistics, i.e. I = 1/2). Experimental proof is given in the work of Yamada et al. [5] were no transitions were observed for K=0 and J odd in the 2_0^1 band, J even in the 2_1^2 band and J odd in the 2_2^3 band. At low temperature then

$$Q_{SUM} = \sum_{J=0}^{\infty}\sum_{K=0}^{J} g_{ns}(2J+1)\exp(-\left[BJ(J+1)+(C-B)K^2\right]\frac{hc}{kT}) \qquad (10)$$

The rotational partition functions for CH_3 (actually Q_{SUM}) calculated from equations (7) and (10) are indistinguishable over a wide temperature range (< 1 % divergence) but deviate below 100 K (Figure 2). The Q_{SUM} from (10) was calculated considering up to 200 levels, more levels do not change the total sum. As expected equation (7) tends to zero as T → 0 while (10) tends to 4, the nuclear statistical weight of the lowest rotational level.

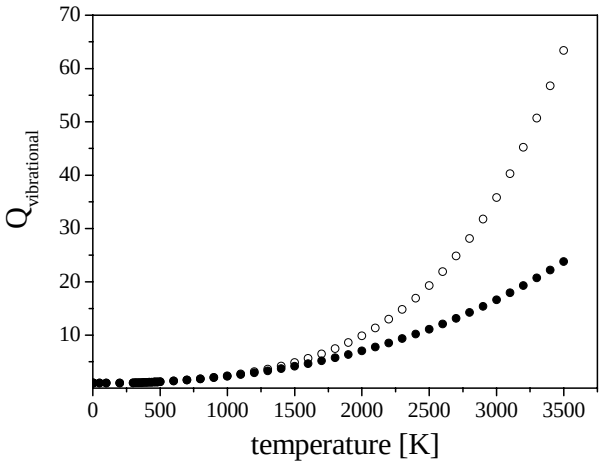

Figure 1. Temperature dependencies of $Q_{vibrational}$, considering vibrational modes: ν_2, ν_4 (•); ν_1, ν_2, ν_3, ν_4 (o).

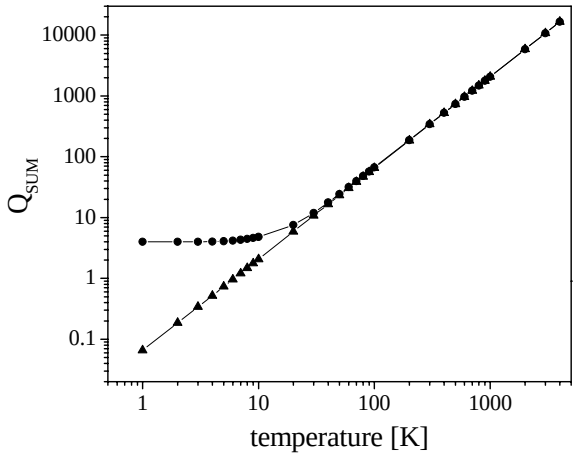

Figure 2. Q_{SUM} as a function of temperature: (▲), approximation given by equation (7); (●), exact summation given by equation (10).

3. Line strengths temperature dependence

The choice of the vibration rotation line to optimise the sensitivity of infrared absorption spectroscopy for detecting the methyl radical is an important issue in practical applications. The temperature dependence of the line strength is given for Q(3,3), Q(6,6) and Q(12,12) in figure 3. These lines were chosen because the levels involved in these transitions have high statistical weights (K = 3, 6, 12) and thus the measured absorption coefficients are large. A useful aspect, which can be obtained from figure 3., is the choice of the temperature regions where one of the line strengths becomes dominant. The plot can be separated into three regions. The first region is for temperatures below 300 K. In this domain Q(3,3) has the highest line strength and therefore this line is recommended for use in this region. In the work of Bezard et al. [2] the methyl radical was observed in the atmosphere of Neptune. The temperature of the upper atmosphere of Neptune is estimated to be about 170 K. In their recorded spectra the measured intensity of Q(3,3) is shown to be higher in comparison with Q(6,6). This agrees with the present calculations. The second temperature region which is considered is between 300 K and 1000 K where Q(6,6) is the strongest line. The third region is higher than

1000 K where the Q(12,12) line strength becomes stronger. This line was used in the experimental work of Lombardi et al. [1] where the temperature in their diamond deposition reactor was above 2000 K.

Detection of methyl in the interstellar medium at temperature of 17 K has recently been reported by Feuchtgruber et al. [6]. Absorption features of the Q-branch and the R(0,0) transition were detected. The temperature was obtained from the absorbance ratio of these features. The R(0,0) transition occurs from the lowest energy level of the methyl radical and is expected to have the largest line strength for very low temperature. Thus, it is of interest to see the behaviour of the line strengths of the transitions which occur between the lower energy levels. Figure 4 shows the temperature dependence of the line strengths of several transitions from the lower energy levels. The line strengths have been calculated using formula (2). It can be seen that all line strengths tend to zero as $T \rightarrow 0$ except for the transition R(0,0) which is the only transition from the lowest level (v = 0, J = 0, K = 0, $E_m = 0$ *J*). Above 10 K, Q(1,1) and R(1,1) are the first lines which can be detected with substantial line strengths. Over 25 K several transitions such as Q(3,3), R(2,0) and so on have greater line strengths and should be detectable at such temperatures.

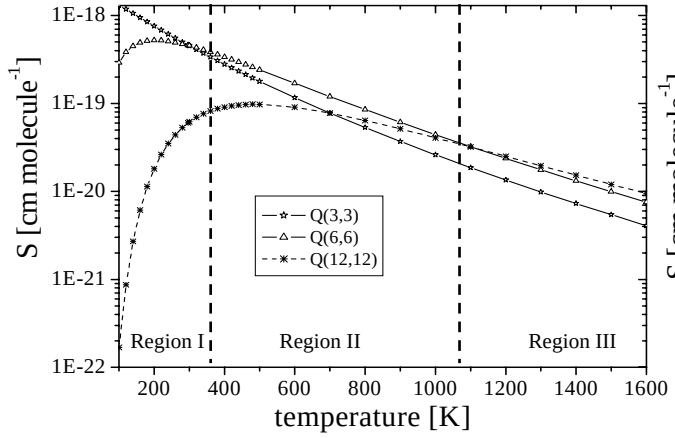

Figure 3. Temperature dependencies of the line strength of the transitions Q(3,3), Q(6,6) and Q(12,12).

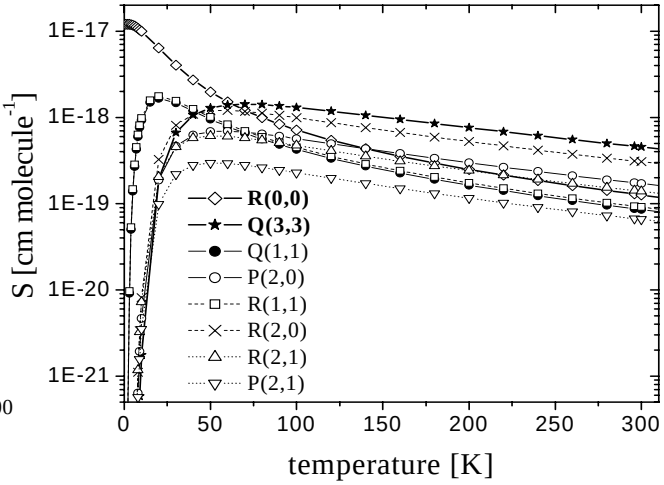

Figure 4. Q(3,3) has the highest line strength over 50 K R(0,0) is the strongest transition below 50 K

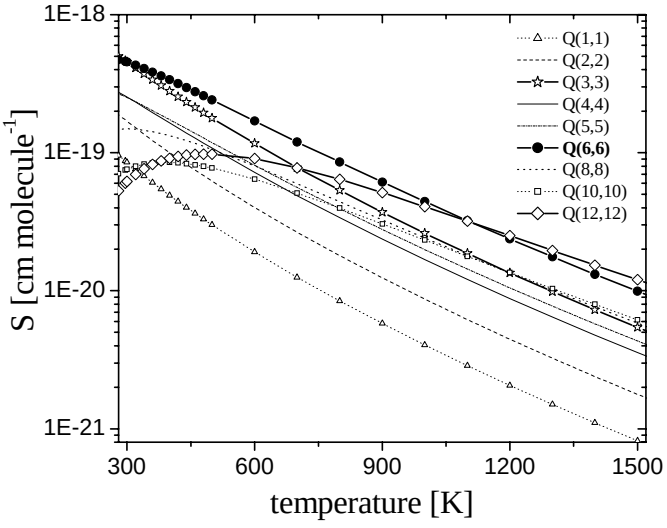

Figure 5. Temperature dependencies of line strengths in the range 300 – 1500 K. Q(6,6) is the most sensitive transition for this temperatures range.

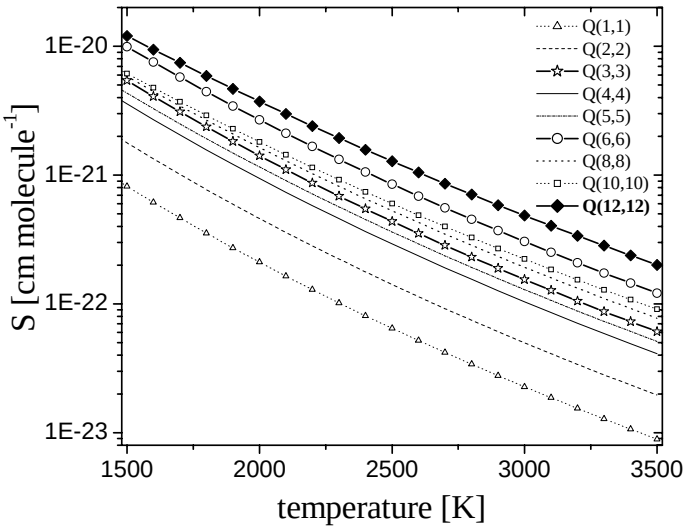

Figure 6. Temperature dependencies of line strengths in the range of 1500 – 3500 K. $Q_{(12,12)}$ (largest S) is recommended for this temperatures range.

The line strength dependence can be used to determine concentrations as well as the gas temperature if at least two absorption coefficients are measured. Based on formula (1), measuring the ratio of two absorption coefficients is the same as the ratio of their line strengths. Taking a measured absorption coefficients ratio, the temperature for which their line strength ratio is the same will determine the rotational temperature. In recent measurements which were done in a hot filament diamond deposition reactor [7] the gas temperature was determined from the ratio of Q(6,6) to Q(12,12). The gas temperature was found to be about 800 K near the deposition substrate, which is essentially the same as the temperature measured by a thermocouple probe. Figures 5 and 6 contain line strength temperature dependencies for some of the most intense transitions of the CH_3 ν_2 fundamental band, for laboratory plasma applications.

References

[1] G. Lombardi, G.D. Stancu, F. Hempel, A. Gicquel, J. Röpcke, Plasma Sources Sci. Technol. **13**, 27 (2004).

[2] B. Bezard, P.N. Romani, H. Feuchtgruber, T. Encrenaz, Astrophysical Journal, **515**, 868 (1999).

[3] G.D. Stancu, J. Röpcke, P.B. Davies, J.Chem. Phys. **122**, 014306 (2005).

[4] G. Herzberg, Molecular Spectra and Molecular Structure Vol. II-Infrared and Raman Spectra of Polyatomic Molecules, Van Nostrand, New York (1945) Reprint ed. Krieger Publishing Company, Malabar, Florida, (1989).

[5] C. Yamada, E. Hirota, K. Kawaguchi, J. Chem. Phys. **75,** (11) 5256 (1981).

[6] H. Feuchtgruber, F.P. Helmich, E.F. van Dishoeck, C.M. Wright, The Astrophysical Journal, **535** L111-L114 (2000).

[7] J. Hirmke, F. Hempel, G.D. Stancu, J. Röpcke, S.M. Rosiwal, R.F. Singer, (to be published) Diamond and related Materials 11

Surface characterization of plasma oxidized tin films

Z. Stryhal[1], J. Pavlik[1], T. Vagner[1] and P. Hedbavny[2]

[1] *Department of Physics, Institute of Science, J. E. Purkyne University, Usti nad Labem, Czech Republic*
[2] *Vakuum Praha, Prague, Czech Republic*

Abstract
In this paper, we have studied surface properties of SnO_2 thin films produced by thermal evaporation of Sn films followed by in situ plasma oxidation with additional substrate heating. The oxide layer properties were studied by Atomic Force Microscopy (AFM) and Secondary Ion Mass Spectrometry (SIMS). The plasma oxidation with additional substrate heating is a possible alternative method for preparing stochiometric SnO_2 layers.
Keywords: plasma oxidation, SnO_2 thin films, AFM, SIMS.

1. Introduction

The phenomenon that the adsorption of some gases on the surface of oxide semiconductors can results in a significant change in the electrical resistance of the material was discovered several decades ago [1]. The SnO_2 thin films are widely used for gas sensor application. The gas sensing properties of the films are strongly dependent on the morphological properties, like as surface roughness, grain size, grain geometry, and chemical composition. The material properties depend on the preparation procedure [2], [3], [4] and [5]. In this work we have studied the properties of tin oxide films prepared by plasma oxidation of thin tin films [6].

2. Experimental conditions

The experiments were carried out in the system for plasma-chemical surface modification of thin films, see Fig. 1.

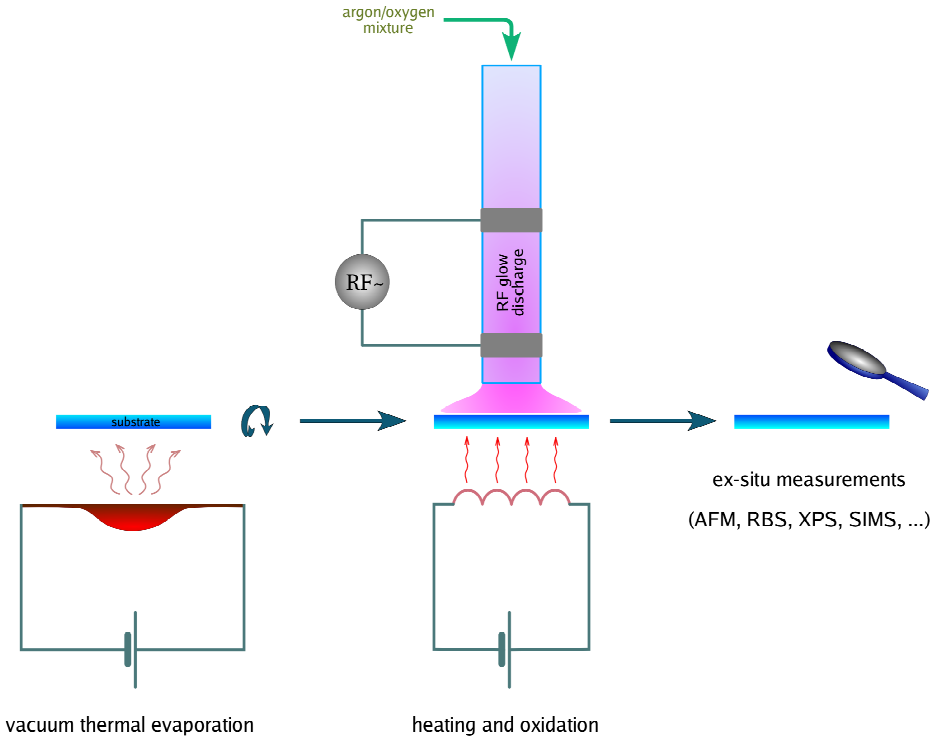

Fig. 1: . The schematic view of the experimental set-up for plasma oxidation of thin metal films

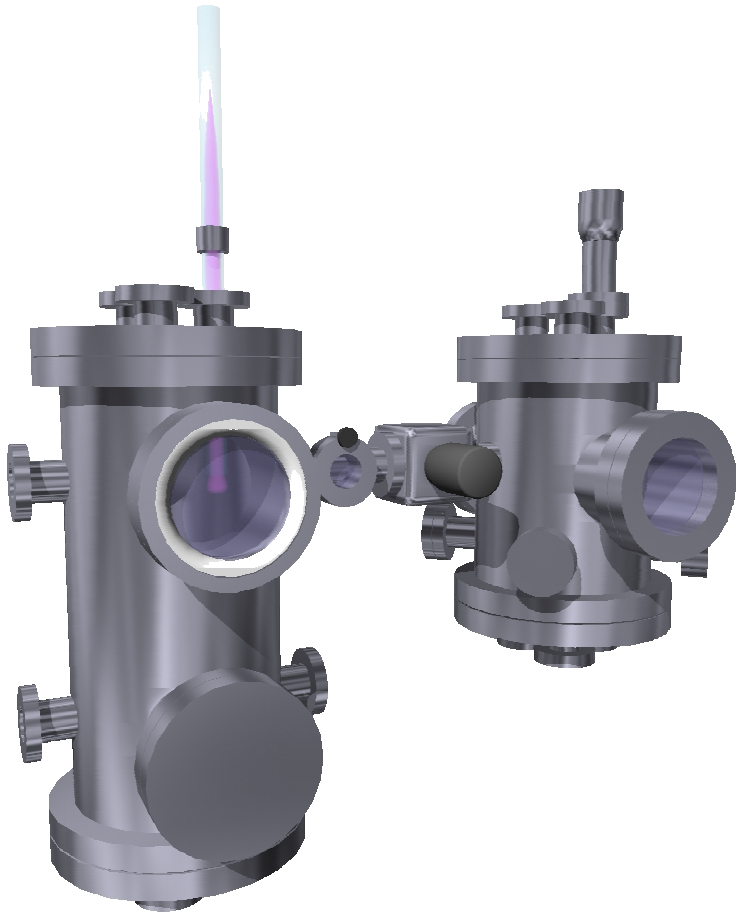

Fig. 2: Experimental system for plasma oxidation with RF discharge

Tin metal films were evaporated in an UHV chamber from Mo boat. The SiO_2 substrates were used. The tin oxide films were then obtained by in situ plasma oxidation in the flowing post-discharge. The RF discharge (13.56 MHz) was applied in oxygen or oxygen/argon mixture (purity: argon 99.9999 %, oxygen 99:995 %). Flow rates were adjusted in order to obtain a total mixture pressure of 50 – 100 Pa which was found to be the optimum pressure for the plasma ignition (RF power 35 W). The substrate was held on the plasma floating potential during plasma oxidation (oxidation time 30 – 120 min). The experimental system has an incorporated heater (the quartz lamp 20 W mounted in a polished stainless steel reflector) which allows an indirect heating of the substrate holder by radiation to temperatures within the range of 100 - 250 °C. The substrate holder temperature was determined directly by an attached resistance temperature detector Pt 100.

3. Characterization techniques

The surface topography and roughness were measured by the Atomic Force Microscopy (AFM - Metris – 2001A – NC, Burleigh Instruments Inc.). A commercially available pyramidal probe of silicon nitride (Si_3N_4) was used. All AFM measurements were carried out in the contact mode at the ambient atmosphere and at room temperature. The scan area varied from 1.2 μm x 1.2 μm to 25 μm x 25 μm.

The depth profiles were measured by the Secondary Ion Mass Spectrometry (ATOMIKA 3000 SIMS system). The SIMS analysis was made using a Cs^+ ion gun, 3.3 keV. The primary beam current was 80 nA and the scan area was 0.5 mm x 0.5 mm.

4. Experimental results

The morphology of the tin films prepared by thermal evaporation on SiO_2 substrates, is a near flat-grain structure (roughness R_q ~ 12 nm). The typical grain size of the film deposited by thermal evaporation was about 0.5 μm. The thickness of Sn films was derived from the AFM images of surfaces with a mechanical scratch and was changed from 10 nm to 80 nm.

The morphology of the tin oxide surface after plasma oxidation is characterized by a sharper grain structure with a higher roughness [6].

Our previous measurements [7] indicate that the ratio of oxygen concentration to the tin concentration varies from 1.5 to 1.8, thus the thin oxide films (thicker than 20 nm) prepared by plasma oxidation contain a mixture of SnO, and SnO_2 oxides. Therefore we prepared a set of samples oxidized at different substrate temperatures (100 °C, 150 °C, 200 °C and 250 °C). The AFM measurements indicate that the increase of the substrate temperature during plasma oxidation causes a higher surface roughness (R_q ~ 25 nm), see Fig. 3. The electrical properties of SnO_2 thin films depend on the distribution and nature of the grain boundaries. The grain dimension does not change appreciably with recpect to substrate temperature.

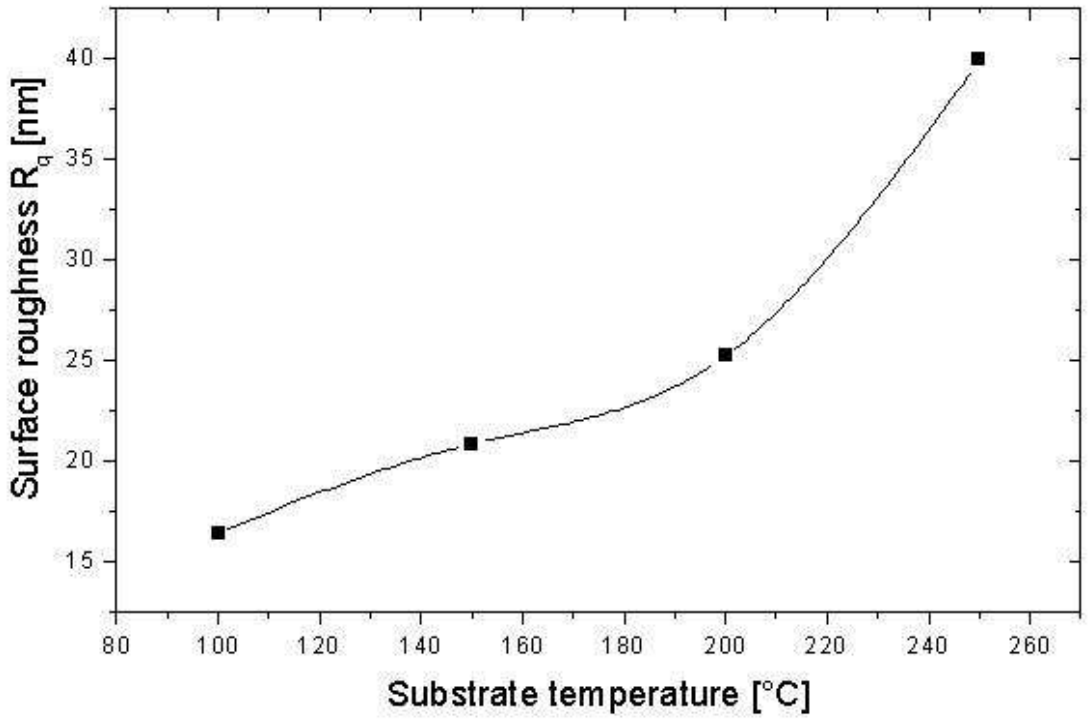

Fig. 3: The dependence of root mean square roughness R_q on substrate temperature

The SIMS measurements indicate that the stoichiometry is better at higher substrate temperatures. The oxide stoichiometry seems not to be influenced by film thickness up to 180 nm at higher substrate temperature (about 250°C), see Fig. 6.

The plasma oxidation without an additional substrate heating produces only thin oxide layers, no matter how long the oxidation time is.

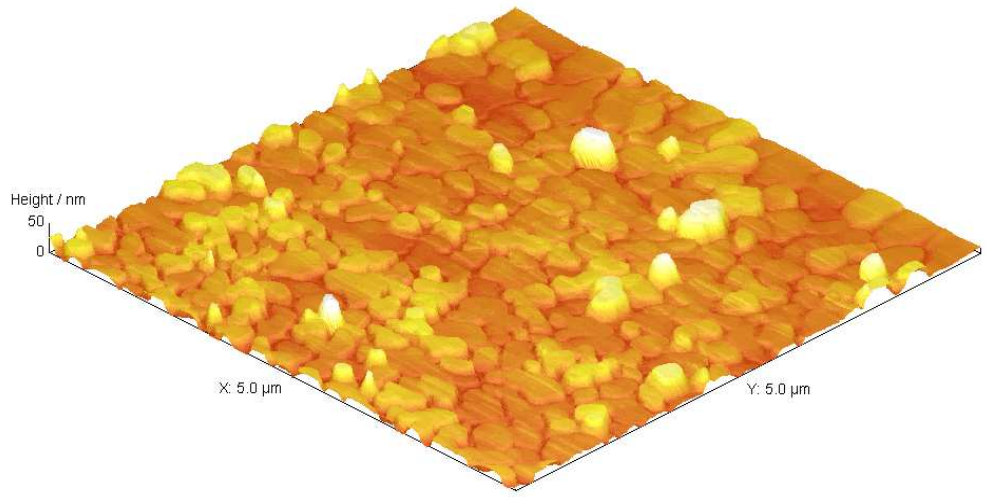

Fig. 4. AFM 3D image of oxidized tin layer prepared without additional substrate heating - mixture of SnO_2, SnO and Sn when thicker than approx. 20nm.

.

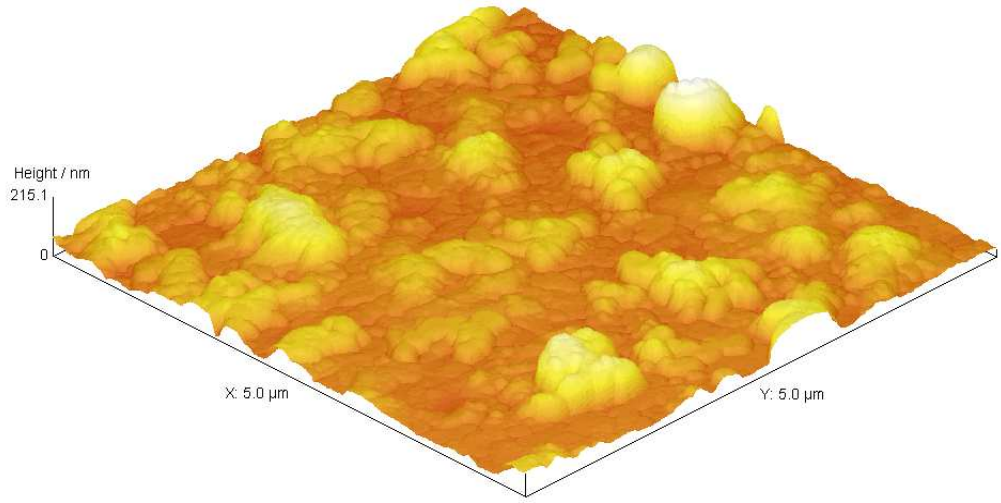

Fig. 5: AFM 3D image of oxidized tin layer prepared with additional substrate heating (~250 ^{o}C) – better stoichiometry in case of thick layers, higher surface roughness.

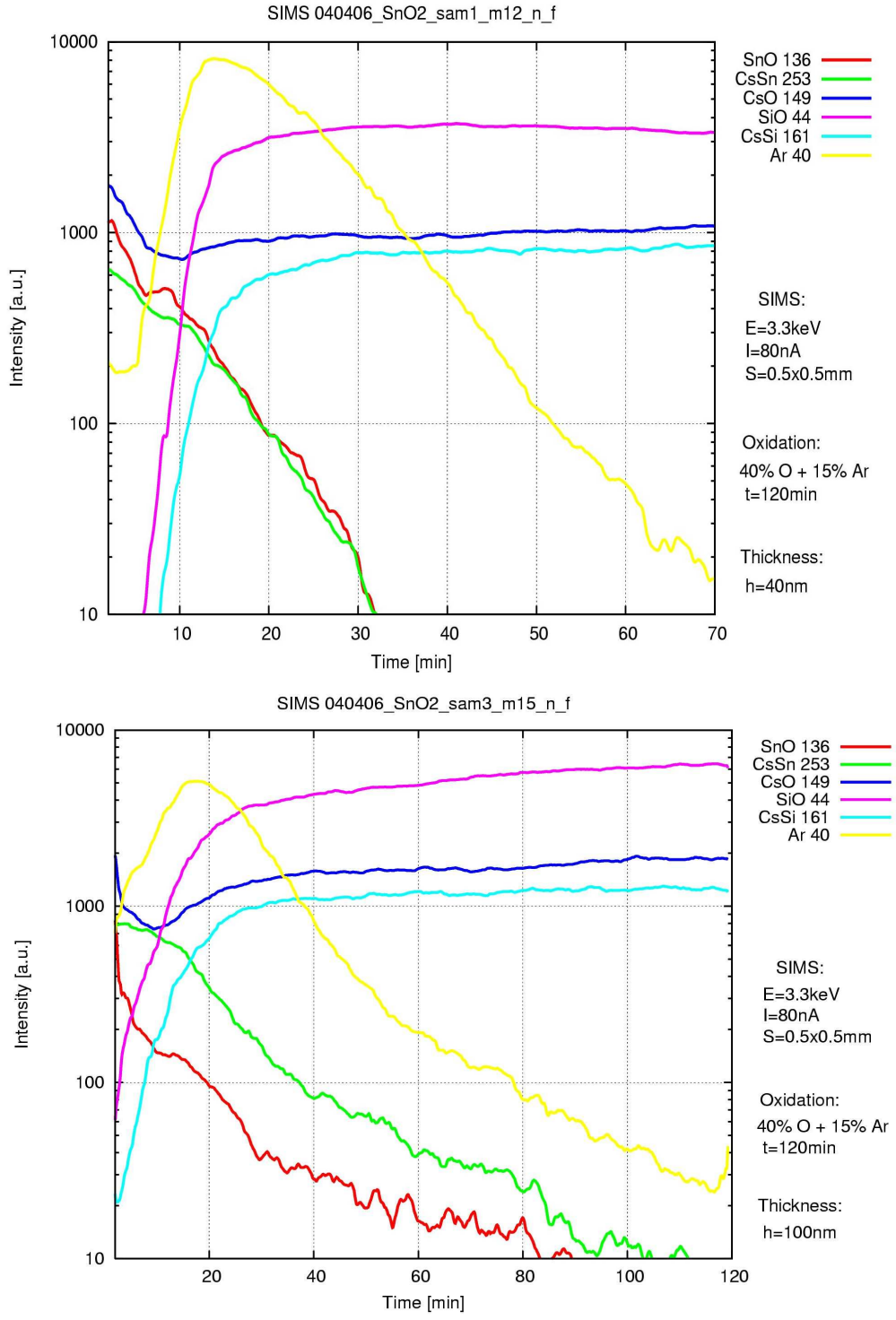

Fig. 6: The depth profiles obtained from SIMS measurements of two samples prepared by plasma oxidation of thin tin films (thickness 40 nm and 100 nm) at higher substrate temperature during oxidation (about 250°C). The cesium ion source has been used.

5. Conclusion

It has been proven that the method of plasma oxidation is a applicable alternative method for preparing thin SnO_2 films. We can prepare pure samples with surface topography different from samples prepared by other techniques. Our experimental results indicate dependence of SnO_2 surface morphology on substrate properties, evaporation conditions and parameters of plasma oxidation. Plasma oxidation without additional substrate heating produce only thin stochiometric oxide layers. On the other hand the plasma oxidation with additional substrate heating seems to be able to produce oxide layers whose stoichiometry seems not to be influenced by film thickness up to 180 nm at higher substrate temperature.

6. Acknowledgements

This work was supported by The Ministry of Education of Czech Republic (Projects COST OC 527.50, OC 527.30 and 1P05OC013, 1P05OC019). The autor T. Vagner acknowledges the support of the grant VAKUUM PRAHA.

References

[1] N. Barsan, M. Schweitzer-Berberich, W, Göpel – Fressenius J. Anal. Chem. p. 287, **365**, (1999).
[2] B. Correa-Lozano, C. C. Comminellis, A. Battisti – J. Electrochem. Soc. 143, 203 (1996)
[3] P. Serini, V. Briois, M. C. Horrillo, A. Traverse, L. Manes – Thin Solid Films. 304, 113 (1997)
[4] Y. S. He, J. C. Campbell, R. C. Murphy, M. F. Arrendt, J. S. Swinnea – J. Mater. Res. 31, 131 (1993)
[5] J. Lancok, M. Jelinek, F. Vyslouzil, M. Vrnata, V. Myslik, A. Santoni – Fine Mech. Opt. 45, 336 (2000)
[6] Z. Stryhal, J. Pavlik, S. Novak, A. Mackova, V. Perina, K. Veltruska – Vacuum 67, 665 (2002)
[7] Z. Stryhal, J. Pavlik, A. Mackova, V. Perina – Proceedings of the 14th Symposium on Application of Plasma Processes, SAPP XIV, Liptovsky Mikulas, Slovak Republic. 144 (2003)

Induction Coil-Plasma Coupling and Power Flow Measurement in RF Induction Thermal Plasmas

Y. Uesugi[1], H. Yamada[1], E. Hanaoka[1], Y. Tanaka[1], H. Ukai[2], M. A. Razzak[2] and S. Takamura[2]

[1]*Department of Electrical and Electronic Engineering, Kanazawa University, Kakuma-cho, Kanazawa, Japan*
[2]*Department of Energy Science and Engineering, Nagoya University, Furo-cho, Chikusa-ku, Nagoya, Japan*

Abstract
Transient response of the induction coil loading impedance and the RF inverter power supply in the initial startup of RF induction thermal plasmas and the power flow in the steady state condition were studied experimentally. This dynamic transition of the discharge can be seen both from the fast camera observation and the RF coupling between induction coil and generated plasma. The plasma coupling characteristics of the induction coil was analyzed using a simple equivalent circuit model.

1. Introduction

Radio frequency induction thermal plasmas(RF ITPs) around atmospheric pressure range have been widely used for plasma metallugy, material processing, hazardous waste treatment and so on[1, 2]. In these engineering applications efficient generation and controllability of functional thermal plasmas are very important engineering issues. So far, studies on fundamental properties of RF ITPs have not been done deeply in contrast to intensive studies on their engineering applications. Efficient production of atmospheric RF ITPs has already done by using semiconductor inverter for RF generator[3, 4]. RF inverters using MOSFETs and static induction transistors(SIT) have a very high DC-RF power conversion efficiency of about 0.9 at several hundreds kHz and 0.8~0.9 below 2 MHz, respectively. An easy power control of RF inverters has been also demonstrated in pulse amplitude modulation experiments[4]

In the present study the electrostatic and electromagnetic coupling between induction coil and generated plasma is analyzed by simple equivalent electric circuits of the induction coil-plasma system. A dynamic mode change from electrostatic discharges to electromagnetic discharges can be seen clearly in the coil loading impedance. In addition to the circuit analysis calorimetric measurements of the RF ITP system are carried out to study the power flow from the RF generator to the plasma, and the heat and particle loss mechanisms of generated plasmas.

2. Experimental Setup

The SIT RF circuit which comprises of an RF inverter, an impedance matching transformer, a tuning capacitor bank and an induction coil is shown in Figs. 1(a) and (b). The loading impedance of the induction coil including the impedance transformer and tuning capacitors is calculated from the inverter output voltage v_1 and current i_1 shown in Fig. 1(b). The DC-RF conversion efficiency η is calculated by

$$\eta = \frac{1}{T}\int_0^T v_1(t) i_1(t) dt \,/\, P_{DC}, \qquad (1)$$

The power losses from the plasma are measured by calorimetry in the plasma torch and the reaction chamber. Heat loads to the plasma torch and the reaction chamber are separately measured by temperature and flow meters in each water cooling section.

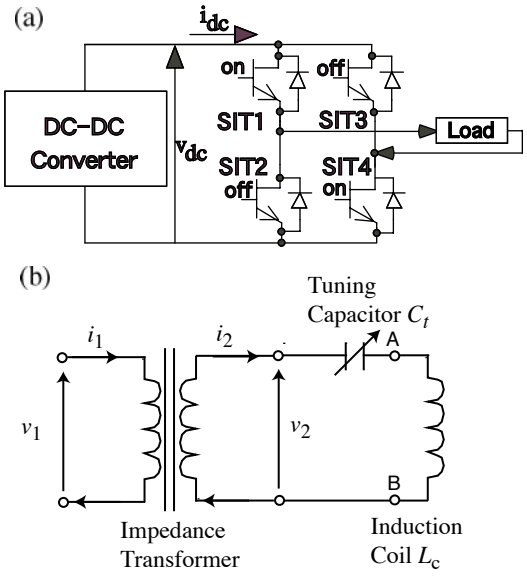

Fig. 1 SIT inverter(a) and induction coil circuit(b)

3. Initial Breakdown and Growth of Argon ITP

3.1 Discharge Mode and Coil Loading

Fast camera pictures of the initial startup of ITP discharges are shown in Fig. 2, where streamer-like electrostatic discharges are generated near the coil conductor inside a quartz glass tube and a ring-shape electromagnetic discharges start to grow at the inner surface of the glass tube. This mode transition from the electrostatic to electromagnetic discharges can be seen clearly in the coil loading impedance shown in Fig. 3. For a few milliseconds after breakdown the discharge is capacitive and the resultant LCR series impedance becomes slightly inductive, which is shown in Fig. 3(d). The discharge current is limited by the dielectric quartz tube, which leads a weak power coupling between the induction coil and the generated plasma. After enough growth of the streamer-like electrostatic discharges the discharge mode transition occurs and the loading resistance rises abruptly, which means the plasma absorbed power increases. The growth of the inductive discharge also changes the LCR series impedance capacitive. The positive feedback mechanism of the induction coil-plasma coupling brings these dynamic plasma response. In the present experiments the inverter output voltage is saturated just after the mode transition since the DC voltage fed to the inverter is limited to 400 V in the present SIT inverter system , and the inverter output power is strongly reduced after voltage saturation. This power reduction comes from the large detuning of the LCR series circuit and the increase of the inverter loss by capacitive inverter load. Preliminary frequency tracking experiments have shown to improve the power coupling efficiency successfully.

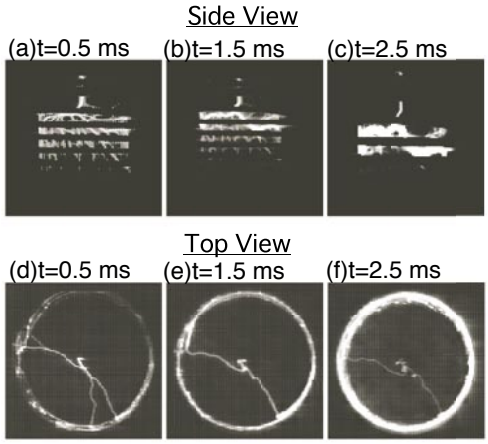

Fig. 2 Fast camera picture of the initial startup of argon ITP. Discharge tube diameter is 70 mm and argon gas pressure is 30 kPa.

3.2 Equivalent Circuit Analysis of Induction Coil Loading Impedance

The dynamic behavior of the induction coil loading impedance is analyzed using simple equivalent circuits of the induction coil both in the electrostatic and electromagnetic discharges discussed previously. Equivalent circuits of the induction coil are shown in Fig. 4. In the electrostatic discharge phase the discharge current is driven by the electrostatic field between coil conductor through the dielectric glass discharge tube. This barrier type electrostatic discharge gives a parallel capacitance in the coil equivalent circuit shown in Fig. 4(a). In the electrostatic discharge phase the primary coil impedance given by $Z_1=V_1/I_1$ in Fig. 1(b) becomes slightly inductive between the ignition and E-H discharge transition as shown in Fig. 3. The coil reactance in Fig. 4(a) is given by

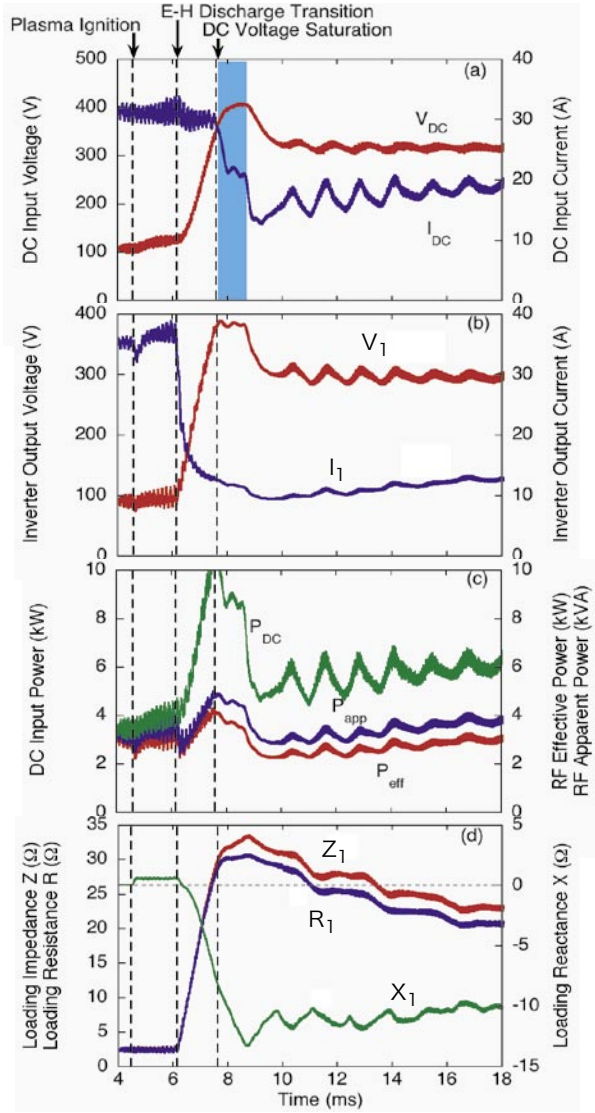

Fig. 3 Inverter response and coil loading impedance in the initial startup phase of argon ITP. (a)Inverter DC voltage and current, (b)Inverter RF voltage and current, (c)Inverter DC input power, apparent RF power and effective RF power and (d)coil loading impedance. The discharge is different from that of Fig. 2.

$$\mathrm{Im}[Z_L] = \frac{1-\omega^2 L_c C_p^{es} + (\omega C_p^{es} R_p^{es})^2}{(1-\omega^2 L_c C_p^{es})^2 + (\omega C_p^{es} R_p^{es})^2}\omega L_c \ , \qquad (2)$$

When $\omega^2 L_c C_p^{es} < 1$, the coil reactance becomes more inductive than the vacuum reactance ωL_c. Rough estimation gives R_p^{es}=3~8 kΩ and C_p^{es}=20~40 pF in the typical argon discharge shown in Fig. 3.

In the electromagnetic discharge a ring shape discharge plasma works as a ring conductor, which has a mutual inductance M. Then the coil impedance is given by

$$Z_L = (R_C + \frac{\omega^2 M^2 R_p^{em}}{(R_p^{em})^2 + \omega^2 (L_p^{em})^2}) + j\omega(L_C - \frac{\omega^2 M^2 L_p^{em}}{(R_p^{em})^2 + \omega^2 (L_p^{em})^2}) \ . \qquad (3)$$

The effective coil inductance decreases and the primary coil impedance Z_1 becomes capacitive as shown in Fig. 3. The effective coil inductance decreases by

$$\frac{\omega^2 M^2 L_p^{em}}{(R_p^{em})^2 + \omega^2 (L_p^{em})^2}, \qquad (4)$$

and the Z_1 becomes more capacitive as shown in Fig. 4.

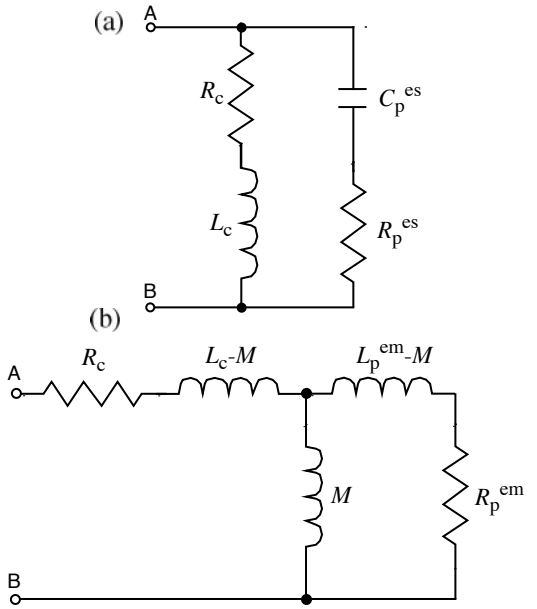

Fig. 4 Equivalent circuits of the induction coil in the electrostatic (a) and electromagnetic discharges(b).

4. Heat Load Measurement and Power Flow Analysis

Heat load to various components of the RF plasma torch is measured by calorimetric method in 450 kHz ITP powered by MOSFET inverter[5]. Preliminary heat load measurements are summarized in Table 1. The inverter output power P_1 and the effective power fed to the induction coil were calculated from measured RF voltage and current. Heat Loads to the torch separately measured are also summarized in Table 2. The coil loading resistance is an effective resistance which indicates the electromagnetic coupling between the induction coil and the generated thermal plasma. In the present experiments shown in Table 1 ~85 % of the fed power to the induction coil is effectively coupled to

Table 1 RF power, induction coil impedance and measured total heat load in 450 kHz RF torch.

Argon Pressure (Torr) Flow Rate (slpm)	Inverter Output (kW)	Induction Coil EffectivePower (kW)	Induction Coil Resistance (Ω)	Induction Coil Reactance (Ω)	Measured Total Heat Load (kW)
230 100	14.4	10.5	0.71	11.7	9.3
230 40	13.7	10.9	0.76	11.1	9.2
25 20	13.5	11.1	1.05	10.9	9.4

Table 2 Measured heat loads and heat flux in various part of the RF torch.

Argon Pressure (Torr) Flow Rate (slpm)	Fed RF Power (kW)	Quartz Tube (kW) and (kW/m^2)	Metal Chamber (kW) and (kW/m^2)	Probe (kW) and (kW/m^2)	Torch Head (kW) and (kW/m^2)
230 100	10.5	2.4 34.4	4.6 14.2	0.75 44.2	0.16 8
230 40	10.9	2.4 34.4	4.6 13.9	0.77 45.4	0.15 7.5
25 20	11.1	2.5 35.4	4.7 14.5	0.77 45.4	0.15 7.5

generate the thermal plasmas. The total power coupling efficiency of the present MOSFET ITP system, which is shown in Fig. 5 is about 60 %. Conversion loss in Fig. 5 means RF conversion efficiency of the MOSFET inverter. The total RF circuit loss is about 30~35 % in the present system. The coil loading resistance is very sensitive to the gas pressure. In the pressure range where the argon thermal plasmas are generated, the coil loading resistance decreases significantly with increasing the gas pressure as shown in Fig. 6.

The preliminary calorimetric measurements shown in Table 2 give that roughly 50 % of the absorbed RF power is carried to the downstream reaction chamber through the convective flow of the argon gas and 25 % of the absorbed power goes to the quartz tube through the convective, conductive and radiative heat flow in the pure argon ITP. When the gas flow rate is increases to improve the heat transfer between hot thermal plasma and cold gas, however, the fraction of the power flow from the hot thermal plasma does not change significantly. Further experimental studies are necessary to clarify the power flow mechanism in the RF ITPs.

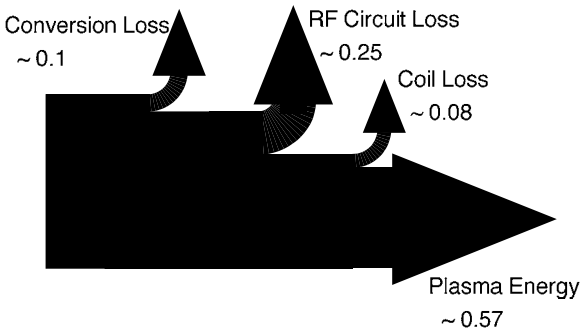

Fig. 5 RF power flow of the 450 kHz MOSFET ITP system. AC input power is about 15 kW. Argon plasma, P=20 ~ 230 Torr.

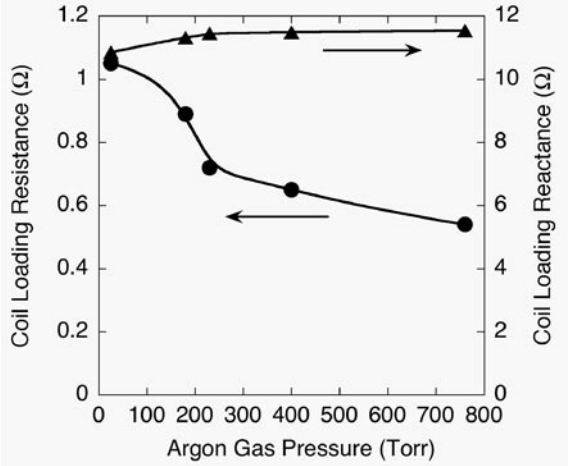

Fig. 6 Induction coil loading resistance and reactance as a function of the gas pressure. AC input power is about 15 kW.

5. Summary

Dynamic startup characteristics of RF ITP were studied by fast camera observations and the equivalent circuit analysis of the induction coil. The initial mode transition from the electrostatic to electromagnetic discharges can be clearly seen both in the visible light observation and the coil loading impedance. The equivalent circuit analysis of the induction coil can clearly explain the transient impedance change of the induction coil during electrostatic to electromagnetic discharge mode change. Initial results of calorimetric measurements of the heat load to the torch and reaction chamber show that the coupling efficiency of the MOSFET ITP system calculated by the electric measurements of the RF voltage and current agrees well with that estimated by plasma heat load measurements.

Calorimetric measurements is done to study the thermal plasma energy transfer to the torch wall through the conductive, convective and radiative heat transfer. About 25~30 % of the thermal energy is delivered to the quartz tube near the plasma production area and about 55~60 % is carried to the down stream reaction chamber mainly through the convective heat transfer. The experimental result that the portion of the delivered heat load of the argon RF ITP does not depend strongly on the gas flow rate is still an open question. Further experiments will be done in near future to study the heat transfer mechanism of the RF thermal plasmas and to improve their performance.

References

[1] M. I. Boulos, P. Fauchais and E. Pfender, *Thermal Plasmas*, Vol. 1, Chap. 1, Plenum Press, New York(1994).

[2] *Thermal Plasmas for Hazardous Waste Treatment* edited by R. Benocci, G. Bonizzoni and E. Sindoni, World Scientific Publishing, Singapore(1996).

[3] Y. Uesugi, T. Adachi, K. Kondo and S. Takamura, Trans. IEE Japan, 461, **122-A**(2002)(in Japanese).

[4] T. Ishigaki, X. Fan, T. Sakuta, T. banjo and Y. Shibuya, Appl. Phys. Letters, 3787, **71**(1997).

[5]T. Sakuta, K.C. Paul, M. Katsuki and T. Ishigaki, J. Appl. Phys., 1372, **85**(1999).

PREPARATION OF CARBON NANOTUBES ON CATALYSIS ORGAN-METAL SOLUTION BY USING PLA/CVD HYBRID SYSTEM

S. Aoqui[1], T. Ohshima[2], H. Kawasaki[2], Y. Suda[2], A. Tanaka[3], Y. Suda[3], T. Ikegami[4], K, Ebihara[4], T. Sakai[5]and T. Uematsu[6]

1 Department of Electrical System & Computer Eng., Sojo University, Kumamoto, Japan
2 Department of Electrical Eng., Sasebo National College of Tech., Sasebo, Nagasaki, Japan
3 Graduate School of Information Science and Technology, Hokkaido University Sapporo, Japan
4 Department of Electrical & Computer Eng., Kumamoto University, Kumamoto, Japan
5 Kumamoto Technology and Industry Foundation, Kumamoto, Japan
6 ELIONIX INC,Tokyo, Japan

Abstract

Thin films preparation which an organ-metal solution was used for has very long history, but there is a little use to that new device materials. We used the solution for the catalyst, and carried out the preparation of carbon nano-tubes or (CNTs). In this paper, we investigated intensively about PLA/CVD hybrid system for CNTs growth. Those were deposited in the temperature range from R.T. to 1100 °C. The deposited CNTs were characterized by a 3D-FE-SEM and a Raman spectrophotometer.

Keywords

carbon nanotubes, pulsed laser ablation, organ-metal solution

1. Introduction

Ever since the discovery of carbon nanotubes (CNTs), a lot of efforts have been given to utilizing their unique electric and structural properties [1]. That is to say, CNTs have been focus of considerable attention because of many possible applications in nanostructure, super strong materials, semiconductor, electron emitting device and hydrogen storage [2]. Several process methods such as arc discharge, chemical vapor deposition (CVD) and pulsed laser ablation (PLA) have been used to produce CNTs. However, as for which methods as well, it isn't easy to apply it the catalyst metal which is necessary for the CNTs growth. In this study, the way that we applied a catalysis organ-metal solution to a substrate and then it was burned out was used [3]. This method is very unique, especially it has almost never used as the catalyst for the nanotubes. Nano size dots of catalytic metal such as platinum (Pt), Nickel (Ni), mixture of Pt/Gold (Au) and mixture of Ni/Au, on Silicon or quartz glass substrate preparation technique by burning of catalysis organ-metal solution had already been developed. Also two apparatus were used for the growth of CNT by this study. One was a traditional thermal CVD system, the other hand was a PLA and CVD hybrid system. When a catalysis organ-metal solution was used, the thermal CVD could obtain the CNTs very easily but high process temperature (less than 1000 °C.) was necessary. On the other hand, when the PLA/CVD hybrid system was used, we obtained CNTs in low temperature relatively.

In this paper, we investigated intensively about PLA/CVD hybrid system for CNTs growth; those were the wavelength of laser (Nd-YAG: λ = 1064nm and 532 nm, pulse duration of 3.5 ns and ArF

excimer laser: λ = 193 nm, pulse duration of 20 ns), the influence of laser fluence and substrate temperature on crystallization and characteristics of the CNTs. The CNTs were deposited in the temperature range from room temperature (R.T.) to 1100 ℃ and laser fluences ranging from 2 to 30 J/cm^2. The deposited CNTs were characterized by an electron probe surface roughness analyzer (3D-SEM: Elionix model ERA 8900FE and ERA 8800) and a field-emission scanning secondary electron microscope (FE-SEM: JEOL model JSM-6301F) and a Raman spectrophotometer (JASCO model NRS-3300).

2. Experiments

Fig. 1 shows a schematic diagram of the PLA/CVD hybrid system used in this study. After the chamber (ϕ = 300 mm) was exhausted by a turbo-molecular pump to a base pressure of 1.3x10^{-4} Pa. In the chamber a sintered pure graphite target (purity 99.99%) of 30 mm in diameter and 5 mm thickness was mounted on the rocking holder. Three kinds of pulsed laser beam was introduced into the chamber through lenses and a quartz window. The laser beam impinges on the target at an incident angle of 0° or 45°. In order to prepare CNTs, n-type Si(100) wafers or quartz glass substrates, which an organ-metal solution was spread, were positioned 30 mm apart from the graphite target. The substrates were heated with a block heater or an electric furnace or an IR lamp, which was mounted on the exterior of the vacuum chamber, from room temperature to 1100 °C. Substrate temperature (Ts) was measured by using a thermocouple. The gas pressure was varied from the base pressure to 1 Torr with 100sccm flow rate by feeding pure methane (CH_4) gas (in case of Nd-YAG laser use) or 500 Torr with 750 sccm flow rate by feeding pure Ar gas (in case of ArF Excimer laser use) into the reaction chamber.

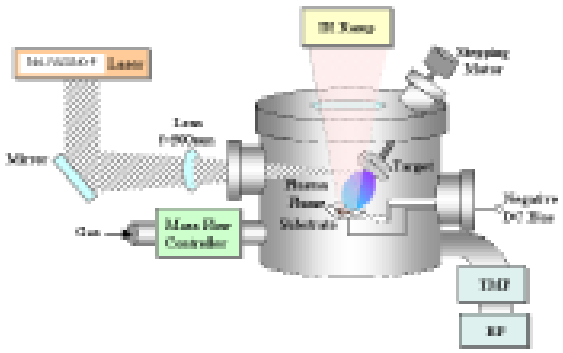

Fig. 1 Schematic diagram of experimental apparatus.

3. Results and discussions

The surface morphology of Pt catalytic metal dots on the Si substrate which should be used for the CNTs growth was examined by 3D-SEM, as shown in Fig. 2(a) and (b). When the burning temperature was 300 °C, it was a very smooth morphology with a silver mirror condition. When temperature rises up to 900 °C, Pt makes an dot type island-shape structure. Moreover dot can be classified in three kinds of diameter, such as about 30 nm, 100nm and 200 nm. Now we consider that these dots have a different

surface direction from the observation of XRD measurement (it is not listed), such as (220), (200) and (111) respectively.

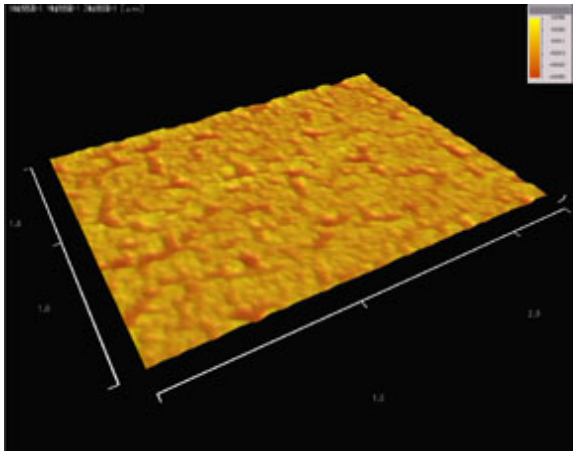

Fig.2 (a)

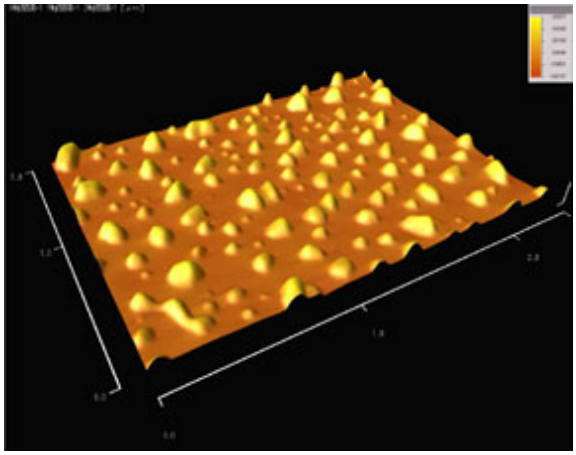

Fig.2 (b)

Fig2(a) burning temperature 300°C at atmospheric ambient condition. Roughness: 0.5 nm.
Fig2(b) burning temperature 900°C at atmospheric ambient condition. height of dots: about 30nm.
Fig.2 3D-SEM images of Surface morphology of Pt nano dot on Si substrate (2.2 μm*1.8μm)

Fig. 3(a) and (b) show FE-SEM images of the CNTs prepared by simple CVD using Pt and Ni catalyst, substrate at 1000 °C, CH_4 ambient gas condition. CNTs growth can be confirmed both catalyst. Tube diameters were 60 nm and 80 nm respectively. Although CNTs grows very long and flexibly with a Ni catalyst, it seems to be hard to grow with a Pt catalyst. This is based on the difference in effect on the catalyst, but in case of Pt, improvement of flexible growth should be possible for that by control of reaction temperature and ambient gas kinds and flow rates.

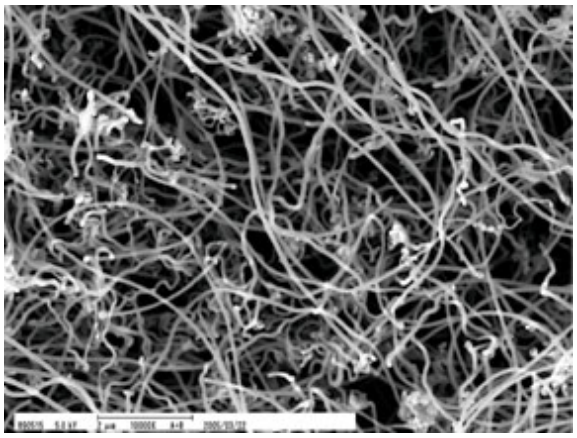

Fig. 3 (a) CNTs on Ni catalyst

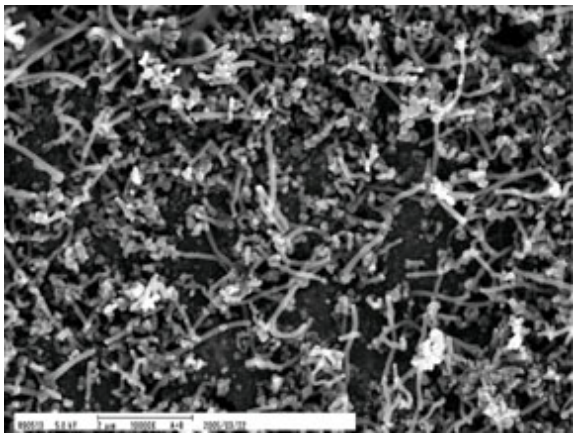

Fig. 3(b) CNTs on Pt catalyst

Fig.3 FE-SEM images of CNTs
(CH_4 ambient gas condition with Ts = 1000 °C)

Fig. 4 shows FE-SEM image of the CNTs prepared at laser fluence of 5 J/cm^2 (λ = 1064 nm), Ts = 650 °C, and 1 Torr CH_4 ambient condition by PLA/CVD hybrid system using Ni catalyst substrate. Though very few CNTs were confirmed, an aspect ratio of tube is large and doesn't curve. Tube

diameter was about 120 nm. However the growth of the CNTs could not be confirmed with this PLA/PLD hybrid system with Pt catalyst.

Accordingly we carried out completely another condition of PLA/CVD hybrid system. Extremely high Ar gas pressure of 500 Torr was given on PLA target ablation. The condition that CNTs were composed of the gaseous phase was considered. Because Ar pressure is very high, plasma plume hardly to spread out. On this condition, ejected carbon atoms and particles were slowed down suddenly. Fig.5 shows EF-SEM images of CNTs on Pt catalyst (pre-burning substrate temperature of 900 °C). (a) and (b) are same images but resolution is different. Average tube diameter was 80 nm.

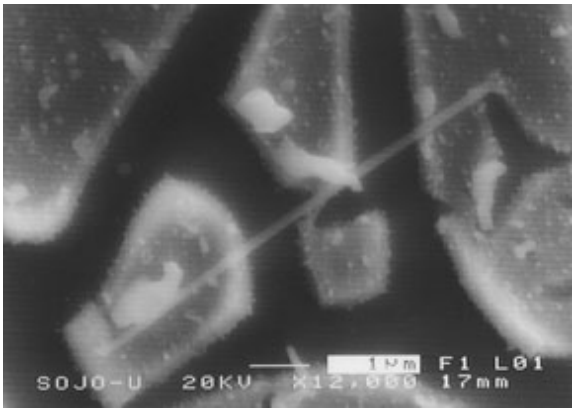

Fig. 4 FE-SEM image of CNTs by PLA/CVD hybrid system
CNTs prepared by PLA/CVD with Nd-YAG laser (λ = 1064 nm) on organ-metal-Ni solution.

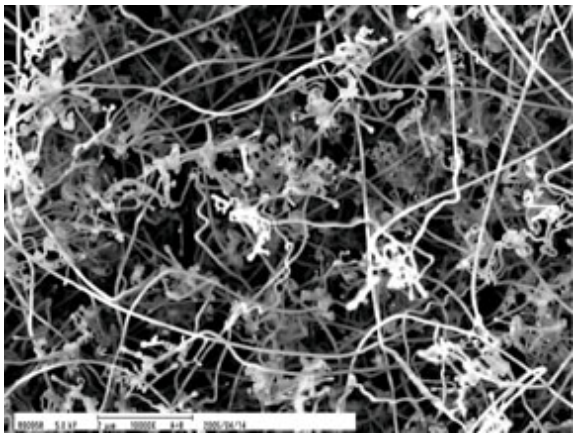

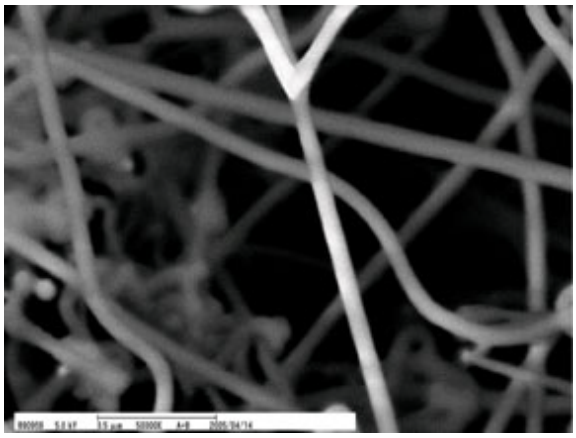

Fig. 5 (a) CNTs on Pt catalyst Fig. 5(b) CNTs on Pt catalyst
Fig. 5 FE-SEM image of CNTs by high Ar pressure PLA/CVD hybrid system
CNTs prepared by PLA/CVD with ArF excimer laser (λ = 193 nm)

Also we carried out the experiment of the selective growth of the CNTs. Because it doesn't have a effect of catalyst with Au, the substrate that the solution on which mixed a little (about 2 weight %) Ni or Pt to Au organ-metal solution was used for was burned out at 900 °C on 100 Torr Ar ambient condition.

Fig.6 shows selective growth of the CNTs by using high Ar pressure PLA/CVD hybrid system on Ni/Au and Pt/Au substrate. CNTs grows around the Ni and Pi island-shape particles. Therefore selective CNTs growth was confirmed in both Ni/Au and Pt/Au substrate. In case of high pressure PLA/CVD Hybrid system, there is no difference

with the appearance of the CNTs between Ni and Pt catalyst. Both average tube diameter was 60 nm.

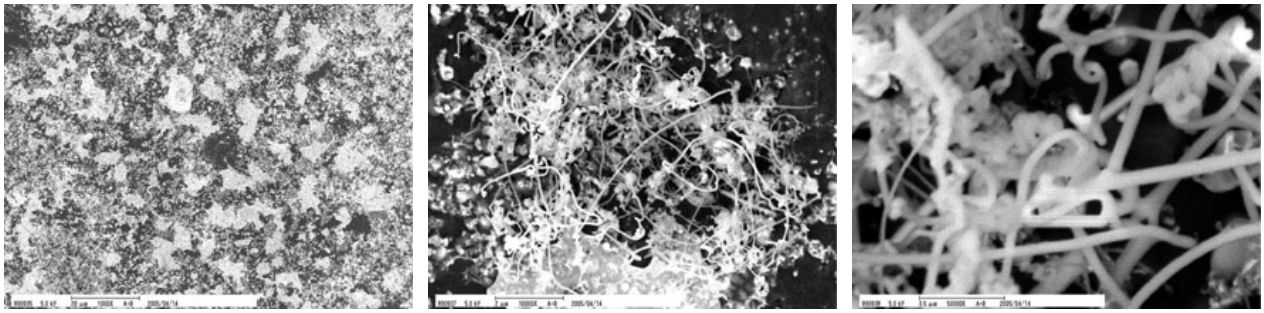

Fig.6(a)CNTs on Ni/Au catalyst

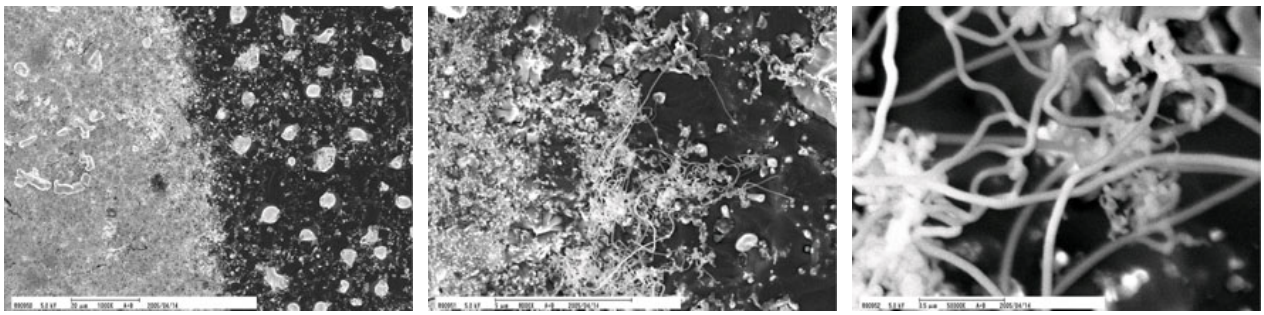

Fig.6(b)CNTs on Pt/Au catalyst

Fig. 6 FE-SEM image of CNTs by high Ar pressure PLA/CVD hybrid system
CNTs prepared by PLA/CVD with ArF excimer laser (λ = 193 nm)

We also measured G band and D band peak ratio of all CNTs by using Raman spectrophotometer. A G/D ratio was almost close to 1, it confirmed that the element which was close to DLC existed in the substrate surface. Therefore it has a possibility to be the mixture of the CNTs and carbon nano fiber.

4. Conclusions

In this study, CNTs were prepared using very new technique which makes an organ-metal solution departure catalytic material. This technique is very simple therefore, it has a possibility of large-scale composition with lower cost. Also it has the possibility to have process temperature reduced by using PLA/CVD hybrid system. Moreover we carried out high pressure PLA/CVD hybrid system. This system had high yield rate of CNTs growth. Also we confirmed selective growth of CNTs.

Acknowledgment

This research was supported in part by RSP program of Kumamoto Technology and Industry Foundation.

References

[1]S. Iijima, Nature 354 (1991) 56-59.
[2]P.M. Ajayan, O. Stephan, Ph. Redlich, C. Coltrex, Nature 375181 (1995) 564.
[3]Naval avionics center, USA, Metallo-organic materials for impredection film reliability. (1980)

REMOVAL OF NO_X AND DUST PARTICLES FROM EXHAUST OF DIESEL ENGINE POWER GENERATOR BY PLASMA-CATALYST SYSTEM

D. Brocilo[1], S. Iwasaki[1,2], K. Yamada[1,3], M. Ara[1], K. Urashima[1],
D. Ewing[1], J. Hoard[4], H. Ehara[2], S. Ono[2], T. Ito[2], M. Itoh[3] and J.S. Chang[1]

[1]*Department of Engineering Physic,, McMaster University, Canada*
[2]*Department of Electrical , Musashi Inst. Tech., Japan*
[3]*Dept. Chem. Eng. And Material Sci, Doshisha University, Japan*
[4]*Ford Motors Company, USA*

Abstract
Experimental investigations have been conducted to study the simultaneous removal of NO_x and diesel soot particulate matter (DSPM) from the exhaust of a diesel engine power generator using a electrostatic precipitator (ESP) and magneto-trench barrier discharge reactor (MT-BDR) placed upstream of Na-Y catalyst. The ESP prevented fouling of MTBDR by removing over 99.9% of DSPM. However, results showed that presence of DSPM in MTBD reactor may assist in NO_2 and NO_x removals which were 35-70% and 6-45%, respectively.
Keywords Plasma Catalyst, NO_x Removal, Diesel Exhaust, Power Generator, Particulate Removal

1. Introduction

Increased use of diesel engines (diesel cars, diesel generators, tracks, and marine ships) motivated the development of various technologies for lowering gaseous pollutant emissions especially for NO_x emissions [1]. The major pollutants in diesel exhaust emissions are a direct result of the diesel combustion process itself. The most toxic gases present in diesel exhaust include carbon monoxide (CO), sulfur dioxide (SO_2) and nitrogen oxides (NO_X). The CO concentration is a function of the air excess ratio, combustion temperature and air/fuel mixture while SO_2 is a function of fuel oil sulphur content. Hydrocarbons (HC) are very engine dependant but a function of the amount of fuel and lubrication oil left unburned during combustion due to insufficient temperature or air supply. Diesel soot particulate matter (DSPM) originates from unburned fuel, ash content in fuel and lub-oil. While the type of fuel used and combustion strategy play a major part in determining the composition of the emissions, other important factor that determines the amount of NO_x is engine speed and load.

There are a number of methods for reducing the NO_x concentrations in exhaust gases that can be divided into three basic categories namely: pre-treatment, internal measures, and after-treatment. Pre-treatment methods are focusing on lowering the combustion temperature by denitration of fuel, use of alternative fuels or adding water to the fuel. Internal measures include changes to the combustion process, such as modification of combustion, the scavenge/charging air or water injection or exhaust gas recirculation. After-treatment methods are applied directly to the combustion gases and can be categorized as re-burning, selective catalytic reductions and plasma assisted reduction methods. In the later case, of interest here, oxidation reaction dominate during the plasma discharges so that the plasma alone is ineffective in reducing NO_x. A combined strategy with a plasma and a catalysis system can enhance the catalyst NO_x removal efficiency by oxidizing NO to NO_2 that are more easily reduced by downstream catalyst. Recently, Szanyi et al [2] have showed that Na- and Ba-Y based catalyst in conjunction with a non-thermal plasma results in a high level of NO_x reduction at relatively low temperatures (~200°C). In this work, NO_x and dust particle removals by combined electrostatic precipitator and trench type barrier dischartge-Na-Y catalyst system were investigated for real diesel engine power generator exhaust gases.

2. Experimental set-up

The experimental test facility, as shown in Fig. 1, consists of diesel engine, electrostatic precipitator (ESP) for DSPM treatment, plasma-catalyst reactor system for gas treatment, flow control devices, and gas sampling system. The diesel exhaust, generated by a 5W single-cylinder diesel generator, was carried to the hybrid

reactors, consisting of magneto-trench barrier discharge [3], schematically shown in Fig. 2, and Na-Y catalyst, approx. 1m downstream of the generator via Ø35 mm tube. The discharge characteristics of MT-BDR and ESP shown in Figs.3 and 4 were conducted for the engine load from 0 to 2.4kW, exhaust gas flow rates from 2 to 5kg/h and applied voltages from 0 to 22kV at fixed magnetic field of 0.5kG. Removal performance of pollutant gases and DSPM by ESP-plasma-catalyst reactors has been evaluated for ESP dc applied voltage of -20kV, reactors flow rate of 2kg/h and trench reactor ac operating voltages with peak to peak values from 5 to 15 kV.

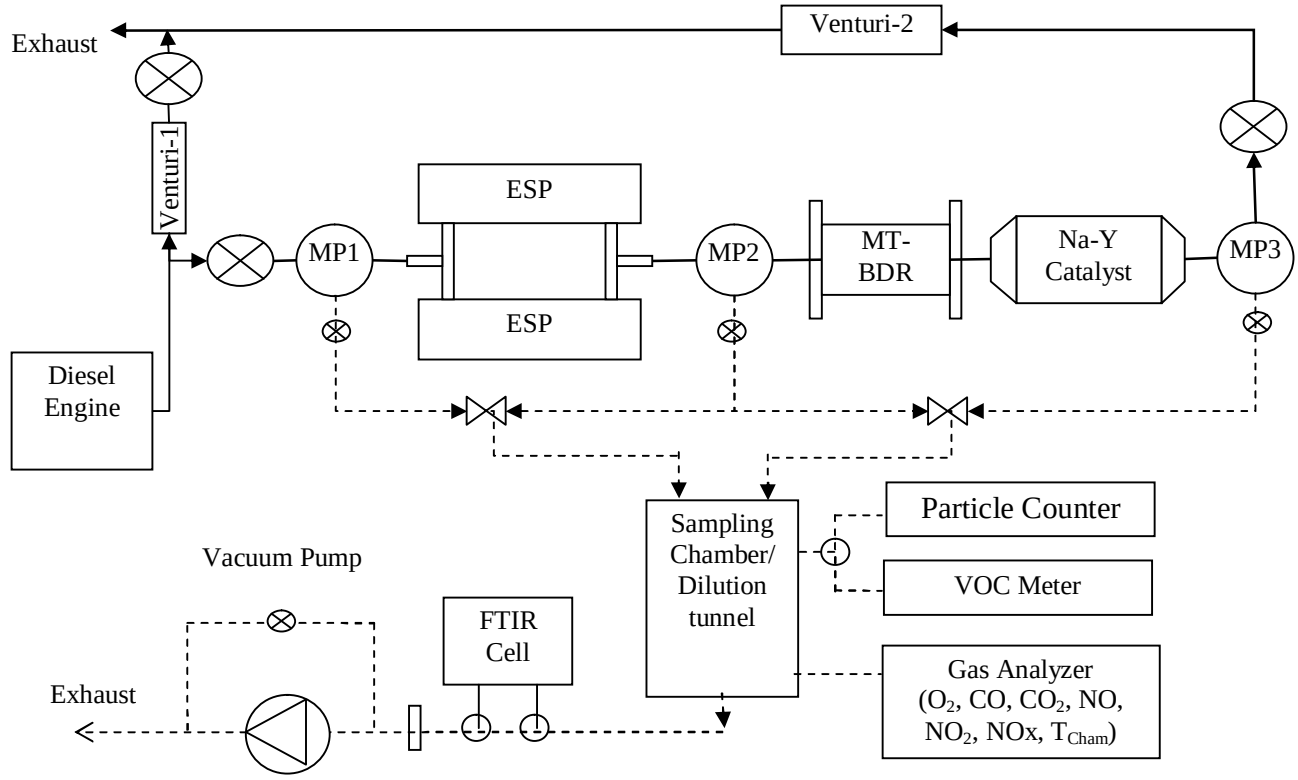

Figure 1. Schematics of experimental test facility.

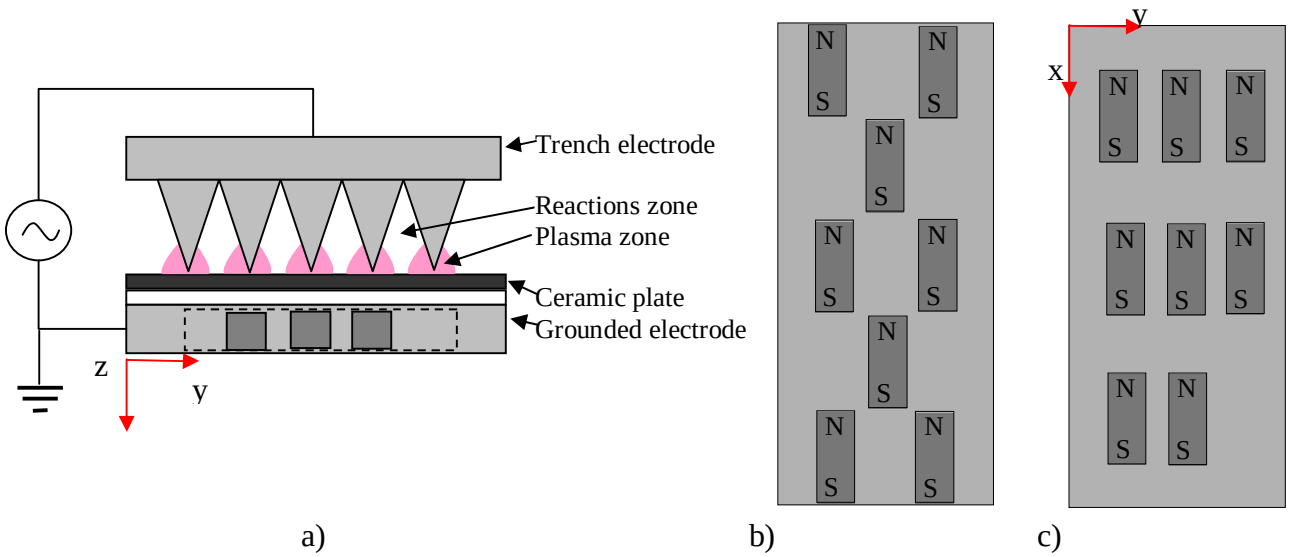

a) b) c)

Figure 2. (a) Cross-section of trench-type-barrier reactor, and (b) staggered and (c) parallel arrangements of permanent magnets.

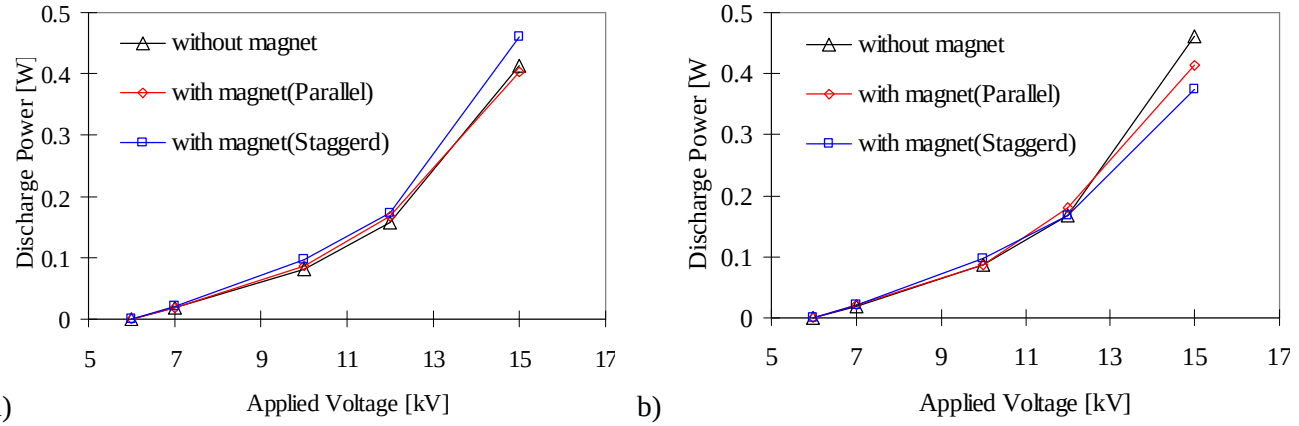

Figure 3. MT-BDR Discharge power versus peak to peak applied voltage with and without permanent magnets for the air flow rates of : (a) 28 l/min, and (b) 56 l/min.

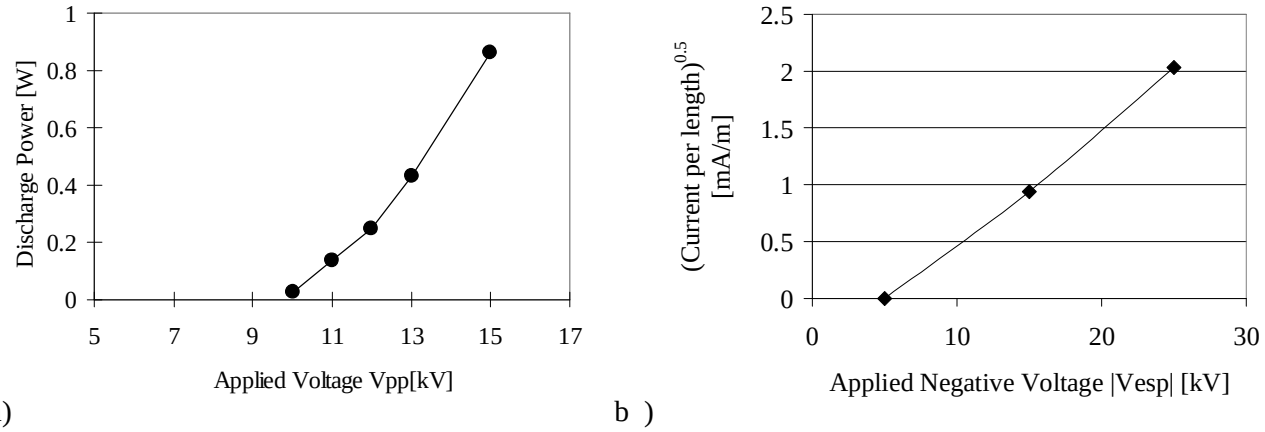

Figure 4. a) MT-BDR discharge power versus peak to peak applied voltage (Vpp), and (b) current-voltage characteristic of ESP for the exhaust flow rate of 2kg/h and engine load of 1.5kW.

3. Results

Figure 5 shows the removal efficiency of DSPM by ESP that was operated at voltage magnitudes lower than 20kV in order to avoid spark discharge. For ESP operating voltage of -15kV more than 99.99% of DSPM was removed. Figure 6 shows the removal of pollutant gases by MT-BDR for cases of : (a) clean and (b) soot-deposited trench reactor. The results show that the NO_x, (NO and NO_2) decreases immediately after non-thermal plasma treatment. However, by increasing the discharge power of trench reactor, the removal rate of NO_x and NO_2 were slightly decreasing.

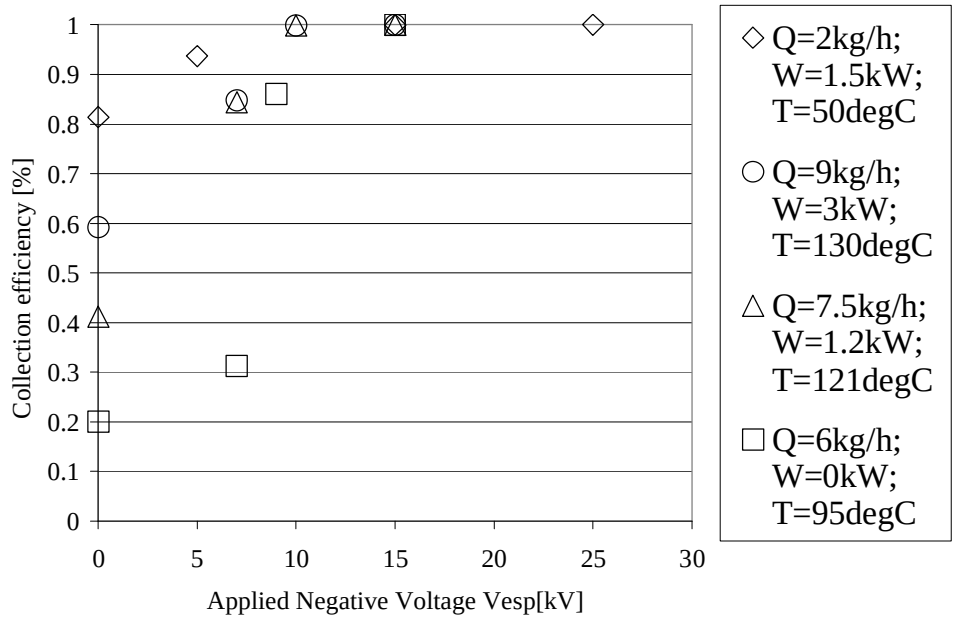

Figure 5. DSPM collection efficiency by ESP for exhaust flow rates (Q) from 2 to 9kg/h and the engine loads (W) from 0 to 3kW (T…average ESP temperature).

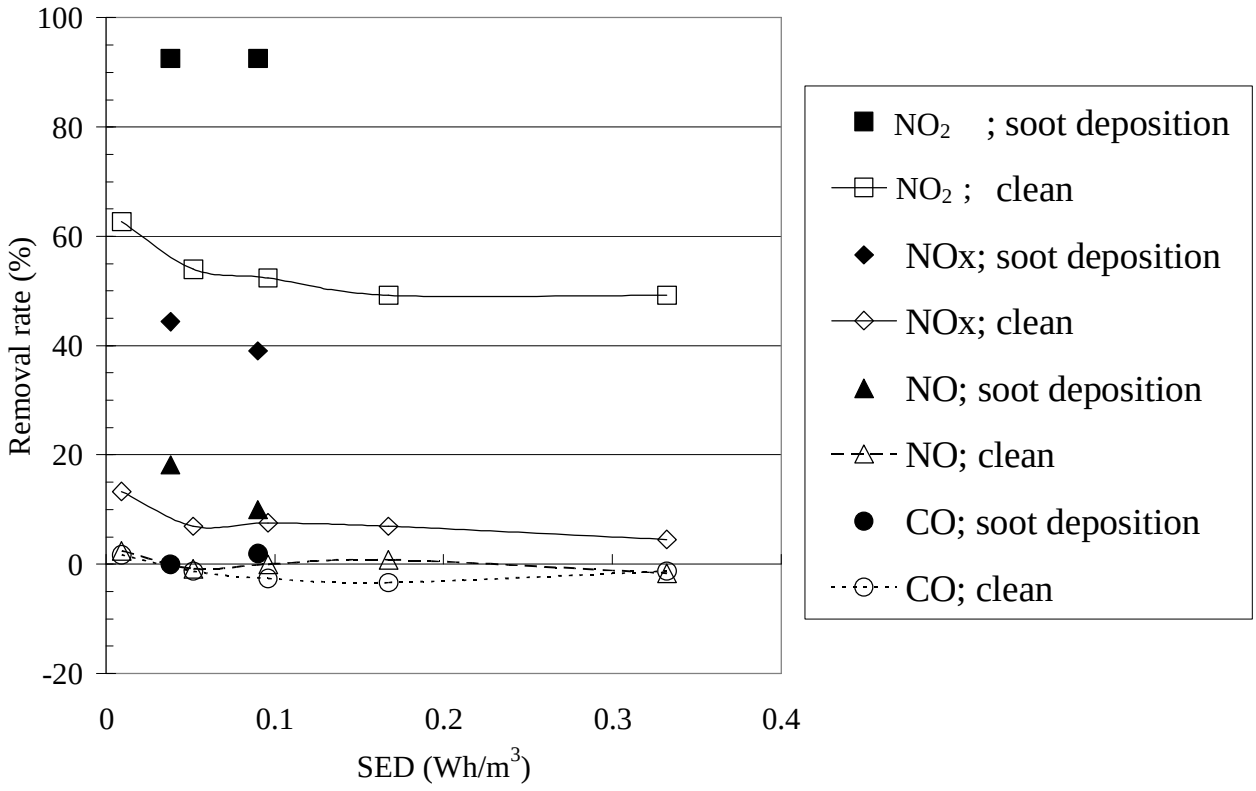

Figure 6. Pollutant gas removal efficiencies as a function of specific energy density for clean and soot deposited trench reactor.

4. Conclusions

Experimental investigations have been conducted to study the simultaneous removal of NO_x and diesel soot particulate matter and the results show that: a) Staggered magnet arrangements can increase the discharge power from 10 to 17% and the improvement is highest at the lowest applied discharge voltage; b) The power improvement decreases with increasing flow rate; c) The NO_2 and NO_x removal rates were 35-70% and 6-45%, respectively. It seems that soot deposition in plasma-catalyst reactors assist in NO_x removals; d) The ESP successfully removed over 99.9% of DSPM from exhaust.

Acknowledgment

Authors thank S. Teii, F. Charles, N. Debacher, M. Uckai, C.Y. Ching, G.D. Harvel, L. Guan for valuable discussion and comments. This work was supported partially by NSERC Strategic Grant and Ford Motors Company.

References

[1] J. Hoard and R.G. Tonkyn., "Two stage plasma–Catalysts for Diesel NOx Emission Control," J. Adv. Oxid. Tech., Vol.6, No.2, 2003, pp. 158-165

[2] Szanyi J, J Kwak, and CH Peden. 2004. "The Effect of Water on the Adsorption of NO2 in Na- and Ba-Y,FAU Zeolites: A Combined FTIR and TPD Investigation." Journal of Physical Chemistry B, Vol. 108, No.12, pp.3746-3753.

[3] Y. Uchida, K. Urashima, J.W. Hoard and J.S. Chang, "Characteristics of Magnetized Trench Type Dielectric Barrier Discharges,", J. Inst. Electrostat. Japan, 2002,Vol. 26, No.6, pp.281-282.

[4] J.S. Chang, Simultaneous removal of NOx, SOx and VOCs from engine combustion generated waste gas streams by non-thermal plasma technologies; International Symposium Plasma -2001 on "research Applications of Plasma"; Warsaw, Poland, September 19-21, 2001

[5] K. Urashima, J.S. Chang, J. Y. Park, D.C Lee, A. Chakrabarti, and T. Ito, "Reduction of NOx from natural gas combustion flue gases by corona radical injection techniques," IEEE Industry Applications, September/October 1998, Vol. 34, No, pp. 934-939.

[6] T. Kuroki , M. Tasayoshi, M. Okubo, and T. Yamamoto, "Single stage plasma –chemical process for particulates, NOx, and SOx simultaneous removal," IEEE Industry Applications, September/October 2002, Vol. 38, No. 5:pp 1204-1209.

[7] A. Mizuno, K.Shimizu, A Chakrabarti, L. Dascalescu, and S. Furuta, "NO_x removal process using pulsed discharge plasma", IEEE Industry Applications, September/October 1995, Vol. 31, No. 5:pp 947-963

[8] R. Ono and T. Oda, " OH radical measurement in a pulse arc discharge plasma observed by LIF method," IEEE Industry Applications, May/June 2001, Vol. 37, No. 3, pp 709-714.

[9] B.R. Locke, A. Ichihashi, H.H Kim, and A. Mizuno, " Diesel engine exhaust treatment with a pulsed streamer corona reactor equipped with reticulated carbon electrodes," IEEE Industry Applications, May/June 2001, Vol. 37, No. 3, pp 715-723

[10] H. Burtscher, S. Kunzel and C. Huglin, "Characterization of particles in combustion engine exhaust, "Journal of Aerosol Science, . April 1998, Vol. 29, No. 4, pp 389-396.

[11] Szanyi J, J Kwak, and CH Peden. 2004. "The Effect of Water on the Adsorption of NO2 in Na- and Ba-Y,FAU Zeolites: A Combined FTIR and TPD Investigation." Journal of Physical Chemistry B, Vol. 108, No.12, pp.3746-3753.

[12] Y. Uchida, K. Urashima, J.W. Hoard and J.S. Chang, "Characteristics of Magnetized Trench Type Dielectric Barrier Discharges,", J. Inst. Electrostat. Japan, 2002,Vol. 26, No.6, pp.281-282.

ELECTRON-BEAM PLASMA IN THE PRODUCTION OF BIOACTIVE AGENTS AND DRUGS

M. Vasiliev[1], T. Vasilieva[2]

1 Moscow Institute of Physics and Technology, Moscow region, Russia
2 Hematological Scientific Center, Moscow, Russia

Abstract
The modification of some biopolymers and amino-acids by the Electron-Beam Plasma was studied experimentally. The plasma was generated by injecting the continuous electron beam in gaseous or vapor media. Due to the treatment the powders of the substances under consideration were found to change their physical-chemical and biological properties. In particular, the modified synthetic derivative of 2-aminopropanoic acid was proved to acquire the anti-aggregation activity for platelets of human blood.
Keywords. Electron-beam plasma. Plasma treatment. Plasma modification of biomaterials.

1. Introduction

The Electron-Beam Plasma (EBP) is generated by injecting an electron beam (EB) into a gaseous medium. Under typical conditions of the EBP generation (the medium pressure $0{,}1 < P_m < 10$ kPa and moderate EB power $N_b < 1$ kW) the plasma is strongly non-equilibrium and cold. Being injected into the gas the EB ionizes the gas, excites the gas molecules and is able to cause the molecule dissociation. As a result, the EBP composition is complicated and there are a lot of chemically active particles that don't exist under equilibrium conditions. With respect to non-equilibrium plasmas generated in conventional ways (for instance, the plasma of gas discharges) the EBP has the following advantages:

- the EB can be injected into any gases, vapors and gas-vapor mixtures; the EBP bulk doesn't contract even at very high gas pressures ($P_m \sim 10$ kPa and higher).
- the solid powders and liquid droplets injected into the gas don't prevent the EBP generation; large-size bodies can be inserted into the plasma bulk.

The EBP was proved to effectively modify properties of materials thanks to the plasma chemical activity, complicated organic and polymer molecules being the most modifiable even at low temperature.

2. The Electron-Beam Plasmachemical reactor and the treatment procedure

Fig. 1 illustrates a typical way of the EBP generation. The focused EB 3 generated by the electron-beam gun 1 located in the high vacuum chamber 2 is injected into the working chamber 6 filled with the molecular gas through the injection window (IW) 4. In passing through the gas the EB is scattered in elastic collisions and the energy of fast electrons gradually diminishes during various inelastic interactions with the medium (ionization, excitation, dissociation). Eventually the EB power transforms into the heat increasing the temperature of the medium and heating the unit elements. It may also cause the phase transformations or is radiated. As a result the plasma cloud 5 is generated, all plasma parameters being functions of *z*- and *r*-coordinates.

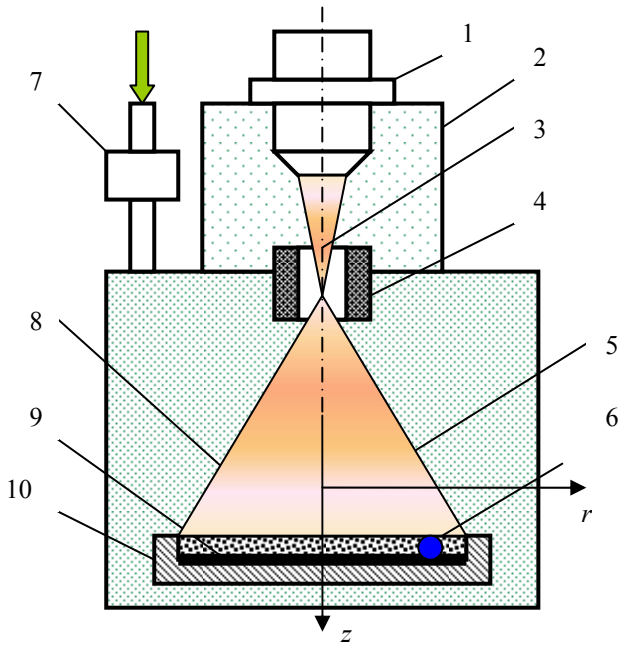

Fig.1.

The working chamber is preliminary evacuated to pressure $\sim 10^{-3}$ kPa and then filled with the plasma generating gas through the feeder 7. The pressure P_m varied within the range 1-10 kPa depending on the gas composition and treatment conditions required. The following gases were used to

generate the EBP: air, nitrogen, oxygen, noble gases (He and Ar), gaseous hydrocarbons, CO_2, water vapor and vapors of some organic liquids. Gaseous and vapor-gas mixtures were used as well.
A specially designed double-stage gas-dynamic window is used to transport the EB of energy E_b = 20-40 keV from high vacuum ~1 Pa (that is a typical pressure required for the operation of electron guns with thermionic cathodes) into the working chamber filled with the gas.

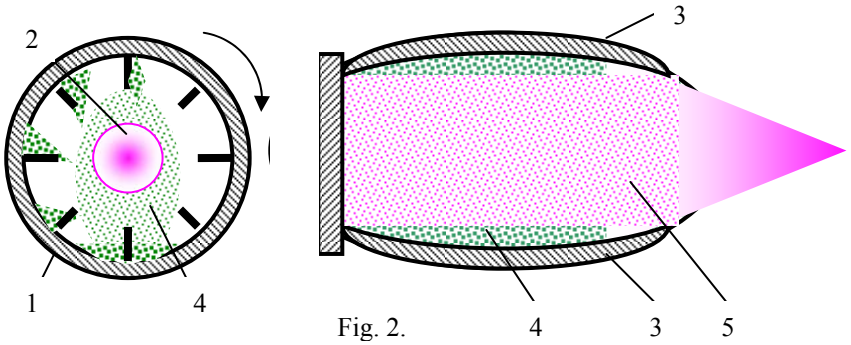

Fig. 2.

The powder of the substance to be treated is filled in the glass container 10. Thin plate 9 made of piezoelectric ceramics is placed on the container bottom. Being fed with AC voltage the plate vibrates, throws up the powder particles and forms the mixing layer 8 of the treated material. The miniature thermo-sensor 9 is inserted into the container to monitor the material temperature T_s during the treatment. Adjusting the EB power the temperature T_s could be varied within the range 300-450 K, no additional heaters or coolers being used to maintain the constant T_s-value. Note that the power is heated by the EB more effectively than the gas and usually $T_s > T_m$, where T_m is the plasma generating medium temperature.
Another version of the reactor developed to treat larger amounts of the biomaterials is illustrated by in fig. 2. The general axis of this reactor (and the axis of the EB injection) is horizontal, the reaction chamber being a cylindrical or barrel-shape vessel 1 equipped with internal ribs 3. The EBP cloud is formed in the vessel hollow by the EB 2 injected throught the open end of the chamber. The powder 4 of material to be treated is mixed by means of the vessel rotation; as a result the aerosol reaction zone 5 is formed inside the chamber. Note, the reaction chamber 1 is placed inside the working chamber (that isn't shown in fig. 2) filled with the plasma generating gas at required pressure P_m.

3. The biopolymers treatment in the Electron-Beam Plasma

The plasmachemical modifications of cellulose materials (pure cellulose, wooden sawdust and crushed paper), peat and chitosan in EBP of O_2, He, H_2O, NH_3, CO_2, SF_6 are studied in detail. The yield (S, %) and the average molecular mass (M, amu) of water-soluble products extracted from the solution were taken to be the quantitative criteria for the modification. Note, typical content of water-soluble substances in untreated cellulose materials does not exceed 1-2%. The molecular mass of the cellulose may reach several million.

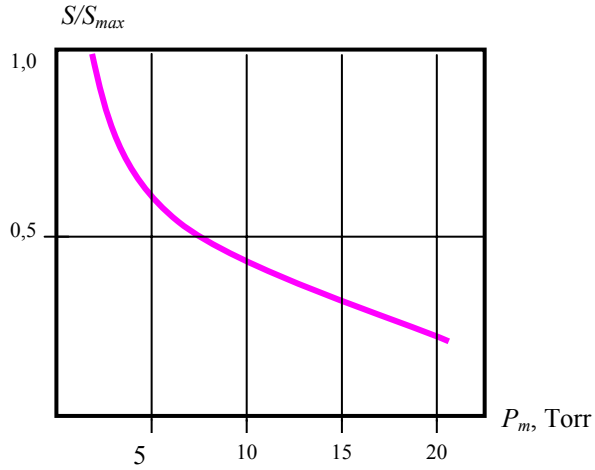

Fig. 3.

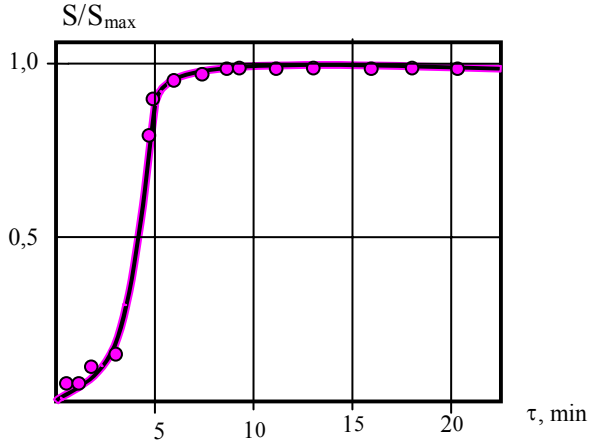

Fig. 4.

The water-soluble products yield depends upon the processing conditions and has a maximum value S_{max} for each plasma-generating gas: for O_2 plasma $S_{max} \approx 45$ %, for H_2O-plasma $S_{max} \approx 56$ %, for (H_2O + NH_3) plasma $S_{max} \approx 70$ % which are reached during certain time periods of the treatment τ_0. At first the dependence $S(\tau)$ increases smoothly, then – steeply close to τ_0 after which the yield of the water-soluble products does

not change whatever the time of the treatment could be (fig. 3). The dependence between S and the pressure of O_2 - plasma is shown in fig. 4. The NMR- and IR-spectroscopy analyses showed the final water-soluble products of the cellulose modification to be β-($C_1 \rightarrow C_4$)-tetrasaccharide, the molecule structure and chemical bonds of the products being identified [1].
The products of the EBP modification of all substances mentioned above turned out to be bioactive. For instance, modified cellulose and peat are effective substrates for microorganisms and fungi: the yield of the yeastrel on the plasmachemically treated peat attained 0,14 kg per 1 kg of the peat, whereas productivity of the untreated substrate was only 0,053 kg. The yield of water-soluble products from plasmachemically modified chitosan achieves 75-80% whereas the efficiency of conventional technologies doesn't exceed 35-40%. Preliminary tests showed the water-soluble products of the chitosan modification to be promising for skin therapy.

4. The amino-acids treatment in the Electron-Beam Plasma

Plasmachemically modified organic substances were supposed to be active agents for drug production. Some natural α-amino acids with artificially inserted pirozolidine cycles into their structures were used as original substances and the products of their modification in the EBP of helium and water vapor were tested as inhibitors of the human platelet aggregation. Preliminary analysis showed the substances of this class to be promising as active agents for medical therapy of acute coronary events, and cardiovascular diseases that remain the leading cause of the mortality. Their advantages are due to selectivity of the pharmacology action and limited side effects.
Biological effect appearing due to plasmachemical modification can be detected by means of the standard techniques *in vitro*, the aggregation degree being chosen as the quantitative characteristics of the biological effect. The platelet aggregation A (%) were measured by the turbodimetric method and A was defined as the ratio of the light transparency of the platelet suspension after ceasing the aggregation process to the initial value of the light transparency [2]. The aggregation was monitored by the aggregometer *Biola* (Russia), ADP (final concentration 1×10^{-5} M; *Boechringer Mannheim*, Germany) being used as an aggregation agent.
The experimental data were statistically analyzed by Student′s test, P-values smaller than 0,05 were considered as reliable. Table presents the results of the statistical analysis.
The powder samples (≈ 50 mg in mass) of the original substance were treated in the EBP of water vapor at pressure $P_m \approx 2$ kPa for variable time duration τ = 45-300 s. The monolayer of the powder to be treated was filled on the glass substrate and placed into the reaction chamber of the electron beam plasmachemical reactor. The typical EB power was $N_b \approx 0{,}1$ kW, the sample temperature T_s under the treatment could be varied within the range 30-110 °C.

Table. The effect of the plasma modification in the EBP of water vapor on the antiaggregation activity of the tested α-amino acid (*in vitro*): the aggregation degree A as a function of the treatment duration τ and temperature of the substance T_s under the treatment procedure.

ADP	ADP + untreated amino acid	ADP + treated amino acid				
		τ = 45 s, T_s = 38 °C	τ = 90 s, T_s = 38 °C	τ = 180 s, T_s = 38 °C	τ = 180 s, T_s = 55 °C	τ = 300 s, T_s = 55 °C
56±2%	46±2%	41±3%	41±3%	34±3%	32±3%	31±3%

The treated substance became partially water-soluble at room temperature and the solution at maximum concentration was added to the platelet suspension to measure the aggregation degree. The main results are:

- The untreated derivative of the α-amino acid decreased human platelet aggregation *in vitro* from 55,82±2,53% (control experiments) to 45,97±3,51%. The untreated compound wasn't dissolvable in distilled water at room temperature and the water heating up to 90 °C followed by cooling to 25 °C was required to carry out the control experiments.
- The water-soluble products of plasma treatment reduced the aggregation degree up to ≈ 30 %, i.e. being treated by the EBP for 5 min the studied substance reduced the platelet aggregation activity by approximately 45 %.
- The effect of the treatment duration on their anti-aggregation activity increased as the treatment prolonged, the anti-aggregation activity rising sharply at $90 < \tau < 180$ s. Our previous experiments

with cellulose, starch, chitosane show that the yield of the plasmachemically modified products began to rise abruptly at some duration τ_0. At shorter durations $\tau < \tau_0$ the plasma didn't modify the original substance and the longer treatment $\tau > \tau_0$ resulted in insignificant additional effect (see fig. 4 and [1]).

- Moderate sample heating amplified the treatment effect slightly, i.e. plasmachemical processes are responsible for the modification. Cellulose and chitosane modification was found to occur due to plasmachemical processes, whereas the substance heating was a minor factor only.

5. Mechanisms of the plasmachemical modification of biomaterials

The properties modification of biomaterials and, in particular, the higher anti-aggregation activity of the α-amino acid after EBP-treatment is assumed to be due to the following reasons:

- Plasma treatment increases the solubility of the studied substance. Regarding the anti-aggregation activity, it means that the concentration of the active agents in platelet suspension during the aggregation degree measurements was inherently higher in comparison with the non-soluble original substance.
- Possible chemical transformations of substances are also supported by the observed changes of the original color due to the plasma treatment. Fig. 5 illustrates the color transformations in the powder of studied amino acid due to the treatment in the EBP of helium and water vapor, the solutions of the treated products and products in solid phase being of the same color.
- Changes of the compound conformation could occur without alteration of its structure. This could improve the affinity of the substance under consideration to the platelet GPIIb/IIIa-receptors.
- Some new chemical groups might be included into the molecule structure during the treatment in the EBP. For instance, the EBP of the water vapor is enriched with H, OH and H_2O_2 radicals that can react with the amino acid molecules.

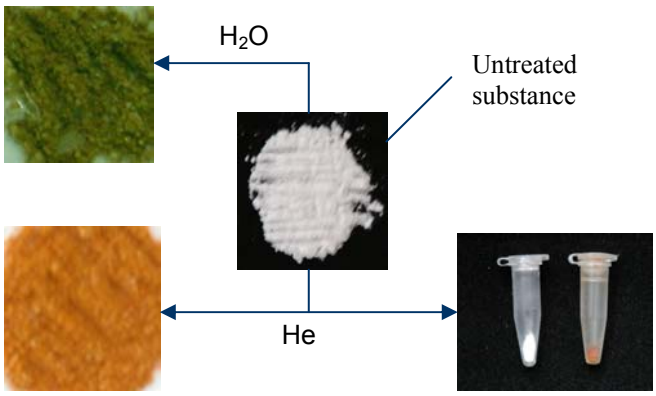

Fig. 5.

These explanations seem to be reasonable and qualitatively correspond to the data of our previous experiments on biopolymers modification by the EBP. Undoubtedly, the higher effect of the plasma modification can be attained by optimizing the treatment regimes and adjusting the design of the plasmachemical reactor.

Conclusions.

- The plasmachemical treatment of natural organic materials and substances is very promising for bioactive agents production and electron beam plasmachemical reactors are able to change the product properties controllably. For instance, the technique involved is likely to be useful for the platelet aggregation antagonists development since inhibitors that can reduce the aggregation activity by fifty percent are considered to be effective.
- The modification of the natural α-amino acid derivatives in the EBP of the water vapor can be explained by the same plasmachemical mechanisms that were found and confirmed in the experiments with cellulose, peat and chitosane.

References

[1] Aleksandrov I.V., Bychkov V.L., Vasiliev M.N. - Chem. of High Energies (in Russsian). **31**, 1, P. 82 - 88 (1997).

[2] Born G.V. Nature (London). **194**, P. 927-929 (1962).

GENERATION AND APPLICATIONS OF THE ELECTRON-BEAM PLASMA OF AEROSOLS

A. Mahir, M. Vasiliev

Moscow Institute of Physics and Technology, Moscow region, Russia

Abstract
The plasma generation by means of the electron beam injection in aerosols was studied, both dispersed liquids and solid powders being used to produce the aerosol medium. Stable and unstable aerosol clouds and aerosol flows (both sub- and super-sonic) were obtained in the electron beam plasma. The plasma-assisted ignition and combustion of dispersed liquid propellants were realized in trans-sonic air flows. The electron beam plasma was found to influence the ordered dust-plasma structures remotely.
Keywords. Electron-beam plasma; plasmachemical reactors; dusty plasma; plasma-assisted combustion.

1. Introduction

Usually the Electron-Beam Plasma (EBP) is generated by injecting an electron beam (EB) into a gaseous medium, the typical range of gas pressure being ~ 0,1–10^3 Torr. In general, the properties of the generated EBP and the geometry of the plasma bulk are due to the parameters of the EB being injected (electron energy E_b, beam current I_b and current density j_b) and the gas properties (composition, pressure P_m and temperature T_m). Many industrial and aerospace applications of the EBP, which will be further considered, result from the following peculiarities of the EBP generation procedure:

- The EB can be injected into any gases and vapors or gas-vapor mixtures. There are no physical restrictions as to the density of the gaseous medium since the EBP bulk doesn't contract even at very high gas pressures (P_m ~ 10^2 Torr and higher).
- Being added to the plasma-generating gas the solid powders and liquid droplets don't prevent the EBP generation. Large-size bodies can be inserted into the plasma bulk. Liquid jets can be injected into the EBP as well.
- The EB can be injected in both still gas and gas streams; the EBP flows appear to be stable.
- When the EB is injected into preliminary generated plasmas, so called Hybrid Plasma (HP) is produced. Experiments showed the EB to be compatible with gas discharges. The HP of aerosols and the HP flows can be generated as well.

To describe the EBP of the aerosol two interrelated problems should be considered: the propagation of the EB through the aerosol cloud (scattering and absorption of the EB) and the behavior of the aerosol irradiated by the EB (electrostatic charging, particle motion, heating, and phase transitions). Plasmachemical reactions both on the particle surface and in the gaseous phase can occur. In developing the EBP plasmachemical reactors, aircraft on-board units and other applications all these problems have to be considered as well.

2. Experimental unit

The experimental complex specially developed to study the aerosol EBP and its applications is shown in fig. 1 and described in detail in [1]. The complex consists of the generator of the EBP, which is the main part of the complex, and accessory systems such as a vacuum system, a gas feeding system, radiation protection and others. The EBP generator characteristics are as follows: E_b = 20-30 keV, I_b = 1-100 mA, j_b = $5\cdot10^3$-$5\cdot10^5$ A/m^2, P_m = 0,1-50 Torr, T_m = 260-600 K.

The focused EB 3 (j_b ~ $5\cdot10^3$-$5\cdot10^5$ A/m^2) was generated by the electron gun 1 inside the high-vacuum chamber 2. The EB was injected into the working chamber 5 through the gas-dynamic Injection Window (IW) 4. Compact and reliable one-, two- and three-stage windows were developed for various ranges of the P_m-value. The EBP cloud 6 was generated due to the interaction of the EB and the gas the working chamber was filled with.

The high-voltage power source fed the three-electrode electron gun. It produced the accelerating voltage (U = 25-60 kV) and the additional negative potential (U_{contr} = 0 ÷ –5 kV) that was supplied to the controlling electrode of the gun to change the EB current within the range I_b = 1-50 mA. The controlling module #1 controlled the power source operation and changed the I_b and E_b values (E_b = U).

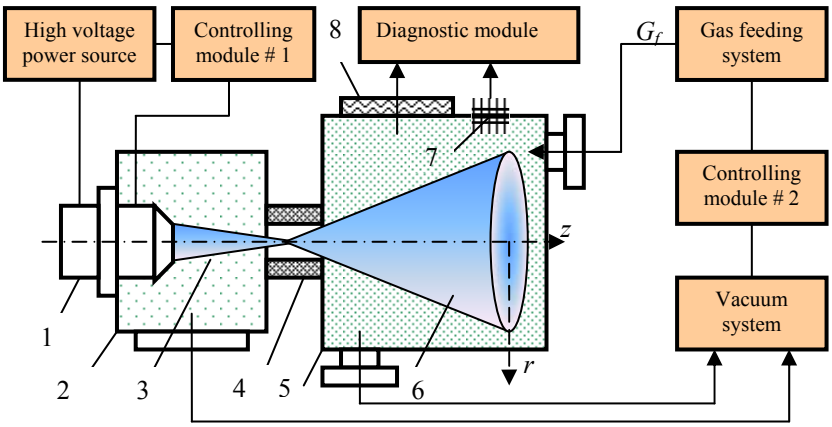

Fig. 1. The scheme of the experimental complex

The large volume working chamber ($V \sim 0{,}5$ m^3) was used to study free EBP clouds that didn't contact the chamber wall. To study localized plasma bulks special reaction chambers (cylinders 30-300 mm in diameter) were placed inside the working chamber, the EB being injected along the cylinder. The cylinder was made of both metallic and dielectric materials. The working chamber was equipped with holders to insert the large-size models in the EBP flow (aerodynamic experiments) or to place a sample of materials to be treated (industrial technologies development). The glass window 8 was used for optical plasma diagnostics. The sensors placed inside the working chamber were connected with the external devices through the hermetic plug and socket units 7. The controlling module #2 was responsible for the operation of the vacuum and gas feeding systems. Operating together they kept the pressure in the high vacuum chamber $\leq 10^{-4}$ Torr and varied the gas pressure in the working chamber within the range $P_m = 1\text{-}10^2$ Torr. EB jets were generated by means of nozzles of different kinds. Usually EB was injected through the choking section of the nozzle along the jet axis. Cylindrical (subsonic), Laval (supersonic) shortened (non-adapted supersonic) and center-body (both sub- and supersonic) nozzles were used. EBP generation by means of the shortened maladapted nozzles is illustrated by fig. 2. The EB 5 was injected through the throat of the nozzle 4 combined with the IW 6 along the gas flow 3. As a result the EBP jet 2 was formed.

The dispersed particles were injected into the working chamber of the experimental unit to produce the aerosol clouds or aerosol flows. The mechanical sprayers were used to introduce powders; liquids were injected by means of centrifugal sprayers or sprayed pneumatically as shown in fig. 2. The liquid jet 7 was injected in the EBP flow 2 which was generated in the supersonic gas flow 3 by the center- body nozzle 4 combined with the IW. The zone 1 is the flow of the aerosol EBP.

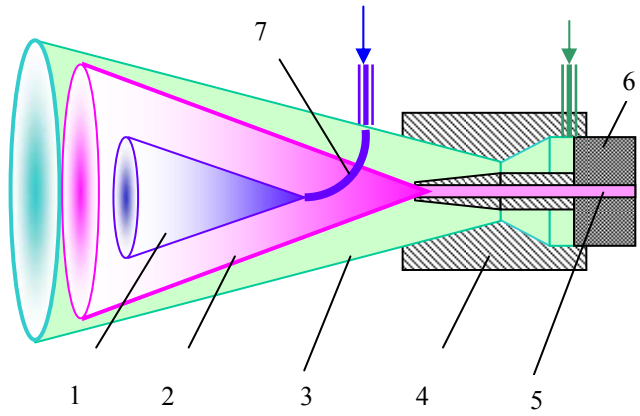

Fig. 2. A supersonic EBP plasma jet generation and pneumatic spraying of the liquid jet in the supersonic EBP flow

The dust layers were formed upon a vibrating membrane, piezoceramic plates and metallic foils equipped with electromagnetic shockers were used as the membrane. The dust clouds were formed in the large-size working chamber by spilling the powder from a vibrating sieve or inside the small-size spinning reaction chamber like a concrete mixer. To produce the aerosol of droplets either liquid jets or liquid films were injected into the gas flow. The centrifugal nozzles were used to generate still aerosol clouds as well.

The working chamber was equipped with the electrode that generated the electrostatic or RF-electromagnetic field in the working chamber. The electrodes of various designs were used:

- to generate HP of aerosol (both still plasma clouds and HP flows);
- to ignite the aerosol of liquid fuels;
- to form ordered dust-plasma structures in the RF-electromagnetic field.

The ordered dust plasma structures (fig. 4) were found to appear above the RF-electrode of a special design [2]. By injecting the EB over the structure the properties of the HP and spatial distribution of the field near the electrode can be changed (see section 4).

3. Stability of the aerosol cloud irradiated by the EB

The stability of the aerosol clouds irradiated by the EB was investigated experimentally to develop the electron beam plasmachemical reactor for the powders treatment. The aerosol particles motion in the EBP of various gases was studied, the gas pressure being varied as well. The aerosol particles were found to begin to fly apart at some the P_m-value due to the EB action i.e. being injected the EB destroyed the aerosol cloud and scattered the solid particles toward the working chamber walls (fig.3). The particle acceleration reduced as the gas pressure rose. The aerosol cloud dispersion was supposed to be explained by electrostatic charging of the powder particles and special experiments were carried out to measure the particle charge as a function of the pressure P_m. A spherical probe, imitative a single aerosol particle, was inserted into the plasma cloud and the potential difference ΔU_p between the probe and the ground was measured. The ΔU_p-value was found to be very small at higher pressures (P_m > 5 Torr) but it began to increase rapidly at $P_m \approx$ 1-2 Torr (see fig. 4). At P_m < 0,5 Torr the potential could reach 100 V and higher. The typical values of the gas pressure at which the $\Delta U_p(P_m)$-function changed its behavior were in agreement with the P_m-values at which the character of the aerosol particles motion changed. Therefore, the electrostatic charging of the aerosol particles irradiated by the EB was responsible for the aerosol flight and scattering.

Fig. 3. The solid aerosol fly apart, P_m = 0,3 Torr

The radial distribution $\Delta U_p(r)$ in the EBP cloud at various distances z from the IW was studied and fig. 5 illustrates the results of these measurements. The figure shows that the points of the plasma cloud located far from the axis z acquire a sufficiently high negative potential.

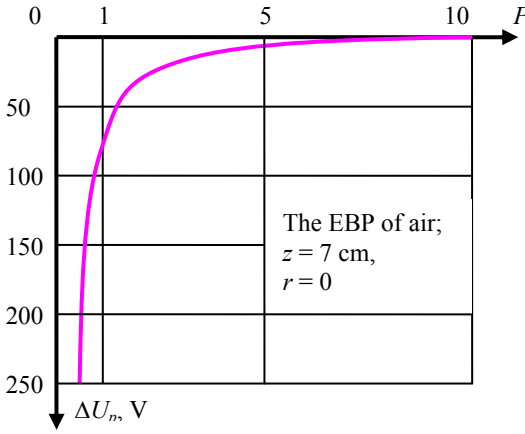

Fig. 4. The potential of the point z = 7 cm on the EBP axis as function of the gas pressure.

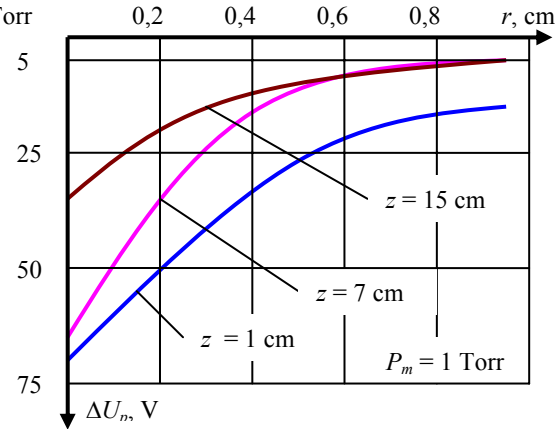

Fig. 5. The potential of various points of the air-EBP at pressure P_m = 1 Torr.

4. The formation of the dust-plasma structures and the remote control of the structures by the EBP

The ordered dust plasma structures are known to be formed in the RF gas discharge [2]. When a small amount of the powder was filled on the active electrode of the RF-discharge system the particles could levitate over the electrode as shown in fig. 7. Certainly, appropriate power of the RF-generator and the gas pressure value should be found and the powder must be introduced carefully. Vibrating membranes or sieves are usually used to introduce various powders: ceramics, glass, polymers and others. Note that the dust plasma structures were proved to exist at sufficiently low pressures P_m < 2-5 Torr only.

The ordered dust structure formation by means of condensation of the evaporated materials was observed as well (see fig. 6). The powerful EB pulse evaporated a target of a solid material in the working chamber filled with the noble gas to create the dense gas + vapor mixture. The vapor condensation resulted in the formation of the ordered dust structures above the RF-electrode. When polymer targets were used the stable dust-plasma crystals were formed during ~15 s after the EB cutoff. In comparison with the dust structures formed by directly introduced powders, the condensed dust-plasma structures were denser and the particle size didn't exceed 5 μm, whereas typical sizes of available solid powders were ~10-20 μm (compare fig. 6 and 7; the

figures present the ordered dust structures of the polymer material in the helium plasma that were formed by vapor condensation and direct introduction of the powder respectively).

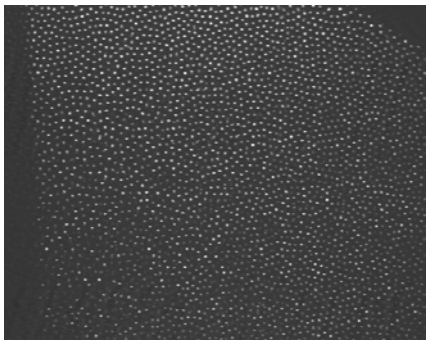

Fig.6. The ordered dust structure formed by condensation of the polymer vapor in the EBP of helium, P_m = 1 Torr.

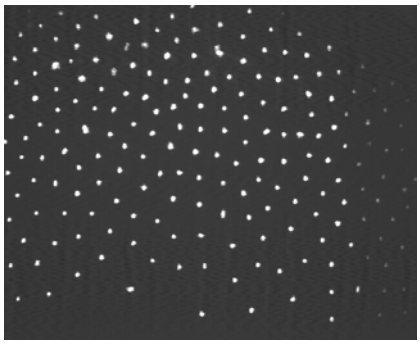

Fig. 7. The ordered dust structure of the polymer powder formed by means of the vibrating sieve in the HP of helium, P_m = 1 Torr.

Though our experiments showed that no ordered dust plasma structures are formed in the pure EBP (in the plasma without gas discharge component), the EBP is able to control the dust-plasma structures. The following phenomena were observed when the EB was injected above the structure but didn't touch it:
- the particles density was changed and the uniformity of the powder layer was violated;
- the structure, as a solid crystal, followed the EB when the beam scanned over the structure slowly.
Thus, the EBP controlled the dust plasma structures remotely and the observed phenomena can be attributed to the electrostatic potential that occurs on the periphery of the EBP bulk (see section 3 and fig. 5).

5. Ignition and combustion of the aerosol in the EBP

The ignition and combustion of liquid aerosols stimulated by the EBP were studied experimentally within the range of the air pressure $10 < P_m < 30$ Torr. The automobile gas and aircraft kerosene were sprayed into the subsonic and supersonic airflow to produce flammable mixture. The aerosol flow of the dispersed liquid propellants was formed as shown in fig. 2 and the EB was injected along the airflow axis. Being preliminary excited by the EB the aerosol flow was ignited by a high voltage RF-electrode introduced in the flow. The kerosene-air mixture was found to combust only if the EB was switched on (fig. 8). When the EB was cut off the flame was extinguished, i.e. the EB really assisted the combustion. Fig. 9 illustrates the luminescence of the kerosene aerosol excited by the EB before ignition. In this experiment the fuel jet was injected toward the airflow and the ignition electrode wasn't fed.

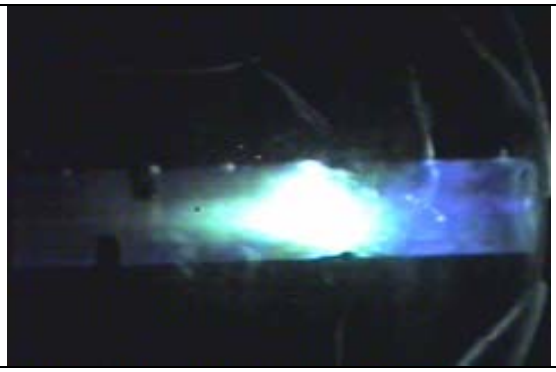

Fig. 8. The EBP-assisted combustion of kerosene in trans-sonic airflow.

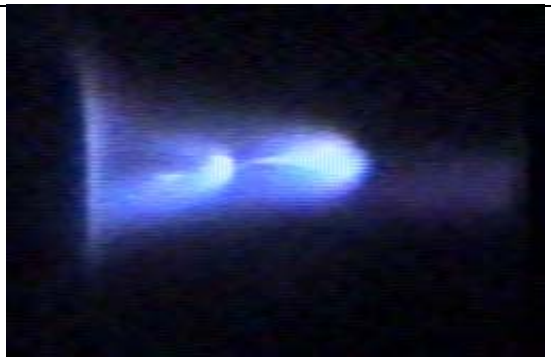

Fig. 9. The luminescence of dispersed kerosene in the trans-sonic air-EBP flow; the mixture isn't ignited.

References

[1] A. H. Mahir, S.L. Lysenko, M.N. Vasiliev - Contributed papers of the 22-nd Summer School and Int. Conf. on the Ionized Gases, August 23-27, 2004, National Park Tara, Serbia and Montenegro. P. 473-476.
[2] L.M. Vasilyak, M.N. Vasiliev, S.P. Vetchinin, D.N. Polyakov, V.E. Fortov. - J. of Exper. and Theor. Physics, **96**, 3 (2003). P. 440-443.

Auger depth profiling optimization on plasma-deposited C/C:N multilayers.

V. Micheli, N. Laidani, R. Bartali, G. Gottardi and M. Anderle

ITC-IRST, Divisione Fisica Chimica delle Superfici e Interfacce, via Sommarive 18, Povo, Trento, Italy

Abstract

In the attempt to produce thin carbon films with attractive mechanical properties we found out that combining different materials in a multilayered structure can result in a significant improvement of the properties of the whole system (low stress for example). In order to relate the film macroscopic properties to its chemical composition and architecture an optimization of the in-depth Auger analysis conditions were studied. An optimal resolution of the 7 nm half-period layered structure has been obtained.

Keywords: AES; Depth profiling; Depth resolution; Sputtering and PACVD deposition, Carbon multilayer

1. Introduction

Recent development of the in-depth distribution and chemical composition analysis along the third dimension perpendicular to the surface has been significantly stimulated by the progress in thin films technology as well as in the opto-electronic and semiconductor materials. A great number of material properties and macroscopic phenomena depend on the atomic scale properties of materials interfaces [1]. For example, friction, wear, hardness and elastic modulus are governed by the structure and composition of inner interfaces. In multi-layered structures, mechanical, thermal and chemical stability of interfaces between different materials (hetero-interfaces) are fundamental for the functioning reliability of technological products such as sensors, microelectronic devices, tools and medical prosthesis, and protective coatings [2]. Although the correlation between macroscopic behavior and structure, properties and composition represents a difficult and a not completely well understood task, it is commonly accepted that the chemical and structural characterization has to be considered as a close link with the preparation and synthesis of a structured sample [1,3]. A number of techniques have been developed for this purpose. Surface and interface analysis methods (ESCA, AES, XPS, etc.) combined with ion sputtering are the most commonly used since they can be easily applicable to nearly all kind of materials.

In multi-structured samples a detailed compositional characterization of the single layer and interface is more than ever crucial if a correlation between film mechanical properties and its chemical composition is required. In depth profiling analysis of thin film or multilayer samples an important figure of merit that defines the accuracy and precision of the in-depth distribution of elements concentration is the depth resolution (Δz) that could be definitely considered as the key parameter for the quality of a depth profile measurement.

The commonly definition of the depth resolution, recommended by the International Union of Pure and Applied Chemistry (IUPAC) and by committee E 42 of The American Society of Testing and materials (ASTM-E42) is given by the distance over which the difference between 84% and 16% of the maximum intensity of the profile at the interface is measured [4-6]. The relative depth resolution is defined by $\Delta z/z$ where z is the depth value measured at interface.

In the case of a more structured sample multilayer of constant ½ period thickness (d) an evaluation of the depth resolution may also be derived by the normalized amplitude of I_m/I_0 [5,6] where I_m represents the difference between the maximum (I_0) end the minimum (I_s) of the signal on both sides of an interface profile.

It has been experimentally demonstrated that in Auger depth profiling (Δz and I_m/I_0) is affected by a large number of factors (instrumental, sample characteristics, beam interaction with a specific sample, etc.) [1,5,7,9].

These effects may lead to a distortion of the shape of the profile, broadening of interface and consequently a degradation of the depth resolution. The primary ion beam nature [8], the ion beam energy [1,5,7] and the ion beam incident angle [1,5,8,10] are the most important experimental aspects which should be taken into account to avoid detrimental contributions to the achievement of an appropriate depth resolution.
In order to find out the more appropriate experimental conditions to optimize the depth resolution in the AES depth profiling of multilayered films both film/substrate and single layers interfaces have been considered.

2. Experimental

Sputtering and PACVD (Plasma Assisted Chemical Vapor Deposition) processes were used in alternate order to deposit, on a n-doped silicon substrate, nanometer-thick carbon films. Samples structured in 2, 4, 8, 16, 32 layers, with single layer thickness varying from 100 to 7 nm ½ period, have been characterized. The two kinds of carbon materials differ by their structural properties. The carbon layers (hereafter indicated as C layers) obtained by graphite sputtering in Ar-H_2 (16%) discharge was hard (hardness ~ 8 GPa), while those prepared by PACVD exhibited polymer-like properties (hardness ~ 1 GPa). During the PACVD process nitrogen was introduced in the hydrocarbon-hydrogen gas process as a marker element, therefore these layers are named C:N. Nitrogen is switched off during the subsequent sputtering deposition process, but some remnant amount is detected in the hard C films and for this reason N concentration varies in an oscillating way along the film depth. The thickness of the single layers of the structure has been reduced when increasing the number of layers in order to approximately maintain the same total thickness of the films (Table 1).
Both kind of films contain hydrogen and would be better described as C:H and C:H:N, however for simplicity we omit it in their nomenclature.

Sample	Total number of layers	Measured film thickness (nm)	Theoretical single layer thickness (nm)
A	2	257	128
B	4	249	62
C	8	254	32
D	16	205	13
E	32	225	7

Table 1
Film thickness, interface width and depth resolution for C/C:N multilayer sample deposited on Si using sputtering and PACVD process.

AES (Auger Electron Spectroscopy) depth profiling is one of the most important and extensively used sectioning methods used for the tree-dimensional analysis of thin films. The technique combines a focused ion beam that is scanned over a sample surface and the measurement of the secondary Auger electron that can be done either discontinuously after the sputtering process or simultaneously with it..
Measurements presented here were performed in a PHI model 4200 system, equipped with a variable resolution cylindrical mirror analyzer (CMA) and a W electron emitter coaxial electron gun. The system base pressure was in the low 10^{-8} Pa. Auger spectra was excited by a 3 keV, 8.75 10^{-4} Acm^{-2} current density electron beam that was scanned over an area of 400 μm^2. A differentially pumped ion gun, model 04-300, was used for the sputtering process. Ion gun gas pressure has been fixed at 20 mPa and positive Ar^+ ions were accelerated to different energies (2, 3 and 4 keV). The 800 μm diameter ion beam has been rastered over an area of 1x1 mm enabling a better uniformity of the beam intensity leading to a more flat bottom of the sputtering crater which is necessary for improving the depth resolution [1] The incidence angle of the ion beam to the surface sample, θ, has been varied with respect to the sample surface from 28 to 68 degrees. C_{KLL}, N_{KLL}, Si_{LMM} and O_{KLL} Auger lines has been acquired and an elemental quantification applying the Physical Electronics manufacturer's relative sensitivity

factors has been obtained. The depth distribution of the elements was recorded as a function of the depth, assessed on the basis of the erosion time and the film thickness.
Films thickness was obtained using a KLA-Tencor P-15 stylus profilometer and an atomic force microscopy (AFM) was applied in the contact mode to investigate the surface roughness.

3. Results and Discussion

As a first step, a carbon film (121 nm thick) material with similar chemical and compositional characteristics to the samples has been used as a reference in the attempt to find out the appropriate experimental ion gun setting giving the best Δz at the Si/film interface and $\Delta z/z$ value. These etching parameters were subsequently applied to the in-depth measurements of the multi-layered samples. With this purpose a thin a:C film has been deposited on Silicon by graphite sputtering.
A number of AES depth profiles obtained by varying both ion beam incidence angle θ with respect to the sample surface and ion beam energy have been acquired. The latter parameter has shown better results at low energy value (2 keV) as largely reported in the literature [1,5,8,10,11].
In Table 2 the Δz and $\Delta z/z$ values measured from the Auger depth concentration profiles of the reference sample are reported as a function of the ion beam incidence angle.

Ion beam incidence angle (°)	Depth resolution Δz (nm)	Relative depth resolution $\Delta z/z$ (%)
68	7	5,8
53	8	6,4
38	6	4,8
28	5	4,1

Table 2.
Dependence of the depth resolution (Δz) at film/Si interface and the relative depthresolution ($\Delta z/z$) for a 121 nm Carbon film on different ion beam incident angle.

A number of phenomena and in particular sputtering-induced effects and escape depth of Auger electrons as well as the experimental ion gun set-up may be the primary causes of a broadened depth profile interface and of a degradation of the depth resolution. The initial surface roughness can greatly influence the depth from which the analytical information is obtained and the AES elemental signal intensities as well. Shadowing effect due to a rough surface may prevent the secondary electrons from reaching the analyzer and they may be recaptured after leaving such a surface. For an initially smooth surface the etching-induced roughness is certainly the prevailing factor for the degradation of the depth resolution and it generally appears as the result of different local etching rates which depend on the crystallographic grain orientation whenever and ion incidence angle [1,9,12]
An increasing trend of depth resolution and relative depth resolution is observed when decreasing the incidence angle down to 28 degrees. The best values of Δz and $\Delta z/z$ obtained at the smallest angle (28°) of Ar^+ ions incidence can be explained taking into consideration the above phenomena. It has been experimentally demonstrated that surface roughness induced by sputtering process, atomic mixing and shadowing that have detrimental effects for the depth resolution and the relative depth resolution can be minimized using a low ion beam incident angle if the sample surface is relatively rough [1].
An Atomic Force Microscope (AFM) has been used to attain information about surface roughness of the samples. Before etching, preliminary results show, for all the samples, a relatively smooth surface (< 10 nm) that is in agreement with the previously statement. For the following reasons a thorough examination of surface roughness and sputtering-induced effects is though required since they are considered one of the most important causes of degradation of the depth resolution [1,9].

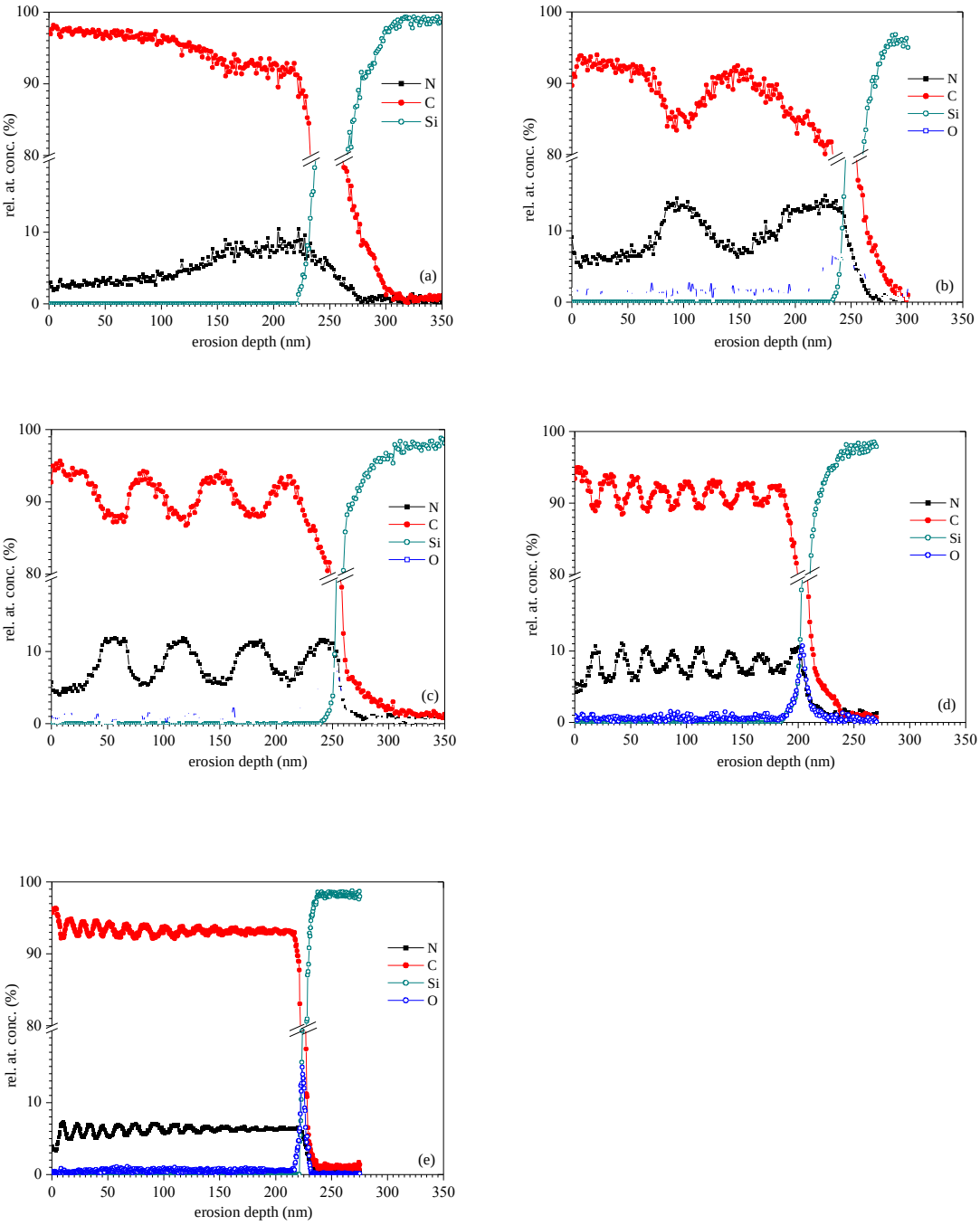

Fig. 3 AES depth profiles of the C/C:N multilayer samples on silicon: (a) 2 layers, (b) 4 layers, (c) 8 layers, (d) 16 layers, (e) 32 layers. All measurements were acquired using a 3 keV, 8.75 10^{-4} Acm^{-2} current density electron beam. Alternating mode sputtering was performed with a 2 KeV, 800µm diameter ion beam which rastered over a 1x1 mm^2 area and the samples were tilted to obtain a 28° ion beam glancing angle respect to the surface sample.

Experimental ion gun set-up which have been adjusted in order to achieve an optimization of Δz and Δz/z parameters on the reference material, low ion beam energy (2 keV) and 28° argon ions incidence angle with respect to the sample surface, have been consequently used to perform the Auger depth profiles on the multilayered structured C/C:N samples.In order to obtain a satisfactory number of C/C:N profile data points, the etching time between two acquisitions during the depth profile has been also reduced from 0.5 to 1.0 min when analyzing the more structured samples (16 and 32 layers).The Auger depth profile raw data expressed as elemental intensity signal as a function of the sputtering time has to be converted to a more universally used in-depth quantification image: elemental composition versus erosion depth. Figure 3 shows the Auger depth profiles through the 2, 4, 8, 16 and 32 C/C:N multilayer samples after conversion of the sputtering time to eroded depth. The Y axis has been expanded in order to emphasize the elements signals trend and to get a better visualization of the layers definition.

In first approximation we have assumed a constant sputtering rate through the depth profile but obviously this estimation may be liable to systematic errors due to both the accuracy of total film thickness measurement using the mechanical stylus ()and the different sputtering yield when analyzing not uniform matrix [1].

In all depth profiles the alternating layers are satisfactorily well defined and this is also confirmed by the normalized amplitudes of I_m/I_0, calculated for every single layer of the structure which shows values that are in agreement with the definition of good in-depth multilayer resolution given in literature [1,4]. In a structured sample with constant single layers thickness the depth resolution in fact may be evaluate by the decreasing of I_m defined as the difference between the maximum and the minimum signal on the both side of an interface, compared to I_0, which is the maximum intensity of the signal (fig. 4a). I_0 has been here defined as the average value calculated on the first carbon layer since t Nitrogen is present, in an oscillatory trend, all through the depth profile. The more reasonable explanation of this effect could be given by the presence of N_2 residual gas in the deposition chamber and the diffusion and mixing phenomena during the layer deposition process.

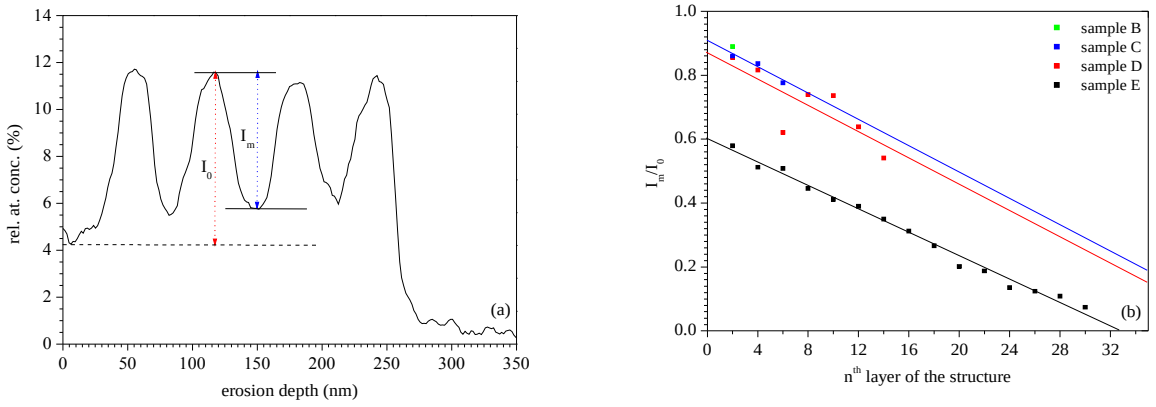

Fig. 4 Schematic picture of the determination of the resolution in a multilayer structure as I_m/I_0 ratio calculated on the Nitrogen profile (a) and evolution of the I_m/I_0 ratio through the multi-layer samples.
B, C, D, E: refer to the samples described in Table 1.

Regarding the analyzed I_0 and I_m may be obviously evaluated only when the number of layers is more than 2. A I_m/I_0 decreasing trend is observed (fig. 4a) when increasing the number of layers and this is an indication that the depth resolution deteriorates with the number of layers. This trend could be better observed in figure 5b where the I_m/I_0 final and the initial ratio has been represented for each

sample as a function of the total number of layers. Up to 16 layers this value is remarkable larger than 0.5 and this is a good indication of well defined adjacent layers. For sample DE (7nm half-period), the resolution is still maintained ($I_m/I_0 > 0.5$) up to 6^{th} layer of the structure, after which it falls drastically.

4. Conclusion

In this work we have optimized the Auger analysis depth resolution parameters (Δz and I_m/I_0) on a number of multilayer structured samples consisting of a sequence of hard and soft thin carbon films on a silicon substrate. Incident ion beam angle and ion beam energy used for the film in-situ erosion during the analysis have been appropriately chosen in order to achieve a good in-depth film-substrate (< 10 nm) and interlayer resolution. Even in the 16-layers structured sample good results have been obtained and every single layer (12 nm thick) could be easily defined with a good degree of accuracy. Measurements have been also performed on a more structured system (7 nm half-period). The depth profile shows satisfactory results as to the Δz but further experiments have to be done in order to improve the I_m/I_0 ratio and the interlayer resolution. Data are not presented in this work as a more detailed evaluation of the factors and experimental conditions which influence the resolution parameters have to be considered.

Acknowledgments

The authors are thankful to “Fondo Unico per la Ricerca-Provincia Autonoma di Trento” who financed this work in the frame of “PPD-Carbon” project.

5. References

1. S. Hofmann, Rep. Prog. Phys. 61 (1998) 827-888
2. A. Zalar, S. Hofmann, Surf. Interface Anal., 12 (1988) 83
3. E.D. Hondros, M.P. Seah, S. Hofmann, P. Lejcek, Physical Metallurgy, (1996),ch 13, 1201
4. S. Hofmann, Surf. Interface Anal. 27, 825-834 (1999)
5. S. Hofmann, Surf. Interface Anal. 2, 148-160 (1980)
6. S. Hofmann, Practical Surface Analysis, ed. D. Briggs and M.P. Seah, 141-179 (1983)
7. S.S. Andrew, et al., Thin Solid Film 263 (1995) 169-174
8. J. Linday, V. Kliment, P. Vogrincic and S. Tomek, Vacuum 46, 53-55(1995)
9. T. Wohner, G. Ecke, H Roβler and S. Hofmann, Surf. Interface Anal., 28, 1-8 (1998)
10. S. Hofmann, J. Vac. Sci. Technol. A 9 (3) May/Jun 1991, 1466-1476
11. S. Hofmann, W. Hosler and R. von Criegern, Vacuum, 41 (1990) 1790
12. I. Ferguson, Auger microprobe analysis, IOP Publishing Ltd 1989

Plasma Reforming Enhanced Methane Combustion

M. Vega[2], T. Kappes[1], G. Lins[1], T. Hammer[1], F. Dinkelacker[2]

1 Siemens AG, Corporate Technology, Erlangen, Germany
2 Friedrich-Alexander-Universität Erlangen-Nürnberg, Lehrstuhl für Technische Thermodynamik, Erlangen, Germany

Abstract
Hydrogen enriched premixed methane combustion was investigated using a compact burner set-up with an integrated plasma reforming unit. A part of the fuel is transformed to syngas by a gas discharge in a fuel rich mixture and then added to the very lean methane air mixture before combustion. The hydrogen enrichment has a strong influence on the combustion behavior with regard to flame stability and flame offgas composition. The blow-off limit could be extended from an air number of 1.67 without plasma application to 2.01 with plasma.

Keywords
methane combustion, hydrogen enrichment, plasma reforming, flame stability, emissions

1. Introduction

Natural gas plays an important role as a fuel in combustion processes for power generation, e.g. in gas turbines, and for other industrial applications. Due to the increasing restrictions regarding the emission of noxious pollutants, huge investments are made in order to improve current combustion technology and fulfill those requirements.

Characteristic properties of hydrocarbon combustion such as efficiency, flame stability, emission of unburnt fuel and pollutants, which are formed in the flame, depend strongly on the relative air-to-fuel ratio, which is also referred to as air number. But there is a trade-off between some of these properties. For example, increasing the air-to-fuel-ratio can reduce pollutant emissions, but at the same time reduces the flame stability.

Various approaches to increase flame stabilization at high air-to-fuel ratio have been made by fluidic means with a co-axial jet flame burner for highly turbulent premix flames [1], by application of electric fields [2,3] and by generating electrical discharges in the flame [4,5]. The difference between the two latter methods is whether the electric field strength is kept below the breakdown value or not. In the first case, the electromagnetic forces act only on the radicals formed in the flame by chemoionization, whereas in the second case charged particles are generated additionally by gas discharges and the effect on the combustion characteristics is much stronger in general.

Hydrogen combustion differs considerably from methane combustion due to a much broader flammability range and a higher flame speed. Even the addition of a few percent hydrogen to methane fuel can improve the combustion characteristics significantly [6]. Hydrogen can be generated from methane and oxygen or water vapor in a catalytic reaction or by plasma treatment. Several plasma techniques have been studied for hydrogen generation from hydrocarbons ranging from dielectric barrier discharges, spark discharges, electron beam, gliding arc and microplasmatron discharges [7-9]. It has been shown that among plasma methods the most efficient are those with high power density and a certain gas heating capability.

The aim of this work was to combine a methane premix burner with a plasma methane reformer to improve the combustion by in situ hydrogen generation, with special regard to blow-off limits and pollutant emissions. The work was divided into two parts. The first one consisted of designing and testing a plasma reactor producing a gas discharge of the gliding arc type in a coaxial configuration, with the intention of finding the most appropriate operating condition. The second part of the work consisted of the integration of the plasma reforming unit in a gas burner and testing by measuring the blow-off limits, pollutant emission and evaluation of the plasma input power in comparison to the thermal input power of the combustion process.

2. Experimental

The heart of the experimental set-up was a burner with an integrated plasma reforming reactor assembled in a coaxial configuration which is sketched in Fig. 1. The plasma unit was removable in a way that a separate characterization and optimization of the reformer could be done. The advantages of this integrated configuration of the reforming unit inside the burner are on the one hand the compact structure of the set-up and on the other hand the fact that the heat energy which is released from the plasma reformer and which would otherwise be lost can be recovered by the lean gas mixture passing the reformer unit.

The plasma reformer consisted of a tubular housing with 10 mm o.d., 8 mm i.d. and a lateral gas inlet for the rich methane air mixture to be treated in the plasma. A section at the downstream end of the housing had a narrower inner diameter of 2.2 mm with a diverging axial gas outlet. A stainless steel wire electrode with 1.5 mm diameter insulated by a ceramic tube was placed in the center of the housing with one end protruding into the narrower section forming the beginning of the discharge zone between the electrode tip and the grounded housing with a gap of 0.35 mm. The high voltage power supply was connected to the back end of the electrode outside the housing. A baffle plate in front of the reformer outlet facilitated the slowing of the plasma flow by diverting it to a radial direction. This way, the treated gas gets mixed with the lean mixture flowing up from the bottom of the burner.

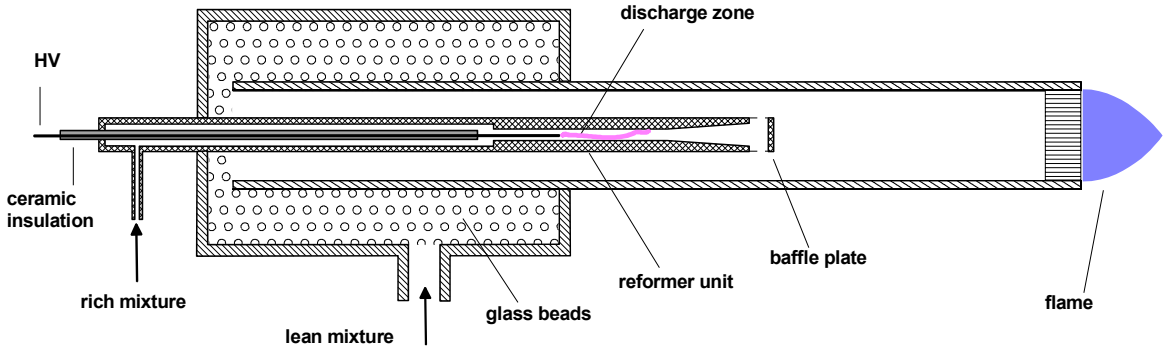

Fig. 1: Burner with integrated plasma reforming unit

The burner was made of a stainless steel tube with 240 mm length and 22 and 25 mm inner and outer diameter, respectively. A perforated plate is located at the outlet of the burner in order to stabilize the flame. The open back end of the burner tube is inserted into a container which has an inlet opening for the lean methane air mixture. The container is filled with glass beads in order to achieve a homogeneous gas distribution all over the cross section of the burner.

A dc power supply (9000-6K-2000 from EA-Elektro-Automatik) was used in the experiments with maximum voltage and current output of 6 kV and 350 mA respectively. It is equipped with an internal electronic system which allows limiting the current and thus the electrical power applied to the gas stream. Voltage and current measurement were performed by means of an 11 kΩ shunt resistor between the power supply and the reactor and two HV probes (LeCroy) connected to a digital storage oscilloscope (LeCroy Waverunner 6030, 2.5 GS/s).

Methane (99.995 %) from gas cylinders as well as O_2 and N_2 from the in-house pressurized-gas network was used for the experiments. The gas flows were adjusted using mass flow controllers (MKS). Samples of the off gas were drawn for analysis, in the case of the open burner flame from a point about 20 cm above the burner head, and piped through heated tubes to the analytical instruments without removing water or other condensable compounds. An FTIR spectrometer (Bruker Tensor 27) with a heated long way gas cell was used to measure the concentrations of CH_4, CO, CO_2, NH_3 and HCN. During plasma reformer characterization a Shimadzu GC-14B gas chromatograph was used to measure the concentrations of H_2, N_2, O_2, CH_4, C_2H_2, C_2H_4, C_2H_6, CO and CO_2. The concentration of NO_x in the burner off gas was measured with a flue gas analyzer based on electrochemical sensors (Testo 300 XL).

3. Results and Discussion

Three different gas mixtures (λ=0.4, 0.5 and 0.6) were tested under different gas flow rate in the range between 2 and 4 l/min (STP) and mean discharge current values between 50 and 100 mA corresponding to electrical power values of 45-75 W. With these air number values of the feed gas, the stoichiometry is between that of partial oxidation to syngas and complete combustion, so a mixture of carbon monoxide, carbon dioxide, hydrogen and water could be expected as reaction products. In fact, only CO, H_2 and H_2O were formed to a major extent, whereat the latter could not be quantified reliably. However, carbon dioxide appeared only in traces, as well as C_2 hydrocarbons (< 0.5 %), ammonia and hydrogen cyanide (< 100 ppm each).

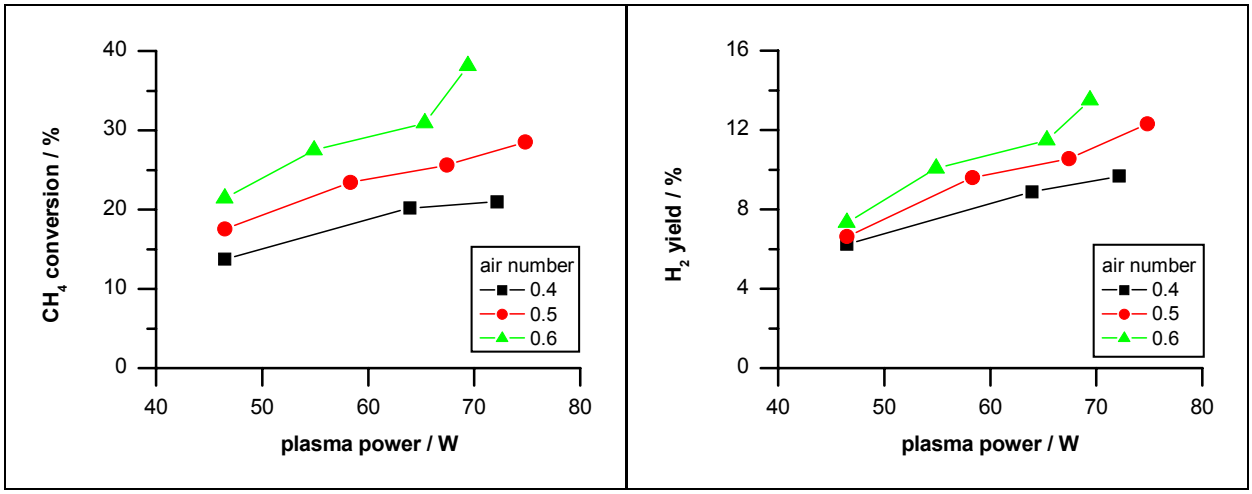

Fig. 2: Influence of plasma power and air number on methane conversion and hydrogen yield

Fig. 2 (left) shows the influence of plasma power and air number λ on the methane conversion at a total gas flow of 3.4 l/min. Methane conversion shows a growing tendency with rising electrical power. The results can be explained in terms of a higher amount of energy transferred to the gas flow, which allows the reaction of a larger amount of methane. Also an increasing air number leads to increasing methane conversion, not only in relative terms as displayed in the diagram but also in absolute terms, i.e. the decreasing methane concentration cannot explain this increase. It is rather due to a higher reaction enthalpy of the leaner mixture, which results in a higher gas temperature in the reaction zone.

The corresponding hydrogen yields are shown in Fig. 2 (right). With regard to the air number, the results show that the yield improves when excess air is supplied. It must be taken into account that since the composition was varied while the gas flow was maintained constant, methane concentration in the gas feed varied from experiment to experiment. Therefore, the influence of the air number on the hydrogen yield is not as strong as shown in Fig. 2 (left). While H_2 selectivity is about 50 % for λ=0.4, it decreases to below 40 % with λ=0.6. However, with regard to the generated hydrogen amount, it can be affirmed that the yield increases with growing air number.

Compared to the H_2 yield, the CO yield was almost twice as high over the whole range of reaction conditions; in other words, the carbon selectivity of CO reached almost 100 %.

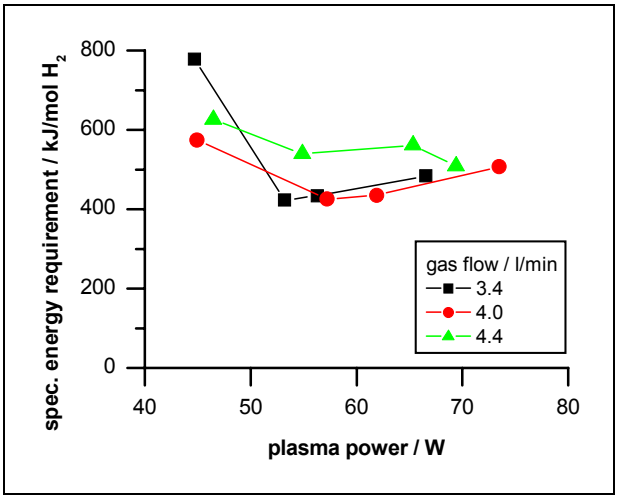

Fig. 3: Specific energy requirement for H_2 formation depending on plasma power and gas flow (λ=0.6)

The energy requirement for the hydrogen generation has been also studied, the influence of plasma power and gas flow are shown in Fig. 3. A decreasing tendency with increasing electrical input power is observed, but above 50 W the three studied gas flow values seem to reach a plateau between 400 and 600 kJ/mol, being somewhat higher at the highest gas flow. At electrical input power below 50 W the energy requirement is also higher. This is attributed to the fact that methane conversion (between 20 and 30 %) and hydrogen yield (between 6 and 9 %) do not reach very high values. This led us to work subsequently at higher electrical power values (current limited to 70 and 90 mA) in order to minimize the energy requirement.

It can be concluded that it is reasonable to work under the conditions which permit the highest hydrogen yield and methane conversion with the lowest possible energy requirement. These requirements are fulfilled under operating conditions with an air number of 0.6, a gas flow of 3.4 l/min and an electrical input power of about 55 W. The electrical input power was subsequently varied to study its effect on the blow-off limits of the combustion process, the above-mentioned conditions are the most adequate to continue the work.

A series of experiments has been carried out with lean methane-air flames in the presence and absence of a plasma in order to establish a comparison between both states, with special regard to blow-off limits, unburnt methane as well as CO and NO_x emissions. Since the methane flow rate was kept constant, the air number increase from experiment to experiment was made by raising the air flow rate and thus increasing the flow velocity. The experimental set-up permitted the air entrainment, which caused a dilution of the exhaust gas. The values of the offgas concentrations have been corrected by individual factors obtained from calculating the carbon balance.

Various series of experiments were carried out to study the influence of the electrical input power on the extension of the flammability limits. The procedure was the following: the flame was ignited at $\lambda = 1.2$ and subsequently – except in the first series – the power supply system was connected in order to ignite the discharge and then the air flow was continuously increased until the extinction of the flame. The overall air number is calculated for fuel and air of both, inner (plasma) and outer flow together.

The highest achievable air number (blow-off limit) without plasma reforming reaches 1.67 under the given experimental conditions. When a gas discharge was applied the blow-off limit increased linearly with increasing plasma power up to an air number of 2.01 with 56 W. This corresponds to 8.5 % of the thermal power of the flame, which was calculated to be 663 W, based on the higher heat value.

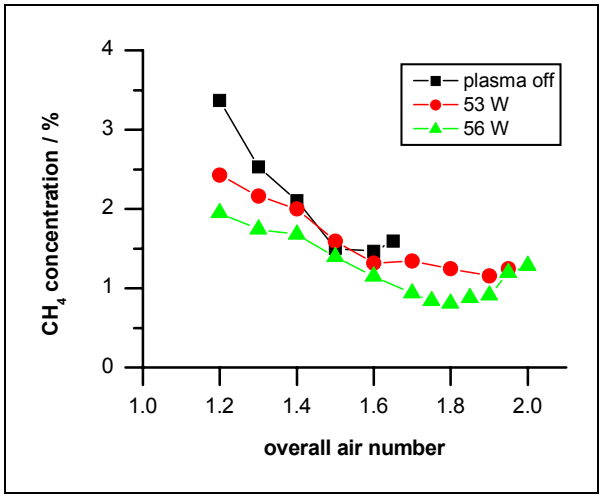

Fig. 4: Concentration of unburnt methane in the flame

The concentration of residual methane, which is measured in the offgas, is displayed in Fig. 4. It is observed that the methane concentration decreases in general with increasing plasma power. This is on the one hand due to the fact that a part of the methane from the inner flow reacts in the reforming unit; on the other hand, the increase in burning velocity in the presence of plasma causes better methane utilization and thus lowers its concentration in the exhaust gas.

With increasing air number the concentration of unburnt methane decreases corresponding to a lower methane concentration of the starting mixture. However, just below the blow-off limit, it rises again forming a minimum in the curve, which lies at $\lambda = 1.8$ at a plasma power of 56 W.

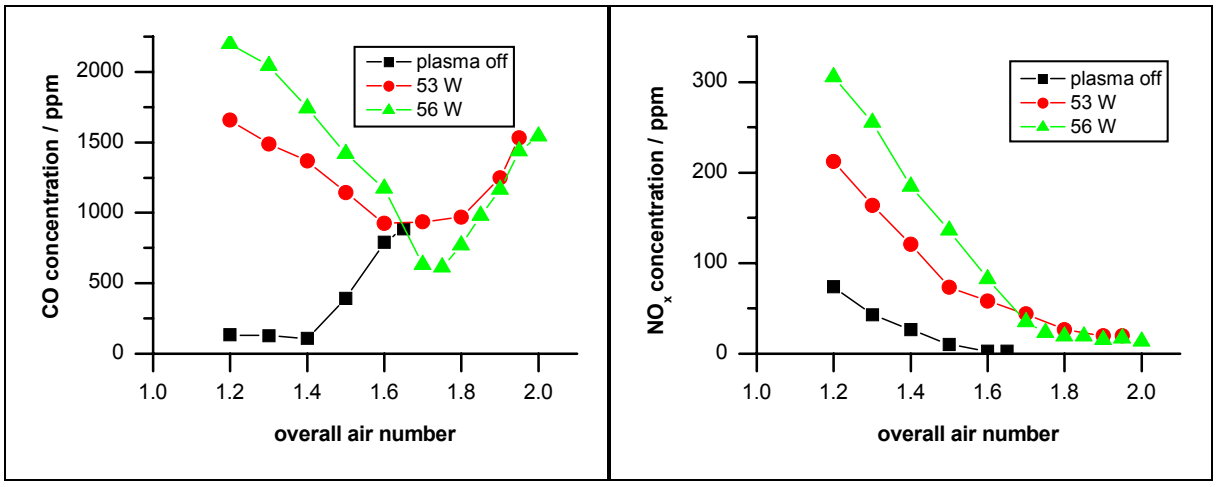

Fig. 5: Concentration of carbon monoxide and nitrogen oxides in the flame

The concentration of carbon monoxide and nitrogen oxides in the flame offgas is represented in Fig. 5 in dependence on the overall air number and plasma power. Without plasma operation the CO concentration remains at a constant and low level of about 100 ppm as long as $\lambda < 1.4$. Nevertheless, at higher air numbers the CO concentration rises rapidly. The reason can be sought in the increasing dilution with air, which reduces the flame temperature and therefore the reaction speed, so that CO cannot be oxidized completely.

In the presence of plasma, the CO concentration is very high at low air numbers, the higher the plasma power the higher the residual CO concentration. This is obviously an effect of the high amount of CO formed in the plasma. However, at $\lambda = 1.6$ approximately, the three curves intersect and the 56 W curve decreases further to

reach a minimum value at about $\lambda = 1.7$. Here the increase of the reaction velocity due to hydrogen combustion could compensate the high feed flow of CO due to plasma reforming.

NO_x emissions show the same tendency without plasma and with varying plasma power applied: a continuous decrease at rising air numbers. This is due to a dilution effect caused by the increase of air flows with growing air number. Moreover, since a higher air flow reduces the combustion velocity and thus also the heat release, the flame temperature decreases. Since the most important NO formation mechanism is that the thermal NO, which, as mentioned, takes only place at very high temperatures, a great part of the emissions could be eliminated by lowering the combustion temperature.

Although the blow-off limits are extended in the presence of plasma, a comparison between the two cases shows that NO_x emissions are always higher than without plasma. This can be mostly attributed to an increase in the burning temperature caused by the additional electrical energy input of the gas discharge and the higher total methane conversion. On the other hand, NO can be generated by the oxidation of ammonia and hydrocyanic acid formed in the plasma reforming step (prompt NO_x).

4. Conclusion

Hydrogen enrichment of lean methane premix flames is a powerful instrument to influence and control the combustion behavior. By integrating a plasma reformer into the burner, the hydrogen enrichment can be done in a compact and flexible way and allows the control of the flame properties with a very low response time. Furthermore the heat loss in the reforming step can be immediately recovered by the lean air mixture.

Blow-off limits can be extended proportionally to the applied discharge power up to values higher than 2, which gives a high flexibility in the choice of operating conditions for the combustion process. The electric power necessary for plasma generation amounts to a maximum of 8.5 % of the chemical input power which is determined by the heat value of the fuel. The emission of unburnt methane can be reduced by nearly a factor of 2, whereas CO and NO_x emissions are higher, at least in the low air number range. An optimum operating point with regard to fuel utilization and reduction of noxious emissions is at an air number 1.8.

References

[1] T.W. Lee, A. Mitrovic - 26th Symposium on Combustion, Naples, Italy (1996).

[2] R.I. Noorani, R.E. Holmes - AIAA Journal, 23, 9 (1984).

[3] H.B. Palmer, J.M. Beér, in: *Combustion technology: some modern developments,* Academic Press New York and London (1974).

[4] E.I. Mintoussov, A.Yu. Starikovskii - 17th International Symposium on Plasma Chemistry, Taormina, Italy (2003).

[5] L.A. Rosocha, D. Platts, D.M. Coates and S. Stange – 1st International Workshop on Plasma-Assisted Combustion, Albuquerque, NM, USA (2003).

[6] J.N. Phillips, R.J. Roby - International Gas Turbine & Aeroengine Congress & Exhibition, Indianapolis, Indiana, USA (1999).

[7] T. Kappes, T. Hammer - 4th International Symposium on Non-Thermal Plasma Technology for Pollution Control and Sustainable Energy Development, Panama City Beach, FL, USA (2004).

[8] A. Czernichowski - Pure & Appl. Chem., **66**, 6 (1994) 1301-1310.

[9] L. Bromberg, D.R. Cohn, A. Rabinovich - Energy & Fuels, **12** (1998) 11.

Hydrogen formation by methane cracking in a cusp plasma device

G. Gervasini[1], M. De Angeli[1], P. Amedeo[1], G. Angella[2], G. Gatto[1], R. Schiavone[1], E. Signorelli[2], N. Spinicchia[1]

[1] *Istituto di Fisica del Plasma "P. Caldirola" Association EURATOM/ENEA/CNR, Milano, Italy*
[2]*Istituto per l'Energetica e le Interfasi CNR, Milano, Italy*

Abstract
A newly approach to the hydrogen recovery from methane by a cusp plasma device is presented. The cusp magnetic geometry is attractive because its high stability on plasma confinement. The paper comments the preliminary results regarding the CH_4 conversion and H_2 selectivity rates (up to 98% and 49% respectively) for different gas mixtures (90-10% to 10-90% of Ar-CH_4) at different fluxes (from 10 to 30 cm^3/min). A study of the influence of the magnetic field is presented too. Future improvements regard the application of an rf signal to increase the hydrogen selectivity, besides the use of a membrane in the plasma phase to recovery the converted H_2 is proposed.
Keywords: methane conversion, hydrogen production, plasma, cusp confinement.

1. Introduction

Hydrogen is supposed to have an important role in the future worldwide energy vector supply and environmentally safe technologies. In the last years plasma has becoming a great alternative for hydrogen production [1]. The addition of a static magnetic field increases the particle confinement time and, consequently, the hydrogen production rate. In this view a plasma device with a cusp magnetic field configuration has been built to investigate the cracking of methane in a plasma environment.
The cusp magnetic configuration approach is very attractive for the purpose of cracking of methane; it has a very simple geometry and the high magnetohydrodynamic stability of the plasma allows to obtain high plasma concentrations with a high dissociation of the CH_4 molecules, besides technique for plasma processing (e.g. radiofrequency ion plugging [2] or hydrogen recovery by permeation membranes [3]) can be easily combined in order to increase the confinement time and allow the recovery of the converted H_2 , they are proposed as improvements of the device.

Here the preliminary results concerning the dissociation of methane in the cusp plasma, measured by quadrupole mass spectrometers and an optical spectrometer, are presented. A large fraction of the converted methane has been deposited along the line cusp vacuum wall as amorphous carbon (a-C) film. The surface morphology of the film has been observed and the results indicate that the film has a prevalently amorphous structure with a significant presence of crystalline clusters.

2. Experiment layout

The experiments have been carried out on the cusp plasma device, developed at the Institute of Plasma Physics in Milan. The cusp magnetic field configuration is obtained by two identical bundles of coaxial solenoids where each bundle carries the same electric current intensity but with opposite directions. The static magnetic field can reach a maximum intensity of 0.5 T at the point cusp and 0.3 T at the line cusp. The experimental apparatus with the vacuum system is shown in Figure 1 (the electromagnets are depicted in dash lines).

The plasma source (labeled PS in the figure) is located at one point of the cusp and is fed with gas (a mixture of Ar and CH_4) through a mass flow controller (FC, model MKS M-200) that maintains a discharge pressure between 10^{-3} and 10^{-2} mbar under a flow rate spanning from 2 to 40 cm^3/min (NTP). The plasma source is a cylindrical rf capacitor composed by an inner tube with 10 mm diameter, 460 mm length, and an outer electrode (ground) represented by the vacuum chamber tube (internal diameter of 60 mm). The plasma source is powered by a commercial 13.56 MHz rf generator with a maximum power of 300 W (Huttinger mod. PFG 300 RF) connected to an automatic impedance matching network. Additional rf power can be coupled to the plasma by means of two ring-shaped electrodes (RSE) which enclose the thin plasma located at the line cusp.

At the second point cusp, opposite to the plasma source, is situated a permeation membrane holder (PR), which is placed at a proper distance from the cusp centre, to allow the plasma, enriched in hydrogen atoms, to strike on the membrane itself. The holder is arranged to mount a 60 mm diameter membrane and is provided with heaters and a thermocouple to monitor the membrane temperature. The permeation membrane is supposed to have a selectivity for hydrogen only (see section 6).

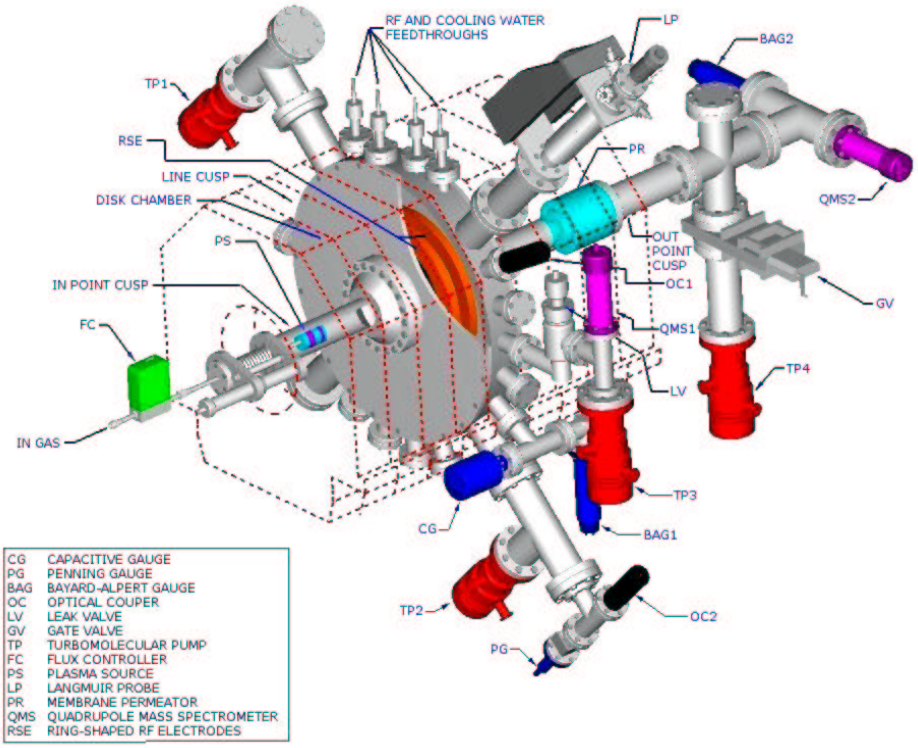

Figure 1 3D layout of the apparatus.

The total pressure in the line cusp chamber is determined by a hot cathode gauge (BAG1) type Bayard-Alpert and by a capacitive manometer (CG) with measuring ranges from 10^{-7} to 10^{-3} mbar and 10^{-3} to 10 mbar respectively. A Langmuir probe (LP), located near the rf ring plates, provides plasma parameters as the electron temperature and the plasma density.
Spectral lines intensities, emitted from the plasma, are provided by a VIS-NUV optical spectroscopy (OC1), model Triax 320 – Jobin Yvon. In particular, the optical collimator OC1 collects the light radially emitted from the centre of the cusp.
The gas composition at the exits of the line cusp chamber and at the second point cusp can be determined by two quadrupole mass spectrometers (QMS1, QMS2) type Balzers QMA 125 adequately screened against the magnetic field [4]. Here gas samples from the cusp chamber are admitted by means of leak valves to the quadrupole volumes; additional turbomolecular pumps provide the gas pumping in these volumes.
Films of the deposited hydrocarbon are obtained from a specimen holder located along the line cusp.

The device is taken under vacuum by two 60 L/s and one 230 L/s single rotor turbopumps. The two 60 L/s (TP1 and TP2) are located at the line cusp and the other pump (TP4) at the second (exit) point cusp.

3. Experimental procedure

The quadrupole mass spectrometers (QMS1, QMS2) are here used for a quantitative analysis of the conversion of methane to hydrogen by measuring the gas partial pressures in the cusp chamber volume (CV). The quadrupoles have been calibrated (determination of the characteristic spectra) for the gases of main concern: hydrogen, argon and methane; while the characteristics spectra of other gases have been taken from literature data. The acquired mass spectra have been analyzed by a multiple linear regression

algorithm that at first automatically detects the gases present in the volume, successively it calculates the gas partial pressures [5].

Before the experiment the CV was pumped at a base pressure of nearly 10^{-7} mbar, the quadrupoles measurements indicate a residual gas composition mainly of water and smaller amounts of CO, CO_2 and hydrogen. Next a known gas mixture of argon and methane is injected inside the source region of the CV volume at a constant flow rate. Quadrupole measurements in these conditions give the reference composition of the introduced gas before the plasma conversion of methane.
Since the methane cracking phenomena is influenced by several parameters (characteristics of the inlet gas mixture, generated plasma and cusp magnetic configuration), some introductory experiments have been performed to maintain nearly constant the influence of the applied static magnetic field (SMF) against the variation of the other parameters. The results are showed in Figure 2 where QMS1 detected ion currents are given respect to the SMF intensity at the point cusp. The detected H_2 signal increases with the SMF intensity and reaches a nearly constant value for SMF larger than 0.1 T; this behavior agrees with the similar decreases of the CH_4 signal. In the following duties, the SMF has been fixed to 0.2 T at the point cusp.

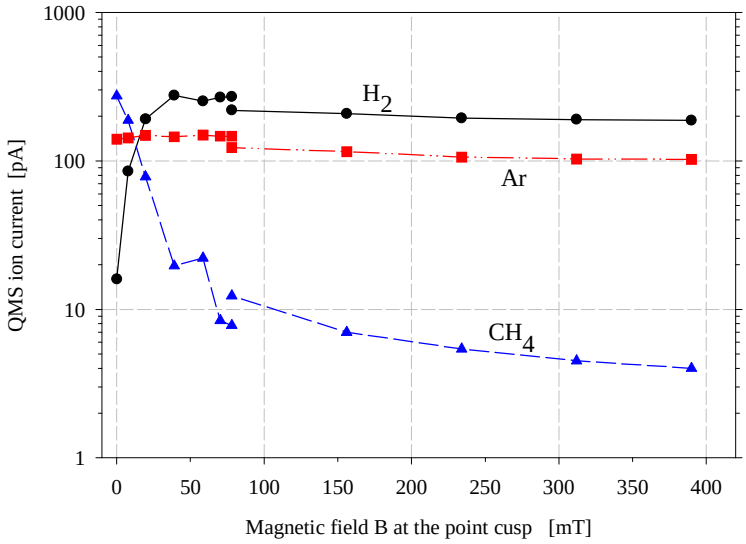

Figure 2 QMS1 detected ion current versus the SMF applied for a mixture of 50% Ar and 50% CH_4. The gas flux is 2 cm^3/min with an rf plasma source power of 100 W.

4. Results and discussion

Plasma parameters have been calculated from Langmuir probe data. The traditional analysis of the voltage-current characteristic has been revised to include the influence of the static magnetic field.
Reliable results have been obtained with argon plasma, since the presence of methane determines a contamination of the probe by carbon deposition. The computed electron temperature is comprised between 5-10 *e*V and the plasma density is within 10^8 - 10^9 cm^{-3}.

The conversion of methane to other compounds is defined as:

$$CH_4 \text{ conversion } (\%) = (\text{moles of } CH_4 \text{ decomposed / moles of } CH_4 \text{ injected}) \times 100. \quad (1)$$

Assuming small differences between the gas temperature with and without the plasma and assuming the hypothesis of perfect gas, the above relationship can be written again in terms of methane partial pressures P_{CH4}:

$$CH_4 \text{ conversion } (\%) = (1 - P_{CH4}/P^0_{CH4}) \times 100 \quad (2)$$

where P^0_{CH4} is the methane partial pressure calculated in absence of plasma.
The conversion of methane to hydrogen is expressed by the hydrogen selectivity according to:

$$H_2 \text{ selectivity} = (\text{moles of } H_2 \text{ produced} / (2 \times \text{moles of } CH_4 \text{ decomposed})) \times 100. \quad (3)$$

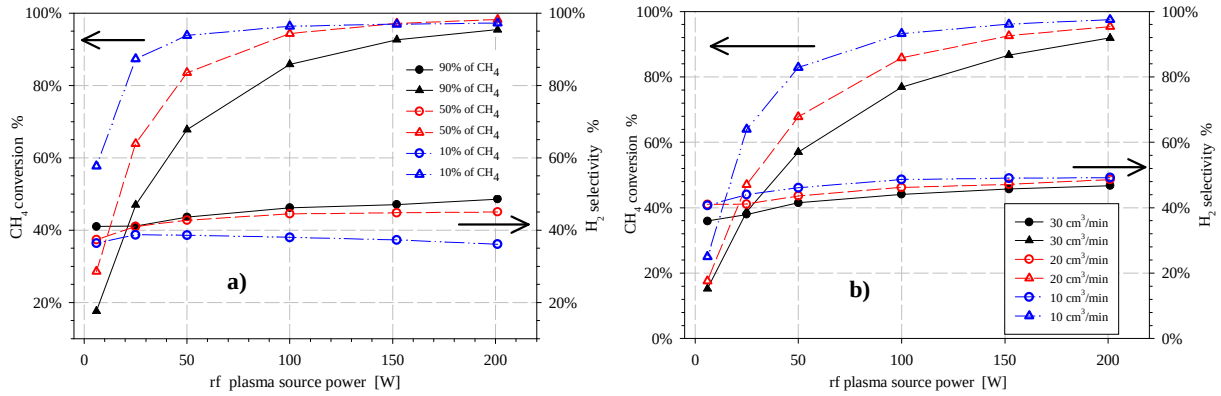

Figure 3 CH_4 conversion (left axes) and H_2 selectivity (right axes) for: a) different inlet gas mixtures at a constant flux of 20 cm^3/min; b) different fluxes of inlet gas mixture at a constant concentration of 10% Ar and 90% CH_4.

The CH_4 conversion and H_2 selectivity are shown in Figure 3a as function of the applied rf power for a constant inlet flux of 20 cm^3/min. At constant rf power discharge, the methane conversion increases with the concentration of argon of the introduced gas mixture. Qualitatively this occurrence can be ascribed to a high concentration of argon atoms in a metastable state [6]. These atoms are characterized by a lifetime comparable or longer respect to the gas or ions collision times. The quenching of the metastable atoms occurs mainly by collisions with methane molecules, with the dissociation of methane in hydrogen atoms and molecules plus methane radicals. Argon metastable states are generated by electron impact excitation.
All these reactions have rates proportional to the electron and argon densities. Besides the SMF configuration of the plasma contributes to increase the overall hydrogen production by expanding the reaction volume (plasma volume) and the confinement time of ions and electrons.
The results in Figure 3a show that above 150 W the methane conversion approaches to 85% while the hydrogen selectivity is less dependent on the rf power and it is comprised between 35-45%. Besides mass spectrometers results have indicated that acetylene and other alkenes compounds are formed, only at high methane flow rate, with concentrations less than 1%.
Figure 3b reports the data relative to an initial 90% CH_4 – 10% Ar gas mixture at different inlet mass flow rates. The methane conversion increases as the gas flow is diminished, that can be supported by a longer residence time of the gas mixture in the plasma volume at lower mass flow rates.

The results from optical spectroscopy are shown in Figure 4 relative to the same set of measurements of Figure 3. The hydrogen emission line at 656.2 nm (H_α of Balmer series) increases with the applied rf power and with the methane concentration in the inlet gas mixture, besides it remains always higher respect to the molecular hydrogen emission line (463.4 nm) which exhibits a less dependence on the applied rf power. Although, from these data, it is not possible to discern the content of atomic hydrogen respect to molecular hydrogen; the results suggest that the applied rf power (in addition to enhance the reactivity in the plasma with a consequent increase of the methane conversion), enriches more and more the concentration of atomic hydrogen of the plasma which is favorable for the foreseen upgrade of the experimental device with permeation membranes working in the plasma phase (see section 6).

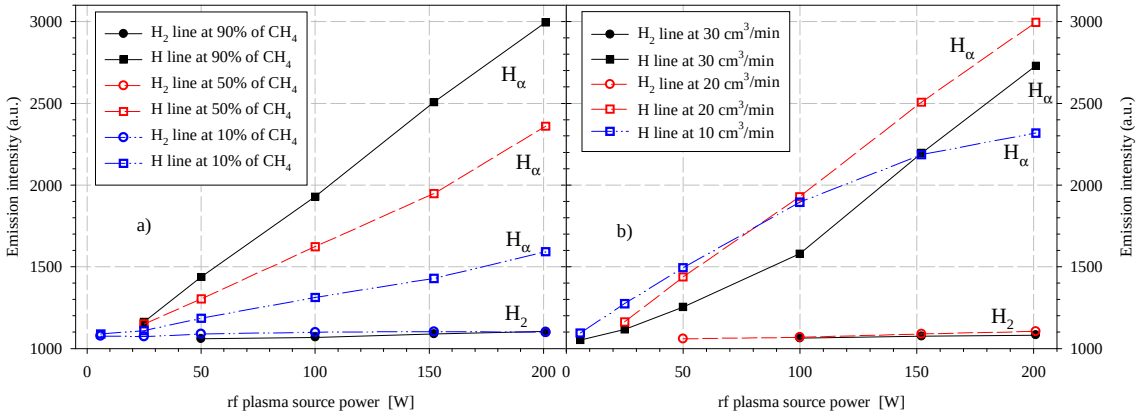

Figure 4 H_α (656.2 nm) and H_2 (463.4 nm) emission lines for: a) different inlet gas mixtures at a constant flux of 20 cm^3/min; b) different fluxes of inlet gas mixture at a constant concentration of 10% Ar and 90% CH_4.

5. Film deposition

A large flux of energetic neutral particles, ions, and thermal radicals is produced and escape from the magnetic field along the line cusp. A portion of such flux has been deposited, as a thin film, on the target/sample mounted along the line cusp.

Observations on the films, by a Fourier Transform Infrared Spectroscopy (FTIR) analysis, showed that a fraction of the converted methane was deposited on the samples as amorphous carbon (a-C) film. In order to investigate the films characteristics and the deposition proprieties, the surface morphology of the films have been examined by scanning electron microscopy (SEM), see Figure 5, while the transmission electron microscopy (TEM) has been used to determine the structure of the films. The results indicate that the films have a significant presence of crystalline clusters embedded in the amorphous structure.

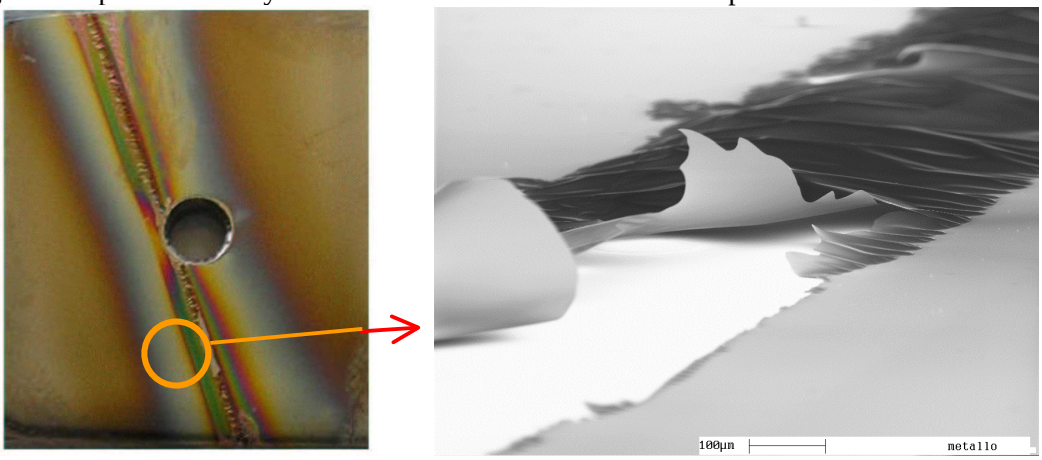

Figure 5 Film deposited on the sample (left) and the enlargement of the rounded particular (right) obtained by SEM.

6. Future improvements

After the preliminary tests on the plasma device here presented, some improvements are under way. They regards: increase of the hydrogen ions confinement time by rf coupling to the plasma and the recovery of hydrogen by means of permeation membranes.

An additional rf signal can be applied to the plasma by the ring-shaped rf electrodes (RSE in Figure 1) which are powered by a broad band rf generator at a frequency close to the ion cyclotron frequency of hydrogen. The rf field generated by the electrodes will be perpendicular to the plasma disk of the line cusp and, according to the theory [7], a repulsive ponderomotive force (directed from the line cusp to the cusp

centre) acts on the plasma species depending on their mass to charge ratio. It will be possible increase the concentration of hydrogen ions against other ions species.
A niobium superpermeable membrane can be mounted inside the permeation holder (PR) at the exit point cusp. This kind of membrane, that can be heated at a temperature around 400 °C, has a high permeation coefficient for *atomic* hydrogen (almost the whole flux pass through the membrane) and negligible for the other species. Moreover, a partial poisoned surface (e.g. with monolayer of deposited carbon atoms) has a beneficial effect to increase the hydrogen atoms permeation [3,8]. The membrane in touch with the plasma is a great way to separate the hydrogen atoms from other particles before their recombination outside the plasma phase.
The increase of the plasma characteristics, density and degree of ionisation, will be achieved by a new plasma source antenna powered at a higher rf frequency (40.68 MHz). The source will allow to operate at higher gas flow rates respect to the values here investigated, in this conditions it is expected a further increase in the methane conversion efficiency.
Besides more advanced diagnostics (e.g. ion mass spectrometer with ion energy analyser, and gas chromatograph) will allow a more comprehensive analysis of the methane cracking phenomena.

7. Conclusions

The plasma device, here proposed, for the decomposition of methane and the hydrogen production presents many advantages:

- a high reaction rate which is enhanced by the cusp magnetic confinement;
- the presence of water and oxygen in the system in negligible quantities exclude the formation of greenhouse gas (like CO_2) by methane steam reforming reactions;
- since the device is based on a physical principle, the possibility to operate with other gases; e.g. hydrogen formation from water vapor.

The results, here presented, may be considered preliminary since they are limited to a low methane flow rate regime. The most significant achievements are: methane decomposition higher than 90% and hydrogen selectivity close to 50%

Some upgrades of the experimental device are in realization, they will allow: to operate with higher plasma densities (and with higher inlet gas flow rates) and to increase the selectivity and production of hydrogen. One improvement employs rf coupling to the plasma to increase the confinement time of hydrogen ions. Another improvement takes advantage of the composition of hydrogen plasmas that present a high content of hydrogen in atomic form. In this case the use of superpermeable membranes will increase the selectivity of hydrogen thanks to their high permeation rate for atomic hydrogen, and no-permeability respect to other gases.

Acknowledgement

This work was supported by the Euratom Communities under the contract of Association between EURATOM/ENEA/CNR. The views and opinions expressed herein do not necessarily reflect those of the European Commission.

References

[1] H. Nagazoe, H. Naito, M. Kobayashi, T. Yamaguchi, H. Rimuro, K. Onoe – Proceedings of the 16th International Symposium on Plasma Chemistry, June, 22-27, 2003, Taormona, Italy.
[2] T. Watari, S.Hiroe, T. Sato, S.Ichimaru – Phys. Fluids **17**, 2107 (1974).
[3] A.I. Livshits, F. Sube, M.N. Solovyev, M.E. Notkin, M. Bacal – J. Appl. Phys. **84**, 2558 (1998).
[4] M. De Angeli, G. Gervasini, G. Gittini - proceedings of "*Atti del XVII congresso dell'Associazione Italiana del Vuoto*", June 28 – July 2, 2005, Venezia, Italy; Editrice Compositori, Bologna, Italy.
[5] G. Gervasini – Vuoto **27**, 19 (1999); see also: www.aiv.it/eng/pubblicazioni
[6] S. V. Avtaeva, M. Z. Mamytbekov, D. K. Otorbaev – J. Phys D Appl. Phys. **30**, 3000 (1997).
[7] T. Watari, S.Hiroe, T. Sato, S.Ichimaru – Phys. Fluids **17**, 2107 (1974).
[8] Y. Nakamura, A. Busnyuk, H. Suzuki, Y. Nakahara, N. Ohyabu, A. Livshits - J. Appl. Phys. **89**, 760 (2001).

Atmospheric pressure dusty plasmas

V.E. Fortov[1], A.V. Filippov[2], V.N. Babichev[2], A.F. Pal[2], A.N. Starostin[2]
[1]*Institute for High Energy Densities, Russian Academy of Sciences, Moscow, Russia*
[2]*Troitsk Institute for Innovation and Fusion Research, Troitsk, Moscow reg., Russia*

Abstract
It is reported about the results of studying the stationary non-self-sustained discharge controlled by a fast electron beam in atomic and molecular gases containing dusty particles of microns in size. It was predicted and experimentally found that there occurred the formation of stable dusty structures in this plasma. Modelling of the non-self-sustained gas discharge has been performed according to the non-local transport model of plasma charged particles with electron diffusion taken into account.
Keywords: dusty plasma, e-beam ionization, non-self-sustained discharge, cathode sheath.

1. Introduction

At present, small-sized 1 – 10 kW autonomous sources of electric energy with an operating lifetime of the order of several years are in demand. Such sources are needed for electric power supply of spacecraft, automatic weather stations, antisubmarine buoys, and for other similar users [1]. At present, such sources are provided by photoelectric converters of solar energy, thermoelectric sources with fuel elements of Sr^{90}, Pu^{238}, or Po^{210}, and thermionic converters with a U^{235} reactor used as a heat source. All of these sources suffer from a number of disadvantages; in particular, they have a very low efficiency. In addition, a nuclear reactor is very complex in fabrication.

Given in this paper are the results of investigations aimed at developing the physical principles of a current source for nuclear-to-electric energy conversion. It is suggested to accomplish this conversion owing to the photovoltaic effect in wide band-gap semiconductors based on CVD of diamond and boron nitride. The operating principle of the novel atomic battery is as follows [2]. High-energy particles, which are formed during decay of radioactive materials in the form of dust grains, ionize an inert gas such as xenon at a pressure of about an atmosphere or higher. The dissociative recombination of formed diatomic xenon ions results in an effective excitation of xenon excimers which emit vacuum ultraviolet (VUV) photons with a wavelength of about 172 nm. These photons fall on a wide band-gap diamond-based photoconverter and generate electron-hole pairs which are separated and develop an electromotive force. Estimates indicate that the total efficiency of a battery utilizing this principle may be as high as 25 – 35%.

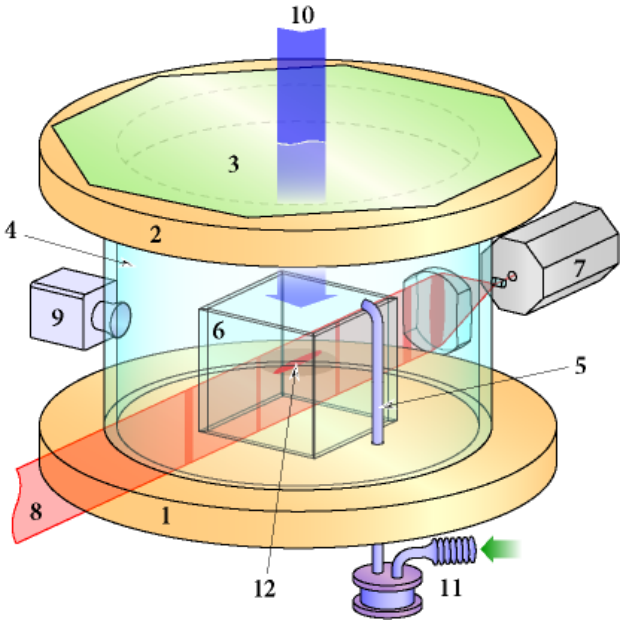

Fig.1. The picture of the experimental setup. (1) the Cu electrode, usually cathode; (2) the top electrode; (3) the Al foil; (4) the cylindrical chamber; (5) the dust particle injection tube; (6) the glass cubic; (7) the He-Ne laser; (8) the laser "knife"; (9) the digital video camera; (10) the e-beam; (11) the dust particles injection system; (12) the dust particles.

One of the key problems in developing such an energy source is creating homogeneous gas dusty mixture with the suppressed sedimentation and/or the hindered deposition of dusty particles on the walls. To solve this problem as well as to decrease the loss of ultraviolet quanta formed under the action of high energetic radionuclide decay particles in the noble gas medium when these quanta are transported to the photoelectric converter it is necessary to create an ordered structure of dusty particles. The present work is devoted to studying the dusty plasma created by the injection of dusty particles into the gas ionized by an electron beam under atmospheric pressure.

2. Experiments

The scheme of the experimental setup is presented in the fig.1. The electron beam (10) with energy varied within 85-115 kV was formed by the vacuum gun with the heated cathode and was then directed through the aluminum foil (3) of 14 μm in thickness into the cylindrical chamber of 7 cm in diameter and 3 cm in height. To suppress the convection, in the central area of the chamber there was a glass cube (5) that was top (from the direction of the electron beam) and bottom (above the bottom electrode) open, the cube's edge being about 1.5 cm. The massive bottom Cu electrode (1) was under the constant negative voltage of 200-4000 V. The anode was a grounded grid on the top of the glass cube. The beam current density in experiments was varied within 0.1-1.0 μA/cm^2. The electron gun operated in the stationary regime. The injection of dusty particles from the storage was performed by the gas flow. The behavior of dusty particles lighted by a laser "knife" (8) was observed with a digital video camera (9).

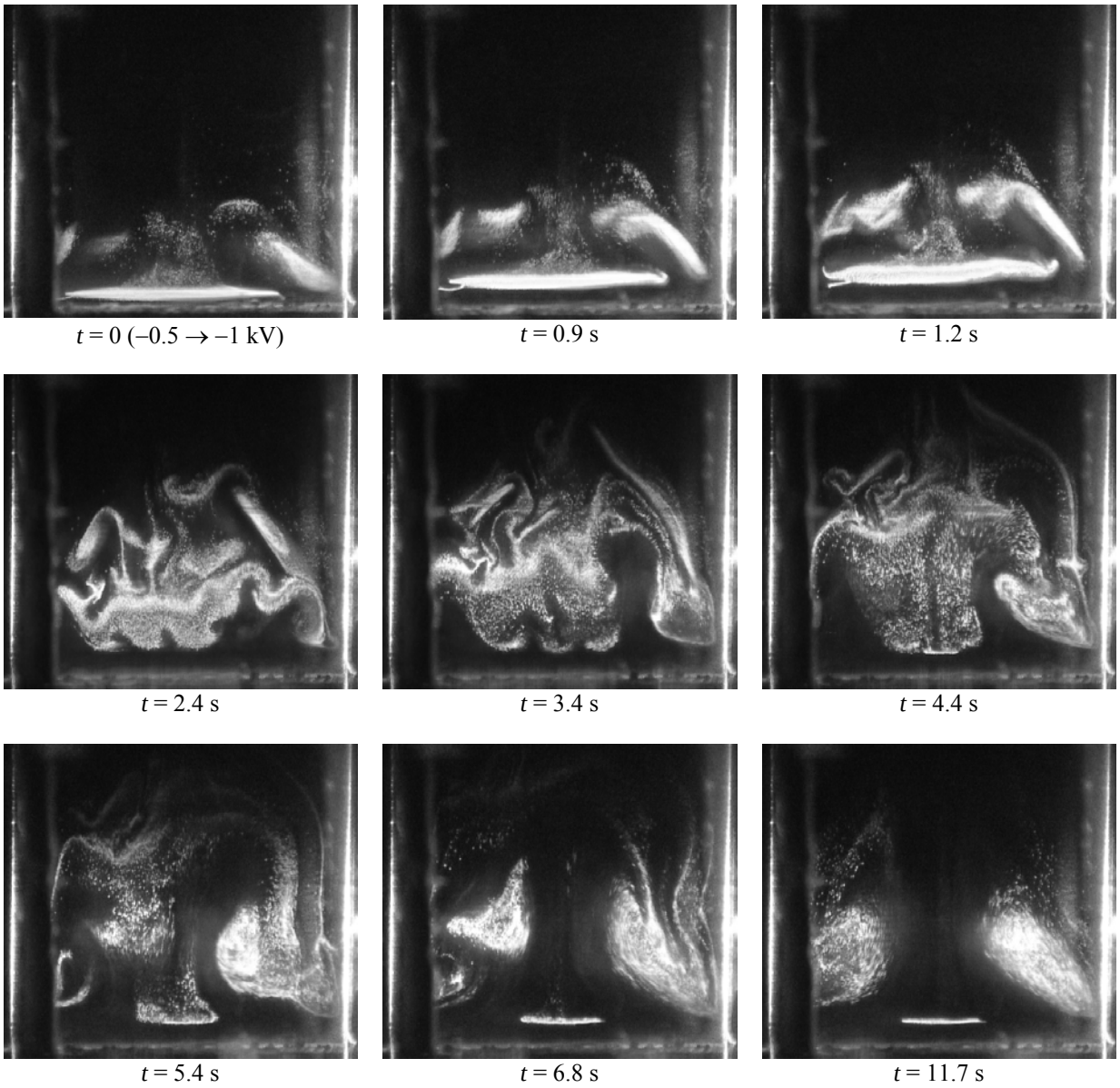

Fig.2. Video frames of the dusty structure evolution in the non-self-sustained discharge in nitrogen when the voltage in the discharge gap is changed from 500 V to 1000 V ($p = 10^5$ Pa, the beam current at the output window of the electron gun is j_b=22 μA/cm^2).

In fig.2 there are frames from a video-film which was made under the accelerating voltage of the electron gun of 115 kV, the beam current density of 100 μA in nitrogen under the pressure of 10^5 Pa with polydisperse CeO_2 dusty particles with the mean size of 1 μm. The first frame in fig.1 shows a stable plate-like structure of dusty particles. The following frames show the evolution of the plate under the step change in the voltage in the discharge gap. The voltage on the bottom electrode, –500 V, was changed to –1000 V under $t = 0$ that resulted in the explosion of the dusty cloud, which 12 seconds later ended in the formation of a plate with a clear-cut side boundary at another height. Above the plate near the side walls of the cube there formed stable vortices whose bottom boundary practically coincided with the location of the plate.

When the bottom electrode was grounded, all dusty particles were deposited on it in about 0.1 s, and when the grounding was removed and the initial voltage supplied there occurred a throwing of dusty particles upward. In this case the plate was not restored, but vortices appeared at the former sites. After the injection of a new portion of dusty particles there formed a more developed plate and vortices at the same sites. It should also be noted that no dusty particles penetrated into the cube area lower than the plate either after the injection or in the course of the following movement. However, in the discharge chamber outside the cube where the vortex motion of dusty particles is more accelerated due to the convective flux the particles could be observed near the bottom electrode. For unchanged parameters the picture described above about dusty particles moving in the discharge gap in the cube also remained unchanged.

Replacing nitrogen by argon in the experiments caused the formation of more stable dusty structures without auxiliary vortical motion of dust particles that more adequately simulated the working regime necessary in the atomic battery. In fig.3 there are dust particle structures which form in argon. In fig.3a there is a CeO_2 particle structure, and in fig.3b there is a structure from polydisperse spherical carbonglass particles whose average radius is 3 μm. Fig.3c shows the image of the low central area of fig.3b dust plate with a five-fold magnification. It is seen that there formed a structure similar to the crystal one with the average inter-particle distance of 150-250 μm.

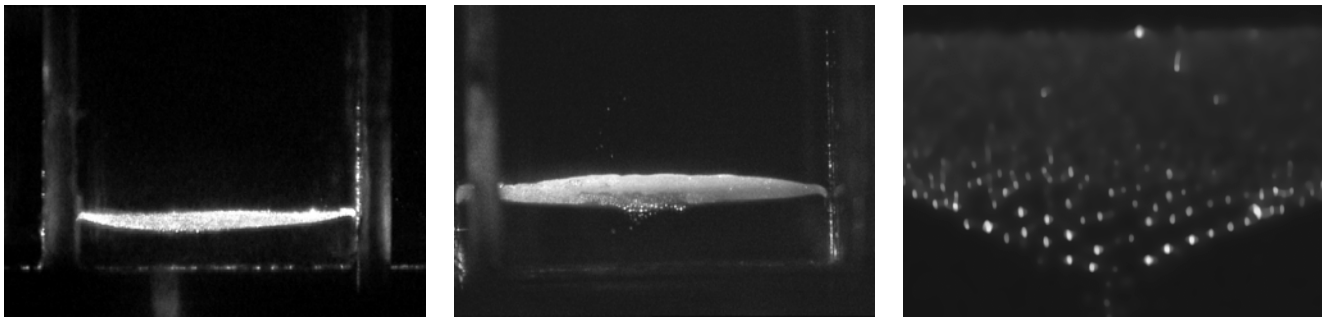

(*a*) (*b*) (*c*)

Fig. 3. Video images of dusty structures in the non-self-sustained discharge in argon under the pressure of $p = 10^5$ Pa, the voltage at the low electrode of U_d=–0.5 kV. and of 22 μA/cm^2. (*a*) CeO_2 particles, j_b=22 μA/cm^2; (*b*) carbon glass spherical particles, j_b=15 μA/cm^2 and (c) the magnified central bottom part of dusty plate from (b).

It was shown in [3] that it was at low gas ionization rates of about 10^{14} cm^{-3}s^{-1} that the formation of ordered plasma-dusty structures was possible. In order to determine the fulfillment of a condition for the levitation of dusty particles in the non-self-sustained discharge in nitrogen the numerical simulation of the cathode sheath was performed according to the non-local model for transport processes, we had developed this model to study the charging of dusty particles [4]. The non-local model of the non-self-sustained discharge consisted of electron and ion number balance equations, the balance equation for electron temperature and the Poisson equation. The numerical simulation offers a clearer view of formation mechanism of dusty trap in the non-self-sustained discharge and verification of fulfillment of a condition for the levitation of dusty particles.

3. Discussion

In the experiments the typical transverse size of the discharge area was 5 times as large as the size of the cathode layer, and the gas ionization according to the calculation by the Monte-Carlo method and by the analytical theory developed by us was quite homogeneous along the radius, therefore, the modelling was performed within one-dimension plane geometry. Fig.4 shows the distribution calculated within the analytical theory for the gas ionization rate in nitrogen and argon under the pressure of 10^5 Pa along the discharge symmetry axis.

Fig.5 shows the distribution of electrical field strength and potential in the cathode layer. The produced pictures are in good agreement with the results of the analytical consideration [5]. It is seen that the field is weak in the positive column, and in the cathode area the field sharply grows. In the anode area in argon there forms a region with the negative electrical field strength, which is due to the diffusion component of the electron flow to the anode when the field in the positive column is weak. When the discharge voltage is increased the non-self-sustained discharge transfers into the normal regime with the self-sustained ionization in the cathode layer and the region with a negative field near the anode disappears. In nitrogen this region also forms, but the absolute values of the field there are much lower than those in argon.

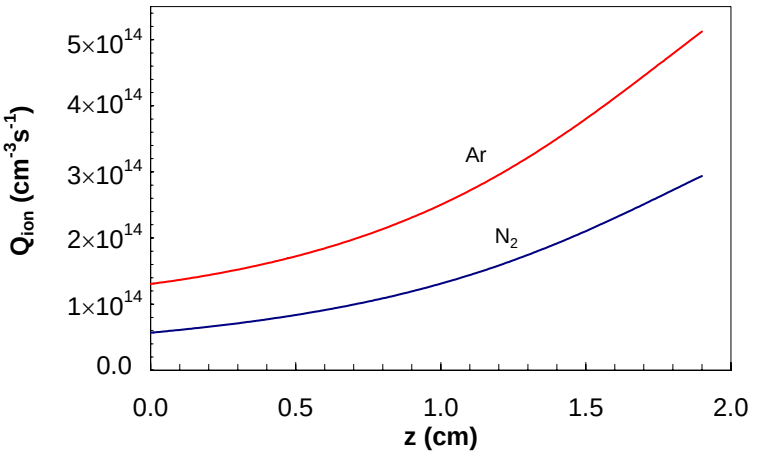

Fig. 4. Distribution of the gas ionization rate under the electron beam current density of 22 μA/cm^2 at the output window of the electron gun and the accelerating voltage 120 kV at the pressure of 10^5 Pa.

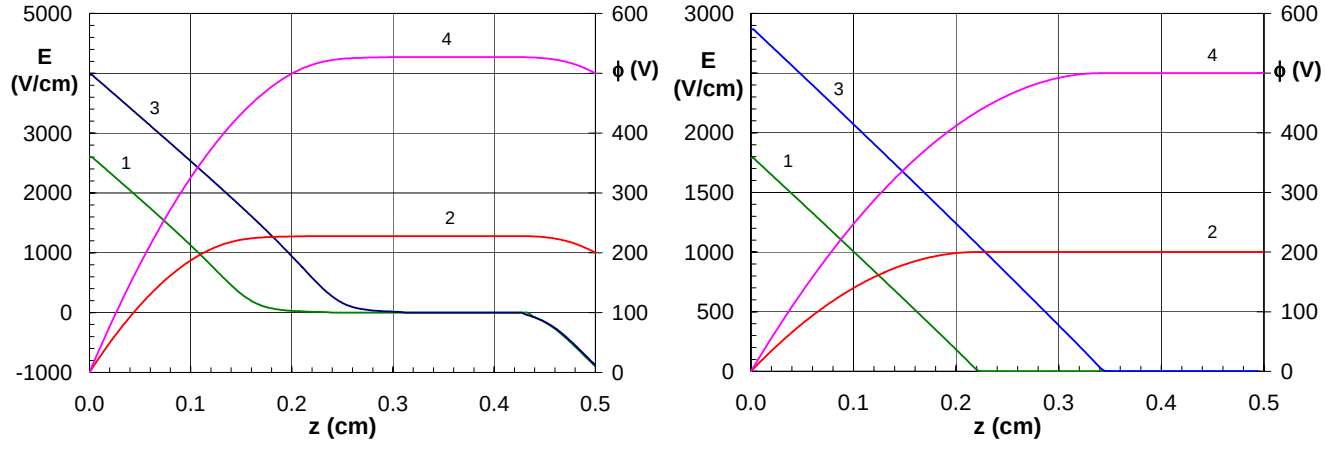

Fig. 5. Distribution of the electrical field strength (1,3) and potential (2,4) in the cathode layer under different voltages at the cathode in Ar (**a**) and N_2 (**b**) for $p = 10^5$ Pa, $L = 0.5$ cm, $j_b = 22$ μA/cm^2. 1, 2 – $U_d = 200$ V, 3, 4 – $U_d = 500$ V.

Let's estimate the electrical force acting upon dust particles in the cathode layer. As it was shown in [2], when the gas ionization rate is low the electron distribution in the vicinity of a dust particle is well described by the Boltzmann distribution, and the flow of ions to the dust particle rather well coincides with the Langevin one. For this case we have the following transcendental equation to estimate the charge of dust particles with taking into account the difference between the density of electrons and ions in the cathode layer

$$j_e = 4\pi r_0^2 \cdot \tfrac{1}{4} n_e \mathrm{v}_{T,e} = \pi r_0^2 n_{e0} \mathrm{v}_{T,e} \exp\left(e\phi/T_e\right) \equiv j_i = -4\pi e k_i q n_{i0}$$

where r_0 is the radius of dust particles, n_{e0}, n_{i0} is the density of electrons and ions in the considered point of the cathode layer far from the dust particle, $v_{T,e}$ is the thermal velocity of electrons, ϕ is the potential of a dust particle, T_e is the temperature of electrons, k_i is the mobility of ions, q is the charge of a dusty particle in elementary charges. On the assumption of vacuum-type relation between the charge and the potential $\phi = eq/r_0$ this equation can be easily numerically solved. The calculations showed that near the cathode where there were practically no electrons the charge of dusty particles became positive. In fig.6 there is dependence of forces acting on CeO_2 dust particles of r_0=1 μm in nitrogen and carbonglass dust particles of r_0=3 μm in argon in the cathode layer upon the distance from the cathode. It is seen that in the cathode layer there considerably increases the force making dusty particles move upwards. The points where curves 1,3 intersect curve 5 and curves 2,4 intersect curve 6 determine the equilibrium position of dusty particles in the cathode layer. The dust particle equilibrium positions determined from the video images and from the calculation data are given in the table.

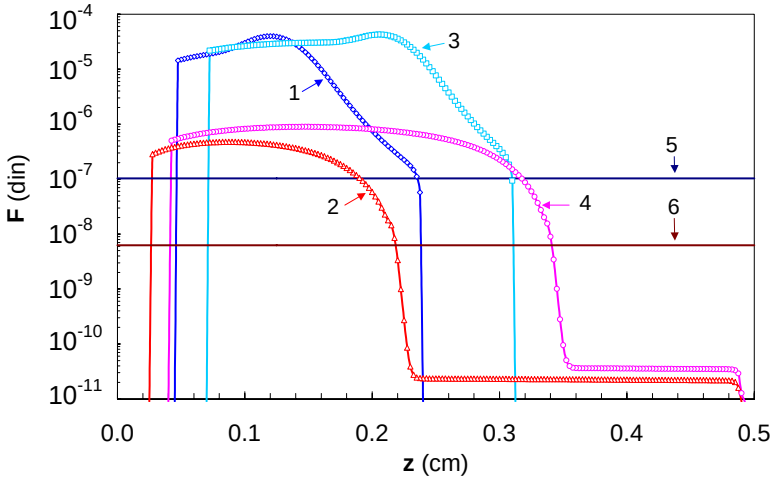

Fig. 6. Forces, acting upon dusty particles in the cathode layer, as a function of the distance from the cathode under different voltages at the discharge gap in Ar (1,3) and N_2 (2,4) for p = 1 atm. 1,2 – the Coulomb force for U_d = 200 V and 3,4 – that for U_d = 500 V; 5,6 – the gravity force for carbonglass dust particles of r_0=3 μm and for CeO_2 dust particles of r_0=1 μm respectively.

It is seen that in argon there is a satisfactory agreement of the experiment with the calculation, and that in nitrogen the disc forms at a much lower level than in the calculation. Neither the addition of oxygen to the plasma model (up to 1%), nor the change in the electron recombination coefficient by an order of the magnitude, nor the consideration of the additional gas ionization by a fast electron beam reflected from the cathode resulted in the better agreement of the calculation with the experiment in nitrogen. The reason for the divergence can be due to the fact that the gas in the near cathode region is highly heated that is most clearly seen in nitrogen.

Table. Experimental and calculation values for the equilibrium height of the dust plate structure in the cathode layer.

Gas	U_d	–200 V	–500 V
Argon	Experiment	0.12	0.18
	Theory	0.23	0.31
Nitrogen	Experiment	–	0.06
	Theory	0.22	0.34

Let's carry out estimations of the non-ideality parameter of the dusty component in the structure given in fig.3c. The non-ideality parameter of the Debye plasma is determined by the following expression [3]

$$\Gamma_s = \frac{e^2 q^2}{a T_d} \exp\left(-a / R_{sh}\right),$$

where $a = \left(n_d\right)^{-1/3}$ is the mean inter-particle distance, n_d is the dust particle density, T_d is the temperature of the dust component in energetic units, R_{sh} is the shielding radius. It was shown in paper [6] that the shielding radius in non-isothermal plasma with the external ionization source for the condition $\beta_L > \beta_{ei}$ was determined by the expression

$$R_{sh} = R_{De}\sqrt{\frac{\beta_L}{2\beta_{ei}}} = \sqrt{\frac{k_i T_e}{2\beta_{ei} e n_{e0}}},$$

where β_{ei} is the coefficient of electron-ion recombination, $\beta_L = 4\pi e k_i$ is the coefficient of Langevin recombination of ions. The calculations showed that in the area of the structure levitation given in fig.3c the electron temperature changes within the range of 0.1-1.0 eV, decreasing with the increase in the distance from the cathode. In argon under atmospheric pressure the basic ion in plasma is Ar_2^+, whose dissociative recombination coefficient is [6]

$$\beta_{ei} = 0.85\times10^{-6}\ (0.025/T_e)^{0.67}\ \mathrm{cm^3/s}$$

(T_e is in eV) and whose mobility under atmospheric pressure is $k_i = 2.1\ \mathrm{cm^2/V\cdot s}$ [6]. Thus we obtain that $\beta_L = 3.8\times10^{-6}\ \mathrm{cm^3/s}$, and the shielding radius

$$R_{sh} \approx 200\ T_e^{0.67}\ \mu\mathrm{m}$$

(T_e is in eV) changes from 200 μm in the low part of the structure down to 40 μm in the top part. It should be noted that the electron Debye radius for our plasma parameters changes as

$$R_{De} \approx 38.5\ T_e^{0.33}\ \mu\mathrm{m}$$

(T_e is in eV) and varies from 38.5 to 18 μm in the high ordered dust structure. Taking into consideration that the charge of dust particles is directly proportional to the electron temperature and is equal to $q \approx -3000T_e$ (T_e is in eV) for carbonglass particles, we obtain that the non-ideality parameter decreases from 1000 down to 2 with the increase in the distance from the cathode, and the critical value of the non-ideality parameter [3] changes from 54 down to 15. Therefore, we can come to the conclusion that the observed structure is similar to the crystal one in the low area and turns to liquid and then gas at the increase in the distance from the cathode.

This work was supported by Russian Foundation for Basic Research, projects 04-02-16883 and 04-02-08085.

References

[1] V.Yu. Baranov, A.F. Pal', A.A. Pustovalov, at al - Radioisotope Sources of Energy. In "Isotopes: properties, production and application", Ed. by V.Yu. Baranov, Moscow: Fizmatlit, v.**2**, p.259 (2005).

[2] L.V. Deputatova, P.P. D'yachenko, N.A. Dyatko, at al - Atomic Battery Based on Ordered Dust-Plasma Structures. TRINITI Preprint 113-A (2004)

[3] A.F. Pal', D.V. Sivokhin, A.N. Starostin, A.V. Filippov, V. E. Fortov - Plasma Phys. Rep. **28,** 28 (2002)

[4] A.V. Filippov, N.A. Dyatko, A.F. Pal', and A.N. Starostin - Plasma Phys. Rep. **29**, 190 (2003)

[5] J.J. Thomson, G.P. Thomson - Conduction of Electricity Through Gases, 3rd ed., Cambridge University Press (1928).

[6] A.V. Filippov, A.G. Zagorodny, A.F. Pal', A.N. Starostin - JETP Letters **81** (4), 146 (2005).

Copolymerization of Chloroform with Heteroaromatic Polymers by Plasma

G.J. Cruz[1], M. Vásquez[1], M.G. Olayo[1], J. Morales[2], R. Olayo[2]

[1]*Departamento de Síntesis y Caracterización, Instituto Nacional de Investigaciones Nucleares, Ocoyoacac, México.*
[2]*Departamento de Física, Universidad Autónoma Metropolitana Iztapalapa, D.F., México.*

Abstract
This work presents a study on the processes of copolymerization by plasma of polypyrrole and polythiophene with chloroform. The main objective was to study the interaction of halogens with heteroaromatic polymers from the point of view of the transport of electric charges along the material. This kind of polymerization can be seen as a hybrid combination of fragmentation, polymerization and doping processes, because some of the fragments resulted from the decomposition of chloroform by plasma can be considered as dopants in the chemical reactions.

Introduction
The polymerization by plasma usually involves particles with energy that can go beyond the level of most of the chemical bonds found in organic compounds (3-6 eV). The amount of collisions with high energy particles break bonds and promotes the creation of new ones in such a way that the polymerization occurs in a sea of fragments of molecules, free radicals and ions. In those conditions, the chemical reactions have to be directed to obtain a reasonable proportion of the expected results, and they can only be manipulated by controlling the electric and the thermodynamic variables. In the same scheme, the doping of polymers occurs by the inclusion of different atoms, molecules or excited species and, depending on the electronic configuration of the dopants, they modify the electronic balance in the material. In a traditional doping, the dopants release the polymers along time or under strong conditions; however, if sufficient energy is applied to a dopant-polymer system, as in a plasma environment, chemical bonds could appear between them, transforming the doped material in different chemical compounds, making the function of the dopants far more complex [1].
In this work we studied the possibility of using chloroform and their fragments, resulted from the high energy collisions with the plasma particles, to form copolymers doped in-situ to modify the electronic configuration in pyrrole and thiophene polymerized by plasma in order to enhance the electric conductivity of the final material. Chlorine in these polymers can be seen in the same way as the traditional solid state dopants, whose fundamental function is to modify the clouds of charges through the entire polymeric network in order to facilitate the electric conduction. The chlorinated polypyrrole (PPy-Cl) and polythiophene (PTh-Cl) were synthesized in this way with resistive glow discharges at 12 W and $7x10^{-2}$ Torr.

Results

Elemental composition
The elemental analysis is discussed in this work to evaluate the participation of the chloroform in the polymers. The atomic carbon/nitrogen (C/N) ratio in PPy and the sulphur/carbon (C/S) ratio in PTh should have the same proportion as in the respective monomers, 4. However, considering the additional C atoms from the chloroform in the polymerization, those ratios should be slightly greater than 4. Table 1 presents the elemental composition of PPy-Cl and PTh-Cl synthesized by plasma. The atomic proportion in the polymers shows that the C/N ratio in PPy-Cl is 4.44, whereas the C/S ratio in PTh is 4.12.

Polymer	C	N	O	S	Cl	C/N	C/S
PPy-Cl	70.8	15.9	9.3	----	4.0	4.4	---
PTh-Cl	70.2	----	9.4	17.1	3.3	---	4.1

Table 1. Elemental composition of PPy-Cl and PTh-Cl.

The oxygen atoms can be attributed to the reaction of the residual radicals in the polymers, which survive at the end of the reactions, with the atmospheric oxygen. As the conditions at the end of the syntheses in both polymers are approximately the same, the oxygen percentages in both polymers are also approximately the same.

Structure

The IR and XPS spectra of both polymers suggest that some chlorine atoms are chemically linked to the pyrrole or to the thiophene rings. The absorption at 613 cm^{-1} in the spectra of Fig. 1 belongs to C-Cl bonds in both polymers. This absorption is part of a wide band involving also the C-S bonds in PTh-Cl and the substitutions of C-H bonds in the heteroaromatic rings.

The C-H aliphatic bonds can be found between 2927 and 2969 cm^{-1}. These groups can be originated from the fragments of chloroform, pyrrole and thiophene due to the high energy discharges. The absorption around 3037 cm^{-1} indicates the presence of C-H aromatic bonds. In both polymers, the aliphatic and aromatic absorption of C-H groups have approximately the same magnitude, indicating, by analogy, that the polymers could be composed with the same proportion of aliphatic and aromatic fragments of chloroform and their respective polymers.

The peaks at 1654 and 1685 cm^{-1} belong to the C=C bonds of PPy-Cl and PTh-Cl, respectively. Both absorptions are partially overlapped by the C-N and C-S groups.

The absorption at 1041 cm^{-1} can be attributed to the oxidation resulted from the interaction of the last free radicals, at the end of the polymerization, with the atmospheric oxygen. The oxygen groups can recombine with hydrogen atoms to form alcohols, C-O-H. This possibility appears also in the XPS analysis. The N-H and/or O-H groups are located in the wide band involving the 3353 cm^{-1} and 3216 cm^{-1} region.

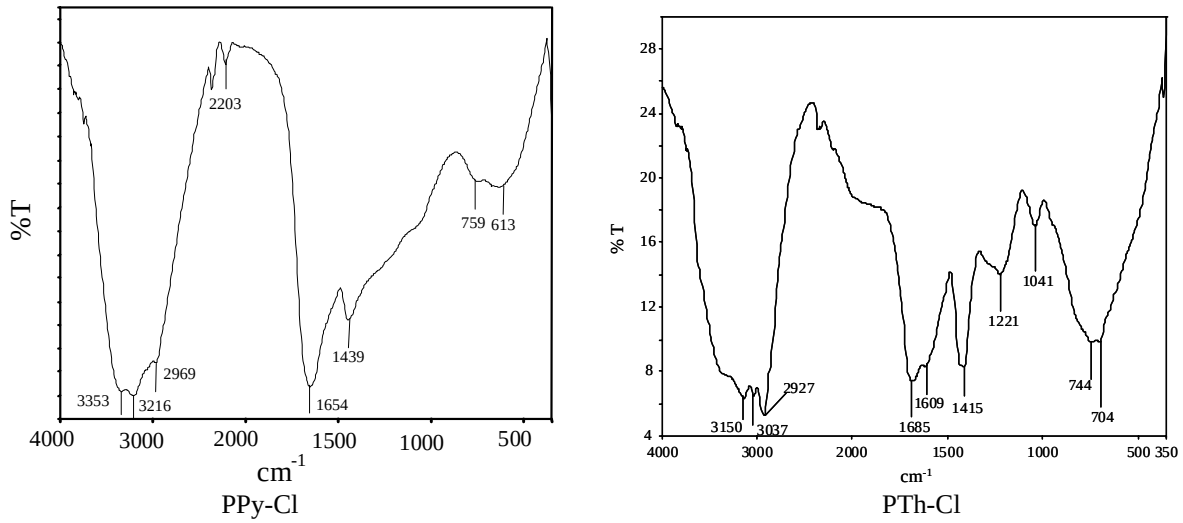

Figure 1 - FT-IR transmission spectra of PPy-Cl and PTh-Cl.

Figure 2 shows the binding energy of the C 1s, N 1s, O 1s and Cl 2p peaks of PPy-Cl and PTh-Cl. Each contribution was deconvoluted with the most probable groups in the polymers. The C1s spectrum of PPy-Cl can be resolved in five peaks. The energy at 284.4 eV can be assigned to the C=C bonds in the pyrrole rings. The peak at 285.0 eV belongs to the C-C and C-H groups; they include the aliphatic carbon bonds. The peak at 286.4 eV implies contributions of C=N and C-O bonds, most probably as a consequence of the polymer oxidation at the end of the reactions. It includes also the contributions of the chlorine atoms as C-Cl bonds. The fourth peak, at 287.7 eV, can be assigned to the C=O groups. The last peak at 288.6 eV can be assigned to C-O and C-N groups.

There are two contributions in the adjustment for the N 1s spectrum. The first one is centered at 399.2 eV and corresponds to both N-C and N-H bonds. The second peak is found at 400.5 eV and is related to the contributions from amine groups. The S 2p signal was adjusted with two contributions. The first one in 163.5 eV represents the S-C groups [2], and at 165.0 eV, the vibration of the sulfur into of the thiophene rings is found [3].

The O 1s signal can include two contributions: the main signal is found at 531.8 eV which belongs to C-O and

C=O groups, whereas the other contribution at 533.6 eV represents the C-O bonds. The C12p signal can be resolved into two doublets, the first one at 197 eV corresponding to chlorine anions, while the other at ~200 eV corresponding to covalent chlorine [4].
Both, XPS and IR analysis suggest that the energy of the plasma is sufficient to break the chloroform molecules and that the fragments combine with the polymers to form chains with aliphatic fragments bonded to them. The fragments come from the chloroform and from some pyrrole and thiophene rings that break during the polymerization. Both techniques suggest the presence of oxygen in the polymers which could be as alcohol groups.

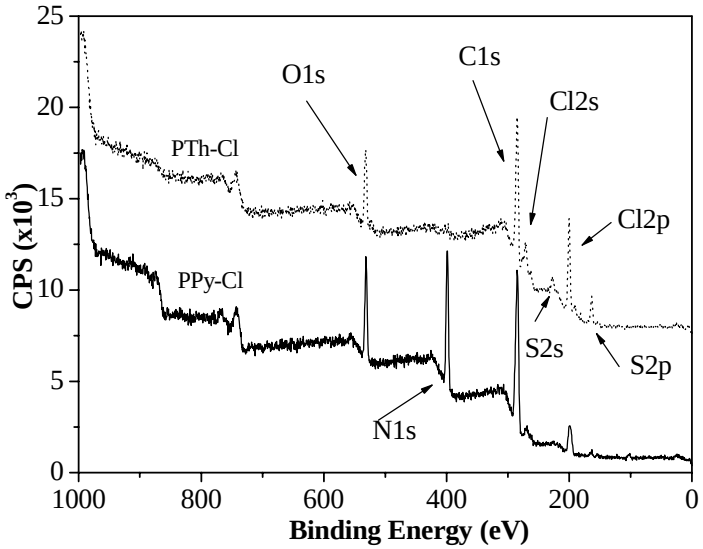

Figure 2 - XPS spectrum of PPy-Cl and PTh-Cl.

Conductivity
The conductivity of PTh-Cl and PPy-Cl is presented in Figure 3 as a function of the relative humidity (RH). The results indicate that PTh-Cl has higher electric conductivity than PPy-Cl in the 30-95% RH range studied. PTh-Cl shows approximately 10^{-5} S/cm conductivity at 40% RH and reaches up to 10^{-3} S/cm at 75% RH. Although it has only an increase of 2 orders of magnitude as a consequence of humidity, its tendency suggests only one mechanism of conduction. PTh without doping has conductivity of approximately 10^{-10} S/cm at 40% RH.

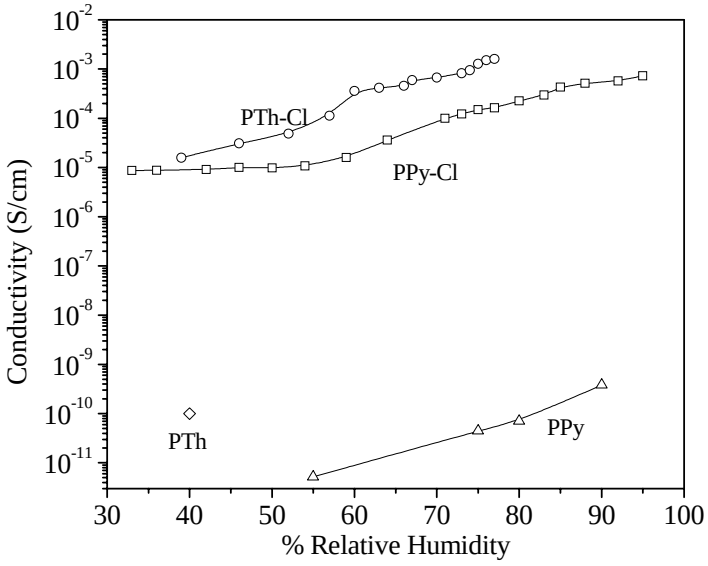

Figure 3 - Conductivity of PTh-Cl and PPy-Cl.

PPy-Cl presents an approximately constant electric conductivity of 10^{-5} S/cm from 35% to 50% RH and after that, increases continuously up to 10^{-3} S/cm at 95% RH. This behavior suggests two conduction mechanisms, the first one at low humidity that could be predominantly electronic and the second, at high humidity, which could be a combination of electronic and ionic transference of charges. Plasma PPy without doping has low conductivity and has been studied, among other reasons, because of its dielectric properties [5]. However, other studies have shown that iodine doped PPy exhibits an exponential response in conductivity with respect to the water content in the structure that makes PPy, or its derivatives, suitable to be used in wet conditions [6].
Chlorine and iodine atoms, combined with water, give better conditions for the transport of electric charges in polypyrroles. The interaction of water in the structure of some semiconductor plasma polymers is important because these polymers can be used as biosensors or in biocompatible materials and, inside the body fluids; the polymers are immersed in an aqueous medium [7]. Figure 3 contains also the conductivity of PPy and PTh without doping. The difference resides in the level of conductivity, 10^{-10}-10^{-11} S/cm for PPy and PTh.

Discussion

PTh-Cl and PPy-Cl were synthesized by plasma in simultaneous copolymerization and doping processes that involves chloroform molecules and its chlorined derivatives which are incorporated to the polymers in formation. The structural analyses indicate that some Cl atoms are chemically bonded to the structure of both polymers and other Cl atoms behave as anions. The chlorine content increases the conductivity of PTh and PPy in approximately 5 or 6 magnitude orders compared with the same polymers without doping. The mechanism of transference of charges has two tendencies in PPy-Cl, one that predominates up to 55% RH and another that rules above that point. The transference of charges in PTh-Cl has a unique tendency along the RH interval studied.

References

[1] – M.G. Olayo, G.J. Cruz, E. Ordoñez, J. Morales, R. Olayo, Polymer, 45, 3565-3575, (2004).
[2] – D.T. Clark, H.R. Thomas, J. Pol. Sci. Part A. Pol. Chem., 16, 791-820, 1978.
[3] – C.D. Wagner, W. M. Riggs, L.E. Davis, J.F. Moulder, Handbook of X-ray photoelectron spectroscopy, Perkin-Elmer Corporation, Physical Electron Division.
[4] – A. Godoy, H. M´Harzi, G. Safoula, P. Molinie, J.C. Bernede, F. Diaz, A. Conan, Polymer, 36 (3), 665-669, 1995.
[5] – D.S. Kumar, Y. Yoshida, Surface and Coatings Technology, 169-170, 600-603, (2003).
[6] – G.J. Cruz, J. Morales, R. Olayo, Thin Solid Films, 342, 119-126, (1999).
[7] – A. Hiratsuka, H. Muguruma, S. Sasaki, K. Ikebukuro, I. Karube, Electroanalysis, 11, No. 15, 1098-1100, (1999).

Soil Sterilization Using Ozone Generated By Dielectric Barrier Discharge

K. Ebihara[1], M. Takayama[1], T. Ikegami[1], H.D.Stryczewska[2],
Y.Gyoutoku[3] , T.Yokoyama[3], N.Gunjikake[3], H. Mizukami[3], S.Araki[3],
M. Tachibana[4], and T. Sakai[5]

1 Department of Electrical and Computer Engineering and Graduate School of Science and Technology, Kumamoto University, Kurokami 2-39-1, Kumamoto 860-8555 Japan

2 Faculty of Electrical Engineering and Computer Science , Lublin University of Technology, Nadobystrzyccka street 38A,20-618 Lublin,Poland

3.Kumamoto Prefecture Agricultural Research Center, Sakae 3801, Goshi, Kikuchi,Kumamoto 861-1113,Japan

4.Dojinglocal,Co.,Tabaru 2081-25,Kamimashiki,Kumamoto 861-2201,Japan

5.Kumamoto Technology and Industry Foundation, Tabaru 2081-01, Mashiki, Kamimashiki, Kumamoto 861-2202, Japan

Abstracts

The soil sterilization was studied by using ozone which is generated by the coaxial dielectric barrier discharge. We developed here the ozonizer with water-cooled screw type electrode and generated the high ozone concentration of 80g/m^3 at 0.3liter/min. Time evolution of injected ozone in the soil and the sterilization of the agricultural soil under various ozone dosages and treatment intervals were investigated. The ozone treated volume and the sterilization rate were clarified from several analytical method such as pH and electrical conductivity measurement.

Keywords: ozone, soil sterilization, dielectric barrier discharge

Introduction

The pressing need to develop environmentally benign alternatives to methyl bromide for soil sterilization requires new technologies for the agricultural and horticultural fumigation. The objective of soil sterilization is to destroy/eliminate microbial cells without significantly altering the chemical and physical characteristics of the soil. Numerous methods including autoclaving (moist heat), dry heat and microwaves have been used to sterilize soil or inhibit microbial activities in soil.[1-3] Ozone has oxidative and germicidal.

Ozone also has many benefits based on on-site generation, minimum human toxicity, low persistent chemicals in the soil. Ozone has been generated by many processing technologies such as dielectric barrier discharge, pulsed discharge, corona discharge and surface discharge. We have developed the ozone generation system suitable to soil sterilization which provides wide range of ozone concentration till 40gO_3/m^3 by varying applied voltage. The coaxial dielectric barrier discharge using the pyramid type electrode or the screw type electrode produced the ozone with high concentration at high efficiency. [4-6] Injection of the on- site generated ozone gas into the soil resulted in decreasing soil pathogen and changing chemical properties of the soil.[6-8]

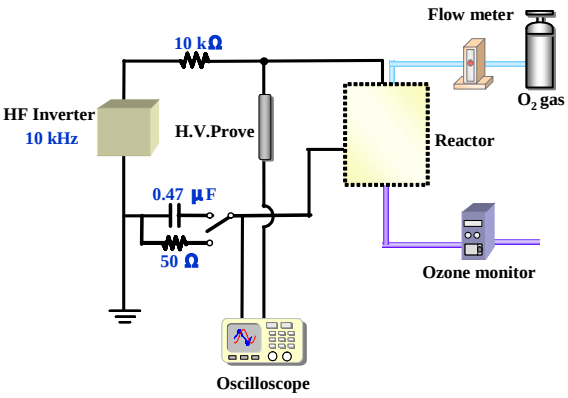

Fig.1 Ozone generation system.

We report here ozone diffusion and sterilization of agricultural soil when it is treated by varying ozone dosages and process duration. The temporal and spatial properties of the soil were investigated using the pH

and electrical conductivity. The bacteria populations , pathogen and soil-borne fungi after ozone treatment were determined and correlated with the processing conditions.

Experimental

Fig.1 shows the outline of the ozone generation system. An electric power of high frequency inverter (10kHz) was applied to the electrodes in the range of applied voltage (1.7 kV-5.5 kV). Material gas (oxygen 99.9 %) was supplied to the reactor of the dielectric quartz glass tube (ϕ 8 mm) with an inner electrode. The inner electrode is the structure of a water-cooled screw type electrode (in Fig.2) and a pyramid type electrode of stainless steel rod (ϕ 6 mm) . The ground electrode is cupper foil wrapped around the quartz tube. The gap separation between the inner electrode and the insulator tube was kept at 1 mm.

Fig.3 shows the ozone concentration as a function of applied voltage. The ozone concentration for the water–cooled electrode changed gradually from 4 g/m^3 to 38g/ m^3 by increasing the applied voltage.

Fig.4 shows the relationship between the ozone generation efficiency and ozone concentration when oxygen flow rate was changed. The high ozone concentration around 80g/ m^3 is generated at a low gas flow rate of 0.3 liter/min. This level of ozone is enough to sterilize bacteria and fungi in the soil. The high value of ozone generation efficiency of 220g/kWh was obtained at 1-2 liter/min where a low ozone concentration of 10g/m^2 was generated.

Fig.5 shows the ozone injection system into the agricultural soil (Audisols: Kumamoto soil). Ozone was introduced into the soil through the drip tube of 1/4 inch Teflon pipe. Two sets of the pH sensor and the electrical conductivity (EC) probe were placed at appropriate separation. The treatment container was arranged in an incubator of which temperature and light illumination can be automatically controlled. These measured data can be transmitted to the PC through the wireless network system.

Results

Fig.6 shows time evolution of pH and EC when the soil was treated by the ozone of 100gO_3/m^3 in 2 liter/min O_2 during 60min (a commercialized ozonizer was used). Decrease of the pH value and increase of EC are clearly shown during the ozone treatment. Agricultural soil consists of mud, sand, organic matter, minerals and water. Electrical conduction in the soil is mostly due to cation (Ca^{2+},Mg^{2+}, K^+, Na^+) and anion (Cl^-, NO_3^-, SO_4^{2-}) originated from mineral components in the

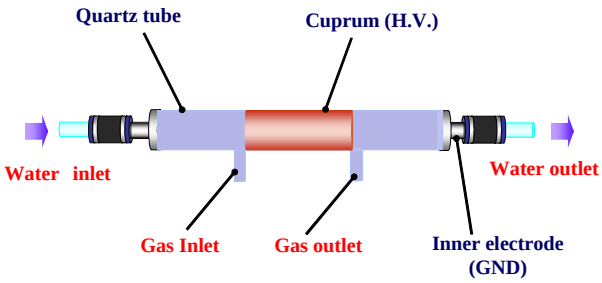

Fig.2 Water cooled screw type electrode

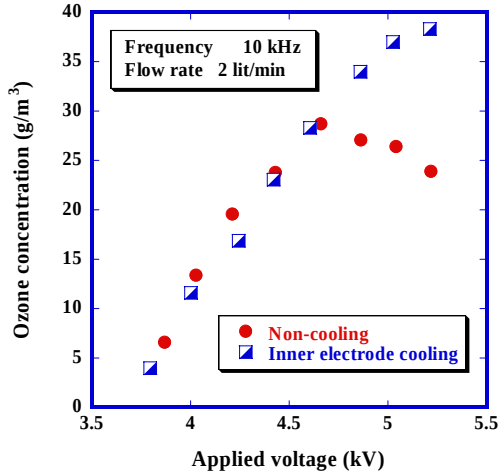

Fig.3 Ozone concentration as a function of applied voltage

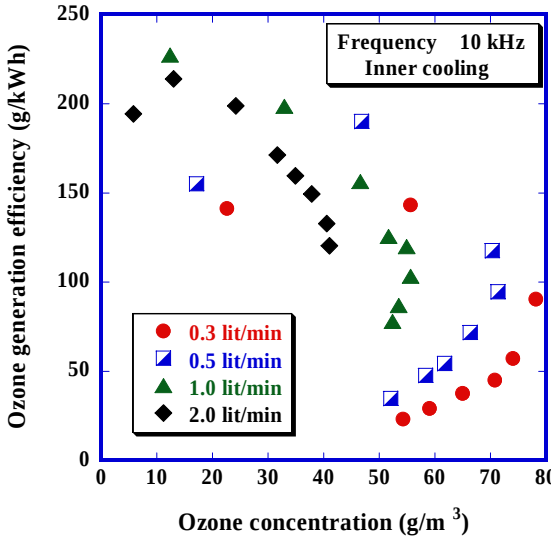

Fig.4 Ozone generation efficiency as a function of ozone concentration

soil. Gradual increase of the EC after treatment is attributed by complicated chemical reaction with ozone. We confirmed that the sterilization terminated in initial 30 minutes by referring the diagnostic results of microbial cells. The behavior of the EC and the pH is expected to be one of indexes for estimation of the sterilization level.

Fig.6 indicates that ozone can diffuse near 30mm away from the gas outlet embedded in the agricultural soil.

In order to apply the proposed system to large area of agricultural land, the ozone supply system with many gas tubes is required. Fig.7 is the double injection system to study the diffusion length between two gas outlets(separation:100mm) in the soil. Time development of EC is shown in Fig.8. The value of EC measured at the center of two sensors shows abrupt increase during ozone injection.

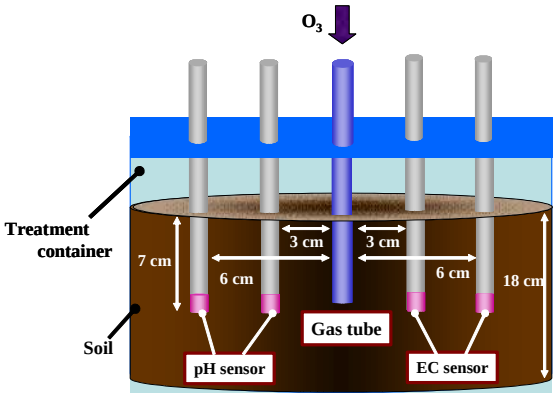

Fig.5 pH sensor and EC probe arrangement

Fig.9 shows the ozone sterilization results when the agricultural soil (50g) was treated varying the ozone dosages (0-40gO_3/m^3) and the duration (1-60min). In this experiment the agricultural soil was filled in an chamber(ϕ 70mm) and ozone gas was supplied from the top of the chamber and evacuated from the bottom exit.[6-7] The soil samples subjected to the sterilization process were sterile. Fasarium oxysporum of 10^6 conidal/mL was inoculated into the soil. The CFU(colony forming unit) counting was used to evaluate the number survivors after 72 hours. The total ozone amount (g) is calculated from the product of ozone concentration, gas flow rate, and treatment duration. For example, the test soil of $7.2x10^6$ CFU shows $1.7x10^2$ CFU after the treatment of ozone dosage of 6.39g where ozone concentration of 38.5 g/m^3 at gas flow rate of 3 liter/min and treating time of 60min were used. The resulting sterilization rate is 100% as shown in Fig.9 (left end data).

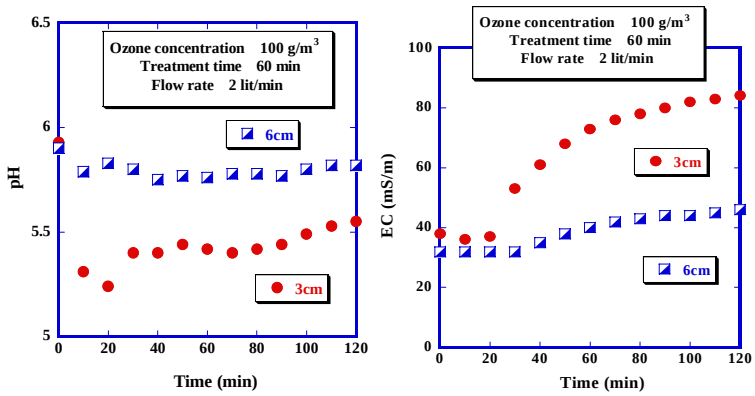

Fig.6 Soil properties during and after ozone treatment at different positions (3,6cm from the gas outlet).

It is shown that the sterilization by ozone injection is effective when the ozone dosage becomes over 0.3g for the 50g soil.

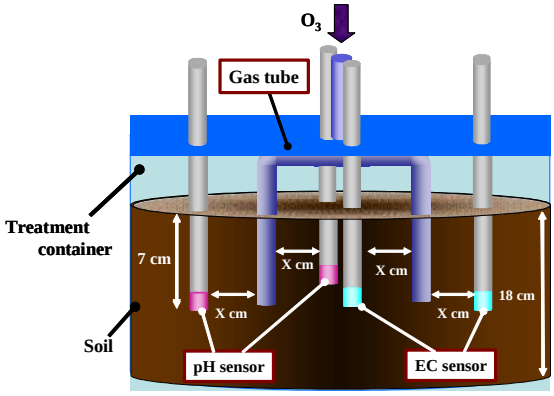

Fig.7 Two ways gas pipe system for ozone supply

Conclusions

We have studied the soil sterilization by using ozone which is generated by the coaxial dielectric barrier discharge. We developed here the ozonizer

with water-cooled screw type electrode and generated the high ozone concentration of 80g/m^3 at 0.3liter/min. Ozone diffusion and the sterilization of the agricultural soil were investigated using ozone injection into the soil. The ozone treated volume and the sterilization rate were clarified from several analytical method.

Acknowledgement

This work have been supported by the Advanced Research Program for Agricultural Technology of the Ministry of Agriculture, Forest and Fisheries , and the Strategic Research Promotion Program of Information Technology of the Ministry of Internal Affairs and Communications.

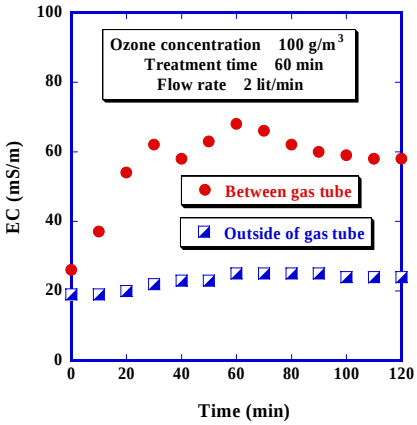

Fig.8 Time development of EC during and after ozone treatment at different positions (5 cm from the gas outlet)

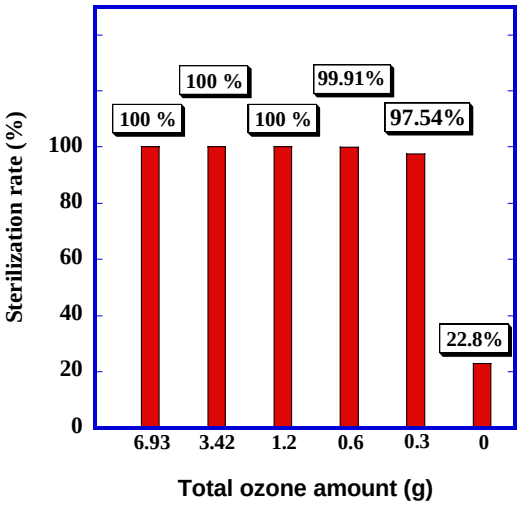

Fig.9 Sterilization as a function of ozone amount. The inoculated soil initially has 4-7x10^6 CFU/cc of Fasarium oxysporum.

References

[1].W.A.Rutala and D.J.Weber, "New disinfection and sterilization methods",CDC,Vol.7,No.2,Mar-April,2001.

[2].J.T.Trevors,"Sterilization and inhabitation of microbial activity in soil", Journal of Micorobiological Methods, Vol.26,pp.53-59(1996).

[3].California Energy Commission: Consultant Report "Ozone gas as a soil fumigant",Nov.2002.

[4].K.Ebihara,Y.Shibuya,H.D.Strycewska, Y.Gyoutoku, K.Kubo andM.Tachibana, "Soil treatment process using ozone and NO generated by Electric discharges", The 21st Symposium on Plasma Processing(Hokkaido,2004.Jan.28-30),P2-35, pp.268 – 269(2004).

[5].M.Takayama, K.Ebihara, H.Strycewska, T.Ikegami, Y.Gyoutoku, K.Kubo and M.Tachibana,"Ozone generation by high frequency dielectric barrier discharge for soil sterilization", Abstracts of 7th APCPST and 17th SPSM(Fukuoka,June29-July2,2004), 30p-85(2004).

[6].H.D.Stryczewska,K.Ebihara, Y.Shibuya, Y.Gyoutoku, M.Tachibana, "Non-thermal plasma based technology for soil sterilization", Ninth International Symposium on High Pressure, Low temperature Plasma Chemistry (Padova,Italy, Aug23-27,2004),No.7.06(2004).

[7].Henryka D.Stryczewska, Kenji Ebihara, Masahiro Takayama, Yutaka Gyoutoku, Mashiro Tachibana, "Non-thermal plasama-based technology for soil treatment", Plasma Processes and Polymers, Vol.2, No.3,pp.238-245(2005).

[8]M. Takayama, K. Ebihara, H. Stryczewska, T. Ikegami, Y. Gyoutoku, K. Kubo and M. Tachibana, "Ozone generation by dielectric barrier discharge for soil sterilization ", Thin Solid Films,2005(in press).

Advanced patterning architectures and dry etching: study of interaction between mask material and plasma in a RIE

D.Piumi, M.R. Boccardi[1], O. Donghi, R. Morandi, S. Alba
STMicroelectronincs, Central R&D, via C.Olivetti 2, Agrate Brianza MI, Italy
[1]Lam Research, Centro Direzionale Colleoni,v.le Colleoni 11, Agrate Brianza MI, Italy

Abstract
Different kinds of hard masks have been evaluated to pattern oxide lines for 90 nm and 65 nm technology nodes application. The materials studied as hard mask and ARC have been TiN and SiON, as well as a Bi-layer and an AHM (Ashable Hard Mask) approach. The main focus of this work has been the characterization of the interaction between the RIE plasma and the mask material surface, in order to understand the weak and the strength points of every architecture choice.
Keywords: RIE, Hard mask, plasma

Introduction

Technological nodes evolution in semiconductor devices requests to both litho and etch to pattern pitches which become more aggressive from time to time. Lithography is forced to use materials (such as 193 nm photoresist) with low resistance to etch, whose thicknesses are to be thinner than they were for previous technological node. This means that the resist mask itself is not enough to make possible an etching process. In addiction to that, very often BARC is not enough to avoid interference effects due to light reflection from the underlying layers, so making necessary the use of thicker BARC or additional anti-reflecting layers.
These layers can be chosen and characterized to be able to work both to drop the interference effects and to act as a hard mask to make the etching process feasible. Hard masks are used for many applications.[1,2]
In this work, inorganic and organic hard masks have been evaluated to pattern oxide lines with pitches for 90 nm and 65 nm technology nodes application. The materials used as inorganic hard mask and ARC have been TiN and SiON. For the organic hard masks, a Bi-layer and an AHM (Ashable Hard Mask) approach have been studied. The main focus of this work has been the characterization of the interaction between the plasma and the mask material surface, in order to understand the weakness and the strength points of every architecture choice.

Experimental

Hard masks under characterization have been studied analyzing their response while used to pattern lines in a single damascene approach. The etched pattern has been an array for 90 nm technology for TiN, SiON and Bi-layer, its shrink to further node (65 nm) for SiON and AHM. Pitches were ranging from 210 nm to 140 nm.
The film to be etched was made of PECVD FSG 4%. A chemistry based on $Ar/C_4F_8/O_2/CO$ was used to etch such a film, selectively landing on Si_3N_4.
The samples have been etched in a DFC (Dual Frequencies Coupled) RIE (27MHz and 2 MHz).
The Hard mask opening for TiN has been performed in a Inductively Coupled Plasma reactor (Cl_2-based chemistry), while the same RIE used for FSG has been used for he others.

Inorganic Hard Masks

Inorganic materials are a very common choice when a hard mask is needed. These materials are usually already present in device's process flow, so neither new tools nor new precursor gases are needed for their deposition. So, as far as they are able to support technological shrink, they are the easiest and less expensive choice. Among them, PVD TiN and PECVD SiON are the most common choices.
PVD TiN is well known for its anti-reflective properties; in addiction to that, from the selectivity point of view, a metallic material is the best mask when a dielectric film is to be patterned. This means that a thin hard mask could be enough to transfer the pattern, so no dramatic increases of final aspect ratio are caused by it.
The first trials done to pattern a TiN-masked FSG showed a very hard etch stop issue to deal with. This was probably due the Ti presence in the polymer. In order to make the Ti-based by-products more volatile and to avoid them to enter the polymer, wafer temperature have been increased. Figure1 shows how an increase of

35°C moved the process latitude from a severe etch stop region (etch stop occurred after 150A of FSG were etched) to an etch stop-free region.

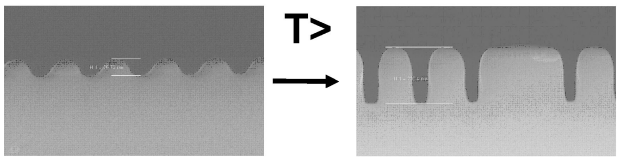

Figure 1: temperature effect on etch stop process window

The need of heating up the wafer during the etching process means that the RIE is to be dedicated for such a process, so making it more expensive from the manufacturing point of view. In addiction to that, if a bipolar ESC is used, it requires an optimization for chucking and dechucking voltages and time, in order to take into account ESC resistance increase with temperature (ESC capacitance does not change), which make narrower the window against wafer re-clamp.
After the first wafer was etched, Ti contamination in the reactor has been evaluated; a bare Si wafer has been exposed to an Ar plasma, then measure by TXRF. The dose revealed on its surface is assumed to be directly correlated to the Ti content in the chamber's hardware.

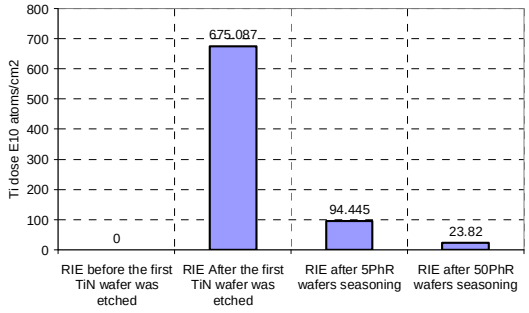

Figure 2: Ti dose monitored by TXRF

Ti presence in the tool can be partially recovered by a standard seasoning, but no complete recovering was possible.Figure2 shows the dose measured on bare Si test chips and its evolution after seasoning; Ti contamination can be decreased of several orders of magnitude, but never completely recovered once a TiN wafer have been processed. In order to estimate Ti effect, a baseline process, not using hard mask but instead a standard resist, has been ran before and after RIE contamination. Results are shown in figure3.

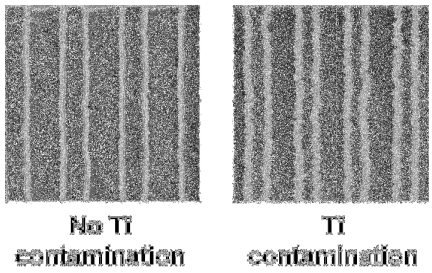

Figure 3: Ti contamination effect evaluated on baseline process.

This result demonstrated that a Ti presence modifies the performances of an etching process. Having observed the effect of Ti on the baseline process, a marathon has been done in order to evaluate the self-contamination risk for the etching process on TiN hard mask. Test chips have been processed by Ar plasma along the TiN marathon to monitor the Ti content of the RIE. Bare Si wafers are supposed to efficiently simulate the top electrode behaviour with respect to Ti contamination (Top electrode is made of Silicon). A ToF-SIMS analysis has been carried on for Si surface and Ti profile (Fig4).

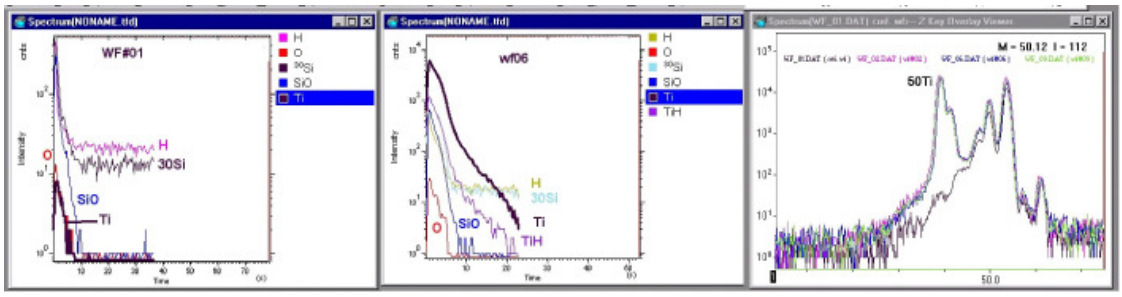

Figure 4: ToF-SIMS analysis of bare Si wafers processed during the marathon

According to ToF-SIMS results, after the first wafer of TiN is processed the Ti content directly goes to its saturation value. The surface spectrum shows that the ^{50}Ti peak, absent before the RIE is contaminated, starts appearing after the first TiN wafer is etched. Its intensity does not change while processing other TiN wafers. Independent XRF measurements carried on the same Si chips, confirm that the saturation level is reached after the first wafer. Ti profile measurement shows that, accordingly to the small diffusion coefficient of Ti in Si bulk, Ti contamination in Si is only at its surface. Considering bare Si behavior as descriptive for top electrode, it can be argued that a thin Ti film is growing on it. So, ESC contamination could take place during WAC (Waferless Auto Clean, a cleaning plasma ran after the process of each wafer to clean the reactor from etch by-product deposited on RIE walls).

No self-contamination in TiN hard mask-based etching process has been revealed from both morphological and electrical data.

As a conclusion for studies on TiN, it seems clear that a TiN hard mask choice would lead to several manufacturing problem. Although the process is not affected by self-contamination, the RIE cannot be shared with other applications for contamination issues. Dedicated ESC temperature is required in order to let the process work.

PECVD SiON has been in parallel evaluated as an alternative to the TiN hard mask. Such a material is known for the extreme tunability of its physical and chemical-physical properties: tuning its stoichiometry, in fact, it is possible to change its optical properties (allowing good performances as ARC) and its response to the etching process.

A first trial have been done to transfer the pattern using the dielectric hard mask; the material chosen as starting point showed a very bad etch resistance (Fig 5). So, a study has been carried on to understand whether it was possible or not to use such a material to pattern lines for 90 nm node. PECVD precursor gases have been tuned, so tuning Si-Si, Si-N and Si-O content in the film, in order to determine the best working range.

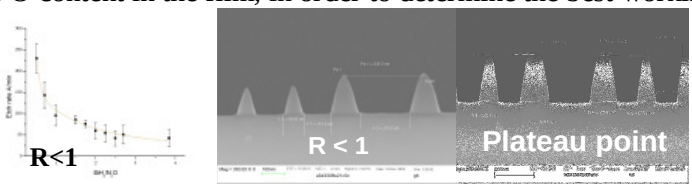

Figure 5: Etch rate for the main etch step on blanket SiON wafers (stoichiometry tuning) and correlated result on patterned wafer

Figure 5 shows the results in term of etch rate for the main etch step on the "tuned" SiON blanket wafers. Increasing the SiH_4/N_2O ratio in deposition step, the etch rate for the correspondent material decreases until it reaches a plateau. Within this plateau, it is still possible to tune optical properties for the film, so its performances as anti reflective coating. Figure 5 also shows results on patterned wafer; the sample with R<1 was the starting point, with a SiON coming from the zone in which SiH_4/N_2O ratio is lower than one. Moving closer to the plateau, the selectivity becomes high enough to allow an efficient pattern transfer. A μ-Auger analysis has been carried on in order to understand which is the microscopic parameter impacting such an etching response. If $Si_xO_yN_z$ is the generic material stoichiometry, it has been found that selectivity FSG-to-SiON increases with x/y ratio, keeping z constant. According to this trend, it is reasonable that, increasing Si/O

ratio keeping constant N, part of Si-O bonds are converted in Si-Si bond. It can be inferred that moving into the plateau means to move far from an “oxide-like” chemical structure. As a consequence, a chemistry to etch oxide becomes more selective to it, so improving the material performances while used as a mask.
Etching data also showed that not always is necessary to move in the plateau zone. Once feasibility is observed for a point out of the plateau, fine tuning on SiON stoichiometry can be used, as shown on fig 6, to tune CD bias; if a CD shrink is necessary and an issue on polymerization process window is present, the desired morphological result can be obtained by a fine tuning for the hard mask material.

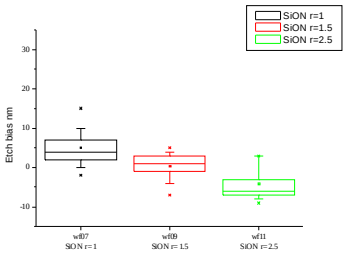

Figure 6: CD bias response to SiON modification

This is a very important strength point for such an approach: hard mask can be tuned as a further degree of freedom in order to reach the right dimensional result without losing in process window width from the etching process point of view.
After the right SiON modification has been found, very good results have been obtained for line patterning in term of profile, dimension, striations and process window. Standard temperature set up allows the definition of a good working point, and no issues have been revealed from marathon test. This demonstrates a strength point of SiON with respect to TiN: while its more expensive in term of characterization work (the stoichiometry is to be tuned to find the best material for each application), it becomes then less expensive in terms of manufacturing, allowing to share the tool with other applications.
Data from the etching characterization showed another issue hard mask-related: selectivity FSG-to-SiON of the main etch depends on pitch. As far as the pitch is shrunk, in fact, the mask faceting effect becomes an additional part of its etch rate during line patterning, so causing a higher mask loss in dense zones. In order to evaluate whether SiON can support a technological shrink or not, a comparative feasibility has been evaluated for 65 nm technology node.

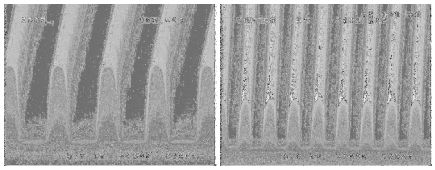

Figure 7: morphological result for the 90 nm and 65 nm technological node

Figure 7 shows the morphological result of the comparative study: once a material is tuned to be enough etch resistant, it is able to support a shrink for at least the next technological node.

Organic Hard mask

Organic hard masks are an alternative to inorganic material for advanced patterning transfer. The main advantage in an organic choice is that the mask can be stripped after the pattern is transferred to FSG. A simple and standard stripping step completely removes the mask. This is not possible if an inorganic material is used, so its presence is to be taken into account making more complicated the integration schemes.
Bi-layer resist for 193 nm lithography has been evaluated for array patterning in 90 nm node. A Bi-layer approach consists of a thick anti-reflective organic coating, called underlayer, and a thin photo resist Si-rich (called Imaging Layer). Silicon presence in the imaging layer allows the etching process to reach a good selectivity imaging-to-under layer, so the pattern can be transferred from the first one to the second one, which acts as the real hard mask to pattern the FSG. A dry development for the underlayer followed by an FSG etch

step has been used for the analysis. Having a Si-rich imaging layer film, it has been observed since the beginning an issue profile-related. In order to have CD control and a vertical profile in the hard mask, H_2 is needed in the mask opening step. Hydrogen in the plasma can react with Si present in the underlayer to generate volatile Si-H compounds, then re-deposited on large areas as Si-based compound, whose composition depends on the overall chemistry of the step. This re-deposition leads to a micromasking effect while etching the oxide by a step selective to Si_3N_4. To avoid this process marginality, a H_2-free chemistry has been chosen. As a consequence, a CD bias always positive and a bowed mask profile are to be accepted.

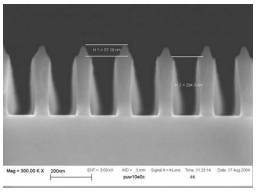

Figure 8: underlayer profile after mask dry development

Figure 8 shows the profile in the underlayer after the dry development step was applied. An average CD bias of 10 nm has been measured for this wafer.

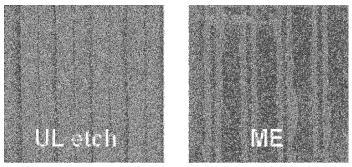

Figure 9: Top view after underlayer etch and after Main Etch followed by O_2 strip

Figure 9 shows the result after a full etch trial: after main etch and strip, strange "shadows" appeared at line bottom. Further analysis demonstrated they are made of oxide. The hypothesis done to explain such an issue is a hard mask reflow mechanism or a chemical modification in the film structure taking place during ME, probably driven by Ar sputter. To support this explanation, it has been observed that strip is not able to remove the underlayer after etch from large unpatterned zones, while the stripping is effective when applied on the same material directly after deposition (Figure 10).

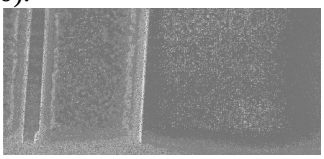

Figure 10: hard mask residuals after strip on large oxide stripes

As a consequence, while no concerns have been found for selectivity and pattern transfer, stronger defectivity problems and questions about post etch strip are open for this organic material. An Ashable Hard Mask (AHM) has been evaluated as well. AHM approach consists of a triple step: a thick α-C layer, a thin Inorganic anti-reflective layer (usually a SiON), called DARC, and then a resist mask. The sequence is: the pattern is transferred from the resist mask to the inorganic layer, which is then the mask to transfer the pattern to α-C. This film is the real hard mask for the etching process; the inorganic layer is thin enough to be completely consumed during FSG etch, so the hard mask can be removed by ashing after the full process is terminated. The evaluation for this approach has been directly done for 65 nm technology application. Again, a H_2-based chemistry would give re-deposition issue in large zone, so a bowed profile has been accepted. While for Bi-layer approach a positive CD bias was to be accepted, the AHM approach allows a CD tuning by modulating both BARC etch step and DARC opening. In general, inorganic material, such s TiN or SiON, are able to allow very high selectivity to oxide, while selectivity is always lower with an organic hard mask. As a consequence, organic hard mask are always thicker. Dealing with very dense arrays, it is important to characterize the process windows against hard mask collapse during main etch, which would give severe electrical failure. CD tunability for AHM approach allowed such a characterization

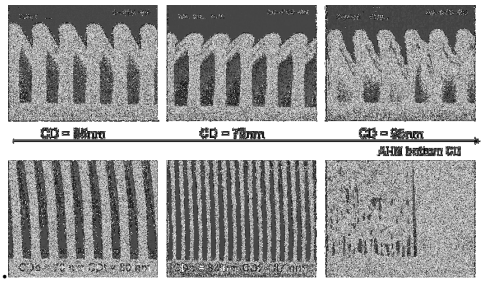

Figure 11: Line collapsed evaluation versus CD bias during mask opening

Figure 11 shows the results for this characterization. The bowed profile has probably a role in making narrower the process window, but it seems very hard to make the profile vertical without generating problem on large areas. As a consequence, depending on pitch and CD target, hard mask thickness is not a degree of freedom but its highest allowed thickness depends on collapse process window. Depending on dimensional requirement, this upper limit can cause selectivity issues, so leading to the need of a high polymerization process, with a consequent issue of narrower process window with respect to etch stop.
When a "collapse-free" condition was realized (in term of CD and carbon thickness) and the pattern was transferred to oxide, no issue related to strip has been observed.

Conclusions

In this work organic and inorganic hard masks have been studied for advanced microelectronic technology node (90 and 65 nm). In particular four layers have been characterized (TiN, SiON, bi-layer and Ashable Hard Mask) and the advantages and disadvantages of each one have been discussed.
For inorganic hard mask it has been showed how PVD TiN is the one able to guarantee the best selectivity (almost no consumption during dielectric etch, no pitch dependence on final oxide line height) but several constraint related to process manufacturability are present. PECVD SiON, on the other side, requires a fine optimization for each application, so it costs more in term of process development time; nevertheless, the final optimized process is a standard one from the RIE point of view, so it's easier to manufacture. Final oxide stripe height depends on pitch, so denser areas are expected to undergo higher consumption than isolated lines, but it has been demonstrated this approach can support at least the 65 nm-node shrink.
Organic hard masks are the easiest choice from integration point of view. After a standard strip, they are supposed to be completely removed, so no particular process flows are needed to manage the residual hard mask. Poor dimensional tuning window has been observed for Bi-layer approach, coupled with severe defectivity and stripping problems. AHM tri-layer guarantees a CD tuning feasibility, but, moving along the technological roadmap, it has been demonstrated its thickness has to decrease with pitch, in order to be free from line collapse problem. Feasibility is proven for 65 nm technological nodes, but its extension to further shrink could be affected by this limit.

Acknowledgments:
The authors would like to thank Laura Aina and Sonia Pirotta for PVD TiN deposition, Roberta Piva for PECVD SiON, Simona Spadoni for ellipsometric characterization, Stefano Alberici for TOF-SIMS measurements, Lam Research for technical support in etching characterization.

References:

[1] O. Donghi, "Application of TIS2000 bi-layer resist to 0.13 mm flash memory gate definition: litho and dry development", Proceedings of 6th CREMSI, Fouveau, November 13-14 2003
[2] S. Regini, "New hard mask approaches for Si dry etch for 90 nm and below flash memory technology", Proceedings of 16th IVCI, Venezia, June 28-July 02 2004

Diagnostics of pulsed mercury free low pressure fluorescent lamps

E. Robert, C. Cachoncinlle, R. Viladrosa, S. Dozias, S. Point and J.M. Pouvesle

GREMI, CNRS-Polytech'Orléans, 14 rue d'Issoudun, BP 6744, 45067 Orléans Cedex 2, France

Abstract This work deals with the development of mercury free low pressure glow discharges likely to be used for publicity lighting. The experiments are performed in neon xenon mixtures powered by a pulsed electronic driver delivering electrical pulses of microsecond duration at repetition rate of a few kHz. Time resolved spectroscopic and electrical measurements are presented during the pulse application and in the afterglow phase of the discharge. The population of NeI, XeI and XeII representative lines is described in correlation with the current pulse development across the sign.

Keywords: mercury-free lamp, fluorescent lamp, glow discharge, UV-VUV, pulsed discharge, plasma kinetics

1. Motivation

This work presents a time resolved spectroscopic and electrical study of new rare gas based fluorescent signs, likely to be used in publicity lighting, powered by a pulsed electronic driver.
The search for efficient and environmentally friendly substitutes for mercury is today a key issue in many light source technologies, such as automotive lamps and fluorescent lighting systems [1].
In a first research and development program, the use of neon-xenon based low pressure discharges appeared as the best solution for the excitation of phosphors [2,3]. A strong trade off between the luminous flux and the setup lifetime was also measured [4,5] and shown to be the result of a very efficient removal of the xenon from the gas mixtures during the sign operation [5]. Furthermore, the increase of the mean current leads to a saturation of the luminous flux extracted from rare gas based signs for injected powers higher than about ten watts when using conventional ballasts on the contrary to the linear behaviour of mercury based devices.
The development of a pulsed electronic driver delivering high repetition rate current pulses in the microsecond time range allow to achieve a three to four times enhancement of both the luminous flux and efficiency of mercury free signs [5]. Besides this significant improvement, the use of pulsed excitation also indicates that high luminous fluxes can be obtained for higher mixture pressures and/ or higher xenon concentrations than those necessary for the AC excited signs, which could be a key factor for the long lifetime operation. Finally, the study of the plasma kinetics induced through pulsed excitation of low pressure rare gases mixtures appears as a crucial issue for the development of efficient and long-living mercury free fluorescent lamps. A first approach for the description and optimization of the pulsed binary rare gas mixtures properties is obtained through time resolved emission spectroscopy by measuring the population of the excited levels of both neon and xenon neutral and ionic states during the current pulse and in the afterglow.

2. Experimental results

The search for the better operating conditions (mixture composition and pressure, pulse amplitude, duration and repetition rate, etc.) of pulsed rare gas based signs is investigated in this work through time resolved spectroscopic diagnostics of the near by electrode and positive column plasmas in relation with electric probe measurements. The spectroscopic measurements have been performed with a 13 mm inside diameter neon xenon sealed sign which radiation is dispersed through a spectrometer equipped with either a photomultiplier tube or a fast ICCD camera. Two probes record the voltage across the sign, with typical amplitudes of a few kV, and the voltage pulse across a resistive shunt providing the current flowing through the cold hollow cathode pulsed discharge. The lab-developed electronic driver allows the selection of the voltage pulse amplitude, duration and repetition rate and as

a consequence the current pulse properties. Each cycle of the driver consists in one positive polarity pulse and one negative polarity pulse to allow a symmetrical operation of the two hollowed electrodes.

2.1. Neon - xenon emission during the electrical pulse

As an illustration of the parametric study, the figure 1 presents the voltage and current waveforms together with the temporal evolution of three emission lines representative of the neon xenon plasma species. The spectroscopic measurement was performed with the spectrometer entrance slit aligned with the close vicinity of the hollow electrode. About 0.4 µs after the onset of the voltage pulse across the sign, a short current spike is observed in relation with the strong emission of neon lines. While this current spike is measured with the same amplitude but a reverse polarity through a complete cycle, following the mode of operation of the electronic driver, it appears that the neon line emission spike exhibits a large and very reproducible amplitude modulation with the pulse polarity. This peculiar relationship, between the current and the plasma emission during the very first stage of the pulsed discharge, also evolves in close correlation with the moderate heating of the electrodes during a few minutes after the sign ignition. These observations are supposed to be correlated with the electron emission processes at the electrodes, essentially monitored by the ion fluxes which also induce the electrode heating and sputtering.
During the time gate spanning from about 0.5 to 2 µs, the neon lines are largely quenched at the benefit of neutral xenon emission radiation. The third phase of the pulsed discharge results in the quenching of the neutral xenon radiative states, the repopulation of neon transitions, and the production of high energy xenon ionic levels. Simultaneously with this plasma kinetics, a strong and nearly linear increase of the current amplitude is measured during the third phase of the pulsed discharge.

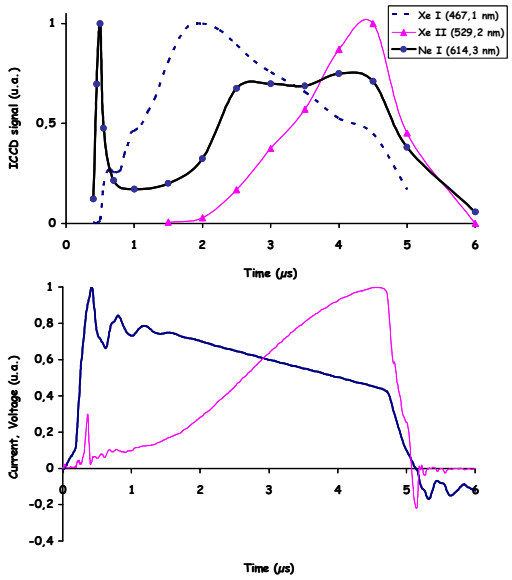

Figure 1 Temporal evolutions of the NeI ($3s[1^1/_2]°$ - $3p[1^1/_2]$, 16,62-18,63 eV, bold line), XeI ($6s[1^1/_2]°$ - $7p[2^1/_2]$, 8,31-10,97 eV, dotted line) and XeII ($6s^4P$ -$6p^4P°$, 23,67-26,02 eV, thin line) emission lines. The spectroscopic diagnostics is performed in a 10 mbar sign powered by a pulse driver delivering the voltage (bold line) and current (thin line) waveforms presented in the bottom diagram. Each data point is measured by averaging over a few thousands of current pulses, the light collected by the ICCD detector set with a 50 ns width intensifying gate.

The figure 2 presents the temporal evolution of the same NeI, XeI and XeII lines for a 4 microseconds pulse delivered at 500 Hz and 1 kHz. On the contrary to the experiment described in figure 1, the spectroscopic diagnostics is performed in the middle part of the sign positive column. It was observed that when the pulse repetition rate is high enough to measure an early current spike, the NeI and Xe I

lines exhibit such a temporal spike only in the electrode zone. This radiative spike rapidly decreases with the distance from the electrode so that it is no more observed in the positive column region for high repetition rate conditions. On the other hand, for the lower repetition rate operation, the current waveform does not exhibit the early spike described in figure 1 while both the XeI and NeI emissions present such a short spike at 500 Hz even at long distance (a few tens of centimetres) from the electrodes. These observations tend to indicate that the spikes observed for the Ne and Xe lines reveals the existence of strong electric field gradients in the electrode region, so called electrode fall, which amplitude and spatial extension is strongly dependent on the pulse repetition rate and also probably pulse duration in our experimental conditions. For the higher pulse repetition rate the field gradient are probably strong enough to result essentially in the production of ionic species in the electrode region and the appearance of the strong current spike. The temporal evolution of the XeII line exhibits a small spike for the 1 kHz measurement. It was also measured that the spike amplitude observed for the NeI lines is correlated with the upper level of the radiative transition. In figure 2, the XeI line maximum is measured at shorter time during the current pulse in correlation with the earlier appearance of the XeII lines and the faster rise of the current pulse. The population of the XeII lines can process through various processes such as electronic excitation from the neutral xenon, from the excited levels of xenon or through collisions between xenon ion and excited states of the neon. The fast production of the XeII lines, on microsecond timescale, indicates that the two first processes seem to be more relevant for the population of the ionic xenon states. Work is in progress to study the effect of the mixture partial pressures on the production of XeII lines and the current increase during the pulse application.

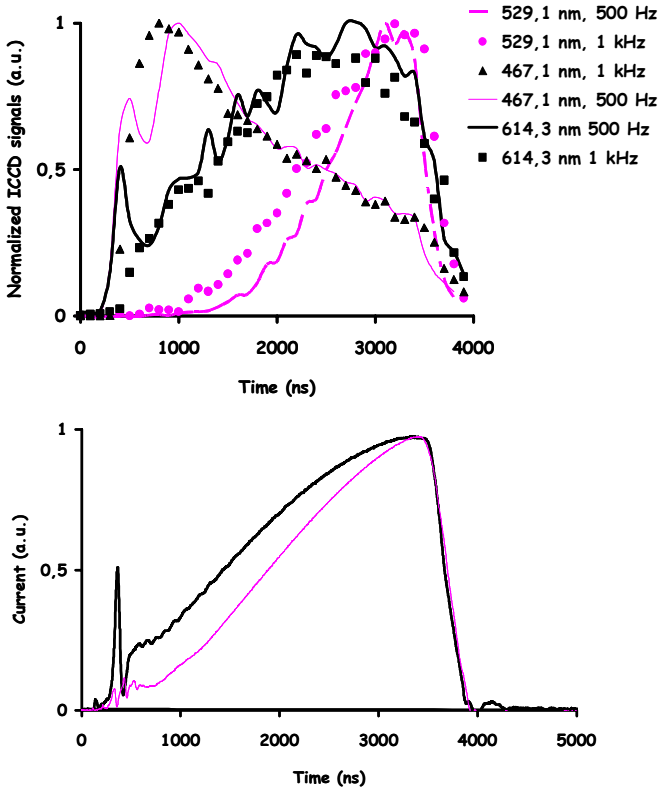

Figure 2 Temporal evolutions of the NeI, XeI, and XeII lines (labelled in fig.1) at 614,3 nm (squares for 1 kHz, bold line for 500 Hz), 467,1 nm (triangles for 1 kHz, thin line for 500 Hz) and 529,1 nm (dots for 1 kHz, dashed line for 500 Hz). The spectroscopic diagnostics is performed in a 10 mbar sign powered by a pulse driver delivering the current (bold line for 1 kHz, thin line for 500 Hz) waveforms presented in the bottom diagram.

2.2 Neon-xenon afterglow

The figure 3 presents the temporal evolutions of the XeI (467,1 nm) and XeII (529,1 nm) lines over 22 microseconds measured in the 10 mbar sign powered by the current pulse shown in fig.2 at 500 Hz.

The line intensities are sampled on one microsecond intensifying gate and averaged over a few thousand pulses. The XeI and the NeI (not shown in fig. 3) lines are populated during the afterglow while the XeII does not exhibit such a behaviour. After the current pulse extinction, in the time window between 5 to 8 microsecond, no signal is measured and the peak of the afterglow signal is observed around 16 microsecond both for XeI and NeI lines for 500 Hz and other pulse repetition rates. The afterglow contribution is about three times larger than the radiation emitted during the pulse application. This features explain in a large extend the considerable improvement in sign performance (output flux and efficiency) when using pulsed excitation in comparison with conventional AC excitation. The zero signal window (5-8 microsecond) is usually explained by the electron cooling, after the current pulse application, necessary for the recombination processes to be efficient. The recombination of molecular ions is known to be one the main processes likely to induce a strong population of the atomic excited states during the afterglow. The recombination for the neon lines has been measured to be at least five times smaller than that of the xenon lines. Work is in progress to study the afterglow to pulse signals ratio versus the mixture partial pressures, the formation of molecular ions in low pressure conditions being strongly dependent on the gas mixture pressure.

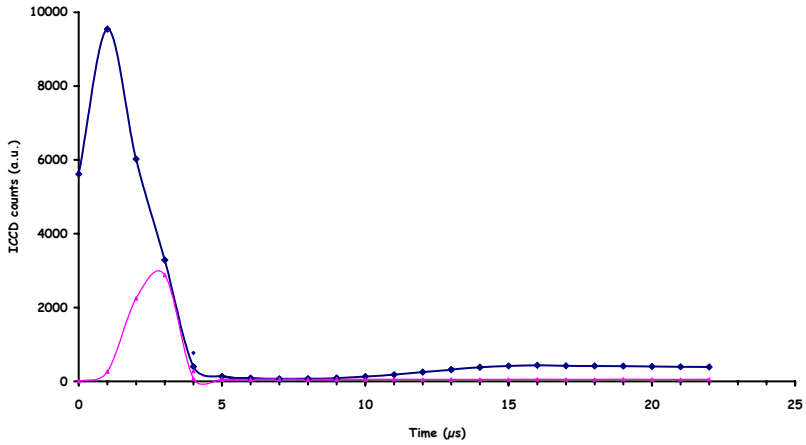

Figure 3 Temporal evolutions of the XeI (467,1 nm) line (bold line) and the XeII (529,1 nm) line (thin line) for a 10 mbar sign powered by 4 microsecond pulses delivered at 500 Hz.

Finally, in the later stage of the afterglow phase, time window ranging from 20 to 500 microseconds, a quasi exponential decay of both NeI and XeI lines is measured. While the XeI lines decay curves are almost similar whatever the radiative states considered in this work (spectral domain ranging from 400 to 600 nm) and for different pulse repetition rate operation modes, the NeI lines decay curves are faster for the lower lying levels (in the range 18,96 to 18,55 eV) and present a strong dependence on the pulse repetition rate.

Conclusion

The pulsed excitation of neon xenon mixtures allowed a three to four times enhancement of the optical flux and efficiency issued from low pressure signs in comparison with the conventional AC excitation scheme. This feature is essentially obtained by the strong emission occurring in the afterglow phase of the discharge. During the pulse application, fast kinetic processes, evolving on microsecond time scale, lead to the population of NeI, XeI and XeII radiative states. The appearance of the XeII lines occurs in correlation with the decay of XeI states and the quasi linear rise of the current amplitude. After the application of the electrical pulse, the plasma cooling allow recombination reactions to occur leading to the efficient population of XeI levels and in a much smaller extend of the NeI lines. The decay of the radiative levels during the afterglow appeared to be sensitive to the pulse repetition rate for neon transition while being quite independent on the radiative states and electronic driver operation mode for the xenon transition. The understanding of all the cross correlated spectroscopic and electrical observations reported in this work are thought to be a key issue for the development of

efficient and long living mercury free signs presenting both high illuminance and controlled photometric (chromatic coordinates) characteristics.

Acknowledgments

This work is supported by AUPEM SEFLI, rue Lavoisier, 45504 Gien Cedex, FRANCE.

References

[1] Proceedings 11th Intl Symp.on the Science and Technol. of Light Sources, IOP Conf. Series n° 182, 2004.
[2] H. Capdeville, Ph. Guillot, L.C. Pitchford, J. Galy, H. Brunet, proc. XXIV ICPIG, **vol. III**, 5, 1999.
[3] H. Sarroukh, E. Robert, C. Cachoncinlle, R. Viladrosa, J.M. Pouvesle, proc. 9th Intl Symp.on the Science and Technol. of Light Sources, 353, 2001.
[4] D. Uhrlandt, R. Bussiahn, S. Gortchakov, H. Lange, D. Loffhagen, proc. 11th Intl Symp.on the Science and Technol. of Light Sources, 15, 2004.
[5] E. Robert, H. Sarroukh, C. Cachoncinlle, R. Viladrosa, V. Hochet, S. Eddaoui, J.M. Pouvesle, Pure Appl. Chem., 77 (2), 463, 2005.

Surface modifications of cotton fabrics by Atmospheric Pressure Plasma (APP)

G. Rombolà[1], F.Parisi[2], G. Apostolo[2], D. Daprà[3], M. Perucca[4], C.F. Pirri[1]

1 Department of Physics, Polytechnic of Turin, Turin, Italy
2 Grinp s.r.l. – Thin film technology, sistemi e processi,, Turin, Italy
3 Department of Electronics, Polytechnic of Turin, Turin, Italy
4 Environment Park, Turin, Italy

Abstract
The aim of this work is to show preliminary results from the characterization of cotton fabric samples chemically and physically modified by Atmospheric Pressure Plasma (APP). The surface properties of cotton fibres were characterized by capillarity test, Attenuated Total Reflectance – Fourier Transform Infrared (ATR-FTIR), X-ray Photoelectron Spectroscopy (XPS), and Atomic Force Microscopy (AFM). The results provide a strong evidence that all APP treatments enhance capillarity diffusion of dye liquid and chemical oxidative process on the surface of cotton fibres.

1. Introduction
The general reactions to be achieved by plasma treatment of cotton fibres are the surface oxidation, the generation of radicals and the edging of surface. Both the surface chemistry (confinement of functional groups to the surface) and the surface topography may be influenced to result in improved hydrophilization, wettability and wickability properties of cotton fabrics, as well as printability and dye uptake [14-15].
Instead of traditional low-pressure plasma treatments, APP is a very promising technique to treat cotton fabrics because it doesn't require a vacuum equipment and it can be applied directly on-line in a textile industrial process. The realization of an industrial APP prototype able to treat cotton fabric two-meters in width is the main result reported in the present work.

2. Experimental
A roll-to-roll system has been mounted around the APP system, in order to make the homogeneous plasma treatment on cotton fabrics. The roll-to roll system moves the cotton fabrics in a speed ranging from 1 to 10 m/min and can simulate the industrial process. This type of simulation is useful to show off how several plasma treatments could be used for many on-line applications, such as dyeing phase or mercerization or any kind of finishing treatment on cotton.
Textile fabrics run under the treatment zone, represented by a short gap (1-5mm) between a high voltage powered electrode, commonly called cathode, and a grounded electrode, anode. As shown in Fig. 1, in this configuration called Dielectric Barrier Discharge (DBD), the cathode is fixed while the anode is a free rotating cylinder, dragged by the fabrics.
Before the treatment, textile fabrics are opportunely dehumidified thanks to three big steel cylinders heated by an internal steam flow at a pressure of 5 bars. Humidity absorbed by cotton fabrics must be as low as possible, in order to avoid discharge instabilities and filamentary discharge appearance.
A gas manifold with two manual flow meters, with a full range scale of 6 m^3/h, has been used to control the inlet of many gases and their mixtures: N_2, CO_2, He, Ar, N_2O_2, dry air. The gas inlet is an integral part of the cathode, and the more diffuse is the gas distribution, the more effective is the plasma treatment.
The equipment for high voltage signal generation is constituted by a low-medium frequency signal generator and a high voltage transformer, both exactly designed for DBD applications by Grinp s.r.l. Common AC 220-380 V at 50 Hz signals are properly processed by the generator and sent to the transformer, which amplifies them up to 20 kV peak voltages. The generator provides the maximum of electrical power to the load electrode when the system resonance frequency is reached.

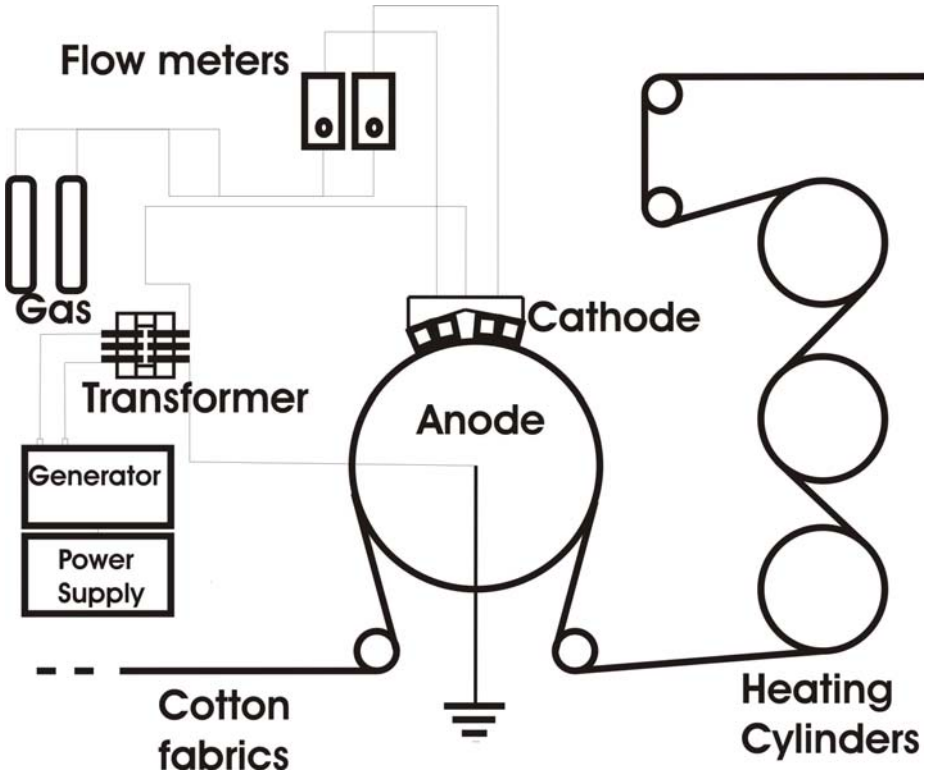

Fig. 1: Experimental arrangement for fabric plasma treatment

Capillarity test has been used to evaluate the diffusion coefficient D of a dyeing liquid into the cotton fabrics. This is a quantitative measurement of wickability, i.e. the bulk absorptivity of cotton fabrics.
The results were treated on the basis of the general wettability relationships [1-4], according to Washburn's equation, the squared rate of liquid capillary rise in porous media is given by:

$$h^2 = \frac{r\gamma\cos\vartheta}{2\eta}t \tag{1}$$

where h is the height by the liquid at the time t, $r = \frac{R_D^2}{R_S}$ is the ratio between R_D the mean hydrodynamic radius of pores and R_S the mean static radius of pores, η the viscosity of the liquid, θ the advancing contact angle of the liquid on the solid and γ is the surface tension of the liquid. The static radius is equal to the geometrical radius of pores, whereas the hydrodynamic radius depends also on the tortuosity of these pores.
Hence, h^2- values must vary linearly with time:

$$h^2 = Dt \tag{2}$$

where the slope D is a capillary diffusion coefficient related to the size of the capillaries r and to the physicochemical characteristics of the liquid. Therefore, a surface treatment of a fabric that modifies r and contact angle causes some variation of this diffusion coefficient D and a set of height adsorption values vs time allows qualitative characterization of fabric sample wettability and wickability. The dye liquid is represented by a chemical inert blue pigment that does not react with the surface of the fibres. This allows to appraise the distribution of the dye liquid along the height of the analyzed samples.
A SensIR Technologies Attenuated Total Reflection – Fourier Transform Infrared (ATR-FTIR) spectrometry was used to provide valuable information related to the chemical structure of sample surface [4,5]. The IR radiation actually penetrates a short distance (~0,5 μm).
X-ray Photoelectron Spectroscopy (XPS) were carried out using a XPS spectrometer equipped with a monochromatised Al K X-ray source (1486.6eV) at 15kV and 10mA.

Physical surface changes on the samples were detected with a SPM DualScope Scanner DS -200Digital Atomic Force Microscopy (AFM). Since cotton fibre surface is very jagged measurements were carried out in non-contact mode.

3. Results and Discussion

Within the limits of consequential variability (due to small electrical instabilities at very high voltages on a two-meters-wide DBD system), the same electric parameters have been maintained (Table 1), mainly in order to study the effects of the type of gas and flows on plasma treatments. In some cases, a treatment has been repeated several times to appraise the effects on the fabrics caused by the plasma exposure time.

Voltage (kV)	**Frequency** (kHz)	**Power** (W/cm^2)
11	30	11

Table 1: electrical parameters

Table 2 provides a summary of the capillarity test results; for each sample the discharge evidence mainly drawn from electrical data is reported. In some cases a specific treatment was repeated to establish a relation between D and the time of plasma exposure and to verify the existence of a saturation exposure time.

In general, an increase of D is appreciable for all plasma treatments compared to an untreated sample. But D is obviously influenced by the gas used for the discharge and the homogeneity of the discharge, and by the gas flow. In each situation considered N_2 plasma gives an homogeneous (diffuse) discharge at atmospheric pressure, commonly called Atmospheric Pressure Glow Discharge (APGD); this plasma regime is related to a high D values. A similar discharge behaviour can be observed when He is added to the gas mixture because He metastable species help obtaining a diffuse discharge characteristic by Penning ionization effect.

It has been shown that presence of CO_2 in the gas mixture drastically influences D because all the Oxygen containing species such as molecular oxygen, ozone or water vapour lead to a filamentary discharge mode because of production of ozone, nitrogen metastable species loss, due to an increased dielectric barrier surface conductivity.

Under the same electrical conditions, an identical small amounts of N_2 and CO_2 (0,2 m^3/h) corresponds to a D = 10,91 mm^2/s and D = 1,41 mm^2/s respectively. The diffuse characteristic of a N_2 discharge progressively disappears when CO_2 flow increases in a mixture of the two gases; D decreases simply by adding CO_2, in agreement with previous deductions.

Nevertheless, D doesn't increase with nitrogen flow values as it could be expected. Enriching the atmosphere with N_2, most of the atmospheric oxygen (existing as impurity in the unevacuated reactor and brought by the cotton fabrics movement) doesn't reach the process zone.

Oxygen is the source of highly chemical reactive species, and, provided that it doesn't exceed certain concentrations to induce discharge instabilities, it is very important in surface oxidation treatment and in surface ablation (etching).

The last evidence can be verified by comparing samples #74 – #77 (table 2). He makes the diffused characteristic of the Townsend discharge to strongly increase with a concentration of only 4,5% in a nitrogen/helium mixture (sample #74 and #75), but at the same He concentration in the mixture (sample #76 and #77), the capillarity effect is more evident when the N_2 concentration is lower.

In fig. 2 there is an overlapping of four spectra concerning four different samples. The spectral region involves typical vibrational activities due to cellulose chemical bonds. In fig. 2a it can be noticed that the use of CO_2, as seen in samples #31 #71, increase the superficial oxidation of the cotton fibres. That activity is bound to the peak at 984 cm^{-1} of vibrational stretching of C=O carbonyl bond. Sample #5 (fig. 2b), obtained by a nitrogen plasma treatment, shows a weak variation of the same peak if compared to the untreated sample [6]. Thus, the surface oxidation is related to the presence of oxygen precursor, such as CO_2 gas or other Oxygen containing mixtures.

However, even if the carbonyl peak is the most evident vibrational activity, it has a very weak intensity, and this is in accordance with the fact that the plasma treatment doesn't penetrate deeply into the bulk fibre [5].

Table 3 sums up measurement data of XPS analysis on some samples. Untreated and plasma treated samples are compared with a "test" sample obtained with wet chemical treatment in highly concentrated NaOH solution (mercerization).

Sample	Velocity	N treat	Discharge	N_2	CO_2	He	D
	(m/min)			(m^3/h)	(m^3/h)	(m^3/h)	(mm^2/sec)
1	3	1	Diffuse	0,2			10,91
5	3	1	Diffuse	2,6			10,34
8	3	1	Diffuse	4,4			9,04
9	3	1	Diffuse	5			8,75
31	3	1	Filamentary		0,2		1,41
36	3	1	Filamentary		3,2		1,13
39	3	1	Filamentary		5		0,86
40	3	1	Filamentary		5,6		0,79
49	3	1	Diffuse	4	0,2		3,24
50	3	1	Diff/Filam	4	1		2,02
51	3	1	Filamentary	4	3		0,38
67	2,5	1	Diffuse		0,4	0,2	0,82
68	2	1	Diffuse		0,4	0,2	1,39
69	1,5	1	Diffuse		0,4	0,2	4,08
70	1	1	Diffuse		0,4	0,2	10,55
71	2,5	1	Diffuse		0,4	2	11,13
72	3	1	Diff/Filam		2	0,2	3,31
74	2	1	Diffuse	2,6			7,79
	2	2	Diffuse	2,6			17,18
	2	3	Diffuse	2,6			19,77
	2	4	Diffuse	2,6			20
75	2	1	Diffuse	2,6		0,06	9,69
76	2	1	Diffuse	2,6		0,12	9,89
77	2	1	Diffuse	1,4		0,06	12,92

Table 2: capillarity test results

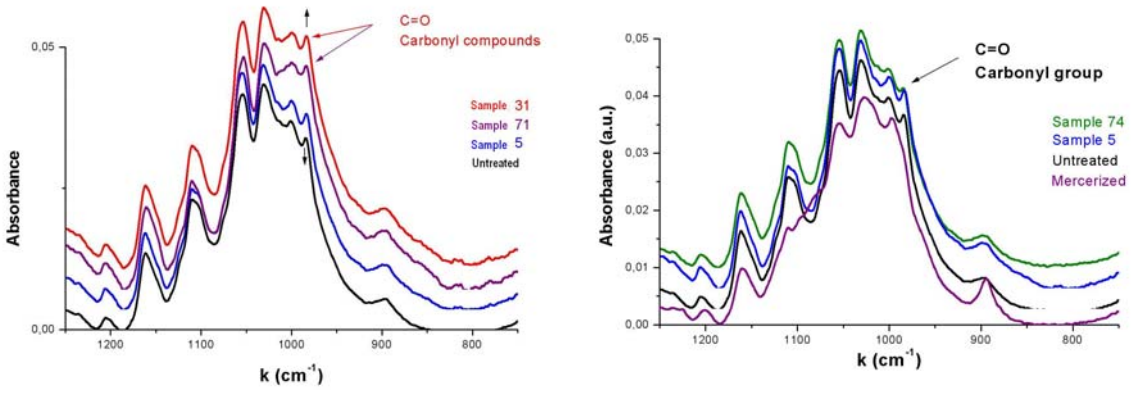

(a) (b)

Fig.2: ATR-FTIR analysis. Comparison of different samples

Conc. at %	C	O	N
Untreated	83.4	14.2	0.9
Test	70.4	27.7	0.3
Sample 74	74.4	20.2	4.0
Sample 75	77.9	18.3	2.8

Table 3: percentage concentration of chemical elements on cotton fibres

The XPS data show that the treatment in plasma increases the superficial concentration of nitrogen and oxygen [8,7]. N_2 plasma treatment increases the nitrogen surface concentration, maybe in the form of $–NH_2$ group or similar (primary or secondary amino groups). Nitrogen content doesn't seem to exceed a saturation value after four times treatment duration as in sample #74.
Oxygen content on the surface of cotton fibres comes from impurities in the processing atmosphere, due to the bad isolation of the plasma reactor. However, also a small O_2 amount in the gas feed leads to an increase of oxygen signal [7]. Many studies on the role of gas composition [10-13] in the DBD treatment of polymers show that O_2, even when present in small quantities, can significally affect the surface chemistry and hence the level of surface transformation.
The fittings of the carbon peak C1s have been carried out for sample #74 and sample #75. It is possible to isolate three components of the carbon peak: the first two are typical of the cellulose (286.7 eV and 288.1 eV), while the third one belongs to a carbossyl or carbonyl groups (290 eV).

	-C-**C**H_2-OH	-O-**C**-O-	HO-**C**=O
Test	69 %	22 %	9 %
Sample 74	63 %	26 %	11 %
Sample 75	62 %	29 %	9 %

Table 4: percentage concentration of the chemical bonded carbon

Table 4 shows the fractions percentages of the three components for the single analyzed samples.
From the point of view of superficial carbon compounds the two samples treated with plasma are quite similar. This is the evidence that N_2 or N_2/He plasma treatments do not strongly affect surface chemistry over a certain limit. The contribution of the 290 eV signal doesn't exceed 11% even after a high time exposure to the plasma. The plasma action is strictly closed to the surface region [5].
Atomic force Microscopy (AFM) provides information about the topography of to the cotton fibres. AFM analyses are carried out comparing topographical images of plasma treatment with untreated samples. AFM measurements of treated samples generally show some changes in surface roughness: it increases if compared to untreated samples. Fig. 3 shows the comparison between sample #74 and an untreated sample. Samples #74 was treated four times with a nitrogen plasma, gradually caused more wrinkled surface. Such superficial wrinkleness can be correlated to the capillarity increase and to the diffusion coefficient D of the sample #74.

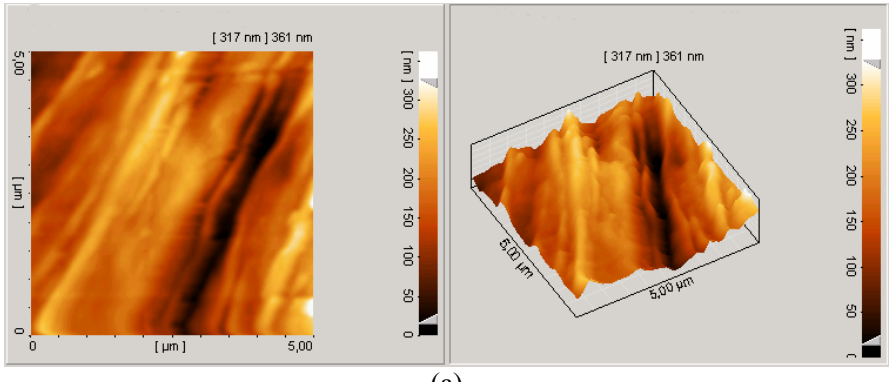

(a)

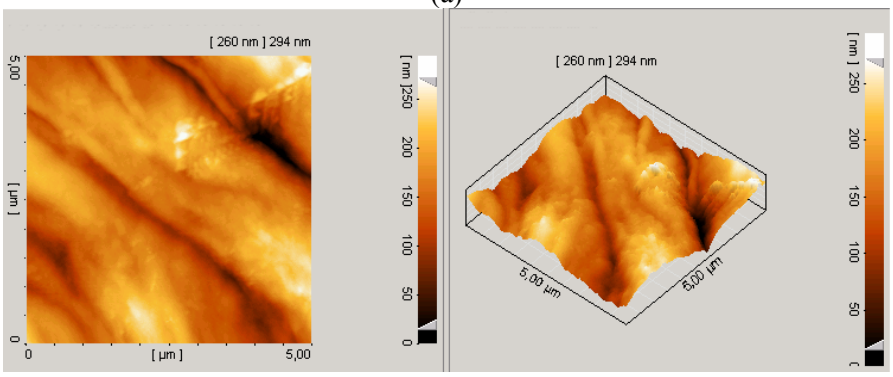

(b)

Fig. 3: comparison between sample #74 treated by nitrogen plasma (a), and untreated sample (b)

4. Conclusions

APP industrial prototype system has been assembled in order to treat textile fabrics in movement.
The morphology of cotton fibres is affected by Plasma treatment. AFM measurements show a notably change in surface roughness and a characteristic wrinkled surface on N_2 plasma treated fibre. Improvement of roughness and wrinkled characteristic can be related to higher D coefficient.
Plasma treatments generally increase wickability properties of cotton fabrics, but wickability is strictly correlated to homogeneity of discharge rather than to surface chemical changes. On the other hand wettability (fig. 1) is related both to homogeneity of discharge and surface chemical changes due to different precursors.
The aim of this work was to demonstrate how the plasma can be an interesting industrial application for textile processes. In the future new plasma processes will be investigated, in order to find the best processes for each type of dyeing substance, to find new kind of surface functionalization for different textile application by plasma grafting or plasma polymerization, and to optimize plasma pre-treatment processes.

5. Aknowledgments

The authors would like to thanks Prof. F. Geobaldo, Dott. G. Ieluzzi, and J. Rocci of Polytechnic of Turin in Italy for ATR-FTIR and AFM measurements, Dott. L. Meda of Polimeri Europa – Istituto Donegani of Novara in Italy for XPS measurements, Dott. C. Ricciardi of Polytechnic of Turin in Italy for his valuable discussion and advice.

References:

[1] F. Ferrero – Polymer Testing 22 (2003), 571-578
[2] P. Stahel, J. Janca, D.P. Subedi – "Surface modification of non-fabricated polypropylene textile in low-temperature plasma at atmospheric pressure" – Dep. Phys. Electronics, Masaryk University, Brno, Czech Republic – Internet source
[3] J. Wiener, P. Dejlova - AUTEX Research Journal, Vol. 3, N°2, June 2003, 64 – 71
[4] K. Chi-Wai, et al. – AUTEX Research Journal, Vol. 3, N°4, December 2003, 194 – 205
[5] H.U. Poll, et al. – Surf. Coat. Techn. – 142-144 (2001), 489-493
[6] C.M. Pastore, P. Kiekens – "Surface characteristics of Fibers and Textiles" – Marcel Dekker, Inc., New York (2001), pp. 203-218
[7] X.J. Dai, L. Kviz – Textile Institute 81st World Conference – Melbourne, Australia, April 2001
[8] C. Penache, et al. – "Plasma Printing: Patterned Surface Functionalization and coating at Atmospheric Pressure" – Fraunhofer Institute (IST – IAP) – Internet source
[9] J. Verschuren, P Kiekens – IX International Izmir Textile & Apparel Symposium, October 2001, Cesme-Izmir, Turkey
[10] R. Dorai, M.J. Kushner – J. Phys. D: Appl. Phys. – 36 (2003), 666-685
[11] F. Poncin-Epaillard, et al. – J. Adhesion Sci. Technol. – 8 (1994), 455
[12] S. Guimond, et al. – Plasmas Polym. – 7 (2002), 71
[13] F. Poncin-Epaillard, et al. - Plasmas Polym. – 7 (2002), 1
[14] Roth R.J. – "Industrial plasma engineering, Vol 1: Principles" – UK:IOP Publishing, 2000/2002
[15] Roth R.J. – "Industrial plasma engineering, Vol 2: Applications to non-thermal plasma processing" – UK:IOP Publishing, 2000/2002

Growth of amorphous thin-films on dental prostheses for the improvement of their performance

M. Perucca[1], C.F. Pirri[2], P. Mandracci[2], C. Carossa[3], P. Ceruti[3]

[1]*Environment Park S.p.A., Clean NT Lab Division, Torino, Italy*

[2]*Department of Physics, Material and Microsystems Laboratory, Politecnico di Torino, Torino, Italy*

[3]*Department of Biomedical Sciences and Human Oncology, Università di Torino, Torino, Italy*

Abstract

TiN, TiAlN, TiAlSiN and nanostructured TiN films were deposited on samples and on prostheses components by DC-ARC-DC LARC™ with a growth rate of 2.5-3 μm/hr, while a-SiO_x coatings of about 6 μm thickness were grown by RF-PECVD on dental materials with a growth speed of about 1.4 μm/hr; the films were characterized respect to their surface properties by means of Electron Scanning Microscopy and high resolution Surface Profilometry.

Keywords: Dental prostheses; plasma assisted deposition; thin films

1. Introduction

Thin-film coatings are extremely important as enabling technology for the fabrication of prostheses to be implanted in the human body [1, 2]. Nanocomposite thin films support several organism functionalities and allow significant enhancement of prostheses performance in different ways. First of all, ceramic and amorphous coatings have excellent barrier properties and they can substantially improve the bio-compatibility of the prosthesis that are directly in contact with the living tissues, avoiding the contact with potentially dangerous materials and blocking the diffusion in the human body of poisonous or allergenic elements coming from the massive material such as Chromium, Nickel and Cobalt, which are present in 95% of alloys (i.e. stellite) for dental prostheses and implants applications. Ceramics coatings also exhibited very good osteogenic properties when applied on artoplastic implants [3]. Ceramic coatings considerably extend also the overall reliability and longer components life cycle, since they can avoid the deterioration of the prosthesis, that is responsible for the formation of particles that can diffuse in the body, with potentially harmful effect on the human health. In the case of dental applications deposition of amorphous or ceramic bio-compatible thin films can also protect the prosthesis from the corrosive action of the saliva and some by-products of food mastication. Durability of ceramic and amorphous coatings functional properties constitutes a major source of reliability for the medical implants and movable prostheses. TiN and ZrN ceramics coatings deposited on OT58 substrate were proven [4] to provide excellent chemical barrier against very aggressive acid agents such as HF, HCl, H_2SO_4 as well as against strong bases such as NaOH. Salt test spray guaranteed resistance of such coatings in extreme environmental conditions [4]. This provides a good reliability of such materials when exposed to less extreme pH and salty environments such as the oral one. Another aspect in which thin film coatings can be helpful is the one of aesthetic features of the prostheses, regarding their colour and brightness selection and preservation in time against ageing. Thin-film coatings can greatly improve the aesthetic features of the prostheses by changing their chromatic properties and light reflection in a controllable way, thus achieving the proper colour and increasing the surface brightness. Typical colour accepted for these applications are within the gold chromatic range. For this reasons TiN and ZrN-containing coatings were developed. For the above

mentioned reasons nanotechnological coatings determine an innovative enabling solution to cure patients allergic to heavy metals contained in prostheses bulk material as well as for providing long life materials preserving the same good looking characteristics. Along with chemical inertness, ceramic coatings were also considered for other functional enhanced properties such as high hardness (up to 3500 micro-HV), fatigue resistance, flexibility, toughness, and good adhesion properties over a large number of materials.

The amorphous silicon-oxygen alloys (a-SiO_x) are also among the most suitable materials for achieving this tasks due to their physical properties such as chemical inertness, high hardness, transparency and good adhesion properties over a large number of materials, together with good properties against diffusion. This kind of materials can be deposited by means of various growth techniques, such as Physical Vapor Deposition (PVD), Chemical Vapor Deposition (CVD), Plasma Enhanced Chemical Vapor Deposition (PECVD). The most suitable techniques for the deposition of thin films on dental prostheses are plasma assisted techniques, since they allow the material growth at a very low temperature. This is particularly important because the materials of which the prostheses are made cannot usually stand high temperatures without a sensible degradation of their properties. Among plasma assisted techniques, PECVD offers the advantages of simplicity, relatively low cost, versatility and allows the deposition of composite materials (such as a-SiO_x), varying the ratio of the different components in a wide range, while deposition of PVD coatings proves to be the best process for attaining highly dense and packed coatings with minimal content of micro-particles, flexible nano- and micro-structure design.
Films of a-SiO_x where grown in a Radio Frequency (13.56 MHz) PECVD (RF-PECVD) reactor using SiH_4 and N_2O as precursor gases at temperatures lower than 100°C on substrates of different materials used for the fabrication of dental prostheses; the films were characterized respect to their surface morphology by Scanning Electron Microscopy (SEM) and profilometry. Moreover, binary, ternary and quaternary Nitrides where grown by PVD on metal alloy substrates for dental frames and implants: the fluxes of reactive gases, arc currents and bias voltages were changed in order to test the properties of the coatings characterised by different chemical compositions.

2. A-SiO_x films

Films of a-SiO_x where grown on two different dental materials by a RF-PECVD reactor using silane (SiH_4) and nitrous oxide (N_2O) as silicon and oxygen precursors respectively. The deposition system was a standard capacitively coupled PECVD system, composed by two electrodes of 144 cm^2 area each, located at a relative distance of 20 mm. A RF potential at a fixed frequency of 13.56 MHz was applied between the electrodes in order to light the plasma discharge. The gas precursors were injected in the space between the electrodes by a Mass Flow Controller (MFC) driven injection system, ensuring a controlled gas flux inside the reactor. The reaction byproducts and exhausted gases were pumped away by a pumping system consisting of a turbo-molecular and a downstream mechanical base pump.

The substrates, having the shape of small square pieces of dimensions 10 mm x10 mm x 2 mm, were cleaned before the growth process rinsing them in a acetone ultrasonic bath for 5 min; two types of microcomposite dental materials were used as substrates for the film deposition: Gradia from GC and Signum from Haeraeus-Kulzer. All the samples were put together in the deposition chamber; each substrate was partially covered with a mask in order to obtain a step between the film and substrate surfaces (see fig. 1).

The gas flow ratio and total gas flow were kept fixed to the following values: $[N_2O]/[SiH_4] = 40$; $[N_2O+SiH_4] = 61.5$ sccm. The total pressure inside the reactor was 400 mTorr, the power density applied to the plasma discharge was 20.8 mW cm^{-2}, while the substrate temperature was about 70 °C in order to avoid the risk of degradation of the substrate material.

A Tencor PL-10 mechanical profilometer was used to evaluate the film thickness by measuring the height of the step between the film surface and the uncovered substrate surface: the deposition rate, obtained by dividing the measured film thickness by the deposition time, was found to be about 1.4 μm/hr. The same instrument was also used for the evaluation of the roughness of the samples surfaces before and after the film deposition. A Scanning Electron Microscope was used to get images of the surface morphology of the film and substrate

surfaces; before the microscope analysis the samples were covered by a thin metal film in order to improve the detection signal, as shown in fig 1.

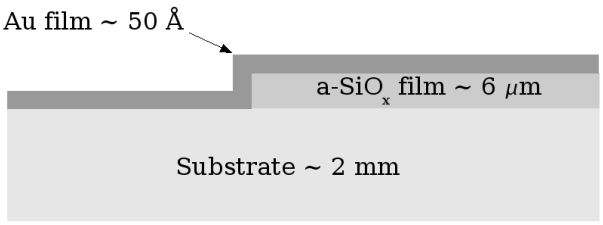

Fig.1. Structure used for the investigation by SEM of a-SiO_x films deposited on dental materials

Tab.1 shows the results of roughness measurements, performed on two different types of dental materials (Gradia and Signum Heraeus) before and after the deposition of a a-SiO_x film. The measurement was performed by acquiring the surface profiles along five different paths for each sample; the paths lengths were kept in range 4-5 mm and were taken in the central part of the sample. The measured surface profiles were filtered in order to separate the long-wave component (waviness) from the short-wave one (roughness); the separation was performed by a software filter provided by the data acquisition software of the profiler. The roughness was evaluated for each path as the RMS of the surface profile and the mean value of the five paths is reported in last table row. It is clear from the measured data, that the surface roughness was not significantly modified by the presence of the film; this fact is due to the high roughness value of the given substrates, that cannot be reduced by a film of this thickness.

Fig. 2 shows two SEM images, taken in the area surrounding the step between the film and the uncovered substrate surface; the darkest area on the right is covered by the a-SiO_x film, while the lighter area is uncovered. As can be seen, the surfaces of the samples present several kind of structures, such as stripes and holes, that are probably due to the mechanical surface polishing procedure. The same structure are still present after the film coverage, confirming that the film thickness is not sufficient to reduce the substrate roughness, as shown by profilometry.

Tab.1. Roughness measurements performed on dental materials before and after a-SiO_x growth

	Gradia	***Gradia+a-SiO$_x$***	***Signum***	***Signum+a-SiO$_x$***
Path#	*RMS / nm*	*RMS / nm*	*RMS / nm*	*RMS / nm*
1	361	627	741	592
2	490	449	606	594
3	392	300	565	349
4	695	406	508	307
5	1154	325	384	436
Mean	***618***	***421***	***561***	***455***

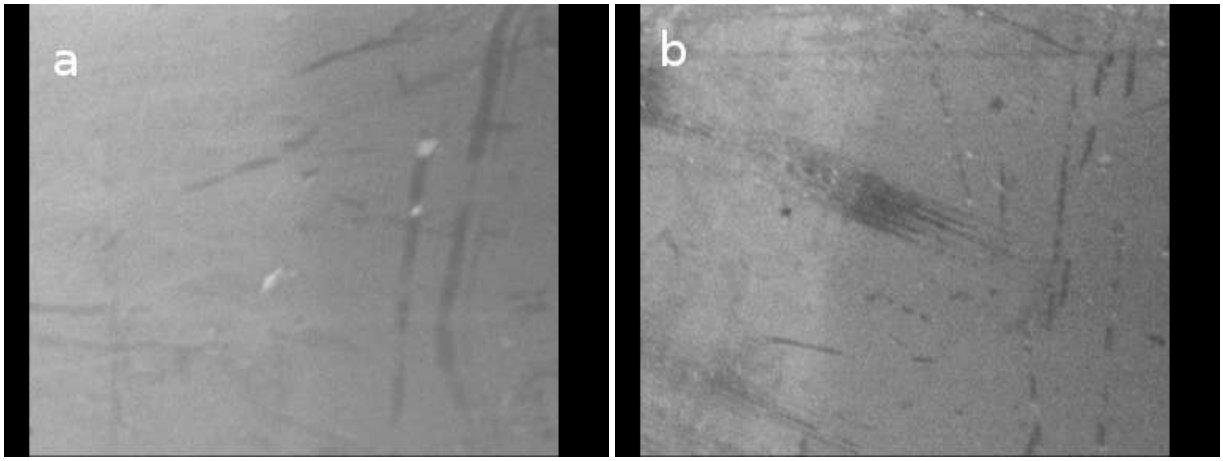

Fig.2. SEM images of two different dental materials partially covered by a a-SiO_x film (a: gradia; b: signum).

3. Ceramic films

Binary, ternary and quaternary nano-composite ceramics coatings of the family TiN, TiAlN and TiAlSiN were deposited on samples and on prostheses components defining a new class of thin films applicable to bio-medical metal alloy substrates. In particular, nano-structure and composition in which nano-cristals of TiN (n-TiN) are dispersed in a amorphous matrix of Si_2N_3 (a-Si_2N_3) determined enhanced wear resistance and hardness; multilayered and graded microstructure and composition allow for maximum barrier efficiency against migration of undesirable chemical compounds and elements. Stoichiometry determining chromatic characteristics has been devised in such a way to fulfil the aesthetic requirements (colours were limited in the 'gold range') also for coatings naturally not displaying such chromatic variety . The final layer of the developed coatings has been heavily loaded by either TiN or by ZrN non-stoichiometric compounds.

Fig.3. Images of different typical dental materials prostheses with complex geometry coated with TIN

Among different technical solutions (sputtering, evaporation, etc.) the PVD ARC-DC LARC™ process was chosen in order to grow complex, dense-packed, microparticle-free ceramics thin films. LARC™ is a innovative evolution of the existing standard PVD ARC-DC deposition techniques in that it allows dramatically decreasing the output of micro-particles, although preserving efficient growth rates (about 2,5-3,0 microns/hour). Indeed the LARC™ technology provided by the Clean NT Lab Platit-PL55 unit with rotating cathodes proved to be an efficient solution to deposit thin ceramic films on stellite three dimensional complex substrates. The innovative cathode geometry increases the cathode surface and assures uniform and controlled

target consumption. Cathode surface may be kept at low temperatures (15-30°C) through an efficient closed loop cooling system, spot trajectory is controlled by adjustable magnetic fields which minimize the spot residence time on the target surfaces, determining uniform evaporation and decreased microparticles yield.

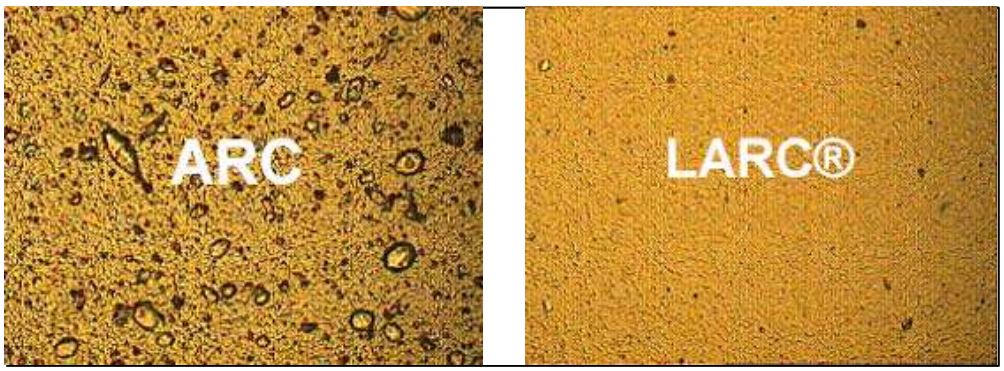

Fig.4. Comparative optical microscope Images in the 10 microns range of two TiN coated substrates showing dramatic decrease of microparticle content in LARC® deposited ceramics coatings

The coating quality in terms of low macro-particles content is quite important for avoiding stress concentration at discrete positions on the coated surface, which may determine an adhesion fault or substantial depletion of barrier property, as well as for aesthetic requirements, especially for what pertaining surface gloss. The process was run in the 200-450°C temperature range at pressures in the order of 10^{-5} mbar, thus assuring the growth of high quality and dense-packed layers columnar- free micro and nano-structures

One or two cathodes were used according to the required stoichiometry. For binary and ternary coatings one Ti or Zr target was employed with Nitrogen as process gas (for binary coatings), Nitrogen and Acetylene as process gases for ternary ones were employed. For quaternary coatings deposited Stoichiometric and non-stoichiometric compounds were realized by employing two cathodes in the same process. For specified process parameters it was possible to deposit nano-structured and nano-composite ceramic thin films. These films were realized by exploiting the spinoidal decomposition occurring in the specified temperature and pressure range. Nano-structured coatings were realized by growing a Si_2N_3 amorphous matrix in which nanocrystals of the metal employed (i.e. Titanium) are dispersed. These films belong the family of super-hard coatings, displaying hardness values exceeding 3500 micro-Vickers, deriving from the grain boundary interactions with the amorphous matrix.

Particular attention was devoted to find the optimal bias voltage in order to avoid excessive energetic impacts of ions on the substrates, characterised by geometries in which at least one of the typical substrate scale lengths was much smaller than the others. This allowed avoiding the possibility of damaging such components by overheating them or by performing a too energetic etching of the surface and bulk material.

Testing and characterization to bio-compatibility requirements of the developed coatings are in progress.

References

[1] R. Max, O. Paar, F.U. Niethard, M. Weber, D.C. Wirtz, BioMedical Engineering OnLine, **2**:15 (2003)
[2] R. Thull, Othopade, **32**, 51 (2003).
[3] H. Matsuno, A. Yokoyama, F. Watari, M. Uo, T. Kawasaki, Biomaterials **22**, 1253 (2001).
[4] CLEAN DECO - LIFE00 ENV/IT/000213 Clean-Deco -Mid Term Report

AMORPHOUS THIN-FILMS GROWN BY PLASMA TECHNIQUES FOR BIOLOGICAL ANALYSIS

M. Cocuzza[1], S.Bianco[1], S. Ferrero[1], E. Giuri[1], C.F. Pirri[1], A. Ricci[1], G. Piacenza[2], M. Perucca[2], D. Bich[3], P. Schina[3], A. Merialdo[3]

1 Department of Physics, Polytechnic of Turin, Turin, Italy
2 Environment, Park S.p.A. Clean NT Lab divisiion
3 Olivetti-I-jet, Arnad (Aosta) Italy

Abstract
This work is focused on the developing and validation of materials grown by plasma techniques, processed for the realization of micro and nano-structures for advanced devices and sensors for genomics, post-genomics and proteomics analyses. Carbon, silicon and titanium based alloys - deposited by means of Physical Vapor Deposition (PVD) - were implemented in miniaturized cantilever microbalances produced with a 2-masks bulk micromachining process.
Keywords: cantilever, micromachining, PVD, genomics

1. Introduction

The recent scientific and technological advances in micro- and nano-technologies, in material and surface science (particularly concerning the interaction between synthetic materials and biologic molecules) in connection with the exceptional developments in the area of genomics and proteomics pave the way to the development of highly innovative methods for DNA, RNA, protein, other biologic molecules and cell analysis, and open new perspectives for the application of molecular diagnostics methods into bio-medical, pharmaceutical and agro-food areas [1]. However, in these areas, the technology is still requiring the availability of fundamental research on materials in order to realize devices which are able to carry out quickly thousands of complex biochemical assays at high resolution down to the femtogram level [2]. Present knowledge and technologies meet clear limitations in satisfying this demand, limitations that also hamper some of the potential application of molecular diagnostics into still unexplored and unexploited fields.
Aim of the research activity is to develop microgravimetric technologies employing cantilevers in order to build MEMS/NEMS-based arrays of microbalances ("cantarray") by means of different plasma processes that allow reaching the sensitivity sufficient to detect and identify nucleic acid molecules. This sensor technology, to be developed as nano-balances with integrated readout, holds great promises as a fast and cheap 'point of care' device (avoiding polymerase chain reaction - PCR [3]), as well as a powerful research tool. This promising technique proves to be quite efficient since does not involve labelling of the molecules by fluorescent, magnetic or radioactive markers and bulky detection schemes are avoided, with consequent relevant time and cost saving. The possibility of realising parallel operation [4] through hybridisation, detection and analysis of different nucleic acid sequences allows a dramatic speed-up in basic and applied research of identified carcinogenic mechanisms and specific genetic pathologies.
This work proposes the optimisation of physical- and chemical-plasma processes for suface and bulk microbalances functionalisation in order to develop arrays of cantilevers (so named cantarrays) to be employed as nanobalances on which cDNA or oligonucleotides will be spotted, to hybridise with complex molecular probes and to characterize the abundance of single cDNA by "weighting" the cantilever after hybridisation. This technology is potentially more sensitive and faster than classical micro-array, and thus it offers the opportunity to analyse rare transcripts or transcripts obtained from a few cells. The analysis of very small quantities of materials [4] and the enhanced reliability deriving by the direct measurement process determine several expectations on plasma processes as enabling technology in new application fields. Moreover, in spite of traditional microarrays, this method allows the precise quantification of cellular transcription, thus opening the way to a number of new applications.

2. Cantilever process, simulation and characterization

Arrays of cantilever structures have been realized through MEMS techniques by using a reactive ion etching on the front of the wafer, for the definition of the cantilever shape, and a back-side bulk micromachining technique for the release of the cantilever structure (2-masks process). The advantage of an array of cantilever, instead of a single device, is the possibility to perform contemporarly different measurements with increased speed in collection of data and complexity of elaboration, but also the opportunity to neglect noise effects due to the environment, by subtracting the output signal of a functionalised cantilever from a non-functionalised one. The process is illustrated in fig. 1. (100)-oriented silicon wafers with a thermally grown 500 nm thick SiO_2 layer on both sides were used as starting substrates (fig. 1a). RIE of SiO_2 and silicon was used on the front of the wafer to define the cantilever array (fig. 1b and c). A thermal oxidation was performed to produce a 500 nm thick SiO_2 etch-stop layer on the lateral sides and on the bottom of the square window hosting the cantilever array (fig. 1d). Then, access to the back-side silicon was obtained through BHF wet etching of the back SiO_2 masking layer (fig. 1e). A time controlled TMAH anisotropic wet etching, assisted by the front SiO_2 etch-stop layer, was used to produce a thin diaphragm made by SiO_2 and the same silicon array of cantilever (fig. 1f). The array was finally released by BHF dipping (fig. 1g).

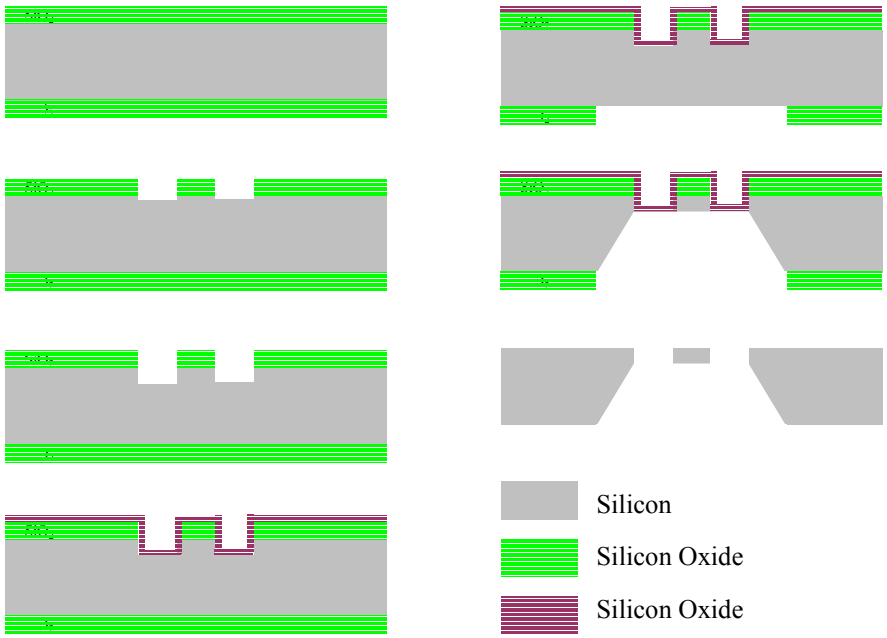

Fig. 1 - Process steps for the fabrication of the cantilevers.

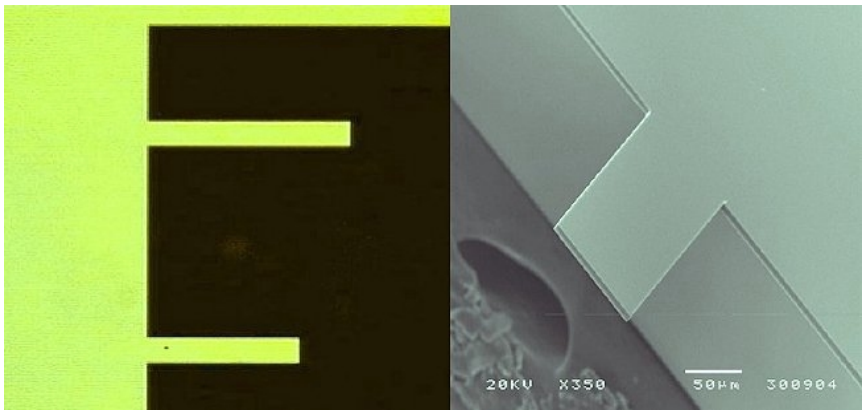

Fig. 2 - Optical and SEM micrographs of the cantilevers.

This solution allows the realization of cantilevers deriving from the same bulk silicon, with a good control on their thickness (defined by RIE etching), and most of all, avoiding stress due to structural films deposition. Cantilevers of different dimensions in a quite broad range were produced (width = 5 ÷ 100 μm; length = 30 ÷ 800 μm; thickness = 5 ÷ 20 μm) to investigate different vibrational properties such as stiffness and oscillation eigenmodes as well as static mode bending for free cantilevers. Actually a SOI wafer solution is under study as an alternative to the described process, to obtain thinner and better controlled cantilevers. In fact thickness is a key point to increase the sensitivity of the cantilevers to be used as functionalised microbalances.
Also simulations of structures behaviour have been carried out by means of finite difference analysis for design purpose. We use the Finite Element Method to develop cantilever suitable surface functionalisation in order to maximize the sensibility of the resonant DNA-microbalance. Dynamic model of such a system provided relevant indications in order to select few among the most efficient nanostructured LARC PVD ceramic thin films (mono and gradient nanostructured layers) capable to increase the resonance frequency of the beam-sensor to be employed as a mass-sensor.
We used the FEA Coventorware™[1] software to build (Process editor), discretize (Pre-processor) and simulate (MemMech) the undamped mechanical modal frequencies and mode shapes of the single-crystalline silicon (SCS) rectangular single clamped cantilever-beams: the mechanical properties used are listed in table 1 with the properties of the PVD coatings.

Material	**Density**	**Young modulus**	**Poisson ratio**
	[g·cm^{-3}]	[MPa]	
Si (SCS)	2,331	1,30E+05	0,278
Ti	4,5063	1,10E+05	0,333
TiN	5,21	5,90E+05	0,232
Cr	7,1	1,62E+05	0,21
CrN	6,4	6,40E+05	0,28

Table 1 - Material properties of silicon and other PVD materials.

Thanks to the flexibility of the Coventorware™ package we were able to design our model from the common bulk process from chip on a silicon <100> wafer: i.e the bulk with the negative sidewall angles obtained from a TMAH backside wet etch up to the thickness of cantilever and ideal simple rectangular base cantilever beams with 5 μm thickness, as from an etch of the residual silicon oxide membrane.

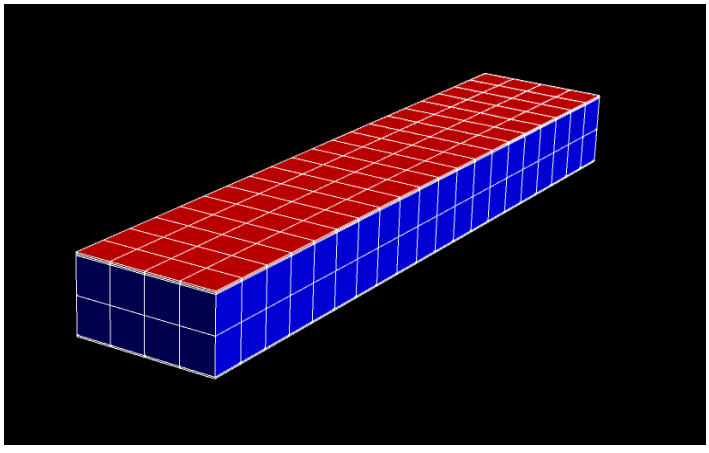

Fig. 3 - 50x10x5 μm cantilever discretized model.

[1] Coventor, Inc., 4000 CentreGreen Way, Suite 190, Cary, NC 27513

In our simulation we used 20-node parabolic brick elements to discretize our system and the mesh optimal density was obtained from convergence studies.
Modal equilibrium undamped mechanical simulations provided the first ten modal frequencies and mode shapes that characterised the silicon cantilever beams.

Mode	Frequency [Hz]	Generalized Mass [kg]
1	2,424803E+06	1,460608E-12
2	4,754558E+06	1,492998E-12
3	1,471628E+07	1,530242E-12
4	2,207229E+07	1,186352E-12
5	2,660810E+07	1,758468E-12
6	3,753118E+07	2,893665E-12
7	3,939249E+07	1,626596E-12
8	6,537417E+07	2,096587E-12
9	6,625503E+07	1,129921E-12
10	7,289934E+07	1,741993E-12

Table 2 - First 10 modal natural frequencies of the 50x10x5 μm cantilever beam (l-w-t).

Comparative analysis between uncoated cantilevers and coated cantilevers where done considering:

- double and single side uniformally metal/LARC PVD (i.e Ti/TiN) coated models;
- lower side metal PVD-coated and upper uniformly metal-coated with a micrometric PVD coating near the cantilever free end.

Comparative analysis have showed as the most sensible cantilevers are the LARC-PVD coated silicon with ceramics geometrical structures[2] at the cantilever free end. The subsequent simulation and experimental steps will be to evaluate the cantilever damping and energy loss in the DNA biological solution in order to extract their Q factor and their mass sensitivity.

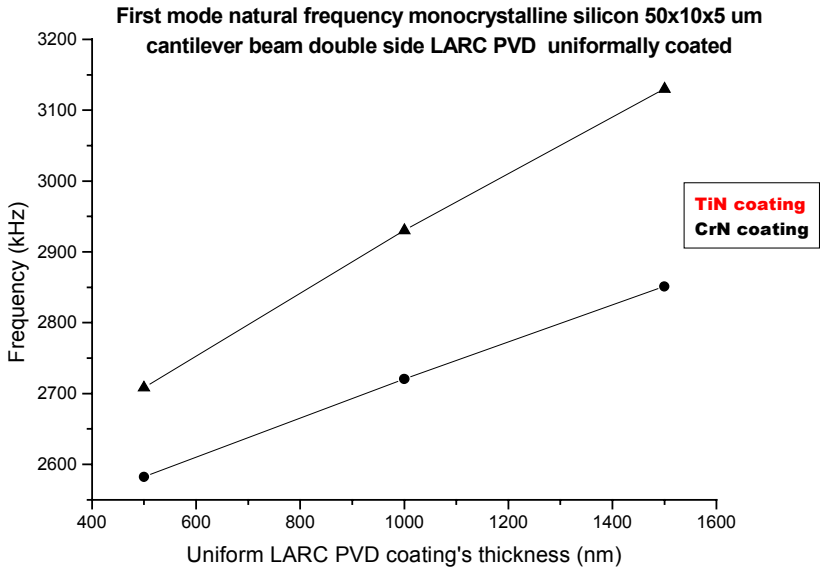

Fig. 4 – First mode natural frequency of uniform LARC PVD coated double side cantilever beams as function of film thickness and material properties.

[2] B. Ilic, H.G. Craighead, S. Krylov, W. Senaratne, C. Ober, P. Neuzil, J. Appl. Phys., Vol. 95, No. 7, 1 April 2004

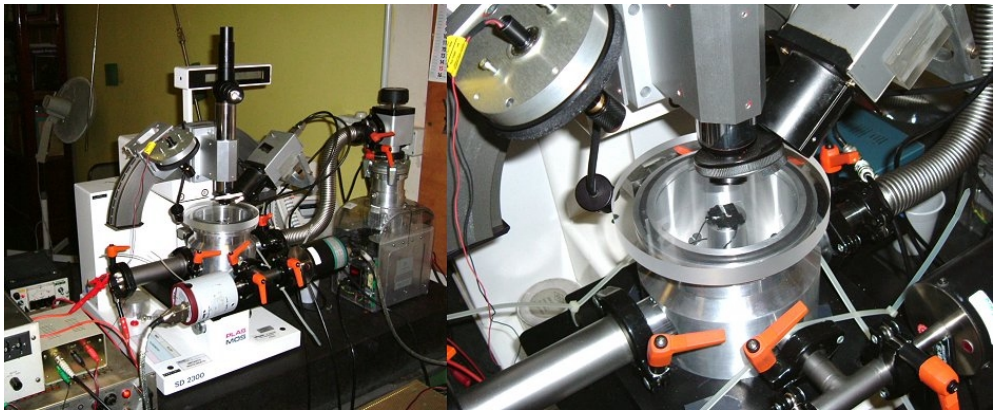

Fig. 5 – Photographs of the measurement setup and a close view of the holding cell with a cantilever die.

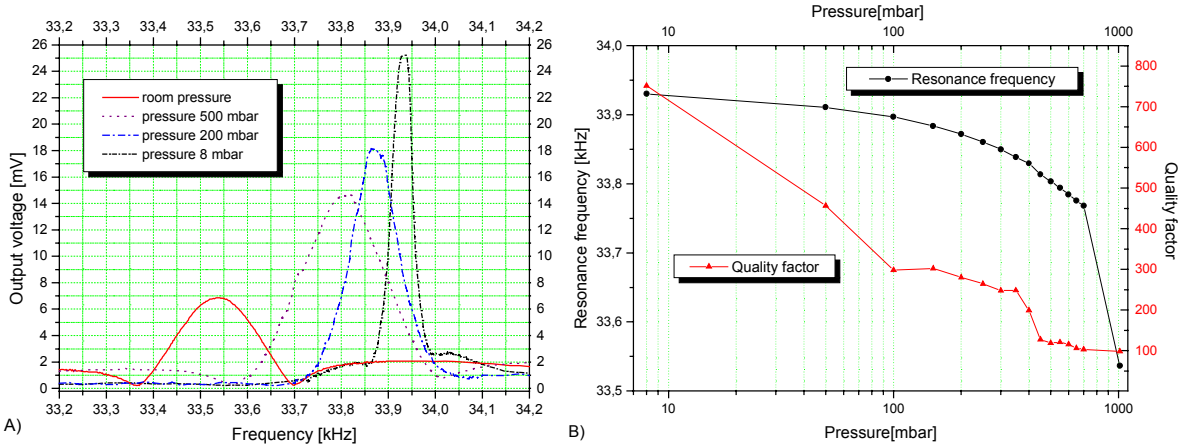

Fig. 6 - (A) Measured resonance spectra at different pressure levels for the 400x100x5 µm cantilever and (B) its corresponding resonance frequency and quality factor vs applied pressure.

The air damping mechanism, and consequently the quality factor of the cantilever, are functions of both the surrounding environment pressure and the internal friction in the cantilever material. Therefore, a systematic investigation of the cantilever resonance behaviour as a function of pressure was performed to develop a deep insight into the response of a cantilever used as a sensor. For the excitation of the microstructures, a small piezoelectric disc was used. A function generator (HP 33120A) produced a sinusoidal signal that first was amplified and then sent to the piezoelectric actuator. The actuator was linked to a holding cell, the test die with the array of cantilevers was attached to the actuator with double-sided tape and the cell was evacuated by a series of a membrane and turbomolecular pump (fig. 5). A needle valve with incorporated micropositioner was used to maintain a precise level of pressure, ranging from 10^{-8} bar to atmospheric pressure. Cantilever vibrational characteristics are measured with the 'optical lever' technique. The position of a focused laser beam reflected off the top side of the cantilever onto a position sensitive detector (PSD) is monitored. The current output of the PSD was amplified and converted into a voltage output, sent to a lock-in amplifier (EG&G 7260) for signal extraction and filtering and stored to a PC, together with the stimulus signal for the function generator. The procedure is controlled in a Labview® environment. The resonant frequency of each cantilever was measured by sweeping through frequencies with the function generator, observing the amplitude of the waveform at the output of the lock-in amplifier, and recording the frequency at which the first peak occurred. Calculation of the quality factor is performed by the Labview code. A vacuum level of 1 mbar implies an increase of the quality factor from less than 100 to about 1000 (fig. 6). Quality factors in excess of 40000 can be obtained in high vacuum conditions. Relative resonance frequency variations are of the order of 1÷1.5 % when shifting from room pressure to 1 mbar (under 1 mbar a saturation behaviour occurs and no more shift in the resonance frequency can be registered).

3. Thin functional film deposition by PVD processes

One of the major issues in the development of advanced cantilever systems for achieving high resolution assays down to the femtogram level is to realise cantilevers with high resonance frequencies. Two different (non mutually exclusive) approaches may be pursued to achieve this goal: improving geometric and/or physical parameters. The 'geometric' solution considers reducing the length of cantilever structures in order to get stiffer beams. The 'physical' approach considers attaining enhanced mass detection resolution by increasing the beam rigidity while keeping the beam inertia to convenient limited values, such that the resonant fundamental harmonic frequency may increase by some orders of magnitude. To tackle this issue, we applied thin ceramic films deposition processes on silicon via Physical Vapour Deposition (PVD). Development of binary, ternary and quaternary ceramics thin films with variable chemistry, stoichiometry and microstructure allows attaining cantilever stiffness enhancement of some orders of magnitude. Specific geometry and mass localisation was indicated by numerical simulations. Materials to be deposited where chosen according to the values of their Young modulus and on the basis of the numerical simulations results. Different types of microstructures were considered: single layered, gradient, multilayered thin films and combination of them. Various film thickness were grown in order to exploit to the maximum extent the cantilever stiffness possible increase. Single (upper) side PVD coated crystalline silicon cantilevers as well as double side coated cantilevers were realised in order to assess possible exploitable benefits from symmetric or asymmetric micro-structural configurations.

Among different technical solutions (sputtering, evaporation, etc.) the PVD ARC-DC LARC^{TM} process was chosen in order to grow complex, dense-packed, microparticle-free ceramics thin films. LARC^{TM} is an innovative evolution of the existing standard PVD ARC-DC deposition techniques in that it allows dramatically decreasing the output of micro-particles, although preserving efficient growth rates (about 2,5-3,0 μm/hour). Indeed the LARC^{TM} technology provided by the Clean NT Lab Platit-PL55 unit with rotating cathodes increases the cathode surface and assures uniform and controlled target consumption. The process was run in the 200-450°C temperature range at pressures of the order of 10^{-5} mbar. The silicon substrates where electrically connected to the substrate bias by a conductor frame, in which the samples have been allocated. This allowed to bypass the hampering question of ARC-DC deposition on non conducting material. The PVD process is run in high vacuum assuring the growth of high quality, dense-packed layers without columnar micro-nano-structures.

One or two cathodes were used according to the required stoichiometry. For binary and ternary coatings one target of Ti, Zr or Cr was employed with nitrogen as process gas (for binary coatings), nitrogen and acetylene as process gases for ternary ones. For quaternary coatings deposited stoichiometric and non-stoichiometric compounds were realised by employing two cathodes in the same process. Different bias voltages and deposition pressures were tested in order to decrease the residual thin film stress. Surface prefunctionalisation etching phases were run with Ar/H_2 mixture for assessing better silicon surface passivation.

For specified process parameters it was possible to deposit nano-structured and nano-composite ceramic thin films. These films were realised by exploiting the spinoidal decomposition occurring in a specified temperature and pressure range. Nanostructured coatings were realised by growing a Si_2N_3 amorphous matrix in which nanocrystals of the metal employed (i.e. titanium) are dispersed. These films belong to the family of super-hard coatings, displaying hardness values exceeding 3400 micro-Vickers deriving from the grain boundary interactions with the amorphous matrix.

Deposition uniformity and process reliability was analysed in order to comply with the stringent quality parameters for these applications. Overall characterisation and analysis of thin film adhesion properties, relevance to the resonance frequency increase, film compliance to the dynamic regime (presence of critical frequencies compromising film adhesion or stiffness, resistance to cyclic loading) are still in progress. Some of the first test results shown good agreement with simulations predicting convenient frequencies up-shifts

References

[1] Guanghua Wu et-al, PNAS 1560-1564, 98, n.4 (2001)
[2] N.V.Lavrik and P.G.Datskos, Appl Phys. Lett. 82, 16, (2003)
[3] Andreas Gyorffy, IEEE 2002 Polytronic Conference
[4] R.Raiteri, MGrattarila and R.Berger, Materials Today, January (2002)

Correlation between processing parameters, microstructure and optical properties for plasma-sprayed yttria-stabilized zirconia coatings

V. Debout[2], E. Bruneton[1], E. Meillot[1], S. Schelz[1]
P. Abélard[2], P. Fauchais[2], A. Vardelle[2]

1 Thermal Spray Laboratory, CEA Le Ripault, Monts, France
2 Laboratoire Sciences des Procédés Céramiques et de Traitement de Surface, University of Limoges, France

Abstract. The optical behavior of yttria-stabilized zirconia (YSZ) plasma-sprayed coatings made under various plasma operating conditions has been investigated over the 0.25-20 µm wavelength range. The oxygen loss in the sprayed material during the deposition process has a strong effect on the reflectivity level as it brings about an increase of absorption. Annealing the coatings at 500 °C for 1h results in an increase in reflectivity over the 1.0-5.0 µm wavelength range. More investigations are required to point out the influence of the microstructural features.
Keywords. Optical properties; Plasma spraying; Microstructure; Stoichiometry; Yttria-stabilized zirconia.

1. Introduction

An extensive effort has been carried out to engineer yttria stabilized zirconia (YSZ) plasma-sprayed deposits as thermal-barrier coatings (TBCs) [1]. Most of studies are about the correlation of the spraying parameters to coating microstructure and macrostructural properties such as thermal conductivity and mechanical resistance [1, 2]. Since the major heat transfer process at high temperature is radiation, the development of high performance TBCs requires a better knowledge of the infrared (IR) properties of thermal-sprayed YSZ coatings. However, only a few studies have dealt with this topic. Eldridge and al. [3] investigated the optical behavior of plasma sprayed YSZ coatings over the 0.25-15 µm range: although YSZ does not provide intrinsic barrier to radiation at wavelengths shorter than 5µm, it is possible to engineer high reflecting TBCs with high volume scattering due to microstructural defects such as porosity and microcracks.
Indeed, thermally-sprayed coatings exhibit a lamellar microstructure resulting from impinging, flattening and solidification of semi or fully molten particles on the substrate. This build-up mechanism induces a large variety of different length-scale defects [2]: rapid solidification and curling up of lamellae result in interlamellar pores; high cooling rates (10^5-10^7 K/s) provide interlamellar microcraks due to stress relaxation; unmelted or partially melted particles included in the coating and poor inter-splat contact lead to spherical pores. Moreover, plasma-sprayed deposits can present bulk chemical modifications as the sprayed particles are exposed in flight to high temperatures and reducing gases. Since the microstructure of thermal-sprayed coatings is process-dependent, it is essential to establish correlations between microstructure and optical properties and determine the heterogeneities that may interact.
Optical properties of homogeneous materials can be described by the complex refractive index $\tilde{\mathbf{n}}$ with a real part **n** and imaginary part **k** related to the phase velocity and attenuation of waves in the matter, respectively. In the case of heterogeneous materials, the scattering of the incident light modifies the optical properties. When an incident ray strikes an interface between heterogeneities and material matrix, some of the light radiation is transmitted; some is reflected due to backward scattering; some is absorbed. The total reflectance **R** and transmittance **T** can be defined as the sum of two contributions: diffuse and spectral. Besides, it is necessary to distinguish the surface scattering from the volume one: the former is due to surface imperfections (mainly roughness), the latter to defects in matter volume (heterogeneities).
The volume scattering process depends on the nature, size, shape and distribution of scattering elements. A general approach of scattering is formulated in the Mie theory for powder beds or spherical dispersions included in materials. A dimensionless quantity **Q,** called scattering efficiency, can be introduced to quantify scattering. It can be regarded as the ratio of two cross sections: the *scattering cross section* defined as the total energy flux abstracted from incident light by scattering versus the incident irradiance (energy flux per unit area) and the *geometrical cross-section* of scattering elements. Q depends on two important factors [4]:

- the relative refractive index **m** between the scattering particles and medium which is equal, for pores ($n_{pore}=1$) embedded in YSZ matter ($n_{YSZ}=2.16$), to $\mathbf{m=n_{pore}/n_{YSZ}}=1/2.16=\mathbf{0.46}$,
- the relative size **x** between the radius **r** of particles and the wavelength of incident light with $\mathbf{x=2\pi r/\lambda}$.

For plasma-sprayed coatings, the scattering centres exhibit flattened shape due to the built-up mechanism. Only assumptions can be made on the role of scattering centres for such a microstructure. Inter and intra-lamellar pores should play a key role because of an important refractive index gap with that of the medium. Their size and distribution have to be managed to improve the radiative properties. At first glance, the contribution of splat boundaries appears to be quite limited insofar as there are no impurities or second phases in these sites. Nevertheless, the characteristics of lamellae should be addressed as they act as separation between inter-lamellar pores. Consequently, porosity was chosen in first approach as an arbitrary criterion in order to engineer coatings with different optical properties.
The purposes of the present study are the following: investigate the effect of process parameters on microstructure characteristics and establish relationships between deposit microstructure, chemistry, reflectance and transmittance measurements. The first section of the paper describes the plasma-spraying experimental set-up and the tools used to characterize the microstructure and optical properties of coatings. The second section presents the experimental results and discusses the determination of the effect of stoichiometry, translucent thickness and microstructure on optical properties.

2. Experimental set-up

2.1. *Plasma spraying*

Plasma spraying has been carried out with a F4-VB Sulzer Metco torch. Agglomerated-and-sintered 7 wt.% Y_2O_3-stabilized ZrO_2 powder (Table 1) has been sprayed on stainless steel substrates located at 120 mm downstream of the nozzle exit. Particles were injected through a 1.5-mm internal diameter injector perpendicular to the plasma torch axis and located at 6 mm from the nozzle exit. The powder injection conditions was fixed according to particle size range and torch operating conditions in such a way that the median particle trajectory was nearly the same whatever were the spraying conditions. During spraying, the substrate temperature maintained around 200-250 °C was monitored using a pyrometer and controlled by an argon cryogenic system.
The particle temperature and velocity at the substrate stand-off distance were measured using a DPV-2000 equipment (Tecnar Automation Ltd, Canada). For each combination of spray parameters, the data from a total of about 5000 individual particles in the highest-flow particle density were acquired and averaged. Velocity and temperature measurement errors are 5% and 20%, respectively [5].
The operating conditions were selected in order to have a large range of particle velocities and temperatures at impact. The following operating parameters were been varied: torch nozzle internal diameter (6 and 8 mm), arc current (320 to 600 A), gas mixture (binary or ternary mixtures of argon, hydrogen and helium) and flow rates. About 25 sets of spraying conditions were investigated. Only two spraying conditions resulting in significant differences in coating microstructure are reported in this paper (Table 2).

Table 1: Feedstock characteristics – ZrO_2-7%wtY_2O_3

Powder reference	Manufacturer	Powder type	Manufacturing Process	Particle size distribution (µm)
827.054	H.C Stack GmbH & Co	Agglomerated and sintered (A&S)	Spray-dried and sintered	10-45

Table 2: Spraying conditions, in-flight particle parameters and coating porosity

Spraying parameter set number	Plasma gas flow rates (slm)	Arc current (A)	Arc Voltage (V)	Nozzle diameter (mm)	Particle in-flight parameters		Coating open porosity
					T (°C)	V ($m.s^{-1}$)	
I	Ar: 45 H_2: 15	600	75	6	3014±185	224±62	10±2%
II	Ar: 12 H_2: 3 He: 45	450	52	6	2598±130	126±30	23±1%

2.2. *Porosity measurement*

Deposit cross-section observations were performed by optical microscopy and digital image analysis was used to estimate the amount of pore in a 3.5-mm^2 cross section. The coating porosity was analyzed by using two volume methods: Archimedes and mercury intrusion porosimetry. The latter provides both open porosity level and pore size distribution. Acidic dissolution was used to remove the coating from the stainless steel substrate.

2.3. *Annealing treatment*

In order to evaluate the effect of oxygen content on optical properties, the samples were annealed in air at 500 °C for 1h. To dismiss any phase and microstructural transformation, the porosity measurements and X-ray diffraction were carried out before and after annealing. The annealing time was evaluated by performing thermogravimetric recordings. It was defined as the time from which no more change in coating weight was measured.

2.4. *Optical characterization tools*

The coating hemispherical reflectance and transmittance were measured over the 0.25-20 µm wavelength range by using two spectrometers. For the 0.25-2.5 µm range, measurements were performed with a Varian Cary 5000 spectrometer equipped with a 11-cm diameter integrating sphere. The inner wall is covered with a white diffuse, homogenous Teflon paint in order to allow multiple reflections.

For the 1.5-20 µm range, a Mid-IR Bruker IF66v/S spectrometer was used. It includes a Fourier Transform IR (FTIR) double-beam spectrometer with a globar source, KBr beam splitter and mercury-cadmium-telluride MCT nitrogen-cooled detector. A 7.6-mm diameter integrating sphere with a gold inner coating (Fig. 1) has been mounted in order to collect hemispherical radiation. A "diffuse" gold sample was used as calibration reference. To acquire the reflectance data, the incident radiation was alternatively directed toward the gold reference and plasma-sprayed sample by switching a mirror. The sample room was maintained under secondary vacuum (P<2000Pa) to avoid the absorption bands of atmospheric gases, mainly CO_2 and H_2O.

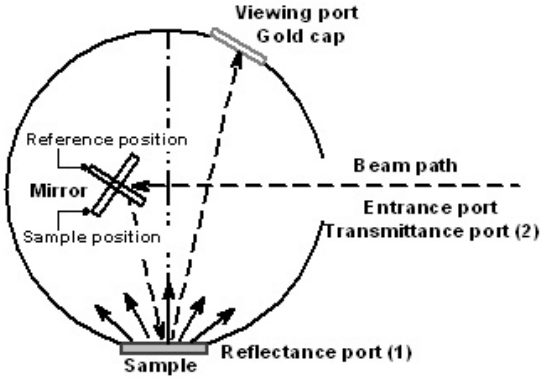

Fig 1: Diagram of IR integrating sphere reflectance (1) and transmittance (2) positions

To examine the optical properties over the entire wavelength range, the Bruker data were adjusted and merged with the Varian data between 1.5 to 2.5µm, using the OPUS software (Bruker Optik GmbH).

3. Results and discussion

3.1. *Darkening of plasma-sprayed zirconia*

The as-sprayed YSZ coatings exhibited various colors depending on the operating conditions. Indeed, the sprayed particles undergo severe reducing conditions i.e. high temperatures and reducing atmosphere (H_2). Chemical modifications may take place and induce a darkening of the YSZ plasma-sprayed coatings. Although the darkening of YSZ materials is commonly noticed under such reducing conditions, controversial causes have been proposed. Few authors attribute the black color to the migration and reduction of impurities (Fe, Li, Ti…) within grain boundaries [6], but most of them assume that the depletion of oxygen induces a modification of the neighbourhood of Zr^{4+} and change in the electronic state to Zr^{3+} [7].

The difference in YSZ deposit color can be regarded as oxygen stoichiometry variation. The spray type I condition led to dark coatings while type II condition resulted in bright yellow coatings. This discrepancy arises from the difference in particle temperature and dwelling time and plasma chemistry i.e. hydrogen content. Figure 2 shows the reflectance spectra of these two as-sprayed coatings. Low reflectivity is observed for sample I over the 1-8µm wavelength range contrary to sample II. However, this significant difference in optical features can be linked to coating stoichiometry as well as microstructural features.

To distinguish these two contributions, the annealing of coatings was performed coupled with thermal gravimetric (TG) experiments at 400°C and 500°C, under air with a 10°C/min rise in temperature. The water evaporation induced a weight loss of 0.04% from the ambient temperature to 330°C. Beyond, a slight weight gain of 0.03% was measured; it could be attributed to an oxygen gain during reoxidization. After one hour at 400°C, no weight variation was observed and the reoxidization process was considered to be completed. Only half hour was required at 500°C to observe the same evolution. In order to allow the diffusion of oxygen in material, the oxidation time was doubled: one hour at 500°C, two hours at 400°C. No microstructural modification was observed under these annealing conditions. So, all coatings were annealed at 500°C during one hour. After annealing, the dark specimens became pale-gray and not white as expected. Some substantial variation in oxygen stoichiometry may remain even after annealing. The re-oxidation ability seems to depend both on initial under-stoichiometry condition and microstructure.

3.2. *Effect of annealing on optical properties*

The reflectance of coatings before and after annealing is shown in Fig. 2. The annealing process had a marked effect on high under-stoichiometric materials (sample I) with a substantial increase in reflectance level over the 1-5µm range. Nearly no variation was observed for initially white coatings (sample II). The different behaviors of reflectance with annealing treatment can be explained by the competition between K, the absorption coefficient and S, the scattering coefficient. Assuming a diffuse incidence of radiation, even though it is not the case in the commonly-used spectrometers, the Kubelka-Munk's theory [8] can be used in first approximation to evaluate the ratio of these two coefficients as a function of the reflectance R :

$$\frac{K}{S} = \frac{(1-R)^2}{2R} \quad (1)$$

For semi-transparent medium, reflectance values (R) lower than 27% (K/S>1) indicate that absorption is dominant; beyond scattering becomes important. Thus, the absorption is predominant for as-sprayed sample I. After annealing, the reflectance increases, K/S ratio decreases and scattering plays a major role.

In the UV-visible range, the radiation absorption results in electronic polarization. In dielectrics, electronic absorption occurs for photons with energies higher than the band gap: in zirconia, the gap energy is estimated around 5.2 eV [9] namely in the near UV (250 nm). Different optical behaviors must be contemplated as a modification of the electronic environment in the matter. Under reducing atmosphere, using the Kröger-Vink notation, the oxygen incorporation equilibrium can be described as follows:

$$O_o^x \Leftrightarrow V_o^{\bullet\bullet} + 2e' + \frac{1}{2}O_{2(g)} \quad (2)$$

where O_o^x is an oxygen atom in normal oxygen site, e' is an electron and $V_o^{\cdot\cdot}$ is a doubly ionized oxygen vacancy. No-stoichiometric coatings exhibit high content of oxygen vacancies which can capture one or two electrons to form neutral or single ionized vacancies. The vacancy creation induces changes in the electronic band structure of materials by acting as donor levels. Zirconia containing oxygen vacancies show additional bands between the valence and conduction bands [10]. Such bands called "vacancy energy bands" are located at a depth around 2.5 eV below the conduction gap which corresponds to absorption around 600nm. The thermoreduction during plasma spraying increases drastically the oxygen deficits and leads to a filling by the electrons of the empty vacancy energy levels. Transitions between this additional band and conduction band may occur. Such a transition requires low energy photons and absorption can take place in the near IR wavelength range (1-5µm) as observed for as-sprayed type I coatings (Fig. 2).

3.3. *Determination of translucent thickness*

The translucent thickness can be defined as the thickness for which the optical transmission falls below 1% [11]. A preliminary study was carried out on freestanding deposits (type I coatings) 300, 500, 800 and 1100-µm thick. For coatings thicker than 500 µm, the transmittance was equal to zero. For thinner coatings, the transmittance values varied between 2% and 5% in the 1-5 µm wavelength range. Thus, all the optical measurements (Fig. 2) were performed with 500-µm thick coatings since it seems to be enough to insure the opaqueness of YSZ coatings.

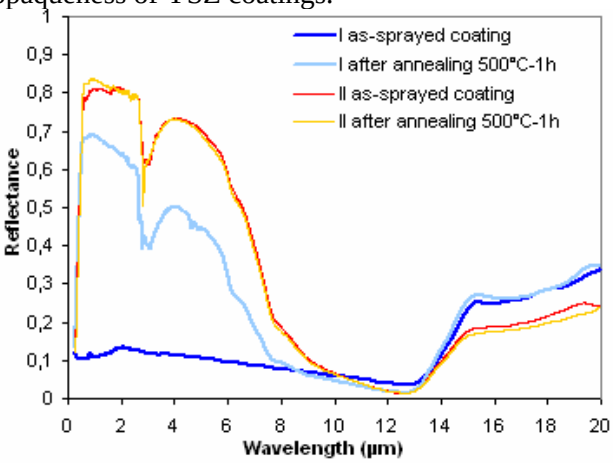

Fig 2: Reflectance spectra for as-sprayed and annealed coatings (sample I and II).

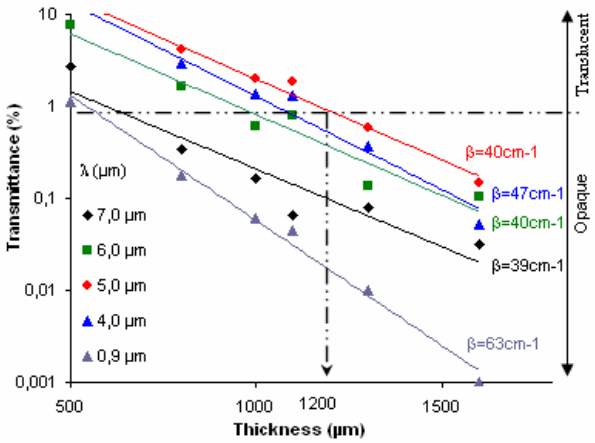

Fig 3: Effect of thickness on transmittance at given wavelength. Sample I annealed at 500°C for 1h.

Nevertheless, the type I coating exhibits oxygen-deficient. Therefore, the absorption contribution might be predominant and scattering restricted according to the Kubelka-Munk's model. As the translucent thickness is sensitive to stoichiometric effects; new investigations were made on type I coatings after annealing. These results are compiled in Fig. 3 where the transmittance *T* is plotted versus coating thickness x in µm at given wavelength values. As expected, the light attenuation takes place according to the Beer-Lambert law:

$$T=\exp(-\beta x) \quad (3)$$

where β is the extinction coefficient. As the extinction coefficient is a measure of the decrease in intensity of the incident beam due to matter absorption and scattering of the light, it can be defined as the sum of the absorption coefficient ($K=4\pi k/\lambda$) and scattering coefficient S. The translucent thickness of annealed type I coating can be evaluated around 1200µm (see Fig. 3).

The translucent thickness is also microstructure-dependent and the evolution of extinction coefficient can be regarded as microstructure effects. Indeed, a slight increase in absorption coefficient K has been reported by Makino and al. [12] for zirconia in the 1-5µm range: $K=0.1cm^{-1}$ at 1.0µm; $K=0.5cm^{-1}$ at 5µm. Conversely, in this wavelength range, YSZ coatings exhibit a decrease of the extinction coefficient β (Fig. 3) which implies a decline in the scattering contribution. This feature can be understood through the evolution of the size of heterogeneities *d* relative to wavelength λ: the increase in wavelength leads to a decrease in the parameter size $x=\pi d/\lambda$. Consequently, the scattering efficiency Q may be reduced around 5µm for lack of suitable size of heterogeneities compared to the wavelength.

3.4. *YSZ optical behavior*

A typical reflectance spectrum of annealed YSZ coating is shown in Fig. 4. The optical behavior can be divided into three radiative regions.

In region **I** ($\lambda<5$ µm), the refraction index n is higher than 1 and the extinction index k is very low (<<1); volume scattering is predominant. The hemispherical reflectance is mainly composed of the diffuse reflectance due to scattering centres like pores or other discontinuities in the matter. Around 3 µm, the absorbed water causes absorption bands and a consistent drop in reflectivity. In region **II** ($6<\lambda<12.5$ µm), the increase in light wavelength brings about a drop in reflectance caused by the decrease in the relative size of the scattering centers compared to λ. Besides, n decreases and k begins to increase due to lattice vibration.

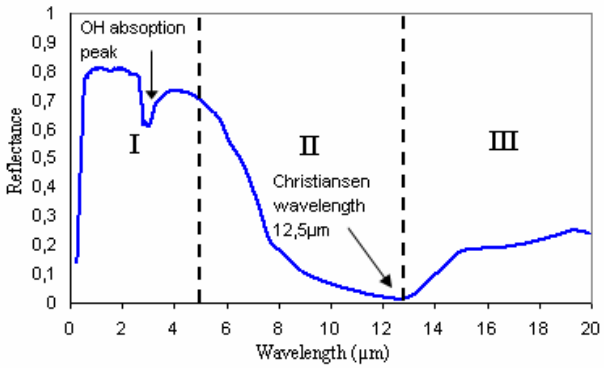

Fig 4: Typical reflectance spectrum of YSZ plasma-sprayed coatings

When n is equal to the refractive index of air (n=1), no scattering occurs and the radiation spreads freely in the material with little absorption due to k value. This phenomenon is a remarkable property of dielectric materials and is called the Christiansen feature. It results in a minimum of transmittance T and reflectance R and a maximum of emissivity ε (Kirchhoff's law: ε=1-R-T). This feature is nearly independent of temperature and texture; its value is fixed by lattice vibration. Christiansen point of YSZ is around 12.5 µm. In region **III** ($\lambda>12.5$ µm), k is large (>0.1) and the resonant lattice vibrations play a key role in such a way that the incident radiations can not enter further than the first surface layers. The scattering process must originate from coating surface.

3.5. *Microstructural effects*

While keeping in mind the preponderant effect of stoichiometry, part of the observed differences after annealing might be indicative of a microstructural dependence of the optical spectra. Figure 2 shows the spectra after annealing for two different microstructures. The type II coating exhibits high reflectivity in the 1-6µm wavelength range except around 3µm where a sharp drop is observed owing to OH absorption. According to the Kubelka-Munk ratio (K/S), scattering is predominant for these two kinds of coatings after annealing. High reflectivity values can be related to an increase in diffuse backward reflection around scattering centres. Compared with type I spectrum, higher reflectivity seems to come along with higher porosity values (see Table 2). Although the deposit porosity seems to be the main cause of diffuse reflection, it could be inadequate to consider only porosity levels. A global description of the optical

properties of porous media needs also the knowledge of scattering centres characteristics: pore size, distribution and shape. The measurement of porosity by mercury intrusion and microscopic observations are in progress to evaluate the mean size of pores and their distribution.
The effect of microstructure can be illustrated in an indirect way by the reoxidation process and also water absorption. The latter can be related to the specific area of open porosity. OH bondings cause absorption around 3 µm which is still present after annealing with a narrower and sharper peak (Fig. 3). Some OH bondings may survive the water desorption or some water could be absorbed again [3].

4. Conclusions

Under-stoichiometry inherent to YSZ plasma-sprayed coatings has a major effect on the optical behaviour of resulting coatings. Dark coatings (i.e. deficient in oxygen) exhibit low reflectivity below 12.5µm due to two kinds of electronic absorption: in the UV-Visible range, a transition occurs between the valence and conduction bands; in the near IR range, the absorption may be due to transition from the vacancy energy and conduction bands. The latter depends on oxygen deficiency. It can be removed by annealing the coatings at 500°C for 1 h. However, such annealing can not guarantee the stoichiometry of coating and, therefore, the intrinsic optical properties of the media (n and k values). The study of the diffusion of oxygen into YSZ coatings is in progress to investigate the reoxidation mechanisms.
The OH bondings cause strong absorption near 3µm and may be reduced by high-temperature annealing.
Annealed coatings exhibit substantial volume scattering that induces a high reflectivity below 5µm. The reflective discrepancy between the two types of coatings used in this study is of particular interest as it can be contemplated as microstructural effects. Further studies of scattering centre characteristics are necessary to understand the scattering phenomena and resulting optical behaviour. The size, distribution and shape of pores must be investigated to engineer highly reflective thermal barrier plasma sprayed coatings.

References

1. A. Kulkarni, A. Vaidya and al., *Processing effects on porosity-property correlations in plasma sprayed yttria-stabilized zirconia coatings,* Materials and Engineering, 2003, **A359**, pp.100-111.
2. A. J. Allen, J. Ilavsky and al., *Microstructural characterization of yttria stabilized zirconia plasma-sprayed deposits using multiple small-angle neutron scattering,* Acta mater., 2001, **49**, pp.1661-1675
3. J.I Eldridge, C.M Spuckler and al., *Infrared radiative properties of yttria-stabilized zirconia thermal barrier coatings,* Ceram. Eng. Sci. Proc., 2002, **23(4)**, pp.417-429.
4. J.G.J. Peelen, *Relation between microstructure and optical properties of polycristalline alumina,* Science of ceramics, **6**, 1973, pp.1-13.
5. C. Moreau, P. Gougeon and al., *On-Line Control of the Plasma Spraying Process by Monitoring the Temperature, Velocity and Trajectory of In-Flight Particles,* Proceedings of the 7th National Thermal Spray Conference, Boston, Massachusetts, Ed. by C.C. Berndt and S. Sampath, 1994, pp.431-437.
6. J.S Moya, R. Moreno and al., *Black Color in Partially Stabilized Zirconia,* Journal of The American Ceramic Society, 1988, **71(11)**, pp.479-480.
7. Gabriel Maria Ingo, *Origin of Darkening in 8wt.% Yttria-Zirconia Plasma-Sprayed Thermal Barrier Coatings,* Journal of The American Ceramic Society, 1991, **74(2)**, pp.381-386.
8. T. Burger, J. Kuhn and al., *Quantitative Determination of the Scattering and Absorption Coefficients from Diffuse Reflectance and Transmittance Measurement: Application to Pharmaceutical Powders,* Applied Spectroscopy, 1996, **51(3)**, pp.309-317.
9. P. Camagni, P. Galinetto and al., *Optical properties of cubic stabilized zirconia,* Solid State Communications, 1992, **83(11)**, pp.943-947.
10. V.I. Aleksandrov, S.Kh. Batygov and al., *Influence of composition and heat treatment on charge states of intrinsic and impurity defects in ZrO_2-Y_2O_3 solid solutions,* Sov. Phys. Solid State, 1984, **26(5)**, pp.799-803
11. V.R. PaiVerneker, A.N. Petelin and al., *Color-center-induced band-gap shift in yttria-stabilized zirconia,* Physical Review B, 1989, **40(12)**, pp.8555-8557.
12. T. Makino, T. Kunitomo and al., *Thermal Radiation Properties of Ceramic Materials,* Transactions of the Japan Society of Mechanical Engineers, 1984, **50(452)**, 1045-1052.

Pulsed Corona Plasma Pilot Plant for VOC Abatement in Industrial Streams as Mobile and Educational Laboratory

Giyoung Tak, Alexander Gutsol, and Alexander Fridman

Department of Mechanical Engineering, Drexel University, Philadelphia, USA

Abstract

High –volume pulsed corona discharge system, which is able to treat up to 750 m^3/h of gas, has been developed at the Drexel Plasma Institute as a core of the mobile Pilot Plant to demonstrate promising technology in paper and wood industry for treatment of high volume – low concentration (HVLC) industrial ventilation streams contaminated by Volatile Organic Compounds (VOC). In this paper, the experimental results for the removal efficiency are presented with respect to several parameters.

Keywords: VOC control, pulsed corona, air cleaning, methanol, dimethylsulfide, alpha-pinene.

1. Introduction

Since Volatile Organic Compounds are the major causes of many environmental problems due to their toxicity and their contribution to the global warming mechanism, many researchers have put their efforts into cleaning of gaseous streams containing VOCs in various ways. Many different industrial processes produce VOCs. In the paper industry, VOCs are mainly contained in solvents, chemical binders, bleaching chemicals for paper production; they are also contained in the wood itself and they released into the exhaust gases during the processing of the wood paste. These emissions are classified as high volume – low concentration (HVLC) gas streams.

Major traditional techniques for VOC removal include biological filters, two stage absorbers and, most important, regenerative thermal incineration or regenerative thermal oxidation (RTO). These methods for the treatment of the dilute off-gases require relatively high energy consumption and result in high treatment costs [1]. Gas phase hazardous organic wastes can be destroyed by oxidation to non-hazardous compounds, such as carbon dioxide and water. The most effective way of oxidizing organics is to use highly reactive species, i.e. reactants with a high oxidizing potential, such as ·OH, ·O, ·H, O_3, and H_2O_2. The hydroxyl radical is especially known to play an important role in oxidative purification and degradation of organic compounds [2]. In a combustion process, efficiency of production and concentration of these free radicals and active species depend on the process temperature. In order to attain the required temperature, a considerable amount of energy must be spent for direct heating of the gas (e.g., by incineration or thermal plasma). To perform incineration of HVLC gas streams, some quantity of fuel must be added to promote effective combustion, since the concentration of organic material is not sufficient to sustain combustion by itself. To uniformly heat the whole gas stream by thermal arc, a high amount of electric energy must be spent. Both these methods are inefficient in terms of production of active species [3].

Low-temperature non-equilibrium (non-thermal) plasma discharges represent an alternative technology for gas phase de-pollution. Here most of the energy (up to 99.9%) is directed in the production of high-energy electrons [3], rather than in heating the gas. Radicals, ions and other active species, which oxidize, reduce or decompose the pollutant molecules, are efficiently produced mainly via electron-impact dissociation, excitation and ionization of the background gas. Non-equilibrium discharges have been tested for the removal of a number of different toxic or environmentally hazardous compounds, such as SO_x, H_2S, VOCs, PAHs (Polycyclic Aromatic Hydrocarbons), heavy metals, and others, like chemical warfare gases such as nerve gas [3].

The feasibility of non-thermal plasmas for VOC control application in the paper and forest products industry was studied by Harkness and Fridman [3]. In that work, published data from all non-thermal processes being currently developed were reviewed to estimate the applicability of the process to contaminants and conditions typical for forest products applications. Four non-thermal plasma technologies appeared to promise both lower capital costs and operating costs than the incineration-type process currently available. They are: 1) dielectric packed bed corona discharge; 2) electron beam discharge; 3) non-thermal gliding arc discharge; and 4) heterogeneous pulsed corona discharge. After investigation sponsored by Department of Energy (DOE), the heterogeneous pulsed corona discharge was chosen as the best non-equilibrium plasma technology for control of the vent emissions from HVLC Brownstock Washers. While the research was conducted, laboratory experiments were carried out using installation with the average power up to 20 W. For the compounds of interest in the DOE project (methanol, acetone, dimethylsulfide and α -pinene), high removal efficiencies were obtained with power levels competitive with the present technologies for the VOCs removal [4]. As continuation of the DOE project, trailored pilot plant as shown in Figure 1, which can treat up to 750 m^3/h of gas stream, was built for testing in industrial conditions [5]. Experiments with the pilot plant were performed with average plasma power up to 3.5 kW. Different design of the laboratory and pilot plant pulsed coronas, as well as different analytical methods revealed many new peculiarities of the VOC abatement process. The work reported herein describes the experimental results for the VOCs removal efficiency with respect to energy consumption, residence time, water effect and initial concentration. In addition, generation of organic byproducts which are hardly removable by plasma is discussed.

Fig. 1. Photograph of the Mobile Plasma Pilot Plant

2. Experimental Setup

Figure 2 illustrates the schematic diagram of the pilot plant including sampling, measuring and calibration equipment. Basically the pilot plant process consists of three stages of gas treatment:

1. Preliminary washing of the exhaust gas stream by a water shower for removing particulates and soluble VOCs such as methanol and acetone.
2. Exhaust stream treatment by dry or wet pulsed corona discharge for VOC oxidation.
3. Removal of the balance of ozone and VOC by self-cleaning adsorbent.

The first stage is similar to scrubbing. For maximum removal of soluble VOCs, the direction of the water flow is opposite to that of the gas stream. System and water flow rate were optimized to reach highest scrubbing efficiency of the soluble VOCs with expected gas flow rates and to prevent water droplets from being carried over by the gas stream. It was presented in the previous laboratory experiments and modeling that it was

possible to remove nearly all the soluble VOCs using this technique [4, 5]. The scrubber volume is about 1 m^3 and is filled with special low density-high surface packed bed material.

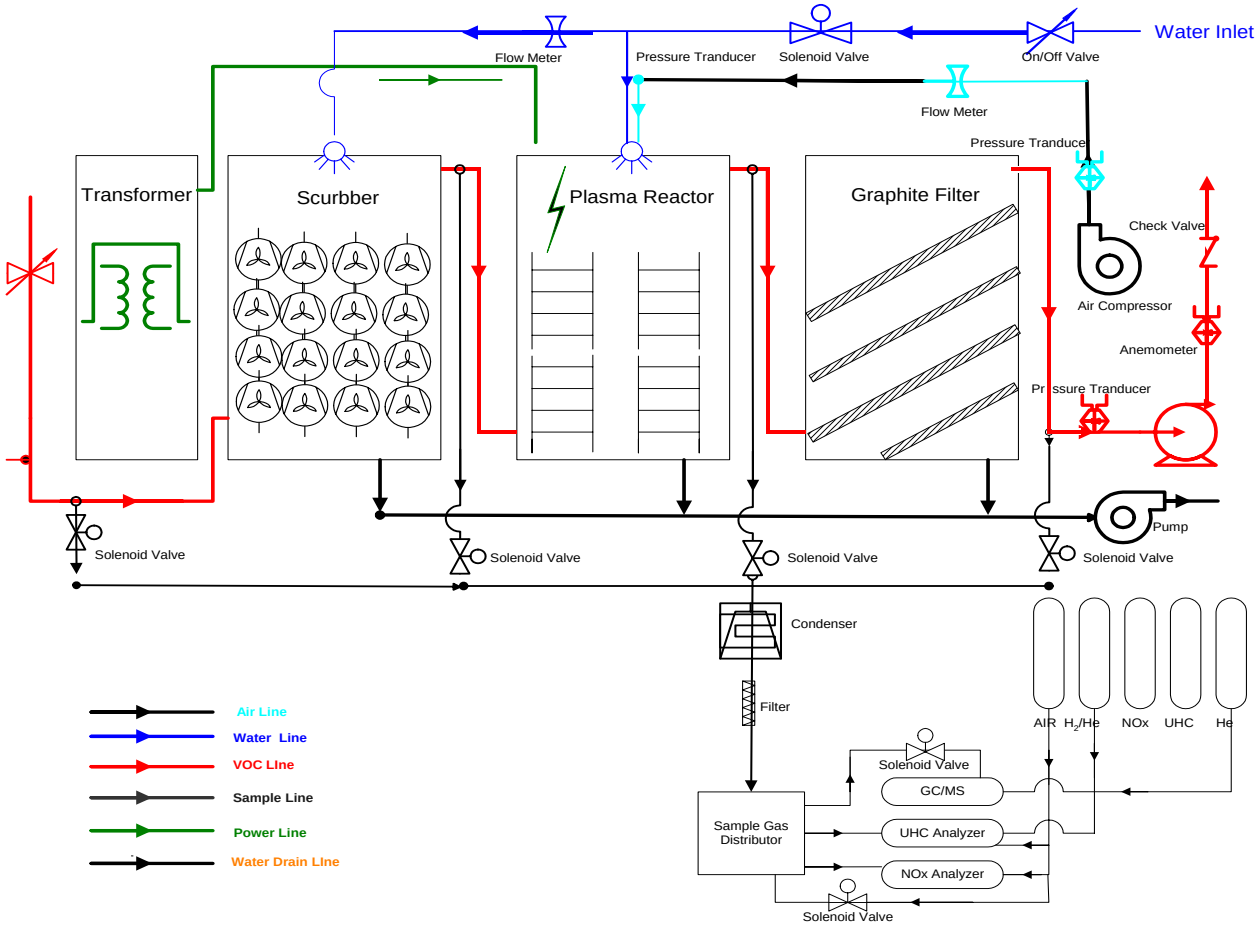

Figure 2. Process Schematic Diagram of the Pilot Plant

In the second stage, the gas stream is treated in the pulsed corona discharge plasma reactor, which includes an option of supplying a water spray flow into the discharge volume. Compressed-air atomizers are used for spray formation. The pulse corona discharge unit consists of 12 units (channels), and each of them includes high-frequency converter with an intermediate frequency of 25 kHz on the base of field (IGBT) transistors, pulse high-voltage transformers, work capacitance and special high-voltage self-firing discharge gap for high voltage pulse formation on the corona electrodes. Discharge power is regulated by stepwise changing of the pulse repetition frequency in the range 20-100% (20%, 40%, 60%, 80%, and 100%). The main parameters of the corona discharge are the followings: peak voltage is about 40 kV, pulse repetition frequency is up to 1 kHz, and pulse duration is of 200-250 ns. The structure of the pulsed corona discharge blocks (Fig. 3) consists of alternate rows of grounded and high-voltage electrodes. Such a structure provides transparency of the discharge volume for the water spray. Plasma discharge zone is formed by 12 corona blocks installed in three layers. Total discharge volume is about 3.6 m^3.

Figure 3. Corona Block

The last cleaning stage includes adsorption and oxidation of any remaining VOCs with filter. The filter is formed by activated charcoal particles of 3 mm size in layers of 2 cm thickness. Total area of the layers is about 2 m^2. This filter contributes to enhance complete removal of any remaining VOCs, ozone and nitrogen oxides.

The pilot plant has three sampling ports after the three cleaning stages for precise analysis of the removal efficiency. Soluble VOC and products of the plasma-chemical destruction may be removed by industrial wastewater. Additionally clean water flow is necessary for cooling electronic equipment.

3. Results and Discussion

Fig. 4 shows overall combination effect of scrubber and plasma on removal of methanol. Temperature of the plasma reactor is kept constant (room temperature). It is possible to reach desirable level of Destruction and Removal Efficiency (DRE) (for example 98%, according to the new U.S. regulations for paper and wood industry) by two ways: just by plasma power increase, or by combination of small plasma power level with scrubbing. If scrubbing and following water treatment is acceptable (as in paper mills), the second approach looks much more promising. If water discharge is not permitted (as in U.S. wood industry), plasma treatment should be applied without preliminary scrubbing, or additional water treatment system should be built. Plasma treatment of methanol is relatively expensive process, even for low concentrations, because as it was shown earlier [4, 5] energy cost of one VOC molecule oxidation by plasma rises enormously with VOC concentration decrease. Our results are a little better but comparable to that obtained with small 20 W system [4, 5]: energy cost is about 300 eV per methanol molecule for 12 ppm initial concentration.

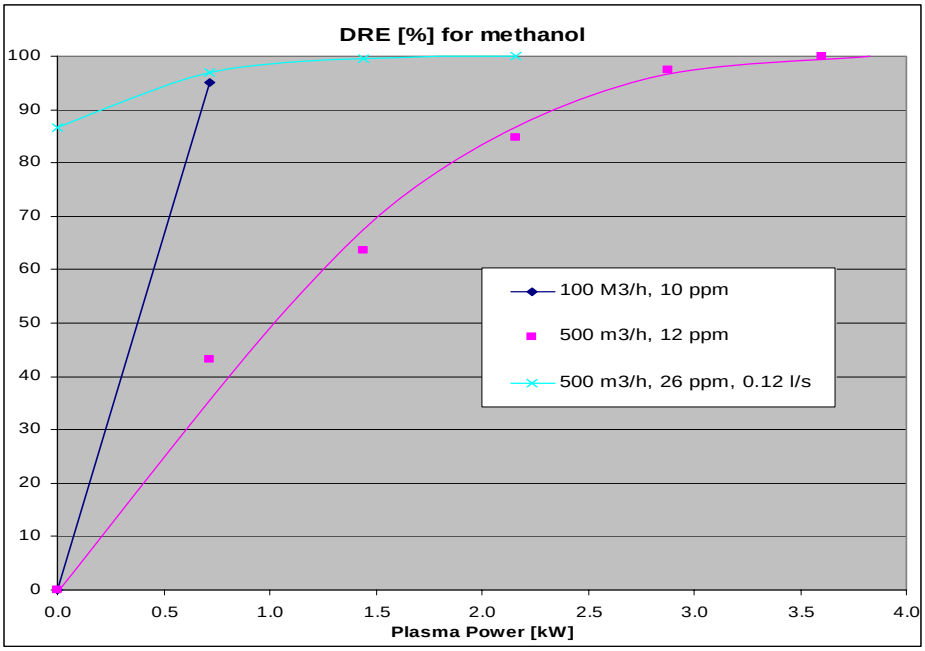

Figure 4. Methanol destruction and removal efficiency depending on plasma power without and with water scrubbing under 0.12 l/s of water flow rate in scrubber (upper blue curve).

The main analytical tool at the pilot plant is a California Analytical Model 300HFID/MHFID Heated Hydrocarbon Analyzer, in contrast to a gas chromatograph used in lab experiments [4, 5]. Thus, instead of direct measurement of concentration for particular VOC we measured cumulative concentration of the initial VOC and all hydrocarbon byproducts. Methanol oxidation (Fig. 4) in plasma is going without formation of any byproducts [4, 5], so interpretation of these results is very simple. As it was demonstrated earlier [4, 5] oxidation of dimethilsulfide (DMS, Fig. 5) in plasma is going faster than oxidation of methanol, but is accompanied by

formation of byproducts – methanol and acetone. It is possible to distinguish two parts on concentration curves in Fig. 5: initially concentration of total hydrocarbons going down relatively fast (mostly DMS oxidation with energy cost about 200 eV per DMS molecule for 10 ppm initial concentration), and then much weaker dependence on power (compare with Fig. 4) that corresponds to oxidation of byproducts. It was shown earlier [4, 5] that elimination of DMS in plasma is going considerably easier than elimination of methanol and much easier than acetone. Addition of NaOH solution spray (0.13 l/s, pH =11.5 and 12.1) into pulsed corona reactor does not change DMS oxidation process considerably.

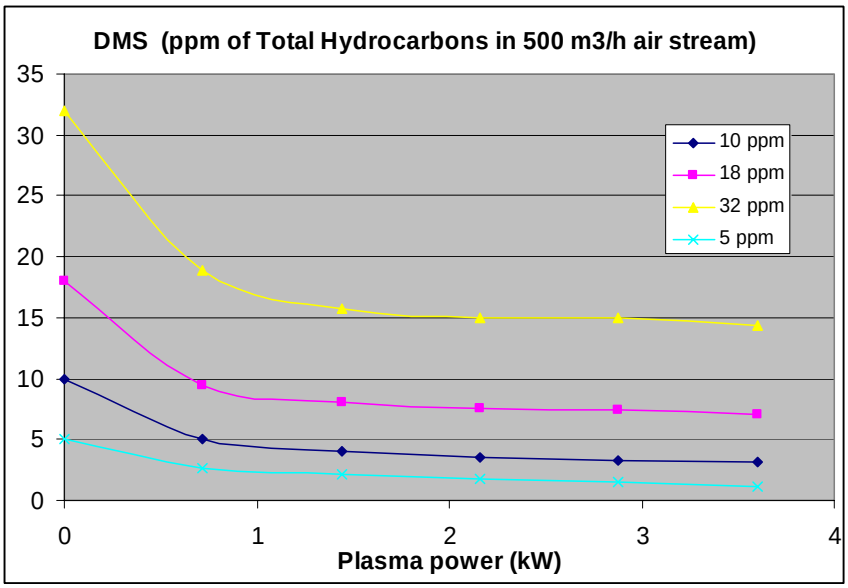

Figure 5. Dimethylsulfide oxidation in plasma: concentration of total hydrocarbons depending on plasma power.

When we considered alpha pinene ($C_{10}H_{16}$) destruction, influence of by-products formation was not so obvious (Fig. 6) while we used relatively high concentration of alpha-pinene (note that 1 ppm of $C_{10}H_{16}$ corresponds approximately to 10 ppm of total hydrocarbons). Nevertheless, control of by-products using GS-MS (HP5890A gas chromatograph with HP5970 Mass Selective detector) revealed high-molecular byproducts (like $C_{25}H_{46}$) than contained cyclopentane rings in molecular structure, which seems hardly to decompose, as these molecules can be considered as soot precursors. Strong influence of these by-products was found in experiments with low concentration of alpha-pinene (Fig. 7). This very specific picture hints us to suggest that there are two very different mechanisms of alpha-pinene interaction with plasma products: chain oxidation that starts by some radical and goes without formation of stable by-products; and decomposition by plasma particles (electrons, first of all) with following formation of soot precursors. We are going to test this suggestion, and if confirmed this leads to reconsideration of the optimal process organization scheme. Water spray in the corona reactor reduces efficiency of the alpha-pinene elimination process (Fig. 6). Energy cost is about 300 eV per alpha-pinene molecule for 2 and 7 ppm initial concentration (probably the most correct figure is for 2 ppm, see Fig. 7) and 40 eV per molecule for 64 ppm initial concentration. The last figure is in a good agreement with the data obtained using 20 W pulsed corona [4, 5].

As it was mentioned earlier, energy price is strongly related to the initial concentration. For relatively low VOC levels, high energy price is required. This is due to the fact that not all the active species produced in the gas discharge can actually target VOC molecules, i.e. not all the electric energy to create active species is consumed for oxidation of organic compounds; some of these species undergo reactions with each other or lose their energy on walls. Reactions with VOC molecules are statistically more frequent if the concentration of VOC is relatively high; in this case, the fraction of energy spent for the purpose of removing the molecules is higher and the energy spent for the elimination of each single molecule decreases.

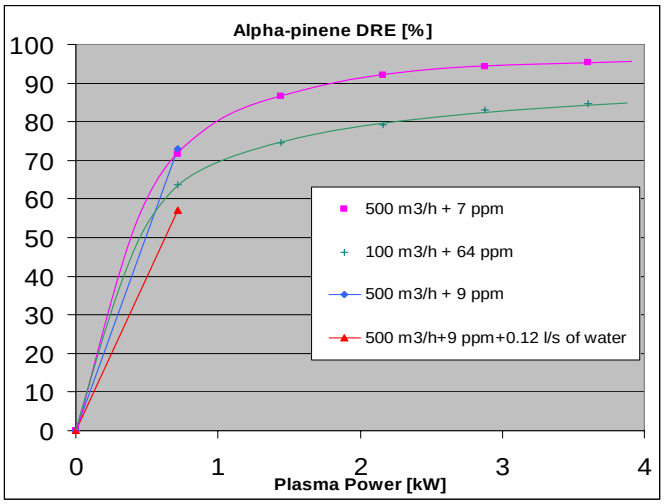

Figure 6. Alpha-pinene destruction and removal efficiency depending on plasma power without and with presence of water spray in the corona reactor.

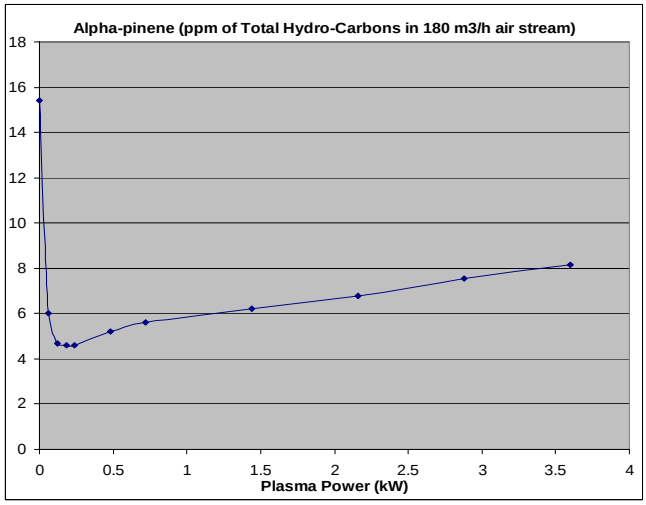

Figure 7. Alpha-pinene oxidation process accompanied by production of stable by-products.

4. Application

The Pilot Plant or Mobile Environmental Plasma Laboratory (Fig. 1) was built to demonstrate this promising plasma technology for VOC emissions control on paper mills. This work was supported by U.S. Department of Energy (project DE-FC07-00ID13868). Later it was decided to use the same Pilot Plant for the test on wood product plant to treat the Oriental Strandboard (OSB) press ventilation stream (US DOE project DE-FC36-04GO14052/A000). Meanwhile the Mobile Laboratory is used for educational purposes at Drexel University, Goodwin College of Professional Studies, as laboratory equipment in the special course AET 380: "Plasma Environmental Laboratory". This laboratory introduces students to the engineering principles of non-thermal plasma application to air cleaning from VOCs and other methods of VOC control and measurements, by combining hands-on laboratory experience with lectures. Specifically, the students learn the engineering and physical principles of non-equilibrium plasma systems operation using the unique pulsed corona system and carry out experiments on plasma cleaning of VOC contaminated air, measure dependence of DRE of particular VOC on plasma power and other system parameters, calculate the energy cost of VOC removal compare to other methods. The work in the laboratory enhances the fundamentals taught in the classroom sessions

References

[1] Paur, H.R.: Removal of Volatile Hydrocarbons from Industrial Off-Gas. Non-Thermal Plasma Techniques for Pollution Control, eds. B.M.Pentrante and S.E. Schulthesis, pp.277-289. Berlin, Springer-Verlag, 1992.

[2] Sun,B., Sato, M., Clements, J.S.: Use of Pulsed High-Voltage Discharge for Removal of Organic Compounds in Aqueous Solution. Journal of Applied Physics, 32:1908-1915, 1999.

[3] The Technical and Economic Feasibility of Using Low-Temperature Plasma to Treat Gaseous Emissions from Pulp Mills and Wood Products Plants", John B. L. Harkness and Alexander A. Fridman, NCASI Technical Bulletin No. 795, September 1999.

[4] M. G. Sobacchi , A. V. Saveliev , A. A. Fridman, A. F. Gutsol, L. A. Kennedy, "Experimental Assessment of Pulsed Corona Discharge for Treatment of VOC Emissions", Plasma Chemistry and Plasma Processing, Vol. 23, No. 2, 2003, p. 347-370.

[5] Sobacchi, M. G., Saveliev A. V., Kennedy, L. A., Lock, E., Fridman, A., Gutsol, A., Desai, A., Tak, G., Gutsol, K., Korobtsev, S., Shiryaevsky, V., Medvedev, D. and Abolentsev, V. "Pulsed Corona Plasma Technology for Treating VOC Emissions from Pulp Mills" 2004 TAPPI Paper Summit, Spring Technical and International Environmental Conference, May 3 – 5, 2004, Atlanta, GA, USA, Electronic Proceedings, PS04169.pdf.

Synthesis of nano materials using pulsed arc discharge and pulsed laser ablation in liquid

H. Kawasaki, Y. Suda, T. Ohshima, Y. Matsunaga, T. Kaneko

Department of Electrical and Electronic Engineering, Sasebo National College of Technology
Okishin 1-1, Sasebo, Nagasaki 857-1193, Japan

Abstract

Carbon nanomaterials have been prepared using a simple production method of pulsed arc discharge and pulsed laser ablation in liquid. Field emission scanning electron microscopic observation revealed that most of nanomaterials produced by arc discharge were sphere shape nanoparticles. On the other hand, small amount of products like nanofiber can be produced using pulsed laser ablation method. The ratio of the products like nanofiber produced in the deionised water with SDS is high compared with those produced in the deionized water. The size of the particles produced by pulsed laser ablation was slightly small, and the density of the particles produced by pulsed laser ablation is high compared with those of produced by arc discharge.

1.Introduction

Recently, several kinds of arc in liquid method have been developed as a cost-effective technique to fabricate various kinds of nanomaterials [1–6]. The method has some advantages in the mass production of carbon nanomaterials compared with any other well-known conventional methods, such as vacuum arc, laser ablation and plasma enhanced chemical vapor deposition. In the past few years, carbon nano-onions, multi-wall carbon nanotubes, single-wall carbon nanotubes (SWNTs), single-wall carbon nanohorns (SWNHs), and their metal included forms, have been successfully synthesized by the arc in liquid method using water and liquid nitrogen to host arc discharge. However, the high-quality single-walled structures such as SWNTs and SWNHs have been produced only when liquid nitrogen was used in the simple arc in liquid method, and the value of those nano materials was small. On the other hand, pulsed laser ablation in liquid method has been also developed for fabricating high quality nano materials [6-8]. Sugiyama et. al. prepared oxo(phtalocyaninato)vanadium(IV) (VOP) nanoparticles dispersed in water by using femtosecond laser ablation of its bulk crystals. They found that the mean size of the VOP nanoparticles was 17 nm, estimated by a scanning electron microscope (SEM) analysis. Furthermore, they suggest that nanoparticle formation process can be controlled precisely by pulsed width, wavelength, repetition rate and fluence using this laser ablation method.

In this paper, carbon nanomaterials have been prepared using arc discharge and pulsed laser ablation methods in the same liquid condition. Morphology, size and density of the particles are observed by field emission scanning electron microscopy (FESEM), and analyzed using computer software. Measurements of optical emission spectra were performed to estimate the processing plasma state in liquid using high speed photonic multichannel spectral analyzer.

2.Experimental

A schematic of the pulsed arc discharge equipment is shown in Fig. 1. In our arc discharge method in liquid, a direct current (DC) arc discharge was generated between two high purity carbon rod electrodes (purchased from Nilaco Corp., Japan; 99.99% purity). Our apparatus consisted of two electrodes (anode 5mmϕ × 50mm, and cathode 20mmϕ × 30mm) in a vertical alignment submerged in 500 ml of deionized water (0.2 mS/m conductivity) or ethanol in a Pyrex beaker. These carbon electrodes were connected to a DC power supply. Arc discharge was

generated by touch and release of these carbon electrodes. The gap distance between the two cylindrical carbon electrodes was initially set to 3 mm, but eventually changed by arc-induced erosion. The discharge current and voltage were set at about 40 A and 5–15 V, respectively. The repetition rate of the pulsed arc discharge was about 0.5 Hz. Nanomaterials formed in the arc plasma region are collected on the water surface and in the water bottom.

A schematic of the pulsed laser ablation system is shown in Fig. 2. High purity carbon target (purchased from Nilaco Corp., Japan; 99.99% purity, 30mmϕ × 5mm) are suspended in 30 ml of a deionized water, ethanol and deionized water (30cc) with sodium dodecyl sulfate ($CH_3(CH_2)_{11}OSO_3Na$; SDS: 3mg) as anionic surface active agent. In the present work, we demonstrate the formation of carbon nanoparticles by using a pulsed Nd:YAG laser (Continuum SureliteIII; wavelength of 532 nm, pulse duration of 3.5 ns, maximum output energy of 340 mJ). The laser beam was focused on the center of the target with a lens, and the spot size was about 3 mm^2. Repitition rate of the pulsed laser was 10 Hz, and nanomaterials were produced at 6000 shots.

Morphology, size and density of those nanomaterials were observed by FESEM (Joel JSM-6800, 3kV, 8μA). Optical emission spectra in the arc plasma were observed by high speed photonic multichannel spectral analyzer (PMA-11: Hamamatsu Photonics) with ICCD detector (C8808-01: Hamamatsu Photonics). Simultaneous measurement wavelength range of this system was from 200nm to 860nm. Effective light-receiving area of optical fiber was 1mmϕ and A/D resolution was 16bits.

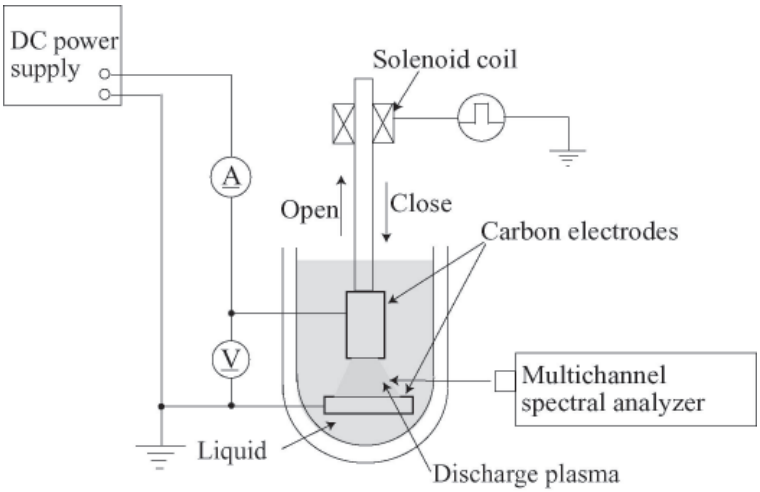

Fig. 1 A schematic of the pulsed arc discharge equipment.

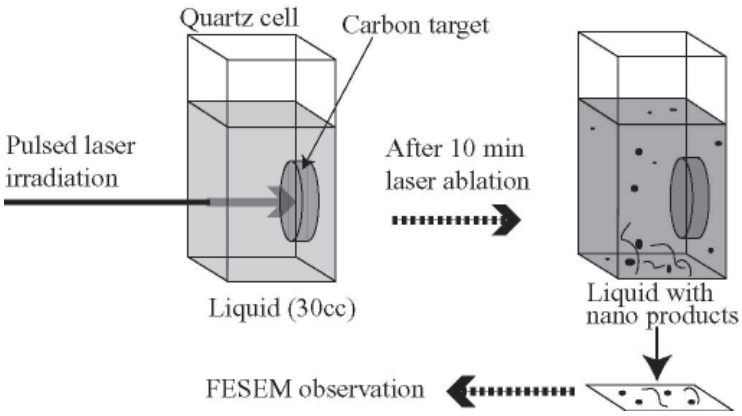

Fig. 2 A schematic of the pulsed laser ablation system.

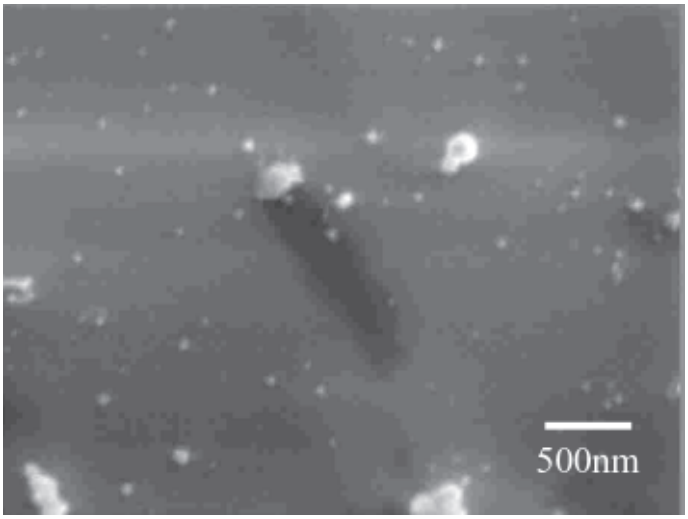

Fig. 3 FESEM image of the nano material products using arc discharge in deionized water.

3.Results and discussion

Figure 3 shows the FESEM images of the nanomaterial products using arc discharge in

deionized water. After the arc discharge experiments, there are two kinds of nano products can be obtained. One of them is powdery products floating on the water surface, and another one is bulky deposits sank down in the water bottom. This result is agree with our previous experiment measured by high resolution transmission electron microscopy (HRTEM; Hitachi H-9000 operated at 300 kV) [9]. In this obserbation, most of the products are the sphere shape particles and some of them are coagurated each other. The FESEM images were further analyzed using computer software (Mitani Syoji ; Winroof) to obtain the diameter distribution of individual nanofibers. The diameter of the nanofiber was distributed from 5 nm to 300 nm. Mean diameter of the particles was approximately 100 nm, and the value is slightly larger than that of our previous results. FESEM images of the nanomaterial products produced in ethanol and deionized water with SDS, not shown here, have almost same images of those produced in pure deionized water. These results suggest that the nanomaterials produced by arc discharge method are independent on the liquid.

Figure 4 shows the FESEM images of the nanomaterial products using pulsed laser ablation in pure deionized water. As shown in Fig. 4, two kinds of nanomaterial products can be observed in the liquid. One of them is sphere shape nanoparticles, and another one is products like nanofiber. In the pure deionized water, many nanometer size sphere shape particles were frequently observed, and some of them were aggregates. The size of the particles produced by pulsed laser ablation was small, and the density of the particles produced by pulsed laser ablation is high compared with those produced by arc discharge. In addition, small amount of nanofibers are observed. The FESEM images were further analyzed using Winroof to obtain the diameter distribution of the particles. The diameter of the particles was distributed from 10 nm to 200 nm. Mean diameter of the particles was approximately 70 nm. FESEM images of the nanomaterial products in ethanol, not shown here, have almost same images.

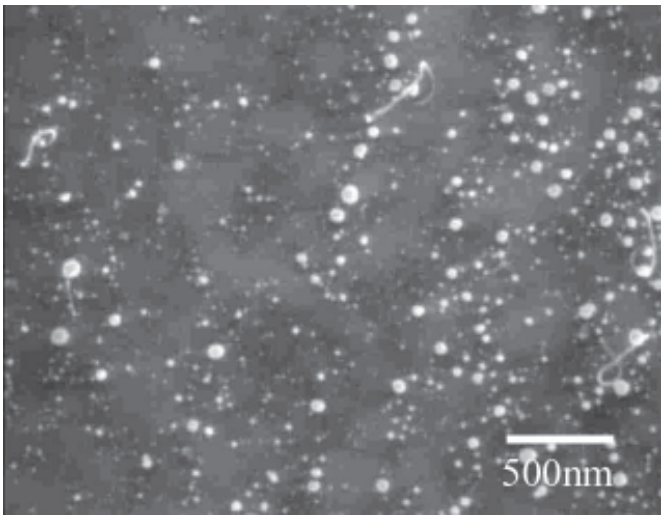

Fig. 4 FESEM image of the nanomaterial products using pulsed laser ablation in pure deionized water.

Figure 5 shows the FESEM images of the nano material products in deionized water with SDS. The shape of the particle is not always spherical compared with that in the pure deionized water and ethanol, and the ratio of the nanofibers increased. The reason of this tendency is not clear yet, but it is considered as follows. SDS molecules with a negatively charge encloses the nano particles which are positive charge. Therefore, products like micell are produced at some part of the particles, and the growth of the particles may be changed as compared with the other liquids.

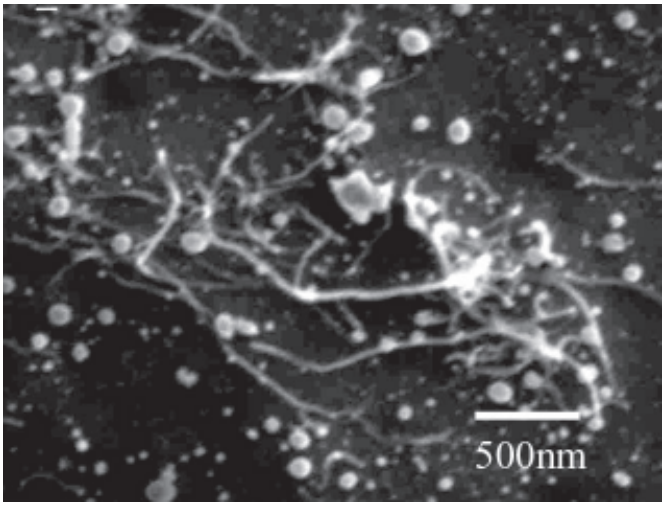

Fig. 5 FESEM images of the nano material products in deionized water with SDS.

Figure 6 shows the emission spectroscopy of the arc discharge plasma in the deionized water with SDS. As the results, C^+(426.7nm), H_β(486.1nm), H_γ(434.0nm) and C_2 swan bands can be observed. Strong peak of H_α(656.3nm) can be also observed, not shown here. Emission spectroscopy from the arc plasma is almost same compared with that in the deionized water described elsewhere [9].

Figure 7 shows the FESEM images of the nano material products by pulsed laser ablation using carbon with metal catalyst (Ni/Co; 1.2at.%) target in deionized water. There are a lot of nanofibers and nano particles, and they are bundled. The reason of the phenomenon is also not clear yet, but it may be due to the metal catalyst.

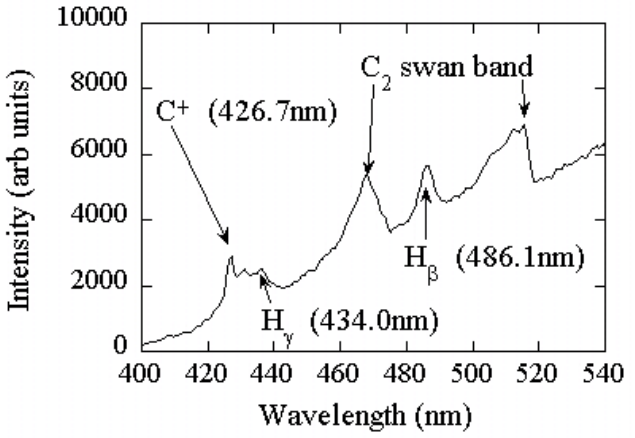

Fig. 6 Emission spectroscopy of the arc discharge plasma in the deionized water with SDS.

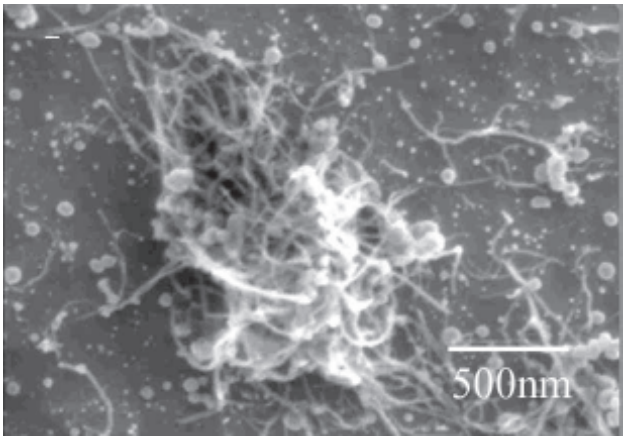

Fig. 7 FESEM images of the nano material products by pulsed laser ablation using carbon with metal catalyst (Ni/Co 1.2at.%) target in deionized water.

4.Conclusion

Carbon nanomaterials have been prepared using pulsed arc discharge in liquid and pulsed laser ablation. FESEM observation revealed that most of nanomaterials produced by arc discharge were sphere shape nanoparticles. On the other hand, small amount of products like nanofiber can be produced using pulsed laser ablation method. The ratio of the products like nanofiber produced in the deionized water with SDS is high compared with those produced in the deionized water and ethanol. The size of the particles produced by pulsed laser ablation was small, and the density of the particles produced by pulsed laser ablation is high compared with those produced by arc discharge.

References

[1] H. Lange, M. Sioda, A. Huczko, YQ. Zhu, HW. Kroto, DRM. Walton, Carbon **41** (2003) 1617.

[2] L. A. Montoro, R. C. Z. Lofrano, J. M. Rosolen, Carbon **43** (2005) 200.

[3] N. Sano, Carbon **43** (2005) 450.

[4] N. Sano, J. Nakano, T. Kanki, Carbon **42** (2004) 686.

[5] H. Lange, M. Sioda, A. Huczko, YQ. Zhu, HW Kroto, D. Walton, Carbon **41** (2003) 1617.

[6] T. Sugiyama, T. Asahi and H Masuhara, Chem. Lett., **33** (2004) 724.

[7] Y. Tamaki, T. Asahi, and H. Masuhara, J. Phys. Chem. A, **106** (2002) 2135.

[8] Y. Tamaki, T. Asahi, and H. Masuhara, Jpn. J. Appl. Phys. **42** (2003) 2725.

[9] Y. Suda, H. Kawasaki, T. Ohshima, S. Nakashima, S, Kawazoe, T. Yoma, Mater. Res, Soc., **829** (2005) B9.17.1.

Study of neutrals and ions transport in a Highly Ionized Sputter Deposition Process (HISDP)

L. de Poucques, J. C. Imbert, M. Mrazkova[1], C. Boisse-Laporte, J. Bretagne, M. Ganciu, L. Teulé-Gay and M. Touzeau

Lab. de Physique des Gaz et des Plasmas, Université Paris-Sud, 91405 Orsay Cedex, France

[1]Department of Physical Electronics, Masaryk University, Kotlarska 2, 61137 Brno, Czech Republic

Abstract

Highly Ionized Sputter Deposition Process is a new technique of magnetron sputtering working in high power pulsed regime. The high current densities obtained with this process ensure a high ionization ratio of the sputtered vapour. This work deals with the study of the transport of titanium ions and neutrals in such a discharge. Current measurements were completed by time and space resolved absorption spectroscopy and by a simple diffusion model.

Keywords: pulsed magnetron sputtering, absorption spectroscopy, titanium diffusion

1. Introduction

In magnetron discharges, the cathode mainly emits sputtered species as neutral particles. Due to gas phase collisions, these particles have relatively low energy when hitting the substrate and lead to deposited films with poor qualities. To improve the film quality as well to deposit materials on complex surfaces for industrial applications [1] (tools, connectors, vias and trenches for highly integrated microelectronics …), works were developed on Ionized Physical Vapor Deposition (IPVD). Classical magnetron devices were then equipped with additional source of vapor ionization using RF loops [2] or microwave antennas [3] in the region between the target and the substrate.

More recently, an alternative technique was explored using magnetron discharges working in high power pulsed regimes [4]. Typical pulsed current density values of the order of 3 A/cm^2 were achieved (two orders of magnitude higher than in continuous DC magnetrons). These high current densities ensure a high ionization ratio of the sputtered vapour.

2. Experimental set-up

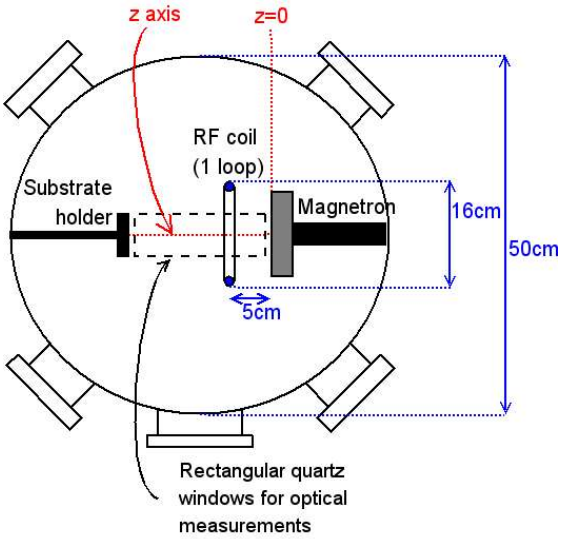

Fig. 1: Diagram of the reactor

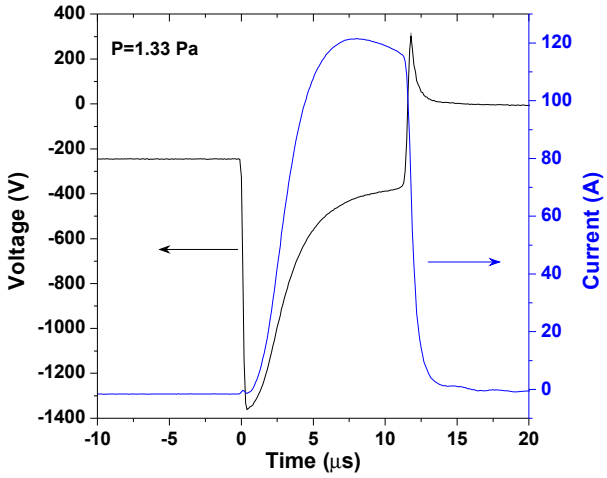

Fig. 2: Typical current and voltage shape during the pulse

The reactor is presented on Figure 1. It is a 50 cm diameter and 45 cm height cylinder. It contains a 10 cm diameter planar circular magnetron cathode and a 16 cm diameter radio-frequency coil with one loop. The "z axis" is the magnetron-substrate holder axis. The "z=0" position corresponds to the target surface. Buffer gas

was argon and the materials of the target was titanium. Working pressure values were 1.33 Pa and 4 Pa. The distance between the titanium target and the substrate-holder was z=14 cm. The quartz windows on top and bottom of the reactor allow spatially resolved optical measurements.

The magnetron cathode was supplied by a high power adapted pulsed generator [5,6]. Typical pulse shapes of the applied magnetron voltage and current are presented on figure 2. The pulse has the following characteristics: the time duration can vary between 5 and 50 µs, the frequency between 20 Hz and 1 kHz, the cathode voltage can reach -1400V and the current 120A. The radio-frequency coil was supplied with a 13,56 MHz – 1600 W generator.

In order to investigate the transport of ions during and after a high power pulse, the ion current on the substrate holder was measured. In order to avoid a great negative current on the substrate holder, a negative bias of -60V was applied.

Spatially resolved absorption measurements were carried out using a titanium hollow cathode lamp. The light emitted by the lamp entered the reactor through the top quartz window and the absorption signal was collected through the bottom quartz window. This lamp was operated in pulsed regime (100µs duration, 100Hz frequency) using a generator developed in our laboratory. In pulsed regime, the absorption signal is clearly separated from the plasma emission and the enhancement of the ionic line emission in the pulse allows the determination of Ti^+ densities by absorption. The method involves the use of the three titanium neutral ground state sub-levels. This allows the determination of titanium densities if thermalisation is achieved [7]. However, the temperature value is needed to deduce absolute densities. In the present study, the density was not determined because we were unable to precisely measure the titanium temperature. We will only discuss the evolution of the absorption coefficient. This coefficient is calculated with the following formula: $A=1-I_t/I_0$, where I_0 is the lamp intensity and I_t is the transmitted intensity through the plasma.

3. Transport of species to the substrate

Time resolved current measurements at 1,33 Pa and 4 Pa are presented on Figures 3 and 4. Two majors contributions to the ion current can be observed and explained.

The first peak is attributed to Ar^+ which are created during the pulse by the electron avalanche near the substrate-holder. They are collected during the pulse and at the beginning of the post-discharge. In this first contribution, the fast Ti^+ (a few $km.s^{-1}$) reaching the substrate-holder without collisions also have to be taken into account (ballistic regime).

The last maximum of each curve is attributed to ions slowed down and thermalized through collisions with argon atoms (classical diffusion regime).

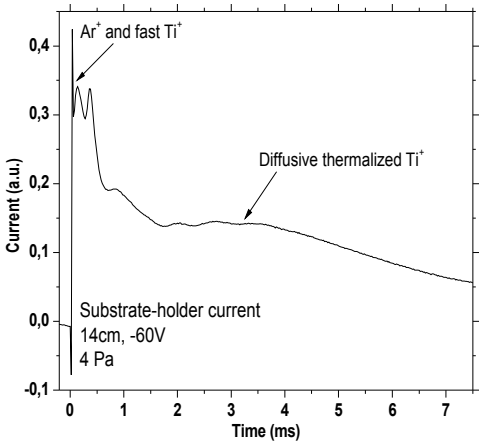

Fig. 3: Current measured on the substrate holder at 4 Pa

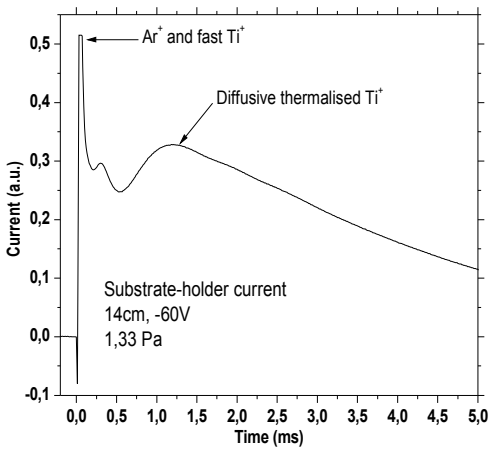

Fig. 4: Current measured on the substrate holder at 1,33 Pa

In order to investigate the first contribution of Ti^+, we made time-resolved current measurements while moving the substrate-holder along the "z" axis. This measurement was only made at 1,33 Pa because the signal was too noisy at 4 Pa to make a correct analysis. We observed that the time delay between the pulse and the arrival of the first peak on the substrate-holder was strongly dependant to the distance between the magnetron and the substrate-holder. We present on Figure 5 a plot of this delay versus the distance. This plot is linear and we can deduce a speed of 6,7 $km.s^{-1}$ which is consistent with magnetron ejection speed reported in [1].

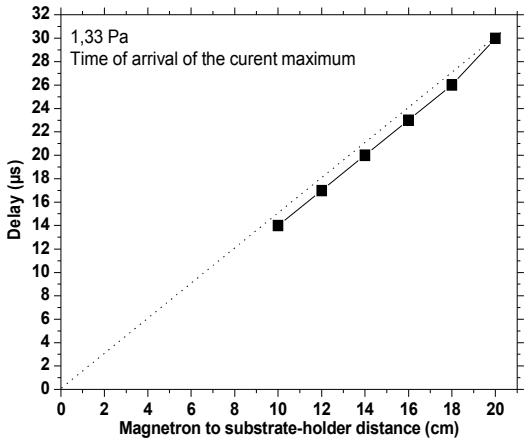

Fig. 5: Delay of the current maximum versus the magnetron to substrate holder distance

We then made time resolved optical absorption measurements at 14 cm to determine the absorption coefficient of titanium species (neutral ground state and ion ground state). On Figures 6 and 7, we compared the absorption coefficient for ionized titanium to the current measurement. It appears that at both pressures, the last maximum of the substrate-holder current effectively corresponds to the maximum of absorption.

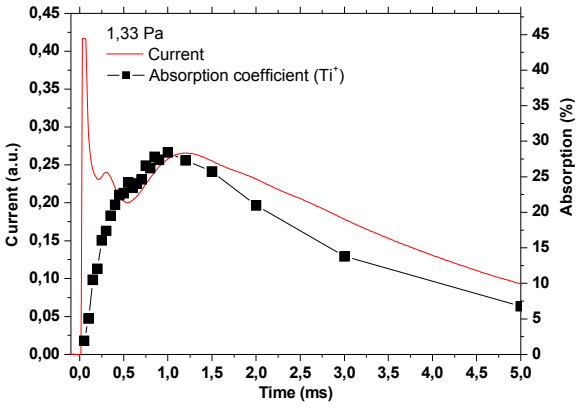

Fig. 6: Comparison between current measurement and absorption measurement at 14cm for 1,33Pa

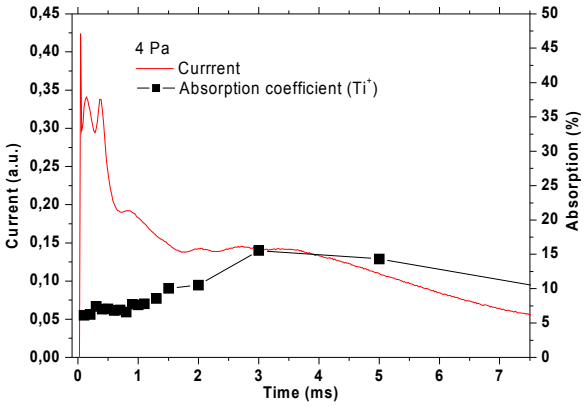

Fig. 7: Comparison between current measurement and absorption measurement at 14cm for 4Pa

In order to have a better understanding of the transport of Ti species, we have made absorption measurements at other distances from the magnetron (6, 8 and 10 cm). The results of these measurements are presented on Figure 8 for 4 Pa. The first interesting result is the translation of the maximum of the absorption

coefficient with the distance. As awaited, the maximum is seen later for longer distances from the magnetron. Furthermore, the peak is widening with an increasing distance. It suggests that for this time scale of several ms, Ti and Ti^+ are transported to the substrate -holder by diffusion.

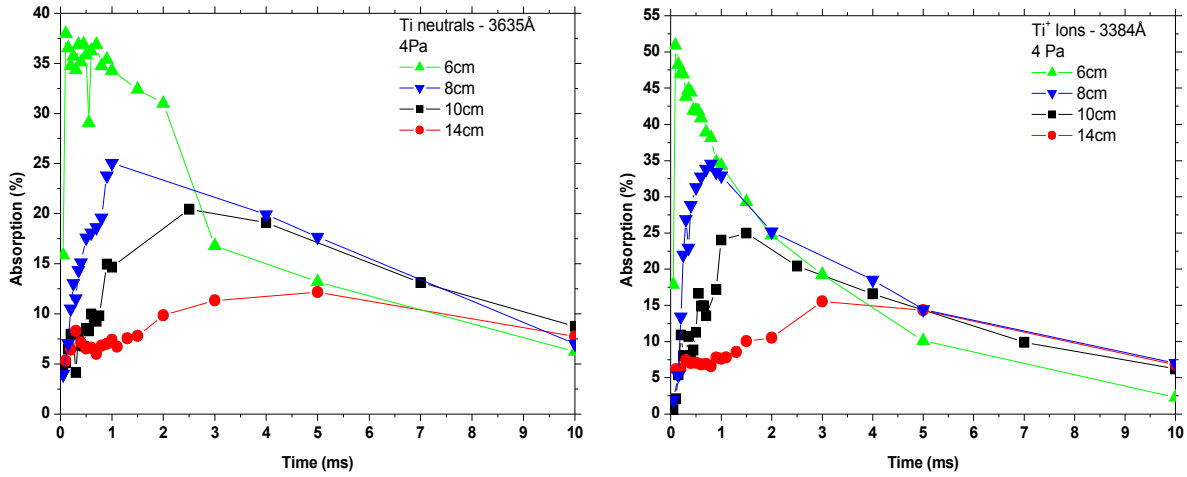

Fig. 8: Absorption measurements on a neutral (3635Å) and an ionic (3384Å) titanium line at 4 Pa for various distances

To investigate this diffusion regime, we have made a very simple 1D simulation of particle diffusion in the reactor. Only diffusion in the *z* direction was taken into account. We neglected the losses in radial direction because the distance between the magnetron and the substrate is lower than the radius of the reactor. The equation is the following:

$$\frac{\partial n}{\partial t} = D \frac{\partial^2 n}{\partial z^2}$$

The calculation of the diffusion coefficient is made using the formula: $D=D_0.k.T/P$. The value of D_0 is given in [8] at 300K: $D_0(300K)=3,1.10^{20}$ atoms.cm^{-1}.s^{-1}. Since D_0 dependence against the temperature is a square root function ([8]), we can easily convert this given value to the wanted temperature. The limit conditions are: n=0 cm^{-3} at z=0cm and z=15cm because the titanium atoms are stuck on the wall without reflection. The initial conditions are:

- the density profile is a Gaussian centred at 4cm with a half-width of 1 cm (see Figure 9) because we estimate that at this distance, the majority of the titanium population is thermalised, and the initial maximum density value is estimated at 1.10^{12} cm^{-3} from the absorption values at 6 cm,
- the initial temperature profile is presented on Figure 9. The simulation was made with this profile for the first 100 µs. After t=100 µs, the temperature is taken constant T=350 K. This is a very simple way to render the duration of the pulse and the temperature decrease with time.

The calculation was only made at 4 Pa because the thermalisation distance at this pressure is low enough to consider that the diffusion model is valid on the length of the reactor (approximately 15cm). In other words we consider that the distance between two collisions is lower than the z-stepping in the model (0,1 mm).

The results are shown on Figure 10. The times found for the maximum at each distance are really close to the times observed previously (neutrals on Figure 8). This very simple model confirms that the last maximum on the current measurement is consistent with a diffusive transport.

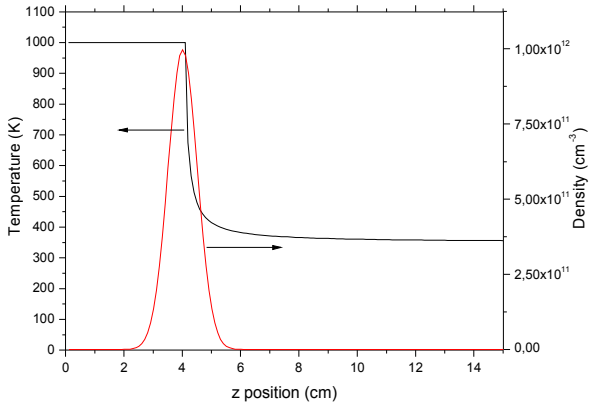

Fig. 9: Initial temperature and density profiles used for the diffusion model

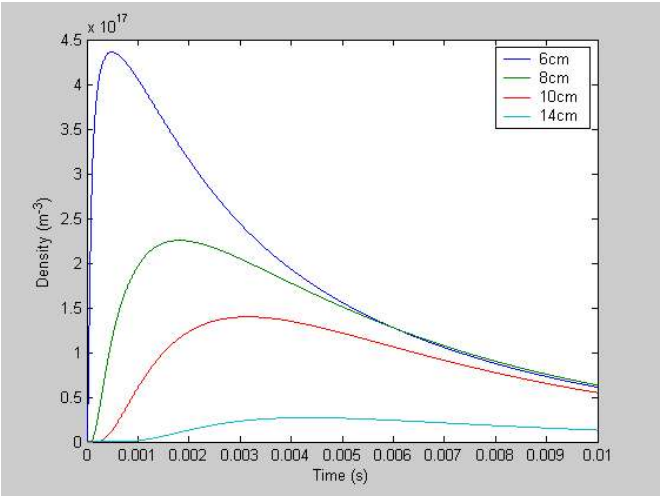

Fig. 10: Density results given by the diffusion model at a pressure of 4 Pa for titanium neutrals

4. Conclusion

Highly Ionized Sputter Deposition Process is a recent alternative technique ensuring a high ionization ratio of the sputtered species. However, the transportation of species in such a discharge is not commonly studied. We were able to make various time and space resolved measurements on our experiment. Current measurements showed two distinct contributions of ions: fast Ti ions and diffused ions.

The first population was investigated with current measurements and the ballistic regime of these ions was confirmed by a measured velocity similar to the ejection speed. The supposed diffused regime (second population) was investigated using resonant absorption spectroscopy. We showed that the behaviour of the measured absorption coefficient was consistent with a diffusion regime. Moreover, the use of a simple diffusion model confirmed this assumption.

Future works will imply the study of the effect of an additional ionization device (the radio-frequency coil) on the transport of species. Preliminary results are presented on Figure 11: when increasing the RF power, the maximum of the current is arriving sooner after the magnetron pulse. This can be due to the creation of a conductive region with an effect similar to an unbalanced magnetron. The potential distribution has to be determined and time resolved Langmuir probe measurements are going to be undertaken.

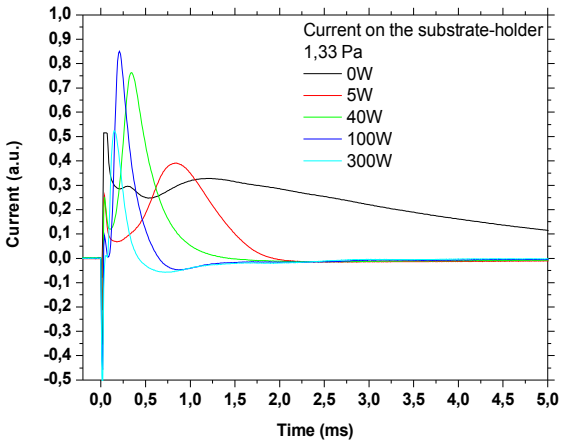

Fig. 11: Current measurements at 1.33 Pa for an increasing additional RF power

An improvement of the model, taking into account the temperature diffusion, as well as a precise measurement of the initial profiles (density as well as temperature) is also to be undertaken.

[1] S.M. Rossnagel, J. Hopwood, Appl. Phys. Lett., 63, p.3285 (1993).

[2] T. Nakamura, K. Okimura, Vacuum, 74, p. 391 (2004).

[3] C.Boisse-Laporte, O. Leroy, L. de Poucques, B. Agius, J. Bretagne, M. C. Hugon, L. Teulé-Gay, M. Touzeau, Surf. and Coat. Tech., 179, p.176 (2004).

[4] V. Kouznetzov, K. Macak, J. M. Schneider, U. Helmersson, I. Petrov, Surf. and Coat. Tech., 122, p. 290 (1999).

[5] M. Ganciu, M. Hecq, S. Konstantinidis J.P. Dauchot, M. Touzeau, L. de Poucques, J. Bretagne, European Patent Appl., No. 4447072.2 / 22.03. (2004).

[6] M. Ganciu, S. Konstantinidis, Y. Paint, J.P. Dauchot, M. Hecq, L. de Poucques, P. Vašina, M. Meško, J.C. Imbert, J. Bretagne and M. Touzeau, 17th ESCAMPIG, Constanţa, 2004, Conf. Proceedings, p. 227

[7] O. Leroy, L. de Poucques, C. Boisse-Laporte, M. Ganciu, L. Teulé-Gay and M. Touzeau, J. Vac. Sci. Technol., A, 22, p. 192 (2004).

[8] D. Ohebsian, N.Sadeghi, C. Trassy and J.M. Mermet, Optics Communications, 32 (1) (1980)

Narrow Tube Inner Coating by Low Pressure Micro Plasma Sputtering

H. Uchida[1], M. Kumamoto[1], H. Fujiyama[1], M. Shinohara[2] and Y. Matsuda[2]

[1]Graduate school of Science and Technology, Nagasaki University, Japan

[2]Department of Electrical and Electronic Engineering, Nagasaki University, Japan

Abstract

For the inner surface coating of narrow tubes, we have investigated pulsed coaxial sputtering process with the 2nd harmonic electron cyclotron resonance (ECR) plasmas. As a result of detailed investigation of temporal evolutions of the target ions current and the pulse voltage, we found that the selection of pulse bias voltage and gap length was very important. As a result, we have succeeded in coating Ag films onto the inner surface of an insulated narrow tube with 1.75mm inner diameter.

Keywords: Sputtering, Micro plasma, ECR, Inner coating, Narrow tube

1. Introduction

Materials with properly modified surface can be used under severe environment. The surfaces modification technique should be used to prolong the lifetime of narrow tubes, which are used in engineering plants and medical instruments such as the catheter. In recent years, there are few examples of researches on tube inner coating [1-8].

The coaxial electron cyclotron resonance (ECR) plasmas and 2nd harmonic ECR plasmas are high-density in spite of generation in low-pressure and narrow gap condition. We have already reported the generation of Xe micro plasmas with the minimum gap length of 500μm at the pressure of 0.01 Torr under the 2nd harmonic ECR condition. Recently, we have succeeded in coating Ag films onto the inner surface of an insulated tube of 1.75mm inner diameter using pulsed coaxial sputtering with the 2nd harmonic electron cyclotron resonance (ECR) plasmas. Pulsed target biasing was indispensable for this process. In this paper, we report the experimental results of temporal behaviors of the target ion current against the pulsed target biasing.

2. Experimental details

Figure.1 shows the experimental setup used in this research. Microwave source of 2.45GHz has been used. The three-stub tuner was used to control microwave transmission. In the present experiments, Ar gas and small coaxial tube as electrodes has been used. Inner electrode was transmitted TEM mode microwave and applied pulse bias voltage. Outer electrode is grounded. Plasma was generated in narrow area between outer electrode and inner electrode.

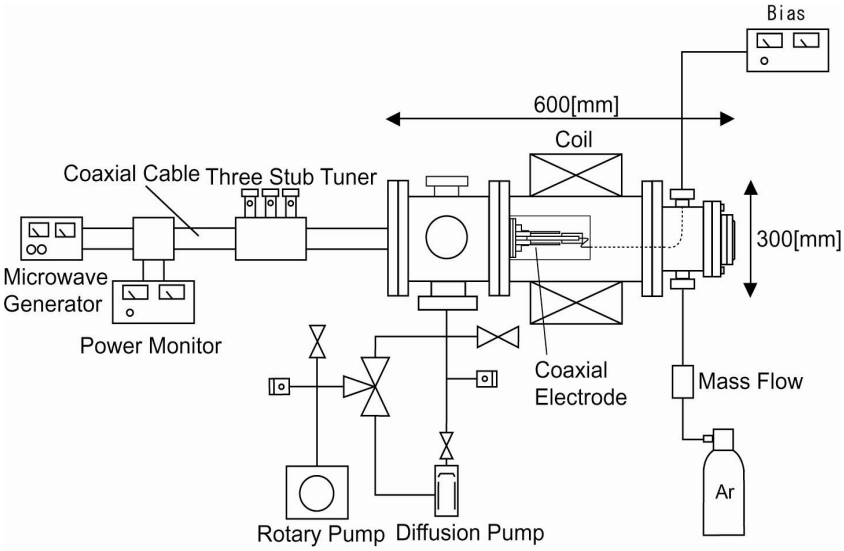

Fig.1 Schematic of Experimental setup

Figure. 2 shows a cross section view of the coaxial sputtering system used in this study. Inner electrode is impressed with TEM mode microwave and pulse bias voltage. Outer electrode is grounded. Plasma is generated between the inner and outer electrodes. In this system, a narrow insulator tube (equal to a substrate) was inserted in the outer electrode and films were deposited on the inner surface of the narrow tube by sputtering. In addition, in order to coat substrates with smaller diameters, a wire target with a smaller diameter was used. However, since the wire target was bent by heat and gravity, the spring was used to always apply a tension to a wire. As a result, the wire was maintained at the center axis of the tube.

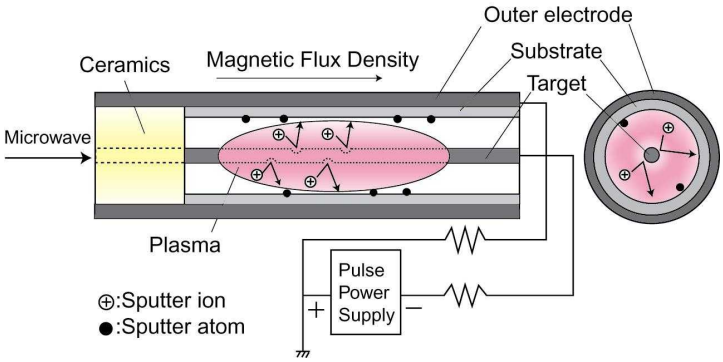

Fig. 2 Coaxial sputtering system

3. Results and discussion

A current probe measured temporal evolution of the target ion current. The target ion current vs. pulse bias

voltage was shown in Fig.3. In this figure, the ion current is decreased with increasing the target bias voltage. Expansion of a sheath can be considered as this cause. When the magnitude of target pulse voltage is increased, sheath width expands, resulting in the decrease in the ions current flowing into a target.

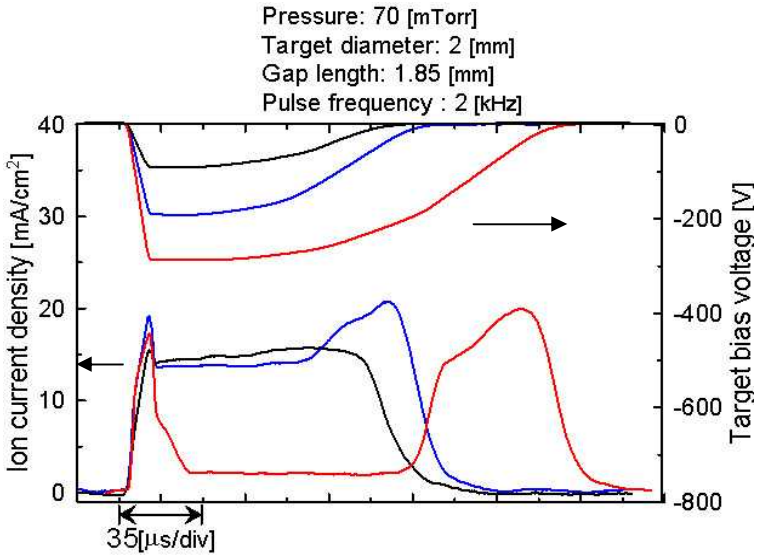

Fig.3 Target ion current vs. pulse bias voltage
(Gap length 1.85mm)

Fig.4 shows the temporal behaviors of the target ion current and the target bias voltage for different gap lengths of 1.85mm and 3.5mm. The ion current is decreased with decreasing the gap length. From this result, it is understood that the gap length has a large influence on plasmas. When the gap length becomes short, the influence of the sheath width is enhanced. In addition, it is noted that the target ion current is increased again at the falling time of the pulse bias voltage, indicating a restoration of plasma density.

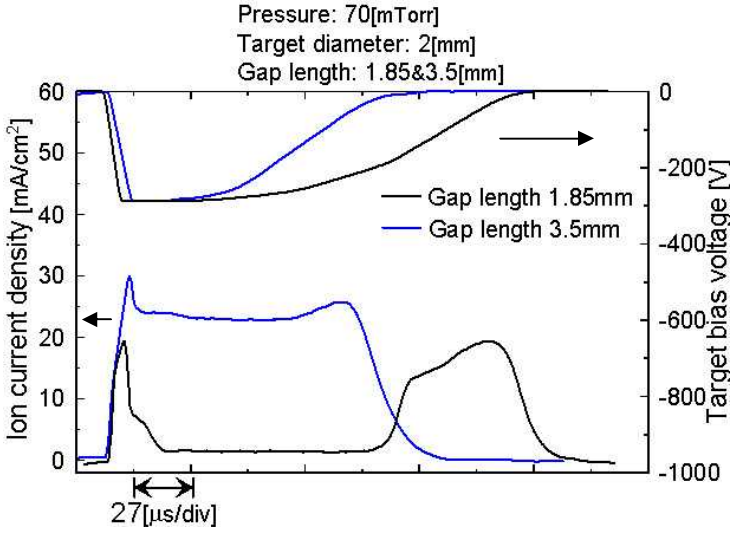

Fig.4 Compared target ion current of gap length 1.85mm with 3.5mm

Based on the above-mentioned experimental results, we have tried to coat Ag thin films onto the inner surfaces of insulated narrow tubes using pulsed coaxial sputtering with the 2nd harmonic electron cyclotron resonance (ECR) plasmas. As a result, we have succeeded in coating Ag films onto the inner surface of an insulated narrow tube with 1.75mm inner diameter. However, in order to keep the reproducibility of the sputter-deposition process for the narrow tubes, geometrical alignment of the center target is indispensable. Further improvements of a mechanical setting of both the target and substrate are necessary.

4. Conclusion

For the inner surface coating of narrow tubes, we have investigated pulsed coaxial sputtering process with the 2nd harmonic electron cyclotron resonance (ECR) plasmas. When the magnitude of target pulse voltage is increased, sheath width expands, resulting in the decrease in the ions current flowing into a target. When the gap length becomes short, the influence of the sheath width is enhanced, resulting in the decrease in the ions current. The target ion current is increased again at the falling time of the pulse bias voltage, indicating a restoration of plasma density. Based on these experimental results, we have succeeded in coating Ag films onto the inner surface of an insulated narrow tube with 1.75mm inner diameter.

This work was supported financially by Grant-in Aid for Scientific Research (B) (Grant No.16340184) from the Ministry of Education, Culture, Sports, Science and Technology.

References

[1] T. Shigemizu et al: Materials Science & Engineering, Vol.A139, pp.312-318 (1991).
[2] H. Kawasaki et al: Materials Science & Engineering, Vol.A140, pp.682-686 (1991).
[3] H. Fujiyama et al: Surface Coatings and Technology, Vol.59, pp.140-143 (1993).
[4] E. Morisaki and H. Fujiyama:Surface and Coatings Technology, Vol.98, pp.834-838 (1998).
[5] Y. Uchikawa et al: Thin Solid Films, Vol.112, pp.185-188 (1999).
[6] T. Nagano and H. Fujiyama: Jpn. J. Appl. Phys, Vol.38, pp.4338-4341 (1999).
[7] S. Sugimoto et al: Jpn. J. Appl. Phys, Vol.38, pp.4342-4345 (1999).
[8] H. Fujiyama: Surface and Coatings Technology, Vol.131, pp.278-283 (2000).

The 2nd Harmonic ECR Low Pressure Micro Plasmas

H. Fujiyama[1], H. Inoue[1], D. Kurogi[1], Y. Furue[1], M. Shinohara[2] and Y. Matsuda[2]

[1]Graduate school of Science and Technology, Nagasaki University, Japan

[2]Department of Electrical and Electronic Engineering, Nagasaki University, Japan

Abstract

Plasma generation has been succeeded for the pressure of 0.01Torr and gap length of 500μm in xenon gas for the 2nd harmonic Electron Cyclotron Resonance (ECR). Resonant confinement of electrons at the 2nd harmonic ECR leads to interesting micro plasma characteristics: the higher electron density, the lower plasma potential, the lower electron temperature and the effective power absorption. PIC-MC simulation of low pressure micro plasma supported such plasma characteristics obtained by the experiments.

Keywords: Micro plasma, 2nd Harmonic ECR, Low-Pressure, Narrow Tube Inner Coating

1. Introduction

Recently, much attention has been paid to microscale science and technology in various fields.

We are developing the low-pressure microplasma to realize the inner coating of narrow tube by the sputter processing and/or EUV source with less self absorption [1].

By our past researches, it was found that the 2nd harmonic ECR micro plasma could be generated for low pressure condition [2].

In the present paper, we will report on the results of measurement of the plasma parameter for the low-pressure micro plasma developed previously. In addition, the experimental results have been estimated by PIC-MC simulation.

2. Experiment

2.1 Experimental Setup

Figure 1 shows the experimental setup. Microwave with frequency of 2.45GHz was emitted by the coaxial TEM mode, which had no cut-off, so that the microwave can propagate through metallic tube of any size. Figure 2 shows the electrode structure. The diameter of an inner electrode was 5mm, and the gap length was adjusted by changing the diameter of an outer electrode. Plasma generation point was located at about 25mm from the edge of electrodes. It is located in the center of the magnetic coil.

2.2 Results and Discussion

As a result of our previous experiment, we have succeeded the low-pressure microplasma generation. The plasma has been mainly generated for the condition of the 2nd harmonic ECR ($\omega_c/\omega=0.5$).

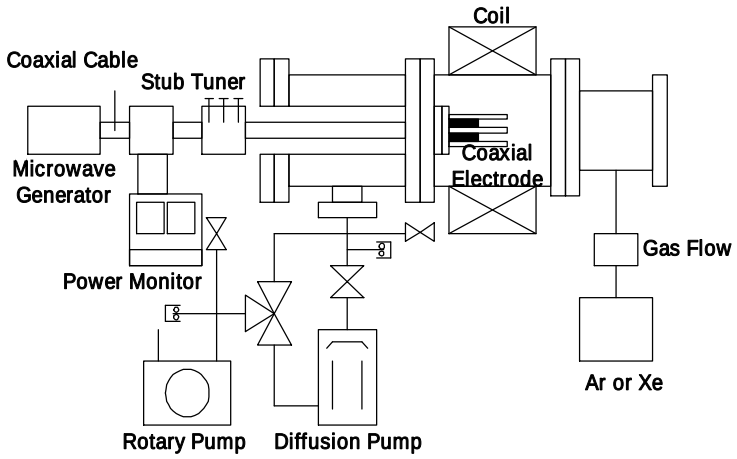

Fig. 1 Experimental setup.

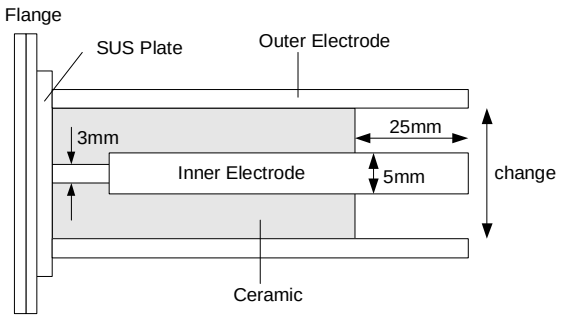

Fig. 2 Electrode structure

Probe measurement has been performed for the conditions of Are pressure 0.03Torr, gap length 3.5mm and incident microwave power 30W. Figure 3 shows the probe system. The cylindrical tungsten rod (diameter 0.3mm) has been used as a Langmuir probe in the plasma, which was generated between the coaxial electrodes. (From the edge of the electrodes to 12.5mm) The top surface of the probe has been insulated to prevent the charged particles flowing to the direction perpendicular to the magnetic field.

Figures 4 and 5 show that the magnetic field dependence of electron density and electron temperature measured by the probe. From these experimental results, the higher electron density and the lower electron temperature has been confirmed at the 2^{nd} harmonic ECR condition. In our previous calculation [2], it was suggested that the electron orbit was very small (<20μm) at the 2^{nd} harmonic ECR condition. Therefore it may be considered that highly efficient ionization by trapped electron collision can be performed at the 2^{nd} harmonic ECR condition because of the "resonant confinement".

In micro plasma world, ECR has rather disadvantage for plasma generation because of the fast electron loss to wall by the resonant acceleration.

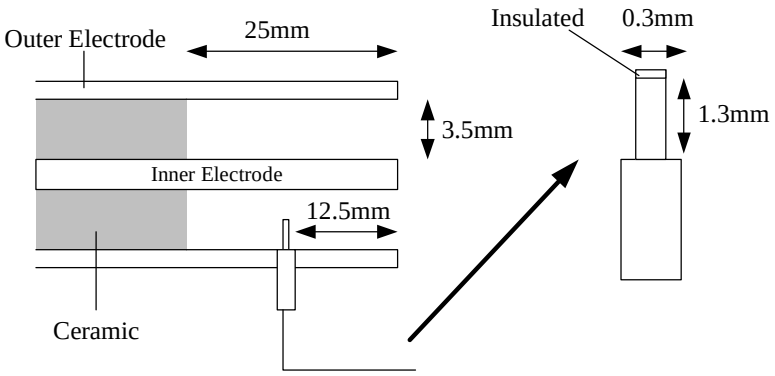

Fig. 3 Probe system

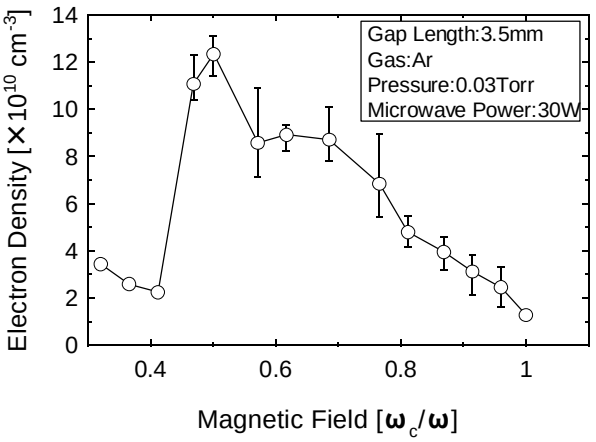

Fig. 4 Magnetic field dependence of the electron density

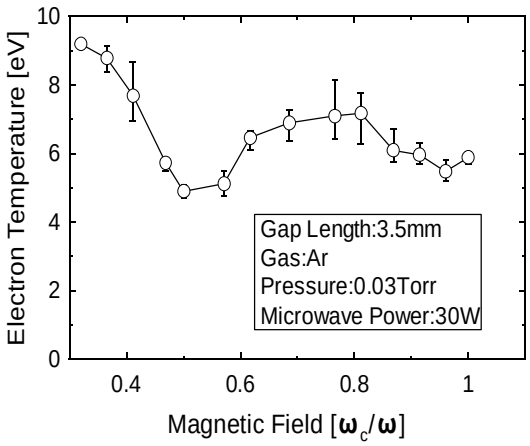

Fig.5 Magnetic field dependence of electron temperature

3. PIC-MC Simulation

3.1 Calculation model

By using the xpdp1 and xpdc1 codes developed at the PTSG, it has been investigated the characteristics of the ECR and the 2nd harmonic ECR micro plasmas. At the xpdc1 code, electrode is Coaxial Tube. Plasma generation region is between inner electrode and outer electrode. Inner electrode radius r_0 is 2.5mm which is connected with 2.45 GHz microwave generator. Outer electrode radius r_1 is 4.5mm that is connected to ground. So that means gap length is 2mm. Source is 2.45GHz microwave power supply ($A \cdot \sin\omega t$, A=30V). Gas is Ar and the pressure is 0.05 Torr.

3.2 Results and Discussion

The simulation result clearly shows that the electron density at the 2nd harmonic ECR become higher than that at ECR condition, as shown in Figure 6. It was also found that the total absorbed power for 2nd harmonic ECR condition was over 10 times higher than the ECR condition.

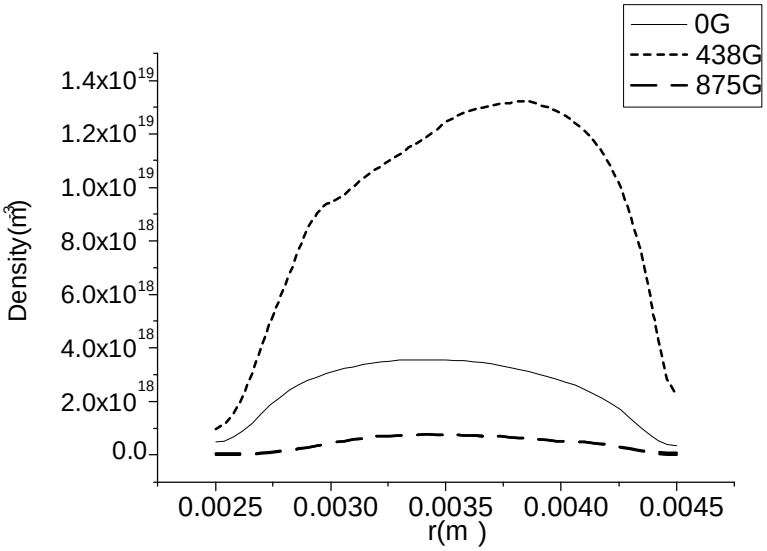

Fig. 6 Simulation results using xpdc1:Electron density

4. Conclusion

Low-pressure micro plasmas generated at the 2nd harmonic ECR have been characterized by the probe measurement and PIC-MC simulation. In spite of the measurement in the gap length of 3.5mm to decrease the probe disturbance, it has been confirmed that the 2nd harmonic ECR plasma has the higher electron density and lower electron temperature compared with the ECR plasma.

Acknowledgments

This work was supported by a Grant-in-Aid for Scientific Research on Priority Area (Grant No.16040214) by the Ministry of Education, Culture, Sports, Science and Technology in Japan.

References

[1]M. Saigoh, N. Ohno, and H. Fujiyama, Materials Science & Engineering, A139 (1991) pp.307-311.

[2]M. Matsushita, Y. Matsuda and H Fujiyama:, Thin Solid Films, Vol.435, (2003) pp. 285-287.

Investigation of the plasma-activated catalytic formation of ammonia in N_2-H_2 plasmas

J.H. van Helden, P.J van den Oever, W.M.M. Kessels, M.C.M. van de Sanden, D.C. Schram and R. Engeln

Department of Applied Physics, Eindhoven University of Technology, P.O. Box 513, 5600 MB Eindhoven, The Netherlands

Abstract

Plasma-surface interactions play an important role in the production of molecules in plasmas. We investigated the plasma-activated catalytic formation of ammonia in N_2-H_2 plasmas. Using different diagnostic techniques, we measured the N, H, NH, NH_2 and NH_3 densities under varying plasma conditions. From the results obtained, we conclude that NH and NH_2 radicals are formed by reactions of the formed NH3 and N+ ions and H atoms emitted by our plasma source.

Plasma-surface interactions, NH, NH_2, expansion

1. Introduction

In applications in which plasma is used for chemical conversion, but also for surface treatment or deposition newly formed molecules are often detected in the background gas. It has been acknowledge for quite some time that plasma-surface interactions are of great importance in the production of these molecules. To gain a better understanding of the plasma-surface interactions, we have investigated this formation of molecules from atomic sources in more detail. Previously, we showed that ammonia can be formed efficiently in plasmas generated from mixtures of hydrogen and nitrogen, i.e. 11% of the total background pressure became ammonia [1]. The ammonia density as a function of the relative hydrogen flow rate was also measured in a low pressure N_2–H_2 flowing discharge [2] and was predicted fairly well from a self-consistent model assuming that NH_3 is mainly produced at the vessel wall [3].

The formation of ammonia is generally ascribed to stepwise addition reactions from absorbed nitrogen and hydrogen radicals at the surface. NH_3 is formed by subsequently hydrogenation of absorbed nitrogen atoms and the intermediates NH and NH_2 at the surface [4]. To obtain further insight in the ammonia formation mechanism, the plasma chemistry was studied in more detail. More specifically, the densities of the atomic radicals (N, H), and the molecular radicals (NH, NH_2) as well as the NH_3 density were determined using various diagnostic techniques. Results on the N and H radical fluxes emitted by the source as measured using two-photon absorption laser induced fluorescence (TALIF) will be presented. The role of the NH_x radicals in the N_2–H_2 plasma was studied by measuring their densities on various positions from the nozzle using cavity ring down spectroscopy. These nitrogen and hydrogen containing plasmas are also of interest in other fields of research, e.g. the deposition of amorphous silicon nitride (a-SiN_x:H) films and the plasma assisted atomic layer deposition of TaN thin films [5].

2. Experimental setup

In the experiments, a high pressure cascaded arc is used as a plasma source to generate N_2-H_2 containing plasmas (Figure 1). This plasma expands supersonically into a low pressure vessel, leading to high fluxes of hydrogen and nitrogen radicals. Via an injection ring monomers can be injected into the background. These monomers undergo charge transfer, and subsequently dissociative recombination reactions with ions (Ar^+, N^+) emanating from the source, leading to atomic and/or molecular radicals. Most of the radicals will arrive at the surface at which they will adsorb. At the surface, new molecules can be generated which subsequently desorb. This process is called plasma-activated catalysis, because a plasma is used to produce the radicals for the molecule production and the almost fully covered (metallic) wall is used as a catalyst [6]. In this so-called remote source approach,

the dissociation and ionization in the plasma source are geometrically separated from the plasma chemistry in the vessel. In this way the plasma conditions can be controlled independently from the downstream plasma chemistry. The plasma is produced with both nitrogen and hydrogen applied through the cascaded arc with a total flow of 1 standard liter per minute. The arc pressure is typically at 0.1-0.2 bar and the current is 55 A and the plasma vessel is kept at 20 Pa.

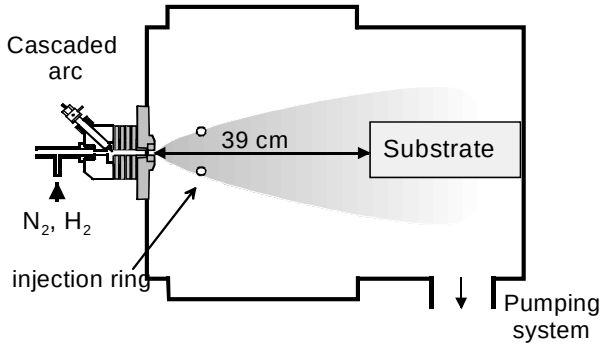

Figure 1: Sketch of the setup in which the thermal plasma expansions are created.

Cavity ring down spectroscopy was used to measure the density of NH and NH_2 radicals on various positions from the nozzle (z = 10, 21, 35 cm). CRDS is an absolute absorption technique based on the measurement of the decay rate of a light pulse confined in a high-finesse optical cavity rather than the magnitude of the absorption. The optical cavity is formed by two highly reflective plano-concave mirrors. The mirrors were directly flanged onto the stainless steel vessel, in which the plasma expands. The light leaking out of the cavity was detected by a photo multiplier tube. When there is an absorbing medium present in the cavity, the intensity of the light pulse will decay faster. From the difference in decay time, (ring-down times) between an empty cavity and a cavity with absorbing species can be related to the density of the absorbing species in the cavity, when information on the cross section and the partition function (state sum) of the absorbing species is known.

The NH radical density was determined using the isolated $A^3\Pi(v'=0) \leftarrow X^3\Sigma^-(v''=0)$ $P_{3,3}(9)$ transition at 339.52 nm. The NH_2 radical was detected at the isolated $\tilde{A}^2A_1 \leftarrow \tilde{X}^2B_1$ $(0,9,0) \leftarrow (0,0,0)$ $\Sigma^P Q_{1,7}$ absorption line at 597.21 nm. The density information is determined by scanning the laser over the absorption line and using the integrated absorption cross-section, which is deduced from the oscillator strengths reported in literature. The Doppler broadening was used to determine the kinetic gas temperature of the radicals by deconvoluting the experimental absorption lines into a Lorentzian laser-line-width and Gaussian Doppler contribution. The laser line-width was 0.11 ± 0.01 cm^{-1} at 339.52 nm and 0.054 ± 0.01 cm^{-1} at 597.21 nm. The temperature was determined for two reasons. Firstly, in order to determine the total density one has to take into account the density distribution in all possible states (determined by the temperature). Secondly, the temperature gives an indication of the possible reaction mechanisms leading to NH and NH_2 radicals.

The densities and fluxes of the atomic radicals (N, H) emitted by the source were measured using two-photon absorption laser induced fluorescence (TALIF). In the case of hydrogen atoms, 205 nm photons are used to excite the H atoms from the $1s^2S$ ground state to the $3d^2D$ and $3s^2S$ states. The resulting non-resonant fluorescence on the Balmer-α transition at 656 nm is detected by a photo multiplier tube. From a spectral scan over the two-photon transition, the H atom density, temperature and velocity along the laser beam are obtained. In all of the measurement the dye laser wavelength is calibrated by the simultaneous recording of the well-known absorption spectrum of molecular iodine. The densities are calibrated using a two-photon transition in a known amount of krypton.

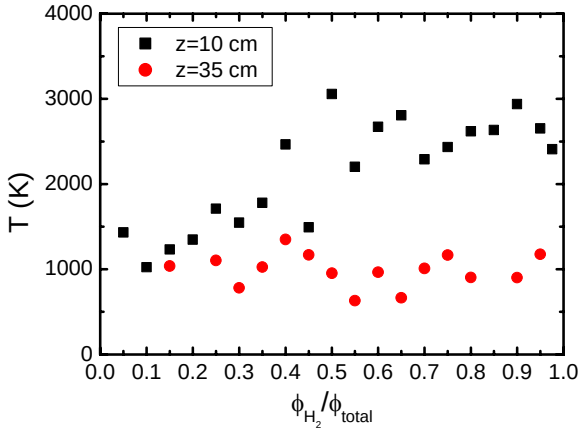

Figure 2: The temperature of the NH_2 radicals at two different positions from the nozzle, i.e. z = 10 and 35

3. Results

The temperature of the NH radicals as determined for z = 10 and 21 cm, is the same as the plasma temperature, i.e. about 1500 K. The temperature of the NH_2 radicals as measured at z = 10 and 35 cm are plotted in Figure 2 as

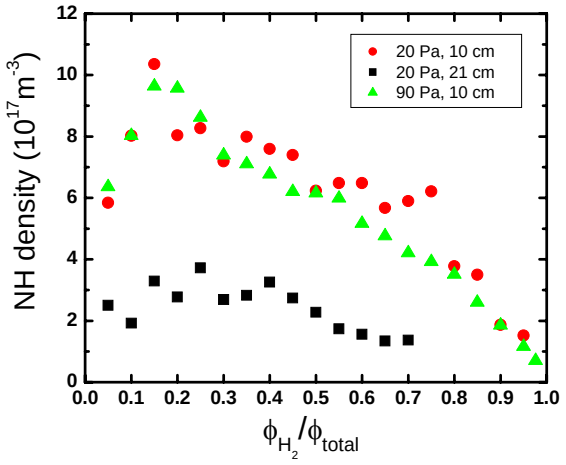

Figure 3: NH density as function of the relative hydrogen flow at two different z-positions and pressures.

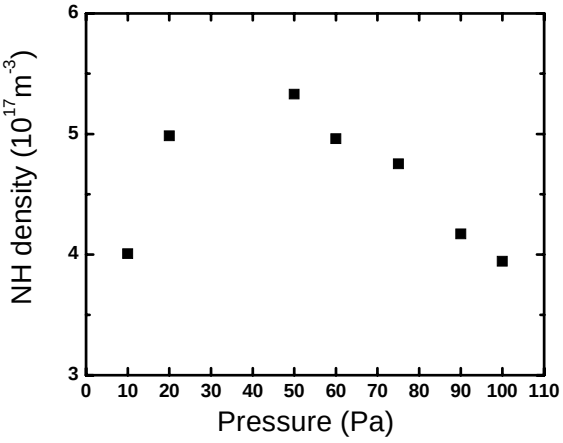

Figure 4: NH density as function of the background pressure. Both nitrogen (5 sccs) and hydrogen (11.67 scs) are applied through the arc.

function of the relative hydrogen flow. The temperature at z = 10 cm increases from 1400 K at almost full nitrogen plasmas to 2500 K for plasmas containing more than 50% hydrogen. The temperature behaviour of NH_2 as function of the relative hydrogen flow, is due to a different plasma temperature at z = 10 cm for different relative hydrogen flows. At low relative hydrogen flows, the plasma is dominated by N atoms and N_2 molecules. Therefore, the formed NH_2 undergoes enough collisions with heavy particles to be thermalized, i.e. the NH_2 radicals have the same temperature as the other particles in the plasma, which is around 1500 K. At high relative hydrogen flows, the temperature of the H atoms is higher than at low relative hydrogen flows and the formed NH_2 radicals undergo mainly collisions with H atoms. Due to the fact that H atoms have a small mass, it takes more collisions and thus time before the plasma is thermalized. At z = 10 cm, the NH_2 radicals didn't undergo enough collisions to be thermalized, i.e. have a temperature around 1500 K. At z = 35 cm, the temperature is 1000 K, independently of the relative hydrogen flow. At z = 35 cm the plasma is completely thermalized, so no dependence on the relative hydrogen flow is expected. Furthermore, a temperature of 1000 K is expected, since z = 35 cm is 2.5 cm in front of the substrate, and a temperature drop takes place from 1500 K in the plasma a few centimetres before the substrate to 600 K at the substrate.

The density of NH shows a maximum at a 80%/20% N_2/H_2 flow, which decreases with increasing distance from the nozzle (Figure 2), in contrast to the NH_3 density which shows a maximum at 30%/70% N_2/H_2 flow. In Figure 3, also the NH density at z = 10 cm is depicted for two different pressures, i.e. 20 and 90 Pa. For the condition, which shows the most NH_3 production in the background, also the pressure dependence of the NH density was measured (Figure 3). The maximum of the NH_2 density occurs at around 15%/85% N_2/H_2 flow. We note that the NH and NH_2 densities (both in the order of a few times 10^{17} m^{-3}) are only about 1% of the maximum ammonia density.

As already mentioned, the temperature of the NH_x (x=1,2) radicals indicates that the NH_x radicals are produced in the plasma expansion. From a comparison of the rate coefficients of neutral-neutral reactions and charge exchange (CE) reactions in the N_2-H_2 plasma expansion, we conclude that charge exchange reactions are dominant in the production of the NH_x radicals at low hydrogen flows. We note that under optimal conditions a significant amount of background gas in our vessel is ammonia, which can diffuse into the plasma beam. The NH_3 originates from surface reactions of plasma produced N and H radicals [6]. A possible reaction path for the formation of NH_x radicals is a CE reaction between ammonia and N^+ from the source. To underpin this idea, the formation of NH_x radicals was studied in Ar-NH_3 plasma expansions in which a CE reaction with Ar^+ is the most important source for NH_x formation [7]. With the outcome of this study, we can explain the NH_x trends we observed.

The charge exchange reaction of N+ with NH_3 produces mainly NH_3^+:

$$N^+ + NH_3 \rightarrow N + NH_3^+. \quad (1)$$

Subsequently, the ammonia ions recombine dissociatively with electrons leading to the formation of NH and NH_2:

$$NH_3^+ + e \rightarrow NH_2 + H \quad (2)$$
$$\rightarrow NH + pH_2 + (2\text{-}2p)H \ (p=0,1),$$

with a 50%-50% branching ratio.

At low hydrogen flows, the decrease of the NH density with increasing hydrogen flow rate can be explained by the decrease in N^+ flux emanating from the source with increasing hydrogen flow rate. The fact that the trend of the NH density as a function of the hydrogen flow rate is independent of the pressure (Figure 3) indicates that indeed N^+ is reacting with ammonia. The N^+ flow emanating from the arc is independent of the background pressure, and thus reaction (1) is the limiting step in the production of NH. However, at high hydrogen flows, the produced N^+ ions are immediately consumed due to reactions with H_2, thus no N^+ ions are left at z = 10 cm. Still, NH is observed at high hydrogen flows. This indicates that a second mechanism has to be taken into account, especially at high hydrogen flows. The mechanism responsible for NH at high hydrogen flows is the reaction between H and NH_3 leading to NH_2 and subsequently the reaction between H and NH_2 leading to NH. This is underlined by the behaviour of the NH_2 density. The NH_2 density has a maximum around 15%/85% N_2/H_2 flow. This is the regime in which no N^+ ions are available and NH_2 can only be formed by:

$$H + NH_3 \rightarrow NH_2 + H. \quad (3)$$

That NH and NH_2 are formed out of ammonia is illustrated in Fig. 4, in which the NH density is shown as a function of pressure (10-100 Pa). The pressure dependence can be explained by recognising that the ammonia density increases with increasing background pressure, leading to a higher NH density. However, when the pressure is even higher, the diffusion of ammonia into the plasma beam becomes more difficult, which counteracts the effect of a higher NH_3 density and leads to a decreasing trend in the NH density as a function of pressure.

4. Conclusions

We have shown that the NH and NH_2 radical densities in N_2-H_2 plasma are in the order of a few times 10^{17} m^{-3}. This is only about 1% of the maximum ammonia density. This indicates that NH and NH_2 play only a minor role in N_2-H_2 plasma in which ammonia is formed. From our results, we conclude that at low relative hydrogen flows the NH_x radicals are mainly formed by charge exchange reactions between N^+ and NH_3 with subsequently dissociatively recombination of NH_3^+ with electrons. At high relative hydrogen flows, the reactions between NH_x (x=2,3) and H lead to the production of NH and NH_2 radicals.

Acknowledgement

The authors acknowledge C.C.H. Lamers for her contribution during the measurements of the NH radicals and M.J.F. van de Sande, J.F.C. Jansen, A.B.M. Hüsken and H.M.M. de Jong for the technical assistance. This work is part of the research program of the Foundation for Fundamental Research on Matter (FOM), which is financially supported by the Netherlands Organization for Scientific Research (NWO).

References

[1] J.H. van Helden, W. Wagemans, P. Vankan, T. Rutten, D.C. Schram and R. Engeln – *Proceedings of the 16th International Sysmposium on Plasma Chemistry*, June 22-27, Taormina, Italy, 2003.
[2] J. Amorim, G. Bavarian, G. Sultan - Appl. Phys. Lett. **68**, 1915 (1996).
[3] B. Gordiets, C.M. Ferreira, M.J. Pinheiro, A. Ricard - Plasma Sources Sci. Technol. **7**, 379 (1998).
[4] J. L. Jauberteau, I. Jauberteau and J. Aubreton, J. Phys. D: Appl. Phys. **35**, 665 (2002).
[5] H. Kim, A.J. Kellock, S.M. Rossnagel, J. Appl. Phys. **92**, 7080 (2002)
[6] P. Vankan, T. Rutten, S. Mazouffre, D.C. Schram, R. Engeln - Appl. Phys. Lett. **81**, 418 (2002).
[7] P.J. van den Oever, J.H. van Helden, J.H. van Hemmen, R. Engeln, D.C. Schram, W.M.M. Kessels and M.C.M van de Sanden - abstract submitted to ISPC 17.

Study of the formation of molecules in N and O containing plasmas

J.H. van Helden[1], G. Lombardi[2], R. Zijlmans[1], G.D. Stancu[2], J. Röpcke[2], D.C. Schram[1] and R. Engeln[1]

[1]*Department of Applied Physics, Eindhoven University of Technology, P.O. Box 513, 5600 MB Eindhoven, The Netherlands*
[2]*INP-Greifswald, Friedrich-Ludwig-Jahn-Str. 19, D-17489 Greifswald, Germany*

Abstract
Mass spectrometry studies on (Ar–)N_2–O_2 and Ar–NO plasmas revealed the tendency of the systems to produce the most thermodynamically favorable molecules in wall association processes. This means that in these plasmas mainly O_2 and N_2 are formed. Still, in plasmas containing mixtures of nitrogen and oxygen a significant amount of nitric oxide (NO) is formed, i.e. up to 4% of the O_2 and N_2 are converted in nitric oxide, as also measured by means of Tunable Diode Laser Absorption Spectroscopy (TDLAS).
Plasma-surface interactions, nitric oxide

1. Introduction

In applications in which plasma is used for chemical conversion, but also for surface treatment or deposition, newly formed stable molecules are often detected in the background gas. It has been acknowledged for quite some time that plasma-surface interactions play a key role in the production of these new stable molecules. To gain a better understanding of the plasma-surface interactions that take place during the formation of stable molecules, we have chosen to investigate the formation of molecules from atomic sources in more detail. We studied the molecule formation processes in plasma containing nitrogen and hydrogen, in which ammonia is formed in large amounts [1], and plasma containing nitrogen and oxygen, in which NO is formed. To better understand the dynamics leading to the production of NO, also the dissociation of NO has been investigated in Ar–NO plasma.

Here, the formation of molecules in plasmas containing nitrogen and oxygen will be discussed. These kind of plasmas are nowadays extensively studied, because of their relevance in various fields of research, e.g. understanding of atmospheric and ionospheric physics, in re-entry studies of orbital space vehicles [2] and as sources of active species for applications in plasma chemistry. Examples of the latter include such as air pollution cleaning by atmospheric pressure discharge treatment [3], sterilization [4], and surface treatment of materials, like etching [5]. From various studies, it was concluded that NO molecules are formed in these kind of plasmas [6]. Furthermore, the results showed that the densities of e.g. NO are strongly influenced by plasma-surface processes [7].

In this paper, we report on the study of the formation of molecules in recombining plasmas generated from mixtures containing N_2 and O_2 using the expanding thermal plasma (ETP) technique. A main advantage of the Expanding Thermal Plasma (ETP) technique is the fact that the plasma is a recombining plasma in which the energy is contained in the ions in the expansion; the electron temperature T_e is too low for electronic collisions to play a role in dissociation or excitation processes. Furthermore, due to the remote nature of the technique, the plasma production, plasma transport and plasma-surface interactions are separated, which allows independent studies of the different aspects of the process. This in contradiction to almost all previous studies on N_2-O_2 plasmas which were performed in non-equilibrium systems, which are driven by electron collisional excitation, and in which the knowledge of electron and ion densities and energy distributions, as well as of the density and internal state distributions of reactants and products, is necessary to generate a kinetic model explaining the plasma behavior. Moreover, the large number of processes that has to be taken into account leads to the development of complex kinetic models.

The density of the molecules generated, were determined with Tunable Diode Laser Absorption Spectroscopy (TDLAS) and mass spectrometry. We detected molecules like NO, N_2O, N_2 and O_2, formed in expanding plasmas generated from: (a) Ar plasma to which mixtures of N_2 and O_2 are admixed; (b) N_2 plasma to which O_2 is added in the background of the vessel. Our measurements revealed the tendency of the systems to

produce the most thermodynamically favorable molecules in wall association processes. This means that in these plasmas mainly O_2 and N_2 are formed. Still, in plasmas containing mixtures of nitrogen and oxygen a significant amount of nitric oxide (NO) is formed, i.e. 4% of the O_2 and N_2 are converted in nitric oxide. Moreover, in N_2–O_2 mixtures, the interaction of the plasma with a substrate leads to an orange glow around the substrate. Emission spectroscopy has revealed that the emission is ascribed to the formation of molecules in an excited state by association of N and/or O atoms at the substrate.

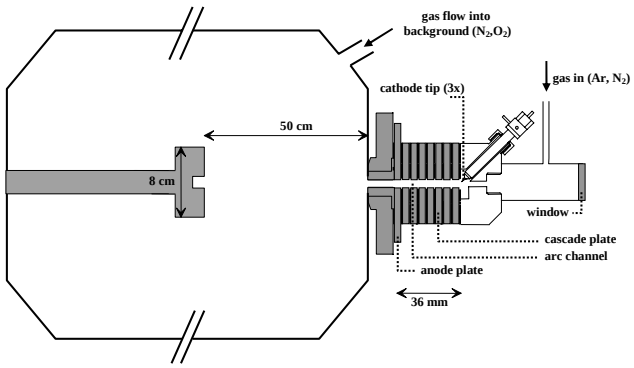

Figure 1: Sketch of the setup in which the thermal plasma expansions are created.

2. Experimental setup

The setup consists of a thermal plasma source in which a high-density argon or nitrogen plasma is created (Figure 1). This plasma expands supersonically into a low-pressure vessel. The pressure gradient between source and the process chamber (0.1-1 mbar) causes, after a supersonic expansion and a stationary shock, a subsonic expansion towards the substrate. Monomers, like oxygen and/or nitrogen are injected into the background. In this way the dissociation and ionization in the plasma source are geometrically separated from the plasma chemistry in the vessel. In this way, the plasma conditions can be controlled independently from the downstream plasma chemistry. Charge transfer reactions between plasma created ions (Ar^+, N^+) or radicals (N) and the monomers, and subsequent dissociative recombination reactions, lead to the production of atomic radicals. Most of the atomic radicals will arrive at the surface at which they will adsorb. At the surface new molecules can be generated which subsequently may desorb. Since the plasma is used to produce the radicals for the molecule production and the almost fully covered (metallic) wall is used as a catalyst, the process is called plasma-activated catalysis [8].

In typical experimental conditions, the cascaded arc source is operated on Ar flows of typically 50 sccs (standard cubic centimeters per second). In argon, a typically ionization degree of 10% is reached with an arc current of 45 A , equivalent to 10^{20} ions/s (and electrons) emanating from the source. The current of the arc can be set to 30-90 A and the voltage over the arc ranges from 100 to 300 V. We studied the formation of molecules like NO, N_2O, N_2 and O_2, in expanding plasmas generated from: (a) Ar plasma to which mixtures of N_2 and O_2 are admixed; (b) N_2 plasma to which O_2 is added in the background of the vessel.

The density of the molecules generated, like NO, N_2O, N_2 and O_2, were determined with Tunable Diode Laser Absorption Spectroscopy (TDLAS) and mass spectrometry. For the Tunable Diode Laser Absorption Spectroscopy (TDLAS) measurements, the so-called infrared multi-component acquisition (IRMA) system based on infrared absorption spectroscopy was used [9]. The IRMA system consists of four independent tunable diode lasers, which can be temporally multiplexed. Rapid scan software measures the mole fractions of several molecules simultaneously with millisecond time resolution. The setup was equipped with a quadrupole mass spectrometer (Balzers QMS 421C) on top of the reactor to analyze the stable species present in the background. The mass spectrometer was calibrated (absolute) by injecting a controlled NO mass flow rate into the N_2-O_2 flow while the plasma is off.

3. Results

Results of TDLAS measurements on NO, formed when an Ar plasma expands in the low-pressure vessel and mixtures of N_2 and O_2 (total flow of 1800 standard cubic centimeters per minute (sccm)) are injected in the background, are depicted in Figure 2. The plasma source is operated at 75 A and a flow of 3000 sccm Ar is applied. The NO mole fraction is defined as: $n[NO]/(n[O_2] + n[N_2])$ (closed symbols) and the efficiency of use of N_2 and O_2 as: $n[NO]/n[N_2]$ (cross) resp. $n[NO]/n[O_2]$ (open circle). In this way 100% means maximal conversion to nitric oxide of the nitrogen (cross) and oxygen molecules (open circle). The results show that a significant

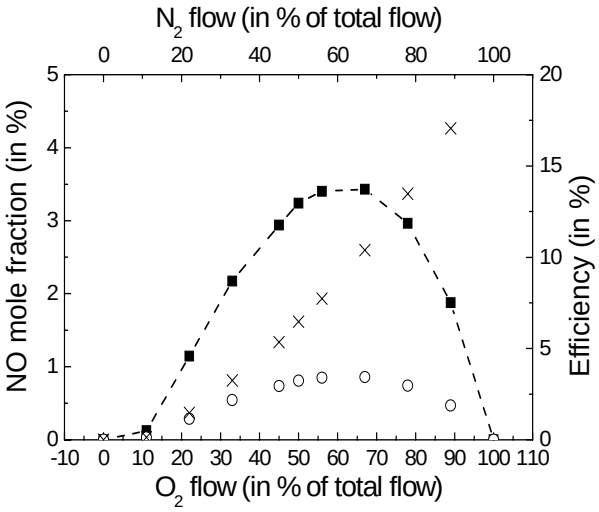

Figure 2: NO mole fraction produced in an Ar plasma expansion to which mixtures of N_2 and O_2 are added. The background pressure in the vessel was 20 Pa (see text for details).

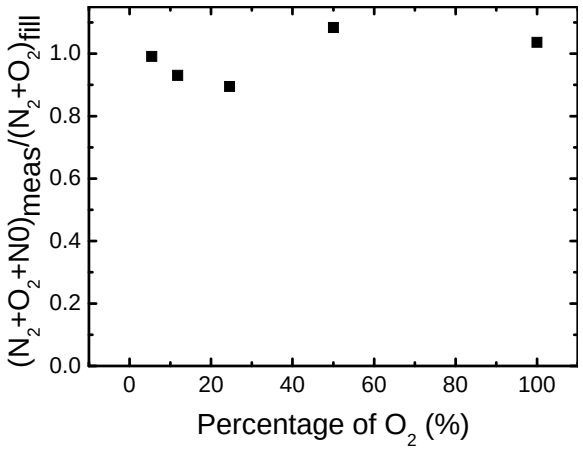

Figure 3: Ratio of the measured densities over the input gas densities for the three main molecules N_2, O_2 and NO.

amount of nitric oxide (NO) is formed, i.e. up to 4% of the O_2 and N_2 was converted in nitric oxide Under our conditions NO is mainly formed by wall association of N and O atoms to NO. The main loss mechanism of NO is:

$$N + NO \rightarrow N_2(X, \nu\sim3) + O. \quad (1)$$

This loss mechanism is responsible for the asymmetry in Figure 2, as it is more effective for higher nitrogen flows. The threshold observed for low oxygen flows is also attributed to this reaction, but also the following reaction could play a role:

$$N + NO_{ads} \rightarrow N_2O. \quad (2)$$

Mass spectrometry data measured under the same conditions show that the ratio of the measured densities over the input gas densities for the three main molecules N_2, O_2 and NO is around one (Figure 3). This indicates that atomic and molecular radicals present in the plasma are converted back into molecules. This is even stronger shown in the case NO is injected in the background, mass spectrometry measurements showed that when the Ar ion flow is larger than the NO flow, 90 % of the NO is converted to N_2 and O_2, which are thermodynamically more favorable than NO. This result clearly shows that the system has the tendency to produce the most thermodynamically favorable molecules in wall association processes. Under the same experimental conditions during which the data of Figure 2 were obtained, no nitrous oxide (N_2O) was detected by means of TDLAS.

Next N_2 plasmas with O_2 injected in the background were studied. In a nitrogen expanding plasma, N^+ and N are emitted by the cascaded arc source. The charge exchange reaction of N^+ with N_2 leads to N_2^+, which partially dissociatively recombines to N atoms. When oxygen is injected in the background, the O_2 undergoes charge exchange reactions with N^+ and N_2^+, which leads to O atoms.

In this case, when after NO measurements the O_2 flow was stopped, N_2O was observed with a time behavior as shown in Figure 4. The two time traces shown in Figure 4 are recorded after 1 minute (black line) and after 5 minutes (gray line) of N and O exposure of the vessel. After exposure times longer than 5 minutes, no change in the trend of the

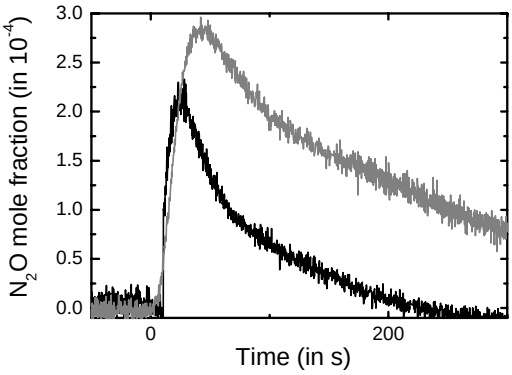

Figure 4: Time behavior of the N_2O mole fraction after switching off the O_2 flow (see text for details).

N_2O mole fraction is observed. Both time traces show a maximum of which the height depends on the time the vessel was exposed to N and O fluxes. Once the maximum is reached, it takes minutes before the density of N_2O is below the detection limit. Since the residence time of the gasses in the vessel is in the order of a second, N_2O is most probably produced in a surface association process of N radicals from the plasma and NO at the surface.

Furthermore, emission spectroscopy and imaging studies on the light emission of N_2–O_2 plasma revealed an intensification of the light around the substrate (Figure 5). The plasma brightness on the right side of Figure 5, (source side) decayed due to dissociative recombination of molecular ions and by mutual recombination of negative and positive ions.

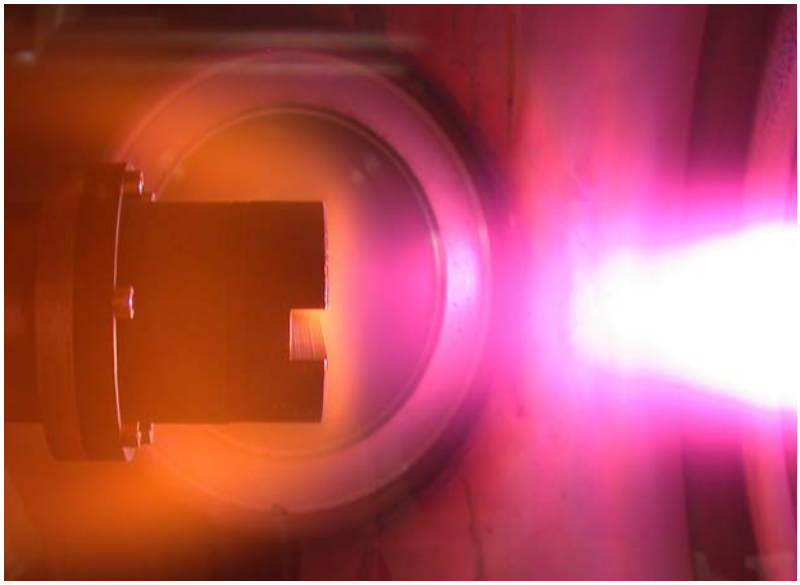

Figure 5: Enhanced emission around a substrate exposed to an N_2/O_2 plasma expansion.

A second clear result is the appearance of an orange glow at and around the substrate. The thickness of the light layer indicates a transition with a lower transition probability, which would be consistent with a broadband feature observed in spectral analysis of the emission. Under certain conditions this light has a remarkable resemblance with the emission observed during the reentry of space vehicles. This light is tentatively attributed to the formation of excited NO_2 in an association reaction of O radicals from the atmosphere and NO adsorbed at the surface of the space vehicle [10]:

$$O(^3P)_{atm} + NO_{ads} \rightarrow NO_2\{^2B_1\} \rightarrow NO_2\{^2A_1\} + h\nu \quad (3)$$

In our plasma vessel the substrate is exposed to high fluxes of oxygen and nitrogen atomic radicals. As shown before, NO can become adsorbed at the surface during N/O exposure, and thus a similar process as in the space vehicle experiments can lead to NO^*_2 emission. However, recombination of N and O atoms to a high vibrational excited B state of NO can also contribute to the radiation.

4. Conclusions

The densities of NO, N_2O, N_2 and O_2 were determined using Tunable Diode Laser Absorption Spectroscopy (TDLAS) and mass spectrometry in on the (Ar–)N_2–O_2 and Ar–NO plasmas. From our results, we conclude that the plasmas reveal the tendency of the systems to produce the most thermodynamically favorable molecules in wall association processes. This means that in these plasmas mainly O_2 and N_2 are formed. Still, in plasmas containing mixtures of nitrogen and oxygen a significant amount of nitric oxide (NO) is formed, i.e. 4% of the O_2 and N_2 are converted in nitric oxide.

Acknowledgement

The authors acknowledge M.J.F. van de Sande, J.F.C. Jansen, A.B.M. Hüsken and H.M.M. de Jong for the technical assistance. This work is part of the research program of the Foundation for Fundamental Research on Matter (FOM), which is financially supported by the Netherlands Organization for Scientific Research (NWO).

References

[1] J.H. van Helden, W. Wagemans, P. Vankan, T. Rutten, D.C. Schram and R. Engeln – *Proceedings of the 16th International Sysmposium on Plasma Chemistry*, June 22-27, Taormina, Italy, 2003.
[2] M. Capitelli (Ed) - *Molecular Physics and Hypersonic Flows (NATO ASI C-482)*, Kluwer, Dordrecht, 1996.
[3] B.M. Penetrante, E. Schultheis (Ed), *Non-Thermal Plasma Techniques for Pollution Control: Part A—Overview, Fundamentals and Supporting Technologies and Part B---Electron Beam and Electrical Discharge Processing*, Springer-Verlag, Berlin, 1993.
[4] C.D. Pintassilgo, J. Loureiro, V. Guerra, J. Phys. D: Appl. Phys. **38**, 417 (2005).
[5] G.J.H. Brussaard, K.G.Y. Letourneur, M. Schaepkens, M.C.M. van de Sanden, D.C. Schram, J. Vac. Sci. Technol. B **21**, 61 (2003).
[6] J. Nahorny, C.M. Ferreira, B. Gordiets, D. Pagnon, M. Touzeau, M. Vialle, J. Phys. D: Appl. Phys. **28**, 738 (1995)
[7] B. Gordiets, C.M. Ferreira, J. Nahorny, D. Pagnon, M. Touzeau, M. Vialle, J. Phys. D: Appl. Phys. **29**, 1021 (1996)
[8] P. Vankan, T. Rutten, S. Mazouffre, D.C. Schram, R. Engeln - Appl. Phys. Lett. **81**, 418 (2002).
[9] J Röpcke, L. Mechold, M. Kaning, J. Anders, F.G. Wienhold, D. Nelson, M. Zahniser, Rev. Sci. Instrum. **71**, 3706 (2000).
[10] E. Murad - Annu. Rev. Phys. Chem. 49, 73 (1998).

Etching of a-C:H films by thermal Nitrogen atoms

D. Douai[(1)], J. Berndt[(1)], S. Hong[(1)], H. Becker[(2)] and J. Winter[(1)]

[(1)]*Institute of Experimental Physics II, Faculty for Physics and Astronomy, Ruhr-University Bochum, D-44780 Bochum, Germany*
[(2)]*Institute of Experimental Physics III, Faculty for Physics and Astronomy, Ruhr-University Bochum, D-44780 Bochum, Germany*

This contribution deals with the etching of amorphous hydrogenated carbon films by thermal nitrogen atoms. The flow rate of nitrogen atoms which is a crucial parameter for any quantitative analysis of the etching process (i.e.for the determination of the erosion yield) is determined by means of Threshold Ionization Mass Spectroscopy (TIMS). The etch rate of the amorphous hydrogenated carbon films is determined by means of a multi-wavelength-ellipsometer which allows the measurement of film thickness and refractive index.

Introduction

Amorphous hydrocarbon films (a-C:H films) have found an increasing number of applications. They are used as protective coatings for optical devices, as wear or corrosion resistant coatings and for biomedical applications (coating of stents, hip and knee joints for example). Depending on the deposition conditions (as gas composition and ion energy) the properties of a-C:H-films can vary from soft polymer-like to hard diamond-like carbon (DLC) [1].

A newer development concerns the incorporation of nitrogen atoms in the carbon network. Stimulated by the work of Liu and Cohen [2] a lot of work has been done to produce and study the properties of such carbon nitride materials [3,4].

In this paper we investigate the interaction of (soft) a-C:H films with a flowing afterglow of a nitrogen plasma. The etching capability of N-atoms is studied for different substrate temperatures by means of ex-situ- ellipsometry. The flux of nitrogen atoms that is impinging on the film is determined quantitatively by means of modulated beam mass spectroscopy. The knowledge of etching rate and N-atom flux allows to determine the erosion yield of the nitrogen atoms. The diffusion of nitrogen atoms into the carbon network-during the etch process- is investigated by means of sputter-XPS-measurements.

Experimental set up

In this contribution we are using the flowing afterglow of a nitrogen discharge to study the etching of amorphous hydrocarbon films. Figure 1 shows a sketch of the experimental set up which consists mainly of two parts: the discharge, where the N-atoms are created, and a differentially pumped process chamber. The discharge is created in a quartz tube (inner diameter 10 mm) by a travelling surface wave at 2,45 GHz, which is excited by a Waveguide-Surfatron structure [5]. The total gas throughput does not exceed 500 sccm, resulting in an upstream pressure in the glass cylinder between 1 and 10 mbar. A 1500 liter/sec turbomolecular pump ensures a downstream pressure of about 10^{-3} mbar in the process chamber. The flow rate of nitrogen atoms which is a crucial parameter for any quantitative analysis of the etching process is determined by means of Threshold Ionization Mass Spectroscopy (TIMS). Losses of N atoms at the inner wall of the mass spectrometer are taken into account by a modulation technique (Modulated Beam Mass Spectroscopy MBMS [6]). The mass spectrometer (Hiden HAL PSM 300) can be moved axially and the substrate holder is mounted on an edge welded bellow which allows radial translation with respect to the axis of the tube. The latter is provided with a Nickel Chromium 80/20 heating wire (Thermocoax 1Nc type) pressed between two copper plates in order to ensure a reasonable heat transfer to the sample.

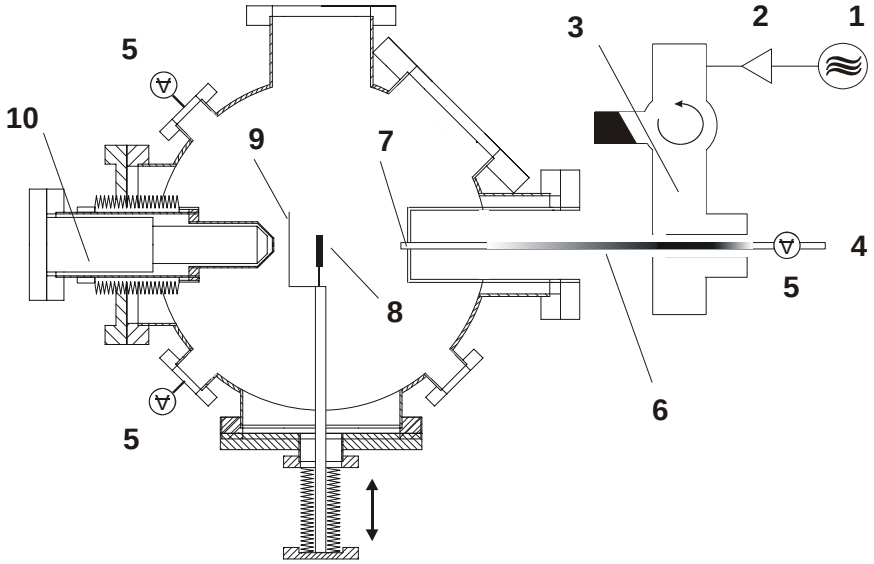

Figure 1 : Experimental arrangement: 1. Microwave Generator, 2. Klystron and Pre-amplifier (+70 dB), 3. Waveguide-Surfatron, 4. Gas inlet, 5. Baratron. 6.Quartz tube (d_{in}=10 mm, d_{out} = 12 mm), 7. Post-discharge 8. Temperature-controlled substrate holder, 9. steel plate, 10. Mass Spectrometer.

The sample which is to be treated (a-C:H films deposited on a Si-substrate, dimensions : 20 mm x 25 mm) by the N radicals is placed on the substrate holder. Both the temperature of the substrate and of the substrate holder are measured by a thermocouple, ensuring good thermal transfer from the sample to the thermocouple. The samples can be heated to a temperature of 600° C. The proximity of the mass spectrometer makes it necessary to enclose the substrate holder with steel plates for thermal shielding.

Experimental results

The thickness d and the refractive index n of the films are measured by ex-situ- ellipsometry before ($d_{initial}$) and after (d_{final}) the treatment in the remote plasma. The deposited films are polymer-like films, with an averaged refractive index of about 1,7 in the spectral range 300-800 nm and are typically 100 nm thick. At temperatures above 300°C (which was measured directly at the surface of the films), they become thermally unstable. At 350 °C, significant thermal desorption of the films occurs under the absence of atmosphere, leading to a diminution of the film thickness with a rate of 0,1 nm/min. After an exposure time Δt to the remote N_2 plasma, the etch rate is determined from the measurement of the thickness d_{final} of the treated film .

$$R = \frac{d_{initial} - d_{final}}{\Delta t} \qquad (1)$$

The thermal activation of the etch reaction was studied by controlling the temperature of the substrate The results are shown on figure 2. The exposure time of the films to the remote plasma was varied between 1 hour at 300°C and 5 hours at 130°C. As can be seen, the etch rate depends strongly on the substrate temperature and varies between 0,14 ± 0,03 nm/min. at 130°C and 1,04 ± 0,25 nm/min. at 300°C. The N flux was approximately 5.10^{16} cm^{-2}/s in all cases.

The etch rate R can be described by an Arrhenius behaviour :

$$R = R_0 \exp\left(-\frac{E}{k_B T}\right) \quad (2)$$

where the pre-factor R_0 depends on the N atom flux, k_B is the Boltzmann constant and T is the substrate temperature. The activation energy E of the etching reaction is deduced from the best fit of equation (2). The value is E = 0,25 ± 0,06 eV.

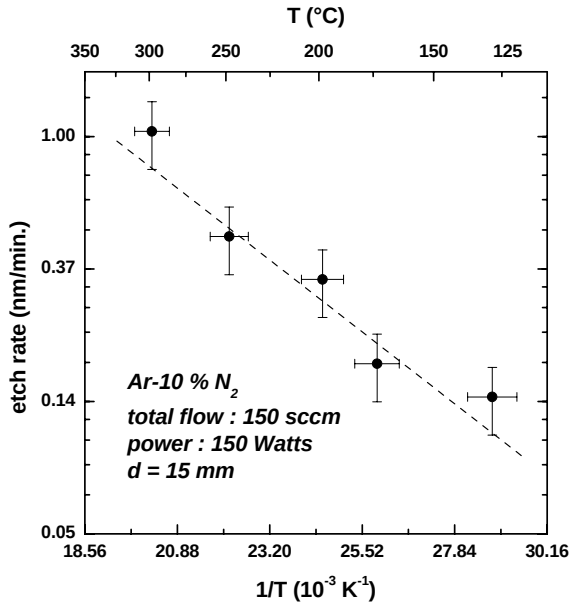

Figure 2 : Arrhenius plot of the temperature dependent etch rate.

Since the C atom density in the film is known from previous Rutherford Backscattering measurements [7], (revealing [C] = 4.10^{22} cm^{-3}) the above etch rates and atomic nitrogen fluxes allow to determine quantitatively an erosion yield (defined as the yield of C atoms removed per impinging N atom). The obtained values are varying between $1{,}9.10^{-4}$ C/N^0 at 130°C and $1{,}4.10^{-3}$ C/N^0 at 300°C. These values are similar to those reported in [8] for carbon erosion by thermal hydrogen atoms on graphite (about 10^{-3} to $5.\ 10^{-3}$ C/H^0).

The nitrogen content of the films is determined by means of Sputter X-ray photoelectron spectroscopy. For the typical kinetic energy of the ejected electrons, the escape depth is about 2 nm in the present case. The films are sputtered by an energetic Ar^+ beam (1 keV). When the film has been sputtered away, the Si substrate is exposed to X-ray radiation, and the spectrum exhibits two signatures at 99 and 151 eV, typical for Si. Thus, given the initial film thickness and the sputtering time, the sputter rate was approximately 2 nm/min. With this method, the depth profile of the relative concentration of the constituents in the films was obtained.

The results show that the surface nitrogen content represents up to 15 % of the carbon content. After 30 sec. sputtering, the N(1s) peak is observed at 398,5 eV, the standard value of N in carbon networks, leading to [N[/[C] = 5 %. Even after 10 minutes of sputtering N atoms are present in the film with a relative concentration of about [N[/[C] = 1 %.Thus, under the experimental conditions (60 min. exposure time, J_N = 5.10^{17} cm^{-2}/s, $T_{substrate}$ = 250°C), the N atoms are diffusing into the carbon network. The presence of N atoms in the film results from a competition between etching and diffusion processes, making it difficult to achieve high values of the [N]/[C] ratio in the bulk of the film

References

[1] J.C. Angus and Y. Wang in ,Diamond and Diamondlike Films and Coatings, edited by R:E: Clausing, L.L. Horton, J:C. Andus and P.Koidl (NATO ASI Series **B 266,** Plenum Press, New York,1991) p.173.
[2] A.Y Liu, M.L. Cohen, *Science* **245** p. 841 (1989).
[3] Vepřek S., *J. Vac. Sci. Technol. A* **17**-5 (1999) pp. 2401-2420.
[4] Muhl S., Mendez J. M., *Diamond and Related Materials* **8** (1999), pp. 1809–1830.
[5] M. Moisan ,Z. Zakrzewski , *J. Phys. D : Applied Physics* **24**, pp. 1025-1048, (1991)
[6] D. Douai., J. Berndt and J. Winter, *Plasma Sources Sci. Technol.* **11**, pp. 60–68, (2002)
[7] S.H. Hong, D. Douai, J. Berndt and J. Winter, 2001 *ISPC 15, vol. 6, p.2379*
[8] Vietzke E., Haasz A. A., in *Physical Processes of the Interaction of Fusion Plasmas with Solids* edited by H.O. Hofer and J. Roth Academic Press, San Diego (1996).

Experimental study of an RF-IPVD process: contamination by the RF coil.

J.C. Imbert, L. de Poucques, C. Boisse-Laporte, J. Bretagne, M. Ganciu, M.C. Hugon,
L. Teulé-Gay and M. Touzeau
Laboratoire de Physique des Gaz et des Plasmas, Bât. 210, Université Paris Sud, 91405 ORSAY cedex, France

Abstract
When dealing with thin film deposition, contamination of the material is an important parameter. In this paper, we present results concerning contamination of the deposited material in an RF-IPVD reactor by the internal coil. We have worked in argon and the sputtered material was titanium. The film contamination is explained by comparing the flux of deposited titanium to the flux of titanium sputtered by argon and titanium ions on the RF coil.
Keywords: IPVD, radio-frequency, contamination, thin film deposition

1. Introduction

Ionised Physical Vapour Deposition (IPVD) has been developed since the 1990s to obtain deposited film coatings that are more conformal and of better quality than those obtained with conventional sputtering technique [1]. The main goal of IPVD is to ionize a significant fraction of the neutral species sputtered from the magnetron target. The ionized sputtered particles can then be collimated by applying an electric bias on the substrate. IPVD reactors consist of a magnetron discharge assisted by an additional plasma source which ionises the sputtered vapour flowing from the magnetron. Reactors using helicon [2] or ECR coupled discharge [3] have already been studied but most of the IPVD reactors use radio-frequency coils to create the additional ionisation [4].

One of the main constraints when working with the deposition of materials, is the control of the purity of the deposited layer. The goal of this work is to point out the problem of contamination by the internal coil in an RF-IPVD reactor and to propose an explanation of the phenomenon.

2. Experimental set-up

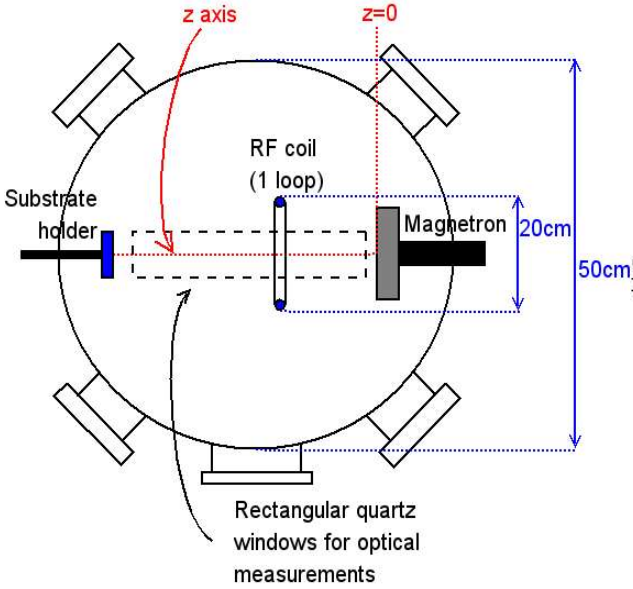

Fig. 1: Diagram of the RF assisted magnetron reactor

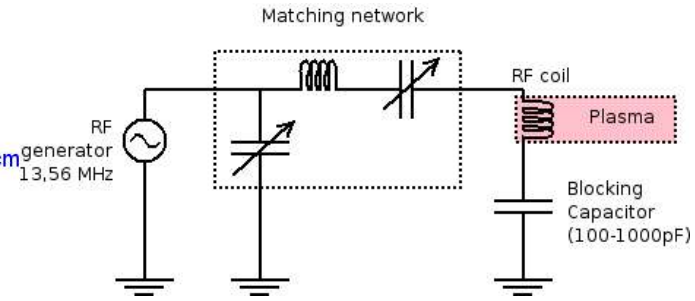

Fig. 2: Electric connection of the coil

The reactor is presented on Figure 1. It is a 50 cm diameter and 45 cm height cylinder, and contains a 10 cm diameter planar circular magnetron cathode. The “z axis” is the magnetron-substrate holder axis. The “z=0” position corresponds to the target surface. Buffer gas is argon and the materials of the target is titanium. The

distance between the titanium target and the substrate-holder is z=14 cm. The quartz windows on top and bottom of the reactor allow spatially resolved optical measurements.

The magnetron cathode is powered by a DC 500V-3A generator. The reactor is flexible enough to allow the use of different RF coils, with 1 or 3 loops, with different coupling to the ground (either grounded or capacitively coupled). The coils are supplied with a 13.56 MHz - 1600W radio-frequency generator. In the present study, we used a 1-loop coil capacitively coupled to the ground. The electric set-up used in this case is presented on Figure 2.

An RF compensated Langmuir probe (manufactured by Scientific Systems) was used to determine the plasma potential, the electron density and the electron temperature. The probe was inserted in place of the substrate holder and it was possible to translate it along the z-axis to make spatially resolved probe measurements.

Various optical diagnostics are possible with this experiment. Spatially resolved optical emission spectroscopy was performed using a collimator, taking light through the bottom quartz window. The emitted light was collected by an optical fibre and analysed through a photomultiplier tube by a Jobin-Yvon HR1000 spectrometer (1200 grooves.mm^{-1} grating, 1000mm focal length). Spatially resolved absorption measurements were carried out using a titanium hollow cathode lamp. The light emitted by the lamp entered the reactor through the top quartz window and the absorption signal was collected through the bottom quartz window. This lamp worked in pulsed regime (100µs duration, 100Hz frequency) using a generator developed in our laboratory. In pulsed regime, the absorption signal is clearly separated from the plasma emission and the enhancement of the ionic line emission in the pulse allows the determination of Ti^+ densities by absorption. The complete method and algorithm used for the determination of densities are described in [6].

Rutherford Backscattering Spectroscopy (RBS) was used to determine the composition of our thin films.

3. Contamination by the RF coil

One problem with the RF-IPVD method when the coil is grounded is the high value of the plasma potential. In our case, in standard deposition conditions (2A magnetron and 450W_{RF}), the plasma potential was measured to be 130V. In these conditions, the potential difference between the plasma and the grounded chamber walls is high enough to allow sputtering of the material deposited on the walls.

A solution to this problem is to use a capacitor to modify the coupling between the coil and the ground [5]. This method gives a much lower plasma potential: in the same conditions as before, we measured a plasma potential of 20V. We therefore have no more sputtering of the walls. However, even if the plasma potential has been lowered, the coil potential still remains high with a mean value of -130V for 450W_{RF}. The phenomenon of sputtering can now happen on the coil.

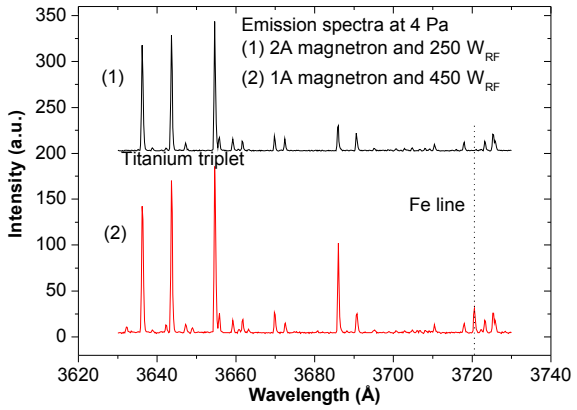

Fig. 3: Emission measurements in the plasma

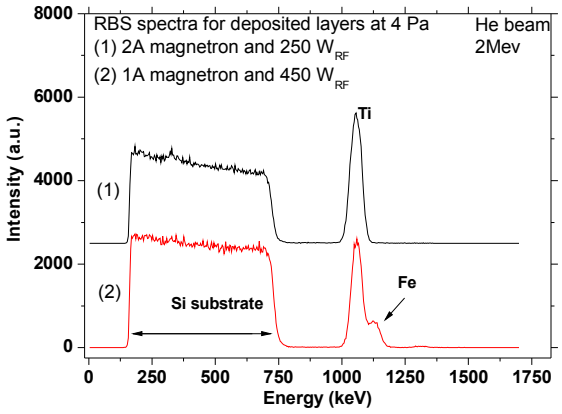

Fig. 4: RBS measurements on a deposited layer

We present, on Figure 3, results obtained by optical emission spectroscopy in two different conditions

of deposition. In the first condition, the Fe emission line was not visible. But when increasing the RF power while decreasing the magnetron current, this emission line became visible. Same observations can be made with surface analysis.

We present, on Figure 4, results obtained by RBS measurements on two deposited layers in the two previous conditions. With 2A on the magnetron and 250W on the RF coil, the RBS spectrum shows only a large band corresponding to the silicon substrate and a single peak corresponding to the Ti deposited thin film. On the other hand, with 1A on the magnetron and 450W on the RF coil, a third peak, indicating the presence of iron in the film, is visible. What does it mean?

In the first case, the lack of iron in the layer means that the flux of titanium depositing on the coil is higher than the flux of material leaving the coil (either titanium or iron), there is enough titanium deposited on the coil to mask the stainless steel of the coil. In the second case, the magnetron current is lower, inducing a lower flux of titanium toward the coil, while the RF power is higher, inducing more sputtering and a higher flux of species leaving the coil, the titanium layer deposited on the coil is progressively removed and the stainless steel can be sputtered.

4. Calculation of the fluxes and correlation with contamination

In order to confirm these assumptions, we have to precisely determine the fluxes reaching and leaving the coil. We suppose an isotropic direction distribution for titanium species around the coil. The absolute densities of Ti species were measured using optical absorption spectroscopy. The magnetron was used without RF power on the coil prior to every absorption measurement in order to avoid the sputtering of the material of the loop. The procedure described in [6] allows to determine a titanium temperature by assuming that the three fundamental sublevels of titanium are in equilibrium. With the RF additional ionization, we found that this assumption was clearly not possible because of a too high electron density, so we had to use another way to measure the titanium temperature. Laser absorption measurements were performed on Ti (λ = 8435,68 Å) metastable and a titanium temperature was deduced using Doppler broadening. The experimental set-up used for the laser measurements is presented on Figure 5. We used a dual passage in order to have a high enough signal, the Fabry-Pérot was used to have a frequency reference.

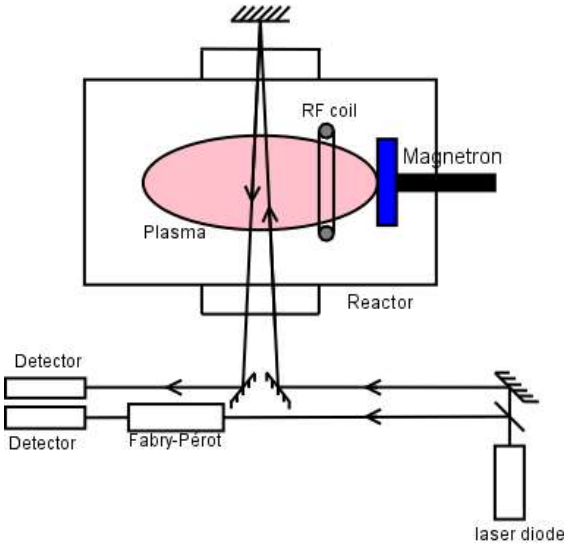

Fig. 6: Diagram of the laser measurement set-up

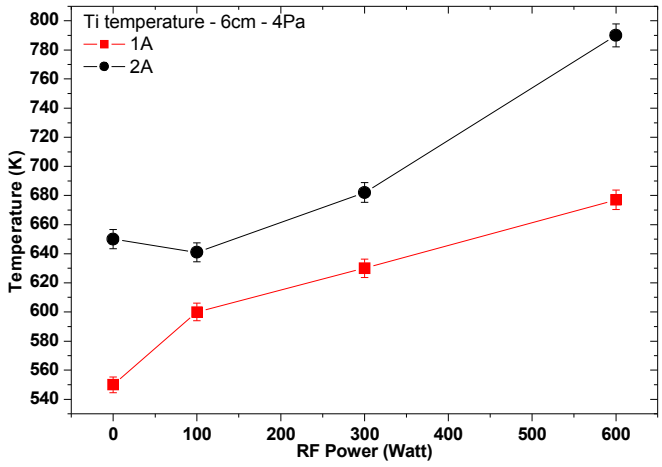

Fig. 5: Temperature determined by laser absorption versus RF power near the RF coil

We present results obtained with this laser measurements on Figure 6 for both 1A and 2A magnetron. We see that the increase of the RF power leads to an increase of the titanium temperature. Combining these temperatures and optical absorption results, we can calculate the absolute densities of species. These densities are reported on Figure 7 and show a decrease of the total titanium density with an increasing RF power. This decrease in density is due to a combination of a decrease of the sputtering yield (coupling between the RF and

the magnetron plasma) and the increase of the temperature (rarefaction of titanium) [8].

We now have all measurements needed to calculate the fluxes. We first consider the flux of atoms depositing on the coil. For neutral titanium atoms depositing on the coil, we consider that their velocity is the mean thermal velocity. Concerning the titanium ions, we consider that they are accelerated in the pre-sheath and reach the Bohm velocity when entering the sheath. Since the flux of species entering the pre-sheath and the flux of species arriving on the coil are equal, the flux of deposited titanium can then be calculated with:

$$\Phi_d = \frac{[Ti]+[Ti^m]}{4}\sqrt{\frac{8\,kT_{Ti}}{\pi\, m_{Ti}}} + [Ti^+]\,e^{-1/2}\sqrt{\frac{kT_e}{m_{Ti}}}$$

where [Ti] is the titanium neutral ground state density, [Ti^m] is the titanium neutral metastable state density and [Ti^+] is the titanium ion density.

Second, we consider the sputtering of the coil. Argon and titanium ions must be taken into account for the sputtering. The titanium ion density is given by absorption spectroscopy, and we consider the argon ion density to be equal to the electron density minus the titanium ion density. The final parameter needed to calculate the flux of species leaving the coil is the sputtering yield. This parameter is calculated using the formula given in [7]. The flux of titanium sputtered from the coil can now be calculated using:

$$\Phi_s = Y_{s,Ti^+}[Ti^+]\,e^{-1/2}\sqrt{\frac{kT_e}{m_{Ti}}} + Y_{s,Ar^+}[Ar^+]\,e^{-1/2}\sqrt{\frac{kT_e}{m_{Ar}}}$$

The parameters needed for the flux calculation are reported in table 1.

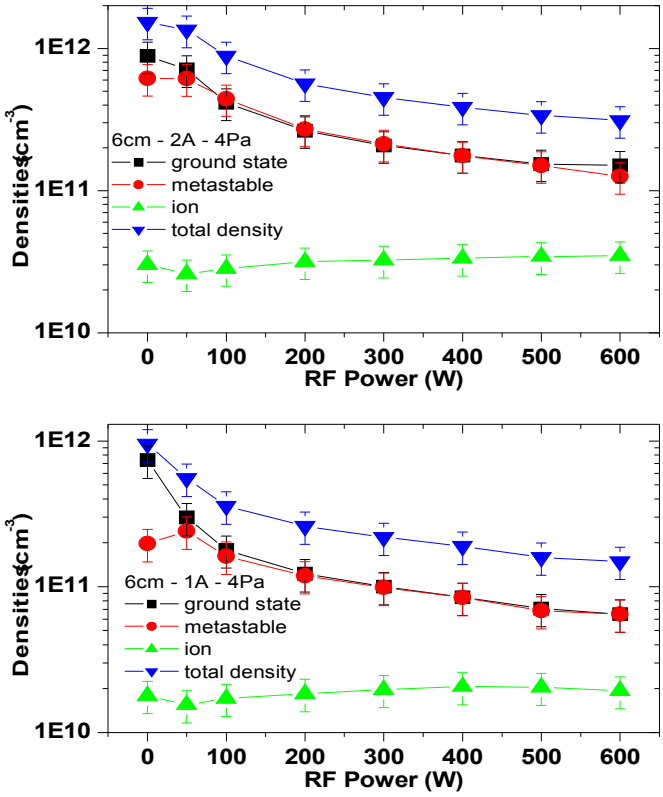

Fig. 7: Densities (titanium ground state, metastable state and ions) evolution versus RF power near the RF coil

With 2A magnetron and 250 W of RF power, the total flux of deposited species is: Φ_d=9,4.10^{22} $cm^{-2}.s^{-1}$ while the total flux of ejected species is Φ_s=1,1.10^{23} $cm^{-2}.s^{-1}$. On the other hand, the same calculation in the case

of an applied magnetron current of 1A and an applied RF power of 450W gives: $\Phi_d=5{,}8.10^{22}$ $cm^{-2}.s^{-1}$ and $\Phi_s=3{,}1.10^{23}$ $cm^{-2}.s^{-1}$.

We clearly see that in the case of a high RF power and a low magnetron current, the flux of species leaving the coil is five times higher than the flux of species deposited on the coil. This result corresponds to the RBS analysis of the deposited layer showing contamination of the film (see Figure 4). On the other hand, in the case of a low RF power and a high magnetron current, the fluxes are similar and iron should not be seen in the deposited layer. This is consistent with the RBS results.

	1A - 450W	2A - 250W
n_e	$5{,}6.10^{11}$ cm^{-3}	$2{,}8.10^{11}$ cm^{-3}
T_e	1,7 eV	1,66 eV
T_{Ti}	653 K	622 K
$[Ti^n]+[Ti^m]$	$2{,}2\pm0{,}6.10^{11}$ cm^{-3}	$4{,}8\pm1{,}2.10^{11}$ cm^{-3}
$[Ti^+]$	$2{,}1\pm0{,}5.10^{10}$ cm^{-3}	$3{,}2\pm0{,}8.10^{10}$ cm^{-3}
$[Ar^+]$	$5{,}4.10^{11}$ cm^{-3}	$2{,}5.10^{11}$ cm^{-3}
V_p	15,4 V	15,3 V
V_{RF}	-161 V	-141 V
$Y_{s,Ti+}$	0,16	0,13
$Y_{s,Ar+}$	0,18	0,15
Φ_d	$5{,}8\pm1{,}5.10^{22}$ $cm^{-2}.s^{-1}$	$9{,}4.10^{22}\pm2{,}4$ $cm^{-2}.s^{-1}$
Φ_s	$3{,}1\pm0{,}8.10^{23}$ $cm^{-2}.s^{-1}$	$1{,}1.10^{23}\pm0{,}3$ $cm^{-2}.s^{-1}$

Table 1: Parameters used for flux calculation

5. Conclusion

Purity of the deposited layers is a parameter of great importance when dealing with material deposition. We have found with layer analysis that this contamination is occurring when the power applied on the radio-frequency coil is rather high while the magnetron power is quite low. In order to quantify this “high” and “low” powers, we determined the flux of species deposited on the coil and the flux of species sputtered from the coil. This calculation has required different experimental studies (Langmuir probe, optical absorption spectroscopy and laser absorption) to measure all the parameters needed. We showed that the contamination can be explained by the comparison of the two fluxes: if the flux of sputtered species is higher than the flux of depositing species, then contamination occurs. At the studied pressure of 4 Pa, the isotropic distribution assumption seems correct.

Further work will consist in other deposited layers analysis at different pressures to check the validity range of the methods presented in this paper especially concerning the isotropic assumption at lower pressure.

6. Acknowledgements

The authors would like to thank N. Sadeghi for his decisive help for the laser absorption measurements and the interpretations of the results.

References

[1] S.M. Rossnagel, J. J. Cuomo and W. D. Westwood, "Handbook of Plasma Processing Technology" 1990 Park Ridge, New Jersey, USA, Noyes Publications

[2] J. Q. Zhang, Y. Setsuhara, T. Ariyasu and S. Miyake, J. Vac. Sci. Technol. A **14** (1996) 2163

[3] A. Yonesu, T. Kato, H. Takemoto, N. Nishimura and Y. Yamashiro, Jpn. J. Appl. Phys. **38** (1999) 4326-

[4] J. Bretagne, C. Boisse-Laporte, L. de Poucques, G. Gousset, M.-C. Hugon, J.-C. Imbert, O. Leroy, L. Teulé-Gay, M. Touzeau, P. Vasina, O. Voldoire "Nanostructured Thin Films and Nanodispersion Strengthened Coatings", Chapter 11, (2004) Kluwer Academic Publishers

[5] K. Suzuki, K. Konishi, K. Nakamura and H. Sugai, Plasma Source Sci. Technol. **9** (2000) 199-204

[6] O. Leroy, L. de Poucques, C. Boisse-Laporte, M. Ganciu, L. Teulé-Gay and M. Touzeau, J. Vac. Sci. Technol. A22 (2004) 192-200

[7] Y. Yamamura and H. Tawara, Atomic Data and Nuclear Data Tables, Vol. 62, No. 2, March 1996

[8] L. De Poucques, J.C. Imbert, C. Boisse-Laporte, P. Vasina, J. Bretagne, L. Teulé-Gay and M. Touzeau, Plasma Source Sci. Technol. **14** (2005) 321-328

Characterization of cathode materials for IT-SOFC synthesized by induction plasma

F. Gitzhofer[1], D. Bouchard[2], L. Sun[2] and G.M. Brisard[2*]

[1] *Department of Chemical Engineering, Université de Sherbrooke, Sherbrooke, Canada*
[2] *Department of Chemistry, Université de Sherbrooke, Sherbrooke, Canada*
[1,2] *Research Center for Electrochemistry, Plasma and Energy*
Université de Sherbrooke,
2500 Boulevard Université, Sherbrooke, Québec, Canada J1K-2R1

Abstract:

In this paper, nanopowders of perovskite cathode materials ($La_{0.8}Sr_{0.2}MnO_{3-\delta}$, $La_{0.8}Sr_{0.2}FeO_{3-\delta}$ and $La_{0.8}Sr_{0.2}CoO_{3-\delta}$), for use in solid oxide fuel cells (SOFCs), were successfully synthesized using induction plasma techniques. Their compositions, structures, morphology, particle size distributions, and BET specific surface areas were determined for comparison with their counterparts which were prepared by the Pechini method and by the glycine-nitrate combustion (GNC) technique. The particle sizes of the plasma-synthesized powders are mostly around 63 nm. These plasma-synthesized powders are generally globular, their BET specific surface areas being about 26 m^2/g, approximately twice those of powders prepared by the glycine-nitrate combustion and Pechini methods. These plasma-synthesized powders are readily reproducible. Their individual particle sizes and distributions are independent of their composition.

*Corresponding author. Tel.: +1-819-821-7093; fax: +1-819-821-8017. E-mail address: Gessie.Brisard@USherbrooke.ca (G. Brisard).

Keywords

Induction plasma synthesis, nanoparticles, ceramic powders, SOFC, perovskite cathode materials

1. Introduction

Recently, nanotechnology has become one of the most important and exciting fields in the forefront of many sciences and technologies. It is widely felt that nanotechnology will be at the “leading edge” of the next industrial revolution [1]. Ceramic nanopowders demonstrate improved or unique characteristics in comparison with conventional ceramic materials. The method of synthesis for nanoscale particles has received considerable attention because of the potential for the fabrication of new materials possessing unique properties. These novel properties and the numerous applications for nanophase materials, especially with respect to ceramic nanopowders, have attracted many scientists and engineers to invent and explore the applications of the now many ceramic nanoparticle preparation methods. Plasma synthesis is one of them.

Being based on oxide-ion conducting electrolytes, solid oxide fuel cells (SOFCs) offer a clean and low-pollution level technology to electrochemically generate electricity at high efficiencies, and are thus very promising energy conversion systems. The fabrication of SOFC components and cells have, to the present, been conducted through a series of sintering processes that are both time consuming and costly. To solve these problems, many efforts are being made to develop a number of new techniques. Among them, as an effective and relatively inexpensive process (no intermediate sintering process or post-treatment, and easy scale-up to mass production) for fabrication of porous and dense thin metal oxides films, thermal plasma technology is a promising and innovative technology, capable of being applied to the development of novel SOFCs [2].

In this paper, nanopowders of SOFC cathode materials ($La_{0.8}Sr_{0.2}MnO_{3-\delta}$, $La_{0.8}Sr_{0.2}FeO_{3-\delta}$ and $La_{0.8}Sr_{0.2}CoO_{3-\delta}$) synthesized by induction plasma technique is described. For comparison purposes, their structure, morphology, and particle size distributions were determined and compared with their counterparts, as prepared by the previously mentioned Pechini [3] or glycine-nitrate combustion (GNC) techniques [4-6].

2. Experimental

2.1. Powder synthesis methods of various cathode materials

2.1.1. Induction plasma technique

Powders of the perovskites $La_{0.8}Sr_{0.2}MnO_{3-\delta}$, $La_{0.8}Sr_{0.2}FeO_{3-\delta}$ and $La_{0.8}Sr_{0.2}CoO_{3-\delta}$, were synthesized by the induction plasma technique from corresponding metal nitrate solutions.
The stoichiometric ratio metal nitrates of $La_{0.8}Sr_{0.2}MO_{3-\delta}$ (M= Mn, Fe or Co) were dissolved to obtain a concentration of 1.1 M solution. Glycine was added to the solution at a concentration of 1.45 M.

The induction plasma synthesis technique was used for production of the $La_{0.8}Sr_{0.2}MnO_3$, $La_{0.8}Sr_{0.2}CoO_3$ and $La_{0.8}Sr_{0.2}FeO_3$ powders. Figure 1 shows a scheme of the induction plasma system. The atomization probe was used to inject the atomization gas (Ar) and the nitrate metal solution. In this system, the plasma was generated by means of a copper induction coil included in the torch body, as shown in Figure 2. The plasma torch was a TEKNA PL50 unit, the coil of which was connected to a LEPEL HF power generator. The plasma jet was formed inside the torch by ionization of input Ar and O_2. Argon, as the central gas and oxygen, as the sheath gas are supplied via the upper part of the torch body and they are initially separated by a concentric quartz tube.
The induction plasma synthesis was performed under conditions of low pressure (75 Torr), input power of 35 kW, and an argon flow rate of 20 l/min as the central gas. In addition, there was a 90 l/min flow rate of oxygen as the sheath gas and 35 l/min of argon as the probe gas. Metal nitrate solution was pumped into the torch at a rate of 15 ml/min. At the end of a synthesis run, the plasma was shut down and the generated powders were recovered from the surfaces of the double walled reactor and the heat exchanger.

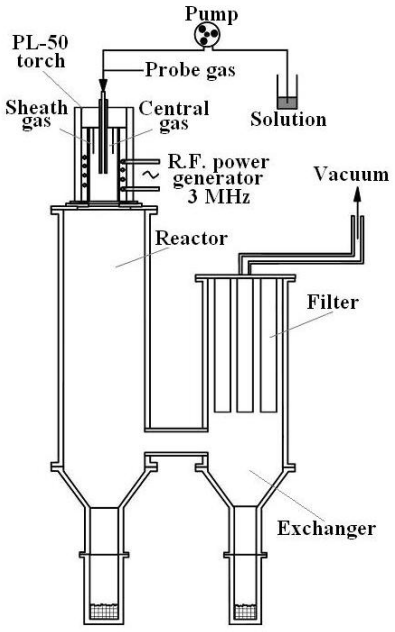

Figure 1: Schematic of nanopowder plasma synthesis system

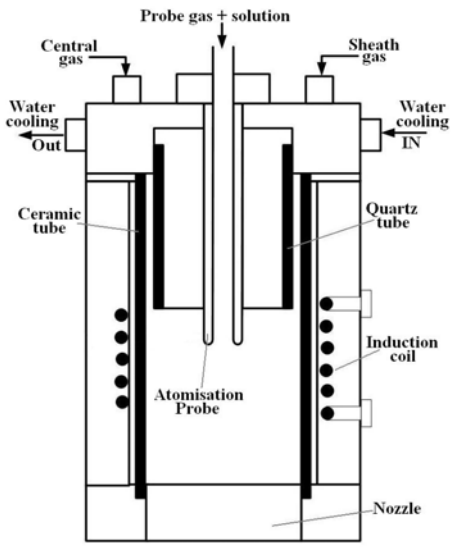

Figure 2: Schematic details of the plasma torch and the atomization probe

2.1.2. Pechini and glycine-nitrate combustion methods

In order to compare the structure, morphology and particle size distribution of plasma-synthesized cathode materials, the Pechini and glycine-nitrate combustion methods have been used to prepare the counterparts of the cathode powders.

A glycine-nitrate combustion technique [4-6] was employed for synthesis of the $La_{0.8}Sr_{0.2}FeO_{3-\delta}$ and $La_{0.9}Sr_{0.1}MnO_{3-\delta}$ powders. The desired molar ratio of La, Sr, Mn or Fe nitrates (as the nitrate salts) were dissolved in water to provide one mole of the final perovskite. 2 moles of glycine were added to this mixture as a chelating agent and aid combustion. Water was subsequently evaporated from the resulting solution using a hot plate maintained at 95 °C until the 'onset of combustion' was achieved. Powders so synthesized were subsequently calcinated at 800ºC for 4 hours.

The Pechini method [7] was employed for the synthesis of the $La_{0.9}Sr_{0.1}MnO_{3-\delta}$ and $La_{0.9}Sr_{0.1}Mn_{0.7}Fe_{0.3}O_{3-\delta}$ powders. Nitrate salts of La, Sr, Fe and/or Mn were dissolved in water in the required molar ratios, equimolar amounts of ethylene glycol and citric acid were then added to the metal ion solutions. These were then heated at 80 ^{o}C to 100 °C for 2 to 3 hours to induce polymerization. After this step, the residue was "charred" at 300 °C for 2 hours and calcinated at 800 °C for 4 hours.

3. Results and discussion

3.1. Morphologies of the synthesized powders

Figure 3 shows high resolution SEM micrographs of powders ($La_{0.8}Sr_{0.2}MnO_{3-\delta}$,) synthesized by the plasma process. All particles shown in this micrograph are close to being globular in shape. Figure 4 is a SEM micrograph of $La_{0.8}Sr_{0.2}FeO_{3-\delta}$ powders, as formed by the glycine-nitrate combustion technique, in which the powder's skeletal structure is illustrated. These powders are very porous, due to the nature of the combustion process. The powders, as formed by the Pechini method also have a porous structure.

Figure 3: SEM micrographs of the plasma synthesized powders: ($La_{0.8}Sr_{0.2}MnO_{3-\delta}$)

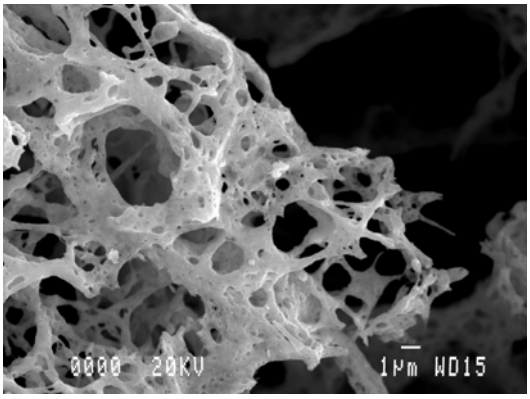

Figure 4: SEM micrographs of powders synthesized by glycine-nitrate combustion technique ($La_{0.8}Sr_{0.2}FeO_{3-\delta}$)

3.2. Particle size distributions and specific surface areas

Figure 5 shows a typical particle sizes distribution of the plasma-synthesized powders. The distribution of particle sizes is independent of their composition. Most of the particles of these plasma-synthesized powders have sizes of 63 nm in average. The distribution of particle size of chemically synthesized powders is shown in Figure 6. The particle sizes of the chemically synthesized powders are bigger than the plasma-synthesized powders (120 nm).

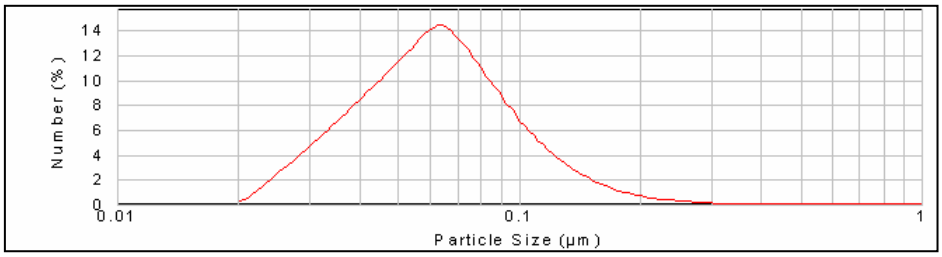

Figure 5: Distribution of particle size of powders formed by plasma synthesis

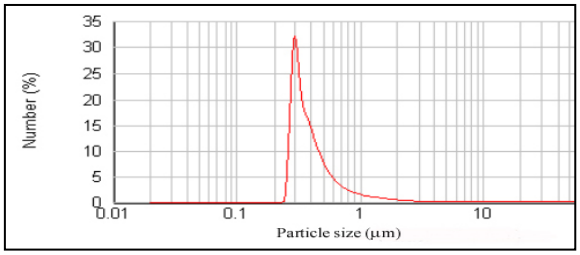

Figure 6: Distribution of particle size of powders formed by glycine-nitrate combustion technique

Table 2 lists the BET specific surface areas of some cathode powders, as synthesized by the three methods. BET specific surface areas of plasma synthesized $La_{0.8}Sr_{0.2}MnO_{3-\delta}$, $La_{0.8}Sr_{0.2}FeO_{3-\delta}$ and $La_{0.8}Sr_{0.2}CoO_{3-\delta}$ nanopowders are the same, about 26 m^2/g. This is approx. twice that of $La_{0.8}Sr_{0.2}FeO_{3-\delta}$ powders, prepared by the glycine-nitrate combustion method and $La_{0.9}Sr_{0.1}MnO_{3-\delta}$ powders, synthesized by the Pechini method. As a result, plasma-synthesized powders have the smallest particle size and the largest BET specific surface area values found in this paper.

Table 2. BET specific surface areas for some cathode powders.

Synthesis methods	Compositions	BET specific surface area (m^2/g)
Plasma synthesis	$La_{0.8}Sr_{0.2}MnO_{3-\delta}$	27
	$La_{0.8}Sr_{0.2}FeO_{3-\delta}$	25
	$La_{0.8}Sr_{0.2}CoO_{3-\delta}$	26
Glycine-nitrate combustion	$La_{0.8}Sr_{0.2}FeO_{3-\delta}$	14
Pechini method	$La_{0.9}Sr_{0.1}MnO_{3-\delta}$	13

3.3. Structures of the synthesized powders

Figure 7 shows a typical X-ray diffraction pattern of ceramic powders formed by plasma synthesis or chemical synthesis technique. All peaks in this figure are labeled by the Miller index of the perovskite The X-ray diffraction patterns of the synthesized perovskite powders have been compared to standards and the crystal systems obtained are orthorhombic for $La_{0.8}Sr_{0.2}FeO_3$, monoclinic for $La_{0.8}Sr_{0.2}MnO_{3-\delta}$, and rhombohedric for $La_{0.8}Sr_{0.2}CoO_{3-x}$ and $La_{0.9}Sr_{0.1}MnO_3$. However, plasma-synthesized $La_{0.8}Sr_{0.2}CoO_{3-\delta}$ powders are a pure perovskite phase, indicating that it is possible to directly synthesize pure perovskite cathode composition materials, as nanosized particles by the induction plasma synthesis technique. Both GNC and Pechini methods can also produce perovskite cathode materials without significant content of impurities.

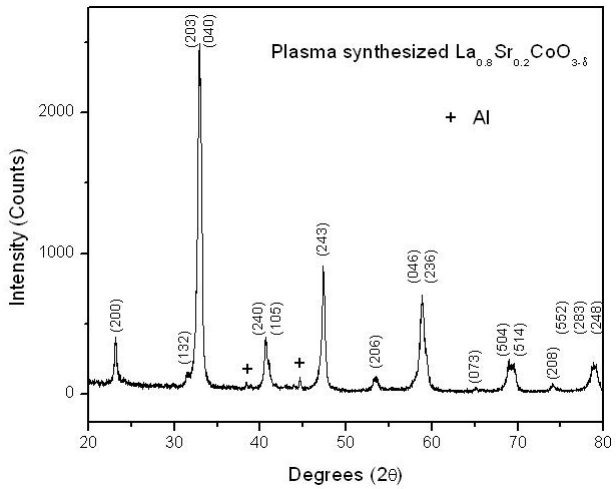

Figure 7: Typical X-ray diffraction patterns of plasma and chemically synthesized powders ($La_{0.8}Sr_{0.2}CoO_{3-\delta}$)

4. Conclusions

Through the use of three different synthesis methods (induction plasma technique, Pechini method, and Glycine-nitrate combustion technique), the nanopowders of target SOFC perovskite cathode materials ($La_{0.8}Sr_{0.2}MnO_{3-\delta}$**,** $La_{0.8}Sr_{0.2}FeO_{3-\delta}$ and $La_{0.8}Sr_{0.2}CoO_{3-\delta}$) were successfully produced with accurate stoichiometry. Most particles of the plasma-synthesized powders are around 63 nm in size. The plasma-synthesized powders are almost globular in shape and their BET specific surface areas are about 26 m^2/g, i.e. about 2 twice that of powders prepared by the glycine-nitrate combustion and Pechini methods. The plasma-synthesized powders are fully reproducible in composition and sizing and are not agglomerated. Particle size and size distribution are independent of particle composition. The next step in this project will be the combination synthesis and the spray projection of these powders onto an electrolyte substrate to form a good electronic and ionic conducting interface between the electrolyte and the cathode. The plasma projection of ceramic nanopowders is a time efficient process. The most immediate practical application lies in the fabrication of SOFC fuel cells, to be performed by the plasma spray projection technique.

References

1. B. Bhushan, introduction, *Springer Handbook of Nanotechnology*, Springer-Verlag, Berlin, New York, 2004, pp. 1

2. Gitzhofer, F., Boulos, M., Heberlein, J., Henne, R., Ishigaki, T., and Yoshida, T., "Integrated fabrication processes for solid-oxide fuel cells using thermal plasma spray technology," *Mrs Bulletin*, Vol. 25, No. 7, 2000.

3. M.P. Pechini, N Adams US Patent 3,330,697 (1967)

4. Chick, L. A., Pederson, L. R., Maupin, G. D., Bates, J. L., Thomas, L. E., and Exarhos, G. J., "Glycine Nitrate Combustion Synthesis of Oxide Ceramic Powders," *Materials Letters*, Vol. 10, No. 1-2, 1990.

5. Hess, N. J., Maupin, G. D., Chick, L. A., Sunberg, D. S., Mccreedy, D. E., and Armstrong, T. R., "Synthesis and Crystallization of Yttrium-Aluminum-Garnet and Related-Compounds," *Journal of Materials Science*, Vol. 29, No. 7, 1994.

6. Murphy, M. W., Armstrong, T. R., and Smith, P. A., "Tape casting of lanthanum chromite," *Journal of the American Ceramic Society*, Vol. 80, No. 1, 1997.

7. Choi, J. H., Jang, J. H., and Oh, S. M., "Microstructure and cathodic performance of $La_{0.9}Sr_{0.1}MnO_3$/yttria stabilized zirconia composite electrodes," *Electrochimica Acta*, Vol. 46, No. 6, 2001.

Non-Catalytic Direct Amination of Carbon Double Bond Using Atmospheric Non-Thermal Plasma

H.Ito, Y.Suga and H.Sekiguchi
Department of Chemical Engineering, Tokyo Institute of Technology, Tokyo, Japan

Abstract

This study investigated the non-catalytic amination of 1-decene using atmospheric pressure glow discharge (APGD). The reaction was carried out by exposing ammonia plasma jet to the substrate of 1-decene. The experimental results indicated that the productions of 1-decylamine and 2-decylamine were identified. This study suggested the APGD was attractive for the amination of organic compounds having carbon double bond under atmospheric pressure without catalysts.

Key words,

Atmospheric non-thermal plasma, Amination, Ammonia, 1-decene

1. Introduction

Plasma has been widely used in processing technique such as welding, etching, thin film formation as well as in the field of energy and environment issues. However, in chemical synthesis, most of them have not been put into practical use except ozone synthesis which has been done for a long time. One of the reasons is that consecutive reactions take place because the products formed in the plasma are also activated by the plasma, resulting in low selectivities of the products.

The development of atmospheric pressure glow discharge (APGD) in recent years has made it possible to generate plasma including electron, ion and radical at room temperature under atmospheric pressure. The APGD can be formed with a simple equipment and has outstanding characteristics, for example, reactor material is hardly restricted by lower pressure and higher temperature, and it can be exposed directly on the surface of liquid and solid having temperature-sensitive properties. Heterogeneous reactions of the plasma with liquid surfaces are expected to have higher selectivity than in gas phase homogeneous reactions because rapid quenching of hot primary products is achieved and consecutive reactions are suppressed due to continuous elimination of them from the surface layer. These characteristics of APGD lead to the creation of new chemical synthesis tool. We have already achieved the epoxidation of carbon double bond by exposing oxygen plasma directly on liquid olefin without catalysts [1]. The study expected a possibility on different reactions using other plasma gas or liquid. Therefore, in this research, mixture of argon and ammonia was used as a plasma gas for direct production of amine with olefin. Some researches on plasma amination have been reported using silence discharge [2-5]. Being different from these researches, our technique seems to have an advantage in no decomposition and no fragmentation of the substrate since the high energy electron does not impact the substrate.

There are a lot of ways to produce amine and currently main methods are (1) hydrogenation of nitrile for alkylamine having carbon number below 5 (R-CN $\rightarrow$ RCH_2NH_2), and (2) amination of alcohol for alkylamine with carbon number over 5 (R-OH $\rightarrow$ RNH_2). The proposed amination technique dose not require catalysts and other additives, therefore, it is expected to be a simple method as compared with the general ways mentioned above.

2. Experimental

The experimental apparatus shown in Fig.1 is almost the same as reported in [1]. The plasma gas was a mixture of argon (Ar) and ammonia (NH_3). The discharge was generated between a tungsten rod at center of quartz tube (high voltage) and aluminum foil on outer wall (ground) by applying rf power (770kHz, 20W). Quartz tube was used as a dielectric material. The electrode configuration is shown in Fig.2 with its dimension. 1-decene ($C_{10}H_{20}$) was chosen as a model of olefin having a straight carbon chain with relatively high boiling point. The batch operation was performed in which the plasma was irradiated to 1-decene as illustrated in Fig.1. The reactant was stirred and its temperature was kept constant with a thermostat. The products in gas and liquid phases were analyzed by gas chromatography (GC) and gas chromatography mass spectroscopy (GCMS). The products including 1-decylamine, 2-decylamine and decane were observed in both exhaust gas and liquid remaining in the reactor in the experiment. Hence conversion, products yield and selectivity are defined as followed:

$$Conversion = \frac{C_{g,i} \times F \times t + C_{l,i} \times V}{n_{init,decene}} \quad , i=1\text{-}decene \tag{1}$$

$$Yield = \frac{C_{g,i} \times F \times t + C_{l,i} \times V}{n_{init,decene}} \quad , i=1\text{-}decylamine,\ 2\text{-}decylamine,\ decane \tag{2}$$

$$Selectivity = \frac{Yield}{Conversion} \tag{3}$$

where $C_{g,i}$ and $C_{l,i}$ respectively indicate the concentrations of species i in the exhaust gas and liquid remaining in the reactor, F represents the volume feed rate, V means the volume of the samples after the experiments, and $n_{init.\ decene}$ is the amount of initial 1-decene. The experiments were performed with changing reaction time, distance between the tip of the tube and the liquid surface and flow rates of NH_3 and Ar as summarized in Table 1.

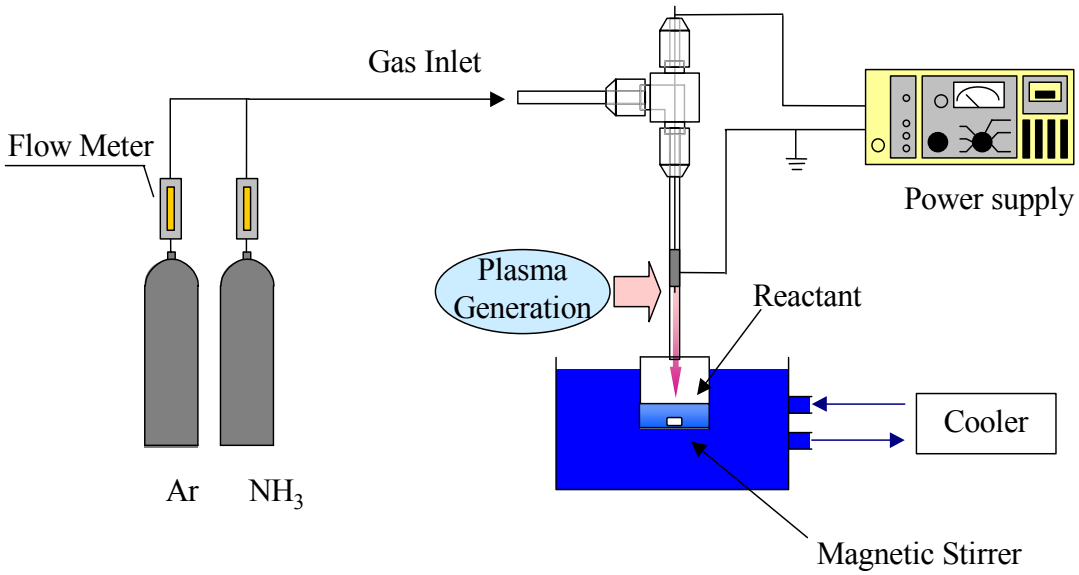

Fig.1 Experimental apparatus

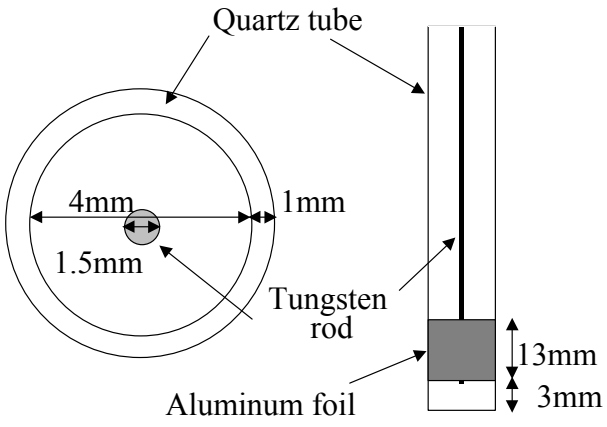

Fig.2 Detail of plasma jet

Table1 Experimental conditions

Sample Volume	2ml
Discharge Power	20 W
Discharge Frequency	770kHz
Thermostat Temperture	-6℃
Reaction Time	0 – 130 min
Ar Flow Rate	3.0 – 4.5 l/min
NH_3 Flow Rate	10 – 90 ml/min
Exposing Distance	1 – 11 mm

3. Results and Discussion

The productions of 1-decylamine, 2-decylamine and decane were clearly observed in all the experimental conditions. Therefore we carried out quantitative analysis on these three products. Many slight peaks were also detected, one of which was assigned to dimerization of 1-decene, however, we couldn't identify them clearly.

3.1 Dependence of reaction time

Figures 3 and 4 show the time dependence of 1-decene conversion and the products yield, respectively. The conversion and products yield increased with reaction time and these increases drew slack curves. This was because the evaporation of liquid 1-decene lengthened the distance between the plasma and reactant surface, resulting in the reduction of the reactivity. As shown in Fig.4, decane was most produced. The production of 2-decylamine was dominant as compared with 1-decylamine. Figure 5 shows the time dependence of the selectivity. The selectivities of decane and 2-decylamine were about 50% and 20% respectively, and they hardly changed with the reaction time elapsed.

3.2 Dependence of distance between the tip of the tube and liquid surface

Figure 6 shows the effect of the distance between the tip of the tube and the liquid surface on the products yield. All the yields decreased gradually as distance became longer. It was expected that active species generated in the plasma were diminished by collision each other and irradiation itself when it was distant from discharge area. This phenomenon was also observed in Figs.3 and 4 as mentioned above.

3.3 Dependence of Ar flow rate

The effects of Ar flow rate on the products yield are shown in Fig.7. The products yield increased with Ar flow rate. The increase in Ar flow rate extended the plasma jet, which increased the flux of active species to the liquid surface. The dilution by Ar might also promote the dissociation of NH_3.

3.4 Dependence of NH_3 flow rate

The effects of NH_3 flow rate on the products yield are shown in Fig.8. The products yield decreased with increasing NH_3 flow rate. The plasma jet became shorter as ammonia flow rate increased. These results suggested that the flux of active species might be reduced even if ammonia flow rate increased.

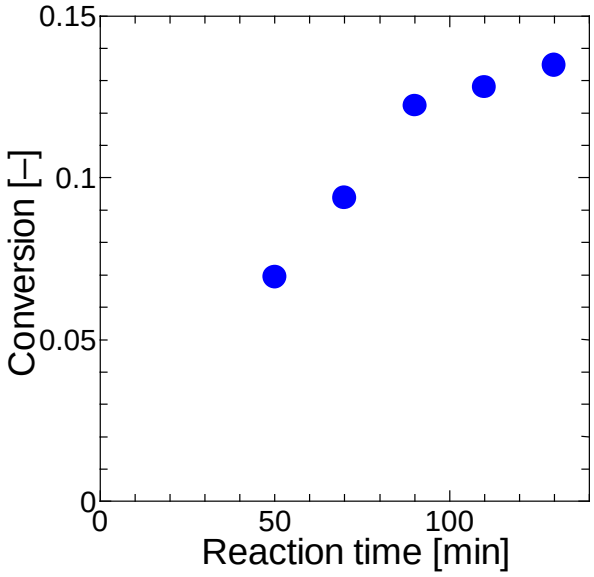

Fig.3 The effect of reaction time on the conversion;
Ar = 3.0l/min, NH_3 = 30ml/min, distance = 5mm.

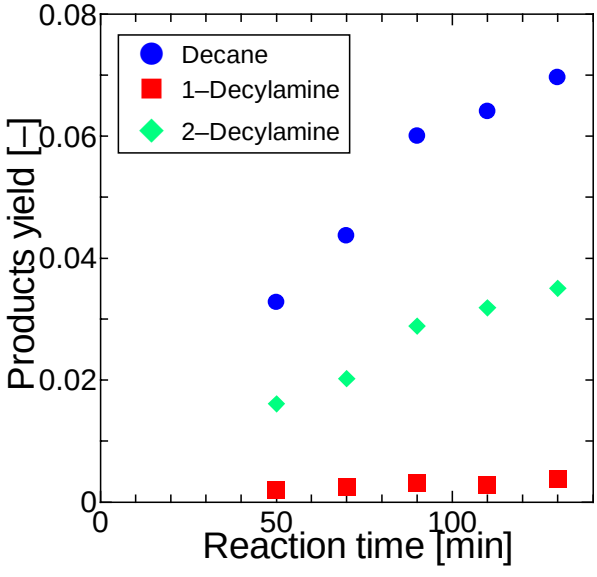

Fig.4 Effects of reaction time on the products;
Ar = 3.0l/min, NH_3 = 30ml/min, distance = 5mm.

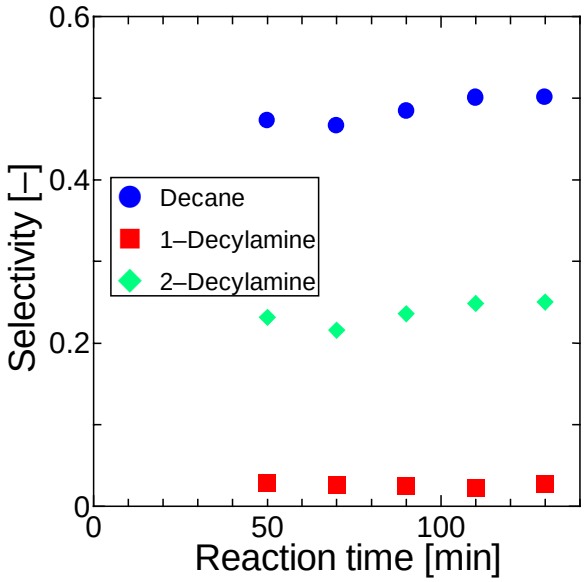

Fig.5 Effects of reaction time on the selectivity;
Ar = 3.0l/min, NH_3 = 30ml/min, distance = 5mm.

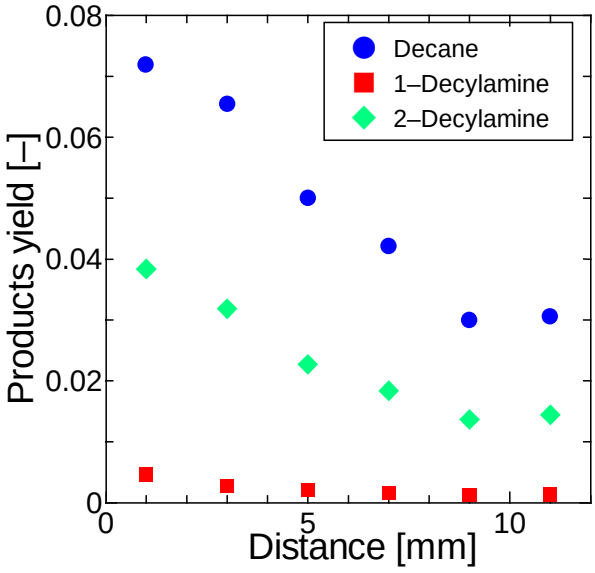

Fig.6 Effects of distance on the products yield;
Ar = 3.5l/min, NH_3 = 30ml/min, reaction time = 70min.

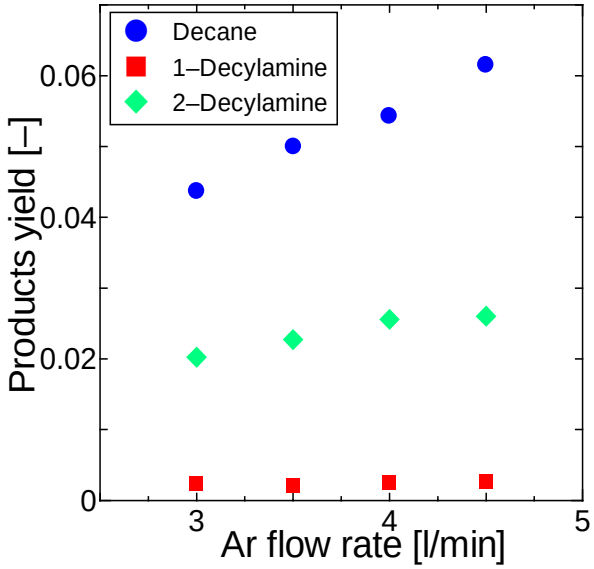

Fig.7 Effects of Ar flow rate on the products yield;
NH_3 = 30ml/min, reaction time = 70min, distance = 5mm.

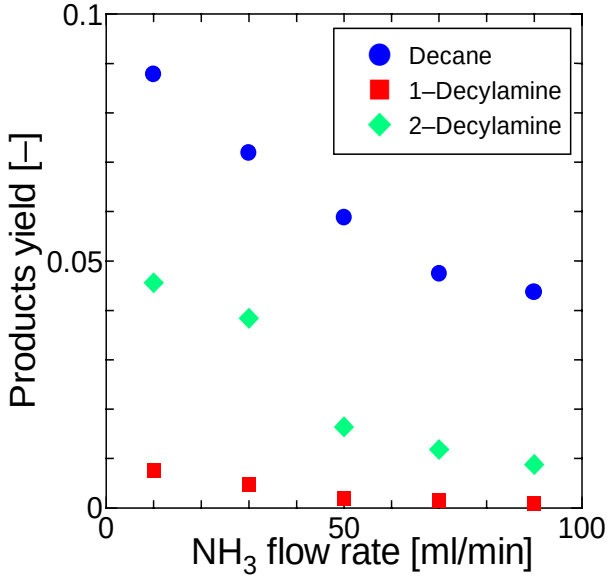

Fig.8 Effects of NH_3 flow rate on the products yield;
Ar = 3.5l/min, reaction time = 70min, distance = 1mm.

3.5 Reaction mechanism

It is expected that the reactions at least occur by two steps because two substituents of carbon double bond would be added to form the amine. The following reaction scheme in Fig.9(a)(b) is proposed to explain the plasma amination where the key radicals are both H and NH_2 generated by APGD:

(a) Hydrogen addition followed by NH_2 attachment

In the case of the addition reaction of H radical to the carbon double bond at the first step, H can be added to the secondary or terminal carbon of the olefin, resulting in forming the primary and secondary radical intermediates, respectively. However, since the secondary radical intermediate is more stable than primary one, the secondary intermediate is produced dominantly. Consecutive addition reactions with H and NH_2 give decane and 2-decylamine, respectively.

(b) NH_2 addition followed by H attachment

When NH_2 radical is added at the first step, similarly to the above case, the secondary radical intermediate is more produced than the primary one. The reaction of the intermediate with H produces 1- decylamine dominantly, hence, 1-decylamine is likely formed in this case. If NH_2 reacts with the intermediate, 1,2-didecylamine will be produced. However, we did not detect its production in the experiment.

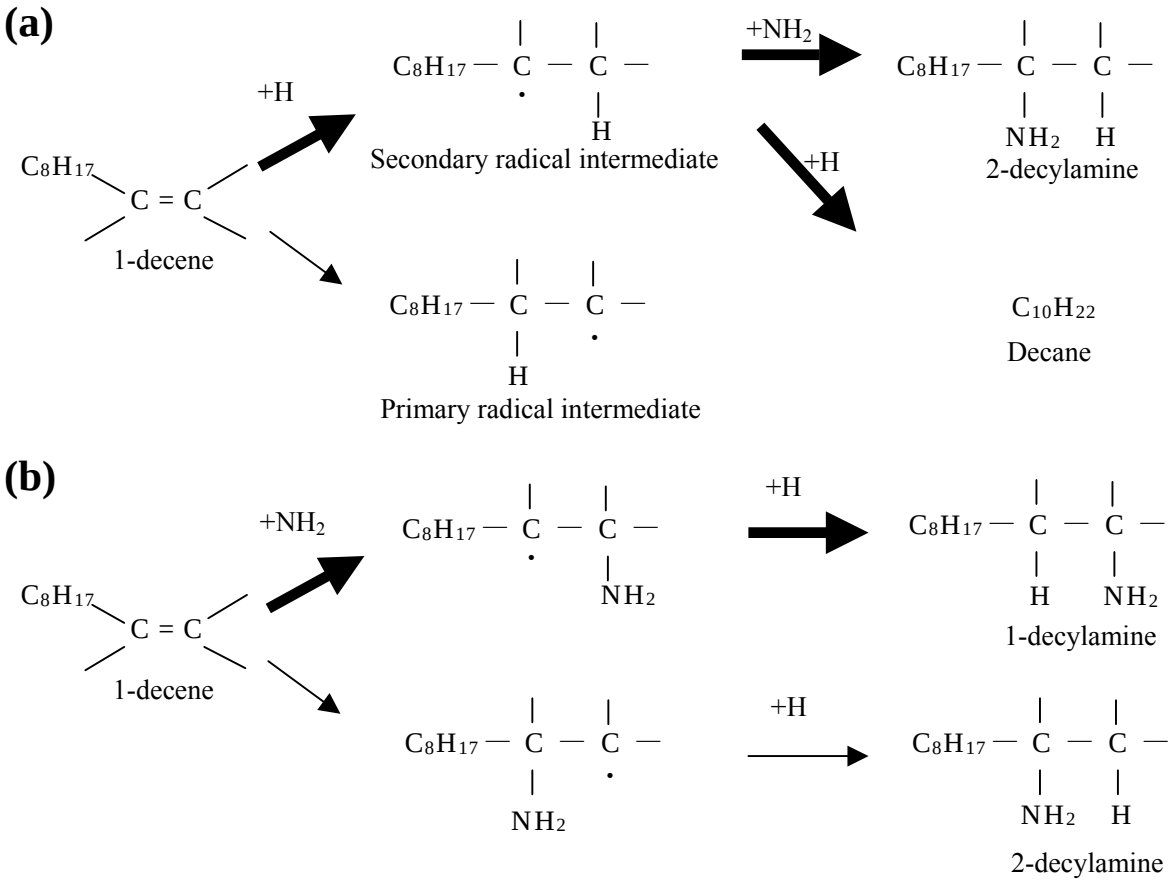

Fig.9 Reaction mechanism proposed;
(a) Hydrogen addition followed by NH_2 attachment,
(b) NH_2 addition followed by H attachment.

Considering the yields of the three products explained above, the concentration of H was higher than that of NH_2 in the plasma. Furthermore, the reactivity of H might be higher as well. Since other radicals such as NH and N would exist in the plasma, further discussion on the mechanism should be done with precious investigations of the plasma and by-products.

From the results of the present study as well as the previous one, the APGD could carry out the addition reactions to carbon double bond without catalyst in two different gases of O_2 and NH_3. Therefore the APGD would be a powerful tool for organic synthesis.

4. Conclusion

The APGD was applied to the non-catalytic amination of 1-decene. The results showed that the amination was successful. The simple reaction mechanism was proposed with the experimental data. This study suggested the possibility of a new organic synthesis technique using APGD.

Reference

[1] Y.Suga and H.Sekiguchi, 2004 7th APCPST 17th SPSM,p344(300-344)
[2] T.Matuda, K.Odo and K,Sugino, 1958 Nippon Kagaku Zasshi,79.p324
[3] K.Sugino and E,Inoue, 1949 J.soc.org.Synth.Chem.Jpn 7.p198
[4] U.Mueller and A.Greiner, 1996 Chem.Tech.18 p327
[5] J.Darleson, St Charles and William.F.Yates, 1970 Uni.Sta.Pat.Off 3518178

DIRECT SYNTHESIS OF METHANOL FROM WATER VAPOR AND METHANE THROUGH DIELECTRIC-BARRIER DISCHARGE

Baowei WANG*, Hua SONG, Genhui XU

Key Laboratory of Green Chemical Technology of State Education Ministry, School of Chemical and Technology, Tianjin University, Tianjin 300072, People's Republic of China

Abstract: The direct synthesis of methanol from methane and water vapor mixtures in a continuous flow reactor through dielectric-barrier discharge of non-equilibrium plasma reaction was studied. Technology conditions including flow rate of reactants, diameter of inner electrode, temperature of water, discharge voltage, dilution ratio and length of outer electrode were investigated through orthogonal experiment. The results showed the selectivity to methanol is as high as 50% and the methanol yield is more than 10% under optimal conditions.
Keywords: plasma; methane; water; methanol; dielectric-barrier discharge.

1 Introduction

Direct synthesis of methanol from methane and water vapor mixture has a high possibility to realize a highly sophisticated energy utilization system with energy regeneration. Nevertheless, this process can never occur by conversional thermo-chemical methods due to the large increase of Gibbs free energy [1]. Direct conversion of water and methane into useful chemicals and clean energy remains to be a big challenge in catalysis in the 21st century [2-5]. Although a large number of studies have contributed to the direct decomposition of conversion of methane in the past decade and many new methods and catalysts have been developed for the direct activation and conversion of methane, there is still no direct process with commercial viability at this moment [6].

In this investigation, direct synthesis methanol from methane and water vapor mixture has been successfully realized via a clean, low power, low-temperature and non-equilibrium plasma trans-normal chemical reaction developed a novel plasma reactor with dielectric-barrier discharge at room temperature and under atmospheric pressure. The effects of flow rate of reactants, the diameter of inner electrode, the temperature of water, the peak voltage, the length of outer electrode and the ratio of methane with water vapor and dilution gas on the methanol formation characteristics has been investigated.

2 Experimental

2.1 Experimental apparatus

Fig.1 shows a reactor and schematic of experimental apparatus. The plasma reactor is a concentric cylinder with an inner stainless steel electrode and an outer electrode of copper foil around a quartz glass thin glass. The length of reactor is 300mm, and its diameter 19.4mm; the wall of reactor is 2.3mm. A high-voltage triangular wave is applied between the inner stainless steel electrode and an outer electrode of copper foil. Power consumption by the plasma reactor is between 5 and 40W; the Ljssajous figure method is used for measurement. A Tektronix TDS 210 digital real-time oscilloscope（Tektronix 2440,500M）with a Tektronix P6015A high voltage probe monitors is used to measure the discharge voltages. The flow rates of methane and dilution gas argon/hydrogen were regulated by mass flow controllers (Jianzhong Instrument, Model D07). The water was heated up through electrical power. The temperature of water was controlled with WMZK-01 temperature display and controller. The feed gases were mixed and then downward introduced a reactor for all experiments.

The exhaust gases were cooled with ice and then analyzed by gas chromatograph (HP Agilent 4890D) on-line. A thermal conductivity detector (TCD) with H_2 carrier gas was used. The liquid products were detected with GC-MS (HP5971A). MSC200 quadrupole mass spectrograph (Switzerland Balzers Quadstar^{TM}) is used for the qualitative detection of hydrocarbon and hydrocarbons produced on line. The analytical condition is EI source, measuring range 0~200amu, electron multiple detector, vacuum chamber press 1.2×10^{-5}Pa, ion-current

* E-mail: wangbw@tju.edu.cn

1.0mA, scan speed 5 amu·s^{-1}, resolution 84.

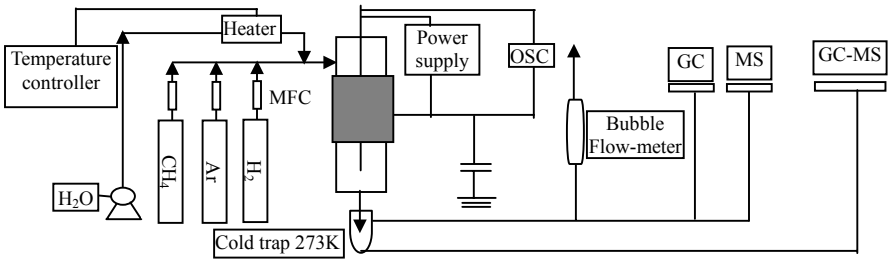

Fig.1 Plasma reactor and measurement apparatus

2.2 Experimental method

A one-pass yield is described as products generated without recycling and separation of initial feedstock. The reaction lasts out one hour at every data points. The exhausted gases were analyzed every six minutes. Thus, every data point was analyzed ten times. The average values were used calculated. The liquid products were analyzed every one-hour. Methane conversion, product selectivity, yield, and ratio of dilution are defined as follows.

%conversion of CH_4=[1- $M_{CH4}\mid_{outlet}$/($M_{CH4}\mid_{outlet}$+$M_{CH3OH}\mid_{outlet}$+2$M_{C2H4}\mid_{outlet}$+$M_{C2H6}\mid_{outlet}$+$M_{C2H2}\mid_{outlet}$)]

%selectivity of methanol=$M_{CH3OH}\mid_{outlet}$/($M_{CH3OH}\mid_{outlet}$+2$M_{C2H4}\mid_{outlet}$+$M_{C2H6}\mid_{outlet}$+$M_{C2H2}\mid_{outlet}$)

%yield of methanol =selectivity×%conversion of methane

DR(ratio of dilution)= $F_{total}\mid_{inlet}/F_{CH4}\mid_{inlet}$

Those results were compared to the total weight of liquid products and changes in total gas flow for consistency. The carbon balance was consistent with 9% error throughout the experiment.

This experimental factor is rather more, such as flow rate of reactants (F), ratio of dilution gas (DR), discharge voltage (U), temperature of water (T), inner electrode diameter (d), length of outer electrode (L). The distributing of data point will be equality if the whole arrange in pairs method was used. However, suppose that the experimental factor have six and three levels of every factor, the needed experimental times will be reach 2187 times. The orthogonal experiment method was selected in order reduce the experimental times. The main purpose of this experiment is that the technology parameters were optimized and the selectivity/yield of methanol can be improved.

The factors and levels used in this experiment are shown in table 2-1. First, the interaction of all factors was not taken into account. Thus, the orthogonal table $L_{16}(4^4\times2^3)$ can be used. Its table head designed is shown in 2-2.

Table 2-1 Experimental factors and level

Factor Symbol	Flow/ml/min F	Ratio of dilution DR	Voltage/kV U	Inner diameter s /mm d	Outer length/mm L	H_2O temp./℃ T
Level						
1	17.26	1	40	0.7	34.5	80
2	23.01	2	45	2.0	69.0	95
3	28.76	3	50	5.0		
4	34.51	4	55	12.0		

Table 2-2 $L_{16}(4^4\times2^3)$ table head designed

Number column	1	2	3	4	5	6	7
Symbol	F	DR	U	d	L	Empty column	T

3 Results and discussion

The experimental results are listed in table 3-1, which were obtained from the orthogonal table $L_{16}(4^4\times2^3)$.

Table 2-3 tells us that the less of selectivity and yield of methanol, the more of total feedstock flow rate. That is to say, the selectivity and yield of methanol is better when the residence time is longer. The reason is that it entrains water vapor increases when total feedstock flow rate increases and other conditions are constant. Water is a type elimination ionization reagent, the energies of absorbed by water vapor increases for its absorb

electrons character; these lead the amount of dissociative water vapor to reduce and the selectivity of methanol decreases if the input energy is not enhanced. Meanwhile, the residence time decreases, the conversion of methane also decreases, so the yield of methanol decreases.

Table 3-1 the $L_{16}(4^4 \times 2^3)$ orthogonal experimental results

No. column	1	2	3	4	5	6	7	Experimental results		
Symbol	F	DR	U	d	L	e	T	X%	S/%	Y/%
No. experiment										
1	1	1	1	1	1		1	25.46	0	0
2	1	2	2	2	1		2	33.42	4.04	1.35
3	1	3	3	3	2		2	24.25	16.00	3.88
4	1	4	4	4	2		1	24.87	64.78	16.11
5	2	1	2	3	2		1	20.68	0	0
6	2	2	1	4	2		2	16.98	18.73	3.18
7	2	3	4	1	1		2	29.93	31.74	9.50
8	2	4	3	2	1		1	31.01	13.77	4.27
9	3	1	3	4	1		2	19.39	4.59	0.89
10	3	2	4	3	1		1	34.79	4.11	1.43
11	3	3	1	2	2		1	25.55	2.74	0.70
12	3	4	2	1	2		2	24.58	8.91	2.19
13	4	1	4	2	2		2	32.17	1.15	0.37
14	4	2	3	1	2		1	35.47	1.72	0.61
15	4	3	2	4	1		1	15.01	8.53	1.28
16	4	4	1	3	1		2	19.27	1.09	0.21

We can see from table 3-1, the selectivity of methanol increases when the ratio of dilution is increasing. The probably reason is that the concentration of argon gas in feedstock gases increases when the ratio is increasing and other conditions are constant. This indicates argon can promote water and methane to dissociate.

Table 3-1 also indicates that the selectivity and yield of methanol increases when the discharge voltage is increasing. It suggests that the OH* and O* produced from water are propitious to synthesis methanol when the degree of dissociation of water remarkably increases after the discharge voltage is more than 50kV.

We can see from table 3-1, for the inner electrodes, the thickest hollow stainless steel tube is best, the filamentary inner electrode is better, the solid stainless steel tube with the diameter 2mm and 5mm, respectively, are last of all. This indicates the inner electrode surface have no effect on the yield and selectivity of methanol.

Table 3-1 suggests that the selectivity of methanol and yield increases with the length of outer electrode extending. Therefore, the levels of outer electrode should be increase and ulteriorly studied. The reason is that the effective plasma zone extends when the length of outer electrode is extending and other condition are constant.

Table 3-1 also suggests that the selectivity and yield of methanol is better under the temperature 80℃ than that under 95℃. The reason is that it entrains water vapor increases when the temperature of water increases. It also indicated the levels of the water temperature should be increase.

The experimental data listed in table 3-1 were obtained without taking into account the interaction of all factors. Therefore, in the next experimental process, the interactions of some factors have to be considered. For interaction of the diameter of inner electrode with total feedstock flow rate, they each can influence the residence time. In addition, the levels of the temperature of water and the length of outer ought to be increased. Thus, the orthogonal table $L_{27}(3^{13})$ was selected to used. The factors and levels are shown in table 3-2. Its table head designed is shown in 3-3.

Table 3-2 Experimental factors and level

Factor Symbol	Flow/ml/min F	Ratio of dilution DR	Voltage/kV U	Inner diameter/mm d	Outer length/mm L	H_2O temp./℃ T
Level						
1	17.256	2	45	0.7	34.5	40
2	25.884	3	50	2.0	69.0	60
3	34.512	4	55	12.0	87.0	80

Table 3-3 $L_{27}(3^{13})$ table head designed

Number column	1	2	3	4	5	6	7	8	9	10	11	12	13
Symbol	F	d	$(F\times d)_1$	$(F\times d)_2$	T	$(F\times T)_1$	$(F\times T)_2$	$(T\times d)_1$	U	DR	$(T\times d)_2$	e	L

Table 3-4 the $L_{27}(3^{13})$orthogonal experimental results

Number column	1	2	3	4	5	6	7	8	9	10	11	12	13	Experimental results		
Symbol	F	d	F×d	F×d	T	F×T	F×T	T×d	U	DR	T×d	e	L	X/%	S/%	Y/%
No. experiment																
1	1	1	1	1	1	1	1	1	1	1	1	1	1	35.35	0.54	0.19
2	1	1	1	1	2	2	2	2	2	2	2	2	2	33.83	1.86	0.63
3	1	1	1	1	3	3	3	3	3	3	3	3	3	30.45	10.01	3.05
4	1	2	2	2	1	1	1	2	2	2	3	3	3	32.11	1.20	0.39
5	1	2	2	2	2	2	2	3	3	3	1	1	1	35.48	3.92	1.39
6	1	2	2	2	3	3	3	1	1	1	2	2	2	32.93	3.69	1.21
7	1	3	3	3	1	1	1	3	3	3	2	2	2	32.44	15.02	4.87
8	1	3	3	3	2	2	2	1	1	1	3	3	3	29.04	5.11	1.48
9	1	3	3	3	3	3	3	2	2	2	1	1	1	26.31	8.23	2.17
10	2	1	2	3	1	2	3	1	2	3	1	2	3	29.42	8.99	2.64
11	2	1	2	3	2	3	1	2	3	1	2	3	1	33.72	0.49	0.17
12	2	1	2	3	3	1	2	3	1	2	3	1	2	24.85	1.32	0.33
13	2	2	3	1	1	2	3	2	3	1	3	1	2	34.45	0.66	0.23
14	2	2	3	1	2	3	1	3	1	2	1	2	3	34.00	2.25	0.77
15	2	2	3	1	3	1	2	1	2	3	2	3	1	32.31	4.96	1.60
16	2	3	1	2	1	2	3	3	1	2	2	3	1	24.72	1.61	0.40
17	2	3	1	2	2	3	1	1	2	3	3	1	2	23.41	8.27	1.94
18	2	3	1	2	3	1	2	2	3	1	1	2	3	28.08	5.51	1.55
19	3	1	3	2	1	3	2	1	3	2	1	3	2	32.83	0.85	0.28
20	3	1	3	2	2	1	3	2	1	3	2	1	3	25.62	5.87	1.50
21	3	1	3	2	3	2	1	3	2	1	3	2	1	31.85	0.73	0.23
22	3	2	1	3	1	3	2	2	1	3	3	2	1	27.90	1.07	0.30
23	3	2	1	3	2	1	3	3	2	1	1	3	2	33.66	0.95	0.32
24	3	2	1	3	3	2	1	1	3	2	2	1	3	32.73	3.87	1.27
25	3	3	2	1	1	3	2	3	2	1	2	1	3	27.63	0.43	0.12
26	3	3	2	1	2	1	3	1	3	2	3	2	1	23.52	2.29	0.54
27	3	3	2	1	3	2	1	2	1	3	1	3	2	14.14	31.91	4.51

Table 3-4 tells us that the conversion of methane decreases; the selectivity and yield of methanol first increase and then decrease when the total feedstock flow rate is increasing and other conditions are constant.

Table 3-4 also tells us that that the conversion of methane first increases and then decreases, the selectivity and yield of methanol first decrease and then increase when the diameter of inner electrode is increasing and other conditions are constant.

From table 3-4, we can see that the conversion of methane decreases with the temperature of water increase. The selectivity and yield of methanol hardly increase when the temperature of water changes from 40℃ to 60℃, however, they suddenly move up when the temperature of water changes from 60℃ to 80℃ and other conditions are constant.

From table 3-4, we can see that firstly the conversion of methane linearly rises with the discharge voltage increasing; however, it changes little after the discharge voltage is more than 35kV. The change of the yield of C_2 hydrocarbons (mainly ethane) is not too. The selectivity and yield of methanol firstly linearly rise with the discharge voltage increases, they reach their maximum when the discharge voltage is more than 45k, and then gradually decreases.

Table 3-4 indicates that the conversion of methane linearly rises with the ratio of dilution gas increasing. The reason is that the concentration of methane reduces and argon can promote methane and water activation. Firstly, the selectivity of yield of methanol slowly increases, and then they quickly go up when the ratio of dilution is more than three.

We can see that it is not significant for the conversion of methane when the significance level a=0.25. It suggests that the length of outer electrode has no obviously effect on the conversion of methane. However, when the length of outer electrode changes from to 34.5mm to 87mm, the selectivity and yield of methanol each have a maximum. It suggests that the yield of methanol is mainly controlled by the selectivity of methanol. It also suggests that most methanol can be decomposed if the length of outer electrode is too long.

The significance test was calculated according to the data in table 3-4. The significance test results are shown in table 3-5.

Table 3-5 significance of every factor

Symbol	F	d	F×d	T	U	DR	T×d	L
Significance	4	4	2	3	4	4	2	0
	0.01	0.01	0.10	0.05	0.01	0.01	0.10	0.25

Table 3-5 indicates that it is significant for the total feedstock flow rate, the diameter of inner electrode, the discharge voltage and the ratio of dilution when the significance level is a=0.01. It is significant for the temperature of water when the significance level is a= 0.05. It is significant for the interaction of the total feedstock flow rate with the diameter of inner electrode (F×d) and the interaction of the temperature of water with the diameter of inner electrode (T×d) when the significance level is a= 0.10. However, it is not significant for the length of outer electrode when the significance level is a=0.25.

According to the orthogonal experimental analyses after taking into account the interaction of some factors, the appropriate technology parameters are listed in table 3-6.

Table 3-6 the appropriate technology parameters

Symbol	F	d	T	U	DR	L
unit	ml/min	mm	℃	kV		mm
Optimal parameters	17.256[a] 28.76[b]	12.0	80	45	4	69.0

[a] Feedstock flow rate is 17.256ml/min, the selectivity and yield of methanol are the biggest.

[b] Feedstock flow rate is 28.760ml/min, the output of methanol in the same time is the biggest.

4 Reaction mechanisms

In general, a unique feature of low temperature plasma is that at least four different types of radicals from

methane and three different types of radicals from water vapor are shown to be produced simultaneously by electron swarm, which is a group of electrons having a wide distribution of energies: the impact of high-energy electrons produces excited methane and water vapor for which the internal excited energy (9~13eV and 12.6eV, respectively) is much higher than the methane and water vapor dissociative threshold (4.51eV and 5.0eV, respectively).

$H_2O+e \rightarrow H_2+O^*$ (1)

$H_2O+e \rightarrow H^*+HO^*$ (2)

$CH_4+e \rightarrow H^*+CH_3^*+e \rightarrow CH_2^*+H_2+e \rightarrow CH^*+H^*+H_2+e \rightarrow C+2H_2$ (3)

Methanol can be produced through HO* and CH_3* reaction or CH_4 and O* reaction after methane was dissociated into CH_3* and water vapor was dissociated into H* and HO* or H_2 and O*. Methanol can be produced through reaction (4) and (5). C_2 hydrocarbons and hydrogen are by-products. The detail reaction mechanism of C_2 hydrocarbons synthesis from methane through plasma reaction was expatiated in the papers [7-8].

$HO^*+CH_3^* \rightarrow CH_3OH$ (4)

$CH_4+O^* \rightarrow CH_3OH$ (5)

5 Conclusions

1. The direct synthesis of methanol from methane and water vapor is doable with continuous flow reactor through dielectric-barrier discharge non-equilibrium plasma under atmosphere press.
2. The selectivity and yield of methanol decrease with the total feedstock flow rate increasing. The selectivity and yield of methanol first decrease, and then increase with the radius of inner electrode increasing. The selectivity and yield of methanol decrease with the water temperature increasing. The selectivity and yield of methanol increase with the discharge voltage increasing, the ratio of dilution increasing, or the length of outer electrode increasing.
3. The appropriate technology condition is d=12.0mm, T=80℃, U=55kV, DR=4, L=69.0mm. When the total feedstock flow rate is 17.256ml/min, the selectivity and yield of methanol is as high as 50% and 10%, respectively. When the total feedstock flow rate is 28.760ml/min, the output of methanol in the same time is the biggest.

Reference

[1] K.Okazaki, T.Kishida, K.Ogawa, *et al*. Direct conversion from methane to methanol for high efficiency energy system with exergy regeneration, Energy Conversion and Management, 43: 1459~1468,(2002)

[2] Yao S L, Takemoto T, Ouyang F, et al. Selective oxidation of methane of methane using a non-thermal pulsed, Energy & Fuels, 14(2): 459~463,(2000)

[3]T. Nozaki, A. Hattori, K. Okazaki. Partial oxidation of methane using a microscale non-equilibrium plasma reactor, Catalysis Today, 98: 607~616,(2004)

[4] Hijikata K, Ogawa K, Miyakawa N. Methanol conversion from methane and water vapor by electric discharge (Effect of electric discharge process on methane conversion), Heat Transfer-Asian Research, 28(5): 404~417, (1999)

[5] Baowei Wang, Genhui Xu. Direct synthesis of oxygenates from water and methane via dielectric-barrier discharge, Chinese Chemical Letters, 15(7): 779~780,(2004)

[6] T. V. Choudhary, E. Aksoylu, D. W. Goodman. Nonoxidative activation of methane, Catal. Rev., 45(1): 151~ 203,(2003)

[7] Wang Baowei, Xu Genhui. Conversion natural gas to C_2 hydrocarbons through dielectric-barrier discharge plasma catalysis, Science in China (B), 45(3): 299~310,(2002)

[8] Yang EnCui, Hao JinKu, Tang TingHua, *et al*. The theoretical study of reaction paths and transition states on coupling reaction of methane through plasma, J. of Mole. Structure: THEOCHEM, 626(1-3): 121~126, (2003)

SYNTHESIS OF NANOSIZED ZINC FERRITES IN RF THERMAL PLASMA REACTOR

L. Gál[1], I. Mohai[1], Z. Károly[1], J. Szépvölgyi[1], J. Gubicza[2]
[1] *Institute of Materials and Environmental Chemistry, Chemical Research Center, Hungarian Academy of Sciences H-1525 Budapest, POB 17, Hungary*
[2] *Department of Solid State Physics, Eötvös University H-1518 Budapest, POB 32, Hungary*

Abstract
In this work synthesis of nanosized zinc ferrites was studied under thermal plasma conditions. Mixture of oxide powders and ethanol solution of corresponding salts were used as precursors. The products were characterized by ICP-OES and XRD methods. Morphology was studied by SEM and TEM. Magnetic properties were characterized by saturation magnetization. Nanosized zinc ferrite particles having ferromagnetic properties were produced which refers to the formation of zinc ferrites of inverse spinel structure in particular conditions.

Keywords: Zinc ferrite; $ZnFe_2O_4$; Thermal plasma; XRD; SEM; TEM; Saturation magnetization

1. Introduction

Ferrite spinels crystallize in face centered cubic lattice. In the normal zinc ferrite structure, Zn^{2+} ions are in tetrahedral, while Fe^{3+} ions are in octahedral positions. Zinc ferrites having normal spinel structure exhibit paramagnetic properties. They are used as pigments, catalysts and adsorbents for desulphurization [1].
Under extreme conditions, such as mechanochemical activation or rapid quenching, position of Zn^{2+} and Fe^{3+} cations in the crystal structure can be partially or even completely reversed [2]. The resulted structure, referred as inverse spinel one, is ferromagnetic with a high saturation magnetization. Thus, inverse zinc ferrites can be used as electrical and magnetic materials. Zinc-ferroferrites ($Zn_xFe_{3-x}O_4$, where $x \leq 0.5$), in which the Fe^{2+} ions are partially substituted by Zn^{2+} ions, have the highest saturation magnetization among spinel ferrites.
Inverse zinc ferrite spinels of ultrafine particle size can be produced in RF thermal plasma conditions due to high processing temperature and the rapid quenching of the formed, meta-stable phases [3-4]. In addition, thermal plasma synthesis makes production of ferrite devices from powders simpler.
In this report, results of the thermal plasma synthesis of zinc ferrites from different precursors are presented. Research was aimed to reveal correlations among properties of products and parameters of processing and to optimize conditions of zinc ferrite production.

2. Experimental

The experiments were performed in an RF thermal plasma reactor operating at a maximum plate power of 30kW (3÷5 MHz). Experimental set-up is shown in Fig. 1. Argon was used as plasma gas with a flow rate of 20 $l \cdot min^{-1}$. The sheath gas was a mixture of Ar and O_2 with flow rate of 23 $l \cdot min^{-1}$ and 20 $l \cdot min^{-1}$, respectively. The oxide precursors were fed using PRAXAIR powder feeder, while the ethanol solutions were injected by a TEKNA suspension feeder. Both mixture of solid oxides and ethanol solution were atomized by argon with flow rate of 3 $l \cdot min^{-1}$. Injection probe was positioned as shown in Fig. 2.
Precursors were prepared by two methods:

- Analytical grade Fe_2O_3 and ZnO powders were thoroughly mixed in a Fritsch laboratory agate mortar grinder
- Analytical grade $Fe(NO_3)_3 \cdot 9H_2O$ and $Zn(NO_3)_2 \cdot 6H_2O$ were dissolved in technical grade ethanol using a magnetic stirrer.

The Fe to Zn molar ratio was set to 2:1 in all cases. In the tests the following parameters were varied:

- Type of precursor
- Plate power
- Position of injection probe
- Concentration of salts in the ethanol solution.

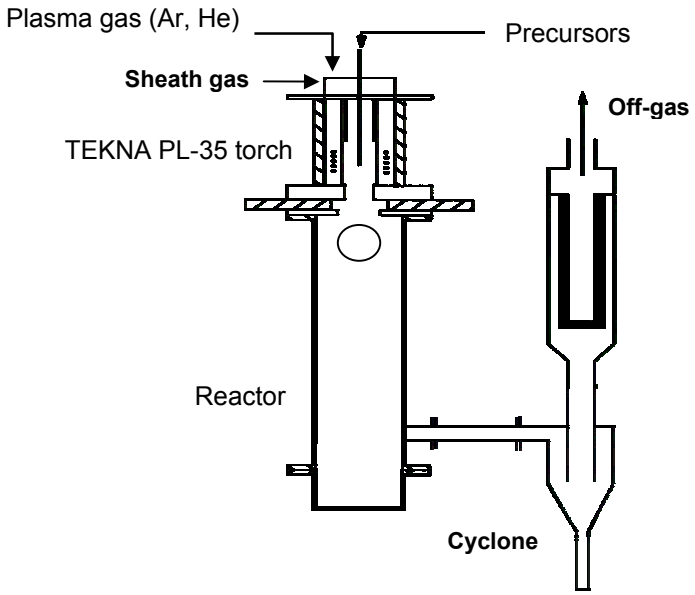

Figure 1 Scheme of the experimental set-up

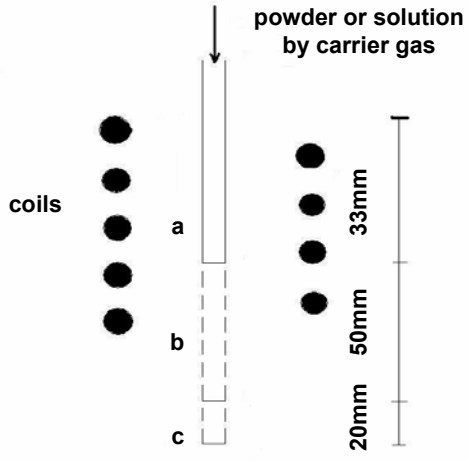

Figure 2 Positions of the injection probe

The experimental conditions are summarized in Table 1.

Table 1 Experimental conditions

Sample No.	Plate power (kW)	Probe position	Molar concentration (M)	Feed rate
Powder				
1	15	a		0.460 g/min
2	25	a		0.360 g/min
Solution				
3	15	b	1.3	0.010 l/min
4	15	c	1.3	0.014 l/min
5	25	c	1.3	0.014 l/min
6	25	c	0.65	0.021 l/min
7	15	b	0.65	0.019 l/min
8	25	b	0.65	0.019 l/min

The reaction products were collected from the reactor wall. Their chemical composition was analyzed by ICP-OES (Thermo Jarrell Ash Atomscan 25). A Philips Xpert XRD apparatus operating with Cu K_α radiation was used to analyze the phase composition. The lattice parameters (a) of the crystalline phases were determined from the positions of the particular diffraction peaks. The mean particle size was calculated from the peak broadening. Product morphology was studied by SEM (Philips XL30 ESEM) and TEM (Philips CM20). Magnetization measurements were performed at room temperature by means of a vibrating-sample (Foner-type) magnetometer varying the external magnetic field up to 2 Tesla. The saturation magnetization was determined by extrapolating the linear high-field part of the magnetization curve to zero fields.

3. Results and discussion

The experimental results are summarized in Table 2. Plasma treatment resulted in extensive spinel formation from both precursors (Figs. 3 and 4). However, in most of the cases, the spinel phase contained magnetite (Fe_3O_4), as well. XR diffractograms indicated some ZnO (zincite) and Fe_2O_3 (hematite) phases in the products. In order to compare results of different experiments, the most intense reflections of the by-products were related to the $ZnFe_2O_4$ 311 reflection. Ratio of Fe_3O_4 to $ZnFe_2O_4$ was calculated by deconvoluting the 731 spinel reflection.

Table 2 Properties of zinc ferrite powders

Sample no.	Zinc ferrite phase				Other phases				Fe : Zn ratio	Saturation magnetization ($emu \cdot g^{-1}$)
					Magnetite		Zincite	Hematite		
	a (Å)	Composition	D (nm)	RI	D (nm)	RI	RI	RI		
Powder										
1	8.439	$ZnFe_2O_4$	53	100	-	0	15	15	2.2 : 0.8	19
2	8.439	$ZnFe_2O_4$	70	100	62	46	19	5	2.1 : 0.9	36
Solution										
3	8.440	$ZnFe_2O_4$	70	100	15	54	8	2	2.0 : 1.0	25
4	8.441	$ZnFe_2O_4$	70	100	18	58	10	2	2.0 : 1.0	26
5	8.441	$ZnFe_2O_4$	62	100	24	13	4	1	2.0 : 1.0	20
6	8.440	$ZnFe_2O_4$	50	100	28	84	14	2	2.0 : 1.0	28
7	8.438	$ZnFe_2O_4$	80	100	39	31	10	1	2.0 : 1.0	28
8	8.441	$ZnFe_2O_4$	70	100	16	128	7	2	2.24 : 0.76	32

RI – relative intensity

Starting from solid precursors, the product contained relatively high amount of un-reacted oxides. At plate power of 15 kW, the product consisted of spinel phase ($ZnFe_2O_4$) only. However, at plate power of 25 kW a remarkable amount of magnetite could be detected in the product, as well. In both runs, practically same concentrations of un-reacted precursors were detected. Increase of the plate power, and hence, the specific energy (kWh/g, applied energy related to the mass unit of precursor) seems to be unfavorable regarding formation of single spinel phase. For the pure $ZnFe_2O_4$ spinel (Sample 1) a saturation magnetization of 19 $emu \cdot g^{-1}$ was measured. This refers to inverse spinel structure.

The mixture of nitrates, as precursor was transformed into spinel with a good efficiency (Fig. 4.). The low relative intensity of ZnO and Fe_2O_3 phases, respectively, refers to more complete formation of ferrites as compared to solid precursor. However, intensity of magnetite reflection is very close to (Sample 6), or even higher (Sample 8) than that of zinc ferrite. This means that the spinel structure contains less zinc than required. A plate power of 25 kW and diluted solution may favor the zinc loss. The highest $ZnFe_2O_4$ formation was observed in Sample 5. This material was produced from a 1.30 M nitrate solution that was fed at a probe position of "b" at plate power of 25 kW.

Crystallites in $ZnFe_2O_4$ had sizes in the range of 50-80 nm for all cases. Size of magnetite particles was smaller. It should be emphasized that these data refer to particles below 1 μm, because particles being greater than 1 μm do not exhibit line broadening of XRD peaks.

SEM and TEM micrographs confirmed calculations of mean particle size based on XRD data. Products from ethanol solutions consist of slightly agglomerated grains having particle size below 200 nm (Fig. 5(a)). In the TEM micrographs (Fig. 5(b)) particles can be classified into three groups, namely those having smallest (5-10 nm), medium (~50 nm) and largest (100-300 nm) sizes.

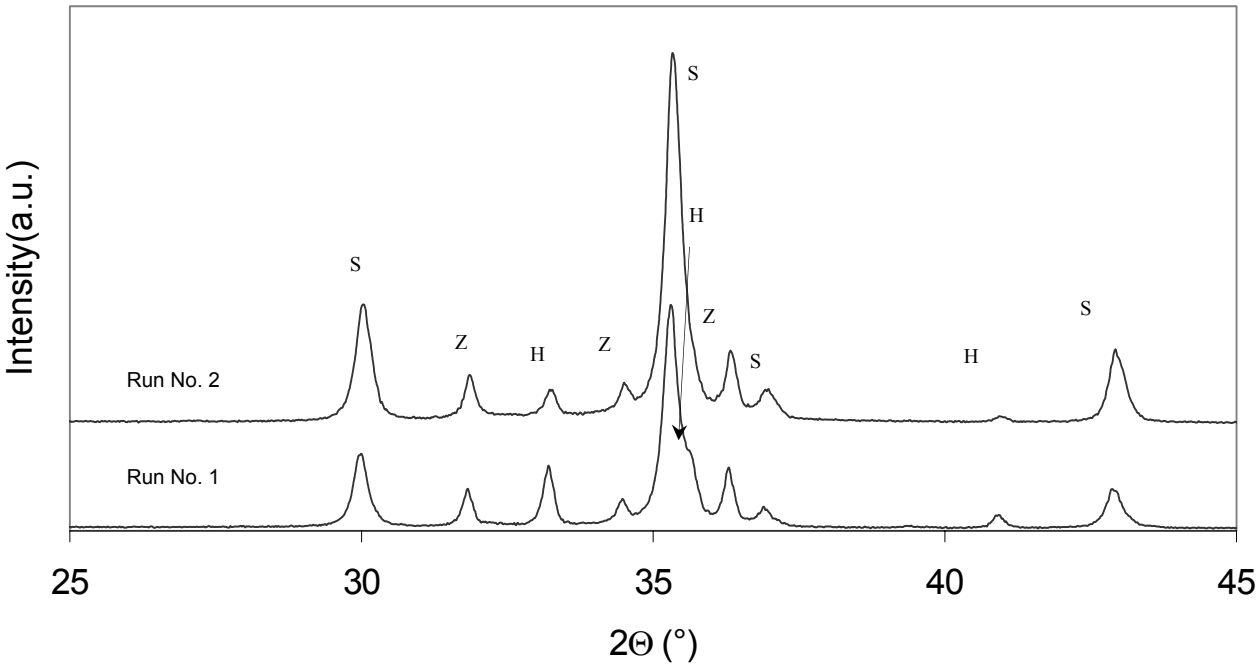

Figure 3 XRD patterns of products from powder mixtures (S: Spinel, H: Hematite, Z: Zincite)

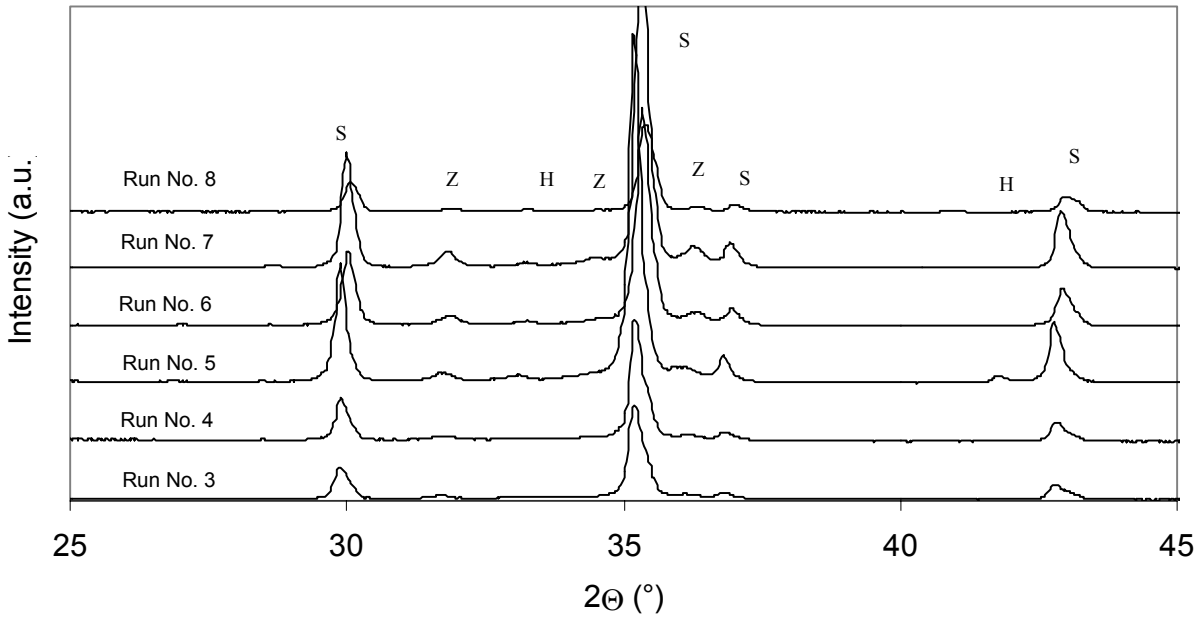

Figure 4 XRD patterns of products from ethanol solutions (S: Spinel, H: Hematite, Z: Zincite)

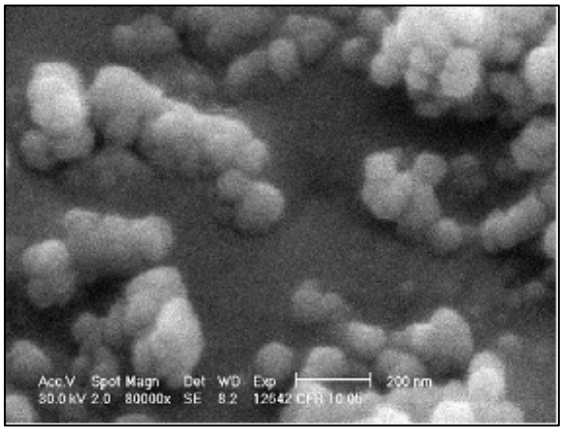

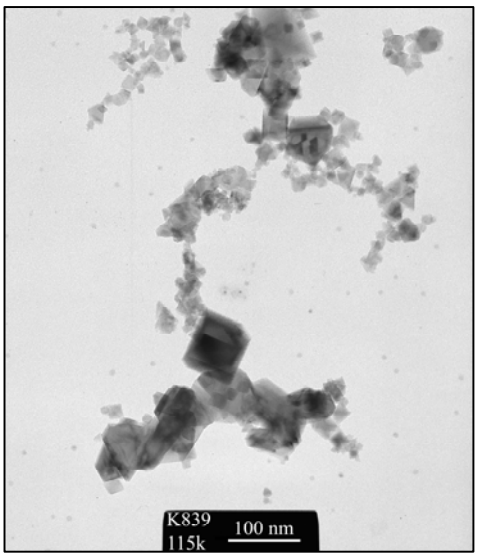

(a) (b)

Figure 5 SEM and Tem microphotograph of a typical product from ethanol solution of metal salts

4. Conclusions

RF plasma treatment of the mixture of Fe_2O_3 and ZnO, and also the ethanol solution of the metal nitrates resulted in an extensive spinel formation. The main reaction product was $ZnFe_2O_4$. However, different amounts of magnetite (Fe_3O_4) were formed, as well. Starting from solid precursors, considerable amount of oxides did not react in particular conditions. Using ethanol solution of metal nitrates, transformation of precursors to spines was much more complete. Thus, for the synthesis of ferrite spinels of well defined composition, use of solutions of metal salts as precursors is recommended. Small particles in the size range of 5-300 nm were produced in this case at specific energies of 0.05-0.1 $kWh \cdot g^{-1}$. Particular energies are less of one order of magnitude as compared to the solid precursors (0.6-1.1 $kWh \cdot g^{-1}$). Saturation magnetization exhibited rather poor correlation with the $Fe_3O_4/ZnFe_2O_4$ intensity ratio. It suggests formation of inverse $ZnFe_2O_4$ spinel with ferromagnetic properties.

Acknowledgements

This work was supported by the Hungarian Scientific Research Foundation (OTKA No. T047360).

References

[1] A. T. Atimtay - Clean Utilization of Coal, NATO ASI Series 370, Kluwer, (1992).
[2] B. D. Cullity - Introduction to Magnetic Materials, Addison-Werley, Reading, MA (1972).
[3] I. Mohai, J. Szépvölgyi, I. Bertóti, et al. - Solid State Ionics 141 (2001).
[4] J. Szépvölgyi, I. Mohai, J. Gubicza, et al. - Key Engineering Materials Vols. **264-268** (2004)

Rotating Non-Equilibrium Gliding Arc Plasma Disc for Enhancement in Ignition and Combustion of Hydrocarbon Fuels

Shailesh Gangoli, Alexander Gutsol, Alexander Fridman
Department of Mechanical Engineering & Mechanics, Drexel University, Philadelphia, PA

Abstract

The best plasma discharge system for combustion applications should generate non-equilibrium plasma with high concentration of active species and intermediate temperatures, high enough to support chain in propagation reaction. The non-equilibrium Gliding Arc (GA) aptly suits this application. A novel, non-equilibrium gliding arc plasma disc reactor has been developed to study possibility of flame speed increase, flammability limit extension for hydrocarbon fuel and oxidizer mixture.

Introduction

The motivation for this work has come from analyzing the two major sources of problems in supersonic combustion: ignition and flame stabilization in supersonic flow. From the viewpoint of chemical kinetics, combustion is a chain process with two limiting reactions: chain-initiation and chain-continuation. Plasma as a source of free radicals and ions can significantly reduce the chain initiation time. Plasma enhanced combustion devices developed in the past have ranged from using plasma torches [1] to nanosecond high voltage discharges. [2, 3] These devices enhance combustion characteristics in supersonic flow significantly, but at the cost of high power consumption.

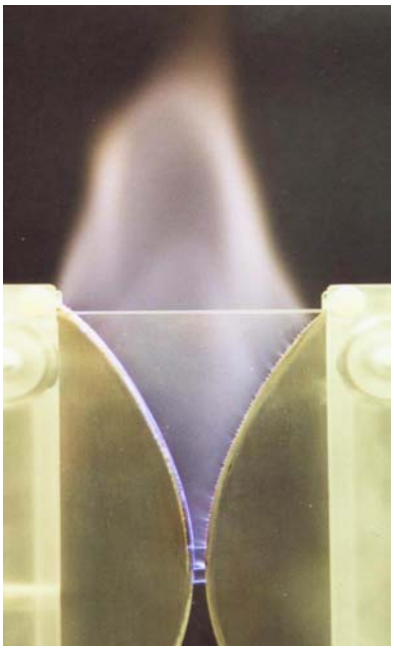

Figure 1: Conventional Gliding Arc discharge in flat geometry.

At low temperatures, equilibrium concentration of radicals reduces very fast and to ignite the combustible mixture within reasonable time, it is necessary to provide some heat to the mixture, in addition to radicals. So, the best discharge system should generate non-equilibrium plasma with high radical concentration and intermediate (better adjustable) temperature, high enough to support chain continuation reaction. The discharge that aptly suits these requirements is the non-equilibrium Gliding Arc (GA). In conventional GA system, as shown in figure 1, the arc starts at the smallest gap between two diverging electrodes under an electric field of approximately 3kV/mm in air and elongates as it is pushed by air. During this elongation period, the thermal arc changes its ionization mechanism into a non-thermal one. Hence it is also known as a transitional discharge.

Non-thermal plasma generated by this unique discharge has relatively high plasma density, power and operating pressure in comparison with other non-equilibrium discharges; high electron temperature (about 1.5eV), relatively low gas temperature (<3000K) and good chemical selectivity in comparison with thermal discharges. High temperature electrons are more efficient in producing ions, radicals, excited and dissociated molecules than those in equilibrium plasma (<1eV). The discharge can be divided into various regions qualitatively, shown in figure 2.

Evolution of conventional flat GA

The evolution of GA can be best explained in the following manner. The arc ignites at the shortest gap and is

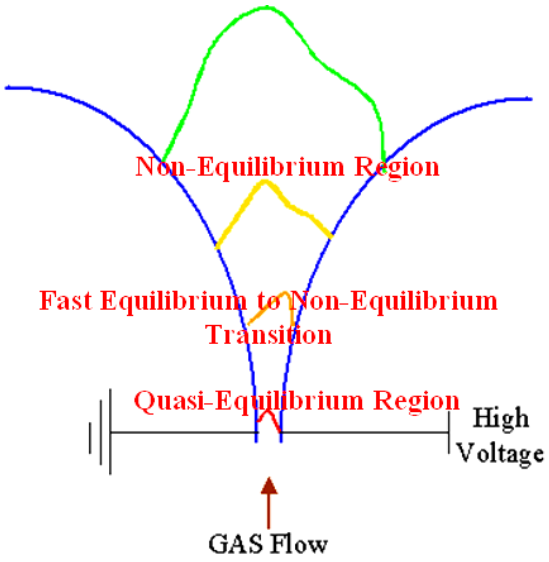

Figure 2: (top) Qualitative classification of regions in the flat GA discharge.

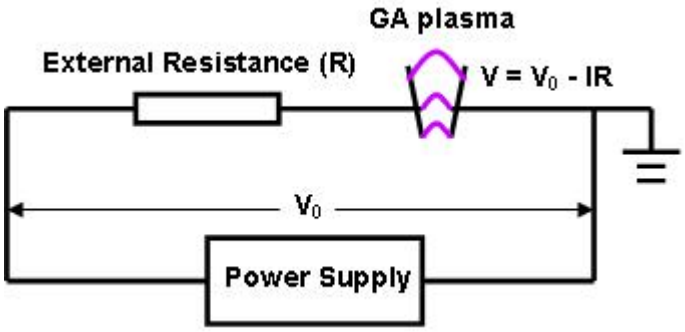

Figure 3: (top right) Electrical scheme for conventional flat GA.

elongated by air flow. Within a short time (microseconds), the arc current *I,* reaches its maximum value $I_{max} \leq V_0/R$, while the voltage drops to almost zero. As the gas flow pushes the arc, its voltage increases and current starts to decrease. The elongating arc demands more power to sustain itself, until it reaches a maximum that the power supply can provide. For the electrical configuration shown in figure 3, by Ohm's law, the power dissipation in plasma reaches its maximum $W_{max} = (¼)\ V_0^2/R$ when the plasma resistance equals the external resistance *R*. The length of arc continues to grow, but the power supplied by the source is insufficient to balance the energy losses to the surrounding gas. If the electric field is sufficiently high (meaning the power supply can provide sufficiently high voltage), the arc changes its ionization mechanism to a non-thermal one. Due to instability the arc cools down and finally extinguishes marking the end of one cycle. The next cycle of arc evolution begins as voltage in the gap reaches its breakdown value. Transition from thermal to non-thermal can be verified from figure 4 [10], wherein the electric field increases i.e. slope of dV/dL increases, after a certain arc length elongation, which in turn explains the increase in electron energy as the arc propagates. The non-thermal zone of the discharge can be considered to be in the normal glow discharge [11], as we can make a visual comparison between snapshots of atmospheric pressure flat GA and atmospheric pressure glow discharge as shown in figure 5.

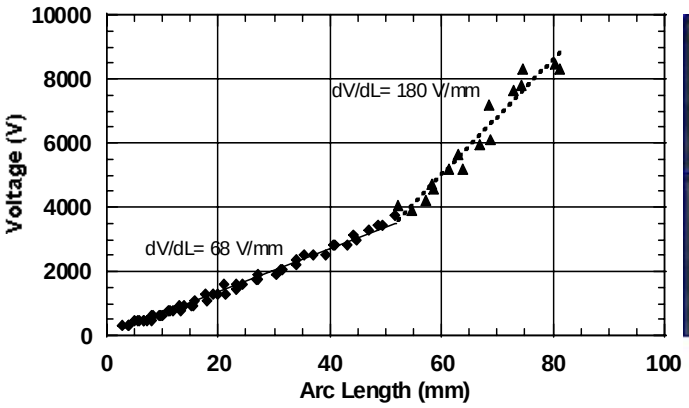

Figure 4: Arc voltage vs length during evolution of GA [10]

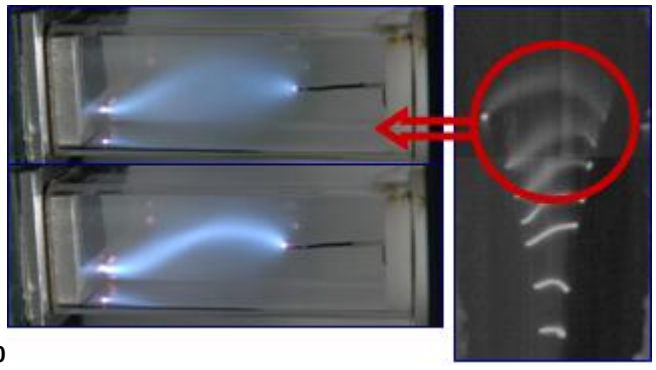

Figure 5: Visual comparison of atm. pressure glow discharge (left) and atm. pressure GA (right)

However, it was recently found that after the GA reaches maximum power and before it quenches, it is still stable in the most non-equilibrium regime [4]. This "overshooting" regime is observed at sufficiently low arc currents. It is possible to extend "life" of the extremely elongated non-equilibrium GA infinitely if we can stop its elongation just before extinguishing. One of the technical solutions to achieve this "infinite life" of the non-equilibrium GA is to rotate it in a magnetic field inside the gas flow.

Principle & Design of Magnetic Gliding Arc (MGA)

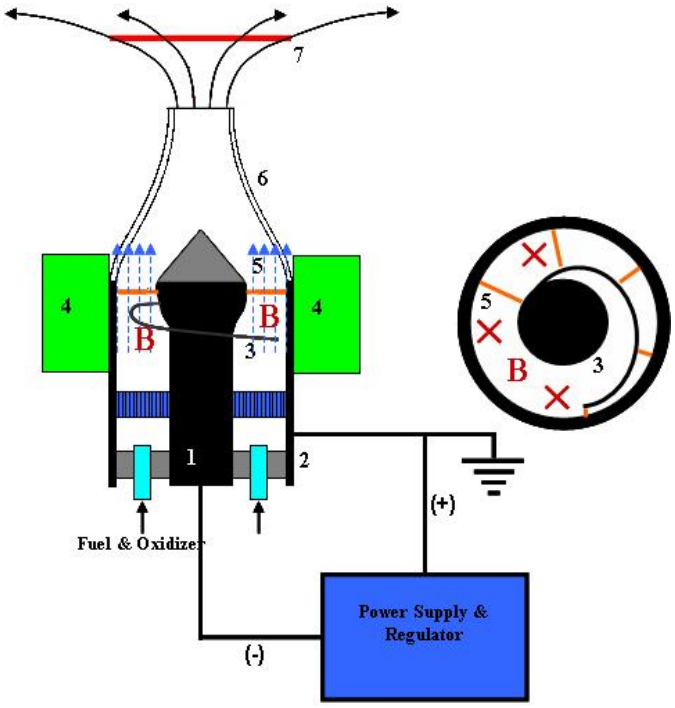

Figure 6: Diagram of newly developed non-equilibrium plasma enhanced counter flow burner: 1. Anode, 2. Cathode, 3. Wire for gliding arc initiation, 4. Circular magnet, 5. GA plasma discharge, 6. Nozzle

The MGA is based on the principle of Ampere force, which is experienced by a current carrying conductor in a magnetic field. The Ampere force is given as $F = IL \times B$, where, F – Ampere Force, I – Current through the conductor, L – Length of the conductor and B – Strength of magnetic field.

The schematic of the MGA setup is as shown in figure 6. Just as in the conventional GA, the arc is initiated at the shortest gap between the spiral wire (connected to the central cathode) and the anodic cylinder. The arc is then rotated by the magnetic field to cause it to move (rotate) upwards along the spiral wire, until it stabilizes on top of the cathode. The arc then rotates in the cross-section of the flow. The stabilized non-equilibrium plasma arc is still just one arc between the electrodes in the plasma device, but depending upon the strength of the magnetic field, the arc is rotated at a high enough rate to pass through a significant portion of the fuel mixture and provide quasi-uniform activation of the flow. The stabilized non-equilibrium plasma arc constantly produces some amount of heat and high density of electrons that produce radicals and active species for maximum flame enhancement.

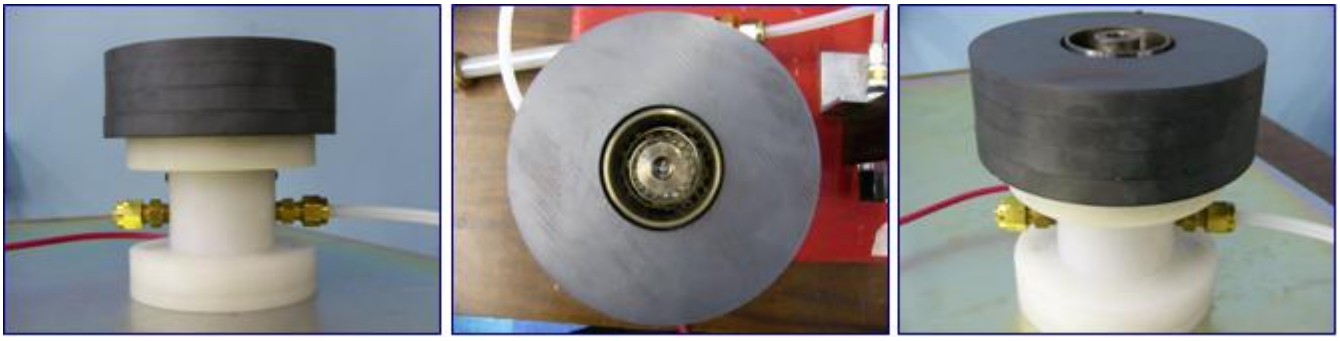

Figure 7: Photographs of the MGA from (left to right) front, top and isometric views, respectively.

Uniformity of Treatment

The frequency of rotation of arc depends on the arc current and magnetic field within the reactor. A simple model can be formulated to predict the flow rate of gas passing through the plasma that can be 'uniformly' treated by it.

For the current MGA configuration: Outer diameter of central electrode Di= 1cm; Inner diameter of anodic cylinder Do= 5cm; Hence, Arc Length ≈ (Di-Do)/2 ≈ 2cm

For a particular case of operation: Current = 130 mA; Magnetic Field = 0.15 T

We make an assumption that the arc is "*not transparent*" to the surrounding air i.e. it experiences a drag force as it rotates. Hence, the plasma arc behaves like a current carrying cylinder (wire) which experiences two sets of forces namely, Ampere Force per unit length = IB = F_a and Drag Force per unit length = $C_d \rho d V^2 = F_d$. Under equilibrium conditions; $F_a = F_d$.

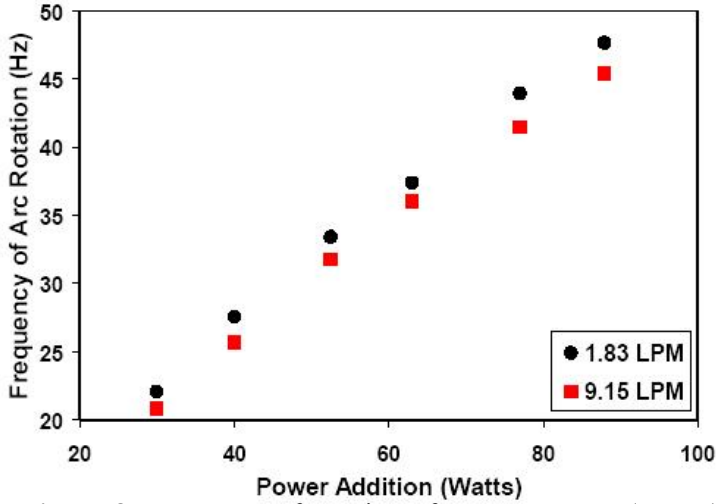

Figure 8: Frequency of rotation of arc vs. Power (current) addition at varied flow rates.

Figure 9: Reactive Capacitive Resistance based power supply, specially developed for GA's

Using this relation we can approximate the velocity of propagation of the arc ~ 4.5 m/s. Hence, the frequency of arc rotation would be ~ 60 Hz. The arc, which is at least 2mm in diameter, appears at the same position 60 times in one second; thus, the velocity of gas that would be treated 'uniformly' is < 12 cm/s. This gives in turn gives us the flow rate of gas that would be treated uniformly < 903 cm^3/s. Figure 8 shows the experimentally measured frequency of arc rotation at different power (current) levels, which conforms to our simplistic model for frequency of arc rotation [9].

Power Supply

As discussed earlier, maximum power is supplied to the GA when the plasma resistance equals the external resistance in the circuit. Even in this case the conventional power supply with the serial resistor (fig. 3) can use only 1/2 of available energy to support the Gliding Arc. All other energy is dissipated in the serial resistor. A new power supply has been developed, which incorporates a reactive capacitive resistance circuit that imitates active resistance, but does not consume significant power. This ensures that it operates more or less in the non-thermal regime of operation. Also, during operation the current can be reduced manually (causing corresponding increase in voltage), to as low value as possible before it extinguishes and restarts again. Figure 9 shows the power supply that specially constructed for this purpose.

MGA Snapshots

Snapshots of the MGA were taken at different shutter speeds to obtain the images (RGB and Grayscale) as shown below. At $1/1000^{th}$ sec, we see a discharge column with a cathode glow.

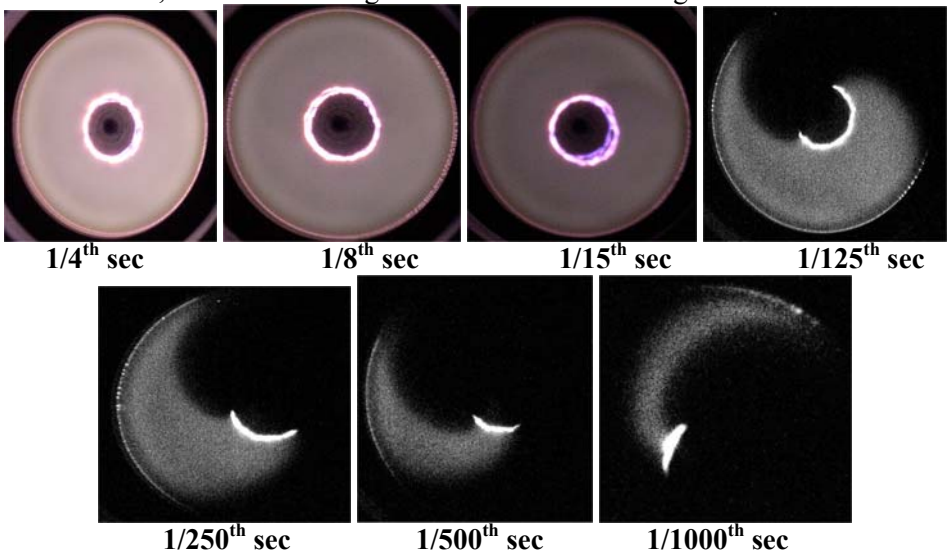

Figure 10: Snapshots of the MGA

Gliding Arc Discharge Diagnostics

Figure 11. Spectra obtained for MGA in 200-450 nm wavelength range

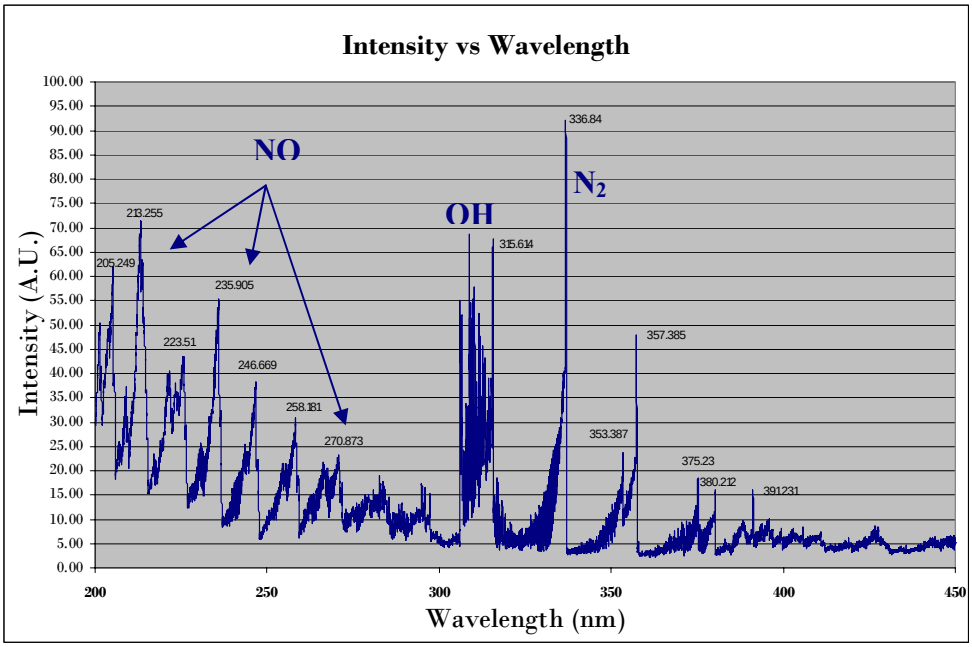

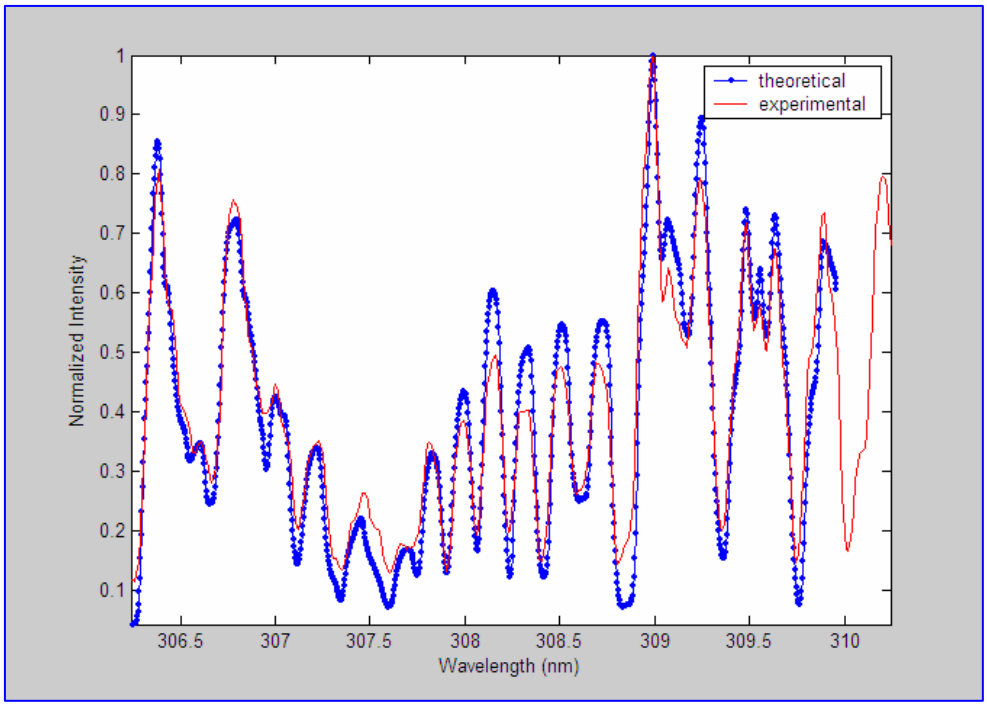

Figure 12: Comparison between experimental and theoretical OH spectra generated for temperature T= 2300K

In our earlier work, we had conducted microwave diagnostics conventional flat GA, and the results for electron density obtained were in the range, $\mathbf{n_e = (1\text{-}3).10^{11}\ cm^{-3}}$ [5]. Figure 11 shows the experimental spectral diagnostic results obtained for the MGA. A theoretical OH spectrum was developed based on data obtained from [6] and methodologies suggested in [7, 8]. Figure 12 shows the comparison between experimental spectrum and a simulated one for the temperature 2300K (theoretical spectra were generated for the temperature range 1000K - 8000K), and then a best fit procedure was applied to find MGA temperature).

Using the data rotational gas temperature ≈ **2300K**, and using BOLSIG, Boltzmann equation solver (Kinema Research) we obtain the average electron energy in the MGA to be ~ **1.56 eV**. This high electron energy is conducive to efficient dissociation and ionization of species that cause 'plasma enhancement effect.'

Experimental Result

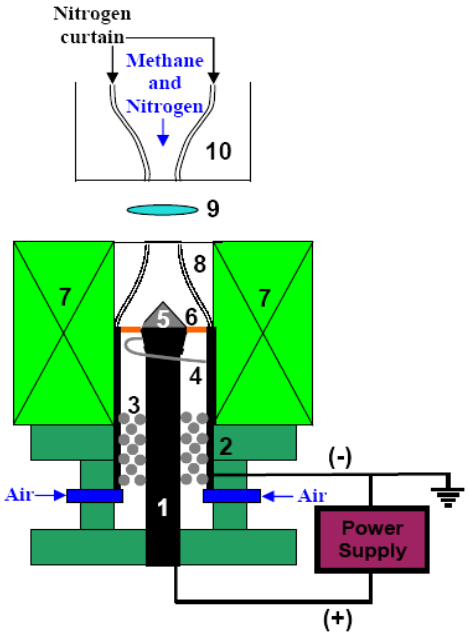

Experiments with opposite diffusion flame were conducted [9] using the MGA. The schematic of the setup is as shown in figure 13. The results obtained are shown in figure 14. We see that the air flow rate, required to cause blow-out of the diffusion flame increases with increase in plasma power.

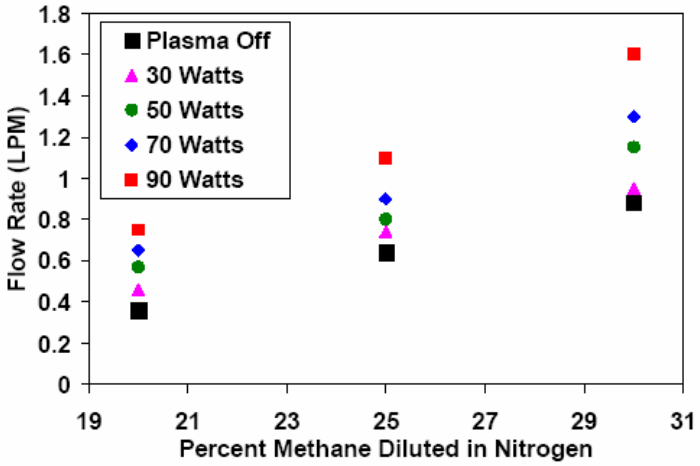

Figure 13: (left) Diagram of newly developed non-equilibrium plasma enhanced counter flow burner: 1. Cathode, 2. Anode, 3. Laminarizer, 4. Spiral, 5. Ceramic arrestor, 6. Stabilized GA plasma, 7. Magnets, 8. Nozzle, 9. Diffusion flame, 10. Fuel nozzle

Figure 14: (right) Flow Rate of Air vs Percentage Methane Diluted in Nitrogen at different plasma powers.

References

[1] Takita, Kenichi, Moriwaki, Atsushi, Kitagawa, Tomoaki, Masuya, Goro, Twenty-Ninth Symposium (International) on Combustion, the Combustion Institute.

[2] Bozhenkov, S. M., Starikovskaia, S. M., Sechenov, V. A., Starikovskii, A. Yu., Zhukov, V. P., "Combustible Mixtures Ignition In A Wide Pressure Range Nanosecond High-Voltage Discharge Ignition," AIAA, 2001.

[3] Bozhenkov, S. M., Starikovskaia, "Chemical Reactions and Ignition Control by Nanosecond High-Voltage Discharge," AIAA, 2002.

[4] Kuznetsova, I.V, Kalashnikov, N. Y., Gutsol, A. F., Fridman, A. A., and Kennedy, L. A., "Effect of 'Overshooting' In The Transitional Regimes Of The Low Current Gliding Arc Discharge," Journal of Applied Physics, 92(2002), 4231-4237.

[5] Kossitsyn, M., Gutsol, A., Fridman, A., "Generation and Diagnostics of Non-Equilibrium Plasma in Gliding Arc Discharge"

[6] Dieke, G.H., Crosswhite, H.M., "The ultraviolet bands of OH, Fundamental Data", J. Quant. Spectrosc. Radiat. Transfer, Vol.2, pp.97-199, 1961.

[7] Pellerin, S., Cormier, J.M., Richard, F., Musiol, K., Chapelle, J., "A spectroscopic diagnostics technique using UV OH band spectrum", J. Phys. D: Appl. Phys. 29 (1996) 726-739.

[8] Charles de, I., "UV OH spectrum used as a molecular pyrometer", J. Phys. D: Appl. Phys. 33 (2000) 1697-1704.

[9] Ombrello, T., Qin, X., Ju, Y., Gutsol, A., Fridman, A., "Enhancement of Combustion and Flame Stabilization using stabilized non-equilibrium plasma", AIAA 2005 conference, Reno.

[10] Ozlem, M.Y., Saveliev A.V., Porshnev, P.I., Fridman, A., Kennedy, L.A., Non-Equilibrium Effects in Gilding Arc discharge".

[11] Staack, D., Farouk, B., Gutsol, A., Fridman, A., "Atmospheric pressure normal glow DC microplasma in air", ISPC 2005, Toronto, Canada.

Plasma heat flux to asymmetric anodes in a hot refractory anode vacuum arc

I. I. Beilis*, A. Shashurin*, A. Nemirovsky*, R. L. Boxman* S. Goldsmith**

Electrical Discharge and Plasma Laboratory, Tel Aviv University

P. O. B. 39040, Tel Aviv 69978, ISRAEL

** Department of Interdisciplinary Studies, School of Electrical Engineering, Fleischman Faculty of Engineering*

*** School of Physics and Astronomy, Raymond and Beverly Sackler Faculty of Exact Science*

Abstract

The transient heat flux to an asymmetric graphite anode in a Hot Refractory Anode Vacuum Arc (HRAVA) was determined using three-dimensional numerical simulation of a thermal anode model and the experimentally measured anode temperature distribution. The HRAVA anode is initially heated by the plasma flux from cathode plasma jets (t<30 s), and then from the dense anode plasma plume in the developed arc stage (t>1min). It was shown that asymmetry parameter of the heat flux increases with anode asymmetry.

Keywords: vacuum arc, hot asymmetric anode, anode plasma plume, heat flux, anode temperature.

1. Introduction

The Hot Refractory Anode Vacuum Arc (HRAVA) is a high current electrical discharge between a consumable cathode and a non-consumable refractory anode, and may be used to deposit coatings of the cathode material with low macroparticle contamination on substrates facing the anode [1,2]. The mechanism of plasma generation in the HRAVA is different from that in the well know hot evaporated anode vacuum arc [3,4]. The plasma configuration would be similar to that which occurs in an arc with non-condensable gas such as argon [5]. Initially (about 1min after ignition), the cathode spot plasma jets heat the refractory anode and then later, in the developed stage of the arc, a dense anode plasma plume is formed [6]. Simultaneously, cathode material is deposited on the refractory anode surface during the initial stage, and then, during the developed stage, the deposited material is re-evaporated from the heated anode. The anode plasma plume appears as a result of cathode material re-evaporation from the anode surface and its ionization by cathode jets dissipated in the plasma plume [6]. Previously, a one-dimensional (1-D) [7] model of the HRAVA anode was considered and the heat flux to a symmetric graphite anode was determined using the 1-D model and measured anode temperatures. The radial distribution of temperature on the symmetric anode surface was taken into account using a 2-D mode for graphite and molybdenum anodes [8]. Anode plasma plume propagation may be directed [9] using anodes with inclined facing surface. However, heretofore, a 3-D model considering asymmetric HRAVA anodes was not developed.

This work presents a 3-D thermal model of asymmetric graphite anodes. The time-dependent heat flux was determined numerically using the measured anode temperature distribution.

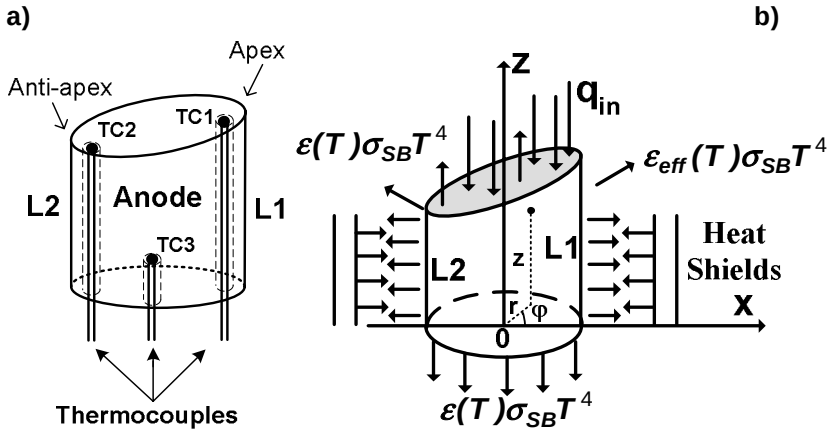

Fig 1. Schematic diagram of anode: a) thermocouple locations; b) heat flux.

2. Experimental Setup

The anode geometry and its heating are presented in Fig. 1. Cylindrical graphite anodes with radius R_a=16 mm and arc currents I=175 and 225 A were considered. The front surface of the anodes was inclined so that the maximal (apex) and minimal (anti-apex) anode

lengths (L1, L2) were: (1) (30, 25), and (2) (30, 20) mm, whereas the length of the symmetric anode was 30 mm (Fig.1a).

The anode temperature was measured using three high-temperature thermocouple probes (W/Re 26%, W/Re 5%) placed in cylindrical cavities with diameter 4 mm in the anode body: TC1 and TC2 - 2mm inside from the front anode surface near the apex and anti-apex, and TC3 – 7 mm from the back anode surface as shown on Fig. 1a, so that thermocouples TC1 and TC2 measured the temperature at two points near to the front anode surface (T_1 near the anode apex and T_2 near the anti-apex, see Fig. 1a) and TC3 at a point near the rear anode surface (T_3). Boron Nitride tubes were used to electrically insulate the thermocouples.

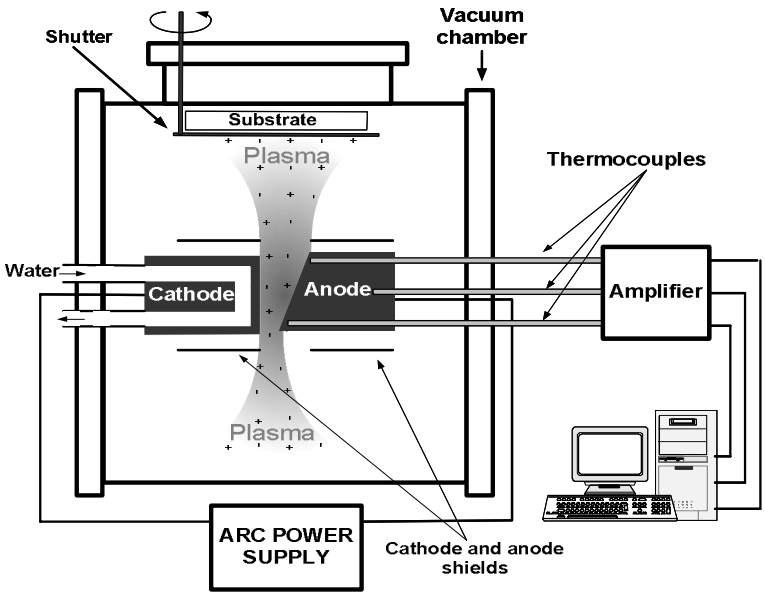

Fig 2. Schematic diagram of the HRAVA experimental setup, plasma expansion and temperature measurement.

Experiments were conducted in a cylindrical vacuum chamber (400 mm length, 160 mm diameter), as shown schematically in Fig.2. The chamber was pumped by a diffusion pump to 2.6×10^{-3} Pa. During the arc, the pressure in the chamber was 2.6×10^{-2} Pa. The discharge was ignited between a water-cooled copper cathode and a co-axial anode. The anode was produced from graphite (POCO DFP-1). The electrodes were surrounded by shields as shown in Fig. 1b and Fig. 2: the cathode by a boron nitride shield and the anode by two cylindrical Mo radiation shields with diameters 60 and 70 mm. The distance between the cathode surface and the anode apex was 18 mm. The arc duration was ≤150 s.

3. Calculation model

The heat flux from the interelectrode plasma to the anode surface was determined using a numerical solution of the heat conduction equation for anode body and the experimentally measured anode temperature distribution.

3.1 Anode temperature calculation

A thermal model of the asymmetric anode considered the 3-D time dependant heat conduction equation in cylindrical coordinates (z,r,φ, Fig.1b) taking into account the temperature T dependence of the thermophysical coefficients of the anode material and the Stefan-Boltzmann radiation from the front, rear and lateral surfaces (Fig.1b):

$$\rho(T)c(T)\frac{\partial T}{\partial t} = \frac{\partial}{\partial r}(\lambda(T)\frac{\partial T}{\partial r}) + \frac{1}{r}\lambda(T)\frac{\partial T}{\partial r} + \frac{\partial}{\partial z}(\lambda(T)\frac{\partial T}{\partial z}) + \frac{1}{r^2}\frac{\partial}{\partial \varphi}(\lambda(T)\frac{\partial T}{\partial \varphi}) + \rho_e(T)J^2 \qquad (1)$$

with the following initial conditions:

$$T(z,r,\varphi,t=0) = T_0 = 300K\ ;$$

and boundary conditions:

$$\lambda(T)\frac{\partial T}{\partial z} = q_{in}(r,z,\varphi,t) - \varepsilon(T)\sigma_{SB}T^4 \qquad \text{at the front anode surface;}$$

$$\lambda(T)\frac{\partial T}{\partial z} = \varepsilon(T)\sigma_{SB}T^4 \qquad \text{at z=0;}$$

$$-\lambda(T)\frac{\partial T}{\partial r} = \varepsilon_{eff}(T)\sigma_{SB}T^4 \qquad \text{at } r = R_a \qquad (2)$$

where ρ, c, λ, ρ_e, ε are the mass density, heat capacity, thermal conductivity, electrical resistivity and emissivity of the anode material, $J = \frac{I}{\pi R_a^2}$ is the current density and $q_{in}(r,z,\varphi,t)$ is the unknown incoming heat flux from the plasma to the front anode surface. The effective emissivity ε_{eff} used in the boundary condition at $r=R_a$ takes into account the heat flux returning from the heat shields to the lateral anode surface [7].

3.2 Anode heat flux model

The observed plasma plume was largely concentrated at the anode apex as shown in Fig. 3.

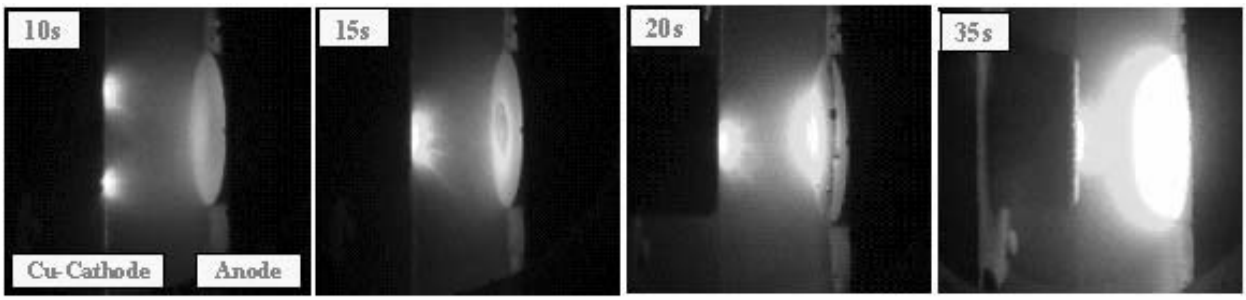

Fig 3. Selected frames demonstrating HRAVA discharge development for I=175A, h=18mm, L2=25mm.

It was assumed that the heat flux incident to the asymmetric anode surface is asymmetric. A simple linear approximation of heat flux was assumed $q_{in}^{asym}(r,\varphi,t) = q_{in}^{sym}(t)\cdot\left[1 + k_{as}^{flux}\frac{r\cos\varphi}{R_a}\right]$ where k_{as}^{flux} is a coefficient of asymmetry for the heat flux, $q_{in}^{sym}(t)$ is the previously defined incoming heat flux for the symmetric anode [7], in the form $q_{in}^{sym}(t) = q_{ss} + q_0 e^{-t/\tau}$, where q_{ss} is the steady state heat flux, ($q_{ss} + q_0$) is the initial heat flux (i.e. at t=0), and τ is the characteristic time for the anode plume to reach the cathode and is obtained from visual observation. The expression of $q_{in}^{asym}(t)$ is obtained assuming that the total net heat fluxes (Q_{in}) for symmetric and asymmetric anodes are equal: $Q_{in}(t) = Q_{in}^{asym}(t) = Q_{in}^{sym}(t) = q_{in}^{sym}(t)\pi R_a^2$. The heat flux may be characterized by an effective anode potential $U_{eff}(t) = \frac{Q_{in}(t)}{I}$ where $Q_{in}(t)$ is the net input power to the anode surface and I is the arc current. Thus heat flux could be expressed finally as:

$$q_{in}^{asym}(r,\varphi,t) = \frac{\left(U_{eff}^{ss} + U_{eff}^{0}e^{-t/\tau}\right)I}{\pi R_a^2}\cdot\left[1 + k_{as}^{flux}\frac{r\cos\varphi}{R_a}\right] \qquad (3)$$

where $U_{eff}^{0} + U_{eff}^{ss}, U_{eff}^{ss}$ are the initial and steady state effective anode potentials, respectively.

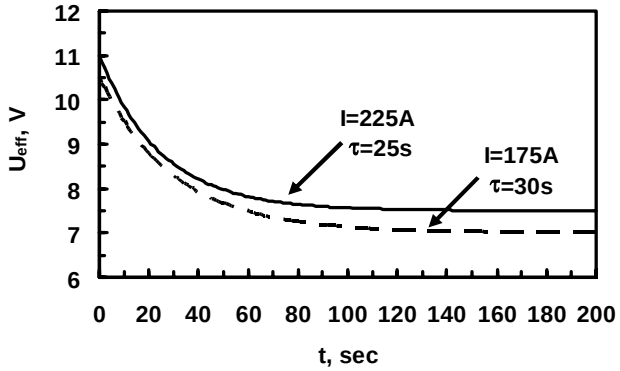

Fig 4. Effective anode potential vs. time

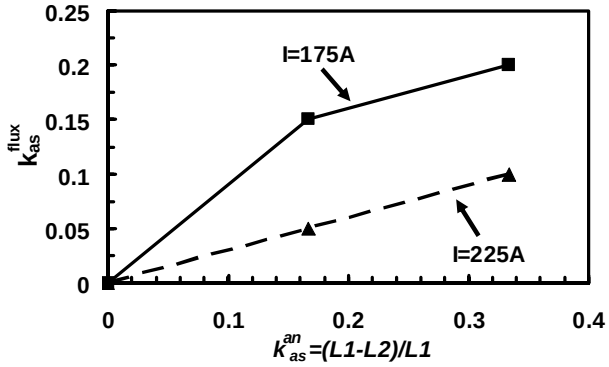

Fig 5. Incoming heat flux asymmetry vs. anode body asymmetry

$U_{eff}^{0} + U_{eff}^{ss}, U_{eff}^{ss}$ were determined from symmetrical anode simulations (with $k_{as}^{flux} = 0$) using the temperature measurements. These values were used for the asymmetric anode simulations. The parameter k_{as}^{flux} was determined by fitting the calculated temperatures (solving the system of equation (1)-(3)) at the thermocouple locations to the measurements.

Eq. (1) was numerically simulated with initial and boundary conditions (2) using a finite-difference method.

4. Results

The dependence of U_{eff} on time is shown in Fig. 4. It is seen that U_{eff} decreased from 10.5 V at t=0 to 7 V in steady-state for I=175A. U_{eff} slightly increased with arc current (up to 11 V at t=0 and 7.5V at steady state for I=225A). k_{as}^{flux} is presented in Fig. 5 as a function of the anode body asymmetry coefficient defined as $k_{as}^{an} = \frac{L1 - L2}{L1}$. It can be seen that heat flux asymmetry increased for more asymmetric anodes.

The time dependent anode temperature T_1 (apex) and T_3 (rear surface) are shown in Fig. 6 for *I=175 A* and *L2=20 mm*. The apex temperature increased with time reaching saturation of about 2000 K at t~80 s after arc ignition. The radial temperature distributions on the front and rear anode surfaces (along the *x-line* as shown in Fig. 1b) are shown in Fig. 7 for symmetric and asymmetric anodes with L2=20 mm. In the case of the symmetric

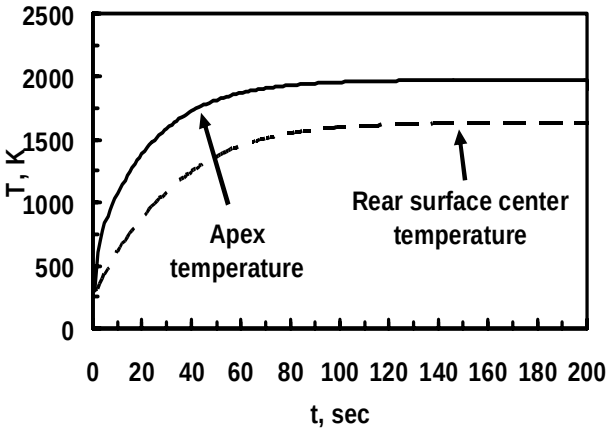

Fig. 6. Asymmetric anode temperature evolution (L2=20mm, I=175A)

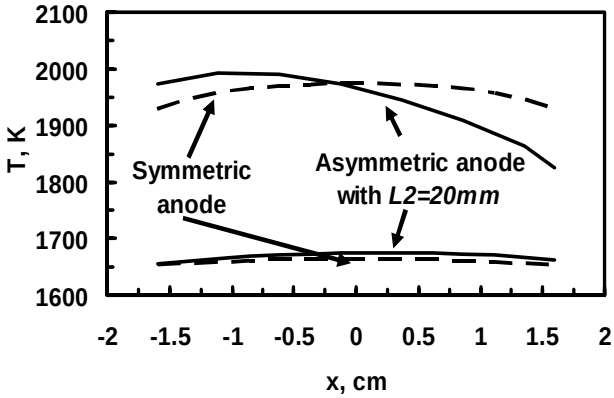

Fig 7. Radial anode temperature distribution. Upper and lower curves - front and rear surfaces, respectively. Solid and dashed curves - asymmetric and symmetric anodes, respectively (*I=175A* and *L2=20mm)*

anode, the maximum surface temperature was at the anode axis ($T_{max}^{sym} = 1975K$), and the temperature decreased slightly in the radial direction.

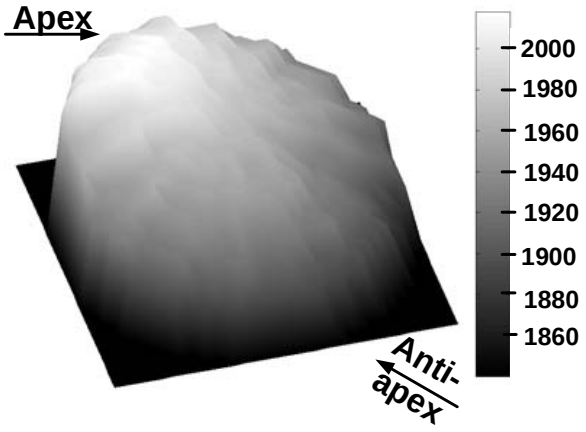

Fig 8. An illustration of face anode surface temperature distribution (*I=175A* and *L2=20mm)*.

The temperature distribution for the asymmetric anode was asymmetric, with the maximum ($T_{\max}^{asym} = 2000K$) shifted from the anode axis in the apex direction (Fig.7). The temperature at the anode boundary near the apex was lower than $T_{\max}^{asym}$. The difference between the maximal and minimal surface temperatures increased from 50 K for the symmetric anode up to 150 K for an asymmetric anode with L2=20 mm for I=175 A. The rear surface temperatures for both anode geometries were close.

A typical front anode surface temperature distribution obtained from 3D calculation is shown in Fig. 8 for *I=175 A* and *L2=20 mm* shows the asymmetry of the anode temperature distribution.

4. Discussions

According to the time dependence of $U_{eff}(t)$, the heat flux to the anode decreases with time. This dependence is a characteristic of a transition from the conventional arc mode to the HRAVA mode. During the transition, the plasma plume developed in the interelectrode gap, expanding and increasing its density. The cathode plasma jets are dissipated in the anode plasma plume [6]. As a result, the radial energy loss from the gap increases while the cathode jet energy impinging on the anode decreases during the transition. Slight increasing of U_{eff} with I may be associated with the previously observed increasing of the plasma temperature with I [6].

The obtained 20% increasing of heat flux from anode center to the apex may be caused by change of the interelectrode distance and therefore the plasma distribution change due to the gap geometry. Slight decreasing of k_{as}^{flux} with I indicates that the plasma distribution in gap was more uniform for higher I.

The sharply increasing anode temperature with time during the initial stage is due to linear heat conduction in the anode body during this stage of arcing when the incoming heat flux was much higher than the energy losses by the radiation. During non-linear heat conduction (anode radiation is important), the rate of temperature rise decreases with time and then the anode temperature reached the saturation determined by the balance of incoming and radiated heat fluxes.

The asymmetric heat flux distribution for the asymmetric anode produced an asymmetric anode temperature distribution. Heat flux was maximal at the anode apex and therefore the maximal temperature was shifted from the anode axis (for the symmetric anode) in direction to the apex (for the asymmetric anode). However, the calculated anode surface temperature located at the anode boundary (see Fig. 7 at x=-1.6) was lower than the maximal apex temperature due to the lateral anode surface radiation.

As the anode body asymmetry reduced with distance from the asymmetric anode face to rear surfaces then the radial temperature distribution is more symmetric in direction to the rear surface and it is close to that at the rear surface for symmetric anode.

Acknowledgments

The research was supported by a grant from Israel Science Foundation

References

[1] I.I. Beilis, R. L. Boxman and S. Goldsmith - Surface and Coatings Technology, **133-134**, issues 1-3, 91 (2000).

[2] I.I. Beilis, A Shashurin, D Arbilly, S. Goldsmith and R. L. Boxman - Surface and Coatings Technology, **177-178**, issues 1-3, 233 (2004).

[3] H.C. Miller, in "Handbook of Vacuum Arc Science and Technology", Ed by R.L. Boxman, e*t.al.* Noyes, Park Ridge NJ, (1995).

[4] H. Ehrich, B. Hasse, M. Mausbach, M. Muller - J. Vac. Sci. Thechnol. **A8**, 2164 (1990)

[5] N. Sanders, K. Etemadi and E. Pfender - J. Appl. Phys., **53** (6) 4136 (1982).

[6] I.I. Beilis, S. Goldsmith, R.L. Boxman - Phys. Plasmas. **9**, 3159 (2002).

[7] H. Rosenthal, I.I. Beilis, S. Goldsmith, R.L. Boxman - J. Phys. D: Appl. Phys. **28**, 353 (1995).

[8] I.I. Beilis, A. Nemirovsky, S. Goldsmith, R.L. Boxman - IEEE Trans. Plasma Sci., **31**, N5, Part 1, 958 (2003)

[9] I.I. Beilis, A Shashurin, A. Nemirovsky, S. Goldsmith and R.L. Boxman - Surface and Coatings Technology, **188-189**, 228 (2004).

Effect of SiO_x -like films deposited by plasma from O_2/HMDSO mixtures on morphology and wettability of polypropylene films

A. Bellel[1], S. Sahli[1], P. Raynaud[2], Y. Segui[2], Z. Ziari[1], D. Eschaich[2]

[1] *Laboratoire de Microsystèmes et Instrumentation, Université Mentouri, Route de Ain El Bey, 25000 Constantine, Algérie*
[2] *Laboratoire de Génie Electrique, Université Paul Sabatier, 118 rte de Narbonne, Bat 3R3, 31062 Toulouse Cedex, France*

Abstract

Polypropylene (PP) foils were coated with thin SiO_x layer elaborated in DECR plasma reactor from a mixture of hexamethyldisiloxane and oxygen. According to contact angle measurements, the surfaces of PP become hydrophilic after the deposition of ultra thin SiO_x film. AFM analysis revealed the formation of irregular structures, which disappear with increasing film thickness. XPS showed that the films composition transforms into more oxidized state as the deposited film thickness increases.
Keywords: Polypropylene; SiO_x films; Contact angle; XPS; AFM

1-Introduction

Polypropylene (PP) is one of the common polymers with very wide field of applications due to their low density, flexibility, chemical inertness and cost-effectiveness. However, PP has very low surface energy which has limited the widespread use of this material. Therefore, the surface modification techniques that can transform these inexpensive materials into highly valuable products have become an important part of the polymers industry. Various surface treatment techniques have been developed to improve the wettability and adhesion properties of PP surfaces without affecting their excellent bulk properties. Some of the common used surface treatment techniques include: plasma, corona discharge, ion beam and microwave irradiation [1-4]. In many cases, surface treatment tends to create an increased surface tension, which is often explained by the formation of new functional groups on the surface of the polymer such as hydroxyl (OH) and carbonyl (C=O) groups [5]. However, it is well established that these surface modifications are degraded in time (aging effects), when exposed to the atmospheric conditions [6]. Hence, new surface modification technique is required to get the polymer surfaces free of damage and having good wettability with a long lifetime. A coating of polymer surface was found to be relatively successful in enhancing the wettability of polymers yielding a more stable hydrophilic treatment.

In this study, surface modification of PP films was carried out via the deposition of thin SiO_x film using plasma enhanced chemical vapor deposition (PECVD). Such films find great potential in biomaterial application and in microelectronics industry [7-8]. The films were elaborated in a microwave DECR plasma reactor from a mixture of hexamethyldisiloxane (HMDSO) and oxygen.

2. Experimental details

PP films of 100 µm thickness were used in all plasma deposition experiments. The polymer was cut into square shaped samples (20 x 20 mm^2) and they were washed with acetone in an ultrasonic washer and dried in an ambient air prior to plasma deposition. The precursor used for PECVD deposits was the hexamethyldisiloxane (HMDSO) which chemical formula is $(CH_3)_3$-Si-O-Si-$(CH_3)_3$.

The PECVD coating experiments were performed in a DECR reactor (2.45 GHz) illustrated in figure 1. The apparatus and its main features have been fully described in more detail in ref [9]. During deposition, the PP substrates were located 18 cm below the glow discharge zone. The deposition was carried out from a mixture of HMDSO and O_2 in the 1:9 proportions. The microwave power and the gas pressure were kept constant at 400 W and 2 mTorr respectively. According to these discharge parameters, the deposition rate was estimated to be 0.047 nm/s [10]. Deposition time was varied in order to observe different stages of the film growth on the polymer substrate.

Films deposited on PP substrates were characterized by contact angle measurements in order to investigate direct effects of the plasma treatment on their wetting property. The measurements were

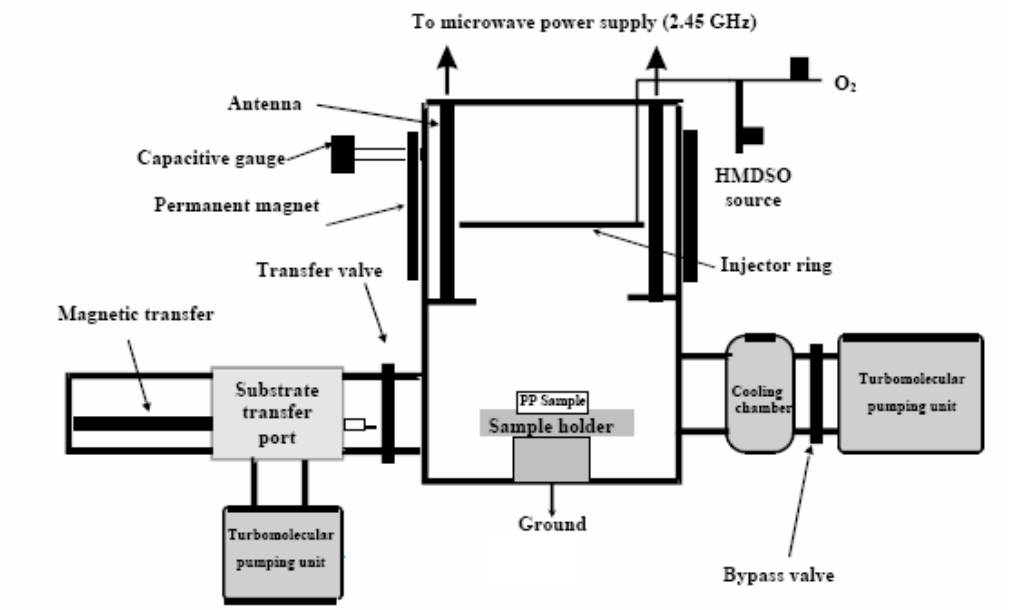

Figure 1: Schematic view of the DECR reactor.

performed using Digitrop contact angle meter made by GBX scientific. Mean value of all contact angles data were averaged from three to five replicates. The measurements were carried out immediately after plasma deposition, at room temperature and atmospheric pressure. For surface energy estimation, different test liquids with different surface free energy values have been used (de-ionized water, formamide, and diiodomethane). The surface energy and its related components were calculated using Owens and Wendt model [11].

The morphology of the deposited film surfaces was studied by atomic force microscopy (AFM) technique. The AFM images were recorded by an Autoprobe CP from Park Scientific Instruments using tapping^{TM} mode and scan rate of 1Hz/line. All scans were characterized by measuring the root-mean-square roughness (R_{rms}) and the arithmetic average of the absolutes values of the surface height (R_{av}) [12]. In order to obtain representative information, different areas were studied on each sample.

Atomic composition was determined by X-ray photoelectron spectroscopy (XPS). The measurements were performed on a VG Scientific photoelectron spectrometer using the monochromatic AlKα X-ray source ($h\upsilon$=1486.6 eV) at normal photoelectron emission angle. The XPS spectra were referenced with respect to the carbon C1s core level at binding energy of 284.4 eV to eliminate charging effects. A constant value of full width at half maximum (FWHM) was used for spectral deconvolution, using a Gaussian type of fitting. The Si 2p peaks were resolved into three components according to the method described by Alexander et al [13].

3. Results and discussion

The extent of surface modification of PP films achieved because of plasma coating has been evaluated by using the contact angle measurement. Surface free energy and its related components for untreated and coated PP films were calculated by measuring the contact angles for three testing liquids (water, formamide and diiodomethane). Figure 2 shows the variation of the contact angle as a function of the deposited film thickness. The values of contact angle decreased rapidly with increasing deposited film thickness for all testing liquids and then reached a constant minimum level. For untreated PP film, the water contact angle was in the order of 99° then decreased significantly to only 27° after the deposition of about 6.6 nm thick SiO_x film on PP substrate. Increasing film thickness to about 28 nm did not improve the hydrophilicity much further. The obtained values of water contact angle were in the range of that found for glass substrate [14]. Figure 3 shows the variation of the surface free energy and its related components as function of deposited film thickness. The results derived from the calculations using the Owens and Wendt model [11], showed that the surface tension of untreated PP was about 27 mJ/m^2. Especially the polar part is near 0.5 mJ/m^2 only. After the deposition of ultra thin SiO_x layer of about 3 nm, there is a considerable increase in the total surface energy and the polar part, which reached a maximum value of about 35 mJ/m^2

and 64 mJ/m^2 respectively. The dispersion component remains practically unchanged, which indicates that the polar component is responsible for the wettability of the material. Increasing film thickness did not improve the hydrophilicity much further. The loss of PP surface hydrophobicity during DECR plasma deposition is believed to arise from the formation of polar SiO_x layers.

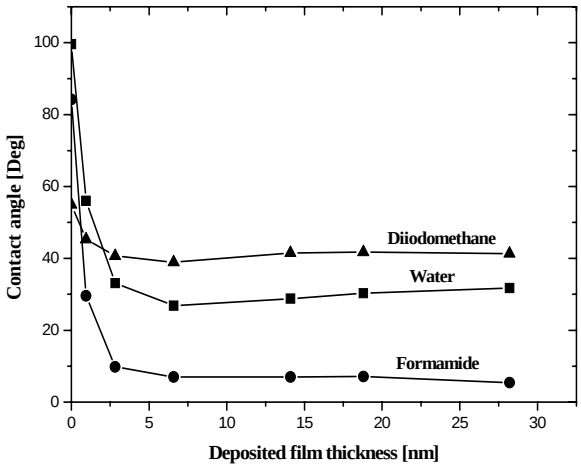

Figure 2: Measured contact angle of untreated and SiO_x coated PP as a function of deposited film thickness.

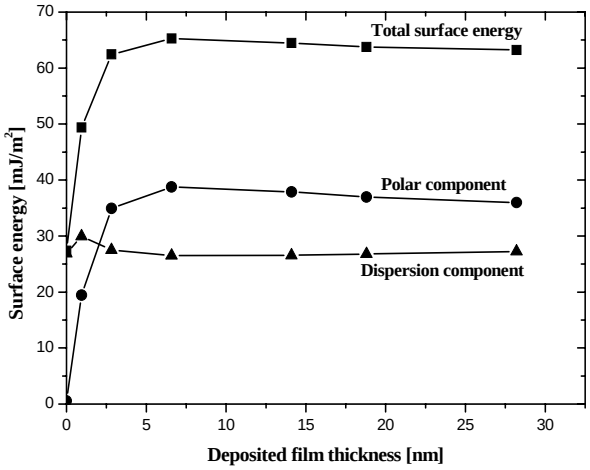

Figure 3: Computed surface energy and its related components.

AFM images of PP surface before and after plasma coating are presented in figure 4. The analyzed area was 2x2 μm^2. The topography shown in Figure 4a is typical of that found for untreated PP samples [15]. The surface roughness (R_{rms}) was in the order of 4.8 nm. For PP coated with 6.6 nm thick SiO_x layer, AFM image showed the formation of irregular structure on PP surface (Figure 4b). This AFM image also shows the presence of microvoids of considerable depth. The surface roughness (R_{rms}) was slightly increased from 4.8 to 6.2 nm. This kind of topography structure has also been observed by Segundo et al [16] for SiO_x films grown by microwave method. The topographical modification induced by plasma deposition is attributed to the ablation effect (etching effect) operating during the early phase of the deposition process in presence of oxygen active species. The ablation process is also supported by the VUV radiation. For thicker coating (28 nm), the irregular surface topography structure has vanished and replaced by the growth of nearly regular ripple structure as can be seen in Figure 4c. The roughness of the surface is however, not changed (R_{rms} = 6.5 nm).

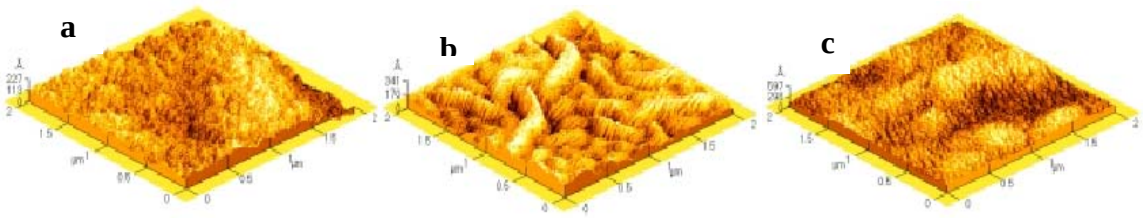

Figure 4: Surface roughness of: (a) untreated PP (R_{rms} = 4.8 nm), (b) PP coated by a 6.6 nm thick SiO_x film (R_{rms} = 6.2 nm) and (c) 28 nm thick SiO_x film (R_{rms} = 6.5 nm).

Table 1 summarizes the Si, O and C content in at.%, obtained from XPS data, of SiO_x films with various film thicknesses. For ultra thin layers, the detected signal of carbon may include also the carbon of the PP substrate. The deposited films were characterized by high proportions of C, which decrease with increasing film thickness. The significant carbon content may be attributed to the existence of an interlayer

between the organic substrate and the PECVD coating. This interlayer has been revealed by many workers [17]. The origin of this interphase was found to be ablation/redoposition process involving volatile organic fragments from the polymer substrate during the first instants of the deposition process. This region was found to consist of cross-linked layer with varying chemical composition. The ablation (etching) of the polymer may be resulted from the action of oxygen active species and VUV photons.

SiO_x film thickness (nm)	Si 2p (%)	O 1s (%)	C 1s (%)	Si 2p peaks components (%)		
				102.1 eV	102.8 eV	103.4 eV
2.8	16	32	52	33	44	23
6.6	21	38	41	22	58	20
28	27	50	23	34	30	36

Table1: Atomic composition and results of the curve fitting of Si 2p peak for SiO_x coated PP.

High resolution of the Si 2p peaks has been performed in order to quantify the silicon environments of the deposited layers. A constant value of full width at half maximum (FWHM) was used for spectral deconvolution, using a Gaussian type of fitting. The Si 2p peaks were resolved into three components (Figure 5) at different binding energies according to a method described by Alexander et al [13]. The 102.1 eV peak was associated with Si bound to two oxygen atoms (unoxidized environment $Si(O-)_2$), the 102.8 eV peak was associated with Si bound to three oxygen atoms (partly oxidized environment $Si(-O)_3$) and the 103.4 eV peak was associated with Si bound to four oxygen atoms (silicon dioxide $Si(-O)_4$). The remaining bonding requirements of the silicon are fulfilled by a various combination of carbon and hydrogen atoms [18]. Figures 5a, 5b and 5c show the effect of film thickness on the distribution of the Si 2p peak amongst the three Si environments. The deconvolution results show that the Si 2p peak shifts toward the high binding energy values as the film thickness increases. For 2.8 nm thick SiO_x films, the partly oxidized environment ($Si(-O)_3$ binding energy 102.8 eV) is the major component (Table 1). When the films thickness is increased, the proportion of unoxidized Si environment ($Si(-O)_2$ binding energy 102.1eV) decreases in favor of the partly oxidized Si environment. At the thickness of about 28 nm, the proportion of partly oxidized Si environment decreases in favor of the oxidized Si environment ($Si(-O)_4$ binding energy 103.4 eV). The deconvolution of the Si 2p peak indicates that the deposited film transforms into more oxidized state when the film thickness increases.

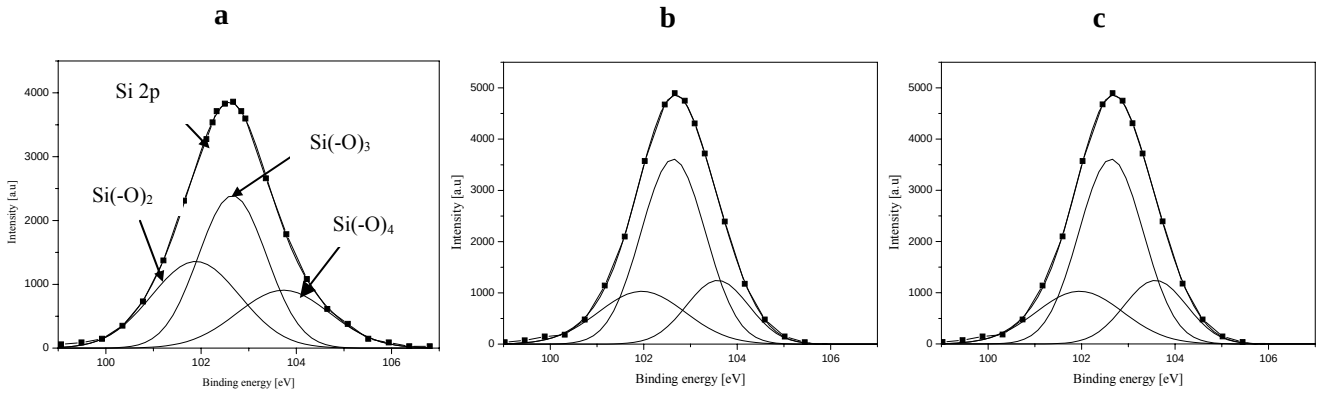

Figure 5: Distribution of the Si 2p signal among the three silicon environments for: 2.8 nm thick SiO_x film (a), 6.6 nm thick SiO_x film (b) and 28 nm thick SiO_x film (c).

4. Conclusions

DECR plasma deposition of thin SiO_x films elaborated from mixture of hexamethyldisiloxane and oxygen on highly hydrophobic PP surface, induces the formation of polar layers. According to the contact angle measurements, the polar component of the surface energy showed a considerable increase from about 0.5 to 35 mJ/m^2 after the deposition of ultra thin SiO_x layer and then stayed nearly at the same level still for

thicker coating. For ultra thin SiO_x layer, AFM images showed the formation of irregular in shape and size structure, due to substrate ablation effect which operates during the very first instants of the film growth. Increasing film thickness, the irregular structure was replaced by the growth of regular ripple structure. The surface roughness was increased from 4.8 nm to 6.2 nm. XPS results show that the deposited films are characterized by high proportions of carbon which decrease with increasing film thickness indicating the presence of an interlayer between the SiO_x film and the polymer substrates. High resolution of the Si 2p peak indicated that as the deposited film thickness increases, the films composition transforms into more oxidized state. The observed improvement in PP wettability may result from the combination of topology modifications (revealed by AFM images) and the chemical composition of the SiO_x deposited layer.

Acknowledgements

This work was supported by CMEP and CNRS/DEF programs. The authors are grateful to Dr D. Hegemann from Swiss Federal Laboratories for Materials Testing and Research (EMPA) for AFM measurements and helpful discussions.

References

[1] N. V. Bhat, D. J. Upadhyay, J. Appl. Polym. Sci. **86**, 925 (2002).
[2] N. Dumitrascu, G. Borcia, G. Popa, J. Appl. Polym. Sci. **81**, 2419 (2001).
[3] A. Saha, V. Chakraborty, S. N. Chintalapudi, Nucl. Instr. and Meth. B **168**, 245 (2000).
[4] S. M. Mirabedini, H. Rahimi, Sh. Hamedifar, S. M. Mohseni, Int. J. Adhes. Adhes. **24,** 163 (2004).
[5] T. N. Murakami, Y. Fukushima, Y. Hirano, Y. Tokuoka, M. Takahashi, N. Kawashima, Colloids and surfaces **29**, 171 (2003).
[6] [1] S. Süzer, A. Argun, O. Vatansever, O. Oral, J. Appl. Polym. Sci. **74**, 1846 (1999).
[7] N. Inagaki, S. Tasaka, T. Nakajima, J. Appl. Polym. Sci. **78**, 2389 (2000).
[8] J. Schwarz, M. Schmidt, A. Ohl, Surf. Coat. Technol. **98,** 859 (1998).
[9] S.Sahli, S.Rebiai, P. Raynaud, Y. Segui, A. Zenasni, S. Mouissat, Plasmas Polym. **7,** 327 (2002)
[10] G. Dennler, A. Houdayer, P. Raynaud, I. Seguy, Y. Segui, M.R. Wertheimer, Plasmas Polym. **8**, 43 (2003.
[11] D.K. Owens, R.C. Wendt, J. Appl. Polym. Sci. **13**, 1741 (1969).
[12] E. Finot, S. Roualdes, M. Kirchner, V. Rouessac, R. Berjoan, J. Durand, J.-P. Goudonnet, L.Cot, Appl. Surf. Sci. **187**, 326 (2002).
[13] M.R. Alexander, R.D. Short, F.R. Jones, W. Michaeli, C.J. Blomfield, Appl. Surf. Sci. **137**, 179 (1999).
[14] L.D. Eske, D.W. Galipeau, Colloids and Surf. A **154**, 33 (1999).
[15] N. Cui, M.D. Brown, Appl. Surf. Sci. **189**, 31 (2002).
[16] A. Zuriga-Segundo, F. Ruiz, C. Vazquez-lopez, J.Gonzalez-Hemandez, J. Vac. Sci. Technol. A**12**, 2572 (1994).
[17] G. Dennler, A. Houdayer, P. Raynaud, I. Seguy, Y. Segui, M. R. Wertheimer, Nucl. Instr. and Meth. B **208**, 176 (2003).
[18] F. Bosc, J. Sanchez, V. Rouessac, J. Durand, Separ. Purif. Technol. **32**, 371 (2003).

Photographing Impact of Plasma-Sprayed Zirconia and Amorphous Steel Particles on Hot and Cold Glass Substrates

A. McDonald[1], M. Lamontagne[2], S. Chandra[1], C. Moreau[2]

[1]*Department of Mechanical Engineering, University of Toronto, Toronto, Ontario, Canada*
[2]*Industrial Materials Institute, National Research Council Canada, Boucherville, Québec, Canada*

Abstract

Plasma-sprayed molten yttria-stabilized zirconia and armorphous steel (38 – 55 μm diameter) were photographed during impact (velocity 135 – 220 m/s) and spreading on a smooth glass surface that was maintained at either room temperature or 400°C. As a droplet approached the surface, it was sensed by a photodetector and after a known delay, a laser was triggered to illuminate the spreading splat. The splat was photographed with a CCD camera. A rapid two-color pyrometer was used to collect the thermal radiation from the impacting and spreading particles to follow the evolution of their temperature and size. The molten particles that impacted a surface at room temperature ruptured and splashed after impact leaving only a small central core adhering to the substrate. On a surface held at 400°C, there was no splashing and a circular splat remained on the surface. Splats on a glass surface held at room temperature had a large maximum spread diameter, almost three times that on a hot surface. The cooling rate on a cold surface was significantly lower than that on a hot surface, suggesting that thermal contact resistance was much greater.

1. Introduction

Plasma spraying is used to deposit coatings that protect against material degradation processes such as wear, erosion, or corrosion. A high-temperature ionized gas jet is used to melt and accelerate metal or ceramic particles to coat a substrate. The molten or partially molten particles impact the substrate, spread while cooling down, and solidify on the substrate or on previously deposited layers. The quality and strength of the coating depends on the size and degree of splashing of the particles after impact. Many experimental studies have been conducted to identify the parameters that influence the size and morphology of the droplets after impact. Aziz and Chandra [1] have presented photographs of tin droplets spreading on cold and heated stainless steel surfaces in intervals of a few milli-seconds after impact. They found that as the droplet impact velocity increased, the maximum diameter of the splat increased and significant splashing occurred. Bhola and Chandra [2] also found that large impact velocities caused impacting droplets to fragment. They used the Rayleigh-Taylor instability to determine the number of satellite droplets formed after impact.

Fukumoto, et al. [3] found that, for nickel and copper droplets in a thermal spray simulated experiment, increasing the substrate temperature reduced the occurrence of splashing and produced disk-like splats. They defined a "transition temperature" as the temperature of the substrate at which 50% of the splats changed from a splash morphology to a disk-like morphology. Since it was shown that impact on cold substrates enhance splashing and fragmentation [3], Jiang, et al. [4] have shown that removal of condensates and/or adsorbates from a cold stainless steel substrate may eliminate splashing and splat fragmentation of impacting molten ZrO_2 and produce contiguous, disk-like splats. The formation of the disk-like splats were attributed to improved contact between the splat and substrate, in the absence of the condensates and adsorbates. It was also shown that the same contiguous, disk-like morphology occurred for splats on a substrate held at 500°C.

Many images have been presented of the impact and spread of low velocity (1 - 10 m/s) droplets on flat surfaces. However, it is difficult to capture images of the spreading particles in the actual plasma-spray process (100 – 250 m/s). Mehdizadeh, et al. [5] and McDonald, et al. [6] have photographed plasma-sprayed molybdenum droplets impacting cold and hot glass by using a CCD camera and long-range microscope. A rapid two-color pyrometer was also used to obtain the size and temperature evolution during spreading. The two-color pyrometric method, as described by Vardelle, et. al [7], calculates the splat size and temperature from the ratio of the intensities of radiation collected at two different wavelengths. The two-color pyrometric method was used by Moreau, et al. [8] to show that there is a period of rapid decrease of the size of the splat after reaching the maximum extent. This was attributed to contraction and fragmentation of the splat due to surface tension forces.

Studies of the microstructure of splats and coatings have shown that the cooling rates of splats on cold substrates differ significantly from those on heated substrates. Fukumoto, et al. [3] found that the

microstructure of the splat on the hot substrate was fine, columnar, flat, and non-porous, while on the cold substrate it was composed of isotropic coarse grains. The transitional change of grain size and quality with increasing substrate temperature indicated that the cooling rate of the splat on the hot substrate was larger than that on the cold substrate. However, actual temperatures during the cooling of the splat were not measured. McDonald, et al. [6] measured the cooling rates of molybdenum splats on cold and heated glass from the temperature evolution obtained from two-color pyrometry. It was found that the cooling rate on hot glass was an order-of-magnitude larger than that on glass held at room temperature.

This study extends the work of McDonald, et al. [6] by photographing the impact and spread of zirconia and steel droplets on glass held at room temperature and at 400 ^{o}C. The steel used in this study is an amorphous iron-chromium based alloy with chemical composition, 44% Cr, 48% Fe, 6% B, 2% Si, and traces of C and S and melting point at ~1550 ^{o}C. A CCD camera was used to capture images of the splat at several instances during spreading. The maximum spread diameter was measured from the images. The temperature evolution of the splat during spreading was used to calculate the cooling rate. A high speed two-color pyrometer was used to measure the temperature of the particles after collision and during spreading on a flat, smooth glass surface.

2. Experimental Method

The experimental assembly and method have been described in detail by Mehdizadeh, et al. [5] and McDonald, et al. [6]. A schematic diagram of the experimental setup is shown in Figure 1.

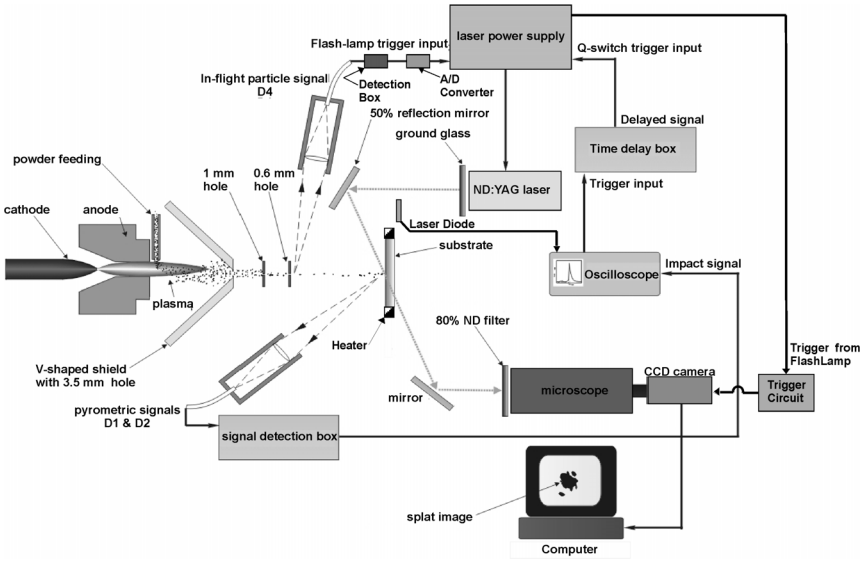

Figure 1. Schematic of the experimental assembly.

A SG100 torch (Praxair Surface Technologies, Indianapolis, IN) was used to melt and accelerate the dense, amorphous steel (LMC-M, Liquidmetal Technologies, USA) and zirconia (#825, Amperit, USA) powder particles, seived to +38 –55 µm. The powder feed rate was less than 1 g/min. The substrate was a glass microscope slide (Fisher Scientific, Pittsburgh, PA) that was washed with water and ethanol and dried in an oven at 140°C for 30 minutes.

The plasma torch was passed rapidly across the glass substrate. In order to protect the substrate from an excess of particles and heat, a V-shaped barrier was placed in front of the torch.

The thermal radiation of the particle was measured with a rapid two-color pyrometric system.This system included an optical sensor head that consisted of a custom-made lens, which focused the collected radiation, with a 0.21 magnification, on an optical fiber with an 800 µm core [5,6]. This optical fiber was covered with an optical mask that was opaque to near infrared radiation, except for three slits. The two smaller slits, with dimensions of 30 µm by 150 µm and 30 µm by 300 µm, were used to detect the thermal radiation of the particles in flight. The radiation was used to calculate the temperature, velocity, and diameter of the in-flight particle [9]. The largest slit, measuring 150 µm by 300 µm, was used to collect thermal radiation of the particle as it impacted and spread on the substrate. With the thermal radiation from this slit, the splat temperature, diameter, and cooling rate were calculated at 100 ns intervals after impact.

The collected thermal radiation was transmitted through the optical fiber to a detection unit that contained optical filters and two photodetectors. The radiation beam was divided into two equal parts by a beam splitter. Each signal was transmitted through a bandpass filter with wavelength of either 785 nm or 995 nm and then detected using an avalanche silicon photodetector. The ratio of the radiation intensity at these wavelengths (referred to as D_1 and D_2, respectively) was used to calculate the particle temperatures with an accuracy of ± 100°C [9].

The thermal emission signals captured by the photodetectors showed the temporal positions of the particle as it passed through the field of view of each of the optical slits. When the particle was not in an optical field of view, the signal voltage was zero. Two small peaks were produced by thermal emissions from the particle as it passed through the first two small slits. The droplet average in-flight velocity was calculated by dividing the known distance between the centers of the two slits by the measured time of flight. A plateau on the thermal emission signal corresponded to the presence of the in-flight particle in the field of view of the third and largest optical slit before impact. Upon impact, the signal increased as the particle spread and eventually decreased as the particle cooled down and/or splashed out of the field of view.

To illuminate the impacting particle, a 5±2 ns duration pulse of light from a Nd:YAG laser (Continuum Minilite, Santa Clara, CA) was used. Since the flashlamp of the laser had to be triggered at least 150 μs before it was pulsed, an optical sensor (labelled D_4 in Fig. 1) was positioned to detect thermal radiation from a particle immediately after it exited the 0.6 mm hole in the third shielding plate (Fig. 1). When the particle entered the third slit field of view of the optical fiber, a signal was sent to trigger the laser after a controlled time delay. This permitted illumination of the substrate at different time intervals after impact and during spreading of the droplet.

A 12-bit CCD camera (QImaging, Burnaby, BC) was used to capture images of the spreading particles. The electronic shutter of the camera was triggered to open by a signal from the flashlamp of the laser. The camera was connected to a long-range microscope (Astro-optics Division, Montpelier, MD) that had an 80% neutral density (ND) filter to attenuate the intensity of the laser beam. The images captured by the camera were digitized by a frame grabber and recorded on a personal computer. Since the images were not photographed directly, but rather, their reflection in a mirror that was at an angle relative to the substrate, the digitized images were rotated and shortened on both dimensions.

3. Results and Discussion

Impact on glass at room temperature

Typical thermal emission signals and images showing the evolution of the splat size and morphology after impact on cold glass are shown in figures 2a and 3a, respectively for zirconia and steel. The average impact velocities of the zirconia and steel particles were 200 m/s and 175 m/s, respectively. The average in-flight temperatures were 2750 ^{o}C and 2910 ^{o}C for zirconia (melting point: 2700 ^{o}C) and steel (melting point: 1550 ^{o}C), respectively. According to the signals, between points *a* and *b*, the splat reaches the maximum spread diameter within 2 μs after impact. As determined from the images collected with the CCD camera and the thermal emission signals, the average maximum diameter of the zirconia splats on cold glass is approximately 450 μm and that of steel is approximately 400 μm. The images show that as the particles on cold glass spread to the maximum extent, they become thin film liquid splats that begin to disintegrate, approximately 1.5 μs after impact (Fig.2a and 3a). The splat material eventually splashes out of the fields of view of the camera and the thermal emission detectors, leaving a central solidified core on the glass surface.

Impact on glass at 400 ^{o}C

Figures 2b and 3b show that on glass held at 400 ^{o}C, there was almost no splashing or break-up. The splats, for both materials, spread to a maximum diameter of approximately 200 μm. Beyond the maximum extent, the splats receded to a diameter smaller than the maximum diameter. In figure 3b, it is evident that the diameter of the steel splats decrease significantly, possibly due to surface tension forces that pull back the liquid film before significant solidification occurs. Some investigators have found that the splat does not begin to solidify until after reaching the maximum splat diameter [10], enabling the liquid to recoil due to

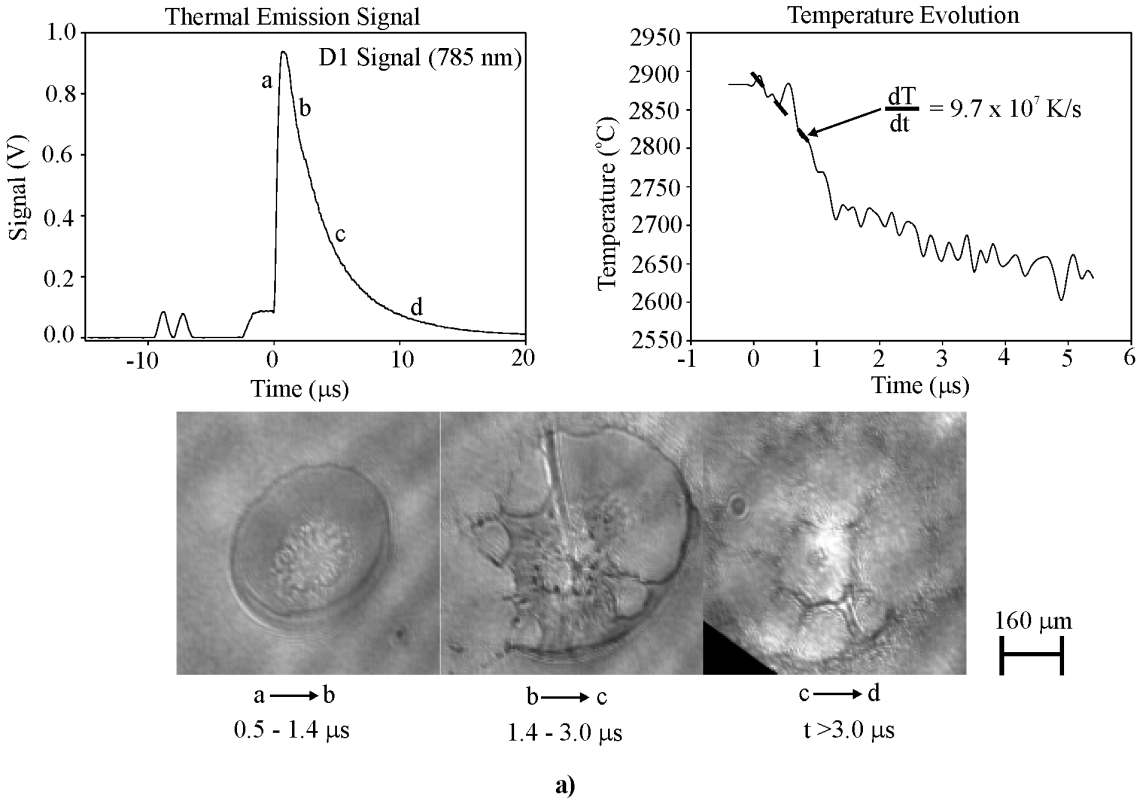

a)

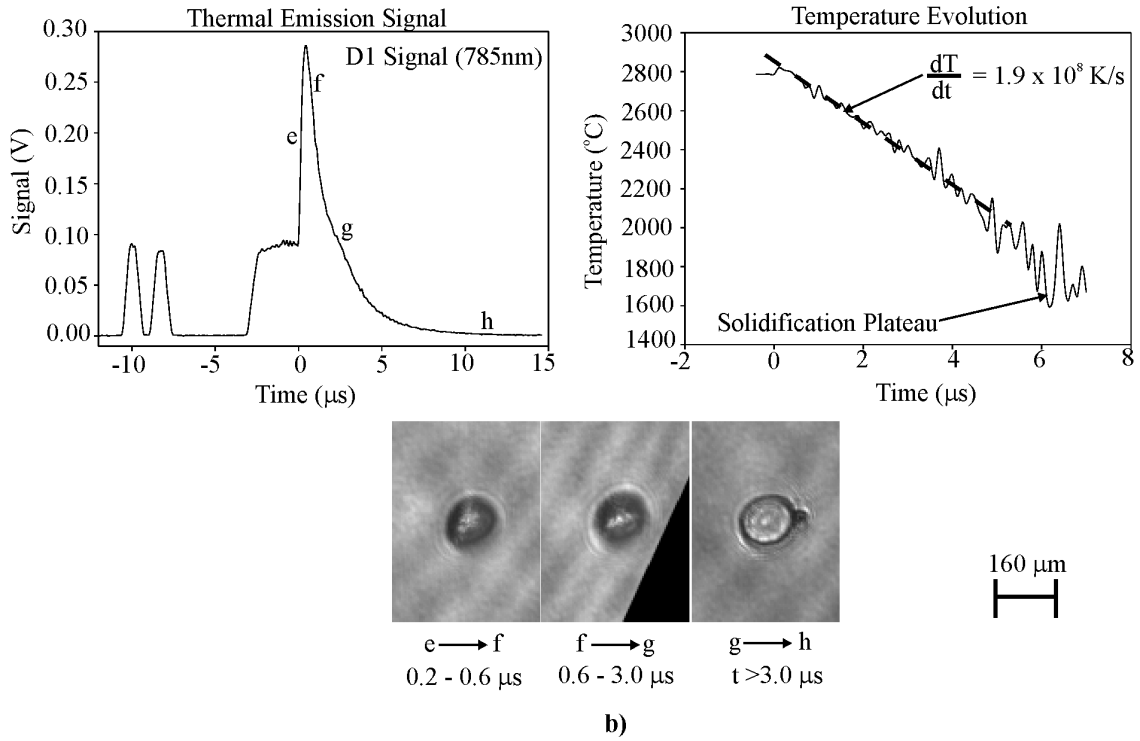

b)

Figure 2. Photodetector signals and images of zirconia at different times after impact on glass at a) room temperature and b) 400 °C

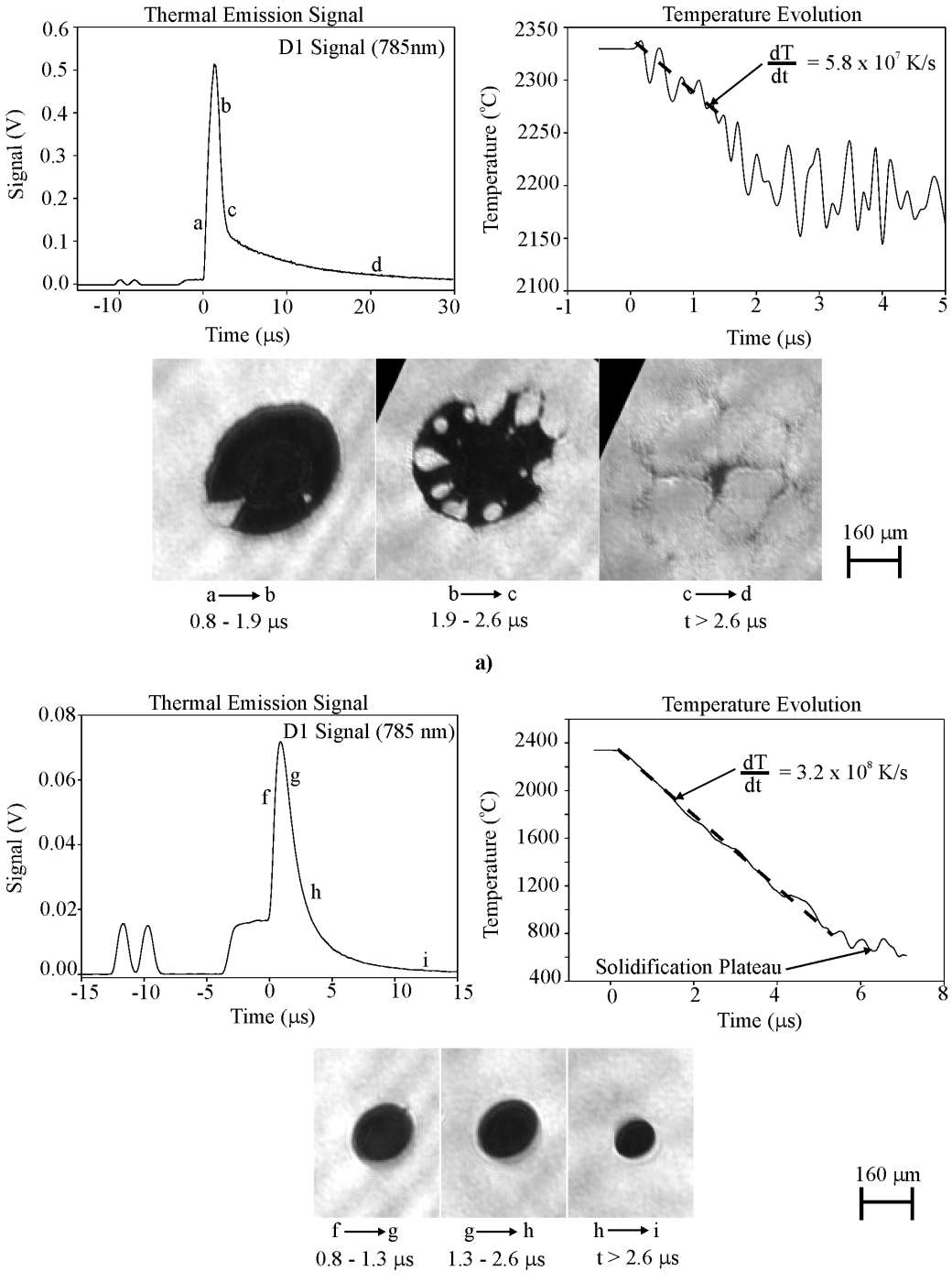

Figure 3. Photodetector signals and images of armacor at different times after impact on glass at a) room temperature and b) 400 °C.

surface tension forces after reaching the maximum spread extent. The thermal emission signals show that the maximum extent occurs within 0.5 μs after impact for both materials. Comparison of the images and thermal emission signals for the splats on cold and hot glass, shows that the maximum spread diameter on cold glass is almost three times larger than that on hot glass. McDonald, et al. [6] and Moreau, et al. [8] have found similar results for molybdenum impact on hot and cold glass.

Splat Temperature Evolution

The splat temperature evolution and the average liquid cooling rates are shown in figures 2 and 3. The cooling rates on the hot glass (order of 10^8 K/s) were much larger than that on the cold glass (order of 10^7 K/s), suggesting that there is lower thermal contact resistance between the splat and the hot glass. The contact resistance between the cold glass and splat may be due to a gas barrier composed of vaporized adsorbates/condensates [4] and entraped air [11].

On the cold glass, the splat liquid cooling rates were calculated from temperatures at the point of impact to the maximum spread extent and before splashing, to ensure that the temperature decrease was not due to loss of material out of the pyrometric fields of view. Since significant splashing did not occur on hot glass, the cooling rate was calculated from temperatures at the point of impact to the solidification plateau (Fig. 2 and 3). The solidification plateau for zirconia occurred at a temperature that was approximately 10% lower than the melting point. For the amorphous steel, the plateau occurred at a temperature that was about 65% lower than the melting point. This, coupled with the large cooling rates, indicates that there was undercooling of the splats on hot glass [12].

4. Conclusion

The influence of substrate temperature on the splat morphology, the maximum spread diameter, and the cooling rate of plasma-sprayed zirconia and steel particles was studied. The flattening of the droplet was monitored by a rapid two-color pyrometer and the thermal emission signals were used to calculate the splat temperatures and cooling rate.The splat was photographed after impact with a CCD camera.

Molten particles that impacted a surface at room temperature disintegrated and splashed after impact leaving only a small central portion adhering to the substrate. On a surface held at 400°C, there was no splashing and a circular splat remained on the surface. Splats on a glass surface held at room temperature had a large maximum spread diameter, approximately three times that on a hot surface. The cooling rate on a cold surface was much lower than that on a hot surface, suggesting that thermal contact resistance was much lower on the hot surface.

5. References

[1] S. Aziz and S. Chandra, "Impact, recoil, and splashing of molten metal droplets", *Int. J. Heat Mass Transfer*, (2000), **43**, pp. 2841 – 2857.

[2] R. Bhola and S. Chandra, "Parameters controlling solidification of molten wax droplets falling on a solid surface", *J. of Material Science*, (1999), **34**, pp. 4883 - 4894.

[3] M. Fukumoto, E. Nishioka, and T. Matsubara, "Flattening and solidification behavior of a metal droplet on a flat substrate surface held at various temperatures", *Surface Coatings and Technology*, (1999), **120 – 121**, pp. 131 – 137.

[4] X. Jiang, Y. Wan, H. Hermann, S. Sampath, "Role of condensates and adsorbates on substrate surface on fragmentation of impinging molten droplets during thermal spray", *Thin Solid Films*, (2001), **385**, pp. 132 – 141.

[5] N. Mehdizadeh, M. Lamontagne, C. Moreau, and S. Chandra, "Photographing impact of molten molybdenum particles in a plasma spray", due for publication in *J. Thermal Spray Tech.*, (2005).

[6] A. McDonald, M. Lamontagne, C. Moreau, S. Chandra, "Visualization of impact of plasma-sprayed molybdenum particles on hot and cold glass substrates", *International Thermal Spray Conference*, (2005).

[7] M. Vardelle, A. Vardelle, P. Fauchais, and C. Moreau, "Pyrometer system for monitoring the particle impact on a substrate during a plasma spray process", *Meas. Sci. Technol.*, (1994), **5**, pp. 205 – 212.

[8] C. Moreau, J. Bisson, R. Lima, and B. Marple, "Diagnostics for advanced materials processing by plasma spraying", *Pure and Applied Chemistry,* in the press.

[9] C. Moreau, P. Cielo, M. Lamontagne, S. Dallaire, M. Vardelle, "Impacting particle temperature monitoring during plasma spray deposition", *Meas. Sci. Technol.,* (1990), **1**, pp. 807 – 814.

[10] T. Watanabe, I. Kuribayashi, T. Honda, and A. Kanzawa,"Deformation and solidification of a droplet on a cold substrate", *Chemical Engr. Science*, **47**(12), (1992), pp. 3059 – 3065.

[11] V. Mehdi-Nejad, J. Mostaghimi, and S. Chandra, "Air bubble entrapment under an impacting droplet", *Phys. of Fluids*, **15**(1), (2003), pp.173 – 183.

[12] R. McPherson, "The relationship between the mechanism of formation, microstructure, and properties of plasma-sprayed coatings", *Thin Solid Films*, **83**, (1981), pp. 297 – 310.

Spectroscopic Diagnostics of Dielectric Barrier Discharges at Atmospheric Pressure

V. Poenariu[1], R. Bartnikas[2] and M.R. Wertheimer[1*]

[1]*Groupe des Couches Minces and Department of Engineering Physics, Ecole Polytechnique, Montreal, Quebec, H3C 3A7, Canada*
[2]*Hydro-Quebec Research Institute, Varennes, QC J3X 1S1, Canada*
[*]*Corresponding author: michel.wertheimer@polymtl.ca*

Abstract
We present optical emission spectroscopy studies of atmospheric pressure glow discharges in flowing pure helium (He), and He/nitrogen (N_2) mixtures. Two different metallic high-voltage electrode geometries have been examined, namely planar and cylindrical, the grounded dielectric-covered electrode being planar. The gap distributions of gas temperature have been evaluated from rotational spectra of molecular nitrogen ion emissions.

Keywords: Atmospheric pressure**,** dielectric barrier, glow discharge, non-thermal plasma, helium, rotational temperature, optical emission spectroscopy

1. Introduction

Dielectric barrier discharges (DBD) at atmospheric pressure are steadily gaining importance since they obviate the need for expensive vacuum systems and can thereby reduce production costs [1]. The gas temperature, T, in the discharge is evidently of great importance, because an excessively high T value can damage thermally-sensitive materials, for example polymers. The purpose of this research has therefore been to measure T in DBDs using optical emission spectroscopy (OES), which has the great advantage of being non-intrusive and non-perturbing. This is accomplished by analyzing high-resolution rotational bands in the emission spectra of suitable electronically-excited molecular species in the discharge. Several molecules have been used in the past for this purpose, but the most frequently studied are nitrogen bands from the Second Positive System (SPS) of N_2 and the First Negative System (FNS) of N_2^+. The latter has the advantage that rotational structure can be fully resolved even with a spectrograph of average performance, and that the rotational temperature, T_{rot}, can be determined from a conventional Boltzmann plot [2].

2. Experimental arrangement

Using the glass-walled DBD apparatus (Fig. 1) described by Radu et al. [3], we have studied atmospheric pressure discharges in flowing He and He/N_2 mixtures, these being excited by audio-frequency (1 to 10 kHz) high voltage (HV). Two different metallic HV electrode geometries have been examined, namely a planar, polished stainless steel electrode with rounded edges, 2.54 cm in diameter, and a cylindrical steel electrode with a radius of 3.15 mm and a length of 26.3 mm. The grounded dielectric-covered electrode is a 1.6 mm thick Al_2O_3 ceramic plate, metallized on its bottom surface.

Optical emission spectroscopy (OES) was studied using a 0.5 m focal length spectrometer (Acton Research SpectraPro 500i), coupled to an ICCD array detector (Roper Scientific PI-MAX 512RB). The spectrometer has a resolution of 0.05 nm at 435.8 nm using a 1200 g/mm grating and a 10-μm slit. Light from the discharge was directed to the spectrometer slit by a mobile optical system, which can provide a (one-dimensional) spatial resolution down to 100 μm. However, to achieve an acceptable signal-to-noise ratio, most of the experiments had a spatial resolution of 250 μm. The rotational band spectra were recorded using an entrance slit width of 10 μm.

Using the R branch of FNS $N_2^+(B^2\Sigma_u^+, v'=0 \rightarrow X^2\Sigma_g^+, v''=0)$ bands near 391 nm, we have measured spatial distributions of T_{rot} for different electrode geometries, gap spacings and gas mixture compositions.

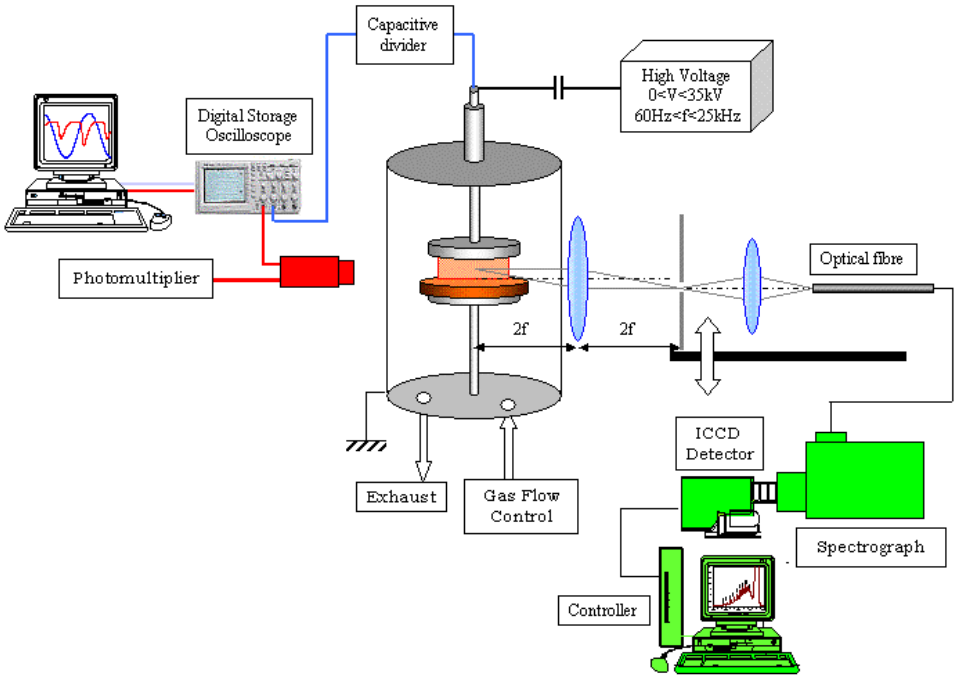

Figure 1. Experimental set-up.

3. Results and Discussion

The optical emission spectrum (Fig. 2) taken between 350 nm and 860 nm of an atmospheric pressure glow discharge (APGD) in high purity helium is very similar to that reported in the literature [4]. This spectrum was obtained in the plane-plane configuration, but it differed little from that obtained in the other configuration. The only differences between the two configurations or between two different axial positions are the relative intensities of the various emission lines. The frequency and amplitude of the voltage applied to the upper electrode and the gap length were also found to influence emission line intensities. However, in each of the discharges emission lines from SPS $N_2(C^3\Pi_u - B^3\Pi_g)$ and FNS $N_2^+(B^2\Sigma_u^+ - X^2\Sigma_g^+)$ bands, triplet oxygen at 777 nm ($3^5P \rightarrow 3^5S$), and the $3^3S \rightarrow 2^3P$ transition at 706.5 nm from helium could be clearly identified.

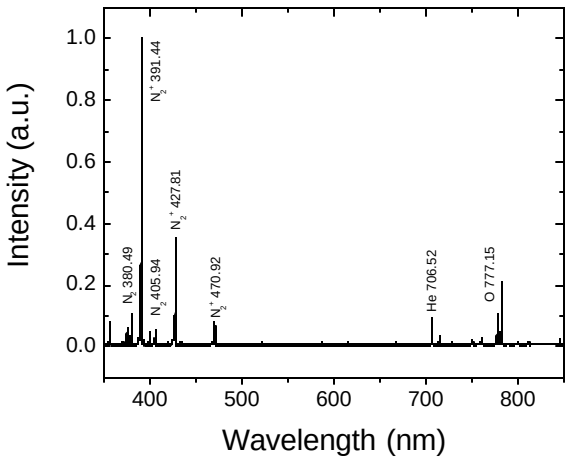

Fig. 2 A typical emission spectrum from high purity helium APGD.

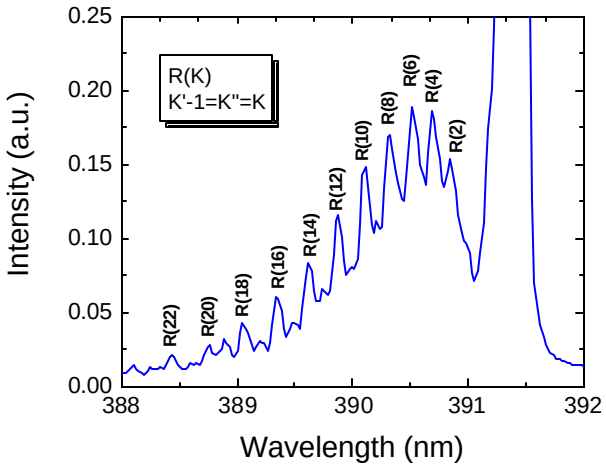

Fig. 3 A typical $N_2^+(B^2\Sigma_u^+, v'=0 \rightarrow X^2\Sigma_g^+, v''=0)$ spectrum from helium APGD.

The most intense emission is the headband of P branch from the $N_2^+(B^2\Sigma_u^+, v'=0 \rightarrow X^2\Sigma_g^+, v''=0)$ transition at 931.44 nm, while helium lines were observed at 667.8 nm ($3^1D \rightarrow 2^1P$), 587.6 nm ($3^3D \rightarrow 2^3P$), or 388.8 nm ($3^3P \rightarrow 2^3S$). The latter is positioned between the R(19) and R(20) lines of the rotational emission spectrum from FNS of N_2^+ (0,0).

Clearly, even in a flow of nominally very pure He, N_2 impurity at the ppm level is sufficient to yield high enough spectral intensity for accurate T_{rot} measurements (Fig. 3). This temperature was determined from the R branch of $N_2^+(B^2\Sigma_u^+, v'=0 \rightarrow X^2\Sigma_g^+, v''=0)$ using the Boltzmann plot method (Fig. 4). The intensities of emission lines from the rotational spectrum are given by the equation

$$\ln\left(\frac{I_{K'K''}}{n\,\nu^4_{K'K''}S_{K'}}\right) = A - \frac{B_{v'}K'(K'+1)hc}{kT_{rot}} \qquad (1)$$

where A is a constant for all lines in a same band (v', v'') for a given rotational temperature, v' and v'' are the vibrational quantum numbers of the upper and lower vibrational states, K' and K'' are the rotational quantum numbers of the upper and lower rotational states, $I_{K'K''}$ is the intensity of a line originating from the same electronic and vibrational level, $\nu_{K'K''}$ is the corresponding wave number, $S_{K'}$ is the line strength, $B_{v'}$ is the molecular rotational constant of the upper vibrational state, h is Planck's constant, c is the velocity of light, and k is Boltzmann's constant. Therefore, by plotting $ln(I_{K'K''}/\nu^4_{K'K''}\,S_{K'})$ against $B_{v'}K'(K'+1)$, a straight line of slope hc/kT_{rot} is obtained [2]; knowing the line intensities and the rotational constants, one can readily determine T_{rot}.

However, some precautions have to be taken to reduce the error in evaluating T_{rot}. Each line of the R branches is overlapped by rotational lines of the folded-back portion of the P branches, that is, R(K) and P(K+27). As a result, at high gas temperatures the P branch lines begin to have an appreciable influence on the measured intensity of low quantum number R branch lines, resulting in lower apparent T_{rot}. Occasionally, between the R(19) and R(20) lines, the emission from the $3^3P \rightarrow 2^3S$ helium transition at 388.865 nm is quite strong; this may artificially increase the intensity of R(20) and result in a higher apparent T_{rot} value.

Each value of T_{rot} has been determined by plotting the average intensities obtained from 25 recorded emission spectra. The standard deviation of the emission line intensities from the R branch is usually between 2 and 5%. We have found that a standard deviation of 5% results in an uncertainty of less than 5% in T_{rot} and we assume that this is close to the average gas temperature, like other authors [5, 6].

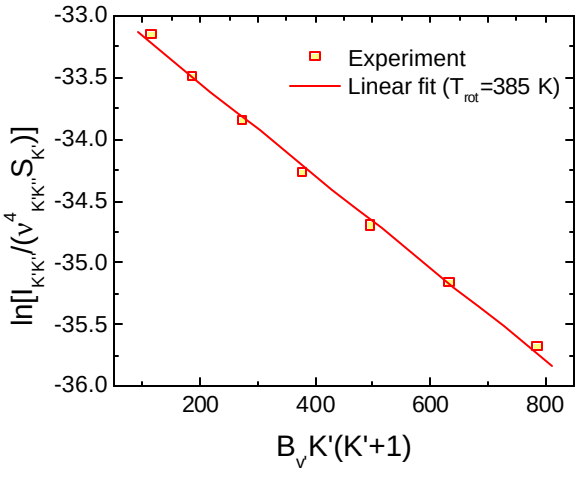

Fig. 4 A typical Boltzmann plot of R(6)-R(14) line intensities from the R branch of $N_2^+(B^2\Sigma_u^+, v'=0 \rightarrow X^2\Sigma_g^+, v''=0)$ versus the energy of the upper rotational levels.

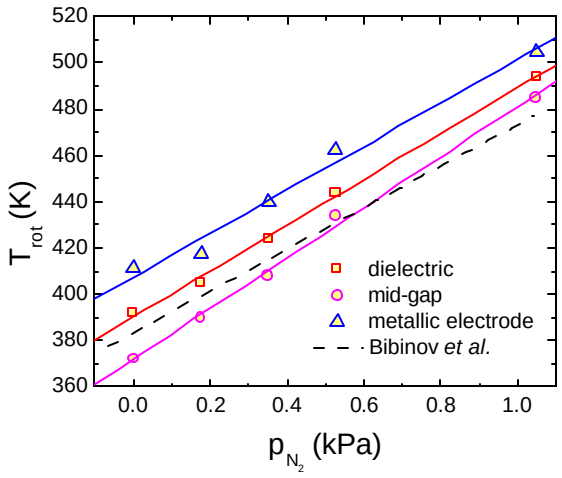

Fig. 5 T_{rot} versus partial pressure of N_2 in He/N_2 mixture obtained in 1.5 mm gap length plane-plane discharges.

Presumably, the presence and types of impurities in the discharge-cell can influence temperature values and their distribution. Because N_2 (from air) appears to be the dominant impurity in our experiments, we increased its concentration in order to evaluate its influence on T_{rot} values. In Fig. 5 we present the evolution of T_{rot} at three different gap positions, namely at the metallic electrode, at mid-gap, and at the dielectric, as a function of N_2 concentration in the He, along with comparable data reported in the literature [5, 6]. Both our and Bibinov's experiments relate to 1.5 mm plane-plane gaps, 1.5 ÷2 kV/19.7 kHz and 2 kV/10 kHz in Bibinov's and our case, respectively. In their case, both electrodes were covered with dielectric (glass) plates.

Figure 5 shows that T_{rot} increases linearly with rising N_2 concentration (up to ~ 1 vol%), and the T_{rot} distribution in the 1.5 mm gap. Mid-gap T_{rot} values are seen to agree well with literature data [5, 6], while those at the two electrode surfaces appear to be appreciably higher, the highest being at the metallic electrode. During sustained discharge the two electrodes heat up, and because they have a higher heat capacity than the gas, their temperature increases with time to a steady-state value that depends on the experimental conditions. With increasing N_2 concentration, the specific heat of the gas, the discharge propagation time and the spatiotemporal distributions of charge carriers and metastable species all are altered. It is interesting to note that the temperature differences between the three locations (at the two electrodes and in the mid-gap) gradually decrease with rising N_2 concentration.

Figure 6, for the case of the cylinder-plane discharge configuration, also shows a linear increase of T_{rot} with rising N_2 concentration (up to ~ 1.4 vol%); here, the APGD was produced in a 1 mm gap, but the temperature was found to be nearly constant throughout the gap, i.e. independent of axial position.

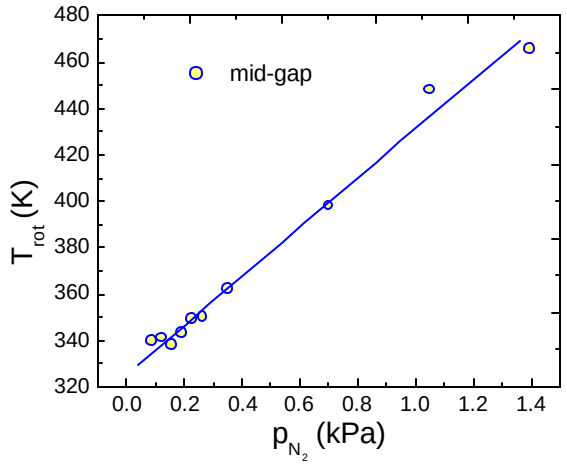

Fig. 6 T_{rot} versus partial pressure of N_2 in He/N_2 mixture discharges in the cylinder-plane electrode configuration.

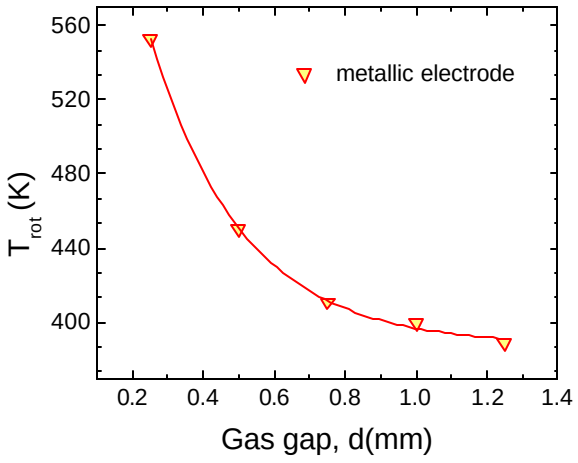

Fig. 7 T_{rot} near the metal electrode in a pure He DBD, versus gap width in the plane-plane configuration.

Finally, if the plane-plane interelectrode gap is narrowed, T_{rot} in a pure He discharge is seen to rise substantially (Fig. 7); this is to be expected, on account of reduced heat transfer. We present the temperature near the upper (metal) electrode, but T_{rot} is almost constant in the gap for gap widths less than 1 mm.

4. Conclusions

In this paper we present systematic investigations of gas temperature in different electrode configurations in short-gap helium APGD under uniform and non-uniform field conditions. The gas temperature is assumed to be equal to the rotational temperature, T_{rot}, which was determined from conventional Boltzmann plots using the R branch of FNS $N_2^+(B^2\Sigma_u^+, v'=0 \rightarrow X^2\Sigma_g^+, v''=0)$ bands near 391 nm. The influence of the N_2 partial pressure in He on T_{rot} in plane-plane and cylinder-plane discharge geometries has been examined, and T_{rot} was found to increase linearly with rising N_2 concentration (up to ~ 1 vol%).

Acknowledgement
This work is supported by grants from the Natural Sciences and Engineering Research Council of Canada (NSERC)

References
[1] U. Kogelschatz - Plasma Chem. Plasma Process **23**, 1 (2003)
[2] G. Herzberg – I. Spectra of Diatomic Molecules, 2nd edn., New York, Van Nostrand (1950)
[3] I. Radu, R. Bartnikas, M.R. Wertheimer - J. Phys. D: Appl. Phys. **36**, 1284 (2003); **38,** 539 (2005)
[4] F. Massines, P. Segur, N. Gherardi, C. Khamphan, A. Ricard – Surf. and Coatings Technol. **174 –175,** 8 (2003)
[5] N.K. Bibinov, A.A. Fateev, K. Wiesemann - Plasma Sources Sci. and Technol. **10**, 579 (2001)
[6] N.K. Bibinov, A.A. Fateev, K. Wiesemann - J. Phys. D: Appl. Phys. **34,** 1819 (2001)

The effect of electric arcs on carbon based electrodes

H.Pálsson[1], G.A.Sævarsdóttir[1], M.Þ.Jónsson[1] and J.A.Bakken[2]

[1]University of Iceland, Dept. of Mechanical Engineering, Hjardarhaga 6, 107 Reykjavik, Iceland
[2]Dept. of Materials Technology, Norwegian University of Science and Technology, Norway

Keywords: Søderberg electrodes, FeSi production, Thermal stresses, Plasma arc

Abstract

The purpose of this paper is to analyze the thermal effects of an electric arc on the surface of a carbon based electrode.The thermal conditions are then used to examine stress conditions in the vicinity of an arc.

Results show that the electrode surface is heated quickly up to a maximum temperature and for a specific test case, the surface can only withstand the load for about $10\,\mathrm{s}$. Also, the thermal stresses on the surface are very high which will increase erosion on the surface in addition to normal evaporation.

1 Introduction

Ferro Silicon is most frequently produced in submerged arc furnaces with Søderberg electrodes, see [1]. The metal is produced in a chemical process which receives energy from an electric arc. Carbon based electrodes are needed for that purpose. The uniqueness of the Søderberg process originates from the fact that these electrodes are manufactured during and in connection with the production itself.

In order to understand better the part of the process that has to do with the energy flow into the metal, fairly accurate mathematical models have been derived. The focus in most of these models has been the electrode, see e.g. [2], as well as the arc, see [3],since most of the production problems are located in these areas. An one-dimensional model was presented in [4] with the main purpose of describing the phase transition at the arc surface. A more complex two dimensonal model was furthermore used in [5] where the focus is on conditions that prevail in the initiation phase of a cathode spot. The results of this work indicates an overheating area of the spot, inside the surface itself, due to ohmic heating and heat losses at the surface.

The purpose of this paper is to focus on the electrode near the spot where the electric current leaves the electrode and forms an electric arc. This can be done with a relatively simple heat transfer model, similar to the model in [4], where a solid with alternating current flowing through it is modelled. The solid is semi-infinite and therefore only one surface (or boundary) is included in the analysis. The current flows out of the solid at the surface at one single area, which is circular with a given radius. Therefore it is assumed that the current density in the whole solid is pointed at this single area, which simplifies the problem.

The problem is furthermore analyzed by using an axi-symmetric finite element model in two dimensions. This is done primarily in order to verify the one dimensional model, and also to compute structural stresses in the arc vicinity.

This particular problem definition corresponds to a conductor with a single electric arc burning from the circular area as shown in figure 1. The figure also shows the model domain near the arc.

The paper is organized as follows. In section 2 a mathematical model is posed, which describes the problem. This is followed by some general results in section 3 and the by a real case study in section 4. Finally, conclusions are drawn in section 5.

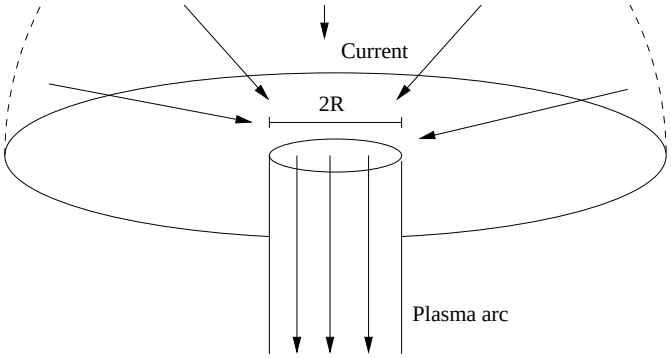

Figure 1: Semi-infinite solid with an electric arc on the surface

2 Mathematical models

2.1 The one dimensional case

A dynamic representation of the temperatures in the solid is described mathematically as an initial value problem. A general formulation of this problem is

$$\rho c_p \frac{\partial T}{\partial t} = k\nabla^2 T + \frac{J^2}{\sigma} \tag{1}$$

where ρ is density, c_p is specific heat, k is thermal conductivity, J is current density, σ is electric conductivity and T is the temperature.

The general problem can be simplified considerably by assuming spherical symmetry in the problem. This implies the following:

- All variables and parameters are constant at a given distance from the center of the arc area.
- It is assumed that a total current I flows directly towards the center and is uniform at a fixed distance.
- A spherical hole is assumed to be present at the arc center, so the solid is bounded by a half-sphere with radius R_s.
- The surface is insulated if the distance from the center is greater than R_s.

These assumptions allow for a model in spherical coordinates where the radius r is the only spatial variable. If the total current is given as I, then the current density becomes $J = \frac{I}{2\pi r^2}$ as it goes through a half-sphere. The initial value problem for the heat equation, (1), then becomes

$$\rho c_p \frac{\partial T}{\partial t} = \frac{k}{r^2}\frac{\partial}{\partial r}\left(r^2 \frac{\partial T}{\partial r}\right) + \frac{I^2}{4\pi^2 \sigma r^4} \tag{2}$$

2.2 Dimensionless form of the heat equation

It is convenient to use dimensionless variables in (2) where it is possible. Consequently the following dimensionless variables are defined

$$\theta = \frac{T - T_\infty}{T_0 - T_\infty} \qquad \eta = \frac{R_s}{r} \qquad \tau = \frac{k}{\rho c_p R_s^2} t$$

where T_0 is a reference temperature at the boundary and T_∞ is the temperature far away from the center (when $r \to \infty$).

The spatial differential operator is transformed into the dimensionless variable η and the time variable becomes t. Therefore the differential operators become

$$\frac{d}{dr} = \frac{d\eta}{dr}\frac{d}{d\eta} = -\frac{R_s}{r^2}\frac{d}{d\eta} = -\frac{\eta^2}{R_s}\frac{d}{d\eta} \qquad \text{and} \qquad \frac{d}{dt} = \frac{d\tau}{dt}\frac{d}{d\tau} = \frac{k}{\rho c_p R_s^2}\frac{d}{d\tau}$$

When θ and η are inserted into (2) the result is

$$\frac{\rho c_p k(T_0 - T_\infty)}{\rho c_p R_s^2}\frac{\partial\theta}{\partial\tau} = \frac{k(T_0 - T_\infty)R_s}{r^4}\frac{\partial}{\partial\eta}\left(R_s\frac{\partial\theta}{\partial\eta}\right) + \frac{I^2}{4\pi^2\sigma r^4}$$

$$\Rightarrow \quad \left(\frac{r}{R_s}\right)^4 k(T_0 - T_\infty)\frac{\partial\theta}{\partial\tau} = k(T_0 - T_\infty)\frac{\partial^2\theta}{\partial\eta^2} + \frac{I^2}{4\pi^2\sigma R_s^2} \quad \Rightarrow \quad \eta^{-4}\frac{\partial\theta}{\partial\tau} = \frac{\partial^2\theta}{\partial\eta^2} + 2\beta \quad (3)$$

where

$$\beta = \frac{I^2}{8\pi^2\sigma k(T_0 - T_\infty)R_s^2} \quad (4)$$

It is clear from (3) and (4) that all the physical properties of the problem can be gathered into a single parameter, β. This simplifies further analysis of the problem, since the solution to the partial differential equation in (3) can be developed as a single parameter function, which includes all the characteristics of the physical problem.

2.3 Finite element modeling

In order to compare the one dimensional model to a more realistic case, a finite element representations of an electrode has been built.

A two dimensional axi-symmetric model is considered, where it is assumed that the current flows from the electrode bottom. The accuracy of this model can be increased by using a very dense mesh, and it is appleciable for both static and dynamic analysis.

3 One dimensional analytical results

3.1 A steady state solution

An extreme case of an arc flowing out from a surface is where the arc does not move, and thus all time changing conditions converge to a steady state solution. This corresponds to setting $\frac{\partial\theta}{\partial\tau} = 0$ and thus the equation to be solved is

$$\frac{\partial^2\theta}{\partial\eta^2} + 2\beta = 0$$

By assuming the boundary conditions $\theta(1) = 1$ ($T(R_s) = T_0$) and $\theta(0) = 0$ ($T(\infty) = T_\infty$), the solution becomes

$$\theta(\eta) = \eta(1 + \beta(1 - \eta))$$

Some interesting values can be derived from the solution. The first one is the maximum value of θ and the position of that value. Differentiation gives

$$\eta_{max} = \frac{1}{2} + \frac{1}{2\beta} \qquad \theta_{max} = \frac{(1+\beta)^2}{4\beta}$$

Another interesting value is the maximum value of η, where $\theta \leq 1$. This corresponds to the minimum radius r where $T \leq T_0$. The solution to this problem is

$$\eta < \frac{1}{\beta} \quad (5)$$

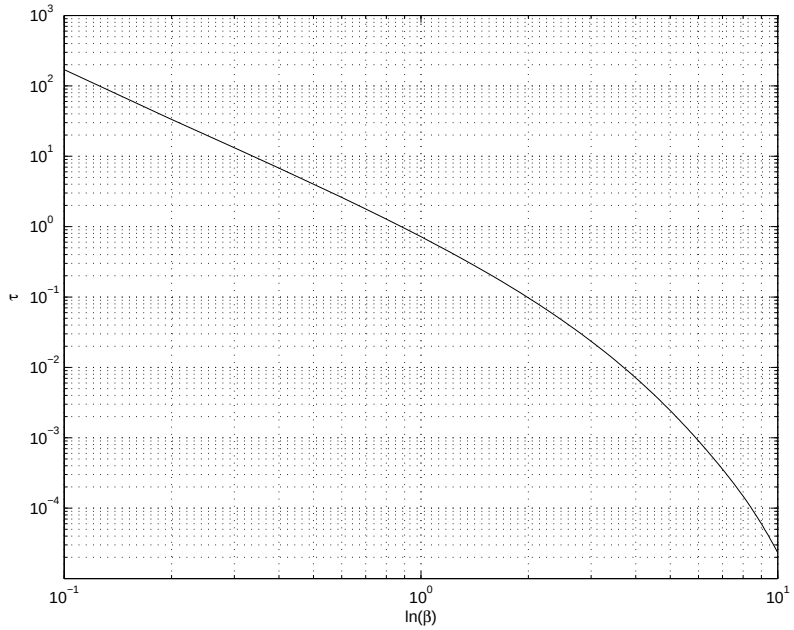

Figure 2: Dimensionless time until temperature penetration occurs as a function of $\ln(\beta)$.

which corresponds to the intrusion of temperatures higher than T_0 in to the solid. The assumption of $\theta \leq 1$ is justified by realizing that the maximum temperature of the material is $\theta = 1$, since it will sublimed into gas at higher temperature. Values of $\theta > 1$ are therefore outside the physical frame of the problem.

3.2 A time dependent solution

It is clear that the steady state solution can only be used as a reference, since it is clear that a realistic case study would not have an arc flow out from the same spot forever. Therefore it is necessary to solve the time dependent problem and thus solve (3) with appropriate boundary conditions.

It turns out that (3) is hard (or impossible) to solve analytically, and numerical methods must be used. This is done by discretizing the space derivative with finite differences and then integrating the result as a system of ordinary differential equations.

The discretization is performed by dividing the interval $0 \leq \eta \leq 1$ into N spaces, such that θ_j is an approximation of θ for $j = 0 \ldots N$. The result is a set of equations

$$\frac{\partial \theta_j}{\partial \tau} = \eta^4 N^2 (\theta_{j-1} + \theta_{j+1} - 2\theta_j) + 2\eta^4 \beta \tag{6}$$

which are mutually dependent. This is then integrated by using a numerical method, in this case a Runge-Kutta method for stiff systems.

The solution of (6) is dependent on β and therefore there is not much point in plotting it as a general solution. But there are some derived quantities that are of special interest and can be shown as a single graph with respect to β.

The first study involves a problem where the initial condition $\theta(\eta, 0) = 0$ is applied, as well as the boundary conditions $\theta(0, \tau) = 0$ and $\theta(1, \tau) = 1$. Thus the temperature at the boundary is raised suddenly to T_0, which is what happens if an arc is suddenly started at the surface. It is of interest to find out how long time passes until this surface temperature starts penetrating the surface (and thus generating abnormally high temperatures inside the solid). Figure 2 show this relationship for a wide range of β.

Result	$R = 5\,\mathrm{cm}$	$R = 3.54\,\mathrm{cm}$
Static R_{max} (based on η_{max})	$9.5\,\mathrm{cm}$	$9.7\,\mathrm{cm}$
Static T_{max} (based on θ_{max})	$16500\,^{\circ}\mathrm{C}$	$30400\,^{\circ}\mathrm{C}$
Static penetration of T_0 (based on (5))	$0.93\,\mathrm{m}$	$1.86\,\mathrm{m}$
Time until penetration starts	$10.5\,\mathrm{s}$	$2.2\,\mathrm{s}$

Table 1: Results for an one dimensional model

It can finally be concluded that figure 2 shows that the time until penetration occurs decreases with increasing arc current I and with decreasing electric conductivity of the electrode material.

4 A real world case study

A realistic case study is analysed in this section, where a baked carbon paste of a Søderberg electrode is considered. Real material parameters are used and the applied current is assumed to be $I = 115\,\mathrm{kA}$. It is further assumed that $T_0 = 4000\,^{\circ}\mathrm{C}$ and $T_\infty = 1000\,^{\circ}\mathrm{C}$. For a discussion of material parameters in Søderberg electrodes see e.g. [7] and [8].

4.1 The one dimensional model

It is assumed that the arc has a radius of $R = 5\,\mathrm{cm}$ and therefore a natural choice would be to set $R_s = R$. But it should be noted that the surface area of the half-sphere bounded by R_s is not the same as the surface are of an arc flowing from the bottom. Therefore, a correction is also considered which results in $R_s = \frac{R}{\sqrt{2}} = 3.54\,\mathrm{cm}$. Both these cases are examined and the results are shown in table 1.

Apparently there is a considerable difference between the two chosen values of the radius, so a comparison to a more complete finite element model should indicate which method should be used.

4.2 Time dependent results from an axi-symmetric finite element model

A model was constructed with the purpose of focusin on the electrode bottom and compare time dependent simulation to the results from the one dimensional model.It is assumed here that the current flows from the bottom in a circular pattern with radius $5\,\mathrm{cm}$.

Figure 3(a) shows the temperature near the arc after $10\,\mathrm{s}$ of simulation time. Here it is clear that the temperature is in some points larger than T_0, but this can be analysed further by choosing two points near the arc and plotting the temperature as a function of time. This is shown in figure 3(b) where the maximum temperature is reached at time from about $9\,\mathrm{s}$ to $20\,\mathrm{s}$. This is close to the result found with the one dimensional model where $R_s = 5\,\mathrm{cm}$.

It should be noted that the edge of the arc (the outer surface for a circular arc) is a problematic spot for the finite element solution because of the fact that the current is forced to flow out perpendicularly to the surface. Nevertheless, this only affects the solution near the problem spot.

4.3 Structural stresses in an axi-symmetric model

The final study here is to look at structural stresses which are the result of temperature changes in the electrode. As before, it is assumed that this effect mostly occurs near the arc, and the results support this fact.

Figure 4(a) shows the stresses at the electrode bottom at a given time points. This time is the same as in figure 3(a), which is $10\,\mathrm{s}$ after the start of the arc at the bottom. It is clear that the stresses are closely related to the temperatures, and appear to be very high, several magnetudes higher than the stress that the electrode is supposed to withstand. This is the case in the contour region, but only penetrated about $2\,\mathrm{cm}$ into the electrode.

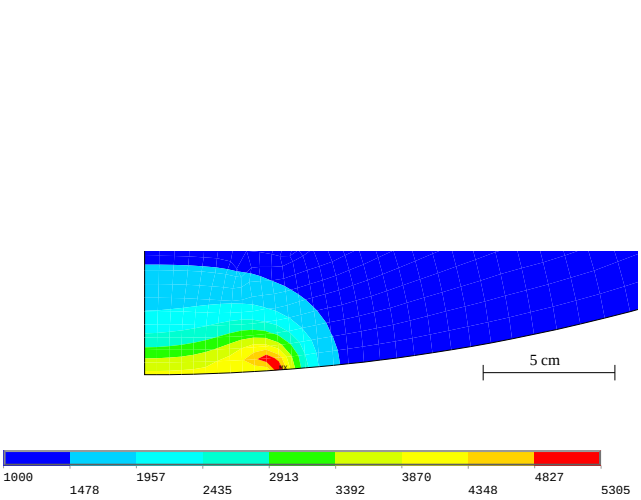

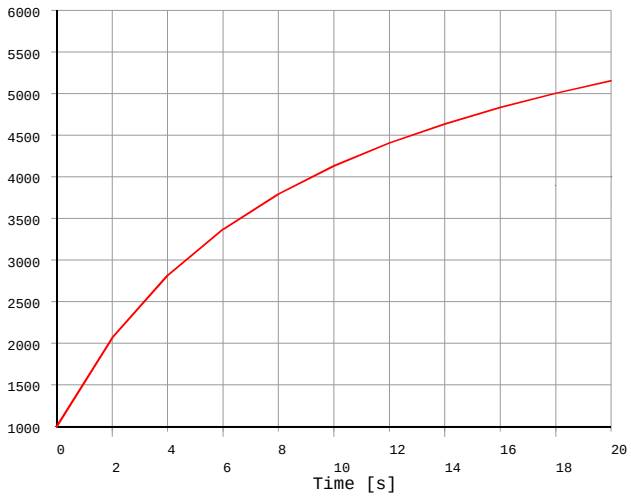

(a) Distribution after 10s

(b) As a function of time

Figure 3: Temperature in an axi-symmetric model [°C].

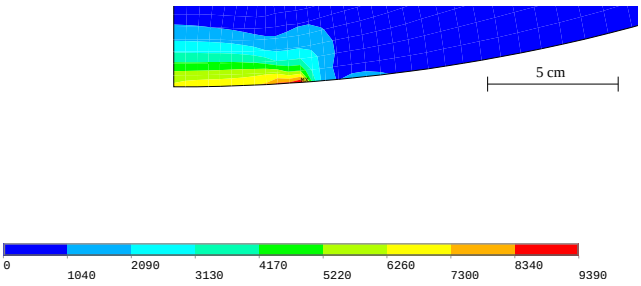

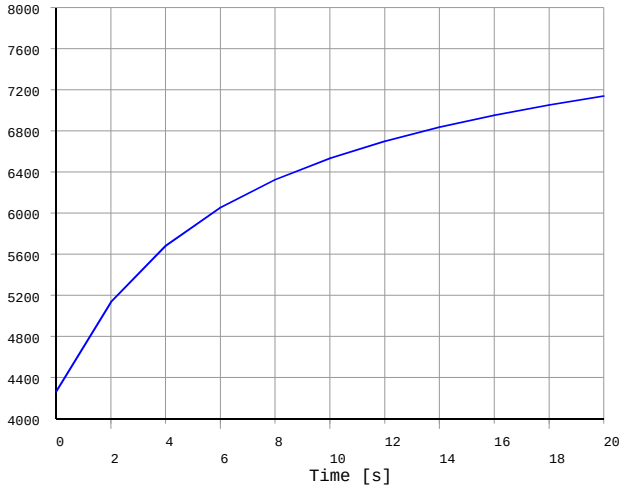

(a) Distribution after 10s

(b) As a function of time

Figure 4: Equvalent stresses near the arc outlet in an axi-symmetric electrode [MPa].

Finally, figure 4(b) shows the changes in stresses with respect to time. This follows the change in temperatures very well, as expected.

5 Conclusions

A spherical model of thermal conditions in a semi-infinite solid has been developed in this paper. This model is in reality one dimensional since changes are only considered in the radial direction. Furthermore, more complex finite element models have been built and compared to the one dimensional model.

The model seems to agree with the more complex two and three dimensional models, and is applicable in the vicinity of an electric arc. This indicates that the results found in figure 2 can be used to analyze the time dependent effect of an arc, burning at the bottom of an electrode. The key parameter here is β, which was defined in (4).

The results indicate that when an arc is formed with a relatively high current, then it affects the surface of the electrode greatly, both with respect to temperatures and structural stresses. Particularly, it is apparent that an electric arc with a current over $100\,\mathrm{kA}$ flowing from a Søderberg electrode would burn at the same point for only up to $10\,\mathrm{s}$, since the material cannot withstand higher temperatures than $4000\,^{\circ}\mathrm{C}$. It is then likely that the arc is moving around within such a time frame, or that more than one arc are present at once.

Furthermore, analysis of the thermal stresses due to the arc heating near the surface show very high stresses, which indicates that the erosion at the surface would considerably support erosion of the electrode.

The combined findings of this paper are an important addition to research on arc movement and electrode consumption. Further work could focus on the somewhat complex plastic behaviour of the electrode material.

Finally, the authors would like to thank for the financial support of this research, which was funded jointly by The Research Council of Norway , The Norwegian Ferroalloy Producers Research Association, and The Icelandic Centre for Research.

References

[1] A. Schei, J. K. Tuset, and H. Tveit, *Production of High Silicon Alloys*. N-7005 Trondheim, Norway: TAPIR forlag, 1998.

[2] M. Þ. Jónsson and H. Þ. Ingason, "Three dimensional simulation model for søderberg electrode," in *INFACON 8*, (Beijing, China), 1998.

[3] G. A. Sævarsdóttir, *High Current AC Arcs in Silicon and Ferrosilicon Furnaces*. 2002. Dr.Ing thesis,Norwegian University of Science and Technology.

[4] T. Klein, J. Paulini, and G. Simon, "Time-resolved description of cathode spot development in vacuum arcs," *J. Phys. D: Appl. Phys.*, vol. 27, pp. 1914–1921, 1994.

[5] Z.-J. He and R. Haug, "Cathode spot initiation in different external conditions," *J. Phys. D: Appl. Phys.*, vol. 30, pp. 603–613, 1997.

[6] H. Pálsson, M. T. Jónsson, and H. Þ. Ingason, "A three dimensional finite element model for the baked part of a søderberg elektrode," tech. rep., University of Iceland, July 1996. Internal Report.

[7] A. G. Arnesen, S. Oekstad, R. Innvær, and L. Olsen, "Operation of søderberg electrodes," 1978. Ilafa-Congres, Acapulco.

[8] R. Innvær, K. Fidje, and R. Ugland, "Effect of current variations on material properties and thermal stresses in soderberg electrodes," in *INFACON 86*, (Rio De Janeiro), 1986.

Analysis of initial layer growth process for CVD plasma polymerization

Prof. Dr.-Ing. E. Schmachtenberg[1], Dipl.-Ing. D. Binkowski[1], Dipl.-Ing. S. Göbel[1]

1 Institute of Plastics Processing at Aachen University, Aachen, Germany

Abstract
Films for barrier improvement of polymers (e.g. PET-bottles) deposited by Plasma enhanced CVD at low pressure are being investigated. For the microwave assisted plasma polymerization of C_2H_2 the correlation of morphology, barrier properties and process parameters is being studied on PET-substrates as well as on Si-Wafers. The AFM analysis shows structures which suggest island growth. ESCA measurements indicate that a high amount of C-C bonds is essential for barrier improvement.

Keywords
Plasma enhanced CVD, layer growth, morphology, barrier properties, acetylene

Introduction

Plasma assisted coating of polymers is a well know process e.g. for barrier improvement of polymers. The initial growth processes are determining the morphology and the further layer growth of thin films. Mechanical and physical properties depend highly on the film morphology. To optimize film properties such as permeation barrier a good understanding of the initial layer growth process is necessary. Previous studies show that the barrier quality of films deposited by Chemical Vapor Deposition (CVD) depends on the film morphology [1, 2]. Defects in the film are one reason for a higher gas permeation. Aim of the presented studies is to identify reasons for the occurrence of defects and to identify a correlation between process parameters, film morphology and barrier properties.

For the deposition of thin films using Physical Vapor Deposition (PVD) processes a broad base and wide variety of research work and papers are existent [3, 4, 5, 6]. However, for Chemical Vapor Deposition this is not the case, even though the industrial use of CVD processes is increasing at a high rate. To optimize the functionalities of the deposited thin films (e.g. anti scratch, anti fog or barrier coatings) a deeper understanding of the processes during layer growth is necessary. This is also essential to improve manufacturing methods.

Thin film deposition

The deposition of thin films can be divided into three different phases. In a first step the particles which will be forming the film are being transported to the surface. In a second step those particles are being absorbed on the substrate respectively on the growing film. The particles diffuse over the substrate and are either being implemented in the film or being removed from the surface by vaporization or sputtering. In a third step the particles migrate to their final position in the film [7].

For the creation of thin films three different models are being found in the literature (fig. 1). These models can also be used to describe growth of plasma polymerized films. These can be a growth in layers as described by Frank-van der Merwe [9], an island growth known as Volmer-Weber [8] growth or a combination of both, described by Stranski-Krastanov [10]. Bauer describes a thermodynamic approach [11, 12] and defines surface energy of the substrate (γ_s), absorbed particles (γ_a) and an energy for the intermediate layer (γ_i). He indicates that island growth occurs when $\gamma_s - \gamma_i < \gamma_a$. If not, layer growth occurs. Stranski-Krastanov growth is described by variation of γ_i with growing film thickness. This approach may not be feasible for low pressure CVD processes due to the lack of a thermodynamically balance.

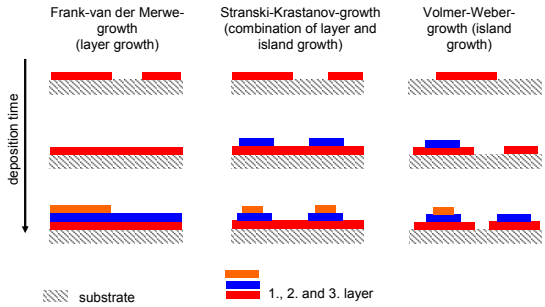

Figure 1: Different models of thin film creation

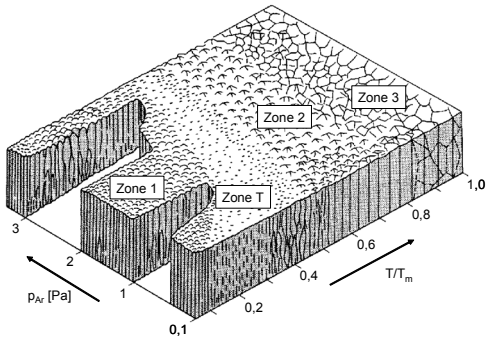

Figure 2: Structural zone model according to [13]

Movchan and Demchishin [5] observe that the morphology of evaporated films can be described by a function of the ratio of substrate temperature T to the melting point of the coating T_m. They describe three different zones in this structural zone model. Zone 1 ($T/T_m < 0{,}3$) is described as zone consisting of tapered crystallites with domed tops. Zone 2 can be observed for $0{,}3 < T/T_m < 0{,}45$ and describes columnar grains. Zone 3 consists of equiaxed grains for $T/T_m > 0{,}45$. [13] observes in addition to that a transition zone T of tightly packed fibrous grain (fig. 2). [6] extends the model with the interdependence on the energy of the deposited particles. Increasing energy leads to a shift of the zones to lower T/T_m values. Thus the two components of the adatom mobility are taken into account. Those components are the thermally induced mobility and the mobility induced by the bombardment with particles of high energy.

Results and Discussion

For microwave assisted plasma polymerization of C_2H_2 at low pressure there are few papers found, which discuss the different produced microstructures during the process, excluding the deposition of diamond like carbons (DLC). Studies on how a variation of the process parameters influences the morphology of the deposited films and how this has an effect on the barrier properties are being made at the Institute of Plastics Processing at Aachen University.

The coatings using acetylene (C_2H_2) as process gas and argon (Ar) as carrier gas are being deposited on two different substrates. For industrial use (especially barrier coatings) the polymer polyethylene terephthalate (PET) is an interesting substrate to investigate. To differentiate the plasma polymerized C_2H_2 from the substrate during ESCA (Electron Spectroscopy for Chemical Analysis) and to have an ideal surface without almost any defects Si-Wafers are being used as second substrate to be coated. The thin films are being deposited using a microwave CVD laboratory plant for barrier coating. The process parameters which are being varied are microwave power, gas flow and composition as well as coating time. To increase the quality of the results and to reduce the number of trials the methodology for design of experiments is being used. This also allows to display the effects of the different parameters in a Pareto chart of effects, which shows also a vertical line to indicate the minimum magnitude of statistically significant parameter estimates. All effects beyond this limit are statistically significant according to the chosen 95% confidence interval.

To have a good bases for correlating barrier, morphology and process parameters with each other barrier measurements of coated PET-bottles against CO_2 are being made in a first step. Secondly the morphological and chemical analysis is being conducted.

The barrier measurements spread for the used parameter range between barrier improvement factor (BIF) 1 and 3,6. This factor represents the ratio of the permeation coefficients of a reference material to the barrier material. Main effects on barrier of deposited C_2H_2/Ar coatings have pressure, gas flow and gas flow ratio as well as process time (fig. 3). Interactions of those can also be observed.

To see whether there is a correlation between barrier and morphology or not Atomic Force Microscopy (AFM) is being used. The AFM analysis shows no significant influence of surface properties to barrier quality. In addition to that could no Frank-van der Merwe growth be observed at any time. The AFM scans rather show structures, which suggest island growth. Figure 4 shows height pictures of coated samples compared to the uncoated Si-Wafer. Also the phase contrast analysis underlines that. A growth as described by Stranski-Krastanov may occur, but this observation could not be exactly determined by the AFM scans. An analysis of a cross section will eventually provide more information. To examine the correlation between barrier and morphology the surface structures of samples with high BIF values are being compared to those with low values for BIF. No significant correlation was found, even though samples with a good BIF seemed to have a more flat and smooth surface.

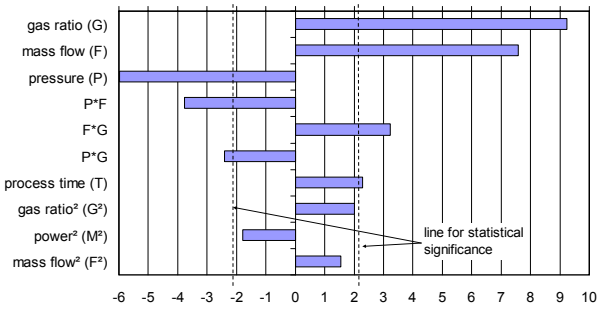

Figure 3: Pareto chart of standardized effects on BIF (R^2=0,90)

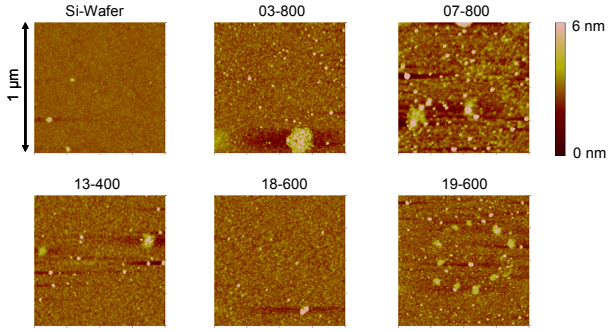

Figure 4: 1µm AFM scans of different samples (height pictures)

The analysis of coating thickness gives a more clearly picture of the effects (fig. 5). As expected the process time has the biggest effect on the thickness of the film. Also the distinct effect of gas ratio and mass flow is accountable, because C_2H_2 is being implemented very fast in plasma when there is sufficient energy to stimulate the gas particles. Of interest is the derived value called layer growth rate (growth rate = d(layer thickness) / dt). A time dependency of the layer growth rate could be observed. The shorter the process time is, the higher the growth rate. Also gas flow and gas ratio have a statistical significant influence on layer growth rate (fig. 6). One reason for this observation may be that not enough monomer gas is present during the whole process, so that after the initial surplus of gas is being used the growth rate decreases.

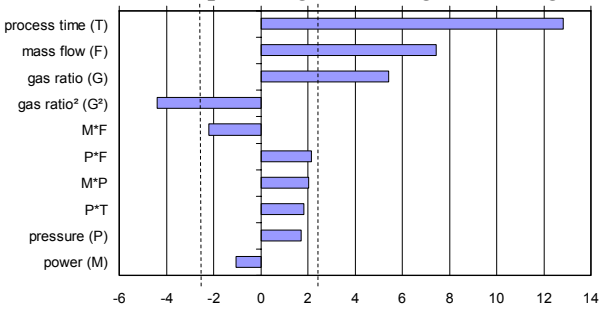

Figure 5: Pareto chart of standardized effects on film thickness (R^2=0,99)

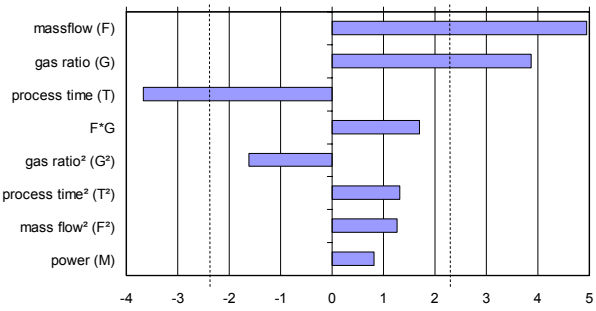

Figure 6: Pareto chart of standardized effects on growth rate (R^2=0,96)

ESCA measurements show that the chemical composition of the thin films is almost identical for all deposited coatings for the conducted design of experiments. Table 1 shows the average elemental composition of the deposited films using acetylene in combination with argon on Si-Wafers. The presence of fluorine may be due to the gas inlet of the coating plant, which is made of PTFE. The nitrogen is either being implemented at the beginning of the process due to some residual nitrogen, which has not been properly removed from the process or it has been implemented after the deposition due to the share of radicals on the film surface. Furthermore ESCA analysis did not verify the existence of covalent Si-C bonds, which suggests a sudden change from Si-Wafer to the film without any transition. Also no change in the film composition could be observed with

increasing film thickness. The wide range of measured barriers with a variation up to factor 3,6 indicates that barrier properties depend solely on the morphology of the films. In addition to that the existence of C-C bonds seems to be a necessary but not sufficient criteria to get a good barrier (fig. 7). Significant influences of process parameters on the occurrence of C-C bonds were found for the gas ratio, the mass flow and the pressure at which the coatings were deposited.

element	C	O	Si	N	F
average [atomic-%]	78,1	14,9	4,8	1,6	0,7
standard deviation	6,3	2,4	4,5	1,6	1,3

Table 1: Average elemental composition of the DOE

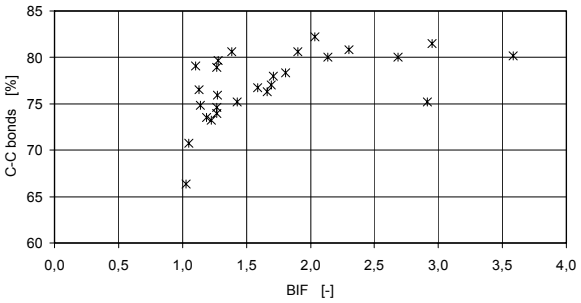

Figure 7: Share of C-C bonds vs. measured BIF

Perspective

AFM analysis shows for C_2H_2/Ar-films on Si-Wafers island growth. If the film growth as described by Volmer-Weber (island growth) or has a growth mechanism based on Stranski-Krastanov (combination of layer and island growth) can not be decided. If Stranski-Krastanov growth occurs, the transition layer is rather thin. Frank-van der Merwe growth could not be observed. To get a better understanding and a more detailed picture additional analysis of a cross-section should be taken into account.

The chemical composition of the deposited films is for all investigated films almost identical, yet the barrier improvement factor varies from 1 – 3,6. This indicates that a good BIF depends solely on the morphology of the deposited films. As described by the structural zone models a higher ion bombardment may lead to a film with lesser defects, thus a better barrier against permeation.

Acknowledgements

The investigations set out in this report received financial support from the Federal Ministry of Economics and Labor (BMWA) by the AiF (No. 13753N), to whom we extend our thanks.

References

[1] Tropsha, Y. G.; Harvey, N. G.: Activated rate theory treatment of oxygen and water transport through silicon oxide/poly(ethylene terephthalate) composite barrier structures. In: Journal of Physical Chemistry B 101 (1997), No. 13, p. 2259-2266

[2] Dahlmann, R.: Permeation durch plasmapolymerisierte Schichten und Plasmabeschichtung von Kunststoffrohren und –hohlkörpern. RWTH Aachen, Dissertation, 2001

[3] W. K. Burton, N. Cabrera, F. C. Frank - The growth of crystals and the equilibrium of their surfaces. In: Philosophical Transactions of the Royal Society of London, Series A 243 (1951), p. 299-358

[4] Z. Zhang, M. G. Lagally - Atomistic Processes in the Early Stages of Thin-Film Growth. In: Science 276 (1997), No. 5311, p. 377-383

[5] B. A. Movchan, V. A. Demchishin - Study of the structure and properties of thick vacuum condensates of Ni, Ti, W, Al2O3 and ZrO_2. In: Fiz. Metal. Metalloved 28 (1969), p. 653-660.

[6] R. Messier, A. P. Giri, R. A. Roy - Revised structure zone model for thin film physical structure. In: Journal of Vacuum Science and Technology A 2 (1984), No. 2, p. 500-503

[7] J. A. Thornton - The microstructure of sputter-deposited coatings. In: Journal of Vacuum Science and Technology A 4 (1986), No. 6, p. 3059-3065

[8] M. Volmer, A. Weber - Keimbildung in übersättigten Gebilden. In: Zeitschrift für physikalische Chemie 119 (1926), p. 277-301

[9] F. C. Frank, J. H. van der Merwe - One-Dimensional dislocations. II Misfitting monolayers and oriented overgrowth. In: Proceedings of the Royal Society of London A 198 (1949), p. 216-225
[10] I. N. Stranski, L. Krastanov - Zur Theorie der orientierten Ausscheidung von Ionenkristallen aufeinander. In: Sitzungbericht der Akademie der Wissenschaften Wien 146 (1938), p. 797-810
[11] E. Bauer - Phänomenologische Theorie der Kristallabscheidung an Oberflächen I. In: Zeitschrift für Kristallographie 110 (1958), p. 372-394
[12] E. Bauer - Phänomenologische Theorie der Kristallabscheidung an Oberflächen II. In: Zeitschrift für Kristallographie 110 (1958), p. 395-431
[13] Thornton, J. A.: Influence of apparatus geometry and deposition conditions on the structure and topography of thick sputtered coatings. In: Journal of Vacuum Science and Technology 11 (1974), Nr. 4, S. 666-670

Ablation of polymers by plasma and by VUV photons: a mass spectrometry study

V. Nelea[1], F. Truica-Marasescu[2], M. R. Wertheimer[2]

[1]*Laboratory for Biomaterials and Bioengineering, Laval University, Quebec, Canada*
[2]*Department of Engineering Physics, Ecole Polytechnique, Montreal, Canada*

Abstract

We report a mass spectrometry study of volatile fragments emanating from the surfaces of several types of hydrocarbon and heteroatom-containing polymers under direct exposure to (i) low-pressure glow discharge plasma, and to (ii) VUV radiation. Depending on the polymer composition and structure, in some cases types (i) and (ii) spectra show substantial differences. In others, the same mass peaks appear, but with different intensity ratios.

Keywords: Polymers, Glow discharge plasma, Vacuum ultraviolet radiation, Mass spectrometry.

1. Introduction

Surface modification of polymers, for example for enhanced adhesion, is now indispensable [1]. One of the main methods involves their exposure to glow discharges, but these are also strong emitters of ultraviolet (UV) and even vacuum ultraviolet (VUV) radiation [2]. In view of this fact, it is of scientific and technological interest to distinguish a possible VUV-induced contribution to the overall interaction between the plasma and a polymer surface. An important effect resulting from this interaction is the scission of macromolecular bonds and the ensuing liberation of volatile organic fragments. These can readily be detected and identified with the help of mass spectrometry, as we have shown in the past [3]. The purpose of the present work has been to compare mass spectra of volatile fragments emanating from the surfaces of several types of polymers under two different conditions, namely (i) direct exposure to low-pressure glow discharge plasma, and (ii) exposure to VUV radiation generated by a low-pressure radiofrequency (r.f.) discharge, but shielding the polymer surface from the active particles of that discharge.

2. Experimental Methodology

In order to accomplish tasks (i) and (ii), we use a specially-designed plasma reactor, coupled to a quadrupole mass spectrometer (QMS) via a small (100 μm) orifice [3]. By means of differential pumping of the reactor and the QMS, one enables the extraction of volatile species from the former to the latter. For all experiments the pressure in the reactor was adjusted within the 50-150 mTorr range, for example by controlling the gas flows. The pressure in the QMS was always kept to about 10^{-7} Torr (Fig. 1).

In the case of type (i) experiments, perforated polymer foil specimens were placed directly onto the orifice plate of the QMS, where they were exposed to active particles (electrons, ions, excited metastables) and photons from the 13.56 MHz r.f. He or Ar plasma, generated with the help of a concentric, powered electrode at 150 W of r.f. power.

Regarding type (ii) experiments, a commercial VUV lamp (Resonance Ltd, Barrie ON, Canada) with a flow of Ar or He + 1% H_2 generated strong, near-monochromatic VUV Lyman α radiation from atomic hydrogen (λ=121.5 nm) [4]. The lamp was placed a short distance from the polymer surface (see the inset of Fig. 1), but the activated gas stream was deviated towards the pumps by a MgF_2 window. In this way, the volatile species detected by the QMS were practically only attributable to VUV-induced bond scissions in the polymer surface region [5]. Figure 2 shows the emission spectrum of the Ar + 1% H_2 flow-lamp at 150 mTorr pressure, as an example. The flows of argon and hydrogen were 99 sccm and 1 sccm, respectively.

We have examined the mass spectra of hydrocarbon polymers (polyethylene, PE; polypropylene, PP; polystyrene, PS), and of others containing heteroatoms (polyethylene-terephthalate, PET; polyethylene-naphthalate, PEN; polycarbonate, PC; and nylon-6 polyamide, PA).

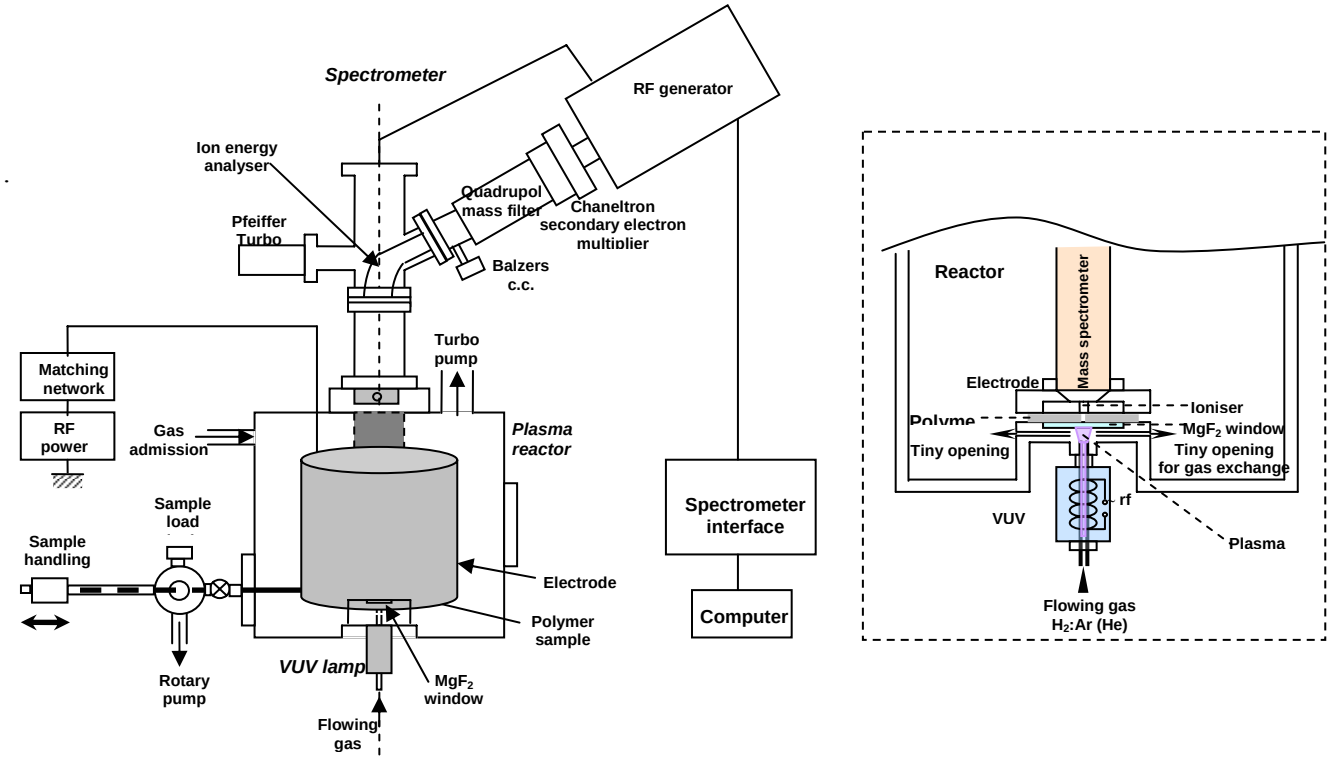

Figure 1. Schematic representation of the experimental set-up. Detail of the VUV lamp (inset)

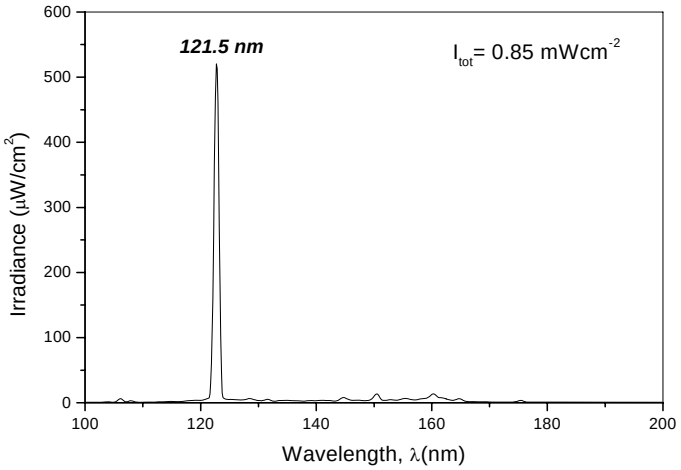

Figure 2. Emission spectrum of the flow-lamp with Ar +1% H_2

3. Results and Discussion

3.1 Plasma experiments

Figure 3 depicts the mass spectra recorded in the mass range 0-150 amu during He plasma exposure without any sample, and with samples of PE or PP. The intensities were normalized to that of the highest intensity peak, He^+. The recorded background spectrum (plasma ignited without any sample) shows mass lines that are characteristic for He plasma, i.e. He^+ (m/e=4 amu) and He^{2+} (m/e=2 amu), and of some contaminants. The latter include desorbed water vapour (H_2O^+, m/e=18 amu; OH^+, m/e=17 amu; O^+, m/e=16 amu; and H_2^+, m/e=2 amu), carbon dioxide (CO_2^+, m/e=44 amu; CO^+, m/e=28 amu), molecular oxygen (O_2^+, m/e=32 amu; O^+, m/e=16 amu) and

some hydrocarbons, of which $C_2H_3^+$ (m/e=27) dominates. However, even though the filament of the QMS ionization source was cleaned by repeated heating cycles, it is not excluded that it may have contributed some of these detected species.

When aliphatic hydrocarbons, in our case PE and PP, were exposed to the He (or Ar) plasma, many C_xH_y hydrocarbon peaks were observed in the mass spectra. They include light species, like carbon (C^+, m/e=12), methylene, (CH_2^+, m/e=14), methyl (CH_3^+, m/e=15) and methane (CH_4^+, m/e=16). One can observe that mass spectral lines appeared as groups (bands) between 38-46, 50-60, 64-73, 77-85 and 95-99 amu, respectively, with diminished intensity for heavier species. Among the most intense mass lines we note 27, 28, 29, 41, 42, 43, 55, 56, 57, 69, 70, 71, 83, 84 and 85. These are recurrent values of ions of alkenyl carbenium ($C_nH^+_{2n-1}$), alkene C_nH_{2n}, (n≥2) and alkyl carbenium ($C_nH^+_{2n+1}$), when a methylene group (mass 14) is eliminated from the polymer backbone. Similar hydrocarbon fragments were reported as by-products for Ar plasma-exposed polyolefins [3]. However, compared with Ar plasma, for PE there are differences of relative intensities within the groups of spectral lines. Moreover, in the case of PP, the mass spectral lines are more numerous and have a greater intensity in the He plasma than their Ar plasma counterparts. These findings suggest that more fragments of heavier masses are formed when polyolefin samples are exposed to the He plasma. As helium has an ionization potential ($1s\ ^2S_{1/2}$, 24.48 eV) higher than that of argon ($3p^5\ ^2P_{3/2}$, 15.76 eV), a higher efficiency of excitation and ionization is expected in the helium plasma leading to the formation of more energetic metastable species that bombard the polymer surface [6].

.

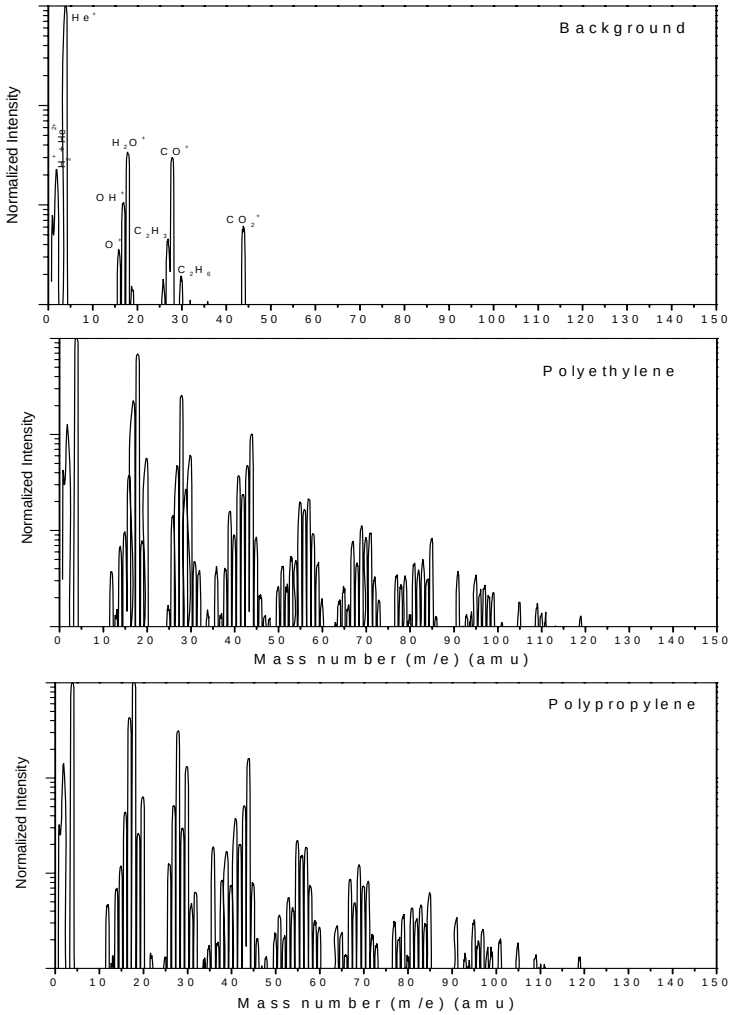

Figure 3. Mass spectra recorded during a He plasma treatment without (a) and with samples of polyethylene (b) and polypropylene (c). Intensities are normalized to the highest intensity peak, He^+.

For aliphatic hydrocarbons the main fragmentation mechanism is the elimination of H_2 and the creation of mid-chain and/or end-chain double bonds (the so-called molecular path); they are easily identifiable in the mass spectrum as alkene species (Fig. 3). Note that in the configuration we used, no measurable signals were detected for masses exceeding 150 amu.

3.2 VUV versus Plasma

In the case of exposure to VUV from the flow lamp, the mass spectra of a given polymer manifested peaks in the same positions as those observed under exposure to inert gas plasma. However, there were systematic differences in the peak intensities, as we now show.
Figure 4 represents the ratio of mass spectral intensities under types (i) and (ii) experimental regimes (I_{plasma}/I_{VUV}) versus the mass number of H_2 and of hydrocarbon fragments liberated from (a) PE, and (b) PP.

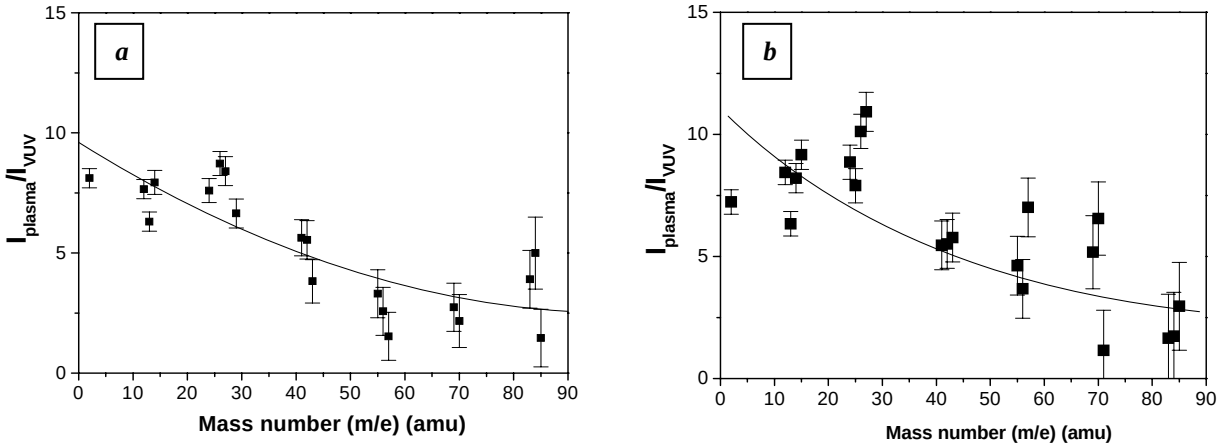

Figure 4. Ratio of mass spectral intensities under types (i) and (ii) experimental regimes vs the mass number of H_2 and of hydrocarbon fragments liberated from (a) PE, and (b) PP

A rather different picture emerged in the case of polymers with aromatic structure and those containing heteroatoms, namely PS, PET, PEN, PC and PA. Here, the signals of the lighter species were found to have lower intensity when exposed to the VUV radiation (regime (ii). In order to examine systematic differences of mass intensities between the two exposure regimes, we present the I_{VUV}/I_{plasma} ratios; Figure 5 shows the evolutions for PC, PS and PA.

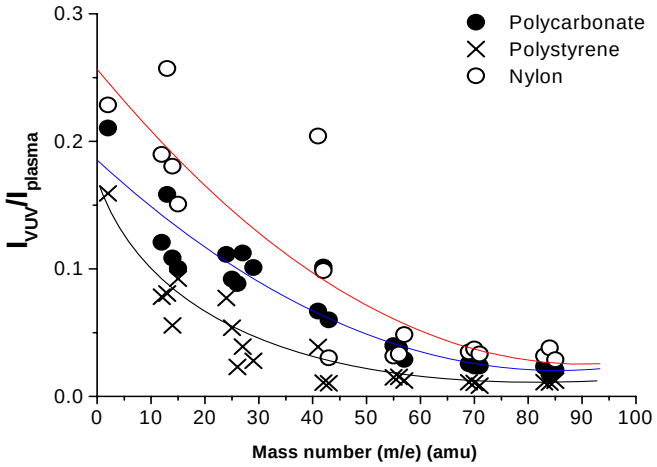

Figure 5. Ratio of mass spectral intensities under types (ii) and (i) experimental regimes vs the mass number of H_2 and of hydrocarbon fragments liberated from polycarbonate, polystyrene and nylon-6 polyamide

4. General Discussion and Conclusions

Figure 4 clearly shows that for the case of polyolefins, PE and PP, exposure to inert gas plasma (type (i) treatment) favours the formation of "lighter" fragments, compared with type (ii), VUV irradiation. In the case of polymers containing aromatic structure (PS, PC), however, Fig. 5 suggests that the opposite appears to apply. While these data must still be considered preliminary, they nevertheless illustrate that bond-breaking events at a given polymer surface are quite different in types (i) and (ii) excitations.

All polymers strongly absorb VUV photons below 160 nm, for example the present Lyman α radiation at 121.5 nm, on account of C-C and C-H σ bond scissions [5]. However, aromatic polymers like PS are far less susceptible to VUV-induced ablation than their aliphatic counterparts. The reason for this is that aromatic structures can dissipate the excitation energy through fluorescence [5]. In the cases of PE and PP, on the other hand, plasma (type (i)) and VUV (type (ii)) excitations both give rise to much bond scission in surface-near layers of the polymers, hence to many volatile fragments. In the case of type (i), however, these are further fragmented in the plasma before entering the QMS, and this explains the trends illustrated by Figs. 4(a) and (b). The reverse behaviour, Fig. 5, is currently the object of further investigations.

Acknowledgement

This work is supported by grants from the Natural Sciences and Engineering Research Council of Canada (NSERC).

References

[1] M. R. Wertheimer, L. Martinu, J. E. Klemberg-Sapieha, G. Czeremuszkin, "Plasma Treatment of Polymers to Improve Adhesion", in "Adhesion Promotion Techniques – Technological Applications", K. L. Mittal and A. Pizzi, Eds., Marcel Dekker Inc, New York (1999).
[2] A. C. Fozza, J. E. Klemberg-Sapieha, M. R. Wertheimer, Plasmas and Polymers **4**, 183 (1999).
[3] J. Hong, F. Truica-Marasescu, L. Martinu, M. R. Wertheimer, Plasmas and Polymers **7**, 245 (2002).
[4] A. C. Fozza, M. Moisan, M. R Wertheimer, J. Appl. Phys. **88**, 20 (2000).
[5] F. Truica-Marasescu, M. R. Wertheimer, Macromol. Chem. Phys. **206**, 744 (2005).
[6] K. Wagatsuma, Spectrochim Acta B: Atom. Spectr, **56**, 465 (2001).

Photocatalytic Activity of Plasma Treated Titania Precursors

V. Brozek[1], J. Matejicek[1], Z. Srank[2], L. Mastny[2], J. Janca[3]

[1]*Institute of Plasma Physics, Academy of Science of the Czech Republic, Za Slovankou 3, 182 21 Praha 8, brozek@ipp.cas.cz*
[2]*Institute of Chemical Technology, 16628 Prague 6, Technicka 5, CZ zlatko.srank@vscht.cz*
[3]*Department of Physical Electronics, Faculty of Science, Masaryk University Brno, Kotlářská 2, 611 37 Brno, jan92@physics.muni.cz*

Abstract
By plasma spraying of titanium carbide and diboride using water stabilized plasma torch and CVD deposition of titanium nitride, followed by their surface oxidation, compact photoactive ceramic parts of chemical reactors can be produced. Photocatalytic efficiency of TiC, TiN and TiB_2 and the products of their oxidation at 450°C and 1000°C in air and at 450°C in oxygen plasma was determined and compared with plasma treated TiO_2 and Ti_2O_3.

Keywords
Photocatalytic activity, titania precursors, water stabilized plasma, oxygen plasma, titanium diboride, titanium carbide, titanium nitride, titanium oxide

1. Introduction

In recent years, a lot of attention is paid to photocatalytic reactions taking place on catalysts based on titania, especially its anatase modification [1,2]. During photocatalysis, intense degradation of organic substances and bacteria takes place on the photocatalyst surface under UV radiation. In study [3] we found that rutile modification also possesses photocatalytic properties, when processed by thermal plasma to obtain oxygen deficiency or defective crystal structure. It was also found that ilmenite, reduced in a hydrogen plasma (in a C/RF reactor under experimental conditions P_{H2} = 350 - 1010 Pa, P_{Ar} = 50 - 100 Pa, T_n = 600-720 K, T_e ~ 11 000K) to metallic iron and TiO_2 with highly disordered structure, exhibits measurable photoactivity [4].
Fabrication of large, strong free-standing parts (FSP) or free flight particles (FFP) from photoactive anatase by plasma spraying is not feasible, due to the low temperature of its transformation to rutile. This is in the 460-600°C range, depending on pressure.

The objective of this study is to produce free-standing parts from such titanium compounds that can be plasma sprayed and then transformed, either in bulk or superficially, to a photocatalytic base. For example, titanium boride, carbide and nitride are such compounds. The working hypothesis assumed that mechanically strong catalytic components of chemical reactors can be prepared using surface oxidation of such compounds under the anatase-rutile transformation temperature.

2. Experimental

Thick, compact coatings of TiB_2 and TiC [5] and TiO_2 were produces by plasma spraying onto graphite substrates using water stabilized plasma generator WSP®. TiN coating was produced by a CVD method. From these coatings, powder samples were prepared by milling after the graphite removal; these were sieved to <50 μm. Further, commercial Ti_2O_3 powder (HiChem Ltd. Praha, CZ) with <50 μm size was used. These powders were subjected to thermal gravimetry analysis in ambient air. It was found that oxidation starts already at 600°C, spontaneous oxidation occurred between 900-1000°C. To obtain information of the process kinetics, they were then oxidized isothermally in ambient air at 450°C and 1000°C and, for comparison, in a barrel rotating plasma chemical reactor in an oxygen plasma, generated by capacitively or inductively driven RF generator [6]. The RF generator (Fig. 1) operated at a frequency of 27 MHz with a power output of 1-4 kW. Total flow rate of oxygen controlled by mass flowmeters was 100 sccm, which corresponds to a pressure of 150 Pa. For plasma-assisted oxidation or reduction in plasmachemical reactors, the kinetic and energy conditions can be varied to obtain the same yield at lower temperatures (up to hundreds of degrees), which is particularly advantageous for low temperature phase transitions.

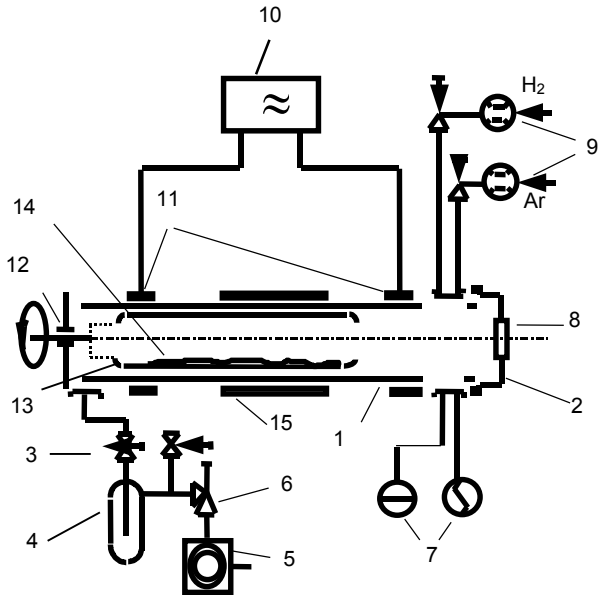

1 outer quartz reactor tube
2 gas inlet flange
3 throttle valve
4 cold trap
5 vacuum pumping system
6 valve
7 vacuum gauges (membrane, Pirani)
8 quartz observing window
9 flow meters
10 RF generator (13.56 MHz, 500 W)
11 external electrodes (capacitive coupling)
12 outlet flange with sample holder
13 inner quartz rotating cylindrical tube
14 pulverized sample
15 oven

Fig.1. RF barrel reactor with capacitive coupling.

Variations in morphology, surface state, structural defect concentration of the reactants and products were characterized by SEM, XRD, BET and IR spectrometry. Photocatalytic activity of the materials was determined by colorimetry, based on the measurements of changes of optical parameters L*, a*, b* and DE* of an indicator (3,3´,5,5´-Tetrabromophenolsulfonphthalein (Bromophenol Blue) and 2-nitroso-1-naphtol) mixed with a powder sample, under UV radiation with a dominant wavelength of 360 nm. A Color Quest XE (Hunter Lab USA) instrument was used at D65 (daylight) and 10° viewing angle. The DE* values were obtained as

$$DE^* = [(DL^*)^2 + (Da^*)^2 + (Db^*)^2]^{½}.$$

The yellowness index, characterizing the degradation processes, was calculated according to the ASTM E313-98 standard. The products of titanium carbide and nitride oxidation were measured as received. However, oxidation of titanium diboride produced – besides TiO_2 – also boron oxide, causing surface sintering of the powder. Thus, boron oxide was removed by water leaching prior to photoactivity measurement.

3. Results and discussion

X-ray diffraction on powders and deposits oxidized in air showed that all samples oxidized at 1000°C for 1 hour transformed, in agreement with theory, to the high-temperature titania modification, rutile. Depending on the exposure time, the oxidation products at 450°C were mixtures of the reactants with a varying amount of rutile and anatase. When the oxidation time was extended to 4 h, all remainders of anatase transformed to rutile. Informative data on the oxidation kinetics are presented in Table 1.

Table 1 - DE* values in dependence on time and temperature of oxidation in air.

	oxidation temperature 450°C				oxidation temperature 1000°C			
sample	0,5 h	1 h	2 h	4 h	0,5 h	1 h	2 h	4 h
Ti_2O_3	15	17	18	18	4	9	10	10
TiC	8	12	12	-	3	4	4,5	-
TiB_2	14	15	15	-	4	5	5.5	5.5

The results of photoactivity measurements of the original and treated samples are shown on Figs. 2-4. The measurements were performed on samples oxidized for a constant time of 1 hour.

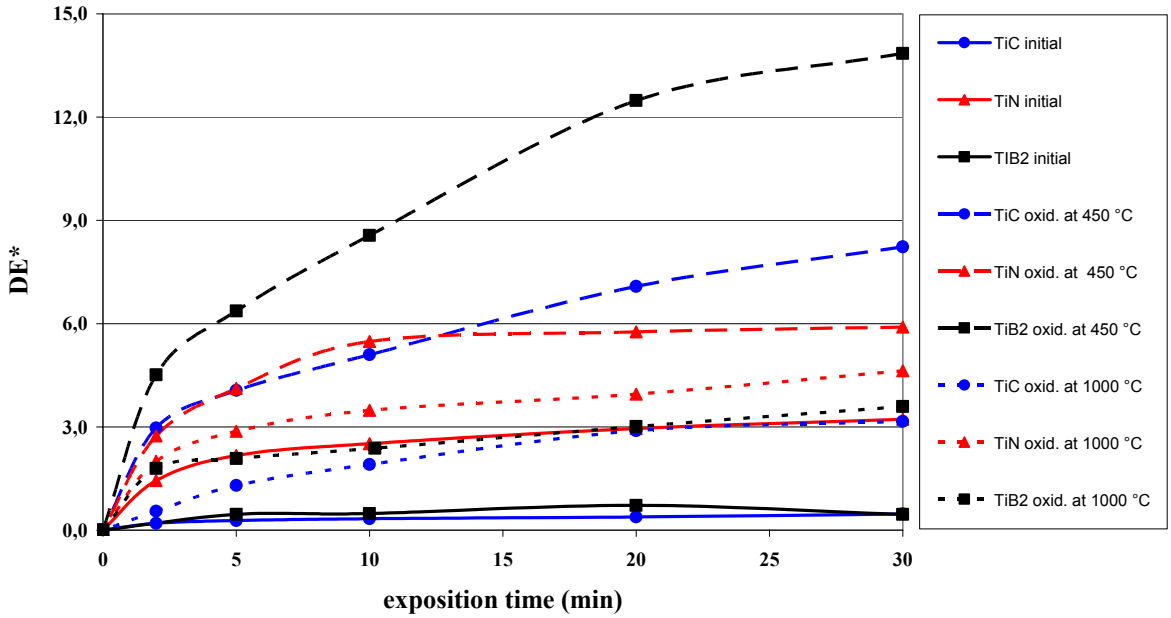

Fig.2 Dependence of a color change DE* of TiC, TiN a TiB_2 coatings colored by 2-nitroso-1-naphtol on the time of exposure by UV light (360 nm) in contact with atmospheric oxygen.

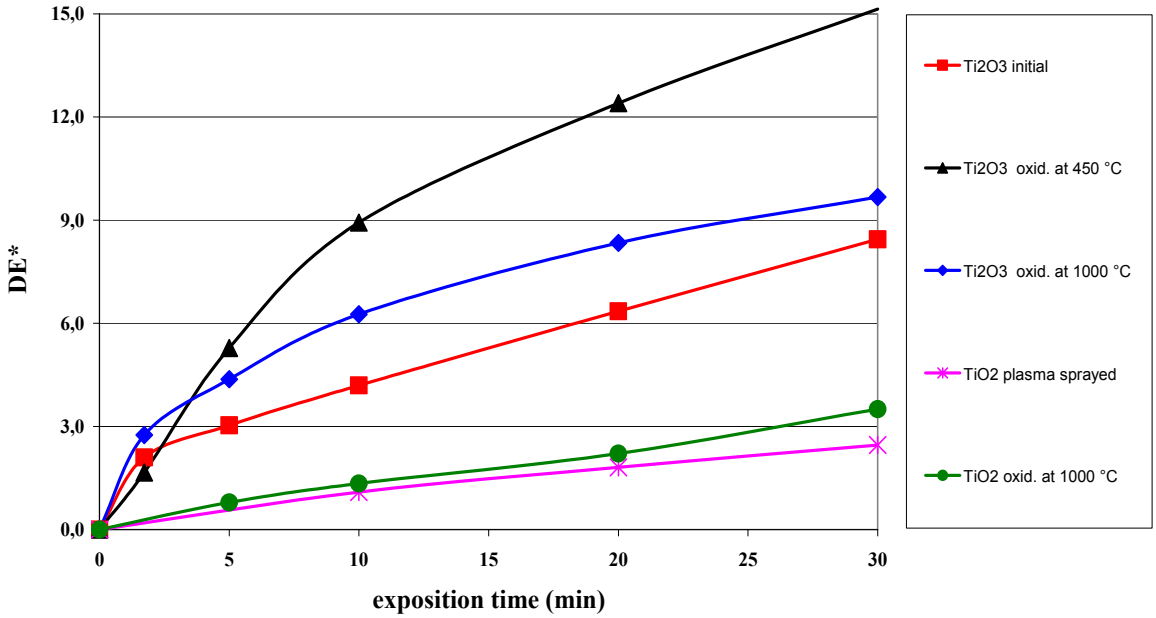

Fig.3. Dependence of a color change DE* of TiO_2 and Ti_2O_3 coatings colored by 2-nitroso-1-naphtol on the time of exposure by UV light (360 nm) in contact with atmospheric oxygen.

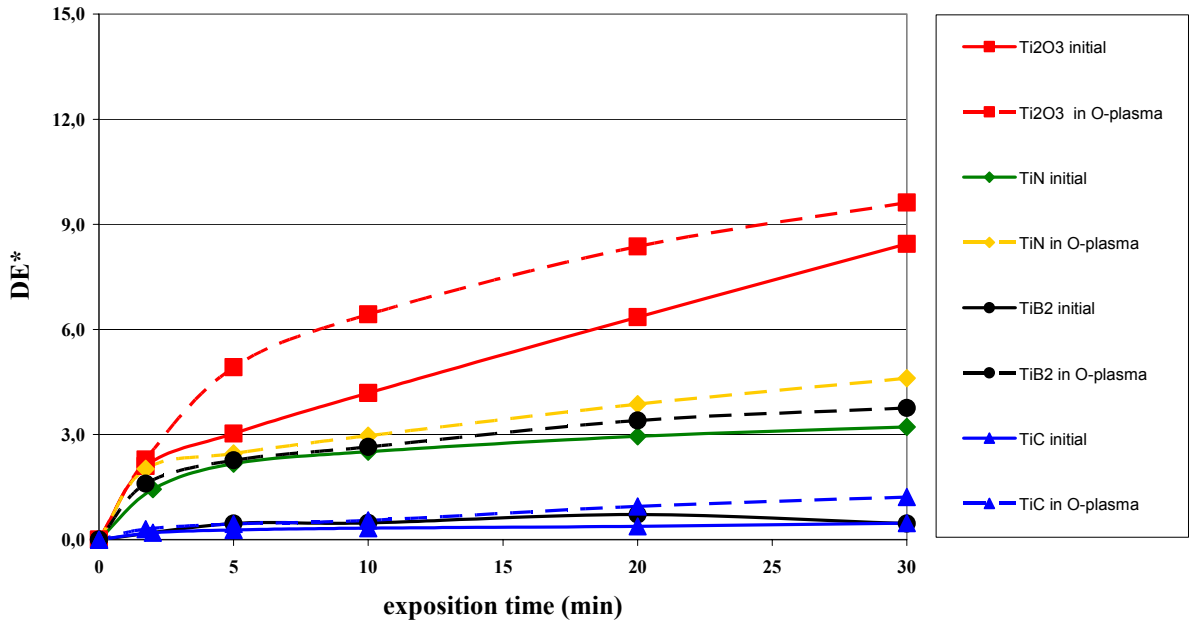

Fig.4 Dependence of a color change DE* of samples oxidized in oxygen plasma, colored by 2-nitroso-1-naphtol, on the time of exposure by UV light (360 nm) in contact with atmospheric oxygen.

From the measured DE* values and YI E313-98 curves, one can see that from the untreated compounds, only Ti_2O_3 (DE* 9/30 min) and TiN (DE* 3/30 min) exhibited moderate photoactivity. T his is probably a result of the TiN production, yielding TiN with 0.04 % oxygen. Plasma sprayed TiC and TiB_2 did not exhibit a distinct photoactivity; the measured values of DE* = 1–3 (see Fig.2) could not be unambiguously attributed to the effect of these non-activated substances.

Oxidation at both 450°C and 1000°C increased photoactivity in all studied substances. The photoactivity of all samples oxidized at 450°C was significantly higher than of corresponding samples oxidized at 1000°C. This corresponds to the presence of highly photoactive anatase in the 450°C oxidation products and presumed higher concentration of lattice defects and surface roughness, caused by lower processing temperature. Analysis of the surface layer of the 450°C samples showed anatase as the major phase and rutile as a minor phase. This influenced the DE* parameter. Maximum photocatalytic effect was observed in oxidized TiB_2 (DE* 15/30). Minimal effect was found in TiN (DE* 6/30), where, due to its high thermal resistance, only minute surface oxidation took place. In its diffractogram, only rutile was weakly identified. Photoactivity of TiC is characterized by DE* = 8/30 min.

Oxidation in the oxygen plasma at an outer wall temperature of 450°C confirmed the order of activity, but with a higher efficiency. The increase was up to fifteen-fold for TiB_2 and TiC and two-fold for TiN, after a 5-10 min exposure. Comparison with a photoactivity of titanium(III) oxide was not possible in this case, because of its intense black color.

SEM images of the deposit surfaces indicated a relationship between photoactivity, thermal treatment and powder morphology. Oxidation leads to increased surface roughness – for example, in TiN oxidized at 450°C, particles with needle-like protrusions 0,1–1 μm were observed. Higher oxidation temperature increases the rutile content in the surface layer and rounds the powder particles. This reduces the specific surface and the number of surface defects, leading to a further decrease in photoactivity. The defects and changes in oxidation state are currently studied also by EPR [7].

4. Conclusions

To obtain compact photocatalytically active materials, we verified the preparation of new titanium oxide forms by oxidation of various titanium compounds (precursors) with different crystal structures and titanium oxidation degree. Four model substances were chosen – titanium boride, carbinde, nitride

and titanium(III) oxide. These compounds can be prepared either as powders with high specific surface, or in the form of large area compact parts, using CVD, PVD and especially plasma spraying (except Ti_2O_3). After the treatment at high temperatures, reached by the water stabilized plasma generator WSP®, measurable photoactivity appears, which can be further controlled by a post-treatment under 450°C. Oxidation in an RF generated oxygen plasma initially seemed more efficient, especially regarding shorter reaction time. However, experiments have shown that although the outer wall temperature was controlled (450°C), uncontrolled temperature increase inside the reactor occurred during the reaction of oxygen plasma with the titanium compounds, leading to the formation of the less active rutile phase. Further process optimization is foreseen especially in the capacitively driven plasmachemical reactor, where the oxygen plasma concentration can be varied, but it is currently difficult to maintain a constant temperature and a stable discharge, due to the electrical conductivity of some precursors.

This study was part of research programme MSM 6046137302 “Preparation and research of functional materials and material technologies”.

References

[1] A. Fujishima, K. Hashimoto, T. Watanabe, *TiO2 Photocatalysis*, *Fundamentals and Applications,* BKC Inc., Tokyo (1999)

[2] T.K. Kim, M.N. Lee, S.H. Lee, Y.C. Park, C.K. Jung, J.-H. Boo, Development of surface coating technology of TiO_2 powder and improvement of photocatalytic activity by surface modification. Thin Solid Films, Vol 475 Iss 1 - 2 2005 171-177

[3] V. Brozek, K. Neufuss, Z. Srank, L. Mastny, M. Vacik, R. Hofman. Photocatalytic properties of plasma sprayed titanium dioxide Chem. Listy *98*, 759 (2004) ISSN 0009-2770

[4] V. Brozek, Z. Srank, L. Mastny, K. Neufuss, Photocatalytic properties of plasma sprayed ilmenite Summaries CHISA 2004, Praha 22-26 August, Vol.I, P1.87 p.295 (CD ROM Abst. 0935) ISBN 80-86059-40-5

[5] V. Brozek, J. Dubsky, B. Kolman, K. Neufuss, P. Chraska, Plasma Sprayed Coatings of Borides, Carbides and Silicide, Ceramic adding the value, AUSTCERAM '92, 777 (1992)

[6] V. Brozek, J. Janca, Plasmachemical reactors for special synthesis and decompositions, 4th European Congress of Chemical Engineering, Granada, Spain 21-25 September 2003 P-6.1-024, p.62, ISBN 84-88233-23-0

[7] Z. Prasil, K. Vacek, Z. Srank, L. Mastny, V. Brozek, Chem. Listy 98, 572 (2004)

IMPROVED PLATELET ADHESION ON GAS-DISCHARGE PLASMA MODIFIED POLYSTYRENE FOR A MICROTITRE PLATE ASSAY

R. Ihrke[1], B. Großjohann[2], J. Freier[2], L. E. Lubenow[2], A. Greinacher[2], S. Santoso[3], K. Schröder[1], A. Ohl[1]

[1] *Institute of Low Temperature Plasma Physics, Greifswald, Germany*
[2] *Ernst-Moritz-Arndt University, Department of Immunology and Transfusion Medicine, Greifswald, Germany*
[3] *Justus-Liebig-University, Institute of Immunology and Transfusion Medicine, Giessen, Germany*

Abstract
Control of blood platelet adhesion on biomaterials requires high-quality equipment of surfaces with signal molecules. Here, these requirements are investigated for the case of the development of a new blood platelet assay in microtitre plates made from polystyrene (PS). PS surfaces modified in ammonia plasma were found to improve the adsorption and enable the covalent coupling of collagen I (Coll I), which causes high and reproducible platelet adhesion.

Keywords
Polymer, biomaterial, ammonia plasma, microwave plasma, surface modification, blood platelet

Motivation
Gas-discharge plasmas are widely spread applied for the mass production of surface modified polystyrene (PS) disposables. The products are called "tissue-culture treated" PS (TCPS) [1] and they possess different oxygen-containing surface groups, and in some cases additional nitrogen-containing groups. In certain applications including the one presented here this is not sufficient and surface modifications become necessary, which are aimed at increased densities of selected chemical functional groups and controlled biomolecule coupling.
In the present case blood platelet adhesion has to be quantified in a multi-well plate. Such a quantification is important to detect enhanced risk of vascular disorders caused by increased platelet adhesiveness, or by a reduced platelet adhesion compromising the haemostatic process. Platelet adhesion can be measured with perfusion chambers [2, 3], but this method is technically complex, very time-consuming and demands a lot of material and man power. In addition, although a number of platelet adhesion assays have been established, most of them need high amounts of expensive extracellular matrix biomolecules, still. Furthermore, instability of the adsorbed layer due to "unspecific" coating procedure was observed during platelet adhesion measurements.
To avoid these problems, here a new platelet adhesion assay was developed utilizing plasma-induced surface modifications, which improve specific adsorptive or covalent immobilization of extracellular matrix proteins.

Experimental
Polystyrene microtitre plates for fluorescence experiments (96 well flat bottom, high binding, black, non-pyrogenic, DNase and RNase free) were purchased from Greiner Bio one (Frickenhausen, Germany). The plates were treated in ammonia plasma generated in a microwave reactor V55G (Plasma Finish, Schwedt, Germany) using 500 W power, 40 ml NH_3 per minute gas flow at a constant pressure of 0.2 mbar for 30 s. This special experimental setup was found to possess enhanced selectivity concerning the formation of amino-functional groups on polymer surfaces [4]. Following this treatment, Collagen I (Coll I) was deposited to account for the needs of specific, selective adhesion. Here, Coll I served as model biomolecule for assay development, only. More specific and more expensive platelet adhesion stimulating substances could be applied in a high-throughput assay. Two different coupling methods (see Fig.1) were tested since it is well known, that functionality of biomolecules can be strongly impaired by immobilization and a prognosis of functionality for a certain method is difficult due to the complexity of polymer surfaces and biomolecules. Here, amino groups of the proteins were linked to polymer surface bound amines. The first route investigated is the reaction of glutardialdehyde (GDA, 2 % in water, Sigma, Taufkirchen, Germany) with amines to form Schiff bases. The second route utilizes a water soluble

carbodiimide (CDI, EDC, 0.12 mol/l, Sigma, Taufkirchen, Germany) as a catalyst for the coupling of acid groups of the spacer polyethylene glycol diacid (PEG-DA) with the amines. The methods mainly differ in the functionality of spacer molecule. While GDA is a short-chain molecule prone to ring formation and protein cross-linking by intermolecular condensation reactions, PEG-DA is a long-chain substance with self-organizing capability according to the repeating ethylene oxide groups. This means, GDA links the protein more rigid than PEG-DA, which additionally enables a higher disposability of the acidic head groups.

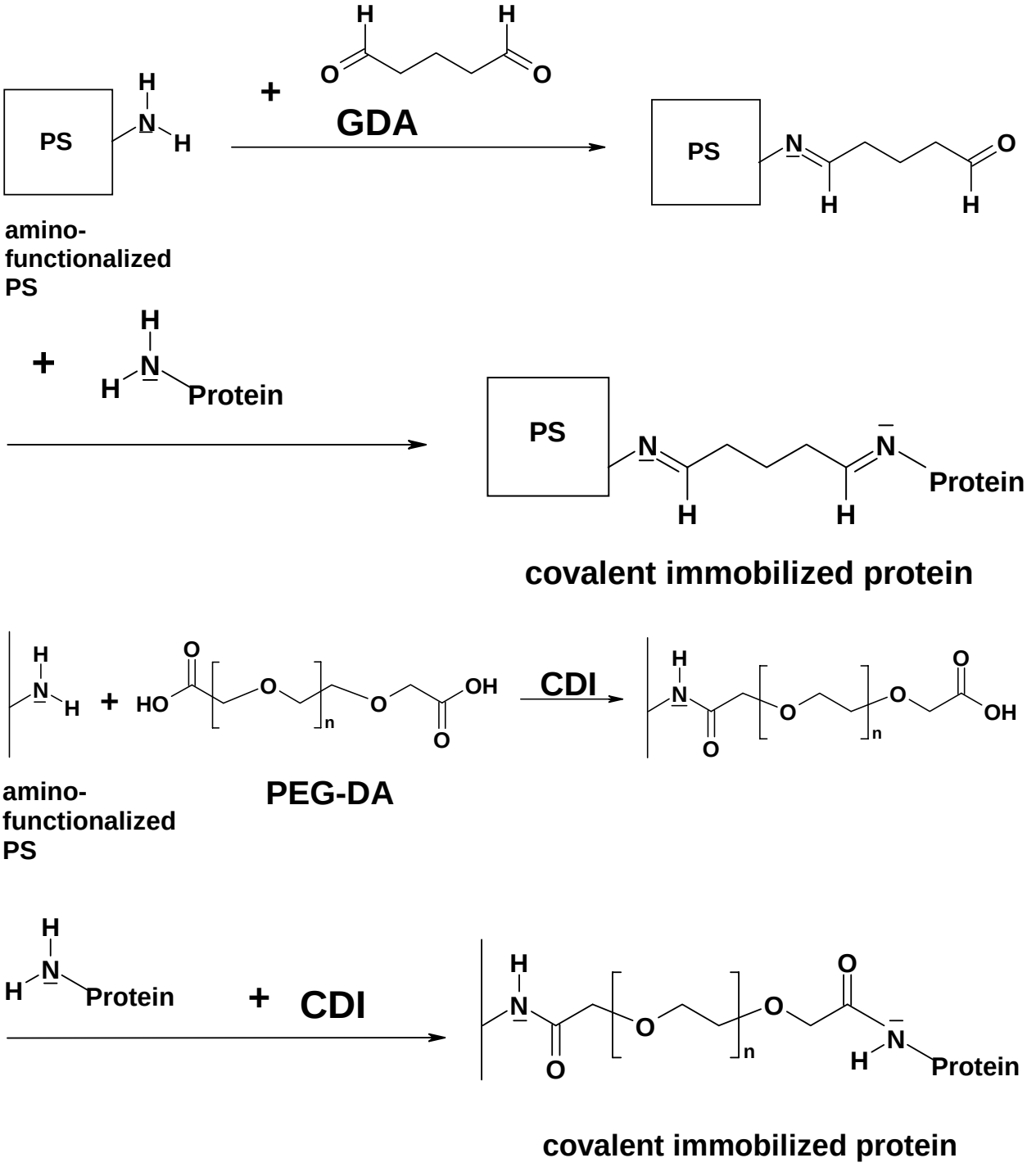

Fig.1: Schematic description of covalent protein-coupling to amino-functionalized PS surfaces by use of glutardialdehyde-method (GDA) and carbodiimide-method (CDI) with polyethylene glycol diacid (PEG-DA), respectively.

For XPS measurements, plane pieces of the bottoms of the wells with a diameter of about 5 mm were cut out. XP spectra were taken with an Axis Ultra (Kratos, Manchester, UK) with monochromatic Al K_α irradiation, charge neutralization and a spot size of about 700 µm diameter.
Human platelets were isolated from whole blood, which was obtained from healthy volunteer donors. Briefly, platelets were harvested from blood by centrifugation and platelet rich plasma (PRP) was transferred into the same volume washing buffer composed of NaCl, KCl , citric acid, $MgCl_2$, $CaCl_2$, glucose (pH 6.5). The PRP was incubated for 15 min at 37°C and centrifuged afterwards. The platelets were gently resuspended in 2 ml washing buffer containing PGE1 and apyrase. Again, washing buffer was added, incubated and centrifugated.

For the adhesion tests, 100 µl of fluorescence labelled platelets (calcein labelling, 100.000/µl) were incubated per well in the dark at 37 °C for 30 min. The number of adherent platelets was determined fluorometrically (Microplate-Reader, FLX 800, BIO-Tek, Winooski, Vermont, U.S.) after three washings.

Results and Discussion
The availability of surfaces with enhanced amino-functionalization is a useful starting point for coupling of biomolecules [5]. The effects of coupling can be approximately characterized by XPS-measurements. In Fig.2 results of such measurements are summarized which are relevant for the present investigations.

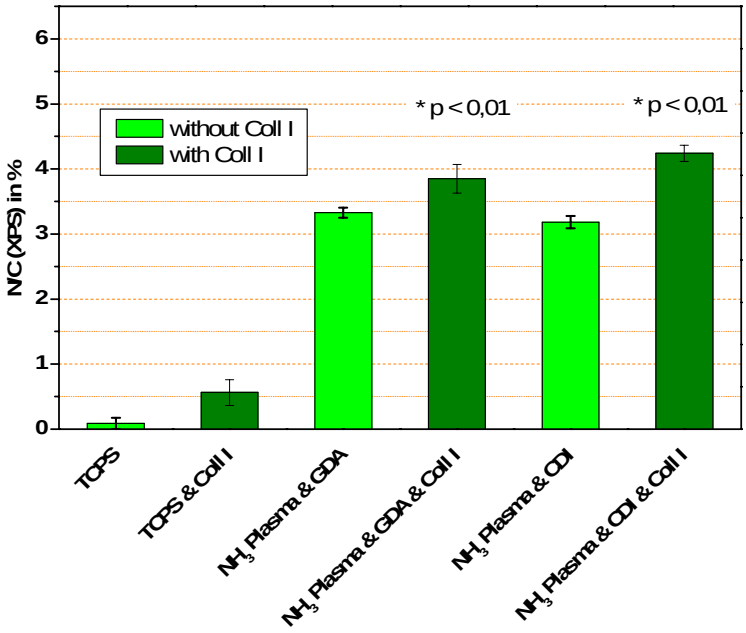

Fig. 2: XPS measurements for comparison of covalent bonding of Coll I from a highly diluted solution (0.01 µg/ml) on ammonia plasma treated surfaces via GDA- and CDI-PEG-DA-method with TCPS surfaces.

Here, the amount of nitrogen on the surface is taken as an indication for the presence of positively charged nitrogen-functional groups in general. Clear differences can be seen between the starting material TCPS (0.1±0.1 % N/C), and the ammonia plasma treated samples (> 3 % N/C). The nitrogen detected on the surfaces coupled with Coll I and the nitrogen detected on surfaces covered with GDA or PEG-DA may stem from different sources. In the latter case it is an indication of nitrogen functional groups generated by the ammonia plasma treatment since both GDA and PEG-DA do not contain any nitrogen. For the Coll I coated surfaces the nitrogen signal may originate from the Coll I, likewise. At least the surplus of nitrogen in comparison to the respective uncoated samples should arise from it. This assumption is supported by the results of additional coupling experiments which used different concentrations of collagen in the coating solution. A high concentration of collagen of 5 µg/ml resulted in surface nitrogen content as high as 17 % for GDA coupling and 13 % for carbodiimide polyethylene glycol diacid (CDI-PEG-DA) coupling. A strong reduction of the concentration to 0.1 µg/ml resulted in a substantial reduction of this signal to about 5 % in both cases with a difference of 1 % to the uncoated

materials (NH_3-plasma + GDA or PEG-DA, respectively). This difference did not change anymore for a further strong reduction of the concentration to 0.01 µg/ml, as can be seen from Fig. 2. Hence, it seems reasonable to assume that for these very low concentrations a certain similar amount of Coll I is deposited on the surfaces for the cases of pure adsorptive coating on TCPS and for both routes of covalent coupling.
In Fig. 3, the results of the respective platelet adhesion investigations are presented. Obviously, Coll I coating on TCPS is much less effective than the other coating methods. That means Coll I possibly adsorbed to TCPS in these small amounts is not active or washed during platelet adhesion assay.
The tenfold platelet adhesion on Coll I immobilized by the PEG-CDI method demonstrates significant advantages of covalent coupling. Also, covalent coupling by the GDA-method shows advantages. But it is not as efficient as the PEG-method. This can be interpreted as an effect of the more rigid coupling of the collagen to the surface which can influence its conformation in a way limiting its activity. Interestingly, a high platelet adhesion is also achieved, if Coll I is applied directly to ammonia plasma treated microtitre plates. The adhesion is similar to the PEG-method. This suggests the conclusion that Coll I is only adsorbed to the surface since otherwise its activity would be limited due to close and rigid surface contact. Vice versa, the similar activities suggest, that covalent coupling by the PEG-method results in optimum conformation of Coll I for platelet adhesion.

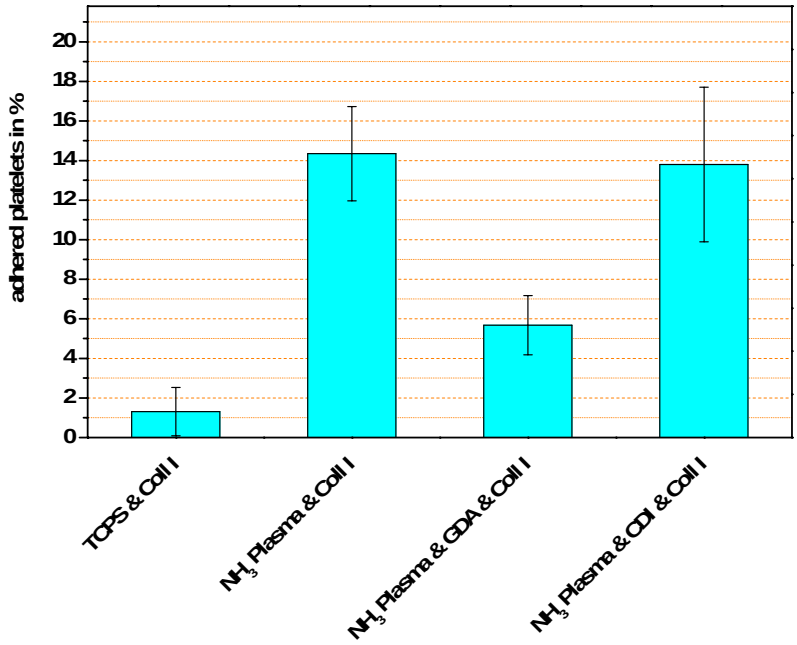

Fig. 3: Coll I coating from diluted solution (0.01 µg/ml): Analysis of platelet adhesion.

For the purpose of assay development, such a combination of low consumption of platelet adhesion stimulating substances and high platelet adhesion is highly desired. It would be of interest to know whether improvements are possible or not. One possibility to test this is to change the concentration of the Coll I solution. In Fig. 4 the results of adhesion tests are given for much more concentrated solutions (5 µg/ml) compared to Fig. 3. With the exception of Coll I on TCPS, only small improvements of adhesion are obtained. This means, that collagen bonding by PEG-DA and high quality ammonia plasma surface treatment may result in an enormous potential to save expensive signal molecules.

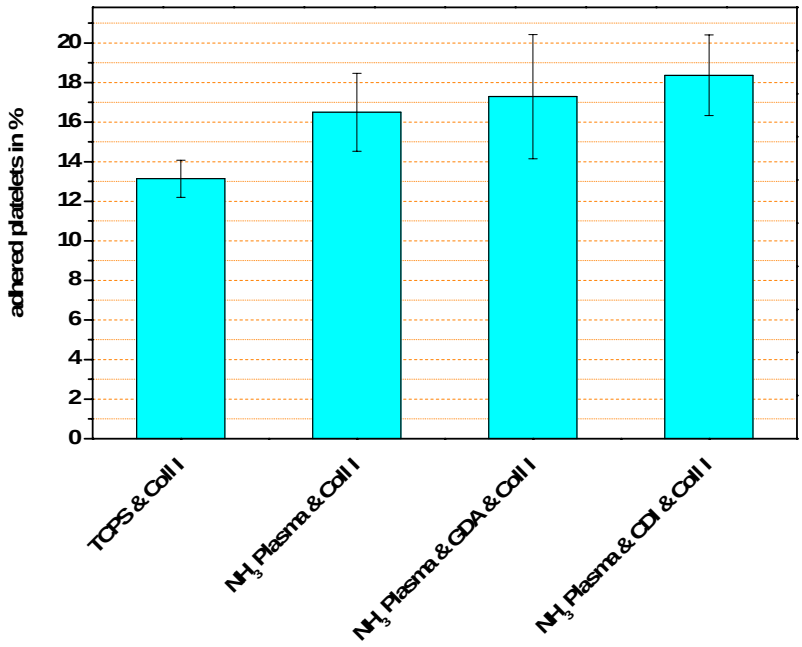

Fig.4: Coll I coating from concentrated solution (5 µg/ml): Analysis of platelet adhesion.

The here observed effects follow the predictions of a very general concept of understanding of the biological responses at non-physiological interfaces, which is known for a long time. According to this understanding, cationic electrostatic forces exhibit a low complement activation and coagulation, but very high platelet adhesion [6]. Also platelet adhesion on plasma polymers agree with it, as e.g. earlier investigation using plasma polymerized allylamine deposits on polyethylene (PE) [7] and polyethyleneterephthalate (PET) [8] demonstrated. These polymeric deposits were found to be more thrombogenic, i.e. adherent for platelets, than the untreated polyethylene, acrylic acid plasma polymers or PET and polyurethane. Similar effects were obtained in an investigation of hydrogels for the improvement of interfacial biocompatibility of polymers. Once more, a positively charged surface (introduced via dimethylaminoethyl DMAEMA copolymers) increased platelet adhesion compared to the nonionic hydrogel polyacrylamide (PAAm) [9]. Mostly, in the literature the increased adhesion is believed to be a consequence of fibrinogen adsorption due to ionic interactions between the positively charged amino groups on the surface and the fibrinogen molecule [8]. More recently, a comparison of the effects of pure fibrinogen, fibronectin, vitronectin and von Willebrand's factor preadsorbed on polystyrene substrates demonstrated that all of these biomolecules are able to support platelet adhesion. Except for fibrinogen, a dependence on the substrate surface pretreatment, whether untreated, fluorinated or positively charged, was found. Also it was reported, that very low amounts of fibrinogen were sufficient to support full-scale platelet adhesion [10].
The here reported results seem to extend the validity of all of these findings for the case of surfaces equipped with covalently bound biomolecules.

References

[1] P. LaRocca, S. Baker, Tissue Culture Surface Treatments, CellLine 6 (1996), 1.

[2] P. Hainaud, J. P. Brouland, P. Andre, G. Simoneau, C. Bal Dit Sollier, L. Drouet, J. Caen, S. Bellucci, Dissociation between fibrinogen and fibrin interaction with platelets in patients with different subtypes of Glanzmann's thrombastenis: studies in an ex vivo perfusion chamber model, Br. J. Hematol, 119 (4) (2002), 998-1004.

[3] M. R. Hernandez, R. Tonda, M. Pino, M. Serradell, G. Arderiu, G. Escular, Evaluation of effects of rofecoxib on platelet function in an in vitro model of thrombosis with circulating human blood, Eur. J. Clin. Invest. 34 (4) (2004), 297-302.

[4] A. A. Meyer-Plath, K. Schröder, B. Finke, A. Ohl, Current trends in biomaterial surface functionalization - nitrogen-containing plasma assisted processes with enhanced selectivity, Vacuum 71 (3) (2003), 391-406.

[5] K. Schröder, R. Ihrke, A. Diener, B. Nebe, J. Rychly, A. Ohl, Defined biologization of artificial polymer surfaces using covalent coupling strategies, Biomaterialien 4(2003), 136.

[6] T. Matsuda, Biological Responses at non-physilogical interfaces and molecular design of biocompatible surfaces, Nephrol. Dial. Transplant. 4 (1989), 60-66.

[7] T.-M. Ko, S. L. Cooper, Surface properties and platelet adhesion characteristics of acrylic acid and allylamine plasma-treated polyethylene, J. Appl. Polym. Sci. 47 (1993), 1601-1619.

[8] J. Chinn, B. D. Ratner, T. A. Horbett, Adsorption of baboon fibrinogen and the adhesion of platelets to a thin film polymer deposited by RFGD of allylamine",
Biomaterials 13 (1992), 322-332.

[9] E. Kulik, Y Ikada, *In vitro* platelet adhesion to nonionic and ionic hydrogels with different water contents, J. Biomed. Mater. Res. 30 (1996), 295-304.

[10] W.-B. Tsai, J. M. Grunkemeier, C. D. McFarland, T. A. Horbett, Platelet adhesion to polystyrene-based surfaces preadsorbed with plasmas selectively depleted in fibrinogen, fibronection, vitronectin, or von Willebrand's factor, J. Biomed. Mat. Res. 60 (2002), 348-359.

Materials processing at atmospheric pressure: non-equilibrium effects on nano-technology and mega-industries

Tomohiro Nozaki* and Ken Okazaki

Department of Mechanical and Control Engineering, Tokyo Institute of Technology.
**Corresponding author: tnozaki@mech.titech.ac.jp*

Abstract: Applications of atmospheric pressure non-equilibrium plasmas, now exclusively produced in the form of filamentary barrier discharges, atmospheric pressure glow discharges, and microplasmas, is spreading out into various engineering fields of not only material processing, but also energy and environment due to its special advantages of forming highly reactive plasmas at atmospheric pressure using simple reactor system. Our research group has been focusing on not only the development of new applications of those plasma sources, but also the establishment of appropriate modeling that enable us to characterize and optimize given plasma processes. This paper overviews our recent projects that range from nano-fabrication in materials processing to fuel upgrade in mega-industries.

1. Introduction

Atmospheric pressure non-equilibrium plasma has been exclusively produced in dielectric barrier discharges (DBDs), and historically used in ozone industry since 1857 [1]. DBD is now recognized as viable processing plasma for chemical conversion processes and applications are spreading out into many fields such as gas cleaning and fuel reforming with growing concern of global environment. In the late 80s, S. Okazaki and co-workers has explored atmospheric pressure glow discharge known as APG that gives spatially diffuse non-equilibrium plasma at high pressure [2]. Research activities and applications in this new field of plasma science and technology have been expanding into not only gas treatments, but also surface modifications, coatings, and PECVDs. The primarily interest of APGs is emphasized in practical applications since it minimizes vacuum system and allows to handle bulky materials in continuous process. It even enables us to use liquid precursors to deposit functional films [3]. From fundamental viewpoint, broad range of operating pressures from 10^{-1} Pa to 10^{5} Pa bring us to the comprehensive understanding of fundamental processes in both gas phase and boundary phenomena in plasma materials processing: it is believed to create greater value-added plasma processing in various industries where processing plasma is currently too expensive to introduce. Atmospheric pressure non-equilibrium plasmas have made a recent remarkable progress in formation techniques in the filed of microplasma. Efficient generation method and diagnostics of microplasma and the development of new applications including light sources of ultra-short wavelengths, three-dimensional micromachining tools, and other plasma devices are now being investigated [4].

This paper overviews materials processing in atmospheric pressure non-equilibrium plasmas based on our recent work. In section 2 and 3, authors devote ourselves to introduce fundamental character of both filamentary and diffuse barrier discharges known as dielectric barrier discharge (DBD) and atmospheric pressure glow discharge (APG), respectively. Optical emission spectroscopy, 1-D simulation of streamer formation, energy balance analysis, and gas chromatographic analysis are provided in order to distinguish DBD and APG from the viewpoint of “thermalization of non-equilibrium plasma”. Novel applications using DBD, APG, and microplasma are briefly introduced in section 4: (1) Low-temperature fuel reforming due to radical injection, (2) Non-equilibrium chemical reaction control in micro-scale reactor, (3) Deposition of carbon nanotubes in atmospheric pressure glow discharge, and (4) Microplasmas and application to nanoparticle formation. Concluding remark is presented in section 5.

2. Atmospheric pressure non-equilibrium plasmas

Generation methods of atmospheric pressure non-equilibrium plasma can be classified into several ways. Filamentary discharges: (I) Barrier discharge type: At least one of two metallic electrodes must be covered by insulating material in order to limit discharge currents and extinguish them within 1-10 ns. An insulating barrier also enables to disperse filamentary discharges over the gap. (II) Corona discharge type: Non-uniform electric

field such as point-to-plane geometry creates sufficiently large electric field that locally breaks down the gap and produces weakly ionized discharge at atmospheric pressure. Corona discharge does not transform into spark discharge as long as voltage and current relationship maintains positive differential characteristics (i.e. $dV/dI > 0$). (III) Pulsed discharge type: Fast response switching device or pulse forming network is applied in order to limit power input to the discharge channel. The pulse duration is generally of the order of 100 ns to avoid arcing, but optimum pulse duration depends on voltage polarity, ignition delay, and streamer propagation period. Homogeneous discharges: (IV) Penning ionization type: If Penning ionization or cumulative ionization becomes a major source of secondary electrons, avalanche-to-streamer transition would be suppressed and Townsend-like break down takes place. This type of plasma is exclusively produced in He, Ar, and N_2. High frequency operation (RF~MW) increases plasma density and helps this mechanism. (V) Microplasma type: As reactor dimension gets smaller than effective $(pd)_{min}$ at given pressure, operating pressure must inevitably increases in order to sustain self-maintaining discharge. Here, $(pd)_{min}$ expresses Paschen minimum and typical value is given by $(pd)_{min} \sim 1$ mmHg cm in ordinary gases [5]. Unlike transient discharges such as DBD and APG, microplasma could be characterized by effective dc approximation when operating frequency exceeds 100 MHz at atmospheric pressure.

It does not necessarily mean that each type of discharge appears in a single reactor. Two or more of them are need to be appropriately combined in a single plasma reactor for desired purpose. The next section exclusively describes fundamental properties of dielectric barrier discharges in both filamentary and diffuse modes which are customary recognized as DBD (dielectric barrier discharge) and APG (atmospheric pressure glow discharge). These two types of discharge are clearly distinguished by not only current waveforms and emission distribution, but also heat transfer characteristics and thermal structures.

2.1. Dielectric Barrier Discharge

A peculiarity of DBD is the presence of a dielectric insulator on one or both metallic electrodes, which leads to a formation of large number of filamentary microdischarges of nanosecond duration. Figure 1 shows typical voltage and current waveforms observed in DBD. It also shows a photograph of streamers taken with high-speed intensified CCD camera (i-Star DH712; Andor Technology). A large number of nanosecond current pulses are observed at every half cycle of applied voltage. The immediate termination of developing discharge due to charge built up on dielectric barrier creates a highly reactive non-equilibrium condition at atmospheric pressure. Due to the charge accumulation on the barrier, streamers are randomly dispersed between electrodes. The gas breaks down based on streamer breakdown mechanism. The velocity of propagating streamer is ten times higher than the drift velocity of electrons at given reduces electric field (10^8~10^9 cm/s). Each filament corresponds to a nanosecond current pulse appearing in the current waveform. DBD has been extensively studied in ozone production and detailed characteristics of individual filamentary discharge have been investigated by many researchers [6-8]. It is not too much to say that electrical and chemical properties of DBD reactor are determined by those of an individual filamentary discharge. Unfortunately, principle parameters such as electron density and electron energy in individual filament are hardly controlled by external parameters because streamer propagation time is too short to establish electrical coupling with external driving circuit. Operating conditions such as frequency and voltage amplitude simply change the number of filaments per unit time and unit area. This kind of robustness, however, may propose some advantages: DBD reactor is operated with variety of power source from commercial frequency to several hundreds kHz without having matching problem. Once reactor is optimized in a laboratory, it is easily scaled up to large scale industry installation.

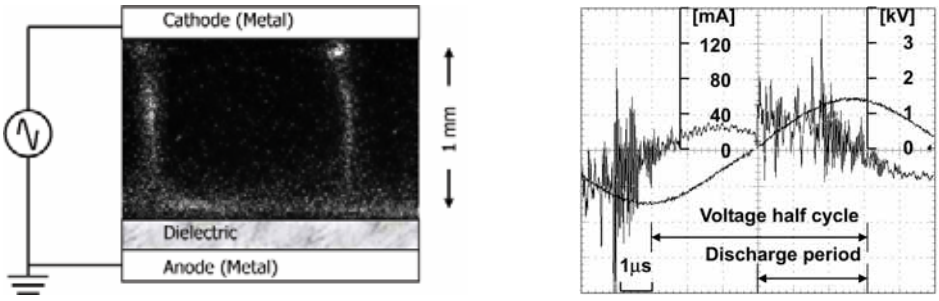

Fig. 1 Voltage and current waveforms in DBD (AC-80 kHz) and Photograph of a single streamer produced in pure methane (10 ns exposure time).

2.2. Atmospheric pressure glow discharge

The discovery of atmospheric pressure "glow" discharge dates back to the early 30s and its history is well described by Kogelschatz [9]. This paper focuses on recent development of atmospheric pressure "diffuse" barrier discharge, in which S. Okazaki and co-workers called atmospheric pressure glow discharge (APG) [2]. Recent progress in formation technique and applications has been published in the journal [10]. Figure 2 shows AC-80 kHz high voltage and current waveforms obtained in APG (CH_4:He=2:98). APG in Fig. 2 was produced in identical barrier discharge reactor using the same power supply shown in Fig. 1. Only difference is that feed gas is diluted by helium. With minimum over voltage, a single current pulse with 500 ns duration appeared at every half cycle of the voltage. A single current pulse became multiple pulses with increasing over voltage [1]. Corresponding emission distributions in the visible spectrum are described in Fig. 2 (a) - (b). Figure 2 (a) shows a superposition of 100 discharge events synchronized with negative discharge current with 1 μs exposure time (metallic cathode - dielectric anode). Figure 2 (b) was recorded during positive discharge current. Light distribution is not localized in the radial direction, but intense emission layer is created near the temporal cathode in both pictures. The emission distribution of APG has the structure similar to that of low pressure glow discharge [12]. Faraday dark space, positive column, and cathode glow are established at the time when a single current pulse reaches its maximum. At this moment, electron density in the temporal cathode region reaches $10^{11}cc^{-1}$ [12,13]. Production of metastable state helium by electron impact and associated Penning ionization becomes important source of secondary electrons. Electron avalanche does not transform into streamer since operating voltage is sufficiently lowered in helium, and Townsend-like breakdown takes place. N_2-based APG attracts broad attention from practical point of view. Formation mechanism also relies on Penning ionization; however, the presence of gaseous admixture is limited below 0.1%, and electron density (10^8cm^{-3}) doesn't reach high enough to produce cathode region. Increasing frequency improves stability of APG, but radio frequency may not be suitable for large scale plasma reactor which extends over 1 m.

3. Thermal structure of atmospheric pressure non-equilibrium plasmas

As briefly described above, DBD and APG are characterized as weakly ionized plasma with properties resembling transient high-pressure glow discharge. The immediate termination of developing plasma due to charge built up on dielectric material realizes highly reactive non-equilibrium conditions at atmospheric pressure. On the other hand, the electrical energy put into atmospheric pressure plasma easily transforms into thermal energy via large number of particle collisions that may lead to serious gas heating. The energy efficiency of material conversion in those plasma process is normally less than 10%. From this point, we paid special attention to the analysis of energy distribution mechanisms in methane-fed DBD and APG by focusing on energy balance analysis, emission spectroscopy of the rotational band of CH ((0,0) $A^2\Delta \rightarrow X^2\Pi$), and gas chromatographic analysis [14,15]. For the best understanding of microscopic energy deposition characteristics and improving energy efficiency by molecular scale optimization, we also analyzed thermal structure of methane-fed DBD and APG by focusing on time averaged gas temperature profiles across discharge gap.

3.1. Relationship between rotational temperature and gas temperature

As shown in current waveforms in Fig. 1 and Fig. 2, feed gas repeatedly breaks down at regular intervals. Therefore, the following relation can express net gas temperature increase between gas gap.

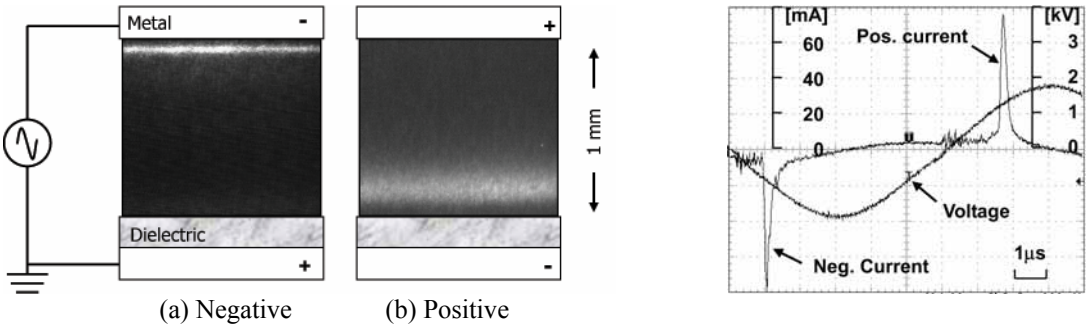

(a) Negative (b) Positive

Fig. 2 Voltage and current waveforms in APG (AC-80 kHz) and photographs of APG synchronized with (a) negative discharge current, (b) positive discharge current with 1 μs exposure time.

$$\Delta T_{net} \approx (T_{rot} - T_0) \approx \Delta T_{ave} + \Delta T_{plasma} \quad [\mathrm{K}] \qquad (1)$$

Here, T_{net} represents net temperature increase between gap, T_{rot} refers to rotational temperature, T_0 is initial gas temperature, ΔT_{ave} represents average temperature increase of feed gas, and ΔT_{plasma} is local temperature increase due to microdischarge or glow discharge formation. The rotational temperature was derived by the Boltzmann plot of rotational band of CH emission [14,16]. Average temperature increase (ΔT_{ave}) depends on not only plasma properties, but also various engineering factors such as flow field, external cooling conditions, and total input power, whereas ΔT_{plasma} is closely related to local energy deposition into transient discharges. In order to characterize thermal structure of DBD and APG, we need to separate ΔT_{ave} and ΔT_{plasma} from net temperature increase (ΔT_{net}).

Rotational temperature versus initial gas temperature (see Eq.1) in methane-fed DBD is shown in Fig. 3 [15]. Rotational temperature is 100-150 K higher than initial gas temperature because microdischarges are localized in narrow filamentary region, but it showed enough sensitivity to the variation of initial gas temperature. The results shown here is much higher than those provided by Luque et al. [17]. They concluded that temperature increase in a streamer is close to 10 K in CH_4/CO_2 barrier discharges operated by 14 kHz pulsed voltage (FWHM: ~2μs). Comparison between these two conclusions suggests important aspect. High frequency operation conducted in our experiment (80 kHz) induces microdischarges that excessively heats up discharge channels. High frequency operation is desirable to design compact reactor and increase throughput, but it might work more like heat source than radical source. It was further investigated in DBD and APG by focusing on energy balance and heat transfer analysis [15,18]. Excess temperature increase in DBD (i.e. ≈100 K) was also observed with respect to input power and gas velocity as shown in Fig. 4 and Fig. 5, while rotational temperature in APG is fairly close to average gas temperature since diffused discharge decreases power density. From Fig. 3 to Fig. 5, ΔT_{plasma} is nearly constant regardless of initial gas temperature (300-400 K), input power (0.5-3.8 Wcm^{-2}), and gas velocity (1-6 ms^{-1}) as long as gas gap (0.5 mm), dielectrics (0.5 mm Pyrex), and pressure were unchanged. Raising the input power for a given configuration generates increasing number of microdischarges per unit of electrode surface, whereas energy spent in an individual microdischarge, on average, does not change significantly. On the other hand, ΔT_{ave} depends mostly on input power and external cooling conditions.

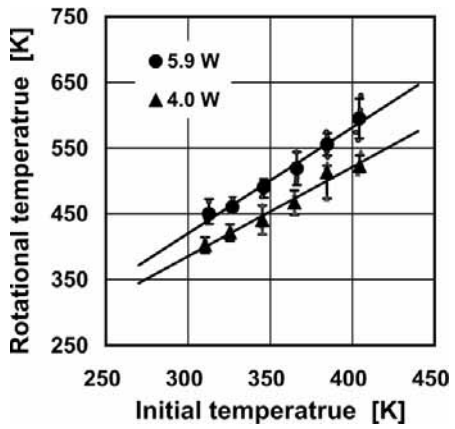

Fig. 3 Rotational temperature vs. initial gas temperature in DBD. Discharge area; 10×80 mm^2, gap; 0.5 mm, dielectric; 0.5 mm Pyrex, gas velocity, 1.0 ms^{-1}, and AC-80 kHz.

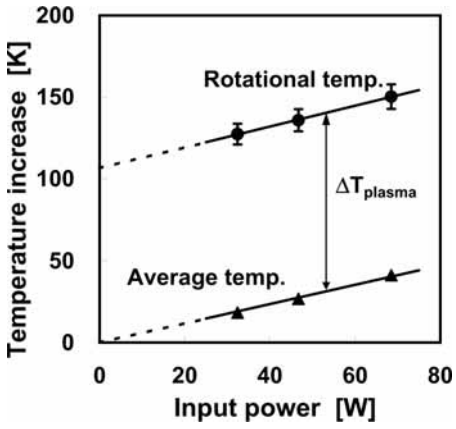

Fig. 4 Comparison between average gas temperature and rotational temperature in DBD. Discharge conditions: see Fig. 3.

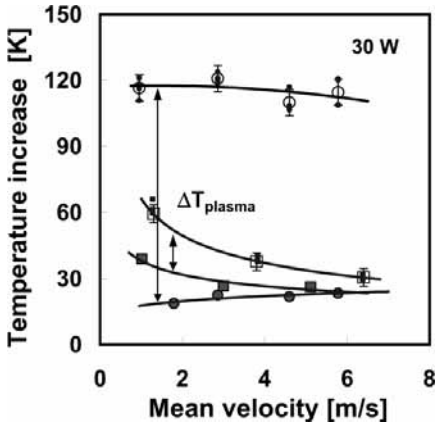

Fig. 5 Average temperature for (●) DBD and (■) APG. Rotational temperature for (○) DBD and (□) APG. Discharge conditions: see Fig. 3.

3.2. Net temperature distribution across discharge gap ($\Delta T_{ave}+\Delta T_{plasma}$)

In the practical interest, net temperature increase ($\Delta T_{ave}+\Delta T_{plasma}$) also poses important issues. Figure 6 (a) shows net temperature increase in DBD obtained by using AC-80 kHz high voltage. When increasing input power, net temperature (ΔT_{net}) in the middle of the gap remarkably increases because of poor cooling condition. Net gas temperature does not approach electrode temperature (20°C) even when decreasing input power to zero since energy spent in individual microdischarge does not continuously approach zero with decreasing input power. This means that gas temperatures increase on both electrodes should correspond to $\Delta T_{plasmae}$. In fact, $\Delta T_{plasmae}$ (~100 K) shown in Fig. 4 corresponds to the temperature increase on both electrodes. In addition, these temperatures are uniquely independent of input power. ΔT_{ave} could be minimized by improving external cooling condition of the reactor. However, memory effect due to high frequency operation induces significant gas heating which reached 100-150 K higher than initial gas temperature. In APG, net temperature increases near metallic electrode was remarkable as shown in Fig. 6 (b), and significantly increase with increasing input power. Temperature distribution is broadened by heat conduction through gas media (main component is helium). Local temperature increase near dielectric barrier becomes clear with input power even though magnitude is still moderate.

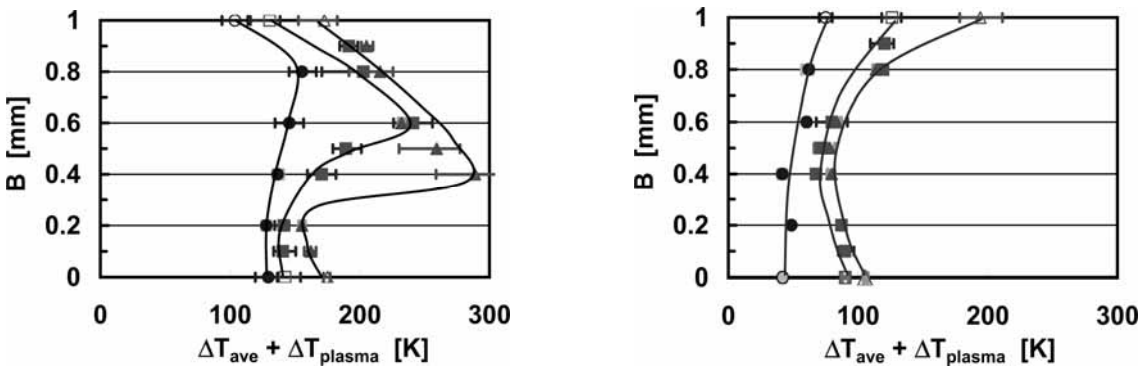

(a) DBD (▲25 W, ■20 W, ●17 W) (b) APG (▲15 W, ■10 W, ●6 W)

Fig. 6 Net temperature distribution in DBD and APG

4. Applications

4.1. Fuel upgrade using filamentary barrier discharges

4.1.1. Streamer formation and related chemistry in methane

We performed numerical simulation on streamer propagation in pure methane for the best understanding of elementary electronic and chemical processes [19,20]. The model consists of two different stages: streamer propagation and related chemistry where ionization, excitation, and dissociation of methane by electron impact are evaluated along with time evolution of field strength and electron density. We adopted complete set of cross sections of methane compiled by Davies et al [21] as recommended by Morgan [22]. During streamer development, electric energy input and radical formation efficiency were analyzed in detail. After the termination of streamer development, the second stage, ionic and free radical chemistry that would last for 10 ms was performed with the reaction scheme proposed by Tachibana et al [23]. The model includes 16 neutral species, 4 positive ions, and 2 vibrationally excited species. Temperature and pressure were 300 K and 760 Torr, respectively. We simulated Anode Directed Streamer (ADS) [24] ignited from tiny plasma spot which is initially located in front of the cathode. We assumed streamer was one-dimensional cylinder with 100 μm diameter. Basic equations were continuity equations for electron, ions, and neutral species, and Poisson's equation. 38 elementary reactions including 8 inelastic collisions were simultaneously solved. Physical modeling and mathematical procedure are presented by many researchers [25-27].

Figure 7 shows temporal development of radical species and products. All radical species including electron are rapidly increases with streamer propagation. Electron density reaches $10^{14}cc^{-1}$ when stream hits the anode. C, CH, CH_2, and H are quickly consumed after streamer termination to form C_2H_2, C_2H_4, and H_2. CH_3 remains relatively high population since hydrogen subtraction from CH_4 by CH_4^+ ($CH_4+CH_4^+=CH_3+CH_5^+$) makes

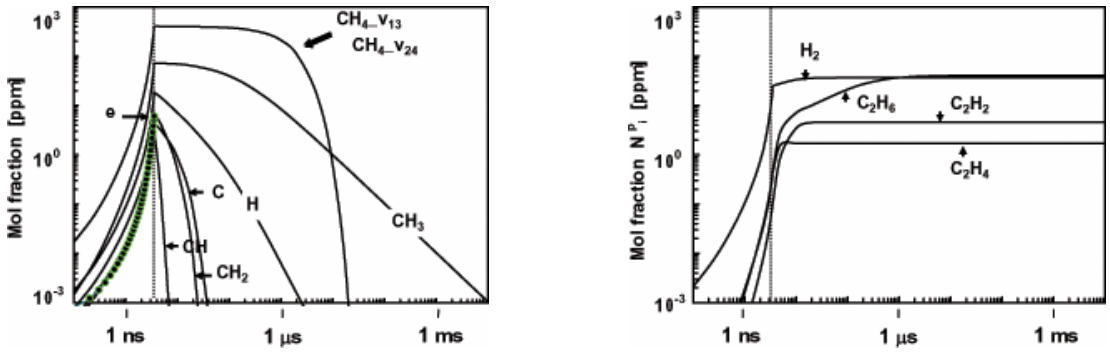

Fig. 7 Evolution of radical species and final products. 200 Td, 760 Torr, 300 K.

Table 1 Fundamental electronic processes. 200 Td, 760 Torr, 300 K, streamer propagation time≈3.5 ns, $N_e \approx 10^{14} cc^{-1}$

Reaction (CH_4 + e)	ε_i [eV]	Density	Energy branch %	k_i/W_e [cm^2] (500 Td)
→ CH4(v24) + e	0.162	$150N_e$	11.9	372×10^{-18}
→ CH4(v13) + e	0.361		24.5	316
→ CH_3 +H + e	9.0	$10N_e$	17.0	88.4
→ CH_2 +H_2 + e	10.0	~N_e	13.2	79.6
→ CH + H_2 + H + e	11.0		10.8	71.5
→ C + 2H_2 + e	12.0		9.3	64.5
→ CH_4^+ + e + e	12.6	N_e	9.4	70.7
→ CH_3^+ + H + e + e	14.3		4.0	46.6

W_e: drift velocity of electrons [cm/s]

radical chain, which eventually produces C_2H_6. From this point, formation of streamer is considered as radical injection phase. The most abundant species are vibrationally excited methane that reached 100 times higher than electron density. However, it can not participate further reactions because of low reactivity. Therefore, production of vibrationally excited methane leads to remarkable energy loss. Approximate radical density and energy distribution are summarized in Table 1 along with excitation threshold. Excitation threshold for vibrational excitation is of the order of 0.1-0.3 eV, however, nearly 40% of input electric energy was consumed since rate constants are 10 times larger than other reactions. From this point, decomposition of vibrationally excited methane during reforming reaction may significantly increase energy efficiency of the process.

4.1.2. Low-temperature fuel reforming due to radical injection

Although industrial applications of C_1 chemistry depend mostly on catalytic conversion processes, plasma catalysis are highlighted as unique technique for energy saving and environment safe purposes with increasing demand of hydrogen and synthesis gas [28-30]. More recently, atmospheric pressure non-thermal plasmas such as Plasmatron [31] and Glidarc [32,33] are recognized as economically competitive plasma fuel converters. Electrical energy consumption of those plasma reactors is normally less than 10% of heating value of the initial fuel when combined with partial oxidation. Driving force of reforming reaction essentially depends on heat released by partial oxidation, while the plasma preliminary enhances the combustion process of initial fuel/air mixtures.

We have developed a barrier discharge and catalyst hybrid reactor for the low temperature reforming of methane [19,20]. This technique allows utilizing low temperature thermal energy wasted from industries, which eventually provides variety of energy utility options. The idea behind the project is that low-calorie fuels such as biogas can be upgraded in the temperature range of 300°C to 400°C, which corresponds to the exhaust gas from internal combustion engine, by the help of non-equilibrium plasma. The resulting hydrogen enriched gas is then available to improve the ignition stability of poor fuels and drives a megawatt internal combustion engine. Figure 8 illustrates the configuration of barrier discharge and catalyst hybrid reactor. The basic idea of hybrid reactor was first developed by Mizuno and Yamamoto [34,35]. The rod-to-tube (ϕ_r 3 mm × ϕ_i 20 mm) reactor was packed with catalyst pellets of 12wt%/γ-Al_2O_3 (3 mm) in the volume of ϕ_i 20 mm × 50 mm. Bipolar pulsed voltage (+/-20 kV at 1-5 kpps with FWHM:~2μs) was applied between center and external ground electrode. The discharge is ignited at pellet contacts, and then propagates covering pellet surface, providing best interaction between plasma

and catalyst. We used simulated biogas which includes 60% methane and 40% nitrogen (CH_4:N_2 = 6:4). Steam and methane ratio (S/C) was set to one (S/C = H_2O/CH_4 = 1). The plasma hybrid process needs to convert 20% of initial methane that enriches hydrogen in output gas by 32% (dry base). It remarkably enhances combustibility of "poor" biogas and is able to drive internal combustion engine.

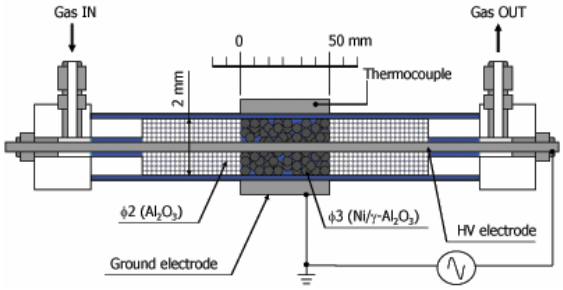

Fig. 8 DBD/Catalyst hybrid reactor

Figure 9 compares methane conversion obtained by three different conditions. The results clearly show that methane is hardly decomposed by barrier discharge since discharge power was limited in order to avoid excess gas heating, i.e. input power was carefully adjusted so as not to exceed endothermic enthalpy of the reaction. Input power density with respect to methane flow rate was smaller than 120 kJ/mol$_{CH4}$ (~13% of HHV of CH_4). According to Fig. 9, Ni/γ-Al_2O_3 catalyst is more effective than barrier discharge, but result does not reach equilibrium because the space velocity is high (SV = 10000 hr^{-1}). On the other hand, combined result reached equilibrium all the way through the temperature tested. Figure 10 schematically presents potential curve for methane molecule, showing tentative reaction mechanisms [18]. Thermal dissociation of methane to H and CH_3, for example, follows the ground state potential curve. This process requires high temperature heat source (> 800°C) and consumed 4.26 eV dissociation energy. Methane dissociation by electron impact must follow upper electronic state that is expressed as dissociation curve. The great benefit of electronic process is that methane decomposition proceeds independently of temperature and pressure, but main drawback is that electrons have to lose twice as much energy as dissociation energy by single collision (9-12 eV >> 4.26 eV). Excess energy fed into methane molecule increases kinetic energy of H and CH_3. Based on our numerical simulation (see 4.1.1), 50% of electric energy can be utilized for dissociation collision to form CH_i (i = 0,1,2,3) and H radicals. However, 60% of those excited energy must be released for gas heating as an excess input energy. This is the main reason that energy cost of plasma fuel conversion is much higher than that for thermal processes. Plasma enhanced catalytic reaction is explained by two-step process as shown in Fig. 10. Two vibrational states of methane are produced by inelastic electron collision. Dissociative chemisorption of vibrational methane takes place at low temperature (400°C ~ 600°C) [36]. This kind of electronic process does not accompany excess energy input since a series of reaction takes place within a ground state potential curve. In addition, number density of vibrational species is 100 times higher than electrons. The utilization of vibrationally excited methane in plasma catalysis potentially increases the efficiency on chemical conversion process in large degree.

4.1.3. Non-equilibrium chemical reaction control in micro-scale reactor

The great benefit of partial oxidation of methane, particularly direct synthesis of methanol, has attracted

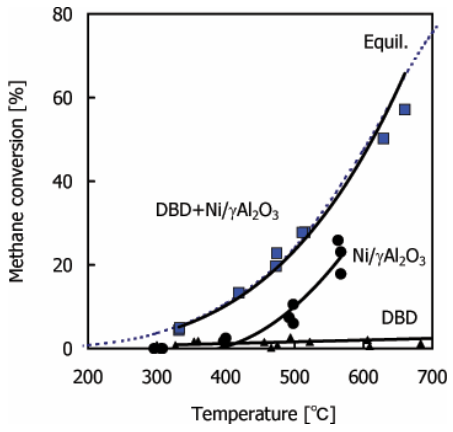

Fig. 9 Methane conversion vs catalyst bed temperature which is measure by infrared camera.. SV = 10000 hr^{-1}, $CH_4/N_2/H_2O$ = 1100/733/2200 sccm (S/C = 1). Power = 25-120 kJ/mol $_{CH4}$.

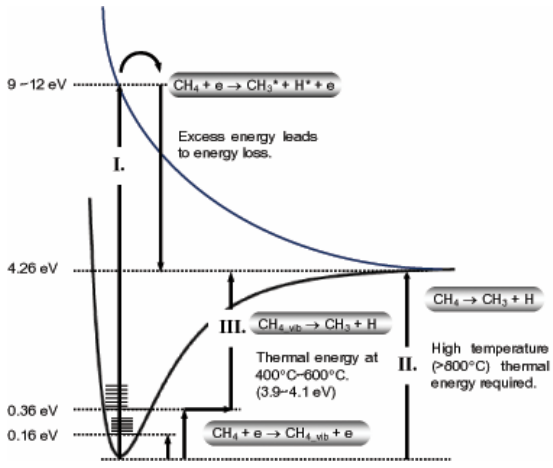

Fig. 10 Methane activation by thermal energy, electron impact, and their combined effect

substantial effort over the past decade because increasing demands for energy and environmental protection are incompatible with a modern two-step liquefaction process, which includes energy intensive syngas ($CO+H_2$) manufacturing. Nevertheless, one-pass yields of organic oxygenates in thermal reaction are generally no more than 5% [37]. More promising results that have claimed a 10% yield have proved difficult to reproduce [38]. One promising solution to achieve a higher yield of useful oxygenates such as methanol is to provide extreme quenching conditions within a single reactor even at elevated temperature and pressure (450~500°C and 3~6 MPa) to avoid successive destruction of highly reactive oxygenates [37,39]. The great benefit of barrier discharge is its simplicity: filamentary discharges can go through sub-micron gap or even liquid phase without particular matching device. Taking advantage of this point, a microscale barrier discharge reactor was developed for low temperature partial oxidation of methane ($CH_4 + O_2 \rightarrow H_2$, CO, CH_3OH, etc). The reactor is designed so that discharge gap becomes larger than Paschen minimum [5], but smaller than quenching distance of CH_4/O_2 flame [40]: i.e., 10 μm < d <1000 μm. Plasma does not have to be used as energy source. Plasma only needs to stimulate chemical conversion process at low temperature with minimum power consumption. A wide range of oxygen and methane mixtures was directly processed without dilution or explosion at ambient temperature because the microscale plasma reactor efficiently removes excess heat generated by partial oxidation, thereby maintaining a reaction field at temperatures near room temperature. Consequently, the least reactive methane was excited by high-energy electrons, whereas successive destruction of reactive oxygenates was minimized simultaneously within the extremely confined environment. A highly reactive and quenching environment is thereby obtained within a single reactor: these are paradoxical conditions in conventional thermochemical processes.

Figure 11 illustrates microplasma reactor used in this experiment [41,42]. A major product among liquid oxygenates was methanol, whose selectivity reached 34% at 30% of methane conversion (Fig. 12 [41]). Selectivity of oxygenates depends on the fragmentation pattern of methane dissociation by electron impact. Selectivity of methanol would reach 60% when the applied electric field corresponds to the breakdown field of methane (~80 Td) [43]. Active ionic oxygen species such as O^-, O_2^-, and O_2^{2-} are also believed to initiate dissociation of alkanes' C-H bonds [37,44]. In addition, atomic oxygen radicals such as O(3p) and O(1D) are recognized as important radical species in discharge chemistry. Along with dissociative excitation of methane by electron impact, production of ionic and atomic oxygen species must play an important role in moderate oxidation of methane in low-temperature plasma catalysis. Detailed mechanistic studies that involve labeled molecules with isotopic atoms are now being conducted in our laboratory for further understanding of reaction mechanisms.

4.2. Nano-fabrication in materials processing using atmospheric pressure homogeneous discharge

4.2.1. Deposition of carbon nanotubes in atmospheric pressure glow discharge

Atmospheric pressure enhanced chemical vapor deposition has great benefits in practical applications since it minimizes vacuum system and allows to handle bulky materials in continuous process. Our group has developed atmospheric pressure plasma enhanced CVD for nanotube deposition [45]. In the previous study, authors pointed out that the existence of energetic cathode region is important to grow nanotubes.

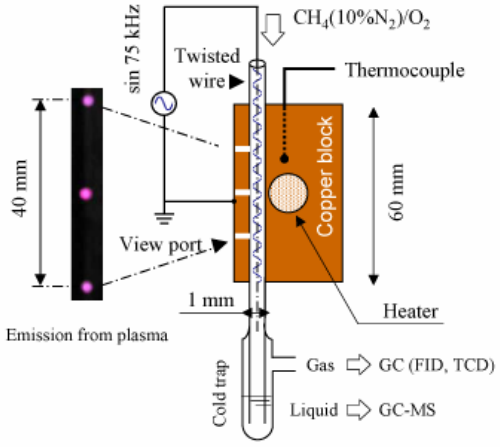

Fig. 11 Micro-plasma reactor setup and emission from view ports

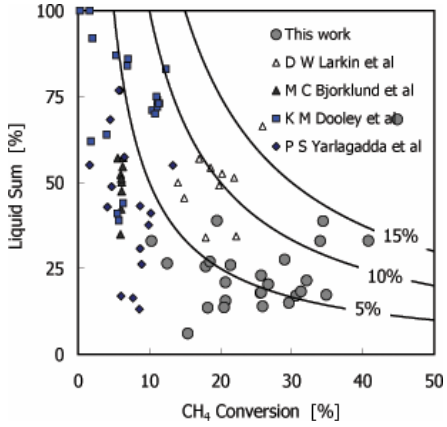

Fig. 12 Methane conversion vs. methanol (+formaldehyde) selectivity. Discharge power: 5 W. Glass inner diameter: 1 and 2 mm. Total gas flow rate: 5-20 sccm. CH_4/O_2 ratio: 1.0-5.0. Temp.: 25-120°C. (●, Δ); barrier discharges, (▲, ■, ♦); thermal reaction.

However, quality of nanotubes such as diameter, number density, and orientation was hard to control with ordinary APG which is operated with 10 kHz - 130 kHz frequency [46]. Main drawback is that APG is temporarily generated with much lower duty cycle. In our experiment effective deposition occurred when the bottom electrode was temporal cathode where discharge current flows for 500 ns (see Fig. 2). High frequency (e.g. RF) operation has several advantages [47,48]. It generates continuous plasma in atmospheric pressure which is probably the minimum requirement for the growth of vertically oriented nanotubes. In addition, operating voltage is significantly reduced due to electron and ion trapping in the discharge gap which minimizes the formation of filamentary discharges. In fact, a stable glow discharge is sustained between two metallic electrodes without dielectric barrier, thus it enables to apply external DC bias to the substrate. This technique especially becomes important in the deposition of nanotubes since high electric field near substrate is necessary to align growing nanotubes [49-51]. However, the role of highly collisional cathodic sheath for the alignment is not fully understood: not only electric field, but also the directionality of ion movement as well as ion energy may also become important parameters in the atmospheric pressure PECVD.

Figure 13 shows atmospheric pressure radio frequency discharge reactor (APRFD) for carbon nanotubes deposition. RF power source was connected to the upper electrode, while DC power supply is to the bottom electrode. Figure 13 (a) and (b) show carbon nanofibers deposited on silicon substrate at 700°C. The substrate was initially coated with Cr underlayer (20 nm) and Ni catalyst layer (20 nm). He, H_2, and CH_4 mixture was fed at constant flow rate of 1000, 4, 2 sccm, respectively. A sample shown in Fig. 13 (a) was obtained in normal APRFD, while (b) was deposited in APRFD with DC-50 V. The result clearly shows that alignment of nanofibers is improved by applying negative DC potential to the substrate. Negative potential attracts positive ions to the substrate, creating cathodic dark space near the substrate. Although actual bias potential is not known since plasma potential has not been identified yet, external DC bias seems to impose sufficient electric field on cathodic sheath. Well-oriented nanofibers also seem to grow in highly collisional cathodic sheath as long as strong electric field is imposed on substrate. Further investigation is being performed.

4.2.2. Microplasmas and application to nanoparticle formation [4]

In this paper, we specifically define microplasma as a non-filamentary, continuous, high-density ($N_e >> 10^{11} cc^{-1}$), reactive non-equilibrium plasma. As reactor dimension gets smaller than effective $(pd)_{min}$ at given pressure, operating pressure must inevitably increases in order to sustain self-maintaining discharge. Here, $(pd)_{min}$ expresses Paschen minimum and typical value is given by $(pd)_{min} \sim 1$ mmHg cm in ordinary gases [5]. Unlike transient discharges such as DBD and APG, effective dc approximation could be assumed when operating frequency exceeds 100 MHz at atmospheric pressure. We explore the new applications into the field of nanoparticle synthesis using such unique plasma source.

Figure 14 shows schematic diagram of microplasma reactor equipped with water-jacket in down stream where reactive microplasma is rapidly quenched. The process starts with the creation of supersaturated radical

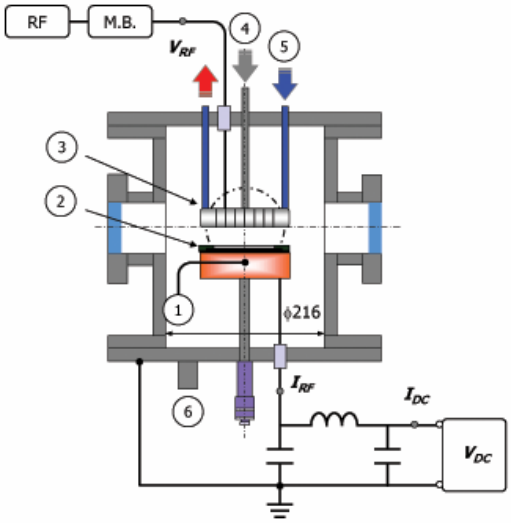

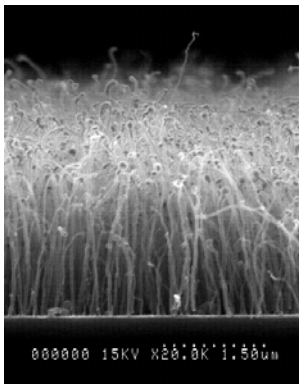

(a) DC-50 V

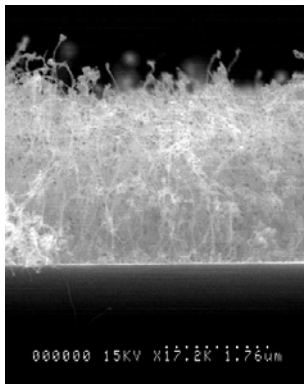

(b) without DC bias

Fig. 13 atmospheric pressure radio-frequency discharge reactor. Background pressure: 5×10^{-3} Torr, 1: Electrical heater and Thermocouples, 2: Sample and sample holder, 3: Shower head electrode, 4: Gas inlet, 5: Cooling water (<1Ωcm), 6: Vacuum pump, metering valve, and pressure gage. Gap: 4 mm, P_{RF}: 50W

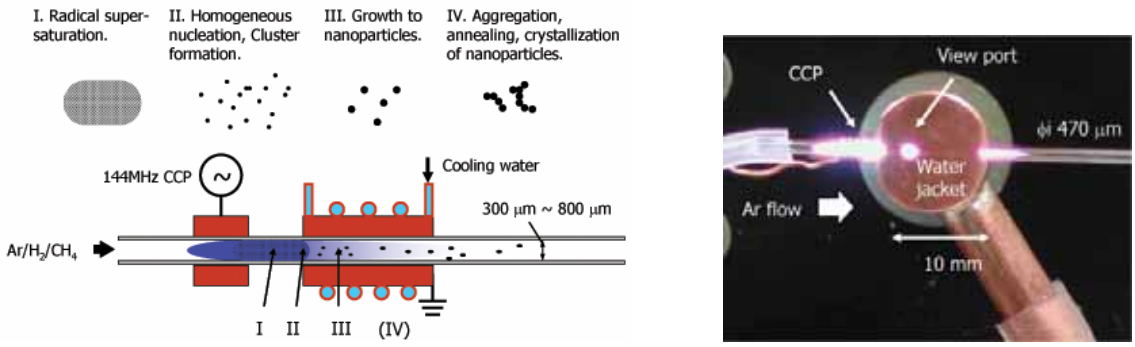

Fig. 14 Schematic diagram of microplasma reactor and fundamental processes of nanoparticle formation.

condition (I) followed by homogeneous nucleation (II), cluster formation and/or particle growth (III), and annealing including aggregation of particles (IV). The proposed microplasma reactor has several advantages over these processes: (1) Microplasma under high frequency operation easily provides supersaturated environment, and also increases throughput of the process, (2) Micrometer scale reactor equalizes radical density and temperature, realizing uniform nucleation, (3) Charged particles prevent aggregation [52], (4) Particle synthesis due to consecutive reaction is easily optimized with short-residence time reactor (~μs). We have developed capacitively coupled VHF (144 MHz) microplasma shown in Fig. 15. At the moment, production and characterization of the microplasma has been carried out. Reynolds number, electron density, and rotational temperature increased with decreasing internal diameter of capillary tube: e.g. Re: 1200 [-], N_e: 4×10^{15} [cc^{-1}], and T_{rot}: 1800 [K] at 290 μm inner diameter. This process is now being developed for diamond and silicon nanoparticle synthesis.

5. Concluding remark

Authors discussed fundamental processes of atmospheric pressure non-equilibrium plasmas, and various applications based on our recent work were briefly overviewed. Industrial application of atmospheric pressure non-equilibrium plasmas will continue to grow into various engineering fields. At the same time, a number of technical challenges are being emerged. The major challenge that authors would like to emphasize is to suppress the thermalization of non-equilibrium plasmas [53]. Although atmospheric pressure non-equilibrium plasma is recognized as weakly ionized low-temperature plasma from the fact that electron temperature is much higher than gas temperature, electrons are likely to lose their energy through rotational, vibrational, and even momentum transfer collisions. Radical species produced by energetic electrons is the main driving force of chemical conversion process; however, heat generated by non-equilibrium plasma also accelerates thermal reactions as discussed in section 4.1.2. Modern plasma reactors become compact and operated at higher frequency (500-500 kHz). Specifically in filamentary barrier discharges, increasing power density simply increases the generation rate of heat, while electron energy and electron density in each filamentary discharge seems to remain unchanged: input power is preferably distributed to thermal energy rather than radicals. Non-equilibrium plasma may lose non-equilibrium nature and may become more like heat source. On the other hand, microplasma developed in our lab reaches the gas temperature of 1000-2000 K, while plasma density gets highly supersaturated at given temperature and pressure (see 4.2.2). Although temperature reaches much higher than room temperature, it is able to provide highly chemical non-equilibrium status. Scientific understanding of thermodynamic non-equilibrium nature of those plasma sources is strongly needed for further development of new field of plasma science and technology.

Acknowledgement

The authors greatly appreciate Professor Joachim Heberlein and Professor Uwe Kortshagen (Dept of Mechanical Engineering, University of Minnesota, Minneapolis). Atmospheric pressure radio frequency discharge has been jointly developed by JH, UK, and TN when TN stayed at U of M as a post-doc during 2003-2004.

References

1. U Kogelschatz, Plasma Chemistry and Plasma Processing, 23(1) (2003) 1-46.
2. S Kanazawa, M Kogoma, T Moriwaki, S Okazaki, J. Phys. D: Appl. Phys., 21 838-840 (1988).
3. W Castagna, K, S O Shea, A Herbert, Hakone IX, Padova, Italy, August 23-27 (2004) CD-ROM.
4. http://plasma1.kuee.kyoto-u.ac.jp/~tokutei429/

5. von Engel, Ionized Gases (Oxford University Press, 1965).
6. B Eliasson, M Hirth, U Kogelschatz, J. Phys. D: Appl. Phys., 20(11) (1987) 1421-1437.
7. K V Kozlov, H-E Wagner, R Brandenburg, P Michel, J. Phys. D: Appl. Phys. 34 (2001) 3164-3176.
8. V I Gibalov, G J Pietsch, J. Phys. D: Appl. Phys. 33 (2000) 2618–2636.
9. U Kogelschatz, IEEE Trans. on Plasma Sci., 30(4) (2002) 1400-1408.
10. Special cluster on atmospheric pressure non-thermal plasmas for processing and other applications, Guest editor: F Massines, J. Phys. D: Appl. Phys., 38(4) (2005) 504-575 (including 8 papers).
11. L Mangolini, K Orlov, U Kortshagen, J Heberlein, U Kogelschatz , Appl. Phys. Lett., **80** (2002) 1722-1724.
12. F Massines, P Segur, N Gherardi, C Khamphan, A Ricard: Surface and Coatings Technology 174-175 (2003) 8-14.
13. L Mangolini, C Anderson, J Heberlein, U Kortshagen, J. Phys. D; Appl. Phys. **37** (2004) 1021-1030.
14. T Nozaki, Y Unno, Y Miyazaki, K Okazaki, J. Phys. D; Appl. Phys., 34(16) (2001) 2504-2511.
15. T Nozaki, Y Miyazaki, Y Unno, K Okazaki, J. Phys. D; Appl. Phys., 34(23) (2001) 3383-3390.
16. G. Herzberg, Molecular Spectra and Molecular Structure, (London 1950), p32.
17. J Luque, M Krausa, A Wokaun, K Haffner, U Kogelschatz, B Eliasson, J. Appl. Phys. 93(8) (2003) 4432-4438.
18. T Nozaki, Y Unno, K Okazaki, Plasma Sources Science and Technology, 11 (2002) 431-438.
19. T Nozaki, N Muto, S Kado, K Okazaki, Catalysis Today, 89 (2004) 57-65.
20. T Nozaki, N Muto, S Kado, K Okazaki, Catalysis Today, 89 (2004) 67-74.
21. J Davies, C J Evans, F L Jones, Proc. R. Soc. London Ser. A 281 (1964) 164-183.
22. W L Morgan, Plasma Chemistry and Plasma Processing 12(4) (1992) 477-493.
23. K Tachibana, M Nishida, H Harima, Y Urano, J. Phys. D: Appl. Phys. 17 (1984) 1727-1742.
24. Raizer Yu P, Gas discharge physics (Berlin: Springer) 1991.
25. J Li, S K Dhali, J Appl Phys 82 (1997) 4205-4210.
26. R Morrow, L E Cram, J Comp. Phys. 57 (1985) 129-136.
27. D Braun, V Gibalov, G Pietsch, Plasma Sources Sci. & Tech. 1 (1992) 166-174.
28. J M Cormier, I Rusu, J. Phys. D; Appl. Phys., 34 (2001) 2798-2803.
29. M Kraus, W Egli, K Haffner, B Eliasson, U Kogelschatz, A Wokaun, Phys. Chem. Chem. Phys. 4(4) (2002) 668-675.
30. J.G. Wang, C.J. Liu, B. Elaisson, Energy and Fuels (2004), 18(1), 148–153.
31. L Bromberg, D R Cohn, A Rabinovich, J Heywood, Int. J. of Hydrogen Energy, 26(10) (2001) 1115-1121.
32. http://www.glidarc-tech.com/
33. Mutaf-Yardimci, A V Saveliev, A A Fridman, L A Kennedy, J. Appl. Phys., 87(4) (2000) 1632-1641.
34. H Kim, A Mizuno, Y Sakaguchi, Energy & Fuels, **16**(4) (2002) 803-808.
35. T Yamamoto, M Okubo, K Hayakawa, K Kitaura, IEEE Trans. Ind. Appl., **37**(5) (2001) 1492-1498.
36. L B F Juurlink, P R McCabe, R R Smith, CL DiCologero, A L Utz, Phys. Rev. Lett. 83(4) (1999) 868-871.
37. K Otsuka, Y Wang, Appl. Catal. A-Gen., 222 (2001) 145.
38. N R Hunter, H D Gesser, L A Morton, P S Yarlagadda, Appl. Catal., 57 (1990) 45.
39. W C Danen, M J Ferris, J L Lyman, R C Oldenborg, C K Rofer, G E Steit, Prep. Petro. Chem. Div. (ASC) 36 (1991) 166.
40. B Lewis, Combustion, Flames and Explosions of Gases (Academic Press, Inc., 1987).
41. T Nozaki, A Hattori, K Okazaki, Catalysis Today, 98 (2004) 607-616.
42. T Nozaki, K Okazaki, S Kado, A Hattori, Method for partial oxidation of light hydrocarbons and micro reactor, Jpn. Kokai Tokkyo Koho, (2004).
43. W M Thornton, Phil. Mag. 28, 666-678, 1939.
44. Y Moro-oka, Catal. Today, 45 (1998) 3-12.
45. T Nozaki, Y Kimura, K Okazaki, J. Phys. D; Appl. Phys., 35 (2002) 2779-2784.
46. T Nozaki, Y Kimura, K Okazaki, S Kado, Plasma Processes and Polymers (Wiley-VCH Publisher), 477-487 2004.
47. A Schutze, J Y Jeong, S E Babayan, J Park, G S Selwyn, R F Hicks, IEEE Trans. on Plasma Science, **26**(6) (1998) 1685-1694.
48. J Park, I Henins, H W Hermann, G S Selwyn, J. Appl. Phys., 89(1) (2001) 20-28.
49. M Meyyappan, L Delzeit, A Cassell, D Hash, Plasma Sources Sci. Technol., **12** (2003) 205-216.
50. V I Merkulov, A V Melechko, M A Guillorn, D H Lowndes, M L Simpson, Appl. Phys. Lett. **79**(18) (2001) 2970-2972
51. R Hatakeyama, G-H Jeong, T Kato, T Hirata, J. Appl. Phys. 96(11) (2004) 6053-6060.
52. A Bapat, C Anderson, C R Perrey, C B Carter, S A Campbell, U Kortshagen, Plasma Phys. Control. Fusion 46 (2004) B97–B109.
53. A Fridman, A Chirokov, A Gutsol, J. Phys. D: Appl. Phys. 38 (2005) R1–R24.

Research on Gliding Arc Discharge Driven by Magnetism

Yuhan Zhao, Qiang Ma, Weidong Xia[1]

Department of Thermal Science and Energy Engineering, University of Science and Technology of China, China, HeFei

[1] *Email: xiawd@ustc.edu.cn*

Abstract: The diameter of non-thermal arc plasma is one of the main parameters that determine the current density of arc, so as to the temperature and the density of electrons. The imagines of gliding arc discharge driven by magnetism at atmosphere are captured observed and its dimension is measured by commercial CCD. The diameter projecting in the direction of motion of the arc (diameter in positive direction) is attained. And the relationship between diameter and current, magnetic field is analyzed, too.

Keywords: Magnetically driving gliding arc, Non-thermal arc, Arc diameter

1. Introduction

Non-equilibrium plasma at atmosphere is a kind of non-thermal plasma which is between thermal and cold plasma. Compared with the thermal plasma, non-equilibrium plasma produced by gliding arc, which needs relatively less power input and has higher energy efficiency, can operate without vacuum system and is suitable to work under atmospheric or higher pressure. Non-equilibrium plasma has extensive application potential in the chemical industry, material preparation, surface modifying and environmental engineering, and etc. [1-3]. Gliding arc discharge is one of the main methods to produce non-equilibrium plasma at atmosphere [4-7].

Electron density n_e and non-equilibrium degree $K_{NE}=(T_e-T_h)/T_e$ (T_e and T_h are electron temperature and heavy particle temperature, respectively.) of non-thermal plasma are important parameters which determine the chemical reaction rate and energy efficiency [8]. In the case of magnetically driving gliding arc which moves fast with little diameter as a kind of non-thermal arc plasma at atmosphere, it's hard to measure the electron temperature and density directly. Electron temperature and density can be calculated by using the parameters as current density, electric field value, and heavy particle temperature [9-11]. And arc diameter is important for calculating current density. Therefore, there are many literatures about non-thermal arc diameter. The measuring methods of arc diameter mainly include hi-speed camera shoot [12,13], CCD imaging, and utilizing electron-multiplier phototube. Leland M. Nicolai chose a certain optical density as representing the edge of the arc, and determined the characteristic arc dimensions from densitometer scans of the arc photographs [12]. At the present time, researches on non-thermal arc diameter mostly focus on the arc diameter in side direction which is observed and measured from the side the electrodes plane. Reports about arc diameter in positive direction which is observed and measured from the end of motion of the arc is not seen now [14].

The magnetically driving gliding arc is observed by commercial CCD camera and arc diameter in positive direction is obtained. And also the dependences of diameter and current, magnetic flux density are analyzed here.

2. Experimental

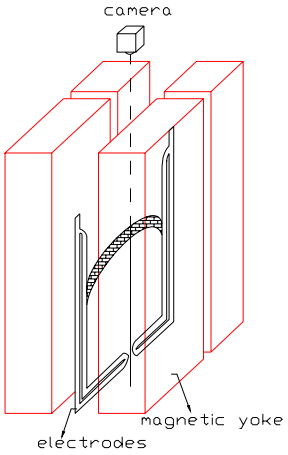

Fig. 1. Arc diameter measurement setting

Fig. 2a. Colorized arc photo (arc current 0.7A, magnetic field 0.8T)

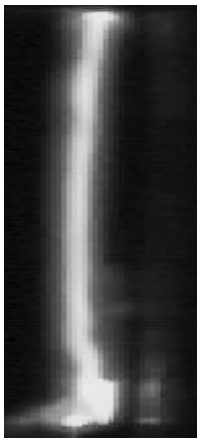

Fig. 2b. Arc grey-scale photo (arc current 0.7A, magnetic field 0.8T)

The arc diameter is investigated by using the experiment device of magnetically driving gliding arc presented by Li lei, Xia weidong et al. [4]. The set-up contains a adjustably constant current source and a magnet providing uniform magnetic field. The sketch of arc diameter measurement is shown in Fig.1. The space between the parallel parts of the electrodes made of copper is 30 mm. The gap between electrodes is 2 mm. The arc moves upward along electrodes. The plane containing electrodes is vertical to the magnetic field. The camera (Samsung VP-D99i , time of exposure is 0.1 ms, F2.0, 12 times optical zoom, 25 fps) is placed in the symmetry axes of electrodes, lens facing the arc. The typical photographs of the arc in the positive direction of arc are shown in Fig. 2a, and Fig. 2b shows the picture converted from Fig. 2a.

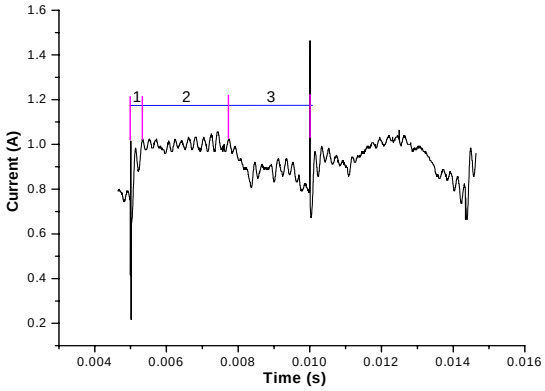

Fig. 3. Arc current waveform

There are three stages in the periodic arc evolution (arc current waveform is shown in Fig. 3): 1. Arc starting stage, before moving into the parallel parts of electrodes; 2. Arc moving along parallel electrodes stage; 3. Arc shifting out of parallel electrodes stage. The arc current ripple ratio is less than 1% in stage (2), thus it is able to determine the relation between arc current and arc diameter without synchronous electric signal and shooting signal.

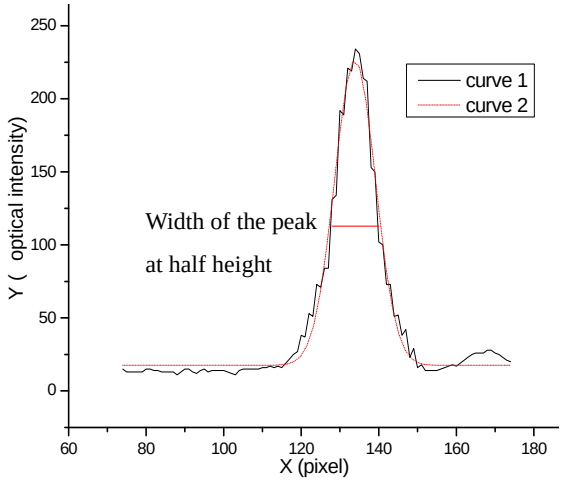

Fig. 4. Radial distribution of sensitization intensity

There was no specific diameter on gliding arc, because of the gradient radial distribution of temperature, current density, optic intensity and etc. Here, we determine arc diameter according to the distribution of absolute value of optic intensity (grey-scale value). First, convert the colorized photo (JPEG file) to BMP file (Fig. 2a), then switch to grey-scale one (Fig. 2b) through applying formula: **gray = 0.2990 * r + 0.5870 * g + 0.1140 * b**. And then by reading out the grey-scale value of every pixel point arraying along the axis of electrodes, one can attain the radial distribution of sensitization intensity

integral of all kinds of beam projected on CCD by arc column, as the curve 1 shown in Fig. 4.

Gauss Function:
$$y = y_0 + (A/(\omega \bullet \sqrt{\pi/2}))e^{\frac{2(x-x_0)^2}{\omega^2}} \quad (1)$$

where y_0: baseline offset , A: total area under the curve from the baseline, x_0= center of the peak, w= approximately 0.849 the width of the peak at half height, is applied to fit curve 1 to Gauss Fit Curve(Curve 2). Two times of the width of the peak at half height is defined as the diameter projecting to CCD of the arc column. Thus, after conversion of length picketage corresponding arc diameter is obtained.

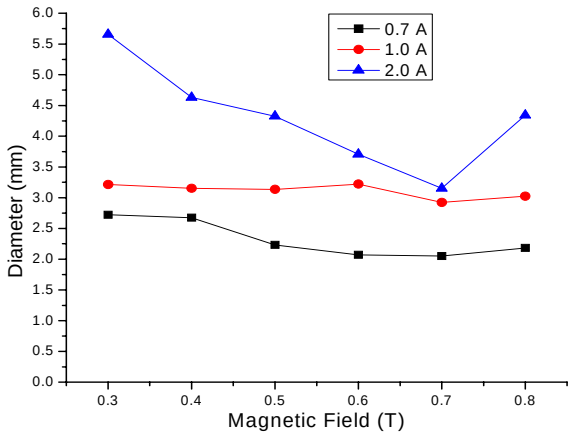

Fig. 5. Diameter-magnetism characteristics of a gliding arc

3. Results and Discussion

The effect of magnetic field and arc current is analyzed and results are given in Fig. 5. For the figure, arc current switch among 0.7A, 1.0A and 2.0A; the range of magnetic flux density is 0.3~0.8 T. One can see that arc diameter in positive direction increases with arc current increasing under constant magnetic field. And when arc current is invariable, arc diameter tends to decrease with the magnetic field value increasing.

4. Conclusions

The figuration and dimension of gliding arc discharge driven by magnetism at atmosphere are observed and measured. The effect of magnetic field and arc current on arc diameter in positive direction is analyzed, too. The following conclusions are reached:

Diameter in positive direction of arc increases due to increases in arc current when magnetic field is constant. And when arc current is invariable, diameter tends to decrease with the increasing magnetic field.

References

[1] S.Brethes-Dupouey, R.Peyrous, B.Held. Removal of H_2S in air by using gliding discharges[J]. Eur.Phys.J.AP, 2000, 11: 43-58.

[2] Krzysztof Krawczyk, Michal Mlotek. Combined plasma-catalytic processing of nitrous oxide[J]. Applied Catalysis B: Environmental, 2001, 30: 3-245.

[3] J.Janca, A.Czernichowski. Wool treatment in the gas flow from gliding discharge plasma at atmospheric pressure[J]. Surface and Coatings Technology, 1998, 98: 12-1115.

[4] Li Lei, Xia Weidong, Zhao Yuhan, Research on non-equilibrium plasma of gliding arc driven by magnetic field at atmospheric pressure, Nuclear Techniques, Vol. 27, No. 5, May 2004.

[5] Czernichowski A, Oil & Gas Science & Technology, 2001, 56(2): 181-190.

[6] Pellerin S, Comier J-M, Richard F et al., J. Appl. Phys D: Apply Phys., 1999, 32: 891-897.

[7] Czernichowski A. Pure Appl. Chem, 1994, 66(6): 1301-1306.
[8] Lin lie, Wu chengkang, Nclear fusion and plasma physics, Vol. 18, No.2, June 1998
[9] O. Mutaf-Yardimci, A. Saveliev, A. Fridman, L. Kennedy, J. of Appl. Phys., 87(4), 1632(2000)
[10] C. Tesar, J. Janca, V. Kapicka, Proc. 11th Int. Symp. On Phys. of Swithcing Arc, Brno (1994), 74
[11] J. R. Roth, Industrial Plasma Engineering, IOP Publishing Ltd, 1995
[12] V.Dalaine, J. M. Cormier, and P. Lefaucheux, JOURNAL OF APPLIED PHYSICS, Vol.83, Num.5
[13] Leland M. Nicolai, THE PHYSICS OF FLUIDS, Vol 13, Num 12, 1970.
[14] A.SATHEESH KUMAR, BHUMESH GUPTA and D. P. TEWARI, Energy Convers. Mgmt Vol. 39, No 14, pp. 1483-1495, 1998

Double Arcs Phenomena of Rotating Arc Driven by Magnetism

Weidong Xia[1], Baihe Du, Lincun Li, Qiang Ma, Quan Chen

Department of Thermal Science & Energy Engineering, University of Science & Technology of China, Hefei, Anhui, China
[1]Email: xiawd@ustc.edu.cn

Abstract:

Large scale arc plasma generator has been developed to processing carbon black and nano-particle [1-3]. To get large-scale homogeneous plasma by arc discharge, an experiment equipment is designed for researching the probability of arc diffused [4]. The plasma generator is of coaxial inner cathode (15mm diameter) and outer anode (80mm diameter), both of them are made of graphite. Currents through the coil wrapping on the anode produce axial magnetic field, which drives the arc fast rotating. The plasma gas is Argon. Hi-speed CCD camera (4000fps, 0.1msec exposure time) is opposite to the spout of the generator, by which continuous end-on imagines of arcs and arc movements are captured.

Fig.1 and Fig.2 are consecutive end-on images of moving arcs. The experiment conditions are as follow: arc current 195A, gas flux 8SNL/min, lengthways magnetic induction 72 Gauss, CCD camera 1000 frames per second with 0.1ms exposure time.

Fig.1 shows the production and alteration progress double arc roots. On frame 1 of Fig.1 one anode arc root is situated on "r1". The greatest curvature of arc is at "c1", from here arc expands fast towards the wall of the anode along radial direction at the greatest curvature, so as that new anode arc root appears (r2, image 2). Double arc roots r1, r2 coexist on frame 2. The central angle between two arc roots is about 60 degree. Frame 3, 4 show the same results. But the double arc roots could not been proved to be steady. Two arc roots coexist less than 1 millisecond-the interval of two frames. In general, the phenomenon of double arc roots was considered as the alternating progress of arc root flopping[5] called as "arc shunting" and the current alternating progress from one root to another is less than 1ms[6].

Differing from Fig.1, Fig.2 shows the parallel double arcs coexist between the cathode and the anode. In the Fig.1 arc column from the cathode to root "r2", "r1" (Fig.1, image 2) on the anode is like in series. The double arcs in parallel astonishingly coexist about 4~5 milliseconds stably, known from frame 2 to frame 6 in Fig.2. Being digressive V-I characteristics and many factors of plasma instability, one arc of parallel two arcs always quickly extinguishes and current transfers to another arc column, or double arcs with common root prestissimo join from the common root [7] (at the cathode). To our knowledge, it is the first time that one reports the stable parallel arcs in large-scale arc plasma generator with rotating arc driven by magnetism.

Waves of arc voltage and arc currents have been measured. The both descending and of single arc and parallel double arcs appear. The ascending V-I characteristics always goes with steady double arcs. The great fluctuation of arc voltage arises from the large scale break of arc column to anode wall and result in breaking of parallel double arcs.

How to be generated the parallel double arcs? Why is the arc V-I characteristics some time ascending and some time descending? And why dose ascending V-I maintain more than 5ms during which without great fluctuation? They will be researched further.

References

[1] Fulchery L, Flamant G, Variot B, and et al., *ISPC 12*, August 21-25 1995
[2] Weidong Xia, Shude Wan, Dazhi Wang and et al., *J. Univ. of Sci. & Tech. of China*, 33**,** 5 (2003)
[3] Weidong Xia, Dazhi Wang, Shude Wan and et al., *Chinese J. Chem. Phys.*, 16 1 (2003)
[4] Baihe Du, Weidong Xia, Lincun Li, and et al., to be pub in *Nuclear Technique (Chinese)*
[5] Zengyuan Guo, *Electric arcs and thermal Plasmas* (in Chinese),
[6] J. L. Dorier, M. Gindrat, CH. Hollenstein and et al., *IEEE Transactions on plasma science*, 29, 3, (2001)
[7] Weidong Xia, Fulchery L, José G A and et al., Characterization of a 3-phase AC Free Burning Arc Plasma, Will be pub in *Plasma Science & technology*.

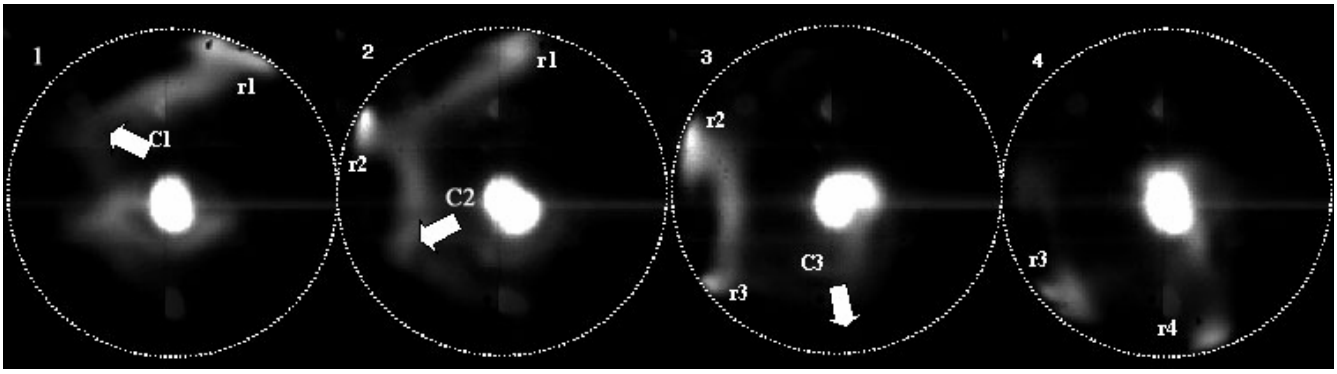

Fig.1 Double arc roots on the anode

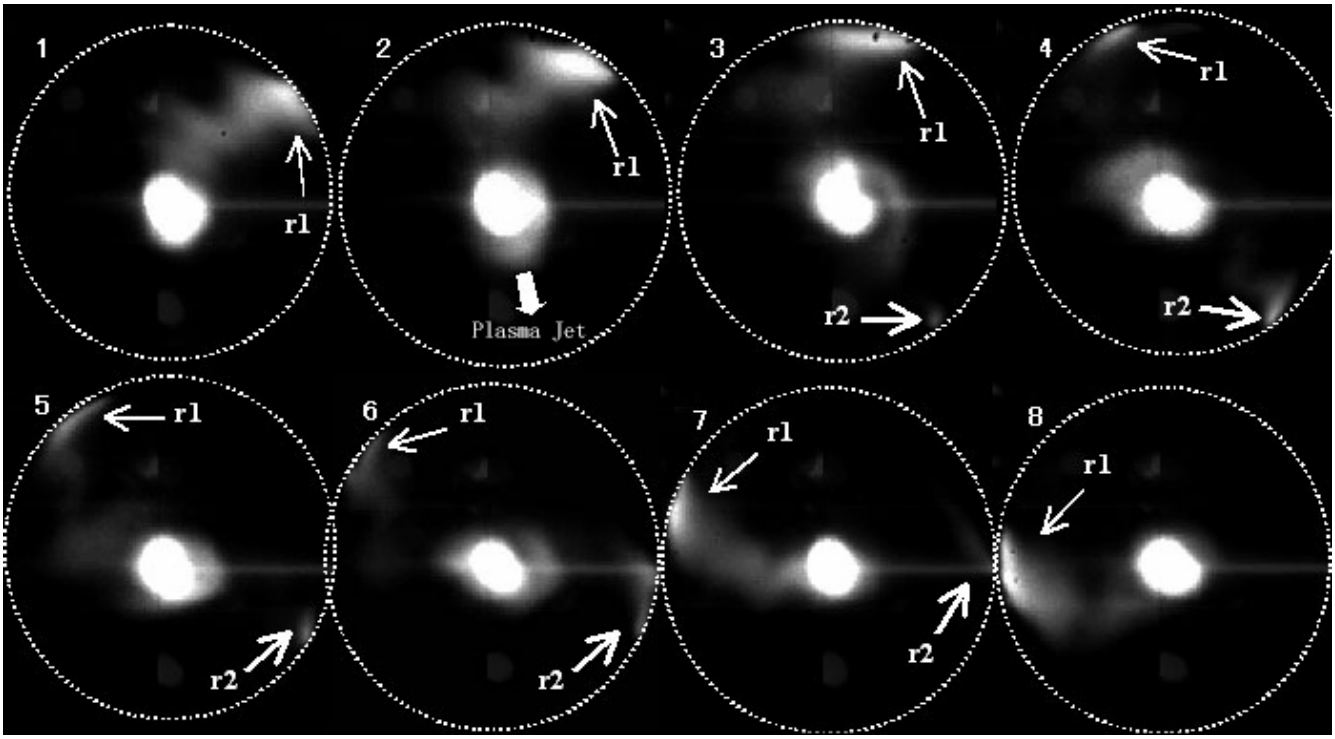

Fig.2 Double arcs parallel between the anode and the cathode

Ozone generation of combined surface discharging and catalysis

Huang Weidong[1], Ren Tingting[1], and Xia Weidong[2]

1. Department of Earth and Space Science, USTC, Hefei, Anhui, PRC 230026

2. Department of Thermal Science and Engineering, USTC, Hefei, Anhui, PRC 230026

(Responsible Author, email: huangwd@ustc.edu.cn)

Abstract

A new method combines catalyst and plasma to produce ozone is provided with lower energy consumption and higher ozone production efficiency. Factors which can affect the ozone production efficiency and concentration were studied, such as power, frequency, gas flow rate and catalysts. The ozone concentration and production increases as discharge power increasing，and decrease as gas flow rate increasing. The correlation between power and energy consumption is significant, and the energy consumption increases as increase of the discharge power. Spherical γ-Al_2O_3 is a nicer catalyst because it is likely to participate in surface discharge as a sort of dielectric.

1. Introduction

Ozone has been harnessed for beneficial purposes such as water treatment, odor and color control because of its strong oxidations. In these applications, ozone is almost always produced at high rates in dielectric barrier discharges in pure oxygen[2]. It is also known that broad application of ozone is hindered primarily because of its low efficiency of generation. The value of 1200g/kWh is the theoretical ozone generation efficiency calculated by thermochemical theory. In a practical ozonizer, the discharge energy is dissipated not only in producing ozone but also in heating the electrodes of the ozonizer and gas. In order to improve the efficiency, a lot of attempts have been made[1-8]. In this paper, a new kind of ozonizer combined hybrid discharge with catalysis is proposed to improve the ozone generation efficiency. The hybrid discharge includes corolla discharge, surface discharge and DBD discharge.

2. Experimental apparatus

The laboratory-scale reactor was made of a quartz tube with an inner diameter of 12mm and wall thickness of 1.0 mm. The inside electrode (hi-voltage electrode), made of a molybdenum wire with a diameter of 0.1 mm, was aligned horizontally along the centerline of the reactor. The outside of the quartz tube is surrounded by water inserted copper wire, which served as the outside electrode (ground electrode). The packing materials were filled in the quartz tube. The packing length was the same as the length of the outside electrode, 15 cm. To hold the packing materials in the tube, glass wool is placed at the front and rear of

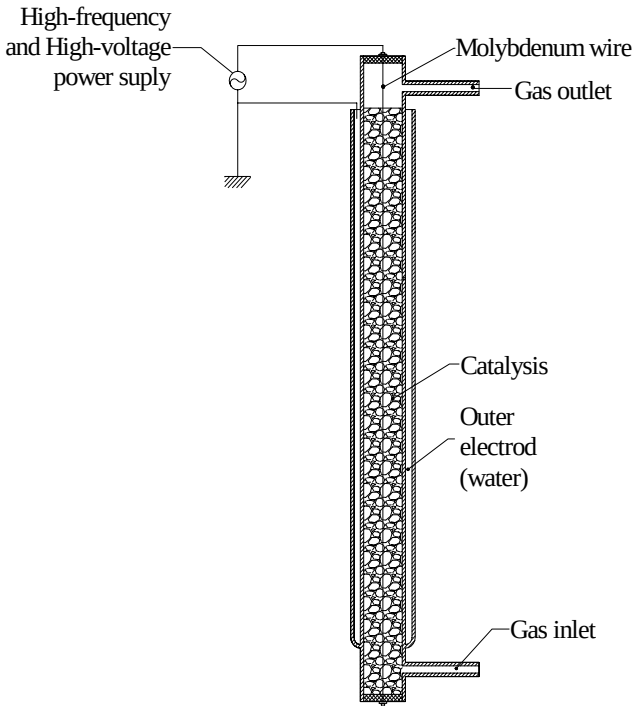

Fig .1. structure of ozone generator

packing material. Power for the non-thermal plasma generating system was supplied by a variable voltage with the range of 0–20 kV (rms value) and the frequency of 10–50 kHz. The plasma reactor was packed with the spherical palletized γ-Al_2O_3 as catalysts in 3–4 mm diameter and 200m^2/g surface proportion. The bed porosity was about 0.4. The packing volume was 17 cm^3 in the reactor with a 15 cm length.

Power supply voltage, discharge currents and charges are measured by a digital oscilloscope (Tektronix TDS2014). The discharge power is calculated according to Lissajous Figure of voltage-charges. The ozone concentration was determined according to CJ/T3028.2-94 (Chinese Standard). The flux of air is determined with flowmeter.

3. Results and discussion

A. Effect of the Gas Flow Rate on the Ozone Concentration and production

The effect of the gas flow rate on the ozone concentration is shown in Fig. 2. The gas flow rate has a great effect on the ozone concentration, which decreases with increase of the gas flow rate. When the gas flow rate is 0.16Nm3/hr, the ozone concentration reaches the value of 1.5g/Nm^3 and production is 0.53g/h. When the gas flow rate is 0.4Nm^3/hr, the ozone production reaches the value of 0.4g/h and concentration is 1.0g/Nm^3.With the rising of the gas flow rate, the reduced trend of ozone concentration becomes generally slow because of the gas cooling.

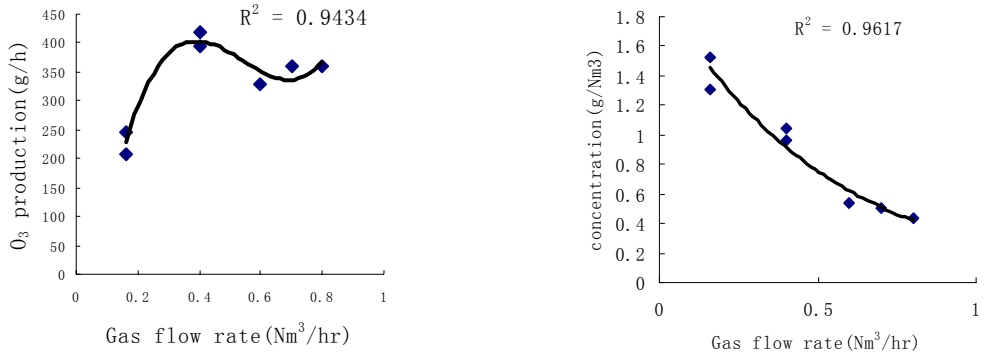

a b

Fig. 2. Gas flow rate vs. (a)ozone concentration,(b)production with gas pressure is 0.12MPa, temperature of inlet air gas is 298K, power is 4w and frequency is 40kHz.

B. Effect of the power on the Ozone Concentration and production

The effect of the power on the ozone concentration is shown in Fig. 3. The power has a great effect on the ozone concentration and production, which increases with increase of the power. When the power is 1.1w, the ozone concentration reaches the value of 0.2g/Nm^3 and production is 0.13g/h. When the power is 12.5w, the ozone production reaches the value of 0.76g/h and concentration is 1.3g/Nm^3.

C. Effect of the frequency on the Ozone Concentration and production

The effect of the frequency on the ozone concentration is shown in Fig. 4. Ozone concentration and production increases with increase of the frequency when the frequency value is between 25kHz and 35kHz.But when the frequency value reaches 40kHz, the rule is changed.

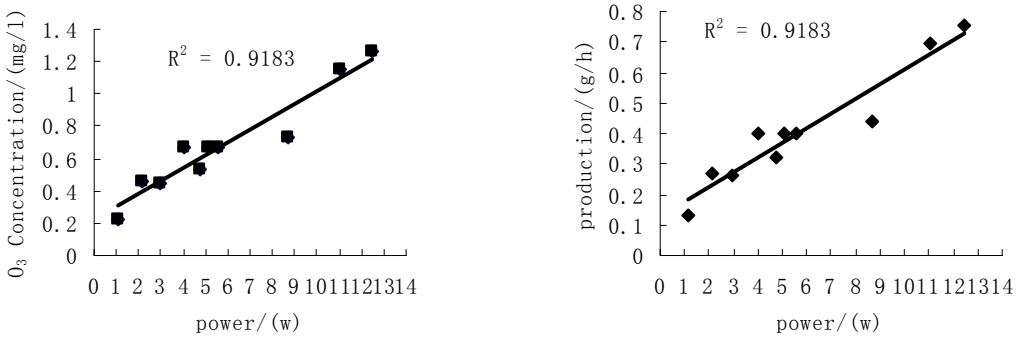

a b

Fig. 3, power vs. (a)ozone concentration ,(b)production with gas pressure is 0.12 MPa, temperature of inlet air gas is 298 K, Gas flow rate is 0.6Nm^3/hr and frequency is 40kHz.

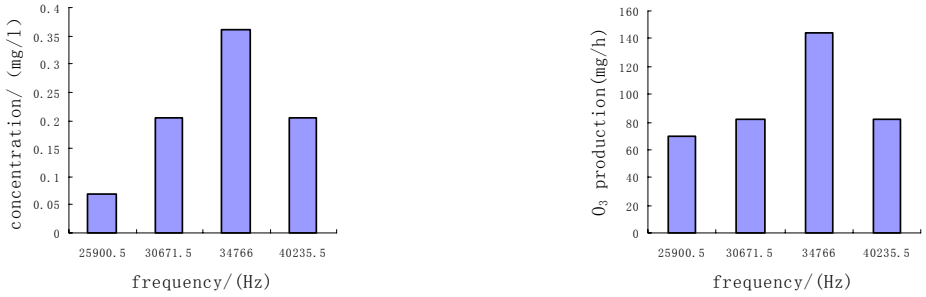

a b

Fig. 4, frequency vs.(a) ozone concentration, (b) production with gas pressure is 0.12 MPa, temperature of inlet air gas is 298 K, Gas flow rate is 0.4Nm^3/hr and power is 2.5w.

4. Energy Efficiency of Ozone Production

Currently, the energy consumption (kWh/kgO_3) is used to exhibit the ozone production efficiency. The effect of the ozone concentration on the energy consumption is shown in Fig.5.

Both power and frequency can affect ozone production efficiency.The effect of power and frequency on the energy consumption is shown in Fig.6. The experimental conditions are as follows: gas pressure, 0.12 MPa; temperature of inlet air gas, 298 K; Gas flow rate, 0.6Nm^3/hr.The correlation of power and frequency with energy consumption has been analyzed and shown in Table.1. The Pearson Correlation is 0.838 between power and energy consumption,and it is -0.242 between frequency and energy consumption.Therefore the correlate between power and energy consumption is significant.

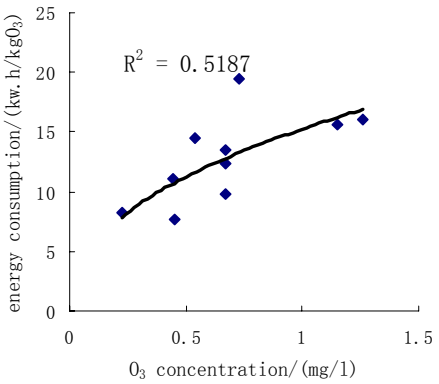

Fig. 5, Ozone concentration vs. energy consumption with gas pressure is 0.12 MPa, temperature of inlet air gas is 298 K, Gas flow rate is 0.6Nm^3/hr and Frequency is 40kHz.

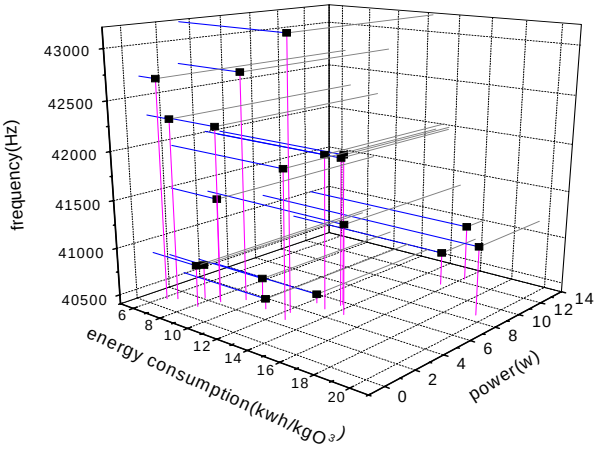

Fig. 6,power and frequency vs. energy consumption with gas pressure is 0.12 MPa, temperature of inlet air gas is 298 K and Gas flow rate is 0.6Nm^3/hr.

Table.1 Analysis of correlations

		power	frequency	energy consumption
power	Pearson Correlation	1.000	-.347	.838**
	Sig. (2-tailed)	.000	.146	.000
	N	19	19	19
frequency	Pearson Correlation	-.347	1.000	-.242
	Sig. (2-tailed)	.146	.	.318
	N	19	19	19
energy consumption	Pearson Correlation	.838**	-.242	1.000
	Sig. (2-tailed)	.000	.318	.
	N	19	19	19

**. Correlation is significant at the 0.01 level (2-tailed).

The effect of the power on the energy consumption is shown in Fig.7. The experimental conditions are as follows: gas pressure, 0.12 MPa; temperature of inlet air gas, 298 K; Gas flow rate, 0.6Nm^3/hr; Frequency,40kHz. The energy consumption increases with increase of the power. When the power is 1.1w, the energy consumption reaches a quite finer value of 8.2kwh/kgO_3. When the power is 12.5w, the energy consumption reaches the value of 16.1kwh/kgO_3.

The effect of the gas flow rate on the energy consumption is shown in Fig.8. The experimental conditions are as follows: gas pressure, 0.12 MPa; temperature of inlet air gas, 298 K; power, 4.5w;

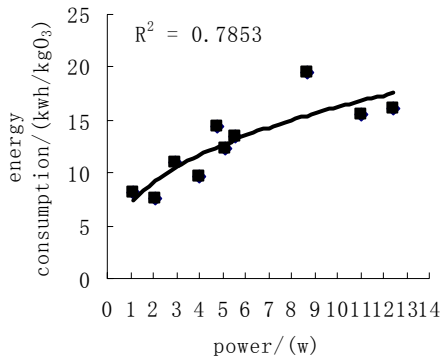

Fig. 7, power vs. energy consumption with gas pressure is 0.12 MPa, temperature of inlet air gas is 298 K, Gas flow rate is 0.6Nm^3/hr and Frequency is 40kHz

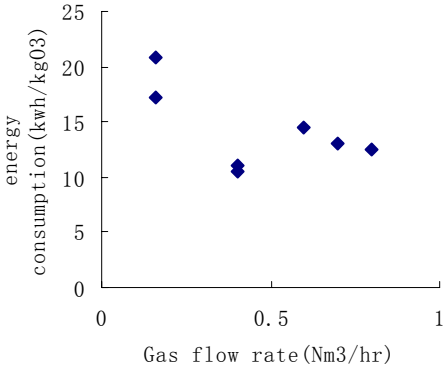

Fig.8,gas flow rate vs. energy consumption with gas pressure is 0.12 MPa, temperature of inlet air gas, is 298 K, power is 4.5w and Frequency is 40kHz

Frequency,40kHz.Between the gas flow rate and the energy consumption,we haven't found a overt correlation.

Efficiency of Ozone Production on other different parameters is shown in Table.2. When the gas flow rate is 0.6Nm^3/h,the power is 0.9w and the frequency is 45kHz, the energy consumption and the production efficiency reaches the best value of 6.2 kWh/kg and 160.9 g/kWh. Therefore the ozone production efficiency is higher than the commercial ozone generator.

Table.2 Efficiency of Ozone Production on the different parameters

frequency（kHz）	power(w)	energy consumption(kwh/kgO3)	O3 production efficiency(g/kwh)	gas flow rate(Nm3/hr)
41	1.1	8.2	121.5	0.6
41	2.1	7.6	131.4	0.6
44	1.2	6.6	150.6	0.6
45	0.9	6.2	160.9	0.6
40	2.7	8. 1	124. 2	0.4

5. Experiment of different catalysts

The plasma reactor was packed with the spherical palletized γ-Al_2O_3 as catalysts. Because of the high surface proportion of the spherical γ-Al_2O_3 in 200m^2/g, catalysts may adsorb large number of oxygen molecules, which will react with oxygen atom produced by discharge to form ozone. Moreover, spherical γ-Al_2O_3 is one sort of dielectric in the plasma besides the function of adsorption and catalysts, that means, other function may exist such as affect the property of plasma formed by the discharge.

Spherical molecular sieves,as a substitute of spherical γ-Al_2O_3, packed in the plasma reactor is studied.The different effect of the two kinds of catalysts is shown in Table.2. When The plasma reactor was packed with the spherical palletized γ-Al_2O_3 as catalysts in 3–4 mm diameter， the ozone concentration is 0.96g/Nm^3,the production is 0.38g/hr and the energy consumption is 9.8kwh/kgO_3; when The plasma reactor

was packed with the spherical molecular sieves type 5A as catalysts in 3–5 mm diameter，the ozone concentration is 0.78g/Nm^3,the production is 0.31g/hr and the energy consumption is 12.1kwh/kgO_3.Therefore spherical γ-Al_2O_3 is better than the spherical molecular sieves because spherical γ-Al_2O_3 is likely to participate in surface discharge as a sort of dielectric.

Table.3 Characteristic of Ozone Production on the different catalysts

Catalysts	ozone concentration (g/Nm^3)	Production （g/h）	production efficiency （g/kwh）	energy consumption （kwh/kgO_3）
. γ-Al_2O_3	0.96	0.38	103.1	9.80
molecular sieves	0.78	0.31	82.4	12.14

The experimental conditions are as follows: gas pressure, 0.12MPa; temperature of inlet air gas, 298K;power，3.8w. Gas flow rate, 0.4Nm^3/hr; Frequency ,40kHz.

The diameter of catalysts can affect the characteristic of ozonizer.We currently use the spherical palletized γ-Al_2O_3 as catalysts in 3–4 mm diameter.**W**hen The plasma reactor was packed with the spherical palletized γ-Al_2O_3 in 0.5–1mm diameter，there are hardly any ozone produced.

6．Conclusions

Ozone generation of combined surface discharging and catalysis is a new method,which is provided with lower energy consumption and higher ozone production efficiency in comparison with the technology of present commercial ozone generator. The plasma reactor was packed with the spherical palletized γ-Al_2O_3 as catalysts.Because of the high surface proportion of the spherical γ-Al_2O_3, catalysts can adsorb oxygen molecule,which will react with oxygen atom to form ozone.At the same time, spherical γ-Al_2O_3 can participate in surface discharge as a sort of dielectric.As a result, the ozone production efficiency are significantly improved in comparison with a ozone generator without catalysts, which the energy consumption and the production efficiency reaches the highest value of 6.2 kWh/kg and 160.9 g/kWh.

Acknowledgenents:

This work is supported by National Nature Science Foundation of China under project 10375065.

Reference:

[1] Yukihara Nomoto et al, ieee transactions on industry applications, vol 31, No.6, 1995, 1458-1462

[2] Ulrich Kogelschatz, Plasma chemistry and plasma processing, Vol23,No.1, 2003, 1-46

[3] Zhitao Zhang et al, Plasma Chemistry and Plasma Processing, Vol. 23, No. 3, 2003, 559-568

[4] John T. Herron and David S. Green, Plasma Chemistry and Plasma Processing, Vol. 21, No. 3, 2001,459-481;

[5] I. Revel, Ph. Belenguer, J. P. Boeuf, and L. C. Pitchford, Pure Appl. Chem. 71, 1837(1999).

[6] R. T. Wegh, H. Donker, E. V. D. van Loef, K. D. Oskam, and A. Meijering, J. Luminesc.87–89, 1017 (2000).

[7] Moo Been Chang, How Ming Lee, Catalysis Today 89 (2004) 109–115

[8] B. M. Penetrante, R. M. Brusasco, B. T. Merrit, and G. E. Vogtlin, Pure Appl. Chem.,71, 1829 (1999).

National sciece foundation of china project:10375065

EFFECT OF OXYGEN RATIO ON FABRICATION OF DIAMOND NANO-WHISKERS IN RADIO FREQUENCY PLASMAS

C.Y. Li and A. Hatta

Department of Electronic and Photonic Systems Engineering, Kochi University of Technology, Japan

Abstract
Diamond nano-whiskers were fabricated by means of reactive ion etching in O_2 or Ar/O_2 radio frequency plasmas. Metal particles were coated onto diamond films to serve as micro-masks before etching. The results showed that the population densities and the distributions of diamond whiskers were dependent on the volumetric ratio of O_2 to Ar. The whiskers were still diamond after etching. Field emission characteristics of the whiskers were also inspected.
Keywords: Diamond, Etching, Radio frequency plasma, Micro-mask, Whisker.

I. Introduction

Diamond has drawn a great deal of attentions because of its outstanding properties such as extremely high mechanical hardness, high thermal conductivity, chemical inertness, the smallest coefficient of thermal expansion, and negative electron affinity characteristics [1]. All these properties are advantageous to various applications [2]. Recently, the negative electron affinity characteristics of diamond films are considered to be highly promising for applications in electron field emission devices [3]. However, the key point remains how to achieve an efficient electron field emission [4]. It has been reported that the electron field emission will be enhanced at the micro-tips of diamond [5]. Therefore, fabrication of sharper field emission tips is still a challenging issue. Among the various approaches, reactive ion etching (RIE) is considered as an efficient method to sharpen diamond into micro-rods or nano-whiskers [6]. In this paper, a novel method for fabrication of nano-whiskers using reactive ion etching in Ar/O_2 or O_2 plasmas was reported. Metals coated on diamond surfaces served as masks during the etching process. Furthermore, a comparison of the morphologies of diamond surfaces before and after etchings demonstrated that the properties of whiskers were dependent on the reacting gas. Field emission characteristics of the whiskers were also examined and a low turn-on field was obtained.

2. Experimental details

N-type Si (100) substrates were abraded with 5-12 μm diamond grits in a ultrasonic agitator for 30 min in order to enhance diamond nucleation before deposition. Polycrystalline diamond films were deposited onto Si substrates using a microwave plasma chemical vapor deposition (CVD) reactor system ASTeX (AX-6350). The deposition process was carried out under pressure of 124 torr, microwave power of 5 kW, and flow rates of 25 and 475 sccm for CH_4 and H_2, respectively. During the deposition, the substrate temperature was kept at 900–950 ℃, monitored by a spot thermometer.

After the diamond films grew to 3 μm in thickness, Al particles were coated on them for 10 min using a DC sputtering device (SANYUDENSHI, SC701HMC Quick Coater).

The etching process was performed for 60 min in a self-assembled radio frequency (RF) plasma reactor with frequency of 13.56 MHz. The chamber pressure was maintained at 22 Pa. Reacting gases were introduced through mass flow controllers. In this study, the gas compositions examined were O_2 (10 sccm)/Ar (90 sccm), O_2

(20 sccm)/Ar (35 sccm), O_2 (100 sccm), and Ar (100 sccm). The RF power was 100 W, corresponding to a DC self-bias voltage of -510 V for each sample. The substrate temperature was kept below 200 ℃ using a water cooling system.

Raman spectroscopy was carried out in a spectroscopic system (JASCO, NR-1800), with a 514.5 nm Ar ion laser (Coherent, K-70) in order to examine the changes in the properties of the diamond films. The samples were also inspected using an S-3000N scanning electron microscope (SEM). Energy Dispersive X-ray Spectroscopy (EDS) was used to analyze the surface composition after etching.

3. Results and discuss

Figures 1-3 present the SEM images of the diamond surfaces after 60 min of etching. From the top views, whiskers were found in each sample. An interesting phenomenon was that the distribution of whiskers was not random. Fig. 1(a) illustrates the result for etching in Ar/O_2 plasma with 10% O_2 (vol/vol). Whiskers with diameter of 150 nm and height of 200 nm were formed only at the grain boundaries, suggesting that the whiskers may form preferentially at the grain boundaries between diamond crystals. This can be explained, most probably, by the presence of non-diamond sp^2 inclusions (e.g., graphite) [7]. However, with increasing O_2 concentration (O_2: 36%), the roots of the whiskers extended gradually into the diamond grains, as shown in Fig. 2(a). It could be noticed that the height of the whiskers remarkably increased to 900 nm. The population density of whiskers increased with the concentration of O_2. When O_2 ratio approached to 100%, the whiskers had the highest population density (about 40 μm^{-2}), as shown in Fig. 3(a). The average diameter of the whiskers reduced to 100 nm with a height of 1 μm. In inert gas Ar (100 sccm), whiskers could not be formed on the surfaces after etching.

In general, there were two processes during the RF plasma etching [8]. Pure Ar plasma only caused physical bombardment etching which could explain why whiskers could not be obtained in pure Ar. The diamond surface would be polished completely if the RF power was higher enough. However, the etching process was different in the Ar and O_2 mixture plasmas. Whiskers obtained in this kind of plasma could be ascribed to the processes of ion-enhanced chemical etching and physical bombardment etching. O_2 would dissociate into O radicals accompanied by the formation of volatile products of CO and CO_2 [9], while Ar would contribute to bombarding the diamond surfaces. In the case of pure O_2 plasma, although O_2 contributed to both physical and RIE etchings, the effect of RIE was apparently predominant [10-11].

The above results suggested that the density and height of the whiskers increased with the flow ratio of O_2 to Ar. However, the diameters of the whiskers were quite different. It is conceivable that the formations of whiskers could be controlled by changing the concentration of O_2 in the reacting gas.

After etching, the EDS measurements were carried out to examine the composition of the etched diamond surfaces. The EDS spot measurements showed that Al remained on the top of the whiskers, as shown in Fig. 4. Because Al was used as coating material on the diamond surfaces before etching, it would react with O_2 to form Al_2O_3 islands on the tops of the whiskers, inhibiting the etching underneath. Some other metals, such as Pt and Au, although could not react with O_2, but could attach to the diamond surfaces and serve as masks due to their incomparably lower etching rate, comparing to that of the carbon substrate [12]. In addition to the whiskers, the bottom areas between the whiskers were also measured using the same method. It was found that there was no presence of Al particles because the diamond film was over etched without the protection of the Al coating.

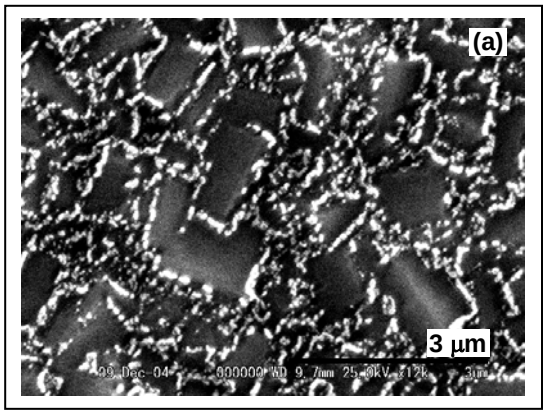

Fig. 1 SEM images of diamond whiskers obtained from etching in O_2 (10 sccm)/Ar (90 sccm). (a) top view, and (b) perspective view.

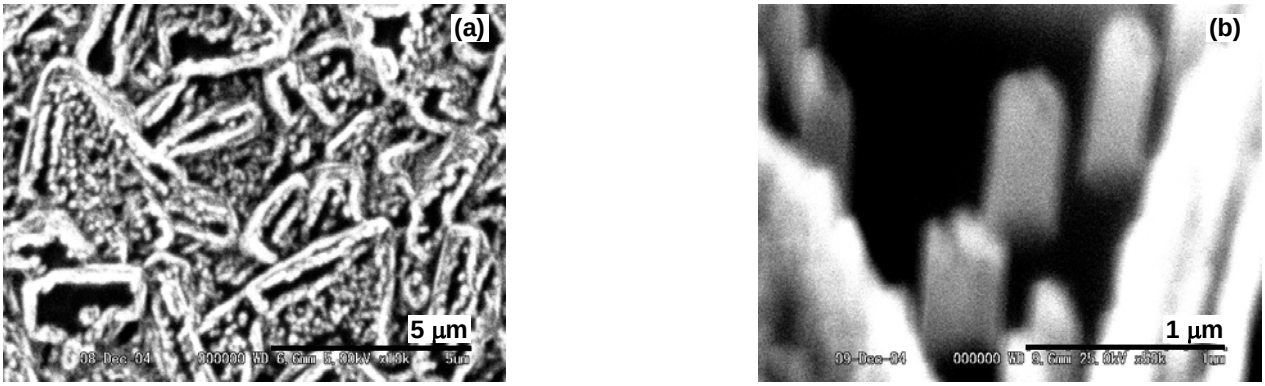

Fig. 2 SEM images of diamond whiskers obtained from etching in O_2 (20 sccm)/Ar (35 sccm). (a) top view, and (b) perspective view.

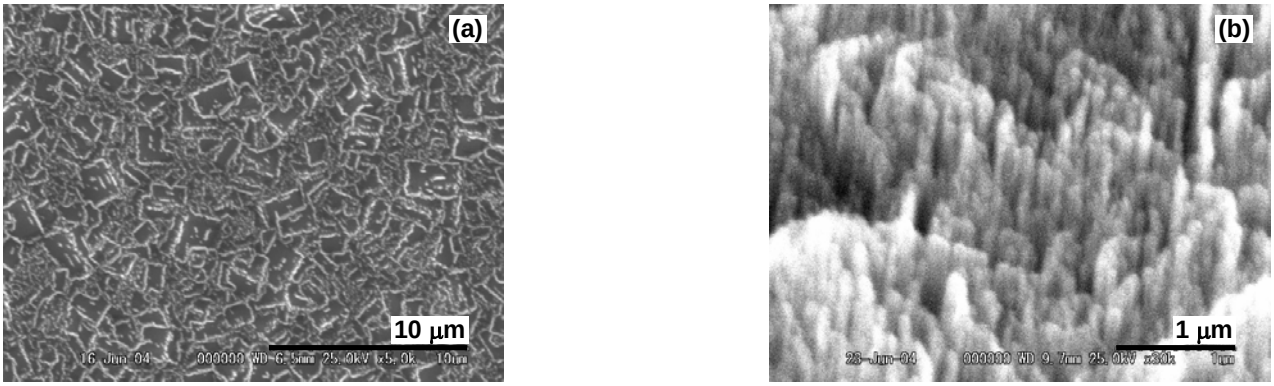

Fig. 3 SEM images of diamond whiskers obtained from etching in O_2 (100 sccm). (a) top view, and (b) perspective view.

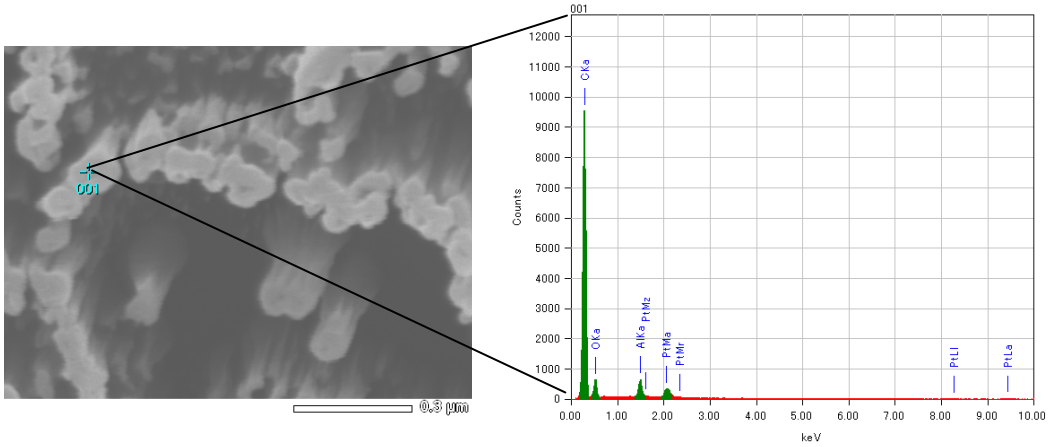

Fig.4. EDS spot measurement showed Al particles remaining on the top of diamond whiskers

It was necessary to inspect the graphitic transformation of diamond after etching. In order to determine the structures of whiskers, Raman spectroscopy was performed for the samples before and after etching. The whiskers were scraped off the substrate and collected on a piece of transparent glass. Scanning electron microscope was used to examine if there were diamond particles mixed with the whiskers in the collected diamond powders, and no diamond particles were found. In Fig.5, the Raman spectra showed a typical diamond (sp^3 bonding) peak at 1332 cm^{-1} along with a low broad non-diamond (sp^2 bonding) peak at 1580 cm^{-1}.

Theoretically, the Raman scattering cross-sections of the graphite should be 50 times higher than that of the diamond. If there were same quantity of sp^2 graphitic carbons, their peaks should be much stronger than that of the diamond. Obviously, for our samples, the diamond peak was much strong than the non-diamond peaks, suggesting that the whiskers had not changed their bonding structures after etching. The presence of a weak graphite peak could be attributed to a small amount of local transformation from sp^3 to sp^2. Most of the bonding structures were kept on sp^3 diamond structures during the etching process. Therefore, we could conclude that the whiskers were still diamond after etching.

Field emission characteristics of the whiskers etched in the pure O_2 plasma were shown in Fig. 6. The samples after etching were treated in hydrogen plasma for 8 min before the field emission measurement in order to get conductive surface. The field emission measurement system was installed in an SEM observation chamber with a gap size of 10 μm. A turn-on field of 10 V/μm was obtained for the whiskers. It was much lower than the original diamond film of 40-50 V/μm which we measured in other experiments.

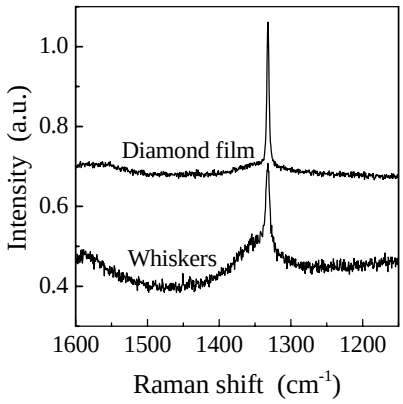

Fig. 5 Raman spectra for the diamond film and the whiskers (Al coated, O_2 100 sccm, etched 60 min).

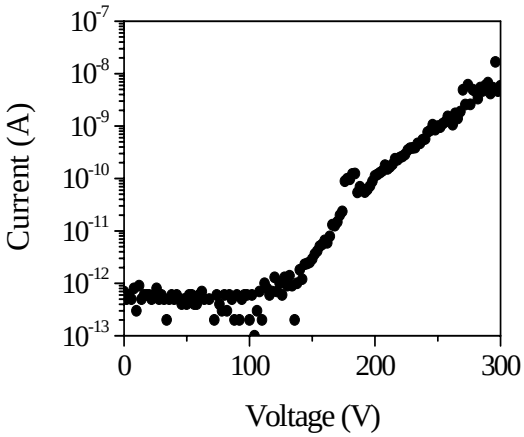

Fig. 6. Current-voltage curve from Al masked diamond whiskers (Al coated, O_2 100 sccm, etched 60 min).

4. Conclusion

Reactive ion etching in RF plasmas is an effective method to obtain diamond whiskers. The population densities and the distributions of whiskers could be controlled by adjusting the volumetric ratio of O_2 to Ar. The bonding structures of the whiskers were not affected by etching process. The turn-on field of the whiskers was as low as 10 V/μm. Therefore, it is possible to use diamond nano-whiskers as cathode emission devices.

Acknowledgement

This work was partly supported by the Grant-in-Aid for Specific Research of Priority Areas “Generation of Micro-scale Reactive Plasmas and Development of Their New Applications” (#15075209) from the Ministry of Education, Culture, Sports, Science and Technology. The help with Raman spectroscopy measurements provided by Dr. Kanda is gratefully acknowledged.

References

[1] C. Nuzenadel, O. Groning, and L. Schlabach, American Institute of Physics, **S003-6951,** 02644-7 (1996).

[2] P. W. May, Endeavour Magazine, **19**, 101-106 (1995).

[3] M.-Y. Teng, K.-S. Liu, H.-F. Cheng, I.-N. Lin, Diamond and Relat. Mater., **12**, 450 (2003).

[4] V. V Zhirnov and J. J. Hren, MRS Bulletin, **9**,42 (1998).

[5] T. Tyler, V. V. Zhinov, A. V. Kvit, D. Kang, and J. J. Hren, Appl. Phys. Lett., **82**, 2904 (2003).

[6] A. S. Barnard, S. P. Russo, and I. K. Snook, Phys. Rev., B**68**, 235407 (2003).

[7] T. Tyler, V. V. Zhirnor, A. V. Kvit, D. Kang, and J. J. Hren, Appl. Phys. Lett., **82**, 2901 (2003).

[8] E. S. Baik and Y. J. Baik, J. Mater. Res., **15**, 924 (2000).

[9] P. W. Leech, G. K. Reeves, A. Hollolland, J. .Mater. Sci., **36**, 3453-3459 (2001).

[10] Y. Ando, Y. Nishibayashi, K. Kobashi, T. Hirao, K. Oura, Proceedings of the Ninth ISAM, Tsukuba, 53 (2002).

[11] M. Berrnard, A. Deneuville, L. Ortega, K. Ayadi, P. Muret, Diamond and Related Materials, **13**, 290 (2004).

[12] S.W. Lee, Applied Surface Science, **215**, 267 (2003).

PECVD of nanocrystalline Si layers on high T_g polymer substrates

L. MacQueen[1], J. Zikovsky[1], G. Dennler[2], M. Latreche[3], G. Czeremuszkin[3],

and M. R. Wertheimer[1*].

1 Groupe des Couches Minces and Department of Engineering Physics, École Polytechnique, Montréal, QC, Canada

2 Linz Institute for Organic Solar Cells (LIOS), Johannes Kepler University, Linz, Austria

3 Nova-Plasma Inc., Montréal, QC, Canada

**Corresponding author: michel.wertheimer@polymtl.ca*

Abstract

Nanocrystalline silicon (nc-Si) was deposited by plasma-enhanced chemical vapor deposition (PECVD) on transparent polymers in order to qualify these for possible use as electronic substrates. Thermally induced failure of the nc-Si/polymer composite was avoided within a range of deposition conditions, permitting structural and electrical characterization of the deposits. Good quality nc-Si films could be deposited on all substrates under appropriate conditions.

Keywords

PECVD, nanocrystalline silicon, flexible electronics, high T_g plastics, OLED

1 Introduction

The advantages of using polymer substrates instead of glass for electronic applications include light weight, flexibility and conformability, and low cost with the possibility of roll-to-roll processing. So far, the adoption of polymers for electronic applications has been slow due to their limited compatibility with semiconductor fabrication processes. In particular, the relatively high linear expansion coefficient, α, and low glass transition temperature, T_g, of most polymers restrict the process window to "low" substrate temperatures ($T_s < 300^{\circ}C$). Plasma-enhanced chemical vapor deposition (PECVD) is an attractive process in the present context since the crystalline volume fraction of deposited Si films can be varied within the said range of "low" temperatures [1-3]. Several high-T_g polymers ($220^{\circ}C < T_g < 330^{\circ}C$) with optical transparency, good chemical resistance and barrier properties have recently been developed for use in organic (OLED) display technology [4], and these have motivated the present research. Our goals have, therefore, been to deposit nc-Si films at the lowest possible T_s values, and to characterize their structural and electrical properties.

2 Experimental Methodology

2.1 Etching and Deposition

The substrate materials used in this work and some of their essential properties (α and T_g) are presented in Table 1. Since nc-Si films must not be contaminated by unwanted impurities, the polymer substrates must be resistant towards ablation (etching) in the H_2-rich plasma during the PECVD process. It was, therefore, deemed necessary to investigate possible etching of the polymer substrates as a preliminary step. Both etching and deposition experiments were performed in a "Reinberg-type" parallel-plate RF-PECVD reactor, operating at 13.56 MHz.

Table 1 Properties of the substrates investigated

Substrate	Symbol	T_g (°C)	α (ppm/°C)*
APPEAR® (cyclic polyolefin)	PO	330	60 + T/4
ARYLITE® (polyarylate)	PA	325	50 + T/15
SUMILITE® (polyethersulfone)	PS	223	50 + T/14
KAPTON® (polyimide)	PI	360	20
Glass (Corning 2947)	G	-	9.5
* T-dependent α values are linear approximations of data from ref. [4].			

Etch rates were determined by partially masking the substrates with 50 nm Au layers before exposing them to H_2 plasma at various RF power densities (25 mW/cm^2 < P < 350 mW/cm^2), and then profiling the etched areas by Atomic Force Microscopy (AFM). Such experiments were carried out with the substrates on the grounded or powered electrodes. In the case of depositions, P was 30 mW/cm^2, with substrates on the grounded electrode only. The SiH_4 and H_2 partial pressures were 8 mTorr and 120 mTorr, respectively (SiH_4 concentration, C_{SiH4} = $[SiH_4]/([SiH_4] + [H_2])$ = 6.25%). The chamber pressure was p = 150 mTorr (20 Pa), while the substrate temperature, T_s, was varied between 25°C and 250°C. Typical deposition durations were 200 minutes, and film thicknesses, d_f, measured by ellipsometry, were 120 $\pm$ 15 nm.

2.2 Characterization of nc-Si Films

Thin Si films deposited by PECVD were then subjected to structural and electrical characterizations, by micro-Raman spectroscopy (MRS) and DC conductivity measurements, respectively. MRS was used to estimate the films' crystalline volume fraction, I_c, by comparing the crystalline (c) and amorphous (a) transverse optical lattice vibrations (c-TO and a-TO) [2, 5]. We used an argon-ion laser, λ=514 nm, in Stokes configuration, calibrated with a c-Si sample displaying a c-TO peak centered at 520.5 cm^{-1} with a FWHM of 3.886 cm^{-1}. Data analysis (spectral deconvolution and area integration) was done using BOMEM GRAMS software. DC conductivity was measured by the four-point-probe method, with samples mounted on a temperature-controlled substrate holder and using computer-automation. This system allowed us to measure sheet conductivity during repeated thermal cycling. Other components of this system include a Keithly 220A current source, an Agilent 33101 Multimeter, and a Temptronic temperature controller. For the case of very low conductivity samples (σ < 10^{-6} S/cm), planar aluminum electrodes (with a 100 μm gap) were evaporated on the Si films, and measurements were carried out under vacuum.

3 Results

3.1 Etching and Deposition Rates

Figure 2 presents etch rates of three polymers in pure H_2 plasma, for samples placed either on the grounded or powered electrodes: Higher etch rates are seen to occur on the latter electrode (P < 0, in Fig. 2). Etch rates were negligibly small for low power densities (|P| < 50 mW/cm^2), especially in the absence of ion bombardment, that is, on the grounded electrode. When SiH_4 was added to the H_2 flow (C_{SiH4} = 6.25%, see Section 2.1), nc-Si films were grown on the grounded electrode only, at typical rates of 0.6 nm·min^{-1}.

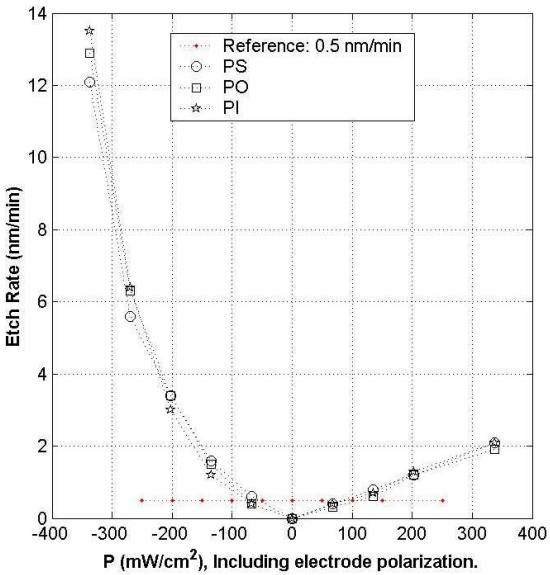

Figure 2 Etch rates for three polymers

3.2 Raman Spectroscopy

The TO spectral feature in our a-Si (a-TO) was Gaussian, centered at ~480 cm^{-1} with a FWHM of ~40 cm^{-1}. The c-TO feature was Lorentzian, centered at ~520 cm^{-1} with a FWHM ~12 cm^{-1}. Intermediate peaks centered at ~505 cm^{-1} with FWHM ~30 cm^{-1} were also detected. The crystalline volume fraction, I_c, can be been estimated using the formula [2]

$$I_c = \frac{A_{520}}{A_{520} + A_{480}} \tag{1}$$

where A signifies the areas under the respective peaks. Figure 3 plots I_c vs. T_s: Films are seen to be amorphous ($I_c \approx 0$) for $T_s < 100°C$, but I_c then rises near-linearly with increasing T_s values. The deviation of TO peak centers (see Fig. 4) is attributed to residual stresses [5].

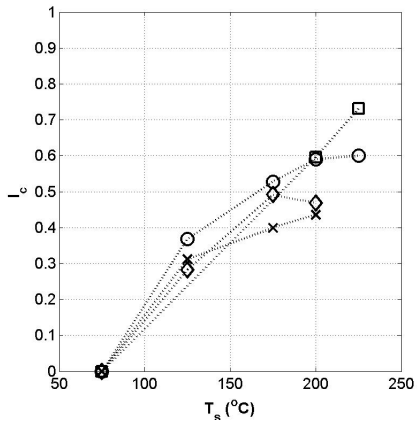

Figure 3 : I_c vs. T_s

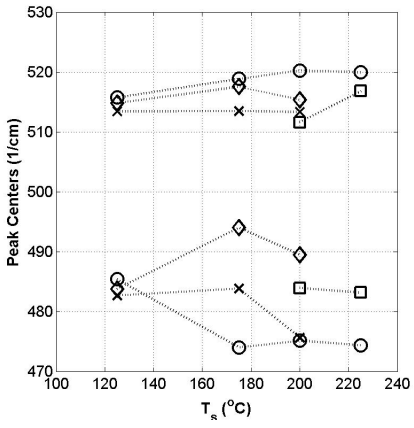

: Glass

: PI

: PO

: PA

Figure 4 : Raman peak-centers (cm^{-1}) vs. T_s

3.3 DC Conductivity

The electrical conductivity of semiconductors like nc-Si, $\sigma(T)$, is thermally activated and therefore obeys the Arrhenius relation [3]

$$\sigma(T) = \sigma_0 \exp\left(\frac{-E_a}{kT}\right) \tag{2}$$

where σ_o is the pre-factor, E_a is the activation energy and k is Boltzmann's constant.

Values of σ and E_a for nc-Si films grown at fixed conditions were very similar, whether deposited on polymers or on glass. "Arrhenius-like" behavior in the range $40^{\circ}C < T < 140^{\circ}C$ was observed for all films deposited at $T_s \leq 175^{\circ}C$, except for those grown on the PO material (see below).

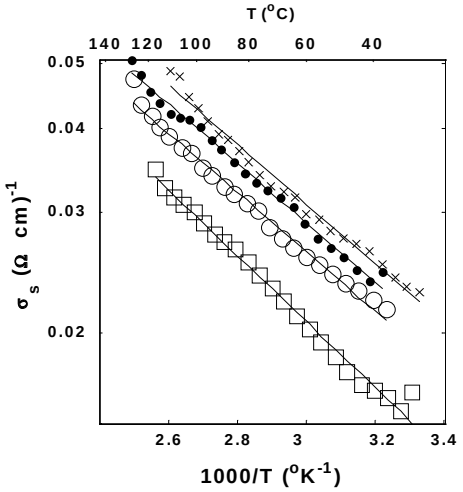

Figure 5

$T_s = 175\ ^{\circ}C$: x = PI; • = PS; ○ = Glass; □ = PA.

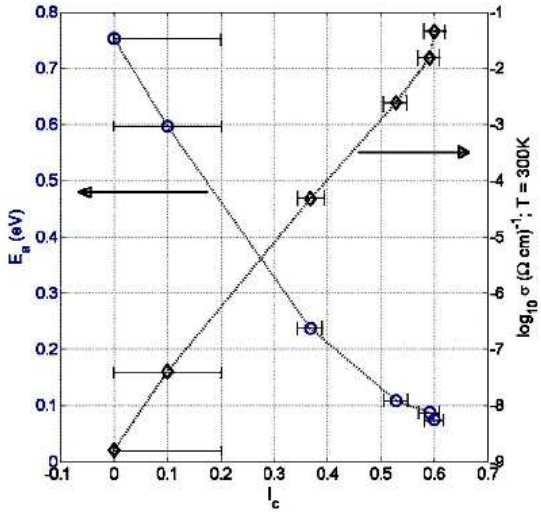

Figure 6 : (nc-Si on glass)

Activation energies and room-temperature dark conductivities for nc-Si films grown on Corning 2947 Ca-lime glass.

The present measurements correlate well with published results for nc-Si films on glass, if we take into account some doping by oxygen. This is known to occur on account of trace quantities of O_2 and H_2O in the reactor, and its extent depends on I_c since oxygen is reported to migrate preferentially within the grain boundaries [6].

3.4 Differential Thermal Expansion

The substrates were in thermal equilibrium at T_s during the nc-Si deposition, but they shrank upon return to ambient conditions. The differential thermal contraction between the substrates and the films can be approximated by

$$\delta = (\alpha_s - \alpha_f)\Delta T \tag{3}$$

where α_s and α_f are the respective coefficients of thermal expansion. Since the thickness of our nc-Si deposits was 10^3-fold less than that of the substrates, stress relaxation of the composite structure gave rise to curvature, which may be expected to follow the Stoney formula up to $Y_f/Y_s \approx 100$, where Y is Young's modulus [7]. This

condition is met, since $Y_f \approx 150$ GPa [8] and $1.9 < Y_s < 5$ GPa [4]. Since $d_s Y_s / d_f Y_f > 10$, we can use the following expression to estimate the interfacial stress in the film due to differential thermal contraction [9]

$$s_f = \frac{Y_f (\alpha_s - \alpha_f) \Delta T}{(1 - \nu_f)} \tag{4}$$

where ν_f is Poisson's ratio of the film. Films deposited on PO, the material with by far the highest value of α_s (see Table 1), at $T_s \geq 200\ ^\circ$C were observed to delaminate; using eq. (4), the compressive strain $\alpha_s \Delta T \approx 1.7\%$ resulted in a stress value $s_f \approx 3.6\, GPa$ that clearly exceeded the f-s adhesion strength. These may, therefore, be considered the limiting conditions for successful film deposition. The PO material undergoes a structural transition at $T \approx 65^\circ$C that was observed to result in anomalous (hysteretic, non-Arrhenius) behavior of nc-Si deposited at $T_s \geq 150^\circ$C.

4 Discussion

Previous research had elucidated the micro-structural evolution of thin Si films, deposited by PECVD, using highly diluted SiH_4 mixtures in H_2. With a suitable choice of C_{SiH4} (5%-9%, 6.25% in the present case) the microstructure of deposited films can be effectively controlled by varying a single parameter, T_s [1-3]. Our results (micro-structural and electrical) demonstrate that a wide range of material properties can be obtained by varying T_s within a range tolerated by the substrates we used. Thermal expansion, α, of these substrates is clearly the greatest challenge for the development of high-stability f-s structures. The nc-Si films nevertheless showed resilience against delamination, as evidenced by the stability of their electrical behavior during thermal cycling, when repeatedly subjected to ~ GPa stresses both in tension and compression. The limiting T_s value above which films delaminate from the substrate of highest α, suggests that the f-s structure can tolerate compressive stresses up to about $s_f \approx 3\, GPa$.

Contamination of the nc-Si by trace amounts of O_2 and H_2O resulted in n-doped behavior of our films, particularly for those deposited at $T_s \geq 150^\circ$C.

The low deposition rate of our process also calls for improvement. This situation was necessitated by minimal ablation of polymers through low power, and by the high dilution of SiH_4 required to produce "good" nc-Si. A feed-gas other than SiH_4 (for example, Si_2H_6) could help overcome this problem.

5 Conclusions

The polymers we have used as substrates fulfill the requirements of electronic applications, for example in OLED technology. Their high T_g values and resistance to ablation have allowed us to deposit satisfactory nc-Si films by RF-PECVD, subject to deposition parameters. The high α of some polymers remains the main obstacle for reliable devices, yet the resilience of nc-Si films is encouraging. Relationships between deposition conditions and structural and transport properties show similarity between nc-Si films grown on glass and on polymer substrates.

Acknowledgement

This work is supported by grants from the Natural Sciences and Engineering Research Council of Canada (NSERC). We thank the staff at the LMF and LCM laboratories of École Polytechnique and the Université de Montréal for valuable assistance.

References

[1] U. Kroll, J. Meier, A. Shah, S. Mikhailov, J. Weber, J. Appl. Phys. **80**, 4971 (1996).

[2] O. Vetterl, A. Gross, T. Jana, S. Ray, A. Lambertz, R. Carius, F. Finger, J. Non-Cryst. Sol. **299-302**, 772 (2002).

[3] S. K. Ram, S. Kumar, R. Vanderhagen, P. Roca I Cabarrocas, J. Non-Cryst. Sol. **299-302**, 411 (2002).

[4] S. Angiolini, M. Avidano, R. Bracco, C. Barlocco, N.D. Young, M. Trainor, X-M. Zhao, SID Digest, **47.1** (2003).

[5] V. Paillard, P. Puech, P. Roca I Cabarrocas, J. Non-Cryst. Sol. **299-302**, 280 (2002).

[6] P. Torres, J. Meier, R. Fluckiger, U. Kroll, J.A. Anna Selvan, H. Keppner, A. Shah, S.D. Littelwood, I.E. Kelly, P. Giannoules, Appl. Phys. Lett. **69**, 1373 (1996).

[7] Z. Suo, E.Y. Ma, H. Gleskova, and S. Wagner, Appl. Phys. Lett. **74**, 1177 (1999).

[8] H. Gleskova, S. Wagner, Z. Suo, Appl. Phys. Lett. **75**, 3011 (1999).

[9] M. Ohring, “Material Science of Thin Films”, Second Edition, Academic Press, San Diego (2002).

Carbon Nanotubes/Nanofibers by Plasma Enhanced Chemical Vapour Deposition

K. B. K. Teo[1], D. B. Hash[2], M. S. Bell[1], M. Chhowalla[3], B. A. Cruden[2], G. A. J. Amaratunga[1], M. Meyyappan[2] and W. I. Milne[1]

1 Department of Engineering, University of Cambridge, Cambridge, UK
2 Center for Nanotechnology, NASA Ames Research Center, Moffett Field, California, USA
3 Department of Ceramics and Materials Engineering, Rutgers University, Piscataway, New Jersey, USA

Plasma enhanced chemical vapour deposition (PECVD) has been recently used for the production of vertically aligned carbon nanotubes/fibers (CN) directly on substrates. These structures are potentially important technologically as electron field emitters (e.g. microguns, microwave amplifiers, displays), nanoelectrodes for sensors, filter media, superhydrophobic surfaces and thermal interface materials for microelectronics. A parametric study on the growth of CN grown by glow discharge dc-PECVD is presented. In this technique, a substrate containing thin film Ni catalyst is exposed to C_2H_2 and NH_3 gases at 700°C. Without plasma, this process is essentially thermal CVD which produces curly spaghetti-like CN as seen in Fig. 1(a). With the plasma generated by biasing the substrate at –600V, we observed that the CN align vertically during growth as shown in Fig. 1(b), and that the magnitude of the applied substrate bias affects the degree of alignment. The thickness of the thin film Ni catalyst was found to determine the average diameter and inversely the length of the CN. The yield and density of the CN were controlled by the use of different diffusion barrier materials under the Ni catalyst. Patterned CN growth [Fig. 1(c)], with 1σ variation in CN diameter of 4.1% and 6.3% respectively, is achieved by lithographically defining the Ni thin film prior to growth. The shape of the structures could be varied from very straight nanotube-like to conical tip-like nanofibers by increasing the ratio of C_2H_2 in the gas flow. Due to the plasma decomposition of C_2H_2, amorphous carbon (a-C) is an undesirable byproduct which could coat the substrate during CN growth. Using a combination of depth profiled Auger electron spectroscopy to study the substrate and in-situ mass spectroscopy to examine gas phase neutrals and ions, the optimal conditions for a-C free growth of CN is determined.

The role of the plasma in a dc plasma enhanced chemical vapor deposition system for carbon nanofiber growth is investigated with a 1-D radially averaged computational model [1]. Equations for the conservation of species mass, ion momentum, and ion, electron, and neutral gas thermal energy are solved axially between the anode and cathode. The model includes 28 species and 200 reactions. The plasma decomposes the ammonia and acetylene feedstock through electron impact dissociation and ionization along with the endothermic ion-molecule sheath reactions of dissociative proton abstraction and collision-induced dissociation. These plasma reactions generate radicals that further contribute to decomposing the feedstock by way of radical exchange reactions (e.g. $NH_3 + H \rightarrow NH_2 + H_2$ and $C_2H_2 + N \rightarrow CH + HCN$). The result is the conversion of the feedstock to the more stable species of H_2, N_2, and HCN. The dramatic impact of this plasma-sponsored conversion on carbon nanofiber growth has been previously demonstrated [2], whereby, at the same substrate temperature, higher plasma power conditions result in much shorter nanofibers relative to lower power growth conditions. This is attributed to acetylene decomposing more readily on Ni catalyst than HCN given that the C-N triple bond strength [3] is 748 kJ/mol and the H-CCH bond strength is only 556 kJ/mol. In-situ mass spectrometry was used to confirm the simulation findings/model as shown in Fig. 2, which displays the mole fraction trends with plasma power for the three main plasma products. The trends are reproduced well where hydrogen and hydrogen cyanide increase with increasing power and nitrogen remains relatively flat. Furthermore, the simulation model has been used to predict the surface temperature at the PECVD cathode for various plasma powers, and this has been experimentally verified.

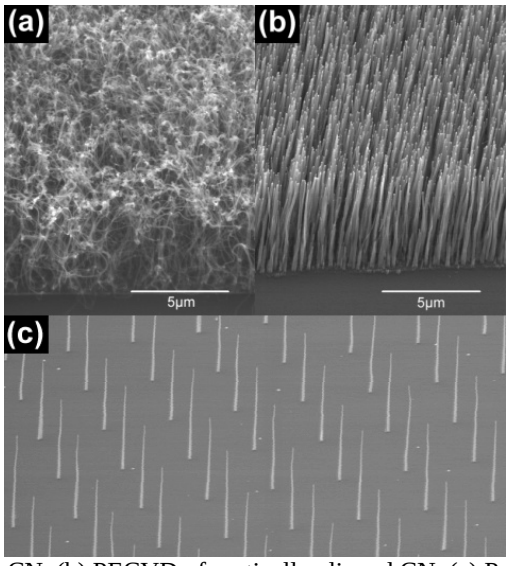

Figure 1. (a) Thermal CVD of curly CN. (b) PECVD of vertically aligned CN. (c) Patterned deposition of highly uniform CN.

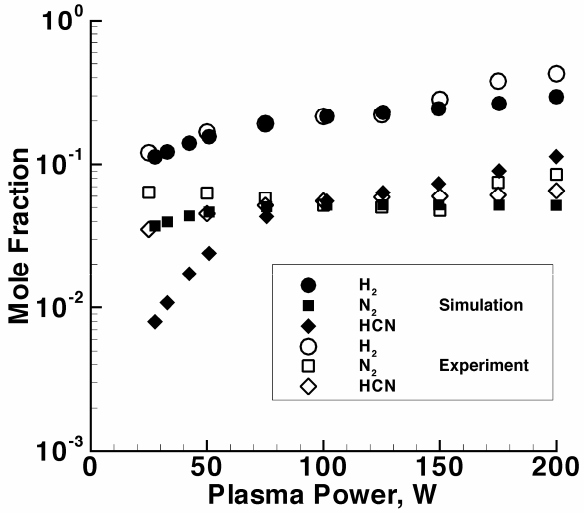

Figure 2. Mole fraction trends of main plasma products from simulation and experiment at 1 cm from cathode.

[1] D. Hash, D. Bose, T. R. Govindan, and M. Meyyappan, J. Appl. Phys. **93**, 6284 (2003).

[2] K. B. K. Teo, D. B. Hash, R. G. Lacerda, N. L. Rupesinghe, M. S. Bell, S. H. Dalal, D. Bose, T. R. Govindan, B. A. Cruden, M. Chhowalla, G. A. J. Amaratunga, M. Meyyappan, and W. I. Milne, Nano Lett. **4**, 921 (2004).

[3] D. R. Lide (Ed.), *CRC Handbook of Chemistry and Physics*, 81st Edition (CRC Press, Boca Raton, 2000).

Two-dimensional self-consistent modeling of Ar microwave-surface-wave plasma at atmospheric pressure

Y. Kabouzi†, D. B. Graves†, E. Castaños Martinez‡, K. Makasheva‡ and M. Moisan‡

†Department of Chemical Engineering, University of California, Berkeley, California 94720
‡Groupe de Physique des Plasmas, Université de Montréal, Montréal, Québec H3C 3J7

Abstract

A self-consistent two-dimensional argon fluid-model coupled with Maxwell's equations is presented. The atmospheric-pressure argon discharge is sustained by the propagation of an electromagnetic surface wave. In addition to the plasma equations, the model takes into account the gas flow and temperature by solving the mass, momentum and energy balance equations for neutral particles. It is found that the gas temperature is a key parameter in modeling surface-wave discharges sustained at atmospheric pressure because it determines both wave propagation characteristics and radial contraction of the plasma column.

1. Introduction

Surface-wave discharges (SWDs) sustained at atmospheric pressure have recently began to be systematically investigated [1,2] because of their potential and current use in industrial applications. However, the properties of atmospheric-pressure SWDs are much less well understood than those of low-pressure surface-wave discharges. This is mainly due to complex phenomena involved in the modeling of SWDs at high pressure such as radial contraction and filamentation. In a recent study [2], we have shown that radial contraction is due to the influence of nonuniform gas heating on the kinetic of molecular ions and, therefore, on the radial distribution of the electron density [2]. To adequately describe the phenomena of radial contraction, one needs to couple Ar atom kinetic processes to Ar molecular ion (MIs) kinetic processes through dissociative recombination. The later recombination process not only controls charged-particules losses but also charged-particles creation, since one of the resulting atoms of the dissociative recombination is in an excited state (a metastable or radiative state), therefore, enhancing step ionization. In this study, a self-consistent two dimensional argon fluid-model coupled with Maxwell's equations is presented. The atmospheric-pressure argon discharge is sustained by the propagation of an electromagnetic surface wave at the frequency of 915 MHz. The tow dimensional plasma model is solved numerically using the commercial code FEMLAB®[3].

Results and conclusion

Figure 1 shows the calculated two-dimensional distributions of plasma and surface wave parameters, for an argon discharge sustained at atmospheric pressure at 915 MHz in a fused silica tube of 3 mm radius and 80 cm length. The total absorbed microwave power is 400 W. In this modeling, the wave-field distribution is obtained using the dielectric description of the plasma. The plasma is then represented by its dielectric permittivity, which is self-consistently calculated from the plasma density and the total elastic collision frequency (dependent on gas and electron temperatures). Figure 1(a) clearly shows that the plasma column is radially contracted: the electron density decreases exponentially, by more than an order of magnitude, form the axis towards the tube wall. In the axial direction, the electron density is almost constant except at the very end of the plasma column where its value decreases rapidly because the decrease of the wave power flux (not shown). The electron temperature is also constant over the whole length of the plasma column, while it decreases very rapidly at the edges of the plasma column (see Fig. 1(c)). Figure 1(b) shows that the gas is heated to

approximately 2500 K at the center of the plasma column where the electron density is the highest. The gas temperature axial and radial distributions follow those of the electron density, since the heating of the gas occurs through elastic collisions. Figure 1(d) shows the two-dimensional distribution of the total electric filed intensity. We observe that the field intensity presents strong inhomogeneities in both directions. While the radial inhomogeneity is related to the skin effect the axial inhomogeneity is due to fact that the electron density approaches the critical density when going towards the plasma column ends.

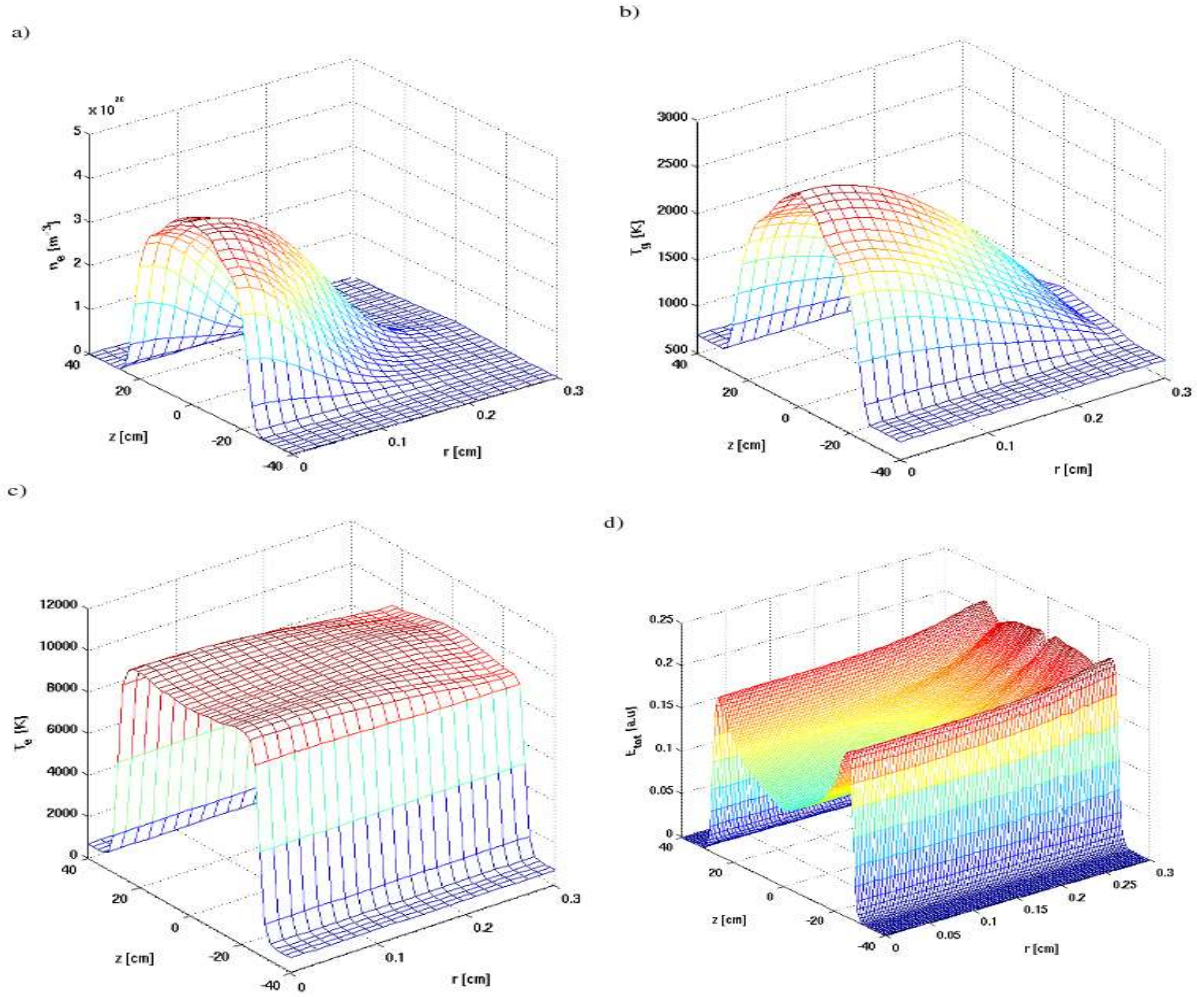

Fig. 1: Calculated two-dimensional distributions of plasma and surface wave parameters. Electron density (a), gas temperature (b), electron temperature (c) and total electric field intensity (d). The argon surface-wave discharge is sustained at 915 MHz in a silica tube of 3 mm radius and 80 cm length. The absorbed microwave power is 400 W.

References

[1] Y. Kabouzi, M. D. Calzada, M. Moisan, K. C. Tran and C. Trassy, J. Appl. Phys. 91, 1008 (2002).

[2] E. Castanos Martinez, Y. Kabouzi, K. Makasheva and M. Moisan, Phys. Rev. E, in press, 70, 066405 (2004).

[3] FEMLAB®, COMSOL, www.comsol.com

Loss mechanisms of atomic hydrogen identification in the afterglow of pulsed microwave discharge thanks of gas temperature LIF measurements

T. Lamara , R. Hugon, J. Bougdira, G. Henrion, M. Belmahi and M. Rémy

Lab. Physique des Milieux Ionisés et Applications – CNRS UMR 7040
Université Henri Poincaré – BP 239
54506 Vandoeuvre-lès-Nancy Cedex, France

Abstract

The present work deals with studying the loss kinetics of atomic hydrogen in a H_2/CH_4 pulsed MPACVD reactor. Time resolved LIF measurements of H-atoms relative density being in the ground state and observed by H_α transition have been established. The decay of H-atoms density in the afterglow was investigated to clarify the involved loss mechanisms. The effect of the diffusion coefficient on the local H-atoms density was studied thanks of time resolved gas temperature LIF measurements, deduced from Doppler broadening.

Keywords

Pulsed MPACVD reactor, LIF, Atomic Hydrogen, Diffusion, Gas temperature.

A) Introduction

There is a particular interest of using H_2/CH_4 gas mixture for diamond growth purpose. It's well known in such plasma that several hydrocarbon spices (C_xH_y) and atomic hydrogen (H-atoms) have an important influence on film quality and deposition rate [1-7]. Atomic hydrogen has a special significance as a major etcher of non-diamond phases, and hence its production and loss mechanisms should be well understood. It has been also shown that operating in pulsed regime increases the enhancement of gas molecules dissociation [10-16]. The kinetic of diamond growth process is very rich under this functional mode, due to the time variations of gas temperature and species density. That is why, the efforts aiming to better understanding these phenomena have been undertaken.

Previous studies on hydrogen pulsed microwave or radio-frequency discharges [5-9], have pointed out the main mechanisms leading to H-atoms loss and creation, which is very important for diamond film growth. Two-photon Laser Induced Fluorescence (LIF) is the best appropriate method to curry out such study, as we can have access to the density of hydrogen atoms being in the ground state. This technique, due to its high spatial and temporal resolution, makes also possible the measurement of radicals flow at the close vicinity of the walls. Moreover, LIF measurements give additional information on the gas temperature as can be deduced from Doppler broadening. The temperature determination in such a plasma can give a helpful information about complex hydrogen loss processes.

B) Experimental arrangement

B.1. Plasma reactor

A big part of the experimental arrangement has been described previously [15-16], it was used mainly for diamond films growth. For more precision, the plasma reactor is a cylindrical stainless steel vessel, home-built MPACVD reactor, of which the configuration is close to the AsTex system §Fig 1. The 2.45 GHz microwave power (600 W - 6 kW), operating in either continuous or pulsed mode, is injected into the cavity by means of a water cooled antenna and a cylindrical wave guide through a upper quartz window. The plasma is, then, generated and adjusted to be localised in the centre of the reaction chamber, closely above the molybdenum substrate holder §Fig 1. The feed gas used for these experiments is either H_2 only or a H_2/CH_4 mixture, it's driven by mass flow-meters, controlled by a host computer in order to maintain both gas

flow ratios and the total pressure. In the whole cases the pressure was maintained at 120 Torr, and the total flow rate at 325 sccm. The pulsed power is controlled by means of wave form generator thus allowing the adjustment of the output peak power, the pulse duration and the pulse repetition rate. The pulsed discharge is ignited by injecting a high peak power (3.5 kW) which lasts 28 ms, followed by an afterglow of 12 ms duration.

B.2. Diagnostic LIF

The plasma characterisation is carried out by means of time-resolved laser induced fluorescence (LIF). The laser source is a tunable pulsed YAG-pumped dye laser, working at 615 nm, providing the photoexcitation. The required 205 nm beam is obtained by tripling the frequency of the dye laser, with an output energy of 1.2 mJ/pulse [16].

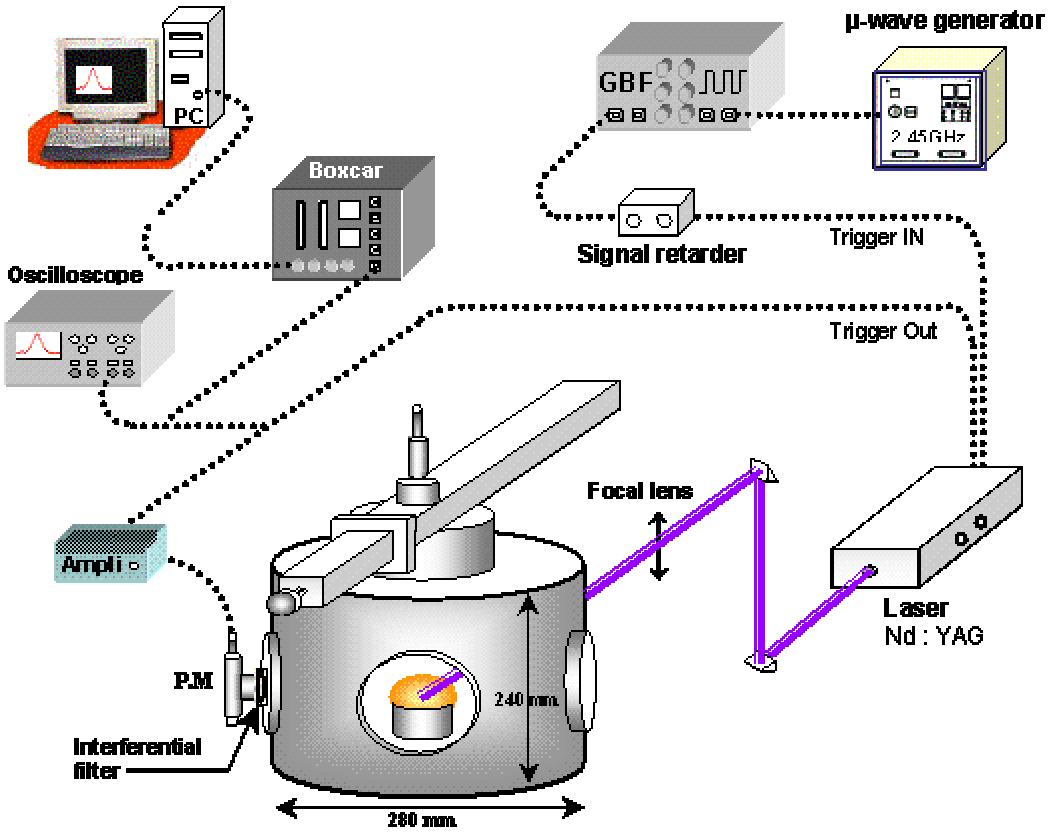

Figure 1: Experimental arrangement

The laser beam is guided to the bottom of the plasma by means of an optical system consisting of prisms and focusing lenses. The laser beam travels across the plasma in parallel to the substrate surface at a position of 4 mm above it. The spatial resolution is determined by the beam width at the focal point (0.5 mm). As we observe only the atomic hydrogen emission represented by H_α line at 656.28 nm, the monochromator was replaced by an interferential filter centred around 656 nm fixed at the entrance of photomultiplier tube (PM). The emitted light is filtered through this filter, and then, the selected H_α beam hurts the PM photocells. The output of the PM is connected to both devices of acquisition: an oscilloscope and a boxcar averager through a current amplifier (SRS 570) as shown in the figure 1.

C) Density and gas temperature measurements

Thanks to its high space and time resolution, we studied by LIF the evolution of the relative density of H-atoms in the center of plasma and the close vicinity of the substrate. A first study was curried out for different parameters, such as the pressure, the power and the gas composition.
The LIF technique, was extremely useful, firstly, for the quantitative study of H-atoms behaviour in the afterglow by measuring the relative density of H-atoms being at the ground state, from the profile observed by H_α transition ($n=3 \rightarrow n=2$) according to the reaction :

$$H\ (n=1)\ +\ 2h\nu_L\ \rightarrow\ H\ (n=3)\ \rightarrow\ H\ (n=2)\ +\ h\nu_f \qquad (1)$$

- ν_L et ν_f are, respectively, the laser excitation and the fluorescence (emission) frequencies

then for the gas temperature measurement, from Doppler broadening of LIF signal around the central wavelength λ_0 :

$$\Delta\lambda_{DH} = 7.167\times10^{-7}\,\lambda_0\sqrt{\frac{T_H}{M_H}} \qquad (2)$$

- T_H is the gas temperature and M_H is the atomic mass of hydrogen.

The temperature measurement was rather difficult because the effective bandwidth ($\Delta\lambda_m$) from the measured LIF profile is often a convolution of two principal contributions. The Broadening caused by Doppler effect and the laser apparatus function ($\Delta\lambda_L$) (convolution product of 2 gaussian profiles).

$$\Delta\lambda_m^2 = \Delta\lambda_{DH}^2 + 2\Delta\lambda_L^2 \qquad (3)$$

The laser contribution is counted two times because we have two-photons laser excitation.
In reality, we have not enough precision on the laser apparatus function, even if we know the spectral width. Because of the instabilities of the excited laser properties over multi-pulses, and the experimental consequences of these power and frequency fluctuations on the two-photon absorption LIF measurement of H-atoms is now being observed [17]. It is found that the averaging over a few tens of laser pulses to calculate the effective bandwidth of two-photon absorption LIF of H-atoms at 205 nm could underestimate the real contribution from the spectral line width of the fundamental laser radiation.

The method proposed to overcome this difficulty is based on measuring the spectral response of the atomic hydrogen and deuterium in H_2 + D_2 microwave discharge by scanning the excited laser frequency [16-17]. The hydrogen and deuterium atoms are supposed to be in thermal equilibrium ($T_H = T_D$) and their excitation frequencies are very close. The excitation wavelengths of hydrogen and deuterium are respectively 102.5722 nm and 102.5443 nm . The advantage of these very close values is that we can obtain two LIF profiles in a narrow frequency range [Fig. 2]. Combining the equations (2) and (3) one can deduce the laser apparatus function $\Delta\lambda_L$.

$$\Delta\lambda_L = \sqrt{\frac{2\cdot(\Delta\lambda_{mD})^2 - (\Delta\lambda_{mH})^2}{2}} \qquad (4)$$

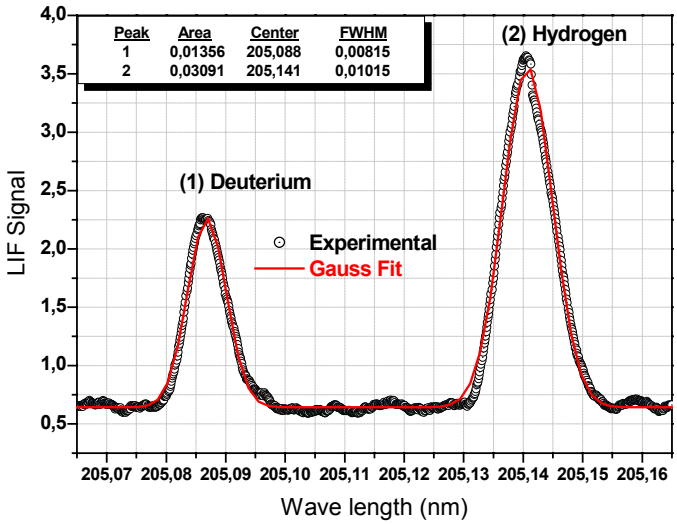

Figure 2: LIF Spectral profile of H_α and D_α lines, plasma H_2-D_2 37.5 % D_2 ; 200 sccm, 2500 W, 120 Torr.

D) Results and discussion

D.1. experimental results

The H-atoms relative concentration was evaluated by calculating the area under curve of LIF signal which has a gaussian profile. The relative density evolution in the afterglow was studied for two positions, at the close vicinity of the substrate (4 mm above the surface) and at the plasma centre (15 mm above the substrate surface), as we can see on the figure 32-a. We must keep in mind that all values are normalised to the value measured at the end of the discharge. One can notices the same evolution in the early afterglow till 2 ms, then a slight difference in benefit of the density near the surface. The most important point lies on the figure 3-b where the evolution is presented in logarithmic scale. At the first sight, we can assume that the decay of H-atoms density in the afterglow happens following tow distinguished regimes. Firstly, a fast loss regime till 2 ms, followed by a slow decay. This behaviour was already observed by several authors that sometimes interpreted by two different phenomena as a double exponential decay. While the classical kinetic theory forecasts only one slope (exponential decay), the existence of two slopes became a serious question to be answered.

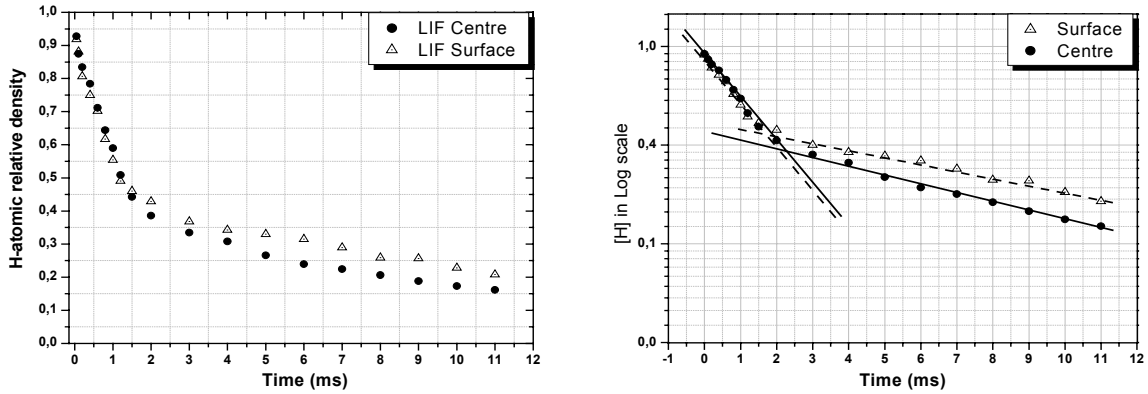

Figure 3: a) Evolution of H-atoms relative density in the afterglow.
b) the same evolution represented in logarithmic scale.

D.2. Kinetic of H-atoms evolution in the afterglow

The equation describing the temporal evolution of H-atoms local density is written:

$$\frac{\partial[H]}{\partial t} + \vec{\nabla}([H]\times\vec{v}) = Sources - Losses \qquad (1)$$

In the afterglow there is no creation process of atomic hydrogen, so no sources. In the probed volume, only volume recombination can contribute to the H-atoms consumption. This kind of recombination needs a third particle:

$$H + H + M \longrightarrow M + H_2 \qquad (2)$$

The local volume recombination rate of atomic hydrogen is given by term of losses : $2k_r[H]^2[H_2]$. with a reaction constant k_r, given by Baulch, $kr = 19.3\times10^{-31}T^{-1}$ ($m^6mol^{-2}s^{-1}$) [18].

To summarise other loss processes under our experimental conditions, which are surface recombinations, we should consider the diffusion term. This phenomenon is generated by the presence of gradient of density and is characterised by a flow of hydrogen atoms to the walls intended to homogenise this concentration. The relative term to this process can be written:

$$div([H]\times\vec{v}) = \frac{D}{\Lambda^2}[H]. \qquad (3)$$

where D is the diffusion coefficient (cm^2s^{-1}), which is considered constant in first approximation to simplify the analytical resolution of the kinetic equation, and Λ the characteristic length of diffusion.

The kinetic equation takes the following form:

$$\frac{\partial[H]}{\partial t} = -\frac{D}{\Lambda^2}[H] - 2k_r[H_2][H]^2 \tag{4}$$

The characteristic length of diffusion is calculated not only considering the reactor dimensions and geometry, but also from the different values of sticking coefficient given in the literature [19]. The reactor walls are made mainly from stainless steel, cooper and quartz windows with a sticking coefficients $\gamma \approx 10^{-4}$ - 10^{-1} at the room temperature [2-3,20]. The sticking coefficient can vary strongly with the surface conditions and for carbon substrate we take a typical value at 900°C $\gamma \approx 0.15$ [21].

Taking in account the reactor dimensions and the sticking coefficient values, we can conclude that the reactor walls loss contribution is too weak because of their big diffusion characteristic length. The carbon substrate situated in the close vicinity of the plasma with a high sticking coefficient has a strong contribution in H-atoms surface recombination, which is very useful for diamond film purity.

This term associated to the volume recombinations is proportional to the square of H-atoms density [H] and also depends on the local density of molecular hydrogen [H_2]. Under our working conditions, we assume that the volume recombinations are at least 100 times lower than surface losses, and hence they can be neglected.

The kinetic equation is reduced to :

$$\frac{\partial[H]}{\partial t} = -\frac{D}{\Lambda^2}[H] \tag{5}$$

where the solution, according to the classical kinetic theory, is an exponential decay if we consider the diffusion coefficient constant. This is not in agreement with the experimental curve of H-atoms density decay in the afterglow, as it can be observed on the figure 3. This evolution was usually interpreted by a double exponential decay.

Thanks of time resolved gas temperature LIF measurements, we studied the evolution of the diffusion coefficient (D) in the afterglow (Figure 4-a) according to the formula used by Lede [22] :

$$D = 1.25\times10^{-4}\frac{T_{gaz}^{1,72}}{P(atm)} \quad (\mathrm{cm}^2 s^{-1}) \tag{6}$$

As-estimated H-atoms density decay, taking into account the variations of diffusion coefficient, was compared to direct measured values from LIF profile as shown on the figure (4-b), where we can observe a good agreement.

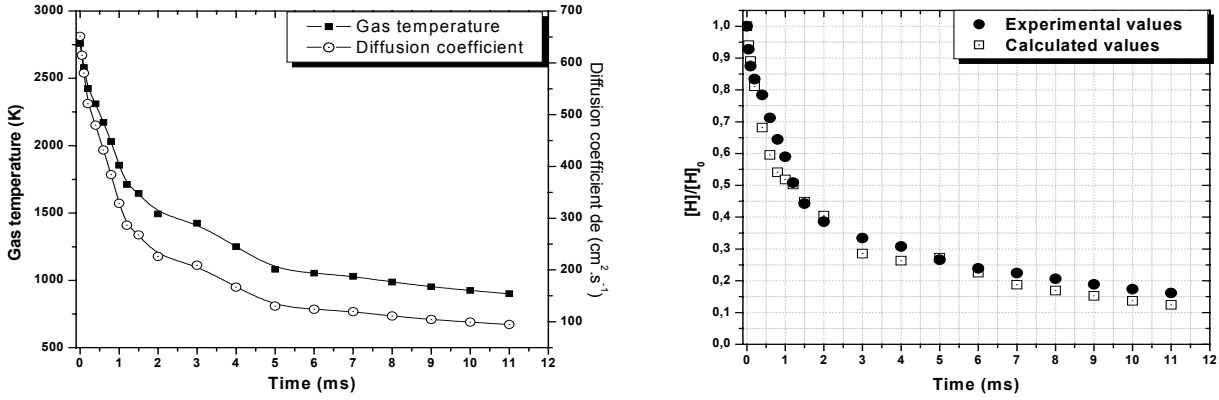

Figure 4: (a) Evolution of the gas temperature and the diffusion coefficient in the afterglow.
(b) The decay of H-atoms density in the afterglow, calculated and experimental evolutions.

Conclusion

In this study we have presented some new results based on the LIF technique which is a powerful diagnostic method for studying pulsed microwave discharge. We have explained, in the case of CH_4/H_2 plasma, the existence of only one loss mechanism of atomic hydrogen, governed by diffusion and recombination on the substrate surface.
The gas temperature and, then, the diffusion coefficient variations are of big interest for studying loss mechanisms at any discharge conditions.
This study shows also the importance of neutral dynamics study, especially gas heating and cooling phenomena for a better understanding of creation and loss processes.

References

[1] J. Deson, F. Haloua, C. Lalo, A. Rousseau, V .Veniard, J. . Phys. D : Appl. Phys. 27 (1994) 2320.
[2] L. Tomasini, A. Rousseau, G. Baravian, G. Gousset, Appl. Phys. Lett. 69 (1996) 1553.
[3] A. Rousseau, E. Teboul, P. Leprince, J. Phys. IV France 8 (1998) 287.
[4] L Chérigier, U Czarnetzki, D. Luggenhölscher, V. Schulz-von der Gathen, H. Döbele, J. Appl. Phys. 85 – 2 (1999) 696.
[5] S. F. Adams and T. A. Miller, Plasma Sources Sci. Technol. 9 (2000) 248.
[6] H. Döbele, U Czarnetzki, A Goehlich. Plasma Sources Sci. Technol. 9 (2000) 477.
[7] A. Rousseau, G. Carty, X. Duten, J. Appl. Phys. 89 – 4 (2001) 2074.
[8] S. Takashima, M. Hori, T. Goto, A. Kono, K. Yoneda, J. Appl. Phy. 90 – 11 (2001) 5497.
[9] A. Rousseau, E. Teboul, N. Sadeghi. Plasma Sources Sci. Technol. 13 (2004) 166.
[10] S. Takashima, M. Hori, T. Goto, A. Kono, K. Yoneda, J. Appl. Phy. 90, 11 (2001) 5497.
[11] J. Larjo, J. Waleweski, R. Hernberg, Appl. Phys. B, 72 (2001) 455.
[12] H. Chatei, J. Bougdira, M. Remy, P. Alnot. Surf. & Coat. Technol. 116-119 (1999) 1233.
[13] L de Poucques, J Bougdira, R Hugon, G Henrion, P Alnot, J. Phys. D: Appl. Phys. 34 (2001) 896.
[14] R. A. Akhmedzhanov, A. L. Vikharev, A. M. Gorbachev, V. A. Koldanov, D. B Radishchev, Diam.& Relat. Mater. 11 (2002) 579.
[15] T. Lamara, M. Belmahi, J. Bougdira, F. Bénédic, G. Henrion, M. Rémy, Surf. & Coat. Technol. 174-175 (2003) 784.
[16] T. Lamara, M. Belmahi, G. Henrion, R. Hugon, J. Bougdira, M. Fabry, M. Rémy, Surf. & Coat. Technol. *In Press, Corrected Proof, Available online 7 April (2005*).
[17] X. R. Duan and H. Lange, J. Phys. B: At. Mol. Opt. Phys. 37 (2004) 427.
[18] D. L. Baulch, J. Phys. Chem. Ref Data, 21 (1992) 411.
[19] P. J. Chantry, J. Appl. Phys. 62 (1987) 1141.
[20] T.P. Chiang, H.H. Sawin, C.V Thompson, J. Vac. Sci. Technol. A 15-5 (1997) 2766.
[21] L. N. Krasnoperov, I. J. Kalinovski, H. N. Chu, D. Gutem, J. Phys. Chem. 97 (1993) 11787.
[22] J. Lede and J. Villermaux, J. Chimie Physique 71 (1974) 85.

Simultaneous determination of heavy metals in airborne particulate matter by ICP-AES following co-precipitation pre-concentration with sodium diethyldithiocarbamat

S. M. Talebi and M. Abedi
Department of Chemistry, Isfahan University, Isfahan 81744, Iran

Abstract

The concentrations of heavy metals in airborne particulate matter in the atmosphere of the city of Isfahan were determined by ICP-AES. Two different digestion procedures were investigated for decomposition of airborne particulate matter. A pre-concentration procedure was developed for the sensitive determination of heavy metals in samples collected with at lower sampling period and also for the samples collected from rural arrears. A comparison was made between the concentrations of heavy metals were determined by FAAS and ICP-AES.and an excellent agreement was found between them. ICP-AES was found to be a quite suitable technique for air pollution studies where a huge number of samples should be analyzed in a short period of time.

Keywords

Inductively coupled plasma atomic emission spectrometry, air pollution, heavy metals, pre-concentration of heavy metals, simultaneous determination of heavy metals.

Introduction

Heavy metals occur in the urban atmosphere mainly in particulate form originating from the mixing of finely divided materials from various sources[1]. Although both natural and anthropogenic sources contribute to distribution of heavy metals into urban atmosphere, the role of human activities is more important [2]. The major sources responsible for releasing heavy metals into urban atmosphere include; metallurgical processes, power plants, garbage incineration, consumption of fossil fuels in automobiles engines [3]. The determination of heavy metals associated with airborne particulate matter is very important in air pollution studies. During the last decades, an extensive database has been published providing different techniques for the determination of heavy metals in environmental samples [4-6]. Among the different techniques, atomic absorption spectrometry is the most popular one, but the single-element analytical methods are time-consuming and tedious. In air pollution studies that a large number of samples should be analyzed in a short period of time, the multi-elemental techniques of analysis are preferred. Because of low concentration some heavy metals and the complexity of the airborne particulate matrix, using a sensitive and accurate method for analysis is of greaty importance.

In this paper, ICP-AES as a popular multi-elemental technique method has been used for the determination of heavy metal concentrations in atmospheric total suspended particles (TSP).

Experimental

Sample collection

Airborne particulate matter from the atmosphere of the city of Isfahan was collected on quartz fiber filter (Whatman QM-A) using a conventional high-volume air sampler. Samples were collected from both urban and rural areas. Samples were collected from a height of 1.5 m above the ground level. Sampling flow rate and sampling period were 1 m^3 min^{-1} and 12 hours respectively. A continuous sampling was also performed for a couple of weeks in order to investigate the day to day variation in concentrations of heavy metals.

Reagents

All chemicals were analytical grade or better

Standard stock solutions (1000 mg/L) of Pb, Cd, Cr, Cu, Ni, Zn and Fe for atomic absorption spectrometry (Varian Company) were used.

Standard solutions in the working range were prepared from the stock standard solution by proper diluting with 5% v/v nitric acid.

The 0.1M solution of sodium diethyldithiocarbamate was prepared by dissolving 2.253 g of the reagent in 100 ml doubly distilled water.

Distilled de-ionized water was used for preparation of standard solutions and washing the dishes.

Standard reference material of airborne particulate matter, NIST, SRM-1648 was used for evaluation of the recovery of digestion procedures and capability of analytical methods.

Sample preparation

The exposed filters were with two different leaching procedures including; 1) digestion with a mixture of nitric acid and hydrogen peroxide as a proposed method , and 2) digestion with a mixture of nitric acid and hydrofluoric acid as a recommended method for releasing of heavy metals from airborne particulate matrix.

Digestion with a mixture of HNO_3 and H_2O_2

The exposed filter was folded and placed in a 100 ml conical flask. 15 ml nitric acid 1:1 (v/v) was added and the flask was then placed on a hot plate for digestion at a temperature below the boiling point of the mixture. When the volume of the solution was reduced to a half, a further 10 ml (v/v) nitric acid and 5

ml of 30% hydrogen peroxide were added to oxidize any organic compounds, and the mixture was heated again at sub-boiling temperature to reduce the volume down to about half. The solution was finally filtered into a 25 ml volumetric flask and made to the volime with de-ionized distilled water with rinsing. From the conocal flask.

Digestion with a mixture of HNO_3 and HF

The exposed filter was folded several times and placed in a PTFE beaker and moisturized with a few ml of de-ionized distilled water, and then 15 ml of Aristar nitric acid was added. The lid of the beaker was screwed and the beaker was heated on a hot plate and refluxed for 8 hours until all organic material be oxidized. The PTFE lid was then unscrewed and the beaker heated at 90 ^{0}C. When the volume was reduced to a half, 8 ml of nitric acid and 5 ml of hydrofluoric acid were added and the mixture was refluxed again to dissolve the material completely. The lid was then removed and the mixture evaporated to near dryness. After removing the remainder of HF (by adding HNO3 and heating) the digest was extracted in nitric acid 1:1 (v/v), transferred into a 100 ml volumetric flask and made to the volume by de-ionized distilled water

Pre-concentration of heavy metals

100 ml of the digest was transferred into a pyrex beaker and the its pH was adjusted to 5 and 50 ml. of the sodium diethyldithicarbamate solution was added on that and the solution was allowed to stand for 30 min. Then 1 ml 1% H_2O_2 was added and allowed to stand for 5 hours. The precipitate was filtered on a narrow pore filter paper and finally dissolved in concentrated nitric acid. The solution was transferred into a 10 ml volumetric flask and diluted to the volume with doubly distilled water.

Instrumentation

ICP-AES determinations were carried out on a Maxim system (Applied Research, Fisons Instruments) fitted with an axial viewing of torch. Axial viewing of the torch gives more light, better ability, and allows determination of easily ionized elements with high sensitivity and precision. Control of the Maxim ICP-AES spectrometer was affected from a suite of software program called Plasma Vision. The system was linked to a DECP 450, D2LP computer and an IBM 238 printer. The ignition, shut down, and sample uptake rate were computer-controlled. The wavelengths used for the determination of heavy metals include; 220.35 nm for lead, 228.80 nm for cadmium, 213.86 for zinc, 267.72 nm for chromium, and 324.75 nm for copper. The background correction was performed using two different positions. Position No. 1 in negative offset and position No. 2 in a positive offset from the analytical wavelength of the element of interest. The instrumental conditions are summarized in Table1.

Table 1: ICP-AES Scanning measurement parameters

Starting mirror	-60
Ending mirror	+60
Step size	4
Pre-integration time	0 (s)
Integration time	1 (s)
Plasma flow	0.8 (L/min)
Forward power	1100 (W)
Carrier flow	0.4 (L/min)
Analysing pump speed	2.0 (L/min)
Transport pump speed	20.0 L/min)
Transport time	30 (s)
Sample type	aqueous

The following analytical lines were used for analysis

Pb 220.35 nm, Cd 228.80 nm, Cr 267.72 nm, Cu 324.75 nm, Ni 231.60 nm, Zn 213.86 nm, and Fe 259.94 nm

Results and discussion

In order to evaluate the efficiencies of the digestion procedures, a standard sample (NIST, SRM-1648) was digested with both of the digestion procedures. The results were compared with certified value and showed that for complet decomposition using a mixture of nitric and hydrofluoric acid was necessary (Table 2).

In order to investigate the variation in concentrations of heavy metals in day and night times, we had to to reduce the sampling tine from 24 hours to 12 hours and in such a circumstance pre-concentration was necessary for sensitive determination. The pre-concentration was performed using co-precipitation of interest cations with sodium diethldithiocarbamate at optimized condition (pH, amount of sodium diethyldithicarbamate, standing time). The precipitate was then decomposed in concentrated nitric acid and analyzed by ICP-AES system. The recovery of heavy metals after pre-concentration was more than 96% at pH=5.

Table 2: The efficiencies of two decomposition methods for releasing heavy metals (µg/g) from NIST-SRM 1648

	HNO_3, H_2O_2 procedure		HNO_3, HF procedure		
Element	Mean	SD	Mean	SD	Certified value
Pb	5430	51.2	6530	62.5	6550
Cd	70	1.9	71	1.9	75
Cr	115	4.1	185	4.9	403
Cu	589	19.5	605	18.4	609
Ni	76	3.3	82	2.5	82
Zn	4711	31.3	4752	30.1	4760
Fe	32289	500	38700	589	39100

Several samples were digested and analyzed by FAAS and ICP-AES. The results were in excellent agreement. Although FAAS is known as a popular method for determination of heavy metals, it is time-consuming and tedious. ICP-AES with the same sensitivity especially after pre-concentration offers the same results at the shorter time. Comparison of the capabilities of FAAS and ICP-AES and the regression equation for the results obtained by the two techniques are summarized in Table 3.

Table 3: Comparison of FAAS and ICP-AES by a linear regression analysis

Element	Regression equation	X,Y pairs
Pb	Y = 1.221 + 0.981 X	26
Cd	Y = 0.132 + 1. 054 X	26
Cr	Y = 0.021 + 1.004 X	26
Cu	Y = 0.387 + 0.991 X	26
Ni	Y = 0.042 + 1.014 X	26
Zn	Y = -0.110 + 1.002 X	26
Fe	Y = 0.021 + 0.998 X	26

The pre-concentration procedure made it possible to reduce the sampling period from 24 hours and investigate the variation in concentration of atmospheric pollutants. Figure 1 shows the variation in concentrations of heavy metals in days with two rush hours and at night times.

.

Figure 1; Day and night time concentrations of heavy metals

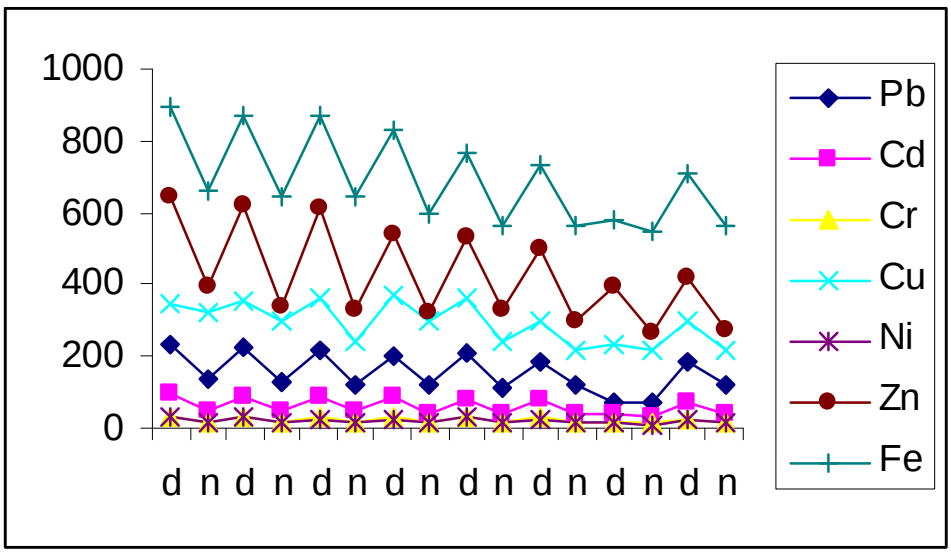

References

1- R. Chester, F. J. Lin, and K. I. T. Morphy, *Environ*. *Technol. Lett*., **10**, 887 (1989).

2- J. Sneddon, *Talanta***, 30**, 631 (1983).

3- H. A. Trindade, W. C. Pfeiffer, H. Londres, and C. L. Costa-Ribeiro, Envir*on*. *Sci. & Technol.*, **15**, 84 (1981).

4- S. Tokalioghu, S. Kartal, and L. Elci, *Anal. Chim. Acta*., **413 ,** 33 (2000).

5- B. Ye, X. Ji, H. Yang, X. Yao, , C. K. Chan, S. H. Cadle, T. Chan, and P. A. Mulawa, *Atmos. Environ.*, **37**, 499 (2003).

6- Q. Zhang, H. Minami, S. Inoue, and L. Atsuya, *Fresenius J. Anal. Chem*., **370**, 860 (2001).

Adhesion and growth of cells at the surface of plasma deposited nanostructured fluorinated coatings

E. D'Aloia[1], G.S. Senesi[2] , R. Gristina[2], R. d'Agostino[1,2], P. Favia[1,2]

[1] Department of Chemistry, University of Bari, Via Orabona 4, 70126, Italy
[2] Institute of Inorg. Methodology of Plasma, (IMIP) CNR, Via Orabona 4, 70126, Italy

**contact author: e.daloia@chimica.uniba.it*

Abstract
Modulated RF glow discharges fed with C_2F_4 were used to deposit nanostructured "teflon-like" coatings characterized by ribbon-shaped structures on a less fluorinated background. In continuous regime smooth samples were obtained. The coatings were analysed by means of X-rays Photoelectron Spectroscopy (XPS) and Atomic Force Microscopy (AFM). Nanostructured and smooth coatings were used in cell growth experiments with 3T3 fibroblast. The density of adhering cells depends on the roughness of the coatings.

1. Introduction

Non equilibrium, low-temperature plasma deposition (Plasma Enhanced-Chemical Vapour Deposition, PE-CVD), treatment and etching processes are nowadays extremely popular in Materials Science Technology for their ability to adapt surface chemistry and properties of materials in a wide range of applications at room temperature, in a controlled way, without changing their bulk [1], at negligible impact for the environment.
PE-CVD, in particular, allows to vary continuously the composition of treated surfaces and, consequently, their physical and chemical properties in a very broad range, by depositing thin (10-1000 nm) coatings of tuneable composition and properties, ranging from those with high retention degree of the monomer structure to those with a fully "scrambled" atomic distribution. PE-CVD allows to tune many surface properties of biomedical interest; Radiofrequency (RF, 13.56 MHz) driven Glow Discharges are the most utilized plasma sources for biomedical applications.
Thin coatings deposited in glow discharges fed with fluorocarbon gases have been investigated since years as source of thin films characterized by surface properties such as low surface energy and wettability, high hydro-phobic and oleo-phobic (stain resistance) character, low friction coefficient, high chemical inertness, low (k) dielectric constant and interesting interactions with biological systems [2]. Such coatings can be plasma-deposited in RF Glow Discharges both in continuous wave (CW) and modulated discharge (MD) regimes to obtain films with different surface properties.
Fluorocarbon films obtained in CW conditions are characterized by a variable fluorination degree and cross-linking character, depending on the experimental parameters, and by low roughness. In recent years PECVD processes have been also investigated in MD conditions; modulating the discharge (pulsing the discharge on/off at defined time intervals) [2-6], it is possible to improve the process control for both the plasma phase [7] and the deposited films [8, 9]. Previous papers [10-12] have shown that MD films, deposited from tetrafluoroethylene (C_2F_4), exhibit very rough surfaces and high fluorination degree. More specifically, low duty cycles in modulated plasma processes results in progressively less branched films and in an increased retention of the monomer structure in the coating including crystalline poly-tetrafluoroethylene (PTFE) nanostructures randomly distributed on an amorphous fluorocarbon background.
In this contribution we present results on the behaviour of cells cultured on fluorocarbon surfaces produced through RF (13.56 MHz) glow discharges fed with fluorine-carbon gases in CW and MD regimes, characterized by identical chemical surface composition, and different roughness determined by peculiar surface topographical features. It has been found, in fact, that the presence of random/oriented morphological features on biomedical materials can drive the behaviour of cells.
3T3 murine fibroblasts were cultured on two kinds of samples, flat and nanostructured, with different topographical features in order to study how the adhesion and growth of cell lines was influenced by topographical parameters. It is known, in fact, that cells adhering at the surface of biomedical materials are sensible to surface topography [13-15].

Data relative to X-ray Photoelectron Spectroscopy (XPS), Water Contact Angle (WCA) and Atomic Force Microscopy (AFM) measurement are presented. The correlation between cells adhesion, spreading and growth and the topography of the processed substrates is discussed.

2. Materials and Methods

RF Glow Discharges fed with C_2F_4 were conducted in CW and MD regimes to deposit flat and rough nano-structured ribbon-like fluorocarbon coatings [13] on 10 mm diameter PET (Goodfellow) circular substrates. Depositions were carried out in a parallel plate stainless steel reactor. The reactor is described in detail in previous papers [10-12]. The upper electrode (12 cm circular dia, stainless steel, shielded) and the lower one (19 cm circular dia, stainless steel, substrate holder, grounded) were 5 cm far. Discharges were ignited in the interelectrode gap with a 13.56 MHz generator (RF Power Products model RF5) connected to the upper electrode through an impedance matching network. A pulse generator was used in MD regimes.
Smooth fluorocarbon coatings were deposited in CW regime, in the following experimental condition: 6 sccm C_2F_4 flow rate, 100 W RF power, 200 mTorr pressure and 5 min of deposition time; this kind of substrates were called as FLAT.
Fluorocarbon coatings with controlled roughness and density of nano-structures were deposited on PET in the following MD experimental condition: 10 sccm C_2F_4 flow rate, 100 W RF power, 5% duty cycle (16 ms time on; 304 ms time off; total period 320 ms), 200 mTorr pressure and 60 min deposition time. These conditions result in ribbon-like nano-structured fluorocarbon coatings called as ROUGH surfaces. Figure 1 shows AFM images of the two different fluorocarbon coatings; smooth surfaces obtained in CW regime and nanostructured ones produced in MD at low duty cycle.

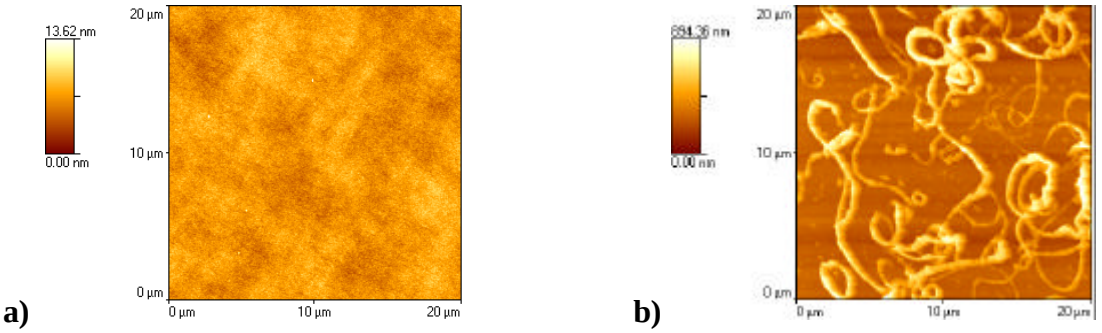

Fig1. AFM images of fluorocarbon coating deposited from C_2F_4 in CW **a)** and MD **b)** conditions showing the pronounced topographical difference between FLAT and ROUGH coatings.

Since a slightly different surface chemical composition was found between ROUGH and FLAT coatings, as known from previous publications [10-13], after the MD deposition process, the substrates were coated in the CW conditions described above for 50 s, in order to deposit a thin conformal (60 nm) CW coating on the nanostructured surface. The resulting substrates were characterized by a defined roughness value and by the same FLAT chemical composition. FLAT and ROUGH substrates were utilized in the same cell-culture experiments to compare in detail cell-surface interactions on fluorinated nanostructured coatings without and with nanostructures at their surface.
Surface chemical analysis of substrates were obtained by X-ray Photoelectron Spectroscopy (XPS). A PHI 5300 instrument (non-monochromatic MgKα X-rays, 1253.6 eV) was used. Only Carbon and Fluorine were detected. The surface chemical composition of FLAT and ROUGH coatings was expressed as F/C ratio; a deeper description of surface chemistry and properties of such coatings is reported in refs.10-12.
Static Water Contact Angle (WCA, 2 µl drops, double-distilled water) measurements were performed with a Ramé-Hart A-100 goniometer, to probe the hydrophobic character of the surfaces used in cell-culture experiments. AFM measurements (SPM - Autoprobe CP Research, Veeco, Sunnydale, CA) were run in non contact mode on 20µm x 20µm sample areas to better evaluate the roughness of the substrates. An a-step (KLA Tencor) instrument was utilized to measure the thickness of the coatings.
3T3 fibroblasts were used for cell culture experiments. Cells were obtained from stocks routinely grown in Dulbecco Modified Eagles Medium (DMEM, Sigma, UK), supplied with 10% fetal bovine serum and 200

mM glutamine, under 5% CO_2/95% air atmosphere at 37°C. ROUGH and FLAT samples were placed, modified side up, in 24 well (Iwaki) culture plates. Cells were obtained after trypsinization of confluent or near-confluent culture, then seeded at 1 x 10^4 cells/well in suspension on all materials. After incubation, cells were fixed with a 4% formaldehyde/PBS solution (15 min) and stained (3 min, Coomassie blue in methanol/acetic acid/water) at different time (3h, 24h, 48h, 96h), to carefully evaluate by means of optical microscopy, the percentage of substrate area covered by cells on different samples. Automated detection of cell outline was used to calculate individual and total cell areas. The Image J (National Institute of Health, US) image analysis software was used; 50÷100 cells were counted for single cell area analysis.
The unpaired Student's t-test was used to evaluate statistical significant differences among tests performed on at least four replicated samples. Differences were considered significant for $p<0.01$.

3. Results and Discussion

PE-CVD of FLAT and ROUGH fluorocarbon coatings

The surface chemistry of FLAT and ROUGH fluorocarbon coatings deposited on PET substrates, as defined in the previous section, are analyzed by XPS, WCA and AFM to detect their surface chemical composition, wettability and roughness, respectively.
An F/C ratio of 1.62±0.03 is detected by XPS on FLAT substrates, and WCA values of 105°±3°. From AFM analysis a root-mean-square roughness value (RMS) of 2.0 ± 0.2 nm is measured on FLAT coatings, confirming a very smooth surface, and a thickness of 300±15 nm of the deposited film.
MD plasma coated PET substrates resulted in a XPS F/C ratio of 1.89±0.03 and WCA values of 155°±5°. The very high WCA value is explained with the presence on the surface, at the same time, of a high fluorination F/C degree, and of the nanostructures; this combined effect of chemistry and roughness on the hydrophobic character of a surface is quite common and well known, and has been reported also in previous papers [11-14] on plasma-deposited MD fluorocarbon coatings. Due to the presence of the ribbon-like structures a RMS roughness value of 130±15 nm is measured by AFM on top of such coatings, which are characterized by a thickness, excluding nanostructures, of 160±15 nm.
In order to obtain surfaces with very similar F/C surface chemistry and different roughness, nanostructured surfaces are conformally coated in the same CW conditions used for FLAT coatings. In this way ROUGH surfaces obtained, have an F/C ratio of 1.61±0.03 measured very similar to FLAT samples.
XPS analysis demonstrate that the C1s spectra of ROUGH (MD) and FLAT (CW) films, before the conformal coating, are quite different. Nanostructured ROUGH films show a sharper C1s band with a predominant contribute of the CF_2 moieties. The smooth FLAT surface, instead, present a broader C1s band with comparable contribution of all CF_x components (Figure 2a). After the homogeneous CW deposition on nanostructured surfaces (MD+CW), the C1s bands of ROUGH and FLAT coatings overlap perfectly (Figure 2b).

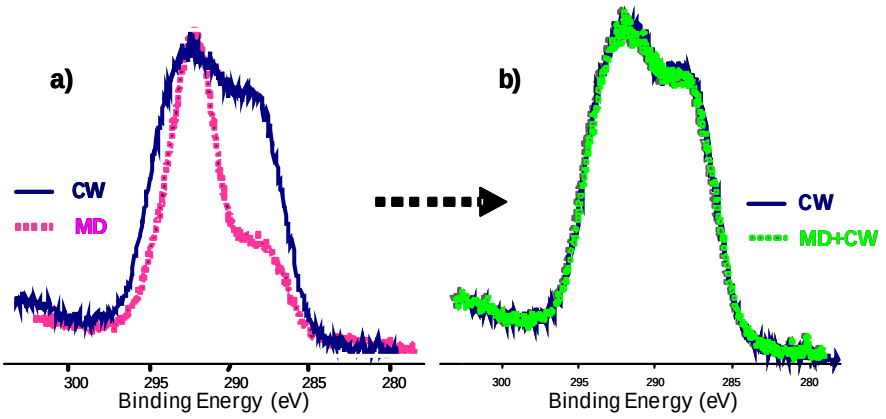

Fig.2 XPS C1s signal of FLAT (CW) and ROUGH (MD) samples before **a)** and after **b)** the conformal CW coating.

After the conformal coating a RMS roughness value of 120±15 nm is found on ROUGH surfaces, with WCA values of 140±5° and a thickness of 220±20 nm, excluding nanostructures. Respect to MD plasma coated

surfaces RMS roughness values and WCA values of ROUGH substrates are reduced due to the conformal deposited fluorocarbon layer.
These results attest that FLAT and ROUGH fluorocarbon surfaces exhibit the same chemistry but different density of nano-structures, so they can be used in cell-culture experiments for investigating in detail the effect of roughness on cell surface interactions.
FLAT and ROUGH fluorocarbon substrates are utilized in cell growth experiment in order to detect different behaviors as a function of the roughness of the substrates underneath.
3T3 fibroblast cells are seeded on FLAT and nanostructured ROUGH samples and the area of samples covered by cells is evaluated by optical microscopy analysis at different time of cell culture (3h, 24h, 48h, and 96h). As it's shown in Figure 3, after 48 hours of cell culture the area covered by cells on ROUGH surface becomes larger than on FLAT fluorinated substrates.
The effect is much more pronounced after 96 hours of culture, since 3T3 cells are almost confluent on nanostructured ROUGH samples, while on FLAT samples there are still large areas of the substrate where cells are not adhered.

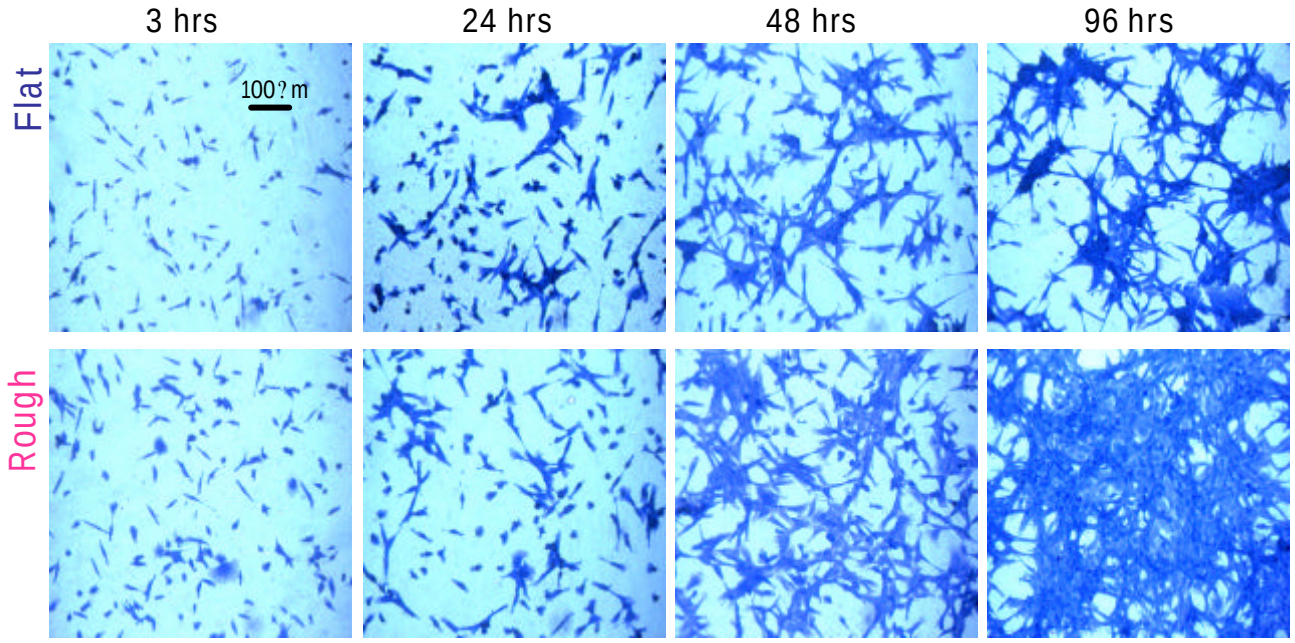

Fig. 3 Optical microscopy pictures showing differential adhesion of 3T3 Fibroblast cells on FLAT and ROUGH surfaces after different period of cell culture (3 h, 24h, 48h, 96h).

The mean values (± SD) of the sample surfaces covered by cells at different time points, shown in Figure 4, confirm the better attitude of cells to adhere on nanostructured ROUGH samples respect to the FLAT ones.

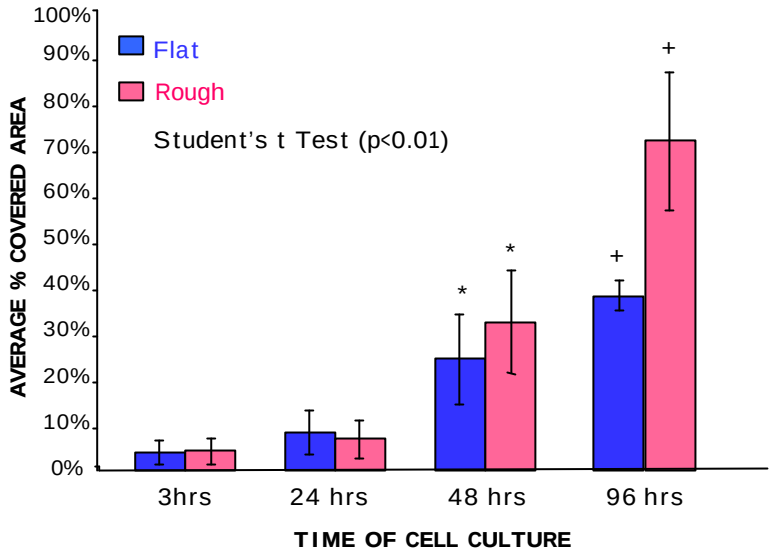

Fig.4 Graph showing % of area covered by 3T3 fibroblast/area 2.8mm^2 (n>10) on FLAT and ROUGH samples at different time of cell culture.

4. Conclusion

Adhesion and morphology of 3T3 murine fibroblasts appeared to be influenced by the topography present at the surface of the plasma deposited coatings. The used cell lines adhered in different way to nanostructured ROUGH samples and to FLAT samples. These results suggest that fluorinated smooth surfaces (FLAT) are not the best substrate for cells thus the increase surface roughness (ROUGH) result in improving the adhesion and growth of cells. Nanostructured coatings with different roughness surface can be modified by the plasma deposition of a thin film with different chemistry in order to observe the behaviour of cells adhered at their surface both to different chemistry and topography.

Acknowledgments

We gratefully acknowledge the MIUR-FIRB RBNE01458S_006 (ITA)and NANOMED QLKE-CT-2000-01500 (EC) projects for the financial support.

References

[1] R.d'Agostino, P. Favia, C. Oehr, M.R. Wertheimer; *Plasma Processes and Polymers*, **2(1)**, 7-15, (2005).
[2] P. Favia; *Plasma polymers and related materials*, H. Biederman ed., Imperial College, 25-55, (2004).
[3] V. Panchalingam, Bryan Poon, Hsiao-Hwei Huo, C.R. Savage, R.B. Timmons, R.C. Eberhart; *J. Biomater. Sci. Polymer Edn*, **Vol.5**, No.1/2, pp. 131-145 (1993).
[4] Han, R.B. Timmons; *J.Vac. Sci. Technol. B*, **18(2)**, Mar/Apr (2000).
[5] Chen, K. Rajeshwar, R.B. Timmons, J.-J. Chen, O.M.R. Chyan, *Chem. Mater.*, **8**, 1067, (1996).
[6] S.J. Limb, K.K. Lau, D.J. Edell, E.F. Gleason, K.K. Gleason, *Plasma and Polymers*, **4**, 21, (1999).
[7] T. Yoshida, Y. Ichikawa, H. Sakai; *Proceedings of the 9th European PV Solar Energy Conference (Freiburg);* Palz.W. Wrixon, G.T., Helm, P., Eds.; Kluwer Academic Publisher: Dordrecht, The Netherlands, 1006-1009, (1989).
[8] X. Chen, K. Rajeshwar, R.B. Timmons, J.-J. Chen, O.M.R. Chyan; *Chem. Mater.*,**8**, 1067-1077, (1996).
[9] S.J. Limb, K.K. Lau, D. Edell, J.E.F. Gleason, K.K.Gleason; *Plasma Polym.;* **4**, 21-32, 1999.
[10] G. Cicala, A. Milella, F. Palumbo, P. Rossini, P. Favia, R.d'Agostino, *Macromolecules*, **35,** 8920, (2002).
[11] P.Favia, G. Cicala, A. Milella, F. Palumbo, P. Rossini R. d'Agostino; *Surf. Coat. Tech.*, **169**, 609, (2003).
[12] Milella A., Palumbo F., Favia P., Cicala G., d'Agostino R., *Pure and Applied Chemistry* submitted.
[13] R. Gristina, E. D'Aloia, G.S. Senesi, E. Sardella, R. d'Agostino, P. Favia; *European Cells & Materials*, Vol **7** Suppl. 1, 8, (2004).
[14] M.J. Dalby, M.O. Riehle, D.S. Sutherland, H. Agheli, A.S.G. Curtis, *Biomaterials*, **25**, 5415-5422, (2004).

[15] E. Sardella, R.Gristina, G.S.Senesi, R.D'Agostino, P.Favia, *Plasma Processes and Polymers* **1(1)**, 63-72, (2004).

Negative Ion Reactions with Atoms for Plasma Processes

A. J. Midey,[a] T. M. Miller,[a] T. H. Thompson, R. A. Morris, and A. A.Viggiano

Air Force Research Laboratory, Space Vehicles Directorate, Hanscom AFB, MA 01731-3010
[a]Boston College, Institute for Scientific Research, 140 Commonwealth Ave., Chestnut Hill, MA 02467

Abstract
Rate constants and product branching ratios for the reaction of $PO_xCl_y^-$ and $SO_xF_y^-$ ions with H atoms were measured in a selected ion flow tube (SIFT) from 298-500 K. The reactive ions underwent halogen abstraction to form HX (X=Cl, F) as the major reaction pathway, having rate constants of around 2×10^{-10} cm^3 s^{-1} from 298-500 K. Preliminary results show that the $PO_xCl_y^-$ ions did not react with N, N_2 or NO. Associative detachment of H atoms did not occur except for F^-, SO_2^- and PO^- ions.

1. Introduction

Phosphorus-containing compounds are potential contaminants in the plasmas of coal-fired magnetohydrodynamic (MHD) electric generators.[1] Anions produced by these compounds such as PO_3^- have also been observed in the mass spectra of numerous pesticides.[2] In addition, flames doped with $POCl_3$ have been observed to produce PO_3^- and PO_2^- as the major terminal ions,[3] and oxyphosphorus compounds have also been used as fuel additives in flame tests for hydrogen-fueled scramjet combustors, demonstrating a measurable increase in thrust by enhancing H, O, and OH recombination kinetics.[4] Nevertheless, the detailed chemistry involved in reaching the PO_2^- and PO_3^- terminal species has not been explained and the reactions of oxyphosphorus ions with atoms have not been extensively studied. This anion chemistry is equally useful for models of plasma-assisted combustion, where the role of negative ion chemistry is not well understood.[5]

An analogous situation concerns discharges where SF_6, O_2 and H_2O are present, leading to $SO_xF_y^-$ anions such as SOF_2^-, $SO_2F_2^-$ and SO_2F^-.[6, 7] The available kinetics for the formation and reactivity of these species are also sparse, despite some recent studies from our laboratory to begin understanding the plasma chemistry.[8, 9] Data on the reactions of the sulfur oxyfluoride anions with atoms is similarly lacking.

To address the dearth of information on the plasma chemistry of these anions, rate constants and branching ratios for $PO_xCl_y^-$ and $SO_xF_y^-$ anions reacting with relevant atomic species were measured in a selected ion flow tube (SIFT) from 298-500 K. Reactions between H atoms and $PO_xCl_y^-$ and $SO_xF_y^-$ ions are discussed as are preliminary results on reactions with O and N atoms.

2. Experimental

The selected ion flow tube (SIFT) has been described in detail elsewhere.[10] Therefore, only a brief description will be provided. $PO_xCl_y^-$ anions were generated in a remote ion source chamber by electron impact on $POCl_3$ and the subsequent ion-molecule reactions of these ions with remaining $POCl_3$.[11-13] All of the $SO_xF_y^-$ ions were similary generated by electron impact; however, various combinations of source gases were used to achieve the requisite source chemistry as follows. SF_6^- and SF_5^- were created from SF_6. SO_2^- was generated from SO_2 while $SO_2F_2^-$ and SO_2F^- were generated from a mixture of SF_6 and SO_2. A mixture of SF_6 and H_2O introduced into a source block cooled to 262 K was used to produce SOF_4^- and SOF_3^-.[8]

Once generated, the desired reactant ion was mass selected with a quadrupole mass filter and injected into a fast flow of helium buffer gas introduced into the temperature-controlled flow tube through a Venturi inlet. After thermal equilibration, atoms created using a microwave discharge on a gas mixture passing through a Pyrex tube were introduced into the reaction region of the SIFT. For H atoms, a mixture of H_2 in He was used in the discharge. For the initial O atom experiments, a microwave discharge on N_2 produced N atoms that were titrated with NO to produce O atoms.[14] Consequently, the reactions with the H_2, N_2 and NO gases used with the

microwave discharge atom source were studied first. After the reaction occurs over a known distance for a previously measured reaction time, a blunt nose cone aperture samples the remaining reactant ions and any product ions. These ions are analyzed with a second quadrupole mass filter and detected with an electron multiplier.

As the neutral reactant concentrations were in excess of the reactant ions, the decay of the reactant ion could be followed using pseudo-first order kinetics, giving the reaction rate constant with a relative uncertainty of $\pm$20% and absolute uncertainty of $\pm$30% for the atom reactions.[15] The product branching ratios as a function of reactant concentration were extrapolated to zero concentration to account for any secondary chemistry that might have occurred at higher concentrations. The branching ratios have uncertainties of $\pm$10%.

To address the issue of possible direct routes to PO_2^- and PO_3^- formation, the secondary reactions of $POCl^-$ product ions with O_2 and O_3 were also studied. $POCl^-$ ions were first created by the $POCl_2^-$ + H reaction and then pure O_2 and, subsequently, a 3% O_3 in O_2 mixture was introduced at an inlet upstream of the initial H atom reaction to react with $POCl^-$. Corrections were made to the branching ratios to account for the product contributions from the O_3 reaction with $POCl_2^-$ ions that could not be completely reacted away at the H atom concentrations achieved here. The operating conditions for this experiment also precluded the determination of whether Cl^- products came from the reactions of $POCl^-$ with O_2 and O_3.[15]

3. Results and Discussion

a. $PO_xCl_y^-$ Reactions with H atoms

The kinetics results for the reactions of $PO_xCl_y^-$ ions with H atoms are summarized in Table 1. All of the $PO_xCl_y^-$ ions in Table 1 were unreactive with H_2, giving a limit to the rate constant of $<5\times10^{-12}$ cm^3 s^{-1}. The rate constants for the reactions of these ions with H atoms were not dependent on temperature from 298-500 K, having rate constants of roughly 2×10^{-10} cm^3 s^{-1}, which are <20% of the capture collision rate constants, k_c, shown in brackets in Table 1.[16, 17]

As seen in Table 1, halogen abstraction from $PO_xCl_y^-$ producing HCl was the primary reaction pathway, resulting in a more energetically stable, less reactive anionic species. The enthalpies of reaction at 298 K in Table 1 were determined from *ab initio* geometry optimizations[15, 18] at the G3 level of theory[19, 20]determined using Gaussian 03W.[21] None of the primary $PO_xCl_y^-$ reactant ions underwent associative detachment with H atoms, which would have produced a neutral molecule and electrons, even though this reaction pathway is slightly exothermic for $POCl_2^-$ for either of the two $HPOCl_2$ isomers shown in Table 1. Associative detachment was observed for H atoms reacting with PO^- ions that were formed by the secondary reaction of H with the $POCl^-$ ions from the $POCl_2^-$ + H reaction. However, the PO^- channel was only observed at high H atom concentrations. A similar detachment channel for $POCl^-$ + H giving HPOCl with the H atom bound to the phosphorus was 48 kJ mol^{-1} exothermic, but the presence of PO^- ions in the flow tube precluded a definitive observation of this process with $POCl^-$. The lowest energy structures for HPO_xCl_y neutral molecules, determined using G3 theory, show the H atom bound to the O, with an O-H bond distance of ~0.98 Å for all of the molecules. The only exception is HP=O, which is ca. 1.5 eV lower in energy than POH.[15]

b. Routes to PO_2^- and PO_3^-

To further probe for reactive channels that directly produce PO_2^- and PO_3^-, the secondary reactions of $POCl^-$ product ions with O_2 and O_3 were studied. The results for this secondary chemistry are also shown in Table 1, where the final branching ratios given were corrected as described in the Experimental section above. Both O_2 and O_3 reacted with $POCl^-$ to directly produce PO_3^- and PO_2^-, respectively, with rate constants of $8.9\pm1.1\times10^{-11}$ and $5.2\pm3.3\times10^{-10}$ cm^3 s^{-1}.[15] These products were only minor channels with $POCl_2^-$ and $POCl_3^-$ reacting with O_3.[18]

Table 1. Kinetics Results for the Reaction of $PO_xCl_y^-$ + H

			Rate Constant, [k_c] ($\times 10^{-9}$ cm^3 s^{-1})	
			Branching Ratios	
Reactants	**Products**	ΔH^0_{298K} **kJ mol^{-1}**	**300 K**	**500 K**
			0.36 [1.9]	*0.37 [1.9]*
PO_2Cl^- + H →	PO_2^- + HCl	-222	1.00	1.00
	HOPOCl + e^-	7		
			<0.005 [1.9]	*<0.005 [1.9]*
$PO_2Cl_2^-$ + H →	PO_2Cl^- + HCl	-27	No Rxn.	No Rxn.
			0.16 [1.9]	*0.16 [1.9]*
$POCl_2^-$ + H →	$POCl^-$ + HCl	-45	0.94	0.96
	Cl^- + HPOCl	-6	0.06	0.04
	$HOPCl_2$ + e^-	-10		
	O=$PHCl_2$ + e^-	-3		
			0.38 [1.9]	*0.37 [1.9]*
$POCl_3^-$ + H →	$POCl_2^-$ + HCl	-275	1.00	1.00
	$HOPCl_3$ + e^-	44		
Secondary	**Chemistry**			
			0.089 [0.62]	
$POCl^-$ + O_2 →	PO_3^- + Cl	-408	>0.99	
	PO_2^- + ClO	-116	<0.01	
			0.52 [0.92]	
$POCl^-$ + O_3 →	PO_2^- + ClO_2	-45	~0.80	
	PO_2^- + Cl + O_2	-32		
	PO_2Cl^- + O_2	-240	~0.20	

c. $SO_xF_y^-$ Reactions with H atoms

The kinetics results for the reactions of $SO_xF_y^-$ ions with H atoms are summarized in Table 2. All of the $SO_xF_y^-$ ions in Table 2 were unreactive with H_2, with an upper limit to the rate constant of $<5\times10^{-12}$ cm^3 s^{-1}. The rate constants for the reactions of these ions with H atoms were weakly dependent on temperature from 298-500 K, with a slightly negative trend with increasing temperature. The rate constants for the reactive ions were roughly 2.5×10^{-10} cm^3 s^{-1}, which was also <20% of the capture collision rate constant.[16, 17] The F^- reaction with H was the exception, reacting at almost 90% of the collision rate at 500 K. This measurement at 500 K was the first for the F^- + H reaction above room temperature.

As seen in Table 2, halogen abstraction from $SO_xF_y^-$ producing HF was the primary reaction pathway, resulting in an unreactive anionic species, analogous to the $PO_xCl_y^-$ reactions. The enthalpies of reaction at 298 K in Table 2 were determined from the experimental literature values where available[22] and extensive G2 theoretical calculations of the thermochemistry.[8, 23, 24] The reactivity trends of $SO_xF_y^-$ ions with H atoms

were identical to those observed in the reactions of these ions with O_3 in the SIFT.[8, 9] In the O_3 reactions, the reactivity of the anion correlated with the bond order of the S atom in the ion, *n*, defined as the sum of the total number of S-F bonds and twice the total number of S-O bonds. Species with an even-numbered *n* such as $SO_2F_2^-$ (*n*=6) and SO_2^- (*n*=4) were reactive and species with an odd-numbered *n* such as SF_5^- and SO_2F^- (*n*=5) were unreactive. While a number of unreactive ions had exothermic reaction pathways with O_3, they were often spin forbidden. This partially explained the observations, e.g. the lack of a reaction for $SO_2F^- + O_3$.[8, 9] Spin did not completely explain the reactivity and it appeared that a kinetic bottleneck also existed. As seen in Table 2, the reactive sulfur oxyfluoride anions have highly exothermic product channels for producing HF. However, as discussed above, the rate constants are <20% of the theoretical limit.[16, 17] The unreactive $SO_xF_y^-$ species had exothermic pathways as well and all of these reaction channels were spin-allowed with H atoms. Therefore, a similar kinetic bottleneck must have contributed to the reactivity trends observed with the H atom reactions as well.

Table 2. Kinetics Results for the Reaction of $SO_xF_y^-$ + H

			Rate Constant, [k_c] ($\times 10^{-9}$ cm^3 s^{-1})	
Reactants	**Products**	ΔH^0_{298K} **kJ mol^{-1}**	**298 K**	**500 K**
$F^- + H \rightarrow$	$HF + e^-$	-242	*1.6 [2.0]*	*1.4 [2.0]*
$SF_5^- + H \rightarrow$	No Reaction		*<0.005 [1.9]*	*<0.005 [1.9]*
$SF_6^- + H \rightarrow$	$SF_5^- + HF$	-431	*0.31 [1.9]*	*0.25 [1.9]*
$SOF_3^- + H \rightarrow$	No Reaction		*<0.005 [1.9]*	*<0.005 [1.9]*
$SOF_4^- + H \rightarrow$	$SOF_3^- + HF$	-470	*0.18 [1.9]*	*0.12 [1.9]*
$SO_2^- + H \rightarrow$	$HSO_2 + e^-$ *cis*-HOSO + e-	38 -62	*0.23 [1.9]*	*0.26 [1.9]*
$SO_2F^- + H \rightarrow$	No Reaction		*<0.005 [1.9]*	*<0.005 [1.9]*
$SO_2F_2^- + H \rightarrow$	$SO_2F^- + HF$	-388	*0.32 [1.9]*	*0.26 [1.9]*

The only ions that underwent associative detachment with were F^- and SO_2^-. Associative detachment of H with SO_2^- produced HSO_2. The different isomers of HSO_2 were observed in both gas phase mass spectrometry experiments[25, 26] and matrix-isolated experiments[27, 28] and were also characterized by extensive theoretical calculations of the HSO_2 doublet potential energy surface.[23-29] Two main isomers were observed, a non-planar HSO_2 with H bound to the S atom and a planar *cis*-HOSO with H bound to the O atom. The *cis*-HOSO isomer is the global minimum on the potential surface and a *trans*-HOSO isomer was shown to be a first-order transition state on the surface. A large barrier exists for isomerization from *cis*-HOSO to HSO_2 and for dissociation from *cis*-HOSO to SO_2 + H. However, it is essentially barrierless to form HSO_2 from H + SO_2. RRKM calculations showed that the rate constant for isomerization from HSO_2 to *cis*-HOSO was much larger than the rate constant for the reverse process.[24, 25] Consequently, HSO_2 would preferentially be formed at

temperatures below ca. 700 K, above which *cis*-HOSO could increasingly be produced.[24, 25] These considerations are important as new preliminary G2 theoretical calculations[30] using Gaussian 03W[21] on the structures of HSO_2^- isomers show that it is 188 kJ mol^{-1} exothermic to form HSO_2^- and 168 kJ mol^{-1} exothermic to form non-planar $HOSO^-$ from SO_2^- + H. The structures of SO_2^-, HSO_2^- and HSO_2 are very similar. At the G2 level of theory, the electron affinity (EA) of HSO_2 is 2.41 eV, which is close to the vertical detachment energy (VDE) of 2.68 eV for forming HSO_2 with the HSO_2^- structure.

Based on our new G2 calculations and the known HSO_2 potential surface, a preliminary mechanism for the SO_2^- + H reaction can be given. The structural similarity of SO_2^-, HSO_2^- and HSO_2 indicate that barriers to forming HSO_2^- with subsequent electron loss should be minimal and that this pathway would require the least amount of structural rearrangement, consistent with the close values of the EA and VDE. However, the reaction to form HSO_2 from SO_2^- + H is 38 kJ mol^{-1} endothermic as shown in Table 2. At 298 K, the thermal energy in HSO_2^- is approximately equal to the endothermicity, making this reaction pathway energetically accessible. This analysis of the energetics is consistent with the observed rate constant being only ~12% of the collision rate constant. While the overall reaction to form *cis*-HOSO is 62 kJ mol^{-1} exothermic, considerably more rearrangement would be necessary to form $HOSO^-$ from SO_2^- + H. This rearrangement would be followed by further rearrangements either before or after electron detachment to form the planar *cis*-HOSO structure. Further calculations are being conducted to search for transition states that could connect the ionic and neutral HSO_2 structures.

c. O atom reactions – Preliminary Results

Oxygen atoms may also react with $PO_xCl_y^-$ ions to generate PO_2^- and PO_3^- directly. To examine this possibility, experiments were begun using the titration of N atoms with NO to produce O atoms for studying these reactions as discussed in the Experimental section. The reaction of $PO_xCl_y^-$ ions with N_2 and NO must be studied first to see if any background reactions must be accounted for in the N and O atom experiments. However, none of the $PO_xCl_y^-$ primary reactant ions shown in Table 1 reacted with either N_2 or NO, nor did PO_2^- and PO_3^- react with N_2 or NO, again giving a limit to the rate constant for these reactions of $<5\times10^{-12}$ cm^3 s^{-1}. In addition, none of the ions just mentioned reacted with N atoms either. The lack of reactivity with N, NO and N_2 meant that any products that would arise during the titration must come from O atom reactions. Initial attempts at reacting O atoms with $PO_xCl_y^-$ ions were hindered by issues surrounding the effect of O atoms on the ion sampling as well as O atom loss processes that need to be minimized.

4. Conclusions

The rate constants and branching ratios for the reactions of $SO_xF_y^-$ and $PO_xCl_y^-$ ions with H atoms were measured in a SIFT from 298-500 K. The rate constants for these reactions were in general about 2×10^{-10} cm^3 s^{-1}, which was <20% of the capture collision rate constant and displayed little or no temperature dependence over the limited range studied. Halogen abstraction from $SO_xF_y^-$ and $PO_xCl_y^-$ producing HF and HCl, respectively, was the primary reaction pathway, resulting in a more energetically stable, less reactive anionic species. Associative detachment of H to produce electrons was only observed with F^-, SO_2^- and PO^-. The structures and thermochemical properties of the relevant molecules were determined using *ab initio* geometry optimization calculations that aided in understanding the experimental results, particularly for the mechanism of the associative detachment reaction of SO_2^- + H. $POCl^-$ product ions reacting with O_2 and O_3 showed that these reactions produce the important PO_2^- and PO_3^- flame ions directly. Preliminary results for the reactions of these anions with O atoms generated via titration of N atoms with NO showed that N_2, NO and N atoms do not react with $PO_xCl_y^-$. However, further work is needed to perfect the experimental method for measuring the O atom reactions themselves.

5. References

[1] J. C. Wormhoudt and C. E. Kolb, *Proceedings of the 10th Materials Research Symposium, Characterization of High-Temperature Vapors and Gases*, U.S. Government Printing Office, 1979, 457-477.
[2] C. Tomlin, *The Pesticide Manual* (British Crop Protection Council, Alton Hampshire, 2003).
[3] J. M. Goodings and C. S. Hassanali, Int. J. Mass Spectrom. Ion Proc., **101**, 337-354 (1990).

[4] G. L. Pellett, NASA Technical Report 1996, 1-16 (1996).
[5] S. Williams, A. J. Midey, S. T. Arnold, T. M. Miller, P. M. Bench, R. A. Dressler, Y.-H. Chiu, D. J. Levandier, A. A. Viggiano, R. A. Morris, M. R. Berman, L. Q. Maurice and C. D. Carter, *AIAA 2001-2873, 4th Weakly Ionized Gases Workshop*, hah, 2001.
[6] I. Sauers and G. Harman, J. Phys. D: Appl. Phys., **25**, 774-782 (1992).
[7] R. J. Van Brunt and J. T. Herron, IEEE Transactions on Electrical Insulation, **25**, 7594 (1990).
[8] S. T. Arnold, T. M. Miller and A. A. Viggiano, J. Phys. Chem. A, **106**, 9900-9909 (2002).
[9] A. A. Viggiano, S. T. Arnold, S. Williams and T. M. Miller, Plasma Chem. and Plasma Proc., **22**, 285-295 (2002).
[10] A. A. Viggiano, R. A. Morris, F. Dale, J. F. Paulson, K. Giles, D. Smith and T. Su, J. Chem. Phys., **93**, 1149-1157 (1990).
[11] T. M. Miller, J. V. Seeley, W. B. Knighton, R. F. Meads, A. A. Viggiano, R. A. Morris, J. M. Van Doren, J. Gu and H. F. Schaefer III, J. Chem. Phys., **109**, 578-584 (1998).
[12] D. H. Williamson, C. A. Mayhew, W. B. Knighton and E. P. Grimsrud, J. Chem. Phys., **113**, 11035-11043 (2000).
[13] R. A. Morris and A. A. Viggiano, J. Chem. Phys., **109**, 4126 (1998).
[14] F. C. Fehsenfeld and E. E. Ferguson, J. Chem. Phys., **56**, 3066 (1972).
[15] A. J. Midey, T. M. Miller, R. A. Morris and A. A. Viggiano, J. Phys. Chem. A, In Press (2005).
[16] T. Su and W. J. Chesnavich, J. Chem. Phys., **76**, 5183-5185 (1982).
[17] T. Su, J. Chem. Phys., **89**, 5355 (1988).
[18] A. I. Fernandez, A. J. Midey, T. M. Miller and A. A. Viggiano, J. Phys. Chem. A, **108**, 9120-9125 (2004).
[19] L. A. Curtiss, P. C. Redfern, K. Raghavachari and J. A. Pople, J. Chem. Phys., **109**, 42 (1998).
[20] L. A. Curtiss, P. C. Redfern, K. Raghavachari, V. Rassolov and J. A. Pople, J. Chem. Phys, **109**, 7764-7776 (1998).
[21] M. J. Frisch, *et al.*, *Gaussian 03, Revision B.02* (Gaussian, Inc., Pittsburgh PA, 2003, 2003).
[22] P. J. Linstrom and W. G. Mallard, *NIST Chemistry WebBook, NIST Standard Reference Database No. 69* (National Institutes of Standards and Technology, Gaithersburg, MD, 2003).
[23] D. Laakso, C. E. Smith, A. Goumri, J. D. R. Rocha and P. Marshall, Chem. Phys. Lett., **227**, 377-383 (1994).
[24] A. Goumri, J. D. R. Rocha, D. Laakso, C. E. Smith and P. Marshall, J. Phys. Chem. A, **103**, 11328-11335 (1999).
[25] A. J. Frank, M. Sadilek, J. G. Ferrier and F. Turecek, J. Am. Chem. Soc., **118**, 11321-11322 (1996).
[26] A. J. Frank, M. Sadilek, J. G. Ferrier and F. Turecek, J. Am. Chem. Soc., **119**, 12343-12353 (1997).
[27] E. Isoniemi, L. Khriachtchev, J. Lundell and M. Rasanen, J. Mol. Struct., **563-564**, 261-265 (2001).
[28] E. Isoniemi, L. Khriachtchev, J. Lundell and M. Rasanen, Phys. Chem. Chem. Phys., **4**, 1549-1554 (2002).
[29] J. X. Qi, W. Q. Deng, K. L. Han and G. Z. He, J. Chem. Soc., Faraday Trans., **93**, 25-28 (1997).
[30] L. A. Curtiss, K. Raghavachari, G. W. Trucks and J. A. Pople, J. Chem. Phys., **94**, 7221 (1991).

Behaviors of Fluorocarbon Radicals in 60 MHz Capacitively Coupled Plasma

M. Nagai, M. Hori, and T. Goto,

[1] *Department of Quantum Engineering, Graduate School of Engineering, Nagoya University, Japan*

Abstract

Optical emission spectroscopy and infrared diode laser absorption spectroscopy were applied to measure rotational temperatures of CF radical in 60 MHz capacitively coupled $Ar/C_4F_8/N_2$ plasmas. The rotational constant Y of $^2\Delta$state of CF radical was evaluated to be 0.58 from the emission intensities using the line strength of Kovacs. The addition of N_2 gas to the Ar/C_4F_8 gases increased CF rotational temperatures. It was found that the rotational temperatures in the excited state were equilibrium with those in the ground state.

I. Introduction

Fluorocarbon gas chemistry is essential in a lot of fields of plasma processing, that is an etching of silicon dioxide (SiO_2) films, decomposition of polymers, and chamber wall cleaning. Generally, the SiO_2 etching is performed with Ar, C_4F_8, and O_2 gas mixtures for the purpose of realizing the vertical etch profile without eching stop. The etchings have been developed in high-density capacitively coupled plasma (CCP) in order to get the etching rate uniformly over 300 mm wafer. Recently, low dielectric (low-k) films such as organosilicate, SiOCH, and SiLK^{TM} are used for the solution of the resistance-capacitance (RC) delay in ULSI. The low-k films etching have been developed with N_2 addition to Ar/C_4F_8 plasma [1]. One of the most serious problems of low-k films etching is a line edge roughness of resists [2], which is considered to be closely related with the behaviour of the radical in $Ar/C_4F_8/N_2$ plasmas.

Plasma parameters such as the density of ion, radical, and electron are strongly influenced on the etch properties. Behaviours of radical have not investigated enough in $Ar/C_4F_8/N_2$ plasmas. Diagnostics of the fluorocarbon plasma is necessary to clarify the correlations between material processings and fluorocarbon gas chemistries.

Recently, several techniques have been employed to measure fluorocarbon plasma. For example, fuorocarbon radicals with plasma have been detected by infrared diode laser absorption spectroscopy (IRLAS) [3], and broadband absorption spectroscopy (BAS) [4,5] and so on. Some of these methods were applied to measure the radical temperatures. Optical emission spectroscopy (OES) is a powerful tool to measure the radical temperatures because it does not require complicated system such as a laser.

The rotational temperatures of CF radical were measured from the optical emissions by other studies [6-8]. In this study, the line strengths expressed by Kovacs were adapted to the calculation of the emission spectra $B^2\Delta$ - $X^2\Pi$ (0-1) and (1-2) band [9]. The line strengths could be used for the coupling of the intermediate case of both the excited state and the ground state. The rotational constant Y of CF $B^2\Delta$ state was evaluated to be 0.58 from the emission intensities in this work. The measurement was performed in $Ar/N_2/C_4F_8$ plasma. Furthermore, it was found that the rotational temperature in the excited state using OES was equilibrium with the temperature in the ground state.

II. Experiment

A. Experimental setup

60 MHz capacitively coupled plasma (CCP) was employed in this study. The power of 60 MHz was applied to the upper electrode. Ar, N_2, and C_4F_8 gases were introduced through the shower head on the upper electrode. The electrode was 30 cm in diameter. The gap distance between upper electrode and lower electrode was 3.5 cm. The electrode was cooled and kept at a temperature of 20 ℃.

Optical emission spectroscopy (OES) measurements were performed using an intensified charge-coupled device (ICCD) spectrometer (model PI-MAX1300RB-25-FG, focal length 750 mm, grating 1200 lines/mm, Rober) for measuring a rotational temperature in the excited state of CF radical and N_2 molecular. Generally, the rotational temperature in the excited state was known to equilibrate with the rotational temperature in the ground state. However, the temperature in both the excited state and ground state has never been measured simultaneously. In this study, the relation of the excited state with the ground state was investigated on the basis of measurement of radicals.

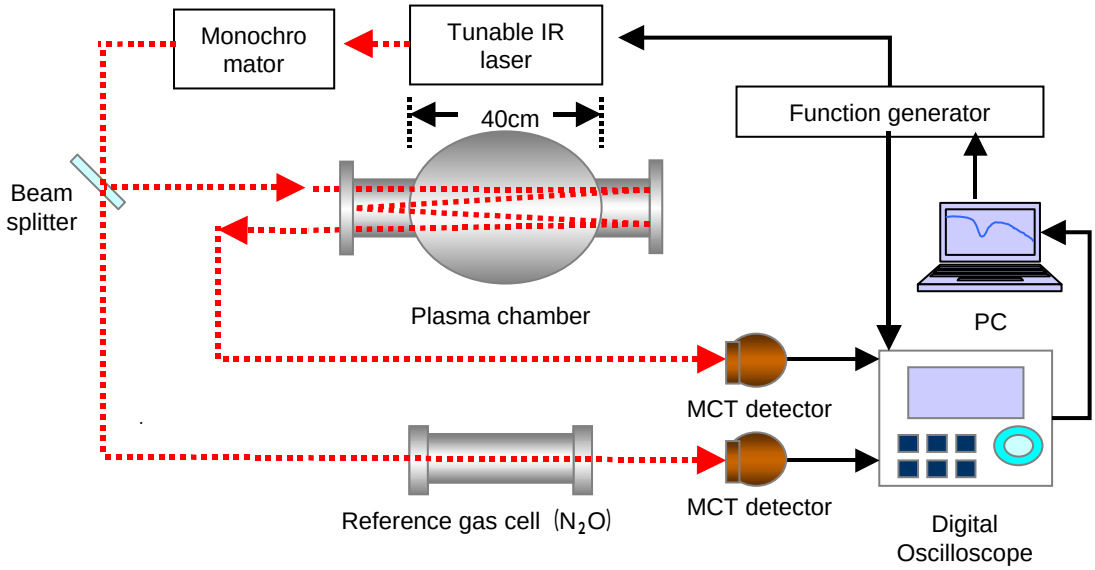

Fig. 1. Shematic diagram of IRLAS measurement in this study.

Infrared laser diode absorption spectroscopy (IRLAS) was performed for measuring the rotational temperature and density of CF radical in the ground state. Figure 1 shows shematic diagram of IRLAS measurement in this study. The infrared diode laser was introduced through NaCl windows into the White-type multiple reflection cell. The laser passed 32 times for the measurement of CF radical through the plasma. Absorption signals were detected by a mercury-cadmium-telluride (MCT) detector and collected by digital oscilloscope. Function generator was used for the tunable laser. The tunable laser and absorption signal were controlled by personal computer (PC) in order to get a high S/N with the accumulation, average, and filtering of the noise. N_2O gas was used for the reference of wavelengths.

B. Method of calculating the rotational temperature in emission

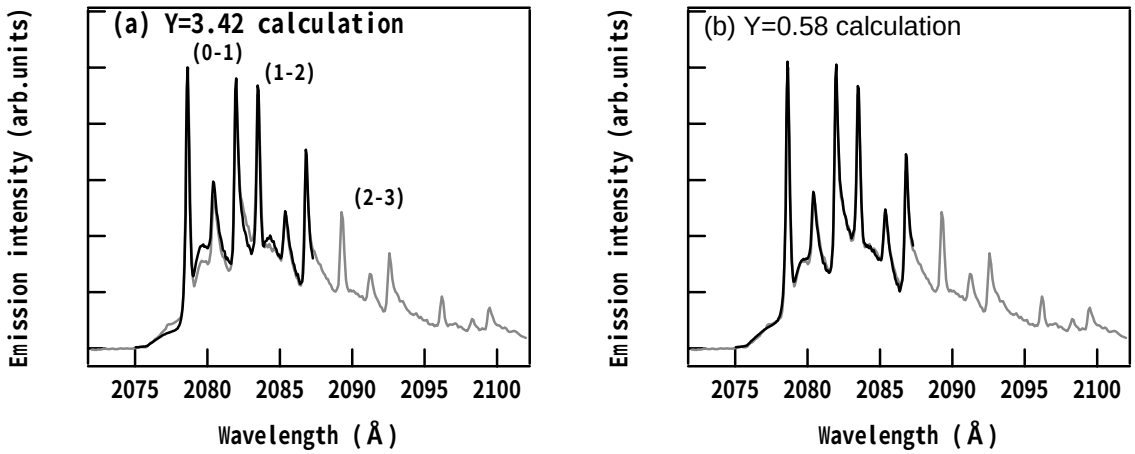

Fig. 2. The measured spectral (gray line) and calculated spectra (black line) of CF $B^2\Delta - X^2\Pi$ electric transition at a reported different coupling constant of (a) Y = 3.42 and (b) 0.58.

The rotational temperatures of CF radical were determined by simulating optical emission spectra of $B^2\Delta$ - $X^2\Pi$ electronic transition. The procedure was as following. (1) Calculation of the energy levels for the $B^2\Delta$ state and the $X^2\Pi$ [10]. (2) Calculation of the transition wavelengths for each branch using the selection rules. (3) Calculation of the line strengths for each transition wavelengths. (4) Simulation of the spectrum line shape and the population distribution as functions of the spectrum width and the rotational temperature [11].

In this study, the line strengths expressed by Kovacs were adapted to the calculation of the emission spectra of CF $B^2\Delta$ - $X^2\Pi$ (0-1) and (1-2) band. The line strengths were used for the coupling of the intermediate case of both the excited state and the ground state. Though the line strength was a function of the rotational constant Y, the rotational constant of CF $B^2\Delta$ state was not determined. The two coupling constants Y of $B^2\Delta$ state of (0-1) band were reported as 3.42 or 0.58 by Carroll and Grennan observing the spin splitting in high resolution emission spectra [12]. In this study, the rotational constant Y of $B^2\Delta$ state was investigated from the emission intensities. The simulation fitted with measured spectra of (0-1) and (1-2) band was executed between 2075 Å and 2087 Å. Figure 2 shows the measured spectra and calculated spectra in Ar/C_4F_8 plasma of CF $B^2\Delta - X^2\Pi$ (0-1) and (1-2) electric transition at a different coupling constant (a) Y=3.42 or (b) Y=0.58. The constant value Y of $B^2\Delta$ state of the (1-2) band was estimated as the same value with the (0-1) band. In the case of Y=3.42 calculation, the rotational temperature was evaluated to be 270 K for the (0-1) band and 230 K for the (1-2) band. In the case of Y=0.58 calculation, the rotational temperature was evaluated to be 290 K for both the (0-1) band and the (1-2) band. The calculated spectra of Y=0.58 was a good fit with the measured spectra as compared with the calculated spectra of Y=3.42. Therefore, the value of the coupling constant Y was 0.58 from emission intensities.

The calculating of CF emission spectra was applied to (0-0) band around 2027 Å as well as (0-1) band. It was found that the coupling constant Y of 0.58 was adapted to (0-0) band.

The rotational temperatures of N_2 were evaluated by simulating the optical emission spectra of $C^3\Pi_u$ - $B^3\Pi_g$ electronic transition. The rotational temperature was used well for neutral gas temperature in plasma [11,13,14]. The rotational constant used was found as a reference [15]. In this event, Honl-London factors were used as the intensity distribution, and Hund's case (a) was assumed.

C. Theory of infrared diode laser absorption spectroscopy (IRLAS)

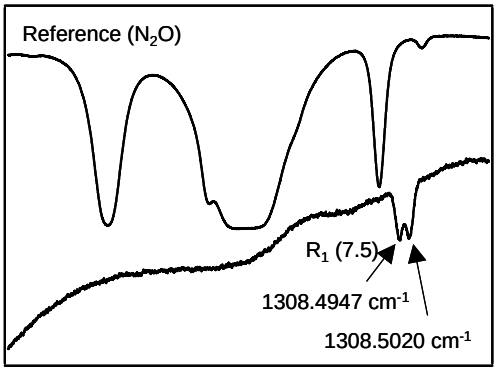

Fig. 3. The absorption spectral of the CF radical and N_2O molecule.

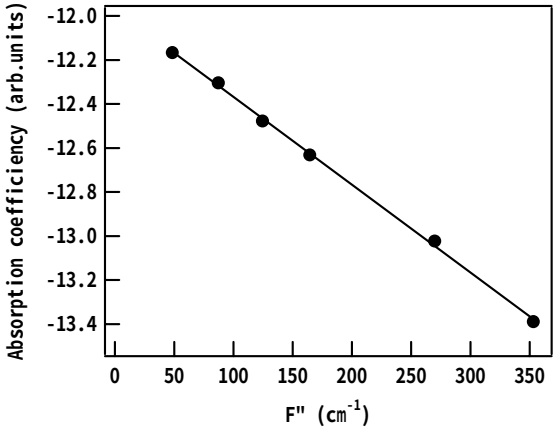

Fig. 4. Boltzmann diagram of CF radical in $X^2\Pi$ state in $Ar/C_4F_8/N_2$ plasma. The slope gives $-hc/k_BTr$ = -0.00399, which corresponds to Tr=360 K.

The rotational temperature and density of CF radical in the ground state were measured by Infrared laser absorption spectroscopy (IRLAS). Detailed observation of vibration-rotation bands of CF radical in the $X^2\Pi$ state have been carried out by Kawaguchi *et al* [16]. Figure 3 shows the absorption spectral of the CF radical of $R_1(7.5)$. The integrated absorption coefficient is related to the radical density n and the line strength S for the measured transition by

$$\int_{-\infty}^{\infty} k(v)dv = S \cdot n \tag{1}$$

The Honl-London factor for the line strength was given by other study [17]. The formula of the line strengths [18] is rewritten approximately as

$$\int_{-\infty}^{\infty} k(v)dv = Cv_c Ag'' exp\left(-\frac{F'' hc}{k_B T_r}\right) \tag{2}$$

where C is constant, v_c is the wavenumber at the center of the absorption line profile, A is the Honl-London factor, g'' is the statistical weight for the lower state of transitions, F'' is the rotational term value for the lower state of transitions, h is Planck constant, c is the light velocity, k_B is Boltzmann constant, and T_r is the rotational temperature. Eq. (2) is transformed into

$$ln\left[\frac{1}{v_c A g''}\int_{-\infty}^{\infty} k(v)dv\right] = -\frac{hc}{k_B T_r}F'' + C' \quad (3)$$

If the distribution of radical density over the rotational levels follows the Boltzmann distribution, a plot of the left-hand side of Eq. (3) against the rotational term value F'' for several transitions becomes a straight line and T_r can be derived from the slope of the plot.

The transition lines of $R_1(5.5)$, $R_2(5.5)$, $R_1(7.5)$, $R_2(7.5)$, $R_1(13.5)$, and $R_2(13.5)$ were measured in the condition at a pressure of 10 Pa, a gas flow rate of $Ar/N_2/C_4F_8$ = 900/100/6 sccm, a 60 MHz power of 1200 W. Figure 4 shows Boltzmann diagram of CF radical in $C^2\Pi$ state. The slope gives $-hc/k_BT_r$ = -0.00399, which corresponds to T_r=360 K.

The CF radical density was measured using the value of the band strength of 1.0 X 10^{-17} cm/molecule.

3. Results and Discussions

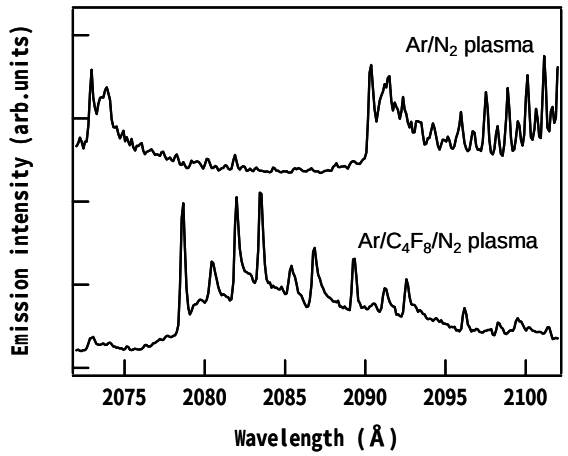

Fig. 5. Emission spectra of Ar/N_2 plasma and $Ar/N_2/C_4F_8$ plasma. N_2 spectra was not covered with CF (0–1) and (1-2) band spectra for calculating the CF rotational temperature.

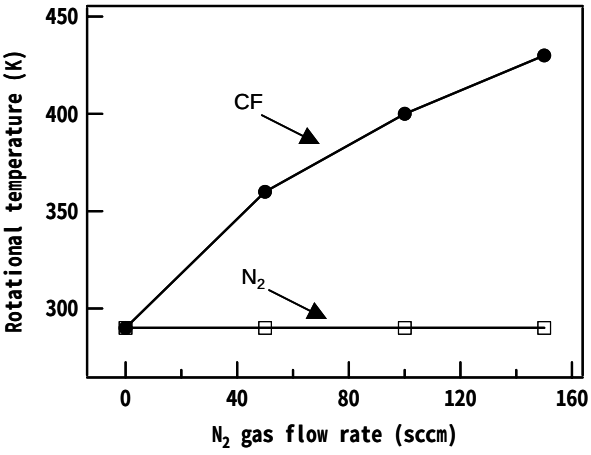

Fig. 6. Rotational temperatures of CF radical and N_2 molecular as a function of N_2 gas flow rate.

Fluorocarbon radical temperatures in $Ar/C_4F_8/N_2$ plasma were investigated using OES and IRLAS measurement. Figure 5 the emission spectra of Ar/N_2 plasma and $Ar/N_2/C_4F_8$ plasma in the condition at a pressure of 10 Pa, a gas flow rate of $Ar/N_2/C_4F_8$ = 900/100/6 sccm, a 60 MHz power of 1200 W. As compared with the emission spectra of Ar/C_4F_8 plasma in Fig. 3, the spectra due to the N_2 plasma were covered with the emission spectra of CF $B^2\Delta - X^2\Pi$. Though some peaks were reported around the (0-1) and (1-2) band of CF $B^2\Delta - X^2\Pi$ [19,20], the peaks seemed to be weak peaks in this plasma. Therefore, it was possible to calculate the emission spectra of the (0-1) and (1-2) band of CF $B^2\Delta - X^2\Pi$. The rotational temperature of CF radical was 360 K for the both the (0-1) and (1-2) band. The temperature was equilibrium with the temperature in Fig. 4. It was found that the rotational temperatures in the excited state were equilibrium with the rotational temperatures in the ground state.

Figure 6 shows the CF rotational temperature and N_2 rotational temperature as a function of N_2 gas flow rate in the condition of a in the condition at a pressure of 10 Pa, a gas flow rate of $Ar/N_2/C_4F_8$ = 1000-x/x/6 sccm, a 60 MHz power of 1200 W. The N_2 rotational temperature was used for the neutral gas temperature in plasma. The gas temperature was constant at 290 K, and the CF rotational temperature was increased from 290 K to 430 K with increasing N_2 flow rate. It was found that the CF rotational temperature was not equilibrium with the gas temperature. Radicals are mainly produced with collisions between molecular and energetic electron, and as a result the radicals are heated by Franck-Condon heating [21]. The radicals were dissociated with the energy of the difference between the excited energy and the electron

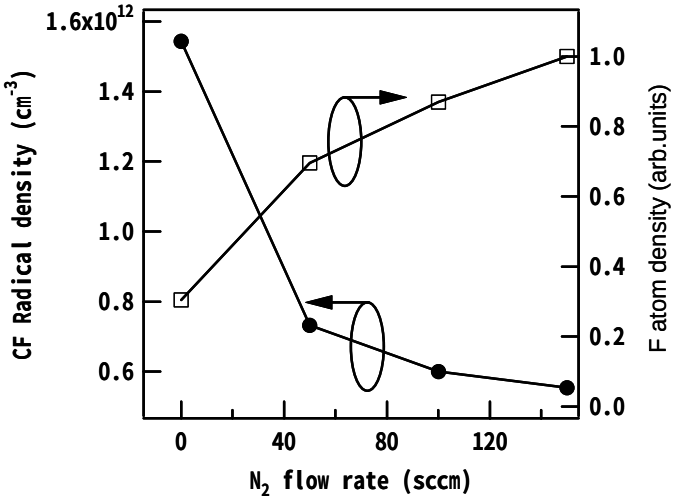

Fig. 7. CF radical and F atom densities as a function of N_2 gas flow rate.

dissociation energy of the neutral molecule. Therefore, it is considered that radical temperatures are related to electron energy distributions. The addition of N_2 was known to influence the electron energy distribution function (EEDF) in Ar plasma due to the vibrational rotational structure of the molecules [22,23]. N_2 leads to increase the electron temperature in the high energy region. One of the mechanisms of the incresion of the CF rotational temperature was the incresion of Franck-Condon effect due to the incresion of the electron temperature with N_2 addition.

It was considered that the difference between CF redical temperature and gas temperature was due to the excess energy of CF radicals from Franck-Condon heating.

The CF radical and gas temperatures in this 60 MHz capacitively coupled plasma (CCP) was much less than the temperatures in inductively coupled plasma (ICP) [6,7]. The cooling mechanism of species is due to losing the kinetic energy by the elastic collision with parent molecule gases, and the heat transfer by the diffusion to the cold wall. The cooling efficiency is dependent on the electrode temperature, the kinds of electrode materials, and the structure of chamber walls. In this 60MHz CCP, plasma was generated between the top electrode and the bottom electrode. The energetic species seemed to be cooled due to the abundant collisions with the electrodes with the mean free pass about 1 cm at a pressure of 10 Pa. It was considered that the difference of CF rotational temperature between CCP and ICP derived from the cooling efficiency and EEDF.

Figure 7 shows CF radical and F atom densities as a function of N_2 gas flow rate. CF radical density was decreased from 1.5 X 10^{12} cm^{-3} to 0.6 X 10^{12} cm^{-3}, and F atom density was increased with increasing N_2 gas flow rate. The decrease of the CF radical density was due to the recombination with CF radical and N atom. The generation of CNF molecule in plasma was reported [24]. The recombination and the excess dissociation due to the high electron temperature with N_2 addition were one of the mechanisms of increasing F atom density in $Ar/N_2/C_4F_8$ plasma.

4. Conclusions

Optical emission spectroscopy and infrared diode laser absorption spectroscopy were applied to measure CF rotational temperatures in both the excited state and the ground state at 60 MHz capacitively coupled $Ar/C_4F_8/N_2$ plasma. The CF rotational temperature was determined in the optical emission spectra by fitting the calculated spectra with the measured spectra. The rotational constant Y of $^2\Delta$state, which was estimated to be 0.58 or 3.42 by Carroll, was determined to be 0.58 from the emission intensities using the line strength of Kovacs. It was found that the rotational temperatures in the excited state were equilibrium with those in the ground state. The CF rotational temperatures in $Ar/C_4F_8/N_2$ plasma were increased from 290 K to 430 K with increasing N_2 flow rate.

References

[1] X. Hua, X. Wang, D. Fuentevilla, G. S. Oehrlein, F. G. Celii, and K. H. R. Kirmse, J. Vac. Sci. Technol. A **21**, 1708 (2003).

[2] D. L. Goldfarb, A. P. Mahorowala, G. M. Gallatin, K. E. Petrillo, K. Temple, M. Angelopoulos, S. Rasgon, H. H. Sawin, S. D. Allen, M. C. Lawson, and R. W. Kwong, J. Vac. Sci. Technol. B **22**, 647 (2004).

[3] K. Miyata, M. Hori, and T. Goto, J. Vac. Sci. Technol. A **15**, 568 (1997).

[4] B. A. Cruden, K. K. Gleason, and H. H. Sawin, J. Appl. Phys. **89**, 915 (2001).

[5] J. Luque, E. A. Hudson, and J. P. Booth, J. Chem. Phys. **118**, 622 (2003).

[6] B. A. Cruden, M. V. V. S. Rao, S. P. Sharma, and M. Meyyappan, J. Appl. Phys. **91**, 8955 (2002).

[7] B. A. Cruden, M. V. V. S. Rao, Surendra P. Sharma, and M. Meyyappan, Appl. Phys. Lett. **81**, 990 (2002).

[8] J. Luque, and E. A. Hudson, and J. P. Booth, J. Appl. Phys. **118**, 622 (2003).

[9] I. Kovacs, Rotational Structure in the Spectra of Diatomic Molecules, edited by Adam Hilger, London, 115 (1969).

[10] E. Hill and J. H. Vleck, Phys. Rev. **32**, 250 (1928).

[11] D. M. Phillips, J. Phys. D: Appl. Phys. **8**, 507 (1975).

[12] P. K. Carrroll and P. K. Grennan, J. Phys. B **3**, 865 (1970).

[13] J. Lefebvre and A. Ricard, Rev. Phys. Appl. T **10**, 137 (1975).

[14] V. M. Donnelly and M. V. Malyshev, Appl. Physics. Lett. **77**, 2467 (2000).

[15] A. Budo, Z. Phys. **98**, 437 (1936).

[16] K. Kawaguchi, C. Yamada, Y. Hamada, and E. Hirota, J. Mol. Spectrosc. **86**, 136 (1981).

[17] R. J. M. Bennett, Mon. Not. Astr. Soc. **147**, 35 (1970).

[18] J. J. Orlando, J. Reid, and D. R. Smith, Chem. Phys. Lett. **141**, 423 (1987) and **147**, 300 (1987).

[19] Y. Tanaka, T. Namioka, and A. S. Jursa, Canad. J. Phys. **39**, 1138 (1961).

[20] B. A. Lofthus, Canad. J. Phys. **34**, 780 (1956).

[21] R. A. Alberty, and R. J. Silbey, Physical Chemistry, 1st ed. (Wiley, New York, 1992).

[22] B. C. Bell and D. A. Glocker, J. Vac. Sci. Technol. A **6**, 2047 (1987).

[23] N. A. Gorbunov and A. S. Mel'nikov, Tech. Phys. **44**, 361 (1999).

[24] K. Miyata, H. Arai, M. Hori, and T. Goto, J. Appl. Phys. **82**, 4777 (1997).

Study of the Low-Pressure RF Hollow Cathode Plasma Jet During Deposition of $Ba_xSr_{1-x}TiO_3$ Thin Films

P. Virostko[1,2], Z. Hubička[1*], J. Olejníček[1], M. Čada[1], P. Adámek[3], M. Šícha[1,2], M. Tichý[1,2], M. Chichina[1,2]

[1] *Institute of Physics, Academy of Sciences of the Czech Republic, Na Slovance 2, 182 21 Praha 8, Czech Republic*
[2] *Charles University in Prague, Faculty of Mathematics and Physics, Ke Karlovu 5, 121 16 Praha 2, Czech Republic*
[3] *Department of Physics, University of South Bohemia, Jeronýmova 10, 371 15 České Budějovice, Czech Republic*

Abstract

Pulse modulated RF plasma jet system was used for deposition of $Ba_xSr_{1-x}TiO_3$ (BSTO) and $SrTiO_3$ (STO) thin films on Si and on multi-layer $Si/SiO_2/TiO_2/Pt$ substrates. Time resolved Langmuir probe measurements were done for determination of plasma parameters at substrate position. Plasma emission spectroscopy was used for control of concentration of particles sputtered from the hollow cathode. Deposited thin films were analyzed by X-ray diffraction, which confirmed presence of BSTO and STO perovskite phase in the films.

Keywords: hollow cathode sputtering, Langmuir probe, emission spectroscopy, ferroelectric thin films.

1. Introduction

The low-pressure RF plasma jet sputtering system was already used for many PVD thin films depositions as for example TiN [1], TiO_2 [2], Cu_3N [3], CN_x [4], ZnO [5], and $LiCoO_x$ [6] thin films. Usually a metallic or single component hollow cathode was reactively sputtered in a suitable working gas in these applications. In the work presented in this paper, the RF hollow cathode was made of $SrTiO_3$ (STO) and $BaTiO_3$ (BTO) composed nozzle and reactively sputtered in Ar and O_2 gas mixture, in order to form $SrTiO_3$, or $Ba_xSr_{1-x}TiO_3$ films on Si and multi-layer $Si/SiO_2/TiO_2/Pt$ substrates.

BSTO thin films have wide range of application. They have, for example, potential use for capacitors due to their high dielectric constant. BSTO material is also very promising for microwave components as for example microwave varactors, phase shifters, or tunable filters. Many methods were used up to now for BSTO films deposition as presented for example in [7], [8], [9], [10], [11], [12], [13], and other works. BSTO thin films are usually prepared by CVD, MOCVD [10], sol-gel, or magnetron sputtering [7], [8]. Usual methods use elevated substrate temperatures above 600–900 °C or thermal post-deposition treatment for proper crystallization and oxidation of BSTO films. This paper describes preliminary results of deposition of BSTO and STO thin films by pulsed RF hollow cathode plasma jet sputtering system without post-deposition annealing and with substrate temperature below 600 °C during deposition.

For better control and reproducibility of the deposition process, plasma parameters at the substrate position should be measured. Langmuir probe measurements are suitable for determination of plasma parameters, which have influence on deposited thin films, as for example plasma potential, electron density, electron distribution function, or electron temperature. Time resolved Langmuir probe measurements are required in pulsed discharges in order to know these parameters in active part of the duty cycle (the pulse) and also their change in the non-active part of the duty cycle (between pulses). Further, plasma emission spectroscopy could be used for determination of concentration of sputtered particles from the hollow cathode.

Properties of the deposited thin films should also be studied and compared with plasma parameters measured at deposition conditions. Chemical composition of deposited thin films was investigated by electron microprobe and compared with plasma emission spectra in this work. Crystalline structure of the films was studied by X-ray diffraction (XRD) in grazing incidence geometry to find out if the desired perovskite phase of BSTO was deposited.

*Corresponding author. Tel.: +420-2660-52995; fax: +420-2865-81448. E-mail address: hubicka@fzu.cz

2. Experimental

The low-pressure plasma jet configuration for BSTO thin films deposition can be seen in Fig. 1. The reactor chamber was continuously pumped by combination of Roots and rotary vane pumps. The composed cylindrical nozzle acted as RF hollow cathode, which was reactively sputtered. The internal diameter of the nozzle was 3 mm. The length of the nozzle was 30 mm. In order to deposit $SrTiO_3$ thin films the nozzle was homogeneous; made of pure $SrTiO_3$ ceramic. In order to deposit $Ba_xSr_{1-x}TiO_3$ thin films one part of the nozzle was made of $SrTiO_3$ and one part from $BaTiO_3$, as it can be seen in Fig 1. Since it was known that STO ceramics has lower sputtering rate than BTO ceramics, the STO part was placed at the nozzle outlet, where the hollow cathode plasma has the highest density. The STO part was also made longer than the BTO part. The length of the STO part was 25 mm and the length of the BTO part was 5 mm. An intensive RF hollow cathode discharge [4] was generated inside the nozzle, on the background of the primary capacitive RF discharge excited in the volume of the reactor. Incoming working gas forced this RF hollow cathode discharge out of the nozzle into the reactor chamber and this plasma jet interacted with the substrate. The substrate was placed perpendicularly to the plasma jet axis in the distance of 20 mm from the hollow cathode outlet. The thin films were deposited simultaneously on Si wafers and on the Pt top layer of multi-layer $Si/SiO_2/TiO_2/Pt$ substrate. Five samples prepared at different deposition conditions are presented in the paper (see Table 1).

Pulse modulated mode was used for plasma jet excitation for all STO and BSTO samples. The length of the active part of the duty cycle was T_w = 1.4 ms. The length of the non-active part was T_0 = 4 ms. Power P_{RF} = 150–300 W was applied on the hollow nozzle electrode during the active part, and P_{RF} = 0 W appeared on the electrode during the non-active part of the duty cycle. The advantage of pulse-modulated mode was enhancement of plasma density and hence the sputtering process by virtually higher applied RF power during the active part. On the other hand, the average applied RF power was low enough to avoid hollow cathode overheating and destruction of ceramic nozzle.

A fraction of pulse-modulated RF power was fed through a tunable capacitance on the substrate (see Fig. 1) in order to generate a controllable pulsed DC bias around the substrate. Current and voltage probes with calibrated RF amplitude response and phase shift up to 100 MHz in combination with digital oscillograph Agilent Infinium 600 MHz 4 GS were capable to measure RF power, RF current and RF voltage on the nozzle, and DC self-bias on the substrate.

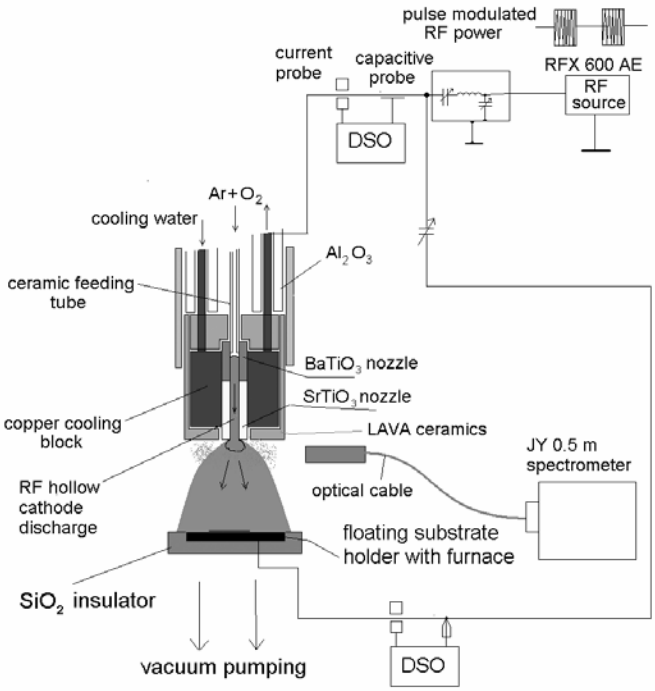

Figure 1. Experimental set up for the plasma jet deposition of STO and BSTO thin films.

Table 1. Deposition conditions for different deposited thin films. Q_{Ar} and Q_{O2} are Ar and O_2 flow rates through the nozzle. P_{RF} is RF power absorbed in the plasma. I_{RF} and U_{RF} are amplitudes of RF current and RF voltage on the nozzle.

Sample no.	Q_{Ar} [sccm]	Q_{O2} [sccm]	P_{RF} [W]	Used nozzle	I_{RFm} [A]	U_{RFm} [V]
1	85	64	178	STO	3.6	259
2	85	64	219	STO, BTO	4.11	232
3	42	32	—	STO, BTO	—	—
4	42	13	180	STO, BTO	4.0	217
5	42	64	—	STO, BTO	—	—

The DC self-bias on the substrate was set to $U_{DC} = -50$ V relative to the grounded reactor. The substrate was held on temperature 500–550 °C. Total gas pressure in the reactor was held at $p = 6$ Pa. These conditions were identical for all presented samples. Deposition conditions, which were different for the five presented samples are in Table 1. Power P_{RF} absorbed in the plasma was calculated from RF current and voltage waveforms taking into account their relative phase shift. RF power P_{RF}, amplitude of RF current I_{RFm}, and amplitude of RF voltage U_{RFm} on the nozzle electrode presented in Table 1 were recorded approximately at the time corresponding to the middle of the active part of the discharge cycle.

Time resolved Langmuir probe was used for determination of plasma parameters during the whole cycle. Probe characteristic at the time t within the cycle was obtained by averaging measurements taken at time t from the start of the pulse in several consequent duty cycles. The Langmuir probe measurements were done at the deposition conditions, but with the substrate holder not present in the reactor. Platinum cylindrical Langmuir probe with diameter $d_p = 200$ μm and length $l_p = 2$ mm was used. The probe was placed at the substrate position. High impedance filters and a metallic hollow cylindrical compensation electrode, connected with the probe through a capacitor, were used as a passive compensation of RF oscillations of probe current. The grounded metallic reactor worked as a voltage reference for the Langmuir probe. The probe surface was cleaned from deposited films by applying high negative voltage on the probe between probe characteristic measurements. This high negative voltage on the probe caused ion bombardment and sputtering of material deposited on the probe surface. Plasma emission spectroscopy was used for control of sputtered particles contained in the plasma jet channel during deposition. For this purpose, Jobin Yvon spectrometer with CCD detector and optical cable were used. Experimental set up can be seen in Fig 1.

Chemical composition of deposited films was measured by electron microprobe JXA 733 of JEOL. Energy of primary electrons in the beam was set to 10 keV. Electron microprobe method provides information about average composition over the whole profile of the analyzed films. Accuracy of this method for thin film atomic concentration analysis is not better than 5%. Therefore, electron microprobe measurements were always done on several points on the surface of the film. The analysis of films structure was performed by XRD in grazing incidence geometry using CuK_α radiation.

3. Results and discussion

Plasma parameters were measured in the position of the substrate by Langmuir probe. Electron energy probability functions (EEPFs) determined from the Langmuir probe measurements for different times can be seen in Fig. 2. The EEPFs were calculated from the second derivative of the electron probe current, according to the Druyvesteyn formula:

$$F(E) = \frac{2\sqrt{2em_e}}{e^3 A_p}\left|\frac{d^2 I_e}{dU_p^2}\right|, \qquad (1)$$

where $E = -eU_p$ is the kinetic electron energy, e is the elementary charge, m_e is the electron mass, A_p is the probe area, I_e is the electron probe current and U_p is the probe voltage relative to the plasma potential. Plasma potential was determined as zero crossing of the second derivative of the probe current. Plasma potential was approximately $V_{pl} = 45$ V in the active part and approximately $V_{pl} = 2$ V in the non-active part of the duty cycle. The EEPF is normalized on the electron density n_e according to the equation

$$n_e = \int_0^\infty F(E)\sqrt{E}\,dE\,. \qquad (2)$$

The EEPFs are depicted in semi-logarithmic scale in Fig. 2, because in this scale an ideal Maxwellian EEPF is linear. It can be seen that in both active and non-active part of the discharge cycle the electron distribution was not Maxwellian. In the active part of the on-off cycle, the EEPFs differed just slightly from Maxwellian; they were a bit rounded. On the other hand, in the non-active part of the discharge on-off cycle, the EEPFs were strongly non-Maxwellian. There was some excess of electrons with the energy around 3 eV in the latter case. The process behind forming of this electron group is not quite clear to us now and would be subject of further investigation.

The time dependence of electron density n_e determined from Langmuir probe measurements is depicted in Fig. 3. Electron density was calculated from the EEPF according to equation (2). This method of electron density evaluation is not very precise because of some disturbance of the second derivative of electron probe current near the plasma potential. However, this error in determination of the second derivative in equation (1) is partly compensated by multiplication by the factor $\sqrt{E}$ in equation (2), because this factor is low near the plasma potential, which corresponds to $E = 0$ eV. The big advantage of this method of electron density evaluation is that it does not require Maxwellian electron energy distribution. Therefore it is suitable for our case. For verification of results obtained by this method, the electron density in the active part of the discharge on-off cycle was also calculated from the electron current in plasma potential I_{e0}, according to the equation

$$n_e = \frac{4I_{e0}}{A_p e v_e}, \qquad (3)$$

where v_e is the mean electron velocity. The mean electron velocity was calculated for Maxwellian distribution. Effective electron temperature was determined from the slope of linear Maxwellian approximation of the second derivative of electron probe current in the semi-logarithmic scale. The effective electron temperature was approximately 4 eV in the active part of the discharge on-off cycle. Electron density in the substrate position during the active part of the cycle determined by both methods was quite similar (see Fig. 3) and its value was relatively high $n_e \approx 2.5\times10^{10}$ m^{-3}. In the non-active part of the duty cycle only first method was used, because electrons had strongly non-Maxwellian distribution there. The electron density decayed approximately exponentially after the end of active pulse (linear decay in semi-logarithmic scale – see Fig. 3).

It was possible to deposit $SrTiO_3$ and $Ba_xSr_{1-x}TiO_3$ thin films on Si and Pt surfaces. Maximum growth rate achieved was 250-300 nm/hour. Electron microprobe measurements showed that chemical composition was close to $SrTiO_3$ for sample no.1 and to $Ba_xSr_{1-x}TiO_3$ for samples no. 2-5 (see Table 2), with some excess of Ti and O atomic concentrations in both cases.

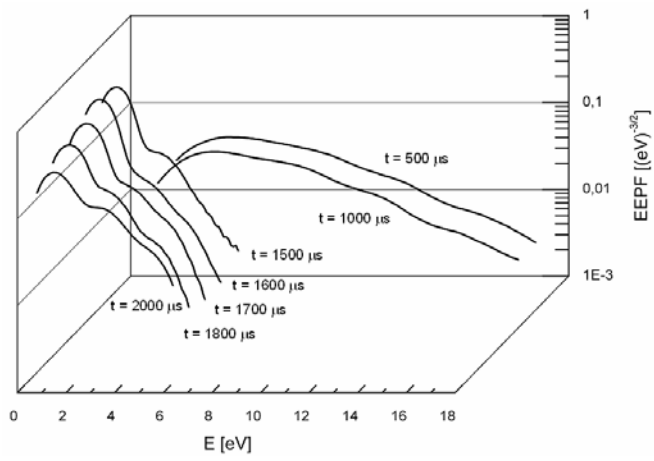

Figure 2. Electron energy probability function (EEPF) in the active part (in t = 500 μs, t = 1000 μs), and in the non-active part of the duty cycle (in t = 1500 μs, t = 1600 μs, t = 1700 μs, t = 1800 μs, t = 2000 μs). The active pulse starts at t = 0 s and ends at t = 1400 μs.

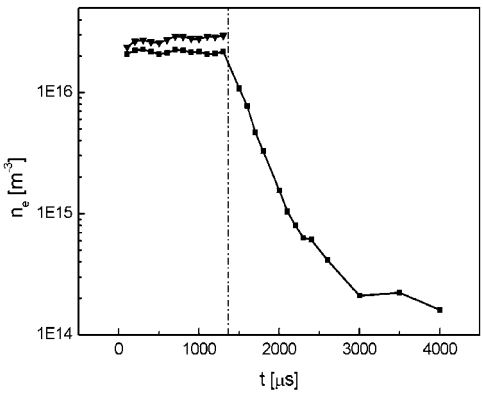

Figure 3. Time dependence of electron density n_e at the position of substrate. The active pulse starts at t = 0 s and ends at t = 1400 μs (indicated by a vertical dash dot line). -■- electron density computed from the integral of the EEPF [equation (2)]. -▼- electron density computed from the plasma potential [equation (3)].

Table 2. Thickness and chemical composition of deposited samples. STO and BSTO are desired values according to the respective chemical formulae: $SrTiO_3$ and $Ba_xSr_{1-x}TiO_3$.

Sample no.	Thickness [nm]	Atomic %(O)	Atomic %(Ti)	Atomic %(Sr)	Atomic %(Ba)
STO	—	60	20	20	0
1	644	60.1	20.2	19.7	0
BSTO	—	60	20	x	20 – x
2	823	61	22	7.4	9.1
3	286	61	22	7.6	9.25
4	232	60	21.5	9.2	8.3
5	215	61	22	9.2	7.3

XRD pattern of sample no. 2 obtained from measurement in grazing incidence geometry can be seen in Fig. 4. Several diffraction peaks belonging to BSTO perovskite phase were found. The BSTO peaks are located in the middle between STO and BTO standard peaks (see Fig. 4). It means that BSTO mixture contained approximately similar amount of Ba and Sr. This result was in agreement with electron microprobe measurement of elemental composition (see Table 2). From the accurate position of detected BSTO diffraction peaks, it was possible to calculate lattice parameter a = 3.980 Å. Furthermore, it was possible to estimate the grain size of crystallites from the width of the diffraction peaks. The estimated grain size was 30 *nm*. However, this estimation is valid only in case that we can neglect the internal stress in the films, which cannot be done with certainty in our case.

It was possible to identify spectral lines belonging to sputtered excited particles Ba, Sr, Ba^+, and Sr^+ in emission spectra taken during deposition. Intensities of these lines were roughly proportional to the deposition rate. The dependence of ratio of emission spectral line intensity of Ba and Sr excited atoms and ions on atomic concentration of Ba and Sr in the deposited films is depicted in Fig. 5. The ratio of emission spectral line intensities and the ratio of thin film concentrations were approximately proportional. This result means that it was possible to control the stoichiometry in deposited thin films by controlling conditions in the plasma for constant geometry of the system. This is important for future possibility of deposition of compositional gradient BSTO films.

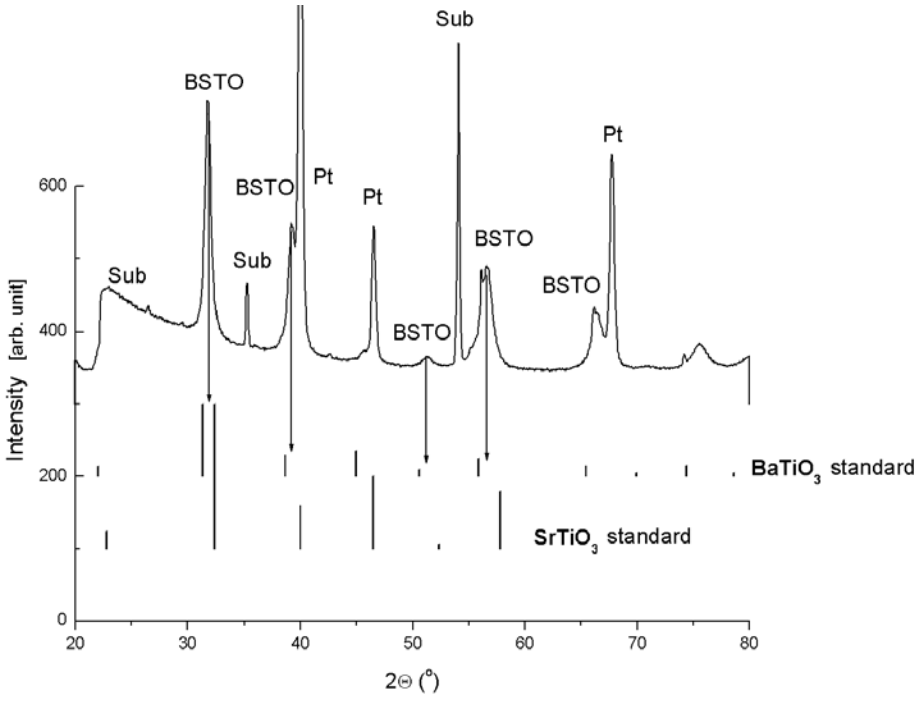

Figure 4. X-ray diffraction patterns measured in grazing incidence geometry. Sample no. 2; BSTO on Pt surface.

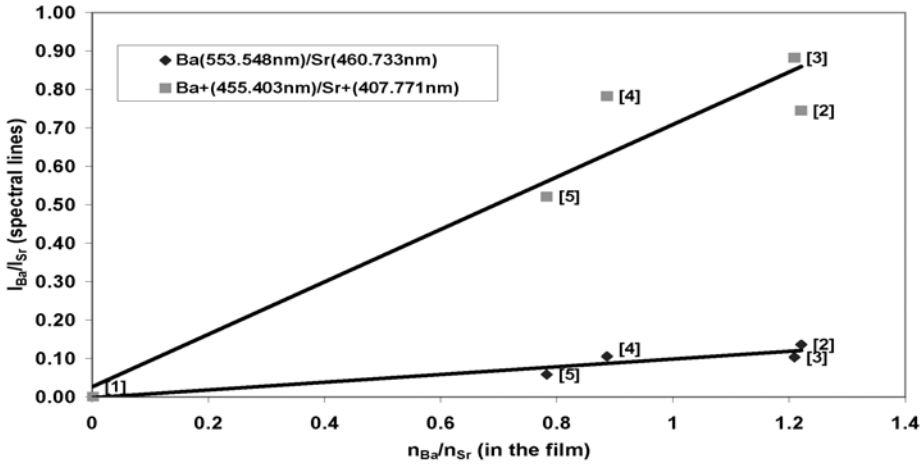

Figure 5. Dependence of the ratio of intensity of Ba and Sr (neutrals and ions) emission spectral lines taken during deposition on the ratio of Ba and Sr atomic concentrations in the deposited films. In the brackets there are numbers of the samples.

4. Conclusion

Low-pressure plasma jet system was investigated during the $SrTiO_3$ and $Ba_xSr_{1-x}TiO_3$ thin films deposition. Time resolved plasma parameters were determined by Langmuir probe measurement at the substrate position during the whole discharge on-off cycle. Electron energy distribution was non-Maxwellian during the whole cycle, with a strong deviation from Maxwellian in the afterglow plasma of the non-active part of the cycle.

$SrTiO_3$ and $Ba_xSr_{1-x}TiO_3$ thin films were successfully deposited. Electron microprobe measurements showed that chemical composition of deposited films was relatively close to desired one in all cases. X-ray diffraction revealed crystalline perovskite structure in all deposited samples.

Plasma Emission spectra measurements showed that the deposition rate of the thin films growth and the thin films stoichiometry can be better controlled by observing the atomic and ion spectral lines. Especially by setting the ratio of intensity of Ba and Sr or Ba^+ and Sr^+ spectral lines we can approximately set the ratio of Ba and Sr concentration in the deposited films. This is very promising for deposition of compositional gradient BSTO layers.

5. Acknowledgement

This work was supported by junior grant KJB1010302 of the grant agency of the ASCR.

References:

[1] L. Bárdoš, S. Berg and H. Baránková – J. Vac. Sci. Tech. **A 11**, 1486 (1993).
[2] L. Bárdoš, H. Baránková – Surf. Coat. Tech. **46**, 463 (2001).
[3] L. Soukup, M. Šícha, F. Fendrych, Z. Hubička, L. Jastrabík, D. Chvostová, H. Šíchová, V. Valvoda, A. Tarasenko, V. Studnička, T. Wagner, M. Novák – Surf. Coat. Tech. **116-119**, 321 (1999).
[4] Z. Hubička, M. Šícha, L. Pajasová, L. Soukup, L. Jastrabík, D. Chvostová, T. Wagner – Surf. Coat. Tech. **142**, 681 (2001).
[5] M. Čada, Z. Hubička, P. Adámek, P. Ptáček, H. Šíchová, M. Šícha, L. Jastrabík – Surf. Coat. Tech. **174**, 627 (2003).
[6] Z. Hubička, M. Čada, I. Jakubec, J. Bludská, Z. Málková, B. Trunda, P. Ptáček, J. Přidal, L. Jastrabík – Surf. Coat. Tech. **174**, 632 (2003).
[7] N.K. Pervez, P.J. Hansen, R. A. York – Appl. Phys. Letters **85**, 4451 (2004).
[8] J. Im, O. Auciello, S.K. Streiffer – Thin Solid Films **413**, 243 (2002).
[9] F. Tcheliebou, H.S. Ryu, C.K. Hong, W.S. Park, S. Baik – Thin Solid Films **305**, 30 (1997).
[10] C.Y. Jin, Y.P. Ding, Z.Y. Meng – J. Inorganic Material **15**, 287 (2000).
[11] B. Vukasinovic, S. Sundell, M. Oljaca – Surface Engineering **19**, 179 (2003).
[12] F. Weiss, J. Lindner, J.P. Senateur, C. Dubourdieu, V. Galindo, M. Audier, A. Abrutis, M. Rosina, K. Frohlich, W. Haessler, S. Oswald, A. Figueras, J. Santiso – Surf. Coat. Tech. **133**, 191 (2000).
[13] K. Abe – J. Ceramic Society Jap **109**, 58 (2001).

Langmuir probe diagnostics of Ar planar magnetron discharge with reactive admixtures N_2 and O_2

V. Straňák[1,2,3], J. Blažek[2], S. Wrehde[1], H. Steffen[1], M. Tichý[3], P. Špatenka[4], R. Hippler[1]

[1]*University of Greifswald, Institute of Physics, Domstrasse 10a, 174 89 Greifswald, Germany*
[2]*University of South Bohemia, Department of Physics, Jeronýmova 10, 371 15 České Budějovice, Czech Republic*
[3]*Charles University in Prague, Faculty of Mathematics and Physics, V Holešovičkách 2, 180 00 Praha 8, Czech Republic*
[4]*Technical University of Liberec, Faculty of Mechanical Engineering, Hálkova 6, 461 17 Liberec, Czech Republic*

Abstract
Plasma is often used to assist deposition of thin layers of different types and properties. Magnetron sputtering deposition is one of the methods used for this purpose. Our work is focused on diagnostics of DC planar magnetron plasma creating by ionisation of working gas. Mixture of Ar (carrier gas) and N_2 or O_2 (reactive gas) was used in our case. Plasma was investigated by means of Langmuir probe and basic plasma parameters (plasma potential V_{pl}, mean electron energy E_m, electron density n_e, density of negative ions n_n) were determined.
Keywords
planar magnetron, Langmuir probe, plasma parameters, negative ion density, TiO_x and TiN_x layers

1. Introduction

Magnetrons are known for a long time in two basic configurations: as a cylindrical [1] or planar [2] magnetron, used in our case. Planar magnetrons can be operated in two modes – balanced and unbalanced mode [3]. The balanced mode is characterised by a conventional configuration of magnetic field. The field lines are well confined around the cathode and electron loss is reduced to a minimum. The basic principle of the unbalanced magnetron is to allow electron release from the magnetic trap (which is typical for balanced magnetron) in order to create plasma also further away from the magnetron cathode and close to the substrate. Elementary processes as electron and ion transport, energetic electron transport, sputtering processes and effects caused by electric and magnetic fields were studied and modeled in Monte Carlo several times [4]. The properties of thin solid films produced by plasma activated deposition are strongly influenced by the ions behaviour. Some works where ion interactions were studied and simulated were published in [5].

The fundamental aspects of magnetron discharges were studied e.g. in [6]. For practical applications, i.e. the layer deposition, mixtures of working gases and specific target materials are mostly used. Composition of gas mixture (carrier gas with reactive gases) determines most properties of deposited layer. Very often nitride layers (N_2 is added) or oxide layers (O_2 is added) are deposited because of their wide utilization range. Rare gases, e.g. Ar, are mostly used as carrier gases. Discharges in Ar+N_2 mixtures were experimentally investigated by optical emission spectroscopy in [7] and by Langmuir probe in [8]. The Ar+O_2 plasma discharges were investigated also by optical emission spectroscopy e.g. in [9] or by Langmuir probes in [10]. Langmiur probe diagnostic of plasmas, where O_2 is added, is not so easy. Problems arise mostly by deposition of non-conducting layers on the probe surface, which causes deformation of probe VA characteristics. Also possible presence of negative ions, when part of the mixture is electronegative gas, complicates interpretation of Langmuir probe data. In our case we carried out the complex diagnostics of pure Ar discharges and mixtures Ar+N_2, Ar+O_2 plasmas. The basic plasma parameters - plasma potential (V_{pl}), mean electron energy (E_e), electron density (n_e) - were determined by standard ways typical for probe measurements. Density of negative ions (n_n), in case of Ar+O_2 discharges, was revealed by simple method based on comparison of two probe characteristics – the one measured in electropositive and the second measured in slightly electronegative plasma [11,12].

2. Experimental setup and experiments

Our experiments were carried out in spherically-shaped stainless-steel vacuum chamber, see Fig.1. Magnetron of the type Vtech 75 by Genco-A was situated in the lower part of the chamber. The magnetron can be operated either in balanced or in unbalanced mode by mechanically changing permanent magnet configuration. This change of modes can be done when discharge is on by the external micrometer screw. Target made of Ti (Ti 99.9 % purity grade, diameter 3") directly connected with the cathode is used for deposition of TiX layers. Water cooling protects the cathode from overheating and consequent destruction. During the Langmuir probe measurements the probe was situated in the substrate plane. The vacuum chamber is pumped by a turbomolecular pump backed by rotary vacuum pump down to ultimate pressure 10^{-8} Pa. Pressure can be adjusted by a throttle valve installed between the chamber and the turbomolecular pump. The flow rate of working gas or mixture of carrier and reactive gases is controlled by MKS mass flow controllers. For our experiments the flow rate of carrier gas (Ar) was 19.3 sccm and rate of reactive gases (N_2, O_2) was kept at 1.5 sccm. The total pressure in the chamber during the experiment was p = 0.7 Pa. Ar gas injection line is fitted to the magnetron cathode. This allows directing the argon gas over the target surface. Pipe for reactive gases is inserted into the chamber with its nozzle end situated close to the target. The mass flow controllers, the throttle valve and magnetron were PC-controlled via their control units.

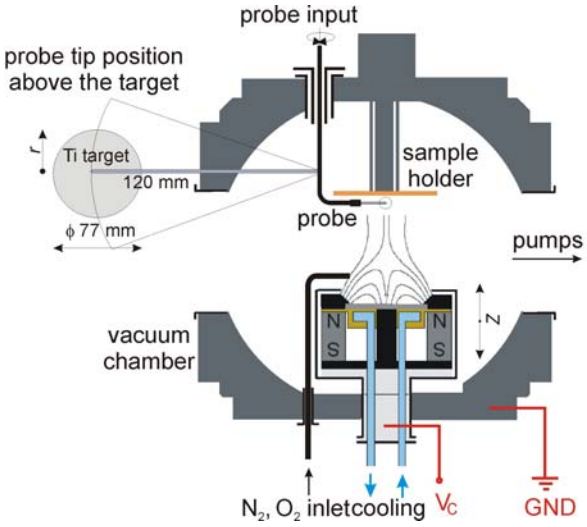

Fig.1. Schematic view of experimental setup. Magnetron is situated in lower part of the chamber, probe is in the position of substrate.

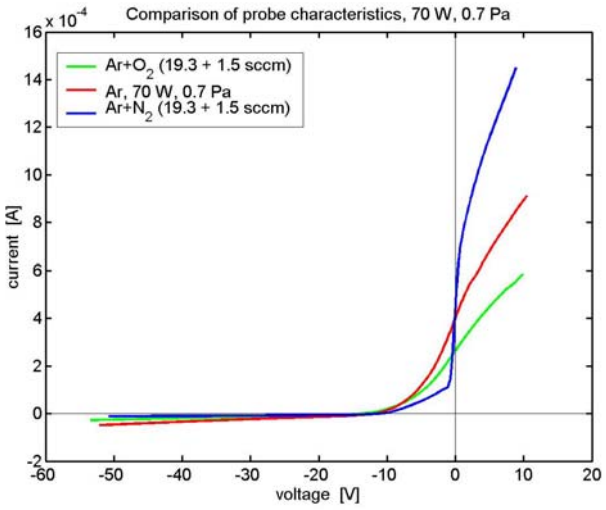

Fig.2. Comparison of three different VA characteristics in Ar, Ar+O_2, Ar+N_2 at the same total pressure and discharge power. The characteristics are shifted along the voltage axis so as $V_s = 0$.

Cylindrical Langmuir probe made of tungsten wire, diameter 50 μm and active length 6 mm was used for the plasma diagnostic. The probe wire was sleeved by a double capillary glass tube. The outer capillary was longer than the inner one. This arrangement prevented the probe from short-circuiting to the sleeve by the metal sputtered during the deposition process. The probe was situated near the plane of the substrate. The probe tip was positioned perpendicular to the magnetic field lines. This arrangement minimizes the effects of magnetic field on the probe measurements. In addition the magnetic field in the plane of measurement is relatively weak - in the order of 1 mT - in both operating modes. The mean gyroradius (r_{Le}) for electrons is in such case much larger than the radius of probe wire (r_p): we can write $r_{Le} >> r_p$. Probe measurement in magnetron discharges can be affected by E×B drift too [13]. This effect was also minimised by using configuration where the probe tip was parallel with E×B drift. For measurement of power dependences in the presented experimental study the probe was kept at the axis of the target and vertical coordinate (distance from magnetron cathode) was z = 65 mm. Probe diagnostics became more difficult when reactive gas was added into carrier gas. Then the probe was covered by deposited layer and the measured data were influenced. Because of this reason the probe was

cleaned by positive ion bombardment; high negative voltage was applied on the probe. In the case of Ar+N_2 discharge the layer (TiN_x) on the probe was electrically conductive and the cleaning process had not to be so aggressive. The powerful cleaning process had to be used when Ar+O_2 discharge was investigated because of non-conductivity TiO_x layer; negative voltage bias about – 190 V for 7 second was applied. Cleaning process minimized the influence of the layer being deposited on the collected experimental data but somewhat reduced life time of the probe. The measuring probe bias voltage was generated by Source Meter Keithley 2400 over the range from – 50 V to + 10 V with step 0.1 V. The acquired data were processed by program code written in Matlab. No noise reducing methods were applied.

3. Determination of plasma parameters

For understanding of elementary processes in the discharge as well as interaction of active particles with substrate knowledge of plasma parameters is necessary. Basic plasma parameters in electropositive discharges – Ar and mixture Ar+N_2 - were revealed by standard ways: the plasma potential (V_{pl}) was determined from the abscissa of the zero-cross of probe characteristics second derivative with respect to probe voltage. The mean electron energy (E_e) was calculated by numerical integration of measured second derivative and the electron density (n_e) was estimated from I_e^2 vs. V plot in electron acceleration regime of the probe characteristic.

Former plasma monitor measurements confirmed the presence of negative oxygen ions in Ar+O_2 discharge. However, direct estimation of negative ion density from Langmuir probe data is difficult. In slightly electronegative plasma, it is almost impossible to determine the n_n directly from measured data since the negative ions (n_n) density is low and the effect on the probe characteristic is almost not discernible. In other words it seems that estimation of charged particle density from characteristics taken in the discharge in pure argon and in the slightly electronegative mixture would yield very similar results. However, under certain (at low pressure fairly acceptable) assumptions it is possible to determine negative ion density by comparing probe characteristics measured in pure electropositive (Ar) plasma and in slightly electronegative (Ar+O_2) plasma at otherwise same conditions. Comparison of three different VA characteristics measured in pure Ar, Ar+N_2 and Ar+O_2 can be seen in Fig.2. The different shape of the curves is caused by different composition of gas mixture; not by presence of negative ions. Comparison of measured and modeled characteristics showed us that all VA characteristics obtained from experiments are similar to modeled characteristics computed based on the "double Maxwell" electron energy distribution, which was observed experimentally in *pure Ar* discharge.

4. Estimation of negative ion density

One possible way to estimate the negative-ion density is based on the charge neutrality condition $n_p = n_e + n_n$, where the subscripts *p, e* and *n* indicate quantities concerning positive ions, electrons and negative ions, respectively. To avoid difficulties concerning correct interpretation of positive-ion current we have taken into consideration two characteristics. The characteristic measured in electronegative mixture of Ar with trace of O_2 was evaluated with the aid of the reference characteristics measured in the pure electropositive Ar plasma [11, 12].

The total current normalized to the unit probe area consists of the electron and positive-ion part, $j = j_e - j_p$. The presence of negative ions, e.g. O^- disclosed by plasma monitor measurements, does not require taking into account their contribution to the total current in the electronic part of the probe characteristics. Indeed, the thermal current of negative ions is comparable to the electronic thermal current only for large n_n densities satisfying relation

$$\frac{n_n}{n_e} \sim \sqrt{\frac{T_e}{T_n}\frac{m_n}{m_e}}\,. \qquad (1)$$

For ratios $T_e / T_n \sim 10^2$ and $m_n / m_e \sim 10^3$ (typical discharge plasma) relation (1) gives the negative-ion density by approximately two orders of magnitude higher than the electron one. Such highly electronegative plasmas were not met in our measurements. Assuming Maxwellian electron energy distribution and the cylindrical probe, the electron current density in electron retarding region can be described by equation

$$j_e(V, n_e, T_e) = e n_e \cdot \sqrt{\frac{eT_e}{2\pi m_e}} \cdot \exp\left(\frac{V}{T_e}\right), \quad V < 0\,, \qquad (2)$$

where m_e and e are the electron mass and elementary charge, respectively, and T_e is the electron temperature measured in volts ($=kT_e^{Kelvin}/e$, T_e^{Kelvin} measured in Kelvins). In the above equation we denoted $V = V_p - V_s$, where V_p and V_s are the probe and the space (plasma) potential, respectively. Quite a few theories have been proposed for the description of the positive-ion probe current. We assume here the approximate formula of the general form [14]

$$j_p(V, n_p, T_e) = en_p \sqrt{\frac{eT_e}{M_p}} \cdot \left(\frac{|V|}{T_e} \right)^{\kappa} f(V), \quad V < 0 \tag{3}$$

with multiplicative factor f that is either constant or depends only on the voltage V. The parameters f and κ can be chosen on the basis of theoretical consideration or determined empirically. The simplest collision-less orbital motion model [15,16] suggests $\kappa = 0.5$, $f = 1$. The factor $\sqrt{eT_e / M_p}$ expresses the Bohm velocity v_B of positive ions at the sheath – presheath edge for the collision-less plasma sheath.

The key assumption of the proposed method is that the positive-ion current is for both electropositive and electronegative plasma expressed by the formula (3) with the same factors f, κ. Assuming that we can write for the ratio of positive-ion currents in electropositive and slightly electronegative plasma (at otherwise similar experimental conditions) the expression

$$\frac{j'_p(V)}{j_p(V)} = \frac{n'_p}{n_p} \sqrt{\frac{M_p}{M'_p}} \cdot \left(\frac{T_e}{T'_e} \right)^{\kappa - 1/2} . \tag{4}$$

Here the dashed quantities are related to the electronegative plasma. The formula (4) together with the quasineutrality conditions $n_p = n_e$, $n'_p = n'_e + n'_n$ results in expression for negative ion density in slightly electronegative plasma:

$$n'_n = \sqrt{\frac{M'_p}{M_p}} \cdot \left(\frac{T'_e}{T_e} \right)^{\kappa - 1/2} \left\langle \frac{j'_p(V)}{j_p(V)} \right\rangle n_e - n'_e . \tag{5}$$

The brackets $\langle\ \rangle$ denote averaging over a suitable chosen interval in the region $V < 0$, where the ratio of ion currents is approximately constant. The electron temperatures and densities are determined from the electronic parts of characteristics. With formula (5) there are associated two error sources. One error arises due to the uncertainty of the effective positive-ion mass M'_p in the electronegative plasma. The second error is connected with accuracy of the positive-ion current model (3). Nevertheless, the computation error was estimated about 35 % from systematic measurements.

5. Experimental results and discussion

In this part of the paper there are presented results of probe measurements in DC planar magnetron discharge. Mainly power dependences of basic plasma parameters are depicted in the plots. In each plot one can compare dependences measured in balanced (BLM, solid lines and full symbols) with dependences measured in unbalanced (UNB, dashed lines and open symbols) mode at the same experimental conditions (pressure, mixture of working gas). At the beginning pure Ar discharge was investigated. Then reactive admixtures N_2 and O_2 were subsequently added. The pressure in the chamber was kept constant at p = 0.7 Pa. Ratio of flow rates of the gas mixture components was kept constant as follows: 19.3 sccm of Ar and 1.5 sccm of N_2 or O_2. All represented results were performed at the axis of the discharge in substrate plane distanced from the target by about 65 mm.

One of the most important physical quantities is energy contained in the discharge. In our case we determined mean electron energy E_m; the dependence of E_m on power can be seen in Fig. 3. It is seen that all dependences have pronounced local maximum at 70 W especially in BLM mode. This fact probably corresponds with geometry of magnetic trap. Decrease of electron energy with incoming power higher at 70 W can be caused by geometry of the system; higher power more confines plasma to cathode. Another effect which can cause fall of

E_m with high incoming power is ionization of Ti particles. Plasma monitor measurements indicated that density of Ti^+ and Ti^{++} increased exponentially with discharge power. Presence of oxygen in the discharge increases E_m; the highest E_m was determined in Ar+O_2 discharge. From previous plasma monitor results we could deduce that negative ions were created by dissociative electron attachment to O_2. The energy equal to electron affinity of particular specie is released at the time of negative ion creation process. For O_2 it has resonance at electron energy around 6.5 eV. Most of the electrons with such energy spend therefore their energy on the dissociative electron attachment of O_2. At the same time the low energy electrons can efficiently transfer their energy to O_2 vibrations, i.e. they heat the oxygen gas. Lower E_m of Ar+N_2 discharge is probably caused by lower ionization potential of N particles and consequent higher ionization rate. In Ar+N_2 discharge the n_e was highest, see Fig.5.
Plasma potential V_{pl} is important plasma parameter especially for understanding plasma - wall interaction processes. Precise discussion of V_{pl} power dependences is difficult in our case. One of the reasons is the fact that voltage applied on the cathode was not constant when the discharge power was varied. Incoming power ($P = U.I$) was held constant (this was advantageous during layer deposition experiments) and cathode voltage as well as discharge current changed with discharge power. The second reason was connected with unwanted deposition of the substrate holder near to the probe. This effect also somewhat influenced measured values of plasma potential. By minimizing these undesirable effects we obtained dependences of V_{pl} on the power deposited in the discharge, which are depicted in the Fig.4. One can see qualitatively similar shapes of V_{pl} curves and E_m courses with distinct maxima around 70 W DC absorbed power. In all three cases we can clearly distinguish between UNB and BLM mode; V_{pl} (UNB) > V_{pl} (BLM) roughly by about 70 %. Neither quantitative nor qualitative differences between V_{pl} in pure Ar and in Ar+O_2 discharge were observed. On the other hand the V_{pl} of Ar+N_2 discharge was lower for both modes compared to that in pure Ar discharge.

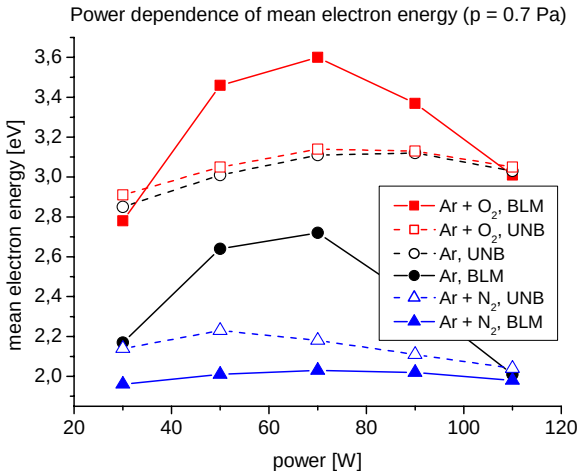

Fig.3. Power dependence of mean electron energy. Conditions: p = 0.7 Pa, Ar – 19.3 sccm, N_2, O_2 – 1.5 sccm

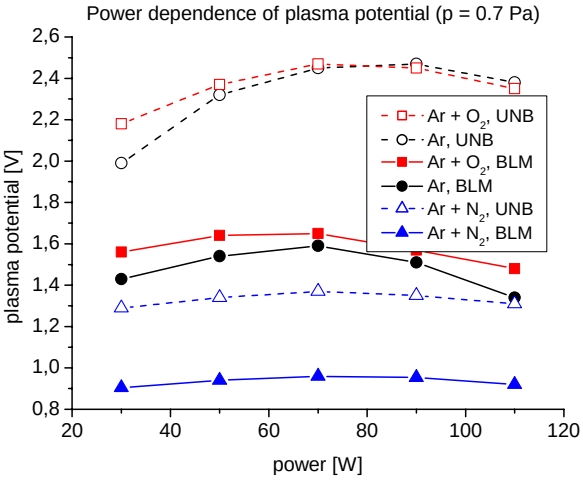

Fig.4. Power dependence of plasma potential. Conditions: p = 0.7 Pa, Ar – 19.3 sccm, N_2, O_2 – 1.5 sccm

Knowledge of charged particle density in the discharge is necessary for keeping reproducible technological properties of created layers (homogeneity of layers, deposition rate etc.). We determined electron density n_e in pure Ar discharge as well as in the mixture of Ar with oxygen. In electronegative Ar+O_2 plasma the negative ion density n_n has been determined by the method described in previous section.
Power dependences of electron density in semi-logarithmic scale are depicted in Fig.5. Generally, the n_e is higher in UNB than in BLM mode and increases almost exponentially with power dissipated in the discharge. This fact probably corresponds with shape of magnetic field which influences the free path of particles necessary for ionization. The highest $n_e \approx 10^{16}$ m^{-3} was estimated in Ar+N_2 discharge which could be caused by enhanced ionization of nitrogen particles via argon metastables. On the contrary the lowest $n_e \approx 10^{14\text{-}15}$ m^{-3} was revealed in Ar+O_2 discharges. This fact is connected with electron losses due to creation of negative ions by

electron attachment. The presence of negative ions, important for deposition of TiO_x layers, was confirmed by plasma monitor measurements. The density of negative ions $n_n \approx 10^{14}$ m^{-3} is lower by one or two orders of magnitude when compared to electron density in discharges in electropositive gases (Ar, Ar+N_2), see Fig.6. The n_n is higher in UNB mode and increases almost linearly. The computational error was estimated to about 30%.

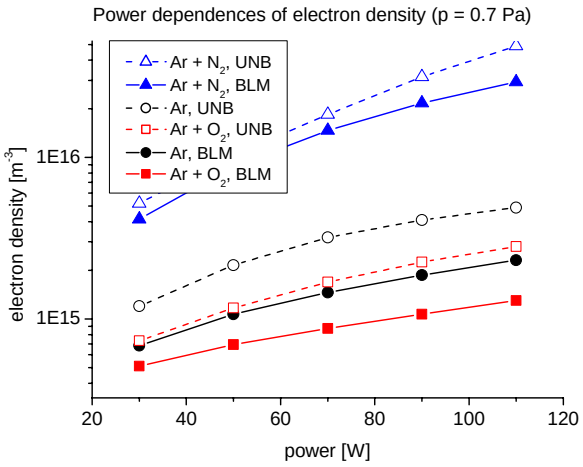

Fig.5. Power dependence of mean electron energy. Conditions: p = 0.7 Pa, Ar – 19.3 sccm, N_2, O_2 – 1.5 sccm

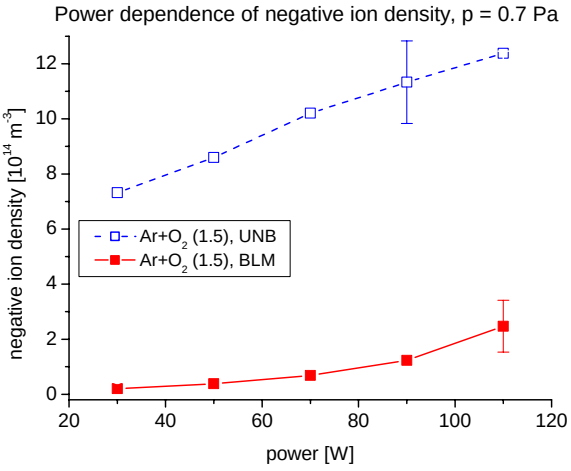

Fig.6. Power dependence of negative ion density. Conditions: p = 0.7 Pa, Ar+O_2 (19.3 + 1.5 sccm).

6. Conclusion

Ar plasma generated by DC planar magnetron with reactive admixtures N_2 and O_2 was investigated by Langmuir probe technique. Dependences of mean electron energy ($E_m \approx 3$ eV), plasma potential ($V_{pl} \approx 1.5$ V) and electron density ($n_e \approx 10^{15\text{-}16}$ m^{-3}) on discharge power were determined. Novel method for determination of negative ion density from probe measurement in slightly electronegative plasma was suggested and applied. In that manner estimated negative ion density was substantially lower ($n_n \approx 10^{14}$ m^{-3}) than electron density.

7. Acknowledgment

This work was financially supported by DFG through SFB 198/A11. This work is a part of the research plan MSM 0021620834 and MSM 467488501 that is financed by the Ministry of Education of the Czech Republic. Partial financial support of Ministry of Education by projects OC 527.60 and 527.70 are also acknowledged.

8. References

[1] J. A. Thorton, J. Vac. Sci. Technol., Vol. **15**, No.2, (1978).
[2] R. K. Waits, J. Vac. Sci. Technol., Vol. **15**, No.2, (1978).
[3] B. Window, N. Savvides, J. Vac. Sci. Technol. A**4(3)** (1986).
[4] T. E. Sheridan, M. J. Goeckner, J. Goree, J. Vac. Sci. Technol., **A.8** (**3**), (1990).
[5] C. H. Shon, J.K. Lee, Appl. Surf. Sci. **192** (2002).
[6] J. Bretagne, C. B. Laporte, G. Gousset et al, Plasma Sources Sci. Technol. **12** (2003).
[7] F. Debal, J. Bretagne, J. P. Dauchot, M. Hecq, M. Wautelet, Plasma Sources Sci. Technol. **10** (2001).
[8] V. Straňák, H. Steffen, S. Wrehde, R. Hippler, M. Tichý, Czech. J. Phys. Vol. **54** (2004), Suppl. C.
[9] W. Trennpohl, J. Bretagne, G. Gouset, D. Pagmon, M. Touzeau, Plasma Sourses Sci. Technol. **5** (1996).
[10] J. T. Gudmundsson, T. Kimura, M. Lieberman, Plasma Sources Sci. Technol. **8** (1999).
[11] M. Shindo, Y. Kawai, Surf. and Coat. Technol. **142-144** (2001).
[12] M. Shindo, S. Hiejema, Y. Ueda, S. Kawakami, N. Ishii, Y. Kawai, Surf. and Coat. Technol. **116-119** (1999).
[13] T. E. Sheridan, M. J. Goeckner, J. Goree, J. Vac. Sci. Technol. A **16**(**4**), (1998).
[14] S. Klagge, M. Tichý, Czech J. Phys. B **35** (1985).
[15] H. M., Mott-Smith, I. Langmuir., Phys. Rev. **28** (1926).
[15] L. Tonks, I. Langmuir., Phys. Rev. **34** (1929).

Comparison of the EDFs and macroscopic properties in the cylindrical magnetron discharges of direct and inverted designs

Yu. B. Golubovskii[1], I. A. Porokhova[1] , V. P. Sushkov[1], M. Holík[2] , P. Kudrna[2], M.Tichý[2]

[1] *St. Peterburg State University, Ulianovskaia 1, 195904 St. Petersburg, Russia*
[2] *Charles University in Prague, V Holešovičkách 2, 18000, Prague, Czech Republic.*

Abstract
Cylindrical dc magnetron discharges in argon in post-cathode (direct) and hollow-cathode (inverted) configurations are studied experimentally and theoretically. The electron component is modelled basing on a non-hydrodynamic solution to the Boltzmann kinetic equation in the radially inhomogeneous electric and axially directed uniform magnetic fields. The absolute values and radial profiles of the EDF and various macroscopic parameters are obtained and compared for the direct and inverted magnetron configurations.
Keywords cylindrical magnetron discharge, Boltzmann equation, non-hydrodynamic model

1. Introduction

The DC cylindrical magnetron discharge (CMD) considered in the present paper consists of two co-axial metallic cylinders serving as electrodes, with radii usually not exceeding several centimeters. The typical working pressures are units of Pa or fewer. The applied voltage has a typical magnitude of hundreds of volts and causes the radially directed electric field. The uniform magnetic field parallel with the discharge vessel axis is created by coils with current. The magnetic field strength in the range from 10 to 40 mT is strong enough to magnetize the electron plasma component, leaving ion motion almost unaffected. The CMD is called post-cathode, or direct magnetron discharge, if the inner electrode is the cathode and the outer one is the anode. In the swapped electrode arrangement, the discharge is called the hollow-cathode, or inverted CMD. Their difference can be attributed to the opposite directions of charged particle fluxes and the different areas of corresponding electrode surfaces. In this paper both configurations will be examined and compared.

The CMDs in inverted configuration are less studied theoretically, while they have been successfully used in technological applications. There are good reasons to believe that the radial courses of collision rates and other characteristics in the inverted CMD will differ from those in the post-cathode discharge.

The planar and cylindrical magnetrons have been simulated by various fluid [1,2], PIC-MCC [3] and non-hydrodynamic models [4,5], based on the Boltzmann kinetic equation for electrons.

In the present paper the cylindrical magnetron discharges in the post- and hollow-cathode configurations are studied, with particular emphasis on the less explored inverted CMD. The analysis of the physical processes and comparison between the two CMD types are performed in terms of the electron distribution functions and relevant macroscopic parameters. Electron plasma component is modelled basing on the spatially inhomogeneous Boltzmann kinetic equation in crossed electric and magnetic fields.

The experimental and simulation results presented here are obtained for the both direct and inverted CMDs of length L=12 cm and radii of the inner and outer electrodes r_0=0.5 cm and R=3 cm, respectively. The working gas was argon, at pressure $p\approx$3 Pa, discharge current $i\approx$100 mA and magnetic field strength B=20 mT.

2. Experimental set-up

The cylindrical magnetron apparatus in the inverted configuration is presented in Fig. 1. The same apparatus was used earlier to study experimentally the discharge in the direct design [6]. Electrodes are arranged co-axially, the anode is placed at the axis of the grounded stainless-steel cylindrical vacuum chamber, which serves as a cathode. The limiters (shields) at both ends of the chamber are connected to the anode. Two magnetic coils are placed symmetrically with the centre of the system to provide the axially directed homogeneous magnetic field. The magnetic coils are energized by a power supply in current-stabilized mode. Each coil has more than 5,000 turns, which results in magnetic field of up to 40 mT at the vessel axis at the winding current around 1 A. Cores of the coils as well as the cathode are water-cooled to avoid overheating at higher currents.

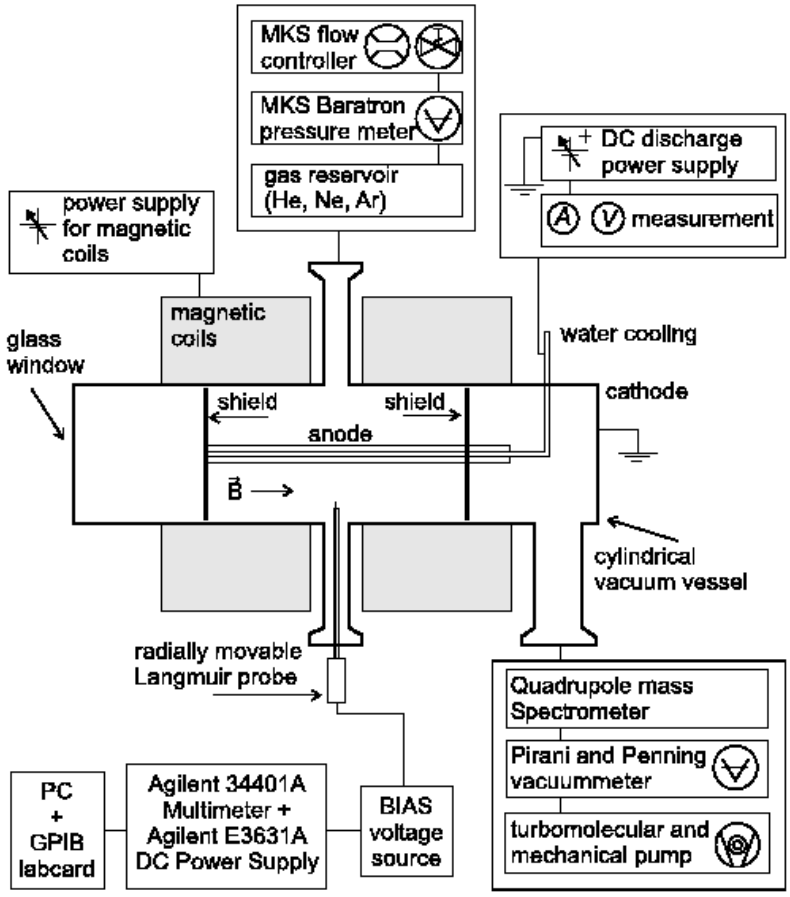

Fig. 1. Schematic diagram of the experimental set-up with the cylindrical magnetron in inverted configuration

The fact that the magnetic field is provided by two coils enables accommodation of several vacuum ports in-between of the coils in the middle of the vacuum chamber. They are used for measurements with radially movable Langmuir probe as well as for pressure measurement and gas inlet. Ports at the ends of the vacuum chamber serve for pumping and electrical feed-through to the anode, accommodation of Pirani and Penning manometers and axially movable Langmuir probe. As the discharge power supply the Advanced Energy MDX 500 unit is used in current-stabilized mode.

The vacuum system is pumped by means of the piston pump Leybold EcoDry M15 and the turbomolecular pump Leybold-Heraeus Turbovac 150. The mechanical piston pump pre-evacuates system down to several Pa and with the turbomolecular pump back-ground pressure of the order of 10^{-3} Pa can be achieved. Research-grade argon (5.6 purity) is introduced into the apparatus via MKS flow controller. Typical gas flow rate is less than 0.5 sccm at working gas pressure of units Pa.

Radially movable Langmuir probe is used to measure parameters of the discharge plasma. Probe holder is made of two Degusit pipes inserted tightly into each other and has special construction to prevent to highest degree the unwanted effect of the sputtered cathode material (short-circuiting of the deposited conducting layer on the ceramic probe holder with the probe wire). Probe measurement circuit consists of computer-controlled DC power supply (Agilent E3631A), which serves as probe bias voltage ramp generator and multimeter (Agilent 34401A), which measures the probe current. Probe bias can be further amplified by high-voltage operational amplifier to a range needed. PC equipped by the GPIB interface card controls the measurement circuit. It has to be noted that the probe bias voltage ramp requires additional dc bias in series to bring the range of the probe voltage up to approximately anode voltage. Most of the discharge voltage (in our case around 300 volts) falls in the cathode region and hence the plasma potential in most part of the positive column keeps close to the anode voltage. The entire probe data acquisition system is driven by control program written in the Agilent VEE Pro iconic programming environment. With this system it is possible to get one probe characteristics consisting of 300 experimental points in about one minute.

3. Theoretical model

The spatially inhomogeneous steady-state Boltzmann equation for the electron distribution function (EDF) $F(\mathbf{v},\mathbf{r})$ states

$$\mathbf{v}\cdot\nabla_{\mathbf{r}}F(\mathbf{v},\mathbf{r})-\frac{e}{m}(\mathbf{E}+[\mathbf{v}\times\mathbf{B}])\cdot\nabla_{\mathbf{v}}F(\mathbf{v},\mathbf{r})=C(F(\mathbf{v},\mathbf{r})).$$

Here m and $-e$ are the electron mass and charge, $\mathbf{E}$ and $\mathbf{B}$ are the electric and magnetic field strengths. $C(F)$ is the collision integral.

Under assumption of weak anisotropy the EDF can be represented in the form $F(\mathbf{v},\mathbf{r})=F_0(v,\mathbf{r})+\mathbf{F}_1(v,\mathbf{r})\cdot\mathbf{v}/v$, where only two first terms of the spherical harmonic expansion are retained. We consider cylindrically

symmetrical and axially uniform CMD plasma with the crossed configuration of the radial electric and axial magnetic fields. Application of the Boltzmann equation to the specified geometry yields the following set of equations, written in variables of the kinetic energy $U=mv^2/2$ and the radial coordinate r

$$\frac{U}{3}\frac{1}{r}\frac{\partial}{\partial r}rf_{1r}(U,r)-\frac{eE(r)}{3}\frac{\partial}{\partial U}Uf_{1r}(U,r)=S(f_0) \tag{1}$$

$$\begin{aligned} f_{1r}(U,r)&=\frac{UNQ_\Sigma(U)}{(NQ_\Sigma(U))^2U+m\omega_{eB}{}^2/2}\left[-\frac{\partial f_0}{\partial r}+eE(r)\frac{\partial f_0}{\partial U}\right] \\ f_{1\theta}(U,r)&=\frac{\sqrt{m/2}\cdot\omega_{eB}}{NQ_\Sigma(U)\sqrt{U}}f_{1r}(U,r); \qquad f_{1z}(U,r)=0 \end{aligned} \tag{2}$$

with $Q_\Sigma(U)$ being the total cross section of all collision types and $\omega_{eB}=eB/m$ denoting the cyclotron frequency. The functions f_0 and $\mathbf{f}_1$ differ from the corresponding functions F_0 and $\mathbf{F}_1$ by the factor $2\pi(2/m)^{3/2}$. The term $S(f_0)$ denotes the sum of the elastic, excitation and ionization collision operators $S(f_0)=S_{el}(f_0)+S_{ex}(f_0)+S_{ion}(f_0)$.

The elastic and excitation collision operators are taken in a customary form. If $Q^{el}(U)$ is the momentum transfer cross section for elastic collisions of electron with heavy neutral particles of mass M and density N, the corresponding operator is

$$S_{el}(f_0)=2\frac{m}{M}\frac{\partial}{\partial U}\left[U^2NQ^{el}(U)f_0(U,r)\right]$$

The excitation collision operator is

$$S_{ex}(f_0)=-UNQ^{ex}(U)f_0(U,r)+(U+U_{ex})NQ^{ex}(U+U_{ex})f_0(U+U_{ex},r),$$

with $Q^{ex}(U)$ denoting the excitation cross section with the threshold U_{ex}.

Integral representation [7] of the ionization operator employs the differential cross section $\sigma(U'',U')$ that defines a continuous spectrum of energies U' of the secondary electrons appearing in ionizing collisions produced by an electron with the incident energy U''

$$\begin{aligned} S_{ion}(f_0(U,r))=&-Uf_0(U,r)\int_0^{(U-U_i)/2}N\sigma(U,U')dU'+\int_{2U+U_i}^{\infty}U'N\sigma(U',U)f_0(U',U)dU' \\ &+\int_{U+U_i}^{2U+U_i}U'N\sigma(U',U'-U_i-U)f_0(U',U)dU', \end{aligned}$$

where U_i is the ionization potential.

The system of equations (1) and (2) can be considerably simplified by introducing a new variable ε being the total energy $\varepsilon = U-e\varphi(r)$, $e\varphi(r)$ is the potential energy. To solve the resulting system numerically it was discretized using implicit finite difference scheme on the two-dimensional non-equidistant grid in variables (ε,r). The resulting EDFs were normalized to the current density at the anode, depending on the discharge current. The discharge current i in the CMD is related to the total current density $ej_0(r)$ according to $i=2\pi Lrej_0(r)$.

The electron density n_e, radial flux j_{er}, excitation W and ionization I rates can be evaluated from the EDF according to

$$\begin{aligned} n_e(r)&=\int_0^{\infty}U^{1/2}f_0(U,r)dU \\ j_{er}(r)&=\frac{1}{3}\sqrt{\frac{2}{m}}\int_0^{\infty}f_{1r}(U,r)UdU \\ W(r)&=\sqrt{\frac{2}{m}}\int_{U_{ex}}^{\infty}UNQ^{ex}f_0(U,r)dU \\ I(r)&=\sqrt{\frac{2}{m}}\int_{U_{ex}}^{\infty}UNQ^{ion}f_0(U,r)dU \end{aligned} \tag{3}$$

Here $Q^{ion}(U)$ is the total ionization cross section $Q^{ion}(U)=\int_0^{(U-U_i)/2}\sigma(U,U')dU'$.

4. Results and discussions

The radial profiles of the electric field $E(r)$ and potential $e\varphi(r)$ used in the present kinetic analysis are reproduced in Fig. 2 for the direct and inverted configurations of the magnetron discharge. The profiles were chosen so, that the simulated electron densities fit the experimentally measured curves and the discharge voltages agree with the experimental values. Thus, a significant difference in the radial field distributions is observed for the direct and inverted CMDs, that influences essentially the formation of the EDF and macroscopic characteristic.

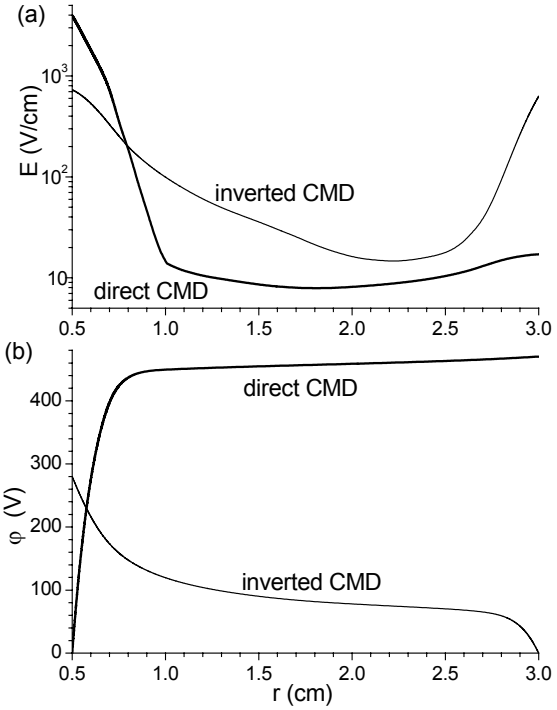

Fig. 2.Radial profiles of the electric field strength (a) and potential (b) in the direct and inverted CMDs used in calculations of the EDFs and macroscopic quantities.

The electron distribution functions calculated from the system of equations (1) and (2) are shown in Fig. 3 for both cylindrical magnetron configurations.

A beam of high-energy electrons accelerated by the cathode fall of the potential is formed in the cathode region. The EDF's tail extends to the energies of the order of the cathode fall, which is considerably larger in the direct CMD. In the positive column these fast electrons loose their energy in inelastic collisions mainly, and the EDF relaxation leads to depletion of the high-energy part.

Distinctions of the EDFs in the anode regions of the post- and hollow-cathode designs are connected with the different magnitudes of the anode fall. In the direct CMD the anode fall is small (≈1 V) and the EDF decreases smoothly to the anode due to electron sinking on the absorbing electrode. The simulations performed for the inverted CMD reveal a large value of the anode fall (≈100 V). In this case electrons, before having escaped to the anode, are accelerated by the action of a strong field in the anode region and populate the EDF in high energies. The EDF extends to the energies corresponding to the anode fall.

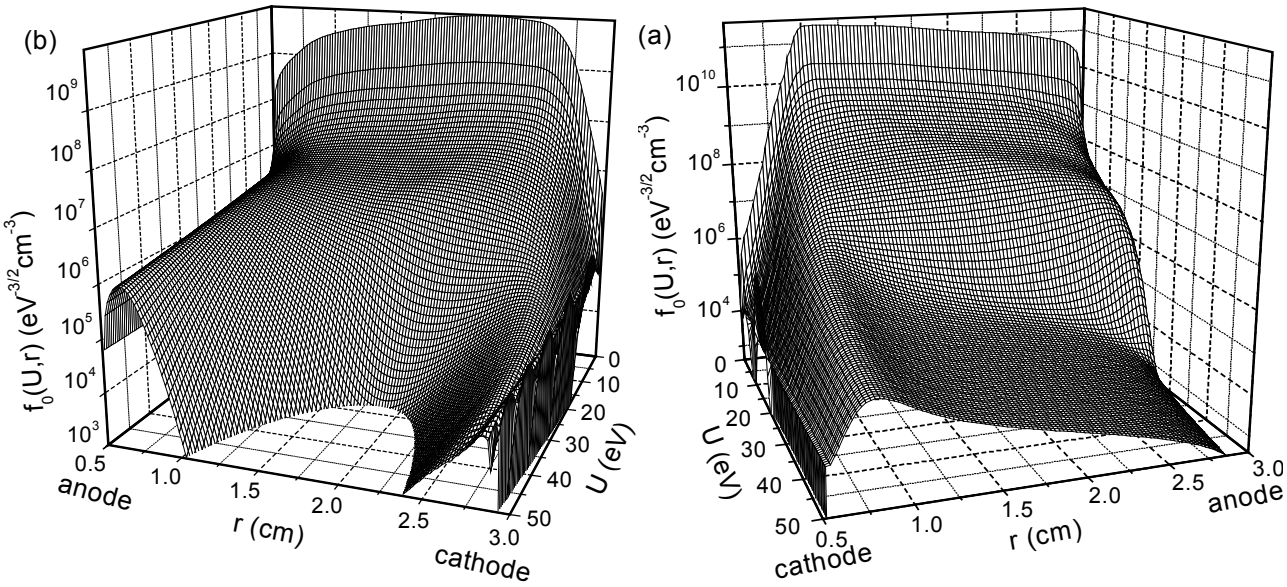

Fig. 3. The EDFs in the direct (a) and inverted (b) CMDs calculated in the corresponding fields shown in Fig. 2. Discharge conditions: (a) B=20 mT, p=3 Pa, i=90 mA and (b) B=2 mT, p=3.3 Pa, i=100 mA.

The general feature of the radial courses of electron density is the maximum located at almost equal distances from the cathode for both CMD configurations. At these distances the electric field strength has a minimum and large electron density values are required to sustain the discharge current in the quasi-neutral plasma. The radial course of the electron density in the direct and inverted CMDs resembles mirror-like pictures. The absolute value of the electron density in the inverted CMD is, however, smaller compared to that in the direct configuration under comparable experimental conditions.

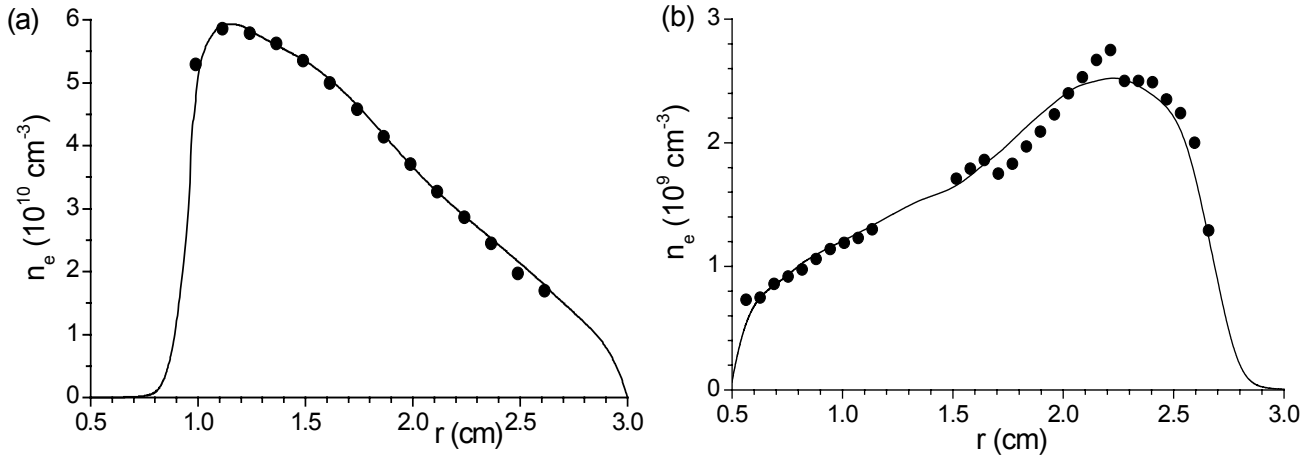

Fig. 4. The radial profiles of the electron density experimentally measured (circles) and calculated (solid lines) in the direct (a) and inverted (b) CMDs.

Along with the electron density $n_e(r)$, the excitation $W(r)$ and ionization $I(r)$ rates as well as the fluxes of charged particles $j_{er}(r)$ and $j_{ir}(r)$ have been calculated in both investigated types of the magnetron discharge.

The radial profiles of the excitation and ionization rates in the direct and inverted magnetrons are compared in Fig. 5. It should be noted, that the maxima of ionization and excitation and, consequently, those of spectral line emission, are formed in the vicinity of the inner electrode for the both CMDs. The electron density maximum is positioned, though, in the cathode vicinity. This can be attributed to the fact, that ionization and excitation rates are governed by the fast electrons concentrated mainly near the inner electrode in both configurations, as indicated in Fig. 3. The electron density is determined by the bulk of the distribution function and by slow electrons concentrated in the positive column. This phenomenon apparently illustrates the non-hydrodynamic regime of the plasma electron component formation.

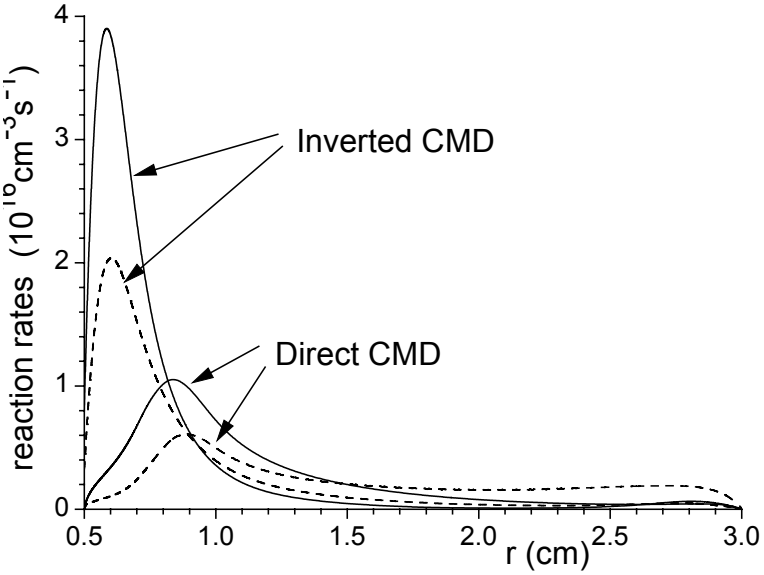

Fig. 5. The radial profiles of the direct ionization rate (solid lines) and the excitation rate (broken lines) in the direct and inverted CMDs.

In spite of the observed discrepances in the absolute values and radial distributions of the ionization rates, the total number of ionization events in the volume per unit time, written in terms of the discharge current $2\pi L\int_{r_0}^{R} I(r)rdr = i/\left[e(1+\gamma)\right]$ is the same in the direct and inverted configurations at equal currents.

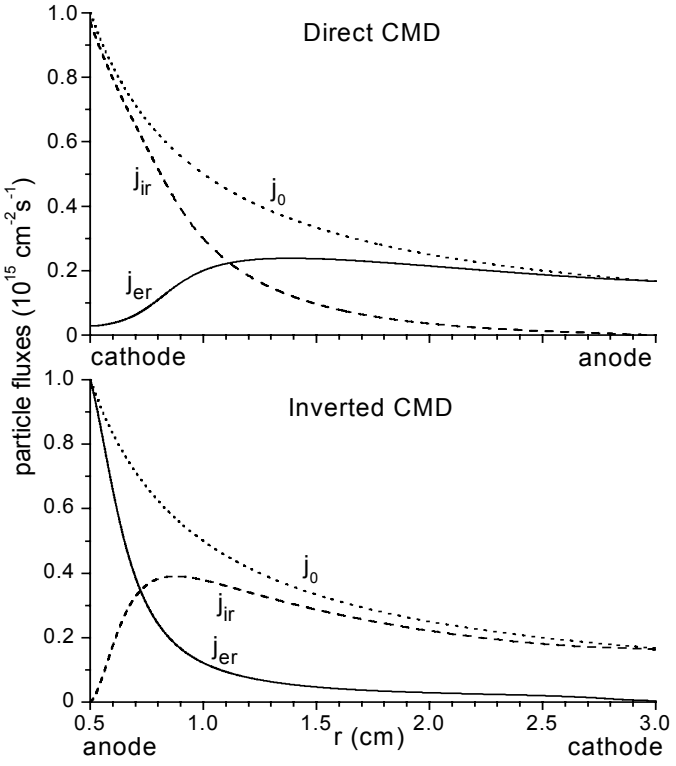

Fig. 6.The radial profiles of the electron $j_{er}(r)$, ion $j_{ir}(r)$ and total $j_0(r)$ current densities in the direct (a) and inverted (b) CMDs normalized by the total current density on the inner electrode: (a) $j_0(r_0)=1.49\cdot10^{16}$cm^{-2}s^{-1}, (b) $j_0(r_0)= 1.66\cdot10^{16}$cm^{-2}s^{-1}.

The transport of the discharge current in both magnetron configurations is demonstrated in Fig. 6, where the radial dependences of the electron $j_{er}(r)$, ion $j_{ir}(r)$ and total j_0 fluxes are reproduced. Electrons are the dominant current carriers in the direct magnetron, as opposed to the inverted CMD where the ion current is the main part of the discharge current. This ratio is valid for the whole discharge gap except for the regions adjacent to the inner electrode in both magnetrons, where intensive ion production takes place. The ions move to the cathode and their flux gives largest contribution to the total current density. For the inverted CMD the ion current dominates both in the cathode region and the positive column.

5. Conclusion

The present study addressed the issues of the plasma electron component formation in the direct (post-cathode) and inverted (hollow-cathode) CMDs. The calculations of the electron distribution functions, absolute values and radial distributions of the electron density, excitation and ionization rates and charged particle fluxes are carried out. The maxima in the electron density radial distribution are shown to be formed in the cathode vicinity in both CMD configurations, whereas the maxima of the ionization rates are situated in the vicinity of the inner electrode independently of its polarity. This fact is indicative of the non-hydrodynamic character of electron kinetics. The role of the electron and ion current densities in discharge current transport is analysed for both configurations.

6. Acknowledgements

The work in St.Petersburg was partially supported by Grant No. A04-2.9-630 of the Russian Ministry of Education. The work in Prague was partially financially supported by the Czech Science Foundation, Grant No. 202/03/0827, 202/04/0360, 202/03/H162, by project COST action 527.70, by the research project MSM 0021620834 and by EURATOM. We thank the University of Greifswald for providing us with the cylindrical magnetron system.

References

[1] J W Bradley – *Plasma Sources Sci. Technol*. **5**, 622 (1996).
[2] C. Costin, L. Marques, G. Popa and G. Gousset – *Plasma Sources Sci. Technol.* **14,** 168 (2005).
[3] T. A. van der Straaten, N. F. Cramer, I. S. Falconer and B. W. James – *J. Phys. D.* **31**, 177 (1998).
[4] I. A. Porokhova, Yu. B. Golubovskii, J. Bretagne, M.Tichý and J. F. Behnke – *Phys. Rev. E* **63** 056408 (2001).
[5] I. A. Porokhova, Yu. B. Golubovskii, M. Holík, P. Kudrna, M. Tichý, C. Wilke and J. F. Behnke – *Phys. Rev. E* **68** 016401 (2003).
[6] M. Holík, O. Bilyk, A. Marek, P. Kudrna, J. F. Behnke and M.Tichý – *Contributions to Plasma Physics* **44**, 613 (2004).
[7] J. Bretagne, G. Delouya, J. Godart and V. Puech – J. *Phys. D: Appl. Phys.* **14,** 1225 (1981).

Carbon thin film deposition on inner wall surface of polymeric-tube, and Langmuir probe measurements

Y. Ohgoe, K. K. Hirakuri, S. Kobayashi, K. Sato, and O. Miyashita

Department of Electronic & Computer Engineering, Tokyo Denki University
Ishizaka, Hatoyama, Saitama 350-0394, Japan
E-mail: yas@f.dendai.ac.jp

Abstract

In this study, to deposit diamond-like carbon (DLC) films on a polycarbonate-inner wall using radio frequency (r.f.) plasma chemical vapour deposition (CVD) techniques, we have developed the cylindrical electrode plasma process. The plasma state was stably generated inside the polycarbonate tube. The thickness of the deposited-DLC film was 300 ~ 350 nm, and the structure was uniform. The cylindrical electrode process is expected to apply to 3-dimensional insulator structures such as polymeric tubes.

Keywords: inner wall surface of polymeric-tube, cylindrical electrode process, r.f. plasma CVD, diamond-like carbon film

Introduction

Radio frequency (r.f.) plasma chemical vapor deposition (CVD) technique can be used on most substrates at low temperatures, and it is possible to control characteristic of deposited films [1]. In common r.f. plasma CVD system, it consists of two planar electrodes. These planar electrodes have advantage of uniformly depositing films over large area [2]. In spite of these extensive advantages, application of r.f. plasma CVD technique has been limited to flat substrates, such as silicon or glass wafers, etc. Therefore, to achieve uniform deposition of thin films is impossible since it is difficult to generate the uniform plasma around complicated (3-dimensional) structure surfaces. For this reason, industrial acceptances of r.f. plasma CVD technology have been restricted. In this study, we have developed cylindrical electrode to deposit diamond-like carbon (DLC) film on inner wall of commercial polycarbonate-tube, using r.f. plasma CVD process. Since characteristics of DLC films depend strongly on plasma conditions, success of uniform DLC films deposition to 3-dimensional structures indicates that this deposition process is applicable to other thin film deposition techniques.

Plasma measurements

The schematic diagram of cylindrical electrode process is shown in Fig. 1. This process consists of an aluminum cylindrical electrode that is put on a cathode side electrode, an anode side electrode, an r.f. generator (model SS-301AAE, Fuji Electronic Industrial Co., Ltd.), a matching box (model HC-2000, Tokyo Hy-power Labs., Inc.), and a vacuum pump (model 1397, Sargent-Welch Scientific Co.). The cylindrical electrode, which is electrically conducted to the cathode side electrode and the power generator, holds the outside of polycarbonate-tube (internal diameter: 11 mm, length: 100 mm, thickness: 1 mm) completely. In this way, it is possible to impress the cylindrical electrode r.f. power to the polycarbonate-tube and to generate glow discharge plasma on the inside of the polycarbonate-tube.

The plasma states (the distributions of electron temperature T_e and electron number of density N_e) of the tube length direction at the central axis were measured using the double-probe data analysis system (Fig. 1). The position at the tips of two probes was kept at the central axis of the tube. The double-probe data analysis system consists of two Langmuir probes (platinum wires with 400 μm in diameter) and the power supply of the probes (model R6243, ADVANTEST CORPORATION). The two probes were positioned parallel to each other at a distance of 10 mm, and the probes outsides were shielded with glass. The experiments were performed with helium (He) plasma, an r.f. power of 13.56 MHz at 30 W. In order to keep the polycarbonate-tube inner wall clean and the Langmuir probe tip without any contamination, He gas was used for estimating the plasma states. The gas pressures were 50, 100, and 150 Pa. These experimental conditions were possible to keep plasma generation inside the polycarbonate-tube.

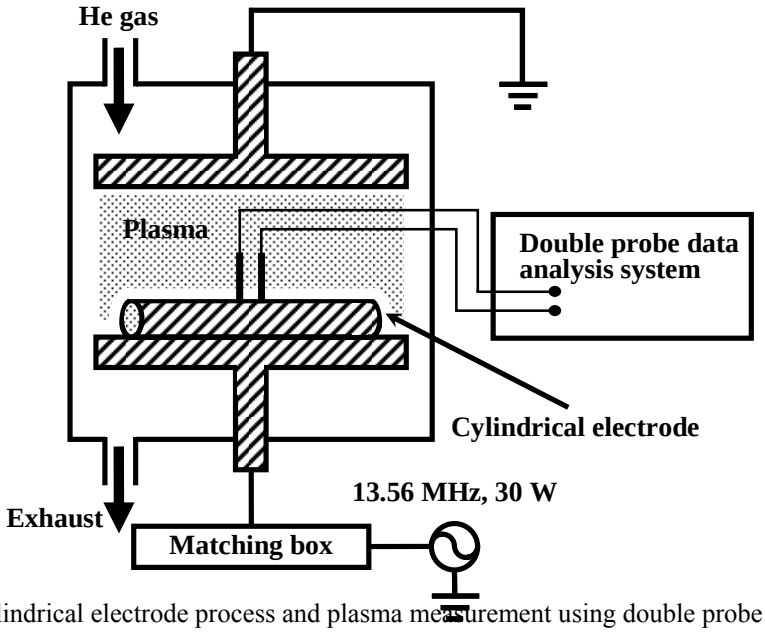

Fig. 1 Schematic of cylindrical electrode process and plasma measurement using double probe method.

Figure 2 shows the distributions of T_e and N_e, which were measured along the length direction at central axis of the polycarbonate-tube. Although the central axis profiles of T_e were higher at the edges part than at the center of the polycarbonate-tube with cylindrical electrode, under the all gas pressure conditions, the profiles of T_e were almost uniform inside the whole tube (Fig. 2-a). Moreover, the profiles of N_e were also measured. The profiles of N_e observed the same tendencies as well as the profile of T_e (Fig. 2-b). That is, both profiles of T_e and N_e were higher at the edges part than at the center of the polycarbonate-tube with the cylindrical electrode. From these results, it is considered that the plasma inside, which was in the hollow cathode discharge at the inner wall surface of the polycarbonate-tube, was generated from the both edges of the tube. Although the plasma inside was defused in the states of T_e and N_e which is show in Fig. 2, it was stably generated inside the whole tube.

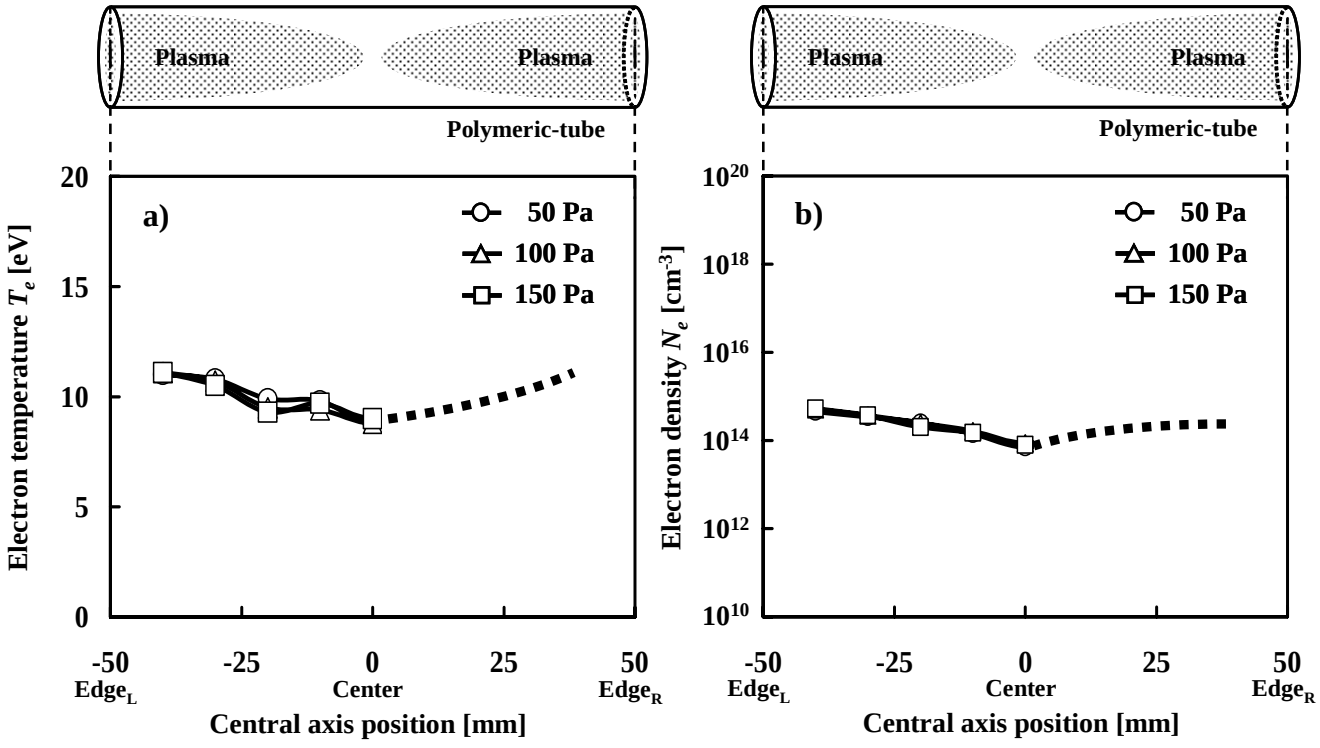

Fig. 2 Distribution of electron temperature T_e and density N_e, which were measured using double probe method.

DLC film deposition on polycarbonate-tube inner wall

The cylindrical electrode process with r.f. plasma CVD technique deposited DLC films on the polycarbonate-tube inner wall. The 13.56 MHz plasma of the electrical power was held constant at 30 W this decomposed the hydrocarbon gas (CH_4), and deposited DLC film on polycarbonate-tube inner wall under the following condition: CH_4 gas pressure at 10 Pa with a deposition time of 10 minutes.

The distribution of the film thickness was measured using the cross section of scanning electron microscope (SEM: JEOL, JSM-5310LVB) images. Additionally, the structure of the DLC film was investigated using infrared spectroscopy (IR: JASCO, FT/IR-620), and Ar-laser Raman spectrophotometer (Raman: JASCO, NRS-2100). Moreover, the chemical composition and bonding states of the DLC films were measured with X-ray photoelectron spectrometer (XPS: JEOL, JPS-9000MC). The monochrometer was used with *Al* K_α. DLC films contain a mixture of sp^3-bonds (tetrahedral or aliphatic), sp^2-bonds (trigonal or aromatic), and sometimes sp^1-bonds (linear or acetylenic) coordinated carbon atoms in a disordered network [2-4]. The properties of DLC films are determined by measuring bonding hybridization of the carbon atoms and relative concentration of the different bonds. Due to the importance of ratio of the sp^3/sp^2 hybridized carbon and hydrogen content in determining the properties of DLC films; it is of primary interest to characterize these two properties. IR, Raman, and XPS spectroscopy are most often used for study of DLC film structures [2]. In order to estimate the structure of DLC film satisfactorily, in this experiment, DLC film was deposited on silicon {100} substrates that were put on at the center and both edges (three different positions) of the polycarbonate-tube inner wall.

The DLC film thickness was decreased at the center of the polycarbonate-tube, it was kept at approximately 300 ~ 350 nm. The structure of the DLC film was investigated using IR, Raman, and XPS analysis. The IR spectra are shown in Fig. 3-a. These spectra were compared to the structure of the DLC film deposited at each different position (the $edge_L$ position, the center position, and the $edge_R$ position) on the inner wall surface. The main peak of all the spectra was the waveform of around 2920 cm^{-1}, and the sp^3 and sp^2 bonding spectra peak was observed at 2855 ~ 3000 cm^{-1} [2,4-7]. All the IR spectra at 3 different positions were similar; moreover, the ratios of sp^3/sp^2 were approximately at 2.4 ± 0.1. In this IR analysis, it is expected that the cylindrical electrode process produced uniformity of the DLC film deposition. The Raman spectra are shown in Fig. 3-b. As for the Raman spectra of all the positions on the inner wall surface of the polycarbonate-tube, each spectrum was of the same form. It is observed that all the spectra of the DLC film on the polycarbonate-tube inner wall were similar. The ratios of I_D/I_G that are ratio of intensities of *G*-peak and *D*-peak were approximately at 0.47. As well as the IR analysis, the cylindrical electrode process is expected to deposit the DLC films uniformly on the polymeric tube inner wall.

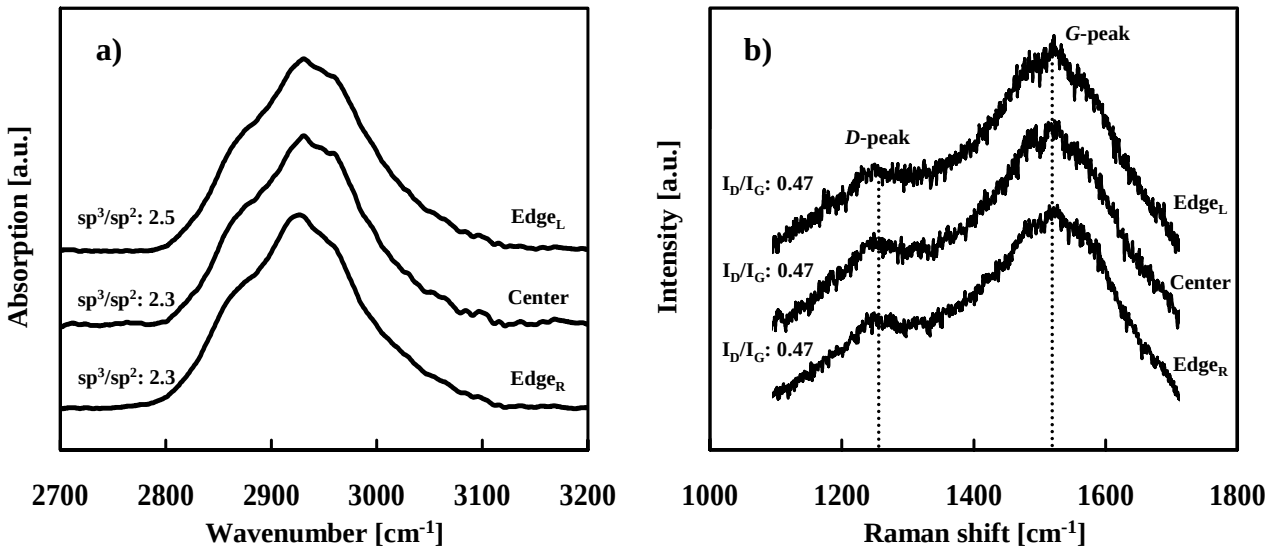

Fig. 3 IR and Raman spectra of the DLC film on the polycarbonate-tube inner wall.

In XPS analysis for the DLC film, carbon (C_{1s}) spectra have peak at 284.4 eV, and these asymmetric spectra were caused from π-bonding. XPS spectra of DLC films are decomposed into two types of peaks, sp^3-bonds (C-C bonds) and sp^2-bonds (C=C) [8,9]. All the FWHM for XPS spectrum of the DLC film were approximately at 1.55, there is no clear difference in these spectra including main peak positions. In this XPS analysis, it was revealed that the deposited DLC film on the polycarbonate-tube inner wall was uniform in structural characterization.

Conclusions

In this study, the DLC films were deposited on the polycarbonate-tube inner wall using the cylindrical electrode process. With the cylindrical electrode it is possible to generate hollow cathode discharge plasma inside the polycarbonate-tube. Based on the double-probe measurements of the plasma, it was expected that the plasma existed stably inside the tube. Additionally, the deposited DLC film on the polycarbonate-tube inner wall was uniformity. Due to the uniform film deposition, it is possible to guess that the plasma states were stable, during deposition, too.

The success of uniform DLC film deposition indicates that the cylindrical electrode process is applicable to other thin film deposition techniques and 3-dimensional structures such as polymeric tubes. Moreover, the cylindrical electrode process is expected to be adapted to slenderer and longer objects such as tubular medical devices. In that case, this process would be widely applied in industries.

Acknowledgment

We would like to thank Mr. Junya SHIROTO and Mr. Tsuneo TOYA for the discussion of the plasma measurements and analysis for DLC film structures. This work was supported by the Frontier Research and Development Center, Tokyo Denki University.

Reference

1. V. M. Tiainen, Diamond Relat. Mater. **10,** 153 (2001).
2. K. E. Spear and J. P. Dismukes, Synthetic Diamond: Emerging CVD Science and Technology, eds. (John Wiley & Sons, Inc., New York, USA, 1994), pp. 91-141
3. Y. Taki, and O. Takai, Thin solid films **316,** 45 (1998).
4. A. Grill, and V. Patel, Appl. Phys. Lett. **60,** 2089 (1998).
5. M. Ban, M. Ryoji, T. Hasegawa, Y. Mori, S. Fujii, and J. Fujioka, Diamond Relat. Mater. **11,** 1353 (2002).
6. K. K. Hirakuri, T. Minorikawa, G. Friedbacher, and M. Grasserbauer, Thin Solid Films **302,** 5 (1997).
7. L. Martinu, A. Raveh, D. Boutard, S. Houle, D. Poitras, N. Vella, and M. R. Wertheimer, Diamond Relat. Mater. **2,** 673 (1993).
8. I. Jimenz, R. Gago, and J. M. Albella, Diamond Relat. Mater. **12,** 110 (3003).
9. A. Kimura, Y. Azuma, T. Suzuki, T. Saito, and Y. Ikuhara, Diamond Relat. Mater. **11,** 1436 (2002).

The recombination in deuterium containing plasma at temperatures 130 – 300 K

O. Novotný[1], R. Plašil[1], P. Hlavenka[1], P. Macko[2], G. Bano[3], A. Pysanenko[1], J. Glosík[1]

[1]*Charles University, Faculty of Mathematics and Physics, Department of Electronics and Vacuum Physics, V Holešovičkách 2, 180 00 Prague 8, Czech Republic,oldrich.novotny@st.mff.cuni.cz*
[2]*Comenius University, Department of Experimental Physics, Bratislava, Slovak Republic*
[3]*Research Institute for Solid State Physics and Optics, HAS, Budapest, Hungary*

Abstract

The paper is covering part of our systematic experimental study of recombination of D_3^+ and D_5^+ ions with electrons in a He-Ar-D_2 afterglow plasma at temperatures T = 130–300 K. The data were obtained using Flowing afterglow (FALP) and stationary afterglow experiments. The experimental data are covering a large extend of buffer gas pressures and a large range of reactant partial number densities: $[D_2] = 10^{12}$-$3\cdot10^{15}$ cm^{-3}. Preliminary data on NIR-CRDS absorption spectroscopy of $D_3^+(v=0)$ are also reported.

Keywords: deuterium, **D_3^+ ions** recombination, rate coefficient, afterglow

1. Introduction

The ions H_3^+ and D_3^+ play important roles in the kinetics of media of astrophysical interest (interstellar molecular clouds [1, 2], and planetary atmospheres [2]) and also in laboratory produced plasmas (discharges, fusion plasmas at walls [3], etc.). The recent discovery of H_3^+ in diffuse interstellar molecular clouds has confirmed the presence of H_3^+ in space and has opened a problem of the observed high column density, which critically depends upon the recombination rate for H_3^+ with electrons at low energies [1, 4]. This problem was again discussed in the connection with very recent new experimental results [5]. The problem gets more complicated by taking into account the H_3^+ deuteration processes [2]. Recently several multiply deuterated species have been detected in interstellar medium, including some triply deuterated molecules e.g. ND_3. Deuterated species in some regions have been observed to have abundance >10% of their un-deuterated analogues, this is very high if we realise that abundance of D is ~10^{-5} with respect to H. Such large enhancement in the abundance of deuterated molecules and ions can be connected with gas-phase fractionation. The kinetics of the formation of H_3^+ and D_3^+ ions in hydrogen and deuterium containing plasmas is well understood (see e.g. [6]). Equally important for hydrogen and deuterium containing plasmas is to understand the processes of destruction of these ions in collisions with electrons. Differences in rates and products branching ratios of dissociative recombination of deuterium and hydrogen containing ions can be also partly responsible for enhancement of population of deuterium in some regions (for details see [7],[8]). Stimulation for present study is coming also from recent very successful theoretical studies of dissociative recombination of H_3^+ and D_3^+ made by V. Kokoouline and Ch. Greene [9].

However, despite enormous efforts, the results of experimental studies determining the rate of recombination of H_3^+ and D_3^+ ions with electrons have been found to yield values that vary by at least one order of magnitude from 1×10^{-8} to 3×10^{-7} cm^{3}s^{-1} for H_3^+ [10, 11, 12, 13] and 2×10^{-8} to 2×10^{-7} cm^{3}s^{-1} for D_3^+ [14, 15, 16, 17]. Moreover H_3^+ and D_3^+ as the simplest triatomic ions, are important examples for testing new quantum-theoretical calculations, but the agreement between theory, experiment and astronomical observations over a large range of energies has not yet been confirmed [9, 18, 19, 20, 21].

In our previous studies of recombination of D_3^+ ions with electrons in deuterium containing plasmas we observed the dependence of recombination rate coefficients on partial pressure of deuterium in the buffer gas. The dependencies were similar to one observed for rate coefficients of ternary ion molecule association reactions. In analogy with other ternary processes we expected strong temperature dependence of observed process, study of this dependence was the main goal of the presented experiment. The results of similar studies carried out in hydrogen plasma are reported in our previous paper [22, 23]. As follows from previous studies rate

coefficient of recombination of D_3^+ ions with electrons is at thermal energies of order of ~1-10x10^{-8} cm^3s^{-1} [25]. Because these values are too small to be measured in standard Flow Tube experiment (FALP), we have built a new version of the FALP with possibility to control temperature of the flow tube (FALP-VT). In the built FALP-VT high pressure and slow velocity of the buffer gas are used in order to be able to measure reliably rate coefficients of the order of ~10^{-8} cm^3s^{-1}. Previous measurements of recombination of D_3^+ with the Advanced Integrated Stationary Afterglow (AISA) apparatus [25] were supplemented and extended to lower temperatures (T=130–300K) and higher pressures of He buffer gas (6–8 Torr). A large range of reactant partial number densities was covered: $[D_2] = 10^{12}$ - $3 \cdot 10^{15}$ cm^{-3}.

The paper is covering part of our systematic study of recombination in low temperature deuterium containing plasmas. Reported is recombination of D_3^+ and D_5^+ ions with electrons in a He-Ar-D_2 afterglow plasma at temperatures T=130–300 K. These studies, [6, 24, 25] are complementary to recent very intensive experimental studies using large storage ring facilities [26, 27, 28]. Very recent experiments with rotationally cold ions indicate (in agreement with theory) that rotational excitation of H_3^+ can have influence on rate of recombination of these ions [20, 29]. In order to contribute to these studies we build near infrared cavity ring-down absorption spectrometer (NIR-CRDS) to monitor decay of H_3^+(v=0) and D_3^+(v=0) in decaying plasma [30] Preliminary data on NIR-CRDS absorption spectroscopy of D_3^+(v=0) are also reported.

2. Experiments

2.1. FALP – Flowing Afterglow

The *Flowing Afterglow Langmuir Probe (FALP)* technique is based on the so-called chemical reactor principle: The buffer gas flowing along the flow tube carries the plasma created upstream in the plasma source. We have built a high-pressure version of this apparatus – *VT-FALP*. The output nozzle at the end of the flow tube allows the working pressure to be increased up to 20 Torr. For ion identification and ion formation studies, we use a mass spectrometer placed statically down stream of the flow tube behind differential pumping. The electron and ion concentrations decay along the tube through diffusion and recombination losses. A *Langmuir Probe* (tungsten wire 18 μm in diameter and 7 mm long) movable along the axis of the flow tube is used for electron concentration measurements. Saturated electron current region of the probe characteristic is used to determine the electron number densities. Considering the constant velocity of the flowing gas (or plasma respectively) one can convert the position of the probe to the duration of the plasma decay. The well-understood recombination reaction of O_2^+ with electrons is used to validate *Langmuir probe* data (calibration procedure) at given temperature, pressure and gas flow rate. In order to minimize losses of ions under study in reactions

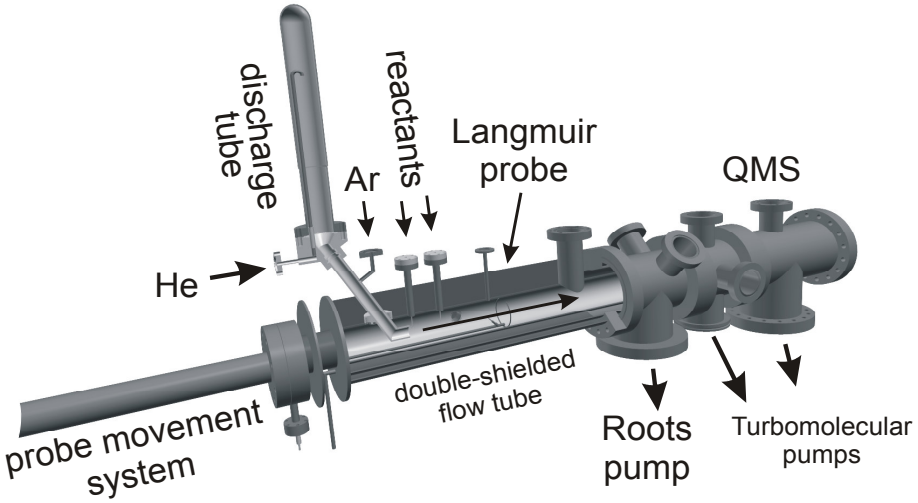

Figure 1. 3D design of the new *Flowing Afterglow Langmuir Probe – Variable Temperature (VT-FALP)* apparatus body. Discharge tube and flow tube is opened to show the internal arrangement. Total displayed length is approximately 1.5 m.

with impurities the gas handling system and the flow tube are using UHV technology and a buffer gas is cleaned by passing through the liquid nitrogen zeolite traps. The schematic 3D picture in Fig. 1. outlines the essential parts of present version of *VT-FALP*. The actual flow tube is embedded in cooling liquid (ethanol or liquid nitrogen) and thermally insulated by double shielding.

2.2. CRDS – absorption spectroscopy

As it was already mentioned possible differences between storage ring and afterglow data are due to differences in rotational excitation of recombining ions in different experiments. The identification of internal state of recombining ions can solve the problem. To study recombination of H_3^+ and D_3^+ ions we have built recently NIR Cavity Ring-Down Absorption spectrometer (NIR-CRDS). To measure recombination rate coefficient one has to determine absolute values of ion number densities. The transitions for D_3^+ were calculated [31], but there are not too many measurements in NIR of $D_3^+(v=0)$ ions. Short description of CRDS together with a configuration of "Test discharge tube" used in these measurements is given in Fig. 2. For more details see our recent papers [30, 32].

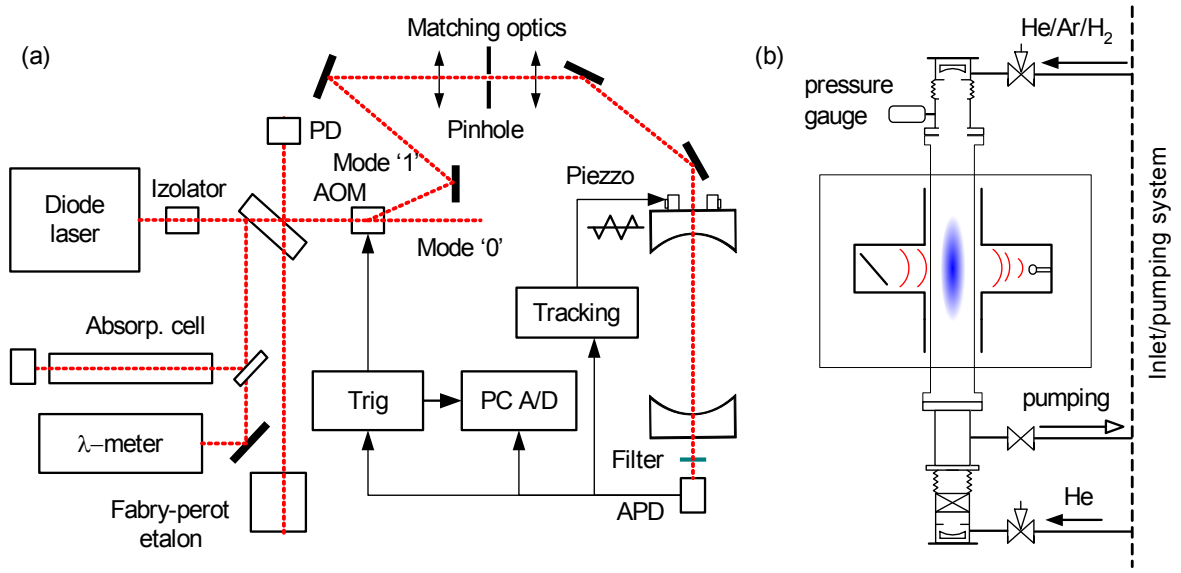

Figure 2. The schematics of the absorption experiment. a) The optical setup of NIR-CRDS spectrometer. The principle and details have been described elsewhere [33]. Light from a near IR diode laser (used in 1450 – 1470 nm region) was coupled into the high finesse optical cavity composed of spherical mirrors. The intensity decay of the light leaking from the cavity after interrupting the feeding beam by acousto-optic modulator (AOM) is recorded. b) Test discharge tube with microwave cavity (2.45 GHz, 30 W), optical cavity and gas handling system. The optical cavity is inside a pyrex tube (d = 4 cm, 72 cm long). The plasma column (5 cm long) is created in He (7 mbar) with small admixtures of D_2 and Ar in typical flow ratio 1100:3:1 (in sccm).

3. Results and discussion

In the present afterglow experiment (FALP-VT) a decay of the electron number density during recombination controlled afterglow is monitored and an effective rate coefficient, α_{eff} is calculated. In these calculations we are considering the deionisation process:

$$D_3^+ + e^- \xrightarrow{\alpha_{eff}} products\,, \qquad (1)$$

The rate coefficient α_{eff} was measured as a function of $[D_2]$ at several temperatures and pressures of the buffer gas. The obtained data together with previous data [6, 25] obtained in stationary afterglow (AISA) experiment are plotted in Fig. 3. Note significant dependence of the effective recombination rate coefficient on $[D_2]$ at all temperatures. We assume here that at very high $[D_2]$ and low temperatures α_{eff} is influenced by enhanced formation of D_5^+ ions and their consequent recombination (with rate coefficient α_5). At low $[D_2]$ and higher

temperatures formation of D_5^+ ions is not so effective and plasma is decaying mainly due to binary recombination of D_3^+ ions (with rate coefficient α_3). In intermediate region recombination of both D_3^+ and D_5^+ with electrons take place and simultaneously (if plasma is close to thermodynamic equilibrium) the number densities of both ions are coupled by van't Hoff equation. The overall dependence of the measured α_{eff} on He pressure, $[D_2]$ and temperature is given by three processes (corresponding rate coefficients are indicated):

$$D_3^+ + D_2 + He \underset{k_{-3}}{\overset{k_3}{\leftrightarrow}} D_5^+ + He\,, \tag{2}$$

$$D_3^+ + e^- \xrightarrow{\alpha_3} products\,, \tag{3}$$

$$D_5^+ + e^- \xrightarrow{\alpha_5} products\,. \tag{4}$$

where k_3 is the rate coefficient for three-body association and k_{-3} the rate coefficient for clusters destruction by collision-induced dissociation (CID) in collisions with He atoms. When considering processes (1) – (4) and diffusion losses (ambipolar diffusion with characteristic diffusion time τ_D), the balance equation for electrons is:

$$\frac{dn_e}{dt} = -\alpha_3 n_e [D_3^+] - \alpha_5 n_e [D_5^+] - ([D_3^+] + [D_5^+])/\tau_D\,, \tag{5}$$

Let us introduce the ratio $R=[D_5^+]/[D_3^+]$ and realize that $n_e = [D_5^+] + [D_3^+]$. Equation (5) can then be rewritten:

$$\frac{dn_e}{dt} = -(\alpha_3 + R\alpha_5)\frac{n_e^2}{1+R} - n_e/\tau_D = \alpha_{eff} n_e^2 - n_e/\tau_D\,, \tag{6}$$

If we consider: $R = \dfrac{[D_3^+]}{[D_5^+]} = \dfrac{k_3[D_2]}{k_{-3}} = K_C[D_2]$ the effective recombination rate coefficient can be written as

$$\alpha_{eff} = \left(\alpha_3 + \alpha_5 K_C [D_2]\right)\frac{1}{1+K_C[D_2]}\,. \tag{7}$$

where $K_C=k_3/k_{-3}$ is the equilibrium constant given by van't Hoff equation. The equilibrium constant has exponential dependence on temperature that is why dependence of α_{eff} on T is so strong. By fitting measured data values of α_3, α_5 and K_C corresponding to particular temperature can be obtained, see e.g. curve through data obtained at 190K in Fig. 4.

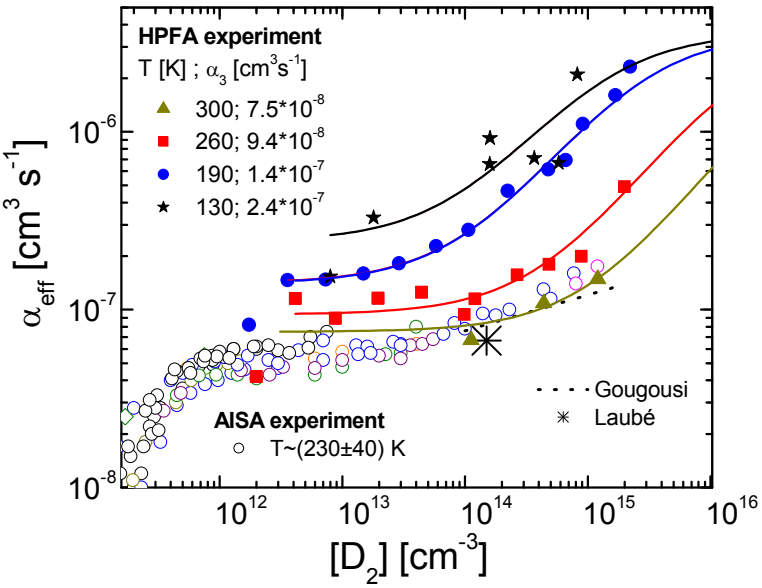

Figure 4. The effective recombination rate coefficients α_{eff} measured over a very broad range of hydrogen number densities on *AISA* (open symbols) and on *VT-FALP* (closed symbols) in a He-Ar-D_2 plasma mixture. The measurements on *AISA* were carried out at the temperature (230±40) *K*.

The obtained results are very similar to one obtained in previous measurements in the He-Ar-H_2 afterglow plasma [22]. Both hydrogen and deuterium plasma were successfully studied at similar conditions using Cavity Ring-Down Spectroscopy (CRDS) and preliminary results will be presented and compared with FALP and AISA studies. As was already mentioned spectra of D_3^+ ions were calculated [31] but not measured in frequency range covered by our diode laser. We have made first preliminary measurements of IR absorption spectra of $D_3^+(v=0)$ using continuous microwave discharge (see Fig. 2) and NIR-CRDS. Obtained spectra are plotted in Fig. 5. Using parallel absorption cell corresponding absorption spectra of H_2O molecule were also measured to increase accuracy of estimation of transition frequencies of $D_3^+(v=0)$.

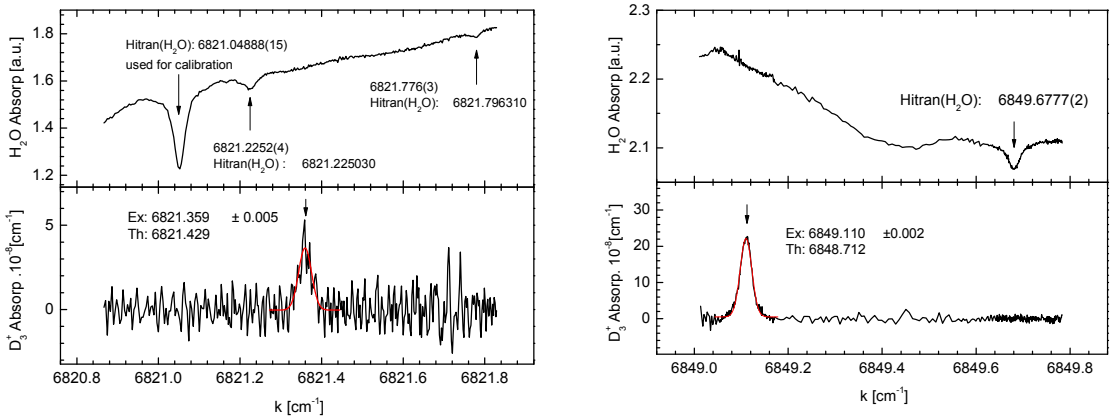

Figure 5. IR absorption spectra of $D_3^+(v=0)$ measured by NIR-CRDS. Ions were generated in continuous microwave discharge (see Fig. 2). In upper panels are plotted measured absorption spectra of H_2O molecule. Hitran tables, λ-meter and Fabry-perot etalon were used to measure frequency of transition.

Table 1. Notations of measured transitions together with theoretical [31] and experimental frequencies.

Re	J2	J1	E1	Th. Freq	Exp. Freq		
A1	1	1	43.609	6821.429	6821.359	±	0.005
E	3	2	85.627	6848.712	6849.05	±	0.050

Note excellent agreement of measured and calculated data. Agreement is far better as was agreement obtained in $H_3^+(v=0)$ studies, see CRDS study in ref. [32] and laser induced reaction study in ref. [34]. Obtained spectroscopic data will be used to measure recombination rate coefficient of $D_3^+(v=0)$.

Acknowledgments

This work is a part of the research plan MSM 0021620834 that is financed by the Ministry of Education of the Czech Republic and partly was supported by GACR (202/03/H162, 205/05/0390, 202/05/P095), GAUK-278/2004 /B-FYZ/MFF, GAUK-226/2005 /B-FYZ/MFF.

References

[1] T.R. Geballe: Phil. Trans. R. Soc. London, **A 358** (2000)
[2] T. J. Millar, H. Roberts, A. J. Markwick, S. B. Charnley: Phil. Trans. R. Soc. London, **A 358** (2000)
[3] R.K. Janev: Proceedings of the 1999 Conference on Dissociative recombination, Theory, Experiment and Applications IV, World Scientific, Singapore, **40** (2000)
[4] J. H. Black: The abundance and excitation of interstellar H3+, Phil. Trans. R. Soc. London, **A 358** (2000)

[5] B. J. McCall, A. J. Huneycutt, R. J. Saykally, N. Djuric, G. H. Dunn, J. Semaniak, O. Novotny, A. Al-Khalili, A. Ehlerding, F. Hellberg, S. Kalhori, A. Neau, R. D. Thomas, A. Paal, F. Österdahl, M. Larsson, Journal of Physics: Conference Series **4**, IOP Publishing (2005)
[6] R. Plašil, J. Glosík, V. Poterya, P. Kudrna, J. Rusz, M. Tichý, A. Pysanenko, Inter. J. Mass Spec. **218** (2002)
[7] H. Roberts, E. Herbst and T.J. Millar, Astronomy and Astrophysics, **424** (2004)
[8] Le Petit F, Roueff E, Herbst E, Astronomy and Astrophysics, **417** (3) APR (2004)
[9] Kokoouline V, Greene CH, Physical Review Letters **90** (13): Art. No. 133201 APR 4 (2003)
[10] M. Larsson: Phil. Trans. R. Soc. London, **A 358** (2000)
[11] M. J. Jensen, H. B. Pedersen, C. P. Safvan, K. Seiersen, X. Urbain and L. H. Andersen: Phys. Rev. A, **63** (2002)
[12] D. Smith D., P. Spanel, Int. J. of Mass Spectr. and Ion Processes **129** (1993)
[13] A. Canosa , J.C. Gomet, B. R. Rowe, J.B.A. Mitchell and J.L.Queffelec: J. Chem. Phys., **97** (1992)
[14] S. Laube, A. Le Padelleck, O. Sidko, C. Rebrion-Rowe, J.B.A. Mitchell and B.R. Rowe, J. Phys.: At. Mol. Opt. Phys., **31** (1998)
[15] T. Gougousi, R. Johnsen, M.F. Golde, Int. J. Mass Spectr. Ion Proc. **149/150** (1995)
[16] D. Smith, P. Spanel, Chem. Phys. Lettt., **211** (1993)
[17] M. Larsson et al., Phys. Rev. Lett., **79** (1997)
[18]A.E. Orel, I.F. Schneider, A. Suzor-Weiner, Phil. Trans. R. Soc. Lond. **A 358** (2000)
[19] D.R. Bates, M.F. Guest and R.A. Kendall.: Planet. Space. Sci., **41**, 9 (1993)
[20] B. J. McCall, A. J. Huneycutt, R. J. Saykally, T. R. Geballe, N. Djuric, G. H. Dunn, J. Semaniak, O. Novotny, A. Al-Khalili, A. Ehlerding, F. Hellberg, S. Kalhori, A. Neau, R. Thomas, F. Osterdahl, M. Larsson, NATURE **422**: (6931) APR 3 (2003)
[21] V. Kokoouline, V., C. H. Greene.: Phys. Rev. A, **68** (2003)
[22] J. Glosík, O. Novotný, A. Pysanenko, P. Zakouřil, R. Plašil, P. Kudrna, V. Poterya, Plasma Source Science & Technology, **12 (4)** (2003)
[23] J. Glosík, R. Plašil, A. Pysanenko, O. Novotný, P. Hlavenka, P. Macko and G. Bánó: Sixth International Conference on Dissociative Recombination, Journal of Physics: Conference Series **4** (2005)
[24] J. Glosík, R. Plašil, V. Poterya, P. Kudrna, M. Tichý, Chem. Phys. Letter, **331** (2000)
[25] V. Poterya, J. Glosík, R. Plašil, M. Tichý, P. Kudrna, and A. Pysanenko, Phys. Rev. Lett. 88 (2002)
[26] B.J. McCall , A.J. Huneycutt, R.J. Saykally, T.R. Geballe, N. Djuric, G.H. Dunn, J. Semaniak, O. Novotny, A. Al-Khalili, A. Ehlerding, F. Hellberg, S. Kalhori, A. Neau, R. Thomas, F. Osterdahl, M. Larsson, NATURE 422 APR 3 (2003)
[27] D. Strasser, L. Lammich, H. Kreckel, M. Lange, S. Krohn, D. Schwalm, A. Wolf, D. Zajfman, Phys. Rev. A 69 (6) JUN (2004)
[28] L. Lammich, D. Strasser, H. Kreckel, M. Lange, HB. Pedersen, S. Altevogt, V. Andrianarijaona, H. Buhr, O. Heber, P. Witte, D. Schwalm, A. Wolf, D. Zajfman, Phys. Rev. Let. 91 (14): Art. No. 143201 OCT 3 (2003)
29 H. Kreckel, J. Mikosch, R. Wester, J. Glosik, R. Plasil, M. Motsch, D. Gerlich, D. Schwalm, A. Wolf, Journal of Physics: Conference Series **4** (2005)
[30] R Plasil, P Hlavenka, P Macko, G Bano, A Pysanenko and J Glosık, Journal of Physics: Conference Series 4 (2005)
[31] J. Ramanlal and J. Tennyson, Mon. Not. R. astr. Soc.**354** (2004)
[32] P. Macko, G. Bánó, P. Hlavenka, R. Plašil, V. Poterya, A. Pysanenko, O. Votava, R. Johnsen, J. Glosík, International J. Mass Spectrom, **233/1-3** (2004)
[33] D. Romanini, A. A. Kachanov, N. Sadeghi, F. Stoeckel, Chem. Phys. Lett. **264** (1997)
[34] J. Mikosch, H. Kreckel, R. Wester, J. Glosik, R. Plasil, D. Gerlich, D. Schwalm, and A. Wolf, Journal of Chemical physics 121(22) Dec 8 2004

Plasma etching fabrication of PMMA-based microfluidic devices for bioanalytical applications

N. Vourdas[1,2], A. Tsougeni[1], A. Tserepi[1], A.G. Boudouvis[2] and E. Gogolides[1,*]
[1] *Institute of Microelectronics, NCSR Demokritos, Aghia Paraskevi 15310, Greece*
[2] *School of Chemical Engineering, National Technical University of Athens, Zografou 15780, Greece*
S. Tragoulias[3] and T.K. Christopoulos[3]
[3] *Department of Chemistry, University of Patras, Patras 26500, Greece*

Abstract
Plasma etching of PMMA (poly-methyl methacrylate) for microfluidic channel production has been performed by implementing either a hard-metallic mask or a polymeric *in situ* mask. Through this technique, an 80 μm-depth channel has been formed on PMMA, for application to rapid DNA-based analysis of genetically modified organisms. Plasma etch rate (ER) measurements are presented as function of the process parameters and they are correlated to plasma gas phase parameters. Relatively high ER was achieved (~1.5μm/min) with low voltage bias (-100V) at low pressures (0.53Pa).

1. Introduction

The fabrication of microfluidic devices with features of 10-1000μm size are of great importance in many fields of analytical science, where a small quantity of sample is available, enhanced resolution and sensitivity in separation is needed and increased functional integration is desired (medical, chemical and biochemical analysis, microchemistry etc) [1]. Even though the first microfluidic devices were fabricated on silicon and glass, the need for easy fabrication, low cost and disposability has recently shifted the attention on polymeric materials.

Microfabrication of polymers can be attained through many techniques such as hot-embossing, micro-casting etc [1]. The implementation of these methods entails the need for a mold fabrication, using standard microelectronic processes. Recently, deep plasma etching of polymers [2]-[4] has been proposed for the fabrication of polymeric microfluidic channels, thus introducing, a mold-free method. The implementation of plasma treatment presents some unique merits in that (i) plasma etching is an inherently mass production technique, (ii) the polymer is treated while being in its solid state, (iii) channel formation is performed in rather low temperatures (cold-plasma), and (iv) within the same plasma reactor several surface physicochemical and mechanical properties (wettability, hardness etc) may be modified, towards the requirements of the specific application. Moreover, plasma treatment is already proposed and in fact it is already widely used for the sealing of PDMS trenches with another PDMS or a glass-plate (providing the fourth wall), through what is referred to as 'plasma activation of PDMS'.

Plasma etching employs a patterned layer (above the plastic that will host the trench) which acts as a mask, enabling the plasma to engrave the plastic substrate only where it is required. This patterned layer should provide sufficient etch resistance throughout the plasma treatment. Hitherto, metallic-hard masks have been utilized, that provide outmost plasma resistance, but on the other hand, impose difficulties and complexity (wrinkles, curvatures etc), while sputtering of their surface contributes to channel roughness.

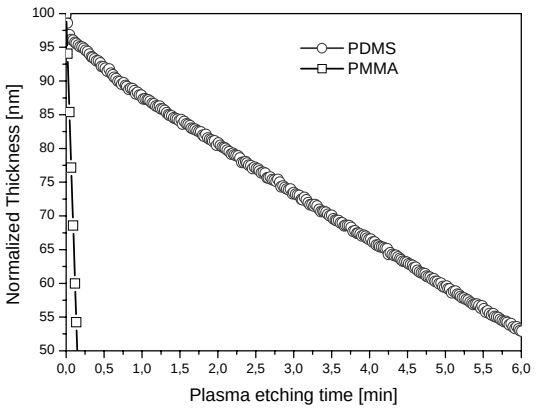

Fig. 1 Differential plasma ER of PMMA and PDMS during oxygen plasma treatment. High selectivity is obtained. Metals are virtually un-etchable in O_2-discharges.

* Corresponding author: Dr. E. Gogolides
Tel. +30 2106503237, Fax: +30 2106511723
e-mail address: evgog@imel.demokritos.gr

In this work we present a method for fabrication of microfluidic devices based on the O_2 plasma etching of polymers -PMMA in particular- using a photosensitive silicon-containing polymeric mask (poly-dimethylsiloxane-PDMS). Our method relies on (i) the ability to lithographically pattern a thin PDMS layer and (ii) the differential plasma ER of the PDMS (top layer) and the underlying PMMA plate, as illustrated in Fig. 1. The etch resistivity of PDMS is attributed to the surface oxide layer formation, during the first seconds of the oxygen plasma treatment [5]. We also carried out plasma etching of PMMA following the conventional procedure; through a metallic -namely Al- mask.

The aim is to fabricate a plastic micro-device for DNA-based analysis of genetically modified organisms (GMOs) *via* capillary electrophoresis (CE) for separation and laser-induced fluorescence (LIF) for detection of GMO-specific sequences [6]. The rapid progress of recombinant DNA technology and its applications to agriculture has resulted in the development of genetically modified plants with herbicide or insect tolerance. In order to allow consumers an informed choice, various countries, including European Union and Japan, have set threshold values above which raw materials and food products must be labeled accordingly. A threshold value of 0.9% GMO content was set for EU. Although GMO testing may be accomplished by detecting either the novel protein synthesized by the transgenic plant or the foreign DNA introduced into the plant's genome, DNA is the preferred analyte due to its greater stability during food processing. Detection of GMO-specific DNA requires amplification of the sequences by using the polymerase chain reaction (PCR) and subsequent analysis of the products. Separation of the amplified fragments by agarose gel electrophoresis and ethidium bromide staining is currently the most widely used method of analysis. However this procedure requires at least 1 hour. We anticipate that by using microchip-based capillary electrophoresis of the amplified fragments we will achieve separation times of less than 1 min. Moreover, plastic chips have low cost and are disposable.

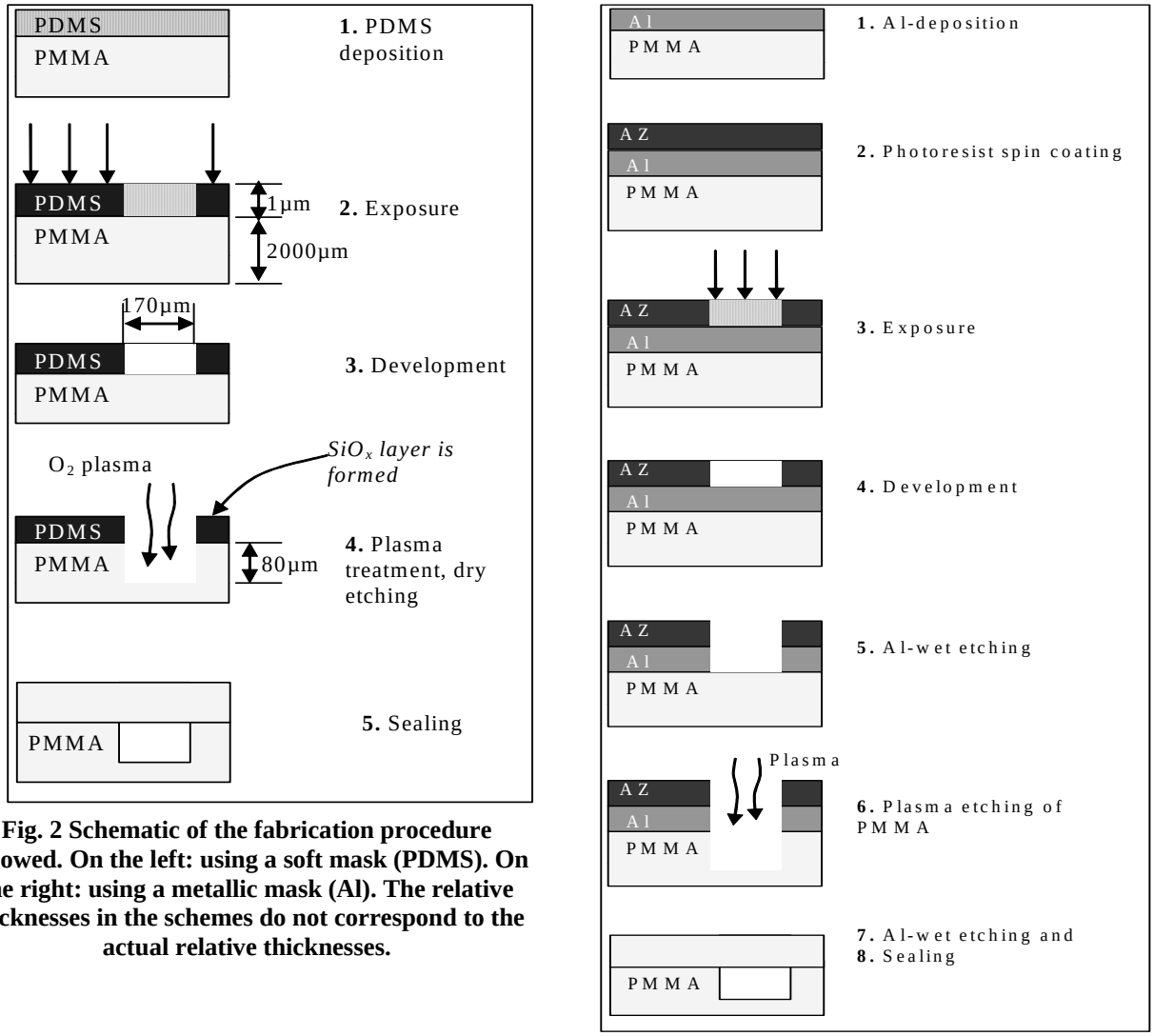

Fig. 2 Schematic of the fabrication procedure followed. On the left: using a soft mask (PDMS). On the right: using a metallic mask (Al). The relative thicknesses in the schemes do not correspond to the actual relative thicknesses.

2. Experimental

All devices are made of PMMA (2mm-thickness) by IRPEN. Two different methods were carried out, for lithographically defined masks that are summarized in Fig. 2. The first employs PDMS as a mask during plasma etching, while the second employs aluminum mask.

2.1 Lithography

With respect to the first one, photosensitive-PDMS solution (PS264, M_w=993k, 5-6% Diphenyl, 0.1-0.3% Methylvinylsiloxane copolymer, Gum from United Chemical Technologies, Inc), was spin coated on the PMMA-sheet. The PDMS layer (~1μm) was exposed through a photo-mask using broadband DUV radiation of an Hg-Xe arc lamp. The soluble part of PDMS was removed (developed) by means MIBK (methyl-isobutyl ketone) and IPA (iso-propyl- alcohol).

With regard to the second one, a thin (200nm) Al-layer was deposited on the PMMA-plate, using an electron gun evaporator. Then a typical photolithography procedure was followed; a commercial photoresist (AZ5214 from Clariant) was spin coated, and exposed through the same photomask as before. After the development of AZ the unprotected aluminum surface was wet-etched, within a thermally controlled tank.

2.2 Plasma etching

Pattern transfer was accomplished by oxygen plasma etching in an inductively coupled (ICP) etcher (MET) from Alcatel. Crucial for our experiments turned out to be the electrode temperature control. In our facilities this is ensured *via* He-backside cooling, which provide adequate temperature stability of the under-treatment specimen. The process variables of this plasma reactor are: plasma source power, bias voltage, gas flow, reactor pressure, and electrode temperature. These variables were properly tuned in order to achieve optimal results (see below in Results and Discussion).

The fourth wall of the channel was provided by another PMMA-sheet, that was thermally bonded to the plasma treated PMMA-plate.

ER was monitored *via in situ* spectroscopic ellipsometry, by J.A. Woollam (M2000), through appropriate procedure that has been described in detail elsewhere [7].

After the plasma etching the channels were sealed by thermal bonding with another PMMA-sheet (providing the fourth wall).

2.3 Gas phase characterization

Gas phase monitoring was performed by means of:

(i) Optical emission spectroscopy, by utilizing an Acton Research SP-500 monochromator with an SBIG CCD detector ST-6i. The subsequent optical actinometry performed by using Ar (actinometric gas) at 5% admixture in oxygen. Oxygen emission lines at 777nm and at 844nm and Argon emission line at 750nm were recorded during the tuning of the process parameters.

(ii) Ion flux measurements, by using an ion-flux probe by Scientific Instruments for determining ion fluxes.

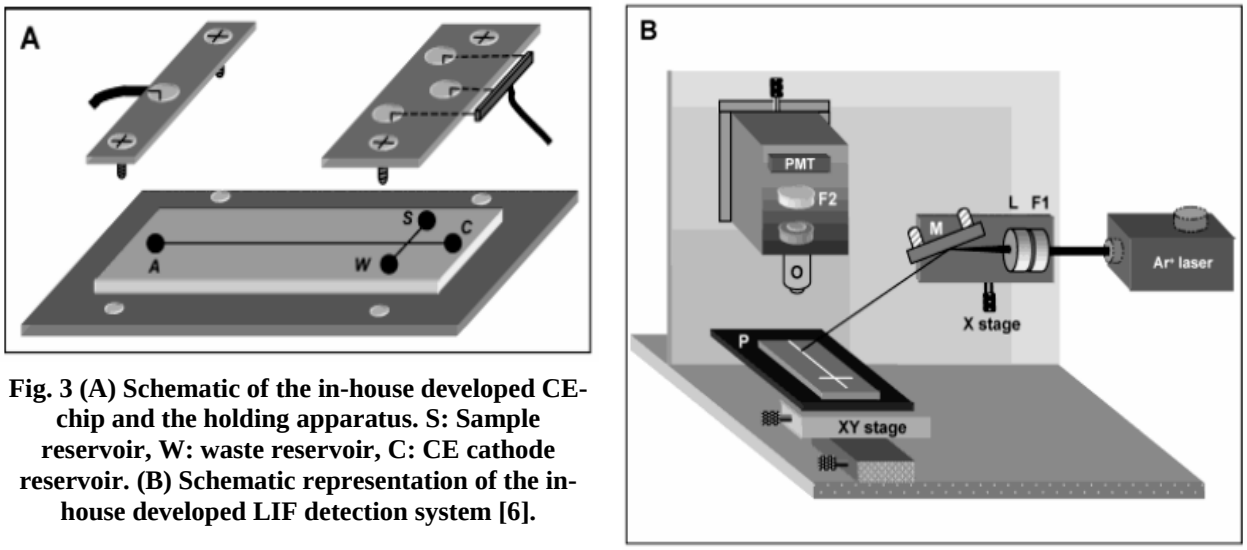

Fig. 3 (A) Schematic of the in-house developed CE-chip and the holding apparatus. S: Sample reservoir, W: waste reservoir, C: CE cathode reservoir. (B) Schematic representation of the in-house developed LIF detection system [6].

2.4 System setup for CE

The assembly of the chip is demonstrated in Fig. 3. In Fig. 3A the installation of the access holes and electrodes is illustrated. The overall analytic device and the detection setup is represented in Fig. 3B.

3. Results and Discussion

3.1 ER dependence on process parameters

In Fig. 4A and Fig. 4B the etch rate (ER) measurements of PMMA in oxygen plasma are presented as a function of the plasma source power and the pressure of the reactor. The aim is to find an optimum process condition set, with regard to the maximization of the ER; the higher the ER the shorter the total time needed for the process. As illustrated in Fig. 4A and Fig. 4B the ER increases vs. plasma source power and exhibits a maximum vs. reactor pressure. The higher achieved ER is ~1.5μm/min, which occurred at 1800W and at 0.53Pa. According to this result, the required time to engrave an 80μm trench would be 53min.

The ER strongly depends on the bias voltage (not shown here), indicating the ion-enhanced nature of the process. Gas phase characterization was performed to explain the above-mentioned variations of ER.

Actinometry was carried out to monitor the [O] variations during plasma treatment. Walkup et al [8] set out that the 844nm emission line must be selected rather than the 777nm emission line in order to follow the [O] profile. In Fig. 4C and in Fig. 4D we provide the information obtained through appropriate analysis of the optical emission data, namely the actinometric ratio $I_{O(844nm)}/I_{Ar(750nm)}$ vs. plasma source power and reactor pressure, respectively.

With respect to the effect of plasma source power, it can be seen that the actinometric ratio increases as the plasma power increases (Fig. 4C), in agreement with the measured ER. On the other hand actinometric ratio presents monotony throughout the measured pressures (Fig. 4D), while ER realizes a maximum. This behavior of the actinometric ratio is in accordance with previous published relevant studies [9], in a low-pressure distributed electron cyclotron resonance (DECR) plasma. This contradiction is solved through resonance absorption measurements in [9] indicating a local maximum of ground-state oxygen atom concentration at about 0.4Pa. The implementation of actinometry that hinges on the fact that only electron impact excitation of [O] occurs, seems to be questionable under these experimental conditions; the dominant mechanism for the production of the 844nm emission line under these conditions is dissociative excitation.

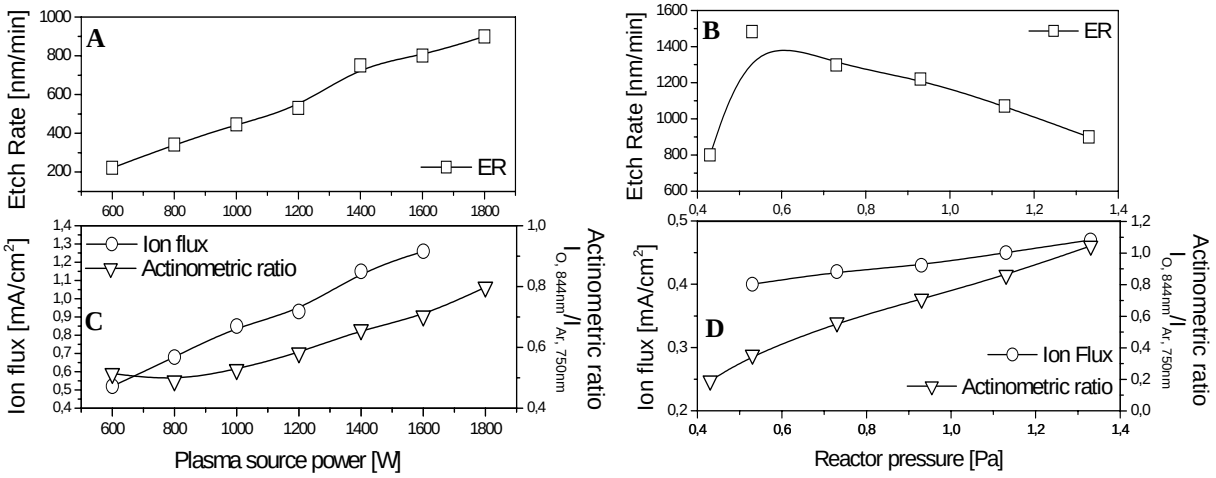

Fig. 4 (A) O_2-plasma etch rate measurements of PMMA vs. plasma source power [Electrode temperature: 15°C, Bias Voltage: -100V, O_2 flow: 100sccm, reactor pressure: 1.33Pa]. (B) O_2-plasma etch rate measurements of PMMA vs. reactor pressure [Electrode temperature: 15°C, Bias Voltage: -100V, O_2 flow: 100sccm, plasma source power: 1800W]. (C) Actinometric ratio $I_{O(844nm)}/I_{Ar(750nm)}$ and ion flux measurements of the oxygen-ICP vs. plasma source power and (D) vs. reactor pressure. The actinometric ratio in (D) has been appropriately treated to include the pressure dependence. In all cases lines are only to guide the eye.

Ion flux measurements designate an increment of J_+ with plasma power (Fig. 4C), which is in correlation with the ER measurements. Increase of plasma source power results in higher electron density and subsequent larger degree of dissociation and ionization. On the other hand J_+ remains practically constant (small increase) with pressure (Fig. 4D), while ER presents a maximum. We suspect that the collisions (mainly charge exchange collisions) in the sheath decrease as the pressure drops resulting in higher energy of the ions and so higher ER. This trend is limited by the decrease of the concentration of the oxygen species (Fig. 4D) as the pressure drops. This trade-off is found to realise a maximum at 0.53Pa.

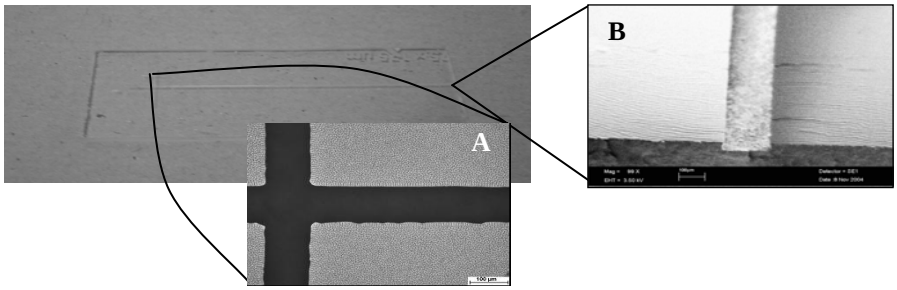

Fig. 5 The microfluidic channel before the sealing. The transparency of PMMA remains intact. (A) Detail of the cross by optical microscopy and (B) cross section of the trench by SEM.

3.2 Surface characterization

The plasma treatment induced manifold changes to the PMMA-plate. First of all PMMA has been patterned according the lithographically defined prototype. Fig. 5 demonstrates the PMMA-plate right after the plasma treatment (before the sealing). Optical microscopy photos (Fig. 5A) reveal the precise pattern transfer (fluctuations at one edge are due to the low quality of the photomask). Secondly, plasma treatment has modified the PMMA surface with regard to its wettability; the initially weakly hydrophilic surface (water contact angle=60^o) became highly hydrophilic (water contact angle=5^o) after the treatment. Finally, plasma treatment caused development of surface roughness (see Fig. 5B). This latter, plasma-induced effect, can be primarily attributed to micro-masking due to Si/Al sputtered material. The highly anisotropic character of plasma etching, due to the ion-enhanced chemical nature of the process, further amplifies/enhance the magnitude of the roughness. This of course is a drawback, imposing difficulties and worries for the subsequent optical detection, if the laser beam goes through the plasma treated plate instead through the non-treated channel cover plate. We are currently working to reduce the surface roughness, by appropriate tuning of the process parameters and/or by a post-etching procedure of the treated surface.

4. Conclusions

A PMMA microfluidic chip was fabricated by means of plasma etching. Thus, patterning and wettability control was accomplished simultaneously. This chip will be evaluated through capillary electrophoresis analysis of DNA (study under way).

Acknowledgments

Funding was partially provided by the European Community Fund (75%) and Public Resources (25%), through the "HERAKLEITOS" program and by the NCSR "DEMOKRITOS"-internal fellowship program.

References

[1] E. Verpoorte, N.F. de Rooij, *Proceedings of the IEEE*¸ **2003**, 91, p. 930
[2] J.S. Rossier, C. Vollet, A. Carnal, G. Lagger, V. Gobry et al, *Lab on a Chip*, **2002**, 2, p. 145
[3] D.F. Weston, T. Smekal, D.B. Rhine and J. Blackwell, *J. Vac. Sci. Technol. B*, **2001**, 19(6), p. 2846
[4] C. Zhang, C. Yang, D. Ding, *J. Micromech. Microeng.*, **2004**, 14, p. 663
[5] A. Tserepi, G. Cordoyiannis, G.P. Patsis et al, *J. Vac. Sci. Technol. B*, **2003**, 21(1), p. 174
[6] P.J. Obeid, T.K. Christopoulos, P.C. Ioannou, *Electrophoresis*, **2004**, 25, p. 922
[7] N. Vourdas, A.G. Boudouvis and E. Gogolides, *Microelectron. Eng.*¸ 78-79, **2005**, p. 474
[8] R.E. Walkup, K.L. Saenger, G.S. Selwyn, *J. Chem. Phys.*, **1988**, 84(5), p. 2668
[9] J.P. Booth, O. Joubert, J. Pelletier, N. Sadeghi, *J. Appl. Phys.*, **1991**, 69(2), p. 618

Toluene destruction by DBD at atmospheric pressure: Identification of reaction pathways by isotopic labeling and use of the plasma DBD as a pretreatment for adsorption

S. Ognier, L. Martin, J. Amouroux
Laboratoire de Génie des Procédés Plasmas et Traitement de Surfaces, 11 rue Pierre et Marie Curie, 75231 Paris Cedex France

Abstract:
An hybrid process combining a plasma DBD discharge and an adsorbent bed was used for the removal of toluene, a mono-aromatic molecule that simulates volatile aromatic pollutant (VOCs). The first objective of the study was to understand the role of active oxygenate species produced by streamers in oxidation and polymerisation mechanisms of aromatic and polyaromatic compounds. The potentiality of plasma pretreatment for optimising the use of adsorbant for the treatment of polluted gaesous effluent was then demonstrated.
Key words:
Dielectric Barrier Discharge, isotopic labeling, toluene, VOC, adsorption

Introduction

Air pollution control is focused by European Union these last years. Two techniques are investigated for treating gaseous effluents containing VOCs at ppm and sub-ppm levels: adsorption [1] and non-thermal plasma [2,3] processes. However, severe limitations still exist in the use of these two techniques. On one hand, plasma processes that are developped with the objective to completely oxidise pollutants in COx encounter two severe limitations: high energetic cost and incomplete oxidation leading to by-products release. On the other hand, adsorption processes are limited by the regeneration costs and the life duration of the adsorbent.

In view of these considerations, a new process coupling a plasma pretreatment followed by an adsorption step is proposed in this study. In a first step, the plasma discharge is used to chemically modify the initial pollutant, to decompose it into smaller molecules or to polymerise it into larger molecules: these reactions contribute to enlarge the distribution of the species. As a result, in the following step, the adsorption process is favored by the large distribution of chemical species : the number of available adsorption sites is increased and therefore the life of adsorbent is enhanced.

In the first part of the study, isotopic labeling experiments were carried out to identify reactional pathways, in particular the role of oxygen in polymerisation and oxidation reactions. The reactor used was a multipoint-to-plane dielectric barrier discharge reactor already used for NOx destruction [4,5]. In the second part, the combination of plasma pretreatment by DBD discharge and adsorption was investigated in a system coupling a wire-cylinder plasma reactor and a fluidized bed of zeolithes.

Experimental

A general view of the experimental setup is presented Figure 1. Gas used to simulate the polluted effluent is a mixture of oxygen (10%), H_2O (1.8%) and toluene in nitrogen. Gas mixture is introduced in the reactor with a flowrate of 3 or 3.5 NL/min heated at 373K (figure 3). Bubbling method was used to set toluene and water concentrations in the gas stream. The concentrations were set by controlling either the flow rate of nitrogen or the temperature of water bath.

In isotopic labelling experiments, a multipoint-to-plane corona discharge reactor was used. Two mixtures were studied: one containing non labeled molecules, with a toluene concentration of 700 ppmv and the other one containing $^{18}O_2$ and toluene three times deutered on methyl group, with a concentration of 200 ppmv. The total mixture flow was 3 l/min.

The second set of experiments consisted of combining a plasma reactor followed by an adsorbant bed. Therefore, the gaseous mixture undergoes first a plasma discharge pretreatment, then it flows through a fluidised adsorbant bed so that the residual toluene as well as the by-products formed from toluene in the plasma discharge are removed by adsorption. The plasma reactor was a wire cylinder reactor. The adsorbant bed is a glass tube of 40 mm diameter filled of 18 g of zeolithes (Mordenite, Si/Al ratio : 60, specific area :

300 m^2/g, density : 0,5 g/cm^3, average diameter : 240 µm). The gaseous flow allows the bed of zeolithes to be at the minimum fluidisation velocity. Gaseous mixtures at toluene concentrations of 100, 400 and 700 ppmv toluene were treated at atmospheric pressure. The total mixture flow was 3.5 l/min.

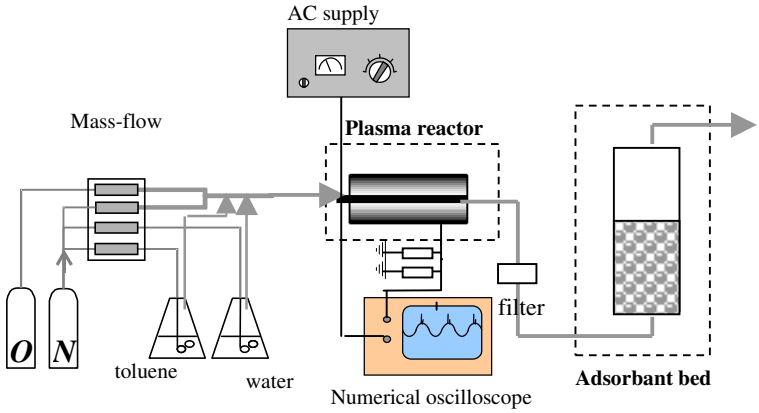

Figure 1: Experimental process and electrical setup

DBD discharge reactors :

The multipoint-to-plane corona discharge reactor is presented figure 2. The stainless steel high voltage electrode is a 4 mm wide and 22 mm diameter disc where thirteen tips are fixed. Each one is 5 mm long, 1 mm diameter and has a 100 µm curving radius. Twelve holes permit gas flowing across the high voltage electrode disc to the inter-electrode zone. The space between tip extremities and dielectric material is fixed at 2 mm. Dielectric used is stumatite, a natural alumino-silicate covering the grounded electrode. It is a 31 mm diameter disc, 4 mm thick; flaps covering the electrode on 4 mm high to center it. The grounded electrode is a stainless steel disc (25 mm diameter, 6 mm thick). Figure 3 presents the wire-cylinder plasma reactor. It consisted of an emitting stainless steal rod (length of 35 mm, diameter of 7 mm) held in the center of a cylinder (internal diameter of 11 mm) made of two layers of dielectric materials (7 mm thick stumatite and 3 mm thick glass) and covered by a copper cylinder. The space between tip extremities of the rod and dielectric material is 2 mm.

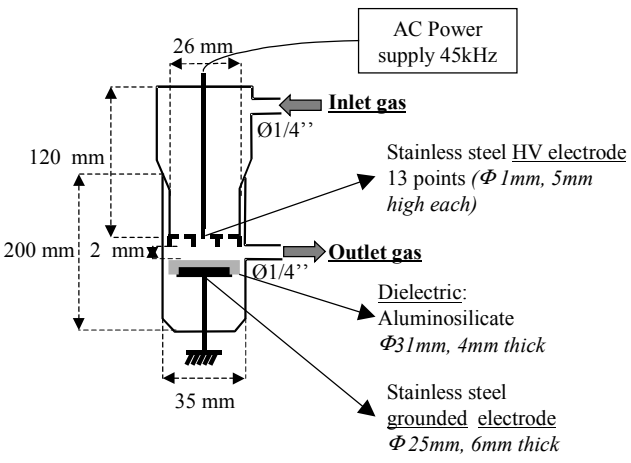

Figure 2: Depollution multipoint-to-plane reactor

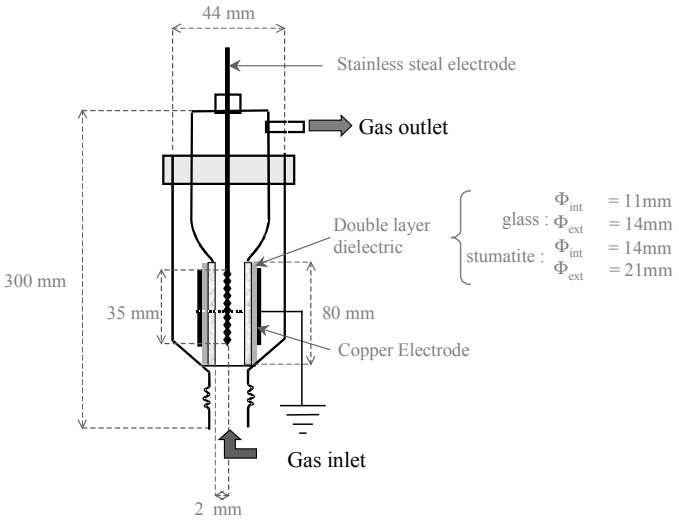

Figure 3 : Wire-cylinder Plasma reactor

Products analyzing:
Toluene and toluene decomposition by-products characterised by a carbon number higher than one were analysed by Gas Chromatography coupled with a Mass Spectrometer (GCtop/Automass II, Porabond Q, carrier gas He,Thermoelectron). CO and CO_2 were quantified with a GC equipped with a TCD detector (IGC, Carboxen, carrier gas He, Intersmat). Gaseous samples were taken at the outlet of the plasma reactor and before the inlet of the adsorbant bed to determine the toluene conversion rate induced by the plasma pretreatment and the nature of the by-products formed. To estimate the performance of the adsorbant bed for trapping toluene and plasma by-products, gaseous samples were as well taken at the outlet of the adsorbant bed. Heavy decomposition by-products were trapped on filters (Teflon ® glass, Pall Gelman DOP 0.3 µm) located at the exit of the plasma discharge zone then extracted into liquid phase (CH_2Cl_2 ¾, acetone ¼) with a soxhlet during 24 hours before being analysed by GC-MS. Labeled and non-labeled molecules are determined by mass spectroscopy analysis, thanks to the ion fragment mass difference.

Electrical setup and pulses characterization:
A high voltage generator supplies from 5 to 30kV peak to peak (U_{pkpk}) alternative voltage while a LeCroy LT 342, 500 MHz digital oscilloscope acquires the electrical characteristics of the corona discharge. A typical oscilloscope screen is presented on figure 4. The pulse currents are responsible of chemical activity.

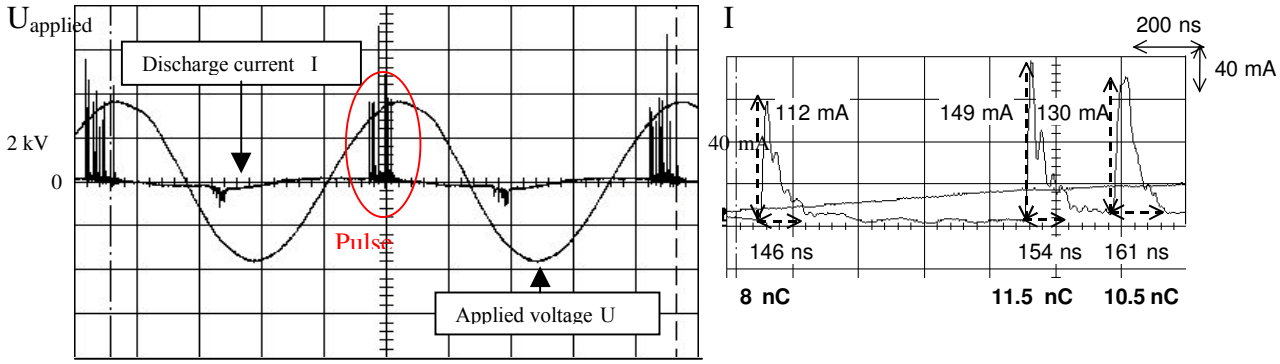

(a) (b)

Figure 4: Oscilloscope screen showing applied tension and reactor electrical response (a) and enlarged oscilloscope screen (b) showing elementary pulses (*multipoint-to-plane reactor, P = 18.15 W, P = 10^5 Pa, D = 3L/min at 373K, [Toluene] = 200 ppm, O_2 10 %, H_2O 1.8 %, N_2 balance*

The discharge power P was computed by the integration on two entire periods of instant applied voltage. Medium tensions of 3.4 kV and 4.85 kV were chosen for the multipoint-to-plane and the wire-cylinder reactors, corresponding to energy densities of 360 J/L and 220 J/L respectively.
Pulse characteristics (duration, current, pulses frequency and number of pulses during one period…) are determined thanks to enlarged oscilloscope screen (figure 4b). Each pulse is the electrical signature of electronic activity in the reactor. The characteristics of the impulsionnal component of the discharge for the multipoint-to-plane reactor are summarized in table 1.

Effective applied tension U_{eff} (kV)	3.40	Average pulse duration (ns)	109
Active power (W)	18.15	Average pulse max current (mA)	123
Energy density (J/L)	360	Average pulse charge (nQ)	6.7
Number of pulses on one period	8	Charge on one period (nC)	50

Table 1: Electrical discharge parameters and pulses characteristics for the labeled test

During one period, the electrical charge collected is 50 nC, what corresponds to $0.5.10^{-12}$ moles of electrons. This quantity is low compared to the quantity of oxygen flowing through the reactor during one period : $3.8.10^{-9}$ moles. That means that electrons are in the minority and that only a small ratio of oxygen could excited if there is accordance between electronic energy distribution function and oxygen excitation cross section. The same procedure allows to obtain an electrical charge collected of 50 nC for the wire-cylinder reactor at an energy density of 220 nC.

Results and discussion

Performance of DBD reactors for toluene decomposition

The performance of the two plasma reactors for toluene destruction was first investigated. Table 2 shows the toluene conversion rates and the quantity of toluene destroyed (ppm) according to the pollutant input concentration for both reactors. The results show that the toluene conversion rate decreases when the toluene input concentration increases. For example, the toluene conversion rate decreases from 85% to 15% when the toluene input concentration increases from 100 to 700 ppm in the wire-cylinder plasma reactor. On the contrary, the quantity of toluene destroyed in the plasma discharge remains almost unchanged whatever the toluene input concentration, about 100 ppm in the wire-cylinder reactor and 150 ppm in the multipoint-to-plane reactor respectively. Therefore, in these experimental conditions, the kinetic of toluene removal does not depend on toluene concentration.The limiting step could be the production of active species by the discharge. The results show as well that for a given energy density, the quantity of toluene destroyed is 50% higher in the MPP reactor compared to the Wire-Cylinder reactor. This result could be explained by the fact that the impulsionnal charge is higher in the MPP reactor (50 nC) than in the Wire-Cylinder reactor (20 nC).

Toluene input concentration	*Toluene conversion rate*	*Quantity of toluene destroyed*
Wire-cylinder reactor (Q = 3.5 l/mn, DE = 220 J/l)		
100 ppm	85 %	85
400 ppm	25 %	100
700 ppm	15 %	105
Multipoint-to-plane reactor (Q = 3 l/mn, DE = 360 J/L)		
700 ppm	20 %	140
200 ppm	80 %	160

Table 2 : Results obtained for toluene conversion in DBD plasma reactor
(P = 13 W, Q = 3.5 l/min)

Figure 7 shows the carbon balance–sheet for treatment of 400 ppm of toluene in the wire-cylinder plasma reactor. Light hydrocarbons CO, CO_2 and heavy by-products condensed on the filter at the exit of the plasma reactor represented respectively less than 20 % and 10 % of the toluene by-products. Among these compounds, monoaromatic compounds with oxygen and/or nitrogen containing groups (benzilic alcohol, benzaldehyde….) were the main by-products of the plasma pretreatment. Lee et al. [6] obtained a similar result using a DBD plasma to treat 100 ppmv of benzene at atmospheric pressure. At a specific energy density of 680 J/L, the benzene conversion rate was 80% but the benzene was not completely but partially oxidised in secondary products such as phenol, benzenediol and more oxidised form of benzaldehyde and benzoic acid.

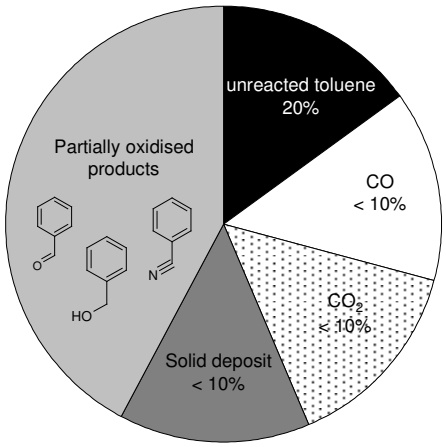

Figure 7: Carbon balance-sheet for treatment of a mixture (O_2 (10 % vol) and H_2O (1.8 % vol) in N_2) with 400 ppm toluene at a Specific Energy Density of 200 J/L in the wire-cylinder reactor

Identification of reaction pathways by isotopic labeling

Isotopic labeling was then used to identify reaction pathways and to understand the role of the different species in the chemical reactivity of the plasma discharge.The by-products identified by GC-MS analysis at the outlet of plasma reactor are presented figure 8. When they are present in a molecule, labeled atoms are pointed out according to : ^{2}H for deuterium and $^{18}0$ for oxygen.

The results show first that there is a large distribution of by-products. The volatile by-products can be classified in linear hydrocarbon compounds (propane, propyne), linear hydrocarbon compounds with oxygen or nitrogen containing groups (acetaldehyde, isocyanomethane), aromatic compounds (benzene, ethylbenzene) and aromatic compounds with oxygen or nitrogen containing groups (benzaldehyde, benzonitrile). Among the condensed by-products, alkans and alkens (linear or ramified, containing from 3 to 22 carbons), polyaromatic compounds and polyaromatics compounds with oxygen containing groups can be distinguished. The presence of oxidized light or heavy molecules confirms oxidation by –OH or –O radical as frequently shown in non thermal plasma discharges.The heavy molecules highlight that polymerization phenomena can take place during plasma treatment. Most of heavy molecules have an aromatic core. Therefore, polymerization is done rather by fragment attachment than by cycle opening.

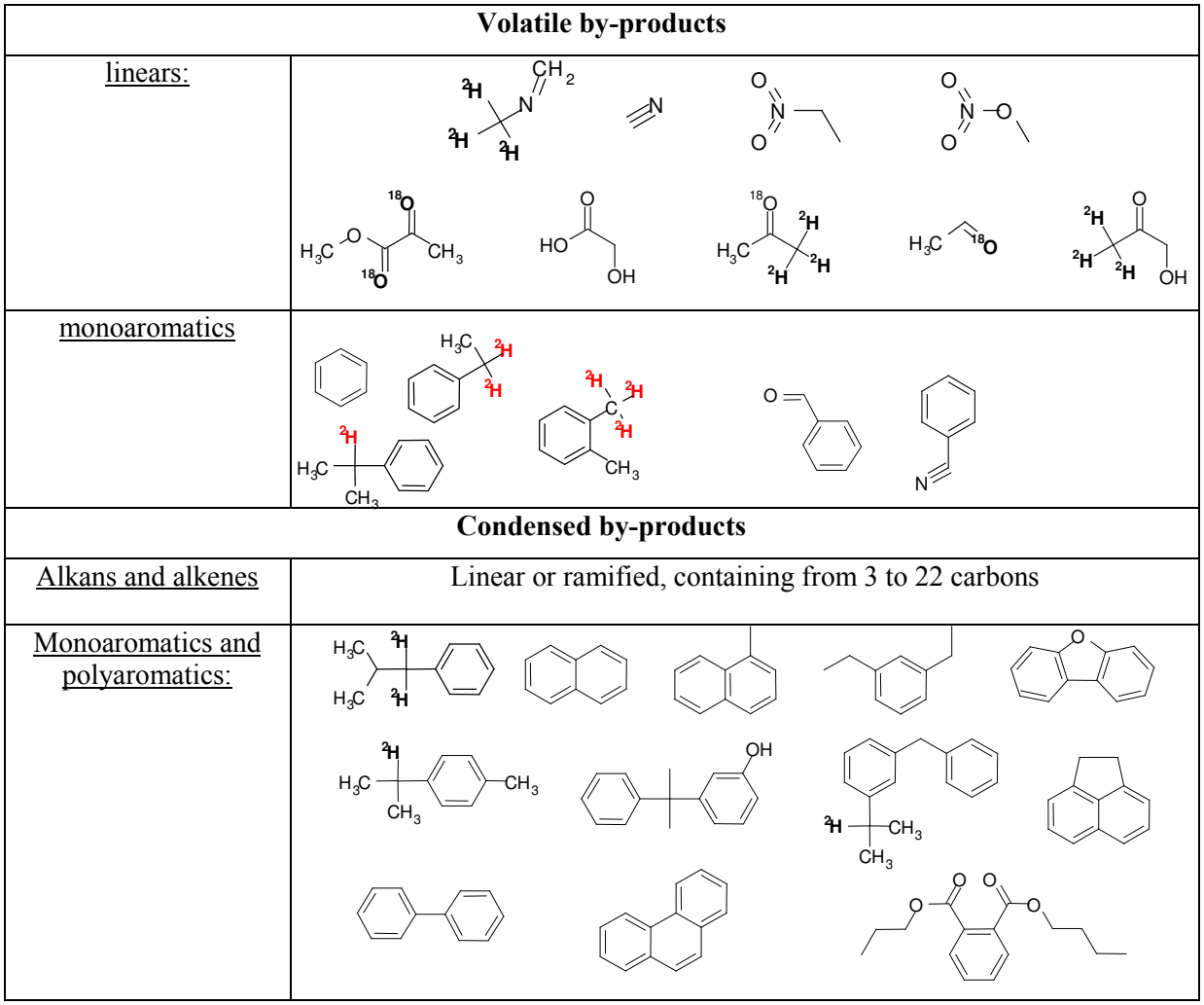

Figure 8: By-products detected by GC-MS analysis

According to these results, the following assumptions can be made about the reaction pathways characterizing the plasma reactivity: First step is the formation of radicals from the toluene compound by direct breaking by the excited species of the DBD reactor (electrons and/or heavy species). Then, radicals formed in the first step are undergoing oxidation and/or recombination reactions. Recombination reactions lead to long carbon chains (alkanes and alkenes) and poly-aromatic compounds. Concerning oxidation reactions, two types of oxidants can be distinguished : oxidants coming from molecular oxygen and oxidants coming from H_2O. The isotopic labeling shows that the nature of the products is highly depending on the

oxygen source. If the distribution of oxygen atoms is investigated, it can be observed that labeled oxygen atoms coming from molecular oxygen are only contained in small-oxidised molecules as ketonic functions. On the contrary, aromatic oxidised compounds contain only unlabeled oxygen atoms coming from H_2O. This result indicates that the active species coming from oxygen lead rather to oxidation reactions with carbon chain cleavage whereas oxidants coming from H_2O (for example hydroxyl radical OH°), less energetic, lead rather to addition reactions. The N-excited atoms react to produce essentially small molecules. Therefore, N-atoms are not involved in macromolecules formation but react only with small molecules and/or radicals. For example, nitrate oxides are formed by reaction of active oxygenate species coming from water with nitrogen and nitrate molecules are formed by reaction of carbon radicals (as $\cdot CH_3$) with ·N radicals. These reactions are usual in plasma medium [7]. Main reactions occuring in the DBD reactor are summarized in Figure 9.

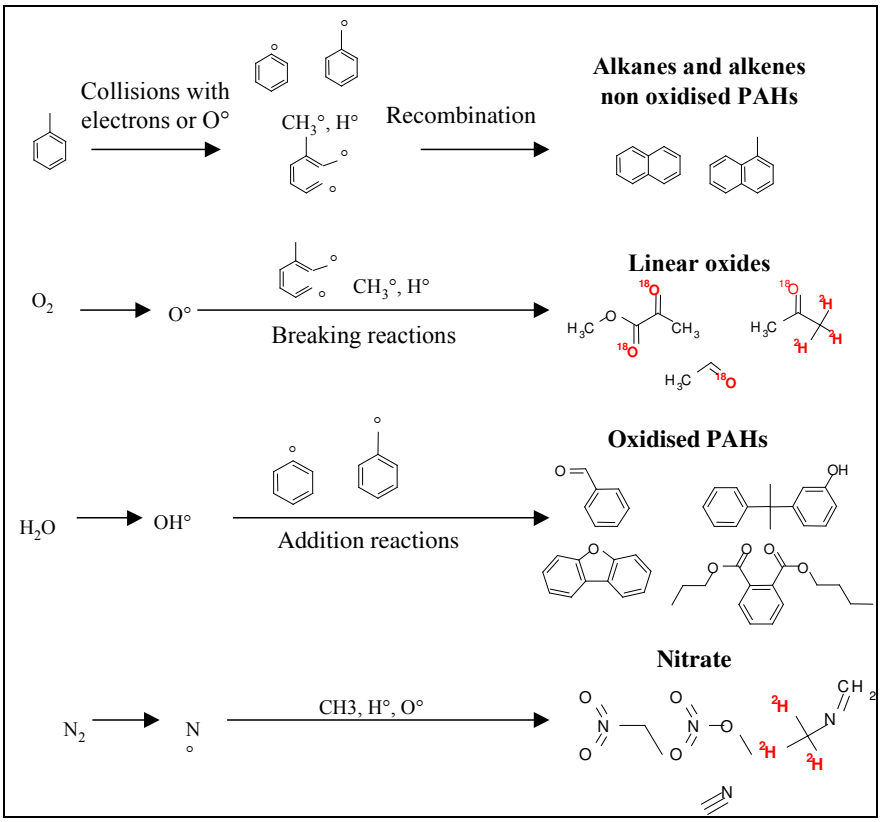

Figure 9 : Reactional pathways

Toluene and toluene by-products adsorption study

To determine wether the plasma discharge can enhance the use of an adsorbant in the treatment of polluted gaesous effluent, the adsorption of toluene and toluene by-products in a fluidized bed of zeolithe located at the exit of the plasma reactor was studied. For 400 ppm toluene concentration at the inlet of the process combining a plasma reactor (wire-cylinder) followed by an adsorbant bed of zeolithes, figure 10 shows the toluene concentrations at the outlet of the plasma discharge and the time evolution of toluene concentration at the outlet of the fluidized bed. The results show that the adsorbant bed is saturated in toluene after about 2 hours.

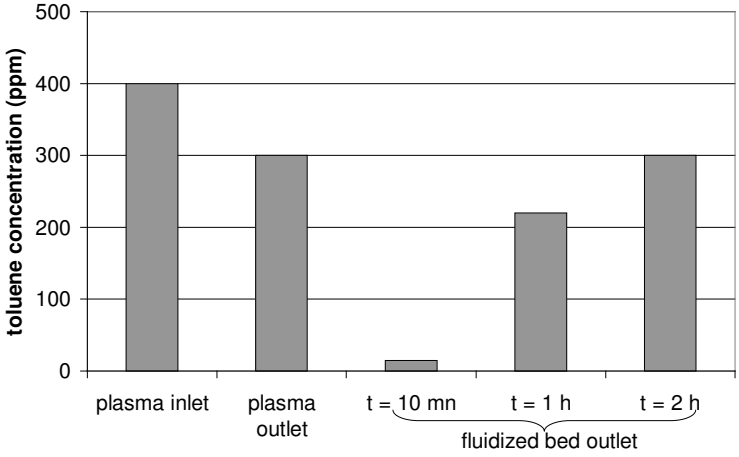

Figure 10 : toluene concentrations at the inlet (a) and at the outlet (b) of plasma reactor and time evolution (c) of toluene concentration at the exit of fluidized bed (Wire-cylinder reactor, Q = 3.5 l/mn, 400 ppm toluene)

The evolution of the relative concentrations of benzene, ethylbenzene, propyne, acetaldehyde, benzaldehyde and benzonitrile for 400 ppm toluene inlet concentration are presented figure 11. The relative concentration is defined as:

$$C_{relative} = \frac{C_{outlet\ of\ adsorbent\ bed}}{C_{inlet\ of\ adsorbent\ bed}}$$

The results show that after 2 hours, benzene and ethylbenzene concentrations at the inlet and at the outlet of the adsorbent bed are equal. This means that there are no more free adsorption sites available for these two compounds. On the contrary, the relative concentrations of linear hydrocarbons and aromatic coumpounds with oxygen or nitrogen containing groups are still lower than 1.0 after two hours of experiment.

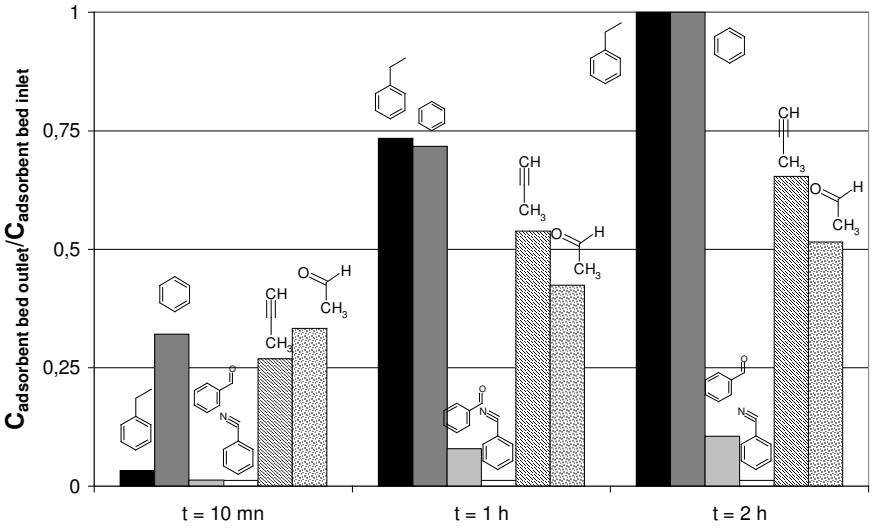

Figure 11: Evolution of relative concentrations of plasma by-products at the outlet of adsorbent bed (gas mixture: 10 % O_2, 1.8 % H_2O, 400 ppm toluene in N_2, Q = 3.5 l/min, Pplasma = 13 W, $m_{adsorbant}$ = 20 g)

These results show that among the different species formed in the plasma, some are trapped on adsorption sites different from those used for toluene adsorption. Aromatic compounds containing oxygen and nitrogen groups such as benzaldehyde and benzonitrile are trapped on adsorption sites different from those used by toluene, benzene or ethylbenzene because of their electrophilic nature. In fact, Vos et al. [8] showed that the adsorption sites are different for hydrophobic and hydrophilic molecules (figure 12). Considering the linear molecules, they can adsorb on adsorption sites which were unavailable for toluene due to steric hindrance.

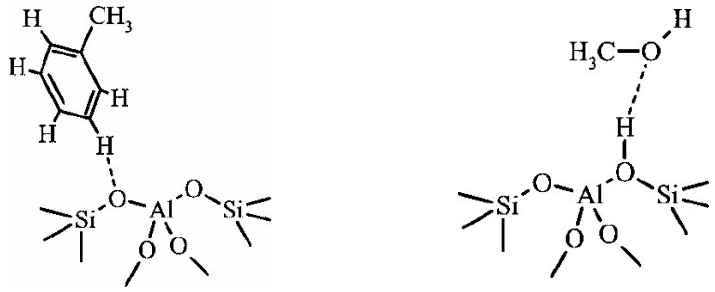

a) b)

figure 13: Interactions between hydrophobic (toluene, a)) and hydrophilic (methanol, b)) molecules and mordenite leading to the trapping of species [9]

Conclusion

In this work, a dielectric barrier discharge reactor was developed to identify depollution mechanisms in a gas mixture air + toluene. A mass balance on by-product was computed in order to underline the importance of oxidation and polymerisation in the process. Toluene and oxygene were labeled by deuterium on methyl group and ^{18}O in order to understand reactional pathways for toluene destruction in the DBD reactor. The oxygen active species lead to the breakage of carbon chains to form light oxidised compounds (C <5) and are also unfavourable in terms of polymerisation reactions. The oxygen atoms contained in heavy (C > 5) oxidised compounds came from H_2O molecules, underlining the role of OH radicals in the formation of these compounds.

The potentiality of plasma pretreatment for optimising the use of adsorbant for the treatment of polluted gaesous effluent was as well demonstrated in this preliminary study. The results showed that the secondary products formed from toluene by the plasma pretreatment were adsorbed on adsorption sites different from those used by toluene due to the chemical and sterical modifications induced in the plasma. As a result, with a plasma pretreatment step, the number of usable adsorption sites is increased compared to the sole adsorption process. Additional experiments are in progress to improve the step of the plasma treatment.

References

[1] P. Dwivedi, V. Gaur, A. Sharma and N. Verma, Comparative study of removal of volatile organic compounds by crypgenic condensation and adsorption by activated carbon fiber, Separation and Purification Technology 39 (2004) 23-37.

[2] R. Vertriest, R. Morent, J.Dewulf, C. Leys and H. Van Langenhove, Multi-pin to plate atmospheric glow discharge for the removal of volatile organic compounds in waste air, Plasma Source and Science Technology, 12 (2003) 412-416.

[3] C. Ayrault, Oxidation of 2-heptanone in air by a DBD-type plasma generated within a honeycomb monolith supported Pt-based catalyst, Catalysis today 89 (2004) 75-81.

[4] F. Daou, A. Vincent and J. Amouroux, Point and multipoint to plane barrier discharge process for removal of Nox fromengine exhaust gases. Understanding of the reactional mechanisms by isotopic labeling, Plasma chemistry and plasma processing, 2003, vol 23 n°2, 309-325.

[5] F. Daou, A. Vincent, S. Robert, E. Francke, S. Cavvadias and J. Amouroux, Removal of Nitric Oxide by point to plane and multipoint to plane DBD in exhaust vehicle gases, ISPC 15 (2001).

[6] B-Y. Lee, S-H. Park, S-C. Lee, M. Kang and S-J. Choung, Decomposition of benzene by using a discharge plasma-photocatalyst hybrid system, Catalysis Today 93-95 (2004) 769-776.

[7] Kareev, Sablier and Fujii, Diagnosis of a CH4/N2 microwave discharge : Ionic and neutral species, J. Phys. Chem. A104 (2000) 7218.

[8] A. M. Vos, X. Rozanska, R. A. Schoonheydt, R. A. van Santen, F. Hutschka and J Hafner, ,J. Am. Chem. Soc., 2001, vol. 123, pp 2799-2809.

Optimization of transfer arc torch operating at low Reynolds number

O.P. Solonenko, K. Takeda(*), A.V. Smirnov
Institute of Theoretical and Applied Mechanics, SB RAS, Novosibirsk, Russia
(*) *– Akita Prefecture University, Honjo, Japan*

Abstract
Transfer arc torch operating at relatively low mass flow rate of a working gas (low Reynolds number) has been developed and optimized in respect to provide a stable arc burning at distance between a nozzle exit and anode surface about 0.1 m. The effect of geometry of the outlet forming nozzle on transfer arc stability has been studied. The torch developed is rather attractive for surface engineering (modification, hard surfacing, etc.) when it necessary to apply a high density surface heat source.
Key words: transfer arc, torch, Reynolds number, stable arcing, optimization

1. Introduction

The plasma guns with a transfer arc are the effective means of surface treatment (cutting, welding, surfacing, surface modification, etc.) since the density of heat flux in the arc spot could reach the value of 10^9 W/m^2 and more. Depending on the functionality the requirements stated to such plasma guns are specified in different ways. For instance, when applying transfer arc for cutting the metals and alloys the continuous evacuation of the material occurred in a resulting molten pool is required. This could be provided only in the case of sufficiently high dynamic pressure of the impinging plasma flow. On the contrary, for welding, surfacing or surface modification one should guarantee a low level of the dynamic pressure at the arc spot providing high level of thermal flux power density. This is to prevent a destruction of fused surface layer.
A similar problem takes place when plasma jet is used to process the surface. Here, the application of the gun with turbulent plasma jet at small stand-off distances (~ 5 gauges between nozzle exit and a surface to be treated) would lead to destruction of the fused surface layer because of high dynamic pressure of plasma jet. If the stand-off distance is increased one is not able to heat the surface up to the given temperature and aggregate state of a surface layer as the length of high-temperature zone of the plasma jet is small owing to high turbulence extent of the jet. Latter results in the reduction of the thermal flux density. In Fig. 1 there are presented experimental data obtained [1] when changing the mass flow rate G of nitrogen and the dimensionless distance $\bar{z} = z / D_n$ between the outlet of nozzle with inner diameter D_n and a flat surface (curve 1 – $\bar{z}$=6, 2 – $\bar{z}$=8, 3 – $\bar{z}$=10; $N=\eta \cdot I \cdot U$ is a thermal power of the torch, and η is its efficiency) at the arc current I=240 A. Value of the Reynolds number $\mathrm{Re} = \bar{u}_{f0} D_n / \bar{\nu}_{f0}$ calculated in the cross section of the nozzle exit varied from 540 to 890. It was calculated at mean–mass plasma velocity and temperature defined by the calorimetric method. As it can be seen from Fig. 1, when G increases from 0.4 g/s to 0.8 g/s (Re number increases from 340 to 580 correspondingly), the linear growth of the integral heat flux into barrier is observed, and it depends on two factors. Firstly, with the increase of G the plasma torch power P increases. Thus, the mean–mass specific enthalpy of plasma at the nozzle exit and consequently the temperature increase and, secondly, the increase of the mass flow rate of the working gas leads to the increase of the heat flux from jet to the surface.

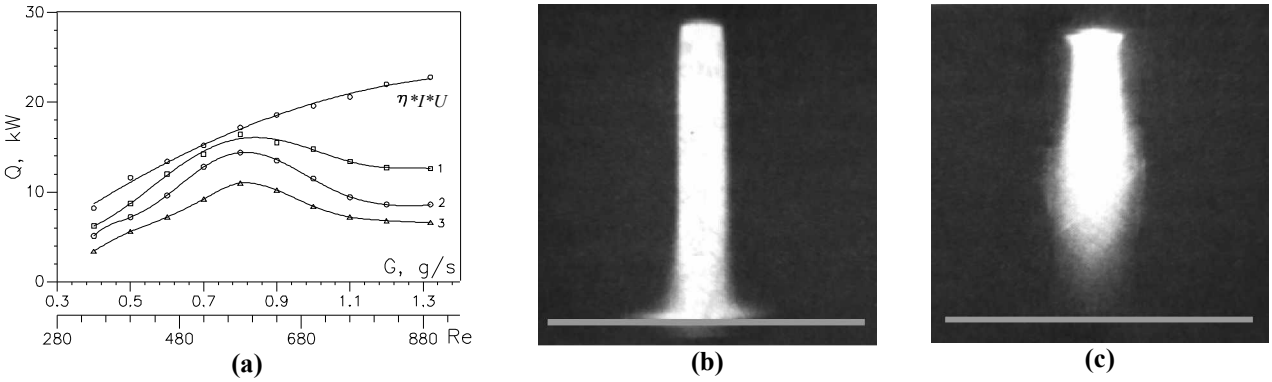

Fig. 1. The integral heat flux from nitrogen plasma jet into obstacle vs. mass flow rate of working gas (Reynolds number) – (a): $\bar{z}$=6 (1), 8 (2), 10 (3). Plasma jet impinging on flat obstacle at $\bar{z}$=8: (b) – Re=580, (c) – Re=820.

With a further increase of G, in spite of the growth of the useful plasma torch power, the decrease of the heat flux into the obstacle begins. The cause of this decrease is the transition of the plasma jet flow from laminar to turbulent regime at Re=580. Consequently, this increases the heat and momentum losses because of more intensive mixing with surrounding atmosphere.

The effect of geometry of the outlet forming nozzle on the stability of plasma jet outflow at reduced Reynolds numbers has been studied in [1, 2]. The following configurations of the outlet nozzle have been tested: cylinder, diffuser and the backward-facing step. The last design has been revealed to show the best result, when the ratio $L/\Delta r$ being ≤ 5 (L is the length of step, and Δr is its height). Here, the flowing out jet does not interact with the wall of the backward-facing step. Besides, within the internal region of a stepped part of the nozzle the additional ambient gas is leaked-in, thus stabilizing the jet. For this design the maximal axial temperatures have been attained in other conditions been equal.

Thereupon, the problem of designing the plasma guns providing a long transfer arc stable operation as well as stable outflow of plasma jet at low Reynolds numbers is to be solved.

The purpose of the paper presented is to study the possibility to develop a transfer arc DC torch providing soft argon arcing at as low as possible Reynolds number when the distance between the outlet of the forming nozzle and water cooled anode is about 100 mm. The Reynolds number is defined by formula $\mathrm{Re} = 4G_{\mathrm{Ar}} / \pi D_{n,i} \mu_{f0}$, where G_{Ar} is the mass flow rate of working argon, $D_{n,i}$ is the inner diameter at inlet of the forming nozzle, and μ_{f0} is the dynamic viscosity of plasma gas at mean-mass temperature at inlet of the forming nozzle. The diapason of arc current is 150–400 A, and flow rate of argon is 5-15 liter/min (0.15–0.4 g/s).

2. Experimental conditions

The plasma gun cathode of 4 mm diameter is made of lanthanum tungsten and is soldered into copper water-cooled holder. Plasma gun forming nozzle (see Fig.3) is made from M1 grade electrical copper. Both the cathode and the nozzle have external water cooling. Positive polarity electrode (anode) was the water-cooled copper disk being simultaneously a sensor of heat flux from an anode arc spot as well as from flowing plasma jet. The schematic of the water-cooled anode is depicted in Figs. 4 and 5. Temperature of anode cooling water at both inflow and outflow points were measured using thermocouples. This allowed one to determine integral heat fluxes into the anode. Concurrently inflow and outflow cooling water temperatures of negative polarity electrode (cathode unit) of the plasma gun were measured. The latter made it possible to estimate total heat losses in the cathode unit and plasma gun forming nozzle as well. Cooling water pressure at plasma gun inflow and anode was 10^6 Pa. In addition, water mass flow rate through the plasma gun was $320 \cdot 10^{-3}$ kg/sec, whereas that value through anode was equal to $733 \cdot 10^{-3}$ kg/sec. Total heat losses in the cathode unit was 5.8 kW. The data of thermocouples were digitized by analog-digital converter (ADC) and acquired for PC processing.

The following study has been carried out for the stable operation of a long soft arc under the above conditions:

1) effects of swirling motion of plasma gas; a cathode tip is fixed by a swirling screw nut; in this case arc stability has been examined by changing the levels of swirling intensity (without swirling, with a soft swirling and with a strong swirling); for this purpose few types of screw nuts were designed and made to produce a various level of swirling intensity (see Fig. 1 and 2),

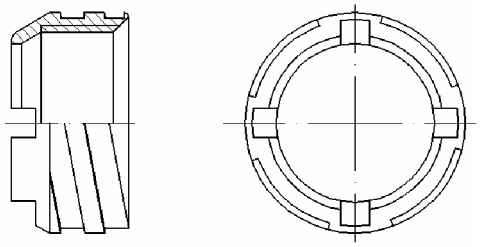

Fig.1. General view of the swirling nut geometry used in the experiments.

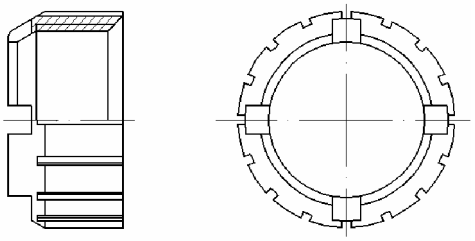

Fig.2. The scheme of the assemblage of the axial working gas supply.

2) effect of the forming nozzle shape; there were tested two types of the cylindrical nozzle with different inlet diameters (4 mm and 6 mm); not only the effect of the orifice diameter but also those of the orifice length and shape (backward-facing step) have been studied (see Fig. 3).
For the practical operation of the plasma torch, data on the life time of the consumable parts such as cathode tip and forming nozzle-anode are required, especially under high current operation. Weight losses and deformation of the parts were measured with time under 400 A operation.
The aim of this experimental course was to investigate an ability of improving the transfer arc stability for minimally possible mass flow rates of working gas (argon) at 100 mm stand-off distance between the forming nozzle exit and the water cooled anode surface. Operating arc current was chosen to be equal 400 A as being maximal current provided by "Plasma-4" power-supply source. The optimization was performed also for variety of the conditions of working gas injection into cathode zone. Here operating gas flow rate was fixed at 0.3 g/sec (different rates of gas swirling, Fig.1, as well as axial gas blowing, see Fig.2), with the forming nozzle geometry being varied (various forms of the backward-facing step, see Fig.3).

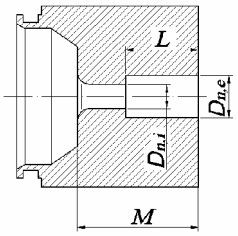

Fig.3. General view of the backward-facing step forming nozzle used in the experiments.

The following legends are used in Fig.3: $D_{n,i}$ is the inlet diameter of the forming nozzle, $D_{n,e}$ is the outlet diameter of the forming nozzle, $\Delta r=(D_{n,e}-D_{n,i})/2$, L is the length of its stepped part, M is the total length of the nozzle–anode.

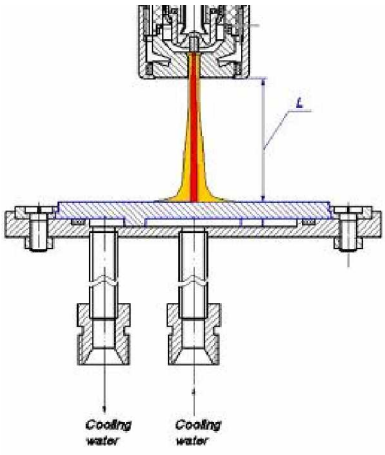

Fig.4. The principal schematic of the plasma gun with transfer arc and water-cooled anode.

3. Results

3.1. Integral characteristics of torch

It is of special interest to investigate the integral characteristics of transfer arc gun depending on the channel diameter of the cathode assembly, the plasma forming gas mass flow rate, the stand-off distance from the forming nozzle outlet section to water-cooled anode surface and its diameter as well. While carrying out the investigation the two sorts of water-cooled anodes were implemented. The diameter of heat transfer surface of the first sort of anode was chosen 100 mm (Figs.4, 5), that of the second one was 200 mm.
The integral characteristics of the transfer arc plasma guns to be compared are plotted in Fig.6, with channel diameter being 4 mm (curve #3) and 6 mm (curve #2).

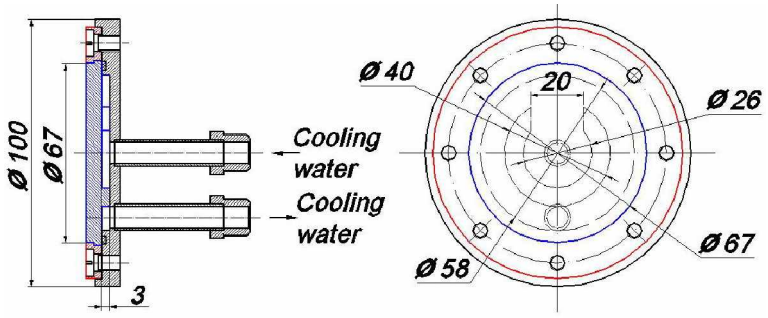

Fig. 5. The principal diagram of the water cooled anode. Blue part corresponds to cooper cooled anode, grey part is stainless steel holder isolated from cooper part by ribbon ring.

It is clearly seen, when reducing the channel diameter from 6 to 4 mm, the electric field intensity of the arc is valuably increased (~50%), other parameters being equal. Still, as arc current is increased (I>250 A) the heat

fluxes into anode are nearly the same. When current I<250 A the heat loss in the cathode assemblage is the smallest for 4 mm channel diameter. On the contrary, for I>250 A and 6 mm channel diameter the situation changes qualitatively. Nevertheless, the value of heat losses in the cathode assembly is small enough and doesn't exceed 6 kW for both cases when the electric arc power is ~60 kW ($D_{n,i}$=4 mm) and ~40 kW ($D_{n,i}$=6 mm). As the arc current is increased the efficiency of the heat transfer into the anode rises and, for instance, at I=300 A is about 40% ($D_{n,i}$=4 mm) and 60% ($D_{n,i}$=6 mm).

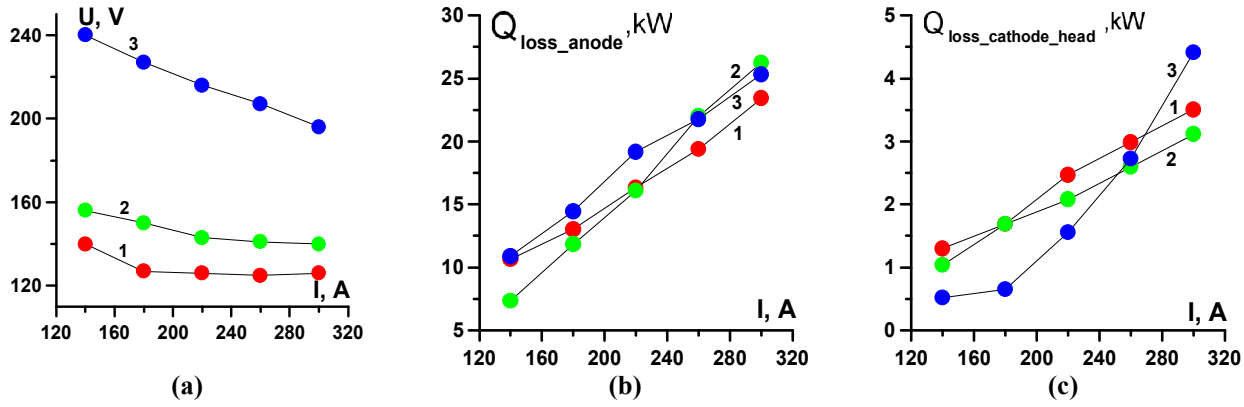

Fig. 6. Volt-amps characteristics – (a), heat flux into water cooled copper anode – (b), and heat losses into cathode assembly – (c) of transfer arc plasma torch. 1 – $D_{n,i}$=6 mm (G_{Ar} =0.3 g/s), 2 – $D_{n,i}$=6 mm (G_{Ar} =0.5 g/s), 3 – $D_{n,i}$=4 mm (G_{Ar}=0.5 g/s). The distance from the nozzle outlet to the anode surface was equal to 100 mm. Diameter of water-cooled anode is D_a=200 mm.

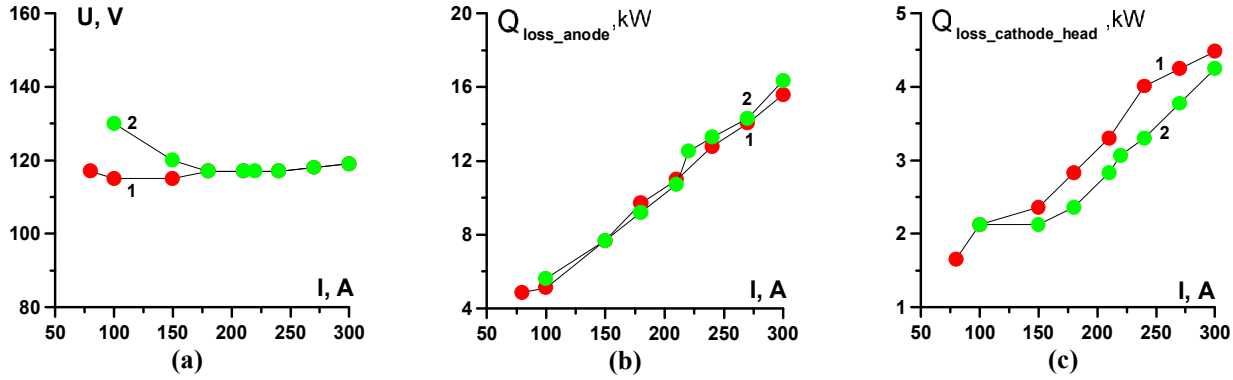

Fig. 7. Volt-amps characteristics – (a), heat flux into water cooled copper plate anode – (b), and heat losses into cathode assembly – (c). The curves (1) and (2) correspond to argon mass flow rate of 0.1 and 0.2 g/sec, accordingly. The distance from the nozzle outlet to the anode surface was equal to 100 mm. Diameter of water-cooled anode is D_a=100 mm.

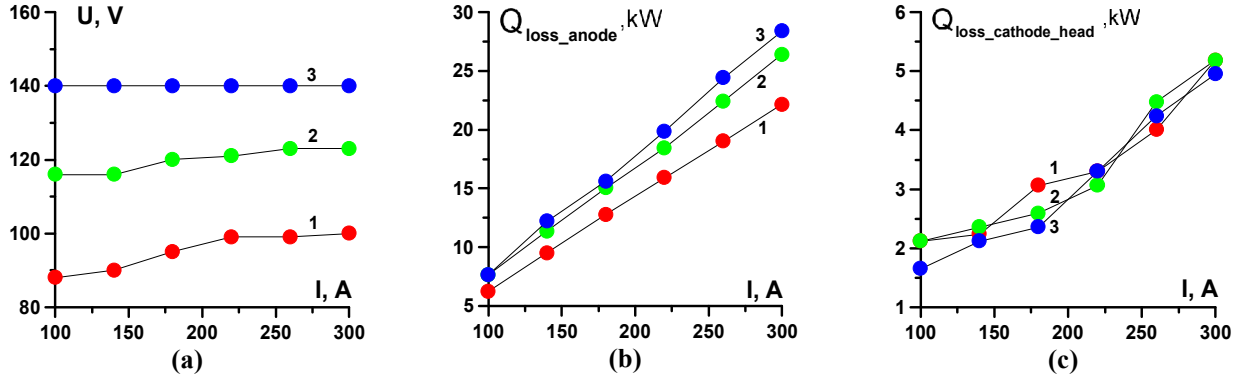

Fig. 8. Volt-amps characteristics – (a), heat flux into water cooled copper anode – (b), and heat losses into cathode assembly. The curves (1), (2) and (3) correspond to the distance from the nozzle outlet to the anode surface of 50, 75 and 100 mm, accordingly. The mass flow rate of argon was equal to 0.3 g/sec. Diameter of water-cooled anode was D_a=200 mm.

In Figs.6, 7 the integral characteristics (curves 1 and 2) of the plasma gun with fixed 6 mm channel diameter are indicated. As seen from Fig.6, increasing the plasma forming gas flow rate as much as almost double resulted in 15-20% increase of the heat transfer into the anode with diameter D_a=200 mm for arc current I>180 A. For lower argon flow rates the difference of thermal fluxes in anode with diameter D_a=100 mm is negligible virtually in the whole range of arc current variation (Fig7, *a,b*) whereas at I>180 A the volt-amps diagrams are coincided.

In Fig. 8 an influence of the distance between outlet cross-section of the cathode assembly and anode surface on the parameters of the transfer arc plasma gun to be studied is illustrated. As the distance becomes larger the increasing volt-amp curve turned to a steady one. When increasing the above distance from 50 to 75 mm the change in anode thermal flux is more noticeable than the change for increasing the distance from 75 up to 100 mm. The subsequent increase of the distance causes the thermal flux to be stabilized to the point of arc break.

The data depicted in Figs.6-8 indirectly point to an influence of the diameter of water-cooled anode on the value of thermal flux being taken. The feature of the transfer arc plasma gun is an air entrainment into plasma jet, and we have a conductive plasma jet flowing onto the wall. It is evidently, the value of the heat flux being taken depends on heat exchange area (i.e. anode diameter). The effectiveness of surface treatment is determined by the power density of the thermal flux in the arc spot where the major power flux is observed. Therefore, it is required to minimize arc spot diameter upon the surface being treated as much as possible. The extreme case is the laminar arc, for which the size of spot of attachment to the surface to be treated is larger a little than the channel diameter of the cathode assemblage. Thereupon, it is interesting to explore the methods of stabilizing the transfer arc at low Reynolds numbers (low mass flow rates of the plasma forming gas).

3.2. Experiments on plasma torch optimization

In these experiments argon flow rate G_{Ar}= 0.3 g/sec, arc current дуги I=400 A. Plasma gun was ignited at 25 mm stand-off distance between nozzle exit section and the water-cooled anode (see Fig.4). Having ignited the plasma gun one increased the stand-off distance to 100 mm.

During plasma gun operating period, along with measuring the heat flux into the water-cooled anode (Fig. 4), the arc root current and voltage were being displayed for each set of investigated operating conditions. This was done in order to analyze their spectral components. The attention was mainly focused on spectra of the voltage fluctuations. The latter can indirectly characterize arc root stability (its length). When valuing the spectral characteristics Blackman-Harris filter was applied. Here spectral amplitude is square root of the sum of squares of real and imaginary parts. Size of the window in which Fast Fourier Transform (FFT) was executed is 16384 counts, total number of counts – 65536, the measuring frequency is 10 kHz. Hence, for FFT upper frequency the resolution is equal to 5 kHz (2 counts per period), for lower one – 0.3 Hz (namely, 100 μsec x 65536 = 6.5 sec, i.e. period is 3 sec).

In Table 1 there are presented the initial parameters of the backward-facing stepped forming nozzles used in the experiments. In each series of the experiments, corresponding to fixed values of $D_{n,i}$ and $D_{n,e}$, the length of step L was varied in the following sequence $L/\Delta r$=6; 5; 4; 3; 2. It was found that for both inlet diameters $D_{n,i}$=4 and 6 mm of the forming nozzle the most stable arcing have taken place at Δr=2.5 mm, $L/\Delta r$=2.4. In other cases, including the forming nozzle without the backward-facing step, erosion of the inner edge at outlet of the nozzle occurred. This erosion is related with intensive micro-shunting of the arc.

Table 1. The geometry of the backward-facing steps investigated

$f_{initial}=L/\Delta r$	$D_{n,i}$	$D_{n,e}$	L	M
6	4	6	6	14
6	4	7	9	17
6	4	8	12	20
6	6	8	6	14
6	6	9	9	17
6	6	10	12	20

The experiments on optimizing the forming nozzle characteristics have shown that this ratio is most appropriate also for mass flow rate of argon of 0.1 and 0.2 g/sec. It is cited from references devoted to plasma jet stabilization using backward-facing step at low Reynolds numbers that above mentioned ratio

should not exceed 5. However in the case under consideration there is an intensive Joule heat release in the limit of nozzle step that would result in an increase of thickness of thermal and velocity boundary layers inside the stepped channel. Therefore the relative length of step has to be shorter in order to avoid a reattachment of the dynamic boundary layer to a wall within the step.
Using the optimal geometry of the forming nozzle the additional experiments have been carried out to study the influence of working gas supply into cathode zone (with and without gas swirling). It was established that axial supply of argon (V_φ=0) provides more stable arcing at L=100 mm. At the same time, the aforesaid micro-shunting was not observed.

3.3. Plasma gun life test

The 10 hour life test of the transfer arc plasma gun optimized have been conducted at arc current I=400 A, with argon mass flow rate being 0.1 g/sec. Taking into consideration the results of cathode unit optimization, in above life tests the axial supply of plasma forming gas in the cathode zone was implemented.
The internal nozzle channel utilized in the life test was the backward-facing steps with channel expansion from $D_{n,i}$=6 mm to $D_{n,e}$=11 mm across diameter. The length of step was 6 mm, this provided the ratio of its length to the height being equal to 2.4. As mentioned above, the experiments for optimizing the forming nozzle have shown that this ratio is most appropriate.
During 10 hours period of plasma gun operating mode the stand-off distance from nozzle cross-section to anode was set of $50 \cdot 10^{-3}$ m. Here the operating voltage was within 80÷85 V, while thermal flux registered by the sensor was about 14.7 kW.
Totally during the life test there were 5 plasma gun runs (4 times plasma gun was switched off). After 10 hour of life test there were no any noticeable erosion of the forming nozzle, the erosion of tungsten cathode was $3 \cdot 10^{-13}$ kg/Coulomb. Such a value of cathode erosion provides its continuous service (up to complete ablation of $1.5 \cdot 10^{-3}$ m length tungsten rod of $4 \cdot 10^{-3}$ m diameter) during more than 500 hours.

Conclusions

As a consequence of the experiments on optimizing soft transfer arc plasma torch it is possible to do the following conclusions:
1) the forming nozzle with inlet diameter of 6 mm, having a backward-facing step with length of 6 mm and diameter of 11 mm provides a maximal stable transfer arc burning at current of 400 A in a diapason of argon mass flow rate 0.1-0.5 g/sec and distance from nozzle exit and anode surface of 100 mm,
2) the axial supply (V_φ=0) of working gas (argon) in the cathode area in comparison with vortex one (V_φ>0) provides the increasing the stability of an arcing in the other conditions been equal,
3) at the optimal conditions found the time life of the cathode continuous operation is not less than 500 hours and time life of the forming nozzle is not worth than cathode.

Acknowledgment

The authors are indebted to Dr. A.A. Mikhal'chenko and Dr. V.I. Kuz'min for supplying the working conditions and support of this work.

References

[1] O.P.Solonenko – Thermal Plasma and New Materials Technology. Vol.2. Investigation and Design of Thermal Plasma Technologies, Ed. by O.P.Solonenko and M.F.Zhukov, Cambridge, England, Cambridge Interscience Publishing (1995), p.7-96.
[2] V.Kuz'min, O.Solonenko, M.Zhukov – Proc. of the 3rd European Congress on Thermal Plasma Processes, Aachen, Germany (1995).
[3] V.Kuz'min, O.Solonenko, M.Zhukov – Proc. of 14th Intern. Thermal Spray Conf., Kobe, Japan (1995).

Synthesis Of Polypyrrole-Like Nanocrystallines By Oriented Plasma Polymerization at Atmospheric Pressure

Xinsheng Fang, Ying Guo, Jinzhou Xu, Jing Zhang*

College of Sciences, Donghua University, Shanghai 200051, China

** Corresponding author: jingzh@dhu.edu.cn*

Abstract

Polymeric polypyrrole-like nanocrystallines were fast synthesized through oriented plasma polymerization at atmospheric pressure and room temperature. The effects of discharge conditions such as discharge time and power on the nanocrystalline morphology and crystallinity were investigated. It was found the nanocrystallines could exhibit various shape such as powders, rods, wires etc at different polymerization conditions. The crystal phase could also change from amorphous to single-crystalline structure. The chemical structure of the nanocrystalline have been studied through FTIR, EDX etc. This novel polymerization method could have great applications in fabricating functional polymeric nanocrystallines.

Keywords

atmospheric oriented plasma polymerization, polypyrrole, nanocrysllines

1. Instruction

It is well known that the properties of materials depend not only on their chemical structures, but also on their morphologies. For example, nanoscale materials possess unique properties on account of their finite small size and have wide-ranging applications to a variety of areas. Especially carbon nanotubes exhibit excellent performance of importance for microelectronic devices and attracted people's great interest in the past 10 years[1,2]. On the other hand, one dimension conjugated conductive polymers are also of great interest[5]. Among these conducting polymers, polypyrrole (PPy) stands out because of its high conductivity, stability in air and array of potential applications [3]. Recently, nano/microwires were synthesized by a chemical and electrochemical method.[4] CNTs/PPY nanocomposites were obtained by in-situ polymerization in the carbon nanotube template.[6]Template-synthesized PPy monodisperse nanowires and tubules were prepared by using an anionic surfactante (diamyl sulfosuccinate) as the dispersing agent[7].

In this paper, PPy-like nanocrystallines were synthesized through oriented plasma polymerization at atmospheric pressure and room temperature. The effects of discharge conditions such as discharge time and power on the nanocrystalline morphology and crystallinity were investigated. The chemical structure of the nanostructures have been studied through FTIR, EDX etc.

2. Experiment

PPy-like thin films were grown on ordinary glass slides, using an oriented plasma polymerization system, which consist of a monomer supply system, an evacuable cylinder reactor (the bottom/top side was 9.0cm is diameter and the height was 20.0cm), housing wire-dielectric-plate geometric electrode that produced a gradient electric field, an argon flow system and a tunable power supply with a high voltage of 10-50 kV and a frequency of 10-100 kHz. The depositions were carried out with atmospheric pressure and ambient temperature by a water cooling system. Pyrrole was used and fed into the reactor through an argon carrier gas at a fixed ratio. After only a few seconds to several minutes, a thin brown film was deposited on the entire substrate, within which a large quantity of nanowires/powders were identified.

A SEM (JSM-5600LV) was used to measure the morphologies of the PPy-like film. Structures and compositions of the samples were investigated on a CM200FEG high-resolution transmission electron microscope (HRTEM) equipped energy dispersive X-ray spectroscopy (EDX) system operated at 200 kV. To obtain electron diffraction patterns from individual nanocrystallines, a nanobeam diffraction mode was used. FTIR (NEXUS-674) was used to characterize the chemical structure of the film.

3. Results and discussion

3.1 Mophorlogy

3.1.1 Effects of discharge time

(a) (b) (c)

Figure 1. SEM photographs of PPy-like thin films prepared by oriented plasma polymerization at atmospheric pressure: (a)t=1min; (b) t=2min; (c) t=3min.

Figure 1 shows SEM photographs of PPy-like thin films deposited during different time. The powders whose diameter was roughly 500nm lay on the surface of a loosely packed nanoparticulate layer. As shown in figure 1(b) and 1(c), the powders would like to link to each other and grow up into wires by molecular force with the elapse of time.

3.2 Effects of discharge power

(a) (b) (c)

Fig. 2 SEM photographs of polypyrrole-like crystals prepared by oriented plasma polymerization at atmospheric pressure: （a）3kV，0.4A，（b）6.5kV，0.7A，（c）8kV，0.8A.

Figure 2 shows SEM photographs of PPy-like thin films deposited at different powers. The length of the nanoswires increases with the increase of discharge power. Fig 2(c) also indicates that the growth rate of the nanowire was considerably high, and it took only 3 minutes to synthesize wires. It is relatively fast process compared to some other meothds[4].

As figure 3 shows, the length/width ratio increase with the discharge power. Since the powders connected and wires formed, there is a sharp increase between 4.5 and 6.5 kW. These photos (Fig. 2, Fig. 5(a)) strongly suggested that 3 min is enough long time to synthesize a single crystalline nanopowder/microwire.

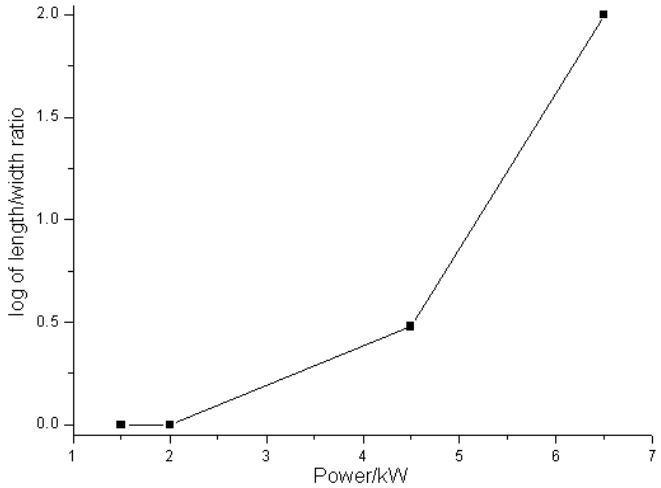

Fig. 3 The effect of the discharge power on the length/width ratio of polyporrole-like crystal wires.

The substrate and its film were immersed into 10mL of absolute ethanol and ultrasonicated for 20 min to completely separate the nanopowders/wires from the substrate. A drop the liquid was placed onto a copper transmission electron microscopy grid, and the solvent was allowed to evaporate. The TEM image obtained after evaporation of the solvent shows that the desired monodisperse nanoweirs were prepared by our method. An anionic surfactant had been used to prevent the aggregation of nanoparticales [7], but our method is fast, simple and immediately.

PPy micro/nanowires with diameters of 50-2000 nm were synthesized by a chemical and electrochemical method[4]. CNTs/PPY nanocomposites with diameters of 80-100nm were obtained by in-situ polymerization in the carbon nanotube template[6]. PPy films were prepared by using a SAMCO plasma polymerizer[11]. It needs to be pointed out that the method proposed by us only needs 3 min, whereas the other method need several hours or even several days. Figure 4 indicates HRTEM photographs of PPy-like nanowire single crystals shown in Fig. 3 (c). Lattice fringes can be seen continuously through the whole particle. The inset in the extended picture is the electron diffraction pattern, which enabled us to confirm that the nanopowder/wire materials were single crystals. The results of EDX shows that the N/C ratio (0.05) of the nanocrystalline is smaller than that of ideal PPy (0.25). From the FTIR and EDX results, it is obvious that the pyrrole rings have been decomposed to some extent in the plasma polymerization precess.

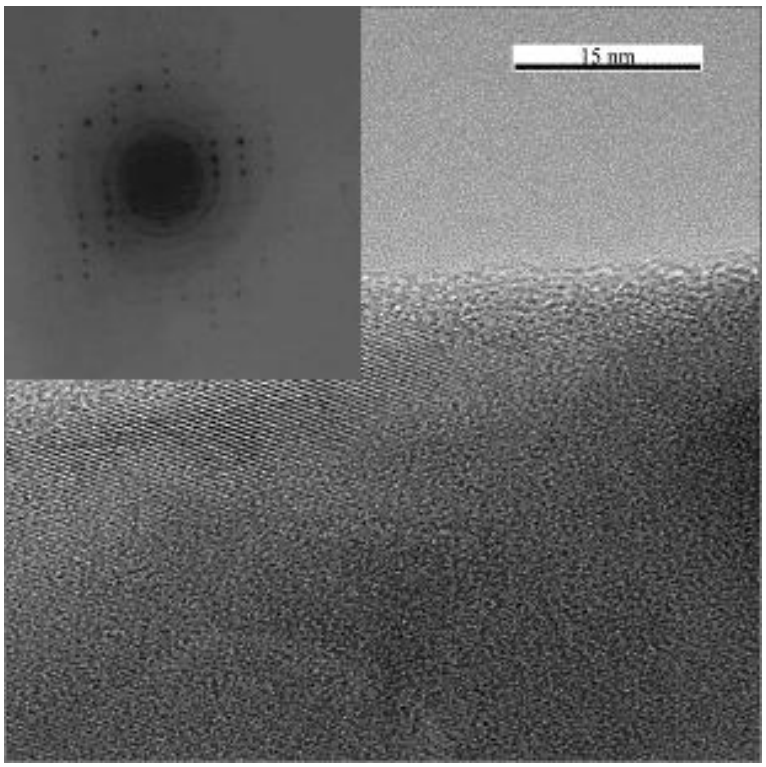

(a)

(b)

Fig. 4 (a) HRTEM image of PPy-like nanowire single crystals shown in Fig. 2(c), the inset is its electron diffraction pattern, (b) EDX spectrum.

3.3 structural characterization

FTIR spectra of pyrrole liquid film and PPy-like film are given in figure 5. The spectra show that the structure of PPy-like film is similar to that of the pyrrole film. In the both spectra, two strong absorptions are observed at 3300-3440 and 745 cm^{-1}. The appearance of broad peak at 3300-3400 cm^{-1} suggests the presence of N-H stretching[9,10]. The other peak at 745 cm^{-1} is due to CH=CH out-of-plane deformation vibration. These suggest

PPy-like film synthesized by our method maintained more C-H, N-H and CH=CH bonds, compared with PPy synthesized by other method[4,11]. On the other hand, in the polymer spectra, peaks around 2900 and 1100 cm^{-1} corresponding C-H stretching vibration and C-H in-plane bending, respectively, are weaker than that of the pyrrole sample. Perhaps related to polymer's high crosslinked structure, C-H bond concentration in PPy-like film is lower than that of the pyrrole molecule. The other peak observed at 1635-1700 cm^{-1} is due to C=N and/or C=C stretching and N-H bending[12,13]. In PPy-like films sample, this peak shifts to high wave number compared with that of the pyrrole sample. The peak shift observed in the PPy-like film is probably due to the formation of C=O by the invasion of the oxygen into the PPy-like film[11]. It is supported by the EDX spectra, which shows an oxygen peak. The absorption peak of C=C in-plane vibration mode at 1384 is more intensive compared to the pyrrole sample. This may result from the structure change, for example, the long conjugation length of the polymer long chain in the PPy-like film. The peak observed at 483 cm^{-1} corresponding to pyrrole ring deformation vibration.

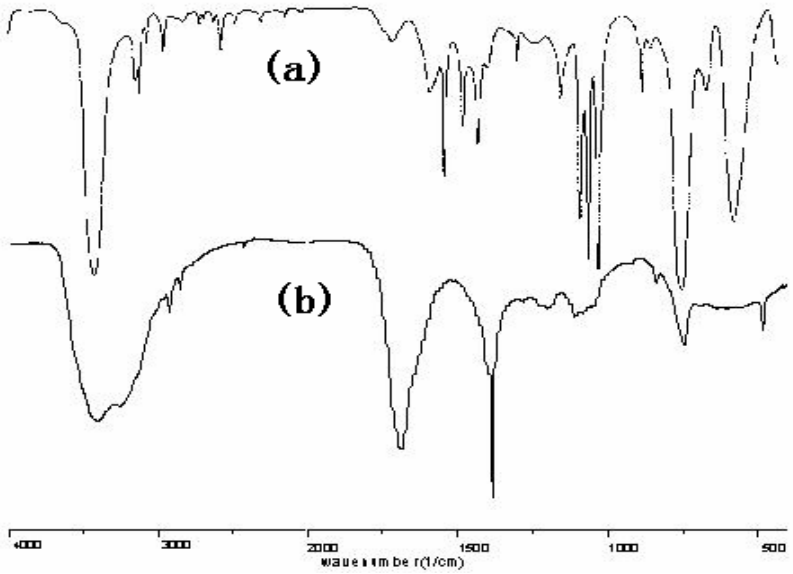

Fig. 5 FTIR spectra of (a) pyrrole liquid film, (b) PPy-like film synthesized by oriented plasma polymerization.

4. Conclusion

PPy-like film with nanostructures was synthesized using the oriented plasma polymerization at atmospheric pressure and room temperature, which was a fast one-step process and could be applied for many different monomers. By controlling the discharge power, the monomer and carrier gas ratio, the flux, etc., the configuration of the naonwires can be closely controlled so that single crystalline and large length/width ratio nanowires can be produced.

References

[1] S. Lijima, Nature 1991;354:56.

[2] A. Bachtold, P. Hadeky, T. Nakanish, C. Dekker, Science 2001;294:1317.

[3] Tanikaw K, Okuao Z, Iwaoka T, Hataso M, J. Appl. Phys. 1997: 2424

[4] Yongsheng Yang, Jin Liu, Meixiang Wan, nanothecnology 2002: 771-773

[5] Y.E. Whang, J.H. Han, H.S. Nalwa, T. Watanabe, S. Miyata, Synth. Met. 1992;41:3043.

[6] B. H. Chang, Z. Q. Liu, L. F. Sun, D. S. Tang, W. Y. Zhou, G. Wang, L. X. Qian, S. S. Xie, Journal of Low Temperature Physics 2000: 41-48.

[7] Silvia De Vito, Charles R. Martin, Chem. Mater. 1998: 1738-1741.

[9] D. Sakthi Kumar, Yasuhiko Yoshida, J. Appl. Phys. 93: 1705(2003)

[10] J. Zhang, M.Z. Wu, T.S. Pu, Z.Y. Zhang, R.P. Jin, Z.S. Tong, D. Z. Zhu, D.X. Cao, F.Y. Zhu, J.Q. Cao, Thin Solid Films 307: 14(1997).

[11] Kouta Hosono, Materials Letters 2004;58:1371.

[12] R.C. Load Jr., F.A. Miller, J. Chem. Phys. 10 (1942) 328.

[13] B. Tian, G. Zerbi, J. Chem. Phys. 92 (1990) 3886.

CHARACTERISATION OF SMART GEL MATERIALS MODIFIED BY GLOW DISCHARGE

Pelin Atillasoy[1], Mehmet Mutlu[1], María D.Landete-Ruiz[2], María D.Romero-Sánchez[2], José Miguel Martín-Martinez[2], Arzu Topacli[3], Cafer Topacli[3]

[1]Plasma Aided Bioengineering and Biotechnology Research Group, Engineering Faculty, Hacettepe University, 06532 Beytepe Ankara/Turkiye
[2]Adhesion and Adhesives Laboratory, Department of Inorganic Chemistry, University of Alicante, 03080 Alicante/Spain
[3]Physics Engineering Department, Engineering Faculty, Hacettepe University, 06532 Beytepe Ankara/Turkiye

Abstract
In this research, it was aimed to modify the structure of Κ-carrageenan by means of air glow discharge to develop smart gel materials. The samples were exposed to 13.56 MHz RF air plasma at a residual pressure of 0.75 Torr. The air plasma produced oxidation and ablation, allowing a decrease in pH values. A noticeably decrease in the viscosity of κ-carrageenan, indicating a depolymerisation.

Keywords: smart gel, Κ-carrageenan, glow discharge, IR-ATR spectroscopy, XPS

1. Introduction

Stimulus-responsive or 'smart' polymers undergo strong conformational changes when only small changes in the environment (e.g. pH, temperature, ionic strength) occur. These changes result in phase separation from aqueous solution or order-of-magnitude changes in hydrogel size. Smart polymers are used in bioseperation and drug delivery, for the development of new biocatalysts, as biomimetic actuators, and as surfaces with switchable hydrophobic-hydrophilic properties. Several types of materials such as carrageenan, sodium alginate, xanthane and chitosan have been reported on literature to prepare smart gels[1]. Most of them had been used in their natural forms.

Low-pressure glow plasma is assumed to provide a waste-less dextrinization of polysaccharides. The destruction of these high molecular weight compounds as a consequence of depolymerisation caused by the reactive electrons, ions and radicals, local temperature increase, as well as oxidation by ozone and/or nitrogen oxides formed in the course of experiments, can be inhibited in some extent [2,3]. Those chemical changes on the bulk structure of the materials produced by plasma treatment encouraged us to check the possible positive changes in the performance of these materials as smart materials.

κ-carrageenan, which is selected as the model macromolecule for this research, consists of linear-sulfated polysaccharide of D-galactose and 3,6-anhydro D-galactose. In this research, it was aimed to investigate the changes in the κ-carrageenan structure by means of glow discharge. The chemical and physical characteristics of the κ-carrageenan prior to and after air plasma modification are reported.

2. Experimental

κ-carrageenan was obtained from Aldrich (Milkwaukee WI 53233, USA).

Exposure of samples to air plasma: A March Plasmod RF plasma Instrument (Concord, CA, USA) with a pyrex glass chamber of 19 cm length and 14 cm diameter was used in the experiments. Synthetic dry air (99.999 % purity) was introduced into the chamber with a flow rate of 16 ml/min. 20 minutes after the air was introduced into the chamber, a uniform air plasma was reached by using a residual pressure of 0.75 Torr. The glow discharge power and the exposure time were 75, 125

Watts and 20, 30 and 40 min, respectively. After plasma treatment, the reactor was placed up to 0.15 Torr for 30 minutes by means of a rotary vacuum pump.

ATR-IR spectroscopy, X-ray Photoelectron Spectroscopy (XPS), Scanning Electron Microscopy (SEM), Energy Dispersive X-Ray Spectroscopy (EDX), Differential Scanning Calorimetry (DSC) techniques, pH and viscosity measurements were used in order to determine the effect of air glow discharge treatment on the κ-carrageenan.

3. Results And Discussion

The effect of the glow discharge technique on the chemical and physical characteristics of the κ-carrageenan were investigated.

χ-carrageenan	**Assignment**
3436	ν(OH)
2963	ν(CH)
2907	ν(CH)
1648	δ(OH)
1379	$\delta(CH_2)$
1266	ν(S=O)Ester sulfate
1069	ν(C-O-C) Glycosidic linkage
1042	ν(C-O-C) Glycosidic linkage
929	ν(C-O)3.6-anhydro-D-galactose
847	ν(C-O-S)D-galactose-4-sulfate

Table 1. Assignment of IR bands (in cm^{-1}) of the as-received κ-carrageenan.

Table 1 shows the assignment of the IR-ATR spectra of the as-received κ-carrageenan (Figure 2). Bands due to OH, CH_2, C-O, S=O and C-O-C can be identified. Furthermore, the broad bands at 1630 and 2160 cm^{-1} in the IR spectrum of Figure 2 are due to inorganic calcium chloride, likely a contaminant in the κ-carrageenan. The air plasma treatment increases the ratio of the intensities of δ (OH)/ν(CH) bands at 1648 and 2907 cm^{-1} in the ATR-IR spectra in a greater extent by increasing the length of treatment up to 30 minutes. The increase is somewhat less important when the air plasma is carried out for 40 minutes. In addition, the intensity of the C-O-C stretching band at 1069 cm^{-1} due to the glycosidic linkage in the air plasma treated κ-carrageenan decreases with respect to the intensity of the OH bands at 1648 cm^{-1} compared to those in the IR spectrum of the as-received κ-carrageenan. These results might indicate that air plasma partially oxidized the κ-carrageenan and some depolymerisation is also produced. In fact, the lower intensity ratios of the C-O-C stretching (at 1069 cm^{-1} and 1049 cm^{-1}) and the OH stretching bands, which are almost similar in the ATR-IR spectra of all air plasma treated samples (Figure 2b) at different exposure time (20, 30, 40 min) and power of the discharge, also confirm the depolymerization of the κ-carrageenan.

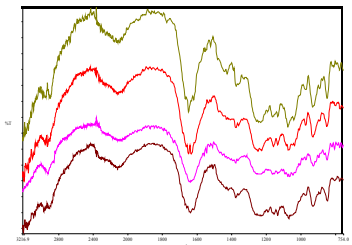

Figure 2a. ATR-IR spectra of a) as-received κ-carrageenan, and plasma treated κ-carrageenan for b) 20 min, c) 30 min, d) 40 min. Power = 75W.

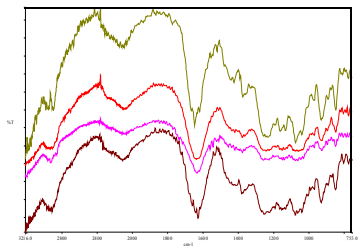

Figure 2b. ATR-IR spectra of a) as-received κ-carrageenan, and plasma treated κ-carrageenan for b) 20 min, c) 30 min, d) 40 min. Power = 125W.

Element	Binding energy (eV)	As-received	Treatment			
			75W-20min	75W-40min	125W-20min	125W-40min
C	285.0	43.8	40.6	37.3	35.6	38.2
O	531.7	30.4	31.6	31.9	30.8	30.5
N	400.0	1.3	0.6	0.4	1.0	0.4
K	292.9	9.9	10.9	11.7	12.9	12.3
S	168.0	2.8	3.5	3.9	3.8	3.5
Na	1072.2	1.8	2.1	2.7	3.1	2.9
Ca	346.9	1.0	1.7	2.1	2.3	2.2
Cl	198.9	9.0	9.0	10.0	10.5	10.0

Table 2a. Atomic percentages (at%) of elements on the as-received and air plasma treated κ-carrageenan.

Element	Binding energy (eV)	As-received	Treatment			
			75W-20min	75W-40min	125W-20min	125W-40min
$(C^*H_2\text{-}CH_2)_n$	283.3	16.9	17.9	20.9	24.6	19.5
C-H, C-C	285.0	65.8	58.1	59.0	46.7	53.8
C-OH, $(CH_3\text{-}C^*H_2)_2\text{-}O$	286.6	17.3	24.0	20.1	28.7	26.7

Table 2b. Percentages of species (at%) obtained from C 1s curve fitting on the as-received and plasma treated κ-carrageenan.

XPS analyses in more details the variation in the surface chemistry of the κ-carrageenan after air plasma treatment. The as-received κ-carrageenan mainly contains carbon and oxygen (Table 2a), although noticeable amounts of chlorine and potassium are also found; furthermore, a small at % of sulphur as expected in the chemical structure and sodium, calcium anions are detected. According to the binding energies, KCl, NaCl and $CaCl_2$ are present on the as-received κ-carrageenan. It has been reported that cations bind to carrageenan's blocking sulfate groups and

affect the balance of attractive and repulsive forces between the molecules so that the optimum gel strength will occur depending on cations such as K, Ca, and Na[4]. Table 2b shows that carbon in the as-received κ-carrageenan is due to –(C^*H_2-CH_2), C-O-C and C-OH. The air plasma treatment decreases the carbon content and slightly increases the oxygen content on the κ-carrageenan, due to surface oxidation. In fact, the amounts of C-OH and C-O-C species (Table 2a) increase after air plasma treatment. The air plasma treatment also changes the amounts of the different carbon species, increasing the –(C^*H_2-CH_2) moieties which is an indication of depolymerisation of the κ-carrageenan. On the other hand, the amounts of Cl, K, Na and Ca increases, indicating the removal of organic material in the κ-carrageenan by treatment with air plasma. The above mentioned modifications produced by air plasma treatment in the κ-carrageenan are more marked by increasing the length of plasma treatment and the power of the discharge.

The air plasma treatment also changes the morphology of the κ-carrageenan. SEM micrographs before and after air plasma treatment (Figures 3a and 3b, respectively) show a noticeable deterioration of the fibre bundles that becomes thinner after air plasma treatment.

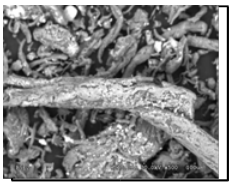

Figure 3a. As-received κ-carrageenan (X500)

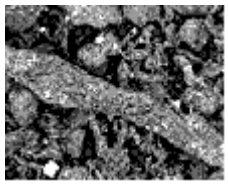

Figure3b. Air plasma treated κ-carrageenan at 125W for 20 min (X500)

pH measurements were carried out to further confirm the oxidation of the air plasma treated κ-carrageenan. Figure 4 shows a decrease in the pH of the κ-carrageenan after air plasma treatment in a greater extent by increasing the power and the length of treatment, supporting the oxidation produced[2].

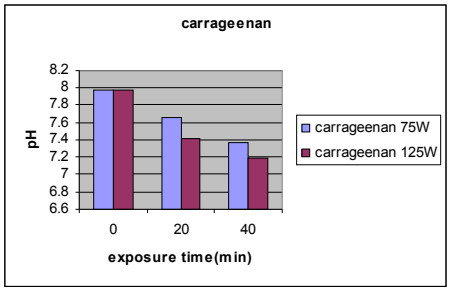

Figure 4**.** pH of aqueous solutions of κ-carrageenan prior to and after air plasma treatment

The air plasma treatment also modifies the viscosity of the aqueous solutions of the κ-carrageenan likely due to the depolymerisation produced (Figure 5). Extended air plasma length of treatment increased the viscosity due to the cross linking of κ-carrageenan fibres.

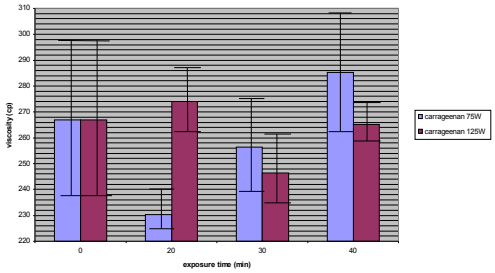

Figure 5. Brookfield viscosity of κ-carrageenan prior to and after air plasma treatment

4. Conclusions

The air plasma affected the structure of the κ-carrageenan by producing oxidation and depolymerization, affecting its pH and viscosity.

The jellification, water adsorption, and swelling behaviour of the air plasma treated polysaccharides for the preparation of temperature and/or pH sensitive smart gels are still under investigation. Further to stagnant modification of polysaccharides by glow discharge method, a rotary glow discharge reactor will also be employed for such powder treatments.

5. References

1) Galaev, Y.I. & Mattiasson, B. (1999). Smart polymers and what they can do in biotechnology and medicine. *Tibtech*, (Vol 17) (pp. 335-340).

2) 2. Lii, C.Y., Liao, C.D., Stobinski, L., Tomasik, P. (2002). Behaviour of granular starches in low pressure glow plasma. *Carbohydrate Polymers*, 49: 499-507 .

3) 3. Lii, C.Y., Liao, C.D., Stobinski, L., Tomasik, P. (2002). Effects of hydrogen, oxygen and ammonia low-pressure glow plasma on granular starches. *Carbohydrate Polymers*, 49: 449-456.

4) 4. Naim S., Samuel B., Chauhan B. and Paradkar A. (2004). Effect of Potassium Chloride and Cationic Drug on Swelling, Erosion and Release from κ-Carrageenan Matrices. *AAPS Pharmaceutical Science Technology,* 5 (2) Article 25.

Dust Particle Dynamics in Plasma Sheath with an Oblique Magnetic Field

M. Davoudabadi and F. Mashayek

Department of Mechanical and Industrial Engineering, University of Illinois at Chicago, Chicago, IL 60607, USA

Abstract
In the presence of a strong oblique magnetic field and under low-pressure limit, a weakly collisional, steady-state, two-fluid model is extended to examine the effect of the bulk plasma density on the structure of the plasma sheath. Conditions under which a single nano-sized dust particle can be trapped in the sheath are considered. While varying the particle density, the ion and electron densities at the particle steady state position and the charge on the particle are calculated for different magnetic field intensities.
Keywords magnetized plasma sheath, dust particle dynamics, fluid simulation

1. Introduction

Dusty plasma is a unique multi-component system composed of dispersed macroscopic charged dust particles that form a colloidal-type suspension in the parent plasma background [1]. It represents the most common configuration in astrophysical, laboratory, and industrial plasmas. The plasma-wall transition, existing for example as a sheath around the surface of a small astronomical body or near the walls of plasma processing reactors, has attracted the interest of the plasma community for many years [2, 3, 4, 5]. The dust charging mechanism and dynamics of dust particles in plasma sheaths have also been topics of many studies [1, 6, 7, 8, 9].

Well-established existing models can provide detailed information on the mechanism of plasma-wall interaction and formation of an electrostatic sheath in an unmagnetized plasma. These models are also being used for simulating the boundary region of *strongly* magnetized plasmas without any modification [10]. However, the extent of such studies involving a magnetic field is very limited and subject to some restrictive assumptions. In this work, we relax some of these assumptions to provide a more comprehensive investigation. In order to simulate the sheath structure, we extend an existing comprehensive model originally developed by Resendes *et al.* [6, 11] for modeling the *unmagnetized* plasma sheath. The model remains valid for a broad range of Larmor radii. After solving for the sheath variables, a single dust particle is considered and it is assumed that the particle does not contribute to the total space charge and, thus, does not modify the sheath structure. For a nano-sized particle with radius R, we consider moderate magnetic field intensities for which the condition $\rho_{e,i} > R$ is satisfied, where $\rho_{e,i}$ are the electron and ion gyroradii. Under these circumstances, following Tsytovich *et al.* [12] and Salimullah *et al.* [13], the orbit motion limited (OML) theory remains intact and is thus utilized to obtain the electric potential difference between the dust particle and the plasma and, consequently, the charge quantity on the dust due to the ions and electrons currents. A complete set of forces acting on the dust particle originating from the electric field in the sheath, the static magnetic field, gravity, and ion and neutral drags is taken into account.

This work is motivated by our ongoing effort in modeling of nanoparticle coating in low-pressure plasma reactors. In our recent paper [14], we fully discussed the effect of presence of a static oblique magnetic field in the plasma sheath and several other parameters on both the sheath structure and dust dynamics. In the present work, we turn our attention specifically towards the effect of bulk plasma number density on the sheath structure and also towards the amount of charge populated on the particle at steady state for various materials with different mass densities under different magnetic field intensities. The particle density ranges from 5,000 Kg m^{-3} to 20,000 Kg m^{-3} representing materials such as steel, copper, silver and gold.

2. Sheath model and dust particle equations

Since the hot electrons are repelled away from the negatively charged wall, their fluid directed velocity v_e is negligible compared to their thermal velocity v_{the}. Therefore, the use of Boltzmann relation as a solution of the electron equations is well justified even in presence of a magnetic field $\vec{B}$ with the intensity B,

$$n_e = n_0 \exp\left(\frac{e\phi}{k_B T_e}\right). \tag{1}$$

Here n_e is the electrons number density, n_0 is the bulk plasma particles number density, e is the elementary electron charge, ϕ is the electric potential in the sheath, T_e is the electron temperature, and k_B is the Boltzmann constant.

To simulate the cold ions concentration and velocity, however, we implement continuity and momentum equations, and include the pressure gradient and drag force due to the collision with neutrals as well as electric and magnetic forces on the ions [6, 15]. In low pressure ranges, ionization in the sheath can be neglected, owing to the low neutral density, n_n, and consequently, an ion mean free path much larger than the sheath thickness, D. Thus, in the present analysis a source-free model is used. We consider the physical parameters changing only along the z (normal to the wall) direction in the sheath region ($\nabla \equiv \hat{k}\frac{\partial}{\partial z}$). The magnetic field is embedded in the x-z plane intersecting the wall (at $z = D$) with an angle θ (see figure 1). We introduce the following normalized variables:

$$\eta = -\frac{e\phi}{k_B T_e}, \qquad \vec{u}_i = \frac{\vec{v}_i}{v_{thi}}, \qquad \xi = \frac{z}{\lambda_{Di0}},$$

where $v_{thi} = \sqrt{8k_BT_i/\pi m_i}$ is the mean ion thermal velocity, and $\lambda_{Di0} = \sqrt{\epsilon_0 k_B T_i/e^2 n_{i0}}$ is the ion Debye length with ϵ_0 denoting permittivity of free space. The steady state fluid equations for the three-dimensional adiabatic ion flow with mass m_i, temperature T_i, and number density n_i, after applying the continuity equation, are described as

$$u_{iz}\frac{\partial u_{ix}}{\partial \xi} = -\alpha u_i u_{ix} + \beta u_{iy}\cos\theta, \tag{2}$$

$$u_{iz}\frac{\partial u_{iy}}{\partial \xi} = -\alpha u_i u_{iy} + \beta(-u_{ix}\cos\theta + u_{iz}\sin\theta), \tag{3}$$

$$u_{iz}\frac{\partial u_{iz}}{\partial \xi}\left(1 - \frac{5\pi}{24}\frac{u_{0z}^{\frac{2}{3}}}{u_{iz}^{\frac{8}{3}}}\right) = \frac{\pi}{8}\frac{T_e}{T_i}\frac{\partial \eta}{\partial \xi} - \alpha u_i u_{iz} - \beta u_{iy}\sin\theta, \tag{4}$$

where $\alpha = n_n\sigma_s\lambda_{Di0}$ is the degree of collisionality and expresses the number of collisions within a Debye length, and the nondimensional parameter $\beta = \sqrt{\pi/8}\lambda_{Di0}/\lambda_{mi}$ is proportional to the magnetic field intensity ($\lambda_{mi} = \sqrt{k_BT_i m_i/e^2B^2}$ is the thermal Larmor radius). Finally, using equation (1) and assuming ions having a single positive charge, the nondimensional Poisson equation can be written as

$$\frac{\partial^2 \eta}{\partial \xi^2} = \frac{T_i}{T_e}\left[\frac{u_{0z}}{u_{iz}} - \exp(-\eta)\right]. \tag{5}$$

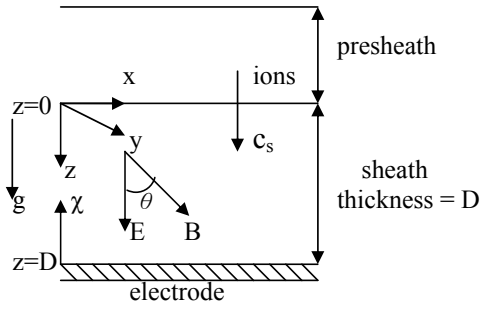

Figure 1: Magnetized plasma sheath configuration.

Chodura [16] proposed that the ions velocity entering the so-called "magnetic pre-sheath" is constrained to be along the magnetic field and to be equal or greater than sonic; while the ion drift velocity at the sheath edge is perpendicular to the solid surface and equal or greater than ion sound speed, $c_s = \sqrt{5k_BT_i/3m_i + k_BT_e/m_i}$. Franklin [17] later proved that in a simplistic fluid model the plasma equations are singular where the Bohm criterion is satisfied. This is regardless of the collision model for the ions and the generation mechanism for the charged particles; therefore, there cannot be a collisionally modified Bohm criterion. (For a detailed discussion on the validity of Bohm criterion at the plasma sheath edge in presence of a magnetic field we refer to [16, 4, 18, 19, 17].) As boundary conditions for the Poisson equation, we take the electric potential at the sheath edge to be zero, where the ion acceleration is also zero, thus giving rise to the other required boundary condition for the potential through the ions z momentum equation (4) [7]. The sheath thickness D is determined by the requirement that the potential takes a given value at the electrode, $\phi(z = D) = \phi_w$. The normalized boundary conditions are summarized as follows:

$$\xi = 0: \qquad u_{ix} = 0, \quad u_{iy} = 0, \quad u_{iz} = u_{0z} = \frac{c_s}{v_{thi}}, \tag{6}$$

$$\xi = 0: \qquad \eta = 0, \quad \frac{\partial \eta}{\partial \xi} = \frac{8}{\pi}\frac{T_i}{T_e}\alpha\left(\frac{c_s}{v_{thi}}\right)^2. \tag{7}$$

Equations (2) – (5) with boundary conditions (6) and (7) are solved using a fourth-order Runge-Kutta method. Starting from the sheath edge at $z = 0$, we march in space until the requirement $\phi = \phi_w$ is fulfilled.

We consider an isolated spherical dust particle of radius $R \ll \lambda_D$ and $R < \rho_{i,e}$, where $\rho_{i,e} = \sqrt{K_B T_{i,e} m_{i,e}/e^2 B^2}$. The latter inequality is satisfied for magnetic field intensities less than a critical value, found in practical units from [12]

$$B^e_{cr}(T)R(nm) > 4137\sqrt{\frac{T_e(eV)}{3(eV)}}.$$

With the above considerations, in the process of tracking the particle in space and time, orbit motion limited (OML) theory [20] can still be utilized to obtain the charge quantity on the dust due to the ion and electron currents and to find the electric force on the particle. Depending on the sign of the normalized potential difference between the particle and the plasma, $y(z, v_p) \equiv e(\phi_p - \phi)/k_B T_e$, in which ϕ_p denotes the particle potential and ϕ the sheath potential at the particle location, the electron and ion currents to the dust particle are given by

$$I_e = -\pi r^2 e \left(\frac{8K_B T_e}{\pi m_e}\right)^{\frac{1}{2}} n_e \exp(y), \qquad I_i = \pi r^2 e n_i v_i \left(1 - \frac{2K_B T_e y}{m_i v_i^2}\right), \tag{8}$$

for $y < 0$, and

$$I_e = -\pi r^2 e \left(\frac{8K_B T_e}{\pi m_e}\right)^{\frac{1}{2}} n_e (1 + y), \qquad I_i = \pi r^2 e n_i v_i \exp\left(\frac{2K_B T_e y}{m_i v_i^2}\right), \tag{9}$$

for $y \geq 0$.

For the ion current, we replace the thermal velocity and energy terms in the OML expression by the mean speed $v_s = \sqrt{v_{thi}^2 + \overline{v}_i^2}$ with which ions approach a dust particle. Here, $\vec{v}_i = (\vec{v}_i - \vec{v}_p)$ is the directed ion speed relative to a stationary dust particle while $\vec{v}_p$ is the particle velocity [21]. By equating the sum of the electron and ion currents to zero, we obtain an implicit equation for $y(z, v_p)$ (see [6, 11]), which depends on the position of the dust particle in the plasma sheath. Assuming a conducting dust particle, the particle charge can be calculated from

$$Q(z, v_p) = \frac{k_B T_e}{e} R y(z, v_p). \tag{10}$$

The main forces on a dust particle in a magnetized sheath are the electric, gravitational, ion drag, neutral drag and magnetic forces. Once the electric field $\overrightarrow{E}$ is calculated from the sheath equations and the charge Q on a dust particle is determined from equation (10), the electric force is simply obtained from

$$\vec{F}_e(z, v_p) = Q(z, v_p)\vec{E}(z). \tag{11}$$

The magnetic force acting on a moving dust particle is obtained via

$$\vec{F}_B = Q\vec{v}_p \times \vec{B}. \tag{12}$$

The ion drag force is given by [21]

$$\vec{F}_{id} = 4\pi n_i v_{thi} \widetilde{v}_s m_i \vec{\overline{v}}_i b^2_{\frac{\pi}{2}} \ln\Gamma, \tag{13}$$

where $b^2_{\frac{\pi}{2}} = e^2 Q^4/m_i^2 \overline{v}_i^4$ and $\ln\Gamma = \frac{1}{2}\ln(1 + b^2_{max}/b^2_{min})$. The maximum and minimum impact parameters, corresponding to maximum and minimum deflection angles, are $b_{max} = \overline{\lambda} = (2n_e\lambda_{De} + n_i\lambda_{Di})/(n_e + n_i)$ and $b_{min} = R$, respectively. Here, ion Debye length and local electron Debye length are defined as $\lambda_{De} = \sqrt{\epsilon_0 k_B T_e/e^2 n_e}$, and $\lambda_{Di} = \left[\epsilon_0(\frac{1}{2}m_i\overline{v}_i^2 + k_B T_i)/e^2 n_i\right]^{1/2}$, respectively.

Neglecting any gas flow, the relative velocity will be v_p, and the drag force due to neutral collisional coupling is given by the Epstein expression [22]

$$\vec{F}_{nd} = -\frac{8}{3}\sqrt{2\pi} R^2 n_n k_B T_n \left(\frac{\vec{v}_p}{v_{thn}}\right), \tag{14}$$

since the typical ratio $v_p/v_{thn} \ll 1$, where v_{thn} is the neutral thermal velocity defined as $v_{thn} = \sqrt{k_B T_n/m_n}$.

The total force acting on a dust particle is $\vec{F}_t = \vec{F}_e + \vec{F}_B + \vec{F}_g + \vec{F}_{id} + \vec{F}_{nd}$, where $\vec{F}_g$ is the gravity force on the particle with magnitude $F_g = m_p g$, where m_p is the dust particle mass and g is the gravitational constant. Having specified the forces, the dust particle Lagrangian equations are described as [11]

$$\frac{d\vec{x}_p}{dt} = \vec{v}_p, \qquad \frac{d\vec{v}_p}{dt} = \frac{\tau_0}{m_p v_{thi}}\vec{F}_t, \tag{15}$$

for particle position and velocity, respectively. Here $\vec{x}_p$ is the displacement normalized by the ion Debye radius λ_{Di} in the plasma, the time is normalized by $\tau_0 = \lambda_{Di}/v_{thi}$, and the velocity by v_{thi}. Initial conditions are provided for each equation having three components in three directions x, y and z.

3. Results and discussion

We consider argon to be the background gas, and the electrode to be held at a constant electric potential $\phi_w = -6V$. Other parameters are $T_e = 1$ eV, $T_i = 0.05$ eV, angle of incidence for the magnetic field $\theta = 20^o$, $P = 10$ mtorr, dust particle radius $R = 620$ nm. With the above parameters, B^e_{cr} is calculated to be 3.8524 T, hence, in the particle dynamics section we consider typical magnetic field intensities of 1.5 and 3 T and the OML theory remains valid. For B=3 T, ρ_i=47,499 nm and ρ_e=794.8 nm, and thus the inequality $R < \rho_{i,e}$ holds.

Figure 2(a), (b), (c) shows the ion velocity normalized by the mean ion thermal velocity, ion density normalized by bulk plasma density, and the normalized electric field as functions of distance from the electrode for different bulk plasma number densities and magnetic field intensities. As the plasma density n_0 increases, ion Debye length decreases; therefore, the degree of collisionality, α, also decreases. Hence, there will be less decelerating ion-neutral drag force but (see figure 2(c)) larger accelerating electric force through the influence of α on the boundary condition for electric potential at the sheath edge (equation (7)). The effect of the latter is dominant especially in the region starting from the sheath edge to near the electrode. This means that in higher n_0 case, ions will be accelerated more effectively and have larger velocity, and because of the continuity a smaller number density for the same distance from the electrode. Thus, the plasma shields the electrode potential more effectively leading to a thinner sheath.

In the present model, there is no restriction on the magnetic field intensity value in modeling the sheath structure. Therefore, to clearly show the effect of the magnetic field on the sheath, typical feasible magnetic field intensities as strong as up to even 4 T have been chosen for the results in this part. The presence of magnetic field induces fluctuations in the ion density. As the ions enter the sheath, they are decelerated by the Lorentz force in the z direction (see the momentum equations (2) – (4)) and thus, the ion density increases. As can be seen from figure 2(a) and (b), higher intensities of the magnetic field (e.g. B=4 T) can cause the ion flow to gyrate; the Lorentz force accelerates and decelerates the ions so the ion density experiences fluctuations. The reason that these fluctuations are more intense for lower plasma number densities can be attributed to the effect of ion Debye length on β which is responsible for the gyration-inducing terms in the momentum equations. For example, β is around 0.9244 for n_0=10^9 cm^{-3} while it is about 2.9233 in the n_0=10^8 cm^{-3} case. Furthermore, from the same figure it can be realized that the plasma sheath is thicker without magnetic field. This trend has been elaborated in details in [14]. Moreover, the indirect influence of magnetic field on the electron number density distribution in the sheath is obvious in figure 2(d).

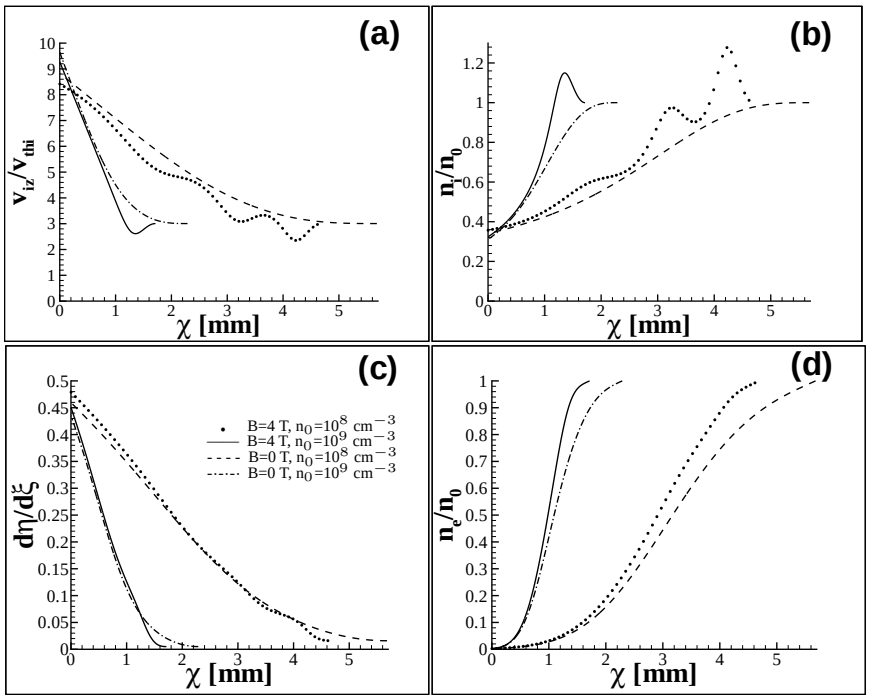

Figure 2: Comparison of plasma variables for different bulk plasma number densities and magnetic field intensities. (a) Normalized ion z-component velocity, (b) normalized ion number density, (c) normalized electric field, and (d) normalized electron number density.

Equations (15) for particle motion have been directly integrated in three directions with zero initial velocity for the dust particle initially released at the sheath edge. At steady state, position and charge of the particle, ion and electron number densities around the particle final position, and the potential difference between the particle and plasma as functions of the particle density are presented in figure 3 for three different magnetic field intensities B=0, 1.5, and 3 T. Since the gravity force on the particle increases with its density, the particle steady state z position, around which the particle oscillates in its transition phase, approaches the electrode. Hence, the number densities of both ions and electrons around the particle decrease (see figure 2(b) and

(d)). In the absence of the magnetic field in the sheath, the difference between these two number densities increases smoothly with the increase of the particle density. From the Poisson equation, this results in a larger negative value of the plasma electric potential ϕ at particle position. Because $(\phi_p - \phi)$ is negative in value and ϕ is also negative throughout the sheath, $(\phi_p - \phi)$ will decrease in magnitude (figure 3(d)). Consequently, according to equation (10), the amount of negative charge collected on the particle at steady state will also decrease in magnitude with the increase of the particle density which is evident in figure 3(a).

In the presence of the magnetic field, however, due to the induced fluctuations in number density of ions (see figure 2(b)), $(n_i - n_e)$ around the particle fluctuates with the increase of the particle density. Let us consider two particles with densities of 6.7×10^3 and 1.4×10^4 Kg m^{-3} both trapped in the sheath with an applied magnetic field intensity of B=3 T. Comparing the corresponding points A and B in figure 3(c), one realizes that ions are more concentrated around the lighter rather than the heavier particle equilibrium point, and thus,

$$(n_i - n_e)|_{z_{p_A}} > (n_i - n_e)|_{z_{p_B}}.$$

Intuitively, more net positive charge exists around particle A, hence less negative charge is expected to be populated on particle A. Furthermore, under the present conditions, it is found that for the case without magnetic field, nanoparticles with radius $R = 620$ nm and densities higher than 17,200 Kg m^{-3} might not be trapped in the sheath, while with the presence of a typical magnetic field intensity of 1.5 T or 3 T and with an angle of incidence of 20^o they can easily be trapped within the sheath.

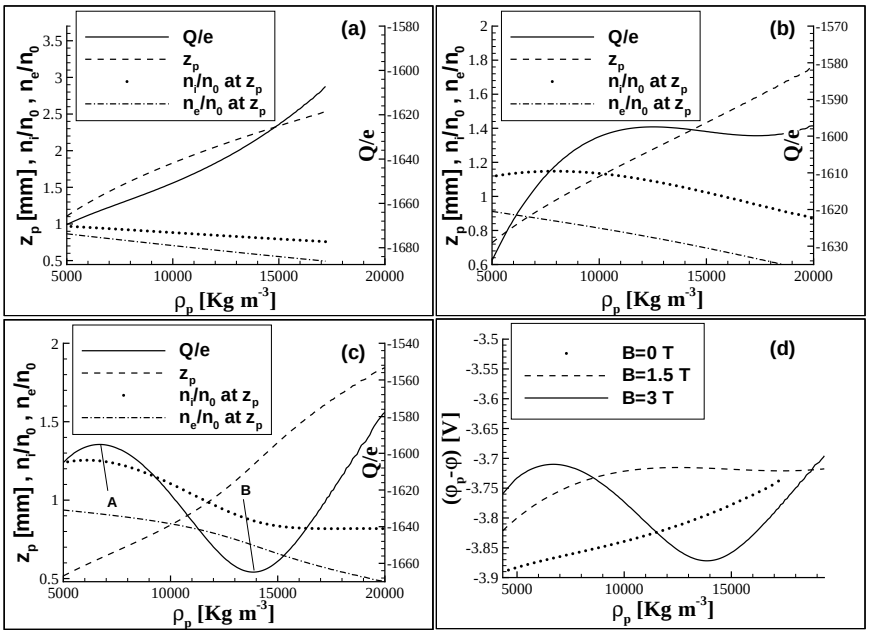

Figure 3: Steady state position and charge of the particle, ion and electron number densities around the particle final position as functions of the particle density for (a) B=0, (b) B=1.5 T, (c) B=3 T. (d) Potential difference between the particle and plasma as a function of the particle density for different magnetic field intensities.

4. Conclusions

The effect of the bulk plasma number density on the structure of a plasma sheath in presence of an oblique magnetic field has been studied by implementing a two-fluid model that adequately accounts for the forces acting on ions in the low pressure range. The primary effect of the magnetic field is to induce oscillations in the spatial variation of ions velocity and density. These oscillations become more pronounced as the magnetic field strength is increased. For varying bulk plasma density, different plasma parameters including the electron and ion densities, ion flow velocity, and electric potential are presented.

The dynamics of a dust particle located within the sheath subject to a moderate oblique magnetic field is examined through implementation of a comprehensive model taking various forces acting on the dust particle into consideration. The influence of the particle density and the magnetic field intensity on the amount of the charge collected on the particle has been discussed. Future studies are recommended to expand the parameter space in order to determine the ranges of various parameters for which particles can be effectively trapped in the sheath. As a practically important result, it is found that without magnetic field present in the sheath, heavier particles with the same size gather less negative charge; while in presence of magnetic field this trend can be violated depending on the field intensity and particle density. In addition, introduction of magnetic field to plasma can help trap heavier particles which could not be trapped in the unmagnetized sheath under the same conditions.

Acknowledgments

This work was supported by grant CTS-0422900 from the U.S. National Science Foundation with Dr. T. J. Mountziaris as the Program Director.

References

[1] S. K. Baishya and G. C. Das, "Dynamics of Dust Particles in a Magnetized Plasma Sheath in a Fully Ionized Space Plasma," Phys. Plasmas **10,** 3733–3745 (2003).

[2] S. R. Seshardi, *Fundamentals of Plasma Physics* (American Elsevier Publishing Company, New York, NY, 1973).

[3] F. F. Chen, *Introduction to Plasma Physics and Controlled Fusion, Volume 1: Plasma Physics* (Plenum Press, New York, NY, 1984).

[4] K. U. Riemann, "The Bohm Criterion and Sheath Formation," J. Phys. D: Appl. Phys. **24,** 493–518 (1991).

[5] T. E. Sheridan and J. Goree, "Collisional Plasma Sheath Model," Phys. Fluids B **3,** 2796–2804 (1991).

[6] D. P. Resendes, G. Sorasio, and P. K. Shukla, "Dynamics of Dust Particles in Plasma Sheaths," Phys. Plasmas **9,** 2988–2997 (2002).

[7] T. Nitter, "Levitation of Dust in RF and DC Glow Discharges," Plasma Sources Sci. Technol. **5,** 93–111 (1996).

[8] D. Winske and M. E. Jones, "Particulate Dynamics at the Plasma-Sheath Boundary in DC Glow Discharge," IEEE Transactions on Plasma Science **22,** 454–464 (1994).

[9] G. C. Das and P. Kalita, "Characteristic Behaviour of Dust Grains in a Magnetized Plasma Sheath," J. Phys. D: Appl. Phys. **37,** 702–708 (2004).

[10] D. Sharma and H. Ramachandran, "Structure of a Source-Driven Magnetized Oblique Presheath," Physical Review E **66,** 026412 (2002).

[11] G. Sorasio, R. A. Fonseca, D. P. Resendes, and P. K. Shukla, "Dust Grain Oscillation in Plasma Sheaths Under Low Pressure," in *Dust Plasma Interaction in Space*, P. K. Shukla, ed., (Nova Publishers, New York, NY, 2002), Chap. 3, pp. 37–70.

[12] V. N. Tsytovich, N. Sato, and G. E. Morfill, "Note on the Charging and Spinning of Dust Particles in Complex Plasmas in a Strong Magnetic Field," New Journal of Physics **5,** 43.1–43.9 (2003).

[13] M. Salimullah, I. Sandberg, and P. K. Shukla, "Dust Charge Fluctuations in a Magnetized Dusty Plasma," Phys. Review E **68,** 027403 (2003).

[14] M. Davoudabadi and F. Mashayek, "Dust Particle Dynamics in Magnetized Plasma Sheath," revised manuscript submitted, Phys. Plasmas .

[15] X. Zou, J. Y. Liu, Z. X. Wang, Y. Gong, Y. Liu, and X. G. Wang, "Electronegative Plasma Sheath Structure in a Magnetic Field," Chin. Phys. Lett. **21,** 1572–1574 (2004).

[16] R. Chodura, "Plasma-Wall Transition in an Oblique Magnetic Field," Phys. Fluids **25,** 1628–1633 (1982).

[17] R. N. Franklin, "The Plasma-Sheath Boundary Region," J. Phys. D: Appl. Phys. **36,** R309–R320 (2003).

[18] K. U. Riemann, "Theory of the Collisional Presheath in an Oblique Magnetic Field," Phys. Plasmas **1,** 552–558 (1994).

[19] P. C. Stangeby, "The Bohm-Chodura Plasma Sheath Criterion," Phys. Plasmas **2,** 702–706 (1995).

[20] B. Walch, S. V. Horanyi, and R. S., "Charging of Dust Grain in Plasma with Energetic Electrons," Phys. Rev. Lett. **75,** 838–841 (1995).

[21] M. S. Barnes, J. H. Keller, J. C. Foster, J. A. O'Neil, and D. K. Coultas, "Transport of Dust Particles in Glow-Discharge Plasmas," Phys. Rev. Lett. **68,** 313–316 (1992).

[22] P. S. Epstein, "On the Resistance Experienced by Spheres in Their Motion through Gases," Phys. Rev. **23,** 710–733 (1924).

Kinetic Rate of Carbon Production in Cold, Vibrationally Excited CO Plasmas

Katherine Essenhigh and J. William Rich

Nonequilibrium Thermodynamics Laboratories, Dept. of Mechanical Engineering, The Ohio State University

The specific rate for the production of carbon by gas-phase Boudouard disproportionation of vibrationally excited carbon monoxide has been measured. The Boudouard disproportionation reaction is

$$CO\ (v) + CO\ (w) \rightarrow CO_2 + C.$$

Here, CO (v) and CO (w) represent carbon monoxide molecules in excited vibrational states v and w, respectively. This reaction has long been observed in various weakly-ionized molecular plasmas containing CO, and has been seen in optically pumped plasmas in which CO is vibrationally excited using a high power laser [1]. In other experiments, the reaction enters plays a role in synthesis of single-walled-carbon nanotubes using optically pumped, non-thermal plasma reactors [2]. Most importantly, the reaction has been known to occur on various metal catalytic surfaces; on iron, for example the reaction causes the carbon particle "pitting" of metal flues containing hydrocarbon/air combustion products. The reaction is not typically studied in the gas phase, however. From various plasma experiments, the activation energy for the gas phase reaction is estimated to be near 6 eV, requiring preparing reactants at a very high temperature for any measurable CO_2 yield by this process.

The experimental setup for the present experiments is shown in the schematic of Fig. 1. In these experiments, cold CO is mixed with an Ar carrier and flows through a reaction cell. The CO is vibrationally excited by the resonance absorption of the radiation from a c.w. CO laser, operating on the CO fundamental infrared bands from 4.7 to 5.3 microns wavelength. The CO rotation/translation modes remain in equilibrium at relatively low gas kinetic temperatures (~ 1,000 K) after vibrational excitation; the translational modes of the Ar carrier are also equilibrated to this temperature. The level of vibrational mode excitation in the CO reactant is measured by IR emission spectroscopy using the first overtone CO band emission. The distribution of energy among the CO vibrational quantum states (the vibrational distribution function, or "VDF") is inferred from these emission spectra. Fig. 2 shows typical VDF's , measured for such reactant preparation, for mixtures of CO in Ar, and for CO/Ar with various amounts of added He diluent. The gas translational/rotational mode temperature is also inferred by emission spectroscopy, from the rotational fine structure of the R-branch emission from the v = 1 – 0 CO fundamental band. It can be seen from Fig. 2 that a very non-Boltzmann distribution of vibrational populations is maintained in steady state; the high populations of vibrational levels near v =25, which are at energies near 6 eV, for example, would only be attained in thermally equilibrated environments at temperatures well above 10,000 K. Critical to the experiment is the ability to control the level of vibrational excitation. As seen in the figure, adding increasing amounts of He results in depopulating upper vibrational levels. This can rapidly decrease the reaction rate. The reaction rate is inferred by passing the mixture from the flow reactor through an FTIR, and inferring the concentration of the CO_2 product by absorption spectroscopy on the V_3 fundamental band. Fig. 3 shows the specific reaction rate inferred for the reaction, as a function of the amount of He added. The decrease in the reaction with the depopulation of higher levels is

easily inferred. It appears that significant reaction occurs only if the total energy in the reactants exceeds ~ 6 eV.

At the 1,000 K translational/rotational temperatures of the present environment, there would be ***no*** gas phase Boudouard reaction if the gas were thermally equilibrated. Indeed, the gas phase Boudouard reaction has only been observed previously by preparation of CO reactant in low-lying excited electronic states (notably, in CO($a^3\Pi$)) in photolytic or electric discharge reactors [3]. The only exception to this has been the measurements reported as CO "dissociation" reaction in very high temperature, shock-tube-generated, thermal environments from 5000 to 15,000 K [4]. No reaction is seen below 5,000 K, much less at the 1,000 K temperature of the present non-equilibrium rate measurements.

Table 1 gives a quantitative summary of the rate data. These data show that the reaction rate falls by an order of magnitude as the populations of vibrational levels above v ~ 25 are reduced by He addition. This reduction occurs although the total energy in vibration is not significantly reduced (see column 4 of Table I). It can be inferred that the effective activation energy of this reaction is approximately the energy of v~25, or, as indicated on the table, E_{act} ~ 5.8 eV. It may not be coincidental that this energy is very close to the ground energy level of the first electronically-excited state in CO, the $a^3\Pi$ state. It is possible that energy transfer from v ~ 25 into the $a^3\Pi$ mediates the reaction whose rate is reported in Fig. 3 and Table I. As we have noted, preparation of CO ($a^3\Pi$) results in a rapid disproportionation reaction. This possible channel is currently being investigated in our group. It is clear, however, why no *thermal* disproportionation is seen unless the gas temperature is above 5,000 K.

References

[1] I. Adamovich, S. Saupe, M.J. Grassi, O. Shulz, S. Macheret and J.W. Rich, "Vibrationally Stimulated Ionization of Carbon Monoxide in Optical Pumping Experiments", *Chemical Physics*, vol. 173, 1993, pp. 491-504

[2] E. Ploenjes, P. Palm, G.B. Viswanathan, V.V. Subramaniam, I.V. Adamovich, W.R. Lempert, H.L. Frasier, and J.W. Rich, "Synthesis of Single-Walled Carbon Nanotubes in Vibrationally Nonequilibrium Carbon Monoxide", *Chemical Physics Letters*, vol. 352, No. 5-6, 2002, pp. 342-347

[3] E.E. Ivanov, Yu. Z. Ionikh, N.P. Penkin, N.V. Chernisheva, Sov. J. Chem. Phys. 7, 1991, 2989

[4] H.-J. Mick, M. Burmeister, and P. Roth, AIAA J., Vol. 31, 1993, 671

Acknowledgement

We wish to thank the U.S. Air Force Office of Scientific Research Space Power and Propulsion Program, and the Ralph W. Kurtz Endowment for support of this research. Very helpful discussions with Profs. Y. Ionikh, W. Urban, and I. Adamovich, and with Dr. Y. Utkin, are also gratefully acknowledged.

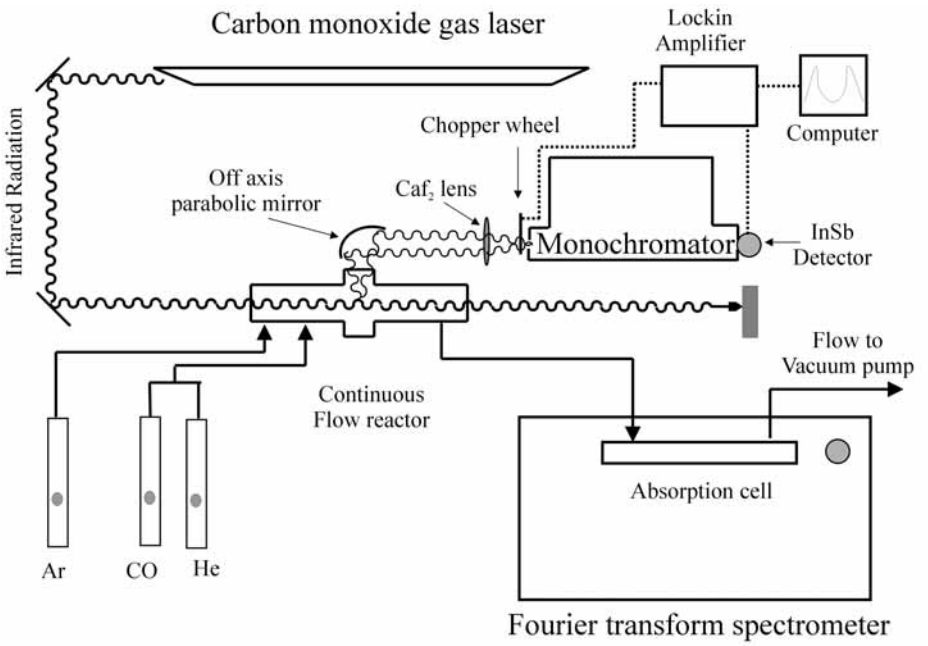

Figure 1: Experimental Set up

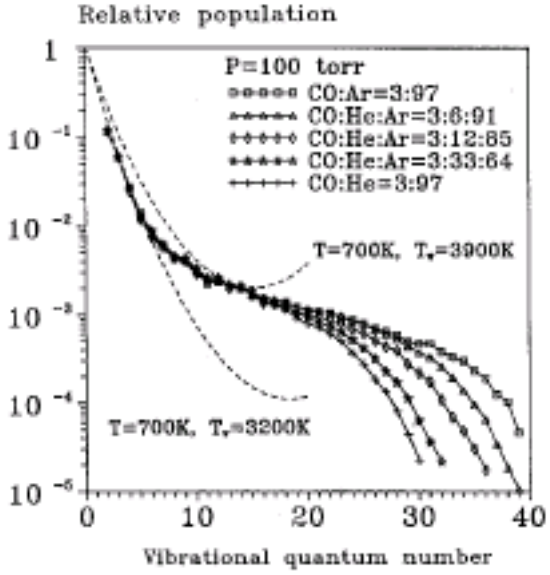

Fig.2 Measured populations of vibrationally excited CO molecules, as the amount of helium diluent is varied.

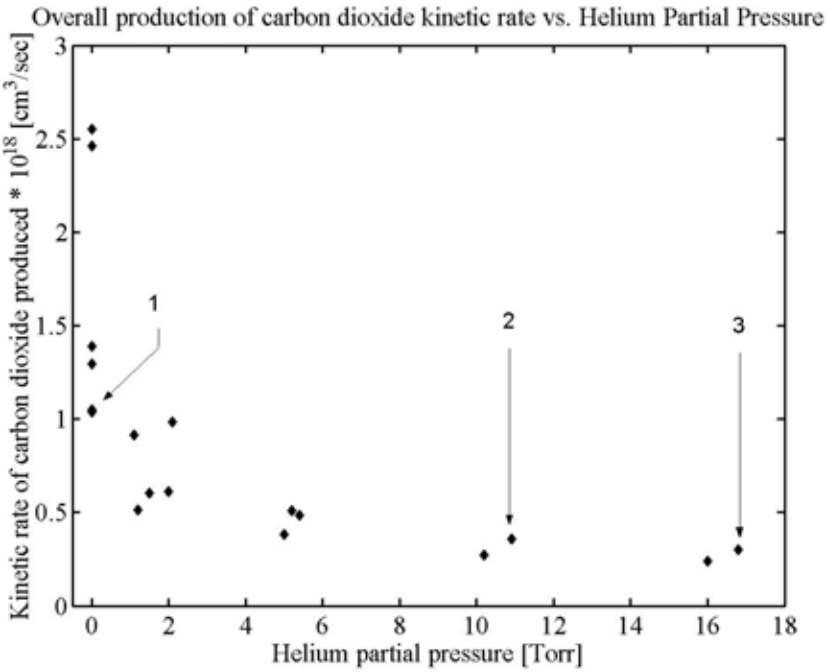

Fig. 3: Specific reaction rate of the gas phase Boudouard reaction, as a function of He addition

Table I: Boudouard Reaction Specific Rate, Dependence on Vibrational Energy Content				
Point, Specific Reaction Rate Constant, cm^3/sec	Total number of carbon monoxide molecules $[cm^{-3}]$	Fractional population (normalized by the population of v = 0) in vibrational levels v > 25	Total energy in all vibrational levels [ev/molecule]	Fractional amount of energy in vibrational levels v > 25 ($E_{v=25}$ = 5.79 ev) [ev/molecule]
1 (He = 0 Torr), $1.5x\ 10^{-18}$	$3.34*10^{17}$	$6.19*10^{-4}$	0.260	$3.95*10^{-3}$
2 (He = 10 Torr), $0.3\ x\ 10^{-18}$	$3.42*10^{17}$	$4.30*10^{-4}$	0.264	$2.67*10^{-3}$
3 (He = 16 Torr) $0.15\ x\ 10^{-18}$	$3.56*10^{17}$	$4.20*10^{-4}$	0.255	$6.51*10^{-4}$

Plasma Removal of Wall Deposited Diesel Soot

D. Brocilo[1], J.S. Chang[1], D. Ewing[2], K. Urashima[1], and J.S. Cotton[3]

[1]Department of Engineering Physics, McMaster University, Hamilton, Canada
[2]Department of Mechanical Engineering, McMaster University, Hamilton, Canada
[3]Dana Canada Corporation, Long Manufacturing, Thermal Products Division, Oakville, Canada

Abstract

An experimental investigation was performed to characterize the soot removal from the internal surface of a tube using a corona radical shower non-thermal plasma system. The corona radical shower non-thermal plasma removed soot from extended regions in the tube, but the removal was more effective near the tube entrance. The soot removal was also more effective for the case when the soot was dry. The emissions of unwanted gaseous by-products were monitored during these tests and found to be small.

Introduction

There has been considerable interest in using non-thermal devices to treat the flue gas in a range of applications [1-3]. Non-thermal plasmas can simultaneously remove the NO_x, particulate matter, and the volatile organic compounds present in the flue gas by promoting the oxidation reactions in the flue gas. Recently, there has been increased interest in using non-thermal plasma systems to oxide particulate matter deposited on surfaces, particularly in diesel exhaust gas pollution control systems. For example, Ohkubo et al. [4,5] considered the regeneration of diesel particulate filters using non-thermal plasmas. They were able to achieve a 85% removal efficiency using a needle-plate electrode configuration.

This investigation focused on developing a non-thermal plasma system to remove the diesel soot deposited in a wire-tube electrostatic precipitator (ESP) system that has been proposed as a possible low-pressure drop alternative for particulate filters[6]. The soot in the proposed system must be periodically removed and rapping can not be used because of concerns of soot reentrainment. There are a number of different designs for non-thermal plasma systems that can be operated in pulsed, flow-stabilized DC corona, dielectric-barrier, or pellet-bed discharge modes[1]. The latter two modes act to promote surface reactions in the reactor after the soot is deposited on the surface so they are not practical in the current application. Thus, it was decided to consider a flow-stabilized corona system with gas injected through the central electrode of the reactor. The flow-stabilized corona non-thermal plasma generates O and OH radicals that act to oxidize the carbon. The O radicals can also oxidize NO in a flue gas passing through the reactor to create NO_2 that could, in turn, oxidize the carbon. The soot oxidization will also result in the production of CO that is an undesired byproduct so that it is useful to characterize this during operation.

In practical applications, the corona radial injection system would have to be designed to optimize the interaction between radicals and the soot on the wall. The objective here was to assess whether the flow-stabilized corona system would be effective in oxidizing the soot so tests were preformed using a small diameter tube to ensure there was interaction between the radicals and the soot on the wall. The optimization for larger diameter tubes would be considered in later investigations. The flow-stabilized corona radical shower system and the experimental facilities used in this investigation are outlined in the next section. The results of the investigation are then presented and discussed.

Experimental Facility

The investigation was performed for a small diameter tube with a length of 200 mm that contained diesel soot deposited from the exhaust gas from a diesel generator described in [7]. After the soot was deposited in the tube, the tube was sectioned by cutting through most of the tube wall and then breaking the remainder of the wall manually. The thickness of the soot in the tube before the tests was

measured using an optical microscope. The sections of the tube were then inserted into a larger diameter tube that held them in place during the tests with the non-thermal plasma system.

The tube was inserted downstream of the non-thermal plasma reactor as shown in Figure 1. The non-thermal plasma reactor consisted of a grounded body tube and a discharge electrode made from a small diameter tube positioned in the center of this reactor. The flow in this system consisted of a main flow through the reactor and an auxillary air flow added through the hollow discharge electrode. The main air flow through the plasma reactor and the auxiliary flow through the electrode were measured using two flowmeters. The auxiliary flow was set so the nominal velocity ranged from 1 to 10m/s.

The discharge electrode was connected to a high-voltage pulsed-type power supply that generated a streamer-type corona discharge from the hollow electrode to the grounded electrode. The reactor was designed so the discharge should be approximately perpendicular to the main gas flow. The pulsed power supply was charged using a low voltage DC power supply. The frequency of the pulsed power supply was controlled using a frequency generator and a triggering circuit. The discharge voltage and current were monitored on a Textronic oscilloscope usaing a high voltage probe connected to the discharge electrode and a current transformer connected to the grounded side.

The experiments to characterize the soot removal were performed by exposing the sooted tube to the flow exiting the reactor for 6 to 11 hours. The gaseous by-products exiting the sooted tube were monitored using a combustion gas analyzer (Eurotron, Greenline 6000). The detection limit for CO, NO and NO_2 was 1 ppm.

Results

The flow stabilized corona system was operated using a pulse high voltage signal generated using an ignition coil, driven by low voltage DC power supply. The typical discharge waveforms of the voltage, the current and the power of the plasma reactor for a pulsing frequency of 200 Hz are shown in Fig.2. In this case, the discharge voltage and current oscillate for approximately 20% of the duty cycle, but the

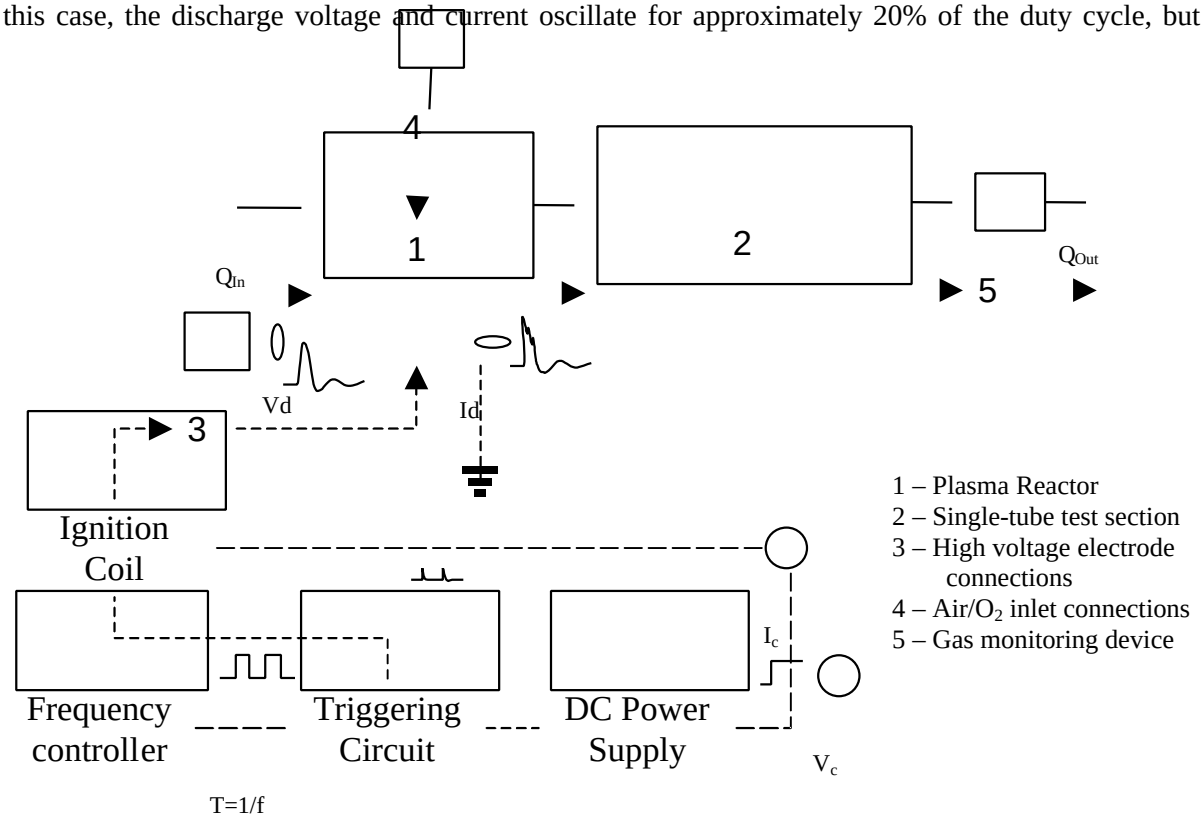

Figure 1 Schematic of experimental set-up of plasma reactor and power supply

discharge power is small after approximately 10% of this cycle. The change in the maximum discharge current and voltage with charging power for the different pulsing frequencies is shown in Fig. 3. The maximum discharge voltage increased rapidly with charging power to a maximum of approximately 15 kV. The charging power required to achieve this discharge voltage increased with frequency, as expected. The maximum charging current that could be achieved with the power supply decreased significantly for frequencies greater than 100 Hz.

The change in the average discharge power with charging power for different pulsing frequencies and air flow rates are shown in Fig. 4. The average discharge power increases with frequencies to 100 Hz before decreasing again as the frequency was increased, particular for frequencies above 200 Hz. The discharge power was relatively independent of the air flow rate for the range of flow rates considered here (Fig 4b), but the spark-over voltage was higher at the higher auxiliary flow rates. The efficiency of the power supply was low in part because no effort was made to impedance match the power supply and load to optimize the performance of the device.

The performance of the non-thermal plasma for soot removal was tested for two cases using

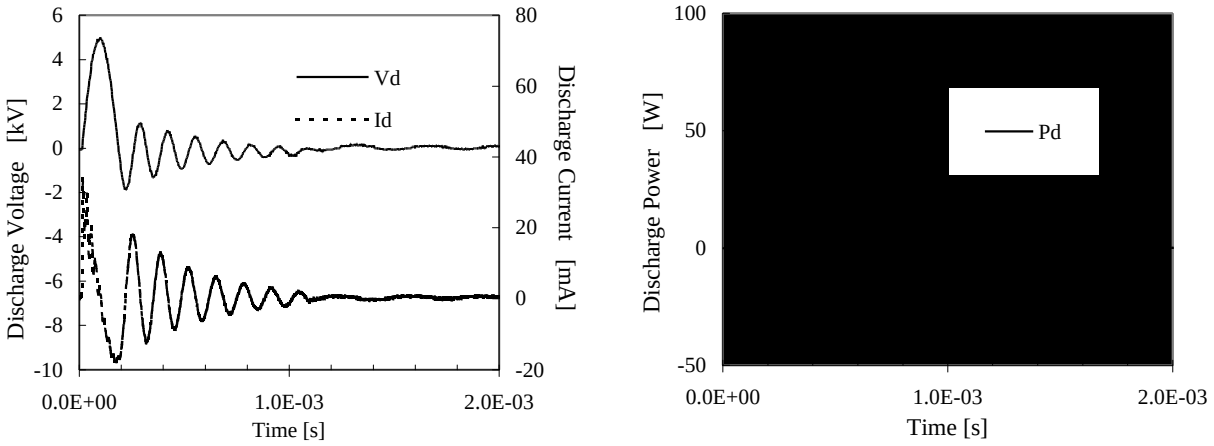

Figure 2. Typical discharge (a) voltage and current waveforms and (b) power waveforms for a charging voltage and current of 2 V and 0.4 A, respectively, a pulsing frequency of 200 Hz , and an air flow of 8 l/min.

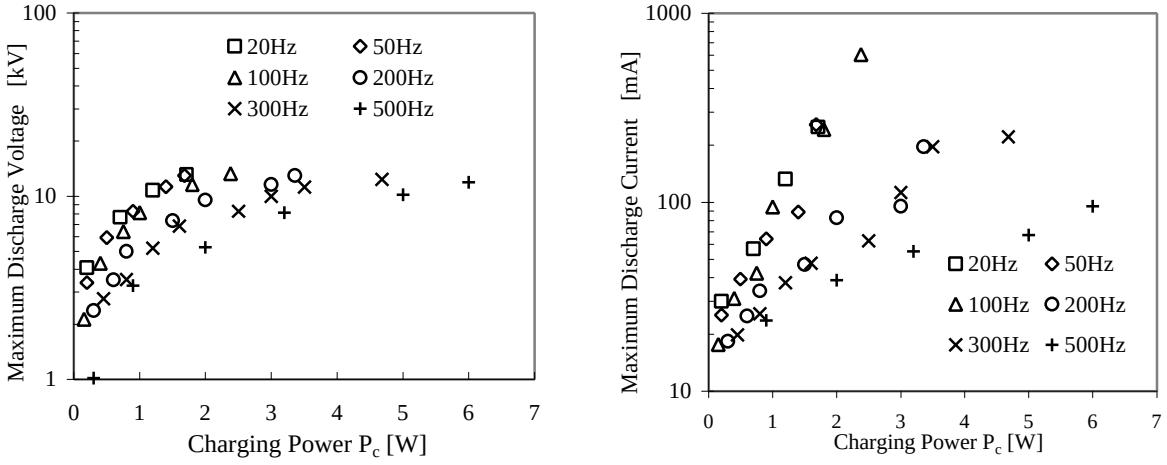

Figure 3. Change in the (a) maximum discharge voltage and (b) maximum discharge current with charging power for different pulsing frequencies.

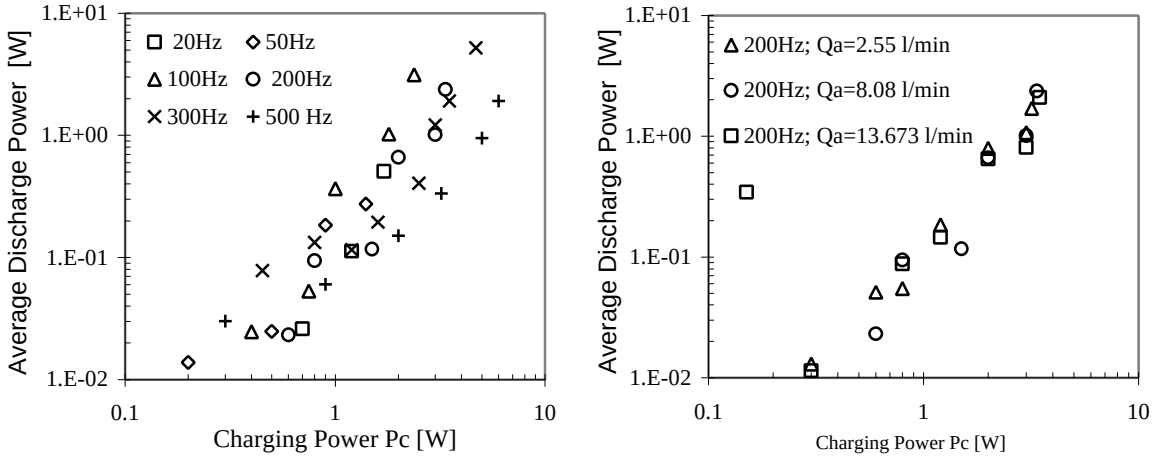

Figure 4. Change in the average discharge power with charging power for different (a) pulsing frequencies and (b) air flow rates.

tubes that had been exposed to diesel exhaust flow for approximately 1 hour of operation. In the first test, the deposited soot layer was treated soon after it was deposited (wet soot condition) for a total time of 11hrs with periodic measurement intervals to weigh the individual tube sections. The plasma reactor was operated at the frequency of 200 Hz, discharge power of 4.5 W. The main and auxiliary air flow rates were 13.7 l/min and 8 l/min, respectively and both were at a temperature of 23^{o}C. The activation of the soot oxidation was monitored by measuring the concentration of the CO in the exhaust gas. It was found that the soot oxidation started 20 to 40 minutes after the non-thermal plasma treatment was initiated. After that, only trace amounts (< 15 ppm) of CO and NOx were observed during the oxidation process.

The removal of the soot layer by the non-thermal plasma treatment was characterized by measuring the soot layer in the tube before and after the test. The deposited soot layer measured at 30 mm and 180 mm downstream of the tube entrance before and after the non-thermal plasma treatment are shown in Figs. 5 and 6. In both cases, the thickness of the soot layer was highly non-uniform around the circumference of the tube before the non-thermal plasma was applied, which was in agreement with the Neutron Radiography 3-D soot deposition thickness measurements in larger diameter tubes reported by Ismail et al. [7]. The thickness of the layer was also significantly thicker near the tube inlet that was also the flow inlet when the tube was in the diesel facility, similar to in Ismail et al. [7]. The application of the non-thermal plasma device reduced the soot layer at both locations near the inlet and the outlet indicating the non-thermal plasma was affecting the soot layer throughout the tube.

The removal of the soot layer throughout the tube was characterized using the circumferentially averaged soot layer thickness determined at the different downstream locations before and after the treatment shown in Fig. 7. The measurements showed that the non-thermal plasma treatment caused a significant reduction in the soot thickness throughout the tube. The soot removal was somewhat larger at the entrance of the tube, but there was significant removal of the soot throughout the tube. It was estimated that approximately 37% of deposited soot was removed after 11 hrs of operation.

In the second test, the soot layer was left undisturbed for more than 24 hours before the tube was treated (dry soot condition). This should remove much of the water and unburnt hydrocarbons absorbed in the layer. In this case, the soot layer was removed more rapidly than for the wet test. The soot layer deposited on the tube in this dry test was not accurately measured so that it was not possible to definitively determine the soot removal rate. It appeared though that over 50% of the soot was removed in 6 hours of continuous plasma treatment. This suggests that the presence of the unburnt hydrocarbons and water vapor in the soot layer had an effect on the oxidation of the soot layer. This difference could be due their presence affecting the diffusion of oxygen into the layer or because in the first experiment

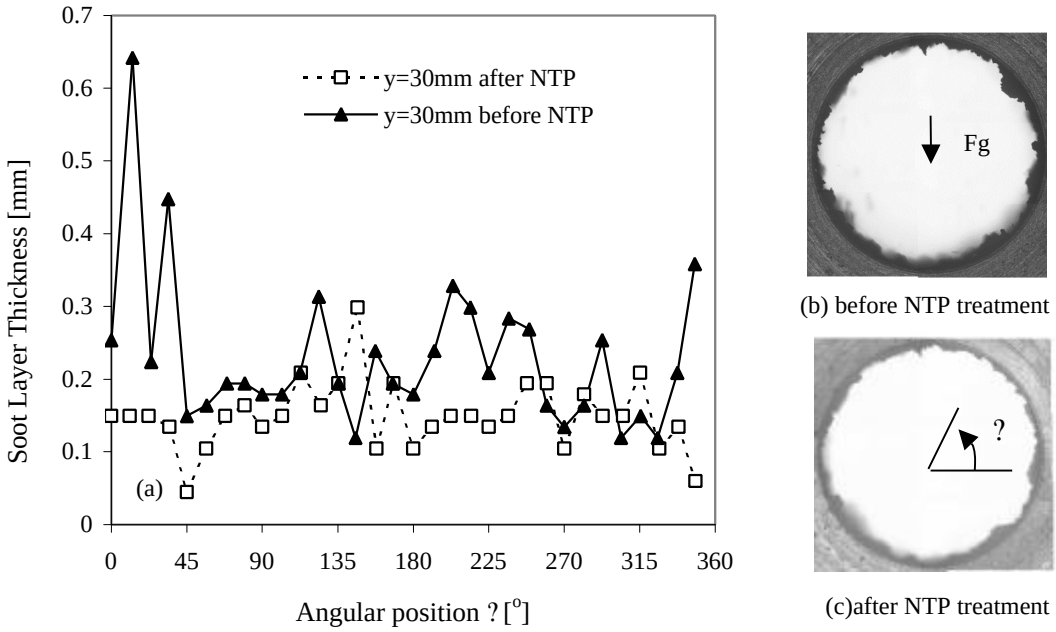

Figure 5. Comparison of the circumferential soot thickness profiles and images of the soot layer thickness at 30 mm downstream of the non-thermal plasma reactor before and after the treatment.

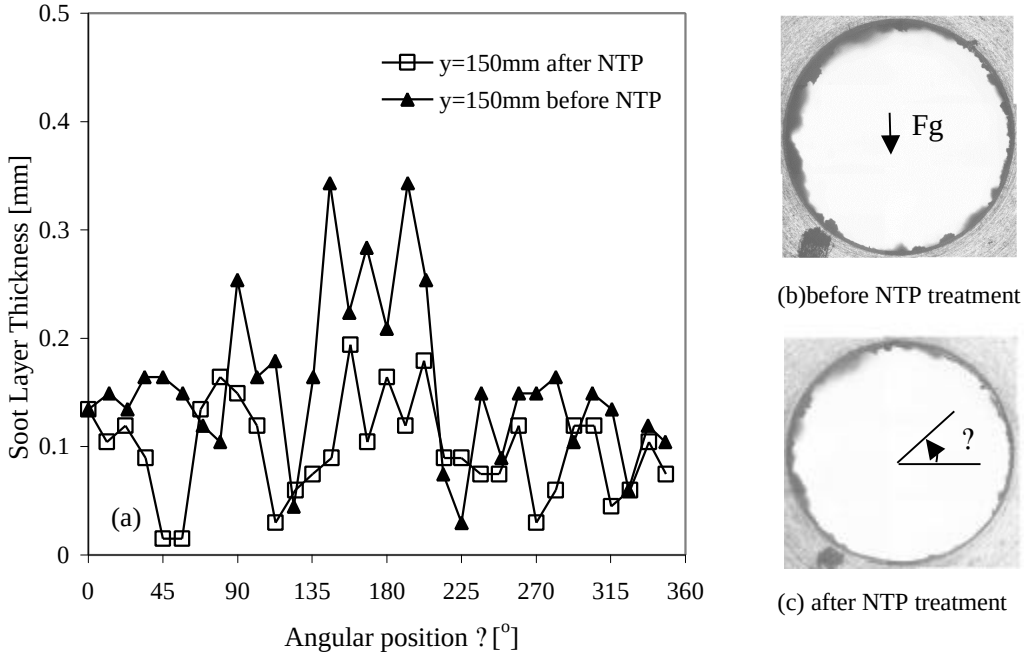

Figure 6. Comparison of the circumferential soot thickness profiles and images of the soot layer thickness at 180 mm downstream of the non-thermal plasma reactor before and after the treatment.

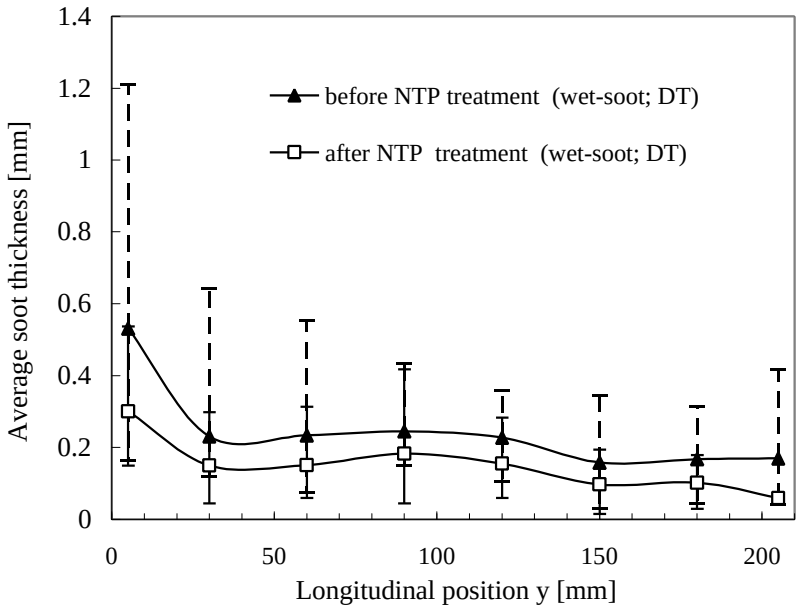

Figure 7. Comparison of the circumferentially averaged soot thickness along the pipe length before and after the 11 hour non-thermal plasma treatment applied immediately after the soot deposition. (The range of thickness at each point is indicated with the bars.)

the unburnt hydrocarbons is oxidized in addition to the carbon soot. In this test, the removal of the soot layer was more non-uniform with a much larger soot removal near the entrance.

Conclusions

Experiments were performed to characterize the removal of diesel soot from a tube using a corona radical shower non-thermal plasma operated using a pulsed-type power supply. The soot could be removed over the entire length of the tube but the soot removal was somewhat larger at the entrance near the corona shower. The measurements of the CO in the exiting flow indicated that the soot oxidation required 20 to 40 minutes to initiate. The tests also indicated that the soot removal rate was larger when the diesel soot had dried for approximately 24 hours.

References

[1] K. Usishima and J.S. Chang, IEEE Trans. DEI, 7, 602 – 614 (2000)
[2] K. Urishima, J.-S. Chang,, and S. J. Kim, J. Adv. Oxid. Tech., 6, 123-131 (2004).
[3] Y. Otsubo, H. Matsuoka, M. Masuda, K. Teraoka, and T. Aiba, JSAE 2004-5440, (2004).
[4] M. Okubo, T. Kuroki, and T. Yamamoto, IEEE Trans. IAS, 40, 1451 - 1458 (2004).
[5] M. Okubo, T. Kuroki, and T. Yamamoto, IEEE Trans. IAS, 40, 1504 - 1411 (2004).
[6] I. Iwasaki, D. Brocila, K. Yamada, K. Urishima, M. Ara, D. Ewing, J. Hoard, H. Ehara, S. Ono, T. Ito, M. Itoh, and J.-S. Chang, Proc. IEJ-ESA Joint Sym. on Electrostatics, 375 – 386 (2004)
[7] B. Ismail, D. Ewing, J.-S. Chang, and J.S. Cotton, J. Aerosol Sci., 35, 1275-1288 (2004).

Non-Thermal Plasma Processing for Dilute Trichloroethylene Decomposition

T.Oda, S.B.Han and R.Ono

Department of Electrical Engineering, the University of Tokyo, Tokyo, Japan

Abstract

Non-thermal plasma process for decomposition of dilute (mostly 250 ppm) trichloroethylene in atmospheric pressure air is experimentally studied. Various kinds of catalysts are tested to improve the decomposition efficiency and the manganese oxide is very effective in decomposing TCE with little energy consumption. The optimal plasma reactor design is also discussed related with the gas flow rate, humidity and oxygen content. Argon gas is also mixed with TCE contaminated air to understand discharge mode effect

Keywords: non-thermal plasma, catalyst, trichloroethylene, manganese oxide

1. Introduction

The atmospheric pressure non-thermal plasma has very strong chemical reactivity and many researchers have been applied that non-thermal plasma to remove environmental pollutants from air or combustion flue gas. Late Masuda developed ultra short pulse generator for the electrostatic precipitator. Florida group or Tokyo group applied that pulse technology to reduce NOx in the combustion flue gas[1,2]. RTI group also reported the VOCs (including CFC113) decomposition[3] by the barrier discharge or the pulse discharge. The authors also reported the CFC113[4] decomposition (maximum is more than 99%) by the surface discharge reactor which was designed as the ceramic reactor ozonizer for high concentration ozone generator. The authors are also engaged in developing the atmospheric pressure nonthermal plasma technology to decompose the dilute volatile organic compounds (VOCs), such as trichloroethylene, acetone and ethylalcohol[5]. The authors investigated the non-thermal plasma reactor not only for VOCs decomposition but also NOx removal from the combustion flue gas[6]. Already many other researchers have also studied on those VOCs decomposition technologies by using the non-thermal plasma[7-9]. Recent interest of those researchers is how to improve the VOCs or NOx decomposition energy efficiency which is very important for the practical usage of the non-thermal plasma. In order to estimate those parameters in the same table, target decomposition material is focused on the trichloro-ethylene ($CHCCl_2$) decomposition which concentration is from 50 to 1,000 ppm. To improve the TCE decomposition efficiency, several experiments have been done and a bolt type reactor (barrier discharge mode and the discharge electrode has sharp edge to generate uniform streamer discharge) and the authors would like to improve their performance more[10]. Many researchers investigated the new type plasma reactor combined with the catalyst[11-13]. The authors also tested the barrier discharge plasma reactor combined with various catalysts[14]. During those researches, the separation of adsorption effect by the catalysts and plasma decomposition effect was very difficult. Moreover, the decomposition efficiency of TCE was affected by the byproduct analysis method. That is; GCMS analysis suggested better decomposition results, compared with normal GC analysis or FTIR. That result suggested the ozone decomposition enhances the TCE decomposition[15]. Einaga et al suggested the usage of manganese oxide[16] and the authors also recognized that effect[15]. The manganese effect to the non-thermal plasma process has been investigated[17] and recent results will be described in this paper.

2. Experimental

There are several ways to realize the non-thermal plasma for the gas decomposition. As the power con-

sumption of DC high voltage discharge is too large, the discharge plasma should be generated by AC or pulse high voltage. Past experiments of the authors suggested that the pulse with ultra short rising time discharge is the best to decompose stable materials. However, the commercial frequency (50 or 60 Hz) high voltage discharge plasma can also decompose VOC (volatile organic compound) with good energy efficiency in most cases. Therefore, the authors usually use 50 Hz discharge because of the simple and economic power supply system.

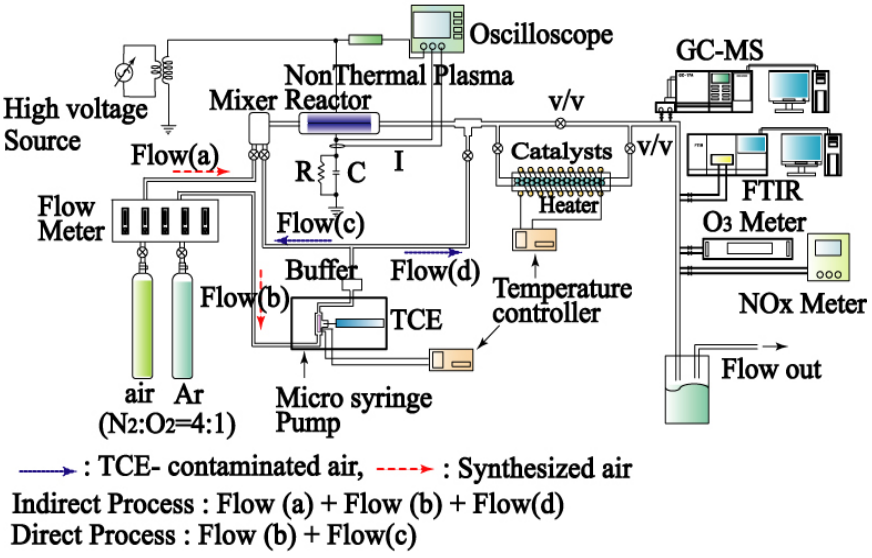

Fig. 1 Experimental setup including the gas flow.

The experimental system including the gas flow is shown in Fig. 1. A calculated amount of TCE is injected into a synthesized air by the micro syringe pump to adjust the TCE concentration. TCE contaminated air passes through non-thermal plasma reactor (Direct method) and passes through catalysts area in need. In another mode (Indirect Method), only pure synthesized air passes through the plasma reactor and is mixed with TCE-contaminated air at the downstream. Other processes are the same as the Direct method. Some times, the catalyst is filled in the plasma reactor. The following experiments are done by that method for Direct Process.

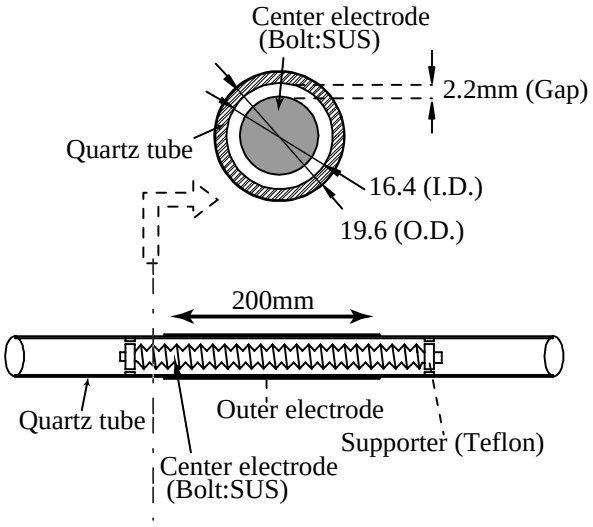

Fig.2 Nonthermal plasma reactor driven by 50 Hz high voltage.

There are many kinds of plasma reactors were fabricated and tested. The surface discharge reactor can generate high density ozone and be injected so much energy to decompose the stable CFC and so on, if the applying voltage frequency increases. As the energy efficiency is very good for the barrier discharge compared with the surface discharge, recent experiments use the barrier type plasma reactor. Typical example reactor is shown in Fig. 2. Various discharge electrode configurations have been tested and the bolt type discharge electrode is the best still now because that generates stable and many streamers from the edge of the plate. Figure 2 shows that example. In that case, the quartz tube (outer diameter 19.6mm and the inner diameter is 16.4 mm (that is; the glass thickness is 1.6 mm. At the center of the tube, 12 mm (in diameter) size stainless steel bolt is located. Ground electrode (Copper film) wounded the tube with 20 cm width. In this paper, the catalyst is filled in that plasma region, if the catalyst is used. As the catalysts, titania (TiO_2), vanadium oxide (V_2O_5), tungsten oxide (W_3O_4), zeolite (Na- or Cu-doped) and manganese oxide (MnO_2) were tested. Typical gas flow rate is 2L/min (1 or 2 L/min) and balance gas is synthesized air (80% nitrogen and

20 % oxygen) The zeolite sintered at low temperature has very large surface area and gas adsorption by the zeolite is too large to separate the adsorption effect and plasma decomposition effect. Finally, the authors decide to use manganese oxide as the ozone decomposition catalyst which also decomposes VOC, maybe by the atomic oxygen effect. That manganese oxide effect to decompose VOC is not yet understood. It is not still unclear whether atomic oxygen radical effect in the gas phase either manganese oxide surface chemical reaction with the ozone and VOC molecule is dominant to decompose VOC.

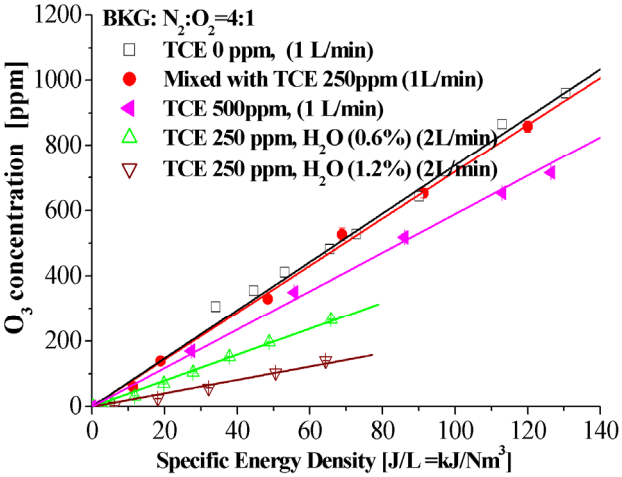

Fig.3 ozone concentration versus the specific energy density for water vapor pressure.

3. Results and Discussions

For ozone generation, humidity is very important. One example is shown in Fig. 3 where dry air without TCE can generate the largest amount of ozone. When the TCE concentration is 250 ppm, the ozone generation is not affected by the existing of TCE but 500 ppm TCE contaminants suppress the ozone generation of about 200 ppm. It is easily recognized that the ozone generation is smaller for artificial addition of water to the air (0.6% or 1.2 %) with 250 ppm TCE than that for dry condition. In that case, atomic oxygen radicals may be consumed to generate OH radicals. If the OH radical is very effective in decomposing TCE, high water content can assist TCE decomposition. At the same condition (without the catalyst), TCE decomposition efficiency is shown in Fig.4 suggesting that water vapor suppresses

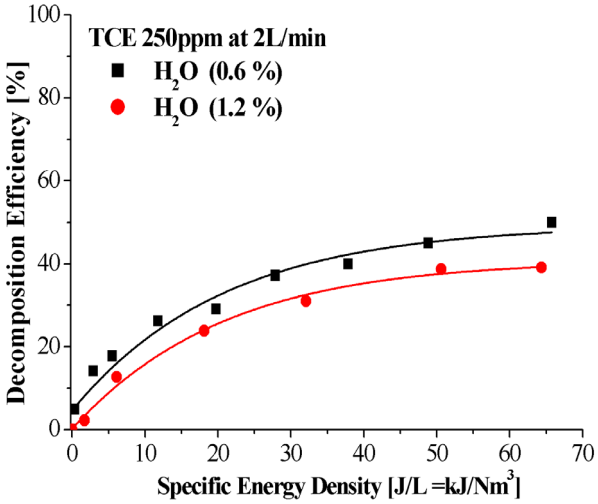

Fig. 4 TCE decomposition efficiency versus the specific energy density(humidity effect)

the TCE decomposition. OH radical is not so strong to oxidize TCE compared with the ozone. However, the decomposition efficiency difference is not so high as estimated from Fig. 3 (ozone suppression). Maybe some part of TCE can be decomposed by OH radicals but real chemical reaction is not yet clear. As byproducts, NO_2 concentration in the processed gas is observed where NO_2 for low water (0.6% H_2O) is rather higher (30 ~40%) than that for 1.2 % water, but total concentration is very low (2~ 4 ppm at high specific energy density; the specific energy density, SED is calculated as electric power consumption(W) / flow rate (L/min) X 60 seconds) observed by chemical luminescence method). Other byproducts

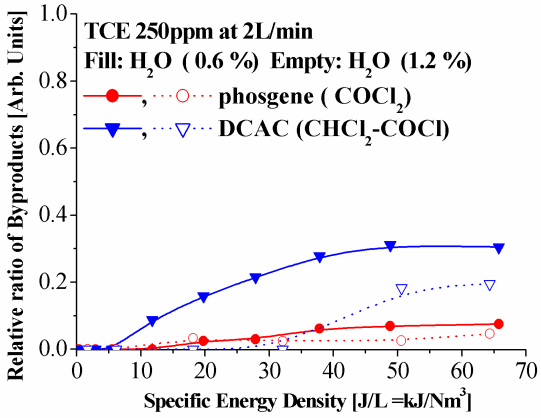

Fig. 5 Byproducts versus specific energy density fro 0.6% and 1.2 % water concentration.

are also measured by a GCMS (gas-chromate-graph mass-spectrometer: Shimadzu GCMS-5000A). Amounts of byproducts; such as DCAC (dichloro-acetylchloride: $CHCl_2$-COCl) and phos-gene ($COCl_2$) are observed for the different spe-cific energy density as shown in Fig. 5. When the specific energy density is less than 30 J/L, DCAC product is negligibly small for 1.2% water in the air, although DCAC for low water concen-tration (0.6%) is pretty high. Increasing the spe-cific energy density from 30 J/L, DCAC byprod-ucts also increases rapidly which does not agree with the Fig.4 where the decomposition efficiency is roughly proportional for both cases. On the other hand, phosgene production is proportional with the TCE decomposition efficiency. This mechanism is not yet clear but the specific energy of 30 J/L should be important. If the processed gas passes through the manganese oxide, the effi-ciency increases more than 98%. Concerning with the byproducts, generation of NO_2 is about 2 ppm for wet condition and 4 ppm for dry condition, at the specific energy of 60 J/L. The oxidation by the ozone with manganese oxide produces lot of TCAA (trichloro-acetaldehyde: CCl_3-CHO) and very little DCAC. Water addition effect should be explained by those results but the energy den-sity is not yet explained. The decomposition mechanism of the ozone on the manganese surface is not yet clear. Maybe some part of the ozone must be trapped on the manganese surface and atomic oxygen will be generated. The behavior of that atomic oxygen radical is not clear. That may stay on the man-ganese oxide surface or that may leave into the con-taminated-air from the surface of the catalyst and attack to VOC molecule to oxidize VOC to water and carbon oxide. Another possibility is that. VOCs themselves also may be trapped on the manganese oxide surface. Those trapped VOCs may be easily oxidized by the ozone with the aid of the manganese oxide catalyst effect. In that model, powder-like zeorite can adsorb VOCs very much but the decomposition of VOCs is not so

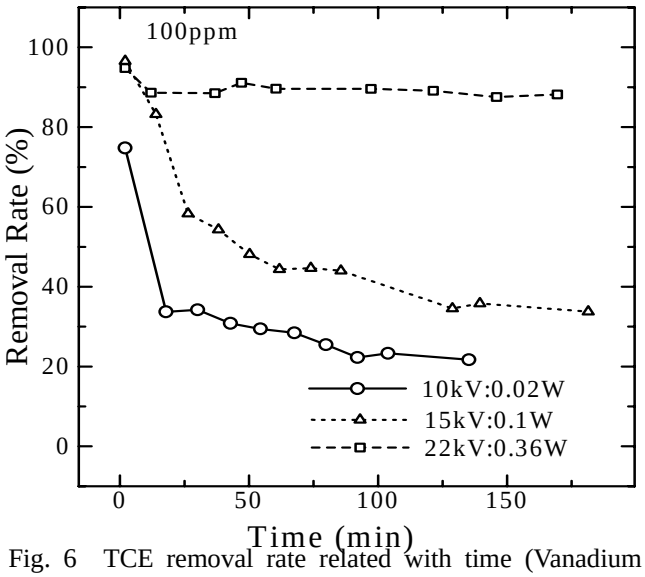

Fig. 6 TCE removal rate related with time (Vanadium Oxide on/in titanium oxide)

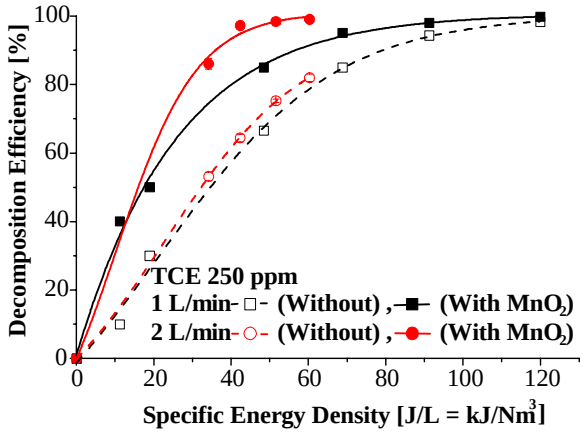

Fig. 7 TCE decomposition efficiency versus SED with/without manganese oxide.

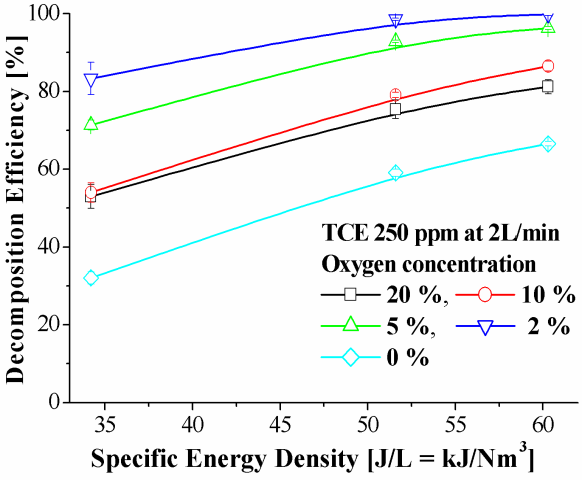

Fig. 8 TCE decomposition efficiency versus SED (oxygen concentration effect)

clear. In previous experiment, VOCs decomposition by the vanadium oxide surface is not clear as seen in Fig. 6 where the flow rate is 0.4 L/min. In this case, adsorption effect continues more than two or three hours except 22 kV plasma where the temperature increases very slowly becouse of the small discharge power and desorption of TCE from the catalyst still increases wit h time.

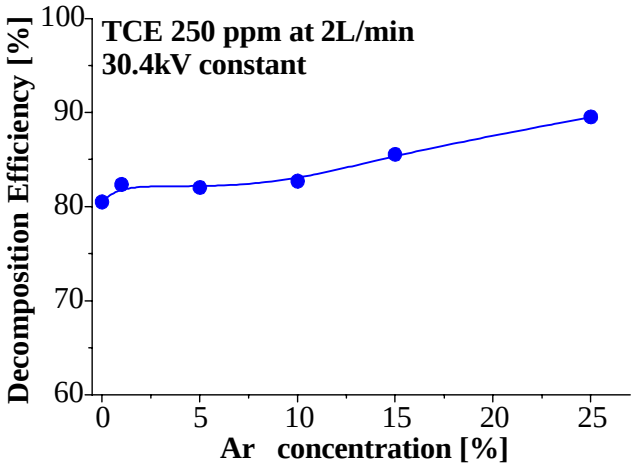

Fig.9 TCE decomposition efficiency (argon partial pressure effect)

Usually the background gas is the air and the oxygen concentration is roughly 20 % and nitrogen is about 80 %. Previous experimental results suggest the importance of the oxygen concentration for the TCE decomposition. However, the optimal oxygen concentration is not yet examined and the authors observe that as shown in Fig.8 where the process is Direct Process without the catalyst. Apparently for the nitrogen ~100% gas (0 % oxygen in Fig. 8), the TCE decomposition efficiency is the worst among all data. That decomposition may be caused by the electron impaction and nitrogen radical effect to disconnect some bondings without oxidation of VOCs. The optimal oxygen concentration is only 2 % which is much smaller value as formerly estimated. This result is in good agreement with atomic oxygen generation observed by TALIF (tow photon absorption laser induced fluorescence) method. Smaller oxygen concentration of less than 2% is not yet tested and this value is not yet optimal value. There is no apparent difference for 10 % and 20 % oxygen concentration. At the SED of 45 J/L, the TCE decomposition efficiency for 20 % oxygen is only 60 % but that for 2 % oxygen is 90 % which value is very useful and practical without manganese oxide. Maybe for further oxidation of VOCs, that oxidation needs much oxygen atom and the performance (for example, most carbon should be oxidized to carbon mono-oxide and carbon dioxide) will be improved for higher oxygen concentrated gas.

For further investigation of gas component effects, pure noble argon gas is added to TCE-contaminated air. That test results is shown in Fig. 9. As the argon gas concentration increases, TCE decomposition efficiency increases a little bit but not so apparent compared with oxygen. (From 80 % to about 90 %,) only 10 % change of TCE decomposition efficiency is recognized, although the decomposition efficiency change is about 20 % from zero to 20 % oxygen. The TCE decomposition efficiency difference is too large of 40 % only for 2 % oxygen concentration change. Since the argon gas is much easily ionized, the discharge energy increases with the increase of the argon concentration, the increase of TCE decomposition efficiency is understood but that value is rather small. If SED is the same, TCE decomposition efficiency will rather decrease. Moreover, the byproduct of phosgene increases with the argon gas concentration. In total, the argon gas addition is not effective in improving the plasma process efficiency, in practice.

4. Conclusions

In order to improve the non-thermal plasma process concerning with the VOCs decomposition efficiency, various parameters are examined. Especially, the balance gas conditions are changed. They are the humidity, the oxygen concentration and the argon gas addition.

4.1 Concerning with the humidity, the dry condition is better than the wet condition although OH radical for-

mation is enhanced by adding the water. Maybe the ozone or the atomic oxygen radical can oxidize the VOCs more than OH radicals. Further investigation must be done for better understanding of the humid plasma process.

4.2 A few percents oxygen contamination to nitrogen is very effective in decomposing TCE compared with normal air (20 % oxygen). That mechanism and the effect to the final oxidation to carbon oxide are not yet recognized.

4.3 Contamination of the argon gas to the air is not so effective in TCE decomposition.

Acknowledgement

This work is partially supported by the Grant-in-Aid for Scientific Research by the Ministry of Education, Culture, Sport, Science, and Technology, Japan.

References

[1] S. Masuda and H. Nakao, Conf. Rec. IEEE-IAS Annu. Meeting, pp. 1173–1182 (1986)

[2] J. S. Clements, A. Mizuno, W. C. Finey, and R. H. Davis, IEEE Trans. Ind. Applicat., vol. 25, pp. 62–69, Jan./Feb. 1989.

[3] T.Yamamoto, K.Ramanathanm P.A.Lawless, D.S.Ensor and J.R.Newsome, IEEE Trans.Ind.Appl., 28, pp.528-534 (1992)

[4] T. Oda, T. Takahashi, H. Nakano, and S. Masuda, IEEE Trans. Ind. Applicat., vol. 29, pp. 787–792, July/Aug. (1993)

[5] T. Oda, R. Yamashita, I. Haga, T. Takahashi, and S. Masuda, IEEE Trans. Ind. Applicat., vol. 32, pp.118–124, Jan./Feb. (1996)

[6] T. Oda, T. Kato, T. Takahashi, K. Shimizu, IEEE Tran. Ind. Appl. 34 , 1998, pp.268–272

[7] S.Futamura and T.Yamamoto, IEEE Trans. Ind.Appl., vol.33, pp. 447-453(1997)

[8] Urashima, J.S.Chang and T.Ito, Conf.Rec.1997 IEEE/IAS Ann.Meeting, pp.1969-1974 (1997)

[9] T.Oda, K.Yamaji and T.Takahashi, Trans.IEEE Ind.Appl., vol.40, No.2, pp. 430-436 (2004)

[10] T. Oda, T. Takahashi, and K. Tada, IEEE Trans. Ind. Applicat., vol. 35, Mar./Apr. pp. 372–379, (1999).

[11] A.Ogata, N.Shintani, K.Mizuno, S.Kushiwada and T.Yamamoto; IEEE Trans. Ind.Applicat., vol.35, No.4, pp.753-759, July/Aug., (1999)

[12] S.Futamura, H.Einaga and A.Zhang; IEEE Trans.Ind.Applicat., vol.37, No.4, July/Aug., pp.978-985 (2001)

[13] T.Ohkubo, D.li, D.Yakushiji, S.Kanazawa and Y.Nomoto, J.Adv.Oxid.Technol., vol.6, No.1, pp.75-79 (2003)

[14] T.Oda and K.Yamaji, J.Adv.Oxid.Technol., vol.6, No.1, pp.93-99 (2003)

[15] T.Oda, T.takahashi and K.Yamaji; IEEE Trans.Ind.Applic., vol.40, No.5, pp.1249-1256(2004)

[16] H.Einaga, T.Ikusuka and S.Futamura, IEEE Trans. Ind.Applicat., vol.37, No.5, pp.1476-1481482 (2001)

[17] S.B.Han and T.Oda, Conf.Rec. IEEE/IAS 2004 Ann.Meeting, 7p3 (2004)

Nonequilibrium Effects in Atmospheric Pressure Electric Arcs

V.A.Zhovtyansky

Plasma Technology Department, National Academy of Sciences of Ukraine the Gas Institute, Kyiv, 03113, Ukraine

Abstract

The nature of nonequilibrium state of plasma in atmospheric pressure electric arcs is investigated by experimental, analytical and numerical methods. The objects of study where a pulse electric arc in argon or helium and a free burning electric arc between evaporating copper electrodes. The state equations of plasma are proposed in the cases if the reason of deviation from local thermal equilibrium (LTE) were radiative transfer or radiation loss in plasma of high degree of ionisation.

1. Introduction

This paper is concerned with study of atmospheric pressure electric arc plasmas being a basis of modern numerous technological applications. The thermal equilibrium model of plasma was accepted in early stage of electric arc quantitative experimental investigation in the 1950s [1].

From the end of 60th some deviations from equilibrium as a result of radiative loss and diffusion processes influence [2 - 4] as well as radiation transfer [5, 6] in various type of arcs were fixed. Yet they were not investigated systematically. So the prior guess that equilibrium occurs in electric arc plasmas in all cases remains dominant. Really, these plasmas are of high density enough to support LTE at the central part of plasma volume as a rule. Nevertheless the bulk plasma is finite with space as any other plasmas in all practical applications. Appearing gradient effects consist in the energy and particles flux to the boundaries and outside of plasma volume.

Four important factors, determining conditions of plasma application, are connected with this.

First, these effects determine electric energy loss in their own transport in discharge channel and, correspondingly, the efficiency of plasma generation. (Really, this channel may be considered as an electric current conductor).

Second, the intensity of energy and particles flux through boundary of plasma determines the efficiency of their influence as a processing agent in technological applications.

Third, diagnostic of plasma is realized through their boundary layer, which influences as a filter on the primary observation results. Therefore to obtain results, adequate to state of plasma, it is necessary to take into consideration this influence correctly.

And finally, fourth, the most important from the viewpoint of physical investigation. Noncompensated energy and particle flux cause detailed balancing violation with respect to some elementary processes and, as a result, to non-equilibrium state of plasma.

2. Experiment

We have studied plasma obtained both in free-burning electric arc between melted cooper electrodes in air atmosphere and in pulse electric arc in discharge section of device type of electric shock tube (EST). The results of the experiments in the wall-stabilized arcs [7 - 9] based on the methods of plasma emission spectroscopy were taken into account to adequately determine the properties of cooper plasma in arc column.

Most complicated were investigations of near channel region of electric arc where the plasma turns into ambient gas gradually in radial direction and medium to be studied is weakly or non-radiating. Moreover, an arc in the absent of stabilization, is spatially unstable. It complicates its diagnostic by alternative methods of absorption spectroscopy. The problem in this case is recording both own spectral radiation of plasma and external source of plasma irradiation as it needs to perform simultaneously by the same image sensor [10].

The arc in cooper vapor was initiated between two noncooled copper electrodes of 6 mm in diameter each (the electrode gap of 2-8 mm). A pulse mode was used to avoid droplet formation. The current pulse of amplitude up to 100 A and duration 30 ms was applied to a pilot (“keep-alive”) low current (3 A) discharge. Investigations were performed in the quasi-stationary stage of the pulse process [11].

In the absence of stabilizing wall this free-burning arc could move chaotically across the working surfaces of electrodes (Fig. 1). That is why the fast scanning tomographic spectrometer was used to study electric arc plasma [12].

A coefficient of recombination of charge particles might be found if near-wall layer of plasma is studying quantitatively. Pulse regime only allows separating with time the specific effects in plasma including mentioned coefficient. Because of this, the relaxing plasma in pulse electric arc has been observed.

In this connection a technique of EST may be used (Fig. 2). They were developed as early as 60th to study plasma extension, including shock and heat waves [13, 14]. The EST was completed of a glass tube (R_t = 0.8 cm) with Kovar ring electrodes E_1 and E_2 1.5 cm wide each spaced at 5 – 7 cm and filled by argon or helium at initial pressure from 65 up to 1330 Pa (Fig. 2). The plasma was produced by a pulse current generator with amplitude up to 20 kA and time duration up to 5 μs. The discharge between electrodes E_1 and E_2 is practically wall-stabilized electric arc. The discharge section E_1 - E_2 was around with symmetrical system of conductors SC (up to 6 ones) to exclude breaks the symmetry of plasma in this section due to own magnetic field action.

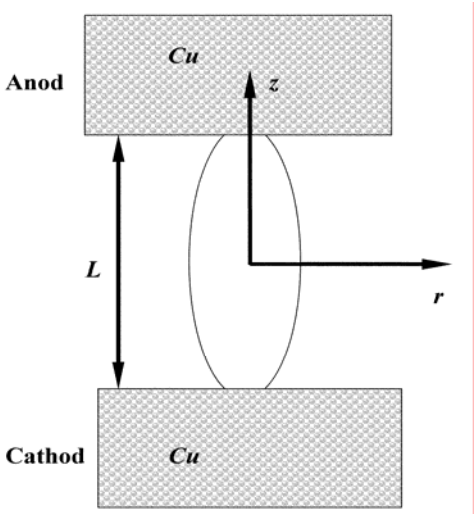

Fig.1. The scheme of free-burning electric arc and system of coordinates

The plasma in discharge section could be bounded by steel pistons every confined in a glass jacked. In this case it was convenient object to study decay of motionless plasma and the influence of near-wall sheath in this decay [15].

Due to sharp increase of plasma temperature up to 1 – 3 eV during pulse discharge, the pressure between electrodes E_1 – E_2 came nearer to atmospheric. If the obtained plasma could extend in enclosing space, there was an additional possibility to study influence of plasma expansion on its equilibrium properties.

The adequate diagnostic of non-stationary plasma was fulfilled by fast scanning emissive and absorb-

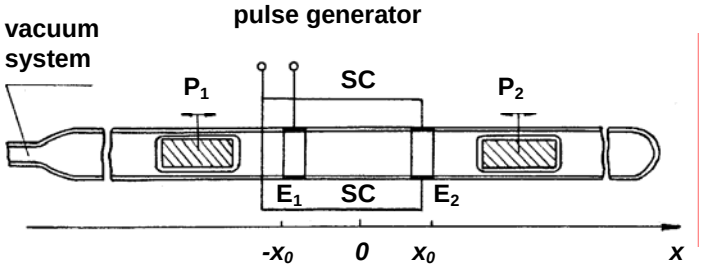

Fig. 2. EST to study plasma decay and system of coordinates:
E_1, E_2 – ring electrodes; SC – symmetrized conductors; P_1, P_2 – steel pistons every confined in a glass jacked

ing tomographic spectrometry. These methods are based on the spatial modulation of radiation of plasma across the section to be studied in combine with using of bifocal optical systems [10, 12]. The spectrometer proposed is suitable for study of short pulse processes, including single one.

Two problems are typical in the research of free-burning electric arc plasma in cooper vapor. First, one of the convenient in diagnostic spectral line 510.5 nm is subject to self-absorption. Second, as will be shown later, just the self-absorption of resonance spectral lines in its turn is the reason of deviation from LTE in plasma in the outer region of electric arc channel. To determine adequately the parameters of plasma in this case the so-called procedure of computational-adaptive spectroscopy was used [16]. In this procedure the initial data of spectroscopic measurements are correcting in the iterative process in accordance with the assumed collisional-radiative model [17] of the arc under study.

The spectroscopic measurements have shown, that N_e changes in a range of $2\cdot10^{16}$–10^{15} cm^{-3} over initial period of plasma decay in EST. The temperature of argon plasma insignificantly changes in a range of 1.3–1.1 eV during this period. In helium plasma the temperature decreases appreciably from 3.5–3 up to 2.5 eV due to electron's high thermal conductivity coefficient $\kappa(T) \sim T^{5/2}$. In all cases a relationship $\gamma = N_e/N_a < 1$ takes a place.

3. Violation of LTE in electric arc plasma due to radiative loss

The LTE-model allows describing the plasma by the same parameters as in complete equilibrium one, except radiation. This model is valid for the real finite plasma of high density where collision-induced proc-

esses of excited states population dominate over radiative ones, which are the factor of non-equilibrium. The population density of the exited states is Boltsmannian, and the distribution of the atoms and their ionization products obeys well-known Saha equation [1, 17]:

$$\omega^{(z)0} = N^{(z+1)} / N^{(z)} = S^{(z)}(T)/N_e. \quad (1)$$

Here $\omega^{(z)0}$ – relative particles density of specified element in sequential charge states (upper index "0" denotes equilibrium state); N - number density of particles in charge state, marked by index in brackets: (0) – for atoms, (1) – for single charged ions and so on; $S^{(z)}$ – depending on temperature function.

Griem [18] and Drawin [19] stated the most common requirements imposed on spatial and temporal non-uniformity of electron density N_e to plasma be in LTE. Biberman *et al*. [17] presented the criteria of various type of non-equilibrium occurrence on the basis of detail consideration of kinetic processes in plasma, including radiative and diffusion loss of charge particles. The restriction on N_e non-uniformity is one of this criterion, with this non-uniformity is some outside factor. Yet in practice most often the radial profile of electric arc itself is a function of plasma state and self-consistent influence of their parameters (first of all temperature and pressure gradients) and processes (diffusion, thermal conductivity, ionization-recombination processes etc). The special role in this context near-wall effects play, and for plasma with free boundary – fluid dynamic effects, determining the dynamic of plasma spatial-temporal structure. It is actually in relaxing plasmas since the specific time of the last ones usually is comparable with the specific time of plasma decay. As a result, the paradox takes a place: criteria of non-equilibrium have sufficiently general character from the one hand and from the other one – owing to these reasons are little acceptable for analysis of concrete processes in real laboratory plasma.

That is why the studying of non-equilibrium factors role in plasmas and determining of their hierarchy are problems of great importance.

Radiative processes begin dominating in the population of individual excited states of atom with decreasing of N_e in LTE-plasma. Thus the plasma changes its state to partial LTE (PLTE) wherein the ground and one or more low-lying exited states are underpopulated toward to equilibrium values for given particles kinetic temperature. The Boltsmann equation is correct only for upper exited states, which are in equilibrium with continuum, in this state of plasma.

The generalized Saha equation, as it is called, can be used as a basis for the state equation in PLTE [17]. This equation includes the additional coefficient $Y^{(z)}(T,N_e)$. It characterizes the deviation of the true value of ionization coefficient $\omega^{(z)}$ for particle of charge number z in PLTE plasma from its LTE-value $\omega^{(z)0}$:

$$\omega^{(z)} = \omega^{(z)0}/Y^{(z)}. \quad (2)$$

The ratio η between rates of collision processes of ground state population from the first exited state and competitive resonance radiation processes is at the hertz of quantitative Greem's criterion of deviation from LTE [18]:

$$\eta = (dN_1/dt)_{\text{рад}}/(dN_1/dt)_{\text{ст}}. \quad (3)$$

It is necessary that this ratio will be $\eta = 0.1$ in order to LTE would be correct with 10% accuracy. Such method corresponds to two-level atom model with two energy levels – ground and exited.

The non-equilibrium factor is $Y > 1$ in a case of radiative loss from plasma and thus decreasing of the ionization degree ω occurs as defined by (2).

The criteria of equilibrium state were refined by Biberman *et al.* [17] within the method of modified diffusion approximation (MDA). In so doing transitions between neighbour states are accounted exactly, and transitions into further states – approximately.

Self-absorption of resonance radiation reduces both the roles of radiative loss and threshold N_e at the same time. It must be emphasized that this effect is typical for electric arc plasmas. Really, the radiation free path is about 10^{-4} – 10^{-2} cm for plasmas of widespread gases at atmospheric pressure. It is substantially smaller than typical arc radius $R \sim 10^{-1}$ – 1 cm. The same parameters range occurs for plasma in vapor of most widespread metals at partial pressure of $0.01 \cdot p_a$, where p_a is pressure of ambient atmosphere. The partial pressure mentioned above just corresponds to their content in free-burning arcs between metal electrodes and also to typical conditions in various experiments [7 – 9, 11].

The problem is that the usual idealization of LTE is applicable only to one degree of ionization of plasma-forming particles. That is why the atom particles are in LTE and ions – in PLTE, as a rule, in high-ionized arc plasmas.

An example is the results of papers [20, 21]. Here the ratio of spectral lines HeII 468.6 and HeI 471.3 *nm* intensities where calculated as a function of T and N_e in plasma with specified characteristic dimensions (radius) in wide parameters range. As it follows from the results presented in Fig. 3, the ratio of mentioned

above intensities doesn't depend practically on N_e in wide parameter range, where $N_e < N_e^{**}$ [22]. This range corresponds to deviation from LTE in helium plasma. Since the densities of radiating particles are connected by generalized Saha equation (2), it follows with account of eq. (1):

$$Y^{(1)} N_e \approx N_e^{**} = \text{const}, \tag{4}$$

where N_e^{**} characterizes the electron density such that the deviations from LTE state become considerable. It allows obtaining simplified state equation for this range of plasma parameters.

If to introduce into the consideration the ionization degree of plasma

$$\omega = N_e/\Sigma N^{(i)} = N_e/N, \tag{5}$$

where N – heavy component densities, so Saha equation can be presented as

$$\omega^2/(1-\omega) = S/N. \tag{6}$$

The only one Saha equation for first ionization degree was used here; therefore (6) is correct only for values $\omega < 1$.

Using of the mass and charge conservation conditions

$$N = N^{(0)} + N^{(1)} + N^{(2)} = N^{(0)} + N^{(1)} (1 + S^{(1)}/N_e^{**}), \tag{7}$$

$$N_e = N^{(1)} + 2N^{(2)} = N^{(1)} (1 + 2S^{(1)}/N_e^{**}), \tag{8}$$

allows generalizing Saha equation into both charge states of particles:

$$\omega^2/[(2-\omega)(1 + S^{(1)}/N_e^{**}) - 1] = S^{(0)}/N. \tag{9}$$

The calculated results [20, 21] are extended by similarity method into other species of plasma forming particle [22]. In doing so the degree of ionization non-equilibrium for helium Y and for any other rare gas Y^* are to be equal if ratios η of collision and radiative resonance processes rates are equal too (see eq. (3)):

$$\eta = \eta^*. \tag{10}$$

The following ratio is the coefficient of similarity on temperature:

$$T^*/T = E_r^*/E_r, \tag{11}$$

where E_r characterize resonance state's excitation energy. Differences in structure of ions of rare gases were taken into account by MDA method [17]. Other coefficients of similarity are determined by concretize of expression (10) [22]. This method allows to find parameter N_e^{**} for other plasma forming gases too.

4. Transfer of radiation and in free-burning electric arc

As was noticed the model of LTE for the dense electric arc plasma was accepted [1]. The natural is tendency to present the object of investigation as is in equilibrium. Really, it allows describing the plasma properties by simple way based on equation (1), (7) and (8).

Nevertheless a lot of experimentors are familiar with the fact that the attempt to determine the pressure in free burning electric arc from experimentally obtained values of T and N_e are accompanied with the mistake by the factor of tens. We have studied gas dynamic process of copper vapor propagation in and out from arc channel to revise the feasible influence of the surplus pressure due to the product of the erosion of electrodes [23]. The result is a weak vary of atmosphere pressure in free burning electric arc channel up to discharge current of 100 A.

The deviation from LTE due to radiation transfer is the reason of this phenomenon. The direct experiment have shown that the area, where the essential absorption of resonance radiation occurs in free burning electric arc copper plasma, and so the excited into the state E_1=1.39 eV cooper atoms exist, is more extended, than the radius of electric arc plasma volume. Over a range of electric arc currents 3.5-30 A and electrode gap 2-8 mm the radius of absorption zone was some times as much than the arc channel radius in all cases. Thus, the resonance irradiation from plasma is screened by external layer of exited atoms with the optical path length

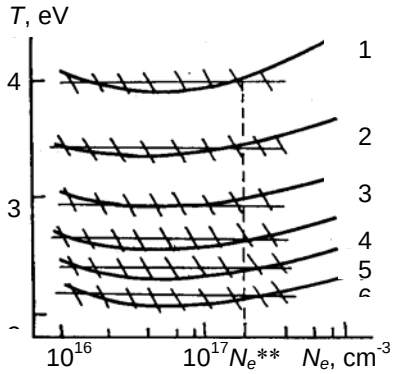

Fig. 3. Lines of the equal ratios $I^{(1)}/I^{(0)} = const$ of the spectral lines HeII 468.6 and HeI 471.3 nm intensities in a plane temperature T – electron density N_e for helium plasma with characteristic dimension (radius) δ = 1 cm: $I^{(1)}/I^{(0)}$ = 10 (1); $I^{(1)}/I^{(0)}$ = 1 (2); $I^{(1)}/I^{(0)}$ = 0,1 (3); $I^{(1)}/I^{(0)} = 10^{-2}$ (4); $I^{(1)}/I^{(0)} = 10^{-3}$ (5); $I^{(1)}/I^{(0)} = 10^{-4}$ (6).

Regions of introduced errors ± 2.5 percent in temperature measurements shown by hatching correspond to approximation of calculated curves 1-6 by straight lines in the range of N_e, where violation of LTE become essential

$\tau \geq 1$. This volume of plasma may be identified as non-equilibrium. Really, the radiation from the hot arc core is able to overpopulate the resonance level of Cu atom at the arc periphery, where temperature is relatively small. It was specified quantitatively too [18].

Two examples of energy levels population distribution in Cu atom in an axis of electric arc channel and in its peripheral area are presented as illustration in Fig. 4. It follows, that the resulting effect from the discussed mechanism of nonequilibrium can be presented through the reduction of effective potential of atom ionization outside of the electric arc axis. Really, as follow from consideration of Fig. 4.b, the ground level of Cu atom would be displaced on a certain potential $\Delta\varphi$ to achiev the same value of population N_0^a of this level in the case of uniform temperature of excited levels equal to local kinetic temperature T_a of plasma particles. This displacement may be treated as the reduction of ionization potential of Cu atom. It is possible to show from geometrical relations in Fig. 4.b or on the basis of Boltsmann equation, that

$$\Delta\varphi_{Cu}(r) = (\varphi_{res} - \varphi_{met})(1 - T(r)/T_0). \quad (12)$$

Here φ_{res} and φ_{met} - exitation potentials of resonance and metastable levels, respectively, of Cu atom.

The simple model of electric arc in copper vapor is proposed in papers [24, 25]. It allows to analyze the character of diffusion processes and heat transfer in plasma both within the limits of the arc channel, and outside of it. However the papers mentioned are developed in LTE assumption.

This part of present paper is devoted to study of the influence on physical properties of free burning electric of plasma non equilibrium arising due to transfer of resonance radiation. The account of this influence is founded in terms of ionization potential reduction according to (12).

At low temperatures the density of electrons in a copper-nitrogen mixture is fully defined by atoms of copper and according to the Saha equation it is proportional to

$$N_e \sim \exp[-\varphi_{Cu}/(2T)]. \quad (13)$$

Using this relationship, electron density N_e' which will take place at effective reduction of ionization potential may be presented in such kind:

$$N_e' = N_e \exp[\Delta\varphi_{Cu}/(2T)]. \quad (14)$$

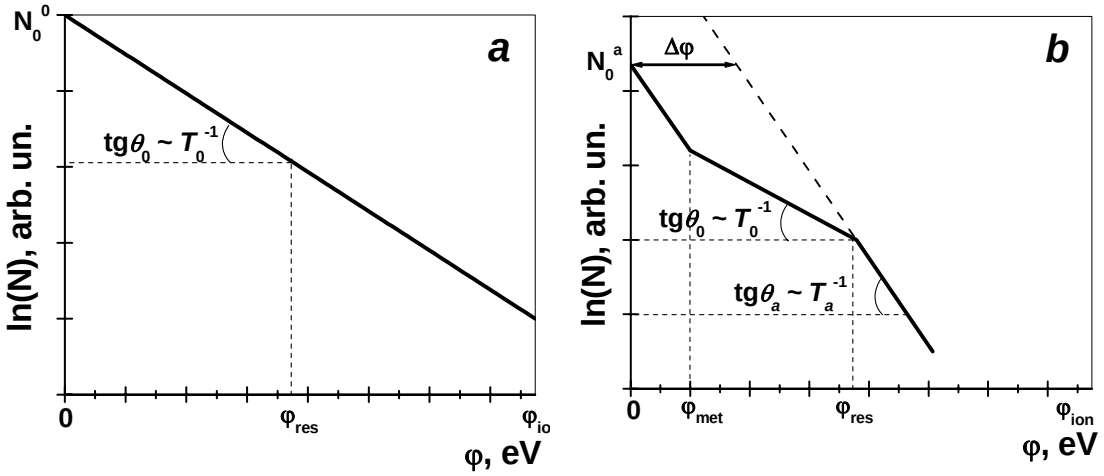

Fig. 4. Distribution of levels population in atom of copper in the electric arc axis (a) and in periphery area (b)

The conductivity of mixture σ' will be presented similarly as $\sigma \sim N_e$:

$$\sigma' = \sigma \exp[\Delta\varphi_{Cu}/(2T)]. \quad (15)$$

The relationships (12) – (15) may be introduced into channel model of electric arc between copper melted electrodes, presented in papers [24 - 27].

Steady existence of a long electric arc assumes, generally speaking, presence of some enclosing wall to heat energy removal. The question of a heat-conducting path in a short arc is solved mainly cooling on electrodes and due to the geometrical factor [28]; nevertheless, it is possible to enter into consideration some effective wall to simplify problem in this case too [26].

The electric current I, temperature T_w and radius r_w of the wall is counted set $I = 30\ A$, $r_w = 3\ mm$, $T_w = 1000\ K$, and distribution of temperature $T(r)$ and an electric field E may be found from the channel model of electric arc. The results of calculation in a case of radiation transfer absence or $\Delta\varphi_{Cu} = 0$ (see Eq.

(12)) are: axis temperature $T_0 = 6843\ K$, radius of electric arc cannel $r_a = 2{,}3\ mm$.

The choice of effective reduction of ionization potential of copper atom $\Delta\varphi_{Cu}$ demands of special remarks. Generally speaking, it can be chosen according to a ratio (12) in all area of existence of electric arc, using experimental data and modeling calculations [11]. The resulting effective reduction of ionization potential is equivalent to significant increase of temperature in the arc channel, taking into account, that the potentials of excitation of resonance levels φ_{res} are 3,71 and 3,82 eV, and metastable one φ_{met} - 1,39 and 1,64 eV for Cu atom. Thus within the framework of chosen channel model to system it is favorable "to establish" very small radius of the channel of an arch which is able to pass all discharge current due to high conductivity in according to exponential relation (15). Such calculation gives, in particular, values $r_a = 0{,}004\ mm$ and $T_0 = 5100\ K$. Nevertheless, it was beyond the channel model.

That is why the calculation with effective value $\Delta\varphi^* = \Delta\varphi_{Cu}/2$ were carried out to establish the tendency of influence of considered effect. The results are $T_0 = 6530\ K$, $r_a = 2{,}2\ mm$. In so doing the power $P = E{\cdot}I$, dissipated in electric arc channel, lowered by a factor 1.3 in comparison with a case without taking into account of radiation transfer.

From this results follows, that a finally the influence of radiation transfer in an electric arc is in the form of additional reduction of power loss on the transport of electric current in its channel. The obtained results open a basic opportunity for the adequate description of power dissipation in free-burning electric arc between melted electrodes (see, for example, [28]).

References

1. W. Finkelnburg, H. Maeker. Handbuch der Physik, **22,** 254 (1956).
2. J.F.Uhlenbusch, E.Fisher. Proceedings of the IEEE, **59,** 578 (1971).
3. J. Bacri, A.M.Gomes, S. Benzaid. J. Phys. D.: Appl. Phys., **9**, 1743 (1976).
4. G.N.Haddad, A.J.D. Farmer. J. Phys. D.: Appl. Phys., **17**, 1189 (1984).
5. V. G. Andropov, E. I. Asinovski, V. M. Batenin and V. F. Chinnov. *Electricity from MHD, 1968.* Vienna: Intern. Atom. Energy Agency. **1**, 117 (1968).
6. L.E. Cram. J. Quant. Spectrosc. Radiat. Transfer, **34**, 353 (1985).
7. I. Miyachi and K. Jaya-Ram. Rev. Sci. Instrum., **42,** 1002 (1971).
8. M. Rahal, B. Rahhaoui, and S.Vacquie. J. Phys. D: Appl. Phys., **17**, 1807 (1984).
9. B. Chemina, R. Gadaud, and P. Andanson. J. Phys. D: Appl. Phys., **20**, 444 (1987).
10. V. A. Zhovtyansky. *Multifunctional absorbed spectrometer.* Patent for invention of Russian Federation №2178875 (7G01J 3/42); application 21.07.1998.
11. I.L.Babich, A.N.Veklich, V.A.Zhovtyansky, A.I.Cheredarchuk. J. Eng. Physics and Thermophysics (translated from Russian), **71,** 127 (1998).
12. V.A.Zhovtyansky. J. of Eng. Phys. and Thermophysics (translated from Russian), **62,** 545 **(**1992).
13. B. Ahlborn, S. Mikoshiba, J.D. Strachan, in *Proc. 10th Int. Shock Tube Symp. (Kyoto, Japan), 336 (1975).*
14. Yu.I.Chutov, V.A.Zhovtyansky. Sov. Journ. Tech. Physics, **45**, 1221 (1975) [in Russian].
15. V.A.Zhovtyansky. Ukrainian Phys. Journ., **44,** 1364 (1999); **45,** 50 (2000) [in Ukrainian].
16. I.L.Babich, A.I.Cheredarchuk, A.N.Veklich, V.A.Zhovtyansky, in *Proc. 12th Inter. Symposium on Plasma Chemistry (August 21-25, Minneapolis, USA), 4, 1861 (Minneapolis, USA, 1995).*
17. L.M.Biberman, V.S.Vorob'ev, I.T. Yakubov. *Kinetics of non-equilibrium low-temperature plasma* (Nauka, Moscow, 1982) [in Russian].
18. H. R. Griem. *Plasma Spectroscopy* (McGraw-Hill Book Company, New York, 1964).
19. H.W. Drawin. Zeit. fur Physik, **228**, 99 (1969).
20. R. Mewe. Brit. J. Appl. Phys., **18,** 107 (1967).
21. М.А.Мазинг, В.А.Слемзин. Труды ФИАН, **119**, 169 (1980) [in Russian].
22. V.A.Zhovtyansky, K.V.Nelep, O.M.Novick. J. Appl. Spectrosc. (transl. from Russian), **49**, 906 (1988).
23. V.A.Zhovtyansky. Ukr. Phys. Journ., **48**, 115 (2003) [in Ukrainian].
24. V. A. Zhovtyansky, A. B. Murphy, V. M. Patriyuk. Indust. Heat Eng., **25**, 5 (2003) [in Russian].
25. V. A. Zhovtyansky, V. M. Patriyuk and A. B. Murphy, in *Proc. 16th ISPC (June 22-27, 2003, Taormina, Italy), Ed. R. d'Agostino, P. Favio, F. Fracassi and F. Palumbo. Paper Po3.45, 6 pp. (Bari, Italy, 2003).*
26. V.A. Zhovtyansky, V. M. Patriyuk, A. B. Murphy, in *Proc.Int. Conf. on Physics of Low Temp. Plasma (May 11-15, 2003, Kyiv, Ukraine), Ed. V.A.Zhovtyansky. Paper 5.2.52, 6 pp. (Kyiv, Ukraine, 2004).*
27. V. A. Zhovtyansky, V. M. Patriyuk, in *Proc. IV Int. Symposium on Theoretical and Applied Plasma Chemistry (May 13-18, 2005,Ivanovo, Russia).* **2**, 564. (2005) [in Russian].
28. V. A. Zhovtyansky, V. M. Patriyuk. Ukrainian Phys. Journ., **45,** 1059 (2000) [in Ukrainian].

The Optimization of Thermochemical Processing of Materials

I.M.Karp, V.G. Nazarenko, O.G.Didyk, V.O. Khomych, V.A.Zhovtyansky

Plasma Technology Department, National Academy of Sciences of Ukraine the Gas Institute, Kyiv, Ukraine

Abstract

The results of study of the volume arc discharge with a plasma source of electrons are presented. The source of electrons is fulfilled as the hollow cathode with gas magnetron heating. The gas discharge plasma is generated in a working gas at pressure 0.1 ÷ 1 Pa and discharge power up to 1300 Wt. The plasma is uniformly enough distributed in the volume of 0.1 m^3; its density is $10^{10} – 10^{11}$ cm^3. Volt-ampere characteristic and distribution of density of an ionic current in working volume depend on discharge conditions are presented, too. Generator of plasma is adapted for joint operation with other sources of the charged particles and plasmas. It may be used in processes of oxidation and nitriding in hydrogen-free atmospheres as well as in energy saving technologies of the combined ionic-plasma processing of constructional materials.

Introduction

The modification of solid materials' surfaces allows obtaining principally new properties of materials and economy of resources. The rather perspective both on ecological cleanness of process, and on energy saving parameters is using of low-temperature discharge plasma for these purposes. The development of the reliable plasma equipment with large operation resource is actual problem in this connection.

The main tendency today is to combine some ionic-plasma processing of constructional materials in single equipment. A number of successive technologies allow obtaining a combination of properties that is impossible in using of these technologies separately [1].

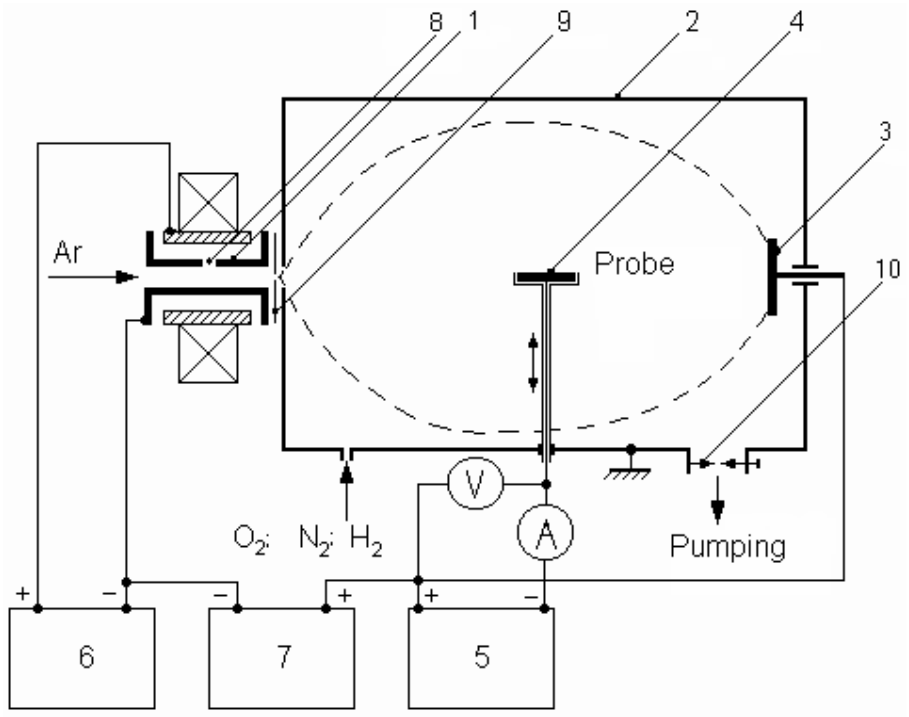

Fig.1

The cleaning and heating of surface is one of the controlling factors in ionic-plasma processing. The rate of cleaning and heating of constructional materials to be processed are defined by plasma parameters. In any case the energy input must all appear as 1 – 3 Wt/cm^2. These conditions are achieved with bias voltage on the material ~1 kV and plasma density $10^{10} ÷ 10^{11}$ cm^{-3}.

Plasma Cathode

The volumetric low pressure arc discharge with a plasma source of electrons may be considered as the most energy efficient device to ionic-plasma processing as estimations implies. In particular, a cathode unit of discharge plasma sources is one of the important elements of plasma devices, defining reliability and the operation resource. The requirements imposed on this unit will increase, if the active gases (N_2, O_2, CH_4 etc.) are applied during plasma processing. Plasma devices with heating tungsten cathode, placed usually in the separate camera and communicated with working volume through the diaphragm have a number of deficiency: the heating of the cathode up to thermoionic emission requires high value filament's currents; the high voltage (1 - 3 kV) is necessary for ignition of the main discharge; small resource due to self-sputtering. The last one is especially critical in a case of operation with large discharge currents (tens of amperes). The use of the hollow cathode allows increasing operation resource of a cathode unit considerably in a mode of an arc discharge. However, the preliminary heating of the hollow cathode is necessary for ignition and maintenance of stable operation of an arc discharge. The gas-magnetron method, on our sight, has the best characteristics in this relation. It is used ordinary in magnetron and ionic sources.

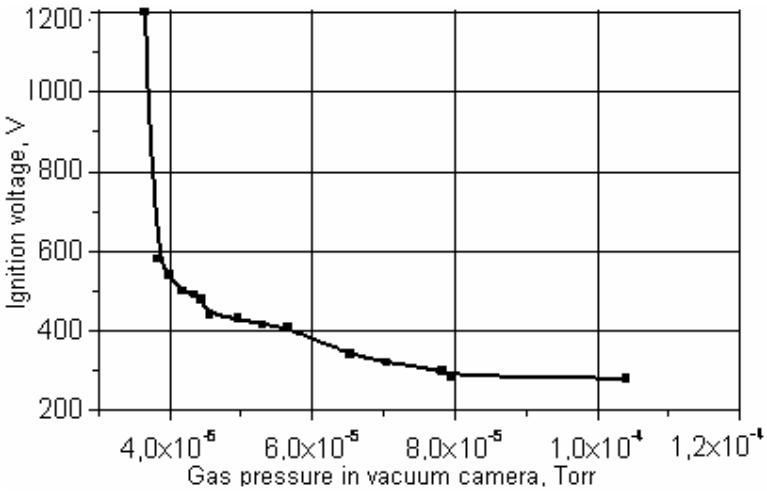

Fig. 2

The arrangement of a cathode unit permitting operation with large currents (tens of amperes) in conditions of significant gas emission from a surface to be processing and the presence of reactive gases (N_2, O_2, H_2 etc.) is presented below. It has additionally a large operation resource.

In plasma device, which scheme is shown in a Fig. 1, the cathode unit 1 is fulfilled as the autonomous system jointed through a ceramic insulator with the vacuum camera 2. Volume of the camera is 100 liters. The processing (reactive) gases are carried immediately into the vacuum camera.

The main discharge gap forms the hollow cathode 1 and main anode 3, located in the vacuum camera. The discharge between these electrodes is initiated by gas magnetron, which cathode is the external surface of the hollow cathode 1 with cathode reflectors in its sides, and anode - the water-cooling outer cylinder [2].

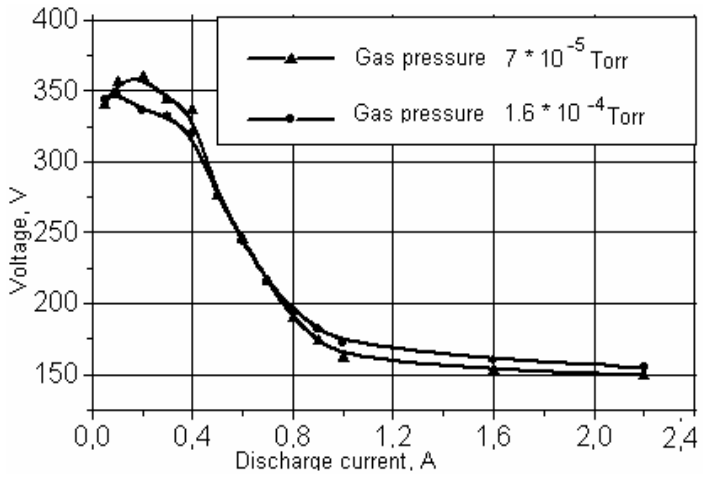

Fig. 3

The electrode system is placed inside a ring permanent magnet with strength of a magnetic field in a working clearance (the hollow cathode - cylindrical anode) ~ 0.1 T. The cathode concavity is connected with discharge gap of auxiliary (gas magnetron) discharge with hole 8. The hollow cathode is communicated with the vacuum camera through the diaphragm 9.

The ignition of the gas-magnetron discharge and transition of a cathode unit to an operating regime is carried out as follows.

With the supply of voltage on an electrode system (the hollow cathode - cylindrical anode) and allow a ballast gas (Ar) to bleed into the hollow cathode, the electrons begin to make rotary movement round the cathode under the influence of crossed electrical and magnetic fields. The length of a free path of electrons therewith is increased, that results in increase of probability of collisions them with atoms. In an outcome fast will increase rates of excitation and ionization of gas that results in ignition of the gas-magnetron

discharge. In a Fig. 2 the dependence of the gas-magnetron ignition voltage discharge on pressure of argon in the vacuum camera is indicated.

The ignition voltage of the discharge decreases with growth of a chamber pressure, achieving acceptable significance smaller than 500 V with the pressure of ballast gas ~ $4.5.10^{-5}$ Torr.

The volt-ampere characteristics of the discharge for various pressure of argon are indicated in a Fig. 3.

In accordance with magnification of a discharge current of the magnetron discharge the temperature of the hollow cathode up to significance of origin of thermionic emission will increase. From discharge gap the plasma of the gas-magnetron discharge will penetrate into the hollow cathode through the holes, thereby considerably improving conditions of ignition of the main discharge.

Ability of the developed cathode unit to work in atmosphere of active gases (N_2, O_2, CH_4 etc.) long time allows to use it in technological processes of nitriding and oxidation as well as in assisting of vacuum - arc processes of coatings deposition.

Arc Discharge

The plasma device is energized with power supplies 5-7 (Fig. 1). The gas discharge plasma is generated in a processing gas at the pressure 0.1 ÷ 1 Pa. The vacuum camera 2 is pumping through the diaphragm 10. The one-sided probe 4 was located in the plasma volume to estimate the distribution of plasma parameters in camera and its effect on a constructional material. The bias voltage was applied between the probe and anode 10.

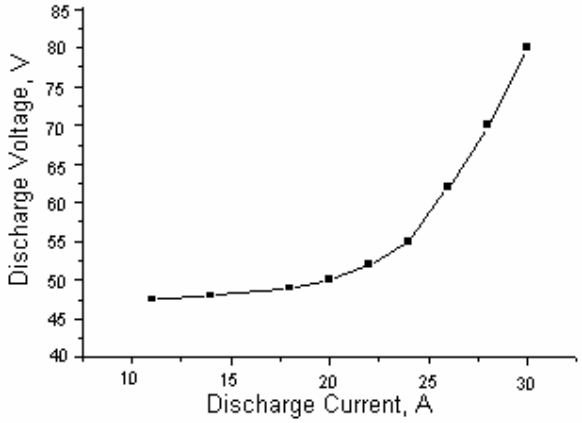

Fig. 4

The plasma generated in magnetron discharge, is penetrating in hollow cathode through the aperture 8. Electrons, emitted from plasma of the hollow cathode, are accelerated under action of the electric field enclosed between the hollow cathode and anode 3 and ionized a working gas in the vacuum chamber. In result the arc discharge in volume mode is initiated. The power delivered into the discharge, is adjusted by reactive impedance of a power unit 7. The density of plasma varies within the $10^{10} \div 10^{11}$ cm^{-3} in a range of working currents 5 ÷ 30 A.

The properties of the volume arc discharge with a plasma source of electrons were investigated experimentally and theoretically. Studies of the basic characteristics of the volumetric discharge were carried out in the following conditions. Electrodes of discharge system - hollow cathode of electrons source 1 and the anode 3 (Fig. 1) - were under the floating potential concerning the working chamber. Ballast gas was argon and reactive gas - nitrogen. Pressure of reactive gas in the working chamber was adjusted within the limits of 0.1 ÷ 1 Pa. The consumption of the ballast gas submitted in hollow cathode was adjusted within the 0.1 - 0.6 cm^3/s.

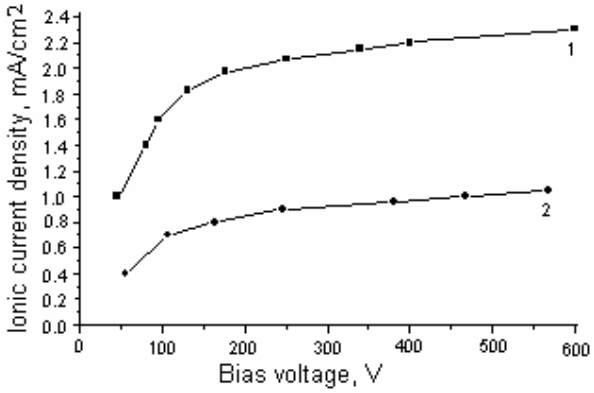

Fig. 5

The operating mode of the volumetric discharge, after its ignition, practically does not depend on parameters of the gas-magnetron discharge to the point of its deenergizing. The consumption of ballast gas had the greatest influence on the characteristics of volumetric discharge. The volt-ampere characteristic of the discharge in argon is indicated in a Fig. 4. The argon consumption was 0.15 cm^3/s in this case.

The working voltage increases with increasing of working current of the volumetric discharge at the constant consumption of ballast gas. This is resulted in instability of the discharge. Stability of the volumetric discharge burning with increase in working currents (from above 30 A) demands increasing of the consumption of ballast gas in

this connection.

An ionic current of saturation on a probe in the center of the chamber is plotted versus voltage bias in Fig. 5. The curves are obtained for the difference plasma-forming gases and pressure at the identical active power delivered into the discharge (1300 Wt). The specific power delivered into the processing constructional material is over 1 Wt/cm^2 (a curve 1) at a voltage bias ~500 V. It allows to make its clearing and heating to working temperature within 450-500^O C effectively. Specific power of heating can be raised and at rather low voltage bias <500 V (to exclude breakdowns) with increase of power delivered into the volumetric discharge. An ionic current of saturation on a probe is plotted versus discharge power in Fig. 6.

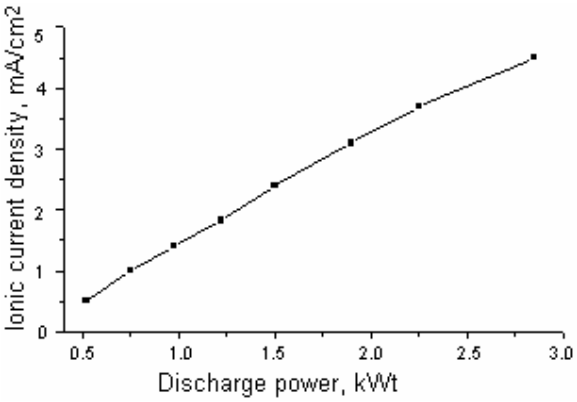

Fig. 6

As may be concluded from the external view of the volt-ampere characteristic in a Fig. 2, the volume recombination processes in plasma are essential to analyze efficiency of this technology. The procedure of thermochemical processing optimization in the device included determination of the base relationship between the plasma parameters and the constructive and technologies characteristics of the apparatus.

The balances of particles and energies in electric discharge plasma were included in treatment. In this case the specific diffusive length Λ for cylindrical camera is defined by

$$1/\Lambda^2 = (2{,}405/R)^2 + (\pi/L^2),$$

where R is radius and L - its length.

It is necessary to take into account also contracting processes in electric discharge plasma. It may be concluded from the distribution of ionic current density on the probe along a radius of camera (Fig. 7). These distributions are obtained for argon as plasma forming gas at the consumption 0.15 cm^3/s and a constant voltage bias 240 V. The power delivered into the discharge was 1300 Wt. The curves of ionic current density distributions in the working chamber at the pressure 0.2, 0.4 and 1.1 Pa are obtained at the fixed consumption of argon by change of diaphragm 10 throughput (Fig. 1).

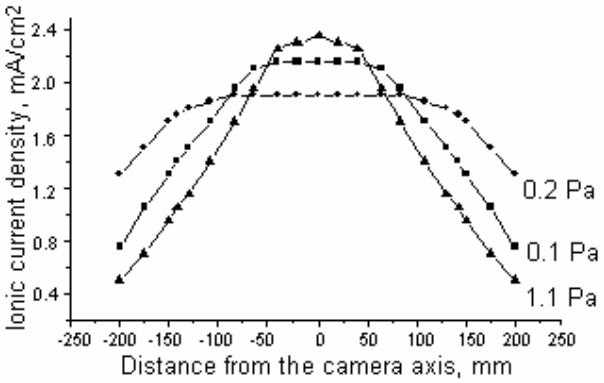

Fig. 7

Conclusion

Generator of plasma adapted for joint operation with other sources of the charged particles and plasmas is proposed. Ability of the developed cathode unit to work long time in atmosphere of active gases (N_2, O_2, CH_4 etc.) allows it using in technological processes of nitriding and oxidation as well as in assisting of vacuum - arc energy saving processes of coatings deposition.

References

[1] T. Bell, H. Dong, Y. Sun. Tribology International, **31**, 127 (1998).

[2] V.O.Khomych, V.G.Nazarenko, O.G.Didyk, V.A.Zhovtyansky, in *Proc. IV International Conf. "Plasma physics and plasma technology" (Minsk, Belarus, 15-19 September, 2003),* **1**, 88 (2003).

Control of the quality of the discharge of low-pressure plasma RF. Application on the synthesis and homogeneity of $LaMnO_3$ Sr-doped layers for SOFC

F. ROUSSEAU[1], M. NIKRAVECH[1], D. MORVAN[1], J. AMOUROUX[1]

[1]Laboratoire de Génie des Procédés Plasmas et Traitements de Surface, ENSCP-Pierre et Marie Curie university, Paris, France

Abstract :
Plasma is a medium with a very high purity, which allows the synthesis of very pure product needed for electrochemical applications such as Solid Oxide Fuel Cell (SOFC). The chemistry in the plasma is very reactive, because of the formation of many reactive species. It can permit to synthesise and to deposit a layer on a substrate without undesirable phase formation, contrary to classical ways of ceramic synthesis which take time and energy. A low pressure plasma process has been developed in the laboratory in order to produce SOFC cathode. In recent works, properties of deposited layer were investigated in order to optimise plasma parameters. But it seemed to be possible to involve the efficiency of the plasma discharge. Plasma generator was equipped with six capacitors. Effects of the generator's modification on the synthesis and on the properties of the layers were studied. The efficiency of the generator was investigated by using calorimetric measurements. Species in the plasma have been characterised by Optical Emission Spectroscopy (OES). The conversion rate of the synthesis has been quantified by IR spectroscopy. Scanning Electron Microscopy and necked observations have been used to see the micro and the macro changes of layer's structure with and without generator's modification.
Keywords : efficiency, plasma discharge, reactive species, SOFC cathode

1. Introduction

Because of the need of respecting environment and decreasing pollutant's concentration in the atmosphere, fuel cells have known a major development. Solid Oxide Fuel Cell (SOFC) exhibits great efficiency for the electrical and thermal power production, as compared to the classical devices. That could permit a better use of fossil fuels like methane. SOFC are going to be essential for the conversion of chemical energy contained in H_2 and O_2 bonds into electrical power for mobile application and power plants [1].
SOFC continue to be investigated for the resolution of many problems, but for the need of material cost reduction too [2, 3]. Usually, process that synthesise ceramic layers needed for SOFC electrodes require two important steps. First, the slurry composed of mixture of commercial powders is screen printed on the electrolyte. Then, the electrode-electrolyte stack is co-fired under high temperature conditions (1200-1300°C during 3h) [4]. High temperatures often lead to undesirable phases formation due to the diffusion of species from each part of the electrode-electrolyte interface. In the case of low-pressure plasma process, reactive species used for the chemical transformation appear at very low temperature as compared to the classical chemistry. Moreover, precursors are injected directly in the plasma reactor with a high velocity, leading to a very strong adherence of the electrode into the electrolyte. A low-pressure plasma process have been developed in order to produce SOFC cathode in one step. The process consists in the synthesis and the deposit of $LaMnO_3$ or $LaCoO_3$ Sr-doped layers on Yttria Stabilised Zirconia [5, 6].
In this paper, results showed the role of induced RF energy on the properties of deposits. It was found that efficiency of plasma coupling was an important factor. In order to enhance the energetic efficiency, inductive coils were equipped with extra capacitors. The aim of this work was to present the behaviour of the plasma process due to these modifications.

2. Experimental set-up

The experimental set-up developed in the laboratory is described in the figure 1. A quartz tube equipped with a convergent nozzle was used as the plasma reactor. A vacuum pump allowed to obtain pressure in the reactor less than 1 mbar. Gas flow-meters controlled the composition and the quantity of gas used in the process. La, Sr, Mn or Co nitrates dissolved in water were used as precursors of the synthesis (ICP-DCP standard solution). An ultrasonic sprayer led to the production of few micrometers droplets containing water and nitrates. A difference in pressure from each part of a pulsed valve permitted the injection of droplets in the plasma reactor. A 40 mHz RF generator was responsible for the plasma discharge by the way of

inductive coils located on the reactor. When nitrates droplets passed through the plasma, nitrates were decomposed into NOx (detected by mass spectroscopy), and La, Sr, Mn or Co ions were oxidised in order to form MnO, SrO, LaO or CoO bonds. Finally, after their flight in the plasma reactor, particles deposited on YSZ.

In order to enhance the efficiency of the plasma discharge, we proceeded in electrical modification on the plasma generator by equipping the inductive coils with five capacitors of 80µF and one of 63 µF as shown on the figure 2.

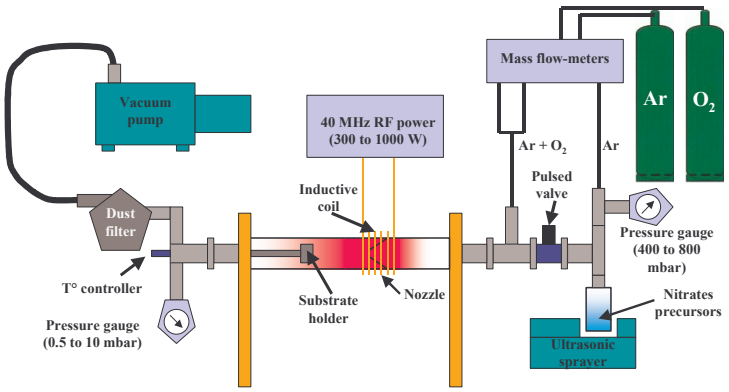

Figure 1 : plasma process experimental set-up

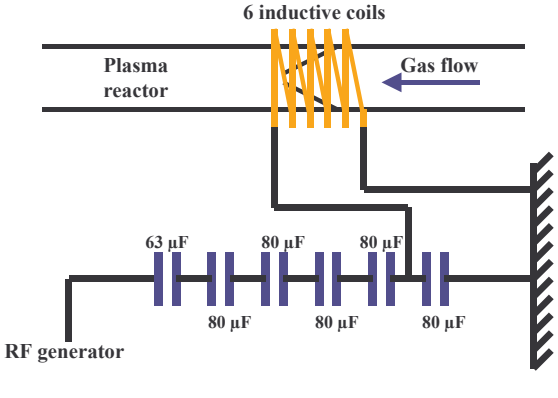

Figure 2 : capacitors add-on on RF generator

3. Effect of generator's modification on the efficiency of the discharge

In order to determine the energetic efficiency of the discharge, a liquid solution was used to simulate the plasma. This method consisted in measuring the electrical current of the generator as a function of the voltage for several electrolyte solutions by applying the inductive RF. Then, it was possible to measure the heat absorbed by the solution representing the same conductivity of plasma. That could be considered as the energy absorbed by the plasma.

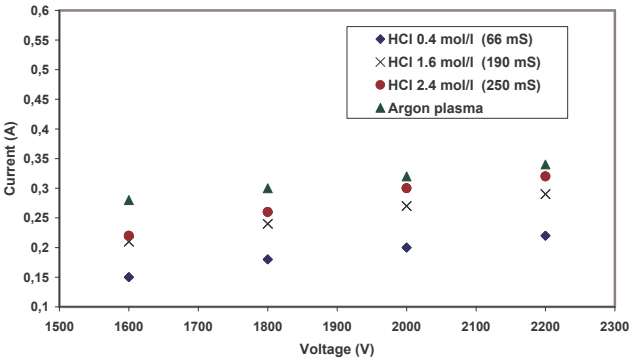

Figure 3 : Current as a function of voltage for different solution containing HCl

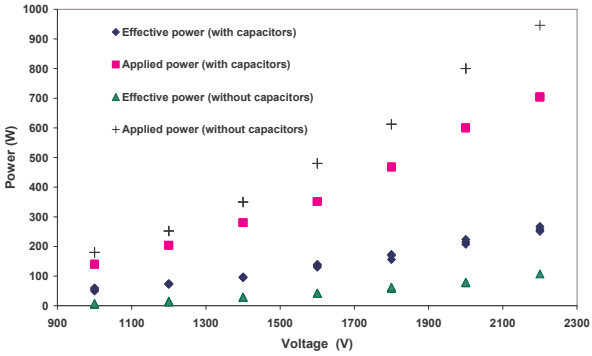

Figure 4 : Power versus plasma generator voltage

Solutions of HCl at different concentrations were elaborated. The conductivity of solutions was measured, showing an increase with the concentration of HCl (maximum for 2.4 mol.l^{-1} HCl). Each solution was placed among inductive coils equipped with capacitors, and the current was measured as a function of voltage on the generator (figure 3). The solution containing 2.4 mol.l^{-1} HCl exhibited almost the same current and voltage values as the plasma at high power. This solution (σ = 250 mS) was the best one which simulated our argon plasma conductivity.

This solution, with almost the same electrical conductivity as our plasma, was chosen to perform measurements of the effective power available in the plasma discharge. The increase of temperature due to the current circulating in coils was measured as a function of voltage. It was performed with and without capacitors on inductive coils. By knowing the heat capacity of the solution, it was possible to determine the

energy transferred into the solution during the working of the generator. The figure 4 represents the evolution of applied power and effective power as a function of the voltage. The results showed that the efficiency of the generator increased with capacitors add-on. Mean efficiency increased from 13 % (without capacitors) to 35 % (with capacitors). Results underlined the fact that quality of plasma discharge strongly depend on electrical characteristics of the generator.
The improvement of plasma coupling by the means of capacitors on inductive coils, resulted in increasing the energetic efficiency of the process. This was checked by comparing the conversion rate of nitrates precursors into $La_{0.7}Sr_{0.3}MnO_3$ in the plasma reactor. For an applied power (3600 W) the conversion rate was measured to be around 70 %. By equipping the inductive coils with capacitors, the conversion rate increased to more than 88 % for an applied power of 800 W [6, 7, 8].

4. Optical emission spectroscopy (OES)

The electrical modification probably had impact on the apparition and the evolution of species in the plasma. It was essential to study the evolution of reactive species like Ar and O as a function of injections in order to understand their role on the synthesis.
OES investigations were carried out on the plasma by equipping the reactor with observation windows of spectrosyl quartz. Spectra acquisitions were performed by using a JOBIN YVON device linked to the reactor with optical fibres.
OES measurements were performed at the exit of the nozzle. Evolution of Ar and O intensities was study as a function of time. Acquisitions were performed with and without capacitors for the same applied power. Figures 5 and 6 show the evolution of intensities for injections of nitrates precursors in an Ar + O_2 plasma (50cc. min^{-1} Ar and 50cc. min^{-1} O_2). Injection of droplets in the reactor resulted in an increase of the light intensity well visible during experiments. Results reported on figures 5 and 6 confirmed the enhancement of energetic efficiency of plasma generator due to capacitors. The light intensity increased highly in the case of inductive coils with capacitors. The higher intensity reached for atomic oxygen underlined the important chemical reactivity of plasma.

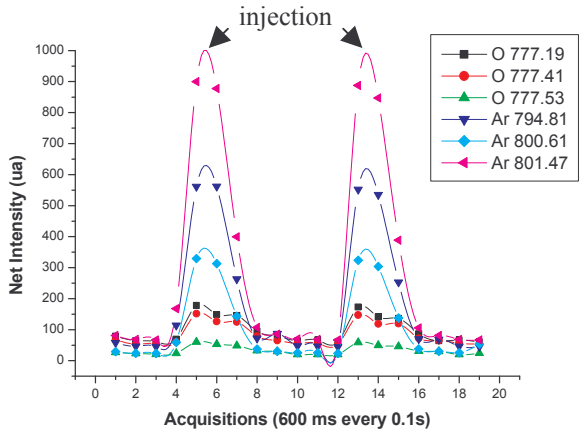

Figure 5 : evolution of intensities as a function of acquisition time (capacitors on inductive coils)

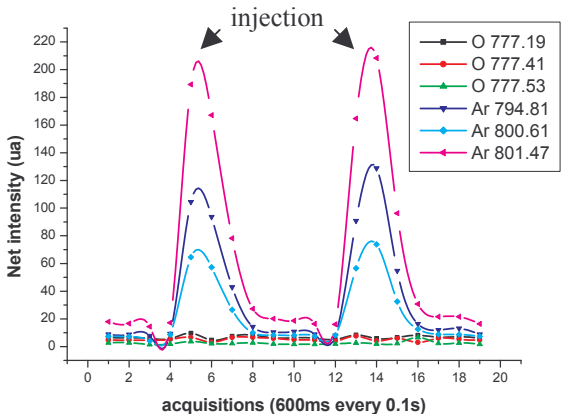

Figure 6 : evolution of intensities as a function of acquisition time (no capacitors)

The ratio of I (Ar 801,47 nm) / I (O 777.19 nm) were calculated in the case of Ar + O_2 + H_2O and Ar + O_2 + H_2O + nitrates as shown on the figure 7. In the case of nitrates precursors injections, it was clear that O intensities decreased as compared to the water injections. Because of respecting pressure, power, and gas composition of plasma for water and water containing nitrates injections, the difference of intensity could be considered as proportional to the concentration of O in the plasma [9]. More investigations on the evolution of O should be done to conclude that the decrease of O intensity was essentially due to the formation of MnO, LaO, SrO or CoO bonds.

Concerning OH radicals from the decomposition of water in the plasma discharge, OH° bands were investigated with and without capacitors on inductive coils. In the case of capacitors add-on, intensity of

OH° bands was more intense. Investigations are currently performed to determine the effect of capacitors on the OH° rotational temperature.

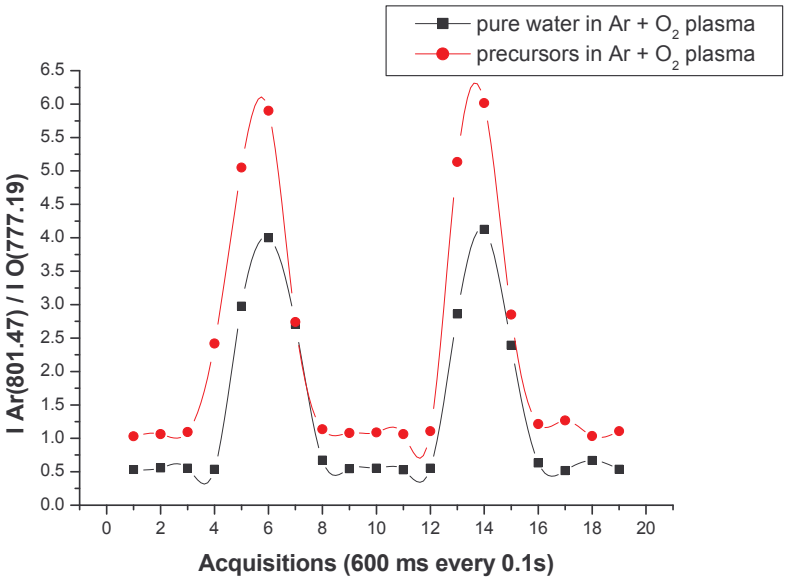

Figure 7 : I (Ar 801,47 nm) / I (O 777.19 nm)
as a function of acquisition time

5. Effect of electrical modification on the deposit

$LaMnO_3$ and $La_{0.7}Sr_{0.3}MnO_3$ layers were deposited with and without capacitors respecting same current and voltage values on the plasma generator. Infrared spectroscopy, neck observations and Scanning Electron Microscopy were used to control the structure of layers and the conversion rate of nitrates precursors into $La_{0.7}Sr_{0.3}MnO_3$.

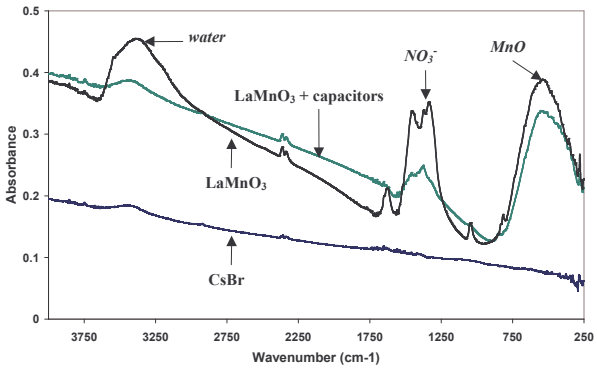

Figure 8 : IR spectra of $LaMnO_3$ deposited with and without capacitors

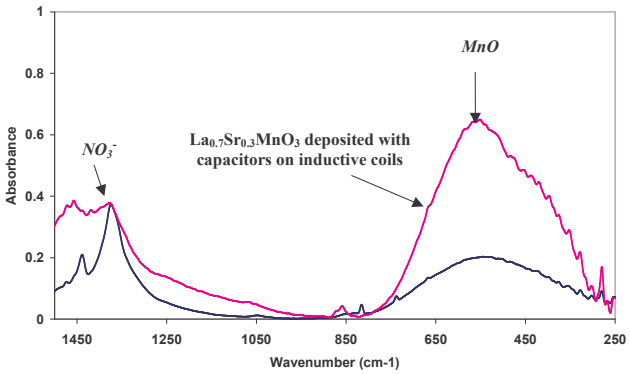

Figure 9 : IR spectra of $La_{0.7}Sr_{0.3}MnO_3$ deposited with and without capacitors

IR spectrum of $LaMnO_3$ deposited with and without capacitors were compared as shown on the figure 8. For same current and voltage values, capacitors add-on increased the efficiency and the power available in the plasma discharge. The effect of power enhancement was clearly visible on IR spectra. In the case of capacitors add-on, NO_3 bond and water intensity was lower and MnO bond intensity were higher, confirming a good oxidisation of nitrates precursors in the plasma. In previous works, IR spectroscopy was used to quantify the conversion rate of nitrates into $La_{0.7}Sr_{0.3}MnO_3$[7,8]. By comparing NO_3^- and MnO bonds intensities, and by using a calibration curve, it was possible to determine the conversion rate. Deposits of $La_{0.7}Sr_{0.3}MnO_3$ were performed in order to study the effect of capacitors on the conversion rate (figure 9).

For a same nitrates intensity, MnO bond intensity was higher for $La_{0.7}Sr_{0.3}MnO_3$ deposited with capacitors on generators. With the capacitors add-on, the conversion rate increased from 52 % to 84%, confirming a better efficiency of the plasma discharge.
Neck observations were used to study the structure of the deposited layer. With or without capacitors, the deposit had the same aspect after the synthesis. But after few days, the layers deposited without capacitors exhibited cracks well visible on the figure 10. This phenomena was probably due to the nitrates present in the deposit. Because of the low conversion rate in the case of no capacitors add-on, a quantity of nitrates were not transformed into NOx and stayed in the deposit. Atmospheric water adsorbed by remaining nitrates caused a swelling of the layer. This phenomena was not visible for layers deposited with capacitors.

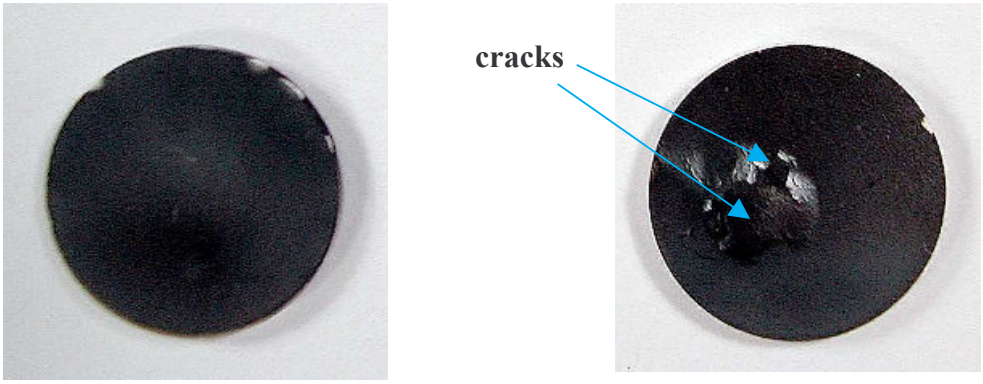

$LaMnO_3$ deposited on YSZ. Capacitors on inductive coils

$LaMnO_3$ deposited on YSZ. No capacitors on inductive coils

Figure 10 : photos of two $LaMnO_3$ samples deposited with and without capacitors

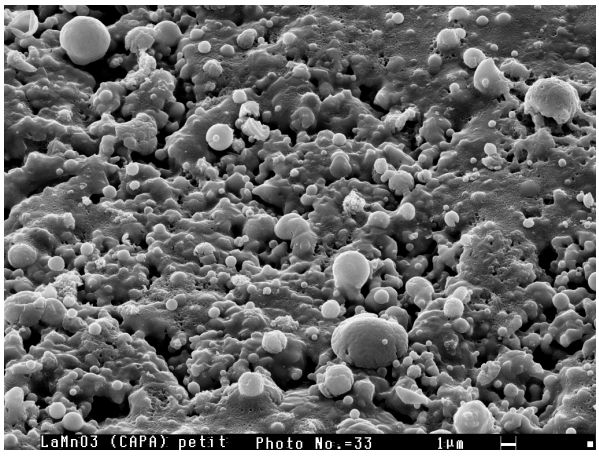

Figure 11 : $LaMnO_3$ layers deposited with capacitors

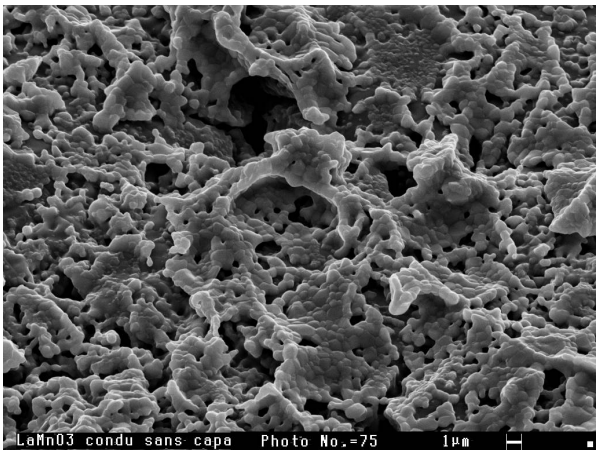

Figure 12 : $LaMnO_3$ layers deposited without capacitors, annealing at 1200°C during 1 hour

Scanning Electron Microscopy was used to study the microstructure of the deposit. The electrical modification of the generator had no visible impact on the aspect of the layers. Layers deposited with or without capacitors were amorphous and had the same structure (figure 11). But after an annealing of 1 hour at 1200°C, the two different layers exhibited an another microstructure (figure 12), probably due to a change of crystalline structure.

6. Conclusion

Electrical modifications on the generator power increased the power available in the plasma discharge. By using solutions of HCl to simulate the plasma, that permitted to determine the yield of RF energy transferred

to the plasma by the inductive coils. Effects of capacitors add-on were well visible on the plasma process. The OES proved that the intensity of activated species were more important in the case of capacitors add-on, probably due to a higher concentration of reactive species in the discharge. Infrared spectroscopy underlined the fact that the conversion rate of nitrates into lanthanum manganite Sr-doped increased with capacitors add-on. Layers deposited without capacitors contained nitrates which caused cracks apparition (due to the adsorption of water into the layers). A microstructure change was not visible by TEM on the layers deposited by using the two electrical configurations, and an annealing led to the apparition of crystalline structure in the two cases. Next studies will consist in a comparison of electronic and gas temperature for the two electrical configurations.

References

[1] : K. Kendall, "Emergence of fuel cell products" europhysics news, , pp 173-175. september/october 2003.
[2] : R. J. Bell, Graeme J. Millar, J. Drennan, "Influence of synthesis route on the catalytic properties of $La_{1-x}Sr_xMnO_3$", Solid State Ionics, 131, pp 211-220, 2000.
[3] : S. C. Paulson, V. I. Birss, "Chromium poisoning of LSM-YSZ SOFC cathodes", J. of Electrochemical Society, 151 (11), pp A1961-A1968, 2004.
[4] : T. Yamada and all, "Development of intermediate-temperature SOFC module using doped lanthanum gallate", J. of Electrochemical Society, 151 (10), pp A1712-A1714, 2004.
[5] : M. Nikravech, F. Rousseau, D. Morvan, J. Amouroux, "Effects of plasma parameters on the properties of $La_{1-x}Sr_xMnO_3$ thin layers deposited in low-pressure RF plasma wave shock reactor", High Temp. Material processes, 7 (2), pp 225-230, 2003.
[6] : M. Nikravech, F. Rousseau, D. Morvan, J. Amouroux, "Production of perovskite deposits for fuel cells by plasma process", J. of Physics and Chemistry of Solids, 64, pp 1771-1775, 2003.
[7] : F. Rousseau, M. Nikravech, E. Francke, J. Milpied, D. Morvan, J. Amouroux, "Investigation on supersonic gas flow coupled with an inductive low-pressure plasma used for the synthesis of SOFC material", High Temp. Material processes, 8 (3), pp 407-416, 2004.
[8] : M. Nikravech, F. Rousseau, D. Morvan, J. Amouroux, "Characteristics of Sr-doped $LaMnO_3$ thin layers deposited with a low-pressure RF plasma wave shock reactor", Proceedings of 5th European Solid Oxide Fuel Cell Forum (1-5 july 2002, Lucerne, Switzerland), 1, pp 377-384.
[9] : A. Grill, "Cold plasma in materials fabrication", IEEE PRESS, 1993.

Effect of convergent nozzle on gases flow and particles behaviour in a low-pressure plasma reactor used for the synthesis of SOFC cathode.

F. ROUSSEAU[1], M. NIKRAVECH[1], D. MORVAN[1], J. AMOUROUX[1]

[1]Laboratoire de Génie des Procédés Plasmas et Traitements de Surface, ENSCP-Pierre et Marie Curie university, Paris, France

Abstract :
Solid Oxide Fuel Cell's (SOFC) development is of high energetic interest. Because of progress toward hydrogen storage and the need of reducing greenhouse gases into the atmosphere, it is clear that SOFC will play a great role in hydrogen-based transports and energy systems. A low-pressure plasma reactor equipped with a convergent nozzle has been developed in the laboratory in order to produce thin perovskite layers that could be used as the cathode for SOFC. Raw materials of La, Sr, Mn or CoO nitrates dissolved in water were introduced into the plasma in order to produce $LaMnO_3$, $LaCoO_3$ or Sr-doped layers on Yttria Stabilised Zirconia (YSZ) substrate. Properties of the layers strongly depend on the chemical reactions and physical phenomena which take place in the plasma reactor. The pressure and the velocity of gases in the reactor played major roles on the porosity and the adherence of the layer on the substrate. It was essential to investigate about the hydrodynamics of the reactor. The study has consisted in two steps : step one was the development of an hydrodynamic model in order to measure gases and particles velocities. The second was the quantification of velocity, concentration and diameter of injected particles by using in-situ measurement technique. Hydrodynamics of the process has been characterised, and the behaviour of particles in the reactor has been described. Model and experimental measurements have underlined the fact that particles were efficiently accelerated due to the depression in the nozzle (from 12 m. s^{-1} to 80 m. s^{-1}. Particles diameters was reduced along the reactor (22 µm to 10 µm from each part of the nozzle).
Keywords : nozzle, hydrodynamic model, Laser Doppler Anemometry, Laser Doppler Granulometry

1. Introduction

Solid Oxide Fuel Cell (SOFC) are promising electrical generator in a near future [1]. Recently, many SOFC prototypes were developed for automotive or power plant applications. But SOFC materials continue to be investigated, in order to solve problems which appear during the synthesis and the working of the cell. Classical ways of ceramic synthesis use the screen printing of a powder on the substrate [2]. But the adherence of the product layers on the substrate is often weak, and lead to bad electrochemical contacts at the interface. A very good adherence is absolutely required for electrochemical applications, such as SOFC.
A plasma process has been developed in order to obtain SOFC cathode materials on YSZ substrate in one step. The principle of this process consisted to a spray of precursors particles injected by a pulsed valve in the plasma. Accumulation of particles on the substrate permitted the growth of the deposited layer. In the case of spray, velocity of particles is a very important parameter, that condition the porosity of the deposited layer and the adherence [3].
In previous works, we observed that nozzle equipping a reactor creates hydrodynamics perturbations. Because of the convergent nozzle, over-pressure waves are created, leading to the acceleration of gases and particles circulating in the reactor. The effect of nozzle was well visible during experiments. For each injection, it was possible to observe shock-wave formation at the exit of the nozzle. The role of the nozzle and the pulsed valve on the gases and particles velocities, was investigated in order to characterise the hydrodynamics of the process.
A numerical model has been developed to determine the velocity and the temperature of gases along the reactor. In the first time, plasma parameters were not considered for the numerical model.
A non-intrusive technique based on the Doppler effect was performed on the reactor to investigate the velocity, the concentration and the diameter of particles along the reactor (Laser Doppler Anemometry LDA – Laser Doppler Granulometry LDG).
The knowledge obtained from these investigations could be used to understand the properties of hydrodynamics on the layer's growth (thickness, porosity and so on…).

2. Experimental set-up

The low-pressure plasma process is described on the figure 1. The plasma reactor consisted in a quartz tube (50 mm in diameter, 600 mm in length) equipped with a convergent nozzle (5 or 3 mm in diameter). A 40 mHz RF generator allowed the plasma discharge by the way of inductive coils (Plasma Ar + O_2 in various composition). Mass flow-meters permitted to control the composition and the flow of plasma and vector gases. The low pressure in the plasma reactor was obtained with a vacuum pump (0.7 – 6 mbar).

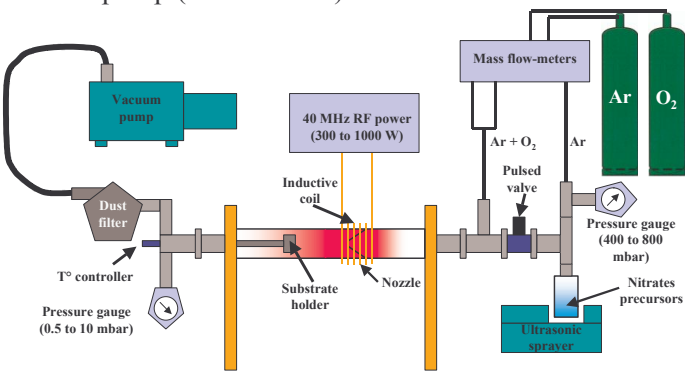

Figure 1 : Experimental set-up

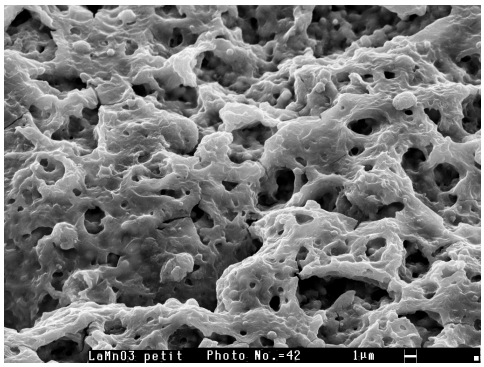

Figure 2 : $LaMnO_3$ deposit on YSZ substrate

The precursors used for the synthesis and the deposit of $LaMnO_3$ and $LaCoO_3$ Sr-doped layers were nitrates of La, Mn, Sr or Co dissolved in water (3 % HNO_3). The solutions were available as commercial product (ICP-DCP standard solution). Few micrometers droplets were formed due to the presence of an ultrasonic sprayer. Particles of water containing nitrates were injected in the plasma reactor by the way of a difference in pressure from each part of a pulsed valve (300 – 600 mbar difference in pressure).

For each injection, argon vector gas and droplets went through the plasma. Reactive species of the plasma (Ar*, O, OH radical from the decomposition of water) permitted the oxidisation of La, Mn, Sr or Co ions in order to form LaO, MnO, SrO or CoO bonds. After their flight through the plasma, particles deposited on YSZ in order to form $LaMnO_3$ and $LaCoO_3$ Sr-doped amorphous layers (figure 2). Between two injections, particles on YSZ continued to be treated by the plasma.

Many investigations had been performed on the plasma process in order to determine the effect of plasma parameters such as power and oxygen quantity in plasma gas on the deposit. Moreover, ex-situ techniques were used to characterise the structure and the electrochemical properties of the layer. Studies of the process and investigations about the deposit were used to optimise the process and to enhance the properties of thin films deposited [4].

3. Hydrodynamic model of the process

A numerical model using FLUENT® [5] software has been developed. By the way of this software, it is possible to calculate velocity, pressure and temperature of gases. Moreover, it is possible to model the evaporation and the trajectory of particles along the reactor.

In order to take into account dimensions and geometry of the reactor and the pulsed valve, different kind of meshes divided in thousands of cells were created, as shown on the figure 3. Meshes were used for the spatial resolution of Navier Stokes equations from the pulsed valve to the exit of nozzle.

The resolution of hydrodynamic equation required boundary conditions. Evolution of pressure from each part of the nozzle was measured in various conditions. By using two pressure gauges connected with a computer interface, it was possible to measure the evolution of pressure as a function of time (injection's pressure equal to 400 mbar) and pulsed valve opening time (figure 3 et 4). Figure 3 shows the evolution of the pressure on front and behind the nozzle. At the beginning of the injection, the curves exhibited a step increase in pressure during nearly 0.3s followed by an exponential decrease during more than 1s. Pressure values showed a maximal ΔP = 8 mbar on both side of the nozzle, probably responsible of shock waves formation. Figure 4 shows the effect of pulsed valve opening

time on the maximal pressure from each part of the nozzle. For opening time less than 0.25 s, max pressures from each part of the nozzle increased. But for opening time more than 0.25s, max pressures decreased. The pulsed valve continued to be open after the sprayer containing water and argon gas was injected. During a short time, the volume before the nozzle increased due to the pulsed valve that connected injection's system with the reactor. The increase of the volume led to a decrease of the pressure.

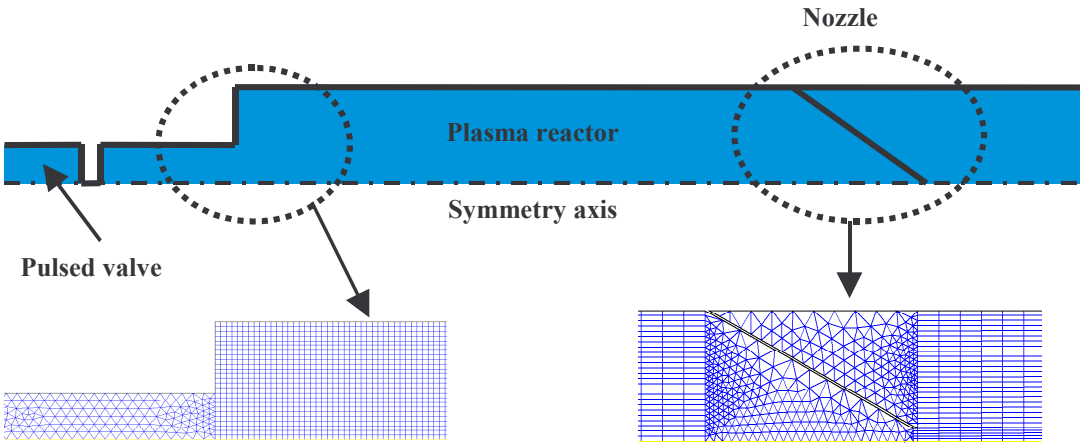

Figure 3 : mesh reactor used for Navier Stokes equation resolution

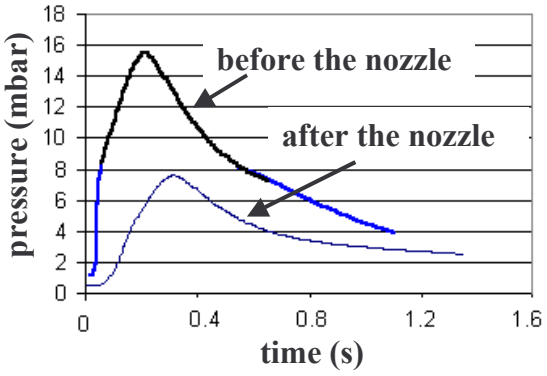

Figure 3 : pressure from each part of the nozzle as a function of time (for one injection)

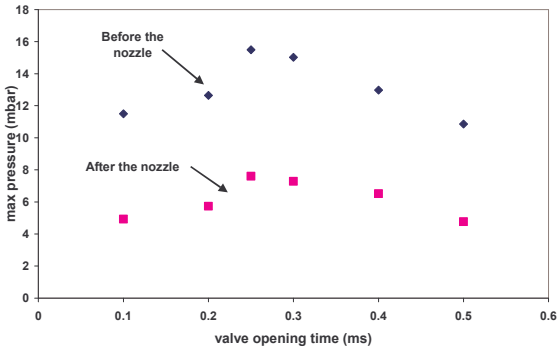

Figure 4 : Maximal pressure from each part of the nozzle as a function of valve opening time

By using pressure measurements as boundary conditions for the resolution of Navier Stokes equation, it was possible to calculate the evolution of velocity and pressure as a function of time (figure 5). The increase of pressure before the nozzle involved the formation of over-pressures waves that reflected against the nozzle. The calculated velocity of these over-pressure waves are shown in the figure 5 (maximal velocity = 380 m. s^{-1}). The over-pressure waves reached supersonic velocities, resulting in shock waves formation. Their velocity and intensity decreased during the different reflection processes. Finally, after a short time (25 ms after the beginning of the injection), the over-pressure waves seemed to disappear.

Concerning the velocity of gases at the exit of the nozzle, the maximal velocity was equal to 710 m. s^{-1} (t = 31 ms after the beginning of injection). High velocity at the exit of the nozzle resulted from the apparition of over-pressure waves before the nozzle. The velocity decreased as a function of time (400 m. s^{-1} at t = 0.2 s after the beginning of injection), due to the disappear of over-pressure waves before the nozzle.

Particles trajectory in the reactor have been modelled using the same boundary conditions. Even if the droplets were dispersed before, a particles jet centred on the reactor's axis was formed at the exit of the nozzle. There was no dispersion effect, so that most of the particles deposited on the substrate.

The evaporation of particles is currently under study using the same computer code The aim is the characterisation of the effect of pressure and gas flow on the vaporisation of injected droplets.

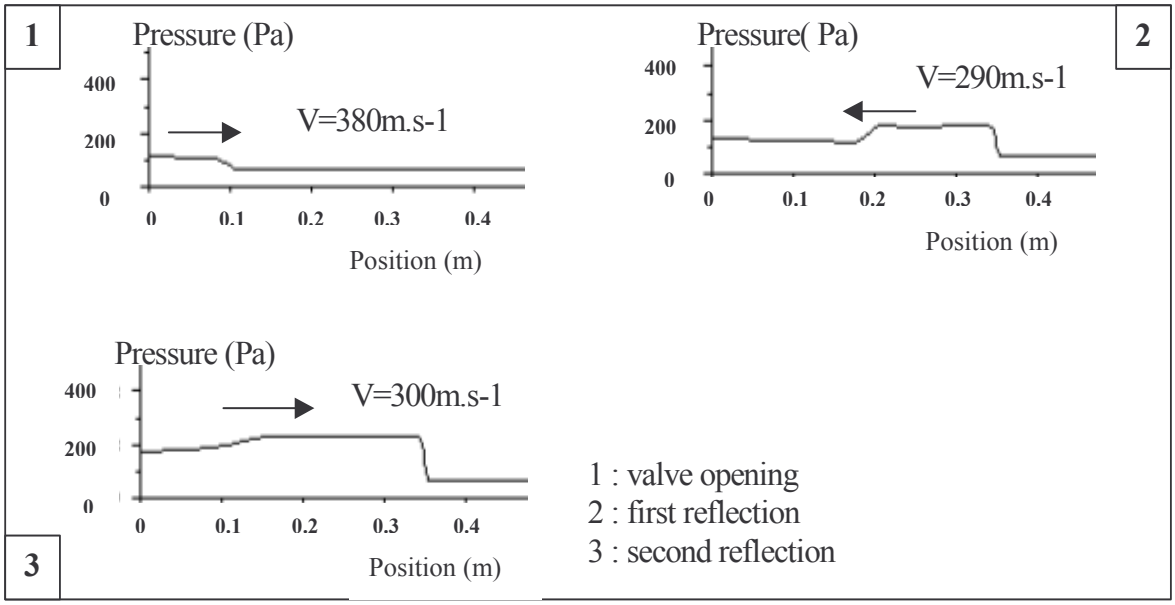

Figure 5 : Profile of pressure along the reactor

4. Laser Doppler Anemometry (LDA) – Laser Doppler Granulometry (LDG) measurements

LDA-LDG technique permitted to measure the velocity, the concentration and the diameter of particles directly on the plasma reactor. For this study, an analytical apparatus manufactured by DANTEC Dynamics corporation was used [6].

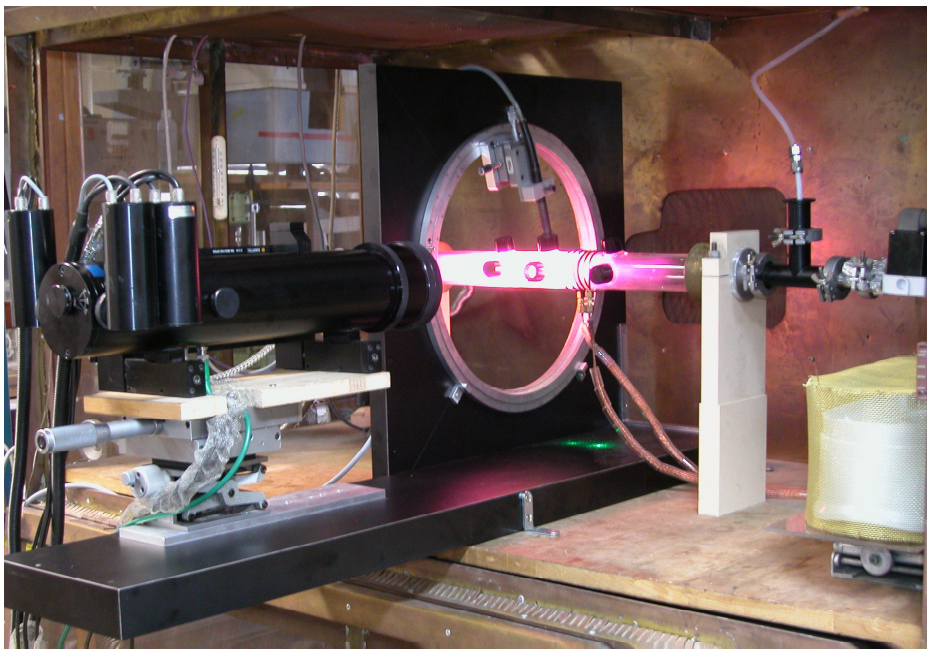

Figure 6 : LDA-LDG experimental set-up

A laser with a well known frequency was split in two beams. The two incident laser beams converged and created a small analytical volume. Each time a particle passed through this volume, it perturbed the frequency of the laser and his perturbation was directly proportional to the velocity of particles. In the case of LDG measurements, the phase difference of three detectors permitted to determine the diameter of particles. A reactor equipped with optical access (quartz spectrosyl) as shown on the figure 6, was specially developed for the measurements, in order to have an accurate detection.

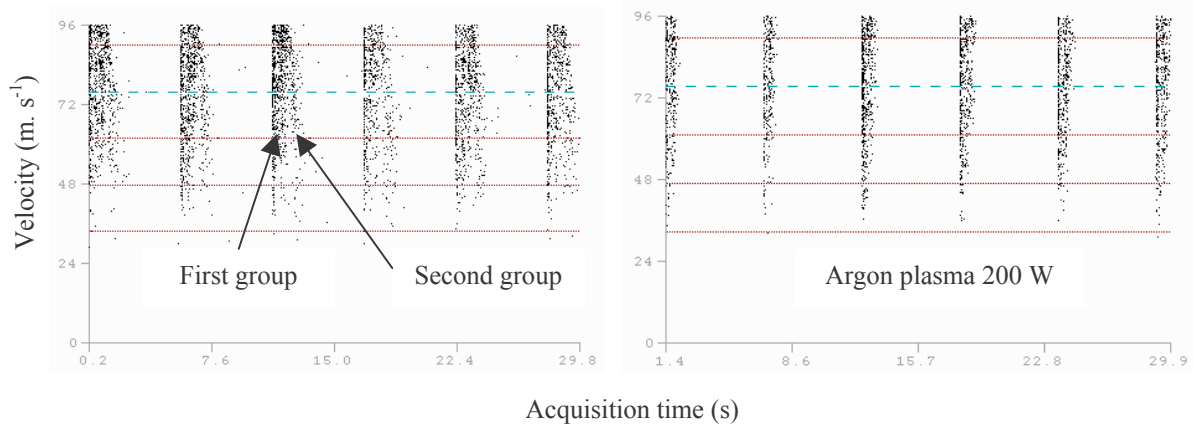

Figure 7 : Velocity of particles as a function of time (right : without plasma, left : with argon plasma 200 W)

Figure 7 shows the particles velocity as a function of time (injection's pressure = 400 mbar), 1 cm downstream of the nozzle exit without and with plasma. In the case of no plasma discharge, particles went through the nozzle in two groups, one following the other, because of shock waves. The second group seemed to be more dispersed than the first one. When the valve opened, the first group quickly was injected in the reactor and underwent the influence of the first over-pressure. Droplets passed through the nozzle with a high swiftness and were detected first. The second group underwent the influence of the pressure waves that were reflected in nozzle, resulting in a more important residence time before the nozzle. Because of re-circulation phenomena (confirmed by positive and negative velocities detected by the LDA before the nozzle), droplets of the second group were detected later.
In the case of plasma discharge application, only one group was detected. The detection of just one group means that the other group underwent a strong vaporisation due to the plasma. Particles of the second group lowered in diameter smaller than one micrometer (limit of detection by LDA). This phenomena, due to the high residence time, resulted from the re-circulation phenomena of particles before the nozzle.

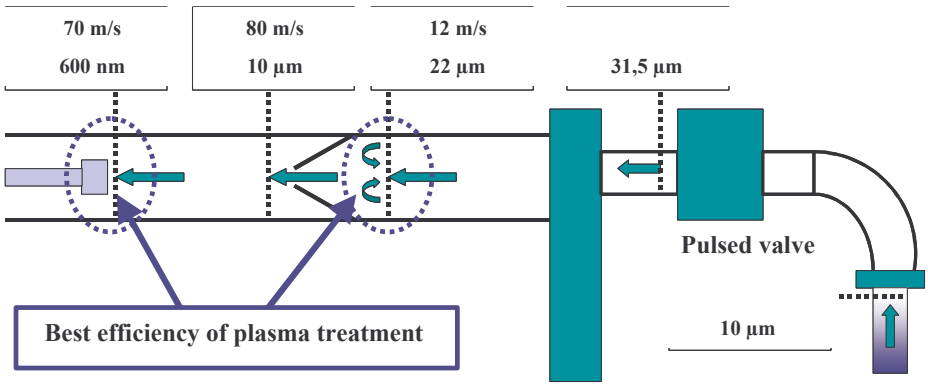

Figure 8 : Mean velocity and mean diameter values at different steps in the plasma reactor

Velocity values obtained at different places on the reactor are summarised on the figure 8. At the exit of the nozzle, the mean velocity was equal to 80 $m.s^{-1}$. Velocities of particles ranged from 20 to 130 $m.s^{-1}$. By comparing the velocities of droplets detected by LDA before the nozzle (12 $m. s^{-1}$) and after the nozzle, it can be assumed that the particles were efficiently accelerated by the gas flow. Particles had a great velocity (70 $m. s^{-1}$) just before they deposited, leading to a great adherence on the substrate.

The diameters of particles were determined by the LDG at different places of the reactor. The figure 9 shows typical velocity and diameter diagrams obtained at the exit of the nozzle (in the case of argon plasma discharge 400W). Diameter of particles was investigated with and without plasma in order to determine the effect of the discharge on the evaporation of droplets. In the two different cases, diameters acquired were the same, confirming that the vaporisation of droplet during the flight in the reactor was essentially due to the vacuum. The evolution of diameters is summarised on the figure 8. The mean diameter before the pulsed valve was equal to 10 µm. The increase of diameter at the exit of the pulsed valve (31.5 µm) was due to the agglomeration of particles. The mean diameter reduced from 22 µm to 10 µm, due to the depression at the exit of the nozzle. That resulted in an evaporation of more than 90 % in volume. Once deposited on the substrate, the mean diameter of particles was equal to 600 nm (determined by Scanning Electron Microscopy).

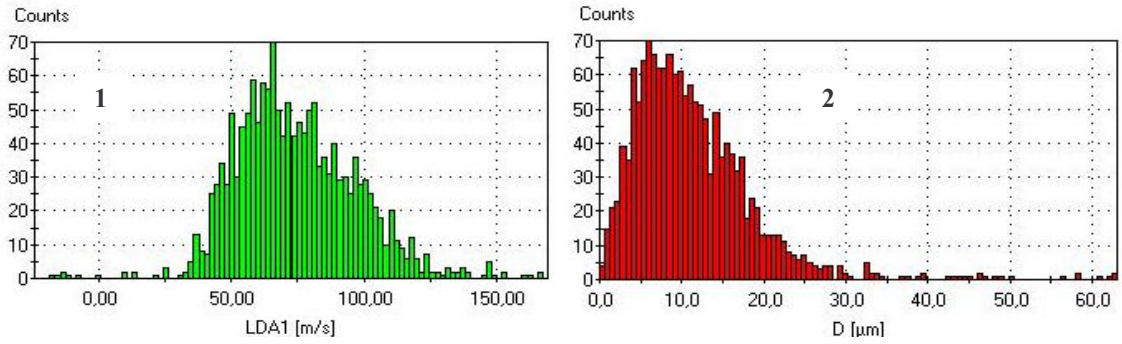

Figure 9 : Velocity (1) and diameter (2) measurements acquired after the nozzle (argon plasma, 400 W)

5. Conclusion

Aerodynamic phenomena taking place into the reactor have been modelled. In order to do that, experimental pressure values were measured and simplifying hypotheses were defined. Velocity and pressure calculations proved shock waves formation in the reactor. Considering some ignored phenomena such as chemical reactions and plasma physics could result in the building of more complex model. Concerning LDA and LDG measurements, it was demonstrated that particles were efficiently accelerated by the gas flow due to the presence of nozzle. Velocity measurements with the LDA were lower than velocity of gases calculated from the model, maybe due to the vacuum present in the reactor. LDA permitted to determine a re-circulation area, that involved the residence time of particles. LDA and LDG results confirmed that particles were strongly submitted to the effect of plasma and vacuum in the reactor.

References

[1] : Science, vol 305, N° 5686, pp 901-1060, august 2004.
[2] : T. Yamada and all, “Development of intermediate-temperature SOFC module using doped lanthanum gallate”, J. of Electrochemical Society, 151 (10), pp A1712-A1714, 2004.
[3] : M. Pasandideh-Fard, Y. M. Qiao, S. Chandra, J. Mostaghimi, “Capillary effects during droplet impact on a solid surface”, Physics of Fluids, 8 (3), pp 650-659, 1996.
[4] : M. Nikravech, F. Rousseau, D. Morvan, J. Amouroux, “Effects of plasma parameters on the properties of $La_{1-x}Sr_xMnO_3$ thin layers deposited in low-pressure RF plasma wave shock reactor”, High Temp. Material processes, 7 (2), pp 225-230, 2003.
[5] : www.fluent.com.
[6] : www.dantecdynamics.com.

Effects of Silent Electrical Discharge Plasma Excitation on the Combustion of Methane, Propane, and Butane

Louis A. Rosocha and Yongho Kim

Plasma Physics Group, Los Alamos National Laboratory, USA

Abstract
We have shown that silent electrical discharge (dielectric barrier discharge – DBD) excitation of methane, propane, and butane can significantly influence their combustion characteristics. In this paper, we compare DBD excitation of the three test fuel gases (in terms of post-plasma, air-mixed-burner combustion and excitation products without combustion). Flame images and mass-spectrometer measurements of decomposition products are presented for representative experiments with the three hydrocarbon test gases.
Keywords: plasma-assisted combustion, silent discharge excitation, flame speed.

1. Introduction

Combustion processes pervade modern life, providing propulsion (automobiles, aircraft, watercraft); generating electricity; and providing heat (homes, water, commercial buildings, industrial processes). Improvements in combustion processes are highly desirable because of the need to achieve better fuel utilization and to reduce pollution.

Over the past five decades, improvements in combustion have been attempted using electric fields, which can affect flame stability, flame propagation speed, and combustion chemistry [1, 2]. Electric-field generated thermal plasmas (usually not efficient and selective in directing electrical energy into the promotion of chemical reactions), have been applied to combustion during the past three or more decades with some success [3], particularly in the conversion of fuel-air mixtures into syngas (H_2 and CO) for use in increasing internal combustion engine efficiency and reducing NO_x emissions [4]. Non-thermal plasmas are potentially more useful tools for promoting combustion. For NTPs, the electrons are energetic ("hot"), whereas ions and neutral gases are near ambient temperature ("cool"), which results in little waste enthalpy (heat) being deposited in a process gas. Typical electron temperatures in such plasmas are of order a few electron volts, which is sufficient to decompose the fuel and to produce free radicals [5]. We consider the silent electrical discharge to be a very promising candidate for combustion enhancement. Two decades ago, Inomata *et al*. [6] demonstrated increases in flames speed when applying a DBD upstream of a methane-air flame. Work performed by Cha, *et al*. [7] during the past few years, showed that applying a DBD to the flame region results in a decrease in flame length and reduced soot formation.

Since 2002, we have carried out research on using DBD plasmas to pre-treat fuels (not fuel-air mixtures) before they are combusted [9-11]. In our technique, fuels are decomposed (cracked) into smaller molecular fragments, boosted into reactive excited states, or made into "free-radicals". The 'plasma-activated' fuel is then mixed with air and combusted. This has shown to stabilize flames, increase flame speed, and allows very lean-burn modes of combustion, highly desirable for the reduction of NO_x. Proof of principle has been demonstrated in experiments using propane as the fuel in a Bunsen-like burner. We have investigated the effects of the plasma on combustion by examining combustion stability under lean-burn conditions, observing increases in flame propagation speed by photography, and by sampling and analyzing the gas residues from combustion [9-11].

In our experiments, combustion is initiated at a place distant (6 cm) from the plasma region. Most previous plasma-assisted combustion works have not separated physical electric field effects (ionic wind) and chemical effects (radicals and fuel fragments) [12, 13]. In contrast to these other works, by having

combustion occur relatively far away from the plasma fuel-excitation region, electric field effects can be greatly reduced, thus providing more insight into the role of plasma chemistry.

In this paper, we report on comparing the effects of DBD excitation on the fuel gases methane, propane, and butane in terms of two characteristics: 1) Flame images indicating changes in flame propagation speed, after the activated gas is mixed with air and combusted in an air-flame burner; 2) Decomposition products resulting from activating the fuel gas, but not combusting it, as measured by mass spectrometry.

2. Experimental Setup

Figure 1 shows the experimental setup for a coaxial DBD fuel-activation reactor and associated burner. In this DBD reactor [10], air flows up through an inner grounded stainless steel tube (outer diameter 0.95 cm) and the fuel gas flows up through the annular region between the quartz dielectric tube (inner diameter 1.25 cm) and the inner metal electrode. This configuration, where the fuel flow encircles the air flow, is known as an inverse flame. The fuel gas and air flows are adjusted to a desired equivalence ration by adjusting gas flowmeters. For example, for a rich-burn equivalence ratio of $\phi = 2$ for propane (C_3H_8), the propane and air flow rates are 0.3 std lit/min and 4.6 std lit/min, respectively. The transparent quartz dielectric tube allows for visual observations of the plasma and flames. A copper mesh electrode, 12 cm in length, surrounds part of the quartz dielectric tube. This outer mesh electrode is powered by a HV AC transformer (Eurocom BHD1530) with a frequency tuned to about 450 Hz.

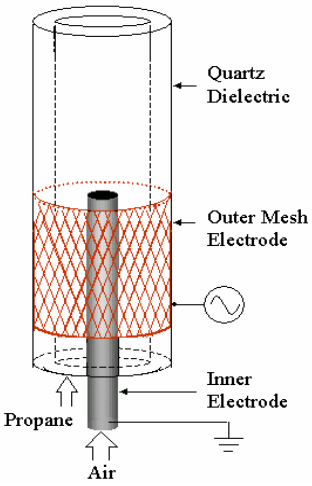

Fig. 1: Schematic diagram of the DBD apparatus.

After a fuel gas is treated with the plasma, it is mixed with the air flow from the inner electrode as it moves to the end of the quartz dielectric. Upon leaving the reactor, the activated fuel-gas-air mixture is used in two types of experiments: 1) it is combusted, with a sample of exhaust being sent to a mass spectrometer (MS), MKS Instruments Model PPT Quadrupole Residual Gas Analyzer; or 2) a sample of activated-fuel mixed with air being directly sent to the MS, without being combusted. We measured the power deposited into the plasma, through the use of well-known Lissajous-diagram techniques (charge-voltage plot) [14]. Flame images were recorded with a digital camera (Nikon CoolPix 3100) to inspect flame quality and stability. The MS was used to identify combustion products (when fuel was combusted) and to correlate them with flame images, or fuel-gas-fragments (when the fuel gas was activated and not combusted). In both cases, the MS was used as a tool to determine if we were indeed decomposing the fuel gas molecules into smaller fragments.

3. Results and Discussion

Initial investigations carried out with the test gases examined how the plasma discharge power affected combustion stability. Previously, we have reported that, in experiments with plasma-activated propane burned in air, flame stability is improved, flame blowout limits are improved (i.e., a leaner burn can be sustained using the plasma), and flame propagation speed is increased [10, 11]. In the previous experiments, an increase in flame speed was determined by observing that the distance a plasma-excited propane/air flame would propagate back toward the plasma region (against the flow of propane and air) increased with plasma power.

In the results reported here, on comparing such an effect for the three different gases, we used a similar technique, namely using flame images to observe the "burnback' phenomenon. Figue 2 shows flame images, taken using the apparatus in Fig. 1, for methane propane, and butane. In this case, the fuel gas flow rate was fixed at 0.3 std lit/min (equivalence ratio set at $\phi = 2$ for each gas by changing the air flow rate) and the plasma power was adjusted to a nominal operating value around 10 W. Methane (CH_4) shows a very slight "burnback" at 10 W (increasing the power further only slightly changes this effect for the methane case. Propane (C_3H_8) shows a substantial effect at 10 W, while butane (C_4H_{10}) shows a dramatic effect at the lower power level of 7 W. For a tube with a 6 cm length above the plasma, as shown in Fig. 1, increasing the power above 7 W causes the flame to reach completely back to the ground center-tube electrode (causing electrical instability in the apparatus). At the beginning of our plasma-assisted combustion investigations, we intuited that more complex hydrocarbons might provide more fragments under plasma excitation, thus showing a larger plasma-assisted combustion effect. For the three test gases examined here, such an assumption seems to be confirmed by the Fig. 2 data.

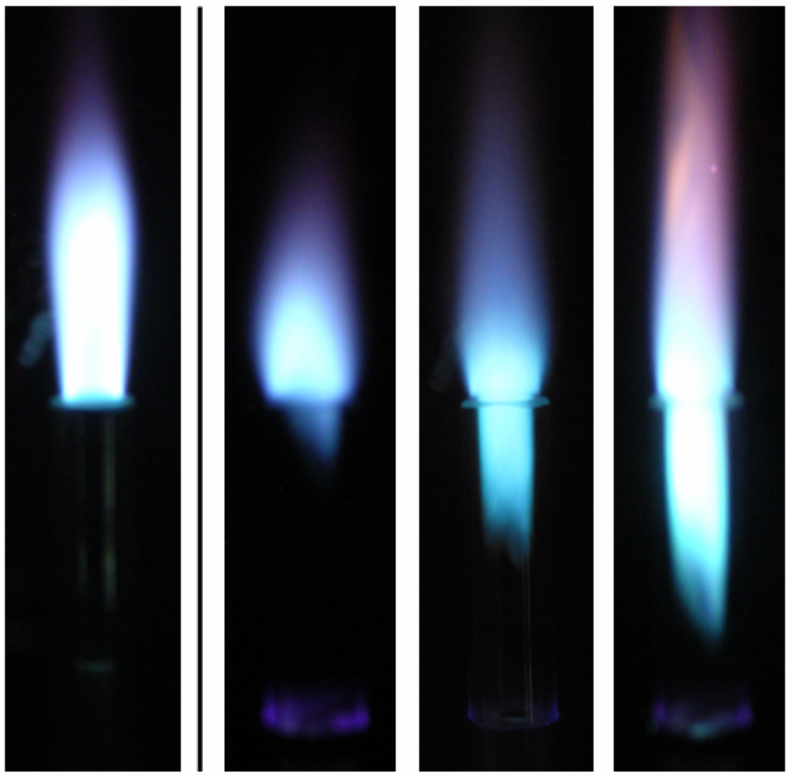

(a) (b) (c) (d)

Fig. 2: Flame images of (a) propane-air without plasma excitation; hydrocarbon-air with plasma excitation, (b) methane, (c) propane, (d) butane; all 10 W, except for butane case of 7 W. "Burnback" is quite significant for propane and butane.

To understand the mechanisms of our observed plasma-enhanced combustion, attempts were made to identify the activated fuel species. In the absence of a flame, and with the air flow through the inner electrode adjusted to give $\phi = 2$ for a flow of 0.3 std lit/min for each test gas, plasma-treated effluent gas was collected at the top of the quartz tube and analyzed with the MS. Figure 3 shows the mass spectra obtained for the three test gases under the flow conditions mentioned above and a plasma power of 10 W for all three plots (plasma specific energy density of 10 W/0.3 std lit/min = 2 kJ/std lit). The plots are created by normalizing the MS signal

values to the total MS pressure and subtracting the spectrum of a normalized air-only background (because air is a co-flow gas for all cases). For both propane and butane, there is a substantial increase in the normalized MS signal for the lower mass peaks M = 15, 26, 27, and 29; but only M = 15 and 16 show a significant increase in the methane case. For all three gases, there is a slight increase in M = 2 (assumed to be hydrogen H_2), which reinforces our notion that the silent discharge behaves like a fuel-molecule decomposer, rather than a fuel converter.

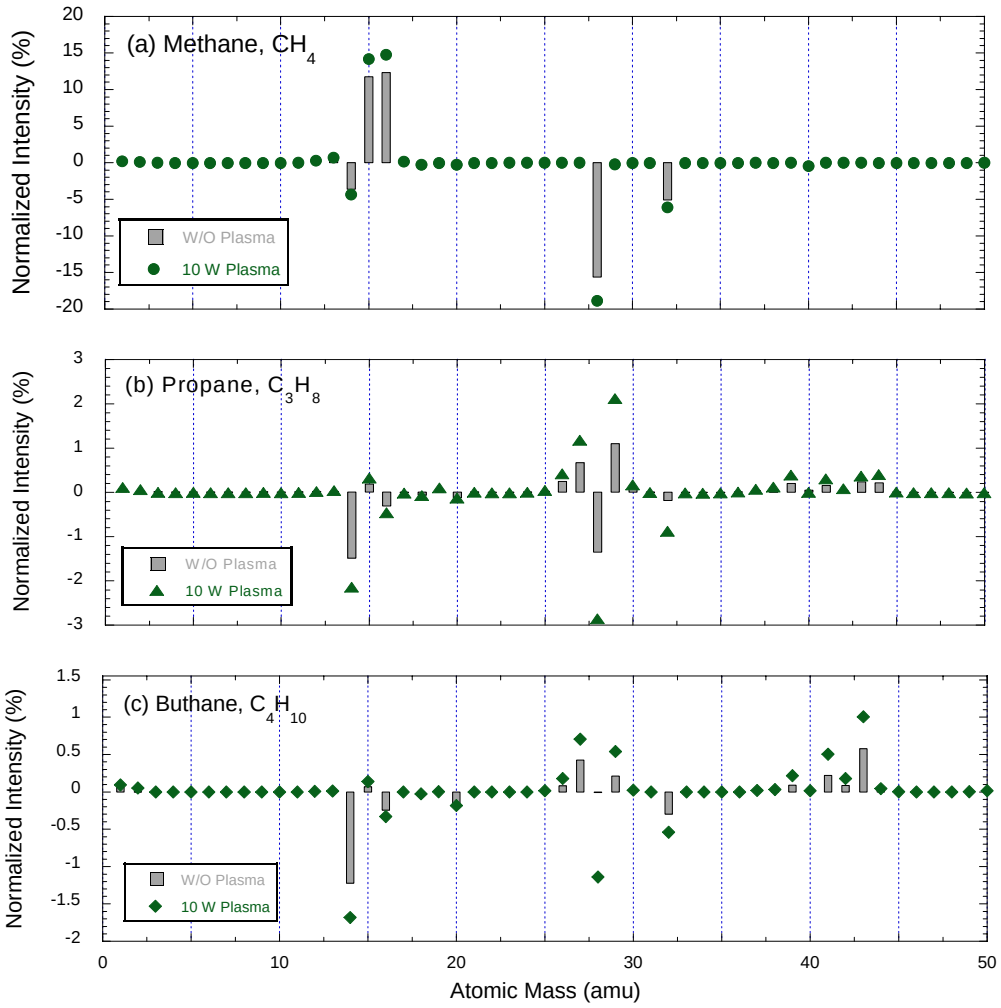

Fig. 3. Normalized mass spectra of (a) methane, (b) propane, and (c) butane under DBD plasma excitation at 10 W (2 kJ/std lit) and $\phi = 2$.

We believe that the fuel gas is decomposed ("cracked) by plasma electron-impact collisions that produce smaller, more easily-combusted fragments and, possibly, free radicals that can propagate combustion reactions. The data presented here in Fig. 3 appears to support that assumption.

In summary, when the hydrocarbons methane, propane, and butane are excited by a silent electrical discharge, mixed with air and combusted, their flame propagation speed increases (butane > propane > methane). In these experiments, the equivalence ratio was set at $\phi = 2$ and the plasma specific energy was relatively modest (2 kJ/std lit for methane and propane, and 1.4 kJ/std lit for butane). We propose that plasma-enhanced

combustion by silent discharges can be explained as an effective increase in the rate of combustion reactions, caused by breaking down fuel molecules and producing radical species in the plasma. In the future, more experiments will be performed to identify reactive species and fuel fragments, and correlate their concentrations with the enhancement of combustion reactions. Silent discharge fuel excitation appears to be a promising technique for enhancing combustion, although more research is needed for practical applications.

4. References

[1] J. Lawton and F. J. Weinberg, *Electrical Aspect of Combustion* (Oxford, Clarendon P., 1969).

[2] H. C. Jaggers and A. von Engel, "The Effect of Electric Fields on the Burning Velocity of Various Flames," *Combustion & Flame*, **16**, 275-285 (1971).

[3] F.J. Weinberg, Ed., *Advanced Combustion Methods* (Academic Press, London, 1986).

[4] L. Bromberg, D.R. Cohn, A. Rabinovitch, and J. Heywood, "Emissions Reductions Using Hydrogen from Plasmatron Fuel Converters," *Int. J. Hydrogen Energy* **26**, 115-1121 (2001).

[5] L. A. Rosocha, "Processing of Hazardous Chemicals using Silent-Electrical-Discharge Plasmas," Chap. 11 in *Plasma Science and the Environment* (AIP Press, New York, USA, 1997).

[6] Y. Kim, W. S. Kang, J. M. Park, S. H. Hong, Y. H. Song, and S. J. Kim, "Experimental and Numerical Analysis of Streamers in Pulsed Corona and Dielectric Barrier Discharges," IEEE Trans. Plasma Sci., **32**, 18-24 (2004).

[7] T. Inomata, S. Okazaki, T. Moriwaki, and M. Suzuki, "The Application of Silent Electric Discharges to Propagating Flames," *Combustion & Flame*, **50**, 361-363 (1983).

[8] M. S. Cha, S. M. Lee, K. T. Kim, S. H. Chung, Y. H. Song, and S. J. Kim "Soot Suppression in Coflow Jet Diffusion Flames using Dielectric Barrier Discharge," Proc. 4th Int. Symp. Non-thermal Plasma Technology, 315-321 (2004).

[9] L. A. Rosocha, D. M. Coates, D. Platts, and S. Stange, "Plasma-enhanced Combustion of Propane Using a Silent Discharge," *Phys. Plasmas*, **11**, 2950-2956 (2004).

[10] S. Stange, Y. Kim, V. Ferreri, L.A. Rosocha, and D.M. Coates, "Flame Images Indicating Combustion Enhancement by Dielectric Barrier Discharges," *IEEE Trans. Plasma Sci*. (to be published 2005).

[11] Y. Kim, S.M. Stange, L.A. Rosocha, V.W. Ferreri, "Enhancement of Propane Flame Stability by Dielectric Barrier Discharges," *J. Advanced Oxid. Technol*. (to be published 2005).

[12] T. Shirai, T. Tabata, H. Tawara, and Y. Itikawa, "Analytic cross sections for electron collisions with hydrocarbons: CH_4, C_2H_6, C_2H_4, C_2H_2, C_3H_8, and C_3H_6," *Atomic Data and Nuclear Data Tables* **80**, 147-204 (2002).

[13] L. Boesten, M.A. Dillon, H. Tanaka, M. Kimura, and H. Sato, "Elastic and vibrational excitation cross sections for collisions with propane," *J. Phys. B: Atomic Mol. Opt. Phys*. **27**, 1845-1855 (1994).

[14] T.C. Manley, "The Electrical Characteristics of the Ozonator Discharge," Tra*ns. Electrochemical Soc*. **84**, 83-95 (1943).

This work supported by the Laboratory Directed Research and Development program at the US DOE/NNSA Los Alamos National Laboratory, operated by the University of California.

Hydrogen production from biomass-ethanol at ambient temperature with novel diaphragm reactor

H. Okutsu[1], S. Asai[1], K. Urasaki[1], E. Kikuchi[1], M. Matsukata[1], S. Kado[2], F. Haga[3] and Y. Sekine[1]

[1] *Department of Applied Chemistry, School of Engineering and Science, Waseda University, Tokyo, Japan*
[2] *Ishikawadai 6-223A, Tokyo Institute of Technology, Ohokayama, Meguro, 152-8552, Tokyo*
[3] *Central Research Center, Nissan, 1, Natsushima, Yokosuka, 237-8523, Kanagawa*

ABSTRACT

We tried direct reforming of ethanol-water mixture using LEP discharge with a novel liquid fuel reforming process. We succeeded to produce hydrogen in high energy efficiency using a diaphragm. So in liquid phase discharge, the most important factor was the diameter of the pinhole on the diaphragm. So, it was important to focus electrons at the pinhole. Moreover, energy efficiency in this discharge reached up to 92 % by HHV based calculations.

INTRODUCTION

Recently, demand of hydrogen is increasing as hydrogen-energy-apparatuses (Fuel-cell) are becoming widely used. It is required to establish hydrogen production process of high efficiency. Some catalytic processes have been considered already, but these had many problems (requirement of high temperature, deactivation of catalyst and coking).

Low energy pulsed (LEP) discharge can solve these problems. This novel technique has noteworthy feature. LEP discharge do not requires high temperature or pressure, thus if reforming using LEP discharge is possible, the reaction takes place at room temperature and atmospheric pressure. This process has many advantages compared to conventional process. We have already succeeded in reforming of hydrocarbon using this LEP discharge [1]-[9].

Additionally, ethanol has a potential for being an alternative fuel replacing fossil fuels because ethanol can be produced from various renewable sources (biomass etc.). And it has many advantages like as transportation, storage and friendly to environment compared to methanol [10]-[11]. Last year, we succeeded to develop a new reforming process from ethanol-water mixture into synthesis gas in vapor phase using electrode of carbon fibers [12]-[13]. So we tried direct reforming of ethanol-water mixture using LEP discharge and purposed to suggest novel liquid fuel reforming process.

EXPERIMENTAL

Diaphragm discharge is a kind of new liquid phase discharge at ambient temperature and atmospheric pressure [14]-[15]. An outline image of the reactor and experimental apparatus are shown in Fig.1. As shown in Fig.1, this reactor consists of two pyrex tubes (inner diameter: 100 mm, outer diameter: 110 mm, total length: 300 mm) and a pair of electrodes is set in the liquid fuel. The insulated teflon-membrane (diaphragm membrane) having single pinhole (diameter: 0.25-2.0 mm) is placed between the two tubes.

This membrane seems to have very important role in this discharge. The pinhole centralized the charge, and by that a discharge in liquid phase was generated, and liquid phase reforming was advanced. We chose ethanol-water mixture as a reforming fuel. The gap distance of electrodes was maintained at 6.0 mm in this study. This novel process is so attractive, because it doesn't require any heaters and pumps. Additionally, the process does not include unreacted ethanol-water mixture in outlet gases.

All products in outlet gases were analyzed by a gas chromatography equipped with FID and TCD (Shimadzu; GC14-B). The liquid fuel after the reaction was analyzed by GC-MS (Shimadzu; GCMS-QP2010). The non-equilibrium pulsed discharge was generated by a DC power supply. Waveforms of current and voltage were observed by a high voltage probe (Textronix), a current prove (Textronix) and a digital phosphor oscilloscope (Textronix).

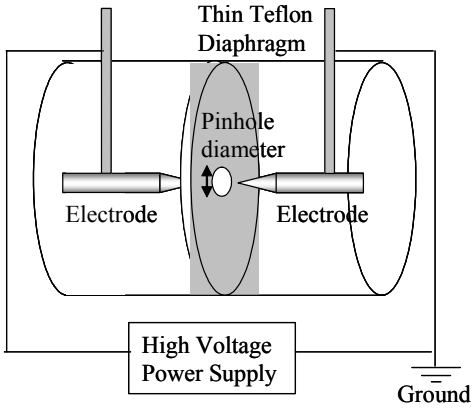

Figure 1. Outline for diaphragm discharge apparatus.

RESULTS AND DISCUSSION

1) Effect of a diaphragm membrane

We examined the diaphragm role in this discharge. So we compared results with and without the diaphragm. After the reaction without the diaphragm, the electrode was corroded and the discharge was not generated. It was considered that the pinhole on the diaphragm allowed electrons to move from high voltage side to ground side while ions and molecules were not allowed. Thereby, it controlled mass transfer and ionic reaction due to electrolysis. On the other hand, in the result with the diaphragm, it turned out that the electrode did not corrode and the discharge could be continued stably for a long time.

2) Shapes of electrodes

We investigated the correlation between shapes of electrodes and formation rates of products. Two types of electrodes which was a needle type (SUS304, outer diameter: 5.0 mm) or a flat-plate type (aluminum, outer diameter: 50.0 mm, thickness: 3.0 mm) were applied for this system. The result is shown in Fig.2, shapes of electrodes had a significant influence on gaseous formation rate in this reaction. In the reaction, hydrogen was generated predominately. In addition to hydrogen, CO, CH_4, C2 compounds (mainly C_2H_2) and small amount of CO_2 were produced. When using a couple of coaxial needle type of electrodes (Type A), the discharge showed the highest value of the formation rate of gaseous products. It was considered that the input power for dielectric breakdown was very low in Type A. It was very similar to the trend of selectivity in vapor phase reaction. On the other hand, diaphragm discharge with a couple of flat-plate electrodes was very difficult to control and the discharge was not generate.

Additionally, energy efficiency calculation based on LHV (lower heating value) is shown in Table 1. Energy efficiency (E_{eff}) based on LHV is defined as Eqn. 1.

$$\text{Energy efficiency} = (\Sigma E_{outoput} / \Sigma E_{input}) \times 100 \qquad (1)$$

Then, energy efficiency based on HHV (higher heating value) is defined as Eqn. 2.

$$\text{Energy efficiency} = ((\Sigma E_{output} + E_{lh}) / (\Sigma E_{input} + E_{lh})) \times 100 \qquad (2)$$

(E_{lh}: the value of latent heat of C_2H_5OH)

Energy efficiency was calculated by Eqn.(1) and Eqn. (2) in the following section. Input power and energy efficiency in this section are shown in Fig.3. Input power in Fig.3 is not the energy consumption of the discharge-gap but the presented value on the high voltage power supply. As the result of that, the energy efficiency was totally low, but type A showed the highest efficiency (LHV: 30.2 %, HHV: 30.8 %) in Fig.3.

Therefore the couple of coaxial needle type of electrodes was selected in the following experiments.

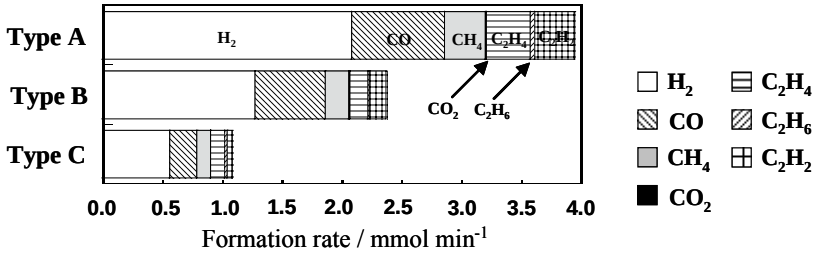

Figure 2. Effect of shapes of electrodes on gaseous products formation rates in diaphragm discharge.
Type A - needle to needle shapes ; Type B - needle to plate shapes ; Type C - plate to needle shapes.

Conditions : discharge gap : 6.0 mm, C_2H_5OH Concentration : 50 mol%, Pinhole diameter : 1.0 mm, Input Current : 15.0 mA, Diaphragm Thickness : 1.0 mm.

Table 1 Energy efficiency calculation based on LHV

Formula	Formation / Consumption rate mmol min^{-1}	ΔHc MJ / mol	Efficiency KJ / min
H_2O	0.069	0.00	0.00
C_2H_5OH	1.303	1.37	1.78
Electricity	82.5 W		4.95
E_{input}			6.73
H_2	2.076	0.242	0.502
CO	0.778	0.283	0.220
CH_4	0.340	0.890	0.303
CO_2	0.013	0.000	0.000
C_2H_6	0.044	1.56	0.068
C_2H_4	0.362	1.41	0.510
C_2H_2	0.332	1.30	0.431
E_{output}			2.035
Efficiency			30.2 %

Conditions : discharge gap: 6.0 mm, C_2H_5OH Concentration : 50 mol%, Pinhole diameter : 1.0 mm, Input Current : 15.0 mA, Diaphragm Thickness : 1.0 mm, shapes of electrodes: Type A

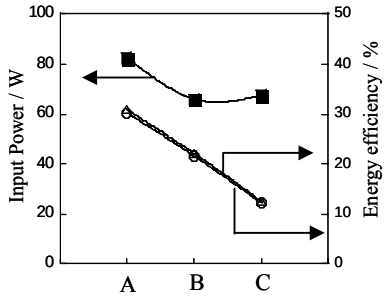

Figure 3. Effect of shapes of electrodes on energy efficiency in diaphragm discharge.
(○: Energy efficiency based LHV, △: Energy efficiency based HHV, ■: Input Power)
Conditions : discharge gap : 6.0 mm, C_2H_5OH Concentration : 50 mol%, Pinhole diameter : 1.0 mm, Input Current : 15.0 mA, Diaphragm Thickness : 1.0 mm.

4) Effect of input power

In this section, we investigated the effect of input power on gaseous formation rates and on carbon-selectivity. In Fig.4, the amount of product increased as the input power increased. The selectivity to carbon monoxide and C2 hydrocarbon were constant despite of the change of the input power. These results showed the same trend like as the gas phase reaction using LEP discharge. So it was proved that the number of electrons in the gap of electrodes serves as an important factor in this liquid phase discharge. In addition, the input power and energy efficiency are shown in Fig.5. The value of input power in Fig.6 was the presented value on high voltage power supply. As the same as Fig.4, energy efficiency increased as input power increased.

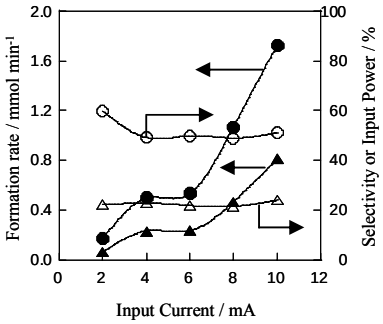

Figure 4. Effect of input current on gaseous formation rates and on carbon selectivity.
(○: H_2 Selectivity, △: CO Selectivity,
●: H_2 formation rate, ▲: CO formation rate)

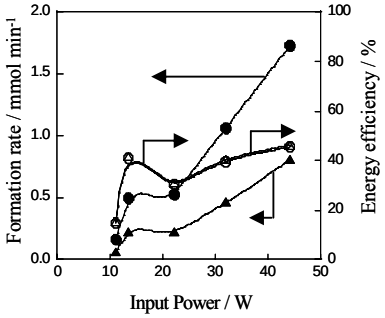

Figure 5. Effect of shapes of electrodes on energy efficiency in diaphragm discharge.
(○: Energy efficiency based LHV,
△: Energy efficiency based HHV,
■: Input Power, ●: H_2 formation rate,

Conditions : discharge gap : 6.0 mm, C_2H_5OH Concentration : 50 mol%, Pinhole diameter : 0.5 mm, diaphragm Thickness : 1.0 mm.

5) Effect of the diameter of pinhole on the diaphragm

The influence of the diameter of the diaphragm pinhole was discussed. The correlation between input power for dielectric breakdown and the pinhole diameter (0.25~2.0 mm) was examined. Results are shown in Fig.6. The power was very high when the pinhole diameter was large. It gave suggestion that focusing electrons on the pinhole was very important. Consequently, we examined the effect of the diameter of pinhole on gaseous formation rates and on energy efficiency. The trend is shown in Fig.7. Even if the diameter of pinhole on the diaphragm was small, gaseous formation rates were not affected because the electron focusing energy was too high. So, the diaphragm membrane was damaged. Therefore, the optimal pinhole diameter was between 0.5 and 1.0 mm. On the other hand, energy efficiency in this range showed very high. When the pinhole was 0.25 mm, the energy efficiency showed as high as 92 % (HHV based).

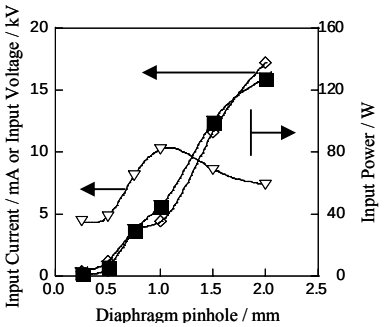

Figure 6. Effect of pinhole diameter on Input power for dielectric breakdown
(◇: Input Current, ▽: Input Voltage,
■: Input Power)

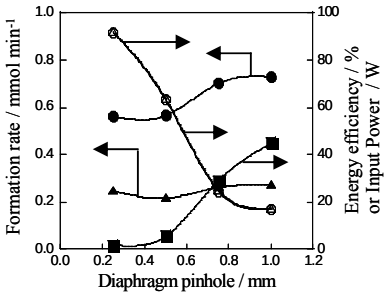

Figure 7. Effect of pinhole diameter on gaseous formation rates and on carbon selectivity.
(○: Energy efficiency based LHV,
△: Energy efficiency based HHV,
■: Input Power, ●: H_2 formation rate,

Conditions : discharge gap : 6.0 mm, C_2H_5OH Concentration : 50 mol%, Diaphragm Thickness : 1.0 mm.

6) Influence of diaphragm thickness

As previously noted, in this liquid phase discharge, focusing electrons on the pinhole was very important. In this section, we investigated the influence of diaphragm thickness (the length of focusing electron's pass) on this discharge. Fig.8 shows the correlation between diaphragm thickness and input power for dielectric breakdown. In Fig.8, we could not observe a remarkable trend. Then, the effect of diaphragm thickness on gaseous formation rate and energy efficiency is shown in Fig.9. As the same as Fig.8, we could not get noteworthy trends. Whereby, the important element in this discharge was not the focused electrons volume, but the focused electrons density.

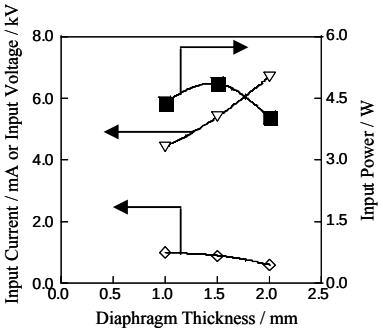

Figure 8. Effect of diaphragm thickness on input power.
(◇: Input Current, ▽: Input Voltage,
■: Input Power)

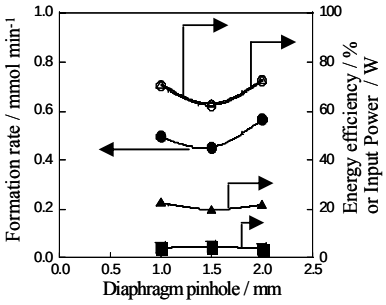

Figure 9 Effect of diaphragm thickness on gaseous formation rates and on carbon selectivity
(○: Energy efficiency based LHV,
△: Energy efficiency based HHV,
■: Input Power, ●: H_2 formation rate,

Conditions : discharge gap : 6.0 mm, C_2H_5OH Concentration : 50 mol%, Pinhole diameter : 0.50 mm

CONCLUSIONS

Using diaphragm membrane, liquid phase discharge was succeeded at ambient temperature and atmospheric pressure. The main gas in products obtained was H_2. In addition to H_2, CO, CH_4, C2 compounds (mainly C_2H_2) and small amounts of CO_2 were produced. First, as a consequence of the effect of shapes of the electrode, a couple of coaxial needle type of electrodes showed the highest yield and stable discharge. Next, we examined the effect of input power on the discharge. The gaseous formation rates showed the trend of increase as increase of input power. This results was as same as the vapor phase discharge (the reforming of C_2H_5OH using the electrode of carbon fibers). Additionally, we investigated the effect of diaphragm pinhole on the discharge. It showed that input power for dielectric breakdown could be very low when diaphragm pinhole was small. Therefore, in this discharge, the most important factor was diameter of diaphragm pinhole, in other words, it was important to focus electrons on the microscopic pinhole. On the other side, diaphragm thickness was not very important in the discharge. Finally, we examined energy efficiency at all conditions. As the consequence of that, energy efficiency in the discharge reached up to 92 % (LHV and HHV based calculations). The ability to generate hydrogen in this condition showed 96 MJ kgH_2^{-1}. And in order to increase energy efficiency, the electrode of coaxial needle type should be selected, and the input power should be increased and the diameter of diaphragm pinhole should be small. It was prospective to use this reformer in the future for hydrogen manufacturing process, because the reformer was very simple and small.

REFERENCES

(1) Y. Sekine, S. Asai, K. Urasaki, M. Matsukata, E. Kikuchi, S. Kado, F. Haga, *Chem. Lett.*, in press.
(2) S. Kado, K. Urasaki, Y. Sekine and K. Fujimoto, *Chem. Commun.*, 415-416 (2001)
(3) Y. Sekine, K. Urasaki, S. Asai, M. Matsukata, E. Kikuchi and S. Kado, *Chem. Commun.*, 78-79 (2005)
(4) Y. Sekine, K. Urasaki, S. Asai, M. Matsukata, E. Kikuchi and S. Kado, *Energy & Fuels*, 18(2), 455-459 (2004)
(5) S. Kado, K. Urasaki, Y. Sekine, K. Fujimoto, T. Nozaki, K. Okazaki, *Fuel,* 82, 2291-2297 (2003)
(6) S. Kado, K. Urasaki, H. Nakagawa, K. Miura and Y. Sekine, *ACS Books Utilization of Green House Gas*, 852, 303-313 (2003)
(7) S. Kado, Y. Sekine, T. Nozaki and K. Okazaki, *Cat, Today*, 89(1-2) 47-55 (2004)
(8) S. Kado, Y. Sekine, K. Urasaki, K. Okazaki and T. Nozaki, *Stud. Surf, Sci, Catal.*, 147, 577-582 (2004)
(9) K. Urasaki, S.Asai, M. Matsukata, E. Kikuchi, S. Kado and Y. Sekine, *abstracts of 16th international symposium on Plasma Chemistry*, 225 (2003)
(10) Y. Sekine, S. Asai, K. Urasaki, E. Kikuchi, M. Matsukata, S. Kado, F. Haga, B. Fabien, *Proc. PCC,* 21-2 (2004)
(11) J. Llorca, P. Ramirez de la Piscina, J. Sales, N. Homs, *Chem. Commun.*, 641 (2001)
(12) R. D. Cortright, R. R. Davda, J. A. Dumesic, *Nature*, 418, 964 (2002)
(13) Y. Sekine, S. Asai, K. Urasaki, E. Kikuchi, M. Matsukata and S. Kado, *abstracts of 16th international symposium on Plasma Chemistry*, 822 (2003)
(14) A.Brablec, P. Slavicek, M. Simor, P. St'ahel, D. Trunec, M. Cernak, *abstracts of 16th international symposium on Plasma Chemistry* 782 (2003)
(15) Zdenka Stara, Frantisek Krcma, Zuzana Raskova, *abstracts of 16th international symposium on Plasma Chemistry* 296 (2003)

Atmospheric Pressure Normal Glow DC Microplasma in Air

D. Staack, B. Farouk, A. Gutsol, A. Fridman
Department of Mechanical Engineering and Mechanics, Drexel University, Philadelphia, PA, USA

Abstract

DC glow discharges were generated between a thin cylindrical electrode and a flat surface in atmospheric pressure air. Voltage-current characteristics and visualization of the discharge indicate operation in the normal glow regime. N_2 emission spectroscopy indicates a non-equilibrium plasma with T_{rot}= 750K to 1550K and T_{vib}= 4500K. Inter-electrode spacing ranged from 20 μm to 1.3 cm. The radius of the positive column is about 100 μm. This size is important in preventing thermal instabilities and the transition to an arc.

DC Glow Discharge, Microplasma

1. Introduction

The formation of spatially uniform, non-equilibrium atmospheric pressure plasma discharges[1] are desirable due to their potential industrial applications [2]. The non-equilibrium translational (T_{trans}), rotational (T_{rot}), vibrational (T_{vib}), and electron (T_e) temperatures ($T_{trans} = T_{rot} < T_{vib} < T_e$) allows them to be used for materials processing applications such as deposition and etching used in the semiconductor manufacturing industry without the need for expensive vacuum systems. One of the most studied non-equilibrium plasma discharge at vacuum pressures is the normal glow discharge [3]. Glow discharges at higher pressures are generally unattainable due to instabilities which lead to a glow-to-arc transition (GAT) [1]. As the pressure is increased the current density increases until reaching the threshold for the development of instabilities leading to a transition to the arc phase and an equilibrium plasma. Generally the thermal instability is suppressed in low pressure discharges by cooling at the walls.

For over 50 years methods to create DC glow discharges at up to atmospheric pressures have been known. Fan [4] used water cooling of the electrodes and stable discharges were achievable in hydrogen and nitrogen at up to 2A. In air, though appearing as a stable glow, even at the lowest currents tested (~100mA) high frequency transitions between glow and arc were noted. Gambling and Edels [5], created glow discharges in air for currents between 10mA and 0.5A noting a stable arc above 0.5A. Several methods have been tried to stabilize the glow discharge and prevent glow to arc transition (GAT). In DC glow discharges at atmospheric pressure, high speed gas flows have been used to provide sufficient cooling of discharges at high pressures [6]. DC microhollow cathode discharges (MHCD) have been reported by Sankaran et al.[7-10] and Stark and Schoenbach [11-13]. The MHCD of Sankaran and Giapis is flow stabilized and operates at up to 20 mA. Stark and Schoenbach operated the MHCD in atmospheric pressure air for current up to 22 mA. Stark and Schoenbach report the discharge being stabilized because the microhollow cathode supplies electrons to the positive column of the discharge rather than the instability-prone cathode region as in a traditional glow discharge.

In this paper, we report recent investigations showing the operation of glow discharges in atmospheric pressure air at lower currents than reported by Gambling and Edels [5]. At lower currents no fluctuating glow-to-arc transitions are seen, and a glow discharge is observable without any surrounding diffuse glow as seen by Gambling and Edels [5]. At these currents the discharge is shown to be stable with diameters of about 100 μm. Current-voltage measurements, visualization and parametric studies of the discharge show it to be a normal glow discharge. Analysis for low pressure normal glow discharges applied to this discharge agree well with experimentally measured values further indicating a normal DC glow discharge. Optical emission spectroscopy shows the discharge to be non-thermal although translational temperatures are between 750K and 1550K. Estimations of the heating and diffusion time show the non-thermal discharge is stable due to its small radius. High pressure discharges stabilized by operating with small characteristic dimension have been termed microplasmas [14].

2. Experimental Setup

The circuit used to generate the glow discharge is similar to that used in low pressure glow discharges. Figure 1 is a schematic of the setup used for creating and analyzing the discharge. A DC power supply is connected in series to a ballast resistor a shunt resistor and the discharge. Various values of shunt resistor, ballast

resistor, power supply polarity, and applied voltage were used depending on the regime of study. For studies in the normal glow discharge regime in air the shunt voltage was 1 kΩ and the ballast was 100 kΩ. The shunt resistor is connected to a voltmeter or an oscilloscope for DC or time dependant current measurements respectively. Typically the power supply voltage was set and the discharge voltage was calculated from the measured current on the shunt and known resistance values. The lower electrode is made from stainless steel. The upper electrode is a steel wire positioning stage which controls the spacing between the wire tip and the lower electrode.

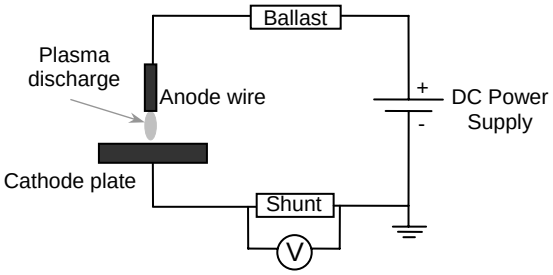

Figure 1: Electrical circuit used to generate and analyze the glow discharge.

For visualizing the discharge a 640x480 resolution Sony CCD-iris color video camera was mounted to a microscope focused on the discharge. The microscope-camera setup provided a variable magnification allowing between a 2mm x 1.5mm and a 20mm x 15mm field of view. For spectroscopy an Acton Research SpectraPro 500i scanning monochromator was used. The entrance slit to the monochromator was placed ~1" from the discharge. Optical emission spectra (OES) of the discharge were taken in a range of 200-450 nm averaging emission from the entire discharge. A roper scientific model 7430 CCD camera was mounted to the exit slit to digitally acquire the spectra at approximately 0.6 nm resolution. Typical acquisition times for the CCD image were 1-5secs. Background images with the discharge off were subtracted and a low pressure mercury lamp was used to determine the slit (apparatus) function and calibrate the spectrometer.

3. Experimental Results and Discussion

Figure 2 shows a series of images of the glow discharge at increasing electrode spacing. The anode is the wire coming from the top of the image and the cathode is the surface along the bottom edge of the image. For electrode spacings of 0.1, 0.5, 1 ,3 and 13 mm the voltages across the plasma required to sustain the discharge were 385, 430, 505, 780, 1450 Volts respectively. Images (a), (b) and (c) were taken at the same magnification; image (d) and (e) were taken at a decreased magnification. Similar to a vacuum glow discharge near the cathode we see the 'Negative Glow' region which maintains approximately the same length as the electrode spacing is increased. Moving up from the 'negative glow' we have the 'Faraday dark space' followed by the 'positive column'. The discharge does not completely cover the electrodes or fill the region between the electrodes. For the same discharge current and same gap spacing with differing electrode sizes the shape and size of the discharge are identical. These general visualizations of our glow discharge match those of a low pressure normal glow. From these images at atmospheric pressure the cathode sheath is unresolved and less than 10 μm in thickness. The occurrence of luminous and non-luminous regions is a major indication that the discharge is a non-thermal discharge. These images are similar to those of Gambling and Edels [5] except that at these low current no diffuse glow surrounding the primary column is seen.

From Figure 2 we see that at increasing electrode spacing the length of the negative glow remains constant while the length of the positive column changes. This is consistent with the discharge being a glow discharge and the electric field in the primary column can be attained by measuring the change in discharge voltage as a function of electrode spacing while maintaining the discharge current constant. For discharge currents of 1.0, 2.1, 5.1 and 10.2 the corresponding electric fields in the positive column were 4.5, 3.8, 2.3 and 1.4 kV/cm. Discharges with large *d* (>1.5mm) as shown in Figures 2 could be created in two ways. If a power supply with sufficient high voltage capability was used the discharge could be directly initiated. An alternative method was to initiate the discharge at smaller *d* and then extend the discharge by moving the upper electrode.

Since the required breakdown voltage was not available in these cases the discharge was only marginally stable. A large disturbance, for example a significant gas flow, could extinguish the discharge. Larger discharge currents were more stable than smaller discharge current.

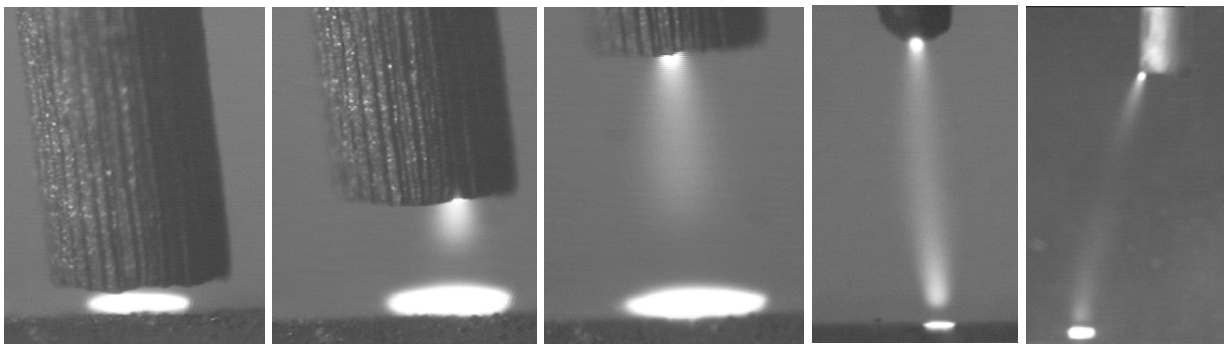

Figure 2: Images of glow discharge in atmospheric pressure air at (a) 0.1 mm, (b) 0.5 mm, (c) 1 mm, (d) 3 mm and (e) 13 mm electrode spacings.

The dimensions of the positive column, and negative glow were estimated from images such as those shown in Figure 2. The cross sectional area of the discharge was then calculated assuming that the negative glow and positive column were cylindrical in shape. Using the measured area and discharge current the current density in the negative glow and positive column regions was calculated. Figure 3a is a plot of the current density in the negative glow and the positive column as a function of current for several different electrode spacings. Figure 5b is a plot of the width of the negative flow and positive. As can be seen from figure 5a the current density in the negative glow region is nearly constant at a value of 5.95 A/cm^2. The occurrence of a constant or normal current density in the cathode region is another hallmark indicating that the discharge is a normal glow discharge. The positive column has increasing current density with increasing current and a nearly constant size of the positive column.

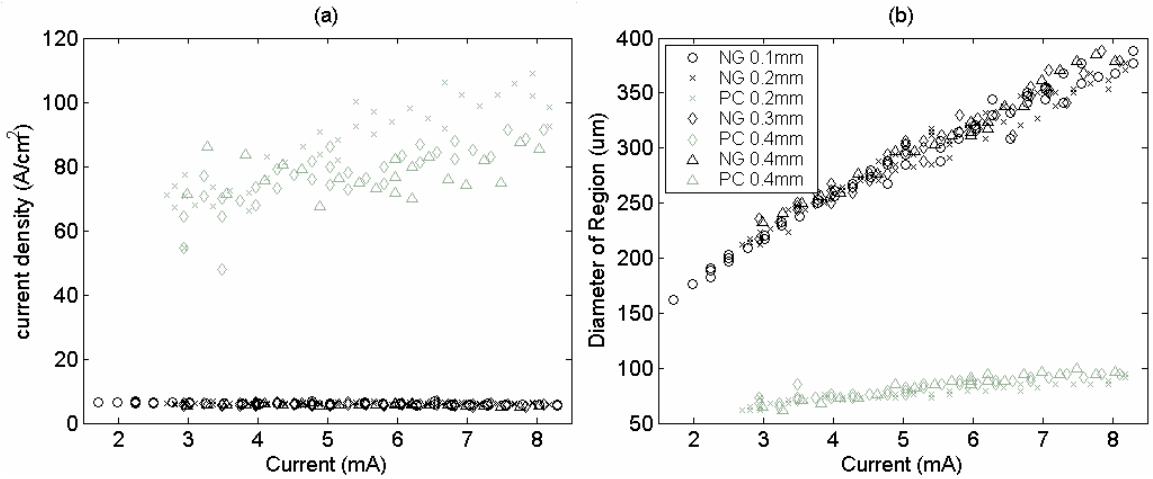

Figure 3: Plot of current density in (a), and diameter of (b) the negative glow (NG) and positive column (PC) regions of the discharge as a function of discharge current for electrode spacings between 0.1 and 0.4 mm. Discharge is in air and conditions correspond to those in Figure 3.

Figure 4 is a plot of discharge voltage vs. discharge current for electrode spacings between 20 μm and 3 mm. Errors in the electrode spacing of +/- 5 μm are due to thermal expansion of the wire and shortening of the gap at higher currents. Errors in current are +/- 20μA and errors in voltage are less than 10V. These plots are for a stainless steel anode and cathode, and with the upper wire electrode 0.8 mm in diameter as anode. The current was varied by changing the DC power supply voltage with a constant ballast resistor. Oscilloscope traces and Fourier power spectrums of the discharge current showed the current to be constant with no significant AC components. Over the range of currents shown all of the discharges were similar in structure to those of figure 2.

Shown in Figure 4 are discharges corresponding to powers between 50 mW to 5W. For the small spacing of electrodes the V-I characteristic is relatively flat. This is consistent with the idea of this being a normal glow discharge and with past measurement in atmospheric pressure glows [4, 5, 12] and MHCDs operating in normal glow mode [12]. For a normal glow discharge in air the normal cathode sheath potential drop is around 270V, the discharge voltage above that occurs mostly in the positive column. For the larger electrode spacing the V-I characteristic the positive concavity and negative slope is more indicative of a subnormal regime. The breakdown voltage to initiate the glow discharge followed the general trends of a Paschen curve. The equation $V_{br} = 940ln(d)+5750$, where d is the electrode spacing in cm and V_{br} is the breakdown voltage, fit our data to within 2% for d between 40μm and 1.5 mm.

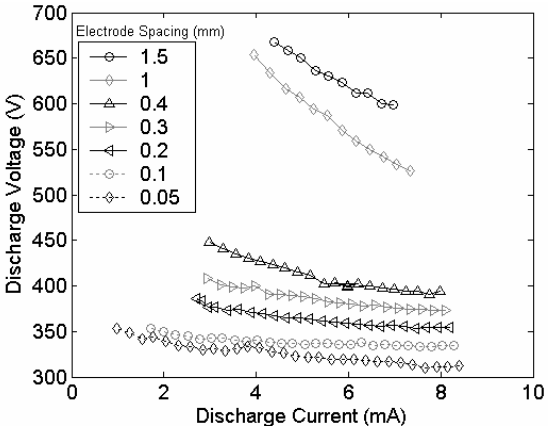

Figure 4: Voltage current characteristics for plasma discharge in air at several electrode spacings.

Figure 5a is the OES from the glow discharge in air between 200 and 450 nm. The brightest lines between 300 and 450 nm are due to the nitrogen 2nd positive electronic transition $N_2(C^3\Pi_u\text{-}B^3\Pi_g)$ and its family of vibrational and rotational level subtransitions. In the ultra violet region between 200 and 300 nm there are weaker NO lines from the $NO(A^2\Sigma^+, v'\text{-}X, v'')$ electronic transition. No OH line which exceeded the height of the tail of the N_2 2nd positive transitions was visible at 308 nm. Some significant N_2+ first negative $N_2^+(B_2\Sigma^+_u\text{-}X^2\Sigma^+_g)$ transitions were also visible in the violet range.

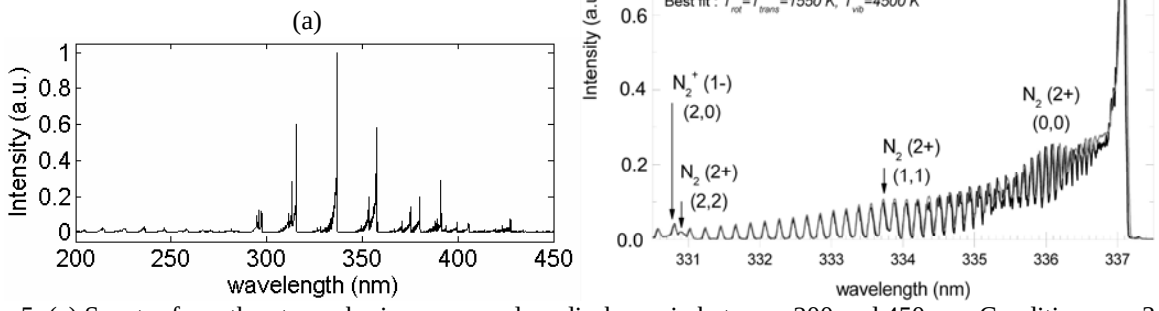

Figure 5: (a) Spectra from the atmospheric pressure glow discharge in between 200 and 450 nm. Conditions are 3.8mA discharge in air with 150 μm electrode spacing. (b) Measured OES and curvefit using SPECAIR for 10mA glow discharge in atmospheric pressure air.

Figure 5b is the measured spectra and a curvefit using SPECAIR at 10mA discharge current. The strongest line is the N_2 2nd+ (0-0) at 337 nm and it overlaps with other lines in the 330 to 337 nm range as listed on the figure. The comb like peaks to the left of 337nm correspond to the rotational sublevels of the transition. The relative heights of these rotational transitions are related to the rotational temperature, T_{rot}. The relative

heights of transitions with different initial vibrational energies are related to the vibrational temperature T_{vib}. SPECAIR[15] a spectroscopic modeling code developed at Stanford was used to model the spectra from these transitions[16]. A least squares curvefit between the modeled spectra and the experimental spectra was using T_{rot} and T_{vib} as fitting parameters. The determined temperatures were 1550K and 4500K for rotation and vibration respectively. These temperatures indicate the non-equilibrium nature of the discharge and are similar to the 1700K-2000K rotational temperature measured in a MHCD [17]. At 0.1mA discharge current similar spectral measurements indicate T_{rot}=750K and T_{vib}=5000K. A decrease in temperature with discharge power is to be expected. At 10mA thermocouples placed 5 mm from the discharge measured an increase from room temperature of about 50K. This indicates temperature gradients on the order of or greater than 2400K/cm.

4. Analysis

Based upon the various measurements detailed above the discharge may be considered a normal glow discharge. Significant formulations are available to describe the parameters of a low pressure normal glow discharge and can be compared to our experimental results. Many of these formulations assume a room temperature gas typical of low pressure glow discharges. Also many of the heuristic invariants are listed in terms of pressure when in fact they are functions of number density. For variable temperatures as high as 1500K in the glow discharge this effect needs to be taken into account. The replacement of p in the relations by an effective pressure $p*T_n/T$ is sufficient in most cases, where p is the pressure in torr, T_n is the normal gas temperature (~293K) and T is the actual gas temperature.

The low pressure normal glow current density for Air and an iron electrode at room temperature from the literature is approximately 300 $\mu A/cm^2\text{-}torr^2$. Using the effective pressure: $j=j_n p^2(T_n/T)^2$ where j_n is the normal current density at room temperature (300 $\mu A/cm^2\text{-}torr^2$). For our conditions of p=760 torr and T=1500K the calculated normal glow current density in the cathode regions is 6.6 A/cm^2. The experimentally measured current density was 6 A/cm^2. The correspondence between the experimentally measured current density and the normal glow current density is further evidence that the discharge is a normal glow discharge at atmospheric pressure. The normal cathode layer thickness and normal cathode potential drop are also consistent with our experimental results as discussed earlier. The electric field can also be estimated. E/p for low pressure glow discharges is typically in the range of 10 to 30 V/cm-torr. Again using an effective pressure, electric fields at 760 Torr and 1500K should be in the range of 1.5 to 4.5 kV/cm. These values are consistent with those measured. E/n can also be determined from the discharge regime. If the discharge is controlled by electron attachment the frequencies of ionization and electron attachment which are both function of E/n will be equal. In air this occurs at $E/n = 13\text{x}10^{-16}$ V/cm^{-2} [18]. At 1550K this corresponds to an electric field of 6.1 kV/cm about a factor four higher than measured at 10mA. If the discharge is controlled by particle diffusion out of the discharge the Engel-Steenbeck relation holds [18]. Taking into account the gas temperature of 1550K and discharge radius of 50μm the electron temperature should be around 1.4eV which corresponds with an E/n of $6\text{x}10^{-16}$ V/cm^{-2} and an electric field of 2.8 kV/cm closer to the experimental value.

These estimations further indicate that the discharge is a normal glow discharge. Building on these estimations we can explain the stability of the discharge. We can show that the discharge is stable due to its small size; a neutral is able to leave the volume of the discharge before it gets too hot. To estimate this consider the diffusion time of a neutral out of a cylindrical volume and the heating time of a neutral in that volume. The time for a neutral to diffuse out of the discharge is the cooling time, τ_c, and is related to the diffusion coefficient, D, and the radius of the cylindrical volume, R. $\tau_c \approx R^2/4D$. D is proportional to the mean free path and the molecular speed and thus has a $T^{3/2}/p$ dependence. D is 0.147 cm^2/sec for N_2 in room temperature atmospheric pressure air.

The heating time for a single neutral is the inverse of the electron density n_e times the rate constant for vibrational excitation of the neutral, k_{ven}. For molecular gases like air the vibrational excitation of the molecule is the fastest mode of energy transfer between the electrons and the neutrals. For nitrogen and 1 eV electrons k_{ven} is $4\text{x}10^{-9}$ cm^3/s. n_e, can be estimated from the current density, j, and the electron drift velocity v_d. The drift velocity corresponding to our E/n is $6\text{x}10^6$ cm/s. The current density, j, calculated before was for the negative glow. In the positive column the current density may be controlled by other mechanisms, the measured current density of

about 80 A/cm^2 corresponds to a n_e of 8x10^{13}cm^{-3}. The heating time for the discharge is thus calculated to be 3 μs. Equating the heating and cooling time gives an estimate for the size of a stable discharge at 45μm. The calculated radius of a stable discharge (45μm) and the experimentally measured discharge radius (30-50μm) are of the same order. This indicates that the discharge can be thermally stable due to its size.

5. Conclusions

We have generated atmospheric pressure microplasma discharges in our laboratories. Several experimentally observed facts lead us to believe this is an atmospheric pressure normal glow discharge. 1) Visualization of the discharge show distinct bright and dark regions corresponding to the 'negative glow', 'Faraday dark space' and 'positive column' of a glow discharge. 2) Voltage-current characteristics of these discharges are relatively flat and are in the regime of a normal glow discharge. 3) Current density measurements indicate a constant current density with increasing discharge current in the 'negative glow' region. Additionally, low pressure normal glow discharge heuristics accurately apply to our atmospheric pressure discharge. Correspondence is seen with experimentally measured values of the current density and electric field. The accurate application of normal glow discharge physics further indicates that the atmospheric pressure discharge is a normal glow discharge. Spectroscopic temperature measurements indicate that the discharge is a non-thermal, non-equilibrium discharge, T_{vib} = 5000K > T_{trans} = 750 to 1550 K. Low pressure normal glow discharges are also non-thermal; however, gas temperatures are lower and typically near room temperature. Estimations also show that the non-thermal glow discharge is stable because of its size. For ~100μm diameter discharges the diffusion time out of the discharge volume is approximately the same as the heating time within the volume.

For low currents and small gap length the discharge the discharge behaves as a normal glow discharge. The breakdown characteristics are also similar to low pressure discharges. However, explorations at high current (greater than approximately 10mA) and large electrode spacing (greater than approximately 1 mm) indicate that the discharge can appear less like a normal glow discharge without transitioning to an arc. At large electrode spacing the discharge begins to bend and is only sustained with higher currents. At larger current the primary column also appears as a diffuse glow.

Acknowledgment: This work reported is supported by the National Science Foundation under Grants DMII-0200062 and DMII-0423409.

6. References

[1] Kunhardt E E 2000 *IEEE Trans. Plasma Sci.* **28** 189
[2] Schutze A, Jeong J Y, Babayan S E, Park J, Selwyn G S and Hicks R F 1998 *IEEE Trans. Plasma Sci.* **26** 1685
[3] Raizer Y P 1997 *Gas Discharge Physics.* (Berlin: Springer)
[4] Fan H Y 1939 *Phys. Rev.* **55** 769
[5] Gambling W A and Edels H 1956 *British Journal of Applied Physics* **5** 36
[6] Yu L, Laux C O, Packan D M and Kruger C H 2002 *J. Appl. Phys.* **91** 2678
[7] Sankaran R M and Giapis K P 2001 *Appl. Phys. Lett.* **79** 593
[8] Sankaran R M and Giapis K P 2002 *Journal of Applied Physics* **92** 2406
[9] Sankaran R M and Giapis K P 2003 *Journal of Physics D: Applied Physics* **36** 2914
[10] Sankaran R M, Giapis K P, Moselhy M and Schoenbach K H 2003 *Appl. Phys. Lett.* **83** 4728
[11] Stark R H and Schoenbach K H 1999 *Applied Physics Letters* **74** 3770
[12] Schoenbach K H, Moselhy M, Shi W and Bentley R 2003 *J. Vac. Sci. Technol, A* **21** 1260
[13] Stark R H and Schoenbach K H 2001 *Journal of Applied Physics* **89** 3568
[14] Hsu D D and Graves D B 2003 *Journal of Physics D: Applied Physics* **36** 2898
[15] Laux C O, Spence T G, Kruger C H and Zare R N 2003 *Plasma Sources Sci. Technol.* **12** 125
[16] Laux CO, 2005, personal communications
[17] Block R, Roedter O and Schoenbach K H 1999 *30th Plasmadynamics and Lasers Conference AIAA-99-3434* Norfolk, VA
[18] Fridman A and Kennedy L A 2004 *Plasma Physics and Engineering* (New York: Taylor & Francis Books Inc)

Electroluminescence of silicon nanoparticles in LED structures.

Jiří Stuchlík [1*], The Ha Stuchlíková [1], Ivan Pelant [1], Anton Fojtík [2], and Jan Valenta [3]

[1] *Institute of Physics, Academy of Sciences of the Czech Republic, Cukrovarnická 10, 16253, Prague 6, Czech Republic.*
[2] *Department of Physical Electronics, Faculty of Nuclear Sciences and Physical Ingineering, Czech Technical University in Prague, V Holešovičkách 2, 18000, Prague 8, Czech Republic.*
[3] *Department of Chemical Physics & Optics, Faculty of Mathematics & Physics, Charles University, Ke Karlovu 3, 12116, Prague 2, Czech Republic.*
[*] *corresponding author: stuj@fzu.cz*

A modified method of synthesis has been used to prepare highly luminescent crystalline silicon nanopaticles (Si-NP).These particles, which are coated by an oxide layer, are prepared by combustion of silane (SiH_4) [1]. Photoluminescence (PL) situated in the red to yellow spectral range 650-850 nm has been activated by etching the Si-NP in two phase cyclohexane /propanol-2 solutions mixed with hydrofluoric acid. A thin homogeneous layer (about 20 nm) of these Si-NP, sized about 2nm and having PL maximum at ~650nm was used to prepared light emitting p-i-n diodes (LED) operated at room temperature. Their cross section is shown in Fig. 1(a). The current-voltage curves show basic properties of good rectifying diodes with rectification factor of about 10^5. Electroluminescence (EL) images and spectra are studied by a microscope connected to an imaging spectrograph with an intensified CCD camera. EL spectra are broad, covering almost all visible range with peak around 600 nm. The decay of EL excited by current pulses is shown to be comparable to photoluminescence decay, i.e. it has stretch exponential form with dominant decay time of tens of microseconds (depending on wavelength). The unique properties of our Si-NC based LED will be compared to other types of Si-NC LEDs.

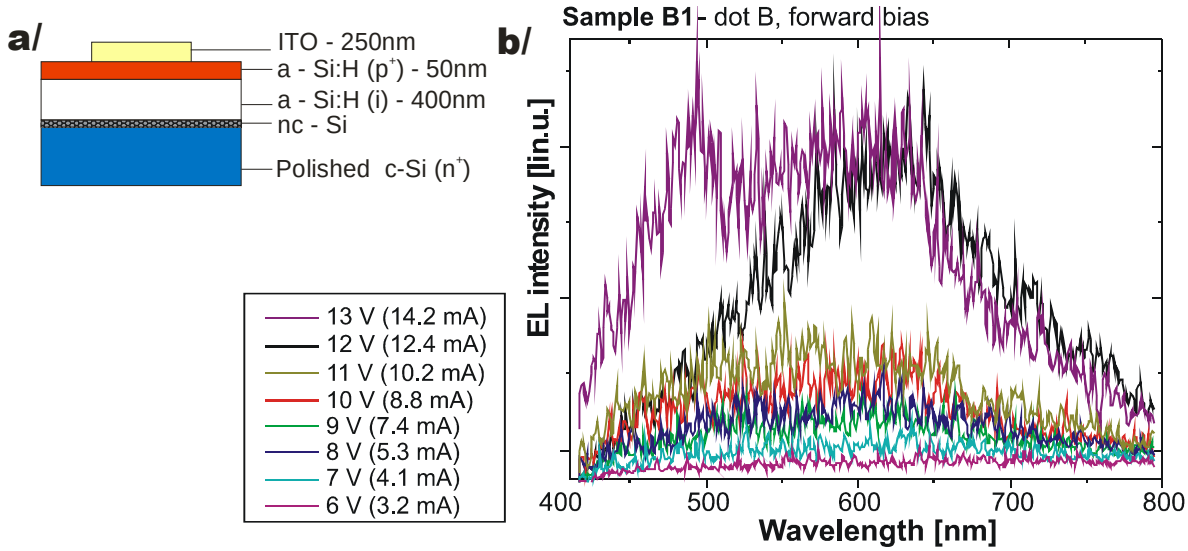

Fig. 1: (a) A schematics of the LED structure. (b) The EL spectra of one emitting spot under various forward bias voltages from 6 to 13 V (indicated in the inserted label).

References

[1] A. Fojtik and A. Henglein, *Chem. Phys. Letters* **221** (1994) 363-367

INFLUENCE OF OZONE TREATMENT ON GERMINATION OF COTTON SEEDS

I.Onishchenko[1], A.Sharudo[2], V.Avtonomov[3], V.Golota[1], P.Ibragimov[3], A.Kamardin[2], A.Khodjaev[2], S.Shilo[1], G.Sotnikov[1], G.Taran[1], L.Zavada[1]

[1] NSC Kharkov Institute of Physics and Technology, Kharkov, Ukraine
[2] Scientific-Technological Center of New Technologies, Tashkent, Uzbekistan.
[3] Institute of selection and seed-growing of cotton, Tashkent, Uzbekistan.

Abstract

The influence of treatment of middle-fiber cotton seeds of C6540 and C6524 sorts (G.hirsutum L.) in ozone-air mixture on germination and energy of germination in dependence of exposition dose and time delay after seed's treatment have been studied. For this purpose the ozonizing installation of productivity 100 g ozone per hour and the technology of seeds treatment by ozone-air mixture have been elaborated. It has been shown that the treatment of cotton seeds by ozone results in enhancing both of germination and energy of germination up to 15-20%.

Introduction

Existing methods of pre-sowing treatment of seeds are based on desinfection of seed material by various toxic reagents, such as: vitavaks, raksil etc.[1]. Providing positive results, these methods have a number of the negative sides connected with the danger of poisoning of operating personnel and environment pollution. Proceeding from this, during the last years in many countries the investigations on search, development and usage of new technologies of pre-sowing treatment of seeds of different agricultural cultures have been carried out. The analysis of different alternate technologies of stimulation of processes of seeds germination has shown, that one of the most effective ways of an activation of seeds material is its treatment in gas atmosphere with some concentration of ozone (ozone treatment) [2]. It is stipulated by that the ozone shows complex influence on seeds, as the actuating and deodorizing agent, and the technologies of ozone application are enough simple, ecological clean and safe. The ozone is received directly at the place of it usage, and after treatment ozone decays up to oxygen, which does not pollute environment.

In the given work our investigations on influence of treatment of middle-fiber cotton seeds of new variety C-6540 and widely cultivated on territory of Central Asia variety C-6524 (G.hirsutum L.), in ozone-air mixture are presented. Investigations at various concentration of ozone depending on exposure time and time of seeds storage after treatment ("binning") have been carried out. The purpose of performed investigations was creation of special ozonizing installations and developing an optimum regime of treatment of cotton seeds that provides energization of process of germination of the seed material, and development on this basis of a new non-polluting technology of pre-sowing treatment and disinfection of cotton seeds with ozone and replacement of the old methods based on chemicals usage.

Technique of investigations

Treatment of seeds by ozone was carried out with help of the compact ozonizing installation "Ozone-Uzb-100" by productivity 100 g ozone per hour that was developed for this aim in NSC «Kharkov Institute of Physics and Technology». This installation is the generator of ozone synthesis of a new generation, which is based on use of the high pressure discharge in oxygen-containing gas, e.g. in air at atmosphere pressure Discharge is ignited in a coaxial system between the tubular cathode and sectioned many needle anode and is supplied by a high-voltage source of direct current. Discharge gap does not contain a dielectric barrier. It favorably distinguishes the developed non-barrier ozonizer from conventional barrier ozonizers as it does not suffer at all of accidental spark breakdowns in discharge gap and is considerably more technological at manufacturing. The main constituents of the generator of ozone "Ozone-Uzb-100" are the block of ozone synthesis, system of high-voltage direct-current feed (voltage up to 18 κV, current up to 65 mA), system of pumping of working gas of efficiency 100 m^3/hour, the monitoring system of electrical and gas

performances, and cooling system.

Treated seeds were loaded into hermetic container by volume of 10 liters, in bottom part of which the ozone-air mixture was fed with the help of oilless compressor. Depending on speed of air flow and a charge current in ozonizers it was possible to receive in working volume the concentration of ozone in a range 0.2 – 9.0 g/m^3. Lots of 600 tomentous seeds were exposed to treatment by ozone. They were settled down in working volume in mesh containers motionlessly. After treatment the seeds were stored required time ("binning") in linen bags at temperature 20-25^{0}C and then were sowed by sets of 150 seeds in standard baths made from the zinced iron of the size 130mm x 260mm x 40mm., filled with sand. Preliminary sand was sifted through special sieves so that to select grains of sand in the size 0.5-1.0mm., then the selected grains of sand were carefully washed out by flowing water after that it was gotten tempered at temperature 400^{0}C during several hours. Treatment of seeds was made at humidity of an environment of 50-60% and temperature 20-25^{0}C. Sprouting was made at average daily temperature 25-28^{0}C and humidity of 65%. Watering of sprouting seeds was carried out in the same time of day by boiled water cooled up to 25^{0}C. Energy of germination was determined on the fifth day, and germination of seeds on the seventh day after their sowing. By results of three measurements average value of germination and energy of germination of seeds for each concentration, exposure time, and time of seeds storage after treatment ("binning") were determined.

It is necessary to note, that in experiments cotton seeds of superstrain of variety C-6540 and C-6524 were used. The seed material is shaped at the collecting of cotton from 2 to 8 simpodial branch. In total for the season of vegetation on a cotton bush can form 16 and more simpodial branches. In our investigations cotton seeds collected from all bush, which did not subjected to any presort and treatment, were used.

Results and discussion

X-ray analysis (fig.1), performed for control untreated seeds of both varieties, selected randomly, has shown, that "fullness" of seeds was equal 97-98 %. This value displayed the maximal possible quantity of viable seeds. Despite of a so high index of vitality the germination of control untreated seeds (average value) was 64 % for variety C-6540 and 72 % for variety C-6524, i.e. about 25-35 % of seeds did not give plantlets.

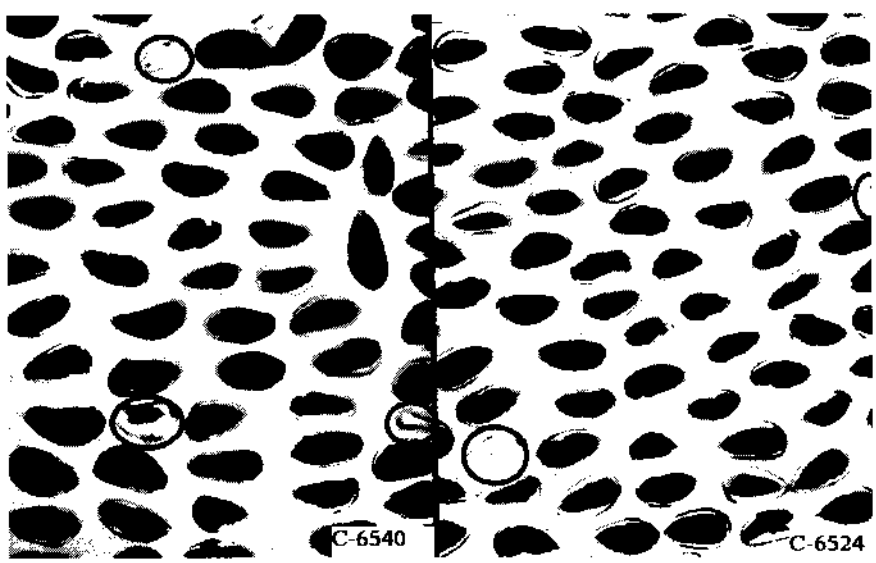

Fig.1. X-ray images of cotton seeds. Empty seeds are marked by a circle.

After treatment of similar seeds in ozone-air mixture the parameters of growth varied. At small concentration of ozone (0.2-2.0 g/m^3) depending on exposure time germination of seeds of variety C-6524 grew approximately by 10-15 % and for variety C-6540 by 5-10% in comparison with the control untreated seeds. The most essential change of germination was obtained not at once, but only after some time delay ("binning" time) after treatment. In that time treated seeds were stored in linen bags at a stationary temperature ~20^{0}C. The most favorable day occurred 5th day and 10th day after treatment for variety C-6524

and for variety C-6540, accordingly. At that energy of germination of seeds of variety C-6540 increased by ~10 %, and seeds of variety C-6524 it was even lower, than for control untreated seeds.

Increase of ozone concentration up to average values (3.0-5.0 g/m^3) resulted in increase seeds germination by value of 15-20% at exposure time 40 minutes. So at treatment of cotton seeds of variety C-6540 by ozone-air mixture with ozone concentration of 5 g/m^3 at exposure time of 40 minutes germination of seeds grew from 64% for the control untreated seeds up to 80 % at time of "binning" 10 days. At the same parameters energy of germination of the above-mentioned seeds increased from 21 % up to 51 % at time of "binning" 7 days and from 21% up to 30% at time of "binning" 10 days. For cotton seeds of variety C-6524 similar results have been obtained: at 7 day of "binning" germination grew from 72% up to 88%, and energy of germination grew from 28 % up to 70%. The increase in exposure time in an ozone-air mixture above 50 minutes and increase in terms of seeds "binning" after treatment more than 10 days, as a rule, resulted in reduction of considered parameters.

In Fig. 2 dependences of germination and energy of germination of cotton seeds treated in ozone-air mixture at ozone concentration of 5 g/m^3 are presented. It is seen that in considered regime of treatment of cotton seeds simultaneous increase of germination and energy of germination was observed.

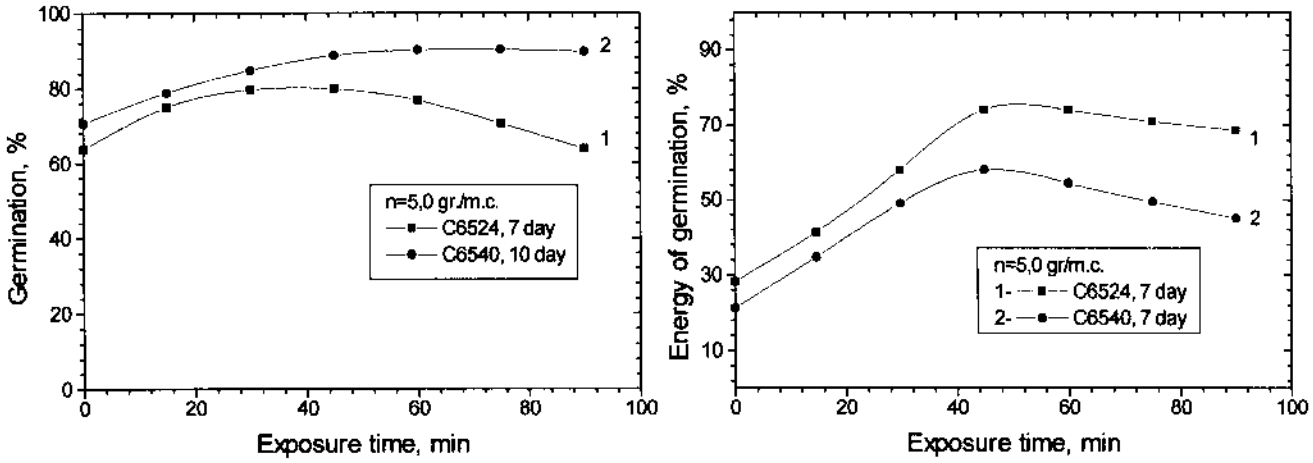

Fig.2. Dependence of germination and energy of germination of cotton seeds subjected to treatment in ozone-air mixture at ozone concentration of 5 g/m^3 on exposure time.

In Fig. 3 the dependences of germination and energy of germination of cotton seeds of both varieties for various terms of "binning" are presented. As it is seen, for cotton seeds of variety C-6524 a maximum of germination and energy of germination were observed at "binning" of 7 day, while for cotton seeds of variety C-6540 a maximum of germination was observed at "binning" of 10 day, and maximum of energy of germination was observed at "binning" of 7 day. The difference in value of germination at "binning" in 7 and 10 day for seeds of variety C-6540 made a value ~2-3 %, but energy of germination for this period varied up to 20%. From our point of view, the peak of seeds activity came for 7 day.

The further increase in concentration of ozone in working volume up to 7,0-9,0 g/m^3 result in more higher germination than for untreated control seeds, but it begins to be reduced in comparison with similar values for medium concentrations of ozone.

General result of the carried out investigations is that fact, that the treatment of cotton seeds in ozone-air mixture results in activation of seeds and enhancement of their growth – energy of germination and germination of cotton seeds.

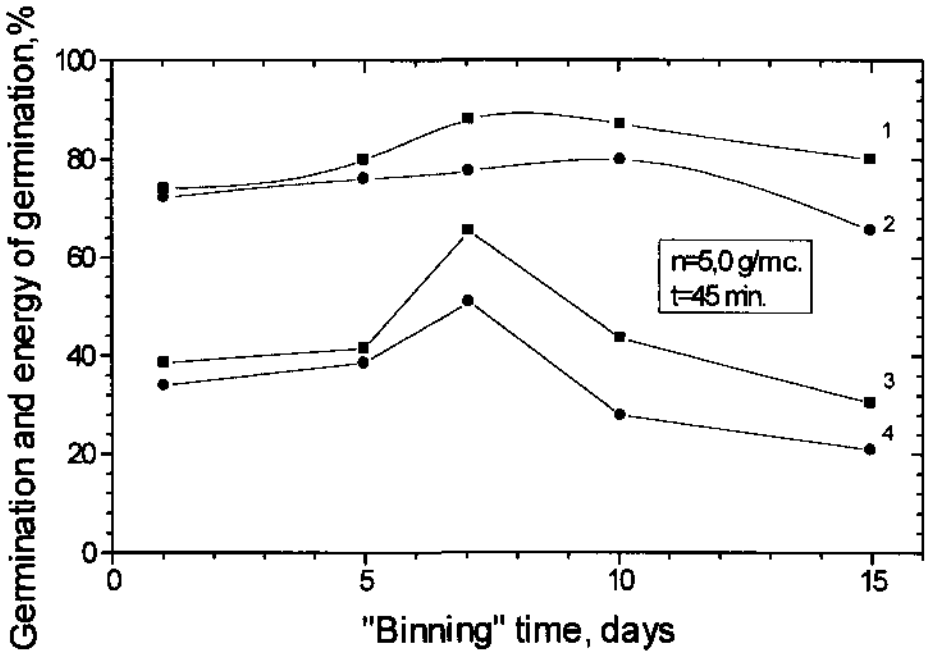

Fig.3. Dependence of growth parameters of cotton seeds from time of "binning": 1- germination of seeds C-6524, 2- germination of seeds C-6540, 3- energy of germination C-6524, 4- energy of germination C-6540

After determination of an optimum regime of cotton seeds treatment the additional experiment on influence of treatment time on germination and energy of germination of cotton seeds was carried out. As it was already noted, increasing in exposure time more than ~50 minutes or increasing of ozone concentration up to 7,0-9,0 g/m^3 results in decreasing of germination of cotton seeds, i.e. the process of depressing of an energy of germination and germination of seeds begins. In the experiment cotton seeds subjected to long-time treatment (2,5-15 hours) in ozone-air mixture at ozone concentration n=5,0 g/m^3. The results on determination of germination of cotton seeds on 7th, 10th and 13th day after their sowing are shown in the Table 1.

Table 1. Germination of cotton seeds treated in ozone-air mixture

№	Variety	Concentration of ozone, g/m^3	Treatment time, hours	Germination, %		
				on 7th day	on 10th day	on 13th day
1	C-6540	0	0	64	70	78
2	C-6540	5	0,6	83	87	88
3	C-6540	5	2,5	57	83	84
4	C-6540	5	5,0	0	78	80
5	C-6540	5	8,0	0	50	76
6	C-6540	5	15,0	0	40	74
7	C-6524	0	0	71	85	93
8	C-6524	5	0,6	95	96	98
9	C-6524	5	2,5	65	81	84
10	C-6524	5	5,0	64	70	72
11	C-6524	5	8,0	0	59	70
12	C-6524	5	15,0	0	52	85

As it is seen from Table 1, the long-time treatment of cotton seeds in ozone-air mixture of medium concentration of ozone, has not resulted in full depressing of seeds growth, and has led only to decreasing of percent of germination and delay in seeds growth. So, if at treatment during 0,6 hours the germination of seeds of varieties C-6540 and C-6524 already on 7th day after sowing was 83% and 95%, accordingly, after treatment during 2,5 hours the germination is reduced up to 57% and 65%. The further increasing in

exposure time reduces the percent of germination even more, down to zero value at 8-15 hour of treatment. But on 10^{th} day even these seeds have sprouted and percent of germination was 40% and 52%, accordingly.

From the table 1 it is seen, that the maximum of germination of control untreated seeds was observed on 13^{th} day after sowing. At the same time after treatment of cotton seeds in ozone-air mixture, already on 7^{th} day the germination was equal 83% and 95%, and in subsequent days this parameter increased some more. It indicated that seeds were more «active» and we saved time of about 6^{th} days. The presence of such "reserve" in time can promote strengthening of sprouted seeds, which subsequently will have an effect on force of the cotton plant.

Thus, the correctly chosen regime of treatment of seed material, can activate the process of seeds growth and increase their germination and energy of germination.

Conclusion

The carried out investigations on influence of treatment of cotton seeds in a ozone-air mixture have shown, that the similar treatment results in activation of process of seeds growth. There is a varietal difference of response of cotton seeds on effect of ozone for different varieties of seeds. It is necessary to take into account at choice of treatment regimes. From the performed investigations optimum regime of treatment of cotton seeds of varieties C-6540 and C-6524 has been determined.

The present work was supported STCU project Uzb-55J.

References

[1] "The method of fungicidal seeds treatment", ISM, 9 (1994).
[2] "Method of fighting against crops' diseases, carrying by seeds", ISM, 8 (1994)

Comprehensive spectroscopic study of argon glow discharge

A.A. Garamoon[1], A. Samir[1], F.F. Elakshar[1], A.Nosair[1] and E.F. Kotp[2]
[1]Center of Plasma Technology, Faculty of Science, Azhar University, Nasr City, Cairo, Egypt
[2]Physics Department, Faculty of Science, Alazhar University, Assuit Branch, Assuit, Egypt

Emission spectra of both positive column and negative glow regions of the DC glow discharge have been measured at different pressures and currents. The intensity of the lines in the negative glow is in the order of five times of that corresponding lines intensity in the positive column region. It is found that the line intensity increases linearly with the discharge current, while it increases as P^{α} with the gas pressure. The electron temperature has been estimated using the line-to-line intensity ratio technique. It is found that the electron temperature in negative glow region is about 3/2 of that in the positive column.

Introduction

The objective of plasma diagnostics is to obtain information about the state of the plasma by means of different experimental techniques. Knowledge of plasma characteristics is required to understand fully the effects of the different physical processes taking place in the plasma and to deduce from them its properties. These diagnostics includes electric probes and optical emission spectroscopy .

Usually, only probes are used routinely for measuring the temperature and density of electrons and ions. However, in magnetized or depositing plasmas in particular, the interpretation of probe characteristics is difficult and can lead to erroneous results **[1]**. Optical methods such as emission, absorption, , laser scattering or fluorescence spectrometry are proven techniques for probing various parts of the plasma without disturbing its state and composition **[2]**.

Among these techniques there is the optical emission spectroscopy **[3]**. This technique is based on the measurement of the optical radiation emitted from the plasma as it reflects the properties of the plasma in the immediate environment of atomic , molecular and ionic radiators **[4]**. The radiation is the result of electron or ion interaction with other particles in the plasma. Because of their high velocity, electron interactions tend to dominate the collisional excitation and ionization processes. Three electron transitions may occur during these interactions:- bound-bound transitions, bound-free transitions, and free-free transitions. The light emitted as a result of these transitions forms line, band, or continuous spectra.

Atoms and ions of the working gas and trace impurities emit radiation when transitions of electrons occur between the various energy levels of the atomic system. The radiation is in the form of narrow spectral lines, unlike the continua of free-electron radiation such as bremsstrahlung **[5]**. Four plasma models, were suggested by **McWhirter** [6], which are dependent on the mechanism of electron interaction. These are The local thermal equilibrium (LTE) model, The steady state corona model , The time dependent corona model and The collisional radiative (CR) model.

The methods used to measure the plasma parameters depend on the plasma model. Three methods are available for electron temperature measurement, these are:-

i- The ratio of two lines intensity.

ii- The ratio of a line to continuum intensity.

iii- The ratio of two parts of continuum intensities.

The first method will be used in the present work for the estimation of the mean electron temperature in the discharge .

Experimental setup

In this experiment a typical DC glow discharge between two parallel copper plates has taken place in a dynamic flow of argon gas the full description of it can be seen in Garamoon **[7].** McPherson scanning monochromator [model 270] with 35 cm focal length has been used, having a diffraction grating of 1200 grooves/mm has been used to scan the spectral lines. The resolution of this monochromator is less than 0.2 Å. The intensity of the light has been measured using a photomultiplier tube (type 9558QB). The output of the photomultiplier was recorded using a digital multimeter (type GDM-8145).

Results and discussion

Figures (1) and (2) show the emission spectrum of argon gas in positive column and negative glow regions respectively.

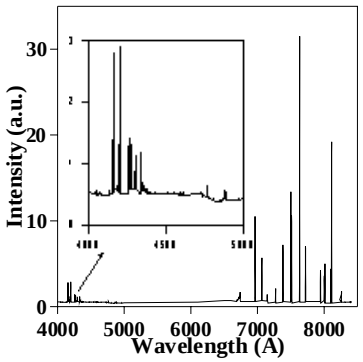

Fig. (1) emission spectrum of positive column at p= 2.25 torr and I= 10mA.

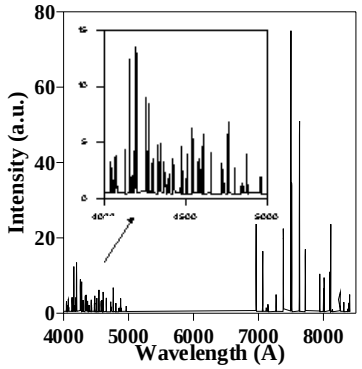

Fig. (2) emission spectrum of negative glow at p= 2.25 torr and I= 10mA.

All lines appeared in the spectrum have been identified as Ar and Ar^+ spectra.

Comparison between Fig (1) and Fig (2) shows that:

i) Intensity of lines in negative glow region is much higher than that in positive column region.

ii) Intensity of the lines in the long wavelength range (7000 - 8000 Å) in negative glow region is in the order two times of that corresponding intensity of lines in the positive column region. At shorter wavelengths (4000 - 5000 Å), however, the intensity of lines in the negative glow region is in the order of five times of the corresponding intensity of the lines in the positive column region.

iii) Lines of Ar^+ appear clearly in the negative glow, while they hardly appear in the positive column region.

The general increase of the intensity of the lines in the negative glow region can be attributed to the increase in the rate of exciting collisions due to both of the higher electron temperature and higher electron density in negative glow region rather than those in positive column. This discussion can explain why the ratio of the intensities of the lines in negative glow to that in positive column is much higher at short wavelengths than those at long wavelengths.

A comparison between the intensities of the two lines of neutral atom Ar and that of the singly ionized ion Ar^+, in positive column and negative glow regions has been represented in Fig. (3).

The intensity of the lines in positive column has been multiplied by a factor of 4, in order to be comparable with that in the negative glow. In negative glow region, the intensity of the line 4348Å is higher than that of the line 4334Å. In positive column region however, the line 4348Å hardly appears and its intensity is much lower than the intensity of the line 4334Å. Since ion density and the mean electron energy in negative glow is much higher than that in positive column region. the intensity of the lines in positive column has been multiplied by a factor of 4, in order to be comparable with that in the negative glow. In negative glow region, the intensity of the line 4348Å is higher than that of the line 4334Å. In positive column region however, the line 4348Å hardly appears and its intensity is much lower than the intensity of the line 4334Å . The intensity of the lines in positive column has been multiplied by a factor of 4, in order to be comparable with that in the negative glow. In negative glow region, the intensity of the line 4348Å is higher than that of the line 4334Å. In positive column region however, the line 4348Å hardly appears and its intensity is much lower than the intensity of the line 4334Å. Since ion density and the mean electron energy in negative glow is much higher than that in positive column, therefore the probability of exciting collisions of electrons with Ar^+ in negative glow region is higher than that in positive column. Consequently most of Ar^+ lines appear clearly in negative glow region and hardly appear in positive column region.

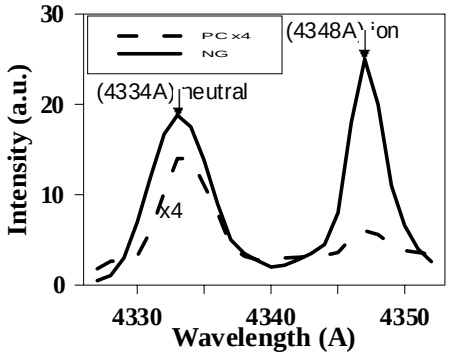

Fig. (3) emission spectrum from PC and NG of two lins; (4334A) neutral atom and (4348A) single Ion.

Figures (4) and (5) represent the line intensity of some lines as a function of the gas pressure in positive column and negative glow where intensity increases by increasing the gas pressure (*p*).

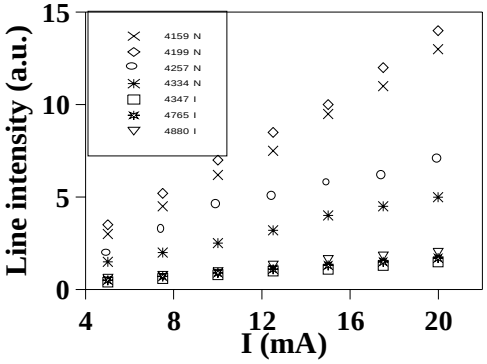

Fig. (4) line intensity, of 4 lines from neutral atom and 3 lines from ion, as a function of discharge current in positive column region P= 0.75 torr.

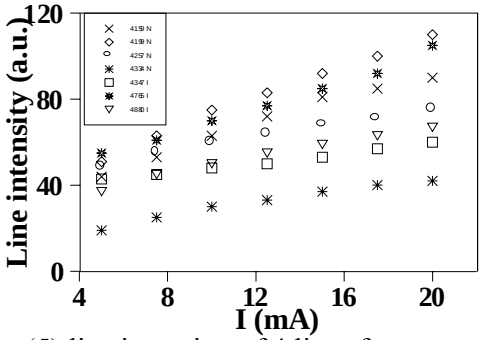

Fig. (5) line intensity, of 4 lines from neutral atom and 3 lines from ion, as a function of discharge current in negative glow region P= 0.75 torr.

The line intensity I_{pq} can be expressed in the form [8]:

$$I_{pq} = N_e N < Q_{pq}(v_e) v_e > \qquad (1)$$

where v_e is the electron velocity $\{v_e=(2kT_e/m_e)^{1/2}\}$, $Q_{pq}(v_e)$ is the excitation cross-section for the p-q transition, N_e is the electron density, and N is the density Ar atoms or the density of Ar^+ ions. As the gas pressure increases;

a) N_e and N increase, consequently the lines intensity increases.
b) T_e decreases and hence the rate coefficient of electron exciting collision $<Q_{pq}(v_e)\ v_e>$ decreases, consequently the intensity of the lines decreases whereas $v_e \sim T_e^{1/2}$.

In the range of p of 0.75 - 12 torr that has been used, the first factor is more effective than the second one. Therefore the intensity of the lines increases by increasing the gas pressure, where the intensity of the lines has been found to be proportional to p^{α}, where α is constant which varies between 0.2 - 0.5, and depends on the wavelength. Figures (6) and (7) show the variations of the line intensities as a function of the discharge current, I.

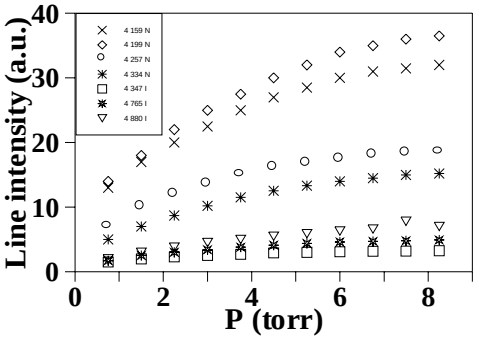

Fig. (6) line intensity, of 4 lines from neutral atom and 3 lines from ion, as a function of gas pressure in positive column region I= 20 mA.

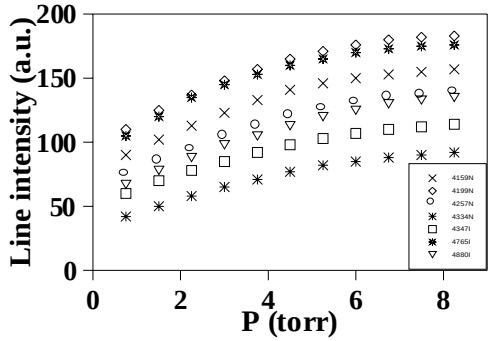

Fig. (7) line intensity, of 4 lines from neutral atom and 3 lines from ion, as a function of gas pressure in negative glow region I= 20 mA.

It can be noticed that, the lines intensity increases linearly by increasing the discharge current, i.e. $I_{pq} \sim I$, in general. This can be attributed to the increase in the electron density N_e which is a linear function of the current where, $I_{pq}=cI$ (mA), c is a constant which found to vary between 0.07 to 0.7 in positive column and 1.2 to 3.8 in negative glow and depends on the wave length.

Electron Temperature by Optical Emission Spectroscopy Technique.

Determination of T_e using optical emission spectroscopy technique the ratio of the intensity of two lines has been adopted here in the present work. For high accuracy it's desirable to choose two spectral lines whereas the ratio of the relative intensity of the two lines is a strong function of T_e; this will be the case if the difference between the transition energy levels of the two lines is large enough. However for neutral atoms, the greatest attainable energy difference yields a minimum uncertainty in temperature of 70 % for argon gas in the range of 0.5 to 1.5 eV **[9]**. The accuracy may

be improved somewhat by measuring several pairs of spectral lines and averaging the resulting temperatures. However this rather time-consuming technique is only partially successful in reducing the experimental uncertainty. A larger energy difference can be obtained if one of the transitions occurs in singly ionized atom, and the other occurs in a neutral atom. Therefore the relative intensity of argon neutral atom (4159 and 4259 Å) and argon singly ionized atom Ar^+ (4348, 4765, and 4880 Å) have been measured at different pressures and discharge currents in both NG and PC regions.

In the first trials if the present work , T_e has been determined assuming LTE model. Using the ratio of two lines intensity T_e can be expressed in the form:-

$$kT_e = \frac{E'-E}{\ln(I\lambda^3 g' f' / I' \lambda'^3 gf)} \qquad (2)$$

where I, λ, g, and f are the total intensity, wavelength, statistical weight, and absorption oscillator strength, respectively, of one line and E its excitation energy. The corresponding quantities for the other line are I', λ', g', f', and E'. The values of the above parameters have been taken from **[10]**.

T_e values obtained by this method, were in the range of 0.3 - 0.9 eV. These results are much smaller than the measurements of the electruc single and double probes. This may be attributed to the fact that the plasma density is so low that the criterion of LTE model is not valid i.e. that:

$$N_e \geq 1.6\times10^{12} T_e^{1/2} X(p,q)^3 \qquad cm^{-3} \qquad (3)$$

One the other hand the criterion of the steady state corona model i.e. that

$$N_e < 5.6\times10^{8} (z+1)^6 T_e^{1/2} \exp(\frac{1.16\times10^3 (z+1)^2}{T_e}) \qquad (4)$$

is valid in the present work. Consequently, steady state corona model has been assumed to estimate T_e. The ratio of two lines intensity T_e is expressed in the form :

$$\frac{I'}{I} = \frac{f' g' \lambda^3}{fg\lambda'^3} \exp(\frac{E'_\infty - E' - E_\infty + E}{kT_e}) \frac{S}{\alpha} \qquad (5)$$

where ; $$\frac{\alpha}{S} = (7.87\times10^{-9}) E'^2_\infty (\frac{E'_\infty}{kT_e})^{3/4} \exp(\frac{E'_\infty}{kT_e}) \qquad (6)$$

Eliminating S/α from equation (5) , therefore ;

$$kT_e = [(7.87\times10^{-9}) E'^{\,7/4}_\infty \frac{fgI'\lambda'^3}{f' g' I\lambda'^3} \exp(\frac{E'+E_\infty - E}{kT_e})]^{4/3} \qquad (7)$$

Values of the parameters used in equation (7) have been taken from **[10],** as tabulated in the following table.

λ (Å)	Transition	E (eV)	**J - J'**	f
4158.6	$1S_3 - 3P_6$	14.47	2 – 2	0.0017
4259.4	$1S_2 - 3P_1$	14.67	1 – 0	0.0022
4348.1	$3P^4 4S - 3P^4(3P)4P$ $[^4P - ^4D^o]$	19.41	5/2 – 7/2	0.43
4764.9	$3P^4 4S - 3P^4(3P)4P$ $[^2P - ^2D^o]$	19.78	1/2 - 3/2	0.37
4879.9	$3P^4 4S - 3P^4(3P)4P$ $[^2P - ^2P^o]$	19.6	3/2 – 5/2	0.35

The ratios of two lines intensities I'/I, one from single ionized atom and the other from neutral atom, have been estimated for six pairs of lines (4159/4348, 4159/4765, 4159/4880, 4259/4348, 4259/4765, and 4259/4880 Å).

Equation (7) shows that, T_e can not be written as an explicit function of the ratio of lines intensity [i.e. $T_e \neq f(I'/I)$]. The implicit function [$T_e = f(I'/I, T_e)$] can be solved numerically. Successive iteration has been curried out to solve equation (7). The guess point has been chosen using single and double probe measurements to accelerate the iteration process.

Figures (8) and (9) show values of T_e as a function of the gas pressure, using the six pairs of lines, in PC and NG respectively.

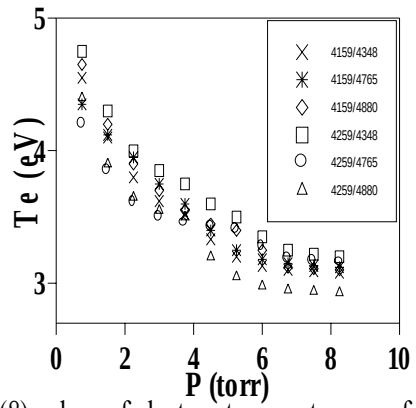

Fig. (8) values of electron temperature as a function of gas pressure in the positive column, using emission spectroscopy technique with different lines ratios.

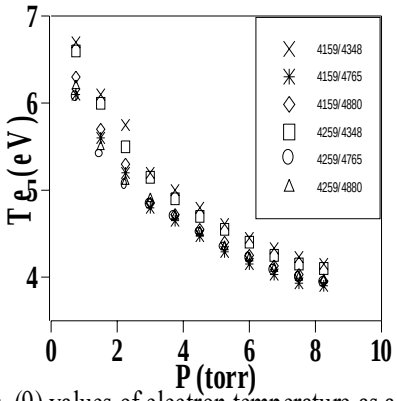

Fig. (9) values of electron temperature as a function of gas pressure in the negative glow, using emission spectroscopy technique with different lines ratios.

Figures (8) and (9) indicate a reasonable agreement of the estimated values of T_e and also that T_e has the same trend of behaviour with pressure using the different pairs of lines, i.e. , T_e decreases by increasing the gas pressure (p). Since the kinetic energy of an electron can be expressed as $mv^2/2 = eE\lambda_e$, where λ_e is the electron mean free path, so T_e is proportional to λ_e and hence inversely proportional to p. Also It can be noticed that the electron temperature in the negative glow region is about 3/2 of that in the positive column.

5-2-4 Comparison between the three techniques used to measure T_e

Figures (10) and (11) represent values of T_e as a function of the gas pressure in positive column and negative glow regions, respectively, using the average values measured by the three techniques i.e. single probe, double probe (the results of which to be published later separate) , and optical emission spectroscopy.

A good agreement between the three techniques is observed.[11} have confirmed a rough agreement between measurements of T_e by optical emission spectroscopy and single probe in Ar positive column. Figures (5-25) and (5-26) prove that, the agreement between optical emission spectroscopy and the probes techniques in the positive column region is much more closer than that in the negative glow region. This may be attributed to the fact that the distribution of electrons in the negative glow region is non-Maxwellian.

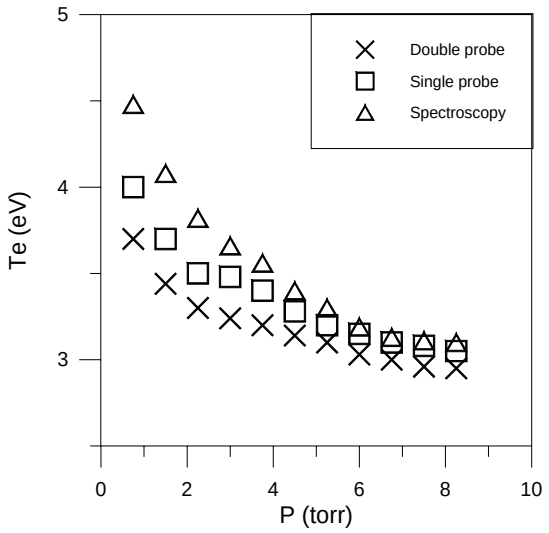

Fig. (10) values of electron temperature as a function of gas pressure measured by different techniques in positive column.

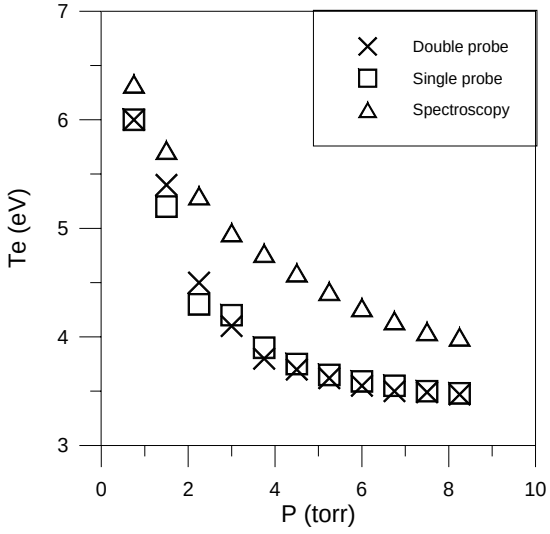

Fig. (11) values of electron temperature as a function of gas pressure measured by different techniques in negative glow.

References

1-Bech A. ,Hemmers D., Schweer H.B. and Uhlenbusch J., J.Phys.D: Appl.Phys.,33 (2000)
2-Hoppstock K. and Harroson W. W. ,Anal.Chem. ,67 (1995)
3- Meulenbroeks R. et al , Phys.Rev. E ,49 (1995)
4- Beheringer K. and Fantz Y. J.Phys. D: Appl. Phys. ,27 (1994)
5- Hutchinson I. H. " Principles of Plasma Diagnostics" , Cambridge Univ. Press (1990)
6- McWhirter R.W.P." Plasma Diagnostics Techniques ", edited by Huddlestone E. and Leonard S. L.,Academic Press , New York (1965)
7- Garamoon A. A. et al, Plasma Sources Sci. Technol., 12 (August 2003)
8- Sovie R. J., Phys. Fluid, 17, (1964)
9- Schmidt P. S. Inst.Tech., 22 (1975)
10- Griem H. R. ," Plasma Spectroscopy " McGraw-Hill , New York (1964)
11- Kano et al (2000, Plasma Sources Sci. Technol.,9 (2000)

Plasma Assisted Combustion of Non-Premixed Hydrocarbon Fuel in High-Speed Airflow

Klimov A., Bityurin V., Moralev I., Tolkunov B., Vystavkin N.
Institute of High Temperature RAS, Moscow, Russia

Abstract

Plasma-assisted combustion (PAC) in high-speed airflow was studied in our previous works [1-6]. Present work is devoted to continuation of internal PAC study. Experiments are carried out in the hot wind tunnel HWT-1. Supersonic airflow (M<2, P_{st}<1 Bar, T_{st}<1000K) is created in test section of this experimental set up. Combined electric discharge (DC+ pulse repetitive discharge, mean power ~1kW) is used for airflow pre-heating and fuel- airflow radical generation. Optical spectroscopy, IR spectroscopy and chromatographic method are used to study plasma and radical generation in PAC zone. Experimental and theoretical results on internal PAC are considered and discussed in this work.

Keywords: combustion, plasma, airflow, radicals, optical spectra

Introduction

It well knows that there are some difficulties connected with ignition, mixing and combustion of hydrocarbon fuel in high-speed airflow. These difficulties are connected with large characteristic ignition time τ_i and combustion time τ_c of hydrocarbon fuel in high-speed airflow at the parameters closed to scramjet ones. Active radical and exited molecule generation in combustion region can decrease these characteristic times considerably [1-6]. The active radicals O, H, CH, OH, NO, CN, CH2 and vibration exited molecules play important role in combustion process. Recently it was revealed that three radicals CN, C2, CH2 play most important role in plasma-assisted combustion namely [1-6]. Non-equilibrium electric discharge can generate these radicals effectively. It was revealed that characteristic propane ignition time τ_I and propane characteristic combustion time τ_c in supersonic airflow M~2 are decreased up to factor 2-3 by non-equilibrium plasma formation (in comparison with the ones at plasma off), [1].

The PAC of *non-premixed* hydrocarbon fuel in high-speed airflow (M<2) was studied in our previous works [1-6]. According obtained experimental background there are two main problems (tasks) in PAC physics, namely

- Fuel PAC completeness in high-speed airflow,
- Fuel mixing in high-speed airflow.

It is revealed that non-premixed PAC is non-homogeneous and non-stationary one as a rule. There is strong plasma-fuel combustion interference in high-speed airflow. Modulation of the discharge and plasma parameters by PAC disturbances and soot particles (carbon clusters) is measured in experiment.

Important role of charged and excited carbon clusters (soot particles) in PAC kinetics and dynamics is considered in the works [1-6]. These particles can accelerate and decelerate the PAC in airflow by its local electric field considerably.

Main experimental results.

1. Internal PAC is studied in experimental set up HWT-1, fig. 1. Hot wind tunnel HWT-1 is designed and manufactured to study PAC in high-speed airflow. Main technical characteristics of HWT-1 are the followings:

- Airflow parameters M<2, P_{st}< 1 Bar
- Airflow mass flux < 100 g/s

- Propane mass flux < 10 g/s
- Gas temperature in arc heater T_o< 1000K
- HF power of the igniter N_d< 2 kW
- Mean power of PG-jet N_d< 3 kW

HWT-1 is consisted of two quartz tubes. This duct design helps us to use optical diagnostic instrumentation in PAC experiment.

Two types of the plasma generators (PGs) are designed, manufactured and tested in PAC experiment, namely:

- Tesla's coil HF plasma generator for HF streamer discharge generation in high-speed airflow,
- PG- Comb for combined electric discharge generation (DC current discharge + high voltage pulses).

Mean power of each PG is about 2-3 kW.

2. Stable internal PAC stimulated by streamer HF discharge and combined discharge (DC discharge + pulse repetitive discharge) is created in a high-speed airflow (M< 2, P_{st}< 1 Bar), fig.2.

   Characteristic plasma parameters of a single HF streamer are the followings:

- Electron concentration N_e<10^{15} cm^3
- Electron temperature T_e=1-2 eV
- Gas temperature T_g=1000-2500K,
- Vibration temperature T_V~2500-7000K
- Specific energy storage ~1-10 J/cm^3
- HF streamer characteristic lifetime T_{str}~50-100 mcs.

   This plasma formation is non-equilibrium one. It has high specific energy storage. So, this plasma formation can stimulate plasma chemical reactions and radical generation in a fuel-airflow mixture.

3. It is revealed that HF streamer discharge has a number of important positive properties (peculiarities) in PAC experiment comparing with other types of electric discharges, namely:

- HF discharge is ignited and burned near a mixing contact surface with high gas density gradient (or near chemical flame front) as a rule, but it never burns inside chemical flame,
- Modulated HF streamer discharge can disturb mixing contact surface considerably and stimulate propane- air mixing (advanced mixing).
- Fuel penetrates through a HF streamer in external airflow deeply. Mean velocity of fuel transportation inside a streamer channel is about V_{fl}~ 10^3 m/s, and more. So, study of this fuel transportation by single HF streamer is very important for advanced fuel mixing.

4. Very small characteristic ignition time τ_1 and combustion time τ_2 are measured in PAC experiment (M< 1,2 , P_{st}< 1Bar, T_o~300K), namely: τ_1~ 30-50 mcs, τ_2~ 100-150 mcs. These experimental values $\tau_{1,2}$ are more than 100-1000 times smaller than traditional chemical ones at plasma off (at the same other conditions).
5. Radical creation by electric discharge is measured in PAC experiment, such as: CH, CH_2, O, O_3, CN, and others. Maximal relative concentration of radicals in PAC experiment is about N*~10^{-2} (our estimations).
6. Final products of PAC are H_2O and CO_2 only in near stoichiometric fuel-airflow mixtures (no toxic impurities and propane).
7. Additional small water vapour injection (propane: water ~ 100: 1) can intensify PAC (increase a mixing rate and combustion rate).
8. It is revealed that small HF power (about ~100W) is needed for the propane-air ignition and PAC. Total chemical power was about N_{ch}~16-17 kW, (it corresponds to propane mass flux M_p~0,4 g/s). So, ratio η= (N_d /N_{ch}) 100%= 0,1-1%.

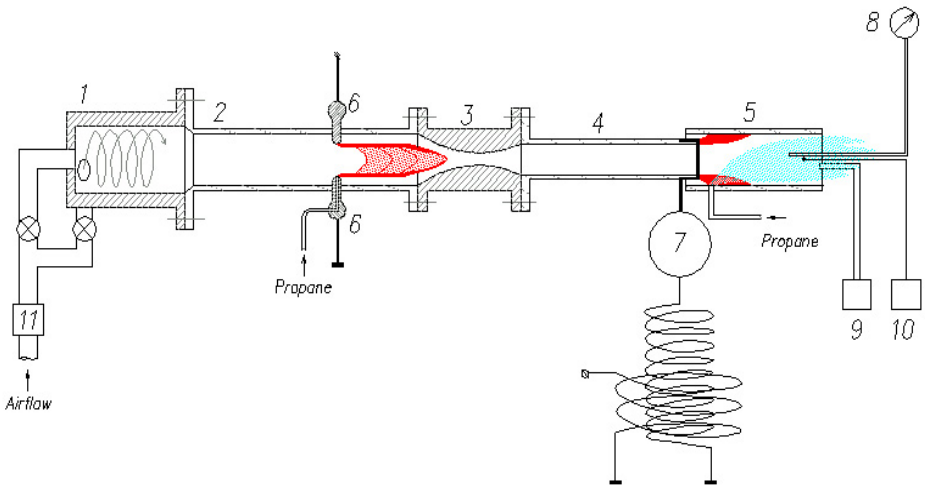

Fig.1. 1,2- fore-chamber with electric arc pre-heater, 3- nozzle, 4, 5- test section, 6-arc electrodes, 7- HF electrode, 8- pressure sensor, 9-chemical probe, 10- thermocouple, 11- mass airflow

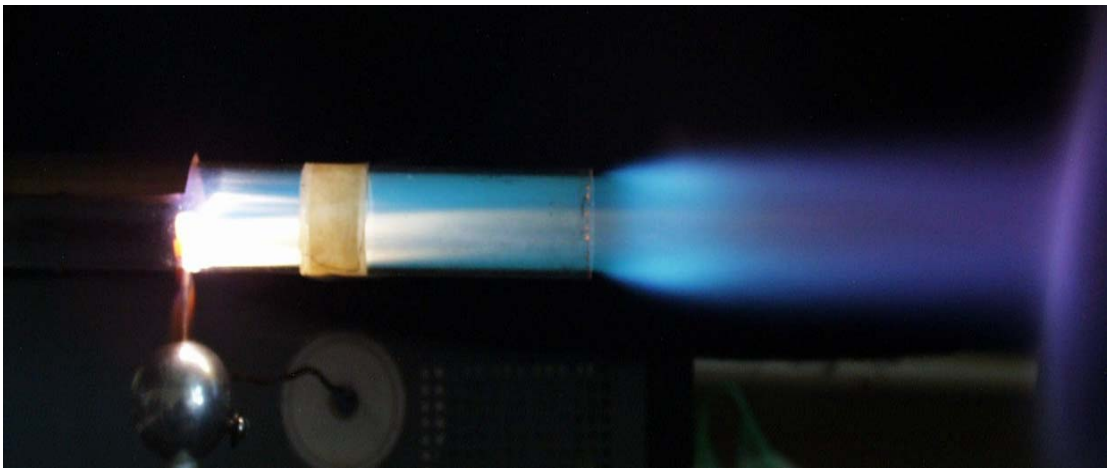

Fig. 2. Stable plasma-assisted combustion in the set up HWT-1 in high-speed airflow (M=0,6; P_{st}=1 Bar), HF discharge (F_{HF}=13,6 MHz), modulation frequency F_i~ 100Hz

9. Extension of fuel combustion concentration limit for rich and lean mixtures up is about 2-4 times at plasma assistance.
10. Combustion temperature limit is decreased up to 2-3 times at plasma assistance.
11. The final PAC specie composition is obtained by IR absorption method and chromatographic method. Partial pressures and concentrations of these species are measured, fig.3.
12. Effective H2, CO, C2H2, CH4…. generation is obtained in rich propane-airflow mixtures at plasma assistance
13. It is revealed that there is high fuel PAC completeness (80-100%) in lean fuel mixture only, fig. 3,4.
14. It is revealed that radical concentration in PAC zone is increased up to 2-3 times at non-intensive external UV radiation created by KrF laser.

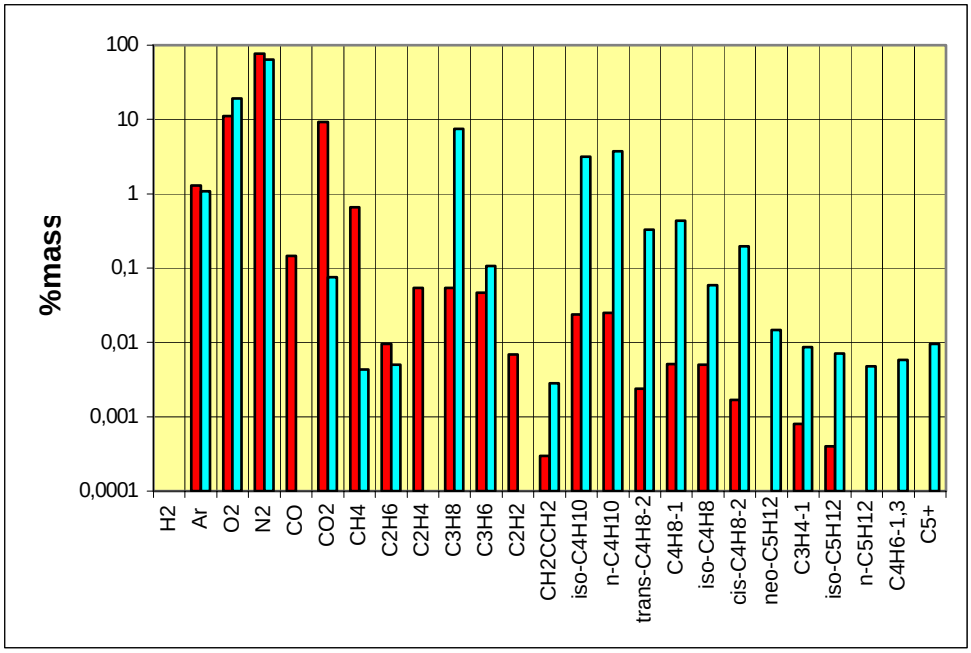

Fig.3. Final PAC species (red): - lean propane-butane mixture at plasma assistance, φ <2, M=0,1; P_{st}=1 Bar. Green - initial mixture at plasma off and combustion off

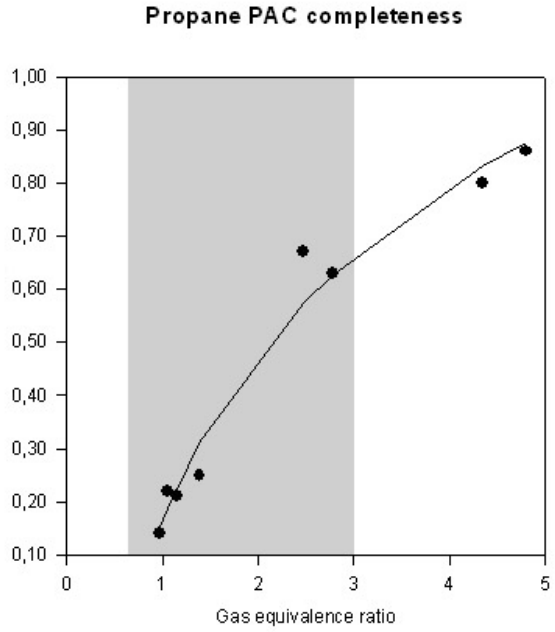

Fig. 4. Propane combustion completeness at plasma assistance in high-speed airflow. Combined electric discharge (DC discharge+ high voltage pulses), I_{DC}=1 Amp, M=0,1; P_{st}=1 Bar

PAC optical spectra

Analysis of optical spectra in PAC region is very important to study of plasma-chemical kinetics and PAC dynamics of hydrocarbon fuel in high-speed airflow. Detail optical spectra have been recorded by spectrometer MS-257 in different cross sections of PAC zone at different operation modes of the plasma generator.

The typical optical PAC spectra are shown in fig.5. These spectra are recorded in the PAC zone created by transverse DC discharge at electric current I_d=1 Amp and voltage U=500-1000 V. These spectra are obtained in stoichiometric, rich, and lean C_3H_8/C_4H_{10}-airflow mixtures (static pressure P_{st}=1Bar, M= 0,1). The following molecular bands are observed and processed:

- CN "violet" system. Sequences Δv= 0 (380-389 nm), Δv= -1 (415-430 nm), and Δ= -2 (455-461nm);
- C_2 Swan system. Sequences Δv=0 (510-517 nm), Δv=1 (467-474 nm), and Δv=-1 (558-564 nm);
- OH $^2\Sigma$-$^2\Pi$ system. Sequences Δv=0 (306-318 nm) and Δv=-1 (280-295 nm);
- NH $^3\Pi$-$^3\Sigma$ system in the 330-345 nm region;
- weak CH $^2\Delta$-$^2\Pi$ (0-0) band.

In some combustion regimes (closed to the stoichiometric one), there are well-pronounced electronic-vibration bands are appeared in the wave range of 597-620 nm (see Fig.5). Their nature is not clarified finally today. However it seems that the following consideration may be of relevant interest. Some of the optical lines in these spectrum are identified as the CH2 ones. Remember that this radical plays very important in PAC kinetics namely [x].

Among atomic lines, most pronounced are WI lines (coming from evaporation of the electrode material) in the regions of 280-305, 320-365, and 407-430 nm. The NI and OI lines in the near IR region.

The rotational T_r temperature and vibration T_v temperature in different regions of a non-uniform combustion zone are determined by performing a global fit of the above-mentioned spectral regions using the line-by-line numerical simulation of the rotational structure of the electronic transitions allowing for the experimentally derived apparatus function, fig.6.

It is revealed that there is the following ration:

$$T_e \geq T_v > T_r \approx 4000\text{-}5000\ K$$

in the cathode plasma filament region. There is the absolutely different relation in the intermediate zone between plasma filaments:

$$T_e \sim T_v \sim T_r \approx 4000\text{-}5000\ K$$

Note that average gas temperature T_g in PAC zone measured by optical pyrometer and thermocouple is about $T_g \sim 2000K$. The same value is obtained by processing of the continuous domain of the optic spectra, fig.x. One can suppose that there is non-homogeneous and non-stationary PAC in the combustor. The analysis of the high-speed video frames recorded in PAC zone proves this conclusion, fig. X.

Anomalous PAC kinetics in some operation mode of plasma generator

Anomalous plasma-chemical kinetics was revealed in lean mixture at some operation modes of plasma generator [x]. Traditional final combustion species (OH, CO, CO2…) were absent behind PAC zone in this regime.

Anomalous soot composition and final gas composition are obtained in rich mixture combustion at plasma assistance, fig.x. There are many carbon and silicon nana-tubes inside soot particles. Remember that high concentrations of the C2H2, C6H6 and other heavy species C7+ are created in this regime also.

High-energy release is measured in propane-argon mixture at plasma assistance. Thermal power of heated final gas flow behind PAC zone is about 6-10 times higher than initial chemical power of propane (its combustion energy in air). Note that this "combustion" is associated with active soot particle generation (high concentration) in PAC zone.

Chemical composition of the soot particles obtained in PAC region is studied by ion mass spectrometer and micro X-ray spectrometer. A number of new elements, such as Na, Al, Si, Cl, P, S, K, Ca, Cr, La and others, are recorded by diagnostic instrumentation inside these particles, fig.7,8. Note that these elements are absent in initial fuel, airflow and electrodes. Molecular ions NAr+, CAr+ , HAr+ and others are recorded inside tested soot particles by ion mass

spectrometer also (in fuel-argon-airflow mixture). There is a question: - how these *unstable ions* conserved inside of these soot particles during *long time period*? It is possible to suppose that different heterogeneous plasma-chemical reactions are realised on the soot particle surface.

It was revealed that charged and excited soot particles play important role in PAC kinetics, PAC completeness, electric discharge stability and flame stability [1-5]. The high local electric potential (up to φ~ 200-1000V) and high local electric field are measured on the surface of these particles (E_S~ E_{br}, where – critical electric breakdown field in gas flow). These particles can accelerate and decelerate fuel PAC in airflow by local electric field considerably.

These experimental results prove the conclusion about possibility of non-traditional anomalous plasma-chemical kinetics in non-premixed hydrocarbon fuel combustion in airflow at plasma assistance. This question will be studied in our future experiment in detail.

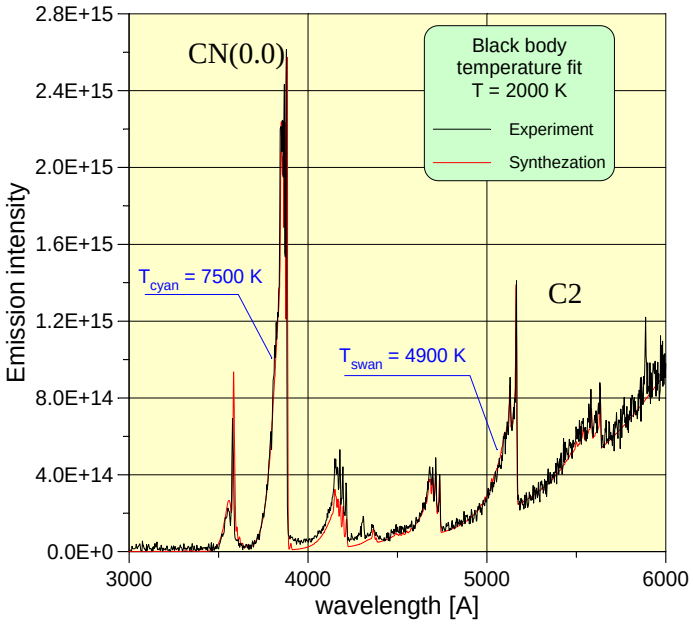

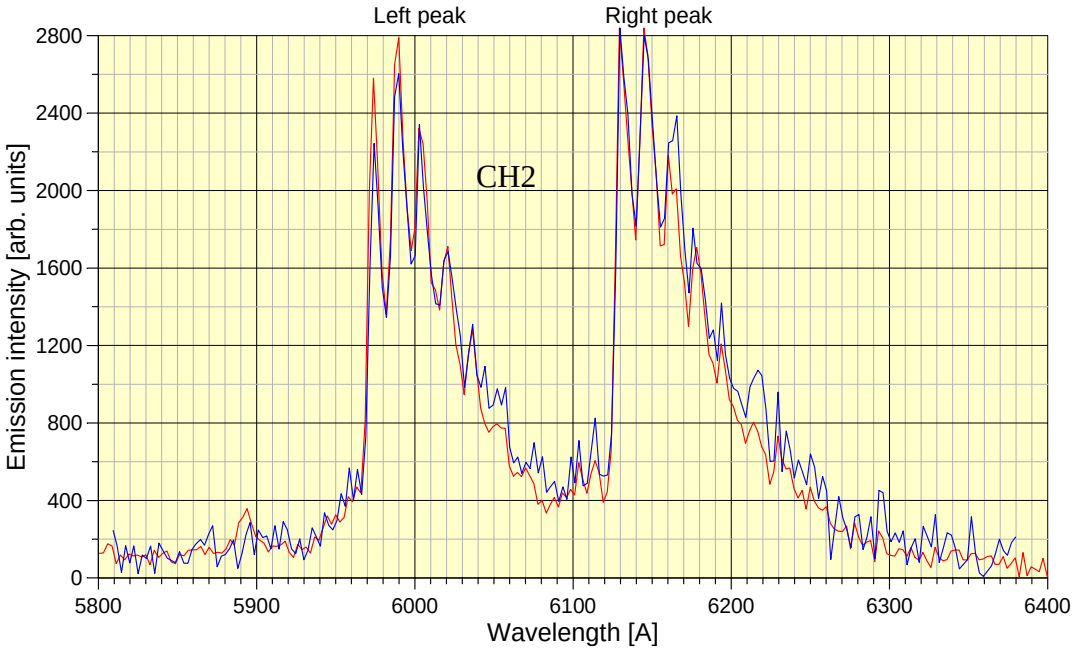

Fig.5. Experimental optical spectra obtained in PAC zone.

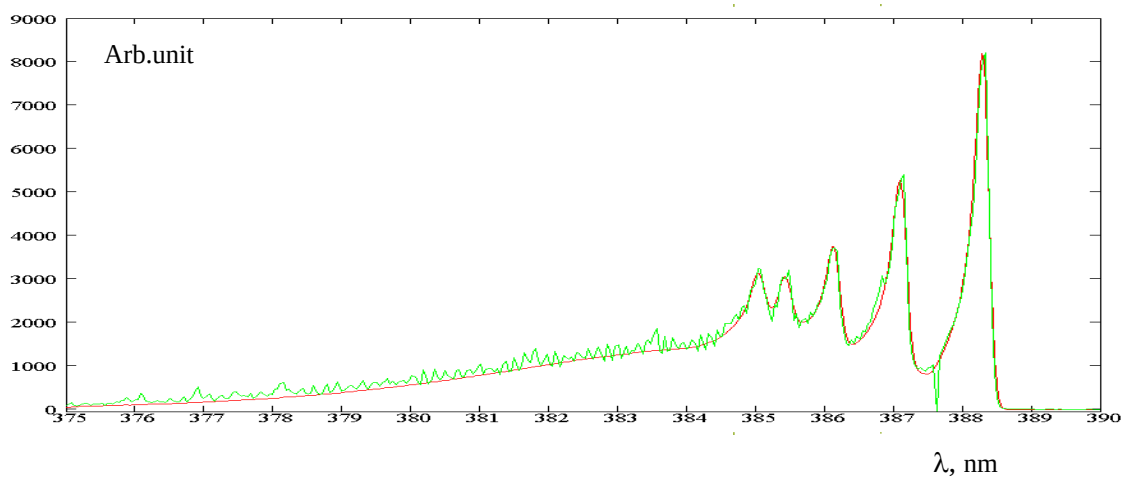

Fig.6. Experimental CN (0,0)- optical spectra (green) and simulated one (red), T_r=5000 T_v=6700K

Conclusions

1. Stable internal PAC regimes are studied in high-speed airflow.
2. Final PAC species are studied by IR absorption method and chromatograph method. Partial pressures and concentrations of these species are measured.
3. It is revealed that that the fuel PAC completeness of the lean propane-airflow mixtures is about η= 90-100%.
4. Optical spectra are obtained in PAC region in airflow and analyzed.

Acknowledgments

This work was supported in part by Russian Academy of Science and European Office of Research and Development (EOARD) under Contract Work 2127P. This Work was supported in part by ONERA under Contract Work #37565/DA/RRAG. We thank Dr. Kolesnichenko Yu., Dr. Khmara D., Dr. Chinnov V., Belevtsev A., for optical spectrum processing and Dr.Velichko A. and Prof. Nikitin A. for IR measurements of final PAC species. We thank Dr. Bilera I., Prof. Lebedev Yu. for soot's composition measurements by ion mass spectrometer and chromatograph. We thank Dr. Brovkin V. for the discussion of obtained experimental results

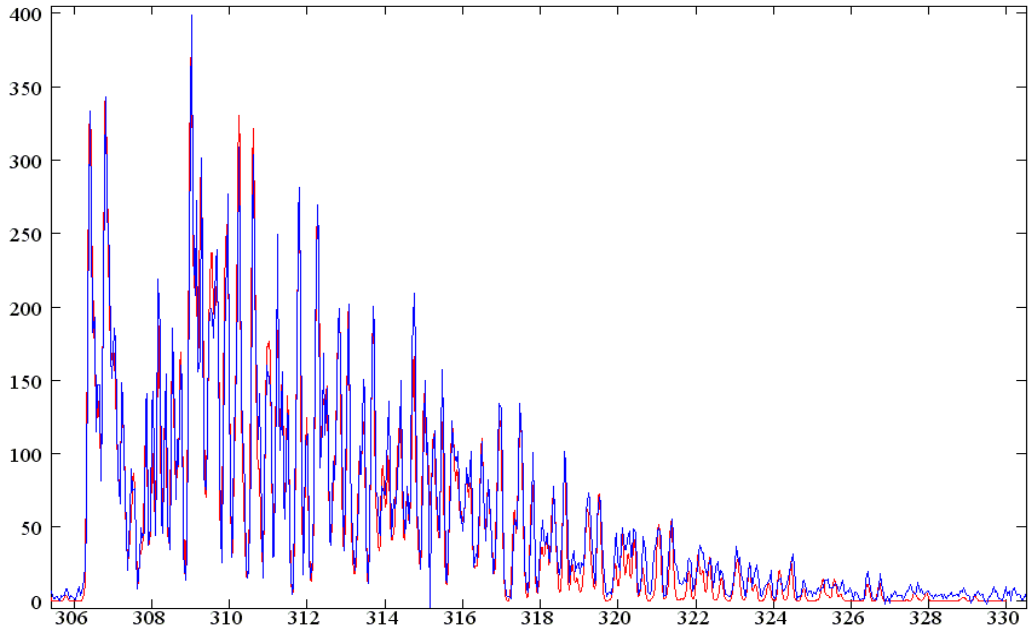

Fig.6b. Experimental OH- optical spectra (green) and simulated one (red), $T_r=T_v=5000K$

References

[1] Klimov A., Bityurin V., Kuznetsov A., Tolkunov B., Vystavkin N., Vasiliev M., External and Internal Plasma- Assisted Combustion, AIAA Paper 2004-1014. Proc. 42nd AIAA Aerospace Sciences Meeting & Exhibit, 4-8 January 2004, Reno, NV, P.10

[2] Klimov A., Bityurin V., VanWie D., at.el., Plasma Assisted Combustion. AIAA Paper 2002-0493, Proc.40th AIAA Aerospace Sciences Meeting & Exhibit, 14-17 January 2002, Reno, NV, P.9.

[3] Klimov A., Byturin V., Kuznetsov A., Sukovatkin N., Vystavkin N, Van Wie D.M., 33rd AIAA Plasma dynamics and Lasers Conference, 11-14 June 2002, Maui, Hawaii, P.10

[4] Klimov A., Byturin V, Brovkin V., Kuznetsov A., Sukovatkin N., Vystavkin N, VanWie D., Optimization of Plasma Assisted Combustion, Proc.4th Workshop on MPA, Moscow 23-25 April, 2002, IVTAN, P.31

[5] Klimov A., Bityurin V., Kuznetsov A., Tolkunov B., Vystavkin N, Sukovatkin N, Serov Yu, Savischenko N, Yuriev A., External and Internal Plasma- Assisted Combustion AIAA Paper 2003-6240. Proc. 41st AIAA Aerospace Sciences Meeting & Exhibit, 6-9 January 2003, Reno, NV, P.9.

[6] Klimov A., Bityurin V., Kuznetsov A., Vystavkin N., Vasiliev M., External and Combined Discharge Plasma in Supersonic Airflow, Paper 2004-0670. Proc. 42nd AIAA Aerospace Sciences Meeting & Exhibit, 4-8 January 2004, Reno, NV, P.33-38

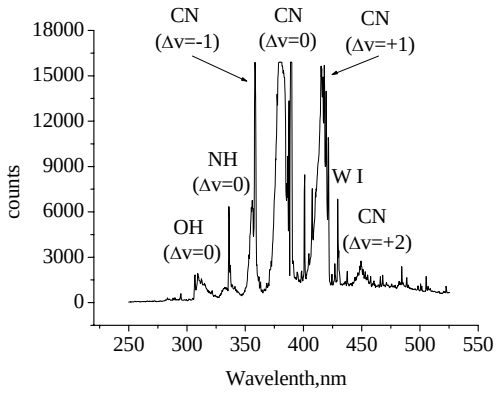

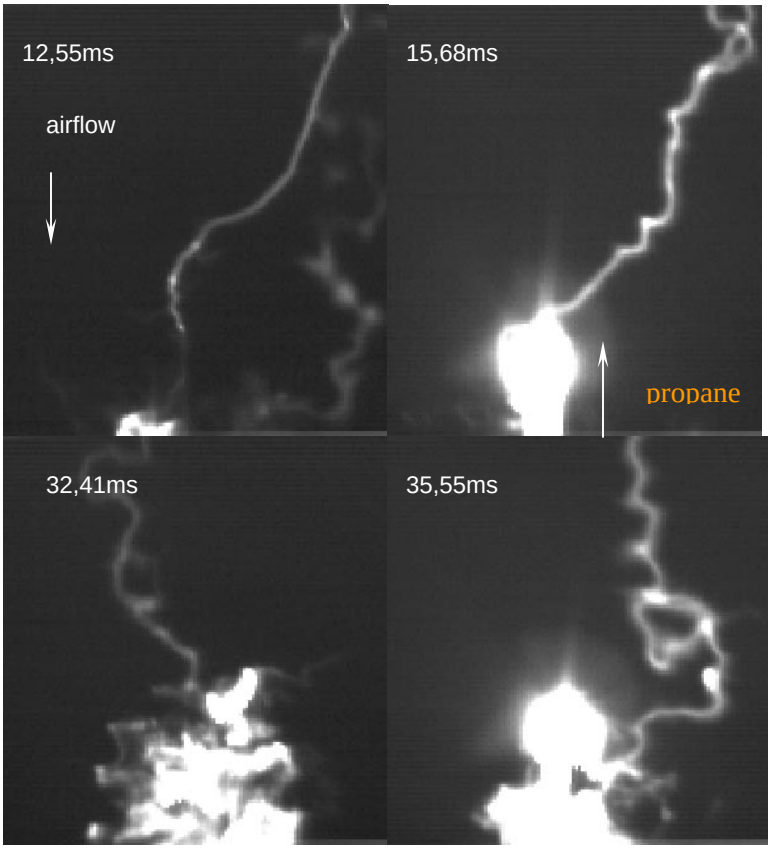

Ignition #1

Ignition #2

Fig. Non-homogeneous and non-continuous PAC. Pulse repetitive ignition. PAC igniter:- hot “balls” in HF streamer. Airflow Mach number M~ 0.1; P_{st}~ 1Bar, F_{HF}~ 1 MHz

EFFECT OF VIBRATIONAL EXCITATION ON OXYGEN ATTACHMENT IN HIGH PRESSURE AIR PLASMAS

K. Frederickson[1], W. Lee[1], I. Adamovich[2], J.W. Rich[2], and W. Lempert[1,2]

[1]*Department of Chemistry, Ohio State University, Columbus, OH*
[2]*Department of Mechanical Engineering, Ohio State University, Columbus, OH*

Abstract

Measurements of electron density decay in high pressure, room temperature pulsed e-beam generated air plasmas demonstrate that vibrational excitation, to T_v ~2,000 K, results in nearly complete mitigation of electron loss by O_2 attachment. Kinetic modeling suggests that two mechanisms may be playing a role simultaneously: i), detachment enhancement by collision of O_2^- (or other negative) ions with vibrationally excited neutrals, and ii), attachment inhibition due to electron heating by superelastic collisions with vibrationally excited neutrals.

1. Introduction and Experimental Results

Recently there has been renewed interest in a variety of potential aerodynamic applications of high pressure air plasmas. In general, such applications require stable, large volume (~1 m^3) non-equilibrium plasmas, with electron density of order 10^{12} - 10^{13} cm^{-3}, which must be sustainable for time periods of order seconds, or more. In addition, practical considerations dictate a total power budget of the order 1-10 MW/m^3. In pursuit of these extremely challenging goals, we have initiated [1] a program to study the influence of vibrational excitation on low temperature electron attachment / detachment / dissociative recombination kinetics in diatomic gases. The essential elements of the experimental apparatus, described in more detail in [1], are shown in Fig. 1. An electron gun is used to generate a pulsed (~ 5-40 microsecond, 80 keV, ~1-2 mamp) electron beam which is introduced through a foil window into a four-armed cross cell containing a variety of room temperature $N_2/O_2/CO$ mixtures, with total pressure between 200 and 760 torr. Perpendicular to the e-beam axis a 10-15 Watt continuous wave (cw) crossed CO laser beam vibrationally excites all diatomic species contained within the laser beam path to vibrational "temperatures" of ~ 2000-3000 K, as confirmed by vibrational (Q-branch) Raman spectroscopy [2]. Time-resolved relative electron density is measured by microwave attenuation, using a 40 GHz oscillator and a pair of 1 cm (length) x 0.20 cm (width) rectangular wave guides, which for clarity are omitted from the figure. The wave guides are located in front and behind the plane of the figure, separated by a gap of 1 cm. The long axis of the wave guide is oriented parallel to the CO laser beam propagation direction in order to maximize the overlap of the vibrationally excited volume with the volume within the gap of the wave guides. In addition, spectrally filtered pure rotational Raman scattering, using a narrow linewidth titanium:sapphire laser in combination with a rubidium vapor filter, [3] is used to obtain accurate (+/- ~10K) spatially resolved heavy species rotational/translational temperature.

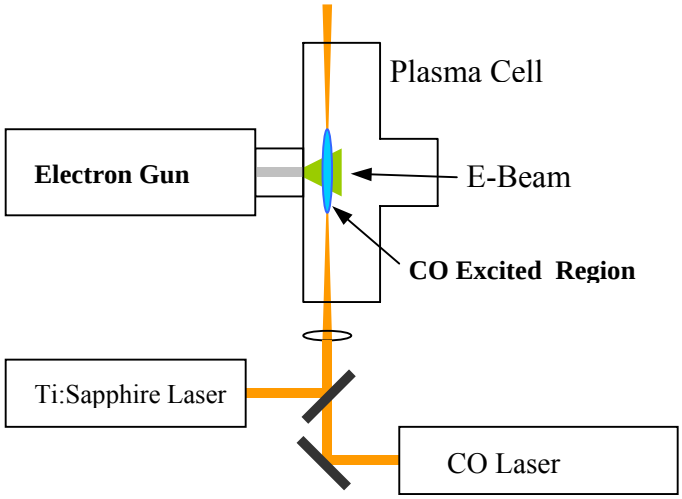

Figure 1: Schematic diagram of nonequilibrium, e-beam sustained plasma apparatus. Microwave waveguides, not shown, are located in front and behind plane of paper.

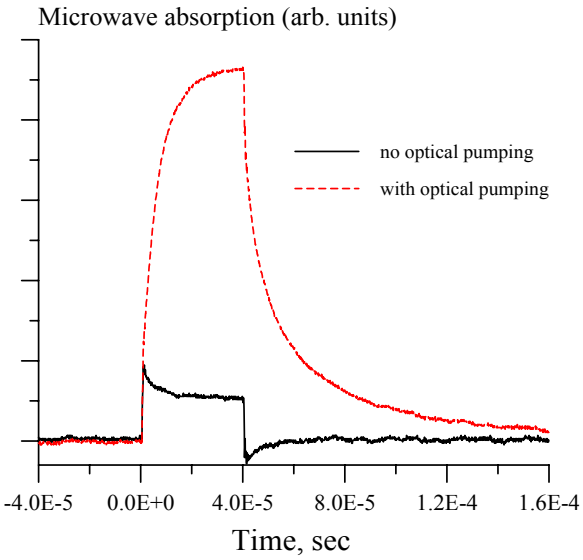

Figure 2. Microwave absorption measurements in e-beam sustained CO/air plasma at P=250 torr, with and without CO laser vibrational pumping. E-beam current and energy are 1 mA and 80 keV.

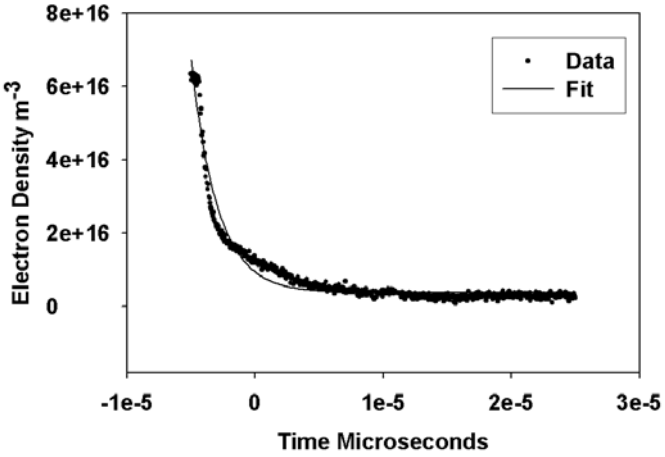

Figure 3. Experimental (dotted) electron density decay and least squares fit (solid) to Eq.(3) for cold gas mixture of 1% O_2 in N_2 at P=300torr. Electron beam current and energy are ~1 mA and 80 keV.

Figure 2 shows a pair of electron density traces obtained from a 7% CO – 93% synthetic air mixture at P=250 torr, with (dashed curve) and without (solid curve) vibrational excitation by the CO laser. It can be seen that when the gas mixture is CO laser pumped, both the plasma rise and decay times increase considerably, from ~0.5 μsec to ~20 μsec, which is similar to the rise/decay time observed in a pure 250 torr nitrogen (attachment-free) plasma [1].

These results can be understood by considering that under equilibrium conditions the electron density in low temperature air plasmas is primarily controlled by rapid three-body electron attachment to oxygen,

$$e + O_2 + M \rightarrow O_2^- + M \qquad (1)$$

In such an attachment-controlled plasma, the time-dependent electron density is described by the simple first order equation

$$\frac{dn_e}{dt} = S - k_a^{(eff)} n_{O_2} N n_e = S - \nu_a n_e \qquad (2)$$

with solution

$$\frac{n_e(t)}{n_\infty} = 1 - \exp\left[-\nu_a t\right] \quad \textbf{(generation)}$$

$$\frac{n_e(t)}{n_\infty} = \exp\left[-\nu_a t\right] \quad \textbf{(decay)} \qquad (3)$$

$$n_\infty = S/\nu_a$$

The attachment frequency, ν_a, is given by $\nu_a = k_a^{(1)} n_{O_2}^2 + k_a^{(2)} n_{O_2} n_{N_2} = k_a^{(eff)} n_{O_2} N$, where $k_a^{(eff)}=6.4\cdot10^{-31}$ cm^6/sec is the effective attachment coefficient for air, defined as 20% O_2 and 80% N_2, and N is the total heavy species number density with rate coefficients $k_a^{(1)}=2.5\cdot10^{-30}$ cm^6/sec for M=O_2 and $k_a^{(2)}=0.14\cdot10^{-30}$ cm^6/sec for M=N_2 [4]. For the conditions of Fig. 2, $\nu_a \sim 10^7$ sec^{-1}, which exceeds the bandwidth of our existing microwave detector. As an alternative the oxygen fraction was reduced in order to yield an attachment rate such that the free electron

decay could be temporally resolved. Figure 3 shows a least squares fit of the experimental electron density decay along with a least squares fit to Eqs. (3) for a 1% O2/N2 mixture at 300 torr and a beam current of 1 mamp. The best fit value of ν_a is 4.8 x 10^5 sec^{-1}, as compared to a prediction of 2 x 10^5, using the oxygen attachment rates from Ref. [4]. While the cause of this discrepancy is not completely understood, it can be seen that the decay curve in Fig. 3 appears to deviate somewhat from a single exponential, an effect which we believe to be a measurement artifact related to small change in wave guide coupling of the microwave signal during the duration of the primary beam current pulse.

Nonetheless, the results illustrated in Figs. 2 and 3 strongly suggest that the O_2 attachment rate in the vibrationally excited, non-equilibrium air plasma is greatly reduced, by two orders of magnitude or more. However, it is well established that the detachment rate of O_2^-, ie, the reverse of (1), is strongly temperature dependent, increasing by a factor of approximately 1,000 when the temperature is increased from 300 K to 600 K [5]. It is essential, therefore, to perform more accurate temperature measurements than were previously possible using low resolution vibrational Raman spectroscopy [2].

Figure 4 (left/right) show the Stokes portion of rubidium vapor filtered pure rotational Raman spectra obtained in the e-beam apparatus corresponding to the lower/upper traces in Fig. 2, respectively, along with least squares fits to a simple sum of Lorentzians spectral model. For the cold gas, the best fit rotational temperature is 308 ± 10 K (2σ) where as for the vibrationally excited gas, the temperature is found to increase slightly, to 350 ± 10 K (2σ).

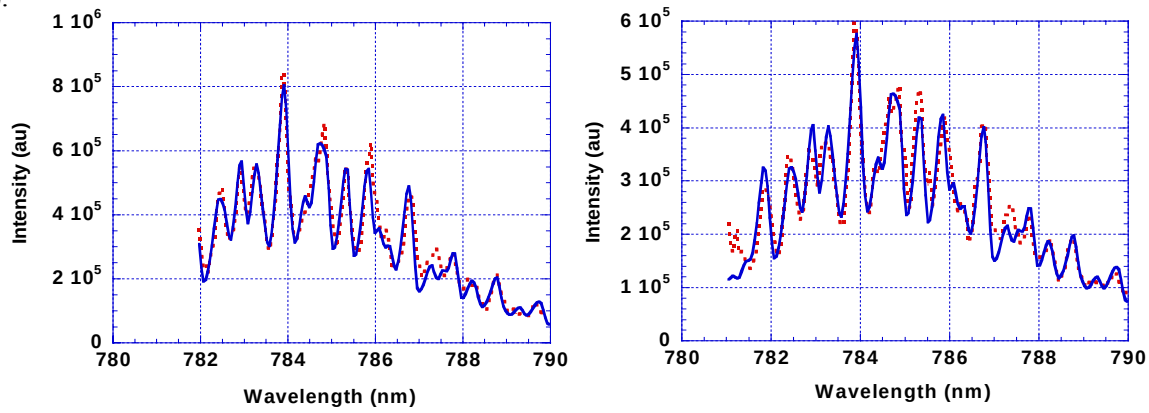

Figure 4: Filtered rotational Raman scattering spectrum obtained from cold (left) and optically pumped (right) gas

In order to determine the extent of the optically pumped region and to verify that the heavy species temperature has been probed at the centerline of the CO laser excitation, a series of filtered rotational Raman spectra were obtained as a function of radial position. This was accomplished by translation of the CO laser beam, while maintaining the alignment of the titanium:sapphire probe laser beam with respect to the image of the exit slit of the spectrometer used to resolve the spectrum. The CO laser was translated in two orthogonal directions, parallel and normal to the plane of the paper in Fig. 1. It was determined that the volume vibrationally excited by the CO laser has a diameter of ~ 0.1 cm, defined as the region in which the rotational temperature exceeds the cold gas value by ~ 10 K or more (the measurement precision). Also note that, unlike previous work performed with a 10 GHz microwave system [6], the diameter of the CO laser excited volume (~0.10 cm) is a significant fraction of the span-wise dimension of the wave guide antennae (0.2 cm).

We conclude, therefore, that although the detachment rate of O_2^- ions is extremely temperature dependent, the attachment mitigation observed previously and confirmed by the data of Fig. 2 is definitively due to a non-thermal mechanism, ie, to vibrational excitation.

2 Kinetic Modeling and Discussion

In order to explore the influence of vibrational excitation on air plasma lifetime more quantitatively we have performed kinetic modeling for two limiting cases, attachment mitigation by i), accelerated detachment and ii), inhibited attachment. First, however, it must be noted that at these conditions the microwave absorption signal is gathered from both the optically pumped and vibrationally non-excited regions of the plasma (See Fig. 1). Since the ambipolar diffusion time at these conditions is $\tau_{diff} \sim R^2/D_a \sim$ 500 μsec, the signal from the optically pumped plasma region can be isolated by a simple subtraction of the microwave signals measured with and without optical pumping. This assumption is justified by the relatively low steady-state electron density in the cold gas region as well as the fact that the optically pumped region fills only a small (~4%) fraction of the total volume between the microwave wave guides.

Limiting case (i), accelerated detachment, is motivated by the fact that the electron affinity of O_2 is only ~0.4 eV. It is reasonable, therefore, that electron detachment from O_2^- (or other negative ions such as O_4^-) is enhanced by collisions with vibrationally excited CO, O_2, and/or N_2 molecules, such as

$$\mathbf{O_2^- + O_2(v \geq 2) \rightarrow e + O_2 + O_2} \tag{4}$$

If it is assumed that the detachment rate for processes such as that described by Eq. (4) are nearly gas kinetic, $k_d \sim 10^{-10}$ cm^3/sec, so that attachment is balanced by rapid detachment, ie $\nu_a << k_d n_d$, one can estimate the required number density, n_d, of "fast detachers", i.e. molecules with vibrational energy sufficient for detachment. To see this more quantitatively, we note that according to this assumption nearly all negative ions formed by attachment are rapidly removed by detachment. In this case ion-ion and electron-ion recombination processes must be included so that the time-dependent electron density is described by

$$\begin{aligned} \frac{dn_e}{dt} &= S - \beta_{ei} n_e n_+ - k_a n_{O_2} N n_e + k_d n_- N \\ \frac{dn_-}{dt} &= k_a n_{O_2} N n_e - k_d n_- N - \beta_{ii} n_- n_+ \end{aligned} \tag{5}$$

where n_- and n_+ correspond to the total number density of negative and positive ions, respectively, and $\beta_{ii}=2\cdot10^{-6}$ cm^3/sec is the ion-ion neutralization rate coefficient [4]. The assumption of rapid detachment implies that the steady-state approximation can be invoked for the time dependence of n_-. The result is

$$[n_-]_{ss} = \left(\frac{\nu_a}{\nu_d + \beta_{ii} n_+}\right) n_e \approx \left(\frac{\nu_a}{\nu_d}\right) n_e \tag{6}$$

where we have assumed that $\nu_d >> \beta_{ii}\, n_+$ and that detachment is dominated by "rapid" detachers. Manipulation and substitution of (6) into (5), assuming that the electron number density is equal to the total positive ion number density, gives

$$\begin{aligned} \frac{dn_e}{dt} &= S - \beta_{ei}^{(eff)} n_e^2 \\ \beta_{ei}^{(eff)} &= \beta_{ei} + \beta_{ii}\frac{\nu_a}{\nu_d} = \beta_{ei} + \beta_{ii}\frac{k_a^{(eff)} n_{O_2} N}{k_d n_d} \end{aligned} \tag{7}$$

with solution

$$\frac{n_e(t)}{n_\infty} = \tanh\left[n_\infty \beta_{ei}^{(eff)} t\right] \quad \textbf{(generation)} \qquad \frac{n_e(t)}{n_\infty} = \frac{1}{1 + n_\infty \beta_{ei}^{(eff)} t} \quad \textbf{(decay)} \tag{8}$$

$$n_\infty = \sqrt{S/\beta_{ei}^{(eff)}}$$

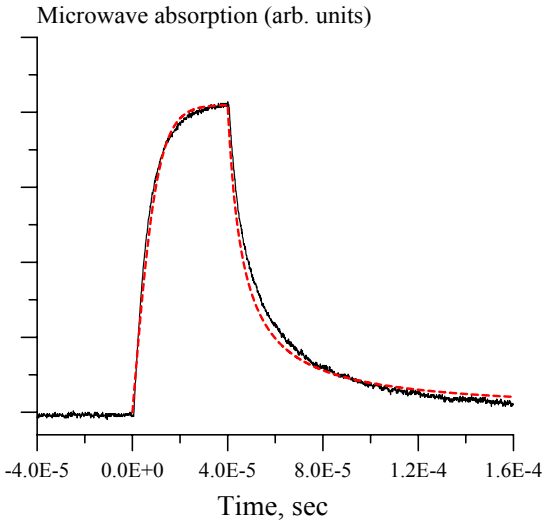

Figure 5. Experimental microwave absorption measurement from Fig. 2 – pumped case (solid line), overlayed with theoretical, rapid attachment model (dashed line) of time-dependent electron

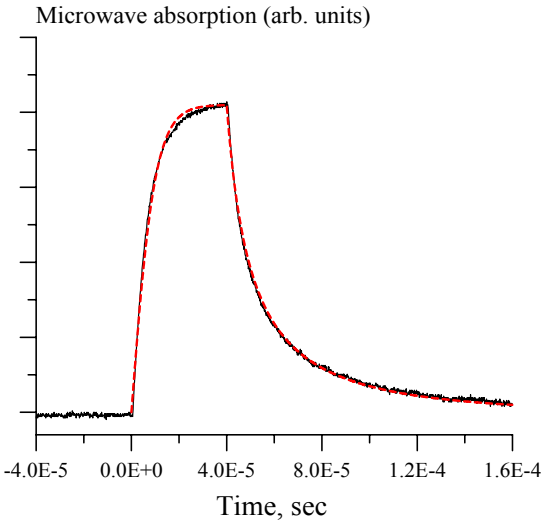

Figure 6. Microwave absorption measurements (solid line) and theoretical time-dependent electron density of Eqs. (10) (dashed line) in e-beam sustained CO/air plasma at P=250 torr (with optical pumping). E-beam current and energy are 1 mA and 80 keV.

Fig. 5 shows the results of fitting the difference between the pumped and non-pumped microwave signals from Fig. 2 to Eqs. (8) (i.e. completely mitigated attachment), assuming an ionization rate of $S=0.3\cdot10^{17}$ cm^{-3}/sec [4]. The best fit to the experimental data is obtained for $\beta_{ei}^{(eff,1)}=3.0\cdot10^{-7}$ cm^3/sec (generation) and $\beta_{ei}^{(eff,2)}=5.0\cdot10^{-7}$ cm^3/sec (decay), which are quite close to the inferred recombination rates in the nitrogen plasma at similar conditions [1]. Clearly to provide such a fit, $\beta_{ii}\,\nu_a/\nu_d$ must be of the same order as $\beta^{(eff)}_{ei}$, or less. Assuming that $\beta_{ii}\,\nu_a/\nu_d = \beta^{(eff)}_{ei} \sim 4\cdot10^{-7}$ cm^3/sec, we find that $n_d/N\sim0.05$. In other words, if only a few percent of all molecules in the plasma are excited to vibrational level v=2 and above, and if such molecules induce detachment with a near gas kinetic rate coefficient, attachment would be completely mitigated. In air this level of vibrational excitation is realized at vibrational temperatures, T_{vob}, of ~2000 K and above, which we have previously measured in optically pumped CO-air mixtures at these conditions [2].

It can be seen, however, that the fit of the plasma decay using Eqs. (8), while very good, is not perfect. This suggests the alternative possibility that electron attachment may remain unbalanced, i.e. a significant fraction of negative ions disappear not by detachment but by ion-ion neutralization. To estimate the effect of the remaining electron attachment, we model the opposite limit to that implied by eqns (5)-(8) and assume that detachment of electrons from O_2^- (or other negative ion) never occurs and that all negative ions eventually neutralize with positive ions. Under this limit, the kinetic equation for electron density is

$$\frac{dn_e}{dt} = S - \beta_{ei} n_e^2 - \nu_a n_e \qquad (9)$$

with analytical solution

$$\frac{n_e(t)}{n_\infty} = \frac{\frac{\Delta}{\nu_a}\tanh\left[\frac{\Delta}{2}t + \tanh^{-1}\left(\frac{\nu_a}{\Delta}\right)\right] - 1}{\frac{\Delta}{\nu_a} - 1} \quad \textbf{(generation)} \qquad \frac{n_e(t)}{n_\infty} = \frac{\exp(-\nu_a t)}{1 + \frac{1}{2}\left(\frac{\Delta}{\nu_a} - 1\right)\left(1 - \exp(-\nu_a t)\right)} \quad \textbf{(decay)}$$

$$\Delta = \sqrt{4S\beta_{ei} + \nu_a^2}$$

$$n_\infty = \frac{\Delta - \nu_a}{2} \qquad (10)$$

Figure 6 shows the best fit of Eqs. (10) to the microwave absorption data for $\beta_{ei}^{(1)} = \beta_{ei}^{(2)} = 3.0 \cdot 10^{-7}$ cm^3/sec and $k_a^{(eff)} = 1.3 \cdot 10^{-33}$ cm^6/sec, which is about 500 times lower then the attachment rate coefficient in room temperature air without optical pumping. It can be seen that taking into account electron removal by both recombination and attachment (although greatly reduced) substantially improves agreement with the experiment. This suggests that the observed increase of the plasma lifetime after the e-beam is turned off may be due not only to fast detachment, but also to slower attachment. Since in the optically pumped plasma the majority of oxygen molecules and third body collision partners participating in the attachment process of Eq. (1) are not vibrationally excited, and the gas temperature remains close to room temperature, slower attachment is most likely due to electron heating in superelastic processes such as

$$\mathbf{e(\varepsilon) + CO(v) \rightarrow e(\varepsilon + \Delta\varepsilon) + CO(v - \Delta v)} \qquad (11)$$

Indeed, experimental measurements [4,7] show considerable reduction of the attachment coefficient as the electron temperature is increased, by about a factor of 10 for $T_e \sim 0.3$ eV.

3 Conclusions

Measurements of the temporal evolution of electron density have been performed in pulsed e-beam generated, high pressure molecular plasmas. Measurements in nonequilibrium air mixtures, vibrationally excited to T_{vib} of order 2,000 – 3000 K by means of CO laser optical pumping, show nearly complete mitigation of the O_2 attachment mechanism, which dominates electron loss in equilibrium systems at these temperatures. Spatially and temporally resolved pure rotational temperature measurements, indicate heavy species rotational/translational temperature is only slightly increased as a result of CO laser pumping, to approximately 350 K. The combination of these two results demonstrates conclusively that the mitigation of electron attachment is due to vibrational excitation, and is not a thermal effect. Kinetic modeling of two limiting cases, accelerated detachment and inhibited attachment, suggests that two mechanisms may be playing a role simultaneously: i), detachment enhancement by collision of O_2^- (or other negative) ions with vibrationally excited neutrals, and ii), attachment inhibition due to electron heating by superelastic collisions with vibrationally excited neutrals.

Acknowledgemenets

This work was principally sponsored by the National Science Foundation – Plasma Physics Division.. Support of the U.S. Air Force Office of Scientific Research – Space, Power, and Propulsion Program, is also acknowledged.

References

[1] W. Lee, K. Frederkickson, P. Palm, I. Adamovich, J.W. Rich, and W. Lempert, AIAA-2257-2004, 35th AIAA Plasmadynamics and Lasers Conference, Portland, OR, 28 June – 1 July, 2004.

[2] W. Lee, I.V. Adamovich, and W.R. Lempert, J. Chemical Physics, vol. 114, No. 13, 2001, pp. 1178-1186.

[3] W. Lee and W. R. Lempert, AIAA Journal, Vol 40, No. 12, 2002, pp. 2504–2510.

[4] Y.P. Raizer, *"Gas Discharge Physics"*, Springer-Verlag, Berlin, 1991

[5] E. W. McDaniel, *Collision Phenomena in Ionized Gases*, John Wiley&Sons, New York, 1964.

[6] P. Palm, E. Plonjes, I.V. Adamovich, V.V. Suramaniam, W.R. Lempert, and J.W. Rich, AIAA-2001-2937, 32nd AIAA Plasmadynamics and Lasers Conference, Anaheim, CA, 11-14 June 2001.

[7] L.M. Chanin, A.V. Phelps, and M.A. Biondi, Phys. Rev. Lett., vol 2, p. 344, 1959.

Production of N-atoms in N2 microwave post-discharge jets for sterilization purposes

S.Cousty, J.Henriques, S.Villeger, J.P Sarrette, A.Ricard

CPAT, Univ. Paul Sabatier, 31062 Toulouse, France

Abstract
The afterglows of N_2 flowing post-discharges have been studied by emission spectroscopy. For post-discharge times of more than 10^{-3} sec., it is observed a late afterglow which is produced by the N+N recombination with enhanced emission of the N_2, 1st pos.band at 580 nm.
At low gas pressure, it is observed a homogenous afterglow in the whole post-discharge reactor.
At high gas pressures, up to 20 Torr, it appeared a post-discharge jet with a N-atom density higher than in the surrounded diffuse afterglow.
The N-atom density has been determined in the post-discharge from the vibrational distribution of N_2, 1^{st} pos. band intensities after calibration by NO titration.
Keywords: Plasma spectroscopy, NO titration, hydrodynamics and kinetics modelling.

1-Introduction

A large interest in flowing microwave N_2-O_2 post-discharge at low gas pressures (1-10 Torr) appeared for sterilization processes of microorganisms [1-4]. In these studies, it was fully destroyed 10^6 spores [1,2] and up to 10^{12} oral bacteria [3,4] after treatment times of 30 minutes in N_2-5%O_2 post-discharges. It was verified that a pure N_2 post-discharge was also effective to sterilize bacteria when N-atoms are reacting on bacteria support heated between 60 and 120°C [5].
In the present paper, it is reported experimental results obtained by emission spectroscopy to characterize a flowing post-discharge with a homogenous afterglow at low pressure (less than 5 Torr) and with a luminous jet at high pressures (10–20 Torr). The density of N-atoms is determined in the jet and in the homogenous afterglows inside a post-discharge chamber of 5 litres for sterilization purpose.

2-The experimental set-up

The experimental set up is reproduced in Fig.1. In the first part of the reactor, a discharge in a quartz tube of 5 mm internal dia. is produced by a 2.45 GHz microwave surfatron at a power of 50-100 Watt. The second part is a treatment chamber in Pyrex of 15 cm dia. and 20 cm height. The gas flow can vary up to 3 Slm and the gas pressure in the reactor can be adjusted between 1 and 50 Torr by means of a throttle valve above the primary pump.
Samples are placed in the center of the post-discharge chamber for sterilization studies.
The optical emission from the plasma and the afterglow is collected by an optical fiber which is connected to a Jobin-Yvon 270M spectrometer with a CCD detector. The optical fiber can be positioned in 1) for the plasma analysis at the surfaguide gap, in 2) for the afterglow detection at the end of the 5 mm post-discharge tube and in 3) for the late afterglow detection inside the 5 liters reactor chamber.
Titration by NO of N -atom densities is performed in the post-discharge chamber.

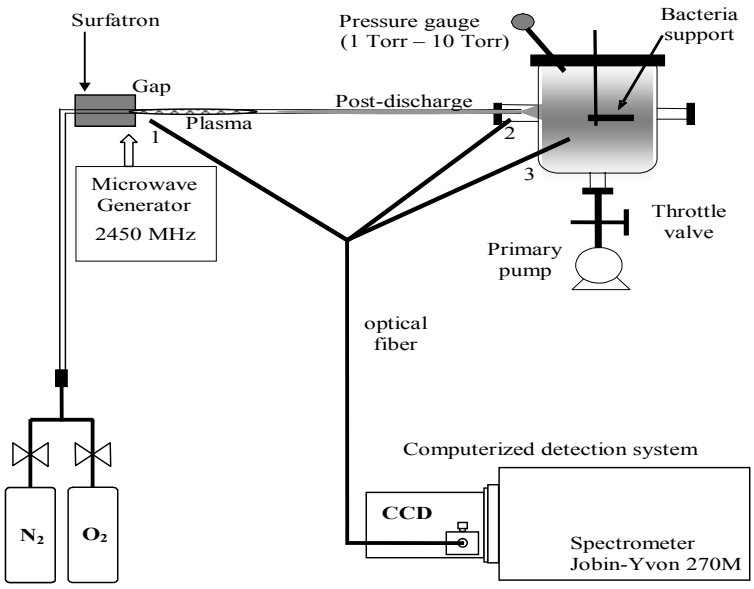

Figure 1 : experimental set up

3-Characterization of N_2 afterglows

With a flow rate higher than 1 Slm, a gas pressure higher than 4 Torr and a microwave power of about 100 Watt, it is observed a post-discharge jet after the end of the 5 mm quartz tube, at the entrance of the reactor chamber. This afterglow jet is surrounded in the reactor chamber by a late diffuse afterglow.

3-1.Characterisation of discharges and post-discharges by emission spectroscopy

The N_2, 1st.pos.emission at 4 Torr, 65 Watt in the plasma, recorded at position 2, at the end of the 5 mm quartz tube (see Fig.1), is reproduced in Fig.2a between 550 and 610nm.
In Fig.2b, it is reproduced the N_2, 1st.pos. at position 3 in the late afterglow. It is clearly observed a peak at 580 nm which characterizes the N+N recombination [6].
The same part of N_2, 1st pos. in the plasma gap (position 1) is reproduced in Fig 2c.

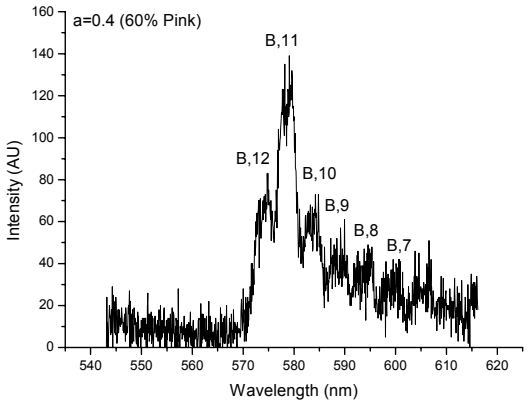

Figure 2a : N_2 1st pos.in the early afterglow

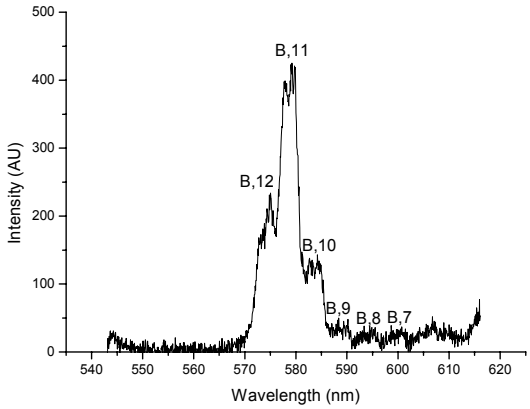

Figure 2b : N_2 1st pos.in the late afterglow

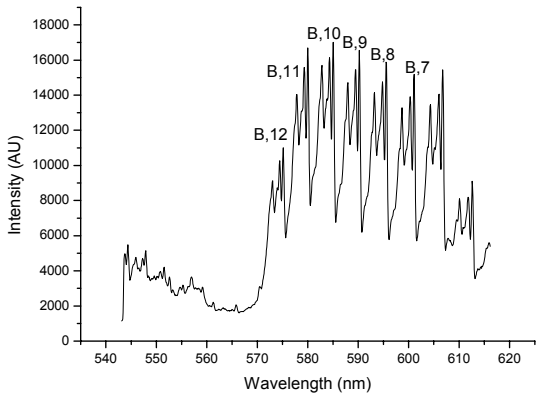

Figure 2c : N_2 1st pos. in the plasma gap

It is observed a broad vibrational distribution of the 1st pos.bands in the plasma gap (position 1), which appeared more and more contracted when going from the discharge tube end (position 2) to the chamber (position 3).

The vibrational distribution of the N_2, 1st pos syst. intensity in the post-discharge can be analysed to characterize the afterglows.

The variations of the normalised vibrational distribution of $N_2(B,v')$ density $r_{B,v'}$

(With $r_{B,v'} = [N_2B,v']/\Sigma_7^{12} [N_2B,v']$) versus v' is reproduced in Fig.3 for several values of a parameter a, with a= 1 for a pure N+N (Lewis-Rayleigh L.R) afterglow and a=0 for an early (pink) afterglow [6,7].

It is written :

$$r_{B,v'} = a\, R_{v'}(N+N) + b\, R_{v'}(Pink) \qquad (1)$$

where $R_{v'}(N+N)$ is the $N_2(B,v')$ vibrational distribution for the pure L.R afterglow (a=1 and b=0 in eq.1) and $R_{v'}(Pink)$ is the corresponding vibrational distribution in pure pink afterglow (a=0 and b=1).

It is presently found the following a–values : a=0.4 at 4 Torr and a=1 at 10–20 Torr, at the end of the 5 mm post-discharge tube which is the beginning of the post-discharge jet in the reactor (see Fig.1). At 4 Torr, it is a 60% pink afterglow. At higher pressures, the N+N recombination appears to be the dominant process at 10 -20 Torr.

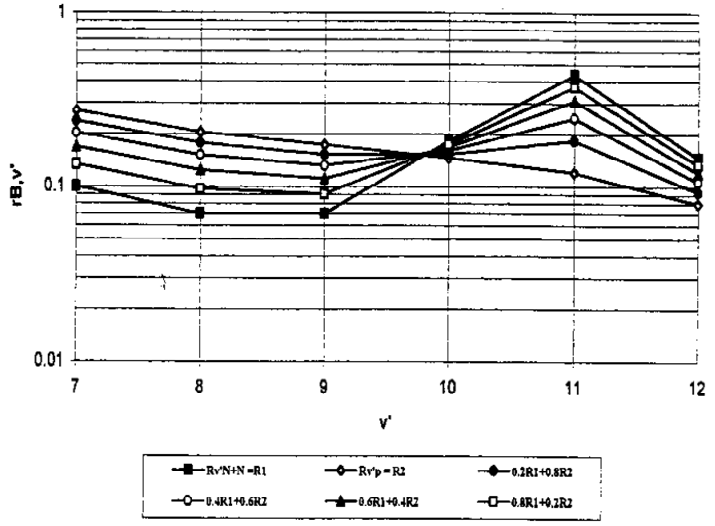

Figure 3 : diagram of $r_{B,v'}$ versus v'

The N_2, 580nm head intensity (I_{N2}) is given by the following equation :

$$I_{N2} = C_1 [N]^2[N_2] k_1 / \nu_1+k_2 [N_2] \quad (2)$$

where C_1 is a coefficient which is related to the photon emission volume, to the spectral response of the spectrometer, to the photon energy and to the band radiative frequencies, the brackets are for the atom and molecule densities, k_1 is the rate coefficients for the N+N recombination, ν_1 is the radiative frequency loss and k_2 is the quenching rate coefficient of the N_2 radiative state by N_2.

The N atom density (in relative unit) is then given by the following equation :

$$[N]^2 = k\, a\, I_{N2} \quad (3)$$

where $k=\nu_1+k_2 [N_2] / C_1k_1[N_2]$ and *a* is the parameter in Fig 3.

At pressure higher than 1 Torr, $\nu_1<k_2 [N_2]$.

3-2.Density of N -atoms after calibration by NO titration

The NO titration has been used to determine the N-atom densities as described in ref 8. An Ar-2% NO gas mixture is introduced through the reactor chamber. It has been checked a satisfactory mixing of the post-discharge and titration flows in the late afterglow for the following conditions : 0.5 slm, 4 Torr, 100 Watt with a measured N-atom density [N]=4(14) cm-3, corresponding to I_{N2}=270cc (spectrometer of Fig.1 with slit of 0.5 mm and integration time of 1s).

The C_1 coefficient in eq.2 has been calibrated to the homogenous late afterglow without afterglow jet at 4 Torr in pos.3 by taking into account the photon emission thickness of 15 cm : C_1=1 with 15 cm in pos.3 and C_1= 0.12 with 1.8 cm in pos.2.

In position 3 (Fig 2b), I_{N2}=350cc, a=1, C_1=1, it is obtained: [N]=4.6(14)cm^{-3} .

In position 2 (Fig 2a), I_{N2}=100cc, a=0.4, C_1=0.12, it is deduced: [N]=4(14)cm^{-3} .

The jet intensity is obtained by subtracting the homogenous emission at 4 cm above the jet from the total intensity in pos.3. Then the intensity of the afterglow jet of dia.1cm at pressure of 10–20 Torr is considered with C_1=6.7 (-2).

Variations of N-atom densities versus the gas pressure are in Fig.4 for the late afterglows (pos.3), inside and outside the plasma jet and for the early afterglow at the end of the 5mm dia.tube (pos.2).

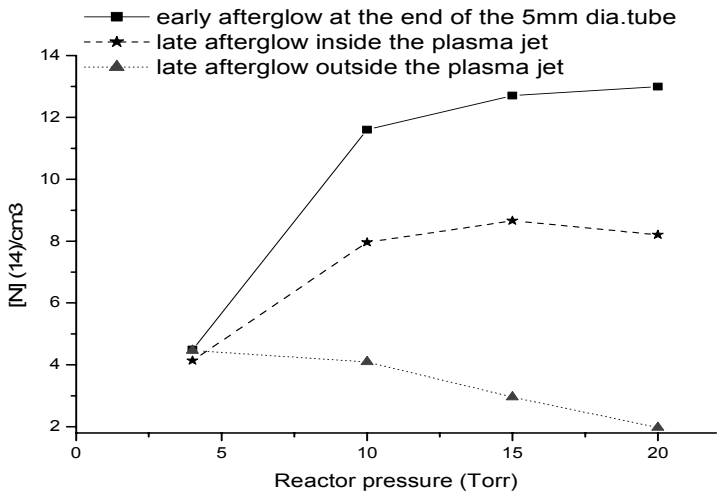

Figure 4: N-atom density versus the gas pressure

There is no difference of density in the late post-discharge at 4 Torr, inside or outside the discharge tube axis, indicating a homogenous late afterglow. Also about the same value of N-atom density is found at the discharge tube exit.

When the pressure is increasing, there is a more and more marked difference in the N-atom densities which are increasing at the discharge tube exit and in the afterglow jet, but which are decreasing in the diffuse afterglow, outside the jet.

3-3.Hydrodynamics and Kinetics modelling of N-atom density

A Fluent modelling of the flowing post-discharge was performed. The N-atom concentration along the reactor diameter (pos.3 in Fig.1) is reproduced in Fig.5, for gas pressures 4, 10, 15 and 20 Torr, at 1 Slm and 65 Watt in the plasma .The hydrodynamics and the loss of N-atoms on the reactor wall are calculated by the Fluent model as described in ref.10. The N-atom densities at the entrance of the reactor are the experimental values as given in Fig.4 (pos.2, black squares). The mean calculated values of N-atom densities along the reactor diameter at pos.3, and the experimental values are presented in table 1.

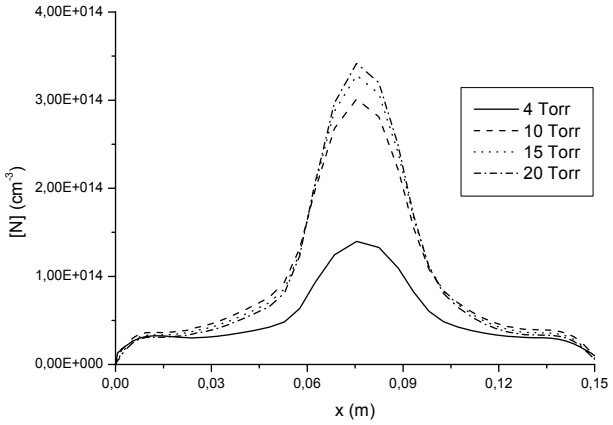

Fig.5 : Spatial distribution of N-atom density along the reactor diameter (position 3 in Fig.1)

	Calculated Values	Experimental Values
4 Torr	4.2 10^{13} cm^{-3}	4.6 10^{14} cm^{-3}
10 Torr	7.1 10^{13} cm^{-3}	4.6 10^{14} cm^{-3}
15 Torr	7.0 10^{13} cm^{-3}	3.7 10^{14} cm^{-3}
20 Torr	6.9 10^{13} cm^{-3}	2.9 10^{14} cm^{-3}

Table 1 : Calculated and Experimental Values, at different pressures, in the reactor chamber

The higher experimental values can be interpreted by a source of N-atoms in the post-discharge, resulting from collisions between excited N_2 molecules, such as $N_2(X, V)$, $N_2(A, a')$ metastables [11].

As shown in Fig.5, the jet of N-atoms in the reactor is enhanced between 10 and 20 Torr.

4 – Concluding remarks

The emission spectroscopy of the afterglows inside a reactor chamber for sterilisation has conduced to the following results :

-At low pressure, typically 4 Torr, with a plasma at 100 Watt in a tube of 5 mm.dia and a flow rate of 1 Slm, it is observed a homogenous post discharge with emission of N_2, 1^{st}.pos.bands which characterizes the N+N atom recombination.

-At higher pressures, up to 20 Torr, it appeared a post-discharge jet, surrounded by a diffuse homogenous afterglow.

The determination of N–atom densities by NO titration was only possible in the late afterglow. These atom densities have also been obtained in the jet post-discharge by calibrating the N_2, 580 nm band intensity, which is the signature of the N+N recombination. The calibration was taken in the best conditions for NO titration that is the late afterglow at 4 Torr, 0.5slm, 100Watt.

The N atom densities have been obtained in the early and late post-discharges. In the homogenous late afterglow at 4 Torr (1Slm, 65W), it has been measured a N-atom density of 4.5(14) cm^{-3}. At 10–20 Torr, the N-atom density in the post-discharge jet was higher than in the diffuse afterglow, outside the jet. The N-atom density increased in the jet but decreased outside as the pressure increased from 10 to 20 Torr.

References

[1]-S.Moreau, M.Moisan, M.Tabrizian, J.Barbeau, J.Pelletier, A.Ricard and L'H Yahia. J.Appl.Phys.88(2000)1166

[2]-M.Moisan et al. Proceedings of the Vth Int.Workshop of Microwave discharges, Greifswald 2003, p.210-221.

[3]-S.Villeger, S.Cousty, A.Ricard and M.Sixou, J.PhysD36, L1 (2003)

[4]-S.Villeger, A.Ricard and M.Sixou, Eur.Phys.J. Applied Phys.26 (2004)203

[5]-S.Villeger, Thèse-Toulouse (2004)

[6]-P.Merel, M.Tabbal, M.Chaker, M.Moisan and A.Ricard, Plasma Sources Sci.Tech.7(1998)550

[7]-S.Bockel, A.M Diamy and A.Ricard, Surf.and Coating Tech.74-75 (1995)474

[8]-A.Ricard, M.Moisan et S.Moreau, J.PhysD 34(2001)1203

[9]-H.Blanchard, J.P Sarrette, S.Villeger, P.Baudel and A.Ricard, Eur.Phys.J. A.P 26 (2004) 22.

[10]-A.Ricard, V.Monna, M.Gaillard, J.P Sarrette and M.Mozetic, Proc.SPIE "Spectroscopy of Nonequilibrium plasmas at elevated pressures" Edit. V.N Ochkin, Vol 4460 (2002)330

[11]-J.Levaton, J.Amorim, AR.Souza, D.Franco and A.Ricard. J.Phys.D. 35(2002)689

Production of active species in N2-O2 flowing post-discharges at atmospheric pressure for sterilisation

Anne-Marie Pointu[1], André Ricard[2], Bénédicte Dodet[3], Emmanuel Odic[3], Juliette Larbre[1], Mihai Ganciu[1,4]

1 – LPGP, Univ. Paris Sud, 91405 Orsay, France
2 - CPAT , Univ. Paul Sabatier, 31062 Toulouse, France
3 – EEI, Supelec, 91190 Gif sur Yvette , France
4 - NILPRP, Low Temp. Plasma Dept., P.O. Box MG-36, Bucharest, Romania

Abstract
A flowing afterglow of pure molecular nitrogen at atmospheric pressure containing some tens to some thousands ppm of molecular oxygen is studied. For flows of 40 Slm, spectroscopic measurements down the discharge allows us to estimate concentrations in N-atoms , O^1S-metastable atoms and in C-atoms in imurity. With UV emission due to nitrogen oxide, the N-atoms and O^1S-metastable atoms are used to sporicidal effects and their relative role is estimated.
Keywords
Plasma spectroscopy, plasma kinetics, plasma sterilization.

1.Introduction

A large interest in flowing N_2-O_2 post-discharge appeared for sterilization processes of microorganisms at low gas pressures (1-10 Torr) [1-4] and at atmospheric pressure [5, 6].
The gas active species have been analysed in low pressure afterglows : N , O-atoms and UV emissions coming from NO(A) radiative states. Their densities have been determined by NO titration [7].The synergetic effects of N and O-atoms with UV and with the substrate temperatures have been reported in [1, 2] and in [3, 4], respectively. The nature and density of active species are less known in flowing post-discharges at atmospheric pressures , except for N-atoms in Ar-N_2 microwave discharges [8] and in pure N_2 post discharge [9,10]. The O, OH and NO_2 active species have recently been detected in atmospheric air DBD plasmas [11].
It is the purpose of the present communication to report the results of diagnostics by emission spectroscopy of radiative species in N_2 flowing post-discharges with a few quantity of O_2 (10^{-5} -10^{-3}) in high N_2 flow (40 Slm) at atmospheric pressure. The density of active species has been determined by using the situated kinetics reactions and after calibration of N atom density by NO titration. Density of O^1S-metastable atoms and of C-atoms in impurity into N_2 is evaluated.
Results of spore sterilization by specific active species are reported.

2.Experimental setup

The experimental set-up is reproduced in Figure1.
It uses the same device described in [9] which has the unique capability of propagating N atoms at atmospheric pressures over long distances in small diameter tube when feeded by pure nitrogen.
A fast pulsed corona discharge is produced between needles at a voltage of some 10 kV, a repetition rate of some 10 kHz and at low average current intensity such as the mean power is near 15 W [9]. Such a power is maintained constant all over the experiment stuffy. The N_2 flow rate (99.995% gas purity) was 40 Slm. A few O_2 quantity at flow rate between 0 and 50 sccm was introduced along the main N_2 flow up the discharge by means of a lateral tube (see Figure1).The post-discharge is in a quartz tube of internal diameter 6 mm where the emission spectroscopy is performed with a Stellarnet EPP 2000 spectrometer (resolution 1.5 nm) in the 200-800nm spectral range. At the same point, the tube is replaced by a 250 cm^3 box containing Bacillus Stearothermophillus spores when post-discharge sterilization effect is experimented.

3. Active species in the N_2 and N_2-O_2 afterglows

3-1 Observed emission spectra

The emission spectra in the afterglow, at a distance x=10 cm from the plasma, is reproduced in Figure 2 for a N_2 discharge (Figure 2a) and for a N_2–(2.5 10^{-5}) O_2 gas mixture (Figure 2b). In Figure 2a, it is observed the N_2, 1^{st}.pos.(580 nm).emission, resulting from the N-atom recombination. Not any other N_2 band appears, neither N_2, 2^{nd} pos nor N_2+, 1^{st}.neg as it is observed in the early (pink) N_2 afterglow [12]. It is concluded that such emission spectrum in Fig. 2a is a characteristic of a late N2 flowing afterglow with emissions of impurity bands such as NH (336 nm) and CN (359nm, 388 nm, 424 nm) bands resulting from reactions of atomic nitrogen with hydrocarbon gas impurities [13]. Such hydrocarbon impurities could come from the N2 gas tank or from a small etching of the polyamide tube by the N-atoms.

These latters disappear as early as O_2 is mixed in N_2, as shown in Figure 2b. Then, besides the always emitting N_2, 580 nm, it can be seen the NOγ (247.9 nm) and NOβ(320.7 nm) bands and a green band at 577 nm. This green band. is produced by the $N_2O(^1S) – N_2O(^1D)$ excimer transitions as reported in [14-16].

3-2. Production of radiative states

The $N_2(B,v'=11)$ state, at the origin of the 580 nm band in Fig.2a,b, is produced by the following N-atoms recombination :

$$N+N+N_2 \rightarrow N_2(B,v'=11) + N_2 \quad (a)$$

The CN–bands as observed in Fig.2a are produced in the afterglow by recombination of N and C-atoms [17] :

$$N+C+N_2 \rightarrow CN(B,v'=7) + N_2 \quad (b)$$

$CN(B,v'=7) \rightarrow CN(A,v'')$, with in particular, the 384.7 nm band for v''=7.

The NO bands in Fig.2b are coming from states NO(B, A). The NO(B) state, emitting the NOβ bands, is produced by the N + O recombination as follows :

$$N+O+N_2 \rightarrow NO(B) + N_2 \quad (c)$$

As for the NO(A), emitting the NOγ bands, the following excitation transfer is efficient :

$$N_2(A) + NO \rightarrow NO(A) + N_2 \quad (d)$$

where $N_2(A)$ are metastable states.

Finally, the $N_2O(^1S)$ excimer, at the origin of the green band, is produced from the $O(^1S)$ metastable as it follows :

$$O(^1S) + N_2 + N_2 \rightarrow N_2O(^1S) + N_2 \quad (e)$$

3-3.Density of radiative states

To determine the density of radiative states, it is necessary to know the loss terms which are by radiative emission and by N_2 quenchings. They are analysed in [7, 8, 10, 17].

It is reproduced here how to determine the $N_2(B,11)$, CN(B,7) and $N_2O(^1S)$ radiative state densities in the post-discharge.

For the $N_2(B,11)$ state, the dominant loss term for pressures higher than a few Torr is by the following quenching [7] :

$$N_2(B,11) + N_2 \rightarrow \text{products} \quad (f)$$

Then the pseudo-stationary state density of $N_2(B,11)$ is given by the following equation :

$$[N_2(B,11)] = k_a [N]^2 / k_f \quad (1)$$

where the brackets are for the specie density and $k_{a,f}$ are the rate coefficient of reactions (a) and (f), respectively.

For the CN(B,7) state, the ν_r^7 - radiative frequency cannot be neglected before the quenching frequency:

$$CN(B,7) + N_2 \rightarrow \text{products} \quad (g)$$

So that the pseudo-stationary state density of CN(B,7) is as follows:

$$[CN(B,7)] = k_b [C][N] k_b / \nu_r^7 + [N_2] k_g \quad (2)$$

As it concerns the $N_2O(^1S)$ excimer, the main loss term is the inverse of reaction (e), with a rate coefficient k_{-e}. The pseudo-stationary density of $N_2O(^1S)$ is then given by the following equation :

$$[N_2O(^1S)] = [O(^1S)][N_2]k_e/k_{-e} \quad (3)$$

3-4. Density of N, C and O(^{1}S) atoms

The N-atom density has been determined in the afterglow by the NO titration method as detailed in [7, 10]. It is obtained a nearly constant value in pure N_2 and in N_2-(0.125-12.5)10^{-4} O_2 gas mixtures of [N] = 4 10^{14}cm^{-3} with an uncertainty of about 30%.

The C-atom density is estimated by comparing the CN(B,7-X,7) , 384.7 nm and the N_2, 580 nm intensities,using the following relations:

$$I_{N2*} = c(\lambda = 580 \text{ nm}) [N_2(B,11)] A(N_2*) \quad (4)$$

$$I_{CN*} = c(\lambda = 384.7\text{nm}) [CN(B,7)] A (CN*) \quad (5)$$

where c(λ) is a coefficient depending of the spectral response of spectrometer and on the energy of emitted photon, A(N_2*) = A(B,11-A,7) and A(CN*) = A(CNB,7-X,7) are the radiative frequencies.

By replacing [CN(B,7)] and [N_2(B,11)] as given by equations 2 and 1, the intensity ratio of the two bands is as follows:

$$I_{CN*}/ I_{N2*} = \alpha_{CN} [C]/[N] \quad (6)$$

with $\alpha_{CN} = [N_2] k_g / \{k_a/k_f (\nu_r^7 + [N_2] k_g)\}$

In conditions of Fig.2a, a C-atom density of about 10^{12} cm^{-3} is estimated from a N-atom density of 4 10^{14} cm^{-3} as obtained by NO titration.

The O(^{1}S) metastable atom densities is now determined by comparing the emission intensity of N_2, 580 nm (I_{N2*}) and $N_2O(^1S)$-$N_2O(^1D)$, 577 nm (I_{N2O*}), with :

$$I_{N2O*} = c(\lambda = 577 \text{ nm}) [N_2O(^1S)] A\{N_2O*) \quad (7)$$

with A(N_2O*) = A(N_2O^1S-N_2O^1D). It is noted that c(λ) has the same value for the two considered bands.

By replacing [N_2O^1S] and [N_2(B,11)] as given by equations 3 and 1, the intensity ratio of the two bands is as follows :

$$I_{N2O*}/ I_{N2*} = [O(^1S)]/ [N]^2 \{[N_2] k_e k_f A(N_2O*) / k_{-e} k_a A(N_2*) \} \quad (8)$$

Variations of N_2, 580 nm, $O^1S.N_2$, 557 nm and NOβ, 321 nm, NOγ, 248 nm band intensities versus the O_2 percentage into N_2 are reproduced in Figure 3.

It is observed a nearly constant intensity of N_2, 580 nm, indicating a constant N-atom density (see eq.1). It is however observed a small flat maximum of the N_2,580 nm intensity which seems to appear at 10^{-4} O2 into N_2. Such a maximum has been previously observed[7] for about 10^{-2} O2 into N2 into a microwave flowing post-discharge at low gas pressure.

The I_{N2O*} at 577 nm shows a peak at 2.5-5.10^{-5} O_2 into N_2 and then sharply decreases.

The NOβ and NOγ band intensities reached maximum values at 20-50 10^{-5} O_2, with a slow decrease up to 130 10^{-5} O_2.

At the peak position of N2O*, the I_{N2O*}/I_{N2*} ratio is about 10. It is taken the following rate coefficients and radiative frequencies :

- $K_eA(N_2O*) / k_{-e}$= 4 10^{-18} cm3s-1 [14], in ref.16 : k_a=1.10^{-33} cm^{6}s^{-1} and k_f = 2.8 10^{-11} cm^{3}s^{-1} [18] and : A(N_2*)= 7.76 10^4 s^{-1} [19].

As [N_2] = 2.4 10^{19} cm^{-3} at the atmospheric gas pressure at room temperature, it is deduced from eq.8 that [O(^{1}S)] = 6 10^{10} cm^{-3} as [N] = 4 10^{14} cm-3.

The O(^{1}S) metastable and N atom dissociation rates are thus [O(^{1}S)]/[O_2] = 10^{-4} for 2.5 10^{-5} O_2 into N_2 and [N]/[N_2] = 2 10^{-5}.

4. Sterlilization results in the N_2 and N_2-O_2 afterglows

Calibrated drops of B-Stear. Spores, diluted in distilled water and dried at 40°C during 30 min., have been deposited on glass plates and then introduced in a 250cc box which is connected to the flowing afterglow.

The numbers of survivors after several times of the post-discharge treatment are reproduced in **Figure 4**. The initial number of B-Stear.spores was 2 10^5.

After a treatment time of 30 minutes, it remained 6 10^2, 2 10^2 and 1 10^2 spores in pure N_2, N_2-(2.5 10^{-4}) O_2 and N_2-(2.5 10^{-5})O_2, respectively.

As shown in **Figure 3**, the N–atoms are alone in pure N_2 post-discharge (with C-atoms in impurity). In the N_2–(2.5 10^{-4}) O_2 gas mixture, the NOγ(248nm) band intensity was at its maximum value. It is the O(^{1}S) metastable atoms which reached their maximum value in the N_2-(2.5 10^{-5})O_2 mixture.

A constant value of N-atom density was obtained in the three studied gas mixtures.
In the results of sterilization as shown in **Figure 4**, it appears that the $O(^1S)$ metastable atoms, coupled to the N-atoms, are the most efficient species to inactivate the B-Stear. spores, in spite of the small quantity of $O(^1S)$ in respect to N-atoms : $O^1S/N=10^{-4}$ as presently found.

5. Concluding remarks

Besides the biocidal effect previously observed in pure nitrogen and attributed to N atoms, working with small admixtures of oxygen in pure N_2 has allowed to evidence separately increasing efficiency of UV radiation and $O(^1S)$ metastable. Density of this latter has been measured.
This exhibits similarities and differences as compared to other studied afterglows. In [1], UV photons and oxygen atoms are shown as being the main inactivating species in N_2-O_2 low pressure mixtures. Owing to steps occurrence in the inactivation glow, their role is assumed to be killing and etching, respectively. In the case of atmospheric air studied in [11], there is no active UV emission but O and OH and NO_2 are present and are evidenced as being highly reactive species, playing the main role in microorganisms destruction. Nitrogen dioxide concentration has been measured around 500ppm.
The present study brings thus new results in the case of a specific atmospheric pressure afterglow with specific kinetic schemes for active species production. It remains however that the reduction effect is still low and has to be increased significantly in view of the chosen application. This could be achieved by increasing oxygen metastable atoms concentration.

References

[1] S.Moreau, M.Moisan, M.Tabrizian, J.Barbeau, J.Pelletier, A.Ricard and L'H. Yahia, 2000, J.Appl.Phys.88, 1166
[2] M.Moisan et al., 2003, Proceedings of the Vth Int.Workshop of Microwave discharges, Greifswald 2003, p.210-221.
[3] S.Villeger, S.Cousty, A.Ricard and M.Sixou, 2003, J.PhysD36, L1
[4] S.Villeger, A.Ricard and M.Sixou, 2004, Eur.Phys. J.Applied Phys.26, 203
[5] IEEE Trans.Plasma Sc.–Special Issue on nonthermal medical/biological application of Ionized gases and EM fields-30 (2002). See M.Laroussi, p.1409
[6] A.Sharma, A.Pruden, Z.Yu, G.Collins and A.M Pointu, 2004, IEEE Trans.Plasma Sc (submitted to publication)
[7] A.Ricard, M.Moisan et S.Moreau, 2001, J.PhysD34, 1203
[8] A.Ricard, A.Besner, J.Hubert and M.Moisan, 1988, J.Phys.B 21, L579
[12] P.Merel, M.Tabbal, M.Chaker, M.Moisan and A.Ricard, Plasmas Sources SC. And Tech.7 (1998) 550
[9] M.Ganciu, A.M Pointu, B.Legendre, J.Orphal, M.Vervloët, M.Touzeau, N.Yagoubi, 2003, USPTO patent request 10/610158
[10] J.Larbre, M.Ganciu, A.M.Pointu, M.Touzeau, J.Orphals, M.Vervloët, 2004, Proc. Int. Workshop on Cold Atmospheric Pressure Plasmas Sources and Applications, Ghent-Belgium, p 93-96
[13] J.Larbre, A.M.Pointu, M.Ganciu, 2004, Bull. American Physical Society **49**, p 714
[11] M.Laroussi, F.Leipold, 2004, Int.J.Mass Spectry 233, 81
[14] G.Black, R.L Sharpless and T.G Slanger, 1975, J.Chem.Phys.63, 4546
[15] D.Pagnon, A.Ricard, S.Cantacuzene and T.Sindzingre, 1987, VIDE-Suppl.284, 20
[16] N.Gherardi, G.Gouda, E.Gat, A.Ricard and F.Massines, 2000, Plasma Sources Sc.Tech.9, 340
[17] C.Jaoul, T.Belmonte, T.Czerwiec, A.Ricard, Eur.Phys J.Appl.Phys.26(2004)227
[18] A.Ricard, J.Tetreault and J.Hubert, 1991, J.Phys.B24, 1115
[19] C.O.Laux and C.H.Kruger, 1992, J.Quant.Spect.Rad.Transfer 48, 9

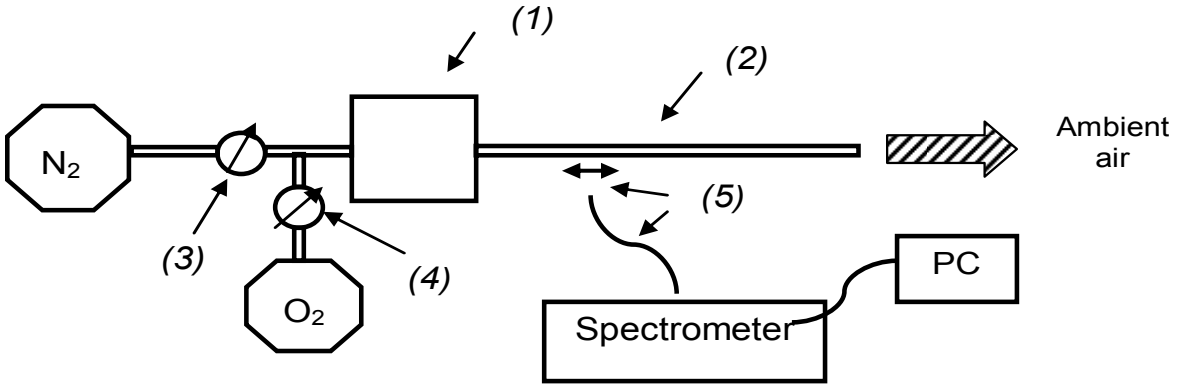

Figure 1 :
Experimental set up
(1) discharge (2) flowing afterglow (3) 0-50000sccm flow-meter (4) 0-50sccm flow-controler (5) optical fiber and collimating lens

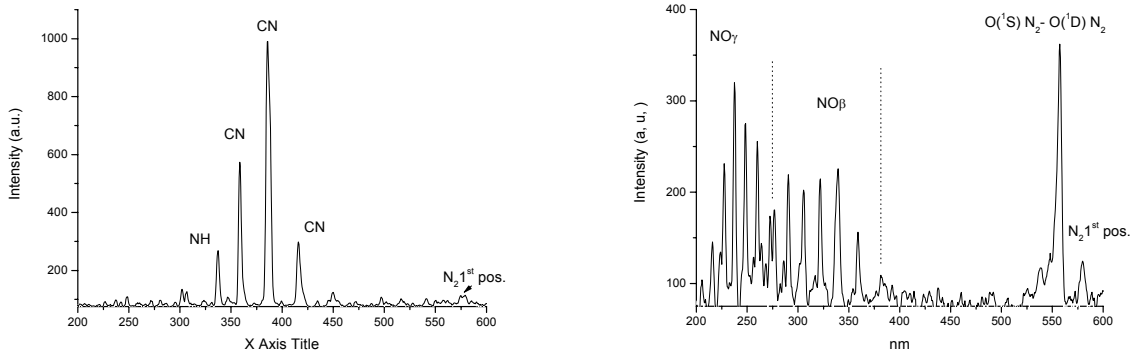

Figure2 : a : "pure" N_2. 99.995% quality b : N_2–(2.5 10^{-2})O_2 mixture
Emission spectra in the afterglow, at a distance x=10cm of the plasma

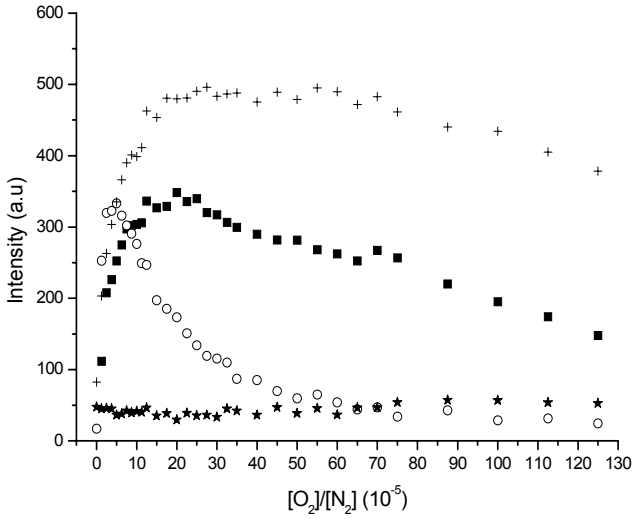

Figure 3 :
Variations of several band intensities versus the O_2 proportion into N_2 :
■ NOγ 248 nm,
o $O(^1S)N_2$-$O(^1D)N_2$ 557 nm,
⁎ N_2 1st pos. 580 nm,
+ NOβ 320.7 nm

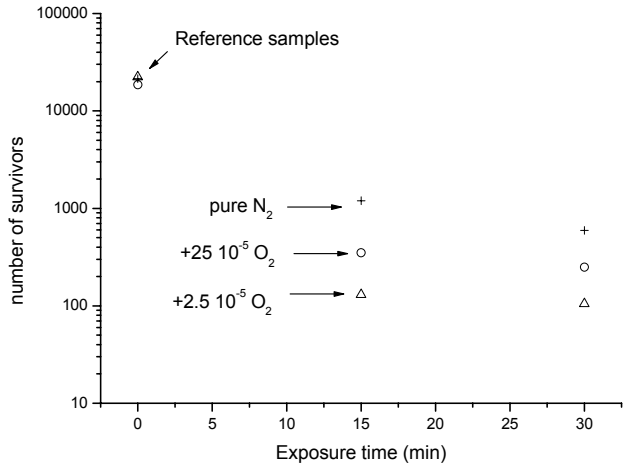

Figure 4 :
Numbers of survivors after several exposure times to the post-discharge

Surface structure and haemocompatibility of N-doped DLC films deposited by hot wire plasma sputtering of graphite.

V.N. Vasilets[1,2], A. Hirose[2], Q. Yang[3], M.N. Foursa[2], F. Boccafoschi[4], D. Mantovani[4], Yu.M. Shulga[5], A. Sarkissian[6], A.V. Kuznetsov[1], V.I. Sevastianov[1]

[1] *The Research Center for Biomaterials, Research Institute of Transplantology and Artificial Organs, Moscow, Russia*
[2] *Plasma Physics Laboratory, University. of Saskatchewan, Saskatoon, SK, Canada*
[3] *Department of Mechanical Engineering, University. of Saskatchewan, Saskatoon, SK, Canada*
[4] *Bioengineering and Biotechnology Unit – St.-Francois d'Assise Hospital Research Center & Laval University, Quebec City, Canada*
[5] *Institute of Problems of Chemical Physics, Chernogolovka, Russia*
[6] *Plasmionique Inc., Varennes, Quebec, Canada*

Abstract

Hot wire plasma sputtering of graphite in a mixture of Ar and nitrogen was used to deposit N-doped DLC films on PTFE and Si supports. The surface and bulk composition of DLC films were analysed by XPS, FTIR, EELS and Auger depth profiling spectroscopy. The relationship between chemical composition, electronic structure and biological performances of deposited films has been investigated.

Keywords: plasma deposition, DLC films, cell adhesion, haemocompatibility

1. Introduction

Plasma assisted deposition of amorphous carbon and diamond-like carbon (DLC) thin films is an attractive technique to improve the surface mechanical properties and biocompatibility of medical polymers. The DLC coating influences in particular the interaction and adsorption of different proteins which in turn, controls the cell adhesion and behaviour. The DLC coatings have been demonstrated to be biocompatible in vitro and vivo in cardiovascular and orthopedic applications [1]. The past few years saw A growing interest in studying the structure and properties of N-doped DLC layers [1,2] has been seen in a past few years. It appears to be a promising coating to improve film properties such as elasticity, electrical conductivity, surface energy and to control biological performance [3].

Earlier [2,3] we reported the possibility of using hot wire plasma sputtering of graphite for deposition of DLC films with high adhesion to the hydrophobic PTFE support. The improved haemocompatibility of PTFE film after DLC coating was obtained on the stage of platelet adhesion. In this article we investigated the influence of nitrogen doping on the chemical and electronic structure of DLC coatings and correlation of a blood compatibility parameters such us platelet adhesion and degree of activation with the surface chemical composition and fraction of sp^3/sp^2 bonded. The other biological parameters of the surface of N-doped DLC films like vascular endothelial and smooth muscle cells attachment and growth, as well as fibrin formation and neutrophils adsorption was also estimated.

2. Experimental details

2.1. Plasma deposition techniques

The film deposition was carried out in hot wire plasma reactor. [2,3]. The square graphite target (25 mm × 25 mm) was located at 10 mm over the round sample holder (diameter 50 mm). The samples of PTFE and Si were exposed to deposition in glow discharge plasma by sputtering the target in the flow of Ar with various percentage of nitrogen (partial pressure 3 – 40 %). The temperature of sample holder during deposition was in the range 180-210^{o}C depending on plasma conditions and hot wire temperature. The last one was controlled by Micro Optical Pyrometer (Pyrometer Instr. Co., USA) and varied in the range 1950 – 2100 K depending on the filament current. The total gas flow and pressure in the plasma chamber was maintained at 25 sccm and 5×10^{-2} torr respectively. The temperature of sample holder during deposition was measured by chromel/alumel thermocouple

and ranged in 180-210 ^{0}C depending on plasma conditions. After deposition the samples were cooled in the reaction chamber under ventilation by Ar flow to the room temperature.

2.3. Surface characterization

The rate of deposition and thickness of carbon films deposited on Si wafer was measured by weighing of the sample before and after deposition on analytical microbalances, Auger depth profiling and AFM measurement of the profile after scratching.

The surface chemical composition before and after deposition on PTFE films was analyzed by XPS spectroscopy (Kratos Axis Ultra spectrometer, USA). The XPS spectra were obtained with 90-degree take-off angle by using monochromatised Al K_α source. The charge neutralizer was on for all the analysis.

The scattering spectra in micro-Raman mode were measured using 633 nm excitation wavelength of helium neon laser. The scattering light was collected in backscattering with CCD camera, using Renishaw Model 2000 Raman spectrometer. The incident laser power on the sample was in the range 0.3 – 1.2 mW.

IR spectra of carbon films deposited on Si substrate in the same run with polymer film were recorded using FTIR spectrometer Perkin-Elmer 1720X (Perkin-Elmer, USA). The IR spectrum of Si support was subtracted from the sample spectrum to obtain the transmittance spectrum of carbon layer.

Electronic structure of carbon coatings was investigated by electron energy loss spectroscopy (EELS). The energy loss spectra were measured in reflection mode using Kratos Axis Ultra spectrometer equipped with Kratos WX-410 electron gun system. The hemispherical electrostatic analyzer is used in retarding mode at the pass-energy 40eV. The primary electron beam energy was 1000eV. The analyzing electron beam is scanned on the area about 2mm x 2mm.

Concentration profiles of C, N and O atoms in the carbon film deposited on the Si wafer were performed with a scanning Auger spectrometer PHI-560. The low energy (1 keV) Ar^+ ions and a grazing sputter angle profiling (80° with respect to the normal) was used to improve the depth resolution and minimize the destruction of surface layer

The surface morphology of the samples was examined by AFM (model PicoSPM, Molecular Imaging, USA) and scanning electron microscopy (SEM) using secondary and backscattered electrons, 5 kV accelerating voltage, and magnification up to 5000 (JSM T330, JEOL, Japan).

2.3. Biological testing

Biological properties of carbon-coated PTFE were investigated using platelet adhesion testing, vascular endothelial and smooth muscle cells attachment and growth, whole blood contact and thrombelastography technique.

Platelet-rich plasma (PRP) was obtained by centrifugation of the whole blood at 100 g for 20 min at room temperature. The small PRP drops (50 µl) were placed onto sample surfaces and incubated in humid atmosphere for different periods (from 5 to 30 min). The samples incubated with PRP for 15 min were chosen for further analysis since the number of platelets adhered to the surface during this time interval was appropriate for quantification. Platelet adhesion patterns were investigated by SEM. The study of platelet adhesion was performed with informed consent of the donors. Five volunteers were included in the series of repeated experiments. The bottom leukocyte rich suspension obtained after centrifugation of blood was used to extract neutrophils. A suspension of $3x10^8$ neutrophils was labelled with 300µCi of In^{111} for 30 minutes at room temperature. Then the suspension was rinsed twice with PBS to remove the unbounded In^{111}. 100µl of the labelled suspension were incubated for 2h at 37°C. After the incubation, samples were rinsed twice with PBS and the amount of neutrophils uptake was evaluated by a gamma scintillation counter

Endothelial cells and smooth muscle cells were isolated from porcine aorta. Smooth muscle cells were subsequently extracted and seeded in tissue-culture flasks coated with porcine gelatine 0.2%. Cells were maintained at 37ºC in 5% CO_2-humified atmosphere and harvested by trypsinization when a monolayer was reached. Cells used as controls were seeded on Petri dishes or cover slides previously treated with porcine gelatine 0.2% (Sigma Aldrich, Milwaukee, USA). Adhesion of blood cells as well as the formation of fibrin on the sample surface was investigated by SEM. Immediately after collection, blood was incubated on the surfaces 30 minutes at 37°C. Than, the samples were washed twice with PBS to remove the non-adherent cells from the

surface and subsequently treated for SEM analysis. The thrombogenicity index was measured using a standard equipment Thrombelastograph D (Hellige GMBH, Germany). The measurement procedure is based on viscoelastic test that characterises formation and strength of the blood clot over the time.

3. Results and discussion

Identification of nitrogen containing groups in the N-doped DLC films was done by FTIR spectroscopy.

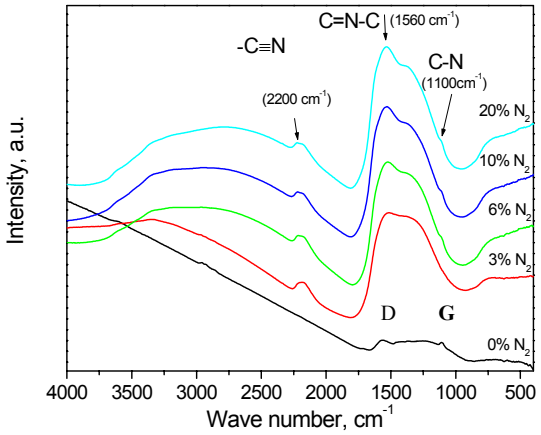

Figure 1 FTIR spectra of DLC films, deposited by sputtering of graphite in (Ar +N_2) plasma at different concentration of N_2 in gas phase (deposition time 2 h)..

Figure 1 shows FTIR spectra of DLC films, deposited by sputtering of graphite in (Ar +N_2) plasma at different concentration of N_2 in gas phase. The broad main band in the region 1000 – 1700 cm^{-1} is appeared with the doping of nitrogen and is attributed to the stretching vibration of CC bonds. Usually CC bonds in pure carbon films are not active in the IR absorption but only detected by Raman spectroscopy due to the high symmetry. However, carbon films doped with different amount of nitrogen reveal Raman-active G (1575 cm^{-1}) and D (1360cm^{-1}) bands in the IR spectra. Symmetric CC bonds become IR-active due to the nitrogen replacement of carbon which breaks the symmetry in six-fold carbon ring structure. The nitrogen replacement gives rise to a net dipole moment and makes active IR absorption. The IR absorption appeared at 2200, 1560 and 1100 cm^{-1} is indicated the formation of -C≡N, -C=N- and –C-N groups respectively in nitrogen doped carbon films.

Raman spectra (see Figure 2a) also show two basic C–C bands around 1575 cm-1 (*G* line) and 1360 cm-1 (*D* line) usually detected in amorphous and diamond-like carbon films. The band at 1575 cm^{-1}, in case of Raman scattering for amorphous carbon and polycrystalline diamond films, is usually assigned to graphite like sp^2 bonded carbon (G peak) while the scattering in the low frequency region around 1300 cm^{-1} has to be interpreted as scattering of sp^3 –bonded carbon plus a possible contribution of a disordered sp^2 phase (D peak). The optical probing depth for Raman spectroscopy, d , is determined by the absorption coefficient α for carbon layer at our excitation wavelength of 633nm, $d=1/(2x\alpha)$. Taking the optical constants for different carbons we could estimate the Raman probing depth to be 100 – 500 nm, which is comparable with the layer thickness. That is why the intensity of Raman bands for the N-doped carbon layers increased with the increase of nitrogen concentration in plasma. According to our measurements the increase of nitrogen concentration in plasma leads to the increase of deposition rate.

Figure 2b shows EELS spectra for N-doped carbon films in comparison with graphite. All curves contain elastic peak and two other peaks whose origin may be attributed to the plasmon excitation of all valence electrons (high energy $\delta+\pi$ plasmon peak) and π-electrons (low energy π-plasmon peak). The intensities and

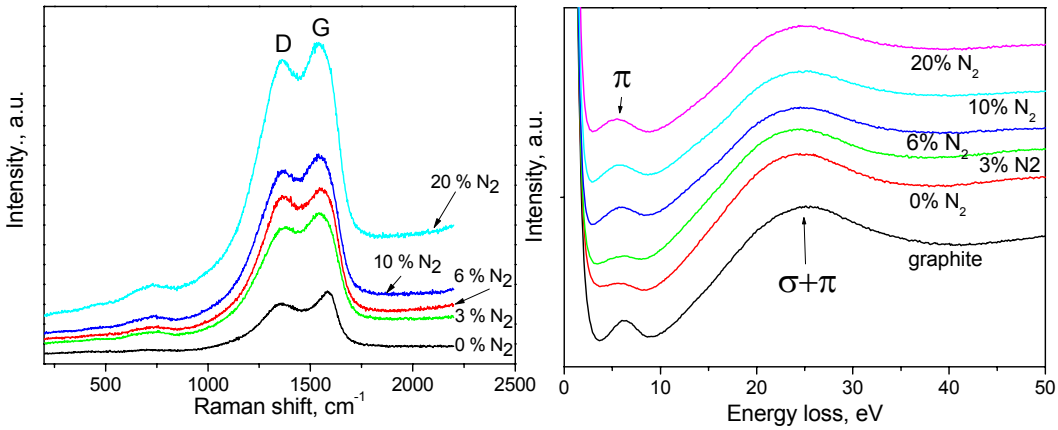

Figure 2 Raman spectra (a) and. energy loss functions (b), obtained for N-doped DLC films, deposited by sputtering of graphite in (Ar +N_2) plasma at different concentration of N_2 in gas phase (deposition time 2 h).

positions of the individual plasmon peaks for graphite and carbon film were calculated after background correction and subtracting the elastic peak, fitted by Gaussian function. The relative intensity ratio for these bands is proportional to the relative number of π-electrons, which is equal to 0.25 for graphite: I(π)/I(δ+π) = k*0.25. By calculating the constant parameter, k, from the graphite energy loss spectrum we can obtain the relative number of π-electrons in our carbon film from the measured intensities of two bands. The percentage of sp^3 value determined from EELS spectra of carbon films deposited at different nitrogen concentrations in plasma are given in Table 1. The substantial fraction of sp^3 bonded carbon around 60% was detected in DLC films deposited at low (3-6%) concentration of nitrogen in plasma. The increase of nitrogen in plasma and on the surface of our carbon film gives rise to the decrease of sp^3 fraction down to 20%. The energy of the main plasmon (δ+π) in carbon materials $\hbar\omega_p$ estimated from the energy loss spectrum along with the known chemical composition allows estimating the specific density of our carbon layers relative to graphite [2]. This value (also shown in the Table 1) is around 1,9 g/cm^3 for all our N-doped DLC films. Such a specific density is rather high in comparison with the density of polymer films but less then that observed for graphite.

The chemical compositions for DLC layers, deposited at different concentrations of nitrogen in plasma determined by XPS are also presented in the Table 1. One can see that the concentration of nitrogen on the surface reaches an upper limit 30,7 at.% with the increase of N_2 concentration in plasma. The presence of a relatively high concentration of oxygen (10 –14 at%) on the carbon layer may be explained by surface contamination and bonding of oxygen in post reactions with free radicals and other chemically active species formed by plasma treatment.

% N_2 in plasma	*depos. rate nm/min*	*C at%*		*N at%*		*O at%*		*sp3/ (sp^3+sp^2) %*	ρ *g/cm^3*
		bulk	*surface*	*bulk*	*surface*	*bulk*	*surface*		
0%N2	4,0	90,2	77,6	6,8	7,8	3,0	14,6	64	1,97
3%N2	7,9	85,9	64,8	11,3	23,8	2,8	11,4	62	1,92
6%N2	6,5	85,5	59,1	12,4	28,9	2,1	12,0	26	1,91
10%N2	6,4	85,7	58,8	12,0	29,6	2,3	11,6	23	1,89
20%N2	9,0	85,4	59,2	12,6	30,7	2,0	10,1	20	1,96
graphite	-	100	100	0	0	0	0	0	2,25

Table 1. Chemical and electronic structure of N-doped DLC films (from XPS, Auger depth profiling and EELS data).

Depth profiling measurements has shown the concentrations of carbon, nitrogen and oxygen atoms in the bulk. Only the traces of oxygen (2 -3 at. %) was observed in the bulk of N-doped DLC films, thus confirmed the post deposition origin of oxygen containing groups on the surface (see Table 1). The interesting finding is that the maximum concentration of nitrogen in the bulk (12,6%) is much less than that detected on the surface (30,7%). Possible explanation to that may be the segregation of nitrogen from the bulk to the surface in the

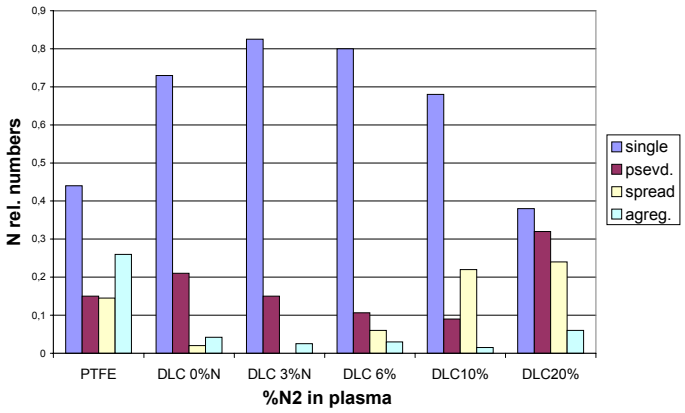

Figure 3. Diagram representing relative platelet quantities for different morphological classes observed by SEM for untreated and N-doped coated PTFE films deposited in different plasma conditions.

process of annealing the sample from 180-200^{0}C to the room temperature after deposition. The higher concentration of nitrogen in the bulk could be thermodynamically non-favourable for the structure of our DLC film at room temperature. Very close maximum concentration of nitrogen (9,7 at%) was reached by the authors [4] in the C:N films deposited in quite different plasma conditions by sputtering of graphite in RF discharge in the mixture of Ar with nitrogen.

To study the haemocompatibility of N-doped DLC film on the stage of cell adhesion the total number and aggregation of adhered platelets was measured. It is generally known, that increased platelet adhesion, activation and aggregation on implant surfaces exposed to blood initiates the formation of thrombus. In vitro analysis shown substantial decrease of total platelet adhesion and suppressed activation for all N-doped DLC coated samples in comparison with untreated PTFE The activation of platelets can be estimated by their morphology analysis. The better blood compatibility of the material is associated with the lower amounts of adhered, activated, spread or aggregated cells. In comparison with the surface of original PTFE which exhibits intensive platelet spreading and aggregation, N-doped DLC coating shows mainly single non-activated platelets and substantially less amount of activated, spread and aggregated platelets (Figure 3). The effect depends on the surface structure and concentration of nitrogen. The minimum activation of platelets was observed for the carbon films deposited with 3% nitrogen in plasma. These films contain 23,8% of nitrogen on the surface and are characterised by the relatively high content (62%) of sp^3 fraction. (see Table 1).

Analysing clotting time changes and trombogenicity factors we have found that N-doped DLC coating do not improve clotting time parameters and blood viscoelastic properties. However, investigation of cell

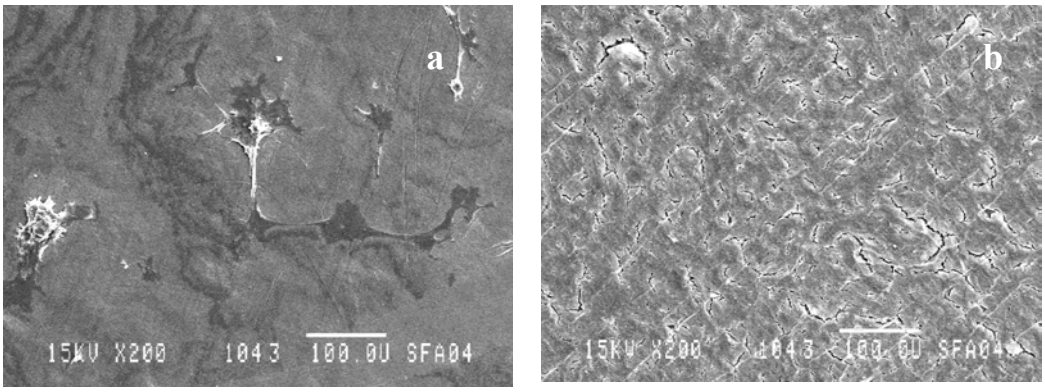

Figure 4. Endothelial cells attachment on virgin PTFE (a) and PTFE coated by N-doped DLC layer (7,8 at.%N) (b) after 72 hours of seeding.

culturing show very promising results. Endothelial and smooth muscle cells were analysed by SEM after 72 hours seeding. Only a low number of cells are able to adhere but not to proliferate on the virgin surface. In fact, even morphology displayed on untreated PTFE shows a bad spreading and numerous cases of apoptotic cells. DLC coated PTFE offers a better environment for cells, showing a good morphology and reaching a confluent monolayer 72 hours after seeding (see Figure 4). Based on these results, we can conclude that DLC coating strongly improves biological performances, allowing the formation of a cellular anti-thrombogenic layer on the surface, miming the natural vascular environment.

Study of the whole blood interaction with the surface allow us to analyse the processes of fibrin formation and red blood cells attachment. DLC-coated PTFE shows a little amount of fibrin and a virtually absent red cells attachment, while a fibrin net with numerous red cells entrapped was found on the untreated surface. Correlating these data with the time required for fibrin formation, we can suppose that fibrin do not strongly attach on DLC-coated PTFE. Thus, also from this point of view, the surfaces after the coating with DLC films are less thrombogenic then the untreated ones.

3. Conclusions.

By doping DLC films with nitrogen, different biological reactions of cells can be continuously adapted to the desired value. The results obtained are promising for further applications of N-doped DLC coating in cardiovascular field.

Acknowledgements. This research has been sponsored by the Canada Research Chair Program and by the Natural Science and Engineering Research Council of Canada.

References

[1] R. Hauert, Diam. Rel. Mat., 12, 583 (2003)
[2] V.N. Vasilets , A. Hirose, Q. Yang, A. Singh, R. Sammynaiken, M. Foursa, Y.M. Shulga, Appl. Phys. A, 79**,** 2079 (2004).
[3] V.N.Vasilets, A.Hirose, Q.Yang, A. Singh, R. Sammynaiken, Yu.M. Shulga, A.V. Kuznetsov, V.I. Sevastianov, Hot wire plasma deposition of doped DLC films on fluorocarbon polymers for biomedical applications, Chapter 5 in Plasma Processes and Polymers, Plasma Deposition of Thin Films, R. d'Agostino, P. Favia, C. Oehr, and M. R. Wertheimer. (eds) , Wiley-VCH, p.65 (2005).
[4] C.J. Torng, J.M. Sivertsen, J.H. Judy, C. Chang, J. Mat. Res., 5, 2490 (1990).

Low Damage Photoresist Material Modification with Electron Beam-Generated Plasmas

S.G. Walton[1], B.J. Orf [2], D. Leonhardt[1], G.S. Oehrlein[2], and R.F. Fernsler[1]

[1]*US Naval Research Laboratory, Plasma Physics Division, Washington, DC 20375-5346*

[2]*University of Maryland, Department of Materials Science and Engineering and Institute for Research in Electronics and Applied Physics, College Park, MD 20742*

Abstract

The Naval Research Laboratory has developed a materials processing system based on plasmas produced by high-energy (≈ 2 keV) electron beams. These plasmas have numerous properties that allow operating regimes not accessible in systems using conventional plasma sources. The system is being used to examine the etching behavior of 193 nm and 248 nm photoresist material in argon plasmas. The initial results of this work are presented.

Keywords: Plasma Source, Electron Beam, Etching, Photoresist

1. Introduction

The Naval Research Laboratory has developed a materials processing system based on electron beam-generated plasmas for use in a variety of processing applications [1]. The systems utilizes a magnetically collimated, sheet of high-energy (≈ 2 keV) electrons to produce a planar plasma. The resultant plasma has unique characteristics when compared to conventional low-pressure plasma sources. When multi-kilovolt electrons pass through a gas, ionization is the dominant mechanism with the cross-sections being similar for most gases. Thus, little energy is consumed by non-ionizing, inelastic collisions and species generation can be regulated by adjusting the background gas concentrations. This in contrast to conventional discharges where the dominant inelastic collisions consume most of the delivered energy and ion production favors the species with the lowest ionization potential.

Also, in conventional discharges, the boundaries of the ionization region are not well defined and can vary greatly with gas pressure and composition or chamber geometry. In electron beam-produced plasmas, the ionization region is limited to the beam volume, which is well defined and uniform when the beam is magnetically confined. Outside the beam channel, the plasma density and ion composition are altered by ion-electron, ion-neutral, and ion-ion reactions and so electrodes (or substrates) can be independently positioned to take advantage of changes in the outwardly diffusing flux of ions and radicals.

Perhaps the most notable difference of electron beam-generated plasmas, is a low electron temperature. Conventional plasma discharges rely on externally applied electric fields to raise the plasma electron temperature so that a fraction of those electrons are energetic enough to ionize the gas and sustain the plasma. Because the electron beam ionizes the gas, no heating of the plasma electrons is required and they are quickly cooled by elastic and inelastic collisions. The resulting plasma electron temperatures are found to be 1.0 eV or lower [2], depending on the background gas. The temperature in molecular gas backgrounds tends to be lower than in noble gases due to the availability of excitation states that extend down to near zero energies. Since the electron temperature determines the plasma potential, ions incident to unbiased surfaces will also exhibit low energies [3], typically below 5 eV.

It is with these attributes in mind that electron beam generated plasmas are being used to investigate the etching behavior of 193 nm and 248 nm photoresist materials. The 193 nm photoresist material is, by necessity, thinner and based on a different polymeric structure than 248 nm photoresist material but has been found to be less robust than 248 nm photoresist material when subject to conventional argon and C_4F_8 based discharges [4]. In this work, we present and discuss experimental characterizations of electron beam-generated plasmas produced in argon, which are used to etch 193 nm and 248 nm photoresist material. The etch behavior of the photoresist materials will also be discussed.

2. Experimental

A number of systems are currently in use for plasma diagnostics and materials processing. While the chamber geometries vary, all systems operate in a similar fashion and consist of a few common components, which are shown in Fig. 1. A sheet-like beam of energetic electrons is produced by pulsing a linear hollow cathode to -2 kilovolts for a fixed pulse width and duty factor. The emergent beam passes through a slot in a grounded anode and is then terminated at a second grounded anode located further downstream. The electron beam volume between the two anodes defines the ionization source volume, with the dimensions set by the slot size (beam thickness and width) and the anode-to-anode distance (beam length). For these applications, the range of a 2 keV electron beam is much larger than the anode-to-anode length. A set of external magnetic field coils produce a coaxial magnetic field of 150 Gauss or higher. Magnetic fields of this magnitude keep the expansion of a 2 keV electron beam in 50 mTorr to less than 0.5 cm at a distance of about 50 cm [5].

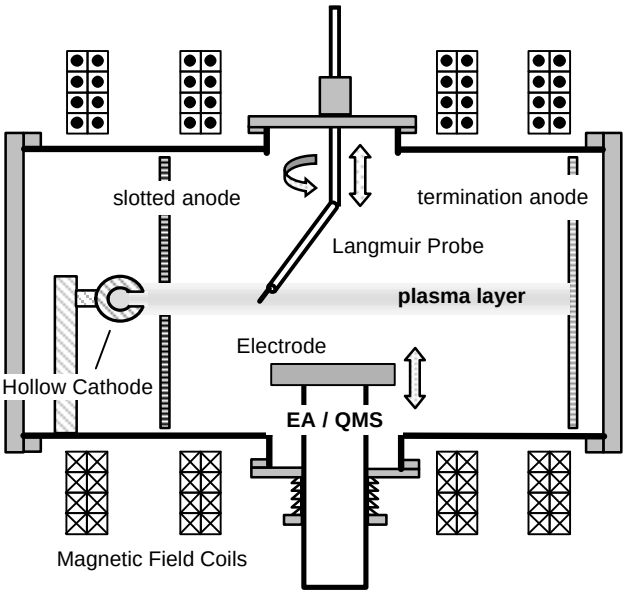

Fig. 1 The experimental apparatus used for plasma characterization.

Plasma Diagnostics

The experimental apparatus has been discussed previously [6] and is shown in the schematic of Fig. 1. The source volume in this system measures approximately 1 cm thick by 25 cm wide by 43 cm long. A dual energy analyzer/mass spectrometer (Hiden EQP 300 Plasma Probe) was used to measure mass-resolved ion energy distributions and ion fluxes sampled through a 20 μm diameter aperture located in the center of a grounded 5.7 cm diameter stainless steel electrode. Because the system was pulsed, all data acquisition was time resolved and the gating techniques have been described elsewhere [6].

The plasma electron temperature and plasma density, were determined using a Langmuir probe that was mounted on a multi-motion feedthrough and constantly heated with an internal resistive element to reduce surface contaminants. The electron temperature and plasma density were derived from a best fit of the I-V trace to a Maxwellian electron energy distribution using time-resolved probe techniques that have also been described elsewhere [7].

Etching Experiments

Details of the electron beam source and reactor used for the etching experiments can be found in [8] and the approach to system operation for etching applications have been previously described [9]. The system was similar to the experimental configuration of Fig. 1 except all diagnostics are absent and the ground electrode was replaced by a biasable stage upon which the photoresist material is mounted. Rf power was applied to the stage through a matchbox by an rf amplifier driven at 13.56 MHz. The rf signal was synchronized to the electron beam pulse so that the rf power was well coupled to the electron beam–produced plasma, thereby minimizing any undesirable rf discharge effects. Stage bias and currents were measured by an oscilloscope probe and current transformer on the atmosphere side of the electrical feedthrough. Forward and reflected powers were determined using an inline directional coupler.

1-2 cm^2 samples of blanket 248 nm (1000 nm thick) and 193 nm (400 nm thick) photoresist films on silicon substrates were adhered to the stage with silver print epoxy, placed in vacuo, and the chamber was evacuated to a pressure of at least ~10^{-5} Torr. The samples were then subjected to plasmas produced in 50-60 mTorr of high-purity argon (50 sccm) with the cathode operating at –2 kV for a range of pulse widths and duty factors in a 150

Gauss magnetic field. The samples were positioned 2.5 cm from the electron beam axis. Post-treatment, the systems was again evacuated to 10^{-5} Torr and then brought to atmosphere with nitrogen. *Ex situ* sample analysis included ellipsometry to determine etch depths and changes in refractive index, contact angle measurements of water drops on the surface, and x-ray photoelectron spectroscopy (XPS) to assess the surface chemical structure.

3. Results and Discussion

Plasma Diagnostics

Plasma diagnostics have been carried out on plasmas produced in 50 mTorr of argon using an electron beam produced by pulsing the hollow cathode to –2 kV for 6 ms at a 10% duty factor. Shown in Fig. 2 are Ar^+ ion energy distributions measured at a grounded electrode positioned 2.5 cm from the electron beam axis. One distribution (open circles) was acquired during a gate extending over nearly the entire pulse period. The other distribution (solid circles) was limited to the last millisecond of the electron beam pulse. The distributions indicate a low incident ion energy but clearly differ in breadth and shape. Complimentary probe data, measured on the beam axis and directly above the electrode, is shown in Fig. 3a. During the course of one period, the electron temperature was characterized by larger values just after the plasma was initiated, followed by a period of near steady-state values, and then a collapse in the afterglow. The electron temperature determines the plasma potential, which then sets the energy range of ions incident to the electrode from the plasmas. It's not surprising then, that the ion energy distribution acquired over the entire period (open circles in Fig. 1) was characterized by a broader energy distribution than the distribution measured when the electron temperature was nearly constant (solid circles in Fig. 1).

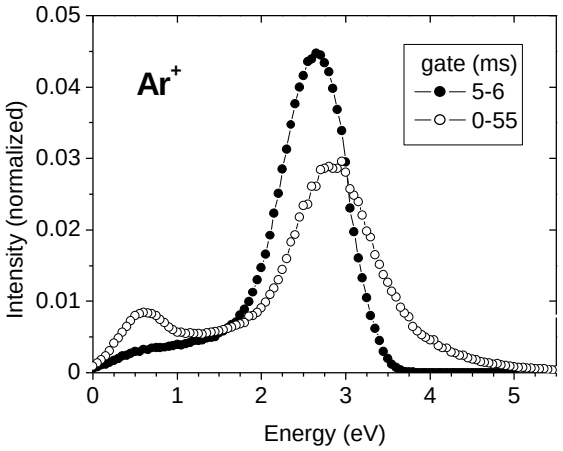

Fig. 2 Ar^+ ion energy distributions measured at a grounded electrode.

Also shown in Fig. 3 are the on axis plasma density and the total Ar^+ ion flux at the electrode. From these plots, it can be seen that the density and flux are reasonably well correlated. The slight temporal difference in relative intensities is expected since the density was measured on-axis and the flux was measured 2.5 cm from the electron beam axis.

A time-dependent ion flux adds a degree of freedom when considering possible surface effects in materials processing applications. A more detailed discussion of the temporal dependencies in argon plasmas can be found in [6]. Important to the etching applications is that the ion flux to the grounded electrode was characterized by low ion energies (< 5 eV). This provides the possibility of exploring the etch response at or near sputtering threshold energies in a high flux, low pressure environment. To explore higher ion energies, an applied bias is required. Previous studies [10] showed this can

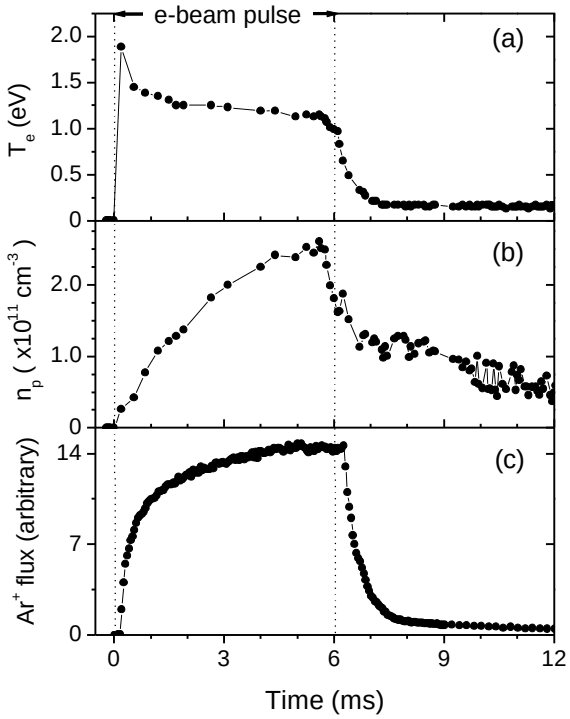

Fig. 3 (a) Electron temperature and (b) plasma density measured on the electron beam axis and (c) the Ar^+ ion flux measured at a grounded electrode located 2.5 cm from the beam axis.

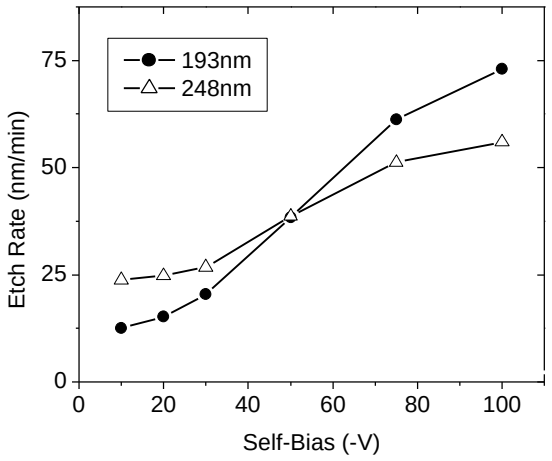

Fig. 4 Photoresist etch rate in electron beam-generated plasmas produced in argon.

be accomplished without altering the electron temperature, thereby providing a narrow energy distribution about a selected energy.

Photoresist Etching

Our work to date has focused on etch rate and limited surface characterization. The etch rate as a function of substrate bias and plasma duty factor for both 248 nm and 193 nm photoresist material are shown in Figs. 4 and 5. The substrate bias is the self-bias induced by the applied rf power, measured by the voltage probe. The experiments of Fig. 4 were carried out using a 4 ms pulse width and a 20% duty factor for a fixed exposure time of 2.5 min. These results are interesting in that the etch rate for the 248 nm photoresist is greater than the rate for the less stable 198 nm photoresist at low self-biases. For self-biases above –50 V the opposite was true, which is consistent with the results found using a transformer coupled plasma source operating at a self-bias of –100 V [4]. The finding of a larger etch rate for the 248 nm photoresist, which is based on a more stable aromatic backbone, compared to the 193 nm material at the low self-bias voltages is surprising. The reason for this behavior is currently being investigated.

The results of Fig. 5 indicate no strong dependence on the duty factor for a fixed pulse width (10 ms) and total exposure time (26 s), using a –10 V self-bias. Note that the relative etch depths shown were normalized by the forward rf power, to eliminate any difference in plasma production caused by operating at widely varying duty factors. Note however, that the slight increase in the etch depth of the 193 nm material with increasing off time suggests the initiation of reactions producing volatile products by the plasma exposure. These reactions, once initiated, will continue without additional particle bombardment and are consistent with a reduced chemical stability of the 193 nm material.

We also have performed ellipsometry, contact angle, and x-ray photoemission studies of plasma-treated photoresist materials. These show increasing surface roughness of both photoresist materials and changes in chemical structure of the 193 nm photoresist material after processing. Results of these studies will be reported in a future publication.

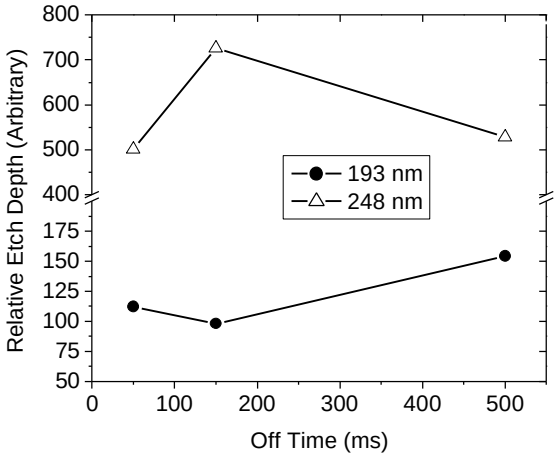

Fig. 5 Photoresist etch rate as function of plasma duty cycle. Off time indicates time between pulses.

4. Summary

Pulsed, electron beam-generated plasmas produced in argon were used to study the etch behavior of 193 nm and 248 nm photoresist material. Plasma diagnostics show the electron temperature, plasma density, and incident Ar^+ have clear time dependencies but in general, the plasmas are characterized by low electron temperatures (1 eV), high densities ($>10^{11}$ cm^3), and low ion energies (< 5 eV) at adjacent grounded electrodes. The etch rates for the photoresist materials were determined for a range of processing conditions. Interestingly, the etch rate of 193 nm photoresist was found to be lower than the etch rate of 248 nm photoresist for low substrate biases (incident ion energies below 50 eV) but was consistent with previous findings at higher bias conditions. Additional work is planned to further explore these behaviors.

5. Acknowledgments

This work was supported by the Office of Naval Research.

References

[1] D. Leonhardt, C. Muratore, S.G. Walton, and R.A. Meger, "Plasma Enhanced Surface Treatments Using Electron Beam-generated Plasmas," *Surf. Coat. Technol*. **188-189**, 299 (2004).

[2] D. Leonhardt, S.G. Walton, D.D. Blackwell, W.E. Amatucci, D.P. Murphy, R.F. Fernsler, and R.A. Meger, "Plasma diagnostics in Large Area Plasma Processing System," *J. Vac. Sci. Technol.* A **19**, 1367 (2001).

[3] S.G. Walton, D. Leonhardt, D.D. Blackwell, R.F. Fernsler, D.P. Murphy, and R.A. Meger, "Ion energy distributions in a pulsed, electron beam-generated plasma," *J. Vac. Sci. Technol. A* **19**, 1325 (2001).

[4] L. Ling, X. Hua, X. Li, G. S. Oehrlein, E. Hudson, P. Lazzeri, N. Coghe, M. Anderle, "Investigation of Surface Modifications of 193 nm and 248 nm Photoresist Materials During Low-Pressure Plasma Etching," *J. Vac. Sci. Technol*. B **22**, 2594 (2004).

[5] W.M. Manheimer, R.F. Fernsler, M. Lampe, and R.A. Meger, "Theoretical overview of the large-area plasma processing system (LAPPS)," *Plasma Sources Sci. Technol*. **9**, 370 (2000).

[6] S.G. Walton, D. Leonhardt, and R.F. Fernsler, "Time-resolved Diagnostics in a Pulsed, Electron Beam-Generated Plasma," *IEEE Trans. Plas. Sci.* **33**, (2005).

[7] D. Leonhardt, W. Amatucci, and G. Gatling, "Temporally resolved Langmuir probe measurements in LAPPS," NRL Memorandum Report NRL/MR/6750—04-8761, 2004.

[8] C. Muratore, D. Leonhardt, S.G. Walton, R.F. Fernsler, D.D. Blackwell, and R.A. Merger, "Low Temperature Nitriding of Stainless Steel in an Electron Beam Generated Plasma," *Surf. Coat. Technol.* **191**, 255 (2005).

[9] D. Leonhardt, S.G. Walton, C. Muratore, F. Fernsler, R.A. Meger, "Etching with Electron Beam Generated Plasmas," *J. Vac. Sci. Technol.* A **22**, 2276 (2005).

[10] S.G. Walton, C. Muratore, D. Leonhardt, R.F. Fernsler, D.D. Blackwell, and R.A. Meger, "Electron beam-generated plasmas for materials processing," *Surf. Coat. Technol*. **186**, 40 (2004).

Plasma polymer-coated pigments for use as corrosion inhibitors in organic coatings

Lin Yang, Hrishikesh Manian and W.J.van Ooij

Department of Chemical and Materials Engineering, University of Cincinnati, Cincinnati, OH-45221, USA

Abstract

Various metal corrosion inhibitors can be added to organic coatings to give them a self-healing property, namely, the corrosion inhibitors can protect the metal, when organic coatings on the metals are damaged, by diffusing to the exposed area. Chromate is one of the most effective and widely used corrosion inhibitors. Unfortunately it has to be replaced, due to its toxicity and carcinogenicity. Many candidates, which can chemically interact with metals and protect them, have been proposed as chromate replacements. However, one of the disadvantages of these pigments is that they are generally too soluble in water. Owing to this, the corrosion inhibition effect cannot be sustained over a longer period of time and the corrosion protection offered by the coating is compromised.

Hydrophobicity and reduced solubility of pigments can be achieved by using a plasma polymerization technique to encapsulate pigments with a hydrophobic film polymerized from fluorine-containing monomers. By tailoring the surface property of pigments in the plasma process, various pigments can be converted into suitable anti-corrosion pigments, which can enhance corrosion prevention for longer periods of time and improve the barring effect of the organic coating system on metal.

In this work, water soluble cerium acetate and sodium vanadate pigments were coated with plasma-polymerized perfluorohexane and octafluorotoluene films. Perfluorohexane does not have a high deposition rate. Therefore, faster-depositing films of octafluorotoluene were used in the latter part of the work. The coated pigments were used as corrosion inhibitors in a water-based organic coating in which the slow release effect of the pigments increases the corrosion resistance of the coating. The coated pigments were tested in an organic primer coating on aluminum alloys for their corrosion inhibiting ability.

Keywords: plasma polymer, corrosion, pigment, hydrophobicity, surface property.

1. Introduction

Corrosion of metals and alloys is a major problem confronting many industries such as automotive, aerospace, and building materials the world over. Organic primer coatings applied on surfaces of metals have been one of the most effective methods to protect metals from corrosion. However, metals may be corroded when any damage happens to organic primer coatings. In this case, inhibitors can be extremely critical in providing corrosion resistance for many metals. Many families of pigments, such as cerium compounds, vanadate, molybdate have been studied and proven to be promising corrosion inhibitors [1-3]. However, one of the disadvantages of these inhibitors is that they are generally soluble in water. Owing to this, those corrosion inhibitors cannot be used in organic coatings on metals and corrosion inhibition effects cannot be sustained over

a long period of time. A slow release property can be achieved by embedding these pigments in a polymer matrix [4]. Plasma polymerization has been explored for obtaining slow release property of organic pigments by coating with a hydrophobic layer of perfluorohexane [5]. Perfluorohexane does not have a high deposition rate and due to this the pigments have to be coated for a long time. In this work we used octafluorotoluene of faster depositing rate. The coated inorganic pigments were tested in organic primer coatings for their slow release property.

2. Experimental

2.1 Plasma polymer coating of the pigments

Perfluorohexane (C_6F_{14}, 95%) and octafluorotoluene (OFT, 98%) provided by Alfa Aesar Inc. were used as monomers to coat cerium acetate (CeAc) pigment and sodium vanadate which were obtained from Alfa Aesar and Fluka, respectively. The process of plasma polymer coating was carried out in a desktop plasma reactor set up with a Pyrex flask set as shown in Figure 1. The top portion was a vertical tube of 130 mm length and 60 mm diameter. The diameter of the flask at the bottom was 75 mm diameter. Two inlets were provided for monomer and pressure gauge. The inductively coupled plasma was excited using an RF generator operating at 13.56 MHz.

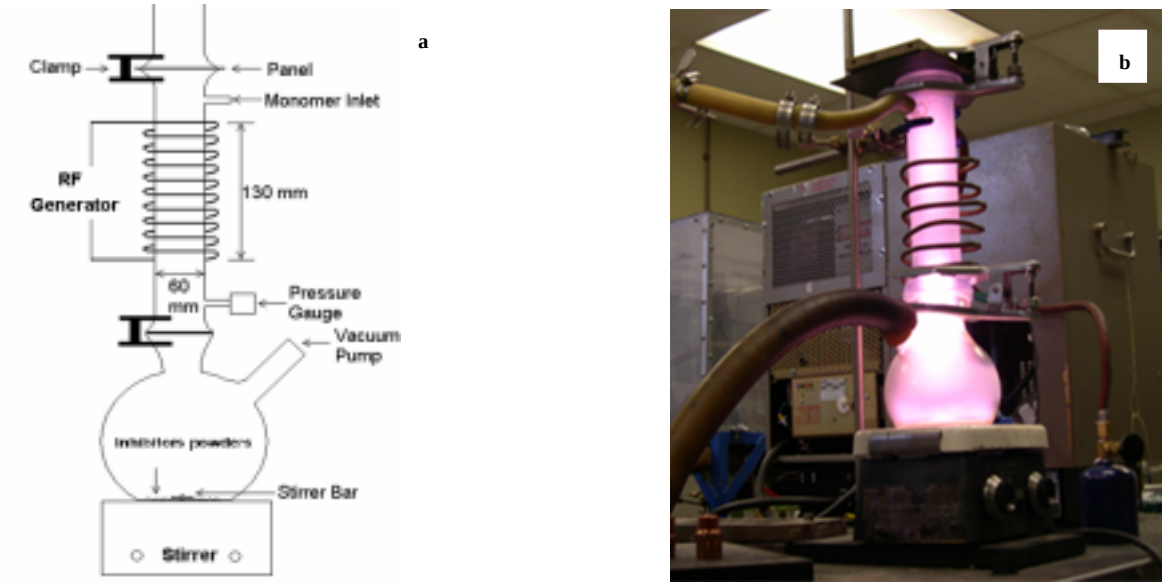

Fig. 1. Schematic view (a) and photograph(b) of the vertical plasma reactor used in this work

Pigment was coated with each monomer respectively. 10 g of the pigment was put in the bottom flask of the reactor. The reactor was pumped down to 7 Pa after which the monomer was introduced till the pressure reading was 45 Pa. The plasma was then generated at a power of 80 W. The pigments were coated for 30 to 60 minutes with continuous stirring by means of a magnetic stirrer.

2.2 Deposition rate study of monomers and characterization of polymer polymerization coating

The deposition rate of the monomers in process of plasma polymer coating was measured by Thermo Gravimetric Analysis (TGA). Ball clay obtained from Kentucky-Tennessee Clay was chosen to be coated in conditions similar to the pigments because it would not decompose before all the plasma polymer coatings were

removed in TGA. The deposition rates were calculated using a similar formula as in [6]. The dynamic wicking properties of pigment particles were measured by using a Lesca dynamic wicking meter. A certain amount of pigment powder was filled in the cylindrical glass tube with an end sealed with nylon mesh. The glass tube was tapped 200 times to ensure the pigment powder was tightly packed. The nylon mesh-sealed end of the vertically placed glass tube was contacted with water in a beaker. By the capillary attraction, water penetrated the pigment powder column through the contact of the nylon mesh with water. The penetration rate of water into the tapped column of pigment was measured using a four digits balance. The contact angle of the powder was calculated using the formula in [7] to determine the increase of hydrophobicity between the surfaces of plasma polymer-coated and uncoated pigment particles.

2.3 Study of slow-release property and durable corrosion inhibition of coated pigments

Fresh AA-2024 T3 substrates were ultrasonically cleaned in ethanol and DC polarizations were carried out on those cleaned AA-2024 substrates in 3.5 w.% sodium chloride solution in the presence of 2000 ppm of the OFT-coated cerium acetate. DC polarization curves were plotted at 10, 100 and 300 hrs. 2000 ppm uncoated cerium acetate and the OFT-coated cerium acetate were added respectively to deionized water to make solutions for conductivity measurement. Conductivities of the freshly prepared solutions were measured using YSI 3200 conductivity meter to verify the slow release properties of plasma polymer-coated pigments.

An organic primer coating was formulated from water based resins and silane. Acrylic resin ECO-CRYL and epoxy resin WD-510 were obtained from Resolution Corporation. Bis-[triethoxysilyl]ethane (BTSE) was provided by Gelest Inc. 1 w.% of pigment was mixed into the organic primer coating by a high shear blender for 5 minutes. The organic primer coating with the pigments uniformly dispersed in it was then applied on the AA-2024 T3 aluminum alloy substrates. Electrochemical Impedance Spectroscopy (EIS) studies were done on these coatings pigmented with plasma-polymer coated pigments by using the ECM8 Electrochemical Multiplexer from Camry Instruments and to test corrosion inhibition of the slowly released pigments over a long period of time.

3. Results and Discussion

3.1 Deposition rate of the monomers

The results of the deposition rate study are shown in Table 1. The OFT shows a deposition rate of 0.335 x 10^{-3} g/cm^2-min, almost three times of the value obtained by perfluorohexane. The deposition rates were calculated by the following formula and listed in Table 1.

Deposition Rate $= \frac{W}{T \times A}$, where, w is weight of deposited film obtained from TGA; T is deposition time; A is total area of pigments used for each run in TGA.

Table 1. The deposition rate results of C_6F_{14} and OFT obtained from TGA

Monomer	Film Weight (mg)	Total Area of Pigments (cm^2)	Treatment time (min)	Deposition rate 10^{-3} (g/cm^2-min)
C_6F_{14}	1.49	185.63	60	0.134
OFT	1.24	123.6	30	0.335

3.2 Wicking Property Studies

The pigments before plasma polymer coating were hydrophilic and of a small contact angle as can be seen from Table 2. The hydrophilic nature of the pigments can impair the corrosion resistance of organic primer coatings. With octafluorotoluene or perfluorohexane, surface modification could be carried out to increase the hydrophobicity of the pigments. As shown in Table 2, the plasma polymer coating from octafluorotoluene increases the water contact angle of the cerium acetate pigment by 60° and for sodium vanadate pigment by 18°. The perfluorohexane increases the contact angle by 42° in the cerium acetate pigment and by 15° for the sodium vanadate pigment. The increased hydrophobicity can be attributed to the presence of fluorine and the highly cross-linked structure in the deposited plasma polymer films.

Table 2. The wicking properties of the untreated and treated CeAC and BTA pigments

Pigment	Penetrating Water Weight (g)	Contact Angle (º)
CeAc	0.62	22
pp-OFT- CeAc	0.31	82
pp-C_6F_{14}- CeAc	0.38	64
$NaVO_3$	0.55	70
pp-OFT- $NaVO_3$	0.14	88
pp-C_6F_{14}- $NaVO_3$	0.22	85

3.3 Slow Release Studies of the Coated Samples

The results of DC polarization studies for 300 hours are plotted in Figure 2. The DC polarization curves for the OFT-coated cerium acetate pigment were shifted to a lower negative corrosion potential as the testing time increases from 10 hours to 300 hours. The cathodic portion of the curve also shifted to the left side, which indicates the pigment was slowly released through the plasma polymer coating and inhibited the cathodic corrosion reactions on the fresh prepared AA-2024 T3.

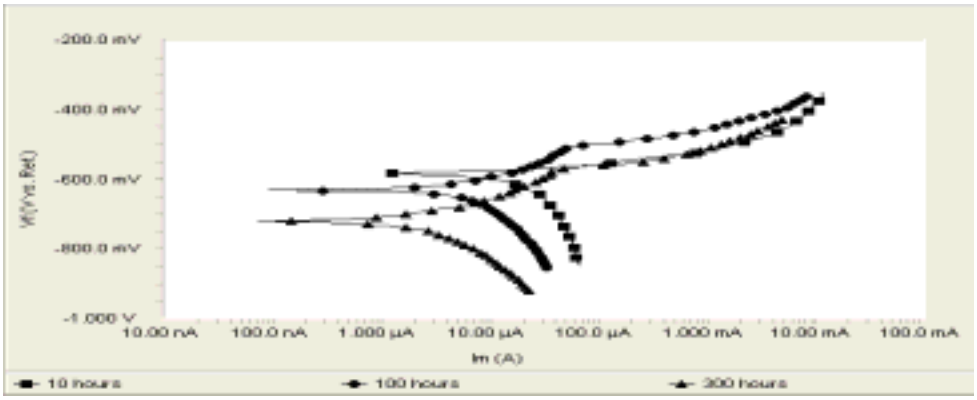

Fig. 2. DC Polarization curves of AA-2024 T3 in the solutions of 3.5% NaCl with 2000 ppm of the OF- coated CeAc for 300 hours

The conductivity measurement curves of cerium acetate and the OFT-coated cerium acetate are shown in Figure 3. The conductivity of uncoated cerium acetate ramped up to 800 μS within 60 seconds and kept constant till measurement was completed. It showed uncoated cerium acetate was very soluble and dissolved quickly on adding to the deionized water. The conductivity of the OFT-coated cerium acetate increased at a much slow rate than uncoated cerium acetate. After 250 seconds, the increasing rate of conductivity remained a constant value which demonstrated the OFT-coated cerium acetate can be slowly released at a certain low rate over a long time.

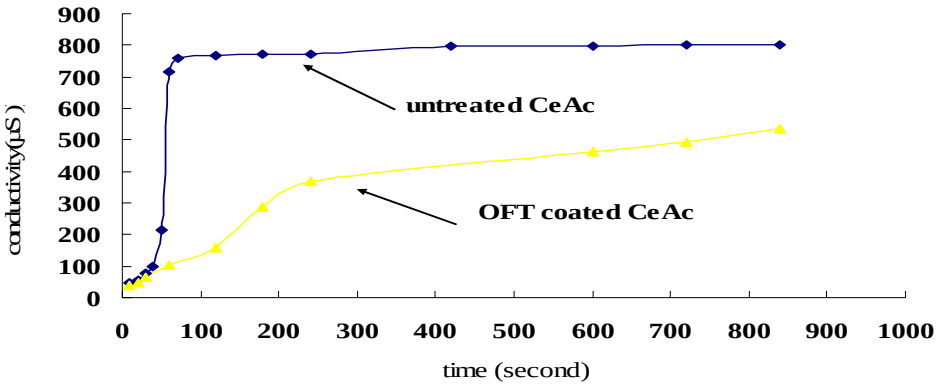

Fig. 3. Conductivity of OFTcoated CeAc and uncoated CeAc

3.4 Corrosion Study

The corrosion performance of pigments in the organic primer coating was characterized by EIS. Figure 4 (a) shows the EIS curves of primer coating pigmented with 1 w.% cerium acetate without plasma treatment. The modulus in low frequency around 10 mHz decreased continuously in the period of test, which indicated the corrosion resistance kept reducing. Also, as test time increased, the curve showed more time constants where the slopes of curve changes. It may probably be caused by considerable amount of water uptake by the hydrophobic cerium acetate pigment. However, the primer coating pigmented with 1 w.% OFT-coated cerium acetate displayed a much better anti-corrosion performance. In Figure 4 (b), the low frequency modulus barely decreased for seventeen days and the slope of curve remained constant indicating little water penetrated the pigmented primer coating and no corrosion products were formed underneath the primer coating. This may be ascribed to hydrophobicity of the OFT-coated pigment which improves the water resistance of whole system and corrosion inhibition of the slowly released pigments. In Figure 4 (c), The OFT-coated sodium vanadate exhibited a slow release property and improved the corrosion resistance of the coating too.

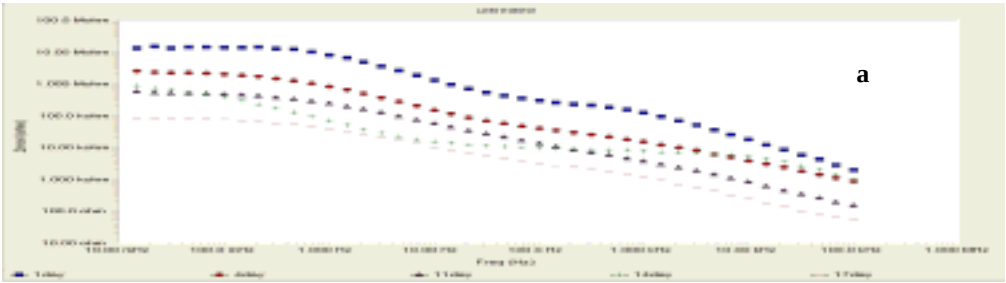

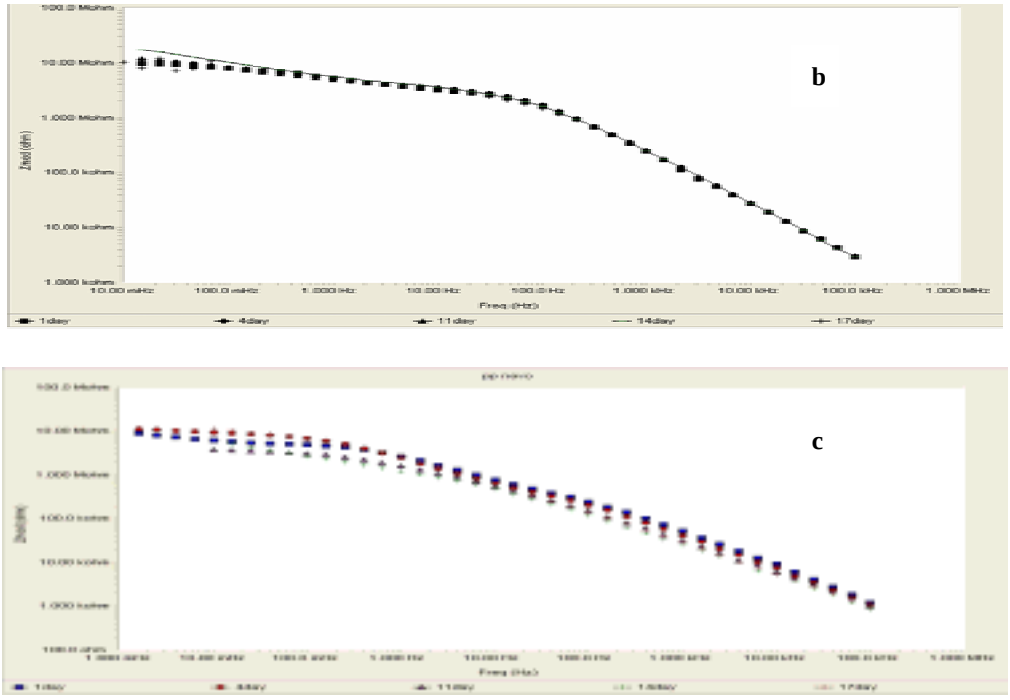

Fig. 4. EIS Bode plots of (a) uncoated CeAc, (b) OFT-coated CeAc, (c) OFT-coated $NaVO_3$ in 3.5% NaCl for 17 days.

4. Conclusions

Plasma polymerization can be used to modify the surfaces of pigments and thus convert hydrophilic pigments to hydrophobic inhibitors for organic primer coatings on metals. The plasma polymer-coated pigments are suitable to be incorporated in primer coating properly and enhance the corrosion protection by slowly be released to the exposed area of the scratched primer coating. By choosing the monomer for plasma polymerization, the deposition rate may be optimized. As demonstrated in our study plasma polymerization of octafluorotoluene has a faster deposition rate as compared to the perfluorohexane.

5. Acknowledgements

The authors would like to thank US AFOSR for funding this research under contract F49620-01-1-0352 (MURI).

6. References

[1] R.L Twite, G. P. Bierwagen, Progress in Organic Coatings, 1998, 33, 91
[2] R.G Buchheit, Electrochem. Soc. Extend. Abstr. ,95-2, Abstr. 182, Chicago, IL, 1995
[3] C. Chen, C. Lin, Analytica Chimica Acta, 1996, 321, 215
[4] V.S Sastri, Corrosion Inhibitors: Principles and Applications, John Wiley and Sons, New York, 1998,
[5] H. Yang, W.J van Ooij, Plasmas and Polymers, 2003, 8, 297
[6] N. Zhang, MS thesis at Chemical and Materials dept. in University of Cincinnati, 2000
[7] N. Inagaki, S. Tasaka, and H. Abe, J. Appl. Pol. Sci., 46, 595 (1992)

Plasma enhanced CVD of hard DLC/SiOx coatings from methane and hexamethyldisiloxane

L. Zajíčková[1], V. Buršíková[1], M. Valtr[1], V. Peřina[2], A. Macková[2], J. Houdková[3]

[1]*Department of Physical Electronics, Masaryk University, Kotlářská 2, Brno 611 37, Czech Republic*
[2] *Institute of Nuclear Physics, Czech Academy of Science, Řež 250 68, Czech Republic*
[3] *Institute of Physics, Czech Academy of Science, Prague 162 53, Czech Republic*

Abstract
In present paper we give some new results on our previously reported hard DLC/SiO_x films deposited from the mixtures of CH_4 and HMDSO and compare them with similar films deposited from CH_4/HMDSO/H_2 mixtures using a different generator. We show that significant drawbacks of the DLC films, high intrinsic stress, bad thermal stability and absorption in the visible range, can be limited by an incorporation of the SiO_x component and we notice that this conclusion is achieved for many DLC/SiO_x films in spite of the different method of preparation and, more surprisingly, of their different structure. However, particular film properties can be further improved by an optimization of the deposition conditions as concluded from the higher hardness of the films deposited from the CH_4/HMDSO/H_2 compared to the CH_4/HMDSO feed.

1. Introduction

The ability of carbon to form three different bonding states, sp^3, sp^2 and sp hybridizations, leads to the variety of synthesized materials containing just this one element. In case of chemical vapor deposition (CVD) where carbon is gained from various hydrocarbon gases we find a broad class of hydrogenated carbon materials, usually amorphous (a-C:H), in which the percentage of hydrogen is additional free parameter varying the material property. Although, there is a little confusion about the term "diamond like carbon" (DLC) we can concluded, according to Robertson [1], that DLC is an amorphous carbon (a-C) or a-C:H material containing high fraction of sp^3 bonding. According to their name the DLC films exhibit properties similar to diamond such as high hardness, good wear resistance, very low friction coefficient, transparency in infrared, good chemical inertness as well as high thermal and low electrical conductivity. Consequently, these films find a variety of applications for example as antireflective coatings, as insulators or semiconductors in microelectronics, biomedical coatings, protective coatings for magnetic recording discs and low friction, wear resistant coatings for micro-electromechanical devices (MEMs). In spite of their valuable properties, however, DLCs have also some drawbacks, namely bad thermal stability, high intrinsic compressive stress and absorption in the visible range. Therefore, the incorporation of other elements like silicon, oxygen, nitrogen or various metals into the amorphous network of DLC has been studied in last decade [2,3].

Based on actual search for nanocomposite materials and their unique properties, the DLCs containing silicon oxides (SiO_x), often referred as DLC/SiO_x nanocomposites, were prepared by various methods and their usefulness was evidenced by low intrinsic stress while keeping the other good mechanical properties of DLCs [4-7] and by improved thermal stability [8]. Moreover, Senkevich *et al.* [9] pointed out that these films exhibit significantly decreased absorption in the visible range that might be necessary for certain applications. The methods for preparation of DLC/SiO_x films can be divided into three categories, (i) hot filament PECVD using for example polyphenylmethylsiloxane [10] or polyvinylsiloxane [11] precursors with r.f. or d.c. biased substrate, (ii) r.f. capacitively [5,8,9] or inductively [7] coupled PECVD using tetraethoxysilane (TEOS) [5,8,9] or hexamethyldisiloxane (HMDSO) [7] and (iii) ion beam assisted deposition with sputtering of Si/SiO_2 target in hydrocarbon gas atmosphere [12]. It should be noted that in the r.f. PECVD approach a hydrocarbon gas (methane, styrene) is added to the organosilicon, besides argon or hydrogen [5,7,8]. Several authors assume that their films, although sometimes prepared by different method, have the same structure of two interpenetrating chemically weakly bonded amorphous networks, a-C:H and a-Si:O, as suggested by Dorfman [4,11]. In some cases, however, the arguments are not quite clear especially when, unlike Dorfman, they found the presence of Si-C bonds in the

films [6,12]. In this sense an exceptional structure of DLC/SiO_x nanocomposites, SiO_x nanoparticles embedded in a-C:H matrix, was reported by Chen and Hong [7].

2. Experimental

The films were prepared in r.f. glow discharges from the mixture of methane (CH_4) and HMDSO. The reactor was a vertically mounted Pyrex® cylinder closed by two stainless steel flanges with two inner parallel plate electrodes made of graphite. A detailed description of the reactor is given in Ref. [13]. The upper electrode was grounded. The bottom electrode was coupled to an r.f. generator (13.56 MHz) via a blocking capacitor. The diameter of the r.f. electrode was 150 mm and the distance between the electrodes was 55 mm. The r.f. voltage of the electrode was superimposed by a negative d.c. self-bias. The self-bias was a result of different electron and ion mobilities and a high asymmetric coupling, i. e. different areas of r.f. driven and grounded and/or floated surfaces in touch with plasma. The substrates for deposition (silicon wafers and glass) were placed on the r.f. electrode in order to achieve the film growth under bombardment of energetic ions. The flow rate of CH_4 was fixed at 1.4 sccm. The flow rate of HMDSO changed in the range 0–0.82 sccm in order to vary the flow rate ratio $q = Q_{\mathrm{HMDSO}}/Q_{\mathrm{CH4}}$.

The first series of the films (denoted as DSi) was prepared from various CH_4/HMDSO feeds using the r.f. generator PG 501 at the fixed power of 250 W as showed on the generator wattmeter. The total pressure before the deposition changed, due to the variation of the total gas flow, in the range 8–11 Pa. The negative self-bias U_{bias} varied from -320 V to -550 V as a function of the gas feed composition and the pressure. The second series of the films (denoted as HDS) was deposited with addition of hydrogen in the amount of 0.35 sccm to the CH_4 and HMDSO mixture using the r.f. generator Dressler. In this series the power was fixed at 50 W as given by the generator wattmeter in order to reach a similar range of the self-biases. The similar self-bias values were taken for the deposition instead of the same r.f. power because it was assumed the self-bias played more important role for the deposition than the power. Moreover, the question about a correct power measurement, especially in case of the generator PG 501, arose in relation to the power and self-bias discrepancy. The decision to keep the self-bias constant rather than power was confirmed by comparing the film properties such as hardness and intrinsic stress.

Films deposited on the silicon substrates were characterized by a UVISEL Jobin-Yvon phase modulated ellipsometer in the spectral range 240–830 nm at the incidence angles 55°–75°. The structure of the films was studied with transmittance measurements in the infrared (FTIR) and X-ray photoelectron spectroscopy (XPS). The complete atomic composition was determined by a combination of Rutherford backscattering (RBS) and elastic recoil detection (ERD) methods. The atomic fractions of C, O and Si were measured by RBS using 2.4 MeV protons perpendicularly bombarding the surface. ERD and RBS with an incident beam of 2.75 MeV α-particles at 75° to the surface normal were simultaneously used to determine the percentage of H.

The depth sensing indentation (DSI) was carried out on the films deposited on the glass substrates using a Fischerscope H100 tester (Vickers). Load-penetration curves were analyzed for several values of maximum applied loads from the whole possible load range of 1–1000 mN to asses the mechanical properties of the films such as hardness H, elastic modulus $Y = E/(1-\nu^2)$, where E is the Young's modulus and ν is the Poisson's ratio of the films and the like. The measured characteristics were corrected for the influence of the low elastic modulus and hardness of the glass substrate as discussed in the next section. The Vickers indentation may introduce substantial cracks and adhesive failures into the thin films. Analyzing the morphology of the indentation prints and measuring the critical load for cracking and/or delamination, it was possible to determine other material characteristics such as the fracture toughness and adhesive properties of the films [14].

3. Results and Discussion

In present paper we give some new results on our previously reported hard DLC/SiO_x films deposited from the mixtures of CH_4/HMDSO, i. e. the first series of the films as described in Experimental (DSi series), and compare them with similar films of the second series (HDS series) deposited from CH_4/HMDSO/H_2 mixtures using a different generator.

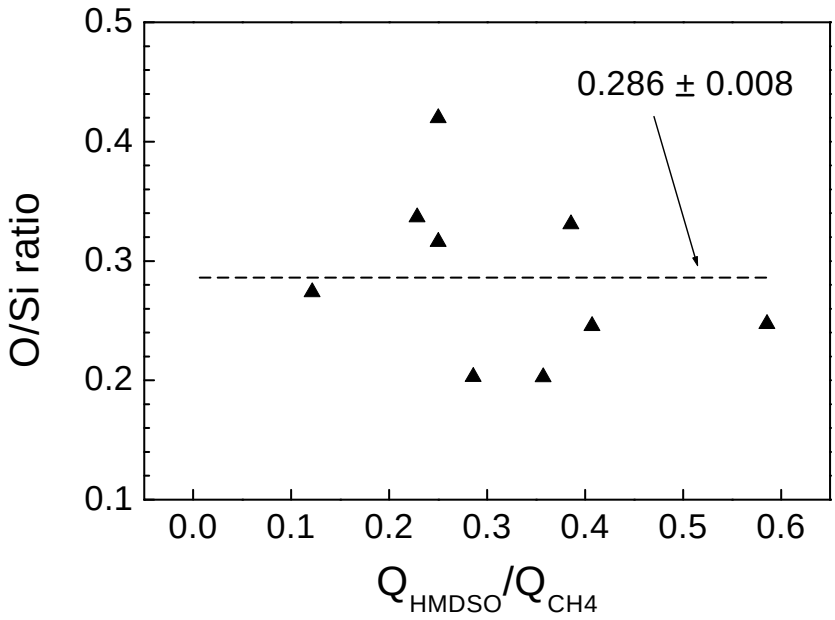

Figure 1: Oxygen-to-silicon ratio in the DLC/SiO_x films (DSi series) as a function of the HMDSO-to-methane flow rate ratio in the deposition mixture.

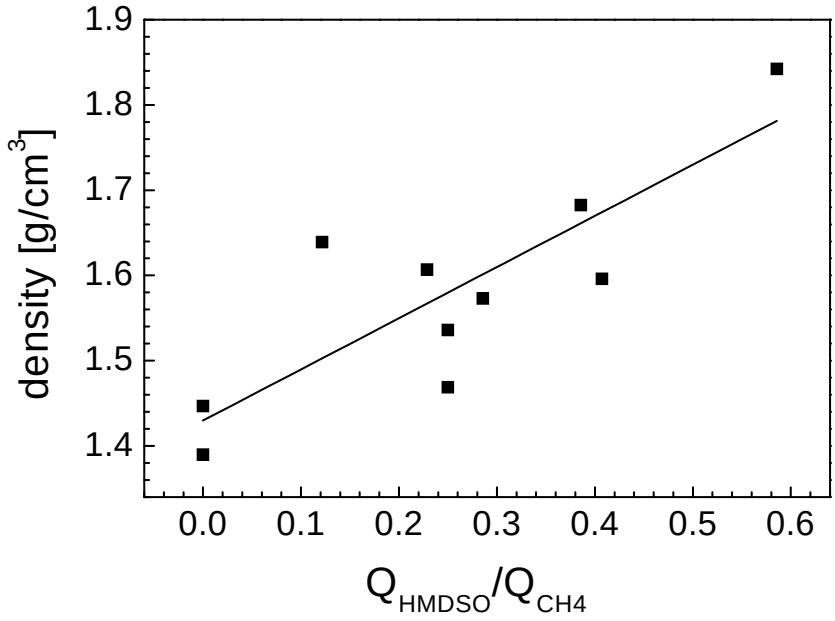

Figure 2: Density of the DLC/SiO_x films (DSi series) as a function of the HMDSO-to-methane flow rate ratio in the deposition mixture.

Table 1: Comparison of DLC and DLC/SiO_x films deposited with or without addition of hydrogen in the gas feed. The flow rate of CH_4 was 1.4 sccm. The atomic concentration of elements denoted by asterisk were obtained by an interpolation between two values for the closest HMDSO flow rates.

film	Q_{HMDSO} [sccm]	Q_{H2} [sccm]	U_{bias} [V]	C at. %	H at. %	Si at. %	O at. %	H [GPa]	Y [GPa]
DSi52	0	0	-320	63.5	35.8	0.3	0.5	23.0	159
HDS33	0	0.35	-544	54.6	42.0	0.6	2.8	25.4	167
DSi50	0.25	0	-460	50.3*	41.6*	5.9*	2.0*	18.8	123
HDS7	0.25	0.35	-460	45.8	44.0	7.2	3.0	23.3	127

As concern the DSi films a correlation between the HMDSO-to-methane flow rate ratio q and their deposition rate, atomic concentrations of C, H, Si and O elements in these films, their optical constants, plastic hardness and elastic modulus as well as the critical indentation depth for initiation of interfacial cracks was presented in Ref. [15]. It was shown that with increasing flow rate ratio q the concentration of Si, O and H increases on the expenses of C. However, the oxygen-to-silicon ratio in the films is scattered around a constant value of 0.286 ± 0.008 as depicted in Fig. 1. One can notice that this value is relatively low when compared with some other authors reporting to have this film component close to silicon dioxide [7,9]. As q varies from 0 to 0.6 the percentage of the $SiO_{0.29}$ component in the film increases up to 14 %. The density of the films is proportional to the q (see Fig. 2). However, all the films containing SiO_x have very similar values of the molar density which is in turn comparatively higher than in the pure DLC films from this series. Since the molar density evidences a degree of film packing the observed instantaneous increase of the film density is caused by replacement of lighter elements (C, H) by heavier Si and O.

The comparison of atomic compositions on the film surface as determined by XPS and in the film bulk by RBS shows that the film surface is more oxidized having the oxygen-to-silicon ratio (O/Si) as high as 2.5 for the lowest addition of HMDSO to CH_4 ($q = 0.17$). Contrary to the constant value in the film bulk the O/Si ratio on the film surface decreases with increasing percentage of HMDSO in the gas feed. This dependence levels out at about $q = 0.3$ reaching the stable, although quite scattered, value in the range 0.8–1.6. The relatively high amount of oxygen, 11.5 at. % (hydrogen excluded from considerations because it cannot be detected by the XPS), is found on the surface of pure DLC films. Moreover, some DLC films contain certain amount of oxygen, 1.6 at. % (excluding hydrogen), even in the bulk. Therefore we believe that the incorporation of the SiO_x component into the structure of DLC prevents a film oxidation since the silicon oxide layer at the surface serves as a barrier for oxygen.

Further information about the chemical structure of the DSi films was obtained from deconvolution of XPS atomic signals and FTIR. Both the methods confirm the presence of Si-C bonds, either on the surface or in the bulk, which is not observed for some DLC/SiO_x nanocomposites [4,7]. The percentage of Si-C bonds on the surface increases from 7 % for $q = 0.17$ up to 28 % for $q = 0.62$ on the expenses of C-C, C-H and C-O bonds. All the silicon related infrared absorption peaks are increasing in intensities with increasing HMDSO in the gas feed. However, the complex absorption band extending from 650 to 900 cm ^{1}, which contains the contribution from Si-C, Si-$(CH_3)_n$, Si-O-Si and Si-CH_2 bond vibrations, does not change its shape suggesting that the relative amount of Si-C bonds with respect to Si-O is stable.

Although the film hardness decreases with increasing q this tendency is very slow for q below 0.25 and the films deposited at q around 0.25 exhibit significantly improved fracture toughness [15]. This means a certain optimum amount of HMDSO in the gas feed can be found where the high hardness of the DLCs is pertained but simultaneously the high compressive intrinsic stress is significantly lowered. This effect can be further improved by an optimization of the deposition conditions as concluded from the higher hardness of the film HDS7 deposited from CH_4/HMDSO/H_2 compared to the film DSi50 deposited from CH_4/HMDSO feed (see Table 1). An example

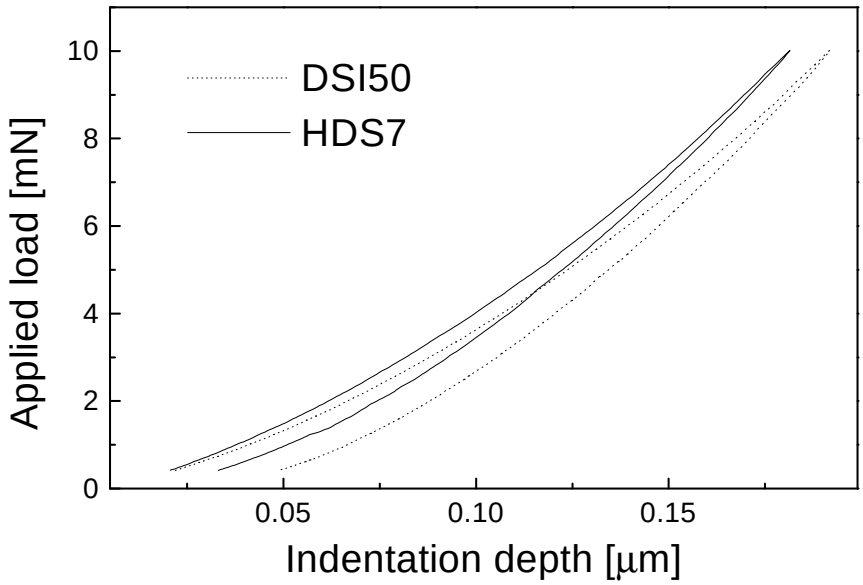

Figure 3: Loading and unloading curves for DLC/SiO_x films deposited at the HMDSO flow rate of 0.25 sccm without (DSi50) or with hydrogen (HDS7) in the gas feed. For the film atomic composition, hardness and elastic modulus of these films see Table 1.

of the loading and unloading curves for these two films is given in Fig. 3. From Table 1 we can see that the higher hardness of the DLC and DLC/SiO_x films deposited from the CH_4/HMDSO/H_2 mixture is related to a lower carbon-to-hydrogen ratio in the films. This effect will be studied in forthcoming paper.

Besides an improved fracture toughness of the DLC/SiO_x films an addition of the SiO_x component improves their thermal stability. This fact was discussed in details for the films from CH_4/HMDSO and CH_4/HMDSO/Ar gas feed in Ref. [16].

A detail study of the optical constants for the films of DSi series by combination of the spectroscopic ellipsometry and reflectometry using the dispersion model based on a parameterization of density of electronics states belonging to the valence and conduction bands showed that the absorption in the visible decreased in the DLC/SiO_x films with respect to the pure DLCs [17]. Similar conclusions were found in Ref. [18] for the films of the HDS series.

4. Conclusion

We have shown above that significant drawbacks of the DLC films, high intrinsic stress, bad thermal stability and absorption in the visible, can be limited by an incorporation of the SiO_x component. It is interesting to notice that this conclusion was achieved for many DLC/SiO_x films in spite of the different method of preparation and, more surprisingly, of their different structure. Here, we have compared two different series of the DLC/SiO_x films, particularly the films deposited from CH_4/HMDSO and CH_4/HMDSO/H_2 mixtures.

Acknowledgment

The present work was supported by the Ministry of Education of the Czech Republic, under the projects 1K05025 and MSM0021622411.

References

[1] J. Robertson - Materials Science and Engineering: R: Reports **37 (5)**, 129 (2002).
[2] Q. Wei, R.J. Narayan, A.K. Sharma, J. Sankar, J. Narayan - J. Vac. Sci. Technol. A **17(6)**, 3406 (1999).
[3] K.-R. Lee, M.-G. Kim, S.-J. Cho, K.Y. Eun, T.-Y. Seong - Thin Solid Films **308-309**, 263 (1997) and references therein
[4] V. F. Dorfman - Thin Solid Films **212**, 267 (1992).
[5] J.H. Lee, D.S. Kim, Y.H. Lee, B. Farouk -Thin Solid Films **280**, 204 (1996).
[6] D. Neerinck, P. Persoone, M. Sercu, A. Goel, D. Kester, D. Bray - Diamond Relat. Mater. **7**, 468 (1998).
[7] L.-Y. Chen, F. C.-N. Hong, Diamond Relat. Mater. **10**, 1058 (2001).
[8] W.J. Yang, Y.-H. Choa, T. Sekino, K.B. Shim, K. Niihara, K.H. Auh - Thin Solid Films **434**, 49 (2003).
[9] J.J. Senkevich, G.-R. Yang, T.-M. Lu, D.W. Sherrer - Appl. Phys. A **77**, 581 (2003).
[10] D. Neerinck, P. Persoone, M. Sercu, A. Goel, C. Venkatraman, D. Kester, C. Halter, P. Swab, D. Bray - Thin Solid Films **317**, 402 (1998).
[11] V.F. Dorfman, A. Bozhko, B.N. Pypkin, R.T. Borra, A.R. Srivatsa, H. Zhang, T.A. Skotheim, I. Khan, D. Rodichev, D. G. Kirpilenko - Thin Solid Films **212**, 274 (1992).
[12] X.-Z. Ding, F.-M. Zhang, X.-H. Liu, P.W. Wang, W.G. Durrer, W.Y. Cheung, S.P. Wong, I.H. Wilson - Thin Solid Films **346**, 82 (1999).
[13] L. Zajickova, V. Bursikova, D. Franta - Czech. J. Phys. **49(8)**, 1213 (1999).
[14] M.J. Matthewson - Appl. Phys. Lett. **49**, 1426 (1986).
[15] L. Zajickova, V. Bursikova, V. Perina, A. Mackova, J. Janca - Surf. Sci. Technol. **174-175**, 281 (2003).
[16] V. Bursikova, V. Navratil, L. Zajickova, J. Janca - Mater. Sci. Eng. A **324**, 251 (2002).
[17] D. Franta, I. Ohlidal, V. Bursikova, L. Zajickova - Diamond Rel. Mater. **12**, 1532 (2003).
[18] D. Franta, I. Ohlidal, V. Bursikova, L. Zajickovakova - Thin Solid Films **455-456**, 393 (2004).

Deflagration-to-Detonation Control by Non-Equilibrium Gas Discharges

Viktor P. Zhukov, Andrei Yu. Starikovskii
Physics of Nonequilibrium Systems Laboratory
Moscow Institute of Physics and Technology
Dolgoprudny, Russia
Corresponding author, V.P. Zhukov: zhukov@neq.mipt.ru

Abstract

An experimental investigation of detonation initiation by high-voltage nanosecond gas discharge was performed. The experiments were carried out in mixtures $C_3H_8+5O_2$ and $C_3H_8/C_4H_{10}+5O_2+xN_2$ ($0 \leq x \leq 10$) at initial pressure 0.15–0.6 atm. The discharge was allowed by an electric pulse with a duration of ∼60 ns and an amplitude of 4–70 kV. The energy deposition in the discharge ranged from 70 mJ to 12 J. Ignition delay time, speed of the flame front, electrical characteristics of the discharge were measured in the experiments. At conditions of the experiment we observed three modes of propagation of flame front: deflagration, transient detonation and Chapman-Jouguet detonation. Observations of discharge development and formation of the flame front were performed with the aid of an ICCD camera. In mixture $C_3H_8+5O_2$ a length of the deflagration-to-detonation transition amounts up to 130 mm at initial pressure of 0.3 atm and initiation energy of 70 mJ.

Experimental

The nanosecond discharge as a source of ignition has a set of advantages [1, 2]: high spatial uniformity, high efficiency of formation of reactive species, high power and coherence.

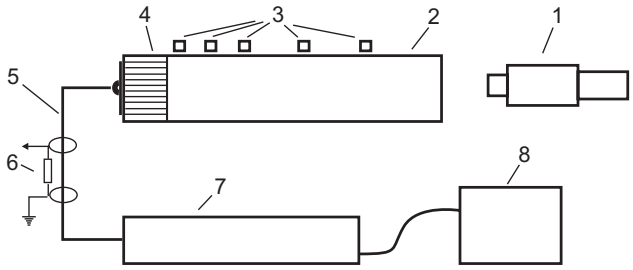

Figure 1: Scheme of experimental setup. 1 – ICCD camera, 2 – detonation tube, 3 – IR detectors, 4 – discharge chamber, 5 – high-voltage coaxial line, 6 – back-current shunt, 7 – high-voltage pulse generator (Marks type), 8 – power supply.

The experimental setup used is shown on fig. 1. The experiments were performed in a detonation tube with a diameter of 140 mm. The discharge device was attached to the end-plate of the detonation tube. The discharge chamber consists from 131 separated sections, which have common high-voltage and grounded electrodes. The discharge device provides uniform excitation at the length of 80 mm. The discharge chamber and the detonation tube are separated by an orifice plate. The orifices are arranged opposite to the each electrode. In the experiments the high voltage electrodes were supplied with a positive pulse with amplitude of 4–70 kV and duration at the half-width of 50 ns. Calculated reduced electric field ranges from 300 Td to 7000 Td near the high-voltage electrode. Given values of the reduced field lies in a range, which is optimal for ignition by discharge [1].

The high-voltage electric pulse was produced by a high-voltage pulse generator. The generator was assembled by Marks scheme. The Marks generator consists of 15 stages with capacity of 6 nF. The amplitude of the output pulse was adjusted by a voltage of a charge power supply. The Marks generator was driven by an auxiliary spark generator. The amplitude and duration of the output pulse were measured by a back-current shunt and capacitive gauge, which were mounted on a high-voltage feed line. The high-voltage line has coaxial geometry with water filling. The electric impedance of line Z was equal to 16 Ohm. The pulse reflected from the high-voltage electrode was not observed. The energy of discharge was calculated from the signal of back-current shunt.

Five IR detectors are placed along the axis of detonation tube. The detectors have a sensitivity range of 0.9–3.5 μm. They record an IR-emission of H_2O and CO_2. The flame speed was calculated from profiles of a voltage on the IR detectors. The speed of the detonation wave was measured with an accuracy of 80 m/s (3%) and the speed of the deflagration wave was measured with an accuracy of 20 m/s (7%).

Initial gas parameters: composition, pressure and temperature were measured in the experiments. The experiments were performed at initial pressures of 0.15–0.6 atm and ambient temperature in fuel mixtures: C_3H_8+5O_2 and C_3H_8/C_4H_{10} + 5O_2 + xN_2 (0≤x≤10), where C_3H_8/C_4H_{10} is a designation of liquified petroleum gas (LPG).

Ignition by Nanosecond Discharge

Firstly, we studied the influence of nitrogen on the ignition under the action of the nanosecond discharge. We measured induction time (fig. 2) and minimal ignition energy in mixtures C_3H_8/C_4H_{10} + 5O_2 + xN_2.

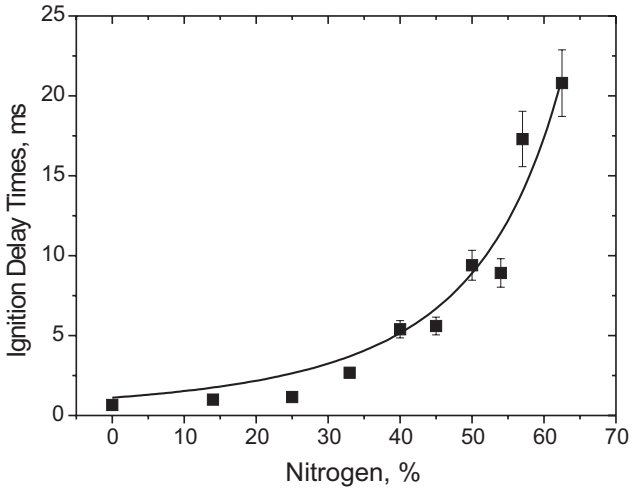

Figure 2: Ignition delay time in mixtures C_3H_8/C_4H_{10}+5O_2+xN_2 at initial pressure 0.3 atm. Line corresponds to eq. (**??**).

The nitrogen dilution: 1) decreases a ratio of the heat of combustion to the heat capacity; 2) decreases the concentrations of the fuel and oxygen; 3) increases a rate of recombination reactions; 4) decreases a formation of active particles. At high temperatures (1200–1800 K) the delay time of auto-ignition depends on the nitrogen dilution at fixed pressure as $\sim (1 - [N_2])^{-x}$, where x=0.45–0.65 [3]. In the case of auto-ignition the second consideration is the main. In our case the nitrogen dilution not only acts on chemical processes, but it reduces the generation of active species in the discharge. Probably, the forth consideration is stronger than others under the discharge ignition.

The induction time and the minimal ignition energy have the same dependence on the percentage of nitrogen in the mixture at a fixed initial pressure (fig. 3). The minimal ignition energy increases from 70 mJ at nitrogen fraction of 25% to 12 J at nitrogen fraction of 62.5%. The values of the energy of 0.07 and 12 J relate to the minimal and maximal operating energy of our discharge device. The energy deposition of 0.07 J corresponds to a heating of fuel mixture on 1 K. Hence the mechanism of the ignition is not a thermal. There is a critical value of active species produced by the discharge. The ignition progresses without an assistance, after the concentration of active particles exceeds the critical value.

The minimal ignition energy extrapolated to an nitrogen dilution of 77% amounts to 25 J. In our case the high value of the minimal ignition energy is explained by a high specific surface of the discharge device. The energy of the discharge is distributed among the 131 discharge section, which is a long tube with a ratio of the diameter to the length of 1/16. The high-voltage nanosecond discharge is characterized by a low energy deposition per an excited volume of a gas in contrast to other types of discharge. In the experiments this value was equal to approximately 0.3 J/l.

Modes of Flame Propagation

The fig. 4 is the summary plot of the experiments in the mixtures C_3H_8/C_4H_{10}+5O_2+xN_2 (0≤x≤10). The fig. 4 depicts the speed of the flame front measured at 412 mm apart from the discharge chamber. At relatively low pressures we observed a deflagration wave with a weak acceleration. At relatively high pressures we observed a C–J detonation wave. At intermediate conditions we observed a transient detonation wave.

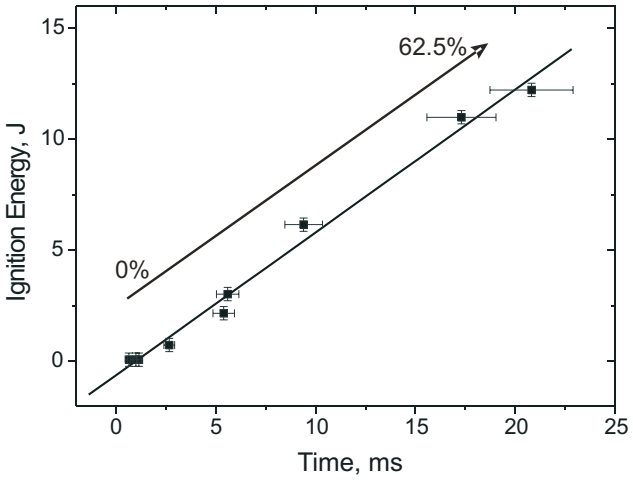

Figure 3: Minimum ignition energy and ignition delay time at difference nitrogen dilutions.

In this mode the flame front accelerates strongly on the motion in the tube. At these conditions the speed of the flame front increases from 500 m/s at position of 150 mm to 2000 m/s at position of 650 mm. It was ascertained that the mode of propagation of flame front is governed by the initial pressure and the mixture composition and the mode is independent of the discharge energy.

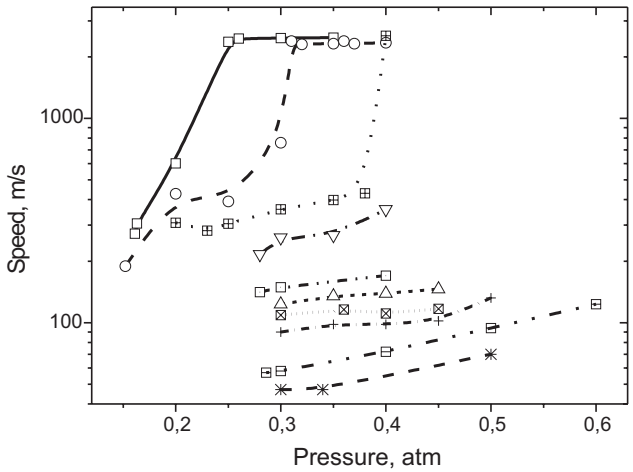

Figure 4: Speed of the flame front at 412 mm apart from discharge chamber in mixtures $C_3H_8/C_4H_{10}+5O_2+xN_2$. $\square$ – x=0 (0%), $\circ$ – x=1 (14%), $\boxplus$ – x=2 (25%), $\triangledown$ – x=3 (33%), $\boxdot$ – x=4 (40%), $\triangle$ – x=5 (45%), $\boxtimes$ – x=6 (50%), $+$ – x=7 (54%), $\boxminus$ – x=8 (57%), $*$ – x=10 (63%).

Formation of Flame Front

We carried out the observation of the discharge development and the formation of flame front through the end-plate of the detonation tube. The observation were performed using ICCD camera "La Vision Picostar 12 HR". The camera registers an emission in the range of wavelength of 300–800 nm. In the discharge the bandwidth $C^3\Pi_u,\ v' = 0 \rightarrow B^3\Pi_g,\ v'' = 0$ of nitrogen at 337 nm makes main contribution to the intensity.

The discharge has three time stages. On the first stage the emission intensity rises sharply. On the second stage the emission intensity falls sharply. The third stage is the after-glow stage. The duration of 1-st, 2-nd and 3-rd stages amounts ∼10, ∼50 and ∼500 ns, consequently. The durations of the stages increase with a rise of an initial pressure. The initial stage of the discharge (up to 10 ns) is spatially quasi-homogeneous, while in the subsequent stages the discharge localized over the few sections of the high-voltage electrode. After 0.5–10 ms (in relation to the initial conditions) from the moment of the discharge the mixture ignites in the discharge chamber. The flame is stronger in some sections of the discharge chamber than in others. Nevertheless the mixture inflames simultaneously and the flame front covers the whole cross-section of the

tube on the end-plate. A position of the flame front was determined by simultaneous measurements through the side-wall with the help of the IR sensors. When the flame front passes from the end-plate the length of the one diameter, the front is spatially homogeneous over the cross-section of the tube.

Initiation of Detonation

It were carried out special experiments to determine the conditions of the detonation initiation. The experiments were performed in $C_3H_8+5O_2$ mixture at initial pressure of 0.3 atm. An optimal conditions for the detonation initiation are reached at initiation energy of the discharge of 70 mJ. In this case the speed of the flame front is constant and is close to the C–J speed. A response (a width of the front) of the first IR detector corresponds to a flame wave that propagates with the supersonic speed. Hence the detonation wave is formed by the time of reaching the first IR detector, which it is confirmed also by the observation with the help of the ICCD camera through the end-plate. The length and time of DDT amount to L_{DDT}=130 mm and t_{DDT}=0.6 ms at initiation energy of the discharge of 70 mJ. In this case the length and time of DDT involve a length of the discharge chamber and the ignition delay time. The initiation energy per the cross-section amounts to 4 J/m^2.

In our case the initiation of detonation proceeds through two stages. On the first stage the nanosecond discharge excites the gas in the discharge chamber. On the second stage a chemical energy of about 1 kJ releases after an ignition delay of 0.5–20 ms. The released energy is enough to initiate the detonation in an appropriate conditions. The discharge produces more the active species near the high-voltage electrode. The gradient of active species [4] and actually the simultaneous energy release [5] assist the initiation of the detonation.

Conclusions

The experimental demonstration of the application of the high-voltage nanosecond gas discharge for the initiation of the detonation was performed. The developed discharge device initiates the detonation at the length of DDT up to 130 mm in a tube with a diameter of 140 mm.

The detonation was initiated by energy of 70 mJ (4 J/m^2) in mixture $C_3H_8+5O_2$ at initial pressure of 0.3 atm.

The measurements of minimal ignition energy and ignition delay time were performed in $C_3H_8/C_4H_{10} + 5O_2 + xN_2$ ($0 \le x \le 10$) mixtures at pressure range of 0.15–0.6 atm. The minimal ignition energy and ignition delay time depend strongly on the nitrogen dilution under the ignition by the high-voltage nanosecond discharge. The extrapolated value of minimal ignition energy amounts 25 J at the dilution level of 77%.

The voluminosity of the discharge is a demerit for ignition and it is a great advantage for detonation.

The discharge device initiate the deflagration wave, the transient detonation wave and the C–J detonation wave in $C_3H_8+5O_2$ and $C_3H_8/C_4H_{10} + 5O_2 + xN_2$ ($0 \le x \le 10$) mixtures. The mode of propagation of flame front is governed by the initial pressure and the mixture composition and the mode is independent of the discharge energy.

The discharge has the different intensity in the sections of the discharge chamber. After the ignition the flame front occupies the whole cross-section of the detonation tube. The non-uniformity of the flame front diminishes completely after passing the length of about the one diameter.

Acknowledgments

This work was partially supported Grants by PR0-1349-MO-02 EOARD/CRDF; grant 02-03-33376 of Russian Foundation for Basic Research.

References

[1] Bozhenkov S.A., Starikovskaya S.M., Starikovskii A.Yu., Combustion and Flame 133 (2003) 133–146.

[2] Starikovskaya S.M., Kukaev E.N., Kuksin A.Yu., et al., Combustion and Flame 139 (2004) 177–187.

[3] Lamoureux N., Paillard C.E., Vaslier V., Shock Waves 11 (2002) 309–322.

[4] Zeldovich Ya. B., Librivich V.B., Makviladze G.M., and Sivashinskii, J. Appl. Mech. Tech Phys., 11 (1970), 76–84.

[5] Schultz, E. Wintenberger, and J.E. Shepherd, In Proceedings of the 16th JANNAF Propulsion Symposium, Chemical Propulsion Information Agency, 1999.